Proceedings of Forum Acusticum - Euronoise 2025

11th Convention of the European Acoustics Association

Edited by

Daniel de la Prida, Jaime Ramis and María Machimbarrena



Chair: Antonio Pedrero
General Secretary: María Machimbarrena

Sociedad Española de Acústica

ISSN 3005-7124
ISBN 978-84-87985-35-5

ORGANIZING COMMITTEE

Honorary President: Antonio Pérez-López (SEA)

Chairman
Antonio Pedrero (SEA)

General Secretary
María Machimbarrena (SEA)

Technical Chairman
Luis A. Azpicueta (UC3M)

Exhibition Chairman
Miguel Ausejo (SEA)

Publications Chairmen
Daniel de la Prida (UPM)
Jaime Ramis (UA)

Forum Laboris Chairman
Roberto San Millán (URJC)

Summer School Chairwomen
Belén Casla (SEA)
Mª Ángeles Navacerrada (SEA)
Laura Estévez (ULE)

Volunteer Coordinators
Juan Negreira (Saint-Gobain Ecophon)
Salvador Luna (UMA)
Cristina Quintero (UMA)

Social Media Coordinator
Lucía Schröder (UMA)

Local Committee
Carolina Gijón (UMA)

CONGRESS COMMITTEE

Ariana Astolfi (EAA)
María Campo (UMA)
Jesús Carbajo (UA)
Teresa Carrascal (IETCC-CSIC)
Alexander Díaz-Chyla (UPM)
Ricardo Hernández (UCA)
Ramón Peral (UMH)
Pedro Poveda (UA)
Samuel Quintana (UCLM)
Carlos Romero (Salford Univ.)
Pedro Salcedo (UMA)
Rosa Mª Alsina (URL)
André Fiebig (EAA)
Fernando Ruiz Vega (UMA)

INTERNATIONAL ADVISORY BOARD

Jorge Arenas
Francesco Asdrubali
Marion Burgess
Torsten Dau
Kristian Jambrošić
Manfred Kaltenbacher
Catherine Lavandier
Luigi Maffei
Carolina Monteiro
Etienne Parizet
Jorge Patrício
Jean-Dominique Polack
Monika Rychtáriková
Brigitte Schulte-Fortkamp
Michael Taroudakis
Nilda Vechiatti
Michael Vorländer
Jo Webb
Jerzy Wiciak

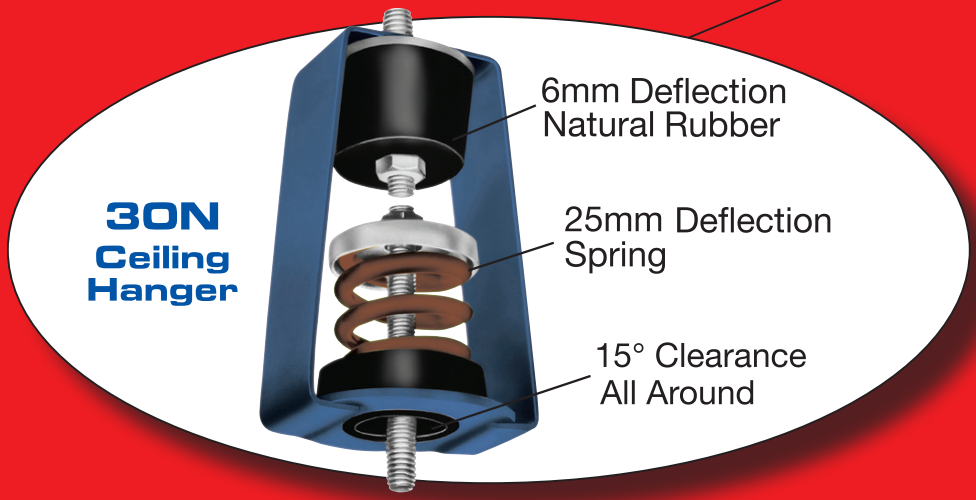
Conference organizer and venue
REVOLUTION EVENTS
Palacio de Ferias y Congresos de Málaga (FYCMA)

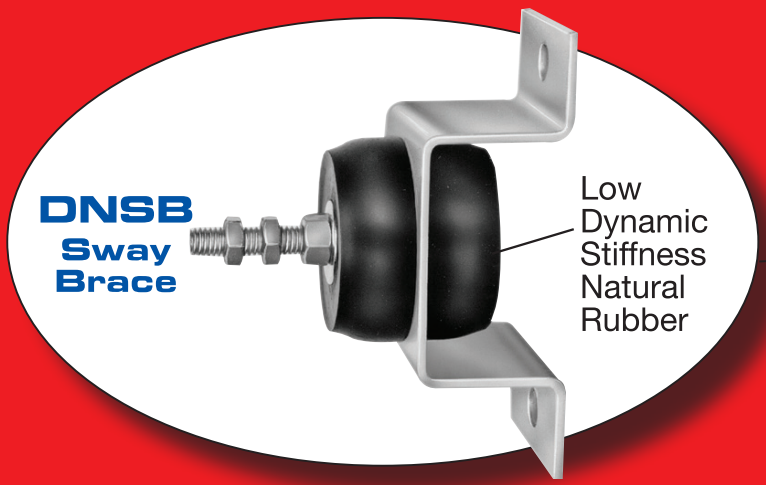
Proceedings of Forum Acusticum - Euronoise 2025
ISSN 3005-7124 | ISBN 978-84-87985-35-5
© European Acoustics Association 2025

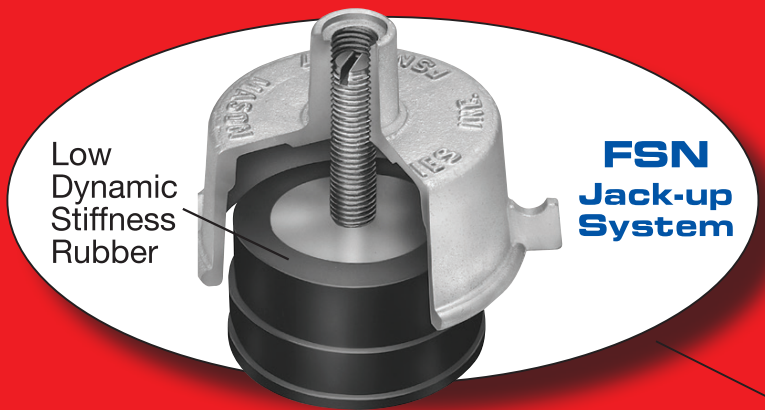
MASON INDUSTRIES, INC.

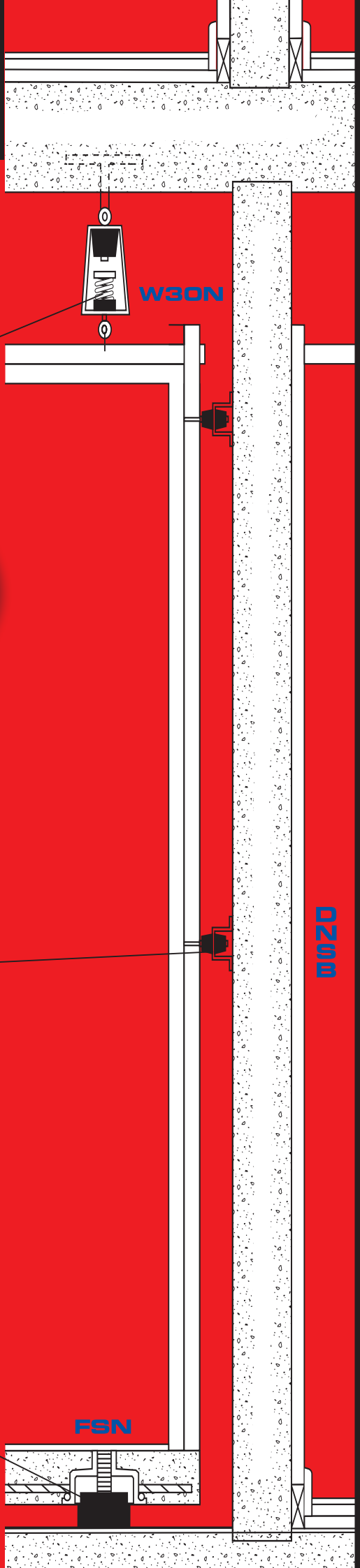
Manufacturers of Noise and Vibration Control Products

We have been designing and improving acoustical isolation products for over sixty years by studying the market and listening to requirements and suggestions from the acoustical fraternity.









350 Rabro Drive, Hauppauge, NY, USA 11788
+1 631 348 0282 • FAX +1 631 348 0279
Email info@Mason-Ind.com • Website www.Mason-Ind.com

MAIN THEME ORGANIZERS

AA01 - Active Control of Sound and Vibration
Jordan Cheer
Teresa Bravo

AA02 - Bio-Acoustics
Bill Davis
David Waddington
Helen Whitehead
Ester Vidaña Vila

AA03 - Building Acoustics
Amelia Romero
Chiara Scrosati
Teresa Carrascal
Carolina Monteiro

AA04 - Education, Public Outreach and History in Acoustics
Montserrat Pàmies-Vilà
Nuria Campillo-Davó

AA05 - Environmental Acoustics
Miguel Arana
Guillermo del Rey
Judicäel Picaut

AA06 - Electro-Acoustics
Hervé Lissek
Libor Rufer
Petr Honzík
Vittorio Ferrari

AA07 - Flow Acoustics
Stefan Becker
Daniele Ragni
Roberto Camussi

AA08 - Industrial Machinery, Equipment Noise and Vibration
Francesco Pompoli
Jaime Ramis

AA09 - Machine Learning and AI in Acoustics
Dick Botteldooren
Rosa María Alsina
Manuel Sobreira

AA10 - Materials and Metamaterials
Jean-Philippe Groby
Rubén Picó

AA11 - Musical Acoustics
Vasileios Chatziioannou
Michele Ducceschi
Vincent Debut

AA12 - Physical Acoustics and Ultrasound
Lynda Chehami
Óscar Martínez-Graullera
Noé Jiménez

AA13 - Physiological and Audiological Acoustics
Deborah Vickers
Maria Milagros J. Fumero
Miriam Isabel Marrufo Pérez

AA14 - Psychoacoustics
Piotr Majdak
Nicola Prodi
Philipp Aichinger

AA15 - Room Acoustics
Monika Rychtáriková
Ingo Witew
Mélanie Nolan

AA16 - Signal Processing
Efrén Fernández Grande
Boaz Rafaelly
Frank Zotter

AA17 - Soundscape, Environmental Quality, Health and Well-Being
André Fiebig
Jerónimo Vida

AA18 - Speech
Laureano Moro-Velázquez
Eugenia San Segundo
Nick Cummins
Phillip Aichinger

AA19 - Numerical, Computational and Theoretical Acoustics
Luis Godinho
Maarten Hornikx
Stefan Schoder
Marcus Mäder

AA20 - Transportation Noise and Vibration
Stephanos Theodossiades
Eduardo Latorre
Ramón Peral

AA21 - Sound Quality and Product Design
Elif Özcan Vieira
Patrick Susini
Georgios Marentakis
Doriana del Palú

AA22 - Underwater Acoustics
Dídac Diego-Tortosa
María Campo

AA23 - Vibro-Acoustics
Jose Roberto de Franca Arruda
Robert Arcos
Arnau Clot
Oriol Guash

AA24 - Virtual Acoustics
Brian Katz
Arcadio Reyes Lecuona
José Javier López Monfort

SESSION ORGANIZERS

Abhayapala T.
A09.06/A16.03 Machine learning for array processing

Aichinger P.
A14.01 Psychoacoustics - General
A18.01 Speech - General

Alsina-Pagès R.M.
A08.07/A09.05 Artificial intelligence for industrial applications
A09.01 Machine learning and AI in acoustics - General
A17.04 Soundscape methods, monitoring and metrics

Altinsoy E.
A14.06 Development of semantic attributes based on psychoacoustic modelling

Amado Mendes P.
A05.07 Outdoor sound propagation
A10.10/A19.08 Numerical methods for wave propagation in complex media

Anda S.
A08.03 Advances in machinery noise and vibration control
A20.02 Automotive noise and vibration

Andreopoulou A.
A16.07/A24.11 Processing/individualization/interpolation of HRIRs or BRIRs

Antunes S.
A03.04 Ground borne noise

Arana M.
A05.01 Environmental acoustics - General
A05.04 Wind turbine noise

Arcos R.
A20.05 Railway noise and vibration
A23.01 Vibroacoustics

Arenas J.
A08.04/A10.04 Materials and systems for noise and vibration reduction

Aspöck L.
A19.07 Validation and benchmarks in computational acoustics

Aspuru Soloaga I.
A17.04 Soundscape methods, monitoring and metrics

Astolfi A.
A15.02 Speech production and perception in rooms

Atamer S.
A14.06 Development of semantic attributes based on psychoacoustic modelling

Aumond P.
A09.07 Events detection and localization, and acoustic scenes, using ML techniques

Ausiello L.
A11.03 Consistency of musical instrument making

Avallone F.
A07.05/A19.06 Methods for advanced computational aeroacoustics

Bai M.R.
A01.06 Signal processing for active control

Barbancho A.M.
A11.05 Instruments, hyperinstruments and beyond

Barros A.
A05.03 Environmental noise perception

Battarra M.
A08.05 NVH damage detection, condition monitoring, diagnostics of machinery

Becker S.
A07.01 Flow acoustics - General
A07.04 Fluid structures acoustic coupling

Bellows S.
A16.06 Source directivity: capturing, processing, and evaluating its effects

Bellucci P.
A05.06 Recent advances in noise mitigation methods
A20.06 Noise barriers and mitigation techniques for road traffic and railway

Ben Tahar M.
A12.02 NDT & SHM Applications

Bernardini G.
A07.05/A19.06 Methods for advanced computational aeroacoustics

Berzborn M.
A15.11/A16.05 Sound field reconstruction in rooms and enclosures

Bottalico P.
A15.02 Speech production and perception in rooms

Botteldooren D.
A09.01 Machine learning and artificial intelligence in acoustics - General

Bravo T.
A01.05/A06.07 Active metamaterials
A10.08 Modeling acoustic wave propagation in viscothermal structures

Brinkmann F.
A24.09/A24.13 Motion and rendering

Camacho J.
A12.03 Biomedical ultrasound

Campillo-Davo N.
A04.01 Education, Public outreach and history in acoustics - General
A04.02 Online resources and simulations
A04.05 Yesterday, today and tomorrow of research in acoustics
A20.04 Tyre/road noise

Campo-Valera M.
A22.03 Communication, positioning and acoustic sensor systems
A22.05 Geophysics and Distributed Acoustic Sensing (DAS)

Camussi R.
A07.01 Flow acoustics - General
A07.02 Aeroacoustics of aircraft and urban air vehicles

Carbajo San Martín J.
A08.04/A10.04 Materials and systems for noise and vibration reduction

Carlosena A.
A06.06 Acoustic-based sensors, actuators and microsystems

Carrascal T.
A03.01 Building acoustics - General
A03.02 Acoustic regulations, classification schemes and standards
A03.08 Reducing neighbour noise by acoustic retrofit in housing

Casalino D.
A07.02 Aeroacoustics of aircraft and urban air vehicles

Chatziioannou V.
A11.01 Musical acoustics - General
A11.04 Articulated musical instrument modelling

Chazot J.D.
A19.01 Numerical, computational and theoretical acoustics - General

Chehami L.
A12.02 NDT & SHM Applications

Chevillotte F.
A10.07/A15.07 Characterization of acoustic materials

Chmelík V.
A03.09 Acoustic and thermal retrofit of office building stock in EU

Cobos M.
A09.06/A16.03 Machine learning for array processing

Cosarinsky G.
A12.02 NDT & SHM Applications

Cuenca J.
A10.03 Metamaterials for noise and vibration reduction

Cummins N.
A18.01 Speech - General

D'Orazio D.
A15.03 Modern offices: challenges and solutions

Dalmont J.P.
A11.03 Consistency of musical instrument making

Davies B.
A02.01 Bio-acoustics - General

Dazel O.
A10.06/A19.05 Numerical methods for acoustic materials and metamaterials

de la Prida D.
A14.07 Robust and unbiased psychoacoustical experimentation
A15.10 Modeling room impulse responses with machine learning

De Marqui Jr C.
A01.05/A06.07 Active metamaterials

Debut V.
A11.01 Musical acoustics - General

Deckers E.
A10.03 Metamaterials for noise and vibration reduction

Declercq N.
A12.01 Physical acoustics and ultrasound - General

Del Palú D.
A21.03 Listening experience in sound-driven design

Del Val L.
A16.04 Airborne sonar

Delle Monache S.
A21.04 Methodologies for sound-driven design and education

Deng J.
A10.05/A23.05 Metamaterials and acoustic black holes in vibro-acoustics

Díaz A.
A03.10 Acoustic consultancy projects and BIM

Diego-Tortosa D.
A22.03 Communication, positioning and acoustic sensor systems
A22.05 Geophysics and Distributed Acoustic Sensing (DAS)

Diviacco P.
A22.04 Traffic ship noises

Ducceschi M.
A11.01 Musical acoustics - General

Duocastella M.
A12.07 Acousto-optics

Dupont S.
A12.07 Acousto-optics

Durand S.
A06.02 Microphones (theory, measurement, MEMS, etc.)

Ech-Cherif El-Kettani M.
A12.02 NDT & SHM Applications

Encina Llamas G.
A18.04 Speech perception pathologies

Engel M.S.
A14.06 Semantic attributes based on psychoacoustic modelling
A17.02 Restorative soundscapes

Estévez-Mauriz L.
A05.05 Urban sound planning
A20.03 Road traffic noise and vibration

Fernández-Grande E.
A15.11/A16.05 Sound field reconstruction in rooms and enclosures

Ferrari V.
A06.06 Acoustic-based sensors, actuators and microsystems

Ferrer E.
A07.04 Fluid structures acoustic coupling

Ferrer Contreras M.
A01.07/A08.06 Innovative noise barriers to enhance acoustic comfort

Fiebig A.
A17.01 Soundscape, environmental quality, health and well-being
A17.02 Restorative soundscapes
A17.03 Soundscape practice and interventions

Fink N.
A13.04 Advancements and challenges in military acoustics

Fraga de Frieta E.
A20.04 Tyre/road noise

Fuente M.
A03.07 Acoustics of wooden buildings

Fusaro G.
A03.11/A05.11 Heat pump sounds in residential settings
A03.12 Ventilation noise in dwellings

Gan W.S.
A01.06 Signal processing for active control

Garai M.
A03.05 Structure-borne sound and noise from building services
A20.06 Noise barriers and mitigation techniques

García Gómez J.Ó.
A15.09 Sound reflections in concert halls

Gautier F.
A10.05/A23.05 Metamaterials and acoustic black holes in vibro-acoustics

Godinho L.
A05.07 Outdoor sound propagation
A10.06/A19.05 Numerical methods for acoustic materials

Gómez-García J.A.
A18.03 Speech production pathologies

González A.
A01.07/A08.06 Innovative noise barriers to enhance acoustic comfort

Guasch O.
A23.01 Vibroacoustics

Guigou Carter C.
A03.04 Ground borne noise

Guillén S.
A11.05 Instruments, hyperinstruments and beyond

Hampton T.
A17.07 Hospital soundscape

Harvie-Clark J.
A03.11/A05.11 Heat pump sounds in residential settings
A03.12 Ventilation noise in dwellings

Hernández-Molina R.
A18.02 Forensic phonetics and acoustics

Hoeller C.
A03.05 Structure-borne sound and noise from building services

Hongisto V.
A15.03 Modern offices: challenges and solutions

Honzík P.
A06.02 Microphones (theory, measurement, MEMS, etc.)

Hopkins C.
A03.03 Prediction of sound and vibration transmission in buildings

Hornikx M.
A15.12/A19.09 Numerical methods for room acoustics
A19.01 Numerical, computational and theoretical acoustics

Izquierdo A.
A16.04 Airborne sonar

Jacob S.
A07.06 Modern experimental techniques in aeroacoustics

Jacob M.
A07.06 Modern experimental techniques in aeroacoustics

Jadoul Y.
A02.07/A09.03 AI and machine learning in bioacoustics

Jaouen L.
A10.07/A15.07 Characterization of acoustic materials
A10.08 Modeling wave propagation in viscothermal structures

Jeon W.
A10.05/A23.05 Metamaterials and acoustic black holes in vibro-acoustics

Jiménez N.
A12.01 Physical acoustics and ultrasound - General

Kang J.
A01.07/A08.06 Innovative noise barriers
A17.03 Soundscape practice and interventions

Katz B.F.G.
A15.04/A24.06 Virtual reconstructions in archaeoacoustic research
A24.01 Virtual acoustics - General

Larrosa-Navarro M.
A14.07 Robust and unbiased psychoacoustical experimentation

Latorre Iglesias E.
A20.01 Transportation noise and vibration - General
A20.05 Railway noise and vibration

Lee P.J.
A17.07 Hospital soundscape

Lenzi S.
A21.02 Applied sound-driven design

Licitra G.
A05.06 Recent advances in noise mitigation methods
A08.07/A09.05 Artificial intelligence for industrial applications

Lissek H.
A01.05/A06.07 Active metamaterials

López Monfort J.J.
A24.01 Virtual acoustics - General

López-Espejo I.
A18.04 Speech perception pathologies

Lostanlen V.
A02.07/A09.03 AI and machine learning in bioacoustics
A09.07 Events detection and localization using ML

Lotinga M.
A05.10/A14.09 Advanced air mobility noise

Maag T.
A05.05 Urban sound planning

Maeder M.
A19.01 Numerical, computational and theoretical acoustics - General
A19.07 Validation and benchmarks in computational acoustics

Majdak P.
A14.01 Psychoacoustics - General
A14.04 Spatial hearing: modeling and applications

Malléjac M.
A10.02 Acoustic, vibroacoustic and elastic metamaterials

Manvell D.
A05.08 Advances in noise mapping

Marektakis G.
A21.03 Listening experience in sound-driven design

Martellotta F.
A15.04/A24.06 Virtual reconstructions in archaeoacoustic research

Martínez-Graullera O.
A12.03 Biomedical ultrasound

Mastino C.C.
A03.10 Acoustic consultancy projects and BIM

Masullo M.
A14.10 Experiments for noise annoyance, comfort, and soundscape

Maury C.
A10.08 Modeling wave propagation in viscothermal structures

Mayer-Kahlen N.
A14.08/A24.05 Virtual acoustics and binaural AR in hearing research

Mayhofer D.
A19.02 Numerical methods for acoustics and vibration

Merino-Martínez R.
A20.07 Aircraft noise

Miniaci M.
A10.02 Acoustic, vibroacoustic and elastic metamaterials

Misdariis N.
A21.02 Applied sound-driven design

Misol M.
A01.02/A01.03 Active sound and vibration control

Montano Rodríguez W.A.
A04.05 Yesterday, today and tomorrow of research in acoustics

Monteiro C.
A03.01 Building acoustics - General

Moro-Velázquez L.
A18.01 Speech - General
A18.05 Speech technologies: diarization, emotion, enhancement

Mucchi E.
A08.05 NVH damage detection, condition monitoring, diagnostics of machinery

Murphy E.
A05.08 Advances in noise mapping

Negreira J.
A15.05 Acoustic comfort in hospitals

Neidhardt A.
A24.09/A24.13 Motion and rendering

Noisternig M.
A16.06 Source directivity

Nolan M.
A10.07/A15.07 Characterization of acoustic materials
A10.08 Modeling wave propagation in viscothermal structures
A15.01 Room acoustics - General

Osses A.
A14.04 Spatial hearing: modeling and applications

Özcan E.
A17.07 Hospital soundscape
A21.02 Applied sound-driven design

P. B. Reynders E.
A03.03 Prediction of sound and vibration transmission in buildings

Pàmies-Vilà M.
A04.01 Education, Public outreach and history in acoustics
A04.02 Online resources and simulations for teaching

Panagiotopoulos D.
A19.02 Numerical methods for acoustics and vibration

Pauletto S.
A21.03 Listening experience in sound-driven design

Pawelczyk M.
A01.02/A01.03 Active sound and vibration control
A01.07/A08.06 Innovative noise barriers
A05.01 Environmental acoustics - General

Peral-Orts R.
A20.01 Transportation noise and vibration - General
A20.03 Road traffic noise and vibration

Pérez Vargas R.
A18.02 Forensic phonetics and acoustics

Pérez-Liva M.
A12.03 Biomedical ultrasound

Pezzoli M.
A09.08/A11.02 Artificial intelligence in musical acoustics

Piana E.
A08.03 Advances in machinery noise and vibration control

Picaut J.
A05.01 Environmental acoustics - General
A05.04 Wind turbine noise

Piñero G.
A15.10 Modeling and estimation of room impulse responses with machine learning

Plumbley M.
A09.01 Machine learning and artificial intelligence in acoustics - General

Pompoli F.
A08.04/A10.04 Materials and systems for noise and vibration reduction

Poveda Martínez P.
A02.02/A22.02 Underwater soundscape and noise
A08.05 NVH damage detection, condition monitoring

Prieto A.
A10.10/A19.08 Numerical methods for wave propagation in complex media

Prinn A.
A19.07 Validation and benchmarks in computational acoustics

Prodi N.
A14.01 Psychoacoustics - General

Puglisi G.
A15.06 Acoustic and multidomain comfort in learning spaces

Rafaely B.
A16.02 Spatial audio signal processing

Ragni D.
A07.01 Flow acoustics - General
A07.02 Aeroacoustics of aircraft and urban air vehicles

Raiola M.
A07.03 Active and passive noise reduction technologies

Ramallo S.
A24.01 Virtual acoustics - General

Ramírez Salado M.
A18.02 Forensic phonetics and acoustics

Ramis-Soriano J.
A02.02/A22.02 Underwater soundscape and noise
A08.03 Advances in machinery noise and vibration control

Rasmussen B.
A03.02 Acoustic regulations, classification schemes and standards
A03.08 Reducing neighbour noise by acoustic retrofit in housing

Reichl C.
A03.11/A05.11 Heat pump sounds in residential settings
A03.12 Ventilation noise in dwellings

Reyes-Lecuona A.
A14.08/A24.05 Virtual acoustics and binaural AR
A24.01 Virtual acoustics - General

Rodríguez P.
A20.07 Aircraft noise

Rodríguez-Montaño V.M.
A18.02 Forensic phonetics and acoustics

Romero A.
A03.01 Building acoustics - General

Romero-García V.
A10.09/A12.10 Acoustic wave propagation in complex media

Rosa González F.L.
A22.04 Traffic ship noises

Rufer L.
A06.03 Loudspeakers and headphones (theory, measurement, MEMS, etc.)

Rus G.
A12.03 Biomedical ultrasound

Russo R.
A09.08/A11.02 Artificial intelligence in musical acoustics

Rychtáriková M.
A03.09 Acoustic and thermal retrofit of office building stock
A15.01 Room acoustics - General

San Segundo E.
A18.01 Speech - General

Sanz Segura R.
A21.04 Methodologies for sound-driven design and education

Sastre J.
A11.06/A24.07 Networked music performances and virtual environments

Schanda U.
A03.05 Structure-borne sound and noise from building services

Schoder S.
A07.05/A19.06 Methods for advanced computational aeroacoustics
A19.07 Validation and benchmarks in computational acoustics

Schoenwald S.
A03.07 Acoustics of wooden buildings

Schulte-Fortkamp B.
A17.06 Soundscape and inclusion, from theory to practice

Schulz A.
A07.03 Active and passive noise reduction technologies

Scrosati C.
A03.01 Building acoustics - General

Sea E.A.
A19.01 Numerical, computational and theoretical acoustics - General

Secchi S.
A15.05 Acoustic comfort in hospitals

Segura-García J.
A24.09/A24.13 Motion and rendering

Shabalina E.
A10.03 Metamaterials for noise and vibration reduction

Siebein K.
A17.03 Soundscape practice and interventions

Širović A.
A02.02/A22.02 Underwater soundscape and noise

Slabbekoorn H.
A02.05 Effects of multimodal stimuli on wildlife

Sobreira M.
A09.01 Machine learning and artificial intelligence in acoustics - General

Spagnol S.
A21.02 Applied sound-driven design

Stoppel F.
A06.03 Loudspeakers and headphones

Susini P.
A21.04 Methodologies for sound-driven design and education

Taghipour A.
A14.10 Experiments for noise annoyance, comfort, and soundscape

Talebzadeh A.
A17.06 Soundscape and inclusion, from theory to practice

Temboury Gutiérrez M.
A13.06 Audiology diagnostic techniques

Thebaud T.
A18.05 Speech technologies: diarization, emotion, enhancement

Theodossiades S.
A20.01 Transportation noise and vibration - General
A20.02 Automotive noise and vibration

Torija Martínez A.
A05.10/A14.09 Advanced air mobility noise

Torrent D.
A10.02 Acoustic, vibroacoustic and elastic metamaterials

Torresin S.
A17.05 Indoor soundscapes

Undurraga J.
A13.06 Audiology diagnostic techniques

Valier-Brasier T.
A10.09/A12.10 Acoustic wave propagation in complex media

Van Belle L.
A10.03 Metamaterials for noise and vibration reduction

Van Damme B.
A10.02 Acoustic, vibroacoustic and elastic metamaterials

Van Renterghem T.
A02.05 Effects of multimodal stimuli on wildlife
A05.03 Environmental noise perception

Van Walstijn M.
A11.04 Articulated musical instrument modelling

Vanhamel J.
A12.07 Acousto-optics

Vida Manzano J.
A17.01 Soundscape, environmental quality, health and well-being - General
A17.04 Soundscape methods, monitoring and metrics

Vidaña-Vila E.
A02.01 Bio-acoustics - General

Villacorta J.J.
A16.04 Airborne sonar

Visentin C.
A15.03 Modern offices: challenges and solutions
A15.06 Acoustic and multidomain comfort in learning spaces

Waddington D.
A02.01 Bio-acoustics - General

Want W.
A09.01 Machine learning and artificial intelligence in acoustics - General

Weger M.
A13.04 Advancements and challenges in military acoustics

Whitehead H.
A02.01 Bio-acoustics - General

Willemsen S.
A11.06/A24.07 Networked music performances and virtual environments

Williges B.
A13.05 Asymmetric hearing loss - clinical solutions and functionality

Witew I.
A15.01 Room acoustics - General

Wrona S.
A01.07/A08.06 Innovative noise barriers

Yorukoglu P.N.D.
A17.05 Indoor soundscapes

Yue Z.
A18.03 Speech production pathologies

Zaffaroni-Caorsi V.
A02.02/A22.02 Underwater soundscape and noise

Zambon G.
A02.02/A22.02 Underwater soundscape and noise

Zirn S.
A13.05 Asymmetric hearing loss - clinical solutions and functionality

Zotter F.
A16.02 Spatial audio signal processing

Plenary Sessions

Plenary Session 1

Sounds of the Ocean: understanding marine life and its interactions with sound



Author: Ana Širović
Affiliation: Norwegian University of Science and Technology, Norway
Date: Monday, June 23rd

Biography:

Ana Širović is a marine bioacoustician and a professor at the Norwegian University of Science and Technology (NTNU) in Trondheim, Norway. Originally from Croatia, she obtained a Bachelor's degree from the University of California Santa Barbara and a PhD in Oceanography from the Scripps Institution of Oceanography at the University of California San Diego in the United States. She is interested in the development and use of new methods to improve understanding of highly exploited and endangered marine species. She also conducts research on ambient sound and the effects of anthropogenic noise on marine life. Her group uses acoustic tools to answer ecological, population-level questions relevant to the management of animal resources. Prior to joining NTNU, Prof. Širović was a faculty member at Texas A&M University at Galveston and Alaska Pacific University, and a research oceanographer at the Scripps Institution of Oceanography. She is the recipient of the Medwin prize from the Acoustical Society of America and the US Antarctic Service Medal.

Abstract:

Sound allows us to investigate the ocean on a much finer time scales than other methods of study as it is feasible to collect continuous underwater recordings over months or years at a time. At the same time, sound is critical for successful functioning of many marine animals. It helps them find food and mates, fend off threats, and sense their environment. I will present case studies that highlight how we have been gaining valuable ecological and biological knowledge about baleen whale and fish species through long-term passive acoustic monitoring effort. Some of these highlights include an improved understanding of animal occurrence and coupling of the occurrence of predators and prey into dynamic ecosystem patterns dynamics, leading ultimately to a fuller understanding of their roles in the ocean. In addition, I will reflect on the concerns that increases in ocean sound levels raise regarding functioning of marine life and ecosystems, again highlighting the issues via several case studies. Effects of exposure to seismic noise studies also show mixed impact across taxa. In lab-based experiments, we found that exposures to sounds of seismic airguns on red drum (Sciaenops ocellatus) juveniles did not induce an increase in water-borne and tissue-measured steroid hormone levels. Pile driving noise often results in hearing impairment in marine mammals and injury in fishes. Currently, impacts from other industrial noise sources are poorly documented across taxa. One such source of increasing interest is offshore wind farms. In 2023 and 2024, we conducted microcosm and mesocosm experiments to investigate the response of plankton community to sounds of operational wind farms. Our preliminary results indicate impacts across trophic levels. Overall, given the limited number of species used in noise impact experiments, development of categorizing principles and modeled response pathways will be necessary to better elucidate mechanistic framework for observed impacts. Combined with multi-stressor impact assessment framework and integration and interplay of effects across ecosystems, improved understanding of underlying impact mechanisms should contribute to a better understanding and ultimately a more efficient management of marine resources.

Plenary Sessions

Plenary Session 2

AI for Acoustics: Recognition, Captioning, Visualization, Separation and Generation of Everyday Sounds



Author: Prof. Mark Plumbley
Affiliation: University of Surrey, UK
Date: Tuesday, June 24th

Biography:

Prof. Mark Plumbley is Professor of Signal Processing at the Centre for Vision, Speech and Signal Processing (CVSSP) at the University of Surrey, in Guildford, UK. He is an expert on analysis and processing of audio, using a wide range of signal processing and machine learning methods. He led the first international data challenge on Detection and Classification of Acoustic Scenes and Events (DCASE), and is a co-editor of the book "Computational Analysis of Sound Scenes and Events" (Springer, 2018). He currently holds a 5-year EPSRC Fellowship "AI for Sound" on automatic recognition of everyday sounds. He is a Member of the IEEE Signal Processing Society Technical Committee on Audio and Acoustic Signal Processing, and a Fellow of the IET and IEEE.

Abstract:

The last few years has seen a rapid increase of interest in the application of AI to everyday sounds. Starting a decade ago with acoustic scene classification and sound event detection, the challenges and workshops on Detection and Classification of Acoustic Scenes and Events (DCASE) have brought together researchers from academia and industry to establish a new research community. In this talk, I will highlight some of the work taking place in this area at the University of Surrey, including pretrained audio neural networks (PANNs), audio captioning, audio visualization, audio source separation and audio generation (AudioLDM). I will also mention some cross-cutting issues such as dataset collection, algorithm efficiency, and large language models (LLMs), and discuss how we might design future AI applications for acoustics, to benefit of people and society.

Plenary Sessions

Plenary Session 3

Standardizing soundscape perception and other tales



Author: Francesco Aletta
Affiliation: University College London, UK
Date: Wednesday, June 25th

Biography:

Dr Francesco Aletta is a Lecturer in Building Physics and Soundscape at Institute for Environmental Design and Engineering, University College London (UCL). His research focuses on environmental acoustics and soundscape studies. Francesco is committed to advancing soundscape research through his contribution to the ISO 12913 series on soundscapes, which provides a comprehensive framework for assessing and managing urban sound environments. Francesco's research has informed international policy discussions. He authored a United Nations Environment Programme report in 2022, addressing emerging environmental concerns related to noise and its impact on public health and urban environments. His work is frequently referred in policy documents and guidelines aimed at promoting healthier and more sustainable sound environments globally. As part of his standardization efforts, Francesco coordinated the Soundscape Attributes Translation Project, an international collaboration of more than 100 scholars worldwide. He is also an active member of editorial boards for leading journals, including the Journal of the Acoustical Society of America (Coordinating Editor for TC Noise), and member of the organizing committee of several international conferences, including the Urban Sound Symposium, and the Lancet UK Public Health Science Conference. Francesco is a member of the Italian Acoustical Society (AIA), the Acoustical Society of America (ASA), and serves as secretary of the Technical Committee Noise of the European Acoustics Association (EAA). With over 200 publications, 6,000 citations and multiple awards, including the ASA Science Communication Award in 2023, Francesco aims to contribute to the global discourse on soundscape design, urban acoustics, and public health.

Abstract:

The way we experience soundscapes is deeply personal, shaped by cultural, environmental, and psychological factors. Yet, as urbanization accelerates and noise management becomes a global priority, the need for standardized approaches to assessing and designing soundscapes has never been greater. This keynote explores the evolving efforts to establish frameworks for soundscape perception, from the development of international standards to the challenges of ensuring their widespread adoption. While standardization provides a necessary foundation for consistency, the reality of soundscape experience is far from universal. People from different cultural and linguistic backgrounds perceive, interpret, and encode sounds in diverse ways, highlighting the limitations of rigid frameworks. Addressing this complexity requires a balance between structured methodologies and adaptability to local contexts. Advances in cross-cultural research and translation efforts are helping to refine these approaches, making soundscape assessment more inclusive and representative. At the same time, new methods for quantifying soundscape quality are emerging, offering ways to integrate perceptual and contextual dimensions into meaningful metrics. These developments not only enhance our ability to compare and evaluate soundscapes but also provide valuable tools for urban planners, policymakers, and designers to create environments that support well-being. This talk will explore the intersection of standardization, perception, and measurement, reflecting on how soundscapes can be assessed in a way that respects both scientific rigor and human experience.

Plenary Sessions

Plenary Session 4

Sculpting sound fields with acoustic holograms



Author: Dr. Noé Jiménez
Affiliation: Spanish Research Council (CSIC), Spain
Date: Thursday, June 26th

Biography:

Noé Jiménez is a Senior Scientist at the CSIC since 2024. He develops his work at the Institute of Instrumentation for Molecular Imaging, a joint centre of the Universitat Politècnica de València (UPV) and the CSIC. He is a Telecommunications Engineer, holds a Master's degree in acoustics and a PhD (2015) from the UPV. He has been a Ramón y Cajal senior researcher, Juan de la Cierva - Incorporation, Juan de la Cierva - Training, has worked at the CNRS (France) as a postdoctoral researcher for two years, and has made stays at Columbia University (NYC, USA), the University of Salford (UK), and the University of Le Mans (France). He has over 15 years' experience in developing imaging and therapeutic ultrasound systems, wavefront shaping techniques and acoustic metamaterials. His recent research interest ranges from the application of acoustic metamaterials for biomedical ultrasound applications, novel therapeutic ultrasound techniques, acoustic holograms, and acoustic vortices.

Abstract:

Using optical holograms, we can modulate light wavefronts to generate visible images. Can we do the same with sound waves? Acoustic holograms can render sonic images, shaping the areas where mechanical waves present a high amplitude, and areas where the media is at rest. In this plenary talk, we will present an overview of the use of acoustic holograms, and how they can be applied in biomedical ultrasound applications, in particular in emerging therapeutic applications of focused ultrasound, but also in other fields like audible engineering acoustics or contactless particle trapping, to tailor sound waves in unprecedented ways.







AMC MECANOCAUCHO

Akustik + sylomer® by getzner

Application BROCHURES

- Building Acoustics
- Solutions for gyms
- Urban Supermarkets
- Machinery in buildings
- Hotels
- Timber constructions
- Floating floors
- and more!

THE BEST STRUCTURAL INSULATION SYSTEM **FOR YOUR PROJECTS**

SCAN ME

Akustik dB Finder

Impact / Airborne Noise Test Results with a simple click on **akustik.com**



AMC Mecanocaucho
The best anti-vibration solutions since 1969

www.akustik.com
www.mecanocaucho.com
sales@amcsa.es
+34 943 69 61 02

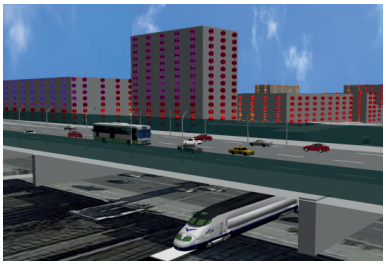
Visit our website **www.akustik.com** to see acoustic results and the full range of insulation products.

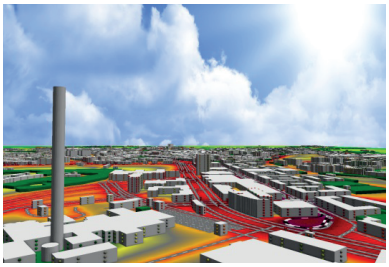
DataKustik

SOFTWARE FOR IMMISSION PROTECTION

STATE-OF-THE-ART NOISE PREDICTION SOFTWARE

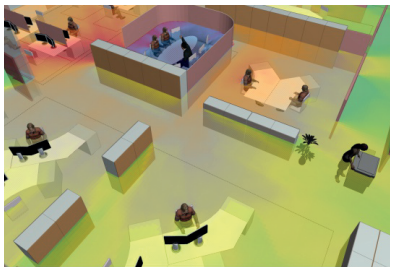
Cadna A®

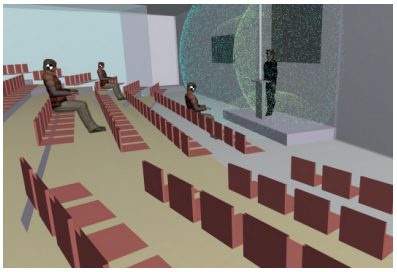




PREDICTION OF SOUND INSIDE ROOMS

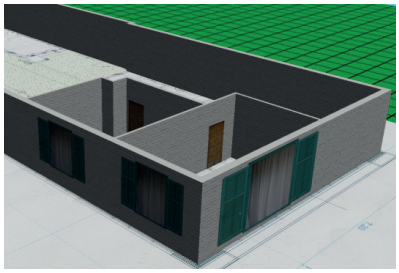
Cadna R®

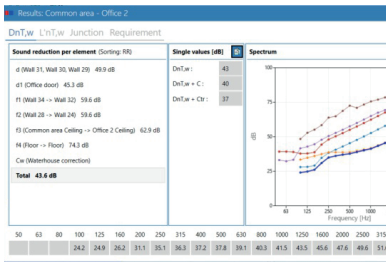




THE BUILDING ACOUSTICS PLANNING SYSTEM

Cadna B®





WWW.DATAKUSTIK.COM


DEMCON
SOUND SOLUTIONS
SOUNDINSIGHT
Sonocat.
• In situ absorption
• In situ transmission
• 3D sound intensity
• Emitted intensity
• Reflected intensity
• Sound power
• Sound pressure
• 3D particle velocity
• 3D impedance
VISIT US AT STAND 12
@ EURONOISE
soundsolutions.demcon.com

HEAD acoustics

soundscape

visit us–
booth
10

What does our environment sound like?

Binaural recordings, mobile measurement systems, and (psycho-)acoustic analyses with HEADscape, along with standardization DIN ISO 12913, represent pioneering soundscape innovation that holistically evaluates noise quality—exclusively from HEAD acoustics.

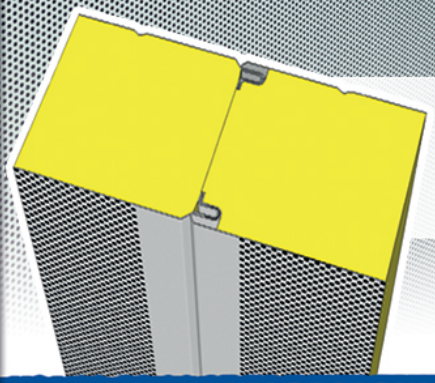
REAL-LIFE-PROOF.

www.head-acoustics.com

meTecno

JETZT NEU!

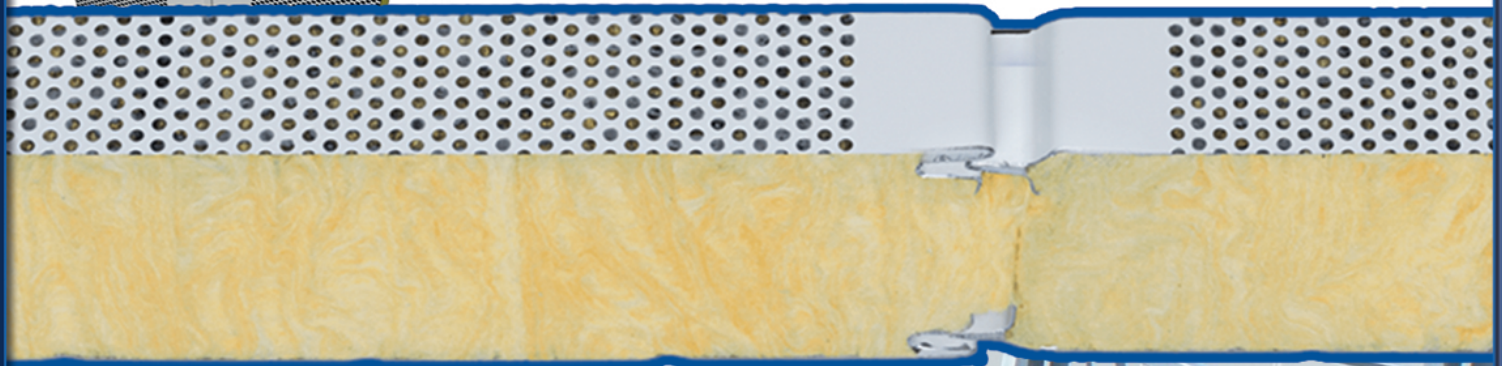
Metecno RC5 high - gelochtes Sandwichelement mit geprüfter Korrosionsschutzklasse RC5



Schallabsorption
α_w = 0,9 - 1,0

Schalldämmung
R_w = 36 - 70 dB

Schallschutz-Sandwichelement mit Dämmkern
aus Glas- oder Steinwolle



Detaillierte Prüfberichte von namhaften Instituten

www.metecno-sound.de

Unerhört gut!

meTecno SOUND

akustik@metecno.de

Norsonic

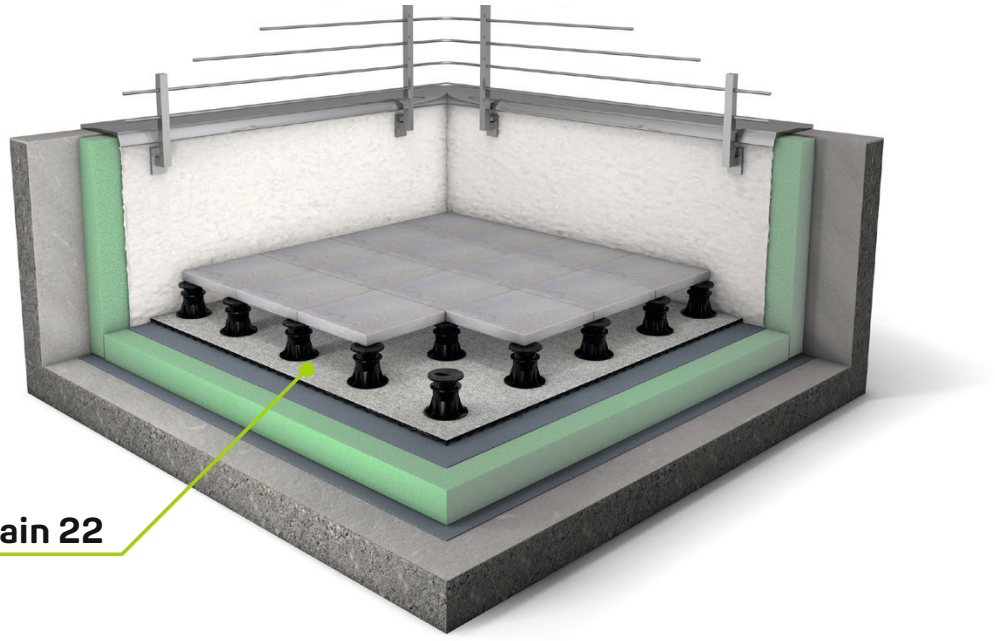


Building Acoustics Measurement Kit

Nor145 Sound Level Meter | Nor283 Dodecahedron Loudspeaker
Nor282 Power Amplifier | Nor850 Software Package

www.norsonic.com





REGUPOL sound and drain 22

Cradle to Cradle Certified®
is a registered trademark of
the Cradle to Cradle Products
Innovation Institute.

acoustics@regupol.eu | www.regupol.com

REGUPOL

climalit SAINT-GOBAIN

ecophon SAINT-GOBAIN

ISOVER SAINT-GOBAIN

placo SAINT-GOBAIN

COMPREHENSIVE ACOUSTIC SOLUTIONS TAILORED TO YOUR PROJECT'S NEEDS

- BUILDING ENVELOPE
- GLAZING
- PARTITIONS
- CEILINGS

Adapted to the needs of each project, providing the greatest acoustic and aesthetic comfort.

We are committed to building better for people and the planet.



360 YEARS YOUNG
MAKING THE WORLD A BETTER HOME

SAINT-GOBAIN

Sealed Air®

Whisper® Acoustic Panels



Noise can be annoying! Just make it Whisper

Whisper is the worlds first commercial metamaterial using networked closed cells to absorb noise resulting in an efficient and durable acoustic solution.

INTERTRAFFIC
GREEN GLOBE AWARD 2024 WINNER
SEE® Brand Whisper® NB-Eco-40-A3

Whisper acoustic panels are designed for recycling in post industrial LDPE packaging foam recycling systems. Whisper offers reduced carbon emissions over traditional mineral wool and polyester acoustic panels in may situations.

IT'S THE COMBINATION OF PERFORMANCE ATTRIBUTES THAT MAKES WHISPER® ACOUSTIC PANELS SO UNIQUE.



YOU CAN CHECK OUT OUR WHISPER EPD HERE:
https://www.environdec.com/library/collection/col151

EPD®
THE INTERNATIONAL EPD® SYSTEM

Visit our website: pages.sealedair.com/uk-whisper

A prueba de fuego.

Un paso más en el aislamiento acústico.

En **SENOR** seguimos innovando en soluciones de **máximo aislamiento acústico** homologadas en laboratorio, ahora con **resistencia al fuego certificada EI120 y EI180.**

Toda la innovación en 3 sistemas:
TECHO / TRASDOSADO / TABIQUE



Accede a las soluciones más avanzadas escaneando este código

www.senor.es

Visit our booth

#29

treble

Next generation acoustic simulations

Fastest simulation engine

Run multiple concurrent simulations, save time, and increase productivity

Treble & BIM

IFC imports with automatic geometry simplification

Highly accurate simulations

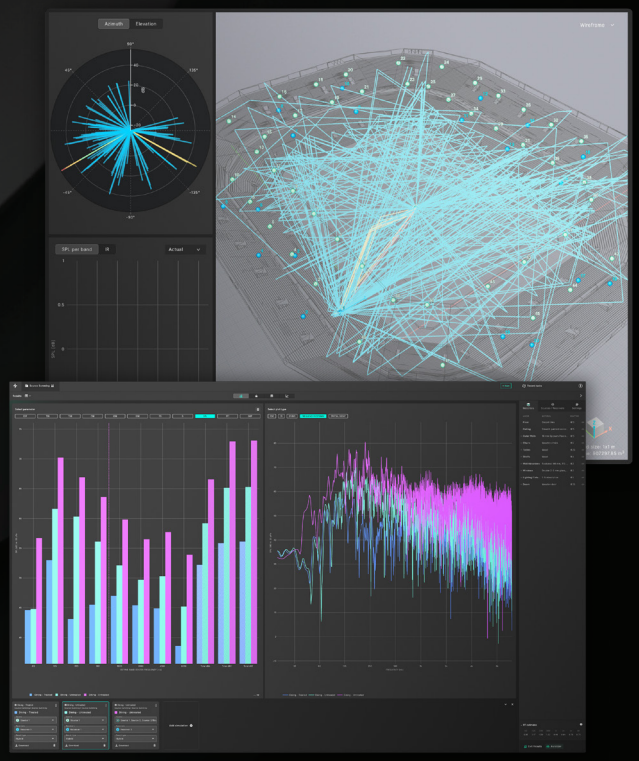
Precise modeling of absorption, phase, diffraction, modes, and coupling

Hybrid solvers for flexibility

Combine fast geometrical and wave-based solvers for flexible simulations

Powerful analysis tools

Experience features like the auralizer, reflection tracking, modal analysis, and many more



Try Treble for free for 14 days

treble.tech

COMPLETE PRECISION. BUILT IN.

With Bedrock Elite, every advanced feature comes standard, because real professionals shouldn't have to choose between options.

Experience inclusive innovation

FAST, ACCURATE, AND FUTURE-READY.

VISIT US TO UNCOVER MORE



www.bedrock-elite.com

BEDROCK ELITE

dBelectronics

Synkro

NOISE CONTROL & MANAGEMENT SMART CITIES IN REAL-TIME



SOUND LIMITER



cap21

SOUND LEVEL METER



SR02

dBnoise

ENVIRONMENTAL NOISE STATION



+34 670 580 725 - info@dbelectronics.es - dbelectronics.es

CASELLA
ESPAÑA
EQUIPAMOS SOLUCIONES

Monitorización de
Ruido y Vibraciones

IMMI
Mapas de Ruido

EARTHSENSE
Smart Cities / ZBE

CRYSOUND
Acoustic Imaging



Síguenos en LinkedIn

stravidB
by CDM Stravitec



Discover Stravi-dB, our free online test data platform!

Stravi-dB is an online library that lets you easily find
the acoustical test reports you're looking for.

SCAN
ME

CDM Stravitec (HQ)
Reutenbeek 9-11
3090 Overijse
Belgium

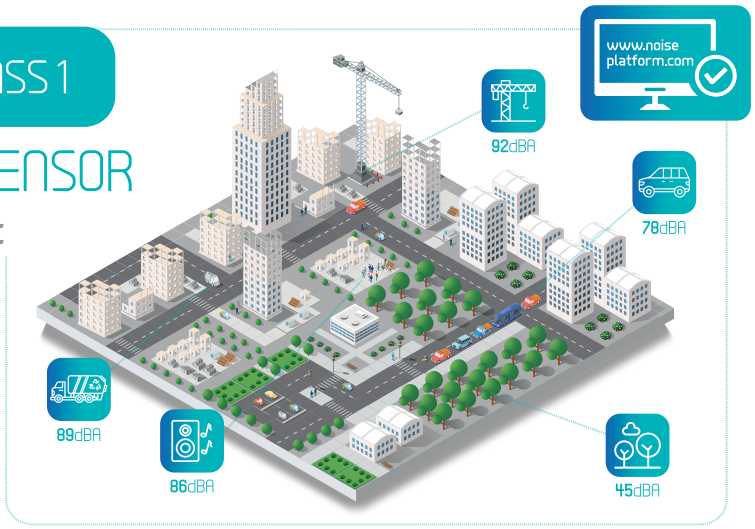
T +32 2 687 79 07
info@cdm-stravitec.com
www.cdm-stravitec.com



TA150 | CLASS 1

NOISE SPECTRUM SENSOR

Smart Noise Management



1 CLASS 1
According IEC 61672-1

Lxy 12 FUNCTIONS
LAeq, LCeq, LZeq and LAleq, LAFmax, LASmax...

AUDIO FILES*
With automatisms (By level, time or emergency)

GPS*
Position Tracker

*OPCIONAL

1/3 OCTAVE*
From 6,3 Hz to 20 kHz

4G*
Modem communication

AI READY*
For event detection and classification

CESVA
NOISE MEASURING INSTRUMENTS SINCE 1969

+ INFO
www.cesva.com



iNoise®

road, rail, industry and wind turbine noise prediction

dGmR SOFTWARE

www.dgmrsoftware.com/inoise

EAA

The European Acoustics Association (EAA) is a non-profit entity established in 1992 that includes in its membership societies predominantly in European countries interested promoting the development and progress of acoustics in its different aspects, its technologies and applications.

The EAA gathers 34 societies of acoustics and serves more than 9000 individual members all over Europe. The EAA is an Affiliate Member of the International Commission for Acoustics (ICA) and of Initiative of Science in Europe (ISE).

Contact: eaa.euracoustics.org

EAA European Acoustics Association
@EAAacoustics



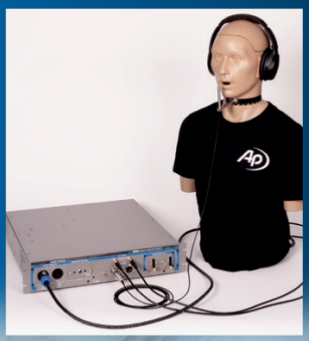
AXIOMETRIX SOLUTIONS

AP | GRAS | imc

Acoustics Solutions









Ingeniería Acústica García-Calderón

Proveedores de equipamiento para medidas de ruido y vibraciones. Diseño y suministro de cámaras anecoicas



CÁMARAS ACÚSTICAS



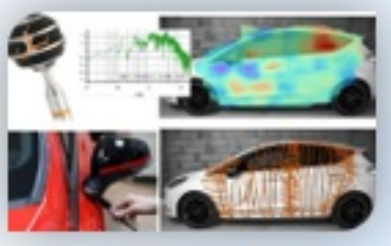
FUENTES SONORAS ULTRALIGERAS



MÁQUINA DE IMPACTOS



MEDIDOR DE ABSORCION Y STL (SONOCAT)



SONDAS INTENSIDAD 3D, PU



ANALIZADORES MULTICANAL

C/ Soto Hidalgo 24, local 8 28042 Madrid, Spain

Telf: +34 91 128 89 47

Email: info@garcia-calderon.com

Web: https://garcia-calderon.com/

IMS

IMS Measurement Systems

Let's Start with Sound and Vibration

Who Are We?

For more than 25 years, we've delivered high-quality sound and vibration solutions with the goal to enhance lives. We offer:

Professional Services:
Our guarantee of highest quality services and equipment.

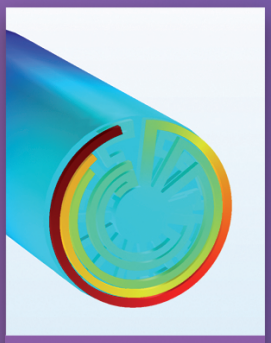
Calibration & Support:
IMS lab calibration for optimal performance and fast turn-around time.

Consulting & Sales:
Expert guidance and premium measuring equipment.

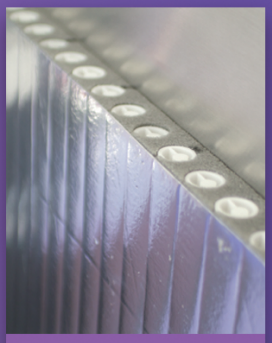
Acoustic and Vibration Measurements:
Precise analyses with our own and HBK measurement solutions.

METACOUSTIC
10TH ANNIVERSARY

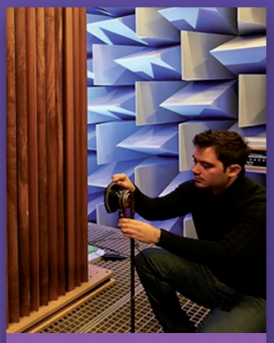
Acoustic R&D Services for industry



Vibro-acoustic simulations



Metamaterial solutions



Experimental validations

Visit us at booth #3

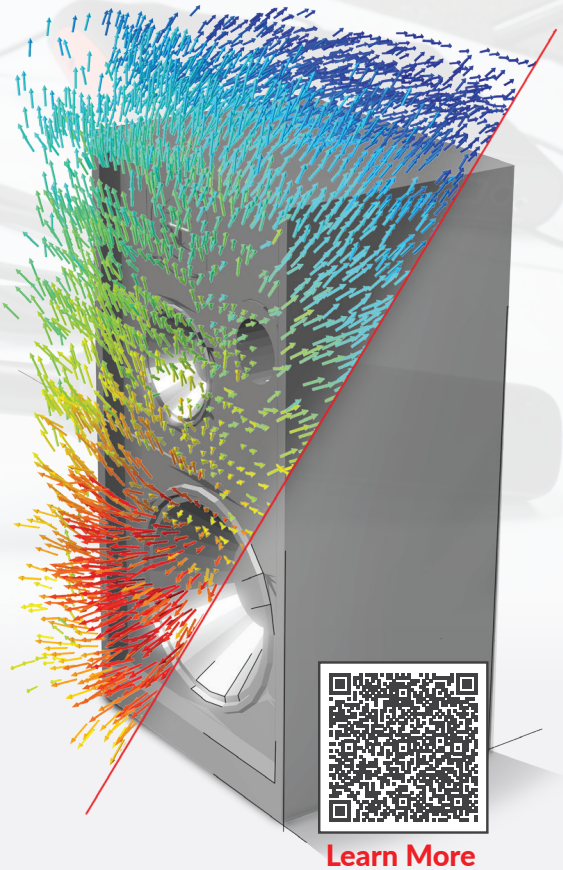
contact@metacoustic.com

MICROFLOWN TECHNOLOGIES

MEASURING 3D SOUND FIELDS WITH MILLIMETER PRECISION

Capture sound intensity data with Scan&Paint 3D to overcome acoustic challenges





Learn More

40 years of development!

The room acoustics software for reliable results

Four decades of development have made **ODEON** a reference software in the field of room acoustics, used by promiment companies in more than **80 countries**.



Odeon
Room Acoustics Software

odeon.dk

MAKE SOUND VISIBLE



LOCALIZE ACOUSTIC CHALLENGES - FAST AND PRECISE.

With the Seven Bel Sound Scanner, you can quickly detect and visualize noise sources – even in the low-frequency range. High-resolution acoustic images support root cause analysis and enable you to focus your time on developing targeted, effective solutions.

www.sevenbel.com

sevenbel
EFFECTIVE SOUND IMAGING

SONITUS SYSTEMS

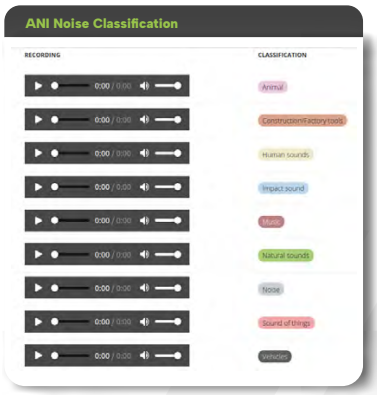
EURO NOISE 2025

23-26 June



Advanced AI-Powered Noise Identification from Sonitus Systems

ANI, Automated Noise Identification, is designed to change the way environmental sounds are monitored. Save time and gain insight into what is really happening on your project using our powerful AI analysis tools.



ANI AUTOMATED NOISE IDENTIFICATION

sales@sonitussystems.com

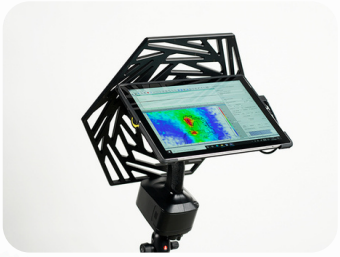
www.sonitussystems.com

TRACK-NOISE

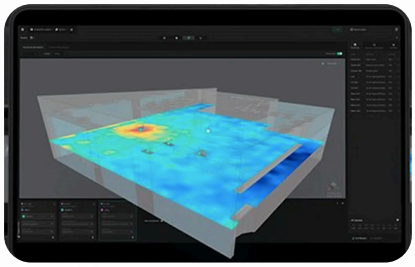
ACÚSTICA - AUDIO - RUIDO - VIBRACIONES

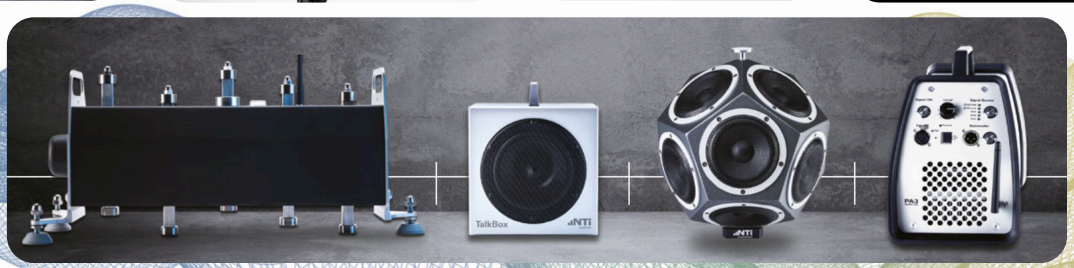
SISTEMAS DE LOCALIZACIÓN SONORA 2D & 3D











www.track-noise.com

www.nti-audio.com

VIBLENS

Silence Engineering

Vibration, shock and noise control

+34 916 483 833
viblens.com info@viblens.com

Engineering | Support & Training | Antivibration Mounts | Instrumentation | Noise Sources & Impact Machines | Vibration, Noise & Temperature Monitors | Acoustic and Vibration Insulation Sheets | Thermal Insulation | Expansion Joints & Compensators

ALPHA ACOUSTIKI

In TUNE with YOUR needs

Architectural acoustics
Sound insulation
Vibration control

www.alphacoustic.com
www.vibro.gr

40+ years

Join us at Booth 5!
FORUM ACUSTICUM EURONOISE 2025
23-26 JUNE 2025

SOCIEDAD ESPAÑOLA DE ACÚSTICA

Impulsando la acústica en España desde 1969

SEA
SOCIEDAD ESPAÑOLA DE ACÚSTICA

Hazte socio y da forma al futuro de la acústica.

Como cualquier sociedad sin ánimo de lucro, la SEA existe por y para sus asociados. Ser socio permite ser partícipe directo del avance y desarrollo de la profesión.

Los asociados son parte activa de la generación de conocimiento, participando en congresos, cursos y actividades.

ORGANIZADORES DE:
FORUM ACUSTICUM EURONOISE 2025

BENEFICIOS EXCLUSIVOS

- **Congresos y Exposiciones**
  Descuentos en Tecniacústicas y otros eventos nacionales, y en congresos internacionales de la EAA.
- **Publicaciones**
  Recepción gratuita de la *Revista de Acústica*.
- **Formación y Ayudas**
  Acceso a becas de estudio y bolsas de viaje para congresos.
  Información sobre ofertas de trabajo en el sector.
- **Red Profesional**
  Conexión con Expertos Senior y Jóvenes Acústicos.
- **Información del sector**
  Actualización en novedades técnicas y normativas.

¡ASÓCIATE!
Visita nuestra web oficial

Escanea para ir al formulario

TABLE OF CONTENTS

Session A01.02/A01.03 Active sound and vibration control

Topology optimisation of microphone arrays for remote microphone virtual sensing in diffuse sound fields
A. Kappis and J. Cheer 3

Control of Transverse Vibrations in Vertically Installed Rotating Shafts Through Active Bearings
J. Song and B. Kim 11

Active Structural Acoustic Control (ASAC) for Vibrating Plates with Openings in Vibro-Acoustic Systems
K. Said Ahmed Maamoun, S. Wrona, M. Pawelczyk and H. R. Karimi 15

A comparison between spatial interpolation approaches in a head-tracked active headrest system
C. K. Lai and J. Cheer 23

Stability Analysis of Stepwise Simultaneous Perturbation Stochastic Approximation for Active Noise Control
C. Liang, F. Ripamonti and H. R. Karimi 31

Spatial Psychoacoustic Analysis of Perceptual Error Shaping in Local Active Noise Control
C. Blöcher, A. Sontacchi and T. Hatheier 37

Enhancing In-Vehicle Speech Intelligibility: A Study On The Benefits Of Active Road Noise Cancellation System
T. Botti, M. Olivieri, J. Gino and A. Oliva 45

Momentum Algorithm And Its Application To Active Control Of HVAC Compressor Noise In Autonomous Bus
S. K. Lee, J. Choi, D. Kim and S. Kim 53

Empirical Study on active noise control in uavs
J. Steiner, F. Hilgemann and P. Jax 61

Session A01.03 Active sound and vibration control

Session A01.05/A06.07 Active metamaterials

Multi-Channel Acoustic Switch via Activation of Evanescent or Propagation Bloch Wave Modes
H. P. Lee, K. M. Lim and Y. Li 69

On-Demand Noise Mitigation With Time-Modulated Active Acoustic Metamaterials
B. Popa 75

Robust spatiotemporal wave localization in piezoelectric metamaterials through programmable topological interface states
B. Alceu Souto, D. Beli and C. De Marqui Jr 79

Active Noise Reduction in Passenger Vehicles with Plasmacoustic Transducers
S. Sergeev, M. Donaldson and H. Lissek 85

Towards plasmacoustic metamaterials
H. Miao, S. Sergeev, R. Vesal and H. Lissek 91

Control of a nonlinear electroacoustic resonator: real-time selection of the equilibrium point
M. Morell, E. De Bono, E. Gourdon, M. Collet, A. Ture Savadkoohi and C.-H. Lamarque 99

Session A01.06 Signal processing for active control

Deep observation filter for virtual sensing in local active noise control
F. Holzmüller and A. Sontacchi 105

Active Noise Control with Extended Quiet Zones using Time-Domain Underdetermined Multichannel Inverse Filters and Kernel Interpolation
M. Anthony and M. R. Bai 113

Spatially Selective Active Noise Control for Open-fitting Hearables with Acausal Optimization
T. Xiao and S. Doclo 117

Using the masking curve of a masker signal to approximate the spectral shape of target speech signal
P. Laffitte, S. Subhra Bhattacharjee, J. Rindom Jensen and M. Græsbøll Christensen 125

Session A01.07/A08.06 Innovative noise barriers to enhance acoustic comfort

Development of ANC secondary source wall arrays assisting with noise barriers
Y. Kwon, S. Jung, H. Kim and J. Kang 135

Emergence Of Indoor Soundscape Studies Focusing On Noise Mitigation: A Bibliometric Review
Z. Rachman, F. Aletta and J. Kang 141

Real-Time Implementation of a User-Selective Active Sound Control Seat Based on Auditory Scene Analysis
T. Islam, J. Garcia, M. J. Garzón Vargas, M. Ferrer, M. De Diego, L. Fuster and A. González 149

Numerical Study Of A Stepped Directional Barrier For Urban Noise Control
N. Campillo-Davo, M. Fabra-Rodriguez, H. Campello-Vicente, D. Abellan-Lopez, E. M. Mora-Saura, D. Clar-Garcia and R. Peral-Orts 155

Optimizing In-Cabin Acoustic Comfort: Psychoacoustic Evaluation of Engine Sound Profiles
M. J. Garzón Vargas, Z. A. Rachman, M. De Diego, A. González, M. Ferrer, J. Kang, F. Aletta and J. Kirchhof 163

Sound attenuation of louvered noise barriers for industrial equipment
N. Kanev and A. Dolger 169

Acoustic Properties of a Louvered Noise Barrier with Tire Rubber Granulate Infill
E. Strazdas and T. Januševičius 175

Session A02.01 Bio-acoustics - General

Bioacustics of ecosystems: insights from multi-component observing stations in Italy and Mozambique
P. F. Moretti, G. Masciandaro, S. Doni, E. Peruzzi, M. Scatena, D. Piccinini and M. Polizzi 183

When The Lab Gets Loud: Testing Noise Effect Of Plants
V. Zaffaroni-Caorsi, S. Caronni, S. Rocca, E. Asnaghi, A. Comotti, L. Assunta Quaglini, F. Angelini, S. Citterio and G. Zambon 191

Enhanced Birdsong Detection Using Multidirectional Beamforming and Automated Source Selection in Low SNR Soundscapes
R. Ikhwanuddin, E. D'Olne, S. S. Sethi and L. Picinali 197

Insights from Deploying Multichannel Acoustic Autonomous Recording Units in Borneo and the UK
N. Le Penru, B. Heath, R. Ewers, S. S. Sethi and L. Picinali 203

A Review On The Potential Interaction Of Vibroacoustic And Electrostatic Plant-Pollinator Communication
I. Sili, A. R. Mohapatra, A. Simona, C. Nerse, D. Navarro-Payá, F. Barbero, G. Pizzio, J. Echeverria, L. Bianco, L. P. Casacci, M. R. Tucci, T. M. José and S. Oberst 207

Classification of Biological Sounds Using Spatial Directivity
J. Prezelj, L. Čurović, J. Murovec and A. Hvastja 215

Session A02.02 Underwater soundscape and noise: modelling, measurements and effects

Session A02.05 Effects of multimodal stimuli on wildlife

'You talking to me!?': The role of visual-acoustic cues in anemonefish social behaviour
L. Yllan and T. Rueger 227

Towards Large-Scale Environmental Noise Mapping in Europe's Natural Areas
S. Rangaswamy Chandrashekar, T. Van Renterghem and D. Botteldooren 235

Low-Frequency Continuous Noise Within The Posidonia Oceanica Key Coastal Ecosystem: Preliminary Results From The North-Western Mediterranean
M. Mulas, S. Ferri, L. Pini, F. Rossi, E. Maggi and F. Caruso 243

Anthropogenic Noise And Artificial Light At Night: Additive And Interactive Effects On Activity Level And Spatial Behaviour
H. Slabbekoorn, C. May, L. Dörner, D. Crowley, K. Te Velde and C. Tudorache 249

Sound communication interference weighting for terrestrial animals
D. Botteldooren, T. Van Renterghem, M. Wood, D. Waddington, B. Davies, C. Palhares Teixeira and R. Klenke 257

Session A02.07 AI and machine learning in bioacoustics

Session A03.01 Building acoustics - General

Towards a simplified periodic testing of tapping machines
V. Wittstock, S. Stange-Koelling, K. Picker and H. Bietz 267

Testing the heavy soft impact source at PTB: setup, calibration and uncertainty
K. Picker, V. Wittstock and M. Kobusch 271

Impact noise from one storey to the next storey – from slab on the ground and slab between floors
B. M. Larsen 277

On the influence of sampling size in the assessment of uncertainty and repeatability of field measurements of impact sound insulation in various floor scenarios
R. San Millán-Castillo, J. Trujillo and A. Romero-Fernández 283

Acoustic properties of biomass bottom ash in different types of recycled concrete
J. Rosales, M. Rosales, M. Cabrera, A. J. Cubero-Atienza, F. Agrela and M. D. Redel-Macías 291

Acoustic performance of raw earth construction systems: State of the art and preliminary results
C. Guigou Carter, P. Glé, T. Blinet, M. Ziapkoff, M. Romagné, L. Le Guen, S. Tochon-Danguy, A. Clément and A. Marcom 295

Acoustic performance of the junction between façades with ETICS and the joinery
L. De Geetere 303

Uniformity of sound fields in large room volumes for the measurement of façade sound insulation
C. Scrosati, F. Bianco, C. Hopkins, A. Nora and L. Barbaresi 311

Proposal for a methodology and calculation to apply in the sound insulation measurement of corner façades using ISO 16283-3 standard
J. Trujillo and A. Romero-Fernández 315

Advanced monitoring for heritage conservation: Technological innovation in preventive maintenance of historic buildings
A. Izquierdo, J. J. Villacorta, L. Del Val, J. Retortillo and A. Lorenzana 323

Double-leaf system sound insulation improvement through embedding resonant elements in the steel studs
J. Idczak and K. Chojnacka 327

Acoustic design of two film sound stages near a train line
J. Sanz Soriano and M. Dunn 331

Shaker-excited LDV measurements of ETFE membranes and cushions: acoustic response to raindrop impacts
M. Lavasani, V. Chmelík, M. Rychtáriková and C. Glorieux 339

The effectiveness of Plenums in Room Acoustic Conditioning
A. E. Espinel Valdivieso, A. Arenaz Gombau, J. I. Riesco García, A. Mena Moreno, J. Gonzalez Nieto and P. Camblor Iglesias 345

Investigating Positional Effects of the Perimeter Frame in Sound Absorption Measurements
G. V. Holøyen 353

Practical Validation Of The Local Plane Wave Method Using A Spherical Microphone Array
D. Borja-Fernández, E. García-Calderón, Y. Wijnant and R. San Millán-Castillo 359

Sound insulation properties of walls equipped with energy storage devices
G. Baldinelli, S. Beozzo, M. Ricci, F. Scrucca, P. Sdringola and G. Murtaza 367

Session A03.02 Acoustic regulations, classification schemes and standards in building acoustics

The legislative leap forward towards regulating the acoustics in buildings in Croatia
M. Horvat, Z. Veršić and K. Jambrošić 375

Revising a national standard on residential acoustic design: science, embedded practices, hearts and minds
B. Fenech and J. Harvie-Clark 383

Acoustic Comfort In Buildings, Saint-Gobain Barometer 2024. Tools For Designing Acoustic Comfort In Buildings
P. González De La Peña and P. Belenguer Rubio 391

Suggestions For The Potential Revision Of The Basic Document On Protection Against Noise Of Spanish Building Code
A. Romero-Fernández, B. Casla-Herguedas and T. Carrascal 397

Technical Specification For Standardized Graphical Presentation Of Acoustic Requirements In Sweden
B. Gärdhagen and N. Jakobsson 405

A Look into the Low Frequency Deficiencies of ISO 717-2
G. V. Holøyen 411

The construction of a standardized acoustic testing room fosters innovative solutions meeting future market technical demands
A. Martinez De Marcos 417

Spatial Variation Of The Sound Pressure Levels Due To HVAC Systems And The Assessment Of Noise
T. Carrascal, A. Romero-Fernández and B. Casla-Herguedas 423

A Survey and Evaluation Method for Speech Intelligibility of Firefighting Radios Considering the Environment of the Fire Site
J. Jeong and I. Yeom 431

Facade Sound Insulation Of Buildings vs Noise Map In Pamplona, Spain
M. Arana 435

Session A03.03 Prediction of sound and vibration transmission in buildings

Finite Element Analysis of Airborne Sound Transmission in Stud-Coupled Lightweight Wall Systems
P. Ayyobi, D. Gomes Andrade, L. Simões Da Silva and L. Godinho 443

Possibility of modelling the receiving room in FEM calculations
A. Lahdensivu, L. Talus, J. Lietzén and M. Kylliäinen 449

Accurate and efficient prediction of sound insulation in multilayer structures: a robust method validated with glazing examples
J. Vastiau, B. Van De Velde and E. P. B. Reynders 455

Bayesian analysis of the Rw based on a parametrized physical model according to EN ISO 12354-1
M. Parzinger and U. Schanda 463

Wave-Based Analysis Of Flanking Sound Transmission Across Junctions With Metamaterial Treatment Using Effective Medium Theory
S. Becuwe, S. Moons, D. Giannini and E. P. B. Reynders 471

Acoustic performance of prefabricated reinforced concrete walls for modular constructions
R. Mohammadi-Firouz and A. Neves E Sousa 479

A statistical regression framework for evaluating noise exposure through outdoor-to-indoor sound propagation models
M. E. Terzakis, C. Van Hoorickx and M. Hornikx 485

Session A03.04 Ground borne noise

Effect of measurement positions on structure-borne noise levels in buildings subject to railway vibrations
C. Guigou Carter and P. Ropars 495

Methodology for assessing structural noise annoyance in buildings caused by rail traffic. Comparative analysis between Portugal and Spain
S. Antunes and J. Patricio 503

Building Base Isolation Design: Quantification Of Vibration Transmission Using Power Flow Analysis
H. Masoumi and J. Talbot 511

Mitigating ground-borne vibrations with a box-in-box solution: feasibility and challenges in a real case study
I. Arana Goenaga, P. V. Rodríguez, A. Isnardo Iglesias, S. F. Frasson Quaresma and H. Masoumi 519

Impact noise horizontally with 80 mm concrete slab and upper 80 mm polystyrene splitted with continuous polystyrene beneath
B. M. Larsen 527

Session A03.05 Structure -borne sound and noise from building services

Preparatory Work Toward Experimental Estimation Of Water Excitation Terms In Wastewater Systems
Y. Aoki, S. Öhler and B. Kaltbeitzel 533

FH-IPTOOLS: Predicting wastewater noise in timber construction – a project introduction
T. Kruse, A. Mayr, U. Schanda and F. Schöpfer 541

From Classification to Prediction: Applying EN14366-1 to Freshwater Systems
L. Däuble, J. Scheck and B. Zeitler 547

On-Site Application of Noise Reduction Technologies for Bathroom Drainage in Apartment Buildings
G.-G. Song, J.-Y. Chung and A.-H. Jo 555

Session A03.07 Acoustics of wooden buildings

Improvement of the airborne and impact sound insulation of a timber stud wall
J. Scheck, U. Schüttler, C. Fichtel and B. Zeitler 561

Sound insulation performance of timber floors with elastically mounted and suspended layers
J. Lietzén, L. Talus, A. Lahdensivu, A. Lopetegi and A. Aldalur 567

Impact Sound Insulation of CLT Floors: Evaluation of Small Scale Specimens and Correlation with Large Scale Systems
M. Puljizevic, T. Poljansek and M. Grasic 577

Influence of gravel on flanking transmission in CLT buildings
A. Dijckmans and C. Crispin 585

Prediction of flanking sound transmission across periodic cross-laminated timber junctions with area couplings
S. Moons, R. Lanoye and E. P. B. Reynders 593

Experimental Modal Analysis of a Cross-Laminated Timber L-Junction with a View Towards Predicting Flanking Sound Transmission
S. Vallely, A. Esposito and S. Schoenwald 601

Load effects in flanking transmission of CLT structures with resilient interlayer
V. Pettoni Possenti, C. Crispin, A. Dijckmans and L. Barbaresi 611

Modelling Cross-Laminated Timber Plate Connections: A Numerical Investigation On Flanking Sound Transmission Through Angle Brackets
A. Esposito, S. Vallely and S. Schoenwald 619

Suggestion for a round robin test on the measurement of vibration reduction indices on CLT junctions
F. Schöpfer, U. Schanda and C. Chateauvieux-Hellwig 627

Detailed analysis of different software for sound insulation calculations of various structures
K. Hagberg, E. Nilsson and D. Bard 631

Rainfall sound insulation of (lightweight) wooden roof constructions
A. Stenitzer, B. Nusser, C. Lux and H. Müllner 641

Acoustic Comfort Of Lightweight Timber Walls: Correlation Between Subjective Evaluations And Objective Measurements
F. Morandi, A. Speranza, P. Brugnara, F. Cappelletti and A. Gasparella 649

Initial Results of the Research Project Sound and Vibration Protection for Long Span Timber Floors
M. Schneider, J. Ruf, M. Marxt and B. Zeitler 655

Session A03.08 Reducing neighbour noise by acoustic retrofit in housing

Improving sound insulation of old timber floor constructions 1917/1937 in multi-storey housing – Field case study & perspectives
B. Rasmussen 665

Acoustic Insulation in plasterboard systems with Mineral Wool
P. Belenguer Rubio and P. González De La Peña 673

In-situ evaluation of concrete interlayer adhesion by vibration in garaje floors
D. Caballol Bartolomé, A. Pérez Raposo and F. Gil Carrillo 683

Noise Reduction Mat Performance of Apartment Houses according to Slab Conditions
J.-Y. Chung, G.-G. Song, A. Cho and S. Jeong 689

Communication between Caregivers and Children Regarding Inter-floor Noise in Multi-family Housing: A Korean Study
M. Kwon and W. Yang 693

Session A03.09 Acoustic and thermal retrofit of office building stock in EU

ActaReBuild MSCA-DN project - Acoustic and Thermal Retrofit of Office Building Stock in EU
V. Chmelík and M. Rychtáriková 699

Mycelium composites combining different waste sources for sustainable acoustic solutions
T. S. Gomez, L. M. Garcia, N. Escobar, M. D. L. A. Navacerrada and C. Glorieux 705

Exploration of use of Membrane-Type Metamaterial Layer for Application in Building Acoustics
R. Zeng, E. Deckers, C. Glorieux, D. Urbán and B. Chmielewski 713

Effect of Load Plate Mass on Dynamic Stiffness Determination
D. Urbán and M. Neusser 721

Evaluating Recycled PET Filaments As A Sustainable Sound Absorbing Material For Building Retrofitting
J. Garcia, D. Tonetti, E. A. Piana and O. Jiricek 727

Building Envelope Assessment of Airtightness Using an Acoustic Camera: A Case Study in Valladolid, Spain
A. Elsaei, M. Machimbarrena, A. Meiss and S. Herguedas 733

Development of acoustic resonators using recycled plastics
J. Potocar, M. Maaroufi, S. Uncik, C. Glorieux and M. Rychtáriková 741

Rethinking material cycles: Combining mycelium and paper waste for the development of sound absorbers
A. M. Kubiak, T. S. Gomez, C. Glorieux, M. D. L. A. Navacerrada, N. Vasileva Nicheva and D. Sanz Arauz 747

Session A03.10 Acoustic consultancy projects and BIM

IFC Open BIM for noise emission evaluation of the HVAC systems
C. C. Mastino, A. Di Bella, J. Vaičiūnas, P. Raffaello, M. Zavari and M. Piga 755

Building Information Modeling: Example of use IDS file and bSDD data base for acoustic evaluation
C. C. Mastino, A. Di Bella, A. Sygulska, P. Raffaello, A. Frattolillo, M. Zavari and V. Da Pos 761

Acoustic calculations and workflow based on list of acoustically distinguishable spaces
A. Fürjes 767

Introduction of a Grasshopper workflow for the integration of the acoustic analysis in a multi-domain BIM model
A. Gerbotto, L. Shtrepi, F. Favoino and A. Astolfi 775

Session A03.11/A05.11 Heat pump sounds in residential settings: challenges and solutions

Machine Learning-Based Prediction of Air Source Heat Pump Noise Annoyance
V. Acun, S. Graetzer and A. Torija Martinez 781

Characterisation and control of aero-acoustical inflow noise sources of the evaporator fan in Heat Pumps
F. Lörcher and S. Hub 789

Improve heat pump placement considering frequency resolved acoustic directivity data: creation of an open database
C. Reichl, F. Bessac, G. Klein, L. Stöckl and M. Czuka 797

The role of measurement locations in low-frequency noise assessment
L. Čurović and J. Prezelj 803

In-Situ Transfer Path Analysis of a Roof Mounted Air Source Heat Pump
L. Barton, J. Hargreaves, V. Acun, A. Torija Martinez, S. Graetzer and D. Waddington 811

Simulation-based analysis of the sound emissions of decentral air-to-water heat pumps in renovated multi-family buildings
W. Monteleone and F. Ochs 819

A Risk-Based Framework For Acoustic Assessment Of ASHPS - From Domestic To Commercial Applications
J. Harvie-Clark, J. Hill, N. Dobinson and R. Hinton 827

Session A03.12 Ventilation noise in dwellings: challenges, measurements, and solutions

Scalability of Ventilation and Noise Insulation methods for assessing a full-scale Metawindow
G. Fusaro, L. Barbaresi and M. Garai 837

A Silencer Design for a Mechanical Heat Recovery Unit
D. Mullally and J. Kennedy 841

Evaluation of Acoustic Performance in Smart Ventilated Windows with Integrated Heat Storage
A. Gerbotto, L. Shtrepi, F. Favoino and A. Astolfi 845

Session A04.01 Education, Public outreach and history in acoustics - General

The teaching of acoustics at the higher technical school of architecture of Madrid in 1855
A. Díaz Chyla 853

Acoustics in music education: Empowering Music Teachers as STEM Ambassadors
M. Pàmies-Vilà 859

From sounds to architectural design: Acousmatic Spaces
A. Sentop Dumen and Y. Celiker-Cenger 867

Acoustic multi-component monitoring of ecosystems: training for mangroves' conservation in Africa
C. Nhancale, Z. Valgi Macheve, A. Rapino, A. J. Nhampossa, M. Polizzi and P. F. Moretti 875

Session A04.02 Online resources and simulations for teaching and learning acoustics

MOOCs for introductory courses in acoustics at the University of Le Mans: assessment and prospects
J.-P. Dalmont 883

Interactive simulation apps for teaching acoustical phenomena and vibration effects
M. Maeder, M. Buba, M. Dogu, M. T. Bárány, T. Breitkreutz, L. Heggemann, L. E. Roca Paz, S. Kersten and J. D. Schmid 885

Open Educational Resources For Acoustics And Audio Signal Processing Using Jupyter Notebooks And Pyfar
F. Brinkmann, M. Berzborn, A. Heimes, A. Hoyer, X. Karakonstantis, S. Kersten, T. Lübeck, P. Palenda, C. Andrade, J. M. Arend, N. Hahn, T. Jüterbock, N. Meyer-Kahlen, A. Paskiewicz, S. J. Schlecht, F. Schultz and S. Weinzierl 889

Application of room acoustics simulation software in university teaching
L. Aspöck, P. Palenda, J. Fels and M. Vorländer 895

Session A04.05 Yesterday, today and tomorrow of research in acoustics

Al-Ándalus. Spreading acoustic knowledge from Spain to Western Europe
W. A. Montano Rodríguez 901

Music studies in 1254 at the University of Salamanca. An al-Ándalus legacy
W. A. Montano Rodríguez 909

20 years of research on acoustics and vibrations at Miguel Hernandez University of Elche
R. Peral-Orts, N. Campillo-Davo, H. Campello-Vicente, M. Fabra-Rodriguez, D. Abellan-Lopez, D. Clar-Garcia and E. Velasco-Sanchez 915

Psychoacoustics, the long way to be considered into international standards
K. Genuit 921

A historical overview of Higini Arau's proposal for calculating reverberation time (1988)
J. Álvarez, R. Graus and H. Martín-Nieva 925

From acoustic testing and modeling towards multi-physical digital twins: use cases and demonstrators
L. Van Belle, D. Panagiotopoulos, V. Cool, H. Denayer, C. Claeys, W. Desmet, B. Pluymers, K. Gryllias, F. Naets and E. Deckers 933

Session A05.01 Environmental acoustics - General

Case Study: Noise Source Analysis Through Environmental Noise Measurements
O. Odeh, M. Bite and D. Kocsis 943

Obtaining noise levels from projected overpressure levels generated by blasting operations
M. Glisser and B. Vásquez 949

Experimental Assessment of Outdoor Leisure Noise: Sampling Methodology and Annoyance Indicators
A. Hidalgo Otamendi and A. Hernandez 955

Practical noise immission modeling for concerts in stadiums: Santiago Bernabeu - Real Madrid (Spain)
C. V. Viloria-Yzquier, E. García-Calderón and R. San Millán-Castillo 961

Comparative analysis between CNOSSOS-EU and interim methods
M. Ausejo Prieto, R. García Morales and I. Soto Molina 969

Need of a National Noise Strategy in Spain and approach to develop it
M. Á. González García, I. Soto Molina and C. Soriano Pastor 975

Preliminary evaluation of a low-cost device for binaural recording and soundscape monitoring
J. M. Navarro Ruiz and M. Masullo 983

Assessing Acoustic Dynamics in Alpine Ecosystems: The Nivolet Pass Case Study
G. Guagliumi, F. Angelini, R. Benocci and G. Zambon 991

Evaluating Background Noise Criteria For Estimating Outdoor-To-Indoor Levels Via A Statistical Learning Modelling Framework
M. E. Terzakis, C. Van Hoorickx, M. Hornikx, F. Naim, D. Fecht, A. L. Hansell and J. Gulliver 999

Towards the Worlds largest Noise Complaint Database
E. King, E. Murphy, T. Messerer and T. Messerer 1007

Assessment And Analysis Of Vibration Impacts From Underground Railway Tunnelling And Excavation In Sydney, Australia
A. Miller, J. Parnell, V. A. Menon and D. Hanson 1011

Immision Directivity in the frequency domain
J. Murovec, L. Čurović, A. Železnik and J. Prezelj 1019

Session A05.03 Environmental noise perception

Measurement Of The Sound Field Over A Green Roof Using Simultaneous Sound Pressure Recordings
J. Alvarez Chaia, A. Alva and A. M. Lacasta 1029

Optimizing the traffic induced annoyance by public participation; Interaction between questionnaires, model calculations, and measurements
W. Van Keulen 1037

The alleviating role of residential green on road traffic noise annoyance: Insights from the RESTORE project
C. Kawai, J. Dopico, B. Schäffer, M. García-Martín, N. Kolecka, S. Tobias, D. Vienneau, M. Röösli, M. Brink and J. M. Wunderli 1041

Clustering individuals based on performance in audio-visual testing
T. Van Renterghem 1045

Exploring soundscape perception through the italian language: a study on descriptive words for noise and sound
M. Ferretti, D. Chiarella, A. Cinini and P. Cutugno 1051

Key Aspects for Survey Data Processing and Statistical Analysis when Modelling Exposure-Annoyance Relationships
M. Brink, B. Schäffer and D. Schreckenberg 1059

Exploring the acoustic environments of Barcelona's Superblocks: perceptions from soundwalks
A. R. Esperidião, A. Potenza, E. Vidaña-Vila, M. Freixes, A. Radicchi, A. Iarozinski Neto and R. M. Alsina-Pagès 1063

Session A05.04 Wind turbine noise

OFF-COUSTICS: Predicting The Underwater Acoustic Footprint Of Offshore Wind Turbines
E. Eerrer, L. Botero-Bolivar, O. A. Marino, M. De Frutos, D. Huergo, A. Ballout, E. Jané, H. Marbona and G. Rubio . 1073

Long-term Wind Farm Noise assessment over different meteorological conditions
K. Lowe, M. Amatriain and S. Broneske 1079

Optimizing Electricity Production in Wind Farms with Noise Mitigation Strategies
Á. Grilo Bensusan 1087

Noise and vibration measurements emitted by wind towers
G. Iannace, L. Fredianelli, A. Akbaba, G. Ciaburro and F. Artuso 1095

Wind turbine directional tonality
M. Amatriain and M. Arana 1099

Session A05.05 Urban sound planning

Guidelines For An Institutional Proposal For The Creation Of A Noise And Vibration Observatory In Uruguay
L. Marisquirena, E. González and P. Gianoli 1109

Characteristics determining the attractiveness of urban green spaces: Insights from the RESTORE project
J. M. Wunderli, C. Kawai, J. Dopico, M. Röösli, D. Vienneau, M. Brink, S. Tobias and B. Schäffer 1115

Necessary steps to advance research on healthy urban sound planning
T. Haselhoff and S. Moebus 1119

Development of a tool for noise management in LEZs
J. I. Riesco García, S. Herrero, L. Garcia, R. Díez, R. Paredes, A. E. Espinel Valdivieso and M. Lora 1123

Soundscape evaluation of residential outdoor spaces based on a subjective questionnaire and objective acoustical measures
M. Isenegger, T. Steiner, G. Heini, L. Bartha, U. Sturm and A. Taghipour 1131

A Spatial Processing Framework For Mapping Areas Benefiting From Urban Morphology And Building Design In Airport Regions
G. Wuite, M. Lugten, R. Vassallo and A. Van Timmeren 1139

Enhancing Urban Acoustic Comfort: The Role of Free Surfaces, Green Spaces and Water Bodies in Mitigating Road Traffic Noise
C. V. Fiorini, V. Battistini, M. Calanna, L. Quaranta, C. Guattari, A. Tarsitano and A. Vallati 1147

Bringing Soundscape Auralizations To The Urban City Planning
J. Llorca-Bofí, H. H. Au-Yeung, M. Lippold and C. Reicher 1155

Session A05.06 Recent advances in noise mitigation methods

The LIFE SILENT Project: advancing sustainable solutions to mitigate noise in urban environments
P. Bellucci, F. Ciarallo, M. Garai, G. Licitra, T. Onorato and F. G. Praticò 1161

Challenges in Producing Innovative Low-Noise Asphalt Mixtures with Recycled Materials and Additives: Insights from the LIFE SILENT Project
M. Diamantini, P. Bellucci, G. Chidichimo and F. G. Praticò 1169

How sustainable are innovative noise mitigation road pavements? An LCA approach
A. Altobello, F. V. Catania, M. Busti, C. Ravagnan and A. Tani 1173

European Projects For Noise Quality In Florence
A. Melloni, G. Pecchioni and R. Bellomini 1181

Managing environmental noise by bringing together continuous monitoring and simulation models
L. Conde Santos, A. Carvalho, J. Preto, P. Valério, C. Leão and G. Covas 1185

Low-Height Noise Barriers For Railways: Measurement Standardization And Metamaterials Application On Noise Reduction
D. De Salvio, P. Guidorzi and M. Garai 1193

Analysis Of Complex Scenarios In The Noise Mitigation Of Main Infrastructures In Italy In Life Silent Project
M. Cerchiai, M. Bolognese, A. Panci, D. Vatteroni, D. Palazzuoli and G. Licitra 1197

Using Microphones in Outdoor Pass-By Noise Testing for Vehicle Speed Measurement
F. Lo Castro, M. L. Ariza Alvarez, M. De Luca and S. Iarossi 1201

LCA approach to evaluate the sustainability of innovative low-height noise barriers
M. Montesi, A. Tranzi, M. Fantozzi, M. Garai and C. Micheletti 1209

LIFE SILENT: Implementation Of The Solutions Developed In The Pilot Site
C. Relandini, M. Fantozzi, S. Relandini and L. Peruzzi 1217

Environmental Noise Reduction Using Geometric Ground Shaping: Results from Scale Model Experiments
T. Shaked, S. Fishkin, A. Hauptman and F. Nir 1223

Session A05.07 Outdoor sound propagation

Self-shielding windows : scale model measurements and numerical simulations
T. Van Renterghem and P. Thomas 1233

Predicting the effects of ground impedance in long-range low-frequency propagation with the Semi-Analytic Finite-Element (SAFE) Method
R. Castro Mota, P. Williams, R. Kirby and S. Jacob 1239

Improvements in Measuring Acoustic Impedance of Outdoor Ground Surfaces
A. Fuchs and M. Haider 1243

Assessing forest acoustics: A comparison of in-situ and scale model acoustic impulse responses
S. Feng, F. Stevens and A. Chadwick 1251

Key Updates In ISO 9613-2:2024 – What's New In Outdoor Noise Prediction Standards?
O. Odeh, A. Khayyat and D. Kocsis 1259

Session A05.08 Advances in noise mapping

Noise Pollution in Spain: Towards a comprehensive assessment
I. Soto Molina, M. Á. González García, C. Soriano Pastor and R. M. Arce Ruiz 1267

Road Traffic Noise Modelling Near Highway Street Using The CNOSSOS-EU Method
K. Katw, B. Tóthmérész and D. Kocsis 1275

Identifying noise action plan priority locations in Ireland
S. Shilton and T. Dolan 1285

Quality Assurance and Modeling Limitations in Noise Emission Control Using ISO 9613-2 and ISO 17534
J. Schaal and D. Zollitsch 1293

Comparative analysis of strategic noise maps: using heat maps to find why two CNOSSOS-EU implementations (iNoise and CadnaA) differ
A. L. Peña 1301

Defra's Noise Modelling System: A new approach to nationwide modelling in support of research and evidence
J. Trow and H. Notley 1307

CNOSSOS Environmental Noise Analysis By Cloud-Based Model Refinement And Calculation
H. Stapelfeldt and I. Naegelen 1315

Overview of research supporting development of a national noise modelling system for England
S. Shilton, J. Trow, M. Wilczek, K. Fedyk, H. Stapelfeldt, R. Wong, B. Peeters and M. Toward 1321

A Comparative Study of Methods for the Distribution of Populations in Residential Buildings for Noise MAPPING PURPOSES
Y. P. Alvarez Ruiz, T. Jiménez Pérez, V. Puyana Romero, M. Sequera Soto, R. Gey Flores and J. L. Cueto-Ancela 1329

An Open-Source Tool For Aircraft Noise Modeling In The Context Of Spain's Global Noise Assessment (Under Development)
I. Soto Molina and R. M. Arce Ruiz 1333

Can road traffic noise annoyance maps describe the lack of mental well-being in an urban area?
A. Montenegro, A. Zumelzu, G. Leal and G. Licitra 1341

Comparison Of Different Urban Traffic Representations For Road Traffic Noise Indicators Estimation
Y. Gao, S. Baclet, P. Aumond, R. Rumpler and A. Can 1349

Delivering National Scale Noise Calculations with CNOSSOS-EU through cloud computing and software optimisation
H. Stapelfeldt, J. Trow and J. Madden 1357

Comparison of input data collection methods for road traffic noise models in residential area
E. Ascari, L. Fredianelli, M. Cerchiai, G. Licitra, C. A. Neagoe, A.-M. Mitu, T. Sireteanu, D.-C. Baldovin, D. Profumo and S. Kanka 1363

Effect of traffic flow on urban noise modelling
V. Gómez Escobar, S. Palomeque Váquez and G. Rey Gozalo 1369

Session A05.10/A14.09 Advanced air mobility noise

Noise Impact Range Assessment using UAM Noise Hemisphere
S.-M. Lee and C. H. Haan 1375

On-field measurements following the EASA Guidelines on Noise Measurements of Unmanned Aircraft Systems lighter that 600 kg
P. Miguel-Ayala, L. Estévez-Mauriz, C. Ramos-Romero and A. Torija Martinez 1379

Rotor Noise Interference Mechanisms For Side-By-Side Co-Rotating Configurations
T. Pagliaroli, P. Candeloro, F. Del Duchetto, J. Yin and K.-S. Rossignol 1387

Integrated U-space Societal Acceptance Assessment: Energy-based and Perception-based Acoustic Metrics
C. Ramos-Romero, M. J. B. Lotinga and A. Torija Martinez 1395

Noise impact of drone parcel delivery scenario over Madrid
I. Legriffon, E. Ruaud, J. Kuljanin and E. Ganic 1403

The effects of time-variant characteristics of unmanned aircraft system noise on reported annoyance
Z. Podwinska, C. Ramos-Romero, M. C. Green and A. Torija Martinez 1409

Review of the effects of drone noise on people
J. Li, B. R.C. Molesworth and M. Burgess 1417

A novel procedure to minimize the acoustic and environmental impact of eVTOL vehicles for intra-city mission profiles
C. Poggi, G. Bernardini and M. Gennaretti 1421

Differences in sound emission level of multi-rotor UAS during hover and cruise
J. Meister, J. Jäggi, T. Van Renterghem and R. Pieren 1429

Prediction of Environmental Noise from Rotorcraft using a Noise Hemisphere with Time-Domain Data
Y. Jo and S.-Y. Wie 1435

Influence of surface roughness on the aerodynamic, aeroacoustic and psychoacoustic performances of drone propellers
G. Capobianchi, A. Di Marco, E. De Paola and L. G. Stoica 1439

Mid-Fidelity Framework for Rotor Noise Prediction and Perception in Maneuvering flight
M. Picillo, M. Barbarino and F. Avallone 1447

Psychoacoustic Characterization Of An Isolated Propeller At Different Inflow Turbulence Conditions And Collective Pitch Angles
R. Merino-Martinez and L. N. Quaroni 1457

Machine Learning-Based Modelling Of UAV Noise Metrics In Real Conditions
C. I. Andino Cappagli, A. Amiri-Simkooei, S. Luesutthiviboon, T. Meiser, A. Morin, M. Zajacík, M. Rollo and M. Snellen 1465

Assessment of the Psychoacoustic Performance of the VENUS Project Distributed Electric Propellers Configuration
A. Di Marco, L. G. Stoica and G. Capobianchi 1473

Comparative Drone Noise Flight Test Campaign Using Conventional Precision Microphones and an Artificial Head
G. Fasulo, F. Petrosino, M. Barbarino and L. Federico 1481

Exploring socio-spatial pattern of noise impact of advanced air mobility – A case study in West Yorkshire, England
L. Jiang 1489

UAS-NoiseCheck - A System Implementing the EASA Guidelines on Drone Noise Measurement
M. Blass, S. Grebien and F. Graf 1495

Noise Modeling of UAM around Vertiports by Sound Barrier
S.-M. Lee and C. H. Haan 1501

Session A05.11 Heat pump sounds in residential settings: challenges and solutions

Session A06.02 Microphones (theory, measurement, applications, MEMS technology, etc.)

Nonlinear Behavior of Condenser Microphones: Analytical Modeling and Experimental Validation
J. Placek and P. Honzík 1507

Characterization of Planar Circular and Square MEMS Microphone Arrays for Low-Power Acoustic Applications
R. Moreno, J. Ortigoso-Narro, M. Raiola, L. A. Azpicueta-Ruiz and D. De La Prida 1515

Pressure-Comparison Calibration Of MEMS Microphones In The Reverberation Chamber
F. Saba, M. Campo-Valera, M. Corallo and G. Durando 1523

Noise Source Direction Estimation using Flow-Sensing MEMS Microphones
T. Röck, M. Hagmüller and F. Zotter 1529

Amplitude modulation discrimination in cochlear implant listeners: Effects of carrier frequency and 'interfering' modulated signals
N. Haywood, B. Moore, B. Williges, P. Boyle, M. Salorio-Corbetto, J. Schlittenlacher, C. Harbottle and D. Vickers 1537

Session A06.03 Loudspeakers and headphones (theory, measurement, applications, MEMS technology, etc.)

Acoustic metamaterials for attenuating unwanted wave phenomena in loudspeaker enclosures
B. Chojnacki, A. Chojak, W. Binek, J. Pawlik and J. Idczak 1543

Flat and curved parametric acoustic loudspeakers measured with exponential sine sweeps
A. Fantinelli and M. Arnela 1547

Influence of coil winding material on the performance of electrodynamic loudspeakers
J. Martinez-Iranzo, C. Martinez-Pia, J. Carbajo San Martín, P. Poveda Martinez, J. Ramis-Soriano and E. G. Segovia-Eulogio 1553

Optimization of Cavities and Suspensions in Underwater Acoustic Projectors: Analytical and Experimental Study
J. Martinez-Iranzo, J. Carbajo San Martín, P. Poveda Martinez, J. Ramis-Soriano, E. G. Segovia-Eulogio and C. Martinez-Pia 1559

Investigating Spatial Aliasing and Fresnel Zones of Line and Planar Sources for Sound Reinforcement
L. Gölles and F. Zotter 1565

A Simulation Framework for Piezoelectric MEMS Speakers: Modeling, Integration, and Validation
F. Bachl and S. Horvath 1573

Mechanically-open and acoustically-closed MEMS loudspeakers for in-ear applications
C. Gazzola, F. Perli, F. Cerini, S. Adorno, P. Lotton, M. Melon and A. Corigliano 1581

Impact of Impedance Mismatch on Crosstalk Cancellation with Micro-Speaker Arrays
F. Veronesi, F. Fazi and J. Hollebon 1585

Development of a omnidirectional cylindrical sound source with a Corona Discharge Transducer
H. Lissek, T. Wang and R. Vesal 1593

Session A06.06 Acoustic-based sensors, actuators and microsystems for diverse applications

On biotelemetry's bidirectional acoustic tag
G. Batet, D. Sarria, S. Gomariz, I. Masmitja and J. Del Rio 1603

Low Order Lateral Modes Of Plate Transducers As Basis For Effective And Reproducible Acoustofluidic Devices
A. Fuchsluger, A. De Pastina and B. Jakoby 1607

Acoustic Levitation in Air: novel techniques and applications
A. Marzo 1609

Piezoelectric MEMS Temperature Sensor based on Acoustic Flexural Plate Waves
S. Bertelli, A. Nastro, M. Baù, M. Ferrari, L. Rufer, S. Basrour and V. Ferrari 1613

Productization challenges of acoustic MEMS sensors and actuators
A. Lagosh, A. Piot, S. Nayak, R. T. Rocha and H. Campanella 1619

Comparative Study of the Frequency Response of Smartwatch Sensors for Human Movement Assessment
M. Centeno-Cerrato, C. Polvorinos-Fernandez, G. De Arcas, L. Sigcha and I. Pavón 1625

Session A06.07 Active metamaterials

Session A07.01 Flow acoustics - General

Comparison of wavepacket models for supersonic twin jets against near-field pressure measurements
I. Padilla-Montero, D. Rodríguez, V. Jaunet and P. Jordan 1637

Matching Pursuit decomposition of jet near-field pressure data
R. Camussi, M. Mancinelli and E. De Paola 1645

Impact Of The Nozzle Exhaust Temperature On The Near-Field Noise Emitted By Subsonic Jets
S. Meloni, G. Palma, R. Camussi and C. Bogey 1653

Revisiting the effects of mean velocity profiles shape on sound propagation through two-dimensional ducts
L. Bonomo, J. A. Cordioli and E. Brambley 1661

GPU-based aeroacoustic simulation of low-speed axial fans across their characteristic fan curves
A. Verza, P. Altmann and L. Erbig 1669

Investigating the Acoustic Radiation of Coherent Structures in a Subsonic Jet
Y. Fang, Z. Song, X. Yang and J. Liu 1677

Session A07.02 Aeroacoustics of aircraft and urban air vehicles

Aeroacoustics of UAV propellers with unequally spaced blades
D. Usov, A. Filippone, C. Poggi and G. Bernardini 1683

Flow characterisation using PIV to optimise microphone windscreens for on-board self-noise measurements of a multicopter (UAV) under different flight conditions
J. Benz, C. Heigl, D. Gruetzner, F. Czwielong, A. Gruender, J. Franke and S. Becker 1689

Anechoic Noise Characterization Of Sub-7kg Multi-Rotor Drones: Configuration Effects And Spl Scaling Models
R. Cao, Z. Zhang, Z. Peng, Z. Ma, W. Chen, P. Zhou and X. Zhang 1697

Numerical Investigation on Tonal Noise Directivity in Distributed Propulsion Systems
A. Zarri and F. De Prenter 1705

Effects of boundary layer ingestion on ducted propeller noise
M. Daroukh, F. Ahmed, T. Le Garrec, M. Azarpeyvand and E. Manoha 1711

Wall Pressure Fluctuations and Impact on the Noise from Distributed Electric Propellers
L. G. Stoica, E. De Paola, G. Capobianchi, A. Di Marco and R. Camussi 1719

Analytical Investigation Of Rotor-Strut Potential Interaction Noise
R. Zamponi, A. Zarri and J. Christophe 1725

Hovering small-scale low Reynolds number rotor-beam source localization using both nearfield and farfield measurements
H. Parisot-Dupuis, B. Mellot, N.' Gariglio and F. Méry 1729

On the Impact of Turbulent Inflow on the Noise Generated by a Propeller Operating at Low Reynolds Number
M. Ali, A. Piccolo, R. Zamponi, D. Ragni and F. Avallone 1737

A Study Of Urban Air Mobility Rotor Noise At Moderate Reynolds Numbers With Collective Pitch Control
C. Tinney, J. Valdez and Y. Zhao-Dubuc 1745

Session A07.03 Active and passive noise reduction technologies

On the Interaction of Grazing Acoustic Waves and Turbulent Boundary Layer over Acoustic Liners
A. Paduano, F. Scarano, D. Casalino, J. A. Cordioli and F. Avallone 1755

Relevance of radiator installation on the efficacy of noise reduction strategies in an industrial engine cooling fan
F. Bellelli, R. Arina and F. Avallone 1763

Rotor Noise Control Using Coaxial Co-Rotating Rotors
C. Tinney, Y. Zhao-Dubuc and J. Valdez 1771

Further Investigation of the Simplified Septa Acoustic Liner Concept
B. Howerton and J. Kreitzman 1779

Turbulence effect on the acoustic boundary layer of perforated acoustic liners
A. Schulz and D. Ronneberger 1787

On the impact of the orifice geometrical features on the performance of an acoustic liner
F. Avallone, A. Khedr, A. Paduano, F. Scarano, L. Meirelles and J. A. Cordioli 1793

Experimental Investigation into the Suppression of Propeller Noise Using Over-Tip-Rotor Liners
S. Palleja Cabre, J. Ballgjati, C. Paruchuri, P. Joseph and F. Avallone 1801

Identification of an actuation manifold for open-loop control of subsonic jet noise with acoustic-based excitation
L. Franceschelli, M. Raiola, A. Ianiro and S. Discetti 1809

Numerical Investigation on Noise Reduction of Distributed Propellers by Phase Synchronization
Z. Yang, M. Meinke, D. Krug and W. Schröder 1817

Mitigation Strategies For Acoustic Reflections Generated By An Axisymmetric Wind Tunnel Nozzle
L. N. Quaroni and R. Merino-Martinez 1825

Session A07.04 Fluid structures acoustic coupling

Suppression of an aeroacoustic feedback mechanism in a complex pipeline
E. Quaranta and M. Smith 1835

Impact of resonance loading on the sound generation from in-duct point sources
M. Behn and U. Tapken 1843

Parametric study of turbulence ingestion noise for marine propellers
R. Lavanant, B. Cotté, G. Serre and J.-F. Mercier 1851

Effects of inflow conditions on turbulence-ingestion noise prediction
A. Piccolo and R. Zamponi 1859

A Vibro-Acoustic Calibration for the FEM Simulation of a Thin-Walled Duct System and Fan Housing
P. Heidegger, F. Czwielong, S. Schoder, S. Becker and M. Kaltenbacher 1867

Shape Optimisation For The Aeroacoustics, Aerodynamics And Heat Transfer Of Round Holes
Y. Wang, J. Guzman-Inigo and A. Morgans 1871

Flow-acoustic coupling in vortex whistle
M. Amielh, D. Mazzoni, Y. Pley and J.-J. Lasserre 1879

Session A07.05 Methods for advanced computational aeroacoustics

Session A07.06 Modern experimental techniques in aeroacoustics

Experimental Investigation of Rotor Shielding Effects on Axial Flow Fan Using Interstage Array
M. Adhikary, A. Pereira, M. Jacob, R. A. Blazquez Navarro and J. Thisse 1891

Stochastic approach for estimating the sound power of tonal mode components in flow ducts based on azimuthal mode analysis
M. Behn and U. Tapken 1899

Instrumentation and measurement validation approach for an aero-acoustic circular testrig based on temporal, frequency, and modal criteria
J. Derré, N. Aujogue and P. Rodríguez Garcia 1907

Numerical assessment of a mode detection array for azimuthal decomposition
H. Vincent, A. Pereira and M. Jacob 1915

Application of atmospheric wind filter arrays for acoustic monitoring UAVs
R. R. Subramanyam, C. Gerasch and S. Jacob 1923

Session A08.03 Advances in machinery noise and vibration control

A Study On The Transfer Characteristics Of The In-Wheel Motor System Based On EV Platform
S. Park, J. Lee, M. Lee, J. Woo, J. Jung, S. Lee and B. Sohn 1933

Relationship among Noise, Cavitation Structure and Erosion Risk in Industrial Centrifugal Pumps with a Fan-type Inducer
S. Narimatsu, H. Utsumi, S. Ejiri and M. Miyabe 1939

The influence of helix angle and gears width on the noise radiated by a gearbox
F. Mori, A. Santoni, N. Zuccherini Martello, R. Grimaldi, S. Chiari and P. Fausti 1949

LpScan – A project to standardize sound power determination from sound pressure scans
F. Heisterkamp, V. Wittstock and D. Brosig 1953

Analytical and Experimental Investigation of Stator Assembly Vibrations in Electric Motors
P. Andreou, A. Z. Hajjaj, M. Mohammadpour and S. Theodossiades 1961

Psychoacoustic investigation of the sound radiation of rotary drilling rigs
J. Riedel, G. Beer, F. Froschmeir, T. Uhlemann and S. Becker 1965

Acoustic measurements and employee feedback: addressing noise in industrial work environments – a case study
P. Van Dort 1969

Comparison Of Control Logic Driving Inverter Compressors In Refrigerators And Potential Impact On Customer Sound Quality Assessment
P. Kosowski, S. Atamer and M. E. Altinsoy 1977

Double And Single Elastic Support For Large Generator Sets
S. Anda 1985

Combined thermal and acoustic design of enclosures for outdoor applications
E. A. Piana, J. J. Garcia, D. Tonetti and R. Spezie 1991

Active Structural Acoustic Control With Remote Microphone Technique For Noise Radiated By A Thin Plate
F. Mori, A. Santoni, C. Marescotti, P. Fausti, F. Pompoli, P. Nataletti and P. Bonfiglio 1997

Design of a tripod vibration actuator for active reduction methods
S. Wrona, F. Caroppo, R. Scarano and M. Pawelczyk 2001

Noise measurements performance guarantee on a Floating Liquified Natural Gas plant
B. Crivelli and D. Vincent 2007

Session A08.04/A10.04 Materials and systems for noise and vibration reduction

Experimental Approaches for the Characterization of the Vibroacoustic Behaviour of a Domestic Coffee Apparatus
F. Castellini, A. Cavallo, M. Rossoni, F. Ripamonti, G. Colombo, R. Corradi and G. Cimmino 2013

Development of Sustainable Sound Absorbing Panels Made of Jute Fibers
F. Pompoli, P. Dagø, C. Marescotti, A. Santoni and P. Fausti 2021

Low-frequency acoustic and vibroacoustic treatments to reduce sound transmission within ducts
C. Lagarrigue, D. Lecoq, J. Perchaud and M. Fruchart 2025

Towards a unified approach to characterize ventilated acoustic metamaterials
F. Martellotta, C. Rubino, S. Liuzzi, F. Bianco and C. Scrosati 2031

Demonstrating the effectiveness of a multi-layer thin mineral sound absorber for courtyard noise reduction
B. Van Damme, J. M. Wunderli, L. Zambila and T. Cavalieri 2035

A Study on the Prediction Method of Bush Dynamic Characteristics in Used and High Frequency Domain
Y. E. Ahn 2039

Measurements Of The Acoustic Properties Of Mycelium-Based Materials Using An Impedance Tube
G. Wersényi, Z. Németh and A. Schweighardt 2045

Recycled materials as absorbent layer in acoustic ceilings: non-woven polypropylene
M. Galindo, E. Alberdie, M. A. Sánchez-Burgos, F. J. Nieves and I. Flores-Colen 2051

Session A08.05 NVH damage detection, condition monitoring, diagnostics of machinery

A Vibration Based Health Monitoring System For An Automatic Packaging Machine
I. Rizioli, G. Cristofori, M. Battarra and E. Mucchi 2061

A mathematical model based digital twin for gearboxes operating at variable speeds
S. Hashim, S. K. Mishra and P. Shakya 2065

A new feature extraction framework for source-free domain adaptation in bearing fault diagnosis
S. Arunagiri, S. K. Mishra and P. Shakya 2073

Analysis of Defects in Rolling Bearings Using Vibroacoustic and Ultrasonic Techniques
E. Voltolini, M. Monaco, E. Armelloni, M. Cocconcelli, A. Toscani, F. Immovilli and E. Manconi 2079

Tool Wear Prediction in CNC Turning Operations using Ultrasonic Microphone Arrays and CNNs
J. Steckel, A. Aerts, E. Verreycken, D. Laurijssen and W. Daems 2087

Session A08.06 Innovative noise barriers to enhance acoustic comfort

Session A08.07 Artificial intelligence for industrial applications

Session A09.01 Machine learning and artificial intelligence in acoustics - General

Neural Network-Based Solutions for the Linearized Euler Equations in Outdoor Sound Propagation
H. Juliust, K. Baumann, A. Schady, S. Gharbi and F. Dietrich 2099

Utilizing Large Language Models for Optimizing Sound Selection in Dementia Care Environments
A. Talebzadeh 2107

Comparative analysis on the use of linear and non-linear methods for auditory attention decoding (AAD)
I. García Ugarte, R. Eguinoa, C. Vidaurre, D. Paternain and R. San Martín 2113

Comparison of Deep Learning and Psychoacoustic Models to Predict UAV Noise Impact in Soundscapes
M. W. Ellis, M. C. Green, M. J. B. Lotinga and A. Torija Martinez 2121

Open-Source System for Multilingual Translation and Cloned Speech Synthesis
M. Cámara, J. Gutierrez, M. P. Daza and J. L. Blanco 2129

A model for improving the performance of large language models on soundscape description tasks
Z. Yuan and D. Botteldooren 2137

Sound environments classification of an university campus using unsupervised machine learning techniques
J. Montoya Belmonte, A. Pita Lozano and J. M. Navarro Ruiz 2143

Session A09.03/A02.07 AI and machine learning in bioacoustics

Automated Ecoacoustic Monitoring: Evaluating Classifier Performance For Common Cuckoo (Cuculus Canorus) Detection
H. Whitehead, W. Davies, S. Gashchak and M. Wood 2149

Clustering and Novel Class Recognition: Evaluating Bioacoustic Deep Learning Feature Extractors
V. Kather, B. Ghani and D. Stowell 2153

Development of an Ear Tag System for Diagnosing Swine Respiratory Diseases Using Long Short-Term Memory Networks
Y. Matoba, S. Ishimitsu, S. Yumoto, O. Mikama, Y. Ogawa, H. Inoue, M. Ishida and D. Tanaka 2161

Automated Data Curation for Self-Supervised Learning in Underwater Acoustic Analysis
H. Hummel, S. Bhulai, B. Ghani and R. Van Der Mei 2165

Preliminary Results on Audio Event Classification Applied to a University Square in Milan (Italy) Before an Urban Regeneration Project
A. Potenza, E. Vidaña-Vila, A. Afify, R. Benocci, R. M. Alsina-Pagès and G. Zambon 2171

Hardware acceleration of Convolutional Neural Network for Lung Ultrasound segmentation
A. Rubio, M. Muñoz, G. Cosarinsky and J. F. Cruza 2179

Cross-Domain Transfer Learning for Segmentation of Lung Ultrasound images
M. Muñoz, A. Rubio, G. Cosarinsky and J. Camacho 2185

Session A09.05/A08.07 Artificial intelligence for industrial applications

Reinforcement Learning To Enhance Computational Fluid Dynamic Simulations With Acoustics
D. Huergo, M. De Frutos, O. A. Marino, E. Jané, G. Rubio and E. Ferrer 2193

Soundscape system based on passenger emotion and conversation perception of autonomous vehicles
K.-J. Chang, J. Kang, D. Park, G. Cho and C. W. Ahn 2201

Automatic classification of packaging waste at source using acoustic technology
M. Arnela, E. Vidaña-Vila, A. Fantinelli, A. Moñux-Bernal, J. Vaquerizo-Serrano, S. Rubio-Garcia and J. C. Socoró ... 2207

Deep Learning-Aided Design Of A Broadband Low-Frequency Meta-Absorber For Room Acoustic Applications
O. Ogun and J. Kennedy 2213

Detection of Operational Regimerelated Faults in Air Compressor Systems Using Acoustic Analysis and Machine Learning
A. Hvastja and J. Prezelj 2221

Monitoring of Manufacturing process, using unsupervised Sound Event Classification with application of Sound Directivity
J. Prezelj, A. Hvastja and T. Berlec 2225

Fault Detection in C-EPS Bearings Based on Unsupervised Learning
H. Jo, J. Park, I.-J. Cho, J. Seo, S.-S. Yoo, S. Lee, S.-J. Bang, J.-L. Oh, C.-H. Jung and S.-Z. Cho 2233

Deep learning for ultrasound surface echo detection with matrix arrays
M. Larrea, M. Muñoz, A. Rubio, J. F. Cruza and G. Cosarinsky 2241

Session A09.06 Machine learning for array processing

Session A09.07 Events detection and localization, and acoustic scenes, using ML techniques

Does Source Directivity Influence Neural Network-Based Speech Position Estimation?
R. A. Viveros-Munoz and S. Guajardo-Herrera 2253

Speech position estimation using neural networks from acoustic signals of hearing aids
S. Guajardo-Herrera and R. A. Viveros-Munoz 2259

Leveraging Pre-Trained Foundational Audio Models for Acoustic Event Detection in Driving Scenarios
M. Moghimi, P. Healy, C. Castorena, F. J. Ferri and M. Cobos 2263

Exploring the Potentialities of Machine Learning Techniques for the Analysis and the Forecast of Road Traffic Noise Levels
D. Rossi, A. Mascolo, D. Singh and C. Guarnaccia 2271

Urban sound classification on the edge: exploring the accuracy-efficiency trade-off
L. Cassens, M. Kroesen, S. Calvert and S. Van Cranenburgh 2279

Automatic detection of roadway noise using AI classifiers and sound level features
E. Betton-Ployon, A. Kacem, J. Mars and N. Martin 2285

Enhanced Environmental Sound Event Classification through Transfer Learning with CLAP Model
F. Artuso, G. Pompei, A. Akbaba, G. Iannace, F. D'Alessandro, F. Fidecaro, G. Licitra and L. Fredianelli 2289

A Comparative Analysis of Interior vs. Exterior Vehicle Microphone Placement for Acoustic Event Detection in Driving Environments
C. Castorena, L. Banchero, J. A. De Rus, F. Vacalebri, S. Roger, J. M. Mossi, J. J. López, F. J. Ferri and M. Cobos ... 2295

Session A09.08 Artificial intelligence in musical acoustics

Session A10.02 Acoustic, vibroacoustic and elastic metamaterials

High bulk modulus pentamodes: the three-dimensional metal water
S. Cominelli, G. Brambilla, M. Verbicaro, M. Pozzi, G. Cazzulani and F. Braghin 2305

Increasing Helmholtz resonator stability against non-linear resistance increments using chamfers
D. Jun, J. Plasek, M. Rychtáriková, Z. Fisarova and C. Glorieux 2309

Switching Room Acoustics with causality-driven dual-function passive metamaterials for broadband sound absorption and diffusion
E. Ballestero, Y. Meng, P. Sheng, V. Tournat, V. Romero-García and J.-P. Groby 2315

Rotatable Phononic Crystal with Multiresonant Scatterers for acoustic switching applications
D. Ramírez-Solana, V. Sangiorgio, R. Picó, J. Redondo, M. Gulzari and M. P. Fanti 2317

Additive Manufacture of Flexible Lattice Absorbers for Enhanced Low Frequency Performance
C. Neill and J. Kennedy 2323

Tunable Envelope Solitons in a Piezoelectric Metamaterial Obeying the Nonlinear Schrödinger Equation
C. Wang and A. Erturk 2327

Optimizing locally resonant elements distribution on isotropic plate for increased sound insulation and mass reduction
K. Chojnacka 2331

Initial Analytical Attempts to Handle the Sound Absorption using Segmented Oblique Perforations
T. D'Orazio, D. Ramos, L. Godinho, C. Guattari and F. Asdrubali 2335

Transfer matrix modelling of folded quarter-wavelength resonators with 90° bends
F. De Bie, H. Denayer and E. Deckers 2341

Session A10.03 Metamaterials for noise and vibration reduction: novel applications and experimental methods

Reduced-order modeling analysis of random geometric changes on the vibroacoustic behavior of metamaterials
Y. Pillot, R. Boukadia, L. Van Belle and E. Deckers 2347

Shape optimization of inertia-amplified mechanical resonators for vibration damping of mounted plate
L. Mardini, A. Bergamini, E. Deckers, C. Claeys and B. Van Damme 2355

Design and experimental characterization of multi-modal metamaterial panels achieving broadband sound transmission and radiation reduction
D. Giannini, L. Van Belle, E. Deckers and E. P. B. Reynders 2361

Psychoacoustical design optimization for acoustic metamaterials using global sensitivity analysis
J. Zhang, J. Cuenca, L. De Ryck, L. Van Belle and E. Deckers 2369

Numerical And Experimental Study Of Acoustic Performance Of Phononic Crystals-Based Ventilated Noise Barriers For Traffic Noise
N. Ahsan, N. Herrera, L. Sangiuliano, P. Amado Mendes and L. Godinho 2375

Validating the use of acoustic metamaterials in industrial applications for low-frequency noise reduction
E. Cierco, M. Janer, D. Suárez and P. V. Rodríguez 2383

Reciprocity Driven Omni-directional Absorption
J. P. Escudero, J.-P. Groby and V. Pagneux 2389

Experimental and Numerical Analysis of Sonic Crystal Noise Barriers with Hybrid Scatterers
N. Herrera-Leon, N. Ahsan, L. Godinho, L. Sangiuliano and P. Amado Mendes 2393

Comparative Analysis of Lightweight Metamaterial Partitions for Enhanced Acoustic Performance and Perceptual Sound Evaluation
M. Ribera, B. Van Damme, A. Pereira, P. Amado Mendes, J. Zhang and L. Godinho 2401

Hierarchical labyrinthine metamaterials for low frequency noise absorption applications
E. Pérez Compte, F. Nistri, L. Zambila, A. Bergamini, A. Gliozzi, L. Shtrepi and F. Bosia 2407

The Influence Of Sample Size On The Results Of Sound Insulation Measurement Conducted In Small Coupled Reverberation Rooms
D. Mlynarczyk, K. Baruch-Mazur and A. Szelag 2411

Injection moulded locally resonant rings for vibration mitigation in pipes
K. Steijvers, U. Arasan, C. Claeys, L. Van Belle and E. Deckers 2415

On the Relationships Between Manufacturing Parameters, Geometrical Accuracy, and Vibrational Properties of Selective Laser Sintered PA-12 Beams
A. Kryuchkov, M. Pavan, C. Claeys and E. Deckers 2423

Quantifying the impact of injection molding process parameters on the vibroacoustic performance of manufactured locally resonant metamaterials
A. Karaman, L. Van Belle and E. Deckers 2431

Using 3D printed labyrinthine inclusions to improve the low-frequency performance of a thin, conventional sound absorbing panel
M. Niedzielczyk and T. G. Zielinski 2439

Rainbow Trapping Resonator Array for High-Level Sound Absorption
A. Cavanagh, O. Umnova and D. Akiwate 2447

Session A10.04 Materials and systems for noise and vibration reduction

Session A10.05/A23.05 Metamaterials and acoustic black holes in vibro-acoustics

Additive acoustic black holes to suppress acoustic energy in a resonant cavity
J. Deng, O. Guasch and X. Chen 2457

Predicting the acoustic response of a resonant cavity coupled to sonic black holes by means of patch transfer functions
P. De Campos Muradas Cerântola, L. Maxit, O. Guasch and J. Deng 2461

Ultra-thin and Ultra-lightweight Meta-panel for Broadband Noise Insulation
J. Kim and W. Jeon 2469

Ventilated acoustic metamaterial for noise reduction in a duct with non-uniform cross sections
D. Kim, J. Kim and W. Jeon 2471

Design of a metamaterial plate with acoustic black hole absorbers and its application to floating raft system
S. Hao, H. Li and Q. Ding 2473

Effects of acoustic black hole pillars on the acoustic energy of a water-filled cavity
J. Li, J. Deng and O. Guasch 2481

Vibration control in a honeycomb sandwich metapanel made up of periodic cells with an ABH-like thickness profile
S. Avetisov, F. Gautier, A. Pelat, S. Sorokin, G. Gabard, M. Versaevel and J. Mardjono 2485

Absorption and scattering of bending waves by an Acoustic Black Hole embedded in a honeycomb sandwich panel
A. Besse, O. Aklouche, F. Ablitzer, A. Pelat and F. Gautier 2489

Efficiency of an Acoustic Black hole embedded into a honeycomb sandwich panel
A. Besse, O. Aklouche, F. Ablitzer, A. Pelat and F. Gautier 2493

Session A10.06 Numerical methods for acoustic materials and metamaterials

Session A10.07/A15.07 Characterization of acoustic materials

Uncertainties in parameter estimation of porous media in tube measurements
Z. Chen and N. Xiang 2501

Characterisation of acoustic metamaterials allowing airflow
G. Memoli, M. Puttock-Brown, J. Eccles, B. Pearce and E. Greenland 2505

Multi-Density Inversion Characterisation Method for Fibrous Material
A. Santoni, F. Pompoli, C. Marescotti and P. Fausti 2511

Measurements and simulations of a double-porosity material under variation of perforation parameters
M. Isenegger, T. Graf, M. Sonderegger, A. Bonnard, S. Fleischli and A. Taghipour 2515

A novel algorithm for estimating Biot parameters in acoustic simulation of fibrous materials based on raw material composition
M.-T. Hoang, M. Tiengo and E. Harry 2523

A multi-modal analysis of anisotropy in porous media
M. Nolan, S. Félix and J.-P. Groby 2529

Combining absorption coefficient measurements in reverberation rooms with different volumes
H. Bietz and V. Wittstock 2533

Analysis of the relationship between sound field isotropy and errors in the results of Sabine's absorption coefficient
M. Berzborn and M. Vorländer 2541

Estimating the Impedance of a Material Sample at Low Frequencies
A. Prinn, R. Maestro-Vallejo, M. L. López Ibañez, M. Larrosa-Navarro and E. Latorre Iglesias 2549

The measurement of the sound absorption of an array of baffles
J. L. Davy, M. Debevc, D. Truett, J. Payne and J. Watson 2557

A data-driven two-microphone method for measuring the sound absorption of finite absorbers
L. Emmerich, P. Aste, E. Brandão, M. Nolan, J. Cuenca, U. P. Svensson, M. Maeder, S. Marburg and E. Zea 2563

Diffusion Equation-Based Estimation Of Spatially Non-Uniform Surface Absorption Coefficients
A. Prinn and E. Habets 2569

Comparative analysis of acoustic absorption testing methods for different Layers of Cotton Wadding
M. Mastoori, A. M. Lacasta, I. R. Cantalapiedra, F. Merli and C. Buratti 2577

An experimental data set focused on methodologies for the in situ characterization of acoustic materials
J. V. Pontalti, E. Brandão, W. D.'A. Fonseca, P. H. Mareze, G. Netto and E. Fernandez-Grande 2585

Measurement Of Sound Absorption Of Wood Chip-Based Materials For Noise Barriers: Effects Of Testing And Casting Conditions
L. Shtrepi, V. Buggè, S. Fasana, M. Zerbinatti and A. Astolfi 2593

Sound absorption prediction of high-density foam-formed softwood fibers
J. Heldmann, J. Cucharero Moya and T. Lokki 2599

Characterization Of The Sound Absorption Properties Of A Fibrous Biomaterial: A Key Input For Room Acoustic Simulation Software
J. Garcia, P. Alloza and E. A. Piana 2605

Characterization of the Acoustic Behavior of Raw Earth Coatings
M. Ziapkoff, P. Glé, A. Héllouin-De-Ménibus, T. Blinet and C. Guigou Carter 2611

Streaming over Micro-Perforated walls submitted to acoustic plane wave
D. Mazzoni, M. Amielh, L. Genevay, T. Bravo and C. Maury 2619

Method for assessing the impact of aging of selected building materials on their acoustic properties
E. Nowicka 2627

Influence Of Moisture Content On The Acoustic Properties Of Textile Materials
L. Euler, A. Mehrem and E. Shabalina 2631

Study of some influences on the acoustic behaviour of disintegrated samples of used cigarettes
C. Moreno González, V. Gómez Escobar and G. Rey Gozalo 2635

A practical approach to the determination of reproducibility precision (σtarget) in the field of sound absorption measurements: Evaluation of Proficiency Testing data according to ISO 354:2003
P. Rosario and J. L. Martínez 2641

Acoustic characteristics of a hydroponic material
G. Iannace, A. Bevilacqua, A. Trematerra and G. Amadasi 2647

Session A10.08 Modeling acoustic wave propagation in viscothermal structures, including porous materials

Boundary Element Method with visco-thermal losses: development, improvements and applications
V. Cutanda Henriquez 2653

Low-drag rainbow-trapping filters for broadband sound dissipation in a low-speed ducted flow
C. Maury, T. Bravo, F. Ali, D. Mazzoni and M. Amielh 2655

Tunable Microperforated Panel Acoustic Absorbers with Coupling Effects Under Grazing Flow
Y. Li and Y. S. Choy 2663

Modelling Sound Absorption Of Vegetal Wools: Consideration Of Fibre Polydispersity
L. Mutel, C. Piégay, P. Glé, E. Gourdon and C. Segovia 2671

Evaluation Of Methods For Modelling The Impact Of Flame-Retardant Treatments On The Acoustic Performance Of Hemp Wools
C. Piégay, T. Schatzmayr Welp Sa, H. Bossert, L. Mutel, S. Marceau, P. Glé and C. Segovia 2677

Multi-functional rainbow trapping filters for particle acoustic agglomeration
T. Bravo, C. Maury, M. Amielh and D. Mazzoni 2683

Multi-resonant material based on channels with contrasting tortuosity
T. G. Zielinski and M.-A. Galland 2691

Session A10.09/A12.10 Acoustic wave propagation in complex media

Numerical simulations of elastic wave propagation in solid materials containing a random distribution of spherical particles
T. Bertels, T. Valier-Brasier and J.-M. Conoir 2701

Dynamic Wave Manipulation in Spatiotemporal Interfaces and Slabs for Acoustic Control
R. Picó, J. Galiana Nieves, J. Redondo and V. J. Sánchez-Morcillo 2705

Ultrasonic Hologram for Bi-directional Diffusion by Phase Controlling the Scattering Coefficients
E. Ballestero, J. Rodríguez-Sendra, V. Romero-García, J.-P. Groby and N. Jiménez 2709

Conditions for weak scattering and the Born approximation in beams with multiple resonators
M. Lázaro, R. Wiltshaw, R. Craster and V. Romero-García 2713

Session A10.10 Numerical methods for wave propagation in complex media

Session A11.01 Musical acoustics - General

Acoustical Behaviour of Vent Holes on Brasswind Instruments
M. Aragó Bishop, A. Myers and M. Campbell 2721

Embouchure Parameter Variations Across Brass Musicians Of Different Levels Of Proficiency
P. Amann, V. Chatziioannou, P. Nicolay and R. Willmann 2727

Modal approaches for modelling nonlinear acoustics in 2D axisymmetric domains: application to brass instruments
F. Soares, B. Cochelin, V. Fréour, C. Vergez and K. Arimoto 2733

Estimating Sound Radiation Characteristics of Complex-Shaped Plates Using Reduced Sets of Elementary Sources
F. Soares and V. Debut 2739

Effects of Different Auditory Monitoring Conditions on Vocal Intonation Accuracy
A. P. Pietrzak 2747

Absolute Pitch among non-global possessors - Timbre and Categorization
É. Resende De Souza 2751

A measurement system to capture the player's control in the natural playing condition of single-reed musical instruments: Application to the performance log of a beginner player
T. Shoji, Y. Wada, Y. Takahashi and K. Arimoto 2757

Session A11.02/A09.08 Artificial intelligence in musical acoustics

A procedure for evaluating the softness of sound played on the Clarinets
N. Yasui 2763

Psychoacoustic Analysis of Viscoellastically Damped Membranes Using Physics-Informed Machine Learning
C. F. Martínez Orellanos and R. Bader 2767

The Revolution is Here: Deep Audio Processing Redefines Offline and Real-Time Audio Experiences
B.-Y. Yossi, T. Yami and F. Nir 2775

Individual violin sound identification using audio features and machine learning
H. Pauget Ballesteros, P. Lalitte and C. Fritz 2783

A Data-Driven Transfer Matrix Model for the Design of Saxophone Mouthpieces
G. Greco, X. Luan, A. Bernardini, F. Antonacci and A. Sarti 2787

Session A11.03 Consistency of musical instrument making

Evaluating the Reproducibility of Impedance Measurements of Wind Instruments
J.-P. Dalmont, A. Ernoult, J. Cabaret, H. Boutin, T. Colinot, V. Fréour and R. Viala 2797

Assessing the consistency of numerical models for wind instrument impedance
A. Ernoult, J. Cabaret, J. Chabassier, T. Colinot, J.-P. Dalmont, J.-B. Doc, V. Fréour and R. Viala 2801

Is it possible to predict single cane reed mouthpiece interaction by measuring the reed alone?
A. Gaillard, M. Tahon, C. Urban, E. Brasseur and B. Gazengel 2807

Reproducibility in the construction of traditional wooden and 3D-printed plastic soundboards for string instruments
S. Labraña, V. Correa, A. Montoya and C. Espinoza 2815

Design, Construction, and Acoustic Characterization of a Fully Functional 3D-Printed Guitar
C. Espinoza, C. Adasme, V. Correa and J. Baeza 2821

Perceptual Comparison Between a Low-Cost Guitar and a 3D-Printed Guitar
C. Espinoza, T. Ibanez, C. Adasme, M. Denzer, C. Díaz and T. Moreno 2827

Numerical design of a trumpet lead pipe: from the numerical model to the evaluation of the hardware prototype
J.-F. Petiot, V. Fréour and K. Arimoto 2833

Session A11.04 Articulated musical instrument modelling

Real-time bowing parameter sensing methods for articulated bow-string physical modelling
E. Ó Néill, M. Van Walstijn and M. Ortiz 2843

A two-register haptic interface for articulated control of harpsichord physical models
M. Hamilton, R. Russo, C. Webb and M. Ducceschi 2851

Real-time demonstrators to exhibit, investigate and teach transient behaviors in nonlinear dynamics, focused on musical instruments
T. Colinot 2859

Influence of the basins of attraction in the register jumps of the clarinet
N. Szwarcberg, T. Colinot, C. Vergez and M. Jousserand 2863

Imaging based saxophone reed modelling
D. Tonetti and E. A. Piana 2871

Vocal tract turbulence and recorder sound – a CFD approach
N. Nordblom and R. Bader 2877

Dynamical Behavior of a Brass Instrument Around a Double Hopf Bifurcation
M. Pégeot, T. Colinot, J.-B. Doc, V. Fréour and C. Vergez 2885

Session A11.05 Instruments, hyperinstruments and beyond

Musical Acoustics students faced with the challenge of building new musical instruments
A. M. Barbancho, I. Barbancho and L. J. Tardón 2891

What do bells made from lunar regoliths sound like?
A. M. Barbancho, I. Barbancho, L. J. Tardón and C. Traginer 2897

Acoustic Design of a Dual-Purpose Sound Tube Organ
E. Pérez, S. Guillén, A. M. Barbancho, I. Barbancho and L. J. Tardón 2905

Enhancing Music Visualization with Haptic Feedback to Ease Perception for DHH Listeners
N. Mauri, M. Sacchetto, P. Bagnus, C. Nicora, M. Zanoni, A. Bianco and C. Rottondi 2913

MeloPad, a portable device for music composition based on the Bela audio and interaction platform
J. Thieme and L. Molina-Tanco 2921

Alfonso and Theresa: Merging Traditional Lutherie with Modern Electronics in the Design of an Expanded Lute and Contrabass
C. Betancur Gutierrez and L. Valentin 2929

Session A11.06 Networked music performances and virtual environments

Session A12.01 Physical acoustics and ultrasound - General

Ultrasonic Imaging for Quantifying Microplastic Concentrations in Liquids
O. Martinez-Graullera, P. Moreno, C. Pinillos Boralla, J. Huecas, R. Shaporin, M. Parrilla and L. Elvira 2943

Ultrasonic intensification reactor applied to the agri-food and pharmaceutical industry
R. Fernández-Clement, F. J. Pastor-Rodríguez, F. J. Navarro-Brull, P. Poveda Martinez and R. Gómez 2949

Preliminary Study On Theoretical Corrections To The Equation Of State In Single-Bubble Sonoluminescence And Extension Of The Minimum Radius Stage
R. Fernández-Clement, P. Poveda Martinez and R. Gómez 2955

Session A12.02 NDT & SHM Applications

Modelling of the Acoustic Emission (AE) wave propagation using the AE transmitting sensors' responses
V.-D. Le, M. Perrin, L. Espinosa, M.-L. Pastor and Y. Le-Maoult 2965

Adaptive 3D Plane Wave Imaging through interfaces
G. Cosarinsky, A. Rubio, M. Muñoz, J. F. Cruza and J. Camacho 2973

Ultrasonic pulse-echo system for measuring the inter-plate distance of an irradiated fuel element
R. Mrabti, E. Le Clézio, T. Delaunay, Y. Calzavara and G. Despaux 2981

Impact of phase anisotropy-related shifts on the contrast of defect localization images in reverberant plates
L. Chehami, O. Bouchakour, E. Moulin and E. Farha 2989

Viscoelastic Model: The Memory Of Cement
J. Gosalbez, V. J. Ruiz, J. Madrigal, R. Miralles, I. Bosch, J. Quiroga and J. Payá 2995

Acoustic Resonance Spectroscopy Using FBG Sensors Embedded in Mortars
J. Gosalbez, V. J. Ruiz, J. Madrigal, A. M. Macian, J. E. Carcel and J. Payá 3003

Characterization of the adhesion quality in an aeronautical assembly by acoustic microscopy
Y. Ezziani, D. Leduc, P. Marechal, M. Ech-Cherif El-Kettani, M. Ducousseau and N. Cuvillier 3009

Ultrasonic maging of layer on substrate structures using high-frequency acoustic field correlation
N. Ben Jafela, L. Chehami, M. Duquennoy, E. Moulin, N. Smagin, D. Fall and Z. Oumekloul 3017

Session A12.03 Biomedical ultrasound

Can acoustic vortices fragment kidney stones?
S. Maldonado-Ortega, E. González-Mateo, A. Cebrecos, C. D. Vera-Donoso, A. Carrión, F. Camarena and N. Jiménez . 3025

Blood-brain-barrier opening in small animals using focused ultrasound
J. Limens-Pinaque, J. Rodríguez-Sendra, J. J. Rodríguez-García, A. Arándiga, J. L. Alonso-Ramos, D. Panadero Soler, N. Jiménez, P. Rico, S. Canals and F. Camarena 3029

Non-Invasive and Low-Cost Photoacoustic/Ultrasound Dual-Modal Imaging System for Carotid Plaque Imaging
A. Ariza-Carrasco, J. G. Muñoz, J. F. Cruza, L. Elvira, J. L. Herraiz, J. M. Udías, M. A. De Laciñana, J. Rodriguez-Pardo, P. Ibáñez García and M. Pérez-Liva 3035

Impact of spatiotemporal excitation parameters in laser diode-based photoacoustic microscopy
J. Á. Navarro-Calvo, I. Pi-Martín, V. Company-Rubio, A. Arándiga, A. Cebrecos and J. J. García-Garrigós 3039

Designing Acoustic Holograms Without Ionising Radiation For Wearable Transcranial Ultrasound Therapy Devices
A. Eroles-Simó, V. Vegas-Luque, A. Carrión, J. A. Pineda-Pardo, J. J. Rodríguez-García, J. L. Alonso-Ramos, F. Camarena and N. Jiménez 3043

Generating acoustic holograms beyond the hyperbolic approximation
V. Vegas-Luque, D. Andrés, A. Eroles-Simó, J. J. Rodríguez-García, F. Camarena and N. Jiménez 3049

Sparse Arrays for 3D Ultrasound Microstructure Imaging
O. Martinez-Graullera, J. Camacho, J. Huecas, G. Cosarinsky, L. Elvira and A. Ibañez 3053

Modular and flexible hardware architecture for real-time 3D ultrasound imaging
J. F. Cruza, R. Mateos, R. G. Bueno, G. Montaldo and J. Camacho 3059

Numerical Framework for Deep Learning Photoacoustics Image Reconstruction
J. G. Muñoz, A. Ariza-Carrasco, J. F. Cruza, L. Elvira, J. Camacho, J. M. Udías, M. A. De Laciñana, J. Rodriguez-Pardo, P. Ibáñez García and M. Pérez-Liva 3067

Session A12.07 Acousto-optics

Towards broadband lateral BAW excitation in a low-velocity anisotropic substrate
K. B. Yushkov, N. Naumenko and V. Y. Molchanov 3073

Uncertainty relations for broadband ultrasonic waveforms: the case of acousto-optic femtosecond laser pulse shaping
K. B. Yushkov and V. Y. Molchanov 3075

Characterization of optoelectronic oscillator based on collinear acousto-optic cell
E. Kostyleva, S. Mantsevich, N. Polikarpova and E. Dyakonov 3077

Acousto-optic spatial frequency filter with phase control for reconfigurable dark optical traps
V. Y. Molchanov, A. Chizhikov, D. Obydennov and K. B. Yushkov 3081

Tailored ultrasound fields for acousto-optic light control directly within a sample
J. Torres-Durall and M. Duocastella 3083

Enhancing Eye Imaging Modalities with Acousto-optic Interaction
I. Grulkowski and D. Ruminski 3089

Recording neuronal activity in 3D using calcium and voltage genetically encoded indicators
W. Akemann, J. Morizet and L. Bourdieu 3093

Design and Validation of an Acousto-Optic Tunable Filter for Spectro-Polarimetry Analysis
S. Dupont, J. Vanhamel and J.-C. Kastelik 3097

Optimization algorithm for AOTF parameter characterization
J. Vanhamel, A. Pavlov and S. Dupont 3103

Exploiting the Acousto-Optic Effect for Advanced Optical Microscopy
M. Duocastella, C. Alexandropoulos, J. Torres-Durall, B. Mestre-Tora, L. Rodriguez-Sune and M. Colom 3109

Session A12.10 Acoustic wave propagation in complex media

Session A13.04 Advancements and challenges in military acoustics: physiological and audiological perspectives

Two hybrid directivity models of muzzle blasts to describe the frequency and distance dependency
P. Bechtel, C. Kleinhenrich and K.-W. Hirsch 3117

Virtual and experimental acoustical comfort testers for earplugs
F. Sgard, K. Carillo, S. Kersten, R. Richert and O. Doutres 3125

Auditory damage risk due to indoor and outdoor shooting
F. Van Der Eerden, E. Van Pruissen, E. Salomons, P. De Krom and A. Van Heijningen 3133

Beyond the Standard Audiogram: The Need for Comprehensive Assessment of Combat Noise Auditory Trauma
S. Chordekar, D. Brand, C. Adelman, R. Frankael, N. Horev and F. Nir 3141

Squad-level operational performance under varying hearing protection devices and simulated hearing loss
B. Sheffield, R. Bieber, S. Turcios and D. Brungart 3145

Impact of Acoustic Test Fixture Ear Stiffness on Earplug Attenuation of Impulsive Sounds
C. Ruzyla, C. Blondé-Weinmann, P. Hamery, F. Sgard and S. Roth 3153

Sound Attenuation with Double Hearing Protection: A Comparison of Real-Ear and Behavioral Hearing Threshold Measurements
A. Hauptman, S. Chordekar, C. Dirks, L. Fostick and F. Nir 3157

Evaluation Of A Novel Sound Enhancing Connecting Tube Apparatus For Improving Sound Localization Of Occluded Ears
A. Benn, L. Grushko, G. Banta and F. Nir 3163

Design and Analysis of Mobile Microphone Arrays for Acoustic Drone Tracking
M. Blass and F. Graf 3173

Acoustic Detection of Drones: A Machine Learning and Psychoacoustic Approach
D. Tejera Berengué, G. Corral García, F. Zhu-Zhou, M. Zurera-Rosa, R. Gil-Pita and M. Utrilla-Manso 3181

Investigating the Impacts of Cockpit Noise Exposure on Human Decision-Making
E. Fox, A. Cook, F. Mobley, G. Bowers, H. Gallagher and Z. Ennis 3189

Comparison of REAT and insertion loss measurements using headphone audiometry
V. Zimpfer, P. Hamery and C. Blondé-Weinmann 3197

The Relationship Between Damage Risk Criteria for Impulse Noise Explained by Simple Acoustical Descriptors
M. Weger 3201

Session A13.05 Asymmetric hearing loss - clinical solutions and functionality

Speech intelligibility in noise of single-sided deaf cochlear implant users for near and distant talkers
T. Wesarg 3211

Effect of reducing the static interaural time difference in bimodal listeners
S. Zirn, S. Roth, F.-U. Mueller, W. Hemmert and J. Angermeier 3215

A comparative study of four directional microphones and directivity steering for bimodal cochlear implant users
H. C. Stronks, N. Langerak, A. J. Schrijver, R. Koning, J. Briaire and J. Frijns 3219

Better-Ear-Listening vs. Combined Bilateral Information Across Ears in Asymmetric Hearing
B. Williges, N. Sadok, D. Arweiler-Harbeck and T. Jürgens 3227

Speech perception and sound localization in CI subjects with electric-acoustic stimulation and contralateral normal hearing
T. Weissgerber, M. Bandeira, T. Stöver and U. Baumann 3231

Session A13.06 Audiology diagnostic techniques

Evaluating Test Time in Simultaneously Recorded ABRs
S. G. B. Kristensen, S. Laugesen, T. Dau and J. A. Undurraga Lucero 3237

Diagnosing hearing loss using air- and bone-conducted parallel auditory brainstem responses
M. Polonenko and R. Maddox 3243

The binaural interaction component is enhanced with chirps relative to clicks and produces better behavioral lateralization
K. A. Walker, C. A. Sammeth, M. Mavandi, N. T. Greene and D. J. Tollin 3247

A Pilot Study on Assessing Auditory Masking Using Auditory Steady- State Responses
A. Sergeeva and P. Kidmose 3255

How frequency-based processing may help clinicians improve sound quality perception in cochlear implant users?
L. Villejoubert, L. Picinali, K. Faulkner and D. Vickers 3263

Evaluation of Hyperacusis and Loudness Estimates as part of an Extended Audiological Test Battery
L. Vinceslas, V. Drga, J. L. Verhey and I. Yasin 3267

Advancing Objective Assessment of Spectral Discrimination using EEG: Amplitude Roving Minimizes Loudness Confounds
M. Rekswinkel, J. Hjortkjær, A. Kressner and J. A. Undurraga Lucero 3275

Neural Responses Akin to ABRS Measured During Natural Speech Listening for Hearing Aid Assessment
F. L. Bachmann, J. P. Kulasingham, K. Eskelund, M. Enqvist, J. Hjortkjær, E. Alickovic and H. Innes-Brown 3281

Optimising Parameters For Measuring The Acoustic Change Complex With Amplitude-Modulated Stimuli Using A Clinical Evoked-Potential System
W. Ellis, D. Vickers, N. Haywood, N. Mehta, M. Keshavarzi and E. De Groote 3287

Alterations in steady-state synchronisation between Acute and Chronic Tinnitus suggests reduction in the neural correlates of tinnitus over time
A. Umashankar, W. Sedley, K. Alter and P. Gander 3295

Numerical analysis of minimum resonance bandwidths in input impedances of human ear canals
R. Roden and M. Blau 3303

Single-Trial Electroencephalographic Analysis of Front-Back Confusions in Free-Field and Headphone-Based Listening Conditions
N. Marggraf-Turley, M. Shiell, N. Pontoppidan, D. Cappotto and L. Picinali 3307

Evaluation of Microphone Nonlinearities in Probes for Measurement of Otoacoustic Emissions
P. Honzík and V. Vencovský 3309

Methodology For The Neurocognitive Study Of Acoustic-Perceptual Abilities And Linguistic Function In Preterm Infants
R. Hernández-Molina, C. Varo Varo, V. M. Rodríguez-Montaño, R. Pérez Vargas, F. Fernández-Zacarías, V. Puyana Romero, T. Denisenko, J. L. Cueto-Ancela and P. Zafra Rodríguez 3315

Session A14.01 Psychoacoustics - General

Binaural fusion as a special case of auditory object formation
J. Aronoff, J. Lapapa, P. Bk, I. Oyebamiji and N. Gustafson 3321

Modeling fluctuation strength based on the Sottek Hearing Model
R. Sottek 3325

Does a frequency mismatch between infrasound and modulator affect their interaction?
B. Friedrich and J. Verhey 3333

A Study On Sound Level Differences In Working Modes Of A Refrigerator With An Inverter Compressor
P. Kosowski, S. Atamer and M. E. Altinsoy 3337

Does Audibility Mediate The Effects Of Binaural Beats On Working Memory And Mental Workload?
K. Van Den Bosch, C. Schmidt Von Wolkahof and T. Sarampalis 3345

Psychoacoustics of Remixing Music: Catering to Hard-of-Hearing and Normal-Hearing Audiences for Enhanced Experiences
F. Nir, T. Yami and B.-Y. Yossi 3349

Impact of real and synthetic lip-sync-related visual cues on speech intelligibility in a highly reverberant conference hall
A. Galletto, A. Guastamacchia, F. Riente, L. Shtrepi, G. Puglisi, A. Albera, F. Pellerey and A. Astolfi 3355

Modelling the interaction of infrasound and low-frequency sounds
J. Verhey and B. Friedrich 3361

Association Between Speech in Noise Performance and Inferred Cochlear Response Functions
L. Vinceslas, V. Drga, J. Verhey and I. Yasin 3365

Humming and rumbling: Experiments and model predictions
M. Gottschalk and J. Verhey 3373

Verified implementations of the Sottek psychoacoustic Hearing Model standardised sound quality metrics (ECMA-418-2 Loudness, Tonality and Roughness)
M. J. B. Lotinga, M. Torjussen and G. Felix Greco 3377

Evaluation Of The Episodic Audiovisual Memory In A Gamified Experiment
G. Wersényi 3385

Session A14.04 Spatial hearing: modeling and applications

Distance perception of nearby sources located around the subject in echoic rooms
N. Kopco and G. Andrejková 3393

Towards predicting binaural audio quality in listeners with normal and impaired hearing
T. Biberger and S. Ewert 3399

Comparing Measures of Information in Head-Related Transfer Functions
N. Meyer-Kahlen, K. Pollack and P. Lladó 3405

Subjective evaluation of the first incoming reflection - revisiting and extending Barron's study
A. Neidhardt, T. Surdu, P. Lladó and E. De Sena 3413

On comparing auditory models and perceptual assessment when rating head-related transfer functions
R. Daugintis, M. Geronazzo and L. Picinali 3421

Vertical Sound Localization: Influence of Age, Ear Size, Sex, and Hair
V. I. Schneider, B. Bugl and A. Sehr 3425

Vertical Sound Localization: Precision and Robustness to Reverberation in a Large-Scale Study
B. Bugl, V. I. Schneider and A. Sehr 3431

Spiking neural networks for sound localization: A new perspective on auditory spatial perception
Q. Liu, S. Laurent, H. Wuthrich and H. Lissek 3435

Does Source Directivity Influence Human Perception of Speech Position?
C. E. Contreras-Saavedra and R. A. Viveros-Munoz 3443

Binaural Localization Model for Speech in Noise
V. Tokala, E. Grinstein, R. Brooks, M. Brookes, S. Doclo, J. Jensen and P. A. Naylor 3449

Spatial Audio Models' Inventory To Cover The Attributes From The Spatial Audio Quality Inventory
P. Lladó, A. Neidhardt, F. Brinkmann and E. De Sena 3457

Spatial release from masking and listening effort: differences between binaural and free-field presentation
N. La Magna, K. Poole and L. Picinali 3465

Session A14.06 Development of semantic attributes based on psychoacoustic modelling

Estimation of interpretable non-linear Sound Quality Metrics using Kolmogorov-Arnold Networks (KANs)
T. Lobato and F. Kamp 3471

Psychoacoustic Modelling of AVAS Sounds: Consumer-Centric Semantic Attribute Development for Electric Vehicles
B. Kullukcu, M. S. Engel, S. Atamer and M. E. Altinsoy 3477

Auditory-Perceptual and Emotional Matching with Psychoacoustic Indicators of Urban Soundscapes
M. S. Engel, M. L. D. U. Carvalho and M. E. Altinsoy 3485

Comparative Analysis of Acceleration Sounds from Electric and Internal Combustion Vehicles Using Discomfort Indices
N. Misaki and S. Ishimitsu 3493

Quantifying and Mitigating Motion Sickness in Autonomous Vehicles through Psychoacoustic Modeling and Neurophysiological Insights
J. Y. Jeon, H. Lee, M. Ji, B. B. Santika, S. U. Choi and H. Moon 3499

Session A14.07 New trends and research for robust and unbiased psychoacoustical experimentation

On the need for homogeneous and standardized methodologies for perceptual testing in acoustics
D. De La Prida, M. Larrosa-Navarro, L. A. Azpicueta-Ruiz and A. Pedrero 3505

Rendering complex acoustic scenes for perception experiments
L. Aspöck, M. Vorländer and J. Fels 3513

Footstep Sounds Recording and Evaluation in Outdoor Environments
A. D'Adamo, K. Srinivasan, D. De La Prida, L. A. Azpicueta-Ruiz and A. Tajadura-Jimenez 3517

Robustness of an equal loudness paradigm to stimuli, environment and participants
M. Geluykens, H. Müllner, V. Chmelík and M. Rychtáriková 3525

Influence of participant training on the discriminability of clarity changes
M. Larrosa-Navarro, D. De La Prida and A. Pedrero 3533

Experimental Design Considerations for Proximity Perception of Binaural Action Sounds in Anechoic and Reverberant Environments
M. M. Rahmani, M. Roel Lesur, D. De La Prida, L. A. Azpicueta-Ruiz, J. R. Diaz Duran, A. D'Adamo and A. Tajadura-Jimenez
3541

The Impact of Looming Sound Duration on Peripersonal Space Measurement
M. M. Rahmani, M. Roel Lesur and A. Tajadura-Jimenez 3549

Optimal Pairwise Comparison Procedures for Subjectic Evaluations
J. Webb and L. Picinali 3557

Session A14.08 Virtual acoustics and binaural AR in hearing research: challenges of a new paradigm

Session A14.09 Advanced air mobility noise

Session A14.10 Psychological and physiological experiments for noise annoyance, acoustic comfort, and soundscape evaluation

Development and psychoacoustic evaluation of a curving noise classification method
M. Isenegger, L. Bartha, S. Emmenegger, C. Jeckelmann-Imhof and A. Taghipour 3567

Spatial Analysis of Axial Fan Psychoacoustic Metrics
N. Cerkovnik and J. Prezelj 3575

Measuring Human Noise Sensitivity: Psychometric Evaluation in an Online Survey
E. Song, W. Ellermeier, C. Marquis Favre, K. Zimmer, S. H. Park and R. Strebel 3583

An Approach for Evaluating Time-varying Annoyance Caused by Railway Noise
J. Egeler, C. Huth, A. Schlesinger, M. Liepert, C. Ende, D. J. Meyer, T. Koch, J. Bartnitzek, L. Höhle, B. Schlüter and R. Böhme 3589

Association of stress biomarkers with road traffic noise exposure and residential green: Insights from the RESTORE study
B. Schäffer, J. Dopico, M. Brink, D. Vienneau, M. Röösli, T. M. Binz, S. Tobias, N. Bauer and J. M. Wunderli 3597

Experimental Design to Map Brain Areas Involved in Sound Recognition Process
J. Donnerer, M. Kaltenbacher and C. Adams 3601

Annoyance of shooting sounds: Re-evaluation of ISO/PAS 1996-3 penalty procedure
A. Kuusinen, E. Rantanen and V. Hongisto 3605

Drone pass-by noise perception across various urban environments settings
N. Gravina, M. Masullo and L. Maffei 3609

Diversity in Sound Perception in Survey to Noise Sensitive People and Relevance for Experimental and Field Studies
C. Rosas-Pérez, L. Galbrun, S. R. Payne and M. E. Stewart 3613

The Role Of Sound Valence In Shaping Taste Perception Across Different Sound Environments
N. F. F. Istiani, M. Masullo, G. Ruggiero and L. Maffei 3621

Investigation into the Effect of Horizontal Source Direction on Psychoacoustic Annoyance
S. Dickinson and H. Lee 3627

Session A15.01 Room acoustics - General

Measurement of room acoustic parameters with an omnidirectional parametric loudspeaker in an converted chapel for choral music performance
M. Arnela, G. Quaranta, M. Avelar and L. H. Sant'Ana 3637

Speech Intelligibility Evaluation and Acoustic Performance of the Madrid Assembly Plenary Hall Combining Traditional and AI-based Methods
E. García-Medina, M. Centeno-Cerrato, J. Trujillo and C. Asensio 3645

Large public database of room acoustic responses
A. Fürjes 3653

Effect of Installation Method and Thickness on the Sound Absorption Performance of Melamine Foam
Y. Chun, S. Kim and S. Lee 3655

Acoustic characterization of Theater Ribeiro Conceição (Lamego, Portugal)
M. Gomes, A. Carvalho and A. Costa 3657

Acoustic characteristics of Gugak (Korean music) practice rooms
J. Jeong and Y. Kim 3665

Technology-Enhanced Methods For Indoor Acoustic 3D Modelling
E. Gómez Parrado, C. Aguado Tienda and Á. Grilo Bensusan 3669

Acoustic design of Church of Our Lady of Fatima in Poland
A. Sygulska 3677

Comparative Analysis of the Acoustic Modeling using Various Room Acoustic Simulation Software
C. H. Haan and C.-H. Han 3681

Quantum-inspired Reverberation using Ray Tracing Method
J. Tudoce, A. Reserbat-Plantey, R. Yamada and M. Lewenstein 3685

Acoustic analysis of a single-nave hall with an apse in the Cellars of Diocletian's Palace in Split
M. Nosil Mešić, Z. Veršić, M. Horvat and K. Jambrošić 3689

Echoes In Iberian Bullrings
M. Martín-Castizo, M. Galindo and S. Girón 3697

Session A15.02 Speech production and perception in rooms

Acoustic refurbishments in a university lecture room: Effects on speaker's comfort and voice strain
N. Cansu, G. Öhlund-Wistbacka, E. Arvidsson, J. Christensson, S. Holmqvist-Jämsén, R. Rydell and V. Lyberg-Åhlander 3707

Sensory-Driven Voice Modulation: Effects of Auralized Acoustics and Visual VR on Voice Outcomes
C. J. Nudelman, A. Tunuguntla, N. Ha, I. Rogala, K. House-Henry, B. Lopez, R. Perez Guerrero and P. Bottalico 3711

The effect of different simulated reverberant environments on cochlear implant users' binaural fusion
J. Aronoff, P. Bk and N. Gustafson 3719

Contribution of auditory detection thresholds to speech recognition in temporally and spectrally degraded environments for older adults
D. Fogerty and J. Dubno 3723

The role of speech directivity in speech perception
B. Monson 3727

On-axis sound pressure levels and sound power of normal speech for speech intelligibility, privacy and security
C. Hopkins, S. Graetzer and G. Seiffert 3731

Investigation on the acoustic conditions of active classrooms in accordance with the students and classroom activities
Y.-J. Choi 3735

Assessing sound levels of student activity in primary school classrooms
C. Visentin and N. Prodi 3741

Speech intelligibility and acoustic conditions in university classrooms for the teaching of Quechua as a second language
H. D. Lazarte Reátegui, W. A. Montano Rodríguez, H. S. Guerrero Arias, M. F. Siguas García, V. L. Palomino Franco and K. L. Huamani Quiquinlla 3745

Binaural speech intelligibility in practice
N. Prodi and M. Begotti 3749

Session A15.03 Modern offices: challenges and solutions

Effects of music on cognitive performance: from the workplace to the laboratory to open-plan offices
A. Smith 3757

Noise in open-plan offices: A holistic research strategy
A. Smith, J. Langer and J. Taylour 3761

Objective method for predicting office noise annoyance
V. Hongisto, R. Alakoivu, J. Keränen and J. Laukka 3769

Enhancing Acoustic Design in Open-Plan Offices: Practical Applications of the Simplified ISO 3382-3 Prediction Model
R. Machner, H. Brokmann and A. Klein 3773

Airborne Sound Insulation In Five Office Buildings According To Requirements Of Italian Regulations And Well Building Standard
S. Di Blasio, F. Ferilli, L. Andreozzi, I. Gualdana, E. Stigliano and E. Siciliano 3779

Optimizing Acoustic Privacy in Open-Plan Offices: A Simulation-Based Study of Desk Partition Designs and Material Choices
G. Fratoni and D. D'Orazio 3787

Sound Absorbing Furniture As A Strategy For Acoustic Comfort Optimization
C. Rubino, S. Liuzzi and F. Martellotta 3793

Do frequencies below 160 Hz play a role in speech privacy between rooms?
A. Kuusinen, E. Rantanen and V. Hongisto 3797

Class A booth reduces stress due to office noise
V. Hongisto, J. Keränen, E. Rantanen and J. Radun 3801

How did the addition of soundproof pods influence office employees' experience?
J. Radun, S. Pitkänen, R. Alakoivu, J. Laukka, H. Maula, A. Sivula and V. Hongisto 3805

Session A15.04/A24.06 Virtual reconstructions in archaeoacoustic research

Acoustical features of the Üç Şerefeli Mosque in Edirne (the mosque with three balconies)
Z. Sü Gül 3811

Virtual acoustic completion of the unfinished baroque church of Santuari del Miracle in the Catalan region of Solsonès
M. Arnela, M. Rebollo-Arjona, R. Scoczynski Ribeiro and R. M. Alsina-Pagès 3819

Exploring the Past using Dynamic Auralization of Cultural Heritage: A Case Study on the Theatre of Tyndaris
L. Lavagna, A. Farina, A. Farina, L. Shtrepi and A. Astolfi 3827

Analysis of the reconstructed acoustic environment of a Portuguese Romanic Cathedral in the XVIth century by numerical modelling
P. Amado Mendes, L. Godinho, D. Mateus, A. Pereira, D. Ramos and A. Gaspar 3831

An archaeoacoustic study of the Hoftheater's (1808-1847) history
B. Postma, M. U. Schumann and B. F. G. Katz 3839

Acoustic Characterization Of The "Cueva Del Pájaro Azul": Architectural Reference Of The Sound Heritage Of Gadir
D. Payo, V. M. Rodríguez-Montaño, F. Fernández-Zacarías and R. Hernández-Molina 3847

Measurement and Auralization of Paleoacoustics landscapes in Chauvet Cave
L. Valentin, J. Abel, J. Berger, C. Chafe, J. Chowning, C. Fritz, N. Farzaneh, M. Kolar, R. Michon, S. Martin, P. Svensson and M. Wright 3855

From Measurement to Music: Reviving the Acoustic Heritage of St. Michael's Church, Coventry, UK
I. Ali-Maclachlan, H. Roberts, B. West, S. Hall and J. Savan 3865

Comparison Between the Acoustic Texture Obtained Through In Situ Measurements and That Calculated From Virtual Models of a Pre-Romanesque Church
L. Carrero-Muriel, D. De La Prida, M. Larrosa-Navarro and A. Pedrero 3873

Survey And Acoustic Correction Of The Boboli Amphitheater Using Of Audio-Visual Model
L. Magnini, V. Amodeo, D. Masci, P. Ruggieri, S. Secchi and G. Verdiani 3881

Session A15.05 Acoustic comfort in hospitals

Space For Music: Elements To Incorporate Into Healthcare Designs
A. Ferrentino, C. Rius and R. Torrents Pairo 3889

Impact Of Spatial Organization On Noise Levels In Open-Bay Neonatal Intensive Care Units
V. M. Rodríguez-Montaño, J. L. Beira Jiménez and R. Hernández-Molina 3897

Environmental Noise in Hospitals: a Rapid Review of Trends and Possible Developments
V. Amodeo and S. Secchi 3905

Towards new metrics to characterize the acoustic environment in Intensive Care Units
E. De Ruiter, E. Fasllija, D. Gommers and E. Özcan 3913

Looking at sound together: using VR with Dutch Hospitals - a case study
C. Van Wezel 3921

Sound in Clinical Environments (SILENTS): Overview of a mixed methods intervention to improve acoustic comfort in a hospital ward in London (UK)
C. Rosas-Pérez, A. Hall, C. J.H. Cook, J. Drever, M. Cobianchi and H. Skene 3925

Noise Assessment Within Healthcare Facilities: Annoyance And Intrusiveness Of Sound Sources
D. De Salvio, V. Amodeo, M. Garai and S. Secchi 3933

Preliminary study of a University Hospital outdoor noise environment based on monitoring and soundscape
A. Nora, D. De Salvio, G. Fusaro and L. Barbaresi 3939

Session A15.06 Acoustic and multidomain comfort in learning spaces

Linking Speech Clarity, Reverberation, And Distance For Classroom Design Optimization
D. Mironovs 3949

Case Study: Remodeling of open plan Dutch school - acoustic design and operational challenges
B. Scherpenhuyzen, C. Campbell and J. Vugts 3953

A possible single number universal classroom acoustic criterion
S. Dance 3961

Virtual Reality for Performance Preparation
C. J. Wingfield, Y. G. Gonzales Redman, C. J. Nudelman and P. Bottalico 3965

Children's listening perception and cognitive performance at school
C. Pavarin, I. Pittana, I. Pavanello, P. Ruggeri, A. Di Bella, P. Scimemi, P. Romagnoni and F. Cappelletti 3973

EEG Insights into the Impact of Noise and Dysphonic Speech on Children's Listening Effort and Sentence Comprehension
S. Murgia, M. M. Flaherty and P. Bottalico 3981

Evaluating Noise-Related Stressors in Italian Schools: Aligning Acoustic Environments with the Needs of Neurodivergent Students
A. Marzi, F. Bettarello, M. Caniato and A. Gasparella 3987

Multi-domain sensation and preference of children at primary school: a case study
I. Pittana, C. Pavarin, I. Pavanello, A. Di Bella, P. Scimemi, P. Romagnoni and F. Cappelletti 3993

Combined effect of IAQ and acoustics on calculation in university classrooms
M. Pellegatti, C. Visentin, S. Torresin, F. Babich and N. Prodi 4001

Teachers' Indoor Environmental Satisfaction And Sound Exposure In Enclosed And Flexible Learning Spaces
J. Radun, M. Veermans, S. Rantanen and V. Hongisto 4005

Vocal behavior in different room acoustic conditions, noise, and with sound field amplification system use
N. Cansu, G. Öhlund-Wistbacka, S. Holmqvist-Jämsén, R. Rydell and V. Lyberg-Åhlander 4009

An Acoustic Survey Of Korean School Classrooms
Y.-J. Choi, D.-H. Kim, H.-J. Lim and H.-J. Kim 4013

Session A15.07 Characterization of acoustic materials

Session A15.09 Sound reflections in concert halls

The Support parameters for measurement of sound reflections on concert hall stages
A. C. Gade 4021

On the influence of sound scattering in room acoustic modelling
A. Pereira, A. Gaspar, L. Godinho, D. Mateus and P. Amado Mendes 4029

Robust 3D Localisation of Anomalies in Reverberation Time Signals
T. Rittenschober and A. Decloux 4035

Development of a 3D tool to visualise the lateral energy component within each sound reflection in concert halls
J. Sanz Soriano, C. Day and J. Ó. García Gómez 4043

Forget about the seat dip effect – you have other problems! Early reflections to compensate for broadband grazing incidence attenuation
N. Rummler, E. Green, Y. Jurkiewicz and E. Kahle 4051

Computer-based Construction of Self-similar Acoustic Reflectors
J. O.'K. O'Keefe 4057

Session A15.10 Modeling and estimation of room impulse responses with machine learning

Deep, data-driven modeling of room acoustics: literature review and research perspectives
T. Van Waterschoot 4065

Complex Room Geometry Inference via Acoustic Echoes
I. Yeon and J.-W. Choi 4073

DiffusionRIR: Room Impulse Response Interpolation using Diffusion Models
S. Della Torre, M. Pezzoli, F. Antonacci and S. Gannot 4079

Latent FXLMS: Accelerating Active Noise Control with Neural Adaptive Filters
K. Sarkar, A. Lu, M. Mittal, Y. Zhuang, R. Corey and A. Singer 4087

Evaluating Acoustic Characteristics used by Conditional GANs for Room Impulse Response Modeling
G. Atienza, F. Pastor-Naranjo, D. De La Prida, L. A. Azpicueta-Ruiz, V. Naranjo and G. Piñero 4095

Session A15.11/A16.05 Sound field reconstruction in rooms and enclosures

Tracking of Spatially Dynamic Room Impulse Responses Along Locally Linearized Trajectories
K. Macwilliam, T. Dietzen and T. Van Waterschoot 4103

Experimental Validation of Sound Field Estimation Methods Using Moving Microphones
J. Brunnström, M. B. Møller, T. Van Waterschoot, M. Moonen and J. Østergaard 4111

Introduction of the boostlet transform for acoustic signal processing
E. Zea, M. Laudato and J. Andén 4119

Frequency and spatial limitations of sound field reconstruction methods for navigable reproduction
A. Figueroa-Duran, N. Meyer-Kahlen, S. A. Verburg, T. Lokki and E. Fernandez-Grande 4127

Spatially extended reconstruction of room impulse responses using a generalizable wave model
E. Fernandez-Grande, A. Figueroa-Duran and S. A. Verburg 4135

Stochastic Variational Inference of Directional Decay Times in a Reverberation Room
M. Berzborn and M. Vorländer 4139

Towards Analytical Waveform Transitions in Space-Time Across Different Boundary Conditions
E. Zea, E. Fernandez-Grande and C. E. Yarman 4145

The performance of the cable robot sound field characterisation measurement system
R. Prislan, M. Repek and D. Svenšek 4153

Sound source localization in small-volume industrial reverberant cavities through the Steered Response Power PHAT-β
K. Rousou, D. Panagiotopoulos, D. Chronopoulos and E. Deckers 4161

Session A15.12/A19.09 Numerical methods for room acoustics

A neural network for predicting with the diffusion equation: a case study of long rooms
I. Fichera, A. Deleforge, C. Foy, J.-D. Pascal, C. Prax, M. Tonelli, C. Van Hoorickx and M. Hornikx 4171

Using spherical array receivers to extract scattering coefficients of room surfaces
D. Xie and M. Hornikx 4179

On the Accuracy of the Image Source Method in the Presence of Two Adjacent Impedance Walls
Z. Xu, E. Habets and A. Prinn 4185

Sweeping echoes management in image-method based open-source software
A. Andrijasevic and M. Horvat 4193

Simulation method for shoebox-shaped rooms with absorbing ceilings
U. P. Svensson, K. H. Reigstad and M. Skålevik 4201

Room Modeling In COMSOL Using Finite Elements Method
R. Maestro-Vallejo, E. Latorre Iglesias, M. L. López Ibañez and A. Melis 4207

Evaluating the Applicability of Statistical Reverberation Theory in Rooms with Varying Compactness and Material distributions
W. Wittebol, H. Wang and M. Hornikx 4215

From Theory to Reality: Assessing Predictive Models for Reverberation Time in Built Environments
M. Caniato and F. Bettarello 4223

Towards a community hub for open-source room acoustics software
S. Willemsen, H. Teymoori, I. Fichera, H. Wang, A. Nolte, A. Serebrenik and M. Hornikx 4229

A zero-phase parametric equalization for microphone and loudspeaker impulse response
V. Popa, B. Moroșanu and H. S. Ionita 4237

Session A16.02 Spatial audio signal processing - capture, encoding and enhancement

Cross-Spectral Analysis of Higher-Order Ambisonic Signals for Investigating the Spatial and Statistical Properties of Captured Sound Fields
N. Hahn, F. Fazi, M. Orita, B. Bacila and P. Nelson 4243

Increasing the spatial aliasing frequency of circular arrays via beamformer order reduction
F. Fazi and N. Hahn 4251

Steerable Neural Directional Filtering
W. Huang, M. M. Halimeh, S. R. Chetupalli, O. Thiergart and E. Habets 4259

Dynamic room impulse response measurements with a robotic arm
S. A. Verburg, O. Díaz Gaztelumendi, Y. Pene and E. Fernandez-Grande 4267

Multi-channel Processing for Patient Identification and Audio Analysis in the Context of Group Music Therapy
A. Epure, T. Dietzen and T. Van Waterschoot 4275

Correction of azimuth ambiguities of the GCC algorithm in a uniform circular array
A. Resino Viñas, G. Corral García, D. Tejera Berengué, F. Zhu-Zhou and M. Zurera-Rosa 4283

Tracking of Intermittent and Moving Speakers : Dataset and Metrics
T. Iatariene, A. Guérin and R. Serizel 4291

Relative Transfer Matrix-Based Binaural Signal Denoising of Head-Mounted Microphone Array Recordings
M. Kumar, A. Bastine, L. Birnie, S. Arcos Holzinger, P. Samarasinghe and T. Abhayapala 4299

Neural Network Solvers for Binaural Encoding with Perception-Based Losses
O. Berebi, Z. Ben-Hur, D. Alon and B. Rafaely 4307

Binaural Signal Matching with Wearable Arrays for Near-Field Sources
S. Goldring, Z. Ben-Hur, D. Alon and B. Rafaely 4315

Ambisonics Encoder for Wearable Array with Improved Binaural Reproduction
Y. Gayer, V. Tourbabin, Z. Ben-Hur, D. Alon and B. Rafaely 4321

Session A16.03/A09.06 Machine learning for array processing

Learning Magnitude Distribution of Sound Fields via Conditioned Autoencoder
S. Koyama and K. Ishizuka 4329

Universal auditory scene analysis model for source separation, event localization, and detection
D. Lee and J.-W. Choi 4337

Learning from data-driven sound field estimation using complex-valued neural networks
V. Paul, N. Hahn and P. Nelson 4343

Exploiting Spatial Information for Anomaly Detection in Industrial Machines Using Autoencoders
C. Luzón-Álvarez, A. M. Torres-Aranda, F. J. Ferri and M. Cobos 4351

Acoustic Scene Description Using Acoustic Imaging And Machine Learning
E. Tiffeneau, Q. Leclère and S. Bouley 4357

Elevation and Azimuth Frequency Invariant Beamforming using Autograd and Concentric Circular Microphone Arrays
J. Ortigoso-Narro, J. A. Belloch, M. Morales-Cespedes and M. Cobos 4365

Point Neuron Learning for broadband array processing
A. Bastine, T. Abhayapala and P. Samarasinghe 4373

Deep Learning-Driven Object Tracking for Enhanced Acoustic Beamforming in Dynamic Environments
J. Ortigoso-Narro, J. A. Belloch and M. Cobos 4381

Complex-valued neural networks for the reproduction of linearly superposed sound fields
I. Lambert, V. Paul and P. Nelson 4389

Interpolation of Modal Displacement in Thin Plates Using Physics-Informed Neural Networks
R. Malvermi, F. Zese, M. Pezzoli, F. Antonacci and A. Sarti 4397

Enhancing the Geometrical Calibration of Microphones Arrays : Solutions and Experimental Validation
M. Hartenstein, P. Luizard, H. Moingeon, C. Pinhède, M. Pachebat, C. Ollivon, F. Ollivier and F. Silva 4405

Session A16.04 Airborne sonar

Spatial Characterization of Noise Generated by a Drone in Hovering Flight
A. Izquierdo, L. Del Val, J. J. Villacorta and J. Retortillo 4415

Detection and spatial localization of xylophagous insects in wood structures with acoustic arrays
L. Del Val, A. Izquierdo, J. J. Villacorta and R. D. Martínez 4421

Plant Health Monitoring using Acoustics
J. Vande Velde, B. Da Silva, A. Touhafi and L. Segers 4427

Compressed Sensing for Data Acquisition in Air Imaging Sonar Sensor
A. Sharifa and J. Steckel 4435

Advancing Direction Estimation for Acoustic Drone Detection in Noisy Outdoor Environments
M. Varela and W.-D. Wirth 4443

Pedestrian Detection Using an Active Acoustic Array Embedded in a Car
J. J. Villacorta, A. Izquierdo, L. Del Val and A. Martin 4449

Session A16.05 Sound field reconstruction in rooms and enclosures

Session A16.06 Source directivity: capturing, processing, and evaluating its effects

A robotic system for space-time characterization of parametric acoustic sound sources
A. Fantinelli, M. Arnela, E. Brandão and E. Fernandez-Grande 4457

Sound source directivity estimation via a spherical wave decomposition of the radiated field : application to human voice directivity measurements
M. Hartenstein, P. Luizard, H. Moingeon, C. Pinhède, M. Pachebat, C. Ollivon, F. Ollivier and F. Silva 4465

Impact of leg diffraction and scattering on voice directivity patterns
S. Bellows, B. F. G. Katz and T. Leishman 4473

Analytic expressions for the low-frequency acoustic center of dipole radiators
S. Bellows 4481

Investigating the effects of sound source occlusion in a real dynamic scenario
T. Surdu, L. Treybig, F. Klein, R. R. Ramachandra Rao and S. Werner 4489

Session A16.07 Processing/individualization/interpolation of HRIRs or BRIRs

Session A17.01 Soundscape, environmental quality, health and well-being - General

Soundscaping as a Multidisciplinary Activity
M. Cobussen 4501

Virtual Reality Applications in Urban Soundscape Assessment: An Overview
Ö. Gök Tokgöz and M. E. Altinsoy 4507

Walking vs. Standing: How Dynamic Visuals Impact Soundscape Perception
K. Guo and J. Kang 4515

An Approach To Sensory Heritage Policy Through Soundscape And Smellscape
P. Lindborg, L. H. Lam, Y. C. Kam and J. Xiao 4519

Meta-analyses in noise and health: to update or not?
E. Van Kempen, M. Reedijk, K. Rijs and C. De Bruijn 4525

Up-to-Date Epidemiological Evidence on Health Effects from Transportation Noise for Burden of Disease Assessment
M. Röösli, N. Engelmann, X. Jiang and D. Vienneau 4533

Umbrella+ Review And Discussion Of The Evidence, Gaps, & Research Needs For Quantifying Transportation Noise Impacts On All-Cause Mortality
S. N. Clark, B. Fenech, J. Gulliver, C. Jephcote, O. Williams and C. Clark 4539

Progress In The Translation Of ISO/TS 12913-2:2018 Soundscape Model Into Spanish: New Insights From The Satp Project In Chile
J. Vida Manzano, R. García Quesada, J. A. Almagro Pastor, E. Suárez Silva and J. Cárdenas Mansilla 4547

Linguistic Representations of Soundscapes: Perceptions and Descriptions in Urban and Mountain Contexts in Trentino-South Tyrol
G. Gozzi, S. Torresin and L. Badan 4555

Towards The Creation Of An Ibero-American Urban Soundscape Network For Collaboration, Preservation And Promotion Of Sound Environments
F. Rodriguez-Manzo, E. Suárez Silva and J. Vida Manzano 4563

Inhabiting Gaudí: Integrating Objective and Subjective Acoustic Evaluations for Human Comfort
R. M. Alsina-Pagès, M. Arnela and M. Freixes 4571

Soundscape Analysis And Contribution To Forming Place Identity And Satisfaction Of Users
Z. Al-Bayyar, T. B. Dahham and P. N. D. Yorukoglu 4577

Interventions And Acoustic Nuances In The Soundwalks With Daumal And ISO 12913 Methods In Elche, Cuenca And Faro
F. Daumal I Domènech, J. Vida Manzano, S. Herguedas and S. Silva Antunes 4583

Citizen Science To Analyse The Relationship Between Sounds And Spirituality In A Monastery
E. Vidaña-Vila, A. Ramos Esperidião, M. Freixes, J. Cabó, A. Iarozinski Neto and R. M. Alsina-Pagès 4591

PEMS: People Experience of Mountain Soundscapes
B. Di Donato and I. Mcgregor 4599

Session A17.02 Restorative soundscapes - Sound quality, health and well-being

Tranquillity Islands: Designing restorative soundscapes in urban environments
G. Watts 4609

Silenzi in Quota – An Initiative Promoting Soundscape Protection in Mountainous Natural Areas
T. Oberman, S. Torresin, R. Keller, G. Gozzi and J. Kang 4615

Field study on the restorative potential of small green and blue spaces in densely populated areas
M. Schuck, E. Lüer and A. Fiebig 4621

A citizen science approach to collect combined noise exposure and survey data
L. Dekoninck, P. Thomas and T. Van Renterghem 4629

Restorative Urban Spaces In Europe: Comparisons Of Criteria And Approaches In Germany And Italy
M. Masullo, R. A. Toma, A. Fiebig, S. Sibilio and L. Maffei 4635

A Simple Structured Approach to Urban Greenspace Acoustic Design
B. W. Hohmann 4641

Acoustic quality layers: A systematic review to understand acoustic quality spaces
H. A. Dogan Iseri and A. Ozcevik Bilen 4649

The Influence of Soundwalk Direction on Healthy Street Metrics
Z. S. Ozturk, J. Kang and F. Aletta 4657

Comparison of methodological approaches for investigating urban parks soundscape restoration: A case study of Curitiba, Brazil
M. S. Engel, K. F. K. Maciel, B. Szeremeta and P. H. T. Zannin 4661

Perceptions Of Chinese Temples Through Soundscape And Smellscape: A Case Study At Wong Tai Sin
L. H. Lam, R. Yue, Y. C. Kam and P. Lindborg 4667

Listening to the High-Tech City and its Vehicles: Auditory Perception of Electric Vehicles Embedded in Shenzhen's Urban Soundscape
Q. Xiang, Z. Liu and M. Z. Sagesser 4673

Restorative Soundscape Design for Resting Places in Purpose-Built Vehicles: Enhancing Relaxation and Well-being through Audio-Visual Environments
J. Y. Jeon, H. Lee, B. B. Santika, D. Park and J. Kim 4681

Mitigating Noise Annoyance Through Green Spaces: Health Impacts in European Urban Environments
X. Jiang, J. Fons-Esteve, M. Sáinz De La Maza, N. Blanes Guàrdia, E. Peris, M. Röösli and D. Vienneau 4685

Courtyard trees and aircraft noise: Investigating the effect of Urban Greenery on aircraft noise perception using Virtual Reality (VR)
R. Vassallo, G. Wuite and M. Lugten 4691

Session A17.03 Soundscape practice and interventions

Soundscape Practice And Interventions: A Framework
J. Kang, X. Fang, F. Aletta, A. Mitchell, T. Oberman, G. Cerwén, X. Chen, J. Xiao and P. Mittal 4699

Defining urban soundscape design means and tools
M. Haberl, T. Kusitzky and S. Alves 4707

Architecture as Soundscape Intervention Design Process and Strategies
M. Gold, G. W. Siebein and K. Siebein 4713

Exploring Soundscape Methods and Interventions in Urban and Suburban Soundscapes
G. W. Siebein, K. Siebein, M. Gold, G. Siebein Jr and M. Roa 4721

A Tale of Two Cities: Soundscape Analysis and Planning
G. W. Siebein, K. Siebein, M. Gold, G. Siebein Jr and M. Roa 4725

The Soundscape of an ICU
K. Siebein, G. W. Siebein, L. Lorusso, D. Rittenbacher, T. Orozco, J. Miller, M. Vetterick and I. Jones 4731

Measuring short-term changes in perceived soundscapes due to localized interventions
G. Memoli, L. Chisari, M. Boerger, J. Eccles, V. Apicella and B. Carambia 4739

Listening to the Built Environment: Cultural and Social Urban Soundscape
L. Tsaih, S.-I. Juan, R. Ghadiri, J. C.-P. Chen, T.-Y. Yu, V. Prawira, C.-H. Chen and Y.-T. Yen 4747

The Sonic (Re)Design Of Urban Places: Auditory Transformations In The Hague (Nl) And Kiruna (S)
M. Cobussen, S. Östersjö, P. Craenen, J. Bennett, R. Zentschnig, I. Ruipérez Canales and J. Berg 4755

Exploring green façades as complex systems and their relationships with soundscape quality through a system thinking approach
S. Torresin, F. Aletta, E. Gasparri, K. Zhou, T. Astell-Burt, A. Brambilla, T. Parkinson, S. Yuksel Dicle and A. Kuru . 4761

Towards Designing Pleasant Urban Soundscape: An Acoustic Metamaterial-Based Multi-Objective Psychoacoustic Analysis
X. Fang, P. Mittal, T. Oberman, F. Aletta, S. Subramanian and J. Kang 4767

Sonic Citizenship and the feeling of awe in urban space
S. Raahede Lundgård, M. Koldkjær Højlund and L. Stenfeldt 4773

The Soundscape of Animal Care Facilities
K. Siebein, G. W. Siebein, S. Boman and H. Lewis 4781

Session A17.04 Soundscape methods, monitoring and metrics

The Prediction Of Environmental Noise, Using Arcmap, (NMSIM-GIS) And ISO 9613, For Commercial Jet Boat Operations
J. Pearse, J. Lee, B. Donohue and G. Watts 4791

Noise in the High-Tech City: Listening to Shenzhen Through a Participatory Phone-Based App
X. Fu, S. Li and M. Z. Sagesser 4799

Introducing NORBAERT – an open source software to facilitate the research on complex networks from the acoustic environment
T. Haselhoff, M. Jedrusiak, F. Weichert and S. Moebus 4807

A revised Web Application for Interactive Exploration and Visualization of ISO 12913 Soundscape Datasets
M. Erdmann, S. Versümer and J. Steffens 4813

Proposal For A Scale To Measure Psychosocial Cobenefits Of Natural Soundscape In Urban Areas
K. Herranz-Pascual, P. Anchustegui, I. Aspuru Soloaga and I. Iraurgi 4817

Polish version of soundscape attributes: translation process and preliminary validation results
J. Dumanowski, J. Felcyn and A. Preis 4823

Comparison of Text-Based and Graphical Methods for Soundscape Assessment
Y. Kim, D. Kim and J. Ryu 4827

Effects of audio-visual interactions on the soundscape in urban shopping streets
J.-Y. Jeon, G. Kim and J.-Y. Hong 4833

Comparative Analysis of Visual and Auditory Perceptions in Urban Environments Using Mental Mapping
G. Kim, J.-Y. Jeon and J.-Y. Hong 4835

Clustering analysis of human perceptual responses to birdsongs
J.-Y. Hong, K. Ooi, B. Lam, Z.-T. Ong and W.-S. Gan 4839

Developing a linguistic corpora-based soundscape questionnaire: addressing translation challenges in the ISO Standard
M. Ferretti, D. Chiarella, A. Cinini and P. Cutugno 4843

The role of pleasantness mapping in a University campus for studying soundscape subjective perception in evolving environments
A. Mascolo, D. Rossi, M. Grimaldi and C. Guarnaccia 4847

Psychoacoustic Assessment of loud vehicles recorded by a noise radar
A. Fiebig, M. Diechmann, P. Kolingba-Froidevaux, A. Mundt and M. Schuck 4855

Soundscape analysis according to ISO/TS 12913-2:2018: A case study for areas of high heritage value in Coimbra
L. Oliveira, A. Pereira, P. Amado Mendes and L. Godinho 4863

Collaborative learning in the diagnosis of the soundscape of the Historic Center of Morelia, Mexico
F. Rodriguez-Manzo and J. Á. García-Márquez 4869

Questionnaires and Acoustic Measurements in Longyearbyen Area During Winter and Summer Seasons
J. Wiciak, D. Mlynarczyk, P. Malecki and J. Piechowicz 4877

NoiseSens - a system for identifying noise offenders in road traffic
F. Fuhrmann, R. Ladstädter, M. Blass, A. Maly, A. Gregorac and F. Graf 4883

Session A17.05 Indoor soundscapes

Comparing Teachers' And Students' Perceptions Of School Soundscapes Through A Questionnaire-Based Study
H. Kurukose Cal, F. Aletta, J. Kang and P. Clarke 4889

A Systematic Review Of Perceptual Attributes For Indoor Soundscape Assessment In Primary School Classrooms
S. Syed, S. Torresin and C. Visentin 4897

Cross-modal effects on assessments of soundscape and IAQ in university classrooms
M. Pellegatti, C. Visentin, S. Torresin, F. Babich, P. W. Wargocki and N. Prodi 4905

Adaptive Comfort: Similarities and Differences Between the Acoustic and Thermal Domains
S. Yuksel Dicle, F. Aletta and J. Kang 4909

Thermo-Acoustic Perception In An Open-Plan Office: Influence Of Ventilation, Gender, And Headphones Under Similar Thermal Conditions
L. P. De Souza, A. P. Melo and R. Lamberts 4917

Characterizing New Modalities Of Shared Offices: A Diary-Interview Methodology To Inform Audio Augmented Reality Approaches
C. Boukhemia, N. Misdariis and M. Lagrange 4925

Noise Perception And Cognitive Effort In The New Civic Central Library Of Torino
A. Astolfi, M. Modica, I. Grozeva, D. Cetani, V. Martinelli, L. Shtrepi, L. Lavagna, A. Griginis, C. Pintore and M. Zampini 4933

Prison soundscapes and health effects: Insights from the literature
J. Chieng, L. Woodland, O. Williams and B. Fenech 4941

Soundscape attribute for the assessment of the acoustical environment in apartments
S. Lee, D. Kim and J. Ryu 4949

Clustering residential sound based on soundscape attributes
J. Kim and J. Ryu 4953

Effects of adding a natural and a mechanical sound to a polyclinic soundscape on spatial knowledge performance
D. Dalir 4959

Radiation and Spatial Characteristics of Masking Speaker Reproduced Sound in Residential Spaces and Its Impact on Masking Performance
D. Kim, S. Kim, Y. Kim, C. Yun, C. Eom and J. Ryu 4967

Auditory Processing-Driven Soundscape Design for Dementia: A Systematic Framework for Environmental Intervention
A. Talebzadeh, P. Devos and D. Botteldooren 4971

The Role of Salient Sounds in everyday indoor Soundscapes
S. Versümer, J. Steffens and P. Blättermann 4975

Soundscape experience mapping: A deep listening approach for eliciting older adults' perceptions of indoor soundscapes
T. Deacon, G. Bibbó, A. Singh and M. Plumbley 4983

Contribution to the measurement and assessment of indoor university soundscapes: a classroom experience
J. Vida Manzano, R. García Quesada and J. A. Almagro Pastor 4991

Session A17.06 Soundscape and inclusion, from theory to practice

Diversity In Soundscapes Studies: A Monochromatic Case On Nature
K. Van Den Bosch, K. Chatburn and A. Talebzadeh 5001

Multispecies Soundscape Character: Conceptualising Soundscape Character For/From Multiple Perspectives
U. Ruiz Arana and G. Cerwén 5007

Listening To Hospitals: Towards An Assessment Tool Of Audio Data Ethics For ICUs
A. Giglio, S. Lenzi, S. Spagnol and E. Özcan 5015

Characterizing the soundscape of Oncology Hospital Spaces at University Hospital 'Mother Teresa' (UHCT): Assessment of Patients and Staff
E. Alimadhi, E. Fasllija and A. Cani 5023

Rehabilitation exercises using spatial sound
K. Piątek and D. Mlynarczyk 5031

Exploring pedestrian perceptions of safety through Shared Space soundscapes
F. Pereira, R. Almeida, D. Machado, E. Sousa, W. L. Martens and E. Freitas 5037

Diversity Of Responses And Potential Conflicts In Inclusive Urban Sound Design – Preliminary Results From Interviews In Brighton (UK)
M. Cobianchi, L. Lavia and J. Drever 5045

Sunday Soundscapes: Foreign Domestic Helpers' Acoustic Contributions to Hong Kong's Public Spaces
R. Yue, P. Lindborg, L. H. Lam, A. L. Lin and Y. C. Kam 5053

Session A17.07 Hospital soundscape

The role of critical alarms in the ICU acoustic environment: A Pilot Study
E. Fasllija, E. De Ruiter, D. Gommers and E. Özcan 5061

Impacts of soundscape on healthcare workers' wellbeing
P. J. Lee and Z. Song 5069

Nurses' Interpretation Of ICU Soundscape: An Annotated Sound Level Measurement At Erasmus Medical Center
E. Özcan, K. Bogers, D. Gommers and S. Spagnol 5075

Session A18.01 Speech - General

Masker Type And Speaker Voice Cues Determine Masking Of Speech By A Single Talker
L. Rachman and D. Baskent 5085

Rhythm instruction to enhance ESP students' prosody: An acoustic study
L. Quesada Vázquez 5091

Slicer - A Tool for Efficient Stimuli Extraction from Large Speech Corpora
L. Eckert, S. Wepner and B. Schuppler 5101

The avatars speech intelligibility: comparison between two different speech generation methodologies for facial animation
F. Cioffi, M. Masullo, A. Pascale and L. Maffei 5105

The effect of congruence of virtual image and reverberation-induced speech on speech intelligibility
N. Hodoshima, K. Hamamoto, M. Mizumachi and K.-I. Sakakibara 5111

Session A18.02 Forensic phonetics and acoustics

Acoustic And Comparative Analysis In The Process Of Trans-Voice Hormonal Treatment
J. Alonso Nogales 5117

Digital Voices: An Analysis Of Speech Intelligibility Through Mobile Devices
R. Pérez Vargas and V. M. Rodríguez-Montaño 5125

Human-Machine Speaker Identification According To TOBI Principles
F. Bernal Ortiz 5131

Perception Of Audio Deepfakes In Spanish And Japanese: Effects Of Language, Speaking Style, And Voice Familiarity
A. López-Jareño, J. J. Romero, E. San Segundo and X. Wang 5139

Speech Clarity And Topic Relevance: Forensic Analysis In Varying Acoustic Environments
R. Pérez Vargas 5147

Perceptual evaluation of synthetic voice detection with dysphonic speakers
J. J. Romero, A. López-Jareño, E. San Segundo and J. Delgado 5153

Session A18.03 Speech production pathologies

Texture Analysis In Recurrence Plots For Pathological Voice Recognition
H. Fandiño-Toro, D. Torricelli and J.A. Gómez-García 5163

Automatic Speech Recognition for a Dysarthric Child Speaking Austrian German
L. Eckert and B. Schuppler 5167

Discriminating Parkinson's Disease from Normophonic Voices Using a SincNet model
J.A. Gómez-García, H. Fandiño-Toro and D. Torricelli 5175

Explainable Feature Selection for Dementia Recognition from Acoustic and Linguistic Cues
A. Gallardo-Antolín, I. Oiza-Zapata, J. Ferreiros-López, F. Fernández-Martínez and R. San-Segundo 5179

Session A18.04 Speech perception pathologies

Comparison Of DNN-Based And Traditional Hearing-Aid Algorithms For Sensorineural Hearing-Loss
M. Wouters, C. Wen, A. Fráter and S. Verhulst 5189

Modelling of distortions created by temporal interactions between pulses in CI users
F. Guérit, C. Garcia and R. P. Carlyon 5193

Perceptual evaluation of deep learning-based speech enhancement for hearing aids
M. Baig, E. Gusó, J. Luberadzka and U. Sayin 5197

Audio-Visual Feature Synchronization for Robust Speech Enhancement in Hearing Aids
N. Saleem, M. Gogate, K. Dashtipour, A. Hussain, U. Anwar, A. Adetomi, A. Tughrul and A. Hussain 5205

Assessing Speech Processing HA/CI Advancements for Naturalistic Field Testing: Advancements with the CCi-MOBILE Research Platform
J. H.L. Hansen, J. N. Saba, H. A.F. Younis, T. Lawson, S. O. Okei and H.-T. Chiang 5213

Session A18.05 Speech technologies: diarization, emotion, enhancement

Localize, Filter, Segment: Towards Multi-Microphone Speaker Segmentation
T. Mariotte 5221

Temporal Segmentation Strategy to Improve Speech-Based Anger Detection using YAMNet
F. Zhu-Zhou, R. Gil-Pita, D. Tejera Berengué, G. Corral García, M. Zurera-Rosa and M. Utrilla-Manso 5229

Towards Interpretable Emotion Recognition: Identifying Key Features with Machine Learning
Y. Kaloga and I. Kodrasi 5237

Developing a novel multimodal speech enhancement intelligibility evaluation metric: Addressing the limitation of traditional objective measures
A. Hussain, M. Gogate, K. Dashtipour, N. Saleem, A. Goman, A. Tughrul, A. Sheikh and A. Hussain 5247

Session A19.01 Numerical, computational and theoretical acoustics - General

Optimizing Volume Penalization for Acoustic FDTD Simulations: Modeling Errors and Parameter Selection
Y. Schubert and M. Lemke 5257

Generation of sound waves by nonlinearly evolving two-dimensional coherent structures on a turbulent subsonic mixing layer
Z. Zhang, W. Ji and X. Wu 5261

Data-driven discovery of nonlinear wave equations in weak formulation
A. Furmanová, V. Hruška and T. Filipska 5269

Uncertainties and Efficiency of Bayesian Decay Analysis
N. Xiang and Z. Sü Gül 5275

Acoustic Field Reconstruction in Tubes via Physics-Informed Neural Networks
X. Luan, K. Yokota and G. Scavone 5279

Machine learning for modelling band structure properties
A. Furmanová, V. Hruška and A. Bajicová 5287

Session A19.02 Numerical methods for acoustics and vibration

Identification of acoustic characteristic of tweeter loudspeakers for car cabin sound quality simulations
E. Garofalo, G. Costa, G. Isacchi, S. Talucci, M. Olivieri, M. Ebri and F. Ripamonti 5293

Development and comparative analysis of novel Component Mode Synthesis Methods for structural and acoustic applications
S. El Kadmiri Pedraza, S. Algermissen and H. P. Monner 5301

Reduced-order transient simulations of the convected wave equation with perfectly matched layers
Y. Cai, G. Gabard, S. Van Ophem, W. Desmet and E. Deckers 5309

Application of Craig-Bampton reduction in vibro-acoustic coupling
S. El Kadmiri Pedraza, S. Algermissen and H. P. Monner 5317

Applicability of the Discontinuous Galerkin method for outdoor noise propagation simulations
F. Kraxberger, J. Heinz, A. Wurzinger, M. Kaltenbacher, S. Schoder and C. Adams 5325

Isogeometric FEM/BEM approach for a coupled acoustic fluid-structural interaction systems
A. M. Shaaban and S. Marburg 5329

On the usage of acoustic radiation modes for Krylov subspace reduction of acoustic finite element models in the time domain
S. Van Ophem 5333

Reconstruction Of Radiated Acoustic Fields Using 3D Laser Vibrometry And FEM Simulation: A Comparative Study Of Interpolation Approaches
P. Nieradka, M. Veloso, J. Jóska, B. Chmielewski, M. Kozupa and G. Kmita 5337

Investigation of the influence of slip-operators on ultrasound pulse-based sound generation principles
D. Mayrhofer, T. Wilczacki and M. Kaltenbacher 5343

Investigation of Memory Efficient Convolutional Truncation Methods for the 2D Time Domain Boundary Element Method
D. Kılıçarslan, D. Panagiotopoulos and E. Deckers 5351

Using open software modeling tools for innovative transducer designs
M. Moszyński, I. Pérez Arjona and V. Espinosa Roselló 5359

An Absorbing Boundary Condition Formulation For Fast Frequency Sweep Of Unbounded Acoustic Finite Element Problems
P. Mariotti, H. Mao, S. Schopper and R. Rumpler 5363

Session A19.05/A10.06 Numerical methods for acoustic materials and metamaterials

Design and Optimisation of a Multi-Layer Porous Barrier with Tunable Resonators
L. Sousa, L. Godinho and P. Amado Mendes 5373

Periodic boundary conditions in finite difference time domain
J. Galiana Nieves, R. Picó, D. Ramírez-Solana and J. Redondo 5381

Non reciprocity in spatiotemporal sonic crystals
J. Galiana Nieves, J. Redondo, V. J. Sánchez-Morcillo and R. Picó 5389

A meshfree approach for sound wave propagation in periodic media with multi-layer porous inclusions
L. Godinho, N. Herrera-Leon, P. Amado Mendes, A. Pereira and J. Redondo 5395

Model-based auralization of vibro-acoustic metamaterial partitions
L. Van Belle, F. Di Giusto and E. Deckers 5399

Geometrical optimisation of an acoustic metamaterial for low-frequency sound absorption
M. L. López Ibañez, A. Melis, J. Muñoz-Paniagua, C. Díaz and E. Latorre Iglesias 5407

Investigation of Stop Band Behavior in complex finite Vibroacoustic Metamaterial Structures using a Power-based Method
H. Atzrodt, A. Maniam, N. Kleinfeller and S. Rieß 5415

Session A19.06/A07.05 Methods for advanced computational aeroacoustics

Separating aerodynamic from acoustic-induced velocity on a portion of an acoustic liner through modal decomposition methods
F. Scarano, B. Lyu, A. Paduano and F. Avallone 5423

Prediction of in-duct aeroacoustic noise of a mechanical ventilation system
R. Sevenois 5431

Acoustic Propagation Through Diffuse Interfaces
A. Ballout, O. A. Marino, G. Rubio and E. Ferrer 5437

An Advanced Boundary Integral Formulation for Sound Scattered by Deforming Bodies
B. De Rubeis, M. Gennaretti, G. Bernardini and C. Poggi 5441

Sound source identification based on balance of acoustic energy
J. Kreuzinger and F. Schwertfirm 5449

Stability investigations of solid wall immersed boundary schemes for the linearized Euler equations in multidimensions
M. G.S. Izsak and H.-J. Kaltenbach 5453

Numerical And Experimental Zig-Zag Trip Effects On A Low Reynolds Number Propeller
M. Lattari, A. Beck, G. C. Vicente, F. D. Silva, J. P. L. C. Salazar, J. A. Cordioli and C. J. Deschamps 5463

Session A19.07 Validation and benchmarks in computational acoustics

Validation study of broadband numerical methods for room acoustic simulations and binaural rendering in a furnished room
H. Sampedro Llopis, S. Guðjónsson, M. Cosnefroy, H. Hafsteinsson and F. Pind 5471

Benchmarking Room Acoustic Sound Particle Simulations incorporating Uncertainty-Based Diffraction: Challenges and Strategies
I. Herrero-Durá, T. Judd, S. Weigand, J. Hörmeyer and J. Schaal 5477

Acoustic characteristics of an open-fan model from semi-analytical predictions and wind tunnel measurements
C. Polacsek, V. Daydé-Thomas, S. Fauqueux, J. Mardjono and M. Descamps 5485

Comparing Open Source Room Acoustics Simulation Tools: Performance and Usability Insights
L. Dijkman, N. Hoekstra and M. Hornikx 5493

Input data for room acoustic simulations: ray-based vs hybrid models of a rectangular room
G. Fratoni and D. D'Orazio 5501

Testing of commercial software to generate simulated impulse responses for Personal Sound Zones systems
D. De La Prida, G. Piñero, L. Fuster and L. A. Azpicueta-Ruiz 5505

Measures of validation for computational room acoustics
A. Prinn, Z. Xu and E. Habets 5513

Numerical validation of VLES-LBM for predicting aerodynamic and acoustic phenomena in propeller-wing ultra-tight separation distances
M. Lattari, A. Beck, L. T. Moresco, F. D. Silva, J. P. L. C. Salazar, J. A. Cordioli and C. J. Deschamps 5521

Unlocking the Potential of Open Research Software in Acoustics: lessons learned from the Nantes workshop
M. Hornikx, H. Wang, I. Fichera, S. Willemsen and L. Paganini 5529

Session A19.08/A10.10 Numerical methods for wave propagation in complex media

Streamlined model of porous media for Finite Difference Time Domain schemes
P. Camblor Iglesias, L. Godinho and J. Redondo 5539

Inspection of welding joints using elastoacoustic signals via topological derivative
C. Placinta, S. Muñoz and M.-L. Rapún 5547

Numerical Quantification Of The Bivalve Presence In Granular Sediments On Coastal Seabeds
A. Prieto and P. Rubial 5553

DG-Trefftz method with radiating boundary conditions imposed via the NtD map: Analysis on a waveguide
P. Monk, M. Pena and V. Selgas 5555

A 3D finite element model of ultrasonic waves travelling through pervious concrete
A. Spalvier, N. Pérez, P. Garcén, L. Hernández and G. Cetrangolo 5559

Generalized plane wave quasi-trefftz spaces for wave propagation in inhomogeneous media
I. Fontana and L.-M. Imbert-Gerard 5565

Efficient Simulation Of Time-Domain Acoustic Wave Propagation In Unbounded And Penetrable Media
V. Dominguez, M. Ganesh and F. Le Louër 5573

On the Acoustic Investigation of Complex Buildings materials by Physics Informed Neural Networks (PINN)
S. Ryehan, I. Z. Soma and J. Naumann 5581

Session A19.09 Numerical methods for room acoustics

Session A20.01 Transportation noise and vibration - General

A source model for airborne noise from ship traffic in fairways
A. Genell and A. Gustafson 5593

Rolling resistance and Rolling noise assessment of bituminous mixtures
M. Ramón Martínez, V. Fernández Vázquez, F. J. Terán Sierra, Á. M. Martínez García-Hoz and S. Expósito Paje 5601

Analysing the Effect of undetected flights in the comparison of measured and modelled aircraft noise
R. Van Der Grift, A. S. Jayanthi, M. Snellen and A. Amiri-Simkooei 5607

IOTA: A positional data processing software for aircraft noise simulations
T. Ramseier, M. Gligorijevic, S. Plüss and B. Schäffer 5615

Session A20.02 Automotive noise and vibration

Modeling of the load transmissibility up to 300Hz of an vehicle air suspension
J. Jang, J. Lee, S. Park, J. Jung, S. Lee and B. Sohn 5623

Comparing Measured Pass-by Levels of Accelerating Battery Electric Cars and Combustion Engine Cars
A. Heusser, J. Jäggi, M. Elser, S. Grunder and R. Pieren 5627

Psychoacoustic assessment of synthetic sounds for electric vehicles in a virtual reality experiment
P. Bazilinskyy, M. S. Alam and R. Merino-Martinez 5635

The use of virtual reality for the subjective evaluation of vehicle cabin interior refinement levels
E. Harry and R. M. Kirby 5643

The determination and ranking of interior cabin noise sources via advanced matrix manipulation
E. Harry and R. Morris-Kirby 5647

XAI based Frequency-Time feature Extraction and development of an optimal evaluation method for C-EPS
J. Park, H. Jo, I.-J. Cho, J. Seo, S.-S. Yoo, S. Lee, S.-J. Bang, J.-L. Oh, C. Jeong and S.-Z. Cho 5653

Research on Integrated Virtual Component Sound System
B. Kang, H. Jo, J. Seo, K. Park and K. Baek 5661

Session A20.03 Road traffic noise and vibration

Loudspeaker Array-Based Auralization of Electric Vehicle Noise in Living Environments
L. Müller, J. Ahrens and W. Kropp 5669

Comprehensive Frequency Spectrum Analysis of Metro Rail Noise for Environmental and Acoustic Insights
V. Laxmi and H. Phuleria 5677

Model-Based Approaches for Acoustic Pavement Characterization
U. Pachale, F. Georgiou, J. Jäggi, D. Wöllstein, A. Heusser and R. Pieren 5681

Evaluation Of Road Noise Prediction Models In Ireland: A Comparison Of CNOSSOS-EU And CRTN Source Models
P. Redondo Martinez and E. King 5685

Impact of the choice of road traffic speed data on modelled environmental noise
A. Sheehan, S. Beevers, A. Beddows and J. Gulliver 5693

Microscopic and Dynamic Road Traffic Noise Model Coupled with a Vehicle Recognition and Tracking Video Analysis Tool
D. Rossi, A. Pascale, A. Mascolo, M. Coelho and C. Guarnaccia 5701

Experimental Assessment of Different Car Driving Styles and Their Role in Road Traffic Noise Annoyance Reduction
M. Czuka, A. Fiebig, M. Schuck, M. Conter, C. Moshona, M. Chudalla and F. Strigari 5709

A case study of prediction accuracy of ASJ RTN-Model 2023 on Japanese general roads
K. Yamauchi and K. Yoshimura 5717

Comparison of a Stochastic and Microscopic Road Traffic Noise Models Using Variable Level of Aggregation of Traffic Flows
A. Mascolo, D. Rossi, M. Nigro, B. Gauvreau and C. Guarnaccia 5725

Acceleration Noise From Electric Cars Matters
S. Baclet and R. Rumpler 5733

Design of Vibration Isolation system for Multiple number of Spacecrafts Transportation Container
D. S. Srivastava, S. Sahu, B. P V and R. V. Nadagouda 5741

Relative importance of road traffic in the temporal structure of city noise
J. M. Barrigón Morillas, D. Montes-Gonzáez, G. Rey Gozalo and R. Vílchez-Gómez 5747

Challenges In Real-Time Low-Cost Vehicle Recognition Systems For CNOSSOS-EU Input
L. Fiorella, D. Profumo, F. Petrongolo, G. De León, F. Artuso, L. Fredianelli, G. Licitra and E. Ascari 5755

Audio-Video Acquisition System For Dynamic Road Pavement Monitoring
F. Petrongolo, L. Fiorella, G. De León, D. Profumo, F. Artuso, A. Monticelli, F. D'Alessandro, E. Ascari, G. Licitra and L. Fredianelli 5761

Session A20.04 Tyre/road noise

New road surface source correction factors for Nord2000 calculations in Sweden
A. Genell and A. Gustafson 5771

Image-based prediction of noise: a two-step conceptual model
F. G. Praticò and V. N.K. Mypati 5779

Machine Learning techniques for tyre rolling noise on rubberized asphalt roads
S. Kanka, F. Artuso, A. Moro, F. Fidecaro and G. Licitra 5785

In-situ evaluation of tyre/road noise of a pavement based on footwear waste
N. Campillo-Davo, R. Peral-Orts, H. Campello-Vicente, M. Fabra-Rodriguez, D. Abellan-Lopez, A. B. Muñoz-Milan, B. Mateu-Romero and F. Aran-Ais 5791

Long-term tyre/road noise comparison of different road surfaces measured by CPX method
P. Markova, B. Hablovicova and V. Krivanek 5797

Influence of velocity on the frequency spectra of SMA 11 road surface measured by CPX method
B. Hablovicova, P. Markova and V. Krivanek 5803

Session A20.05 Railway noise and vibration

Method for Railway Noise Event Detection: experiment using Medusas sensors
M. Hellot, M. Sineau and C. Mietlicki 5811

GENIFER feasability study - Assessing railway noise instantaneous annoyance with in-situ listening test
M. Hellot, R. Mafféis, M. Sineau, A.-S. Evrard and J.-P. Regairaz 5817

VibraSIG - Modeling railway structure-borne noise and vibrations and implementation in QGIS geographic information software
R. Walther 5825

Framework for the assessment of uncertainty of high-speed train pantograph aerodynamic noise predictions
E. Latorre Iglesias, G. García Barrios, M. L. López Ibañez, A. Melis, J. Muñoz Paniagua and D. Thompson 5831

BIM-Based Noise Protection Planning in Railway Infrastructure
J. Bartnitzek, L. Höhle, J. Egeler, A. Schlesinger, M. Liepert, C. Huth, C. Ende, D. J. Meyer, T. Koch, B. Schlüter and R. Böhme 5839

The influence of nonlinear behaviour of reinforced concrete structures on numerical modelling for vibration
M. Österreicher 5845

A method for track-independent railway vehicle characterization as ground-borne vibration sources based on blocked forces
R. Arcos, A. Clot, Y. Shafieyoon and J. Meggitt 5851

Study of the effect of ballast properties and wheel geometry on rolling noise
E. M. Sánchez Orgaz, V. T. Andrés, J. Martínez Casas and F. D. Denia 5859

Session A20.06 Noise barriers and mitigation techniques for road traffic and railway

The design of a sonic crystal noise barrier for an evolving urban area
G. Fusaro and M. Garai 5865

Noise barriers: what really matters and what doesn't?
J. P. Clairbois, P. Houtave and M. Garai 5869

Assessment of efficiency of WHIStop diffractor for road traffic noise abatement
E. King, S. Horsman and M. Manohare 5875

The ECODRIVE Project: Traffic Management and Control Measures to Mitigate Road Traffic Noise
T. Onorato and P. Bellucci 5883

Session A20.07 Aircraft noise

AAVT: A Tool To Run Virtual Surveys With Passing Aircraft
G. Isherwood, J. Eccles and G. Memoli 5893

Exposure-response relationships between aircraft noise and annoyance or sleep disturbance for Dutch civil and military airports
M. Reedijk, R. Van Poll, J. Hoekstra, W. Swart, J. Van Der Kassteele, A. Sahai and D. Houthuijs 5901

Sound Characteristics and Perception Study of new Generation of Turbofan Aircraft
R. Aalmoes, N. Sieben and S. Nolet 5907

Indoor and Outdoor Noise perception of communities near Schiphol Airport
N. Sieben and R. Aalmoes 5915

Krueger flap noise generation on a semi-span aircraft model
L. Sanders and M. Pott-Pollenske 5923

Aircraft Noise-Induced Annoyance Analysis Using Psychoacoustic Listening Experiments
R. Merino-Martinez and V. S. Buzetelu 5929

Evaluation Of Audio-Visual Parameters In The Perceived Aircraft Noise Annoyance In Virtual Reality Experiments
S. A. Priboi and R. Merino-Martinez 5937

Low-Noise Propeller Optimization Via Blade Sweep And Uneven Spacing
F. Fruncillo, P. Luchini and F. Giannetti 5945

Community And Cabin Noise Assessment Of A 19-Seater Hydrogen-Electric Airliner
M. Barbarino, G. Fasulo, A. Pagano, A. Visingardi, F. Morlando, F. Petrosino, M. Zupanič and J. Drofelnik 5953

Exploring Acoustic Signatures of Different Aircraft Types and Operations Using Advanced Data Analysis
I. Besnea, A. Amiri-Simkooei, I. Dedoussi and M. Snellen 5961

Session A21.02 Applied sound-driven design

Mitigating Motion Sickness in Electric Vehicles Through Active Sound Design
S. Kim, J. Yang and M. E. Altinsoy 5971

Sound design in beauty tech: improving the sounds of hair dryers
A. Bhatara, A. Suwanto, S. Romagny and D. Morizet 5975

Design and evaluation of the SoundAsleep app: the impact of emotional states on sound preferences for sleep
S. Hallak, A. Choubey and S. Pauletto 5983

SoundAI: Exploring culture-sensitive and environmentally-conscious applications for AI-supported sound-driven design
E. Özcan, S. Mora, F. Duarte and S. Lenzi 5991

From Research to Practice: A Collaborative Approach to Tackling Alarm Fatigue in ICUs
I. Bostan, R. Van Egmond, D. Gommers and E. Özcan 5999

Experimental Evidence Shows that Auditory Icon Clinical Alerts Work Better than Tones
J. Edworthy 6007

Session A21.03 Listening experience in sound-driven design

Rotary Engine Essence Utilization for In-Car Sounds Driven Design
M. Yamamoto, S. Ishimitsu, Y. Mitsuda, S. Fujikawa, K. Iwata, M. Kikuchi, M. Matsumoto, S. Kodama and H. Inaki . 6013

Listening and talking about sound: exploring effective descriptors for everyday sounds with non-expert listeners
D. Larsson Holmgren, N. Misdariis and S. Pauletto 6019

Exploring the benefits and boundaries of auditory representations in service design
A. Kuštrak Korper, J. Blomkvist and V. Rodrigues 6029

Investigating strategies in a sound design for sustainability exercise in an educational setting
G. Marentakis and S. Delle Monache 6033

A Design Guideline For Gamified Intervention For Managing Hyperacusis: Insights From Expert Interview
Q. Liu, T. Wang, H. Yang and E. Özcan 6041

Session A21.04 Methodologies for sound-driven design and education

From framework to practice: Les_Sons, a product sound tool for design education
S. Delle Monache, T. Delfrap, N. Misdariis, D. Murray-Rust and E. Özcan 6051

Designing Sounds For Exhibitions: Tools To Enhance Sound-Driven Design Strategies
M. Riva and R. Trocchianesi 6059

Sound-Driven Design in Astronomy: the long-term impact of design and evaluation activities on the development of astronomical data sonification tools
S. Pauletto and N. Misdariis 6067

Acoustic Design Case Studies Of Educational Spaces For Neurodivergent Individuals
F. Bettarello, M. Di Prisco, G. Scavuzzo and M. Caniato 6075

Session A22.02/A02.02 Underwater soundscape and noise: modelling, measurements and effects

Comparative analysis of three underwater soundscapes
J. Ramis-Soriano, P. Poveda Martinez, J. Carbajo San Martín, A. Forcada Almarcha, C. Valle Pérez and N. Ullah 6083

Numerical modeling of low frequency sound propagation in three dimensional shallow marine environment with solid seabed
P. Klin and U. Tinivella 6091

Acoustic indicators of ecosystems' and energy dynamics in marine environments
A. Pomaro and P. F. Moretti 6095

An Optimized MATLAB Software Package for the Analysis and Characterization of Underwater Sound Produced by Wind Farms
J. A. Díaz, S. Neves and E. Delory 6101

Advanced far-field vibro-acoustic modeling of underwater pile driving for offshore noise mitigation
J. Perchaud, M. Fruchart and C. Lagarrigue 6107

The Hidden Patterns of Marine Soundscapes:A Better Approach for Identifying and Counting Sources of Sound in Marine Areas of Special Conservation
F. L. Rosa González, J. P. Lüke, S. Garcia Beitia and J. Almunia Portoles 6113

New Methods For Studying Underwater Noise Effects On Microscopic Sessile Marine Invertebrates: Challenges And Perspectives
L. Manni, G. Sabbadin, S. Domenichi, L. Ballarin, V. Zaffaroni-Caorsi and G. Zambon 6117

On the problem of underwater sound mapping in shallow waters: a case study
A. Aguirre, E. Robles Arnao and E. Ruiz 6125

Acoustic characterization of Panarea's hydrothermal system
S. Viola, D. Bonanno, L. S. Di Mauro, D. Diego-Tortosa, C. Gomez Garcia, A. Idrissi, G. Riccobene and S. Sanfilippo . 6131

Vibro-Acoustic Study Of A Small Glass Walled Fish Tank: An Experimental And Theoretical Approach
N. Ullah, J. Carbajo San Martín, P. Poveda Martinez and J. Ramis-Soriano 6135

Underwater noise survey in the Turku Archipelago
V. Hongisto, R. Alakoivu, O. Outinen, J. Sahlsten and O. Loisa 6143

Methodology For Underwater Noise Level Measurement From Dredging Activities
S. Nuñez Gutierrez and D.P. Ruiz Padillo 6147

An Open Dataset for Exploring Underwater Soundscapes and Vessel Noise in Barcelona, Constanța and Lagoon of Venice Basins
I. Nou-Plana, A. Teaca, F. Gazzada, M. Freixes, G. Zambon and R. M. Alsina-Pagès 6155

Streamlining Underwater Acoustic Propagation Modeling with a Python-Based Interface
I. Urtiaga Chasco and A. Hernández Guerra 6163

Sounds generated by a fixed offshore oil and gas platform during production periods
N. Pérez Gimeno, J. L. Cueto-Ancela and E. Nava Baro 6169

Acoustic study of diving sperm whales during a week of continuous monitoring in the western Ionian Sea
V. Sciacca, A. S. Briguglio, F. Caruso, L. S. Di Mauro, F. Filiciotto, C. Pellegrino, G. Riccobene, F. Simeone and S. Viola 6177

The Marine Soundscape of Kongsfjorden, Svalbard: Two-Year Study on Spectral Variability and Environmental Drivers
V. Sciacca, M. Azzaro, G. De Vincenzi, F. Giglio, P. Giordano, L. Langone, S. Miserocchi, F. Paladini De Mendoza and F. Filiciotto 6181

Exploratory Study On The Acoustic Characterization Of Transit And Trawling Noise From Fishing Vessels In The Strait Of Sicily
S. Ferri, G. Sorrentino, R. Grammauta, G. Milisenda and F. Caruso 6185

The Project KNOWHALE: Improving Knowledge On Fin Whale Acoustic Occurrence And Behaviour In The Central Mediterranean Sea
G. De Vincenzi, F. Caruso, S. Ferri, F. Filiciotto, L. Beranzoli, V. Cardin, S. Miserocchi, T. Sgroi and V. Sciacca 6191

SOS Bass project: acute and chronic effect of vessel noise disturbance on farmed fish
D. Bertotto, F. Filiciotto, T. Gaggero, L. Marinelli, C. Guérineau, M. Bortoletti, A. Meloni, F. Colotto, V. Sciacca and P. Mongillo 6195

Communicating in noisy waters: how shipping noise and environmental conditions affect blue and fin whale calling activity
Z. Groenewoud, M. Baumgartner and A. Širović 6199

Session A22.03 Communication, positioning and acoustic sensor systems

Time synchronization of long-term underwater acoustic observations: the challenge of autonomous hydrophones without global clock baseline
D. Nazarpour, P. F. Moretti, S. Buogo and A. Pomaro 6205

Design Of An Autonomous Low-Cost Acoustic Acquisition System Based On Intensimetric Sensors For Underwater Acoustics Scenarios
J. D. Pastor Sar, J. Carbajo San Martín, P. Poveda Martinez, J. Ramis-Soriano and E. G. Segovia-Eulogio 6213

Design And Fabrication Of An Acoustic Leaky-Wave Antenna For Underwater Applications
A. Fernández-Garrido, M. Campo-Valera, R. Picó, E. Abdo-Sánchez and R. Asorey-Cacheda 6221

Studies On The Conceptual Design Of An Acoustic Sensors Array For Neutrinos Event Triggering
C. A. Quiroz Rangel, M. Ardid, D. Diego-Tortosa, G. Riccobene and S. Viola 6227

Session A22.04 Traffic ship noises

Interacting Multiple Model Target Tracking Algorithm for Underwater Maneuvering Targets Based on Transformer
Y. Liu, T. Ji, X. Ma, X. Wang, C. Feng, P. Li and Y. Hu 6235

The Spatio-Temporal And Frequency Modeling Of Deep-Sea Surface Reverberation Caused By Different Waveforms
X. Wang, X. Pei, X. Ma, C. Feng and Y. Liu 6243

The Italian Ocean Sound monitoring sub-system for the 'Italian Integrated Environmental Research Infrastructures System (ITINERIS)' project
S. Sanfilippo, D. Bonanno, L. S. Di Mauro, D. Diego-Tortosa, A. Idrissi, G. Riccobene and S. Viola 6251

Impact of Maritime Traffic Noise on Juvenile Dicentrarchus labrax
P. Giner Tarazona, I. Pérez Arjona, J. Ramis-Soriano, V. Espinosa Roselló, M. Mauro, P. Poveda Martinez, V. Arizza, M. Vazzana, A. Vizzini and R. De Luca 6259

The characteristic spectrum of vessels in different European basins
G. Zambon, F. Gazzada, I. Nou-Plana and R. M. Alsina-Pagès 6263

Modeling of a ship sound recorded by an ocean bottom seismometer
S. Pinson 6269

Ship Propeller Non-Cavitating Noise In Non-Uniform Flow
M. Brun, S. Pinson, J. Carpentier and J.-A. Astolfi 6275

The OceanSoundModel: a GUI for shipping noise predictions
O. C. Rodríguez, S. Jesus, H. Chognot and L. O. Júnior 6283

Session A22.05 Geophysics and Distributed Acoustic Sensing (DAS) capabilities

Trans-dimensional Bayesian matched-field inversion for seabed geoacoustic profiles
S. Dosso and J. Bonnel 6293

Optimization Of Sparse Sampling And Interpolation For Seismic Data Compression Using A Genetic Algorithm
N. Giovanardi, L. Lobato, J. Leal Filho and S. Paul 6297

Advances in Optoacoustic Technologies for Monitoring the Ionian Sea
D. Diego-Tortosa, S. Aurnia, G. Cappelli, M.-A. Gutscher, C. Gomez Garcia, A. Idrissi, L. Quetel, G. Riccobene, A. Tricomi and S. Viola 6303

Assessment On The Potential Of Distributed Acoustic Sensing In The Gulf Of Catania
A. Idrissi, D. Diego-Tortosa, L. S. Di Mauro, F. Grenga, C. Gomez Garcia, G. Laudani, G. Riccobene, S. Sanfilippo, A. Tricomi and S. Viola 6311

Pre-stack Seismic Data Compression Using U-net-Based Predictors
J. Leal Filho and S. Paul 6319

Underwater sound detection with taut, vertically suspended fibre-optic cable and distributed acoustic sensing
J. D. Pelaez Quiñones, P. J. Thomas, S. Bjørnstad and P. Lunde 6327

Lossy Compression for Distributed Acoustic Sensing
L. Eckert, V. Dumitru and M. Hagmüller 6331

Session A23.01 Vibroacoustics

Predicting the vibroacoustic response of an elastic hydrofoil in a turbulent flow
P. Williams, M. Karimi, J. Kha, K. Tsigklifis and R. Howell 6341

A Method for Measuring Instantaneous Structural Intensity in Flat Structures
K. Abe, H. Yamada and T. Yamazaki 6345

Finite Element Model Update of an Aircraft Interior Lining Panel
S. Algermissen 6353

Theoretical and experimental analysis of vibro-acoustic coupling at high levels: application to the design of passive absorbing devices
R. Moussa, A. Givois and N. Dauchez 6361

Measurements of flexural wave properties on viscoelastic panels using a laser Doppler vibrometer
N. Xiang, J. Taylor and M. Miller Iii 6369

Session A23.05 Metamaterials and acoustic black holes in vibro-acoustics

Session A24.01 Virtual acoustics - General

Psychoacoustic evaluation of a pilot system for simulating diverse room acoustics for musicians
L. Bartha, M. Isenegger, A. Taghipour, D. Rose, E. Alessandri and S. Köchli 6377

IR64-CAR: A Dataset Of Impulse Responses Captured With A Spherical Microphone Array For Automotive Acoustic Research
J. López-Ballester, G. Greco, S. Roger, J. J. López, F. J. Ferri and M. Cobos 6385

Cylindrical harmonic decomposition of the sound intensity vectors
J. Wang and T. Abhayapala 6393

Hearing Protection Device with AI-Based Sound Detection and Localization
L. Banchero and J. J. López 6401

Addressing Acoustic Simulation Pitfalls in Virtual Reality for Occupational Safety Research
M. Cuevas-Rodriguez, D. González-Toledo, A. Lawson, N. Keren and A. Reyes-Lecuona 6409

Spatial localisation and level accuracy in the detection of a moving source using a delay-and-sum beamformer
A. Osses, B. Ackermans, H. Nuijens, R. Sweep and M. Hornikx 6417

VR-PTOLEMAIC: A Virtual Environment for the Perceptual Testing of Spatial Audio Algorithms
P. Ostan, F. Del Gaudio, F. Miotello, M. Pezzoli and F. Antonacci 6425

Trends in the use of Virtual Reality for acoustic investigation of the built environment
T. Vovk and R. Prislan 6433

Presenting the 'Diamonds Room'
J. Grassi, M. Pellegatti, N. Prodi, C. Visentin, G. Tampone, A. Bertelli and L. Tebaldi 6441

Session A24.05/A14.08 Virtual acoustics and binaural AR in hearing research: challenges of a new paradigm

Impact of Room Acoustic Mismatch on Conversational Dynamics in Virtual One-On-One Conferencing: Preliminary Study
P. Abehsera-Morell, D. Poirier-Quinot and B. F. G. Katz 6447

Relating Room Acoustic Rating Consistency to Binaural Masking Level Difference Scores
F. Stärz, S. Van De Par, L. O.H. Kroczek, S. Roßkopf, A. Mühlberger and M. Blau 6451

New Release of the Binaural Rendering Toolbox: Introducing Version 2.0
D. González-Toledo, M. Cuevas-Rodriguez, L. Molina-Tanco, L. Picinali and A. Reyes-Lecuona 6457

Accommodation to virtual sound rendering in a reverberant room with 3DoF and 6DoF interaction
J. Meyer and L. Picinali 6465

Perceptual sensitivity to the “open window” in late reverberation
B. Seeber, P. Weymar, S. Ewert and S. Van De Par 6473

Vision-To-Audio Vs Audiovision-To-Audio Matching Shows The Difference Between Virtual Acoustics For VR And AR
N. Meyer-Kahlen, L. Qiu, T. Lokki and J. M. Arend 6477

The Extended SONICOM HRTF Dataset And Spatial Audio Metrics Toolbox
K. Poole, J. Meyer, V. Martin, R. Daugintis, N. Marggraf-Turley, J. Webb, L. Pirard, N. La Magna and L. Picinali 6483

Enhancing Photogrammetry Reconstruction for HRTF Synthesis via a Graph Neural Network
L. Pirard, K. Poole and L. Picinali 6487

Session A24.06 Virtual reconstructions in archaeoacoustic research

Session A24.07/A11.06 Networked music performances and virtual environments

Soundcool: Enabling Easy-to-Configure International Collaborative Performances with Minimal Technical Knowledge and AI
J. Sastre, F. Valero-García, R. Dannenberg, J. Andrés, S. Scarani and N. Lloret 6497

Exploring the Acoustic Characteristics that Determine Performance Quality in Opera Singing
H. Kondo, S. Kondoh, S. Kawahara and S. Fujii 6503

Latency evaluation and modeling of a mechatronic display for telematic music
M. Gurevich, R. B. Gillespie, J. Yi, K. Sodum, K. Abellera, J. Granzow, S. Sumner and L. Rogland 6511

Artificial IRs in Dynamic Virtual Acoustics for Music Experimentation
L. Valentin and C. Betancur Gutierrez 6519

Session A24.09/A24.13 Motion and rendering

Dynamic loudspeaker equalization for participant movements in a loudspeaker array
M. Kuntz and B. Seeber 6527

Real-time Virtual Environment and Room Acoustics Simulator
K. De Haas, M. Schutte and S. Ewert 6533

Auralization in a moving base driving simulator as part of a digital twin
A. Genell and T. Lundberg 6541

Train Passing Synthesis in Environments Based on Geospatial Data
M. Liepert, A. Schlesinger, J. Egeler, C. Huth, C. Ende, D. J. Meyer, T. Koch, L. Höhle, J. Bartnitzek, B. Schlüter and R. Böhme 6545

Measurement-Based Sound Source Modeling of Moving Vehicles for Auralizations Utilizing Acoustic Beamforming
T. Kron, D. J. Meyer, T. Koch, C. Ende, J. Egeler, A. Schlesinger, J. Bartnitzek, L. Höhle, B. Schlüter and R. Böhme 6549

A Preliminary Evaluation Of Rendering Techniques For Room Impulse Responses
R. Roy Chowdhury, I. Engel and L. Picinali 6557

Exploring simple methods for room absorption estimation in early reflections for binaural audio rendering
P. Gutierrez-Parera, F. Arrebola, M. Cuevas-Rodriguez, D. González-Toledo, L. Molina-Tanco and A. Reyes-Lecuona 6565

Perception of Simulated Moving Sound Sources in Reverberant Virtual Audio-visual Environments
S. Fichna, S. Van De Par, V. L. Flanagin and S. D. Ewert 6571

Complex room acoustics rendering with multi-zone auralization: Application to Teatro Principal de Valencia
J. López-Ballester, J. Segura-García, M. Cobos, R. Cibrián, S. Cerdá and A. Giménez 6579

Session A24.11/A16.07 Processing/individualization/interpolation of HRIRs or BRIRs

HRTF Database Matching for Localization Accuracy Applications
E. Tavelidou, K. Bakogiannis and A. Andreopoulou 6589

Investigating the Effect of Skin and Hair Absorption on Numerically Simulated HRTFs
F. Brinkmann, T.-N. Wennemann and S. Weinzierl 6597

Evaluating Deep Learning Approaches for Photogrammetric Ear Scan Denoising in Head-Related Transfer Function Computation
F. Di Giusto, F. Lluis, S. Van Ophem and E. Deckers 6605

Session A24.13 Motion and rendering

DOI:

Main theme: A01 Active Control of Sound and Vibration

Session A01.02/A01.03 Active sound and vibration control

Chair(s): M. Pawelczyk, M. Misol

DOI: 10.61782/fa.2025.0899



FORUM ACUSTICUM
EURONOISE 2025

TOPOLOGY OPTIMISATION OF MICROPHONE ARRAYS FOR REMOTE MICROPHONE VIRTUAL SENSING IN DIFFUSE SOUND FIELDS

Achilles Kappis* **Jordan Cheer**
Institute of Sound and Vibration Research, University of Southampton, Southampton, UK

ABSTRACT

Past research has shown that virtual sensing techniques can enhance the performance of active noise control systems by projecting the control points towards remote locations of interest. However, accurate sound field estimation using virtual sensing is critical to the performance of such active control systems and depends on both signal processing and the physical microphone array. Typically, microphone placement is determined by practical considerations such as convenience, spatial constraints and cost, resulting in limited exploration of optimal microphone positioning. The current study employs a genetic algorithm to identify optimal microphone array configurations for accurate estimation of the pressure in a diffuse sound field, utilising the Remote Microphone Technique. The optimality criterion is defined as the estimation performance or the robustness of the derived topologies to practical uncertainties. The resulting optimal configurations are evaluated against a conventional uniform linear microphone array, which consist of sub-array elements capable of utilising both pressure and pressure gradient information for enhanced estimation accuracy.

Keywords: *Virtual sensing*, *Remote Microphone Technique*, *Microphone arrays*

1. INTRODUCTION

Virtual Sensing (VS) has been effectively integrated in to local Active Noise Control (ANC) systems such as the active headrest and has been shown to improve control performance [1, 2].However, this is reliant on accurate estimation of the sound field at the remote location of interest [1, 3]. In general, VS studies have focused on the use of physical microphone arrays with rather straightforward geometries, such as linear or circular arrays [4, 5]. Additionally, in many practical applications, microphone placement is dictated by constraints in the system such as limited space availability and convenience. Thus, limited research has been undertaken investigating more complex or flexible microphone positioning that is solely based on providing optimal estimation performance. The problem of finding the optimal combination of sensor positions, in the ANC context, has been investigated in the past [6] with the use of Genetic Algorithms (GAs) providing promising results [5]. However, in most of the studies presented in the literature the optimal configuration was generated by selecting the combination of microphone positions out of a predefined set. The current work constitutes a preliminary study to investigate the suitability of using a GA to calculate the optimal microphone configurations from a continuous set of available positions. The Remote Microphone Technique (RMT) is used as the VS method employed for the estimation. The estimation error over a grid of virtual microphones and the robustness to uncertainties are used as performance metrics for the calculated microphone configurations and the solutions are compared to a uniform linear array consisting of sub-arrays capable of incorporating pressure and pressure gradient for the estimation of the pressure at the virtual microphones [7–9].

**Corresponding author*: A.Kappis@soton.ac.uk.
Copyright: *©2025 A. Kappis et al. This is an open-access article distributed under the terms of the Creative Commons Attribution 3.0 Unported License, which permits unrestricted use, distribution, and reproduction in any medium, provided the original author and source are credited.*

2. REMOTE MICROPHONE TECHNIQUE

2.1 Virtual sensing formulation

The block diagram of a generalised virtual sensing system using the RMT is shown in Fig. 1. The sound field is generated by N_v primary sources with complex strengths $\boldsymbol{v} = \left[v_1, v_2, \ldots, v_{\mathrm{N_v}}\right]^\mathrm{T}$, with $[\,\cdot\,]^\mathrm{T}$ denoting transposition. The source strengths correspond to realisations of uncorrelated wide sense stationary random processes. The signals at the monitoring microphones, $\boldsymbol{d}_\mathrm{m} = \left[m_1, m_2, \ldots, m_{\mathrm{N_m}}\right]^\mathrm{T}$ and at the virtual microphones, $\boldsymbol{d}_\epsilon = \left[\epsilon_1, \epsilon_2, \ldots, \epsilon_{\mathrm{N}_\epsilon}\right]^\mathrm{T}$, are given by

$$\boldsymbol{d}_\mathrm{m} = \boldsymbol{P}_\mathrm{m}\boldsymbol{v} \tag{1a}$$

$$\boldsymbol{d}_\epsilon = \boldsymbol{P}_\epsilon\boldsymbol{v}, \tag{1b}$$

with $\boldsymbol{P}_\mathrm{m} \in \mathbb{C}^{\mathrm{N_m}\times\mathrm{N_v}}$ and $\boldsymbol{P}_\epsilon \in \mathbb{C}^{\mathrm{N}_\epsilon\times\mathrm{N_v}}$ denoting the frequency response functions from the sources to the monitoring and virtual microphones respectively. The sound field at the virtual microphone positions is estimated by applying the observation filter $\hat{\boldsymbol{O}}$ to the monitoring microphone signals. The estimation error is then given by

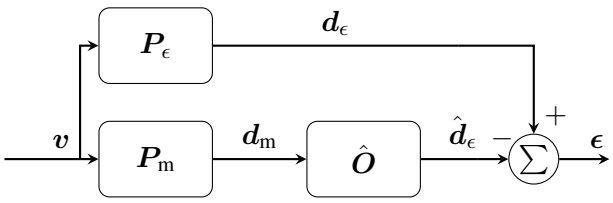


Figure 1. Block diagram of a generalised virtual sensing system. The sound field at the error microphones, $\boldsymbol{d}_\epsilon$, is estimated by applying the observation filter $\hat{\boldsymbol{O}}$ to the signals measured at the monitoring microphones $\boldsymbol{d}_\mathrm{m}$.

$$\boldsymbol{\epsilon} = \boldsymbol{d}_\epsilon - \hat{\boldsymbol{d}}_\epsilon = \boldsymbol{d}_\epsilon - \hat{\boldsymbol{O}}\boldsymbol{d}_\mathrm{m} = \boldsymbol{P}_\epsilon\boldsymbol{v} - \hat{\boldsymbol{O}}\boldsymbol{P}_\mathrm{m}\boldsymbol{v}. \tag{2}$$

The optimal filter, in the least squares sense, is calculated by minimising the cost function [3]

$$\begin{aligned} J_2 &= \mathrm{E}\left[\boldsymbol{d}_\epsilon^\mathrm{H}\boldsymbol{d}_\epsilon\right] \\ &= \mathrm{tr}\left\{\boldsymbol{S}_{\epsilon\epsilon} - \boldsymbol{S}_{\mathrm{m}\epsilon}\hat{\boldsymbol{O}}^\mathrm{H} - \hat{\boldsymbol{O}}\boldsymbol{S}_{\mathrm{m}\epsilon}^\mathrm{H} + \hat{\boldsymbol{O}}\boldsymbol{S}_\mathrm{mm}\hat{\boldsymbol{O}}^\mathrm{H}\right\}, \end{aligned} \tag{3}$$

where $\mathrm{E}[\,\cdot\,]$ denotes the expectation operator, $[\,\cdot\,]^\mathrm{H}$ denotes Hermitian conjugation, the quantities $\boldsymbol{S}_{\epsilon\epsilon}$ and $\boldsymbol{S}_\mathrm{mm}$ correspond to the monitoring and virtual microphone power spectral density matrices respectively and $\boldsymbol{S}_{\mathrm{m}\epsilon}$ is the cross spectral density matrix between the monitoring and virtual microphones. These matrices can be calculated with the help of the power spectral density matrix of the source signals, $\boldsymbol{S}_\mathrm{vv}$, as

$$\boldsymbol{S}_{\epsilon\epsilon} = \mathrm{E}\left[\boldsymbol{d}_\epsilon\boldsymbol{d}_\epsilon^\mathrm{H}\right] = \boldsymbol{P}_\epsilon\boldsymbol{S}_\mathrm{vv}\boldsymbol{P}_\epsilon^\mathrm{H} \tag{4a}$$

$$\boldsymbol{S}_\mathrm{mm} = \mathrm{E}\left[\boldsymbol{d}_\mathrm{m}\boldsymbol{d}_\mathrm{m}^\mathrm{H}\right] = \boldsymbol{P}_\mathrm{m}\boldsymbol{S}_\mathrm{vv}\boldsymbol{P}_\mathrm{m}^\mathrm{H} \tag{4b}$$

$$\boldsymbol{S}_{\mathrm{m}\epsilon} = \mathrm{E}\left[\boldsymbol{d}_\epsilon\boldsymbol{d}_\mathrm{m}^\mathrm{H}\right] = \boldsymbol{P}_\epsilon\boldsymbol{S}_\mathrm{vv}\boldsymbol{P}_\mathrm{m}^\mathrm{H} \tag{4c}$$

$$\boldsymbol{S}_\mathrm{vv} = \mathrm{E}\left[\boldsymbol{v}\boldsymbol{v}^\mathrm{H}\right]. \tag{4d}$$

The unconstrained solution to (3) is then given by [3]

$$\hat{\boldsymbol{O}}_\mathrm{opt} = \boldsymbol{S}_{\mathrm{m}\epsilon}\boldsymbol{S}_\mathrm{mm}^{-1} = \boldsymbol{P}_\epsilon\boldsymbol{S}_\mathrm{vv}\boldsymbol{P}_\mathrm{m}^\mathrm{H}\left(\boldsymbol{P}_\mathrm{m}\boldsymbol{S}_\mathrm{vv}\boldsymbol{P}_\mathrm{m}^\mathrm{H}\right)^{-1}, \tag{5}$$

where $[\,\cdot\,]^{-1}$ denotes matrix inversion. The assumption of uncorrelated sources with equal strengths simplifies the source power spectral density matrix to a scaled identity matrix which can be omitted without loss of generality. This formulation enables the calculation of the filter's expected performance without generating multiple sound field realisations, making it suitable for repetitive calculations, such as those required for the optimisation with a GA used in the this study.

2.2 Performance metrics

The monitoring microphone array configurations calculated with the GA are evaluated based on two metrics, the estimation performance and the robustness to uncertainties. The metric used to evaluate the performance of the estimation is the normalised mean squared estimation error. For a single virtual microphone this is given by

$$L_\epsilon = 10\log_{10}\left(\frac{\mathrm{E}\left[\epsilon\epsilon^*\right]}{\mathrm{E}[d_\epsilon d_\epsilon^*]}\right), \tag{6}$$

where $[\,\cdot\,]^*$ denotes complex conjugation. The estimation error gives negative values for good estimation performance with $-\infty$ denoting perfect estimation.

The robustness of the configurations is reported by the condition number of the monitoring microphone power spectral density matrix, $\kappa\left(\boldsymbol{S}_\mathrm{mm}\right)$. Higher condition numbers signify higher sensitivity to uncertainties with the theoretical maximum value being ∞ for singular matrices and the lowest is unity, for a scaled identity matrix.

3. GENETIC ALGORITHM

A GA is used in this work to perform a search of the microphone positions that will provide optimal estimation performance under certain constraints. The search is performed over a constrained two-dimensional continuous spatial domain with MATLAB's built-in GA algorithm. When non-linear constraints, such as those used in this study are included, the underlying algorithm used is the Augmented Lagrangian Genetic Algorithm (ALGA) [10]. A Lagrangian consisting of the fitness values of the individuals complemented by the sum of a scaled transformation of the constraints is minimised in each generation, and the original problem is approximately solved. The high level flowchart diagram describing the algorithm is shown in Fig. 2, and the steps and their associated parameters are described below.

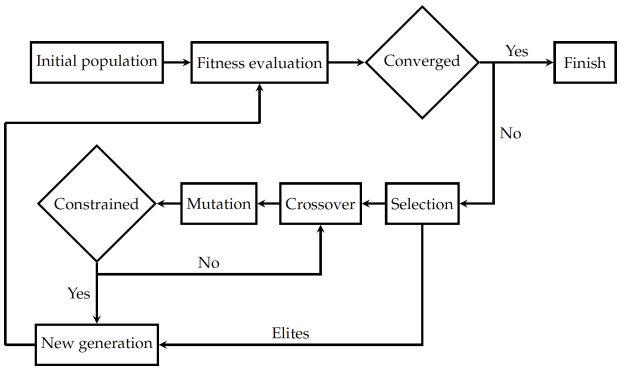


Figure 2. Flowchart diagram describing the genetic algorithm used in the current study.

Population and coding scheme The parameters to be optimised are the positions of the monitoring microphones. The number of microphones is fixed to eight and their x and y coordinates are interleaved in a vector of the form $\boldsymbol{x} = \left[x_1, y_1, x_2, y_2, \ldots, x_{\mathrm{N_m}}, y_{\mathrm{N_m}}\right]$ which constitutes one individual in the population, with one generation consisting of 100 individuals. The population of the first generation is drawn at random from a uniform distribution scaled and shifted to satisfy any imposed constraints.

Fitness function The fitness function defines the performance of each individual. In the current study, two distinct fitness functions are used. The function evaluating the performance of the configurations is defined as the sum of the estimation error values over a spatial virtual microphone grid, given by

$$J_{\mathrm{GA}} = \sum_{i=1}^{N_\epsilon} L_{\epsilon_i}. \tag{7}$$

For the optimisation of the robustness of the configurations, the condition number is used as the fitness function and is directly calculated using the corresponding built-in function in MATLAB. Smaller values denote better performance for both functions so the optimisation is formulated as a minimisation problem.

Selection After the fitness of each individual in a generation has been evaluated, the individuals are ordered based on a scale associated with their performance rank instead of their fitness score. The values are proportional to $\frac{1}{\sqrt{r}}$, where r is the rank of each individual. Ordering the individuals based on their rank removes the effect of the spread of the score values on the convergence of the search [11].

Elitism To ensure useful information is not lost from one generation to the next, the notion of *elitism* is used. The five individuals that scored highest are passed directly to the next generation. This ensures that the best fitness value of each generation cannot be worse than the previous and facilitates convergence to an optimal solution.

Crossover To traverse the search domain, individuals in new generations are created by combining elements of the parameter vectors of solutions in the current generation. After initial trials the percentage of the individuals in the new generation resulting from crossover was set to 80% which provides a good tradeoff between domain search and variability of solutions. For each individual created by crossover five candidates are picked at random and the two with the highest fitness score are chosen as the "parents". To decide which part of the vector will be picked from each parent two integers, n and m in the range from zero up to the number of parameters are picked at random. Elements with indices less than n and greater than m are picked from the first parent and the rest from the second parent.

Mutation The new generation individuals that are not created through crossover result from mutation, which is

the process of applying random changes to some of the values in the parameter vectors of current generation individuals. To perform the mutation, a direction in the space of the parameter vector is picked and scaled at random. If any imposed constraints are not satisfied the direction and scale are adapted.

Constraints and bounds The minimum value of the estimation error given by Eq. (7) has been constrained to be great than -30dB for each virtual microphone, which aims to discourage solutions that achieve effective estimation on average across all positions by achieving extremely low error at a small number of microphone positions.

The values describing the coordinates of the microphones have been constrained to satisfy two conditions. Firstly, the microphones must not be located outside of a specified area to avoid overly favourable positioning overlapping with the virtual microphone grid. Secondly, the minimum allowed distance between the microphones is constrained to be approximately 0.0354m. This constraint serves a twofold purpose: first, to avoid overlapping microphones, and second, to ensure comparability with the "conventional" array against which the solutions are compared.

Termination conditions The optimisation is performed until 300 generations are evaluated, or the best fitness value change is smaller than 10^{-1} for 100 successive generations. At this point, the parameter vector associated with the best fitness values is returned as the optimal solution.

4. SIMULATIONS

4.1 Simulation setup

The GA was used in a scenario where monitoring microphones could be positioned over a rectangular spatial domain with side equal to 0.5m. A rectangular $0.5\text{m}\times0.25\text{m}$ grid of 10×10 virtual microphones was used to evaluate the fitness function of Eq. (7). The complete geometry of the optimisation problem is presented in Fig. 3.

To facilitate comparison with a past study [9], a two element Uniform Linear Array (ULA) of inter-element distance of 0.1m was implemented and positioned parallel to the x Cartesian axis, as shown in Fig. 3. Each array element consists of a sub-array with two pairs of microphones, one orientated parallel to the x-axis and one to the y-axis. The distance between the two microphones of each pair is 0.05m.

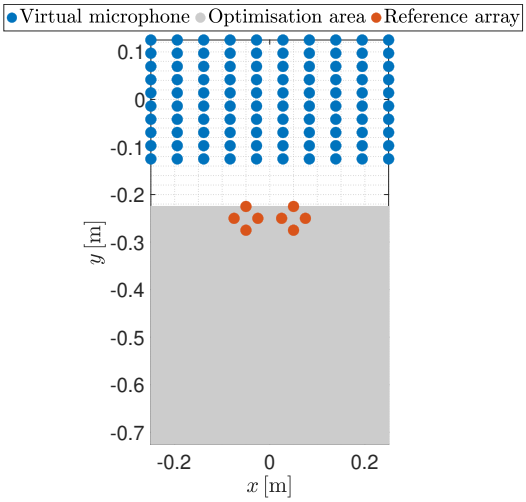


Figure 3. Geometry of the optimisation problem. Virtua microphones are denoted with blue dots and the microphones of the reference linear array with red dots. The grey square denotes the area the algorithm uses for the candidate monitoring configurations.

A diffuse sound field was generated by a constellation of 501 ideal point sources on the surface of a sphere with radius of 10m arranged on a Fibonacci lattice. At low frequencies, the impact of the microphone topology is obscured by the increased performance due to high coherence between the monitoring and virtual microphones [2, 4]. For this reason, the optimisation was performed at a frequency of $f = 1\text{kHz}$, although the performance has been assessed over a broader frequency range.

4.2 Optimising estimation performance

First, the GA was used to calculate microphone configurations that provide optimal performance by minimising the fitness function of Eq. (7). The optimisation was performed five times and the spatial distribution of the estimation error over the virtual microphone grid at the optimisation frequency is presented in Fig. 4, along with the performance of the reference ULA. The black line indicates the area over which the estimation error is less than -10 dB.

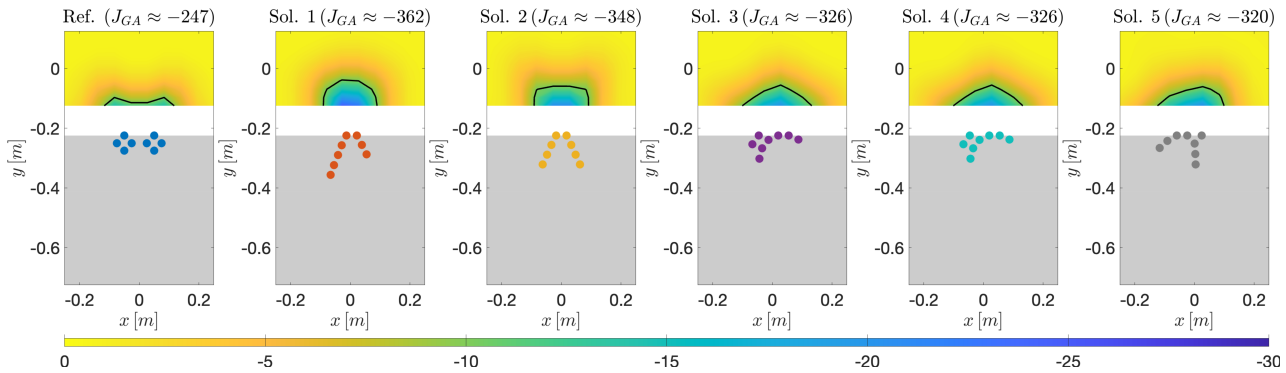


Figure 4. Spatial estimation error distribution for the microphone configurations calculated with the GA at the frequency of 1 kHz. The solid line (–) indicates the area over which the estimation error is less than -10 dB.

The configurations obtained with the GA yield significantly lower fitness values than the reference design. For the GA setups, areas with estimation errors below -10 dB consistently extend further from the microphone array, and the lowest error achieved is consistently lower than that of the reference arrangement.

Distinct patterns are observed in the topologies of the solutions. The configurations with the best fitness scores, solutions 1 and 2, consist of linear sub-arrays oriented toward the estimation area, extending the -10 dB error zone along their axes [5,9]. The other configurations utilise the same mechanism, to a lesser extent, combined with microphone placement near the virtual microphone grid to achieve a low fitness value, resulting in slightly worse estimation spread over a larger area.

The performance gain achieved with the calculated configurations comes at the cost of increased sensitivity to uncertainties, which is reflected in the condition numbers associated with the arrays. Fig. 5 presents the condition numbers for the calculated arrays at frequencies from 50 Hz to 2 kHz. The condition numbers range from about 10^6 for the reference array to approximately 2.5×10^7 for the solution with the lowest fitness score at the optimisation frequency, with the span increasing significantly at lower frequencies. Additionally, it is important to highlight the large range of the fitness scores being 42 dB at the frequency of 1 kHz.

4.3 Optimisation with constrained condition number

An additional constraint on the upper bound of the condition number was introduced to control the sensitivity of

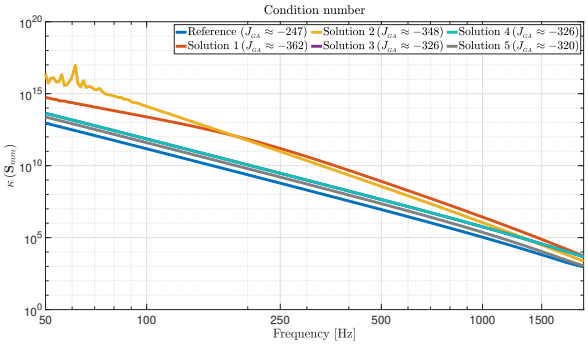


Figure 5. The condition number for the arrays calculated with the genetic algorithm for frequencies from 50Hz to 2kHz.

the calculated arrays. Additionally, solutions 2 and 3 of Fig. 4 were included in the initial population. The optimisation was performed five times for each of the condition numbers from 10^3 to 10^8 with a geometric step of 10. The spatial distribution of the estimation error for the configurations associated with the lowest fitness score from each trial are shown in Fig. 6.

Even with the condition number constrained to low values, the optimised arrays achieve lower function scores than the reference array. The spacing between microphones is larger under strict condition constraints and decreases with more relaxed bounds. The topologies exhibit significant similarities; for condition bounds up to 10^5, the primary difference between configurations is the micro-

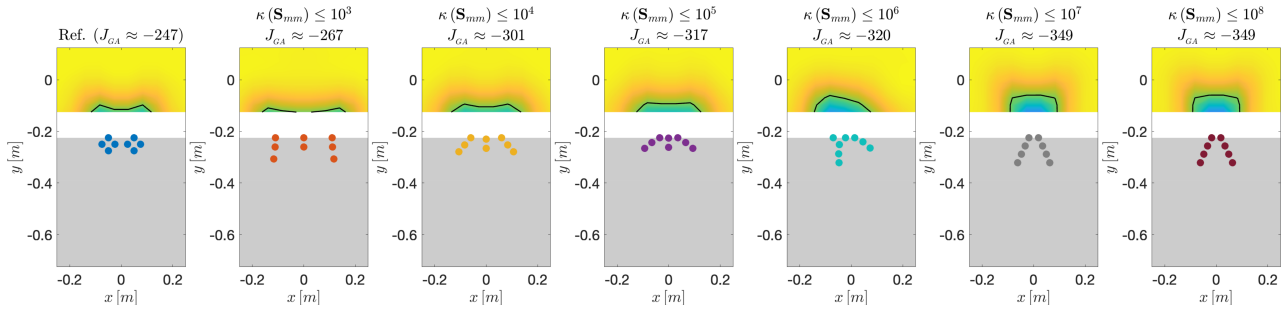


Figure 6. Spatial estimation error distribution for the microphone configurations associated with the lowest fitness score when the condition number is constrained. The solid line (–) indicates the area over which the estimation error is less than -10 dB.

phone spacing. At higher condition constraints, the optimal configurations resemble those calculated without any constraint on the condition, indicating that further relaxation of the bound is unlikely to yield significant performance benefits.

Fig. 7 presents the condition numbers of the microphone configurations of Fig. 6. The conditioning of the arrays is consistent with the imposed constraints up to approximately the optimisation frequency. For constraint values of 10^6 and higher, the configurations with the best fitness scores are those introduced in the initial population, and their condition does not reach the bound. Notably, among the two configurations, only the one returned for $\kappa(\boldsymbol{S}_{\text{mm}}) \leq 10^6$ satisfies this constraint. When the constraint is relaxed, the configuration that achieves the best score is returned instead.

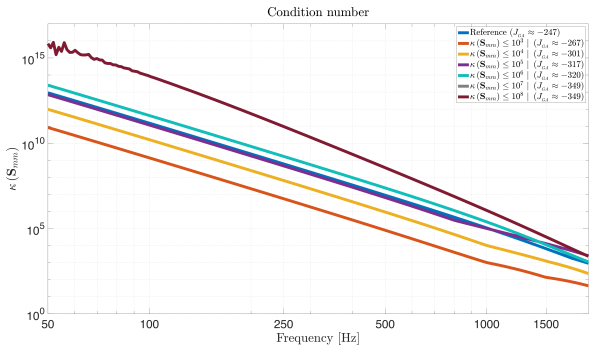


Figure 7. Conditioning of the microphone configurations associated with the lowest fitness score when the condition is constrained.

It is important to investigate the consistency of the GA in calculating the optimal arrays presented in Fig. 6. Fig. 8 presents the spread of the fitness scores for the calculated arrays at each constraint value, revealing a score range of the order of 40 dB for all configurations, consistent with the range for the unconstrained optimisation. The vertical overlap of the boxes indicates that, for a specified constraint, a calculated array may perform worse than those derived with more relaxed condition bounds, which contradicts the purpose of the optimisation.

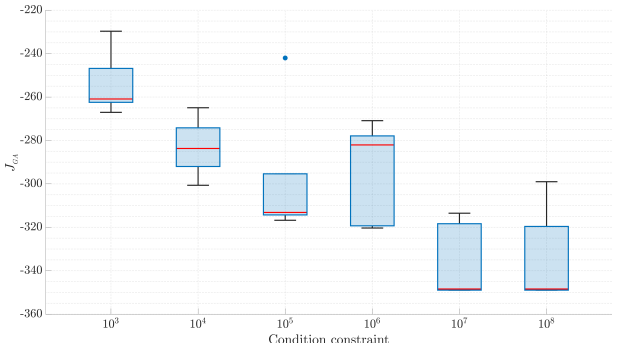


Figure 8. Fitness score spread for the calculated arrays for each condition constraint value.

4.4 Optimisation with constrained estimation error

An alternative approach to the optimisation is to constrain the estimation error to be lower than a specified bound and minimise the condition number. Five trials

were performed with the total estimation error over the virtual microphone grid being upper bounded by values from -100 dB to -400 dB in steps of 50 dB. The same two arrays were included in the initial population for these trials too.

The spatial distribution of the error for the arrays associated with the lowest condition numbers is shown in Fig. 9. The titles indicate the constraint and the actual value achieved by the array. It can be seen that when the bound was set very low, no feasible solution was found and the array that was closest to satisfying the constraint was returend. The minimisation of the condition number leads to distinctively different arrays compared to those acquired by minimising the error, with inconsistencies in the performance. The array associated with the $J_{\text{GA}} \leq -300$ dB has a condition number of about 3.4×10^4, while the array in Fig. 6 associated with a condition number bound of 10^4 achieves an error of $J_{\text{GA}} \approx -301$.

The range and median of the condition number associated with the calculated arrays for each constraint value are presented in Fig. 10. The spread of the values is significant when the consistency in the estimation error is taken into account. The results suggest that the same error values can be achieved with arrays whose conditioning differs significantly from each other. In contrast to the results obtained for the error minimisation, no significant overlap is observed between the condition numbers of the arrays calculated for each constraint bound.

5. SUMMARY

In this study, the applicability of a genetic algorithm for the calculation of optimal microphone configurations used to estimate the pressure in a tonal diffuse sound field at some location remote from the array was investigated.

The sum of estimation errors over a spatial grid of virtual microphones was used as the optimisation criterion. Microphone arrangements with similar topological patterns demonstrated performance gains compared to a reference linear array composed of sub-arrays capable of incorporating pressure and pressure gradient information into the estimation process [9]. However, the performance gains were accompanied by increased sensitivity to uncertainties, as assessed via the numerical conditioning.

Further optimisation trials were conducted with constraints on the condition number or the sum of estimation errors over the grid. Significant inconsistencies were observed in the results, with similar error metrics resulting from distinctly different array topologies. Overall, the range of the fitness values associated with the calculated configurations was found to be excessive with significant overlap for different constraint values in certain situations. Further refinement of the algorithm and its parameters is required if the method is to be used for the calculation of optimal microphone configurations.

6. ACKNOWLEDGMENTS

This work was supported by the project “IN-NOVA: Active reduction of noise transmitted into and from enclosures through encapsulated structures”, which has received funding from the European Union’s Horizon Europe programme under the Marie Skłodowska-Curie grant agreement no. 101073037 and by UK Research and Innovation under the UK government’s Horizon Europe funding agreement with grant number EP/X027767/1.

The authors would also like to acknowledge the use of *IRIDIS* High Performance Computing Facility, and associated support services at the University of Southampton, in the completion of this work. Jordan Cheer was supported by the Department of Science, Innovation and Technology (DSIT) Royal Academy of Engineering under the Research Chairs and Senior Research Fellowships programme.

7. REFERENCES

[1] W. Jung, S. J. Elliott, and J. Cheer, “Estimation of the pressure at a listener’s ears in an active headrest system using the remote microphone technique,” *J. Acoust. Soc. Am.*, vol. 143, pp. 2858–2869, May 2018.

[2] W. Jung, S. J. Elliott, and J. Cheer, “Local active control of road noise inside a vehicle,” *Mech. Syst. Signal Process.*, vol. 121, pp. 144–157, Apr. 2019.

[3] S. J. Elliott and J. Cheer, “Modeling local active sound control with remote sensors in spatially random pressure fields,” *J. Acoust. Soc. Am.*, vol. 137, pp. 1936–1946, Apr. 2015.

[4] P. Zhang, S. Wang, H. Duan, J. Tao, H. Zou, and X. Qiu, “A study on coherence between virtual signal and physical signals in remote acoustic sensing,” *J. Acoust. Soc. Am.*, vol. 152, pp. 2840–2848, Nov. 2022.

[5] X. Zheng, Z. Jia, B. Wan, M. Zeng, and Y. Qiu, “A study on hybrid active noise control system combined with remote microphone technique,” *Appl. Acoust.*, vol. 205, p. 109296, Mar. 2023.

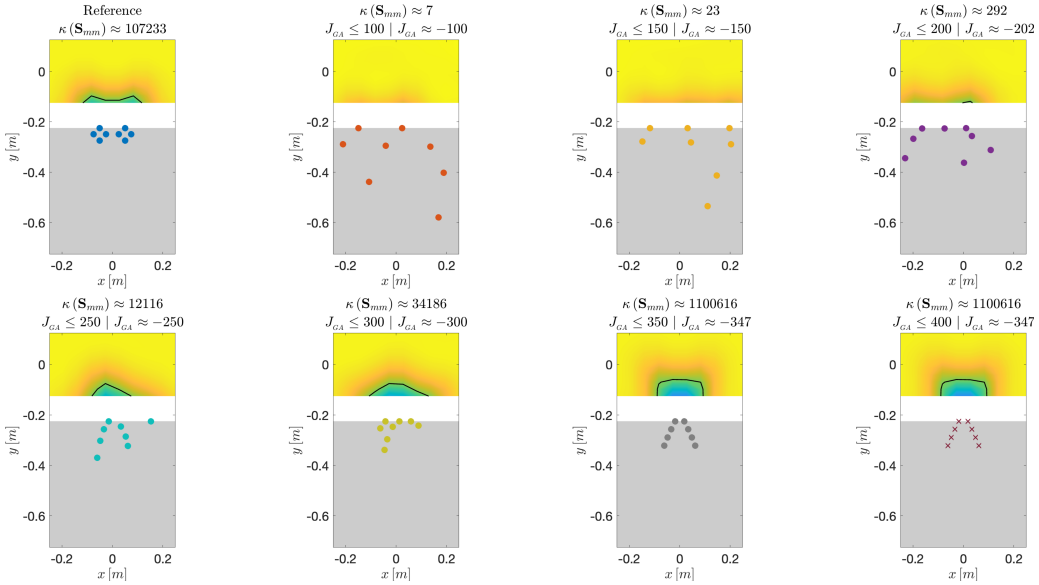


Figure 9. Spatial estimation error distribution for the microphone configurations with the lowest condition number when the total estimation error is upper bounded. The solid line (–) indicates the area over which the estimation error is less than -10 dB.

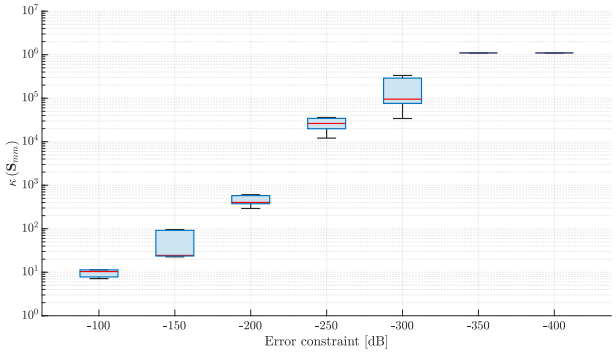


Figure 10. Fitness score spread for the calculated arrays per condition constraint value.

[6] S. L. Padula and R. K. Kincaid, "Optimization Strategies for Sensor and Actuator Placement," Technical Memorandum 209126, NASA, NASA Langley Research Center Hampton, VA 23681-2199, Apr. 1999.

[7] D. J. Moreau, J. Ghan, B. S. Cazzolato, and A. C. Zander, "Active noise control in a pure tone diffuse sound field using virtual sensing," *J. Acoust. Soc. Am.*, vol. 125, pp. 3742–3755, June 2009.

[8] S. Elliott and J. Garcia-Bonito, "Active cancellation of pressure and pressure gradient in a diffuse sound field," *Journal of Sound and Vibration*, vol. 186, pp. 696–704, Oct. 1995.

[9] A. Kappis, J. Cheer, and J. A. Zhang, "Remote Sensing Using Multi-Microphone Configurations for Local Active Noise Control Applications," in *Proc. 30th Int. Congr. Sound Vibr.*, (Amsterdam, Netherlands), June 2024.

[10] A. R. Conn, N. Gould, and P. L. Toint, "A globally convergent Lagrangian barrier algorithm for optimization with general inequality constraints and simple bounds," *Math. Comput.*, vol. 66, pp. 261–289, Jan. 1997.

[11] S. Katoch, S. S. Chauhan, and V. Kumar, "A review on genetic algorithm: past, present, and future," *Multimed. Tool. Appl.*, vol. 80, pp. 8091–8126, Feb. 2021.

DOI: 10.61782/fa.2025.0252

FORUM ACUSTICUM EURONOISE 2025

CONTROL OF TRANSVERSE VIBRATIONS IN VERTICALLY INSTALLED ROTATING SHAFTS THROUGH ACTIVE BEARINGS

Jaewon Song[1] **Byeongil Kim**[1*]
[1] Department of Mechanical Engineering, Yeungnam University, Republic of Korea

ABSTRACT

Machines with vertical shafts, such as generators and electric motors, must address vibration-induced noise and heat. Vertical hydroelectric generators, in particular, are prone to vibrations from water flow and component imbalances, leading to reduced efficiency, early wear, and potential system failure. Controlling shaft vibrations is essential for maintenance and stable operation. This study aims to address these issues by applying active control technology to reduce vibrations in vertical shafts, utilizing active bearings and the NLMS algorithm. To validate the study, simulations were conducted using MATLAB/SIMULINK, and the system was mathematically modeled using the FEM approach. Experiments were conducted at 600 RPM, inspired by the rotational speed of the Porjus U9 generator, and additional analysis was performed across a speed range from 100 RPM to 800 RPM to compare shaft displacement orbits with simulation results. Through this comparison, the reliability of the simulation model was evaluated, and the effectiveness of active control in reducing vibrations was successfully demonstrated. These results suggest that active bearings have the potential to resolve vibration issues in machines with vertical shafts, such as generators and electric motors, thereby extending their operational lifespan.

Keywords: active bearing, finite element method, normalized least mean square algorithm, vertically driven shaft, transverse vibration.

*Corresponding author: bikim@yu.ac.kr.

Copyright: © 2025 First author et al. This is an open-access article distributed under the terms of the Creative Commons At- tribution 3.0 Unported License, which permits unrestricted use, distribution, and reproduction in any medium, provided the orig- inal author and source are credited.

1. INTRODUCTION

Machines equipped with vertically oriented shafts such as hydroelectric generators and electric motors are frequently subject to vibration-related challenges. In particular, vertical hydroelectric generators experience significant transverse vibrations due to water flow disturbances and internal imbalances in components. These vibrations can result in increased noise, heat generation, mechanical wear, and, ultimately, a decrease in system efficiency and reliability. Over time, excessive vibrations may lead to premature failure of critical components, posing serious maintenance and operational risks. Among the various solutions proposed to mitigate these problems, active vibration control technology has emerged as a promising approach. In contrast to passive methods, active control strategies can adapt to varying operational conditions and effectively suppress unwanted vibrations in real time. This study focuses on applying such a method specifically, the use of active bearings combined with the Normalized Least Mean Square (NLMS) algorithm to control transverse vibrations in vertically installed rotating shafts. To evaluate the proposed method, a mathematical model of the system was developed using the Finite Element Method (FEM), and simulations were conducted using MATLAB and SIMULINK environments. The system behavior was analyzed under a rotational speed of 600 RPM, chosen based on the operational characteristics of the Porjus U9 hydroelectric generator. Additionally, a parametric analysis was carried out across a range of speeds (100–800 RPM) to assess vibration responses and compare shaft displacement orbits with simulation results. Through this analysis, the accuracy and reliability of the proposed model were validated, and the effectiveness of the active control strategy was confirmed. The findings of this research highlight the potential of active bearings as a viable solution for reducing vibrations in vertical shaft systems. This

approach not only contributes to the enhancement of machine performance but also extends the operational lifespan of equipment such as generators and electric motors.

2. MODELLING OF ROTOR

In this chapter, we employed the FEM(Finite Element Method) to construct a model of a vertical shaft system comprising a generator and a turbine. The model comprises 15 nodes and 14 elements. Figure 1 below provides a visual representation of this model.

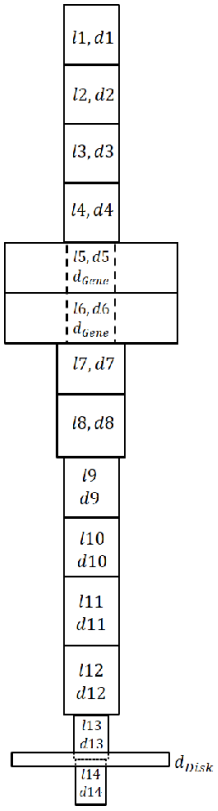


Figure 1. Porjus U9 rotor finite element model.

2.1 Finite element method

For modeling using the finite element method, the shaft model was structured with 14 elements and 15 nodes. The matrices utilized for modeling include the mass, stiffness, and damping matrices. These matrices are detailed as follows.

$$M_i^e = \frac{\rho A_i l_i}{420}\begin{bmatrix} 156+\left(\frac{m_d}{\rho A_i l_i/420}\right) & & & sym \\ 22l_i & 4l_i^2+\left(\frac{I_d}{\rho A_i l_i/420}\right) & & \\ 54 & 13l_i & 156 & \\ -13l_i & -3l_i^2 & -22l_i & 4l_i^2 \end{bmatrix} \quad (1)$$

$$K_i^e = \frac{2EI_i}{l_i^3}\begin{bmatrix} 6+\left(\frac{k_i}{2EI_i/l_i^3}\right) & & & sym \\ 3l_i & 2l_i^2 & & \\ -6 & -3l_i & 6 & \\ 3l_i & l_i^2 & -3l_i & 2l_i^2 \end{bmatrix} \quad (2)$$

$$G_i^e = \begin{bmatrix} 0 & & & sym \\ 0 & I_p\Omega & & \\ 0 & 0 & 0 & \\ 0 & 0 & 0 & 0 \end{bmatrix} \quad (3)$$

2.2 Modelling of active bearing

The active bearing system comprises a rubber grommet and a piezo actuator, illustrated in Figure 2. The modeling process involved utilizing linearized stiffness, with the damping effects from oil films in the bearings disregarded. Furthermore, considering the significant rigidity of the housing, it was treated as a rigid body. In Figure 1, the upper bearing of the turbine has been replaced with an active bearing.

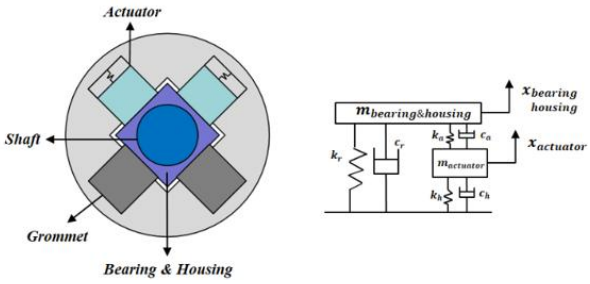


Figure 2. Structure and dynamic model of the active bearing

$m_{bearing\&hosing}$ refers to the mass of the housing attached to the rotor. k_r , c_r express the stiffness and damping of the rubber grommet. Also, $m_{actuator}$ represents the actuator mass. k_a and k_h represent the stiffness of the actuator and the spring located below the actuator, respectively, and c_a and c_h also represent the damping of the actuator and the spring located below the actuator. $x_{bearinghosing}$ and $x_{actuator}$ mean the displacement of the bearing housing and the actuator, respectively.

3. SIMULATION RESULTS

In this study, simulations were conducted at the nominal speed of 600 rpm. The overall system response obtained from the simulation-based control is presented in Figure 3.

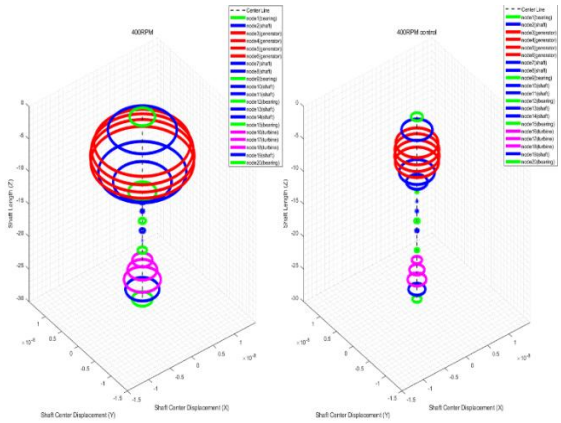


Figure 3. Comparison of system response before and after control at 600 rpm.

The control result at Node 12, which corresponds to the displacement measurement point in the actual experimental setup, is shown below.

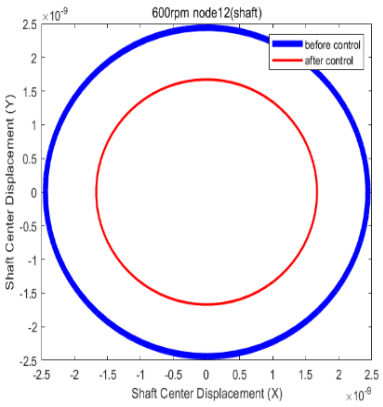


Figure 4. Shaft orbit at 600 rpm before and after control.

In the simulation, it was confirmed that the use of active bearing control effectively reduced vibrations, with a 31.54% reduction in amplitude observed after control.

4. EXPERIMENTAL RESULTS

4.1 Experimental setup

Figure 5 shows the experimental setup for evaluating the active bearing system. It consists of an unbalanced disk and two actuator-sensor modules mounted on a vertical shaft. The actuators apply control forces in the X and Y directions, while the sensors measure shaft displacement. All components are mounted on a rigid frame to reduce external disturbances.

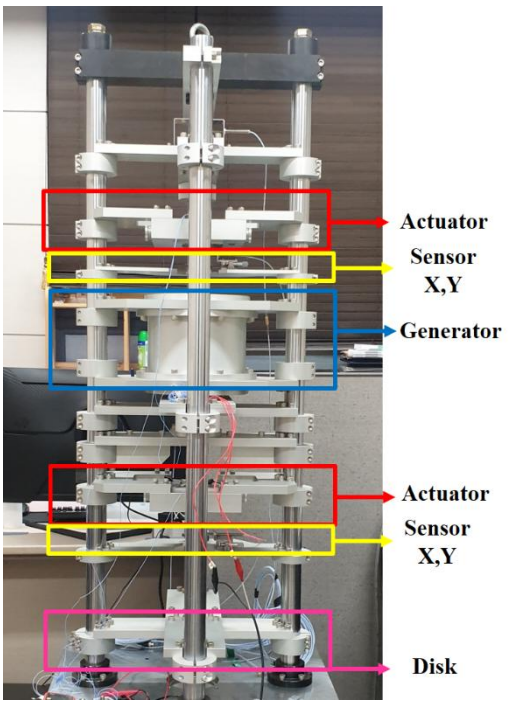


Figure 5. Experimental setup

Acceleration sensors in the X and Y directions send signals to Simulink via the d-SPACE platform. The NLMS algorithm processes the signals to generate control inputs, which are applied to piezoelectric actuators for real-time vibration suppression.

4.2 Experimental Results

Similar to the simulation results, the displacement response at 600 rpm was measured. The orbit plots before and after control are shown in the figure below.

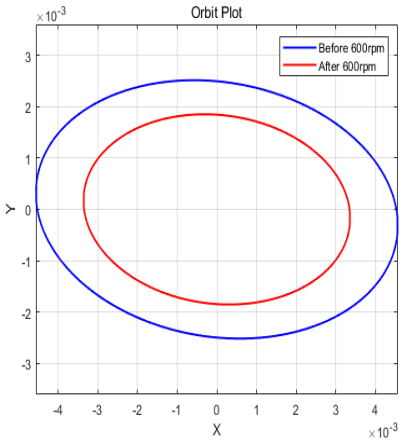


Figure 6. Shaft orbit at 600 rpm before and after control.

A 26.31% reduction in orbit amplitude was observed after applying the control.

5. CONCLUSION

In this study, an active vibration control method combining active bearings and the Normalized Least Mean Square (NLMS) algorithm was proposed to suppress transverse vibrations in vertically oriented rotating shaft systems. A vertical shaft model, including a generator and turbine, was developed using the Finite Element Method (FEM), and simulations were performed at 600 rpm using MATLAB and Simulink. The simulation results confirmed that the proposed method effectively reduced vibration amplitudes. To verify the practical effectiveness of the method, an experimental setup was constructed, featuring piezoelectric actuators and acceleration sensors. A real-time control loop was implemented using the d-SPACE system and Simulink, incorporating the NLMS algorithm. The experimental results showed a similar trend to the simulation, demonstrating significant vibration reduction at 600 rpm. These findings validate the potential of active bearings as a robust solution for vibration control in vertical rotor systems. The proposed approach can enhance operational stability and extend the service life of equipment such as hydroelectric generators and vertical electric motors.

6. ACKNOWLEDGMENTS

This work was supported by the Basic Science Research Program through the National Research Foundation of Korea (NRF), funded by the Ministry of Education (NRF-2021R1A6A1A).

7. REFERENCES

[1] J.-C. Luneno, J.-O. Aidanpää, and R. Gustavsson, “Model based analysis of coupled vibrations due to the combi-bearing in vertical hydroturbogenerator rotors,” Journal of Vibration and Acoustics, vol. 133, no. 6, pp. 061012-1–061012-11, Dec. 2011.

[2] J. Fang, X. Xu, and J. Xie, “Active vibration control of rotor imbalance in active magnetic bearing systems,” Journal of Vibration and Control, published online, Jul. 8, 2013.

[3] M. Chen, X. Ning, Z. Zhou, Y. Shu, Y. Tang, Y. Cao, X. Shang, and X. Han, “LMS/RLS/OCTAVE vibration controls of cold orbital forging machines for improving quality of forged vehicle parts,” World Electric Vehicle Journal, vol. 13, no. 5, p. 76, Apr. 2022

DOI: 10.61782/fa.2025.0098

FORUM ACUSTICUM EURONOISE 2025

ACTIVE STRUCTURAL ACOUSTIC CONTROL (ASAC) FOR VIBRATING PLATES WITH OPENINGS IN VIBRO-ACOUSTIC SYSTEMS

Khaled Said Ahmed Maamoun[1,2*] **Stanislaw Wrona**[1] **Marek Pawelczyk**[1]
Hamid Reza Karimi[2]
[1] Department of Measurements and Control Systems, Silesian University of Technology, Gliwice, Poland
[2] Department of Mechanical Engineering, Politecnico di Milano, Milan, Italy

ABSTRACT

Active Structural Acoustic Control (ASAC) is a well-established technique for managing noise and vibration in vibro-acoustic systems. This study investigates the application of ASAC to vibrating plates with corner openings, a configuration that presents unique challenges due to localized stress concentrations and complex vibro-acoustic coupling. The placement and configuration of inertial actuators, which are integral to ASAC systems, are experimentally analyzed to optimize performance. The results show that the position of the opening significantly influences the overall system response, making the placement of inertial actuators unique to each configuration. Changing the location of the opening alters the vibrational and acoustic characteristics of the plate, requiring a tailored actuator arrangement for effective control. For fully clamped plates, placing actuators near the edges reduces their effectiveness in suppressing sound due to the high stress concentrations and limited vibrational energy at these regions. Additionally, positioning actuators around the openings introduces greater instability and nonlinearities into the system, further complicating the control dynamics. These findings highlight the necessity of considering both the opening location and actuator placement to optimize performance in vibro-acoustic systems.

Keywords: *active noise control, active structure acoustic control, vibro-acoustic systems, noise reduction.*

**Corresponding author*: *Khaled.maamoun@polsl.pl.*
***Copyright**: ©2025 Khaled et al. This is an open-access article distributed under the terms of the Creative Commons Attribution 3.0 Unported License, which permits unrestricted use, distribution, and reproduction in any medium, provided the original author and source are credited.*

1. INTRODUCTION

Openings in plate structures play a vital role in numerous engineering applications, particularly in vibro-acoustic coupled systems. These structures are widely employed across various domains, including household appliances, manufacturing, and vehicle engineering [1]. The shape, location, and relative position of openings concerning the noise source in such systems significantly influence the system's sound power response. For systems where openings are located in high-stress areas of vibrating plates, such as plate corners, additional sound power resonances are expected. Therefore, special attention is required to effectively address these systems [2]. Different techniques are employed to improve sound reduction in such systems, including both passive and active control methods [3].

Active Structural Acoustic Control (ASAC) plays a crucial role in mitigating noise transmission in various engineering applications by actively controlling structural vibrations. When properly implemented, ASAC can not only attenuate noise in localized regions but also achieve global noise reduction [4, 5]. It is generally implemented using a combination of passive noise barriers, vibration actuators, sensors, and a control system, as outlined in [6]. ASAC mitigates noise transmission through a structure by actively controlling its vibrations.

The authors in [7] theoretically evaluated a radiation-mode-based ASAC system for an enclosure with vent openings. However, their study was limited to tonal disturbances and did not explore practical real-world applications. A feedforward ASAC algorithm was later implemented on the lining panels of an aircraft cabin using a low-cost microcontroller, achieving a tonal noise reduction of 23 dB [8]. In [9], the authors examined the ef-

fectiveness of a tonal ASAC strategy that employs an experimentally identified radiation matrix to regulate sound power radiation, demonstrating superior performance over conventional active vibration control methods. However, their study did not consider broadband excitation.

Despite these advancements, the existing literature indicates a notable research gap in ASAC applications for systems with openings compared to fully enclosed structures. This highlights the need for further investigation to enhance ASAC effectiveness in such configurations.

The filtered-x least-mean-square (FxLMS) algorithm is the most popular active control algorithm due to its stability and simple structure [10]. The reference signal to the controller is filtered through the model of the secondary path between the actuator and the error sensors, ensuring effective noise attenuation. More features and have been added to FxLMS to enhance its characteristics, such as the Leaky FxLMS that introduces a small leakage factor to prevent coefficient drift and instability, making it more robust in nonstationary environments [11]. The Normalized FxLMS (NFxLMS) algorithm adjusts the step size based on the filtered reference signal power, ensuring faster convergence and better stability in varying input conditions [12].

The selection of the inertial actuator location on vibrating plates is crucial, as it directly affects the control system's ability to reduce noise [13]. Various studies have addressed this placement problem. Some studies optimize actuator placement based on vibration response [14], while others incorporate radiated sound into the cost function [15, 16]. The main contributions of this paper are twofold: i) an analysis of ASAC's effectiveness in mitigating noise from vibro-acoustic systems with openings, and ii) an investigation into the optimal placement of inertial actuators on vibrating plates, specifically considering corner regions with high stress concentrations.

The reminder of the paper is organized as follows: Section 2 is introduction of the experimental setup. Section 3 presents the results and the discussion. Finally, the conclusion is presented in Section 4.

2. EXPERIMENTAL SETUP

The experimental setup is designed to provide flexibility in testing actuators at various positions. The test plate can be replaced to evaluate systems with openings located at different corners. The laboratory room measures 5.8 meters in length and 3.5 meters in width. While the walls are lined with sound-absorbing materials, the presence of equipment and other objects within the room gives it acoustic characteristics more representative of a typical real-world environment rather than those of a dedicated acoustic chamber. The setup comprises a rectangular steel plate mounted on a concrete enclosure containing a loudspeaker. The plate is composed of steel with a density $\rho = 7850\,\mathrm{kg/m^3}$, Young's modulus $E = 210 \times 10^9\,\mathrm{Pa}$. The dimensions of the plate are $a = 0.42\,\mathrm{m}$, $b = 0.39\,\mathrm{m}$, and $h = 0.001\,\mathrm{m}$, representing its length, width, and thickness, respectively. The loudspeaker generates a random, band-limited noise signal with a position fixed at (0.3 m, 0.1 m, -0.3 m) for all the considered configurations. The concrete enclosure offers substantial sound attenuation, ensuring that the majority of the acoustic energy exiting the enclosure propagates through the plate and the circular opening. The active control system employs three Beyerdynamic MM1 error microphones and three DAEX32EP-4 inertial actuators, as illustrated in Fig. 1.

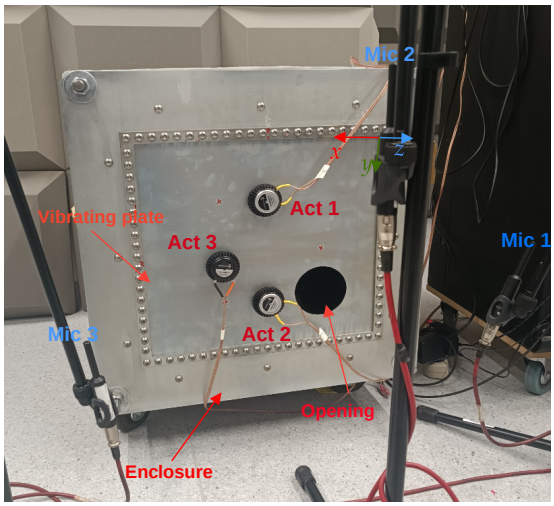


Figure 1: An overview of the experimental setup, showing a vibrating plate that contains a circular opening of a radius 0.05 m with center coordinates at (0.105 m, 0.265 m). Actuators (Act 1, Act 2, and Act 3) are mounted on the plate at (0.2 m, 0.1 m), (0.27 m, 0.2 m), and (0.2, 0.295 m), respectively. Microphones (Mic 1, Mic 2, and Mic 3) are positioned at the coordinates (-0.18 m, 0.12 m, 0.25 m), (0.21 m, -0.1 m, 0.4 m), and (0.53 m, 0.24 m, 0.25 m), respectively.

2.1 Algorithm

For active control, a feedforward multichannel FxLMS algorithm with a leakage factor is employed due to its simplicity and robustness [3], as illustrated in Fig. 2. The system normalizes based on the power of a single reference signal. The reference signal, denoted as $R(n)$, can be artificially generated or obtained via a reference microphone. The adaptive filter coefficients, represented by the vector W, consist of K elements generating the control signals $Y(n)$, while the canceling signals are given by $\hat{Y}(n)$.

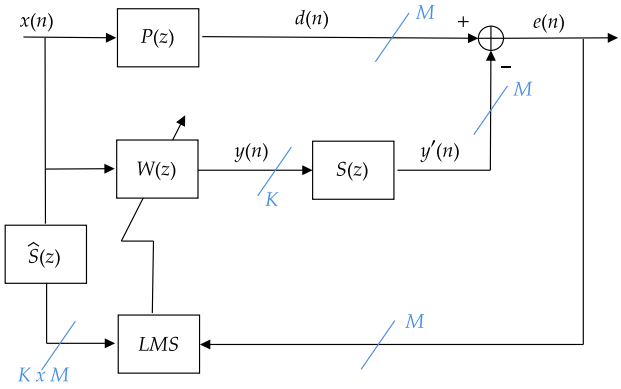


Figure 2: Block diagram of a single-reference multichannel feedforward FxLMS algorithm. M and K denote the number of outputs and secondary sources, respectively.

Since the secondary path matrix S is not directly available, it is approximated using an estimate $\hat{S}$. The $K \times M$ secondary paths are modeled as FIR filter impulse responses and adapted using the NLMS algorithm. The adaptive filter coefficients $W_k(n)$ are updated as:

$$W_k(n+1) = (1-\eta(n)\beta)W_k(n)+\eta(n)\sum_{m=1}^{M} R'_{km}(n)E_m(n), \tag{1}$$

where $R'_{km}(n)$ is the filtered reference signal, $E_m(n)$ is the error signal, and $\eta(n)$ is the normalized step size expressed as follows:

$$\eta(n) = \frac{\mu}{\sum_{k=1}^{K}\sum_{m=1}^{M}\|R'_{km}(n)\|^2}, \tag{2}$$

where μ is the fixed step size, $\|\cdot\|$ denotes the L^2-norm, and β is a leakage regularization factor.

In real-time operation, the total system latency from ADC input to DAC output is approximately 2.16 ms, which is close to the acceptable threshold for active control applications. This delay results from the combined effects of the output buffer (0.33 ms), the group delay introduced by IIR filters during downsampling (to 3 kHz) and upsampling (0.83 ms), and the inherent processing delay of the ADC and DAC at a 48 kHz sampling rate. The system is implemented using the Analog Devices SC598 with an SHARC+ core, integrated with the EVSOMCRR-EZKIT development board [17], featuring a 4-channel, 24-bit ADC and a 12-channel, 24-bit DAC.

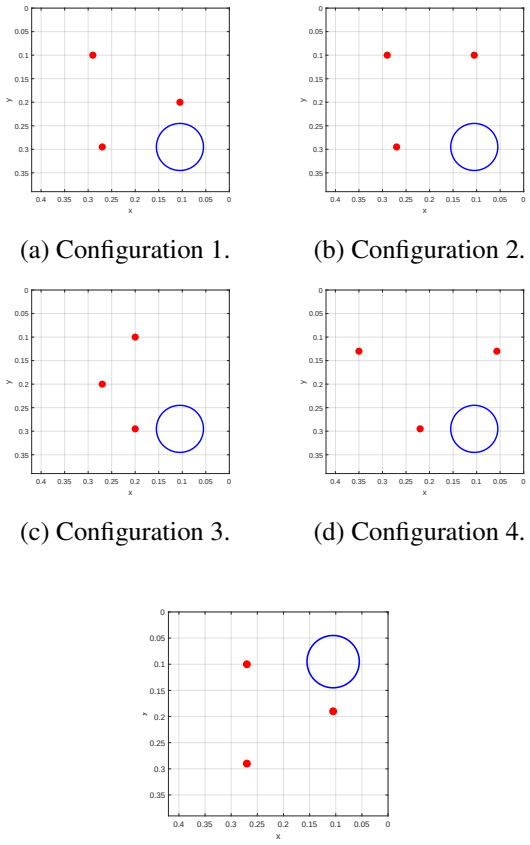
3. RESULTS AND DISCUSSION

This study investigates the effect of actuator positioning on the performance of vibro-acoustic systems by evaluating four distinct actuator arrangements, as illustrated in Fig.3. The selected configurations are designed to reflect both critical and potentially optimal actuator placements, informed by the physical characteristics of the system [2, 15].

The mass of the actuators is approximately 140 g, which can alter the system's response even without control. Fig. 4 compares the power spectral density (PSD) of the three error microphones for the four configurations under consideration.

The difference between Configuration 1 and Configuration 4 is particularly noticeable in the frequency range between 150 Hz and 200 Hz. This is due to the fact that, in Configuration 4, the actuator masses are positioned near the edges of the clamped plate, regions of high stress, resulting in a higher sound power response.

In contrast, Configuration 1 places two of the three actuators closer to the opening, which helps to reduce vibrations in that region, thereby minimizing the radiated sound power. Moreover, Configurations 2 and 3 exhibit similar performance, as the actuators are more concentrated near the center of the plate. To assess the reduction achieved through active control, the four configurations are compared to the average microphone response in the absence of control. As shown in Fig. 5, ASAC effectively minimizes the system's sound power response, indicating that it is not only effective in reducing radiated sound but also in mitigating noise leakage through the opening. The actuator placement near the clamped edges in Configuration 4 restricts the system's ability to vibrate actively. The displacement is constrained, and this helps generate anti-noise waves that counteract sound leakage through



(a) Configuration 1. (b) Configuration 2.

(c) Configuration 3. (d) Configuration 4.

(e) Configuration 5.

Figure 3: An overview of the four configurations of the actuators' arrangements.

the opening.

Configuration 3 demonstrates the best performance across the considered frequency range. This is attributed to one actuator being positioned closer to the opening—allowing greater flexibility for displacement—combined with a central actuator arrangement that provides a balanced response across most mode shapes. Configurations 1 and 2 may be advantageous when targeting specific resonances. For instance, Configuration 2 positions the actuators closer to the anti-nodal regions of the third and fourth mode shapes of the rectangular plate [2], making it more effective in that frequency range.

To evaluate the influence of the relative position of the opening with respect to the excitation source, as well as the effect of actuator arrangement, Configuration 5 is tested and compared with Configuration 1. This comparison is considered fair, as both configurations share a similar actuator arrangement, as illustrated in Fig. 6.

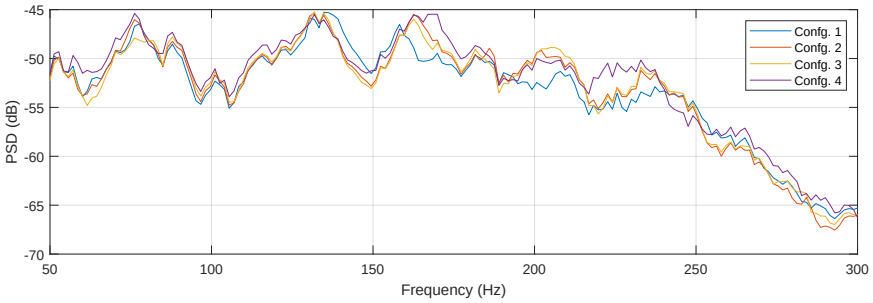
Configuration 5 exhibits lower sound power levels compared to Configuration 4, particularly in the frequency range between 135 Hz and 200 Hz. This improvement is attributed to the fact that the opening in Configuration 5 is positioned farther from the internal noise source, resulting in reduced sound leakage through the opening. When ASAC is applied, Configuration 5 demonstrates enhanced control performance due to the revised opening location, which makes the actuator placement—particularly that of Act 1 and 3—more favorable for inducing effective vibrational displacement near the aperture. As a result, despite having the same actuator arrangement as Configuration 1, the system achieves over 5 dB additional noise reduction in the frequency ranges of 70–125 Hz and 170–200 Hz due to the relocated opening.

4. CONCLUSION

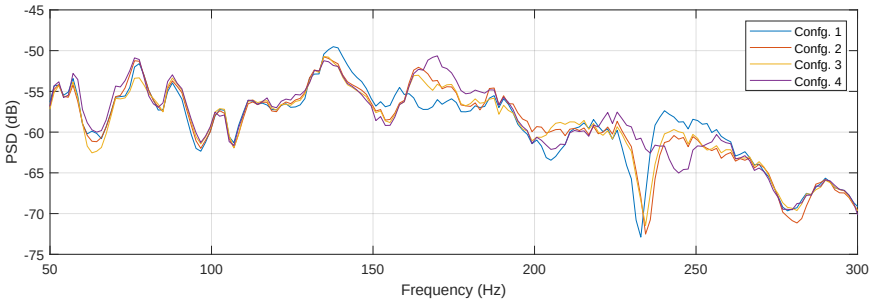
This study experimentally examined the application of Active Structural Acoustic Control (ASAC) in vibro-acoustic systems with structural openings, focusing on the influence of inertial actuator placement and opening location on control effectiveness. Five actuator configurations were evaluated on a fully clamped vibrating plate to assess how spatial arrangement and structural characteristics impact both passive and active noise control performance.

The results demonstrate that actuator positioning significantly affects the system's vibrational and acoustic response. Configurations with actuators placed near the clamped edges—regions of high stress and low vibrational energy—showed limited effectiveness in both passive damping and active control. In contrast, configurations with actuators distributed closer to the plate center or near the opening, such as Configuration 3, provided more balanced control across the frequency range, benefiting from greater displacement flexibility and improved mode shape engagement. Moreover, Configuration 5 revealed that relocating the opening farther from the noise source, even with the same actuator arrangement as Configuration 1, can lead to an additional 5 dB reduction in key frequency ranges. This highlights that the opening's position, in relation to the excitation source and actuators, plays a crucial role in minimizing sound leakage and enhancing ASAC performance.

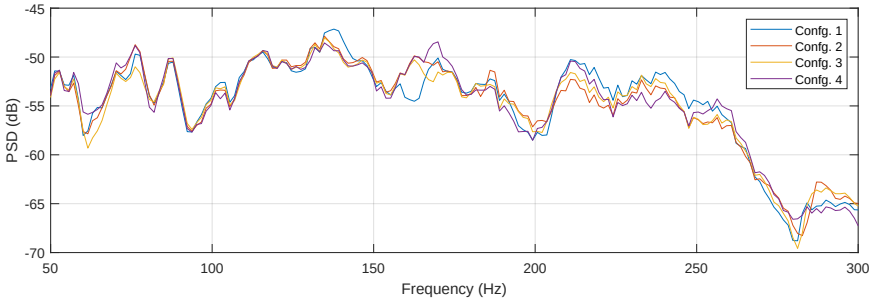
These findings underscore the importance of tailoring



(a) Mic 1

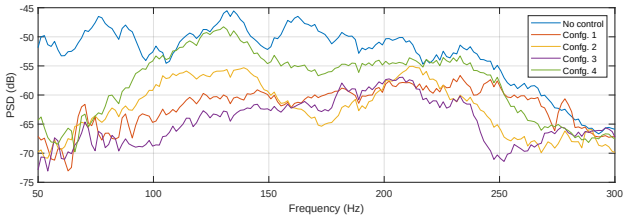


(b) Mic 2

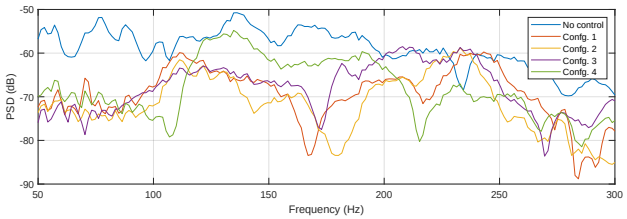


(c) Mic 3

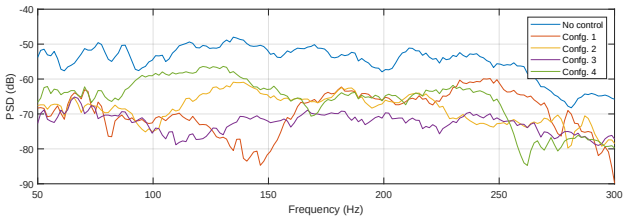
Figure 4: PSD of the three error signals for the configurations without active control.



(a) Mic 1



(b) Mic 2



(c) Mic 3

Figure 5: PSD of the three error signals for the configurations with active control.

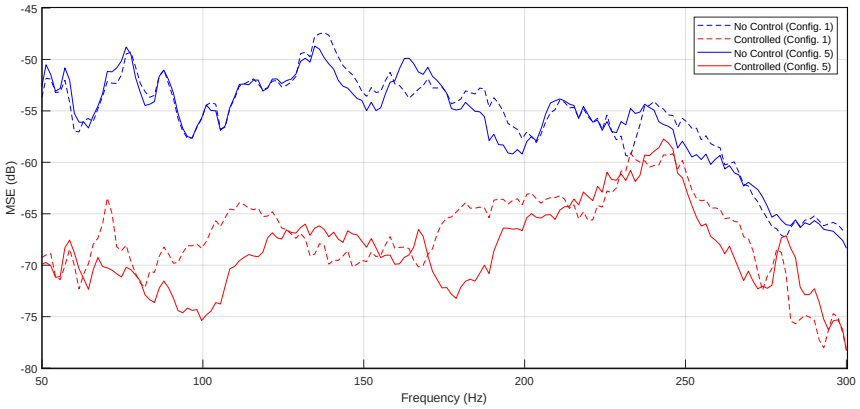


Figure 6: Mean square error (MSE) of the three error microphones signals for Configurations 1 and 5.

actuator placement strategies to the specific structural and acoustic context, particularly in systems with openings, to maximize control efficiency and achieve optimal noise reduction.

5. ACKNOWLEDGMENTS

The work was supported by the project IN-NOVA: Active reduction of noise transmitted into and from enclosures through encapsulated structures, which has received funding from the European Union's Horizon Europe program under the Marie Sklodowska-Curie grant agreement no. 101073037.

6. REFERENCES

[1] Z. Zhu, Y. Song, Y. Zhang, Q. Liu, and G. Wang, "Sound radiation of the plate with arbitrary holes," *International Journal of Mechanical Sciences*, vol. 264, p. 108814, 2024.

[2] K. S. A. Maamoun, S. Wrona, M. Pawelczyk, and H. R. Karimi, "Shaping of the frequency response of vibrating plates with openings for vibro-acoustic systems," *Mechanical Systems and Signal Processing*, vol. 218, p. 111539, 2024.

[3] S. Elliott, *Signal processing for active control*. Elsevier, 2001.

[4] K. Mazur, S. Wrona, and M. Pawelczyk, "Design and implementation of multichannel global active structural acoustic control for a device casing," *Mechanical Systems and Signal Processing*, vol. 98, pp. 877–889, 2018.

[5] A. Chraponska, S. Wrona, J. Rzepecki, K. Mazur, and M. Pawelczyk, "Active structural acoustic control of an active casing placed in a corner," *Applied Sciences*, vol. 9, no. 6, p. 1059, 2019.

[6] S. Wrona and M. Pawelczyk, "Active reduction of device narrowband noise by controlling vibration of its casing based on structural sensors," in *Proceedings of the 22nd International Congress on Sound and Vibration, Florence, Italy*, pp. 12–16, 2015.

[7] O. Jeon, H.-G. Kim, J. Kook, S. M. Kim, and S. Wang, "Active structural acoustic control for radiated sound power reduction of enclosure with vent holes based on radiation modes," *Journal of Mechanical Science and Technology*, vol. 36, no. 7, pp. 3313–3327, 2022.

[8] M. Misol, S. Algermissen, M. Rose, and H. P. Monner, "Aircraft lining panels with low-cost hardware for active noise reduction," in *2018 Joint Conference-Acoustics*, pp. 1–6, IEEE, 2018.

[9] J. Milton, J. Cheer, and S. Daley, "Active structural acoustic control using an experimentally identified radiation resistance matrix," *The Journal of the Acoustical Society of America*, vol. 147, no. 3, pp. 1459–1468, 2020.

[10] P. Song and H. Zhao, "Filtered-x least mean square/fourth (fxlms/f) algorithm for active noise control," *Mechanical Systems and Signal Processing*, vol. 120, pp. 69–82, 2019.

[11] O. Tobias and R. Seara, "Leaky-fxlms algorithm: stochastic analysis for gaussian data and secondary path modeling error," *IEEE Transactions on Speech and Audio Processing*, vol. 13, no. 6, pp. 1217–1230, 2005.

[12] M. T. Akhtar and W. Mitsuhashi, "A modified normalized fxlms algorithm for active control of impulsive noise," in *2010 18th European Signal Processing Conference*, pp. 1–5, 2010.

[13] X. Liu, G. Cai, F. Peng, and H. Zhang, "Piezoelectric actuator placement optimization and active vibration control of a membrane structure," *Acta Mechanica Solida Sinica*, vol. 31, pp. 66–79, 2018.

[14] D. Chhabra, G. Bhushan, and P. Chandna, "Optimal placement of piezoelectric actuators on plate structures for active vibration control via modified control matrix and singular value decomposition approach using modified heuristic genetic algorithm," *Mech. Adv. Mat. Struct.*, vol. 23, no. 3, pp. 272–280, 2016.

[15] S. Wrona, M. Pawelczyk, and J. Cheer, "Acoustic radiation-based optimization of the placement of actuators for active control of noise transmitted through plates," *Mechanical Systems and Signal Processing*, vol. 147, p. 107009, 2021.

[16] Q. Mao and S. Pietrzko, "Control of noise and structural vibration," *Cham, Switzerland: Springer, DOI*, 2013.

[17] Analog Devices, "ADSP-SC598 Product Page," 2025. Accessed: 2025-03-01.

DOI: 10.61782/fa.2025.0008



FORUM ACUSTICUM
EURONOISE 2025

A COMPARISON BETWEEN SPATIAL INTERPOLATION APPROACHES IN A HEAD-TRACKED ACTIVE HEADREST SYSTEM

Chung Kwan Lai* **Jordan Cheer**
Institute of Sound and Vibration Research (ISVR)
University of Southampton, United Kingdom.

ABSTRACT

The integration of head-tracking can improve the achievable performance of active noise control headrest systems by allowing the mismatch between the plant model used by the controller and the physical plant response to be reduced. Although previous studies have shown that the performance improvement achieved through head-tracking is limited by the resolution of the tracking system, this limitation can be addressed by either interpolating between plant models obtained at different head positions and then calculating the required controller, or interpolating between a set of pre-computed controllers optimised for different head positions. The differences in performance between the two approaches to interpolation, however, have not been explored, despite various interpolation strategies being previously utilised in head-tracked active control systems discussed in the literature. This paper presents a comparison between the two approaches to spatial interpolation for a head-tracked active headrest system. Assuming a tonal disturbance, it is shown through numerical simulations that the performance benefit brought by spatial interpolation differs between the two approaches to interpolation.

Keywords: *active headrest system, local active noise control, head-tracker, interpolation*

1. INTRODUCTION

The use of active noise control to provide local control of sound at a listener's ears dates back to the 1950s [1], however, it has recently attracted renewed interest due to the potential for integrating head-tracking techniques to extend the bandwidth of effective control [2]. In the context of an active headrest system [3], where secondary loudspeakers are typically placed near the headrest, a head-tracker can be used to detect the current position of the user's head and update either the plant model, which is then used to compute the controller, or the precomputed controller itself, both of which would be obtained during a calibration stage. In either case, this updating process can reduce the mismatch between the physical and assumed responses for the physical head position, thereby improving control performance in response to head movements. While it is ideal for the head-tracker and corresponding system updates to be as accurate as possible to maximise the control performance, such an approach may not be feasible in practice, as this would require a lengthy calibration process to measure the plant responses and optimal controllers for many head positions. Previous research has been conducted to determine how the tracking accuracy influences the performance and stability of an active headrest system and ultimately to define the required tracking accuracy for a given level and bandwidth of performance [4, 5]. However, rather than utilising an extremely fine tracking resolution, an alternative approach is to interpolate between the responses [6] for a coarser tracking resolution to improve their accuracy. Although it seems relatively straightforward that the performance of the active headrest system will depend on the accuracy provided by the interpolation algorithm used, there are in fact two approaches to interpolation: in the first case, the plant responses corresponding to the coarse measurement grid are interpolated directly and the optimal controller is then calculated using the interpolated plant responses; in the second case, the interpolation is instead performed between the optimal controllers calculated for each head position

**Corresponding author*: C.K.Lai@soton.ac.uk.
Copyright: *©2025 First author et al. This is an open-access article distributed under the terms of the Creative Commons Attribution 3.0 Unported License, which permits unrestricted use, distribution, and reproduction in any medium, provided the original author and source are credited.*

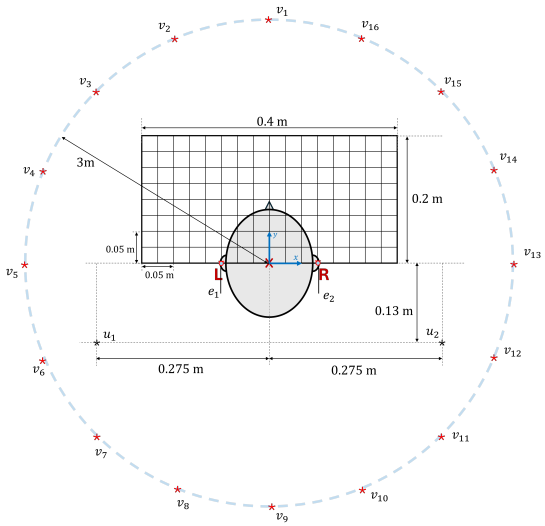


Figure 1: Configuration for the active headrest where the head translates in the sway (left/right) and surge (front/back) direction within a $(0.4\text{ m} \times 0.2\text{ m})$ translational grid. The minimum grid spacing for the translational grid is 0.025 m.

on the coarse measurement grid. This paper presents a comparison between the control performance for the two proposed approaches to interpolation applied to an active headrest system. Sec. 2 describes the active headrest and introduces the two spatial interpolation approaches; Sec. 3 describes the interpolation algorithm used to realise the interpolation in both cases; Sec. 4 presents the results from the simulation study; and conclusions are drawn in Sec. 5.

2. FORMULATION OF ACTIVE HEADREST CONTROL PROBLEM

Fig. 1 illustrates the numerically simulated configuration of the active headrest, which employs a boundary element model of the KU100 head [7] implemented in COMSOL to represent the user's head. Two monopole point sources, driven by control signals u_1 and u_2, simulate the secondary sources in the active headrest; whilst the disturbance sound field is generated by 16 incoherent primary sources, driven by the complex source strengths $v_1 - v_{16}$, positioned around the head, as depicted in Fig. 1. The feedforward control strategy used to minimise the signals at the user's ears is shown in Fig. 2, where each diagram illustrates a different interpolation approach for updating the control filter, $\mathbf{W}$, based on the current location of the head. Assuming that the disturbance signal is tonal, the cost function that aims to minimise the error signals located at the user's ears can be expressed in the frequency domain, as

$$\begin{aligned} J &= \mathbb{E}\left[\mathbf{e}^{\mathrm{H}}\mathbf{e} + \beta\mathbf{u}^{\mathrm{H}}\mathbf{u}\right] \\ &= \mathrm{tr}\left\{\mathbb{E}\left[\mathbf{e}\mathbf{e}^{\mathrm{H}} + \beta\mathbf{u}\mathbf{u}^{\mathrm{H}}\right]\right\} \end{aligned} \tag{1}$$

where $\mathbf{e}$ and $\mathbf{u}$ denote complex vectors of the error signals and control signals, respectively, and $\beta = 0$ is the regularization parameter. Based on the block diagram shown in Fig. 2, the complex vector of error signals is given by

$$\mathbf{e} = \mathbf{d} + \mathbf{G}\mathbf{u} = \mathbf{d} + \mathbf{G}\mathbf{W}\mathbf{x}, \tag{2}$$

where $\mathbf{W}$ and $\mathbf{G}$ are matrices of control filters and the physical plant responses, respectively, and $\mathbf{x}$ is the complex vector of reference signals. Assuming that the physical plant responses are perfectly known, the optimal control filter matrix can therefore be derived as [8]

$$\mathbf{W}_{opt} = -\left[\mathbf{G}^{\mathrm{H}}\mathbf{G} + \beta\mathbf{I}\right]^{-1}\mathbf{G}^{\mathrm{H}}\mathbf{S}_{xd}\mathbf{S}_{xx}^{-1}, \tag{3}$$

where $\mathbf{S}_{xd}$ is the spectral density matrix between the disturbance and reference signals, and $\mathbf{S}_{xx} = \mathbf{I}$ is the spectral density matrix of the reference signals, following the general notation $\mathbf{S}_{xy} = \mathbb{E}\left[\mathbf{y}\mathbf{x}^{\mathrm{H}}\right]$.

During the initial calibration phase, the plant responses were directly obtained for a subset of head positions within a discrete translational grid of $(0.4\text{ m} \times 0.2\text{ m})$, marked by the red crosses in Fig. 3. The corresponding optimal control filters for these head positions were then calculated using Eqn. (3). The use of a coarser resolution reflects the practical constraints encountered on calibration complexity and duration. For the remaining grid points, the control filter can be determined utilising the two different approaches to interpolation, as outlined in Fig. 2. In the controller-based interpolation approach, as shown in Fig. 2a, the control filter is calculated by directly interpolating between the optimal control filters computed for the head positions included in the calibration process, and the interpolated control filter is denoted as $\underset{\sim}{\mathbf{W}}$. In contrast, in the plant-based interpolation strategy, as shown in Fig. 2b, the plant model and spectral density at the target head position are first estimated by interpolating between the responses measured in the calibration, and then the control filters are calculated using the interpolated responses, as

$$\mathbf{W}_o = -\left[\underset{\sim}{\mathbf{G}}^{\mathrm{H}}\underset{\sim}{\mathbf{G}} + \beta\mathbf{I}\right]^{-1}\underset{\sim}{\mathbf{G}}^{\mathrm{H}}\underset{\sim}{\mathbf{S}}_{xd}\mathbf{S}_{xx}^{-1}, \tag{4}$$

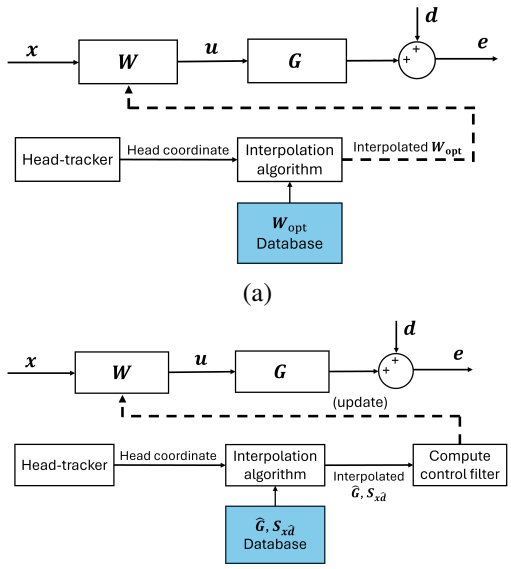


Figure 2: The multichannel feedforward control system used in the head-tracker equipped active headrest system, featuring (a): controller-based interpolation and (b): plant-based interpolation architecture.

where $\underset{\sim}{\mathbf{G}}$ and $\underset{\sim}{\mathbf{S}}_{xd}$ denote the interpolated plant model and spectral density matrices respectively.

To compare the performance of the two approaches to interpolation, the control performance of the active headrest system at the interpolated grid points can be assessed by computing the attenuation performance at the i-th error microphone, given by

$$L_{e,i} = -10\log_{10}\left|\frac{\mathbf{S}_{e_i e_i}}{\mathbf{S}_{d_i d_i}}\right|. \tag{5}$$

3. SPATIAL INTERPOLATION BASED ON KERNEL RIDGE REGRESSION

While various interpolation algorithms are available, to compare the two approaches to interpolation described in the previous section, the Kernel-ridge interpolation method will be utilised. This algorithm has recently been applied to sound-field estimation and a spatial active noise control system [9, 10], and is described in this section.

Consider a general complex matrix $\underset{\sim}{\mathbf{H}}(\boldsymbol{\psi}) \in \mathbb{C}^{(I\times J)}$, where $\boldsymbol{\psi}$ represents the vector of head coordinates, and

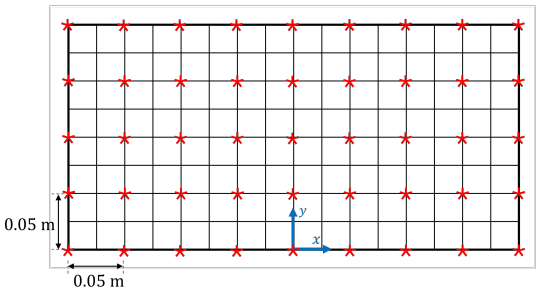


Figure 3: Head positions within the translational grid, marked by red crosses, indicate locations where plant responses were directly measured during the calibration phase.

the element at the i-th row and j-th column is denoted by $\underset{\sim}{h}_{ij}(\boldsymbol{\psi})$. In this context, $\underset{\sim}{\mathbf{H}}$ may represent either the control filter $\underset{\sim}{\mathbf{W}}$, plant model $\underset{\sim}{\mathbf{G}}$, or spectral density $\underset{\sim}{\mathbf{S}}_{xd}$, depending on the interpolation approach being utilised. During the calibration phase, the matrix is measured at discrete grid positions, which are denoted as $\hat{\mathbf{H}}(\boldsymbol{\psi}_n)$ for the n-th position. The goal of interpolation is to estimate each element of $\underset{\sim}{\mathbf{H}}$ at an arbitrary position $\boldsymbol{\psi}$ using the corresponding elements from the pre-measured matrices $\hat{\mathbf{H}}$ at the known positions $\boldsymbol{\psi}_n$. Each element of $\underset{\sim}{\mathbf{H}}$ can be calculated according to the interpolation function given as $\underset{\sim}{h}_{ij}(\boldsymbol{\psi}) = \boldsymbol{\phi}^{\mathrm{H}}(\boldsymbol{\psi})\mathbf{f}$, where $\boldsymbol{\phi}(\boldsymbol{\psi})$ is the input feature vector that is a function of head coordinates $\boldsymbol{\psi}$, and $\mathbf{f}$ is the complex weighting vector containing the coefficients that determine the contribution of each feature vector components. The cost function, which minimises the sum of squared errors between the interpolated and pre-measured elements across all discrete head positions, is defined as

$$\begin{aligned} J_{ij} &= \sum_{n=1}^{N}\left|\underset{\sim}{h}_{ij}(\boldsymbol{\psi}_n) - \hat{h}_{ij}(\boldsymbol{\psi}_n)\right|^2 + \lambda\mathbf{f}^{\mathrm{H}}\mathbf{f} \\ &= \left(\boldsymbol{\Phi}\mathbf{f} - \hat{\mathbf{h}}_{ij}\right)^{\mathrm{H}}\left(\boldsymbol{\Phi}\mathbf{f} - \hat{\mathbf{h}}_{ij}\right) + \lambda\mathbf{f}^{\mathrm{H}}\mathbf{f}, \end{aligned} \tag{6}$$

where N is the total number of discrete grid points used during the calibration phase, and

$$\boldsymbol{\Phi} = \left[\boldsymbol{\phi}^{\mathrm{H}}(\boldsymbol{\psi}_1)\ \boldsymbol{\phi}^{\mathrm{H}}(\boldsymbol{\psi}_2)\ \cdots\ \boldsymbol{\phi}^{\mathrm{H}}(\boldsymbol{\psi}_N)\right]^{\mathrm{T}}, \tag{7}$$

$$\hat{\mathbf{h}}_{ij} = \left[\hat{h}_{ij}(\boldsymbol{\psi}_1)\ \hat{h}_{ij}(\boldsymbol{\psi}_2)\ \cdots\ \hat{h}_{ij}(\boldsymbol{\psi}_N)\right]^{\mathrm{T}}, \tag{8}$$

are the generic input feature matrix and the vector of pre-measured elements across all grid points, respectively, and

λ is the regularisation factor. The optimal $\mathbf{f}$ is therefore given as

$$\mathbf{f}_{opt} = \left[\mathbf{\Phi}^{\mathrm{H}}\mathbf{\Phi} + \lambda\mathbf{I}\right]^{-1}\mathbf{\Phi}^{\mathrm{H}}\hat{\mathbf{h}}_{ij}. \tag{9}$$

However, the value of $\mathbf{f}_{opt}$ depends on the choice of $\mathbf{\Phi}$, which may involve a much higher number of dimensions than the number of grid points. Instead, the cost function can be kernelized to overcome the dimensionality curse imposed by the generic input feature vector [11]. By letting $\mathbf{f} = \mathbf{\Phi}^{\mathrm{H}}\boldsymbol{\alpha}$, where $\boldsymbol{\alpha}$ is the intermediate complex variable vector, the cost function from Eqn. (6) can be expressed in terms of $\boldsymbol{\alpha}$ to give

$$J_{ij} = \boldsymbol{\alpha}^{\mathrm{H}}\left[(\mathbf{K}\mathbf{K} + \lambda\mathbf{K})\right]\boldsymbol{\alpha} - \boldsymbol{\alpha}^{\mathrm{H}}\mathbf{K}\hat{\mathbf{h}}_{ij} - \hat{\mathbf{h}}_{ij}^{\mathrm{H}}\mathbf{K}\boldsymbol{\alpha} + \hat{\mathbf{h}}_{ij}^{\mathrm{H}}\hat{\mathbf{h}}_{ij}, \tag{10}$$

where $\mathbf{K} = \mathbf{\Phi}\mathbf{\Phi}^{\mathrm{H}}$ is the Gram matrix, which is Hermitian and semi-positive-definite i.e. $\mathbf{K} = \mathbf{K}^{\mathrm{H}}$, given by

$$\mathbf{K} = \begin{bmatrix} \kappa(\boldsymbol{\psi}_1, \boldsymbol{\psi}_1) & \kappa(\boldsymbol{\psi}_1, \boldsymbol{\psi}_2) & \cdots & \kappa(\boldsymbol{\psi}_1, \boldsymbol{\psi}_N) \\ \kappa(\boldsymbol{\psi}_2, \boldsymbol{\psi}_1) & \kappa(\boldsymbol{\psi}_2, \boldsymbol{\psi}_2) & \cdots & \kappa(\boldsymbol{\psi}_3, \boldsymbol{\psi}_N) \\ \vdots & \vdots & \ddots & \vdots \\ \kappa(\boldsymbol{\psi}_N, \boldsymbol{\psi}_1) & \kappa(\boldsymbol{\psi}_N, \boldsymbol{\psi}_2) & \cdots & \kappa(\boldsymbol{\psi}_N, \boldsymbol{\psi}_N) \end{bmatrix}, \tag{11}$$

and $\kappa(\boldsymbol{\psi}_m, \boldsymbol{\psi}_n) = \boldsymbol{\phi}^{\mathrm{H}}(\boldsymbol{\psi}_m)\boldsymbol{\phi}(\boldsymbol{\psi}_n)$ is denoted as a kernel function. The optimal value of $\boldsymbol{\alpha}$ that minimises Eqn. (10) can then be obtained as

$$\boldsymbol{\alpha}_{opt} = \left(\mathbf{K} + \lambda\mathbf{I}\right)^{-1}\hat{\mathbf{h}}_{ij}. \tag{12}$$

Finally, the interpolated element at an arbitrary position $\boldsymbol{\psi}$ can then be evaluated as

$$\underset{\sim}{h}_{ij}(\boldsymbol{\psi}) = \boldsymbol{\kappa}(\boldsymbol{\psi})\left(\mathbf{K} + \lambda\mathbf{I}\right)^{-1}\hat{\mathbf{h}}_{ij}, \tag{13}$$

where

$$\boldsymbol{\kappa}(\boldsymbol{\psi}) = \left[\kappa(\boldsymbol{\psi}, \boldsymbol{\psi}_1)\ \kappa(\boldsymbol{\psi}, \boldsymbol{\psi}_2)\ \cdots\ \kappa(\boldsymbol{\psi}, \boldsymbol{\psi}_N)\right] \tag{14}$$

is known as the reproducing Kernel vector.

To gain a preliminary understanding of how different kernel functions affect the controller's performance, two different kernel functions have been used here for interpolation. The first, derived from previous work [10], is constrained by the 3D Helmholtz equation and is given by

$$\begin{aligned}\kappa(\boldsymbol{\psi}_m, \boldsymbol{\psi}_n) &= \mathrm{sinc}(k||\boldsymbol{\psi}_m - \boldsymbol{\psi}_n||_2) \\ &= \frac{\sin(k||\boldsymbol{\psi}_m - \boldsymbol{\psi}_n||_2)}{k||\boldsymbol{\psi}_m - \boldsymbol{\psi}_n||_2},\end{aligned} \tag{15}$$

where $k = \omega/c_0$ is the acoustic wavenumber, and $||\cdot||_2$ denotes the l_2-norm. The second kernel function, adapted from [12], is a Gaussian kernel scaled according to the wavenumber, defined as

$$\kappa(\boldsymbol{\psi}_m, \boldsymbol{\psi}_n) = \exp\left(-k^2||\boldsymbol{\psi}_m - \boldsymbol{\psi}_n||_2^2\right). \tag{16}$$

To evaluate the accuracy of the interpolation, the overall interpolation error between the interpolated matrix $\underset{\sim}{\mathbf{H}}$ and the true matrix $\mathbf{H}$ at the interpolated head position $\boldsymbol{\psi}$ is defined as

$$L_{\mathbf{H}}(\boldsymbol{\psi}) = 10\log_{10}\left|\frac{\sum_{i,j}\left|h_{ij}(\boldsymbol{\psi}) - \underset{\sim}{h}_{ij}(\boldsymbol{\psi})\right|^2}{\sum_{i,j}\left|h_{ij}(\boldsymbol{\psi})\right|^2}\right|. \tag{17}$$

4. COMPARISON BETWEEN SPATIAL INTERPOLATION APPROACHES

This section evaluates the interpolation accuracy for the interpolation algorithm introduced in Sec. 3 and the performance of the active headrest system is then presented in Sec. 4.2, with a comparison between the two interpolation approaches described in Sec. 2.

4.1 Interpolation accuracy

Fig. 4 and Fig. 5 present the overall interpolation error, calculated according to Eqn. (17), for the $\mathbf{G}$, $\mathbf{S}_{xd}$, and $\mathbf{W}$ matrices at all head positions requiring interpolation, corresponding to the unmarked grid points in Fig. 3. To improve the conditioning of the Gram matrix inversion in Eqn. (11), the regularisation parameter for all cases was set to $\lambda = 1 \times 10^{-6}$. When the Helmholtz kernel function from Eqn. (15) is used to interpolate the $\mathbf{G}$ and $\mathbf{S}_{xd}$ matrices, the interpolation error, shown in Fig. 4a, remains below -30 dB across all frequencies. Notably, the error for $\mathbf{S}_{xd}$ is significantly lower than that for $\mathbf{G}$ at all frequencies, highlighting how interpolation accuracy varies between different matrices. In contrast, when using the Gaussian kernel function from Eqn. (16), as shown in Fig. 4b, the estimation error increases with frequency, exceeding -20 dB at some head positions around 900 Hz. This difference arises from the nature of the kernel function itself, as discussed in [10], where the Helmholtz kernel function is better suited for the interpolation of responses that are physically related to the acoustic sound field, such as the acoustic response. While both the plant $\mathbf{G}$ and spectral density $\mathbf{S}_{xd}$ correspond to the secondary and primary acoustic responses, respectively, the differences in interpolation accuracy between the two may arise

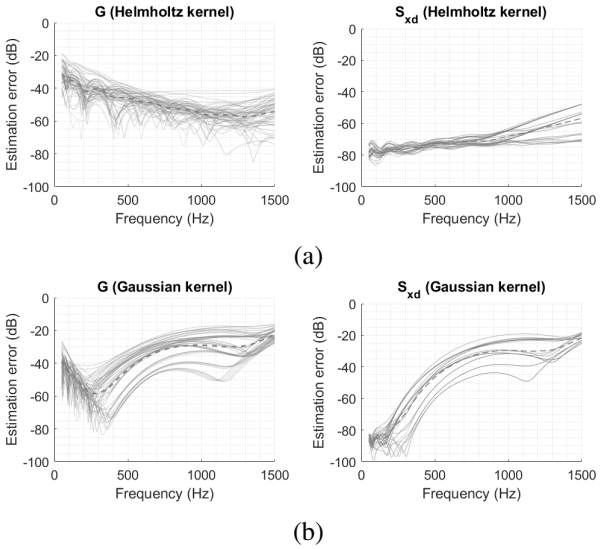


Figure 4: The overall interpolation error, evaluated using Eqn. (17), for the $\mathbf{G}$ and $\mathbf{S}_{xd}$ matrices as a function of frequency at head positions requiring interpolation. Solid lines represent errors for all head positions requiring interpolation using the (a) Helmholtz kernel from Eqn. (15) and the (b) Gaussian kernel from Eqn. (16), while the dotted line indicates the average interpolation error.

from the fact that the head scattering effect varies more spatially in the near-field compared to the far-field. When both the Helmholtz and Gaussian kernel functions are used to interpolate the control filter, the overall interpolation error, as shown in Fig. 5, is significantly lower compared to that of $\mathbf{G}$ and $\mathbf{S}_{xd}$, and increases with frequency. Even though the control filter is directly related to the plant responses, as shown in Eqn. (3), the individual elements of the controller matrix result from the interaction between all elements of the plant due to the matrix inverse and multiplication operation, which results in a lower interpolation accuracy. These results offer valuable insights into how the performance of the active headrest system varies between the spatial interpolation approaches, as further discussed in Sec. 4.2.

4.2 Control performance comparison between spatial interpolation approaches

Fig. 6 and Fig. 7 present the attenuation performance plots for the left error microphone as a function of frequency

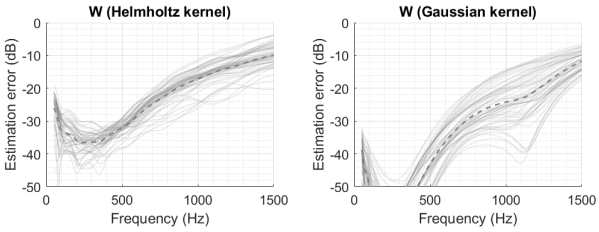
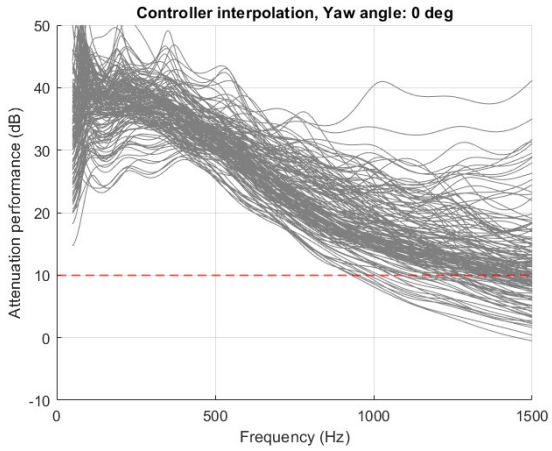
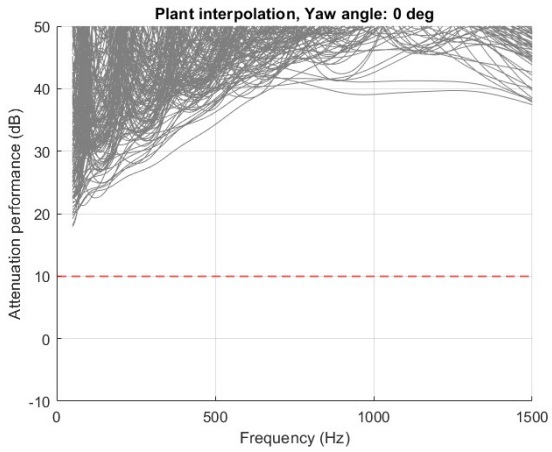


Figure 5: The overall interpolation error, evaluated using Eqn. (17), for the control filter $\mathbf{W}$ as a function of frequency at head positions requiring interpolation. Solid lines represent errors for all head positions requiring interpolation using the (a) Helmholtz kernel from Eqn. (15) and the (b) Gaussian kernel from Eqn. (16), while the dotted line indicates the average interpolation error.

for all head positions requiring interpolation. Depending on the interpolation approach being applied, interpolation is performed on either the plant responses or precomputed controllers obtained from the marked grid points in Fig. 3. When the controller-based interpolation strategy using the Kernel function from Eqn. (15) is applied (Fig. 6a), the attenuation performance generally decreases with increasing frequency, with less than 10 dB performance being achieved for some head positions at around 900 Hz. In contrast, the attenuation performance is significantly improved when the plant-based interpolation strategy (Fig. 6b) is used, with attenuation levels in excess of 20 dB being achieved across all frequencies. This is likely due to the differences in interpolation accuracy between the plant and controller matrices, as discussed in Sec. 4.1, which results in an upper-frequency limit beyond which the performance achieved by interpolating the controller is limited. When the Gaussian kernel from Eqn. (16) is used in the interpolation algorithm, the performance of both interpolation approaches degrades with increasing frequency. The results for the controller-based approach (Fig. 7a) show a slight improvement compared to those obtained using the Helmholtz kernel function (Fig. 6a) for some head positions. Although the plant-based interpolation approach still performs better than the controller-based interpolation approach, the results still highlight the importance of selecting the appropriate kernel function when performing spatial interpolation.

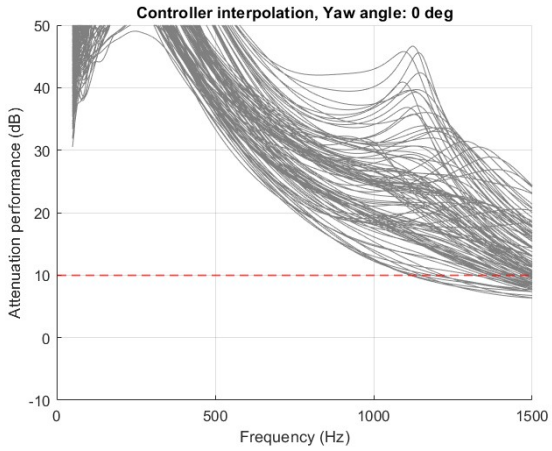


(a)

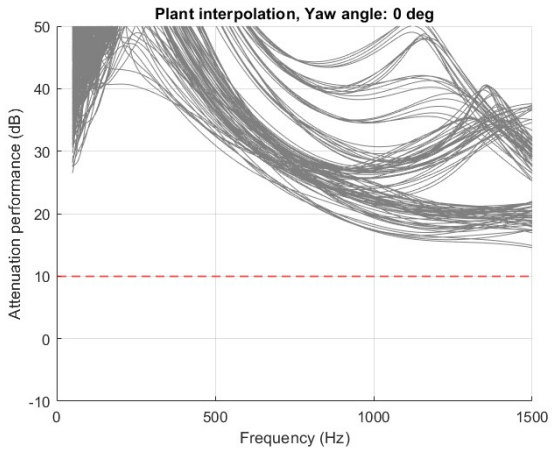


(b)

Figure 6: Attenuation performance plots for the left error microphone as a function of frequency for head positions requiring interpolation using the Helmholtz kernel function given by Eqn. (15), shown for (a) the controller-based and (b) the plant-based interpolation method.



(a)



(b)

Figure 7: Attenuation performance plots for the left error microphone as a function of frequency for head positions requiring interpolation using the gaussian kernel function given by Eqn. (16) , shown for (a) the controller-based and (b) the plant-based interpolation method.

5. CONCLUSIONS

Although integrating head-tracking techniques into active noise control headrest systems has been shown to significant enhance control performance, the performance remains constrained by the resolution of head-tracking, which is limited by the calibration procedure. This limitation can be addressed by applying spatial interpolation techniques to estimate the either the controller or the plant responses at head positions that have not been explicitly calibrated. However, the effectiveness of interpolation depends on both the chosen interpolation approach and the utilised interpolation algorithm. This paper has presented two interpolation approaches: one that interpolates between plant models obtained at different head positions before computing the corresponding controller, and another that interpolates directly between a set of precomputed optimal controllers. In both cases the kernel ridge interpolation algorithm has been utilised with different kernel functions being explored. The results from numerical simulations of an active headrest system with head-tracking have demonstrated that when utilising the kernel ridge interpolation algorithm, a significant improvement in control performance is achieved when utilising the plant-based interpolation approach. It has also been shown that the kernel function has a significant impact on the achieved performance, with the Helmholtz kernel function providing a significant performance advantage when utilised with the plant-model interpolation approach, but providing somewhat inferior performance when applied to the controller-based interpolation approach.

6. ACKNOWLEDGMENTS

The work was supported by the project IN-NOVA: Active reduction of noise transmitted into and from enclosures through encapsulated structures, which has received funding from the European Union's Horizon Europe programme under the Marie Sklodowska-Curie grant agreement no. 101073037. This work was funded by UK Research and Innovation under the UK government's Horizon Europe funding guarantee [grant number EP/X027767/1]. Jordan Cheer was supported by the Department of Science, Innovation and Technology (DSIT) Royal Academy of Engineering under the Research Chairs and Senior Research Fellowships programme.

7. REFERENCES

[1] H. F. Olson and E. G. May, "Electronic Sound Absorber," *The Journal of the Acoustical Society of America*, vol. 25, pp. 1130–1136, Nov. 1953.

[2] S. J. Elliott, W. Jung, and J. Cheer, "Head tracking extends local active control of broadband sound to higher frequencies," *Scientific Reports*, vol. 8, pp. 1–7, Dec. 2018.

[3] B. Rafaely, S. J. Elliott, and J. Garcia-Bonito, "Broadband performance of an active headrest," *The Journal of the Acoustical Society of America*, vol. 106, pp. 787–793, Aug. 1999.

[4] C. K. Lai, J. Cheer, and C. Shi, "The effect of head-tracking resolution on the stability and performance of a local active noise control headrest system," *The Journal of the Acoustical Society of America*, vol. 157, pp. 766–777, Feb. 2025.

[5] H. Jiang, H. Chen, J. Tao, H. Zou, and X. Qiu, "Accuracy requirements of ear-positioning for active control of road noise in a car," *Applied Acoustics*, vol. 225, p. 110164, Nov. 2024. Read_Status: Done Read_Status_Date: 2024-11-11T22:45:18.126Z.

[6] J. Y. Oh, H. W. Jung, M. H. Lee, K. H. Lee, and Y. J. Kang, "Enhancing active noise control of road noise using deep neural network to update secondary path estimate in real time," *Mechanical Systems and Signal Processing*, vol. 206, p. 110940, Jan. 2024. Read_Status: Done Read_Status_Date: 2024-10-16T20:57:28.691Z.

[7] F. Di Giusto, S. Van Ophem, W. Desmet, and E. Deckers, "Analysis of laser scanning and photogrammetric scanning accuracy on the numerical determination of Head-Related Transfer Functions of a dummy head," *Acta Acustica*, vol. 7, p. 53, 2023.

[8] S. Elliott, *Signal Processing for Active Control*. Academic Press, 2000.

[9] S. Koyama, J. Brunnstrom, H. Ito, N. Ueno, and H. Saruwatari, "Spatial Active Noise Control Based on Kernel Interpolation of Sound Field," *IEEE/ACM Transactions on Audio, Speech, and Language Processing*, vol. 29, pp. 3052–3063, 2021. Read_Status: Done Read_Status_Date: 2024-09-22T08:31:58.734Z.

[10] S. Koyama, J. G. C. Ribeiro, T. Nakamura, N. Ueno, and M. Pezzoli, "Physics-Informed Machine Learning for Sound Field Estimation: Fundamentals, state

of the art, and challenges [Special Issue On Model-Based and Data-Driven Audio Signal Processing]," *IEEE Signal Processing Magazine*, vol. 41, pp. 60–71, Nov. 2024.

[11] N. Cristianini and J. Shawe-Taylor, *An introduction to support vector machines: And other kernel-based learning methods*. Cambridge: Cambridge University Press, 2013. OCLC: 1031088649.

[12] N. Ueno, S. Koyama, and H. Saruwatari, "Kernel Ridge Regression with Constraint of Helmholtz Equation for Sound Field Interpolation," in *2018 16th International Workshop on Acoustic Signal Enhancement (IWAENC)*, (Tokyo), pp. 1–440, IEEE, Sept. 2018.

DOI: 10.61782/fa.2025.0826



FORUM ACUSTICUM
EURONOISE 2025

STABILITY ANALYSIS OF STEPWISE SIMULTANEOUS PERTURBATION STOCHASTIC APPROXIMATION FOR ACTIVE NOISE CONTROL

Chao Liang[1*] **Francesco Ripamonti**[1] **Hamid Reza Karimi**[1]
[1] Department of Mechanical Engineering, Politecnico di Milano, 20156, Milan, Italy

ABSTRACT

Active noise control (ANC) is particularly effective in mitigating low-frequency noise, with its primary objective being to achieve maximum noise reduction while minimizing both measurement and computational costs. The filtered-x least mean square (FxLMS) algorithm has been widely adopted due to its effective balance between performance, ease of implementation, and computational efficiency. However, FxLMS relies on accurate secondary path estimation, which can be computationally intensive and time consuming. Recently, as a model-free method, the simultaneous perturbation stochastic approximation (SPSA) algorithm has been successfully applied in broadband, multi-channel, and time-varying environments. Despite its demonstrated effectiveness in noise reduction, the stability of SPSA has received limited attention. Following a recently proposed stepwise SPSA extension, which significantly enhances the stability of classical SPSA, this work investigates its stability characteristics with respect to key algorithmic parameters. The analysis provides insights into the parameter selection process, enabling efficient noise reduction while ensuring stability.

Keywords: *active noise control, stepwise SPSA, stability analysis, parameter optimization*

1. INTRODUCTION

The filtered-x least mean square (FxLMS) algorithm has been widely adopted in industrial active noise control (ANC) applications due to its effectiveness and implementation simplicity [1–3]. However, its performance is highly dependent on an accurate model of the secondary path, making it less suitable for time-varying environments.

As an alternative, simultaneous perturbation stochastic approximation (SPSA) provides a model-free approach to ANC. It updates the controller by estimating the gradient of the loss function using only function evaluations, thereby eliminating the need for explicit secondary-path modeling [4]. This characteristic enables SPSA to better adapt to changes in the acoustic environment.

SPSA has been applied in various ANC scenarios, including early adaptive systems [5], feedback control for periodic disturbances [6], time-varying environments [7], cross-correlation-based enhancements [8,9], second-order variants for faster convergence [10], and multi-channel extensions [11]. Despite these developments, SPSA's performance remains sensitive to parameter tuning, particularly the step size a and the perturbation coefficient c, where inappropriate settings may result in instability.

While prior research has primarily focused on the noise reduction performance of SPSA-based ANC, limited attention has been paid to its stability characteristics. Recently, stepwise SPSA (S-SPSA) was introduced to improve the robustness of the algorithm with respect to the selection of a and c [12]. This paper builds upon that foundation by further analyzing the influence of key algorithmic parameters on system stability and performance.

2. ALGORITHM DESCRIPTION

As illustrated in Fig. 1, the reference signal $x(n)$ passes through the primary path $P(n)$, generating the primary noise $d(n)$, where n denotes the discrete time index. To attenuate $d(n)$, the adaptive filter with weights $\boldsymbol{w}(n)$ gen-

*Corresponding author: chao.liang@polimi.it.
Copyright: ©2025 Chao Liang et al. This is an open-access article distributed under the terms of the Creative Commons Attribution 3.0 Unported License, which permits unrestricted use, distribution, and reproduction in any medium, provided the original author and source are credited.

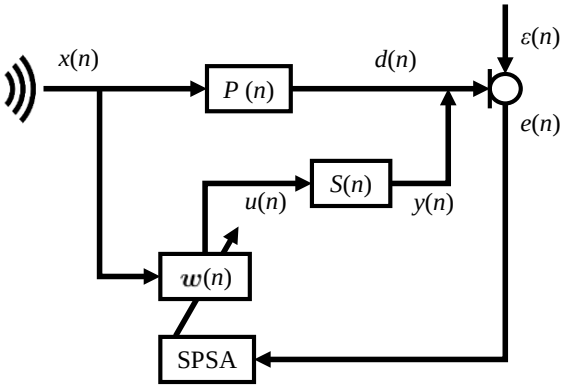


Figure 1: Block diagram of the ANC system using SPSA.

erates a control signal $u(n)$, which passes through the secondary path $S(n)$ to produce the anti-noise signal $y(n)$. The residual error $e(n)$, which also includes background noise $\varepsilon(n)$, is given by

$$e(n) = d(n) - y(n) + \varepsilon(n). \tag{1}$$

SPSA:

To minimize the energy of the residual error, SPSA iteratively updates the filter coefficients using

$$\boldsymbol{w}(k+1) = \boldsymbol{w}(k) - a\hat{\boldsymbol{g}}(\boldsymbol{w}(k)), \tag{2}$$

where k is the block index, a is the step size, and $\hat{\boldsymbol{g}}(\boldsymbol{w}(k))$ denotes the estimated gradient of the loss function.

The gradient is estimated by applying the perturbation $c\boldsymbol{\Delta}(k)$ to the weights $\boldsymbol{w}(k)$ and evaluating the loss function over two consecutive segments within a data block of length 2λ:

$$J^+ = J(\boldsymbol{w}(k) + c\boldsymbol{\Delta}(k)) = \frac{1}{2}\sum_{n=1}^{\lambda} e^2(n), \tag{3}$$

$$J^- = J(\boldsymbol{w}(k) - c\boldsymbol{\Delta}(k)) = \frac{1}{2}\sum_{n=\lambda+1}^{2\lambda} e^2(n), \tag{4}$$

where J is the loss function defined as the sum of squared error signals, c is the perturbation coefficient, $\boldsymbol{\Delta}(k)$ is a random perturbation vector, and 2λ is the block length. This structure ensures that the gradient approximation is based on distinct error responses to positive and negative perturbations, allowing for an efficient stochastic update.

The gradient is then estimated as:

$$\hat{\boldsymbol{g}}(\boldsymbol{w}(k)) = \frac{J^+ - J^-}{2c\boldsymbol{\Delta}(k)}. \tag{5}$$

S-SPSA:

To improve stability and convergence, the stepwise SPSA (S-SPSA) divides each block into $2m$ equal-length segments. Each segment has a length of λ/m. The loss functions for the i-th segment are defined as:

$$J_i^{s+} = \frac{1}{2}\sum_{n=(i-1)\frac{\lambda}{m}+1}^{i\frac{\lambda}{m}} e^2(n), \tag{6}$$

$$J_i^{s-} = \frac{1}{2}\sum_{n=(i-1)\frac{\lambda}{m}+\lambda+1}^{i\frac{\lambda}{m}+\lambda} e^2(n). \tag{7}$$

Each segment computes its own gradient independently:

$$\hat{\boldsymbol{g}}_i^s = \frac{J_i^{s+} - J_i^{s-}}{2c\boldsymbol{\Delta}_i(k)}, \quad \hat{\boldsymbol{g}}_i^s \in R^{\frac{L}{m}}, \tag{8}$$

where $\boldsymbol{\Delta}_i(k)$ is the i-th subvector of the perturbation vector $\boldsymbol{\Delta}(k)$, such that:

$$\boldsymbol{\Delta}(k) = \left[\boldsymbol{\Delta}_1^T(k), \boldsymbol{\Delta}_2^T(k), \ldots, \boldsymbol{\Delta}_m^T(k)\right]^T.$$

Finally, each sub-filter $\boldsymbol{w}_i(k)$ is updated independently as:

$$\boldsymbol{w}_i(k+1) = \boldsymbol{w}_i(k) - a\hat{\boldsymbol{g}}_i^s(\boldsymbol{w}(k)). \tag{9}$$

3. NUMERICAL SIMULATION AND RESULT DISCUSSION

To investigate the influence of parameters on the stability of the algorithms, numerical simulations are conducted using the following default configuration. The sampling rate is set to 16 kHz. The adaptive filter $\boldsymbol{w}(n)$ has a length of $L = 1024$, and the block length is set to $2\lambda = 4000$. For the S-SPSA, each block is divided into $2m$ segments, where $m = 2$.

The reference signal $x(n)$ consists of a sum of tonal components with equal amplitude $A = 1$, at frequencies of 150 Hz, 200 Hz, ..., up to 700 Hz. Gaussian white noise $\varepsilon(n)$ is added as background interference, yielding a signal-to-noise ratio (SNR) of 10 dB between the original primary noise $d(n)$ and the background noise. The

primary and secondary paths are measured experimentally using a Kundt's tube and their frequency responses cover the range from 100 Hz to 750 Hz.

To evaluate the performance of active noise control, the attenuation of noise is quantified using the average noise reduction (ANR), defined as:

$$\mathrm{ANR}(n) = 10\log_{10}\frac{\sum_{i=n-l+1}^{n} e^2(i)}{\sum_{i=n-l+1}^{n}(d(i)+\varepsilon(i))^2}, \quad (10)$$

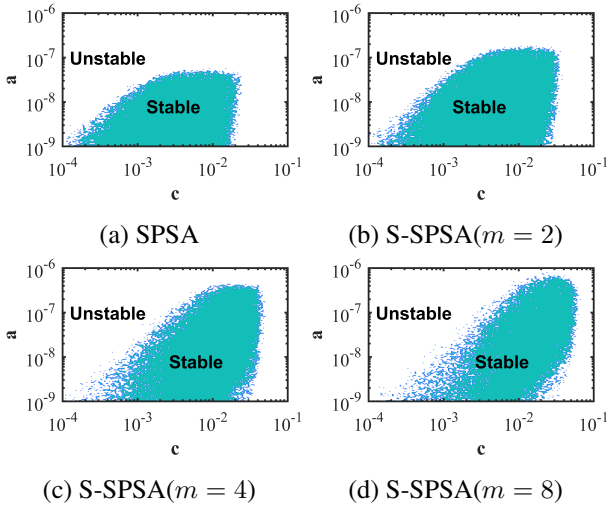
where the window length is set to $l = 2000$ samples.

3.1 Stability Comparison

To evaluate algorithmic stability, each simulation runs for 60 seconds. The system is considered *unstable* if one of the following conditions is met:

$$\begin{cases} \sum_{n=1}^{2\lambda} e^2(n) > 2\sum_{n=1}^{2\lambda} d^2(n), \\ \mathrm{ANR}(t = 60\,\mathrm{s}) \geq 0, \end{cases} \quad (11)$$

and is defined as *stable* otherwise.



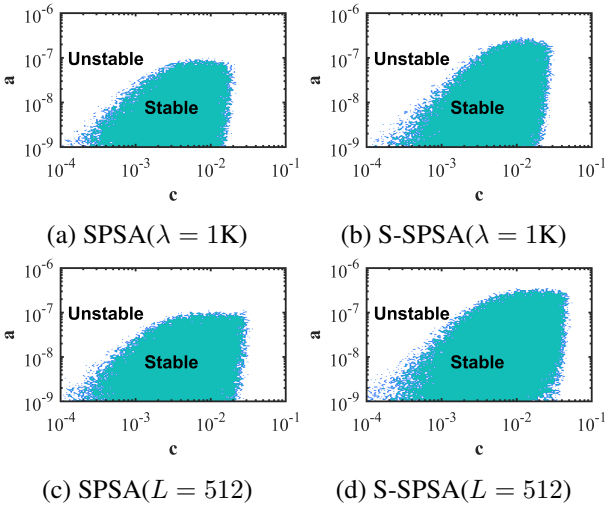
(a) SPSA (b) S-SPSA($m = 2$)

(c) S-SPSA($m = 4$) (d) S-SPSA($m = 8$)

Figure 2: Stability of the algorithms with respect to the parameter m.

As shown in Fig. 2, green regions indicate parameter combinations that lead to stable operation. Compared to the standard SPSA, the stepwise variant S-SPSA with $m = 2$ notably expands the stability region. Further increasing the segment number to $m = 4$ and $m = 8$ raises the upper bounds of stable values for both step size a and perturbation coefficient c. However, S-SPSA with $m = 8$ exhibits a narrower overall stability region, indicating that $m = 2$ and $m = 4$ have better stability.

In Fig. 3, S-SPSA again demonstrates a broader stable region than conventional SPSA. Compared to Fig. 2a and Fig. 2b, it can be observed that reducing either the block length λ or filter length L increases the upper stability boundary for the step size a, implying improved robustness under smaller system dimensions.



(a) SPSA($\lambda = 1$K) (b) S-SPSA($\lambda = 1$K)

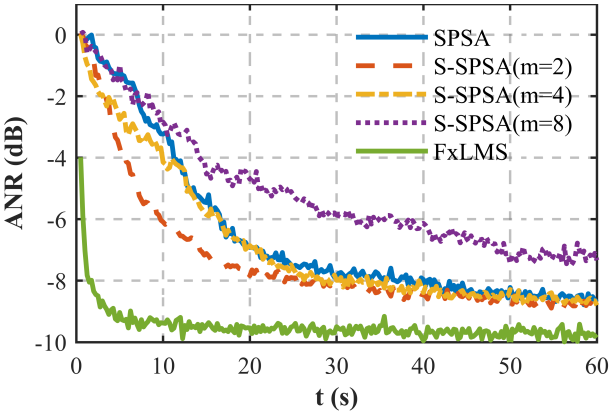
(c) SPSA($L = 512$) (d) S-SPSA($L = 512$)

Figure 3: Stability of the algorithms with respect to the parameters λ and L.

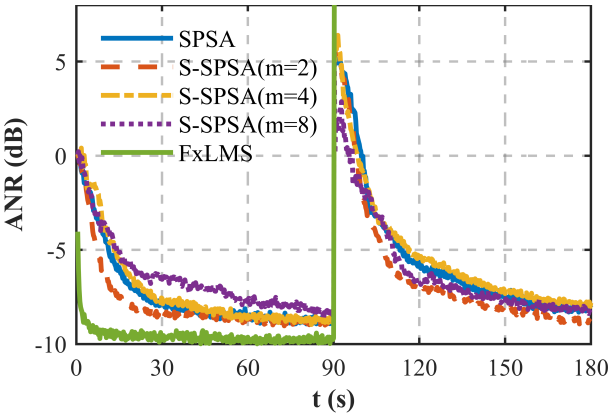
3.2 Performance Comparison

The tracking performance of the algorithms is assessed using the ANR metric, defined in Eq. (10), with optimal parameters a and c. As depicted in Fig. 4a, the convergence behavior of standard SPSA, S-SPSA with $m = 2, 4, 8$, and FxLMS is evaluated over 60 seconds. S-SPSA with $m = 4$ closely approximates the performance of standard SPSA, stabilizing at an ANR of approximately -8.7 dB. The variant with $m = 2$ exhibits the fastest initial convergence among S-SPSA configurations, reaching -6 dB within 10 seconds, while $m = 8$ converges more slowly, stabilizing at a slightly higher ANR of -7.3 dB. In contrast, FxLMS demonstrates superior performance, achieving an ANR below -8 dB within 5 seconds and maintaining a steady-state value near -10 dB.

The robustness of these algorithms to abrupt changes is examined in Fig. 4b, where the secondary path is reversed at $t = 90$ s. After this point, FxLMS diverges

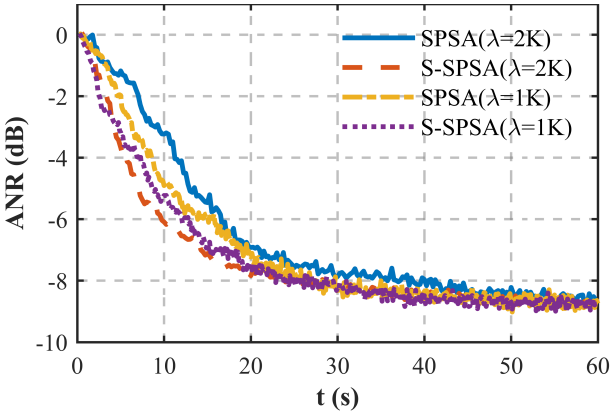


(a) Convergence performance of algorithms

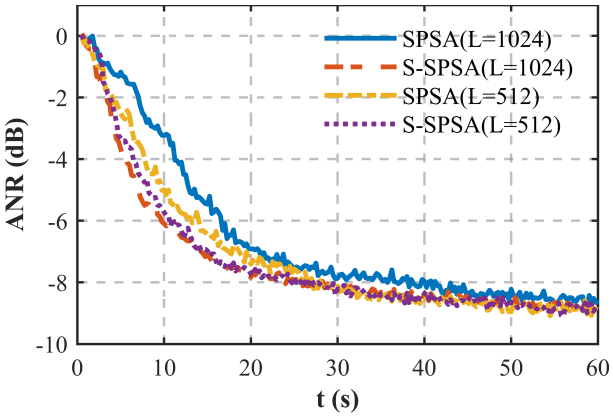


(b) Robustness to secondary path reversal at $t = 90$ s

Figure 4: ANR performance with the parameter m



(a) ANR versus block length λ



(b) ANR versus filter length L

Figure 5: ANR performance with respect to the parameters λ and L

sharply to instability. Conversely, SPSA and S-SPSA variants exhibit adaptivity; their ANR values increase temporarily to over 0 dB but recover gradually over the subsequent 90 seconds.

The influence of block length λ and filter length L on performance is shown in Fig. 5. At $\lambda = 1$K and $L = 512$, the ANR differences across SPSA and S-SPSA diminish, suggesting that shorter block and filter lengths lessen the impact of m on noise reduction performance.

4. CONCLUSION

This paper investigates the impact of the segment number m, half block length λ, and filter length L on the stability and noise reduction performance of the SPSA and S-SPSA algorithms. The results demonstrate that increasing m generally raises the upper stability bound for the step size a, while configurations with $m = 2$ or $m = 4$ are recommended due to their stability and noise attenuation performance.

Additionally, smaller values of λ and L not only enhance algorithmic stability by allowing for larger values of a, but also reduce the performance gap between SPSA and S-SPSA variants. These findings suggest that appropriate segmentation and parameter selection are crucial for robust and efficient adaptive noise control using perturbation-based optimization.

5. ACKNOWLEDGMENTS

The work was supported by the project IN-NOVA: Active reduction of noise transmitted into and from enclo-

sures through encapsulated structures, which has received funding from the European Union's Horizon Europe program under the Marie Sklodowska-Curie grant agreement no. 101073037 and in part by the Italian Ministry of University and Research under grant 'Learning-based Model Predictive Control by Exploration and Exploitation in Uncertain Environments' (PRIN PNRR 2022 fund, ID P2022EXP2W).

6. REFERENCES

[1] L. Lu, K.-L. Yin, R. C. de Lamare, Z. Zheng, Y. Yu, X. Yang, and B. Chen, "A survey on active noise control in the past decade-part i: Linear systems," *SIGNAL PROCESSING*, vol. 183, JUN 2021.

[2] Y. Guo, D. Shi, X. Shen, J. Ji, and W.-S. Gan, "A survey on adaptive active noise control algorithms overcoming the output saturation effect," *SIGNAL PROCESSING*, vol. 222, SEP 2024.

[3] Y. Liu and Z. Lei, "Review of advances in active impulsive noise control with focus on adaptive algorithms," *APPLIED SCIENCES-BASEL*, vol. 14, FEB 2024.

[4] J. C. Spall, "Implementation of the simultaneous perturbation algorithm for stochastic optimization," *Ieee Transactions on Aerospace and Electronic Systems*, vol. 34, no. 3, pp. 817–823, 1998.

[5] Y. Maeda and T. Yoshida, "An active noise control without estimation of secondary-path-anc using simultaneous perturbation," in *INTER-NOISE and NOISE-CON Congress and Conference Proceedings*, vol. 1999, pp. 985–994, Institute of Noise Control Engineering, 1999.

[6] Y. L. Zhou, Q. Z. Zhang, X. D. Li, and W. S. Gan, "On the use of an spsa-based model-free feedback controller in active noise control for periodic disturbances in a duct," *Journal of Sound and Vibration*, vol. 317, no. 3-5, pp. 456–472, 2008.

[7] B. Chen, R. Guo, S. Yu, and Y. Yu, "An active noise control method of non-stationary noise under time-variant secondary path," *Mechanical Systems and Signal Processing*, vol. 149, p. 107193, 2021.

[8] M. Y. Wu, X. G. Liu, H. Meng, and W. K. Li, "Cost function research for spsa algorithm: An application of the cross-correlation function in periodic disturbance energy estimation," *Mechanical Systems and Signal Processing*, vol. 164, 2022.

[9] S. J. Li, G. Y. Jin, M. Y. Wu, Y. K. Chen, and T. G. Ye, "A simultaneous perturbation stochastic approximation algorithm for broadband noise control," *Journal of the Acoustical Society of America*, vol. 153, no. 1, pp. 643–653, 2023.

[10] Z. Duan, N. Han, and T. Zhang, "Model-free active noise control using second-order simultaneous perturbation stochastic approximation algorithm for periodic noise," *Digital Signal Processing*, vol. 158, p. 104923, 2025.

[11] Y. L. Yang, X. G. Liu, M. Y. Wu, F. Feng, and S. W. Wang, "Multiple channel spsa algorithm with improved cost function in active vibration control," *Mechanical Systems and Signal Processing*, vol. 223, 2025.

[12] C. Liang, F. Ripamonti, and H. Reza Karimi, "A stepwise simultaneous perturbation stochastic approximation algorithm for stability improvement of active noise control systems." Under review, 2025.

DOI: 10.61782/fa.2025.0812



FORUM ACUSTICUM
EURONOISE 2025

SPATIAL PSYCHOACOUSTIC ANALYSIS OF PERCEPTUAL ERROR SHAPING IN LOCAL ACTIVE NOISE CONTROL

Christian Blöcher[1*] **Alois Sontacchi**[1] **Thomas Hatheier**[2]
[1] Institute of Electronic Music and Acoustics, University of Music and Performing Arts Graz, Austria
[2] Audio Mobil Elektronik GmbH, Braunau–Ranshofen, Austria

ABSTRACT

To address the frequency-dependent nature of human auditory perception, error shaping can be incorporated into traditional feedforward Filtered-Reference Least-Mean-Squares (FxLMS) local Active Noise Control (ANC) schemes by applying A-weighting to the LMS input signals. Several publications have compared the psychoacoustic properties of noise residuals produced by such Filtered-Error LMS (FeLMS) and FxLMS ANC systems at the point of cancellation. This paper expands previous studies by additionally investigating the surrounding sound field. In a co-simulation, both algorithms are evaluated for fullband and bandlimited control for an active headrest system with two built-in loudspeakers and a head and torso simulator (HATS) positioned in front of the headrest. With white, pink, and real-world driving noise as innovation signals, the sound field after adaptation is evaluated for HATS rotations and transitions to the front, utilizing psychoacoustic- and speech metrics. While the FeLMS algorithm generally produces more coloration for head movements from the reference position than the FxLMS algorithm, performance for synthetic signals is otherwise similar. However, for driving noise, it achieves greater loudness reduction and improved speech intelligibility. The spatial extent of noise control is enlarged for bandlimited compared to fullband ANC systems at the cost of reduced performance near the reference position.

Keywords: *Active Noise Control, Psychoacoustics, Speech Intelligibility.*

*__Corresponding author__: *bloecher@iem.at.*

__Copyright__: *©2025 Blöcher et al. This is an open-access article distributed under the terms of the Creative Commons Attribution 3.0 Unported License, which permits unrestricted use, distribution, and reproduction in any medium, provided the original author and source are credited.*

1. INTRODUCTION

Active Noise Control (ANC) aims at reducing unwanted noise by superimposing a destructively interfering anti-noise played via loudspeakers. The optimization goal of traditional feedforward ANC schemes relying on the Filtered-Reference Least-Mean-Squares (FxLMS) approach is the minimization of the error signal energy [1]. This corresponds to a maximization of the mean noise reduction across the entire controlled frequency spectrum. However, since this criterion ignores the frequency-dependent nature of human auditory perception [2], the achieved noise reduction may be suboptimal. A simple, yet effective way of incorporating the frequency characteristic of our hearing system is perceptual error shaping. In a Filtered-Error LMS (FeLMS) ANC approach [3], a psychoacoustic rating filter, such as A-weighting, can be applied to the LMS input signals to guide the focus of the adaptation towards frequency regions in which our hearing is more sensitive [4]. Previous publications have compared the psychoacoustic properties of noise residuals produced by perceptually motivated FeLMS ANC approaches and FxLMS systems at the point of cancellation [5] or for headphone applications [6]. This paper extends the evaluation by additionally investigating the psychoacoustic properties of the surrounding sound field. In a co-simulation, both FxLMS and FeLMS algorithms are evaluated for fullband and bandlimited local control in an active headrest system for use in vehicles, utilizing both synthetic and real-world innovation signals.

The rest of this paper is organized as follows. Section 2 details the co-simulation by describing the physical measurement setup, specifying the utilized innovation signals, and highlighting the investigated ANC algorithms and adaptation procedure. Section 3 features the metrics used in the spatial psychoacoustic evaluation, before results are presented in section 4. To conclude, section 5 summarizes the findings and provides an outlook.

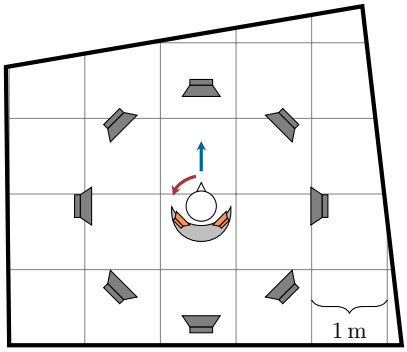
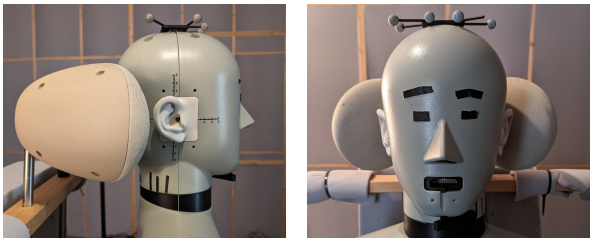


Figure 1. Measurement setup in an anechoic room with primary loudspeakers (grey), and HATS positioned in front of an active headrest with integrated secondary loudspeakers (orange). Arrows indicate directions of HATS rotation (red) and transition (blue).



(a) Side view (b) Front view

Figure 2. Placement of the HATS in front of the headrest at the reference position.

2. CO-SIMULATION

2.1 Measurement Setup

The evaluation took place within a co-simulation based on the physical setup depicted in Fig. 1, extending the approach described in [7]. In an anechoic room, a Brüel & Kjær 4128C HATS was positioned in front of an active headrest situated in the center of a circular arrangement of eight Genelec 8020B loudspeakers with a radius of $1.45\,\mathrm{m}$. While these loudspeakers served as the primary sources, two loudspeakers integrated into the headrest in close proximity to the HATS' ears were utilized as secondary sources. To model this scenario within the co-simulation, both the acoustic primary paths between the loudspeakers in the circular arrangement and the HATS, and the acoustic secondary paths between the headrest loudspeakers and the HATS were measured at a sample rate of $44.1\,\mathrm{kHz}$ using the method of multiple exponential sine sweeps [8]. Starting from the neutral HATS position shown in Fig. 2 as a reference position, the measurement procedure was repeated for rotations of the HATS of up to $30°$ to the left in $1°$ steps and lateral transitions of the HATS of up to $15\,\mathrm{cm}$ to the front in $0.5\,\mathrm{cm}$ steps. To ensure the accuracy of the re-positioning of the HATS, rotations were executed using a motorized turntable and the HATS' position was verified using an optical tracking system (OptiTrack Motive with 6 Flex3 cameras, mean error $\leq 0.5\,\mathrm{mm}$) for both rotations and transitions.

2.2 Innovation Signals

For the co-simulation, both synthetic and real-world innovation signals were utilized. As synthetic test signals, $75\,\mathrm{s}$ of mono white and pink noise were generated at a sample rate of $44.1\,\mathrm{kHz}$. Additionally, a recording of driving noise captured using an NTi MA2230 measurement microphone in a car (combustion engine, $80\,\mathrm{km/h}$) was cut to the same duration. To achieve a diffuse presentation, all innovation signals were processed using the IEM Plugin Suite's [1] Granular Encoder [9] as described by Holzmüller et al. [10] and decoded to the eight-channel loudspeaker arrangement using the AllRAD approach [11]. After application of the primary path transfer functions for the reference position, all spatialized innovation signals were normalized to produce a level of $70\,\mathrm{dB(A)}$ at the HATS. Subsequently, the spatialized signals at the HATS were generated from the normalized innovation signals for all measurement positions.

2.3 Evaluated ANC Systems

Fig. 3 illustrates the extension of the FxLMS algorithm into an FeLMS ANC system, as detailed in [3], for the evaluated setup. In an FxLMS system, the broadband disturbances $\mathbf{d}(n)$ at the HATS' microphones, modeled as the reference signals $\mathbf{x}(n)$ filtered by the respective primary paths $\mathbf{P}(z)$, are superimposed with the control signals $\mathbf{y}(n)$, resulting in the error signals $\mathbf{e}(n)$. With the control signals generated by filtering $\mathbf{x}(n)$ with a set of adaptive linear filters $\mathbf{W}(z)$ and applying the secondary paths $\mathbf{S}(z)$, the error signal at HATS microphone m can be expressed as

$$e_m(n) = d_m(n) + \sum_{i,j} \left(\mathbf{w}_{i,j}^T(n)\,\mathbf{x}_i(n)\right) * \mathbf{s}_{j,m}(n), \quad (1)$$

[1] https://plugins.iem.at

where $*$ indicates the convolution operation, $\mathbf{s}_{j,m}$ denotes the impulse response of $S_{j,m}(z)$ between secondary loudspeaker j and HATS microphone m, $\mathbf{x}_i(n) = [x_{i,0}(n), x_{i,1}(n), ..., x_{i,N-1}(n)]^T$ is the reference signal vector at primary loudspeaker i, and $\mathbf{w}_{i,j}(n) = [w_{i,j,0}(n), w_{i,j,1}(n), ..., w_{i,j,N-1}(n)]^T$ is the coefficient vector of $W_{i,j}(z)$, controlling the reference signal at primary loudspeaker i via secondary loudspeaker j, with filter order N at time n.

The filter coefficients are updated via the LMS algorithm, which takes the error signals $\mathbf{e}(n)$ and the filtered reference signals $\mathbf{r}(n)$ as inputs. Instead of the typical approach of filtering $\mathbf{x}(n)$ via an offline estimate of the secondary paths $\hat{\mathbf{S}}(z)$, in this simulation we can substitute $\hat{\mathbf{S}}(z)$ with our actual secondary paths $\mathbf{S}(z)$. The update equation for the filter coefficients $\mathbf{w}_{i,j}(n)$ is expressed as

$$\mathbf{w}_{i,j}(n+1) = \mathbf{w}_{i,j}(n) - \mu\, \mathbf{r}_{i,j}^T(n)\, \mathbf{e}(n), \qquad (2)$$

where $\mathbf{r}_{i,j} = [\mathbf{r}_{i,j,0}(n), \mathbf{r}_{i,j,1}(n), ..., \mathbf{r}_{i,j,N-1}(n)]^T$ denotes the filtered reference signal vectors for reference signal i, filtered with the secondary paths $\mathbf{S}_j(z)$ from secondary loudspeaker j to both HATS microphones, and μ is the adaptation step size.

In an FeLMS system both LMS input signals are additionally filtered with a weighting filter $H(z)$. Here, $H(z)$ denotes an A-weighting of the LMS input signals, implemented as a 7th order digital IIR filter derived via the improved matched z-transform method [12]. With $\mathbf{r_f}(n)$ and $\mathbf{e_f}(n)$ denoting the perceptually filtered versions of $\mathbf{r}(n)$ and $\mathbf{e}(n)$, Eqn. (2) becomes:

$$\mathbf{w}_{i,j}(n+1) = \mathbf{w}_{i,j}(n) - \mu\, \mathbf{r_f}^T_{i,j}(n)\, \mathbf{e_f}(n). \qquad (3)$$

To improve the convergence behavior of both ANC systems, the Normalized LMS (NLMS) algorithm [13] is employed, normalizing the adaptation step size by the time-smoothed total maximum energy over all $\mathbf{r}_{i,j}(n)$ and $\mathbf{r_f}_{i,j}(n)$, respectively.

As previous studies have shown, that the perceived spatial extent of ANC systems increases when limiting the control bandwidth [10], the evaluation of both FxNLMS and FeNLMS algorithms was conducted for both fullband and bandlimited ANC systems, i.e. at sample rates $f_{s,anc} = \{44.1\,\text{kHz}; 4410\,\text{Hz}\}$ with respective control filter lengths of 512 and 51 taps ($\hat{=}\,12\,\text{ms}$).

2.4 Adaptation

The adaptation for all ANC systems, bandwidth conditions, and innovation signals was conducted for the reference position only. Step sizes for all conditions were set individually to ensure convergence after 70 s of the innovation signal.

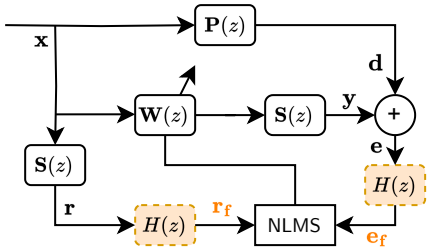


Figure 3. Extension of the FxNLMS algorithm into an FeNLMS system via added weighting filters $H(z)$ (orange) for the evaluated setup.

Fig. 4 shows the semitone-smoothed error power spectral densities (PSD) for the left HATS channel at the reference position both without ANC and after the adaptation process for all conditions. At the point of cancellation, substantial noise reduction is achieved by both FxNLMS and FeNLMS algorithms for white and pink noise in both bandwidth conditions. The FeNLMS PSDs show a bathtub-shaped frequency characteristic due to the applied A-weighting with a slight amplification of very low frequencies, while the FxNLMS algorithm tends to focus more on the reduction of higher frequency components. However, for driving noise, only the FeNLMS algorithm manages to achieve substantial noise reduction, while the FxNLMS algorithm only reduces very low frequency components and some harmonics caused by the car's combustion engine. The error PSDs for the bandlimited condition are in good agreement with the fullband condition up to just below the systems' Nyquist frequency at 2205 Hz, except for the FxNLMS algorithm for white noise, which achieves greater noise reduction in the controlled frequency range in the bandlimited condition.

3. EVALUATION

In order to evaluate the controlled sound field for rotations and transitions of the HATS extending from the sweet spot at the reference position, the control- and innovation signals were superimposed at all measurement positions. For each condition, the spatialized control signals were generated by filtering the normalized innovation signals with the respective converged adaptive filter and then applying the

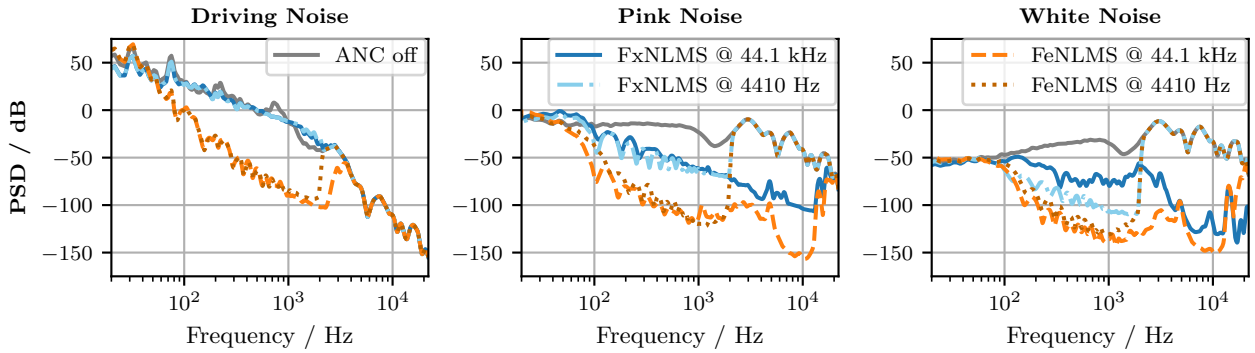


Figure 4. Error power spectral densities (PSD) at the reference position at left HATS channel for all control conditions after convergence. To prevent obscuring any data points, legend items are distributed among subplots.

corresponding secondary paths. The duration of the generated stimuli was 10 s. Afterwards, the following metrics were calculated in MATLAB R2024a at all measurement positions for both the uncontrolled spatialized innovation signals and all control conditions.

RMS. The monaural root mean square (RMS) value for the left HATS channel. Lower is better.

Loudness. The binaural loudness calculated using MATLAB's Audio Toolbox implementation of the Moore-Glasberg model [14] for signals captured at the eardrum. Lower is better.

Sharpness. The monaural acoustic sharpness of the left HATS channel computed using MATLAB's Audio Toolbox implementation of the model in DIN 45692 [15]. Lower is better.

PEMO-Q. The monaural Perceptual Similarity Measure (PSM) calculated by the PEMO-Q [2] [16] between the signal at the left HATS channel at the reference position and all other measurement positions. The PSM is calculated from the correlation between internal representations of level-normalized reference and test signals based on the Oldenburg Perception Model (PEMO). Higher is better.

MBSTOI. The reference-based Modified Binaural Short-Time Objective Intelligibility (MBSTOI) [3] [17] evaluated for a potential communication scenario, in which the adaptation of the ANC filters is paused, and the headrest loudspeakers are used to also play speech signals. To limit potential speaker-related biases the mean MBSTOI was calculated over the first sentence of each of the six speech samples provided in the EBU SQUAM material [4] in English, German, and French, uttered by male and female speakers. With the speech samples spatialized to the HATS using the secondary transfer paths and normalized to 55 dB(A), the MBSTOI was calculated from the speech samples in noise with the reference condition of speech samples spatialized to the HATS without any innovation signal present. Higher is better.

For monaural metrics, only signals at the left HATS channel were evaluated, because for rotations of the HATS greater fluctuations caused by the control signals can be expected at the ipsilateral ear, while for transitions to the front there is little difference between the channels due to the symmetric arrangement of the measurement setup.

4. RESULTS

The evaluated metrics for all ANC and innovation signal conditions are displayed in Fig. 5 for HATS rotations, and in Fig. 6 for transitions of the HATS. Prior to an in-depth discussion of the results, it is possible to discern several general trends from the data. For white noise there is little difference between algorithms, except for sharpness close to the reference position and coloration compared to the reference position expressed via the PEMO-Q values. For white and pink noise, and a translation of 2 cm to 5 cm, an interference effect is visible as the HATS exits the acoustic shadow provided by the headrest against the mid-to-back primary loudspeakers. For driving noise, there is virtually no difference per algorithm between bandwidth conditions due to the strong spectral tilt of the innovation signal. For

[2] https://uol.de/en/mediphysics/downloads/pemo-q
[3] http://ah-andersen.net/code/
[4] https://tech.ebu.ch/publications/sqamcd

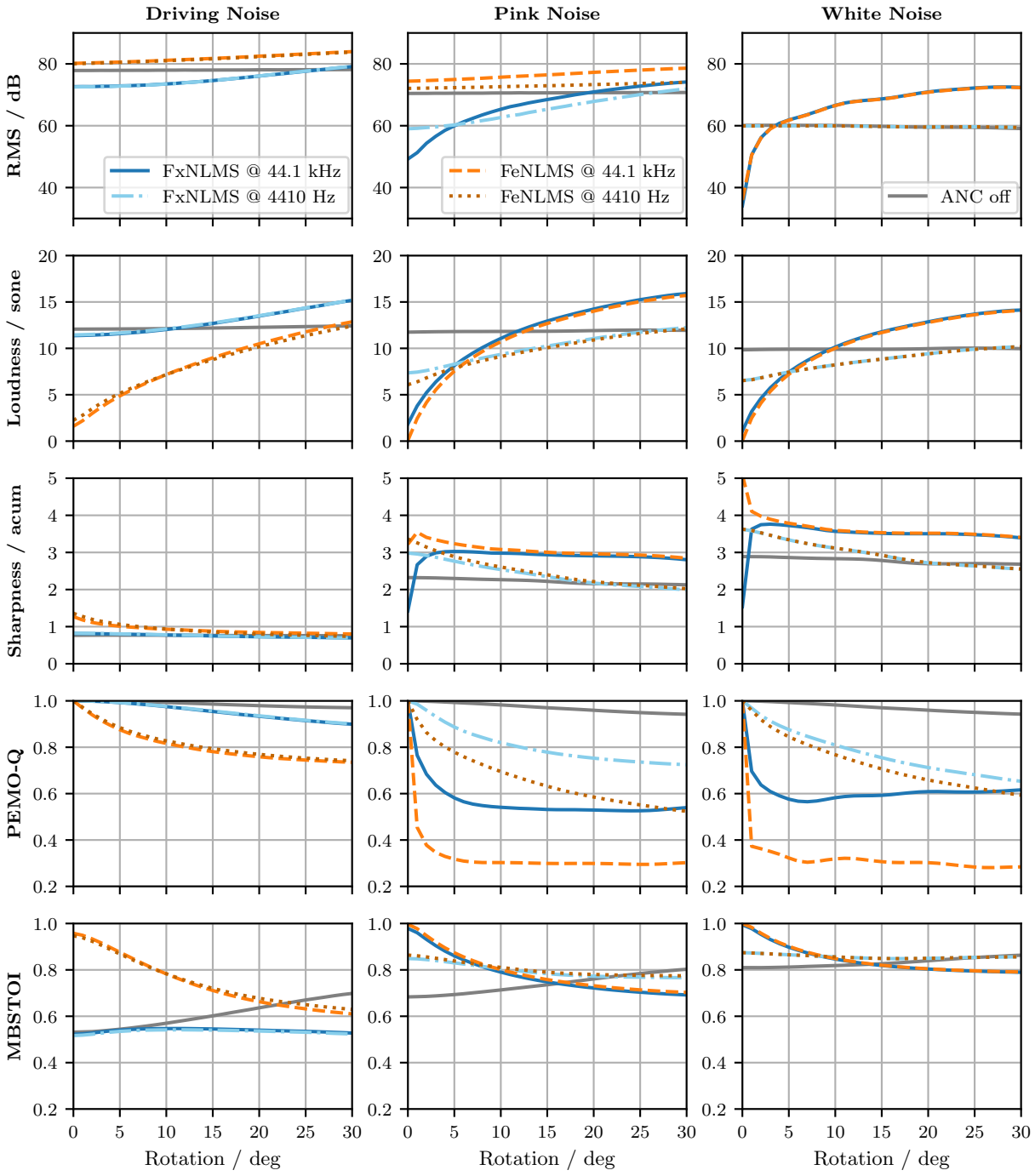


Figure 5. Evaluated metrics (rows) for all innovation signals (columns) as a function of HATS *rotation* from the reference position without ANC, and for fullband and bandlimited FxNLMS and FeNLMS ANC systems. To prevent obscuring any data points, legend items are distributed among subplots.

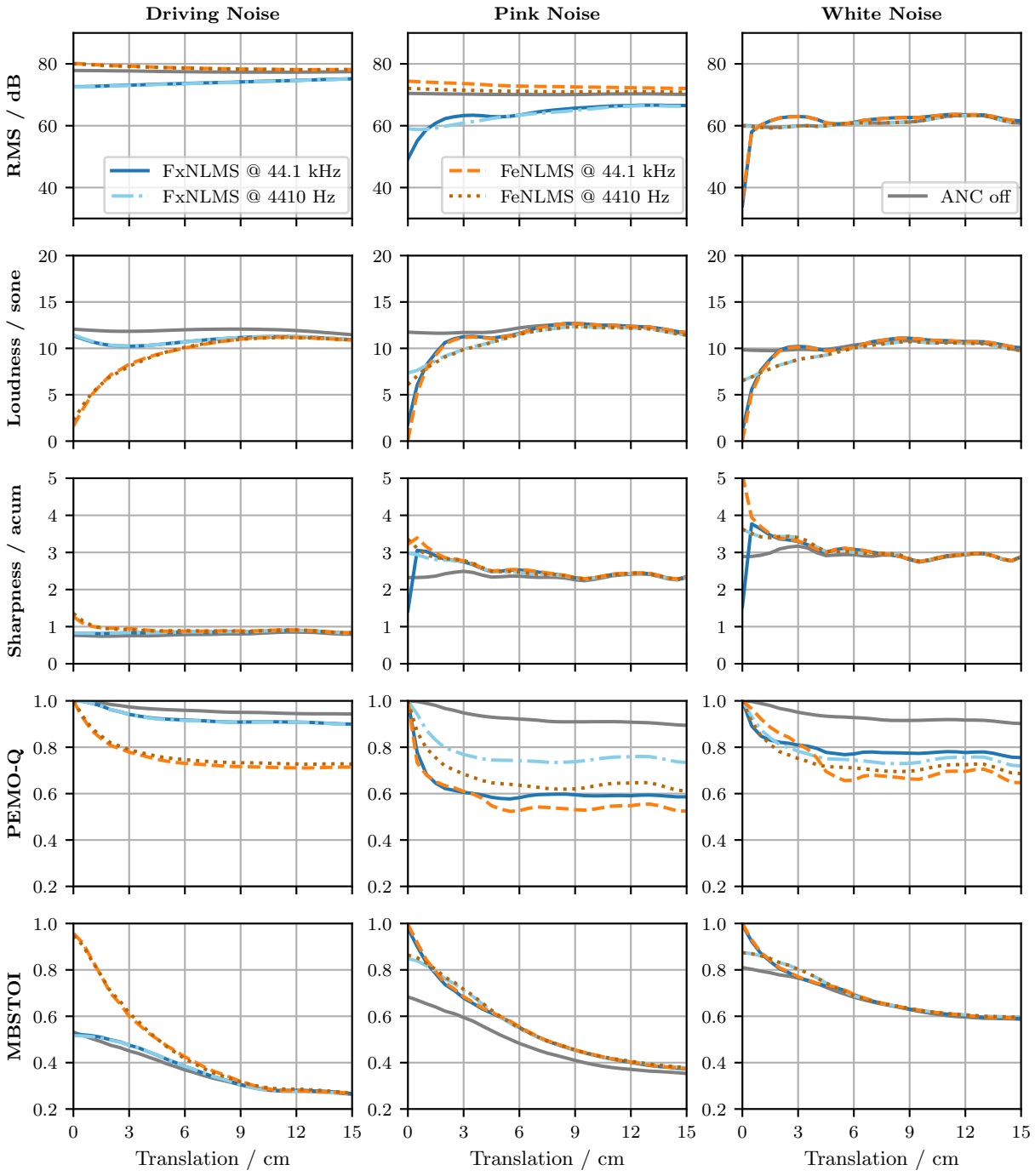


Figure 6. Evaluated metrics (rows) for all innovation signals (columns) as a function of HATS *translation* from the reference position without ANC, and for fullband and bandlimited FxNLMS and FeNLMS ANC systems. To prevent obscuring any data points, legend items are distributed among subplots.

the other innovation signals, compared to the fullband condition, the bandlimited condition generally results in smaller deviations from the data without ANC close to the reference position. The effects of the bandlimited condition also decrease more gradually with increasing rotation and translation from the reference position.

RMS. For white noise, both fullband ANC systems achieve a substantial reduction at the reference position but produce increased RMS values from 4° rotation and from 1 cm to 11 cm translation. The bandlimited ANC systems cause virtually no change in RMS. For pink noise, both FxNLMS systems manage a reduction in RMS that decreases for increasing rotation and translation, with the fullband condition performing better only near the reference position. Both FeNLMS systems cause an increase in RMS, that increases with rotation and slightly decreases with translation. For driving noise, these general trends between algorithms remain. While the FxNLMS systems achieve less reduction in RMS at the reference position compared to pink noise, the decrease in reduction for rotation and translation is more gradual.

Loudness. For white noise, similar trends are visible for the fullband condition as in the RMS results with the area of effect extending slightly further. Not visible in the RMS data, the bandlimited condition achieves some loudness reduction up to 25° rotation and 6 cm translation. Contrary to the RMS results, the FeNLMS algorithm achieves loudness reduction for both pink and driving noise, due to the focus on perceptually relevant frequency regions. While for pink noise, the FeNLMS systems achieve higher loudness reduction at the reference position, similar loudness reduction to the results for white noise is achieved for all conditions for head movements. For driving noise, the FeNLMS algorithm achieves a substantial loudness decrease at the reference position, while the FxNLMS algorithm barely reduces the loudness of the innovation signal. Loudness reduction extends up to 25° rotation and 10 cm translation for the FeNLMS systems, while loudness is increased by the FxNLMS systems from 10° rotation but remains stable across translation.

Sharpness. For white and pink noise, sharpness is reduced at the reference position by the fullband FxNLMS system but increased for all other ANC conditions. For rotations, sharpness remains increased over the condition without ANC for fullband control but reduces to the uncontrolled value for bandlimited control at 17° rotation. For transitions, sharpness reduces to match the value without ANC at 7 cm for all ANC conditions. For driving noise, sharpness is only slightly increased for the FeNLMS algorithm near the reference position.

PEMO-Q. Only slight changes are observed for all uncontrolled innovation signals. For all innovation signals, the sound field produced by the FeNLMS algorithm exhibits lower perceptual similarity to the reference position per bandwidth condition than that produced by the FxNLMS algorithm, with larger differences visible for rotation of the HATS. For fullband control, and white and pink noise, rotations of only 2° already cause a drop in perceptual similarity before values remain constant from 5°, indicating substantial coloration compared to the reference position, especially for the FeNLMS algorithm. An ongoing, more gradual decrease is visible for bandlimited conditions and driving noise. Across translations, the decline in perceptual similarity is less steep and values remain mostly constant from 5 cm translation for all conditions.

MBSTOI. Since the speech audio is played back via the headrest loudspeakers, intelligibility without ANC increases with rotation, because the ipsilateral ear moves towards the left loudspeaker. Similarly, intelligibility decreases with translation, because the HATS moves away from the loudspeakers. For white and pink noise, both fullband ANC systems enable perfect intelligibility at the reference position that decreases to levels observed without ANC by 12° rotation and 3 cm translation for white noise, and 15° rotation for pink noise. For larger rotation, intelligibility values fall below those of the uncontrolled condition. The bandlimited ANC systems cause slightly lower intelligibility at the reference position, but show a more gradual decline with increased rotation, extending the area of effect to 20°. Across translations, intelligibility is the same for all ANC systems from 5 cm. For driving noise, only the FeNLMS algorithm causes a substantial increase in intelligibility with the effect extending to 20° rotation and 8 cm translation.

5. CONCLUSION

In a co-simulation of an active headrest system, a perceptually motivated FeNLMS algorithm using A-weighting was compared to an FxNLMS algorithm for fullband and bandlimited control with white, pink, and driving noise as innovation signals. Extending from the point of cancellation, the sound field produced by the ANC measures was evaluated for head rotations and transitions to the front based on RMS, binaural loudness, sharpness, PEMO-Q, and MBSTOI.

While the FeNLMS algorithm increases RMS values for pink and driving noise, the adaptation focus on per-

ceptually relevant frequency regions causes a substantial reduction in loudness surrounding the point of cancellation.

For white and pink noise, there is only little difference between both algorithms in loudness and speech intelligibility, but the FeNLMS algorithm causes an increase in sharpness at the reference position and an increased coloration for head movements. However, for driving noise, the FeNLMS algorithm achieves vastly better loudness reduction and an increase in speech intelligibility.

While for white and pink noise, both algorithms perform better at the point of cancellation for the fullband condition when examining RMS, loudness, and MBSTOI, differences from the uncontrolled condition decrease more gradually for the bandlimited ANC systems. Further supported by the lower sharpness change and reduced coloration for head movements, an increased spatial extent is suggested for bandlimited control. For driving noise, the bandlimited ANC systems perform equally well as the fullband systems.

Future work will focus on the conduction of listening experiments to verify the simulation results.

6. REFERENCES

[1] S. Kuo and D. Morgan, "Active Noise Control: A Tutorial Review," *Proceedings of the IEEE*, vol. 87, no. 6, pp. 943–973, 1999.

[2] E. Zwicker and H. Fastl, *Psychoacoustics - Facts and Models*. Springer Berlin, Heidelberg, 2007.

[3] S. Kuo and J. Tsai, "Residual Noise Shaping Technique for Active Noise Control Systems," *J. Acoust. Soc. Am.*, vol. 95, no. 3, pp. 1665–1668, 1994.

[4] H. Bao and I. M. S. Panahi, "Using A-Weighting for Psychoacoustic Active Noise Control," in *Proc. of the 2009 Annual International Conference of the IEEE Engineering in Medicine and Biology Society*, (Minneapolis, USA), pp. 5701–5704, 2009.

[5] H. Bao and I. M. S. Panahi, "A Perceptually Motivated Active Noise Control Design and Its Psychoacoustic Analysis," *Etri Journal*, vol. 35, no. 5, pp. 859–868, 2013.

[6] P. R. Benois, U. Zölzer, and V. Papantoni, "Psychoacoustic Hybrid Active Noise Control Structure for Application in Headphones," in *Proc. of the 25th International Congress on Sound and Vibration*, (Hiroshima, Japan), 2018.

[7] C. Blöcher, A. Sontacchi, and T. Hatheier, "Impact of Perceptual Error Shaping in Active Noise Control Across Signals with Diverse Spectral Tilt," in *Fortschritte der Akustik - Proc. of DAS/DAGA 2025*, (Copenhagen, Denmark), 2025. Without peer review.

[8] P. Majdak, P. Balazs, and B. Laback, "Multiple Exponential Sweep Method for Fast Measurement of Head-Related Transfer Functions," *J. Audio Eng. Soc.*, vol. 55, pp. 623–637, 2007.

[9] S. Riedel, M. Frank, and F. Zotter, "The Effect of Temporal and Directional Density on Listener Envelopment," *J. Audio Eng. Soc.*, vol. 71, pp. 455–467, 2023.

[10] F. Holzmüller and A. Sontacchi, "Perceived Spatial Extent of Local Active Noise Control for Broadband Disturbances," in *Proc. of the AES 5th International Conference on Automotive Audio*, (Gothenburg, Sweden), 2024.

[11] F. Zotter and M. Frank, "All-Round Ambisonic Panning and Decoding," *J. Audio Eng. Soc.*, vol. 60, 2012.

[12] D. W. Gunness and O. S. Chauhan, "Optimizing the Magnitude Response of Matched Z-Transform Filters (MZTI) for Loudspeaker Equalization," in *Proc. of the AES 32nd International Conference*, (Hillerød, Denmark), 2007.

[13] D. Slock, "On the Convergence Behavior of the LMS and the Normalized LMS Algorithms," *IEEE Transactions on Signal Processing*, vol. 41, no. 9, pp. 2811–2825, 1993.

[14] B. C. J. Moore and B. R. Glasberg, "Modeling Binaural Loudness," *J. Acoust. Soc. Am.*, vol. 121, no. 3, pp. 1604–1612, 2007.

[15] DIN German Institute for Standardization, "DIN 45692 – Messtechnische Simulation der Hörempfindung Schärfe," 2009.

[16] R. Huber and B. Kollmeier, "PEMO-Q – A New Method for Objective Audio Quality Assessment Using a Model of Auditory Perception," *IEEE Transactions on Audio, Speech, and Language Processing*, vol. 14, no. 6, pp. 1902–1911, 2006.

[17] A. H. Andersen, J. M. de Haan, Z.-H. Tan, and J. Jensen, "Refinement and Validation of the Binaural Short Time Objective Intelligibility Measure for Spatially Dverse Conditions," *Speech Communication*, vol. 102, pp. 1–13, 2018.

DOI: 10.61782/fa.2025.0343



FORUM ACUSTICUM
EURONOISE 2025

ENHANCING IN-VEHICLE SPEECH INTELLIGIBILITY: A STUDY ON THE BENEFITS OF ACTIVE ROAD NOISE CANCELLATION SYSTEM

Tommaso Botti[1] **Marco Olivieri**[2] **Jacopo Gino**[1] **Alfonso Oliva**[2*]

[1] Teoresi S.p.A, Torino, Italy
[2] Ferrari S.p.A., Maranello, Italy

ABSTRACT

The acoustic quality inside vehicles has become a key factor in the overall evaluation of cars, particularly in luxury models. As a result, improving in-cabin communication and overall acoustic comfort has gained significant attention from the automotive industry. Recently technologies, such as Active Road Noise Cancellation (ARNC), have been extensively explored to reduce unwanted noise, effectively lowering acoustic pressure within the vehicle cabin. Beyond noise reduction, these algorithms have the potential to significantly enhance in-vehicle speech intelligibility. In this study, we investigate the impact of ARNC algorithms on person-to-person speech communication, simulating conversations between passengers. Experimental measurements have been conducted in a four-seat vehicle model equipped with a state-of-the-art ARNC system. Passenger communication has been simulated by convolving reference speech signals with measured acoustic impulse responses within the vehicle cabin. Additionally, we compare different metrics to assess speech intelligibility between front and rear seats, evaluating the effectiveness of the ARNC algorithm. The results demonstrate the potential of ARNC in enhancing in-vehicle speech intelligibility, offering valuable insights for future advancements in automotive audio technology.

Keywords: *speech intelligibility, in-car communications, active noise control*

***Corresponding author**: *Alfonso.Oliva@ferrari.com.*

***Copyright**: ©2025 Botti et al. This is an open-access article distributed under the terms of the Creative Commons Attribution 3.0 Unported License, which permits unrestricted use, distribution, and reproduction in any medium, provided the original author and source are credited.*

1. INTRODUCTION

The ability to communicate effectively within a car is crucial for both comfort and safety, making acoustic optimization a key area of research and development [1, 2]. Traditionally, improving acoustic comfort in a vehicle has relied on passive noise control techniques, such as by improving insulation materials, acoustic glazing, and optimized cabin structures. Although these methods effectively reduce overall noise levels, they are often limited by weight, cost, and design limitations. Furthermore, passive solutions are typically more effective at high frequencies, while their insulating properties tend to degrade at lower frequencies, making them less effective against road-induced low-frequency noise.

As an alternative, active solutions have gained significant attention, encompassing a variety of approaches based on advanced signal processing, including personalized audio zones (commonly referred to as ”private bubbles”) and Active Road Noise Cancellation (ARNC). The latter, in particular, aims to reduce low-frequency road noise by generating anti-noise signals, typically through the vehicle’s audio system. Although ARNC has been developed primarily to enhance passenger comfort by reducing background noise levels, its potential impact on speech intelligibility within the vehicle has not yet been fully explored.

In this paper, we assess the indirect benefits of ARNC on the in-car speech intelligibility by analyzing how reduced road noise contributes to clearer in-vehicle communication. We present a series of experimental measurements along with objective and subjective evaluations, aiming to provide insights into the role of ARNC not only as a comfort-enhancing or weight-reduction technology,

but also as a potential enabler of improved speech communication among vehicle occupants.

The rest of the paper is structured as follows. Sec. 2 present the context and background of ARNC and speech intelligibility. In Sec. 3 we present the methodology and experimental scenario to evaluate the impact of ARNC in passanger-to-passanger communications. Results are provided in Sec. 4 along with objective metrics and subjective evaluations. In Sec. 5 we draw final conclusions and considerations.

2. BACKGROUND AND PROBLEM FORMULATION

2.1 Active Road Noise Cancellation

Active Road Noise Cancellation (ARNC) refers to the application of Active Noise Cancellation (ANC) techniques to mitigate low-frequency road noise inside vehicle cabins. ANC techniques actively generate anti-noise signals to counteract unwanted sound waves, leveraging the principle of destructive interference [3, 4]. Unlike passive solutions, which rely on insulating materials and structural modifications, active techniques require an external power source and the implementation of a control strategy.

Most control systems are based on the well-known Filtered-x Least Mean Squares (FxLMS) algorithm [5, 6], which is an extension of the LMS algorithm [7] belonging to the gradient descent [8] family of optimization techniques. These techniques minimize a cost function by iteratively moving in the direction of its negative gradient [9]. FxLMS is a hybrid-feedforward control strategy based on adaptive filtering [7] that iteratively adjusts the filter coefficients to minimize the residual error, i.e., the sound pressure level at the cancellation position. The algorithm employs reference sensors, error microphones, and actuators to find the optimal solution and apply the control action.

A typical ARNC architecture adopted accelerometers mounted on the chassis or suspension system as reference sensors to detect road-induced vibrations before they propagate into the cabin. To measure the residual error, microphones are strategically placed within the cabin. Finally, actuators are typically the loudspeakers of the car's sound system [10].

The ARNC system operates by modeling two main paths: the primary and the secondary [11]. The primary path refers to the sound propagation from the road to the cabin, while the secondary path represents the transfer function from the actuators to the microphones within the cabin. The FxLMS algorithm continuously adapts to these paths to optimize noise cancellation, accounting for plant variations.

2.2 Speech Intelligibility

Speech intelligibility within a vehicle cabin is a critical aspect of passenger communication, particularly in the presence of road noise [12, 13]. High noise levels can mask speech signals, reducing the ability of passengers to understand each other clearly. The assessment of speech intelligibility in noisy environments typically relies on both objective and subjective evaluation methods.

Several metrics are commonly used to quantify speech intelligibility. The Short-Time Objective Intelligibility (STOI) [14] metric provides a prediction of intelligibility by analyzing the correlation between clean and degraded speech signals. The Signal-to-Noise Ratio (SNR) [15] quantifies the relative level of speech against background noise, with higher values indicating improved clarity.

In this paper, we leverage these metrics to quantify the impact of ARNC on speech intelligibility, comparing objective measurements in different road conditions to assess its role in improving in-vehicle communication.

3. METHODOLOGY

In this study, a speaker located in the rear right seat of a car has been simulated, and the impact of an ARNC system on speech intelligibility at the front right passenger position has been assessed. To achieve this, a state-of-the-art active noise cancellation system based on the Filtered-x Least Mean Squares algorithm has been implemented.

3.1 Experimental scenario

In order to evaluate the potential benefits of an Active Road Noise Cancellation (ARNC) system on in-vehicle speech intelligibility, an FxLMS-based algorithm was implemented and tested on the vehicle. The car was instrumented with accelerometers placed at carefully selected locations, while microphones were positioned inside the cabin, near the right front passenger's ears.

We adopted the mouth simulator of a Head and Torso Simulator (HATS) [16] placed on the right rear passenger seat to simulate human speeches. Specifically, the impulse responses (IRs) from the artificial mouth to the left and right microphones at the co-driver's seat, with an occupant

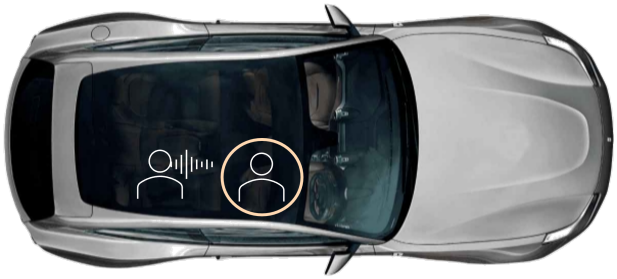


Figure 1. Measurement setup. Speaker at the rear-right seat and listener at the front-right seat along with the ARNC system.

in place, were measured in an anechoic chamber to characterize the acoustic transmission path through the Exponential Sine Sweep (ESS) method [17]. A schematic representation of the experimental setup is shown in Fig. 1. Notice that, in this study we assume the left-right microphones coincide with the co-driver ears, thus the measured IRs correspond to the transfer function from the rear-right talker to the ears of listener position under test.

Firstly, road noise measurements were performed on different road surfaces and at various speeds with the ARNC system deactivated. Then, the same measurements were repeated with the ARNC system enabled. In the rest of the paper, we will refer to those measurements as "*ARNC OFF*" and "*ARNC ON*", respectively. Therefore, this process provided road noise signals at the right front passenger's ears, both with and without active noise cancellation.

Moreover, a speech source at the rear-right passenger seat was simulated by convolving different clean speech signals with the previously measured IRs. The test signal was carefully designed to include both female and male speech segments, with progressively decreasing amplitude levels of $0\,\mathrm{dBFS}$, $-6\,\mathrm{dBFS}$, and $-12\,\mathrm{dBFS}$, respectively.

Finally, the resulting simulated speech signals at the right front passenger's ears were superimposed onto the road noise recordings, both with *ARNC OFF* and *ARNC ON*, allowing for a direct comparison of speech intelligibility under different noise conditions.

4. RESULTS

The impact of the ARNC system in terms of speech intelligibility has been evaluated with objective analysis and perceptual subjective analysis. The former, with the computation of different metrics. The latter, with the evaluation of two different perceptual listening tests. The following sections provide detailed explanations of the results along with insights and interpretations.

4.1 Objective analysis

To quantify the impact of the ARNC system on in-vehicle communication, we compute two different metrics presented in the literature of speech intelligibility, as explained in Sec. 2.2.

First of all, the Short-Time Objective Intelligibility (STOI) has been computed as reported in [14]:

$$STOI = \frac{1}{JM} \sum_{j,m} STOI_{j,m} \quad , \tag{1}$$

where:

$$STOI_{j,m} = \frac{(\boldsymbol{x}_{j,m} - \mu_{\boldsymbol{x}_{j,m}})^T \quad (\bar{\boldsymbol{y}}_{j,m} - \mu_{\bar{\boldsymbol{y}}_{j,m}})}{||\boldsymbol{x}_{j,m} - \mu_{\boldsymbol{x}_{j,m}}|| \quad ||\bar{\boldsymbol{y}}_{j,m} - \mu_{\bar{\boldsymbol{y}}_{j,m}}||}, \tag{2}$$

with

- J is the total number of one-third octave bands
- M denotes the total number of temporal frames
- $\boldsymbol{x}_{j,m}$ represents the clean speech short-time temporal envelope in the $j-th$ frequency band and $m-th$ time frame
- $\bar{\boldsymbol{y}}_{j,m}$ represents the normalized degraded speech envelope in the $j-th$ frequency band and $m-th$ time frame after applying a one-frame temporal clipping
- $\mu_{\boldsymbol{x}_{j,m}}$ and $\mu_{\bar{\boldsymbol{y}}_{j,m}}$ denote the sample average of $\boldsymbol{x}_{j,m}$ and $\bar{\boldsymbol{y}}_{j,m}$

The STOI index has been computed for each speech segment and evaluated at the three amplitude levels. Inspecting the results, we notice that for each segment the ARNC provides an improvement in terms of intelligibility with an increase up to $5\,\%$, and in general higher then $1.1\,\%$. However, to provide a single index for both ears position, the following binaural definition, denoted as BSTOI, has been formulated:

$$BSTOI = \sqrt{\frac{STOI_L^2 + STOI_R^2}{2}}, \tag{3}$$

where $STOI_L$ and $STOI_R$ represent the $STOI$ index computed at the left and right ear microphones position,

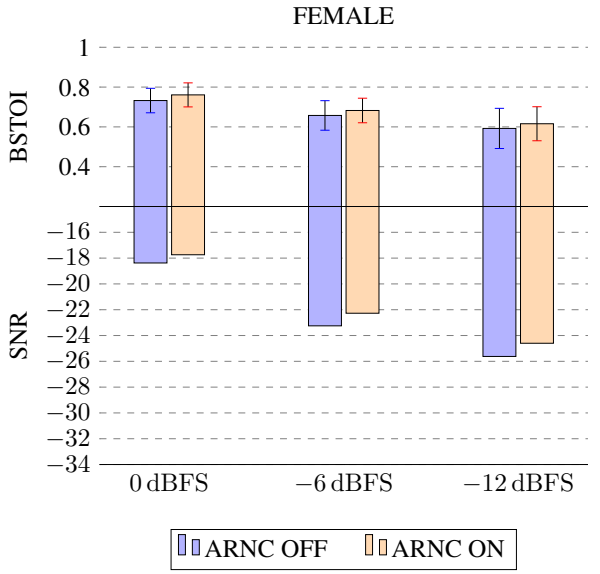


Figure 2. Average and standard deviation of BSTOI and average SNR for Female speakers at different dBFS values.

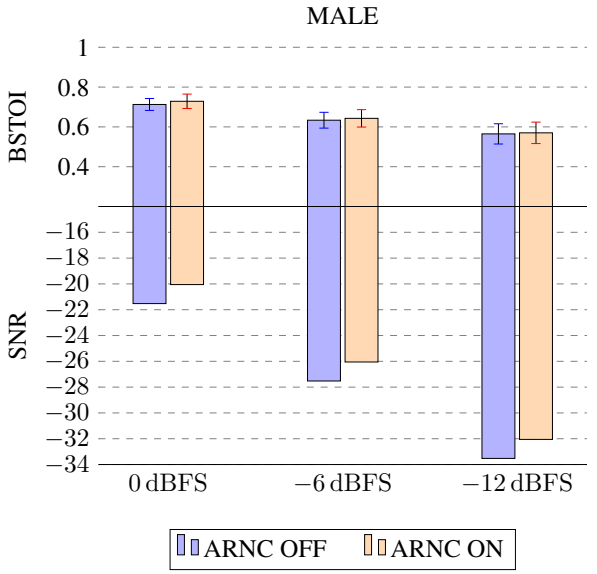


Figure 3. Average and standard deviation of BSTOI and average SNR for Male speakers at different dBFS values.

respectively. Therefore, as for STOI, also BSTOI values are in the range $[0, 1]$, with 1 referring to the highest intelligibility score.

Similarly, the Signal-to-Noise Ratio (SNR) has been computed in dB for all the speech segments and the different amplitude levels as follows:

$$SNR = 10 \log_{10} \left(\frac{P_{signal}}{P_{noise}} \right), \tag{4}$$

where P_{signal} and P_{noise} denote the power of the signal and the noise, respectively. Moreover, we consider as SNR the mean values between the two microphones at the ear positions. It is worth noticing that in our scenario SNR values are negative due to the predominance of the noise compared to the signals.

Fig. 2 and 3 depict the average BSTOI (in the positive y-axis) and SNR data (in the negative y-axis) computed among female and male speakers, respectively, for each different dBFS values.

In general, female speech signals achieve higher values of BSTOI and SNR with respect to the male speech signals, both with ARNC system ON and OFF. This is due to the higher frequency content of female speeches, which is less affected by road noise. Indeed, male voices exhibit more spectral overlap with road noise, which is more dominant at low frequencies, resulting in lower scores, in general. Enabling the ARNC system for female speakers results in an increase of the BSTOI higher than 1.3% for all the three amplitude levels, with a maximum increase of 3.4%. For the case of male speakers, all amplitude levels show an increase of the index higher than 0.3%, with a maximum delta of 2%. In terms of SNR instead, we have a maximum increase of 1% for female speakers, while for the male case a maximum delta of 1.5% is registered.

Finally, the standard deviation of the BSTOI index between females decreases when the ARNC system is activated, indicating more uniform values, while an increment can be observed for the case of male speakers. Therefore, it can be noticed that the ARNC system provides an increase in terms of intelligibility for all the examined cases.

4.2 Subjective analysis

The benefits of the ARNC system on speech intelligibility has been evaluated also through a subjective evaluation campaign. Specifically, two blind tests were conducted:

- **Test 1:** A-B comparison of each speech signal with ARNC system enabled and disabled
- **Test 2:** Progressively increasing level test of speech signals.

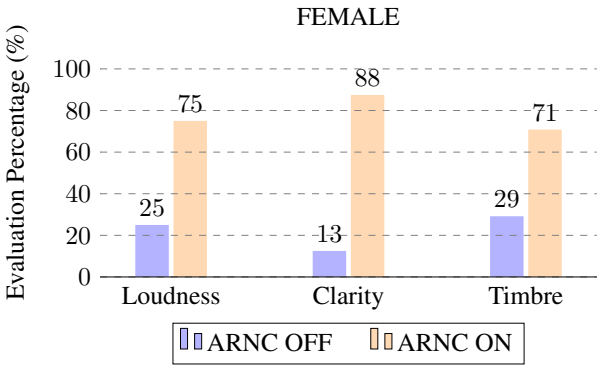


Figure 4. Average KPIs results of the A-B comparison for Female speech signals.

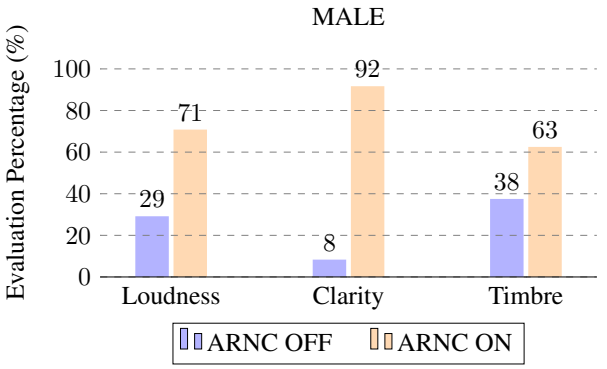


Figure 5. Average KPIs results of the A-B comparison for Male speech signals.

4.2.1 A-B comparison

For this experiment, we focus on four test signals from the simulated speech signals with background road noise described in Sec. 3.1. In particular, we considered the two female and the two male speakers. For each of the selected speech, signal A and signal B have been randomly generated considering *ARNC ON* and *ARNC OFF* conditions.

The blind listening test was conducted on 12 expert-listeners using Audeze high-quality professional headphones [18], and they were given the ability to switch between signal A and signal B for each of the four speech frames. Therefore, for each frame the listeners were asked to express their preference between A and B based on the following three key performance indicators (KPIs):

- Loudness
- Clarity
- Timbre

where *Loudness* refers to the highest perceived loudness of the speech, *Clarity* relies on the precise articulation and correct pronunciation perceived, and *Timbre* evaluated the perceived quality of the speech.

The average evaluation results expressed in percentage between female and male speakers are depicted in Fig. 4 and Fig. 5, respectively. In both cases, the same trend can be noticed with an overall preference to the *ARNC ON* condition for all the three KPIs. Therefore, the activation of the ARNC system implies a perceptual benefits on the rear-to-front speech intelligibility.

It is worth nothing that, considering the *ARNC ON* condition, the *Loudness* and *Timbre* indeces collect higher results for the female speakers with respect to male ones, respectively with $4\,\%$ and $5\,\%$ of difference. Conversely, the *Clarity* with *ARNC ON* has been selected by $92\,\%$ for the case of male speaker, lowering to $88\,\%$ for female speakers. Such results depend on the frequency range of the male and female speech. With lower frequency contents, the male spectra is more affected by the frequency range of the road noises, thus the presence of an ARNC system affects the speech *Clarity*.

The stacked bar plot depicted in Fig. 6 represents the detailed results for the two female speakers (refer to F1 and F2) and the two male speakers (refer to M1 and M2). Interestingly, the sujbective results between *ARNC OFF* and *ARNC ON* present higher variance for the female case with respect to the male one. Such result confirms the impact of the ARNC system to the lower frequency range. Indeed, assessors considered easier the A-B test for male with respect to female speakers. Interestingly, although an overall preference for the case with the algorithm enabled can also be seen for the *Timbre* index, it has been described as the most difficult KPI to be evaluated by the majority of the listeners.

4.2.2 Progressively increasing level test

To further assess the impact of the ARNC system on in-vehicle speech intelligibility, an additional blind test was conducted. In this experiment, the same four speech frames used in the A-B comparison test of Sec. 4.2.1 have been evaluated. However, for each of the speech frames under consideration, assessors have been asked to listen to a progressively increasing level of the speech frames both with *ARNC OFF* and with *ARNC ON*, thus highlighting

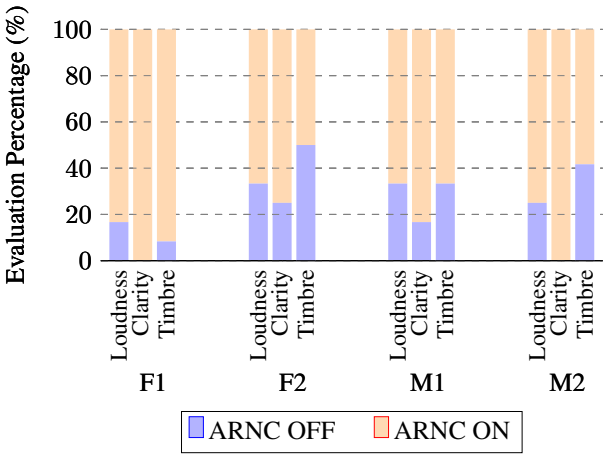


Figure 6. Overall KPIs results of the A-B comparison for Female (F1 and F2) and Male (M1 and M2) speech signals.

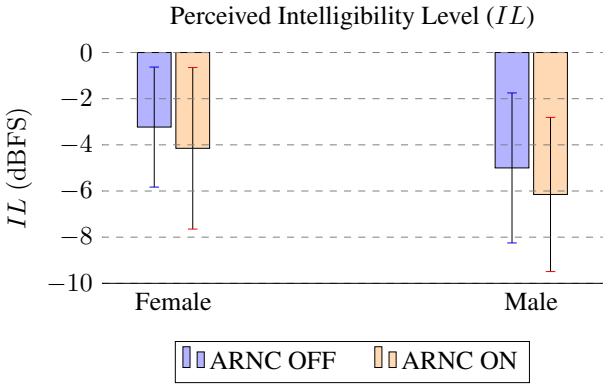


Figure 7. Results of perceived intelligibility level (IL). Avarage and standard deviation are shown with respect to Female and Male speeches with for the case of *ARNC OFF* and *ARNC ON*.

when the signals were intelligible. In particular, the simulated speech has been initially set to a level of -20 dBFS, thus progressively increasing the level at each repetition with a step of 2 dBFS of increments up to 0 dBFS.

A group of 13 expert-listener was selected for the blind test. Assessors have been instructed to stop the audio playback as soon as they were able to understand all the words in each frame, thus identifying a level of perceived intelligibility expressed in dBFS and for the sake of simplicity denoted as IL (intelligibility level). The average results of the perceived IL along with the standard deviation are depicted in Fig. 7 for the case of *ARNC OFF* and *ARNC ON* and differentiating between male and female frames.

In general, assessors were able to fully comprehend the speech content at a lower level in the case of *ARNC ON*, thus confirming the benefits of the road noise reduction for the intelligibility. In particular, the delta level of perceived IL between *ARNC OFF* and *ARNC ON* is equal to 2 dBFS for male speeches and decreases to 1.77 dBFS for female speakers.

It is worth noticing that independently of the ARNC system, male talkers achieved a lower IL then female speeches. The former with -4.15 dBFS and -6.15 dBFS of IL for the case of *ARNC OFF* and *ARNC ON*, respectively. For female speeches, the average results reduced to -3.23 dBFS and -5 dBFS, respectively. Therefore, the delta IL between the disabled and enabled ARNC system increases from 1.77 dBFS for female speakers to 2 dBFS for male speakers. As expected, such result confirms the benefits of the ARNC system in terms of speech intelligibility signals with lower frequency contents that overlap with the ARNC operating frequency range. Moreover, notice that the outcome of this listening test is aligned with Fig. 4 and Fig. 5 of the A-B listening test in Sec. 4.2.1, where male speeches with *ARNC ON* achieved a higher *Clarity* score compared to the female counterpart test.

Another interesting interpretation of the advantages of the ARNC system provided by the results of the devised progressively increasing level test lies in allowing the rear passengers to speak at a lower level but keeping the same speech intelligibility at the front passengers when the ARNC system is enabled.

5. CONCLUSIONS

In this study, the benefits of an Active Road Noise Cancellation (ARNC) algorithm on in-vehicle passenger-to-passenger speech intelligibility have been evaluated through both objective and subjective assessments. Road noise measurements were conducted at the front-right passenger's ear positions in a vehicle instrumented with accelerometers and microphones, using a state-of-the-art ARNC algorithm.

To simulate a speaker inside the vehicle, a Head and Torso Simulator was placed on the rear right-seat, and the impulse response from its artificial mouth to the microphones at the front passenger's ear position has been

measured. A reference speech signal, consisting of both male and female voices at different amplitude levels, was then convolved with the measured impulse responses to replicate how speech from the rear passenger seat would be perceived by the front passenger. Finally, this processed speech signal was superimposed with the previously recorded road noise, both with and without the ARNC system enabled.

Speech intelligibility was assessed using two objective metrics, specifically STOI and SNR, at both ears. Additionally, two blind listening tests were conducted with more than 10 expert-listeners. Specifically, both objective and subjective assessments revealed an increase in speech intelligibility when the ARNC algorithm is enabled, with a stronger perceptual improve for the case of male speakers, where the frequency content of the voice has a major overlap with the one of the road noise. Therefore, results of devised experiments consistently demonstrated the positive impact of the ARNC system on in-vehicle speech intelligibility, confirming its potential in enhancing communication within the vehicle cabin.

6. REFERENCES

[1] C. Lüke, G. Schmidt, A. Theiß, and J. Withopf, "In-car communication," in *Smart Mobile In-Vehicle Systems: Next Generation Advancements*, pp. 97–118, Springer, 2013.

[2] B. Căşeriu and P. Blaga, "Automotive comfort: State of the art and challenges," in *International Conference Interdisciplinarity in Engineering*, pp. 375–387, Springer, 2022.

[3] D. Miljković, "Brief introduction to active noise control," pp. 977–982, 05 2023.

[4] K. Ng, *The Challenges of Active Noise Control*. 11 2023.

[5] S. Elliott and P. Nelson, "Active noise control," *IEEE Signal Processing Magazine*, vol. 10, no. 4, pp. 12–35, 1993.

[6] E. Bjarnason, "Analysis of the filtered-x lms algorithm," *IEEE Transactions on Speech and Audio Processing*, vol. 3, no. 6, pp. 504–514, 1995.

[7] B. Widrow and M. E. Hoff, "Adaptive switching circuits," in *Neurocomputing: foundations of research*, pp. 123–134, MIT Press, 1988.

[8] S. Boyd and L. Vandenberghe, *Convex Optimization*. Cambridge University Press, 2004.

[9] S. Ruder, "An overview of gradient descent optimization algorithms," *arXiv preprint arXiv:1609.04747*, 2016.

[10] Z. Jia, X. Zheng, Q. Zhou, Z. Hao, and Y. Qiu, "A hybrid active noise control system for the attenuation of road noise inside a vehicle cabin," *Sensors*, vol. 20, no. 24, 2020.

[11] S. Kuo and D. Morgan, "Active noise control: a tutorial review," *Proceedings of the IEEE*, vol. 87, no. 6, pp. 943–973, 1999.

[12] N. Samardzic and C. Novak, "In-vehicle speech intelligibility for different driving conditions using the speech transmission index," *Noise Control Engineering Journal*, vol. 59, no. 4, pp. 397–407, 2011.

[13] N. Samardzic and C. Novak, "In-vehicle application of common speech intelligibility metrics," *International Journal of Vehicle Noise and Vibration*, vol. 7, no. 4, pp. 328–346, 2011.

[14] C. H. Taal, R. C. Hendriks, R. Heusdens, and J. Jensen, "An algorithm for intelligibility prediction of time–frequency weighted noisy speech," *IEEE Transactions on Audio, Speech, and Language Processing*, vol. 19, no. 7, pp. 2125–2136, 2011.

[15] P. C. Loizou, *Speech Enhancement: Theory and Practice*. CRC press, 2013.

[16] H. Acoustics, "Head acoustics head and torso simulator (hats) hms ii.3 with ln." `https://www.head-acoustics.com/products/artificial-head-binaural-recording/hms-ii3-ln` [Accessed: (03/2025)].

[17] A. Farina, "Advancements in impulse response measurements by sine sweeps," in *Audio engineering society convention 122*, Audio Engineering Society, 2007.

[18] Audeze, "Audeze lcd-x." `https://www.audeze.com/products/lcd-x` [Accessed: (03/2025)].

DOI: 10.61782/fa.2025.0584

FORUM ACUSTICUM EURONOISE 2025

MOMENTUM ALGORITHM AND ITS APPLICATION TO ACTIVE CONTROL OF HVAC COMPRESSOR NOISE IN AUTONOMOUS BUS

Sang-Kwon Lee[1*] **Junseok Choi**[1]
Doyeon Kim[1] **Seongyeol Kim**[1]
[1] Department of Mechanical Engineering, Inha University, South Korea

ABSTRACT

The compressor is used for a heating, ventilation, and air-conditioning (HVAC) system which provide air conditioning for each passenger in autonomous bus. The sound radiated from the compressor of the HVAC system is a high-frequency annoyance noise caused by vibroacoustic noise due to the shell vibration of the compressor. The dominant frequency components of the vibroacoustic noise are harmonics of the rotation frequency of the reciprocating compressor. The HVAC system generates vibroacoustic noise dominantly in the frequen-cy range between 100 and 600 Hz. Such noise is not only distinctly perceptible but also contributes to passenger discomfort and negatively impacts the perceived quality of the vehicle. The aim of this paper is to attenuate the vibroacoustic noise of the HVAC system by developing an active noise control (ANC) system. Generally, the widely recognized filtered-X least mean squared (FXLMS) algorithm has been successfully implemented to active noise control of reciprocating compressor. However, its performance was found lacking outside the peak frequency of compressor operation noise. To address this, the momentum algorithm was employed to enhance ANC performance. The momentum algorithm has a lower residual error and faster convergence rate compared to the FXLMS algorithm. As a consequence, the implementation of the momentum based ANC algorithm resulted in enhanced noise reduction not only at the peak frequencies, which correspond to the compressor operation frequency, but also in frequency ranges outside these peak frequencies.

[*]***Corresponding author***: *sangkwon@inha.ac.kr*
Copyright: *©2023 First author et al. This is an open-access article distributed under the terms of the Creative Commons Attribution 3.0 Unported License, which permits unrestricted use, distribution, and reproduction in any medium, provided the original author and source are credited*

Keywords: *compressor, vibroacoustic noise,active noise control, momentum algorithm, fast convergence.*

1. INTRODUCTION

HVAC noise profoundly affects passenger riding comfort within electric vehicle cabins. Consequently, extensive re-search efforts have been devoted to analyzing and reduc-ing these noises. Contrasting with typical vehicle HVAC systems, the HVAC system under autonomous bus seats is structurally akin to refrigerator systems, incorporating com-ponents like compressors, evaporators, condensers, and fans. This similarity allows for the application of noise con-trol techniques used in refrigerator systems to be effectively employed in autonomous car seat HVAC systems as shown in Fig.1. Among these HVAC parts, the shell vibration of the compressor generates noise that is harmonic to the rotation frequency of the reciprocating compressor. The hybrid technique, a combination of passive and active techniques, can be used to obtain a reduction in the overall frequency range for this dominant noise.

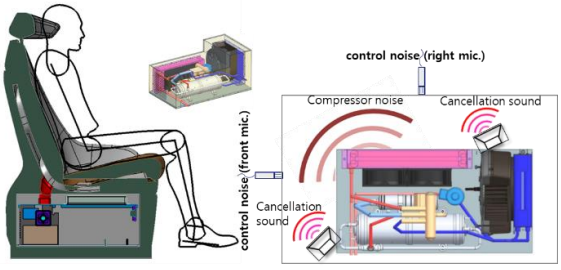


Figure 1. HVAC system of autonomous bus seat.

ANC stands out as a technique for suppressing low-frequency noise, offering the advantage of effective noise reduction without additional weight or space consumption

unlike many passive methods [1]. On the other hand, passive strategies such as sound absorbing materials are more suited for high-frequency noise reduction [2]. For example, the vibration absorber can be designed to reduce such structural vibration in the high-frequency range [3]. ANC operates by producing 'anti-noise' of equal ampli-tude but opposite phase to the primary noise. Adaptive filter-ing, often employing the LMS algorithm, is a cornerstone of ANC systems for addressing time-varying noise characteris-tics [4]. Despite its effectiveness, there are space con-straints within the system that limit the speaker size, affecting low-frequency noise reduction. Therefore, the low-frequency component of the output can be filtered out [5]. In this study, on the other hand, a frequency range between 200 Hz and 600 Hz is targeted for this ANC application since the speaker to be used has a diameter of 2.25 inches. However, this frequency range is relatively high for the ANC ap-plication because the generation of a signal that is out of phase of the high-frequency primary noise signal is chal-lenging due to its short wavelength. Hence, the ANC algo-rithm requires fast convergence. For the ANC algorithm, the FXLMS algorithm is widely used because it is robust and requires low computation. However, the convergence speed of the LMS algorithm is poor due to a phenomenon called eigenvalue spread [6]. The performance of the LMS algo-rithm can be improved using the momentum algorithm [7] with a small increase in computational burden In this study, the momentum algorithm based ANC algorithm will be de-veloped for the HVAC system for autonomous bus seats.

2. FXLMS ALGORITHM

The fundamental objective of the Least Mean Square (LMS) algorithm is to compute the optimal filter coefficients that minimize the mean square error. This optimization employs the iterative steepest descent method, where each iteration proceeds in the direction opposite to the gradient of the error surface [4].

$$\boldsymbol{w}(n+1) = \boldsymbol{w}(n) + \mu(-\nabla_n) \tag{1}$$

The error signal, $e(n)$, is defined as the difference between the desired signal (in this case, noise to be canceled), $d(n)$, and the output signal, $y(n) = x(n)\boldsymbol{w}(n)$.

$$e(n) = d(n) - x(n)\boldsymbol{w}(n) \tag{2}$$

Accordingly, the gradient of the squared error is expressed as

$$\nabla e^2(n) = -2e(n)x(n) \tag{3}$$

Substituting Eq. (3) into Eq. (1), the final form of the LMS algorithm is obtained.

$$\boldsymbol{w}(n+1) = \boldsymbol{w}(n) + \mu x(n) e(n) \tag{4}$$

Here, μ denotes the convergence factor, crucial for the stability and steady-state performance of the algorithm. The algorithm employs a time-varying step size, calculated to be inversely proportional to both the power of the reference signal ($\widehat{P_x}$) and the filter length (L). This is expressed as

$$\mu(n) = \frac{\alpha}{L\widehat{P_x}(n)} \tag{5}$$

Here, the normalized step size α falls within the range of $0 < \alpha < 2$. The power of the reference signal is estimated using the formula.

$$\widehat{P_x}(n) = \frac{1}{M}\sum_{m=0}^{M-1} x^2(n-m) \tag{6}$$

To mitigate divergence issues due to insufficient spectral excitation, a leaky mechanism is integrated into the weight update process. The leaky LMS algorithm is thus formulated as follows.

$$\boldsymbol{w}(n+1) = \nu\boldsymbol{w}(n) + \mu x(n) e(n) \tag{7}$$

In this context, ν denotes the leakage factor, constrained within the range $0 < \nu \leq 1$. Adjusting the leakage factor involves a trade-off between robustness and performance loss [1]. In practical implementations involving electronic components such as microphones, filters, and amplifiers, the signal path from the loudspeaker to the error microphone, termed the secondary path, significantly influences the ANC system's efficacy. Burgess [8] proposed compensating for the secondary path effect to enhance system performance. This is achieved by filtering the reference signal with a filter that mimics the secondary path, leading to the development of the filtered-X LMS (FXLMS) algorithm. The error signal in the FXLMS context is redefined as follows.

$$\hat{x}(n) = s(n) * x(n) \tag{8}$$

where $s(n)$ is the impulse response of the secondary path, $*$ denotes linear convolution. The gradient of squared error can be rewritten as

$$\nabla e(n) = -2\hat{x}(n)e(n). \quad (9)$$

The FXLMS algorithm iteratively updates the filter weights to achieve optimum noise cancellation.

$$\boldsymbol{w}(n+1) = \nu\boldsymbol{w}(n) + \mu\hat{x}(n)e(n) \quad (10)$$

Since the transfer function, $S(z)$ of the secondary path is typically unknown, it can be estimated via a separate LMS algorithm. The adaptive filter output is computed by linear convolution between the optimum filter and the reference signal.

$$y(n) = \sum_{l=0}^{L} w_l(n)\hat{x}(n-l) \quad (11)$$

The block diagram of the FXLMS algorithm is shown in Fig. 2.

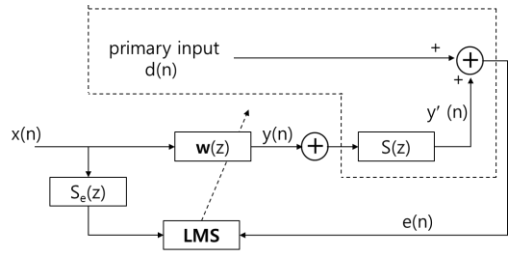


Figure 2. Block diagram of ANC system using FXLMS algorithm.

In this representation, $\hat{S}(z)$ denotes the estimated transfer function of the secondary path, $P(z)$ represents the primary path, and $W(z)$ symbolizes the time-varying adaptive filter.

3. THEORY OF THE MOMENTUM ALGORITHM

The momentum algorithm can also be derived from gradient descent method, where the gradient of gradient descent descends along the surface of cost function ξ which is error surface in the context of ANC. The system can resemble to dynamic system with a mass moving along the error surface. The direction of movement at this time is determined by potential $\nabla\xi$, and can be expressed as [9]

$$\frac{d\boldsymbol{w}}{dt} = \nabla\xi \quad (12)$$

Therefore, in (12), while a local minimum is achieved when $\nabla\xi(\boldsymbol{w}) = 0$, it is not the only equation where a minimum point occurs exactly at $\nabla\xi(\boldsymbol{w}) = 0$ but also governs the system movement. In other words, the system does not converge directly to the target point but rather oscillates and gradually converges. This can be considered as a simple oscillator that takes into account the oscillations that occur. Using this, the resulting second-order differential equation is as

$$\eta\frac{d^2\boldsymbol{w}}{dt^2} = -\nabla\xi(\boldsymbol{w}) - b\frac{d\boldsymbol{w}}{dt} \quad (13)$$

If $\eta \geq 0$, it considers the mass of the particle, and if $b \geq 0$, t considers the damping that occurs during the system's change process. When $\nabla\xi(\boldsymbol{w}) = 0$ as in (12), it reaches a minimum point in the differential equation. When η converges to 0, it results in (12). If η is positive, the trajectory represented by (13) gradually changes direction in the direction indicated by $-\nabla\xi(\boldsymbol{w})$, showing evidence of momentum [9]. A simple finite difference approximation in (13) is as

$$\eta\frac{\boldsymbol{w}(t+\Delta t)-2\boldsymbol{w}(t)+\boldsymbol{w}(t-\Delta t)}{(\Delta t)^2} \approx -\nabla\xi(\boldsymbol{w}(t)) - b\frac{\boldsymbol{w}(t+\Delta t)-\boldsymbol{w}(t)}{\Delta t} \quad (14)$$

In summary,

$$\boldsymbol{w}(t+\Delta t) = \boldsymbol{w}(t) - \alpha\nabla\xi\big(\boldsymbol{w}(t)\big) + \beta(\boldsymbol{w}(t) - \boldsymbol{w}(t-\Delta t)) \quad (15)$$

In the ANC system, signals are processed as discrete signals rather than continuous signals, so $t = n, \Delta t = 1$. Therefore, equation (15) can be rearranged for discrete signals as

$$\boldsymbol{w}(n+1) = \boldsymbol{w}(n) - \alpha\nabla\xi\big(\boldsymbol{w}(n)\big) + \beta\big(\boldsymbol{w}(n) - \boldsymbol{w}(n-1)\big) \quad (16)$$

This algorithm is defined as Polyak's heavy ball method. With slight modifications, a related method called Nesterov's optimization can also be obtained. If ξ is a convex quadratic equation, the approach in (16) (allowing for adaptive choices of α and β that vary with each iteration) is called the Chebyshev iteration method. Additionally, (16) can be redefined as

$$\begin{aligned}\boldsymbol{v}(n) &= \boldsymbol{w}(n+1) - \boldsymbol{w}(n) \\ &= -\alpha\nabla\xi\big(\boldsymbol{w}(n)\big) + \beta\big(\boldsymbol{w}(n) - \boldsymbol{w}(n-1)\big) \\ &= -\alpha\nabla\xi\big(\boldsymbol{w}(n)\big) + \beta\boldsymbol{v}(n-1)\end{aligned} \quad (17)$$

In (17), we can divide it into two equations as follows.

$$\begin{cases} \boldsymbol{w}(n+1) = \boldsymbol{w}(n) + \boldsymbol{v}(n) \\ \boldsymbol{v}(n) = -\alpha \nabla \xi\big(\boldsymbol{w}(n)\big) + \beta \boldsymbol{v}(n-1) \end{cases} \quad (18)$$

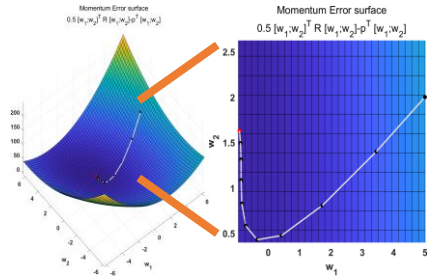
Here, $\boldsymbol{v}$ is the accumulated gradient, $\boldsymbol{\alpha}$ is the step size, and β represents inertia, where $0 < \beta < 1$ and typically $\beta = 0.9$ is used. Additionally, $\nabla \xi(\boldsymbol{w}(n))$can be expressed as $\nabla \xi(n)$ in (12), and $\nabla \xi(\boldsymbol{w}(n))$ in (18) can be expressed by (9) as

$$\nabla \xi(\boldsymbol{w}(n)) = 2[\nabla \mathrm{e}(n)]\mathrm{e}(n) = -2\boldsymbol{x}(n)e(n) \quad (19)$$

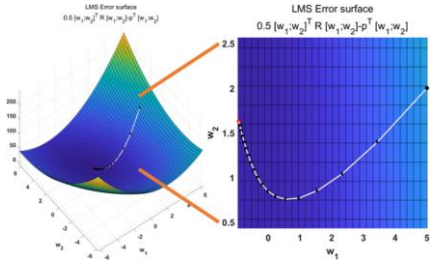
By (19), (18) can be expressed as

$$\begin{cases} \boldsymbol{w}(n+1) = \boldsymbol{w}(n) + \boldsymbol{v}(n) \\ \boldsymbol{v}(n) = \mu \boldsymbol{x}(n)e(n) + \beta \boldsymbol{v}(n-1) \end{cases} \quad (20)$$

μ represents the step size. In other words, μ is a convergence coefficient that is crucial for stability and steady-state performance, much like in the LMS algorithm.



(a) Convergence of the momentum algorithm along the error surface.



(b) Convergence of the LMS algorithm along the error surface.

Figure 3. Comparison of convergence performance the momentum and LMS algorithm along the error surface.

Therefore, the convergence performance depends on this μ value, and an appropriate μ value must be found. For an arbitutary cost function, the convergence pergormance of two algorithms along the error surface was compared and its results are illustrated in Fig. 3.

4. ANC OF HVAC COMPRESSOR NOISE

4.1 Flow Chart of Algorithm

The ANC system employed in this study is characterized as a single reference with a multiple output configuration (1x2x2), as delineated in Fig. 4. The system acquires a reference signal through an accelerometer stuck to the compressor's shell. Two small size speakers were useded for ANC. One speaker positioned at the front side of compressor and the other one is right side. The error signals were captured by microphones strategically placed in the near field of the front and right sides of the HVAC system. These reference and error signals are crucial in the computation of filter coefficients, a process executed utilizing Eq. (10) and Eq. (20). It should be noted that the reference signal undergoes a filtration process before its integration into the algorithm, facilitated by modeled secondary filters. These filters represent transfer functions that cover the characteristics of various electronic components, such as analog filters and amplifiers, as well as the acoustic pathway extending from the speakers to the error microphones. Subsequently, the derived optimal filter coefficients are convolved with the reference signal in accordance with Eq. (11). This process yields the output signal $y(n)$, which functions as the anti-noise of the targeted noise signal $d(n)$.

4.2 Experimental Setup of the HVAC ANC System

The experimental setup entailed the utilization of a notebook computer interfaced with the dSPACE Autobox I/O board as shown in Fig. 5. The dSPACE Autobox plays a crucial role in this setup, facilitating the conversion of signals from analog to digital and vice versa. Additionally, it executes the embedded MATLAB Simulink code designated for Active Noise Control (ANC).
The signals collected from the error microphones and the accelerometer cannot be employed in their raw form due to the indeterminate frequency content. Consequently, it becomes essential to subject these signals to a low-pass filtering process. This step aids in determining the appropriate sampling frequency. The low-pass filters are configured with a cut-off frequency of 400 Hz in this study, marginally exceeding the highest frequency target for ANC.

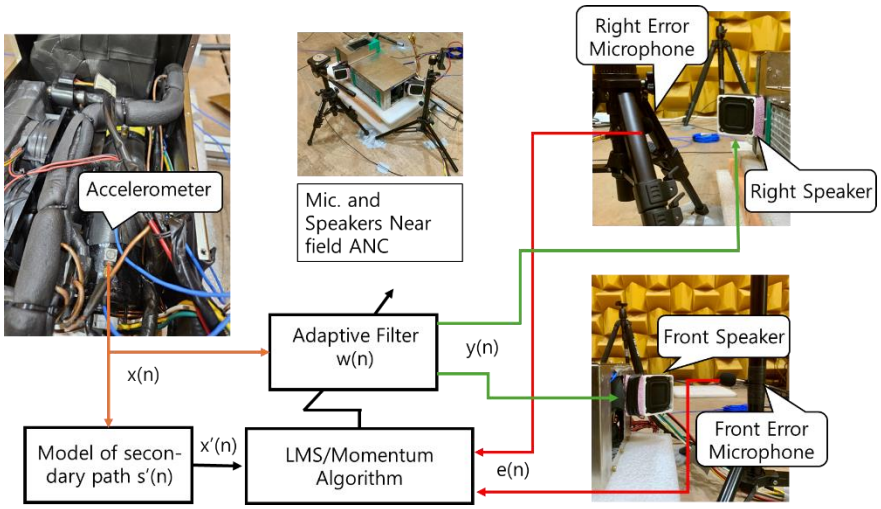


Figure 4. Block diagram of ANC system using FXLMS algorithm.

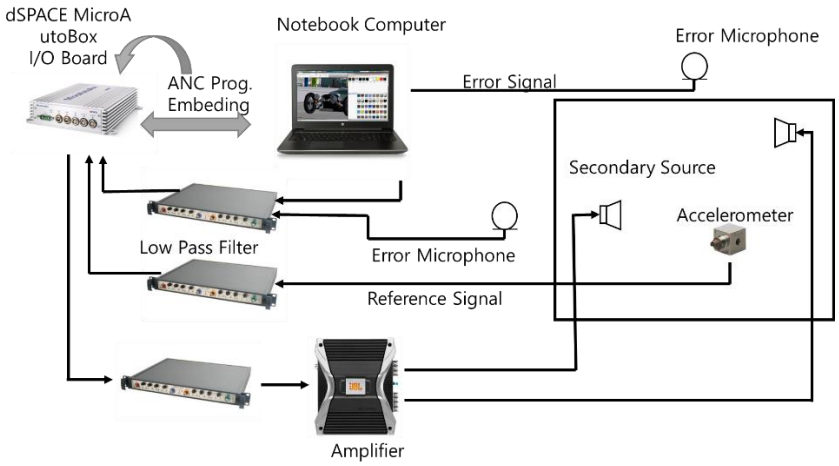


Figure 5. Experimental setup for the implementation of ANC system.

To prevent the occurrence of aliasing which distorts the signal, the sampling frequency must be at least twice the frequency content of the signal according to the Nyquist-Shannon sampling theorem. In this instance, a sampling frequency of 2048 Hz is selected, exceeding the double threshold of the signal's frequency content. Moreover, the output signal $y(n)$, directed towards the speakers, requires filtering to correct any reconstruction errors that may arise during the digital-to-analog (A/D) conversion process. Therefore, the cut-off frequency for this reconstruction filter is set at 400 Hz to eliminate the reconstruction error during the A/D conversion and to prevent the algorithm from diverging due to exciting the speakers outside the target frequency range (100-400 Hz). Finally, this signal is amplified using an amplifier to effectively drive the loudspeakers.

4.3 Placement of Error Microphones

To measure the basic SPL (sound pressure level) of HVAC system, five microphones have been installed within a 1-meter distance from the center of HVAC system in accordance with the stipulated standards [10] as shown in Fig. 6. According to the results of measured SPL, overall A-

weighted SPL in frequency range (0-5000 Hz) was as listed in Tab. 1.

Table 1. A-weighted sound pressure level of all microphones.

Microphones	Front	Right	Left	Rear	Top
Average SPL	80.1 dB	83.2 dB	75.8 dB	77.1 dB	78.3 dB

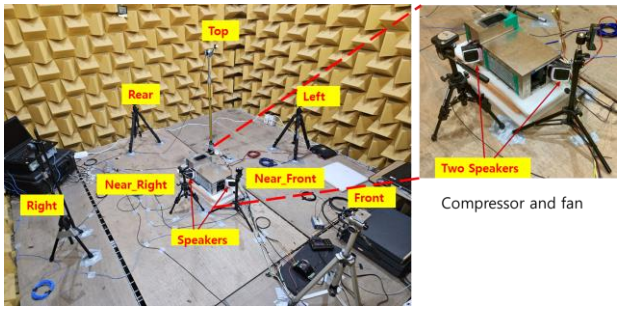


Figure 6. Setup of seven microhones and two speakers for ANC of HVAC system.

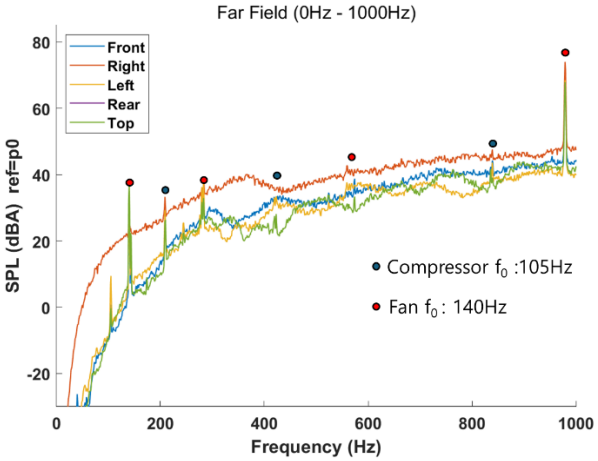


Figure 7. Frequency analysis of the sound pressure measured at the five microphones.

The major frequencies of the measured noise are associated to the rotating frequency of compressor shaft (105Hz) and cooling fan (140Hz) and their harmonics as shown in Fig.7. For the active cancellation of vibroacoustic noise radiated from shell of compressor and fan at nearfield, the error $e(n)$ microphones were installed at the front and the right of test compressor respectively. Two secondary speakers were also installed near to the test compressor as shown in Fig. 6. The frequency band that ANC is possible is from 100Hz to 400Hz due to size limit of secondary speaker and wave length of sound.

4.4 Selection of the Reference Signal

The ordinary coherence function is commonly employed to assess the extent of linear association between two signals, such as input and output signals [11]. The coherence value, therefore, is an important parameter for the performance evaluation of the ANC system [1]. Thus, magnitude-squared coherence can be defined as

$$C_{dx}(f) = |\gamma_{dx}(f)|^2 = \frac{|S_{dx}(f)|^2}{S_{dd}(f)S_{xx}(f)} \quad (21)$$

where f denotes the frequency of interest, $S_{dx}(f)$ is the cross-power spectrum, and $S_{dd}(f)$ and $S_{xx}(f)$ are the autopower spectra of $d(n)$ and $x(n)$, respectively. The coherence values between the accelerometer signal in the z direction and front, right microphone approached unity at the operational frequency of the compressor and its harmonics. This indicates a high degree of correlation, suggesting that the vibroacoustic noise emanating from the compressor can be effectively controlled.

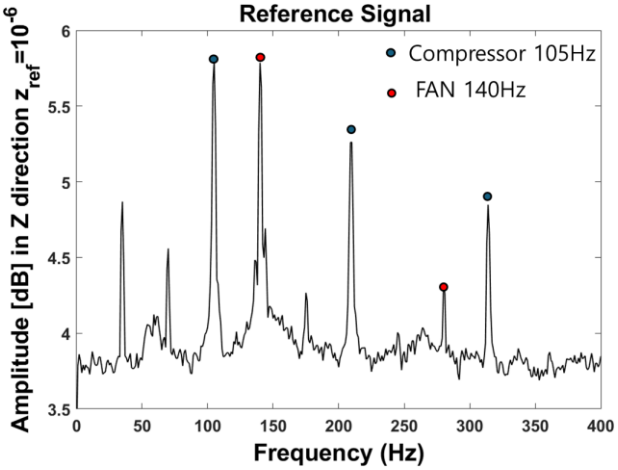


Figure 8. Fourier transform of the reference signal.

This indicates a high degree of correlation, suggesting that the vibroacoustic noise emanating from the compressor can be effectively controlled. According to the coherence results, the accelerometer data specifically collected in the z-axis

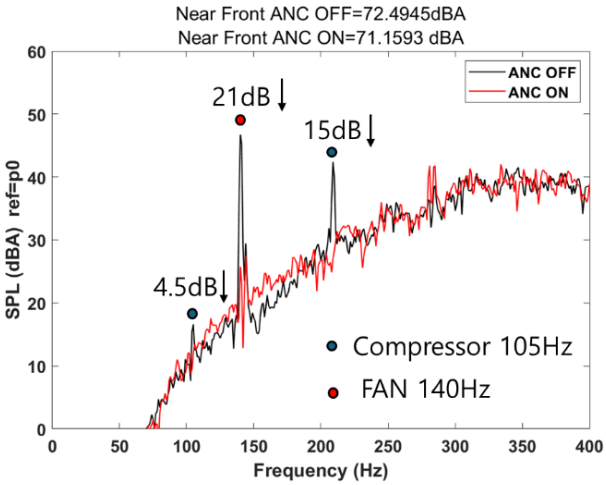
direction has been employed as the reference signal $x(n)$ as shown in Fig. 4. The Fourier transform of this reference signal is presented in Fig.8, offering a detailed spectral representation. The peaks in the graph denote the operation frequency of the compressor and fan.\

4.5 Measurement of Secondary Paths

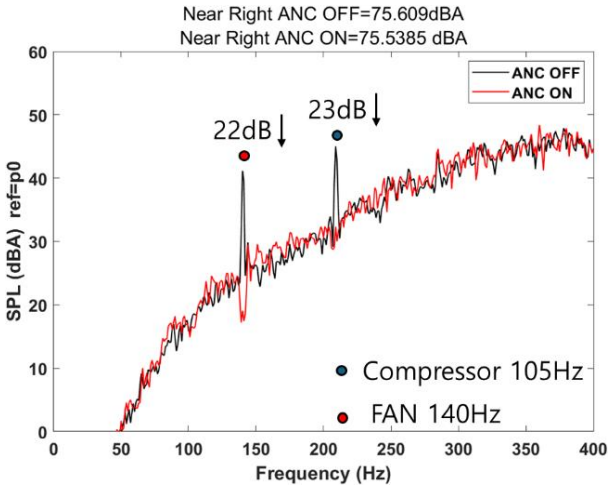
The estimation of the secondary path models, which are the transfer functions between speakers and error microphones, is based on the assumption that these models are time-invariant. Consequently, an offline modeling technique has been implemented to determine these filter coefficients. Broadband white noise, recognized as the ideal signal for such estimations due to its encompassing frequency range, is utilized in this process. This white noise is inputted into the speakers, and the consequent sound pressure is measured by the error microphones. Utilizing adaptive filter algorithms in this context facilitates the determination of the filter coefficients for the secondary paths, thereby allowing for a precise model estimation [12-13].

4.6 Results of the ANC

In this study, the momentum algorithm was used for the ANC of compressor and fan noise. The discrete Fourier transforms (DFTs) of the signals captured by the error microphones are graphically represented in Fig. 9. Within this figure, it is evident that the momentum algorithm exhibits excellent performance, particularly in terms of reducing the peak frequencies. For the front and right microphone, the performance of the peak reduction across the frequency spectrum is notably similar.



(a) Fourier transform of the front error microphone.

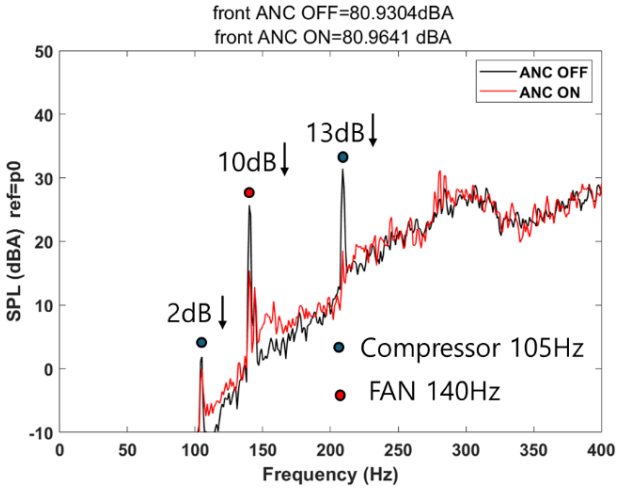


(b) Fourier transform of the right error microphone.

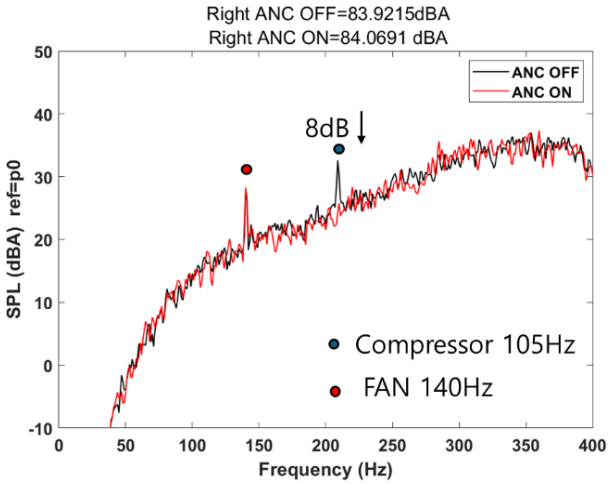
Figure 9. Fourier transform of the error microphones data without and with ANC.

The attenuation level of fan noise is up to 22dB at 140Hz and that of compressornoise is up to 23dB .

Attenuation levels of noise measured by front and right microphone are depicted as shown in Fig.10. Consequently Uncontrolled noise measured at far field microphones was also attended through ANC of near field noise.



(a) Fourier transform of the front error microphone.



(b) Fourier transform of the right error microphone.

Figure 10. Fourier transform of the far field microphones data without and with ANC.

5. CONCLUSIONS

In this study, we present the implementation of a momentum algorithm within the HVAC system of an autonomous bus seat. The HVAC system is a significant source of vibroacoustic noise, predominantly within the 100 to 400 Hz frequency range. This noise is primarily due to the vibration of the compressor's shell at the rotation frequency and its harmonics, resulting in prominent peaks in the frequency response. To control these disruptive noises, an ANC system has been developed. The reference signal for the ANC system was derived from an accelerometer stuck to the compressor's shell. Noise level of HVAC system is attenuated up to 20dB at near filed and 10dB at far field respectively. The study concludes that the momentum algorithm is excellent in reducing the overall noise levels of the HVAC system.

6. ACKNOWLEDGMENTS

This work was supported by the grant funded by the Korea evaluation institute of industrial technology (KEIT) (No. 20018706).

7. REFERENCES

[1] Sen M Kuo and Dennis R Morgan. Active noise control systems, volume 4. Wiley, New York, 1996.

[2] DG Smith, MF Arnold, EW Ziegler, Kh Eghtesadi, and M Brown. A systems approach to appliance compressor quieting using active noise control techniques. 1992.

[3] Hwang, W., Oh, I., Kim, B., Park, S., & Ryu, K. (2006). A study on noise radiation from compressor shell.

[4] Widrow Bernard and D Stearns Samuel. Adaptive signal processing. Englewood Cliffs, NJ: Prentice Hall, 1985.

[5] JM Ku, WB Jeong, and C Hong. Active control of compressor noise in the machinery room of refrigerators. Noise Control Engineering Journal, 67(5):350–362, 2019.

[6] Ku, J. M., Jeong, W. B., & Hong, C. (2020). Controller design for active noise control of compressor by using the time window POCS technique. Journal of Mechanical Science and Technology, 34, 2693-2700.

[7] Meena, Shiv Ram, and C. S. Rai. "Effect of eigenvalue spread in noise cancellation of two sensory systems using adaptive algorithms." Journal of Statistics and Management Systems 23.1 (2020): 157-169.

[8] Burgess, John C. "Active adaptive sound control in a duct: A computer simulation." The Journal of the Acoustical Society of America 70.3 (1981): 715-726.

[9] Goran Nakerst, John Brennan, and Masudul Haque, “Gradient descent with momentum — to accelerate or to super-accelerate?”, arXiv:2001.06472v1, (2020): 1-23.

[10] International Organization for Standardization. (2004). Acoustics — Noise test code for compressors and vacuum pumps — Engineering method (Grade 2) (ISO Standard No. 2151:2004). https://www.iso.org/standard/31316.html

[11] Shin, Kihong, and Joseph Hammond. Fundamentals of signal processing for sound and vibration engineers. John Wiley & Sons, 2008.

[12] Lee, S. K., Lee, S., Back, J., Shin, S. (2018). A New Method for Active Cancellation of Engine Order Noise in a Passenger Car. Appl. Sci. 8, 1394.

[13] H. W. Kim, H. S. Park, S. K. Lee and K. H. Shin, Modified-Filtered-u LMS Algorithm for Active Noise Control and Its Application to a Short Acoustic Duct, Mechanical Systems and Signal Processing 25 (2011) 475-484.

DOI: 10.61782/fa.2025.0338

FORUM ACUSTICUM EURONOISE 2025

EMPIRICAL STUDY ON ACTIVE NOISE CONTROL IN UAVS

Jonas Steiner[1*] **Florian Hilgemann**[1] **Peter Jax**[1]
[1] Institute of Communication Systems, RWTH Aachen University, Aachen, Germany

ABSTRACT

Unmanned aerial vehicles (UAVs) are known for their characteristic noise emissions, which are inevitable during operation, but often perceived as annoying. Current research on UAV noise mitigation focuses on passive technology, but active noise control (ANC), commonly used in headphones and related applications, might prove to be more effective. However, ANC algorithms require comprehensive knowledge of acoustic transfer paths, across all operational modes of the UAV. Commercially available UAVs lack components such as microphones and loudspeakers as required by ANC applications. The purpose of this work is to investigate the estimation accuracy achievable with a simplified linear time-invariant (LTI) model of the generally non-linear aerodynamic system of UAV sound emission. For this, a prototype UAV-ANC system, which extends a UAV with added microphones and loudspeakers, is considered. Extensive measurements are conducted in a controlled indoors environment to assess the applicability of state-of-art system identification methods for estimating the associated acoustic transfer paths. These transfer path estimates can be used to determine the efficacy of ANC algorithms in the considered application through simulation. They are made available online for research purposes.

Keywords: *Active Noise Control, System Identification, Unmanned Aerial Vehicles*

1. INTRODUCTION

The sound produced by UAV quadrocopters is an undesirable byproduct of rotor-based propulsion systems. The subjective impact of this sound depends on the frequency of occurrence of UAV flyby events as well as on the sound pressure level of the noise [1]. Participants of that study perceived scenes that feature UAV noise as highly annoying. The reduction of UAV noise is vital as it has the potential to improve the acceptance of UAV technology, e.g., in urban delivery tasks.

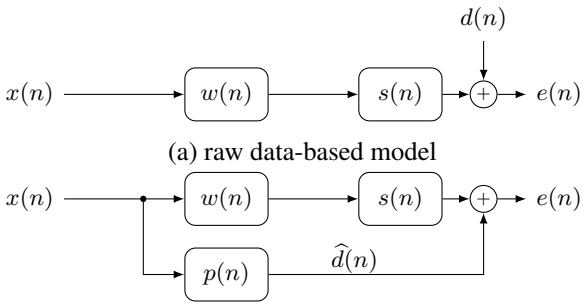
Currently, the mitigation of drone noise receives scientific and practical interest. As an example, In [2], a looped rotor blade that reduces the sound pressure level (SPL) at the blade passing frequency (BPF) by four decibels was proposed. However, the thrust force of the less noisy rotor was also significantly reduced. Another method for reducing the perceived SPL is ANC, which is typically used in headphones [3], and was proposed as a suitable means of mitigating UAV noise [4, 5]. One advantage of active approaches is that they do not interfere with the rotor design.

The working principle of ANC is based on destructive interference, which requires accurate knowledge on the acoustic sound propagation with respect to both, magnitude and phase. In classical ANC applications such as ANC headphones, this sound propagation is modeled using LTI models of the electro-acoustic transfer paths. While these transfer paths were studied thoroughly in headphone applications, fewer results are available for UAVs. For instance, the reproduction of rotor noise was studied using analytic [6] and data driven methods [7], but these approaches lack accurate information about amplitude and phase required by ANC.

This paper presents a database of spatially distributed noise measurements of a commercially available UAV, together with simultaneously recorded reference signals in proximity of the UAV. Impulse responses with corresponding raw data that reflect the primary- and secondary paths are made available online [1]. The main purpose of this data is the analysis of the transfer paths for ANC ap-

*Corresponding author: steiner@iks.rwth-aachen.de.
Copyright: ©2025 Jonas Steiner et al. This is an open-access article distributed under the terms of the Creative Commons Attribution 3.0 Unported License, which permits unrestricted use, distribution, and reproduction in any medium, provided the original author and source are credited.

[1] https://www.doi.org/10.5281/zenodo.15064305



(a) raw data-based model

(b) path-based model

Figure 1: Block diagrams of systems considered.

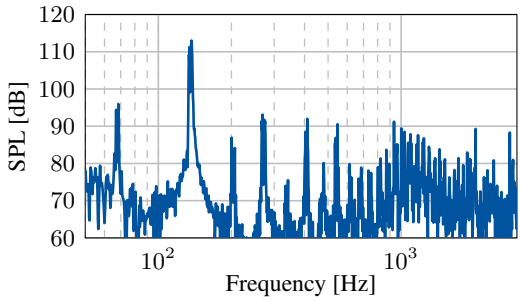


Figure 2: SPL of reference signal for 137 Hz BPF.

plications. For this, the prediction error of a conventional system identification algorithm on the measurement data is analyzed, and a case study of a basic feed-forward ANC system is included. The study brings insight into UAV transfer path modeling and highlights the potential and difficulties of real-world spatial ANC for UAVs.

2. SYSTEM OVERVIEW

The system at hand consists of four main components: a reference microphone and loudspeakers close to the UAV, error microphones further away, and a signal processor. In general, the primary path $p(n)$ models sound propagation from a microphone collocated towards the primary noise source, in this case, the reference microphone signal $x(n)$, to a point in space where noise cancellation is desired. The signal at this point is denoted by $d(n)$ or $e(n)$ when the ANC system is disabled or enabled, and is picked up by one of the error microphones. The secondary path $s(n)$ models the sound propagation to the same point but originating from a loudspeaker that is used to generate the anti-phase signal which achieves the noise reduction [8]. For this analysis, the path-based model from Fig. 1b, which estimates $d(n)$ by the means of the linear model $p(n)$, will be compared with the raw data-based model from Fig. 1a, which uses recordings of $d(n)$ and therefore does not require $p(n)$ explicitly. The latter raw-data approach could turn out as favorable because modeling inaccuracies cannot occur. In practice, the reference signal $x(n)$ is afflicted with acoustic feedback from the loudspeaker, which is not considered here for the sake of a simplified evaluation. In headphone applications, ANC is required to attenuate broadband signals with limited a priori knowledge of the signal source characteristics [8]. Therefore, the objective is to minimize the expected broadband SPL of the remaining noise signal. With UAVs, an estimate of the excitation signal can be measured and exploited in a band limited ANC approach focused on reducing the SPL at the BPF.

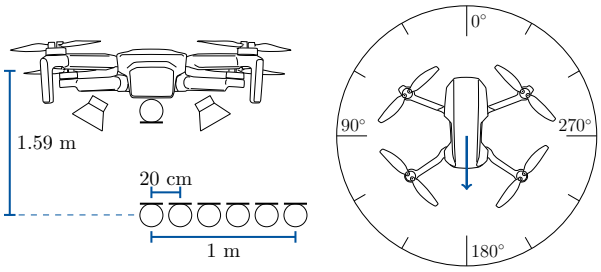
To define electro-acoustic transfer paths, a commercially available drone was extended by loudspeakers and microphones. Generally, the objective is to derive an optimal finite impulse response (FIR) filter $w(n)$ that causes cancellation of the disturbance signal $d(n)$, reducing the signal power of the remaining error signal $e(n)$.

3. MEASUREMENT SETUP

The measurements were done in two parts. In the first part, the propagation of UAV noise was measured, while in the second part, the sound emitted by the loudspeakers was recorded. The objective of each measurement was to gather signal components required for deriving the optimal FIR filters $w(n)$ and subsequent simulation. While the secondary path estimation can be done with optimized excitation signals [9], the primary paths are required to be estimated using the UAV noise, which is inherently tonal (Fig. 2) and therefore not suited for broadband estimation. This excitation complicates the identification of $p(n)$, which could degrade the ANC performance.

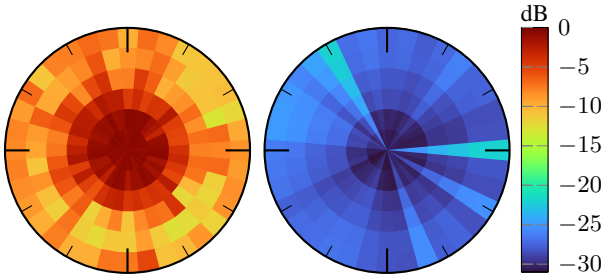
3.1 Measurement Equipment

The measurements were carried out in a controlled indoors environment that follows the base reference ITU-R BS.1116-2 [10], but is subject to adverse acoustic effects such as room echos. A DJI mini 2 SE is equipped with a DPA 4061 omnidirectional condenser type microphone with a pop-filter to protect against wind noise, placed directly on the bottom of the chassis. A RME 12-mic microphone amplifier was used together with the RME MADIface USB as an audio interface running at a sampling frequency of 48 kHz. Six error microphones of the same make and model were placed in a linear array on top of a Head Acoustics HRT I high-precision turntable, to fa-



(a) Front view. (b) Top-down view.

Figure 3: Measurement setup.



(a) primary paths. (b) secondary paths.

Figure 4: Relative approximation error.

cilitate the measurement of $d(n)$ inside a disk directly underneath the DJI mini. These microphones allow to gather the required measurement data, but are unavailable in practice. Multiple independent measurements were performed with varying rotations of the turntable. As secondary sources five Fostex 6301b active studio monitors were placed in proximity to the DJI mini. The error microphones were spaced 20 cm apart. The DJI mini was placed 1.59 m above the microphone array (Fig. 3).

3.2 UAV Noise Measurements

During the UAV noise measurements the loudspeaker array was not present. Measurements were taken at multiples of 10° of turntable angle spanning the entire disk. Figure 3b shows the coordinate system used for the angles. The DJI mini was fixed by a construction mounted to its top, such that arbitrary rotational speeds could be utilized without requiring stable flight conditions. This way, scenarios such as hovering, take off and landing could be simulated by assigning the same rotational speed to all rotors. Here, 10 different rotational speeds were selected, such that the BPF varied between 93 Hz and 233 Hz. For each configuration of angle and rotational speed the reference microphone and all six error microphones were recorded for two seconds. The estimated primary paths have been obtained using the MMSE method [11] and are available as FIR filters of length 8192 (corresp. 170 ms).

3.3 Loudspeaker Measurements

The loudspeakers were placed in a cross-shaped arrangement tightly below the DJI mini. One central loudspeaker was placed directly underneath the DJI mini, with loudspeakers at each of its four sides angled away from the center at about 30°. Exponential sweeps [9] with a duration of 10 s were played back over each of the five loudspeakers in individual measurements. Again, all measurements were repeated for each multiple of 10° of turntable angle. All secondary paths were obtained using the spectral division method with suitable regularization and are available as FIR filters of length 8192.

3.4 Analysis of Estimation Accuracy

One issue with the primary path estimate is the tonal characteristic of the UAV noise, visible in Fig. 2. With a narrow-band excitation signal it is generally not possible to obtain the underlying broadband transfer function. However, the transfer path estimates can be analyzed objectively by their relative estimation error. This measure has no issue with small band excitation, as the same frequencies used for identification are used in the evaluation. A high approximation error indicates insufficient model order or a general lack of applicability of linear models. Figure 4 shows the normalized approximation error in decibels for each primary path estimate at a BPF of 137 Hz, as well as the accuracy of the secondary path estimates averaged over the five speakers. It clearly shows that the estimation of secondary paths is more accurate compared to the primary path. Rotor-induced wind noise is present at the error microphones but not in the reference microphone signal. This deteriorates the estimation accuracy underneath the UAV as can be seen in Fig. 4a, where the approximation error decreases with the radius.

4. CASE STUDY

The case study considers an ANC system which uses five secondary sources and is optimized for one error microphone directly underneath the UAV for a turntable rotation of 0°. The two system models described in section 2, are tested and compared using different rotational speeds. The optimal filters $w(n)$ were determined using the well

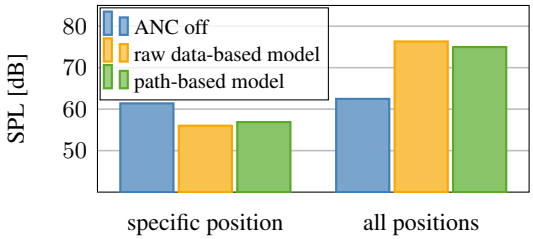


Figure 5: SPL comparison.

known minimum mean squared error approach [11] using a filter length of 8192 samples. The simulation results for a BPF of 137 Hz are presented in Fig. 5, showing the SPL in a third-octave band centered at the BPF at the target location and averaged over all virtual microphone positions. The data includes comparisons of both considered systems to the scenario without ANC. Peak SPL at the target location is reduced by 9 dB and 7 dB using the raw data-based and path-based models, respectively. This evaluation is likely more favorable than a real application, as the secondary path estimates employed for the filter design were also used in the subsequent simulation. Despite this success at the target location, the overall SPL is increased highly using any of the described methods.

5. CONCLUSION

This paper describes a database which contains spatially distributed quadrocopter noise for ANC applications. The data is available online and facilitates the design and simulation of UAV-ANC algorithms. Experiments on reducing the UAV noise within a region of interest were conducted. It was shown that a relatively simple system equipped with a single reference microphone and five secondary loudspeakers, designed to minimize the SPL at a single error microphone, can reduce drone noise at the target location, but is generally not suited for spatial noise reduction.

6. ACKNOWLEDGEMENTS

This work was part of the SILENce project, which was funded by the Federal Ministry of Digital and Transport as part of the mFUND innovation initiative.

Funded by:

Federal Ministry for Digital and Transport

mFUND
Das Startkapital für die Mobilität der Zukunft

on the basis of a decision by the German Bundestag

7. REFERENCES

[1] M. Lotinga, M. Green, and A. J. Torija Martinez, "How do flight operations and ambient acoustic environments influence noticeability and noise annoyance associated with unmanned aircraft systems?," in *Quiet Drones*, (Manchester, UK), Sep. 2024.

[2] J. du Plessis, A. Bouferrouk, and A. Pontillo, "Numerical study of noise reduction on looped propeller blades with bio-inspired tubercles," in *Quiet Drones*, (Manchester, UK), Sep. 2024.

[3] F. Hilgemann, E. Chatzimoustafa, and P. Jax, "Data-driven uncertainty modeling for robust feedback active noise control in headphones," *J. Audio Eng. Soc*, vol. 72, pp. 873–883, Dec. 2024.

[4] D. Miljković, "Methods for attenuation of unmanned aerial vehicle noise," in *International Convention on Information and Communication Technology, Electronics and Microelectronics (MIPRO)*, pp. 0914–0919, 2018.

[5] H. Bi *et al.*, "Spherical sector harmonics based directional drone noise reduction," in *International Workshop on Acoustic Signal Enhancement*, pp. 1–5, 2022.

[6] K. Brentner *et al.*, "Maneuvering rotorcraft noise prediction: A new code for a new problem," in *AHS Aerodynamics, Acoustics and Test Evaluation Specialist Meeting*, 2002.

[7] C. Dreier and M. Vorländer, "Drone auralization model with statistical synthesis of amplitude and frequency modulations," *Acta Acust.*, vol. 8, p. 35, 2024.

[8] S. Kuo and D. Morgan, "Active noise control: A tutorial review," *Proc. IEEE*, vol. 87, no. 6, pp. 943–973, 1999.

[9] S. Müller and P. Massarani, "Transfer-function measurement with sweeps," *J. Audio Eng. Soc.*, vol. 49, no. 6, pp. 443–471, 2001.

[10] ITU-R BS.1116-2, "Methods for the subjective assessment of small impairments in audio systems," recommendation, Geneva, CH, Jun. 2014.

[11] S. Haykin, *Adaptive Filter Theory*. Essex, UK: Pearson Education, 2014.

DOI:

Main theme: A01 Active Control of Sound and Vibration

Session A01.03 Active sound and vibration control

Chair(s): M. Pawelczyk, M. Misol

DOI:

Main theme: A01 Active Control of Sound and Vibration

Session A01.05/A06.07 Active metamaterials

Chair(s): T. Bravo, H. Lissek, C. De Marqui Jr

DOI: 10.61782/fa.2025.0587

FORUM ACUSTICUM EURONOISE 2025

Multi-Channel Acoustic Switch via Activation of Evanescent or Propagation Bloch Wave Modes

Heow Pueh Lee* **Kian Meng Lim** **Yapeng Li**
Department of Mechanical Engineering, National University of Singapore, Singapore

ABSTRACT*

Sonic crystals exhibit interesting phenomena, enabling flexible manipulation of acoustic waves. By leveraging the complex band structure, we propose a wave profile decomposition method to quantitatively predict wave propagation behaviors, revealing that acoustic wave attenuation is influenced by the sound source profile. While earlier studies have demonstrated the feasibility of acoustic switches, the realization of an adjustable multi-channel switch remains unexplored. To address this, a unit cell featuring five Helmholtz resonators is designed to modify sound source profiles by adjusting the orientations of the resonators. This unit cell is connected to three one-dimensional sonic crystals with cylindrical cores to form a multichannel acoustic switch. The ON state of a channel is achieved by activating propagating Bloch wave modes, whereas the OFF state corresponds to the activation of evanescent Bloch wave modes. To enable switching functionality across different frequencies, the orientations of the Helmholtz resonators are optimized to produce desired acoustic source profiles at the outputs. Both experimental and numerical investigations confirm the switching mechanism arising from the activation of evanescent and propagating Bloch wave modes, offering a versatile and tunable platform for advanced acoustic control.

Keywords: *complex band structure, Bloch wave modes, sonic crystal, acoustic switch.*

*__Corresponding author__: mpeleehp@nus.edu.sg.
__Copyright__: ©2025 First author et al. This is an open-access article distributed under the terms of the Creative Commons Attribution 3.0 Unported License, which permits unrestricted use, distribution, and reproduction in any medium, provided the original author and source are credited.

1. INTRODUCTION

Switches and rectification devices constitute essential components for managing energy flow in various applications, including acoustics and vibration control systems. Different operational principles have been explored to design efficient acoustic or vibration switches.
Based on nonlinear mechanism, Boechler et al. demonstrated an acoustic switching and rectification approach using a one-dimensional granular crystal featuring a defect positioned near one end. By exploiting nonlinear Hertzian contact, which induces bifurcations and chaos, vibration energy originating from frequencies within band gaps is redistributed into lower frequencies within the granular crystal's propagation band [1]. Similarly, Li et al. introduced an acoustic switch based on a driven chain of spherical particles exhibiting nonlinear contact forces, where the output signal is modulated by adjusting the amplitude of a low-frequency control wave [2]. Devaux et al. developed a one-way acoustic switch employing acoustic radiation pressure effects at a water-air interface, effectively controlling directional acoustic propagation [3]. Vanhille and Campos-Pozuelo designed a three-channel acoustic switch based on bubbly-liquid channels. In this mechanism, acoustic waves traveling through the bubbly-liquid medium experience significant attenuation due to the presence of bubbles. By strategically positioning acoustic pressure antinodes to relocate bubbles away from the propagation path, acoustic energy can selectively pass through bubble-free channels [4]. Alagoz et al. proposed another approach, utilizing destructive interference between control waves and input waves, thereby facilitating wave-to-wave acoustic switching [5].
The closure of a sonic crystal (SC) band gap can facilitate the transition from an OFF state to an ON state. For instance, Zhu proposed an acoustic wave switch based on phononic crystals with meta-fluid inclusions that were constructed by alternately stacking sound-hard sub-layers. By altering the orientation of these sub-layers, the anisotropic density of the inclusions is modified, and the opened band gap induces an OFF state in the meta-fluid

phononic crystals [6]. Similarly, Babaee et al. employed an array of elastomeric helices in air; in its undeformed configuration, the system exhibits distinct band gaps characterized by strong wave attenuation. When the helices are axially stretched, these band gaps are suppressed, thereby allowing sound to propagate [7]. In another approach, Bilal et al. realized a phononic transistor-like device by utilizing magnetic coupling to adjust the band gap frequency [8]. Cao et al. designed a Kirigami metashell featuring Archimedean spirals, where deformation of the spiral branches closes the band gap, thus switching the metashell to an ON state [9]. Xue et al. introduced an acoustic switch based on a compressible p-type triply periodic minimal surface structure that can be deformed to either open or close the band gap, thereby controlling the OFF or ON state [10]. Finally, Jia-Hao He et al. [11] developed a bidirectionally tunable, multiconfiguration acoustic diode that controls its ON and OFF states by varying the orientation of square scatterers, and Yuanyuan et al. designed a tunable soft chiral-ligament phononic crystal where unit cell deformations adjust the band gaps [12].

2. DEPENDENCE OF TRANSMISSION LOSS ON SOUND SOURCE PROFILE

In this section, we quantitatively examine the relationship between wave attenuation behaviors, the sound source profile and the complex band structure. A one-dimension SC is studied in the following. The one-dimensional SC under investigation consists of a channel filled with air (density: ρ=1.23 kg/m³, sound speed: c=343 m/s) and N periodically arranged rigid cylinders with a radius of r=15 mm. The channel's width is w=60 mm. Figure 1 (a) illustrates the unit cell of the SC, demonstrating periodicity along the x-axis with a lattice constant of a= 60 mm. Sound hard walls are enforced on the upper and lower sides, and Bloch-Floquet periodic boundary conditions are imposed on the left and right boundaries of the unit cell. Figure 1 (b) shows the complex band structure. The influence of the sound source profiles on wave propagation behaviors are studied. The first three Bloch wave modes at 3.0 kHz are illustrated in the left panels of Figure 1 (c). In the right panel of Figure 1 (c), '+' represents that the phase of sound source is π/2 rad and '−' represents that the phase is -π/2 rad. The contours represent the acoustic pressure fields when the SC is excited by these sound sources. The sound source profile is adjusted according to the Bloch wave modes on the left panel. The resulting acoustic pressure fields in the first cell of the SCs (as shown in the right panels of Figure 1 (c)) closely resemble the Bloch wave modes depicted in the left panels.

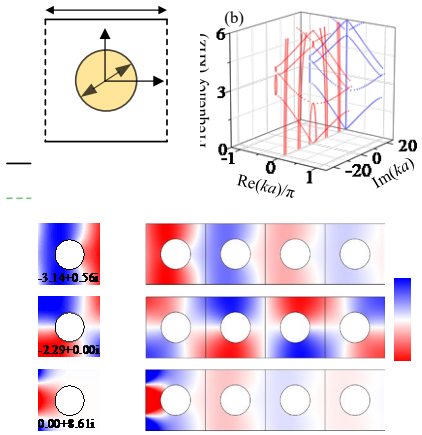


Figure 1. (a) Schematic of the unit cell. (b) Complex band structure. (c) Complex band structure in the Re (ka)-frequency plane (left panel) and Im(ka)-frequency plane (right panel). (c) The first three Bloch wave modes at 3.0 kHz and acoustic pressure fields for three different cases of sound source. The number on the downside of the left panel denotes the value of ka.

Figure 1 (c) demonstrates the feasibility of activating different Bloch wave modes by adjusting the profile of the sound source. Activating a propagating Bloch wave mode enable a large acoustic pressure at the other end of the SC. After sorting the eigen wavenumbers in descending order based on their imaginary part, the m-th order Bloch wave mode can be defined as the mode associated with the m-th eigen wavenumber. Assuming the m-th order Bloch wave mode participates in wave propagation, the acoustic pressure profiles on the left and right boundaries of the unit cell are represented by $p_{m,\mathrm{L}}(y)$ and $p_{m,\mathrm{R}}(y)$, respectively. According to the Bloch-Floquet periodic boundary condition, $p_{m,\mathrm{R}} = p_{m,\mathrm{L}} \exp(-\mathrm{i}k_m a)$ (a is the lattice constant, k_m is the m-th eigen wavenumber). Suppose that a prescribed acoustic pressure is applied on the left boundary of a one-dimensional SC and the profile is $p_{\mathrm{S}}(y)$, this sound source profile can be decomposition into the profiles ($p_{m,\mathrm{L}}(y)$ and (m=1,2,⋯, M)) from different order of Bloch wave modes, expressed as:

$$p_{\mathrm{S}} = p_{\mathrm{L}}^{(1)} = \sum_{m=1}^{M} w_{1,m} p_{m,\mathrm{L}}\,, \tag{1}$$

where $p_{\mathrm{L}}^{(1)}$ represent the acoustic pressure profile on the left boundary of the first unit cell, and M represents that profiles from the first M Bloch wave modes are utilized.

Performing Gram-Schmidt orth-normalization on $p_{m,\mathrm{L}}$ will derive M different basis orthotropic profiles $\hat{p}_{m,\mathrm{L}}$. $p_{m,\mathrm{L}}$ and $\hat{p}_{m,\mathrm{L}}$ are related by:

$$\mathbf{p} = \mathbf{A}\hat{\mathbf{p}}, \tag{2}$$

where $\mathbf{p}$ and $\hat{\mathbf{p}}$ are expressed in column vector forms, expressed as $[p_{1,\mathrm{L}}, p_{2,\mathrm{L}}, ..., p_{M,\mathrm{L}}]^{\mathrm{T}}$ and $[\hat{p}_{1,\mathrm{L}}, \hat{p}_{2,\mathrm{L}}, ..., \hat{p}_{M,\mathrm{L}}]^{\mathrm{T}}$, respectively. $\mathbf{A}$ is a $M \times M$ matrix that transfers orthotropic basis $\hat{p}_{m,\mathrm{L}}$ to basis $p_{m,\mathrm{L}}$ by using Gram-Schmidt orth-normalization, and $A_{i,j} = \langle p_{i,\mathrm{L}}, \hat{p}_{j,\mathrm{L}} \rangle$. According to the Bloch-Floquet periodic boundary condition, the TL can be calculated as:

$$\begin{aligned} \mathrm{TL}^N(\hat{\mathbf{w}}_1) &= -20\log(\left\|\hat{\mathbf{w}}_1\mathbf{A}^{-1}\mathbf{D}^N\mathbf{A}\right\|_2) \\ &= -20\log(\left\|\bar{\mathbf{w}}_1\mathbf{D}^N\mathbf{A}\right\|_2) \end{aligned}, \tag{3}$$

where $\mathrm{TL}^N(\hat{\mathbf{w}}_1)$ represent the TL of a SC with N unit cells and excited by a sound source with a profile of $p_{\mathrm{S}} = \hat{\mathbf{w}}_1\hat{\mathbf{p}}$. In Equation (3), $\|\hat{\mathbf{w}}_1\|_2$ is 1 and $\bar{\mathbf{w}}_1$ is $\hat{\mathbf{w}}_1\mathbf{A}^{-1}$ with $\|\hat{\mathbf{w}}_1\|_2 = 1$.

3. DESIGN METHOD OF THE ACOUSTIC SWITCH

In this section, we propose a design methodology for an acoustic switch. For brevity, the design principle is demonstrated using a single-channel acoustic switch, as illustrated in Figure 2 (a). This configuration comprises a one-dimensional SC with the acoustic switch cell positioned at the left end, where a plane wave is incident. The detailed structure of the acoustic switch is depicted in Figure 2 (b). Central to the switch cell is a C-split resonator—although other scatterer configurations may also be employed—which is characterized by an outer radius of r=15 mm, a thickness (dr) of 2 mm, and a split width of w=2 mm. A plane wave sound source, designated as $p_{\mathrm{in}}(y)$, is applied at the left boundary of the switch cell. As the acoustic waves propagate through the switch cell, the output acoustic pressure profile, $p_{\mathrm{out}}(y)$, is altered. Based on the criteria discussed in Section 2, if $p_{\mathrm{out}}(y)$ excites propagating Bloch wave modes, the acoustic waves continue to propagate through the subsequent SC, thereby placing the switch in the ON state. Conversely, if $p_{\mathrm{out}}(y)$ triggers evanescent Bloch wave modes, the acoustic wave is inhibited from propagating, resulting in an OFF state. By adjusting the orientation (θ) of the C-split resonator, the output acoustic pressure profile can be effectively modulated, thereby controlling the switching state. This approach highlights the feasibility of using geometric and orientation adjustments to achieve tunable acoustic wave manipulation in engineered sonic crystals.

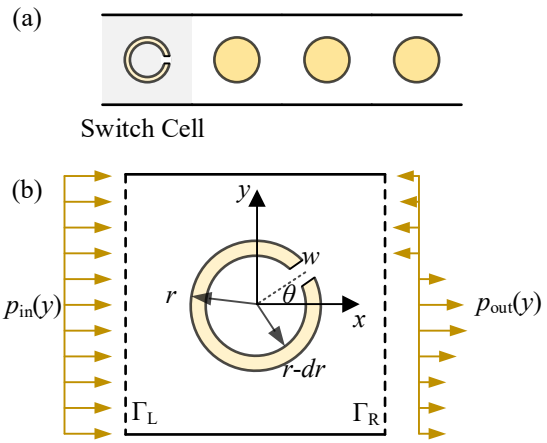


Figure 2. (a) Schematic of the acoustic switch. The cell on the left end is the switch cell. (b) Detail illustration of the switch cell. The switch cell contains a C-split.

According to the design principle—where the activation of evanescent or propagating Bloch wave modes hinges on accurately predicting the output acoustic pressure profile from a given input—the key is to model the wave propagation within the switch cell precisely. Here, we analyze the switch cell illustrated in Figure 2 (b). The left boundary is treated as an acoustic pressure boundary, while the boundaries of the C-split resonator and the upper and lower boundaries are considered sound-hard wall boundaries. Consequently, determining the overall acoustic pressure profile also requires specifying the acoustic boundary condition on the right side (Γ_{R}), which serves as the interface between the switch cell and the sonic crystal. Before defining the precise boundary condition on Γ_{R}, we first examine the acoustic pressure and the normal acoustic velocity at the different interfaces depicted in Figure 3.

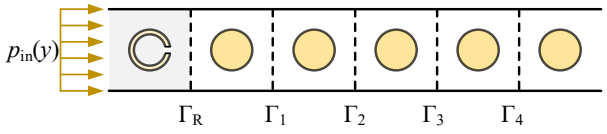


Figure 3. Different interfaces in the acoustic switch.

According to Equation (1), the acoustic pressure and acoustic norm velocity can be decoupled as:

$$p_{\mathrm{R}} = \sum_{m=1}^{M} w_{1,m} p_{m,\mathrm{L}}, \quad v_{\mathrm{R}} = \sum_{m=1}^{M} w_{1,m} v_{m,\mathrm{L}}. \tag{4}$$

After acoustic waves propagate through several unit cells of the sonic crystal, the acoustic pressure and velocity at the

nth interface are characterized by the Bloch-Floquet periodic boundary conditions. The acoustic pressure and velocity can be expressed as follows:

$$\begin{aligned} p_n &= \sum_{m=1}^{M} w_{1,m} p_{m,\mathrm{L}} \exp(-in\,\mathrm{Re}(k_m a)) \exp(-n\,\mathrm{Im}(k_m a)) \\ v_n &= \sum_{m=1}^{M} w_{1,m} v_{m,\mathrm{L}} \exp(-in\,\mathrm{Re}(k_m a)) \exp(-n\,\mathrm{Im}(k_m a)) \end{aligned} . \quad (5)$$

As n increases, the contribution of the evanescent component diminishes, and both the acoustic pressure and acoustic velocity converge to their steady-state values:

$$\begin{aligned} p_n &\approx w_{1,1} p_{1,\mathrm{L}} \exp(-in\,\mathrm{Re}(k_1 a)) \\ v_n &\approx w_{1,1} v_{1,\mathrm{L}} \exp(-in\,\mathrm{Re}(k_m a)) \end{aligned} . \quad (6)$$

This result indicates that the acoustic impedance converges to a constant profile, expressed as:

$$Z = \frac{p_n}{v_n} = \frac{p_{1,\mathrm{L}}}{v_{1,\mathrm{L}}}, \quad (7)$$

where $p_{1,\mathrm{L}}$ is acoustic pressure profile of the propagating Bloch wave mode, and $v_{1,\mathrm{L}}$ is velocity profile of the propagating Bloch wave mode. Hence, we define the propagating Bloch mode impedance as $Z_{\mathrm{PB}} = p_{1,\mathrm{L}} / v_{1,\mathrm{L}}$.

After applying the Bloch mode impedance boundary condition to the right boundary of the switch cell, we can compute the output acoustic pressure profile, $p_{\mathrm{out}}(y)$, for a prescribed input profile. Using Equation (3), the transmission loss (TL) of the acoustic switch can then be determined based on this output pressure profile. To validate the capability of the Propagating Bloch Impedance (PBI) boundary condition in predicting the switch cell's output profile, we examine cases with rotation angles of 0° and 90°. In both scenarios, different SC unit cells are analyzed, as depicted in Figure 4 (a) and Figure 4 (c). Figure 4 (b) and Figure 4 (d) present a comparison between the TL calculated via Equation (3) and that obtained from the commercial software COMSOL. The strong correlation between these results indicates that the PBI boundary condition reliably predicts the output acoustic profile and that the predictive model based on Equation (3) accurately estimates the TL.

Next, we determine the rotation angle of the acoustic switch by solving the following optimization problem:

$$\begin{aligned} \min_{\theta_{\mathrm{ON}},\theta_{\mathrm{OFF}}} \quad & \mathrm{TL}(\theta_{\mathrm{ON}}, f_0) - \mathrm{TL}(\theta_{\mathrm{OFF}}, f_0) \\ s.t. \quad & \theta_{\mathrm{ON}}, \theta_{\mathrm{OFF}} \in [0,\, 180^\circ] \end{aligned} . \quad (8)$$

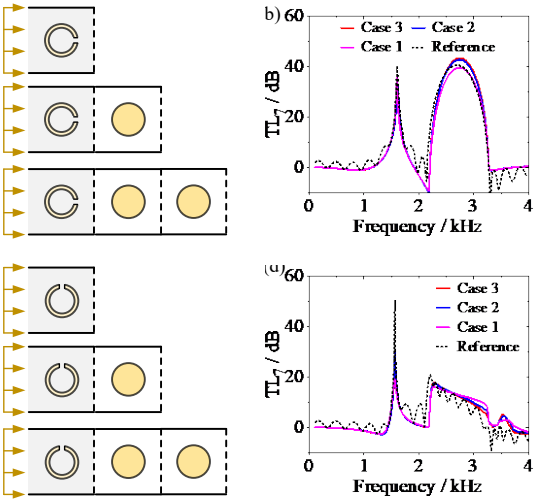


Figure 4. (a) Numerical model to calculate the output acoustic pressure profile $p_{\mathrm{out}}(y)$ of the switch cell when the rotation angle θ is 0°. (b) Comparison of the TL calculated with predicated pressure profile $p_{\mathrm{out}}(y)$ and reference from COMSOL (θ is 0°). (c) Numerical model to calculate the output acoustic pressure profile $p_{\mathrm{out}}(y)$ of the switch cell when the rotation angle θ is 90°. (d) Comparison of the TL calculated with predicated pressure profile $p_{\mathrm{out}}(y)$ and reference from COMSOL. (θ is 90°). PBI indicates propagating Bloch impedance boundary condition. Case 1, 2, and 3 indicates there are zero, one or two unit cells of SC in the prediction model.

where θ_{ON} and θ_{OFF} is the rotation angle when the switch is in ON state and OFF state, respectively. f_0 is working frequency. By setting f_0 as 3.0 kHz, and solving Equation (8) with the PSO algorithm, we derive that θ_{ON} is 100.7°, and θ_{OFF} is 0°. Figure 5 shows the acoustic pressure field when the rotation angle is in OFF (upper panel) state or ON (lower panel) state.

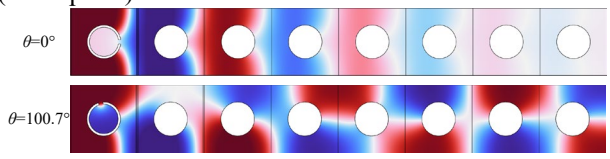


Figure 5. Acoustic pressure of the acoustic switch when the rotation angle is θ_{OFF}= 0° (upper panel) and is θ_{ON}= 100.7° (lower panel).

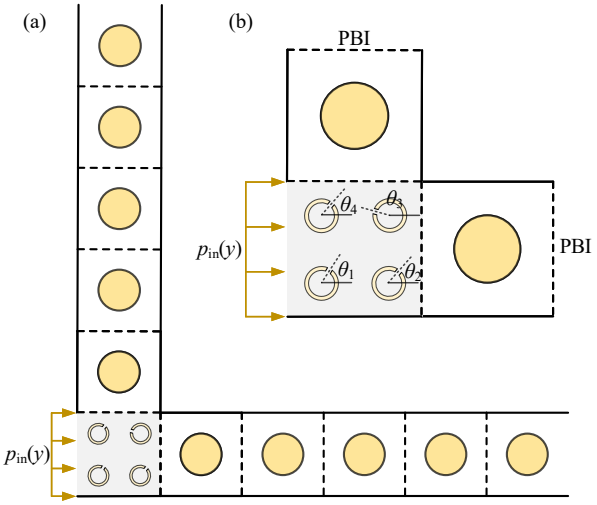


Figure 6. (a) Two-channel acoustic switch. (b) Numerical model to predict the output acoustic pressure profile and TL.

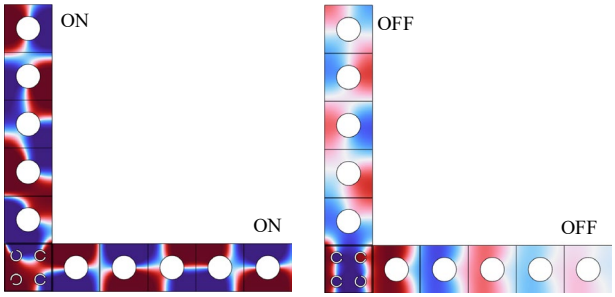


Figure 7. Acoustic pressure of the acoustic switch when both branches are in ON state (left panel with **θ**=[209.6°, 0°, 0°, 107.5°]) or OFF state (right panel with **θ**=[0°, 102.87°, 0°, 0°]).

For a multichannel acoustic switch, as illustrated in Figure 6 (a), Figure 6 (b) shows the corresponding numerical model used to predict the acoustic pressure profiles. In the switch unit cell, four C-split resonators with individually adjustable rotation angles are employed. By varying the orientations of these resonators, the output acoustic pressure profiles directed to the upper sonic crystal (SC) and the left SC can be independently controlled. Here, TL_U represents the transmission loss of the upper SC branch, while TL_L represents the transmission loss of the left branch. To simultaneously control both branches such that they are in the same ON or OFF state, the following optimization problem can be formulated:

$$\begin{aligned} \min_{\theta_{ON},\theta_{OFF}} \quad & \left[\mathrm{TL_L}(\boldsymbol{\theta}_1, f_0) - \mathrm{TL_L}(\boldsymbol{\theta}_2, f_0)\right] \\ & + \left[\mathrm{TL_U}(\boldsymbol{\theta}_1, f_0) - \mathrm{TL_U}(\boldsymbol{\theta}_2, f_0)\right] \\ s.t. \quad & \boldsymbol{\theta}_1 = [\theta_{1,1}, \theta_{1,2}, \theta_{1,3}, \theta_{1,4}] \in [0, 360^\circ] \\ & \boldsymbol{\theta}_2 = [\theta_{2,1}, \theta_{2,2}, \theta_{2,3}, \theta_{2,4}] \in [0, 360^\circ] \end{aligned}, \tag{9}$$

And the design results in shown in Figure 7.

To derive a double-channel switch that one is in ON state and the other is in OFF state, we define he optimization problem as follows:

$$\begin{aligned} \min_{\theta_{ON},\theta_{OFF}} \quad & \left[\mathrm{TL_L}(\boldsymbol{\theta}_1, f_0) - \mathrm{TL_L}(\boldsymbol{\theta}_2, f_0)\right] \\ & + \left[\mathrm{TL_U}(\boldsymbol{\theta}_2, f_0) - \mathrm{TL_U}(\boldsymbol{\theta}_1, f_0)\right] \\ s.t. \quad & \boldsymbol{\theta}_1 = [\theta_{1,1}, \theta_{1,2}, \theta_{1,3}, \theta_{1,4}] \in [0, 360^\circ] \\ & \boldsymbol{\theta}_2 = [\theta_{2,1}, \theta_{2,2}, \theta_{2,3}, \theta_{2,4}] \in [0, 360^\circ] \end{aligned}, \tag{10}$$

And the design results in shown in Figure 8.

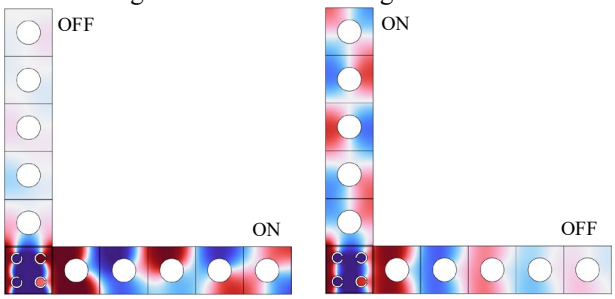


Figure 8. Acoustic pressure of the acoustic switch when the two branches have opposite states. Left panel with **θ**=[42.9°, 0°, 0°, 41.9°] and right panel with **θ**=[0°, 0°, 198.5°, 0°]).

4. ACKNOWLEDGMENTS

The authors would like to acknowledge the financial support from the Ministry of Education MOE Tier 2 grant with the project ID MOE-T2EP50221-0007.

5. REFERENCES

[1] N. Boechler, G. Theocharis, and C. Daraio: "Bifurcation-based acoustic switching and rectification," *Nature materials*, vol. 10, no. 9, pp. 665-668, 2011.

[2] F. Li, P. Anzel, J. Yang, P. G. Kevrekidis and C. Daraio: "Granular acoustic switches and logic elements," *Nature communications*, vol. 5, no. 1, pp. 5311, 2014.

[3] T. Devaux, A. Cebrecos, O. Richoux, V. Pagneux and V. Tournat: "Acoustic radiation pressure for nonreciprocal transmission and switch effects," *Nature Communications*, vol. 10, no. 1, pp.3292, 2019.

[4] C. Vanhille and C. Campos-Pozuelo: "An acoustic switch," *Ultrasonics sonochemistry*, vol. 21, no. 1, pp. 50-52, 2014.

[5] S. Alagoz and B. Baykant Alago: "Sonic crystal acoustic switch device," *The Journal of the Acoustical Society of America*, vol. 133, no. 6, pp. 485-490, 2013.

[6] X. F. Zhu: "Acoustic waves switch based on meta-fluid phononic crystals," *Journal of Applied Physics*, vol. 112, no. 4, pp. 044509, 2012.

[7] S. Babaee, N. Viard, P. Wang, N. X. Fang and K. Bertoldi: "Harnessing deformation to switch on and off the propagation of sound," *Adv. Mater*, vol. 28, no. 8, pp. 1631-1635, 2016.

[8] O.R. Bilal, A. Foehr and C. Daraio: "Bistable metamaterial for switching and cascading elastic vibrations," *Proceedings of the National Academy of Sciences*, vol. 114, no. 18, pp.4603-4606, 2017.

[9] P. Cao, W. Ou, Y. Su, Y. Yin, E. Dong, Z. Song, J. Li and Y. Zhang: "Acoustic switch via kirigami metasurface," *Physical Review Applied*, vol. 18, no. 5, pp. 054040, 2022.

[10] P. Xue, H. Dai and L. Zhou: "Acoustic switch via a compressible minimal surface structure," *Advanced Engineering Materials*, vol. 25, no. 4, pp. 2201144, 2023.

[11] J. H. He and H. H. Huang: "Multiband switching realized by a bidirectionally tunable and multiconfiguration acoustic diode," *AIP Advances*, vol. 8, no. 10, pp.105032, 2018.

[12] Y. Li, K. Huang, M. Gong, C. Sun, S. Gao, Y. Lai and X. Liu: "Realization of acoustic tunable logic gate composed of soft materials," *Results in Physics*, 57, p.107421, 2024.

DOI: 10.61782/fa.2025.0655



FORUM ACUSTICUM
EURONOISE 2025

ON-DEMAND NOISE MITIGATION WITH TIME-MODULATED ACTIVE ACOUSTIC METAMATERIALS

Bogdan-Ioan Popa*
Department of Mechanical Engineering, University of Michigan, USA

ABSTRACT

It is generally accepted that active metamaterials could, in principle, address long-standing challenges in noise mitigation. However, the research of active structures capable to meet these challenges has been slow due to issues of stability and scalability. This work shows that 2D active metamaterials composed of arrangements of sensor-driver pairs can be configured to be excellent sound absorbers very well matched to the background fluid and thus scatter-free. The property is achieved by programming the metamaterial effective mass density and bulk modulus to be complex numbers with matching phases. Moreover, the metamaterials can be switched from being opaque absorbers to transparent media on very small time scales by time-modulating their effective material properties without adverse effects such as ensuing instability. Furthermore, the metamaterial unit cells are completely independent of each other thus promoting scalability.

Keywords: *active acoustic metamaterial, noise control, time modulation, programmable metamaterial*

1. INTRODUCTION

Noise has long been correlated with an increased incidence in cardiovascular diseases [1] making noise mitigation an important area of research. Numerous passive absorbers have been proposed but they tend to be either ineffective, too bulky, narrow band, or scatter sound instead of dissipating it [2, 3]. It has been proposed that metamaterials can advance this strategically important field due to their increased degrees of freedom on sound manipulation. Passive metamaterials have been tried first, but they suffered from the same limitations as conventional passive sound dissipation methods [4]. It was soon realized that active metamaterials can overcome these limitations [5]. A particularly promising active metamaterial architecture consists of arrangements of sensor-driver pairs realizing effective acoustic properties dictated by the chosen transfer function (or gain) between each pair of sensors and drivers [6–8]. These gains are typically set in electronic circuits programmable in real time [9–13]. The advantages of this approach are its scalability promoted by the independence of the sensor-driver pairs (i.e., there is no connection between different pairs) and very low response time and thus broadband operation stemming from the gains being computed apriori for a desired functionality [14] and not adaptively as in conventional controls-based systems [3]. It has recently been shown that active metamaterials composed of sensor-driver pairs achieve very large sound dissipation with minimal scattering [13]. However, the effect has been studied in the steady state regime in which the effective properties of the metamaterial are fixed. Whether switching these properties on-demand can be done in a stable manner is unknown.

Here we show experimentally that active metamaterials following the sensor-driver architecture can be switched instantaneously from scatter-free opaque absorbers to transparent media without adverse effects. To act as a sound absorber, the fabricated metamaterial is designed to mimic the acoustic behavior of a continuous medium with bulk modulus and mass density having complex values with matching phases. We show that these effective properties can be time modulated to switch from

**Corresponding author*: bipopa@umich.edu.
Copyright: *©2025 Bogdan-Ioan Popa This is an open-access article distributed under the terms of the Creative Commons Attribution 3.0 Unported License, which permits unrestricted use, distribution, and reproduction in any medium, provided the original author and source are credited.*

complex to real quantities matching the properties of air on very short time scales thus realizing the remarkable transition from absorber to transparent medium.

2. ACTIVE METAMATERIAL DESIGN

The goal of this work is to realize a time-modulated 2D active acoustic absorbing medium that does not scatter impinging sound. The medium is represented by the red box placed in the air-filled acoustic waveguide shown in Fig. 1a and composed of two parallel plates driven at the fundamental mode by an external speaker placed on the side of the waveguide. The air has bulk modulus B_0, mass density ρ_0, speed of sound c_0 and characteristic impedance Z_0.

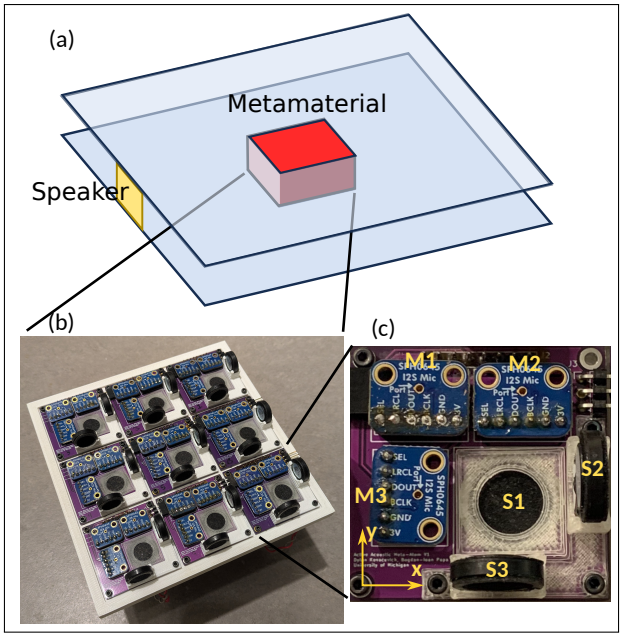


Figure 1. (a) Schematic of the experimental setup showing a homogeneous fluid of bulk modulus B and mass density ρ placed in a 2D waveguide and ensonified by an external speaker. (b) Active metamaterial programmed to realize the B and ρ of the desired fluid. (c) Photo of unit cell showing the labeled microphones Mi and speakers Si, where $i = \overline{1,3}$.

The medium is a very good absorber matched with the background as long as its bulk modulus B and mass density ρ are complex quantities having the following expressions.

$$B = B_0 e^{j\phi}, \quad \rho = \rho_0 e^{-j\phi}, \tag{1}$$

where ϕ is a real phase. Under these conditions, the characteristic impedance of the metamaterial matches that of air ($Z = \sqrt{B\rho} = Z_0$) and the speed of sound inside the metamaterial is complex ($c = \sqrt{B/\rho} = c_0 e^{j\phi}$). High absorption is achieved when the imaginary part of c is large.

This continuous medium is realized with an active metamaterial composed of the 3 by 3 arrangement of active cells illustrated in Fig. 1b. The metamaterial is under a good approximation flat, protruding very little inside the waveguide and thus it is not impeding the flow of air. Consequently, in its off state, the metamaterial has the effective properties of air.

It has been shown that active cells composed of multiple sensor-driver pairs can fully program the effective bulk modulus, mass density tensor, and two Willis coupling vectors depending on the nature of the sensor and driver in each pair [5, 13]. In particular, the bulk modulus is controlled by a monopole sensor capturing the local pressure p and driving a monopole driver whose amplitude is proportional to p. Similarly, each component $\rho_{\alpha\beta}$ of the mass density tensor ($\alpha, \beta \in \{x, y\}$ in 2D) is controlled by a dipole sensor capturing the local particle velocity u_α and driving a particle velocity source parallel to direction β with amplitude proportional to u_α.

Figure 1c shows a 2D metamaterial cell realizing three sensor-driver pairs to control the bulk modulus and all components of the mass density tensor. In this approach, the pressure and particle velocity components are obtained with three microphones Mi sensing the acoustic pressures $p_{\mathrm{M}i}$ and driving the three speakers Si, where $i = \overline{1,3}$. One speaker is horizontal, acting as a monopole pressure source, and two speakers are vertical, acting as dipole sources in the x and y directions. The sensed monopole and dipole quantities p, u_x, and u_y as well as the amplitude of the sound generated by these speakers $A^{\mathrm{S}i}$ are shown in Table 1. The proportionality terms between the sensed and driven quantities (g^m, g_x^{dx}, g_y^{dx}, g_y^{dy}, and g_x^{dy}) are set by a Teensy 4 microcontroller connecting the microphones and speakers of each cell.

Closed-form expressions relating these gain terms to the desired effective material properties B and ρ given by Eqn. (1) are derived elsewhere [13, 14] and implemented in the microcontroller.

In its active state the metamaterial is programmed to have B and ρ given by Eqn. (1), where $\phi = 30°$. As we

Table 1. Driven versus sensed quantities.

Sensed	Driven
$p = \frac{p_{M1}+p_{M2}+p_{M3}}{3}$	$A^{S1} = g^m p$
$u_x = -\frac{\int (p_{M1}-p_{M2})dt}{\rho_0 d}$	$A^{S2} = g_x^{dx} u_x + g_y^{dx} u_y$
$u_y = -\frac{\int (p_{M3}-p_{M1})dt}{\rho_0 d}$	$A^{S3} = g_x^{dy} u_y + g_y^{dy} u_x$

will see in the next section, this phase produces a very large absorption. The microcontroller in each cell can reduce the gains g shown in Table 1 to zero essentially instantaneously.

3. RESULTS

The metamaterial is ensonified by a speaker at 1200 Hz. We programed the metamaterial to switch from the opaque, high absorption state ($\phi = 30°$) to the transparent state ($\phi = 0°$) and back every 1.67 ms, i.e. two acoustic periods at 1200 Hz. Figure 2 shows the time domain acoustic pressure fields measured inside and outside the metamaterial at two time instances separated by 1.67 ms with and without the metamaterial inside the waveguide.

The external speaker excites cylindrical waves in the empty waveguide (Fig. 2 top). The two time instances illustrated in the figure are chosen approximately two acoustic periods apart and thus the two measured acoustic pressure distributions are essentially the same.

The bottom panels represent the acoustic fields measured in the waveguide with the metamaterial inside. The black squares in the figure represent the position of the metamaterial. The same two instances separated by two acoustic periods shows the metamaterial behavior $\phi = 30°$ (absorber state) and $\phi = 0°$ (transparent state), respectively.

In the absorber configuration, the metamaterial dissipates almost all the incident energy as indicated by the very low amplitude pressure inside the structure and behind it (the shadow region). In all other directions, the acoustic pressure looks essentially the same as that measured in the empty waveguide at the same time instant, which confirms the metamaterial's expected scatter-free behavior.

In its transparent state, the metamaterial behaves essentially as air, i.e., the measured fields look like those measured in the empty waveguide, confirming that the effective B and ρ match those of air.

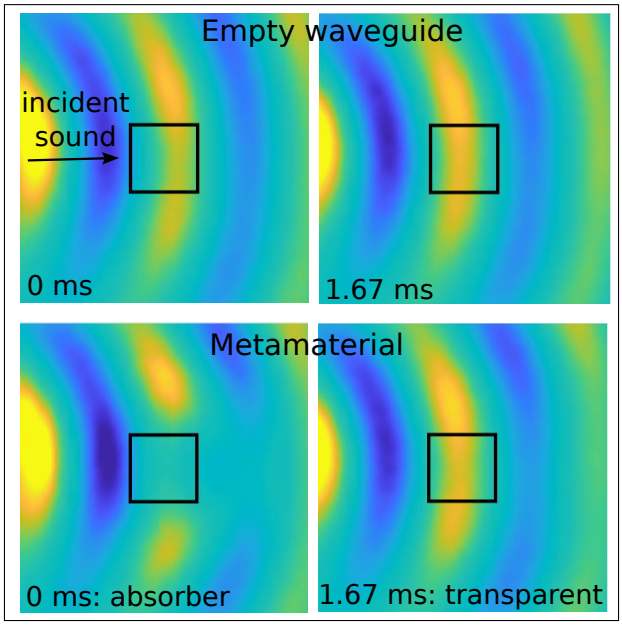


Figure 2. Time domain acoustic pressure measured in the empty waveguide (top) and with the time-modulated programmable metamaterial (bottom). The right pressure fields (transparent state) were measured 1.67 ms later than the left fields (absorber state), i.e. half the modulation period.

4. CONCLUSIONS

This work shows that active metamaterials with carefully tailored effective bulk modulus and mass density behave as highly effective, compact sound absorbers. The metamaterial demonstrated here is composed of independent unit cells composed of sensor-driver pairs that promote scalability, i.e., adding more cells increases the area covered by the metamaterial absorbers without having to change the existing cells. More importantly, the gain between the sensors and drivers in each pair are precomputed from a desired set of effective acoustic properties leading to low dispersion. This approach contrasts with conventional controls methods used in existing noise cancellation devices that use complex, adaptive transfer functions realized with centralized controllers.

Remarkably, this work shows that the fabricated metamaterial can switch functionality essentially instantaneously without any adverse effects such as ensuing instability. This property has been demonstrated experimentally by repeatedly switching the metamaterial from its ab-

sorber to transparent configurations. Active metamaterials based on sensor-driver pairs are thus ideal for noise mitigation, but also for other applications that require very fast time modulation of material parameters recently associated with interesting physical phenomena.

5. ACKNOWLEDGMENTS

This material is based upon work supported by the National Science Foundation under Award No. CMMI-1942901.

6. REFERENCES

[1] T. Münzel, T. Gori, W. Babisch, and M. Basner, "Cardiovascular effects of environmental noise exposure," *European Heart Journal*, vol. 35, no. 13, p. 829–836, 2014.

[2] M. Long, *Architectural Acoustics*. Applications of modern acoustics, Academic Press, 2005.

[3] M. J. Crocker, *Handbook of Noise and Vibration Control*. John Wiley & Sons, 2007.

[4] S. A. Cummer, J. Christensen, and A. Alù, "Controlling sound with acoustic metamaterials," *Nature Reviews Materials*, vol. 1, p. 16001, 2016.

[5] B.-I. Popa, Y. Zhai, and H.-S. Kwon, "Broadband sound barriers with bianisotropic metasurfaces," *Nat. Comms.*, vol. 9, p. 5299, 2018.

[6] A. M. Baz, "An Active Acoustic Metamaterial With Tunable Effective Density," *Journal of Vibration and Acoustics*, vol. 132, p. 041011, 2010.

[7] W. Akl and A. Baz, "Experimental characterization of active acoustic metamaterial cell with controllable dynamic density," *J. Appl. Phys.*, vol. 112, p. 084912, 2012.

[8] B.-I. Popa, L. Zigoneanu, and S. A. Cummer, "Tunable active acoustic metamaterials," *Phys. Rev. B*, vol. 88, p. 024303, Jul 2013.

[9] Y. Zhai, H.-S. Kwon, and B.-I. Popa, "Active Willis metamaterials for ultracompact nonreciprocal linear acoustic devices," *Phys. Rev. B*, vol. 99, p. 220301, Jun 2019.

[10] Y. Zhai, H.-S. Kwon, and B.-I. Popa, "Anomalous Reflection with Omnidirectional Active Metasurfaces Operating in Free Space," *Phys. Rev. Appl.*, vol. 16, p. 034023, Sep 2021.

[11] D. A. Kovacevich and B.-I. Popa, "Programmable bulk modulus in acoustic metamaterials composed of strongly interacting active cells," *Applied Physics Letters*, vol. 121, no. 10, p. 101701, 2022.

[12] D. A. Kovacevich, K. Grosh, and B.-I. Popa, "Stability-derived bounds on the realizable acoustic properties of active metamaterials," *Phys. Rev. Appl.*, vol. 21, p. L051002, 2024.

[13] D. A. Kovacevich and B.-I. Popa, "Active acoustic metamaterials with on-demand bulk modulus and full mass density tensor," *Smart Materials and Structures*, vol. 33, no. 10, p. 105012, 2024.

[14] D. A. Kovacevich and B.-I. Popa, "Transformation acoustics with bulk media composed of polarized sources," *Phys. Rev. B*, vol. 104, p. 134304, 2021.

DOI: 10.61782/fa.2025.0755

FORUM ACUSTICUM EURONOISE 2025

ROBUST SPATIOTEMPORAL WAVE LOCALIZATION IN PIEZOELECTRIC METAMATERIALS THROUGH PROGRAMMABLE TOPOLOGICAL INTERFACE STATES

Bruno Alceu Souto [1*] **Danilo Beli** [2] **Carlos De Marqui Jr**[1]

[1] Department of Aeronautical Engineering, University of Sao Paulo, Brazil
[2] Department of Mechanical Engineering, Eindhoven University of Technology, the Netherlands

ABSTRACT

The emergence of topological states in condensed matter physics has provided reliable mechanisms for waveguiding in phononic crystals and metamaterials. This study introduces a strategy for dynamic wave localization using space-time programmable topological interface states in piezoelectric metamaterials. By dynamically tuning inductive shunt circuits, we induce and modulate interface states in space and time without physical changes in the host structure. By modulating electrical properties, the topological interface can be dynamically moved along the beam, enabling efficient energy transfer. The numerical results clarify the effects of modulation smoothness on wave localization for cases with and without structural damping, identifying the optimal conditions for robust energy transfer.

Keywords: *piezoelectricity, programmable metamaterial, topological interface states, structural damping*

1. INTRODUCTION

The discovery of topological states in condensed matter physics has led to innovative methods for manipulating waves in metamaterials [1, 2]. The topological protection of these states, which confine mechanical waves to edges or interfaces between regions with distinct topological properties [3], provides robustness against backscattering caused by imperfections or disturbances along the propagation path [4]. In contrast to their electronic counterparts [5], acoustic and elastic systems offer greater flexibility in the design, fabrication, and detection of diverse topological phenomena [6]. In this context, breaking the spatial inversion symmetry while maintaining the time-reversal symmetry can be achieved in the subwavelength regime by manipulating piezoelectric inductive shunt circuits [7]. In this sense, connecting two metamaterials with distinct Zak phases allows the emergence of a topological interface state that presents significant vibration energy localization [8].

Recent years have seen significant interest in exploring metamaterials with adaptable and programmable characteristics, particularly due to their potential for versatile control over wave propagation. [9]. Recent studies have concentrated on multi-coupling domains to improve reconfigurability. Within this context, piezoelectric materials have become a popular choice due to their versatility in controlling wave behavior. This is achieved by adjusting digitally controlled analog and digital shunt circuits, as opposed to traditional analog shunts. This advancement has enabled the experimental implementation of programmable metamaterials [10, 11]. This advanced control strategy enables the design of materials with spatiotemporal modulation, enhancing metamaterials by adding an extra dimension of tunability through dynamic adjustments of their properties in both space and time [12].

In this work, we build upon a recently introduced approach that utilizes space-time modulation of trivial de-

*Corresponding author: brunoalceu@usp.br.
Copyright: ©2025 Souto et al. This is an open-access article distributed under the terms of the Creative Commons Attribution 3.0 Unported License, which permits unrestricted use, distribution, and reproduction in any medium, provided the original author and source are credited.

fects [13, 14] and extend it to programmable topological interfaces within an electromechanically coupled metamaterial beam. By applying cosine-based modulations to the electrical properties of the unit cells, we demonstrate that the topological interface can be dynamically repositioned along the beam, enabling efficient energy transfer while preventing energy leakage. Additionally, we discuss the effects of structural damping on the modulation performance and energy availability for further operations.

2. MODEL DESCRIPTION

Fig. 1 depicts the electromechanical metamaterial, which consists of a thin conductive substructure sandwiched by two oppositely poled piezoelectric layers. The outer surfaces of the thin and conductive electrodes covering each piezoelectric layer are periodically segmented, and each segment is connected to an inductive shunt circuit, characterizing a local resonator with the equivalent in-series piezoelectric capacitance. The unit cell highlighted in Fig. 1 comprises four consecutive local resonators with the outer and inner inductances set as L_1 (blue inductances) and L_2 (red inductances), respectively. Thus, the unit cell has a mirror symmetry regarding the central point. A dimerization parameter δ is defined to generate $L_1 = L_r(1+\delta)$ and $L_2 = L_r(1-\delta)$, where L_r is a reference inductance.

The metamaterial beam is discretized into one-dimensional finite elements based on the Euler-Bernoulli assumptions. A third-degree polynomial is employed to approximate the transverse displacement field within each element that has two degrees of freedom per node, denoted as transverse displacement (w) and rotation about the y direction (θ) [15]. In the electrical domain, the non-zero electric field component is assumed to be uniform in the thickness direction of the piezoelectric layers. Consequently, one electrical degree of freedom is sufficient to model the voltage output in each electrode's segment. The structural dissipation is included using Rayleigh's proportional damping model. Consequently, the behavior of the piezoelectric metamaterial beam is governed by the following finite elements equations [16],

$$\mathbf{M}\ddot{\mathbf{u}} + \mathbf{D}\dot{\mathbf{u}} + \mathbf{K}\mathbf{u} - \boldsymbol{\Theta}\mathbf{v} = \mathbf{F} \tag{1a}$$

$$\mathbf{C_p}\mathbf{v} + \mathbf{q} + \boldsymbol{\Theta}^t\mathbf{u} = \mathbf{0} \tag{1b}$$

where $\mathbf{M}$ is the global mass matrix ($n_m \times n_m$), $\mathbf{K}$ is the global stiffness matrix ($n_m \times n_m$), $\mathbf{D}$ is the structural damping matrix ($n_m \times n_m$), $\mathbf{F}$ is the vector of external mechanical inputs ($n_m \times 1$), $\boldsymbol{\Theta}$ is the electromechanical coupling matrix ($n_m \times n_e$), $\mathbf{C_p}$ is the capacitance matrix ($n_m \times n_e$), $\mathbf{v}$ is the vector of voltage output from each electrode segment ($n_e \times 1$), $\mathbf{q}$ is the vector of electrical charges ($n_e \times 1$), $\mathbf{u}$ is the vector of mechanical degrees of freedom ($n_m \times 1$), which contains the transverse displacements and rotations (about the y direction) associated to each node, and n_m and n_e are the number of mechanical and electrical degrees of freedom, respectively. The over-dots represent the derivative with respect to time t.

When considering time-varying inductances in each shunt circuit, the voltage output from each electrode segment is determined by $\mathbf{v}(t) = \dot{\mathbf{L}}_c(t)\dot{\mathbf{q}} + \mathbf{L_c}(t)\ddot{\mathbf{q}}$, where $\mathbf{L_c}$ is a diagonal matrix ($n_e \times n_e$) that contains the inductances connected to each segment of electrode. In this case, the matrix representation of Eqs. 1 is

$$\begin{bmatrix} \mathbf{M} & -\boldsymbol{\Theta}\mathbf{L_c} \\ \mathbf{0} & \mathbf{C_p}\mathbf{L_c} \end{bmatrix} \begin{bmatrix} \ddot{\mathbf{u}} \\ \ddot{\mathbf{q}} \end{bmatrix} + \begin{bmatrix} \mathbf{D} & -\boldsymbol{\Theta}\dot{\mathbf{L}}_\mathbf{c} \\ \mathbf{0} & \mathbf{C_p}\dot{\mathbf{L}}_\mathbf{c} \end{bmatrix} \begin{bmatrix} \dot{\mathbf{u}} \\ \dot{\mathbf{q}} \end{bmatrix} + \begin{bmatrix} \mathbf{K} & \mathbf{0} \\ \boldsymbol{\Theta}^t & \mathbf{I} \end{bmatrix} \begin{bmatrix} \mathbf{u} \\ \mathbf{q} \end{bmatrix} = \begin{bmatrix} \mathbf{F} \\ \mathbf{0} \end{bmatrix} \tag{2}$$

where $\mathbf{I}$ is the identity matrix ($n_e \times n_e$). Equation 2 represents a multiphysical problem, wherein the mechanical and electrical domains are coupled through the electromechanical coupling matrix $\boldsymbol{\Theta}$ (off-diagonal elements of the matrices). In each unit cell, the combination of the inductive shunt L_{c_j} and the effective capacitance of the piezoelectric bimorph C_{p_j} forms a capacitive-inductive circuit whose resonance frequency is $\omega_{n_j} = 1/\sqrt{C_{p_j} L_{c_j}}$.

In Fig. 1, each electrode segment has length l_s and width b equal to 20 mm. The substructure has thickness h_s of 1 mm, the elastic modulus is $c_s = 69$ GPa, and mass density $\rho_s = 2700\,\mathrm{kg/m^3}$. The substructure is sandwiched by two PMN-PT piezoelectric layers, each with a thickness h_p of 0.6 mm. The elastic modulus of the PMN-PT crystal at a constant electric field is $\bar{c}_{11}^E$ of 21.8GPa, an effective piezoelectric stress constant $\bar{e}_{31}$ of $-14.1\,\mathrm{C/m^2}$, a permittivity component at a constant strain $\bar{\epsilon}_{33}^S$ of 33 nF/m, and a mass density ρ_p of $8120\,\mathrm{kg/m^3}$.

The angular frequency axis in the results is normalized by the velocity of the longitudinal wave considering the composite material's average properties. Accordingly, the normalized frequency assumes $\Omega = \omega l_s/(2\pi\sqrt{Y_{avg}\rho_{avg}})$, where $Y_{avg} = v_f/Y_s + (1-v_f)/Y_p$ and $\rho_{avg} = v_f\rho_s + (1-v_f)\rho_p$ are the average modulus and the average mass density, respectively, while

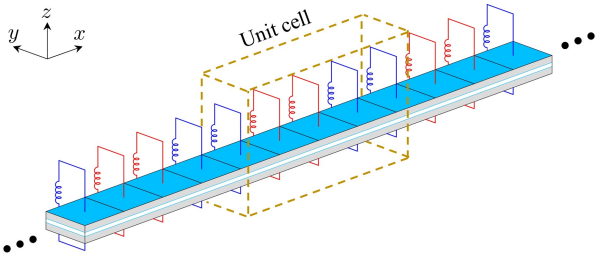


Figure 1. Scheme of the locally resonant electromechanical metamaterial, where the light gray and white regions represent the piezoelectric and substructure layers, the blue regions represent the electrodes. The highlighted region depicts the unit cell, where the blue and red inductances are associated with L_1 and L_2, respectively.

$v_f = h_s/(h_s + 2h_p)$ is the volume fraction of the substructure and $Y_p = 1/s_{11}^E$ is the piezoelectric elastic modulus. In addition, the finite element mesh for the numerical calculations is assumed as 12 elements per unit cell, which gives approximately 1.1 mm for each element. This value corresponds to 3% of the smallest wavelength analyzed, which can capture the studied dynamic behavior effectively.

3. RESULTS

Fig. 2 depicts the band structure for three unit cells, one tuned with $\delta = 0$ (Fig. 2(a)) and tuned with $\delta = \pm 0.05$ (Fig. 2(b)), where $L_r = 0.576$ H. The unit cells tuned with $\delta = 0.05$ are named UCA in this work while the ones tuned with $\delta = -0.05$ are UCB. The numerical procedures combine the Bloch-Floquet periodic conditions with the finite element matrices where the electrical outputs are considered internal degrees of freedom (for more details, see [13]). An inverse eigenproblem (i.e., $\omega(\kappa)$) is solved for each wavenumber κ. According to the presented results, the homogeneous unit cell (i.e., $\delta = 0$) features a locally resonant band gap between $\Omega_l = 0.0153$ and $\Omega_u = 0.0169$. In addition, a folding point appears at $\Omega_f = 0.0150$ (red circle in Fig. 2(a)). The folding point opens to generate a band gap in the subwavelength region (green region) for the non-homogeneous unit cell (i.e., $\delta \neq 0$). Although the band structures of the unit cells tuned with $\delta \pm 0.05$ are identical, they have distinct topological properties due to band transition and inversion, which characterizes a topologically non-trivial band gap [17].

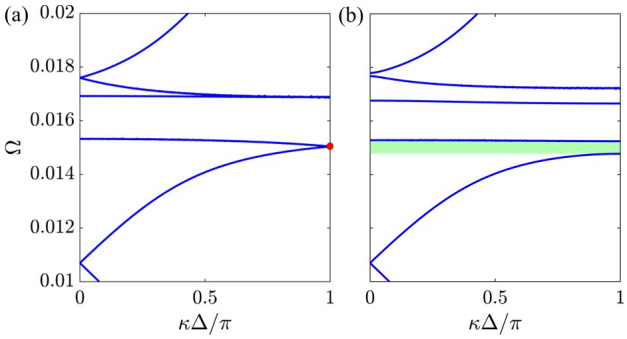


Figure 2. Dispersion relation of the unit cell tuned with $\delta = 0$ (a) and $\delta = \pm 0.05$. The red circle indicates the folding point whereas the green region highlights the non-trivial band gap.

The emergence of a topological interface mode is examined through the harmonic response of a finite piezoelectric metamaterial beam consisting of 16 unit cells — 8 unit cells UCA to the right and 8 unit cells UCB to the left, creating an interface between them. A harmonic point excitation, denoted as $\bar{F}(L/2, \Omega)$ (where L represents the total length of the metastructure), is applied at the interface position. The corresponding harmonic transverse displacements, $\bar{w}(x, \Omega)$, are obtained along the metastructure as well as the amplitude of the transfer functions $20\log_{10}|\hat{w}(x, \Omega)/\hat{F}|$ (dB, reference 1 m/N). Fig. 3(a) shows the harmonic response as a function of space and frequency for the periodic configuration (the metamaterial beam with 16 unit cells tuned with $\delta = 0.05$). Fig. 3(b) displays the harmonic response for the topological metamaterial (metamaterial with 8 unit cells tuned with $\delta = 0.05$ and 8 unit cells tuned with $\delta = -0.05$). Three attenuation zones are observed in the responses of the periodic configuration and the topological metamaterial beam. These consist of two Bragg band gaps and a locally resonant band gap situated between them, which is consistent with the dispersion previously presented for the unit cells. Figure 3(b) displays a resonance peak within the first non-trivial Bragg band gap (green region depicted in Fig. 2(b)), which corresponds to the topological interface state.

After examining the behavior of a topological metamaterial with a fixed interface, we now investigate its pro-

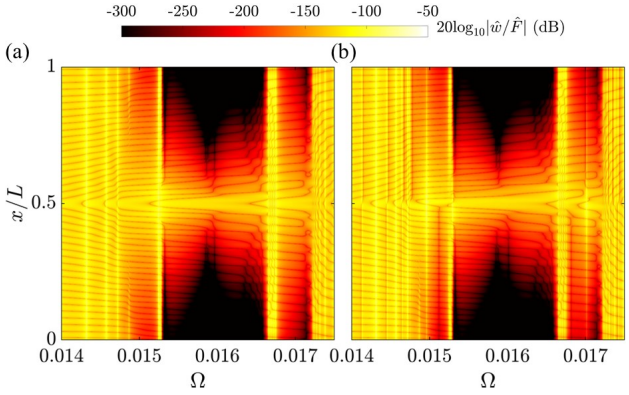


Figure 3. Maps displaying harmonic responses as a function of both spatial position and frequency for the periodic metastructure without topological interface (a) and for the topological metastructure with topological interface (b).

grammable counterpart. We perform the space-time wave localization by dynamically modulating the interface in both space and time. This approach involves transforming one of the unit cells adjacent to the interface into its topological counterpart while keeping the others unchanged. As a result, the interface can only shift between successive unit cell boundaries within a single modulation cycle. In this framework, modifying a unit cell initially set to $\delta = 0.05$ ($\delta = -0.05$) requires that the inner electromechanical resonators are changed from Ω_{t_1} (Ω_{t_2}) to Ω_{t_2} (Ω_{t_1}), while simultaneously updating the outer electromechanical resonators from Ω_{t_2} (Ω_{t_1}) to Ω_{t_1} (Ω_{t_2}). Consequently, vibrational energy is expected to be transferred from the initial interface location to the final interface position.

The essential mechanism for achieving a perfect energy transfer across successive unit cell boundaries involves the smooth and synchronized adjustment of each local resonator's frequency. In this study, cosine functions are employed to modulate the local resonant frequency, affecting the inductance of each shunt circuit during space-time transitions. These functions are of interest in this application since they present zero-time derivatives at the beginning and end of the transition intervals and are continuous throughout the entire domain. For convenience, we denote the unit cells on the left and right of the topological interface with the indices j and $j+1$, respectively. If the interface is intended to move to the right (left) side, then the unit cell represented by $m = j+1$ ($m = j$) is topologically converted. Furthermore, consider Ω_{m_1} and Ω_{m_2} as the frequencies of local resonators, which are initially tuned to Ω_{t_1} and Ω_{t_2} within the unit cell m to be converted, respectively. Therefore, the variation of the locally resonant frequencies defined by Ω_{m_1} from $\Omega_{m_1}/\Omega_{t_1} = 1$ to $\Omega_{m_1}/\Omega_{t_1} = \Omega_{t_2}/\Omega_{t_1} = \eta$ is governed by the following law during the time interval $t_{i_j} \leq t \leq t_{f_j}$:

$$\frac{\Omega_{m_1}}{\Omega_{t_1}}(t) = \frac{(1+\eta)}{2} - \frac{(\eta-1)}{2}\cos\left(\frac{t-t_{i_j}}{t_{f_j}-t_{i_j}}\pi\right) \quad (3)$$

simultaneously, the change in locally resonant frequencies defined by Ω_{m_2} from $\Omega_{m_2}/\Omega_{t_1} = \eta$ to $\Omega_{m_2}/\Omega_{t_1} = 1$:

$$\frac{\Omega_{m_2}}{\Omega_{t_1}}(t) = \frac{(1+\eta)}{2} + \frac{(\eta-1)}{2}\cos\left(\frac{t-t_{i_j}}{t_{f_j}-t_{i_j}}\pi\right) \quad (4)$$

where t_{i_j} and t_{f_j} are, respectively, the initial and final time steps of the transition. Likewise, the transition about the mth unit cell can be characterized through $\delta_m(t) = (\Omega_{m_2}(t)^2 - \Omega_{m_1}(t)^2)/(\Omega_{m_2}(t)^2 + \Omega_{m_1}(t)^2)$. The rate of change of the frequencies of the local resonator, $d\Omega_{m_1}/dt$ and $d\Omega_{m_2}/dt$, affects the energy transfer over space and time. To control the transition smoothness, we define the transition interval as integer multiples N_j of the excitation period T, i.e., $\Delta\tau_j = t_{f_j} - t_{i_j} = N_j T$. In the case involving more unit cells, e.g., the interface displacement from the boundary between the jth and $(j+1)$th unit cells to the boundary between the $(j+3)$th and $(j+4)$th unit cells, the time values must be chosen so that $t_{i_{j+2}} \geq t_{f_{j+1}}$ and $t_{i_{j+3}} \geq t_{f_{j+2}}$, which means that the next transition only begins when the previous has been finished.

The feasibility of the previously discussed strategy is illustrated through simulations in the time domain. The Newmark method at a constant time step configured with $\gamma = 0.5$ and $\beta = 0.25$ (average constant acceleration scheme) [18] was employed to conceive multiple transition scenarios. A point force excitation is applied at the interface position and modeled as a sine burst (sinusoidal envelope) with a central frequency of $\Omega = 0.01496$ (corresponding to the frequency of the topological interface mode). The force magnitude is 0.1 N with a duration of 100 periods (i.e., $100T$, where T corresponds to one period). The interface is initially assumed at the center of the beam, between unit cells 8 and 9. Equations 3 and 4 are used to create the programmable topological interface from the center of the beam to the location between unit cells 12 and 13.

In the first transition unit cell 9 is changed from $\delta = -0.05$ to $\delta = 0.05$, i.e., the inductors are time modulated from the $L_2L_1L_1L_2$ configuration to $L_1L_2L_2L_1$ and, therefore, the space-time vibration energy localization around the new interface position (between unit cells 9 and 10) is observed. Subsequently, unit cell 10 is modified from $\delta = -0.05$ to $\delta = 0.05$ configuration, resulting in space-time vibration energy localization around the new interface position between unit cells 10 and 11. Later, the electrical inductances of the unit cell 11 are updated, resulting in the new tuning $\delta = 0.05$ and, consequently, changing the interface to the new position between unit cells 11 and 12. Finally, unit cell 12 is gradually changed from $\delta = -0.05$ to $\delta = 0.05$, creating a new interface between unit cells 12 and 13 and, finally, vibration energy localization around the new topological interface position.

Fig. 4 displays the transitions for two cases. The first one, displayed in Fig. 4(a), assumes an undamped configuration and $N = 100$. The white dots delimit the modulation intervals, where the stages II to V represent the time modulation of the inductors of unit cells 9 to 12, respectively. The perfect space-time vibration energy transfer along each smooth transition is observed in Fig. 4(a), where the energy initially confined around the center of the metamaterial beam is gradually and perfectly transferred to the final interface position. Fig. 4(b) shows the result for a damped configuration, i.e., $\zeta = 0.002$. Even considering that the amplitude of motion is reduced over time due to dissipation effects, vibration energy is localized at the final interface position. Although not shown in this work, there is a trade-off between modulation speed and the available energy in the final state in the presence of damping [14].

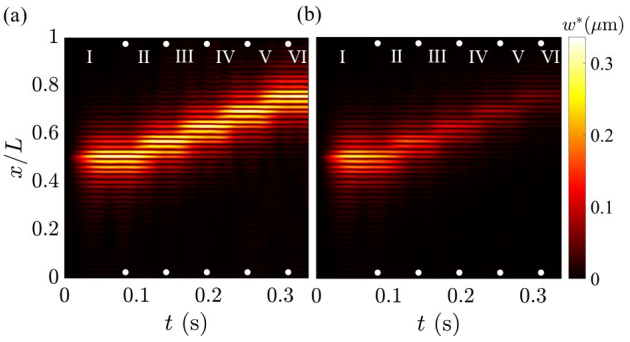


Figure 4. Multiple smooth modulations for the undamped (a) and damped (b) cases.

4. CONCLUSIONS

This study introduced a framework for space-time wave localization using programmable topological interface states in electromechanically coupled metamaterials. Energy transfer between programmable interfaces was successfully demonstrated by smoothly modulating inductive shunt circuits in an undamped metastructure. Although the amount of vibration energy was reduced throughout the modulations, successful modulations could be observed in the presence of structural damping.

5. ACKNOWLEDGMENTS

The authors are grateful to the National Council for Scientific and Technological Development grant # 383782/2022-8 and to the São Paulo Research Foundation grants # 2018/18774-6, # 21/12700-3 and # 2018/15894-0.

6. REFERENCES

[1] G. Ma, M. Xiao, and C. T. Chan, "Topological phases in acoustic and mechanical systems," *Nature Reviews Physics*, vol. 1, pp. 281–294, Apr 2019.

[2] W. Zhu, W. Deng, Y. Liu, J. Lu, H.-X. Wang, Z.-K. Lin, X. Huang, J.-H. Jiang, and Z. Liu, "Topological phononic metamaterials," *Reports on Progress in Physics*, vol. 86, p. 106501, sep 2023.

[3] R. K. Pal and M. Ruzzene, "Edge waves in plates with resonators: an elastic analogue of the quantum valley hall effect," *New Journal of Physics*, vol. 19, p. 025001, feb 2017.

[4] Y. Jin, D. Torrent, and B. Djafari-Rouhani, "Robustness of conventional and topologically protected edge states in phononic crystal plates," *Phys. Rev. B*, vol. 98, p. 054307, Aug 2018.

[5] M. Z. Hasan and C. L. Kane, "Colloquium: Topological insulators," *Rev. Mod. Phys.*, vol. 82, pp. 3045–3067, Nov 2010.

[6] H. Huang, J. Chen, and S. Huo, "Recent advances in topological elastic metamaterials," *Journal of Physics: Condensed Matter*, vol. 33, p. 503002, oct 2021.

[7] Z. Wu, R. Xia, J. Yi, and Z. Li, "Multiple topological interface modes in electromechanically resonant piezoelectric beams," *Engineering Structures*, vol. 281, p. 115716, 2023.

[8] Y. Liu, H. Wang, W. Fang, Q. Han, D. Liu, and Y. Liang, "Tunable control of subwavelength topological interface modes in locally resonance piezoelectric metamaterials," *Composite Structures*, vol. 276, p. 114541, 2021.

[9] Y.-F. Wang, Y.-Z. Wang, B. Wu, W. Chen, and Y.-S. Wang, "Tunable and Active Phononic Crystals and Metamaterials," *Applied Mechanics Reviews*, vol. 72, 02 2020. 040801.

[10] C. Sugino, M. Ruzzene, and A. Erturk, "Digitally programmable resonant elastic metamaterials," *Phys. Rev. Appl.*, vol. 13, p. 061001, Jun 2020.

[11] T. M. P. Silva, M. A. Clementino, V. C. de Sousa, and C. De Marqui, "An experimental study of a piezoelectric metastructure with adaptive resonant shunt circuits," *IEEE/ASME Transactions on Mechatronics*, vol. 25, no. 2, pp. 1076–1083, 2020.

[12] J. Santini and E. Riva, "Elastic temporal waveguiding," *New Journal of Physics*, vol. 25, p. 013031, feb 2023.

[13] R. L. Thomes, D. Beli, and C. De Marqui, "Space–time wave localization in electromechanical metamaterial beams with programmable defects," *Mechanical Systems and Signal Processing*, vol. 167, p. 108550, 2022.

[14] R. L. Thomes, D. Beli, C. Sugino, A. Erturk, and C. D. M. Junior, "Programmable moving defect for spatiotemporal wave localization in piezoelectric metamaterials," *Phys. Rev. Appl.*, vol. 19, p. 064031, Jun 2023.

[15] M. Petyt, *Introduction to Finite Element Vibration Analysis*. Cambridge University Press, 1998.

[16] C. De Marqui Junior, A. Erturk, and D. J. Inman, "An electromechanical finite element model for piezoelectric energy harvester plates," *Journal of Sound and Vibration*, vol. 327, no. 1, pp. 9–25, 2009.

[17] M. Xiao, Z. Q. Zhang, and C. T. Chan, "Surface impedance and bulk band geometric phases in one-dimensional systems," *Phys. Rev. X*, vol. 4, p. 021017, Apr 2014.

[18] N. M. Newmark, "A method of computation for structural dynamics," *Journal of the Engineering Mechanics Division*, vol. 85, no. 3, pp. 67–94, 1959.

DOI: 10.61782/fa.2025.0097

FORUM ACUSTICUM EURONOISE 2025

ACTIVE NOISE REDUCTION IN PASSENGER VEHICLES WITH PLASMACOUSTIC TRANSDUCERS

Stanislav Sergeev[1*] **Mark Donaldson**[1] **Hervé Lissek**[2]
[1] Sonexos SA, Route de la Grotte 6, CH-1003 Lausanne, Switzerland
[2] Laboratory of Wave Engineering, Ecole Polytechnique Fédérale de Lausanne, Switzerland

ABSTRACT

Low-frequency noise in commercial passenger vehicles is difficult to mitigate, as conventional methods often rely on heavy, bulky materials with limited effectiveness at these frequencies. This study investigates the application of plasmacoustic metalayer-enabled transducers for in-cabin noise control. The system employs ten 18x18 cm transducers, strategically distributed within the cabin, and evaluated under static conditions. The transducers, using the corona discharge mechanism, employ active impedance control to regulate the acoustics, enabling direct sound field management through interaction between ionized air and surrounding air particles. These transducers are lightweight and feature a slim form factor, achieving inertia-free operation and an extended bandwidth of sound control. Experimental results demonstrate broadband global noise reduction exceeding 3 dB across an operating frequency range of up to 700 Hz, effectively suppressing low-frequency resonant peaks and attenuating direct sound when transducers are placed along noise propagation paths. These findings highlight the potential for side panels and rear benches integrated with plasmacoustic technology to provide scalable and efficient global noise control solutions in passenger vehicles, reducing weight and eliminating the use of unsustainable materials.

Keywords: *plasmacoustic metalayer, sound absorption, vehicle interior noise.*

**Corresponding author*: *stanislav.sergeev@sonexos.com.*
***Copyright**: ©2025 First author et al. This is an open-access article distributed under the terms of the Creative Commons Attribution 3.0 Unported License, which permits unrestricted use, distribution, and reproduction in any medium, provided the original author and source are credited.*

1. INTRODUCTION

Active noise reduction techniques have advanced significantly over recent decades and have been implemented in commercially mature products. Effective noise cancellation can be achieved across broad frequency ranges in acoustically controlled environments, such as ear canals or waveguides, such as exhaust and ventilation ducts [1–3]. However, active noise reduction remains challenging in generic three-dimensional spaces, where passive solutions, including porous and resonant absorbers, presently dominate. These passive materials often require substantial mass and volume to achieve the desired performance in the lower frequency range [4], limiting their applicability in vehicle cabins, where the added weight affects performance. Active methods, such as active noise cancellation (ANC) [5] and active sound absorption [6, 7], present promising alternatives by improving acoustics without compromising vehicle performance to the same degree.

ANC systems in vehicles typically employ multichannel adaptive feedforward techniques, predominantly using the filtered-x LMS algorithm [8]. These systems rely on multiple reference and error sensors, usually microphones and accelerometers, placed throughout the cabin, along with loudspeakers integrated into the vehicle's interior - typically as part of its audio entertainment system. ANC effectively reduces low frequency engine and exhaust noise, when good corelation of the noise at source and target locations can be measured. Reducing road and wind noise is more challenging due to difficulties in obtaining accurate reference signals, thus necessitating additional sensors and processing powers. Enhancements like remote microphone sensing and passenger head tracking [9] improve performance, but can increase complexity and costs while limiting the effective spatial noise control

area. More research is required to expand the capabilities of the ANC and expand the noise reduction zone.

Active sound absorption modifies the acoustic properties by equipping small surface areas with active transducers designed for perfect or partial sound absorption. Recent research introduced plasmacoustic metalayers [10], which utilize ionized air layers controlled by alternating electric fields, enabling sound absorption without mechanical parts. The tests demonstrated perfect absorption at normal incidence over a bandwidth exceeding 1 kHz, achieved through a compact design adaptable to various shapes and sizes without affecting performance.

In the previous work [11], a respectable reduction in low-frequency broadband noise was achieved in a simplified rectangular volume using just a few plasmacoustic transducers if the volume presents a significant degree of reverberation. Further numerical simulations of more realistic spaces, such as a real vehicle cabin, have indicated that although a larger number of transducers may be needed to achieve similar noise reduction performance, the proportion of the so-called active absorbing area still remains low (below 3%) and can be practically realized. In this work, we attempt to achieve a significant noise reduction in a real vehicle cabin by deploying the prototype plasmacoustic active sound absorption (PASA) system in the vehicle cabin interior.

2. SETUP OF THE EXPERIMENT

2.1 Plasmacoustic transducer

The plasmacoustic transducer used in the experimental setup is illustrated in Figure 1. It consists of two electrodes that create a corona discharge. The corona electrode is a thin tungsten wire arranged in a parallel back-and-forth pattern and secured within a rigid plastic frame. The second electrode, called collector, is made from a perforated metallic plate with a high open-area ratio, ensuring minimal acoustic obstruction. The electrode system is enclosed with an acoustically transparent ozone filter. The gap between the electrode is approximately 5 mm and follows a patented geometry. The active area established between these electrodes measures 180×180 mm^2. The device operates within a voltage range of 5 to 8 kV. The ionized particles generated by the discharge interact with the surrounding air, transferring energy from the discharge zone. A detailed explanation of the operating principles is provided in previous work [10, 12]. Each transducer is powered with a compact electronic control unit (ECU),

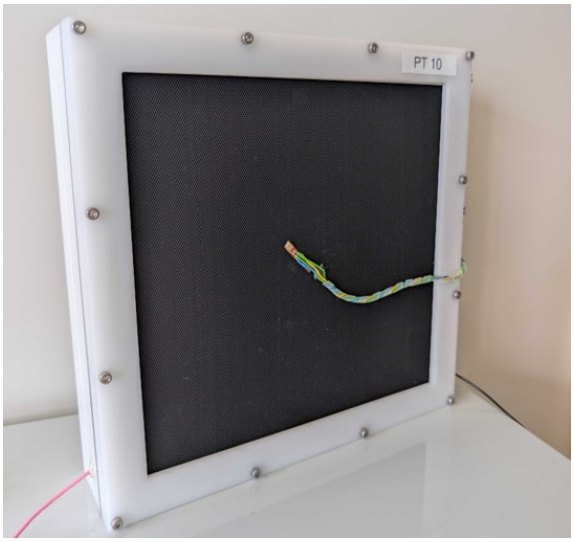


Figure 1. Assembled plasmacoustic transducer covered with the ozone filter. A control microphone is fixed in the middle of the transducer's surface.

which combines a high-voltage amplifier with an embedded electronic controller. The microphone measures the total sound pressure on the front surface of the transducer, providing input to the control algorithm. The closed-loop control aims to establish a target acoustic impedance condition over the active area of the plasmacoustic transducer. In this experiment, the controller was set to achieve an impedance close to the characteristic impedance of air:

$$Z_0 = \rho c, \tag{1}$$

where $\rho = 1.23\ kg/m^3$ is the density of the air and $c = 343\ m/s$ is the speed of sound in the air. The control transfer function is derived analytically [10], discretized and executed on the controller with a sampling frequency of 100 kHz. Thus, each of the plasmacoustic transducers is driven with an independent single-input single-output control system.

2.2 Test environment

The experiment was carried out in the Tesla Model 3 cabin of the model year 2022 as shown in Fig. 2. No changes were made to the original trim or other interior components. This vehicle model was chosen because it represents a midsize BEV deployed with a typical acoustic package. At the same time, its interior design, offering a

number of flat surfaces, allows for a simpler installation of prototype plasma transducers.



Figure 2. Vehicle under test with 10 plasmacoustic transducers placed in the cabin above; schematic locations of the microphones (red dots) and plasmacoustic transducers (blue rectangles) below.

Measurements were performed under static conditions. The sound field in the cabin is excited by a loudspeaker placed in the corner of the trunk. In this configuration, when playing back a broadband noise signal, different low-frequency acoustic modes of the cabin can be excited. Additionally, noise is filtered by the car's trim while passing from the trunk into the cabin, which resembles a dynamic noise spectrum. Sound pressure spectra are captured by measurement microphones that are attached to the headrests of the four seats.

Ten 180×180 mm^2 plasmacoustic transducers are placed in the vehicle cabin (blue rectangles in Fig. 2). They provide a total active area of approximately 0.32 m^2 and 1.5% of the entire surface of the cabin. Four transducers are placed on the dashboard (see Fig. 2), four other are distributed on the back seat shelf, and two are attached to the left and right back doors. Those locations are chosen as reasonable candidates for an actual deployment of the system. The ECUs are connected to the transducers from the outside of the car.

3. EFFECTIVE NOISE REDUCTION

Noise reduction performance is evaluated by comparing the noise spectra at different microphone locations when the PASA system is off and on. These frequency responses with the PASA system in passive and active modes are presented in Fig. 3.

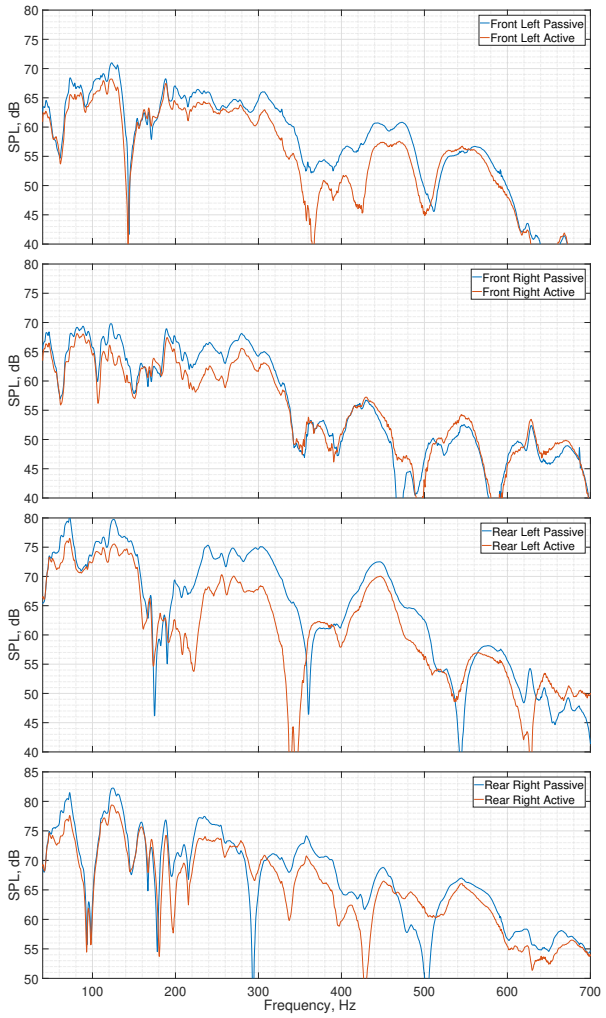


Figure 3. Measured frequency responses at different microphone locations in the vehicle cabin labeled by a seat position. Blue - PASA system is turned off; red - PASA system targets Z_0 impedance.

As discussed in the Introduction, realistic three-dimensional spaces rarely exhibit a high level of reverberation. Typically, they experience considerable acoustic

losses as a result of the vibration of lightweight structural components and air leaks. As a result, only a few first low-frequency cabin modes with limited amplitudes can be identified in the 40 to 140 Hz range. It is also worth noting that the front seat microphones are positioned near the center of the cabin, which is close to a pressure node of the first resonance. Nevertheless, the active plasmacoustic transducers effectively dampen these low-frequency modes. This effect is observable at all measurement locations, though it is more pronounced at the rear seats, where the microphones are placed closer to the cabin boundaries.

At higher frequencies, the cabin also shows limited reverberation. In this range, the mechanism by which the PASA system reduces acoustic noise changes. In addition to dampening the resonances of the cabin, plasmacoustic transducers absorb the direct noise propagating past the panels. As a result, a broad level of noise reduction is observed rather than reduction at the resonant peaks. Overall, while performance varies across frequency bands and measurement positions, the dominant spectral components are attenuated throughout the entire measured frequency range, from 40 to 700 Hz. The global noise reduction achieved well exceeds that possible by traditional ANC techniques, whose effect is limited to specific control locations.

4. CONCLUSIONS

In this study, the PASA system has demonstrated its potential to reduce acoustic noise in compact three-dimensional environments such as vehicle cabins. The application of a plasmacoustic metalayer significantly extends the operational bandwidth of a single device for local acoustic impedance control. Although a realistic environment with considerable inherent damping requires a larger active surface area, effective control can still be achieved with a relatively small number of transducers. In this experiment, only 1.5% of the interior surface area of the cabin was covered by an actively controlled impedance surface provided by the PASA system. With transducers distributed throughout the cabin and tuned to achieve a target impedance close to Z_0, the PASA system successfully reduced noise levels in the 40 to 700 Hz frequency range. Different sound absorption mechanisms dominate in different frequency bands: at low frequencies, resonant peaks are suppressed, whereas at higher frequencies, noise is reduced through the absorption of direct sound. In the latter case, placing transducers in close proximity to potential noise sources enhances effectiveness. Therefore, the ability of plasmacoustic transducers to attenuate higher-frequency direct sound depends on their position relative to the excitation source. This is an important consideration in dynamic driving conditions due to the spatially distributed nature of the noise sources. In summary, the active sound absorption system based on plasmacoustic transducers offers a broadband, global, light-weight, and environmentally sustainable form of active noise reduction, potentially deployable at a significantly lower cost of ownership than conventional active road noise cancellation techniques, which require multiple drivetrain-mounted accelerometers and higher, networked computational demands.

5. CURRENT STATUS AND OUTLOOK



Figure 4. Exterior aesthetics of a commercial version of a plasmacoustic transducer.

Sonexos will be manufacturing a plasmacoustic transducer "Plasmapanel®" featuring reduced operating voltages and enhanced long-term reliability. As illustrated in Fig. 4, the transducer comprises electrodes enclosed within a hermetically sealed plastic housing. The front face of the enclosure is acoustically transparent, enabling effective sound transmission, while maintaining the electrode assembly in a controlled gas environment. This configuration significantly reduces the required operating voltages and protects electrodes from corrosion. Multiple Plasmapanel® units can be assembled into arrays, providing flexible scaling of the active surface area to achieve specific noise reduction targets.

6. ACKNOWLEDGMENTS

The research presented in this document was conducted as part of the PANACHE innovation project, which is supported by Innosuisse, the Swiss Innovation Agency, under grant agreement No. 102.618 IP-ENG.

7. REFERENCES

[1] T. C. Kwong, Y. S. Choy, C. C. H. Chan, and S. W. Mung, "Tunable active noise control circuit topology for multiple-feature applications," *Scientific Reports*, vol. 14, no. 1, p. 18629, 2024.

[2] L. Wu, L. Wang, S. Sun, and X. Sun, "Hybrid active and passive noise control in ventilation duct with internally placed microphones module," *Applied Acoustics*, vol. 188, p. 108525, 2022.

[3] E. de Bono, A. D. Fernandes, G. Petrone, M. Ouisse, and R. Teloli, "On the optimization of (generalized) impedance for acoustic liners," in *34th ICAS (ICAS2024)*, 2024.

[4] T. Cox and P. d'Antonio, *Acoustic absorbers and diffusers: theory, design and application*. CRC press, 2016.

[5] J. Cheer and S. J. Elliott, "Multichannel control systems for the attenuation of interior road noise in vehicles," *Mechanical Systems and Signal Processing*, vol. 60-61, pp. 753–769, 2015.

[6] E. Rivet, *Room Modal Equalisation with Electroacoustic Absorbers*. PhD thesis, Lausanne, 2016.

[7] K. Billon, E. De Bono, M. Perez, E. Salze, G. Matten, M. Gillet, M. Ouisse, M. Volery, H. Lissek, J. Mardjono, *et al.*, "In flow acoustic characterisation of a 2d active liner with local and non local strategies.," *Applied Acoustics*, vol. 191, p. 108655, 2022.

[8] P. N. Samarasinghe, W. Zhang, and T. D. Abhayapala, "Recent advances in active noise control inside automobile cabins: Toward quieter cars," *IEEE Signal Processing Magazine*, vol. 33, no. 6, pp. 61–73, 2016.

[9] H. Su, J. Liu, A. Liu, and B. Li, "A study of an active noise control system with continuous tracking of the human ear and noise segmentation control," *International Journal of Automotive Technology*, pp. 1–17, 2025.

[10] S. Sergeev, R. Fleury, and H. Lissek, "Ultrabroadband sound control with deep-subwavelength plasma-coustic metalayers," *Nature Communications*, vol. 14, no. 1, p. 2874, 2023.

[11] S. Sergeev, M. Donaldson, and H. Lissek, "Ultrabroadband sound control of 3d spaces using plasma-coustic metalayers," in *INTER-NOISE and NOISE-CON Congress and Conference Proc.*, (Nantes, France), pp. 8431–8442(12), 2024.

[12] S. Sergeev, H. Lissek, A. Howling, I. Furno, G. Plyushchev, and P. Leyland, "Development of a plasma electroacoustic actuator for active noise control applications," *Journal of Physics D: Applied Physics*, vol. 53, p. 495202, dec 2020.

DOI: 10.61782/fa.2025.0908



FORUM ACUSTICUM
EURONOISE 2025

TOWARDS PLASMACOUSTIC METAMATERIALS

Han Miao[1] **Stanislav Sergeev**[2] **Rahim Vesal**[1] **Hervé Lissek**[1*]
[1]Laboratory of Wave Engineering, Ecole Polytechnique Fédérale de Lausanne, Switzerland
[2]Sonexos SA, Route de la Grotte 6, CH-1003 Lausanne, Switzerland

ABSTRACT

The ”plasmacoustic metalayer” concept relies on the use of a Corona Discharge Transducer (CDT), transparent towards fluid flows and to light. When used as an actuator within an active control system, it allows manipulating sound waves in transmission/reflection/absorption without resorting to a membrane or any other mechanical intermediate, contrarily to conventional loudspeakers. Moreover, owing to its non-resonant nature, the CDT is an obvious candidate for the development of broadband active acoustic metamaterials, especially since it is transparent to sound in a ”passive” mode.

This presentation aims to showcase some examples of active plasmacoustic metamaterials concepts, through numerical simulations and experimental validations, at the unit-cell level. These preliminary results will allow drawing conclusions on the applicability of the CDT to achieve broadband active acoustic metamaterials, and identifying routes for further development of the concept.

Keywords: acoustic metamaterials, plasmacoustic metalayers, active control

1. INTRODUCTION

Acoustic metamaterials have emerged in the early 2000's inspired by the literature on their electromagnetic counterparts. In its general definition, an acoustic metamaterial is an artificial structure consisting of miniature engineered elements (cavities, ducts, membranes, etc.), assembled in such a way so that the whole exhibits physical properties that mimic or even go beyond physical phenomena occurring in nature. The most important feature of these unit-cells is their subwavelength dimension, namely their size should much smaller than the wavelengths they interact with [1].

However, most of the reported architectures rely on resonant structures (Helmholtz resonators, coiled-space cavities, membranes) [2–4]. Therefore, the resulting anomalous/negative properties are limited to a narrow frequency bandwidth, if not at a single frequency. Also, their inherent losses negatively impact their “transmissibility” capacities (the amount of acoustic energy that can be effectively transmitted “forward” by the artificial structure), and therefore preclude any practical application. More generally, passive linear metamaterials are bound to the Kramers-Kronig relations, eventually leading to trade-offs in terms of bandwidth of operation and transmissibility.

In a view to overpassing the inherent limitations of passive structures, active acoustic metamaterial concepts have been recently investigated. In this paradigm, the unit-cells are composed of electroacoustic transducers (loudspeakers and microphones) connected by a control platform, in a view to adapting their dynamic response to ongoing sound waves. Thanks to such a tunability, it is possible to observe exotic time-varying properties such as time-reversal for sound focusing, non-Hermitian media, acoustic circulators, acoustic diodes, and many other interesting topological phenomena, that were not possible with passive constructions. But conventional loudspeakers are still intherently resonant, thus limited in terms of bandwidth of operation, and more importantly, they are prone to introduce significant losses against which the control should devote a significant par of energy to function. Last, they rely on (opaque) membrane radiators, that cannot avoid scattering (loudspeakers are obstacles to the propagation of sound in a metamaterial structure).

The Plasmacoustic Metalayer recently developed by

*__Corresponding author__: herve.lissek@epfl.ch.
__Copyright__: ©2025 Han Miao et al. This is an open-access article distributed under the terms of the Creative Commons Attribution 3.0 Unported License, which permits unrestricted use, distribution, and reproduction in any medium, provided the original author and source are credited.

Sergeev et al [6, 7] allows interacting with exogenous sound waves in a membraneless manner, thanks to a Corona Discharge Transducer (CDT) [5]. Besides its almost transparency to fluid flows (and light), which makes it non-scattering and lossless in its passive form, the main asset for metamaterial applications is its non-resonant characteristics. In active mode, it has been capable to exhibit almost ideal sound absorption over an ultrabroadband frequency range (20 Hz-2000 Hz), owing to the absence of mechanical interface known to bound the bandwidth of operation in conventional loudspeaker-based active control systems. Moreover, further use of the concept in transmission configuration have been demonstrated, showing also variable broadband reflection/transmission modules and phases. This makes the Plasmacoustic Metamalayer a most promising candidate as unit-cell for active metamaterial applications.

This paper introduces the Plasmacoustic Metamaterial (PM) concept, by leveraging some examples of active sound reflection/transmission results achieved by the plasmacoustic metalayer concept. These examples will be discussed in the light of their application as plasmacoustic metamaterial unit-cells (PMUC), that are the heart of a research project submitted for funding to the Swiss National Science Foundation.

2. THE CORONA-DISCHARGE ELECTROACOUSTIC TRANSDUCER

2.1 Corona discharge transducer in a "wire-to-grid" configuration

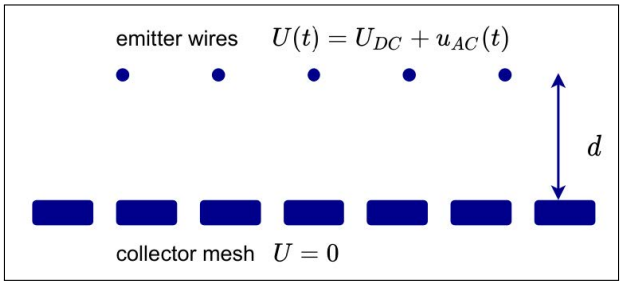


Figure 1. Sketch representing a cut view of the electrode pair: corona electrode (emitter wires)/collector electrode (grounded perforated grid)

Corona discharge transducers (CDT) allow for sound generation due to the ionization of molecules in the surrounding fluid, moved by an intense oscillating electric field. In the "wire-to-grid" configuration, the transducer is constituted by a pair of electrodes (forming two parallel planes, as illustrated in the sketch of Fig. 1): the first one is a perforated metallic grid connected to the ground, and is designated the "collector electrode"; the second one, designated "corona electrode", is made of an ultra thin wire (diameter of the order of 100 μm), arranged in a pattern of parallel lines along a same plane parallel and distant of d to the collector plane, put at a sufficiently high voltage so as to trigger the extraction of electrons from surrounding molecules. The breakdown voltage, above which ionization is possible, is designated U_0 and is of the order of a few kV.

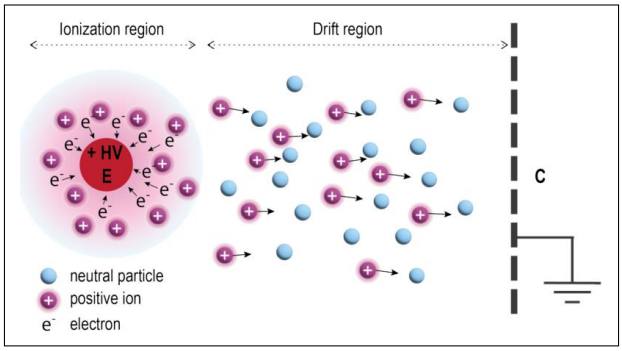


Figure 2. Corona discharge principle

When applying an offset voltage U_{DC} higher than U_0, positive ions are accelerated inside the ionization region towards the collector electrode. They then collide with the neutral particles present in the drift region, which are then moved, giving rise to an "ionic wind" (constant flow).

If an alternating voltage $u_{ac}(t)$, of the order of 1 kV, is superimposed to U_{DC} (while total voltage $U_{DC} + u_{ac}$ still remains higher than the breakdown voltage, as well as not exceeding a value above which arcing may occur), the transducer generates acceleration/deceleration of the surrounding fluid layers, responsible for sound generation.

The preceding studies show that this corona discharge transducer configuration could be modelled as the combination of two volumic sound sources, one monopolar "heat" source H (due to the heat release at the corona electrodes), and another dipolar "force" source F (relative to the electrostatic force moving the surrounding fluid back and forth).

An extremely simple electroacoustic model can be deduced from the coupling equations between the plasma generation and actuation, and the generated sound field.

Indeed, it has been shown that the offset voltage U_{DC} can be linked to the current I flowing through the corona wire according to the Townsend formula:

$$I = CU_{DC}(U_{DC} - U_0) \tag{1}$$

where C is a constant that depends on the transducer geometry, and that can be experimentally determined. It is then possible to express the two sources H and F as a function of the voltage feeding the transducer [5, 6]:

$$\begin{aligned} H &= C(3U_{DC}^2 - U_{DC}U_0)u_{ac}\ [\mathrm{W}] \\ F &= \frac{C.d}{\mu_i}(2U_{DC} - U_0)u_{ac}[\mathrm{N}] \end{aligned} \tag{2}$$

where μ_i designates ions mobility, and d is the distance between the two electrodes (or the plasma thickness). It can be seen that the two sound sources are interdependent. Their individual influence is independent on frequency but on the constant parameters U_0, U_{DC}, C, d and μ_i, and not directly on the transducer cross-section area S. However, the lateral dimensions of the CDT is likely to change the current-voltage law (Eq. (1)), thus C.

In the following, we define the the heat source power density $h = \frac{H}{S.d}$ (in W/m^3), and the dipolar force source density $f = \frac{F}{S.d}$ (in N/m^3), where S is the transducer effective cross-section area, to be used in the expression of the sound fields generated by the CDT.

3. THE PLASMACOUSTIC METALAYER AS A METAMATERIAL UNIT-CELL

Let's consider a 1D waveguide along dimension x being the host of the PMUC, as illustrated in Fig. 3. In the PM paradigm, we will consider a unit-cell integrating a CDT, one ore more microphones (either one on the front side when backed by a rigid cavity, or with at least 2 microphones, one on each sides of the transducer in an open configuration), a control hardware and a power amplifier capable to manage the high voltage DC and the acoustic control voltage u_{ac}, as illustrated on Fig. 3. For the sake of simplicity, the controller part includes the power amplifier, to deliver a given voltage u_{ac} to the transducer.

In the configuration where the CDT is centered at the origing $x = 0$ and oriented so that the collector electrode is located towards the left (with respect to the chosen direction of axis x of the waveguide) and the corona electrode being on the right side, a given ac voltage u_{ac} will give rise to a dipolar force source that will generate out-of-phase (wrt. u_{ac}) sound pressures towards the increasing x direction, while generating in-phase (wrt. u_{ac}) sound pressures towards the decreasing x direction. The different contribnutions to the acoustic field generated by the CDT will then be (distinguised between negative and positive x half-domains):

$$\text{for } x < 0 : \begin{cases} p_h(x) = \dfrac{dc_0}{2C_pT_0}he^{jkx} \\ p_f(x) = \dfrac{d}{2}fe^{jkx} \\ v_h(x) = -\dfrac{d}{2\rho_0C_pT_0}he^{jkx} \\ v_f(x) = -\dfrac{d}{2\rho_0c_0}fe^{jkx} \end{cases} \tag{3}$$

$$\text{for } x > 0 : \begin{cases} p_h(x) = \dfrac{dc_0}{2C_pT_0}he^{-jkx} \\ p_f(x) = -\dfrac{d}{2}fe^{-jkx} \\ v_h(x) = \dfrac{d}{2\rho_0C_pT_0}he^{-jkx} \\ v_f(x) = -\dfrac{d}{2\rho_0c_0}fe^{-jkx} \end{cases} \tag{4}$$

If we consider an exogenous sound field $p_{ac}(x) = p_{ac}^+e^{-jkx} + p_{ac}^-e^{+jkx}$, and the associated particle velocity $v_{ac}(x) = \frac{1}{\rho_0c_0}\left(p_{ac}^+e^{-jkx} - p_{ac}^-e^{+jkx}\right)$, we can derive the total pressure fields on both sides of the unit-cell as:

$$x < 0 : \begin{cases} p_t(x) = p_{ac}^+e^{-jkx} \\ \qquad + \left(p_{ac}^- + \dfrac{dc_0}{2C_pT_0}h + \dfrac{d}{2}f\right)e^{jkx} \\ v_t(x) = \dfrac{1}{\rho_0c_0}\left[p_{ac+}e^{-jkx}\right. \\ \qquad \left. - \left(p_{ac}^- + \dfrac{dc_0}{2C_pT_0}h + \dfrac{d}{2}f\right)e^{jkx}\right] \end{cases} \tag{5}$$

$$x > 0 : \begin{cases} p_t(x) = p_{ac}^-e^{jkx} \\ \qquad + \left(p_{ac}^+ + \dfrac{dc_0}{2C_pT_0}h - \dfrac{d}{2}f\right)e^{-jkx} \\ v_t(x) = \dfrac{1}{\rho_0c_0}\left[-p_{ac}^-e^{jkx}\right. \\ \qquad \left. + \left(p_{ac}^+ + \dfrac{dc_0}{2C_pT_0}h - \dfrac{d}{2}f\right)e^{-jkx}\right] \end{cases} \tag{6}$$

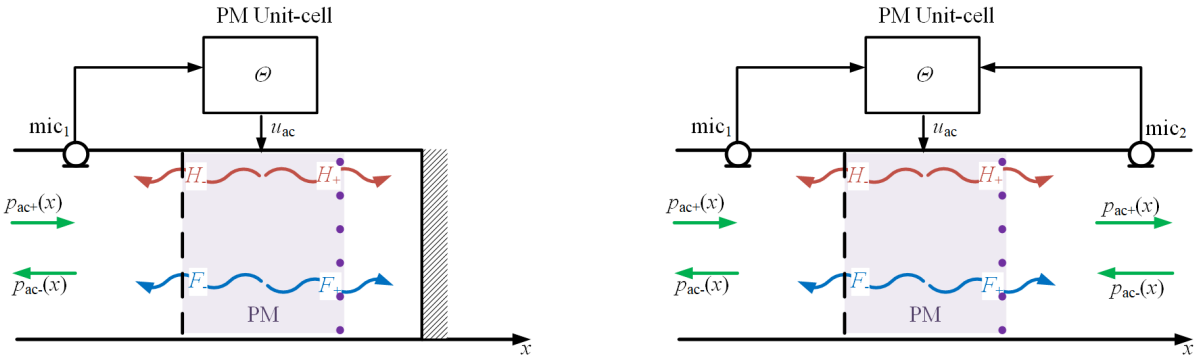


Figure 3. Realizations of a PMUC in a 1D waveguide: left: PMUC backed by a rigid termination; right: PMUC open on both sides

In these sets of equations, h and f are intricate as they both depend on u_{ac}. Still, the control of u_{ac} as a function of one ore more microphone inputs allows achieving interesting acoustic properties over the PMUC. The following section intends to present some of the applications.

4. EXAMPLES OF PLASMACOUSTIC METAMATERIAL UNIT-CELL REALIZATIONS

4.1 PMUC in reflection

The first realization of a PMUC in reflection is reported in [6]. In this experience, the PMUC is in the backed configuration (see Fig. 3-left), with a control microphone located at position $-x_0$ (the PMUC center being at the origin $x = 0$). In this configuration, the left-handed side of the PMUC can simplify, taking into account the reflection at the back wall distant of l from the PMUC center. Accounting for the actual (measurable) specific impedance $Z_l = \frac{p_t(x=l)}{v_t(x=l)}$ at the wall ($x = l$), we derive the reflection coefficient $R = \frac{Z_l - Z_c}{Z_l + Z_c}$ and then the relationships on the left side ($x < 0$) become:

$$\begin{cases} p_t(x) = p_{ac}^+ e^{-jkx} + \Big(R p_{ac}^+ \\ \quad + \dfrac{dc_0}{2C_pT_0}(1 - Re^{-2jkl})h \\ \quad + \dfrac{d}{2} f(1 - Re^{-2jkl})\Big)e^{jkx} \\ v_t(x) = \dfrac{1}{\rho_0 c_0}\Big[p_{ac}^+ e^{-jkx} - \Big(R p_{ac}^+ \\ \quad + \dfrac{dc_0}{2C_pT_0}(1 + Re^{-2jkl})h \\ \quad + \dfrac{d}{2}(1 - Re^{-2jkl})f\Big)\, e^{jkx}\Big] \end{cases} \tag{7}$$

By prescribing a target specific impedance $Z_t(-x_0) = \frac{p_t(-x_0)}{v_t(-x_0)}$ at the control microphone position, we can deduce the transfer function $\Theta(\omega) = \frac{u_{ac}}{p_t(-x_0)}$ to drive the PMUC in order to achieve the targeted impedance:

$$\begin{cases} \Theta(\omega) = \dfrac{1}{A}\dfrac{Z_c}{Z_t}\left(\dfrac{Z_t - Z_{ac}(-x_0)}{Z + Z_{ac}(-x_0)}\right) \\ A = \dfrac{d}{2}\left(f + \dfrac{c_0 h}{C_p T_0}\right)e^{-jkx_0} \\ \quad + \dfrac{d}{2}\left(\dfrac{c_0 h}{C_p T_0} - f\right)Re^{-jk(x_0+2l)} \\ Z_{ac}(-x_0) = \dfrac{p_{ac}(-x_0)}{v_{ac}(-x_0)} \end{cases} \tag{8}$$

In this study, we target a control in reflection with adjustable amplitude and phase, the target impedance being set so as to achieve target reflection coefficient $R_t =$

$|R_t|e^{j\angle(R_t)}$. In that view, we define a dimensionless factor $\zeta \in [01]$ to define a virtual acoustic termination ζZ_l, and a virtual depth of the cavity $l + \Delta l$ leading to an additional delay in the control loop. In this control strategy, the target impedance becomes:

$$Z_t = Z_c \frac{\zeta Z_l + jZ_c \tan(k(l + x_0 + \Delta l))}{Z_c + j\zeta Z_l \tan(k(l + x_0 + \Delta l))} \quad (9)$$

An experimental prototype of PMUC in absorption has been built with lateral dimensions $50\,\mathrm{mm} \times 50\,\mathrm{mm}$ and inter-electrode gap of $6\,\mathrm{mm}$, and placed in a rectangular tube of same cross-section and length $1.1\,\mathrm{m}$, with a back cavity length l =15 mm. The PCB 130D20 quarter-inch ICP microphone used for the control is located at position $x_0 = -10\,\mathrm{mm}$ and input a Speedgoat IO-334 working at $50\,\mathrm{kHz}$. Finally a TREK 615-10 high voltage AC/DC amplifier drives the PMUC with amplification gain of 1000 (accounted for in the transfer function Θ).

The reflection coefficient is measured after ISO 10534-2 standard [12], with two PCB 130D20 ICP microphones distant of $50\,\mathrm{mm}$ from each others, the signals of which are processed by a B&K Pulse Multichannel Analyzer to estimate the transfer functions H_{12} and derive the reflection coefficient in the different control cases.

We measured the reflection coefficient (in amplitude and phase) for two scenarios: one where we set the coefficient ζ to achieve different reflection amplitude of [0.9 0.7 0.4] while keeping $\Delta l = 0\,\mathrm{m}$ (see Fig. 4), and another where we keep the reflection amplitude to 0.4 while adding a virtual cavity depths of [3.7 cm, 9.7 cm, 14.7 cm], namely by adding a delay of [0.22 ms, 0.56 ms, 0.85 ms] (see Fig. 5).

We can then assign any reflection coefficient amplitude and phase to the PMUC in the backed configuration, which gives a unique possibility to control the reflection gratings over a 2D metasurface with an ultra-thin unit-cell (in the range of $1\,\mathrm{cm}$ in the current prototype, but it can be made even thinner), without having to employ acoustic or mechanical resonators with frequency-dependent thickness as reported in the current literature (space-coiling channels [8], Helmholtz resonators [9], or membrane-capped cavities [10]).

4.2 PMUC in transmission

Preliminary investigations on the use of a PMUC in open configuration for active noise reduction have been recently undertaken. In this study, the PMUC consists of a square

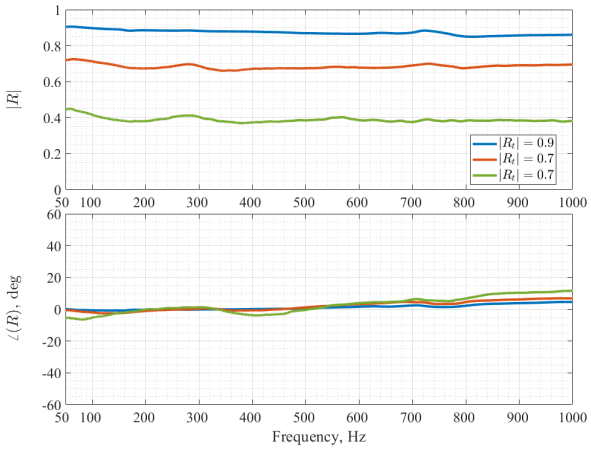


Figure 4. Reflection coefficient measured on the PMUC in an impedance tube with variable amplitude, while the phase is set to 0 degree (source: Sergeev et al [6])

CDT of size $50\,\mathrm{mm} \times 50\,\mathrm{mm}$ and inter-electrodes gap $d = 6\,\mathrm{mm}$, surrounded by two PCB 130D20 quarter-inch ICP microphones as control microphones, distant of x_0 to the center of the CDT. The PMUC is inserted in the middle of an impedance tube with same square cross-section and total length $2\,\mathrm{m}$. One extremity is loaded with a $500\,\mathrm{mm}$ long melamin wedge to ensure anechoic condition, the other hosting a loudspeaker used as the sound source. The PMUC is controlled with a Speedgoat Baseline Real-Time Target Machine to assign the targeted control law. The acoustic properties of the PMUC are measured with two pairs of PCB 378B02 half-inch ICP microphones, the signals and the transfer functions being processed with a 4-channels B&K Pulse Sound and Vibration Analyzer. The Transfer Matrix Method [13] is employed to derive the PMUC transmission properties, such as the effective propagation constant $\gamma = \alpha + j\beta$, transmission loss, or the effective impedance matrix of the small insertion of size $d + 2x_0$.

In this study, the control strategy consisted in synthesizing a target 2-port acoustic circuit comprising a series impedance Z_t, following the same methodology as the one employed for the PMUC with back-cavity configuration. Here it is important to stress on the fact that the PMUC will result in both series impedance and shunt admittance Y_t since the monopolar and dipolar sound

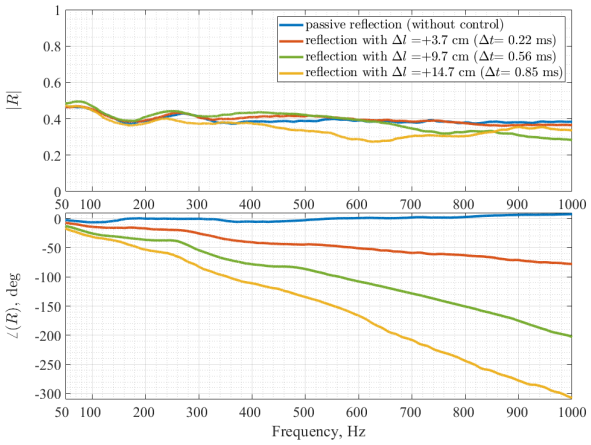


Figure 5. Reflection coefficient measured on the PMUC in an impedance tube with variable delays (source: Sergeev et al [6])

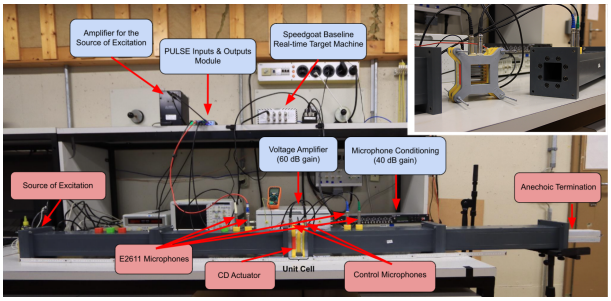


Figure 6. Setup of the PMUC assessment in transmission

sources are intricated. Nevertheless the choice has been made here to ignore the shunt admittance and verify that the control still allows achieving the series impedance, and see how much it is impacted by the resulting admittance. Therefore, the heat source h is set to 0 in the sound field expressions of Eqs. (5) and (6), in order to derive the target control law $\Theta(\omega)$, so as to deliver a prescribed particle velocity as $v_t = \dfrac{p_t(-x_0) - p_t(+x_0)}{Z_t}$.

We decided to assign two target impedances here. The first one corresponds to a layer of porous material wth porosity of 0.75 and flow resistance $1.5\,\mathrm{MPa\,s\,m^{-4}}$ and of thickness $d + 2x_0 = 64\,\mathrm{mm}$, modeled as series resistance R_t (also taking into account the "natural" mass of air $M_p = \rho_0(d + 2x_0)$ without the PMUC, while neglecting the "natural" compliance). The second one targets a single-degree-of-freedom resonator consisting of an acoustic mass M_t and compliance C_t (also taking into account the "natural" mass of air without the PMUC, while neglecting the "natural" compliance). The target impedance in these two cases are

$$\begin{cases} Z_{t,\text{porous}} = R_t + j\omega M_p \\ Z_{t,\text{membrane}} = j\omega(M_p + M_t) + \dfrac{1}{j\omega C_t} \end{cases} \tag{10}$$

where $M_p = 76.8\,\mathrm{g\,m^{-2}}$, $R_t = 0.1\,\mathrm{Pa\,s\,m^{-3}}$, M_t =331 $\mathrm{g\,m^{-2}}$ and $C_t = 6.510^{-6}\ \mathrm{m^{-1}\ N^{-1}}$. The results in terms of achieved normalized impedance $z = \frac{Z}{Z_c}$ are represented on Fig. 7 and Fig. 8.

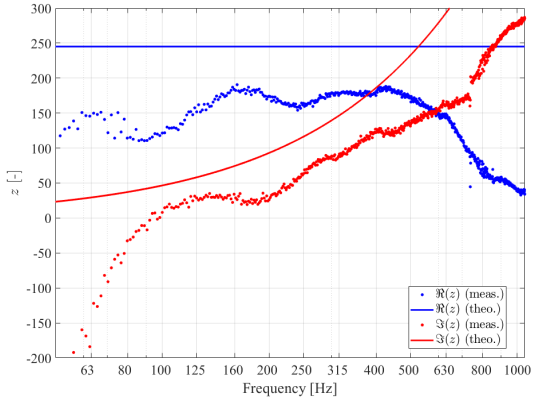


Figure 7. Normalized acoustic impedance (blue: real part; red: imaginary part) when targeting a porous layer (points: measurements; lines: target)

We can observe that the achieved impedance differs from the target one, mainly due to the assumption after which the the CDT is mainly dipolar. However, the behaviour at low frequencies fits reasonably well the target in the second case, while the achieved resistance of the first case is significantly lower than the target. The effect of the monopolar source explains the mismatch with the target, especially at high frequencies.

From these measurements, it is also possible to derive the transmission loss $TL = 10.\log_{10}\left(\dfrac{I_i}{I_t}\right)$ and the propagation contant $\gamma = \alpha + j\beta$. The examples for the case where the target impedance is the one of a porours layer are given in Fig. 9 and Fig. 10

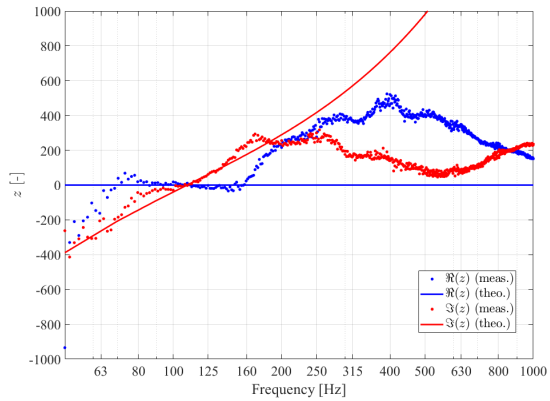


Figure 8. Normalized acoustic impedance (blue: real part; red: imaginary part) when targeting a membrane (points: measurements; lines: target)

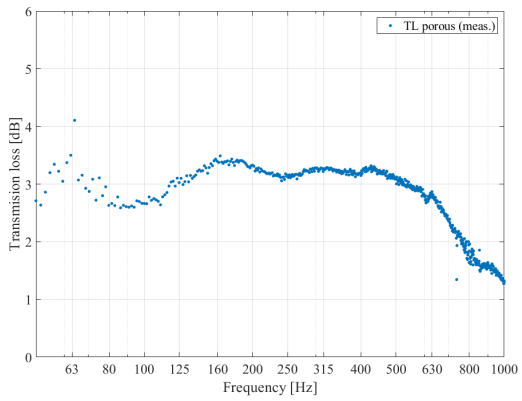


Figure 9. Transmission loss when targeting a porous layer $Z_t = R_t + j\omega M_p$

5. CONCLUSION AND PERSPECTIVES

We have shown that the PMUC allows achieving a wide range of acoustic properties, either in reflection when backed with a closed cavity, or in transmission when open on both ends. The achieved performance is aligned with the targeted one in the case where the PMUC is closed at one side, but differs in the open configuration, due to the intrication of monopolar/dipolar sound sources.

In a follow-up study, we will develop alternative control strategies that allow separating monopolar and dipolar components of the CDT, thus enabling full control on the 2-ports acoustic properties.

6. REFERENCES

[1] S.A. Cummer, J. Christensen, A. Alù, Controlling sound with acoustic metamaterials. *Nat. Rev. Mater.*, 1:16001, 2016.

[2] N. Fang, Ultrasonic metamaterials with negative modulus. *Nat. Mater.*, 5:452–456, 2006.

[3] C. Zhang, X. Hu, Three-Dimensional Single-Port Labyrinthine Acoustic Metamaterial: Perfect Absorption with Large Bandwidth and Tunability. *Phys. Rev. Appl.*, 6:064025, 2016.

[4] S. Lee, C.M. Park, Y.M. Seo, Z.G. Wang, C.K. Kim, Composite Acoustic Medium with Simultaneously Negative Density and Modulus. *Phys. Rev. Lett.*, 104:054301, 2010.

[5] S. Sergeev, H. Lissek, A. Howling, I. Furno, G. Plyushchev, and P. Leyland, Development of a plasma electroacoustic actuator for active noise control applications *Journal of Physics D: Applied Physics*, 53:495202, 2020.

[6] S. Sergeev, Plasma-based Electroacoustic Actuator for Broadband Sound Absorption, EPFL PhD Thesis N. 9784, Lausanne, Switzerland, 2022.

[7] S. Sergeev, Ultrabroadband sound control with deep-subwavelength plasmacoustic metalayers *Nat. Commun.*, 14:2874, 2023.

[8] N. Jiménez, V. Romero-García,L- M. García-Raffi, F. Camarena, K. Staliunas, Sharp acoustic vortex focusing by Fresnel-spiral zone plates. *Appl. Phys. Lett.*, 112: 204101, 2018.

[9] N. Jiménez, T. J. Cox, V. Romero-García,J. P. Groby Metadiffusers: Deep-subwavelength sound diffusers. *Sci Rep* 7: 5389, 2017.

[10] H. Esfahlani, S. Karkar, H. Lissek, J. R. Mosig, Acoustic carpet cloak based on an ultrathin metasurface. *Phys. Rev. B* 94(9):014302, 2016.

[11] F. Bongard, H. Lissek, J. R. Mosig. Acoustic transmission line metamaterial with negative/zero/positive refractive index. *Phys. Rev. B*, 82(9):094306, 2010.

[12] ISO 10534-2:2023. Determination of acoustic properties in impedance tubesPart 2: Two-microphone technique for normal sound absorption coefficient and normal surface impedance, ISO standards, 2023.

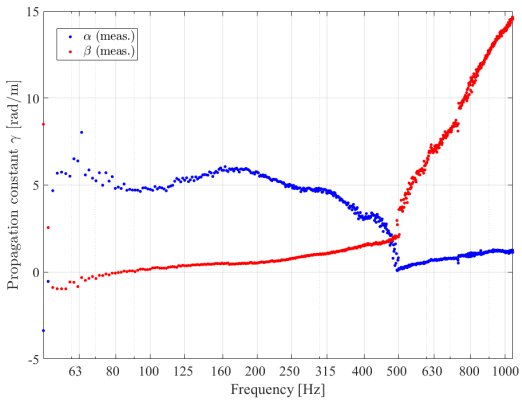


Figure 10. Propagation constant when targeting a porous layer $Z_t = R_t + j\omega M_p$

[13] ASTM 2611-19. Standard Test Method for Normal Incidence Determination of Porous Material Acoustical Properties Based on the Transfer Matrix Method, ASTM standards, 2019

DOI: 10.61782/fa.2025.0846



FORUM ACUSTICUM
EURONOISE 2025

CONTROL OF A NONLINEAR ELECTROACOUSTIC RESONATOR: REAL-TIME SELECTION OF THE EQUILIBRIUM POINT

Maxime Morell[1*] **Emanuele De Bono**[3] **Emmanuel Gourdon**[1]
Manuel Collet[2] **Alireza Ture Savadkoohi**[1] **Claude-Henri Lamarque**[1]
[1] ENTPE, Ecole Centrale de Lyon, CNRS, LTDS, UMR5513, 69518 Vaulx-en-Velin, France
[2] CNRS, Ecole Centrale de Lyon, ENTPE, LTDS, UMR5513, 69130 Ecully, France
[3] Ecole Centrale de Lyon, CNRS, ENTPE, LTDS, UMR5513, 69130 Ecully, France

ABSTRACT

To tackle the issue of adaptability to in-situ conditions while providing efficient acoustic absorption in a large frequency bandwidth, impedance control of loudspeakers has been brought as a solution. To control the impedance of a loudspeaker, one should place microphones collocated to the loudspeaker, supplied with a processor that calculates the needed electrical current to send to the loudspeaker's coil to target a specific impedance. This concept has long been considered in the framework of linear dynamics, however the extension to nonlinear dynamics is a current subject of interest. In this study, nonlinear dynamics are enforced through a feedforward control tracking a setpoint defined by a numeric exosystem. The use of the exosystem allows to synthesize uncommon behaviors such as nonpolynomial nonlinear restoring forces. However, nonlinear resonators may present many stable equilibrium points for a single frequency, which may be targeted via the choice of the initial conditions. The choice of the initial conditions in electroacoustics is challenging and would permit better sound absorption. In this study, a method for targeting the equilibrium point of a nonlinear dynamical system in the framework of electroacoustic resonators is presented, and its experimental implementation is demonstrated, leading to many potential acoustic applications.

*__Corresponding author__: *maxime.morell@entpe.fr.*
__Copyright__: *©2025 Maxime Morell et al. This is an open-access article distributed under the terms of the Creative Commons Attribution 3.0 Unported License, which permits unrestricted use, distribution, and reproduction in any medium, provided the original author and source are credited.*

Keywords: *Programmable, Nonlinear, Feed-forward, Resonator, Exosystem*

1. INTRODUCTION

An electroacoustic resonator (ER) is a loudspeaker collocated to microphones and equipped with a processor running a controller that takes into input the measured pressure, and provides as an output the electrical current to enforce to the loudspeaker [1, 2]. The benefits of an ER lies in its efficiency in a bandwidth around its resonance frequency, leading to the possibility of efficient acoustic absorption at low frequencies. The resonance frequency can be tuned through digital programming of the controller. As this concept is widely studied for linear behaviors enforced to the loudspeaker [3], enforcing nonlinear behavior using a digital control at low excitation amplitudes stands as a current subject of interest [4–7]. A nonlinear resonator offers larger frequency bandwidth of efficiency and features nonlinear phenomena useful of the mitigation of vibrations. However, a nonlinear system may present multiple co-existing equilibrium points at a single frequency, which do not have similar efficiency results in acoustic absorption [7, 8]. indeed, the system converges towards a specific equilibrium point depending on the initial conditions. As a result, the acoustic absorption capabilities of a nonlinear resonator, compared to a linear resonator, lies in the initial conditions. In this study, a nonlinear ER created by a digitally programmed controller is used for the mitigation of acoustic vibrations. As the choice of the initial conditions proves to be difficult, the choice of the equilibrium point might be done in the digital programming. The method for targeting a specific

equilibrium point is presented.

2. THE DIGITAL CONTROL ENFORCING NONLINEAR BEHAVIOR

The linear dynamics are enforced through the infinite input response method, which can not be used to enforce nonlinear dynamics efficiently [4]. As a result, the nonlinear dynamics are enforced through a real-time based feed-forward controller tracking a setpoint defined by an Exosystem (ES).

Considering a loudspeaker collocated with microphones, the ER is created by assuming that the loudspeaker's response is dominated by its first mode, along with the hypothesis of low amplitudes (to keep the resonator in its linear regime) and low frequencies (to keep the excitation frequencies close to the ER's first mode).
The ES simulates the targeted behavior of the loudspeaker under the measured pressure. The ES model contains the dynamic to enforce, and is supplied with the measured pressure. Its numerical resolution can be realized using classical numerical schemes for solving ordinary differential equations. Once the targeted displacement, speed and acceleration are predicted, the electrical current is calculated using the feed-forward controller containing the loudspeaker's model driven by the predictions. The equations of the control are presented in Eqn. (1):

$$\dot{X}(t) = A(X(t), t, f_{ext}(t), u_d(t)) \tag{1a}$$

$$u_d(t) = \varphi(\dot{X}_d(t), X_d(t), t, f^m_{ext}(t)) \tag{1b}$$

$$\dot{X}_d(t) = F(X_d(t), t, f^m_{ext}(t)) \tag{1c}$$

where Eqn. (1a) is the equation of the system to control, here the loudspeaker. The variable X stands for the loudspeaker's modal coordinate of its first mode, t is the time, f_{ext} represents the external forces applied on the loudspeaker's membrane (the pressure), and u_d is the control variable allowing to apply the control, here the electrical current. The Eqn. (1b) is the equation that permits to determine the electrical current to send to the loudspeaker, which is obtained by inversion of the system Eqn. (1a). The variable f^m_{ext} represents the measured external forces. The calculation is done using the variable X_d standing for the desired modal coordinate provided by solving the ES Eqn. (1c). The ES Eqn. (1c) provides the nonlinear desired behavior by solving it using numerical schemes. These control equations are evaluated at each time step.

3. TARGETING SPECIFIC EQUILIBRIUM POINTS

By forcing the ES to target specific equilibrium points, the feed-forward controller then tracks the setpoint to enforce the ES behavior to the loudspeaker. As a result, modifying the basin of attraction of the ES to raise the size of the set of initial conditions to all the set of initial conditions leads to enforcing the targeted equilibrium point.

This goal can be achieved by adding synthetic variables to the ES equation to control the basin of attraction of the solution. Three methods are considered: adding a synthetic desired displacement X^s_d, or a desired speed $\dot{X}^s_d$, or an additional external force f^s_{ext}.
The form of the synthetic added variable should be selected to force the system onto an equilibrium point, and then set to 0 in order to maintain a passive behavior of the ER.

4. NUMERICAL SIMULATION OF THE CONTROL

To demonstrate that the method allows to choose a specific equilibrium point, numerical simulations are conducted. The control is simulated with and without the added synthetic variables, and solved using a fourth order Runge-Kutta with the following control equations:

$$M_0\ddot{x}(t) + R_0\dot{x}(t) + K_0x(t) = f_{ext}(t) - Blu_d(t) \tag{2a}$$

$$u_d(t) = \frac{1}{Bl}(-M_0\ddot{x}_d(t) - R_0\dot{x}_d(t) - K_0x_d(t) + f^m_{ext}(t)) \tag{2b}$$

$$M_d\ddot{x}_d(t) + R_d\dot{x}_d(t) + K_dx_d(t) + K_d\beta x_d(t)^3 = f^m_{ext}(t) \tag{2c}$$

with $\dot{\bullet}$ corresponds to a time derivative. The parameters M_0, R_0, K_0 stand for the modal mass, damping and stiffness of the loudspeaker without electrical current, and M_d, R_d and K_d represent the desired modal mass, damping and stiffness of the ES model. The parameter β is the nonlinear constant coefficient of the cubic nonlinearity. The simulations are conducted with the parameters $M_d = M_0 = 3.89 \times 10^{-4}$ kg, $R_d = R_0/8 = 3.29 \times 10^{-2}$ kg.s^{-1}, $K_d = K_0 = 4.34 \times 10^3$ kg.s^{-2} and $\beta = 10^{10}$ m^{-2}. The excitation is chosen to be a mono-harmonic sine excitation of amplitude 1.5 Pa. The initial conditions are taken as $(x_d(0), \dot{x}_d(0)) = (0, 0)$. The sampling frequency is chosen to be 50 kHz, with a 20 seconds duration of the

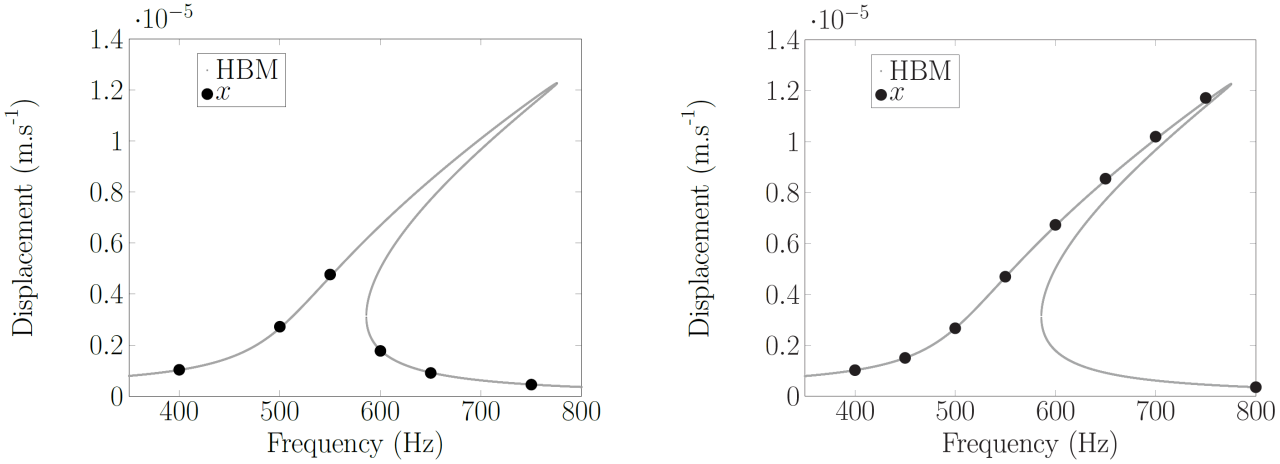


Figure 1: Comparison of the analytical solution of Eq. (1c) obtained with a Harmonic Balance Method (HBM) and the obtained equilibrium point with the numerical simulation of the control with (a) the classical control; (b) the added synthetic variables.

mono-harmonic sine excitation.
The synthetic added variable is chosen as an added external force of the form:

$$f_{ext}^{s} = 200\big(1 - \tanh(t-2)\big) \tag{3}$$

The results of the simulations are presented in Fig. 2. The obtained equilibrium point after 15 seconds of simulation is represented as a black dot. The numerical solutions are compared with a Harmonic Balance Solution (HBM) of the ES equation. One can observe in Fig. 2a that the control without the added synthetic variables targets the lower energy equilibrium point. However, with initial conditions at (0,0), and with the added synthetic variable in Fig. 2b, the control enforces the higher energy equilibrium point. It is due to the control of the basin of attraction of the ES equation with the added variable.
Numerical simulations validates the method, demonstrating its ability to drive the system towards a higher energy equilibrium point, which offers improved acoustic absorption capabilities. The results showed that without the synthetic control variable, the system naturally settled at a lower energy equilibrium point, while the added external synthetic force successfully guided the system toward the desired state.

5. CONCLUSION

In this study, we introduced a novel digital control strategy to enforce nonlinear behaviors in electroacoustic resonators for enhanced acoustic absorption. By leveraging an exosystem to generate targeted nonlinear dynamics, the feed-forward controller successfully tracks and enforces the desired equilibrium state of the loudspeaker. A key challenge of nonlinear systems, the coexistence of multiple equilibrium points with varying efficiency, was addressed by incorporating synthetic variables into the ES equation. This approach effectively reshaped the system's basin of attraction, enabling the selection of a specific equilibrium point through digital programming rather than relying on initial conditions. The proposed approach paves the way for digitally controlled nonlinear resonators with tunable properties, opening new possibilities for vibration and noise mitigation in advanced engineering systems.

6. ACKNOWLEDGMENTS

The authors thank Abdelhakim Ezzerouki for providing helpful assistance in the electronic realization of the experiment. The authors would like to thank the following organizations for supporting this research: (i) The "Ministère de la transition écologique" and (ii) LABEX CELYA (ANR-10-LABX-0060) of the "Université de

Lyon" within the program "Investissement d'Avenir" (ANR-11- IDEX-0007) operated by the French National Research Agency (ANR).

7. REFERENCES

[1] E. Rivet, S. Karkar, and H. Lissek, "Broadband low-frequency electroacoustic absorbers through hybrid sensor-/shunt-based impedance control," *IEEE Trans. Control Syst. Technol.*, vol. 25, pp. 63–72, 1 2017.

[2] E. D. Bono, M. Collet, G. Matten, S. Karkar, H. Lissek, M. Ouisse, K. Billon, T. Laurence, and M. Volery, "Effect of time delay on the impedance control of a pressure-based, current-driven electroacoustic absorber," *J. Sound. Vib.*, vol. 537, p. 117201, 10 2022.

[3] S. Karkar, E. D. Bono, M. Collet, G. Matten, M. Ouisse, and E. Rivet, "Broadband nonreciprocal acoustic propagation using programmable boundary conditions: From analytical modeling to experimental implementation," *Phys.Rev. Appl.*, vol. 12, 11 2019.

[4] X. Guo, H. Lissek, and R. Fleury, "Improving sound absorption through nonlinear active electroacoustic resonators," *Phys.Rev. Appl.*, vol. 13, 1 2020.

[5] X. Guo, H. Lissek, and R. Fleury, "Observation of non-reciprocal harmonic conversion in real sounds," *Commun. Phys.*, vol. 6, p. 93, 5 2023.

[6] E. De Bono, M. Collet, and M. Ouisse, "The advection boundary law in absence of mean flow: Passivity, nonreciprocity and enhanced noise transmission attenuation," *J. Sound. Vib.*, vol. 590, p. 118603, 2024.

[7] M. Morell, E. Gourdon, M. Collet, A. Ture Savadkoohi, E. De Bono, and C.-H. Lamarque, "Towards digitally programmed nonlinear electroacoustic resonators for low amplitude sound pressure levels: Modeling and experiments," *J. Sound. Vib.*, vol. 584, p. 118437, 2024.

[8] M. Morell, M. Collet, E. Gourdon, A. T. Savadkoohi, and E. De Bono, "Experimental validation of the analytical modelling of a digitally created duffing acoustic nonlinear oscillator at low amplitudes," *Mech. Ind.*, vol. 26, p. 2, 2025.

DOI:

Main theme: A01 Active Control of Sound and Vibration

Session A01.06 Signal processing for active control

Chair(s): M. R. Bai, W.-S. Gan

DOI: 10.61782/fa.2025.0263

FORUM ACUSTICUM EURONOISE 2025

DEEP OBSERVATION FILTER FOR VIRTUAL SENSING IN LOCAL ACTIVE NOISE CONTROL

Felix Holzmüller* **Alois Sontacchi**
Institute of Electronic Music and Acoustics
University of Music and Performing Arts Graz, Austria

ABSTRACT

Local active noise control (ANC) algorithms are often based on adaptive filters, requiring an error signal to operate. For optimal performance, this error signal should be captured at a position as close as possible to the desired point of cancellation. However, in many situations, this is not feasible without invading the listener's space. In such cases, virtual sensing algorithms such as the remote microphone technique (RMT) can be employed to estimate the signal using nearby sensors and domain knowledge. The RMT relies on filters, calculated in a training phase based on recorded scenarios. To ensure sufficient performance under varied acoustic conditions and geometrical configurations, a suitable filter set must be selected during operation from a pre-calculated database encompassing all potential scenarios. This paper proposes a novel approach for an online estimation of the observation filter in the RMT, based on a convolutional neural network. By providing correlation metrics and coordinates as input features, efficient asynchronous computation on external processing units is possible. Handling various acoustic scenarios with variable virtual error microphone position, this approach renders the use of any filter selection logic obsolete.

Keywords: *active noise control, virtual sensing, remote microphone technique, convolutional neural network, generalized cross correlation*

**Corresponding author*: *holzmueller@iem.at.*
***Copyright**: ©2025 Felix Holzmüller et al. This is an open-access article distributed under the terms of the Creative Commons Attribution 3.0 Unported License, which permits unrestricted use, distribution, and reproduction in any medium, provided the original author and source are credited.*

1. INTRODUCTION

Active noise control (ANC) is a widely used technique for noise reduction [1]. Secondary sources emit control signals that mimic the primary disturbances at a point of interest with an inverse phase. When executed properly, this approach can lead to a substantial reduction in noise through destructive interference. While global ANC approaches aim to reduce disturbances throughout the entire space, local ANC targets selected points of cancellation. The latter technique has been shown to control a larger frequency bandwidth with fewer transducers [2]. An inherent issue of local ANC is its limited spatial extent, often referred to as "zone of quiet" [3–5], which corresponds to the area where at least 10 dB noise reduction can be achieved. The extent of this region usually scales inversely with the controlled bandwidth in diffuse sound fields [3, 5]. Outside this zone of quiet, the ANC system can actually increase the sound pressure [3]. Another position-dependent issue arises when considering common ANC system architectures. Many implementations are based on adaptive filters [6–8] to compensate for slight changes in the scenario during operation. However, adaptive filters for ANC usually require the residual error signals and transfer functions between the secondary sources and the points of cancellation [1, 9]. A mismatch between the estimated and actual error signals or transfer paths can lead to a deterioration in noise reduction performance or even render the system unstable [10, 11].

As it is often not possible to place sensors at the desired points of cancellation without invading the listener's space [12], so-called *virtual sensing* techniques [13–15] are employed to estimate the signal of virtual error microphones at the points of cancellation, using signals from nearby physical microphones and domain knowledge. Due to the limited spatial extent of local ANC and the sensitivity of certain virtual sensing algorithms to changes in the

acoustic scenario [16], a large variety of filters for different situations is calculated in advance and either switched [11] or interpolated [17] during operation to account for time-variant changes.

The dependency on position and acoustic scenario spans a multivariate space, requiring a large database of precomputed filters as well as a filter-selection mechanism during operation. Recently, neural networks have been utilized to handle some of these challenges - for example for modelling secondary paths [18], selecting filters from a database with a classifier network [19], or applying physically informed neural networks for virtual sensing in simple, static acoustic scenarios [20].

We propose a method for the online estimation of the observation filter in the *remote microphone technique* (RMT) [14] with variable virtual microphone position, based on a lightweight convolutional neural network (CNN). The underlying RMT is explained in section 2 before describing the proposed approach in section 3. It is tested for different source and receiver configurations in sections 4 and 5, followed by a conclusion and outlook in section 6. Code and data are openly accessible [21].

2. REMOTE MICROPHONE TECHNIQUE

The RMT [14] is a commonly used technique for virtual sensing. It is based on the assumption that the residual noise $e[n]$ at the listener's position can be decomposed into contributions from the primary noise sources $d_e[n]$ and the control signals $u[n]$, filtered by the transfer function $G_e(z)$ between the secondary sources and the listener's position. The residual error is expressed as

$$E(z) = D_e(z) + G_e(z)U(z)\,, \tag{1}$$

with $E(z)$, $D_e(z)$, and $U(z)$ being the z-transform of $e[n]$, $d_e[n]$, and $u[n]$, respectively. For simplicity, it is assumed that only a single $d_e[n]$, $e[n]$, and $u[n]$ exist, forming an acoustic single-input-single-output system.

On the other hand, the R physical remote microphones also record a mixture $\mathbf{m}[n] = \begin{bmatrix} m_0[n] & m_1[n] & \dots & m_{R-1}[n] \end{bmatrix}^T$ of primary disturbances $\mathbf{d}_m[n] = \begin{bmatrix} d_{m,0}[n] & d_{m,1}[n] & \dots & d_{m,R-1}[n] \end{bmatrix}^T$ and control signal $u[n]$, filtered by the transfer paths $\mathbf{G}_m(z) = \begin{bmatrix} G_{m,0}(z) & G_{m,1}(z) & \dots & G_{m,R-1}(z) \end{bmatrix}^T$ between the secondary sources and remote microphones. Using these definitions, the remote microphone signals in z-domain are expressed as

$$\mathbf{M}(z) = \mathbf{D}_m(z) + \mathbf{G_m}(z)U(z)\,. \tag{2}$$

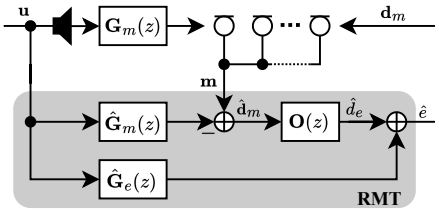


Figure 1. Block diagram of the remote microphone technique (RMT).

A block diagram of the RMT is shown in figure 1. By subtracting the filtered control signal from the remote microphone signals, the primary disturbances at the remote positions

$$\mathbf{D}_m(z) = \mathbf{M}(z) - \mathbf{G}_m(z)U(z) \tag{3}$$

can be extracted. As the actual secondary paths $\mathbf{G}_m(z)$ are usually unknown, a modelled $\hat{\mathbf{G}}_m(z)$ is used to calculate $\hat{\mathbf{D}}_m(z)$. The latter signals are then processed by a so-called *observation filter* $\mathbf{O}(z) = \begin{bmatrix} O_0(z) & O_1(z) & \dots & O_{R-1}(z) \end{bmatrix}$ to get an estimate for the primary disturbances at the virtual error microphone

$$\hat{D}_e(z) = \mathbf{O}(z)\hat{\mathbf{D}}_m(z)\,. \tag{4}$$

Finally, the control signal $U(z)$, filtered by a model for the secondary path $\hat{G}_e(z)$ to the virtual error position, is added to get an estimate for the residual error signal

$$\hat{E}(z) = \hat{D}_e(z) + \hat{G}_e(z)U(z)\,. \tag{5}$$

The secondary paths $\hat{\mathbf{G}}_m(z)$ and $\hat{G}_e(z)$ can be estimated relatively easily by measuring the transfer function between secondary loudspeakers and the remote microphones or a temporarily placed microphone at the virtual position, respectively. The observation filter is computed in a training phase using recordings of the primary disturbances at the remote and virtual microphone positions. The filters themselves are estimated for example via cross-correlations [22] or cross spectral densities (CSDs) [23] between remote and virtual error microphones, forming an inverse problem. To cover several virtual microphone positions and acoustic scenarios, different filter sets must be obtained and switched during operation [23].

In the next section, an approach to estimate the observation filter during operation using a CNN is described. The neural network is capable of estimating filter coefficients for variable virtual microphone positions as well as various primary source configurations.

3. NEURAL OBSERVATION FILTER

We propose an approach to estimate the finite impulse response (FIR) coefficients for the observation filter using a CNN. An overview of the system architecture is shown in figure 2.

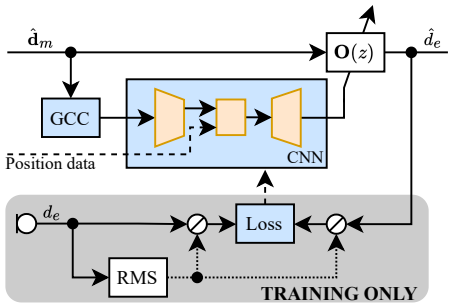


Figure 2. Architecture of the proposed deep observation filter.

3.1 Input features: GCC-PHAT

Applying a neural network to a raw audio signal is generally associated with high computational complexity [24]. As ANC with virtual sensing is often deployed on embedded and low-power hardware, we chose to pre-process the inputs by calculating the generalized cross-correlation functions (GCC) [25] between all unique combinations of remote microphones. A similar approach is commonly used in acoustic beamforming applications [26]. This approach enables us to update the observation filter coefficients asynchronously to the filter process itself.

The GCC $r_{x_1x_2}[k]$ with lag k between two signals $x_1[n]$ and $x_2[n]$ is calculated as

$$r_{x_1x_2}[k] \xleftarrow{\text{IDFT}} \psi(f) S_{x_1x_2}(f)\,, \tag{6}$$

where $S_{x_1x_2}(f)$ refers to the CSD between $x_1[n]$ and $x_2[n]$, f to a frequency index, and $\xleftarrow{\text{IDFT}}$ to an inverse discrete Fourier transform (IDFT). $\psi(f)$ is an additional frequency weighting to sharpen peaks in the GCC [25]. A widely used weighting is the so-called *phase transform* (GCC-PHAT) [25]

$$\psi_{\text{PHAT}}(f) = \frac{1}{\left|S_{x_1x_2}(f)\right|}\,. \tag{7}$$

This measure has proven to be useful in a pilot study [27] and is also applied in the here presented model. To further reduce the number of input parameters for the neural network, only the values of the GCC covering the microphone array aperture around zero lag are considered [1].

The GCC-PHAT is computed online during operation to account for time-variant changes. Let $\tilde{S}_{x_1x_2,t}(f)$ be the CSD estimated using only the signals in a current time frame t. An exponentially weighted moving average

$$\hat{S}_{x_1x_2,t}(f) = \alpha\tilde{S}_{x_1x_2,t}(f) + (1-\alpha)\hat{S}_{x_1x_2,t-1}(f) \tag{8}$$

with smoothing factor α is applied to average over a larger time scope as well as to put an emphasis on recent values in order to track time-variant changes.

Additionally, the neural network receives the Cartesian coordinates of the virtual error microphone as well. These coordinates can be obtained for example by head-tracking systems [23, 28] in real-world applications.

3.2 Model architecture

The network itself has an encoder-decoder-like architecture. In this publication, four remote microphones with an aperture of less than 30 cm are used for virtual sensing. This means, that six GCCs for the unique microphone combinations with 29 values each [2] are computed and used as input for the neural network.

The encoder consists of four sequential stages, compressing the temporal input dimension while expanding channels. Each stage comprises two 1D convolutional layers with a padding of 1. Kernel size and stride are configured to compress the temporal dimension.

The encoding stage operates independently of the virtual microphone position. To track the virtual microphone's position, the output of the encoder is flattened and concatenated with the three Cartesian coordinates before being passed to two linear layers. The output of these bottleneck layers is then reshaped and expanded again in the decoder. The latter consist, similarly to the encoder, of four stages with two transposed 1D convolutional layers each. The layer parameters are adjusted such that the output shape corresponds to 4 sets of FIR filters with 65 coefficients each. All layers use leaky ReLU activation functions. An overview of the model architecture with its parameters is provided in table 1. The CNN has in total 366.94 k parameters and requires 1.34 M operations per inference.

[1] E.g. if the maximum time-of-flight between microphones in the array corresponds to 10 samples, only the 21 central values of the GCC are used.

[2] $\left\lceil \frac{0.3\,\text{m}}{343\,\text{m/s}} \cdot 16\,000\,\text{samples/s} \right\rceil = \pm 14$ samples around zero lag

4. TRAINING

To train and assess the model, a synthetic dataset is created in pyroomacoustics [29]. Four remote microphones are positioned at the Cartesian coordinates $(0.1, 0.1, 0.1)$, $(0.1, -0.1, -0.1)$, $(-0.1, 0.1, -0.1)$, $(-0.1, -0.1, 0.1)$ m, forming as tetrahedral arrangement with an aperture of 28.3 cm. A single virtual microphone is placed near the origin of coordinates. Its exact position is randomly varied for each scene with a distance of up to 5 cm from the centre of the tetrahedron. A single primary source is positioned at a distance of 1 m with random direction of arrival in free field conditions. The source emits coloured broadband noise with a power spectral density proportional to $1/f^{\beta}$, where $\beta \in [0; 2]$ and the root mean square (RMS) level between -40 dB and -10 dB are randomly selected. All random variables are drawn from uniform distributions. In total, 50 000 scenes were generated, each lasting 10 s at a sample rate of 16 kHz and a speed of sound of $c = 343$ m/s. The dataset has been split for training and validation with an 80/20 ratio.

Table 1. Structure of the neural network, consisting of 1D convolutional (Conv1d), linear, and transposed 1D convolutional layers (ConvT1d).

Layer	Shape		Kernel	Stride	Pad
	In	Out			
Conv1d	6×29	16×29	3	1	1
Conv1d	16×29	16×14	4	2	1
Conv1d	16×14	32×14	3	1	1
Conv1d	32×14	32×7	4	2	1
Conv1d	32×7	64×7	3	1	1
Conv1d	64×7	64×3	4	2	1
Conv1d	64×3	128×3	3	1	1
Conv1d	128×3	128×3	3	1	1
Flatten	128×3	384			
Linear	384 + 3	256			
Linear	256	384			
Unflatten	384	128×3			
ConvT1d	128×3	64×9	5	3	2
ConvT1d	64×9	64×9	3	1	1
ConvT1d	64×9	32×17	3	2	1
ConvT1d	32×17	32×17	3	1	1
ConvT1d	32×17	16×33	3	2	1
ConvT1d	16×33	16×33	3	1	1
ConvT1d	16×33	4×65	3	2	1
ConvT1d	4×65	4×65	3	1	1

The network is trained by minimizing the mean squared error (MSE) loss between the predicted primary disturbances $\hat{d}_e[n]$ at the virtual microphone and the known target signal $d_e[n]$. Since the MSE is calculated in time domain, phase errors which are critical for ANC are inherently accounted for. For a level invariant loss [30], the signals are normalized by the target signal's RMS value.

The CSDs for the GCC are estimated using Welch's method [31] with a FFT size of 128, 50 % overlap and a Hann window. The GCC estimates are exponentially weighted as described in equation (5) with $\alpha = 0.01$ as all presented scenes are stationary. Given the aperture of the remote microphone arrangement, only the central 29 values of the GCCs between the six unique microphone combinations are used as input for the neural network as described in section 3.2.

The observation filter is modelled as FIR filter using the overlap-save method. For this simple anechoic scenario, a filter length of 65 taps is chosen. The overlap-save algorithm operates with a segment length of 128 samples and a stepsize of 64 samples. Coefficients are updated every 500 ms, meaning that the neural network is inferred twice per second. To enhance robustness, the network is trained to estimate past samples of the primary disturbances instead of the current ones, as seen in the *delayed RMT* [22, 32]. With a delay of 25 samples, all relevant parts of the FIR coefficients are shifted into a causal region.

The model has been trained using the Adam optimizer [33] at a learning rate of 1e−4. A weight decay of 1e−8 was applied to prevent overfitting and exceedingly large filter coefficients. Training was conducted for 1000 epochs in PyTorch with a batch size of 100, requiring approximately 16 h on a single NVIDIA GeForce RTX 3080 GPU.

5. RESULTS

The presented model is evaluated regarding the influence of position information, as well as for different primary disturbance directions and virtual microphone positions. It is assessed using a normalized mean square error (NMSE)

$$NMSE = 10\log_{10}\left(\frac{\sum_{n=0}^{\infty}\epsilon[n]^2}{\sum_{n=0}^{\infty}d_e[n]^2}\right) \tag{9}$$

as single-value broadband metric, where

$$\epsilon[n] = d_e[n] - \hat{d}_e[n]\,. \tag{10}$$

The estimation error [23]

$$E(f) = 10\log_{10}\left(\frac{S_{\epsilon\epsilon}(f)}{S_{d_e d_e}(f)}\right), \tag{11}$$

based on the power spectral densities $S_{\epsilon\epsilon}(f)$ and $S_{d_e d_e}(f)$ of $\epsilon[n]$ and $d[n]$, respectively, is used to analyse the spectral properties of the presented approach.

5.1 Availability of position data

In a first experiment, the potential improvement in estimation accuracy by providing the virtual microphone position is assessed. As mentioned in section 3.2, the position of the virtual error microphone is provided in Cartesian coordinates both during training and validation. As a baseline for comparison, the same model is validated without accurate position data by supplying only the centre coordinates of the microphone arrangement as virtual microphone position, regardless of its actual location. Additionally, another model is trained and validated entirely without valid position data as well. All experiments are performed on the same dataset.

Table 2. Mean validation NMSE in dB with standard deviation (SD) with and without provided coordinates of the virtual microphone.

Position data	NMSE in dB	
	Mean	**SD**
train+val	**-33.53**	9.90
train only	-17.67	14.35
none	-13.42	12.24

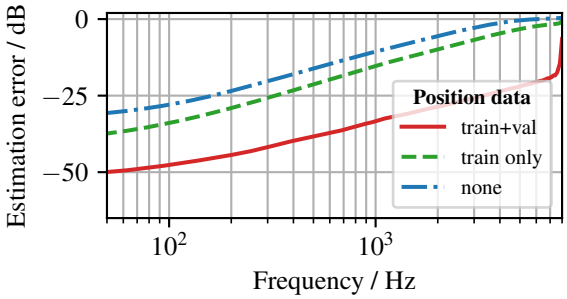


Figure 3. Validation estimation error in dB for models trained and validated with and without accurate position data of the virtual microphone.

As seen in table 2, the NMSE increases by more than 15 dB when the network is supplied with inaccurate position data during validation. This result is expected, as other authors have demonstrated that accurate tracking of the (virtual) error microphone position can significantly improve ANC performance [11, 13, 23]. If the network is even trained without position data, the mean NMSE rises further, but its variance slightly decreases. The mean estimation error in frequency domain in figure 3 can provide more insights into the model's characteristics. It performs best towards low frequencies with an estimation error around −50 dB, but still maintains less than −20 dB error even at the upper end of the assessed spectrum. The spectral tilt can be attributed to the spectral distribution of the primary disturbances during training, which emphasises low frequencies, ranging from brown to white noise. The estimation error for the conditions without accurate tracking data exhibits a constant bias across the whole assessed spectrum, indicating that accurate tracking information enhances performance even towards very low frequencies.

5.2 Virtual error position

In a second evaluation, the effect of the actual position of the virtual error microphone on estimation performance is investigated. For this analysis, the validation set is divided into five distinct subsets based on the distance r of the virtual microphone from the centre of the arrangement. Table 3 shows only a minor decline in estimation performance and a slight increase in variance as the virtual microphone moves away from the centre. The mean NMSE rises by approximately 0.5 dB to 1 dB per cm of distance from the centre. Larger deviations occur at both the start and end of

the assessed range, meaning the increase of NMSE is not strictly proportional to absolute distance.

Table 3. Mean validation NMSE in dB with standard deviation (SD) for different virtual position distance r from the tetrahedron's centre.

Range	NMSE in dB	
	Mean	**SD**
$r \in [0.0, 1.0)$ cm	**-35.02**	9.55
$r \in [1.0, 2.0)$ cm	-34.07	9.57
$r \in [2.0, 3.0)$ cm	-33.48	10.00
$r \in [3.0, 4.0)$ cm	-33.05	9.97
$r \in [4.0, 5.0)$ cm	-32.06	10.14

5.3 Primary source direction

Finally, the influence of the primary disturbance direction is examined. Two extreme cases are considered:

1. Sound arriving from the direction of a remote microphone, and
2. Sound propagating along the normal vector of the tetrahedron's surfaces.

For both cases, a tolerance margin of 10° is applied to the direction of arrival.

As table 4 shows, only minor differences in NMSE are observed depending on the primary source direction. The difference in mean NMSE is not statistically significant ($p = 0.762$) according to an independent samples t-test. This suggests that estimation performance is unaffected by the primary disturbance direction.

6. CONCLUSION

In this article, a neural network-based method for estimating the observation filter in the remote microphone technique for local active noise control has been presented. It features an encoder-decoder-like architecture implemented as a convolutional neural network.

For efficient operation, the neural network receives GCCs between all remote microphones, along with the coordinates of the virtual microphone, as input features. It computes the FIR coefficients of the observation filter, which can be used in conventional filter architectures. With

Table 4. Mean validation NMSE in dB with standard deviation (SD) for primary sources in direction of a single remote microphone or normally to the tetrahedron surfaces with 10° tolerance.

Direction	NMSE in dB	
	Mean	**SD**
mic	-34.31	9.36
surface	**-34.58**	9.62

this structure, filtering can be performed on low-latency hardware while allowing asynchronous coefficient estimation on an external (co-)processor or neural processing unit (NPU) for optimal performance.

It has been demonstrated that supplying the network with accurate position information of the virtual microphone significantly enhances estimation accuracy. The lowest NMSE is achieved when the virtual microphone is positioned near the centre of the tested arrangement, whereas NMSE only slightly increases with distance from the centre. However, no statistically significant differences dependant on the primary source direction could be observed.

In future studies, the presented model will be expanded to handle time-variant scenarios with moving virtual positions and primary disturbances. It is anticipated that recurrent architectures will yield noticeable improvements for these cases. Additionally, the model's capability to process scenarios with multiple primary sources and narrowband signals will be evaluated, especially in conjunction with an adaptive ANC algorithm to assess noise reduction performance.

7. REFERENCES

[1] S. J. Elliott, *Signal Processing for Active Control*. Signal Processing and Its Applications, Academic Press, 1 ed., 2001.

[2] J. Cheer, "Active Sound Control in the Automotive Interior," in *Future Interior Concepts* (A. Fuchs and B. Brandstätter, eds.), pp. 53–69, Cham: Springer International Publishing, 2021.

[3] S. J. Elliott, P. Joseph, A. Bullmore, and P. A. Nelson, "Active cancellation at a point in a pure tone diffuse

sound field," *J. Sound Vib.*, vol. 120, pp. 183–189, Jan. 1988.

[4] J. Garcia-Bonito, S. J. Elliott, and C. C. Boucher, "Generation of zones of quiet using a virtual microphone arrangement," *J. Acoust. Soc. Am.*, vol. 101, pp. 3498–3516, June 1997.

[5] B. Rafaely, "Zones of quiet in a broadband diffuse sound field," *J. Acoust. Soc. Am.*, vol. 110, pp. 296–302, July 2001.

[6] J. Buck and D. Sachau, "Active headrests with selective delayless subband adaptive filters in an aircraft cabin," *Mech. Syst. Signal Process.*, vol. 148, p. 107164, Feb. 2021.

[7] L. Yin, Z. Zhang, M. Wu, Z. Wang, C. Ma, S. Zhou, and J. Yang, "Adaptive parallel filter method for active cancellation of road noise inside vehicles," *Mech. Syst. Signal Process.*, vol. 193, p. 110274, June 2023.

[8] C. L. Ferrari, J. Cheer, and M. Mautone, "Investigation of an engine order noise cancellation system in a super sports car," *Acta Acust.*, vol. 7, p. 1, 2023.

[9] D. R. Morgan, "An analysis of multiple correlation cancellation loops with a filter in the auxiliary path," *IEEE Trans. Acoust., Speech, Signal Process.*, vol. 28, pp. 454–467, Aug. 1980.

[10] C. Boucher, S. J. Elliott, and P. A. Nelson, "Effect of errors in the plant model on the performance of algorithms for adaptive feedforward control," *IEE Proceedings F (Radar and Signal Processing)*, vol. 138, no. 4, p. 313, 1991.

[11] C. K. Lai, J. Cheer, and C. Shi, "The effect of head-tracking resolution on the stability and performance of a local active noise control headrest system," *J. Acoust. Soc. Am.*, vol. 157, pp. 766–777, Feb. 2025.

[12] S. K. Behera, D. P. Das, and B. Subudhi, "Head movement immune active noise control with head mounted moving microphones," *J. Acoust. Soc. Am.*, vol. 142, pp. 573–587, Aug. 2017.

[13] D. Moreau, B. Cazzolato, A. Zander, and C. Petersen, "A Review of Virtual Sensing Algorithms for Active Noise Control," *Algorithms*, vol. 1, pp. 69–99, Nov. 2008.

[14] A. Roure and A. Albarrazin, "The remote microphone technique for active noise control," in *INTER-NOISE 1999*, (Fort Lauderdale, FL, USA), pp. 1233–1244, Dec. 1999.

[15] J. Zhang, S. J. Elliott, and J. Cheer, "Robust performance of virtual sensing methods for active noise control," *Mech. Syst. Signal Process*, vol. 152, p. 107453, May 2021.

[16] S. J. Elliott, W. Jung, and J. Cheer, "Causality and Robustness in the Remote Sensing of Acoustic Pressure, with Application to Local Active Sound Control," in *ICASSP 2019*, (Brighton, United Kingdon), pp. 8484–8488, IEEE, May 2019.

[17] D. J. Moreau, *Spatially Fixed and Moving Virtual Sensing Methods for Active Noise Control*. PhD thesis, The University of Adelaide, Australia, 2010.

[18] J. Y. Oh, H. W. Jung, M. H. Lee, K. H. Lee, and Y. J. Kang, "Enhancing active noise control of road noise using deep neural network to update secondary path estimate in real time," *Mech. Syst. Signal Process.*, vol. 206, p. 110940, Jan. 2024.

[19] R. Xie, A. Tu, C. Shi, S. Elliott, H. Li, and L. Zhang, "Cognitive Virtual Sensing Technique for Feedforward Active Noise Control," in *ICASSP 2024*, (Seoul, Korea), pp. 981–985, Apr. 2024.

[20] Y. A. Zhang, F. Ma, T. Abhayapala, P. Samarasinghe, and A. Bastine, "An Active Noise Control System Based on Soundfield Interpolation Using a Physics-informed Neural Network," *arXiv:2309.106055 [eess.AS]*, Sept. 2023.

[21] F. Holzmüller and A. Sontacchi, "Deep Observation Filter - Code." `https://zenodo.org/records/15147273`, Apr. 2025.

[22] W. Jung, S. J. Elliott, and J. Cheer, "Local active control of road noise inside a vehicle," *Mech. Syst. Signal Process.*, vol. 121, pp. 144–157, Apr. 2019.

[23] W. Jung, S. J. Elliott, and J. Cheer, "Combining the remote microphone technique with head-tracking for local active sound control," *J. Acoust. Soc. Am.*, vol. 142, pp. 298–307, July 2017.

[24] H. Purwins, B. Li, T. Virtanen, J. Schlüter, S.-Y. Chang, and T. Sainath, "Deep Learning for Audio Signal Processing," *IEEE J. Sel. Top. Signal Process.*, vol. 13, pp. 206–219, May 2019.

[25] C. Knapp and G. Carter, "The generalized correlation method for estimation of time delay," *IEEE Trans. Acoust., Speech, Signal Process.*, vol. 24, pp. 320–327, Aug. 1976.

[26] X. Xiao, S. Watanabe, H. Erdogan, L. Lu, J. Hershey, M. L. Seltzer, G. Chen, Y. Zhang, M. Mandel, and D. Yu, "Deep beamforming networks for multi-channel speech recognition," in *ICASSP 2016*, (Shanghai, China), pp. 5745–5749, Mar. 2016.

[27] F. Holzmüller and A. Sontacchi, "Pilot study on virtual sensing for active noise control," in *Annual Meeting on Acosutics - DAS|DAGA 2025*, vol. 51, (Copenhagen, Denmark), Mar. 2025.

[28] Y. Liu, H. Li, H. Zou, Z. Lin, and J. Lu, "Active headrest combined with a depth camera-based ear-positioning system," *J. Acoust. Soc. Am.*, vol. 157, pp. 519–526, Jan. 2025.

[29] R. Scheibler, E. Bezzam, and I. Dokmanić, "Pyroomacoustics: A Python Package for Audio Room Simulation and Array Processing Algorithms," in *ICASSP 2018*, (Calgary, Alberta, Canada), pp. 351–355, Apr. 2018.

[30] S. Braun and I. Tashev, "Data Augmentation and Loss Normalization for Deep Noise Suppression," in *SPECOM2020*, (St. Petersburg, Russia), pp. 79–86, 2020.

[31] P. D. Welch, "The use of fast Fourier transform for the estimation of power spectra: A method based on time averaging over short, modified periodograms," *IEEE Trans. Audio and Electroacoust.*, vol. 15, no. 2, pp. 70–73, 1967.

[32] D. Treyer, S. Gaulocher, S. Germann, and E. Curiger, "Towards the implementation of the noise-cancelling office chair: Algorithms and practical aspects," in *ICSV23*, (Athens, Greece), July 2016.

[33] D. P. Kingma and J. Ba, "Adam: A Method for Stochastic Optimization," *arXiv:1412.6980 [cs]*, Jan. 2017.

DOI: 10.61782/fa.2025.0096

FORUM ACUSTICUM EURONOISE 2025

ACTIVE NOISE CONTROL WITH EXTENDED QUIET ZONES USING TIME-DOMAIN UNDERDETERMINED MULTICHANNEL INVERSE FILTERS AND KERNEL INTERPOLATION

Michael Anthony[1*] **Mingsian R. Bai**[1]
[1] Department of Electrical Engineering, National Tsing Hua University, Taiwan

ABSTRACT

This paper proposes a novel Active Noise Control (ANC) framework that exploits time-domain underdetermined multichannel inverse filters (TUMIF) with kernel-based sound field interpolation to enhance the spatial coverage of noise suppression. While TUMIF is effective in reducing noise at the measured control points, its performance degrades elsewhere, limiting its application in extended spatial regions. To solve this problem, a kernel ridge regression method is used to interpolate the Acoustic Transfer Functions (ATFs) of the secondary loudspeakers and the unmeasured control points, based on the Helmholtz equation. The interpolated control points enable the creation of extended quiet zones with a limited number of measured control points. The simulation results showed that the proposed approach achieved significant broadband noise reduction in an extended control region.

Keywords: *active noise control, sound field interpolation, kernel method.*

1. INTRODUCTION

Active Noise Control (ANC) is an effective technique for reducing unwanted noise, especially in the low frequency range, by generating anti-noise signals through secondary loudspeakers [1]. Adaptive filtering techniques, such as the widely used filtered-x least mean squares (FxLMS), handle time-varying issues but suffer from increasing computational complexity as the number of secondary loudspeakers and control points increases [1–2]. Moreover, these approaches are constrained by the overdetermined inverse filtering problem, which limits their achievable noise reduction performance. To address this, time-domain underdetermined multichannel inverse filtering (TUMIF) is introduced [3].

A major limitation of traditional ANC systems is that noise cancellation is confined to measured control points, with performance deteriorating in between these locations [4]. Broader quiet zones can be achieved by increasing the amount of measured control points. However, measuring a large number of measured control points is often impractical due to the time-consuming calibration process and physical constraints in real-world environment [5]. To overcome this challenge, the kernel ridge regression method [6] is proposed to estimate the Acoustic Transfer Functions (ATFs) at unmeasured locations, so-called interpolated control points. These interpolated control points enable broader noise suppression without requiring additional physical sensors.

In this work, we propose a novel ANC framework that integrates TUMIF with kernel interpolation to achieve spatially extended noise control. This combination enhances the noise suppression at interpolated control points while maintaining the performance at measured control points.

2. RELATED WORK

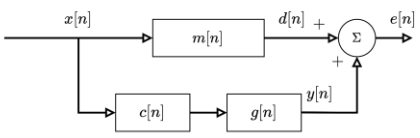


Figure 1. Block diagram of a single-channel feedforward ANC system.

[*] ***Corresponding author***: michaelzhang220@gmail.com.
Copyright: *©2025 First author et al. This is an open-access article distributed under the terms of the Creative Commons Attribution 3.0 Unported License, which permits unrestricted use, distribution, and reproduction in any medium, provided the original author and source are credited.*

Single-channel feedforward ANC system can be seen as a model-matching problem as illustrated in Fig. 1. Under the assumption that both the secondary path $g[n]$ and the controller $c[n]$ are FIR systems, their linear convolution should match the primary path $m[n]$ such that the residual error signal $e[n]$ tends to zero, with n denoting the discrete time index. Let L_p, L_s, and L_c be the impulse response length of, respectively, primary path, secondary path, and controller, the matrix form of the linear convolution relation is modeled as

$$\mathbf{G}\mathbf{c} = -\mathbf{m} \tag{1}$$

where

$$\mathbf{m} = [m[0] \quad m[1] \quad \cdots \quad m[L_p - 1]]^T \tag{2}$$

$$\mathbf{c} = [c[0] \quad c[1] \quad \cdots \quad c[L_c - 1]]^T \tag{3}$$

$$\mathbf{G} = \begin{bmatrix} g[0] & 0 & \cdots & 0 \\ g[1] & g[0] & & \vdots \\ \vdots & g[1] & \ddots & \\ g[L_s-1] & \vdots & & 0 \\ 0 & g[L_s-1] & & g[0] \\ \vdots & 0 & \ddots & g[1] \\ & \vdots & & \vdots \\ 0 & 0 & \cdots & g[L_s-1] \end{bmatrix} \tag{4}$$

Note that $L_p = L_s + L_c - 1$ and $\mathbf{G}$ is a $L_p \times L_c$ convolution matrix. The least square (LS) solution is computed as:

$$\mathbf{c}_{LS} = -\mathbf{G}^{+}\mathbf{m} = -\left(\mathbf{G}^T\mathbf{G}\right)^{-1}\mathbf{G}^T\mathbf{m} \tag{5}$$

The fact that Eqn. (1) is an overdetermined system ($L_p > L_c$) generally leads to a non-zero minimum residual error. The TUMIF approach [3] has proven effective in mitigating this problem by introducing additional secondary loudspeakers.

3. PROPOSED METHOD

The proposed method is divided into two stages: calibration stage and testing stage. At the calibration stage, the ATFs between J microphones and K secondary loudspeakers G_F are measured. ATFs at interpolated control points $\hat{G}_F$ are estimated using kernel ridge regression based on the measured one and then inverse transformed into time-domain impulse reponses (IRs). Both the interpolated and measured IRs are fed onto TUMIF to compute the coefficients of the controllers $\mathbf{c}$. The microphones are detached at the testing stage and the proposed ANC framework suppresses unwanted noise in a widened region, resulting in broader quiet zones.

3.1 Sensor interpolation using kernel method

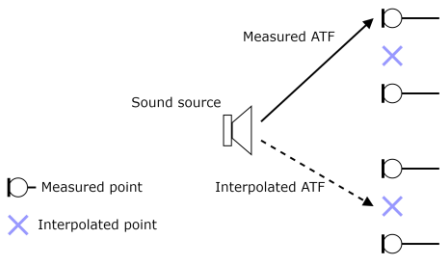


Figure 2. Block diagram of the sensor interpolation problem.

As shown in Fig. 2, kernel interpolation is utilized to estimate the ATFs in between measured control points, as written as the following optimization problem:

$$\min_{G_F} \mathfrak{I} = \sum_{j=1}^{J} \left|\hat{G}_F(\mathbf{r}_j) - G_F(\mathbf{r}_j)\right|^2 + \alpha \left\|\hat{G}_F\right\|_{\mathcal{H}}^2 \tag{6}$$

where $\hat{G}_F(\mathbf{r}_j)$ and $G_F(\mathbf{r}_j)$ are, respectively, the interpolated and measured ATFs at position vector $\mathbf{r}_j$ of the j microphone, α is the regularization parameter, and $\|\bullet\|_{\mathcal{H}}^2$ is the squared L_2-norm within the Hilbert space $\mathcal{H}$. By deriving the reproducing kernel, the solution of Eqn. (6) can be obtained as [6]

$$\hat{G}_F(\mathbf{r}) = \kappa^T(\mathbf{r})\left(\mathbf{K} + \alpha\mathbf{I}_J\right)^{-1}\mathbf{G}_F \tag{7}$$

where

$$\mathbf{K} = \begin{bmatrix} j_0\left(k\|\mathbf{r}_1 - \mathbf{r}_1\|_2\right) & \cdots & j_0\left(k\|\mathbf{r}_1 - \mathbf{r}_J\|_2\right) \\ \vdots & \ddots & \vdots \\ j_0\left(k\|\mathbf{r}_J - \mathbf{r}_1\|_2\right) & \cdots & j_0\left(k\|\mathbf{r}_J - \mathbf{r}_J\|_2\right) \end{bmatrix} \tag{8}$$

$$\kappa^T(\mathbf{r}) = \left[j_0\left(k\|\mathbf{r} - \mathbf{r}_1\|_2\right) \quad \cdots \quad j_0\left(k\|\mathbf{r} - \mathbf{r}_J\|_2\right)\right] \tag{9}$$

are the Gram matrix and kernel function, respectively, in which k is the wave number, $\mathbf{I}_J$ denotes the $J \times J$

identity matrix, $\mathbf{r}$ is position vector of the interpolated control point, and $j_0(\bullet) = \sin(\bullet)/(\bullet)$ denotes the zeroth-order spherical Bessel function, also known as the sinc function.

3.2 TUMIF

Let J_t be the total number of both interpolated and measured control points. The multichannel version of Eqn. (1) can be formulated as

$$\begin{bmatrix} \mathbf{G}_{11} & \cdots & \mathbf{G}_{1K} \\ \vdots & \ddots & \vdots \\ \mathbf{G}_{J_t 1} & \cdots & \mathbf{G}_{J_t K} \end{bmatrix} \begin{bmatrix} \mathbf{c}_1 \\ \vdots \\ \mathbf{c}_K \end{bmatrix} = \begin{bmatrix} -\mathbf{m}_1 \\ \vdots \\ -\mathbf{m}_{J_t} \end{bmatrix} \tag{10}$$

where

$$\mathbf{m}_j = [m_j[0] \quad m_j[1] \quad \cdots \quad m_j[L_p - 1]]^T \tag{11}$$

$$\mathbf{c}_k = [c_k[0] \quad c_k[1] \quad \cdots \quad c_k[L_c - 1]]^T \tag{12}$$

$$\mathbf{G}_{jk} = \begin{bmatrix} g_{jk}[0] & \cdots & 0 \\ g_{jk}[1] & & \vdots \\ \vdots & \ddots & 0 \\ g_{jk}[L_s - 1] & & g_{jk}[0] \\ 0 & \ddots & g_{jk}[1] \\ \vdots & & \vdots \\ 0 & \cdots & g_{jk}[L_s - 1] \end{bmatrix} \tag{13}$$

for $j = 1, 2, \ldots, J_t$ and $k = 1, 2, \ldots, K$.

An underdetermined system can be established if the following requirement is satisfied:

$$L_p = L_s + L_c - 1 < KL_c \tag{14}$$

or

$$L_c > \frac{L_s - 1}{K - 1} \tag{15}$$

By satisfying Eqn. (15), exact solutions that result in zero residual errors exist. It also follows that an infinite number of exact solutions exists, providing additional freedom to achieve other objectives [3]. The minimum-norm solution can be wriitten as

$$\mathbf{c}_{LS} = -\mathbf{G}^{+}\mathbf{m} = -\mathbf{G}^T\left(\mathbf{G}\mathbf{G}^T\right)^{-1}\mathbf{m} \tag{16}$$

However, the Gram matrix $\mathbf{G}^T\mathbf{G}$ may be ill-posed at some frequencies, resulting in high gain controllers. This problem can be mitigated, at some cost in model fitting performance, by using the TIKR approach [7]

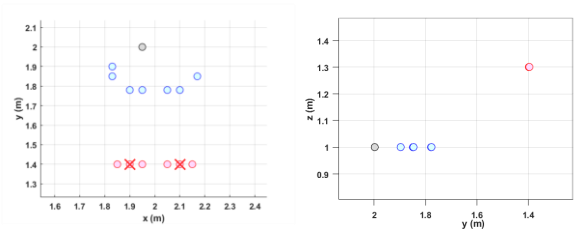
$$\mathbf{c}_{TIKR} = -\left(\mathbf{G}^T\mathbf{G} + \beta^2\mathbf{I}\right)^{-1}\mathbf{G}^T\mathbf{m} \tag{17}$$

where β is the regularization parameter.

4. SIMULATION

4.1 Simulation setup

A $4 \times 4 \times 3$ m^3 rectangular room is considered in this simulation. Fig. 3(a) illustrates the location of primary loudspeaker (grey circle), secondary loudspeakers (blue circles), measured control points (red circles), and interpolated control points (red crosses). As displayed in Fig. 3(b), the loudspeakers are located one meter above the ground and another 30 cm higher for the microphones to mimic laptop user behavior. The ATFs are generated by using Image Source Method (ISM) [8] with a reverberation time (T60) of 120 ms and white noise is used as the primary noise.



(a) (b)

Figure 3. Loudspeakers and microphones placement (a) x and y axes and (b) y and z axes.

The control points are numbered incrementally to the right starting from the first red circle on the left. The kernel interpolation parameter α and regularization parameter β are set as, respectively, 10^2 and 10^{-4}. The L_p, L_s, and L_c are configured as, respectively, 1024, 512, and 1024.

In order to verify the performance, MSNR [9] is used as the evaluation metric which is defined as

$$MSNR = 10\log_{10}\frac{\sum_{n=0}^{N}\left|d_j[n]\right|^2}{\sum_{n=0}^{N}\left|e_j[n]\right|^2} \tag{18}$$

where $d_j[n]$ and $e_j[n]$ represent the primary noise signal and and the error signal at the j-th control point. The larger the MSNR, the better the noise control performance.

4.2 Simulation results

Tab. 1 presents the MSNR values measured on each control point, comparing the performance of the proposed method with TUMIF. The combination of TUMIF and kernel interpolation achieves better performance at the unmeasured control points while maintaining its effectiveness at the measured control points. The power spectrum density (PSD) is plotted in Fig. 4, demonstrating that the proposed method controls noise more effectively than TUMIF.

Table 1. Comparison of MSNR (dB).

Control points	TUMIF	Proposed method
Measured #1	28.88	31.12
Unmeasured #2	-27.72	8.49
Measured #3	27.63	26.68
Measured #4	28.15	27.32
Unmeasured #5	-22.5	4.22
Measured #6	29.43	30.52

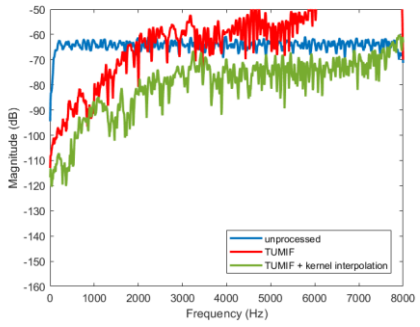


Figure 4. Power Spectrum Density (PSD) at unmeasured control point #2.

5. CONCLUSIONS

This study explored the integration of TUMIF with kernel interpolation to extend the quiet zone beyond measured control points. While TUMIF effectively suppresses noise at these points, its performance degrades at unmeasured locations. Kernel ridge regression was employed to interpolate ATFs, enabling broader noise suppression without additional physical microphones. Simulations demonstrated significant noise reduction at both measured and unmeasured control points for the proposed method, leading to an extended quiet zone. Real-time validation will be conducted in future work.

6. REFERENCES

[1] Y. Kajikawa, W.-S. Gan and S. M. Kuo, "Recent applications and challenges on active noise control," in *8th International Symp. on Image and Signal Processing and Analysis*, Trieste, Italy, 2013.

[2] P.-L. Zhong, Y.-S. Chen and M. R. Bai, "Multichannel learning-based spatially extended active noise control via model matching and sensor transfer function interpolation," in *Asia Pacific Signal and Information Processing Association Annual Summit and Conference*, Taipei, Taiwan, 2023.

[3] M. R. Bai, H.-Y. Chen, L. Yang and S.-C. Huang, "Active control of noise in a duct using the sparsely coded time-domain underdetermined multichannel inverse filters," *The Journal of the Acoustical Society of America,* vol. 146, no. 2, pp. 1371-1381, 2019.

[4] H. Ito, S. Koyama, N. Ueno and H. Saruwatari, "Feedforward spatial active noise control based on kernel interpolation of sound field," in *International Conference on Acoustics, Speech, and Signal Processing*, Brighton, UK, 2019.

[5] W.-L. Lin, Y.-S. Chen, B.-R. Lai and M. R. Bai, "Multichannel room response equalization with a broadened control region using a linearly constrained approach and sensor interpolation," *The Journal of the Acoustical Society of America,* vol. 153, no. 4, pp. 1960-1973, 2023.

[6] N. Ueno, S. Koyama and H. Saruwatari, "Kernel ridge regression with constraint of helmholtz equation for sound field interpolation," in *International Workshop on Acoustic Signal Enhancement*, Tokyo, Japan, 2018.

[7] A. N. Tikhonov, "Solution of nonlinear integral equations of the first kind," *Dokl. Akad. Nauk SSSR,* vol. 156, no. 6, pp. 1296-1299, 1964.

[8] J. B. Alley and D. A. Berkley, "Image method for efficiently simulating small-room acoustics," *The Journal of the Acoustical Society of America,* vol. 65, no. 4, pp. 943-950, 1979.

[9] D. P. Das and G. Panda, "Active mitigation of nonlinear noise processes using a novel filtered-s LMS algorithm," *IEEE Transactions on Speech and Audio Processing,* vol. 12, no. 3, pp. 313-322, 2004.

DOI: 10.61782/fa.2025.0817

FORUM ACUSTICUM EURONOISE 2025

SPATIALLY SELECTIVE ACTIVE NOISE CONTROL FOR OPEN-FITTING HEARABLES WITH ACAUSAL OPTIMIZATION

Tong Xiao* **Simon Doclo**
Department of Medical Physics and Acoustics and Cluster of Excellence Hearing4all,
Carl von Ossietzky Universität Oldenburg, Germany

ABSTRACT

Recent advances in active noise control have enabled the development of hearables with spatial selectivity, which actively suppress undesired noise while preserving desired sound from specific directions. In this work, we propose an improved approach to spatially selective active noise control that incorporates acausal relative impulse responses into the optimization process, resulting in significantly improved performance over the causal design. We evaluate the system through simulations using a pair of open-fitting hearables with spatially localized speech and noise sources in an anechoic environment. Performance is evaluated in terms of speech distortion, noise reduction, and signal-to-noise ratio improvement across different delays and degrees of acausality. Results show that the proposed acausal optimization consistently outperforms the causal approach across all metrics and scenarios, as acausal filters more effectively characterize the response of the desired source.

Keywords: active noise control, spatial selectivity, causality, beamforming

1. INTRODUCTION

Active noise control (ANC) hearables create a quiet environment by using secondary sources to generate anti-noise, which minimizes sound at specific positions when superimposed on the primary noise (leakage) [1, 2]. Based on their fit, hearables can be categorized as closed-fitting (completely occluding the ear), open-fitting (partially occluding the ear), and open-ear (no occlusion, e.g., smart glasses). Open-fitting and open-ear designs, in particular, reduce the occlusion effect and improve the physical comfort. Recent research focuses on designing intelligent ANC hearables with spatial selectivity, particularly for complex acoustic environments like cocktail-party scenarios involving multiple sound sources from different directions [3–5]. In these scenarios, listeners may wish to focus on desired sounds from a specific direction (e.g., the front) while blocking out undesired sounds from other directions.

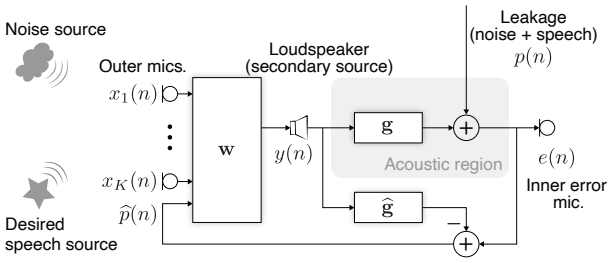


Figure 1: Block diagram of an ANC system with K outer microphones, one inner error microphone and one loudspeaker (i.e., secondary source). The control filter is denoted by $\mathbf{w}$, the secondary path is denoted by $\mathbf{g}$, and its estimate by $\widehat{\mathbf{g}}$.

Modern ANC hearables are commonly equipped with multiple microphones, i.e., microphones on the exterior of the hearable and error microphones in the interior close to the eardrum. On the one hand, conventional ANC algorithms suppress all leakage measured by the inner error microphones, including desired speech. On the other hand, multi-microphone noise reduction algorithms perform spatial filtering by reducing all noise while preserving speech from the desired direction [6–8]. However, these algorithms typically ignore the leakage and do not

*Corresponding author: Tong.Xiao@uni-oldenburg.de.
Copyright: ©2025 Tong Xiao and Simon Doclo. This is an open-access article distributed under the terms of the Creative Commons Attribution 3.0 Unported License, which permits unrestricted use, distribution, and reproduction in any medium, provided the original author and source are credited.

exploit the inner error microphones. Recent advancements have proposed integrating spatial filtering into an ANC system so that sounds from a desired direction are preserved and sounds from undesired directions are actively suppressed [9–17]. A recent study demonstrated that, when the speech component from an outer reference microphone signal is desired, a small delay is required to satisfy causality. The optimal delay is the acoustic delay between the reference microphone and the inner error microphone for the desired source [17]. These findings were derived using a system with *causal* relative impulse responses (ReIRs). However, under more flexible design constraints, *acausal* ReIRs may give a better performance.

In this paper, we present an improved approach to spatially selective ANC (SSANC) that leverages *acausal* ReIRs in the optimization process, thereby substantially improving performance over the causal optimization approach. We analyze the signal distortion, noise reduction, and signal-to-noise ratio (SNR) improvement of the inner error microphone signal when the speech component of an outer microphone signal is desired. We identify both the optimal range of delays and the optimal degree of acausality based on these evaluation metrics. These insights guide the design of a more effective SSANC for open-fitting hearables.

2. SIGNAL MODEL

As shown in Fig. 1, we consider a hearable with K outer microphones. Without loss of generality, we consider one loudspeaker as the secondary source and one inner error microphone, resulting in a total of $K+1$ microphones. We assume that the acoustic feedback paths between the loudspeaker and the outer microphones are known, such that acoustic feedback can be canceled. In addition, we assume that an estimate of the secondary path between the loudspeaker and the inner error microphone is available. Subscripts $(\cdot)_s$ and $(\cdot)_v$ denote the speech and noise components in signals, respectively.

The inner error microphone signal $e(n)$, with n the discrete time index, is given by

$$e(n) = p(n) + (\mathbf{G}\mathbf{w})^{\mathcal{T}}\mathbf{x}(n), \tag{1}$$

where $(\cdot)^{\mathcal{T}}$ denotes the transpose operator. The leakage (including noise and desired speech) at the inner error microphone is denoted by $p(n)$, and the anti-noise component at the inner error microphone is given by $(\mathbf{G}\mathbf{w})^{\mathcal{T}}\mathbf{x}(n)$, where $\mathbf{w}$ is the stacked control filter, $\mathbf{x}(n)$ is the stacked input vector, and $\mathbf{G}$ represents the secondary path convolution matrix. The stacked control filter $\mathbf{w}$ is defined as

$$\mathbf{w} = [\mathbf{w}_1^{\mathcal{T}} \quad \mathbf{w}_2^{\mathcal{T}} \quad \dots \quad \mathbf{w}_{K+1}^{\mathcal{T}}]^{\mathcal{T}} \in \mathbb{R}^{(K+1)L_w}, \tag{2a}$$

$$\mathbf{w}_k = [w_{k,0}\ w_{k,1}\ \dots\ w_{k,L_w-1}]^{\mathcal{T}} \in \mathbb{R}^{L_w}, \tag{2b}$$

where L_w denotes the control filter length for each channel. The convolution matrix of the secondary path is defined as

$$\mathbf{G} = \text{blkdiag}\,(\mathbb{G}\dots\mathbb{G}) \in \mathbb{R}^{(K+1)L\times(K+1)L_w}, \tag{3a}$$

$$\mathbb{G} = \begin{bmatrix} g_0 & \cdots & 0 \\ \vdots & \ddots & \vdots \\ g_{L_g-1} & \ddots & g_0 \\ \vdots & \ddots & \vdots \\ 0 & \cdots & g_{L_g-1} \end{bmatrix} \in \mathbb{R}^{L\times L_w}, \tag{3b}$$

where $L = L_g + L_w - 1$, and L_g denotes the secondary path filter length. As input signals to the control filter we consider the K outer microphone signals $\mathbf{x}_k(n)$, $k = 1,\dots,K$, and an estimate of the leakage $\widehat{\mathbf{p}}(n)$, i.e., the stacked input vector $\mathbf{x}(n)$ is defined as

$$\mathbf{x}(n) = [\mathbf{x}_1^{\mathcal{T}}(n)\ \dots\ \mathbf{x}_K^{\mathcal{T}}(n)\ \widehat{\mathbf{p}}^{\mathcal{T}}(n)]^{\mathcal{T}} \in \mathbb{R}^{(K+1)L}, \tag{4}$$

with

$$\mathbf{x}_k(n) = [x_k(n)\ \dots\ x_k(n-L+1)]^{\mathcal{T}}, \tag{5a}$$

$$\widehat{\mathbf{p}}(n) = [\,\widehat{p}(n)\ \dots\ \widehat{p}(n-L+1)]^{\mathcal{T}}. \tag{5b}$$

The estimated leakage $\widehat{p}(n)$ can be computed from the inner error microphone signal $e(n)$, the loudspeaker signal vector $\mathbf{y}(n) = [y(n)\dots y(n-L_g+1)]^{\mathcal{T}}$, and an estimate of the secondary path $\widehat{\mathbf{g}}$ as

$$\widehat{p}(n) = e(n) - \widehat{\mathbf{g}}^{\mathcal{T}}\mathbf{y}(n). \tag{6}$$

Assuming a perfect estimate of the secondary path to be available, i.e., $\widehat{\mathbf{g}} = \mathbf{g} = [g_0\ g_1\ \dots\ g_{L_g-1}]^{\mathcal{T}}$, the leakage can be written as $p(n) = \widehat{p}(n) = \mathbf{q}^{\mathcal{T}}\mathbf{x}(n)$, with

$$\mathbf{q} = [\mathbf{0}^{\mathcal{T}}\ \dots\ \mathbf{0}^{\mathcal{T}}\ \boldsymbol{\delta}^{\mathcal{T}}]^{\mathcal{T}} \in \mathbb{R}^{(K+1)L}, \tag{7a}$$

$$\boldsymbol{\delta} = [1\quad 0\quad \dots\quad 0\,]^{\mathcal{T}} \in \mathbb{R}^{L}. \tag{7b}$$

Hence, the inner error microphone signal in (1) can be rewritten as

$$e(n) = (\mathbf{q} + \mathbf{G}\mathbf{w})^{\mathcal{T}}\mathbf{x}(n). \tag{8}$$

Assuming that the speech and the noise components are uncorrelated, then we have

$$e_s(n) = (\mathbf{q} + \mathbf{G}\mathbf{w})^{\mathcal{T}}\mathbf{x}_s(n), \tag{9a}$$

$$e_v(n) = (\mathbf{q} + \mathbf{G}\mathbf{w})^{\mathcal{T}}\mathbf{x}_v(n). \tag{9b}$$

3. ACAUSAL OPTIMIZATION

In the SSANC system, the objective is to minimize the power of the inner error microphone signal while preserving the delayed desired speech component of an outer reference microphone signal. This can be achieved by imposing the constraint

$$e_s(n) = x_{\mathrm{ref},s}(n-\Delta). \tag{10}$$

For each channel, the speech component can be represented as the convolution of the speech component of the reference microphone signal and an acausal ReIR filter, that is,

$$x_{k,s}(n) = \sum_{l=-L_a}^{L_h-1} h_k(l)\, x_{\mathrm{ref},s}(n-l), \tag{11}$$

where the ReIR has L_a-tap anti-causal part and L_h-tap causal part. The stacked input vector for all the channels can then be written as

$$\mathbf{x}_s(n) = \mathbf{H}^{\mathcal{T}}\, \mathbf{x}_{\mathrm{ref},s}(n), \tag{12}$$

where

$$\mathbf{H} = [\mathbf{H}_1 \dots \mathbf{H}_{K+1}] \in \mathbb{R}^{(L_a+L_h+L-1)\times(K+1)L}, \tag{13a}$$

$$\mathbf{H}_k = \begin{bmatrix} h_{k,-L_a} & \cdots & 0 \\ \vdots & \ddots & \vdots \\ h_{k,L_h-1} & \ddots & 0 \\ 0 & \ddots & h_{k,-L_a} \\ \vdots & \ddots & \vdots \\ 0 & \cdots & h_{k,L_h-1} \end{bmatrix} \in \mathbb{R}^{(L_a+L_h+L-1)\times L}, \tag{13b}$$

$$\mathbf{x}_{\mathrm{ref},s}(n) = [x_{\mathrm{ref},s}(n+L_a) \dots x_{\mathrm{ref},s}(n-L_h-L+2)]^{\mathcal{T}} \in \mathbb{R}^{L_a+L_h+L-1}, \tag{13c}$$

and $\mathbf{x}_s(n) \in \mathbb{R}^{(K+1)L}$ is similarly defined as (4).

We rewrite (10) as

$$e_s(n) = \boldsymbol{\delta}_\Delta^{\mathcal{T}} \mathbf{x}_{\mathrm{ref},s}(n), \tag{14}$$

where

$$\boldsymbol{\delta}_\Delta = [\underbrace{0 \dots 0}_{L_a}\ \underbrace{0 \dots 0}_{\Delta}\ \underbrace{1\, 0 \dots 0}_{L_h+L-1-\Delta}]^{\mathcal{T}} \in \mathbb{R}^{L_a+L_h+L-1}. \tag{15}$$

Thus, using (9a), (12) and (14), we reformulate (10) as

$$\mathbf{H}(\mathbf{q}+\mathbf{G}\mathbf{w}) = \boldsymbol{\delta}_\Delta. \tag{16}$$

It is important to note that although the ReIRs, e.g., $\mathbf{H}$ and $\boldsymbol{\delta}_\Delta$, are modeled to be *acausal*, the SSANC control filter $\mathbf{w}$ for generating the anti-noise is still *causal*.

Therefore, the optimization problem for an SSANC system can be defined as

$$\underset{\mathbf{w}}{\text{minimize}} \quad \mathcal{E}\left\{e^2(n)\right\} + \beta \mathbf{w}^{\mathcal{T}}\mathbf{w} \tag{17a}$$

$$\text{subject to} \quad \mathbf{H}(\mathbf{q}+\mathbf{G}\mathbf{w}) = \boldsymbol{\delta}_\Delta, \tag{17b}$$

where $\mathcal{E}\{\cdot\}$ denotes the mathematical expectation operator. β denotes a regularization factor. The solution is found to be

$$\begin{aligned}\mathbf{w} = &-\left[\mathbf{I}-\boldsymbol{\Phi}_{\mathbf{rr}}^{-1}\mathbf{G}^{\mathcal{T}}\mathbf{H}^{\mathcal{T}}\left(\mathbf{H}\mathbf{G}\boldsymbol{\Phi}_{\mathbf{rr}}^{-1}\mathbf{G}^{\mathcal{T}}\mathbf{H}^{\mathcal{T}}+\rho\mathbf{I}\right)^{-1}\mathbf{H}\mathbf{G}\right]\boldsymbol{\Phi}_{\mathbf{rr}}^{-1}\boldsymbol{\phi} \\ &+\boldsymbol{\Phi}_{\mathbf{rr}}^{-1}\mathbf{G}^{\mathcal{T}}\mathbf{H}^{\mathcal{T}}\left(\mathbf{H}\mathbf{G}\boldsymbol{\Phi}_{\mathbf{rr}}^{-1}\mathbf{G}^{\mathcal{T}}\mathbf{H}^{\mathcal{T}}+\rho\mathbf{I}\right)^{-1}(\boldsymbol{\delta}_\Delta-\mathbf{H}\mathbf{q}),\end{aligned} \tag{18}$$

where

$$\boldsymbol{\Phi}_{\mathbf{xx}} = \mathcal{E}\left\{\mathbf{x}(n)\mathbf{x}^{\mathcal{T}}(n)\right\}, \tag{19a}$$

$$\boldsymbol{\Phi}_{\mathbf{rr}} = \mathbf{G}^{\mathcal{T}}\boldsymbol{\Phi}_{\mathbf{xx}}\mathbf{G} + \beta\mathbf{I}, \tag{19b}$$

$$\boldsymbol{\phi} = \mathbf{G}^{\mathcal{T}}\boldsymbol{\Phi}_{\mathbf{xx}}\mathbf{q}, \tag{19c}$$

and ρ denotes a small regularization factor, $\mathbf{I}$ denotes the identity matrix.

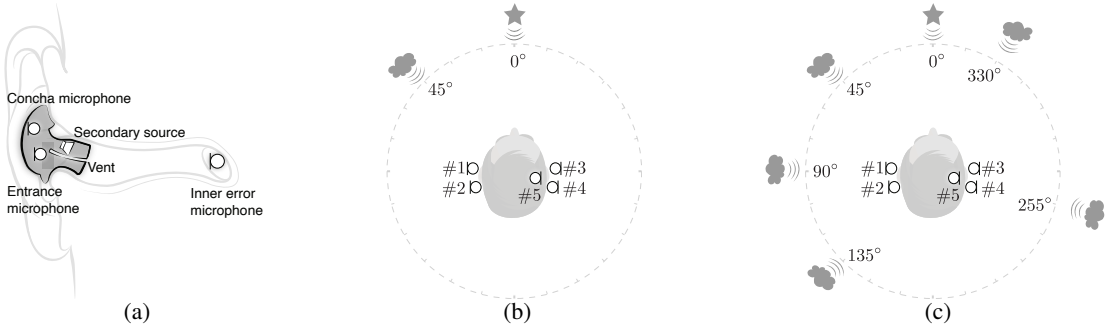
It should be noted that the solution is similar to the previous studies [15, 17]. The major difference is that the ReIR matrix $\mathbf{H}$ is acausal now containing L_a-tap anti-causal part of the ReIR for all channels. When $L_a = 0$, the solution becomes causal, as in the previous approach.

4. SIMULATIONS

4.1 Setup

For the simulation, we considered a pair of open-fitting hearables [18, 19] inserted into both ears of a GRAS 45BB-12 KEMAR Head & Torso simulator, as shown in Fig. 2(a). We used four outer microphones (entrance microphones and concha microphones at the left and right ears, labeled as #1– #4), one inner error microphone (located at the right ear, labeled as #5), and the outer receiver at the right ear as the secondary source. The inner error microphone was assumed to be at the eardrum.

Two acoustic scenarios were considered. In the first scenario, as shown in Fig. 2(b), we considered a desired speech source at 0° and an undesired speech source at 45°



(a) (b) (c)

Figure 2: (a) Illustration of the open-fitting hearable. (b) First acoustic scenario. A desired speech source is at $0°$, and one undesired speech source is at $45°$. (c) Second acoustic scenario. The desired speech source is at $0°$, and five babble noise sources are at $45°$, $90°$, $135°$, $255°$ and $330°$.

("p361_005" and "p243_018" from the VCTK dataset [20], respectively). In the second scenario, as shown in Fig. 2(c), the same desired speech source remained at $0°$, and five noise sources were placed at $45°$, $90°$, $135°$, $255°$ and $330°$ (babble noise from the NOISEX-92 database [21]). The desired speech and noise components in all microphone signals were generated by convolving source signals with measured anechoic impulse responses from the database [19]. All signals were 5 seconds in duration and sampled at 16 kHz. The desired speech and noise components were mixed such that the signal-to-noise ratio (SNR) of the leakage at the inner error microphone was set to -5 dB. In the second scenario, all noise sources contributed the same energy. As the secondary path estimate we used the measured impulse response between the outer receiver and the inner error microphone at the right ear (from [19]).

We set the filter lengths to $L_w = 600$, $L_g = 280$, and $L_h = 262$. The acausal ReIRs were computed using the least-mean-squares adaptive filter (after convergence) from microphone signals simulated with white noise at $0°$, using the entrance microphone #3 as the reference microphone. Similar to the previous studies [15, 17], we were only interested in the frequency range above 100 Hz. Therefore, a minimum-phase high-pass filter with a cut-off frequency at 100 Hz was applied to the desired signal $x_{\mathrm{ref},s}(n-\Delta)$. The effects of delay ($\Delta$) and acausality ($L_a$) on system performance were investigated.

4.2 Evaluation metrics

The following three metrics are used for evaluation. The intelligibility-weighted spectral distortion is used to assess the amount of speech distortion [9, 22, 23]. It is defined as

$$\mathrm{SD}_{\mathrm{intellig}}\,(\mathrm{dB}) = \sum_{b=1}^{B} I(\omega_b)\, 10\log_{10}\frac{\mathcal{P}_{\epsilon}(\omega_b)}{\mathcal{P}_{\mathrm{ref},s}(\omega_b)}, \quad (20)$$

where the band importance function $I(\omega_b)$ expresses the importance of the b-th one-third octave band for intelligibility [24], and B denotes the total number of bands. $\mathcal{P}_{\epsilon}(\omega_b)$ is the power spectral density of $\epsilon(n)$ in the b-th band, where $\epsilon(n) = e_s(n) - x_{\mathrm{ref},s}(n-\Delta)$. $\mathcal{P}_{\mathrm{ref},s}(\omega_b)$ is the power spectral density of $x_{\mathrm{ref},s}(n-\Delta)$ in the b-th band.

The noise reduction is defined as the difference between the power of the noise component of the leakage $p_v(n)$ (without control) and the noise component of the inner error microphone signal $e_v(n)$ (with control), i.e.,

$$\mathrm{NR}\,(\mathrm{dB}) = 10\log_{10}\sum_{n=1}^{N} p_v^2(n) - 10\log_{10}\sum_{n=1}^{N} e_v^2(n), \quad (21)$$

where N denotes the total signal length.

The SNR improvement (ΔSNR) is defined as

$$\Delta\mathrm{SNR}\,(\mathrm{dB}) = 10\log_{10}\frac{\sum_{n=1}^{N} e_s^2(n)}{\sum_{n=1}^{N} e_v^2(n)} - 10\log_{10}\frac{\sum_{n=1}^{N} p_s^2(n)}{\sum_{n=1}^{N} p_v^2(n)}. \quad (22)$$

4.3 Performance for different delays

First, we investigate the effect of delay Δ on performance. The speech distortion, the noise reduction and the SNR improvement are shown in Fig. 3 for different delays ranging from zero to 80 samples (5 ms) for the first scenario.

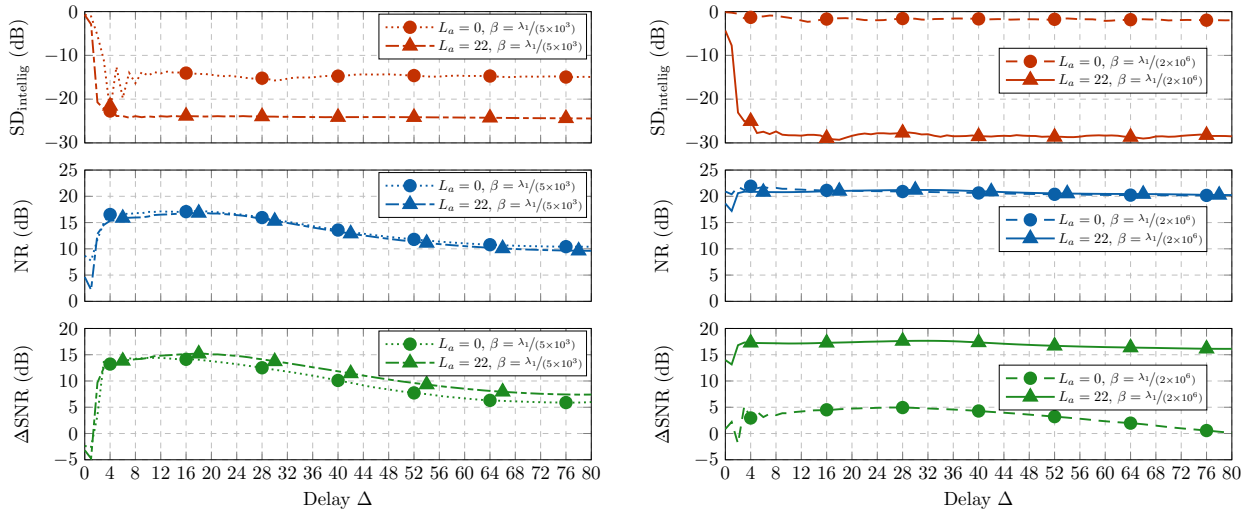


Figure 3: Speech distortion, noise reduction, and SNR improvement for the first simulation scenario for different delay Δ when (a) $L_a = 0$ and $L_a = 22$, with $\beta = \lambda_{\max}(\mathbf{G}^T\mathbf{\Phi_{xx}}\mathbf{G})/(5\times10^3) = \lambda_1/(5\times10^3)$, (b) $L_a = 0$ and $L_a = 22$, with $\beta = \lambda_1/(2\times10^6)$. In all cases, $\rho = \lambda_{\max}(\mathbf{HG}\mathbf{\Phi_{rr}}^{-1}\mathbf{G}^T\mathbf{H}^T)/(1\times10^5)$.

Four design choices are considered. When $L_a = 0$, $\beta = \lambda_{\max}(\mathbf{G}^T\mathbf{\Phi_{xx}}\mathbf{G})/(5\times10^3) = \lambda_1/(5\times10^3)$ and $\rho = \lambda_{\max}(\mathbf{HG}\mathbf{\Phi_{rr}}^{-1}\mathbf{G}^T\mathbf{H}^T)/(1\times10^5)$ as shown in Fig. 3(a), where $\lambda_{\max}(\cdot)$ denotes the largest eigenvalue, this design corresponds to the previous causal optimization [15, 17]. It can be observed that there is very high speech distortion, low noise reduction and low SNR improvement for $\Delta < 4$. This is due to the delays between the reference microphone and the inner error microphone from the desired source, which has a 4-sample delay. The causality constraint requires the delay to be at least four samples. For $4 \leq \Delta \leq 30$, the speech distortion is about -15 dB, the noise reduction has about 15–17 dB, and the SNR improvement is about 14 dB. However, further increases in delay result in degraded noise reduction, which in turn leads to reduced SNR improvement. These results agree with the previous findings.

When $L_a = 22$ with the same β and ρ as shown in Fig. 3(a), it can be observed that the speech distortion is reduced to a much lower level for $\Delta \geq 4$, reaching about -24 dB. However, the noise reduction and the SNR improvement do not show significant benefits compared to the previous results.

The main advantage of acausal optimization is its ability to achieve better performance with a smaller β value, i.e., when less constraint is imposed on the secondary source. The results are shown in Fig. 3(b) when $\beta = \lambda_1/(2\times10^6)$. In the causal case ($L_a = 0$), the system

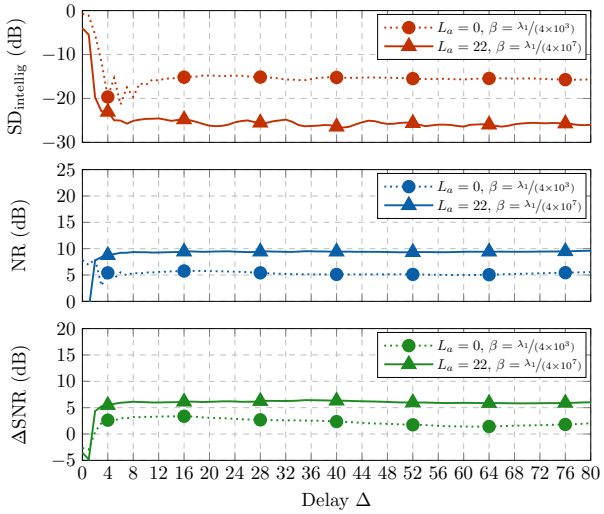


Figure 4: Speech distortion, noise reduction, and SNR improvement for the second simulation scenario for different delay Δ when $L_a = 0$, $\beta = \lambda_1/(4\times10^3)$, and when $L_a = 22$, $\beta = \lambda_1/(4\times10^7)$. In both cases, $\rho = \lambda_{\max}(\mathbf{HG}\mathbf{\Phi_{rr}}^{-1}\mathbf{G}^T\mathbf{H}^T)/(2\times10^5)$.

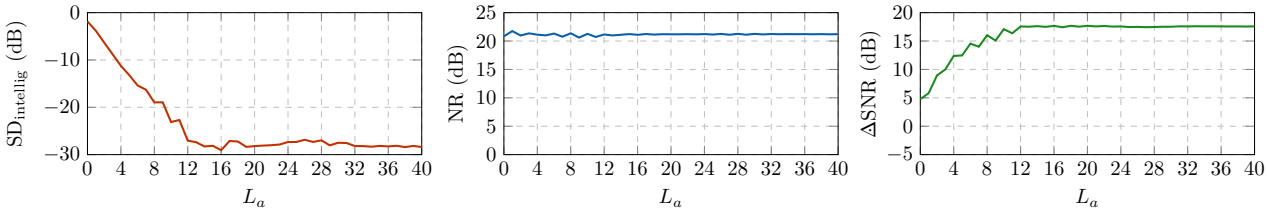


Figure 5: Speech distortion, noise reduction, and SNR improvement for the first simulation scenario for different L_a values when $\Delta = 32$, $\beta = \lambda_1/(2\times10^6)$ and $\rho = \lambda_{\max}(\mathbf{H}\mathbf{G}\mathbf{\Phi}_{\mathbf{rr}}^{-1}\mathbf{G}^{\mathcal{T}}\mathbf{H}^{\mathcal{T}})/(1\times10^5)$.

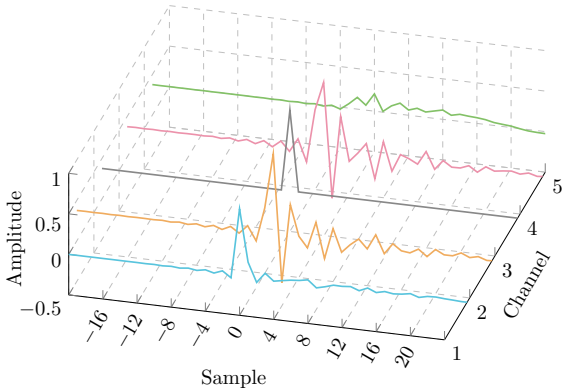


Figure 6: Acausal ReIRs for all five channels.

achieves a high level of noise reduction (21 dB), but at the cost of significant speech distortion (approximately -2 dB), resulting in an SNR improvement of just under 5 dB. In this configuration, the SSANC system fails to operate as intended and instead behaves similarly to conventional ANC, reducing both speech and noise components of the leakage. In contrast, the acausal design ($L_a = 22$) achieves much lower speech distortion (around -28 dB for most delays), maintains a similar level of noise reduction (21 dB), and delivers an SNR improvement exceeding 17 dB for most delays. Furthermore, the acausal approach yields consistent performance across varying delays, reducing the sensitivity to delay selection and thus imposing fewer constraints on the system compared to the causal design, which requires careful tuning of delay parameters.

The results for the second scenario are shown in Fig. 4. The performance reduces overall compared to the first scenario, which is expected since the scenario is much more challenging. However, the general trend remains the same. The speech distortion is reduced from about -15 dB to about -26 dB, the noise reduction increases from approximately 6 dB to around 9.5 dB, and the SNR improvement is increased from about 3 dB to about 6 dB.

4.4 Performance for different degrees of acausality

The results above show the performance for the causal design ($L_a = 0$) and one acausal design ($L_a = 22$). We now investigate the effect of different degrees of acausality, i.e., different lengths of anti-causal part L_a on performance. For this analysis, we use the first scenario and fix the delay to $\Delta = 32$ (2 ms), with $\beta = \lambda_1/(2\times10^6)$ and $\rho = \lambda_{\max}(\mathbf{H}\mathbf{G}\mathbf{\Phi}_{\mathbf{rr}}^{-1}\mathbf{G}^{\mathcal{T}}\mathbf{H}^{\mathcal{T}})/(1\times10^5)$. The results for different L_a values are shown in Fig. 5.

It can be observed that noise reduction remains consistent across all L_a values. However, speech distortion is high when L_a is small. As L_a increases, the speech distortion decreases and stabilizes when L_a reaches approximately 12. The SNR improvement follows a similar trend.

By examining the ReIRs for all five channels, as depicted in Fig. 6, it can be observed that the amplitude of the impulse responses also stabilizes around $L_a = 12$. Thus, using acausal filters to model the response from the desired source enables the SSANC system to achieve better performance than that of a purely causal design.

5. CONCLUSION

This paper has presented an improved approach to spatially selective active noise control that incorporates acausal relative impulse responses into the optimization process, leading to a substantial performance improvement over the causal optimization approach. Using a pair of open-fitting hearables in two acoustic scenarios, we demonstrated that the speech distortion under acausal optimization remains consistently lower than that of the causal optimization. Furthermore, both noise reduction and SNR improvement are significantly higher with acausal optimization. This indicates that acausal relative impulse responses offer a more accurate representation of the desired source, leading to improved noise control performance.

6. ACKNOWLEDGMENTS

This research was funded by the Deutsche Forschungsgemeinschaft (DFG, German Research Foundation) – Project-ID 352015383 – SFB 1330 C1.

7. REFERENCES

[1] S. J. Elliott, *Signal processing for active control*. Academic Press, 2000.

[2] C. Hansen, S. Snyder, X. Qiu, L. Brooks, and D. Moreau, *Active Control of Noise and Vibration*. CRC Press, 2 ed., Nov. 2012.

[3] Y. Kajikawa, W.-S. Gan, and S. M. Kuo, "Recent advances on active noise control: open issues and innovative applications," *APSIPA Transactions on Signal and Information Processing*, vol. 1, e3, pp. 1–21, 2012.

[4] C.-Y. Chang, A. Siswanto, C.-Y. Ho, T.-K. Yeh, Y.-R. Chen, and S. M. Kuo, "Listening in a noisy environment: Integration of active noise control in audio products," *IEEE Consumer Electronics Magazine*, vol. 5, no. 4, pp. 34–43, 2016.

[5] R. Gupta, J. He, R. Ranjan, W.-S. Gan, F. Klein, C. Schneiderwind, A. Neidhardt, K. Brandenburg, and V. Välimäki, "Augmented/mixed reality audio for hearables: sensing, control, and rendering," *IEEE Signal Processing Magazine*, vol. 39, no. 3, pp. 63–89, 2022.

[6] B. Van Veen and K. Buckley, "Beamforming: a versatile approach to spatial filtering," *IEEE ASSP Magazine*, vol. 5, no. 2, pp. 4–24, 1988.

[7] S. Doclo, W. Kellermann, S. Makino, and S. E. Nordholm, "Multichannel signal enhancement algorithms for assisted listening devices: Exploiting spatial diversity using multiple microphones," *IEEE Signal Processing Magazine*, vol. 32, pp. 18–30, Mar. 2015.

[8] S. Gannot, E. Vincent, S. Markovich-Golan, and A. Ozerov, "A consolidated perspective on multimicrophone speech enhancement and source separation," *IEEE/ACM Transactions on Audio, Speech, and Language Processing*, vol. 25, no. 4, pp. 692–730, 2017.

[9] R. Serizel, M. Moonen, J. Wouters, and S. H. Jensen, "Integrated active noise control and noise reduction in hearing aids," *IEEE Transactions on Audio, Speech, and Language Processing*, vol. 18, no. 6, pp. 1137–1146, 2010.

[10] R. Serizel, M. Moonen, J. Wouters, and S. H. Jensen, "Output SNR analysis of integrated active noise control and noise reduction in hearing aids under a single speech source scenario," *Signal Processing*, vol. 91, no. 8, pp. 1719–1729, 2011.

[11] D. Dalga and S. Doclo, "Combined feedforward-feedback noise reduction schemes for open-fitting hearing aids," in *Proc. IEEE Workshop on Applications of Signal Processing to Audio and Acoustics (WASPAA)*, (New Paltz, NY, USA), pp. 185–188, 2011.

[12] D. Dalga and S. Doclo, "Theoretical performance analysis of ANC-motivated noise reduction algorithms for open-fitting hearing aids," in *Proc. International Workshop on Acoustic Signal Enhancement (IWAENC)*, (Aachen, Germany), pp. 1–4, 2012.

[13] C.-Y. Ho, K.-K. Shyu, C.-Y. Chang, and S. M. Kuo, "Integrated active noise control for open-fit hearing aids with customized filter," *Applied Acoustics*, vol. 137, pp. 1–8, 2018.

[14] V. Patel, J. Cheer, and S. Fontana, "Design and implementation of an active noise control headphone with directional hear-through capability," *IEEE Transactions on Consumer Electronics*, vol. 66, pp. 32–40, Feb. 2020.

[15] T. Xiao, B. Xu, and C. Zhao, "Spatially selective active noise control systems," *The Journal of the Acoustical Society of America*, vol. 153, pp. 2733–2744, May 2023.

[16] H. Zhang, J. Zhang, F. Ma, P. N. Samarasinghe, and H. Sun, "A time-domain multi-channel directional active noise control system," in *Proc. European Signal Processing Conference (EUSIPCO)*, (Helsinki, Finland), pp. 376–380, 2023.

[17] T. Xiao and S. Doclo, "Effect of target signals and delays on spatially selective active noise control for open-fitting hearables," in *Proc. IEEE International Conference on Acoustics, Speech and Signal Processing (ICASSP)*, (Seoul, Republic of Korea), pp. 1056–1060, 2024.

[18] F. Denk, M. Lettau, H. Schepker, S. Doclo, R. Roden, M. Blau, J.-H. Bach, J. Wellmann, and B. Kollmeier, "A one-size-fits-all earpiece with multiple microphones and drivers for hearing device research," in *Proc. AES International Conference on Headphone Technology*, (San Francisco, USA), pp. 1–9, Aug. 2019.

[19] F. Denk and B. Kollmeier, "The hearpiece database of individual transfer functions of an in-the-ear earpiece for hearing device research," *Acta Acustica*, vol. 5, no. 2, pp. 1–16, 2021.

[20] C. Veaux, J. Yamagishi, and K. MacDonald, "CSTR VCTK corpus: English multi-speaker corpus for CSTR voice cloning toolkit," 2017.

[21] A. Varga and H. J. Steeneken, "Assessment for automatic speech recognition: II. NOISEX-92: A database and an experiment to study the effect of additive noise on speech recognition systems," *Speech Communication*, vol. 12, no. 3, pp. 247–251, 1993.

[22] A. Spriet, M. Moonen, and J. Wouters, "Spatially preprocessed speech distortion weighted multi-channel Wiener filtering for noise reduction," *Signal Processing*, vol. 84, no. 12, pp. 2367–2387, 2004.

[23] S. Doclo, A. Spriet, J. Wouters, and M. Moonen, "Frequency-domain criterion for the speech distortion weighted multichannel Wiener filter for robust noise reduction," *Speech Communication*, vol. 49, no. 7, pp. 636–656, 2007.

[24] Acoustical Society of America (ASA), "Methods for Calculation of the Speech Intelligibility Index," ANSI/ASA S3.5-1997 Standard, American National Standards Institute (ANSI), 1997.

DOI: 10.61782/fa.2025.0946

FORUM ACUSTICUM EURONOISE 2025

USING THE MASKING CURVE OF A MASKER SIGNAL TO APPROXIMATE THE SPECTRAL SHAPE OF A TARGET SPEECH SIGNAL*

Pierre Laffitte[1*] **Sankha Subhra Bhattacharjee**[1] **Jesper Rindom Jensen**[1]
Mads Græsbøll Christensen[1]
[1] **Audio Analysis Lab, Aalborg University, Denmark**

ABSTRACT

This work attempts to provide a novel look at speech privacy preservation, by proposing a solution based on sound masking as an alternative or a complement to traditional sound control and noise cancellation methods. We propose a framework for generating a masker signal whose masking curve approximates the spectral shape of the target speech to be masked. The approximation is done by Gradient Descent-based optimization, to minimize the distance between the magnitude spectrum of the target speech and the masker. The results show that the proposed algorithm exhibits the desired effect, reducing the measured annoyance when other metrics are kept constant. Although proper implementation in a real-world system is out of the scope of this paper, it serves to validate the theoretical background proposed here.

Keywords: *psychacoustic annoyance, signal masking, block processing, numerical optimization*

1. INTRODUCTION

Unwanted noise in open-plan offices, healthcare facilities, and residential spaces disrupts concentration, compromises confidentiality, and increases stress. Sound masking technology mitigates these effects by generating a low-level, unobtrusive background sound that conceals conversations and auditory distractions, enhancing privacy and acoustic comfort. It is widely applicable in both controlled sound zones and open acoustic spaces [1–6]. As an alternative, traditional noise control methods, such as active noise control [7, 8] and sound zone control [9, 10], though effective under optimal conditions, rely on precise reference signals or *a priori* information that are often impractical to obtain. In contrast, sound masking leverages the natural masking effect, where one sound renders another less perceptible, without requiring detailed information about the acoustic channels. While most studies evaluate the psychological impact of various fixed masking signals — such as white noise, pink noise, or speech-shaped noise [11] — few explore the creation of a masker tailored to the specific acoustic environment. This work focuses on generating a dynamic masker designed to optimize both privacy and listening comfort by adapting to the characteristics of the speech to be masked.

*__Corresponding author__: pl.laffitte@gmail.com.
__Copyright__: ©2025 Pierre Laffitte et al. This is an open-access article distributed under the terms of the Creative Commons Attribution 3.0 Unported License, which permits unrestricted use, distribution, and reproduction in any medium, provided the original author and source are credited.

2. RELATED WORK

Research on masking sounds for privacy dates back to the 1970s [12, 13]. Early approaches often relied on predefined noise types such as white, pink, babble, or speech-shaped noise [5]. Other sounds, like nature sounds [4,6] or music [6, 14], have been explored, but pink noise remains the most common. To evaluate masker efficiency, metrics like the speech transmission index (STI) [4–6, 15] and articulation index (AI) [16] are frequently used. However, we opted for the short-time objective intelligibility (STOI) [17], designed to better handle time-frequency processing. The key premise of this work is that optimal masking requires tailoring the sound to the speech being masked. While constant noisy sounds are more efficient for masking, they are less tolerable. Psychoacoustic research re-

veals that masking is a frequency-dependent phenomenon [18]. By reducing energy in spectral regions that do not contribute to masking and ensuring enough energy where it does, we can maintain masking efficiency while minimizing annoyance. The Masking Curve [18] describes a signal's masking capability across the frequency spectrum, providing a threshold dB value for each frequency that a given signal can mask. This psychoacoustic approach forms the foundation of our method, balancing intelligibility reduction and listener comfort.

3. PROBLEM FORMULATION

We aim to mask a speech signal $x(n)$ with a masker signal $y(n)$, such that the mixture $x(n) + y(n)$ is unintelligible. To avoid trivial solutions where louder maskers provide better masking, we fix the masker energy $E_y = C$, where C is a constant determined by practical considerations (e.g., desired SNR limits). Since the speech signal $x(n)$ typically has a non-flat spectrum, the masker $y(n)$ does not need uniform energy across all frequencies to effectively mask it. The total masker energy, expressed as:

$$E_y = \sum_{-f_s/2}^{f_s/2} S_{xx}(f) \tag{1}$$

can be minimized by reducing spectral components where little or no masking energy is required. Psychoacoustic research shows that the masking effect is governed by frequency and energy [18]. A masker's energy spectral density $Y(f)$ defines its masked threshold $\nu(f)$ —the minimum energy level required to mask a signal at each frequency. To create a masker $y(n)$ that matches the target speech spectral shape, we iteratively adjust $y(n)$ to minimize the distance between $X(f)$ and $\nu(f)$: This leads to the optimization problem:

$$\min_{y(n)} (\|X(f) - \nu(f)\|)^2 \tag{2}$$

where $\nu(f)$ is nonlinearly dependent on $y(n)$ [18]. To avoid intelligibility leakage, we reset the phase to zero at each frame, simplifying the problem to spectral magnitude only. A block diagram of the process is shown in Fig. 1.

4. PROPOSED METHOD

To achieve this, we choose to generate a control signal $\epsilon(n)$ and shape its spectrum by multiplying it with a

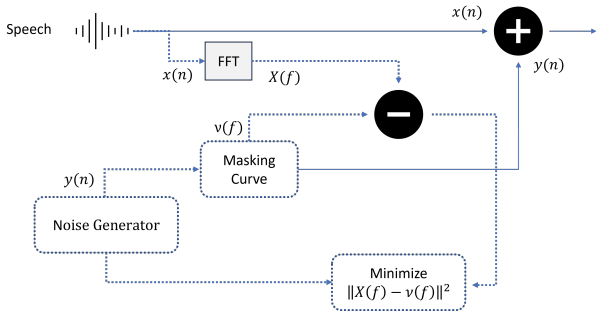


Figure 1: Optimization framework to produce a masker signal, using its masking curve to approximate the speech' spectrum. Dashed lines represents the optimization loop.

weight vector $\vec{W}$ in the frequency domain. The masking curve $\nu(f)$ then depends directly on the resulting time domain signal. The STOI and PA metrics being based on third-octave bands, we choose $\vec{W}$ to have a component along each third octave band, meaning that each filter weight represents an octave band. Our objective is to find the set of filter weights $\vec{W}$ which minimizes the distance between the target speech spectrum and the masked threshold of our masker:

$$\min_{\vec{W}} \sum_{k}^{M} (\|X_k - \nu_k\|)^2 \tag{3}$$

$\tilde{X_k}$ is the k-th third octave band amplitude of the windowed speech frame and ν_k is the masked threshold for the k-th third-octave band with M the total number of bands. When the optimization is finished, the final weight vector $\vec{W}$ is used to filter a raw masker sound, at a power determined by the pre-defined Masker to Signal Ratio (MSR).

4.1 Block processing

We use block-based processing; the target speech to be masked is windowed in the time domain, and each windowed block of signal is then analyzed in the frequency domain. The windowing process uses a classic Hanning window, e.g.,

$$\tilde{x}(x) = \omega(n)x(n) \tag{4}$$

where $\omega(n)$ is the Hanning window function, $x(n)$ the sampled input signal and $\tilde{x}(n)$ the windowed signal frame.

The Hanning window exhibits constant overlap-add property (COLA) thereby allowing reconstruction of the signal in the time-domain after frequency-domain processing [19]. Since this process is block based, each block is adjusted to the desired MSR value, resulting in a fluctuating energy, following the envelope of the input speech maskee.

4.2 Optimization

We frame the problem as an unconstrained optimization problem in which we try to minimize the error or distance between a desired variable and an estimated variable. The desired variable is defined as the speech spectrum, $X(f)$, and the estimated variable is the masking curve calculated from the produced masker, $\nu(f)$. The cost function is the l_2-norm of the difference

$$J(\mathbf{W}) = \sum_{k}^{M} (\|X_k - \nu_k\|)^2 \tag{5}$$

which for simplicity is assumed to be convex. To find a global minimum for this function, we use the gradient descent method. Since there is no closed-form solution to the derivative of our error function, we employ a numerical optimization scheme, namely the Finite Difference Method (FDM). In this method, the derivative is approximated by

$$\frac{df}{dx} = \frac{f(x+h) - f(x-h)}{2h} \tag{6}$$

following a rewriting of Taylor's first order decomposition of differentiable functions. For our cost function $J(\mathbf{W})$, this gives the following gradient computation:

$$\Delta = \frac{J(\mathbf{W} + \epsilon) - J(\mathbf{W} - \epsilon)}{2\epsilon} \tag{7}$$

The update equation for weight vector $\mathbf{W}$ is then:

$$\mathbf{W}_{i+1} = \mathbf{W}_i - l_{\text{rate}}\Delta \tag{8}$$

where l_{rate} is a hyper-parameter whose value is chosen empirically.

4.3 Smoothing filter

Once the optimal third-octave band weights are found, we design a filter whose frequency response matches these weights. Applying this filter to the raw masker sound shapes its frequency domain according to the weight values.

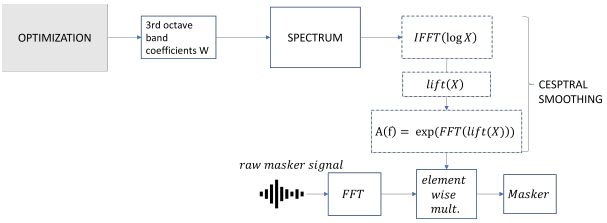


Figure 2: Cepstral windowing method used to smooth the spectrum before converting it to a filter for the raw masker sound

We call this the smoothing filter because we want to avoid a rough masking sound or one that resembles the original speech too closely, as that would compromise intelligibility. To achieve this, we transpose the weights from the third-octave basis to a linear frequency axis, take the cepstrum, and apply a "liftering" filter to retain only the slow spectral variations.

We then return to the frequency domain via the Fourier transform, taking the exponential to reverse the log transformation of the cepstrum. This produces a smoothed spectrogram, which we use to derive the filter for the raw masker sound by taking the inverse Fourier transform.

$$S(f) = \exp(FFT(w * IFFT(\log(FFT(x))))) \tag{9}$$

where w is the "lifter" (i.e. the filter), we apply to the cesptrum to only keep the first few values.

This spectral smoothing technique is called the "cepstral windowing method", for which a graphical description is given in Fig. 2 and is explained in [19].

4.4 Metrics

In this work, we rely on three metrics to evaluate the performance of our framework, which correspond to the two subjective criteria in which we are interested, namely the intelligibility of the speech and the annoyance of the noise.

4.4.1 STOI

Short-term objective intelligence (STOI) is a metric proposed to measure the objective intelligibility of a given speech signal. The subjective evaluation carried out in [17] shows that the STOI objective metric correlates with perceived annoyance. A value of STOI of 0.20 correspond

roughly to a subjective intelligibility score of less than 10%, with a correlation coefficient of 0.95. We noticed from our experimental results that the STOI function does not distinguish very well between two different maskers at low values of intelligibilities, for instance when increasing the volume of the masker. That is, the function exhibits a bit of saturation in the low range (below 0.20), while another metric such as CSII was able to make clearer distinctions between maskers. This is why we chose to also use CSII in addition to STOI.

4.4.2 CSII

Proposed to measure the intelligibility of a speech signal [20], Coherence Speech Intelligibility Index (CSII) computes speech intelligibility, by eq.(14) [20]. According to the paper's finding, a CSII value of 0.10 corresponds roughly to a subjective intelligibility score of less than 10%, with a correlation coefficient of 0.98.

4.4.3 Annoyance

We consider the Annoyance derived in [21] to measure the degree of annoyance incurred by the masker, given by:

$$PA = N_5(1 + \sqrt{\omega_S^2 + \omega_{FR}^2}) \tag{10}$$

where $\omega_S = (S - 1.75) \times 0.25 \log(N_5 + 10)$ and $\omega_{FR} = \frac{2.18}{N_5^{0.4}}(0.4F + 0.6R)$ and the following variables are defined as follows:

- N_5 relates the perceived loudness of the signal
- S is the sharpness (in acum)
- R measures the roughness (in asper)
- F measures the fluctuation strength (in vascil)

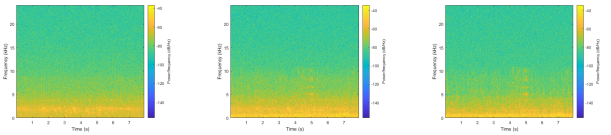
It was shown [21] that this objective annoyance metric correlates with the perceived annoyance.

4.5 Masker signal composition

It was reported in [11] that babble noise is the least annoying type of masker when compared to white noise, pink noise, and speech-shaped noise, so we decided to use it as our masker sound. Additionally, in order to add content/energy in some parts of the spectrum, we added nature sounds to complement the babble sound, which were mostly field recordings from the forest, containing sounds of a river flowing, the rain, and birds chirping. Different combinations of raw sounds were tested, using different mixing proportions, as shown in table 1. Sound a consists of nature sounds and white noise, sound b consists of nature sounds, babble sounds and white noise, sound c consists of babble sounds and white noise, while sound d (noise) was composed of white noise only.

Table 1: Proportion of the raw sounds in the different masking sounds generated and used as input to the optimization process. 'noise' denotes white noise, 'bab' stands for babble noise and 'nat' stands for nature sounds.

sound	noise	bab.1	bab.2	bab.3	nat.1	nat.2	nat.3
a (1)	0.1	0	0	0	0.5	0.5	0.5
b (6)	0.1	0.5	0.5	0.5	0.5	0.5	0.5
c (8)	0.1	0.5	0.5	0.5	0	0	0
d (noise)	1	0	0	0	0	0	0



(a) 'a' (b) 'b' (c) 'c'

Figure 3: Spectra of 'a' (left), 'b' (center), and 'c' (right)

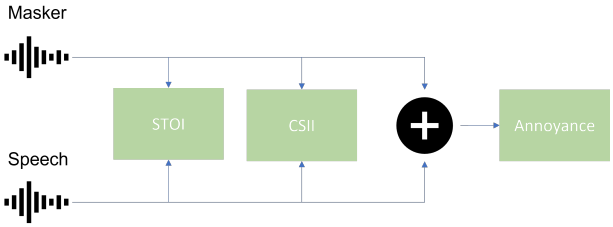


Figure 4: Experimental setup

The spectra of each of the raw masker sounds are given in fig.3; with sound 'a' at the top, sound 'b' second to top, and sound 'c' at the bottom. One can see some sonic patterns in the spectrum; at second 5, for example, between 5 kHz and 10 kHz for sounds 6 and 8. The same pattern is not visible in sound 1, however sound 'a'and sound 'b' seem to share similar content in the 1 kHz-2 kHz frequency band. Similarly, sound 'b' and 8 have similar content in the 0-1 kHz band. sound 'b' seem to be the sound sharing patterns with most other sounds, which is

confirmed by the information provided in Table1. In that sense, sound 'b' is the closest to white noise because it is the "fullest" in frequency.

5. RESULTS

This section presents the measured Intelligibility (STOI and CSII) as well as the annoyance of the masker generated by the proposed methods.

The masker and the input speech are combined to simulate the resulting acoustic signal heard in practice. Annoyance is computed on this signal, while the clean input speech and the masker are used to calculate the intelligibility metrics, as shown in Fig. 4.

All experiments were conducted with a fixed Masker to Signal Ratio (MSR) of -3 dB, meaning the masker power is adjusted at each frame according to the input speech power. This value was chosen as it produced reasonable intelligibility levels.

5.1 Hyper parameter selection

5.1.1 Window length

We tested analysis windows of 25 ms, 50 ms, 100 ms, 200 ms, and 400 ms at an MSR of -6 dB for four masker sounds (Table 1). A 100 ms window consistently provided the best balance between low annoyance and low intelligibility. At -6 dB, it produced the lowest annoyance for sounds 6 and 8, the second lowest for white noise (by only 0.3), and a mid-range value for sound 1. At -3 dB, the 100 ms window again gave competitive annoyance levels, remaining close to the lowest values across all sounds. Intelligibility variations were small at -6 dB, staying low (under 0.2 for STOI and 0.10 for CSII), except for sound 1, where the 100 ms window produced the lowest scores—both below the 10% word recognition threshold (as explained in 2). At -3 dB, the 100 ms window again yielded the lowest STOI and CSII scores for sound 1 and remained highly competitive for other sounds. These results lead us to conclude that a 100 ms window is the most suitable for our experiment.

5.1.2 Number of Cepstral Coefficients

The number of cepstral coefficients for spectral smoothing affects the signal reconstruction and thus the masker, by controlling spectrum smoothness. We tested various coefficient counts to assess their impact on intelligibility and annoyance.

Table 2: Effect of window length at MSR of -6dB.

	Sound 'a'			Sound 'b'			Sound 'c'			Noise		
Window	STOI	CSII	PA	STOI	CSII	PA	STOI	CSII	PA	STOI	CSII	PA
25ms	0.15	0.12	99.8	0.10	0.06	93.2	0.11	0.06	87.2	0.10	0.08	99.8
50ms	0.15	0.10	94.1	0.10	0.05	88.4	0.11	0.06	83.1	0.11	0.07	95.6
100ms	0.11	0.05	75.7	0.11	0.07	61.2	0.13	0.08	58.8	0.10	0.07	68.0
200ms	0.14	0.09	73.7	0.11	0.05	66.7	0.11	0.05	64.7	0.11	0.06	68.8
400ms	0.18	0.10	67.9	0.15	0.05	62.9	0.15	0.05	60.3	0.16	0.07	67.7

Table 3: Effect of window length at MSR of -3dB.

	Sound 'a'			Sound 'b'			Sound 'c'			Noise		
Window	STOI	CSII	PA	STOI	CSII	PA	STOI	CSII	PA	STOI	CSII	PA
25ms	0.27	0.45	75.0	0.16	0.13	77.8	0.17	0.13	76.6	0.21	0.36	76.5
50ms	0.18	0.18	80.4	0.16	0.12	66.2	0.16	0.12	66.4	0.18	0.26	67.5
100ms	0.14	0.10	64.8	0.15	0.12	52.1	0.18	0.17	50.6	0.15	0.14	58.1
200ms	0.17	0.14	62.6	0.14	0.09	51.7	0.15	0.08	52.6	0.15	0.11	59.5
400ms	0.24	0.14	54.9	0.25	0.19	50.4	0.24	0.14	49.8	0.23	0.21	57.6

Table 4 show the metrics for three different raw masker sounds. In most cases, intelligibility was only slightly affected, except for the CSII values for sound 'c'. The general trend is that for sounds 6 and 8, higher coefficients lead to higher intelligibility and lower annoyance. For sound 'a', intelligibility remains constant while annoyance decreases with more coefficients. In contrast, for noise, intelligibility decreases and annoyance increases with more coefficients. Based on these results, we selected 250 coefficients as a good compromise between annoyance and intelligibility.

5.2 Evaluation of the proposed optimization method

To validate our method, we evaluated its performance in different iterations to confirm that optimization improved the metrics as expected. We repeated the experiment with four masker sounds (Table1) to ensure consistency. Fig.5 shows the metric evolution for these sounds, with the origin on the x-axis representing 0 iterations (i.e., the raw masking signal as the baseline). For mixes 6, 8 and Noise, optimization decreased intelligibility (STOI and CSII), while mix 1 showed the opposite. However, annoyance decreased significantly for all cases, resulting in more agreeable maskers. This effect likely arises from the algorithm shaping the raw sound by retaining energy where speech is present and omitting regions without signal, producing a quieter and more tolerable masker. Interestingly, for three out of four sounds, the masking power diminished with optimization. We interpret this as the algorithm potentially failing to fully mask speech due to fixed window sizes or frequency-domain errors. If speech is present beyond the frame duration analyzed, it may remain un-

Table 4: Effect of the number of Cepstral coefficients on the measured metrics, at -3 dB.

N. Coef	Sound 'a'			Sound 'b'			Sound 'c'			Noise		
	STOI	CSII	PA	STOI	CSII	PA	STOI	CSII	PA	STOI	CSII	PA
16	0.14	0.12	67.7	0.15	0.12	56.8	0.18	0.17	54.9	0.17	0.22	54.8
32	0.15	0.11	66.8	0.16	0.12	57.1	0.19	0.17	54.8	0.16	0.16	56.5
64	0.14	0.11	64.7	0.16	0.14	53.2	0.20	0.21	52.3	0.15	0.12	59.3
128	0.13	0.10	65.0	0.17	0.16	52.8	0.20	0.23	51.1	0.15	0.13	58.3
256	0.13	0.10	63.1	0.18	0.18	51.2	0.21	0.28	49.3	0.15	0.13	57.9
512	0.14	0.11	60.5	0.18	0.18	50.1	0.21	0.28	48.8	0.16	0.17	56.4

masked. This suggests a weaker than expected correlation between the masking curve in [17] and the actual intelligibility: Despite producing a theoretically better masker, the algorithm did not achieve lower intelligibility as anticipated.

5.3 Evaluation against the baseline

As a baseline, we measured intelligibility and annoyance metrics for a pink noise masker, used as the control signal for our optimization framework. To ensure a fair comparison, we block-processed the pink noise masker to adjust its energy according to the maskee's power, keeping the SNR constant. Fig. fig. 6 shows the metric evolution for different SNR values. To achieve a CSII of 0.5, we need an MSR of about -2.5 dB, yielding an Annoyance of around 56. The graphs also reveal that while CSII follows SNR monotonously, STOI shows discontinuities in the low-intelligibility range, suggesting saturation. For clearer comparison, Fig. 7 places the baseline and proposed method side-by-side, showing that our method consistently achieves lower annoyance for similar intelligibility at any SNR level. This confirms that our framework produces more efficient and less annoying maskers without compromising intelligibility, a highly successful outcome.

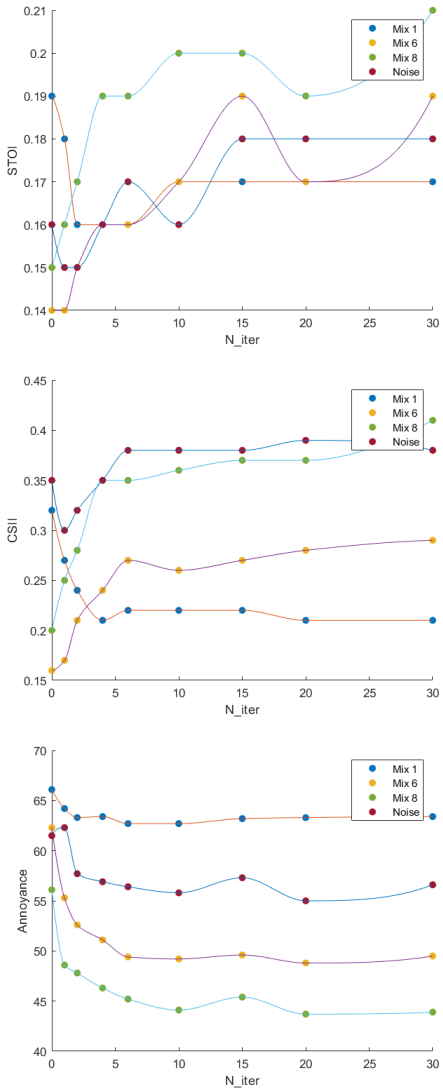


Figure 5: STOI, CSII and Annoyance metrics variation with the number of iterations, for masking sound 1

6. CONCLUSION

We have introduced a framework which optimizes the level of a masker sound at different frequency bins, in order to reduce the total energy of the masker by concentrating it only in frequency regions where it is needed. This is achieved by comparing the masking curve of the masker to the target speech maskee's spectrum, and finding a filter to shape the masker's spectrum so that the masking curve matches the maskee's spectrum. Using some intelligibility metrics as well as annoyance metrics from the literature (CSII, STOI, PA), our experimental results show that the masker signal produced by this framework exhibits lower annoyance at similar levels of intelligibility. Therefore this can find practical use in the design of masking systems for speech privacy, or at least guide the design of such systems, as used in office spaces or in cars for example.

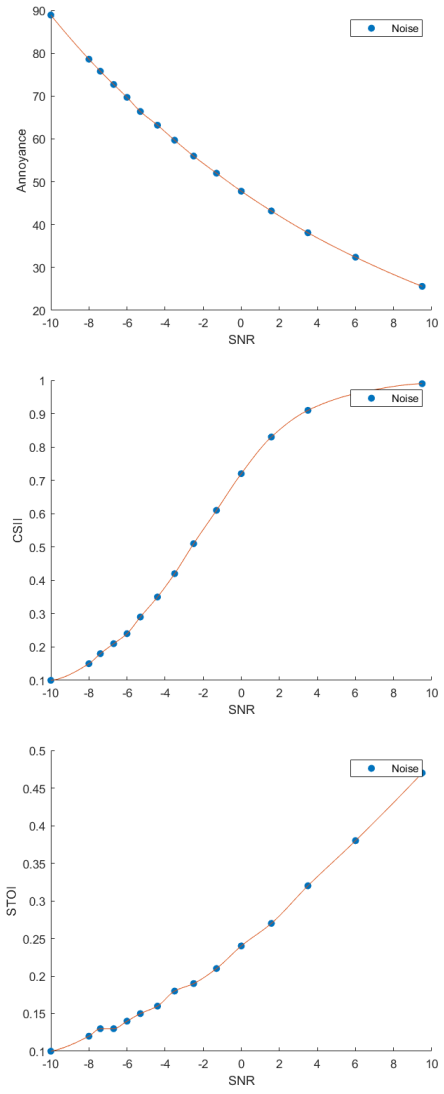


Figure 6: Evolution of STOI, CSII and Annoyance values for a pink noise masker vs. SNR.

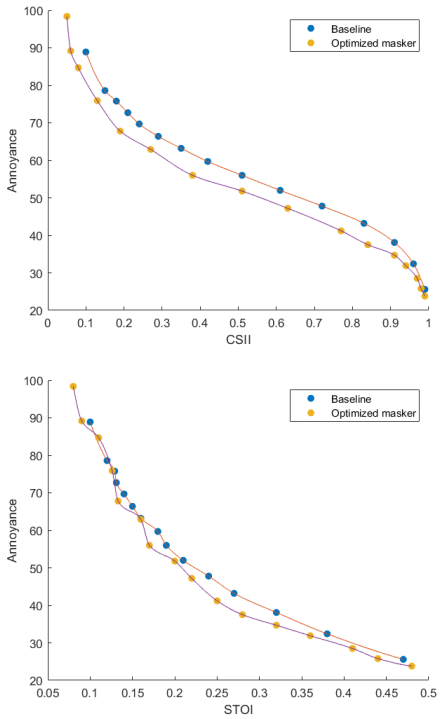


Figure 7: Comparison of baseline masker and optimized masker performance by looking at their corresponding Annoyance and SNR levels in function of CSII and STOI.

7. REFERENCES

[1] J. Donley, C. Ritz, and W. B. Kleijn, "Improving speech privacy in personal sound zones," in *2016 IEEE International Conference on Acoustics, Speech and Signal Processing (ICASSP)*, pp. 311–315, 2016.

[2] J. Donley, C. Ritz, and W. B. Kleijn, "Multizone soundfield reproduction with privacy- and quality-based speech masking filters," *IEEE/ACM Transactions on Audio, Speech, and Language Processing*, vol. 26, no. 6, pp. 1041–1055, 2018.

[3] D. Wallace and J. Cheer, "Optimisation of personal audio systems for intelligibility contrast," 05 2018.

[4] J. Carlsson, "Evaluation of masking sounds in an existing open-plan office master's thesis in the master's programme in sound and vibration," tech. rep.

[5] V. Hongisto, "Effect of sound masking on workers in an open office," tech. rep.

[6] A. Haapakangas, E. Kankkunen, V. Hongisto, P. Virjonen, D. Oliva, and E. Keskinen, "Effects of five speech masking sounds on performance and acoustic satisfaction. implications for open-plan offices," *Acta Acustica united with Acustica*, vol. 97, pp. 641–655, 7 2011.

[7] W. Zhu, L. Luo, J. Sun, and M. Christensen, "A new variable step size algorithm based hybrid active noise

control system for gaussian noise with impulsive interference," in *2020 IEEE 6th International Conference on Computer and Communications, ICCC 2020*, (United States), pp. 1072–1076, IEEE, Dec. 2020. Publisher Copyright: © 2020 IEEE.; 6th IEEE International Conference on Computer and Communications, ICCC 2020 ; Conference date: 11-12-2020 Through 14-12-2020.

[8] R. Serizel, M. Moonen, J. Wouters, and S. Jensen, "A speech distortion weighting based approach to integrated active noise control and noise reduction in hearing aids," *Signal Processing*, vol. 93, p. 2440–2452, Sept. 2013.

[9] S. Bhattacharjee, L. Shi, G. Ping, X. Shen, and M. Christensen, "Study and design of robust personal sound zones with vast using low rank rirs," in *International Conference on Acoustics, Speech, and Signal Processing*, (United States), IEEE Signal Processing Society, May 2023.

[10] T. Lee, L. Shi, J. Nielsen, and M. Christensen, "Fast generation of sound zones using variable span trade-off filters in the dft-domain," *IEEE/ACM Transactions on Audio, Speech, and Language Processing*, vol. 29, pp. 363–378, 2021.

[11] D. Wallace, "Practical audio system design for private speech reproduction thesis for the degree of doctor of philosophy," tech. rep., 2020.

[12] R. Waller, "Office acoustics—effect of background noise," *Applied Acoustics*, vol. 2, no. 2, pp. 121–130, 1969.

[13] A. C. C. Warnock, "Acoustical privacy in the landscaped office," *Journal of the Acoustical Society of America*, vol. 53, pp. 1535–1543, 1973.

[14] S. J. Schlittmeier and J. Hellbrück, "Background music as noise abatement in open-plan offices: A laboratory study on performance effects and subjective preferences," *Applied Cognitive Psychology*, vol. 23, pp. 684–697, 2009.

[15] Y. Zhang, D. Ou, and S. Kang, "The effects of masking sound and signal-to-noise ratio on work performance in chinese open-plan offices," *Applied Acoustics*, vol. 172, 1 2021.

[16] F. Zarei, J. Lee, R. Mackenzie, and V. L. Men, "Evaluation of the uniformity of sound-masking systems in an open-plan office," *Applied Acoustics*, vol. 186, 1 2022.

[17] C. Taal, R. Hendriks, R. Heusdens, and J. Jensen, "A short-time objective intelligibility measure for time-frequency weighted noisy speech," *ICASSP, IEEE International Conference on Acoustics, Speech and Signal Processing - Proceedings*, pp. 4214 – 4217, 04 2010.

[18] S. V. D. Par, A. Kohlrausch, R. Heusdens, J. Jensen, and S. H. Jensen, "A perceptual model for sinusoidal audio coding based on spectral integration," *Eurasip Journal on Applied Signal Processing*, vol. 2005, pp. 1292–1304, 6 2005.

[19] J. O. Smith, *Spectral Audio Signal Processing*. `http`:http://ccrma.stanford.edu/ jos/sasp//–`ccrma.stanford.edu/~jos/sasp/`, accessed 2023. online book, 2011 edition.

[20] J. M. Kates and K. H. Arehart, "Coherence and the speech intelligibility index," *The Journal of the Acoustical Society of America*, vol. 117, pp. 2224–2237, 4 2005.

[21] U. Widmann, "A psychoacoustic annoyance concept for application in sound quality," *The Journal of the Acoustical Society of America*, vol. 101, pp. 3078–3078, 05 1997.

DOI:

Main theme: A01 Active Control of Sound and Vibration

Session A01.07/A08.06 Innovative noise barriers to enhance acoustic comfort

Chair(s): M. Pawelczyk, J. Kang, A. González, S. Wrona, M. Ferrer

DOI: 10.61782/fa.2025.0295

FORUM ACUSTICUM EURONOISE 2025

DEVELOPMENT OF ANC SECONDARY SOURCE WALL ARRAYS ASSISTING WITH NOISE BARRIERS

Youngmin Kwon[1*] **Seongmo Jung**[1] **Hyounsuk Kim**[2] **Jonggyu Kang**[2]

[1] SAMSUNG C&T, Seoul, S. Korea
[2] ARE Inc., Daejeon, S. Korea

ABSTRACT

Outdoor noise outstanding at the boundaries of residential areas are perceived disagreeably and therefore managed strictly in accordance with the national or local noise ordinances. In many cases around high density urban areas, large scale solid noise barriers along residential boundaries are to intervene to lessen noise pollution downstream of road traffic, industrial facilities, or in particular, construction sites. Noise barriers are also required for power plants whose noise sources present across a broad site of plant facilities, even though they reside in suburban or low density remote areas. This study explored active noise control (ANC) against propagation of such environmental noise pollution and a way to shorten height and/or length of or even entirely replace desired physical noise barriers. A total of 4 arrays of anti-phase signal generating secondary sources in 6 test cases atop or around a 3-meter high temporary noise barrier were designed and investigated. Up to 12 secondary sources were engaged in those arrays. Noise reduction performance of their ANC schemes was evaluated at 8 locations along a distance of 20m. Multi-row arrays either on top of or lay on the barrier was found best among others. Their performance attained up to 5.6dB reduction on average.

Keywords: *active noise control, active noise reduction, active noise barrier, active wall array, environmental noise*

[*] ***Corresponding author***: *iam0min.kwon@samsung.com*
Copyright: *©2025 First author et al. This is an open-access article distributed under the terms of the Creative Commons Attribution 3.0 Unported License, which permits unrestricted use, distribution, and reproduction in any medium, provided the original author and source are credited.*

1. INTRODUCTION

The outdoor noise mitigation measures typically applicable for environmental noise, which originates particularly in road traffic or construction sites, as well as for industrial noise call into question their effectiveness against noise propagation in the urban context. Such measures include noise barrier walls and temporary barrier panels. The noise barrier walls can be effective only on a massive solid scale. The temporary barrier panels that are commonly set up along the perimeter of a construction site in S. Korea are made of either galvanized iron within 1mm thick or recycled plastic. Two main purposes of those panels are 1) to reduce construction noise getting through; and 2) to screen the construction site from the view outside. However, the former is in fact not very practical due to their thin profile, causing lacking in sound insulation performance.

Noise barrier walls along the main roads and busy thoroughfares that are adjacent to a dense residential area are not unusual in S. Korea. Those barrier walls are employed profusely and erected higher than 10m oftentimes for high-rise residential buildings against roadway noise. If those barrier walls required to be higher than 10m, then their foundation structure shall be reinforced, increasing in construction cost. Such massive barrier walls whether transparent or not bring about many other issues: limited views and daylight at the lower floors of residential buildings; impeded air circulation across residential areas; and bird collisions. In some cases, tuned acoustic resonators are placed on top of the barrier walls to reduce diffraction of sound traveling around, escalating construction cost.

This study pioneered an active noise control (ANC) method to assist with such noise barrier walls or panels by attenuating sound waves traveling over and at the same time possibly weakening sound transmission passing through them. Eventually, it can be expected to scale down or replace a barrier structure entirely.

2. DEVELOPMENT OF ACTIVE WALL ARRAYS

Multi-row arrays of 8 to 12 anti-phase signal generating secondary sources (loudspeakers) were studied in close collaboration with the existing temporary barrier panels. Acoustic sample data acquisition and secondary path modeling were conducted to estimate the acoustic characteristics and behavior of outdoor sound propagation around the barrier panels. Based on this modeling, 4 arrays were designed atop or either side of the barrier panels and their active noise reduction performance was investigated.

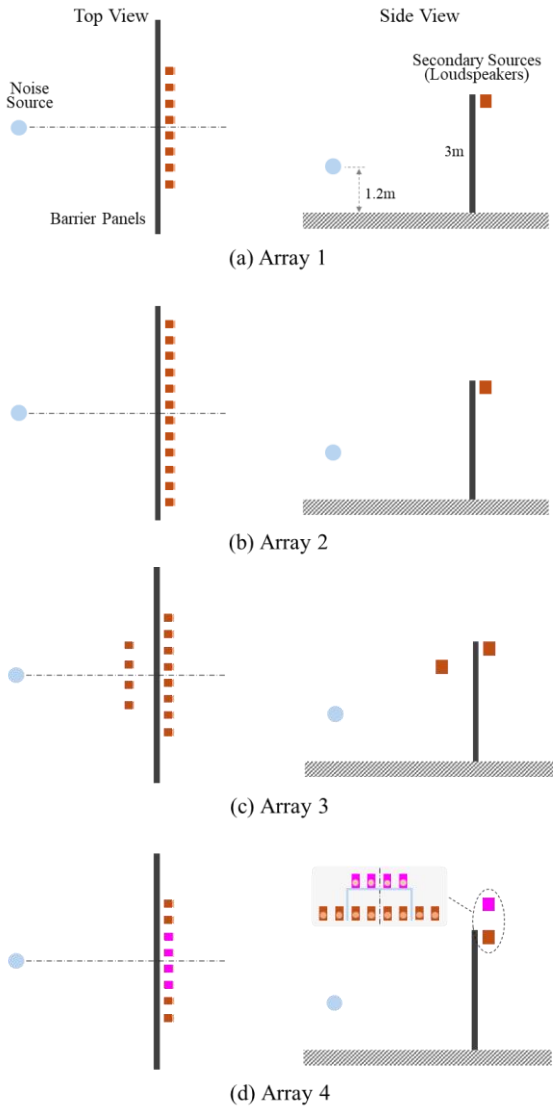


Figure 1. Active secondary source wall arrays.

Arrays 1 and 2 aligned the secondary sources along the other topside of the barrier panels against the noise source. While Array 1 accommodated 8 secondary sources, Array 2 did 12 ones. Array 3 aligned 8 secondary sources as same as Array 1 but with 4 other ones on the barrier panels facing the noise source. Array 4 employed 2 rows with 12 secondary sources on top of the barrier panels: 8 ones at the lower row and 4 ones at the upper row. See Fig. 1.

3. TEST SETTINGS AND PROCESS

3.1 Test site

The designed active secondary source wall arrays were tested at an inactive construction site, which has been no ground breaking, under free-field conditions. The site is surrounded at its boundary by 3-meter high temporary barrier panels that are made of recycled plastic. They are two-layer sandwich panels with an air cavity in a total thickness of 35mm. Each layer is 2mm thick and their sound transmission loss is unknown. See Fig. 2 and Fig.3..

3.2 Noise source

A dodecahedron omni-directional loudspeaker was used as a single point noise source. The test signal was white noise, which is a random continuous noise type that contains broadband spectrum. The noise source was set up at 1.2m high above ground and 3.5m from the barrier panels with a sound pressure level of 100dB as measured at 1m away.

3.3 Microphone settings

A number of microphones were employed for different purposes. They were assigned as reference microphones; error microphones; and observation microphones. Error microphones were designated as physical ones and virtual ones. In due course, the former remain for good with their original purpose, whereas the latter are to be removed upon tuning of a designed active noise control scheme.

A reference microphone (RM) was placed between the noise source and the secondary sources to pick up incoming signals from the noise source. Physical error microphones (PMs) were placed at the other side of the barrier panels to pick up the residual signals and increase their correlations with those at the virtual error microphones. On the other hand, virtual error microphones (VMs) were placed away in the designated active noise controlled zone or so-called quiet zone to fine-tune the perceived signals in line with those signals at the PMs. Plus, 8 observation microphones (OMs) were placed in a row at 1.6m intervals within the farthest distance of 20m for acoustic measurements.

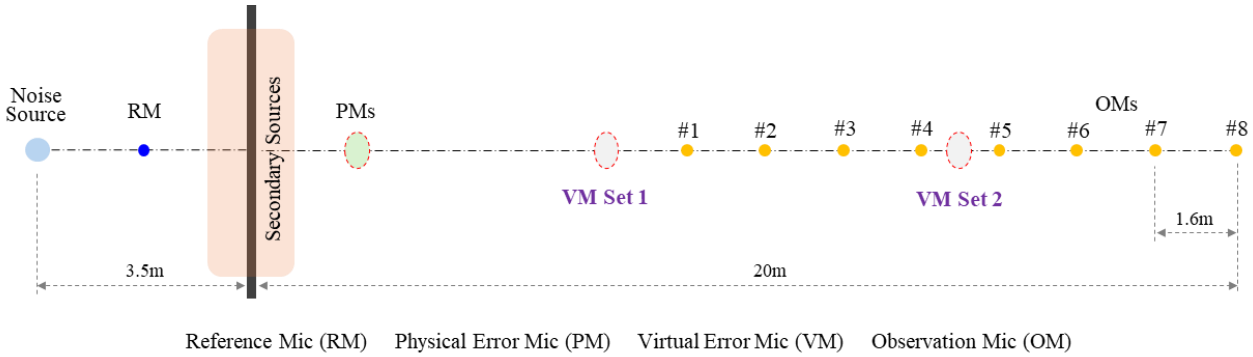


Figure 2. ANC test equipment setup plan (not to scale).



(a) At sound source side (b) At receiver side

Figure 3. ANC test setup example: Array 3.

3.4 Test method and process

A set of virtual error microphones (VMs) was placed either ahead or in the middle of the observation microphones (OMs). A total of 6 cases were tested and evaluated in combination with 4 designed active secondary source wall arrays and with those 2 locations of the VM set. Arrays 1 and 2 were evaluated only with the VM set located ahead and in the middle of the OMs respectively. Arrays 3 and 4 were done with the VM set at both locations.

Acoustic measurements of frequency-domain spectral responses up to 1kHz were carried out to evaluate noise reduction performance of the designed active secondary source wall arrays. Two measurement sets were taken for each array: one without and the other with an adaptive active noise control scheme up and running. In addition, a background noise measurement was taken for each array to review any eccentric acoustic events that might occur at the time of testing. Finally, noise reductions in dB were computed on the basis of the acoustic data obtained from the OMs.

4. TEST RESULTS

Spectral analyses were carried out across the frequency range of 30Hz through 500Hz where ANC filtering was applied. Noise reductions were computed from these analyses on the acoustic data obtained at each of the OMs and their performance by distance was examined within the designated active noise controlled zone. In addition, noise reductions of both all of 8 OMs and the last 3 OMs were tabulated on average and compared with each other. See Tab. 1.

Table 1. Summary of noise reductions on average.

Arrays	Test Cases	VM Locations		Average Reductions (dB)	
		Set 1	Set 2	Overall	End 3 OMs
1	1	●		3.0	1.6
2	2		●	4.8	5.1
3	3-1	●		4.2	3.0
	3-2		●	5.3	5.3
4	4-1	●		5.3	3.4
	4-2		●	5.6	4.6

Among the frequency range of interest, noise reduction performance was beginning to take effect from about 130Hz and it was effective up to 500Hz. Note that the designed ANC scheme performed ably between 200Hz and 450Hz but did not perform well at the lower frequencies than 130Hz. See Fig. 4. This noise reduction performance was observed broadly from most of the test cases coupled with those active secondary source wall arrays.

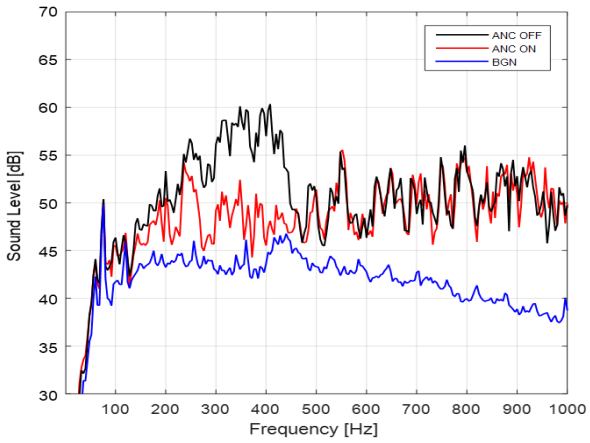


Figure 4. Spectral responses measured at the OM #6 from Test Case 3-2 with Array 3.

According to the test results of noise reduction by the active secondary source wall arrays, it is obvious that the more secondary sources are employed, the better noise reduction performance is achieved. The noise reductions of Arrays 2 through 4 which were with 12 secondary sources were 2 or 3dB higher than that of Array 1 which was with 8 ones. It appears that diffraction effect of sound decreases as the coverage by secondary sources widens either vertically or horizontally.

Next, it was found that the noise reduction performance improves as the virtual error microphones are set farther back in the active noise controlled zone. Among Arrays 3 and 4, Test Cases 3-2 and 4-2 that employed the VM Set 2 made 1 to 2dB or even more reductions than Test Cases 3-1 and 4-1 that employed the VM Set 1 except for the OMs at #1 and #2, which were the closest to VM Set 1. See Fig. 5

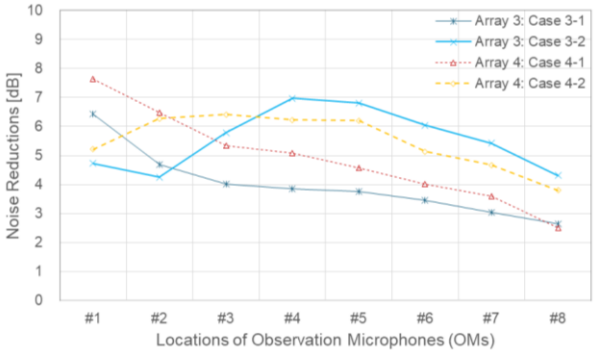


Figure 5. Noise reductions of Arrays 3 and 4 across the OMs by distance

Lastly, the noise reduction performance of Array 3 was comparable to that of either Array 2 or Array 4. Although the number of secondary sources was rather small, those residing at the sound source side of the barrier panels would come into play as the first line of active noise control directly on sound propagation from the noise source.

To summarize, for the cases of Arrays 2 through 4 tested with the VM Set 2, the overall noise reductions averaged from all of 8 OMs were 4.8, 5.3 and 5.6dB respectively and the noise reductions averaged from the last 3 OMs were 5.1, 5.3 and 4.6dB respectively.

5. CONCLUSION

The average noise reductions made by each of the active secondary source wall arrays, Arrays 2 through 4, that were equally with 12 secondary sources and tested with the VM Set 2 were shown comparable to each other in this study. Based on the overall noise reductions resulted from all of 8 measurement locations, the noise reduction performance of Array 4 appeared to be only marginally better than others. On the other hand, that of Array 3 was slightly higher if only the last 3 measurement locations were taken into account. However, it should not be suggested that Array 2 is to be considered least.

It is obvious that noise reduction performance becomes more effective as the virtual error microphones are placed as farther away from the noise source or the barrier panels back in the designated active noise controlled zone where the actual receivers reside to perceive the resulted sound. In addition, it should be noted that a set of the secondary sources accommodated near to the sound source can be of an initial role in noise reduction performance.

6. REFERENCES

[1] R. Javahersaz, S. Mohamady, and A. Montazeri, "Recent technological advances in spatial active noise control systems," in *Proc. of the 51st International Congress and Exposition in Noise Control Engineering (Inter-noise)*, (Glasgow, Scotland), 2022.

[2] S. M. Kuo and D. R. Morgan, "Active noise control: a tutorial review," in *Proc. of the IEEE*, vol 87, no. 6, pp. 943-973, 1999.

[3] Z. Han, M. Wu, Q. Zhu, and J. Yang, " Three-dimentional wave-domain acoustic contrast control using a circular loudspeaker array," *Journal of Acoust. Soc. Am.*, vol 145, no. 6, pp. EL488-493, 2019.

[4] X. Tang, J. Zhang, and T. D. Abhayapala, "Active noise control over multiple zones: adaptive algorithm in time domain," *Proc. of Asia-Pacific Signal and Information Processing Association Annual Summit and Conference (APSIPA ASC)*, (Auckland, New Zealand), pp. 288-292, 2020.

[5] B. Lam, W. Gan, D. Shi, M. Nishimura, and S. Elliott, "Ten questions concerning active noise control in the built environment," *Building and Environment*, vol 200, p. 107928, 2021.

[6] J. Tao, X. Qiu, and J. Pan, "Control of transformer noise using an independent planar virtual sound barrier," in *Proc. of Acoustics 2015*, (Hunter Valley, Australia), 2015.

[7] L. Zhang, J. Tao, and X. Qiu, "Performance analysis of decentralized multi-channel feedback systems for active noise control in free space," *Applied Acoustics*, vol 74, pp. 181-188, 2013.

[8] E. Leboucher, P. Micheau, A. Berry, and A. L'Esperance, "A stability analysis of a decentralized adaptive feedback active control system of sinusoidal sound in free space," *Journal of Acoust. Soc. Am.*, vol 111, no. 1, pp. 189-199, 2002.

DOI: 10.61782/fa.2025.0337

FORUM ACUSTICUM EURONOISE 2025

EMERGENCE OF INDOOR SOUNDSCAPE STUDIES FOCUSING ON NOISE MITIGATION: A BIBLIOMETRIC REVIEW

Zulfi Rachman[1*] **Francesco Aletta**[1] **Jian Kang**[1]
[1] UCL Institute for Environmental Design and Engineering, The Bartlett, University College London (UCL), Central House, 14 Upper Woburn Place, London WC1H 0NN, United Kingdom

ABSTRACT

Soundscape methodologies are increasingly recognised as effective approaches to address noise-related challenges. This study presents a bibliometric analysis of soundscape research focusing on the emerging domain of indoor soundscapes. Data were retrieved from the Scopus database using the keywords: "noise" AND ("noise barrier*" OR "noise control*" OR "noise reduction") AND "soundscape". After applying inclusion and exclusion criteria, 188 documents were selected for analysis, which included trend analysis, keyword co-occurrence mapping using VOSviewer (v1.16.19), and distribution analysis of indoor soundscape studies across different settings. Results show a notable growth in publication activity beginning in 2010. The highest number of studies was recorded in 2014 (n = 16), and citations peaked in 2016 (n = 518). Keyword analysis reveals that indoor soundscape remains an emerging topic, represented in only three papers (5.4%), mostly linked to terms such as "health" and "well-being" without a direct connection to "soundscape" as the central term. Further analysis identified 23 studies directly addressing indoor soundscapes, with open-plan offices being the most underrepresented setting, with only one study, followed by commercial spaces (e.g., retail shops, restaurants, cafes), with two studies.

Keywords: *Indoor soundscape, Indoor Acoustic Research, Noise control, Bibliometric analysis, soundscape research trends*

[*] ***Corresponding author***: *Zulfi.rachman.22@ucl.ac.uk*
Copyright: *©2025 Rachman et al. This is an open-access article distributed under the terms of the Creative Commons Attribution 3.0 Unported License, which permits unrestricted use, distribution, and reproduction in any medium, provided the original author and source are credited.*

1. INTRODUCTION

Noise is considered one of the most widespread environmental pollutants, with the World Health Organization (WHO) and European Environment Agency (EEA) identifying it as a significant public health concern [1]. Exposure to community noise has been associated with hearing discomfort, cardiovascular issues, sleep disruption, reduced cognitive and work performance, and increased annoyance [2]. Traditional noise management in buildings has focused mainly on airborne and structural noise transmitted through building elements or generated by activities and operations within the building [3], with treatment approaches primarily aimed at reducing or isolating noise through physical interventions and active noise control systems.

Various standardised methods are available to evaluate noise reduction or isolation performance, such as sound absorption coefficient, transmission loss, sound transmission class, weighted sound reduction index, and weighted normalised impact sound pressure level [4], [5], [6], [7]. However, researchers have long questioned whether these objective parameters adequately reflect human perception of acoustic comfort [3]. This gap has prompted a shift towards more holistic, user-centred approaches to acoustic design, notably the soundscape approach.

Within this context, the present study is conducted as part of the INNOVA Doctoral Network, a collaborative research initiative that addresses noise challenges in encapsulated structures. This doctoral project, titled *"Noise Barriers with a Soundscape Approach,"* aims to extend the traditional concept of noise barriers by integrating soundscape principles with a focus on indoor applications. Rather than treating noise barriers solely as physical structures that block sound propagation, this project adopts a soundscape perspective to explore broader strategies that not only

reduce noise but also enhance how users perceive and experience the acoustic environment [8].

The soundscape concept bridges the divide between physical measurements and subjective experience by considering the perceptual and contextual dimensions of sound [9]. Defined by ISO 12913 as the *"acoustic environment as perceived or experienced and/or understood by a person or people, in context* [10]*,"* soundscape studies integrate both objective measurements and subjective evaluations [10], [11], [12]. This approach recognises that the impact of sound is not solely determined by its intensity but also by how listeners interpret and appraise it.

Over the past two decades, soundscape research has marked a significant shift in environmental acoustics, extending beyond traditional noise control engineering [13]. While early studies focused on urban and outdoor settings, recent years have seen growing interest in indoor soundscapes to address perceived acoustic quality in interior environments [3].

To explore the positioning of this emerging area, the present study conducts a bibliometric review of soundscape research applied to address noise-related challenges. The review includes a trend analysis to examine how the focus of publications has evolved over time, a keyword co-occurrence mapping to identify recurring concepts and relationships between research topics, and a distribution analysis to investigate how indoor soundscape studies are represented across different settings.

2. METHODS

This study employed a literature search to identify relevant publications for inclusion in the bibliometric review. All records were retrieved from the Scopus database using the following search query:

"noise" AND "noise barrier*" OR "noise control*" OR "noise reduction" AND "soundscape"

The search was conducted on January 28, 2025, resulting in an initial dataset of 264 documents. Subsequently, preliminary filtering was applied directly within Scopus by limiting the results based on subject area, document type, and language, which reduced the dataset to 199 documents. Further screening was performed by reviewing the titles and abstracts to assess their relevance, specifically focusing on studies addressing soundscape and noise control. After this screening process, 188 documents were identified and selected for inclusion in the bibliometric analysis. The document selection process is illustrated in Figure 1.

The dataset was manually analysed to identify trends and examine indoor soundscape studies across various settings. A keyword co-occurrence analysis was performed using VOSviewer (version 1.16.19) to visualise the network of authors' keywords. The full counting method was applied, where each keyword occurrence was counted equally. A minimum threshold of three keyword occurrences was set to refine the analysis and focus on the most significant terms. This approach produced a keywords network map highlighting the selected authors' keyword relationships and research clusters.

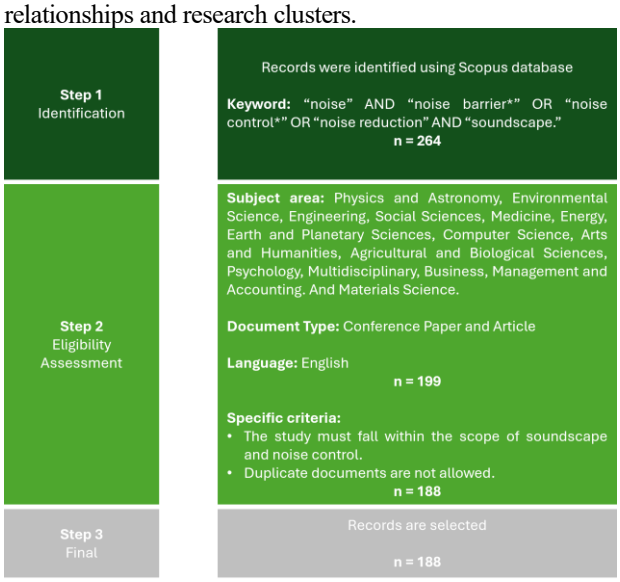


Figure 1. Study selection process

3. RESULTS AND DISCUSSIONS

This section presents and discusses the results of the bibliometric analysis, highlighting key trends, research clusters, and the distribution of indoor soundscape studies across various settings. These findings offer insights into the evolution and current state of research in the field.

3.1 Trends in Studies and Citations Over Time

The trend of soundscape research addressing noise issues shows a gradual increase in studies and citations over time, as illustrated in Figure 2. Early activity was limited, with only a few publications in the 1990s and early 2000s—for instance, just two studies appeared in 1993, and some years, such as 2001 and 2006, recorded only a single study.

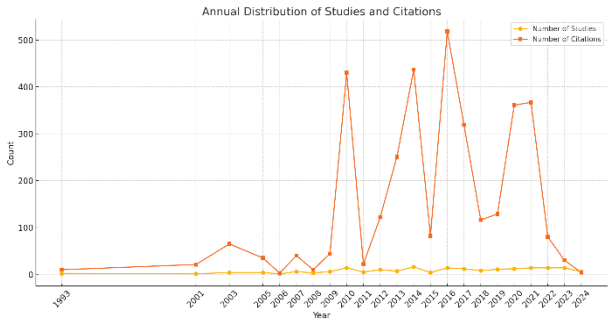


Figure 2. Annual distribution of studies and citations in soundscape and noise control research.

A noticeable rise began around 2010, when the number of studies reached 14, accompanied by 430 citations, marking a turning point in research interest. This upward trend continued, with 2014 standing out as the year with the highest number of studies (n=16) and 437 citations, indicating increased productivity and strong academic attention. The peak in citations occurred in 2016, with 518 citations across 14 studies, suggesting the presence of influential works that gained wide recognition.

The years 2017 to 2021 showed consistent research activity, with publication counts ranging from 12 to 14 studies per year and high citation levels, maintaining the visibility of the field. However, a decline is observed in the most recent data: while in 2023 sustained high output with 14 studies, citation counts dropped to 30, and in 2024, the number of studies decreased sharply to 6, with only four citations. This drop may reflect the limited time for newer publications to accumulate citations and the possibility that many 2024 studies have yet to be indexed or published.

3.2 Keyword Co-occurrence Analysis

This section presents a keyword co-occurrence analysis to explore the relationship between authors' keywords in soundscape research addressing noise issues. The analysis helps identify central themes, research clusters, and potential gaps in existing literature.

Figure 3 illustrates the network visualisation of each cluster, distinguished by colour coding. The colours used include red, green, blue, yellow, purple, light blue, orange, brown, and pink. In the keyword co-occurrence network, coloured circles represent individual keywords, with their node size corresponding to their frequency of occurrence. Keywords with higher frequencies appear with larger text and circles [14]. The bibliometric mapping of studies addressing noise challenges and innovative soundscape approaches yielded ten clusters, as shown in Table 1.

The central node, "soundscape", is the most frequently occurring term, underscoring its centrality in the analysed research. Closely related terms such as "noise", "environmental noise", "health", and "noise control" are prominently connected, reflecting their strong relevance to the field. Table 1 shows that the cluster with the fewest cluster occurrences is Cluster 9. However, its close proximity to the central node suggests that, despite its lower frequency, it holds significant conceptual relevance [15].

The next smallest is Cluster 7, whose relative distance "soundscape" highlights its position within an emerging subfield of soundscape research—distinct from outdoor or urban studies. This cluster centres on subjective evaluations, linking annoyance to perception and connecting health and well-being to environmental noise and control strategies. Notably, the keyword "indoor soundscape" is not directly linked to "soundscape" but instead connected through "health" and "well-being". This indirect pathway suggests a conceptual gap, indicating that indoor soundscape research has yet to be fully integrated into the broader soundscape discourse. Addressing this gap could help establish more holistic frameworks for designing health-supportive acoustic environments, particularly in indoor settings.

While limited in number, the three studies identified within the "indoor soundscape" theme provide valuable insights into how indoor soundscapes are perceived and evaluated. These works employ different methodological approaches—from experimental setups to qualitative inquiry and interventions using materials and active noise control—but share a common emphasis on subjective perception, acoustic comfort, and well-being.

- Lam, Bhan, et al. (2023) conducted an experimental study to assess the effectiveness of an anti-noise window using Active Noise Control (ANC) and biophilic maskers (birdsong and water sounds) in naturally ventilated urban dwellings. The findings revealed that ANC significantly reduced perceived loudness and annoyance, even with minimal objective sound level reduction. The addition of birdsong was more effective than water in further reducing annoyance, and perceptual metrics better predicted subjective comfort than by physical acoustic data alone [16].

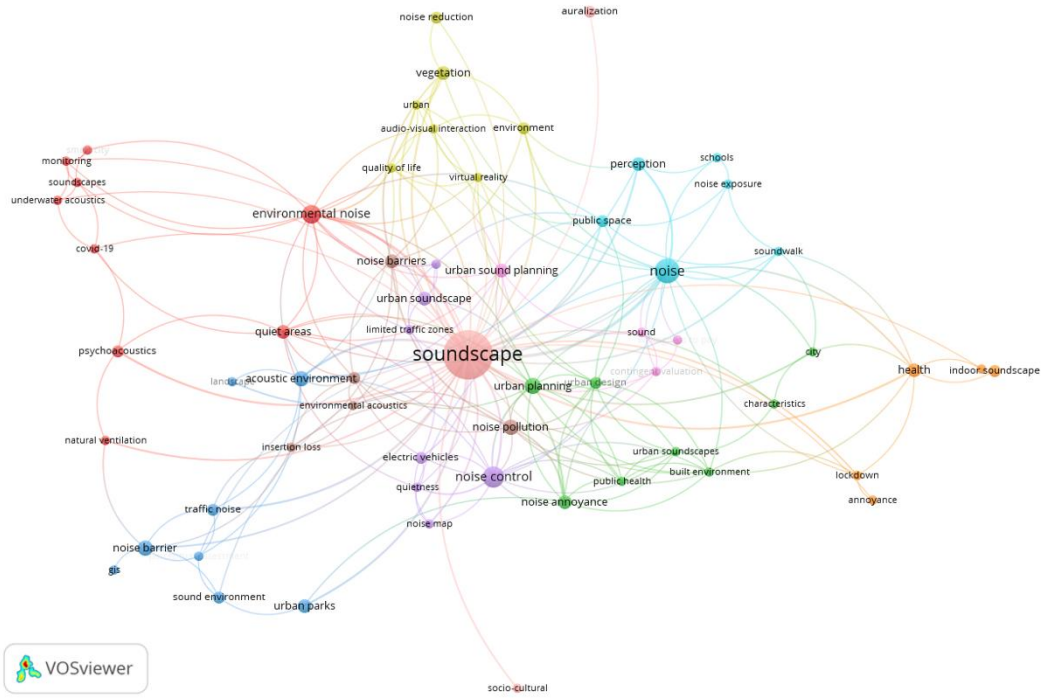


Figure 3. Keywords Network Visualisation

Table 1. Keyword Clusters Identified from Co-occurrence Analysis

Cluster	Keywords	Occurrence (%)
Cluster 1	covid-19, environmental noise, monitoring, natural ventilation, psychoacoustics, quiet areas, smart city, soundscapes, underwater acoustics	11.3%
Cluster 2	built environment, characteristics, city, noise annoyance, public health, urban design, urban planning, urban soundscapes	9.6%
Cluster 3	acoustic environment, GIS, landscape, noise barrier, perceptual assessment, sound environment, traffic noise, urban parks	10.4%
Cluster 4	audio-visual interaction, environment, noise reduction, quality of life, urban, vegetation, virtual reality	7.5%
Cluster 5	electric vehicles, limited traffic zones, noise control, noise map, noise perception, quietness, urban soundscape	10.4%
Cluster 6	noise, noise exposure, perception, public space, schools, soundwalk	10.8%
Cluster 7	annoyance, health, indoor soundscape, lockdown, well-being	5.4%
Cluster 8	environmental acoustics, insertion loss, noise barriers, noise pollution, soundscape design	6.7%
Cluster 9	contingent valuation, sound, urban sound planning, willingness to pay	4.2%
Cluster 10	auralization, socio-cultural, soundscape	23.8%

- Torresin, Simone, et al. (2020) employed a qualitative approach, using expert interviews to explore how user-centred acoustic design can enhance well-being in buildings. Their study identified perceptual dimensions of indoor soundscapes—spanning acoustic, visual, and thermal domains—and promoted the integration of soundscape-based methods into Post-Occupancy Evaluation (POE). They advocated a shift from noise elimination toward strategies that enhance positive sound experiences and increase user agency [17].
- Li, Feng, et al. (2022) presented a case study examining ceramic passive amplifiers as a design-based strategy for improving indoor soundscapes. Their results showed that these amplifiers enhanced pleasant sounds and contributed to multisensory comfort by combining visual and tactile elements. The study highlights that acoustic comfort improvements were influenced by sound level reduction, aesthetic coherence, and emotional resonance [18].

Collectively, these studies underscore the multidimensional nature of indoor soundscape research, demonstrating that soundscape quality is shaped not only by objective acoustic parameters but also by contextual, perceptual, and affective factors. This growing body of work supports the development of soundscape assessment frameworks that integrate both quantitative acoustic data and qualitative user experience—advancing more human-centred approaches to indoor acoustic design.

3.3 Distribution of Indoor Soundscape Studies Across Different Settings

A secondary screening was conducted from the 188 studies included in the main analysis to further understand the contextual scope of indoor soundscape research. This step involved selecting studies whose content directly addressed indoor soundscapes, resulting in 23 studies.

Figure 4 displays the distribution of these 23 studies across different indoor settings. The most commonly identified category was general indoor setting (n = 5), which includes studies that explored indoor soundscapes without specifying a particular type of space.

This is followed by residential, educational settings (e.g., schools, universities, libraries), and vehicle-related environments, each with four studies. The hospital category accounts for three studies, while commercial spaces (such as retail shops, restaurants, or cafés) are represented by two studies. Open-plan offices were the least represented, with only one study included. Further exploration of existing soundscape assessments and the factors involved has been conducted through a systematic review carried out by the authors [19].

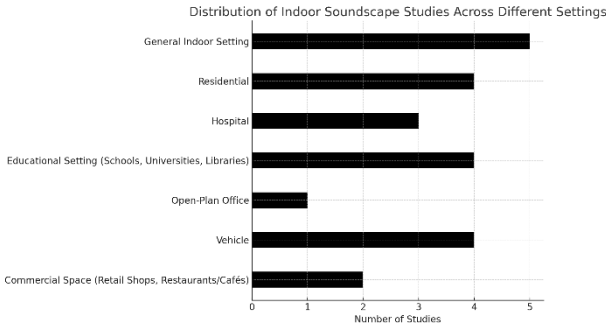


Figure 4. Distribution of Indoor Soundscape Studies Across Different Settings.

The distribution indicates that indoor soundscape research has been applied across various settings with varying degrees of attention. While some environments have received more focus, others—particularly office and commercial spaces—appear underexplored in the existing literature. This suggests potential directions for future research, especially in contexts where sound environments may significantly influence user experience and activity.

4. CONCLUSION

This bibliometric review examined indoor soundscape as an emerging topic in soundscape research, increasingly recognised for its potential to address noise-related issues. Research trends show a notable rise in interest beginning around 2010, marked by an increase in both publications and citations (n = 14 studies, 430 citations). Research productivity peaked in 2014 with 16 studies and 437 citations, while 2016 recorded the highest citation count, with 518 citations across 14 studies. From 2017 onward, research activity remained steady. However, a noticeable decline was observed in 2023, when citations dropped to 30 despite a consistent output of 14 studies. In 2024, the number of publications and citations further declined (n = 6 studies, 4 citations). This decrease may reflect the limited time for newer studies to gain recognition or delays in indexing.

Keyword occurrence analysis further confirms the status of indoor soundscape as an emerging area. The term appeared in Cluster 7 alongside annoyance, health, and well-being, with the second-lowest occurrence rate (5.4%). The “indoor soundscape” node was not directly linked to

the central "soundscape" node but connected through health and well-being. This suggests a conceptual gap and indicates that this area has yet to integrate into the broader soundscape discourse fully. Only three documents represented this node, emphasising the multidimensional nature of indoor soundscape research, which considers both acoustic parameters and contextual, perceptual, and affective factors.

Finally, the distribution of indoor soundscape studies across settings reveals limited exploration in open-plan offices and commercial spaces, represented by only one and two studies. This highlights a research gap and the need for further investigation in these underrepresented environments.

5. ACKNOWLEDGMENTS

This research was supported by the UK Research and Innovation (UKRI) under the IN-NOVA project, Active reduction of noise transmitted into and from enclosures through encapsulated structures (Project reference: EP/X027341/1). The authors gratefully acknowledge this support.

6. REFERENCES

[1] O. Hahad *et al.*, "Noise and mental health: evidence, mechanisms, and consequences," *J Expo Sci Environ Epidemiol*, vol. 35, no. 1, pp. 16–23, Jan. 2025, doi: 10.1038/s41370-024-00642-5.

[2] J. K. A. Tan, Y. Hasegawa, S.-K. Lau, and S.-K. Tang, "The effects of visual landscape and traffic type on soundscape perception in high-rise residential estates of an urban city," *Applied Acoustics*, vol. 189, p. 108580, Feb. 2022, doi: 10.1016/j.apacoust.2021.108580.

[3] S. Torresin *et al.*, "Indoor soundscape assessment: A principal components model of acoustic perception in residential buildings," *Building and Environment*, vol. 182, p. 107152, Sep. 2020, doi: 10.1016/j.buildenv.2020.107152.

[4] ASTM International, *Test Method for Sound Absorption and Sound Absorption Coefficients by the Reverberation Room Method*, ASTM C423-2, West Conshohocken, PA, USA., 2022. doi: 10.1520/C0423-22.

[5] ASTM International, *Classification for Rating Sound Insulation*, ASTM E413-22, West Conshohocken, PA, USA., 2022. doi: 10.1520/E0413-22.

[6] International Organization for Standardization (ISO), *ISO 717-1:2020 - Acoustics — Rating of sound insulation in buildings and of building elements — Part 1: Airborne sound insulation*, Geneva, Switzerland., 2020.

[7] International Organization for Standardization, *ISO 717-2:2020 - Acoustics — Rating of sound insulation in buildings and of building elements — Part 2: Impact sound insulation*, Geneva, Switzerland., 2020.

[8] "Active reduction of noise transmitted into and from enclosures through encapsulated structures - INNOVA Project," CORDIS | European Commission. Accessed: Apr. 01, 2025. [Online]. Available: https://cordis.europa.eu/project/id/101073037

[9] Ji. Kang and B. Schulte-Fortkamp, *Soundscape and the Built Environment*, vol. 525. Boca Raton: CRC Press, 2016.

[10] International Organization for Standardization (ISO), *ISO 12913-1: Acoustics — Soundscape — Part 1: Definition and conceptual framework*, Geneva, Switzerland., 2014.

[11] International Organization for Standardization (ISO), *ISO 12913-2: Acoustics — Soundscape — Part 2: Data collection and reporting requirements*, Geneva, Switzerland., 2018.

[12] International Organization for Standardization (ISO), *ISO 12913-3: Acoustics — Soundscape — Part 3: Data analysis*, Geneva, Switzerland., 2019.

[13] J. Kang, "Soundscape in city and built environment: current developments and design potentials," *City Built Enviro*, vol. 1, no. 1, p. 1, Jan. 2023, doi: 10.1007/s44213-022-00005-6.

[14] N. J. van Eck and L. Waltman, "Software survey: VOSviewer, a computer program for bibliometric mapping," *Scientometrics*, vol. 84, no. 2, pp. 523–538, Aug. 2010, doi: 10.1007/s11192-009-0146-3.

[15] Q. Liu, N. L. Ali, and H. Y. Lee, "Applying VOSviewer in a bibliometric review on English language teacher education research: an analysis of narratives, networks and numbers," *Cogent Education*, vol. 12, no. 1, p. 2449728, Dec. 2025, doi: 10.1080/2331186X.2025.2449728.

[16] B. Lam, K. C. Q. Lim, K. Ooi, Z.-T. Ong, D. Shi, and W.-S. Gan, "Anti-noise window: Subjective perception of active noise reduction and effect of informational masking," *Sustainable Cities and*

Society, vol. 97, p. 104763, Oct. 2023, doi: 10.1016/j.scs.2023.104763.

[17] S. Torresin *et al.*, "Acoustics for Supportive and Healthy Buildings: Emerging Themes on Indoor Soundscape Research," *Sustainability*, vol. 12, no. 15, p. 6054, Jul. 2020, doi: 10.3390/su12156054.

[18] F. Li, J. Xiang, T. Li, D. Shen, and T. Li, "Active Indoor Soundscape Design: A Case Study of Ceramic Passive Amplifiers," *IJERPH*, vol. 19, no. 18, p. 11251, Sep. 2022, doi: 10.3390/ijerph191811251.

[19] Z. Rachman, F. Aletta, and J. Kang, "Exploring Soundscape Assessment Methods in Office Environments: A Systematic Review," *Buildings*, vol. 14, no. 11, p. 3408, Oct. 2024, doi: 10.3390/buildings14113408.

DOI: 10.61782/fa.2025.0728



FORUM ACUSTICUM
EURONOISE 2025

REAL-TIME IMPLEMENTATION OF A USER-SELECTIVE ACTIVE SOUND CONTROL SEAT BASED ON AUDITORY SCENE ANALYSIS

Tahmida Islam* **Juan Garcia** **Maria Garzon** **Miguel Ferrer**
Maria de Diego **Laura Fuster** **Alberto Gonzalez**
Inst. of Telecommunications and Multimedia Applications (iTEAM)
Universitat Politècnica de València, València
Spain

ABSTRACT

Environmental noise can harm people's health, leading to issues such as hearing loss, increased stress levels, and reduced overall well-being. This noise pollution is a growing concern in urban environments, where constant exposure to sounds from traffic, construction, and other sources can create an uncomfortable living situation. We can implement active sound control techniques to address these challenges, which offer a promising solution to reduce unwanted noise. This method uses loudspeakers to change the sound in an area and create a specific sound field. However, real-time active sound control is challenging. There are limitations based on where we place microphones and loudspeakers and how we select sound sources to create a comfortable environment for users. This paper presents a user-selective active sound seat that addresses these design challenges. This seating solution combines the principles of active sound control with advanced techniques derived from the Auditory Scene Analysis framework. These techniques help separate individual sound sources from a mix by analyzing the position and characteristics of different sounds in a room. As a result, users of the active sound seat can selectively mask unwanted sounds in their vicinity.

Keywords: *active sound control, sound separation, spatial filtering*

**Corresponding author*: tislam@upv.edu.es.

Copyright: *©2025 First author et al. This is an open-access article distributed under the terms of the Creative Commons Attribution 3.0 Unported License, which permits unrestricted use, distribution, and reproduction in any medium, provided the original author and source are credited.*

1. INTRODUCTION

Active Sound Control (ASC) is an acoustic technology that manipulates sound waves using secondary sources (loudspeakers) to shape the acoustic environment. A key application of ASC is Active Noise Control (ANC), where the system generates a sound field that destructively interferes with unwanted noise, effectively reducing it. Beyond noise reduction, ASC can also enhance auditory experiences, such as through spatial audio reproduction and zonal sound control [1, 2]. These capabilities allow ASC to suppress noise and selectively amplify or modify specific sound fields, improving sound quality in complex environments. In automotive applications, ASC technologies are increasingly used to reduce in-cabin noise and enrich the driving experience through powertrain sound enhancement or infotainment features [3].

A key enabler of such user-focused ASC systems is Auditory Scene Analysis (ASA), a perceptual process by which the human auditory system separates and identifies individual sound sources in a complex acoustic environment [4]. ASA helps us understand and focus on specific sounds even in noisy surroundings [5] but selectively listening to different sounds in an acoustic mixture remains a challenge in machine hearing [6]. Spatial cues, such as interaural time and level differences, play a crucial role in localizing sound sources—analogous to how microphone arrays can be used in machines to separate overlapping sources based on spatial filtering [7].

Spatial filtering techniques like beamforming are widely used for sound source separation. Traditional beamformers focus on sounds from a specific direction, but modern implementations must address more complex environments with reverberation and multiple sources. In

this broader context, beamformers are viewed as multiple-input single-output systems that combine spatially filtered microphone signals to enhance desired sources and suppress interference [8]. Recent advancements incorporate neural networks (NNs) to estimate beamforming parameters or directly predict filter coefficients [9–11]. Some architectures combine NNs with traditional spatial filters [12–14], followed by post-filtering stages for further enhancement [15, 16].

After separating sound sources using ASA-inspired techniques, ANC is applied to suppress unwanted noise and maintain an ambient acoustic environment around the listener. Among various ANC algorithms, the Filtered-X Least Mean Square (FxLMS) algorithm is favored for its simplicity and real-time adaptability [17–19]. Most real-time ANC systems use the FxLMS algorithm or its modifications [20–24] due to its proven effectiveness. In recent years, many researchers and engineers have chosen the Speedgoat platform to implement and test different acoustic models. Speedgoat supports machine-in-the-loop experiments, real-time simulation, and control validation under dynamic conditions [25, 26].

This work presents a real-time implementation of a user-selective Active Sound Control (ASC) seat that integrates Auditory Scene Analysis (ASA) principles. An NN-based spatial filtering system separates sound sources captured via a microphone array. After sound separation, a multi-channel FxLMS ANC system actively cancels unwanted noise around a selected user. The system is implemented and tested on the Speedgoat platform to validate performance under real-time conditions and ensure a targeted acoustic response around the seat.

2. METHODOLOGY

2.1 Multi-channel Active Noise Control System

The proposed system is based on a generic multi-channel Active Noise Control (ANC) framework consisting of I reference signals, J secondary sources, and K error sensors. The adaptive filtering approach used in this system follows the MultiChannel Filtered-X Least Mean Squares (MFXLMS) algorithm [27], which is detailed as follows.

The adaptive filter output at the j-th secondary source is expressed as:

$$\mathbf{y}_j(n) = \sum_{i=1}^{I} \mathbf{w}_{ji}^T(n)\mathbf{x}_i(n)\,. \tag{1}$$

The adaptive filter coefficient vector is given by:

$$\mathbf{w}_{ji}(n) = [w_{ji,0}(n), w_{ji,1}(n), \ldots, w_{ji,N-1}(n)]^T\,, \tag{2}$$

where N is the number of filter coefficients.

The input tap vector is defined as:

$$\mathbf{x}_i(n) = [\mathbf{x}_i(n), \mathbf{x}_i(n-1), \ldots, \mathbf{x}_i(n-N+1)]^T\,. \tag{3}$$

The update equation for the adaptive filter coefficients is given by:

$$\mathbf{w}_{ji}(n) = \mathbf{w}_{ji}(n-1) + \mu \sum_{k=1}^{N} e_k(n)(\hat{\mathbf{S}}_{kj}(n) * \mathbf{x}_i(n))\,. \tag{4}$$

Here, $\hat{\mathbf{S}}_{kj}(n)$ represents the estimated secondary path between the kth error sensor and the jth secondary source.

For example, a 2×2 MFXLMS system block diagram is shown in Figure 1. The proposed control system consists of two main modules: an **ASA Module** and an **ANC Module**. Both modules work together to create a personalized acoustic environment by suppressing unwanted noise while preserving desirable sounds such as music, alarms, and voice alerts.

The ANC module implements real-time noise cancellation using the MFXLMS algorithm. It operates on a sample-by-sample basis to minimize the error signal at the error microphones, thereby ensuring an ambient acoustic zone around the user.

2.2 Auditory Scene Analysis and Source Separation

The system must first isolate desired and undesired sound sources to enable user-selective noise cancellation. This separation is accomplished using a *Filter-and-Sum Beamformer* (FASB) [28], which enhances signals originating from a particular direction while suppressing others.

The FASB beamformer processes the signals captured by an array of microphones as follows:

- The beamformer individually filters each microphone signal.
- The filtered signals are then summed to generate a reference signal representing the selected noise source.

This reference signal is fed into the ANC system to cancel user-specified noises selectively.

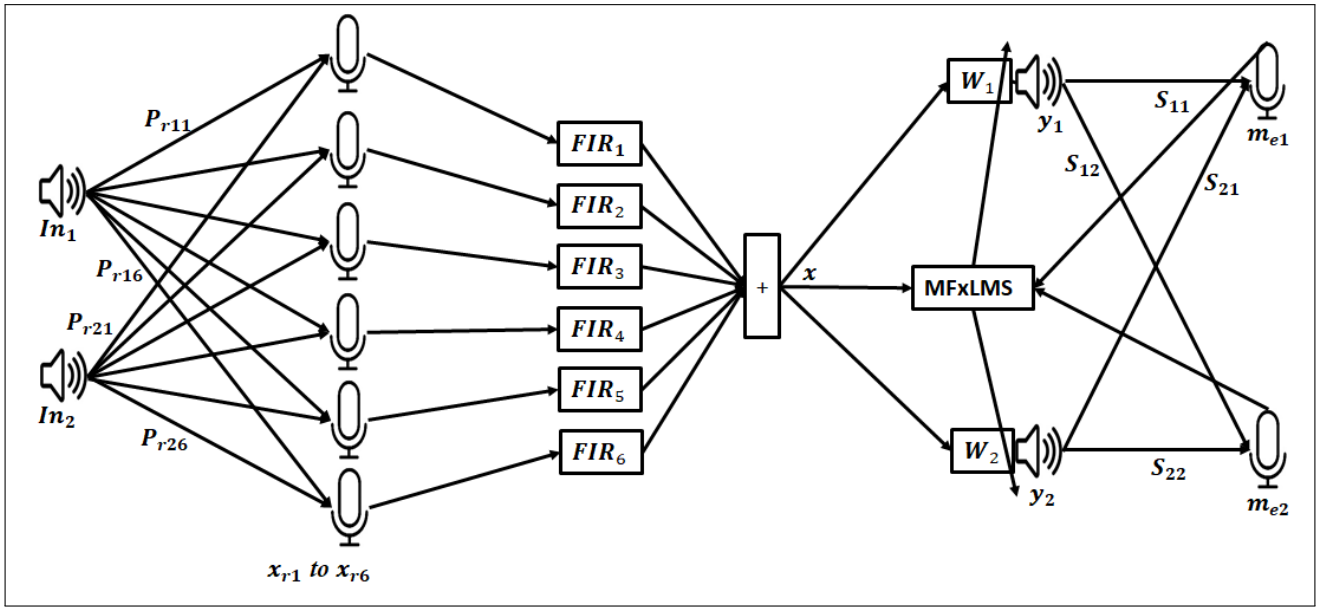


Figure 1. A block diagram illustrating an example of ASA with multichannel ANC system.

2.3 Neural Network-Based Beamformer Optimization

The beamformer filters are designed using an NN to optimize spatial filtering performance. The objective is to extract a single target sound source while suppressing others.

Consider an experimental setup with two independent sound sources located at different positions. The signals captured by the microphone array can be expressed as:

$$x_{rm}[n] = In_1[n] * \mathbf{P}_{r1m} + In_2[n] * \mathbf{P}_{r2m}\,, \quad (5)$$

where $\mathbf{P}_{rim}$ represents the acoustic path between the i-th source and the m-th microphone and $In_i[n]$ defines the primary signals at time instant n.

The signals from all microphones are linearly combined using a set of beamformer filters to extract the target source:

$$x[n] = \sum_{m=1}^{M} x_{rm}[n] * \mathbf{h}_m\,. \quad (6)$$

Here, $\mathbf{h}_m$ are the beamformer filter coefficients to be optimized.

The ideal objective is to recover only the target signal, i.e.,

$$x[n] = In_1[n]\,. \quad (7)$$

However, direct inversion of the acoustic propagation paths is highly complex. Instead, a relaxed objective is defined as:

$$x[n] = In_1[n] * \mathbf{P}_{r1m}\,. \quad (8)$$

This relaxed objective avoids the need for deconvolution while still achieving effective separation.

A neural network model is used to optimize the beamforming filters. The NN takes as input the raw signals from multiple microphones and processes them through a set of 1D convolutional layers. The outputs of these filters are summed to generate the beamformed signal.

The loss function used for training is the Mean Squared Error (MSE) between the network's output and the desired reference signal:

$$\mathcal{L} = \frac{1}{T}\sum_{n=1}^{T}\left(x[n] - In_1[n] * \mathbf{P}_{r1m}\right)^2\,. \quad (9)$$

The neural network learns optimal beamformer filter coefficients that maximize target source extraction by minimizing this loss function.

2.4 Real-Time Implementation on Speedgoat

The system, including the ASA-based source separation and MFXLMS-based ANC, is deployed in real time using

the Speedgoat rapid control prototyping platform. Speedgoat allows for hardware-in-the-loop testing and real-time validation of the proposed algorithm under practical conditions.

The real-time implementation involves:

- Estimating multi-microphone acoustic paths $\mathbf{P}_{rim}$ to perform the offline design of beamformers using the trained neural network.
- Extracting the selected noise source using the designed beamformers and feeding it into the ANC system.
- Applying the MFXLMS algorithm to generate anti-noise signals in real time.
- Continuously adapting the ANC system to changing acoustic conditions to ensure effective noise suppression.

3. EXPERIMENTAL RESULTS

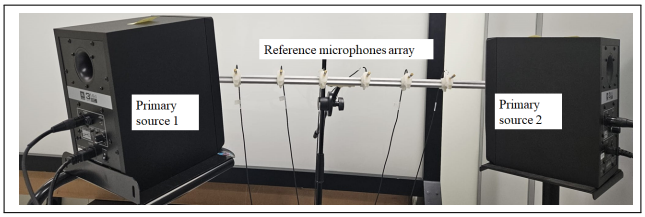


Figure 2. An array of six reference microphones for sound source separation.

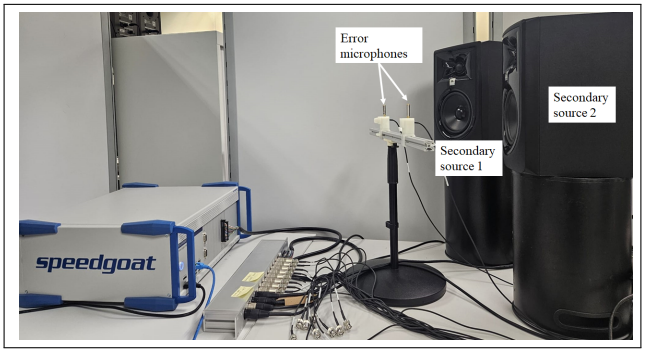


Figure 3. Control Area of the real time implementation.

This experiment utilized two primary sources to generate white noise and speech signals, where white noise was regarded as an undesired signal. An array of six microphones served as reference microphones (see Figure 2). The beamformers filtered the signals from these microphones to create a reference signal that represented the chosen noise source. In the control area, two secondary sources and two error microphones were employed to achieve user-selective Active Sound Control (ASC) at the car seat (see Figure 3).

The real-time experiments were conducted in three stages to assess the performance of the proposed ASA system, Only speech playing (Baseline Measurement): This scenario establishes a reference for clean speech signals without interference.

- Only speech playing (Baseline Measurement): This scenario establishes a reference for clean speech signals without interference.
- Speech and noise playing, ANC off: This represents a real-world noisy environment where the desired speech signal is masked by background noise.
- Speech and noise playing, ANC on: The ANC system is activated to suppress undesired noise while preserving the speech signal.

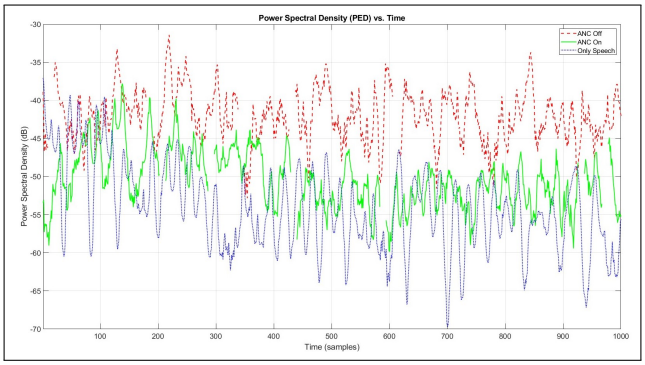


Figure 4. Power Spectral Density (PSD) of the signal at the error position with the ANC system Off, On, and with only a speech signal.

The measured signals from the error microphone in these scenarios are visualized in Figure 4. The dashed line represents when ANC is turned off, showing higher power spectral density due to noise. The dotted line corresponds to the clean speech signal without noise as a reference for ideal speech quality. The solid line represents the scenario with ANC enabled, illustrating the noise

reduction. In the ANC off condition, the noise significantly raises the power spectral density across the frequency spectrum, confirming that speech intelligibility is negatively impacted. When ANC is activated, there is a noticeable reduction in noise levels, as seen by the decrease in power spectral density (solid line curve compared to dash line). This demonstrates that the ANC system effectively reduces unwanted noise while preserving the desired speech signal.

4. CONCLUSION

The experimental results confirm that the proposed Active Sound Amplification (ASA) system significantly improves the acoustic environment by reducing unwanted noise while preserving desired sounds. The offline neural network processing used to obtain beamformer information simplifies the ASA, making it less computationally demanding for real-time implementation. This design makes ASA a promising solution for applications that require personalized sound zones, such as in-vehicle communication or selective noise control in shared spaces. However, some residual noise is still present even when active noise cancellation (ANC) is activated. This suggests that while the ASA-based sound separation performs well, further refinements in spatial filtering or active noise cancellation could enhance its effectiveness.

5. ACKNOWLEDGEMENTS

This project is supported by Horizon Europe Marie Skłodowska-Curie Actions (MSCA) Doctoral Net-work under the European Union's funding scheme. The project title is 'Active reduction of noise transmitted into and from enclosures through encapsulated structures' and is identified by project number 101073037.

6. REFERENCES

[1] F. Rumsey, "Sound field control," *Journal of the Audio Engineering Society*, vol. 61, no. 12, pp. 1046–1050, 2013.

[2] F. Rumsey, *Spatial audio*. Routledge, 2012.

[3] J. Cheer, "Active sound control in the automotive interior," *Future Interior Concepts*, pp. 53–69, 2021.

[4] A. S. Bregman, *Auditory scene analysis: The perceptual organization of sound*. MIT press, 1994.

[5] B. T. Szabó, S. L. Denham, and I. Winkler, "Computational models of auditory scene analysis: a review," *Frontiers in Neuroscience*, vol. 10, p. 524, 2016.

[6] I. Kavalerov, S. Wisdom, H. Erdogan, B. Patton, K. Wilson, J. Le Roux, and J. R. Hershey, "Universal sound separation," in *2019 IEEE Workshop on Applications of Signal Processing to Audio and Acoustics (WASPAA)*, pp. 175–179, IEEE, 2019.

[7] D. Markovic, A. Defossez, and A. Richard, "Implicit neural spatial filtering for multichannel source separation in the waveform domain," *arXiv preprint arXiv:2206.15423*, 2022.

[8] E. Vincent, T. Virtanen, and S. Gannot, *Audio source separation and speech enhancement*. John Wiley & Sons, 2018.

[9] A. A. Nugraha, A. Liutkus, and E. Vincent, "Multichannel audio source separation with deep neural networks," *IEEE/ACM Transactions on Audio, Speech, and Language Processing*, vol. 24, no. 9, pp. 1652–1664, 2016.

[10] J. Heymann, L. Drude, C. Boeddeker, P. Hanebrink, and R. Haeb-Umbach, "Beamnet: End-to-end training of a beamformer-supported multi-channel asr system," in *2017 IEEE International Conference on Acoustics, Speech and Signal Processing (ICASSP)*, pp. 5325–5329, IEEE, 2017.

[11] W. Zhang, A. S. Subramanian, X. Chang, S. Watanabe, and Y. Qian, "End-to-end far-field speech recognition with unified dereverberation and beamforming," *arXiv preprint arXiv:2005.10479*, 2020.

[12] J. Wu, Z. Chen, J. Li, T. Yoshioka, Z. Tan, E. Lin, Y. Luo, and L. Xie, "An end-to-end architecture of online multi-channel speech separation," *arXiv preprint arXiv:2009.03141*, 2020.

[13] Y. Fu, J. Wu, Y. Hu, M. Xing, and L. Xie, "Desnet: A multi-channel network for simultaneous speech dereverberation, enhancement and separation," in *2021 IEEE Spoken Language Technology Workshop (SLT)*, pp. 857–864, IEEE, 2021.

[14] W. Liu, A. Li, C. Zheng, and X. Li, "A neural beam filter for real-time multi-channel speech enhancement," *arXiv preprint arXiv:2202.02500*, 2022.

[15] Z.-Q. Wang and D. Wang, "Multi-microphone complex spectral mapping for speech dereverberation,"

in *ICASSP 2020-2020 IEEE International Conference on Acoustics, Speech and Signal Processing (ICASSP)*, pp. 486–490, IEEE, 2020.

[16] Z.-Q. Wang, P. Wang, and D. Wang, "Multi-microphone complex spectral mapping for utterance-wise and continuous speech separation," *IEEE/ACM transactions on audio, speech, and language processing*, vol. 29, pp. 2001–2014, 2021.

[17] J. Lorente, M. Ferrer, M. de Diego, and A. Gonzalez, "The frequency partitioned block modified filtered-x nlms with orthogonal correction factors for multichannel active noise control," *Digital Signal Processing*, vol. 43, pp. 47–58, 2015.

[18] D. Shi, W.-S. Gan, B. Lam, and C. Shi, "Two-gradient direction fxlms: An adaptive active noise control algorithm with output constraint," *Mechanical Systems and Signal Processing*, vol. 116, pp. 651–667, 2019.

[19] M. Tufail, S. Ahmed, M. Rehan, and M. T. Akhtar, "A two adaptive filters-based method for reducing effects of acoustic feedback in single-channel feedforward anc systems," *Digital Signal Processing*, vol. 90, pp. 18–27, 2019.

[20] X. Mu, J. Ko, and J. Rheem, "Modified fxlms algorithm for active noise control and its real-time implementation," *Journal of the Institute of Electronics and Information Engineers*, vol. 50, no. 9, pp. 172–176, 2013.

[21] J. Lorente, M. Ferrer, M. De Diego, and A. González, "Gpu implementation of multichannel adaptive algorithms for local active noise control," *IEEE/ACM Transactions on Audio, Speech, and Language Processing*, vol. 22, no. 11, pp. 1624–1635, 2014.

[22] M. Ferrer, A. Gonzalez, M. de Diego, and G. Pinero, "Convex combination filtered-x algorithm for multichannel active noise control,"

[23] D. Sachau and S. Jukkert, "Real-time implementation of the frequency-domain fxlms algorithm without block delay for an adaptive noise blocker," *Proceedings of the ISMA, Leuven, Belgium*, pp. 15–17, 2014.

[24] L. Liu, Q. Su, W. Li, and S. M. Kuo, "Real time implementation and experiments of multi-channel active noise control system for icu," in *2021 IEEE International Conference on Electro Information Technology (EIT)*, pp. 395–400, IEEE, 2021.

[25] A. Pelletier, P. Micheau, and A. Berry, "Implementation of a self-sensing piezoelectric actuator for vibro-acoustic active control," in *Sensors and Smart Structures Technologies for Civil, Mechanical, and Aerospace Systems 2014*, vol. 9061, pp. 1093–1102, SPIE, 2014.

[26] X. Xu, Y. Lu, C. Lan, Z. Xing, and M. Shao, "Experimental research on global active rotor noise control using near-field acoustic holography and sound field reproduction," *Mechanical Systems and Signal Processing*, vol. 206, p. 110930, 2024.

[27] T.-H. Jung, J.-H. Kim, K.-J. Kim, and S.-W. Nam, "Active noise reduction system using multi-channel anc," in *2011 11th International Conference on Control, Automation and Systems*, pp. 36–39, IEEE, 2011.

[28] M. Kajala and M. Hamalainen, "Filter-and-sum beamformer with adjustable filter characteristics," in *2001 IEEE International Conference on Acoustics, Speech, and Signal Processing. Proceedings (Cat. No. 01CH37221)*, vol. 5, pp. 2917–2920, IEEE, 2001.

DOI: 10.61782/fa.2025.0636

FORUM ACUSTICUM EURONOISE 2025

NUMERICAL STUDY OF A STEPPED DIRECTIONAL BARRIER FOR URBAN NOISE CONTROL

Nuria Campillo-Davo[1*] **Miguel Fabra-Rodriguez**[1] **Hector Campello-Vicente**[1]
David Abellan-Lopez[1] **Elicio M. Mora-Saura**[1] **David Clar-Garcia**[1] **Ramon Peral-Orts**[1]
[1] Engineering Research Institute of Elche (I3E), Miguel Hernandez University of Elche, Elche, Spain

ABSTRACT

Acoustic barriers are structures used to block or reduce noise propagation, improving people's quality of life. Barriers installed to mitigate traffic noise traditionally consist of continuously installed acoustic panels. In contrast, this work proposes the development of a directional barrier consisting of discrete cylindrical elements of stepped height distributed in the form of a sonic crystal. The barrier is designed to suppress transversely especially the frequency of 1000 Hz, the frequency at which the sound peak of rolling noise occurs. In order to test the sound effect of this barrier, numerical simulations of acoustic propagation are performed using FEM/BEM. The final objective aims to develop a sound barrier for application in urban environments that fulfils a dual application: mitigating noise pollution, but allowing a certain directivity of the noise from the transit of a vehicle to act as an acoustic warning element for pedestrians.

Keywords: *noise barrier, tyre road noise, sonic crystal, electric vehicle, traffic noise.*

1. INTRODUCTION

Noise emission generated by road traffic is one of the main sources of noise in urban and interurban environments. The noise emitted by a vehicle is generated by different sub-sources, commonly grouped into three categories: noise generated by the engine and traction system, noise produced by the interaction between tyre and road surface -tyre/road noise-, and aerodynamic noise. The gradual introduction of hybrid-electric and pure electric vehicles in road traffic can contribute to improving noise environments in cities by reducing engine noise, whereas tyre/road noise emission remains. However, the low detectability of the new generation of vehicles, mainly at low speeds - i.e. sound pressure levels below 56 dB at 10 km/h [1] - is of great concern for the most vulnerable groups [2] such as pedestrians, especially children and elderly people and people with blindness or low vision [3], cyclists or scooter users, as well as drivers of other vehicles [4]. Therefore, the coexistence of both types of vehicles (ICE vehicles and electric vehicles) will require technical solutions that allow adequate noise control in urban environments.

The use of acoustic barriers as a corrective measure for noise generated by road traffic has been used for decades [5-7]. Classical noise barriers, understood as continuous flat elements whose noise control mechanism is mainly based on reflection, have a series of drawbacks, some of which are caused precisely by the reflected sound [8,9]. This has led to the evolution of barrier designs through different solutions, either based on their material composition with the incorporation of absorbent materials, or based on their geometric definition with the inclusion of elements that disperse the reflected sound, for example through the use of sonic crystals [10,11].

Sonic crystals are materials formed by a regular distribution of repeated basic elements that allow the waves impinging on them with a certain frequency to suffer a destructive interference. Currently, the optimization of this type of materials is focused on different lines [12], such as the inclusion of resonances within their elements to analyze the interaction of both phenomena [13-15], the design of the geometry of the section of the discrete elements that form

[*] ***Corresponding author***: ncampillo@umh.es.
Copyright: *©2025 First author et al. This is an open-access article distributed under the terms of the Creative Commons Attribution 3.0 Unported License, which permits unrestricted use, distribution, and reproduction in any medium, provided the original author and source are credited.*

the barrier [16-18], the configuration of the position of the elements within the barrier [19-21], the composition of the materials of the elements that form the barrier [22-25], or the height of the elements [26].

The diffraction of sound waves that occurs at the upper edge of the barriers is one of the main factors that reduce their performance, and one of the main lines of work in the optimization of classical barriers [8]. However, this aspect has also been considered in other barrier proposals, such as in [27] where the effect of diffraction at the edge of a sonic crystal-based barrier was analyzed, observing the possibility of varying its attenuation level by modifying the design of the upper edge of the barrier. In [28] the effect of diffraction was also considered, working with a barrier design based on sonic crystals made up of nested elements.

Therefore, this paper presents a preliminary study of a low height stepped directional acoustic barrier (SDAB) system. The purpose of the design of this barrier is to create an interference in the propagation of sound in the transverse direction, but at the same time to allow sound transmission at a certain angle in both the horizontal and vertical planes. Thus, the stepped directional acoustic barrier SDAB is based on a two-dimensional sonic crystal of circular elements of 0.125 m diameter arranged as a three-row square Bravais grid. Each of these rows has been assigned a different height: 0.4, 0.7 and 1 m. In this way, a three-dimensional barrier of staggered cylindrical elements has been achieved, where the elements with the lowest height are located on the emitter's side. The barrier is designed to mainly block the propagation of the 1000 Hz frequency in its transverse direction, the frequency at which the highest peak sound energy is produced in the tyre/road noise emission. Given that the rolling sound emission occurs at a very low height, hence the low height of the barrier elements. The grid parameter “a” has been set according to Bragg's law at 0.17 m, as half the wavelength of the interest frequency transmitted by the air.

The study has been based on the numerical modelling of a set composed by a point sound emitter, located at a distance of twice the parameter “a” from the axis of the first cylindrical dispersing element of the barrier. The objective of the work will be to study the ability of the SDAB barrier to reduce the sound propagation in the transverse direction, while at the same time allowing the sound transmission to reach a receiving area located towards the end of the barrier. Fig. 1 shows the source assembly in front of the SDAB, at the center of the barrier. The figure shows the area to be protected from sound transmission - the protected area - in a transverse direction to the barrier, as well as the area where it is desired that the barrier allows sound transmission - the receiving area-.

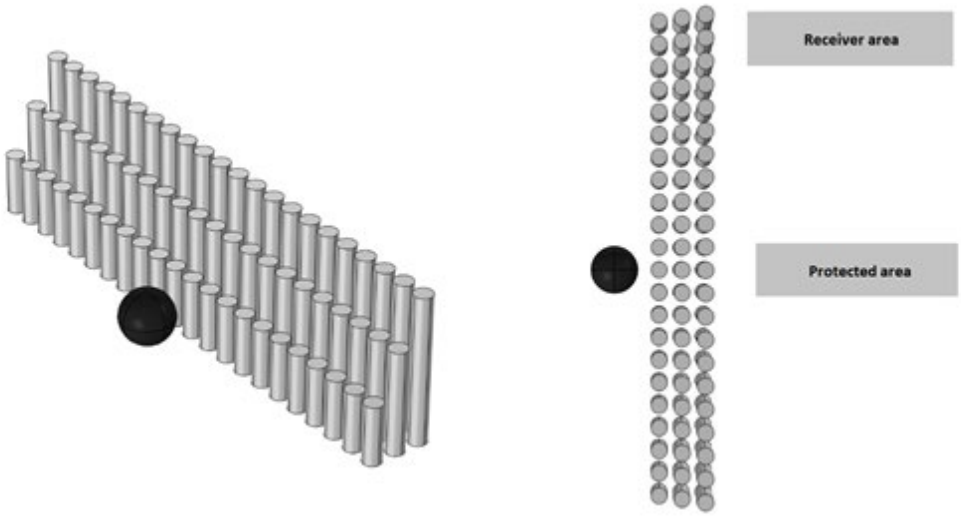


Figure 1. Noise source and SDAB barrier set. Left: isometric view. Right: plan view.

2. SIMULATION METHODOLOGY

The model developed to study the effect of the SDAB barrier on the acoustic propagation of an emitter, has been implemented in the COMSOL Multiphysics software. It is a BEM model where a sound source is placed in front of the acoustic barrier in an open field. Fig. 2 shows the geometry of the barrier as well as a detailed grid layout. The advantage of the BEM methodology is that it does not need to discretize the air volume, which is computationally advantageous for calculating sound propagation in open spaces. In this preliminary study, the emitter has been defined as a static omnidirectional sound source, located in front of the central area of the barrier. For this purpose, a point monopole has been placed at a height of 0.25 m, same height as the center of a commercial dodecahedral sound source, and separated by a distance of twice the parameter "a" from the axis of the first cylindrical dispersing element. To simulate the omnidirectional sound source, this monopole has been placed inside a 0.36 m diameter air sphere whose interior has been discretized by FEM. For the study, a barrier of 22 cylindrical elements for each of the rows has been used, giving a total barrier length of about 4 m. The surface of the sphere serves as a connection between the FEM environment and the BEM environment used for the study of acoustic propagation by imposing a continuity in the generated sound pressure field. The sides and top caps of the cylindrical elements of the barrier are established as fully reflective surfaces. In turn, the effect of the ground is modelled as a plane which is also considered as fully reflective.

3. RESULTS

The numerical model implemented in COMSOL Multiphysics has been run in a stationary analysis at the frequency of 1000 Hz with a sound source power of 5 W. Fig. 3.a) shows the effect of the directional SDAB barrier on the sound propagation of the acoustic field generated by the omnidirectional source. Additionally, the sound field produced by a conventional continuous flat barrier of rectangular geometry, 1 m high, placed at the same distance from the source as the highest row of cylindrical elements, see Fig. 3.b), has been simulated.

In the vertical plane of both simulations in Fig. 3 (lower images), it can be seen how the SDAB barrier is able to reduce, more effectively than the conventional barrier, the sound propagation from a distance of 1 m in the transverse direction of the barrier. In addition, the conventional barrier reflects, to a greater extent than the SDAB barrier, the sound field produced on the source side, instead of scattering it. In the horizontal plane (images above), there is also a different behavior between the two types of barriers. While the conventional barrier blocks the sound propagation similarly along its entire length, the SDAB barrier is more effective in the transverse direction, for which the distance between cylinders presents a destructive interference for the 1000 Hz wavelength. As the angle of incidence increases, the distance between elements increases, allowing more sound propagation.

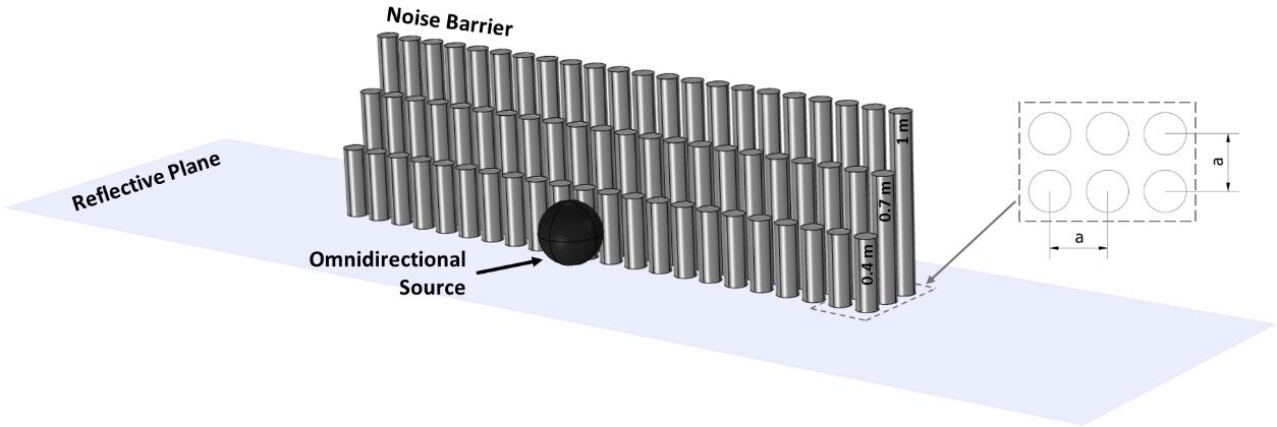


Figure 2. Geometric characteristics of the SDAB acoustic barrier and modelling in COMSOL Multiphysics.

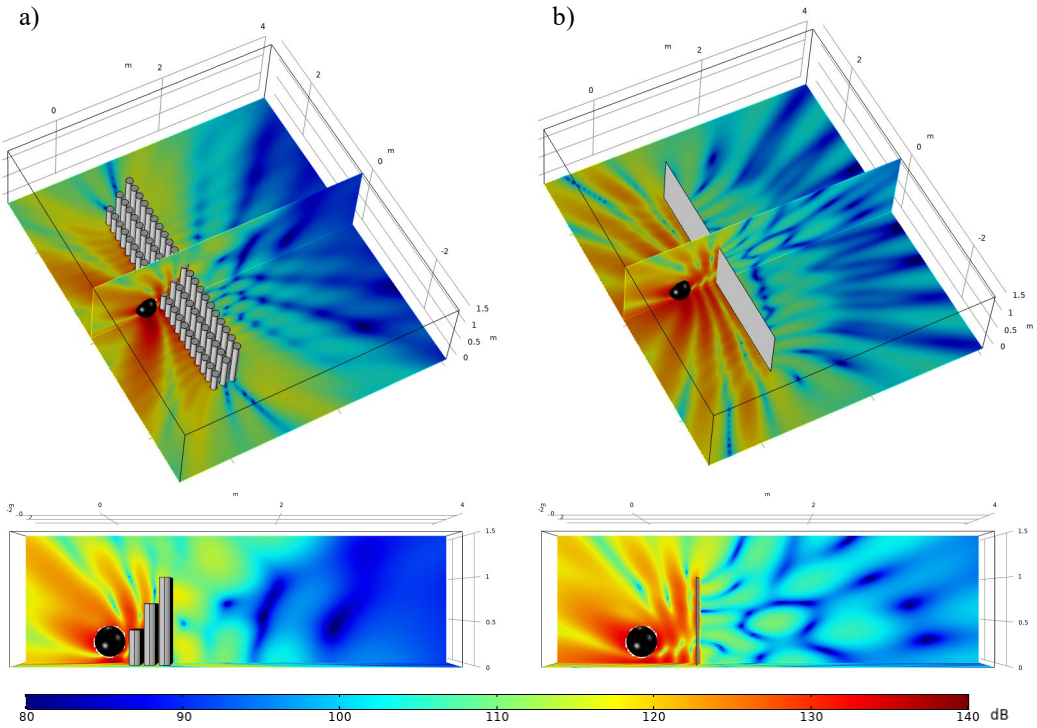


Figure 3. Sound Pressure Level of the simulated sound field at 1000 Hz: a). Directional barrier with cylindrical elements. b). Conventional rectangular barrier.

To better quantify the propagation in the horizontal plane, Fig. 4 shows a polar plot of the Sound Pressure Level, evaluated over a circumference of 4 m radius, centered on the source at 1.2 m height, thus lying above both barriers. In the transverse direction, at 0°, a receiver at a height of 1.2 m would perceive 90 dB for the SDAB barrier and 95 dB for the traditional barrier. The SDAB barrier is more effective than the rectangular barrier up to an angle of 50°, where it has a lobe of greater acoustic propagation. A difference of 5 dB can also be quantified at 180° due to the higher reflection of the traditional barrier towards the source itself.

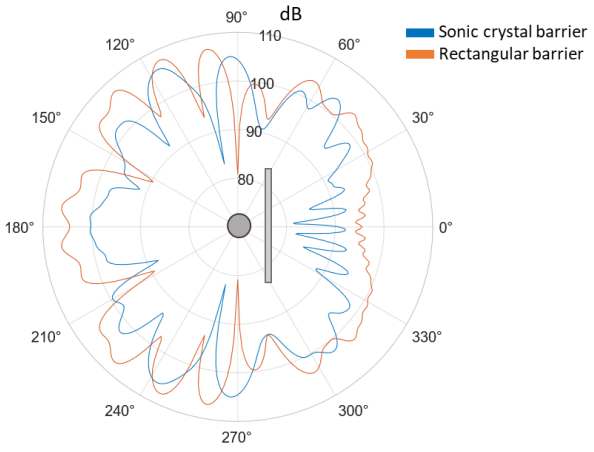


Figure 4. Polar plot of the Sound Pressure Level of the simulated sound field at 1000 Hz, at a height of 1.2 m and with an evaluation radius of 4 m.

4. CONCLUSIONS AND FURTHER WORK

The SDAB stepped acoustic barrier presented in this work has been designed in order to favor sound directivity at a frequency of 1000 Hz. In the horizontal plane, greater directivity has been achieved at an angle of 50º with respect to the transverse direction of the barrier, while it is reduced in the direction of 0º. In turn, in the vertical plane, the stepped barrier produces a more effective attenuation below the angle formed by its stepped elements. In this sense, the group is working on the experimental validation of a prototype SDAB stepped barrier, as shown in Fig. 5. This figure has been obtained using an acoustic camera that allows the sound field generated by the source, with an emission of 1000 Hz, and located at a distance of 4 m, to be seen graphically.

The behavior of the barrier at other frequencies is also being studied experimentally by obtaining the Insertion Loss in different positions in space. The final objective will be to achieve three-dimensional directivity by placing the barrier in the proximity of an urban traffic flow.

5. ACKNOWLEDGMENTS

This work has been supported by the Conselleria de Educación, Cultura, Universidades y Empleo, de la Generalitat Valenciana (GVA), by means of the research call "Convocatoria de Subvenciones a grupos de investigación emergentes – Convocatoria GE 2023" - project CIGE/2022/1.

GENERALITAT VALENCIANA
Conselleria d'Educació, Universitats i Ocupació

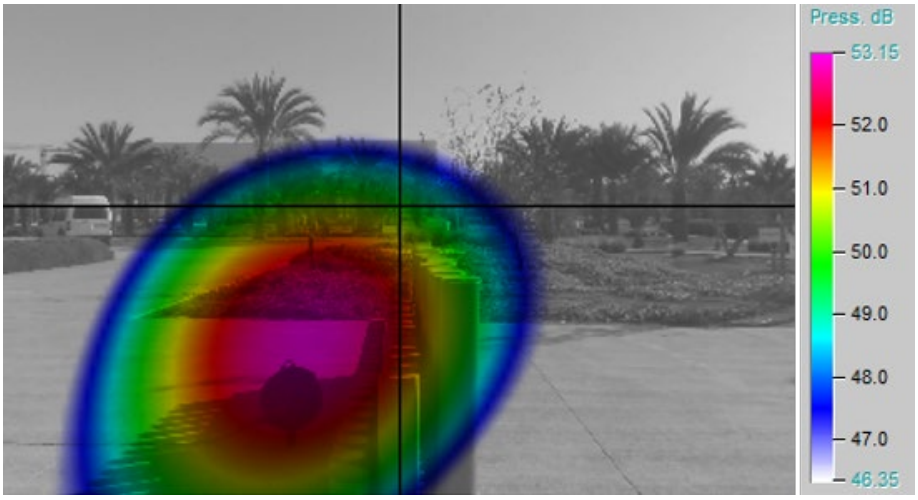


Figure 5. Acoustic camera study of the effect on sound propagation of a prototype SDAB barrier.

6. REFERENCES

[1] P. Egia, O. Abarrategi, A. Bilbao, D. Cubert, A. Diez, M. Gorriaran, A. Iriondo, I. Martinez, and D. Martinez, "The electric vehicle: Solving the silent problem", in *Proc. of the 18th International Conference on Renewable Energies and Power Quality - ICREPQ'20*, (Granada, Spain), 2020.

[2] S. Brenda, M. Petria, Ph. Haasa, Ch. Kretteka, and C. Haasper: "Hybrid and electric low-noise cars cause an increase in traffic accidents involving vulnerable road users in urban areas", *International Journal of Injury Control and Safety Promotion*, vol. 20(4), pp. 339-341, 2012.

[3] L. Garay-Vega, A. Hastings, J. Pollard, M. Zuschlag, M. Stearns: "Quieter cars and the safety of blind pedestrians: Phase I", report DOT HS 811 304, Tech.rep., National Highway Traffic Safety Administration, U.S. Department of Transportation, 2010.

[4] M.C. Pardo-Ferreira, J.A. Torrecilla-García, C.L. Heras-Rosas, J.C. Rubio-Romero: "New risk situations related to low noise from electric vehicles: perception of workers as pedestrians and other vehicle drivers", *International Journal of Environmental Research and Public Health*, vol. 17(18):E6701. 2020.

[5] S.W. Redfearn: "Some acoustical source-observer problems", *Philosophical Magazine*, Series 7, vol. 30, pp. 223-236, 1940.

[6] Z. Maekawa: "Noise reduction by screens", *Applied Acoustics*, vol. 1 (3), pp. 157-73, 1968.

[7] U.J. Kurze: "Noise reduction by barriers", *Journal of the Acoustical Society of America*, vol.55, pp. 504-518, 1974.

[8] M.P. Peiró-Torres, J. Redondo, J.M. Bravo, J.V. Sánchez Pérez: "Open noise barriers based on sonic crystals. Advances in noise control in transport infrastructures", *Transportation Research Procedia*, vol. 18, pp. 392-398, 2016.

[9] Elitsa Gieva, Ivelina Ruskova, Krasimir Nedelchev, and Ivan Kralov: "Comparative analysis of the acoustic efficiency of classical and sonic crystal noise barriers", *IOP Conf. Ser.: Mater. Sci. Eng.*, vol. 1002, 012014, 2020.

[10] R. Martinez-Sala, J. Sancho, J. V. Sanchez, V. Gomez, J. Llinares, and F. Meseguer: "Sound attenuation by sculpture", *Nature*, vol. 378, pp. 241, 1995.

[11] J. V. Sánchez-Pérez, D. Caballero, R. Mártinez-Sala, C. Rubio, J. Sánchez-Dehesa, F. Meseguer, J. Llinares, and F. Gálvez: "Sound Attenuation by a Two-Dimensional Array of Rigid Cylinders", *Physical Review Letters*, vol. 80, no. 24, pp. 5325-5328, 1998.

[12] Luca Fredianelli, Lara Ginevra Del Pizzo, and Gaetano Licitra: "Recent Developments in Sonic Crystals as Barriers for Road Traffic Noise Mitigation", *Environments*, vol. 6, 14, 2019.

[13] Javier Redondo, David Ramírez-Solana, and Rubén Picó: "Increasing the Insertion Loss of Sonic Crystal Noise Barriers with Helmholtz Resonators", *Applied Sciences*, vol. 13, 3662, 2023.

[14] Ho-Chul Shin, Shahram Taherzadeh, and Keith Attenborough, "Ground effect due to periodic and resonant roughness structures", in *Proc. of Internoise 2014 Conference*, (Melbourne, Australia), 2014.

[15] T. Cavalieri, A. Cebrecos, J.-P. Groby, C. Chaufour, and V. Romero-García: "Three-dimensional multiresonant lossy sonic crystal for broadband acoustic attenuation: Application to train noise reduction", *Applied Acoustics*, vol. 146, pp. 1-9, 2019.

[16] Alireza Tajsham, Davood Younesian, Javad Goodini, and Ali Hosseinkhani: "A new polyhedral sonic crystal for broadband sound barriers: Optimization and experimental study", *Applied Acoustics*, vol. 218, 109881, 2024.

[17] Elitsa Emilova Gieva, and Ivelina Nikolaeva Ruskova, "Models in COMSOL of Attenuation of Sonic Crystal Noise Barrier depend on Different Form", in *Proc. of XXIX International Scientific Conference Electronics - ET2020*, (Sozopol, Bulgaria), 2020.

[18] D. P. Elford, L. Chalmers, G. M. Swallowe, and F. Kusmartsev, "Matryoshka locally resonant sonic crystal", in *Proc. of the Acoustics 2012 Nantes Conference*, (Nantes, France), 2012.

[19] Hsiao Mun Lee, Kian Meng Lim, and Heow Pueh Lee: "A maze structure for sound attenuation", *Applied Acoustics*, vol. 115, pp. 88-92, 2017.

[20] David Ramírez-Solana, Jaime Galiana-Nieves, Rubén Picó, Javier Redondo, Valentino Sangiorgio, Angelo Vito Graziano, and Nicola Parisi: "Sonic Crystal Noise

Barrier with Resonant Cavities for Train Brake Noise Mitigation", *Applied Sciences*, vol. 14, 2753, 2024.

[21] F. Koussa, J. Defrance, P. Jean, and P. Blanc-Benon: "Acoustical Efficiency of a Sonic Crystal Assisted Noise Barrier", *Acta Acustica united with Acustica*, vol. 99, pp. 399-409, 2013.

[22] Antonella Bevilacqua, Gino Iannace, Ilaria Lombardi, and Amelia Trematerra: "2D Sonic Acoustic Barrier Composed of Multiple-Row Cylindrical Scatterers: Analysis with 1:10 Scaled Wooden Models", *Applied Sciences*, vol. 12, 6302, 2022.

[23] Tommaso D'Orazio, Francesco Asdrubali, Luís Godinho, Matheus Veloso, and Paulo Amado-Mendes: "Experimental and Numerical Analysis of Wooden Sonic Crystals Applied as Noise Barriers", *Environments*, vol. 10, 116, 2023.

[24] Gioia Fusaro, and Massimo Garai: "Acoustic Requalification of an Urban Evolving Site and Design of a Noise Barrier: A Case Study at the Bologna Engineering School", *Applied Sciences*, vol. 14, 1837, 2024.

[25] M. Veloso, M. Pereira, L. Godinho, P. Amado-Mendes, and J. Redondo: "Insertion loss prediction of sonic crystal noise barriers covered by porous concrete using the Method of Fundamental Solutions", *Applied Acoustics*, vol. 211, 109543, 2023.

[26] Faouzi Koussa, Jérome Defrance, Philippe Jean, Philippe Blanc-Benon, "Transport noise reduction by low height sonic crystal noise barriers", in *Proc. of the Acoustics 2012 Nantes Conference*, (Nantes, France), 2012.

[27] Constanza Rubio, Sergio Castiñeira-Ibáñez, Vicent Romero-García, and Juan Vicente Sánchez-Pérez, "Characterization of the diffraction on the upper edge of acoustic barriers based on sonic crystals. Comparison with the case of classic barriers", in *Proc. of Euronoise 2012 Conference*, (Prague, Czech Republic), 2012.

[28] Xiaochun Qin, Weijie Yang, Zijian Zhang, and Zhenghao Chen: "Research on the design and noise reduction performance of periodic noise barriers based on nested structure", *Journal of Cleaner Production*, vol. 476, 143708, 2024.2012.

DOI: 10.61782/fa.2025.0665



FORUM ACUSTICUM
EURONOISE 2025

OPTIMIZING IN-CABIN ACOUSTIC COMFORT: PSYCHOACOUSTIC EVALUATION OF ENGINE SOUND PROFILES

Maria Juliana Garzón Vargas[1*] **Zulfi Aulia Rachman** [2] **María de Diego Antón**[1]
Alberto González Salvador[1] **Miguel Ferrer Contreras**[1] **Jian Kang**[2]
Francesco Aletta[2*] **Jan Kirchhof** [3]

[1]Institute of Telecommunications and Multimedia Applications (iTEAM), Universitat Politécnica de Valencia (UPV), Valencia, Spain

[2] UCL Institute for Environmental Design and Engineering, The Bartlett, University College London, United Kingdom

[3] Müller-BBM Active Sound Technology GmbH, Munich, Germany

ABSTRACT

Achieving acoustic comfort inside the vehicle cabin typically requires a combination of Passive and Active Noise Control techniques, methods that have been effective at modifying the resulting sound field in a closed enclosure. [1] From a subjective point of view, not all noise sources are equally disturbing to passengers, and engine and road noise are often perceived as the most unpleasant noise sources, due to the presence of low-frequency components. This paper presents a subjective evaluation test designed to determine the most effective filter configuration that could improve the perception of engine noise inside a vehicle. Filtered engine noise samples are rated using the Bradley-Terry pairwise comparison method, allowing participants to express their preference between the original sound and three filtered versions of it. Recordings were captured under different operating conditions, including: driving state, gear shift and engine RPM configuration. Three perceptual attributes were chosen along with preference by default: pleasantness, power and naturality. This work aims to contribute to the development of Sound Quality Evaluation strategies that improve in-cabin acoustic comfort.

*__Corresponding author__: *mjgarva1@upvnet.upv.es.*

__Copyright__: *©2025 Maria Juliana Garzón Vargas et al. This is an open-access article distributed under the terms of the Creative Commons Attribution 3.0 Unported License, which permits unrestricted use, distribution, and reproduction in any medium, provided the original author and source are credited.*

Keywords: *psychoacoustics, sound quality, jury test, engine noise, in-cabin noise, acoustic comfort.*

1. INTRODUCTION

Numerous efforts have been made to study and deal with the acoustic comfort and driving experience of users over time. Relevant publications in this field include [2], [3], [4], [5], [6], [7], [8]. Psychoacoustics in the automotive industry plays a crucial role in reflecting the audible preferences of drivers and passengers to ensure sound quality subjectively; this along objectively indices are the two ways noise experienced in the car can be assessed. [9] Through subjective evaluation methods, researchers can determine the level of comfort in the driving experience, having in mind a positive outcome for it. [10] In the beginning, the interior development of the vehicle was mainly focused on achieving objective indices and quantitative metrics given by airborne and structure-borne noise paths. [11] However, this idea has gradually evolved over time, as a result of different challenges faced by manufacturers due to trends such as lighter and more efficient automobiles, but also the integration of Electric Vehicles (EV). [12] Sound Quality Design (SQD) is introduced in this field when engineers on customized solutions, including comfort and power. Various approaches such as digital signal processing and adaptive algorithms have been explored, more recently through Deep Learning (DL). [13]

2. METHODS

The following section briefly describes how the audio recordings were obtained, selected, analysed, processed and presented.

2.1 Data acquisition

Data were acquired with a four-cylinder gasoline engine research vehicle on public roads of Neue Gautinger Strasse, Germering, Germany. Audios were provided by researchers at Müller-BBM Active Sound Technology GmbH. All windows were kept closed during the measurements. Eight microphones were strategically placed in the vehicle compartment at the following positions: microphones 1 to 4 were placed on the ceiling of the car in the front left (FL), front right (FR), rear left (RL), and rear right (RR) positions, while microphones 5 to 8 were placed on the inner side of the headrests at the same locations. The sampling frequency was set to 8192 Hz. Each individual operating point was set and measured for approximately 1 minute and 30 seconds.

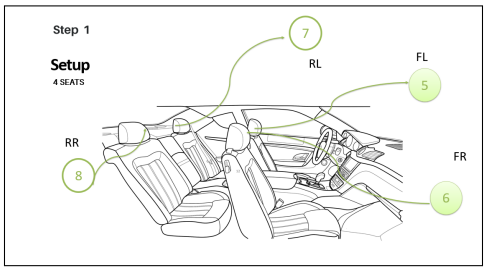


Figure 1. Setup Arrangement. M5-M6: Front seat microphones placed at the inner side of the headrests. M7-M8: Rear seat microphones.

2.2 Auditory Stimuli

From the original dataset, a total of 5 measurements were thoroughly selected for the test. Each driving operating mode was measured under different conditions: the first one reflects a smooth and constant ramp-down during the transition from 3rd to 4th gear. The second was recorded at constant speed while shifting from 3rd to 4th gear, starting at 1300 RPM (revolutions per minute). The third recording represents a smooth and continuous ramp-down in 5th gear. The fourth captures the initial ramp-up phase and, lastly, the fifth corresponds to a gradual ramp-down. All audio recordings were presented to participants in.wav format, through stereo reproduction and with normalized amplitude.

2.2.1 FIR Filters

Finite impulse response (FIR) filters are digital filters that are used to shape the frequency content of audio signals with high precision and stability. Due to their linear phase response, FIR filters keep the original shape of audio signals, which is ideal for applications such as equalization and noise reduction. Traditionally, are widely used in professional audio systems and digital audio workstations to ensure transparent sound processing without introducing phase distortion. FIR filters are also beneficial for loudspeaker correction and room compensation, where accurate control over both magnitude and phase is essential. Authors in [14] validate the effectiveness of FIR filters in modifying the frequency content of the noise signals. [15]

2.2.2 Frequency-based analysis

Power Spectral Density (PSD), also known as the power spectrum, describes how the power of a signal is distributed between different frequencies. It is widely used in signal processing applications because it helps identify dominant frequencies, noise levels, and other important signal characteristics. [16] The normalized cut-off frequency is determined based on the Nyquist theorem, which states that the maximum frequency that can be accurately represented is half the sampling rate. For the purpose of this study, 3 FIR filters were designed using the Hamming windowing method: a low-pass filter of order 800 and two high-pass filters of order 500.

2.3 Questionnaire

2.3.1 Evaluation Method

The pairwise comparison method was selected due to its effectiveness in facilitating listener evaluations by limiting judgments to two stimuli at a time, S1 and S2. This approach improves sensitivity to perceptual variations while minimizing cognitive load and individual bias, thereby increasing the reliability and consistency of the collected data. In contrast to rating scales or direct ranking procedures, pairwise comparisons are particularly well-suited for experiments aiming to establish a robust preference structure and to detect small differences in sound quality with more accuracy. [17] The order in which comparisons are presented has been manually configured based on a specific criterion: ensuring that the two most similar signals were not evaluated consecutively. This deliberate

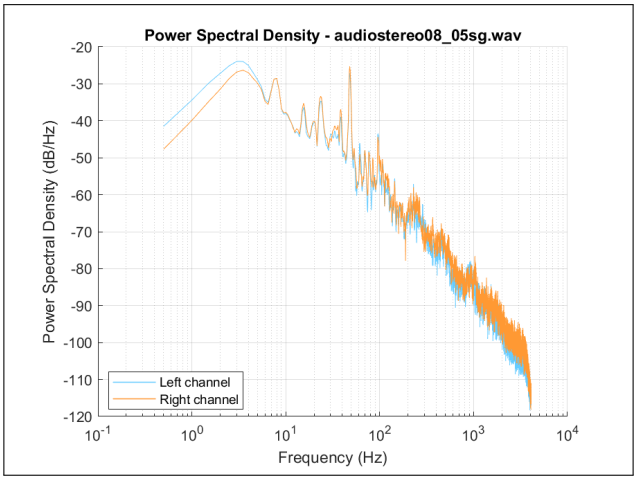


Figure 2. Power Spectral Density (PSD) of signal No. 08, measured at microphones 5 (Front Left) and 6 (Front Right). Driving operation condition: 5th gear, ramp-down. Length: 5 seconds. Sampling rate: 8192Hz.

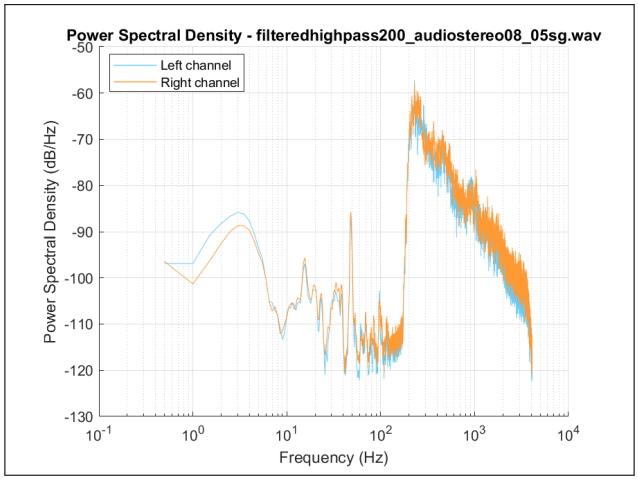


Figure 3. Powerspectral density (PSD) of signal No. 08, measured at microphones 5 (Front Left) and 6 (Front Right). Driving operation condition: 5th gear, ramp-down. Length: 5 seconds. Sampling rate: 8192Hz. Filter: High-pass, Cut-off frequency: 200Hz, Order: 500.

separation prevented potential listener bias and facilitated a more accurate and robust auditory assessment.

2.3.2 Perceptual attributes

According to [17], Pleasantness refers to the overall subjective acceptability or enjoyment of a sound, often influenced by tonal balance, loudness, and the absence of disturbing elements. Power is associated with the perceived strength or intensity of a sound, and is often linked to attributes such as loudness and spectral content that convey a sense of engine performance. Meanwhile, naturality refers to how realistic or lifelike a sound appears and whether it aligns with the listener's expectations based on prior experience with similar auditory events. These attributes were chosen based on the frequency components of the audio samples prepared. For instance, a filtered engine sound that is more pleasant may reduce listener fatigue during driving, while maintaining sufficient power ensures that the vehicle still provides a sense of performance. Additionally, preserving naturality is crucial, as overly artificial-sounding modifications can lead to user dissatisfaction, even if the sound is technically improved. Together, these attributes allow for a holistic evaluation of sound quality that balances subjective enjoyment with perceptual fidelity. [18]

2.4 Experiment

2.4.1 Tools

To avoid external and internal noise sources were perceived by listeners during the playback step, the experiment was carried out in the anechoic room of the GTAC Laboratory at UPV. Due to the low-frequency content of the noise signals, Senheiser HD600 headphones with a frequency response ranging from 12 to 40500 Hz were employed, as well as the M-Audio Track Quad sound card connected to an ASUS laptop.

2.4.2 Process

To ensure consistency, a total of 30 participants (25 Male and 5 Female) with normal hearing abilities were invited to participate in the test. Since 5 audios with different configuration were selected, 5 sets of stimuli were presented consecutively, one set of stimuli per driving mode. First, each jury was explained the step by step of the experiment and was given an example. The software application was then launched, and the subjects were asked to read the disclaimer that describes the task to be completed and their agreement to it. As the test started, volunteers were asked to listen to two signals and rate them according to their perceptual auditory preference. During every com-

parison, signals S1 and S2 are continuously played until the jurors tick the available checkboxes. The instruction provided to volunteers was: "Between signal one (S1) and signal two (S2), please select the one that you find to be most pleasant/powerful/natural, than the other based on the rating scale provided".



Figure 4. Jury inside the anechoic room, reading the agreement disclaimer prior to beginning the test.

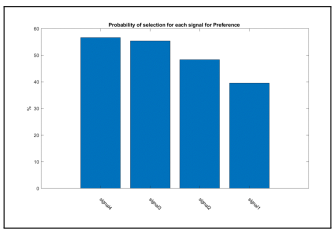


Figure 5. Probability of selection for each signal based on Preference attribute. Signal1 (original audio) was the least preferred, followed by Signal2 (low-pass filtered at 50 Hz). Signal3 and Signal4, processed with high-pass filters (200 Hz and 100 Hz respectively), received the highest preference scores.

3. RESULTS

3.1 Ratings

3.1.1 Preference ratings

The original audio signal, Signal1 received the lowest rating, indicating that it was the least preferred among the 4 available. Signal2, corresponding to the low-pass filtered signal (50 Hz, order 800), also received a negative rating, though less severe than the original, suggesting a slight improvement in perceived preference. Signal3 and Signal4, both processed with high-pass filters, demonstrated a significant increase in preference. Signal3 (high-pass filter at 200 Hz, order 500) achieved a positive rating, while signal4 (high-pass filter at 100 Hz, order 500) received the highest overall score. These results suggest that attenuating lower frequencies and preserving higher frequency content, particularly above 100 Hz, contribute positively to the subjective perception of the signal, making high-pass filtering a promising approach to improving sound quality in this context. Interestingly, this result has revealed that improved perceptual assessments can be obtained through FIR Filtering.

3.2 Acoustic EQ profile

Active Noise Control (ANC) and Active Noise Equalization (ANE) are similar schemes. While ANC focuses on reducing unwanted noise by generating anti-noise signals, ANE aims to shape the sound field to achieve a desired profile. ANE is based on ANC by not only canceling noise, but also enhancing sound quality through spectrum shaping. Relevant publications have focused on shaping the spectral content of engine noise in the vehicle interior cabin. At the same time, they highlight the importance of designing and choosing the suitable filters for the algorithms implemented in this systems. [19], [20], [21] The ultimate goal after obtaining the test results of this subjective test is to use the most pleasant filter as our Shaping filter: $C(z)$ inside the Adpative Noise Equalization algorithm.

4. ACKNOWLEDGMENTS

The authors would like to thank Noise Control experts at Müller-BBM Active Sound Technology GmbH, researchers at the GTAC Lab and the Acoustics Group in UCL, as well as all participants for their valuable time. This paper is the outcome of a research visit at the Acoustics Group of the UCL Institute for Environmental Design and Engineering, within the Bartlett School of Environment, Energy and Resources, The Bartlett Faculty of the Built Environment at University College London (UCL), in London, UK. The home institution is Universitat Politècnica de València (UPV), research center The Institute of Telecommunications and Multimedia Applications (iTEAM), The Audio and Communications Signal Processing Group (GTAC). This work is fully supported by Horizon Europe, Marie Skłodowska-Curie Actions, Doctoral Networks (MSCA-DN), INNOVA Project titled: "Active reduction of noise transmitted into and from enclosures through encapsulated structures".

5. REFERENCES

[1] P. N. Samarasinghe, W. Zhang, and T. D. Abhayapala, "Recent advances in active noise control inside automobile cabins: Toward quieter cars," *IEEE Signal Processing Magazine*, vol. 33, pp. 61–73, Nov 2016.

[2] D. VÄSTFJÄLL, M.-A. GULBOL, M. KLEINER, and T. GÄRLING, "Affective evaluations of and reactions to exterior and interior vehicle auditory quality," *Journal of Sound and Vibration*, vol. 255, no. 3, pp. 501–518, 2002.

[3] M. de Diego, A. Gonzalez, G. Pinero, M. Ferrer, and J. Garcia-Bonito, "Subjective evaluation of actively controlled interior car noise," in *2001 IEEE International Conference on Acoustics, Speech, and Signal Processing. Proceedings (Cat. No.01CH37221)*, vol. 5, pp. 3225–3228 vol.5, 2001.

[4] M. J. M. Nor, M. H. Fouladi, H. Nahvi, and A. K. Ariffin, "Index for vehicle acoustical comfort inside a passenger car," *Applied Acoustics*, vol. 69, no. 4, pp. 343–353, 2008.

[5] D. Maiberger, E. Strasser, U. Letens, and S. Par, "Contextual aspects in subjective vehicle sound assessment," *Acta Acustica united with Acustica*, vol. 105, pp. 530–544, 05 2019.

[6] J. Yoshida, F. Völk, H. Fastl, and G. Rigoll, "Influence of vehicle-exterior image on sound quality evaluation of japanese and german drivers," *Acoustical Science and Technology*, vol. 37, pp. 123–128, 05 2016.

[7] A. Wolfindale, G. Dunne, and S. Walsh, "Vehicle noise primary attribute balance," *Applied Acoustics*, vol. 73, no. 4, pp. 386–394, 2012.

[8] D. Vigé, "13 - vehicle interior noise refinement – cabin sound package design and development," in *Vehicle Noise and Vibration Refinement* (X. Wang, ed.), pp. 286–317, Woodhead Publishing, 2010.

[9] A. Miśkiewicz and T. Letowski, "Psychoacoustics in the automotive industry," *Acta Acustica united with Acustica*, vol. 85, pp. 646–649, 09 1999.

[10] Z. Wang, P. Li, H. Liu, J. Yang, S. Liu, and L. Xue, "Objective sound quality evaluation for the vehicle interior noise based on responses of the basilar membrane in the human ear," *Applied Acoustics*, vol. 172, p. 107619, 2021.

[11] M. Harrison, "4 - interior noise: assessment and control," in *Vehicle Refinement* (M. Harrison, ed.), pp. 145–233, Oxford: Butterworth-Heinemann, 2004.

[12] M. Münder and C.-C. Carbon, "A literature review [2000-2022] on vehicle acoustics: Investigations on perceptual parameters of interior soundscapes in electrified vehicles," *Frontiers in Mechanical Engineering*, vol. 8, 08 2022.

[13] H. B. Huang, R. X. Li, M. L. Yang, T. C. Lim, and W. P. Ding, "Evaluation of vehicle interior sound quality using a continuous restricted boltzmann machine-based dbn," *Mechanical Systems and Signal Processing*, vol. 84, pp. 245–267, 2017.

[14] A. R. Hamza and M. A. H. E. Shiekh, "Vehicle's cabin noise reduction techniques by cost-effective embedded processor," *International Journal of Intelligent Systems and Applications in Engineering*, vol. 11, pp. 416–429, Aug. 2023.

[15] S. D. Stearns, "Fir filter design," in *Digital Signal Processing with Examples in MATLAB*, ch. 5, pp. 111–133, CRC Press, 1 ed., 2003.

[16] A. Dwivedi, S. Ghosh, and N. Londhe, "Review and analysis of evolutionary optimization-based techniques for fir filter design," *Circuits, Systems, and Signal Processing*, vol. 37, 10 2018.

[17] N. Otto, S. Amman, C. Eaton, and S. Lake, "Guidelines for jury evaluations of automotive sounds," *S V Sound and Vibration*, vol. 35, 04 2001.

[18] P. Jennings, G. Dunne, R. Williams, and S. Giudice, "Tools and techniques for understanding the fundamentals of automotive sound quality," *Proceedings of The Institution of Mechanical Engineers Part D-journal of Automobile Engineering - PROC INST MECH ENG D-J AUTO*, vol. 1, pp. 1–16, 10 2010.

[19] M. de Diego, A. Gonzalez, M. Ferrer, and G. Piñero, "Multichannel active noise control system for local spectral reshaping of multifrequency noise," *Journal of Sound and Vibration*, vol. 274, no. 1, pp. 249–271, 2004.

[20] A. Gonzalez, M. de Diego, M. Ferrer, and G. Pinero, "Multichannel active noise equalization of interior noise," *IEEE Transactions on Audio, Speech, and Language Processing*, vol. 14, no. 1, pp. 110–122, 2006.

[21] M. Ferrer, M. de Diego, A. Hassani, M. Moonen, G. Piñero, and A. Gonzalez, "Multi-tone active noise equalizer with spatially distributed user-selected profiles," *IEEE/ACM Transactions on Audio, Speech, and Language Processing*, vol. 30, pp. 3199–3213, 2022.

DOI: 10.61782/fa.2025.0780

FORUM ACUSTICUM EURONOISE 2025

SOUND ATTENUATION OF LOUVERED NOISE BARRIERS FOR INDUSTRIAL EQUIPMENT

Nikolay Kanev[1,2*] **Alexander Dolger**[2]
[1] Research Institute of Building Physics, Russia
[2] Moscow State University of Civil Engineering, Russia

ABSTRACT

An industrial equipment is often noise source in urban spaces and disturbs people everyday activities. The usual way to reduce noise level is application of barriers surrounding the equipment. On the other hand, any obstacles can interfere with the normal operation of the equipment, for example, they can block the air flow. Therefore, the barrier should provide both significant sound attenuation and sufficient ventilation. For this reason, the louvered noise barriers are used in practice to protect residential areas and other noise sensitive spaces. In the paper we study their sound attenuation performance in dependence on acoustic properties of the louvre blades. It is shown that the rigid blades are not so effective because sound energy penetrates through the barrier, whereas the dissipative louvre blades reduce sound more effective. In addition, we consider the other two boundary conditions for the louvers. It is found that the reactive impedance shows the highest performance at low frequencies.

Keywords: *simulation, impedance, diffraction, noise control*

1. INTRODUCTION

Technological and industrial equipment for various purposes continues to be one of the major sources of man-made noise in buildings and surrounding areas. Exposure to elevated noise levels reduces acoustic comfort and has a negative impact on human health, leading to physiological and psychological consequences. These factors highlight the need for effective noise reduction measures, making this an important area of focus in architectural and building acoustics.

One of the issues is shown in Fig. 1. Dry coolers are placed on the roof and emit noise around. To reduce noise radiated downwards the equipment is surrounded by a heavy brick barrier. The noise level on the lower floors and on the ground is appropriate, whereas on the upper floors the noise acts directly on the windows and terrasses and its level is still too high. It is impossible to cover the equipment with a solid roof, as this would prevent ventilation. Therefore, a ventilated barrier is required, and a louvered-type noise barrier can be used to achieve this.

The sound attenuation of louvered barriers has been studied [1-6], and this research continues these investigations. In this paper we focus on the acoustic properties of louvers. Using simulation, we study the attenuation of sound transmitted through the barrier depending on the acoustic impedance of the louvre surfaces.



Figure 1. Dry coolers on the roof.

[*] ***Corresponding author***: *nikolay.kanev@mail.ru*
Copyright: *©2025 First author et al. This is an open-access article distributed under the terms of the Creative Commons Attribution 3.0 Unported License, which permits unrestricted use, distribution, and reproduction in any medium, provided the original author and source are credited.*

2. LOUVERED NOISE BARRIERS

2.1 Sound diffraction by barriers

Sound attenuation by barriers is usually calculated using a classical diffraction theory [7]. The sound transmitted through the louvered barriers with a finite height can be divided into two components (Fig. 2). The first component T_1 is the sound that propagates around the upper edge of the barrier. The second component T_2 is the sound that penetrates through the barrier. By separating these two components, we can simplify the diffraction problem. The transmission coefficient T_1 can be found using the known results of diffraction by a rigid finite barrier. The calculation of the transmission coefficient T_2 can be fulfilled for the infinite louvered barrier. This approach allows us to focus on the second component of the transmitted sound and find the parameters of the barrier for maximum sound attenuation.

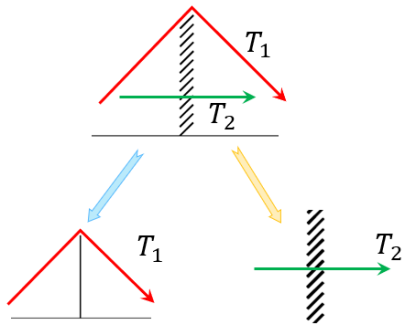


Figure 2. Simplification of the problem of sound diffraction by the louvered barrier.

In this paper, we examine the infinite louvered barrier and investigate the impact of its acoustic properties on sound attenuation.

2.2 Attenuation of sound transmission

The formulation of the sound diffraction problem by an infinite louvered barrier is illustrated in Fig. 3. The louvers are rectangular in shape with dimensions of h and L, with a spacing of H between the edges of the louvers. The inclination angle of the louvers is denoted by α. These four geometrical parameters completely define the barrier.

Acoustic properties of the louvers are described by the impedance Z normalized to ρc, where ρ is a density of the medium and c is a sound speed. All louver surfaces have the same acoustic impedance.

The incident sound is a harmonic plane wave with the wavenumber $k = \omega/c$, where ω is frequency. We are interested in the sound field behind the barrier.

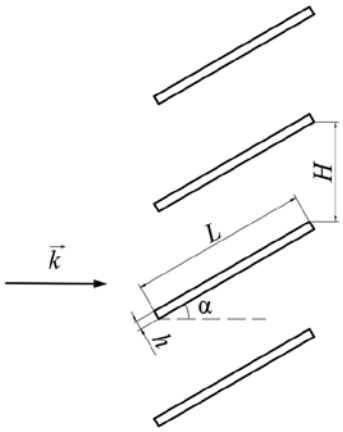


Figure 3. Formulation of the diffraction problem.

If the sound energy density of the incident wave is E_1 and the sound energy density behind the barrier is E_2, then the sound attenuation due to the barrier is determined as

$$T = 20\lg\frac{E_1}{E_2}. \quad (1)$$

We will use simulation to calculate the sound attenuation coefficient T.

3. SIMULATION

The scheme of the numerical experiment is shown in Fig. 4. We consider a two-dimensional case with a rectangular domain of dimensions 20 x 10 m. One side of the domain is a plane oscillating at frequency ω with a velocity normal to that side. All other sides of the domain have the impedance $Z_0 = 1$ and slightly reflect sound waves. Therefore, the oscillating side acts as a source for a plane wave.

A louvered barrier is placed in the middle of the domain. Each louver has dimensions $h = 0.05$ m and $L = 1$ m. The distance between the louvers edges is $H = 0.45$ m, resulting in a period of 0.5 m for the structure. The parameters h, H and L are fixed in this experiment, while the inclination angle α can take on different values. The impedance of the louver surfaces will be changed as well.

A probe domain is a rectangular area located behind the barrier. The sound energy density is calculated in the entire simulation domain without the barrier, and E_1 is the average of this value over the probe domain. To calculate the sound energy density E_2 with the barrier, the same process is followed, but with the addition of the barrier. The sound attenuation of the barrier is then found using Eqn. (1).

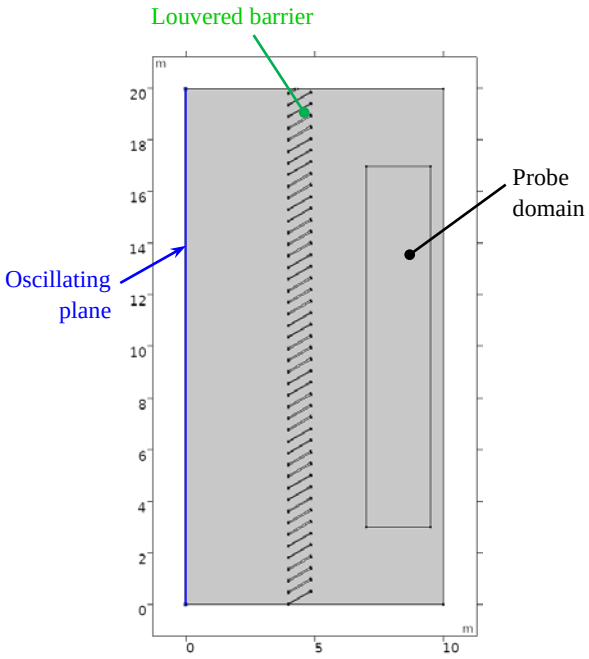


Figure 4. Scheme of the numerical experiment.

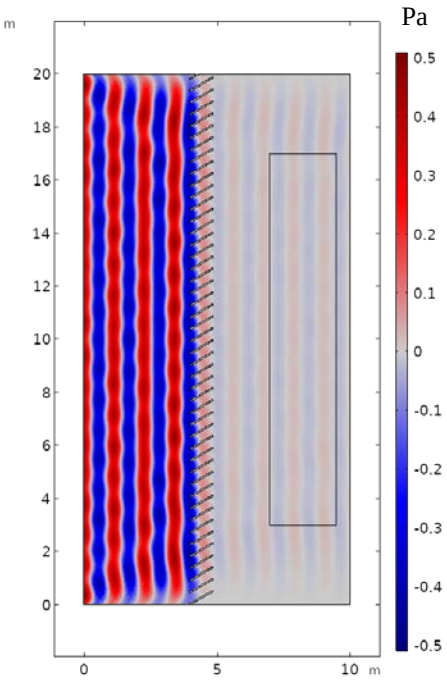


Figure 5. Sound pressure at 300 Hz with Z =1 and α = 30°.

Fig. 5 shows an example of calculating the sound pressure field at 300 Hz with the incilnation angle α = 30° and the surface impedance Z = 1. The sound field appears to be a set of the plane waves with slight distortions caused by reflections from the boundaries of the calculation domain. We can see that the transmitted wave has a smaller amplitude in comparison with the incident one. Therefore, the barrier effectively attenuates sound.
The following calculations of T are made in a similar way for different values of the louver impedance. We will use the frequency range 100-1000 Hz with a step size of 100 Hz.

3.1 Rigid surface

The first issue we consider is the louvers with the rigid surfaces. The standard boundary condition is $\partial p/\partial n = 0$, where p is the sound pressure, n is a normal to the surface. The sound attenuation defined by Eqn. (1) for the inclination angles α = 0, 30°, 60° is given in Fig. 6.

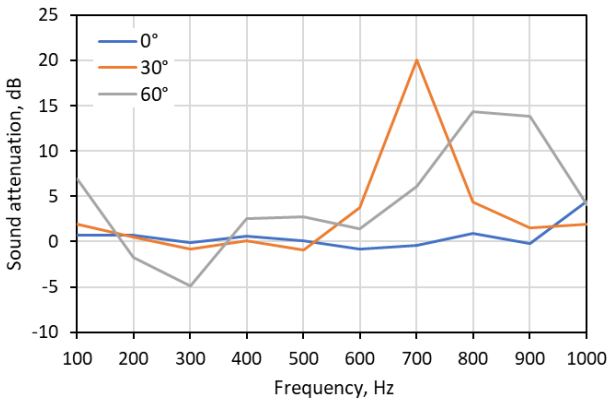


Figure 6. Sound attenuation for the rigid louvers.

If the louvers are parallel to the wavevector (α = 0) the sound attenuation is close to zero at all frequencies, whereas the inclined louvers reduce transmitted sound at certain frequencies. But their effect is narrowband, so the rigid louvers are not very effective.

3.2 Absorbing surface

Next type of the louvers is a sound absorber with the surface impedance Z_a = 1. This surface completely absorbs a normally incident sound wave. The calculated sound attenuation is shown in Fig. 7. The barrier reduces sound at all frequencies and the reduction increases with the increase of the angle α.

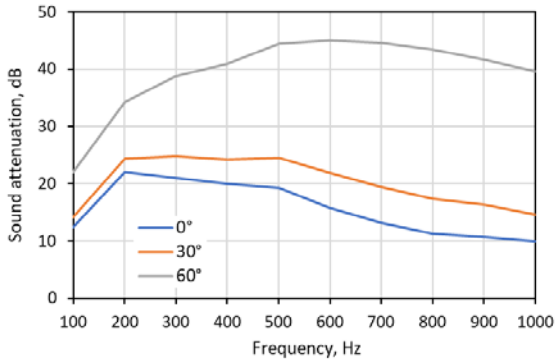


Figure 7. Sound attenuation for the absorptive louvers.

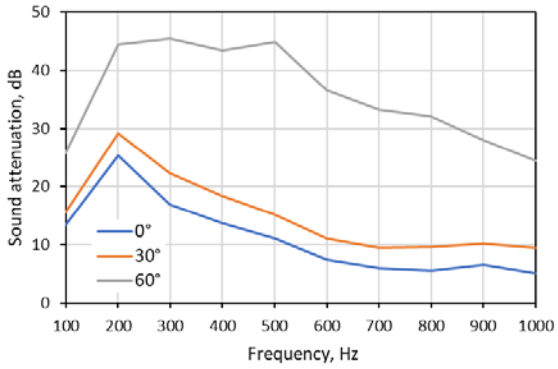


Figure 8. Sound attenuation for the louvers with the Creamer's impedance.

It is important to note that the distance between the louvers changes with the angle α, because the space period H is fixed. The distance is $H\cos\alpha$, it decreases with increase of α. So, the better attenuation for α > 0 is related to a smaller distance.

The non-inclined louvers have the performance of 10-20 dB in the entire frequency range. The maximum sound attenuation is at frequencies 200-500 Hz. The frequency characteristic resembles the performance of a plate muffler used for ducts [8].

3.3 Cremer's impedance

Sound propagation in a duct has a maximum attenuation coefficient if the duct surfaces have the Cremer's or optimal impedance [9,10]. Using the formula for the optimal impedance derived in [11] we can find it in dependance on the duct width d as follows

$$Z_c = kd(0.15 + 0.12i). \quad (2)$$

We can hope that the optimal sound decay in the duct between the louvers will provide a good performance of the sound attenuation by the barrier. At 500 Hz the optimal impedance as given by Eqn. (2) is Z_c = 0.61+0.49i. The simulation results for this impedance are presented in Fig. 8. The maximum attenuation for α = 0, 30° occurs at 200 Hz, rather than 500 Hz. It means that the short duct with the length L can not be considered as an infinite duct. Anyway, the found effect is comparable to that of the absorbing surfaces, but at high frequencies the sound attenuation is lower.

The large inclination angle as seen in Fig. 7 and 8 provides very high sound attenuation for both the absorptive louvers and the ones with the Cremer's impedance. At all frequencies the effect is greater than 20 dB.

3.4 Reactive impedance

The final type of impedance is a reactive impedance with Re Z = 0. The louvers do not dissipate sound energy, but at low frequencies, under certain conditions, all eigenmodes in the gap between the louvers are non-uniform. Above a certain frequency there are uniform modes and sound propagates through the gap. This physical principle allows us to hope that the barrier effectively isolates sound waves at low frequencies.

Fig. 9 shows the sound attenuation for the louvers with the impedance Z_r = –0.1i. For α = 0, 30° the barrier reduces the transmitted sound at frequencies below 500 Hz. At higher frequencies sound propagates between the louvers without attenuation. For α = 60° the effectiveness of the barrier is significant up to 1000 Hz.

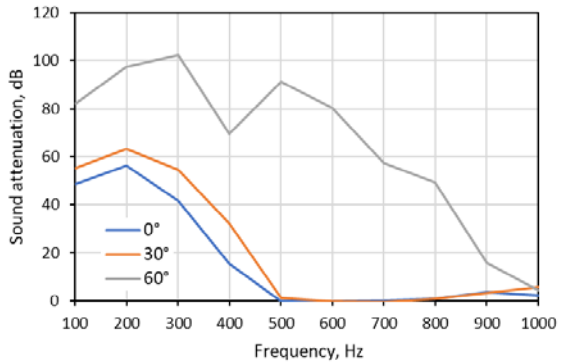


Figure 9. Sound attenuation for the louvers with the reactive impedance.

3.5 Comparison of different impedances

To compare the sound attenuation for different boundary conditions on the louver surfaces, we present the results for $\alpha = 0°$ and three types on the impedance are presented in Fig.10. We can see that the Cremer's impedance has the lowest performance, while the absorptive impedance provides significant attenuation over a wide frequency range. Louvers with reactive impedances have a very high reduction in transmitted wave at low frequencies, but their performance is negligible at higher frequencies.

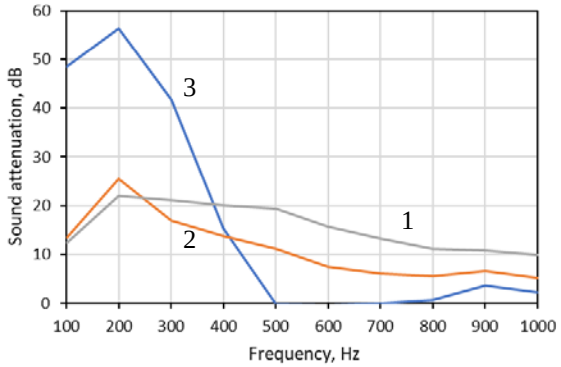


Figure 10. Sound attenuation for the louvers with different impedances for $\alpha = 0°$: $1 - Z_a$, $2 - Z_c$, $3 - Z_r$.

4. CONCLUSION

The findings of this study demonstrate the importance of selecting the acoustic properties of the louvers for designing ventilated barriers. Based on our findings, we can conclude that absorptive louvers can be used for wide-band sound attenuation. Industrial equipment typically emits low-frequency noise, so in this case, louvers with reactive impedance may be more suitable.

To generalize the findings, additional simulations and a theoretical study of infinite louvered barriers are required. The dependence of sound attenuation on the length, thickness of louvers, and the distance between them needs to be investigated in order to determine the optimal parameters for the barrier.

5. REFERENCES

[1] R. Lyons: "Sound insulation of acoustic louvre and open screens," *Build. Acoust.*, vol. 1, no. 2, pp. 105–124, 1994.

[2] G.R. Watts, D.C. Hothersall, K.V. Horoshenkov: "Measured and predicted acoustic performance of vertically louvred noise barriers," *Appl. Acoust.*, vol. 62, pp. 1287-1311, 2001.

[3] E.B. Viveiros, B.M. Gibbs, S.N.Y. Gerges: "Measurement of sound insulation of acoustic louvres by an impulse method," *Appl. Acoust.*, vol. 63, pp. 1301-1313, 2002.

[4] J.L. Horner, S.J. Walsh: "Prediction of the spatial characteristics of higher mode sound transmission through a periodic slit screen," *Appl. Acoust.*, vol. 83, pp. 47-56, 2014.

[5] B. He, X.B. Xiao, X. Zhou, J. Han, X.S. Jin: "Characteristics of sound insulation and insertion loss of different deloading sound barriers for high-speed railways," *Notes on Numerical Fluid Mechanics and Multidisciplinary Design*, vol. 126, pp. 345-352, 2014.

[6] T. Astrauskas, P. Baltrėnas, T. Januševičius, R. Grubliauskas: "Louvred noise barrier for traffic noise reduction," *The Baltic journal of road and bridge engineering*, vol. 16, no. 1, pp. 140–154, 2021.

[7] H. Kuttruff: *Acoustics*. London, New York: Taylor & Francis, 2007.

[8] D.V. Chugunkov, E.A. Zhuravlev, G.A. Seyfelmlyukova, K.C. Fomenko: "Study of the acoustic efficiency of a plate silencer of the original design," *IOP Conf. Ser.: Mater. Sci. Eng.*, vol. 976, 012029, 2020.

[9] L. Cremer: "Theory regarding the attenuation of sound transmitted by air in a rectangular duct with an absorbing wall, and the maximum attenuation constant produced during this process," *Acustica*, vol. 3, pp. 249-263, 1953.

[10] B.J. Tester: "The optimization of modal sound attenuation in ducts, in the absence of mean flow," *J. Sound Vib.*, vol. 27, no. 4, pp. 477–513, 1973.

[11] N.G. Kanev: "Optimum sound attenuation in a rectangular duct with impedance walls," *Acoust. Phys.*, vol. 68, no. 4, pp. 403-407, 2022.

DOI: 10.61782/fa.2025.0084

FORUM ACUSTICUM EURONOISE 2025

ACOUSTIC PROPERTIES OF A LOUVERED NOISE BARRIER WITH TIRE RUBBER GRANULATE INFILL

Edgaras Strazdas[1*] **Tomas Januševičius**[2]
[1] Department of Environmental Protection and Water Engineering, Vilnius Gediminas Technical University, Lithuania
[2] Research Institute of Environmental Protection, Vilnius Gediminas Technical University, Lithuania

ABSTRACT

To ensure comfortable working and living conditions, various systems such as heating, ventilation, heat pumps, and generators are employed, all of which require high air permeability for optimal performance. Consequently, conventional noise barriers are often unsuitable in these contexts. This study aims to design a louvered noise barrier with high air permeability by incorporating recycled tire rubber granulate as the sound-absorbing material. This approach supports the principles of the circular economy and sustainability by promoting the reuse of secondary materials. The barrier's acoustic performance was evaluated in a semi-anechoic noise reduction chamber. The influence of the number of louvers and their inclination angles on sound attenuation was investigated. Experimental measurements were used to determine the sound reduction index (R'), sound insertion loss (IL), and equivalent sound level loss (L_{Aeq}). The structure achieved a maximum weighted sound reduction index (R'_w) of 4.0 dB. The apparent sound reduction index reached up to 10.2 dB at high frequencies (4000 Hz). The highest recorded sound insertion loss was 12.63 dB at 2500 Hz, while the maximum equivalent sound level loss (L_{Aeq}) was 9.4 dB(A).

Keywords: *acoustic louvers, noise barrier, tire rubber granulate, anechoic chamber, insertion loss.*

[*] ***Corresponding author***: *edgaras.strazdas@vilniustech.lt.*
Copyright: *©2025 Strazdas et al. This is an open-access article distributed under the terms of the Creative Commons Attribution 3.0 Unported License, which permits unrestricted use, distribution, and reproduction in any medium, provided the original author and source are credited.*

1. INTRODUCTION

Noise is emitted by air-cooling equipment, water cooling units, fans, and diffusers due to the movement of exhaust and intake airflow, as well as the operation of condensers and compressors. Acoustic comfort issues can be addressed using conventional noise barriers. However, these enclosures are not suitable for ventilation equipment, which must exhaust or intake air to function properly. Increasingly strict noise regulations are prompting many manufacturing and commercial companies to seek effective solutions to avoid exceeding the prescribed noise levels in their environments.

Noise barriers are among the most effective and widely used methods for mitigating noise [1-4]. The selection of a specific type of barrier in each case is usually determined by the position of the noise source, the characteristics of the noise it emits, and the terrain of the site under consideration [5]. The effectiveness of an installed barrier depends on the materials used in its construction, the height of the barrier, surface geometry, shape, acoustic properties of additional elements installed on top of the barrier, as well as the surrounding terrain and meteorological conditions [6-8].

The operation of noise barriers is based on the principle that a sound wave loses its original energy and becomes attenuated when passing directly through an obstacle. A portion of the wave's energy is reflected upon impact, another portion is absorbed and converted into thermal energy, and the remainder is either transmitted through the material or diffracted. This residual energy can reach the receiver, either separately or as a combination of transmitted and diffracted waves [7].

One effective way to reduce noise is through sound absorption. Sound-absorbing materials are often used in combination with perforated plates made from materials such as steel, glass, plastic, and others. Many of these

materials are effective at reducing medium and high-frequency noise but are less effective at controlling low-frequency noise. To increase air permeability or provide adequate shading, scientists have proposed several types of noise barriers, such as sonic crystals or louvered structures. Researchers have found that sonic crystals can achieve noise attenuation levels between 16 and 25 dB(A) [9]. Louvered structures are often used as façade elements or structural components of buildings. They provide necessary light and air permeability while also offering sound attenuation properties [10]. Sound-attenuating louvers can be used to reduce noise from engineering equipment or road traffic [11]. One alternative for reducing noise from ventilation equipment is the use of sound-absorbing louvers made of perforated panels filled with absorbent material. The operating principle of a louvered noise barrier is based on the reflection, absorption, and refraction of incoming sound waves. Reflection occurs when a wave traveling through one medium encounters another medium and is partly scattered such as when a sound wave moves from a liquid to a gaseous medium, or from a solid to a liquid, and so on. Part of the wave passing through different media is reflected back into the original medium, while another part is absorbed and thus enters the new medium. Upon impact, the sound wave also undergoes refraction, changing its propagation trajectory in the new medium. This occurs due to the sudden change in the speed at which the sound wave travels. Sound absorption is directly related to the frequency of the sound waves and also depends on the angle at which the sound waves enter the material. Vilniškis et al. conducted a study examining three different louver configurations. The best noise-reduction performance was observed in louvers covered with glass wool panels, achieving sound insulation values ranging from 10.8 to 12.5 dB. Meanwhile, louvers covered with polystyrene foam panels achieved values between 5.4 and 8.4 dB [12]. Vilniškis also found that increasing the tilt angle of the panel structure increased the pressure near the structure from 45 Pa to 9 kPa, and the air velocity passing through the structure changed from 13 m/s to 70 m/s [13]. Astrauskas et al. found that the noise attenuation of the louvered barrier was greatest in the 2500 Hz and 3150 Hz octave frequency bands. Depending on the tilt angle of the louvers, sound attenuation in these bands reached up to 28 dB(A), and the equivalent sound pressure level was reduced by up to 17 dB(A) [11].

The aim of this paper is to design a louvered noise barrier with high air permeability, incorporating recycled tire rubber granulate as the sound-absorbing material. The paper is organized as follows: Section 2 describes the materials and methods; Section 3 presents the main results; and Section 4 provides the conclusions.

2. MATERIALS AND METHODS

The main research object of this study is a louvered barrier composed of a specific number of identical louvers filled with sound-absorbing recycled tire rubber granulate. The noise barrier consists of horizontal louvers inclined at a specified angle. The horizontal louvers are 30 mm thick and 860 mm long, and are made from bent metal sheets. The upper part of each louver is a solid metal plate, while the lower part is a perforated metal plate. Inside the louvers is the sound-absorbing material. The perforated plate is placed on the underside of the louver to protect the sound-absorbing material from environmental factors such as precipitation, dust, and icing. The structure of the louver is shown in Figure 1.

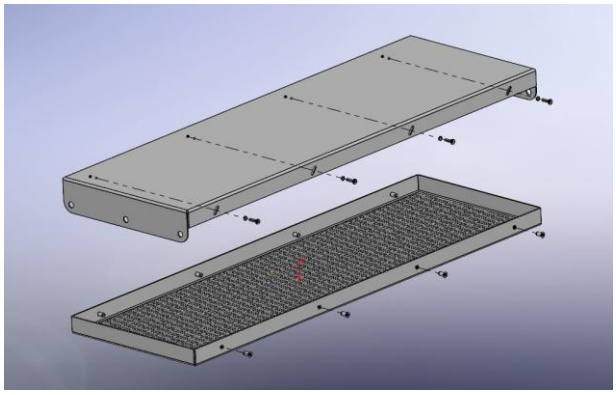


Figure 1. The structure of the louvers in the noise barrier.

The louvers are made from two 2 mm thick bent metal sheets. The upper sheet is a solid metal plate, while the lower one is a perforated metal plate. The parameters of the perforated sheet include 35% open area with round perforations, 5 mm in diameter, and 8 mm centre-to-centre spacing. After the louvers are filled, the metal sheets are joined together using rivets or bolts.

The louver infill consists of two layers of recycled tire rubber: a 10 mm thick rubber granulate plate for sound insulation and a 20 mm thick layer of rubber granules (granule size 2–5 mm) for sound absorption (Figure 2). The rubber granulate plate made from shredded tire rubber granules (1 mm in size), mixed with polyurethane glue in a 30/70% ratio. To prevent the granules from falling out

through the perforated sheet, a metal mesh with 1x1 mm openings is placed on top.

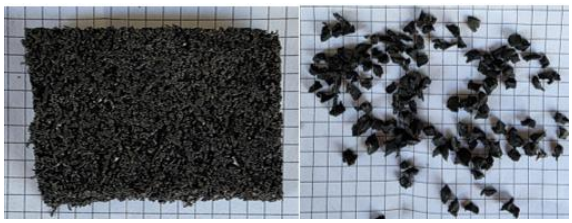


Figure 2. Louvers infill: 10 mm thick rubber granulate plate and 2–5 mm tire rubber granules.

The filled louvers are placed into a wooden frame measuring 900x970 mm and secured with screws from the sides. The frame with louvers is then placed into the window of a semi-anechoic chamber (Figure 4, Figure 5). A general view of the semi-anechoic chamber is shown in Figure 3.

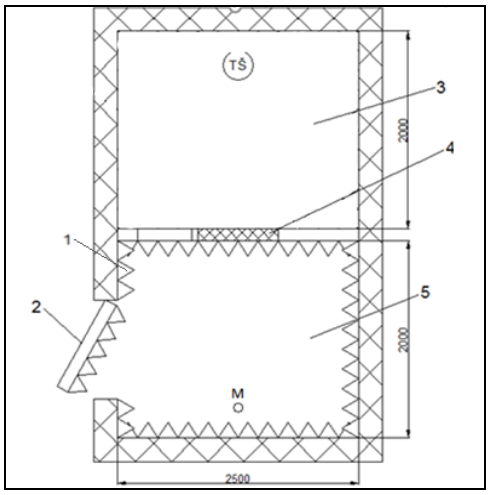


Figure 3. General view of the noise reduction chamber. 1 – walls covered with foam rubber, 2 – door, 3 – room for outgoing sound, 4 – location of structure, 5 – room for receiving sound, M – microphone position, TŠ – noise source.

Three different configurations of the louvered barrier were investigated: structures with 5, 6, and 7 louvers. Each configuration was tested with the louvers tilted at angles of 0, 15, 30, and 45 degrees. In total, 12 different louvered barrier configurations were tested.

The experimental studies were conducted using high-precision equipment from the manufacturer Brüel & Kjær: the sound source "Brüel & Kjær The Omni-Power Sound Source Type 4292-L," the amplifier "Brüel & Kjær Type 2734," and the sound level analyser "Brüel & Kjær 2270." The measuring device complies with standards IEC 61672, IEC 60651, and IEC 60804. During the tests, the sound level was measured using a one-third octave band filter.



Figure 4. Tested louvered noise barrier from room for outgoing sound.



Figure 5. Tested louvered noise barrier from sound receiving room.

The following parameters were determined during the experimental measurements:

- sound reduction index (R').
- sound insertion loss (IL).
- equivalent sound level loss (L_{Aeq}).

According to the [14], the sound insulation level of a louvered noise barrier was determined. This standard provides all the main measurement methods and procedures required to determine sound insulation under laboratory conditions. Sound pressure levels are measured in both the source and receiving rooms. The average sound pressure level is calculated in both rooms (applying background noise correction), and the sound reduction index the barrier is determined. The weighted sound reduction index (R'_w) is determined by fitting a standard reference curve to the measured sound reduction index values across various frequencies, as specified in [15].
Insertion loss was calculated as the difference between the sound pressure level without the louvers and the sound pressure level with the louvers. Insertion loss was calculated according to Eqn. (1) as described in [16].

$$IL = L_{p1} - L_{p2} \quad (1)$$

where L_{p1} is the sound pressure level without the louvers and L_{p2} is the sound pressure level with louvers.
Equivalent sound level loss (L_{Aeq}) is the difference in equivalent noise level between the sound emitted by the noise source, measured in the receiving room without the louvers, and the sound level measured after the louvers have been installed.

3. RESULTS

First, sound reduction measurements of the barrier were performed. Figure 6 presents the results of sound reduction measurements for constructions with 5, 6, and 7 louvers in 1/3 octave frequency bands, ranging from 100 to 5000 Hz. From the obtained results, it can be observed that in the low-frequency range to 500 Hz, the apparent sound reduction index is similar across the all barrier configurations. Additionally, the measured index is relatively high at low frequencies. However, these results may be affected by room or measurement effects. The chamber may have standing waves at low frequencies that "trap" energy, making the insulation performance appear better than it actually is. Moreover, since low frequencies have longer wavelengths, if the microphone is positioned at a node or null point, it may register lower sound levels, thereby artificially increasing the perceived sound insulation. In the mid-frequency range from 500 to 1600 Hz negative sound reduction index values are observed, which is caused by interference resulting from standing waves in the chamber. For these reasons, the most reliable results were obtained when analyzing the sound reduction at high frequencies, ranging from 2000 to 5000 Hz. When examining the barrier composed of 5 louvers, the apparent sound reduction index in these frequencies ranged from 0.1 dB with the louvers positioned at a 0-degree angle, to 5.1 dB when tilted at a 45-degree angle. The weighted sound reduction index (R'_w) ranged from 0.1 dB to 1.5 dB. The barrier with 6 louvers showed sound reduction of up to 8.2 dB at a frequency of 3150 Hz when the louvers were tilted at a 45-degree angle. The weighted sound reduction index (R'_w) ranged from 0.4 dB to 2.1 dB. The construction consisting of 7 louvers achieved the highest results, with the apparent sound reduction index reaching up to 10.2 dB at 4000 Hz when the louvers were tilted at a 45-degree angle. When the louvers were tilted at 30 degrees, the result at high frequencies reached up to 5.3 dB; at 15 degrees, up to 3.1 dB; and up to 2.4 dB at 0 degrees.

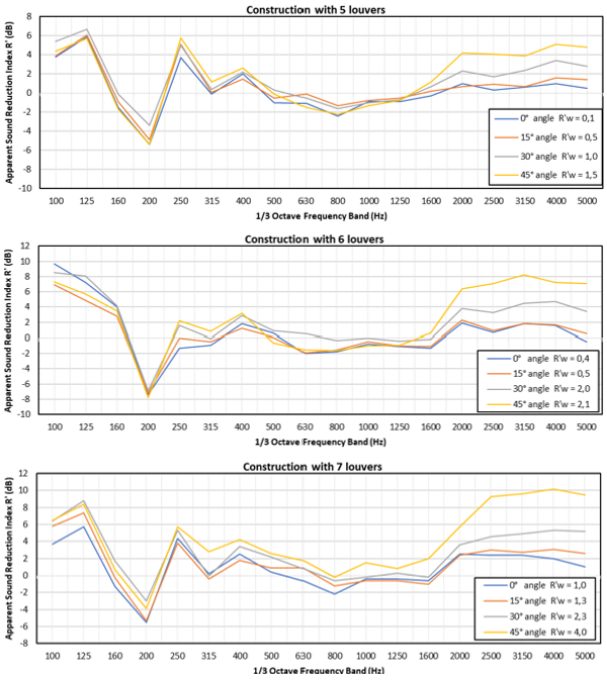


Figure 6. Louvered noise barrier sound reduction.

The weighted sound reduction index (R'_w) of construction with 7 louvers ranged from 1.0 dB to 4.0 dB at inclination angle from 0 to 45 degrees.

Another parameter examined was the sound insertion loss (IL). The insertion loss results for the louvered barrier are presented in Figure 7. For the barrier with 5 louvers, the results at low frequencies (100–500 Hz) reached up to 6.01 dB at 100 Hz when the louvers were tilted at a 15-degree angle. At 400 Hz, the highest IL was measured at 5.08 dB with the louvers tilted at 45 degrees. As with the previously analyzed parameter, results at low frequencies can be influenced by room or measurement effects. In the mid-frequency range (500–1600 Hz), the IL reached up to 6.26 dB at 1600 Hz. The highest IL was observed in the high-frequency range, reaching up to 8.35 dB near 5000 Hz with the louvers tilted at a 45-degree angle. At high frequencies, the influence of increasing the tilt angle on achieving higher insertion loss is clearly noticeable.

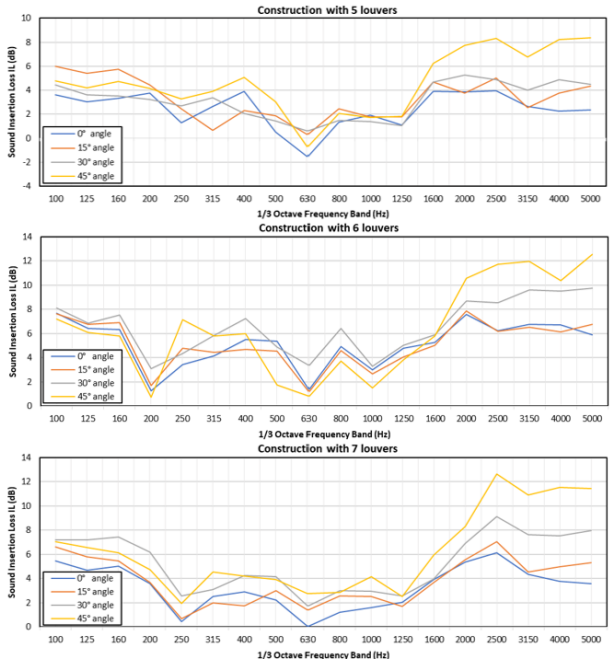


Figure 7. Louvered noise barrier sound insertion loss.

For the barrier with 6 louvers, the results of insertion loss at low frequencies (100–500 Hz) reached up to 7.52 dB at 160 Hz when the louvers were tilted at a 30-degree angle. In the mid-frequency range (500–1600 Hz), the IL reached up to 6.41 dB at 800 Hz with the louvers tilted at a 30-degree angle. The highest insertion loss (IL) was observed in the high-frequency range, reaching up to 12.55 dB at 5000 Hz with the louvers tilted at a 45-degree angle. The construction consisting of 7 louvers achieved the highest IL results overall up to 7.45 dB at low frequencies, 5.96 dB in the mid-frequency range, and up to 12.63 dB at 2500 Hz.

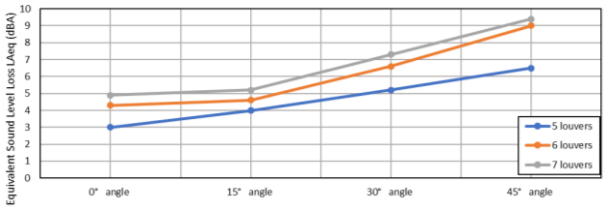


Figure 8. Equivalent sound level loss (L_{Aeq}) results.

Another parameter analyzed to evaluate the effectiveness of the louvered barrier was the Equivalent Sound Level Loss (L_{Aeq}). The results are presented in Figure 8. According to the data, when the number of louvers increased from 5 to 7 with a louver tilt angle of 0 degrees, the results changed from 3.0 dB(A) with 5 louvers to 4.3 dB(A) with 6 louvers, and 4.9 dB(A) with 7 louvers. When the louvers were tilted at a 15-degree angle, the results were 4.0, 4.6, and 5.2 dB(A), respectively. Increasing the tilt angle to 30 degrees, the equivalent sound level loss reached 5.2 dB(A) with 5 louvers, 6.6 dB(A) with 6 louvers, and 7.3 dB(A) with 7 louvers. The highest equivalent sound level loss in all cases was obtained when the louvers were tilted at a 45-degree angle, with results reaching 6.5 dB(A) for 5 louvers, 9.0 dB(A) for 6 louvers, and 9.4 dB(A) for 7 louvers.

In summary, it can be stated that the main parameter determining the effectiveness of the louvered barrier in all cases is the inclination angle of the louvers. The highest efficiency of louvered barrier is achieved when the louvers are tilted at a 45-degree angle and the structure consists of 7 louvers, as this increases the sound-absorbing surface area and reduces the gap between louvers. The louvered barrier is most effective at attenuating noise in the high-frequency range, from 1600 to 5000 Hz. Similar conclusions were reached by researchers who studied a similar type of louvered noise barrier with sound-absorbing materials applied to the louvers [11-12, 17].

4. CONCLUSIONS

This study evaluated the acoustic performance of a louvered noise barrier incorporating recycled tire rubber granulate as a sound-absorbing material. The experimental results demonstrated that both the number of louvers and their

inclination angle significantly affect the barrier's effectiveness in reducing noise. The most influential parameter across all configurations was the louver tilt angle, with the highest performance observed at 45 degrees. Increasing the number of louvers from 5 to 7 consistently improved sound attenuation results, due to the greater surface area of sound-absorbing material and reduced spacing between louvers. Among the tested configurations, the barrier with 7 louvers tilted at 45 degrees exhibited the best acoustic performance, achieving a maximum apparent sound reduction index of 10.2 dB at 4000 Hz, a sound insertion loss of 12.63 dB at 2500 Hz and an equivalent sound level loss (L_{Aeq}) of 9.4 dB(A). The barrier is most effective in the high-frequency range (1600–5000 Hz), aligning with the typical operational noise range of HVAC and similar equipment. These findings confirm the potential of louvered barriers using sustainable infill materials for application in ventilation-related noise control.

5. REFERENCES

[1] H. M. Ariff, T. T. Dele-Afolabi, T. H. Rafin, D. W. Jung, Z. Leman, K. A. M. Rezali, and R. Calin, "Temporary sound barrier system from natural fiber polymeric composite," *Materials Today: Proceedings*, 2022. DOI: 10.1016/J.MATPR.2022.11.142.

[2] A. I. Komkin and G. M. Nazarov, "Features of sound diffraction by a noise absorbing screen," *Acoustical Physics*, vol. 67, no. 3, pp. 298–301, 2021. DOI: 10.1134/S1063771021030076.

[3] A. Nowoświat, J. Bochen, L. Dulak, and R. Zuchowski, "Study on sound absorption of road acoustic screens under simulated weathering," *Archives of Acoustics*, vol. 43, no. 2, pp. 323–337, 2018. DOI: 10.24425/122380.

[4] V. Zaets and S. Kotenko, "Investigation of the efficiency of a noise protection screen with an opening at its base," *Eastern-European Journal of Enterprise Technologies*, vol. 5, no. 5(89), pp. 4–11, 2017. DOI: 10.15587/1729-4061.2017.112350

[5] I. Ekici and H. Bougdah, "A review of research on environmental noise barriers," *Building Acoustics*, vol. 10, no. 4, pp. 289–323, 2003. DOI: 10.1260/135101003772776712.

[6] S. Grubeša, K. Jambrošić, and H. Domitrović, "Noise barriers with varying cross-section optimized by genetic algorithms," *Applied Acoustics*, vol. 73, no. 11, pp. 1129–1137, 2012. DOI: 10.1016/J.APACOUST.2012.05.005.

[7] V. Laxmi, C. Thakre, and R. Vijay, "Evaluation of noise barriers based on geometries and materials: a review," *Environmental Science and Pollution Research*, vol. 29, no. 2, pp. 1729–1745, 2022. DOI: 10.1007/S11356-021-16944-2.

[8] G. Watts, "Factors affecting the performance of traffic noise barriers," in *Proc. of Internoise 2000 – DC/ConfOrg*, pp. 3–4, 2000.

[9] S. M. Dimitrijević, V. M. García-Chocano, F. Cervera, E. Roth, and J. Sánchez-Dehesa, "Sound insulation and reflection properties of sonic crystal barrier based on micro-perforated cylinders," *Materials*, 2019.

[10] J. Lee, J. D. Chang, and R. Coffeen, "Acoustical evaluations of a double skin façade as a noise barrier of a naturally-ventilated facade," *Journal of Acoustics*, vol. 2, no. 1, 2020.

[11] T. Astrauskas, P. Baltrėnas, T. Januševičius, and R. Grubliauskas, "Louvred noise barrier for traffic noise reduction," *The Baltic Journal of Road and Bridge Engineering*, 2021. DOI: 10.7250/bjrbe.2021-16.519.

[12] T. Vilniškis, P. Baltrėnas, and T. Januševičius, "Case study: Evaluation of noise reduction in frequencies and sound reduction index of construction with variable noise isolation," *Noise Control Engineering Journal*, 2020. DOI: 10.3397/1/376817.

[13] T. Vilniškis and T. Januševičius, "Modelling of acoustic louvers aerodynamic drag," in *Conf. for Junior Researchers: Science – Future of Lithuania*, 2018. DOI: 10.3846/aainz.2018.021.

[14] ISO 10140-2:2021, *Acoustics – Laboratory measurement of sound insulation of building elements – Part 2: Measurement of airborne sound insulation*, 2021.

[15] ISO 717-1, *Acoustics – Rating of sound insulation in buildings and of building elements – Part 1: Airborne sound insulation*, latest edition.

[16] ISO 11691:2020, *Acoustics – Measurement of insertion loss of noise barriers in situ*, 2020.

[17] J. Lee, J. D. Chang, and R. Coffeen, "Acoustical evaluations of a double skin façade as a noise barrier of a naturally-ventilated façade," *Journal of Acoustics*, vol. 2, no. 1, 2020. DOI: 10.20900/joa20200001.

DOI:

Main theme: A02 Bio-acoustics

Session A02.01 Bio-acoustics - General

Chair(s): B. Davies, D. Waddington, H. Whitehead, E. Vidaña-Vila

DOI: 10.61782/fa.2025.0178

FORUM ACUSTICUM EURONOISE 2025

BIOACUSTICS OF ECOSYSTEMS: INSIGHTS FROM MULTI-COMPONENT OBSERVING STATIONS IN ITALY AND MOZAMBIQUE

Pier Francesco Moretti[1*] **Grazia Masciandaro**[2] **Serena Doni**[2]
Eleonora Peruzzi[2] **Manuele Scatena**[2] **Davide Piccinini**[3] **Marta Polizi**[4]

[1] CNR-Department of Earth System Sciences and Environmental Technologies, National research Council of Italy, P.le A. Moro 7, 00185 Rome, Italy

[2] CNR-Research Institute on Terrestrial Ecosystems, Via Moruzzi 1, 56124 Pisa, Italy

[3] INGV-National Institute of Geophysics and Volcanology, Via Cesare Battisti 53, 56125 Pisa, Italy

[4] UNESCO Chair of Management of Conservation Areas, Europastrasse, 4, 9500 Villach, Austria

ABSTRACT

Human activities impact the environment, prompting science to help create policies for responsible use of natural resources. Environmental sustainability, biodiversity, and ecology are interconnected and crucial for healthy ecosystems. This means we need to study the ecosystems as a whole, not just as an integration of individual parts.

Sound is present in all environments and can help us understand the relationship between biodiversity and environmental conditions. Scientists usually study sounds in the air, focusing on how living organisms behave in different situations. However, the biosphere includes air, soil, and water, each requiring different methods based on available technology.

We investigated the potential of an instrumental set-up to simultaneously record sounds in air, soil, and water in two ecosystems: mangroves in Mozambique and a humid forest in Italy. Preliminary results allowed to identify common traits and differences between the different components, and suggest we should move beyond traditional methods that only analyze frequencies or acoustic indicators.

[*]***Corresponding author***: *pierfrancesco.moretti@cnr.it*

Copyright: *©2025 Moretti, P.F. et al. This is an open-access article distributed under the terms of the Creative Commons Attribution 3.0 Unported License, which permits unrestricted use, distribution, and reproduction in any medium, provided the original author and source are credited.*

Keywords: *bioacoustics, biodiversity, ecosystems, soundscape ecology, hydrophones.*

1. INTRODUCTION: WHY

Environmental sustainability, biodiversity, and ecology are interrelated foundations crucial for the well-being of ecosystems and the overall health of our planet. Safeguarding biodiversity, which refers to the variety of life on Earth, has received large attention as a key to contribute in the functioning of ecosystems. Every species has in fact a specific role in maintaining the equilibrium of the system, ranging from pollination to soil regeneration. Ecology, the study of interactions between organisms and their environments, helps us understand how ecosystems operate and how human activities impact on it. The integrity of ecosystems relies therefore on a rich tapestry of biodiversity [1] and the interrelationships between organisms and physical conditions [2-4]. Disrupting ecosystems through deforestation, habitat destruction, and the spread of invasive species endangers biodiversity and weakens ecological resilience. Protecting biodiversity is not just about saving individual species but preserving the intricate web of life that sustains ecosystems and the services they provide, such as air, water, soil, and food. In this context, it is essential to incorporate the monitoring of all the different components of biosphere to gain insights into the functioning of ecosystems. However, in many cases, these processes are technically complex, time-consuming, and challenging when needed for feeding models and simulations.

Since biological resources, natural events and human activities are pervading the acoustic field, we focused on monitoring the soundscape of the different components of the environment and look for emergent properties.

We investigated the potential of an instrumental set-up to simultaneously record sounds in air, soil, and water in two ecosystems: mangroves in Mozambique and a humid forest in Italy. Preliminary results allowed to identify common traits and differences between the different components, and suggest we should move beyond traditional methods that only analyze frequencies or acoustic indicators.

2. METHODOLOGY: WHERE, WHAT AND HOW

2.1 Locations

An instrumental set-up to monitor simultaneously the soundscapes in air, soil, and water has been developed and installed in Italy and in Mozambique.

One observing station was positioned in the Regional Park of Migliarino, San Rossore, Massaciuccoli, central Italy, 4 m above sea level (43°43'18.2"N, 10°17'4.8"E). The Park extends on a coastal alluvial plan, characterized by a coastal dune system [5]. In this environment, superficial aquifers are present, and the study area was selected within a coastal oak forest dominated by Quercus ilex L., typical of the Mediterranean forest ecotype of the Regional Park. The access to the Park is limited and very few cars can enter every day.
Data were acquired from March 2024 to July 2024.

Another station was installed in the island of Inhaca, in Mozambique, in two different locations (26°2'49.2"S, 32°54'3.6"E, and 26°3'8.22"S, 32°53'53.56"E). Both locations are characterized by the presence of mangroves and are included in a reserve area in Inhaca, where human activities are limited to few passages by foot, and they can be considered as pristine environments.
Data were acquired for two weeks during a summer school of the ManGrowth project held in October 2024 [6].

2.2 Instrumentation

A system consisting of four acoustic sensors were used and positioned accordingly to the geomorphology of the environments we selected for the observations.
The signals were amplified using the four channels of a Zoom P4 Podtrack, and the respective gains were adjusted to maintain the mean signals within the available dynamic range. Simultaneous recordings at 16 bit and 44100 Hz sampling frequency were saved as successive files of 3h 22m 53s duration each.
The overall system, excluding the sensors and the power supply, has a weight less than 1 Kg and dimensions of less than 20x20x20 cm3.

2.3 Positioning

One microphone (model Maono model PM 320), protected from atmospheric agents such as rain and wind, was positioned above the ground at approximately +60 cm in Italy, while hanging at approximately +120 cm on a mangrove branch in Mozambique.
Three other sensors (hydrophones Aquarian model H2a) were positioned.
In Italy, one hydrophone was at -15 cm depth from the ground level, and other two hydrophones, aligned vertically, at -15 cm and -80 cm respectively and both at a distance of approximately 13m from the first hydrophone. The hydrophone at -80 cm was immersed in the aquifer.
In Mozambique, one hydrophone was hanged on a mangrove's root, and at a height that allowed the sensor to be in air or in water accordingly to the tide cycle, another hydrophone was buried in the soil, that in our case was mainly in the mud, the last hydrophone was a few meters apart from the other two, ad always in the water. The first location was on a flat area, while the second close to a river.

In Fig. 1 and Fig. 2, the three different locations and positioning of the sensors are shown.
We will refer at signals from the four different positions of the sensors in the three locations as specified in Table 1.

Table 1. The four different positions of the sensors in the three locations. Colours refer to sensors in Fig.1.

REFERENCE NAMES	Location	Position
HUMFOR_AIR	Humid forest, IT	AIR
HUMFOR_SOIL1	Humid forest, IT	-15 cm
HUMFOR_SOIL_2	Humid forest, IT	-15 cm
HUMFOR_AQUIFER	Humid forest, IT	-80 cm
MANFLAT_AIR	Mangroves, MZ	AIR
MANFLAT_BRANCH	Mangroves, MZ	Branch
MANFLAT_SOIL	Mangroves, MZ	Mud
MANFLAT_WATER	Mangroves, MZ	Water
MANRIVER_AIR	Mangroves, MZ	AIR
MANRIVER_BRANCH	Mangroves, MZ	Branch
MANRIVER_SOIL	Mangroves, MZ	Mud
MANRIVER_WATER	Mangroves, MZ	Water

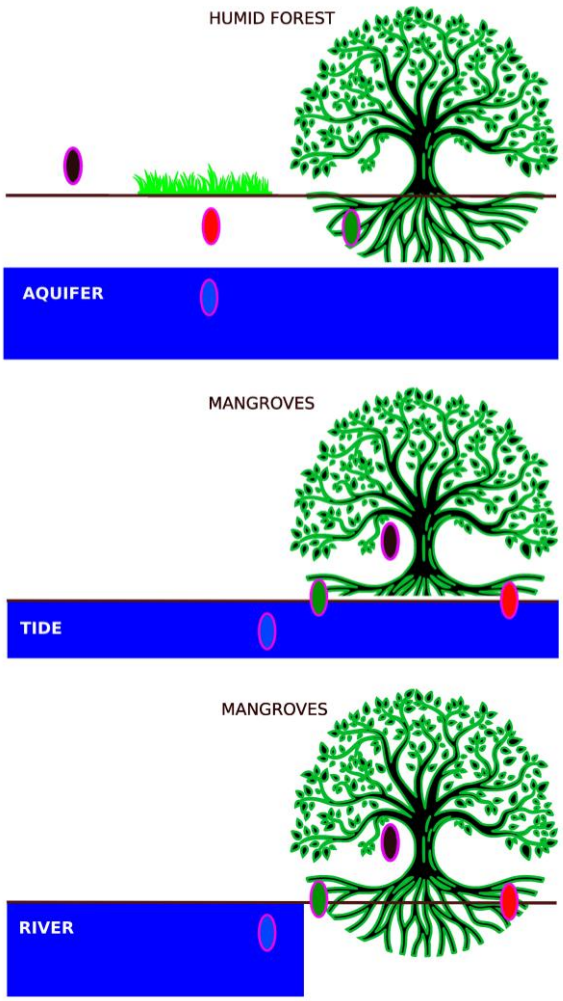


Figure 1. A schematic representation of the three locations (from upper to lower panels) and the four different positions of the sensors (colours refers to the positions described in Table 1).

2.4 Data analysis

Signals were analyzed via Fast Fourier Transform, using first the software *Audacity* for a preliminary check of frequencies and main traits. Timeseries, power spectra and further analysis were obtained with *IDL* software package. Additional elaboration of the signals to compute the acoustic indexes was performed using different software packages (soundecology [7-8], *warblerR* [9], *tunerR* [10] *seewave* [11]).



Figure 2. The observing stations in the three locations (from top to bottom, respectively: the humid forest in the Park of San Rossore, the first and second stations in Inhaca).

3. RESULTS

What immediately emerged from the analysis is that the dynamics of the soundscape in Inhaca MANRIVER is much richer than MANFLAT and richer than in the Park of San Rossore. Some samples are shown in Figures from 3 to 8.

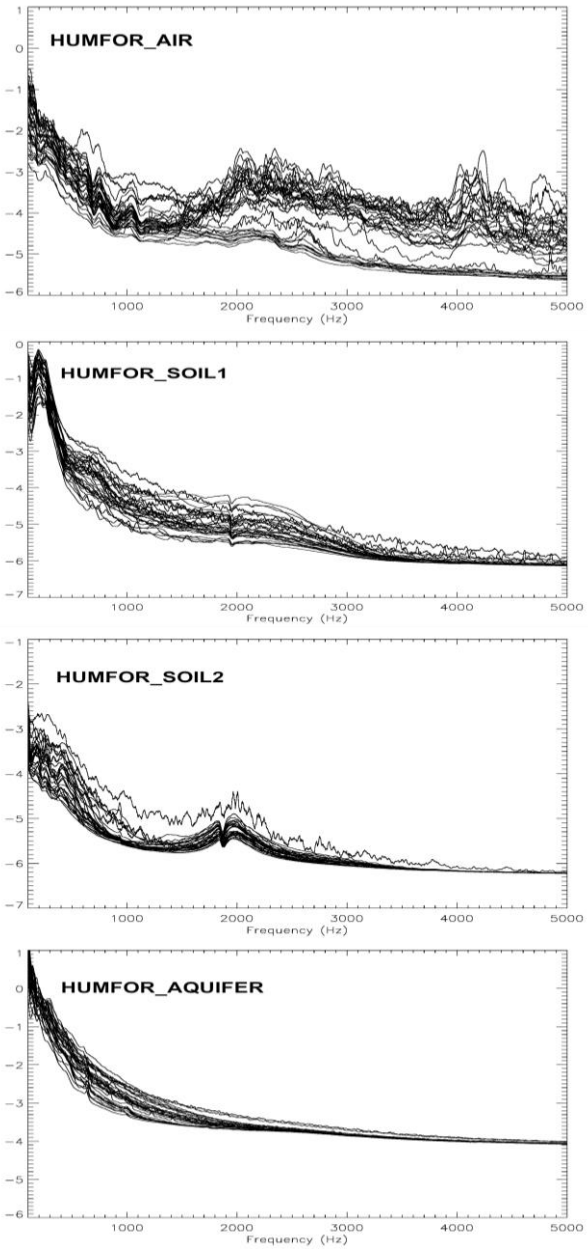


Figure 3. The log in base 10 of the power spectra (centred between 1 and 5 kHz to better show the details) of the signals from HUMFOR_AIR,HUMFOR_SOIL1,HUMFOR_SOIL 2,HUMFOR_AQUIFER (from top to bottom panels respectively). Each curve corresponds to a power spectrum of a set of 43 files of 3h 22m 23s duration, starting from 24 May 2024. On y-axis arbitrary units.

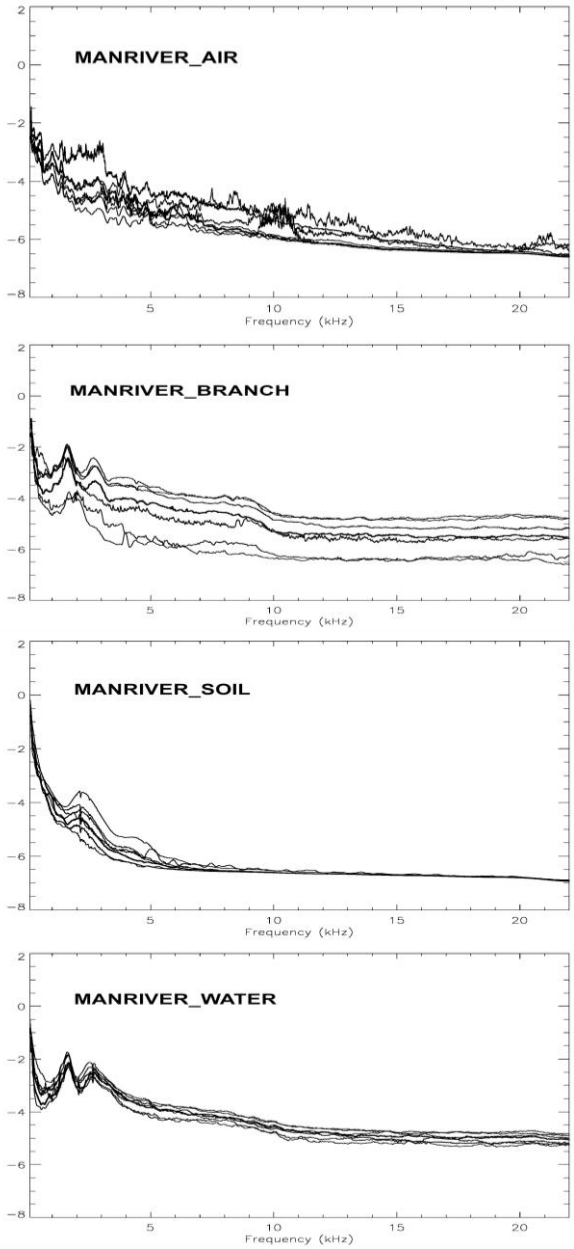


Figure 4. The log in base 10 of the power spectra (up to the Nyquist Frequency) of the signals from MANRIVER_AIR,MANRIVER_BRNCH,MANRIV ER_SOIL,MANRIVER_WATER (from top to bottom panels respectively). Each curve corresponds to a power spectrum of a set of 7 files of 3h22m23s duration, starting from 6 Oct 2024. On y-axis arbitrary units.

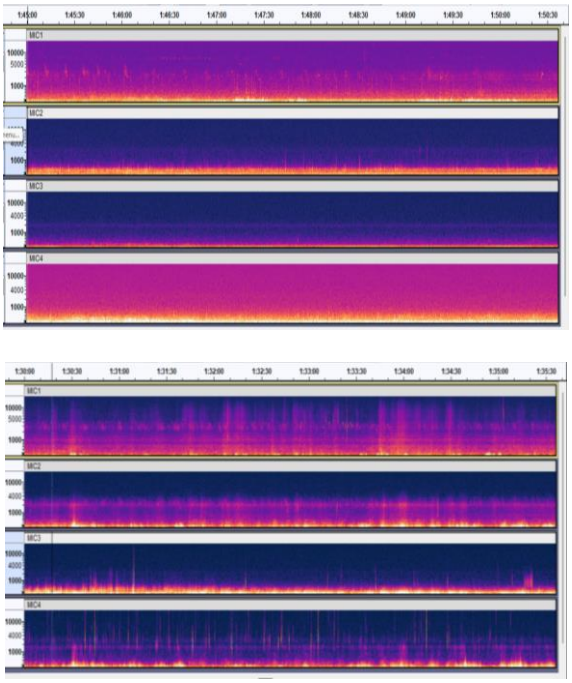


Figure 5. Examples of traits of power spectra for the 4 sensors in Park of San Rossore (upper panel) and in Inhaca (bottom panel). Panels show a 5-min zoom of the power spectra of a 3h22m23s run. On y-axis, frequencies in Hz. White and reddish colours refer to more powerful signals.

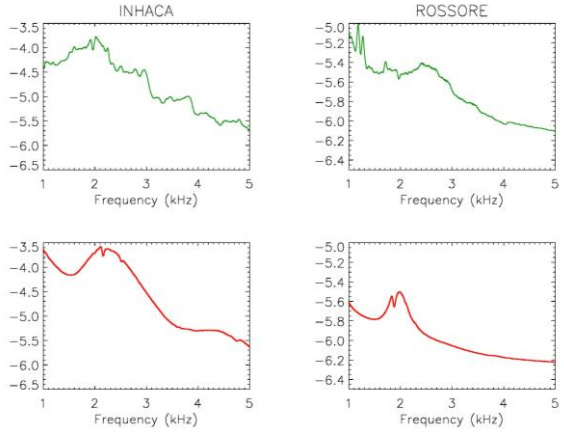


Figure 6. The log in base 10 of the power spectra (centred between 1 and 5 kHz) of the signals from MANRIVER_BRANCH and MANRIVER_SOIL (on the left, in green and red respectively), HUMFOR_SOIL1 and HUMFOR_SOIL2 (on the right, in green and red respectively), for a 3h22m23s temporal window. On y-axis arbitrary units.

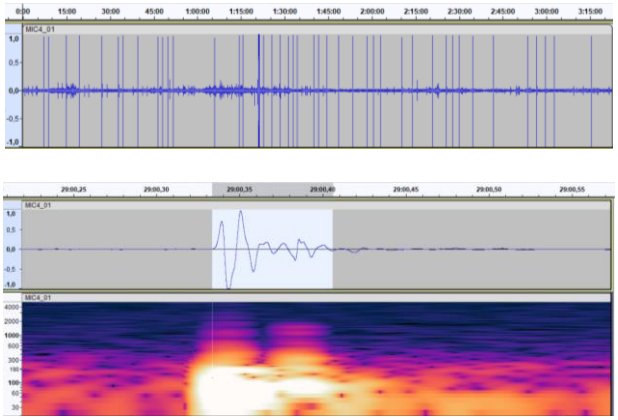


Figure 7. Examples of impulsive signals (i.e. spikes) detected in the aquifer in Park of San Rossore on 19th March 2024. Upper panel: a 3h22m23s run. Bottom panel: a zoom on one of the impulses with the associated power spectrum (on y-axis, frequencies in Hz). The impulses are not periodically occurring, show always the same signature, and last approximately 0.07s.

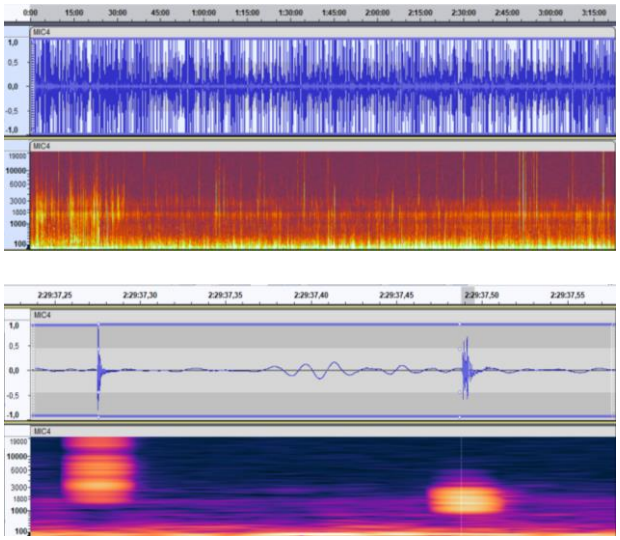


Figure 8. Examples of impulsive signals (i.e. spikes) detected in the river in Inhaca on 6th October 2024. Upper panel: a 3h22m23s run with the associated power spectrum (on y-axis, frequencies in Hz). Bottom panel: a zoom on a couple of successive impulses with the associated power spectrum (on y-axis, frequencies in Hz). The impulses are not periodically occurring, show different signatures with durations between 0.02 and 0.08s.

4. DISCUSSION AND CONCLUSIONS

Investigation of soundscapes in air relies on an historical large experience in the recognition of acoustic sources. Signatures of natural sources (e.g. rain, thunders, earthquakes), biological (mainly birds) and anthropogenic ones (e.g. cars, aircrafts) have been catalogued and many tools are available. It is not the aim of this paper to list the species that have been identified. As an example for one of our locations, some reports are available for the identification of birds In Inhaca [12].
Many acoustic indexes have been proposed for the extraction of information from the data, and their values have to be interpreted accordingly to the benefits and limitations that each of them can provide [13-14].

Despite of the large experience in acoustics in air, the identification of signals to the respective sources is a real challenge in soils and water.
In fact, when an acoustic signal is difficult to be clearly recognized in the spectrum, the experience as humans embedded in soundscapes in air facilitates the recognition via listening directly the sound. In soils and water this is very rare.
Acoustic studies in various terrains have traditionally focused on investigating movements within the Earth's mantle or rock layers. Beyond seismic applications, acoustic measurements served to monitor changes in soil characteristics, as well as capture sounds related to flowing water, cracks, and other indicators of physical conditions or habitats for flora and fauna. Generally, the methodologies to observe the biosphere within soils are not fully developed, and only a few examples have been documented. Our understanding of soil soundscapes at higher frequencies than those typically measured by geophones (20–20,000 Hz) remains limited, likely due to the increased attenuation of sound. In fact, soil structures strongly attenuate acoustic wave propagation above 2 kHz [15].
Few examples of acoustic studies of biodiversity in soils reported, mainly in forests [13,16]. Acoustic traits were associated with abiotic parameters and soil communities, Diurnal and seasonal trends were observed. Additional experiments in laboratory have been implemented to associate soundscapes and biotic sources in soils [17]. All the mentioned observations used sampling frequencies below 50kHz.
Some progress has been made in studying soundscapes within aquatic environments, particularly in marine ecosystems. The Wenz curves [18] still serve as the primary framework for understanding marine soundscapes, outlining the key characteristics of the spectral distribution of acoustic sources. However, most studies focus on the effects of maritime traffic at low frequencies, and many biological sources remain difficult to identify, with the exceptions of mammals' vocalism and fish chorus. Innovative approaches have been proposed for understanding the links between acoustic sources and processes that govern the equilibrium of the marine ecosystems [19-20].

For these reasons, when approaching the soundscape of ecosystems as a whole, we need to reflect on the limitations of the used instrumentation and the previous knowledge that can suggest any interpretation.

We installed acoustic observing stations in different ecosystems, and we took advantage of the high sensitivity of hydrophones installed in humid or aquatic media.
The system has already proven its potential to monitor the different components of the biosphere in a mangrove ecosystem in a remote island in Mozmbique [6].
Now we compared the data acquired also in a humid forest in a Reserve Area in Italy.
We focused on the main traits, commonalities and differences between the soundscapes, looking at clues for the identification of signatures of the ecosystems as a whole, that when signals are acquired simultaneously in air, soil and water.

Having in mind that is not the aim of this paper to describe in detail the identification of the signatures of the acoustic sources, we summarize the main results as follows.
Commonalities: the signals from the soil and vegetation show clear acoustic signatures at frequencies between 1 and 4 kHz. The power spectra show a characteristic "bell" shape with details that are slightly different between the stations, suggesting that they refer to a distribution of contributing acoustic sources (see Fig. 6).
Differences: the locations are very different in terms of ecosystems, with the African one characterized by a richness of biodiversity and the influence of tides. The aquifer in Italy is poor of living organisms, in contrast with the river in Africa. In terms of acoustic noise, the Italian ecosystem, despite embedded in a reserve area, is largely impacted at low frequencies by the aircraft passages that are detected in all the components, while the human impacts in Inhaca have not been detected and can therefore be considered a true pristine environment for acoustic monitoring.
Impulsive events in the aquatic media have been recorded in both locations: they are both aperiodic but their nature is very different.

Those in the aquifer shows a constant temporal profile, while those in the river not. We suggest that those in the aquifer are related to the relaxation of energy associated to the physical properties of the system, while those in the river are associated to the crustaceous and crabs.

In this context, we proceed to a comparison of the information extracted via acoustic indexes and other indicators produced by algorithms that were built ad-hoc to extract different information. Power spectra of 0.27s time intervals have been computed and, at different frequencies, powers above 10 standard deviations were selected and identified as events. The number of spikes has been averaged over a 5 min interval and named EVENTS.

We report the temporal behaviour of classical acoustic indexes and one indicator (EVENTS) in Fig. 9 and 10.

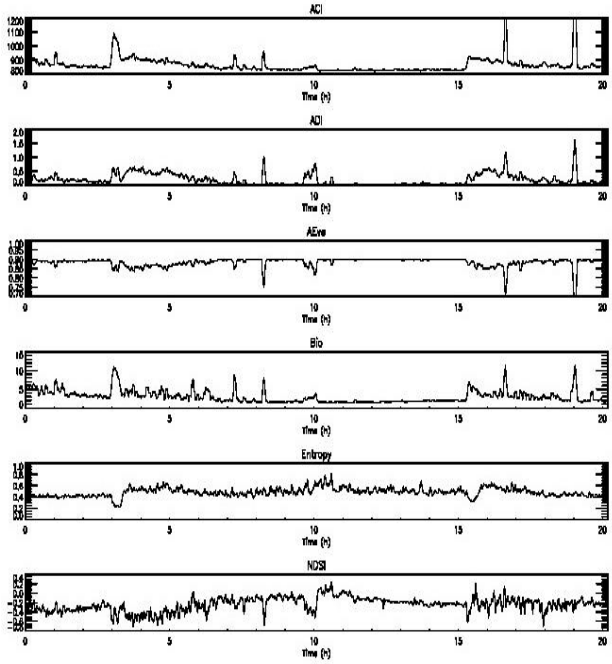


Figure 9. The values of different acoustic indexes (from top to bottom: ACI, ADI, AEve, Bio, Entropy and NDSI) computed for MANRIVER_WATER on 1st Oct 2024.

To conclude, we showed that the soundscape at frequencies between 1 and 4 kHz *in soils* from different ecosystems can be a useful tool to describe the characteristics of biotic sources and their health.

We also showed that the information on biodiversity usually extracted via acoustic indexes can be misleading, as already referred [21] when applied to soils and aquatic environments, suggesting to look at different data analysis for a better understanding of the interconnected components of the ecosystems.

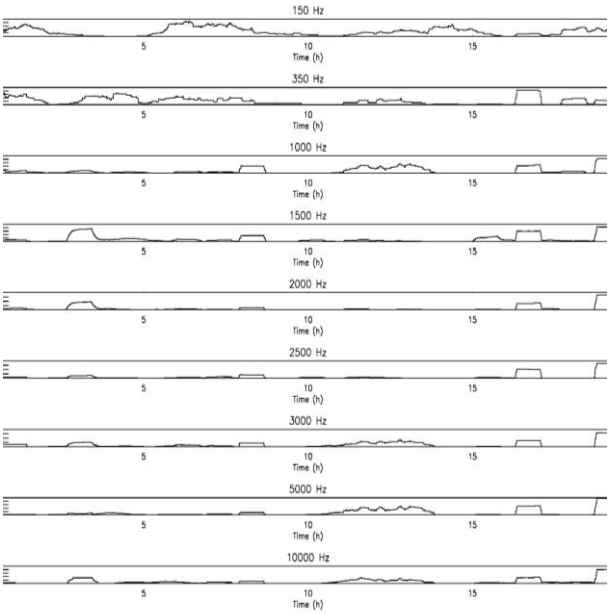


Figure 10. The values of the indicator named EVENTS (see text) at different frequencies (MANRIVER_WATER on 1st Oct 2024). Temporal coincidences at many different frequencies suggest impulsive events. Different time cycles are shown, preliminarily associated to biological sources and/or physical processes. On y-values are arbitrary units, aiming to show time cycles.

5. ACKNOWLEDGMENTS

This research was conducted within the framework of the ManGrowth Project (Preservation of Ecosystems for Sustainable Development – AID 012432/01/2), funded by the Italian Agency for Development Cooperation, and the project AFONIA, funded by the National Research Council of Italy.

We thank Paolo Ramoni for his valuable and outstanding support in Inhaca. We thank Augusto Nhampossa, Aura Rapino, Clotilde Nhancale, Lavinia Scepi, and Zaira Macheve for their help in the installation of the stations in Inhaca, and Damiano Biagini and Michele D'Ambrosio in the installation of the station in Park of San Rossore. We thank the Regional Park of San Rossore for their collaboration, the authorization to install the observing station and their valuable support in logistics and management of the activities.

6. REFERENCES

[1] J.E.M.Watson, T. Evans, O. Venter, B. Williams, A. Tulloch, C. Stewart, and et al.: "The exceptional value of intact forest ecosystems" Nat Ecol Evol., 2, pp. 599–610, 2018.

[2] Y. Liu, J. Bi, J. Lv, Z. Ma, and C. Wang: "Spatial multi-scale relationships of ecosystem services: A case study using a geostatistical methodology", Sci Rep., 7, 9486, 2017.

[3] P.J. Carrick, and K.J. Forsythe: "The species composition—ecosystem function relationship: A lobal meta-analysis using data from intact and recovering ecosystems", PLoS One, 15, 7: e0236550, 2020.

[4] G. Steur, H. ter Steege, R.W. Verburg, D. Sabatier, J.F. Molino, O.S. Banki, and et al.: "Relationships between species richness and ecosystem services in Amazonian forests strongly influenced by biogeographical strata and forest types", Sci Rep., 12, 5960, 2022.

[5] N.P. Psuty: "The Coastal Foredune: A Morphological Basis for Regional Coastal Dune Development", in *Coastal Dunes. Ecological Studies*, Martínez & Psuty eds, Springer, Berlin, vol. 171, pp. 11-27, 2008.

[6] A. Nhampossa, A. Rapino, C. Nhancale, M. Polizzi, L. Scepi, Z. Macheve, and P.F. Moretti: "Exploring the potential of a bioacoustic monitoring station in the mangrove ecosystem of Inhaca", in *Proc. of the Summer School ManGrowth 2023: Ecology and conservation* (Inhaca, Mozambique), in press, 2025.

[7] B.C. Pijanowski, L.J. Villanueva-Rivera, S. Dumyahn, A. Farina, B. Krause, B. Napoletano, S. Gage, and N. Pieretti: "Soundscape Ecology: The Science of Sound in Landscapes", BioScience 61, 203-216, 2011.

[8] L.J. Villanueva-Rivera, B.C. Pijanowski, J. Doucette, and B. Pekin: "A primer of acoustic analysis for landscape ecologists", Landscape Ecology, 26, 1233-1246, 2011.

[9] M. Araya-Salas, and G. Smith-Vidaurre: "warbleR: an r package to streamline analysis of animal acoustic signals", Methods Ecol Evol, 8, 184-191, 2017.

[10] U. Ligges, S. Krey, O. Mersmann, and S. Schnackenberg: "tuneR: Analysis of Music and Speech", https://CRAN.R-project.org/package=tuneR, 2023.

[11] J. Sueur, T. Aubin, and C. Simonis: "Seewave: a free modular tool for sound analysis and synthesis" Bioacoustics, 18, 213-226, 2008.

[12] E. Candeago, J.F.A. César, C. Foggia, and D.S.C. Odorico: "The sound of mangroves", in *Proc. of the Summer School ManGrowth 2023: Ecology and conservation* (Inhaca, Mozambique), pp. 38-46, 2023.

[13] J.M. Robinson, M.F. Breed, and C. Abrahams: "The sound of restored soil: using ecoacoustics to measure soil biodiversity in a temperate forest restoration context", Restoration Ecology, 31, 5, e13934, 2023.

[14] T. Bradfer-Lawrence, N. Gardner, L. Bunnefeld, N. Bunnefeld, S.G. Willis, and D.H. Dent: "Guidelines for the use of acoustic indices in environmental research", Meth Ecol Evol, 10, pp. 1796–807, 2019.

[15] M.L. Oelze, W.D. O'Brien, and R.G. Darmody: " Measurement of attenuation and speed of sound in soils", The Journal of the Acoustical Society of America, 66, pp. 788-96, 2022.

[16] M. Maeder, X. Guo, F. Neff, D. Schneider Mathis, and M.M. Gossner: "Temporal and spatial dynamics in soil acoustics and their relation to soil animal diversity", PLoS ONE, 17, 3, e0263618, 2022.

[17] M. Lacoste, S. Ruiz, and D. Or: "Listening to earthworms burrowing and roots growing – acoustic signatures of soil biological activity", Sci Rep., 8, 10236, 2018.

[18] G.M. Wenz: "Acoustic ambient noise in the ocean: spectra and sources", J Acoust Soc Am, 34, pp. 1936-56, 1962.

[19] P.F. Moretti, and A. Affatati: "Understanding the Impact of Underwater Noise to Preserve Marine Ecosystems and Manage Anthropogenic Activities", Sustainability, 15, 10178, 2023.

[20] P.F. Moretti, A. Pomaro, and S. Buogo: "Metrology for underwater acoustics: rethinking measurement strategies for the assessment of the environmental status", in *Proc. of IEEE Metrology for the Sea* (Portorose, Slovenia), pp. 546-551, 2024.

[21] I. Alcocer, H. Lima, L.S.M. Sugai, and D. Llusia: "Acoustic indices as proxies for biodiversity: A meta-analysis", Biological Reviews, 97, 6, 2209–2236, 2022.

DOI: 10.61782/fa.2025.0970

FORUM ACUSTICUM EURONOISE 2025

WHEN THE LAB GETS LOUD: TESTING NOISE EFFECT OF PLANTS

Valentina Zaffaroni-Caorsi*[1] Sarah Caronni[1] Sofia Rocca[1] Emanuele Asnaghi[1] Arianna Comotti[1] Lara Assunta Quaglini[1] Fabio Angelini[1] Sandra Citterio[1] Giovanni Zambon[1]

[1] Department of Earth and Environmental Sciences, University of Milano-Bicocca, Milan, Italy

ABSTRACT

Noise pollution is increasing in both scope and intensity due to the growth of the human population and urban development, significantly impacting terrestrial and aquatic habitats. Anthropogenic noise is pervasive in nature and has been shown to affect a wide range of animal taxa. Recent studies, however, reveal that noise and vibrations can also influence plants, altering their morphological, physiological, and genetic traits. This suggests that noise pollution may exert effects on ecosystems at more complex levels than previously understood. In this study, we investigated the effects of broadband noise (pink noise) on two plant species (one herbaceous and one tree species) to explore its potential impact on vegetation. Laboratory experiments were conducted under controlled conditions at the Department of Earth and Environmental Sciences, University of Milano-Bicocca, Italy. Seeds were planted in soil-filled pots and placed within two phytotrons -one designated as the treatment chamber, where pink noise was continuously emitted through a speaker, and the other as the control chamber, with no noise exposure. We assessed whether noise influenced germination rates, growth and survival of plants. Preliminary results show an effect on germination and development of the herbaceous species.

Keywords: *anthropogenic noise, laboratory experiment, plant, soil, microbiome.*

1. INTRODUCTION

The rapid expansion of urban areas has led to a significant increase in noise pollution, which now poses a serious threat to both terrestrial and aquatic ecosystems [1]. Among the various sources of anthropogenic noise, traffic and industrial activities are particularly disruptive to biodiversity [2–3]. While noise pollution is widely recognized as an environmental stressor, its impact extends beyond animals to affecting a broad range of organisms [4]. Previous research has extensively documented how noise interferes with animal communication, reproduction, and spatial behaviors [1–5–6].

More recent findings indicate that plants, too, can perceive and respond to sound stimuli [7–8]. Unlike animals, plants are immobile and must endure environmental stressors, relying on complex signaling networks and adaptive mechanisms to cope with fluctuating conditions [9]. Studies suggest that exposure to certain sound frequencies can alter seed germination, plant growth, oxidative stress levels, and the expression of stress-related genes [8]. Prolonged noise exposure has also been linked to reductions in photosynthetic and transpiration rates, ultimately affecting plant development and survival, particularly in urban environments [10–11].

Beyond physiological changes, noise pollution may also interfere with ecological interactions, such as plant-pollinator relationships. Excessive noise can disrupt pollinators' ability to detect floral cues, which may negatively impact pollination success and, consequently, plant reproduction [10].

Despite growing concern about noise pollution, most studies have focused on specific sound frequencies (e.g., 0.4kHz, 1kHz, 5kHz), limiting our understanding of the effects of broader noise exposure [12] as road traffic noise. Research on noise-induced changes in plant physiology is still scarce, with only one study examining how traffic noise affects urban vegetation [13]. Given the increasing presence of anthropogenic noise across landscapes, further research is needed to assess its potential effects on plants [14].

This study investigates the impact of broadband noise (pink noise) on an herbaceous and a tree species to evaluate how noise pollution may influence plant-microbe interactions and overall ecosystem dynamics.

*Corresponding author: valentina.zaffaronicaorsi@unimib.it

Copyright: ©2025 First author et al. This is an open-access article distributed under the terms of the Creative Commons Attribution 3.0 Unported License, which permits unrestricted use, distribution, and reproduction in any medium, provided the original author and source are credited.

2. MATERIAL AND METHODS

2.1 Species studied

This study focused on two species, one herbaceous, *Trifolium pratense L.* and one woody *Ulmus minor L.* The first one, commonly known as red clover, is a temperate perennial herb commonly growing wild in meadows throughout Europe and Asia. The second one is also widely planted in both countryside and urban areas, across almost all Europe. Both species are known for their tolerance to adverse environmental conditions and stress [15–16].

2.2 Experimental design

The study took place in 2023 at the University of Milan-Bicocca, Italy, in two phytotrons (growth chambers - Sanyo, 180Hx80Lx55W), maintaining a temperature of 25°C and a day/night cycle from 9 a.m. to 9 p.m. (light) and 9 p.m. to 9 a.m. (dark). The experiment was conducted using a speaker (JBL Control 1 Pro) placed on the top shelf X (Fig.1) emitting pink noise continuously for 24 hours (stimulus constructed using Audacity software). To mimic natural conditions, fluorescent lights alternated between 12-hour light/dark cycles. Seeds of *T. pratense* and *U. minor*, certified by research institutions, were sown in 24 soil-filled pots (12 per species, 50 seeds per pot). The pots were placed in shelfs Y and Z (Fig.1).

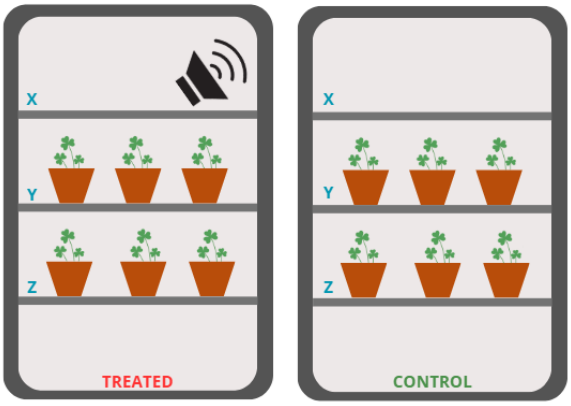


Figure 1. Treat phytotron (left) with a pink noise signal continuously emitted by a loudspeaker in shelf X, 24h a day and control phytotron (right) with no noise.

2.3 Acoustic data collection and analysis

Acoustic data collection was carried out using a Class 1 calibrated sound level meter (SLM -Larson Davis - 831C) equipped with a wired microphone, allowing precise placement inside the phytotron to record noise levels. To characterize the noise perceived by the plants both background and treatment noise levels were measured. The growth chamber was divided into four sections by three horizontal shelves: the speaker was placed on the first shelf (Figure 1), while the plants were positioned on the second and third shelves (three pots per species per shelf). Nine measurements were taken for each shelf (column A, B, C, row 1, 2, 3 - see Figure 2), following a regular grid in the treated and control conditions, with lights on/off, totaling 36 measurements per phytotron. Each recording lasted one minute, with a sampling rate of 48.000 Hz.
The acoustic data collected was extracted from the SLM and analyzed using its corresponding software, BZ5503 and Evaluator 7820. Data exported included LeqZ 1/3 octave bands . Sound pressure levels were measured at each points to characterize levels of noise arriving to the plants for both treatment and control phytotrones.

2.4 Acoustic data collection and analysis

The following plant morpho-functional traits were measured for both species: total and thorough time emergence (%), survival and growth (in terms of plant height, number and area of leaves).

2.5 Statistical analysis

We performed a linear mixed-effects model (LMM) using treatment, light condition and shelf as fixed factors and dB level as response variable. Data exploration followed the protocol described in [17]. We ran the models using packages “lme4” [18]. Visual analysis and figures were computed with R Studio (RStudio). Regarding biological parameters, univariate analyses (ANOVA and SNK tests) were conducted with GMAV software to analyze data regarding the morpho-functional traits considered for the two species and the bacterial abundances.

3. RESULTS

3.1 Acoustic characterization of the phytotrons

The Linear Mixed Model (LMM) analysis (Fig.2; Tab.1) revealed that background noise levels (dBZ) in treated phytotron were higher compared to control ($p < 0.001$).

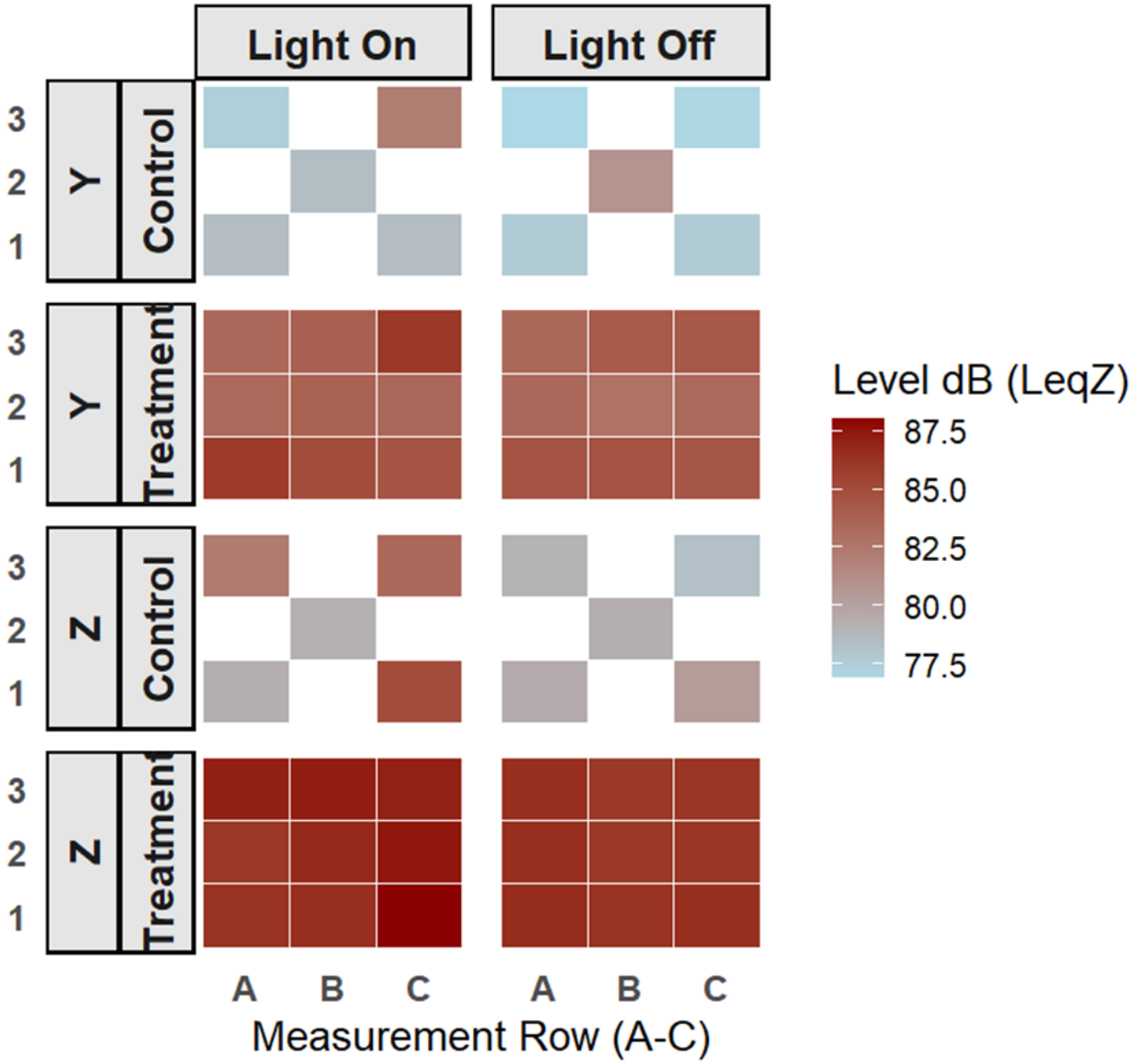


Figure 2. Heatmap of Noise Level dB (Z) by measurement site per shelf per treatment under light on/off condition.

Table 1. Summary of the Generalized Linear Mixed Model. Baseline reference: control, light off, shelf Y.

Factor	Estimate	SE	df	t-value	p-value
Intercept	78.9	0.55	28.45	143.90	<.0001
Treatment	5.37	0.636	44.4	8.453	<.0001
Light On /Off	-0.95	0.720	43.9	-1.313	0.196
Shelf (Y/Z)	2.83	0.720	43.9	3.934	<.0001
Treatment × Light	0.50	0.89	43.9	0.559	0.579
Treatment × Shelf	-0.23	0.89	43.9	-0.257	0.798
Light × Shelf	-1.59	1.018	43.9	-1.529	0.133
Treatment × Light × Shelf	1.36	1.27	43.9	1.077	0.288

Furthermore, the shelf position also influenced the level's noise with the higher levels in Z respect to Y ($p < 0.001$). On the contrary, the light condition, although a bit higher in the light condition, was not significantly different ($p = 0.196$). Regarding interactions, no significant two-way or three-way interactions were found (p-values > 0.05). This suggests that the effects of Treatment, Light, and Shelf Position were largely independent rather than influencing each other. These differences in noise distribution between shelves and treatments could influence plant physiological responses. For this reason, the pots were rotated within the phytotron throughout the experiment to ensure equal exposure to noise.

3.2 Effect of noise treatment on plant species

The effect of the treatment exposure on the target species showed that noise negatively affected the germination of *U. minor*, causing a significant delay and a reduction in the number of germinated seeds compared to the control. In contrast, *T. pratens*e showed no significant differences between the two conditions. At the end of the experiment, no significant differences in plant survival were observed between species and treatments, although *U. minor* showed slightly lower values under noise exposure. However, with regard to the growth, *U. minor* displayed significantly lower values for the height, the leaf number and area under noise exposure. In contrast, for *T. pratense* no significant variations between the noise exposure and the control treatment were observed.

4. DISCUSSION

The results from the acoustic characterization highlight key factors for improving experimental design when studying noise effects on plants. As expected, the treated phytotrons had significantly higher noise levels than the controls. However, the shelf position also influenced the noise distribution by having higher levels observed on the lower shelf. Meanwhile, light conditions showed no significant effect. The absence of significant interactions indicates that treatment and shelf position acted independently. These findings emphasize the need to account for spatial noise variability. Rotating pots, as done in this study, helps ensure equal exposure, reducing bias. Future experiments should integrate such controls to improve reproducibility and isolate noise effects more effectively.

Our results showed an effect of noise mainly on one of the considered plants, *Ulmus minor*, suggesting that species-specific responses to noise occur. This supports previous findings by [19], who observed varied plant reactions to different sound frequencies, with noise having both negative and, in some cases, positive effects on growth. Similar to other environmental factors like moisture, light, wind, and temperature, plant responses to noise appear to be primarily physiological and dependent on species-specific traits and functional groups [20].

5. CONCLUSION

Our results bring two important conclusions regarding both experimental design and noise impact on plants:

- Phytotrons represent a good environment for testing the effect of noise on plants, provided pot rotation is considered, as noise distribution is not homogeneous.
- Noise had an effect on plants, particularly on *Ulmus minor*, suggesting species-specific responses. These findings confirm previous studies and indicate that plant responses to noise, as well as to other environmental factors, depend on the species' physiological and functional traits.

6. ACKNOWLEDGMENTS

This research was funded by MUSA 654 – Multilayered Urban Sustainability Action – project, funded by the European Union – NextGener-655 ationEU, under the National Recovery and Resilience Plan (NRRP) Mission 4 Component 2 Invest-656 ment Line 1.5: Strengthening of

research structures and creation of R&D "innovation ecosystems", 657 set up of "territorial leaders in R&D.

7. REFERENCES

[1] R. Sordello, F. Flamerie De Lachapelle, B. Livoreil, and S. Vanpeene, "Evidence of the environmental impact of noise pollution on biodiversity: a systematic map protocol," *Environmental Evidence*, vol. 8, no. 1, pp. 8, 2019.

[2] T. Lengagne, "Traffic noise affects communication behaviour in a breeding anuran, Hyla arborea," *Biological Conservation*, vol. 141, no. 8, pp. 2023–2031, 2008.

[3] J. T. Mason, C. J. W. McClure, and J. R. Barber, "Anthropogenic noise impairs owl hunting behavior," *Biological Conservation*, vol. 199, pp. 29–32, 2016.

[4] D. G. E. Gomes, C. D. Francis, and J. R. Barber, "Using the Past to Understand the Present: Coping with Natural and Anthropogenic Noise," *BioScience*, vol. 71, no. 3, pp. 223–234, 2021.

[5] V. Zaffaroni-Caorsi, C. Both, R. Márquez, D. Llusia, P. Narins, M. Debon, and M. Borges-Martins, "Effects of anthropogenic noise on anuran amphibians," *Bioacoustics*, vol. 32, no. 1, pp. 90–120, 2022.

[6] G. Shannon, M. F. McKenna, L. M. Angeloni, K. R. Crooks, K. M. Fristrup, E. Brown, K. A. Warner, M. D. Nelson, C. White, J. Briggs, S. McFarland, and G. Wittemyer, "A synthesis of two decades of research documenting the effects of noise on wildlife," *Biological Reviews*, vol. 91, no. 4, pp. 982–1005, 2016.

[7] J. Y. Kim, H.-J. Lee, J. A. Kim, and M.-J. Jeong, "Sound Waves Promote Arabidopsis thaliana Root Growth by Regulating Root Phytohormone Content," *International Journal of Molecular Sciences*, vol. 22, no. 11, pp. 5739, 2021.

[8] H. C. de Melo, "Plants detect and respond to sounds," in *Planta*, vol. 257, no. 3, Springer Science and Business Media Deutschland GmbH, 2023.

[9] B. Fernández-Marín, J. Gulías, C. M. Figueroa, C. Iñiguez, M. J. Clemente-Moreno, A. Nunes-Nesi, A. R. Fernie, L. A. Cavieres, L. A. Bravo, J. I. García-Plazaola, and J. Gago, "How do vascular plants perform photosynthesis in extreme environments? An integrative ecophysiological and biochemical story," *The Plant Journal*, vol. 101, no. 4, pp. 979–1000, 2020.

[10] J. R. Barber, K. R. Crooks, and K. M. Fristrup, "The costs of chronic noise exposure for terrestrial organisms," *Trends in Ecology & Evolution*, vol. 25, no. 3, pp. 180–189, 2010.

[11] K. Lohrey and P. Talarczyk, "The Impact of Traffic Noise Pollution on Plant Growth Within Urban Community Gardens," *Journal of Student Research*, vol. 10, 2021.

[12] B. Li, J. Wei, X. Wei, K. Tang, Y. Liang, K. Shu, and B. Wang, "Effect of sound wave stress on antioxidant enzyme activities and lipid peroxidation of *Dendrobium candidum*," *Colloids and Surfaces B: Biointerfaces*, vol. 63, no. 2, pp. 269–275, 2008.

[13] Z. H. Kafash, S. Khoramnejadian, A. A. Ghotbi-Ravandi, e S. F. Dehghan, "Traffic noise induces oxidative stress and phytohormone imbalance in two urban plant species," *Basic and Applied Ecology*, vol. 60, pp. 1–12, 2022.

[14] C. A. Guerra, A. Heintz-Buschart, J. Sikorski, A. Chatzinotas, N. Guerrero-Ramírez, S. Cesarz, et al. "Blind spots in global soil biodiversity and ecosystem function research," *Nat. Commun*, vol 11, pp. 3870, 2020.

[15] J. Primorac, V. Kozumplik, L. Barba, Z. Knezović, e S. Bolarić, "Morphological and agronomic characteristics of Croatian red clover (*Trifolium pratense* L.) breeding populations tolerant to abiotic stress," *Cereal Research Communications*, vol. 35, no. 2, pp. 953–956, 2007.

[16] J. A. Martín, J. Sobrino-Plata, B. Coira, D. Medel, C. Collada, and L. Gil, "Growth resilience and oxidative burst control as tolerance factors to *Ophiostoma novo-ulmi* in *Ulmus minor*," *Tree Physiology*, vol. 39, no. 9, pp. 1512–1524, 2019.

[17] A. F. Zuur, E. N. Ieno, and C. S. Elphick, "A protocol for data exploration to avoid common statistical problems," *Methods in Ecology and Evolution*, vol. 1, no. 1, pp. 3–14, 2010.

[18] D. Bates, M. Maechler, B. Bolker, S. Walker, R. H. B. Christensen, H. Singmann, B. Dai, G. Grothendieck, P. Green, and M. Ben Bolker, "Package 'lme4'," *Convergence*, vol. 12, no. 1, p. 2, 2015.

[19] R. H. E. Hassanien, T. Z. Hou, Y. F. Li, and B. M. Li, "Advances in Effects of Sound Waves on Plants," in *Journal of Integrative Agriculture*, vol. 13, no. 2, pp. 335–348, 2014.

[20] M. Pagano and S. Del Prete, "Symphonies of Growth: Unveiling the Impact of Sound Waves on Plant Physiology and Productivity," *Biology*, vol. 13, no. 5, p. 326, 2024.

DOI: 10.61782/fa.2025.0339

FORUM ACUSTICUM EURONOISE 2025

ENHANCED BIRDCALL DETECTION USING MULTIDIRECTIONAL BEAMFORMING AND AUTOMATED SOURCE SELECTION IN LOW SNR SOUNDSCAPES

Rifqi Ikhwanuddin[1,4*] **Emilie D'Olne**[2] **Sarab S Sethi**[3] **Lorenzo Picinali**[1]
[1] Dyson School of Design Engineering, Imperial College London, United Kingdom
[2] Electrical and Electronic Engineering, Imperial College London, United Kingdom
[3] Department of Life Sciences, Imperial College London, United Kingdom
[4] Engineering Physics, Institut Teknologi Sumatera, Indonesia

ABSTRACT

In forest ecosystems, detecting birdcalls is hindered by high environmental noise and multiple sound sources, complicating species identification. Beamforming techniques can enhance signal-to-noise ratio (SNR) by focusing on specific directions but face challenges with numerous, unpredictably located sources. This study proposes a novel methodology integrating multidirectional beamforming with automated source selection to address these issues. Our approach sequentially scans multiple directions and employs BirdNET (a machine learning-based platform for bird recognition) confidence scores to identify optimal detection sectors, improving accuracy. Using a Multichannel Acoustic Autonomous Recording Unit (MAARU), experiments were conducted in a controlled virtual sound environment with simulated Eurasian Blue Tit calls under varying SNR conditions (+30dB to -30dB). Results demonstrate a significant enhancement in species detection accuracy compared to single-channel recordings, especially at low signal-to-noise ratio, with beamforming achieving up to 588% improvement in detection counts at -20 dB ($p < 0.0001$) and consistently higher confidence scores ($p < 0.05$). The findings highlight the potential of combining multidirectional beamforming with AI-based detection for biodiversity monitoring in challenging acoustic environments. Future work will extend these methods to field deployments to validate their effectiveness in real-world conditions.

Keywords: *birdcall, passive acoustic monitoring, multidirectional beamforming, & ecoacoustics.*

Corresponding author: *r.ikhwanuddin23@imperial.ac.uk.*
Copyright: *©2025 Rifqi Ikhwanuddin et al. This is an open-access article distributed under the terms of the Creative Commons Attribution 3.0 Unported License, which permits unrestricted use, distribution, and reproduction in any medium, provided the original author and source are credited.*

1. INTRODUCTION

Passive Acoustic Monitoring (PAM) offers promising capabilities for biodiversity assessment through IoT sensors and AI analysis [1]. However, practical implementation faces challenges from overlapping sound sources and environmental noise [2, 3].

While autonomous recording units are increasingly used for monitoring bird occurrences in remote areas, multi-channel sensor devices remain uncommon due to data size constraints and their relative novelty in ecological applications [4]. Traditional single-channel systems struggle in low signal-to-noise ratio (SNR) environments, where target bird vocalisations are often obscured by background noise, making species identification difficult without spatial information [4, 5].

Multi-channel recording systems with beamforming techniques present an effective solution by enabling focused listening in specific directions. These techniques can be implemented through either dynamic steering, which continuously adjusts to sound source movements, or static steering, which maintains fixed directional focus points [6].

This research integrates multidirectional static steering beamforming with BirdNET, an AI-based detection system, aiming to enhance biodiversity monitoring accu-

racy in challenging acoustic environments with overlapping sound sources and significant background noise.

2. MATERIALS AND METHODS

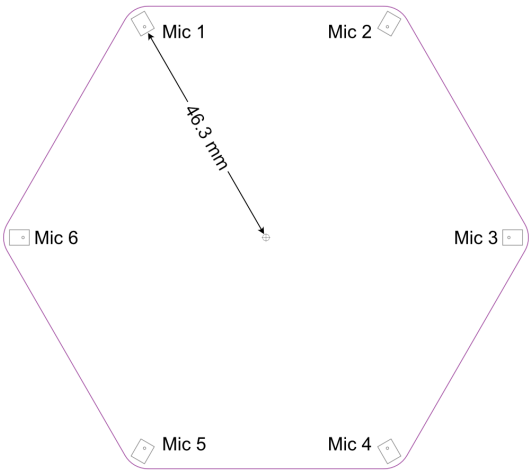


Figure 1. Circular microphone array configuration with six microphones (Mic 1-6) positioned at the vertices. Each microphone is positioned at an equal distance of 46.3 mm from the centre point of the array.

We used the Multichannel Acoustic Autonomous Recording Unit (MAARU) [4,7], which integrates a Raspberry Pi 3 Model B+ with a ReSpeaker 6-microphone circular array containing omnidirectional MEMS microphones (see Fig. 1) [8]. Complete instructions are available on GitHub [9]. The MAARU sampled audio at 16kHz during all experiments [10, 11].

Testing employed a Virtual Sound Environment (VSE) with third-order Ambisonics recordings reproduced through a 31-loudspeaker system [12]. Our experimental scenario combined an 8-minute background soundscape with Eurasian Blue Tit (EBT) calls (*Cyanistes caeruleus*) reproduced sequentially from 31 different positions at progressively decreasing sound pressure levels (70dB to 10dB in -10dB steps). The EBT call was selected for its frequency range (3-8kHz) which aligns with common bird vocalisations (see Fig. 2) [10].

For beamforming implementation, we measured 3D impulse responses using time-stretched pulse signals generated from 31 spatial positions at a fixed distance of 1.5 meters. These measurements incorporated azimuth angles

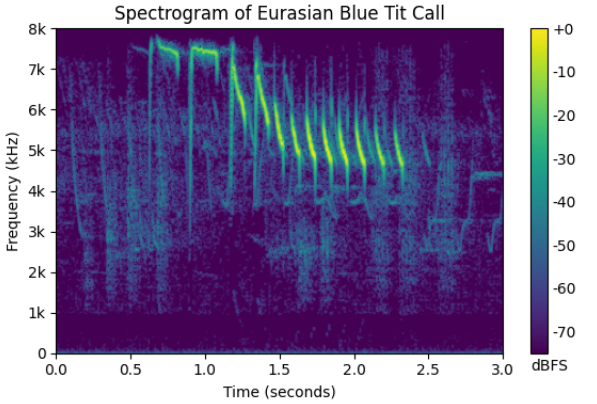


Figure 2. Spectrogram of a Eurasian Blue Tit (Cyanistes caeruleus, XC28208) call showing its distinctive frequency pattern. The characteristic high-frequency modulations (3-8kHz) are visible between 0.5-2.5 seconds.

from 0° to 360° (40° increments) and elevations of -45°, 0°, 45°, and 90°.

Our processing pipeline employed a Butterworth high-pass filter (500Hz cutoff) followed by an Impulse Response-based Filter-and-Sum beamformer, using measured impulse responses as steering vectors rather than analytical models. This data-driven approach captures complex acoustic environment characteristics including room reflections and array imperfections.

For automated source selection, we processed 3-second segments independently through beamforming, `birdnetlib` [13], and `BirdNET-Analyzer` model v2.4 [14]. For determining successful detections, we applied a confidence score threshold of 0.4, which represents a balance between detection sensitivity and false positive reduction as recommended in previous ecological monitoring studies [15, 16]. All detection events that exceeded this threshold were counted in our analysis of detection performance across varying SNR conditions. Our system automatically selects the direction yielding the highest BirdNET confidence score for each time segment, creating a comprehensive spatial acoustic map. For baseline comparison, we extracted single-channel audio from the same recordings and processed it directly with BirdNET without beamforming.

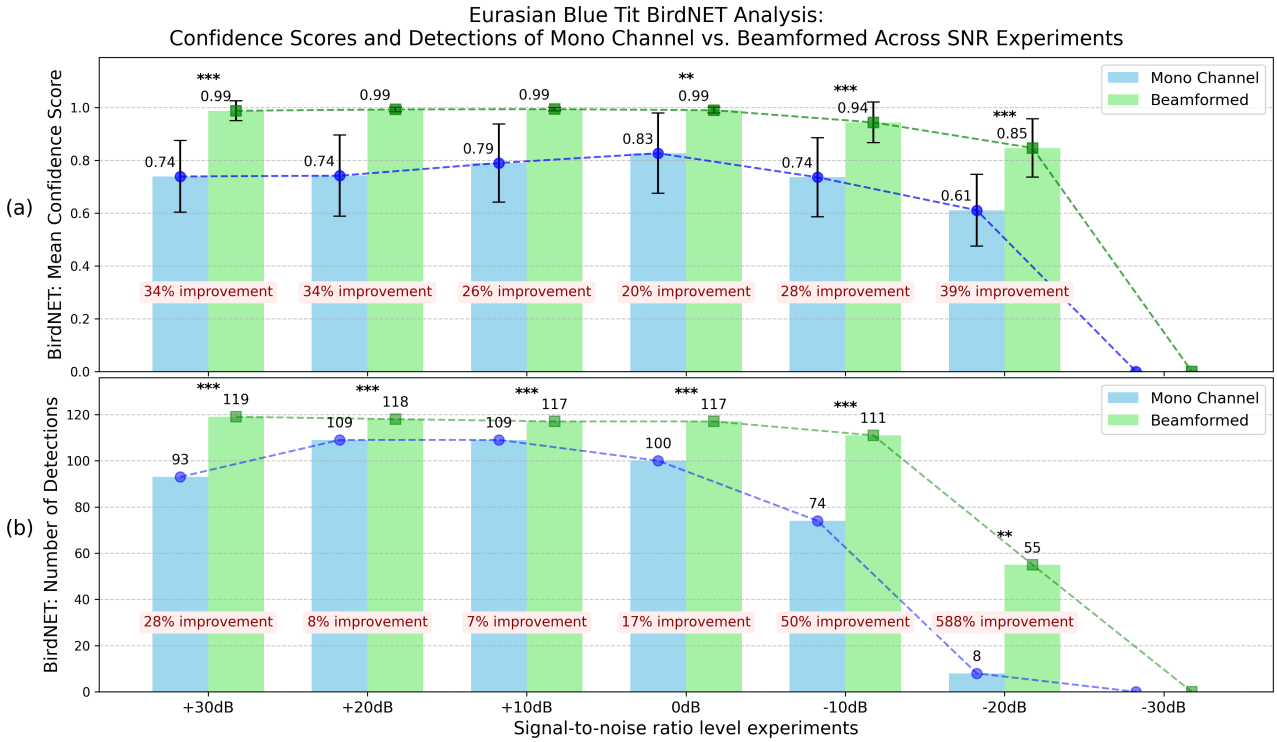


Figure 3. Performance comparison between mono channel recording and multidirectional beamforming for Eurasian Blue Tit detection across decreasing SNR levels. Panel (a) shows BirdNET confidence scores (0-1 scale), while panel (b) displays the number of successful detections (out of 124 possible events). Percentage values indicate the relative improvement of beamforming over mono channel recording. Error bars represent standard deviation.

3. RESULTS AND DISCUSSIONS

3.1 Detection Performance Comparison

Results demonstrate a clear superiority of multidirectional beamforming over conventional mono-channel recordings for birdcall detection. Higher BirdNET confidence scores were consistently achieved with the beamforming approach across various SNR levels (Fig. 3). Paired T-tests revealed significant differences in confidence scores at all SNR levels tested ($p < 0.05$), with Beamformed outperforming Mono Channel by 20-39% (Fig. 3). For instance, at +30dB, Beamformed achieved a mean confidence score of 0.9882 compared to 0.7392 for Mono Channel ($t = 17.0666$, $p < 0.0001$, ***; Fig. 3), with a large effect size (Cohen's $d = 2.6246$). This trend persisted even at lower SNRs, such as -20dB, where Beamformed maintained a confidence score of 0.8466 compared to 0.6107 for Mono Channel ($t = 4.3936$, $p = 0.0022$, **; Cohen's $d = 2.0474$). It is important to note that confidence scores are not direct probabilities and remain specific to the experimental setting and Eurasian Blue Tit species [16].

Both recording approaches showed declining confidence scores at extreme low SNR levels (-20dB and -30dB), with no detections recorded at -30dB where the birdcalls became virtually inaudible, aligning with our experimental design expectations.

3.2 Species Detection Accuracy at Varying SNR Levels

The experimental design incorporated 124 distinct birdcall events. At favourable SNR conditions (+30dB to -30dB), the beamforming approach detected up to 119 calls while mono-channel recordings detected a maximum of 109 calls (Fig. 3). Chi-square tests confirmed signifi-

cant differences in detection rates at several SNR levels. For example, at +30dB, Beamformed detected 119 calls compared to 93 by Mono Channel (χ^2 = 20.3092, p < 0.0001, ***; Cramer's V = 0.2862), indicating a moderate effect size.

A pronounced performance gap emerged at lower SNRs. At -10dB, mono-channel detection dropped to 74 calls while beamforming maintained 111 detections (χ^2 = 27.5768, p < 0.0001, ***; Cramer's V = 0.3335). This disparity widened dramatically at -20dB, with beamforming detecting 55 calls compared to only 8 with the mono-channel approach (χ^2 = 45.0251, p < 0.0001, ***; Cramer's V = 0.4261), corresponding to a 588% improvement in detection counts (Fig. 3). At -30dB, neither method detected any calls, causing statistical analysis infeasible at this level.

These findings, supported by significance stars in Fig. 3, demonstrate the beamforming technique's capacity to maintain reliable detection in challenging acoustic environments, simulating scenarios where birds are at considerable distances from recording equipment.

3.3 Key Performance Trends

Analysis of the performance data reveals several important patterns that highlight the practical advantages of beamforming:

Increasing advantage at lower SNR levels: The most striking trend is how the performance gap between beamforming and mono-channel recording widens dramatically as SNR decreases. While beamforming shows modest improvements (7-28%) at high SNR (+30dB to 0dB), where differences in detection counts were sometimes not statistically significant (e.g., at +20dB, χ^2 = 3.3296, p = 0.0680), this advantage increases exponentially at challenging SNR levels. At -10dB, beamforming achieved 50% improvement in detection counts, which surged to a remarkable 588% improvement at -20dB, supported by a highly significant Chi-square test (χ^2 = 45.0251, p < 0.0001, ***; Fig. 3).

Robustness across varying SNR conditions: Beamforming maintains consistently high performance (confidence scores >0.94 and detection counts >110) across the +30dB to -10dB range, while mono-channel performance fluctuates more dramatically even at favourable SNR levels. For instance,, at 0dB, Beamformed detected 117 calls compared to 100 by Mono Channel (χ^2 = 9.4378, p = 0.0021, **; Cramer's V = 0.1951), highlighting greater stability and reliability regardless of source distance.

Extended detection threshold: The beamforming approach extends the practical detection threshold by approximately 10dB, maintaining useful detection capabilities (55 detections) at -20dB where mono-channel recording nearly fails completely (8 detections). This effectively increases the functional detection range of the recording system, as evidenced by the significant difference at -20dB (p < 0.0001, ***).

These trends suggest beamforming's greatest value lies in extending reliable detection to challenging acoustic environments, effectively increasing monitoring range and providing more consistent data quality regardless of source distance in field deployments.

3.4 Limitations and Practical Considerations

The multidirectional beamforming approach faces three primary challenges:

Computational requirements: Processing an 8-minute recording required approximately 14 minutes (2 minutes for beamforming across 31 directions plus 12 minutes for BirdNET classification), potentially limiting large-scale deployments.

Storage demands: The process generates 31 WAV beamforming files (15MB each) plus a mono file (3MB) from a single 45MB FLAC file, necessitating substantial storage capacity for extensive field deployments.

Complex Impulse Response Characterisation Requirements: An additional significant limitation is the complexity involved in measuring impulse responses for multichannel devices. This process requires specialised equipment (such as precision turntables and calibrated loudspeaker arrays), anechoic or controlled acoustic environments, and considerable technical expertise. The full characterisation of 3D impulse responses across multiple azimuth and elevation angles is time-consuming and must be repeated for each new recording device configuration. This represents a substantial barrier to implementation compared to single-microphone deployments, which require no such calibration procedures.

4. CONCLUSION

This study demonstrates that integrating multidirectional beamforming with AI-based species detection significantly enhances birdcall identification in challenging acoustic environments. Statistical analysis confirmed that Beamformed outperformed Mono Channel across all SNR levels, with highly significant differences in both confidence scores (p < 0.05) and detection counts (p < 0.1

at significant levels), as indicated by significance stars in Fig. 3. Our approach maintained high detection accuracy at SNRs as low as -20dB, far outperforming traditional mono-channel recordings.

The methodology offers a promising framework for developing more sophisticated PAM systems capable of providing valuable behavioral and ecological insights across various species. While focused on birds, the approach could be adapted for other species with vocalisation frequencies below 8kHz.

This initial study demonstrates promising results, but several important areas require further investigation. Field testing in real-life environments with unknown sound source positions is essential to validate performance under natural reverberation conditions and diverse forest soundscapes. A more comprehensive analysis examining how beamforming affects other ecological metrics beyond simple detection is also needed. Additionally, deeper analysis of how detection performance varies with source location could provide valuable insights for optimizing array designs. Parallel to these ecological validations, optimising the computational efficiency of the BirdNET classification process would enhance the practical applicability of this method for large-scale monitoring. These extensions would strengthen the ecological applications of the multidirectional beamforming approach and better quantify its advantages over conventional recording methods across diverse monitoring scenarios.

5. ACKNOWLEDGMENTS

This work is funded by the Indonesia Endowment Fund for Education / Lembaga Pengelola Dana Pendidikan (LPDP), Indonesia (Scholarship Identification Number: 20230522097975).

We are grateful to Neel Patrick Le Penru for granting us permission to use his field recordings in our experiment to recreate the forest soundscape in a virtual sound environment.

6. REFERENCES

[1] S. S. Sethi, R. M. Ewers, N. S. Jones, C. D. L. Orme, and L. Picinali, "Robust, real-time and autonomous monitoring of ecosystems with an open, low-cost, networked device," *Methods in Ecology and Evolution*, vol. 9, pp. 2383–2387, Dec. 2018.

[2] S. R. P.-J. Ross, D. P. O'Connell, J. L. Deichmann, C. Desjonquères, A. Gasc, J. N. Phillips, S. S. Sethi, C. M. Wood, and Z. Burivalova, "Passive acoustic monitoring provides a fresh perspective on fundamental ecological questions," *Functional Ecology*, vol. 37, pp. 959–975, Apr. 2023.

[3] I. Tolkova and H. Klinck, "Source separation with an acoustic vector sensor for terrestrial bioacoustics," *The Journal of the Acoustical Society of America*, vol. 152, p. 1123, Aug. 2022.

[4] B. E. Heath, R. Suzuki, N. P. Le Penru, J. Skinner, C. D. L. Orme, R. M. Ewers, S. S. Sethi, and L. Picinali, "Spatial ecosystem monitoring with a Multichannel Acoustic Autonomous Recording Unit MAARU," *Methods in Ecology and Evolution*, vol. 15, pp. 1568–1579, Sept. 2024.

[5] J. P. Ethier and D. R. Wilson, "Using microphone arrays to investigate microhabitat selection by declining breeding birds," *Ibis*, vol. 162, no. 3, pp. 873–884, 2020.

[6] F. Grondin, D. Létourneau, C. Godin, J.-S. Lauzon, J. Vincent, S. Michaud, S. Faucher, and F. Michaud, "ODAS: Open embeddeD Audition System," *Frontiers in Robotics and AI*, vol. 9, p. 854444, May 2022.

[7] N. Le Penru, A. Borrelli, B. Heath, R. Ewers, S. Sethi, and L. Picinali, "Development and Validation of a Test Platform for Spatial EcoAcoustic Technologies," in *Proc. of the 10th Convention of the European Acoustics Association Forum Acusticum 2023*, (Turin, Italy), pp. 4671–4674, European Acoustics Association, Jan. 2023.

[8] Seeed Studio, "ReSpeaker 6-Mic Circular Array Kit for Raspberry Pi | Seeed Studio Wiki." https://wiki.seeedstudio.com/ReSpeaker_6-Mic_Circular_Array_kit_for_Raspberry_Pi/, Jan. 2023.

[9] B. E. Heath, "MAARU - Multichannel Acoustic Autonomous Recording Unit." https://beckyheath.github.io/MAARU/index.html, 2024.

[10] H. S. S. C. Sagar, A. Anand, M. E. Persche, A. M. Pidgeon, B. Zuckerberg, Ç. H. Şekercioğlu, and Z. Buřivalová, "Global analysis of acoustic frequency characteristics in birds," *Proc. of the Royal Society B: Biological Sciences*, vol. 291, p. 20241908, Nov. 2024.

[11] N. P. Le Penru, B. E. Heath, J. Dunning, L. Picinali, R. M. Ewers, and S. S. Sethi, "Towards using virtual acoustics for evaluating spatial ecoacoustic monitoring technologies," *Methods in Ecology and Evolution*, vol. 16, no. 1, pp. 108–125, 2025.

[12] D. G. Malham and A. Myatt, "3-D Sound Spatialization using Ambisonic Techniques," *Computer Music Journal*, vol. 19, no. 4, pp. 58–70, 1995.

[13] J. Weiss, "Birdnetlib v0.18.0 documentation." https://joeweiss.github.io/birdnetlib/, 2025.

[14] S. Kahl, C. M. Wood, M. Eibl, and H. Klinck, "BirdNET: A deep learning solution for avian diversity monitoring," *Ecological Informatics*, vol. 61, p. 101236, Mar. 2021.

[15] D. Funosas, L. Barbaro, L. Schillé, A. Elger, B. Castagneyrol, and M. Cauchoix, "Assessing the potential of BirdNET to infer European bird communities from large-scale ecoacoustic data," *Ecological Indicators*, vol. 164, p. 112146, July 2024.

[16] C. M. Wood and S. Kahl, "Guidelines for appropriate use of BirdNET scores and other detector outputs," *Journal of Ornithology*, Feb. 2024.

DOI: 10.61782/fa.2025.0480

FORUM ACUSTICUM EURONOISE 2025

INSIGHTS FROM DEPLOYING MULTICHANNEL ACOUSTIC AUTONOMOUS RECORDING UNITS IN BORNEO AND THE UK

Neel P. Le Penru[1,2*] **Becky E. Heath**[3] **Robert M. Ewers**[2]
Sarah S. Sethi[4] **Lorenzo Picinali**[1]
[1] Dyson School of Design Engineering, Imperial College London, UK
[2] Georgina Mace Centre for the Living Planet, Imperial College London, UK
[3] Department of Zoology, University of Cambridge, UK
[4] Department of Life Sciences, Imperial College London, UK

ABSTRACT

Multichannel acoustic monitoring uses recorders with multiple microphones to capture the spatial distribution of sounds, potentially providing an enhanced understanding of ecosystems. However, due to practical barriers such as high power demands, large data needs, and ingress protection challenges, there have been few, long-term deployments of autonomous multichannel recorders (i.e., without manual intervention). Here, we describe new, 2 to 22 week long deployments of the Multichannel Acoustic Autonomous Recording Unit (MAARU) in temperate (UK) and tropical (Borneo) environments. MAARU is a custom six-microphone recorder that uses solar power and 4G data transmission for fully autonomous monitoring. We first outline updates to MAARU's weatherproofing and field installation, including a redesigned enclosure with improved robustness to insect ingress, and share lessons for future deployments. In particular, we found that the membranes that seal microphone holes in the recorder casing fail under heavy rain if not sheltered and that 3D-printed polymer parts with a low glass transition temperature may warp due to heat from the electronics. We also discuss MAARU's capacity to amplify sounds from target directions via beamforming, and consider its application to distinguishing bird communities in neighbouring areas of different land use. In all, we hope these insights advance the successful adoption of this powerful technology.

Keywords: *Spatial Ecoacoustics, Microphone Arrays, Passive Acoustic Monitoring, Beamforming, Bioacoustics*

1. INTRODUCTION

Capturing natural soundscapes with multichannel recorders can unlock a range of information about the behaviour and distribution of animals. For instance, sounds' direction of arrival can be calculated, facilitating estimates of species abundance or tracking of individual movement [1, 2]. Beamforming can also be used to hone in on sounds from target directions, producing a higher signal-to-noise ratio (SNR) and allowing enhanced bird call classification and other analyses [2–5].

A growing number of commercial and custom multichannel field recorders have been developed (see an overview in [3]), including stereo units [6] and those with four or more microphones [3–5]. However, many remain costly and/or are not designed for fully autonomous deployments, with self-sufficient powering and data transmission alongside robustness to prolonged environmental exposure. Such features are necessary to obtain the large-scale insights of long-term continuous Passive Acoustic Monitoring (PAM) and/or for monitoring ecosystems and illegal activity in near real time (e.g., [7]).

MAARU was designed to fill this gap: it is open source, built from mostly off-the-shelf (OTS) components, and can employ solar powering and cellular data transmission [3]. Building on an existing fully autonomous, open source recorder [8], MAARU's core hardware consists of a Raspberry Pi (2B v1.2, 3B or 4B)

*Corresponding author: neel.le-penru16@imperial.ac.uk.
Copyright: ©2025 Le Penru et al. This is an open-access article distributed under the terms of the Creative Commons Attribution 3.0 Unported License, which permits unrestricted use, distribution, and reproduction in any medium, provided the original author and source are credited.

with a sound card and circular array of six omnidirectional MEMS microphones (full details in [3]). The existing MAARU design features two weatherproofing options: an affordable, modified OTS container and a custom 3D-printed enclosure for semi-autonomous deployment.

We present a new hybrid weatherproofing design, with modified OTS and 3D-printed parts for improved robustness and ease of use and manufacture. We deployed MAARUs with this updated weatherproofing for up to 5 months at temperate sites in the UK and in the tropical forests of Malaysian Borneo, to validate the revised design and further investigate the applications of beamforming in ecoacoustics. Here, we review how these deployments went, suggest further improvements to MAARU's design and deployment, and discuss forthcoming analyses.

2. MATERIALS AND METHODS

2.1 Weatherproofing Redesign

MAARU's original modified OTS weatherproofing was designed to be highly affordable and require no specialist tools to build. Early deployments revealed robustness challenges, though, in particular from animal interference, such as rodents chewing on power cables, and impacts, such as falling from height. The existing 3D-printed version addressed some of these issues with a sturdier enclosure. However, it was cumbersome to print (>15 hr on a *Prusa* MK3S) and required applying a coat of resin to fully seal against water, limiting accessibility for users without access to a well-equipped workshop. The water resistant ePTFE vents used to cover the microphone holes in both original designs were also found to be susceptible to insect ingress – specifically, termites chewing through the vents – during deployments in the Brazilian Amazon.

For the redesigned weatherproofing, we thus opted for a durable polycarbonate, water-resistant case (*Tactix* Water Proof Case (L), ∼10–15 USD depending on vendor) to house the core electronics (Raspberry Pi, sound card, microphone array, 4G dongle and a 12–5 V step-down converter). The case lid hinges for easy access to the internals. To prevent insect ingress, we used much smaller microphone holes and ePTFE vents, as the MEMS microphone ports are <0.5 mm in diameter. We also attached patches of fine stainless steel woven mesh (100 mesh, 0.15 mm hole size) over each microphone hole on the exterior of the case, using a water- and UV-resistant adhesive (Fig. 1A).

To accurately align the microphone ports with the corresponding holes in the case, we designed a 3D-printed mounting frame that sits near-flush against the base and sides of the case. The frame attaches to the case via velcro and the electronics mount to it without adhesives, allowing all parts to be removed with ease. The Raspberry Pi, sound card and microphone array form a sub-assembly, joined by screws and metal standoffs, that rests on springs glued into the mounting frame. A 3D-printed ring also sits around the microphones and flush with the top of the case. It contains a small hole for each microphone port and acts as an additional physical barrier to insect ingress. The springs prevent excessive force being placed on this sub-assembly when the case lid is closed.

A single power cable enters the case via a watertight cable gland. This can either be a USB cable connected to the Raspberry Pi, or, for solar powered deployments, a two-core power cable (AWG 17 was suitable for our powering setup), which connects to the step-down converter via bullet-style crimp connectors. Wherever possible, appropriately-specified crimp connectors were used instead of soldering to make electrical connections, as they can be easily dis/re-connected. The holes for the microphones and cable gland are all manually drilled and accurately located using 3D-printed jigs that can attach to the *Tactix* case. The electronics power cable's other end attaches to a 30 A solar charge controller which is housed with a lithium iron phosphate (LiFePO4) battery in a separate IP56-rated polypropylene box (supplier: *Solent Plastics*, product code: WBAT-S, ∼10 USD). Both the electronics power cable and a heavier duty power cable that runs to the solar panel (in our case, AWG 13 was suitable) enter this box via cable glands in manually-drilled holes. Where possible, we wrapped cables in a semi-rigid plastic cable tidy and nylon cable mesh to protect them from rodents and other animals. If costs permit, we recommend using armoured cable for long-term deployments.

2.2 UK and Borneo Deployments

MAARUs were deployed at four temperate sites at Imperial College's Silwood Park campus (Ascot, UK) for various periods of time (from 14 to 125 days) between February and July 2024. MAARUs and 60 W solar panels were mounted to custom-built metal frames fixed to the ground, with the battery box placed underneath (Fig. 1B). In September 2024, MAARUs were deployed at six tropical sites spanning a land-use gradient in and around the Danum Valley Conservation Area in Sabah, Malaysia. Two devices were deployed in each of: old-growth forest, logged forest, and smallholder oil palm plantations.

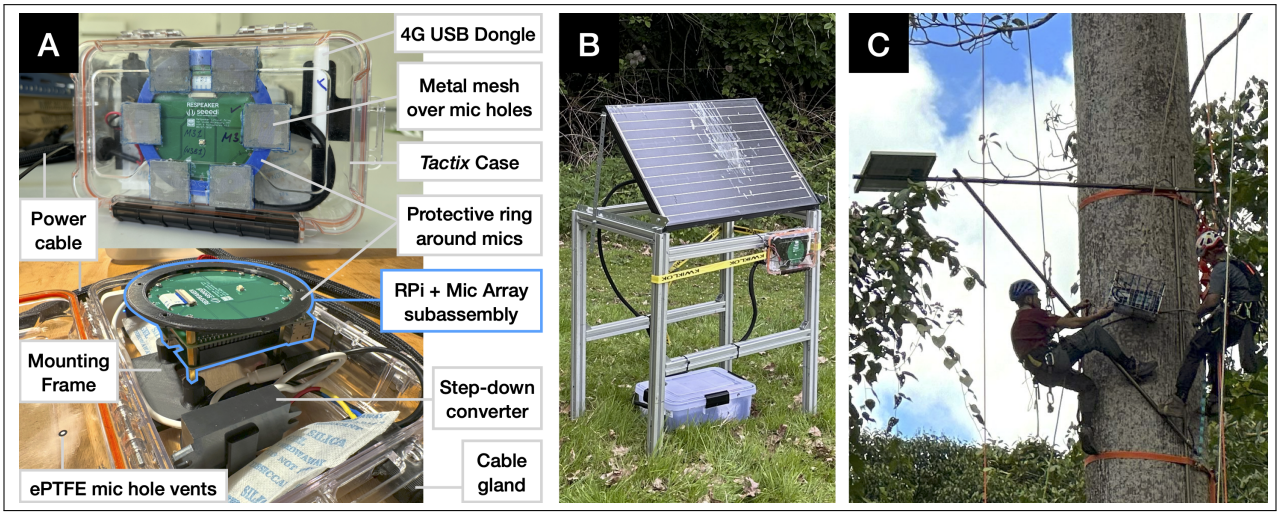


Figure 1. **A:** Redesigned MAARU weatherproofing enclosure. **B:** MAARU deployment in the UK. **C:** Professional tree climbers Jamiluddin Jami and Louis Makhluf mount a MAARU to a tree in Malaysian Borneo.

Data were collected between approx. two weeks and five months, depending on devices' survival time (see Section 3). For access to sunlight and protection from animals on the ground (e.g., elephants), the old growth and logged forest devices were mounted to trees by professional tree climbers. Solar panels (three 55 W and one 100 W) were attached to triangular structures assembled from aluminium poles (Fig. 1C). MAARUs and battery boxes were placed in a cage built from six steel grills (supplier: *DAISO*, ∼6 USD per cage), to protect them from animals in the trees (e.g., monkeys). The cages and pole structures were fixed to trees with heavy-duty ratchet straps. For the oil palm sites, the device cage and 100 W solar panels were mounted to slotted angle bars inserted in the ground.

Across all sites, MAARUs were deployed near the edges of different habitats or land-use types and/or within audible range of roads or other sources of anthropogenic noise from prevailing directions, so as to explore various applications of beamforming. All recordings were compressed to FLAC on-device and streamed over 4G to *Box* Cloud Storage via FTPS. For continuous 24/7 recording, this creates ∼8 GB/day of data (∼250 GB/month), so all devices had a minimum 300 GB/month cellular data plan.

3. RESULTS AND CONCLUSIONS

MAARU's redesigned weatherproofing improves robustness to previous failure modes while enabling better access to internals and easier manufacturing than the previous 3D-printed enclosure. However, new failure modes have been discovered. For the UK deployments, the 3D-printed parts were made from PLA, which is safe (minimal fumes) and straightforward to print, but has a fairly low glass transition temperature (T_g) of ∼57°C [9]. This was expected to be sufficient, however parts in three units warped due to heat from the electronics, damaging several microphones in these units (sometimes in just two weeks after deployment). The Raspberry Pi and 4G dongle can generate considerable heat, which was likely exacerbated by both being housed in a clear, sealed enclosure exposed to sunlight. For the Borneo deployments, these parts were printed from ABS, which has a T_g of ∼107°C [9], and did not warp. We thus recommend using ABS or other materials with a similar or higher T_g in future.

In Borneo, the old growth and logged forest units failed after ∼2-4 weeks. This appears to be due to water ingress from heavy rainfall piercing the ePTFE microphone vents (not all units have been retrieved yet). All old growth and logged forest units were deployed horizontally (i.e., with the ePTFE vents perpendicular to rainfall) to provide the freedom to beamform in any horizontal direction. MAARUs were deployed vertically in the UK and oil palm and did not face this issue. The oil palm devices were also sheltered by the solar panels. As such, we recommend either sheltering any units deployed horizontally (e.g., with the solar panel or some other cover [4]) or

deploying the MAARU units upside down, which should allow for equivalent beamforming and localisation capabilities. Finally, for all deployments, the 55 W and 60 W panels did not provide enough power for continuous 24/7 monitoring (perhaps due to lower insolation in the UK and some obstruction from trees and clouds in Borneo), whereas the 100 W panels in Borneo did, hence we recommend the latter for such monitoring efforts in future.

Despite device failures, sufficient data was gathered to investigate beamforming to distinguish neighbouring habitats/land-use types and to steer recordings away from reasonably directional unwanted noise (e.g., road traffic) towards directions of interest. For the UK deployments, there is also an opportunity to evaluate MAARU's beamforming capacity with fewer microphones undamaged by parts warping. Existing tests with MAARU showed improved confidence scores of avian call classifier BirdNET (which correlate with probability for many species) when beamforming in generic directions [3], likely owing to a higher SNR. Leveraging knowledge of habitat and site structure should allow for scaling these benefits to more ecologically relevant applications. Beamformed audio will also be analysed with acoustic indices and machine learning model embeddings as part of a representative ecoacoustic toolkit. While it is harder to define an improvement in these metrics without ground truth biodiversity data, we hypothesise that they should significantly differ for directions corresponding to different land-use. Should beamforming with MAARU successfully distinguish neighbouring habitats/land-use types, there is a notable opportunity for ecologists to monitor land-use gradients with fewer devices, and thus less cost and disturbance, than if single-channel, omnidirectional recorders are used (many of which cost a similar amount to MAARU). Overall, we hope these forthcoming analyses show that beamforming can segment soundscapes for more efficient and accurate ecosystem monitoring.

4. ACKNOWLEDGMENTS

We thank Jamiluddin Jami, Johnny Larenus, Ahmad Jelling, Yehezkiel Jahuri, and Louis Makhluf for invaluable assistance with the Borneo deployments. We are grateful to the Sabah Biodiversity Council for granting an access license and the Danum Valley Management Committee for providing a fieldwork permit. We also thank Dr. Henry Bernard, the South East Asia Rainforest Research Partnership, Silwood Park's field manager and technicians, and the Imperial AXD, ACE Workshop and IDEAS Lab teams for their support. N.P.L.P. was funded by NERC [NE/S007415/1] via the SSCP DTP and a UK Acoustics Network Plus Early Career Travel Grant.

5. REFERENCES

[1] D. T. Blumstein *et al.*, "Acoustic monitoring in terrestrial environments using microphone arrays: Applications, technological considerations and prospectus," *J. Appl. Ecol.*, vol. 48, no. 3, pp. 758–767, 2011.

[2] T. A. Rhinehart, L. M. Chronister, T. Devlin, and J. Kitzes, "Acoustic localization of terrestrial wildlife: Current practices and future opportunities," *Ecol. Evol.*, vol. 10, no. 13, pp. 6794–6818, 2020.

[3] B. E. Heath *et al.*, "Spatial ecosystem monitoring with a Multichannel Acoustic Autonomous Recording Unit (MAARU)," *Methods Ecol. Evol.*, vol. 15, no. 9, pp. 1568–1579, 2024.

[4] M. Wijers, A. Loveridge, D. W. Macdonald, and A. Markham, "CARACAL: A versatile passive acoustic monitoring tool for wildlife research and conservation," *Bioacoustics*, vol. 30, pp. 41–57, Nov. 2019.

[5] P. Chwalek, M. Coblentz, S. Montague, M. Kuronaga, I. Zhu, and J. A. Paradiso, "Acoustic data collection in arctic environments during the midnight sun using multi-channel SoundSHROOMs," *Sci. Data*, vol. 12, p. 318, Feb. 2025.

[6] Wildlife Acoustics, "Song Meter SM4 Wildlife Audio Recorder."

[7] S. S. Sethi, R. M. Ewers, N. S. Jones, A. Signorelli, L. Picinali, and C. D. L. Orme, "SAFE Acoustics: An open-source, real-time eco-acoustic monitoring network in the tropical rainforests of Borneo," *Methods Ecol. Evol.*, vol. 11, pp. 1182–1185, Oct. 2020.

[8] S. S. Sethi, R. M. Ewers, N. S. Jones, C. D. L. Orme, and L. Picinali, "Robust, real-time and autonomous monitoring of ecosystems with an open, low-cost, networked device," *Methods Ecol. Evol.*, vol. 9, pp. 2383–2387, Dec. 2018.

[9] E. Sirjani, P. J. Cragg, and M. K. Dymond, "Glass transition temperatures, melting temperatures, water contact angles and dimensional precision of simple fused deposition model 3D prints and 3D printed channels constructed from a range of commercially available filaments," *Chem. Data Coll.*, vol. 22, p. 100244, Aug. 2019.

DOI: 10.61782/fa.2025.0030

FORUM ACUSTICUM EURONOISE 2025

A REVIEW ON THE POTENTIAL INTERACTION OF VIBROACOUSTIC AND ELECTROSTATIC PLANT-POLLINATOR COMMUNICATION

Ivan Sili[1*] **Abhishek Ray Mohapatra**[1] **Alberti Simona**[2]
Can Nerse[1] **David Navarro-Payá**[3] **Francesca Barbero**[2]
Gastón Pizzio[3] **Jone Echeverria**[3] **Lorenzo Bianco**[2]
Luca Pietro Casacci[2] **Maria Rosaria Tucci**[3] **Tomás Matus José**[3]
Sebastian Oberst[1]

[1] Faculty of Engineering and Information Technology, University of Technology Sydney, Ultimo NSW 2007, Australia
[2] Department of Life Sciences and Systems Biology, University of Turin, 10123, Turin, Italy
[3] Institute for Integrative Systems Biology (I2SysBio), CSIC-Universitat de Valencia, Paterna, 46908, Valencia, Spain

ABSTRACT

Pollinators, like bees, use various cues to locate flowers with rewards such as nectar and pollen. While most research focuses on olfactory and optical signals, vibroacoustic and electrostatic cues may be more critical in pollination. Studies on honeybees, bumblebees, and hoverflies indicate that the electrical charges insects accumulate assist in navigating, identifying, and potentially communicating with flowers rich in nectar or pollen. Vibroacoustic signals and cues, such as buzzing, further enhance pollen extraction. However, the interplay between vibroacoustic and electrical signals in bees, including wild bees and eusocial Australian stingless bees, remains poorly understood. Additionally, the impact of insect morphology on their ability to acquire charge through triboelectric interactions with air and plants is unclear. This study examines vibroacoustic and electrostatic communication between plants and pollinators, with a focus on analysing existing literature. We hypothesise that Australian stingless bees have evolved a mechanism like honeybees for obtaining an electrical charge, though likely smaller due to their morphology. The review aims to facilitate the first experimental measurement of electrical charge in stingless bees.

Keywords: *electroreception, vibroacoustic, communication, stingless bee, pollination.*

[*] ***Corresponding author***: *ivan.sili@uts.edu.au.*

Copyright: *©2025 Ivan Sili et al. This is an open-access article distributed under the terms of the Creative Commons Attribution 3.0 Unported License, which permits unrestricted use, distribution, and reproduction in any medium, provided the original author and source are credited.*

1. INTRODUCTION

Navigation is essential for pollinators because it enables them to locate flowers efficiently, return to their nests, and ensure successful pollination, which is critical for ecosystem health and biodiversity [1]. Pollinators, including insects (bees, wasps, moths etc.), birds, and certain mammals, navigate between plants and the nest, enabling plant fertilisation through pollination between flowers. However, apart from navigation, recent research [2-5] shows that pollinators seem to communicate with the plants and make foraging decisions based on food availability and preference.

These navigation and communication mechanisms are highly diverse, encompassing a variety of sensory and cognitive strategies that allow them to find their way in complex environments. Some animals can orient themselves using the Earth's magnetic field, a process known as magnetoreception [6]. In addition to magnetoreception, animals rely on other advanced systems for navigation, such as infrasound, ultrasound, echolocation

[7] or biotremology (vibrational communication) [8]. Many insects rely heavily on their visual systems to navigate, locate food sources, and recognise landmarks [1]. Pollinators, particularly bees, see colours differently than humans. They can perceive ultraviolet (UV) light, which is invisible to the human eye. Many flowers have patterns in the UV spectrum that may enhance their attractiveness to pollinators [9].

We can classify the sensory mechanisms of communication and pollinator navigation into the following categories: olfactory, optics, vibroacoustic and electromagnetism [7]. The interaction of patterns, visual, vibrational, acoustic, and electromagnetic cues forms a complex communication network between plants and pollinators, greatly influencing the pollination process.

Communication cues are distinguishable based on their distance and timing [7] summarised in Table 1. Typically, long-distance communication occurs over a large time scale (lasting for hours), while medium- and short-distance signals are more likely to occur within minutes or seconds.

Table 1. Summary of observed common cues in the distance-time domain.

Cue Type	Distance range	Time of occurrence	Example
Olfactory	Long-range (m)	min to h	Floral scents and volatile production.
Optics	Medium-range (cm)	min	Bright colours, UV patterns.
Vibro-acoustic	Short-range (mm)	s	Buzz pollination, sugar increase to specific pollinator.
Electro-magnetism		ms	Pollen adhesion due to charge differences.

Apart from well-documented cues, researchers are investigating potential indications of an additional level of communication in plant-pollinator interactions. Recent evidence [10] indicates that the low-frequency motion of a flower (1 Hz to 2 Hz) serves as a distinct optical cue, independent of the object's shape. Experiments carried out by Desai et al. [11] suggest that foraging honeybees (*Apis mellifera*) can detect and identify both stationary and oscillating flowers, exhibiting a preference for the moving one. Further research is needed to determine whether a moving object can serve as an additional salience factor and whether pollinators use it in their decision-making.

While much research has focused on optical and olfactory cues in these interactions, the roles of vibroacoustic and electrical communication have garnered increasing interest in recent years [2-5, 12-15]. In the domain of electrical communication, publications predominantly focus on charge-measuring experiments involving honeybees [2, 16], bumblebees [17], hoverflies [5] and moths [18]. This current review aims to synthesise current knowledge regarding the significance of electrostatic fields in pollinator behaviour and plant-pollinator dynamics, as well as the potential coupling of this field with vibroacoustic cues to contribute to the field of plant-pollinator electro-acoustic (multimodal) communication.

2. ELECTROSTATIC FIELD AND CHARGE

2.1 Bee`s charge

Non-biological substances are known [19] to acquire an electric charge as they move through the atmosphere due to triboelectric charging. Experimentally observed raindrops [19] carry an electrical charge, typically ranging from 5 pico Coulombs (pC) to 100 pC, as they fall from the clouds during rainfall. With a diameter of approximately 4 mm, they are comparable in size to Australian native stingless bees, which are three to four times smaller than honeybees (Fig. 1). We assume that bees become highly triboelectrically positively charged while traveling through the atmosphere, in contrast to sessile and negatively charged flowers.

The first experiments providing some evidence of electrically charged insects were conducted in 1929 by Heuschmann [20], and bees specifically in 1975 by Erickson [21]. The last research shows that worker honeybees (*Apis mellifera*) possess a surface electrical charge when entering and leaving the hive, and the amount of the charge varies on their daily rhythm, peaking at midday or early afternoon. The experimental setup included two concentric conductive tubes with outer diameters of 12 mm and a length of 5 mm, separated by a 2 mm gap.

The calculated average charge shows that a bee returning from active flight had a charge of about 12 pC. However, due to the full contact between the bee and the tubes in this experiment and the inevitable transfer of charge while passing through the tube, the obtained results are likely lower compared to the actual value. A bee's surface can acquire and carry an electrical charge emanating a static electric field, similar to any physical object exposed to friction, pressure, or other external forces.

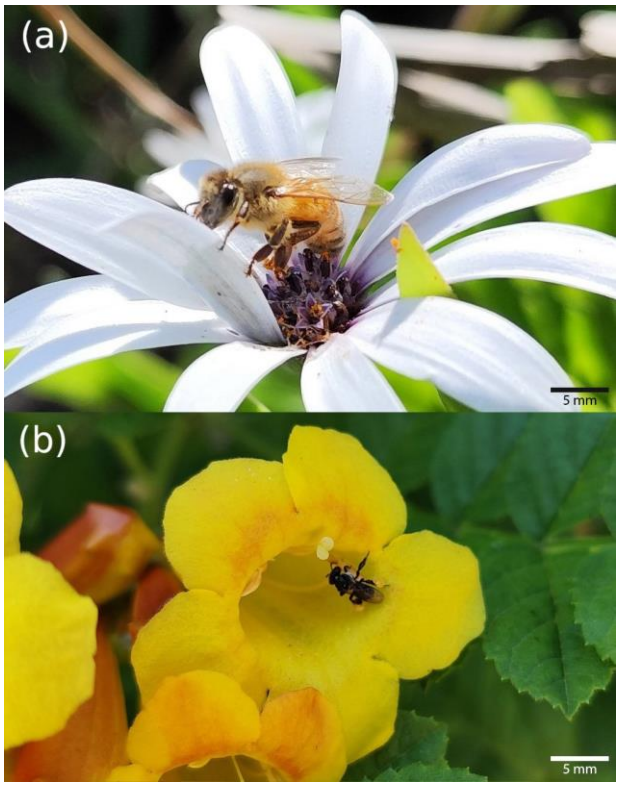


Figure 1. An equal-scale view of (a) the Western honeybee *Apis mellifera* and (b) the Australian stingless bee *Tetragonula carbonaria* foraging near local flowers in the northern region of Sydney, Australia (photo credit: Ivan Sili, November 2024)

As a result of this interaction, one entity gains additional electrons and becomes negatively charged, while the other becomes positively charged.

Over time, insects have learned to utilize the electrical charge they carry on their bodies. This charge varies based on the bee's activity, environmental conditions, and body size. There is evidence [21], that an inactive honeybee may carry a negative charge as well, typically ranging from −1.8 pC to +2.9 pC, inside the beehive at 70% humidity. An active bee, such as a dancing bee near the hive entrance, is usually positively charged up to 45 ± 4.3 pC, with a maximum charge reaching around 80 pC [21].

Colin et al. [16] measured the electrical potential of winter-clustered *Apis mellifera* and compared this to foraging bees in the spring, proposing a new technique with an induction ring. The same method and device were used in subsequent studies [17, 18]. The charge sensor consisted of two coaxial rings electrically insulated by a dielectric material. An electrometer connected to the inner ring measured the electrical current induced by the passage of a charged insect. It was observed that foraging bees typically possess smaller charges (mean = 29 ± 40 pC) than winter bees (mean = 153 ± 105 pC). Most bees carry a positive charge; however, 7% of measured bees were negatively charged, and less than 1% neutrally charged. These measurements align with findings published by Clarke et al. [22] for foraging bumblebees (mean = 32 ± 35 pC). Variations in body size among the measured bees did not significantly affect individual net charge variability, likely because fluctuations in bee size do not exceed 20%, except for the queen (whose net charge varies between +159.6 pC and +240.5 pC with a one-day delay measurement) [16]. However, the fact that the queen carries a higher amount of charge may correspond to a size-dependent charging effect, which has not been investigated yet.

Recent research by Montgomery et al. [23] suggests that the electric charge possessed by bumblebees stimulates volatile emissions. Findings indicate that *Petunia integrifolia* slightly increases the emission of behaviourally and physiologically active compounds in response to visits from positively charged bumblebees ~121 pC. Stronger emissions correlate with higher levels of electrical stimulation.

2.2 Humidity and the charge

Weather conditions, particularly relative air humidity, can significantly influence the charge carried by bees. Triboelectric charging, a primary factor in bees acquiring charge, is highly dependent on humidity levels. In [24] has shown that increasing humidity often corresponds to a decrease in bee charge, following an exponential decay relationship. The assumption is that water allows higher conductivity between two dielectric surfaces, thereby facilitating charge transfer. In conditions of high humidity, bees may have difficulty charging efficiently, which could result in reduced communication between plants and pollinators.

The only experimental study on the relationship between humidity and charging bees that we are aware of is that of Montgomery et al. [25]. The mathematical model derived as observed in the cited experiment can be represented as follows:

$$Q_{bee} = 0.26 + (5.73 - 0.022RH)\int Idt,\ [pC] \qquad (1)$$

where Q_{bee} – represents bee charge; RH – relative humidity; and I – induced electric current in the ring sensor.

Relative humidity also noticeably reduces a bee's charge retention time. An insect is likely to dissipate half of its charge within the first 30 seconds at humidity levels over 70%, while retaining 90% of its original charge when the relative humidity is below 70% [24]. Badger et al. reported [26], that a hummingbird's charge is also highly dependent on relative humidity, with net charge generally decreasing as humidity increases. Temperature, however, has no significant effect on the acquired charge. Previous research suggests that the variability of bee charges under different humidity levels should be considered when modelling future environmental experiments.

2.3 Foraging distance and the charge

One of the most common pollinators in the world, the western honeybee (*A. mellifera*), tends to visit only one type of flower while foraging in a specific direction and is highly flower-constant [27]. Bees can quickly learn all multimodal attributes of a specific plant and use this information while foraging. More than two thousand years ago, the Greek scientist Aristotle in his work "Historia Animalium" [28], remarked that a beekeeper could predict weather conditions based on the flight distance of bees. Bees can sense the approach of rain, as evidenced by their shorter flight distance. However, even under optimal weather conditions, their flight range is limited. In our current understanding, honeybee foraging range can reach up to 10 km from the hive, with a mean of 5.5 km. About 50% of bees foraged at distances more than 6 km, 25% more than 7.5 km, and only 10% more than 9.5 km [27].

Relevant work in this research line includes that of Es'kov and Sapozhnikov [29], which showed no evidence that foraging distance affects a honeybee's electric charge. Bees that flew 5 meters and 200 meters from the hive carried similar charges, varying between +0.98…+0.96 ± 0.13 pC. Controversially, in an experiment conducted by Montgomery [24], bumblebees had significantly higher charges when flying compared to walking, with positive charge increasing after more than 10 seconds of flight, assuming that flying activity impacts the positive charging of insects. This impact is expected to be logarithmic and can be approximated with:

$$Q_{bee} = 17.3 - 16.4e^{-0.17t}, \ [pC] \qquad (2)$$

where Q_{bee} - charge of the bee, and t – flight time.

Montgomery suggests [24] that a bee already carrying a positive charge is unlikely to gain additional charge during either short or long flights, emphasizing the limited electric charge saturation for an individual.

3. VIBROACOUSTICS COMMUNICATION

Vibroacoustic communication also is a crucial aspect of the interactions between pollinators, particularly bees, and flowering plants. This form of communication involves the use of vibrational and acoustic signals that can convey important information about foraging, mating, and environmental conditions.

Flight and non-flight vibrations produced by the rapid contraction of thoracic muscles in bees can be classified. To encourage bee visits, plants have evolved a mechanism to produce nectar rich in sugar and pollen, which bees collect and process to produce honey. However, certain plants, such as tomato, potato or snapdragon families, release pollen only under specific conditions, with precisely tuned vibrations being one of these requirements [12]. These vibrations are often produced by certain species of bees, known as "buzz-pollinators" [12]. This is an evolutionary adaptation that ensures more precise pollination, as only specific types of pollinators can access the pollen.

Buzz pollination is a documented yet not fully understood process employed by insects to efficiently extract pollen. The vibrations produced during buzz pollination are typically generated by the thoracic muscles through direct physical contact between the bee and the flower. During this process, a bee typically assumes a C-shaped position around the anthers and produces rapid, millisecond-long vibrations in the frequency range of 100 Hz to 400 Hz [30], often coinciding with the peak or dominant frequency, along with multiple harmonics of rapidly decreasing magnitude. This phenomenon is likely to occur in species within the families *Apidae* and *Melittidae*; meanwhile, only 6% of flowering plant species possess flowers with anthers that open in response to vibrations [31].

Bumblebees are known to transmit vibrations to flowers through various morphological structures, including the thorax, mandibles, and possibly legs [31]. Research [31] suggests that bee size is positively associated with vibration amplitude, but not necessarily with frequency. Morgan et al. [32] demonstrated that bees adjust the frequency, amplitude, and duration of their vibrations as they gain experience manipulating the same plant. Vallejo-Marín et al. [33] in their research conducted across North America, Europe, and Australia, found that the body size of bees, specifically thorax width, during non-flight defensive activity positively correlates with the acceleration amplitude of their buzzes, while it has no significant effect on buzz frequency. Non–flight (floral) vibrations exhibit also higher frequencies and greater amplitudes compared to the vibrations generated during flight. The frequency and amplitude of these vibrations play a crucial role in

determining the rate of pollen release. Observed in [34] was a positive correlation between vibration amplitude and the rate of pollen release, with a similar relationship found between higher vibration frequencies and increased pollen release and plant parts are likely grown with preferred resonance frequencies to accommodate a maximum of pollen release [35].

The most common eusocial Australian stingless bees, *T. carbonaria* and *A. australis*, have not been observed performing buzz pollination [36], likely due to their small body size. In contrast, some solitary bees, like blue-banded bees (*A. cingulata*) or carpenter bees (*Xylocopa* spp.), are recognized as native buzz pollinators in Australia [36].

While buzz-pollination is well studied, vibroacoustic signals (VAs) produced by pollinator`s wing beats could cause a potentially adaptive plant response, even before the contact between the plant and the insect. King [37] reported that after landing on a plant, the bee flaps its wings and rapidly contracts its flight muscles. The wingbeat frequency [30] of *Xylocopa* bees affects the amount of pollen removed from *Senna spectabilis*, maintaining constant values between 250 Hz and 500 Hz. In the range of 300 Hz to 400 Hz, an ejection of 0.02 to 0.10 mg of pollen was observed in flowers that received only one visit, with a tendency for less pollen to be ejected at frequencies greater than 500 Hz. The aforementioned study showed that different species of bees exhibit distinct buzzing patterns, which are related to their wingbeat frequency. Bees may modify their wingbeat frequency to approach the natural frequency of the plant they visit, optimizing the pollination process. Nerse et al. [38] studied the biomechanical properties of the snapdragon (*Antirrhinum litigiosum*) and showed how the features of flower organ material are flexible and respond to pollinator vibro-acoustic stimuli. While buzz-pollination behaviour is restricted to specific plant-insect interactions (such as those involving poricidal anthers), the responses gathered by Veits et al. [4] suggest that VA could serve as a signal potentially in all plant-insect interactions, hypothesised to be a basal plant mechanism for sensing and responding to vibrations.

4. DISCUSSION

From the analysis of the literature, we can conclude that recent research investigating the intricate communication between plants and pollinators has confirmed that electrostatic fields and vibroacoustic serve as additional cues in plant-pollinator communication.

Bees are known [39] to emanate both static and modulated electric fields. The static electric field is generated by the static charge possessed by the bee, while the modulated field is likely influenced by insect activity, with wing flapping being the most crucial factor. Although some studies have suggested this relationship [39, 40], there is no strong evidence supporting the idea that wing flapping alone modulates a bee's electric charge to a significant extent. While electrostatic interactions have been studied, the dynamic, real-time modulation of a bee's electric charge by its wing movements remains an underexplored area. Experimental research measuring both the acquired electric charge (e.g. emanating electric field) and wing flapping frequency simultaneously could provide a clearer understanding of this phenomenon.

An increase in wingbeat rate during a bee's foraging activity may enhance the positive charge it carries. Consequently, a higher charge could generate stronger electrostatic forces between the pollinator and pollen, enabling the insect to more efficiently analyse potential outcomes. Based on the measured electrical charge carried by the bees, we also aim to question whether flowers may have evolved to manipulate their electrical charges to ensure the loyalty of specific pollinators. If plants can manipulate their own electric charge in response to an approaching pollinator, this could open a new area of exploration. This trait may have evolved in a way similar to buzz pollination, but within the electrostatic realm, attracting specific pollinators to collect the pollen.

The morphology of bees determines its vibroacoustic properties. In cases where buzz-pollination is possible, the size of the thorax regulates the amplitude of the vibrations [33]. The frequency of these vibrations, however, is not influenced by body size but is instead determined by the wing flapping frequency. Additionally, bees can adjust the vibration frequency depending on the context, such as floral interaction or defensive behaviour. The potential influence of thorax size and musculature on the electrostatic charge acquired by bees, in a manner similar to their effect on vibrational properties, remains an open question. Future research is needed to investigate whether the amplitude of the electric signal, like that of vibroacoustic signals, is influenced by the size of the wing, wingspan or musculature of the thorax, clarifying the biomechanical interactions between body morphology and electrostatic charge.

A review of the literature reveals that the relationship between pollinators' morphology and their ability to acquire charge remains poorly understood. In [17] suggested that insect cuticle accumulates surface electric charge. While some evidence [14, 16] suggests that larger body size and wingspan correlate with increased charge, specific values vary among species. For instance, honeybees have been reported to possess an average charge of 29 pC [16],

bumblebees 32 pC [22], hoverflies 37 pC [5], butterflies 49 pC [18], and hummingbirds 66 pC [26]. Conversely, wasps have been reported to carry a smaller average charge of 8 pC [40], despite being larger in size compared to honeybees or bumblebees.

Why do wasps deviate from this trend? Could it be an evolutionary trait that wasps did not develop, as pollen and nectar collection are not their primary activities? Wasps have less triboelectric interaction with petals and sepals but still acquire some charge while flying through the air. Does physical contact with the flower play a more significant role in charge acquisition compared to airborne charging during flight? And what morphological features of wasps determine their small electric charge? One potential explanation is their smoother shape, with fewer body hair. In [41], researchers removed hair from the thorax of hoverflies, which reversed the polarity of the obtained charge or resulted in a neutral charge when hair from the propleuron was removed, concluded that the presence and distribution of hair on the thorax play a crucial role in determining both the amount and polarity of the induced charge. The idea that a larger surface area with longer hair could influence electric charge acquisition is also reasonable and should be further studied across different pollinator species.

But which species should be considered optimal for investigating the influence of morphological characteristics on charge acquisition? An Australian stingless bee *Tetragonula carbonaria* is a dominant candidate for such studies. These bees are approximately three to four times smaller than honeybees in terms of body size, have fewer hair on the thorax compared to honeybees or bumblebees, and possess a chitin-covered, smoother abdomen (Fig. 2a, b). We currently have no research on the average electric charge possessed by stingless bees, but considering their morphology, it could be of a lower magnitude than that of honeybees or bumblebees. The open question is whether this small charge could be sufficient for pollen adhesion via electrostatic forces. We also don't know whether stingless bees rely on vibroacoustic and electrostatic cues or both while foraging or if they prefer to use other sensory modalities or their combination. As this species deviates from *Apis* genus, they have evolved some important features to succeed in pollen and nectar collection: possession of corbiculae with hairy areas for attaching pollen grains (Fig. 2c), similar frequency of wing flapping, and, as a hypothesis, emit vibroacoustic and electrostatic stimuli to target flowers (Fig. 2d) to indicate their presence. Flowers are likely to respond to these stimuli by releasing pollen or increasing sugar concentration [4].

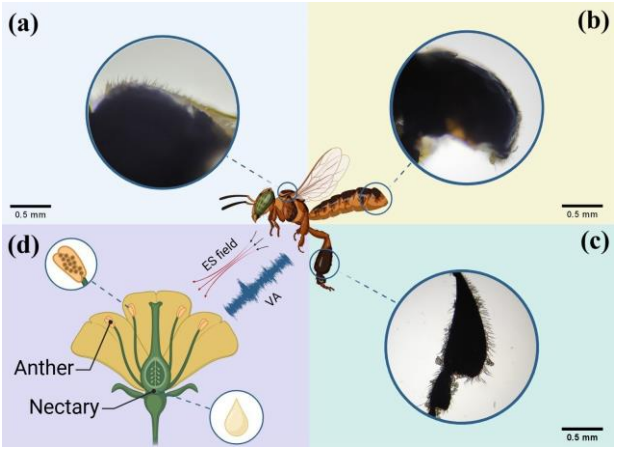


Figure 2. Morphological traits of the Australian stingless bee *Tetragonula carbonaria* and their potential impact on charge acquisition and vibroacoustic stimuli under a 40× magnification microscope view (photo credit: Ivan Sili, image created with BioRender.com). Circles indicate sampling positions on various parts of the bee's body, highlighting the detailed structure of the bee's anatomy. (a) Thorax sparsely covered with short hair. (b) Smooth hairless chitin abdomen. (c) Hairy corbicula with densely attached pollen. (d) The vibroacoustic (VA) and electrostatic (ES) stimuli emitted by a bee are hypothesized to trigger a plant's response, aiding in assessment outcomes and potentially leading to pollen release and an increase in nectar sugar concentration.

Airborne acoustic waves, thoracic vibrations, and electrostatic fields modulated by wing flapping may create a complex multimodal communication system between plants and pollinators. As a pollinator approaches a flower, it likely utilizes all available sensory modalities to evaluate the interaction and distinguish a rewarding flower. This leads to another hypothesis suggesting that a bee, upon landing a flower, may first sense the amount of pollen in the anther. Shortly after assessing the pollen, possibly through its electric charge, the "buzz bee" may either employ a vibroacoustic strategy—such as thoracic vibrations upon landing on the flower—which requires energy expenditure to obtain the reward, or choose to search for another flower that offers a more rewarding outcome without expending energy, while an increase in sugar concentration will help maintain the preferred pollinator's loyalty to the same flower.

5. ACKNOWLEDGMENTS

Work supported by Research Grant RGP0003/2022, Good vibes: how do plants recognise and respond to pollinator vibroacoustic signals?, funded by HFSP https://doi.org/10.52044/HFSP.RGP00032022.pc.gr.153605

6. REFERENCES

[1] M.A.F. Sanjuan, "Physics of animal navigation." *Eur. Phys. J. Spec. Top.* 232, pp. 231–235, 2023. https://doi.org/10.1140/epjs/s11734-023-00795-8

[2] U. Greggers, G. Koch, V. Schmidt, et al. "Reception and learning of electric fields in bees." in *Proc Biol Sci.* Vo. 280, 2013. doi: 10.1098/rspb.2013.0528.

[3] D. Robert, "Aerial electroreception". *Current Biology*, vol. 34, Issue 20, pp. R1018-R1023, 2024. https://doi.org/10.1016/j.cub.2024.06.028

[4] M. Veits, I. Khait, U. Obolski et al "Flowers respond to pollinator sound within minutes by increasing nectar sugar concentration." *Ecol. Lett.* Sep;22(9), pp. 1483-1492, 2019. doi: 10.1111/ele.13331.

[5] S.A. Khan, K.A. Khan, S. Kubik et al. "Electric field detection as floral cue in hoverfly pollination." *Scientific Reports*, vol. 11, 2021. https://doi.org/10.1038/s41598-021-98371-4

[6] J. L. Gould, "Magnetoreception." *Current Biology*, Volume 20, Issue 10, pp. 431-435, 2010. https://doi.org/10.1016/j.cub.2010.03.045

[7] R. Karban, "Plant Sensing and Communication." University of Chicago Press, 251 p. 2015. https://doi.org/10.7208/9780226264844

[8] S. Oberst, J.C.S. Lai, T. A. Evans, et al., "Physical Basis of Vibrational Behaviour: Channel Properties, Noise and Excitation Signal Extraction. In Biotremology: Studying Vibrational Behavior." *Springer International Publishing*. https://doi.org/10.1007/978-3-030-22293-2_5

[9] C. Grüter: Stingless Bees. Their Behaviour, Ecology and Evolution. Cham, Switzerland: *Springer Nature* Switzerland, 2020.

[10] G. Hennessy, C. Harris, C. Eaton, et al. "Gone with the wind: Effects of wind on honey bee visit rate and foraging behaviour." *Animal Behaviour*, vol. 161, pp. 23-31, 2020.

[11] R. Desai, M.A. Garratt, M.V. Srinivasan and S. Ravi "Honey bee foraging behaviour can be influenced by preferences for oscillating flowers." *Animal Behaviour*, vol. 214, pp. 147-156, 2024. https://doi.org/10.1016/j.anbehav.2024.06.005

[12] M. Vallejo-Marin, D. L. Field, J. Fornoni, et al "Biomechanical properties of non-flight vibrations produced by bees." *J Exp Biol*. Vol. 227 (12), 2024. doi: https://doi.org/10.1242/jeb.247330

[13] F. Barbero, T. Matus, and S. Oberst, "Good vibes: How do plants recognise and respond to pollinator vibroacoustic signals" Human Frontier Science Program. 2022 Retrieved from https://www.hfsp.org/node/74710

[14] Y. Vaknin, S. Gan-Mor, A. Bechar, B. Ronen, and D. Eisikowitch, "The role of electrostatic forces in pollination." *Plant Syst. Evol.* vol. 222, pp. 133–142, 2000. https://doi.org/10.1007/bf00984099

[15] C. E. Morley, and D. Robert, "The bee, the flower, and the electric field: electric ecology and aerial electroreception". *J Comp Physiol A* vol. 203, pp. 737–748, 2017. https://doi.org/10.1007/s00359-017-1176-6

[16] M. E. Colin, D. Richard, S. Chauzy. "Measurement of Electric Charges Carried by Bees: Evidence of Biological Variations." *Journal of Bioelectricity*, 10(1–2), pp. 17–32, 1991. https://doi.org/10.3109/15368379109031397

[17] C. Montgomery, K. Koh, and D. Robert. "Measurement of electric charges on foraging bumblebees (Bombus terrestris)". *Journal of Physics: Conference Series.* vol. 1322, 2019. DOI 10.1088/1742-6596/1322/1/01200

[18] S. J. England, D. Robert, "Electrostatic pollination by butterflies and moths." *Journal of the Royal Society Interface.* vol. 21, issue 216, 11 p., 2024. https://doi.org/10.1098/rsif.2024.0156

[19] S. Chauzy, S. Despiau, "Rainfall rate and electric charge and size of raindrops of six spring showers", *J. Atmos. Sc.*, vol.7, pp.1619-1627, 1980. https://doi.org/10.1175/1520-0469(1980)037<1619:RRAECA>2.0.CO;2

[20] O. Heuschmann, "über die Elektrischen Eigenschaften der Insektenhaare." *Journal of Comparative Physiology A: Neuroethology, Sensory, Neural, and Behavioral Physiology*, vol. 10, pp. 594-664, 1929.

[21] E.H. Erickson, "Surface electric potentials on worker honeybees leaving and entering the hive", *J. Apic. Res.*, pp. 141-147, 1975.

[22] D. Clarke, H. Whitney, G. Sutton, and D. Robert, "Detection and Learning of Floral Electric Fields by Bumblebees." *Science*. vol. 340, pp. 66-69. 2013. DOI:10.1126/science.1230883

[23] C. Montgomery, J. Vuts, C.M. Woodcock, et al. "Bumblebee electric charge stimulates floral volatile emissions in Petunia integrifolia but not in Antirrhinum majus." *Sci Nat* 108, 44. 2021. https://doi.org/10.1007/s00114-021-01740-2

[24] C. Montgomery, "The electric ecology of bumblebees", Student thesis: Doctoral Thesis › Doctor of Philosophy (PhD), 2020.

[25] C. Montgomery, K. Koh, and D. Robert, "Measurement of electric charges on foraging bumblebees (Bombus terrestris)", *J. Phys.: Conf. Ser.* vol. 1322, 2019. DOI 10.1088/1742-6596/1322/1/012002

[26] M. Badger, V.M. Ortega-Jimenez, L. von Rabenau, et al, "Electrostatic Charge on Flying Hummingbirds and Its Potential Role in Pollination." *PLoS ONE*, vol.10, 2015. https://doi.org/10.1371/journal.pone.0138003

[27] M. Beekman, F. L. W. Ratnieks, "Long-range foraging by the honey-bee, Apis mellifera L." *Functional Ecology*, vol. 14, pp. 490-496, 2000. https://doi.org/10.1046/j.1365-2435.2000.00443.x

[28] Aristotle: Historia Animalium, Harvard Univ. Press, Cambridge, 1970.

[29] Ye. K. Es'kov, A. M. Sapozhnikov, "Mechanisms of generation and perception of electric fields by honey bees." *Biofizika*. pp. 1124-1130. 1976.

[30] R. A. A. Martins, J. A. A. Martins, "Buzz Pollination in Three Species of the Genus Senna: Bioacustics Characteristics of the Vibrations." *International Journal of Science and Research*. pp. 758-764, 2022 DOI: 10.21275/SR221109174906.

[31] M. Vallejo-Marín, "Buzz pollination: studying bee vibrations on flowers." *New Phytol*, vol. 224, pp. 1068-1074, 2019. https://doi.org/10.1111/nph.15666

[32] T. Morgan, P. Whitehorn, G.C. Lye, and M. Vallejo-Marín, "Floral sonication is an innate behaviour in bumblebees that can be fine-tuned with experience in manipulating flowers." *Journal of Insect Behavior*. vol. 29, pp. 233–241, 2016. https://doi.org/10.1007/s10905-016-9553-5

[33] M. Vallejo-Marin, D.L. Field, J. Fornoni, D. Montesinos, et al. "Biomechanical properties of non-flight vibrations produced by bees." *J Exp Biol*. vol. 227(12), 2024. doi: 10.1242/jeb.247330.

[34] C. Woodrow, N. Jafferis, Y. Kang, and M. Vallejo-Marín, "Buzz-pollinating bees deliver thoracic vibrations to flowers through periodic biting". *Current Biology*, vol. 34, pp. 4104-4113, 2024. https://doi.org/10.1016/j.cub.2024.07.044.

[35] C. Nerse, S. Oberst, D. Navarro-Payá, et al, "Propensity to efficiently transmit vibrations in snapdragons in response to vibroacoustic signalling". in *Proc. of the Inter. Cong. on Sound and Vibration*. Society of Acoustics, (Prague, Czechia), 2023.

[36] T. Heard, A. Dollin, "The Australian native bee book: keeping stingless bee hives for pets, pollination and sugarbag honey". Sixth edition. Sugarbag Bees. pp. 246. 2019.

[37] M.J. King, "Buzz foraging mechanisms of bumble bees." *Journal of Apicultural Research* vol. 32, pp. 41–49, 1993.

[38] C. Nerse, A. R. Mohapatra, S. Oberst, et al., "Model updating of flowering snapdragon (Antirrhinum litigiosum) biomechanical responses to vibro-acoustic stimuli." *J. Acoust. Soc. Am.*, 2023. https://doi.org/10.1121/10.0023171/

[39] U. Greggers, G. Koch, V. Schmidt V, et al, "Reception and learning of electric fields in bees." in *Proc. Biol. Sci.* Mar 27; vol. 280(1759), 2013.

[40] S.J. England, D. Robert, "Prey can detect predators via electroreception in air", in *Proc. Natl. Acad. Sci.* U.S.A. vol. 121, 2024.

[41] S. A. Khan, A. Ahmad, and M. Tanveer, "A new horizon in electrostatic charge induction on hoverflies", *J. Appl. Entomol.*, vol. 1, no. 1, pp. 09–14, 2021.

DOI: 10.61782/fa.2025.0816

FORUM ACUSTICUM EURONOISE 2025

CLASSIFICATION OF BIOLOGICAL SOUNDS USING SPATIAL DIRECTIVITY

Jurij Prezelj* **Luka Čurovič**[1] **Jure Murovec**[2] **Andrej Hvastja**[1]

[1] Faculty of Mechanical Engineering, University of Ljubljana, Slovenia
Aškerčeva 6, 1000 Ljubljana, Slovenia

ABSTRACT*

Bioacoustic methods for biodiversity monitoring face limitations, particularly when relying on single-channel recordings, that lack spatial context. To address this, we tested a novel approach that incorporates spatial directivity into biological sound classification using a network of microphone arrays. Each array, comprising of four microphones, estimates the Direction Of sound Arrival (DOA), attributing spatial features to sound events. By combining these spatial features with conventional acoustic features, in combination with unconventional use of K-means clustering, we developed a methodology for classifying biological sound events. Our approach employs iterative adjustment of the number of clusters to refine classification, filter out noise (e.g., traffic), and reveal tree-like class structures that separate between species and even individuals within same species. Experimental data from a multi-day field recording using synchronized 8-channel microphone systems demonstrates the method's ability to separate sound events and identify individual organisms. The results highlight the potential of spatially informed acoustic analysis to overcome some limitations of bioacousticaly based diversity assessment.

Keywords: *Direction Of Arrival, Sound Event Classification, Bioacoustics, Microphone Array, K-Means, PCA analysys, Sound signal features.*

*Corresponding author: jurij.prezelj@fs.uni-lj.si
Copyright: ©2025 First author et al. This is an open-access article distributed under the terms of the Creative Commons Attribution 3.0 Unported License, which permits unrestricted use, distribution, and reproduction in any medium, provided the original author and source are credited.

1. INTRODUCTION

In recent years, bioacoustic monitoring has emerged as an essential tool for assessing biodiversity, particularly in ecosystems where visual observation is limited or impractical. Acoustic signals generated by insects, amphibians, birds, and mammals provide rich information that can be used to estimate biodiversity, identify ecological changes, and support conservation efforts [1,2]. While the development of passive acoustic monitoring systems has enabled long-term, non-invasive data collection, the accurate classification of biological sound events remains a significant challenge. In many environments, the acoustic landscape is also heavily contaminated with anthropogenic noise sources such as traffic, aircraft, and industry noise [3]. These noise sources contaminate biologically relevant acoustic signals, reducing the effectiveness of automated classification. Traditional sound classification methods rely heavily on spectral features (e.g., energy levels at specific frequencies), temporal characteristics, and time-frequency representations such as spectrograms [4,5]. However, these approaches often fall short when biologically similar signals, such as calls from different individuals of the same species, exhibit overlapping frequency content. In such cases, additional information is required to improve classification accuracy. Promising and underexplored direction in acoustic monitoring is the use of spatial directivity. i.e. the direction from which sound event originates and how it changes over time. Direction Of sound Arrival (DOA), typically employed in microphone arrays, offers the ability to extract spatial features associated with sound sources [6,7]. This can be particularly useful in field conditions where multiple individuals of the same species are active simultaneously, or where moving sources produce time-varying spatial signatures.

In this study, we investigate the potential of combining conventional acoustic features with spatial directivity features for the classification of biological sound events, with a focus on insect species, specifically crickets. We hypothesize that spatial features such as mean direction, deviation of direction, and imaginary/real components of DOA vectors, when added to standard spectral features, can improve the separation between different individuals, even within the same species, under real environmental conditions. The proposed methodology is based on K-means algorithm with adaptive number of classes for unsupervised feature evaluation and classification. The aim is to develop a framework for distinguishing biologically relevant events from background noise, and for assessing biodiversity by estimating the number and identity of individual signal sources. By integrating spatial analysis into the bioacoustic feature space, this work contributes a novel perspective to acoustic biodiversity monitoring, particularly in complex and noisy environments. The results may have practical implications for automated species detection, behavioral studies, and long-term ecological assessments in increasingly urbanized and acoustically polluted habitats.

2. EXPERIMENTAL SETUP

2.1 Study Site and Recording Conditions

The selected study site is located in Zaplana, a rural area in Slovenia that offers stable infrastructure for long-term acoustic monitoring. This location was chosen primarily due to access to continuous electrical power, reliable on-site supervision, and controlled environmental conditions that minimize the risk of equipment damage or theft. The site provides a natural acoustic environment yet is close enough to human activity to also include anthropogenic noise, which is important for the development of separation techniques, as shown in Figure 1.



Figure 1: Data acquisition location with measurement systems

Eight Behringer ECM8000 measurement microphones, selected for their flat frequency response and omnidirectional pickup pattern, which are well suited for capturing complex environmental soundscapes. Four microphones, forming one system, were spatially distributed in a square array of 40mm, optimized for Direction Of Arrival (DOA) calculations in frequency range from 60 to 6000 Hz. Two systems, i.e. arrays, were used.
All eight microphones were connected to a MOTU Stage B 16-channel stage microphone preamplifier, with integrated AD converter and USB3 connection. Such a setup ensured phase-synchronized signal acquisition across all channels, a prerequisite for subsequent beamforming and directionality analysis. The AD converter was connected to a custom LabVIEW-based acquisition system that managed signal recording and real-time data processing. The software was developed in-house to enable robust control over file handling, signal normalization, and metadata logging.
The microphone array and hardware were housed in weather-protected enclosures and mounted at fixed positions throughout the measurement campaign to maintain geometric stability. The entire system operated autonomously over the 36-hour recording period, powered by the site's reliable local electricity supply, with occasional human supervision for maintenance and monitoring. Recordings were acquired in 30-second intervals, with a pause of 5 to 10 seconds between each segment due to WAV file saving time to disk. This led to the generation of 3880 multi-channel WAV files, each containing eight synchronized audio channels. Such temporal segmentation was a compromise between disk write speed and uninterrupted monitoring, and it ensured sufficient data quality for post-hoc feature extraction and classification analysis.

2.2 Signal Processing and Feature Extraction

A major challenge in biodiversity acoustics is the extraction of meaningful information from large volumes of long-term, multichannel audio recordings. The aim of this study was to identify and classify biological acoustic events using both spectral and spatial characteristics of sound. The following signal processing steps were implemented to transform raw waveform data into a structured set of acoustic features suitable for classification.

2.2.1 Data Preprocessing

The raw recordings consisted of 30-second-long multichannel WAV files. Due to constraints in disk writing speed, a gap of 5 to 10 seconds existed between consecutive files, resulting in discontinuous but time-stamped data. Each recording contained eight synchronously recorded channels, enabling spatial analysis. All recordings were

preprocessed using the custom LabVIEW-based software developed specifically for this application. Preprocessing included: Amplitude normalization of all signals to the same reference level, DC offset removal, Segmentation of the recordings into fixed intervals for time-aligned feature extraction, Filtering for optional band-limiting to biologically relevant frequency ranges.

2.2.2 Feature Extraction

Feature extraction was performed for each segment and on each channel independently unless otherwise specified. A total of over 100 acoustic features were computed, categorized into the following domains:

Spectral Features: including power spectral densities across third-octave bands, dominant frequency, spectral centroid, spectral roll-off, skewness and kurtosis of the normalized spectrum.

Cepstral Features: calculated from the real cepstrum of each segment, including the frequency and amplitude of the dominant peak, the cepstral centroid, and energy measures.

Time Domain Features: such as zero crossing rate, short-term signal energy, crest factor, skewness and kurtosis of the waveform, and amplitude envelope characteristics.

Autocorrelation Features: including number of zero crossings of the autocorrelation function, integral properties of its shape, and geometric descriptors (e.g., string length of normalized autocorrelation curve).

Spatial Features: derived from direction-of-arrival (DOA) estimation algorithms applied to the microphone array data. These included average and deviation of real and imaginary DOA components, and instantaneous DOA angle estimation using phase-difference methods.

Each feature was computed within a 125 ms time window with no overlapping, selected as a compromise between temporal resolution and stability of DOA and spectral statistics. Importantly, the spatial features were calculated from twelve DOA snapshots within each 125 ms frame, to account for the rapid directional fluctuations in low-SNR conditions.

2.2.3 2.3.3 Feature Selection and Dimensionality Reduction

Given the high dimensionality of the feature space, a series of statistical techniques were employed to reduce redundancy and highlight relevant dimensions for classification. These included:

- Principal Component Analysis (PCA) to identify dominant modes of variance,
- Singular Value Decomposition (SVD) to rank feature importance,
- Correlation analysis to remove colinear features,
- Expert-driven selection, particularly for features known to be relevant for distinguishing between insect species (e.g., 2576 Hz and 8000 Hz bands).

The final feature set used in classification experiments typically consisted of 4 to 6 features, balancing interpretability with classification accuracy. These included a mix of spectral bands, signal shape descriptors, and spatial DOA deviations. The extracted features formed the basis for further analyses, including unsupervised clustering (K-means) and biodiversity assessment discussed in the next section.

2.3 K-Means Classification

Unsupervised K-means classification algorithm was selected to assess the separability of different types of sound events and to support biodiversity monitoring. This method partitions the dataset into a specified number of clusters by minimizing the within-cluster variance and is widely used for its efficiency and interpretability of data [16].

In our study, a selected subset of features was used as input for clustering. These included both classical acoustic features such as signal energy levels at selected frequencies (e.g., 2576 Hz and 8000 Hz) and temporal characteristics (e.g., zero crossing rate), as well as spatial features related to the direction of arrival (DOA) and its variability.

The initial number of clusters was estimated using the Elbow method, which plots the within-cluster sum of squares (WCSS) against the number of clusters. A visible 'elbow' in the curve typically indicates the appropriate number of clusters. This method was implemented using MATLAB. In our data, the elbow typically occurred between 4 and 6 clusters. Initial results showed that traffic noise and biological signals often clustered separately, confirming that classical spectral features are sufficient to isolate low-frequency anthropogenic noise. Further subdivision of clusters revealed differences between different insect species calls.

An interesting aspect of the approach was the tree-like splitting of clusters when the number of clusters gradually increased. For instance, starting with three clusters often separated background, traffic, and biological signals. Increasing to five or six clusters revealed distinctions between insects. This exploratory method provided insights into both the structure of the dataset and the potential for unsupervised identification of acoustic diversity in the environment.

These findings highlight that unsupervised learning, when guided by expert's selected feature vector, can serve as a robust tool for separating meaningful acoustic events from environmental noise.

3. RESULTS

To better illustrate the challenges associated with classifying biological sounds in natural environments, Figure 2 presents a representative 10-second recording from two spatially separated microphone array systems, located 12 meters apart. Figure 2 shows the spectrograms for both systems (top and bottom panels) alongside the corresponding Direction of Arrival (DOA) estimates over time. DOA results are plotted between the two spectrograms, with red dots representing System 2 and blue dots representing System 1. DOA calculations were performed on filtered signals, using a band-pass filter (2000–4000 Hz) to isolate the frequency range of interest, the calling frequencies of cricket of species A. This filtering helps suppress environmental noise and focuses on the DOA of crickets. Accurate DOA tracking corresponds with cricket calls, while scattered DOA values appear during silent intervals.

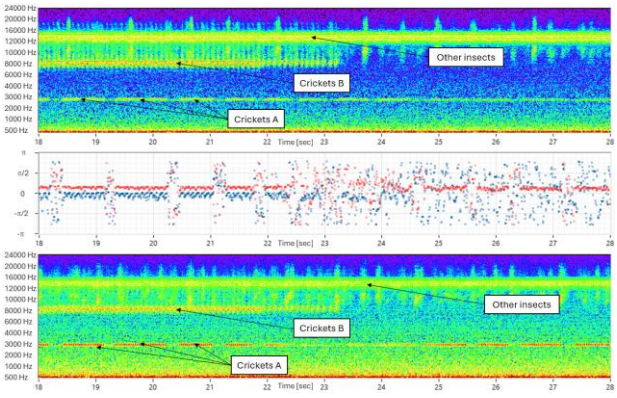


Figure 2: Example of a 10-second recording showing spectrograms of two synchronized microphone systems placed 12 meters apart. Red and blue dots represent DOA estimates from System 1 and System 2, respectively, in the 2000–4000 Hz range, specificly tuned to detect crickets of species A.

The visualization demonstrates that when a cricket is actively producing sound, the DOA algorithm accurately tracks its spatial position. However, during silent periods or low signal-to-noise conditions, the system yields scattered direction estimates with high deviation, suggesting that direction estimates are essentially random in the absence of a clear signal. This behavior underlines one of the key limitations of DOA based approaches in natural environments: direction estimation requires some minimal signal to noise ratio to be reliable.

An additional challenge is the temporal structure of cricket calls. Each call (approximately 1 second in duration) consists of a sequence of 12–30 short chirps, each lasting only a few milliseconds. These brief chirps are separated by short pauses. During these pauses, the DOA algorithm frequently registers spurious directions due to the lack of acoustic energy, which cannot be easily averaged due to the circular nature of angular data. This causes angular "jumps" or artifacts, making the differentiation between multiple crickets of the same species particularly challenging.

Despite these limitations, the system shows strong potential for spatially resolving biologically relevant sounds. This example sets the stage for the subsequent sections, which evaluate various feature extraction methods and classification strategies, including unsupervised learning.

3.1 PCA Analysis of the Whole Dataset

To assess the relative contribution of features in the dataset and to identify dominant patterns of variability, we performed principal component analysis (PCA) on the full dataset, comprising 108 features extracted from synchronized 8-channel acoustic recordings. Prior to the analysis, all features were normalized using min-max scaling to the [0,1] range.

This ensured that features of differing physical dimensions (e.g., signal amplitude, spectral centroid, direction deviation) contributed comparably to the analysis. PCA was then performed on the normalized dataset. The first principal component (PC1) alone explains approximately 30% of the total variance, while the first two components together account for more than 50%.

3.1.1 Feature Contributions to PC1

By examining the loadings of each feature on PC1, we can identify which features contribute most to this dominant source of variance. Among the most influential features were zero crossing rate, and its two derivatives (crossing at 0.125 and 0.25), high-frequency spectral components (e.g., 15608 Hz, 13664 Hz), and spectral centroid. Zero crosing of Autocorelation function and Cepstrum based features also proved to be important. Spatial features extracted during DOA calculation however showed only moderate influence.

The PCA results support our hypothesis that a combination of signal energy, zero-crossing, and spatial features collectively governs the variance in the overal acoustic dataset. Notably, individual frequency bands used for species classification (e.g., 2576 Hz and 8000 Hz) did not emerge as dominant contributors in PC1. This reinforces the need to integrate spatial directivity metrics when aiming to distinguish between acoustically similar species or individuals. These findings suggest that both spectral and

temporal discontinuity features are key discriminators in the data. However, the moderate loadings of spatial features also imply their relevance, particularly for distinguishing between individual sources of similar spectral character.

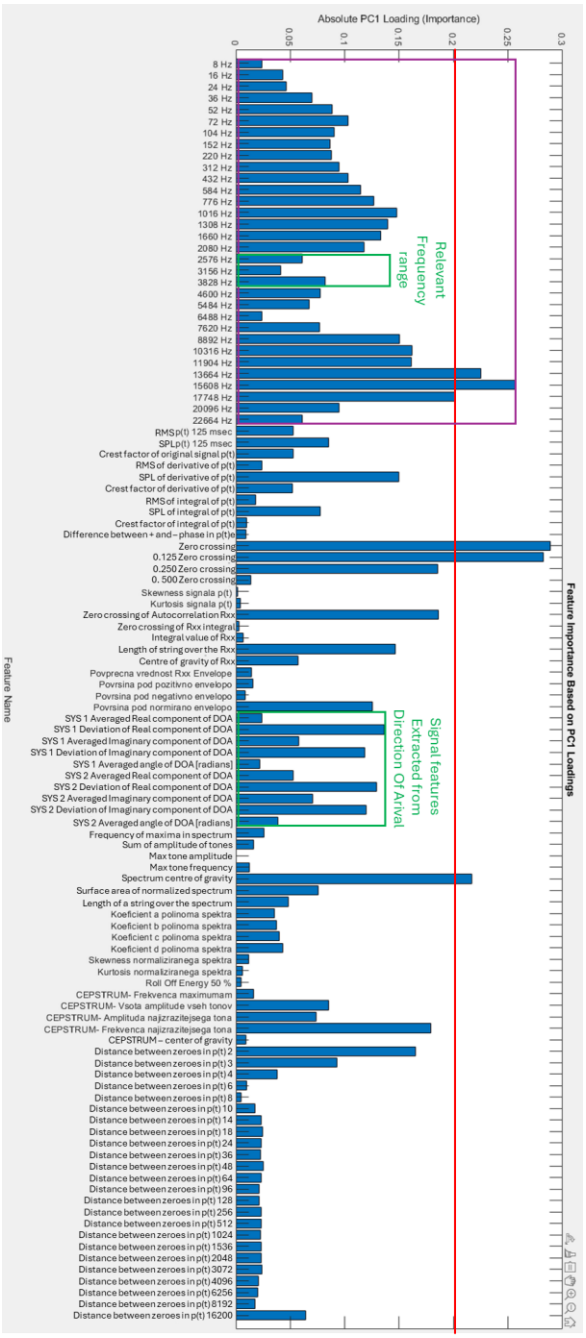


Figure 3: Bar chart of absolute PC1 loadings for all features

3.1.2 Subjective Feature Selection

Following the initial inspection of the recordings and DOA behavior, we performed a subjective selection of features for the unsupervised classification. Subjective approach was motivated by our experience, by the structural complexity of crickets calls, and the known limitations of automated feature selection methods in low signal-to-noise environments. To reduce data dimensionality while preserving relevant information, we selected a subset of features: from the complete dataset based on three criteria: (1) domain knowledge about cricket call characteristics, (2) visual correlation of features with known biological events (e.g., active chirping), and (3) interpretability and temporal stability of the feature across multiple recordings. The following eight features were chosen for initial analysis:
Level of signal derivative (captures abrupt energy changes in short-duration chirps)

1. Level at 2576 Hz
2. Level at 8000 Hz
3. Direction Of Arrival on System 1
4. Deviation of DOA on System 1
5. Direction Of Arrival on System 2
6. Deviation of DOA on System 2
7. Zero Crossing Rate (ZCR),

These features were selected not only for their statistical relevance but also for their interpretability. For example, signal derivative and zero-crossing features respond to the pulse-like nature of chirps, while DOA deviation provides a strong inverse indicator of consistent sound sources (i.e., crickets). Frequency-specific features were chosen to separate overlapping frequency bands used by different species. The subjective selection was further validated through data visualization and initial clustering tests. This manual step proved essential in capturing meaningful biological structure in a highly complex acoustic environmet.

3.2 K-Means Clustering

Several established methods exist to estimate the “optimal” number of clusters in K-means clustering, including the elbow method (which identifies a knee in the within-cluster sum of squares), silhouette analysis, and the gap statistic. More advanced criteria such as the Calinski-Harabasz, Davies-Bouldin, and Dunn indices, or model-based tools like Bayesian Information Criterion (BIC), are frequently employed in automatic model selection.
However, in the context of bioacoustic field recordings, these methods proved insufficient. They consistently suggested a relatively small number of clusters (typically fewer than six), which did not reflect the nuanced structure

of the biological acoustic environment. In our case, the goal was not to discover a fixed, singular classification scheme, but to explore the hierarchical relationships between sound events, and incrementally refine the detection and separation of biological signals from environmental noise.
To that end, we adopted a progressive and semi-supervised clustering approach. Starting with a subset of recordings that contained known biological activity (observed directly during data collection), we applied K-means repeatedly, increasing the number of clusters step by step. This revealed a tree-like evolution of classes, where larger clusters gradually split into finer subgroups as the number of clusters increased. Importantly, this process exposed meaningful patterns:

- A small number of clusters (e.g., k = 2–3), K-means already separates high-energy signals, such as traffic noise, from ambient biological sounds.
- As the number of clusters increased (k > 5), we began to see separation between different types of biological signals, including cricket chirps of different species, and eventually between individual crickets of the same species based on spatial and temporal features.

Figure 4 demonstrates how the separation between traffic noise and biological signals improves with an increasing number of classes, specifically in the context of filtering out peaks (e.g., traffic) while preserving fluctuating ambient sounds (e.g., insects). Based on this insight we structured our classification process into three stages as depicted in a series of figures from Figure 5 to 9.

1) Noise Filtering: Low-frequency traffic noise was excluded from the data based on spectral and temporal features. Consequently, higher-frequency traffic noise overlaping bioacoustic sound was removed as well.

2) Species Identification: By selecting key spectral features (SPL at 2576 Hz and 8000 Hz) we were able to distinguish between cricket of species A and B. Narrowband filtering alone was insufficient; classification relied on the overall feature vector and clustering behavior.

3) Individual Discrimination via DOA: By incorporating spatial features of direction of arrival (DOA) and deviation of DOA, K-means could distinguish signals from different individuals of the same species A, even when their spectral profiles were similar.

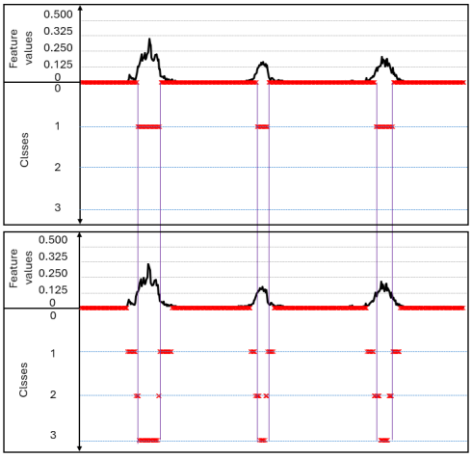


Figure 4: By increasing the number of classes in K-Means algorithm, the separation between background noise and signal is more effective. In our case we are interested into exclusion of pulses, representing traffic noise and to maintain background noise composed from biological sounds.

The presented approach effectively combines unsupervised clustering with subsequent supervised refinement, allowing us to separate traffic noise from biological signals and then further differentiate among species or members of species based on sound directivity data (DOA). The gradual increase in the number of clusters to form a tree-like structure is particularly insightful, as it provides a visual and quantitative means to identify the minimal number of classes required for effective discrimination. This multi-step process, first filtering out traffic noise, then distinguishing species based on spectral features, and finally resolving individual variation using spatial features, demonstrates a robust strategy for addressing the complexities inherent in bioacoustics data.

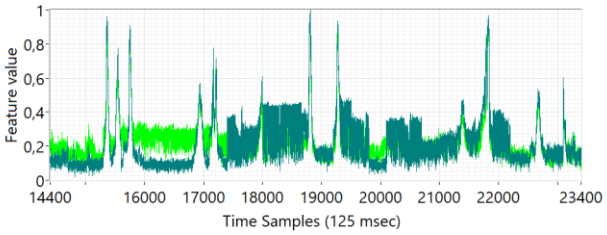


Figure 5: Recorded signal @ 2576 Hz and 8000 Hz, with pronounced spikes due to the traffic noise

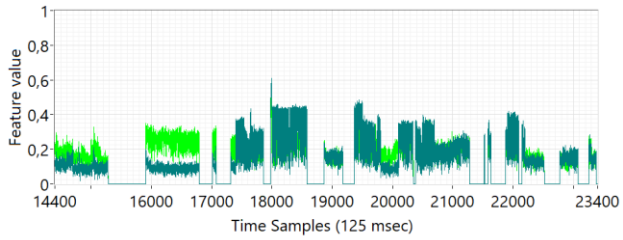


Figure 6: The first step: Exclusion of unappropriate samples, containing traffic noise 2576 Hz and 8000 Hz, that is in frequency range of cricket's calls.

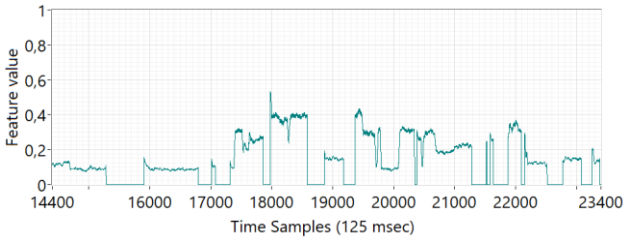


Figure 7: Second step was to smooth the data by moving average, while maintaining the exclusion of corrupted data by traffic noise

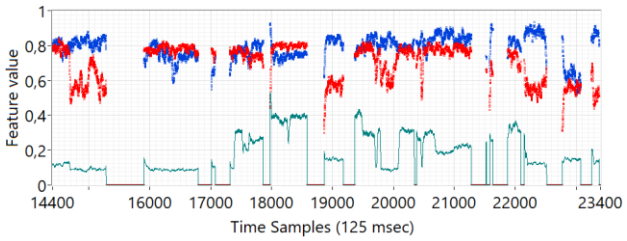


Figure 8: Third step was to implement the spatial directivity (DOA) from two systems into the classsification

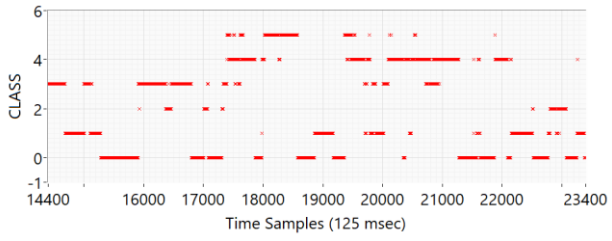


Figure 9: Results of Classification to 6 clases (evaluated by the elboww method) and using subjectivly selected features.. Classification includes DOA based features, hence classification of biological sounds using spatial directivity.

The use of K-means clustering in this study extended beyond traditional unsupervised classification. Through iterative refinement and adaptive manipulation of the number of clusters, we were able to explore the latent structure in the dataset and identify practical thresholds for signal separation. Notably, K-means classification was not only used as a final output but also as a tool for feature selection and filtering—enabling us to progressively refine the data by first removing traffic noise and later isolating biologically relevant events.

Despite promising results, some limitations were encountered. While spatial directivity (DOA) features significantly contributed to distinguishing individual sources, they were insufficient on their own for the complete classification of cricket species. Chirp structure and signal continuity played a crucial role in DOA reliability. The DOA subwindowing approach proved sensitive to brief signal gaps within cricket chirps, leading to erratic directional estimates during the pauses. This reduced the classification resolution and introduced variability into the spatial feature set.

A key insight from these challenges is the importance of synchronization between signal segmentation and DOA estimation. Future work should focus on optimizing the trade-off between subwindow duration and averaging period during feature extraction. For example, preliminary tests suggest that using a 25 ms subwindow and averaging over 250 ms may offer a better balance between time resolution and directional stability than the currently used 10 ms / 120 ms configuration. This will be crucial for capturing species-specific calling patterns while preserving spatial integrity.

Nonetheless, the integration of spatial features, particularly deviation metrics, demonstrated clear value in enhancing the separability of overlapping sound sources, especially for individuals within the same species. This directionally informed classification represents a novel addition to conventional bioacoustic methods, which often rely solely on spectral or temporal descriptors.

4. CONCLUSION

This study presents a novel approach to the classification of biological sounds by integrating spatial directivity information into the feature set. We demonstrated that alternative applications of unsupervised K-means classification algorithm, by iterative clustering with different number of classes can improve classification accuracy in complex outdoor acoustic environments.

We found that spatial features, particularly DOA and deviation of DOA within 125 msec, can successfully add information to traditional spectral features. While direct classification based solely on DOA remains challenging due to signal intermittency, combining directionality with

spectral features enables the identification of both species and individual callers in limited range.

This integrative methodology offers a promising framework for scalable, autonomous biodiversity monitoring, particularly in habitats affected by overlapping biological and anthropogenic sounds. The results not only highlight the potential of spatial information in bioacoustics but also lay the groundwork for future improvements in sensor design, feature synchronization, and hybrid supervised-unsupervised classification strategies.

With further development, such techniques may significantly advance acoustic biodiversity assessment, contributing to conservation science, species tracking, and real-time ecosystem monitoring.

5. ACKNOWLEDGMENTS

Authors would like to thank Slovenian Research Agency ARIS for their funding of the project J7-50042: Acoustic monitoring of urban noise and biodiversity for green future using IoT-Sound-Radar and AI for event classification

6. REFERENCES

Depraetere, M., et al. (2012). Monitoring animal diversity using acoustic indices: Implementation in a temperate wood. Ecological Indicators, 13(1), 46–54. https://doi.org/10.1016/j.ecolind.2011.05.006

Pijanowski, B. C., et al. (2011). Soundscape Ecology: The Science of Sound in the Landscape. BioScience, 61(3),203–216. https://doi.org/10.1525/bio.2011.61.3.6

Hedley, R. W., et al. (2017). Direction-of-arrival estimation of animal vocalizations for monitoring animal behavior and improving estimates of abundance. Avian Conservation and Ecology, 12(1), 6. https://doi.org/10.5751/ACE-00963-120106

Stevenson, B. C., et al. (2014). A general framework for animal density estimation from acoustic detections across a fixed microphone array. Methods in Ecology and Evolution, 6, 38–48. https://doi.org/10.1111/2041-210X.12291

Heath, B. E., et al. (2024). Spatial ecosystem monitoring with a multichannel acoustic autonomous recording unit (MAARU). Methods in Ecology and Evolution. https://doi.org/10.1111/2041-210X.14390

Verreycken, E., et al. (2021). Bio-acoustic tracking and localization using heterogeneous, scalable microphone arrays. Communications Biology, 4(1), 1–11. https://doi.org/10.1038/s42003-021-02746-2

Farina, A., et al. (2011). The soundscape methodology for long-term bird monitoring: A Mediterranean Europe case-study. Ecological Informatics, 6(6), 354–363. https://doi.org/10.1016/j.ecoinf.2011.07.004

Jensen, M. E., & Miller, L. A. (1999). Echolocation signals of the bat Eptesicus serotinus recorded using a vertical microphone array. Behavioral Ecology and Sociobiology, 47(1–2), 60–69. https://doi.org/10.1007/s002650050650

Hill, A. P., et al. (2019). AudioMoth: A low-cost acoustic device for monitoring biodiversity and the environment. HardwareX, 6, e00073. https://doi.org/10.1016/j.ohx.2019.e00073

Stowell, D., & Plumbley, M. D. (2014). Automatic large-scale classification of bird sounds is strongly improved by unsupervised feature learning. PeerJ, 2, e488. https://doi.org/10.7717/peerj.488

Nieto-Mora, D. A., et al. (2023). Systematic review of machine learning methods applied to ecoacoustics and soundscape monitoring. Heliyon, 9(10), e20275. https://doi.org/10.1016/j.heliyon.2023.e20275

Laurijssen, D., et al. (2018). Low-cost synchronization of high-speed audio and video recordings in bio-acoustic experiments. Journal of Experimental Biology, 221(4), jeb173724. https://doi.org/10.1242/jeb.173724

Sumitani, S., et al. (2021). Fine-scale observations of spatio-spectro-temporal dynamics of bird vocalizations using robot audition techniques. Remote Sensing in Ecology and Conservation, 7(1), 18–35. https://doi.org/10.1002/rse2.152

Rhinehart, T. A., et al. (2020). Acoustic localization of terrestrial wildlife: Current practices and future opportunities. Ecology and Evolution, 10(13), 6794–6818. https://doi.org/10.1002/ece3.6216

Ross, S. R. P. J., et al. (2018). Listening to ecosystems: Data-rich acoustic monitoring through landscape-scale sensor networks. Ecological Research, 33(1), 135–147. https://doi.org/10.1007/s11284-017-1509-5

MacQueen, J. (1967). Some methods for classification and analysis of multivariate observations. In Proceedings of the Fifth Berkeley Symposium on Mathematical Statistics and Probability (Vol. 1, No. 14, pp. 281-297).

DOI:

Main theme: A02 Bio-acoustics

Session A02.02 Underwater soundscape and noise: modelling, measurements and effects

Chair(s): J. Ramis-Soriano, G. Zambon, A. Širović, P. Poveda Martinez, V. Zaffaroni-Caorsi

DOI:

Main theme: A02 Bio-acoustics

Session A02.05 Effects of multimodal stimuli on wildlife

Chair(s): T. Van Renterghem, H. Slabbekoorn

DOI: 10.61782/fa.2025.0001

FORUM ACUSTICUM EURONOISE 2025

"YOU TALKING TO ME!?": THE ROLE OF VISUAL-ACOUSTIC CUES IN ANEMONEFISH SOCIAL BEHAVIOUR

Lucia Yllan[1*], Theresa Rüeger[1]

[1]School of Natural and Environmental Sciences, Newcastle University, UK

ABSTRACT

Acoustic communication is integral to the social dynamics of many animal species, yet fish remain underrepresented in bioacoustics research despite their ecological diversity and environmental importance. This study investigates the vocalisations and associated behaviours of anemonefish, focusing on the orange clownfish (*Amphiprion percula*). Through in situ audio-video recordings of wild populations in Papua New Guinea, we documented a diverse repertoire of sounds and their behavioural contexts, highlighting their critical role in social hierarchy maintenance, group cohesion, and territorial interactions. To understand how anemonefish integrate sensory information, we conducted a visual-acoustic cue manipulation experiment, showing the reliance on multisensory cues for social behaviours. Our findings reveal the diversity and functional significance of fish vocalisations while highlighting potential vulnerabilities to underwater noise pollution. By combining behavioural ecology and experimental manipulation this work provides new perspectives on sensory ecology in marine systems and emphasizes the need for conservation strategies in increasingly noisy underwater environments.

Keywords: *visual-acoustic cues, size hierarchy, vocalisations, size assessment, behaviour*

**Corresponding author: l.yllan2@newcastle.ac.uk.*
Copyright: ©2025 First author et al. This is an open-access article distributed under the terms of the Creative Commons Attribution 3.0 Unported License, which permits unrestricted use, distribution, and reproduction in any medium, provided the original author and source are credited

1. INTRODUCTION

Despite fish representing 35% of the total chordate biomass and half of vertebrate species [1], knowledge about acoustic communication in fishes is limited compared to other taxa. The main reason for this bias is fishes' apparent limitation of acoustic signalling which is restricted to certain families and species [2]. Nevertheless, several fish taxa use acoustic signals for a variety of functions.

Anemonefishes (genus *Amphiprion*) are ideal to study acoustic communication in wild fish populations since. They display a complex array of behaviours both interacting with other species and within their social groups with strict size hierarchies and mutualistic relationship with their sea anemone host, which makes them extremely site attached [3]. Anemonefish groups are formed by unrelated individuals and have a strict size-based social hierarchy where individuals queue for the breeding position [4]. The largest anemonefish is the dominant female and the second largest is the sub-dominant male, the breeding pair, which can also have non-reproductive subordinates [5]. Acoustic cues may be key to maintain their strict hierarchical social structure within groups [6], by signalling dominance/submission and allowing group members to be differentiated.

Anemonefishes can hear sounds between 75 and 1800 Hz [7] and produce sounds using their jaw teeth and vibrations from their rib cage, which generates variation in their vocalisations related to their body size [8]. Consequently, these acoustic features may convey information on the social rank of the emitter within the group [9]. In addition, individuals might use their side vision or mechanosensors to assess conspecifics size through lateralisation or side-by-side swimming [11-12]. Thus, anemonefish can obtain information form visual and acoustic cues to assess a conspecifics' size and visual-

acoustic cues might be essential to maintain hierarchy stability within the group. However, the relative importance of these cues and their role in social interactions has not been studied.

This study examines the acoustic communication of orange clown anemonefish (*Amphiprion percula*) in natural reef habitats in Papua New Guinea, with the goal of advancing our understanding of acoustic communication in wild fish populations. The specific aims of this study are to: (1) characterize the vocal repertoire and associated behavioural contexts of *A. percula*; and (2) evaluate the integration of visual and acoustic cues in social interactions through sensory manipulation experiments.

2. METHODS

2.1 Baseline data collection

The study was conducted Kimbe Bay, Papua New Guinea. Anemonefish groups were recorded using GoPro Hero 9 action cameras and AudioMoths version 1.7.1 which were placed in front of groups on stationary tripods set close to the anemone to obtain video and audio data. A total of 142 vocalisation trains (594 individual vocalisations) were recorded *in situ* from *A. percula* groups. All individuals of the group were caught and measured underwater to obtain their standard length (SL) in mm.

2.2 Visual-acoustic cues experiment

For this experiment, three treatments (with three trials each, Tab. 1) manipulating different sensory cues were conducted: I) congruent visual-acoustic cues (A, E, I), II) constant visual cues (B, E, H) and III) constant acoustic cues (D, E, F). To simulate different size conspecifics (difference of less than 1cm, 25% larger, and 25% smaller) we used mirrors with different lenses and UW30 underwater speakers to playback sounds from different size individuals, previously recorded from the same population. The trials were recorded using GoPro cameras. For the experimental trials, only the subordinates (rank 3) of 18 groups were used. The dominant individuals, rank 1 and 2 were removed to remove effects of gender and social status as studies have shown that individual behaviour is influence by social rank [12].

Table 1. Table showing the combination of visual-acoustic cues used in the experiment.

		Visual cues		
		Smaller size	*Similar size*	*Larger size*
Auditory cues	*Smaller size*	A	B	
	Similar size	D	E	F
	Larger size		H	I

2.3 Behavioural and acoustic data

Video recordings from the baseline and experimental data were used to score individuals behaviour using BORIS (v. 7.12) (Tab. 2). Unwanted noise interferences present in the acoustic data were removed using a low-frequency filter in Audacity. Acoustic data in format *.wav* was cut in smaller clips and imported to Raven Pro v 1.6 to extract the acoustic parameters of all vocalisations, which were exported in selection tables. Vocalisations were labelled in relation to the behaviours that were displayed by the vocalising fish and the social rank of the fish.

Table 2. Ethogram used in the study showing the behavioural categories and descriptions of each behaviour.

Behaviour	**Description**
Aggression	Fish rapidly swims towards the mirror and bumps into it
	Fish rapidly darts and turns prior to or during aggressive contact.
Submission	Fish shakes body side to side in jolty fashion.
Social Interactions	Fish simultaneously approach, stay or follow each other within 1 body length
Territorial displays	Fish with stiffened body posture while vocalising
Lateralisation	Fish turns on their side within a body size of distance to the mirror
Time outside anemone	Fish swims outside the perimeter of the anemone
Out of sight	Fish cannot be seen because it enters anemone, moves under or behind anemone, or swims beyond the video frame.

2.4 Statistical analysis

All statistical analyses were performed in R v. 4.4.2 [13]. We used package *seewave* [14] to visualize the acoustic data, creating spectrograms and oscillograms. Using the packages *warbleR* and *Rraven* [15-16], we imported the selection tables created in Raven to analyse the parameters of the spectrograms. We used the *glmmTMB* package to fit generalised linear mixed models (GLMM) that accounted for zero-inflation in the data [17], using treatment, cues size and focal individual size as fixed effects. Individual ID as random effect to account for non-independence of individuals' behaviour. We used Akaike's Information Criterion (AIC) [18] for model selection. The *emmeans* package [19] was used to perform pairwise comparisons and the *performance* package was used to calculate the marginal R^2 (provides the variance of the model explained by the fixed effect) and conditional R^2 (provides the variance explained by both fixed and random effects) using Nakagawa's R^2 [20].

3. RESULTS

3.1 Vocalisations and behavioural context

We found that *A. percula* vocalisations are composed by pulses of sounds with a frequency range between 0.2 and 1.08 kHz and a duration between 0.007 and 0.361 ms. The pulses of sound could be produced individually or in a train of consecutive pulses that could range from 2 to 20 pulses, with an average of 0.036 ms of pause between pulses.

We identified five behaviours that were associated with vocalisations of *A. percula*: Interspecific aggression (aggressive displays to other fish species), intragroup aggression (aggressive displays to other fish within the social group), social interactions (non-agonistic interactions between members of the social group), submission (submissive displays to other members of the social group) and territorial displays, in which individuals would get close to the edge of the anemone and produce vocalisations without a direct interaction with another fish.

The pulse number analysis revealed several significant differences between behavioural categories. Submissive vocalisations were significantly different from aggressive (estimate = -1.899, $p < 0.01$, Fig. 1), competitive (estimate = -1.094, $p < 0.05$), territorial (estimate = 1.240, $p < 0.01$) and social vocalisations (estimate = -1.269, $p < 0.01$). However, no significant differences were found between vocalisations associated with other behaviours. These results suggest that the submissive sounds differed significantly from vocalisations associated with other behaviours.

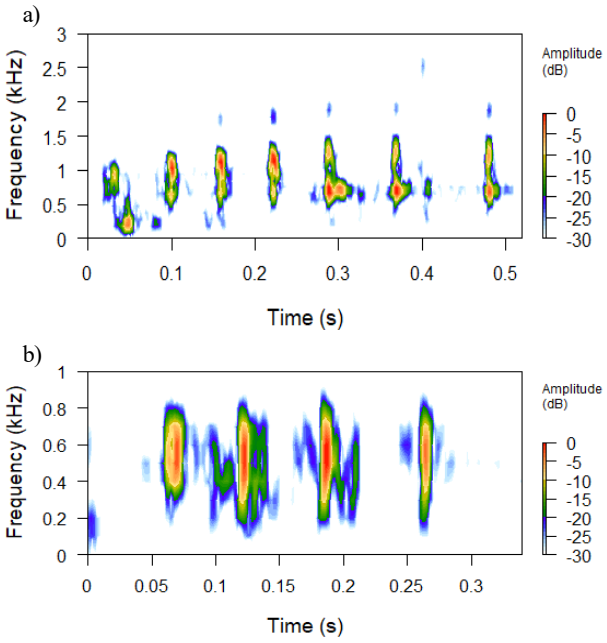


Figure 1. Spectrograms of *A. percula* vocalisation trains showing the frequency in kHz and the duration of the call in seconds (s). The spectrogram (a) correspondence with a submissive vocalisation while the spectrogram (b) corresponds with an aggressive vocalisation.

3.2 Visual-acoustic cues manipulation experiment

Focal fish exhibited different rates of display between behaviours and a higher interaction rate when visual-acoustic cues were congruent (Fig.2). There were significant differences in behavioural category (χ^2_3 = 60.355, $P < 0.001$) and experimental treatments (χ^2_2 = 6.407, $P < 0.01$). Aggressive, lateralisation, and territorial behaviours had positive estimates (Aggression: 0.498 ± 0.283 behaviour/min; Lateralisation: 1.083 ± 0.276 behaviour/min; Territorial: 0.509 ± 0.275 behaviour/min), while submission had a negative estimate (-0.414 ± 0.343 behaviour/min). Among treatments, the congruent cues experiment had the highest behavioural rate (0.498 ± 0.283 behaviour/min), compared to constant acoustic (0.126 ± 0.117 behaviour/min) and constant visual cues (-

0.184 ± 0.123 behaviour/min). There was no significant interaction between behavioural category and treatment. The fixed effects explained 30.1% of the variance (R^2m = 0.301, R^2c = 0.395).

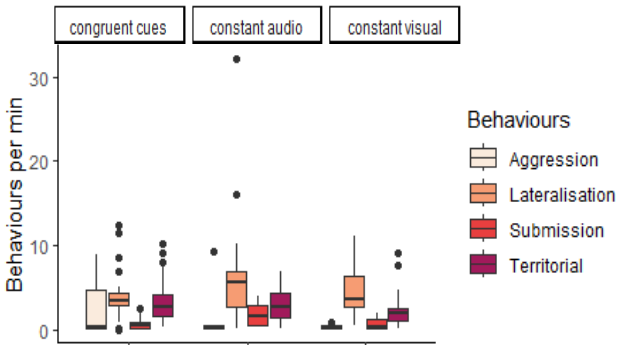


Figure 2. Distribution of behavioural rates (behaviours per minute) across treatments (congruent visual-acoustic cues, constant acoustic cues, and constant visual cues) for four behaviours: aggression, lateralization, submissions and territorial displays. Each box represents the interquartile range (IQR), with the median indicated by the horizontal line.

Lateralisation rates were significantly different between trials in the congruent (χ^2_2 = 10.774, P < 0.01, Fig. 3) and constant acoustic cues treatments (χ^2_2 = 15.126, P < 0.001). Individuals displayed higher lateralization rates when presented with similar-sized cues (congruent cues: 1.591 ± 0.609; constant acoustic cues: 2.535 ± 0.680), compared to cues from larger (congruent cues: -1.706 ± 0.625; constant acoustic cues: -2.126 ± 0.705) or smaller conspecifics (congruent cues: 0.634 ± 0.672; constant acoustic cues: 1.266 ± 0.692). This suggests that visual cues representing similar-sized conspecifics led to more pronounced lateralisation behaviours. In contrast, in the constant visual cues treatment, lateralization rates were the lowest when individuals were presented with similar-size cues, with the highest rates displayed when presented with small acoustic cues. However, these differences were not significant.

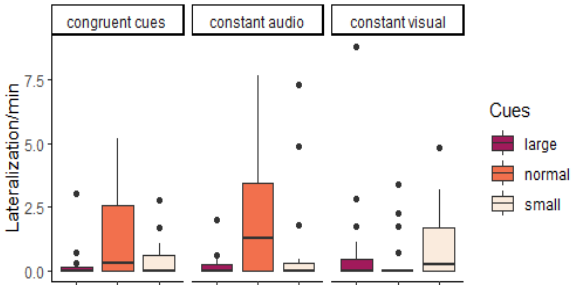


Figure 3. Lateralization events per minute across different cue sizes (larger cues, normal/similar size cues, and smaller cues) and treatments (congruent visual-acoustic cues, constant acoustic cues, and constant visual cues). Boxplots show the distribution of lateralization behaviour for each cue size within each treatment group. Each box represents the interquartile range with the median shown as a horizontal line; whiskers extend to 1.5× the IQR.

Territorial display rates were significantly influenced by focal individual standard length (Fig. 4). Territorial rates decreased with standard length increase in both the congruent treatment (χ^2_1 = 4.959, P < 0.05, -0.091 ± 0.040). This trend was also observed in the constant acoustic and constant visual treatments, however, there were not significant effect found.

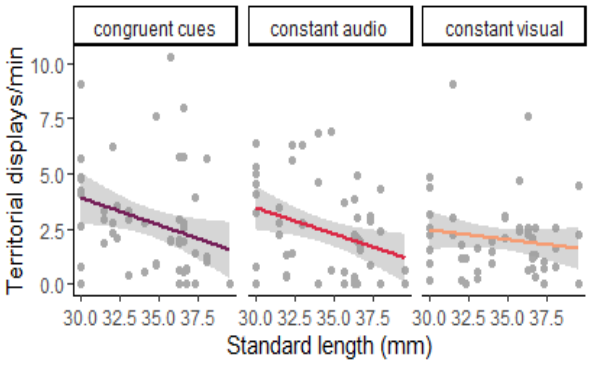


Figure 4. Relationship between standard length (mm) and frequency of territorial displays (displays per minute) across experimental treatments. Grey points indicate individual observations, while coloured lines represent linear regression with 95% confidence intervals.

Aggressive and submissive displays were primarily observed when individuals were presented with similar-size cues across all treatments. However, only the submission rate in the congruent cues treatment showed significant differences between trials ($\chi^2_2 = 10.774$, $P < 0.01$).

4. DISCUSSION

Our findings highlight the complexity of social communication in *A. percula*, emphasizing the critical role of multimodal signals—particularly the integration of visual and acoustic cues—in conspecific size assessment and social interactions. Across experimental treatments, individuals displayed distinct behavioural responses depending on the type and congruency of the sensory stimuli, with congruent visual-acoustic cues eliciting the strongest reactions. These included increased rates of interaction, heightened body shakes and lateralisation, and more time spent outside the anemone, suggesting that multimodal input enhances signal reliability and informs decision-making during social and agonistic encounters [22-23].

We demonstrated that vocalisations are used frequently in natural settings and across diverse social contexts—not only during aggression, but also in neutral interactions and interspecific encounters. These results expand upon previous research by showing that vocal signals are not limited to conflict scenarios but also serve broader social functions [24]. Notably, we observed vocalisations occurring independently of direct interaction, such as at the edge of the anemone or during interspecific interactions—an observation not previously reported in anemonefish bioacoustics literature. This broader range of social contexts highlights the limitations of laboratory settings, where social complexity is often reduced [25].

Lateralisation also emerged as a key behaviour, especially in response to similar-sized visual cues. This supports the hypothesis that lateralisation allows individuals to monitor conspecific size and evaluate their social status [10-11], potentially influencing their decision to engage in conflict [29]. This is consistent with findings in anurans, where vocal frequency is used to assess body size [30-31]. Interestingly, lateralisation was also increased in response to smaller acoustic cues under constant visual treatment, suggesting that individuals rely more on acoustic cues when visual differences are subtle.

Territorial display rates were inversely related to focal fish size, with smaller individuals showing higher rates, particularly in response to larger conspecific cues. This suggests that smaller individuals may use indirect strategies, such as territorial displays, to signal presence or dominance without engaging in direct conflict [32]. These displays may also serve as alert signals to other group members, though further research is needed to clarify their role in group-living contexts.

Behaviourally, body shakes and aggression were more frequent when individuals were exposed to similar-sized conspecific cues, particularly under congruent visual-acoustic treatments. While only body shakes showed statistically significant increases, this trend aligns with predictions that individuals engage in either aggressive or appeasing behaviours when size differences are minimal [26-27]. These behaviours may appear contradictory, but reflect strategic decisions based on social context and perceived dominance, as body size is a strong predictor of conflict outcomes [28].

Overall, our study reinforces the importance of multimodal sensory integration in social interactions and hierarchy maintenance among *A. percula*. Congruent visual-acoustic cues prompted stronger behavioural responses, supporting their role in enhancing recognition, reducing uncertainty, and guiding social decisions. While visual cues often dominated in conflict scenarios, acoustic cues provided critical size information when visual assessment was ambiguous. These findings contribute to a broader understanding of how sensory systems mediate social behaviour in complex group-living animals and underscore the need for future research that integrates ecological realism, individual variation, and dominance structure. Importantly, the reliance on acoustic signals in diverse social contexts highlights the potential vulnerability of these animals to anthropogenic noise, emphasizing the need to consider acoustic pollution as a disruptive force in reef fishes social dynamics.

5. ACKNOWLEDGEMENTS

We thank the Mahonia Na Dari Research and Conservation Centre (Kimbe Bay, Papua New Guinea)

for supporting the fieldwork for this study and the Tamare-Kilu communities which granted us access to work in their local coral reefs. This research was funded by the School of Natural and Environmental Sciences, at Newcastle University.

6. REFERENCES

[1] Y. M. Bar-On, R. Phillips, and R. Milo, "The biomass distribution on Earth," Proc Natl Acad Sci U S A, vol. 115, no. 25, pp. 6506–6511, 2018, doi: 10.1073/pnas.1711842115.

[2] F. Ladich and H. Winkler, "Acoustic communication in terrestrial and aquatic vertebrates," Journal of Experimental Biology, vol. 220, no. 13, pp. 2306–2317, 2017, doi: 10.1242/jeb.132944.

[3] D. G. Fautin, "The Anemonefish Symbiosis: What is Known and What is Not," Symbiosis, vol. 10, pp. 23–46, 1991.

[4] P. M. Buston and M. A. Cant, "A new perspective on size hierarchies in nature: Patterns, causes, and consequences," Oecologia, vol. 149, no. 2, pp. 362–372, Aug. 2006, doi: 10.1007/s00442-006-0442-z.

[5] J. T. Moyer, A. Nakazono, and S. Species, "of the Anemonefish Amphiprion in Japan," Japanese Journal of Ichthyology, vol. 25, no. 2, pp. 101–106, 1978.

[6] T. Rueger, R. Branconi, C. Y. M. Froehlich, S. J. Heatwole, M. Y. L. Wong, and P. M. Buston, "The Next Frontier in Understanding the Evolution of Coral Reef Fish Societies," Front Mar Sci, vol. 8, no. May, p. 665789, 2021, doi: 10.3389/fmars.2021.665780.

[7] E. Parmentier, O. Colleye, and D. Mann, "Hearing ability in three clownfish species," Journal of Experimental Biology, vol. 212, no. 13, pp. 2023–2026, 2009, doi: 10.1242/jeb.030270.

[8] O. Colleye and E. Parmentier, "Overview on the Diversity of Sounds Produced by Clownfishes (Pomacentridae): Importance of Acoustic Signals in Their Peculiar Way of Life," PLoS One, vol. 7, no. 11, 2012, doi: 10.1371/journal.pone.0049179.

[9] E. Parmentier and D. Lecchini, "Sound Communication," Evolution, Development and Ecology of Anemonefishes, no. Schneider 1964, pp. 95–102, 2022, doi: 10.1201/9781003125365-12.

[10] S. M. Stieb et al., "A detailed investigation of the visual system and visual ecology of the Barrier Reef anemonefish, Amphiprion akindynos," Sci Rep, vol. 9, no. 1, Dec. 2019, doi: 10.1038/s41598-019-52297-0.

[11] L. Desrochers, R. Branconi, E. Schlatter, B. Dent, and P. Buston, "Sensory cues underlying competitive growth in the clown anemonefish (Amphiprion percula)," Behavioural Processes, vol. 181, Dec. 2020, doi: 10.1016/j.beproc.2020.104276.

[12] L. Yllan, S. Heatwole, M. Wong, and T. Rueger, "Effect of social context on behaviour in anemonefish hierarchies," Anim Behav, vol. 209, pp. 83–93, Mar. 2024, doi: 10.1016/j.anbehav.2023.12.014.

[13] RStudio Team, "RStudio: Integrated development for R," 2023, RStudio, PBC.

[14] J. Sueur, T. Aubin, and C. Simonis, "Seewave: a free modular tool for sound analysis and synthesis.," 2008, Bioacoustics.

[15] M. Araya-Salas, "Rraven: connecting R and Raven bioacoustic software.," 2020, R package version 1.9.

[16] M. Araya-Salas, "warbleR: an r package to streamline analysis of animal acoustic signals," 2017, Methods in Ecology and Evolution.

[17] A. Kassambara and F. Mundt, "factoextra: Extract and Visualize the Results of Multivariate Data Analyses." 2020, R package version 1.0.7.

[18] D. Bates, M. Mächler, B. Bolker, and S. Walker, "Fitting Linear Mixed-Effects Models using lme4," Jun. 2014. Available: http://arxiv.org/abs/1406.5823

[19] Y. Sakamoto, M. Ishiguro, and G. Kitagawa, "Akaike information criterion statistics.," Dordrecht, The Netherlands: D. Reidel, vol. 81, no. 10.5555, p. 26853, 1986.

[20] Lenth R, "emmeans: Estimated Marginal Means, aka Least-Squares Means," 2024, R package version 1.10.6.

[21] S. Nakagawa, P. C. D. Johnson, and H. Schielzeth, "Appendices S1-S5 and S7 for 'The coefficient of determination R 2 and intra-class correlation ICC from

generalized linear-mixed effects models revisited and expanded' Appendix S1 Deriving the observation-level variance σ 2 ε using log-normal approximation," pp. 1–11, 2017.

[22] N. E. Munoz and D. T. Blumstein, "Multisensory perception in uncertain environments," May 2012. doi: 10.1093/beheco/arr220.

[23] A. J. W. Ward and T. Mehner, "Multimodal mixed messages: The use of multiple cues allows greater accuracy in social recognition and predator detection decisions in the mosquitofish, Gambusia holbrooki," Behavioral Ecology, vol. 21, no. 6, pp. 1315–1320, Nov. 2010, doi: 10.1093/beheco/arq152.

[24] E. Parmentier and D. Lecchini, "Sound Communication," in Evolution, Development and Ecology of Anemonefishes, CRC Press, 2022, pp. 95–102. doi: 10.1201/9781003125365-12.

[25] D. L. M. Campbell, S. A. Weiner, P. T. Starks, and M. E. Hauber, "Context and control: behavioural ecology experiments in the laboratory," 2009.

[26] M. Wong, C. Uppaluri, A. Medina, J. Seymour, and P. M. Buston, "The four elements of within-group conflict in animal societies: an experimental test using the clown anemonefish, Amphiprion percula," 2016.

[27] R. Bergmüller and M. Taborsky, "Experimental manipulation of helping in a cooperative breeder: Helpers 'pay to stay' by pre-emptive appeasement," Anim Behav, vol. 69, no. 1, pp. 19–28, Jan. 2005, doi: 10.1016/j.anbehav.2004.05.009.

[28] O. Domínguez-Castanedo, "Agonistic interactions with asymmetric body size in two adult-age groups of the annual killifish Millerichthys robustus (Miller & Hubbs, 1974)," J Fish Biol, vol. 99, no. 3, pp. 773–781, Sep. 2021, doi: 10.1111/jfb.14757.

[29] A. R. Reddon, C. J. Dey, and S. Balshine, "Submissive behaviour is mediated by sex, social status, relative body size and shelter availability in a social fish," Anim Behav, vol. 155, pp. 131–139, Sep. 2019, doi: 10.1016/j.anbehav.2019.06.026.

[30] M. A. Bee, S. A. Perrill, and P. C. Owen, "Size assessment in simulated territorial encounters between male green frogs (Rana clamitans)," 1999.

[31] B. Gingras, M. Boeckle, C. T. Herbst, and W. T. Fitch, "Call acoustics reflect body size across four clades of anurans," J Zool, vol. 289, no. 2, pp. 143–150, Feb. 2013, doi: 10.1111/j.1469-7998.2012.00973.x.

[32] M. V. Noël, J. W. A. Grant, and J. G. Carrigan, "Effects of competitor-to-resource ratio on aggression and size variation within groups of convict cichlids," Anim Behav, vol. 69, no. 5, pp. 1157–1163, 2005, doi: 10.1016/j.anbehav.2004.07.019.

DOI: 10.61782/fa.2025.0906

FORUM ACUSTICUM EURONOISE 2025

TOWARDS LARGE-SCALE ENVIRONMENTAL NOISE MAPPING IN EUROPE'S NATURAL AREAS

Rangaswamy Chandrashekar, Shreyas[1*] **Van Renterghem, Timothy**[1] **Botteldooren, Dick**[1]
[1] WAVES research group, Department of Information Technology, Ghent University, Belgium

ABSTRACT

Sound propagation outdoors involves complex physics, posing significant challenges for accurate computational modelling and environmental noise mapping in natural areas. This study uses the advanced Harmonoise point-to-point sound propagation model, which incorporates key features for natural environments, such as acoustically soft surfaces, terrain variations, meteorological effects, and their interactions. Considering the model requirements, the study leverages remotely sensed data featuring high spatial and temporal resolution. Relevant datasets such as elevation, land use and meteorological parameters are integrated into the modelling framework, allowing to produce detailed exposure level maps. Standard noise emission spectra for anthropogenic traffic sources such as roads, railways and aircrafts, together with wind turbine and mining activities, are of interest. By utilizing open input data only, the study ensures applicability over various countries to arrive at the challenging task of producing anthropogenic noise exposure maps in all of Europe's natural areas. In this paper, focus is on road traffic noise, where traffic parameters are based on road categorization, and an update of the progress is reported.

Keywords: *noise mapping, road traffic noise, analytical harmonoise point-to-point model, environmental noise*

[*] ***Corresponding author:*** *shreyas.rangaswamychandrashekar@ugent.be.*

***Copyright**: ©2025 First author et al. This is an open-access article distributed under the terms of the Creative Commons Attribution 3.0 Unported License, which permits unrestricted use, distribution, and reproduction in any medium, provided the original author and source are credited.*

1. INTRODUCTION

Environmental noise is increasingly recognized as a significant pollutant with adverse effects not only on human health but also on wildlife and biodiversity in natural areas. Following the Environmental Noise Directive (END) [1] and other European policies, there have been crucial efforts for human-centric large-scale noise mapping, consequently focusing on urban areas. However, natural regions-many of which fall under the Natura2000 network-remain underrepresented in these assessments.

Noise propagation in natural environments is influenced by factors such as undulated terrain, varying ground cover types, and dynamic meteorological conditions [2]. In remote areas, sources of noise, such as road traffic, wind turbines, railways or mining operations are often located at a distance from the natura2000 sites, i.e., away from the biodiverse habitat, necessitating models that accurately capture long-range sound propagation.

This study addresses these gaps by developing a methodology for large-scale environmental noise mapping across Europe's natural areas using exclusively open data sources. To simulate sound propagation with physical realism, the advanced analytical Harmonoise point-to-point model [2], [3] is employed. Unlike simpler methods, Harmonoise incorporates detailed ground characterization, impedance discontinuities, and terrain diffraction effects, which are critical for accurately estimating noise levels in complex natural environments, while keeping computing times within reason.

Ultimately, this work aims to contribute to the development of comprehensive, biodiversity-conscious noise mapping strategies that can inform environmental management and policy decisions across Europe.

2. DATA

This study uses open data sources, primarily derived from remote sensing. The key inputs to the model include ground cover, elevation (digital terrain model), meteorological datasets, and road traffic networks, each obtained from distinct sources.

For ground cover information, the study utilizes the Dynamic World land cover dataset. This dataset provides a spatial resolution of 10 meters across Europe, with a temporal resolution of 2 to 5 days, depending on the location [4]. The dataset delineates different types of ground cover class efficiently.

For large-scale environmental noise modeling across Europe, an essential input is accurate elevation data in the form of a digital terrain model (DTM), which represents the bare-earth surface without vegetation, buildings, or other surface features. While the EEA-10 dataset provided by the European Environment Agency [5] offers pan-European coverage at 10-meter resolution, it represents a digital surface model (DSM) rather than a true terrain model and is therefore less suitable for precise noise propagation modeling.

Ongoing research is exploring the derivation of DTMs from Sentinel-1 SAR data, which could potentially enable consistent terrain modeling across the continent. However, for the purpose of this study, a high-resolution regional DTM from the Flemish government (DHMV II) was used [6]. This dataset, based on LiDAR data, collected between 2013 and 2015, offers 1-meter spatial resolution and accurately captures ground elevation. While this limits the geographic scope of the current case study, it provides a robust testbed for assessing modeling methodologies with high-quality elevation inputs.

In this study the focus is on road traffic noise. The road network is obtained from the Open Street Map (OSM). OSM road data is categorized into different types to which appropriate traffic parameters were assigned. [7].

3. METHODOLOGY

The analytical Harmonoise point-to-point model (HP2P) was implemented in Python 3 [2]. Taking advantage of the available versatile geospatial manipulation libraries, such as the rasterio, osmnx, and shapely, the data processing and preparation were streamlined to serve as efficient inputs to the model. In this paper, as an example, a natura2000 site with coordinates 50.98° N 4.42° E in the Flemish province of Brabant, in Belgium, is chosen.

The study area is a relatively flat ground terrain with elevation varying between 9 m and 14 m above sea level. The site under observation is a mixture of ground cover, with dominant ground cover types forest floor, grass, shrub and scrub. Figure 1 and figure 2 shows ground cover and elevation maps in the study area, respectively.

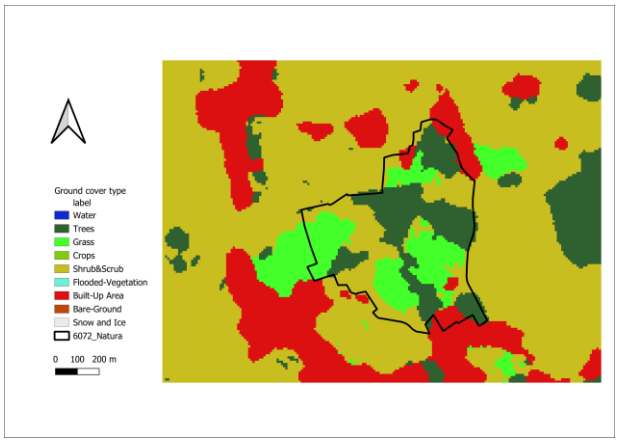


Figure 1. Ground cover map of the natura2000 site under study.

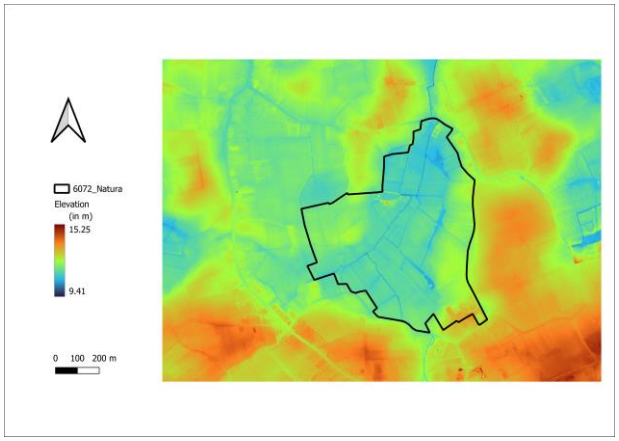


Figure 2. Elevation map of the natura2000 site under study.

3.1 Spatial ETL (Extract, Transform & Load) Pipeline

A buffer of 3.2 km is created around the Natura2000 site, i.e., the study area. Within this buffer, the existing road networks are downloaded. This network is then used to calculate the betweenness centrality [8] of each edge, assigning a corresponding value to each road segment.

Each road is then assigned a traffic intensity, vehicle speed and share of heavy vehicles based on the OSM category

(e.g., motorway, primary, secondary), as well as additional attributes such as the presence of tunnels, the number of lanes, and max speed. The constants linking road categories to traffic parameters are derived from observed traffic patterns in the Flanders region in Belgium. The betweenness values and assigned traffic intensity levels are combined to generate a final traffic-weighted road network.
Since we focus on Natura 2000 sites, we often don't find major road networks that pass through these areas. The following map (fig. 3) shows the road network. Most of the roads here belong to the tertiary or residential category.
Around the current Natura 2000 site, a grid of receiver points is generated at a resolution of 10 × 10 meters. The density of these points was decreased with increasing distance from the major road network (i.e., motorway, primary, secondary and tertiary) to optimize computational efficiency. Indeed, further away from the road, spatial variations in exposure levels become limited.
From each receiver point, cross-sections are drawn to the nearby road segments. The receiver points are divided into groups based on their distance to the road. For each group, a different discretisation of the roads segments in source points is applied. For example, as shown in the figure 3 below, the group of points closest to the major road have been assigned source separations along the road segments of 10 m, while the points furthest away 90 m. This approach strongly increases computational efficiency.

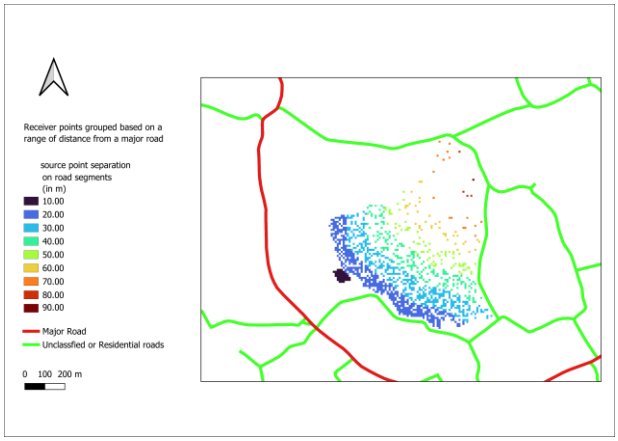


Figure 3. The solid black lines indicate the roads, the red region is the natura2000 site (study area) and the green dots are the receiver points, where the sound pressure levels are computed.

For a given receiver, only those road segments falling within four times the distance from the nearest line source are selected for generating the cross-sections.

The cross-sections are then used for sampling the elevation and ground cover values at a fine spatial resolution of 1 meter. Each of these cross-sections were then subject to the Douglas-Pecker algorithm for simplification to linear segments. With an allowed maximum deviation set at 0.1 m, the profiles preserve the topological features that are relevant for the sound propagation.
Therefore, the final simplified profile carries information on elevation, ground cover type, and the distance from the source. While preserving the topological structure of the profile, it is also essential to retain the exact positions where ground cover transitions occur. These points are explicitly included in the profile, along with the updated ground cover type. This ensures that the Harmonoise model correctly accounts for ground impedance discontinuities by assigning the appropriate acoustic parameters—such as porosity and flow resistivity—on a segment-wise basis. Including these transitions enables accurate Fresnel-zone-based weighting and avoids unrealistic attenuation estimates that could arise from assuming uniform ground conditions along the propagation path. The table 1 below summarizes different ground cover classes available in the ground cover dataset [4] and their associated effective porosity and flow resistivity values.

Table 1. Different types of ground cover and the associated effective flow resistivity and porosity values for using the Zwikker and Kosten ground impedance model [9]

Ground cover type	Flow resistivity ($kPas/m^2$)	Porosity
Water	10^7	10^{-7}
Forest-floor	20	0.5
Grass	300	0.75
Crops	200	0.9
Shrub & Scrub	100	0.45
Flooded Vegetation	10^7	10^{-7}
Built – Up Area	10^7	10^{-7}
Bare Ground	450	0.35

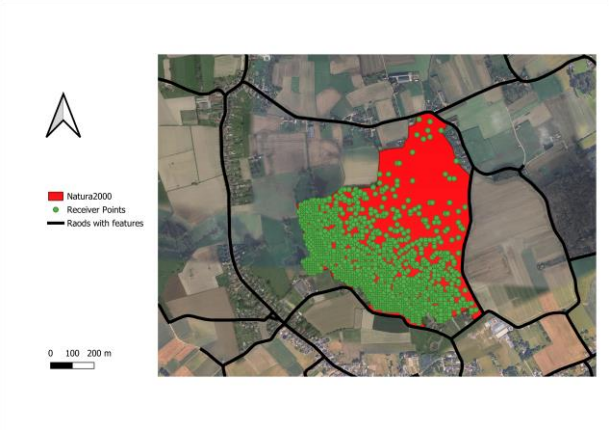


Figure 4. The solid black lines indicate the roads, the red region is the natura2000 site (study area) and the green dots are the receiver points, where the sound pressure levels are computed.

3.2 Computing Sound Pressure Levels at receiver points

The sound pressure levels (SPL) are computed for 1/3 octave bands with center frequencies ranging from 25 Hz till 10 kHz.

Table 2. Input parameters used to run the Harmonoise propagation model

Parameters	Values
Air temperature	15 ° C
Relative Humidity	70%
Atmospheric Pressure	101.325 kPa
Speed of Sound	340 (ms^{-1})
Turbulence scattering strength	5e-6
Source Height	0.03 (m)
Receiver Height	2 (m)

Following the Harmonoise/IMAGINE source power level model [3], [10], the sound pressure level at each receiver location is computed by first determining the source power level based on the traffic parameters (more precisely : traffic intensity, share of heavy and light vehicle, and vehicle speeds) for each road segment.

As the analytical model provides sound pressure levels relative to free field sound propagation, the geometrical spreading term is added afterwards to calculate the total attenuation towards a receiver. Additionally, an A-weighting correction is applied. Future research should explore alternative weighting schemes to better capture the effects on wildlife and biodiversity.

To look at the impacts of elevation and ground cover on the final sound pressure levels, the simulations were run with different simplifications. Test cases involve free field sound propagation only, neglecting terrain elevation by using a fixed elevation, and using a fixed ground cover. All other parameters remain the same as mentioned in Table 1. For simplicity, no refraction was considered in any noise map in this paper, although the Harmonoise analytical point-to-point model is able to model this accurately and efficiently.

4. RESULTS

The sound pressure levels are stored as a feature of the receiver points and are used in creating the noise maps. The outputs are stored as a separate vector files for each test case. The vector shape files are converted to raster pixels with a pixel size of 10 m in the georeferenced units, in our case it is EPSG:3035. The simulations for 4 different test cases are discussed below with fixed level axes. In a first step, interpolation is not applied and only the locations with actual calculations are shown (raw sound pressure level maps).

4.1 Case 1: Free field propagation

The simplest map, only accounting for free field propagation, is depicted in Fig. 5.



Figure 5. Sound pressure level map under free field propagation for the natura2000 site.

4.2 Case 2: Elevation and ground cover is kept constant

In this case, the elevation is kept at a constant value throughout the sampling locations. The ground cover is taken as forest floor, which was assigned a flow resistivity value of 20 kPas/m^2 and porosity value of 0.5 (From table 1).

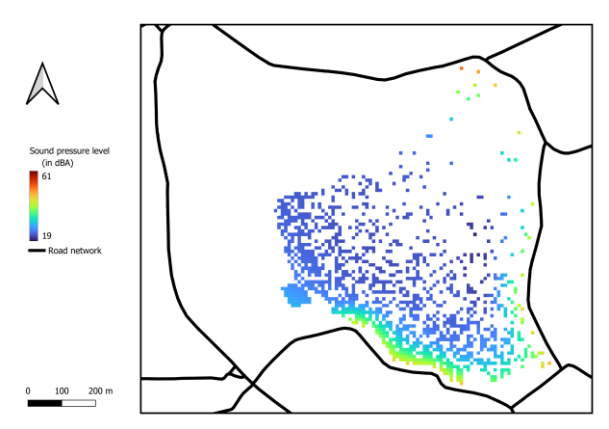


Figure 6. Sound pressure level map for flat forest floor ground

4.3 Case 3: Flat terrain with actual ground cover

Here, the actual ground cover from the dynamic world dataset [4] was used in case of flat terrain.

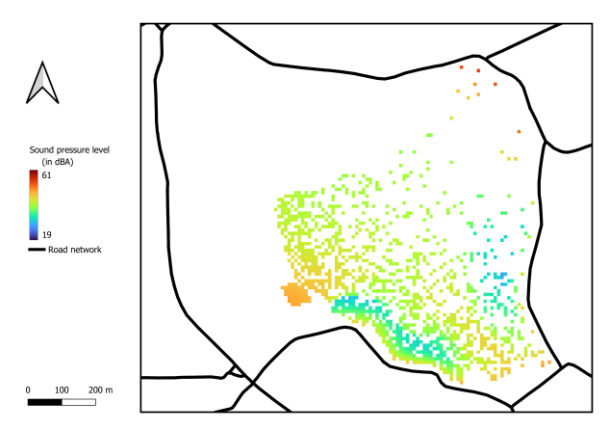


Figure 7. Sound pressure level map for constant elevation and actual ground cover values. The solid black lines indicate the roads

4.4 Case 4: Actual ground cover and actual elevation

In the final test case, actual elevation and ground cover are used, and represents the most accurate map.

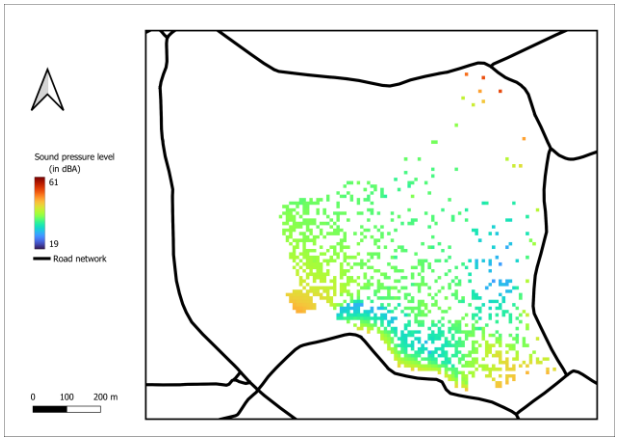


Figure 8. Sound pressure level map for actual ground cover and elevation values. The solid black lines indicate the roads.

4.5 Comparison map

Along with these 4 simulation cases, the difference map between the most simple free field propagation map and the most detailed one, including actual ground cover and elevation, is presented in fig. 9.

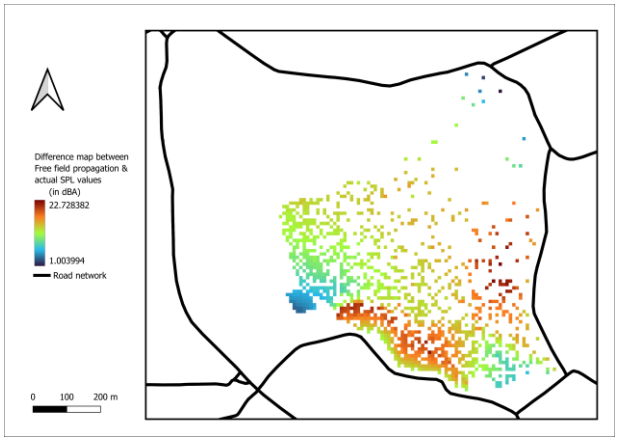


Figure 9. The difference map between the free field propagation and actual sound pressure level.

5. DISCUSSION

From the simulation test cases, it is found that both elevation and ground cover significantly affect the exposure levels. Table 3 summarizes the average differences and standard deviations in sound pressure levels.

Table 3. Average difference between the first three test cases and the final detailed exposure levels

Test case	Average difference (dBA)	Standard deviation (dBA)
Case 1: Free Field	13.5	3.5
Case 2: Flat terrain + forest-floor	10.8	5.4
Case 3: Flat terrain + actual ground cover	2.9	1.8

These variations highlight that ground-related excess attenuation is not merely an additive correction but a dominant propagation mechanism in vegetated and uneven terrain. Notably, the largest attenuation was seen in the final scenario, where both actual elevation and ground cover were used, suggesting synergistic attenuation effects between soft ground and terrain diffraction. Figure 9 illustrates that terrain and ground effects become increasingly important at greater distances, implying that simplified free-field approximations may severely overpredict noise exposure, thereby limiting the practical usefulness of noise mapping efforts. Free field maps, although they might seem attractive from a computational point of view, will not provide meaningful noise maps, with limited use in biodiversity studies.

The Harmonoise model's ability to account for ground attenuation and diffraction proves to be a critical advantage over simpler models like ISO 9613-2 or CNOSSOS - EU, which may underpredict attenuation in soft, vegetated environments [11].

6. FUTURE WORK

Future work will focus on reducing computational time through parallel processing, machine learning, and interpolation strategies. Parallel processing and machine learning methods can improve computational efficiency by optimizing noise modeling workflows, while interpolation techniques will help identify the minimum number of receiver points required to accurately estimate noise exposure across larger areas. These methods will be systematically tested by comparing their results against full calculations across a wider set of input parameters and scenarios, ultimately supporting more efficient large-scale environmental noise mapping for Europe's natural areas.

ACKNOWLEDGMENTS

This study is part of the PLAN-B project "The Path Towards Addressing Adverse Impacts of Light and Noise Pollution on Terrestrial Biodiversity and Ecosystems', funded by the European Union under the Horizon Europe program (project n°101135308).

7. REFERENCES

[1] European Commission, "Environmental Noise Directive (END) 2002/49/EC," [Online]. Available: https://ec.europa.eu/environment/noise/. [Accessed: Apr. 3, 2025].

[2] D. van Maercke and J. Defrance, "Development of an analytical model for outdoor sound propagation within the Harmonoise project," Acta Acustica united with Acustica, vol. 93, pp. 201–212, 2007.

[3] G. J. van Blokland and H. A. van der Toorn, "The Harmonoise/IMAGINE Sound Power Model," TNO Report HARMONOISE WP1, 2005.

[4] Google and World Resources Institute, "Dynamic World: Near real-time 10m land use land cover dataset," 2022. [Online]. Available: https://dynamicworld.app/about. [Accessed: Feb. 10, 2025].

[5] European Space Agency, "Copernicus Digital Elevation Model (Copernicus DEM)," [Online]. Available: https://dataspace.copernicus.eu/explore-data/data-collections/copernicus-contributing-missions/collections-description/COP-DEM. [Accessed: Apr. 3, 2025].

[6] Agentschap Digitaal Vlaanderen, "Digitaal Hoogtemodel Vlaanderen II, DTM, raster, 1 m," 2014. [Online]. Available: https://www.vlaanderen.be/datavindplaats/catalogus/digitaal-hoogtemodel-vlaanderen-ii-dtm-raster-1-m. [Accessed: Apr. 1, 2025].

[7] OpenStreetMap, "About OpenStreetMap," [Online]. Available: https://www.openstreetmap.org/about. [Accessed: Apr. 2, 2025].

[8] A. Kirkley, H. Barbosa, M. Barthelemy et al., "From the betweenness centrality in street networks to structural invariants in random planar graphs," Nature Communications, vol. 9, Art. no. 2501, 2018, doi: 10.1038/s41467-018-04978-z.

[9] T. Van Renterghem, F. Huyghe, and K. Verheyen, "Effect of tree species and season on the ability of forest floors to abate environmental noise," Applied Acoustics, vol. 184, p. 108349, 2021, doi: 10.1016/j.apacoust.2021.108349.

[10] B. Peeters and G. J. van Blokland, "The Noise Emission Model for European Road Traffic," IMAGINE Deliverable 11, Jan. 11, 2007. [Online]. Available: https://www.imagine-project.org/bestanden/IMA55TR-060821-MP10%20-%20IMAGINE%20Deliverable%20D11.pdf [Accessed: Apr. 2, 2025].

[11] K. Attenborough and T. Van Renterghem, "Adequacy of Engineering Predictions of Soft Ground Effect," *Forum Acusticum*, Lyon, France, pp. 863–868, Dec. 2020. doi: 10.48465/fa.2020.0278.

DOI: 10.61782/fa.2025.0535

FORUM ACUSTICUM EURONOISE 2025

LOW-FREQUENCY CONTINUOUS NOISE WITHIN THE *POSIDONIA OCEANICA* KEY COASTAL ECOSYSTEM: PRELIMINARY RESULTS FROM THE NORTH-WESTERN MEDITERRANEAN

Martina Mulas[1*] **Sara Ferri**[2,3] **Lucia Pini**[1]
Francesca Rossi[4] **Elena Maggi**[1] **Francesco Caruso**[2]
[1] Department of Biology, University of Pisa, Italy
[2] Department of Marine Animal Conservation and Public Engagement (CAPE), Stazione Zoologica Anton Dohrn, Naples, Italy
[3] Department of Life Sciences and System Biology, University of Turin, Italy
[4] Department of Integrated Marine Ecology (EMI), Genova Marine Center, Stazione Zoologica Anton Dohrn, Genoa, Italy

ABSTRACT

Coastal marine ecosystems are increasingly exposed to sensory pollutants such as anthropogenic noise and artificial light at night. Within the AquaPLAN project framework, in summer 2024 we characterized the noise pollution levels within shallow *Posidonia oceanica* seagrass meadows. Sampling occurred at an urbanized light-polluted site (port) as well as at three naturally dark sites at different level of protection within marine protected areas (MPAs), along the Tuscan coastline (Italy). Acoustic data were recorded up to 192 kHz sampling frequency applying a 16% duty cycle (5 mins recording every 30 mins) by passive acoustic monitoring. Here, we present some preliminary results of a subset of data (96 files) from recordings of 3 days, considering 2 recordings each per 4 parts of the day (nighttime; dawn; daytime; dusk), per day (N=3), per site (N=4). These were processed focusing on the low-frequency continuous noise. Noise was louder and more frequent within the meadow situated close to the port of Capraia, while meadows within MPAs exhibited variable noise pollution levels. These findings provide critical baselines for long-term initiatives assessing noise pollution exposure along with quantitatively measured light pollution levels and then developing mitigation strategies for key-habitats.

Keywords: *Mediterranean Sea, Posidonia oceanica, Noise pollution*

1. INTRODUCTION

Coastal zones are densely populated and largely exposed to human-induced global and local stressors [1]. With the fast pace at which coastal urbanization goes, some novel human-related stressors have become more common, including sensory pollutants like anthropogenic noise and artificial light at night [2,3,4].
The Horizon Europe project AquaPLAN (Aquatic Pollution from Light and Anthropogenic Noise: Management of Impacts on Biodiversity) aims to characterize, both spatially and temporally, anthropogenic noise and artificial light at night and their effects in aquatic habitats. The interest of the Italian project partners, University of Pisa and Stazione Zoologica Anton Dohrn, focus on the impacts of the before-mentioned pollutants on subtidal coastal ecosystems, such as those sustained by the seagrass *Posidonia oceanica*, forming extensive meadows which provide several ecosystem services. This species, endemic to the Mediterranean Sea, is protected together

[*] ***Corresponding author***: martina.mulas@biologia.unipi.it
Copyright: *©2025 Mulas et al. This is an open-access article distributed under the terms of the Creative Commons Attribution 3.0 Unported License, which permits unrestricted use, distribution, and reproduction in any medium, provided the original author and source are credited.*

with its peculiar habitat type (Habitat 1120) [5] and, to date, only a few studies have directly investigated the anthropogenic noise levels to which this is exposed [6].
Here, we present preliminary data collected in summer 2024 at four sites, selected by an *a-priori* qualitative assessment of potential differences in noise pollution levels, as related to recreational boating and the proximity to a marina where light pollution also occurred.
Following the Marine Strategy Framework Directive (MSFD; 2008/56/EC), our goal was to describe the anthropogenic low-frequency continuous noise levels present in these sites and to assess the possible threatened status of the investigated meadows. The MSFD is one of the few legislations directly mentioning noise as the 11th descriptor for a good environmental status (GES) and it defines it as '*anthropogenic sound that has potential to cause negative impacts on the marine environment, including component biota but not necessarily the whole environment*' [7]. Anthropogenic noise sources in water can be distinguished into impulsive and non-impulsive (continuous), with the latter being mainly associated with noise pollution (NP) produced by shipping, sonar and recreational boats often continuously emitting at low frequencies <1-kHz [8]. Regarding this, the 11.2.1 indicator defined the average level centered at 63- and 125-Hz of the 1/3 octave frequency bands (TOLs) as representative of the non-impulsive low-frequency noise ('shipping bands' *sensu* [9]).

2. MATERIAL AND METHODS

2.1 Study area

Field monitoring activities were conducted between July and September 2024, where *Posidonia oceanica* is at its maximum growth [10]. Among the selected sites, three were located around Capraia Island (Capraia Port - CP, Cala del Moreto - CM, and Peraiola – PER - this latter being part of a no-take zone), and one offshore the Leghorn port, on a shallow bank called 'Secche della Meloria - MEL – within a Marine Protected Area (MPA) (Fig.1).

2.2 Data acquisition and processing

Acoustic recordings were collected via Passive Acoustic Monitoring technique (PAM) using an autonomous recorder (Hydromic384K, DODOTRONIC) with sensibility of -156.1 dB re. 1 V/µPa. Acoustic data were acquired up to a sampling frequency of 192 kHz and 16-bit dynamic range, with a 16% duty cycle (5 mins of recording every 30 mins). This was selected to balance battery time-consumption and data storage limitation. The recorders were mounted and tidily assured on a seabed station and deployed at around 10 m depth for 14 days at Capraia Port (672 files), 19 days at Peraiola (912 files), 20 days at Cala del Moreto (960 files) and 21 days at Secche della Meloria (5040 files). Sea state conditions were similar among sites (<3 Beaufort scale) and wave height field (2-3 Douglas scale). The temperature at the three sites at Capraia island was 26.67±1.30°C, while at the Secche della Meloria site was 23.88±1.89°C. Salinity was constant at around 37-38 ppm.

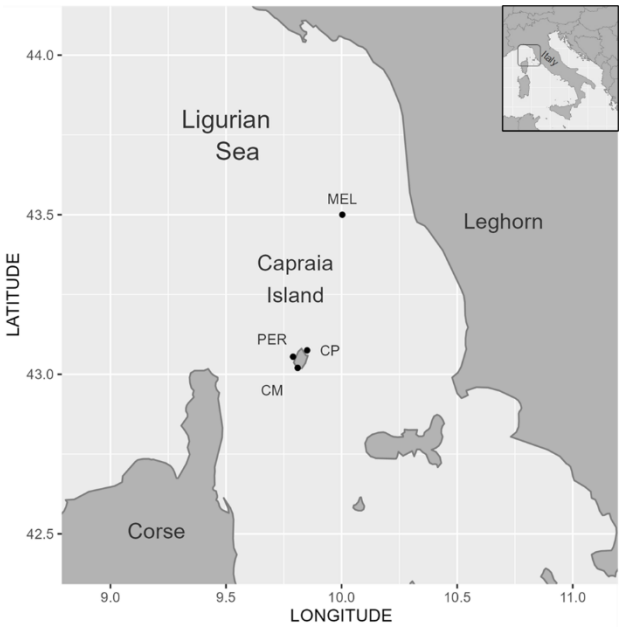


Figure 1. Map of the study area located in the Ligurian Sea (Italy), on the northwestern Mediterranean Sea: MEL - Secche della Meloria; CP – Capraia Port; CM – Cala del Moreto; PER – Peraiola. Map obtained in R Studio version 4.3.3 [11-14].

To this preliminary study, we extracted one subsampled dataset following a procedural scheme: two 5-min recordings per hour per four slots per day from three randomly chosen days per site. The three days included at least one weekend-day (N=6) and the whole subset consisted of 40 minutes a day for a total of 480 minutes. The four slots were the following: 'night'– from midnight to 1am; 'dawn' – from 6 to 7am; 'day' – from noon to 1pm;

'dusk' – from 6 to 7pm. Data were collected as .wav files and no pre-amplification or filtering was applied. Firstly, the audio files were aurally and visually inspected using the free software Raven Lite (from the Cornell Laboratory; www.birds.cornell.edu/home/). The Sound Pressure Level (SPL dB re: 1µPa-rms) was calculated for seventeen 1/3 octave bands (TOLs - frequency range 25 Hz – 1 kHz) using a toolbox in MATLAB [15], with Hann window type with 1 second window length, 50% window overlap and 300 second time-average data (one value for each single file). Special attention was given to the two 1/3 octave bands highlighted by the MSFD and centered at 63-Hz and 125-Hz. Statistical analyses and plots were run in RStudio v.4.3.3 [11,14]. Data was processed with generalized additive mixed effect models (GAMMs) through the 'mgcv' package [16] for the two bands separately. The additive mixed model was chosen to address the non-linear relationship between time of the day and SPL (rms) per site, with the former as the smooth part and days as the random intercept. Due to the limited set of data here processed, we set a flexibility of 4 knots to avoid overfitting.

3. RESULTS

The variations of the SPLs centered at the two shipping bands of the 1/3 octave bands per site are shown in Figure 2. Overall, the 125-Hz band was louder than the 63-Hz at all sites and time slots. Both shipping bands' values showed a similar diel trend, except for the Capraia Port site, where at noon and at dusk higher values were recorded at both bands (Fig. 2). The diel trend of the root-mean-square sound pressure levels at both 63- and 125-Hz bands showed non-linear patterns with variation over time at Capraia Port and Cala del Moreto, while at Peraiola the trend was linear and no temporal pattern was observed (GAMM, $p<0.05$). Meloria site showed a significantly different temporal trend at 63-Hz, but not at the 125-Hz band. The Capraia Port site was the loudest with peak values recorded at dusk for the 63-Hz and at noon in the 125-Hz band. Following the Capraia Port site, Cala del Moreto was the second loudest with the highest peak recorded at noon at both bands, being three- and two-fold lower than the Capraia Port value at 63-Hz and 125-Hz, respectively. The models explained 68.7% and 81.3% of the diel variance for the 63-Hz and 125-Hz bands. As for the random terms, days resulted significantly different at Capraia Port at both bands, and at Meloria when considering the 63-Hz band. For both TOLs, the difference in the medians of the loudest and quietest sites was around 18-22 dB and about 34 dB at 63- and 125-Hz, respectively.

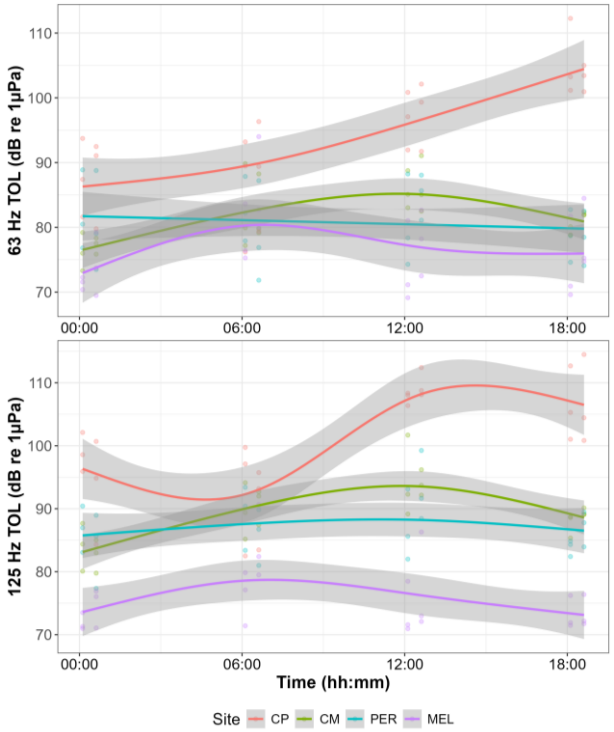


Figure 2. Temporal trend of the two shipping bands TOLs centered at 63- and 125-Hz (dB re: 1µPa). Coloured points and lines represent the SPL (rms) values per site, recorded at a six-hour interval per three days per site (N=2 per time slot). Shaded lines represent upper and lower 95% confidence intervals.

4. DISCUSSION

The preliminary data here shown are, to date, the first related to the anthropogenic noise exposure level of the *P. oceanica* meadows of the Tuscan coast (north-western Mediterranean Sea, Italy) and expressed in terms of TOLs sound pressure levels [17]. Here, our interest was addressed to the diel variation of the two shipping bands, the 63-Hz and 125-Hz, at four different sites, including two MPAs. Not surprisingly, the Capraia Port site was the loudest with the highest median values recorded at noon (92.73 dB re 1µPa and 105.89 dB 1µPa) and at dusk (92.02 dB 1µPa and 103.15 dB 1µPa) at 63- and 125-Hz bands, respectively, when most human activities happen. Moreover, our values were comparable to those obtained in other noisy coastal areas within the Mediterranean Sea (e.g., Gulf of Naples, Civitavecchia port, and the North Adriatic Sea) characterized by intensive human presence [18,19,20,21].

Cala del Moreto, the site on the western coast of Capraia island, was significantly different from Capraia Port and showed significant non-linear temporal trends, possibly due to its site location facing several naval routes as well as small vessels traffic [22]. The highest value at Cala del Moreto was recorded at noon for both bands with 81.03 and 88.40 dB 1µPa at 63- and 125-Hz, respectively. Interestingly, the two MPAs, Peraiola and Secche della Meloria, had two different temporal trends. The former was constant along the diel cycle spanning from 73.40 and 79.11dB 1µPa, and 82.81 and 87.63 dB 1µPa at 63- and 125-Hz, while the latter had a significantly different temporal behavior at 63-Hz, and no differences were recorded at 125-Hz. The lowest rms SPLs at the 125-Hz band were also recorded at Meloria, spanning from 71.34 dB 1µPa at dawn to 71.74 dB 1µPa at noon, respectively (median values). The overall louder 125-Hz band could be due to the combination of shallow sites, high number of recreational boats and less favorable propagation conditions for low frequencies, affecting the contribution from distant shipping as suggested by Garrett et al (2016) [23].

5. FUTURE REMARKS AND CONCLUSION

Drawing conclusions regarding the anthropogenic noise pollution of these sites require further investigation integrating PAM data with automatic identification system (AIS) data [17,19,20]. Follow-ups will consist in processing the remaining recordings, which span a period of ~2-3 weeks and expanding the analyses to natural biological sounds (biophony). This will contribute to widening soundscape information related to the Mediterranean Sea and, more in particular to *Posidonia oceanica* meadows. Furthermore, soundscape analysis, considering both anthropony and biophony, combined to naval traffic information may allow us to detect possible effects of noise pollution on species associated to the meadows. Urbanized sites such as the Capraia Port are also affected by several other threats such as artificial light at night, so that investigating the two factors in multiple stimuli research will provide further insights towards a more comprehensive characterization of sensory pollutants exposure levels [24]. Finally, because the amelioration of sensory polluted sites can be immediate by limiting the naval traffic in certain areas and switching off/to light emission at certain wavelengths, knowledge of their combined effects can help to quickly act and mitigate their impacts within the purpose of the here-presented AquaPLAN project.

6. ACKNOWLEDGMENTS

We would like to thank Dr. Simone Bava, Dr. Miriam Ferretti and Dr. Roberta Minetti for their help during the field campaign. Additional thanks to the Unit of Marine Biology and Ecology of the Pisa University Biology Department. The work of Sara Ferri was supported by the PhD program of the Stazione Zoologica Anton Dohrn and by the University of Turin through the SUSTNET PhD scholarship (No. 39-033-31-DOT21BX3F7-8932). This research was funded by the European Union under the Horizon Europe Programme, Grant agreement No. 101135471 (AquaPLAN).

7. REFERENCES

[1] Q He and BR Silliman (2019) Climate Change, Human Impacts, and Coastal Ecosystems in the Anthropocene. *Current Biology* 29: R1021–R1035. 10.1016/j.cub.2019.08.042

[2] JA Hildebrand (2009). Anthropogenic and natural sources of ambient noise in the ocean. *Marine Ecology Progress Series* 395:5-20. 10.3354/meps08353

[3] C Duarte, L Chapuis, SP Collin, DP Costa, RP Devass, et al (2021) The soundscape of the Anthropocene ocean. *Science* 371: eaba4658. 10.1126/science.aba4658

[4] TW Davies, JP Duffy, J Bennie and KJ Gaston (2014) The nature, extent, and ecological implications of marine light pollution. *Frontiers in Ecology and the Environment* 12:347-355. 10.1890/130281

[5] European Community (1992) Council Directive 92/43/EEC of the European Council of 21 May 1992 on the conservation of natural habitats and of wild fauna and flora. Official journal of EC, N°L206/7.

[6] M Ceraulo, E Papale, F Caruso, F Filiciotto, R Grammauta et al (2018) Acoustic comparison of a patchy Mediterranean shallow water seascape: *Posidonia oceanica* meadows and sandy bottom habitats. *Ecological Indicators* 85: 1030-1043. 10.1016/j.ecolind.2017.08.066

[7] European Marine Strategy Framework Directive Good Environmental Status (MSFD-GES) Report of the Technical Subgroup on Underwater Noise and other forms of energy, pp. 31.

[8] T Gotz, G Hastie, LT Hatch, O Raustein, BL Southall et al (2009) Overview of the impacts of anthropogenic

underwater sound in the marine environment. OSPAR Biodiversity Series, London 134.

[9] P Blondel, B Dell and C Suriyaprakasam (2020) Acoustic Signatures of Shipping, Weather and Marine Life: Comparison of NE Pacific and Arctic Soundscapes. *Proceedings of Meetings on Acoustics* 40(1): 070011. 10.1121/2.0001312

[10] A Peirano, S Cocito, V Banfi, R Cupido, V Damasso et al (2011) Phenology of the Mediterranean seagrass *Posidonia oceanica* (L.) Delile: Medium and long-term cycles and climate inferences. *Aquatic Botany* 94 (2): 77-92. 10.1016/j.aquabot.2010.11.007.

[11] [RStudio] R Core Team (2024) R: A Language and Environment for Statistical Computing. R Foundation for Statistical Computing, Vienna, Austria. https://www.R-project.org/

[12] A South (2011) rworldmap: A New R package for Mapping Global Data. The R Journal 3(1): 35-43. 10.32614/RJ-2011-006

[13] A South (2012) rworldxtra: Country boundaries at high resolution. https://CRAN.R-project.org/package=rworldxtra

[14] H Wickham (2016) ggplot2: Elegant Graphics for Data Analysis. Springer-Verlag New York.

[15] N Merchant, KM Fristrup, MP Johnson, PL Tyack, MJ Witt et al (2015) Measuring acoustic habitats. *Methods in Ecology and Evolution* 6(3): 257-265. 10.1111/2041-210X.12330

[16] SN Wood (2017) Generalized Additive Models: an introduction with R, 2nd edition. Chapman and Hall/CRC, Boca Raton, FL.10.1201/9781315370279

[17] G Buscaino, M Ceraulo, N Pieretti, V Corrias, F Filiciotto et al (2016) Temporal patterns in the soundscape of the shallow waters of a Mediterranean marine protected area. *Scientific Reports* 6:34230. 10.1038/srep34230

[18] N Pieretti, M Lo Martire, C Corinaldesi, L Musco, A Dell'Anno and R Danovaro (2020) Anthropogenic noise and biological sounds in a heavily industrialized coastal area (Gulf of Naples, Mediterranean Sea). *Marine Environmental Research* 159: 105002. 10.1016/j.marenvres.2020.105002

[19] V Cafaro, D Piazzolla, C Melchiorri, C Burgio, G Fersini et al (2018) Underwater noise assessment outside harbour areas: The case of Port of Civitavecchia, northern Tyrrhenian Sea, Italy. *Marine Pollution Bulletin* 133:865-871. 10.1016/j.marpolbul.2018.06.058

[20] A Codarin and M Picciulin (2015) Underwater noise assessment in the Gulf of Trieste (Northern Adriatic Sea, Italy) using a MSFD approach. *Marine Pollution Bulletin* 101(2):694-700. 10.1016/j.marpolbul.2015.10.028

[21] M Picciulin, A Petrizzo, F Madricardo, A Barbanti, M Bastianini et al (2023) First basin scale spatial-temporal characterization of underwater sound in the Mediterranean Sea. *Scientific Reports* 13: 22799. 10.1038/s41598-023-49567-3

[22] L Wilson, MK Pine and CA Radford (2022) Small recreational boats: A ubiquitous source of sound pollution in shallow coastal habitats. *Marine Pollution Bulletin* 174: 113295. 10. 1016/j. marpo lbul. 2021. 113295

[23] J Garrett, P Blondel, B Godley, S Pikesley, M Witt and L Johanning (2016) Long-term underwater sound measurements in the shipping noise indicator bands 63 Hz and 125 Hz from the port of Falmouth Bay, UK. *Marine Pollution Bulletin* 110(1):438-448. 10.1016/j.marpolbul.2016.06.021

[24] W Halfwerk and P Jerem (2021) A systematic review of research investigating the combined ecological impact of anthropogenic noise and artificial light at night. *Frontiers in Ecology and Evolution* 9:765950. 10.3389/fevo.2021.765950

DOI: 10.61782/fa.2025.0139

FORUM ACUSTICUM EURONOISE 2025

ANTHROPOGENIC NOISE AND ARTIFICIAL LIGHT AT NIGHT: ADDITIVE AND INTERACTIVE EFFECTS ON ACTIVITY LEVEL AND SPATIAL BEHAVIOUR

Hans Slabbekoorn[1*] Christina May[1,2] Lisa Dörner[1]
Danielle Crowley[1] Kees te Velde[1] Christian Tudorache[1]
[1] Institute of Biology Leiden, Leiden University, the Netherlands
[2] BC Cancer Research Institute, Vancouver, BC, Canada

ABSTRACT

Visual and auditory sensory capacities play an important role in the animal kingdom in communication and orientation. For most animals, sound and light are most prominent in relatively long-range signaling and in gathering information about their local and more distant environments. Natural conditions for each modality have therefore continuous impact on general activity level and on spatial decisions to get closer, go further away, or stay put. Insight into these fundamental processes is critical to understand the potential effects of pollution from anthropogenic noise throughout the day and artificial light at night. The impact of sound and light on animal responsiveness roughly follows the same principles and the effects may add up or show interactive effects. We will address fundamental and applied insights into the potential effects of noise and light pollution, by themselves and in concert, and we present an early case study on Lake Victoria cichlids with experimental exposure to elevated intensity levels of both sound and light. We conclude with addressing the specific conditions of migratory fish, and we argue that it is critical to study them for potentially negative consequences of short- and long-term effects of anthropogenic noise and artificial light at night.

*Corresponding author: h.w.slabbekoorn@biology.leidenuniv.nl
Copyright: ©2025 First author et al. This is an open-access article distributed under the terms of the Creative Commons Attribution 3.0 Unported License, which permits unrestricted use, distribution, and reproduction in any medium, provided the original author and source are credited.

Keywords: *multi-modality, phonotaxis, phototaxis, skyglow, soundscape*

1. INTRODUCTION

Sound and light play an important role in the life of animals. Natural sound and light background intensities and spectra determine general activity levels and affect circadian or seasonal rhythms. Specific sound and light sources can also influence spatial decisions: drawing animals closer (attraction) or driving them away (deterrence). This is also referred to as positive and negative phonotaxis and phototaxis [1,2]. For many species, sound and light are the principal modalities used to communicate with conspecifics and to extract information from their environment. Sounds are generated in a variety of ways, propagate through the environment, dependent on habitat- and condition specific scattering and absorption, after which they have communicative potential within the audible range of conspecifics. Behavioural displays and colouration only become visible in the presence of light and when reflected light meets the eye. Objects in the habitat and context will also play a role in detection probability, next to visual attention. Auditory and visual stimuli are often used in concert for communication, and also typically co-occur as environmental cues. Their perceptual prominence varies as with communicative signals with the environmental conditions, behavioural context, and focus (hearing is continuous and omnidirectional, watching is restricted to a particular angular focus and field of vision. In the Anthropocene, both light and noise pollution have altered the world and thereby also the

multi-modal perception of communicative signals and environmental cues.

1.1 Sounds of sexual selection and survival

Natural soundscapes include all that is audible in the environment for an individual animal in a particular habitat at a specific time of day [3,4]. The onset of vocalizations of conspecifics or heterospecifics in the morning may wake up animals and stimulate them to do the same or start other activities, such as foraging or nest-building (Figure 1). Also gradual fluctuations over the day in audible presence of local animal communities may affect vocal and other activity levels. Vocal activities are fluctuating seasonally, driven by hormonal variation over the year, likely stimulated by day length and temperature. The acute effect of natural soundscapes per day may therefore also contribute to longer-term, stimulating effects on physiological and behavioural cycles related to seasonal migration and reproduction. The ability to respond and participate in vocal interactions can for example be critical for reproductive development and mate choice in birds and thereby affect breeding success. Natural soundscapes may also suppress activities when they indicate potential danger by the presence or arrival of a predator. Responsiveness in slowing down activity can then directly translate into survival. Conversely, the resurgence of natural level and composition of local soundscapes may signal the apparent release of danger and trigger revival of halted activities. Abiotic sounds of rain or wind can also affect vocal or other activity levels, likely related to the masking effect on their own vocalizations or on audibility of predator risk, or through learned association with rain or wind, which may be unfavourable to many activities.

1.2 Ambient light by day and night

Light intensity as perceived by animals depends on their visual abilities and the species-specific sensitivity for parts of the light spectrum. The response to light intensity in terms of general activity level is determined by their nocturnal, crepuscular, or diurnal life style (Figure 1), which varies among and within species [5,6]. The length of daylight varies by season and latitude and tunes the biological clock of animals in such a way that their activity levels are optimally timed to ecological opportunities related to feeding and breeding, and to risks of predation and disease. This means that light conditions not only have acute effects, but also influence longer-term physiological and behavioural cycles, such as migratory and reproductive seasons. Acute effects of natural daylight could be regarded as stimulating when triggering activity of diurnal animals, but also as suppressing when making nocturnal animals seek shelter. Twilight and moonlight have a different spectrum and intensity and may also be stimulating or suppressing, depending on species and context. Nocturnal and crepuscular animals typically have special visual adaptations to see at low light intensities (scotopic vision), usually correlated to declines in colour vision or shifts in spectral sensitivities towards colour ranges that are relevant at the dim hours of the day.

1.3 Anthropogenic noise and artificial light at night

Noisy conditions due to human activities [7,8] and artificially lit up nights [9,10] typically disturb or distract animals, generally leading to lower activity levels of whatever they would have done at the time and place (Figure 1). Anthropogenic noise is typically louder, more repetitive, and lower in frequency, than natural sounds. Any time of day, such noisy conditions may elicit fear, stress, or anxiety, making animals to reduce activities that would be risky under the acoustic conditions of perceived threat. Noisy conditions may also just distract, as animals of various taxa have been shown to be unable to avoid processing audible sound, and they thereby lower activity levels of behaviours that require attention for appropriate performance. Finally, masking may yield decreased activity levels through lower stimulating effects of natural soundscapes or reduced opportunities for auditory predator scanning. Lower vocal activity levels may also be the result of lowered auditory feedback from hearing less of their own sounds or of vocal responses from conspecifics. Interestingly, there are also birds and frogs that are vocally triggered by anthropogenic sound events and many species that elevate their vocal intensity and sound production rate in response to more continuously elevated noise levels due to human activities.

Artificial light at night takes away the safety of dim and dark conditions that allow many prey animals to room around with lowered predation rates. Despite intensity typically being much less than natural day time light levels, direct light from lamps, and even indirect light reflected from clouds and air of high humidity (skyglow), usually outcompetes by far any natural light at night from moon or stars. Even though not all diurnal predators become active at night at lit up places, many nocturnal prey species may be less active under artificially elevated conditions and spend less time on critical activities such as foraging, exploring, socializing, and courting. Interestingly, artificial light at night may

also trigger or stimulate activity levels. Birdsong is known to be starting earlier and to end later during the day at territories lit up by artificial light. Predatory fish and birds like herons or grebes may go hunting for fish at times of day that would naturally be too dark to see their prey.

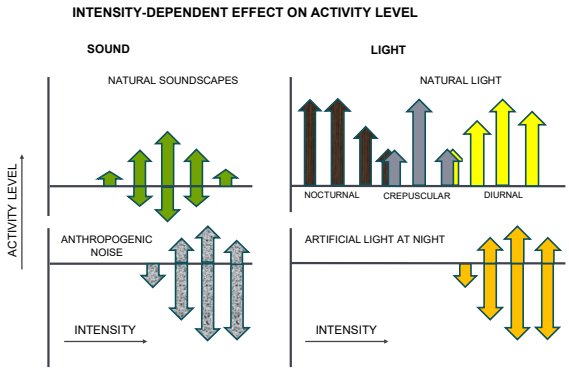


Figure 1: Sound and light conditions can affect general activity level. Soundscapes of conspecific and heterospecific sounds indicating safe conditions for foraging or social activities may elevate activity level in a parabolic way from modest to familiar to extreme sound levels. Natural light levels may stimulate activity depending on whether species are nocturnal, crepuscular, or diurnal. Anthropogenic noise and artificial light at night can also trigger or stimulate activity of animals that are usually not or less active at night, but more often suppress activity of nocturnal and crepuscular species with increasing intensity.

2. CICHLID CASE STUDY

A study with Lake Victoria cichlids (*Pundamilia nyererei*) at Leiden University in August and September 2009, provides a nice example of suppressing effects of sound and light on activity level [11]. Christina May exposed solitary males to noisy or ambient quiet conditions, in bright or dark conditions, and scored their swimming activity and style. After that, she added a female and quantified the courtship behaviour and male calls per pair under the four combinations of sound and light exposure treatments. Earlier studies in this species had shown that both noisy conditions [12] and light intensity and spectrum [13] affect swimming patterns and spatial preferences respectively, likely through familiarity, stress, or anxiety related tendencies to engage in explorative activity. Furthermore, both male sound production [14] and male colouration during behavioural displays [15] have been shown to play a role in communication among male cichlids and in female mate choice.

2.1 Cichlid methodology

We used 40 unique pairs of cichlids from our Leiden stock at the time. These fish were three-year-old, lab-raised individuals [c.f. 14]. All recordings and behavioural observations were made in the same experimental tank (300 x 100 x 100 cm, water level at 90 cm, swimming area restricted to 200 cm, away from both ends). Housing conditions and all experimental procedures were in accordance with guidelines of the Association for the Study of Animal Behaviour and licensed by approval from the ethical committee on animal experimentation of Leiden University (licence number: UDEC 08055). Male and female cichlids within a test pair always came from different stock tanks and were unfamiliar to each other. Relatively large or small males were paired with relatively large or small females respectively, and randomly assigned to sound and light conditions. At the end of the test, fish were transferred back to the stock tank, where they resumed normal activities, and were kept alive as breeding stock.

During the experimental exposure, cichlids experience ambient sound levels at 116 dB re 1 uPa, from the ambient building conditions in the aquarium facilities at the Gorlaeus building of Leiden University. We used an ING 32mV amplifier with an MR23333-000 waterproof speaker (Knowles Electronics, Itasca, IL), in the center of the tank, 10 cm below the water surface, connected to a desktop computer for playing back sound underwater. The speaker was in the water and turned on, but not playing back any sound for the ambient sound treatment. During elevated noise conditions, we played back white noise between 500 and 2000 Hz to generate sound levels of 119 re 1 uPa, which reflects possible conditions for nearby human machinery or boat presence in natural waters. Cichlid calls center around 500 Hz, and they readily respond to playback of calls and white noise of the same frequency range and temporal pattern [14,16]. This made it likely that they would also hear the artificially elevated noise levels in the current set-up, while we would not miss any courtship calls due to masking. Bright and dark light levels in the aquarium were adjusted to 19,800 and 770 Lux, respectively (measured with a light meter and nAmp converted to Lux). The measurements and light levels corresponded with samples taken at Lake Victoria close to the surface and at 6 meters depth (~21,000 and 325 Lux) respectively (Frans Witte, unpublished data).

For the experiment, male and female were introduced in the 200 cm tank arena, on either side of an opaque divider, with a sandy bottom and a three-rock shelter on the male side. After an hour of acclimatization, the male swimming behaviour was observed and scored for 15 min, using JWatcher V6.1. After another two hours, the opaque divider between male and female was removed and we observed courtship interactions for 15 min and recorded any male calls, using an HTI 96-min hydrophone (High-Tech, Inc, Gulfport, MS), with a 20-dB amplifier, and a digital recorder (Marantz PMD 660, WAV-format, 44.1-kHz sampling rate). We analyzed our data with JMP (version 8.0) and R (version 2.10.1) statistical software. Shapiro-Wilk tests revealed that our data were not normally distributed and we applied general linear models, using a Gaussian distribution and identity link for continuous response variables (swimming and window swimming) and a Poisson distribution and log identity for count data (courtship quivers and calls). Male size caused variability, but did not affect treatment dependent patterns.

2.2 Cichlid results

General swimming behaviour of solitary males appeared to go down but was not significantly affected by sound treatment ($F = 0.09$, $p = 0.77$). In contrast, during the dark conditions the male cichlids were significantly more away from their rock shelter and swam significantly more than during the bright conditions ($F = 23.39$, $p < 0.0001$, see Figure 2). In the time swimming, they also exhibited a stereotypical window-swimming behaviour, with their noses against the glass, going up and down and left and right, usually regarded as an indication of discomfort. Of the time swimming, they swam significantly more in this mode of window swimming in noisy compared to ambient quiet conditions ($F = 4.30$, $p < 0.05$), which was not affected by light treatment ($F = 0.02$, $p = 0.88$).

Courtship behaviour of the pairs of cichlids was affect by both sound and light treatments (Figure 2). The noisy treatment yielded significantly less lateral quiver displays than the quiet treatment ($F = 5.02$, $p < 0.05$) and the bright significantly less than the dark treatment ($F = 5.20$, $p < 0.05$). As, two out of the ten pairs for the quiet and dark condition were highly active, with only modest activity for the 30 pairs in the other conditions, there also was a significant interaction ($F = 6.38$, $p < 0.02$). Vocal activity of the males was especially low for the bright conditions, and not very different for the sound treatments in the dark conditions, which yielded a non-significant effect of sound on call rate ($F = 1.66$, $p = 0.20$) and a significant impact of light on call rate ($F = 17.10$, $p < 0.0001$), and no interaction effect.

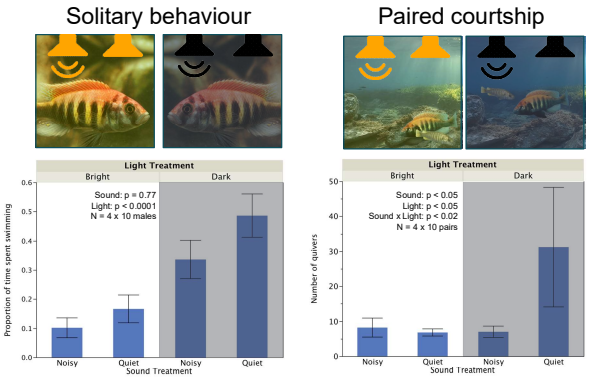


Figure 2: Multi-modal exposure experiment with *Pundamilia nyererei* cichlids. Male cichlids were exposed to playback-induced noisy conditions or ambient control conditions (2 x 2 design) and to bright or dark light conditions. Both sound and light reduced activity levels in a way: cichlids swam significantly less under bright light than dark conditions (left graph), and were involved more in window swimming under noisy than quiet conditions. When a female was introduced, modest levels of courtship where observed, except for two out of the ten pairs in the dark and quiet conditions, which were very active with quivers, and hence the significant effect of both light and sound and a significant interaction (right graph). Courtship call rate was also significantly reduced by light, not by sound.

3. EFFECTS ON SPATIAL DECISIONS

3.1 Looming and luring sound conditions

Besides the effects on activity level, anthropogenic noise and artificial light at night can also affect spatial decisions. Many studies investigated the potentially negative effects of anthropogenic noise on aquatic animals and deterrence is probably one of the most reported effects. Noise exposure level is often varying in amplitude, as vessels are for example moving, and approaching vessels may acoustically suggest a looming threat. Driving away in fear is also the focus in acoustic deterrent studies, in which responsiveness to human-made sounds is investigated as application for herding marine mammals away from fishing nets [17] or guiding fishes away from harmful pumping stations [18]. Variation in acoustic features may determine effect sizes, but typically deterrent capacity is assumed to be positively related to sound intensity (Figure 3).

However, anthropogenic sounds can also be audible and not drive animals away and even attract them out of curiosity or after experience with positive rewards when human activity underwater yields feeding opportunities. Although even loud deterrent devices like pingers have been shown to be successful in their targets at first and become a dinner bell after dolphins find out that they are associated with full nets of fish, amplitude levels of attractive sounds are likely to be relatively low amplitude (Figure 3).

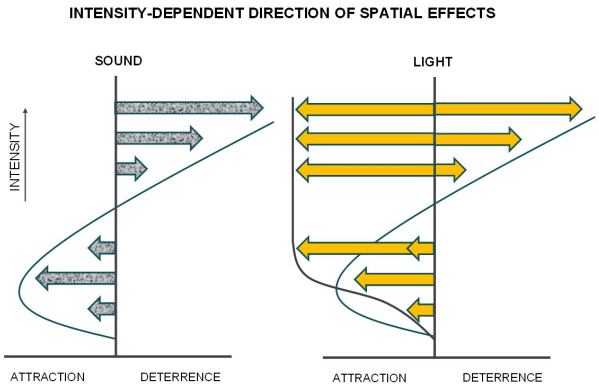


Figure 3: Generalized and schematic illustration of spatial responsiveness to sound and light relative to intensity. At low intensity, animals may just detect sound or light and become interested and be drawn towards the source. At higher intensities, this phonotactic or phototactic behaviour may get stronger, up to an optimum level at which the attractive power starts to decline again. Sound and light may also become deterrent and get stronger towards more extreme intensities. For some animal groups, intense light seems not to become aversive and phototaxis can even become stronger, persistent, maladaptive, and often fatal.

3.2 Fatal attraction: blinded by the light

The spatial effects of artificial light at night can have a similar pattern as anthropogenic noise (Figure 3). Animals with nocturnal habits or living in dark habitats typically avoid bright areas and move away from light sources. The higher the light intensity, the higher the probability of spatial deterrence. However, also at lower intensities of light, animals may be drawn towards the source out of curiosity and the explorative nature of the species or caused by positive experience with food-associated light sources. Actually, there are many examples, in contrast to sound in which the attractive effect of light does not fade with intensity. Moths and many nocturnal insects are attracted to bright lamps at night. Also migratory birds are known to be attracted to brightly lit oil platforms at sea [19] or exceptional beacons of light, such as the Tribute in light, an annual art installation at the Twin tower memorial site. The insects and birds seem to blinded by the light or at least loose the capacity to escape the light source site as long as the light is on. Another fatal attraction is found in marine turtles, where juvenile animals, just out of the egg, crawl on the beach into the wrong direction: towards lamps of coastal roads or buildings, away from the ocean which they used to find by going for the bright side with most open sky [20].

3.3 Multimodality

Given that most animals have perceptual abilities for both sound and light, they are likely to be affected by both all the time [21]. Responsiveness to playback of conspecific song may yield a different response strength depending on amplitude and other acoustic features, but may also vary between bright and dark conditions. Similarly, the response strength to a visual display of a fish during particular light conditions may be modified by ambient sound levels from nearby conspecific or heterospecific vocalizations or by the rustling of leaves in the wind. Consequently, also the effects of noisy conditions and artificial light at night will depend on multimodality. Noise and light pollution may co-occur at night, such as with passing cars or brightly lit highways or industrial areas, but each may also occur independently of each other. Noise and light pollution may have unimodal, cross-modal, and multimodal effects [21]. Multimodal effects may be in the same or opposite direction [22], with respect to stimulation or suppression of activity level and with respect to attraction or deterrence (Figure 4).

3.4 Additive and interactive effects

The co-occurrence of both anthropogenic noise and artificial light at night may yield additive effects, where the combined effect is equal to the sum of each separately (Figure 4). If the effect is in the same direction, they add up, if they are in opposite direction, they get subtracted. The effect of sound and light exposure on swimming activity in the cichlid case study suggested such an additive effect in the suppression of activity. The effect of courtship quivers seemed to be more dramatic and either of the stressors seemed to have a similar suppressive impact as the two together, although this may also be due to a bottom effect. The pattern yielded a significant interaction, as the absence

of noisy conditions was only yielding high activity levels in dark and not in bright conditions. More interactions are possible, for which there are no or limited examples available at the moment, where there may be antagonism and synergism [22], leading to variable patterns for effects in the same and different direction (Figure 4).

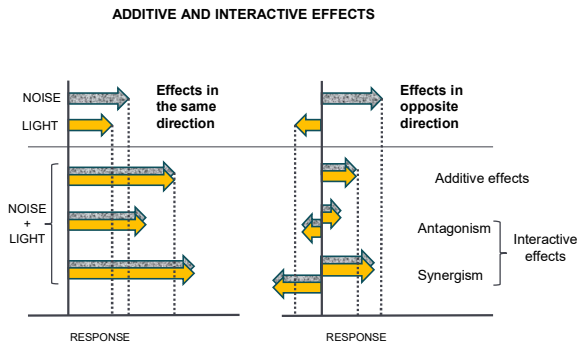


Figure 4: Spatial responsiveness to light and sound can involve attraction and deterrence, depending on the intensity (figure 2), and co-occurrence of both modalities can thus result in responsiveness into the same (left panel) or opposite direction (right panel). The combined effects of both can be additive and yield the sum or subtraction of both of the directional responsiveness. Sound and light can also interact and yield antagonistic or synergistic effects that are more complex (after [22]).

3.5 Particle motion of sound and polarized light

Sound and light can be characterized by intensity and spectrum, but there are additional features with similar aspects and consequences for animal species that can perceive these. For most aquatic invertebrates and fish, sound is perceived through the particle motion aspect of sound [23,24], which makes sound pressure level measurements less reliable in terms of exposure conditions, especially when close to boundaries with air, rock, or bottom. The sensitivity to particle motion can be extended with pressure sensitivity in case there is a gas-filled cavity such as a swim bladder. In both cases, the animals perceive directionality through the particle motion. Relative particle motion levels of a sound from a source at a particular distance and angle are dependent on ambient noise from just the same direction. Signal-to-noise ratios are therefore favorable compared to sound pressure of an unidirectionally arriving signal and omnidirectionally accumulated ambient noise. There is also a special role for polarized light for some species groups: the oscillation of the electric field vector of light can be detected by many invertebrates. Insects can for example use the polarization of light to detect water, improve visual contrast, undermine camouflage, navigate through landscapes, and even to signal during mating [25]. Many animals that also exploit the direction of light polarization as a source of information may be detrimentally affected by light that has been polarized through interaction with human-made objects, such as reflective windows at large office buildings, car window screens, or specific parts of wasted bottles [26].

4. THE CASE FOR MIGRATORY FISHES

In this final section, we would like to draw attention to migratory fish. Migratory fish provide an interesting case for studying the effect of both sounds and light in terms of activity level and spatial decisions, as done in the context of the EU Horizon-project AquaPLAN. We lack fundamental insights into the role of natural soundscapes and natural light during day and night. Furthermore, the expansion of noise and light pollution in and around aquatic habitats is spreading worldwide and may warrant the label acoustic climate change [7]. Freshwater ecosystems are among the most vulnerable in the world and the protection of especially migratory fish is a major challenge, because their decline is often caused by multiple stressors. These stressors include blockage of migratory routes, overfishing of populations, water quality changes and habitat deterioration [27].

4.1 Noisy conditions on migration

On top of the many recognized stressors, both noise and light pollution may add significant problems. The habitat of migratory fishes has been increasingly affected by anthropogenic noise worldwide, especially due to an increase in the number and size of shipping vessels [28]. Natural soundscapes are increasingly recognized as an important ecological feature of critical importance to animals [3,29]. Sounds audible to freshwater fish may include sounds of mammals, fish, frogs, and aquatic invertebrates, gas bubbles produced by aquatic plants and decomposing bacteria, but also physical disturbance of the substrate or water surface by animal or water currents and wind [28]. However, high levels of shipping and recreational activity may render the acoustic cues about the river environment inaudible and this may also be true when rivers flow through noisy urban areas. Migratory fish are therefore constantly challenged acoustically, as spatial details, temporal dynamics, and directionality of natural auditory cues can be masked and become inaccessible.

4.2 Light on short- and long-term effects

Also light pollution along rivers and coastal areas has spread worldwide. Natural light cycles are increasingly disrupted by artificial light pollution [30]. Currently, ~80% of the global population resides under light-polluted skies, and artificial sky brightness continues to rise. Artificial light at night impacts freshwater ecosystems both directly, via illuminated infrastructure like bridges and vessels, and indirectly through skyglow caused by atmospheric light scattering [31], and might disrupt specifically light-dependent biological processes such as migration. In species such as Atlantic salmon (*Salmo salar*) and European eel (*Anguilla anguilla*), artificial light at night has already been linked to various detrimental short-term and long-term effects, such as increased predation, disorientation, and delayed migration timing [32]. The alignment with the biological clock is likely to be especially vital during migration, but more studies are needed to shed a better light on problems and potential solutions.

5. CONCLUSIONS

Sound and light play an important role in the live of all animals and especially migratory fish. Sound and light conditions affect general activity levels and may influence spatial decisions. Noise and light pollution can detrimentally affect these natural processes and undermine adaptive responsiveness to the natural environment. More studies are required to gain insight into the fundamental nature of positive and negative phono- and phototaxis, both to natural and artificial conditions. Studies in captivity such as in the cichlid case study may be suitable to explore additive and interactive effects and migratory fish may provide a suitable and important model system to investigate responsiveness to experimental exposure to anthropogenic noise and artificial light at night in their natural habitat.

6. ACKNOWLEDGMENTS

HS received funding through AquaPLAN and SATURN; LD is PhD-student for AquaPLAN; DC is PhD-student for BioClock; KtV is PhD-student for SATURN. CT received funding through BioClock. AquaPLAN and SATURN are funded by the European Union, Horizon Europe, Research and Innovation Programme: grant No.101135471 (AquaPLAN) and No. 101006443 (SATURN). BioClock is funded by the Dutch Research Council (NWO) in the framework of the National Research Agenda (NWA): grant No. NWA.1292.19.077.

7. REFERENCES

[1] G. Jekely: "Evolution of phototaxis," in *Phil. Trans. of the Roy. Soc. B-Biol Sci.,* 364, pp. 2795-2808, 2009.

[2] N. Ando, Shidara, H., and H. Ogawa: "Auditory virtual reality for insect phonotaxis," in *J. of Robotics and Mechatr.,* 33, pp. 494-504, 2021.

[3] H. Slabbekoorn, and N. Bouton: "Soundscape orientation: a new field in need of sound investigation" in *Anim. Behav.,* 76, pp. 5-8, 2008.

[4] C.D. Francis, J.N. Philips, and J.R. Barber: "Background acoustics in terrestrial ecology" in *Ann. Rev. Ecol. Evol. Syst.,* 54, pp. 351-373, 2023.

[5] D.E. Nilsson: "The diversity of eyes and vision," in *Ann. Rev. Vision Sci.,* 7, pp. 19-41, 2022.

[6] D.M. Dominoni, S. Åkesson, R. Klaassen, K. Spoelstra, and M. Bulla: "Methods in field chronobiology," in *Phil. Trans. of the Roy. Soc. B: Biol. Sci.*, 372, 20160247, 2017.

[7] H. Slabbekoorn: "Noise pollution," in *Current Biology,* 29, pp. R942-R995, 2019.

[8] C.M. Duarte, L. Chapuis, S.P. Collin, D.P. Costa, S., & Harding, H. R. "The soundscape of the Anthropocene ocean," *Science,* 371, eaba4658, 2021.

[9] T. Longcore, and C. Rich: "Ecological light pollution", in *Front. Ecol. Environm.,* 2, pp. 191-198, 2004.

[10] L.F.B. Marangoni, T. Davies, T. Smyth, A. Rodriquez, M. Hamann, C. Duarte, K. Pendoley, J. Berge, E. Maggi, and O. Levy: "Impacts of artificial light at night in marine ecosystems – a review," in *Global Change Biology,* 28, 5346-5367, 2022.

[11] H. Slabbekoorn, C. May, and M.N. Verzijden: "Cichlid courtship acoustics: signals and noise influence reproductive behaviour" in A.N. Popper and A. Hawkins (eds.), *The Effects of Noise on Aquatic Life*, 407 Adv. Exp. Med. Biol. 730, DOI 10.1007/978-1-4419-7311-5_93, 2012.

[12] S. Shafiei Sabet, K. Westdorp, J. Campbell, P. Snelderwaard, and H. Slabbekoorn: "Behavioural responses to sound exposure in captivity by two fish

species with different hearing ability," in *Anim. Behav.* 116, pp. 1-11, 2016.

[13] D. Mameri, C. van Kammen, T.G.G. Groothuis, O. Seehausen, and M.E. Maan: "Visual adaptation and microhabitat choice in Lake Victoria cichlid fish" in *Roy. Soc. Open Sci.,* 6 (3), 2019.

[14] M.N. Verzijden, J. van Heusden, H. Slabbekoorn: "Sound of male Lake Victoria cichlids vary within and between species and affect female mate preferences," in *Behav. Ecol.,* 21, pp. 548-555, 2010.

[15] M.E. Maan, O. Seehausen, L. Söderberg, L. Johnson, E.A.P. Ripmeester, H.D.J. Mrosso, M.I. Taylor, T.J.M. van Dooren, and J.J.M. van Alphen: "Intraspecific sexual selection on a speciation trait, male colouration, in the Lake Victoria cichlid *Pundamilia nyererei*," in *Proc. Roy. Soc. B-Biol. Sci.,* 271, pp. 2445-2452, 2004.

[16] N. Estramil, N. Bouton, M.N. Verzijden, K. Hofker, K. Riebel, and H. Slabbekoorn: "Cichlids respond to conspecific sounds but females exhibit no phonotaxis without the presence of live males," In *Ecol. Freshw. Fish,* 23, pp. 305-312, 2014.

[17] J.V. Carretta, and J. Barlow: "Long-term effectiveness, failure rates, and ''dinner bell'' properties of acoustic pingers in a gillnet fishery," *Marine Techn. Soc. J.,* 45, pp. 7-19, 2011.

[18] M. Bomford, and P.H. Obrien: "Sonic deterrents in animal damage control – a review of device tests and effectiveness," in *Wildlife Soc. Bull.,* 18, pp. 411-422, 1990.

[19] C. Gjerdum, R.A. Ronconi, and T.E. Hamer: "Bird strandings and bright lights at coastal and offshore industrial sites in Atlantic Canada," in *Avian Cons. Ecol.,* 16 (1), 2021.

[20] M. Brei, A. Perez-Barahona, and E. Strobl: "Environmental pollution and biodiversity: Light pollution and sea turtles in the Caribbean," in *J. Environm. Econom. Managem.*, 77, pp. 95-116, 2016.

[21] W. Halfwerk, and H. Slabbekoorn: "Pollution going multimodal: the complex impact of the human-altered sensory environment on animal perception and performance," in *Bio. Lett.,* 11 (4), 2015.

[22] W. Halfwerk, and P. Jerem: "A systematic review of research investigating the combined ecological impact of anthropogenic noise and artificial light at night," in *Front. Ecol. Evol.,* 9, 2021.

[23] S.L. Nedelec, J. Campbell, A.N. Radford, S.D.Simpson, and N.D. Merchant: "Particle motion: the missing link in underwater acoustic ecology," *Meth. Ecol. Evol.,* 7, pp. 836-842, 2016.

[24] A.N. Popper, and A.D. Hawkins: "The importance of particle motion to fishes and invertebrates," in *J. Acoust. Soc. Am.,* 143, pp. 470-488, 2018.

[25] R.R. Cezário, V.M. Lopez, and R. Guillermo-Ferreira: "Polarized vision in the eyes of the most effective predators: dragonflies and damselflies (Odonata)," in *Sci. Nature,* 112 (1), 2025.

[26] G. Horváth, G. Kriska, and B. Robertson: "Polarized light pollution: a new kind of ecological photopollution," in *Front. Ecol. Environm.,* 7, pp. 317-325, 2009.

[27] K. te Velde, A. Mairo, E.T.H.M. Peeters, H.V. Winter, C. Tudorache, and H, Slabbekoorn: "Natural soundscapes of lowland river habitats and the potential threat of urban noise pollution to migratory fish," in *Environm. Poll.,* 359, 124517, 2024.

[28] M.B Kaplan, and S. Solomon: "A coming boom in commercial shipping? The potential for rapid growth of noise from commercial ships by 2030," in *Marine Policy,* 73, pp. 119–121.

[29] R.R. Fay: "Soundscapes and the sense of hearing of fishes," in *Integr. Zool.* 4, 26-32, 2009.

[30] D. Khodasevich, S.S. Tsui, and M.E. Martinez: "Characterizing the modern light environment and its influence on circadian rhythms," in *Proc. Roy. Soc. B-Biol. Sci.,* 288 (1955), 2021.

[31] F. Hölker, A. Jechow, S. Schroer, K. Tockner, and M.O Gessner: "Light pollution of freshwater ecosystems: principles, ecological impacts and remedies," in *Phil. Trans. Roy. Soc. B-Biol. Sci.,* 378 (1892), 2023.

[32] A.S. Vowles, and P.S. Kemp: "Artificial light at night (ALAN) affects the downstream movement behaviour of the critically endangered European eel, *Anguilla anguilla*," in *Environm. Poll.,* 274, 2021.

DOI: 10.61782/fa.2025.0783

FORUM ACUSTICUM EURONOISE 2025

SOUND COMMUNICATION INTERFERENCE WEIGHTING FOR TERRESTRIAL ANIMALS

Dick Botteldooren[1*] **Timothy Van Renterghem**[1] **Mike Wood**[2]
David Waddington[2] **Bill Davies**[2] **Camila Palhares Teixeira**[3] **Reinhard Klenke**[4]
[1] Department of Information Technology, Ghent University, Belgium
[2] Acoustics Research Centre, University of Salford, UK
[3] University of Minas Gerais State, Av. São Paulo Rod MG 040 URB, 3996, Ibirité - MG/Brazil
[4] Institut für Biologie Geobotanik
Botanischer Garten , Martin-Luther-Universität Halle-Wittenberg , Germany

ABSTRACT

In epidemiological research on the effects of noise on terrestrial animals (primarily birds and mammals), A-weighted sound levels are often used for convenience. However, A-weighting is based on human loudness perception and is not well-suited for this purpose. The plan-B project explored alternatives, as assessing perceived loudness across multiple species is impractical. Two alternatives used in humans are hearing level weighting and communication interference weighting. These could also be applied for terrestrial animals. The former is a conservative approach covering all sound uses, while the latter can be easily extracted from the vast database of recorded animal communications. Different weightings were applied to two-week recordings at 40 suburban and urban locations, where traffic is the dominant noise source. The Spearman correlation between 15-minute equivalent levels with different weightings was very high. Thus, for a Europe-wide assessment, the specific weighting applied may not be critical. However, for specific locations, sources, or particular (endangered) species, the chosen weighting may affect conclusions.

Keywords: *weighting curves, bird communication interference, biodiversity*

**Corresponding author*: dick.botteldooren@ugent.be.
Copyright: *©2025 Dick Botteldooren et al. This is an open-access article distributed under the terms of the Creative Commons Attribution 3.0 Unported License, which permits unrestricted use, distribution, and reproduction in any medium, provided the original author and source are credited.*

1. INTRODUCTION

The effects of noise on terrestrial biodiversity have become a critical area of ecological research. Anthropogenic noise, stemming from urbanization, industrial activities, and transportation, poses a significant threat to the persistence of many species [1] [2]. Studies have shown that noise pollution can influence physiology [3], increase costs of communication, and disrupt various biological functions, leading to changes in species interactions and altering community structures [4] [5].

Sound plays vital roles in the lives of many organisms, similar to its functions in humans. It serves as a tool for passive monitoring, enabling situational awareness by detecting danger, confirming safety, and identifying opportunities for food and water. Additionally, sound facilitates active communication, essential for mate finding, establishing territorial boundaries, and sharing experiences. However, task-irrelevant sounds can interfere with these primary functions, causing masking effects or making auditory scene analysis more challenging.

To measure the interference caused by noise, various strategies have been developed. One approach focuses on what can be heard being disturbing, while another emphasizes the impact on active communication. In humans, the former approach led to the adoption of A-weighting, a method that adjusts sound measurements to reflect the relative loudness perceived by the human ear [6]. Historically, speech interference weighting has also been used to assess how background noise affects speech communication.

This study investigates the potential to calculate com-

munication interference weights for terrestrial animals using analysis of recordings in 1/3 octave band spectra. By clustering these spectra, we can decrease the diversity of variants and simultaneously exclude recordings contaminated by extraneous sounds. In Section 3, the derived weighting curves are utilized on a variety of noise recordings from suburban and urban areas, while Section 4 provides a discussion of our key results.

2. DERIVING SOUND COMMUNICATION INTERFERENCE WEIGHTING

For deriving communication interference a representative amount of bird sounds had to be collected. For this, we used one of the primary sources for bird song recordings, Xeno-canto, a collaborative website dedicated to sharing wildlife sounds from around the world. For deriving a weighting curve, only the spectral content of the song is relevant. Hence, 1/3 octave band spectra are calculated for each recording and normalized to obtain an rms-value of one for the highest 1/3 octave band while ignoring temporal structure.

However, several bird species produce songs with comparable spectra. This similarity can be explored to reduce the number of weighting curves that one could obtain. Hence, the spectra in the frequency range 160 Hz to 10000 Hz were mapped to two dimensions using UMAP (Uniform Manifold Approximation and Projection) [7] and subsequently clustering based on DBSCAN(Density-Based Spatial Clustering of Applications with Noise) [8] was applied. This procedure also allows to identify outlier spectra that could be caused by noisy recordings. the resulting mapping to two dimensions is shown in Figure 1. In this figure, different symbols refer to automatically identified clusters while colors are related to species. The prevalence of species in each cluster is further analyzed in Figure 3.

Figure 2 illustrates the mean spectral data grouped by bird clusters, revealing three prominent classifications: the extensively populated cluster 5 along with its numerous variants, cluster 4, and cluster 0. As depicted in Figure 3, cluster 5 and its variants encompass recordings of songbirds, cluster 0 is characterized by doves and pigeons, while cluster 4 includes species such as the mallard, grey heron, Eurasian jay, Eurasian coot, and common buzzard. The birds in this last group utilize vocalizations not for marking territories but for interactions such as mutual communication, signaling danger, or expressing aggression. Notably, the coot is recognized for its high-pitched

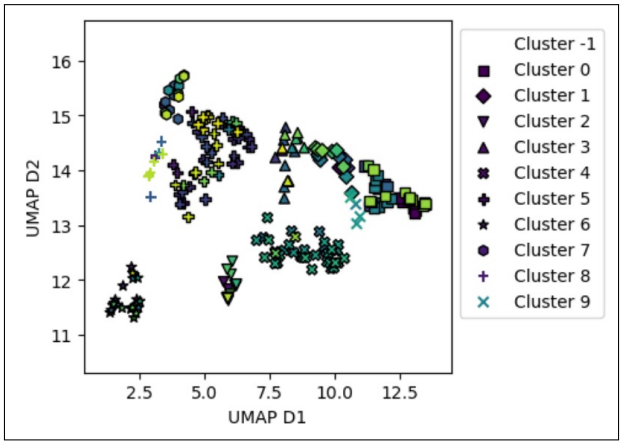


Figure 1. Clusters of bird song spectra based on 250 recordings from 25 bird species, mapped in 2 dimensions.

vocalizations at elevated pressure levels. A shared feature within this group may be their body size, which influences the ability to produce sound at lower frequencies [9]

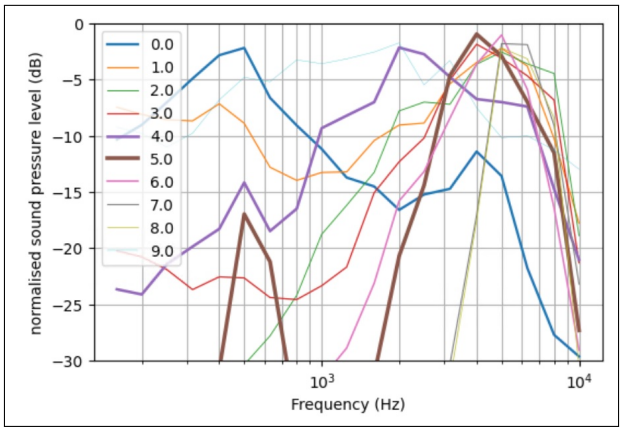


Figure 2. Song spectra averaged over each cluster; line width is proportional to the number of exemplars in the cluster thus thinner lines may refer to clusters of noisy or poor quality measurements.

Based on the communication spectra, three different weighting curves are proposed: CI1, CI2, CI3 (Figure 4). They are described by analytical functions similar to the ones used for describing A, B, and C-weighting. These functions correspond to filters with sets of complex conjugate poles and zeros, and can thus be implemented easily

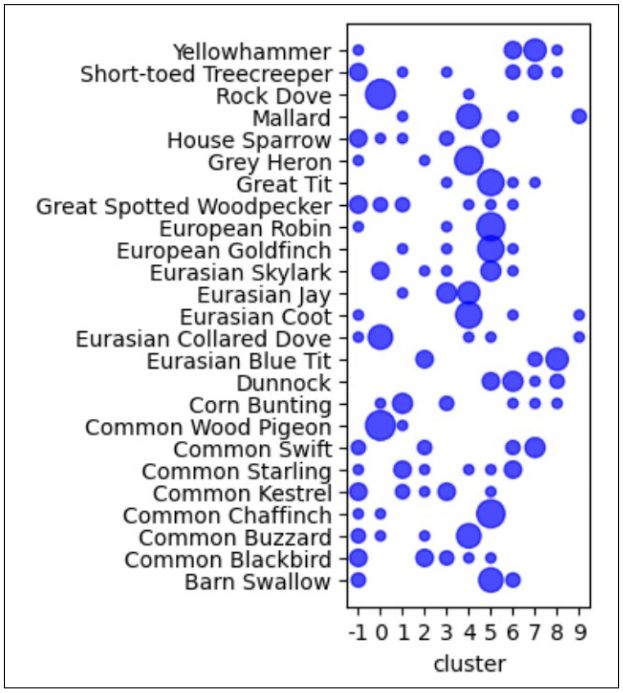


Figure 3. Distribution of the species over the clusters; the size of the circle is proportional to the number of recordings of that species in that cluster; cluster -1 refers to recordings that do not fall in one cluster

in measurement equipment.

3. INTERFERENCE WEIGHTED NOISE LEVELS

3.1 Effect of weighting on biodiversity surveys

To investigate how the selection of weighting curves could influence large-scale biodiversity studies, this research compares 15-minute equivalent noise levels using both A-weighting and CI-weighting. Approximately two weeks of data were gathered from 40 sites within the broader Ghent (Belgium) area. Each measurement was taken at the facade of a building, with environments varying from suburban to urban.

In Figure 5, a scatter plot is depicted illustrating the comparison between A-weighted and CI1-weighted levels (for songbirds) and A-weighted and CI2-weighted levels (for doves). To assess the monotonic relationship within these data points, we have determined Spearman's correlation coefficients: 0.898 for A-weighted vs. CI1-

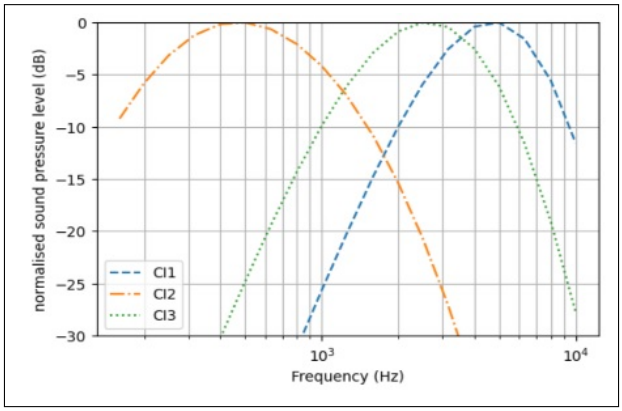


Figure 4. Communication Interference weighting curves proposed for three groups of bird species.

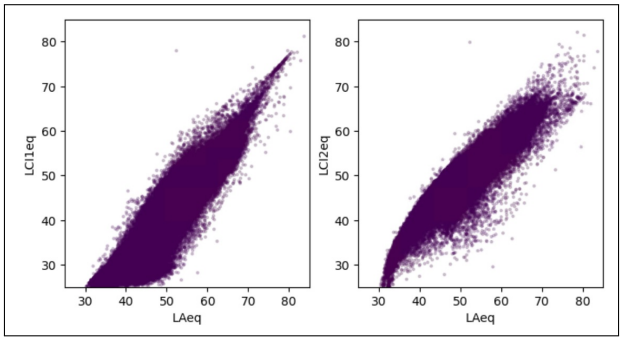


Figure 5. Scatter plot of 15-minute CI1 and CI2 weighted Leq versus A-weighted Leq; each dot represents a single observation at any time during the day at any of the 40 locations.

weighted, 0.928 for CI2-weighted, and 0.965 for CI3-weighted. The substantial correlation values suggest that on a broad scale, such as biodiversity surveys across an entire continent, using existing A-weighted noise maps could be an acceptable approach, particularly given the prevalence of anthropocentric noise mapping. With traffic being a primary contributor to anthropogenic sounds, especially in the suburban and urban areas examined here, either weighting scheme would indeed effectively highlight these human-induced auditory disturbances.

3.2 Temporal patterns

When examining specific situations, communication interference weighting can highlight differences between

recording sites. Figure 6 illustrates the effect of weighting by comparing measurements at two suburban gardens. At the first measurement location (until day 115), the CI1-weighted levels exhibit a pattern over the day that is clearly influenced by the light/dark cycle. On certain days (depending on the weather), the CI1-weighted level shows a distinct increase in the early morning, linked to the morning bird chorus, which is the primary communication interference for songbirds. This pattern is not as evident in the A-weighted level plot (left part of the figure). At the second location (after day 115), a clear diurnal anthropogenic noise pattern is visible in A-weighted levels, including typical daily and weekly variations. The CI1-weighted level shows a more uniform pattern throughout the day. Interestingly, the highest CI1-weighted levels at this second location are lower than the levels observed during the morning chorus at the first location.

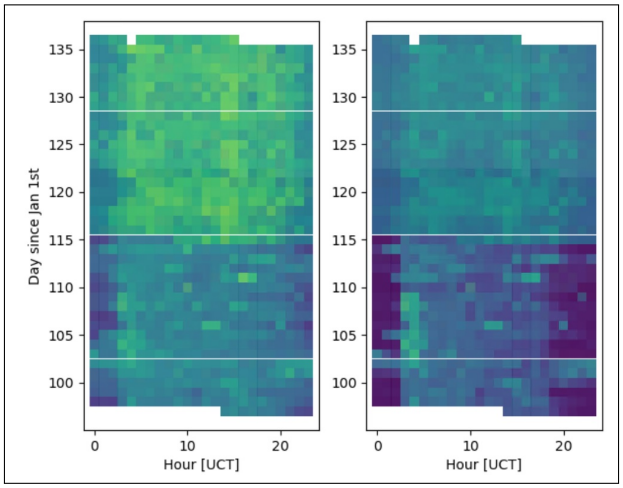


Figure 6. Heat map of noise levels at two suburban gardens (location change on day 115); left: A-weighted, right: CI1-weighted.

4. DISCUSSION

Communication interference weighting curves extracted in this publication are extracted from recordings of the communication of several bird species. These species were selected based on their estimated abundance in Belgium, hence the resulting weighting curves might not be applicable in different climatological zones and different continents. The database used for collecting the sounds was Xeno-canto. This sound collection contains contributions from lay persons and is not carefully checked for origin of the data nor the recording conditions are carefully checked. It can be expected that most recordings originate from suburban neighborhoods and thus song bird frequencies may already have been shifted to higher frequencies because of the presence of anthropogenic sounds [5].

The importance of appropriate frequency weighting is explored based on measurements in the Ghent area, Belgium. Belgium is situated at the crossroads of Europe, with two major roads, E40 and E17, intersecting near Ghent. Several air corridors pass over the measurement area, and although the nearest airport is 60 km away, aircraft noise is often clearly audible in the more tranquil areas. Within this context, and considering measurements at different hours of the day, a monotonous relationship was observed between A-weighted levels and CI-weighted levels. Thus, at times and locations with significant noise, whether anthropogenic or natural, a high noise level will be obtained regardless of the weighting. From this, one could conclude that for identifying zones with high disturbance, A-weighting might still be an acceptable alternative for assessing effects of noise on wildlife and biodiversity, even though it lacks a logical foundation. Although we would not advise doing so, it could be a cost-effective alternative for lengthy calculations when A-weighted noise maps are available.

More detailed analysis of the diurnal pattern of CI1-weighted noise level reveals the relative importance of other bird sounds compared to anthropogenic noise. Indeed, not only anthropogenic environmental noise has to be considered as a source of disturbance but also natural soundscapes can be noisy because of wind, waves, or other species, e.g. such as frogs [10]. Animals have adapted to noisy environments by selecting a specific window of opportunity for singing. This can include optimal meteorological conditions for acoustic transfer [11], diurnal pattern of other bio-phonic sounds, or waiting for a specific short time window [12]. Based on the above, one could expect that some birds have the ability to select optimal singing strategies to avoid anthropogenic noise as well as bio-phonic sound. Literature on birds adapting their singing behavior to urban sound environment [3] has gained a lot of attention, also in lay literature. Some experimental work is not so univocal [13] and point at the role of overlapping spectra. Observed pitch changes might not be the adaptive strategy but rather a side effect of singing louder in noisier environment [14], comparable to the Lombard effect in humans.

As a general conclusion, both theoretical considera-

tions and measurement examples show that using a specific weighting curve for assessing communication interference in animals could be beneficial. This could allow for a more targeted impact assessment of new initiatives and interventions, in particular if the species of interest are known. This could also lead for more efficient noise mapping as the frequency range that needs to be modeled is usually less extended than for human-related A-weighting. Hence, for new biodiversity-related noise mapping the use of CI-weighting should be preferred.

5. ACKNOWLEDGMENTS

This study is part of the PLAN-B project "The Path Towards Addressing Adverse Impacts of Light and Noise Pollution on Terrestrial Biodiversity and Ecosystems', funded by the European Union under the Horizon Europe program (project n°101135308). We would like to thank Andreas Van Ranst, Audric De Backer, and Louis Peirs, Engineering Physics students at Ghent University for their help in collecting and processing data.

6. REFERENCES

[1] R. Sordello, O. Ratel, F. Flamerie De Lachapelle, C. Leger, A. Dambry, and S. Vanpeene, "Evidence of the impact of noise pollution on biodiversity: A systematic map," *Environmental Evidence*, vol. 9, pp. 1–27, 2020.

[2] M. M. Sander and D. T. Tietze, "Impacts of traffic infrastructure on urban bird communities: A review," *Sustainability*, vol. 14, no. 24, p. 16805, 2022.

[3] R. Amjad, T. Ruby, K. Ali, M. Asad, A. Imtiaz, S. Masood, M. Q. Saeed, M. Arshad, S. Talib, Q.-t. A. Alvi, A. Khan, and M. M. Sharif, "Exploring the effects of noise pollution on physiology and ptilochronology of birds," *PLOS ONE*, vol. 19, p. e0305091, June 2024.

[4] A. Kok, B. Berkhout, N. Carlson, N. Evans, N. Khan, D. Potvin, A. Radford, M. Sebire, S. Shafiei Sabet, G. Shannon, *et al.*, "How chronic anthropogenic noise can affect wildlife communities. front ecol evol. 2023; 11: 1130075."

[5] Z. Hao, C. Zhang, L. Li, B. Gao, R. Wu, N. Pei, and Y. Liu, "Anthropogenic noise and habitat structure shaping dominant frequency of bird sounds along urban gradients," *Iscience*, vol. 27, no. 2, 2024.

[6] D. S. Houser, W. Yost, R. Burkard, J. J. Finneran, C. Reichmuth, and J. Mulsow, "A review of the history, development and application of auditory weighting functions in humans and marine mammals," *The Journal of the Acoustical Society of America*, vol. 141, no. 3, pp. 1371–1413, 2017.

[7] L. McInnes, J. Healy, and J. Melville, "Umap: Uniform manifold approximation and projection for dimension reduction," *arXiv preprint arXiv:1802.03426*, 2018.

[8] E. Schubert, J. Sander, M. Ester, H. P. Kriegel, and X. Xu, "Dbscan revisited, revisited: why and how you should (still) use dbscan," *ACM Transactions on Database Systems (TODS)*, vol. 42, no. 3, pp. 1–21, 2017.

[9] J. I. Friis, J. Sabino, P. Santos, T. Dabelsteen, and G. C. Cardoso, "The allometry of sound frequency bandwidth in songbirds," *The American Naturalist*, vol. 197, no. 5, pp. 607–614, 2021.

[10] H. C. Gerhardt, "Sound pressure levels and radiation patterns of the vocalizations of some north american frogs and toads," *Journal of Comparative Physiology*, vol. 102, no. 1, pp. 1–12, 1975.

[11] A. Guibard, F. Sèbe, D. Dragna, and S. Ollivier, "Influence of meteorological conditions and topography on the active space of mountain birds assessed by a wave-based sound propagation model," *The Journal of the Acoustical Society of America*, vol. 151, no. 6, pp. 3703–3718, 2022.

[12] L. M. Chronister, T. A. Rhinehart, and J. Kitzes, "When birds sing at the same pitch, they avoid singing at the same time," *Ibis*, vol. 165, no. 3, pp. 1047–1053, 2023.

[13] E. Bermúdez-Cuamatzin, M. López-Hernández, J. Campbell, I. Zuria, and H. Slabbekoorn, "The role of singing style in song adjustments to fluctuating sound conditions: a comparative study on mexican birds," *Behavioural processes*, vol. 157, pp. 645–655, 2018.

[14] E. Nemeth and H. Brumm, "Birds and anthropogenic noise: are urban songs adaptive?," *The American Naturalist*, vol. 176, no. 4, pp. 465–475, 2010.

DOI:

Main theme: A02 Bio-acoustics

Session A02.07 AI and machine learning in bioacoustics

Chair(s): Y. Jadoul, V. Lostanlen

DOI:

Main theme: A03 Building Acoustics

Session A03.01 Building acoustics - General

Chair(s): A. Romero, C. Scrosati, T. Carrascal, C. Monteiro

DOI: 10.61782/fa.2025.0901

FORUM ACUSTICUM EURONOISE 2025

TOWARDS A SIMPLIFIED PERIODIC TESTING OF TAPPING MACHINES

Volker Wittstock [1*] **Sylvia Stange-Kölling** [1] **Kevin Picker** [1]
Heinrich Bietz [1]
[1] Physikalisch-Technische Bundesanstalt, 38116 Braunschweig, Germany

ABSTRACT

ISO-tapping machines are used as a standardised excitation when measuring impact noise. It is required that 5 hammers with a mass of 500 g each impact the floor at a velocity of 886 mm/s at time intervals of 0.1 s. There are several other requirements like the distance between the hammers, the hammer diameter and the radius of the impact surface of the hammer. These requirements are today defined in different international standards but there is an activity ongoing to develop a new standard ISO/PWI 21791 "Acoustics – Sound sources for building acoustics" which shall also cover the testing of tapping machines.
The current standards prescribe that some of the parameters have to be measured only once like the distance between the hammers whereas other parameters shall be checked regularly like the velocity at impact and time between impacts.
The contribution introduces an alternative periodic test of ISO tapping machines which is based on a simultaneous measurement of the acting force at each of the five hammer positions. Results of test measurements are presented and conclusions with respect to the applicability of such a method are derived.

Keywords: *tapping machine, blocked force, direct force measurement*

[*] ***Corresponding author**: volker.wittstock@ptb.de*
***Copyright**: ©2025 Volker Wittstock et al. This is an open-access article distributed under the terms of the Creative Commons Attribution 3.0 Unported License, which permits unrestricted use, distribution, and reproduction in any medium, provided the original author and source are credited.*

1. INTRODUCTION

It has been agreed that a new standard ISO/PWI 21791 "Acoustics – Sound sources for building acoustics" is developed. This standard shall contain all information for different types of sound sources used for measurements in building acoustics which are currently described in the different standards. Possible extensions to the currently standardised situation are also discussed. One of these possible extensions is a simplified method for a periodic testing of tapping machines. The motivation for this is that the verification of the current requirements for tapping machines is laborious, which may be one of the reasons why periodic testing of tapping machines is avoided quite often.

2. FORCE EXERTED BY TAPPING MACHINES

A straightforward way of testing tapping machines is to measure their force directly and to compare this to a required force. This leads directly to the question how large the force of a tapping machine should be.
Starting point to answer this question is the blocked force level $L_{F,\mathrm{b}}$ of a tapping machine. It could be shown in [2] that this can be described by a sum of two terms

$$L_{F,\mathrm{b}} = L_{F,\mathrm{b},1} + \Delta L_{F,\mathrm{b}} \tag{1}$$

Here $L_{F,\mathrm{b},1}$ is the level of the blocked force when each hammer impacts the receiver only once in each cycle. It is calculated from

$$L_{F,\mathrm{b},1} = 20\,\mathrm{lg}\left[\frac{m\,v_{\max}\,(1+k)}{F_0}\sqrt{\frac{2\,(10^{1/20}-10^{-1/20})\,f}{T}}\right]\mathrm{dB} \tag{2}$$

with the hammer mass m, the velocity at impact $v_{\max}$, the restitution coefficient k, the reference force $F_0 = 10^{-6}$ N, the centre frequency of the one-third octave band f and the time between impacts T. The second summand $\Delta L_{F,\mathrm{b}}$

in eq. (1) is the increase of the force level due to double or triple impacts. It is

$$\Delta L_{F,\mathrm{b}} = \begin{cases} 10\,\mathrm{lg}\,[1+k^2+k^4]\,\mathrm{dB} & \text{for } k<k_1 \\ 10\,\mathrm{lg}\,[1+k^2]\,\mathrm{dB} & \text{for } k_1<k<k_2 \\ 0\,\mathrm{dB} & \text{for } k>k_2 \end{cases} \quad (3)$$

with

$$k_1 = -0{,}5 + \sqrt{0{,}25 + \frac{t_{\mathrm{lift}}\, g}{2\sqrt{2\, g\, h}}} \quad (4)$$

and

$$k_2 = \frac{t_{\mathrm{lift}}\, g}{2\sqrt{2\, g\, h}} \quad (5)$$

In eqs. (4) and (5), g is the gravitational acceleration, h is the hammer falling height and t_{lift} is the time between impact and lift of the hammer. The standard [1] requires that t_{lift} is smaller than 80 ms. This ensures that $\Delta L_{F,\mathrm{b}}$ is smaller than 0.8 dB [2].

For a mobility mismatch situation, i.e. the hammer mobility is sufficiently large compared to the receiver mobility, the exerted force is equal to the blocked force of a tapping machine. Then equations (1) to (5) clearly show that the force exerted by tapping machines depends on the required quantities of the current standard [1] (hammer mass, hammer impact velocity, time between impacts) but also on additional quantities, namely the restitution coefficient and the occurence of double or triple impacts. These additional quantities are not known and can not be predicted easily [2].

3. TEST MEASUREMENTS

To test a direct measurement of the force of tapping machines, a brass plate with five force sensors [2] is used. The hammers of the tapping machine hit directly on the force sensors. Six different tapping machines are used. Prior to the measurements, their properties (impact velocity, time between impacts) had been tested. Five tapping machines were within the specifications from [1], one tapping machine revealed an impact velocity which was too small. For the force sensors, the sensitivity provided by the manufacturer is used.

Fig. 1 shows the difference between the measured force level and the calculated blocked force level for five hammers of one tapping machine. The measurement has been performed three times. Between the measurements, the tapping machine was dismounted and remounted, in some cases several days were between the measurements. The result of the second measurement is shifted by -1 dB and the results of the third measurement by -2 dB for a better graphical representation. For the comparison, the restitution coefficient is set to 0.65 and $\Delta L_{F,\mathrm{b}}$ to 0. The impact velocity, the time between hammer impacts and the hammer mass are set to the default values from the standard. This input for the calculation of the blocked force level is the same for all tapping machines. The measured force levels are close to the calculated blocked force level for all five hammers between 20 Hz and 1 kHz. At higher frequencies, the measured force levels become smaller than the calculated blocked force level due to the mobility ratio [2]. In all three measurements, a certain pattern is observed. Hammer 3 always exhibits the largest force, hammer 1 always the smallest.

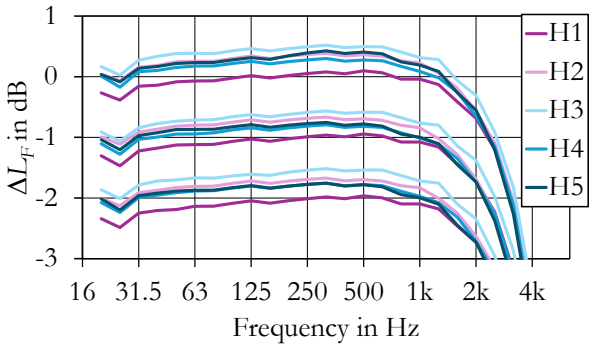


Figure 1. Difference between the measured force level and the calculated blocked force level for five Hammers of a tapping machine; Measurements were repeated three times and the results shifted by -1 dB (second measurement) and -2 dB (third measurement) for better visibility.

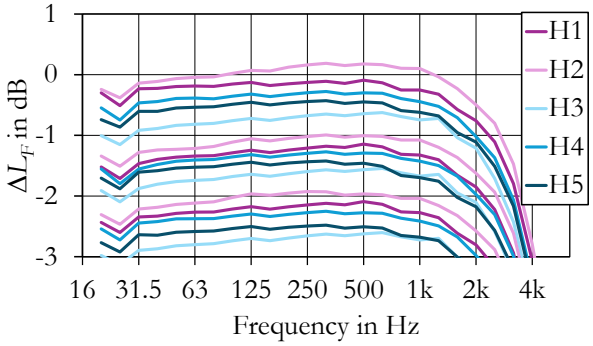


Figure 2. Same as Fig. 1 but different tapping machine.

The observed pattern may suggest that the sensitivity of the force sensors may show some systematic deviation. Fig. 2 proves that this is not the case since the pattern is very

different for another tapping machine. The reason is probably that the restitution coefficient is not identical for different tapping machines. In [2], a standard deviation of the restitution coefficient of about 10 % had been observed when different tapping machines act on the same position of the same receiver.
It is now interesting to see which force is measured for the tapping machine where the impact velocity was too small. This result is displayed in Fig. 3. Hammer 1 clearly shows a much smaller force than the other hammers.

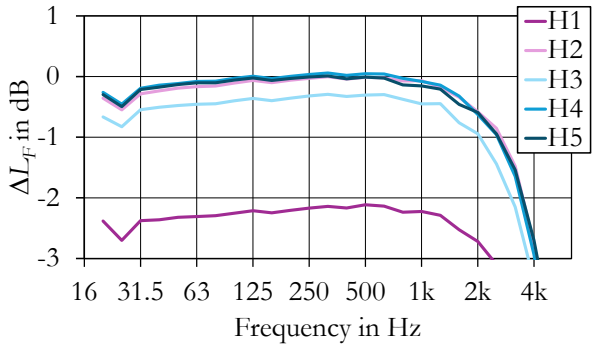


Figure 3. Same as Fig. 1 and Fig. 2 but tapping machine not complying to the specifications from [1] and no repeated measurement shown.

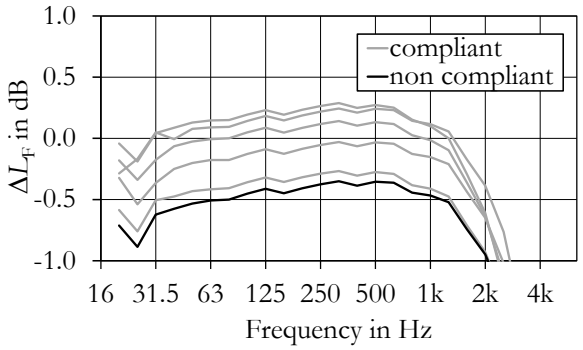


Figure 4. Deviation between the measured force level and the calculated blocked force level averaged over all five hammers for the six tapping machines tested.

Finally, the differences of the measured force levels to the calculated blocked force levels were averaged for the five hammers of one tapping machine. This result is shown in Fig 4. At frequencies from 50 Hz to 1 kHz, this difference is between -0.5 dB and 0.3 dB for the tapping machines complying to the standard requirements. For the tapping machine not complying to the standard requirements, this difference is only slightly larger. The reason is that only one out of five hammers has a much smaller force level which is largely compensated by the averaging over 5 hammers.

4. CONCLUSIONS

A periodic testing of tapping machines by measuring their force levels seems to be possible. An application of a criterion for each single hammer and for the average of all five hammers seems to be appropriate. It is essential for the method that the occurring restitution coefficients are determined, possibly by a set of tapping machines which are known to meet the requirements from [1]. Before such a method can be standardised, further investigations need to be performed, e.g. on the reproducibility of the results and on the uncertainty of the measured force levels compared to the uncertainty of the calculated blocked force level.

5. REFERENCES

[1] ISO 10140-5:2021 Acoustics — Laboratory measurement of sound insulation of building elements, Part 5: Requirements for test facilities and equipment.

[2] V. Wittstock, H. Bietz, and M. Schmelzer: The influence of the restitution coefficient and multiple impacts on the force exerted by ISO tapping machines, *Acta Acustica*, 2025, 9, 14

DOI: 10.61782/fa.2025.0852

FORUM ACUSTICUM EURONOISE 2025

TESTING THE HEAVY SOFT IMPACT SOURCE AT PTB: SETUP, CALIBRATION AND UNCERTAINTY

Kevin Picker [1*] **Volker Wittstock** [1] **Michael Kobusch** [1]
[1] Physikalisch-Technische Bundesanstalt (PTB), Bundesallee 100, D-38116 Braunschweig, Germany

ABSTRACT

The heavy soft impact source is a rubber ball with a mass of 2.5 kg which is used as a standard device to excite floor constructions. This device is dropped from a height of 1 m in the source room, and the maximum sound pressure level is measured inside the receiving room either in one-third octave bands from 50 Hz to 630 Hz or in octave bands between 63 Hz and 500 Hz. The A-weighted sum of these values together with some corrections for reverberation time and room volume is finally used to assess the acoustic insulation against impact noise.
From a metrological point of view, the rubber ball is an absolute standard. Its properties are defined mainly by the force exerted on a hard receiver in octave bands between 31.5 Hz and 500 Hz. At PTB, a new facility for testing rubber balls was set up to measure this force. In the contribution, the setup is described, the calibration of the force sensor by a calibrated impact hammer is explained and a first estimate of the measurement uncertainty is derived.

Keywords: *heavy soft impact source, ball impact, dynamic force measurement, in-situ calibration, uncertainty estimation.*

1. INTRODUCTION

There are two standards, [1] and [2], which describe the measurement of sound insulation in buildings or laboratories. In both standards there are proposals for at least two impact sources and the characteristics or requirements of those. One is the tapping machine, which is the more commonly used device for measurements according to the named standards in Europe. However, the heavy soft impact source is gaining attention more and more. It is discussed whether this source can simulate certain everyday situations, such as jumping children and dropping objects, better than the tapping machine.
At PTB, a test setup for tapping machines already exists, but due to increasing interest a test setup for the heavy soft impact source is also required.

2. MEASUREMENT SETUP

The measurement setup at PTB consists of a force sensor mounted on a heavy base mass, and both are placed on a concrete floor (Figure 1). The force sensor is attached to the base mass via an adapter plate, and an aluminium impact plate measuring 100 mm in diameter is mounted at the top using a second adaptor.

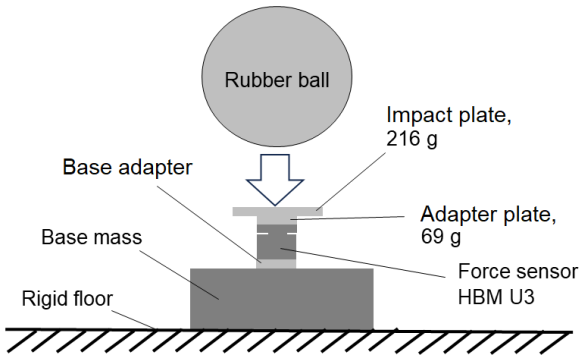


Figure 1. Measurement setup for impact forces.

Thanks to a wall-mounted spacer (not shown in Figure 1), the ball to be tested can be dropped onto the centre of the impact plate from a height of 1 m with good repeatability.

[*] ***Corresponding author***: *kevin.picker@ptb.de.*
Copyright: *©2025 First author et al. This is an open-access article distributed under the terms of the Creative Commons Attribution 3.0 Unported License, which permits unrestricted use, distribution, and reproduction in any medium, provided the original author and source are credited.*

The strain gauge force sensor is connected to a bridge amplifier before the input signal is fed into a measurement unit for further analysis.

3. CALIBRATION OF THE SETUP

The force measurement setup was calibrated in-situ by applying several hammer strokes (approx. 25) with a traceably calibrated impact hammer of a head mass of 500 g. The method of the in-situ dynamic force calibration by means of an impact hammer (see Figure 2) is described in [3].

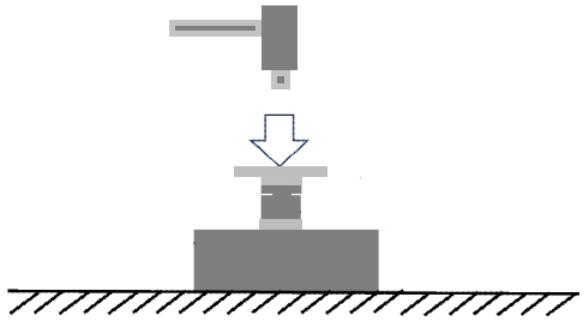


Figure 2. Calibration of the measurement setup with an impact hammer.

The measurements were made with three hammer tips of different stiffness (soft, medium, hard), and the force spectra for the hammer and force sensor were analyzed in octave bands from 31.5 Hz to 500 Hz. The calibrated sensitivity of the considered hammer tip configuration was also determined in the frequency domain. Therefore, the respective sensitivity S_{cal} of the force measurement setup could be calculated.
In Figure 3, the deviation ΔL_{S} from the nominal sensitivity S_{nom} is visualized. The average of the frequency-dependent sensitivity was used to scale the measured time signals. However, it became clear that it makes a difference which hammer tip is used.

$$\Delta L_{\mathrm{S}} = 20\,\mathrm{lg}\frac{S_{\mathrm{cal}}}{S_{\mathrm{nom}}}\ \mathrm{dB} \tag{1}$$

For better estimation, the difference between the individual values and the nominal sensitivity was determined in dB according to Equation (1). The nominal sensitivity for the measuring chain of force sensor and bridge amplifier is 0.1 mV/N. For the octave bands up to 250 Hz, the sensitivity differences between different hammer tips are below ± 0.2 dB and show a smooth shape. This changes at 250 Hz, as the differences with all the tips become larger. Hirakawa et al. made a similar discovery in their work [4] (Page 5, Figure 7). They were using only a hard hammer tip to calibrate their setup, but the difference is also getting larger with increasing frequencies. At 500 Hz the difference is about 1 dB in [4]. It is assumed that the impulse generated by the hammer no longer produces a force that is sufficiently large compared to the noise at these frequencies. This applies more to softer tips than to harder ones.

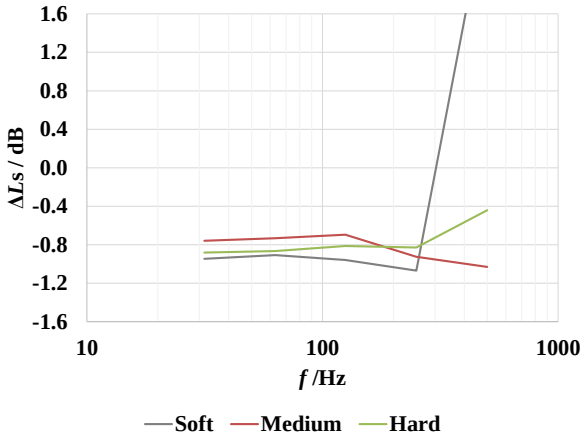


Figure 3. Calibrated sensor sensitivity for different hammer tips in octave bands.

$$u_{\mathrm{cal}} = 20\,\mathrm{lg}\left(1+\frac{\sigma}{S_{\mathrm{cal}}}\right)\ \mathrm{dB} \tag{2}$$

Finally, the uncertainty for the sensitivity of the force measurement setup was estimated according to formula (2) from the experimental standard deviation σ of repeated hammer impacts (Figure 4), which is 0.2 dB at the lower octave bands and increases towards higher octave bands for the medium and soft hammer tips. The variations in sensitivity due to different hammer tips shown in Figure 3 are well covered by this estimated uncertainty.

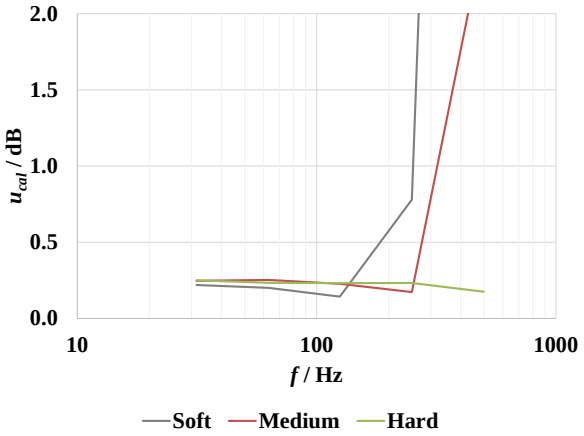


Figure 4. Estimated uncertainty of the sensitivity of the force measuring setup.

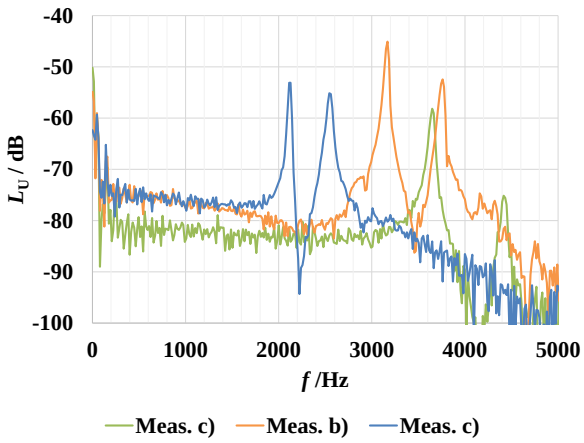


Figure 5. Sensor response for different mass loads.

4. TEST MEASUREMENTS

4.1 Sensor response

The aluminium impact plate and adapter mounted on the force sensor are required to enable impact measurements with the dropping ball. However, these components provide additional mass that acts on the sensor element and changes its dynamic response. This effect was investigated by measuring the pulse response of the force sensor using different mass loads. A narrowband spectrum was measured for the following mechanical configurations:

a) Force sensor without mass load
b) Force sensor with upper adapter plate (69 g)
c) Force sensor with adapter and impact plate (mass 285 g)

The results can be seen in Figure 5. All three narrowband spectra exhibit two resonances, which are shifted towards lower frequencies with increasing mass. However, these resonances should not have any significant influence on the octave band analysis, as these are well below 2 kHz.

4.2 Time signals of ball drops

A series of test drops with three rubber balls was performed (Table 1). Ball 3 is a prototype that is about 30 years old, while the two other balls are newer types that can be purchased today. Also, ball 3 is slightly heavier than the other two balls. Each ball was dropped ten times onto the force measuring setup and the time signals were recorded (Figures 6 to 8).

Table 1. Mass values of the rubber balls under test.

	Ball 1	Ball 2	Ball 3
m / kg	2.448	2.364	2.589

The time signals of balls 1 and 2 have more in common than those of ball 3: their pulse shape is similar, the force reaches a peak value of around 1.6 kN, and the pulse duration is around 20 ms for both balls. Ball 3 generates impacts with a considerably larger peak force, more than 3.5 kN, and the duration here is approximately 10 ms.

Another aspect can be seen in all time signals. The force pulses exhibit a superposed wavy disturbance, especially on the rising slope. To estimate the frequency of this ripple, the time interval between two maxima or minima was determined. The values show that we deal with the resonances of the system previously presented in Figure 5c), which occur in the range from 2 kHz to 3 kHz. The same effect can actually be observed in the pulse curves shown in the standards [1] and [2], or in similar studies with other force sensors [4].

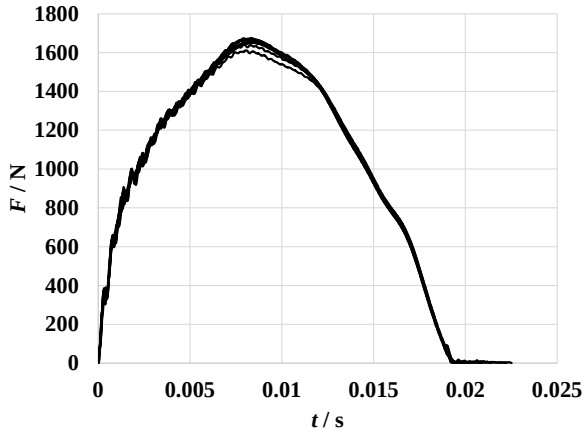


Figure 6. 10 force pulses obtained with ball 1.

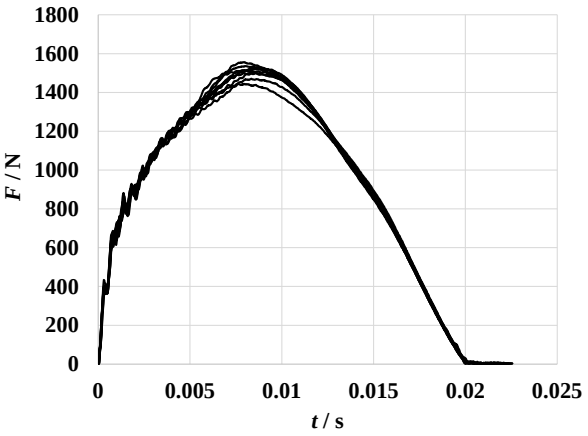


Figure 7. 10 force pulses obtained ball 2.

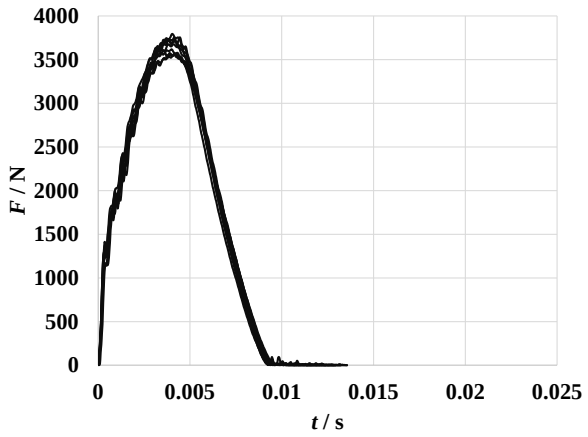


Figure 8. 10 force pulses of obtained with ball 3.

4.3 Integration time for octave band measurement

The ball impacts have a duration of up to 20 ms. However, the main criterium for the validation of a heavy soft impact source is the impact force exposure level measured in octave bands. Depending on the filter centre frequency f, the filters require a settling time depending on $1 / B$ with a bandwidth of $B = f / \sqrt{2}$. It is therefore necessary to investigate which integration time is appropriate.

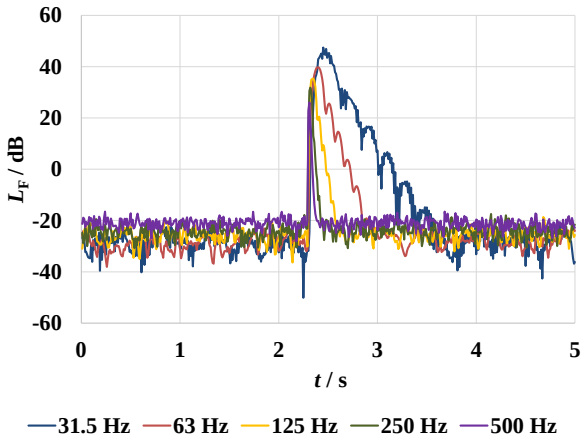


Figure 9. Force levels over the measurement time for different octave bands.

For one ball drop, the time history of the octave bands was measured for a duration of 5 s. Figure 9 shows the time history of the filter output for five octave bands. With increasing frequency, the filters need less time to process the impact. While the lower bands require more time, this will be a disadvantage for the higher bands, as the amount of noise increases. This is illustrated in Figure 10. Here, the impact force exposure level $L_{F,E}$, according to Equation (3), is shown as a function of the integration time T_{av} for each octave band. The data in Figure 9 has been split so that the pre-impact part of the measurement is included in the analysis as background noise (dashed, shorter curves). An integration time of less than 50 ms results in distorted impact force exposure levels for the lowest frequency bands; for all octave bands above 63 Hz, the levels reach a constant value more quickly. Again, the noise curves show that the influence of noise increases with integration time. For example, for the highest octave specified in the standard at 500 Hz, the SNR is approx. 24 dB.

$$L_{\mathrm{F,E}} = L_{\mathrm{F}} + 10\,\mathrm{lg}\left(\frac{T_{\mathrm{av}}}{T_{\mathrm{ref}}}\right)\ \mathrm{dB} \tag{3}$$

To make a decision on the required integration time, the difference between each force exposure level and the level at the longest integration time of 2.7 s was determined for each octave band. Figure 11 shows that for all octaves of the standard (31.5 Hz to 500 Hz) the deviations after 1 s are very small. Such an integration time also has the advantage that the reference value of Equation (3) is 1 s, so the measured impact force level is equal to the desired impact force exposure level.

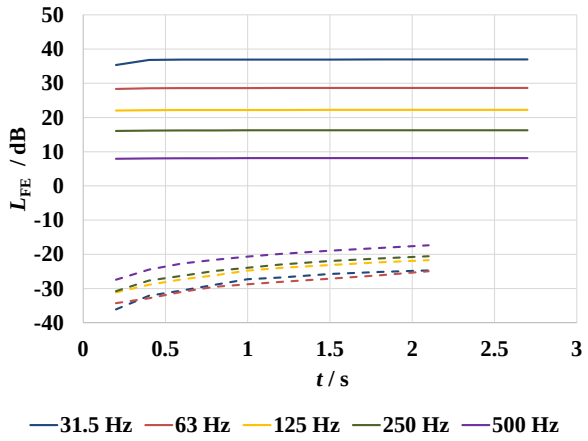


Figure 10. Impact force exposure level and noise level in dependance of integration time.

4.4 Results of octave band measurements

With the knowledge presented in the previous section, the triggered measurement was set to 1 s integration time and the results of 10 ball drops were analyzed in octave bands. Figure 12 shows the difference between the average of the measured octave band levels and the required level of the standards [1] and [2] for each ball. The results for ball 1 and ball 2 are between the limits, with a small deviation at 500 Hz for ball 1. The impact force exposure levels of ball 3 are outside the limits in every octave band.

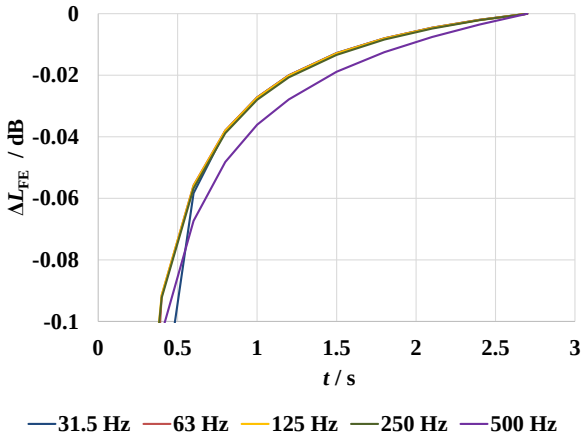


Figure 11. Dependence of the impact force exposure level on integration time for each octave band, plotted as deviation ΔL from the longest integration time of 2.7 s.

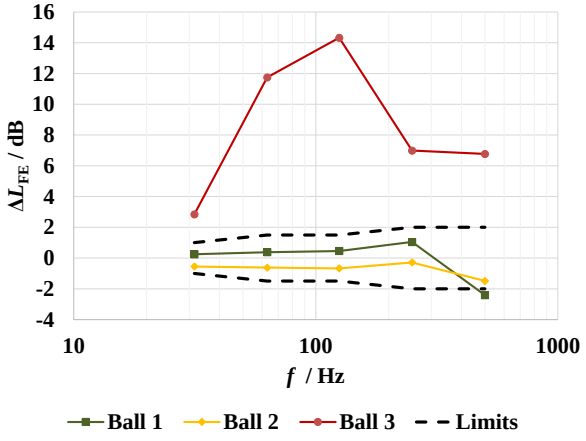


Figure 12. Impact force exposure level of the three balls in comparison with the limits.

The standard deviations of the impact force exposure levels from the 10 ball drops were also calculated. The values are between 0.1 dB and 0.5 dB (Figure 13). For the two balls complying with the standard requirements, they are below 0.3 dB.

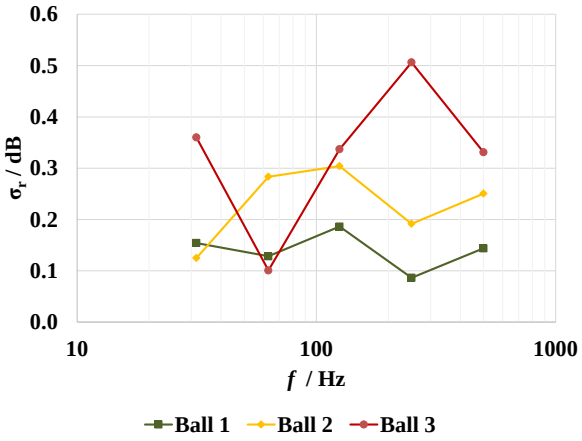


Figure 13. Standard deviation of the impact force level determined from ten repeated ball drops.

5. UNCERTAINTY ESTIMATE

To estimate the uncertainty of the measured force exposure level, the mean value from the 10 ball drops is used as the measurand. A first uncertainty estimate for this measurand is determined by using the uncertainty estimate of the calibration u_{cal}, the standard deviation of repeatability σ_{r} and the influence of the noise due to the averaging. The latter is estimated from Figure 11 to be $u_{\mathrm{N}} = 0.05$ dB.

$$u(L_{\mathrm{F,E}}) = \sqrt{u_{\mathrm{cal}}^2 + \frac{\sigma_{\mathrm{r}}^2}{n} + u_{\mathrm{N}}^2} \tag{4}$$

The resulting uncertainty is about 0.3 dB for the calibration with the hardest hammer tip (Figure 14). For the soft hammer tip, the uncertainty is much larger at 250 Hz and 500 Hz, and the medium hammer tip is between these two cases. In view of the standard's tolerance range for the impact force exposure level of ±1.0 dB to ±2.0 dB, this uncertainty is comparatively large and must be investigated further.

6. SUMMARY

A new setup for measuring the impact force exposure levels of heavy soft impact sources has been installed at PTB. It consists of a strain gauge sensor with a bridge amplifier and an octave band analyzer. This device was calibrated by an impact hammer which had been traceably calibrated at PTB. The uncertainty of the measured force exposure level of heavy impact sources was estimated to be about 0.3 dB. This very first uncertainty estimate indicates that the uncertainty is not negligible when comparing measured force exposure levels to the requirements from the standard. Further investigations are necessary before a test service can be established at PTB.

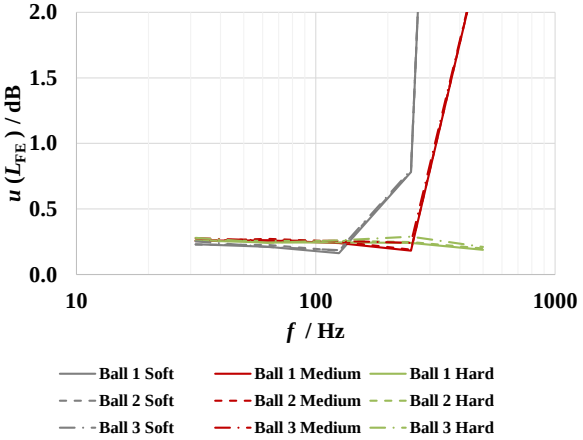


Figure 14. Uncertainty estimates for the measured force exposure level.

7. REFERENCES

[1] DIN EN ISO 10140-5, "Acoustics - Laboratory measurement of sound insulation of building elements - Part 5: Requirements for test facilities and equipment", First edition 01 September 2010

[2] DIN EN ISO 16283-2, "Acoustics – Field measurement of sound insulation in buildings and of building elements – Part 2: Impact sound insulation", German edition EN ISO 16283-2:2020

[3] M. Kobusch, L. Klaus: "In-Situ dynamic force calibration using impact hammers", Acta IMEKO, December 2020, Volume 9, Number 5, Page 118 - 123

[4] S. Hirakawa, C. Hopkins: "Verification procedures for the impact force applied by the rubber ball used for impact sound insulation measurements", 29th International Congress on Sound and Vibration (ICSV), 9 – 13 July 2023

DOI: 10.61782/fa.2025.0444

FORUM ACUSTICUM EURONOISE 2025

IMPACT NOISE FROM ONE STOREY TO THE NEXT STOREY – FROM SLAB ON THE GROUND AND SLAB BETWEEN FLOORS

Bernt Mikal Larsen[1*]
[1] Multiconsult Norway, Fjellgata 6, 4612 KRISTIANSAND S, NORWAY

ABSTRACT

There are few studies or little information in the literature about impact noise from one storey to the next storey above. The issue is important when designing shopping centres or other facilities below apartments, when deciding the flooring to be used above the concrete slab. Measurement from apartment building in Kristiansand in Norway shows $L'_{n,w}$ 26 dB to the floor above (from one storey to the next storey above) when a 150 mm thick slab is used on the ground with gap to walls and columns. When slab on ground is in contact with concrete wall (no gap), $L'_{n,w}$ of 51-54 dB is measured to the floor above from a 90 mm slab on ground. Between floors with a main construction of 250-260 mm concrete, $L'_{n,w}$ of 61-65 dB is measured to the floor above. The measured impact level is higher from slab between floors than from ground, and no contact between wall and slab reduces the impact level significantly.

Keywords: *impact noise between floors, impact noise to floor above, impact noise from slab to above*

1. INTRODUCTION

Few or no studies have been made in field on impact noise from one storey to the next floor above [1]. This paper shows impact noise levels from slab on ground to the floor above, and from slab between floors to the next storey above. The issue is important when designing apartments or offices above shopping centres and other facilities. All measurements and analyses are from finished buildings in field with construction as summarized below.

2. MEASUREMENT METHOD

The impact noise levels were measured with tapping machine Norsonic 211 in finished buildings. The results are given for bare concrete slab, corrected for damping effect of floor coating or floating floor and to receiving room volume of 100 m^3. Above the concrete slab, there were different flooring for all the measurements as summarized in each chapter. The frequency spectrum is also given in figures for all measurements.

3. SLAB ON GROUND, IMPACT NOISE TO FLOOR ABOVE

3.1 Slab with airgap to surrounding walls and columns

One measurement was done in a building with parking basement on the ground and apartments in the floor above. For this situation the measurement was done directly on the bare concrete floor in the parking basement. The concrete floor was with gap to surrounding walls and all columns in the parking basement. The construction of the floor in the basement was:

- 150 mm thick concrete slab on 2 layers of plastic and gravel
- Gap to surrounding walls and columns

The receiving room volume was 100 m^3, and the measured $L'_{n,w}$ 26 dB. In general the impact levels are low, and in the lowest frequencies close to 30 dB. In figure 1 the measurement curve is given. The impact levels in the floor above are supposed to be due to movements in polystyrene and/or ground transferred up through walls and columns.

[*] ***Corresponding author***: bernt.mikal.larsen@multiconsult.no.
Copyright: *©2025 First author et al. This is an open-access article distributed under the terms of the Creative Commons Attribution 3.0 Unported License, which permits unrestricted use, distribution, and reproduction in any medium, provided the original author and source are credited.*

This construction is transferring the highest levels in the low-frequency range.

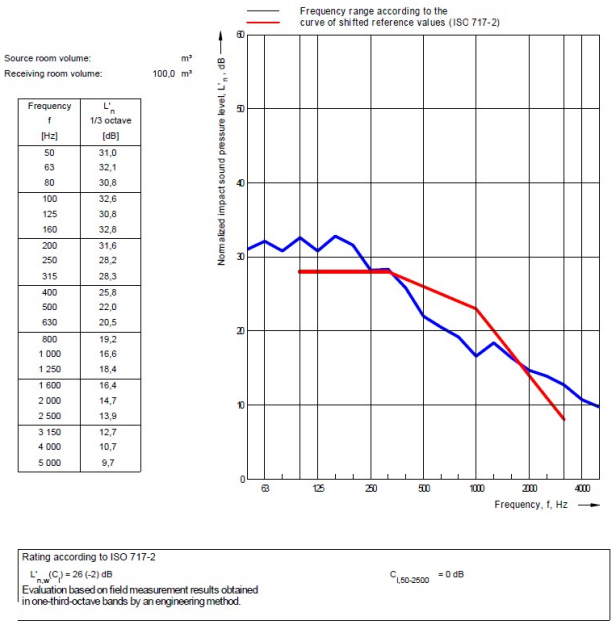


Figure 1. Impact noise from slab on ground to floor above. 150 mm concrete slab on 2 layers of plastic and gravel with gap to surrounding walls and columns.

3.2 Slab in contact with concrete wall

Other measurement for ground slab was done when the slab had contact with a concrete wall. Such a measurement was done in building with apartments on the ground floor and the floor above. The basement construction was as follows:

- Hard oak parquet
- 2 mm Selit pro parquet flooring
- 90 mm concrete slab
- 300 mm polystyrene

The measured L'$_{n,w}$ was 34 dB to receiving room volume of 100 m^3. The damping effect of the floor coating consisting of oak parquet and 2 mm parquet flooring is 17-20 dB [2] according to experiences in Norway. The impact noise level to the floor above is then L'$_{n,w}$ 51-54 dB for bare concrete slab in contact with concrete wall. In figure 2 it can be seen a much steeper curve from highest to lowest frequencies than in figure 1, and almost similar levels as in figure 1 for the highest frequencies. The effect of splitting a concrete slab against walls and columns is 25-28 dB for the L'$_{n,w}$-value. In the lowest frequencies the levels are 10-20 higher with contact between slab and wall than for the situation with no contact between ground slab and surrounding walls and columns.

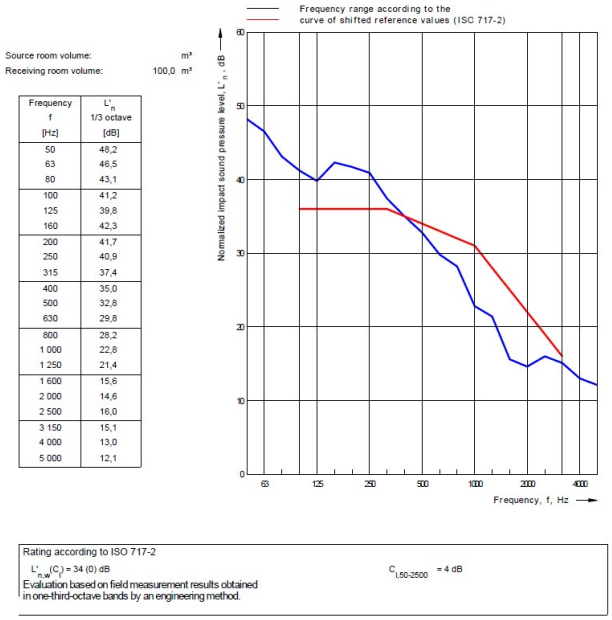


Figure 2. Impact noise from slab on ground to floor above, when the ground slab has contact with concrete wall. Measurement done on oak parquet.

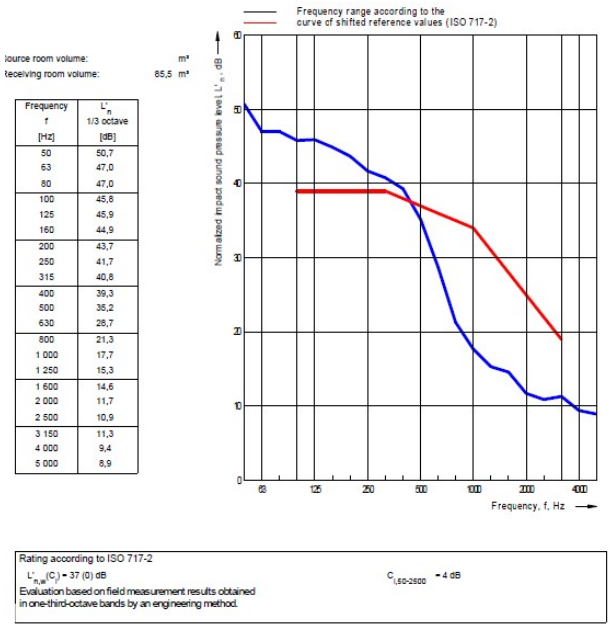
3.3 Slab on ground – lightweight walls

In a building with lightweight walls between apartments, two different measurements of impact noise to living room in the floor above were done. The lightweight walls were in contact with the concrete slab, and mounted directly to the concrete slab. Construction was as follows:

- laminate
- wool cardboard
- 100 concrete slab
- 100 mm polystyrene
- plastic film due to radon gas
- 150 mm polystyrene

The measured L'$_{n,w}$ was 37 dB and given in figure 3. The damping effect of the floor coating consisting of laminate on wool cardboard is 13-15 dB [2] according to experiences in Norway. The impact noise level to the floor above is then

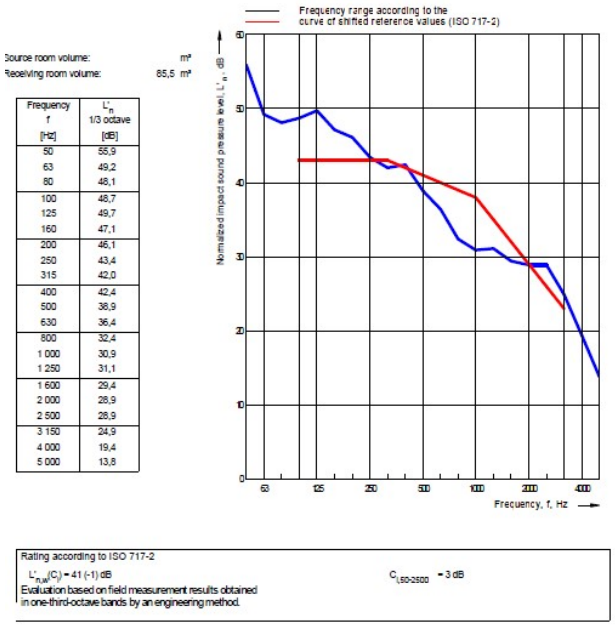
L'$_{n,w}$ 51-53 dB for bare concrete slab in contact to the floor above in building with lightweight walls.



Frequency f [Hz]	L'n 1/3 octave [dB]
50	50,7
63	47,0
80	47,0
100	45,8
125	45,9
160	44,9
200	43,7
250	41,7
315	40,8
400	39,3
500	35,2
630	28,7
800	21,3
1 000	17,7
1 250	15,3
1 600	14,6
2 000	11,7
2 500	10,9
3 150	11,3
4 000	9,4
5 000	8,9

Figure 3. Impact noise from slab on ground to floor above, in building with leightweight walls. Measurement done on laminate floor .

Similar result in the same building is from bathroom to living room, where the flooring was with vinyl coating. The measured L'$_{n,w}$ was 41 dB and given in figure 4. The damping effect of the floor coating consisting of vinyl coating is 7-10 dB [2] according to experiences in Norway. The impact noise level to the floor above is then L'$_{n,w}$ 49-52 dB for bare concrete slab in contact to the floor above in building with lightweight walls.



Frequency f [Hz]	L'n 1/3 octave [dB]
50	55,9
63	49,2
80	48,1
100	46,7
125	49,7
160	47,1
200	46,1
250	43,4
315	42,0
400	42,4
500	38,9
630	36,4
800	32,4
1 000	30,9
1 250	31,1
1 600	29,4
2 000	28,9
2 500	28,9
3 150	24,9
4 000	19,4
5 000	13,8

Figure 4. Impact noise from slab on ground to floor above, in building with lightweight walls. Measurement done on vinyl coating.

By comparing figure 3 and 4 with figure 1, it may be observed that the levels in the lowest frequencies (100-160 Hz) transferred through walls and columns in contact with a slab, are much higher than what is transmitted through movements in polystyrene or ground (figure 1).

4. SLAB BETWEEN FLOORS – IMPACT NOISE TO FLOOR ABOVE

4.1 Slab with no apartment (free space) below

Measurement was done for a slab between 3rd and 4th floor in apartment building, In this case, there was free space below the apartment in 3rd floor. The situation is shown in figure 5. The situation will affect the stiffness of the construction and the levels in the lowest frequencies. The floor construction was as follows:

- 15 mm parquet
- 35 mm putty compound
- 25 mm polystyrene

- 260 mm concrete slab
- 115-145 mm airgap with mineralwool
- 12 mm gypsum

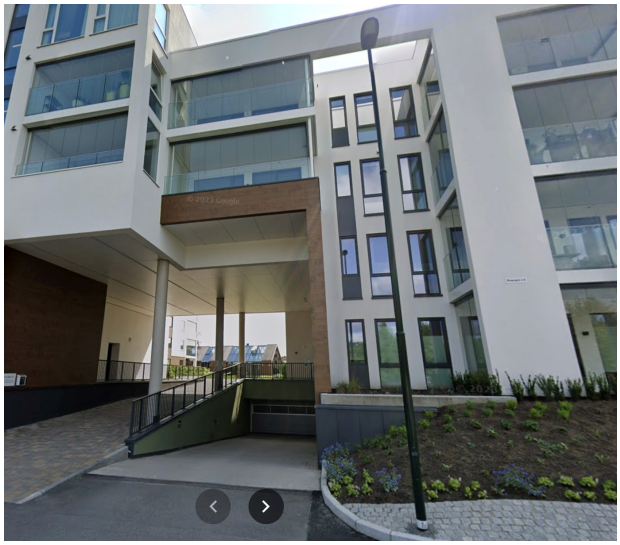


Figure 5. Picture of apartment with free space below where impact measurement was done to floor above.

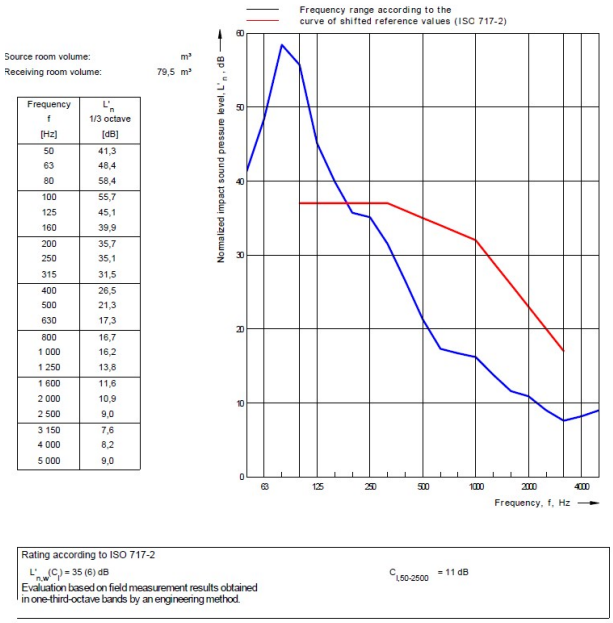


Figure 6. Measurement result to floor above with free space below.

The measurement was done to a room with receiving room volume of 80 m^3. The damping effect of the floor coating consisting of parquet, putty compound and polystyrene is 25-28 dB [2] according to experiences in Norway. The impact noise level to the floor above is then $L'_{n,w}$ 61-64 dB for bare concrete slab of thickness 260 mm and with receiving volume of 100 m^3. This shows that there in general is a need for a coating or floating floor, to satisfy the demands for impact noise values to the floor above in Norway. The impact levels to the floor above are quite high in 80 and 100 Hz compared to surrounding frequencies. Comparison of figure 6 with figure 1 and 2 verifies that there will be much more annoyance due to low frequency noise from a general slab between different floors than from a slab on ground.

4.2 Slab between floors – stiff fastened to concrete walls

Impact noise for a situation with concrete slab between floors of thickness 250 mm was measured. In this case there were concrete walls in the building with the concrete slab stiff fastened to these concrete walls. The construction was as follows:

- parquet
- 35 mm putty compound
- 25 mm polystyrene
- 250 mm concrete slab

The damping effect of the floor coating consisting of parquet, putty compound and polystyrene is 25-28 dB [2]. The impact noise level to the floor above is then $L'_{n,w}$ 62-65 dB for bare concrete slab of 250 mm and corrected to receiving room volume of 100 m^3. The result is shown in figure 7 below. Even with a floating floor (with no contact to walls) on slab between floors, there is still significant level of low-frequency noise transferred to the floor above.

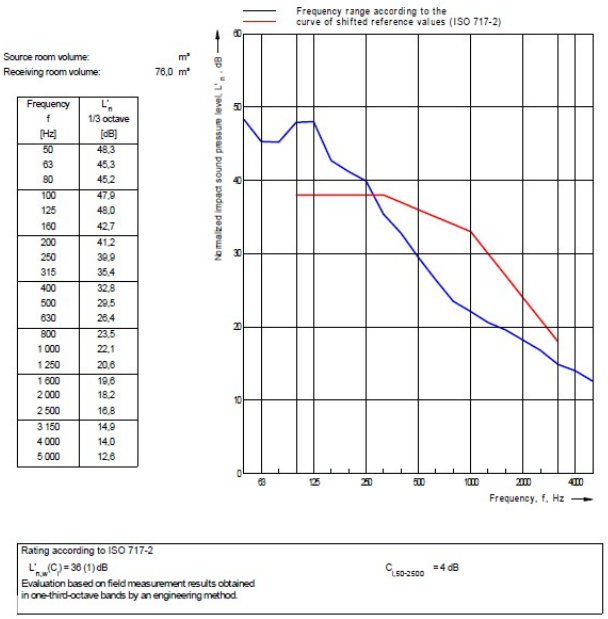


Figure 7. Measurement result to floor above from 250 mm slab between floors, stiff fastened to concrete walls in the building

4.3 Hollow core slab between floors – lightweight walls in building

Impact noise for a situation with hollow core slab between floors of thickness 200 mm was measured, between 1st and 2nd floor. In this case there were lightweight walls in the building between apartments. The construction was as follows:

- parquet
- 40 mm putty compound
- 30 mm impact reducing plate
- 280 mm polystyrene
- 200 mm hollow core slab

The damping effect of the floor coating consisting of parquet, putty compound and polystyrene is 30 dB [2]. The impact noise level to the floor above is then $L'_{n,w}$ 64 dB for bare hollow concrete slab of 200 mm and corrected to receiving room volume of 100 m^3. The result is shown in figure 8 below.

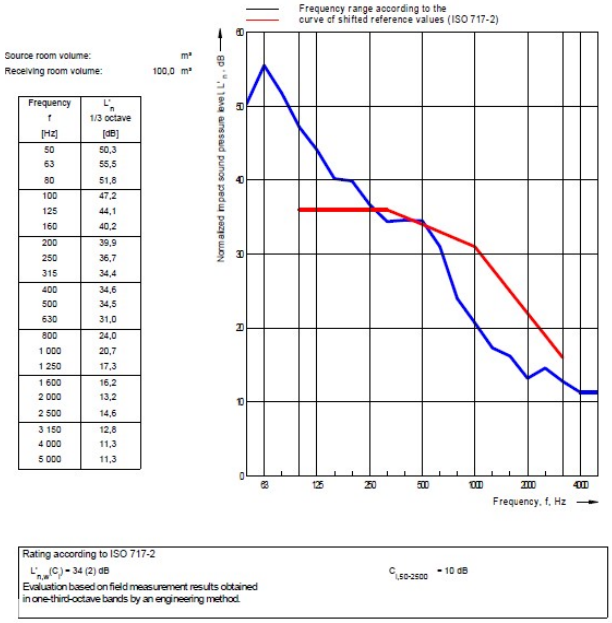


Figure 8. Measurement result to floor above from 200 mm hollow core slab between floors, lightweight walls in the building. The levels below 100 Hz is due to stiffness of the construction.

5. CONCLUSIONS

5.1 Slab on ground to floor above

Measurement shows $L'_{n,w}$ of 26 dB when slab on ground is with airgap to surrounding walls and columns, and with low levels of low frequency noise. When the concrete slab is in contact with concrete wall, columns or lightweight walls, the $L'_{n,w}$ for bare concrete slab to the floor above increases to 51-54 dB. The difference is 25-28 dB with connections to walls and colums, compared with the situation with airgap. To fulfill demands in Norwegian standard from shopping centre or parking basement to apartment ($L'_{n,w} \leq 48$ dB), there is a need for thick enough slab or a flooring reducing impact noise with 6 dB or more, when the slab is in contact with surrounding walls and columns.

5.2 Slab between floors

From slab between floors of concrete and thickness 250-260 mm to the floor above, impact noise from bare slab is

$L'_{n,w}$ 61-65 dB. There will then be a need for impact noise reduction of 13-17 dB to fulfill the requirement of $L'_{n,w} \leq 48$ dB from shopping centre to apartments above.

The measurements show approximately 10 dB higher $L'_{n,w}$ from a slab between floors to the floor above than from a slab on ground to floor above. The reason for this difference is thought to be due to different stiffness. By comparison of the levels from slab on ground with slab between floors, the main difference is related to the levels in the frequency range from 100-160 Hz. It can be seen that a slab between floors stiff fastened to concrete walls gives lower levels to floor above than other situations and is closer to impact noise from slab on ground. By comparison of concrete slab in buildings stiff fastened to concrete walls with concrete slab in buildings with lighweight walls, it can be seen much higher levels in the lowest frequencies for building with lightweight walls.

5.3 Consequences for solutions in buidlings

The measurements summarized from buildings show a need for a good enough solution with both slab on ground and slab between floors, to satisfy $L'_{n,w} \leq 48$ dB from shopping centre or parking basement to apartments in floor above for combined buildings.

6. SUMMARIZING POEM

Impact noise to storey above is studied by few
That's why this paper passed conference review
A splitted concrete slab on the ground
Is really the best for low impact sound
Connection with walls transfers frequency low
That is what this presentation should show
What damping you need on the slab below
Is after all this something you will know

7. ACKNOWLEDGMENTS

May I give my biggest acknowledgements to the companies Mur I Sør and Aamodt Bygg for data from measurements in their projects. In the future it would be interesting with more results and experiences from finished buildings. This could increase the knowledge and improve the necessary solutions in different buildings.

8. REFERENCES

[1] John LoVerde and Wayland Dong, Measurement of Lateral impact noise isolation, *24th International Congress on Sound and Vibration (2017)*.

[2] SINTEF: "522.513 Lydisolerende tunge etasjeskillere"

DOI: 10.61782/fa.2025.0648

FORUM ACUSTICUM EURONOISE 2025

ON THE INFLUENCE OF SAMPLING SIZE IN THE ASSESSMENT OF UNCERTAINTY AND REPEATABILITY OF FIELD MEASUREMENTS OF IMPACT SOUND INSULATION IN VARIOUS FLOOR SCENARIOS

San Millán-Castillo, Roberto[1*] **Trujillo, Jose Alberto**[2] **Romero-Fernández, Amelia**[3]
[1] Universidad Rey Juan Carlos-Departamento de Teoría de la Señal y Comunicaciones - EIF, Spain
[2] Laboratorio de Ensayos Acústicos (Labenac) - Universidad Politécnica de Madrid, Spain
[3] Instituto de Ciencias de la Construcción Eduardo Torroja. IETcc - CSIC, Spain

ABSTRACT

One of the most widely used standards for field measurements of impact sound insulation is ISO 16283-2: 2020. The assessment of the standard deviation of repeatability must comply with ISO 12999-1, as repeatability is a crucial factor in ensuring reliable test performance. However, in some cases, the frequency band results do not comply with the maximum standard deviation limits for repeatability. These deviations raise concerns about the adequacy of the current repeatability limits and the testing procedures outlined in the ISO standard. This study compares the maximum standard deviation of repeatability between impact sound insulation tests conducted with four and six sound source positions, as well as the limits specified in ISO 12999-1, regarding the one-third octave bands of interest in various typical floor scenarios in Spain. Furthermore, these tests study the effect of increasing the number of tapping machine positions on global uncertainty.

Keywords: *impact sound insulation, field testing, uncertainty, repeatability).*

1. INTRODUCTION

ISO 16283-2 is a widely used standard for field measurement of impact sound insulation [1]. This standard aims at assessing impact sound insulation by measuring sound pressure level in a receiving room employing an impact source [1]. Generally, building acoustics standards require uncertainty by ISO 12999-1 [2].

The measurement uncertainty limits can be determined through reproducibility rates [2]. Moreover, ISO 12999-1 recommends repeatability for verifying the quality of laboratory's testing procedures, on their own. In repeatability conditions, results must remain under the maximum values of the typical deviation of repeatability (σ_r) versus frequency in one third-octaves resolution, from 50 Hz to 5 kHz; higher tolerances in the low-frequency range up to 400 Hz, and in higher frequencies, it remains constant. This limit is the same for airborne sound insulation, façade sound insulation, and impact sound insulation. This differs from previous standards such as EN 20140-2 [3], and even *Case C* of ISO 12999-1: 2020, for inter-laboratory repeatability assessment. An extensive survey in [4, 5] reports significant deviations in impact sound insulation testing for different tapping machine positions, correlated with some types of floor, structure and finish. However, no systematic differences were found in global ratings. The study in [6] on gypsum concrete floors and concrete floors shows that repeatability tests exceed σr limits in ISO 12999-1 at some bands. The structure of wood floors may lead to increases on impact sound pressure level in low frequencies, reaching out from 4 dB to 7 dB, depending on tapping machine location, according to [5]. A previous work by the authors [7], presented some examples for a range of typical Spanish floors and four source positions, in which σ_r exceeded the recommended repeatability limits.

[*] ***Corresponding author***: roberto.sanmillan@urjc.es
Copyright: *©2025 San Millán-Castillo, Roberto et al. This is an open-access article distributed under the terms of the Creative Commons Attribution 3.0 Unported License, which permits unrestricted use, distribution, and reproduction in any medium, provided the original author and source are credited.*

This study provides additional data to this issue by performing tests with a reasonable increase on source positions and related insights about uncertainty.
Current literature suggests that impact source location and building technology may influence testing and requires further research to decrease measurement uncertainty. This work aims at 1) assessing σ_r of four typical Spanish floor scenarios in horizontal and vertical set-up, including four and six impact source locations within the same test; 2) comparing σ_r to the limits of ISO 12999-1 and the impact on measurement uncertainty.
The remainder of this paper is organized as follows. Section 2 describes the measurement procedure and scenarios. After that, Section 3 includes the results and discussion of the testing. Section 4 provides conclusions.

2. MATERIALS AND METHODS

2.1 Measurement procedure and equipment description

Impact sound insulation measurements were performed following ISO 16283-2 [1] in 4 different scenarios (see Section 2.2). In each of them, the measurements were repeated 5 times, under conditions of repeatability, that is, with the same measurement procedure, the same measuring system and the same operators, over a short time; but modifying the source and microphone positions for each repeated measurement and selecting them again more or less randomly.
The magnitude measured was the 'standardised impact sound pressure level' (L'_{nT}), defined in Eqn. (1), in the frequency range from 50 Hz to 5000 Hz in the one-third octave bands. The default procedure ($V > 25$ m^3) and fixed microphone positions were used. A tapping machine was used as an impact source.

$$L'_{nT} = L_i - 10 \cdot \lg \frac{T}{T_0} \quad \text{[dB]} \qquad (1)$$

where L_i is the energy-average impact sound pressure level in the receiving room corrected by background noise; T is the reverberation time in the receiving room [8]; T_0 is the reference reverberation time, in s (for dwellings, $T_0 = 0{,}5$ s).
Six and four different positions of the tapping machine were used, randomly distributed on the floor under test. Likewise, four or six different microphone positions were used, measuring impact noise levels in two of these positions for each source position. The averaging time for the level measurements was 15 s. The location of the tapping machine and microphone positions met the specifications of the reference standard regarding the distances between them, the source positions and room boundaries.

For each tapping machine position, the standardised impact sound pressure level is calculated, and an averaged final value is obtained, according to equation Eqn. (2):

$$L'_{nT} = 10 \cdot \lg \frac{1}{m} \sum_{j=1}^{m} 10^{L'_{nT,j}/10} \quad \text{[dB]} \qquad (2)$$

where m is the number of tapping machine positions; $L'_{nT,j}$ is the standardised impact sound pressure level for tapping machine position j.
For each scenario and each test, two L'_{nT} index results were obtained. The first was derived from the combination of all six tapping machine positions with their associated microphone positions, while the second was obtained by combining only four tapping machine positions with their corresponding microphone positions.
The airborne sound contribution from the tapping machine was also evaluated to determine whether it should be considered negligible or if it might influence the results in some way.
The suitable Class 1 equipment, according to reference standards, for measurements and the tools used for data post-processing are defined in [7].

2.2 Scenarios description

The four measurement scenarios correspond to existing dwellings with a typical separating floor configuration in Spain. This configuration consists of a concrete beam and block floor, likely with some layers of mortar and sand (total thickness ≈ 300 mm). The only difference between them lies in the floor finish: non-floating wood flooring (ID1) and non-floating ceramic tile flooring (ID2, ID3, ID4).
Regarding the relative positioning of the test rooms, ID1 and ID2 are horizontally adjacent, while ID3 and ID4 are vertically adjacent.

3. RESULTS AND DISCUSSION

The following sections present the measurement results for the four scenarios. For each measurement set, compliance with the repeatability requirements of ISO 12999-1 was evaluated.
First, the L'_{nT} spectra for the four measurement scenarios are presented, considering both six and four tapping machine positions during testing (Fig. 1).
Next, the received noise levels in the receiving room are analyzed for each source position in the emitting room and its two corresponding measurement points in the receiving room (Fig. 2).
Finally, the standard deviation of repeatability (σ_r) and the expanded uncertainty (U) are analyzed for the different

scenarios, assessing the differences caused by using six or four tapping machine positions (Fig. 3 and 4).
The airborne sound contribution from the tapping machine and its influence was found to be negligible in most cases. This contribution is usually much more controlled when the rooms are vertically adjacent. In this case, some transmission was found from 630 Hz onwards in scenario ID1, where the rooms are horizontally adjacent.

3.1 Spectra of the 5 repeated measurements of L'$_{nT}$

Fig. 1 shows the L'_{nT} spectra corresponding to the average of the five repetitions in each set-up, comparing results obtained using four and six tapping machine positions.

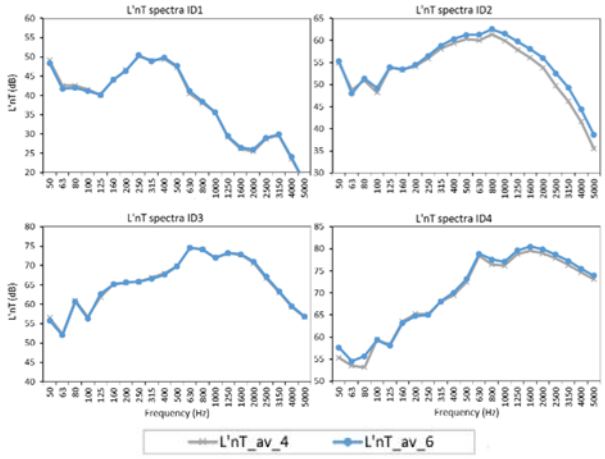


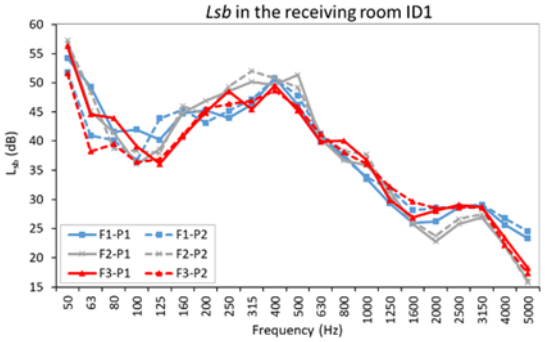
Figure 1. Spectra of the 5 repeated measurements of L'_{nT}.

The L'_{nT} spectra for each scenario remain practically overlapping when using four and six tapping machine positions. This suggests that increasing the sampling size by adding more tapping machine positions has minimal influence on the final result. However, compared to performing the test five times under repeatability conditions, some variations may still be observed, as discussed in section 3.3.

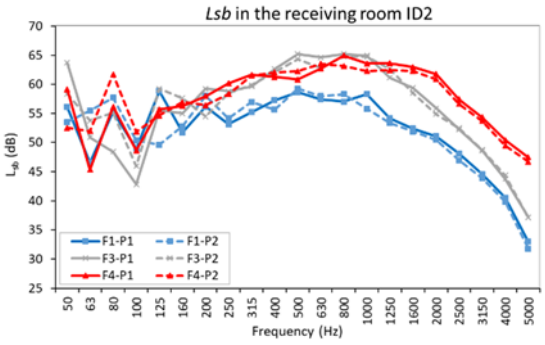
3.2 Analysis of signal and background noise levels (L_{sb}) in the receiving room

The following graphs represent the spectra of the combined signal and background noise level (L_{sb}) measured in the receiving room for the four test scenarios The data correspond to one of the repetitions and represent the combinations of source positions (F_i) and their corresponding microphone positions (P1 and P2).

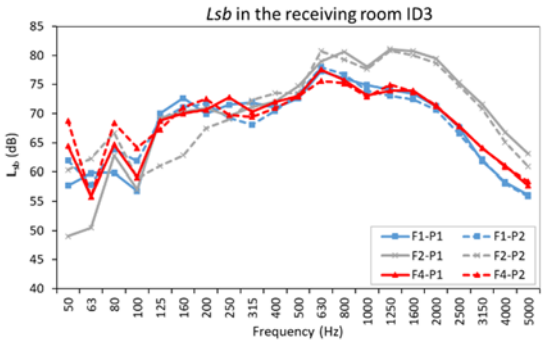
Although four and six tapping machine positions were used for the tests, the graphs only show measurement combinations for three source positions to simplify the representation.



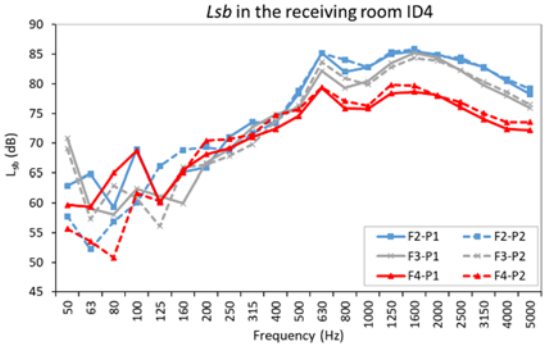
(a)



(b)



(c)



(d)

Figure 2. Combined signal and background noise level (L_{sb}) in the receiving room. Combinations of source position and measurement points for one of the repetitions. (a) ID1, (b) ID2, (c) ID3, (d) ID4.

The data in Fig. 2 can be roughly grouped into pairs, mostly from mid frequencies onwards. Each pair of microphone positions with a similar response in the receiving room corresponds to the same source position. This suggests that the tapping machine positions influence the results of this test and introduce variability in repeatability. The same findings were reported in [7].

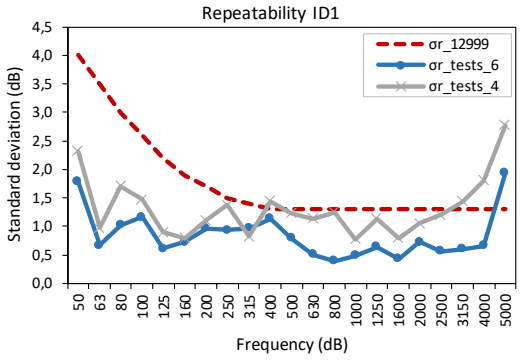
In scenario ID1 (Fig. 2a), the microphone positions can also be roughly paired, but the grouping is less clear compared to the other scenarios. In this case, the floor was more homogeneous, which theoretically allows for a more uniform response of the transmitted impact noise. The separating floor is finished with a non-floating wooden flooring, which might contribute to providing a homogeneous surface for hammer impacts. As a result, the variability between measurement points is lower than in other cases, though small deviations can still be observed at higher frequencies.

The dependence of impact sound levels on the source position is very clear in scenarios ID2, ID3, and ID4 (Fig. 2b, 2c, and 2d), where the curves for P1 and P2 are almost completely overlapped from 1 kHz onwards. This indicates a strong consistency between the measurement points when the same source position is used. However, these scenarios exhibit greater variability, particularly at lower frequencies. In these cases, the separating floor is finished with a non-floating ceramic tile flooring, which might increase the variability of the transmitted noise levels. The differences observed between measurement points could be influenced by the location of the hammer strikes and possible variations in the attachment quality of the tiles. Similar results have been reported in previous studies for both wood and ceramic flooring [5-7].

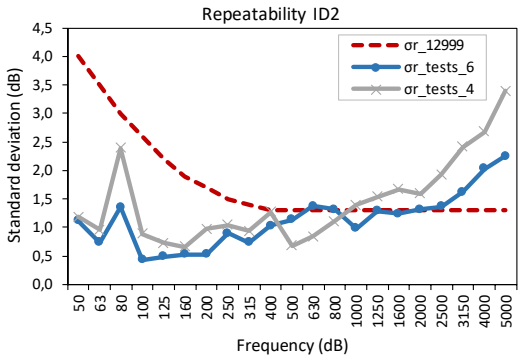
These results reinforce the idea that the positioning of the tapping machine can affect measurement repeatability.

3.3 Analysis of repeatability results (Standard deviation)

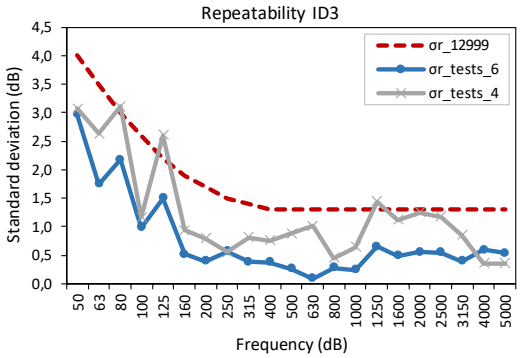
Fig. 3 presents the standard deviation of repeatability (σ_r) for each test scenario, comparing the results obtained using four and six tapping machine positions with the limits given in Table 1 of ISO 12999-1 [2]. When values from measurements are higher than those indicated in the reference standard, they are non-compliant with repeatability requirements.



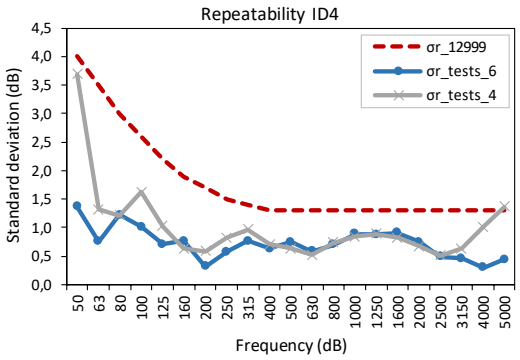
(a)



(b)



(c)



(d)

Figure 3. Standard deviation: ISO 12999-1 vs measurements. (a) ID1, (b) ID2, (c) ID3, (d) ID4.

Overall, a significant improvement in repeatability values is observed when increasing from four to six tapping machine positions. Although this improvement is noticeable across all scenarios, each scenario presents particular nuances depending on the frequency range considered.

Scenarios ID1 (Fig. 3a) and ID2 (Fig. 3b) generally comply with the repeatability requirements up to the highest frequencies. However, at high frequencies, improvements in repeatability can still be observed when increasing from four to six positions. The non-compliance shifts from 2.5 kHz to 4 kHz in ID1 and from 800 Hz to 2 kHz in ID2, indicating a beneficial effect of using more tapping machine positions. In ID2, a peak in the value of σ_r exceeding the limit curve repeatability appears at 80 Hz, which, although still within the standard limits, improves significantly when increasing positions.

Scenario ID3 (Fig. 3c) exhibits the worst repeatability issues at low frequencies (80 Hz, 125 Hz) when using four positions, exceeding the ISO limit. There is also a minor non-compliance with σ_r at 1.25 kHz. Increasing positions significantly reduces these deviations, bringing them below the ISO threshold. At mid and high frequencies (from 500 Hz onwards), repeatability remains stable when using six source positions, with no exceedances of the ISO 12999-1 limit.

Scenario ID4 (Fig. 3d) shows relatively stable repeatability values across the entire frequency range. At 50 Hz, repeatability is quite high with four source positions, nearly exceeding the limit, but this value improves significantly with six positions. A notable improvement is also observed at 5 kHz.

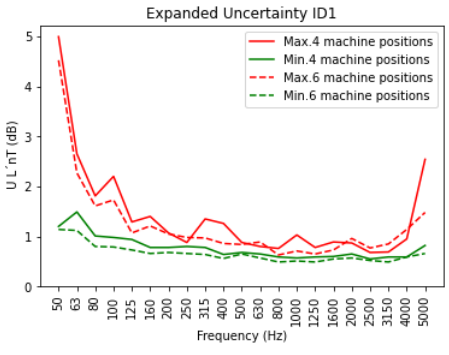
As a summary, it has been observed that compliance with ISO 12999-1 and repeatability values generally improves when increasing from four to six source positions, although issues in ID1 and ID2 remain problematic, exceeding the ISO 12999-1 limit in both cases even with six positions.

The most notable improvement occurs at 50 Hz in scenario ID4, where the repeatability value is significantly reduced when using six positions. Peak repeatability values at 80 Hz and 125 Hz in ID3 and at 80 Hz in ID2 are also significantly reduced.

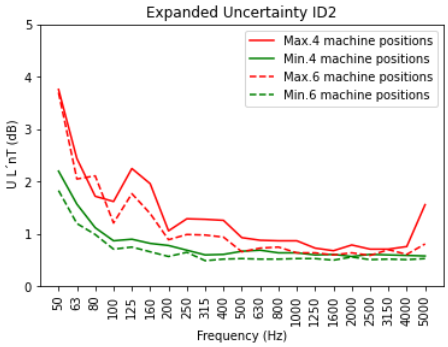
These results confirm that increasing the number of tapping machine positions improves repeatability in most situations. However, remaining high-frequency deviations require further research to determine whether other factors may be influencing the variability.

3.4 Uncertainty

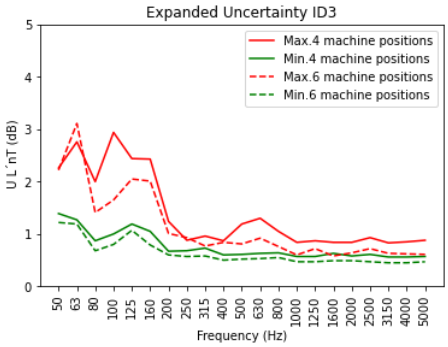
Generally, in building acoustics, expanded uncertainty provides insights of the testing quality and robustness. Fig. 4 presents the expanded uncertainty range vs. frequency for all the scenarios, using four and six source positions, of five test under conditions of repeatability.



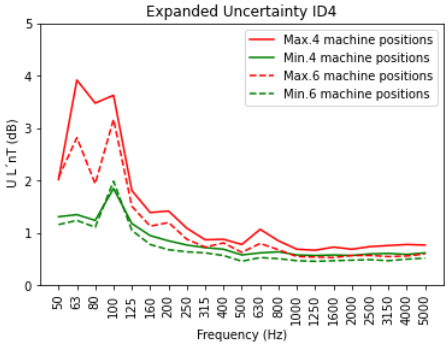
(a)



(b)



(c)



(d)

Figure 4. Expanded uncertainty range for four and six source positions: (a) ID1, (b) ID2, (c) ID3, (d) ID4.

The uncertainty analysis highlights the impact of increasing the number of tapping machine positions. The comparison of expanded uncertainty allows us to evaluate the effect of this increase results in a reduction of both minimum and maximum uncertainty values.

This effect is particularly noticeable in low frequencies, where uncertainty tends to be higher, mainly in the vertical scenarios ID3, Fig. 4(c), and ID4, Fig. 4 (d). In higher frequency the deviations are less prominent.

In the horizontal scenarios ID1, Fig. 4(a), and ID2, Fig. 4 (b), the difference is less relevant than in vertical set-ups. Although the uncertainty improvement is evident, it is not generally substantial.

4. CONCLUSIONS

The results confirm that increasing the number of tapping machine positions from four to six does not introduce significant changes in the averaged L'_{nT} spectra. Therefore, reducing the number of source positions could be considered without significantly affecting the final values of the results in L'_{nT}. However, there is a significant affectation in repeatability values.

A clear dependence of the received noise levels on the tapping machine position was observed. This finding reinforces the idea that increasing the number of microphone positions alone would not contribute to better repeatability. Instead, the key factor in measurement variability appears to be the location of the tapping machine. Given this, future research should explore whether reducing the number of microphone positions to one per source position while maintaining six source positions could still ensure reliable results while optimizing test procedures. Additionally, expanding the dataset with more samples would allow for broader conclusions.

Despite the lack of significant spectral differences, increasing the number of source positions led to a notable reduction in standard deviation in all scenarios, improving repeatability. This confirms that a higher sampling density contributes to more stable and consistent measurements. However, some high-frequency deviations remained, particularly in scenarios ID1 and ID2, indicating that further research is needed to understand whether other factors could be influencing the observed variability.

The results confirm that increasing the number of source positions enhances measurement reliability by reducing the uncertainty range. This is particularly beneficial in cases where uncertainty is initially higher, such as in low-frequency regions. However, at high frequencies, while some improvements are observed, they are less pronounced. When comparing the uncertainty results associated with the tests using four source positions to those obtained using six, it can be observed that, at mid and high frequencies, there is no significant difference between the uncertainties in both cases. However, this trend is not reflected in the repeatability

curves, where the use of six source positions instead of four does show a clear improvement in the levels of repeatability achieved.

The increase of tapping machine positions does not significantly change the final L'_{nT} values, but it plays a relevant role in reducing measurement uncertainty and improving repeatability. This suggests that an optimized balance between source positions and uncertainty reduction should be considered.

5. REFERENCES

[1] International Organization for Standardization. (2020). ISO 16283-2: acoustics: field measurement of sound insulation in buildings and of building elements: part 2: impact sound insulation.

[2] International Organization for Standardization. (2020). ISO 12999-1: Acoustics− Determination and application of measurement uncertainties in building acoustics− Part 1: Sound insulation.

[3] Comité Europeen de Normalisation. (1993). EN 20140-2: Acoustics - Measurement of sound insulation in buildings and of building elements - Part 2: Determination, verification and application of precision data (ISO 140-2:1991).

[4] LoVerde, J., Dong, D. W, "Variations in impact sound level as a function of tapping machine position", The *Journal of the Acoustical Society of America*, vol. 141 (5), 3929-3929, 2017.

[5] Larsson, K., Simmons, C., Amiryarahmadi, N., & Zhang, X, "Influence of tapping machine position on timber joist floors on the low frequency impact sound", in *Proc.of the 41st International Congress and Exposition on Noise Control Engineering*, *Internoise 2012*, (New York, United States), vol. 8, pp. 6620-6630, 2012.

[6] J. LoVerde and D.W. Dong, "Measurement of low frequency impact insulation", *The Journal of the Acoustical Society of America*, vol. 148, no. 4 Supplement, pp. 2513–2513, 2020.

[7] A. Romero Fernández, J. A. Trujillo Gallego, and R. San Millán Castillo, "Assessment of repeatability of field measurements of impact sound insulation in different floor scenarios" in *Proc. of the 55° Congreso Español de Acústica - XIII Congreso Ibérico de Acústica*, pp. 857–866, 2024.

[8] International Organization for Standardization. (2008). ISO 3382-2 - Acoustics - Measurement of room acoustic parameters - Part 2: Reverberation time in ordinary rooms.

DOI: 10.61782/fa.2025.0085

FORUM ACUSTICUM EURONOISE 2025

ACOUSTIC PROPERTIES OF BIOMASS BOTTOM ASH IN DIFFERENT TYPES OF RECYCLED CONCRETE

Rosales, Julia[1] **Rosales, Manuel**[1] **Cabrera, Manuel**[1] **Cubero-Atienza, Antonio José**[1], **Francisco Agrela, Francisco**[1] **Redel-Macías, María Dolores***

[1] Departamento de ingeniería rural, construcciones civiles y proyectos de ingeniería, Spain

ABSTRACT

In Andalusia, the second-largest autonomous community in Spain, energy production through biomass combustion is emerging as one of the most promising alternatives to fossil fuels. This biomass can be incorporated into construction materials. Analyzing the acoustic properties of these new, more sustainable materials is essential. It could contribute to the search for quieter spaces, as noise reduction is key to enhancing comfort in buildings. A wide range of thermal insulating materials, such as rock wool boards, cellulose boards, and wood fibers, are commonly used for acoustic insulation in walls, floors, doors, ceilings, ducts, enclosures, and building installations. Currently, conventional insulating materials dominate the market, while innovative natural and recycled insulating materials are either minimally marketed or not yet commercially available. However, materials like rock wool and glass wool, derived from natural processes, are highly energy-intensive to produce. Additionally, porous materials made from synthetic petrochemicals are widely used as acoustic insulation but pose potential risks to human health and the environment. As a result, there is an increasing demand for environmentally friendly insulation materials to meet noise reduction needs. This study focuses on analyzing the potential of innovative construction materials to enhance sound quality and acoustic insulation.

Keywords: *biomass bottom ash, lightweight concrete, self-compacting concrete, acoustic insulation*

1. INTRODUCTION

Nowadays, there is an increasing demand for quieter spaces in workplaces and residential areas. Reducing noise levels helps improve people's quality of life and comfort [1]. The WHO published a guideline on noise exposure in Europe. This guideline reviews studies that provide evidence on noise exposure, particularly night noise exposure, and its consequences for human health. For night noise exposure caused by road traffic, 45 dB is set as the reference level to avoid health effects. However, noise levels in Europe are well above this value. The health consequences of this night noise exposure range from cardiovascular disorders to menta health problems [2]. For these reasons, soundproofing in construction materiales is increasing being considered. A wide variety of thermal insulating materials, such as rock wool boards, cellulose boards, and wood fibers, are also used for acoustic insulation in walls, floors, doors, ceilings, duct, enclosures, and building installations. Today, insulating materials (e.g. rock wool, polystyrene) are commercially available and more commonly used compared to innovative natural and recicled insulating materials (e.g., rice, cotton, palm oil fiber, glass foam, plastics, recycled textile fibers), which are either barely marketed or not yet available [3]. However, rock and glass wool, derived from natural processes, are energy-intensive building insulation materials during manufacturing. Although porous materials derived from synthetic petrochemicals (e.g., rock wool, glass wool, polyurethane, polyester) are used as acoustic insulationmaterials, they can cause adverse effects on human health and the environment. Consequently, there is a growing demand for environmentally friendly insulation materials [4]

***Corresponding author**: mdredel@uco.es

***Copyright**: ©2025 First author et al. This is an open-access article distributed under the terms of the Creative Commons Attribution 3.0 Unported License, which permits unrestricted use, distribution, and reproduction in any medium, provided the original author and source are credited.*

for noise reduction. It is important to distinguish between sound absorption and sound insulation. The firth refers to a material's ability to absorb sound anergy, thereby preventing echoes and improving indoor quality. In contrast, sound insulation or soundproofing materials pevent sound waves from entering or leaving a space, acting as a barrier to sound. This study will analyze the potential of new construction materials to improve sound quality and acoustic insulation.

2. MATERIALS AND METHODS

The conventional raw materials used were:
Portland cement from Cementos Portland Valderrivas S.A, Alcalá de Guadaíra, Seville, Spain: type I of medium-high strength 42.5 MPa at 28 days with high initial strength R (CEM I 42.5-R). This type of cement is recommended for the production of normal high-performance concrete, very suitable for the industrial manufacture of prefabricated structural elements requiring maximum strength.
For this study a by-product was used as an alternative material replacing natural sand and expanded clay in each type of manufactured concrete. Biomass bottom ash (BBA) is composed of unburned coarse particles produced in the primary combustion chamber during the biomass energy production process [5,6]. In this study the BBA used comes from the biomass power plant located in Linares of the company Sacyr Industrial. The biomass used as fuel supply for electricity generation is composed of 60% wood from pruning almond and olive trees, and 40% olive cake. A pre-processing of the BBA was carried out in the laboratory to obtain different materials for making concrete:
- BBA-D: Oven-dried at 60ºC to constant mass.
- BBA-C: Oven-dried at 60ºC to constant mass and crushed and sieved to obtain a grain size between 0 and 4 mm.

A study was carried out in two separate series. The first series, called SCC, produced self-compacting concrete with partial substitution of sand and limestone filler; the second series, called LC, produced lightweight concrete with partial substitution of sand and expanded clay.
It is essential to evaluate the properties of density, absorption and porosity in order to select the type of concrete for a specific use, as these characteristics affect the long-term performance and durability of the structures. Table 1 shows the results obtained for all the mixes studied.

Table 1. Density, absortion and open porosity of hardened concrete.

	Density (kg/dm3)	Absorption(%)	Open porosity (%)
SCC-CR	2.37	3.16%	7.48%
SCC-15NS	2.33	4.77%	9.68%
SCC-30NS	2.30	5.25%	11.23%
SCC-15NS/30LF	2.32	4.98%	10.66%
SCC-30NS/60LF	2.29	5.80%	12.15%
LC-CR	1.88	6.96%	14.26%
LC/BBA-25NS	1.65	7.45%	15.12%
LC/BBA-50NS	1.52	9.21%	16.15%
LC/BBA-25EC/25NS	1.89	7.16%	8.92%
LC/BBA-50EC/50NS	1.73	9.84%	8.05%

All tests were carried out in a reverberation chamber, following the guidelines of the UNE-EN ISO 10140-2:2022 standard, which establishes a laboratory method for measuring airborne sound insulation in construction materials.
The measurement equipment used complies with the specifications set forth in ISO 10140-5:2022. This includes class 1 sound level meters, as per the IEC 61672-1 standard, and an acoustic calibrator meeting class 1 requirements in accordance with the IEC 60942:2017 standard.
The sound generated in the emitting room must remain stable. In line with standard recommendations, white noise was used during testing, produced by a standardized white noise generator.
According to ISO 10140-4:2022, when performing measurements with fixed-position microphones and a single sound source, at least five microphone positions must be used in each room (both emitting and receiving) for every speaker placement. Additionally, the sound source must be positioned in at least two different locations within the emitting room.
Sound quality refers to how a listener perceives and evaluates a sound. Unlike objective properties such as loudness or frequency, sound quality is inherently subjective and shaped by human perception.
Loudness, a fundamental component of sound perception, describes the perceived intensity or strength of a sound.
To assess sound quality, a Mikado Gfai acoustic camera was used, equipped with 96 MEMS microphones operating within a frequency range of 10 Hz to 24 kHz.

3. RESULTS

Analysing the attenuation efficiency of the concrete plates by frequency, Table 2 shows the acoustic attenuation produced by each concrete plate during the tests.

Table 2. Acoustic attenuation for each concrete plate.

	L_{Aeq} 125Hz	L_{Aeq} 250Hz	L_{Aeq} 500Hz	L_{Aeq} 1000Hz	L_{Aeq} 2000Hz	L_{Aeq} 4000Hz	L_{Aeq} 8000Hz
SCC-CR	36.5	40.0	42.9	40.2	39.3	43.9	44.1
SCC-30NS	38.0	40.8	46.1	47.5	47.5	49.6	51.7
SCC-30NS/60LF	37.8	40.7	45.6	46.1	47.0	46.3	49.2
LC-CR	38.1	40.4	47.7	47.0	49.5	53.4	58.2
LC/BBA-25EC/25NS	38.3	40.6	47.5	47.4	50.3	53.4	57.7
LC/BBA-50EC/50NS	38.2	40.5	47.1	48.5	51.7	54.0	58.0

As can be seen, the main insulation efficiency occurs at high frequencies, 4000Hz and 8000Hz, with LC/BBA-50EC/50NS being more effective and SCC-CR less effective.

Obtaining the average values for each mix concrete, the attenuation values achieved are collected in Table 2.

In Figure 1, it can be seen that the highest loudness corresponds to the concrete (SCC-CR). It is observed that the LC compounds have lower loudness than the SCCs. This may be due to the fact that the LCs have greater absorption and open porosity compared to the SCCs. Open porosity is the ratio of the total volume of open pores to the total volume of the material. High open porosity values correspond to high efficiency in dissipating acoustic energy due to the viscous and thermal effects occurring in the interconnected pores. Additionally, the presence of different scales of porosity enhances sound absorption [7].

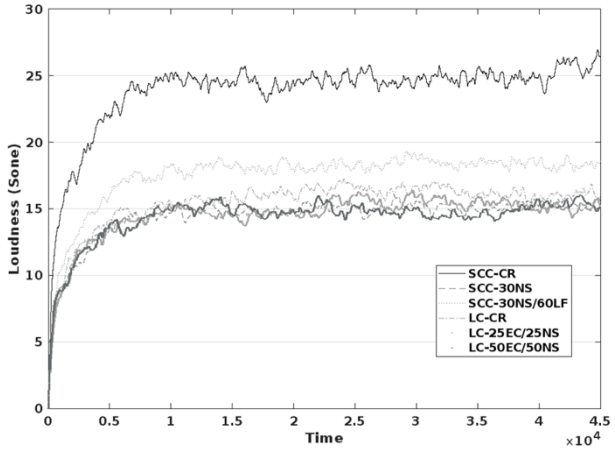


Figure 1. Loudness results.

4. CONCLUSIONS

The conclusions drawn from this study are shown below:

- The level of acoustic insulation of the tested concrete has been determined through comparative analysis. The concrete with the highest acoustic insulation capacity was the one corresponding to LC/BBA-50EC/50NS, and the one with the least acoustic insulation capacity was LCC-CR, which shows that lightweight concrete with a high BBA application rate leads to improved acoustic insulation. The greatest insulation effect occurs at high frequencies (4000Hz and 8000Hz).
- The sound quality of the noise transmitted by the concrete specimens was also studied. The highest level of loudness corresponds to SCC-CR concrete.

5. ACKNOWLEDGMENTS

This work is part of grant projects PID2022-141028OB, PID2019-105936RB-C21 and TED2021-130596B–C22 funded by MCIN/AEI/10.13039/501100011033,
The authors also would like to thank Manuela Santana member of the team at INERCO CORPORACIÓN EMPRESARIAL, S.L.

6. REFERENCES

[1] T. Yinping, R. Musu, Z, Hang, T. Peijs: "Recent progress inacoustic materials and noise control strategies-A review," in *Applied Materials Today, 24*, pp. 1–27, 2021.

[2] O. Hahad, M. Kuntic, S. Al-Kindi, I. Kuntic, D. Gilan, K. Petrowski, A. Daiber and T. Münzel: "Noise and mental health: evidence, mechanisms, and consequences," *J Expo Sci Environ Epidemiol*, 35, pp. 16–23, 2025.

[3] M. Dohmen, E. Braat-Eggen, A. Kemperman and M. Hornikx: *"The effects of noise on cognitive performance and helplessness in childhood: a review,"* Int J Environ Res Public Health, pp. 1-12, 2022.

[4] O. Hahad, M. Kuntic, S. Al-kindi, I. Kuntic, D. Gilan, K. Petrowski, A. Daiber and T. Münzel: *"Noise and menthal health:evidence, mechanisms, and consequences,"* Journal of exposure science and environmental edpidemiology, pp. 1-12, 2024.

[5] M. Cabrera, A.P. Galvin, F. Agrela, M.D. Carvajal and J. Ayuso: *"Characterisation and technical feasibility of using biomass bottom ash for civil infrastructures,"* Construction and Building Materials 58, pp. 234-244, (014.

[6] J. Rosales, M. Cabrera, M.G. Beltrán, M. López and F. Agrela: *"Effects of treatments on biomass bottom ash applied to the manufacture of cement mortars,"* Journal of Cleaner Production 154, pp. 424-435, 2017.

[7] R. Venegas and O. Umnova: *"Acoustical properties of double porosity granular materials,"* The Journal of the Acoustical Society of America 130, 5, pp. 2765-2776, 2011.

DOI: 10.61782/fa.2025.0081

FORUM ACUSTICUM EURONOISE 2025

ACOUSTIC PERFORMANCE OF RAW EARTH CONSTRUCTION SYSTEMS: STATE OF THE ART AND PRELIMINARY RESULTS

C. Guigou Carter[1*] **P. Glé**[2] **T. Blinet**[1]
M. Ziapkoff[2] **M. Romagné**[3] **L. Le Guen**[4]
S. Tochon-Danguy[3] **A. Clément**[3] **A. Marcom**[5]
[1] CSTB, Grenoble / Marne La Vallée, France
[2] CEREMA, Gustave Eiffel University, UMRAE, Strasbourg, France
[3] LASA, Lyon, France
[4] Gustave Eiffel University / MAST-GPEM, Bouguenais, France
[5] Confédération Construction Terre Crue, Montreuil-Le-Gast, France

ABSTRACT

The main objective of the CarAc'Terre project is to remove regulatory and normative obstacles to raw earth construction techniques relative to acoustics. A multi-scale methodology for characterizing the acoustic performance of raw earth construction systems is proposed using both a performance-based and a perceptual approach. A state-of-the-art review on earth-based walls and floors has been conducted as a means of proposing a large experimental design in response to the identified gaps. Measurements are planned at the material, wall as well as building scale, such that contributions from materials formulation, walls composition, system type, and the construction implementation can be investigated.
This paper describes the general outline of the CarAc'Terre project and discusses the preliminary sound insulation results obtained on different types of walls. Measurements to determine material characteristics are described; these material characteristics are subsequently used as input data to numerical models. Comparison between predicted and measured acoustic performance, in terms of sound insulation, is also examined.

Keywords: *acoustic performance, raw earth, building acoustics, measurement, prediction.*

[*] ***Corresponding author***: *catherine.guigou@cstb.fr*
Copyright: *©2025 First author et al. This is an open-access article distributed under the terms of the Creative Commons Attribution 3.0 Unported License, which permits unrestricted use, distribution, and reproduction in any medium, provided the original author and source are credited.*

1. INTRODUCTION

1.1 The CarAc'Terre project

The main objectives of the CarAc'Terre project are to characterize the acoustic performance of raw earth constructions from a physical and sensory perspective, distinguishing the contributions from material formulation, wall composition, and their implementation.
The project, running for 3 years (2024-2027), is carried out with the support of the French Earth National Project [1] which aims to enable a new, large-scale deployment of raw earth constructions by removing cultural, socio-economic, technical, insurance, and regulatory barriers, particularly by involving craftsmen in the earth industry.

1.2 Raw earth in buildings

Environmental regulations strongly influence material choices by imposing strict standards on energy performance and carbon emissions. Raw earth, as a low-carbon material, is a response to these requirements, promoting sustainable construction that respects natural resources. Such a strategic material, naturally abundant and renewable, also offers interesting thermal properties to improve summer comfort, thus impacting the energy efficiency and comfort of buildings.
However, the critical lack of acoustic data on raw earth is a major obstacle to its widespread specification and use. Without this information, architects, acousticians, designers, and construction professionals in general are still hesitant to adopt this material, despite its numerous environmental benefits.

1.3 Acoustic issues and challenges of raw earth

Mastering the acoustic properties of raw earth-based materials and construction systems in buildings necessarily requires a better understanding of the physical phenomena governing acoustic properties at the material, wall, and in situ scales.
This work has been initiated for certain materials for which results are already available. This is the case, for example, of lightweight earth mixtures [2]. These initial studies have raised numerous questions, such as the effect of the earth and plant fillers used, the elastic characteristics of various materials, and the assumptions of isotropy or multi-scale porosity. Beyond understanding performance levels, it is important to be able to model acoustic behavior and extrapolate them to various formulations or implementation configurations. An initial benchmark of available acoustic modeling tools was carried out on various raw earth systems (earth brick walls, lightweight earth walls, partitions with earth plates) [3].

2. PROJECT METHODOLOGY

The main objective of the project is to remove regulatory and normative barriers for all raw earth construction techniques regarding acoustics. The proposed approach is based on the following tasks:

- State of the art and fabrication
- Laboratory measurements
- In situ measurements and surveys
- Modeling at element and building scales
- Knowledge dissemination

The first task aimed to gather all existing data on the subject through a state-of-the-art review in order to define the most appropriate experimental investigation (earth and construction systems choice).
The experimental approach is implemented in two ways: the laboratory level at the material and wall scales under controlled conditions, and the in situ level, with the aim of completing the characterizations while collecting user feedback on their perceptions of the acoustic comfort associated with the raw earth material.
The modeling task will allow the measurement results to be extended to various configurations (formulations, thicknesses, frame types, junctions, etc.) or construction systems.
Finally, the dissemination task intends to communicate the main results in an understandable manner to the raw earth stakeholders in the construction sector. Databases, charts, test reports and standard construction solutions will be widely shared and usable to promote raw earth for different types of buildings, including collective housing.

3. MATERIAL SCALE

3.1 Material types

Raw earth is implemented using numerous and very different techniques. Furthermore, the raw earth material itself can be very diverse, partly due to the nature of the earth in question and partly due to the elements associated with it (plant fillers, wooden frames, etc.).
The following materials are mainly distinguished [4]:

- Lightweight earth: obtained by combining a large proportion of fibers (hemp, straw, flax, etc.) to earth, with a density around 150 to 1000 kg/m^3, implemented through shuttering or projecting, or precast bricks;
- Cob: mixture of clay earth and fibers (usually straw) around secondary frames, with a density from 600 to 1800 kg/m^3;
- Bauge: earth-fiber mixture with density from 1400 to 1800 kg/m^3, applied in a plastic state by lifting directly onto a wall, with or without formwork;
- Rammed earth: earth and gravel (no fibers) mounted by compaction with formwork, with density from 1700 to 2200 kg/m^3;
- Adobes: earth bricks eventually including fibers shaped manually using molds, with density from 1200 to 1800 kg/m^3;
- Earth bricks: generally obtained without fibers through compression or extrusion, with density from 1400 to 2200 kg/m^3;
- Raw earth boards: fiber-reinforced earth boards (similar use as plaster boards) with density ranges from 700 to 2000 kg/m^3;
- Coatings: earth renderings (with or without fibers) are used in addition to all the previously listed materials as a finishing layer to homogenize the appearance of a wall and to protect it, with density from 1500 to 1800 kg/m^3;
- Loose earth for floor: adding weight to wood-based floor systems.

It is desired to be able to use all kind of earths regardless of their origin (quarries, spoil, reuse-deconstruction, etc.). Therefore, the tested samples will be representative of a very wide variability of origins, allowing to generalize the obtained acoustic performance results as much as possible.

3.2 Approach implemented

The material-scale approach is based on measuring the acoustic performance (absorption coefficient, transmission loss) in a Kundt tube on the different selected materials, and simultaneously characterizing the porous (porosity, airflow resistance, tortuosity, etc.) and elastic (Young's modulus, structural damping) parameters.
Once these properties and characteristics have been determined, an initial modeling step is carried out at this scale to identify the most appropriate material model for each case. In this context, acoustic models account for three modes of dissipation: viscous and thermal dissipations linked to the porous nature of the material, but also mechanical dissipations linked to the elastic skeleton [5]. The parameters required for these models can be relatively numerous depending on the complexity of the material, but a satisfactory description is generally possible by retaining only the most significant ones. MATELYS's AlphaCell© software based on the transfer matrix method (TMM) will be used primarily to predict the acoustic performance at the material scale.
In addition to these parameters, there are mechanical parameters, whose effect at the wall/component level can be very significant. The longitudinal dynamic modulus of elasticity is determined according to standard EN 14146. This measurement is primarily used to characterize the elastic properties of "solid" materials such as concrete (standard, lightweight, polymer, etc.), terracotta, various renders, etc. The method is based on measuring the fundamental resonant frequency of a "bar" or "cylinder" specimen subjected to longitudinal vibration (compression mode). The damping factor is obtained based on the width of the resonance peak. The flexural elastic modulus of the boards (plaster based or earth based) is also determined using the standard ISO 16940 (sample sizes being in the order of 600 mm long and 60 mm wide).

4. BUILDING ELEMENT SCALE

Building elements are made from the materials previously studied to form the construction systems for walls, floors, and their coatings. The acoustic challenges for these components and raw earth construction systems are numerous. One of them is to understand their acoustic properties in terms of direct transmission, lateral transmission, and absorption under controlled laboratory conditions, and to successfully maintain these performances once they are installed in situ.
Others are to include the complexity of ensuring peripheral sealing of walls due to shrinkage and settlement as the material dries, the management of wall junctions, the behavior of the systems, and the inhomogeneities of the material that can cause localized weaknesses.
The acoustic and mechanical properties of diffuse-field systems presented below are measured according to building acoustic standards in the CSTB laboratories.

4.1 Mechanical properties

The structural reverberation time Ts (in s) is evaluated according to the EN ISO 10848-1 standard on each supporting wall without finish. The total loss factor, including internal losses, coupling losses, and radiation losses, can then be deduced and used in simulations.
The mechanical mobility Y_{ij} (in m/(Ns)) is the ratio of the velocity response at point i to an excitation force applied at point j, according to the ISO 7626-1 standard. An impact hammer (instrumented for evaluating the injected force) is used to excite the wall (transient excitation), and several measurement points on the wall are considered, along with several excitation positions.

4.2 Acoustic properties

The acoustic behavior of a system (wall, floor, etc.) is characterized in a laboratory from a direct sound insulation perspective by measuring the sound reduction index R, evaluated according to standard NF EN ISO 10140-2 and from a lateral transmission perspective by measuring the standardized lateral sound insulation $D_{n,f}$, according to standard NF EN ISO 10848-1. Sound absorption behavior represents the ability of a material or system to absorb the energy of sound waves, thus reducing sound reflection and limiting phenomena such as acoustic reverberation. It is characterized by the sound absorption coefficient α_s, measured according to the NF EN ISO 354 standard.

4.3 Radiation homogeneity

For non-homogeneous structures of certain raw earth construction systems, such as cob or rammed earth, transmission through the walls has been analyzed using supplementary sound intensity measurements. Areas of greater radiation can be observed locally within the studied walls due to certain cracks, clusters of fibers or aggregates (see Figure 1).

4.4 Boundaries treatment

The shrinkage and settling of the earth during drying can create voids around the edges of the walls, ranging from one to several centimeters (see Figure 2), which must be filled to obtain satisfactory acoustic measurement.

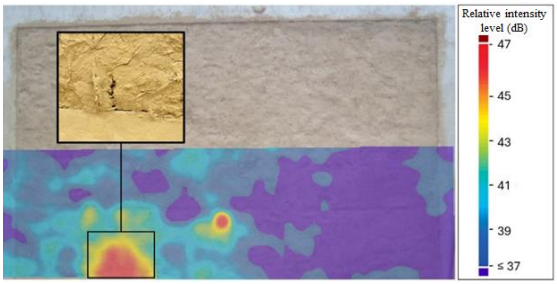


Figure 1. Intensity measurement on the cob wall showing effect of local crack (400 Hz).



Figure 2. Peripheral shrinkage of an earth wall due to drying.

4.5 Modelling

CSTB's AcouSYS software will be used primarily to predict the acoustic performance of multi-layer systems. Calculations are based on the transfer matrix method (TMM) combined with spatial windowing to account for the finite dimensions of the systems. Materials are available: isotropic or orthotropic solid, fluid, porous, perforated, and viscoelastic. Partition assemblies use a frame transmission model with a SEA (Statistical Energy Analysis) approach integrating the distance between studs, the screw pitch, and point contact stiffnesses for frames.
All physical parameters of the materials must be defined.

5. BUILDING SCALE

The difficulty in transposing and maintaining performance at the building scale lies in controlling the direct and flanking transmissions.

5.1 Junctions

Junction characterizations are planned to be conducted on a prototype built from earth bricks and a timber frame specifically, as well as in situ when the configurations encountered allow it. Measurements will be based on the EN ISO 10848 series of standards for the frequency range covering one-third octave frequencies from 50 to 5000 Hz.

5.2 In situ acoustic measurements

Sites containing raw earth construction systems are being identified to conduct in situ acoustic measurements in order to link building elements acoustic performances to the building acoustic performance. The adequacy of the in situ acoustic performance with respect to regulatory criteria and comfort will be verified.

5.3 Perceptive survey

A significant built heritage of raw earth is present in France and around the world [6-7]. Despite a Ph.D thesis on the perception of raw earth including the acoustic aspect [8], the absence of quantitative and qualitative data on projects built with raw earth (heritage or recent projects) is quite notable [9]. Therefore, as part of the CarAc'Terre project, it is intended to collect users perception of acoustic comfort and, more broadly, interior comfort based on a survey methodology to be established. The subjective data collected will be compared with acoustic measurements at the building scale in order to observe the influences and relationships between material-related parameters, implementation parameters and user-related parameters (physical, physiological and psychosocial).

6. PRELIMINARY RESULTS

6.1 Material scale

6.1.1 Acoustic based characterization

For each material, an experimental campaign is first carried out to obtain as many mechanical and acoustic parameters as possible, which are essential for subsequent modelling.
An example of material-scale modelling is proposed for the coating on adobe wall. The material behavior can be considered as purely elastic, porous-rigid, or poro-elastic. In the case of a purely elastic material, considered here as isotropic, only the mechanical contributions come into play. These are described in terms of density ρ, Young's modulus E, Poisson's ratio ν, and damping factor η. The porous-rigid hypothesis, which considers only the porous phase of the material, is based on acoustic dissipation resulting solely from visco-inertial and thermal effects. Finally, poro-elastic behavior combines the three dissipative effects. The porous character modeling proposed here is based on the Boutin-Geindreau granular model [10], requiring only two parameters Φ, the porosity, and R_p, the radius of earth aggregate considered to be spherical, from which all the other acoustic parameters are deduced.
Five cylindrical samples of coating, with an average

thickness of 41 mm and an average diameter of 96 mm, were tested. Considering the elastic parameters given in Table 1, a Poisson's ratio ν = 0.2 [11], and the acoustic parameters obtained, i.e. Φ=40% and R_p=2.1 10^{-5} mm, the absorption coefficient α (-) and the transmission loss TL (dB) of the coating are calculated and compared to the average experimental response measured in a Kundt's tube as shown in Figure 3. Results analysis reveals that the hypothesis of purely porous behavior fails to predict TL, while the one of purely elastic behavior fails to predict α. The poro-elastic behavior hypothesis therefore seems to be the most interesting approaches for TL and α prediction; however, the approach could be refined to improve accuracy.

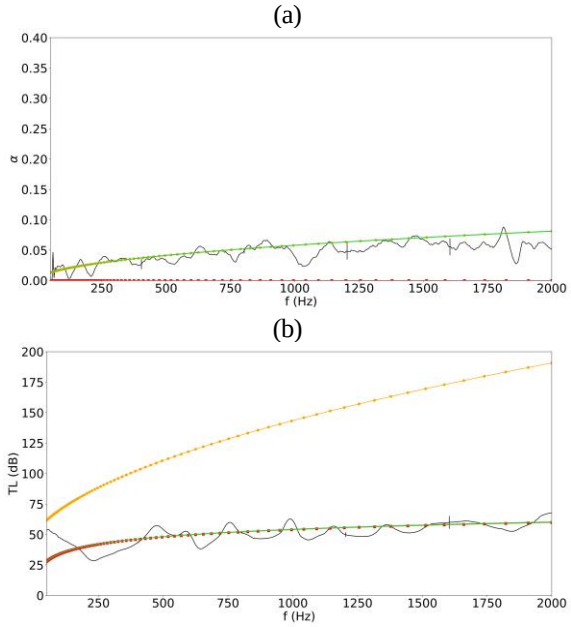


Figure 3. Coating material scale behavior for (a) absorption coefficient α (-) and (b) transmission loss TL (dB); experimental measurement (–), simulation of elastic (■), porous-rigid (●), and poro-elastic (–) approaches.

Concerning the acoustic measurement at the material scale for the adobe samples, difficulties were encountered. On the one hand, it was impossible to machine the adobe bricks with the various tools available (hole saw, diamond core bit) to the desired dimensions. The porosity was however measured on brick fragments and found to be around 36%. On the other hand, the materials proved to be too resistive to characterize directly the resistivity. The order of magnitude for this parameter is 10^7 N.m^{-4}s, and this value allowed to determine the absorption behavior and the correct orders of magnitude for transmission performance during modeling at the material scale. Evaluation of other parameters (tortuosity and characteristic lengths) were also not possible due to this impermeable nature.
Therefore, these different materials will be modelled as elastic materials at the building component scale when transmission loss is concerned.

6.1.2 Structure based characterization

Samples in the form of bars of 210 mm in length and a square cross section of 50 mm x 50 mm, were produced using the same mix as the adobe bricks. They are used to determine the first compressional mode for longitudinal vibration propagation. Similar measurements were carried out for the coating applied to adobe wall as well as the coating on the earth-based boards mounted on the lining. The elastic modulus of the boards (plaster based or earth based) was determined on beam samples. Table 1 presents the determined characteristics.

Table 1. Characteristics determined for the different configurations of the adobe wall.

Material	ρ (kg/m^3)	E (MPa)	η (%)
Adobe	1835	3270	2.3
Coating on adobe	1605	4195	4.2
Plaster board	725	2200	2.0
Earth based board	1480	664	3.9
Coating on earth based board	1738	4360	2.3

6.2 Building component scale

Following the state-of-the-art phase, a first group of laboratory measurements has been conducted on different wall systems. Sound reduction index R was obtained for

- Bauge wall
- Two rammed earth walls: 30 and 40 cm in thickness
- Adobe wall considering the effect of a layer of earth slip, earth coating, and plasterboard or raw earth-based board linings

Absorption coefficient α was obtained for several coatings made of clay and earth-hemp mix. Sound reduction index R and airborne flanking transmission $D_{n,f}$ was obtained for a partition wall made of raw earth boards mounted on a

metallic frame. Figure 4 illustrates some of the laboratory tested systems.

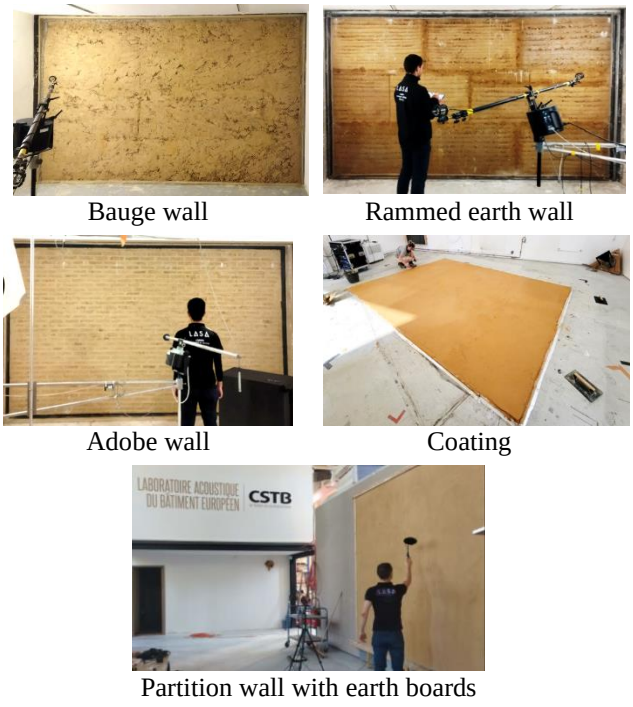


Figure 4. Illustration of the systems tested in laboratory.

These measurement results along preliminary prediction results are presented below in details for the adode wall.

6.2.1 Adobe wall – Laboratory acoustic measurements

The masonry type adobe wall is 110 mm thick, and made of 110 mm x 50 mm x 220 mm bricks composed of clay, with a mass per unit area of 184 kg/m². The adobe wall is 2.5 m in height and 4.2 m in width and the first measurements were performed 56 days after manufacturing. Then, on the emission side, a thin layer (≈2 mm) of earth slip was first put on the wall, and afterwards a complementary layer of earth coating of 22 mm in thickness was applied.
On the receiving side, two types of lining on standard metallic frame independent from the adobe wall, are considered: the first one is a standard plasterboards lining (45 mm of mineral wool and a double layer of 12.5 mm thick plasterboards); the second one uses earth based boards (earth with coco fibers) 22 mm in thickness instead of the plaster boards, and a earth based coating 10 mm in thickness. The first lining corresponds to a surface mass of about 18 kg/m² while the second one to about 49.5 kg/m². Figure 5 presents the sound reduction index measurement results for the different configurations considered.

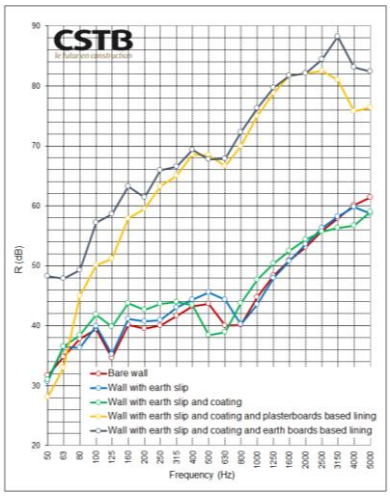


Figure 5. Sound reduction index R for the different configurations of the adobe wall.

It can be observed that the application of the earth slip layer has limited influence of the sound reduction index, meaning that the wall has a low porosity. Adding the earth coating layer increases the mass per unit area of the wall thus modifying the apparent critical frequency and improving the sound reduction index below this critical frequency.
Applying a lining on the other side of the wall greatly improves the acoustic performance. The lining using earth based boards with an earth coating finish being heavier than the standard plaster boards is associated to the better performance especially in the low frequency range. In the high frequency range, a flanking pass (probably related to the concrete frame used to mount the wall system) limits the acoustic performance of the linings.

6.2.2 Adobe wall – Mechanical measurements

Mobility depends on frequency and has peaks corresponding to the resonance frequencies of the structure considered in the low frequency range. In the high frequency limit, the input mobility Y_{ii} is essentially real and determined by the mass per unit area and the bending stiffness. Figure 6 presents the measured input mobility of the bare adobe wall obtained at 5 different positions on the wall, along with the one predicted using AcouSYS software with an elastic modulus of 2.2 GPa and 3.3 GPa. Since the wall is not a thin plate, the predicted input mobility is not independent of frequency.

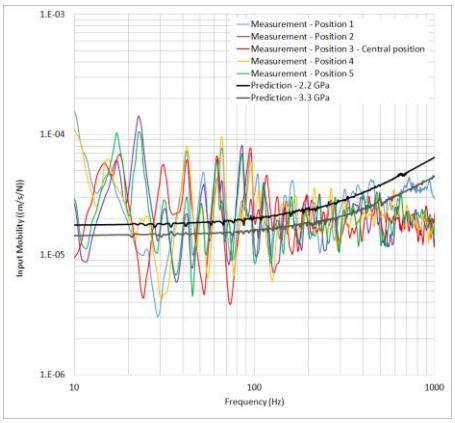


Figure 6. Input mobility for the adobe wall (bare configuration).

6.2.3 Adobe wall – Comparison between measurement and prediction

The comparison between the measured and predicted sound reduction index for the different configurations of the adobe wall is presented in Figures 7 to 10. The corresponding single number quantities are given in Table 2.
It can be observed that the predicted performances are in line with those measured except for the lower frequency range in the case of the bare wall and the wall with coating on one side (Figures 7 and 8). The elastic modulus of the adobe wall is taken to be 2.2 GPa in order to match the critical frequency between measurement and prediction.

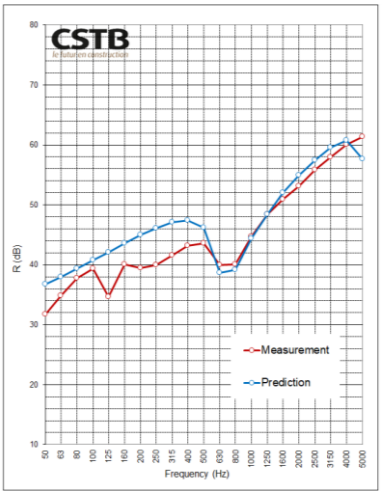


Figure 7. Sound reduction index for the bare adobe wall.

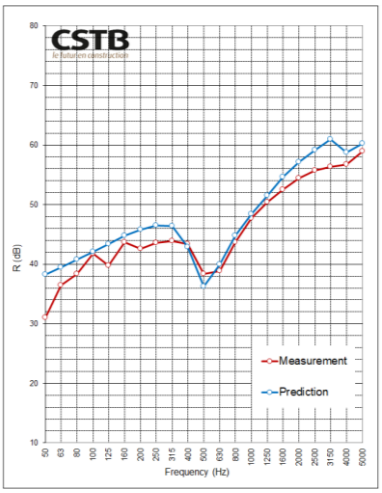


Figure 8. Sound reduction index for the adobe wall with earth coating on one side.

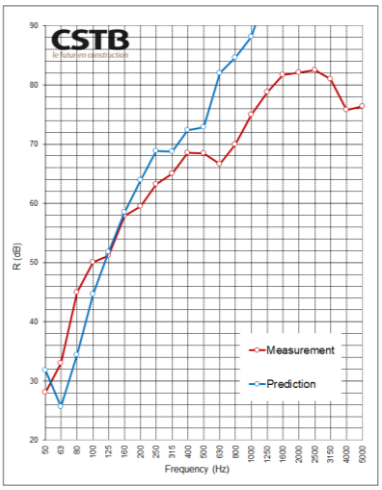


Figure 9. Sound reduction index for the adobe wall with earth coating on one side and with standard plaster board lining on the other side.

The presence of a lining improves greatly the acoustic performance; however, the prediction overestimates the acoustic performance (Figures 9 and 10). This is probably due to a flanking transmission associated to the concrete frame holding the wall and the lining. This is under investigation and will be taken into account in the future prediction. However, the SNQ in the case of the standard lining obtained from the measurement and the prediction is close; this is not the case for the other type of lining tested.

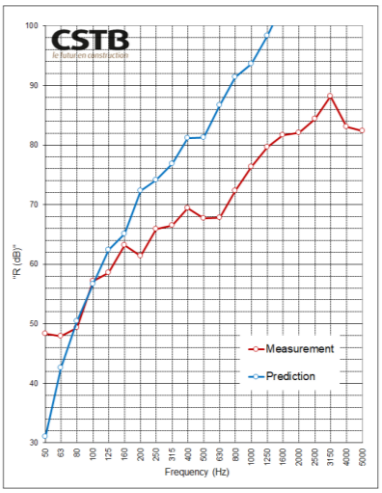


Figure 10. Sound reduction index for the adobe wall with earth coating on one side and with earth based board lining on the other side.

Table 2. SNQ for the different configurations of the adobe wall – Measurement and prediction.

Configuration	R_w+C (dB) Measured / Predicted
Bare wall	45 / 45
Wall with earth slip and coating	46 / 46
Wall with earth slip and coating and plasterboards based lining	70 / 71
Wall with earth slip and coating and earth boards based lining	73 / 81

7. CONCLUSIONS

This paper describes the general outline of the CarAc'Terre project and discusses the preliminary sound insulation results obtained on different types of walls. Measurements to determine material characteristics are described; these material characteristics are subsequently used as input data to numerical models.

Preliminary comparison between predicted and measured acoustic performance, in terms of sound insulation, has been examined for the adobe wall. Similar methodology is applied to the other walls already tested.

More measurements both in laboratory and in situ are planned in 2025, as well as the first occupants survey.

8. ACKNOWLEDGMENTS

This project is supported by the French State as part of France Relance, now integrated into France 2030, and operated by ADEME.

9. REFERENCES

[1] https://projet-national-terre.univ-gustave-eiffel.fr/

[2] T. Blinet, C. Guigou-Carter, P. Glé, A. Héllouin de Ménibus : *Projet report on acoustic performances of light earth (clay and hemp shiv mix) walls* (in French), 2024. https://hal.science/hal-04841720v1

[3] M. Romagné, P. Glé, C. Guigou-Carter, E. Gourdon, "Acoustic performances of earthen walls, review of modeling approaches and tools," *Proceedings of Internoise 2024* (Nantes, France), pp. 4418–4428, 2024.

[4] Collectif terre crue : *Guide des bonnes pratiques de la construction en terre crue*. 2018.

[5] J.F. Allard, N. Atalla: *Propagation of Sound in Porous Media: Modelling Sound Absorbing Materials*, Second Edition, Wiley, 2009.

[6] U. Röhlen, C. Ziegert : *Construire en terre crue*. Le Moniteur Ed., 2013.

[7] F. Volhard : *Construire en terre allégée*. Actes Sud, 2016.

[8] M. Miranda Santos : *La terre crue à l'épreuve des ambiances sonores. Un dialogue entre la mesure physique et les expériences sensibles*, Ph.D thesis ENSA Nantes, 2022.

[9] A.N. Daza, E. Zambrano, J.A. Ruiz, "Acoustic performance in raw earth construction techniques used in Colombia," *Proceedings of EuroRegio2016* (Porto, Portugal), pp. 1–10, 2016.

[10] Boutin, C., Geindreau, C., "Periodic homogenization and consistent estimates of transport parameters through sphere and polyhedron packings in the whole porosity range." *Phys. Rev. E* 82, 2010.

[11] Blinet, T., Falwisanner, T., Glé, P., Guigou-Carter, C., Kadri, E., "Propriétés acoustiques des matériaux biosourcés.",2018.

DOI: 10.61782/fa.2025.0082



FORUM ACUSTICUM
EURONOISE 2025

ACOUSTIC PERFORMANCE OF THE JUNCTION BETWEEN FAÇADES WITH ETICS AND THE JOINERY

Lieven De Geetere[1*]
[1] Buildwise, Kleine Kloosterstraat 23, 1932 Zaventem, Belgium

ABSTRACT

Due to the use of lightweight and often rigid insulation materials in External Thermal Insulation Composite Systems (ETICS), the risk of sound leaks at the junction with the external joinery is real. However, detailed knowledge of the acoustic performance of common connection methods is lacking. Therefore, an acoustic measurement campaign was set up in the acoustic laboratory of Buildwise in Belgium to measure the acoustic insulation performance of the junction $R_{s,Atr}$ $(= R_{s,w} + C_{tr})$ (standardized in ISO 10140-1) for a large number of common connection methods. From this dataset, interesting trends are observed and guidelines for the applicability of the different junction types with respect to the required façade sound insulation are deduced.

Keywords: *ETICS, façades, sound leaks, joinery, junction*

1. INTRODUCTION

External Thermal Insulation Composite Systems (ETICS) are frequently used to improve the energy efficiency and sustainability of buildings, both new and existing. They basically comprise an insulating layer and an external rendering. The insulating layer consists of panels that can be glued or mechanically fixed to the structural façade. These are either made up of fibrous materials (like mineral wool, wood fibers,…) or are foam-based (like EPS, XPS, PU, …). They usually increase the direct façade sound insulation R_{Atr}, but can also lower it, especially when relatively thin and stiff insulation layers are combined with lightweight renderings (see EN ISO 12354-1 [1], Annex D.2.3 for design values of ΔR_{Atr}).

Further, due to their light and stiff character, they are prone to cause sound leaks at the junction with the external joinery. Whether these sound leaks will determine the overall in-situ sound insulation of a composed façade pane, will depend on the (opaque) façade composition, the window composition, the way of mounting the window to the façade, the way of connecting the ETICS to the window and the finishing of the internal reveal. The acoustic performance of the junction can be quantified by the so-called sound reduction index of joints or slits R_s, which is defined in EN ISO 12354-3 [2] and which will be called junction sound reduction index throughout this paper. It represents the sound reduction index that would be measured for a perfectly insulating panel with area of 1 m² in which a joint with a length of 1 m is applied. For façades, the spectral adaptation term C_{tr} (defined in ISO 717-1 [3]) is usually applied to obtain a single number rating representative for urban traffic noise $R_{s,Atr}$ $(= R_{s,w} + C_{tr})$.
Since experimental data on this important junction sound reduction index is hard to find, a laboratory measurement campaign was set up to study a large number of common connection methods used in Belgium.

2. MEASUREMENT SETUP

The measurement method to measure the sound reduction index of joints or slits is standardized in ISO 10140-1 [4], Annex J. Since this method is mainly intended for simple joints filled with fillers or seals, it is not directly applicable to more complicated junctions of ETICS façades with the external joinery. Therefore, a dedicated measurement setup was built, however keeping the same measurement methodology.

[*] ***Corresponding author***: lieven.de.geetere@buildwise.be.
Copyright: *©2025 Lieven De Geetere. This is an open-access article distributed under the terms of the Creative Commons Attribution 3.0 Unported License, which permits unrestricted use, distribution, and reproduction in any medium, provided the original author and source are credited.*

In a standard 10 m² laboratory measurement opening, first a façade wall with an ETICS is constructed. This wall is made up of 19 cm thick massive concrete blocks, plastered on the indoor side. On the outdoor side, the insulating layer is made up of 20 cm thick EPS insulation panels that are glued to the base wall. For practical reasons, the exterior rendering is represented by a 9.5 mm gypsum board lining glued to the insulation panels. The sound reduction index of this ETICS wall is called R_{wall}. By comparing the measured spectra of the wall with and without the ETICS, the mass-spring-mass resonance frequency of the ETICS is estimated to be in the 250 Hz third-octave band.
Secondly, a highly insulating dummy window is assembled. It is made up of a 7 cm thick heavy timber peripheral frame, completely filled with mineral wool. On both sides, it is closed by a composite layer of two 2 mm thick steel plates glued together with a 3 mm thick bituminous layer in between (see Fig. 1). The sound reduction index of this dummy window is measured in the laboratory in a standardized small-sized test opening and called R_{dummy}.

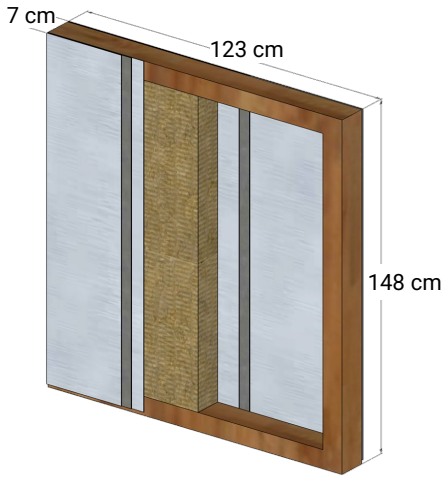


Figure 1. Dummy window.

Finally, an opening is made in the façade wall to host a concrete precast frame to which the dummy window can be mounted using the connection methods to be investigated. Four concrete frames with different opening dimensions make it possible to control the mounting gap width between concrete frame and dummy window very precisely to respectively 0, 2, 4 and 8 cm (see Fig. 2 and Fig. 4, nr. 6). The measured sound reduction index of this composed wall is called R_{tot}.

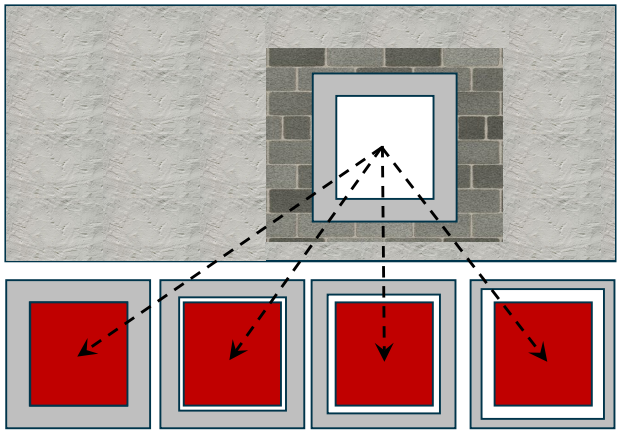


Figure 2. Principle to ensure controlled gap widths of 0, 2, 4 and 8 cm between window and façade wall by using precast concrete frames to mount the dummy window (red).

This total sound reduction index can be calculated by Eqn. (1):

$$R_{tot} = -10log\left\{\frac{1}{S_{tot}}\left[\begin{array}{c} S_{wall}\cdot 10^{\left(\frac{-R_{wall}}{10}\right)}\ldots \\ +S_{dummy}\cdot 10^{\left(\frac{-R_{dummy}}{10}\right)}\ldots \\ +1\cdot l_S 10^{\left(\frac{-R_S}{10}\right)}\end{array}\right]\right\} \quad (1)$$

in which S_{tot} is the area of the laboratory measurement opening, S_{wall} is the area of the façade wall excluding the window opening, S_{dummy} is the area of the dummy window, l_s is the perimeter of the window opening. Here it is supposed that the junction type is the same for all 4 sides of the window panel.
From that equation and the previously measured spectra for R_{wall} and R_{dummy}, the junction sound reduction index can be estimated by Eqn. (2):

$$R_s = -10log\left\{\frac{1}{l_s}\left[\begin{array}{c} S_{tot}\cdot 10^{\left(\frac{-R_{tot}}{10}\right)}\ldots \\ -S_{wall}\cdot 10^{\left(\frac{-R_{wall}}{10}\right)}\ldots \\ -S_{dummy}\cdot 10^{\left(\frac{-R_{dummy}}{10}\right)}\end{array}\right]\right\} \quad (2)$$

In the ideal case where there is no sound leakage across the window junctions, the maximum total sound reduction index can be calculated by omitting the green term in Eqn. (1). It can be seen from Fig. 3 that this ideal sound reduction index is determined by the performance of the façade wall at low

frequencies and by the performance of the dummy window at high frequencies.

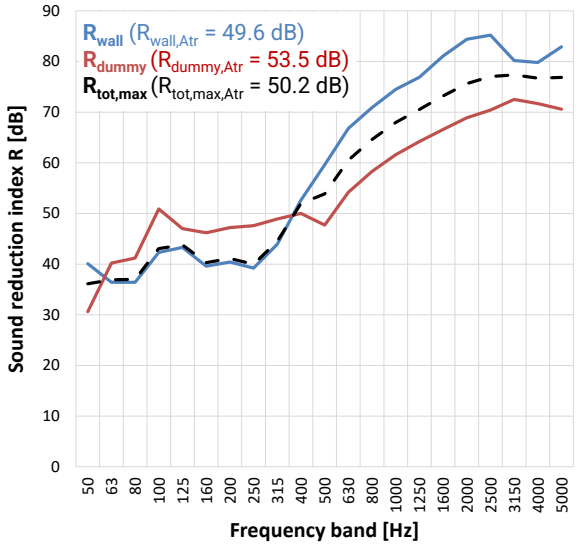


Figure 3. Measured sound reduction index for the façade wall and the dummy window and calculated maximum total sound reduction index.

3. TESTED CONFIGURATIONS

In the Buildwise acoustic lab in Limelette, Belgium, a large number of variants of typical mountings of exterior joinery in an ETICS wall were tested (Fig. 4), both in flush (a) and eccentric (b-f) mounting. Anchoring methods using dowels or angle brackets (a-c), positioning frames (i.e. first attached to the structural wall) (d-e) and installation frames (i.e. first attached to the window) (e-f) were combined with interior finishes made of plasterboard, either fixed directly in the reveal (c) or via mounting blocks where the remaining space between the reveal and the plasterboards is completely filled with standard PU spray foam (a, b, f), or glued on XPS reveal boards (d-e).

4. STUDIED EFFECTS

4.1 General remarks

In the following graphs, a selection of the measured junction sound reduction index spectra R_s are presented. The single number values mentioned in the graphs are $R_{s,Atr}$ values. When some curves are lacking data, it means that the values in these frequency bands could not be calculated by Eqn. (2) because in these bands the measured R_{tot} was higher than the $R_{tot,max}$.

Since the single number value $R_{s,Atr}$ is in most cases largely determined by the value of R_s around the mass-spring-mass resonance frequency of the ETICS, mounting alternatives that give large variations in the 250 Hz band will also reflect large variations in the single number value. Inversely, mounting variations that cause variations only at higher frequencies can show uncorrelated changes in the single number value due to usual statistical variations within the expected measurement uncertainty at 250 Hz.

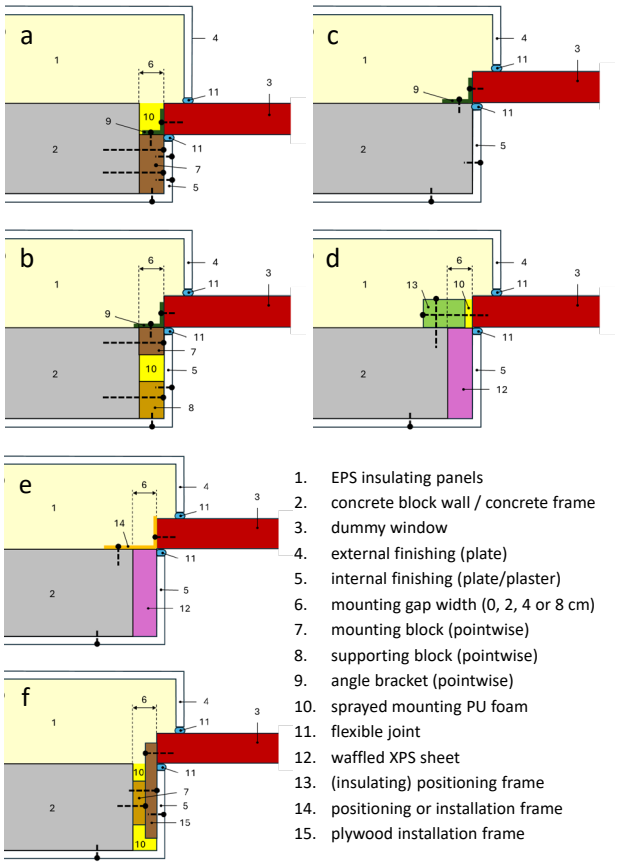


Figure 4. Examples of tested mounting variations.

4.2 Mounting gap width

The mounting gap width (see Fig. 4, nr. 6) is an important parameter, especially when the window is mounted pointwise by dowels or angle brackets, which is illustrated in Fig. 5 and Fig. 6. A mountain gap width of 4 cm or 8 cm

lowers the $R_{s,Atr}$ value by 4 respectively 9 dB compared to the case where no mounting gap was present.



Figure 5. Example of a (partial) mounting using angle brackets on mounting blocks with a mounting gap of 8 cm (exterior side).

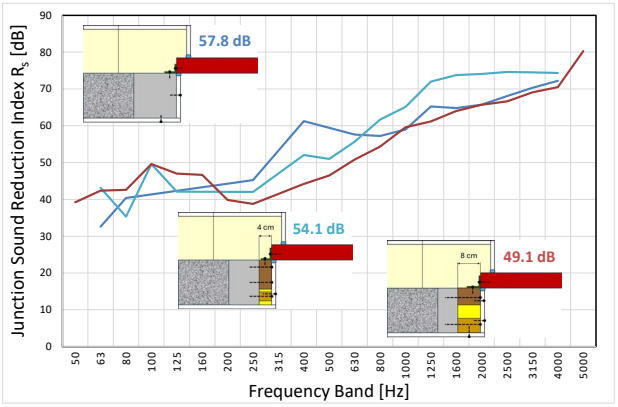


Figure 6. Influence of the mounting gap width.

4.3 Interior finishing

For the cases with spray foamed interior reveals in combination with a pointwise connection of the window panel (Fig. 8), adding an extra gypsum board at the interior side, gives an average gain in $R_{s,Atr}$ of about 1 dB.
However, when in these cases, the sprayed PU foam on the interior reveal is replaced by rigid XPS insulating panels, a large wideband drop of about 9 dB is observed (Fig. 7). This was found to be due to remaining thin air gaps between these insulating panels and the reveal and between the insulating panels themselves.

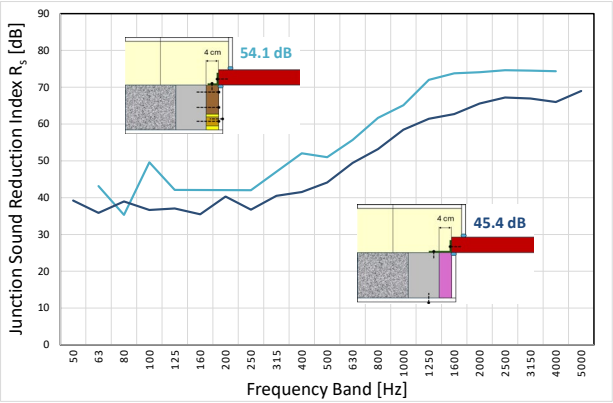


Figure 7. Influence of replacing the PU spray foam at the interior side by rigid XPS insulating panels (case with pointwise mounted windows).



Figure 8. Example of a (partial) mounting using angle brackets on mounting blocks with a mounting gap of 8 cm and spray foamed interior reveals (interior side).

4.4 Flush versus eccentric mounting

When switching from a flush to an eccentric mounting in the case of pointwise mounted windows, the $R_{s,Atr}$ value drops about 2.5 dB and 1 dB in the case of respectively a 4 cm and 8 cm mounting gap. This drop is mainly due to the behaviour in the 250 Hz band and since both curves remain similar in

each case, this difference is more likely to be determined by the measurement uncertainty in this band (Fig. 9).

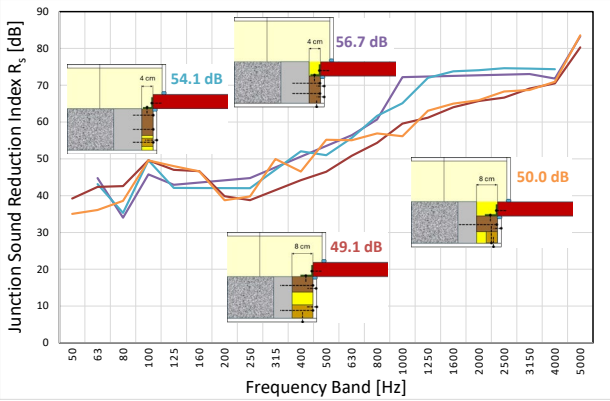


Figure 9. Influence of the mounting depth of the window: flush mounting versus eccentric mounting.

4.5 Installation frame type

Installation frames are commonly used in eccentric mountings to laterally extend the window chassis to enable fixing it to the structural façade while completely covering the mounting gap. They can be made of different materials. However, comparing 60x60 mm² heavy timber battens with L-shaped frames made of a 8 mm thick PES fiberglass composite (Fig. 4e) did not show significant performance differences.

4.6 Plywood installation frame

Another common technique in Belgium to install windows while ensuring airtightness is to apply a plywood installation frame to the window before it is being installed. This installation frame is mounted pointwise on the structural façade wall using mounting blocks. The remaining space between the installation frame and the reveal is then filled with sprayed PU foam (Fig. 4f). No considerable changes in performance are observed compared to pointwise connection methods without installation frame (Fig. 4b), as long as the mounting gap width is comparable.

4.7 Positioning frame density

The insulating positioning frames in Fig. 4d are made of compacted EPS battens with nominal densities of 100, 200 and 400 kg/m³. They have been tested for a mounting gap width of 4 cm and show no remarkable change in performance between these 3 densities.

4.8 Positioning frame filler type

The levelling clearance between the compacted EPS positioning frames and the window panel was filled either by a self-expanding foam tape or by a sprayed PU foam. In all cases, the PU foam performed considerably better (an improvement of about 3 dB in $R_{s,Atr}$) and is additionally more practical to apply (Fig. 10).

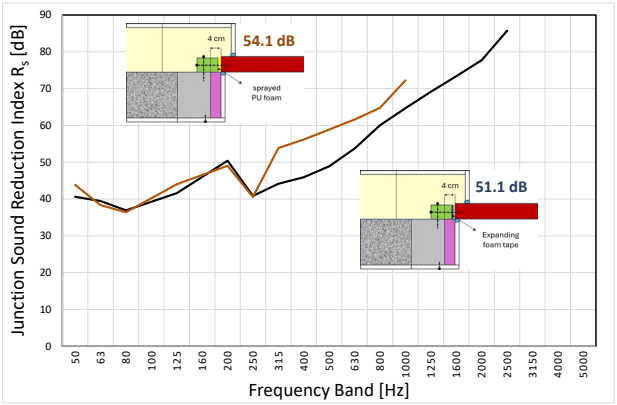


Figure 10. Influence of the filler type for the levelling clearance between positioning frame and window.

4.9 Sealing joints

Sealing joints between the interior and exterior finishings and the window are important to achieve a good air- and rain tightness. They also play an acoustic role at higher frequencies as can be seen in Fig. 11. The influence on the $R_{s,Atr}$ value however remains rather small (1 to 2 dB per joint), since the behavior around the mass-spring-mass resonance frequency of the ETICS remains unaffected.

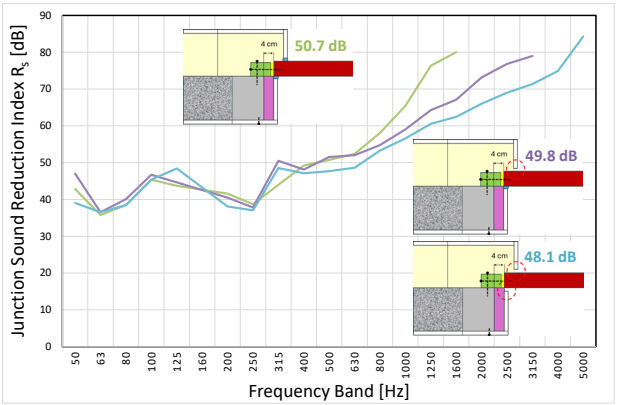


Figure 11. Influence of the sealing joints.

4.10 Exterior and interior finishing

For practical reasons, the external rendering and interior reveal finishing used in-situ were replaced during the laboratory measurements by acoustically equivalent plasterboards. Although not reflecting good practices but interesting from a scientific point of view, the effect of locally removing these lining plates was additionally studied (Fig. 12). Gradually removing these lining boards lowered the junction sound reduction index systematically in the frequency region above the mass-spring-mass resonance frequency of the ETICS. However, no systematic changes were observed around and below this resonance frequency. Since the $R_{s,Atr}$ value becomes more and more dominated by the spectral values at higher frequencies, a gradual decrease of 3 to 5 dB with each step was measured.

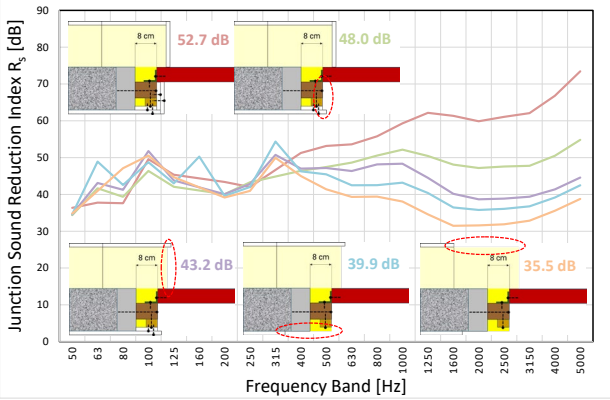


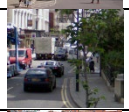
Figure 12. Effect of gradually removing exterior and interior lining boards.

5. APPLICABILITY OF THE TESTED JUNCTIONS IN DIFFERENT OUTDOOR NOISE CLASSES

5.1 Façade insulation requirements

The façade sound insulation requirements in Belgium are specified in the building acoustical standards series NBN S 01-400-x. Four outdoor noise classes are defined, going from a quiet rural environment or quiet residential area (Class 1) to very busy urban traffic (Class 4). For each class, a reference outdoor sound pressure level L_{Aref} is set. For dwellings, most strict requirements are for bedrooms during night. If there are no structural frequent loud passages of vehicles during night along bedrooms, the requirements, expressed in D_{Atr} (= $D_{2m,nT}$ + C_{tr}) for façade panes, are summarized in Table 1.

Table 1. Belgian façade sound insulation requirements.

Outdoor noise class		Day spaces		Night spaces	
		$L_{Aref,day}$	D_{Atr}	$L_{Aref,night}$	D_{Atr}
1		60 dB	≥ 28 dB	55 dB	≥ 28 dB
2		65 dB	≥ 31 dB	60 dB	≥ 32 dB
3		70 dB	≥ 36 dB	65 dB	≥ 37 dB
4		≥ 77 dB	≥ 43 dB	≥ 72 dB	≥ 44 dB

5.2 Use case

To verify what mounting methods can be used in each of the outdoor noise classes, an acoustically rather unfavourable situation of a small bedroom with a large total junction length between the ETICS wall and the joinery is considered (Fig. 13). We assume that the ETICS wall has an $R_{Atr,wall}$ of at least 48 dB. The in-situ façade sound insulation can be calculated according to [2]:

$$D_{Atr,tot} \cong R_{Atr,tot} + 10lg\left(\frac{V}{3S_{tot}}\right), \qquad (3)$$

in which $R_{Atr,tot}$ is the traffic-noise related single number value of the sound reduction index of the composed façade pane, that can be calculated using Eqn. (1) in which R_{dummy} is replaced by R_{window}.

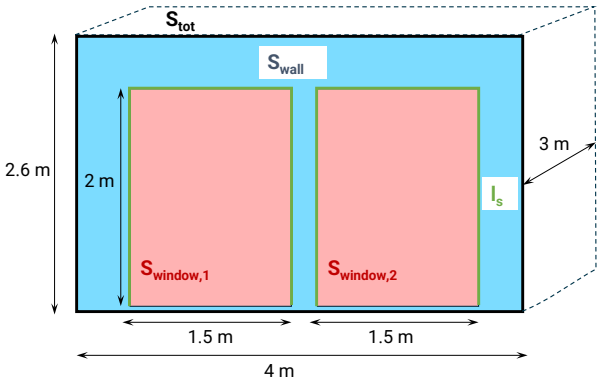


Figure 13. Use case of a small bedroom with S_{tot} = 10.4 m², S_{wall} = 4.4 m², S_{window} = 6 m² and l_s = 11 m.

Since the composed façade sound reduction index $R_{Atr,tot}$ will be largely determined by the sound transmitted through the windows and the junction, the choice of an appropriate window type is quite important. We first need to make a deliberate choice of the glazing, appropriate for the different outdoor noise classes. Then we make the necessary corrections described in EN 14351-1 [5] to estimate the chosen $R_{Atr,window}$ (Table 2).

Table 2. Choice of appropriate windows for the outdoor noise classes 2-4 for the selected use case.

Outdoor noise class	$R_{Atr,\ glazing}$	Area correction [5]	Frame correction [5]	$R_{Atr,\ window}$
2	30 dB	-1 dB	+1 dB	30 dB
3	40 dB	-1 dB	-3 dB	36 dB
4	47 dB	-1 dB	-3 dB	43 dB

5.3 Junction sound reduction index requirements

With these choices for $R_{Atr,wall}$ and $R_{Atr,window}$, the minimum required values for the junction sound reduction index $R_{s,Atr}$ to fulfill the D_{Atr} requirements for the bedroom in Table 1 can be calculated by combining Eqn. (3) and Eqn. (2) in which R_{dummy} is replaced by R_{window}. For classes 2, 3 and 4 this results in minimum $R_{s,Atr}$ values of 42.9, 43.3 and 53.6 dB respectively. Important to note is that in these cases, the fraction of sound energy passing through the windows is quite substantial: 90%, 72% and 72% respectively, while the fraction passing through the junction remains small: 9%, 25% and 11% respectively. This shows that the choice of an appropriate window is of prime importance.

5.4 Eligible junction solutions

From this simple use case, it follows that for the outdoor noise classes 1-3, all studied connecting methods are possible since all measured $R_{s,Atr}$ values were larger than 45 dB. In class 4 however, only the following junction types are eligible:

- connection methods where there is no mounting gap between the chassis and the reveal opening;
- installation methods with positioning frames: the clearance between the positioning frame and chassis must be limited to 1 cm and must be filled with spray foam (swelling strips are not recommended from both a practical and acoustic point of view);
- plywood installation frames in combination with a maximum of 2 cm wide spray foam;
- angle brackets or dowels in combination with a plasterboard interior lining and a max. 4 cm wide spray foam.

6. ACKNOWLEDGMENTS

Buildwise wants to thank all companies that made this research possible by supplying components to build the laboratory setups, in particular Knauf, Buildtechnics and Staduco.

7. REFERENCES

[1] EN ISO 12354-1:2017 *Building acoustics - Estimation of acoustic performance of buildings from the performance of elements - Part 1: Airborne sound insulation between rooms*, CEN, 2017.

[2] EN ISO 12354-3:2017 *Building acoustics - Estimation of acoustic performance of buildings from the performance of elements - Part 3: Airborne sound insulation against outdoor sound*, CEN, 2017.

[3] EN ISO 717-1:2020 *Acoustics - Rating of sound insulation in buildings and of building elements – Part 1: Airborne sound insulation,* ISO, 2020.

[4] EN ISO 10140-1:2021 *Acoustics - Laboratory measurement of sound insulation of building elements - Part 1: Application rules for specific products*, ISO, 2021.

[5] EN 14351-1:2006+A2:2016 *Windows and doors - Product standard, performance characteristics - Part 1: Windows and external pedestrian doorsets*, CEN, 2016.

DOI: 10.61782/fa.2025.0936

FORUM ACUSTICUM EURONOISE 2025

UNIFORMITY OF SOUND FIELDS IN LARGE ROOM VOLUMES FOR THE MEASUREMENT OF FAÇADE SOUND INSULATION

Chiara Scrosati[1*] **Francesco Bianco**[1] **Carl Hopkins**[2]
Alessia Nora[3] **Luca Barbaresi**[3]
[1] Construction Technologies Institute, National Research Council of Italy CNR-ITC, Italy
[2] Acoustics Research Unit, University of Liverpool, UK
[3] Department of Industrial Engineering, University of Bologna, Italy

ABSTRACT

In some countries, it is necessary to measure sound insulation with large receiving rooms that are currently outside the scope of ISO 16283-3. Façade sound insulation needs to be measured in schools, universities and offices, which often have room volumes greater than 250 m^3. In this paper, grid measurements of the sound pressure level are made in a receiving room of about 470 m^3 with a non-uniform absorption distribution. This allows an assessment of the spatial variation of sound pressure level when measuring the façade sound insulation, where the façade includes windows with relatively low sound insulation. The results show high sound pressure levels near the windows. This results in standard deviations for the spatial variation in the mid and high-frequency range that are higher than would be expected due to the direct field from these windows.

Keywords: *large volumes, façade sound insulation, spatial variation*

1. INTRODUCTION

The current version of ISO 16283 all parts is intended for room volumes from 10 m^3 to 250 m^3 in the frequency range from 50 Hz to 5000 Hz. This is a change with respect to the previous version of the ISO 140 relative to the on-site measurements. In fact, the series ISO 140 did not include limits for the volumes of the receiving rooms. In the present version, therefore, it is out of the scope of the standard the measurements of room volumes exceeding 250 m^3. In particular, this can be an issue for façade sound insulation that must be measured in some countries, such as schools or open-plan offices. The main issue in small room volumes, such as in dwellings, is the large variation in the sound pressure level at low frequencies [1]. Although low-frequency issues are potentially less problematic in large rooms, an assessment is needed to check whether there are any issues for façade sound insulation when the receiving room volume exceeds 250 m^3. As a first step, this paper assesses the spatial variation of the sound field inside a large room of about 470 m^3 using grid measurements of the sound pressure level.

The spatial variation of the sound field is often assessed with the sound source inside the room [2, 3]. In the present study, which is focused on façade sound insulation, the sound source is outside the room. The diffuse field theory predicts a uniform sound field in the centre of a room. On the basis that the onset of reflected sound cannot occur prior to the arrival of the direct sound, Barron and Lee [4] developed a revised theory for large-volume concert halls that predicts the average behaviour of sound levels more accurately.

This paper compares the measured standard deviation from the grid of microphone positions with different theories. For a diffuse sound field where the direct field is negligible, Schroeder's theory [5] is used along with the Lubman-Craik approach [6, 7, 8] for low-frequencies where there is a modal sound field. The Gaussian Orthogonal Ensemble GOE approach from Langley and Cotoni [9] is combined with Lubman's theory [6] for the direct field in a source room, as described by Davy [10].

[*] ***Corresponding author***: scrosati@itc.cnr.it
Copyright: *©2025 C. Scrosati et al. This is an open-access article distributed under the terms of the Creative Commons Attribution 3.0 Unported License, which permits unrestricted use, distribution, and reproduction in any medium, provided the original author and source are credited.*

2. MEASUREMENT SET-UP

The measurements were performed in a historical university lecture room of about 470 m^3 volume. The room has 15 rows (see Fig. 1) of continuous school desks and folding chairs with a Class D absorptive ceiling. The floor surface of the room is approx. 141 m^2, and the dimensions are approximately 17 m in length, 8.3 m in depth and 3.5 m high. The two facades of the room are made of 0.7 m plastered double walls with 0.4 m full bricks, an internal air gap, and 0,14 m hollow bricks. Include two wood frame single pane windows 2 m long and 2.7 m high that were not sealed and, therefore, not airtight.

Sound pressure level measurements were made in a three-dimensional grid when the outside sound source pointed towards the windows on the longest façade. The grid points are indicated in Fig. 2. For each point of the grid, four different heights were measured to give a total of 648 grid points.



Figure 1. View from the front of the lecture room with the longest façade wall on the right-hand side.

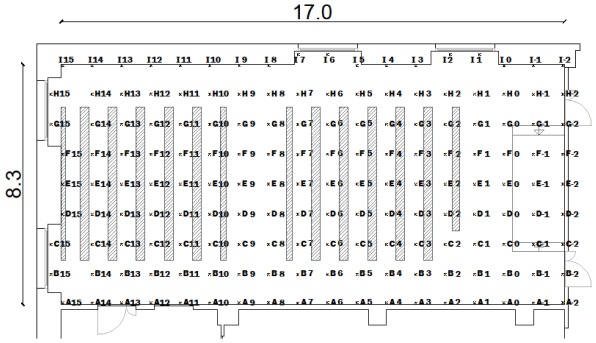


Figure 2. Sketch of the lecture room with grid points.

3. RESULTS

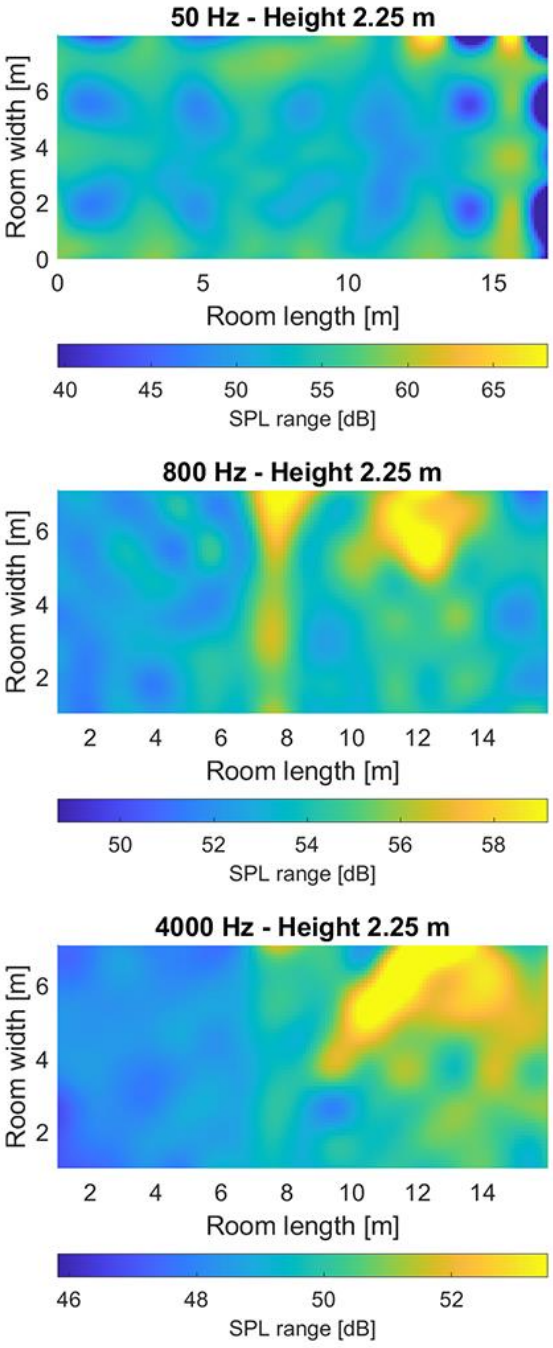


Figure 3. Contour plots of the sound pressure level at a height of 2.25 m. The SPL range shown at the bottom of each plot is a function of the frequency of the surface plot range.

Figure 3 shows contour plots of the sound pressure level at a height of 2.25 m at 50 Hz, 800 Hz and 4 kHz, with the exception of points located on the room's edges. At 50 Hz, there is evidence of modal behaviour. At 800 Hz, there is evidence of strong sound radiation from both windows, with sound transmitted across the room that is reflected across the desks. At 4 kHz there is strong radiation from the right-side window that is expected to be caused by the absence of seals around the window frame and a closing mechanism that causes a gap near the top of the window.

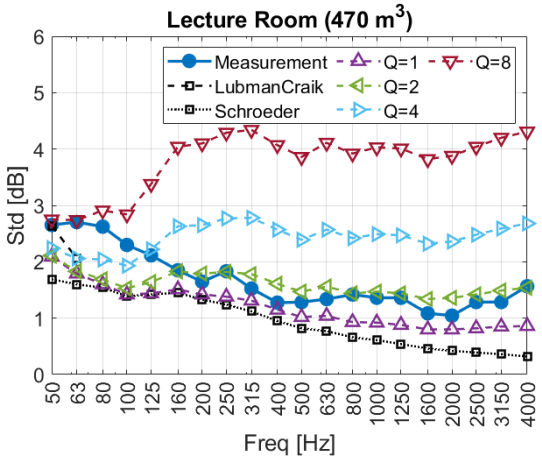


Figure 4. Standard deviations from measurements and theory.

Figure 4 shows the measured standard deviation of the sound pressure levels from the grid, excluding grid points next to the walls, floor and ceiling. At 50 Hz, where there are approximately seven modes, the theory from Lubman-Craik shows the closest agreement with measurements as this theory accounts for low modal density. The Schroeder theory underestimates the standard deviation across the entire frequency range because no account of the direct field from the high levels of transmitted sound from the windows is taken. Ideally, the directivity, Q, needs to be related to a physically meaningfully description for the source. For Q=1 the source would be omnidirectional; hence this would not be appropriate. For Q=2 the source would be sited on a plane and this is a reasonable approximation, but Q=4 might represent a source situated along an edge to represent a leak from the top edge of the window. However, the actual situation is more complex because there is a deep niche of approx. 0.4 m and there could be a two-dimensional reverberant field within the niche above 1 kHz. Comparison of the measured standard deviation with Q=1, 2, 4 and 8 indicates that Q=2 is a reasonable value that the deep niche might justify.

4. CONCLUSIONS

Extending ISO 16283-3 to larger room volumes requires an assessment of the standard deviation for the spatial variation of sound pressure levels. Schroeder theory (or other theories) that only considers the reverberant field underestimate the standard deviation across the entire frequency range because no account is taken of the direct field. The large room considered in this paper had windows with relatively low airborne sound insulation, which led to significant levels of mid- and high-frequency sound radiating from the windows across the room. Therefore, it was necessary to consider the direct field when calculating the standard deviation.

5. ACKNOWLEDGMENTS

This study was developed under the Royal Society grant IEC\R2\232037 - International Exchanges.

We gratefully acknowledge the assistance of Giulia Fratoni, Gioia Fusaro, Vincenzo Pettoni Possenti, Matteo Spinelli and Virginia Tardini in performing the grid measurements.

6. REFERENCES

[1] C. Hopkins and P. Turner. Field measurement of airborne sound insulation between rooms with non-diffuse sound fields at low frequencies, *Appl. Acoust.*, 66(12), 1339-1382, 2005.

[2] M. Vorlander, "Revised relation between the sound power and the average sound pressure level in rooms and consequences for acoustic measurements" *Acustica* Vol. 81, 1995.

[3] S. Chiles and M. Barron. "Sound level distribution and scatter in proportionate spaces" *J. Acoust. Soc. Am.* 116 (3), 2004.

[4] M. Barron and L-J. Lee. Energy relations in concert auditoriums. I , *J. Acoust. Soc. Am.* 84 (2), 1988.

[5] M.R. Schroeder. Effect of frequency and space averaging on the transmission responses of multimode media. J. Acoust. Soc. Am. 46(2), 277-283, 1969.

[6] D. Lubman. Precision of reverberant sound power measurements, *J. Acoust. Soc. Am.* 56(2), 523-533, 1974.

[7] R.J.M. Craik. On the accuracy of sound pressure level measurements in rooms, *Appl. Acoust.* 29, 25-33, 1990.
[8] C. Hopkins. Sound insulation. Butterworth-Heinemann, 2007. ISBN 978-0-7506-6526-1.
[9] R.S. Langley and V. Cotoni. The ensemble statistics of the vibrational energy density of a random system subjected to single point harmonic excitation, *J. Acoust. Soc. Am.* 118(5), 3064-3076, 2005.
[10] J. Davy. The spatial variability of random noise in a reverberant space, *Proceedings of the 24th International Congress on Sound and Vibration*, London, United Kingdom, 23-27 July 2017, 1-8, 2017.

DOI: 10.61782/fa.2025.0706

FORUM ACUSTICUM EURONOISE 2025

PROPOSAL FOR A METHODOLOGY AND CALCULATION TO APPLY IN THE SOUND INSULATION MEASUREMENT OF CORNER FAÇADES USING ISO 16283-3 STANDARD

Trujillo Gallego, Jose Alberto[1*] **Romero Fernández, Amelia**[2]
[1] Laboratorio de Ensayos Acústicos (Labenac) - Universidad Politécnica de Madrid, Spain
[2] Instituto de la Construcción Eduardo Torroja (CSIC), Madrid, Spain.

ABSTRACT

The measurement methodology described in ISO 16283-3:2015 for façade sound insulation allows the use of a loudspeaker as a substitute for real noise sources (road, railway, or aircraft traffic). Using this source, the sound insulation tests of multi-wall façades are conducted wall by wall. The method requires positioning the loudspeaker at an angle of sound incidence of 45°, which, for ground-floor façades necessitates placing the sound source off-center, toward one of the two lateral edges of the wall under test. This situation becomes particularly critical for corner façades with two walls, where the side to which the sound source is shifted may lead to significantly different results due to potential indirect noise transmission into the interior space via the opposite wall. Furthermore, the mathematical approach used to calculate the final sound insulation value does not accurately reflect a real situation.

This study proposes a more appropriate positioning and calculation method to achieve repeatable and representative results under realistic conditions, demonstrated through an example in a real scenario.

Keywords: *ISO 16283-3; façade sound insulation, corner façade, field measurements, repeatability.*

1. INTRODUCTION

The current standard for façade sound insulation, ISO 16283-3 [1], defines a field measurement and calculation method to determine the acoustic insulation of whole façades (global methods). The specified test method is general, meaning that in specific cases, it may lack precision or fail to provide representative results.

This paper studies the specific case of a corner façade with two walls exposed to outdoor noise and how standard testing procedures can yield different results depending on their application. Additionally, it evaluates how the current calculation method may not accurately reflect real conditions in this scenario of a corner façade.

2. SCENARIO

Figure 1 illustrates a typical scenario of a corner façade with two walls on the ground floor.

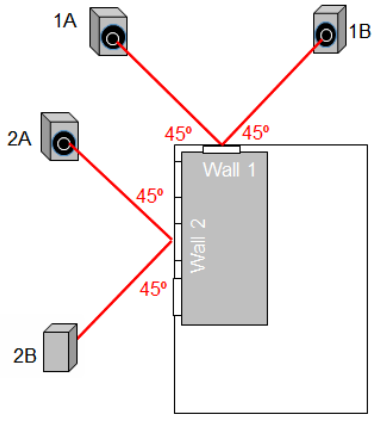


Figure 1. Possible sound source positions per wall.

[*] ***Corresponding author***: jtrujillo@labenac.es.
Copyright: *©2025 First author et al. This is an open-access article distributed under the terms of the Creative Commons Attribution 3.0 Unported License, which permits unrestricted use, distribution, and reproduction in any medium, provided the original author and source are credited.*

According to the measurement standard, when using the global loudspeaker method, each façade wall must be tested separately. To ensure an angle of sound incidence equal to 45°±5° on the wall, the noise source must be laterally displaced from the façade centre. The standard allows for two possible loudspeaker positions: either towards the corner or in the opposite direction (Fig. 1).

2.1 Insulation procedure for Wall 1

For measuring the sound insulation of Wall 1, two noise source positions are possible: 1A, with the source shifted towards the corner (Fig. 2a), and 1B, shifted in the opposite direction (Fig. 2b).

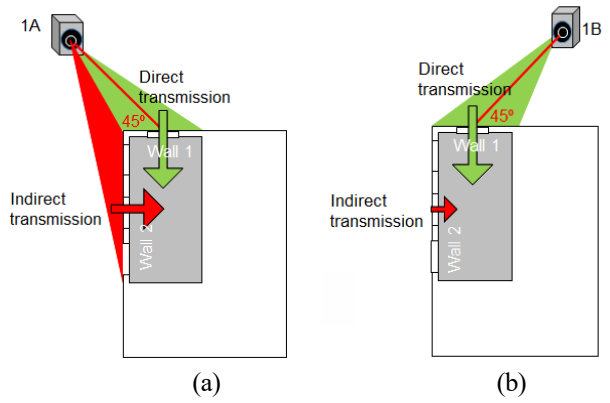


Figure 2. (a) Noise transmission for 1A sound source position. (b) Noise transmission for 1B sound source position.

For source position 1A, due to the small length of Wall 1, the noise source has a direct line of sight to both tested walls. As a result, although the source is directed at Wall 1 (direct transmission), part of the sound beam directly reaches Wall 2. This means that the indoor noise level (L_2) consists of contributions from both the tested wall ($L_{2,W1}$) and the adjacent wall ($L_{2,W2}$), making it impossible to isolate the contribution of Wall 2 in the overall measured levels, without any other additional and specific studies.

$$L_2 = 10Log(10^{(0,1*L_{2,W1})} + 10^{(0,1*L_{2,W2})}) \quad (1)$$

Consequently, the partial insulation of Wall 1 ($D_{nT,W1}$) may be underestimated. However, using source position 1B ensures that most of the loudspeaker's sound beam is transmitted through Wall 1, with significantly lower and negligible indirect transmission through Wall 2. Thus, in this configuration, $L_{2,W1} >> L_{2,W2}$, and consequently, $L_2 \approx L_{2,W1}$.

In conclusion, selecting source position 1B provides a result closer to the real sound insulation of the wall.

2.2 Insulation procedure for Wall 2

As in the previous case, two source positions can be used to characterize the sound insulation of Wall 2: 2A, with the source shifted towards the corner (Fig. 3a), and 2B, shifted in the opposite direction (Fig. 3b).

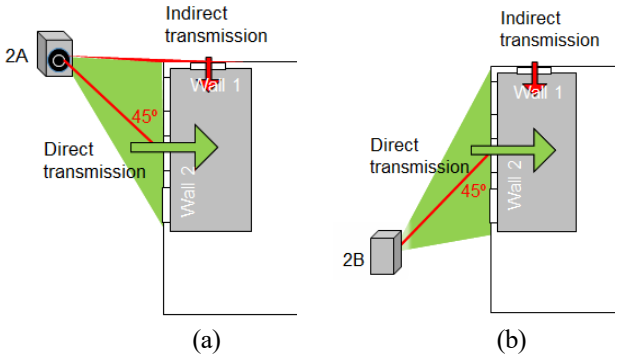


Figure 3. (a) Noise transmission for 2A sound source position. (b) Noise transmission for 2B sound source position.

Due to the greater length of Wall 2, in the least favorable position (2A, near the corner), there is hardly any direct view of Wall 1. Therefore, regardless of whether 2A or 2B is chosen, the direct transmission through Wall 2 will be significantly higher than the indirect transmission through Wall 1 ($L_{2,W2} >> L_{2,W1}$). This means that, in this case, the source position is less critical, and the partial insulation result of Wall 2 ($D_{nT,W2}$) is expected to be similar for both source positions.

2.3 Conclusions on sound source position

Since the measurement procedure in ISO 16283-3 standard [1] requires that façades with multiple walls be tested independently (wall by wall), it is essential to ensure that the measured insulation corresponds exclusively to the tested wall, avoiding noise transmission into the room through the adjacent corner wall. Source positions shifted towards the façade corner may lead to lower-than-actual partial insulation values due to indirect noise transmission, with deviations that cannot be precisely quantified. These deviations depend on factors such as source position, coverage beam, and wall dimensions.

Therefore, to minimize this situation, the best approach is to locate the source away from the façade centre, as far as possible, always in the direction opposite to the corner.
Other authors [2] have also studied the influence of the source position on the final results of the façade insulation of corner rooms, additionally considering the acoustic attenuation due to corner diffraction.

3. ON THE CALCULATION METODOLOGY

ISO 16283-3 [1] allows the use of road traffic (see Fig. 4), railway traffic, and even aircraft noise as sound sources. Conducting tests with these sources provides insulation values that reflect real façade performance under actual noise exposure. However, using traffic noise requires very specific conditions, making the global loudspeaker method the preferred option due to its simplicity and independence from external sources.
The standard's calculation method evaluates each façade wall separately, determining a partial insulation index ($D_{2m,i}$) for each. The final insulation value is then obtained by averaging the individual results, as expressed in Eqn. (2):

$$D_{2m} = -10Log(\frac{1}{n}\sum_{i=1}^{n}(10^{(0,1*D_{2m,i})})) \qquad (2)$$

3.1 Comparison of road traffic and loudspeaker global methods

Next, a theoretical case of a corner façade is evaluated using both global methods: road traffic noise and the loudspeaker.

3.1.1 Theoretical considerations

For the development of this example, the following considerations will be taken into account:

- To simplify the analysis, the examples will use global values rather than one-third octave band frequency spectra.
- The two walls forming the façade are identical in both dimensions and construction characteristics. Each wall provides a sound insulation level of D = 35 dB.
- In both the road traffic noise method and the loudspeaker method, the external measurement point receives the same noise level in all cases: $L_{1,2m}$ = 85 dB.

3.1.2 Test 1. Sound insulation measurement using loudspeaker global method

As mentioned in the previous section, the loudspeaker positions farthest from the corner are selected to avoid indirect transmissions that could affect the results (Fig. 4).

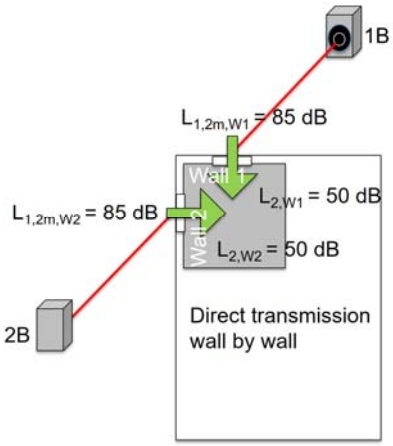


Figure 4. Façade sound insulation calculation using a loudspeaker as a sound source.

As specified by the standard's procedure, each wall is tested separately. For Wall 1, with an outdoor noise level $L_{1,2m}$ = 85 dB and a sound insulation value D = 35 dB, the indoor noise level will be 50 dB ($L_{2,W1}$). Since indirect transmission is negligible, it follows that $L_2 \approx L_{2,W1}$ = 50 dB.
Given that both walls have identical properties, their partial insulation values are:

$$D_{ls,2m,W1} = D_{ls,2m,W2} = 85\ \text{dB} - 50\ \text{dB} = 35\ \text{dB} \qquad (3)$$

Finally, applying Eqn. (2), the overall insulation is $\mathbf{D_{ls,2m}}$ = **35 dB**.

3.1.3 Test 1. Sound insulation measurement using road traffic global method

As previously mentioned, the insulation test must be performed separately for each wall. However, in this case, it is important to consider that outdoor noise enters the indoor space simultaneously through both façade walls.
Since both walls are identical and exposed to the same outdoor noise levels, the insulation calculation for Wall 1 ($D_{tr,2m,W1}$) is also valid for Wall 2 ($D_{tr,2m,W2}$), giving the same result.

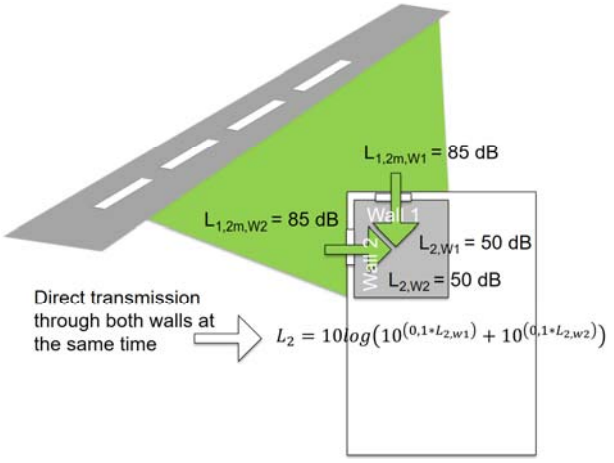


Figure 5. Façade sound insulation calculation using road traffic noise.

For Wall 1, with an outdoor noise level of $L_{2m,W1}$ = 85 dB and a known insulation value $D_{tr,2m}$ = 35 dB, the noise reaching the interior through this wall is 50 dB. However, as the traffic noise excites both walls equally, an additional 50 dB also enters through Wall 2. Therefore, the total indoor noise level (L_2) can be calculated as:

$$L_2 = 10Log(10^{(0,1*L_2,W_1)} + 10^{(0,1*L_2,W_2)}) \quad (4)$$

Resulting in L_2 = 53 dB (Fig. 5).
Thus, the partial insulation values for both walls are:

$$D_{tr,2m,W1} = D_{tr,2m,W2} = 85\ \text{dB} - 53\ \text{dB} = 32\ \text{dB} \quad (5)$$

Finally, applying Eqn. (2), the overall insulation value is **$D_{tr,2m}$ = 32 dB**.

3.2 Conclusions on the calculation method

Therefore, as reflected in the previous theoretical discussion, for the same façade and identical outdoor noise conditions, there is a 3 dB deviation between the traffic noise insulation procedure and the loudspeaker method, despite using the same testing methodology and calculation approach.
The key difference lies in the fact that, during traffic noise insulation measurements, outdoor noise enters through both façade walls simultaneously, regardless of which wall is being tested at a given moment. This results in a higher interior noise level and, consequently, a lower insulation value compared to the loudspeaker method.
Considering that traffic noise insulation measurement better represents real-world conditions and should therefore be used as a reference, two alternative adaptations of the loudspeaker method are proposed to achieve similar results:

Option 1: Modification of the testing method: This approach requires using two identical loudspeakers, each directed towards the centre of one wall, positioned to minimize indirect transmission (Fig. 6), away from the corner. The testing procedure follows the standard method, assessing the partial insulation of each wall. The only difference is that, during the test of each wall, both loudspeakers (sound sources S_1 and S_2) will emit the same noise simultaneously at the same intensity.

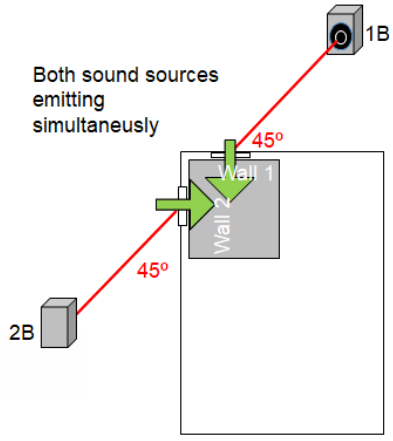


Figure 4. Façade sound insulation measurement using two loudspeakers simultaneously as sound sources.

Option 2. Modification of the Calculation Method: In this case, the standard procedure remains unchanged: each wall is tested separately using a single noise source, positioned sequentially; first for Wall 1 to calculate its partial insulation, then for Wall 2.
To determine the overall insulation, the standard Eqn. (2) is replaced with a new equation that sums the partial insulation values instead of averaging them:

$$D_{2m} = -10Log(\sum_{i=1}^{n}(10^{(0,1*D_{2m,i})})) \quad (6)$$

4. PRACTICAL CASE

To validate the previous findings, a sound insulation test was conducted on a corner façade. Two identical loudspeakers were positioned to excite both façade walls, with their locations shifted away from the corner to reduce indirect transmissions.

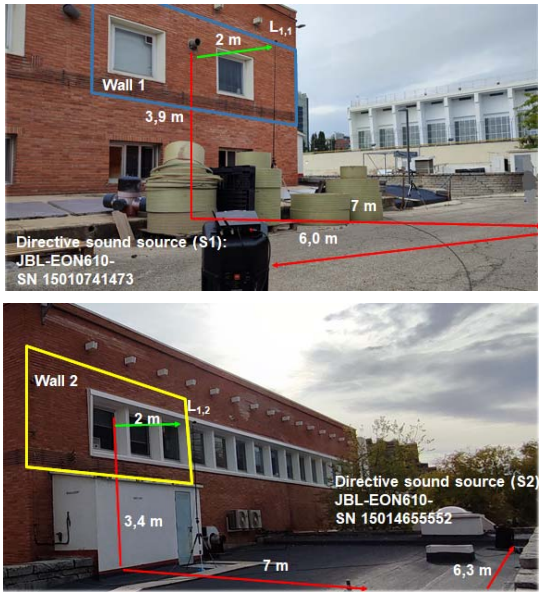


Figure 5. Measurement scenario. Outdoor microphone and sound source positions per wall.

4.1 Measurements

The following tests were performed according to ISO 16283-3 [1]:

- Test 1: "Real-World Scenario". Both noise sources emitted simultaneously during the testing of each wall.
- Test 2: Standard Procedure. Sound insulation measured separately per wall.
- Control Tests: Outdoor measurements taken 2m from Wall 1 while testing Wall 2, and vice versa, to check for indirect transmission.

4.2 Instrumentation

The following equipment was used for the tests:

- Brüel & Kjaer model 2270 dual-channel sound level meter and one-third octave band analyzer.
- Brüel & Kjaer model 2260 dual-channel sound level meter and one-third octave band analyzer.
- Brüel&Kjaer model 4231acoustic calibrator.
- Two JBL model EON610 directive sound sources.
- AKG dual-channel RF transmitter.

5. RESULTS AND DISCUSSION

5.1 Outdoor noise level results

Next, the outdoor results are presented according to

- $L_{1,W1\ (S1\&S2)}$: Outdoor noise level 2m in front of wall 1. Sound sources S1 and S2 emitting simultaneously.
- $L_{1,W1\ (S1)}$: Outdoor noise level 2m in front of wall 1. Only emitting sound source S1.
- $L_{1,W2\ (S1\&S2)}$: Outdoor noise level 2m in front of wall 2. Sound sources S1 and S2 emitting simultaneously.
- $L_{1,W2\ (S2)}$: Outdoor noise level 2m in front of wall 2. Only emitting sound source S2.
- $L_{1,W1\ (S2)}$: Outdoor noise level 2m in front of wall 1. Only emitting sound source S2 (control measurement).
- $L_{1,W2\ (S1)}$: Outdoor noise level 2m in front of wall 2. Only emitting sound source S1 (control measurement).

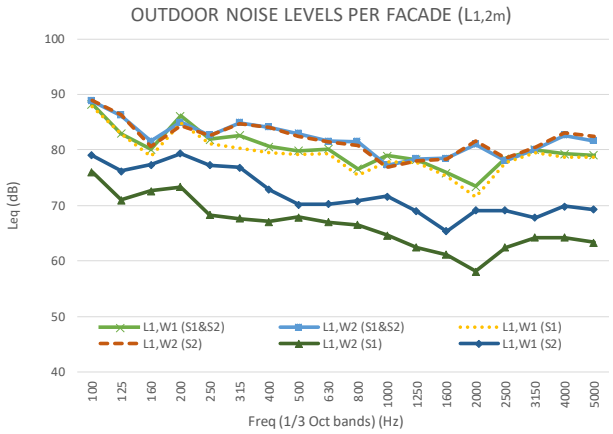


Figure 6. Outdoor levels.

For each wall, the noise spectrum measured at 2m remains similar, whether both sources operate simultaneously or only the one exciting the measured wall is active. This confirms that, with the selected source positioning, the influence of the secondary source on the measured wall is negligible. This effect is particularly evident for Wall 2, where the measured spectra closely align in both test conditions, reinforcing the validity of the experimental setup.

5.2 Indoor noise levels results

The following results were obtained indoors:

- $L_{sb(S1\&S2)}$: Indoor noise level when S1 and S2 emitting simultaneously.
- $L_{sb\ (S1)}$: Indoor noise level when S1 emitting.
- $L_{sb\ (S2)}$: Indoor noise level when S2 emitting.
- L_b: Indoor background noise level.

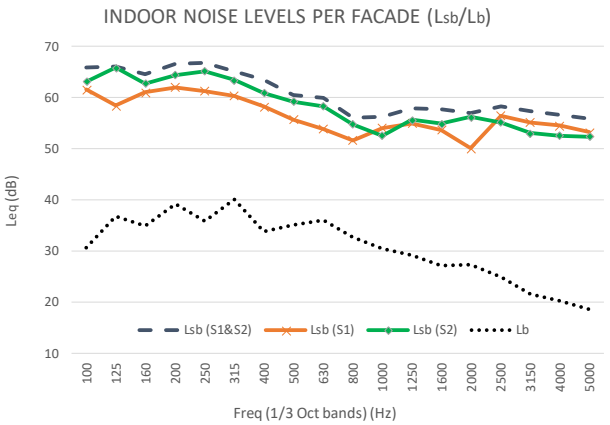


Figure 7. Indoor levels.

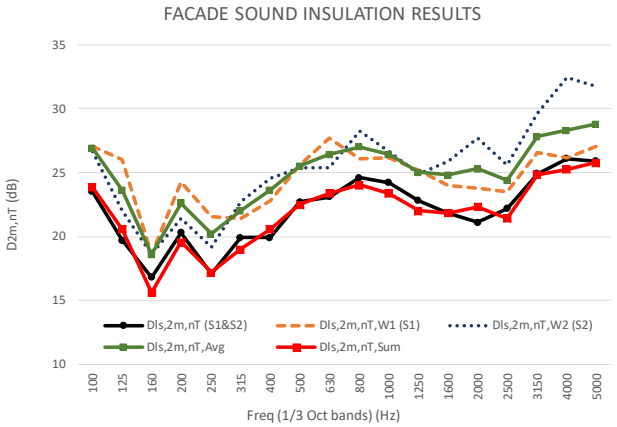


Figure 8. Standardized level difference.

The results confirm no significant background noise influence. As expected, indoor noise levels are higher when both façade walls are excited simultaneously, replicating real-world conditions.

5.3 Standardized level difference ($D_{ls,2m,nT}$)

Graph in Fig. 10 presents the results:

- $D_{ls,2m,nT\ (S1\&S2)}$: Final standardized level difference calculated using Eqn. (2), for sound insulation descriptor $D_{ls,2m,nT}$. when both sound sources are emitting simultaneously.
- $D_{ls,2m,nT,W1\ (S1)}$: Partial standardized level difference for Wall 1 (with only sound source 1 emitting).
- $D_{ls,2m,nT,W2\ (S2)}$: Partial standardized level difference for Wall 2 (with only sound source 2 emitting).
- $D_{ls,2m,nT,Avg}$: Final standardized level difference level calculated using Eqn. (2) based on the partial results $D_{ls,2m,nT,W1\ (S1)}$ and $D_{ls,2m,nT,W2\ (S2)}$.
- $D_{ls,2m,nT,Sum}$: Final standardized level difference calculated using Eqn. (6), summing the partial results $D_{ls,2m,nT,W1\ (S1)}$ and $D_{ls,2m,nT,W2\ (S2)}$.

Considering that the sound insulation curve $D_{ls,2m,nT\ (S1\&S2)}$ represents a real-life scenario (e.g., road traffic noise exciting both walls simultaneously), it can be observed that this curve closely matches the $D_{ls,2m,nT,Sum}$ curve, obtained by summing the partial insulation values using Eqn. (6). This differs from Eqn. (2), currently in the standard, which averages these partial insulation values.

Thus, applying Eqn. (2) to calculate the final insulation from partial insulation values ($D_{ls,2m,nT,Avg}$) results in higher insulation levels across all frequency bands than those observed in a real scenario.

All findings are validated when applying the calculation method for obtaining weighted values according to ISO 717-1 [3], as shown in Table 1.

Table 1. Weighted standardized level difference.

Freq. range (Hz)	$D_{ls,2m,nT,w}$ (C; C_{tr}) (dB)		
	S_1&S_2 simultaneously	Eqn. (2)	Eqn. (6)
Weighted	23	26	23
100-3150	(-1;-1)	(-1;-1)	(-1;-1)
100-5000	(0;-1)	(0;-1)	(0;-1)
50-3150	(-1;-2)	(-1;-2)	(-1;-2)
50-5000	(0;-2)	(0;-2)	(0;-2)

6. CONCLUSIONS

Based on the findings presented in this study, it is concluded that testing façades with two corner walls is a complex process influenced by multiple factors. Additionally, the mathematical approach currently applied in the standard to compute the final insulation from partial insulation values

may not be adequate or representative of real conditions. Therefore, the following recommendations are proposed:

- When using the loudspeaker method, the noise source should be positioned in a way that minimizes indirect transmissions through the adjacent wall while measuring the insulation of the tested wall.
- Whenever possible, the sound source should be placed away from the façade's centre, in the opposite direction of the corner. In some cases, achieving this may require increasing the source-to-façade distance.
- Positioning the source too close to the corner can lead to an underestimated insulation value for the tested wall. Moreover, in such cases, it becomes difficult to quantify the impact of indirect transmissions, as they depend on uncontrollable factors such as façade length, direct visibility of the other wall, and placement of façade elements on the untested wall.

Furthermore, the study confirms that the calculation equation currently used in the standard, Eqn. (2) does not accurately reflect real-world conditions and often leads to an overestimation of façade insulation. Instead, a more appropriate approach is to sum the partial insulation values rather than averaging them, as proposed in Eqn. (6). If indirect transmissions are properly controlled, this equation yields results that are representative of real conditions.

This approach aligns with the calculation methodology of ISO 12354, Part 3 [4], which states that the apparent sound reduction index of a façade is obtained by summing the acoustic power transmitted through each of its components.

Indirectly, similar considerations are already reflected in some European national regulations, such as the Belgian standard NBN S 01-400-1 [5], which establishes sound insulation requirements for residential buildings. In cases of corner façades with elements on both walls, this standard increases the sound insulation requirement by 3 dB.

7. REFERENCES

[1] ISO 16283-3:2016. *Acoustics — Field measurement of sound insulation in buildings and of building elements — Part 3: Façade sound insulation.* International Organization for Standardization, 2016.

[2] N. Granzotto, E. Alessio, "Evaluation method for façade acoustic insulation for a corner room: discussion on the results obtained as a function of the source position", *Applied Sciencies*, vol. 10, no. 21, 7434, 2020. doi:10.3390/app10217434

[3] ISO 717-1:2020. *Acoustics – Rating os sound insulation in buildings and of building elements. Part 1: Airborne sound insulation.* International Organization for Standardization, 2020.

[4] ISO 12354-3:2017. *Building Acoustics – Estimation of acoustic performance of buildings from the performance of elements. Part 3: Airborne sound insulation against outdoor sound.* International Organization for Standardization, 2017.

[5] NBN. NBN S 01-400-1:2022. *Acoustics – Acoustic performance of buildings – Part 1: Dwellings.* Belgian Bureau for Standardization (NBN), 2022.

DOI: 10.61782/fa.2025.0106

FORUM ACUSTICUM EURONOISE 2025

ADVANCED MONITORING FOR HERITAGE CONSERVATION: TECHNOLOGICAL INNOVATION IN PREVENTIVE MAINTENANCE OF HISTORIC BUILDINGS

Alberto Izquierdo[1*] **Juan José Villacorta**[1] **Lara del Val**[1]
Javier Retortillo[2] **Antolin Lorenzana**[2]
[1] Department of Signal Theory and Communications and Telematics Engineering, University of Valladolid, Spain
[2] ITAP (Institute of Advanced Production Technologies), Universidad de Valladolid, Spain,

ABSTRACT

Preventive maintenance of historical buildings through continuous structural monitoring is essential for the preservation of cultural heritage. It enables efficient management of the physical interaction between tourism and architecture and supports early detection of structural anomalies, facilitating data-driven decision-making.
The University of Valladolid has established a multidisciplinary research team composed of architects, mechanical engineers, and telecommunication engineers. This team has developed an innovative, reconfigurable, scalable, and low-cost technological platform based on MEMS (Micro Electro Mechanical Systems) sensors. These sensors allow real-time and synchronous monitoring of vibrations, mechanical stresses, inclinations, temperature, humidity, and crack evolution in structural elements.
The system integrates local and cloud-based data processing and storage using open-source technologies. Advanced signal processing, statistical analysis, and artificial intelligence techniques—including modal analysis and machine learning algorithms—enable the early identification of potential structural issues, reducing the need for costly corrective interventions and ensuring the longevity of historic structures.
A case study of the 45-meter-high tower of the Monastery of San Jerónimo in Granada is presented to demonstrate the effectiveness of the proposed monitoring solution in a real-world heritage setting.

Keywords: *Structural Health Monitoring, MEMS sensors, cultural heritage conservation, preventive maintenance, machine learning.*

1. INTRODUCTION

Preventive maintenance through continuous monitoring of historic buildings is a key factor in the conservation of cultural heritage, as it allows for efficient management of the physical interaction between tourism and architecture. Early detection of structural anomalies facilitates data-driven decision-making, minimizing the risk of severe damage and optimizing the resources allocated to conservation [1-3].
At the University of Valladolid, a multidisciplinary group has been established. It is composed of researchers from the Wood Structures and Technology Group, the Array Processing Group and the Structural Dynamics Group.
This interdisciplinary team combines the knowledge of architects in the field of heritage wooden structures and the expertise of mechanical engineers in vibration analysis and modal characterization of structures. It also leverages the skills of a team of telecommunications engineers who are capable of hardware design and development, as well as algorithm programming and the creation of open-access libraries for data acquisition, processing, and analysis.

.

[*] ***Corresponding author***: *alberto.izquierdo@uva.es.*
Copyright: *©2025 Alberto Izquiedo et al. This is an open-access article distributed under the terms of the Creative Commons Attribution 3.0 Unported License, which permits unrestricted use, distribution, and reproduction in any medium, provided the original author and source are credited.*

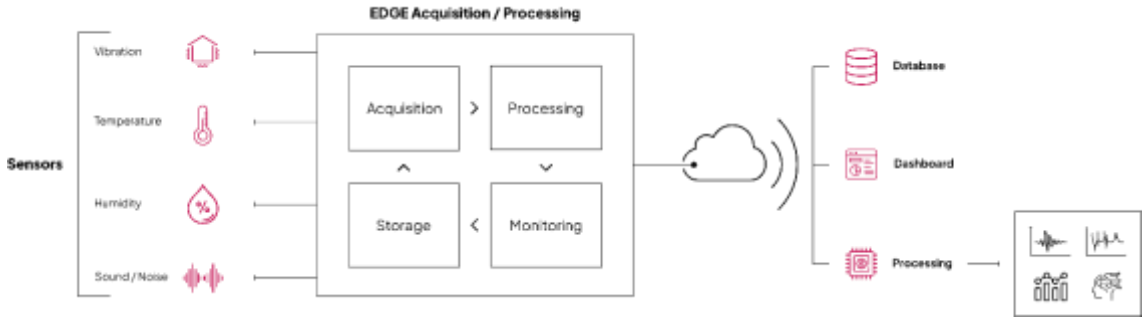


Figure 1. Smart Monitoring System for Architectural Heritage

This team has recently developed an innovative, reconfigurable, scalable, and low-cost technological architecture based on MEMS (Micro-Electro-Mechanical Systems) sensors. These sensors allow precise monitoring of vibrations, mechanical stresses, inclinations, temperature, humidity, and the progression of cracks in the structures. Integrating these data into a synchronous acquisition system provides a detailed and continuous view of the structural condition of the buildings [4-5].

In addition, a platform for processing and analyzing these data has been implemented using open-source technologies. This platform enables the logging, statistical analysis, and remote monitoring of key structural parameters. Thanks to its ability to identify anomalies before they become critical problems, it emerges as an efficient and cost-effective solution for managing preventive maintenance in historic buildings, reducing the need for costly and potentially disruptive corrective interventions.

This paper presents the technical characteristics of the monitoring system and its potential applications in the conservation of architectural heritage. A case study is also discussed: the monitoring of the 45 m tall tower of the Monastery of San Jerónimo in Granada, where the system's capabilities have been evaluated in a real heritage environment.

2. SYSTEM DESCRIPTION

As illustrated in the figure (Fig. 1), the structural monitoring platform is composed of three main components:

1. A set of sensors capable of detecting vibrations, temperature, humidity, and acoustic sources such as ambient noise and sound.
2. A hardware system with embedded software, responsible for four core tasks: data acquisition, local
3. A visualization and storage platform, where data are stored in a database and graphically displayed through a dashboard.

The resulting technological architecture is reconfigurable, scalable, and low-cost, making it suitable for the continuous structural monitoring of heritage buildings.

2.1 Sensors

The system uses MEMS (Micro Electro Mechanical Systems) technology, which integrates both the sensor and the associated electronics on a single chip. These devices capture signals, amplify them, and convert them to a digital format. The multisensor captures variations in mechanical stress, inclination, temperature, humidity, crack development, and even acoustic pressure.

2.2 Data Acquisition

During acquisition, data are collected synchronously (all sensors sample at the same time) and in real time. Preliminary local processing reduces the volume of data to be transmitted, optimizing computational and storage resources.

Several system implementations have been developed, some of which include over 40 triaxial acceleration sensors, operating at sampling rates close to 500 Hz. The large volumes of data generated are processed locally to extract key statistical parameters, which are then uploaded to the cloud for storage and visualization. When required, raw data can be transferred for advanced offline analysis.

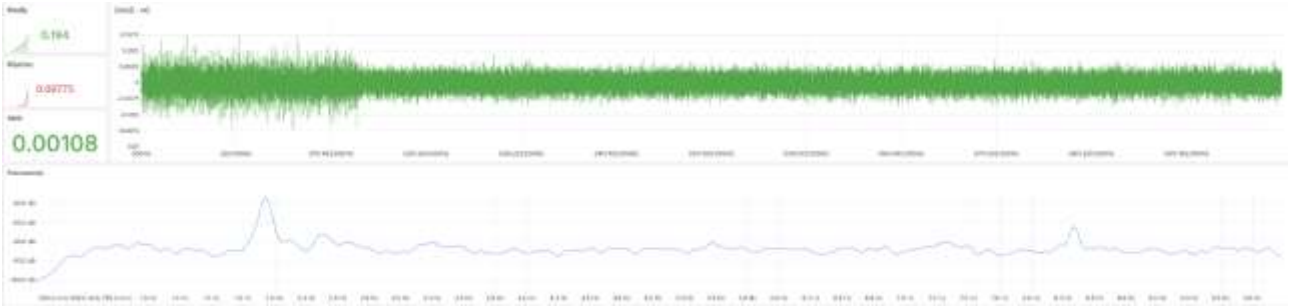


Figure 2. Vibration evolution recorded

2.3 Post-Processing

The system integrates technologies and algorithms across four main areas:

1. Signal processing algorithms that filter data within the desired bandwidth and remove bias.
2. A set of libraries that compute statistical metrics such as mean, variance, maximum, and minimum values.
3. Advanced algorithms including Experimental Modal Analysis (EMA) and Operational Modal Analysis (OMA).
4. AI-based techniques, including machine learning and deep learning classifiers, to support health status assessment and decision-making in heritage conservation.

All sensor data are uploaded to the cloud, where dedicated time-series databases and result visualization dashboards are deployed. Figure 2 shows an example of sensor-recorded vibrations evolution in a monitored building.

3. CASE STUDY

Since May 2024, in collaboration with the School of Civil Engineering at the University of Granada, a structural monitoring project has been carried out on the tower of the Monastery of San Jerónimo, located in the city of Granada (Fig. 3).

A set of five sensors has been installed, measuring triaxial acceleration, temperature, and humidity, along with two additional sensors monitoring the width of two major cracks located between the main nave and the tower. The tower comprises five levels, with the bell chamber located on the penultimate floor. Figure 4 highlights the placement of the five accelerometers within the interior slabs.

The primary objective of this project is to analyze the tower's modal behavior and to correlate crack width evolution with environmental variables (temperature and humidity) as well as the vibrational response of the structure.

Sensor installation was completed in record time, ensuring proper placement on each level. Data acquisition is carried out using a system based on National Instruments' myRIO platform, equipped with 5G cellular communication capabilities. This technology enables real-time data transmission, facilitating the remote structural health monitoring of the tower.

4. CONCLUSIONS

This work presents an innovative technological architecture for the structural monitoring of architectural heritage, characterized by its reconfigurability, scalability, and low cost. The system has demonstrated its capacity to provide continuous and detailed insight into the structural health of historic buildings, enabling early detection of anomalies before they evolve into critical damage.

The developed system integrates advanced MEMS sensors capable of recording vibrations, mechanical stresses, inclinations, temperature, humidity, and crack evolution in heritage structures. Leveraging open-source technologies, collected data are processed in real time and stored in accessible platforms for remote analysis and visualization.

Furthermore, advanced artificial intelligence techniques, including machine learning and deep learning models, have been incorporated to enhance the system's predictive capabilities, optimizing preventive maintenance strategies and supporting informed decision-making in heritage conservation.



Figure 3: Royal Monastery of San Jerónimo (Granada/Spain).

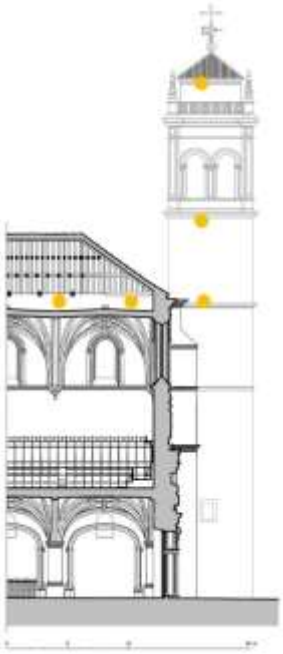


Figure 4. San Jerónimo Tower [6]

5. ACKNOWLEDGMENTS

This project would not have been possible without the multidisciplinary collaboration of architects, industrial engineers, and telecommunication engineers with extensive experience in regional and national research projects, as well as in real-world implementations in partnership with companies from the sector. We also acknowledge the collaboration between the University of Valladolid and the University of Granada

6. REFERENCES

[1] J. Park: "Special Feature Vibration-Based Structural Health Monitoring," *Applied Sciences*, vol. 10, no. 5139, 2020.

[2] N. Iban, J.M. Soria, A. Magdaleno, C. Casado, I.M. Díaz and A. Lorenzana: "Ad-Hoc Vibration Monitoring System for a Stress-Ribbon Footbridge: From Design to Operation," *Smart Structures and Systems*, vol. 22, pp. 13–25, 2018.

[3] W. Wei, S. Watts, T. Seddon and D. Crombie: "Protecting Museum Collections from Vibrations Due to Construction: Vibration Statistics, Limits, Flexibility and Cooperation," *Studies in Conservation*, vol. 63, pp. 293–300, 2018

[4] A. Magdaleno, J.J. Villacorta, L. del Val, A. Izquierdo and A. Lorenzana: "Measurement of Acceleration Response Functions with Scalable Low-Cost Devices. An Application to the Experimental Modal Analysis," *Sensors*, vol. 21, no. 6637, 2021

[5] A. Lorenzana, J.J. Villacorta, A. Magdaleno, L. del Val and A. Izquierdo: "Design of an Instant Vibration-Based Warning System and Its Operation during Relocation Works of Historic Facades," *Buildings*, vol. 14, no. 1889, 2024

[6] A. Almagro Orbea: "Monasterio de San Jerónimo" https://www.academiacolecciones.com/arquitectura/inventario.php?id=AA-814_01. Last access: February 20, 2025.

DOI: 10.61782/fa.2025.0313

FORUM ACUSTICUM EURONOISE 2025

DOUBLE-LEAF SYSTEM SOUND INSULATION IMPROVEMENT THROUGH EMBEDDING RESONANT ELEMENTS IN THE STEEL STUDS

Julia Idczak[1*] **Klara Chojnacka**[1]

[1] Department of Mechanics and Vibroacoustics, AGH University of Krakow, Poland
Faculty of Mechanical Engineering and Robotics
al. Adama Mickiewicza 30, Cracow

ABSTRACT

Lightweight partitions, consisting of two parallel plates connected by steel studs, are commonly used in buildings. While these structures offer clear advantages over heavyweight alternatives, as extensively documented in the literature, they also have drawbacks, notably the reduced sound transmission loss in high frequency range due to the steel studs acting as sound bridges between the two layers. Various solutions have been proposed in the literature to reduce sound transmission through the studs, such as optimizing their shape. This study introduces an innovative approach to achieve high sound insulation in multilayer structures by incorporating resonant elements into the steel junctions. Thorough numerical analysis was performed in COMSOL Multiphysics software. The results highlight the differences in vibroacoustic parameters, especially focus on transmission loss, between structures with standard junctions and those with resonant elements, underscoring the significant potential of new, proposed in this work structures.

Keywords: *double-leaf partition, transmission loss enhancement, resonant elements*

*__Corresponding author__: idczak@agh.edu.pl.

__Copyright__: ©2025 Idczak et al. This is an open-access article distributed under the terms of the Creative Commons Attribution 3.0 Unported License, which permits unrestricted use, distribution, and reproduction in any medium, provided the original author and source are credited.

1. INTRODUCTION

Double-leaf partitions (DL), commonly analyzed in theoretical models as two parallel plates separated by an air cavity or porous material, are often associated with high transmission loss (TL), especially in the high frequency range. However, in practical applications, such constructions require structural supports to ensure stability and stiffness. These supports, known as studs, are typically made of steel and spaced at 60 cm intervals. Although the presence of studs enhances the mechanical stability of the partition, it also facilitates the transmission of impact sound, leading to a reduction in TL due to the introduction of an additional transmission path.

Sharp was one of the first researchers to introduce a comprehensive approach to predict TL [1]. His model presents the decoupled approach, where airborne and structure-borne sound transmission paths are treated as separate, additive contributions. The total transmission coefficient τ is defined as a sum of ratio of power radiated due to the airborne excitation W_a to power inserted to the structure W_i and ratio of power radiated by the sample due to structure-borne excitation W_s to power W_i according to the equation $\tau = \frac{W_a}{W_i} + \frac{W_s}{W_i} = \tau_a \left(1 + \frac{W_s}{W_a}\right)$.

Craik studied double-leaf structures using statistical energy analysis (SEA), separately examining airborne and structure-borne transmission [2, 3]. The TL values for a representative double-leaf structure, analyzed for both transmission paths separately, are shown in Figure 1. Following extended analytical and numerical investigations, one of the first researchers to experimentally examine the influence of studs on TL was J. Poblet-Puig [4], who an-

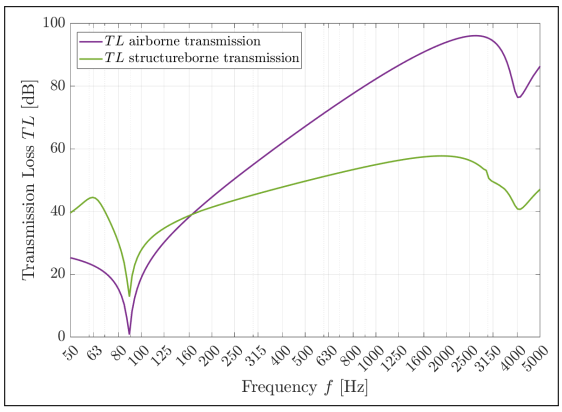


Figure 1. Transmission Loss obtained for DL structure with pure airborne transmission, and pure structureborne transmission.

alyzed the effect of the size and distribution of the stud. Since then, numerous studies have explored various aspects of the vibroacoustic behavior of studs [5] and optimized stud geometry to improve the sound insulation performance of partitions [6]. In this study, a novel approach is proposed in which locally resonant elements are embedded within the studs to enhance sound insulation. By introducing these resonant components, impact sound transmission can be mitigated, leading to improved acoustic performance of the partition.

Metamaterials are artificially engineered geometric structures that, when properly designed and manufactured, can be used to mitigate vibrations and noise across various frequency ranges. One type of metamaterial commonly used for vibration and noise reduction is the locally resonant metamaterial (LRS). These materials consist of small resonant elements which, when attached to a base structure (e.g., a plate), create a stopband for flexural waves propagating through the structure. Within this stopband frequency range, the propagation of flexural waves is significantly suppressed due to the interaction between the base plate and the resonant elements [7].

In the basic configuration, the resonant elements are manufactured separately and attached to the base plate at sub-wavelength distances to induce the stopband effect. However, alternative approaches propose integrating the resonant elements directly into the base structure itself to attenuate the propagation of flexural waves more efficiently. In [8] a matryoshka design of LRS was proposed as a solution for a multi-resonant broadband vibration mitigation solution. Then the same idea was used in [9] in thermoformed plate for noise suppresion in resonance driven environments.

This study examines a double-leaf partition composed of plasterboard plates separated by a layer of porous material and connected by steel studs. To enhance its sound insulation properties, the research explores the carving resonant elements within the studs to reduce the structureborne sound transmission. The results indicate an increase in transmission loss when resonant elements are incorporated into the structure. Numerical simulations of eigenmodes and transmission loss were performed using COMSOL Multiphysics.

2. NUMERICAL ANALYSIS

Numerical analysis of the system was performed using COMSOL Multiphysics with Solid Mechanics and Pressure Acoustics Module. A 3D model is presented in Figure 2. Three configurations were tested in the simulations:

- double-leaf construction with no mechanical connection between two plates and porous material filling an air cavity,
- double-leaf construction with steel studs and porous material,
- double-leaf with steel studs with one and two resonant elements.

The basic structure consisted of two plasterboard plates ($\rho = 1150[\frac{\text{kg}}{\text{m}^3}]$, $E = 3(1 + 0.01i)$ [GPa], $\nu = 0.3$ [-]), each with a thickness of 0.0125 m, separated by a 0.05 m layer of porous material with an air flow resistivity of 11400 $\frac{\text{Pa} \cdot \text{s}}{\text{m}^2}$.

The geometry and dimensions of the stud with resonant elements are illustrated in Figure 3. Two steel studs ($\rho = 7850[\frac{\text{kg}}{\text{m}^3}]$, $E = 205$ [GPa], $\nu = 0.33$ [-]), of height $h_1 = 0.05$ [m], thickness $t_s = 0.002$ [m], and unit cell width of $l_1 = 0.06$ [m], were placed at both boundaries of the sample as shown in Figure 2. Resonant elements were placed at the boundary of the stud that was not attached to the plasterboard. There were two configurations of resonant elements tested: the first with only one resonant element with radius $r_1 = 0.019$ [m], and the second with two resonators of radius r_1 and $r_2 = 0.0126$ [m].

The analysis was performed in COMSOL Multiphysics, focusing on frequency domain analysis within the 100–3150 Hz range, using a step size of 1 Hz. The structure was excited using a boundary load of 1 Pa on

the first plasterboard. Each side boundary of the sample was considered free. The radiating side of the structure was connected to the air domain terminated with Perfecly Matched Layer.

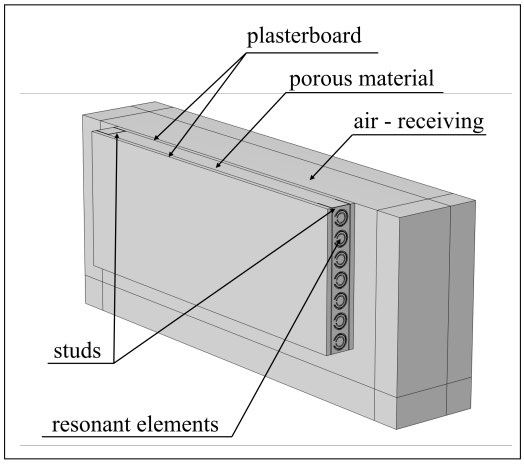


Figure 2. 3D model of the structure with resonant elements embedded in the studs made in COMSOL.

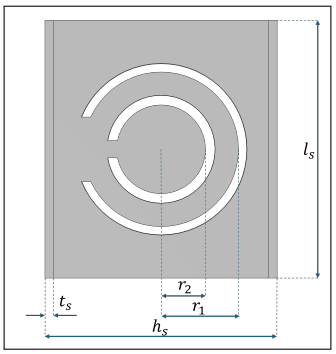


Figure 3. Dimensioning of the stud and resonant elements.

Firstly, eigenfrequencies were calculated for a stud element modeled as one resonant element using periodic conditions and considering the element infinite in one dimension (stud length). In addition, to preserve the mass applied to the stud by the plates, a boundary condition of the added mass was attached. The eigenfrequency analysis was crucial to predict the resonant frequencies of the element and its influence on the TL characteristics of the whole partition. Knowing the eigenfrequencies of the resonant element, a frequency domain analysis was performed. The key parameter most commonly studied in the case of DL structures is Transmission Loss, calculated according to equation $TL = 10\log_{10}(\frac{p_{in}}{p_{out}})$, where p_{in} is the input pressure, defined as the boundary load equal to 1 Pa, and p_{out} is the average value of the acoustic pressure on the radiating side of the sample, calculated from the total area of the plate.

3. RESULTS

The results shown in Figure 4 present eigenfrequencies and modes for the first four natural frequencies of the resonant elements embedded in the studs, within the analyzed frequency range. Analyzing the TL values presented in Figure 5, a significant increase in the parameter is observed at the resonant frequencies of the embedded elements, particularly around 740 Hz and 1375 Hz, therefore, overlapping with the first two natural frequencies of the resonant elements. In both cases, the TL improvement reaches approximately 15 dB for the first stopband around 740 dB, and 20 dB - for stopband around 1375 Hz. These results highlight the crucial role of integrated resonant elements in steel studs, demonstrating their effectiveness in locally enhancing TL values in double-leaf structures.

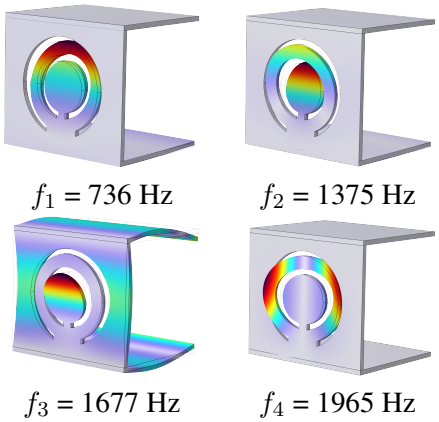


Figure 4. First modes of resonant elements on the steel studs

4. CONCLUSIONS

This paper presents a numerical analysis of double-leaf structures with steel studs. The study compares the Transmission Loss results for a traditional sample with a standard C-shaped steel stud and for studs that incorporate resonant elements. These resonant elements were designed

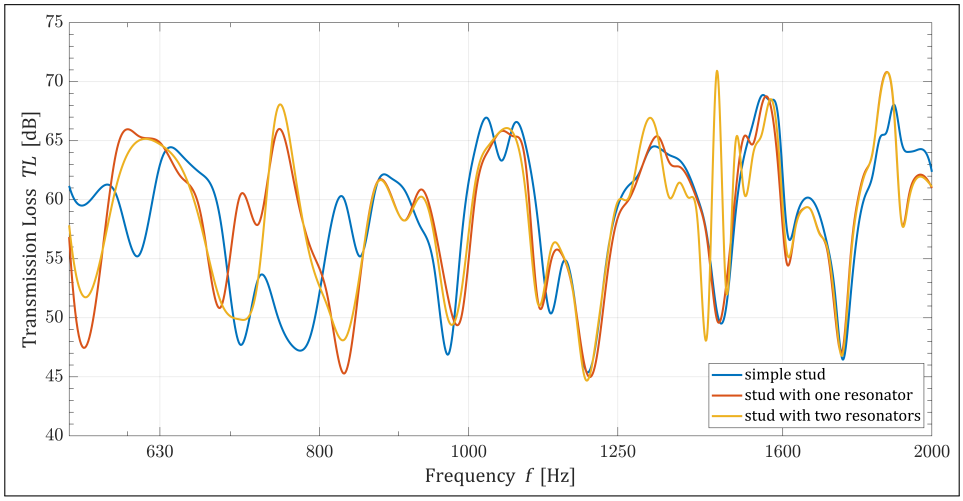


Figure 5. Transmission Loss obtained for DL structure with traditional stud (blue curve), resonator consisted of one ring (red curve), and resonator consisted of two rings (yellow curve).

with frequencies tuned to the frequencies corresponding to the lowest TL values observed in the spectra obtained for the traditional stud. The increase in TL at these specific frequencies is 15 dB, which is a significant improvement. This substantial increase demonstrates the potential for further investigation and practical implementation to improve sound insulation in stud-based partition systems. The follow-up to this study will focus on optimizing the shape of the resonant elements to improve the overall transmission loss characteristics of double-leaf structures, for a significant local enhancement. In addition, an experimental investigation will be conducted to validate the proposed solution in real-world applications.

5. REFERENCES

[1] B. H. Sharp, "Prediction methods for the sound transmission of building elements," *Noise Control Engineering*, vol. 11, no. 2, pp. 53–63, 1978.

[2] R. S. R.Craik, "Sound transmission through double leaf lightweight partitions. part i: Airborne sound," *Applied Acoustics*, vol. 61, no. 2, pp. 223–245, 2000.

[3] R. S. R.Craik, "Sound transmission through double leaf lightweight partitions. part i: Airborne sound," *Applied Acoustics*, vol. 61, no. 2, pp. 247–269, 2000.

[4] J. Poblet-Puig, A. Rodríguez-Ferran, C. Guigou-Carter, and M. Villot, "The role of studs in the sound transmission of double walls," *Acta Acustica united with Acustica*, vol. 95, no. 3, pp. 555–567, 2009.

[5] B. Nguyen, T. Morgan, M. English, and M. Castellucci, "Vibro-acoustic performance of different steel studs in double-leaf walls by finite element analysis," *Building Acoustics*, vol. 22, no. 2, pp. 65–80, 2015.

[6] J. C. Van den Wyngaert, M. Schevenels, and E. P. Reynders, "Shape optimization of studs in double-leaf plasterboard walls for maximal broadband sound insulation and minimal material use," *Applied Acoustics*, vol. 183, p. 108307, 2021.

[7] A. Hall, E. Calius, G. Dodd, E. Wester, and K. Chan, "Development of locally resonant structures for sonic barriers," *Building Acoustics*, vol. 21, no. 3, pp. 199–220, 2014.

[8] D. P. Elford, L. Chalmers, F. V. Kusmartsev, and G. M. Swallowe, "Matryoshka locally resonant sonic crystal," *The Journal of the Acoustical Society of America*, vol. 130, no. 5, pp. 2746–2755, 2011.

[9] N. de Melo Filho, C. Claeys, E. Deckers, and W. Desmet, "Realisation of a thermoformed vibro-acoustic metamaterial for increased stl in acoustic resonance driven environments," *Applied Acoustics*, vol. 156, pp. 78–82, 2019.

DOI: 10.61782/fa.2025.0071



FORUM ACUSTICUM
EURONOISE 2025

ACOUSTIC DESIGN OF TWO FILM SOUND STAGES NEAR A TRAIN LINE

Javier Sanz Soriano[1*] **Malcolm Dunn**[1]
[1] Marshall Day Acoustics, Auckland, New Zealand

ABSTRACT

The Auckland Film Studios (New Zealand) site has recently expanded its facilities with the construction of the Te Pūtahi building. This includes two large sound stages (2,000m^2 each) which provide a word class facility for film production. The project location, situated in an industrial area and near a train line, required careful acoustic consideration of the constructions to ensure a low background noise. While precast concrete walls typically used in soundstages would provide the required sound insulation performance to control airborne noise ingress, reradiated noise from the vibration generated by train pass bys was identified to exceed the design specification with this construction. A simple and robust alternative design, with a double layer construction, was developed to reduce reradiated noise, but still provide adequate airborne sound insulation and reduce the risk of construction errors. Furthermore, an auralisation demonstration of train pass bys was also prepared during the design process to assist the design team and client to understand the effects of building materials in the audibility of trains in the studios. This paper outlines the design process and technical solutions developed to achieve the required design specification.

Keywords: *sound stages, train, reradiated noise, auralisation.*

1. INTRODUCTION

Sound stages are an essential part of the filming production process. These provide a controlled and versatile environment for filmmakers to explore and make their ideas reality. Sound stages are typically large empty rooms with high ceilings, structural grids to support lighting, curtains and other equipment or props used during filming and building sets.

A low background sound and a controlled internal environment are essential in a soundstage. With sound stages often located in industrial areas or main transport areas, the acoustic design is a key element of the success of the sound stages.

Auckland Film Studios in New Zealand, has recently expanded their facilities with the Te Pūtahi sound stages. The Te Pūtahi building, which includes two sound stages (2,000 m^2 each) in one building, is located in a moderately high noise environment, within an industrially zoned area and approximately 25m from a train line. The project was developed by Tātaki Auckland Unlimited and was co-funded by Government and Auckland Council.

Thanks to active client engagement and a detailed and well-coordinated design, an excellent outcome was achieved - a high-performance facility was delivered which readily met the client's expectations.

In this paper the authors describe the design challenges and decisions undertaken during the design of Te Pūtahi sound stages.

[*] ***Corresponding author***: *javier.sanz@marshallday.co.nz*
Copyright: *©2025 First author et al. This is an open-access article distributed under the terms of the Creative Commons Attribution 3.0 Unported License, which permits unrestricted use, distribution, and reproduction in any medium, provided the original author and source are credited.*

2. SITE LOCATION AND EXISTING NOISE ENVIRONMENT

2.1 Site location

The Auckland Film Studios site is located in an industrial zone with the rail corridor approximately 25m from one of the Te Pūtahi sound stages (see Figure 1 and Figure 2).

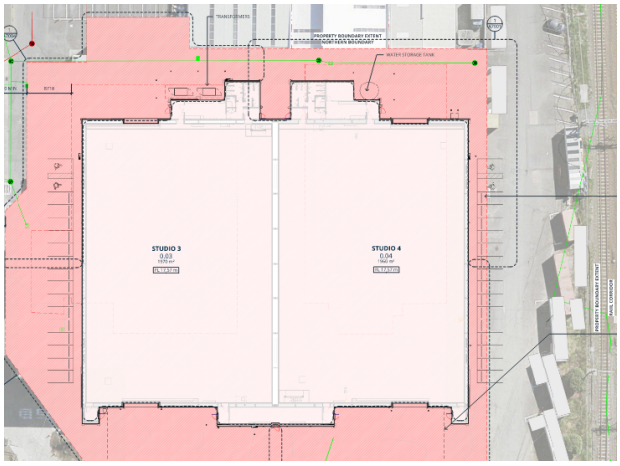


Figure 1. Location of Te Pūtahi sound stages[1]



Figure 2. Te Pūtahi building during construction[2]

2.2 Existing noise and vibration environment

2.2.1 Noise environment

According to the noise regulations, adjacent sites can generate noise levels of up to 65 dB L_{Aeq} at the site boundary of Auckland Film Studios.
The sound stages are exposed to noise from other sites, but also noise from adjacent roads and train pass bys.
A noise logger was installed at the proposed location of the building for one week. A detailed analysis of a representative day was undertaken and the noise sources and design level discussed with the client. An incident level of 72 dBA was decided as the design level - this would cover the noise from passenger trains as well as other ambient sources. The design level is shown in Figure 3 with a horizontal red dashed line. Noise from some film related activities within the site exceeded this level for short durations of time, but we were informed these could be managed and should not be considered. Nevertheless, based on the noise data measured, the ambient noise levels would only exceed 72 dBA approximately 2 minutes per day.

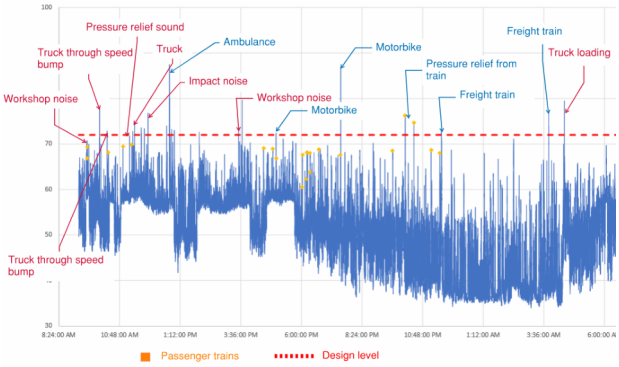


Figure 3. Analysis of noise levels measured

2.2.2 Vibration from trains

There was an existing building in the same location as the proposed soundstages. Vibration levels were measured during one week at this location. Trains pass bys were the main vibration source, and while the vibration was moderately low and subjectively barely perceptible, reradiated noise from train vibration had an important influence on the building construction.

[1] Architecural drawing from Ignite Architects
[2] Photo from Mark Scowen

3. DESIGN CRITERIA

3.1 Background noise criteria

When filming, sound stages require a low background noise to ensure the sound recordings are not affected. A noise criterion on NC 25 during filming was specified as part of the brief. The design brief also indicated that internal noise sources within the site or non-frequent sources (freight trains, ambulance, etc.) would not need to be considered as part of the design.
The Noise Criteria descriptor (NC) is typically used to set a background noise criterion of room from relatively constant noise sources (e.g. mechanical services noise). However, it appears that this descriptor is commonly used in the design of sound stages. In accordance with the measurement standard, ANSI/ASA S12.2-2019 [1], noise is 'averaged' over the room during a measurement period of not less than 20 seconds.
Noise from train pass-bys can be of a short duration and if an average level descriptor, like NC, was to be used, the design criterion could be achieved but noise ingress might not meet the client's expectation. Discussions on the meaning and intent of the NC design criterion specified in the brief and the perception of short duration noise levels were important aspects to ensuring the design would meet the client's expectations. The use of percentile descriptors to communicate the transient nature of the noise sources was investigated, but these can be complicated to understand for non-acousticians. An auralisation of the predicted noise from train pass bys as well as typical background noise levels in the sound stage was undertaken in Marshall Day Acoustics' Listening Room [2]. This process, which is discussed later in this document, played an important in explaining the potential impact of train noise intrusion, enabled the client to fully participate in the decision-making process and gave them assurance about the outcome of the project.

3.2 Vibration criteria

Vibration from HVAC plant and trains also needs to be considered. While not part of the brief, the ASHRAE human comfort criteria was used and a design criteria of 0.14 mm/s was used for 'typical' trains with some minor exceedance of 0.2 mm/s allowed for 'worst-case' trains.
A vibration level of 0.1 mm/s is the limit of perception when placing hands on the floor and are concentrating in a quiet environment, this is 'operating theatre' level. A criterion of 'night-time residential' 0.14 mm/s would mean that vibration would generally not be perceivable during general activities.

4. BUILDING DESIGN

Sound stages' buildings require constructions that provide high levels of sound insulation. The use of precast concrete walls is very frequent in sound stages due to structural durability and sound insulation performance.
Concrete is effective at stopping airborne noise but is unfortunately efficient at radiating ground borne vibration. With building located near the train line, the use of concrete walls would have resulted in a large area of efficiently radiating concrete exposed within the studio. Based on the vibration levels measured, averaged noise levels of NC 23-29 were predicted from reradiated noise. This meant that investigating the use of alternative materials that are less efficient at reradiating ground borne vibration was required.
The design and construction program were only 22 months. This meant that an early contractor involvement was an important aspect in the design. While the design concept was developed early in the design, the exact construction materials were adjusted in close collaboration between all design team members and selected contractor to ensure all requirements were achieved: acoustic performance, procurement times, cost, etc. The design process and solutions proposed are described in the next sections.

4.1 Building constructions to control noise ingress and reradiated noise

4.1.1 External walls

High levels of sound insulation can be provided by either very heavy masonry constructions or from multiple skins of lighter weight materials. As regenerated noise from train vibration with concrete walls was identified early in the design, a double skin facade system spaced by a large cavity and isolated between layers was proposed.
Materials like Korok and Durra panels (see Figure 4) are less efficient at reradiating ground borne vibration and are commonly used in large buildings in New Zealand due to its long spans and quick installation. Durra panels are made of compressed wheat straw, which is a natural and renewable resource. Korok panels are made of a galvanised steel shell with an aerated concrete infill.



Figure 4. Image of Durra panel (left) Korok (right)

The construction below was recommended (see the architectural detail in Figure 5).

- Steel profile cladding on a 45mm ventilated cavity with battens at 1200mm centres
- 78 mm Korok panels
- 500mm cavity with a lightweight fibreglass/polyester blanket (90 mm thick and minimum density of 10 kg/m^3)
- Durra panel to the studios side

To maintain the sound insulation performance of the system it was important to maintain the isolation between the inner and outer layers. A robust and consistent solution, isolating the connection of the Korok panels to the main structure with neoprene pads, was designed between the authors and the architects to ensure this isolation was achieved throughout the building and reduce the risk of construction errors on site.

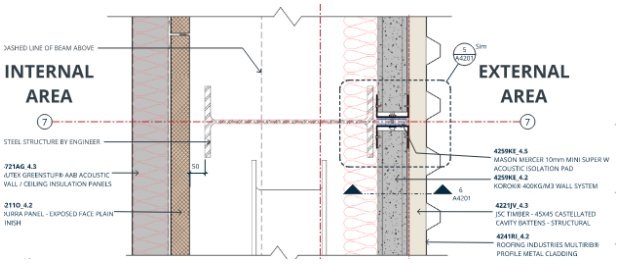


Figure 5. Image of external wall construction[3]

Figure 6 shows a comparison of the predicted sound insulation performance of the system proposed compared to a 200mm thick concrete wall.

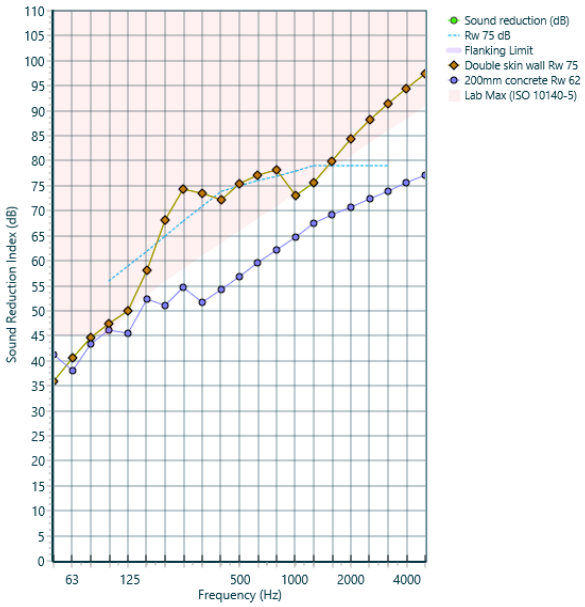


Figure 6. Comparison of sound insulation of concrete wall with double skin system in INSUL

As it can be seen in Figure 1, in one of the external walls, the Korok panel and external cladding had to be replaced with a concrete panel for fire reasons due to the close proximity of a building from another site to the sound stages.

4.1.2 Roof/ceiling

The roof/ceiling represents a very large area, and therefore the sound insulation performance was important too. Furthermore, rainfall is frequent all year round in Auckland with sporadic heavy falls. The client informed that rain noise is a limitation in other sound stages.
With the tight construction period and the roof construction planned for the winter period, the contractor's input in the roof systems to ensure building was weather tight as soon as possible was important. The design team worked collaboratively with the contractor to design a system based on this and met the acoustic performance required. The roof/ceiling system in Figure 7 was proposed, which addresses both noise ingress and controls rain noise.

[3] Architecural detail from Ignite Architects

- Steel warm roof system with a solid mass layer and stone wool core
- 400mm cavity with a lightweight fibreglass/polyester blanket (min 90mm thick and min density of 10 kg/m^3)
- Korok (600 kg/m^3) connected to the roof at no closer than 1200 mm centres

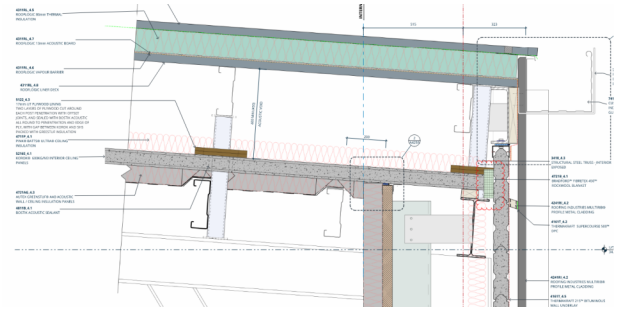


Figure 7. Roof/ceiling construction[3]

4.1.3 Scenery doors

Large scenery / elephant doors (7m x 7m) are required in sound stages for loading and unloading purposes. Doors are typically the weakest point in the sound insulation of a building, but their performance was key to achieving the design criteria.

Two sets of medium performance doors were initially discussed as the most robust solution. However, a single high performance scenery door (STC/R_w 55 and NIIC/D_w 58) was finally selected for cost reasons. Each studio has two of these doors.

The operational mechanism of the doors was an important aspect in the design. Sprinklers are typically not desired in sound stages because a false trigger could destroy the sets, which would have a significant cost implication. Large smoke extract fans connected to the AHU ductwork were used as the fire protection and smoke extract design. This meant that the doors need to be capable of opening quickly to provide enough make up air.

4.1.4 Slab

With the slab on grade, noise reradiated from train vibration through the slab and masonry upstand was predicted to range between NC $_{1sec}$ 23-28 during short periods of time but meet the design criterion of NC 25 when averaged according to the relevant measuring standards (ANSI/ASA S12.2-2019) in the studio closer to the train line.

An example of the noise levels predicted within the studio from the train vibration during a train pass-by with the slab on grade is shown in Figure 8. The approximated duration of the train pass by is 30 seconds. The graph shows the noise levels predicted for each second (NC_{1sec}) in blue, and the averaged noise level when measured/assessed according to ANSI/ASA S12.2-2019 is shown in red. While the averaged noise level for 20 seconds (minimum measurement length) would be NC 20-25, noise from trains would be higher than NC 25 during short periods of time, in this example 8 seconds.

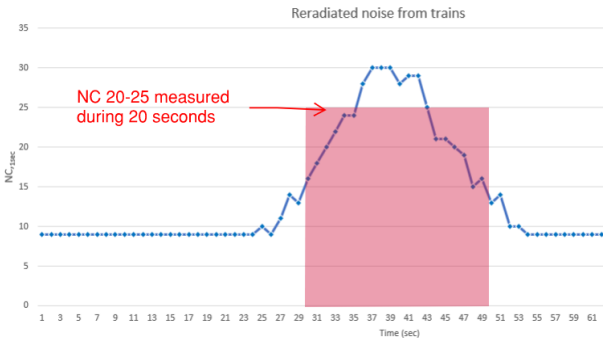


Figure 8. Noise from train pass by in sound stage closer to the train line with slab on grade

Up to approximately 12 trains per hour cross near the sound stages at times. Even though the design was predicted to meet the design criteria without further treatment, additional mitigation measures were explored to reduce the possible disruption from train pass bys: isolating the train tracks (this was not possible for practical reasons), trench along site (the trench to be effective this would need to be very deep, and it was found out this the trench was not possible because of the high water table on site) and isolating the slab of the sound stage.

Due to the elevated cost of isolating the slab, it was important for the client to understand the effects of the noise from the trains in the sound stages. An auralisation of the noise from train pass bys with and without the isolation was demonstrated in Marshall Day Acoustics' Listening Room. The demonstration was presented to representatives of the client. During the demonstration, sound engineers, who would be working in the studios, simultaneously recorded the background noise to verify if this would be disruptive in their recordings. The demonstration included a VR 3D model of the sound stage and sound was reproduced via a calibrated array of speakers providing an immersive as well as accurate experience (see Figure 9).



Figure 9. MDA's Listening Room

Following the demonstration the client decided that the isolation of the slab was required to achieve sufficient protection from train pass-bys.
The slab was isolated using a 50mm Sylomer mat (SR-11) below the entire slab (see Figure 10), which has a natural frequency of 21 Hz. Measurements showed that most of the vibration energy from passenger trains was around 125 Hz. With this design the noise from the trains was predicted to meet the design criteria and be well below NC_{1sec} 25. A minor increase in vibration was predicted at some low frequencies but this was predicted to still be generally imperceptible, only just noticed when lying down still and quietly.

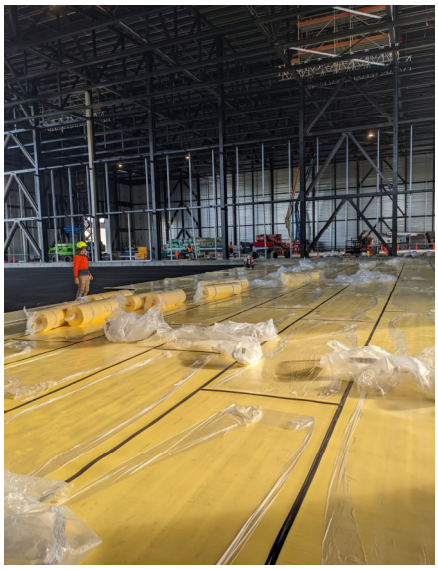


Figure 10. Sylomer mat during construction

4.2 Other design considerations

4.2.1 Sound insulation between studios

The Te Pūtahi building has two sound stages. Each sound stage could be used by a different client and therefore the sound insulation between sound stages needed to be considered.
A concrete wall, similar to other sound stages, was not appropriate due to the reradiated noise from trains. With the use of Durra panels to the internal walls of the building envelope, it seemed logical to use Durra panels for the internal wall. A double Durra panel wall including fibrecement layer with a large cavity and independent structures was proposed (see Figure 11).

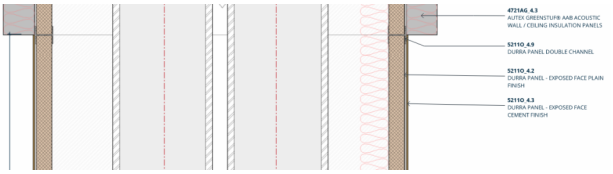


Figure 11. Wall construction between studios[4]

4.2.2 HVAC noise

The design team was informed that the low background noise from mechanical services is only required during critical recording and the mechanical systems would typically be turned off during filming. Nevertheless, the following design criteria for mechanical services noise was agreed for the different uses:

Table 1. Background noise criteria for different uses

Activity	**Background noise criteria (NC)**
Filming preparation with an occupied set and speech communication required	30-35
Scenery construction	35-40
Warehouse/workshop	40-45

Mechanical equipment is typically located in an outdoor plantroom and sections of internally lined ductwork and long attenuators are required to control noise from the HVAC equipment and noise ingress.

[4] Architecural detail from Ignite Architects

4.2.3 Rain noise and noise ingress via the ductwork

With the mechanical equipment located on an external plant platform, rainfall on the external ducts and external noise break-in into the ductwork after the attenuators can compromise the design, particularly in a high rainfall location like Auckland.
Acoustically it would be preferable to locate the attenuators at the penetration of the building envelope, but this was not practicable due to the space constrains. To mitigate the risk of rainfall and noise ingress, a flexible connection in the ductwork and a rain shroud, isolated and spaced away from the ductwork, between the attenuators and building penetrations was built (see Figure 12).

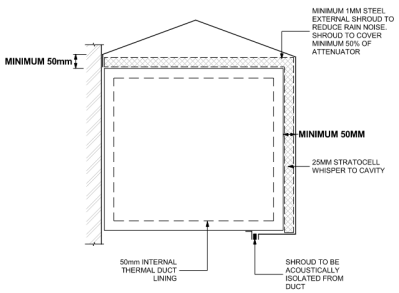


Figure 12. Rain shroud[4]

4.2.4 Absorptive treatment

It is important that sound stages are acoustically 'dead' spaces, and all available surfaces (ceiling and walls) are to be covered with absorptive materials. The lower section of the walls (<2m) is typically not covered with an absorptive material as a robust layer is desirable. This area will be normally obscured by sets during filming, treatment over this section of the wall is not normally required.
A black 100mm high density polyester blanket (density of 48 kg/m^3) was used on the walls and ceiling (see Figure 13).



Figure 13. Internal view of Te Pūtahi sound stages[5]

[5] Photo from Mark Scowen

5. COMMISSIONING RESULTS

Commissioning measurements were undertaken to confirm compliance with the design brief. These included measurements of the background noise from noise ingress and mechanical services at different operation modes, and the sound insulation performance of the doors. Overall, both sound stages perform very well and readily meet the design criteria.

5.1 Noise ingress

Background noise measurements from noise ingress were undertaken with a low noise microphone to ensure the floor noise of the microphone/sound level meter did not limit the measured performance. All HVAC systems were turned off during the measurements. Measurements were undertaken at a time with high train pass-bys to ensure a representative sample of noise sources was captured.
Studio 3 is the sound stage located at a further distance from the railway. The slab in this studio was not isolated as the rail line is located further away and the studio is shielded by studio 4 and other buildings. In this studio noise from trains was the most audible source. Averaged noise levels of NC 12-17 were measured from train pass bys with noise levels typically below $NC_{1,sec}$ 17, with the exception of an event where two trains (one each line) pass by during the measurements and noise levels raised of up to $NC_{1,sec}$ 22 (see Figure 14).

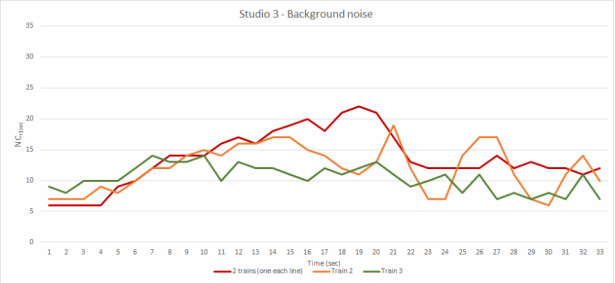


Figure 14. Background noise in sound stage non isolated (further away from train line)

In Studio 4, the isolated soundstage located near the rail line, train noise was barely audible above the background. An averaged noise levels of NC 15 was measured during train pass bys. As shown in Figure 15 (coloured solid lines), noise levels just barely exceeded $NC_{1,sec}$ 15 during some events. Noise from other noise sources (e.g. ambulance or loud motorbikes) were also below NC 20.

While studio 3 is the sound stage located at a further distance from the rail line, measurements show that noise from trains was higher in studio 4. This shows the importance of the reradiated sound from train vibration and effectiveness of the slab isolation.

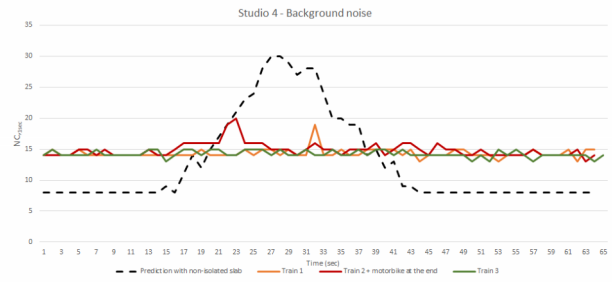


Figure 15. Background noise in sound stage with slab isolated compared with non-isolated prediction

Figure 15 shows a comparison of the noise levels measured in studio 4 (sound stage near the railway) and the predicted noise level from the reradiated noise without the slab isolated (dashed line in Figure 15).

5.2 Mechanical services noise

Noise from mechanical services noise was also measured for the different modes: air conditioning mode (mode with the AHU and fan set to maintain the temperature in the room) and boost mode (mode to cool/heat the sound stages).
The results of the measurements are shown in Table 2. These readily met the design performance recommended.

Table 2. HVAC background noise

Mode	Noise level (NC)
Air conditioning	20
Boost mode	25-26

6. ACKNOWLEDGMENTS

The authors would like to thank Auckland Tātaki Unlimited and Ignite Architects for their support on this paper and facilitating the architectural details shown. The authors would also like to acknowledge the teamwork and collaboration from the design team and contractors (Ignite Architects, eCubed, BGT Structures, Hayden + Rollet, Crossfire/Jensen Hughes, Precon and others) in a challenging but enjoyable project which has resulted in a very successful outcome.

7. REFERENCES

[1] ANSI/ASA S12.2-2019, *Criteria For Evaluating Room Noise*

[2] Marshall Day Acoustics Listening Room, https://marshallday.com/the-listening-room

DOI: 10.61782/fa.2025.0767

FORUM ACUSTICUM EURONOISE 2025

SHAKER-EXCITED LDV MEASUREMENTS OF ETFE MEMBRANES AND CUSHIONS: ACOUSTIC RESPONSE TO RAINDROP IMPACTS

Majid Lavasani[1,2*] **Vojtech Chmelík**[1] **Monika Rychtarikova**[1]
Christ Glorieux[3]
[1] KU Leuven, Department of Architecture, Campus Brussel and Ghent, Belgium.
[2] STU Bratislava, Department of Materials Engineering and Physics, Faculty of Civil Engineering, Bratislava, Slovakia.
[3] KU Leuven, Department of Physics and Astronomy, Laboratory of Soft Matter and Biophysics – Acoustics, Heverlee, Belgium.

ABSTRACT

The elastic properties of ethylene tetrafluoroethylene (ETFE) membranes are of importance for the features of their distinct drum-like acoustic response when subjected to rainfall, which in turn can affect acoustic comfort, speech intelligibility, and cognitive task performance. The spectrum and loudness of the sound caused by rain impact is dependent on the elastic parameters of the membrane, on the membrane tension, and on the geometry. This study addresses the elastic behavior of single-layer ETFE membranes and multi-layer ETFE cushions, using shaker-excited, scanning laser Doppler vibrometry (LDV)-detected guided wave measurements. The dispersion relation of bending waves running along ETFE membranes was determined, enabling the extraction of the applied tension. The findings contribute to a deeper understanding of the acoustic behavior of ETFE systems during rainfall and their implications for architectural design.

Keywords: *ETFE, Rain noise, Tension, Stress, LDV*

1. INTRODUCTION

Ethylene tetrafluoroethylene (ETFE) membranes are widely used in contemporary architecture due to their lightweight properties, durability, and optical transparency. They are commonly implemented in large-span roofs, façades, and stadium enclosures, where their mechanical and acoustic behavior plays a crucial role in overall performance. One of the significant acoustic challenges associated with ETFE structures is the sound generated by impacting raindrops [1,2]. Depending on factors such as membrane tension, material stiffness, and structural configuration, rain-induced noise can range from subtle background sound to disruptive levels that affect acoustic comfort in enclosed spaces. Accurately predicting this noise requires a precise understanding of ETFE's mechanical properties, particularly the in-plane tension, bending stiffness, and Young's modulus.

The in-plane tension of an ETFE membrane directly influences the propagation of bending waves, which in turn affects how vibrations and sound waves are generated upon raindrop impact. However, the exact tension in mounted ETFE membranes is not always well known, leading to uncertainties in acoustic modeling. A more accurate estimation of these mechanical properties allows for better predictions of rain-induced noise and improved numerical simulations of droplet impacts.

To address this, this study investigates the mechanical properties of single-layer ETFE membranes and multi-layer ETFE cushions through wave propagation analysis. The findings will contribute to improving the modeling of the

[*] ***Corresponding author***: majid.lavasani@kuleuven.be
Copyright: *©2025 First author et al. This is an open-access article distributed under the terms of the Creative Commons Attribution 3.0 Unported License, which permits unrestricted use, distribution, and reproduction in any medium, provided the original author and source are credited.*

acoustic response of ETFE membranes under raindrop impact, enhancing the accuracy of predictions for architectural applications.

2. METHODOLOGY

The measurement of ETFE membranes' vibrational properties was achieved through Laser Doppler Vibrometry (LDV), by recording the vibrational response of the membranes under excitation. This setup allows for a detailed analysis of the material's dynamic behavior at various frequencies and distances from the shaker. Figure 1 presents an image of the experimental setup. The measurements were conducted in a semi-anechoic chamber. The sample was placed on a damping material to minimize the transmission of vibrations from the sample through floor to the laser measurement device.

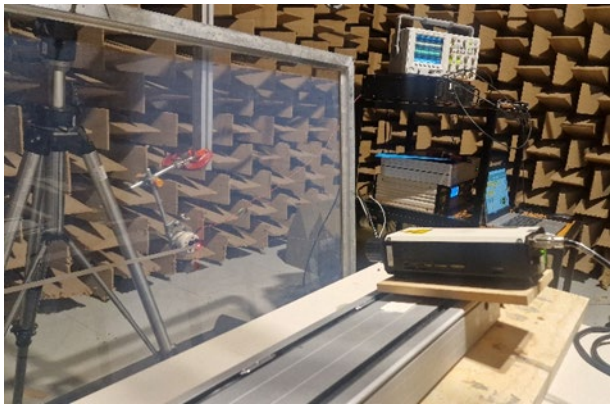


Figure 1. Picture of the measurement setup

A schematic representation of the measurement setup is provided in Figure 2.
The key steps were as follows:

- A swept-frequency signal is generated by a computer and transmitted to the shaker via a sound card, with amplification applied during transmission. The shaker's cylindrical moving element made gentle contact with the membrane, with its circular end (approximately 2 mm in diameter) touching the surface. The sweep covers a frequency range from 10 Hz to 10 kHz. To prevent overloading at low frequencies, the amplitude was fading in from low to high values till 1000 Hz and constant above. The total sweep duration was 20 seconds, which is more than twice of measured structural reverberation time of the sample. Figures 3 and 4 show the waveform and spectrogram of the sweep, respectively.

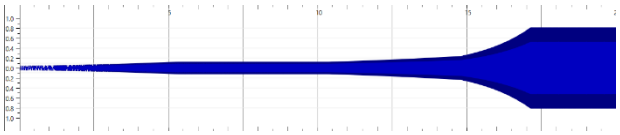


Figure 3. Waveform of the 20 second sweep

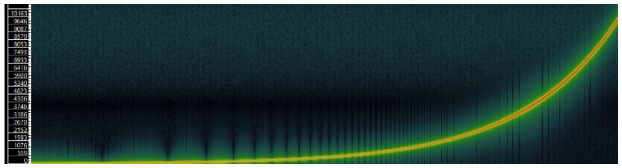


Figure 4. Spectrogram of the sweep

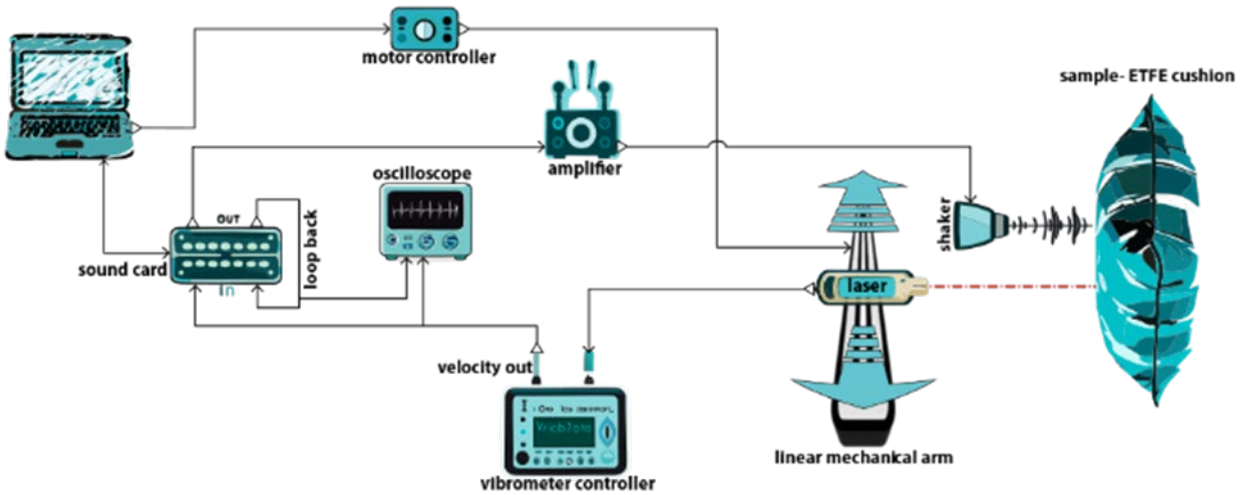


Figure 2. Schematic representation of the Laser Doppler Vibrometry (LDV) setup.

- The vibrational response was recorded with a sampling rate of 44.1kHz . In addition to the normal displacement component of the vibration response with a Laser Doppler Vibrometer (LDV), also the sent signal was looped back to a second recording channel, to serve as reference.
- The vibrations were recorded at different distances from the shaker contact point along a line starting from the excitation point using a linear mechanical arm. For each sample, over 600 recordings were taken along a distance exceeding 60 cm, with a spatial step size of 1 mm, thus obtaining the spatiotemporal dependence of the normal vibration velocities $v_z(r,t)$. The overall measurement range was sufficient to capture the longest wavelengths, while the spatial step size was fine enough to resolve the shortest wavelengths. Table 1 provides detailed specifications of the equipment used in this measurement setup.
- From the sweep recordings, for each detection distance, the spectrum $v_z(r,f)$ was determined. By making use of the sent spectrum, the transfer spectrum was determined and Fourier transformed to get the impulse response for each distance r.
- The impulse responses were windowed in order to select only the direct wave arrivals, and then Fourier transformed back to frequency domain. Finally, the direct signals $v_{z,direct}(f,r)$ were spatially Fourier transformed to obtain the waveumber-frequency dispersion relation $v_{z,direct}(f,k_b)$.
- From the maximum amplitudes in wavenumber-frequency domain, the velocity dispersion was determined.

$$c(f) = \frac{\omega}{k} \tag{1}$$

Table 1. Equipment details

Equipment	Model/Specification	Details
Sound Card	Roland Quad-Capture	24-bit, 192 kHz
Amplifier	EHQ Power VPA2350MB	
Shaker	LDS V100 series	Diameter of moving circular end: 2mm
Velocity Controller(LDV Decoder)	Polytec OFV 3001 Vibrometer Controller	Velocity Range: 1000 mm/s/V
Retroreflective Tape		Thickness: 0.5 mm

Two types of samples were measured: a membrane and a cushion. Both consisted of similar membranes, as shown in Table 1, but differed in structure. The first sample was a single-layer membrane, while the second was a three-layer cushion with an air pressure of approximately 250 Pa in both cavities. The outer layers had a thickness of 250 µm, while the inner layer's thickness is uncertain but is estimated to be between 80 and 120 µm based on the company's production specifications.

3. THEORETICAL MODEL

3.1 Wave propagation in uniaxially stressed membrane

The material properties, specifically Young's modulus and tension, were determined by fitting the obtained c(f) to a theoretical model for Lamb wave propagation in a membrane under stress: for uniaxial stress, the governing dispersion relation for wave propagation is given by [3]:

$$\omega = \sqrt{\frac{\frac{B}{h} * k_b^2 + \sigma_{xx}}{\rho}}\, k_b \qquad (\text{rad.s}^{-1}) \tag{2}$$

where ω is angular frequency(rad/s), h is the membrane thickness (m), k_b is the wavenumber (1/m), σ_{xx} is in-plane tension(Pa), ρ is the material density(Kg/m^3), and B is the bending stiffness(N·m), given by:

$$B = \frac{Eh^3}{12(1-\nu^2)} \qquad (\text{N.m}) \tag{3}$$

E is Young's modulus (Pa) and ν is Poisson's ratio (dimensionless).

Eq. (2) can be rewritten to determine the phase velocity of the propagating bending wave:

$$c_b = \pm\sqrt{\frac{\sigma_{xx} \pm \sqrt{{\sigma_{xx}}^2 + 4\omega^2 \rho B/h}}{2\rho}} \qquad (\text{m.s}^{-1}) \tag{4}$$

where c_b represents the phase velocity. Equation (4) shows that the bending wave velocity is dependent on the in-plane tension of the material, as demonstrated in Figure 5 for an ETFE membrane-the sample used in this experiment, for literature values for the material properties listed in Table 2 and varying values of the tension.

Table 2. Known physical properties of the ETFE sample

Abbreviation	Name	Value	Unit
E	Young's modulus	0.52×10^{9}	Pa
H	Thickness	250×10^{-6}	m
μ	Poisson's Ratio	0.45	-
ρ	Density	1750	kg/m3
η	Loss Factor	0	-

4. RESULTS

4.1 Impulse response(time vs distance plot)

The impulse responses from all measurement positions were combined into a spectrogram, where the color represents the amplitude of the impulse response. The recordings were normalized to ensure that the impulse responses from further positions could be adequately visualized without excessive amplitude variation. Additionally, to mitigate the effects of high-frequency noise and improve signal clarity, low-pass filter was applied to the recordings.

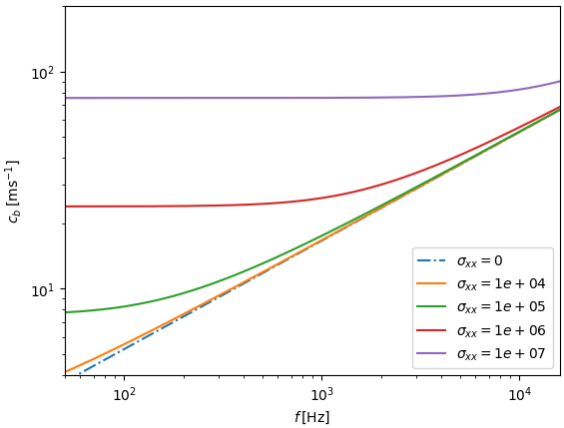


Figure 5. Theoretical relation between bending wave velocity and frequency for different values of the in-plane tension of an ETFE membrane.

The results are plotted as a function of position and time in Figure 6 (single-layer membrane) and Figure 7 (cushion). The signal magnitude is color-coded. The slope of the bright color regions corresponds to the bending wave velocity, with steeper slopes indicating a higher wave velocity. Also reflected waves, particularly in the cushion sample, can be observed, with the 722 mm position marking the edge of the sample.

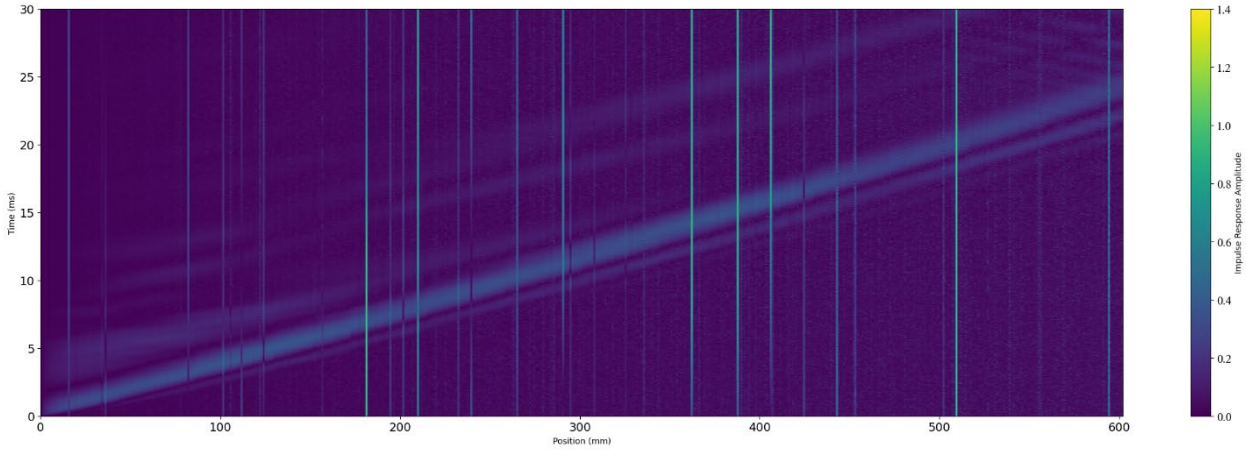


Figure 6. Time-distance plot of the arriving waves of the single-layer membrane.

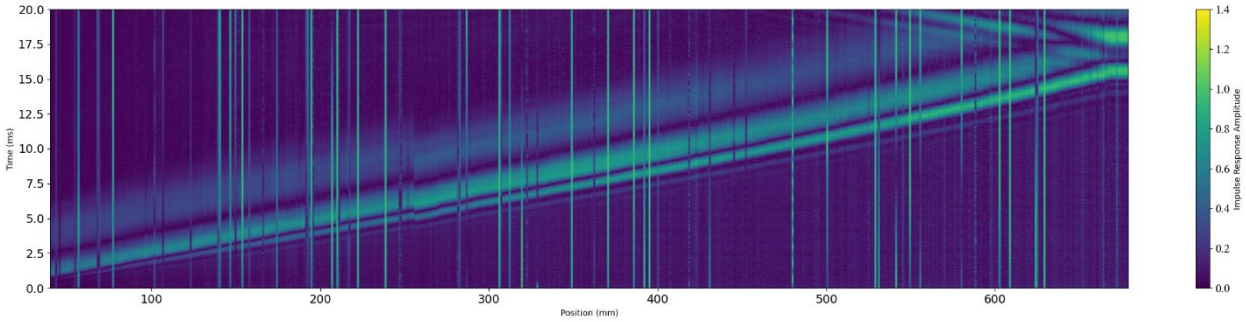


Figure 7. Time-distance plot of the arriving wave of the 3 layers cushion.

4.2 Wavenumber–frequency dispersion curve

After windowing the direct sound from the impulse responses, a 2D Fourier transform was applied, resulting in the wavenumber-frequency spectrum $S(k_b,f)$ in Figures 8 and 9, for the membrane and the cushion, respectively.

4.3 Tension estimation

Eq. (2), the relationship between wavenumber and frequency was used to fit the experimental k-f plot, enabling the estimation of the corresponding in-plane tension. The value of Young's modulus and Poisson' ratio were taken from literature (Table 1). The tension was found to be 1.95±0.03 MPa in the single membrane and 3.30±0.02MPa in the cushion.

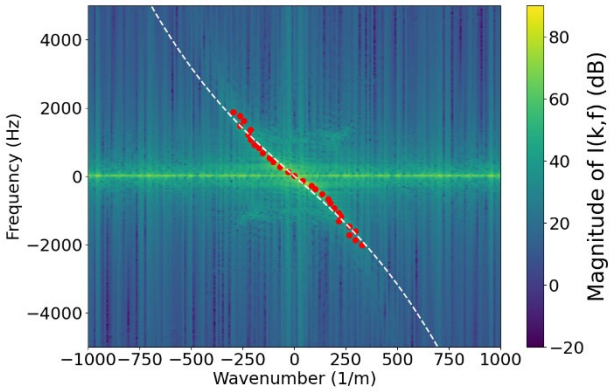


Figure 8. Fitted frequency-velocity plot of the bending wave along the membrane. The white dashed line represents the theoretical dispersion curve fitted using a tension value of 1.95 MPa.

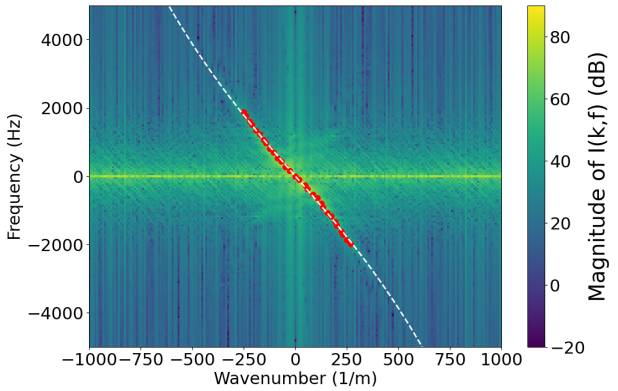


Figure 9. Fitted frequency-velocity plot of the bending wave along the 3 layer-cushion. The white dashed line represents the theoretical dispersion curve fitted using a tension value of 3.30 MPa.

5. CONCLUSION

This study has demonstrated the effectiveness of using shaker-excited Laser Doppler Vibrometry (LDV) to characterize the dynamic behavior and estimate the in-plane tension of ETFE membranes and cushions. We characterized a single-layer membrane with a thickness of 250 microns and a multi-layer cushion, which had an outer layer thickness of 250 microns, with an estimated internal air pressure of approximately 250 Pa. The results reveal a clear and significant difference in mechanical tension between the single-layer membrane (1.95±0.03 MPa) and the multi-layer cushion (3.30±0.02 MPa). These large tension values

strongly affect the dispersion and therefore also the acoustic impedance[4] and radiation efficiency when rain drop impact generated bending waves are running along the surface.

This indicates that the applied tension can be used as a parameter to control or mitigate the loudness and spectral features of rain noise, which can be exploited in architectural design of membrane and cushion based building structures.

6. ACKNOWLEDGMENTS

This work was supported by the Slovak national grant KEGA 033STU-4/2024.
This project acknowledges receipt of funding under number ESG 23-01-09-A, aimed at supporting doctoral students and young researchers at Slovak University of Technology to initiate their research careers.
This project has received funding from the European Union's Horizon Europe research & innovation programme under the HORIZON-MSCA-2021-DN-01 grant agreement No. 101072598 – "ActaReBuild".
We would like to thank Vector Foiltec GMBH for providing us the research samples.

7. REFERENCES

[1] M. Lavasani, V. Chmelík, Y. Sluyts, M. Rychtarikova, And C. Glorieux, (2024). "Sound of natural and artificial rain impact on ETFE membranes." in *proc. of the INTER-NOISE and NOISE-CON*, *270*(2), pp. 9687–9696, 2024.

[2] M. Toyoda, and D. Takahashi: "Reduction of rain noise from Ethylene/TetraFluoroEthylene membrane structures." *Journal of Applied Acoustics*, vol. *74 no.* 12, pp. 1309–1314, 2013.

[3] R. Waitz, S. Nößner, M. Hertkorn, O. Schecker, and E. Scheer: "Mode shape and dispersion relation of bending waves in thin silicon membranes." *journal of Physical Review, vol. B*, no. *85*(3), 2012.

[4] T. E. Vigran: *Building Acoustics*. Oxford: Press, 2008.

DOI: 10.61782/fa.2025.0862

FORUM ACUSTICUM EURONOISE 2025

THE EFFECTIVENESS OF PLENUMS IN ROOM ACOUSTIC CONDITIONING

Espinel Valdivieso, Ana Esther[1*] **Arenaz Gombau, Angel**[1] **Riesco García, Jose Ignacio**[1]
Mena Moreno, Andrea[1] **Gonzalez Nieto, Jairo**[1] **Cambor Iglesias, Pablo**[1]
[1] Audiotec Ingeniería Acústica S.A. C/ Juanelo Turriano, 4. 47151 Boecillo. Valladolid. Spain

ABSTRACT

The same absorbent material behaves differently depending on whether it is installed directly on a surface or if there is a plenum - an air chamber - between the supporting surface and the material.

This fact is particularly relevant in cases where these materials are used with or without a plenum in the acoustic conditioning of rooms, as the acoustic quality of a room can vary considerably depending on this factor.

AUDIOTEC has developed a study in which, in a first phase, was characterized in a reverberation chamber the variation of the sound absorption coefficient of different materials as a function of the plenum used in the tests.

Based on this information, simulations were carried out using ODEON Room Acoustic Software to calculate various room acoustic quality parameters (reverberation time, definition, clarity, STI) as a function of the plenum used.

This study concludes that in the project phase of room acoustic conditioning, the correct definition of the plenum to be used is fundamental, as depending on it, the acoustic quality of these rooms can be significantly improved.

Keywords: *acoustic absorption, reverberation time, inteligibility*

[*] ***Corresponding author***: *ana.espinel@audiotec.es*
Copyright: *©2025 First author et al. This is an open-access article distributed under the terms of the Creative Commons Attribution 3.0 Unported License, which permits unrestricted use, distribution, and reproduction in any medium, provided the original author and source are credited.*

1. INTRODUCTION

The purpose of this study is to evaluate, by means of acoustic modelling, the improvement obtained by the use of plenums in the acoustic conditioning of rooms.
For this purpose, test results of the acoustic absorption of materials with and without plenums, obtained in standardised test chambers, are used, as well as the room acoustic simulation software Odeon © room acoustics simulation software.

2. SOUND ABSORPTION TESTS

As a starting point for carrying out the study, we have used the results of sound absorption tests on materials with and without a plenum, carried out in Audiotec's standardised reverberation chamber at its facilities in the Boecillo Technological Park in Valladolid. These tests were carried out in accordance with the ISO 354 standard.

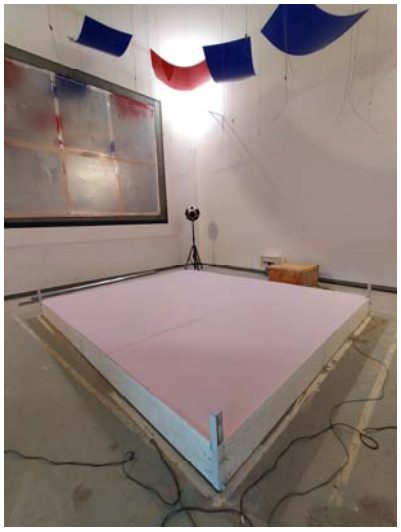


Figure 1. Plenum in reverberation chamber

2.1 TEST RESULTS USED IN THE STUDY

This study used the results of the absorption coefficient of different sound absorbing materials, including PET panels and mineral wool panels.
Firstly, the behaviour of sound-absorbing PET panels was analysed by varying the plenum.
The results obtained for the same material using different plenums

Frec Hz	α 0 mm plenum	α 50 mm plenum	α 200 mm plenum	α 400 mm plenum
125	0,05	0,15	0,35	0,40
250	0,05	0,40	0,65	0,75
500	0,25	0,85	0,85	0,80
1000	0,55	0,80	0,80	0,80
2000	0,85	0,95	0,85	0,85
4000	0,95	0,90	0,85	0,90

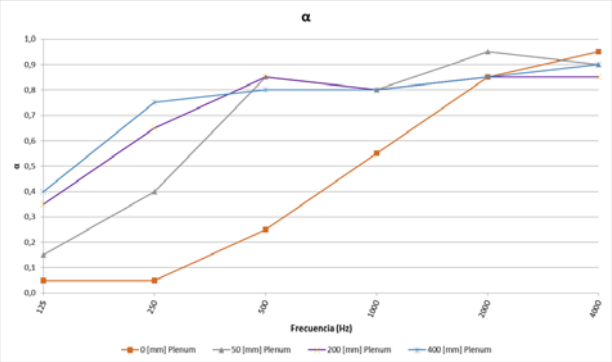


Figure 2. Sound Absorption Coefficient

3. ACOUSTIC CONDITIONING SIMULATION

3.1 The enclosure

In order to carry out the simulations, a multi-purpose enclosure was considered, with the following dimensions Floor area: 56 m2; height: 3 m; volume: 168 m3.

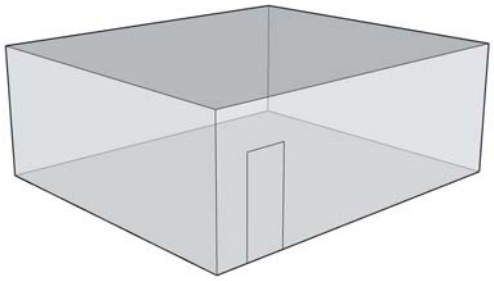


Figure 3. 3D Room Model.

The surfaces of the room are highly reflective: Ceramic tiled floor, smooth concrete walls and ceiling with plaster finish and a wooden door.
For the purposes of the simulation, only the ceiling is modified, leaving the other surfaces unchanged

3.2 Acoustic parameter recommended

Taking into account the intended use of our theoretical The recommended values to be obtained, taking into account the intended use of our theoretical enclosure as a multiple room, are as follows:

Parameter	Value
T20	0,80[s] – 1[s]
STI	≥ 0,65

3.3 Acoustic simulation

The simulations were carried out using the Odeon © acoustic prediction software. This software can be used to characterise various acoustic parameters, the results of which will vary according to the different materials present on the surfaces of the room.

The following parameters were analysed for this study:

- Reveberation timeT20 [s]
- Speech intelligibility STI

3.4 Initial acoustic characterization of the enclosure

As a starting point, we took the 3D model that had been generated to carry out a study of the most important acoustic parameters.

3.4.1 Reverberation time

The average reverberation time obtained (500 Hz, 1000 Hz and 2000 Hz) is 5.48 s, although there are reverberation times of the order of 10 s at low frequencies.
At medium frequencies, the reverberation times are also high, in the order of 6 s, which has a direct impact on speech intelligibility.
Finally, the high frequencies show values in the order of 3 and 4 s.

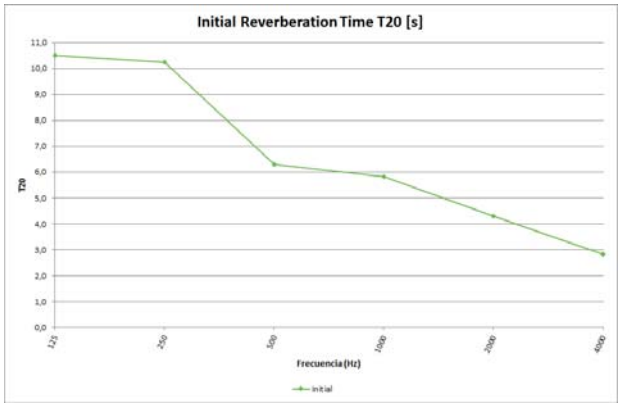


Figure 4. Initial reverberation time.

3.4.2 Speech intelligibility

Another parameter calculated is the speech intelligibility STI, which evaluates the quality of the perception of the spoken word, the initial value obtained is poor, which is consistent with what was observed in the reverberation time:

Parameter	Value
STI	0.30

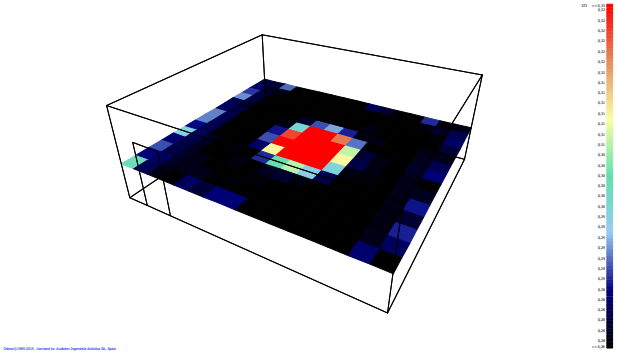


Figure 5. Initial speech intelligibility.

3.5 Acoustic characterisation of the enclosure with the sound-absorbing material installed without a plenum

3.5.1 Reverberation time

The simple application of the material to the ceiling reduces the reverberation time at low frequencies by almost half, with values around 5 [s].
At medium frequencies, the reverberation time is reduced to values around 1.6 [s].
The reverberation time at high frequencies shows a significant reduction with values around 1 second.

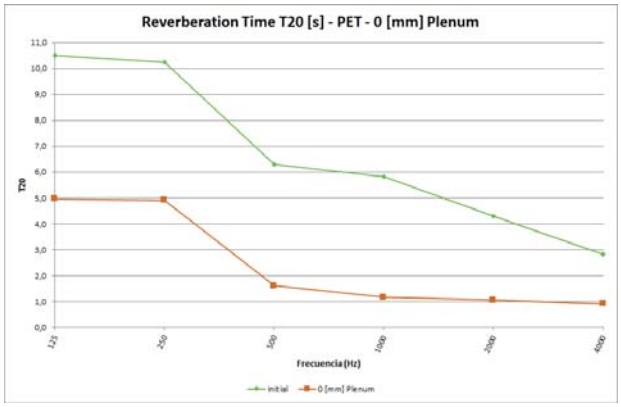


Figure 6. Reverberation time – 0 [mm] plenum

The application of the sound-absorbing material in the enclosure is effective at medium and high frequencies, although its behaviour is not so effective at low frequencies, since the reverberation time, although reduced, is still high for this type of enclosure.

Parameter	Value
T20 mid	1,17 s
T20 125 Hz	5 s
T20 250 Hz	5 s

3.5.2 Speech intelligibility

The impact of installing a non-plenum sound-absorbing material in the enclosure is positive, and speech intelligibility values have improved significantly, although they are still not good.

Parameter	Value
STI	0.55

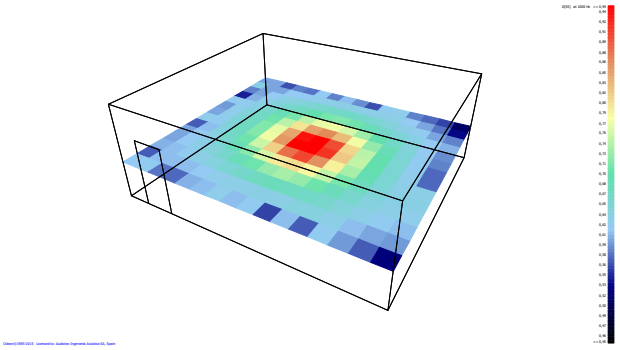


Figure 7. Speech intelligibility STI – 0 [mm] plenum.

3.6 Acoustic characterization of the enclosure with the material installed with 50 mm, 200 mm and 400 mm plenums

In this section we analyse the effectiveness and the improvement offered by the plenum in the acoustic conditioning of the enclosure.

For this purpose, a new simulation was carried out using plenums of 50 mm. 200 mm. and 400 mm. with the same material.

3.6.1 Reverberation time

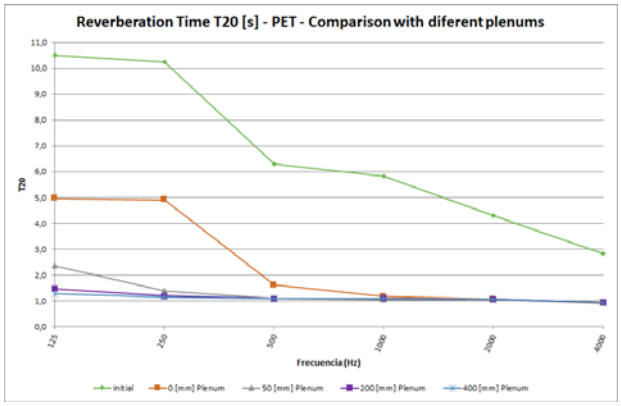


Figure 8. Reverberation time - Comparison according to the use of plenums.

As can be seen, the introduction of plenums with an air chamber improves the reduction of the reverberation time in the low frequency bands. This improvement is progressive as the air space (plenum) behind the material is increased, although there is hardly any difference between the 200 mm and 400 mm plenum.

The mid-frequencies also show a significant improvement with the introduction of an air gap. However, the improvement becomes less noticeable as the air gap increases.

Finally, it is observed that the high frequency is hardly affected by the introduction of the air gap. In other words, the improvement in this range is determined by the surface properties of the material.

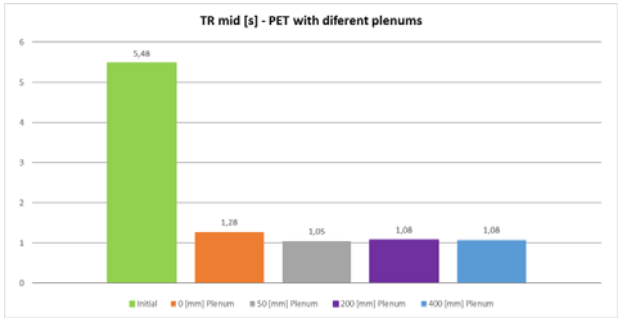


Figure 9. TRmid comparison

When the sound absorbing material is placed in the room without the air chamber, the average reverberation time shows a noticeable improvement.

It should be noted that the TR mid only considers the 500, 1000 and 2000 Hz bands.

mm, we have a decrease in the average reverberation time with respect to the material installed directly, but when the chamber is increased to 200 mm, we have a slight increase and a stagnation for the 400 mm chamber, proving that when the air chamber is increased, the medium and high frequencies are hardly affected, in this case, although an improvement is observed in the low frequencies.

3.6.2 Speech intelligibility STI

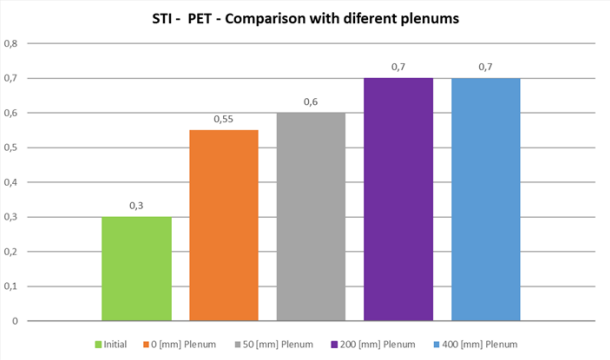


Figure 10. Speech intelligibility STI comparison

Speech intelligibility shows a significant improvement when the material is placed directly without an air chamber, going from a "very poor" value of 0.30 to a "fair" value of 0.55, meaning that the material alone has a positive effect on speech intelligibility.

With the addition of a 50 mm air chamber, the improvement is notable, with values classified as "good" of 0.65, indicating that this configuration provides better control of sound energy in the speech frequency range.

With 200 mm and 400 mm plenums, the values are 0.7 and are considered "very good".

Increasing the size of the air chamber shows little significant improvement, keeping the speech intelligibility values in the "very good" range.

4. COMPLEMENTARY STUDY

4.1 Test results used in the complementary study

A complementary study was conducted with a different material type (mineral wool) to verify the influence of material type on plenum performance.

The absorption coefficient of the material tested with different configurations is as follows:

F Hz	α 0 mm plenum	α 400 mm plenum
125	0,15	0,40
250	0,60	0,70
500	1,00	0,80
1000	0,95	0,90
2000	0,90	0,90
4000	0,90	0,90

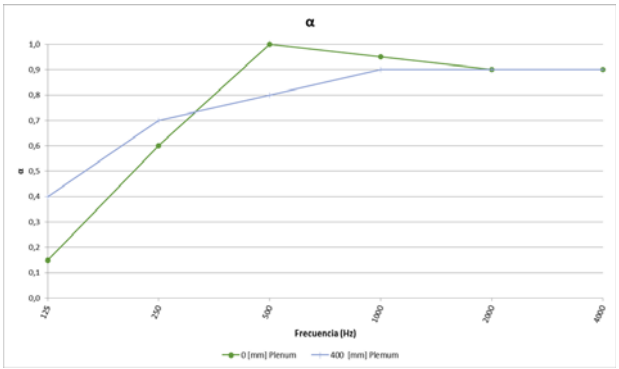


Figure 11. Sound Absorption Coefficient.

4.2 Acoustic characterisation of the enclosure with the sound-absorbing material 2 installed without a plenum

4.2.1 Reverberation time

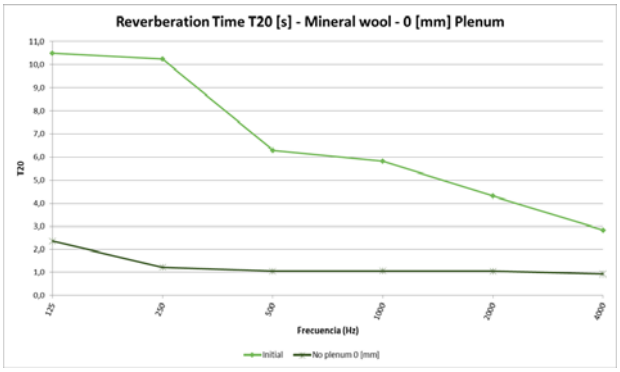


Figure 12. Reverberation time – 0 [mm] plenum.

The effect of using Material 2 in the enclosure without a plenum shows a reverberation curve with adequate values at medium and high frequencies.

The performance of material 2 at low frequencies without enclosure is better than that of material 1, reducing the reverberation time from around 10 [s] to values of 2.3 [s] for 125 Hz and 1.2 [s] for 250 Hz, reaching values of around 1.2 seconds, although still high.

At medium and high frequencies, the improvement in relation to material 1 is not so significant.

The average reverberation time obtained is slightly longer than recommended for this type of enclosure, although this difference is hardly noticeable at practical levels.

Parameter	Value
T20 mid	1,06 s
T20 125 Hz	2,3 s
T20 250 Hz	1,2 s

4.2.2 Speech intelligibility

The average speech intelligibility is rated "good". This indicates that the material has good control of the sound energy in the voice range.

Parameter	Value
STI	0.65

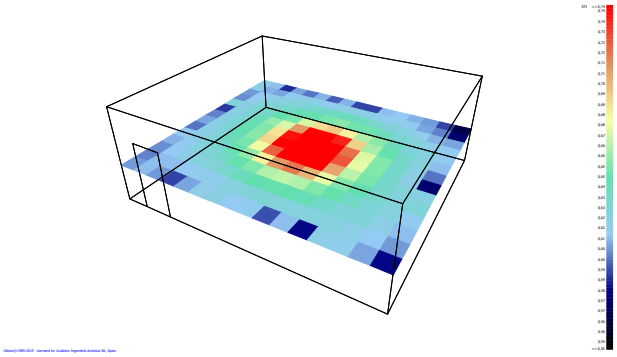


Figure 13. Speech intelligibility STI – 0 [mm] plenum.

4.3 Caracterización acústica del recinto con el material 2 instalado con plenum de 400 mm

4.3.1 Reverberation time

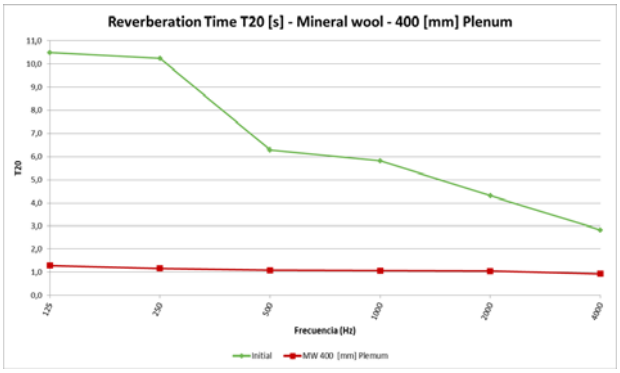


Figure 14. Reverberation time – 400 [mm] plenum.

As in the case of material 1, the reverberation time curve with a 400 mm air chamber stabilises at values close to 1 s over the whole frequency range studied, although a significant improvement can be observed in the 125 Hz band for this material.

4.3.2 Inteligibilidad de la palabra

In terms of speech intelligibility, the results are "very good".

Parameter	Value
STI	0.70

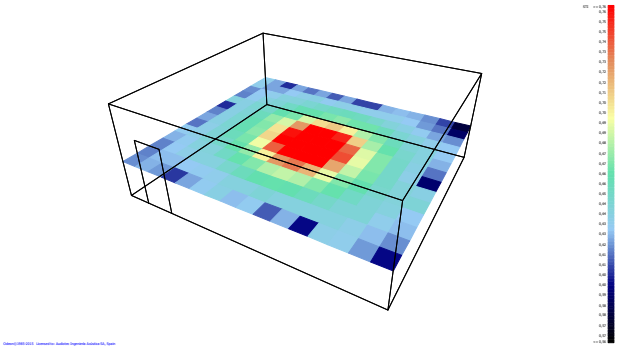


Figure 15. Speech intelligibility STI – 400 [mm] plenum.

5. COMPARATIVE ANALYSIS

5.1 Reverberation time

5.1.1 Materials installed without a plenum

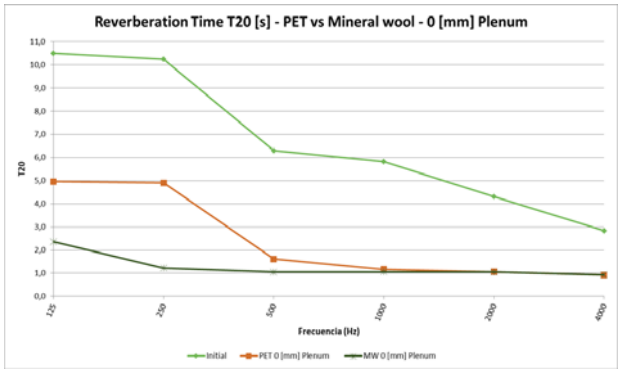


Figure 26. Reverberation time – 0 [mm] plenum comparison.

Material 2 has a better performance in the low frequency range compared to material 1 and controls the low frequency range more efficiently.

There is a slight increase in reverberation time in the 500 Hz band for material 1 at mid frequencies,

Both materials show similar behavior at high frequency, with material 2 being slightly better.

5.1.2 Materials installed with 400 mm plenum

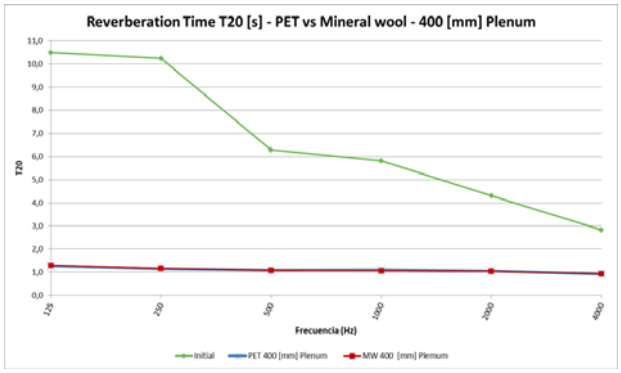


Figure 37. Reverberation time – 400 [mm] plenum comparison

The performance of the two materials with a 400 mm chamber is very similar, and in both cases the control of the low frequencies is significantly improved, while the performance in the mid and high frequencies remains stable.

5.1.3 TR mid comparison

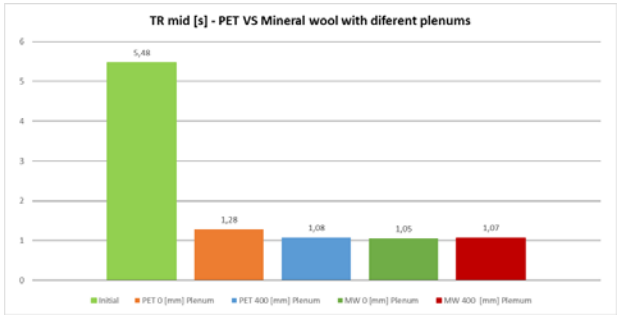


Figure 48. Trmid comparison.

As far as the average reverberation time is concerned, the placement of any sound-absorbing material improves the conditions, with material 2 showing the best performance

without an air chamber, with the most significant improvement at 125 and 250 Hz.

The reverberation time values obtained with a 400mm air chamber show hardly any perceptible differences between the different materials under consideration.

5.2 Speech intelligibility comparison

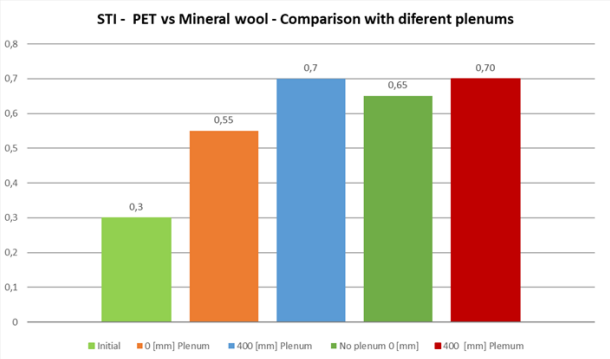


Figure 19. Speech intelligibility STI comparison

In terms of speech intelligibility, when placing the materials without air chamber, we have an improvement but insufficient with material 1.

Under the same conditions, material 2 without air chamber performs better than material 1.

The performance of both materials with 400 mm air chamber is similar, obtaining a "very good" performance.

6. CONCLUSIONS

The air chamber (plenum) is very effective in reducing low frequency reverberation (125Hz and 250Hz) for both materials, although its effect is less at medium and high frequencies than not using a plenum.

Material 2 without plenum shows a better performance at low frequencies than material 1, although this fact does not significantly affect the TRmid value, since it is calculated considering the 500 Hz, 1000 Hz and 2000 Hz bands.

The improvement in speech intelligibility without plenum is more significant with material 2, which has higher absorption results, especially at low frequencies, although the installation of a 400 mm air chamber tends to compensate for the improvement in room intelligibility.

The fact of inserting a plenum improves the speech intelligibility compared to not inserting it, although this improvement is hardly noticeable between the use of a 200 mm plenum and a 400 mm plenum.

7. REFERENCES

[1] Beranek, L.L., Acoustics, 5th edition, Acoustical Society of America, New York, (1954).

[2] Marshall, Long, Architectural Acoustics, Elseiver, California (2006)

[3] Blauert, Jens, Xiang, Ning, Acoustics for Engineers, Troy Lectures, Springer-Verlag, Berlin (2008)

[4] Everest, F. Alton, Pholman Ken c. Master Handbook of Acoustics, fifth edition, Mc Graw Hill (2009)

DOI: 10.61782/fa.2025.0494



FORUM ACUSTICUM
EURONOISE 2025

INVESTIGATING POSITIONAL EFFECTS OF THE PERIMETER FRAME IN SOUND ABSORPTION MEASUREMENTS

Gjermund V. Holøyen[1*]
[1] SINTEF Community, Børrestuveien 3, 0373 Oslo, Norway

ABSTRACT

When measuring the sound absorption coefficient according to ISO 354:2003, the standard commonly requires the use of a reflective frame around the perimeter of the test specimen, to keep the edges from absorbing sound. Logically, this is most important at high and medium frequencies, but previous studies have shown a significant impact also at lower frequencies. At this end of the spectrum, the frame seems to have a positive effect on the measurement results – an effect that persists even when the test specimen is only partially covered by a frame. To get closer to the cause of this phenomenon, reverberation room measurements have been carried out on a partially framed test specimen. Several different configurations of a partial frame have been tested, with a view to observe whether the position of the partial frame relative to the test specimen is of any importance to the measurement results. The results from these measurements are presented and discussed in this paper.

Keywords: *sound absorption measurements, reverberation room, measurement setup, edge effects*

1. INTRODUCTION

In annex B in the standard for measuring the sound absorption coefficient in a reverberation room, ISO 354:2003, rules and guidelines for mounting of different types of sound absorbers are given [1]. Most commonly, sound absorbers are placed directly on the floor during testing, for which the standard normally requires a reflective frame to be built around the perimeter of the test specimen to keep the edges from absorbing sound. However, previous studies have shown that the presence of a frame has a significant positive impact on the measured sound absorption coefficient at the lowest frequencies [2], an impact that seems to be dependent on the placement of the test specimen and its perimeter frame in the reverberation room [3]. To look deeper into this phenomenon, further reverberation room measurements have been carried out – this time with a focus on what happens when a test specimen is only partially covered by a frame.

2. METHODOLOGY

A test specimen of 200 mm melamine foam was used in the measurements. 15 pieces of 0.6 x 1.2 m was assembled into a test object of 3 x 3.6 m. This test specimen size fully complies with the requirements for test specimen size and shape given in ISO 354 when fully framed, however, the absorptive area is larger than 12 m^2 for most of the partially framed measurements.

For the frame, 48 x 195 mm spruce wood was used. Weights were used to keep the frame in place, avoiding air spaces between the frame and the test specimen, and the frame was sealed to the floor with tape. The frame is 5 mm lower than the test specimen, but this is not expected to affect the measurement results at lower frequencies. The test specimen was placed in the room as shown in Fig. 1, and the four parts of the frame named North, South, East and West (abbreviated N, S, E and W). In total, 16 tests were carried out, covering all possible frame combinations, see Tab. 1.

The reverberation room is 8 x 6.65 x 3.76 m, which gives a volume of exactly 200 m^3. It is equipped with 14 diffusers with a total area of 42 m^2. All tests were carried out with the interrupted noise method in accordance

*__Corresponding author__: gjermund.holoyen@sintef.no.
__Copyright__: ©2025 Gjermund V. Holøyen. This is an open-access article distributed under the terms of the Creative Commons Attribution 3.0 Unported License, which permits unrestricted use, distribution, and reproduction in any medium, provided the original author and source are credited.

with ISO 354:2003, with three source positions, four microphone positions per source position and three measurements per microphone position. Ensemble averaging was used to evaluate the reverberation times with T_{20} used as evaluation range.

Finally, the results have been subject to a limited analysis in an attempt to discover any emerging patterns in the data. However, due to time and funding constraints, a deeper analysis is left for future work.

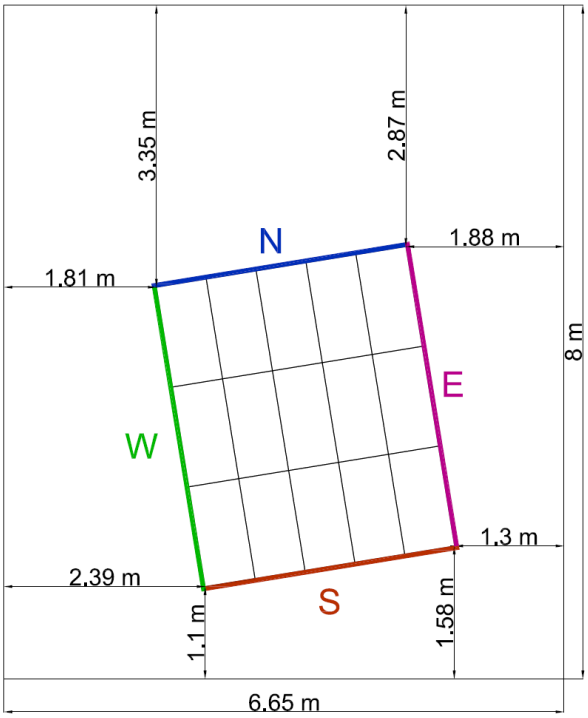


Figure 1. A horizontal view of the reverberation room, the placement of the test specimen and the names of the four parts of the frame.

3. RESULTS

All measurement results are presented, somewhat chaotically, in Fig. 2. The figure shows that between 100 and 160 Hz, the measurements with no frame and full frame act as outliers, with every other measurement inbetween the two. The standard deviation of all 16 measurements is plotted in Fig. 3. Because the low frequencies are the ones at interest, the remaining figures will be limited to the frequency range of 100–315 Hz for the sake of both author and readers.

Table 1. A list of the 16 tests, with frame configurations and exposed absorptive area.

Frame configuration	Exposed absorptive area
No frame	13.44 m^2
N	12.84 m^2
S	12.84 m^2
E	12.72 m^2
W	12.72 m^2
S+W	12.12 m^2
S+E	12.12 m^2
N+W	12.12 m^2
N+E	12.12 m^2
N+S	12.24 m^2
E+W	12.00 m^2
N+E+W	11.40 m^2
S+E+W	11.40 m^2
N+W+S	11.52 m^2
N+E+S	11.52 m^2
Full frame	10.80 m^2

In Fig. 4 the average of the measurement series with one piece of frame, two pieces of frame and three pieces of frame are plotted together with the measurements without frame and with a full frame. Then Fig. 5–Fig. 7 are showing the measurements with one piece of frame, two pieces of frame and three pieces of frame separately.

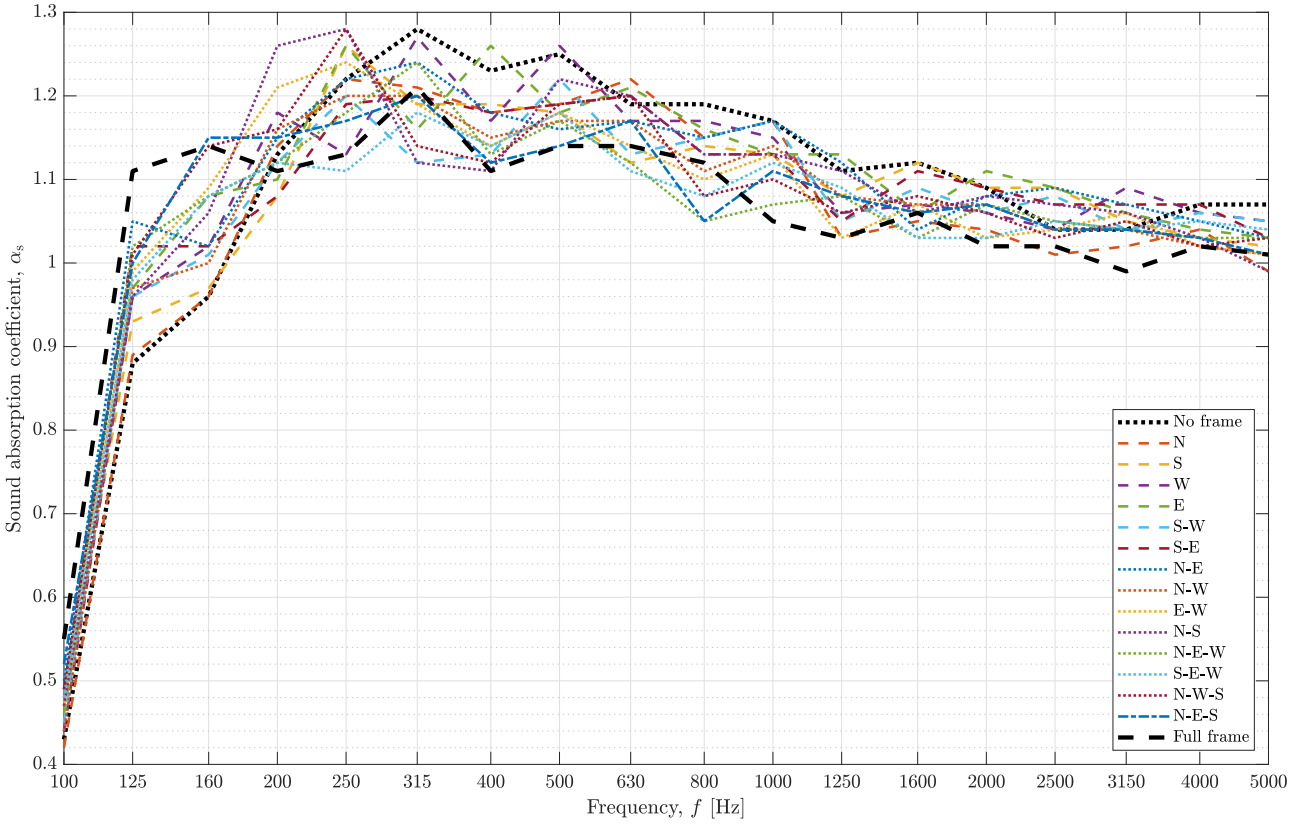


Figure 2. All measurement results as a function of frequency.

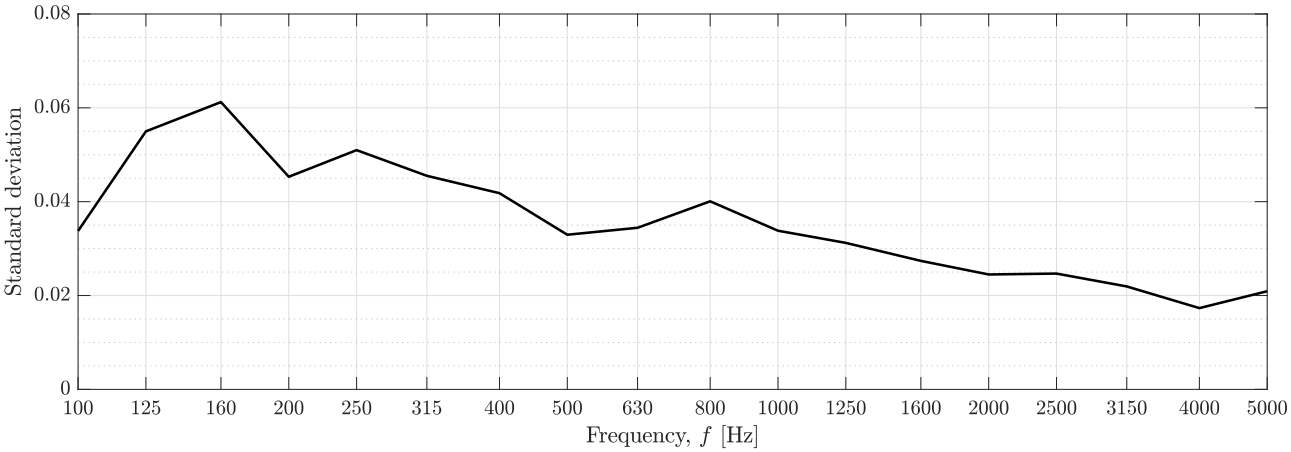


Figure 3. The standard deviation of the 16 measurement series.

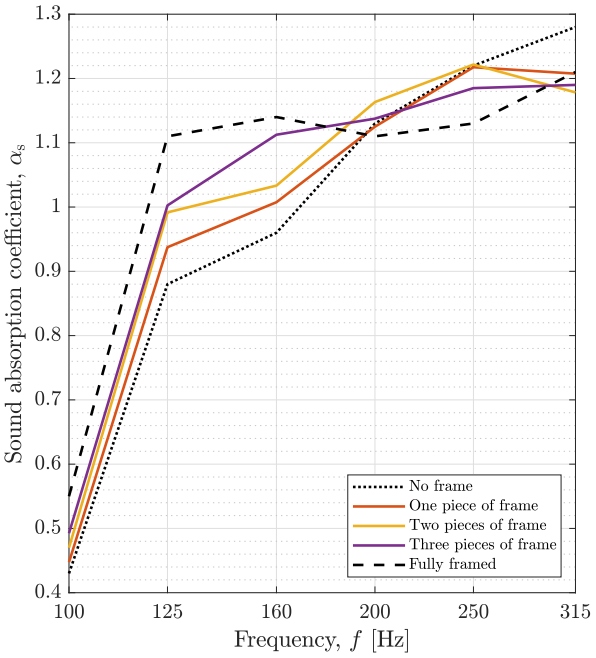


Figure 4. The average of the measurements with one, two and three pieces of frame

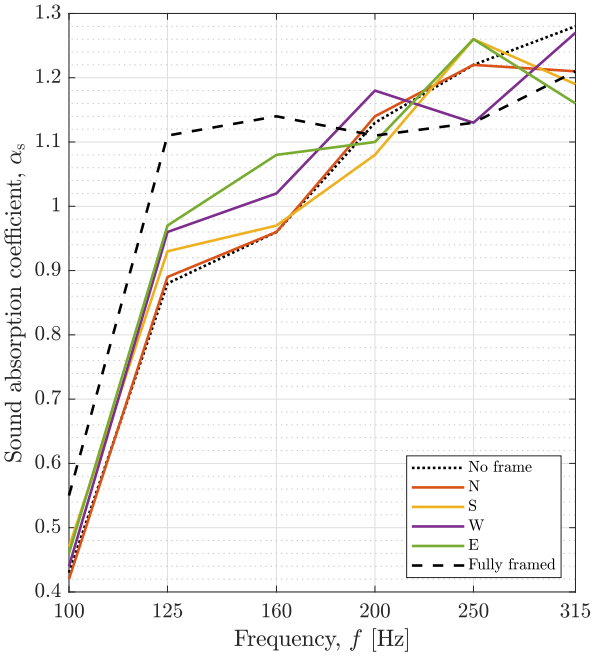


Figure 5. Measurement results with one piece of frame.

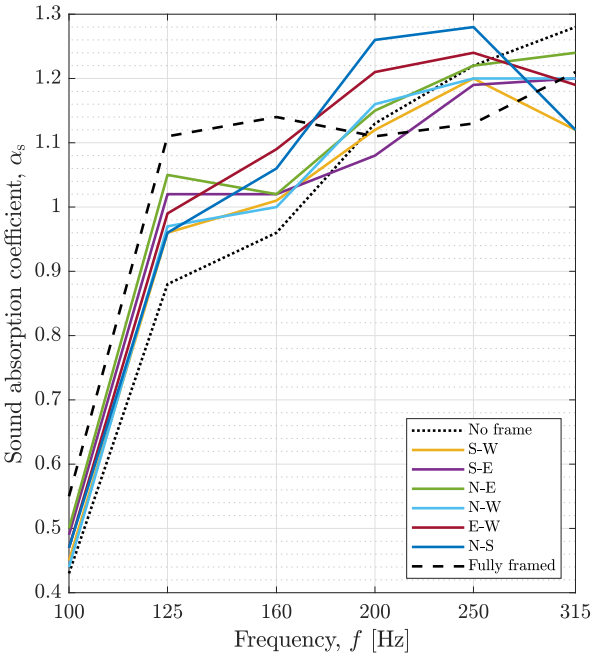


Figure 6. Measurement results with two pieces of frame.

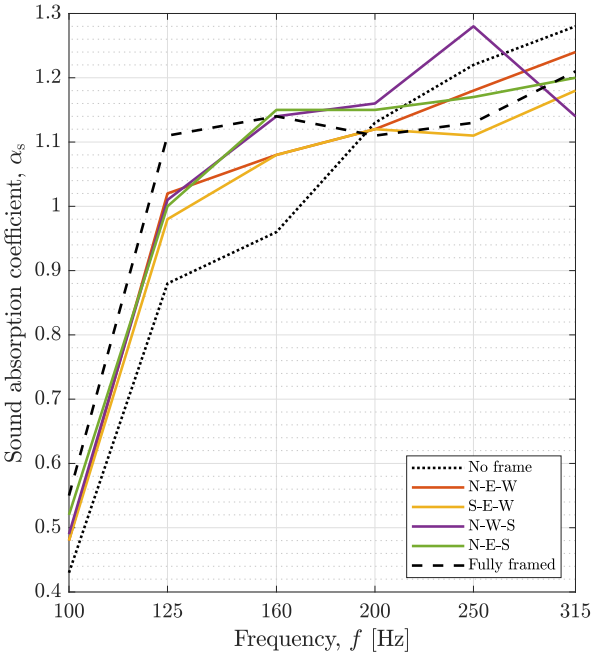


Figure 7. Measurement results with three pieces of frame.

4. DISCUSSION

The results clearly show that the frame has a positive impact on the results at lower frequencies, as seen in previous work. As shown in Fig. 4, when adding an additional piece of frame, the measured sound absorption coefficient increased at 100, 125 and 160 Hz. The difference between the measurements without a frame and with a full frame at these frequency bands were 0.12, 0.22 and 0.18 respectively, which correspond to increases of 28, 26 and 19 % from the worst to best result. At 200 Hz, the curves intersect. This is somewhat lower than in previous experiments [2, 3].

At frequencies above 160 Hz, there are also significant differences between the measurement series, but those differences are seemingly more chaotic, and the clear relationship between levels of framing and the measured sound absorption coefficient that is observed at the lowest frequencies is not observed here. In terms of positional effects, no simple relationship between the position of the frame and which frequencies are affected by its presence has been found. However, the Eastern frame seems to have a generally strong impact on the 125 Hz band, and it was present in all but one measurement series where the 125 Hz band was measured at or above 1. Similarly, it was present in all but one measurement series where the 160 Hz band was measured at or above 1.05. This will be subject to future investigation.

The far and away best result at 125 Hz was obtained with a fully framed test specimen. Similar results were seen at 100 Hz, but less dramatic, seeing as the sound absorption coefficient there were lower to begin with. At 160 Hz, however, the three pieced frame performed strongly, and two of those measurement series were on par with the fully framed one. At 200 and 250 Hz, several partial frame configurations performed better than the fully framed one.

A fascinating observation was that when averaging the results in every third octave band across a measurement series, all measurement series had an average sound absorption coefficient between 1.05 and 1.085. The standard deviation of this average was much lower than in any single third octave band. This points in the direction of randomness playing a significant part in the deviations seen above 160 Hz.

5. FURTHER WORK

The measurement data will lay the foundations for deeper investigations. There are many intriguing tendencies in the dataset, which will be interesting to look at in further detail.

6. CONCLUSION

Reverberation room measurements of sound absorption have been carried out in order to further investigate the positional effects of the frame around a test specimen. The measurement results have shown a clear positive impact from the frame at the lowest frequencies – an impact that at the three lowest third octave bands can be observed to an increasing degree as the test specimen goes from unframed via partially framed to fully framed. The highest standard deviations were found at 125 and 160 Hz, but when accounting for the lower sound absorption coefficient, the 100 Hz band is also significantly affected.

No simple relationship between frame configuration and what frequency bands are affected has been found at the time of writing, and a deeper analysis of the measurement data will be carried out in future work.

7. ACKNOWLEDGMENTS

The measurements covered in this paper has largely been carried out outside of the author's working hours. The work with the paper itself has been funded by the Construction Technology group at SINTEF Community, led by Monica Strøm Nodland. I would like to thank Monica for her support.

8. REFERENCES

[1] ISO. *Acoustics - Measurement of sound absorption in a reverberation room*, ISO 354:2003, International Organization for Standardization.

[2] G. V. Holøyen. Investigation of the Importance of Frame Height Compared to Test Specimen Height During Laboratory Sound Absorption Measurements. In *Proc. of Forum Acusticum 2023*, pages 5575–5582, Torino, Italy, 2023.

[3] G. V. Holøyen. The frame around a test specimen and its influence on the measured sound absorption coefficient. In *Proc. of INTER-NOISE 2024*, pages 8971–8980, Nantes, France, 2024.

DOI: 10.61782/fa.2025.0688

FORUM ACUSTICUM EURONOISE 2025

PRACTICAL VALIDATION OF THE LOCAL PLANE WAVE METHOD USING A SPHERICAL MICROPHONE ARRAY

Borja-Fernández, Daniel[1,3*] **García-Calderón, Eugenio**[1] **Wijnant, Ysbrand**[2]
San Millán-Castillo, Roberto[3]
[1] Ingeniería Acústica García-Calderón (IAG), Madrid, Spain
[2] University of Twente, Demcon sound solutions, The Netherlands
[3] Universidad Rey Juan Carlos - Departamento de Teoría de la Señal y Comunicaciones - EIF, Spain

ABSTRACT

In most environments, the Local Plane Wave (LPW) method estimates the amplitude and phase of the incident and reflects sound waves without making assumptions regarding the global sound field. This study compares the results of standardized ISO tests and LPW tests in some practical cases of airborne sound insulation and acoustic absorption.

The first step in the validation consisted of performing laboratory measurements for all target applications in reverberant or anechoic rooms according to the corresponding ISO standards. Subsequently, the same samples were tested using the LPW method in regular non-laboratory rooms. The results of the LPW method showed reasonable agreement with the ISO results, despite the simplified test environments.

Keywords: *Local Plane Wave, Acoustic measurement, Airborne sound insulation, Sound absorption*

1. INTRODUCTION

In situ measurements of acoustic parameters are crucial for various applications, including the automotive industry and architecture. Traditionally, the determination of acoustic absorption, transmission loss, and sound power has been performed according to ISO standards in controlled laboratory environments. However, these conditions do not always accurately reflect the behavior of materials in real-world applications. Therefore, in recent years, methods have been developed to assess these parameters without prior assumptions about the global sound field.

In this context, the University of Twente and the company Soundinsight (Demcon group) have developed new techniques and devices (Sonocat) to measure the incident sound energy and, separately, the reflected sound energy in any sound field. In doing so, the Local Plane Wave (LPW) method allows the in situ absorption and emission coefficients as well as the transmission loss and radiated power to be estimated. There is no need for a predefined sound field or restrictions on the configuration of the environment [1] [2].

This study compares in situ measurements made with the LPW probe against traditional methods based on ISO standards, intending to validate the accuracy and reliability of the LPW method as an effective alternative for acoustic characterization in practical and in situ applications, which shows good correlation with laboratory-controlled and standardized tests.

2. THEORETICAL BACKGROUND

The LPW method is a novel approach for measuring sound absorption, transmission loss, and sound power in situ, without relying on the assumptions of the global

*__Corresponding author__: d.borja.2021@alumnos.urjc.es.
__Copyright__: ©2025 Borja-Fernández, Daniel et al. *This is an open-access article distributed under the terms of the Creative Commons Attribution 3.0 Unported License, which permits unrestricted use, distribution, and reproduction in any medium, provided the original author and source are credited.*

sound field. This method is particularly useful in practical applications where the sound field is complex and cannot be easily replicated in laboratory settings. The LPW method is based on the assumption that the sound field can be approximated as a combination of incoming and reflected plane waves, that is, the pressure and particle velocity in the normal direction to the surfaces of interest (absorber/partition). By measuring the sound pressure, P, and the normal particle velocity to the absorbing surface, U_n, the complex amplitudes of the incoming wave, A, and the reflected wave, B, can be determined using Eqn. (1) and Eqn. (2). [3]:

$$A = \frac{1}{2}(P + \rho_0 c_0 \overrightarrow{U} \cdot \overrightarrow{n}), \tag{1}$$

$$B = \frac{1}{2}(P - \rho_0 c_0 \overrightarrow{U} \cdot \overrightarrow{n}), \tag{2}$$

where ρ_0 is the density of the medium, c_0 is the speed of sound, and $\overrightarrow{n}$ is the normal vector, with direction pointing into the absorbing surface.

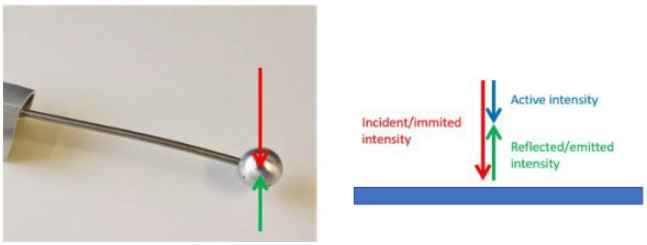


Figure 1. Diagram illustrating the incident, active, and reflected/emitted intensities in the LPW method.

The incident sound intensity I_{in} can then be calculated as in Eqn. (3):

$$I_{in} = \frac{A \cdot \overline{A}}{2 \cdot \rho_0 c_0}, \tag{3}$$

Both, the active and incident power are obtained by spatial integration of the active and incident intensity, respectively. Note that this is an essential part of the LPW method; similar to the active intensity, the incident intensity is now a local quantitative measurement in situ, where $\overline{A}$ denotes the complex conjugate of A. The absorption coefficient α is defined as the ratio of the active power P_{ac} (net acoustic power) to the incident power P_{in}, as shown in Eqn. (4):

$$\alpha = \frac{P_{ac}}{P_{in}}, \tag{4}$$

As illustrated in Figure 1, the LPW method distinguishes between an incident, active and reflected/emitted intensities, which are crucial to accurately determine the absorption coefficient and transmission loss. This distinction allows for more precise measurement of sound energy interactions with surfaces under real-world conditions.

The LPW method can also be applied to measure in situ sound transmission loss. Transmission loss (TL) is defined as the reduction in sound power when a sound passes through a partition, as in Eqn. (5):

$$TL = -10 \log_{10}(\frac{P_{tr}}{P_{in}}), \tag{5}$$

where P_{tr} is the transmitted power and P_{in} is the incident power. Using the LPW method, the incident and transmitted powers can be measured by scanning the pressure and particle velocity on both sides of the partition. This allows for the determination of transmission loss under real conditions, even when the sound field is not diffuse or anechoic [4].



Figure 2. Measurement of incident sound power, scanning the surface approximately at 3 cm of partitions, using Sonocat probe.

3. EXPERIMENTAL PROCEDURES FOR THE ACOUSTIC CHARACTERIZATION

3.1 Evaluation of airborne sound Insulation

3.1.1 Experimental setup

Airborne sound insulation was measured on a separating wall between two dwellings in a building block, following the methodology established in ISO 16283-1 [5]. A pink noise source, dodecahedron (IAG DD5), was used for the test. For data acquisition and processing following the ISO standard procedure, a 01 dB SONO 1/3 octave band analyzer and DB BATI software were used. For the alternative LPW method, the Sonocat probe was used.

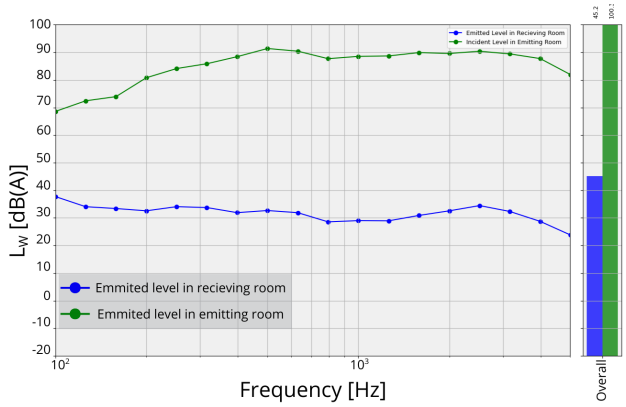


Figure 3. Incident and radiated sound power levels for the partition measured as shown in Figure 2.

3.1.2 Measurement procedure

Measurement of incident sound power. In the emitting room, a diffuse sound field was generated using a pink noise source. The incident sound power on the separation wall was measured by scanning the surface approximately 3 cm from the separating wall (partition) using a Sonocat probe.

Measurement of emitted sound power. In the receiving room, the sound power emitted by the separating partition was measured by scanning the surface again at 3 cm using a Sonocat probe.

Measurement of background noise. The background noise level was recorded by scanning the partition noise radiation in the receiving room once more, but the noise source was turned off to evaluate its influence on the measurements.

Figure 2 shows the scanning of the separating wall using a Sonocat probe. Figure 3 shows the values of the incident (sound power in the emitting room) and radiated (sound power in the receiving room) levels captured by Sonocat. Remarkably, background noise measurements were not performed using the Sonocat probe.

3.1.3 Calculation of acoustic parameters

Calculation of R' (apparent sound reduction index) The apparent sound reduction index R' was calculated in the frequency domain for all frequencies in the 1/3-octave band test range (100 Hz–5 KHz), according to ISO 16283-1, we applied Eqn. (6):

$$R' = L_1 - L_2 + 10log_{10}\left(\frac{S}{A}\right), \qquad (6)$$

where S is the area of the wall and A is the equivalent absorption area of the receiving room.

3.1.4 Comparison with the ISO 16283-1 Standard

The spectrum value of the transmission loss (*TL*) obtained experimentally using the LPW method was compared with the spectrum values obtained following the ISO 16283-1 standard. Deviations were analyzed, and potential sources of variation were discussed.

3.2 Determination of the sound absorption coefficient

3.2.1 Sample selection

The absorption coefficient, measured using the LPW method, was evaluated for various material samples. The method was compared with the absorption coefficients, as characterized by the manufacturer. These samples included several materials that are representative of applications in building acoustics. In addition, the behavior of the absorption coefficient was studied under various conditions, including different sample sizes, different sound incident angles over the sample, and different placement locations.

3.2.2 Experimental setup

An omnidirectional sound source consisting of a dodecahedral loudspeaker (IAG DD5) powered by a pink noise

amplifier (IAG DD400A) was used to measure the absorption coefficient. The experimental setup was designed not only to validate the LPW method using the Sonocat probe against manufacturer-provided data, but also to analyze the influence of sample size and placement location on the measured absorption coefficient.

3.2.3 Measurement procedure

Sample Size Variation. To study the effect of sample size on the absorption coefficient, measurements were taken using four different surface areas of the same material.

Placement configuration variation. The absorption coefficient was measured under three different conditions to analyze the influence of the placement configuration. The sample was placed directly on the floor, placed on a table, and surrounded with another absorbent material. Figure 4 shows the setup for the 45º incidence sound test.



Figure 4. Setup for the measurement of the absorption coefficient with 45º incidence sound.

Measurement with Sonocat probe. Multiple measurements were taken using a Sonocat probe, and the surface of the sample was systematically scanned to capture the necessary levels to calculate the absorption coefficient. Figure 5 shows the in situ absorption measurements for Ecophon Akusto One and Ecophon Master Eg.

Data recording. The absorption coefficient values were recorded in one-third octave frequency bands ranging from 100 Hz to 5 KHz.



Figure 5. Example of measurement setup of the sound absorption using Sonocat.

4. ANALYSIS OF RESULTS

4.1 Airborne sound insulation

4.1.1 Comparison of experimental and reference data

In Figure 6 shows the experimental direct transmission loss of the separating partition (TL), using Sonocat, compared with the in situ R' measurement (according to ISO 16283-1 standard).

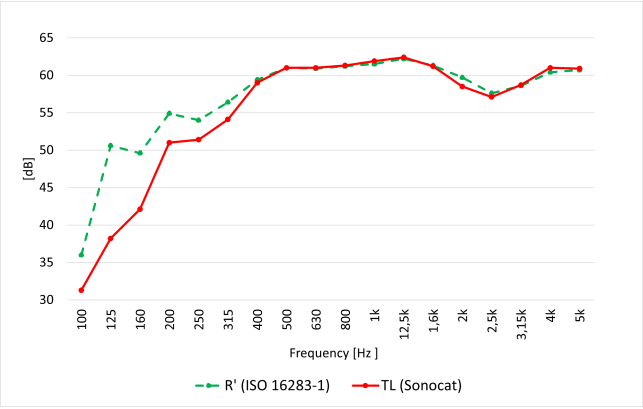


Figure 6. Comparison of TL Values using Sonocat and R' ISO 16283-1.

4.1.2 *Discussion of results*

Low Frequencies (100 Hz - 250 Hz). Deviations were observed between the experimental and reference values. These deviations can be attributed to the difficulties in generating a true or ideal diffuse sound field at low frequencies and the influence of uncontrolled flanking paths (sound transmission through adjacent structures in the wall or receiving room).

Mid and High Frequencies (250 Hz - 5000 Hz). The values calculated using the LPW method were in excellent agreement with reference values. This confirms the accuracy of the LPW method using the Sonocat probe in this frequency range.

4.1.3 *Validation of the Method*

Despite the deviations observed at low frequencies, the experimental results showed a good correlation with the theoretical values in the mid- and high-frequency ranges. This validates the methodology and confirms the usefulness of the LPW method, helping to separately analyze the radiation for different room partitions (floor, walls, and roof) to evaluate the sound insulation in practical applications.

4.1.4 *Recommendations for future studies*

To improve the accuracy of ISO measurements, it is recommended to ensure a completely diffuse sound field, especially at low frequencies. The LPW method does not rely on the diffusivity of the sound field because it directly measures the incoming sound intensity. Hence, it can also be used in non-diffused sound fields. For optimal test accuracy according to the ISO method, a perfectly diffuse sound field was required in both rooms. However, this condition is not necessary when the Sonocat method is used. Consequently, diffuse field conditions are not properly achieved in various scenarios, and variability in the sound pressure levels may occur, particularly at low frequencies. This may lead to higher values than the actual performance when the ISO standard is followed. The LPW method can also be used to evaluate the influence of flaking paths on the sound transmission. Additional measurements must be conducted at lower frequencies to better understand the reasons for these deviations.

4.2 Sound absorption coefficient

4.2.1 *Experimental validation and analysis of measurement conditions*

Behavior of the absorption coefficient in various situations:

Sample size. The area of the sample significantly influenced the measured absorption coefficient, particularly at low frequencies. The results for the different sample sizes are presented in Figure 7. We measured samples of different sizes (e.g. 2400 mm × 1200 mm and 2400 mm × 1800 mm). Analyzing the results, it is observed that if the sample is larger, the effect of the sample size decreases and converges to a value that is also measured by the laboratory ISO 354 absorption test.

Placement configuration. The placement of the samples also affected the measurements. The results for the different placement configurations (table, floor, and surrounded by another absorbent material) are summarized in Figure 8. Samples placed directly on the floor exhibited higher absorption coefficients at low frequencies than those placed on a table, likely because of the interaction with the floor surface and resonances of the table. The similarity between the sample placed on the ground and that surrounded by absorbent material proved that the Sonocat method measures the absorption coefficient of the scanned material regardless of its surroundings.

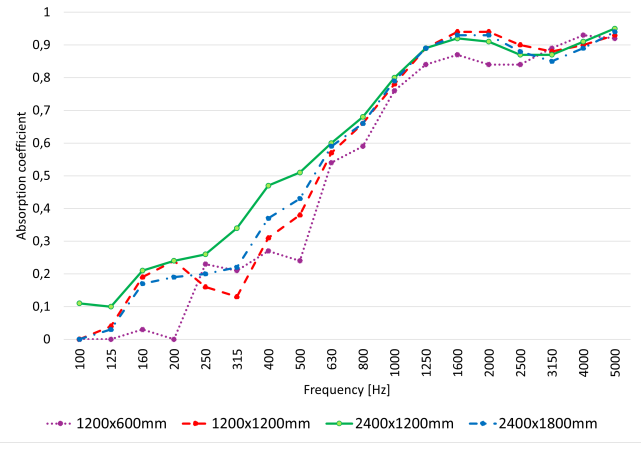


Figure 7. Values obtained by measuring a sample of Geopannel PYL of different dimensions.

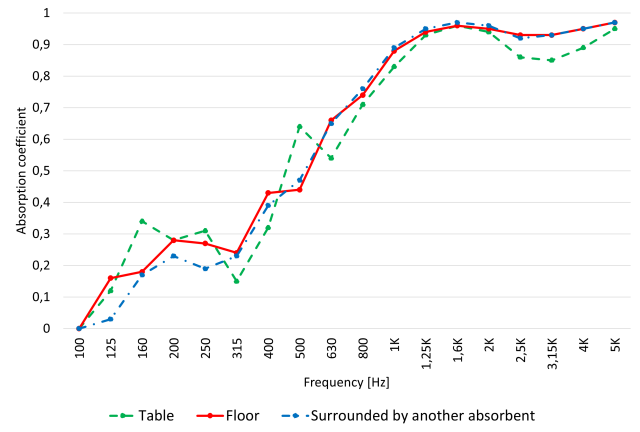


Figure 8. Values obtained by measuring a sample of Basotec G+ of different placement configuration.

Comparison with Manufacturer-Provided Data: The sound absorption coefficient (α) was measured using the Sonocat probe (LPW method) for the same material (Basotec G+) in different configurations. It was concluded that the best way to measure α, such that the LPW method closely resembles the ISO method, is to place a sufficiently large sample (in the experiments, a surface of 1200 mm x 1200 mm was used) on a surface that ensures a fixed position, such as the floor. The results were compared with the α values provided by the manufacturer, which were measured using a reverberation chamber and impedance tube according to the ISO 354 and ISO 10534-2 standards [6] [7].

4.2.2 Discussion of results

Low frequencies (100 Hz - 200 Hz). In this range, the values obtained with the Sonocat method were higher than those obtained with the impedance tube and close to those obtained with the reverberation chamber.

Mid frequencies (200 Hz - 1 KHz). In this frequency range, the values obtained were between those provided by the reverberation chamber and those obtained using an impedance tube.

High frequencies (1 KHz - 5 KHz). In this range, the Sonocat method demonstrated excellent reliability, with absorption coefficients very close to those of both the reverberation chamber and impedance tube.

4.2.3 Validation of LPW method

Currently, there are two standardized test methods for measuring the sound absorption coefficient: the reverberation chamber method and the impedance tube method. Both methods are based on different sound field assumptions (diffuse and normal incident, respectively), different calculation criteria, different sample sizes, and different test environments, the absorption coefficients are different for both methods.

As shown in Figure 9, we compared the spectrum absorption coefficients of the three methods. Sonocat led to intermediate values with respect to the values obtained in the impedance tube and those obtained in the reverberation chamber.

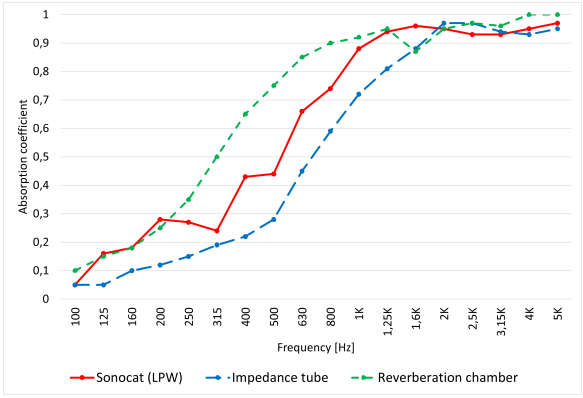


Figure 9. Comparison of α values using Sonocat (LPW method), impedance tube and reverberation chamber.

4.2.4 Recommendations for future studies

To obtain good results, it is recommended that a sample surface of at least 1200 mm x 1200 mm. Measurements should be conducted in a solid basement without radiated sounds.

To obtain results similar to those of the standard methods, future tests should consider the perpendicular incidence of sound waves. A Previous experiment, as shown in Figure 10, showed results that were closer to those in Figure 9, performed with an incidence of 45º. Therefore, it is suggested that a perpendicular sound field impinges on the surface of the sample to compare the standard's

results with those obtained using the LPW method,

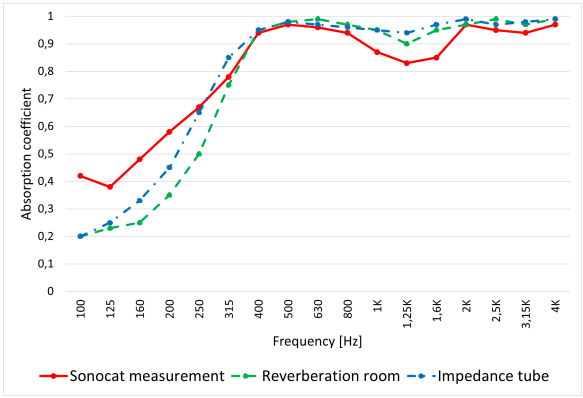


Figure 10. Comparison of α values using Sonocat (LPW method) with normal incident sound field, impedance tube and reverberation chamber.

This type of scenario occurs only when we want to evaluate the manufacturer's samples. However, this fact is not relevant when we perform in situ measurement tests; for example, when we measure complete construction solution areas, such as ceilings, walls, or floors, each covered with different absorption materials, allowing the absorption coefficient of each surface to be measured with this LPW method.

Additional applications can focus on the in situ measurement of the absorption coefficient inside a moving vehicle, where the noise source is the noise generated by the vehicle itself.

5. CONCLUSIONS

In conclusion, it is important to highlight the difference between the in situ method and the ISO method. ISO standards rely heavily on a true diffuse field; however, the reality is different, and the results depend on the diffusivity of the sound field, which we never obtain in real measurements. Therefore, we can conclude that by using the LPW method, we will obtain in situ insulation and absorption values with reliable results that can never be obtained with currently standardized methods. The LPW method is an ideal representative method for determining the acoustic behavior of materials at locations where they are installed.

6. ACKNOWLEDGMENTS

The authors express their gratitude to Juan Negreira from Ecophon (Saint Gobain Group) and Sandra Yaniz from Geopannel for their support in providing the necessary samples and information required for the various experiments conducted in this study. Their kind contributions, including material and technical insights, were relevant to the successful completion of this study.

7. REFERENCES

[1] Y. H. Wijnant, E. Kuipers, and A. de Boer, "Development and application of a new method for the in-situ measurement of sound apsorption," in *24th International Conference on Noise and Vibration Engineering, ISMA 2010*, pp. 1–14, Katholieke Universiteit Leuven, 2010.

[2] Y. H. Wijnant, J.-H. Ho, N. Consten, and A. de Jong, "A novel way to determine sound absorption, sound transmission and sound power," in *42. Jahrestagung für Akustik, DAGA 2016*, pp. 1038–1041, DAGA, 2016.

[3] Y. H. Wijnant, "On the local plane wave methods for in situ measurement of acoustic absorption," in *21st International Congress on Sound and Vibration, ICSV 2014*, International Institute of Acoustics and Vibration (IIAV), 2015.

[4] Y. Wijnant, "On the in-situ measurement of transmission loss using the local plane wave method," in *24th International Congress on Sound and Vibration, ICSV24*, 2017.

[5] International Standards Organization, "ISO 16283-1: Acoustics — field measurement of sound insulation in buildings and of building elements," 2014.

[6] International Standards Organization, "ISO 354: acoustics: Measurement of sound absorption in a reverberation room," 2003.

[7] International Standards Organization, "ISO 354-2: acoustics: Determination of acoustic properties in impedance tubes part 2: Two-microphone technique for normal sound absorption coefficient and normal surface impedance," 2023.

DOI: 10.61782/fa.2025.0788

FORUM ACUSTICUM EURONOISE 2025

SOUND INSULATION PROPERTIES OF WALLS EQUIPPED WITH ENERGY STORAGE DEVICES

G. Baldinelli[1*] **S. Beozzo**[2] **M. Ricci**[2]
F. Scrucca[3] **P. Sdringola**[4] **G. Murtaza**[5]

[1] Department of Engineering, University of Perugia, Italy
[2] Energy Efficiency Department, Italian National Agency for New Technologies, Energy and Sustainable Economic Development (ENEA), Research Center Bologna, Italy
[3] Department for Sustainability, Italian National Agency for New Technologies, Energy and Sustainable Economic Development (ENEA), Research Center Casaccia, Rome, Italy
[4] Energy Efficiency Department, Italian National Agency for New Technologies, Energy and Sustainable Economic Development (ENEA), Research Center Casaccia, Rome, Italy
[5] CIRIAF – Interuniversity Research Center on Pollution and Environment "Mauro Felli", University of Perugia, Italy

ABSTRACT

The integration of electrical energy storage in buildings is a transformative solution for enhancing the efficiency and reliability of the power grid. By installing battery systems, households can store excess energy generated from renewable sources, such as solar panels, during periods of low demand. This stored energy can then be utilized during peak hours, reducing the strain on the grid and mitigating the risk of outages. Energy storage also promotes better utilization of renewable resources by addressing their intermittent nature, ensuring a more stable supply of green energy. A wall equipped with energy storage systems is proposed, to be installed in the external envelope; beyond structural and thermal properties analyses, not described in this research, the acoustic properties of the solution are evaluated, in comparison with an equivalent traditional light-weight wall. In more detail, the airborne sound insulation of these walls has been measured in coupled reverberating rooms, showing a certain improvement respect to light-weight walls, especially at low frequencies. A large space for improvement emerges also as one of the main results.

[*] ***Corresponding author***: *giorgio.baldinelli@unipg.it*
Copyright: *©2025 First author et al. This is an open-access article distributed under the terms of the Creative Commons Attribution 3.0 Unported License, which permits unrestricted use, distribution, and reproduction in any medium, provided the original author and source are credited.*

Keywords: *building insulation, energy storage, reverberating rooms.*

1. INTRODUCTION

Building walls serve structural, insulating, and protective functions, with solutions ranging from traditional masonry to prefabricated panels, dry construction systems, wood, and aerated concrete. Traditional masonry, known for its robustness and durability, is complemented by faster and more sustainable technologies such as wood, valued for its energy efficiency and sustainability. A comparison between masonry and wood highlights the ecological and seismic advantages of wood, despite higher costs and maintenance requirements. The choice fell on wooden construction due to its adaptability to various dimensions and ease of customization for integrating electrical storage.

Prefabricated wooden walls can utilize X-Lam or frame systems as load-bearing elements. The X-Lam system, made of cross-laminated solid wood panels, offers high structural strength. The frame system, lightweight yet strong, consists of wooden studs and insulation materials. Due to its configuration, the frame structure proves more suitable for integrating electrical storage modules.

Energy storage systems are essential for balancing energy production and demand, promoting the use of renewable sources, and supporting electric mobility. Commercially available devices rely on lead-acid or, more recently,

lithium-ion batteries. Lithium batteries offer advantages such as high energy density, long lifespan, and integrated management systems, but they come with higher costs and disposal challenges. A rapidly developing technology is supercapacitors, based on electrochemical double-layer principles, which provide benefits in charge/discharge cycles and versatility, though currently limited by high costs and lower specific energy.

The supercapacitor production and application sector has been expanding rapidly in recent years, particularly due to technological advancements driven by the automotive industry's interest. This has led to significant technological improvements, and increased commercialization is expected to drive down costs.

The prefabricated wall analyzed in this research has been designed using a load-bearing frame structure, with an internal stratigraphy based on the most common commercial configurations (Figure 1) to ensure broad market representation. The wooden studs are spaced at 62.5 cm intervals to accommodate the developing supercapacitor modules.

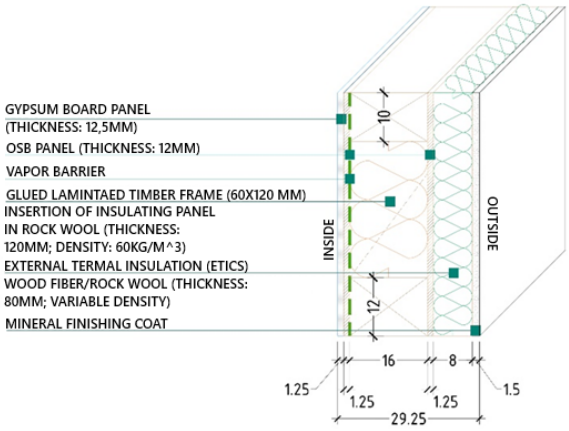


Figure 1. Typical stratigraphy of the prefabricated wooden wall.

The integration of the prefabricated wall's characteristics with the need for a modular supercapacitor system led to the development of an interlocking and lamellar system, featuring high-potential modules.

The proposed solution employs 48V supercapacitor modules with a capacity of 1050 Wh each (Figure 2). These modules are stackable up to 15 units, enabling quick and easy installation of the storage system (Figure 3). The technical specifications are listed in Table 1. Additionally, thanks to the modularity of the final design, the system can cover a wide range of applications and energy needs.

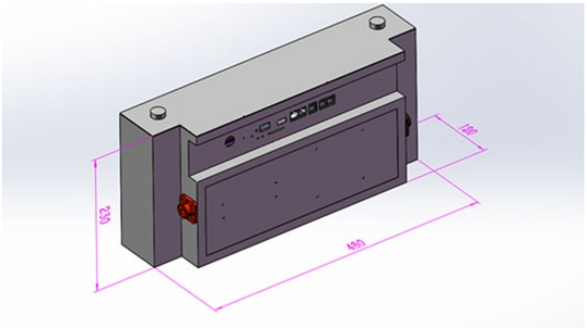


Figure 2. Draw of the storage systems.

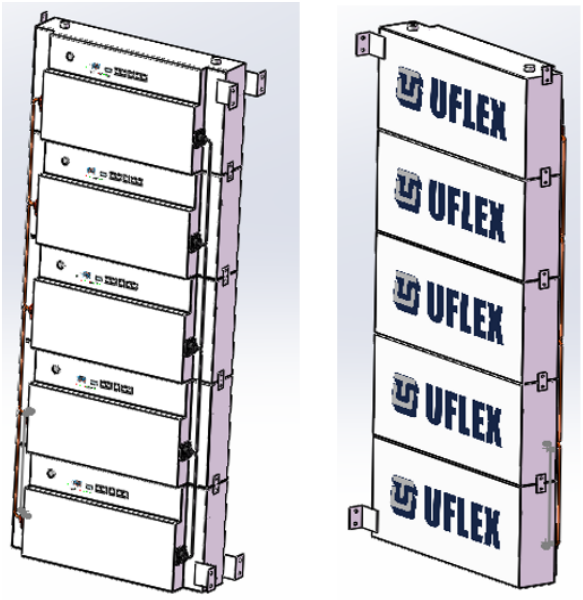


Figure 3. Storage system modules.

Characteristic	Parameter
Nominal Energy	1050 Wh (@10A)
Max Charging Voltage	58.8 VDC
Min Charging Voltage	42 VDC
Charging Current	Standard: 10A, Max: 20A
Discharging Current	Standard: 10A, Max: 20A
Operating Temperature	Charge: 0 °C ~ +60 °C Discharge: -20 °C ~ +55 °C
Life Cycles	20,000 cycles (@10A)
Storage Temperature	-20 °C ~ +45 °C
Parallel Connection	Up to 15 units
Dimensions (W x D x H)	48 x 12 x 23 cm
Weight	12 kg
IP Rating	IP30

Table 1. Supercapacitor module specifications.

The wiring system is designed to avoid occupying additional space within the wall, with the module's shape allowing cables to pass along the edges without exceeding the module's maximum footprint (Figure 4).

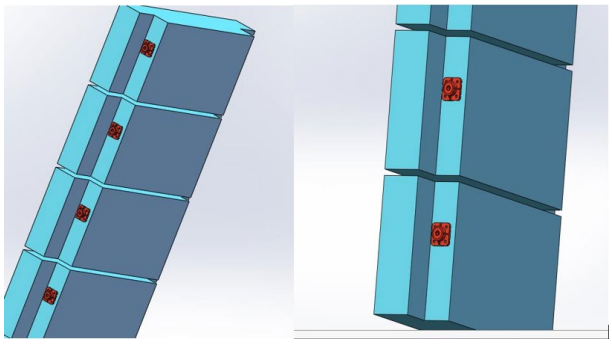


Figure 4. Electrical connection details.

2. DESCRIPTION OF THE REVERBATING ROOMS AND SAMPLE HOUSING PARTITION

The reverberating rooms of Perugia University are characterized by a test opening of the partition between the chambers, with a surface area of 10.5 m^2. Since samples of these dimensions were not available, the opening had to be adapted, reducing the sample area and trying to get as close as possible to the real assembly conditions. For this reason, it was decided to install a masonry wall, which. in the central part, was equipped with a hole where the sample being tested was installed.

It should be emphasized that the partition for housing the samples must have soundproofing properties sufficiently higher than those of the tested sample; for this reason, high mass materials were chosen.

The partition wall between the reverberation chambers was built with 2 rows of Lecablocco Fonoisolante ® elements measuring 20 cm x 20 cm x 25 cm, laid so that the length corresponds to the longest dimension, for a total thickness of 40 cm. The wall was plastered on both sides.

A value of the sound insulation index R_w equal to approximately 60 dB was estimated for this wall, significantly higher than that presumed for the samples under examination.

3. MEASUREMENTS RESULTS

Figure 5 shows the stratigraphy of the walls used for the comparison with the wall equipped with the storage system.



Figure 5. Stratigraphy of the tested walls.

Beyond an external thick coating of wood wall and cement, there is a space that hosts wood wool (or storage devices), to end with a thin inner layer of wood wall, closed with a final layer of plaster.

In figure 6, the traditional wall filled of wood wool is shown during the installation in the reverberating rooms.



Figure 6. View of the traditional sample with rock wool, before internal finishing.

Figure 7 shows the wall with the storage systems, again during the installation in the reverberating rooms.



Figure 7. View of the sample with storage devices, before internal finishing.

Figures 8 and 9 display the traditional sample during the tests both in the emitting and receiving room.



Figure 8. Sample from the emitting room.



Figure 9. Sample from the receiving room.

In figure 10, the trend of the sound insulation power with frequency is reported for both the traditional sample and the sample with the storage system.

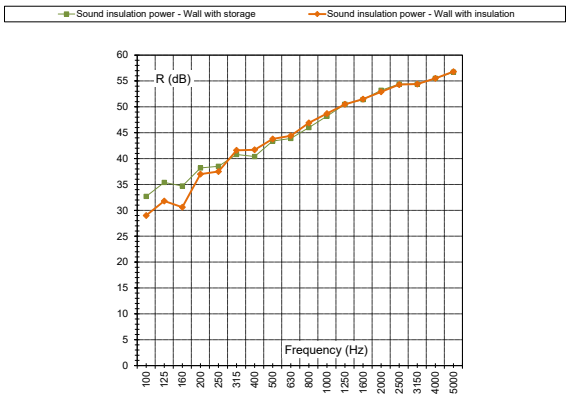


Figure 10. Comparison of the trend of the Sound insulation power R in one-third octave bands between 100 and 5000 Hz for the sample with storage systems and the traditional sample.

It is evident how the addition of mass generates an improvement in the acoustic insulation performance, especially at low frequencies, although the single-number index for airborne sound insulation R_w shows a rather limited growth, moving from 47 to 48 dB.
This circumstance is probably due to the presence of acoustic bridges that interrupt the continuity of the modules of the storage systems.
A more accurate design of the stratigraphy could lead to a more significant improvement in the sound insulation characteristics of the wall with storage systems.

4. ACKNOWLEDGMENTS

This research was funded in the Program Agreement between the Italian National Agency for New Technologies, Energy and Sustainable Economic Development (ENEA) and the Ministry of Environment and Energy Safety (MASE) for the Electric System Research, in the framework of its Implementation Plan for 2022–2024, Project 1.5 “High-efficiency buildings for the energy transition” (CUP I53C22003050001), Work Package 3 “Innovative technologies and components for increasing the energy performance of buildings”. The research was also funded funded by the European Union - NextGenerationEU under the Italian Ministry of University and Research (MUR) National Innovation Ecosystem grant ECS00000041 - VITALITY. We acknowledge Università degli Studi di Perugia and MUR for support within the project Vitality.

DOI:

Main theme: A03 Building Acoustics

Session A03.02 Acoustic regulations, classification schemes and standards in building acoustics

Chair(s): B. Rasmussen, T. Carrascal

DOI: 10.61782/fa.2025.0872

FORUM ACUSTICUM EURONOISE 2025

THE LEGISLATIVE LEAP FORWARD TOWARDS REGULATING THE ACOUSTICS IN BUILDINGS IN CROATIA

Marko Horvat[1*] **Zoran Veršić**[2] **Kristian Jambrošić**[1]
[1] University of Zagreb Faculty of Electrical Engineering and Computing, Croatia
[2] University of Zagreb Faculty of Architecture, Croatia

ABSTRACT

For a long time, acoustics in buildings in Croatia has been poorly regulated in terms of appropriate legislative documents. The future of this field has been brightened by the recent development and completion of a comprehensive technical regulation on the subject matter. This document addresses the aspects of acoustics in buildings that concern room acoustics, building acoustics, and noise, providing a set of requirements for the architects and other involved experts to adhere to, thus facilitating better building design in terms of acoustics in buildings. The aim of this paper is to present the key provisions of this document that will help achieve this goal. Details will be given on the stipulated requirements on sound insulation and permitted noise levels in buildings that are considered acoustically sensitive, such as residential buildings, office buildings, buildings used for accommodation, buildings used for activities on all levels of education, and healthcare buildings. The requirements on the design for optimal room acoustics will be given for rooms used for music, speech, education, and sports, as well as requirements on room acoustics in noise-sensitive spaces focused on reducing excessive reverberance and excessive noise that stems from it.

Keywords: *technical regulation, acoustics in buildings, room acoustics, building acoustics, noise.*

1. INTRODUCTION

Acoustics in buildings is a field that has not been properly addressed during the entire existence of Croatia as a sovereign state, despite several prior attempts that have been made to improve this status quo. The latest efforts to rectify the situation have been encouraged by the European Union, stating that the Croatian regulations in this field are outdated and in need of updating. After 18 months of work, the new Technical Regulation on Acoustics in Buildings has been created. The document has passed scrutinization on all levels and is now ready to be published in the Official Gazette of the Republic of Croatia.

In [1,2] details have been given on the history of the field of acoustics in buildings in Croatia in the past 40 years, explaining the urgent need for creating a comprehensive regulation that has been lacking all these years. A description of the workflow that resulted in the creation of this document has also been given, as well as the description of its scope, and a general overview of its content.

This paper focuses on the technical requirements stipulated by the Regulation in terms of airborne and impact sound insulation, maximum permissible noise levels inside buildings, and the requirements on room acoustics (where applicable). In terms of sound insulation and noise, a detailed overview of these criteria is given for buildings that contain spaces that are deemed as noise-sensitive and must, therefore, be protected from noise. The spaces to be protected are housing units in strictly residential and mixed residential-commercial buildings, office spaces in commercial buildings, commerce spaces in shopping malls, accommodation units in hotels, dormitories, etc., spaces used for activities at all levels of education, spaces in healthcare facilities, and preschool spaces. In terms of room acoustics, the Regulation addresses spaces used for music, speech, education, and sports, for which optimal acoustics

[*] ***Corresponding author**: marko.horvat@fer.unizg.hr*
***Copyright**: ©2025 Horvat et al. This is an open-access article distributed under the terms of the Creative Commons Attribution 3.0 Unported License, which permits unrestricted use, distribution, and reproduction in any medium, provided the original author and source are credited.*

needs to be achieved. In addition, mandatory acoustic treatment is stipulated for certain spaces that are expected to benefit from reduction of excessive reverberance and consequent noise reduction inside those spaces.

2. KEY PROVISIONS IN THE REGULATION

This Regulation is to be applied in design and construction of new buildings, reconstruction of the existing ones, and construction of simple buildings that do not require a building permit, so that the fundamental requirement that concerns the protection from noise is met in every aspect.
The technical requirements in terms of acoustics in buildings are stipulated as:

- $R'_{w,min}$ or $D_{nT,w,min}$ or $R_{w,min}$ as the minimum required value for airborne sound insulation of a building element (door, window, glass wall) or between two spaces in a building
- $L'_{n,w,max}$ as the maximum permissible value for impact sound insulation between two spaces
- $L_{R,Aeq}$ as the maximum permissible noise rating level in dwelling rooms for living and rest, work rooms, and special-purpose rooms
- $L_{AF,max,nT}$ as the maximum permissible level of service equipment noise
- T_{Soll} as the required reverberation time for spaces that require optimal room acoustic conditions
- A/V as the minimum required ratio of the equivalent absorption area and room volume for spaces that require reduction of reverberance

The airborne sound insulation of the outer shell of a building is to be designed to meet the requirements on the maximum permissible noise rating level $L_{R,Aeq}$ in the protected spaces inside the building, taking into account the most exposed spaces and the least favourable conditions during the day, evening or night. The outdoor noise level is to be obtained from (in the given order of priority) noise measurements, calculation estimates, or taken as maximum permissible outdoor noise level in the particular noise zone.
Rooms inside a building that contain service and other equipment or host activities connected with commercial exploitation are divided into three noisiness groups according to the expected, designed, or measured noise rating level $L_{R,Aeq}$:

- N1 – the noise rating level is below 70 dBA
- N2 – the noise rating level is between 70 and 80 dBA
- N3 – the noise rating level exceeds 80 dBA

These designations shall be used in the remainder of the article. In new buildings, no direct contact between N3-rated spaces and critically protected spaces is allowed, in terms of sharing a common party wall or floor.

To prove that the requirements will be met, this Regulation stipulates the use of the EN 12354 series of standards [3-7] in the design process but also allows the use of calculation methods or models (e.g. ray-tracing methods in room acoustics) that are based on verified technical solutions and/or new advancements and solutions in the fields of noise protection and room acoustics. Laboratory reports on sound insulation and sound absorption of materials and constructions may/should be used as input data for the design process.

The proof of meeting the set requirements in the design and construction process shall be obtained through measurements according to relevant standards [8-18]. The "simple acceptance" rule shall be applied. In exceptional cases, the required proof may be obtained through reports provided by all parties that partake in the building process.

3. SOUND INSULATION REQUIREMENTS

The requirements on airborne and impact sound insulation in critical types of buildings are presented in detail in Tables 1 to 7. In specific cases, $D_{nT,w}$ or R_w are used instead of R'_w.

Table 1. Sound insulation requirements for residential and residential-commercial buildings

Residential and residential-commercial use	$R'_{w,min}$ (dB)	$L'_{n,w,max}$ (dB)
Party wall between any two rooms in two housing units (within a multi storey building or in two adjacent buildings in direct contact)	52	
Party wall between dwelling rooms of a housing unit and a technical/commercial space* – N1; N2; N3***	57 62 67	
Party wall between other rooms in a housing unit and a technical/commercial space* – N1; N2; N3	52 57 62	
Party wall between a housing unit and storage rooms, entrance spaces, stairwells	52	
Party wall between a housing unit and garbage rooms, fitness, wellness, other common spaces for residents only	57	
Entrance door to the housing unit (R_w)** - with buffer space with a second door	30	
Entrance door to the housing unit (R_w)** - without buffer space	37	

Party wall with a door between a housing unit and common hallway or stairway ($D_{nT,w,min}$)	42	
Party wall between dwelling rooms of a housing unit and a single garage	55	
Party wall between dwelling rooms of a housing unit and a common garage, common garage entrance or exit	57	
Party floor between all rooms of two housing units	52	55
Party ceiling of a housing unit towards a terrace or a loggia of another housing unit		53
Party ceiling of a housing unit towards a common terrace		50
Party floor of a housing unit towards technical or commercial spaces* – N1; N2; N3***	57 62 67	58
Party ceiling of a housing unit towards technical or commercial spaces* – N1; N2; N2 fitness and sports; N3***	57 62 62 67	48 48 46 46
Party floor of a housing unit towards storage rooms, entrance spaces, stairwells	52	58
Party floor of a housing unit towards garbage rooms, fitness, wellness, other common spaces for residents only	57	58
Party ceiling of a housing unit towards storage rooms, entrance spaces, stairwells	52	48
Party ceiling of a housing unit towards garbage rooms, fitness, wellness, other common spaces for residents only	57	48
Party floor of a housing unit towards a single garage	55	58
Party floor of a housing unit towards a common garage, common garage entrance or exit	57	58
Party floor or floor on the ground of a housing unit towards another housing unit		55
Stairwells, balconies, common hallways, gallery hallways		58
Party floor or floor on the ground of commercial spaces or N2 and N3*** rooms towards a housing unit		48
Party floor or floor on the ground of an N3 room, towards housing unit (no direct contact is allowed!)		42
Outdoor entrance door to a housing unit (R_w)**	30	
Windows and balcony doors (R_w)**	30	

Notes:

*N3 rooms are not allowed in strictly residential buildings

*N3 rooms are allowed in residential-commercial buildings, but they must not be in direct contact with dwellings in the building

**R_w of a door, window, or a glass wall must be 2 dB higher than stipulated by this Regulation

***Not allowed in new buildings; allowed when reconstructing an existing N3 room in an old building, or when such room has already been designed and partially constructed

Table 2. Sound insulation requirements for office-commercial buildings

Office-commercial use	$R'_{w,min}$ **(dB)**	$L'_{n,w,max}$ **(dB)**
Party wall between two different users	52	
Wall between rooms for intellectual work within offices of a single user	44	
Wall between demanding workrooms or between a conference room and other spaces of the same user	47	
Wall between a room for intellectual work and other rooms – N1; N2 and garages; N3	47 52 57	
Wall between a room for intellectual work and communication spaces of a single user	44	
Door between a room for intellectual work and a hallway or other rooms (R_w)*	30	
Door between a demanding workroom or a conference room and a hallway or other rooms (R_w)*	32	
Glass wall between rooms for intellectual work of the same user (R_w)*	30	
Party floor/ceiling between all rooms for intellectual work and rooms of different users	52	58
Party floor of a room for intellectual work towards other rooms – N1; N2; N3	47 52 57	58
Party ceiling of a room for intellectual work towards other rooms – N1; N2; N3	47 52 57	55
Party floor or floor on the ground of service equipment rooms or N2 and N3 rooms towards dwelling rooms		48

Notes:

*R_w of a door, window, or a glass wall must be 2 dB higher than stipulated by this Regulation

Table 3. Sound insulation requirements for shopping malls

Shopping malls	$R'_{w,min}$ **(dB)**	$L'_{n,w,max}$ **(dB)**
Party wall between commerce rooms of two different users*	44	
Wall between a commerce room of a single user and other rooms – N1; N2 and garages; N3	44 47 52	
Party floor/ceiling	44	

Notes:

*The requirement is not set for commerce rooms that are open towards common areas of the shopping mall

Table 4. Sound insulation requirements for hotels, motels, dormitories and other accommodation buildings

Hotels and other types of accommodation	$R'_{w,min}$ (dB)	$L'_{n,w,max}$ (dB)
Party wall between accommodation units (four-star and five-star category)	52	
Party wall between accommodation units (other categories)	47	
Party wall with a door between connected accommodation units (four-star and five-star category) ($D_{nT,w,min}$)	52	
Party wall with a door between connected accommodation units (other categories) ($D_{nT,w,min}$)	47	
Wall between an accommodation unit and a hallway (four-star and five-star category)	52	
Wall between an accommodation unit and a hallway (other categories)	47	
Wall between an accommodation unit and other rooms – N1; N2 and garages	52 57	
Party floor/ceiling between accommodation units	52	58
Party floor of an accommodation unit towards other rooms – N1; N2 and garages	52 57	58
Party ceiling of an accommodation unit towards other rooms – N1; N2 and garages	52 57	48
Party floor or floor on the ground of service equipment rooms towards dwelling rooms		48
Entrance door to the accommodation unit (four-star and five-star category) (R_w)*	35	
Entrance door to the accommodation unit (other categories) (R_w)*	27	

Notes:

*R_w of a door, window, or a glass wall must be 2 dB higher than stipulated by this Regulation

Table 5. Sound insulation requirements for healthcare facilities

Healthcare use	$R'_{w,min}$ (dB)	$L'_{n,w,max}$ (dB)
Wall between hospital rooms	47	
Wall between hospital suites	52	
Wall between a hospital room and other rooms – N1; N2 and garages	52 57	
Wall between a hospital room and a hallway	47	
Wall between a hospital suite and a hallway	52	
Wall between an operating room and other rooms – N1; N2 and garages	52 57	
Wall between operating rooms	42	
Party floor/ceiling between accommodation units	52	58
Party floor of an accommodation unit towards other rooms – N1; N2 and garages	52 57	58
Party ceiling of an accommodation unit towards other rooms – N1; N2 and garages	52 57	48
Party floor or floor on the ground of service equipment rooms towards dwelling rooms		48
Entrance door to the accommodation unit (four-star and five-star category) (R_w)*	35	
Entrance door to the accommodation unit (other categories) (R_w)*	27	

Notes:

N3 rooms must not be in direct contact with hospital rooms/suites

*R_w of a door, window, or a glass wall must be 2 dB higher than stipulated by this Regulation

Table 6. Sound insulation requirements for educational facilities (elementary, middle and higher education; other education)

Educational use	$R'_{w,min}$ (dB)	$L'_{n,w,max}$ (dB)
Wall between classrooms and/or teachers' cabinets	52	
Wall between classrooms, teachers' cabinets or libraries and (class)rooms for physical, technical, or musical education	60	
Wall between classrooms or teacher's cabinets and communication spaces (hallways, stairwells, galleries, etc.) in schools	52 49	
Wall between classrooms or teacher's cabinets and communication spaces (hallways, stairwells, galleries, etc.) in higher education institutions	52	
Wall between a library and communication spaces (hallways, stairwells, galleries, etc.)	52	
Wall between classrooms, teachers' cabinets or libraries and other rooms – N1; N2 and garages, multipurpose spaces, mess halls, sports or multipurpose halls	52 60	
Party floor of classrooms, teachers' cabinets, libraries and communication spaces above – N1 and classrooms and teachers' cabinets; N2 and garages, sports or multipurpose halls, mess halls, and (class)rooms for physical, technical and musical education	52 60	48 58
Party ceiling of classrooms, teachers' cabinets, libraries and communication spaces above – N1 and classrooms and teachers' cabinets; N2 and garages, sports or multipurpose halls, mess halls, and (class)rooms for physical, technical and musical education	52 60	48 46
Party floor or floor on the ground of service equipment rooms, towards dwelling room		48
Other party floors/ceilings towards dwelling rooms	52	48
Door between a classroom and a teacher's cabinet (R_w)*	32	
Door and/or a transom between classrooms, teachers' cabinets or libraries and hallways or other	37	

rooms (R_w)*	
Door to a sports or multipurpose hall (R_w)*	35
Door to a technical room or a service equipment room (R_w)*	37
Wall with a door of a sports or multipurpose hall ($D_{nT,w,min}$)	45
Wall with a door of a technical room or a service equipment room ($D_{nT,w,min}$)	45

Notes:
N3 rooms must not be in direct contact with dwelling rooms
*R_w of a door, window, or a glass wall must be 2 dB higher than stipulated by this Regulation

Table 7. Sound insulation requirements for preschool facilities

Preschool use	$R'_{w,min}$ **(dB)**	$L'_{n,w,max}$ **(dB)**
Wall between rooms for daily dwelling of children and communication spaces or other units	52	
Wall between rooms for daily dwelling of children and other rooms – N1; N2 and garages; N3***	52 60 65	
Party floor of rooms for daily dwelling of children, offices, dwelling rooms, and communication spaces above – N1, rooms for daily dwelling of children or offices; N2, garages, sports or multipurpose halls, and mess halls; N3***	52 60 65	48
Party ceiling of rooms for daily dwelling of children, offices, dwelling rooms, and communication spaces below – N1, rooms for daily dwelling of children or offices; N2, garages, sports or multipurpose halls, and mess halls; N3***	52 60 65	48 46 46
Party floor or floor on the ground of service equipment rooms, towards dwelling room		48
Other party floors/ceilings towards dwelling rooms	52	48
Door to a sports or multipurpose hall (R_w)*	35	
Door to a technical room or a service equipment room (R_w)*	37	
Wall with a door of a sports or multipurpose hall ($D_{nT,w,min}$)	45	
Wall with a door of a technical room or a service equipment room ($D_{nT,w,min}$)	45	

Notes:
N3 rooms must not be in direct contact with dwelling rooms
*R_w of a door, window, or a glass wall must be 2 dB higher than stipulated by this Regulation
***Not allowed in new buildings; allowed when reconstructing an existing N3 room in an old building, or when such room has already been designed and partially constructed

Specific additional provisions stipulate that no requirement is set on the impact sound insulation for the fire escape stairwell if a non-residential building has an elevator. Furthermore, common garages are classified as N2 spaces. Rooms used by the hospitality industry or craftsmen, as well as rooms used for games and fun (movie theatres, game rooms, etc.) are classified as N3 spaces by default, regardless of the predicted or measured A-weighted noise rating level $L_{R,Aeq}$. Engine rooms, technical rooms, and service equipment rooms are also classified as N3 by default, regardless of the predicted or measured A-weighted noise rating level $L_{R,Aeq}$. Finally, the requirements set for impact sound insulation as $L'_{n,w,max}$ are valid for all possible directions of sound propagation.

4. NOISE REQUIREMENTS

The requirements regarding the maximum permissible noise levels in critically protected spaces are given in detail in Tables 8 to 11.

Table 8. Maximum permissible noise rating levels in dwelling spaces used for rest and living

Room type	$L_{R,Aeq,max}$ **(dBA)**		
	day	***evening***	***night***
Dwelling rooms in a housing unit	35	35	30
Dwelling rooms in accommodation units in community housing buildings	35	35	30
Dwelling rooms in accommodation units in buildings used for accommodation or in other buildings	35	35	30
Hospital rooms in healthcare facilities (not including the noise of medical equipment)	30	30	30

Table 9. Maximum permissible noise rating levels in workplace spaces

Room type	$L_{R,Aeq,max}$ **(dBA)**
Doctor's offices, infirmaries, operation rooms, etc.	35
Classrooms, lecture rooms, teachers' and study cabinets, libraries, reading rooms, offices for focused intellectual work, laboratory facilities, etc.	35
Dwelling rooms for children in kindergartens and nurseries, multipurpose halls and mess halls, sports halls in schools and kindergartens	40
Offices, meeting rooms, conference rooms	40

Table 10. Maximum permissible noise rating levels in special-purpose spaces

Room type	$L_{R,Aeq,max}$ (dBA)
Concert halls, theatres, etc.	25
Movie theatres, reading rooms, exhibition rooms	35

Note: The requirement is valid with the electroacoustic equipment switched on, but not reproducing sound.

Table 11. Maximum permissible levels of service equipment noise or noise originating in other spaces, in dwelling spaces

Room type	$L_{AF,max,nT}$ (dBA)	
	Stationary or intermittent noise	Short-term or fluctuating noise
Dwelling rooms in housing units	30	35
Dwelling rooms in accommodation units in buildings used for accommodation or in other buildings	30	35
Dwelling rooms in accommodation units in community housing buildings	30	35
Hospital rooms in healthcare facilities (not including the noise of medical equipment)	30	35
Doctor's offices, infirmaries, operation rooms, etc.	35	40
Classrooms, lecture rooms, teachers' and study cabinets, libraries, reading rooms, offices for focused intellectual work, laboratory facilities, etc.	35	40
Dwelling rooms for children in kindergartens and nurseries,	35	40
Offices, meeting rooms, conference rooms, multipurpose halls and mess halls, sports halls in schools and kindergartens	40	45

Additional provisions stipulate that sound insulation of building parts must be designed to ensure that the requirements given in Tables 8 to 11 are met. The noise rating levels given in these tables are set for fully furnished rooms. The levels of noise in dwelling rooms, coming from service equipment or from other rooms, must not exceed maximum permissible noise levels set in Table 11. Maximum permissible noise levels $L_{AF,max,nT}$ are normalized taking into account the actual reverberation time in the room.

5. ROOM ACOUSTICS REQUIREMENTS

The room acoustics requirements stipulated in this Regulation are based on the HRN DIN 18041:2024 standard [19]. As opposed to sound insulation and noise requirements which are given directly as fixed values, the room acoustics requirements are given implicitly, and the required values need to be calculated based on the size and the type of the room for which they are to be defined. All spaces for which the room acoustics requirements are set in this Regulation are divided into type A and type B.

Type A is further divided into five categories, named and marked as "Music" (A1) "Speech / lecture" (A2), "Education / communication" and "Speech / lecture (inclusive)" (A3), "Education / communication" (inclusive)" (A4), and "Sports" (A5). The technical requirement set on type A rooms is the required reverberation time T_{Soll}, calculated from the room volume V according to the category of the given room. The Regulation provides a general description of each category, and the actual categorization is to be made using the HRN DIN 18041 standard. Figure 1 shows a graphic display of the required reverberation time T_{Soll} depending on the category and the size of type A rooms.

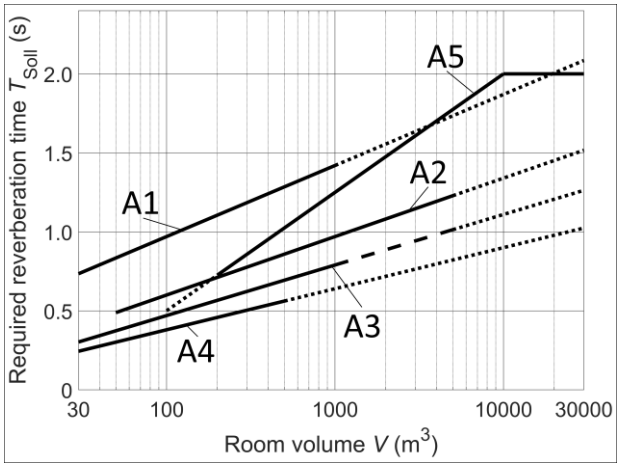


Figure 1. The required reverberation time T_{Soll} for type A rooms, depending on size (room volume) and the category (A1 to A5) of the room.

The obtained value of T_{Soll} is the one the architect/engineer should strive to obtain by designing appropriate acoustic treatment of a room. The tolerances within which the reverberation time T obtained by design should fall are

shown in Figure 2 as values normalized to the required reverberation time T_{Soll}.

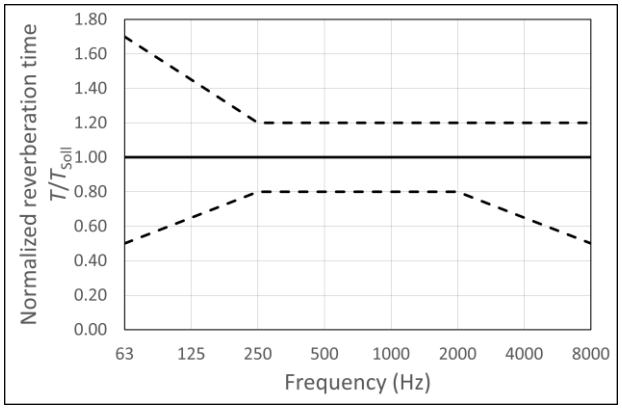


Figure 2. The tolerances of the required reverberation time T_{Soll} in type A rooms.

Type B spaces are defined as the ones that require some sort of acoustic treatment to prevent excessive reverberance. Although the HRN DIN 18041 standard lists the requirements for this type of spaces purely as recommendations, this Regulation stipulates them as mandatory for the following spaces: common rooms in kindergartens and nurseries, teaching cabinets; multipurpose spaces in kindergartens, nurseries, elementary and middle schools; teacher lounges; sports halls in schools; libraries; hallways in front of classrooms and lecture rooms; common hospital rooms; hospital hallways and waiting rooms; open-plan offices and call centres; administrative spaces in which multiple clients are handled simultaneously; entrance halls in public and other buildings (schools, hotels, train stations, airports, etc.). The spaces are categorized into categories B1 to B5 according to the HRN DIN 18041 standard. The technical requirement set on type B rooms is the minimal required ratio *A/V* of the equivalent absorption area *A* and room volume *V*, according to the category of the given room and the ceiling height *h* of the room. No requirement is set for category B1. The illustration of the requirements set for categories B2 to B5 is shown in Figure 3. The minimal required values of the *A/V* ratio are fixed for each category for ceiling heights up to 2.5 metres, and they continuously decrease with the ceiling height increasing above that threshold value.

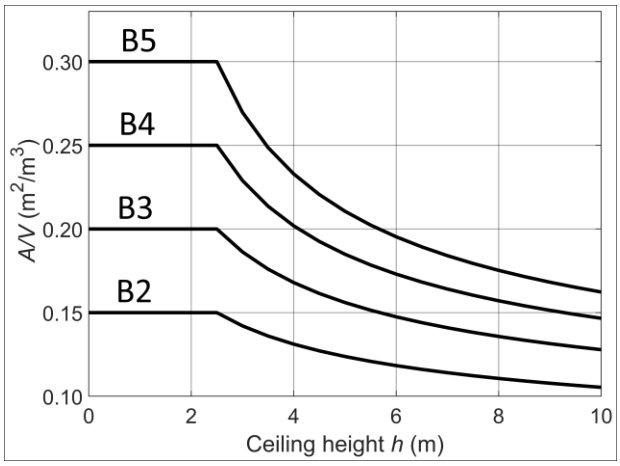


Figure 3. The minimum required value of the ratio *A/V* of the equivalent absorption area *A* and room volume *V* for type B spaces (categories B2 to B5), depending on ceiling height *h* and the category of the room.

6. CONCLUSION

The new Technical Regulation on Acoustics in Buildings that is now awaiting official publication represents a big legislative leap forward towards regulating this particular field in Croatia, after decades of neglect. Prior publications have given an overview of this document, its scope and content, the historical and technical reasons for its creation, and a description of the efforts and the employed workflow that was required to achieve this goal. This technical regulation contains comprehensive information for all who participate in the building process, in terms of the set requirements that need to be met, the methods to be used in the design process for the purpose of meeting the set requirements, and the methods of checking and verifying that the design values have indeed been achieved. For the first time, all the key factors of acoustics in buildings have been addressed in a single document.

This paper has provided key provisions of this Regulation that will facilitate correct building design in terms of acoustic comfort. A detailed overview of the technical requirements stipulated in this document has been given as well, in terms of airborne and impact sound insulation between rooms in critically sensitive buildings, permitted noise levels, and optimal room acoustics conditions depending on the use of a room/space.

The authors hope that the application of this Regulation will improve acoustic design of buildings in Croatia.

7. ACKNOWLEDGMENTS

The authors wish to thank the members of the expert committee engaged in creating this Technical Regulation, as follows: Dunja Magaš, Damir Borović, Slavica Radić-Vuković, Lejla Ahmetašević, and Jelena Svibovec of the Ministry of Physical Planning, Construction and State Assets; Bojan Milovanović of the Faculty of Civil Engineering in Zagreb; Mateo Biluš of the Croatian Chamber of Architects; Hrvoje Damić of the Croatian Chamber of Civil Engineers; Miljenko Henich of the Croatian Standards Institute; and Neno Torić of the Faculty of Civil Engineering, Architecture and Geodesy in Split.

8. REFERENCES

[1] M. Horvat, Z. Veršić, and K. Jambrošić, "The development of a new technical regulation on acoustics in buildings in Croatia," in *Proc. of InterNoise 2024*, (Nantes, France), pp. 001–007, 2024.

[2] M. Horvat, Z. Veršić, and K. Jambrošić, "The new technical regulation on acoustics in buildings in Croatia," in *Proc. of the 10th International Ergonomics Conference*, (Zagreb, Croatia), pp. 001–008, 2025.

[3] HRN EN ISO 12354-1:2017 - *Building acoustics -- Estimation of acoustic performance of buildings from the performance of elements -- Part 1: Airborne sound insulation between rooms*, Croatian Standards Institute, 2017.

[4] HRN EN ISO 12354-2:2017 - *Building acoustics -- Estimation of acoustic performance of buildings from the performance of elements -- Part 2: Impact sound insulation between rooms*, Croatian Standards Institute, 2017.

[5] HRN EN ISO 12354-3:2017 - *Building acoustics -- Estimation of acoustic performance of buildings from the performance of elements -- Part 3: Airborne sound insulation against outdoor sound*, Croatian Standards Institute, 2017.

[6] HRN EN 12354-5:2023 - *Building acoustics -- Estimation of acoustic performance of building from the performance of elements -- Part 5: Sounds levels due to the service equipment*, Croatian Standards Institute, 2023.

[7] HRN EN 12354-6:2005 - *Building acoustics -- Estimation of acoustic performance of buildings from the performance of elements – Part 6: Sound absorption in enclosed spaces*, Croatian Standards Institute, 2005.

[8] HRN EN ISO 16283-1:2014/A1:2018 - *Acoustics -- Field measurement of sound insulation in buildings and of building elements -- Part 1: Airborne sound insulation*, Croatian Standards Institute, 2018.

[9] HRN EN ISO 16283-2:2020 - Acoustics -- *Field measurement of sound insulation in buildings and of building elements -- Part 2: Impact sound insulation*, Croatian Standards Institute, 2020.

[10] HRN EN ISO 16283-3:2016 - *Acoustics -- Field measurement of sound insulation in buildings and of building elements -- Part 3: Facade sound insulation*, Croatian Standards Institute, 2016.

[11] HRN EN ISO 717-1:2021 - *Acoustics -- Rating of sound insulation in buildings and of building elements -- Part 1: Airborne sound insulation*, Croatian Standards Institute, 2021.

[12] HRN EN ISO 717-2:2021 - *Acoustics -- Rating of sound insulation in buildings and of building elements -- Part 2: Impact sound insulation*, Croatian Standards Institute, 2021.

[13] HRN ISO 1996-1:2016 - *Acoustics -- Description, measurement and assessment of environmental noise -- Part 1: Basic quantities and assessment procedures*, Croatian Standards Institute, 2016.

[14] HRN ISO 1996-2:2017 - *Acoustics -- Description, measurement and assessment of environmental noise -- Part 2: Determination of sound pressure levels*, Croatian Standards Institute, 2017.

[15] HRN EN ISO 16032:2024 - *Acoustics -- Measurement of sound pressure level from service equipment or activities in buildings -- Engineering method*, Croatian Standards Institute, 2024.

[16] HRN EN ISO 3382-1:2010 - *Acoustics -- Measurement of room acoustic parameters -- Part 1: Performance spaces*, Croatian Standards Institute, 2010.

[17] HRN EN ISO 3382-2:2010 - *Acoustics -- Measurement of room acoustic parameters -- Part 2: Reverberation time in ordinary rooms*, Croatian Standards Institute, 2010.

[18] HRN EN ISO 3382-3:2022 - *Acoustics -- Measurement of room acoustic parameters -- Part 3: Open plan offices*, Croatian Standards Institute, 2022.

[19] HRN DIN 18041:2024 – *Akustička kvaliteta prostorija – Zahtjevi, preporuke i upute za planiranje (DIN 18041:2016, translation into Croatian)*, Croatian Standards Institute, 2024.

DOI: 10.61782/fa.2025.0750

FORUM ACUSTICUM EURONOISE 2025

REVISING A NATIONAL STANDARD ON RESIDENTIAL ACOUSTIC DESIGN: SCIENCE, EMBEDDED PRACTICES, HEARTS AND MINDS

Benjamin Fenech[1*] **Jack Harvie-Clark**[2]
[1] Noise and Public Health, Radiation Chemical Climate and Environmental Hazards, UK Health Security Agency (UKHSA), London, UK
[2] Apex Acoustics, Gateshead, UK

ABSTRACT

In 2024, Harvie-Clark and Fenech published a set of proposals for updating a British Standard widely used for its residential acoustic design guidance. The proposals suggested a shift from the current approach targeting fixed averaged internal sound levels, irrespective of the sound source. The proposals put stronger emphasis on external sound levels, by assigning facades into sound exposure categories (SEC), informed by the synthesis of epidemiological evidence gathered over the past two decades. The building envelope is then designed with equivalent levels of sound insulation corresponding to equivalent adverse effects from noise, and a holistic consideration of indoor environmental quality. The proposals were accompanied by an extensive programme of dissemination events in the UK. This paper gives an overview of the feedback gathered from these events - with a particular focus on the aspects that were least and most contentious. Some of the areas covered include: differences between the WHO 1999 vs 2018 Guidelines, the relevance of external sound levels to population health, the additional value and underpinning evidence associated with criteria for noise events, specifying a facade acoustic performance vs internal levels, and setting criteria for noise sources other than transport.

Keywords: residential acoustic design, national standards, acoustic regulations.

[*] ***Corresponding author***: *benjamin.fenech@ukhsa.gov.uk*
Copyright: *©2025 Benjamin Fenech et al. This is an open-access article distributed under the terms of the Creative Commons Attribution 3.0 Unported License, which permits unrestricted use, distribution, and reproduction in any medium, provided the original author and source are credited.*

1. INTRODUCTION

The British Standard BS 8233 "Guidance on sound insulation and noise reduction for buildings," [1] provides guidance for the control of noise in and around buildings. It is applicable to the design of new buildings, or refurbished buildings undergoing a change of use within the UK. In this paper we are focusing on the requirements relevant to the acoustic design of new residential development. The standard was last updated in 2014 and is currently undergoing a revision. In 2024, Harvie-Clark and Fenech [2] published proposals that aimed to align the acoustic criteria for residential development with the body of evidence that has been published in the last two decades, including the 2018 WHO Environmental Noise Guidelines for the European region [3]. In brief, the proposals:

a) Introduced the concept of noise source-specific "Sound Exposure Categories", defined by the external sound levels corresponding to specific health outcomes (i.e. percentage of population highly annoyed or highly sleep disturbed);
b) Specified target internal conditions in terms of a facade sound insulation performance, with an equivalent performance requirement for equivalent source-dependent health burden; and
c) Suggested guidance whether opening windows can be used to mitigate overheating, depending on the corresponding Sound Exposure Category.

The rationale for point (a) is the strengthening epidemiological evidence showing that the adverse health risk increases with external sound level, and the availability of exposure response relationships allows the increased risk above a certain threshold to be quantified. The rationale for point (b) is that for a given long-term averaged sound level, aircraft and railway noise are more annoying and sleep disturbing than road traffic noise - this could be partly

explained by the higher instantaneous sound levels during aircraft flyovers and train pass-bys for typical exposure situations. The rationale for point (c) is to emphasize the need for a holistic design of a healthy indoor environment that takes into account safe temperatures, noting the increased risk of overheating from a changing climate[1].

To encourage debate on these proposals, Harvie-Clark and Fenech participated in an extensive programme of dissemination events between September 2024 and March 2025, both in-person and online, targeting members of relevant professional and trade bodies in the UK (Institute of Acoustics (IOA), the Association of Noise Consultants (ANC) and the Chartered Institute of Environmental Health (CIEH)). These events sparked strong interest[2] and a very active debate, with practitioners expressing a broad range of views. In general, there was good agreement with the underpinning principles of the proposed changes during these events (see Annex A). However the discourse outside the events was largely shaped by those that had strong opposing views, which even led to requests for stopping the proposals from going out for a public consultation. In this paper, we present some of the salient points from the debate that has taken place to date.

2. RELEVANCE OF OUTDOOR VS INDOOR SOUND LEVELS TO PUBLIC HEALTH

A letter to the editor [5] published in a bimonthly magazine of the Institute of Acoustics, signed by 33 experienced acousticians, raised important questions about the proposed approach to include external noise levels as key design criteria. Their concern can be summarised by the following extract from the letter [5]:

"To align with public health research the proposal is to assess and control noise exposure via the external sound levels, under the mistaken assumption that this alignment with the evidence base justifies a departure from controlling internal levels.

I don't think anyone has ever actually suggested that the community health impacts from environmental sound on residents in buildings is predicated more on the noise levels outside the buildings in which they are exposed than those they experience internally. It is just much more difficult to do large scale studies on actual internal levels in comparison with the convenience of large-scale noise mapping. Hence all the recent studies refer to external levels as a proxy.

By definition, a proxy is not the parameter we are trying to control to the benefit of residents to deliver suitable internal living conditions. It's like trying to drive a car looking only at the sat-nav screen! This lack of precision – the failure to target the parameter itself rather than the more convenient proxy is uniquely problematic in relation to exposure of individuals to environmental sound."

Similar arguments were made in a position statement published on the website of the Chartered Institute of Environmental Health [6], where it was argued that:

"If we are interested in the design of new homes to provide good or reasonable living conditions indoors then we need to identify the best evidence that relates to internal noise conditions."

Harvie-Clark and Fenech published a response to these points [7]. The response drew on three fundamental concepts that have defined noise and health theory for many decades:

i. Noise is a psychosocial stressor, i.e. '*an environmental factor interacting with social and cultural factors to influence the mind and behaviour*' [8]. Within this framework, noise exposure 'at home' is not limited to the sound levels inside the physical space enclosed within a building envelope. It also covers any outdoor spaces that residents consider part of their home. This is also consistent with how the international standard for measuring noise annoyance [9] defines the wording 'at home' to capture inside the home or outdoors at home, including balconies, gardens, etc.

ii. The mechanistic evidence on the relationship between chronic noise exposure and chronic health outcomes supports a direct pathway and an indirect pathway [3,10]. The indirect (psychological) pathway is mediated by cognitive and emotional responses to the personal experience of the noise, which is not limited to the sound levels experienced when inside the home.

[1] For example, a report by the Climate Change Committee [4] notes that "*Increases in temperature have been linked with an increase in the death rate (particularly amongst older people) across the UK, including in recent heatwaves in every year from 2018 to 2021. Recent estimates suggest that around a fifth of homes in the UK are already overheating in summers today*" and "*Climate projections suggest that a 'hot' summer such as 2018 will become the average summer by 2050, even with deep cuts in global greenhouse gas emissions. The combination of increasing hot weather, and an ageing population, means that heat-related deaths may treble without further adaptation actions.*"

[2] One lunchtime webinar organized specifically for introducing the proposals hit the participants limit of the IOA's Zoom account (500) and was one of the most attended IOA event in its history.

iii. A dwelling is not just a physical structure – it represents a place where people call home [11]. The places where people live have a significant impact on their mental and physical health [12]. When residents feel a deep connection to their place of residence, they are more likely to be satisfied with their living conditions. This relationship is influenced by various factors, including the quality of the physical environment, social interactions and the availability of amenities. Noise has been shown to interact with some of these factors [13, 14]. Socio-acoustic studies from Norway found that the noise levels in the immediate neighbourhood of a home can affect residential noise annoyance, with a similar effect on both outdoor and indoor noise annoyance [15].

To support these theoretical concepts, Fenech and Harvie-Clark drew on evidence from two studies in Sweden [16, 17] that investigated the influence of the external sound environment on disturbances inside the dwelling. For example, in [17], for the same internal averaged noise levels, disturbances to communication, listening to TV/radio, concentration and relaxation were consistently higher with high external levels (windows closed) than with a quieter external environment (windows open). Similar observations were made for sleep disturbance. Other studies on noise annoyance investigated differences between outdoor and indoor annoyance (see for example [18]) and indoor annoyance with windows open and closed (see for example [19]). These studies show that both outdoor annoyance, and indoor annoyance with windows open are important contributors to the overall annoyance reactions and therefore support the relevance of both the external and internal sound exposure at home.

3. RELEVANCE OF WHO ENVIRONMENTAL NOISE GUIDELINES (2018) FOR RESIDENTIAL ACOUSTIC DESIGN

The CIEH statement included the following arguments [6]:
"*The recommendations made in the WHO Community Noise Guidelines were derived using evidence relevant to internal noise conditions, including interference with communication and sleep disturbance effects. It was recognised that the maximum noise level was best correlated with effects on sleep and that is the reason why the recommendations for the protection of sleep inside dwellings included the 45 dB L_{Amax} criterion. In 2018 the WHO reviewed the available scientific evidence and published the Environmental Noise Guidelines European Region 2018* [ENG2018]. *It concluded that:*
"The current environmental noise guidelines for the European Region supersede the CNG [1999 WHO guidelines for community noise] from 1999. Nevertheless, the GDG [Guideline Development Group] recommends that all 1999 CNG ***indoor guideline values*** *and any values not covered by the current guidelines (such as industrial noise and shopping areas)* ***should remain valid****." (Our emphasis)."*
The CIEH statement went on to suggest that the proposals by Harvie-Clark and Fenech departed from WHO recommendations. The statement did not mention that the ENG2018 explicitly state that "*The* [2018] *guidelines are source specific and not environment specific. They therefore cover all settings where people spend a significant portion of their time, such as residences …*". The CIEH statement also did not mention that the 1999 CNG [20] guideline values for residential settings were expressed as both external and internal levels.
In response, Fenech and Stansfeld [21] published an article to clarify the relationship between the WHO 1999 CNG and ENG2018. In summary, Fenech and Stansfeld argue:
"When referring to WHO guidelines to set criteria for residential settings (dwellings) exposed to transport noise, the main reference should be to the WHO Environmental Noise Guidelines for the European Region (ENG2018), because they are the most up-to-date guidelines. Additional consideration can be given to the indoor guideline values in the Guidelines for Community Noise [CNG (1999)], but only if this is done in conjunction with the external guidelines in the ENG2018 and taking into account the source-specific characteristics of the sound (e.g. intermittency, low frequency content, etc). In writing the ENG2018 it was clear that the indoor guidelines from the CNG (1999) could not and should not be quoted or used in isolation."

4. CAN HIGH FAÇADE SOUND INSULATION PERFORMANCE LEAD TO "COMPROMISED LIVING CONDITIONS"?

The letter to the editor by Clarke and Fiumicelli [5] appeared to suggest that up to a certain level, transport noise ingress in buildings with windows closed can have beneficial health effects:
"*If, for example, rather than achieving internal conditions at night of 30dB $L_{Aeq,8hr}$ with L_{max} levels in the low 40s in two apartment buildings, we get one building with 20 $L_{Aeq,8hr}$ (L_{max} in the low 30s) and one building at 40 $L_{Aeq,8hr}$*

(L_{max} in the low 50s) then BOTH sets of residents have dramatically compromised living conditions, due to annoyance and sleep disturbance in the under-attenuated case and high levels of neighbour noise disturbance in the over-attenuated building."

The CIEH statement [6] also included the following statement:

"The proposed revisions to BS8233 place too much emphasis on façade insulation and overheating. This appears to be fundamentally at odds with the guidance contained in the ProPG[3]".

To our knowledge, there is no robust scientific evidence demonstrating that lower internal sound levels due to higher façade sound insulation leads to 'dramatically compromised living conditions' or increased neighbour noise disturbance. While anecdotal reports of increased sensitivity to neighbour noise in quieter environments exist, these have not been substantiated by systematic studies. It is not clear how noise from discrete car/train pass-bys or aircraft flyovers that averages to an internal level of 30dB $L_{Aeq,8hr}$ can be effective at reducing disturbance from an unpredictable and intermittent source such as neighbour noise. External anthropogenic noise ingress with windows closed should not be relied on as a sound source contributing to a positive internal soundscape in homes, because it is completely out of the control of the building occupant. Research by Torresin et al [22] demonstrated the importance of control over one's environment to achieve an ideal indoor soundscape for work and relaxation. We argue that neighbour noise disturbance should be managed by appropriate levels of sound insulation between dwellings and, if acoustic masking is necessary, this should be achieved by sources of sound that are under the full control of the building occupants.

5. THE ROLE OF MAXIMUM SOUND LEVELS IN RESIDENTIAL ACOUSTIC DESIGN

A common argument that came up at several engagement events and was noted in the CIEH statement [6], was the lack of L_{max} criteria in our original proposals, and the perceived lack of protection for sleep disturbance because of this omission.

There is clear evidence that L_{max} correlates better with short-term noise-induced physiological sleep disturbances than long-term averaged noise metrics [24]. However the relationship between single-event noise indicators and long-term health outcomes at the population level remains tentative [3]. Simplistic criteria, such as indoor sound pressure levels not to exceed approximately 45 dB L_{Amax} more than 10–15 times per night, are based on studies from the 1970s-80s [20], and such criteria can be expressed in terms of an energy equivalent level such as $L_{Aeq,8hr}$ [20]. Basner et al. [23] proposed a physiological noise effects criterion for the protection against adverse effects of nocturnal aircraft noise. Applying this criterion requires detailed knowledge of all the noise events and their respective L_{max} throughout the night. Such an approach would be feasible and appropriate to inform decisions on changes around transport hubs such as airports (e.g. new runway, airspace changes or changes to night flights), given that aircraft noise modelling software can predict L_{max} data. However, applying this approach to new residential acoustic design would require comprehensive new guidance on how to obtain representative internal L_{max} distributions throughout the entire night period[4]. Instead, our proposals [2] were derived from source-specific self-reported sleep disturbance evidence, in accordance with the WHO 2018 recommendations [3]. Self-reported sleep disturbance responses take into account additional dimensions of sleep disturbance, such as problems falling asleep at the beginning of the night and falling back to sleep after a conscious awakening [24].

5.1 Practitioners' views on maximum levels

In a questionnaire ran at some of the outreach events (see Annex A), participants were asked to state to what extent they agreed with these five statements (shown from left to right in Fig. 1):

i. I am comfortable specifying and/or complying with L_{max} criteria.
ii. There is good quality evidence linking L_{max} criteria to long term health outcomes.
iii. Including additional L_{max} criteria in BS 8233 will add value to residential acoustic design.
iv. BS 8233 should include L_{max} criteria for all situations.
v. BS 8233 should include L_{max} criteria only for specific situations.

Statements *ii*,*iv* and *v* invited additional free text comments.

Referring to Fig. 1, practitioners were generally comfortable specifying and/or complying with L_{max}

[3] The Professional Practice Guidance on Planning and Noise (ProPG) was published in 2017 to provide practitioners with guidance on a recommended approach to the management of noise within the planning system in England. It was co-produced by the CIEH, IOA and ANC.

[4] In the UK, current national noise modelling tools for road and conventional railway noise do not output L_{max} data.

criteria, despite responses to the second question being mostly neutral or disagreeing that "There is good quality evidence linking L_{max} criteria to long term health outcomes". Most respondents strongly agreed, agreed or were neutral in response to the statement that "*Including additional L_{max} criteria in BS 8233 will add value to residential acoustic design"*. Most respondents were neutral, however, in response to the final two statements suggesting that BS 8233 should include L_{max} criteria for all situations / only for specific situations.

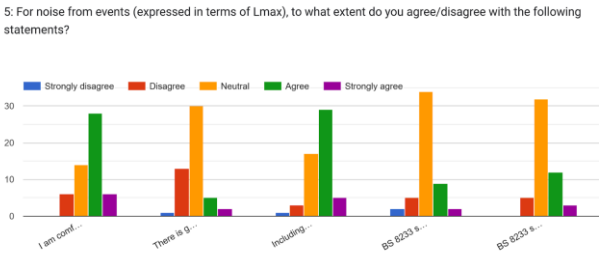


Figure 1 Survey question on noise events - see text for the complete text of the five options.

The following sections summarize the free text responses, categorized under six themes.

5.1.1 Practical Utility Despite Evidential Limitations

A prominent theme in the responses was the suggestion of the practical utility of L_{max} in real-world applications, despite acknowledged limitations in its evidential basis. Many respondents consider L_{max} "well understood" and effective for "giving a resident an appropriate environment", despite the lack of evidence linking this metric with long term health outcomes.
Several comments suggested that L_{max} provides valuable contextual information that benefits "all stakeholders". Respondents highlighted specific applications where L_{max} is particularly useful, such as "nighttime economy in urban areas" and "where residential is located above or adjacent to a significant sound source".

5.1.2 Concern About Evidence Gap vs. Practical Need

Responses acknowledged the tension between the lack of robust evidence linking L_{max} to health outcomes and their perception of its practical importance. Several comments acknowledge the evidence gap we had presented: "You've presented the case that there is insufficient health evidence". However, this was frequently countered with caution: "Lack of evidence of correlation isn't evidence of a lack of correlation". Some respondents remained hesitant about abandoning L_{max}: "not convinced yet that we should be disregarding L_{max} levels altogether".

5.1.3 Source-Specific Applications

Some comments suggested that L_{max} may be more relevant for certain noise sources than others. Specific mentions of "ambulance and police alarm", "lift noise, plant noise," and "wind farms", for example. Several respondents suggested that while our approach for "road, rail, air traffic sources" may be appropriate, guidance is still needed "for other sources". Entertainment venues, "intermittent disturbing noise sources running through the night," and impulsive sounds were highlighted as requiring specific consideration. We acknowledge these arguments, and changes were made to the BS8233 proposals to state that an assessment of noise from events may be appropriate in certain situations.

5.1.4 Pragmatic Regulatory Concerns

Some respondents raised concerns about the practical implications of removing L_{max} criteria in regulatory contexts: "removing L_{max} altogether from BS 8233 might open the door to more unscrupulous developers/ contractors". There were concerns that without L_{max}, some stakeholders "won't pay for a more detailed approach/ or attempt to understand the health effects". There were some suggestions that L_{max} serves as a simple, understood metric that facilitates compliance checks.

5.1.5 International Context and Alternative Approaches

A few responses alluded to international perspectives and alternative approaches. Reference was made to criteria in "some other countries (primarily Australia and particularly Spain/Barcelona)", for example. There were suggestions that further research into L_{max} "ahead of the revision" would have been beneficial, and indications that a comparative analysis of different regulatory approaches might be valuable.

5.1.6 Assessment Challenges

Several comments acknowledged the practical difficulties in using L_{max} as an assessment tool. There was recognition that "L_{max} assessment is fraught with assumptions and uncertainty", and implicit acknowledgment of methodological challenges in applying L_{max} criteria consistently.

5.2 Comparing L_{max} criteria with real-world data

This thematic analysis suggests that while there is acknowledgment of the limited evidence base for L_{max}

criteria in relation to long-term health outcomes, there remains significant attachment to the metric for specific applications and contexts. The responses suggest a desire for better guidance rather than its complete removal.

We carried out simulations based on actual measurements of road traffic noise to test how our proposed internal criterion (façade sound insulation ≥ L_{den} – 32dB) compares with two L_{max} based criteria:

- less than 10 events with L_{AFmax} > 45dB (referred to as "10th highest $L_{AF,max}$ meeting 45dB") [20]; and
- less than one additional awakening per night (referred to as "1AW") [23].

The measurements consisted of 187 24hr sound level profiles, typically made at distances of up to 10m from the kerbside[5]. From each data set, we extracted the following information: L_{den}, $L_{Aeq,16hr}$, $L_{Aeq,8hr}$, and for the night time period: highest $L_{AF,max,8hr}$, 10th highest $L_{AF,max,2\ min}$ and the complete set of $L_{AS,max,2min}$ (i.e. 240 values for each night). We then calculated the façade reduction required to achieve the relevant criterion. The reduction required was calculated as a facade level difference, based on the A-weighted values for the indicators, and assuming a standardised road traffic spectrum[6]. The method used to determine the facade level difference to achieve the 1AW criterion internally is described in [25], using dose response functions from [24].

Figures 2 and 3 show how our original proposals (orange line: equivalent to a Class D classification in ISO/TS 19488:2021) compares to the two different L_{max}-based criteria. Individual markers represent each 24hr dataset. If a marker is above the orange line, the façade insulation requirement to meet the relevant L_{max} criterion is higher than our proposed target, and vice-versa.

Fig. 2 shows that in the majority of cases, a higher level of facade sound insulation is required to achieve less than ten events with $L_{AF,max}$ > 45 dB than to meet an internal level of 35 dB L_{den}. Fig. 3 shows that meeting 35 dB L_{den} achieves the 1AW criterion on average, and in more than 80% of cases. The mean difference between the requirement to meet the 45 dB $L_{AF,max}$ criterion and the 1AW criterion was 4.0 (± 3.2) dB, with a range from + 13 to -5 dB.

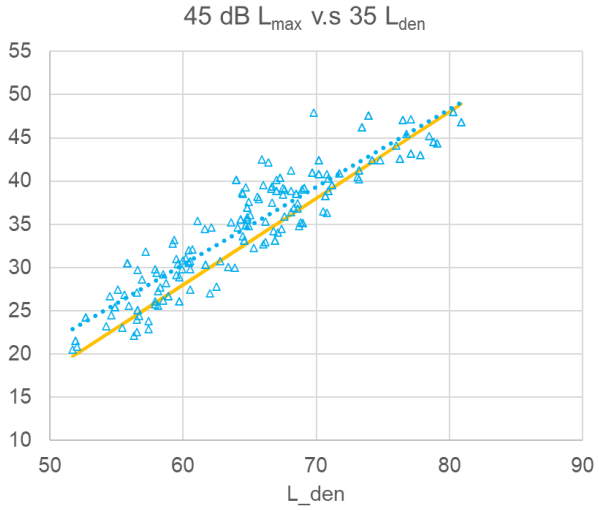


Figure 2 Facade level difference required to ensure the "10th highest $L_{AF,max,inside}$ < 45dB" criterion is met, plotted as a function of external L_{den} level. Each blue marker represents a 24hr measurement. The orange line represents the criterion in our original proposals [2].

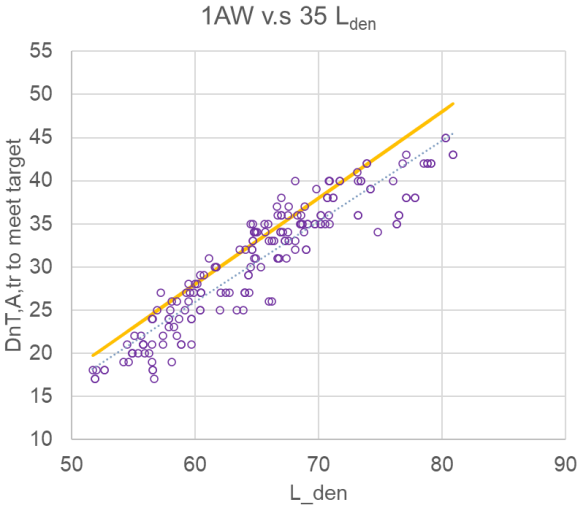


Figure 3 Facade level difference required to ensure the "1 additional awakening per night" criterion is met, plotted as a function of external L_{den} level. Each purple marker represents a 24hr measurement. The orange line represents the criterion in our original proposals [2].

[5] Further details of the measurements can be found in [26].

[6] This is a simplification, as a real facade provides different levels of A-weighted attenuation depending on the frequency content of the incoming sound field. This is particularly relevant for assessing noise from events, for which the frequency content can vary widely.

6. CHANGING THE STATUS QUO – HEARTS AND MINDS

Both the letter to the editor by Clarke and Fiumicelli and the CIEH statement argued in favour of maintaining the status quo. The former argued [5]:

The UK has a reputation for practical delivery against internal criteria. It's what we do really well. As with the delivery of sound insulation between dwellings via pre-completion testing and Robust Details, acousticians in other jurisdictions look on with envy at the UK's track record for effective delivery against measured in-situ performance.

The suggestion that we dispense with this process to align with the proxy parameter used for convenience in the broader-brush epidemiological studies is a reductive and retrograde proposition.

The CIEH statement argued [6]:

"Although the proposed revisions to the standard are based on what the authors consider to be sound scientific studies, the internal and external noise levels have been used for decades without apparent problems or challenges."

Whilst both narratives suggest that current methods work '*without apparent problems*', no evidence was provided in either instance to support these claims. However, there is evidence that current approaches are leading to problems. For example, a Quieter Road-Map published by Sustainable Aviation noted [26]:

"*The development of land near and within areas of high aircraft noise areas around airports for noise-sensitive uses, including residential development continues to be, a major challenge that many UK airports are facing. Many of the measures in the ICAO Balanced Approach are in place at UK airports and are incorporated in airport Noise Action Plans. However, the effectiveness of airport and airline noise control measures can be compromised by competing demands on the planning system to deliver residential development in noise sensitive areas, Some Local Planning Authorities have been forced to prioritise housing targets over exposure to aircraft noise. This has resulted in residential development encroaching in areas around airports that are subject to higher levels of aircraft noise."*

The CIEH statement also argued against any potential conflicts with existing guidance (ProPG), published in 2017, because "*Discrepancies between the ProPG and BS8233 could lead to confusion and hinder the promotion of design outcomes that support good health and quality of life.*" During the engagement events it was noted that there was currently no appetite within the ANC or the CIEH to revise ProPG.

Another criticism of the proposals that came up at some of the events was on the use of the L_{den} metric. Whilst we acknowledge that the L_{den} metric does not fully capture the complex relationships between sound and health, the same can be said of the other metrics in the current standard ($L_{Aeq,16hr}$ and $L_{Aeq,8hr}$). Our original proposals were expressed in terms of L_{den} to align with the large body of epidemiological evidence on sound and health. Whilst conversions between metrics are possible, these introduce additional, and in our view, unnecessary uncertainties.

7. ACKNOWLEDGMENTS

We are grateful for the extensive engagement of the UK acoustics community during the outreach events that took place since September 2024, which has led to further refinement of the proposals. We also acknowledge the constructive "check and challenge" by the BS8233 drafting panel, led by Dr. David Hiller. Special thanks to Weigang Wei, AtkinsRealis for extracting the sound data used in the L_{max} analysis. The views expressed in this article are those of the authors and are not necessarily those of UKHSA or the Department of Health and Social Care.

8. REFERENCES

[1] British Standard 8233:2014 Guidance on sound insulation and noise reduction for buildings, 2014.

[2] Harvie-Clark J, Fenech B (2024). Aligning residential acoustic design guidance with the health evidence: a new proposal for the UK. Proc. Internoise 2024.

[3] World Health Organization. Environmental Noise Guidelines for the European Region. 2018.

[4] Climate Change Committee. Risks to health, wellbeing and productivity from overheating in buildings. 2022.

[5] Clarke E and Fiumicelli D (2024). Reductive proposals for BS 8233 update. IOA Acoustics Bulletin 50(6).

[6] CIEH statement on proposed revisions to BS8233. https://www.cieh.org/media/mi1cdqqk/cieh-statement-on-proposed-revisions-to-bs8233.pdf

[7] Fenech B., Harvie-Clark J. IOA Acoustics Bulletin 51(1).

[8] Clark C, Vienneau D, Aasvang GM (2024) Noise and Effects on Health and Well-Being. In A Sound Approach to Noise and Health.

[9] Clark C, Gjestland T, Lavia L, et al. (2021) Assessing community noise annoyance: A review of two decades of the international technical specification ISO/TS 15666:2003. J. Acoust. Soc. America 150, 3362.

[10] Münzel, T, et al. (2024) Transportation noise pollution and cardiovascular health. Circulation Research 134 (9).

[11] Weidemann S, Anderson JR (1985) A Conceptual Framework for Residential Satisfaction. In: Altman, I., Werner, C.M. (eds) Home Environments. Human Behavior and Environment, vol 8.

[12] NHS England 2018. Putting Health into Place: Introducing NHS England's Healthy New Towns programme.

[13] Appleyard D, Lintell M (1972). The environmental quality of city streets: The resident viewpoint. J. Am. Inst. Planners 38: 84-101.

[14] Peris E, Fenech B (2020). Associations and effect modification between transportation noise, self-reported response to noise and the wider determinants of health: A narrative synthesis of the literature. Science of the Total Environment 748 (2020) 141040.

[15] Klæboe R, Kolbenstvedt M, Fyhri A (2005) The Impact of an Adverse Neighbourhood Soundscape on Road Traffic Noise Annoyance. ACTA ACUSTICA UNITED WITH ACUSTICA Vol. 91.

[16] Öhrström E (2004) Longitudinal surveys on effects of changes in road traffic noise—annoyance, activity disturbances, and psycho-social well-being. J. Acoust. Soc. Am. 115 (2).

[17] Öhrström E, Skånberg A, Svensson H, Gidlöf-Gunnarsson A. (2006) Effects of road traffic noise and the benefit of access to quietness. Journal of Sound and Vibration 295 (2006) 40–59.

[18] Danish Road Directorate (2006) Noise annoyance from urban roads and motorways. Report 565 – 2016.

[19] Preisendörfer P, Liebe U, Enzler HB, Diekmann A (2022) Annoyance due to residential road traffic and aircraft noise: Empirical evidence from two European cities. Environmental Research 206 (2022) 112269.

[20] WHO (1999) Guidelines for community noise. Geneva: World Health Organization.

[21] Fenech B, Stansfeld S (2024). Clarifying the relationship between the WHO 2018 Environmental Noise Guidelines for the European Region and the 1999 Guidelines for Community Noise for dwellings exposed to transport noise. IOA Acoustics Bulleting JAN/FEB 2025.

[22] Torresin S, et al. (2022). The actual and ideal indoor soundscape for work, relaxation, physical and sexual activity at home: A case study during the COVID-19 lockdown in London. Front. Psychol. 13:1038303.

[23] Basner, M, Samel, A, Isermann, U (2006). Aircraft noise effects on sleep: Application of the results of a large polysomnographic field study. J. Acoust. Soc. Am. 119, 5

[24] Basner, M, McGuire, S (2018). WHO Environmental Noise Guidelines for the European Region: A Systematic Review on Environmental Noise and Effects on Sleep. Int. J. Environ. Res. Public Health 2018, 15, 519.

[25] Paxton et al (2019). Assessing L_{max} for residential developments. Proc. IOA 2019.

[26] Sustainable Aviation (2025). Quieter Road-map.

[27] Conlan N, Wei W, Harvie-Clark J. (2021). Empirical Relationship Between L_{night} and L_{Amax} Proc. IOA 43(1).

[28] British Standard BS 0:2021. A standard for standards – Principles of standardization.

[29] Harvie-Clark J. (2025). BS 8233 proposals: what do people really think now? IOA Acoustics Bulletin 51(3).

9. ANNEX A – ENGAGEMENT EVENTS

The development process of British Standards of UK origin is broadly similar to that for international and European standards, although there are no voting stages. The relevant committee overseeing a standard revision is asked to give approval at two stages (for the draft to go to public consultation and for the final version to be published). Public consultation on a 'draft for public comment' is considered an essential part of the process and the responses arising from it are reviewed in the same manner as for international and European projects [28].

The engagement and dissemination events were intended to inform relevant audiences of the main proposed changes to BS 8233 in advance of the public consultation, and to provide more detailed information on the rationale and supporting evidence that informed the proposals.

During four of the events taking place between January and March 2025, we gathered feedback using two separate questionnaires. We obtained 56 and 70 responses to these questionnaires, out of an estimated 150-200 delegates. 50 – 60% of respondents were from the private sector. The majority of the non-private sector responses were from environmental health practitioners working in the public sector, who take a regulating role within the planning system in the UK.

Respondents to the questionnaire were generally supportive of our guiding principles:

- 59% agreed that current knowledge on noise and health warrants more emphasis on external sound levels, reflecting the latest WHO evidence base.
- 89% of respondents supported accounting for how different transportation sources affect health to different extents.
- 75% of respondents viewed Sound Exposure Categories as useful markers for navigating noise impacts in planning.

Concerns were raised about specifying a sound insulation performance instead of internal sound levels, and about the challenges associated with practical implementation. Further details on the survey responses can be found in [29].

DOI: 10.61782/fa.2025.0066

FORUM ACUSTICUM EURONOISE 2025

ACOUSTIC COMFORT IN BUILDINGS, SAINT-GOBAIN BAROMETER 2024. TOOLS FOR DESIGNING ACOUSTIC COMFORT IN BUILDINGS.

Penélope González de la Peña[1*] **Paula Belenguer Rubio**[2]
[1] Saint-Gobain España, Spain
[2] Saint-Gobain España, Spain

ABSTRACT

Does the current Technical Building Code (DB HR) provide the acoustic comfort required by users? In 2024, the 2nd Saint-Gobain Housing Barometer was carried out to answer the many questions that arise about the situation of main residences in Spain and the immediate future expectations of those who live in them. More than 1,000 people between the ages of 18 and 70 were interviewed in five major urban centers and smaller towns, with the help of CAWI methodology, which guarantees a 95.5% confidence interval.

Among the concerns of the users, acoustic insulation concerns half of the respondents and it's linked with the sustainability of the building.

In this paper, we will discuss the survey carried out, the current requirements of the DB HR and its future planned modification, and the Acoustic Classification of Buildings standard, as well as the Saint-Gobain Acustic software, which helps to select construction solutions that meet user requirements, both for renovation and new construction.

Keywords: *CTE DB HR, acoustic comfort, survey, software, Saint-Gobain Acustic.*

[*] ***Corresponding author***: penelope.gonzalez@saint-gobain.com

Copyright: *©2025 First author et al. This is an open-access article distributed under the terms of the Creative Commons Attribution 3.0 Unported License, which permits unrestricted use, distribution, and reproduction in any medium, provided the original author and source are credited.*

1. INTRODUCTION

In 2021, the first Home Barometer was carried out, analyzing the situation of the main residence in Spain and the main concerns of its users. The aim of this Barometer was to answer the many questions that have arisen about the situation of main residences in Spain and the immediate future expectations of those who live in them. The study focused on the main residence buildings, gathering the opinions and evaluations of the household members, who are the current or potential decision-makers, regarding the main residence, such as buying, renting, renovating...

This Barometer was marked by the impact of the pandemic and the post-confinement period, a time when new needs were activated in our homes.

In 2023, the Barometer has been repeated and includes, in addition to the aspects covered in 2021, sustainability and the impact of teleworking on the perception of housing.

2. INSULATION AND ACOUSTIC COMFORT. RESULTS IN THE 2024 BAROMETER

One of the main housing concerns in the Barometer is acoustic insulation, at 48%. When broken down by age, we see that younger generations are most concerned about this aspect of their current home.

Principales preocupaciones sobre la vivienda	Total	18-29 Generación Z	30-44 Millennials	45-59 Generación X	60-70 Boomers
Aislamiento acústico	48 %	51,5 %	53,3 %	47,9 %	35,0 %

Figure 1. Concern about acoustic insulation in the usual residence by age.

When broken down by type of family, the percentage varies according to whether people live alone, with children or with a family member.

Principales preocupaciones sobre la vivienda	Total	tipo de hogar				
		Sólo	En pareja sin hijos	En pareja con hijos	Con mis padres	Con algún familiar
Aislamiento acústico	48 %	54,0 %	44,9 %	53,2 %	40,0 %	33,7 %

Figure 2. Concern about acoustic insulation by family type.

Similarly, the importance of soundproofing changes depending on whether the dwelling user teleworks or not: 55% of teleworkers consider soundproofing to be very important, while this figure falls to 45% for users who do not telework. Teleworking increases the need to improve acoustic insulation, brightness, space and views.

But not only does teleworking increase the amount of time we spend at home, more than 44.8% of respondents say that they spend more time at home since the pandemic, so the need for acoustic comfort in the usual home is also important in this case.

In terms of concern about acoustic insulation by geographical area, the percentages are as follows:

Principales preocupaciones sobre la vivienda	Total	Madrid	Barcelona	Bilbao	Sevilla	Valencia	Resto de España
Aislamiento acústico	48 %	45,9 %	48,6 %	56,1 %	60,0 %	53,1 %	45,9 %

Figure 3. Sound insulation concerns by geographical area.

In the south of Spain, the importance of good acoustic comfort is 15% higher than in other regions.

When it comes to buying a new home, acoustic insulation becomes even more important, with 87.8% of respondents considering soundproofing to be an important aspect when choosing a home.

When asked about renovating their current home, 26.5% of people who have carried out renovations in their home have done so with the motivation of improving its acoustic insulation, and this percentage rises to 31.3% in the case of teleworkers. If we analyze these renovations according to the year of construction of the building, we see that they are the same in houses built before 1979 (before any acoustic regulations) and in houses built after 2007, with the Technical Acoustic Code already in force, so the perception of low acoustic comfort in current houses remains even to be built with acoustic parameters.

Motivos reforma vivienda	año de construcción			
	Total	<1979	1980-2006	2007>
El aislamiento acústico (minimizar/eliminar ruidos)	26,5 %	29,4 %	22,4 %	29,4 %

Figure 4. Percentage of acoustic insulation renovations by year of construction.

As a conclusion of the 2024 Barometer on insulation and acoustic comfort, we can see that the concern for acoustics in the home is not diminishing and is even increasing for those users who telework and need a suitable acoustic environment to concentrate.

3. REGULATIONS APPLICABLE TO HOUSING

3.1 Current regulations. DB HR and UNE 74201

In October 2007, as part of the Technical Building Code, the Basic Document on Noise Protection (DB HR) was published, which became mandatory in 2008, six months after its publication.

In the survey, the year of construction of the buildings was as follows:

Año de construcción vivienda actual	Total
De 1979 o anterior	26,3 %
Entre 1980 y 2006	39,1 %
Entre 2007 y 2012	14,6 %
Entre 2013 y 2019	5,8 %
A partir de 2019	3,1 %
No lo sé, lo desconozco	11,1 %
Nueva	23,5 %
Base	1025

Figure 5. Year of construction of the current home.

Therefore, when we talk about concern for acoustic insulation, we can see that 34.6% of respondents already live in homes built to DB HR and therefore have acoustic insulation built into their construction solutions.

Nevertheless, acoustic insulation is an important issue that stands out despite the fact that they have homes built to DB HR specifications.

Reflecting this concern for acoustic comfort in homes, the UNE 74201 standard was published in September 2021. "Acoustics. Acoustic classification scheme for buildings", which establishes a classification scheme that makes it possible to characterise the level of acoustic comfort in newly constructed buildings and to evaluate the acoustic conditions in existing buildings, offering the possibility of improving them in future renovations. A building that complies with the Technical Building Code in DB HR is generally classified in Class D according to the UNE 74201 standard; this classification is based on sampling carried out in the most unfavourable rooms of the building, taking into account the performance of airborne noise insulation, impact noise, facades and installations.

As noted in the survey, this Class D rating is below what almost half of respondents consider to be acoustic comfort, so there is still room for improvement in new buildings and refurbishment of existing buildings.

3.2 Possible modification of DB HR

The Administration is currently considering changing some aspects of the basic noise protection document.

Table 1. Current insulation limits and possible changes

Constructive element. Protected space	Current requirement	Possible modification
$D_{nT,A}$ room with different unit of use	50 dBA	52 dBA
$D_{nT,A}$ room with installations or activities	55 dBA	57 dBA
$L'_{nT,w}$ room with different unit of use	65 dB	60 dB
$L'_{nT,w}$ room with installations or activities	60 dB	55 dB

With the increase in the requirements for protected spaces, the acoustic classification of the building would move from class D to class C or B. Therefore, the possible modification of DB HR is an advance compared to the current requirements, but it still has room for improvement, as it falls short of the acoustic classification of the building of class A, which would provide optimal acoustic comfort to the users.

In parallel with this modification of the requirements in terms of insulation limit values, the tables of the simplified option for checking DB HR should be modified in the part that concerns plasterboard systems, which are excessively increased in the current standard. In this case, the modification concerns the systems used for internal partitions, where the minimum insulation requirement and the minimum mass must been adapted to the current systems and to the tests made by UNE 102045 test standard "Procedure for monitoring and characterizing the assembly of gypsum plasterboard systems for airborne sound insulation tests in the laboratory".

The change in requirements for partition walls in self-supporting frame systems may change the tables associated with these systems in the simplified option to adapt them.

Table 2. Modification of simplified option tables for self-supporting frame elements

	Current requirement	Possible modification
Internal partitions	33 dBA	39 dBA

3.3 Need to adapt support documents to DB HR changes.

This regulatory change in DB HR must also be reflected in the various support documents and programmes, so that the solutions proposed in them are in line with the current situation of the systems and also with the new insulation values.

3.3.1 DB HR Application Guide.

This guide, which contains interpretation criteria, comments and application examples to assist technicians, develops the DB HR principles and regulatory texts so that they must be adapted to global requirements and to the new Simplified Option tables.

3.3.2 Catalog of Construction Elements (CEC)

The CEC provides users with a database of information on the hygrothermal and acoustic performance of generic building components. This catalogue was created in conjunction with the introduction of DB HR to assist designers in incorporating systems into acoustic studies for which acoustic tests were not available.

Since the publication of the CEC, there has been an update in the testing of different construction systems, with the development of the above-mentioned UNE 102045 standard, which avoids the dispersion of acoustic test results in plasterboard systems and reduces uncertainty between laboratories.

Therefore, the CEC should also be modified and adapted to the new values of the tests carried out with the new protocol, in order to provide more reliable results to acoustic technicians.

4. ACOUSTIC CALCULATION SOFTWARE. SAINT-GOBAIN ACUSTIC

There are several softwares on the market that perform the calculation of the acoustic insulation in buildings using the General Option of DB HR, taking into account all the spaces, construction solutions, types of joints... These programs offer a complete acoustic study of the building, which allows an in-depth analysis, but requires modelling the building in all its spaces and construction solutions, which requires in-depth knowledge of it and also a certain technical knowledge, in addition to being time consuming. Therefore, this calculation using the General Option is more common when dealing with buildings of a certain size or relevance.

Most residential buildings, such as those covered by the Saint-Gobain Barometer, are calculated using the Simplified Option, which offers a simpler calculation model based on tables depending on the construction configuration used and allows the building to be modelled more quickly without requiring extensive acoustic knowledge.

In 2022, the Saint-Gobain Acustic software will be launched as an add-on to the Ce3X building energy certification programme, with the idea of making it easier for technicians to choose different acoustic solutions in the building, checking compliance with the DB HR using the Simplified Option and also performing a pre-classification of the building using the UNE 74201 system, so that in addition to compliance with the regulations, the technician can have an idea of what class of acoustic comfort will be achieved in the building.

4.1 Introduction of Acoustic data of the building in Saint-Gobain Acustic.

The Saint-Gobain Acustic add-on is integrated into the Ce3X software and allows the user to carry out both the energy certification of the building and the verification of compliance with CTE DB HE and DB HR without having to model the building in different software.

Within the add-on, different tabs are opened where the technician must fill in the conditions and construction solutions of the building:

- Acoustic description of the building
- Vertical indoor systems
- Horizontal indoor systems
- Envelope (facades, roofs and external floors)
- Reverberation and facilities

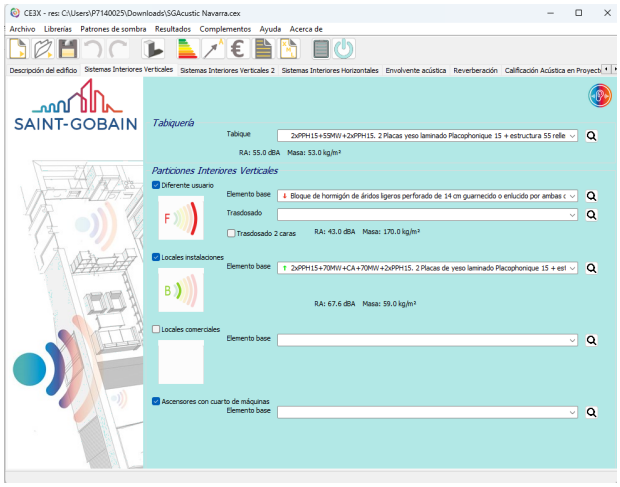


Figure 6. System introduction screen.

The software has a database of acoustically characterized construction solutions, including the CEC and Saint-Gobain acoustic solutions. In addition, the user can introduce their systems with tests or perform the calculation of their own systems.

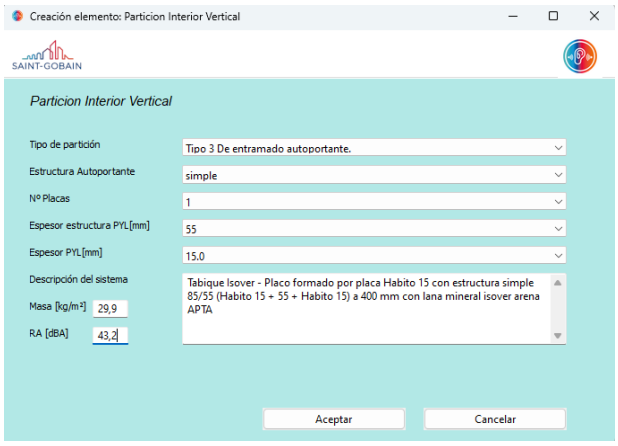


Figure 7. Introduction of new systems with values known to the technician screen.

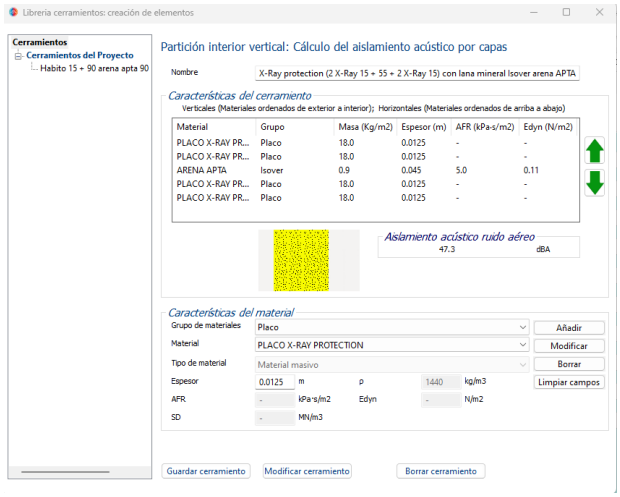


Figure 8. Acoustic calculation construction system screen.

4.2 Checks and reports.

Saint-Gobain Acustic carries out the verification of the CTE DB HR using the simplified option, using the tables and conditions defined in the basic document. In the case of different construction systems for the same use, the least favourable (with lower acoustic performance) must always be introduced in the software to ensure compliance with DB HR.

With regard to the acoustic classification of buildings, Saint-Gobain Acustic carries out an estimated pre-classification based on laboratory tests of the construction elements installed in the building, in accordance with option B of the standard for classification using "in situ" measurements for subsequent classification.

The reports generated by the tool are as follows:

- Acoustic report. With the data of the property, the construction solutions used in the building, and different checklists for the solutions with important points to be checked in the construction site from an acoustic point of view, both construction systems and the facilities.
- Justification Simplified Option DB HR with the format of the Basic Document.
- Acoustic pre-classification according to UNE 74201. Partial and global.
- Building Acoustic label. Similar in format to the energy certification, this label allows, at a glance, to know the acoustic classification of the building, partial and total.

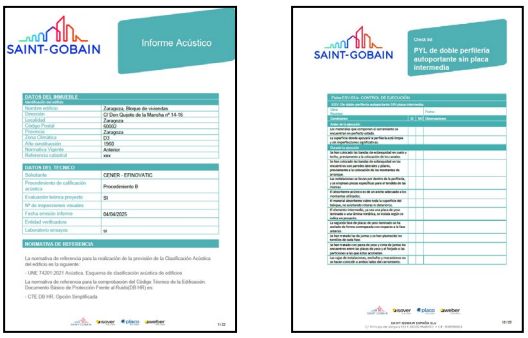


Figure 9. Acoustic report.

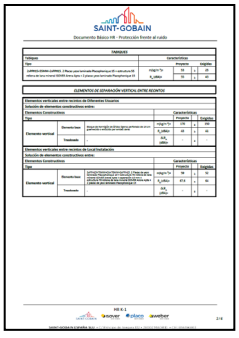


Figure 10. Justification DB HR.

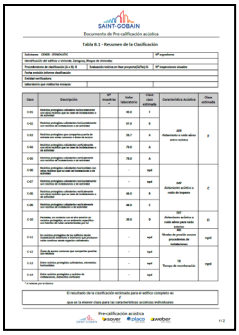


Figure 11. Acoustic pre-classification.



Figure 12. Acoustic label.

5. CONCLUSIONS.

There is a demand from users to achieve adequate acoustic comfort in their buildings, to increase the current requirements for acoustic insulation for both airborne and impact noise and for installations in current dwellings.

The future modification of the CTE DB HR goes in this direction by increasing the requirements to achieve a C or B classification in the Acoustic Classification of Buildings. These new values, although still far from an A classification, will allow greater comfort.

These changes must also be reflected in all the supporting documents of the CTE (Application Guide and Catalogue of Construction Elements), so that technicians have tools to design buildings from an acoustic point of view, both in the design phase and in the execution phase.

In addition, manufacturers of building materials must develop their systems to offer solutions adapted to the new acoustic requirements.

The use of simple calculation tools, such as Saint-Gobain Acustic, allows the democratization of acoustics, making it more accessible to technicians involved in projects and construction.

6. REFERENCES

[1] Código Técnico de la Edificación. Documento Básico de Protección frente al ruido

[2] Catálogo de Elementos Constructivos CEC

[3] Guía de Aplicación del DB HR

[4] UNE 74201 “Acústica. Esquema de clasificación acústica de edificios”

[5] UNE 102045 "Procedimiento para el seguimiento y caracterización del montaje de sistemas de placa de yeso laminado para ensayos de aislamiento acústico a ruido aéreo en laboratorio"

[6] Saint-Gobain Acustic. Complemento para el cumplimiento del DB HR y la pre-clasificación acústica de edificios. https://www.saint-gobain.es/sg-acustic

DOI: 10.61782/fa.2025.0839

FORUM ACUSTICUM EURONOISE 2025

SUGGESTIONS FOR THE POTENTIAL REVISION OF THE BASIC DOCUMENT ON PROTECTION AGAINST NOISE OF SPANISH BUILDING CODE

Romero-Fernández, Amelia[1*] **Casla-Herguedas, Belén**[1] **Carrascal, Teresa**[1]
[1] Instituto de la Construcción Eduardo Torroja (CSIC), Madrid, Spain.

ABSTRACT

In Spain, the Basic Document DB HR Protection Against Noise, part of the Building Code (CTE), regulates the acoustic conditions in buildings. This regulation, in force since 2009, has accumulated 16 years of implementation and experience, during which maintenance tasks and continuous studies have been conducted to explore potential improvements.

As a result, steps are being taken towards a possible new version of the document, which may address the deficiencies identified over the years and expand its content to include aspects previously not considered.

This paper presents some of the proposals currently under study. For instance, updates to the requirements are being considered, including a slight increase in the performance levels for airborne and impact sound insulation, as well as a review of the sound insulation descriptors currently in use. Additionally, new content is being evaluated, such as criteria for applying the DB HR to existing buildings, construction solutions for wooden buildings, noise from building services, and mandatory field acoustic measurements to verify compliance with the requirements.

Keywords: *DB HR, building acoustics regulations, sound insulation requirements, field measurements, noise from building services*.

1. INTRODUCTION

The Basic Document DB HR on Protection Against Noise, part of the Spanish Building Code (CTE) [1,2], establishes the acoustic requirements for buildings, as well as the rules and procedures to ensure compliance. Published in 2009, it represented a significant change from the previous regulation (NBE-CA-88) [3], as it introduced higher sound insulation requirements and adopted a performance-based approach, using in situ acoustic descriptors instead of laboratory test values. This allowed a final performance of the building to be verified.

Acoustic comfort is a key factor in building quality, with a direct impact on the well-being, health, and productivity of occupants. Noise pollution is recognized as a major environmental issue, with proven effects on stress, sleep quality, and cognitive performance [4]. In residential buildings, inadequate sound insulation can affect privacy and lead to conflicts between neighbours, while in work and educational environments, poor acoustic conditions can impair concentration and learning. In addition to airborne and impact noise insulation, controlling noise from building installations, such as elevators, HVAC systems, and plumbing, is essential to ensuring occupant comfort.

Since its implementation, DB HR has accumulated 16 years of application and experience, during which continuous studies and in situ tests have been conducted to assess its effectiveness. These efforts, carried out in collaboration with the building sector and within the regulatory maintenance activities for the Ministry of Housing, have helped verify

[*] ***Corresponding author***: aromero@ietcc.csic.es.
Copyright: *©2025 Romero-Fernández, Amelia et al. This is an open-access article distributed under the terms of the Creative Commons Attribution 3.0 Unported License, which permits unrestricted use, distribution, and reproduction in any medium, provided the original author and source are credited.*

compliance with acoustic requirements, identify challenges in the application of the regulations, and gain experience in using testing standards such as ISO 16283 [5].

Over the years, the evolution of the construction sector and data analysis have revealed certain limitations and areas for improvement within DB HR. Advances in construction techniques, the introduction of new materials, and changing user expectations make it necessary to adapt the regulatory framework to ensure its effectiveness. Additionally, in situ testing has identified implementation difficulties, variations in execution quality, and specific cases where current requirements may be insufficient.

In this context, Spain is currently reviewing its building acoustics standard, exploring possible modifications to optimize their application and enhance acoustic quality in buildings. This paper provides an overview of the ongoing changes under consideration and the new approaches that could be incorporated into the future revision of the regulations.

2. CURRENT STATE OF DB HR: ANALYSIS OF IDENTIFIED AREAS FOR IMPROVEMENT

The current DB HR is structured into different sections that address each of the regulated aspects: sound insulation (airborne, impact, and exterior noise in facades), reverberation time and sound absorption, and noise and vibration from building services. Among these, sound insulation is the most extensively developed, whereas protection against noise from building services is addressed more generally and with less detail.

Scope of application

Currently, DB HR applies exclusively to new buildings and major restorations, without considering other types of interventions in existing buildings. To facilitate the progressive adaptation of the building stock to current quality standards, it would be advisable to define specific criteria based on the type of intervention, distinguishing between major restorations, partial refurbishments, extensions, and changes of use, among others. Additionally, introducing flexibility conditions in the application of these criteria could be beneficial, considering the context of the intervention and the characteristics of the building.

Sound insulation requirements and descriptors

A critical aspect of DB HR is the selection of sound insulation indices and the corresponding regulatory requirements. Across Europe, building codes show significant disparities in the descriptors used to assess airborne and impact sound insulation between dwellings, as well as in the required performance levels [6, 7].

Acoustic descriptors in building regulations are defined in ISO standards [5, 8]. In Spain, the descriptor used to assess in-situ airborne sound insulation is the Standardized level difference, weighted A ($D_{nT,A}$), over a frequency range of 100 Hz to 5000 Hz, which approximately corresponds to $D_{nT,w} + C_{100\text{-}5000}$, where C represents the Spectrum adaptation term for pink noise.

Given the European context, it may be advisable to align these indices with those more commonly used in other countries, such as $D_{nT,w}$ and R'_w (with or without the spectrum adaptation term C) for indoor sound insulation, and $D_{2m,nT,w} + C_{tr}$ for facades, within the 100 Hz to 3150 Hz frequency range.

Regarding fundamental acoustic requirements between adjacent dwellings, the values established in DB HR for airborne sound insulation ($D_{nT,A} \approx D_{nT,w} + C_{100\text{-}5000} \geq 50$ dBA) and impact sound insulation ($L'_{nT,w} \leq 65$ dB) are at the lower end compared to most European countries. Other nations generally impose stricter requirements, often exceeding 53-55 dB for airborne sound insulation and setting impact sound limits below 60 dB. The Spanish regulatory values thus reflect a lower level of acoustic protection.

These requirements have remained unchanged since the publication of DB HR in 2009. However, practical experience suggests that most buildings constructed under this regulation comply with the acoustic requirements [9]. In the case of impact sound insulation, measured values often significantly exceed the minimum requirements. This demonstrates that it is possible to achieve higher acoustic quality levels, suggesting that it may be an appropriate time to consider increasing the regulatory requirements for sound insulation.

Design and dimensioning using the simplified method

DB HR provides two methods for designing acoustic solutions: the simplified and the detailed method, both based on the prediction models outlined in ISO 12354 [10]. While the detailed method requires precise calculations of sound insulation, the simplified method offers predefined construction solutions for building elements, ensuring compliance through their combination.

After several years of application, the simplified method could benefit from review and optimization to enhance its accessibility and efficiency. Although Tables 3.2 and 3.3 in DB HR [1] appear to provide a wide range of solutions, in practice, when translating these laboratory-measured insulation values and surface mass densities into commercially available construction systems, the number of viable solutions is relatively limited.

Moreover, the use of the simplified method is complicated by the requirement to comply with numerous additional conditions to control flanking transmissions. While these constraints ensure the validity of the proposed solutions, they also render the application of the method cumbersome and unintuitive.
Finally, the simplified method does not include solutions for lightweight timber structures, such as CLT (cross-laminated timber), light timber frames, or hybrid timber-concrete structures. Timber construction has experienced significant growth in recent years, including multi-story buildings, yet the lack of predefined solutions in DB HR forces reliance on the detailed method or specific testing for compliance. It would be beneficial for DB HR to incorporate acoustic compliance options for such constructions within the simplified method framework.

Noise from Building Services

As previously mentioned, DB HR addresses building service noise in a very general manner, without establishing specific requirements. Instead, it provides guidelines that can be considered best practices for noise and vibration control. However, acoustic requirements for building services are not explicitly defined within DB HR but are instead referenced in Royal Decree 1367/2007 [11], a regulatory development of Law 37/2003 on Noise [12], which remains pending revision and update [13]. This decree establishes noise limit values to transmit to adjacent rooms caused by building services, as well as the corresponding testing and assessment procedures.
However, these procedures are identical to those applied for commercial and industrial noise, leading to interpretation issues regarding whether building services are indeed covered under this regulation. Moreover, applying the same measurement and assessment methodology to building services may be inappropriate, as it fails to consider key aspects such as: the specific characteristics of each type of installation, operating modes and work cycles, and the nature of the noise generated.
It is therefore necessary for DB HR to provide a more detailed and tailored regulatory framework for building service noise, ensuring clearer guidelines adapted to their specific characteristics, in the context of the building.

Finished Building Control: In-Situ Testing

DB HR does not mandate acoustic testing upon completion of construction. However, if tests are conducted, it specifies the technical standards under which they should be performed [5, 14], along with the acceptable tolerances for verifying compliance with acoustic requirements. The following tolerances are permitted for in-situ measurements: 3dBA for airborne sound insulation, 3dB for impact sound insulation, and 0.1s for reverberation time.
Although acoustic control upon completion is not mandatory at the national level, several autonomous communities and municipalities require in-situ testing as a prerequisite to obtain the first occupation license. These controls include verifying sound insulation in walls, floors, and facades, as well as measuring sound pressure levels generated by building services.
Regions such as Andalucía, Castilla y León, and País Vasco, along with cities such as Barcelona, Murcia, Valencia, and Valladolid, have developed specific regulations governing these tests. In some cases, beyond requiring the tests, they also establish sampling procedures and specific evaluation criteria. Details on how these regulations make this control acoustic testing can be found in [15].
The heterogeneity of these regulations highlights the need for greater standardization in the obligation and methodology of finished building acoustic testing, ensuring a uniform and reliable verification of compliance with acoustic requirements across the country.

3. PROPOSALS CURRENTLY UNDER STUDY FOR THE REVISION OF DB HR

In light of the issues discussed above, this section presents some of the proposals currently under study to address areas identified for improvement. Work is underway on a revised version aimed at refining certain aspects and expanding on topics that have not yet been covered in these regulations.

3.1 Document restructuring

The DB HR document is being restructured into new sections, grouped according to the acoustical characteristics it regulates: Section HR1 for airborne and impact sound insulation, Section HR2 for sound absorption and reverberation time, and Section HR3 for service equipment noise.
This restructuring aims to provide a more systematic and specific approach, ensuring that each section includes its own requirements, scope of application, and specific criteria. Additionally, the original content will be reviewed and adapted accordingly.

3.2 Criteria for application to existing buildings

This section summarizes some of the criteria under study for applying DB HR to interventions in existing buildings, depending on the degree of intervention:

- Full intervention (major restorations): The entire building must comply with the acoustic requirements of DB HR.
- Extension: Any newly added part of an existing building must meet DB HR requirements, and the new separating walls and floors with the existing spaces must ensure compliance.
- Change of use: When the change of use affects the entire building, it must be fully adapted to the requirements. But, when the change of use is partial, affecting only a part of the building, only that part must meet the corresponding requirements. For instance, in a conversion to residential use (a dwelling), the newly created living spaces must comply with DB HR regulations.
- Partial renovation or localized intervention in building elements and installations: The applicable criteria must be defined in greater detail. Depending on whether the intervention significantly affects multiple construction elements, involves simultaneous work in several dwellings, or is more localized, flexibility criteria may be applied to approach DB HR requirements as closely as possible, even if full compliance is not achievable.

In all cases, the non-degradation principle shall prevail, ensuring that the intervention does not reduce the existing acoustic performance before the works.

3.3 Update of requirements and standardization of sound insulation descriptors

In alignment with European regulations, it is proposed to replace $D_{nT,A}$ with $D_{nT,w} + C$ for indoor airborne sound insulation and $D_{2m,nT,Atr}$ with $D_{2m,nT,w} + C_{tr}$ for façades, both within the frequency range of 100 Hz to 3150 Hz.

Additionally, an update to the regulatory requirements is being considered, including a 2 dB increase in airborne sound insulation and a 5 dB reduction in impact noise levels. Table 1 presents the sound insulation requirements currently under study for protected spaces such as living rooms and bedrooms in residential buildings.

Table 1. Sound insulation requirements for protected spaces in dwellings.

Sound insulation	Type of spaces	Current reqs.	New reqs. proposal
Airborne	Between protected spaces and other spaces outside the living unit [1]	$D_{nT,A}$ ≥ 50 dBA	$D_{nT,w} + C$ ≥ 52 dB
	Between protected spaces and noisy areas, such as equipment rooms or activity rooms	$D_{nT,A}$ ≥ 55 dBA	$D_{nT,w} + C$ ≥ 57 dB
Impact	Between protected spaces and other spaces outside the living unit [1]	L'_{nTw} ≤ 65 dB	L'_{nTw} ≤ 60 dB
	Between protected spaces and noisy areas, such as equipment rooms or activity rooms	L'_{nTw} ≤ 60 dB	L'_{nTw} ≤ 55 dB
Façade [2] (Same values)	Bedrooms	$D_{2m,nT,Atr}$ ≥ 30-47 dBA	$D_{2m,nT,w} + C_{tr}$ ≥ 30-47 dB
	Living rooms	$D_{2m,nT,Atr}$ ≥ 30-42dBA	$D_{2m,nT,w} + C_{tr}$ ≥ 30 – 42 dB

[1] A living unit refers to a section of a building designated for a specific function, whose occupants share a functional connection (e.g., dwellings, hospital rooms, hotel rooms, classrooms, etc.). In this case, a living unit is considered a dwelling.

[2] The sound insulation requirements for façades depend on the day noise level (L_{day}) of the area where the building is located.

3.4 Review of the simplified option for sound insulation

The simplified option in DB HR presents several areas for improvement. While its main advantage is ease of application, it also has limitations that need to be addressed in the upcoming revision of DB HR. First, the construction solutions for separating walls and floors (Tables 3.2 and 3.3 in DB HR [1]) must be recalculated to meet the new sound insulation requirements under consideration. Additionally, this simplified option should be reviewed and optimized to make it more accessible and practical, simplifying the adaptation of laboratory sound insulation values to construction elements available on the market. It is also necessary to reduce the complexity of additional conditions for controlling flanking transmissions, aiming for greater flexibility without compromising the technical validity of the proposed solutions. This would facilitate the practical application of viable acoustic solutions in real projects.

Furthermore, the simplified option could incorporate solutions for lightweight timber buildings, such as those built

with CLT, timber frame, or hybrid timber-concrete structures. These should be basic or fundamental solutions, covering the most common cases while ensuring compliance with acoustic requirements. The goal is to integrate these solutions into the regulation without unnecessarily complicating the design and application process, avoiding the need to resort to the general option or conduct specific acoustic tests.

Finally, it is important to clarify that the simplified option is merely a guideline providing examples of possible solutions. Other alternatives exist beyond those explicitly included in DB HR. In its current wording, the simplified option may be mistakenly interpreted as a mandatory requirement, which needs to be addressed.

3.5 Service equipment noise

Currently, DB HR regulates service equipment noise in buildings by referencing Law 37/2003 on Noise [12] and Royal Decree 1367/2007 [11], which sets maximum permissible noise levels in adjacent spaces. However, since building service equipment is an integral part of the building itself, it is necessary to regulate this aspect more specifically within DB HR, adopting a more architectural approach rather than treating it similarly to commercial or industrial activities, as is currently the case.

The objective is to define specific noise requirements for building service equipment by establishing appropriate noise indices, their corresponding limit values, and a measurement method adapted to the characteristics and operating cycles of each type of installation. The testing procedure could be based on ISO 16032 [16], which includes the measurement of both the equivalent continuous sound pressure level (L_{eq}) and the maximum sound pressure level (L_{max}) for different types of installations.

At the same time, maintaining a degree of compatibility with the methodology of RD 1367/2007 is desirable, while incorporating some improvements, such as:

- Averaging measurement points instead of using only the most unfavorable measurement.
- Defining a sampling methodology based on the operating cycles and working modes of each system, instead of the current minimum measurement duration of 5 seconds.
- Applying the corrections for impulsive, tonal, and low-frequency components only when they exceed the hearing threshold [17].
- Normalizing measurement results relative to the reverberation time of the spaces.

A key step is the correct classification of service equipment according to their characteristics and operating conditions, as these factors determine the generated sound pressure levels, the appropriate measurement procedure, and the noise index to be used ($L_{A,max}$, $L_{A,eq,Ti}$, $L_{Aeq,cycle}$, etc.). While some systems operate continuously (e.g., HVAC), others operate intermittently or by events (e.g., plumbing, elevators), making it essential to define specific criteria for their evaluation. In particular, an index based on maximum noise levels is proposed for systems with intermittent operation, as well as those with start-up phases or changing working modes that generate noise peaks.

Finally, while most European countries establish a single noise limit for service equipment (whether in terms of $L_{Aeq,T}$, $L_{A,max}$, or both), Spain differentiates limit values depending on the period (day, evening, night). Aligning this approach with international practice should be considered.

3.6 On-site testing for final compliance verification

It is proposed to establish mandatory in-situ testing at the national level to verify compliance with sound insulation, reverberation time, and service equipment noise level requirements. Currently, some regional governments already require these tests before granting the first occupancy license. Implementing this requirement nationwide would help standardize quality control in building construction.

To ensure proper implementation, a minimum sampling procedure must be defined to guarantee compliance with the DB HR of the CTE without interfering with regional competencies. This minimum approach will allow regions that have already developed their own testing systems to maintain them without regulatory conflicts. Additionally, clear criteria for compliance declarations must be established, studying aspects such as measurement uncertainty and the application of tolerances to limit values.

In this regard, it is proposed to reduce the tolerance in sound insulation compliance measurements from 3dB to 2dB. This proposal is based on an analysis of European regulations [7], where 21 out of 28 countries do not establish any tolerance or uncertainty, requiring strict compliance with the regulatory values. Among the countries that do consider tolerances, Denmark sets a 1 dB tolerance, Austria, Belgium, and Sweden apply 2 dB, while Spain, France, and Portugal allow a 3 dB tolerance.

4. CONCLUSIONS

The analysis of the Basic Document DB HR Noise Protection, part of the Spanish Building Code (CTE), highlights the progress made in the acoustic regulation of buildings since its publication in 2009. However, it also reveals areas that require improvement and updates to meet

current industry demands and align with international practices. In this regard, a series of enhancements have been identified and proposed, starting with the reorganization of the document to facilitate its application.

Regarding the current sound insulation requirements, they are among the lowest in Europe, making it advisable to revise and raise the standards to improve acoustic quality in buildings. Additionally, it is necessary to optimize the simplified option to enhance its applicability and incorporate timber construction solutions, and develop more specific regulations for building service noise, ensuring they are appropriately tailored to the characteristics of each type of project.

Furthermore, it is essential to establish specific criteria for applying DB HR to existing buildings, considering different levels of intervention. It must be ensured that interventions do not degrade the initial acoustic conditions and, when full compliance with the requirements is not feasible, promote improvements that bring the building as close as possible to the established standards.

Finally, the implementation of mandatory field acoustic testing at the national level is proposed to verify compliance with the requirements. This would ensure more uniform and rigorous quality control across the country.

Overall, these proposed revisions to the Basic Document DB HR represent a key opportunity to enhance the acoustic quality of buildings in Spain and ensure greater comfort for users.

5. ACKNOWLEDGEMENTS

This work has been carried out within the framework of the development of building regulations at the national level, specifically the Technical Building Code, with the support of the Ministry of Transport, Mobility, and Urban Agenda (MITMA), which is gratefully acknowledged.

6. REFERENCES

[1] Ministerio de Fomento, *Documento Básico DB HR Protección frente al Ruido. Código Técnico de la Edificación.* 2019.

[2] Ministerio de Fomento, *Real Decreto 314/2006, de 17 de marzo, por el que se aprueba el Código Técnico de la Edificación.* Actualizado en el Real Decreto 732/2019, de 20 de diciembre, de modificación del Código Técnico de la Edificación.

[3] España, Ministerio de Obras Públicas y Urbanismo, *Norma Básica de la Edificación. NBE-CA 88 sobre Condiciones Acústicas en los edificios*. Orden de 29 de septiembre de 1988 por la que se aclaran y corrigen diversos aspectos de los anexos a la *Norma Básica de la Edificación NBE-CA-82 sobre Condiciones Acústicas en los Edificios*. vol. BOE-A-1988-23328. 1988, pp. 29222-29223.

[4] EEA. (2020). *Environmental noise in Europe-2020*. In European Environment Agency (Issue 22/2019). [Online]. Available: https://www.eea.europa.eu/publications/environmental-noise-in-europe.

[5] ISO 16283. *Acoustics. Field measurement of sound insulation in buildings and of building elements - Part 1: Airborne sound insulation*, 2014. - *Part 2: Impact sound insulation*, 2020. - *Part 3: Façade sound insulation*, 2016. International Organization for Standardization.

[6] B. Rasmussen, "Sound insulation between dwellings – Comparison of national requirements in Europe and interaction with acoustic classification schemes", in *Proc. of the 23rd International Congress on Acoustics*, (Aachen, Germany), 2019. [Online]. Available: https://d-nb.info/1215170386/34

[7] B. Rasmussen, M. Machimbarrena, Eds., "Building Acoustics Throughout Europe. Volume 1: Towards a Common Framework in Building Acoustics Throughout Europe". *COST Action TU0901, European Cooperation in Science and Technology*, 2014. [Online]. Available: https://www.cost.eu/publication/building-acoustics-throughout-europe-volume-1-towards-a-common-framework-in-building-acoustics-throughout-europe/

[8] EN ISO 717. *Acoustics – Rating of sound insulation in buildings and of buildings elements. - Part 1: Airborne sound insulation. - Part 2: Impact sound insulation.* International Organization for Standardization, 2020.

[9] A. Romero, T. Carrascal, B. Casla, "Airborne and impact sound insulation performance in Spanish multi-storey housing: 10 years of the protection against noise regulations in the Building Code (2009-2019)", in *Proc. Internoise 2019- 49th International Congress and Exhibition on Noise Control Engineering*, (Madrid, Spain), 2019.

[10] ISO 12354. *Building Acoustics - Estimation of acoustic performance of buildings from the performance of elements - Part 1: Airborne sound insulation between rooms. - Part 2: Impact sound insulation between*

rooms. - Part 3: Airborne sound insulation against outdoor sound. International Organization for Standardization, 2017.

[11] Jefatura del Estado, *Ley 37/2003, de 17 de noviembre, del Ruido*. (BOE 18/11/2003), vol. 276. 2003, pp. 40494 a 40505. https://www.boe.es/eli/es/l/2003/11/17/37

[12] Ministerio de la Presidencia, *RD 1367/2007de 19 de octubre, por el que se desarrolla la Ley 37/2003, de 17 de noviembre, del Ruido, en lo referente a zonificación acústica, objetivos de calidad y emisiones acústicas*. (BOE 23/10/2007), vol. 254. 2007, pp. 42952–42973. https://www.boe.es/eli/es/rd/2007/10/19/1367

[13] A. Romero, B. Casla, T. Carrascal, "Propuestas para la revisión del RD 1367/2007 en el ámbito de la acústica de la edificación. Coordinación con el DB HR del CTE", [Conferencia invitada], in *Proc. Tecniacústica 2023 - 54º Congreso Español de Acústica - XIII Congreso Ibérico de Acústica* (Cuenca, Spain), 2023.

[14] ISO 3382-2:2008. *Acoustics - Measurement of room acoustic parameters. Part 2: Reverberation time in ordinary rooms*. International Organization for Standardization, 2008.

[15] T. Carrascal, B. Casla-Herguedas, A. Romero-Fernández, "Verification of Conformance with Spanish Regulations Acoustic Sampling", in *Proc. of the 10th Convention of the European Acoustics Association Forum Acusticum 2023*, (Turin, Italy), pp. 3709–3715. 2023. doi: 10.61782/fa.2023.1159

[16] ISO 16032:2024. *Acoustics - Measurement of sound pressure level from service equipment or activities in buildings - Engineering method*. International Organization for Standardization, 2024.

[17] ISO 226:2023. *Acoustics - Normal equal-loudness-level contours*. International Organization for Standardization, 2023.

DOI: 10.61782/fa.2025.0848

FORUM ACUSTICUM EURONOISE 2025

TECHNICAL SPECIFICATION FOR STANDARDIZED GRAPHICAL PRESENTATION OF ACOUSTIC REQUIREMENTS IN SWEDEN

Bo Gärdhagen[*1]
Niklas Jakobsson[2]
[1] Akustikverkstan Konsult AB, Göteborg, Sweden
[2] Akustikkonsulten i Sverige AB, Stockholm, Sweden

ABSTRACT

Ten Swedish acoustic consultant companies sent their experts to standardize the graphical presentation of acoustical requirements for buildings, now published as SIS/TS 25261.
The need for a standardized method became quite urgent when the latest Swedish sound classification scheme for healthcare, educational and business premises were published in 2023, which introduced a new approach to defining sound requirements. In the new SS 25268:2023 the requirements are based on the needs of noise control and speech intelligibility that come from the intended usage of the rooms, instead of the designation of the room. To furthermore express requirements based on the need for noise control, the values of sound reduction are presented in a matrix with level differences, $D_{nT,w}$, not reduction indexes, R'_w.
SIS/TS 25261 specifies a working order from acoustical needs analysis, via measurable quantities, to acoustical specifications for building elements. It presents colours, line types and symbols to use, and layout for tables. This unified approach will simplify for architects, property developers, contractors and consultants, and eliminates the need for each acoustic consultant to use their own individual method, leading to misunderstandings and ad hoc solutions.

[*] ***Corresponding author***: *bo.gardhagen@akustikverkstan.se.*
Copyright: *©2025 Bo Gärdhagen et al. This is an open-access article distributed under the terms of the Creative Commons Attribution 3.0 Unported License, which permits unrestricted use, distribution, and reproduction in any medium, provided the original author and source are credited.*

Keywords: requirements, classification, graphic, needs, colours.

1. BACKGROUND

1.1 SS 25268:2023 – Acoustic Requirements Based on Functional Room Use

Contemporary Swedish office buildings rarely consist of a corridor flanked by a row of cellular offices, which formed the basis for the airborne sound insulation criteria in earlier editions of the Swedish acoustic classification standard for non-residential premises. Historically, the standard included separate requirements for room-to-room and room-to-corridor transmission.
Today, office layouts more commonly include various forms of open-plan areas combined with meeting rooms, small rooms for phone calls or focused work, and a limited number of individual offices for specific purposes. Some staff categories are accommodated in shared multi-occupancy rooms. Informal break areas are often located in open zones between enclosed rooms. The same is true for schools in Sweden, where corridors often have been replaced by big open spaces for where students both study and relax.
In the previous version of the standard, it was unclear how to classify a meeting room that adjoins an open-plan office. Some interpreted the requirements as applying to a wall facing a corridor, which resulted in under-specified insulation. Others treated it as a wall between two enclosed rooms, leading to overly stringent requirements, as open-plan offices inherently contribute to sound attenuation.
The adopted solution was to shift the requirement from sound reduction index (R'_w) to weighted standardized level

difference ($D_{nT,w}$), and to define room types based on their functional acoustic needs. This conceptual shift has also been applied to all other acoustic parameters covered by requirements, with an emphasis on the intended acoustic function of each space.

1.2 Variation in Acoustic Requirement Documentation

Acoustic descriptions and noise control specifications previously produced for Swedish construction projects have varied significantly, primarily due to the absence of a unified framework for presenting such requirements. Each consultant has adopted their own approach—even within the same firm—resulting in documentation that is often difficult to interpret consistently.
When previous requirements were expressed as R'_w in 4 dB intervals, many consultants illustrated airborne sound insulation requirements using coloured lines on wall layouts. As most manufacturers specified the expected sound insulation performance of their products under ideal conditions (e.g., "Sound Class R'_w = 44 dB"), this practice appeared convenient—an orange line might then imply both that the partition must meet R'_w = 44 dB and that the corresponding wall product should be selected accordingly.
However, this approach becomes problematic in cases such as partitions incorporating doors, or when cross-laminated timber (CLT) floor slabs are used, which may introduce significant flanking transmission at higher performance levels. Furthermore, when the chosen colours are too similar in hue, it increases the risk of misinterpreting the actual requirement.

1.3 The Solution

Members of the SIS Technical Committee for Building Acoustics, who developed the new standard for non-residential premises, invited numerous acoustics firms across Sweden to participate in a collaborative effort. The objective was to establish a coherent and transparent approach to presenting the new acoustic requirements.
Consensus was reached on a process that begins with end-user needs as defined in a functional room programme, continues through the specification of measurable performance targets, and concludes with the detailed representation of requirements for individual building elements.
A smaller group developed proposals for graphical symbols and colour schemes. These proposals were then reviewed by the broader group, and the result was published as a Technical Specification—a format that allows for faster implementation than a full standard, while maintaining consistency and clarity.

1.4 Room Function vs Spatial Function

A *room* is defined as a volume enclosed on all sides by floor, walls, and ceiling. A *space*, by contrast, refers to either an entire room or a part of a room that serves a specific function.
Since the presence or absence of separating constructions between different areas—i.e., whether they are distinct rooms—has significant implications for acoustic performance, SS 25268:2023 [1] specifies that the stated requirements apply to *spaces*. For this reason, the term *spatial function* is used in place of *room function* throughout the standard.

2. METHOD

2.1 General

The method follows the typical design process used in Swedish construction projects, which is structured in three stages: programme design, system design, and construction documentation.
In many projects, the design is put out to tender for what is known as a design-and-build contract (*totalentreprenad*) at some point during or between the system design and construction documentation phases. In a strictly defined design-and-build contract, the client is responsible for providing layout plans and performance requirements. However, in practice, the level of prescription can be quite extensive—sometimes approaching the level of a detailed construction document. Consequently, the tender documentation for design-and-build contracts often becomes the central legal reference for determining whether a building satisfies the performance requirements at the final inspection.

2.2 Acoustic Spatial Function

During the programme design phase, the organisation intended to occupy the premises specifies its needs for the different room functions the building is required to support. To achieve an appropriate acoustic environment, these acoustic needs must be clearly defined.
In the acoustic standard SS 25268:2023, airborne sound insulation requirements are presented in matrix form, with rows representing the expected noise levels within the space, and columns indicating the space's sensitivity to acoustic disturbances. The acoustic spatial function is expressed in everyday language, such as "normal speech noise level" or "need for speech privacy," combined with the space's sensitivity level—low, normal, elevated, or high.

5.4.2.2 Basic requirements

Table 2 – Minimum weighted standardised level difference, $D_{nT,w}$ [dB] for healthcare premises

Spatial Function	For the receiving space: Need for disturbance protection			
From the source space: Category of airborne noise source	Low	Normal	Elevated	High
2a need for confidentiality of speech	52 I, II	52 I	52 I	52 I
2b need for speech privacy	44 III	44	48	52

I The conditions for requirements to and from other activities are specified in section 5.3.3.2.

II A minimum $D_{nT,w}$ = 40 dB is permitted for separating constructions with a door or glazed partition towards a corridor, passageway, or other space intended for transit only. This deviation may only be accepted where the risk of overhearing or breach of confidentiality is low.

III A minimum $D_{nT,w}$ = 36 dB is permitted for separating constructions with a door or glazed partition towards a corridor, passageway, or other space intended for transit only.

Figure 1. Excerpt from table presenting acoustic spatial function for sound level difference in healthcare premises, as presented in SS 25268:2023, translated into English.

Examples of typical room types associated with each acoustic function are listed in a supporting table. For instance, a meeting room is typically described as having a normal sensitivity to disturbances and a need for speech privacy. A distinction is made between confidentiality—which refers to preventing the intelligibility of speech outside the room even at raised voice levels and under quiet background conditions—and speech privacy, which means that, under normal conditions, conversations inside the room should not be heard outside.

In SIS/TS 25261 [2], the acoustic spatial function may be represented either in tabular form or graphically using a designated symbol (see Graphical Representation below).

2.3 Verifiable Acoustic Requirements

It is essential that the acoustic requirements to be fulfilled at the final inspection of a building are both unambiguous and clearly defined, so that those performing measurements and other forms of verification can readily determine whether the measurement results meet the stipulated criteria.

During the development of SIS/TS 25261, it was concluded that verifiable airborne sound insulation is often more clearly represented not as the tabulated $D_{nT,w}$ value, but rather as the performance required of the separating element, expressed in terms of R'_w. Several reasons support this approach:

- **Standardised procedure:** According to EN ISO 16283-1, measurements should be conducted from the larger room to the smaller one. If the governing requirement for the partition is defined in the opposite direction, this deviates from the standard, and measurement conditions may become suboptimal—especially if the source and receiver positions are forced too close due to limited space.
- **Measurement direction:** R'_w is independent on the direction of measurement. In contrast, $D_{nT,w}$ tends to be higher when measured from a small room into a larger one. If the operator, for practical reasons, chooses the wrong direction, the result may be misleading.
- **Clarity in comparison:** With R'_w, it is clear which target value the measured result should be compared against. For example, from an open-plan office with normal speech activity into a small room for private phone calls, the required $D_{nT,w}$ is 36 dB. In the reverse direction—where speech privacy is needed—the requirement is $D_{nT,w}$ = 44 dB. Although the lower value (36 dB) implies a stricter requirement for the separating structure, it is easy to mistakenly compare the measurement with the higher threshold.

That said, in certain cases it may still be preferable to specify and measure $D_{nT,w}$ directly—particularly when the boundaries of the separating structure are unclear. For instance, when a corridor intersects with a larger room and a corner room has a robust wall facing the open space but a door leading to the corridor, it is the latter that weakens the overall insulation. Measuring $D_{nT,w}$ from the larger space into the corner room provides a clear and unambiguous assessment.

SIS/TS 25261 permits verifiable acoustic requirements to be stated either as R'_w or $D_{nT,w}$. However, when specifying $D_{nT,w}$, it must be in the direction that places the highest demand on the separating construction. In the section Graphical Representation below, corresponding symbols are presented. In addition to airborne sound insulation, there are also standardised symbols for impact sound level, reverberation time, noise from building services, and environmental noise (e.g., from traffic or external sources).

2.4 Requirements for Building Elements

The final step in the design process is to specify the building elements required to meet the defined acoustic performance criteria. If this has not been addressed earlier, it must be done during the preparation of construction documentation. However, in some cases, it may be desirable to establish these requirements earlier in the process—for budgeting purposes or to influence the execution of the design.

Until roughly a decade ago, it was common practice in Sweden to specify the expected in-situ sound insulation (R'_w) for glazed partitions, doors, and windows. This is now less frequent, as it often led to errors: procurement staff from contractors and sales representatives from suppliers frequently overlooked the prime symbol, resulting in products being delivered based on laboratory-tested R_w values instead. This mismatch commonly led to failed field measurements.

As mentioned in the Background section, it has also been standard practice in Sweden for suppliers of gypsum board

partitions to report their products' in-situ performance as R'_w. However, for the reasons discussed above, this practice is increasingly being reconsidered. The recommended approach is now a general transition towards specifying products and systems based on their laboratory-measured values.

SIS/TS 25261 provides clear graphical symbols indicating performance requirements of building products directly on construction drawings. These values must be based on laboratory measurements—or equivalent calculated data. It is the responsibility of the acoustic consultant to ensure that an appropriate safety margin is applied between laboratory data and the expected in-situ sound insulation performance.

3. GRAPHICAL REPRESENTATION

3.1 General

The development of a graphical system for representing acoustic requirements—covering spatial acoustic function, verifiable acoustic parameters, and requirements for building elements—began with an unconventional approach: a designer with expertise in graphic communication, but without prior experience in acoustics or construction drawings, was invited to create an initial concept.

This method was chosen to promote a fresh perspective, unencumbered by established habits or conventions. The initial design was subsequently reviewed and refined by experienced acousticians to ensure its practical applicability in real project environments.

3.2 Toolbox

To facilitate the implementation of standardised symbols and visual conventions, a custom toolbox has been developed for the PDF markup software Bluebeam Revu. This platform offers robust functionality for the purpose and is already widely used by Swedish acoustics consultants. In most cases, consultants add acoustic requirements directly onto architectural PDF drawings.

The graphical symbols have also been designed to be compatible with Revit, and future development plans include dedicated toolboxes for that platform as well.

3.3 Tabular Format

In some cases, it is more efficient to present the acoustic spatial function in tabular form—for example, when the layout has not yet been finalised, or when the number of room types is limited. SIS/TS 25261 provides design guidelines for such tables to enhance legibility and ensure consistency across different consultants.

Table 1. Summary of acoustical spatial functions for large meeting rooms

MEETING ROOMS ≥ 50 M²	SPATIAL FUNCTION	COMMENT
Requirement level	Basic requirements	
Sound level difference	20b Need for speech privacy	
Impact sound level	23b Moderate impact sound load	
Disturbance protection	Elevated need	
Room acoustics	26b Speech communication	Digital meetings[1]
Noise from installations, traffic, etc.	27a, 28a Special requirements for disturbance protection	

[1] Requires $T_{125} \leq 0{,}7$ s and wall absorbers covering ≥ 8 % of wall surface area

Figure 2. Example of table presenting acoustical spatial functions in tabular form, following SIS/TS 25261.

3.4 Colour Scale

SIS/TS 25261 prescribes a colour scale designed to maximise the visual distinction between categories by using primary digital colours from the RGB and CMY colour models:

Magenta – special conditions or requirements and is always accompanied by explanatory text
Blue – exceptionally high-performance requirements
Red – high requirements
Yellow – elevated requirements
Green – standard requirements
Cyan – low requirements
Grey – very low requirements

The intention is to improve readability for individuals with colour vision deficiencies and to support digital readability. With consistent application, this unified colour scale contributes to improved clarity and familiarity over time.

3.5 Symbols for Acoustic Spatial Function

When representing acoustic spatial function on drawings, a specific symbol is used: four or five circles arranged within a rectangle, supplemented by one or two triangles. The circles represent individual acoustic characteristics, while the triangles indicate the space's sensitivity to disturbances regarding sound insulation.

Typically, four circles are used, since requirements for noise from building services and from external sources (e.g., traffic) are often aligned. Similarly, a single triangle is generally sufficient, as sensitivity to airborne and impact sound tends to be coordinated.

Each circle contains a code referring to the corresponding row in SS 25268. For instance, "5b" denotes "Moderate impact sound load" in healthcare premises. The characteristics are listed in the same order as in SS 25268: airborne sound insulation, impact sound insulation, room acoustics, noise from installations, and environmental noise from traffic or other external sources.

3.6 Symbols for Verifiable Acoustic Requirements

A set of graphical symbols—comprising arrows, triangles, 45°-rotated squares, and pentagons—combined with colours and numerical values, is used to represent measurable acoustic requirements on drawings.

The symbols are functionally motivated: a double-headed arrow represents R'_w, which is a reciprocal value, while a single-headed arrow indicates $D_{nT,w}$, which applies in one direction only. There is also a combined symbol for environmental noise from installations, traffic, and other external sources, used when the A-weighted equivalent sound level requirement is the same for all. A perpendicular line is added to sound insulation symbols to indicate extended frequency range down to 50 Hz.

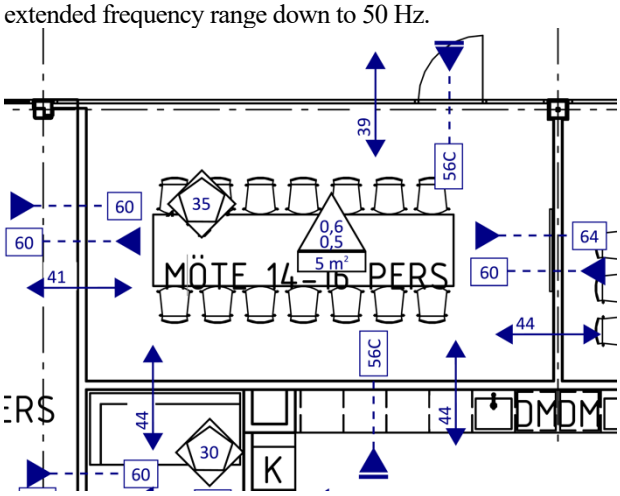


Figure 3. Example of verifiable acoustic requirements in meeting room, following SIS/TS 25261.

3.7 Symbols for Building Element Requirements

Requirements for building elements may be indicated using coloured lines on the corresponding partition, text within a rectangle, or a combination of both. For façade windows, requirements can be represented using coloured areas on the façade drawings or as special coloured lines on plan drawings.

The text inside the rectangle consists of one or two letters indicating the type of building element, followed by two digits representing the minimum laboratory-measured sound reduction index.

The letter codes are as follows:

- V for walls (vägg in Swedish)
- D for doors
- G for glass
- ÖD for transfer air devices (överluftsdon in Swedish).

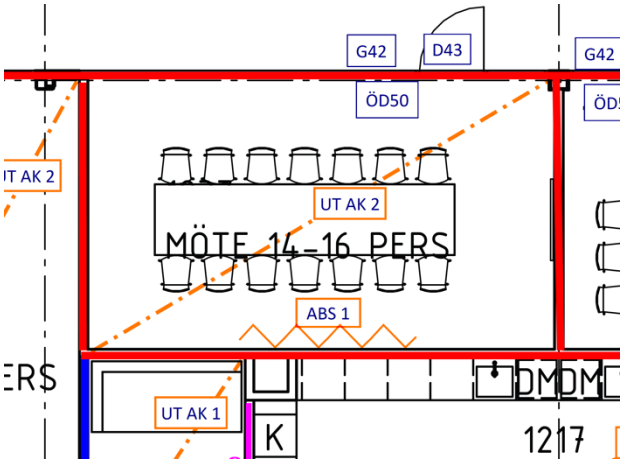


Figure 4. Example of acoustical requirements for building parts for meeting room, following SIS/TS 25261.

3.8 Application in Residential Buildings

Although the symbols for verifiable acoustic requirements also are applicable to residential buildings following SS 25267 [3], it is primarily the symbols representing acoustic requirements for building elements that are relevant for use in residential housing projects.

4. SUMMARY

The introduction of SS 25268:2023 and the associated technical specification SIS/TS 25261:2024 marks a fundamental shift in how acoustic requirements are defined and communicated in Swedish building projects. Instead of focusing on room labels or construction types, the requirements are now derived from functional acoustic needs—expressed in terms of spatial usage and verifiable performance metrics.

SIS/TS 25261 establishes a structured workflow from needs analysis to construction documentation and offers a comprehensive graphical system for representing acoustic requirements. This includes standardised symbols, colour codes, and table formats for acoustic spatial functions, verifiable sound parameters, and building elements. The approach improves clarity, facilitates communication across disciplines, and supports consistent documentation—especially important in large or complex projects.

While developed with non-residential buildings in mind, some of the graphical tools can also be applied in residential contexts following SS 25267. The proposed standard is expected to streamline acoustic coordination in Swedish

construction and serves as a model for harmonisation in future European guidelines.

5. REFERENCES

[1] Swedish Standard SS 25268:2023 Building acoustics – Sound requirements for spaces in buildings – Healthcare premises, rooms for education, preschools and leisure-time centres, rooms for office work, hotels, and restaurants

[2] Swedish Technical Specification SIS/TS 25261:2024 – Building Acoustics – Presentation of sound requirements

[3] Swedish Standard SS 25267:2024 Building acoustics – Sound classification of spaces in buildings – Dwellings

DOI: 10.61782/fa.2025.0013

FORUM ACUSTICUM EURONOISE 2025

A LOOK INTO THE LOW FREQUENCY DEFICIENCIES OF ISO 717-2

Gjermund V. Holøyen[1*]
[1] SINTEF Community, Børrestuveien 3, 0373 Oslo, Norway

ABSTRACT

As the world of building acoustics is moving towards a stronger emphasis on low frequency sounds, certain standards are lagging behind. In particular, the lack of low frequency spectra for the calculation of the weighted improvement of impact sound insulation, ΔL_{w}, in ISO 717-2 might soon prove to be a significant issue as countries are moving in the direction of including the low frequency spectrum adaption term $C_{\mathrm{I},50-2500}$ in their building legislation. However, it is no straightforward task to find a functional solution to this problem, and a simple extension of the spectra given in the standard today, may not alone be enough. In the work leading to this paper, potential solutions for the heavyweight reference floor have been investigated and assessed. The results are presented and discussed in this paper.

Keywords: *improvement of impact sound reduction, floating floor, low frequencies, spectrum adaption terms*

1. INTRODUCTION

In recent years, the focus on low frequency sound insulation has increased. In Norway, the standard NS 8175 was revised in 2019, where a significant change from the previous version was the inclusion of low frequency spectrum adaption terms in class C for dwellings [1]. Class C in NS 8175 is referred to in the Norwegian building code (TEK), and by ensuring compliance with class C in NS 8175, one is also ensuring compliance with TEK [2]. At the time of writing, the 2019-version of the standard is yet to be adopted into TEK, but signals from the authorities are suggesting that an adoption may be on the cards within 2026 or at the latest when TEK is fully revised.

When this eventually happens, low frequency spectrum adaption terms must be considered for both airborne and impact sound, which from a construction technology point of view is likely going to be relatively undramatic [3]. However, one critical issue is the single number quantity ΔL_{w}, which is defined in ISO 717-2 [4]. The calculation procedure for ΔL_{w} relies on reference spectra given in ISO 717-2, which are limited downwards to 100 Hz. That means ΔL_{w} cannot be calculated including frequencies below 100 Hz, and no corresponding low frequency spectrum adaption terms can be calculated either. This could in theory be solved by simply extending the existing spectra down to 50 Hz, but previous studies have shown that it's not quite so straightforward [7]. This paper looks at other options for calculating low frequency spectrum terms to go along with ΔL_{w} for the heavyweight reference floor.

2. METHODOLOGY

Two paths have been considered, both based on $C_{\mathrm{I},50-80}$ as an alternative to $C_{\mathrm{I},50-2500}$. For both, extensions of the current spectrum in ISO 717-2 are essential. For this paper, four possible extensions have been suggested. The extensions, denoted as α, β, γ and δ and presented in Fig. 1, are simple extensions of the current heavyweight reference floor spectrum in ISO 717-2. α represents a linear extension of the current spectrum (a reduction of 0.5 dB per third octave), and the other three extensions with reductions of 2, 3 and 4 dB per octave respectively. For both paths, measurement results from five measurements performed at SINTEF have been used, see Fig. 2. The five floors are all floating floor constructions with a concrete screed. An average of measured impact sound levels from the 140 mm bare concrete reference floor at SINTEF is also shown in Fig. 1.

*__Corresponding author__: gjermund.holoyen@sintef.no.
__Copyright__: ©2025 Gjermund V. Holøyen. *This is an open-access article distributed under the terms of the Creative Commons Attribution 3.0 Unported License, which permits unrestricted use, distribution, and reproduction in any medium, provided the original author and source are credited.*

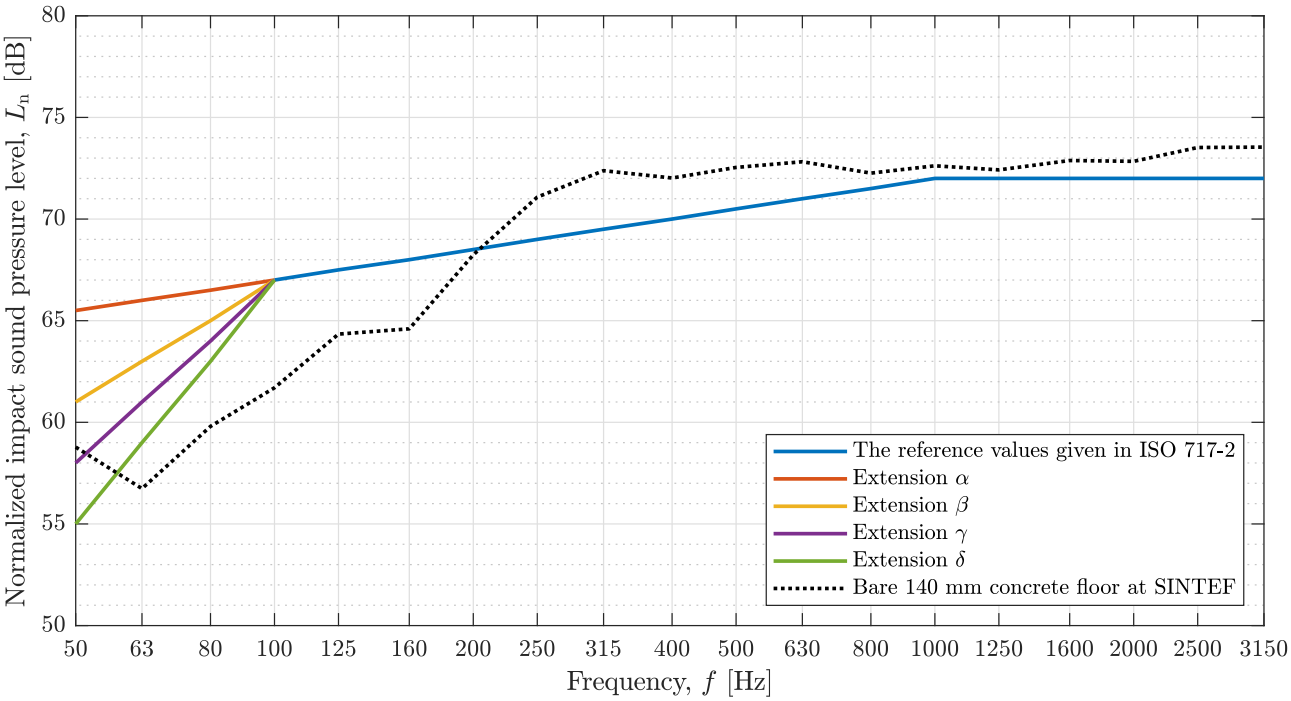


Figure 1. A graphical representation of the suggested extensions of the reference values in ISO 717-2, as well as an average of measured impact sound levels for SINTEF's bare 140 mm concrete floor

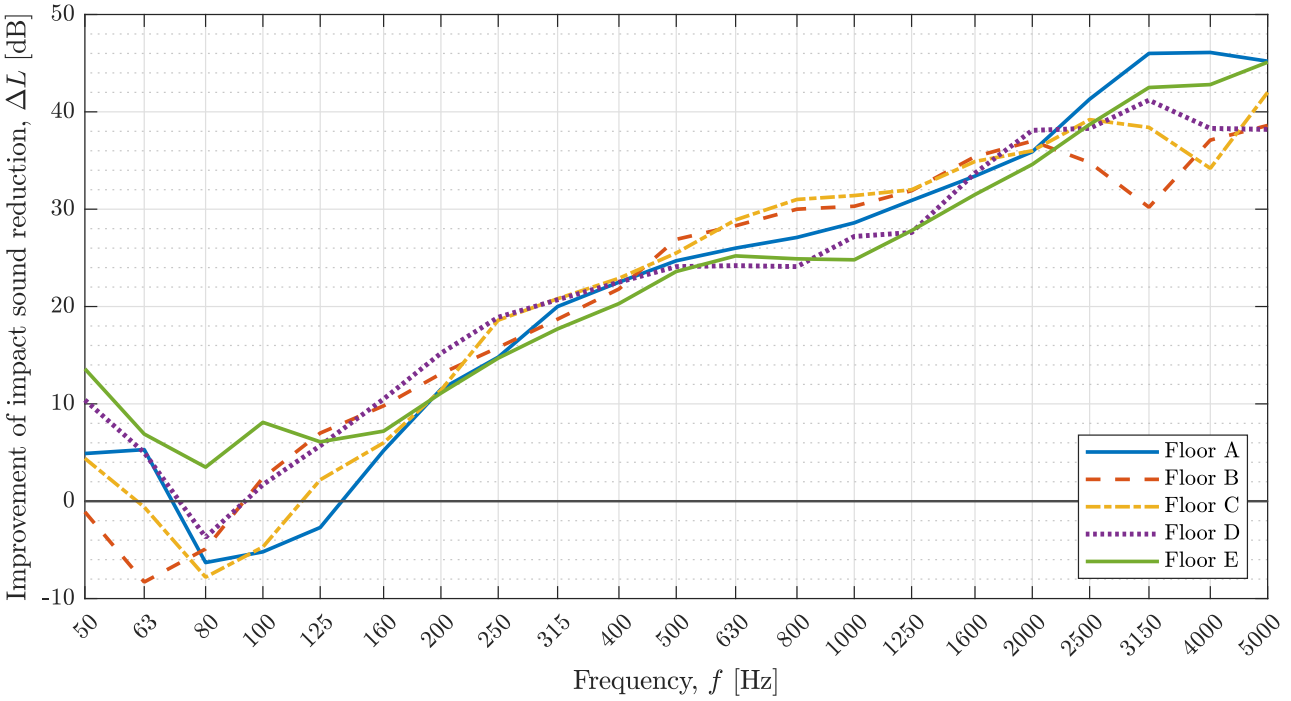


Figure 2. ΔL as a function of frequency for the five floors used in this study.

The first path considers $C_{\mathrm{I},50-80}$ as a direct alternative to $C_{\mathrm{I},50-2500}$. The other path considers calculating $C_{\mathrm{I,r},50-80}$ as a low frequency spectrum adaption term that is tied to ΔL_{w}, without affecting the use of $C_{\mathrm{I},50-2500}$. In essence, for the second path, ΔL_{w} describes 100–3150 Hz while $C_{\mathrm{I,r},50-80}$ works as a tool for an extended frequency range, describing only 50–80 Hz.

The goal is for the measured $L_{\mathrm{n,w}} + C_{50-80/2500}$ for the entire floor to align with the measured $L_{\mathrm{n,0,w}}$ for the bare reference floor minus ΔL_{w} for the floating floor plus the suggested low frequency spectrum adaption term, ideally on the conservative side. Additionally, ΔL_{w} and $C_{\mathrm{I},50-2500}$ are generally favouring floating floors with a low resonance frequency, which is good for the lowest frequencies in the traditional 100–3150 Hz range, but significantly less so for the extended part of the frequency range. A low frequency spectrum adaption term to accompany ΔL_{w} should therefore ideally also reflect how well the floor in question handles the lowest frequencies.

It the follwing, it is important to be aware that $C_{\mathrm{I},50-80}$ or $C_{\mathrm{I},50-2500}$ refers to the spectrum adaption term calculated from the measured $L_{\mathrm{n,w}}$ of a complete floor, while $C_{\mathrm{I,}\mathbf{r}\mathrm{,}50-80}$ or $C_{\mathrm{I,}\mathbf{r}\mathrm{,}50-2500}$ refers to the spectrum adaption term calculated to go alongside ΔL_{w}. The calculation procedures are described in ISO 717-2, and are also briefly explained in chapter 3 below.

3. CALCULATION PROCEDURE

When measuring the weighted improvement of impact sound reduction, ΔL_{w}, according to ISO 10140-1 [5] and ISO 10140-3 [6], a reference measurement is performed on a bare reference floor, and then the measurement is repeated on the test floor. The first set of measurement values are denoted as $L_{\mathrm{n,0}}$ and the latter as L_{n}. The frequency dependent reduction of impact sound pressure level, ΔL, may then be calculated as follows:

$$\Delta L = L_{\mathrm{n,0}} - L_{\mathrm{n}}. \tag{1}$$

Following from this, one can calculate ΔL_{w} with the help of the reference spectra that are defined between 100 and 3150 Hz in ISO 717-2. For the heavyweight reference floor the spectrum is denoted as $L_{\mathrm{n,r,0}}$. This calculation is performed in two steps, with the first being

$$L_{\mathrm{n,r}} = L_{\mathrm{n,r,0}} - \Delta L. \tag{2}$$

At this point, $L_{\mathrm{n,r,w}}$ is calculated from $L_{\mathrm{n,r}}$ using the regular procedure for calculating the normalized weighted impact sound level given in ISO 717-2. Then, the second step is

$$\Delta L_{\mathrm{w}} = L_{\mathrm{n,r,0,w}} - L_{\mathrm{n,r,w}}, \tag{3}$$

where $L_{\mathrm{n,r,0,w}}$ equals 78 dB for heavyweight floors.

As for spectrum adaption terms, they are calculated with the following formula, normally for the frequency range 100–2500 Hz or 50–2500 Hz:

$$C_{\mathrm{I}} = L_{\mathrm{n,sum}} - 15 - L_{\mathrm{n,w}}, \tag{4}$$

where

$$L_{\mathrm{n,sum}} = 10\mathrm{lg} \sum_{i=1}^{k} 10^{L_i/10}. \tag{5}$$

The same calculation can be carried out for $L_{\mathrm{n,r}}$ and $L_{\mathrm{n,r,w}}$, then denoted as $C_{\mathrm{I,r}}$. It is not explicitly stated in the standard that Eqn. (4) may be used for other frequency ranges, but any calculations of $C_{\mathrm{I},50-80}$ and $C_{\mathrm{I,r},50-80}$ in this paper have been performed using this equation.

4. RESULTS AND DISCUSSION

4.1 Measurement and calculation data

Measurement data for the five floors are given in Tab. 1 and Tab. 2. Calculated $C_{\mathrm{I,r},50-80}$ for the five floating floors and four extensions of the reference spectra are shown in Tab. 3.

Table 1. $L_{\mathrm{n,w}}$ and ΔL_{w} for the five floors.

Floor	A	B	C	D	E
$L_{\mathrm{n,w}}$	53 dB	51 dB	53 dB	49 dB	50 dB
ΔL_{w}	22 dB	26 dB	23 dB	28 dB	28 dB

Table 2. $C_{\mathrm{I},50-5000}$ and $C_{\mathrm{I},50-80}$ for the five floors.

Floor	A	B	C	D	E
$C_{\mathrm{I},50-2500}$	4 dB	4 dB	4 dB	3 dB	1 dB
$C_{\mathrm{I},50-80}$	-2 dB	3 dB	0 dB	0 dB	-8 dB

Table 3. Calculated $C_{\mathrm{I,r},50-80}$ for the five floors and four extended spectra.

Floor	A	B	C	D	E
$C_{\mathrm{I,r},50-80,\alpha}$	2 dB	10 dB	5 dB	6 dB	-1 dB
$C_{\mathrm{I,r},50-80,\beta}$	1 dB	7 dB	3 dB	4 dB	-3 dB
$C_{\mathrm{I,r},50-80,\gamma}$	0 dB	5 dB	2 dB	3 dB	-5 dB
$C_{\mathrm{I,r},50-80,\delta}$	-2 dB	4 dB	1 dB	2 dB	-6 dB

4.2 Path one

As Tab. 2 shows, $C_{\mathrm{I},50-80}$ is 0 or lower for four of the floors. which suggests that it's poorly suited as a low frequency spectrum adaption term. Even for Floor B, which is by far the worst performing floors at these frequencies, $C_{\mathrm{I},50-80}$ is lower than the presently used $C_{\mathrm{I},50-2500}$.

However, Tab. 2 also highlights a major weakness in $C_{\mathrm{I},50-2500}$, which is the same for floors A, B and C despite Floor B being very different to the other two. In fact, ΔL for Floor B is negative in all three third octave bands below 100 Hz due to the floor's low resonance frequency, which has a strong positive impact on ΔL_{w}, and a less strong, but nonetheless positive, impact on $C_{\mathrm{I},50-2500}$.

One could, however, consider using a different constant than 15 in Eqn. (4) for the calculation of $C_{\mathrm{I},50-80}$, see Fig. 3.

As the figure shows, it is difficult to obtain values for $C_{\mathrm{I},50-80}$ that show particular likeness with $C_{\mathrm{I},50-2500}$ using this calculation method. Other frequency ranges, like 50–100 Hz or 50–125 Hz could also be considered, but as Fig. 4 shows, $C_{\mathrm{I},50-x}$ moves quickly towards $C_{\mathrm{I},50-2500}$ as x goes above 80 Hz. It is difficult to find good arguments for why any of these alternative spectrum adaption terms are any better than $C_{\mathrm{I},50-2500}$, and therefore it seems sensible to avoid this path.

4.3 Path two

$C_{\mathrm{I},50-80}$ may be a poor choice for a spectrum adaption term to go along with $L_{\mathrm{n,w}}$, but when calculated as a spectrum adaption term to go alongside ΔL_{w}, the numbers in Tab. 3 are showing more promise. An issue with using $C_{\mathrm{I,r},50-2500}$ are the relatively high reference values at 100–160 Hz, which normally lead to very conservative values for $C_{\mathrm{I,r},50-2500}$ no matter how steeply the curve for the reference floor is dropping below 100 Hz [7].

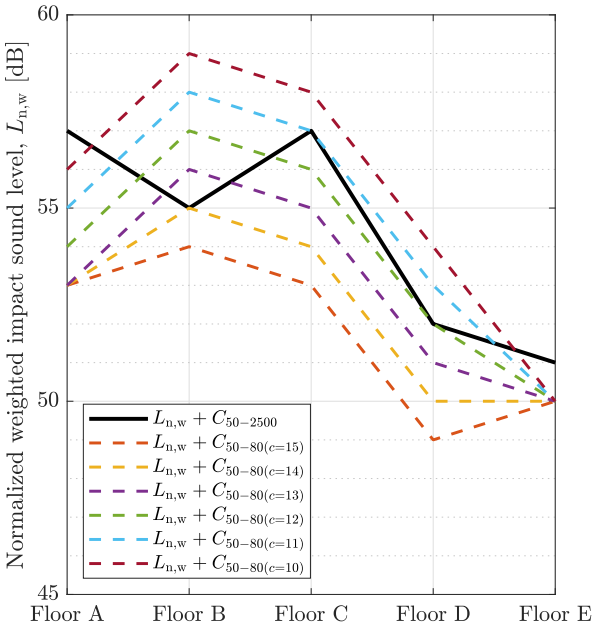


Figure 3. Alternatives for calculating $C_{\mathrm{I},50-80}$.

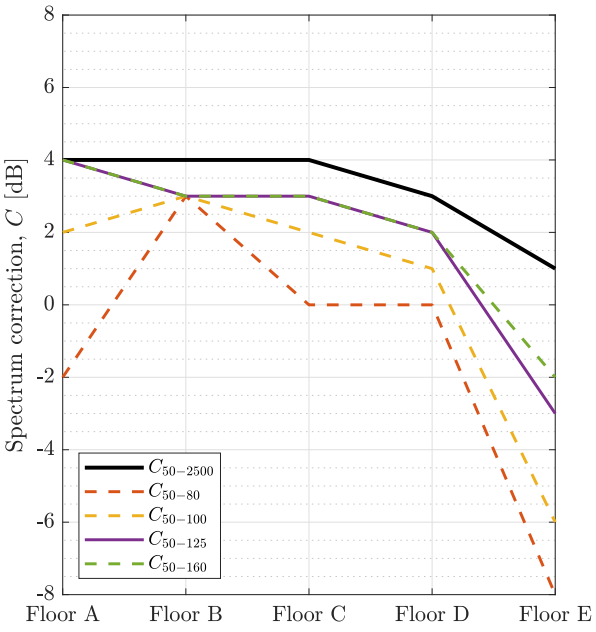


Figure 4. A graphical representation of how different evaluation ranges affect the calculated spectrum adaption terms.

By adding up $L_{\mathrm{n,0,w}}$ for the 140 mm concrete floor, which is 79 dB, ΔL_{w} from Tab. 1 and $C_{\mathrm{I,r,50-80}}$ from Tab. 3 and comparing the numbers with the measured $L_{\mathrm{n,w}} + C_{\mathrm{I,50-2500}}$, relatively similar results are achieved for the more aggressive approaches to the extension of the reference spectrum. This is assuming negative values are not to be counted, which at least is the case in Norway [1]. This is visualised graphically in Fig. 5.

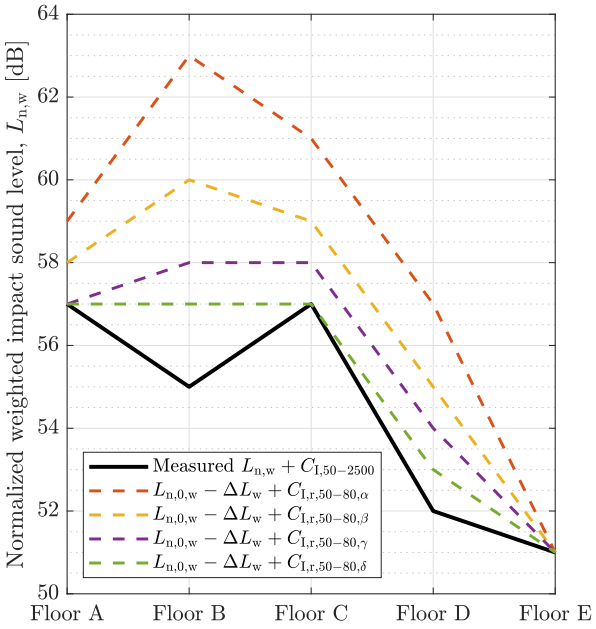


Figure 5. A graphical representation of how the calculated spectrum adaption terms in Tab. 3 align with measured results.

As the figure shows, the results for the δ-spectrum are very close to the measured results, with the exception of Floor B. However, given Floor B's poor low frequency characteristics it can be argued that this is a good thing. In this format, $C_{\mathrm{I,r,50-80}}$ acts as a number that can be added to ΔL_{w} to obtain a relatively good approximation of $L_{\mathrm{n,w}} + C_{\mathrm{I,50-2500}}$, but it can also be used as a comparison tool for the five floating floors. Floor B has the worst low frequency characteristics of the five, and therefore also the highest $C_{\mathrm{I,r,50-80}}$. Floor E, on the other hand, has excellent low frequency characteristics, and $C_{\mathrm{I,r,50-80}}$ for that floor is correspondingly low.

Thus, the values in Tab. 3 can be used as a simple way to rank the low frequency characteristics of a number of floors. The relative low frequency strength of the five floors seems to be generally well represented in Tab. 3, perhaps with the exception of Floor D. However, any low frequency spectrum adaption term is calculated in context of the $L_{\mathrm{n,w}}$ of the floor, meaning that although Floor D's low frequency characteristics in isolation are the second best of the five, they are relatively poor in context of the floor's measured $L_{\mathrm{n,w}}$.

The negative values for Floors A and E can perhaps be used as an argument against this method, but when using the data to calculate the expected $L_{\mathrm{n,w}} + C_{\mathrm{I,50-2500}}$, any negative values will be set to 0. As a tool to compare the different floors, large variations can be positive. It should also be noted that the spectrum adaption terms for floors A and E effectively are 0 for both the δ and γ spectra. This is a cause for concern, but Floor E has $C_{\mathrm{I,50-2500}}$ of 1, so the difference here is small. The difference is significantly larger for Floor A, but Floor A is also somewhat of an outlier, with the largest difference between $L_{\mathrm{n,w}}$ and $L_{\mathrm{n,0,w}} - \Delta L_{\mathrm{w}}$, see Fig. 6.

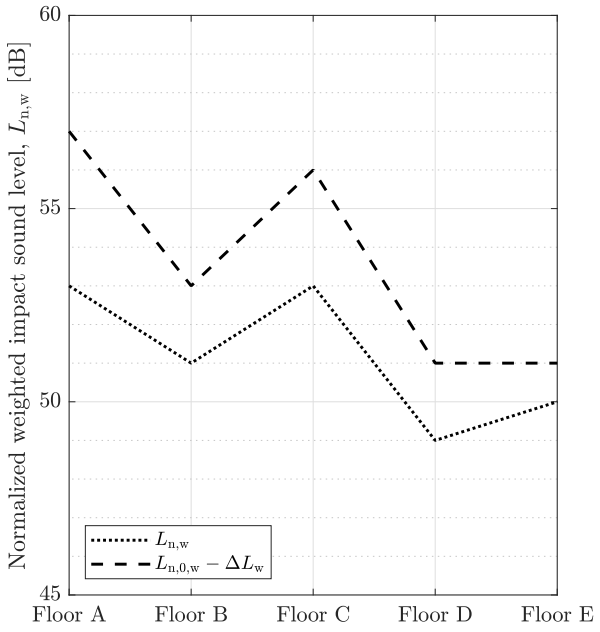


Figure 6. The difference between $L_{\mathrm{n,w}}$ and $L_{\mathrm{n,0,w}} - \Delta L_{\mathrm{w}}$.

4.4 Summary

It has been difficult to find a way to calculate a low frequency spectrum adaption term for ΔL_{w} that is directly comparable to $C_{\mathrm{I,50-2500}}$. Using $C_{\mathrm{I,r,50-2500}}$ is not a

good option because it leads to very conservative results. $C_{\mathrm{I,r},50-80}$ does however give sensible results for some of the suggested extensions of the reference spectra in ISO 717-2, but it isn't directly comparable to $C_{\mathrm{I},50-2500}$, and replacing $C_{\mathrm{I},50-2500}$ with $C_{\mathrm{I},50-80}$ or similar variations does not seem to be a good idea.

As a possible solution, it is suggested to use $C_{\mathrm{I,r},50-80}$ as a term that is strictly connected to ΔL_{w}. For the γ and δ spectrum extensions suggested in this paper, $C_{\mathrm{I,r},50-80}$ provides good differentiation between the different floors. This makes $C_{\mathrm{I,r},50-80}$ suitable as a tool to rank the low frequency performance of different floors as well as to calculate the expected $L_{\mathrm{n,w}} + C_{\mathrm{I},50-2500}$ for a floor construction based on $L_{\mathrm{n,w}}$ for the bare floor, and ΔL_{w} and $C_{\mathrm{I,r},50-80}$ for the floating floor.

5. FURTHER WORK

The findings above suggest that $C_{\mathrm{I,r},50-80}$ may be an option for how frequencies lower than 100 Hz can be tied to ΔL_{w} via a low frequency spectrum adaption term. However, the findings are based on a small sample size from one lab, and to obtain a better basis for decision, deeper studies with more data from several labs are needed.

6. CONCLUSION

When $C_{\mathrm{I},50-2500}$ gets introduced in building legislation, there is a need to update ISO 717-2 to facilitate calculations of a low frequency spectrum adaption term for the weighted improvement of impact sound reduction, ΔL_{w}. To be able to perform such a calculation, an extension of the reference spectra in ISO 717-2 down to 50 Hz is necessary.

In this paper, some alternative extensions for the heavyweight reference floor are suggested, and the low frequency spectrum adaption term $C_{\mathrm{I,r},50-80}$ is assessed as a possibility. The findings show that $C_{\mathrm{I,r},50-80}$ in combination with one or more of the suggested spectra may well be a viable solution. However, since this paper is based on a small sample size from one lab, further and more comprehensive studies are needed.

7. ACKNOWLEDGMENTS

The work with this paper has been funded by the Construction Technology group at SINTEF Community, led by Monica Strøm Nodland. I would like to thank Monica for her support.

8. REFERENCES

[1] Standards Norway. *Acoustic conditions in buildings. Sound classifications of various types of buildings*, NS 8175:2019, Standards Norway.

[2] DiBK. *Regulations on technical requirements for construction works*, TEK17, Direktoratet for byggkvalitet, 2017

[3] A. Løvstad and P. K. Limmesand. Consequences of revised sound insulation requirements between dwellings in Norway. In *Proc. of BNAM 2021*, held digitally, 2021.

[4] ISO. *Acoustics.Rating of sound insulation in buildings and of building elements*, ISO 717-2:2020, International Organization for Standardization.

[5] ISO. *Acoustics – Laboratory measurement of sound insulation of building elements — Part 1: Application rules for specific products*, ISO 10140-3:2021, International Organization for Standardization.

[6] ISO. *Acoustics – Laboratory measurement of sound insulation of building elements — Part 3: Measurement of impact sound insulation*, ISO 10140-3:2021, International Organization for Standardization.

[7] G. V. Holøyen. Extending the frequency range of ISO 717-2 – a look at options and issues. In *Proc. of INTER-NOISE 2024*, pages 9195–9202, Nantes, France, 2024.

DOI: 10.61782/fa.2025.0858

FORUM ACUSTICUM EURONOISE 2025

THE CONSTRUCTION OF A STANDARDIZED ACOUSTIC TESTING ROOM FOSTERS INNOVATIVE SOLUTIONS MEETING FUTURE MARKET TECHNICAL DEMANDS.

Alvaro Martínez de Marcos
Head of Acoustics. Product Manager
Danosa Group S.A., Polígono Industrial Sector, 9, 19290 Fontanar, Guadalajara, Spain

ABSTRACT

The construction of a standardized acoustic testing room is a key development in fostering innovative solutions that meet the current technical demands of the market. This presentation details the design and construction process of a specialized facility that provides controlled conditions for the precise evaluation of acoustic technologies. The room enables the research and enhancement of materials and technologies that improve acoustic comfort and soundproofing, contributing to the advancement of acoustic engineering in key sectors such as construction. Additionally, the presentation highlights how this infrastructure serves as a crucial tool for complying with technical standards and addressing the growing market demands. It also emphasizes the important role manufacturers play in promoting initiatives from technical committees, working closely with governments to ensure that acoustic solutions improve the quality of life for the population. Through this approach, the collaboration between industry and authorities is key to creating healthier and more comfortable living conditions, contributing to the continuous improvement of urban and residential environments.

Keywords: *acoustic testing room, soundproofing, technical standards*, *construction.*

*Corresponding author: ademarcos@danosa.com.
Copyright: ©2025 First author et al. This is an open-access article distributed under the terms of the Creative Commons Attribution 3.0 Unported License, which permits unrestricted use, distribution, and reproduction in any medium, provided the original author and source are credited.

1. INTRODUCTION

This article presents the development of specialised acoustic rooms for the evaluation of construction solutions. The creation of these facilities responds to the growing need to investigate new alternatives within the field of lightweight and industrialised construction, understanding 'lightweight' as one in which the structural elements are mainly composed of wood, sheet metal or other low-mass materials. Furthermore, this initiative is linked to the future update of the Spanish Technical Building Code (Código Técnico de la Edificación), scheduled for 2026, which drives the need to adapt construction solutions to the new regulatory requirements.

2. DRIVING ACOUSTIC INNOVATION BY DANOSA GROUP S.A.

The new acoustic rooms are being constructed in Fontanar, a small village in the province of Guadalajara (Spain) , with a population of just over a hundred inhabitants, where the facilities of Danosa Group S.A. are located, the company behind this project. Founded over 60 years ago, Danosa Group S.A. has been a pioneer in the development of acoustic insulation since the 1980s, specialising in the manufacture of elastic materials such as polyethylene foams and anti-resonant elements like acoustic membranes and multi-layer products.

Throughout its history, Danosa Group S.A. has played a key role in the development of various national technical standards, contributing to the advancement of the industry and the establishment of benchmarks in the sector. Furthermore, the company has introduced innovative solutions to the market by creating integrated acoustic systems that combine different materials to improve both airborne and impact sound insulation in construction. Its approach has always been to provide value-added

proposals, adapting to the growing needs of the sector and contributing to the improvement of acoustic quality in built environments.

3. DEVELOPMETN CONTEXT

3.1 New construction systems

The increasing adoption of new lightweight construction solutions, such as thin sheet metal (1 mm to 1.5 mm thickness), laminated wood panels (CLT), sandwich panels with rigid insulation cores, and traditional timber beam systems, presents significant challenges in accurately modelling their acoustic performance using specialised software. These novel construction methods necessitate substantial research and development efforts from acoustic insulation manufacturers to ensure effective soundproofing. This situation mirrors the developments of the 1980s, when the industry pioneered decoupling solutions for compression layers on floors and structural elements to mitigate impact noise, or replaced lead sheets with bituminous membranes for improved airborne noise insulation. Today, manufacturers are once again called upon to innovate and design new solutions to address the acoustic complexities associated with these lightweight construction systems. This ongoing demand for technological advancements continues to drive the evolution of acoustic insulation products and methodologies.

3.2 Regulatory change

The second factor driving the creation of this project is the knowledge of an imminent significant change in Spanish acoustic regulations[1], which involves an increase of approximately 2 dB in airborne sound levels (DnTa 52 dBA) and a reduction of 5 dB in impact noise (Lntw 60 dB) in protected rooms, along with new restrictions on tolerances in measurements. This change is accompanied by a renewed focus from the National Technical Committees, emphasizing the importance of manufacturers actively collaborating in the development of new acoustically justified solutions. The goal is to create "standard" solution catalogs that can serve as references for designing future constructions, ensuring compliance with the new regulatory requirements.

3.3 Improving quality of life

The involvement of construction manufacturers in technical committees, associations, forums, and various markets, alongside architects and building designers, provides a realistic representation of the impact on people's quality of life. In this context, without delving into purely commercial matters, manufacturers position themselves as innovative entities with the financial capacity to allocate resources towards the development of testing and measurement elements for future systems. Furthermore, they possess extensive knowledge of diverse products and solutions used worldwide, which allows them to contribute to society by providing solutions that enhance quality of life. These solutions are also closely aligned with environmental sustainability, as they often incorporate new materials that reduce the ecological footprint of the products.

3.4 Participants in project development

The following paragraph describes the participants who have directly contributed their expertise to the design and construction of the testing rooms.

3.4.1 Danosa Group S.A.

As the promoting and contracting entity, is represented by Álvaro Martínez, a member of the Technical Standardization Committee CTN-74 and Head of Acoustics at the company. Advocates for the construction of an acoustic measurement facility where new solutions for the market can be developed.

3.4.2 Tecnalia

As one of the leading companies in innovation at the national level and one of the main institutes, it has Marta Fuente as the head of acoustics.

3.4.3 Gikesa

As an acoustic measurement laboratory and a benchmark in technical support for the construction sector.

3.4.4 Maribel Castro (Architect)

Architect in charge of the projects and construction management of the buildings and constructions at Danosa Group S.A.

4. TESTIGN ROOM DESIGN

4.1 Regulation

The design of the testing chambers is based, as expected, on the ISO 10140 standards, both with regard to the requirements for installations and equipment [UNE-EN ISO

[1] Incomming regulation January 2026. New CTE DB-HR

10140-5] and the measurement methodology itself [UNE-EN ISO 10140-2 and 4], enabling the comparison of results with those obtained by other laboratories.
Although the aforementioned standards do not specifically address the design of acoustic transmission chambers, they do specify, either quantitatively or qualitatively, a set of requirements that significantly influence the design, such as:

- Minimum dimensions and volumes.
- Controlled reverberation time in both chambers.
- The need for the acoustic field inside the chambers to be diffuse.
- Minimisation of indirect transmissions between chambers.
- Background noise as low as possible in the receiving chamber.
- Energy dissipation (loss factor) for heavy samples.

4.2 Sizing

Regarding the dimensions and volumes, a separator element measuring 3.4 x 4.6 meters has been chosen, which closely resembles the standard surface area of a residential space. The volume difference between the chambers is maintained within 10%, in compliance with the requirements set out by the standard.

4.2.1 Minimisation of Indirect Sound Transmission

One of the key aspects in the design of an acoustic laboratory is the minimisation of indirect sound transmission between chambers. Unlike real-world construction, where sound is transmitted between spaces through multiple transmission paths, the goal in a laboratory setting is to ensure that the sound only travels through the test sample, thereby characterising the material or construction solution. The joints between elements of the different chambers are specifically designed to achieve this by using structural decoupling components with very low dynamic stiffness. This approach effectively isolates the chambers, ensuring that the measurements accurately reflect the acoustic properties of the sample under test.

4.2.2 Energy Dissipation (Loss Factor)

Another important parameter is the loss factor (energy dissipation) of the sample once placed between the transmission chambers. While this aspect is primarily relevant for heavy samples, it has also been considered in the design to ensure the accuracy and reliability of the test results.

4.2.3 Reverberation Time

The reverberation time is carefully controlled in both chambers, set between 1 and 2 seconds, achieved through the strategic placement of absorbent materials in both the emitter and receiver rooms. The acoustic field within each chamber is diffuse, meaning that a large number of reflected waves, originating from all directions, combine in such a way that, at any given point and in any instantaneous direction of the sound wave, the average density of acoustic energy is equally probable. This is first achieved through appropriate chamber sizing, which accounts for the potential for standing waves or dominant modes, particularly at low frequencies. Additionally, once the laboratory is constructed, this diffuse field is further ensured by the placement of curved reflective elements, whose positioning and orientation are determined through a statistical testing process.

As part of the design development, a model of the potential indirect transmissions has been created, which integrates the defined construction solution. Based on this model, the maximum acoustic parameters R'w and L'nTw have been estimated, yielding a value of 94 dB for R'w and 23 dB for L'nTw.
It is important to highlight that these values represent the measurement limit due to flanking transmissions, but they are subject to the influence of background noise in the receiving room. This factor is controlled through the configuration of the room envelope, as well as by the influence of external noise generated outside.

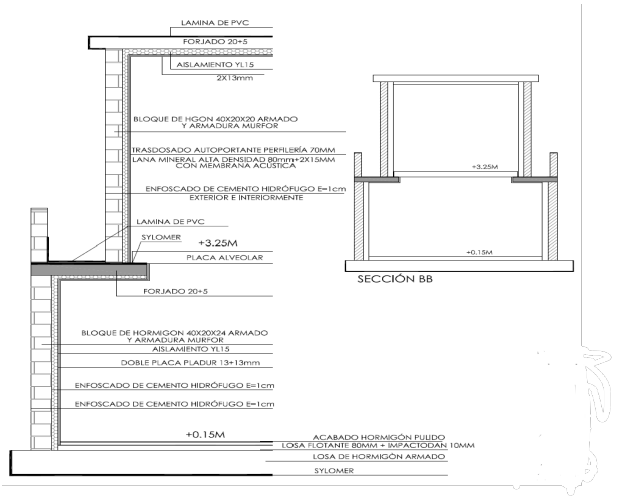


Figure 1. Construction section of the testing rooms (1)

4.2.4 Isolation of the chambers

Finally, yet equally important, the isolation of the chambers from external noise sources ensures the lowest possible background noise in the receiving chamber. This allows for the accurate measurement of high levels of sound insulation without any interference, ensuring the reliability of the test results.

Once the testing room is designed, constructed, and calibrated, the measurement procedure and the equipment to be used will be established. Following this, the results of the insulation tests will be validated. To achieve this, tests will be conducted on various items with known insulation properties, ensuring that the measurements align with the expected values.



Figure 2. Construction interior of the testing rooms (2)

5. SOLUTIONS TO BE TESTED

5.1 Light or industrialised construction

Lightweight construction solutions are increasingly in demand within the sector. The rapid construction time, coupled with the reduced cost of buildings due to the use of fewer materials, has driven the adoption of new building systems. However, the limited acoustic insulation offered by these structures, combined with the rigidity of their connections, necessitates the integration of additional elements with insulating properties. Within the category of "lightweight" systems, the following can be considered.

5.1.1 CLT (Cross-Laminated Timber)

Innovative and sustainable building material that has gained popularity in modern architecture. CLT is manufactured by bonding layers of wood (typically pine, spruce, or other types of wood) arranged in alternating directions (crosswise), which provides greater strength and dimensional stability compared to traditional wood.

5.1.2 Wood beam structure

Construction system primarily used in buildings and other infrastructures to support loads and distribute them efficiently. Beams are horizontal or inclined components responsible for transferring the loads from the structure to the ground or other supporting elements, such as columns or walls. In a wood beam structure, wood is the primary material used due to its mechanical properties, aesthetics, and sustainability.

5.1.3 Deck-type sheet structure

Construction system that uses steel panels (or, in some cases, other metallic materials) to form a strong and continuous surface that serves both to support loads and as part of the structural element of a building, typically in floor or roof slabs. This system is commonly used in the construction of industrial, commercial, residential buildings, and certain infrastructure applications due to its efficiency, speed of execution, and structural performance.

5.1.4 Prefabricated panel structure

A construction system that uses panels manufactured off-site (in a prefabrication plant) which are then

transported and assembled at the construction site. These panels can be made from various materials, such as concrete, wood, steel, or composite materials, and are designed to serve structural, aesthetic, or both functions. Prefabricated panels are modular elements produced in series under controlled conditions, ensuring their quality and dimensional accuracy.

The rigid elements to be used as separation layers and/or supports include OSB boards and fibre cement boards.

The acoustic components employed will consist of cross-linked polyethylene, acoustic membranes, rubber mats, multi-layer panels, anti-resonant elements, and other sound-absorbing materials. These can be placed in structural gaps or used as spring elements between masses. Additionally, vibration isolation systems will be integrated into certain solutions where low-frequency performance is required.



Figure 3. Last days of construction. (2)

6. REFERENCES

[1] Esquema de Construcción. Proyecto constructivo salas de ensayo (Danosa)

[2] Pictures of testing rooms in Danosa, Fontanar (Guadalajara – Spain)

DOI: 10.61782/fa.2025.0814

FORUM ACUSTICUM EURONOISE 2025

SPATIAL VARIATION OF THE SOUND PRESSURE LEVELS DUE TO HVAC SYSTEMS AND THE ASSESSMENT OF NOISE

Teresa Carrascal[1*] **Amelia Romero-Fernández** [1] **Belén Casla-Herguedas**[1]
[1] Eduardo Torroja Institute for Construction Sciences. IETcc- CSIC. Madrid, Spain

ABSTRACT

Regulations in many countries establish limits on noise produced by building services and equipment and refer to international standards such as ISO 16032 and ISO 10052 or to national procedures for the verification of such requirements.
This study analyses the distribution of sound produced by HVAC equipment in an office building. For that purpose, systematic measurements were conducted at multiple locations within a room to determine spatial variations in sound pressure levels produced by internal units. Factors influencing noise assessments such as room geometry, spatial sampling, HVAC equipment settings and the presence of background noise are also examined. The ultimate aim of this work is to study how variations of sound pressure levels affect the assessment of L_{Aeq} and to propose practical recommendations to assess noise from building services to fulfil regulatory requirements.

Keywords: *noise from building services, noise limit, requirements, ISO 16032, HVAC noise, spatial variation.*

1. INTRODUCTION

This communication aims to study the distribution of sound produced by HVAC (Heating, ventilation, and Air Conditioning) systems in a training room located at the Eduardo Torroja Institute for Construction Sciences, which is part of the Spanish National Research Council (CSIC) in Madrid.

Regulations in many countries establish limits on noise produced by building services and equipment and refer to international standards such as ISO 16032[1] and ISO 10052[2] or to national procedures for the verification of such requirements.
Although weighted descriptors used in regulations such as L_{Aeq}, $L_{Aeq,nT}$, $L_{AFmax,}$ etc. provide a general sense of acoustic performance, they often fail to capture the spatial non-uniformities of the sound field, in particular in the low frequency range.
This paper studies the spatial variations of sound pressure levels due to service and equipment in a training room in an office building, and its impact on weighted values.

2. SCENARIO DESCRIPTION

The Eduardo Torroja Institute for Construction Sciences is an entity that conducts scientific research and technological development in the field of construction, its materials, and the performance associated with the pursued approaches. It is housed in a distinctive building inaugurated in 1953, originally serving as the new headquarters for the Technical Institute of Construction and Cement, now known as the Eduardo Torroja Institute for Construction Sciences.
A room belonging to the Eduardo Torroja Institute for Construction Sciences was studied, as described below.
The room was originally the archive of the former library of the Institute. This archive was relocated to the basement of the building, creating a space that began to be used as a training room. An absorbent ceiling was installed, along with a movable partition to divide the room into two sections[3]. The absorbent ceiling improves user comfort and ensures compliance with the acoustic conditioning requirements outlined in the current regulations, specifically the Basic Document DB HR Protection Against Noise of the Spanish Technical Building Code[4]. The current layout

[*] ***Corresponding author***: tcarrascal@ietcc.csic.es
Copyright: *©2025 First author et al. This is an open-access article distributed under the terms of the Creative Commons Attribution 3.0 Unported License, which permits unrestricted use, distribution, and reproduction in any medium, provided the original author and source are credited.*

of the training room is rectangular, with a floor area of 69.8 m² and a height of 2.75 m. See Figure 1.



a) b)

Figure 1. a) Photograph of the training room. b) Detail of one of the three indoor units the room is equipped with.

3. MEASUREMENTS PERFORMED

Equivalent sound level (L_{eq}) measurements were conducted over 15-second intervals at 30 points within the room (Figure 2), at two different heights: 1.20 m and 1.50 m, resulting in a total of 60 measurements. These two heights were chosen because they represent typical positions of the occupants in the room, 1.20 m is the ear height used in standards for acoustic measurements[5]. The height of 1.50 m above floor level below the noise source is specified in ISO 16032 procedure [1].

Additionally, sound levels were taken at three room corners, (separated 50 cm from the walls and the floor) and nine background noise measurements were taken in different positions. These measurements were repeated for the V3 and V5 ventilation modes.

The training room is equipped with three ceiling-mounted variable refrigerant flow (VRF) indoor units positioned at the distances marked in Figure 2. These units consisted on four-way ceiling cassettes that operate simultaneously and have three modes of operation: heating, cooling, and ventilation. Each of these modes has five ventilation speed settings.

For this study, measurements were carried out with the "ventilation" mode at two speeds: the highest (V5) and the medium (V3), while the lowest speed was excluded due to its noise levels being close to the background noise. The ventilation mode was selected because it provides a constant fan speed during operation, in contrast to the heating and cooling modes, where the system automatically regulates fan speed and refrigerant flow to maintain the desired room temperature.

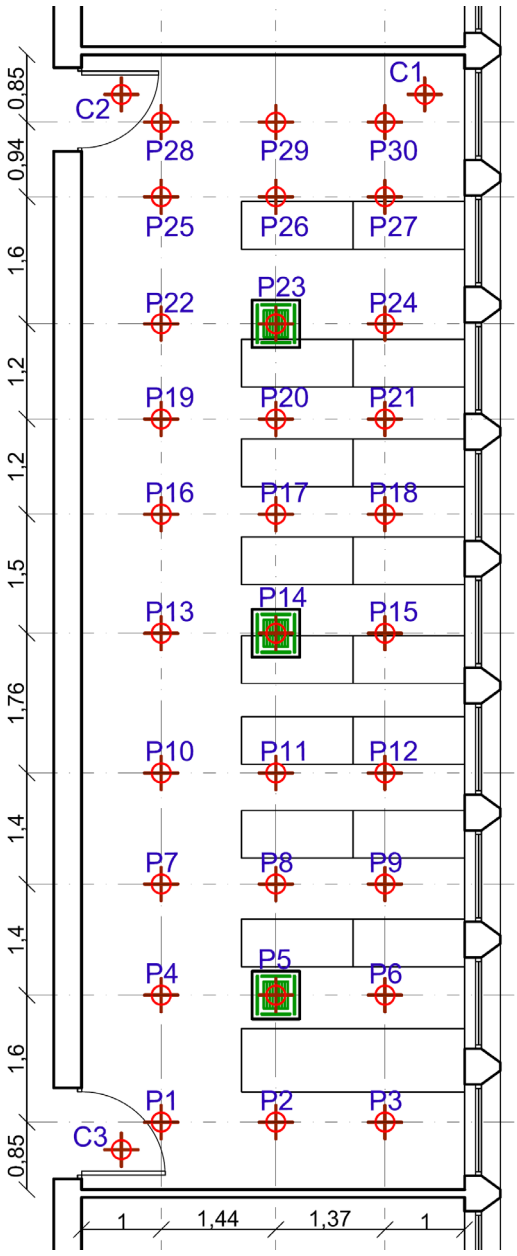


Figure 2. Plan of the room indicating the measurement positions and the location of the VRF cassettes.

The measurements were conducted with two people present in the room, which was furnished with chairs and tables (see test scenario description in Section 2.2). A floor plan of the room with the distribution of the source and microphone positions for the measurements is shown in Figure 2.

The equipment used for the measurements was as follows:

- Environmental sound level meter, Class 1, model CR:171B, by Cirrus Research plc;
- Calibrator model CB006, by Cesva.

Using an acoustic calibrator, sound level checks of the measurement chain were performed before and after the tests, with satisfactory results.

Data processing was carried out using the NoiseTools v1.8.9 software for data downloading, analysis, and reporting, along with Microsoft Excel and MATLAB R2024b update 3.

4. RESULTS

The primary noise sources during the measurements were the fans and the airflow passing through filters, coils and louvers. Refrigerant-related noise was negligible since the compressor was not active, which is why the ventilation mode was chosen for this study.

The sound source remained steady and did not show significant fluctuations over time as the equivalent continuous sound pressure levels (L_{eq}) remained stable throughout the measurement periods.

Table 1 shows the average A-weighted and C-weighted equivalent continuous sound pressure levels obtained for the 30 measurement points, as well as the maximum values and the minimum values of L_{Aeq} and L_{Ceq}, along with the corresponding ranges, for the two fan speed settings and the two measurement heights.

Table 1. L_{Aeq} and L_{Ceq} for the two fan speed settings and the two measurement heights.

Velocity setting		**Velocity 3**		**Velocity 5**	
Height (cm)		**h=120**	**h=150**	**h=120**	**h=150**
$L_{A,eq}$ (dB)	Average	40.1	40.0	44.7	44.8
	Max	41.3	41.9	45.9	47.2
	Min	38.8	38.3	43.5	43.1
	Range	2.4	3.6	2.4	4.1
$L_{C,eq}$ (dB)	Average	52.3	53.4	53.9	54.6
	Max	56.3	59.0	55.4	60.5
	Min	49.4	49.9	52.7	52.3
	Range	6.9	9.1	2.7	8.2

Table 2 shows the values of the equivalent continuous sound pressure level measured at the 3 corner positions. The average background noise levels L_{Aeq} measured at the nine positions were 32.0 dB and 31.4 dB. Two sets of background noise level measurements were obtained, as the measurements for each fan speed setting were conducted different days.

Table 2. L_{Aeq} and L_{Ceq} measured at the 3 corner positions.

Velocity setting	**Velocity 3**			**Velocity 5**		
Corner	C1	C2	C3	C1	C2	C3
$L_{A,eq}$ (dB)	39.4	38.2	38.1	43.9	44.9	43.2
$L_{C,eq}$ (dB)	57.1	53.6	56.7	56.2	56.5	57.2

4.1 Spatial distribution of sound

Figure 3 shows the L_{Aeq} at each measurement position, including the corner positions, for each velocity setting and measurement height. The highest values corresponded to the positions located directly beneath the internal VRF units (P5, P14 and P26). The values of corner positions are represented by crosses.

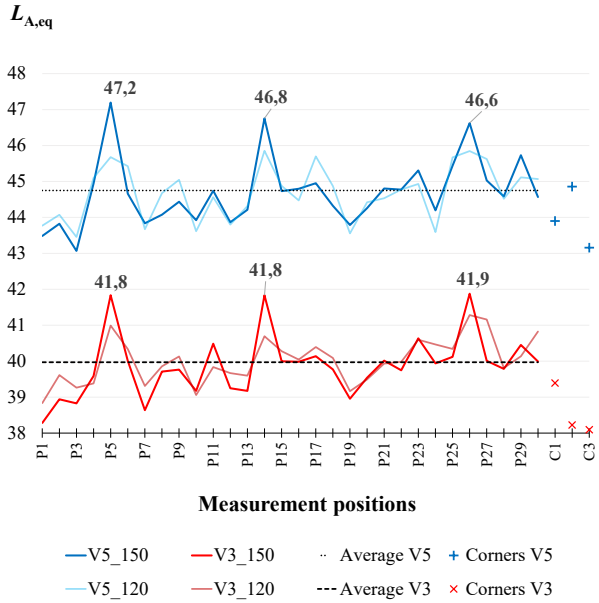


Figure 3. L_{Aeq} at each measurement position.

As seen in Figure 3 and Table 1, the average difference between the measurements performed at 120 cm and 150

cm is 0.4 dB in average. In contrast, the average difference between the measurements performed with V5 and V3 fan speeds is significantly higher 4.7 dB, likely due to the increased air volume and turbulence at V5.

Figure 4 shows the spatial variations of the L_{Aeq} in the room for the fan speed V5 and height 120 cm. It is clearly seen the positions with the highest L_{Aeq}, which are beneath the internal units.

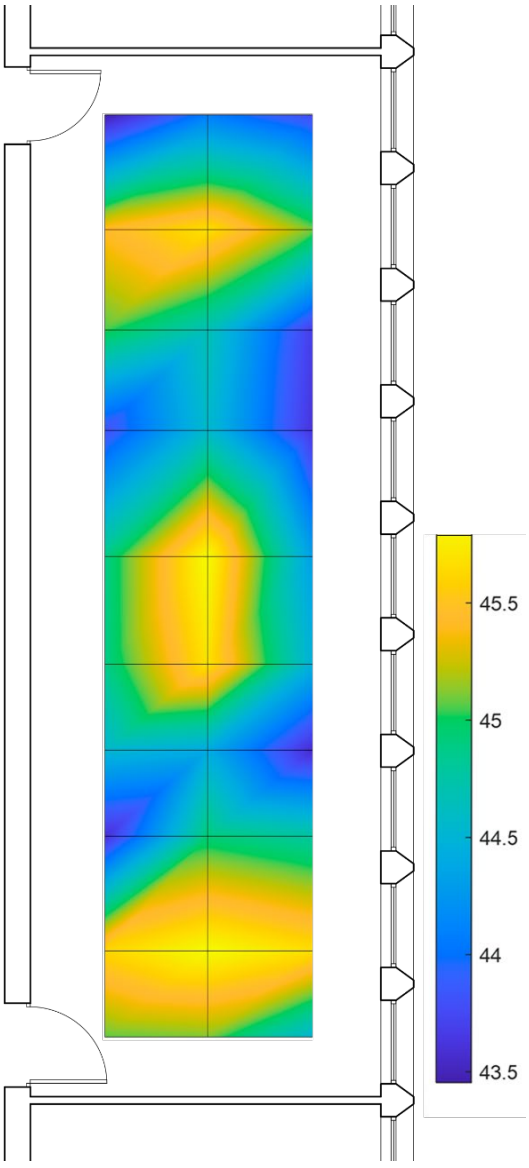


Figure 4. L_{Aeq} spatial variations in the room for the fan speed V5 and height 120 cm. Graph based on measured data. Plan view.

4.2 Frequency spectrum variations

Figure 5 shows the spectra of the average equivalent continuous sound pressure level obtained for the 30 points for the fan speed of V5 and height of 120 cm. The hearing threshold has also been represented, showing that part of the energy in below 50 Hz is below it Similar results were observed for measurements at fan speed V3 and height of 150 cm.

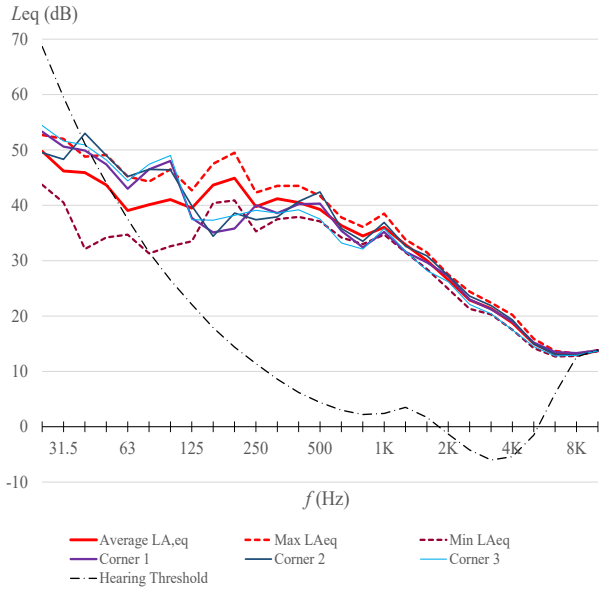


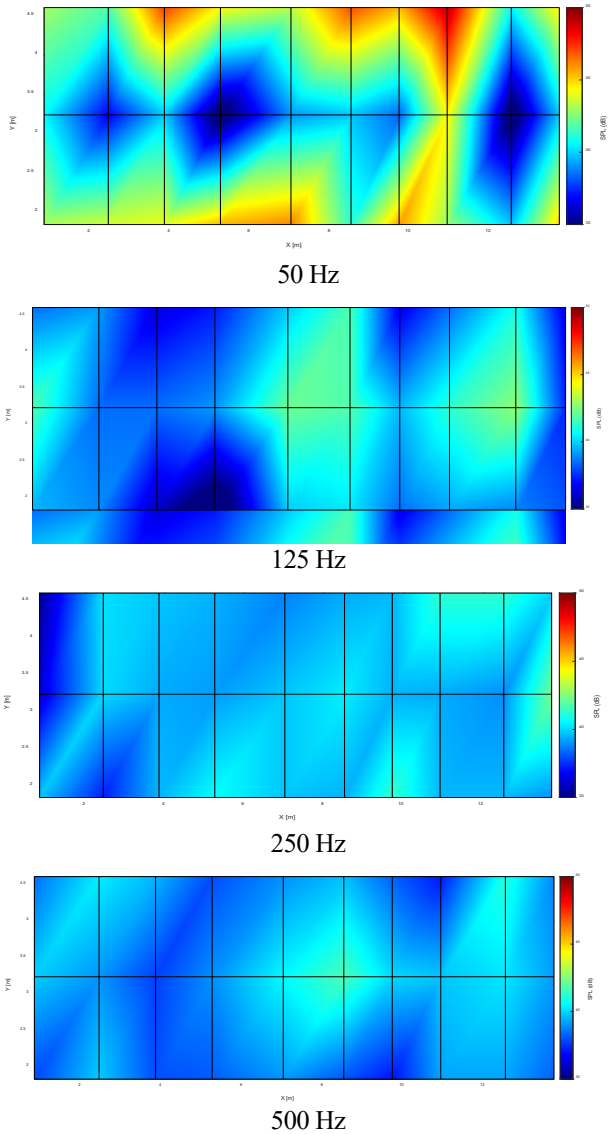
Figure 5. Average L_{Aeq} in the room for the fan speed V5 and height 120 cm.

As seen in Figure 5, most of the acoustic energy emitted by the VRF cassette units is concentrated in the low-mid frequency range.

Even though the A-weighted equivalent sound pressure level differences range from 2.4 to 4.1 dB, a closer look at the spectral results reveals differences of 7 to 15 dB in the low-frequency range (50–250 Hz). See Figure 5, which shows the average equivalent continuous sound pressure level obtained for the 30 points for the fan speed of V5 and height of 120 cm.

The Figure 6 shows the spatial distribution of the sound pressure levels in the room for the frequencies of 50, 125, 250, 500 Hz. The same color scale was used to plot all the graphs, and across the series, it is evident that the largest variations in the sound field occur in the low-frequency range. The Schroeder frequency of the room is 130 Hz, which marks the boundary between the low-frequency

range dominated by discrete room modes and the higher-frequency range where the sound field becomes statistically diffuse. As seen in Figures 5 and 6, the spatial variations become more significant bellow it due to the non- irregular modal behavior. At 50 Hz, the graph may show the influence of background noise coming from outside, caused by traffic.



50 Hz

125 Hz

250 Hz

500 Hz

Figure 6. Spatial distribution of the sound pressure levels in the room for the frequencies of 50, 125, 250, 500 Hz. Graph based on measured data. Plan view.

5. THE ASSESSMENT OF SERVICE AND EQUIPMENT NOISE

ISO 16032[1] contains the engineering method for the measurement of sound pressure levels in rooms from service equipment. It is referred in several European regulations[6] to verify compliance with requirements. This section presents the results that have been obtained using the estimation method described in ISO 16032[1] for the calculation of the average sound pressure level in the room, L_{Aeq}.

The sound pressure level is determined for a specified operating condition and duty cycle. Sound pressure levels are measured in three microphone positions, one position in a selected corner of the room and two positions in the reverberant sound field. All values were corrected for background noise.

Table 3 shows the results of the calculations. They were performed to determine the range of the average sound pressure levels, L_{Aeq}, obtainable in the room. The following criteria was used for the calculations:

- Positions with the highest sound pressure level, which are the ones beneath the internal units (P4, P14)
- Positions with the lowest sound pressure levels (P3, P13)
- Two positions chosen at random (P15, P19).

The corner position chosen was Corner C1, which is the corner that has the highest sound pressure level for both velocities (V3 and V5). This section aims to find the highest and the lowest value of the average L_{Aeq} obtainable, so positions below the VRF units are also included in the calculations, even when they are considered additional measurements in ISO 16032[1].

The differences found are 2.1 dB for V3 and 2.5 for V5.

Table 3. Calculated average L_{Aeq} in the room.

Velocity	Corner	Position 1	Position 2	ISO 16032 L_{Aeq}
V3	C1	P4	P14	40.5
V3	C1	P15	P19	40.0
V3	C1	P3	P13	38.4
V5	C1	P4	P14	45.8
V5	C1	P15	P19	44.0
V5	C1	P3	P13	43.3

5.1 Background noise levels

Background noise was measured at 9 positions across the room. Figure 7 shows a comparison of the sound pressure level of position 5, which is just beneath the internal unit and the background noise levels measured in the same position. Figure 8 shows the sound pressure levels at position 27, which was randomly selected from among the positions with average sound pressure levels. Background noise levels interfered in the positions that were far from the noise sources at fan speed 3 in the low frequency range and from 800 Hz upwards.

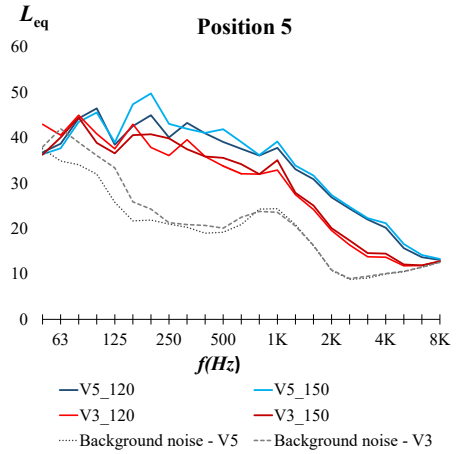


Figure 7. Sound pressure level in position 5 for two fan speed settings (V5 and V3) and two heights in comparison to background noise.

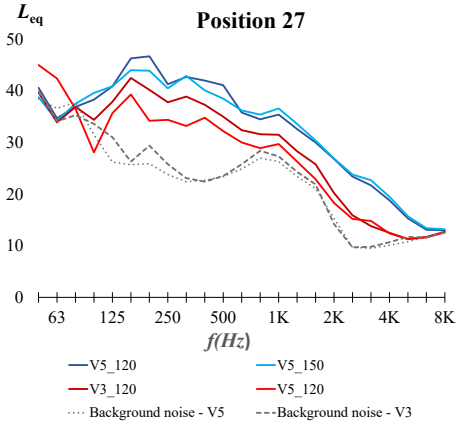


Figure 8. Sound pressure level in position 27 for two fan speed settings (V5 and V3) and two heights in comparison to background noise.

6. CONCLUSIONS

This paper is a study of the variation of the sound pressure levels in a room produced by HVAC equipment and how this affects the values of the average L_{Aeq} defined in ISO 16032.

A room in an office building was selected and measurements were performed in 30 positions, for two fan speed settings and two microphone heights: 120 cm and 150 cm, as these heights are typical occupant positions within this room.

The differences in sound pressure levels have been studied and compared in each position and in each frequency range.

Significant spatial variations of sound pressure levels were observed in the room, particularly in the low-frequency range (50–250 Hz), where differences of up to 15 dB were found between positions.

The average A-weighted differences between the two heights (120 cm and 150 cm) were minimal (~0.4 dB), indicating vertical uniformity at the range 120–150 cm of listener height, whereas fan speed changes (V3 vs. V5) resulted in much greater differences (~4.7 dB), primarily due to increased airflow.

The highest SPL values were consistently measured directly below the internal VRF units, confirming these areas as critical points for acoustic comfort.

When average L_{Aeq} levels were estimated using ISO 16032 method, differences of 2.1 dB and 2.5 dB were found between positions in this room for fan speeds of V3 and V5 respectively. Although the difference is small, it may determine whether the measured values fall within or exceed the limit values specified in national regulations.

In this particular case, it is sensible to take measurements at 1.50 m below the VRF units when assessing noise from building services, as this location represents a typical occupant position during courses and corresponds to a critical point in terms of sound exposure.

This study is part of a broader research carried out at Eduardo Torroja Institute for Construction Sciences, IETcc-CSIC, on service and equipment noise and its assessment. Other critical factors in the assessment of service and equipment noise have also been studied like the reverberation time correction[7].

7. REFERENCES

[1] ISO, ISO 16032:2024. Acoustics - Measurement of sound pressure level from service equipment or activities in buildings - Engineering method, 2024.

[2] ISO, ISO 10052:2021 Acoustics — Field measurements of airborne and impact sound insulation and of service equipment sound — Survey method.
[3] B. Casla Herguedas, T. Carrascal, and A. R. Fernández, 'Caso práctico: Acondicionamiento acústico de un aula de formación en edificio existente', in Proceedings of Acústica 2024, Faro, Portugal, Sep. 2024. [Online]. Available: https://www.spacustica.pt/acustica2024/pdf/livro_comunicacoes_v5.pdf
[4] Ministerio de Transportes, Movilidad y Agenda Urbana, Documento Básico DB HR Protección frente al Ruido. Código Técnico de la Edificación. (DB HR Protection against noise. Spanish Building Code). 2019. [Online]. Available: http://www.codigotecnico.org/cte/export/sites/default/web/galerias/archivos/DB_HR_sept_2009.pdf
[5] ISO, ISO 3382-3:2022. Acoustics - Measurement of room acoustic parameters - Part 3: Open plan offices.
[6] B. Rasmussen and T. Carrascal García, 'Noise from ventilation systems in dwellings - Regulations and field test procedures in selected countries in Europe', INTER-NOISE NOISE-CON Congr. Conf. Proc. InterNoise 22 Glasg. Scotl., vol. 265, no. 1, pp. 6221–6229, Aug. 2022, doi: 10.3397/IN_2022_0926.
[7] T. Carrascal, B. Casla-Herguedas, and A. Romero-Fernández, 'Correction for reverberation time in acoustic measurements from service and equipment - Comparison between different methods', INTER-NOISE NOISE-CON Congr. Conf. Proc. InterNoise 24 Nantes Fr., vol. 270, no. 6, pp. 5086–5094, August, 24, doi: 10.3397/IN_2024_3545.

DOI: 10.61782/fa.2025.0043

FORUM ACUSTICUM EURONOISE 2025

A SURVEY & EVALUATION METHOD FOR SPEECH INTELLIGIBILITY OF FIREFIGHTING RADIOS CONSIDERING THE ENVIRONMENT OF THE FIRE SITE

Jeongho Jeong[1*] **Insu Yeom**[2]
[1] Fire Insurers Laboratories of Korea, Gyeonggi-do, Republic of Korea
[2] National Fire Research Institute, Chungcheongnam-do, Republic of Korea

ABSTRACT

In a firefighting site, the firefighter's radio plays a very important role in not only responding to the situation quickly but also in maintaining the life of the firefighter. In order for firefighters to communicate smoothly using the radio, they must be able to clearly deliver their voices and deliver them to the other firefighters. However, there are various noise sources at the firefighting site, as well as the influence of the main firefighting water, making it difficult to communicate using the radio. In this study, we conducted a survey on the level of speech transmission of radios used at firefighting sites and on-site noise. Firefighters mainly used radios and handy microphones, and responded that it was difficult to hear speech due to various noises at firefighting sites and howling phenomena of several radios in the same place. The main sources of noise at the site were the sirens of fire trucks and equipment noise such as pump cars. The siren sound transmitted into the interior of fire trucks was investigated to be very high at about 83 to 93 dB. In addition, it was investigated that the radio speech sound was affected by the main water supply for firefighting.

Keywords: *speech intelligibility, fire fighting, radio transmission, fire truck noise*

1. INTRODUCTION

In large-scale firefighting operations, swift fire suppression and successful rescue efforts heavily rely on rapid and clear communication between firefighters on the ground and the commanding staff. Communication at the fire site is primarily carried out through radios. Therefore, the radios used by firefighters must be capable of transmitting clear voice messages with sufficient volume. Recently, firefighter radios have evolved to resemble smartphones, incorporating various information and communication functions. There are various noise sources at the firefighting site, as well as the influence of the main firefighting water, making it difficult to communicate using the radio.

This study explores methods for developing information and communication radios that enable clear communication for firefighters at the fire site, focusing on evaluating speech intelligibility considering the noise conditions at the site.

To achieve this, the study first conducted a survey to assess the current state of speech intelligibility in firefighter radios. Secondly, the noise levels and characteristics of key firefighting equipment were investigated. Finally, the study proposes a method for measuring the speech intelligibility of radios by applying the widely used Speech Transmission Index (STI), as s standardized as IEC 60268-16[1] and ISO 3382-3[2], and by simulating the noise characteristics of a firefighting environment.

2. SURVEY ON THE NOISE OF FIRE SITE

A survey was conducted on the satisfaction with the transmission and reception of messages through radios used by firefighters, the causes of poor audibility, and the major noise sources in fire ground environments. The survey was carried out from June to July 2024, involving approximately 500 firefighters. The survey method included both paper questionnaires and an online response option.

Regarding the extent of message transmission through the radios, only 9.8 % of the respondents reported that all messages were successfully transmitted. Furthermore, in terms of satisfaction with the reception of speech, only 39 % of the firefighters expressed satisfaction with the

[*] ***Corresponding author***: jhjeong92@email.ad.
Copyright: *©2025 First author et al. This is an open-access article distributed under the terms of the Creative Commons Attribution 3.0 Unported License, which permits unrestricted use, distribution, and reproduction in any medium, provided the original author and source are credited.*

clarity of the received sound. The most commonly selected reasons for poor audibility of radio messages were the background noise at the scene and the sounds of other firefighters. This suggests that issues related to environmental noise and acoustic phenomena, such as howling, are the main causes of poor reception.

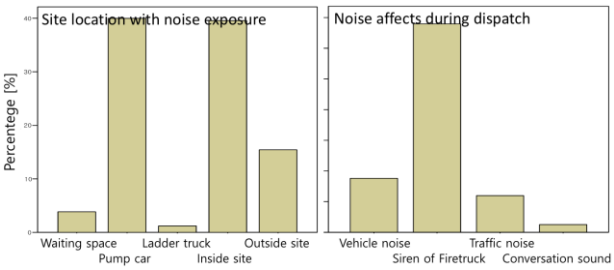


Figure 1. Results of a survey on noise at fire site

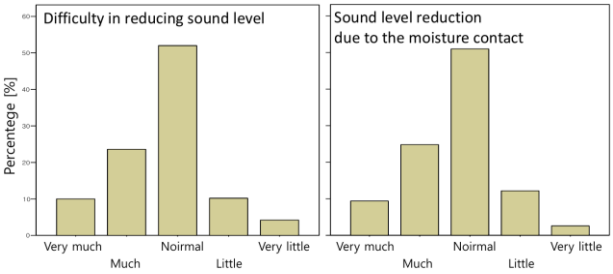


Figure 2. Survey results on difficulty in reducing level and sound level reduction due to the moisture contact

When asked about the locations and equipment that generate the most noise at fire ground operations, the results, as shown in Figure 1, indicated that pump trucks and the interior of fire scenes are the noisiest areas. During the dispatch phase, the siren of the fire truck was identified as the primary source of noise.

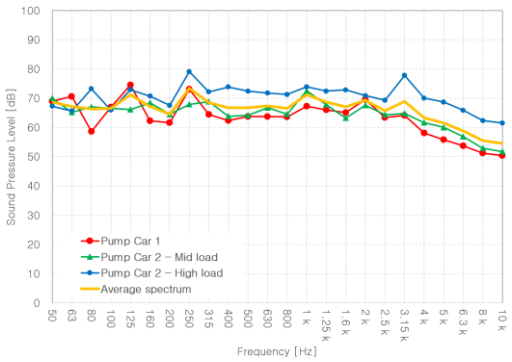
In terms of the reduction in radio volume and the effects of moisture, the survey results, as shown in Figure 2, revealed that 33.6% of respondents experienced difficulty due to low volume on their radios. Additionally, 34. 2% of firefighters reported experiencing difficulties due to moisture-related issues affecting the radios.

3. NOISE CHARACTERISTICS OF FIRE TRUCKS & SIREN

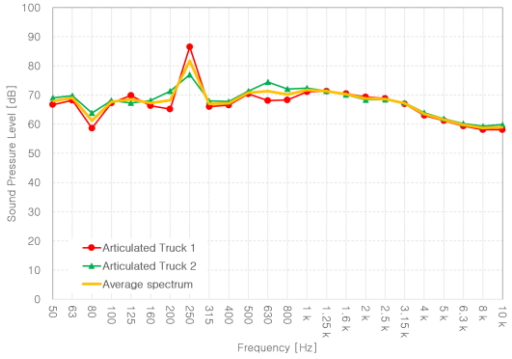
Based on the survey results, the noise characteristics of firefighting equipment were measured. Noise measurements were taken at several locations around the vehicles when operating pump trucks and articulated fire trucks, which are actively used by two fire stations in Gyeonggi Province. The noise from firefighting equipment was recorded throughout the entire training scenario, and noise levels were analyzed based on the operational stages and load conditions of the equipment. Figure 3 shows the firefighter training scenario and the articulated fire truck being measured.



Figure 3. The noise measurement of articulated fire trucks and firefighter training scenarios.



(a) Frequency characteristics of pump car



(b) Frequency characteristics of articulated truck

Figure 3. Sound level measurement results of fire trucks

Figure 3 presents the averaged noise measurement results for the fire pump trucks and articulated fire trucks,

categorized by each vehicle. The noise generated by the fire trucks exhibits a flat frequency characteristic, with specific noise bands occurring due to pump operation for each piece of equipment. The noise generated by a single fire vehicle typically exceeds 70 dB across most frequency bands, with noise levels around 78 dB(A) to 85 dB(A).
Figure 4 shows the frequency measurement results of the siren sound from various fire vehicles. Due to the characteristic nature of siren noise, high sound pressure levels were observed in frequency bands above 400 Hz, with a peak at 630 Hz. As the frequency increases, the sound pressure levels in the respective frequency bands decrease.

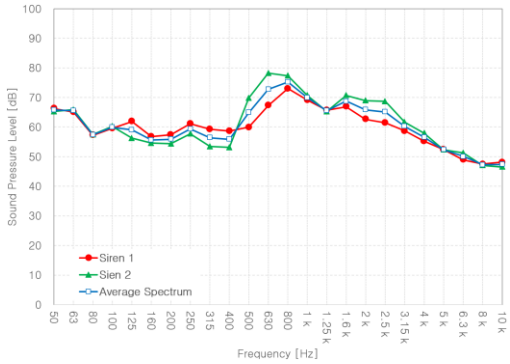


Figure 4. Sound level measurement results of sirens

The results of the firefighting equipment noise characteristics measurement were simplified for use as field sound sources when measuring the speech clarity of radios used by firefighters.

4. SPEECH TRANSMISSION INDEX MEASUREMENT OF FIREFIGHTERS RADIO

For speech intelligibility measurement of fire fighter's radio was conducted using STI (Speech Transmission Index), which is standardized in IEC 60268-16 and ISO 3382-3. The Speech Transmission Index (STI) measurement was based on IEC 60268-16. STI measurements were conducted using the NTI XL2 sound level meter and NTI Talk-Box. The sound source for the STI measurement was generated by the Talk-Box, which simulates human speech, and was then input into the transmission radio's microphone. The STI sound source transmitted through the communication network was received by the radio's speaker, and the STI of the received sound was measured.
Figure 5 illustrates the simplified measurement setup for STI measurement of the radios. The distance between the Talk-Box and the transmitting radio, as well as the distance between the receiving radio and the STI measurement microphone, was set to 10 cm, considering the actual conditions in which firefighters hold and speak into radios or listen to them. The transmission and reception of STI sound sources through the radios were conducted in a soundproofed environment to ensure adequate noise isolation.

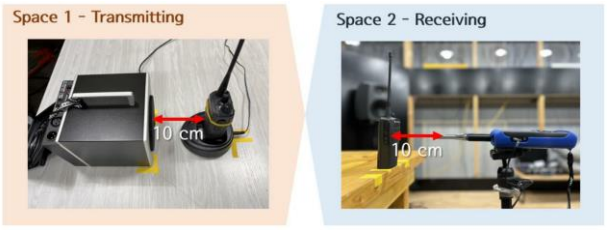


Figure 5. Speech intelligibility measurement set-up for fire fighter's radio

In addition to the STI measurement setup in Figure 5, the simplified noise characteristics of firefighting equipment were reproduced using two loudspeakers to measure the STI of firefighter radios. The noise level of firefighting equipment in the field was approximately 85 dB(A), but considering the test environment and the sound pressure levels generated by the firefighting radios, it was set to from 52 dB(A) to 72 dB(A) for the experiment.
STI measurements were conducted on three types of firefighter radios and one normal radio, comparing the values obtained in a quiet environment without firefighting equipment noise and the values obtained in conditions where firefighting equipment noise was present.

Table 1. STI measurement results of normal radio

BGN condition	STI	STI class
Low-noise	0.78	Excellent
52 dB(A) noise	0.76	Excellent
62 dB(A) noise	0.75	Excellent
72 dB(A) noise	0.42	Bad

Table 2. STI measurement results of fire fighters radio 1

BGN condition	STI	STI class
Low-noise	0.89	Excellent
52 dB(A) noise	0.54	Sufficient
62 dB(A) noise	0.31	Bad
72 dB(A) noise	0.22	Incomprehensible

Table 3. STI measurement results of fire fighters radio 2

BGN condition	STI	STI class
Low-noise	0.78	Excellent
52 dB(A) noise	0.75	Excellent
62 dB(A) noise	0.41	Bad
72 dB(A) noise	0.33	Bad

Table 4. STI measurement results of fire fighters radio 3

BGN condition	STI	STI class
Low-noise	0.92	Excellent
52 dB(A) noise	0.89	Excellent
62 dB(A) noise	0.84	Excellent
72 dB(A) noise	0.78	Excellent

The STI measurement results for the general radio (Type 1) and three types of firefighting radios are shown in Table 1 to Table 4. During the STI measurement, the volume of the receiving radio was set to its maximum. In the case of the general radio, the STI value did not change significantly as the surrounding noise level increased. However, under the 72 dB(A) condition, the STI value decreased to 0.42.
For the two types of firefighting radios, as shown in Tables 2 and 3, an increase in background noise level was found to correlate with a decrease in the STI value. However, for firefighting Radio 3, as shown in Table 4, although the STI value slightly decreased with the increase in background noise level, the evaluation grade remained "Excellent."
The different changes in STI values across the radios with increasing background noise levels are believed to be influenced by the sound pressure levels generated by the radios and the frequency characteristics of the radio microphones and speakers.

5. CITATIONS

In order to ensure rapid response and firefighter safety at fire situation, clear communication through firefighter radios is essential. However, measurement method for speech intelligibility has not been proposed that targets the entire system, including the hardware such as the transmitting radio's microphone and the receiving radio's speaker, as well as the software. Additionally, it is necessary to specify the measurement environment considering the field conditions of radio usage.

This study aimed to establish a method for evaluating speech intelligibility of firefighter radios by identifying the noise sources at fire scenes through a survey. The noise characteristics of selected firefighting equipment were measured and simplified, then presented as background noise during the speech intelligibility evaluation.
The speech intelligibility (STI) of the radios was measured and compared. Differences in speech transmission index (STI) and sound pressure levels between radio models were identified. It was found that the degree of change in speech intelligibility varied across radio models depending on the reproduction of background noise from the fire scene.
In the future, it is necessary to standardize the speech intelligibility (STI) measurement methods for radios and various products, considering the noise environments specific to their intended use.

6. ACKNOWLEDGMENTS

This work was supported by the research project funded By the Nation Fire Research Institute of Korea.

7. REFERENCES

[1] IEC 60268-16:2020, Sound system equipment - Part 16: Objective rating of speech intelligibility by speech transmission index.

[2] ISO 3382-3:2022, Acoustics — Measurement of room acoustic parameters — Part 3: Open plan offices

DOI: 10.61782/fa.2025.0399



FORUM ACUSTICUM
EURONOISE 2025

FACADE SOUND INSULATION OF BUILDINGS VS NOISE MAP IN PAMPLONA, SPAIN

Miguel Arana*
INAMAT[2]. Department of Sciences, Public University of Navarre,
Pamplona, Spain

ABSTRACT

The Spanish Technical Building Code requires minimum insulation of facades according to the acoustic zone in which the building is located. Thus, the airborne sound insulation, $D_{2m,nT,Atr}$ between a protected enclosure (living room/bedroom) and the exterior varies from 30 to 47 dBA. The daytime noise index value, Ld, can be obtained by consulting the strategic noise maps. The urban agglomeration of the Pamplona Region (Spain) has carried out the strategic noise maps in its four phases (2007-2012-2017 and 2022) as well as their associated action plans against noise.

NASUVINSA is the public housing and urban planning company of the Government of Navarre in charge of the management of social housing in the region of Navarre. Over the last decade, numerous protected housing developments have been delivered in the agglomeration of the Pamplona region. Although not exhaustively, it has been possible to access to results of the acoustic insulation of facades since 2011. The overall results of the insulation obtained are presented in this work, as well as the correlation between such insulation and the daytime levels, Ld, obtained from the noise map in force at the date of the building project.

Keywords: *Facade sound insulation, regulations, noise maps, in situ measurements.*

*__Corresponding author__: marana@unavarra.es
__Copyright__: ©2025 First author et al. This is an open-access article distributed under the terms of the Creative Commons Attribution 3.0 Unported License, which permits unrestricted use, distribution, and reproduction in any medium, provided the original author and source are credited.

1. INTRODUCTION

The basic document 'DB-HR Noise Protection' [1] specifies the objective parameters and verification methods whose compliance ensures that basic requirements are fulfilled and that the minimum quality levels of the basic noise protection demands of the Spanish Technical Building Code [2] are exceeded. Internal partition walls, as well as facades, roofs, party walls and floors in contact with the outside air, which make up each part of a building, must have characteristics (in conjunction with the adjacent construction elements) which meet certain minimum requirements. Thus, for example, protection against noise generated in enclosures not belonging to the same property requires that the airborne sound insulation index, $D_{nT,A}$, shall not be less than 50 dBA.

The data over time of the acoustic insulation measured for the interior walls by newly constructed houses in our city (Pamplona, Spain) has already been the subject of previous studies [3-4]. This paper analyses the requirements of the regulations regarding facade sound insulation between a protected enclosure (bedrooms, living rooms, classrooms, offices) and the outside. Results of many measurements over the last decade will be shown.

2. INDEX FOR ASSESSING THE FACADE SOUND INSULATION FROM EXTERNAL NOISE

The acoustic index used in Spanish regulations to assess the sound insulation of facades, roofs and floors in contact with the outside air is the A-weighted standardized level difference, $D_{2m,nT,Atr}$. The final terminology ('tr') refers to the fact that the predominant noise is traffic noise, with a standardized characteristic spectrum. It is defined by the expression:

$D_{2m,nT,Atr} = -10 \cdot log \sum_{1=1}^{n} 10^{(L_{Atr,i} - D_{2m,nT,i})/10}$ [dBA] (1)

where:

$D_{2m,nT,i}$ is the standardized level difference, in frequency band i, in dB.

$L_{Atr,i}$ is the A-weighted standardized traffic noise spectrum figure in the frequency band i, in dBA

i cover all one-third octave frequency bands from 100 Hz to 5 kHz.

The normalized spectrum for traffic noise is identical (at least in the range of frequencies between 100 Hz and 3.15 kHz) with the one used in ISO 717-1:2020 [5] to calculate the adaptation term C_{tr}. If the dominant outdoor noise is aircraft noise, this index is also used for the overall assessment, but using the values of the standard aircraft noise spectrum, A-weighted, $L_{Aav,i}$. Such spectra are shown in Table 1. Of course, the overall power of each spectrum is 0 dB.

Table 1. Normalized spectrum values for traffic and aircraft noise

f_i	$L_{Atr,i}$	$L_{Aav,i}$	f_i	$L_{Atr,i}$	$L_{Aav,i}$
100	-20	-23,8	800	-9	-9,5
125	-20	-20,2	1000	-8	-10,5
160	-18	-15,4	1250	-9	-11
200	-16	-13,1	1600	-10	-12,5
250	-15	-12,6	2000	-11	-14,9
315	-14	-10,4	2500	-13	-15,9
400	-13	-9,8	3150	-15	-18,6
500	-12	-9,5	4000	-16	-23,3
630	-11	-8,7	5000	-18	-29,9

The $D_{2m,nT,Atr}$ index is not a common index in European countries. In the regulations of various countries (DIN 4109 in Germany, NF S 31-057 in France, Resistance to sound_Part E, Building regulation in England, UNI 11367 in Italy, for example) it is more common to use the indices $D_{ne,w}$ and $D_{2m,nT,w}$, together with the spectral adaptation term C_{tr}. It is not common to use the spectral adaptation term for aircraft noise.

3. REQUIREMENTS FOR FACADE SOUND INSULATION AGAINST EXTERNAL NOISE

The facade airborne sound insulation, $D_{2m,nT,Atr}$, between a protected rooms and the outside shall not be less than the values shown in Table 2, depending on the use of the building and the values of the daytime noise index, Ld, of the area where the facade building is located. The value of the Ld index is obtained from the last approved strategic noise map.

Table 2. Minimum values for the $D_{2m,nT,Atr}$ index in Spanish regulation

Ld , dBA	living room, bedroom classroom, office	kitchen, corridor waiting room
Ld≤60	30	30
60<Ld ≤60	32	30
65<Ld ≤70	37	32
70<Ld ≤75	42	37
Ld > 75	47	42

When official data of the daytime noise index value, Ld, are not available, the value of 60 dBA will be applied for the type of acoustic area with predominantly residential land use. Although the indices for assessing outdoor noise insulation could be different, the required facade sound insulation in other countries also depends on the use of the building and the ambient noise levels in the environment where the building is located. For example, in Germany, insulation requirements for facades (R'_w + C_{tr}) range from 30 dB (for Ld up to 55 dBA) to 45 dB (for Ld up to 70 dBA). In England, in areas with outdoor noise levels of 70 dB, a minimum insulation of 40 dB is required for the $D_{ne,w}$ index. In the case of Italy, the regulation UNI 11367 classifies buildings into four classes, depending on the acoustic performance achieved. The minimum facade sound insulation requirements, index $D_{2m,nT,w}$, are 32 (Class IV), 37 (Class III), 40 (Class II) and 43 dB (Class I).

Considering the main single-number quantity descriptors (R'_w , $D_{n,w}$ and $D_{nT,w}$) and their combinations with the spectral adaptation terms, 27 descriptors are obtained for the facade sound insulation index [6]. It will show here results for the descriptor of the Spanish Standard, $D_{2m,nT,Atr}$ and the most used in many European countries, $D_{2m,nT,w}$ (measured with one speaker) together with the adaptation terms C and C_{tr}. In fact, $D_{2m,nT,\ Atr} = D_{1s,2m,nT,w} + C_{tr}$.

4. DATA

Results of acoustic insulation measurements on facades carried out in the period from 2011 to 2022 by 4 accredited laboratories for this type of measurements were provided. The location of the housing developments where these dwellings are found (location described in Table 2) are shown in Figure 1. This figure shows the noise map (Phase IV) of the Agglomeration of Pamplona. All the strategic noise maps carried out in Spain are available in the Noise Pollution Information System (SICA) on the website of the Ministry for Ecological Transition and Demographic Challenge of the Government of Spain [7].

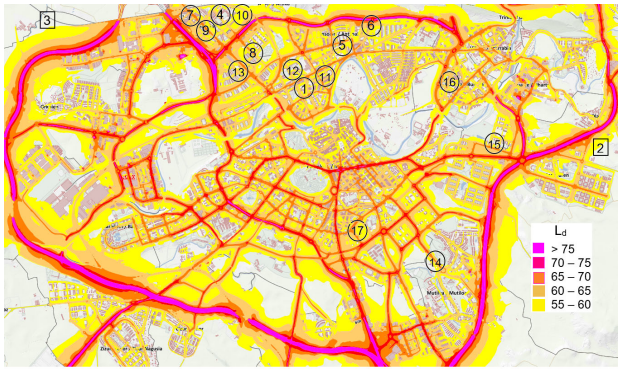


Figure 1. Location of the measurements. Points plotted on the acoustic map (phase IV) of the Agglomeration of Pamplona.



Figure 2. Example of measurement point (in black) and acoustic mapping of the area.

Figure 2 gives an idea of the available data. Location of the house (in black) where the measurements are taken and daytime levels, Ld, obtained from the current acoustic map.

5. RESULTS

Table 3 shows the results obtained for facade sound insulation against exterior noise in the measurements for which results were available.

Table 3. Facade sound insulation

Loc	Meas	Lab	(l-b), m^2	D_{2m}	D_{ls}	Ld
5	2011	1	(b) 6,6	33	36 (-1;-3)	
15	2011	2	(b)	34	37 (-1;-3)	
2	2011	1	(b) 4,1	28	31 (-1;-3)	
2	2011	1	(b) 4,8	32	35 (-1;-3)	
3	2011	1	(b) 6,5	32	35 (0;-3)	
4	2011	1	(b) 6,6	32	36 (-2;-4)	
10	2011	1	(l) 9,12	31	34 (-1;-3)	
5	2011	1	(l) 8,96	32	35 (-1;-3)	
5	2011	1	(l) 9,12	30	35 (-2;-5)	
6	2011	1	(b) 5,6	43	47 (-1,-4)	
6	2011	1	(l) 6,9	43	50 (-2,-7)	
7	2011	1	(l) 7,4	36	38 (0,-2)	
7	2011	1	(b) 7,4	37	39 (0,-2)	
8	2011	1	(l) 22,7	31	35 (-1,-4)	
8	2011	1	(b) 22,7	33	37 (-1,-4)	
9	2011	1	(l) 7,4	37	40 (-1,-3)	
9	2011	1	(b) 7,4	37	41 (-1,-4)	
10	2011	1	(l) 10,8	31	34 (-1,-3)	
10	2011	1	(l) 11,1	34	36 (-1,-2)	
10	2011	1	(l) 19,0	31	34 (-1,-3)	
10	2011	1	(l) 11,1	33	35 (0,-2)	
12	2011	1	(l) 9,4	34	37 (-1,-3)	
12	2011	1	(l) 9,1	35	39 (-1,-4)	
13	2011	1	(l) 7,8	34	38 (-2,-4)	
13	2011	1	(b) 7,9	37	40 (0,-3)	
11	2011	1	(b) 5,9	29	33 (-1;-4)	
11	2011	1	(l) 8.30	29	33 (-1;-4)	
1	2011	1	(b) 5,70	26	31 (-1;-4)	

11	2011	1	(l) 8,65	31	36 (-2;-5)	
1	2011	1	(b) 5,85	29	33 (-1;-4)	
12	2011	1	(b) 6.00	28	32 (-2;-4)	
8	2011	1	(l) 10,8	34	35 (0,-1)	
8	2011	1	(l) 11,1	35	39 (-1,-4)	
12	2011	1	(b) 5,9	34	37 (-1,-3)	

Table 3. Facade sound insulation (cont.)

Loc	Meas	Lab	(l-b),m^2	D_{2m}	D_{ls}	Ld
14	2012	2	(b)	34	37 (-1;-3)	60-65
14	2012	2	(b)	35	39 (-1;-4)	60-65
14	2012	2	(b)	34	35 (1;-1)	60-65
15	2013	2	(b)	31	33 (-1;-2)	55-60
14	2013	2	(b)	35	39 (-2;-4)	65-70
14	2013	2	(b)	34	37 (-1;-3)	65-70
14	2013	2	(b)	33	36 (-1;-3)	65-70
17	2013	2	(b)	32	37 (-2;-5)	65-70
17	2014	2	(b)	29	33 (-1;-4)	65-70
14	2014	2	(b)	28	32 (-2;-4)	65-70
14	2014	2	(b)	30	34 (-1;-4)	65-70
16	2019	2	(b)	35	40 (-1;-5)	65-70
14	2019	3	(b) 6,1	36	42 (-2,-6)	65-70
14	2019	3	(b) 6,1	36	42 (-2,-6)	65-70
15	2020	3	(b)	33	39 (-3;-7)	60-65
16	2021	1	(b) 6,67	46	50 (-1;-4)	65-70
16	2021	1	(b) 4,8	32	35 (-1;-3)	65-70
17	2021	1	(b)	33	39 (-2;-6)	60-65
3	2022	4	(l)	30	36 (-2;-6)	

Legend:
Loc: Location of new housing (see Fig. 1)
Meas: Year of measurements
Lab: Laboratory (accredited) that performed the measurements. There were 4.
(l-b), m^2: Receiving room (**l**iving room/**b**edroom) and wall surface in contact with the outside.
D_{2m}: $D_{2m,nT,Atr}$ (dBA); Standardized level difference, A-weighted, on facades and roofs, when the dominant exterior noise is due to traffic [1].
D_{ls}: $D_{ls,2m,nT,w}$ (C;C_{tr}): Weighted standardized level difference; single-number quantity derived from one third octave band values, measured with one loudspeaker (**1s**) [5]. **C** and **C_{tr}** are the spectral adaptation terms for, respectively, pink noise and traffic noise. It can be assumed that $D_{2m,nT,Atr} = D_{ls,2m,nT,w} + C_{tr}$
Ld: A-weighted long-term average sound levels, determined over all the diurnal period (7 – 19 hours) obtained from the noise map in force at the date of the building design.

6. ANALYSIS

Although the basic document 'DB-HR Noise Protection' was approved in 2007, an adaptation period was granted, and it became mandatory in April 2009. Until this date, the previous regulation on acoustic conditions of buildings, NBE-CA-81 [8], continued to be applied. For this reason, it cannot be concluded whether current facade sound insulation requirements in force were fulfilled for measurements prior to 2012. Although the old evaluation index (R) was not the current index ($D_{2m,nT,Atr}$), the value required at that time (30 dBA) will be assumed to be equivalent (for purposes of compliance with the requirements) to the minimum value required today. It is possible to carry out such an assessment for measurements after 2012, because the sound insulation requirements were already in force and the strategic noise maps were published.

Cells whose results do not strictly comply with the requirements of the sound insulation standard are highlighted with grey background in Table 3. However, in some cases, the non-compliance is only 1-2 dBA, which is within the margin of the error of measurement. In six of the cases, the non-compliance is more than 4 dBA.

7. CONCLUSIONS

After the entry into force of the new building acoustic insulation requirements in Spain (CTE and dB-HR), a notable increase in the acoustic performance of the interior partitions of buildings has become evident. Although an increase has also been noted, it has been much lower in the case of facade insulation against external noise. The facade sound insulation obtained is lower than required in a significant percentage of measurements. In six of the cases, the non-compliance is more than 4 dBA.

More data are required to draw further conclusions. For example, it had not been possible to access to the architectural designs where acoustic insulation of facades was justified, in the light of the dB-HR requirements. This would allow confirming whether strategic noise maps are useful as well as its impact on the required sound insulation. It is the author's opinion that the great uncertainty associated with the results obtained in the elaboration of acoustic maps significantly limits the subsequent decisions that, in theory, they entail.

8. ACKNOWLEDGMENTS

The author wishes to thank 'NASUVINSA' and 'ID Ingeniería Acústica' for their assistance with data collection, which made the study possible

9. REFERENCES

[1] Real Decreto 1371/2007, de 19 de octubre. BOE núm. 254, de 23 de octubre de 2007, pp: 42992-3045. https://www.boe.es/eli/es/rd/2007/10/19/1371 (in Spanish).

[2] Real Decreto 314/2006, de 17 de marzo. BOE núm. 74, de 28 de marzo de 2006, pp: 11816-31. https://www.boe.es/eli/es/rd/2006/03/17/314 (in Spanish).

[3] Miguel A. Arana, Ricardo San Martin, Antonio Vela, and Maria L. San Martin, Acoustic insulation of recent flat buildings in Pamplona, Spain, The Journal of the Acoustical Society of America 112, Issue 5_Supplement, 2429 (2002)

[4] Arana, Miguel; San Martin, Ricardo; Nagore, Iñaki; Pérez, David. Improvements in acoustic insulation of new flats in Pamplona (Spain) after the approval of the current Spanish Technical Building Code. INTER-NOISE and NOISE-CON Congress and Conference Proceedings, InterNoise20, Seoul, Korea, pages 990-1987, pp. 1161-1166(6). (2020)

[5] ISO 717-1:2020. Acoustics. Rating of sound insulation in buildings and of buildings elements. Part 1: airborne sound insulation.

[6] Rasmussen B, Machimbarrena M, Fausti P. COST TU0901 C. Building acoustics throughout Europe. Vol. 1: Towards a common framework in building acoustics throughout Europe; 2014. e-ISBN: 978-84-697-0158-4

[7] Sistema Básico de Información sobre la Contaminación Acústica (SICA) (in Spanish). https://sicaweb.cedex.es/

[8] NBE-CA-81. Norma Básica de la Edificación. Condiciones Acústicas. R.D. 1909/81. B.O.E. 7 de septiembre de 1981. (in Spanish)

DOI:

Main theme: A03 Building Acoustics

Session A03.03 Prediction of sound and vibration transmission in buildings

Chair(s): C. Hopkins, E. P. B. Reynders

DOI: 10.61782/fa.2025.0403

FORUM ACUSTICUM EURONOISE 2025

FINITE ELEMENT ANALYSIS OF AIRBORNE SOUND TRANSMISSION IN STUD-COUPLED LIGHTWEIGHT WALL SYSTEMS

Pedram Ayyobi[1*] **David Gomes Andrade**[1] **Luís Simões da Silva**[1]
Luís Godinho[1]
[1] University of Coimbra, ISISE, ARISE, Department of Civil Engineering, Coimbra, Portugal

ABSTRACT*

Lightweight wall systems, widely used in aerospace and construction, offer advantages such as weight efficiency, rapid construction, and ease of replacement. However, the presence of flexible or rigid studs within these systems complicates their acoustic performance, particularly in terms of airborne sound insulation. This study employs an efficient finite element approach to accurately predict the sound transmission loss of stud-coupled double-leaf lightweight walls. This approach offers a cost-effective and time-efficient alternative to experimental and analytical methods while maintaining acceptable precision. A parametric study was conducted to investigate the sensitivity of sound insulation to various parameters, including panel thickness and stud stiffness. The results provide insights into the influence of effective parameters on the acoustic performance of lightweight coupled wall systems, facilitating the design of more acoustically effective solutions for noise-sensitive environments.

Keywords: *lightweight wall systems, sound transmission loss, stud-coupled double-leaf, finite element, parametric study.*

* ***Corresponding author***: Pedram.Ayyobi@uc.pt
Copyright: *©2025 P.Ayyobi et al. This is an open-access article distributed under the terms of the Creative Commons Attribution 3.0 Unported License, which permits unrestricted use, distribution, and reproduction in any medium, provided the original author and source are credited.*

1. INTRODUCTION

Understanding the impact of studs on the sound insulation of double-leaf walls is relevant for building acoustics [1], [2]. Indeed, double-leaf walls offer improved sound insulation compared to single walls, but their performance may be affected by structural connections like studs, which act as sound bridges [3], [4], coupling the two leaves of the partition. Various approaches have been employed to analyze this effect, including analytical, experimental, and numerical methods [4–8].

Early analytical models simplified the wall system by focusing on airborne transmission through infinite, unconnected leaves, neglecting the influence of studs [9], [10]. Later models attempted to incorporate studs as rigid connections, which proved inadequate for lightweight walls with flexible metal studs [11–13]. To address this, analytical models evolved to include flexible studs, often represented as springs with translational and rotational stiffness [4], [7], [11], [14]. However, these models often required empirically derived stiffness values, limiting their predictive power for new designs [11]. Smeared models offered another analytical approach by distributing stud properties uniformly [7]. Vigran's work [3], reviving and extending Sharp's method, aimed to correct transfer matrix calculations by accounting for stud effects, initially for infinitely stiff studs and later for flexible ones using empirical data. While providing valuable insights into phenomena like mass-spring-mass resonance and coincidence, analytical models often involve simplifications in geometry and boundary conditions [4], [7], [11].

Experimental investigations have been vital for assessing the sound insulation performance of double-leaf walls with various stud configurations [5], [15]. These studies have examined the influence of stud type, spacing, cavity filling,

and the use of resilient elements [15], [16]. Researchers have measured the sound reduction index (R) and weighted sound reduction index (R_w) for different constructions. Studies by Hongisto et al. specifically explored the impact of stud characteristics and resilient channels [5], [8]. While providing real-world data for validation, experimental approaches are resource-intensive and may not offer detailed insights into the dynamic behavior of studs within the assembly [5].

Numerical methods, particularly the Finite Element Method (FEM), offer a more comprehensive approach. FEM allows for detailed modeling of stud geometry, material properties, and the interaction between studs, panels, and the cavity. It can accurately represent fluid-structure interaction (FSI), crucial for understanding sound transmission pathways. But FEM analyses are time consuming and require experts for accurately simulate the complex systems. Numerical models can also incorporate damping and complex boundary conditions. They have demonstrated good agreement with experimental results [2], [17], [18].

This study makes use of a simplified model that efficiently predicts the performance of stud-coupled infinite wall systems with reasonable accuracy while still being time efficient. Moreover, the model is designed to be flexible, allowing for the analysis of various wall configurations and stud shapes. The model tends to be efficient compared to existing FEM or analytical approach while providing acceptable accuracy.

2. FINITE ELEMENT MODELING METHODOLOGY

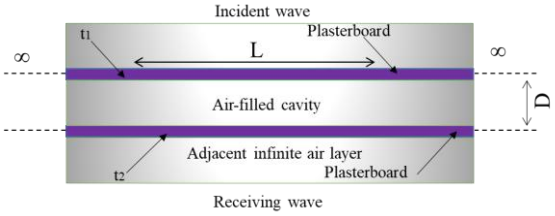
Figure 1 shows the schematic view of un-coupled and coupled wall systems, considering L as periodic unit cell length, t_1 and t_2 are panels thickness and D is cavity thickness. The system is infinite, and an incident plane wave is applied to one side of the panel, while its effect is evaluated in other side by means of nodal displacements. The finite element model uses 1D elements, see Figure 2. The plane strain Euler-Bernoulli beam element has been used to model wall panels. The air inside the cavity and receiving side is modeled using analytical frequency dependent spring, discussed in detail elsewhere [18]. The stud is modeled as equivalent two node bar element. Additionally, infinite panels with a 600 mm stud span are modeled using Bloch–Floquet boundary conditions. The numerical model is organized into two groups, each evaluating wall performance based on panel thickness and stud thickness. Material properties used in the models are listed in Table 1.

The panels' thickness is considered in two cases of identical (0.0125mm) and nonsymmetrical panels (0.0125-0.025 m). the cavity thickness is considered 0.05 m, verification models based on [7] except for experimental studies.

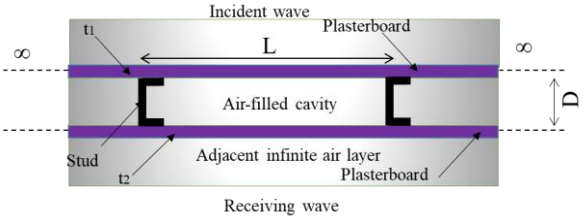
Table 1. material properties

Element	Properties		
Panels	$\rho_p = 790 kg/m^3$	$\nu_p = 0.3$	$E_p = 2.5e9\,Pa$
Stud	$\rho_s = 7850 kg/m^3$	$\nu_s = 0.28$	$E_s = 2.1e11\,Pa$
Air	$\rho_a = 1.21 kg/m^3$	$c = 343 m/s$	

* ρ is density, ν is Poisson ratio and E is module of elasticity. Air density and speed of sound are indicated by ρ_a and c, respectively.



a) Un-coupled wall system



b) Coupled wall system

Figure 1. Schematic view of the wall.

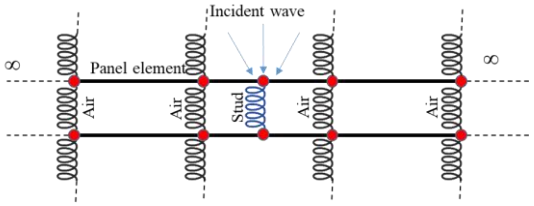


Figure 2. FE model scheme.

3. MODEL VERIFICATION AND VALIDATION

The proposed simulation approach is compared with an existing analytical model [7] in normal and 45 degrees incident angle for un-coupled system (Figures 3 and 4) and coupled systems either analytical or experimental studies (Figures 5-7). For verification, the proposed model is compared against two analytical models [7], [19] and then validated with two experimental studies [3], [19].

The comparison between the proposed numerical model and the analytical model from [7] shows excellent agreement for both 45° and normal incidence (Figures 3 and 4).

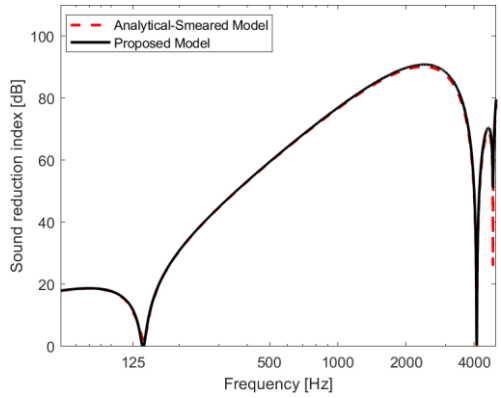


Figure 3. Comparison of Un-coupled proposed model and analytical smeared model ($\varphi = 45^o$).

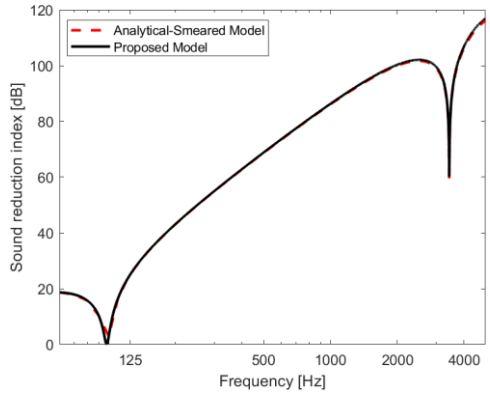


Figure 4. Comparison of Un-coupled proposed model and analytical smeared model ($\varphi = 90^o$).

Figure 5 compares the proposed numerical model with the analytical smeared model from [7]. Despite some differences, the numerical model follows the same trend, predicted the coincidence frequency, and shows acceptable agreement. Moreover, from Figure 6, comparisons with experimental studies (Vigran [3]) reveal that the model accurately predicts the mass–air–mass and coincidence frequencies, although with differences of about 5 dB in high frequency ranges. It also agrees well with the experimental and analytical results of Godinho et al. [19], even though there is an approximate 10 dB difference in the low frequency range (Figure 7).

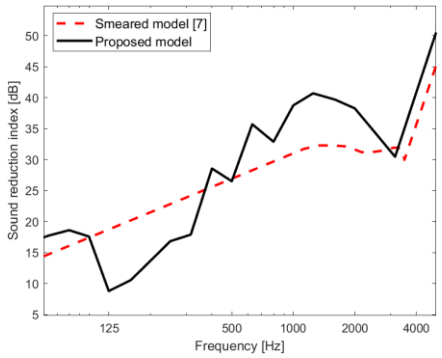


Figure 5. Comparison of proposed model and analytical smeared model (diffuse field).

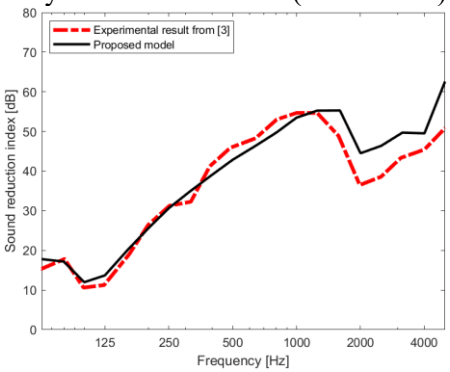


Figure 6. Comparison of proposed model and Experiment [3].

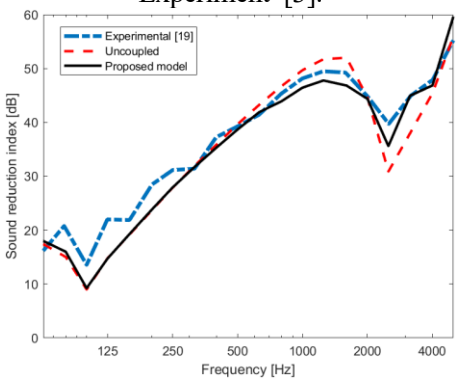
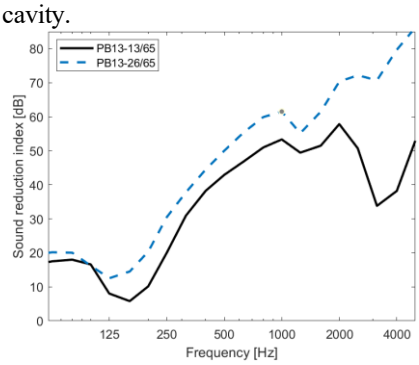


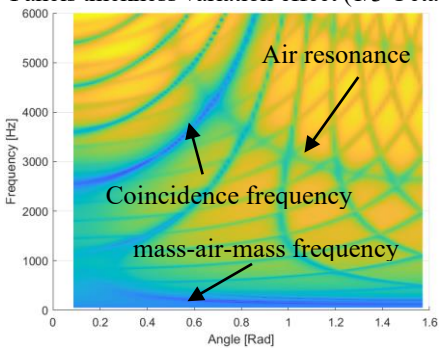
Figure 7. Comparison of proposed model and results of [19].

4. PARAMETRIC STUDY

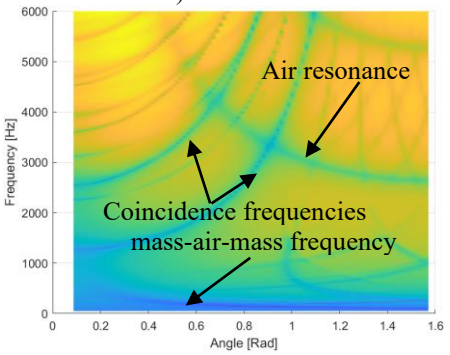
The first part of the parametric study evaluates the effect of wall panel thickness on the model. As expected, using asymmetric panel thicknesses leads to different coincidence resonances. Figure 8 illustrates this effect by comparing configurations with 13 mm and 26 mm panels, both with a 65 mm air gap. The material properties for the panels and studs are provided in Table 1. In this notation, "PB 13-13/65" denotes a wall consisting of two 13 mm panels with a 65 mm cavity.



a) Panels thickness variation effect (1/3 Octave band)



b) PB13-13/65

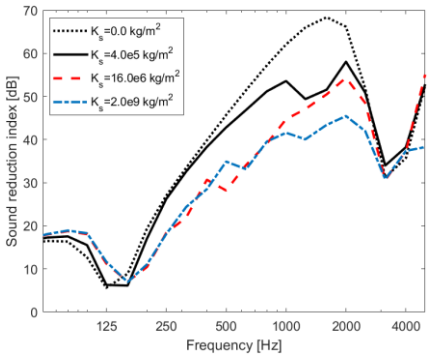


c) PB 13-26/65

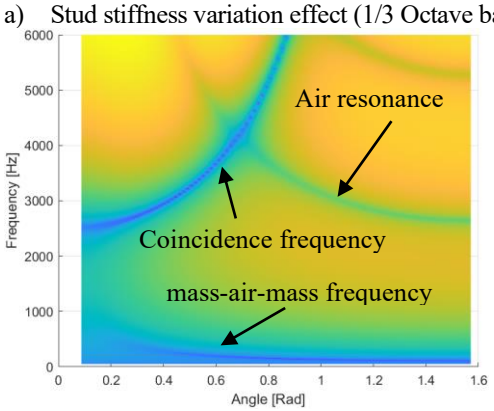
Figure 8. sound transmission index variations of double leaf wall due to geometry differences.

Asymmetric panel thickness produces two distinct coincidence frequencies (Figures 8b and 8c) because each panel responds differently due to its unique mass and stiffness. In accordance with the mass law, an increase in mass and stiffness generally improves sound insulation. Figure 8a illustrates that while the performance is similar at low frequencies—where the response is largely governed by mass—the stiffer, heavier configuration delivers significantly enhanced insulation at higher frequencies, achieving improvements of up to 5–20 dB. This is due to the reduced vibrational transmission and more favorable behavior of the stiffer system.

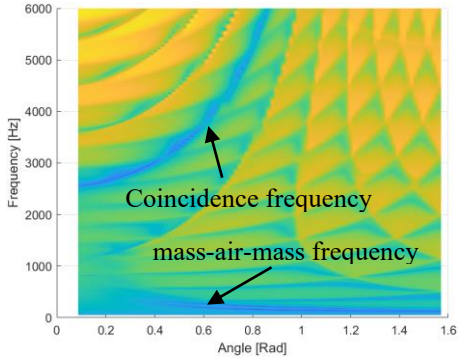
To evaluate the effect of stud stiffness on sound insulation, four cases were examined: one without a stud, two with intermediate and standard steel stud stiffness, and one with a relatively rigid stud ($K_s = 2e9 kg/m^2$, similar to wood studs). Figure 9 presents one-third octave band plots of the sound reduction index for these cases, comparing uncoupled and rigid boundary conditions across various incident angles.



a) Stud stiffness variation effect (1/3 Octave band)



b) Un-coupled system



c) Rigid stud

Figure 9. sound transmission index variations of double leaf wall due to stud stiffness.

Figure 9a shows that as stud stiffness increases, the wall's sound insulation deteriorates. For example, around 1000 Hz, an un-coupled wall achieves roughly 62 dB, while a wall with a softer stud reaches about 53 dB; this gap widens to 10–20 dB with intermediate or rigid studs. At low frequencies, all configurations perform similarly because the system's mass dominates the response. However, at higher frequencies, the increased stiffness in stud-coupled systems enhances vibrational transmission, thereby reducing insulation. Figure 9b displays the resonance frequencies of the un-coupled system, where both mass–air–mass and air resonances are evident. In contrast, Figure 9c—representing a rigid stud-coupled system—exhibits significant oscillations across all frequencies, with only the mass–air–mass and coincidence resonances clearly visible. This behavior indicates that a stiffer connection introduces additional dynamic effects, ultimately compromising sound insulation in the medium and high frequency ranges.

5. CONCLUSIONS

This study presents a simplified FEM-based model that combines finite element analysis with an analytical formulation for the fluid medium. The model shows good agreement with existing analytical and experimental data. Our findings indicate that key design parameters—such as panel thickness and stud stiffness—significantly influence the acoustic performance of stud-coupled double-wall systems. Thicker panels improve performance by increasing mass and introducing asymmetry, while more flexible studs enhance insulation in the medium to high-frequency range. Overall, the model is both efficient and accurate, and it can be further developed to incorporate cavity absorbers or extend to triple-wall systems.

6. ACKNOWLEDGMENTS

This work was partly financed by FCT / MCTES through national funds (PIDDAC) under the R&D Unit Institute for Sustainability and Innovation in Structural Engineering (ISISE), under reference **UID/04029/Institute for Sustainability and Innovation in Structural Engineering (ISISE)**, and under the Associate Laboratory Advanced Production and Intelligent Systems ARISE under reference LA/P/0112/2020.
It was also funded by the Innovation Pact "R2UTechnologies | modular systems" (C644876810-00000019), by "R2UTechnologies" Consortium, co-financed by NextGeneration EU, through the Incentive System "Agendas para a Inovação Empresarial" (Agendas for Business Innovation"), within the Recovery and Resilience Plan (PRR).

7. REFERENCES

[1] A. Arjunan *et al.*, "Development of a 3D finite element acoustic model to predict the sound reduction index of stud based double-leaf walls," *J. Sound Vib.*, vol. 333, no. 23, pp. 6140–6155, 2014, doi: 10.1016/j.jsv.2014.06.032.

[2] A. Arjunan, C. J. Wang, K. Yahiaoui, D. J. Mynors, T. Morgan, and M. English, "Finite element acoustic analysis of a steel stud based double-leaf wall," *Build. Environ.*, vol. 67, pp. 202–210, 2013, doi: 10.1016/j.buildenv.2013.05.021.

[3] T. E. Vigran, "Sound insulation of double-leaf walls – Allowing for studs of finite stiffness in a transfer matrix scheme," *Appl. Acoust.*, vol. 71, no. 7, pp. 616–621, Jul. 2010, doi: 10.1016/j.apacoust.2010.02.003.

[4] J. C. E. Van den Wyngaert, M. Schevenels, and E. P. B. Reynders, "Predicting the sound insulation of finite double-leaf walls with a flexible frame," *Appl. Acoust.*, vol. 141, pp. 93–105, Dec. 2018, doi: 10.1016/j.apacoust.2018.06.020.

[5] V. Hongisto, M. Lindgren, and R. Helenius, "Sound Insulation of Double Walls – An Experimental Parametric Study," *Acta Acust. united with Acust*, vol. 88, pp. 904–923, 2002.

[6] A. J. Price and M. J. Crocker, "Sound Transmission through Double Panels Using

Statistical Energy Analysis," *J. Acoust. Soc. Am.*, vol. 47, no. 3A, pp. 683–693, Mar. 1970, doi: 10.1121/1.1911951.

[7] J. Wang, T. J. Lu, J. Woodhouse, R. S. Langley, and J. Evans, "Sound transmission through lightweight double-leaf partitions: Theoretical modelling," *J. Sound Vib.*, vol. 286, no. 4–5, pp. 817–847, 2005, doi: 10.1016/j.jsv.2004.10.020.

[8] V. Hongisto, "Sound insulation of double panels - Comparison of existing prediction models," *Acta Acust. united with Acust.*, vol. 92, no. 1, pp. 61–78, 2006.

[9] J. M. P. António, A. Tadeu, and L. Godinho, "Analytical evaluation of the acoustic insulation provided by double infinite walls," *J. Sound Vib.*, vol. 263, no. 1, pp. 113–129, 2003, doi: 10.1016/S0022-460X(02)01100-8.

[10] Al. London, "Transmission of reverberant sound through single walls," *Natl. Bur. Stand.*, vol. 42, 1949.

[11] J. Poblet-Puig, A. Rodríguez-Ferran, C. Guigou-Carter, and M. Villot, "The Role of Studs in the Sound Transmission of Double Walls," *Acta Acust. united with Acust.*, vol. 95, no. 3, pp. 555–567, May 2009, doi: 10.3813/AAA.918176.

[12] B. H. Sharp, "Prediction Methods for the Sound Transmission of Building Elements.," *Noise Control Eng*, vol. 11, no. 2, pp. 53–63, 1978, doi: 10.3397/1.2832099.

[13] F. J. Fahy and P. Gardonio, *Sound and Structural Vibration Radiation, Transmission and Response*. Academic Press, 2006.

[14] J. L. Davy, "The sound transmission of cavity walls due to studs," in *INTER-NOISE and NOISE-CON Congress and Conference Proc.*, Institute of Noise Control Engineering, 1993, pp. 975–978.

[15] S. Paul, G. F. Radavelli, and A. R. da Silva, "Experimental evaluation of sound insulation of light steel frame façades that use horizontal inter-stud stiffeners and different lining materials," *Build. Environ.*, vol. 94, pp. 829–839, Dec. 2015, doi: 10.1016/j.buildenv.2015.08.010.

[16] G. QIANG-GUO and J.-Q. WANG, "effect of resilient connection on sound transmission loss of metal stud double panel partitions," *Acta Acust. united with Acust*, vol. 8, no. 1, pp. 1–13, 1983, doi: 10.15949/j.cnki.0371-0025.1983.01.001.

[17] J. C. E. Van den Wyngaert, M. Schevenels, and E. P. B. Reynders, "Broadband acoustic shape optimization of studs in double-leaf walls," *J. Sound Vib.*, vol. 485, p. 115562, Oct. 2020, doi: 10.1016/j.jsv.2020.115562.

[18] P. Ayyobi, D. Andrade, L. Simões da Silva, and L. Godinho, "predicting airborne sound transmission in infinite lightweight double-panel walls : an efficient finite element approach" in *XIII congresso Ibérico de Acústica, Tecniacústica*, (Faro, Portugal), 2024.

[19] L. Godinho, A. B. Santos, R. Luis, and R. Santos, "sound insulation of layered panels : comparision of experimental and theoretical results," in *The thirteenth international congress on sound and vibration*, (Vienna, Austria), 2006.

DOI: 10.61782/fa.2025.0686

FORUM ACUSTICUM EURONOISE 2025

POSSIBILITY OF MODELLING THE RECEIVING ROOM IN FEM CALCULATIONS

Alina Lahdensivu[1*] **Lauri Talus**[1] **Jesse Lietzén**[1]
Mikko Kylliäinen[1]
[1] AINS Group, Department of Acoustical Engineering, Finland

ABSTRACT

Timber partition floors have problems with their impact sound insulation (ISI) at low frequencies under 100 Hz. The Finnish Government has sought to increase construction from timber in recent years, which causes ISI to play an important role in the structural design process of timber floors. Literature indicates the receiving room plays a significant role in the verifiable impact sound insulation of a timber joist floor. There are very few analytical calculation methods for ISI of timber floors, and their solutions are only valid for specific cases. The most common assumptions in analytical equations are about the diffusivity of the sound field and completely rigid room boundaries. This study revisits the theory of a modal sound field in a receiving room and coupling between a simply supported floor and the sound field of a receiving room. The possibility of modelling the receiving room in FEM calculations of ISI is discussed.

Keywords: *impact sound insulation, timber joist floor, modal sound field*

1. INTRODUCTION

In recent decades, timber has become more popular as a building material due to its environmental benefits. Timber floors however have problems with their impact sound insulation at low frequencies. [1–4]
It has long been acknowledged that the sound field of a room affects the verifiable impact sound insulation (ISI) of intermediate floors especially in the low frequencies where the sound field is modal [1,5–11]. Most calculation methods, however, assume a diffuse sound field and completely rigid boundaries causing innate uncertainty [7–8,11–14].
This article is an extract from the Master's thesis of Lahdensivu [15], where the effect of the room size to the ISI was examined, and focuses on the coupling between a plate and the sound field of a receiving room. The purpose of this study is to show how the coupling between the plate and the room affects the sound pressure field in the receiving room.

2. LITERATURE REVIEW

2.1 Sound field of a receiving room

The sound field of a room is divided by the Schroeder limiting frequency into diffuse and modal sound fields [16], [17]. In 1954 Schroeder defined a minimum requirement for a diffuse sound field to have a modal overlap factor of $M = 10$ [18]. In the 1962 article [19] the modal overlap factor was revised to $M = 3$ based on other studies. In a diffuse sound field, it is assumed that the energy density is equal everywhere in the room i.e. sound can propagate from and to any direction with the same probability and reflect to any direction with equal probability. A diffuse sound field can be studied purely statistically, making calculations simpler. [16–17]
The modal overlap factor is not an adequate indicator to assume a diffuse sound field on all frequency bands in a room. A diffuse sound field cannot be assumed in small, enclosed spaces, in rooms where the longest dimension is clearly greater in comparison to the shortest dimension, in rooms with inadequate amount of scattering and diffusing elements, in rooms with many absorbing surfaces with uneven distribution as well as in very large spaces where the sound field acts locally. [16–17]

[*] ***Corresponding author***: alina.lahdensivu@ains.fi.
Copyright: *©2025 Lahdensivu et al. This is an open-access article distributed under the terms of the Creative Commons Attribution 3.0 Unported License, which permits unrestricted use, distribution, and reproduction in any medium, provided the original author and source are credited.*

In a modal sound field, the amplitude of the sound pressure doesn't vary with time. Room modes are found on frequencies where at least one room dimension is a multiple of the half wavelength of the mode. There are three types of room modes: axial, tangential and oblique. [20]
In a room with perfectly rigid and reflective boundaries, room modes can be calculated using Eqn. (1).

$$f_{n_x n_y n_z} = \frac{c}{2}\left[\left(\frac{n_x}{l_x}\right)^2 + \left(\frac{n_x}{l_x}\right)^2 + \left(\frac{n_x}{l_x}\right)^2\right] \quad (1)$$

Where c = 343 m/s, n_x, n_y and n_z are the number of half wavelengths and l_x, l_y and l_z are the dimensions of the room. Eqn. (1) gives a reasonable estimate for the room modes in most rectangular rooms. Lightweight walls, however, cannot be considered rigid [20].
In a room where the boundaries are not completely rigid the eigenvalues of the wavefunction are complex [16–17,20]. Kuttruff [20] has proposed a simplified way to calculate the sound pressure in a receiving position with non-reflective surfaces. However, solving the system of equations requires numerical methods for iteration.
Kuttruff's equation utilizes the surface impedance of a wall, which is dependent on frequency and the material properties of the boundary. A lightweight gypsum board wall can be considered to perform as a plate resonator. The impedance of a plate resonator can be calculated for example using Eqn. (2) [20].

$$Z = r_s + \mathrm{j}\left(\omega m - \frac{\rho c^2}{\omega d}\right) \quad (2)$$

Where r_s is the flow resistivity of the absorbing material in the cavity, $\mathrm{j} = (-1)^{1/2}$, ω is angular frequency, m is surface mass of the plate, ρ = 1,205 kg/m^3, c = 343 m/s, and d is the total thickness of the air cavity.
The absorption of the plate resonator is very localized to its natural frequency. Calculating the absorption coefficient from the plate resonator impedance does not correspond to a measured absorption coefficient of a lightweight wall. The conversion also loses the information about the complex part of the impedance which corresponds to the losses at the boundary.

2.2 Modal coupling between a plate and a room

Multiple different calculation methods for the coupling between the sound field of a room and a structure have been made [7–8,13–14,21]. Most equations predicting the impact sound insulation of timber floors and coupling of the sound field of the room are based on assumptions of diffuse sound field and perfectly rigid room boundaries [7–8,13–14,21].

In 1967 Kihlman [21] suggested an equation to calculate the sound pressure level in the receiving room when the source room is excited with an omnidirectional loudspeaker. Neves e Sousa & Gibbs [7–8] modified Kihlman's [21] equation to research the modal coupling between the receiving room and a homogeneous concrete floor, when the floor is excited by a point force. The sound pressure level in the receiving room in frequency domain can be calculated using Eqn. (3).

$$p(x,y,z) = -\mathrm{j}\omega\rho \sum_{n_x,n_y,n_z=1}^{\infty} \frac{c^2(-1)^{n_z} C_{n_{x1}n_{y1}} \varphi_{n_x n_y n_z}(x,y,z)}{\left[\left(\omega_{n_x n_y n_z} + \mathrm{j}\delta\right)^2 - \omega^2\right] \Lambda_{n_x n_y n_z}} \quad (3)$$

where $\mathrm{j} = (-1)^{1/2}$, ω is the angular frequency, ρ = 1,205 kg/m^3, n_x, n_y and n_z are the number of half wavelengths of the mode, c = 343 m/s, $C_{nx,ny}$ is the coupling factor, φ is the eigenmode function of the room, $\omega_{hx.ny.nz}$ is the angular eigenfrequency of the receiving room, $\delta = 6{,}9/T$ [21], [22], [23] and $\Lambda_{n_x n_y n_z} = \int \varphi_{n_x n_y n_z}(x,y,z)\,\mathrm{d}V = V/8$.
When the floor is excited by a point force, the coupling factor is

$$C_{n_x n_y} = \mathrm{j}\frac{4\omega F}{\pi^2 m} \sum_{n_{x1},n_{y1}=1}^{\infty} \left\{\frac{\varphi_{n_{x1}n_{y1}}(x_0,y_0)}{\omega_{n_{x1}n_{y1}}^2(1+\mathrm{j}\eta) - \omega^2} D\right\}$$
$$D = \frac{[(-1)^{n_{x1}+n_x} - 1][(-1)^{n_{y1}+n_y} - 1]}{n_{x1}n_{y1}\left[\left(\frac{n_x}{n_{x1}}\right)^2 - 1\right]\left[\left(\frac{n_y}{n_{y1}}\right)^2 - 1\right]} \quad (4)$$

Where $\mathrm{j} = (-1)^{1/2}$, ω is the angular frequency, F is the point force, m is the surface mass of the floor, n_{x1} and n_{y1} are the number of half wavelengths of the plate mode, x_0 and y_0 are the coordinates of the point force, ω_{hx1ny1} is the angular eigenfrequency of the floor, $\eta = \eta_i + X/\sqrt{f}$ and n_x and n_y are the number of half wavelengths of the room mode.
According to literature, the modal sound field of the receiving room can have a significant effect on the sound pressure level and therefore on the impact sound insulation. The material properties of the plate affect the plate modes and the coupling between the plate and room modes. From the point of timber construction, it would be beneficial to examine the effect of modal coupling between the floor structure and the room sound field, since the low frequency range has been found to have problems in the ISI.

3. MATERIALS AND METHODS

The modal coupling of CLT and concrete slabs in different room configurations was studied to examine the differences in room response and modal coupling behaviour.

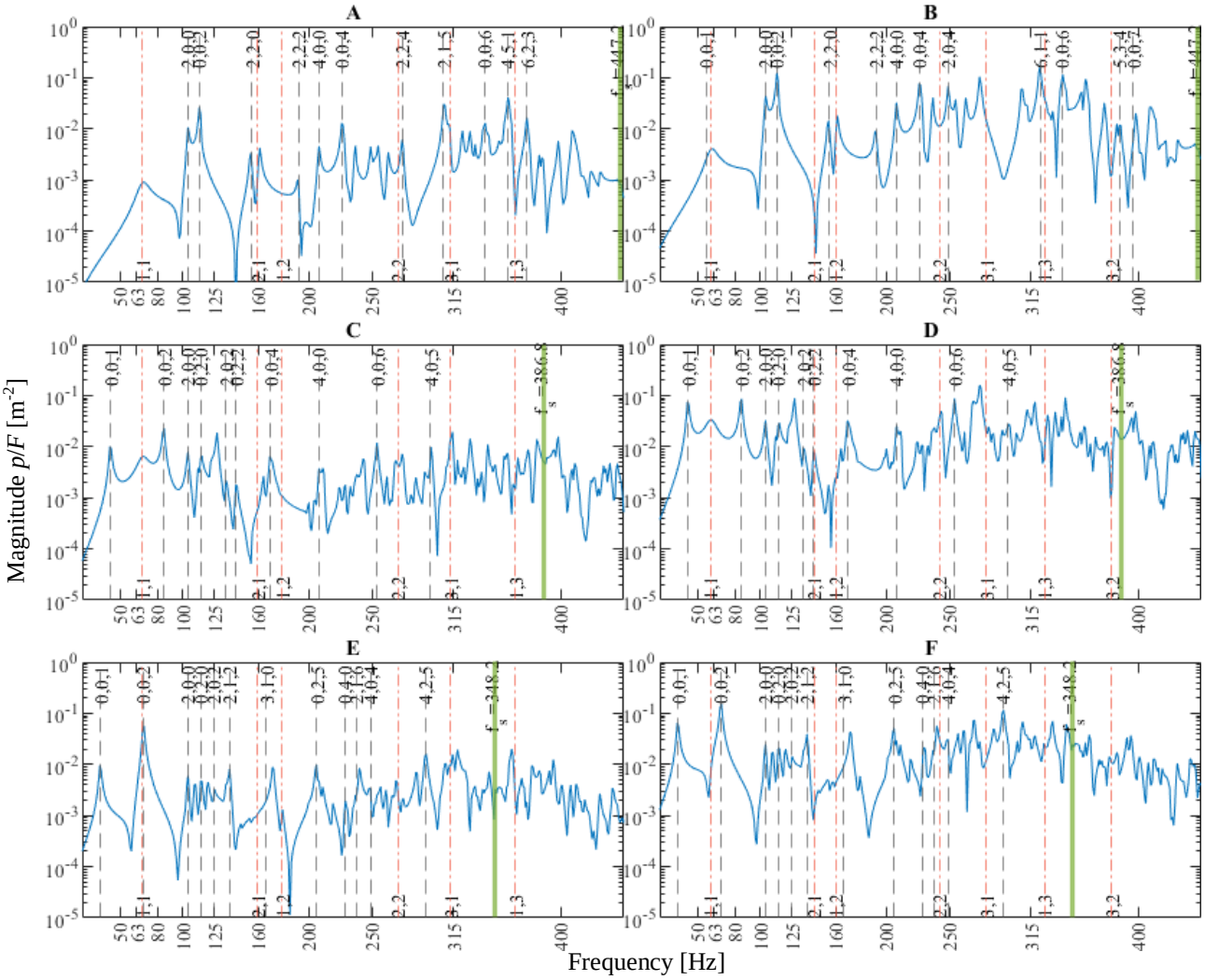


Figure 1. Magnitude of sound pressure in the middle of the receiving room caused by the vibration field of a floor. **A)** Concrete floor V = 30 m^3 **B)** CLT floor V = 30 m^3 **C)** Concrete floor V = 40 m^3 **D)** CLT floor V = 40 m^3 **E)** Concrete floor V = 50 m^3 **F)** CLT floor V = 50 m^3. The room modes are depicted with vertical dashed lines, the plate modes with vertical dotted dashed lines and the Schroeder limiting frequency with a solid vertical line. The corresponding room modes are written on the top of the graph and plate modes at the bottom.

The sound pressure in V = 30 m^3, V = 40 m^3 and V = 50 m^3 rooms were calculated utilizing Eqn. (3) at positions (0,7;0,7;0,7), (0;0;0) and (lx+0,5; ly+0,2; 1,5) from the centre of the room. A CLT and concrete plate with different dimensions were studied. The floors were excited with a 5 N point force from the middle of the floor. Material properties used in the calculations are presented in Tab. 1.

Table 1. Material properties.

Material	ρ [kg/m^3]	E [MPa]	ν [-]	η [-]
Concrete 200 mm [24]	2 500	33 000	0,2	0,015
CLT 200 mm [25]	420	4 539*	0,4	0,015

* Effective value $E_{eff} = \sqrt{E_x E_y}$

4. RESULTS

The magnitude of the sound pressure in the middle of the receiving room for concrete and CLT floors in 3 different room volumes are presented in Fig 1. The highest peaks in the magnitude of the sound pressure are on room modes f_{001} and f_{002}. The shape of the magnitude of the sound pressure is similar between the concrete and CLT slabs in same volume rooms but the magnitude is higher for the CLT slabs. The results are similar with other calculation positions and floor dimensions.

5. DISCUSSION

Neves e Sousa & Gibbs [7–8] found that the 1st vertical room mode f_{001} is the most significant for the ISI of homogeneous concrete floors. However, the calculations suggest that the 2nd vertical room mode f_{002} is significant as well. The peaks in the magnitude in Fig 1. correspond to a weaker sound insulation of the structure. The higher calculated magnitude of sound pressure for CLT floors also points to a weaker sound insulation in comparison to concrete slabs.

The problem with analytical models is the assumptions and simplifications done to derive the wanted equations. With other calculation methods, for example FEM calculations, complex boundary conditions can be considered. However, defining the boundary conditions can be difficult.

In FEM models the studied floor often radiates into an infinite space. Lietzén et al. [26] modelled the ISI of a full timber mock up floor that was also measured in a laboratory setting (V = 56 m^3). The simulated and measured results are in Fig. 2.

The simulated result differs from the measured result especially around 63 and 80 Hz octave bands. The first vertical room mode of the laboratory is f_{001} = 38 Hz and the second room mode f_{002} = 86 Hz. The second room mode could explain the difference in the low frequencies in the results shown in Fig. 2. Modelling the whole receiving room in a FEM software could lead to better agreement with the measured result on low frequencies.

To model the room and study the coupling further, the boundary conditions need to be determined with an adequate precision. Recent studies [27–32] utilising FEM modelling of the room sound field are transient or determine a single value impedance or absorption coefficient for all the surfaces of the room.

The boundary conditions that can be given for the room are impedance, sound hard and sound soft boundaries. Both sound hard boundary and sound soft boundary do not correspond to room sound fields in timber buildings.

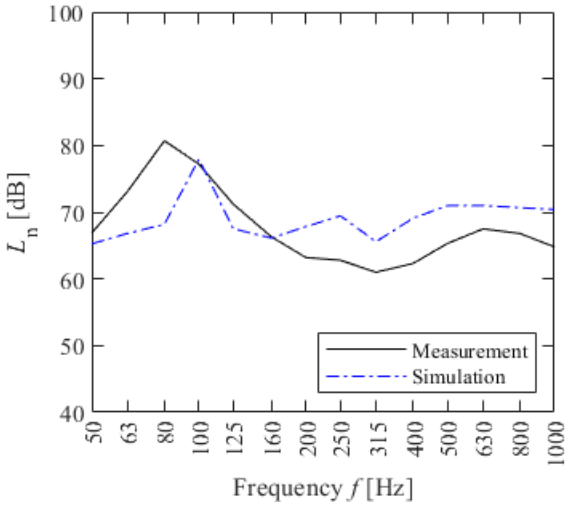


Figure 2. Measurement and simulation result of a timber mock-up floor [26].

Calculating the absorption coefficient from the plate resonator impedance does not correlate to the reverberation time in a room. The boundary condition can also be the absorption coefficient. This however only gives real value results though the reverberation time of the room would be closer to reality. Using the absorption coefficient also loses the information about the phase change.

6. CONCLUSIONS

The 1st and 2nd vertical room modes f_{001} and f_{002} cause the highest peaks in the sound pressure in the room causing the sound insulation of a plate to be weaker. Therefore, modelling the room could improve the agreement between measured and simulated ISI results on low frequencies. However, methods for defining non-rigid boundary conditions are limited to single number values of impedance or absorption coefficient. Other methods for defining non rigid boundary conditions should be investigated further.

7. REFERENCES

[1] C. Johansson, "Low-frequency impact sound insulation of a light weight wooden joist floor", *Applied Acoustics*, vol. 44, no. 2, pp. 133–147, 1995.

[2] C. Hopkins and P. Turner: "Field measurement of airborne sound insulation between rooms with non-

diffuse sound fields at low frequencies", *Applied Acoustics*, vol. 66, no. 12, pp. 1339-1382, 2005.

[3] C. Simmons, "Measurement of Sound Pressure Levels at Low Frequencies in Rooms. Comparison of Available Methods and Standards with Respect to Microphone Positions", *Acta Acustica united with Acustica*, vol. 85, pp. 88–100, 1999.

[4] P. Latvanne, *Puuvälipohjien akustiset ominaisuudet ja laskentamallit*, Tampere University of Technology, 2015. (in Finnish)

[5] H. Goydke, "Guidance for the measurement of sound insulation of building elements in low frequency bands", *INTER-NOISE and NOISE-CON Congress and Conference Proc.*, (Gothenburg, Sweden) pp. 175–178, 1990.

[6] P. Hammer, *Impact sound transmission of wooden-joist floor*. Lund institute of technology, Department of Engineering Acoustics, 1994.

[7] A. Neves e Sousa and B. M. Gibbs: "Parameters influencing low frequency impact sound transmission in dwellings", *Applied Acoustics*, vol. 78, pp. 77–88, 2014.

[8] A. Neves e Sousa and B. M. Gibbs: "Low frequency impact sound transmission in dwellings through homogeneous concrete floors and floating floors", *Applied Acoustics*, vol. 72, no. 4, pp. 177–189, 2011.

[9] S. Y. Yoo, P. J. Lee, S. Y. Lee, and J. Y. Jeon: "Measurement of Sound Field for Floor Impact Sounds Generated by Heavy/Soft Impact Sources", *Acta Acustica united with Acustica*, vol. 96, no. 4, pp. 761–772, 2010.

[10] E. Reynders, "Practical formulas for quantifying the uncertainty of impact sound insulation measurements caused by the diffuse field assumption", *INTER-NOISE and NOISE-CON Congress and Conference Proc.*, (Madrid, Spain) pp. 7405–7415, 2019.

[11] P. Wang, C. Van hoorickx, G. Lombaert, and E. Reynders: "Numerical prediction and experimental validation of impact sound radiation by timber joist floors", *Applied Acoustics*, vol. 162, art. 107182, 2020.

[12] E. P. B. Reynders, P. Wang, C. Van hoorickx, and G. Lombaert: "Prediction and uncertainty quantification of structure-borne sound radiation into a diffuse field", *Journal of Sound and Vibration*, vol. 463, art. 114984, 2019.

[13] A. Osipov, P. Mees, and G. Vermeir: "Low-frequency airborne sound transmission through single partitions in buildings", *Applied Acoustics*, vol. 52, no. 3, 273–288, 1997.

[14] G. Y. Jin, Y. H. Chen, and Z. G. Liu: "A Chebyshev-Lagrangian method for acoustic analysis of a rectangular cavity with arbitrary impedance walls", *Applied Acoustics*, vol. 78, pp. 33–42, 2014.

[15] A. Lahdensivu, *The effect of the modal sound field of a receiving room to the verifiable impact sound insulation of a timber joist floor*, Tampere University, 2024. (in Finnish)

[16] C. Hopkins, *Sound Insulation*, 1st ed. Amsterdam: Elsevier Ltd., 2007.

[17] J. H. Rindel, *Sound Insulation in Buildings*, 1st ed. Cornwall, Great Britain: Taylor & Francis Group, LLC., 2018.

[18] M. R. Schroeder, "Statistik der Frequenzkurve in Räumen", *Acustica*, vol. 1954, no. 4, pp. 594–600, 1954. (in German)

[19] M. R. Schroeder and K. H. Kuttruff: "On Frequency Response Curves in Rooms. Comparison of Experimental, Theoretical, and Monte Carlo Results for the Average Frequency Spacing between Maxima", *The Journal of the Acoustical Society of America*, vol. 34, no. 1, pp. 76–80, 1962.

[20] H. Kuttruff, *Room acoustics*, 5th ed. Abingdon: Spon Press, 2009.

[21] T. Kihlman, "Sound Radiation into a Rectangular Room. Applications to Airborne Sound Transmission in Buildings", *Acustica*, vol. 1967, no. 18, pp. 11–20, 1967.

[22] L. L. Beranek, *Acoustic Measurements*. New York: John Wiley & Sons, Incorporated, 1949.

[23] P. M. Morse and K. U. Ingard: *Theoretical Acoustics*, 1st ed. New York, 1968.

[24] SFS EN 1992-1-1+A1+AC Eurocode 2. Suomen standardoimisliitto SFS, Helsinki, Suomi., 2015. (in Finnish)

[25] J. Zhou, Y. H. Chui, M. Gong, and L. Hu: "Elastic properties of full-size mass timber panels: Characterization using modal testing and comparison with model predictions", *Composites Part B: Engineering*, vol. 112, pp. 203–212, 2017.

[26] J. Lietzén, V. Kovalainen, M. Kylliäinen, and S. Pajunen: "Computational prediction of impact sound insulation of a full-scale timber floor applying a FEM simulation procedure", *Engineering Structures*, vol. 310, art. 118130, 2024.

[27] M. Meissner, "Prediction of low-frequency sound field in rooms with complex-valued boundary conditions on walls", *Vibrations in Physical Systems*, vol. Vol. 30, no. 1, 2019.

[28] M. Meissner, "Application of modal expansion method for sound prediction in enclosed spaces subjected to boundary excitation", *Journal of Sound and Vibration*, vol. 500, art. 116041, 2021.

[29] M. Meissner and T. G. Zielinski: "Impact of Wall Impedance Phase Angle on Indoor Sound Field and Reverberation Parameters Derived from Room Impulse Response", *Archives of Acoustics*, Vol. 47, no. 3, pp. 343–353, 2022.

[30] M. Meissner and T. Zielinski, "Low-frequency prediction of steady-state room response for different configurations of designed absorbing materials on room walls", *Proc. of ISMA and USD*, (Leven, Belgium) pp. 463–477, 2020.

[31] A. Blazejewski, "Modal approach application and significance analysis inside bounded space in a steady state acoustic field condition", *Int. J. Dynam. Control*, vol. 3, no. 1, pp. 50–57, 2015.

[32] R. Tomiku, T. Otsuru, N. Okamoto, and Y. Kurogi: "Direct and modal frequency response analysis of sound fields in small rooms by finite element method", *Proc. of Acoustics*, (Paris, France), pp. 1297–1302, 2008.

DOI: 10.61782/fa.2025.0056



FORUM ACUSTICUM
EURONOISE 2025

ACCURATE AND EFFICIENT PREDICTION OF SOUND INSULATION IN MULTILAYERED STRUCTURES: A ROBUST METHOD VALIDATED WITH GLAZING EXAMPLES

Jasper Vastiau[1*] **Bart Van de Velde**[2] **Edwin P.B. Reynders**[1]

[1] KU Leuven, Department of Civil Engineering, Structural Mechanics Section, Kasteelpark Arenberg, box 2448, B-3001 Leuven, Belgium
[2] SonIQ, Nieuwe Sint-Annadreef 23, 8200 Brugge, Belgium

ABSTRACT

Engineering offices and manufacturers of acoustic building systems or materials often rely on measurement data to estimate whether building solutions will be of sufficient acoustic quality. This typically involves numerous costly and time-consuming laboratory measurements, making it difficult to efficiently explore and optimize various design configurations. In this paper, a method is presented to accurately and efficiently predict the sound insulation of multilayer structures. Accuracy ensures reliability, while efficiency is crucial for optimization, where numerous simulations are needed, for example to identify the ideal layering or material properties of a(n) (inter)layer. The prediction method accounts for arbitrary layering, finite dimensions, boundary conditions and resulting modal behavior, as well as frequency- and temperature-dependent material properties. Extensive validation has been conducted using numerous examples with a specific focus on glazing, demonstrating the model's robustness and reliability. An accuracy of $1-2\,\mathrm{dB}$ in single number rating is generally achieved using default non-product specific material data. The method achieves higher accuracy when material properties are determined from testing.

Keywords: *airborne sound insulation, layered elements, glazing, viscoelastic interlayers*

Corresponding author: *jasper.vastiau@kuleuven.be.*

Copyright: *©2025 Vastiau et al. This is an open-access article distributed under the terms of the Creative Commons Attribution 3.0 Unported License, which permits unrestricted use, distribution, and reproduction in any medium, provided the original author and source are credited.*

1. INTRODUCTION

Engineering offices and manufacturers of acoustic building systems or materials often rely on measurement data since the alternatives regarding existing prediction software are either too slow (e.g. using finite elements), or too inaccurate (e.g. analytical expressions assuming thin plate theory). This typically results in a difficult process of exploration and optimization of various new or existing design configurations, since it involves numerous costly and time-consuming laboratory measurements. The need for sound insulation prediction methods which are both accurate and efficient is therefore of crucial importance.

In this paper, a robust method is presented, which is designed to accurately and efficiently predict the sound insulation of multilayer structures with varying elements such as wall leafs and cavities. Wall leafs can consist of layered elements of elastic, viscoelastic and poroelastic nature and are implemented using elastodynamics theory. The modal Transfer Matrix Method (mTMM) [1, 2] envelops this theory and additionally accounts for arbitrary layering, finite dimensions, simply supported or antisymmetric boundary conditions and the resulting modal behavior. The mTMM also allows for frequency-dependent material properties, which can be especially important in practical applications. Viscoelastic interlayers are a particular type of interlayer that can be present in these layered wall leafs, since the material properties depend both on frequency and temperature. This dependence on temperature is expressed through the Williams-Landel-Ferry equation [3, 4], while the dependence on frequency is accounted for using the Generalized Maxwell-Wiechert model [5]. Cavities are assumed to be 'hard-walled' with

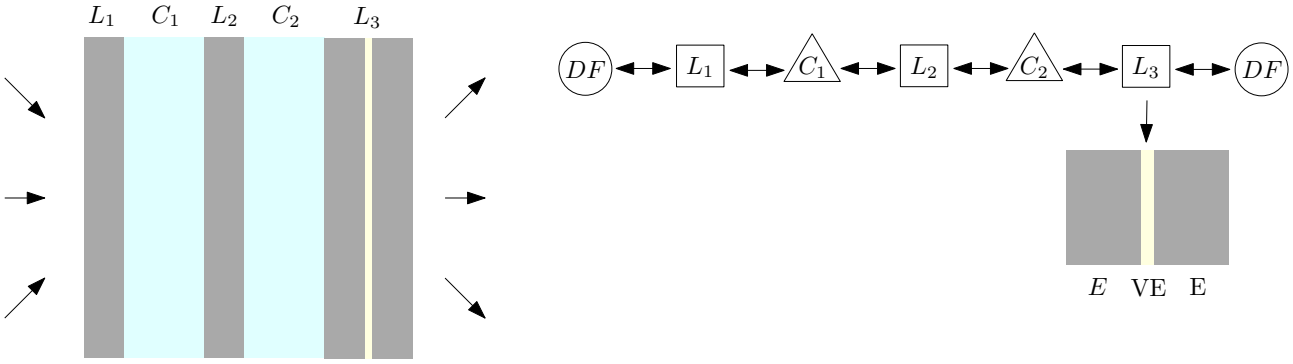


Figure 1. Glazing system with three wall leafs L_1, L_2 and L_3, separated by two cavities C_1 and C_2. The third wall leaf is layered, consisting of two elastic (E) layers with a viscoelastic (VE) in between. The outer wall leafs are coupled to diffuse fields (DF).

finite dimensions and the interaction between cavity and adjoining wall leafs is accounted for [6].

This method enables the exploration and optimization of various design configurations without the need for extensive laboratory testing. The method's robustness and reliability are demonstrated through extensive validation using numerous examples, with a specific focus on glazing. Validation on glazing is particularly interesting since all these elements (wall leafs, cavities, viscoelastic interlayers) can all occur separately or combined in any desired order. The ability to accurately predict sound insulation is crucial for optimizing design configurations and exploring new materials and material properties. By reducing the reliance on costly and time-consuming laboratory measurements for experimental design optimization, this approach facilitates the development of effective acoustic solutions for a wide range of applications.

2. SOUND INSULATION PREDICTION

Walls and floors typically consist of several structural parts, such as leafs and cavities. A wall leaf consists of at least one solid layer, and layered wall leafs can contain varying element types, e.g. an elastic layer or a viscoelastic interlayer which is used in laminated glazing. Cavities are assumed to be hard-walled, and can either be filled with fluid or with porous material. The sound insulation prediction approach is graphically represented in Fig. 1. It starts by indicating all leafs and cavities, and using the corresponding mathematical approach for each leaf or cavity, as will be discussed in the following subsections 2.1 and 2.2. The coupling between wall leafs and cavities is briefly discussed and finally the computation of the diffuse sound insulation is included.

2.1 Wall leafs

Layered elements such as wall leafs or floating floors are implemented using elastodynamics theory, which accounts for longitudinal and shear wave propagation, as well as their interaction in the form of bending waves. One of the main advantages over thin plate theory for the prediction of sound insulation is that thickness effects such as thickness resonances are accounted for due to the presence of the shear waves. The elastodynamics theory also successfully captures key physical phenomena such as the coincidence effect and the mass-air-mass resonance. This theory is enveloped by the mTMM [1, 2], which is used here. Layers with materials of an elastic or viscoelastic nature (also poroelastic layers, but these are not present in glazing) can all be implemented and combined into a single wall leaf. Material properties can be frequency-dependent, but also temperature-dependent in the case of viscoelastic interlayers. The prediction approach for these interlayers is elaborated in detail in section 3, since they are often used in glazing.

In the mTMM, the boundary conditions of a wall leaf are accounted for by decomposing the out-of-plane displacements of the leaf into sinusoidal basis functions [1], which correspond to antisymmetric boundary conditions for thick wall leafs. These basis functions represent mode shapes of the wall leaf and they occur at their respective natural frequencies, making the mTMM a modal approach. Due to the combination of this modal approach

and employing analytical solutions for the wave propagation in each layer in the frequency-wavenumber domain, a high computational efficiency is achieved.

2.2 Cavities

Cavities are modeled as 'hard-walled' three-dimensional cuboid acoustical spaces. A modal approach is applied, where the mode shapes or the basis functions of the cavity are taken to be the normalized mode shapes of a hard-walled, rectangular cuboid cavity [7]. The dynamic stiffness of the cavity is then expressed in terms of its natural frequencies and loss factor, determined by the speed of sound and mass density of the fluid and the reverberation time of the cavity or the loss factor of the fluid. Note that this is an analytical approach, such that the computational efficiency for cavities is very high. A cavity can either be filled with a specific fluid (e.g. air, argon, krypton) or with a porous material. In case of a porous filling, the porous material can be implemented as an equivalent fluid, e.g. by using the Delaney-Bazley-Miki model [8, 9], which employs the flow resistivity to determine the complex, frequency-dependent sound speed and mass density of the equivalent fluid.

2.3 Coupling of wall leafs and cavities

Coupling of the wall leafs and cavities is achieved by employing the acoustical pressure in a cavity as an excitation of the adjoining wall leaf, while the displacements of a wall leaf are used as an excitation of the adjoining cavity. Since modal approaches are used for both the wall leafs and cavities, this coupling strategy is called a modal-interaction model [6].

2.4 Diffuse sound insulation

The modal-interaction model finally allows the calculation of the diffuse sound insulation. This is not straightforward due to the finite wall dimensions, but a correct calculation is achieved by employing the diffuse field reciprocity relationship [12], so that the ensemble mean of the sound transmission coefficient $\hat{\tau}_{12}$ [10, 11] can be evaluated as

$$\hat{\tau}_{12} = \frac{8\mathrm{V}_1}{c\mathrm{S}\pi\mathrm{n}_1}\mathrm{Tr}\left(\tilde{\mathbf{D}}_{\mathrm{dir}}^{(1)}\mathbf{D}_{\mathrm{tot}}^{-H}\tilde{\mathbf{D}}_{\mathrm{dir}}^{(2)}\mathbf{D}_{tot}^{-1}\right), \qquad (1)$$

with V_1 the volume of the sending room, c the speed of sound, n_1 the modal density of the sending room and S the surface area of the interface between structure and room. $\mathbf{D}_{\mathrm{dir}}$ denotes the direct field dynamic stiffness matrix, whereas $\mathbf{D}_{\mathrm{tot}}$ represents the total dynamic stiffness matrix of the structure, including all wall leafs, cavities and their coupling. The imaginary part of a matrix is denoted with a tilde.

3. VISCOELASTIC INTERLAYERS

Laminated glazing makes use of viscoelastic (polymer) PolyVinylButyral (PVB) interlayers. The mechanical properties of these PVB interlayers are not only frequency-dependent, but they also depend on temperature. These effects can be accounted for by using the generalized Maxwell-Wiechert model and William-Landel-Ferry model [3, 4], respectively.

3.0.1 Generalized Maxwell-Wiechert model

At the small-strain regime, viscoelastic effects can be characterized efficiently by using the Generalized Maxwell-Wiechert model, taking into account the time/frequency-dependency of the shear modulus [5]. This model is constructed from parallel combinations of a spring and a damper placed in series, which are placed in parallel with a single elastic spring [13]. The elastic springs in combination with the viscous dampers provide dynamic stiffness in case of fast loading conditions, while the elastic spring represents the quasi-static stiffness. The elements in the Maxwell model can be derived experimentally using dynamic mechanical analysis (DMA) [13]. The time-dependency of the shear relaxation modulus can be expressed as [13]:

$$G(t) = G_\infty + \sum_{i=1}^{n} G_i \exp -t/\tau, \qquad (2)$$

with G_∞ the long-term shear modulus, G_i and τ_i the shear modulus and relaxation time of a viscoelastic unit (spring-damper pair), respectively. The number of viscoelastic units is denoted by n. The properties of the viscoelastic units are inversely related as follows:

$$\tau_i = \frac{\eta_i}{G_i}. \qquad (3)$$

The long-term shear modulus is related to the instantaneous shear modulus G_0 by [13]:

$$G_0 = G_\infty + \sum_{i=1}^{n} G_i. \qquad (4)$$

Substitution of Eqn. (4) into Eqn. (2) yields [14]:

$$G(t) = G_0 - \sum_{i=1}^{n} G_i \left(1 - \exp 1{-}t/\tau_i\right). \quad (5)$$

The shear relaxation modulus in the time-domain G(t) can also be expressed in the frequency domain as [5]:

$$G(\omega) = G_0 - \sum_{i=1}^{n} \frac{G_i}{(\omega\tau_i)^2 + 1} + \mathrm{i}\sum_{i=1}^{n} \frac{G_i \omega\tau_i}{(\omega\tau_i)^2 + 1}. \quad (6)$$

This expression can be subdivided into the real part representing the storage modulus, which determines the elastic behavior. The imaginary part of the resulting expression constitutes the loss modulus, representing the energy dissipation [5]. It has been demonstrated in [5] that the storage and loss moduli of several types of viscoelastic interlayer are subject to high differences due to the use of specific additives and plasticizers, and to differences in the measurement techniques.

3.0.2 Williams-Landel-Ferry equation

The dynamical shear modulus $G(T, \omega)$, which depends on both temperature and frequency, obeys the following relation:

$$G(T, \omega) = G(\mathrm{T}_0, \alpha_T \omega), \quad (7)$$

with $\mathrm{T}_0 = 20°C$ the reference temperature. The horizontal shift parameter α_T [3, 4] is proportional to the loss factor, given by

$$\alpha_T = \frac{\eta(T)}{\eta(\mathrm{T}_0)}. \quad (8)$$

For most polymer systems, the loss factor $\eta(T)$ is well-represented by the empirical Vogel–Fulcher law

$$\eta(T) = B \exp\left(\frac{\mathrm{T_A}}{T - \mathrm{T_V}}\right), \quad (9)$$

with $\mathrm{T_A}$ the activation temperature and $\mathrm{T_V}$ the Vogel temperature. Combining both Eqn. (8) and Eqn. (9) leads to [4]:

$$\log \alpha_T = -C_1 \frac{T - \mathrm{T}_0}{T - \mathrm{T}_0 + C_2}, \quad (10)$$

with two constants C_1 and C_2, defined as

$$C_1 = \log \mathrm{e} \left(\frac{\mathrm{T_A}}{\mathrm{T}_0 - \mathrm{T_V}}\right) \text{ and } C_2 = \mathrm{T}_0 - \mathrm{T_V}. \quad (11)$$

Eqn. (10) was proposed by Williams, Landel and Ferry and is known as the WLF equation. The influence of the PVB temperature and the resulting variations in airborne sound insulation of single laminated glazing is demonstrated in Fig. 2, displaying clear variations up to 4 dB in the frequency range around coincidence.

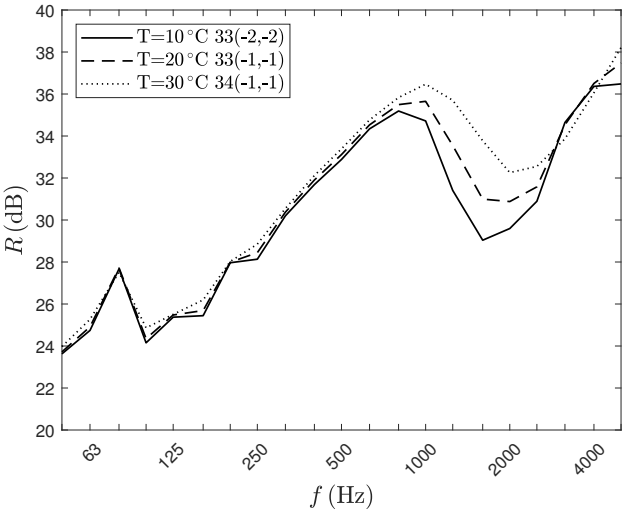


Figure 2. Influence of temperature on the mechanical properties of PVB and the resulting variations in airborne sound insulation of 44.2 glazing.

4. VALIDATION

The model can be showcased effectively using (laminated) glazing examples, since they contain all previously discussed elements: cavities and wall leafs including elastic layers and viscoelastic interlayers. The assumed default material properties of glass and the cavity fluids are listed in Tables 1 and 2, respectively. Note that a loss factor of $\eta = 0.05$ is assumed for the glass panes, which approximately consists of equal parts of internal losses and edge damping [15], i.e. energy loss due coupling of the glass panes through the mounting frame.

Table 1. Material properties of glass: density ρ, Young's modulus E, Poisson coefficient ν and loss factor η.

$\rho\,[\frac{\mathrm{kg}}{\mathrm{m}^3}]$	E [GPa]	$\nu\,[-]$	$\eta\,[-]$
2500	62	0.24	0.05

Table 2. Material properties of air and Argon: density ρ, sound speed c and cavity reverberation time T.

	$\rho\,[\frac{\mathrm{kg}}{\mathrm{m}^3}]$	$c\,[\frac{\mathrm{m}}{\mathrm{s}}]$	$T\,(\mathrm{s})$
Air	1.2	340	2
Argon	1.784	319	2

The simplest examples are single glass panes. Three single glazing examples with thicknesses of 4 mm, 10 mm and 19 mm are simulated and validated with corresponding laboratory measurements in Fig. 3. The simulations successfully capture the physical behavior of the single glazing, including the coincidence effect, resulting in accurate single number ratings with a maximum deviation of 1 dB.

Fig. 4 includes the results of simulations and laboratory measurements of two types of double glazing: 4-10-4 and 6-12-8. Fig. 4 indicates that other than the coincidence effect, also the mass-air-mass resonance is well-predicted, which also results in an accuracy of 1 dB on the single number rating.

Fig. 5 displays two examples of triple glazing: 4-10A-4-10A-4 and 6-14A-4-14A-6. Contrary to the double glazing examples, the cavities are filled with Argon instead of air to increase the airborne sound insulation. The use of argon instead of air mainly affects the anti-resonance peak just before coincidence, so around $1600-2000$ Hz in Fig. 5(a) and at approximately 1000 Hz in Fig. 5(b). Simulations have shown that the inclusion of argon instead of air does indeed improve the sound insulation at the anti-resonance frequency, where Fig. 5(a) indicates that this improvement is underestimated, while Fig. 5(b) suggests that the effect is correctly captured in the simulations. This variance can possibly be attributed to the niche effect [16]. Nevertheless, the prediction accuracy of the simulations for triple glazing is still 1 dB, as this niche effect at coincidence occurs at high frequencies and thus has a small influence on the single number rating.

Several examples are included for laminated glazing, both single (cfr. Fig. 6) and double (cfr. Fig. 7). The frequency and temperature-dependent material properties of the PVB interlayers are taken from [17], and it is assumed that the temperature of the PVB equals 20° C. Three examples of laminated single glazing are displayed in Fig. 6: 33.2, 1212.2 and 10101010.6. The prediction accuracy

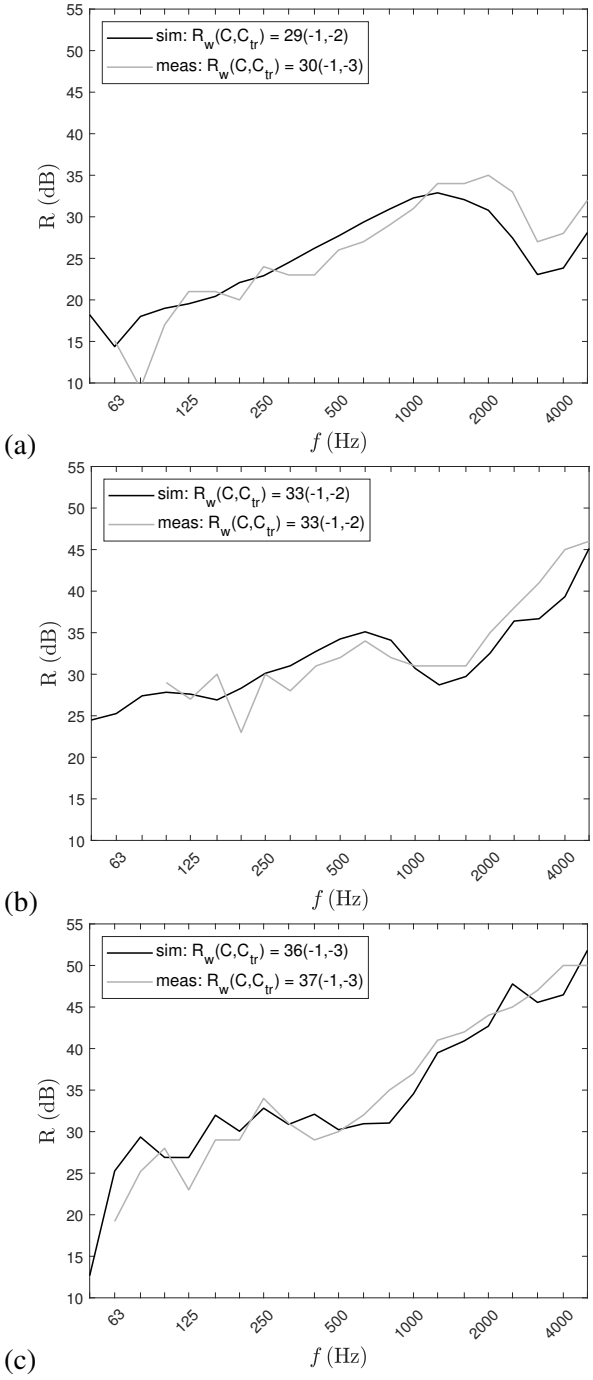


Figure 3. Single glazing: simulation (black) and laboratory measurement (grey). (a) 4 mm, (b) 10 mm and (c) 19 mm.

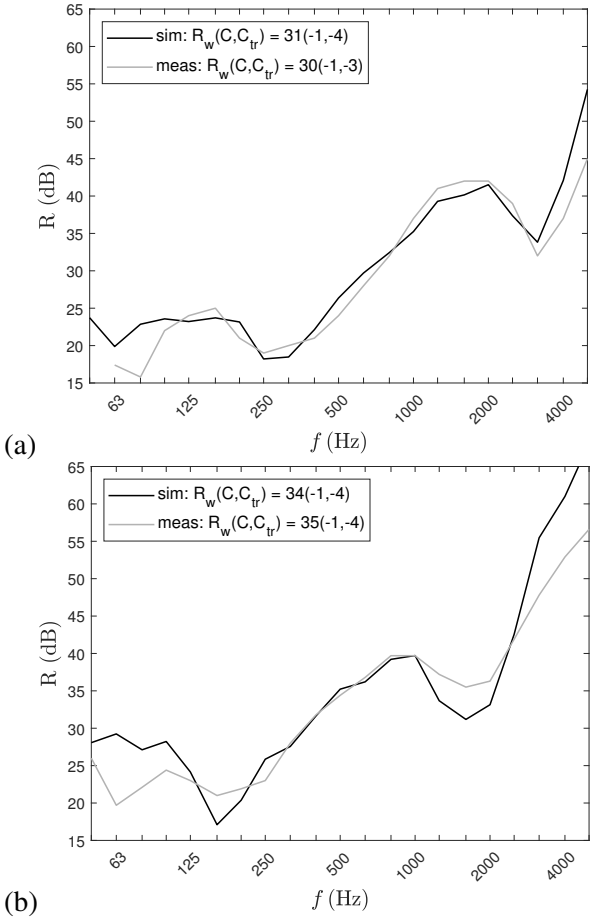


Figure 4. Double glazing: simulation (black) and laboratory measurement (grey). (a) 4-10-4 and (b) 6-12-8.

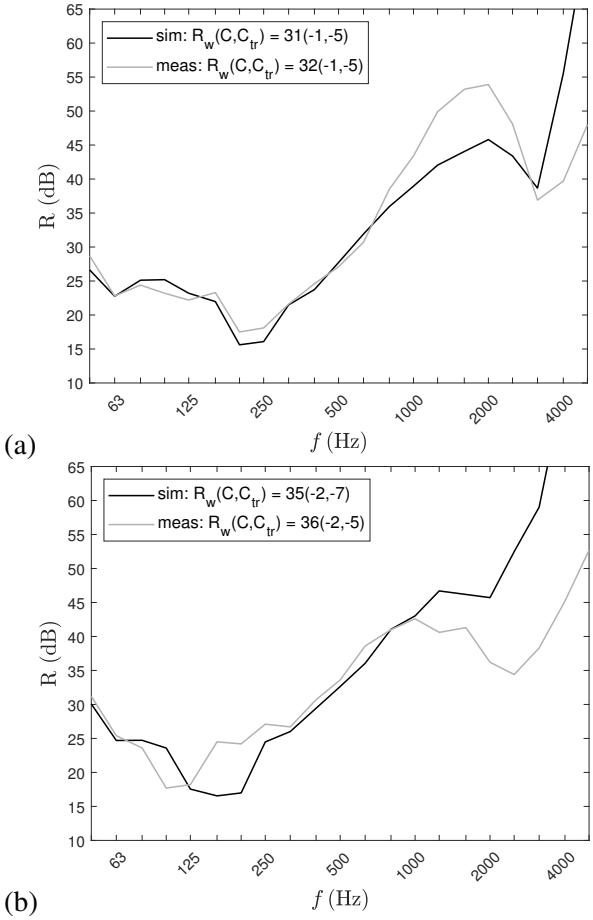


Figure 5. Triple glazing: simulation (black) and laboratory measurement (grey). (a) 4-10A-4-10A-4 and (b) 6-14A-4-14A-6.

for each of the examples is comparable to non-laminated glazing (cfr. $1-2\,\mathrm{dB}$), indicating that both the glazing properties and the assumed frequency and temperature-dependent material properties of the PVB interlayers perform with high accuracy within the prediction model.

The two validation examples for laminated double glazing provide an increasing order of complexity: Fig. 7(a) contains the results for 4-6-33.1 glazing, which has only one laminated glass panel, whereas the results for double glazing with two laminated glass panels (33.2-12-55.2) is displayed in Fig. 7(b). The simulation results for both validation examples contain a spectral shape which is very similar to the measured laboratory values. It is clear that the mass-air-mass resonance and the coincidence phenomenon are correctly simulated and that the sound insulation in the intermediate frequency range as well as low frequencies is accurately predicted. At frequencies above coincidence, however, the simulations indicate a significantly higher sound insulation than measured in the laboratory. This can be attributed to transmission through the mounting frame, which is not included in the simulations. This influence can generally be seen in glazing with high sound insulation, such as the triple glazing in Fig. 5 where this overestimation at high frequencies is also observed. As this effect only appears above coincidence, its influence on the single number rating is very limited, resulting in a prediction accuracy of $2\,\mathrm{dB}$ for both examples of the laminated double glazing.

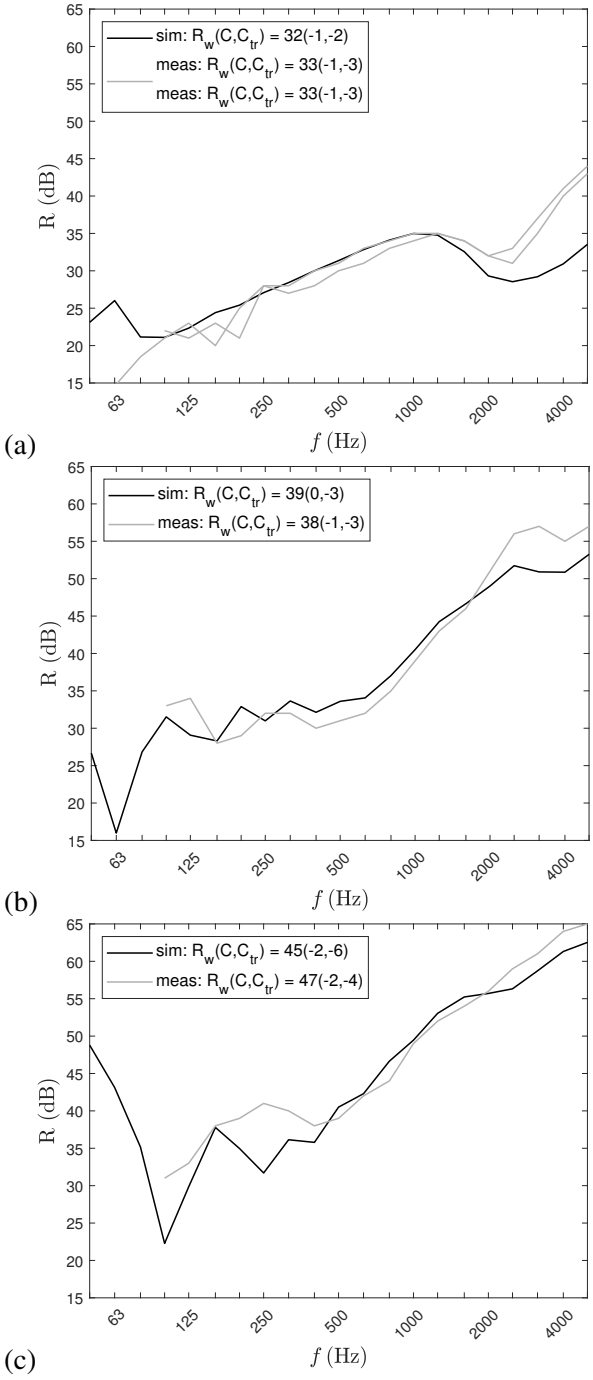


Figure 6. Laminated single glazing: simulation (black) and laboratory measurement (grey). (a) 33.2, (b) 1212.2 and (c) 10101010.6.

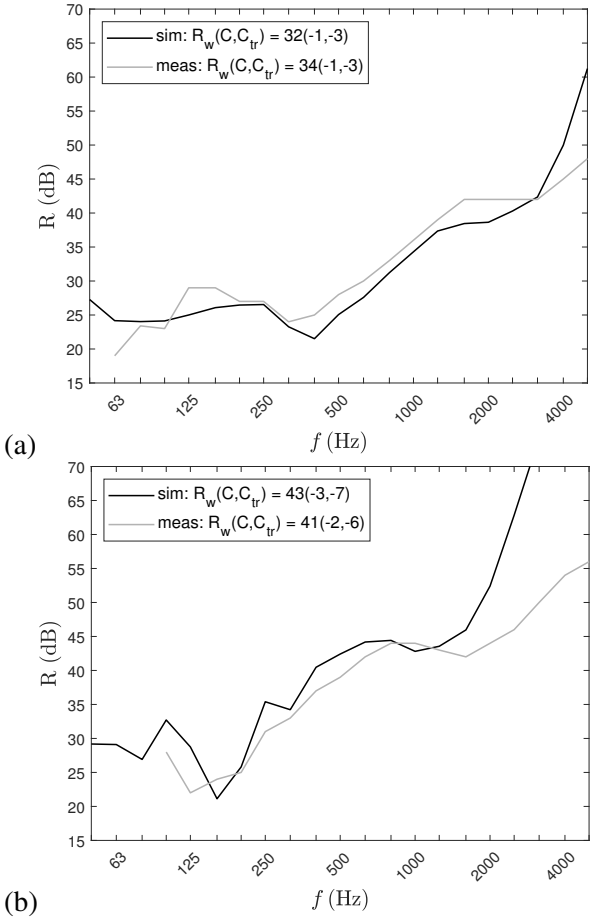


Figure 7. Laminated double glazing: simulation (black) and laboratory measurement (grey). (a) 4-6-33.1 and (b) 33.2-12-55.2.

5. CONCLUSIONS

In this paper, a robust and efficient prediction method for determining the sound insulation of multilayer structures is presented, with a particular focus on glazing examples. The proposed method accounts for various factors such as arbitrary layering, finite dimensions, boundary conditions, and frequency- and temperature-dependent material properties. The results show that the prediction method can achieve an accuracy of $1-2\,\mathrm{dB}$ in the single number rating using predefined values from a material database, and even higher accuracy is attainable when material properties are determined from testing. The method successfully captures key physical phenomena such as the mass-air-mass resonance and the coincidence effect, by using elas-

todynamics and accounting for material properties that may depend on frequency and temperature, providing reliable predictions for (laminated) single, double, and triple glazing configurations. In addition to the accuracy, the predictions maintain a low computational cost due to the modal approach

The ability to accurately and efficiently predict sound insulation is crucial for optimizing design configurations and exploring new materials and various material properties. This method offers a valuable tool for engineering offices and manufacturers, enabling them to reduce the reliance on costly and time-consuming laboratory measurements. By providing a more efficient alternative, the method facilitates the exploration and optimization of acoustic solutions for specific situations. Future work could focus on further expansion of the model to account for additional complexities, such as the influence of frame transmission, double walls with flexible studs, lightweight floors and periodic structures.

6. ACKNOWLEDGMENTS

This research is funded by the European Research Council in the form of the Soprano Proof of Concept grant number 101188255. The financial contribution of the ERC is gratefully acknowledged.

7. REFERENCES

[1] C. Decraene, A. Dijckmans, and E. Reynders, "Fast mean and variance computation of the diffuse sound transmission through finite-sized thick and layered wall and floor systems," *Journal of Sound and Vibration*, no. 422, pp. 131–145, 2018.

[2] J. Vastiau, C. Van hoorickx, and E. Reynders, "Transfer matrix approaches for the prediction of impact sound radiation from layered floors," *Journal of Sound and Vibration*, vol. 569, no. 117992, pp. 1–20, 2024.

[3] J. Ferry, *Viscoelastic properties of Polymers*. New York: John Wiley & Sons, 1970.

[4] G. Strobl, *The physics of Polymers*. New York: Springer Berlin Heidelberg, 2017.

[5] A. Zemanová, J. Zeman, T. Janda, J. Schmidt, and M. Šejnoha, "On modal analysis of laminated glass: Usability of simplified methods and enhanced effective thickness," *Composites Part B*, pp. 92–105, 2018.

[6] F. Fahy and P. Gardonio, *Sound and structural vibration: radiation, transmission and response*. Oxford, UK: Academic Press, 2nd ed., 2007.

[7] J. Van den Wyngaert, M. Schevenels, and E. Reynders, "Predicting the sound insulation of finite double-leaf walls with a flexible frame," *Applied Acoustics*, no. 141, pp. 93–105, 2018.

[8] M. Delaney and E. Bazley, "Acoustical properties of fibrous materials," *Applied Acoustics*, vol. 3, no. 2, pp. 105–116, 1970.

[9] Y. Miki, "Acoustical properties of porous materials - modifications of delany-bazley models," *Journal of the Acoustical Society of Japan*, vol. 11, no. 1, pp. 19–24, 1990.

[10] L. Cremer, M. Heckl, and B. Petersson, *Structure-borne Sound: Structural Vibrations and Sound Radiation at Audio Frequencies, 3rd ed.* Berlin: Springer, 2005.

[11] E. Reynders and C. Van hoorickx, "Uncertainty quantification of diffuse sound insulation values," *Journal of Sound and Vibration*, vol. 544, no. 117404, pp. 1–15, 2023.

[12] P. Shorter and R. Langley, "On the reciprocity relationship between direct field radiation and diffuse reverberant loading," *Journal of the Acoustical Society of America*, vol. 117, no. 1, pp. 85–95, 2005.

[13] P. Hooper, B. Blackman, and J. Dear, "The mechanical behaviour of poly(vinyl butyral) at different strain magnitudes and strain rates," *Journal of Materials Science*, pp. 3564–3576, 2012.

[14] G. Vergassola and D. Boote, "A simplified approach to the dynamic effective thickness of laminated glass for ships and passenger yachts," *Journal on Interactive Design and Manufacturing*, pp. 123–135, 2020.

[15] C. Hopkins, *Sound insulation*. Oxford: Elsevier Ltd., 2007.

[16] A. Dijckmans, *Wave based calculation methods for sound-structure interaction. Application to sound insulation and sound radiation of composite walls and floors*. PhD thesis, KU Leuven, 2011.

[17] D. Lams, *Prediction and optimization of the sound insulation of double and triple laminated glazing*. Master's thesis, KU Leuven, 2021.

DOI: 10.61782/fa.2025.0169



FORUM ACUSTICUM
EURONOISE 2025

BAYESIAN ANALYSIS OF THE RW BASED ON A PARAMETRIZED PHYSICAL MODEL ACCORDING TO EN ISO 12354-1

Michael Parzinger[1*] **Ulrich Schanda**[1]
[1] Laboratory for Sound Measurement, Technical University of Applied Sciences Rosenheim, Germany

ABSTRACT

The EN ISO 12354-1 standard provides a physical model for the sound reduction index R. The results of this model can be used to calculate the weighted sound reduction index for different scenarios, which itself plays an important role in the design of a building element. This raises the question of how well this physical model actually reflects reality. In this work, the physical model is first optimized based on Bayesian inference. The optimized model can then in turn be used to simulate the sound reduction index taking into account uncertainties. These simulations then can provide an analysis of the construction in order to decide whether the minimum requirements on sound insulation will be met with a certain probability. For example, it is checked how thick a calcium silicate brick wall must be so that the weighted sound reduction index is at least 53 dB with a probability of 95 %. This is relevant as, in the best-case scenario, building elements can be optimized concerning the economization of material, which enables a cost-effective and sustainable construction.

Keywords: *Sound reduction index, Rw, Bayesian inference*

1. INTRODUCTION

For new buildings, an optimized construction in terms of sustainability is compulsory. Requirements on sound insulation have to be met as well. Often, the question arises as to how thick a solid wall should be. Thin walls would save material, whereas thick walls guarantee better sound insulation. This paper focuses on the influence of the thickness of a homogeneous wall on the weighted sound reduction index R_w using a Bayesian approach.

To investigate this issue, a physical model for the sound reduction index R is considered. This physical model is first optimized using data from laboratory measurements of walls made of calcium silicate (Ca-Si) blocks. This part was also discussed at Forum Acusticum 2023 [1] and at [2, 3], but has been expanded since then.

With this optimized model, the sound reduction index is simulated by drawing realizations from a corresponding probability distribution. The values for the weighted sound reduction index can then be calculated and analyzed. This procedure is finally used for claims about wall thicknesses that do not occur in the available data. In particular, the probability of whether a wall meets a certain requirement on the weighted sound reduction index is estimated.

2. PHYSICAL MODEL

First, a physical model for the sound reduction index R is discussed, which is based on the model in ISO 12354-1 Annex B [4] and given in equation (1). A few modifications have been implemented and are explained in DAS/DAGA [5]. All quantities in the following equations together with the chosen numerical values are listed in Table 1. The second term in equation (1) denotes the Waterhouse correction.

$$R = -10\lg(\tau) - 10\lg\left(1 + \frac{c_0 S_\mathrm{tot}}{8Vf}\right) \qquad (1)$$

The transmission coefficient in the first term is given

*Corresponding author: Michael.Parzinger@TH-Rosenheim.de.

Copyright: ©2025 Michael Parzinger et al. This is an open-access article distributed under the terms of the Creative Commons Attribution 3.0 Unported License, which permits unrestricted use, distribution, and reproduction in any medium, provided the original author and source are credited.

in equation (2), while the radiation factor σ is defined by the equation (6).

$$\tau = \begin{cases} \frac{Z_0^2}{(m'\pi f)^2}\left(\frac{\pi}{2}\frac{\sigma^2}{\eta_{\text{tot}}}\frac{f_c}{f} + \frac{2\sigma_f}{(1-f^2/f_c^2)^2}\right), & f < 0.89 f_c \\ \frac{Z_0^2}{(m'\pi f)^2}\frac{\pi}{2}\frac{\sigma^2}{\eta_{\text{tot}}}, & 0.89 f_c \leq f \leq 1.4 f_c \\ \frac{Z_0^2}{(m'\pi f)^2}\frac{\pi}{2}\frac{\sigma^2}{\eta_{\text{tot}}}\frac{f_{c,\text{eff}}}{f}, & f > 1.4 f_c \end{cases} \tag{2}$$

$$f_c = \frac{\sqrt{3}}{\pi}\frac{c_0^2}{c_{\text{L}}}\frac{1}{t} \tag{3}$$

$$f_{\text{c,eff}} = f_{\text{c}} \cdot \left(1 + \frac{1}{\gamma^3} \cdot \left(\frac{3.6}{1-\mu} \cdot \frac{tf}{c_{\text{L}}}\right)^{\frac{3}{2}}\right)^{\frac{2}{3}} \tag{4}$$

$$\eta_{\text{tot}} = \eta_{\text{int}} + \text{C}/\sqrt{f} \tag{5}$$

The calculations of the radiation factor are strongly based on ISO 12354-1, only the maximum value is adjusted due to ambiguities in the standard and because past analyses have shown that these adjustments are appropriate.

$$\sigma(f) = \min\left(\tilde{\sigma}(f); \sigma_3(f); \sqrt{1 + \frac{2(l_1+l_2)\cdot f_{\text{c}}}{5c_0}}; 2.0\right) \tag{6}$$

Further adjustments have been made in the high frequency range, where thickness resonances occur. For this purpose, a new quantity τ_0 is introduced in equation (7). The definition of c_{L1} signifies that in this work a distinction is made between the effective value c_{L} and the nominal (material) value c_{L1} for the longitudinal wave velocity.

$$\tau_0 = \left(\cos^2(u) + \frac{1}{4}\left(\frac{\rho c_{\text{L,ex}}}{Z_0} + \frac{Z_0}{\rho c_{\text{L,ex}}}\right)^2 \sin^2(u) + \eta_{\text{int}}^2\right)^{-1} \tag{7}$$

$$u = \frac{2\pi f t}{c_{\text{L,ex}}} \tag{8}$$

$$c_{\text{L,ex}} = c_{\text{L1}}\frac{1-\mu}{\sqrt{1-2\mu}} \tag{9}$$

The following variables are introduced:

$$f_{\text{T}} = \sqrt{3}(1-\mu)\frac{c_{\text{L1}}}{2\pi t} \tag{10}$$

$$\tilde{f}_{\text{T}} = \arg\min_f |\log(f) - \log(2^{2/3} f_{\text{T}})| \tag{11}$$

$$\tau_{\text{plateau}} = \frac{\eta_{\text{ref}}}{\eta_{\text{tot}}}\left(\frac{4Z_0}{\rho c_{\text{L,ex}}}\right)^2 \tag{12}$$

$$\eta_{\text{ref}} = \eta_{\text{int}} + \frac{\text{C}}{\sqrt{2^{2/3} f_{\text{T}}}} \tag{13}$$

$$\tau_{\text{w}}(f) = (\tau_{\text{plateau}}(f)^4 \tau_0(f))^{1/5} \tag{14}$$

Finally, the adjusted transmission coefficient is defined in equation (15).

$$\tau_{\text{adj}}(f) = \begin{cases} \tau(f), & f \leq \tilde{f}_{\text{T}} \\ \tau_{\text{w}}(f) \cdot \tau(\tilde{f}_{\text{T}})/\tau_{\text{w}}(\tilde{f}_{\text{T}}), & f > \tilde{f}_{\text{T}} \end{cases} \tag{15}$$

Table 1. Quantities for the sound reduction index R.

Symbol	Description	Value
f	Frequency in Hz	
c_0	Sound speed in air	340 m/s
S_{tot}	Total surface in reception room	85 m²
V	Reception room volume	50 m³
Z_0	Sound characteristic impedance of air	418 $\frac{Pa}{m/s}$
m’	Mass per unit area	440 kg/m²
σ_f	Radiation factor for forced waves	See ISO 12354-1
$\tilde{\sigma}$	Radiation factor	See ISO 12354-1
σ_3	-	See ISO 12354-1
ρ	Density of the material	1760 kg/m³
μ	Poisson’s ratio	0.25
t	Construction thickness	0.25 m
l_1, l_2	Side lengths of wall	Depends
c_{L1}	Nominal longitudinal wave velocity	2500 m/s
c_{L}	Effective longitudinal wave velocity	Fit parameter
C	Boundary loss constant	Fit parameter
η_{int}	Internal loss factor	Fit parameter
γ	Shear wave contribution factor	Fit parameter

3. DATA DESCRIPTION

For the next step, data from 24 laboratory measurements will be used to further customize the model. These originate from a round robin test carried out by the *Physikalisch-Technische Bundesanstalt* (PTB). The separating components are Ca-Si walls with a thickness of 25 cm including plaster. Further details on the laboratory experiments can be found in [6] and [7]. Figure 1 shows the mean progression of these 24 curves and the range resulting from the mean value ± 1 respectively ± 2 times the standard deviation of the measurement data.

4. BAYESIAN INFERENCE

The data is now the basis for the optimization of the physical model from section 2 by only changing some parameters but not the physics of the model. Bayesian methods are applied for this purpose. The Bayesian concept of probability is characterized by the idea that probabilities are not interpreted as relative frequencies but as degrees of belief that can be updated with new information. For the application, a distribution is assumed which represents the knowledge of our parameter before the data is known. This distribution is referred to as the prior distribution. The data y is then combined with the prior distribution to obtain a posterior distribution. This posterior distribution represents the knowledge of the parameter after the data is taken into account. Since the knowledge is expressed by probability distributions, it also contains all uncertainties of the parameters. To derive this posterior, Bayes' theorem from equation (16) is applied (s. subsection 4.1). The term $\propto$ denotes equality except for factors that do not depend on θ. The concept of Bayesian statistics is further discussed in several books like [8], [9], and [10].

$$\underbrace{\mathbf{p}(\theta|y)}_{\text{posterior}} = \frac{\mathbf{p}(\theta)\,\mathbf{p}(\theta|y)}{\mathbf{p}(y)} \propto \underbrace{\mathbf{p}(\theta)}_{\text{prior}}\,\underbrace{\mathbf{p}(y|\theta)}_{\text{likelihood}} \tag{16}$$

On the one hand, this approach is suitable when there are few data relative to the number of parameters to be estimated. This is because sample size plays a less central role in Bayesian statistics than in classical statistics. On the other hand, some of the parameters are physical quantities for which prior knowledge exists. The term $\mathbf{p}(\theta)\,\mathbf{p}(y|\theta)$ can also be interpreted in such a way that the parameters are pushed away from the data optimum in the direction of physically meaningful values.

This is also the difference to the classical approach, also known as the frequentist approach, in which θ is chosen such that it maximizes the likelihood $\mathbf{p}(y|\theta)$. The analysis using the classic approach was presented at this year's DAS/DAGA [5].

4.1 Definitions and assumptions

First, the physical parameters to be adjusted are selected. These are the internal loss factor η_{int}, the boundary loss constant C, the longitudinal wave velocity c_{L} of the plate, and γ. Therefore, $\phi = (\eta_{\text{int}}, \text{C}, c_{\text{L}}, \gamma)^T \in \mathbb{R}^4$ is defined as the vector of physical fit parameters.

In addition to these, a covariance matrix is also necessary, which is defined as $\Sigma \in \mathbb{R}^{21\times 21}$ and indicates the third-octave band-dependent variances on the diagonal and the covariances between two third-octave bands outside of it. For this purpose, $\theta = (\phi, \Sigma)$ is denoted as the tuple of ϕ and Σ.

The measurement curves are each denoted as y_i with $i = 1, \ldots, 24$. A multidimensional normal distribution is assumed for these if ϕ and Σ are given, i.e. $y_i|\theta \sim \mathcal{N}_{21}(\text{M}_i(\phi), \Sigma)$. Here, $\text{M}_i : \mathbb{R}^4 \to \mathbb{R}^{21}$ denotes the physical model as a function of the physical fit parameters. This results in a potential model curve for each ϕ. The index in M_i indicates that the properties of the i-th wall are taken into account. This refers in particular to the side lengths.

The notation y in equation (16) represents the vector of all 24 measurement curves, i.e. $y = (y_1^T, y_2^T, \ldots, y_{24}^T)^T \in \mathbb{R}^{504}$, where $504 = 21 \cdot 24$ results from the number of third octave bands times the number of measurement curves. It is assumed that the measurement curves are independent of each other.

4.2 Prior distributions

Maximum Entropy Prior (MEP) is applied to convert physical prior knowledge into a prior distribution. The MEP was introduced by Jaynes [11, 12] and further discussed in [13], [14], [15] and others.

If prior knowledge of the expected value, variance, minimum, and maximum is available for a one-dimensional parameter, then the truncated normal distribution results as the prior distribution [15, Page 201].

The prior assumptions for the physical fit parameters ϕ are shown in Table 2. Note that for the longitudinal velocity c_{L} the effective value and not the nominal value is meant. These assumptions are based on individual experience, but this only plays a minor role for the results as long as other prior knowledge does not deviate too much from the Table 2 values.

Table 2. Prior assumptions for the parameters ϕ

Parameter	Mean	Variance	Min.	Max.
η_{int}	0.02	0.01^2	0.005	∞
C	2	1	0.25	5
c_L in m/s	1000	300^2	700	5000
γ	0.77	0.2^2	0.55	0.95

Both the variances and the correlations are required for the prior distribution of the covariance matrix. The variances are based on the work of Wittstock (2015) [16]. With MEP, this results in the exponential distribution with the calculated average as the expected value for each one-third octave band.

The LKJ (Lewandowski, Kurowicka, Joe) [17] distribution is employed to model prior knowledge about correlations. This distribution is given by $\mathbf{p}(\Omega|\nu) \propto |\Omega|^{\nu-1}$ for each correlation matrix Ω. The parameter ν represents the prior knowledge about the correlation. If ν is less than one, high correlations are assumed; if ν is greater than one, low correlations are assumed; and if $\nu = 1$, no prior knowledge of the correlation is assumed. Here, ν is modeled as an exponential distribution with an expected value of one.

The equations (17) show a summary of all prior assumptions. Here, $\mathcal{N}^{\mathcal{T}}$ denotes the truncated Gaussian, where the hyperparameter a_k, b_k, and the support S_k are chosen such that the properties satisfy Table 2 for $k = 1, 2, 3, 4$. While w_j^2 represents the variances calculated in [16] for $j = 1, \ldots, 21$.

$$\begin{aligned} y_i|\theta &\sim \mathcal{N}_{21}(\mathrm{M}_i(\phi), \Sigma), \\ \theta &= (\phi, \Sigma), \\ \phi_k &\sim \mathcal{N}^{\mathcal{T}}(a_k, b_k, S_k), \\ \Sigma &= D\Omega D, \\ D &= \mathrm{diag}(\sigma_1, \ldots, \sigma_{21}), \\ \sigma_j^2 &\sim \mathrm{Exp}(1/w_j^2), \\ \Omega|\nu &\sim \mathrm{LKJ}(\nu), \\ \nu &\sim \mathrm{Exp}(1). \end{aligned} \tag{17}$$

4.3 Posterior sampling

The software STAN [18, 19] is used to derive the posteriors. For the sampling procedure, the No-U-Turn Sampler (NUTS) is applied, which allows random numbers that are distributed like the posteriors to be drawn without calculating them analytically. The notation, $\theta^{(s)}$ represents the sample number s for $s = 1, \ldots, S$. For the following steps, $S = 4000$ samples are utilized for each parameter.

4.4 Posterior results

A summary of the results of the physical fit parameters ϕ is shown in Table 3. While c_L, γ, and η_int are credible, C deviates quite strongly from what is expected.

Therefore, a second model variant under the condition that C = 0.91, and $\eta_\mathrm{int} = 0.01$, which are the values according to ISO 12354-1, was applied. In this case, a shift of the model curve is required. Figure 1 compares these models by visualizing $\frac{1}{S}\sum_{s=1}^{S} \mathrm{M}_i(\phi^{(s)})$. As the model curves are generated for each wall, the thickness of the curves reflects the influence of the wall properties. The Figures 2, 3, 4, and 5 compare the posterior samples between these two model variants with each other and with sampling from the prior densities.

For the future steps, the focus is on the model for which η_int and C are considered as non-fixed parameters since this has the better quality according to measures such as leave-one-out cross validation (LOO-CV) and WAIC [20]. The model with fixed parameters η_int and C only serves as a comparison.

The results of the standard deviations and correlations are summarized in Figures 6 and 7. For the standard deviations, both the median curve and the corresponding quantile ranges are shown. The values are also compared with the calculations according to Wittstock. The correlation was averaged across all sampled matrices. It can be seen that the correlations in the one-third octave bands below the critical frequency ($\approx$ 240 Hz) are rather weak, whereas the one-third octave bands above correlate rather strongly. An explanation might be that below the critical frequency the sound transmission is dominated by the forced transmission. The individual structural behavior does not play a significant role.

Table 3. Posterior summary of fit parameters

Quantiles	η_int	C	c_L	γ
2.5%	0.005	3.44	1019	0.57
25%	0.007	3.91	1047	0.60
50%	0.009	4.16	1061	0.61
75%	0.012	4.41	1075	0.64
97.5%	0.020	4.85	1100	0.68

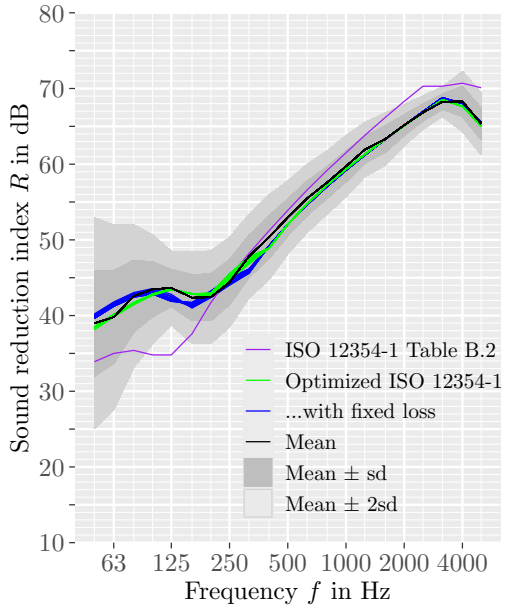


Figure 1. Model comparisons

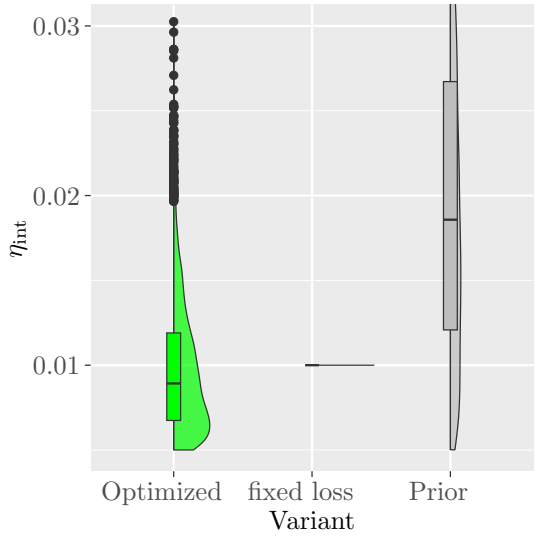


Figure 2. Posterior sample comparison of η_{int}

5. ANALYSIS OF R_{w}

The optimized model discussed is applied to simulate the sound reduction index. Let $W(t)$ be the properties of a Ca-Si wall with a thickness of t meter and the rest as in the data (see Table 1). As before, the notation $\mathrm{M}_{W(t)}(\phi)$ is used for the sound reduction index of a wall with the properties $W(t)$ as a function of the parameters ϕ.

The difference between the model and the measurement curve is simulated by drawing from a $\mathcal{N}_{21}(0, \Sigma^{(s)})$ distribution for each s. These 4000 simulated vectors of differences are each added to the corresponding $\mathrm{M}_{W(t)}(\phi^{(s)})$. This procedure is carried out in steps of one cm with wall thicknesses t from 0.18 meters to 0.36 meters. This results in 4000 simulated shapes of the sound reduction index R for each wall thickness, which can then be used to calculate the weighted sound reduction index R_{w} according to ISO 717-1 [21]. Note that by using all 4000 draws, the distribution and thus the estimation uncertainties of the parameters are taken into account.

The results are shown in Figure 8. The blue points in this figure show a comparison with the model variant in which the internal loss factor η_{int} and the boundary loss factor C are fixed.

These simulated values of the weighted sound reduction index R_{w} can then be utilized to estimate the proba-

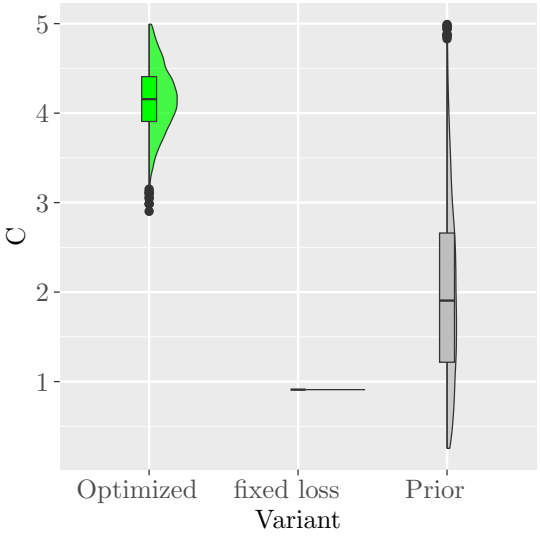


Figure 3. Posterior sample comparison of C

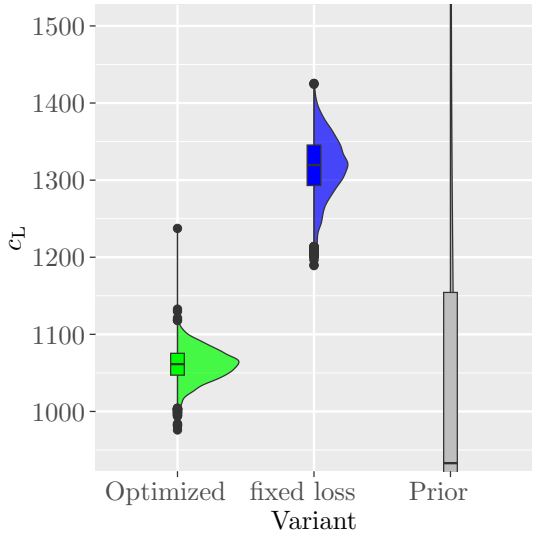


Figure 4. Posterior sample comparison of c_L

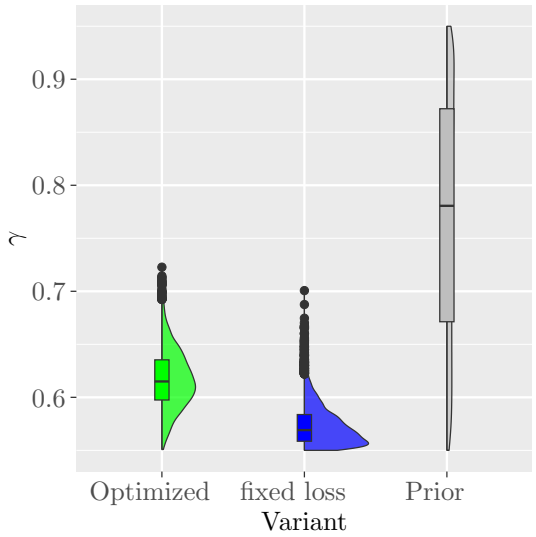


Figure 5. Posterior sample comparison of γ

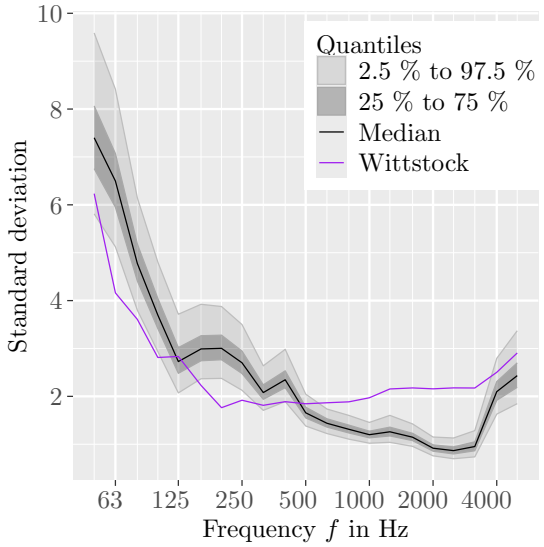


Figure 6. Estimated posterior distribution of the standard deviation in comparison with the calculations according to Wittstock

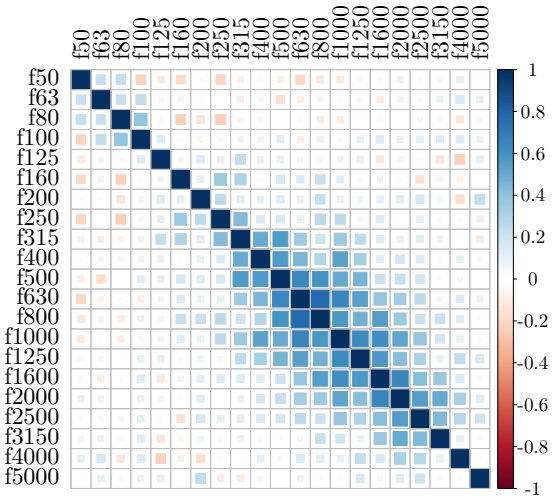


Figure 7. Averaged correlations

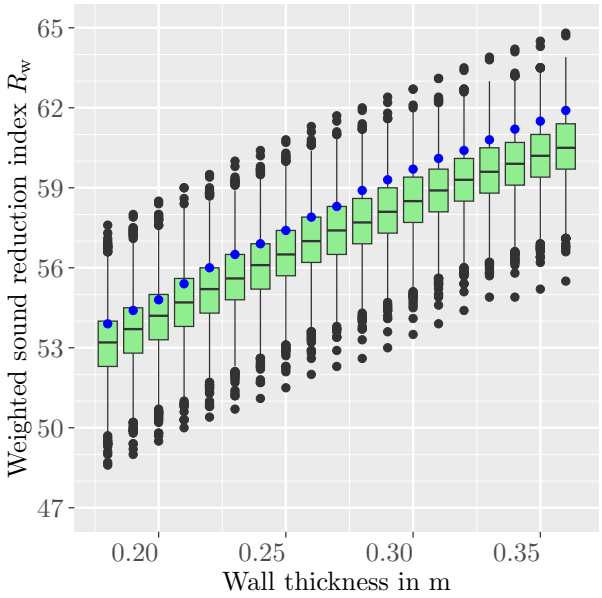


Figure 8. Simulated R_w values

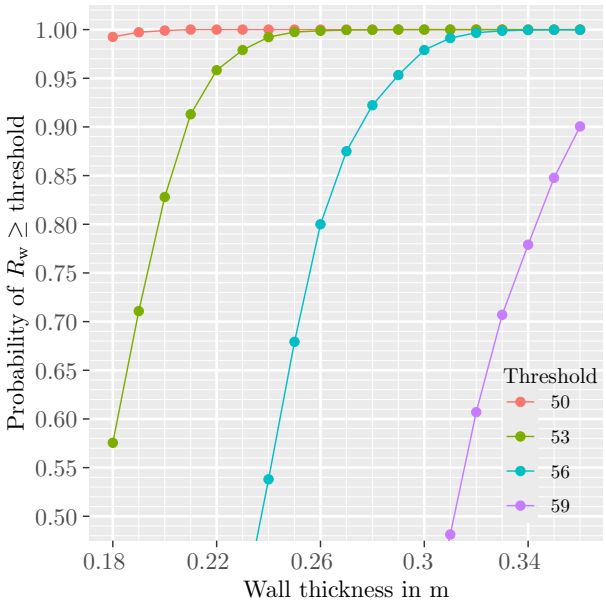


Figure 9. Estimated probability of R_w exceeding a threshold depending on the wall thickness

bility of specified threshold values being exceeded using relative frequencies. These results for probabilities of at least 0.5 are shown in Figure 9.

On the one hand, it can be seen that, according to this analysis, very high requirements of at least 59 dB need correspondingly thick walls of 36 cm to be fulfilled with a probability of about 90 %. On the other hand, low requirements of 50 dB are almost always met also with 18 cm walls.

Assuming 53 dB is set as the threshold value, the question arises as to the probability with which this should be reached. If this is to be fulfilled in at least 90 % of cases, then a thickness of 21 cm is sufficient, and for 95 % it should be 22 cm.

6. DISCUSSION

In this work, the physical model according to ISO 12354-1 was first adapted and then optimized using Bayesian methods. With the help of simulations based on the physical model and probability assumptions, sound reduction index R curves of Ca-Si walls at different thicknesses were simulated. These simulated curves were in turn taken to provide information on the distribution of the weighted sound reduction index R_w depending on the wall thickness.

However, it should be noted that the accuracy of the physical model cannot be verified for wall thicknesses other than 25 cm, but since the model itself is strongly based on the surface area mass, it is credible that the model still fits.

This procedure should therefore be repeated on the basis of other data. In addition to calcium silicate walls with different wall thicknesses, other materials such as reinforced concrete walls or lightweight concrete are also conceivable. In addition, further physical models for the sound reduction index R are to be utilized as a basis, in particular model variants based on the in-situ case.

Overall, it can be stated that this approach provides promising results, but further data and steps for validation are still necessary. However, the procedure itself remains identical regardless of the chosen physical model behind or the exact nature of the data.

7. ACKNOWLEDGEMENTS

We would like to thank the *Physikalisch-Technische Bundesanstalt* for providing the data from the round-robin test. In particular, Mr. Wittstock, who also provided us with his calculations for the one-third-band standard devi-

ations discussed in [16].
Furthermore we would like to acknowledge the funding of the research by the *Bavarian State Ministry of Education, Culture, Science and Arts*.

8. REFERENCES

[1] *Proceedings of Forum Acusticum 2023*, 2023.

[2] Deutsche Gesellschaft für Akustik e.V., ed., *Fortschritte der Akustik - DAGA*, 2024.

[3] Deutsche Gesellschaft für Akustik e.V., ed., *Fortschritte der Akustik - DAGA*, 2023.

[4] DIN EN ISO 12354-1:2017-11, "Bauakustik – berechnung der akustischen eigenschaften von gebäuden aus den bauteileigenschaften: Teil 1: Luftschalldämmung zwischen räumen."

[5] Deutsche Gesellschaft für Akustik e.V., ed., *DAS/DAGA 2025 - 51st Annual Meeting on Acoustics*, 2025.

[6] W. Weise and V. Wittstock, "Using round robin test results for the accreditation of laboratories in the field of building acoustics in germany," *Building Acoustics*, no. 12, pp. 189–206, 2005.

[7] DIN EN ISO 10140-5:2021-09, "DIN EN ISO 10140-5:2021-09, Akustik- Messung der Schalldämmung von Bauteilen im Prüfstand- Teil 5: Anforderungen an Prüfstände und Prüfeinrichtungen (ISO 10140-5:2021); Deutsche Fassung EN ISO 10140-5:2021."

[8] W. M. Bolstad and J. M. Curran, *Introduction to Bayesian statistics*. THEi Wiley ebooks, Hoboken, NJ: Wiley, third edition ed., 2017.

[9] A. Gelman, J. B. Carlin, H. S. Stern, and D. B. Rubin, *Bayesian data analysis*. Texts in statistical science series, Boca Raton, Fla. u.a.: Chapman & Hall/CRC, 2. ed. ed., 2004.

[10] J. Wakefield, *Bayesian and Frequentist Regression Methods*. Springer Series in Statistics, New York, NY: Springer New York, 2013.

[11] E. T. Jaynes, "Information theory and statistical mechanics," *Phys. Rev.*, vol. 106, pp. 620–630, May 1957.

[12] E. T. Jaynes, "Information theory and statistical mechanics. ii," *Phys. Rev.*, vol. 108, pp. 171–190, Oct 1957.

[13] D. Dowson and A. Wragg, "Maximum-entropy distributions having prescribed first and second moments (corresp.)," *IEEE Transactions on Information Theory*, vol. 19, no. 5, pp. 689–693, 1973.

[14] E. T. Jaynes, *Probability Theory - The Logic of Science*. Cambridge: Cambridge University Press, 2003.

[15] P. C. Gregory, *Bayesian logical data analysis for the physical sciences: A comparative approach with Mathematica support*. Cambridge University Press, 2005.

[16] V. Wittstock, "Determination of measurement uncertainties in building acoustics by interlaboratory tests. part 1: Airborne sound insulation," *Acta Acustica united with Acustica*, vol. 101, no. 1, pp. 88–98, 2015.

[17] D. Lewandowski, D. Kurowicka, and H. Joe, "Generating random correlation matrices based on vines and extended onion method," *Journal of Multivariate Analysis*, vol. 100, no. 9, pp. 1989–2001, 2009.

[18] Stan Development Team, "Stan: Stan reference manual," 2024.

[19] Stan Development Team, "RStan: the R interface to Stan," 2024. R package version 2.32.6.

[20] A. Vehtari, A. Gelman, and J. Gabry, "Practical bayesian model evaluation using leave-one-out cross-validation and waic," *Statistics and Computing*, vol. 27, no. 5, pp. 1413–1432, 2017.

[21] DIN EN ISO 717-1:2021-05, "Akustik - bewertung der schalldämmung in gebäuden und von bauteilen: Teil1: Luftschalldämmung," 2021.

DOI: 10.61782/fa.2025.0968



FORUM ACUSTICUM
EURONOISE 2025

WAVE-BASED ANALYSIS OF FLANKING SOUND TRANSMISSION ACROSS JUNCTIONS WITH METAMATERIAL TREATMENT USING EFFECTIVE MEDIUM THEORY

Sofie Becuwe[1*] **Stijn Moons**[1,2] **Daniele Giannini**[1] **Edwin P. B. Reynders**[1]
[1] KU Leuven, Department of Civil Engineering, Structural Mechanics Section, Belgium
[2] CDM Stravitec, 3090 Overijse, Belgium

ABSTRACT

Reducing flanking sound transmission in buildings is challenging, with current options limited to mass increase and structural decoupling. This study explores an alternative approach using resonant metamaterial treatments, where small resonators are added on a subwavelength scale to the building elements connected via the junction. These offer a promising lightweight approach to achieve vibroacoustic attenuation, by creating wave propagation bandgaps that inhibit free-traveling waves within targeted frequency ranges. Wave propagation through the junctions is modeled using an analytical wave approach, in which thin isotropic semi-infinite plates are considered, and equilibrium and compatibility equations are imposed along the junction line. The metamaterial treatment is introduced in a computationally efficient way through effective medium theory, which locally employs homogenized material properties in the connected plates to capture the essential effects of subwavelength resonators. Results show that the structural transmission loss exhibits a significant increase close to the frequency of local resonance. To explore the achievable performance of the proposed treatments, various scenarios are analyzed, by varying the extent of the metamaterial treatment, from a narrow strip close to the junction to the full receiver plate, as well as the local resonator mass and multiple local resonances to address broader band effectiveness.

*__Corresponding author__: *sofie.becuwe@kuleuven.be.*
__Copyright__: *©2025 Becuwe et al. This is an open-access article distributed under the terms of the Creative Commons Attribution 3.0 Unported License, which permits unrestricted use, distribution, and reproduction in any medium, provided the original author and source are credited.*

Keywords: *flanking sound transmission, wave-based analysis, locally resonant metamaterials, effective medium theory*

1. INTRODUCTION

Ensuring a sufficiently high level of sound insulation in buildings is a challenging problem, due to the presence of a multitude of sound transmission paths between the rooms across junctions of building elements, also called flanking transmission paths, through which vibrational energy is transmitted. Current solutions to suppress flanking paths involve mass increase and structural decoupling through elastic interlayers or linings, which however do not always prove to be feasible in renovations or lightweight constructions. To address these limitations, in this paper a new solution for the suppression of flanking sound is researched, based on resonant metamaterials.

Metamaterials are artificial structures, engineered to manipulate wave propagation on the microscopic (i.e., sub-wavelength) scale, such that at the macroscopic scale, an effective material is created with unconventional wave propagation properties that surpass those of conventional materials [1, 2]. Of the various types of metamaterials that have appeared over the years, resonant metamaterials (RMMs) are particularly attractive for noise control in buildings. By small resonators (periodically) added to a host structure on a subwavelength scale, RMMs achieve the suppression of free elastic wave propagation in a targeted frequency range [3, 4], while maintaining a light weight. Furthermore, by employing resonators that possess multiple resonances, known as multi-modal resonators, multiple frequency ranges can be targeted [5].

Recent developments make it possible to efficiently

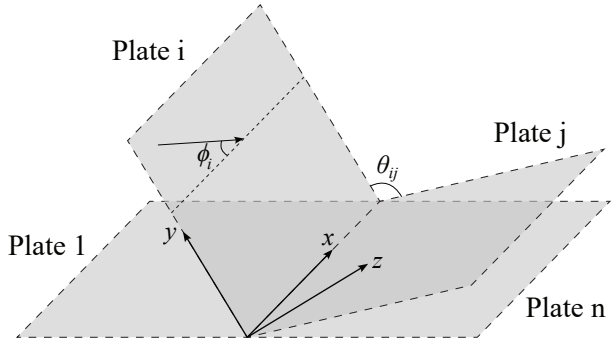


Figure 1: Schematic representation of a system of thin plates connected through a junction.

predict and quantify the influence of flanking sound transmission through junctions [6, 7], however these models only include the application of elastic interlayers, not RMMs. In this paper, the analytical model as described in [8] will therefore be expanded to include RMM applications too, by means of effective medium modeling [9]. With this technique, the effect of the subwavelength resonators is approximated by locally considering equivalent, frequency-dependent, material properties in the host structure [9].

The present paper is organized as follows. Section 2 summarizes the wave-based method to analyze flanking sound transmission across junctions, along with its extension through include RMM treatments. In Section 3, the method is used to analyze flanking transmission across a junction between two steel plates, for which different RMM treatments are considered by varying the width of the treated strip, the resonator mass, and the number of local resonances. Section 4 concludes the work.

2. METHODOLOGY

The used methodology consists of a combination of an analytical wave approach to model wave propagation through junctions [8] with effective medium theory to introduce the metamaterial treatment in a computationally efficient way as described in [9]. The considered system is a junction with n directly connected thin isotropic semi-infinite plates, each inclined at an angle θ_{ij} relative to an arbitrary reference plate (Fig. 1). The corresponding local coordinate system (x', y', z') for each plate is illustrated in Fig. 2. The metamaterial treatment can be applied both on the entire plate surface or a smaller strip close to the junction (Fig. 2). Due to both out-of-plane bending waves and in-plane longitudinal and shear waves, the plates vibrate.

The general aim is to determine the structural transmission coefficients τ_{ij}^{st} between an incident wave type s in plate i and a transmitted wave type t in plate j:

$$\tau_{ij}^{st}\left(\omega, \phi_i\right) := \frac{I_{\mathrm{y},j}^{t}}{I_{\mathrm{y},i}^{s}}. \tag{1}$$

with $I_{\mathrm{y},i}^{s}\left(\phi_i\right)$ the incident intensity and $I_{\mathrm{y},j}^{t}\left(\phi_i\right)$ the transmitted intensity in the local y'-direction per unit length of the connection. The transmission coefficient in Eq. (1) is dependent on the angle of incidence. The diffuse transmission coefficient, independent on the angle of incidence, for homogeneous isotropic plates, can be found as [6]:

$$\tau_{ij}^{st}\left(\omega\right) := \frac{1}{2}\int_0^{\pi} \tau_{ij}^{st}\left(\omega, \phi_i\right) \sin\phi_i \mathrm{d}\phi. \tag{2}$$

We here consider plane incident waves with incident angle $\phi_i = \operatorname{atan}\left(\frac{k_{\mathrm{y},i}^{s}}{k_{\mathrm{x}}}\right)$, frequency ω and wavenumbers k_{x} along the x-direction and k_{y} along the y-direction. Specifically, we consider only bending incident waves. This incident wave causes reflected and transmitted plane waves from the junction to each receiver plate j for any potential wave type t, which is considered to be a bending, shear or longitudinal wave. Compatibility at the junction imposes that the frequency ω and the wavenumber k_{x} along the x-direction, for all reflected and transmitted waves, are equal to the ones imposed by the incident wave.

The structural transmission loss in dB can subsequently be computed from the transmission coefficient as [10]:

$$R_{ij}\left(\omega\right) = -10\log\left(\tau_{ij}^{st}\left(\omega\right)\right). \tag{3}$$

The forces and displacements at the plate edge in the local coordinate system are illustrated in Fig. 2. From these, the incident and transmitted intensity can be computed as [11]:

$$I_{\mathrm{y},i}^{s}\left(\phi_i\right) := -\frac{\omega}{2}\mathrm{Im}\left(\mathbf{f}_{\mathrm{inc},i}^{s\mathrm{T}}\mathbf{u}_{\mathrm{inc},i}^{s*}\right), \tag{4}$$

$$I_{\mathrm{y},j}^{t}\left(\phi_i\right) := -\frac{\omega}{2}\mathrm{Im}\left(\mathbf{f}_{\mathrm{out},j}^{t\mathrm{T}}\mathbf{u}_{\mathrm{out},j}^{t*}\right), \tag{5}$$

with * denoting the complex conjugate. Specifically, the intensities for incident bending and transmitted bending

and in-plane longitudinal or shear waves are [8]:

$$I^{\mathrm{B}}_{\mathrm{y},i}\left(\phi_i\right) = -\frac{\omega}{2}\mathrm{Im}\left(f_{\mathrm{yz,inc},i}u^*_{\mathrm{z,inc},i} + m_{\mathrm{yy,inc},i}\theta^*_{\mathrm{x,inc},i}\right), \tag{6}$$

$$I^{\mathrm{B}}_{\mathrm{y},j}\left(\phi_i\right) = -\frac{\omega}{2}\mathrm{Im}\left(f_{\mathrm{yz,out},j}u^*_{\mathrm{z,out},j} + m_{\mathrm{yy,out},j}\theta^*_{\mathrm{x,out},j}\right), \tag{7}$$

$$I^{\mathrm{L/S}}_{\mathrm{y},j}\left(\phi_i\right) = -\frac{\omega}{2}\mathrm{Im}\left(f_{\mathrm{yx,out},j}u^*_{\mathrm{x,out},j} + f_{\mathrm{yy,out},j}u^*_{\mathrm{y,out},j}\right). \tag{8}$$

2.1 Plate model for plates without RMM treatment

In order to compute the forces and displacements in Eqs. (6) - (8) for plates without RMM treatment, the associated dynamic stiffness matrices need to be derived, which relate the forces and displacements at the plate edge. The plate edge displacements $\mathbf{u}_j\left(x', y', z', t\right)$ and forces per unit length $\mathbf{f}_j\left(x', y', z', t\right)$ for a plate j consist of contributions from the outgoing transmitted and reflected waves at the junction $\mathbf{u}_{\mathrm{out},j}$ and the incident wave $\mathbf{u}_{\mathrm{inc},j}$ [6]:

$$\mathbf{u}_j = \mathbf{u}_{\mathrm{out},j} + \mathbf{u}_{\mathrm{inc},j}, \tag{9}$$

$$\mathbf{f}_j = \mathbf{f}_{\mathrm{out},j} + \mathbf{f}_{\mathrm{inc},j}, \tag{10}$$

where $\mathbf{u}_{\mathrm{inc},j}$ and $\mathbf{f}_{\mathrm{inc},j}$ are only non-zero for the source plate.

The stiffness matrix $\mathbf{D}_j \in \mathbb{C}^{4x4}$ relating the forces $\mathbf{f}_{\mathrm{out},j}$ to the edge displacements $\mathbf{u}_{\mathrm{out},j}$, is composed of a contribution from the in-plane (IP) and out-of-plane (OOP) wave motion, represented respectively by $\mathbf{D}_{\mathrm{IP}}$ and $\mathbf{D}_{\mathrm{OOP}} \in \mathbb{C}^{2x2}$ [6]:

$$\underbrace{\begin{bmatrix} f_{\mathrm{yx}} \\ f_{\mathrm{yy}} \\ f_{\mathrm{yz}} \\ m_{\mathrm{yy}} \end{bmatrix}}_{:=\mathbf{f}_{\mathrm{out},j}} = \underbrace{\begin{bmatrix} \mathbf{D}_{\mathrm{IP}}\left(k_{\mathrm{x}}\right) & \mathbf{0} \\ \mathbf{0} & \mathbf{D}_{\mathrm{OOP}}\left(k_{\mathrm{x}}\right) \end{bmatrix}}_{\mathbf{D}_j\left(k_{\mathrm{x}}\right)} \underbrace{\begin{bmatrix} u_{\mathrm{x}}\left(y'=0\right) \\ u_{\mathrm{y}}\left(y'=0\right) \\ u_{\mathrm{z}}\left(y'=0\right) \\ \theta_{\mathrm{x}}\left(y'=0\right) \end{bmatrix}}_{\mathbf{u}_{\mathrm{out},j}}. \tag{11}$$

For compactness, the dependency from $\mathbf{D}_j$ on k_{x} is omitted in further equations. Eq. (11) can then be substituted into Eq. (10), resulting in the total force per unit length exerted by the plate on the junction:

$$\mathbf{f}_j = \mathbf{D}_j\mathbf{u}_{\mathrm{out},j} + \mathbf{f}_{\mathrm{inc},j}. \tag{12}$$

The stiffness matrices $\mathbf{D}_{\mathrm{IP}}$ and $\mathbf{D}_{\mathrm{OOP}}$ for in-plane and out-of-plane wave motion of isotropic plates can be computed according to [8]:

$$\mathbf{D}_{\mathrm{IP}}\left(k_{\mathrm{x}}\right) = \frac{Et}{k_{\mathrm{x}}^2 + k_{\mathrm{Sy}}k_{\mathrm{Ly}}}\begin{bmatrix} D_{11} & D_{12} \\ -D_{12} & D_{22} \end{bmatrix}, \tag{13}$$

with

$$D_{11} = -\frac{\mathrm{i}\left(k_{\mathrm{Sy}}^2 - k_{\mathrm{x}}^2\right)k_{\mathrm{Ly}}}{2\left(1+\nu\right)}, \tag{14}$$

$$D_{12} = \frac{\mathrm{i}\left(k_{\mathrm{Ly}}^2 + \nu k_{\mathrm{x}}^2\right)k_{\mathrm{x}}}{1-\nu^2} - \frac{\mathrm{i}k_{\mathrm{Sy}}k_{\mathrm{Ly}}k_{\mathrm{x}}}{1+\nu}, \tag{15}$$

$$D_{22} = -\frac{\mathrm{i}\left(\nu k_{\mathrm{x}}^2 + k_{\mathrm{Ly}}^2\right)k_{\mathrm{Sy}}}{1-\nu^2} - \frac{\mathrm{i}k_{\mathrm{x}}^2k_{\mathrm{Sy}}}{1+\nu}. \tag{16}$$

$$\mathbf{D}_{\mathrm{OOP}}\left(k_{\mathrm{x}}\right) = \frac{\mathrm{i}B}{k_{\mathrm{B1y}} - k_{\mathrm{B2y}}}\begin{bmatrix} D_{33} & D_{34} \\ D_{34} & D_{44} \end{bmatrix}, \tag{17}$$

with

$$B = \frac{Et^3}{12\left(1-\nu^2\right)}, \tag{18}$$

$$D_{33} = k_{\mathrm{B1y}}^3k_{\mathrm{B2y}} - k_{\mathrm{B2y}}^3k_{\mathrm{B1y}}, \tag{19}$$

$$D_{34} = \mathrm{i}k_{\mathrm{B2y}}^3 - \mathrm{i}k_{\mathrm{B1y}}^3 + \left(2-\nu\right)\left(k_{\mathrm{B2y}} - k_{\mathrm{B1y}}\right)\mathrm{i}k_{\mathrm{x}}^2, \tag{20}$$

$$D_{44} = k_{\mathrm{B2y}}^2 - k_{\mathrm{B1y}}^2, \tag{21}$$

where E is the Young's modulus, t the thickness of the plate, ν the Poisson's ratio and B the bending stiffness of the plate. k_{B1y}, k_{B2y}, k_{Ly} and k_{Sy} can be found from the equations of motion for OOP and IP motion and are dependent on k_{x} and the bending, longitudinal and shear wavenumbers, given by:

$$k_{\mathrm{B},j} = \left(\frac{\rho_{\mathrm{OOP},j}t_j\omega^2}{B_j}\right)^{1/4}, \tag{22}$$

$$k_{\mathrm{L},j} = \sqrt{\frac{\rho_{\mathrm{IP},j}(1-\nu_{\mathrm{IP},j})^2\omega^2}{E_{\mathrm{IP},j}}}, \tag{23}$$

$$k_{\mathrm{S},j} = \sqrt{\frac{2\rho_{\mathrm{IP},j}(1+\nu_{\mathrm{IP},j})\omega^2}{E_{\mathrm{IP},j}}}. \tag{24}$$

In the case of plates without RMM treatment, the mass densities $\rho_{\mathrm{OOP},j}$ and $\rho_{\mathrm{IP},j}$ are both frequency-independent.

Subsequently, the forces and moment equilibrium and displacement compatibility are imposed at the junction line. The equations are expressed in the global coordinate system, denoted with subscript g, with a transformation matrix $\mathbf{R}_j$ [6]:

$$\mathbf{u}_{\mathrm{g}} = \mathbf{R}_j\mathbf{u}_j, \tag{25}$$

$$\mathbf{f}_{\mathrm{g},j} = \mathbf{R}_j\mathbf{f}_j = \mathbf{R}_j\mathbf{D}_j\mathbf{R}_j^{-1}\mathbf{u}_{\mathrm{g}}, \tag{26}$$

where

$$\mathbf{R}_j := \begin{bmatrix} 1 & 0 & 0 & 0 \\ 0 & \cos\theta_{ij} & -\sin\theta_{ij} & 0 \\ 0 & \sin\theta_{ij} & \cos\theta_{ij} & 0 \\ 0 & 0 & 0 & 1 \end{bmatrix}. \tag{27}$$

For the source plate, $\theta_{ij} = 0$, while for the receiver plate, θ_{ij} is equal to the angle between the source and receiver plate. The displacements and forces exerted on the junction by an incident bending wave are then found as [8]:

$$\mathbf{u_{inc}} = \begin{bmatrix} u_\mathrm{x} \\ u_\mathrm{y} \\ u_\mathrm{z} \\ \theta_\mathrm{x} \end{bmatrix} = \begin{bmatrix} 0 \\ 0 \\ u_{\mathrm{z,inc}} \\ \theta_{\mathrm{x,inc}} \end{bmatrix}, \tag{28}$$

$$\mathbf{f_{inc}} = \begin{bmatrix} f_{\mathrm{yx}} \\ f_{\mathrm{yy}} \\ f_{\mathrm{yz}} \\ m_{\mathrm{yy}} \end{bmatrix} = \begin{bmatrix} 0 \\ 0 \\ f_{\mathrm{yz,inc}} \\ m_{\mathrm{yy,inc}} \end{bmatrix}, \tag{29}$$

with $u_{\mathrm{z,inc}} = \alpha_i$, $\theta_{\mathrm{x,inc}} = i\alpha_i k_y$, $f_{\mathrm{yz,inc}} = -\alpha_i B_1(k_y^3 - (2-\nu_{1\mathrm{OOP}})k_x^2 k_y)$ and $m_{\mathrm{yy,inc}} = \alpha_i B_1(k_y^2 - \nu_{1\mathrm{OOP}} k_x^2)$. α_i represents the amplitude of the incident wave, here taken equal to unity. The incident wave power in the y-direction then becomes [6]:

$$I_\mathrm{inc} = \frac{\rho_{1\mathrm{OOP}} t_1 \omega^3 \alpha^2}{k_{\mathrm{B1}}} \sin\phi_i. \tag{30}$$

In the next step, the equilibrium equation can be rewritten for n plates with a source plate i as the sum of the forces from Eq. (12) exerted by all plates [8]:

$$\sum_{j=1}^{n} \mathbf{f}_{\mathrm{g},j} = \mathbf{0}, \tag{31}$$

$$\sum_{j=1}^{n} \mathbf{R}_j \mathbf{D}_j \mathbf{u}_j = \mathbf{R}_i \left(\mathbf{D}_i \mathbf{u}_\mathrm{inc} - \mathbf{f}_\mathrm{inc}\right). \tag{32}$$

Taking into account the compatibility requirements at the junction, Eq. (25) is substituted into this expression:

$$\left(\sum_{j=1}^{n} \mathbf{R}_j \mathbf{D}_j \mathbf{R}_j^\mathrm{T}\right) \mathbf{u}_\mathrm{g} = \mathbf{R}_i \left(\mathbf{D}_i \mathbf{u}_\mathrm{inc} - \mathbf{f}_\mathrm{inc}\right). \tag{33}$$

Eq. (33) is solved for the displacements $\mathbf{u}_\mathrm{g}$ at the junction. The displacements for every receiver plate j in the local coordinate system can then be found as:

$$\mathbf{u}_j = \mathbf{R}_j^\mathrm{T} \mathbf{u}_{\mathrm{g},j}. \tag{34}$$

From this result, $\mathbf{u}_{\mathrm{out},j}$ can be computed as $\mathbf{u}_j - \mathbf{u}_\mathrm{inc}$ when the considered plate contains the incident wave. Otherwise, $\mathbf{u}_{\mathrm{out},j}$ is equal to $\mathbf{u}_j$. The related forces can be found as $\mathbf{f}_{\mathrm{out},j} = \mathbf{D}_j \mathbf{u}_{\mathrm{out},j}$. In that way, all the input values for Eqs. (6)-(8) are determined.

2.2 Plate-strip model for plates with RMM treatment

To reduce flanking sound transmission through junctions, RMMs can be applied to a full plate or only in a strip close to the junction. When plates are fully treated with RMMs, the same methodology as described in Section 2.1 can be applied, with only one difference: in that case the mass density in Eq. (22) is not frequency-independent anymore. Due to the resonators, the OOP mass density will be influenced by inertial contributions of each resonator mode k. This results in an effective mass density, taking into account the modal effective masses. The effective mass density of a multi-modal metamaterial panel is obtained as [9]:

$$\rho_{\mathrm{eff,z}}(\omega) = \rho + \frac{1}{t} \sum_{k=1}^{n_\mathrm{m}} \frac{m''_{\mathrm{z},k}(1+\mathrm{i}\eta)}{(1+\mathrm{i}\eta) - (\omega/\omega_k)^2}, \tag{35}$$

with ρ the mass density of the host plate, n_m the modes of interest, t the thickness of the host plate, $m''_{\mathrm{z},k}$ the modal effective translational masses, η the damping loss factor of the resonators and ω_k the fixed base natural frequencies of the resonator.

If only a RMM strip close to the junction is considered, this strip has a frequency-dependent OOP effective mass density, while the OOP mass density of the untreated connected plate is frequency-independent. The IP mass density is always frequency-independent, but due to the added resonators, an additional static mass needs to be added to the mass density of the host structure. To include the effect of a RMM strip between the junction and an untreated connected plate, the prediction model as described in section 2.1 needs to be expanded, following the methodology developed in [7, 8] for thin plate interlayers. Contrary to the previously considered plates, the RMM strip has a finite dimension in the y'-direction. Thus not only the displacements and forces at the junction line (2) need to be taken into account, but also the forces and displacements at the interface between the RMM strip and the connected plate (1), as illustrated in Fig. 2. The relation between the forces per unit length $\mathbf{f}_\mathrm{l}$ and the displacements $\mathbf{u}$ at both endplanes of the RMM strip can be expressed in the local coordinate system through a stiff-

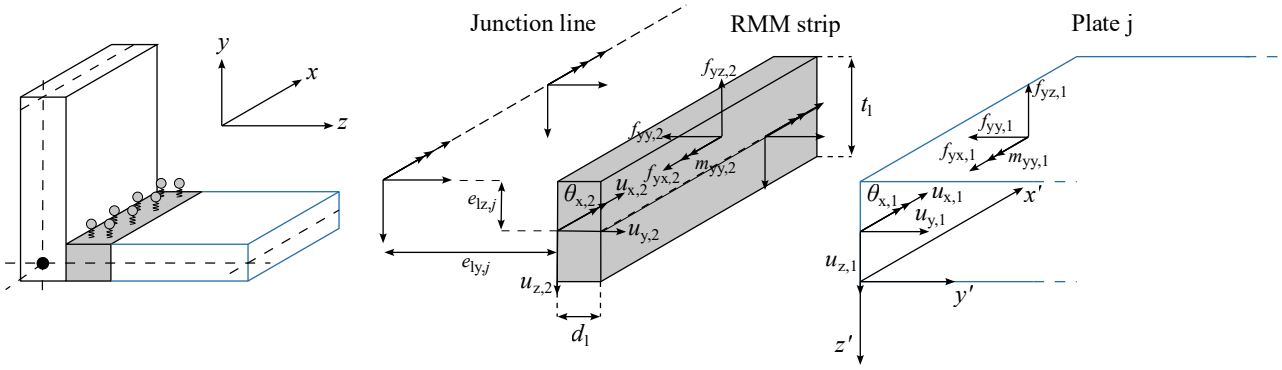


Figure 2: Exploded view of a plate/strip system.

ness matrix $\mathbf{D}_\mathrm{l}$ [8]:

$$\mathbf{f}_\mathrm{l} = \mathbf{D}_\mathrm{l}\,\mathbf{u}, \tag{36}$$

where

$$\mathbf{f}_\mathrm{l} := [\mathbf{f}_{\mathrm{l},1} \;\; \mathbf{f}_{\mathrm{l},2}]^\mathrm{T} = [\mathbf{f}_\mathrm{l}\,(y'=d_\mathrm{l}) \;\; \mathbf{f}_\mathrm{l}\,(y'=0)]^\mathrm{T}, \tag{37}$$

$$\mathbf{u} := [\mathbf{u}_1 \;\; \mathbf{u}_2]^\mathrm{T} = [\mathbf{u}\,(y'=d_\mathrm{l}) \;\; \mathbf{u}\,(y'=0)]^\mathrm{T}. \tag{38}$$

For each plate j connected to the junction through a RMM strip, the exerted forces $\mathbf{f}_{1,j}$ at position (1) and $\mathbf{f}_{2,j}$ at position (2) can be divided into a direct contribution from the plate $\mathbf{f}_{\mathrm{p},j}$ as in Eq. (11) and a contribution related to the RMM strip itself $\mathbf{f}_{\mathrm{l},j}$ [8]:

$$\mathbf{f}_j = \mathbf{f}_{\mathrm{p},j} + \mathbf{f}_{\mathrm{l},j}, \tag{39}$$

$$\mathbf{f}_{\mathrm{g},j} = \mathbf{D}_{\mathrm{g,p},j}\mathbf{u}_\mathrm{g} + \mathbf{D}_{\mathrm{g,l},j}\mathbf{u}_\mathrm{g}, \tag{40}$$

where the subscript g denotes the global coordinate system and

$$\mathbf{D}_{\mathrm{g,p},j} = \begin{bmatrix} \mathbf{R}_j\mathbf{D}_j\mathbf{R}_j^\mathrm{T} & \mathbf{0} \\ \mathbf{0} & \mathbf{0} \end{bmatrix}, \tag{41}$$

$$\mathbf{D}_{\mathrm{g,l},j} = \begin{bmatrix} \mathbf{R}_\mathrm{j} & \mathbf{0} \\ \mathbf{0} & \mathbf{R}_{\mathrm{l},j} \end{bmatrix} \underbrace{\begin{bmatrix} \mathbf{D}_{\mathrm{l},j,11} & \mathbf{D}_{\mathrm{l},j,12} \\ \mathbf{D}_{\mathrm{l},j,21} & \mathbf{D}_{\mathrm{l},j,22} \end{bmatrix}}_{\mathbf{D}_{\mathrm{l},j}} \begin{bmatrix} \mathbf{R}_j^\mathrm{T} & \mathbf{0} \\ \mathbf{0} & \mathbf{R}_{\mathrm{l},j}^\mathrm{T} \end{bmatrix}, \tag{42}$$

with $\mathbf{D}_j$ being the dynamic stiffness matrix for a thin plate j as in Eqs. (13) and (17). The stiffness matrix $\mathbf{D}_{\mathrm{l},j}$ of a RMM strip consists of four block matrices $\mathbf{D}_{\mathrm{l},j,mn} \in \mathbb{C}^{4x4}$. The strip is considered as a waveguide, in contrary to the two steel plates which are considered as halfspaces. Due to the finite y'-dimension, waves in both the positive and negative y'-direction are considered for the deformation of the layer. The stiffness matrices can be computed in a similar way as in section 2.1, and can be found in [8].

Since the endplane of the RMM strip could have offsets $e_{\mathrm{ly},j}$ and $e_{\mathrm{lz},j}$ relative to the theoretical junction line, as illustrated in Fig. 2, the transformation matrix (27) needs to be adapted for the RMM strip as [8]:

$$\mathbf{R}_{\mathbf{l,j}} := \begin{bmatrix} 1 & 0 & 0 & 0 \\ 0 & \cos\theta_{ij} & -\sin\theta_{ij} & 0 \\ 0 & \sin\theta_{ij} & \cos\theta_{ij} & 0 \\ 0 & e_{\mathrm{lz},j} & e_{\mathrm{ly},j} & 1 \end{bmatrix}. \tag{43}$$

where the transformation matrix (27) corresponded to the situation in which these offsets are zero.

The global force equilibrium per unit length is then evaluated both at the junction line and at each interface between a RMM strip and at its connected plate:

$$\sum_{j=1}^{n} \mathbf{f}_{\mathrm{g1},j} = \begin{cases} \mathbf{R}_i\,(\mathbf{D}_i\mathbf{u}_\mathrm{inc} - \mathbf{f}_\mathrm{inc}), & \text{if } j = i \\ \mathbf{0}, & \text{if } j \neq i \end{cases} \tag{44}$$

$$\sum_{j=1}^{n} \mathbf{f}_{\mathrm{g2},j} = \begin{cases} \mathbf{0}, & \text{if } j = i \\ \mathbf{R}_i\,(\mathbf{D}_i\mathbf{u}_\mathrm{inc} - \mathbf{f}_\mathrm{inc}), & \text{if } j \neq i \end{cases} \tag{45}$$

3. APPLICATION

In this Section, the methodology described in Section 2 is applied to a rigidly connected horizontal junction of steel plates, where both fully treated RMM plates and plates with only a small RMM strip close to the junction are considered. The results are compared with the junction models without any RMM treatment, to quantify the attenuation provided by RMM treatments on flanking sound transmission.

The steel plates without RMM treatment are considered isotropic and so the OOP and IP properties are the

same. The properties of the considered steel plates are: $\rho = 7850$ kg/m^3, $E = 210 \cdot 10^9$ Pa, $t = 0.002$ m, $\nu = 0.3$. From these parameters, the surface mass, shear modulus and bending stiffness can be computed as $m = \rho t$, $G = E/2(1+\nu)$ and $B = Et^3/12(1-\nu^2)$ respectively.

A distinction is made between OOP and IP material properties for the parts of the structure with RMM treatment. The IP properties remain the same as for the untreated plate, except for the mass density, where an additional static mass is added due to the presence of the resonators. In this paper, the added static mass due to the resonators will be initially taken equal to 10% of the mass of the host structure belonging to one resonator. The OOP mass density can be found through effective medium modeling with Eq. (35). The resonance frequency of the resonators is set to 500 Hz.

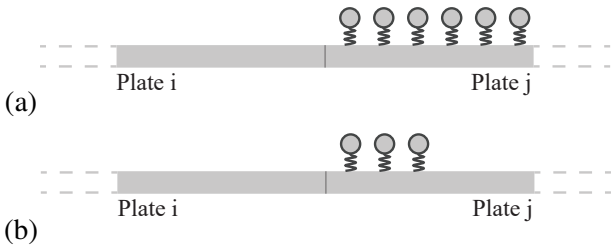


Figure 3: Junction between two plates ($\theta_{ij} = \pi$) with a fully treated RMM receiver plate (a) and with a treated RMM strip close to the junction (b).

3.1 Fully treated receiver plate

The first case we consider, is a junction of two steel plates of which the receiver plate is fully treated with resonators, as illustrated in Fig. 3a. The source plate i is further denoted as plate 1, the receiver plate j as plate 2.

The structural transmission loss for the transmitted bending waves is shown in Fig. 4 for a junction between two plates with an angle $\theta_{12} = \pi$. The receiver plate is fully treated with resonators with a damping of 0 and a local resonator mass of 10 % and 20 % with respect to the mass of the host plate. The structural transmission coefficient for longitudinal and shear waves is very small with respect to the transmission coefficient for bending waves, and therefore the structural transmission loss for these wave-types is not further considered in this paper. The graphs show that due to the RMM treatment of the receiver plate, at the resonance frequency of 500 Hz, less vibrational energy is transmitted from the source into the receiver plate and so the RMM treatment is effective to reduce wave propagation at the targeted frequency.

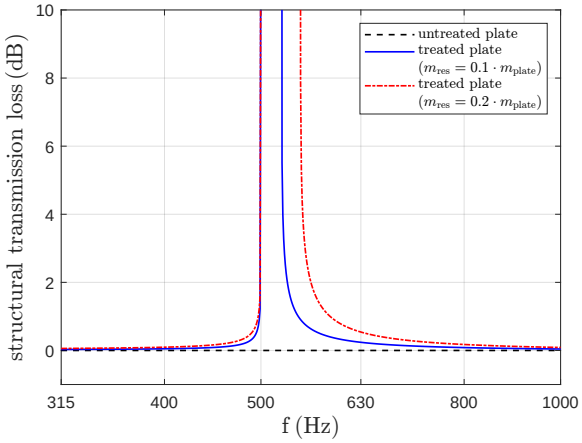


Figure 4: Comparison between the structural transmission loss for the transmitted bending waves through a junction ($\theta_{12} = \pi$) with an untreated and fully treated receiver plate with no damping in the resonators and a local resonator mass of 10 % and 20 % with respect to the mass of the host plate.

3.2 Influence of the local resonator mass

In a second case, the influence of the added resonator mass with respect to the host structure is analyzed, which is also shown in Fig. 4. In a first case, the local resonator mass is taken to be 10 % of the mass of the host structure. In a second case, the local resonator mass is taken to be 20 % of the mass of the host structure. The graphs in Fig. 4 show that in the case of 20 % added mass, the bandgap that inhibit free-traveling waves at the resonance frequency of the resonators widens, resulting in a broader frequency range in which the transmitted vibrational energy is reduced. Even though not shown here, similar results have been obtained for another resonator damping, other angles θ_{12} of the junction and in the case only a strip of resonators is applied.

3.3 Receiver plate with RMM strip

Thirdly, only a small strip of resonators is applied close to the junction, as illustrated in Fig. 3b. The strip is modeled as a part of the junction as discussed in Section 2.2,

and so the structural transmission loss is computed for the transmitted bending waves after the strip. The results are shown in Fig. 5 for a junction between two plates with an angle $\theta_{12} = \pi$, with a resonator damping of 0 (Fig. 5a) and 0.02 (Fig. 5b). The results are shown for a strip with a width of 0.03 m, 0.05 m, 0.10 m, 0.15 m and 0.3 m. From these graphs it is clear that we can achieve already a significant reduction in wave propagation from source to receiver plate at the resonance frequency by applying only a small strip of resonators close to the junction. Fig. 5a shows that the frequency range in which free wave propagation is inhibited becomes larger by increasing the width of the strip. From Fig. 5b it is clear that the larger the width of the strip is, the larger the structural transmission loss through the RMM strip will be. Similar results are obtained for another resonator damping and other angles θ_{12} of the junction. When a strip of resonators with very low damping is considered, additional drops in the structural transmission loss are visible, caused by Fabry-Perot standing waves. However, this is only significant at very low damping values, and thus has no impact in practice.

3.4 Influence of multi-modal resonators

As a fourth case, the influence of multi-modal resonators is examined. Multi-modal resonators allow to have multiple resonance frequencies, resulting in broader band effectiveness. As an example, a junction with an angle $\theta_{12} = \pi$ is considered, with a treated strip of 0.15 m close to the junction in the receiver plate and a damping of 0, 0.02, 0.05 or 0.1 in the resonators. Three resonance frequencies (500 Hz, 460 Hz, 420 Hz) are considered. The results are shown in Fig. 6. A peak is visible at each resonance frequency of the multi-modal resonator, resulting in a more broadband reduction of the transmitted vibrational energy. Even though not shown here, similar results have been obtained for another resonator damping, other angles θ_{12} of the junction and in the case a fully treated receiver plate is applied.

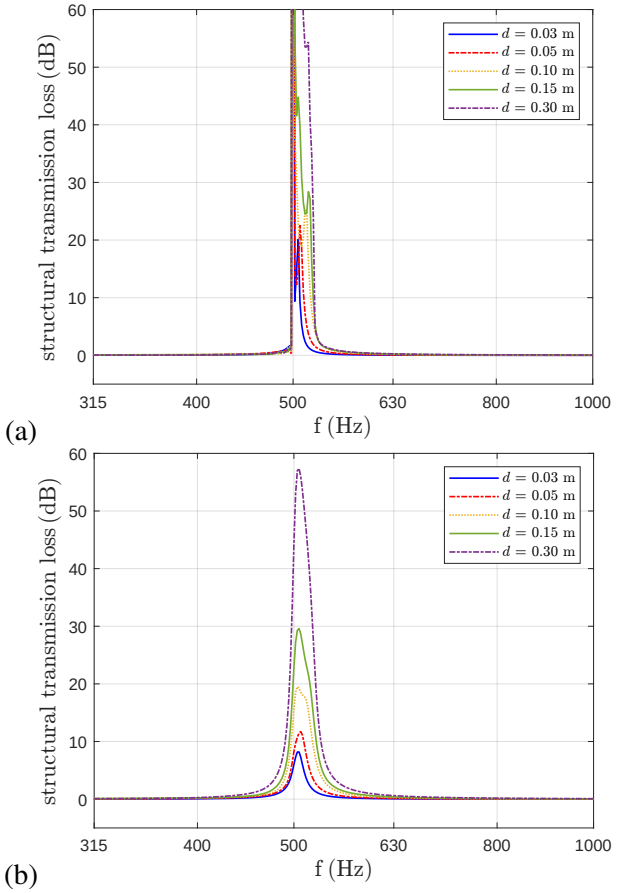


Figure 5: Comparison of the structural transmission loss for the transmitted bending waves between a junction ($\theta_{12} = \pi$) with a treated strip close to the junction in the receiver plate for a damping of 0 (a) and 0.02 (b) in the resonators. Results are shown for a strip width of 0.03 m, 0.05 m, 0.10 m, 0.15 m and 0.3 m.

4. CONCLUSION

In this paper, an analytical wave approach to model wave propagation through junctions was combined with effective medium theory to introduce a metamaterial treatment in the junction design. The proposed model has been used to study flanking transmission across junctions with steel plates, exploring various scenarios in which the width of the treated strip, the resonator mass, and the number of local resonances were changed. Varying the width of the metamaterial strip has proven that already a significant reduction in wave propagation can be obtained for sufficiently wide strips. Increasing the mass of the local resonators broadens the frequency range in which bending wave transmission to the receiver plate is reduced, but it can however conflict with lightweight requirements. Another way of widening the band of effectiveness is therefore to use multi-modal resonators, allowing to include multiple resonance frequencies. The methodology proposed in this work sets a framework to analyze and de-

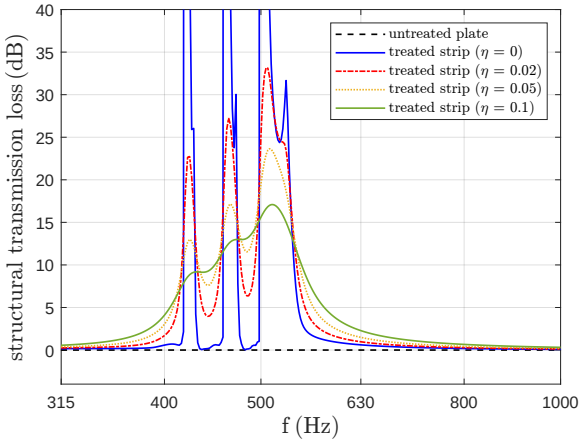


Figure 6: Comparison of the structural transmission loss for the transmitted bending waves through a junction ($\theta_{12} = \pi$) with a treated strip of 0.15 m close to the junction in the receiver plate, for a damping of 0, 0.02, 0.05 and 0.1 in the resonators. Three resonance frequencies (500 Hz, 460 Hz, 420 Hz) are considered.

sign metamaterial treatments for the suppression of flanking sound transmission across junctions of plates. Future research will focus on further validation against numerical and experimental results for practical applications.

5. ACKNOWLEDGMENTS

The presented research has been performed within the framework of the project "Resonant metamaterials for broadband suppression of flanking sound transmission in buildings" (Grant 1S38725N), funded by the Research Foundation Flanders (FWO), Belgium. Stijn Moons gratefully acknowledges the financial support of Flanders Innovation & Entrepreneurship (VLAIO) through the Baekeland fellowship HBC.2022.0712. Daniele Giannini gratefully acknowledges the financial support of the Research Foundation Flanders (FWO) through the postdoctoral fellowship 12A3Q24N.

6. REFERENCES

[1] M. Hussein, M. Leamy, and M. Ruzzene, "Dynamics of phononic materials and structures: historical origins, recent progress, and future outlook," *Applied Mechanics Reviews*, vol. 66, no. 4, pp. 040802–3, 2014.

[2] G. Ma and P. Sheng, "Acoustic metamaterials: From local resonances to broad horizons," *Science Advances*, vol. 2, no. 2, p. e1501595, 2016.

[3] F. Lemoult, N. Kaina, M. Fink, and G. Lerosey, "Wave propagation control at the deep subwavelength scale in metamaterials," *Nature Physics*, vol. 9, pp. 55–60, 2013.

[4] C. Claeys, K. Vergote, P. Sas, and W. Desmet, "On the potential of tuned resonators to obtain low-frequency vibrational stop bands in periodic panels," *Journal of Sound and Vibration*, vol. 332, no. 6, pp. 1418–1436, 2013.

[5] D. Giannini, M. Schevenels, and E. Reynders, "Rotational and multimodal local resonators for broadband sound insulation of orthotropic metamaterial plates," *Journal of Sound and Vibration*, vol. 547, no. 117453, pp. 1–17, 2023.

[6] R. Langley and K. Heron, "Elastic wave transmission through plate/beam junctions," *Journal of Sound and Vibration*, vol. 143, no. 2, pp. 241–253, 1990.

[7] P. Mees and G. Vermeir, "Structure-borne sound transmission at elastically connected plates," *Journal of Sound and Vibration*, vol. 166, no. 1, pp. 55–76, 1993.

[8] S. Moons, R. Lanoye, and E. Reynders, "Prediction of flanking sound transmission through cross-laminated timber junctions with resilient interlayers," *Applied Acoustics*, vol. 228, no. 110317, pp. 1–15, 2025.

[9] D. Giannini and E. Reynders, "Effective medium modelling of real-world multi-modal metamaterial panels achieving broadband vibroacoustic attenuation," *Extreme Mechanics Letters*, vol. 69, p. 102161, 2024.

[10] R. Craik, *Sound transmission through buildings using statistical energy analysis*. Aldershot, UK: Gower, 1996.

[11] L. Cremer and M. Heckl, *Structure-borne sound: Structural vibrations and sound radiation at audio frequencies*. Berlin: Springer, 2nd ed., 1988.

DOI: 10.61782/fa.2025.0080

FORUM ACUSTICUM EURONOISE 2025

ACOUSTIC PERFORMANCE OF PREFABRICATED REINFORCED CONCRETE WALLS FOR MODULAR CONSTRUCTIONS

Reza M. Firouz[1*] **Albano Neves e Sousa**[1]
[1] CERIS, Instituto Superior Técnico, Universidade de Lisboa, Av. Rovisco Pais 1, 1049-001, Lisbon, Portugal

ABSTRACT

Modular construction is being promoted as a solution to the problem of housing crisis as the demand for new construction continues to rise. However, the performance of this construction approach must be competitive with conventional construction methods. Therefore, beyond structural performance and safety features, indoor comfort qualities such as thermal and acoustic insulation should be considered. Acoustic transmission loss phenomena are generally governed by mass, and reinforced concrete (RC) walls are considered massive elements compared to other conventional building materials. However, it is still necessary to enhance such elements with insulation materials. In this study, the acoustic performance of double-layer prefabricated RC wall elements with embedded insulation layers is assessed under different configurations. A 3D harmonic acoustic finite element (FE) numerical model is developed and verified to evaluate the sound reduction capability of the prefabricated double-layered concrete walls with different thicknesses. The effect of using various insulation materials is also discussed.

Keywords: *Acoustic performance, building acoustics, airborne sound, prefabricated RC walls, Finite element analysis.*

1. INTRODUCTION

The construction waste, high labor costs in developed countries, and the sustainability considerations, promote modular construction as a possible approach to tackle these challenges. Adoption of modern techniques for development of mass buildings leads to affordable housing needed today for many countries. Hence, the efforts should generate solutions aiming to save energy and reducing the construction costs [1]. Maintaining quality and the level of comfort, such as thermal and acoustic comfort, etc., is essential and can't be disregarded. Pre-cast buildings minimize the construction time compared to conventional non-precast buildings which usually require multiple different phases for finishing the elements such as floors and walls, separately. However, while minimizing the number of phases in modular construction, the building must meet the construction provisions at the end of these phases [2]. Therefore, besides structural performance, considerations should be for thermal and acoustic isolations. Moreover, it is crucial to carefully configure their structural elements to avoid thermal and acoustic bridges. The insurance could be made by developing numerical analysis models, which are verified by performing experimental studies on scaled samples or using existing research data.

The literature includes limited amounts of data regarding the acoustic performance of concrete floor and wall systems. Proença et. al. [3] performed an experimental, numerical, and analytical study of the acoustic performance of light weight composite sandwich panels as floor system. The sandwich panels were comprised of two identical glass fiber reinforced polymer (GFRP) face sheets and a rigid polyurethane (PUR) foam core and placed firmly between two chambers for the

[*] ***Corresponding author***: reza.mohammadifirouz@tecnico.ulisboa.pt
©2025 First author et al. This is an open-access article distributed under the terms of the Creative Commons Attribution 3.0 Unported License, which permits unrestricted use, distribution, and reproduction in any medium, provided the original author and source are credited.

acoustic test. Weighted sound reduction index (Rw) of 30 dB were reported by the test results. It was concluded that for such lightweight floor systems the performance index values did not fulfill the acoustic requirement of building standards. Ferreira et. al. [4] performed experimental tests of mechanical, fire resistance and airborne sound performance on sandwich panel system for non-loadbearing walls. The sandwich panels were comprised of two face sheets (gypsum board, fire resistant gypsum board, or magnesium oxide), glued to the extruded polystyrene (XPS) core and fixed by galvanized steel profiles. However, despite satisfactory results for other factors, the acoustic performance of the wall panels for the index of sound insulation was insufficient and it was proposed to add acoustic covering layers to the wall systems. Calleri et al. [2] characterized the sound insulation properties of innovative façade made by two-layer cast-in-situ light weight concrete wall with an insulation layer of non-woven fabric in between. Experimental tests were performed to evaluate the acoustic performance of this wall with or without window opening. R_w value of 48 dB were reported from the acoustic test of the façade system. Peng et al. [5], assessed the acoustic behavior of prefabricated composite wall panel, comprised layers of steel wire network, expanded polystyrene foam plastic (EPS), and fine aggregate concrete. It was reported that EPS board can enhance sound insulation in the middle (500 ~ 2000 Hz) and high frequency ranges (<2000 Hz). 42 dB of apparent sound reduction parameters were reported.

In this paper, a study on the acoustic performance of prefabricated double layer RC walls with insulation core is presented. FEM numerical acoustic model has been developed using ANSYS® software package and verified with the existing data on similar models. Then the harmonic acoustic simulation results for different thicknesses and insulation materials are analyzed. Finally, overall conclusions are drawn and suggestions for future work are given.

2. NUMERICAL MODEL

2.1 Materials and methodology

In this study, RC pre-fabricated wall panels featuring an isolation layer were modelled. The RC walls were of 3 m height, including two layers of RC wythe, with an insulation layer in between. The top and the bottom side of the walls were composed of RC section, resembling a beam section. Figure 1 shows the details of the modeled samples. The cross-sectional area as shown in Figure 1 could be of two proposed thickness, 160 mm (P18) or 220 mm (P22), including an insulation layer of 60 mm thick in between which serve as thermal and acoustic isolation, while reducing the weight of the wall system. The material of wall panels includes concrete of class C50/60. The insulation layer of EPS or PUR were considered in the modelling. Longitudinal and transversal steel reinforcement, and spatial trusses were also considered for the cross-section as shown in Figure 1. The proposed wall systems are considered be a segment of multi stories modular buildings.

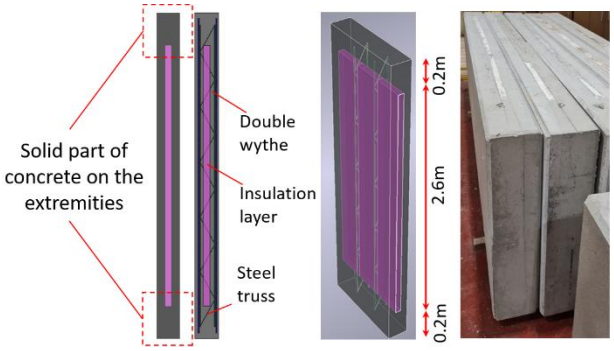


Figure 1. Description of the modelled pre-fabricated RC wall panels.

2.2 Description of the numerical model

A 3D FE model using ANSYS® was used to assess the acoustic performance of the pre-fabricated wall panels. Finite element model for the acoustic harmonic analysis of the airborne sound reduction of the pre-fabricated RC walls are shown in Figure 2. The airborne sound source of 0.01 Kg was simulated as nodal acoustic mass, which was placed in one top corner of the emitting room (Figure 2).

The relevant properties of different materials used in the model are shown in Table 1.

Both emitting and receiving chambers were of 3×3×3 m^3 dimensions. Pre-fabricated RC walls were modelled with 3 m height and 3 m width. The concrete wall panels were considered fixed in top, bottom, and sides as the displacement boundary condition of the geometry. A fluid-structure interface (FSI) was considered at the contact surfaces of the acoustic chambers and the RC wall. Absorption coefficients (α) based on different frequencies (*f*) which are shown in Table 2, were applied in the acoustic medium (air chambers) surfaces.

The model was meshed using ANSYS FLUID220 (20-node acoustic element) and SOLID186 (20-node structural solid element) element types were used, respectively for acoustic and structural domains. Mesh size of 125 mm was adopted for all elements of the geometries which led to a total number of 41580 elements.

As shown in Figure 3, six random nodes in each of the emitting and receiving chambers were considered as microphone positions to report the sound pressure level (SPL). The selection of these nodes was adopted based on the recommendations of BS EN 20140-9 [6].

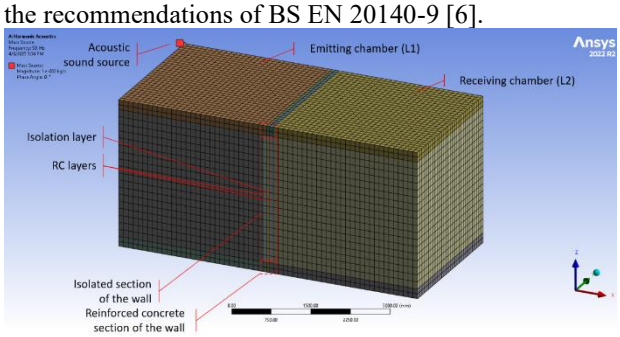


Figure 2. Meshed FE model of the pre-fabricated RC wall, between the two chambers.

Table 1. Material properties of different elements.

Properties	Air medium	Concrete	EPS	PUR
Density [Kg/m³]	1.225	2400	30	100
Elastic Modulus [MPa]	-	30×10^3	3.9	25.9
Poisson's ratio	-	0.2	0.1	0.495
Speed of sound [m/s]	343.2	-	-	-

Table 2. Acoustic absorption coefficient.

f [Hz]	125	250	500	1000	2000	4000
α [-]	0.03	0.03	0.02	0.03	0.04	0.05

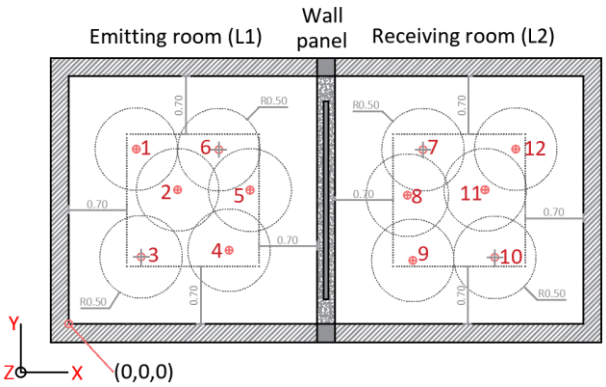


Figure 3. Microphone locations in the emitting and receiving rooms for SPL measurement.

2.3 Model validation

Results from the Proença et al. [3] was used to validate the presented numerical model. The study included experimental and numerical investigation of the acoustic performance of composite sandwich panels with GFRP and PUR core for lightweight floor systems. All the reported data on geometry and mechanical properties of materials were used to develop a FE model for validation. Figure 4 shows the comparison of the FEM model results, presented in this study *vs.* experimental and numerical results reported by Proença et al. It is observed that for frequencies below 1000 Hz, the FEM model shows good agreement with the experimental results. All three curves exhibit a noticeable drop in the 1000–1250 Hz range, likely due to a coincidence frequency, although some slight variations are present. While differences become more apparent at higher frequencies, the overall trend of the FEM model remains consistent with the results obtained by Proença et al., indicating acceptable predictive behavior.

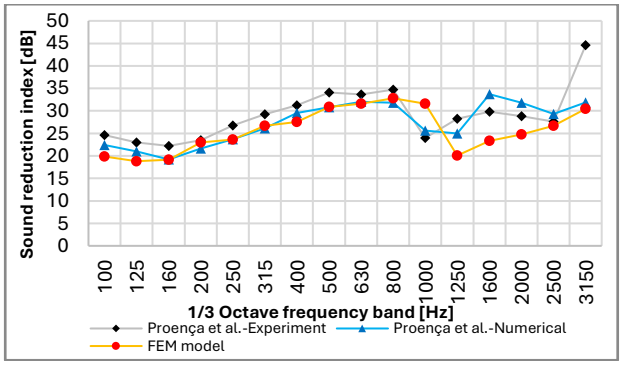


Figure 4. Numerical results of presented FE model vs. the results reported by Proença et al.

3. RESULTS AND DISCUSSION

Figure 5 and Figure 6 show the narrow bound results of the numerical model for pre-fabricated wall panels of 220 mm and 180 mm thicknesses (P22 and P18), with EPS and PUR core insulation layer. The Rw index (Table 3) was calculated using ISO 717-1 reference curve (Figure 5) and based on the methodology provided by this standard [7]. The P22 sample with EPS insulation showed relatively good behavior with Rw equal to 48 dB. Legal requirements for airborne sound transmission in most countries (as Rw indicator) are in the range of 45-55 dB [8]. The P22 sample with PUR core showed a significant acoustic performance of Rw equals to 54 dB. Both P22-EPS and P22-PUR showed a relatively similar behavior in very low and high frequencies. However, in the range of 160-1000 Hz, the P22-PUR outperformed the

P22-EPS sample. For the pre-fabricated walls of 180 mm thickness, both P18-EPS and P18-PUR showed similar behavior in the small frequencies (100-160Hz). However, the P18-EPS showed a higher drop in Rw index at 200 Hz, compared to the other and recovered this difference gradually until 1250 Hz. P18 samples show similar performance in frequencies above 1250 Hz. However, considering their calculated Rw indexes (40 and 42 dB, respectively for P18-EPS and P18-PUR), they can be used as interior walls within dwellings.

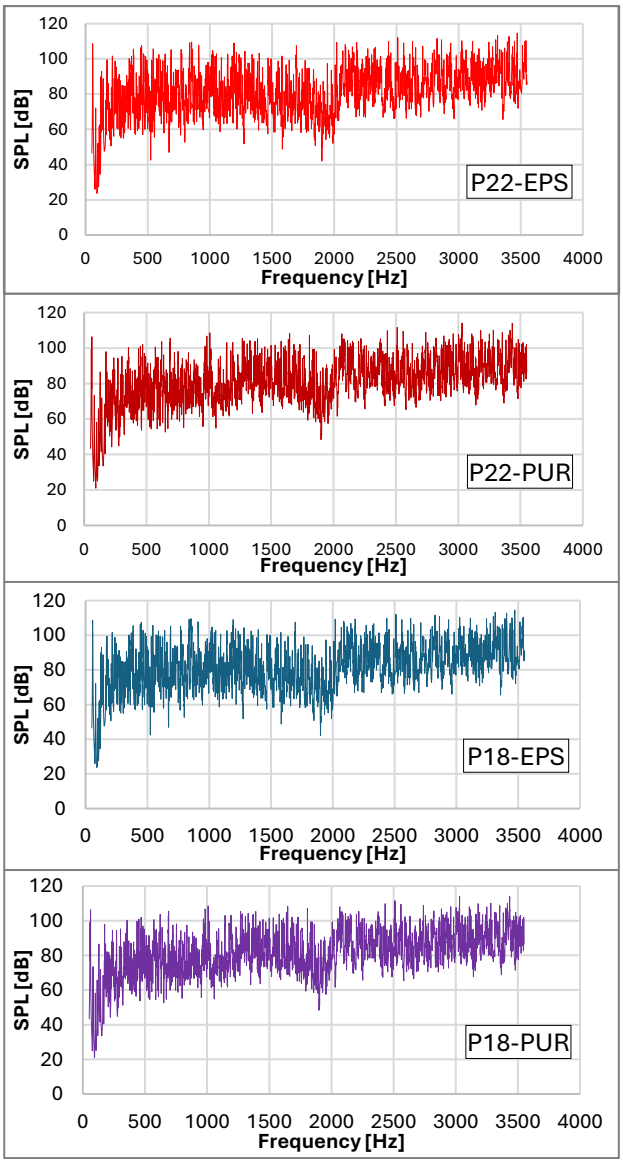


Figure 5. Narrow band results for SPL in receiving room (L2) for different samples.

The critical frequency (f_c) where coincidence effect occurs in a homogenous rectangular plate, can be calculated with the following equation [9]:

$$f_c = \frac{c^2\sqrt{3}}{\pi c_L h} \quad (1)$$

where c is the sound velocity in air (343.2 m/s), c_L is the longitudinal wave speed in plate, and h is the thickness of the plate. Considering h, as 8 mm and 6 mm thick concrete plate, for one layer of the pre-fabricated wall system, and the c_L as 4000 m/s (according to [10] for the relatively similar concrete strength) for the concrete double layer wall here. The critical frequency for the layer of the prefabricated wall where the sound is radiated would be 203 Hz and 271 Hz, respectively for P22 and P18 samples. Therefore, the dip of the transmission loss curve which is shown in Figure 6 might be attributed to the coincidence effect.

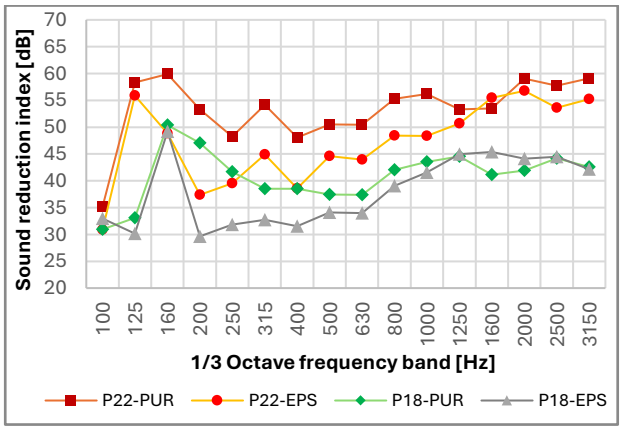


Figure 6. Microphone locations in the emitting and receiving rooms for SPL measurement.

Table 3. Rw index for different modelled samples.

Sample	P22-EPS	P22-PUR	P18-EPS	P18-PUR
Rw [dB]	48	54	40	42

4. CONCLUSIONS

In this paper, a 3D FE numerical model to evaluate the acoustic performance of pre-fabricated double layer RC wall for modular construction was presented. Acoustic performance of pre-fabricated RC walls of 180 mm (P18) and 220 mm (P22) thicknesses, with EPS and PUR as core insulation material, was assessed.

Results showed that core insulation materials have significant influence on acoustic performance. PUR significantly outperforms EPS in both P22 and P18 samples. Moreover, P22 walls shown to offer noticeably better performance in low-frequency insulation, following the mass law principle. P22-PUR was the most robust and versatile for acoustic demands. However, P22-EPS sample also showed a relatively acceptable response, close to the requirements of the building codes. P18 samples may only be viable as internal walls or where cost or weight savings outweigh performance. Moreover, a dip in transmission loss which probably caused by coincidence effect were observed in lower frequencies (about 200 Hz) for all samples.

Future works considering the flanking effects are recommended, since it is an important concern in modular buildings and solutions should be provided to avoid acoustic bridges. This study is part of a bigger project on the development of pre-fabricated concrete wall systems for modular construction. Therefore, further numerical and experimental studies are being carried out to investigate the acoustic performance of the double layer concrete wall system, comprehensively.

5. ACKNOWLEDGMENTS

This article is a result of the Innovation Pact "R2UTechnologies| modular systems" (C644876810-00000019) by "R2UTechnologies" Consortium, co-financed by NextGeneration EU, through the Incentive System "Agendas para a Inovação Empresarial" ("Agendas for Business Innovation"), within the Recovery and Resilience Plan (PRR) of Portugal.

6. REFERENCES

[1] E.M. Generalova, V.P. Generalov, A.A. Kuznetsova, Modular buildings in modern construction, Procedia engineering 153 (2016) 167-172.

[2] C. Calleri, A. Astolfi, L. Shtrepi, A. Prato, A. Schiavi, D. Zampini, G. Volpatti, Characterization of the sound insulation properties of a two-layers lightweight concrete innovative façade, Applied Acoustics 145 (2019) 267-277.

[3] M. Proença, A. Neves e Sousa, M. Garrido, J.R. Correia, Acoustic performance of composite sandwich panels for building floors: Experimental tests and numerical-analytical simulation, Journal of Building Engineering 32 (2020) 101751.

[4] S. Ferreira, M. Morais, V. Costa, A. Velosa, G. Vela, J. Teles, T. Pereira, Modular sandwich panel system for non-loadbearing walls – Experimental mechanical, fire and acoustic testing, Journal of Building Engineering 78 (2023) 107642.

[5] L. Peng, L. Xiaoyong, C. Ying, Y. Zhiwu, Y. Dayou, Thermodynamic and acoustic behaviors of prefabricated composite wall panel, Structures 28 (2020) 1301-1313.

[6] B.S. Institute, BS EN 20140-9:1994, Acoustics - Measurement of sound insulation in buildings and of building elements, 1994.

[7] I. ISO, 717-1; Acoustics—Rating of Sound Insulation in Buildings and of Building Elements—Part 1: Airborne Sound Insulation, International Organization for Standardization: Geneva, Switzerland (2013).

[8] M. Neto, S. Bertoli, Critérios de desempenho acústico em edifícios residenciais, QUALIFICAÇÃO E COMPETÊNCIA PROFISSIONAL EM ACÚSTICA: exigências de um mercado em expansão (2011).

[9] O.A. Hassan, Building acoustics and vibration: theory and practice, World Scientific Publishing Company2009.

[10] W. Xu, H. Li, X. Liu, Study on wave velocity characteristics and compressive strength of concrete under different water pressure, Academic Journal of Architecture and Geotechnical Engineering 3(1) (2021) 46-51.

DOI: 10.61782/fa.2025.0038

FORUM ACUSTICUM EURONOISE 2025

A STATISTICAL REGRESSION FRAMEWORK FOR EVALUATING NOISE EXPOSURE THROUGH OUTDOOR-TO-INDOOR SOUND PROPAGATION MODELS

Michail Evangelos Terzakis* **Cédric Van hoorickx** **Maarten Hornikx**

Building Acoustics Group, Department of the Built Environment,
Eindhoven University of Technology, Eindhoven, The Netherlands

ABSTRACT

Urban noise exposure has been shown to have significant adverse effects on human health. Studies based on outdoor noise levels, rather than indoor levels, risk introducing bias when identifying an exposure-response relationship with health outcomes. This bias is of particular concern for vulnerable groups (e.g., children) who spend most of their time indoors. This highlights the need for a comprehensive approach to modelling outdoor-to-indoor sound propagation for the estimation of indoor noise levels. For both outdoor and indoor propagation, energetic approaches are used, while the facade sound insulation is modeled via the Transfer Matrix Method, incorporating the facade element size and bridge connections. Validation of this modelling approach against sound insulation measurements has revealed good agreement. The employment of the developed models resulted in the generation of datasets, facilitating the implementation of statistical learning (random forest) models for estimating (equivalent) indoor noise levels using predictors associated with outdoor levels and factors related to the indoor and outdoor environment, and facade structure. The proposed approach has the potential to estimate indoor levels for entire cities from predicted outdoor noise levels (noise maps) and built environment characteristics.

Keywords: *outdoor-to-indoor, sound propagation, sound insulation, modelling.*

**Corresponding author*: *m.e.terzakis@tue.nl.*

***Copyright**: ©2025 Terzakis et al. This is an open-access article distributed under the terms of the Creative Commons Attribution 3.0 Unported License, which permits unrestricted use, distribution, and reproduction in any medium, provided the original author and source are credited.*

1. INTRODUCTION

Urban noise exposure has been characterized as a threat for people, showing significant associations with psychophysiological, mental health, cognitive, and sleep aspects [1, 2]. Noise exposure studies are usually conducted via the outdoor noise levels rather than the indoor levels [2]. This may correspond to a systematic risk of bias in the identification of "true" exposure-response relationship with health outcomes [3]. This bias is of particular concern for vulnerable groups (e.g. children) who spend the majority of their time indoors.

To properly characterize the indoor noise exposure, various approaches have been defined to simulate the sound propagation from outdoors to indoors via building façade structures (e.g. [3–6]). In noise exposure studies, the utilisation of the auralisation-based approaches (e.g., [5, 6]) can be regarded as a strategy for characterizing the outdoor-to-indoor sound propagation in a detailed way. For adjacent room settings subjected to diffuse-field conditions, auralization approaches for airborne sound insulation based on ISO 12354-1 [7] were proposed [8,9]. Based on these approaches, auralization models for both adjacent indoor and outdoor-indoor settings were proposed [5], using closed form formulae for sound insulation. For outdoor and indoor settings, an alternative approach was proposed, where the sound insulation was modeled via closed form formulae and a spatial window technique (size correction) [10]. However, the aforementioned approaches were based on single-layer and -component structures.

The objective of this study is to develop a modelling approach for the propagation of sound from outdoors to indoors via multi-layer and multi-component façade structures and apply this approach through generated datasets

for evaluating noise exposure via a statistical regression framework. This approach facilitates the simulation of a broad range of built environments, enabling the estimation of indoor noise exposure levels based on, for instance, noise maps of the outdoor noise exposure level as well as the evaluation of the significance of diverse predictors.

2. MODELING FORMULATION

2.1 Façade Sound Insulation Modelling

Although numerical modelling approaches, such as the Finite Element Method (FEM) [11] and the Boundary Element Method (BEM) [12], can be applied for the computation of sound insulation in a precise way, these modelling approaches require high computational complexity. Alternatively, the Transfer Matrix Method (TMM) can provide a formulation for the calculation of the sound insulation of structures in an efficient way, considering the propagation of sound waves through multi-layered structures [13].

2.1.1 Infinite Incident Sound Transmission Coefficient

In the TMM framework [13], a plane wave impinges on the first layer of a material under an angle of incidence θ (i.e. angle between the direction of propagation of the incident plane wave and the normal to the plane of the layer) and propagates into the cavity, and then to a second material layer, and so on, up to the radiation (last) layer.

Assuming a multi-layer structure subject to thin-plate theory, a simple product among the transfer matrices of thin plates and fluid cavities, including the incident and radiated layer, results in the infinite sound transmission coefficient [13, 14]. However, in structures composed of diverse media (e.g. solid and poroelastic), the aforementioned conventional approach is untenable. Coupling interface matrices are included to global matrix, composed of the transfer matrices of the diverse layers, to satisfy the continuity condition between two adjacent elements and for calculating the infinite sound transmission coefficient [13].

2.1.2 Spatial Windowing Technique

A spatial windowing technique has been introduced to alleviate infinite structure behaviour effects at low frequencies via the radiation efficiency of finite size structure [10]. Considering rectangular surfaces, an efficient methodology for calculating the radiation efficiency was proposed in [15]. Based on this approach, the adjusted radiation efficiency was proposed in [16] for calculating the radiation efficiency of rectilinear surfaces (polygon surfaces in which all sides intersect at right angles) by dividing the rectilinear surfaces into isolated and adjacent (first order correlation) sub-domains (sub-surfaces).

2.1.3 Finite Incident Sound Transmission Coefficient

For calculating the sound transmission coefficient ($\tau_{\text{fin}}(\theta)$) for rectangular surfaces, the spatial windowing technique can be implied to the (infinite) incident sound transmission coefficient. Regarding a single-layer structure, the finite sound transmission coefficient can be obtained as in [17], while for a multi-layer structures, the finite sound transmission coefficient can be obtained as in [10]. For rectilinear surfaces, the same approaches can be applied so that the finite (first-order) sound transmission coefficient to be obtained as in [16].

2.1.4 Bridge Connection

The bridge connection (line or point) can be further incorporated into the finite incident sound transmission coefficient, providing a correction at high frequencies. In double-layer structures, the studs can be incorporated using a thin-plate [18] and a global matrix [19] approach.

2.2 Propagation Modelling

An example room with total dimensions 3m×3m×3m (L×W×H) was considered, assuming that its façade structure consists of a single-layer rectilinear wall (concrete of thickness 0.1m) and a single-layer (1m×1m) rectangular window (glass of thickness 0.006m) component, both of which subject to the thin-plate theory. Their material properties were taken from [16]. Furthermore, 11 sound sources (S1–S11) located in front of the façade structure were considered (road-traffic structure), covering a total length of 14m. These sound sources were positioned at three different distances from the façade (7m, 14m, and 21m), denoting the sound source formats (L1–L3). Finally, five receivers are included indoors. R1: at the centre of the room; R2: at 0.5m from the front and left wall; R3: at 0.6m from the front and right wall; R4 at 0.7m from the back and left wall; R5 at 0.4m from the back and right wall. The height of all receivers was kept constant at 1m from the ground (children's ear seated). An illustration is presented in Fig. 1.

2.2.1 Outdoor-to-Façade Propagation Modelling

For point sources with acoustic power 1W, the free-field mean squared sound pressure at any point of the iso-

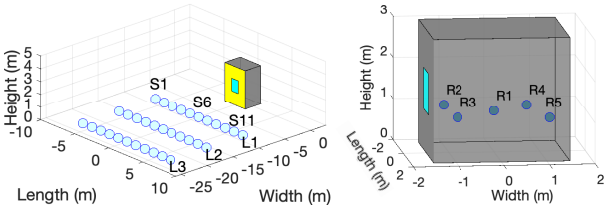


Figure 1. Representation of the example scenario.

lated and adjacent surfaces ss at a distance r_s from the sound source s can be expressed as $p^2_{ss}(f, r_s) = Z_0(\frac{1}{4\pi r_s^2})$. Hence, the incident sound power at any point of façade under free-field conditions can be expressed as [5]

$$W_{inc,s}(f, \theta_s, r_s) = \frac{1}{4\pi} \int_{S_{ss}} \frac{1}{4\pi r_s^2} |\cos(\theta_s)| dS. \quad (1)$$

For small elements and source positions that are far away, a first-order approximation can be made by assuming that θ_s and r_s do not vary significantly in S_{ss}.

2.2.2 *Façade-to-Indoor Propagation Modelling*

In façade-to-indoor propagation modelling, it was assumed that the façade elements act as sound sources. By further assuming that each sub-surface emits sound into a hemisphere, the squared pressure from the wall (p^2_w) and window (p^2_g) surface to the receiver q in the room R can be calculated as [5]

$$p^2_{w,q}(f) = Z_0 \left[\sum_i \sum_{\substack{j \in \epsilon_i \\ j>i}} W_{tr,ij,w}(\theta_{s,ij}) \left(\frac{2}{4\pi r^2_{ij,q}} + \frac{4}{A_R(f)} \right) - \sum_i \sum_i W_{tr,i,w}(\theta_{s,i}) \left(\frac{2}{4\pi r^2_{i,q}} + \frac{4}{A_R(f)} \right) \right] \quad (2)$$

$$p^2_{g,q}(f) = Z_0 \left[W_{tr,i,g}(\theta_{s,i}, r_s) \left(\frac{2}{4\pi r^2_{i,q}} + \frac{4}{A_R(f)} \right) \right], \quad (3)$$

where the transmitted sound power is defined as $W_{tr} = W_{inc,s} \cdot \tau_{fin}$. Note that the τ_{fin} term is defined in Section 2.1.3. Furthermore, $r_{ij,q}$ and $r_{i,q}$ denote the distance between the center of adjacent and isolated sub-domains and receiver q, respectively, and A_R denotes the total absorption area of the room.

2.3 Outdoor-based Indoor Impulse Response

The outdoor-based indoor impulse response per sound source and indoor receiver position can be synthesized via the inverse Fourier Transform of the sum of the frequency responses of the wall ($H_{w,q}$) and window ($H_{g,q}$) surfaces expressed as $h_q(t) = \mathfrak{F}^{-1}\{H_{w,q}(f) + H_{g,q}(f)\}$. The latter frequency responses can be calculated using the approach outlined in [5].

Finally, since the sound transmission coefficient is calculated for 31 1/3-octave frequency bands, ranging from 20Hz to 20kHz, a linear interpolation and a piecewise cubic extrapolation in the sound transmission coefficient is employed within the frequency range from zero to Nyquist frequency. Additionally, a linear (anti-symmetric) phase term based on [20] is added to $H_{w,q}$ and $H_{g,q}$ for synthesizing the outdoor-based indoor impulse response, expressed as [5, 6] $\tau_{fin}(\theta) = |\tau_{fin}(\theta)| e^{j\phi(f)}$.

3. RESULTS AND DISCUSSION

3.1 Modelling Example

Based on the example described in Section 2.2, the finite sound reduction index of the window and wall surfaces is calculated via the methodologies presented in Section 2.1. The results are presented in Fig. 2.

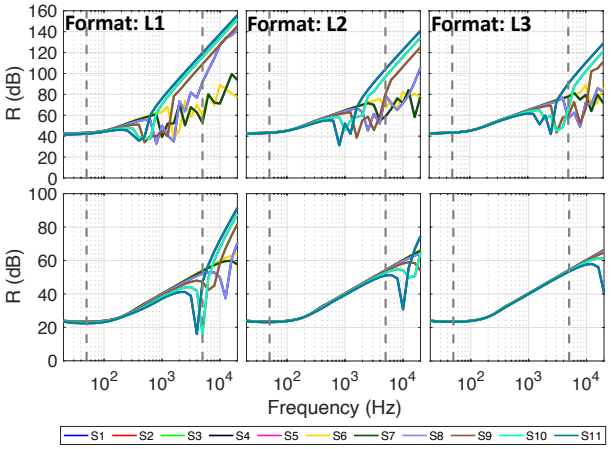


Figure 2. Sound reduction index of the wall (top) and glass (bottom) surface per source and format.

Focusing on Fig. 2 (top), the influence of all adjacent and isolated sub-surfaces to the sound reduction index of the wall surface is illustrated, similar to those presented in [16]. Since the sound source positions S1-S5 are symmetrical to those of S7-S11, the sound reduction indexes of the former are obscured by the latter. For the window surface Fig. 2 (bottom), analogous sound reduction trends to those exhibited by the wall surface are evident.

By incorporating the outdoor and indoor modelling, the outdoor-based indoor impulse and frequency responses can be synthesized with respect to five receiver positions. The results are illustrated in Fig. 3.

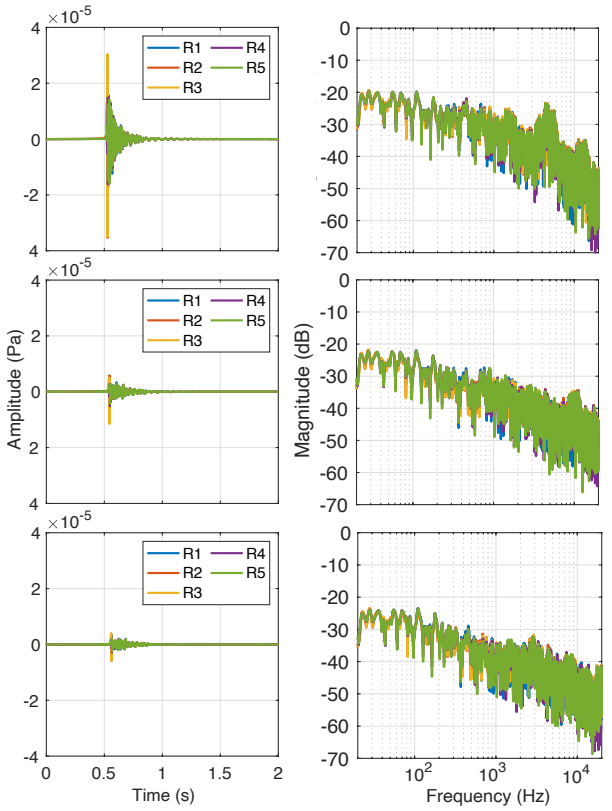


Figure 3. Average impulse and magnitude responses per receiver position across the sound sources (S1-S11) in Format L1 (top), L2 (mid), and L3 (bottom).

Regarding Fig. 3, the presence of multiple peaks in the magnitude responses denotes the (average) sound transmission from the elements of the façade structure. The most prominent peaks are presented in relation to the Format L1 among the three formats. As the distance between the sound source format and façade structure increases (from Format L1 to Format L3), a single incident character is obtained. Finally, the impact of the wall surface is only evident in the coincidence region, while in other regions, the glass surface dominates the wall surface in the total sound reduction index [16].

3.2 Experimental Validation

For validating the modeling methodology, the settings and the results of the case study presented in [21] for a 201.6m^3 lecture room were used with respect to the distribution of sound sources in the linear format. Regarding the characteristics of façade structure from inside to outside, this consists of a plaster layer, a brick layer, a poroelastic layer (mineral wool) and a steel layer with point connections. For simplicity, it was assumed that the façade structure consists of a three-layer structure composed by a brick layer ($\rho = 1900$ kg/m^3, $E = 2.4 \cdot 10^{10}$ Pa, $\mu = 0.1$, $\eta = 0.01$, and $h = 0.050$ m), a poroelastic layer ($\phi = 0.9$, $\alpha_\infty = 1$, $\sigma = 59100$ NS/m^4, $\Lambda = 10\mu$ Pa, $\Lambda' = 36\mu$ Pa, $\rho = 90$ kg/m^3, $E = 7 \cdot 10^5$ Pa, $\mu = 0.01$, $\eta = 0.01$, and $h = 0.070$ m), and a steel layer ($\rho = 7800$ kg/m^3, $E = 2.1 \cdot 10^{11}$ Pa, $\mu = 0.33$, $\eta = 0.01$, and $h = 0.026$ m), assuming that the plaster layer does not significantly influence the sound reduction index. Regarding windows, these consist of a double-leaf structure, where the thickness of each layer is 5mm and the gap between the two panes is 15mm. The reverberation time of the room was obtained via ISO 3382-2 [22]. The comparison between measured and predicted sound insulation is presented in Fig. 4.

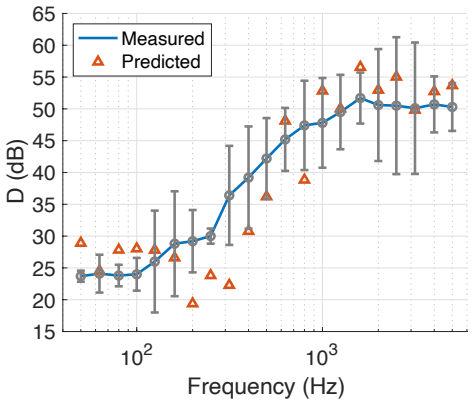


Figure 4. Comparison between the measured and calculated sound insulation, expressed via the level difference (D) in 1/3-octave frequency bands. The error-bars represent the 95% Confidence Interval.

In Fig. 4, the predicted and measured results present a good agreement. The observed discrepancies can be attributed to various factors, including deviations in the material properties, the incident field, the modal behaviour of surfaces and room, and the effect of window frames.

3.3 Application

Based on the developed modelling methodology, datasets can be generated for developing statistical learning prediction models for estimating the indoor noise exposure levels, expressed by the equivalent noise indicators, via various predictors. These predictors correspond to the outdoor noise exposure levels and factors related to outdoor environment, indoor environment, and façade structures. This approach allows for estimating the indoor noise exposure levels in areas with available outdoor levels and built environment characteristics. The block-diagram of application is presented in Fig. 5.

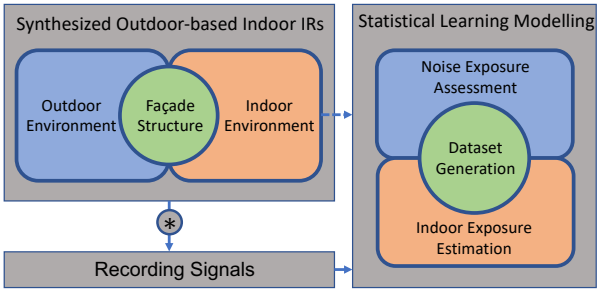


Figure 5. Application of outdoor-to-indoor models. Note that the dashed arrow denotes the additional parameters related to the outdoor and indoor environment as well as façade structure.

3.3.1 Dataset Generation

First, the impact of the room size was considered, defining three rooms (L×W×H): Room 1 (3×3×3), Room 2 (4×4×3), and Room 3 (5×4×4). Second, the façade structures were considered, defining two types of wall structures (i.e., monolithic, and filled-cavity) subject to the global-matrix approach, and three types of windows (i.e., single-leaf, double-leaf, and triple-leaf) subject to the thin-plate approach. In both wall structures, each (solid) leaf has a thickness of 0.1m and 0.2m. In the filled-cavity wall structures, a mineral wool material was considered for the cavity measuring 0.1m, while point connections ($n = 10$) between the leaves were also taken into account. Regarding the window panes, the thickness of the leafs and the (air fluid) cavity depths were set to 4mm, 8mm, and 12mm. The dimensions of the windows per room scenario are presented in Tab. 1. Finally, four façade structures composed of wall and window structures were considered: (a) single-leaf wall with single-leaf window, (b) double-leaf wall with single-leaf window, (c) double-leaf wall with double-leaf window, and (d) double-leaf wall with triple-leaf window. It should be noted that the generated dataset is constrained to the information deemed necessary for a city.

Table 1. Window scenarios (WSc) per room (R).

R	WSc	L_g(m)	H_g(m)	R	WSc	L_g(m)	H_g(m)
R1	W1.1	0.50	0.50	R3	W3.1	0.50	0.50
	W1.2	1.00	1.00		W3.2	1.00	1.00
	W1.3	2.00	2.00		W3.3	2.00	2.00
R2	W2.1	0.50	0.50		W3.4	2.50	2.50
	W2.2	1.00	1.00		W3.5	3.00	3.00
	W2.3	2.00	2.00		W3.6	3.50	3.50
	W2.4	2.50	2.50				

3.3.2 Noise Exposure Assessment

By convolving the synthesized outdoor-based indoor impulse responses with road-traffic (1-minute) recordings, the noise exposure indoors can be estimated. Similarly, the outdoor noise exposure levels can be estimated at the center of the façade structures. For the assessment of the relationship between indoor and outdoor noise exposure, the equivalent noise indicator can be calculated for one second integration time. The assessed relationships with respect to R1, Format L1 (defined in Fig. 1), and window size W1.2 per façade structure (defined in Section 3.3.1) are presented in Fig. 6.

As illustrated in Fig. 6 (top), the improvement of façade configuration with respect to the window surface leads to a reduction in equivalent indoor noise exposure levels. A lack of a significant effect of two wall thicknesses is also evident, as confirmed by the averaged spectral outdoor-to-indoor level difference presented in Fig. 6 (bottom). Although not shown here, as the surface area of window increases, the effect of wall structure is reduced, while the effect of window becomes dominant. The coincidence frequency of the thinner single wall surface is approximately 500Hz, while for the thicker single wall structure, the coincidence frequency is lower, at around 250Hz. Furthermore, it can be observed that their mass-air-mass and mass-air-mass-air-mass resonance frequencies exhibit a concurrence with the lowest coincidence frequencies of the wall surface.

3.3.3 Prediction Modelling and Verification

In order to estimate the equivalent indoor noise exposure levels ($L_{eq,In}$), averaged over a fifteen-second period, the random forest (RF) modelling approach [23] was

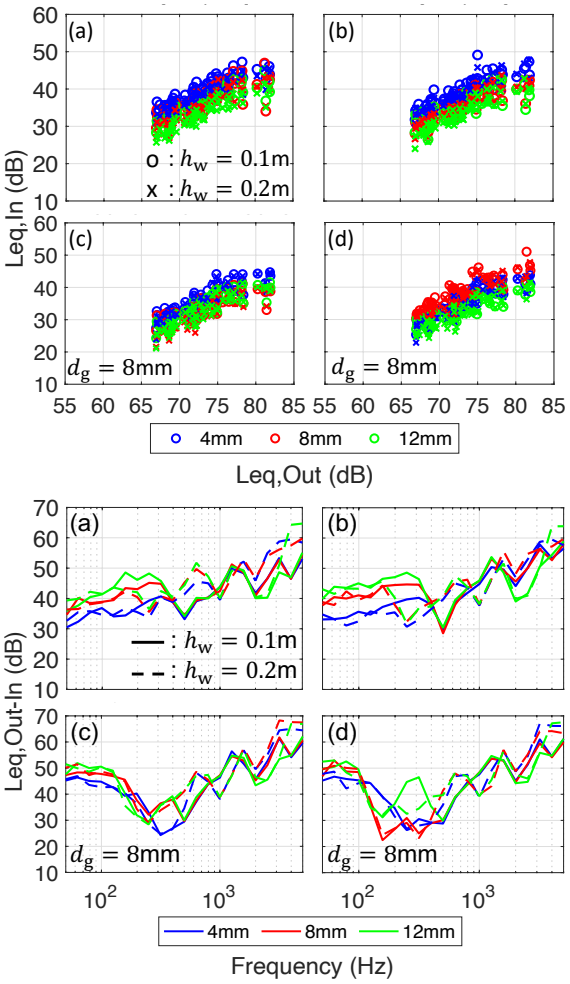


Figure 6. Relationship between the average outdoor and indoor levels (top) and time-averaged equivalent spectral outdoor-to-indoor level differences (bottom) with respect to Format L1, R1, and W1.2 per façade structure (a-d). Note that h_w denotes the thickness of the wall, while d_g denotes the window cavity width.

employed in the generated dataset via the *ranger* package [24] in RStudio. The outdoor noise exposure levels ($L_{eq,Out}$) at the centre of the façade are considered, in conjunction with parameters associated with the outdoor environment (FrmtDist: format distance), the indoor environment (RoomVol: room volume), and façade structure (SRatio: window-façade ratio, hGlass: glass thickness, hWall: wall thickness, dGlass: distance between glass panes, WinStruct: window structure, and WinStruct: wall structure). Note that the WinStruct and WallStruct predictors are categorical predictors while all the others are continuous predictors. The dataset, composed by 28080 observations (sound levels) were split into a 70% for training and a 30% for testing. For tuning of the RF models, the number of trees (n_{tr}) was selected to range from 100 to 1200 trees with an increment of 100 trees, while the number of split-variables (m_{tr}) was set to vary from 3 to 9 variables with an increment of 1 variable. The node size was ranged from 1 node to 15 nodes with an increment of 1 node. Following the tuning procedure, n_{tr} = 900, m_{tr} = 5, predictors = 9, and node size = 4.

For exploring the impact of the various predictors, the (normalized) importance of each predictor in the model was assessed, and the results are presented in Fig. 7.

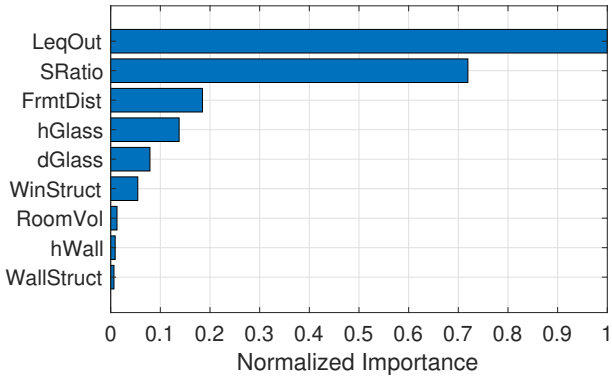


Figure 7. Importance of predictors.

As seen from Fig. 7, the outdoor noise exposure levels and the ratio between the window and façade surface correspond to the most important predictors, indicating that these predictors explained the highest percentage of the unexplained variance in the model. The wall parameters presented the less significant contribution to the model, which is also validated from Fig. 6.

Finally, the k-fold cross-validation procedure for k = 10 was adopted [25], splitting the training dataset into ten equal in-size chunks and adopting a resampling procedure. The model was developed based on nine chunks, with the objective of predicting the tenth treated as a validation set. The performance of the fitting model was evaluated via the R^2 and RMSE metric [26]. The results are presented in Fig. 8.

As seen from Fig. 8, the RF modelling approach presented a RMSE = 1.67dB with respect to the test dataset. By interpreting the error level with the ability of a healthy ear to perceive a change in broadband noise levels, cor-

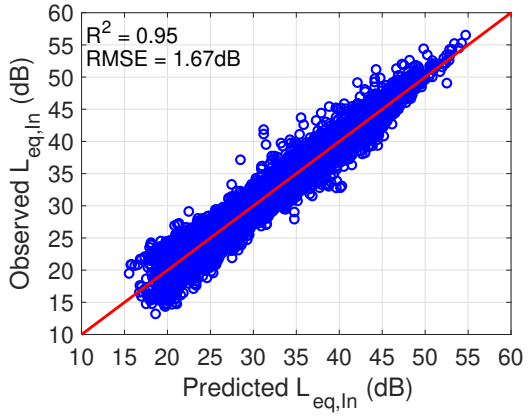


Figure 8. Modelling validation.

responding to the perceptible level difference [27]. An error level around 3dB is associated to a just audible level difference, indicating a good performance of the executed modeling approach, as the RMSE level falls below this threshold.

4. CONCLUSIONS

In this paper, an outdoor-to-indoor modelling framework, validated via sound insulation measurements, was developed. The objective of this approach is to support noise exposure studies via generated (modelling-based) datasets so that the indoor noise exposure levels can be estimated via statistical learning approaches. This approach enables a detailed and controlled characterisation of outdoor-to-indoor sound propagation, which has the potential to estimate indoor levels in cities with available predicted outdoor noise levels and built environment characteristics.

5. ACKNOWLEDGMENTS

This research was funded by the European Union's Horizon 2020 research and innovation program under grant agreement No. 874724, Equal-Life Project, part of the European Human Exposome network.

6. REFERENCES

[1] I. van Kamp, S. Simon, H. Notley, C. Baliatsas, and E. van Kempen, "Evidence Relating to Environmental Noise Exposure and Annoyance, Sleep Disturbance, Cardio-Vascular and Metabolic Health Outcomes in the Context of IGCB (N): A Scoping Review of New Evidence," *International Journal of Environmental Research and Public Health*, vol. 17, p. 3016, 4 2020.

[2] M. E. Terzakis, M. Dohmen, I. van Kamp, and M. Hornikx, "Noise Indicators Relating to Non-Auditory Health Effects in Children—A Systematic Literature Review," *International Journal of Environmental Research and Public Health*, vol. 19, p. 15633, 11 2022.

[3] M. Terzakis, C. Van hoorickx, M. Hornikx, F. Naim, A. Hansell, and J. Gulliver, "Estimation of Low Frequency Outdoor-to-indoor Noise Attenuation Factors Based on Night-time Noise Exposure," in *30th International Congress on Sound and Vibration (ICSV)*, (Amsterdam, The Netherlands), pp. 1–8, 2024.

[4] B. Locher, A. Piquerez, M. Habermacher, M. Ragettli, M. Röösli, M. Brink, C. Cajochen, D. Vienneau, M. Foraster, U. Müller, and J. Wunderli, "Differences between Outdoor and Indoor Sound Levels for Open, Tilted, and Closed Windows," *International Journal of Environmental Research and Public Health*, vol. 15, 1 2018.

[5] I. Muhammad, A. Heimes, and M. Vorländer, "Interactive real-time auralization of airborne sound insulation in buildings," *Acta Acustica*, vol. 5, p. 19, 4 2021.

[6] I. Muhammad, A. Heimes, and M. Vorländer, "Sound insulation auralization filters design for outdoor moving sources," in *PROCEEDINGS of the 23rd International Congress on Acoustics*, (Aachen, Germany), pp. 1721–1728, 2019.

[7] ISO, "ISO 12354-1 Building acoustics Estimation of acoustic performance of buildings from the performance of elements Part 1: Airborne sound insulation between rooms," *International Organization for Standardization*, 2017.

[8] M. Vorländer and R. Thaden, "Auralisation of airborne sound insulation in buildings," *Acta Acustica*, vol. 86, pp. 70–76, 2000.

[9] A. Rodríguez-Molares, "A new method for auralisation of airborne sound insulation," *Applied Acoustics*, vol. 74, pp. 116–121, 1 2013.

[10] M. Villot, C. Guigou, and L. Gagliardini, "Predicting the Acoustical Radiation of Finite Size Multi-layered Structures by Applying Spatial Windowing on Infinite Structures," *Journal of Sound and Vibration*, vol. 245, pp. 433–455, 8 2001.

[11] N. Atalla and F. Sgard, *Finite element and boundary methods in structural acoustics and vibration*. Boca Raton, Florida: CRC Press, 2015.

[12] R. Panneton and N. Atalla, "Numerical prediction of sound transmission through finite multilayer systems with poroelastic materials," *The Journal of the Acoustical Society of America*, vol. 100, pp. 346–354, 7 1996.

[13] J. Allard and N. Atalla, *Propagation of Sound in Porous Media: Modelling Sound Absorbing Materials*. Wiley-Blackwell, 2 ed., 2009.

[14] T. Vigran, *Building Acoustics*. CRC Press, 2 ed., 2019.

[15] Y. Yu and C. Hopkins, "Reduced order integration for the radiation efficiency of a rectangular plate," *JASA Express Letters*, vol. 1, p. 062801, 6 2021.

[16] M. E. Terzakis, C. Van hoorickx, and M. Hornikx, "Spatial windowing for finite-size incident sound transmission coefficient of multi-component surfaces," *INTER-NOISE and NOISE-CON Congress and Conference Proceedings*, vol. 270, pp. 2900–2909, 10 2024.

[17] T. Vigran, "Predicting the sound reduction index of finite size specimen by a simplified spatial windowing technique," *Journal of Sound and Vibration*, vol. 325, pp. 507–512, 8 2009.

[18] T. Vigran, "Sound transmission in multilayered structures – Introducing finite structural connections in the transfer matrix method," *Applied Acoustics*, vol. 71, pp. 39–44, 1 2010.

[19] A. Santoni, P. Bonfiglio, P. Fausti, and N. Z. Martello, "Sound insulation of heavyweight walls with linings and additional layers: numerical investigation," in *EuroNoise 2015*, (Maastricht), pp. 2537–2542, 2015.

[20] J. Proakis and D. Manolakis, "Design of Digital Filters," in *Digital Signal Processing*, ch. 10, pp. 660–664, Pearson, 4 ed., 2006.

[21] M. E. Terzakis, C. Van hoorickx, and M. Hornikx, "Characterization of façade sound insulation by impulse response measurements for various source position formats: a case study," *INTER-NOISE and NOISE-CON Congress and Conference Proceedings*, vol. 270, pp. 2910–2920, 10 2024.

[22] ISO, "ISO 3382-2:2008 Acoustic - Measurement of Room Acoustic Parameters, Part 2: Reverberation Time in Ordinary Rooms," *International Organization for Standardization*, 2008.

[23] G. James, D. Witten, T. Hastie, and R. Tibshirani, *An Introduction to Statistical Learning with Applications in R*. New York, NY: Springer US, 2021.

[24] M. N. Wright and A. Ziegler, "ranger : A Fast Implementation of Random Forests for High Dimensional Data in C++ and R," *Journal of Statistical Software*, vol. 77, no. 1, 2017.

[25] G. James, D. Witten, T. Hastie, and R. Tibshirani, "Resampling Methods," in *An Introduction to Statistical Learning*, pp. 203–205, Springer US, 2021.

[26] E. Bartz and T. Beielstein, *Hyperparameter tuning and optimization applications. In: Hyperparameter tuning for machine and deep learning with R: a practical guide.* Springer, 2023.

[27] E. Murphy and E. A. King, "Principles of Environmental Noise," in *Environmental Noise Pollution*, pp. 9–49, Elsevier, 2014.

DOI:

Main theme: A03 Building Acoustics

Session A03.04 Ground borne noise

Chair(s): C. Guigou Carter, S. Antunes

DOI: 10.61782/fa.2025.0322

FORUM ACUSTICUM EURONOISE 2025

EFFECT OF MEASUREMENT POSITIONS ON STRUCTURE-BORNE NOISE LEVELS IN BUILDINGS SUBJECT TO RAILWAY VIBRATIONS

C. Guigou Carter[1*] **Pierre Ropars**[1]
[1] CSTB, Grenoble, France

ABSTRACT

In the objective of improving the comfort and even the health of occupants of buildings close to railway lines, it is appropriate to predict and measure vibration levels and ground-borne noise levels in order to limit them, particularly in housing.
In this work, the effect of tabulated transfer functions generally used for the vibration impact assessment investigations, measurement positions for both vibration levels and structure -borne noise is studied on the basis of numerical modeling. Concerning vibrations, a measurement at mid-span of the floor is generally considered; however, this position can be difficult to determine or access, especially when the floor supports several rooms, so a measurement in the center of a room is often carried out. The vibration levels can then be used to predict ground-borne sound levels. To set an acceptable threshold for occupants, it is necessary to specify one or more easily identifiable and accessible measurement positions and to adapt the limit threshold to this measurement configuration. The same problem exists for ground-borne noise measurements. Based on the results obtained, proposals concerning impact assessment investigations, measurement and prediction positions for vibrations and ground-borne noise in buildings are formulated.

Keywords: ground-borne noise, railway vibrations, building acoustics, measurement positions.

[*] ***Corresponding author***: catherine.guigou@cstb.fr
Copyright: *©2025 First author et al. This is an open-access article distributed under the terms of the Creative Commons Attribution 3.0 Unported License, which permits unrestricted use, distribution, and reproduction in any medium, provided the original author and source are credited.*

1. INTRODUCTION

In densely populated areas, the rarefication of land leads to the construction of buildings very close to railway tracks. Alternatively, the construction of new railway lines will impact existing buildings. In both cases, vibration, and noise levels especially in lodgings might be severely impacted by the proximity of underground and surface railway traffic. In France, there is still no mandatory requirement regarding limitation of vibration and ground-borne noise levels from railways, even though discussions on the subject have started a few years back. However, developers and city planners are now aware of the necessity to consider these aspects.
Prediction methods are required for designing buildings to protect inhabitants against ground-borne (structure-borne) noise from railway lines or other ground vibration sources, a European task group (CEN/TC126/WG2/TG1) is doing preliminary work on this subject.
The effect of using tabulated transfer function (ground to building foundations and building foundation to building floor) for vibration impact assessment investigations is questioned with respect to a security margin. Furthermore, it is also quite important to be able to verify the vibration and ground-borne noise levels after either a building or a new railway line construction. In this work, the effect of the measurement positions for both vibration levels and ground-borne noise is studied based on numerical modeling. Concerning vibrations, a measurement at mid-span of the floor is generally considered; however, this position can be difficult to determine or access, especially when the floor supports several rooms, so a measurement in the center of a room is often carried out. The vibration levels can then be used to predict ground-borne sound levels. To set an acceptable threshold for occupants, it is necessary to specify one or more easily identifiable and accessible measurement positions and to adapt the limit threshold to this measurement configuration. The same problem exists for ground-borne noise measurements.

2. INVESTIGATED CONFIGURATIONS

Simulations are conducted based on a 2.5D FEM/BEM model (infinite constant geometry in one-direction) implemented in CSTB MEFISSTO software [1]. The ground-borne noise levels are evaluated following the 2.75D approach proposed in [2] also implemented in CSTB MEFISSTO software.

The base configuration is shown in Figure 1: it consists in a concrete based building with an underground level and 3 stories above ground. The underground slab and walls are 40 cm in thickness; the other slabs are 20 cm in thickness, and the façade is 18 cm in thickness. The height between slabs is 2.5 m. The type and thickness of the central wall at the first and second stories are varied; the reference case corresponds to a concrete wall 18 cm in thickness. The ground is either a simple half-space (soft, medium, or hard type), or made of 2 layers (surface layer on a semi-infinite layer). The railway line platform has a height of 50 cm and a width of 6 m; for simplicity, it is assumed to be concrete. The center of railway line is located at 10 m from the building façade. The excitation in the center of the railway platform (red dot in Figure 1) is assumed to be a line of uncorrelated forces applied over the considered train length L_T (geometry infinite in the direction of the train line).

Tables 1 and 2 give the characteristics of different elements used for the prediction.

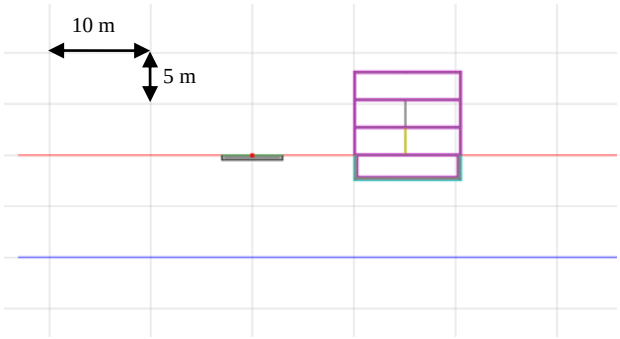


Figure 1. Investigated base configuration.

Table 1. Building component characteristics.

	E (MPa)	ν (-)	ρ (kg/m^3)	η (%)
Concrete	25000	0.3	2500	1
Bricks	20	0.1	1000	1
Equivalent lightweight partition	40	0.1	476.6	2

Table 2. Ground characteristics.

	C_p (m/s)	C_s (m/s)	ρ (kg/m^3)	η (%)
Surface layer	300	150	1800	5
Semi-infinite layer	800	300	1800	5
Soft soil	208	120	1400	5
Medium soil	388	224	1600	5
Hard soil	731	422	1800	5

Figure 2 shows the force density spectrum applied to platform by the train.

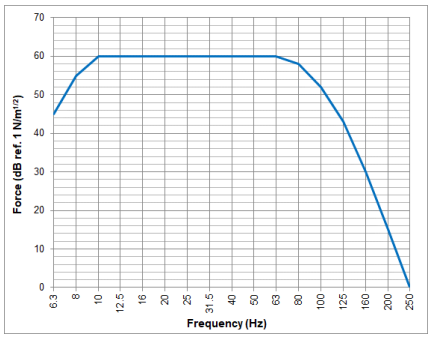


Figure 2. Force spectrum applied to platform by the train.

3. EFFECT OF TABULATED BUILDING TRANSFER FONCTION

In most vibrations impact assessment studies, the building floor velocity needs to be estimated in neighboring buildings of railway tracks. A typical configuration for such estimation is shown in Figure 3.

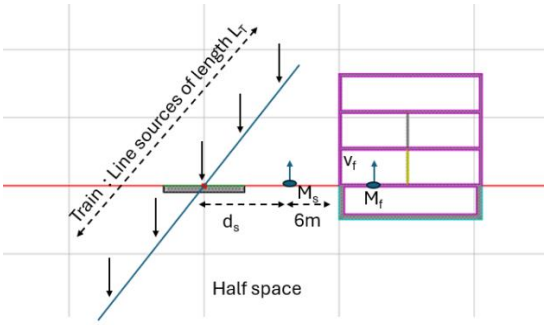


Figure 3. Typical configuration with used notation

In this case, the floor velocity v_f can be computed using a combination [3] of (i) the excitation terms as a force density spectrum (*FDS*, unit N/m$^{1/2}$), (ii) the propagation between the track center and near the building at point M_s given by a line source transfer mobility (*LSTM*, unit m/s/N/m$^{1/2}$) [3] and finally (iii) the dynamic of behavior represented by a correction factor C_b [4] :

$$v_f = FDS \times LSTM \times C_b \quad (1)$$

The correction factor C_b can be estimated by the ratio between the "global transfer function" Y_G (defined by the velocity at the receiver point M_f (floor center) for a "unit" line force applied on the track) and the *LSTM*. Nevertheless, it is not possible to measure Y_G when either the track or the building, does not exist. In practice, the *LSTM* is defined using numerical method and C_b is replaced by measured or tabulated transfer function between points M_s and M_f. Note that C_b includes C_{b2} and C_{b3} in [4] that replace TF2 representing the transfer function from free field ground (at building distance) to building foundations and TF3 representing the transfer function from building foundations to floor, in [3]. In this case, the global transfer function can be misestimated. In general, this error depends on the type of the building, the soil profile, the distance between the track and the building and the train length. Considering the same building and the same soil, the error can be expressed with the sum over the frequency band [8-250] Hz as:

$$Error(d_s, L_T) = 10 \log_{10} [\Sigma Y_G^2 / (LSTM \times C_b)^2] \quad (2)$$

In the following, the error given by Equation (2) is computed for three simple cases of homogenous half space soil (soft, medium, and hard soil type defined in Table 2); the building corresponds to the one described in Section 2. The building correction factor is taken from [4] for medium size building. The error is observed as a function of distance d_s from 7 to 40 m, and train length L_T from 1 to 100 m.

As seen in Figures 4 to 6, the use of the transfer function in place of correction factor does not have an impact on results when the train length L_T is very small. When L_T increases, for building near the track (d_s < 10 m), the transfer function is underestimated, meaning that the floor velocity is underestimated as well. On the contrary, for large distances between building and track, the transfer function and the floor velocity are overestimated. For intermediary distances, a zone for which the global transfer function is correctly estimated, exists (zone in green). The position and the size of this zone depend on soil characteristics. The results show that the zone is larger for stiffer soil; this can be explained by the fact that the transfer function from soil to building foundations (TF2 or C_{b2}) is smoother when the soil stiffness is higher. On the contrary, the transfer function FT2 or C_{b2} for lower soil stiffness has a deeper and large minimum, leading to more impact on the global transfer.

Due to these observations, tabulated transfer function must be used with caution, particularly when issued from measured point to point transfer function. It is more accurate to use a building correction factor C_b measured in situ. If impossible, a security margin of 6 dB should be considered when using tabulated transfer functions in the case of buildings located near the railway track.

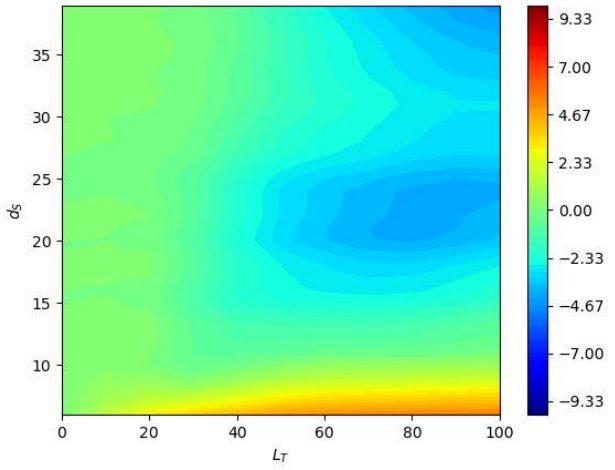


Figure 4. Maps of the error function for a 3-storey building on a soft soil half space

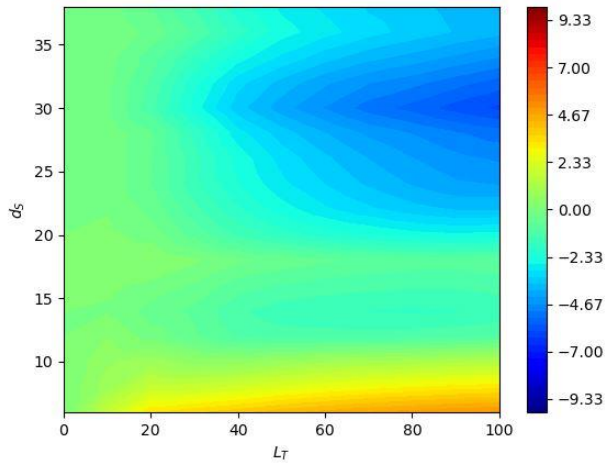


Figure 5. Maps of the error function for a 3-storey building on a medium soil half space

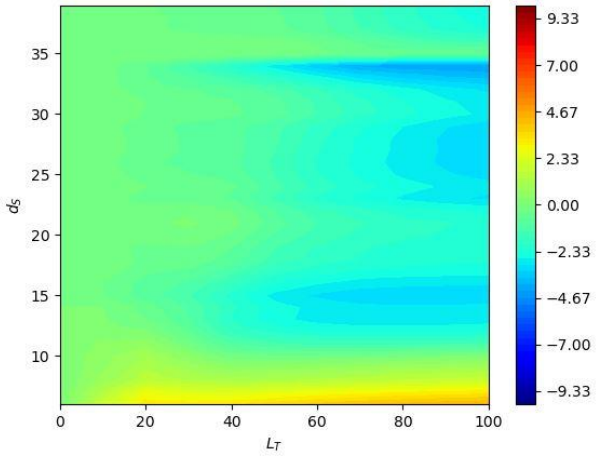


Figure 6. Maps of the error function for a 3-storey building on a hard soil half space

4. EFFECT OF EVALUATION POSITIONS IN BUILDING

In this section, the effect of the middle wall in the first and second building stories is investigated on the floor vibration level as well as on the ground-borne sound pressure level. The train is assumed to be 20, 40 or 100 m in length and the uncorrelated force are applied at 10 m from the building façade at the center of the railway platform. The ground is composed of two layers.

Indeed, it is quite important when fixing a limit for either vibration or ground-borne sound level to verify by the measurements that it is respected. In [5], measurements in the vertical direction at the floor mid-span is mentioned regarding vibration, due relevance in terms of human perception of the train passage event and possible annoyance. Following [5], ground-borne noise measurement is performed using one microphone at the one third point of a room's plan dimension (four options possible) and at a height of 1.2 to 1.5 m.

Since the prediction model is based on 2.5D approach, the vibration levels and the ground-borne sound levels are evaluated is a plane situated at the center of the train.

The middle wall in the first and second building stories can be made of either concrete (18 cm in thickness), lightweight bricks (7 cm in thickness) or an equivalent lightweight partition wall (like plasterboards on metallic frame, 10 cm in thickness). The case of no middle wall on all building stories is also considered.

4.1 Floor vibration levels

The vibration levels are evaluated along the floor slab across the building for the different situations considered. Figure 7 presents the velocity level on the concrete slab for the different investigated configurations in the case of a 100 m long train. It can be seen that the general pattern of the velocity level across the slab is rather similar for the different configurations. The presence of the wall, even for the concrete wall case, on the 1st and 2nd floors does not appear in an obvious way.

Figure 8 shows the one-third octave spectra of the concrete slab velocity for a position at one-quarter, half and three-quarter of slab length (on the left hand-side) and the global level over the frequency range (on the right side). Note that to simplify the spectra graphics the case of the equivalent lightweight partition is not shown; the behavior being close to the one for the brick type wall.

It is interesting to note that the velocity level in the 1st floor slab is pretty much the same regardless of the type of wall and the three selected positions along the slab.

For the 2nd floor slab due to the presence of a wall below and above the slab, the effect of the wall is well observed. At one-quarter of the floor length, the levels are slightly increased (except at 6.3 Hz), and the maxima slightly shifted in frequency for the concrete wall, while it is mostly increased for the other considered wall types (more lightweight). At the half length of the slab (under the wall if present), the velocity levels are lower in the presence of the concrete wall above 25 Hz, while they are higher for the other wall types (more lightweight). At three-quarter of the concrete slab, the velocity levels are generally increased compared to the case without wall.

For the 3rd floor slab and for the concrete wall, the velocity levels are increased above 20 Hz for the positions at one-quarter and three-quarter of the slab length and mostly increased below 25 Hz at the center of the slab (at the wall position). For the other wall types, the levels are increased.

For the top slab, the velocity levels are larger when the lightweight walls (brick wall or equivalent partition) are considered in the building and for the various locations considered (one-quarter, middle, and three-quarter of the slab length).

For lightweight wall, it appears of interest to evaluate the velocity level at the centre of the room (in the present case at one-quarter of the slab length) but to also investigate the center of the slab and if not taking a margin into account (margin of about 3 dB).

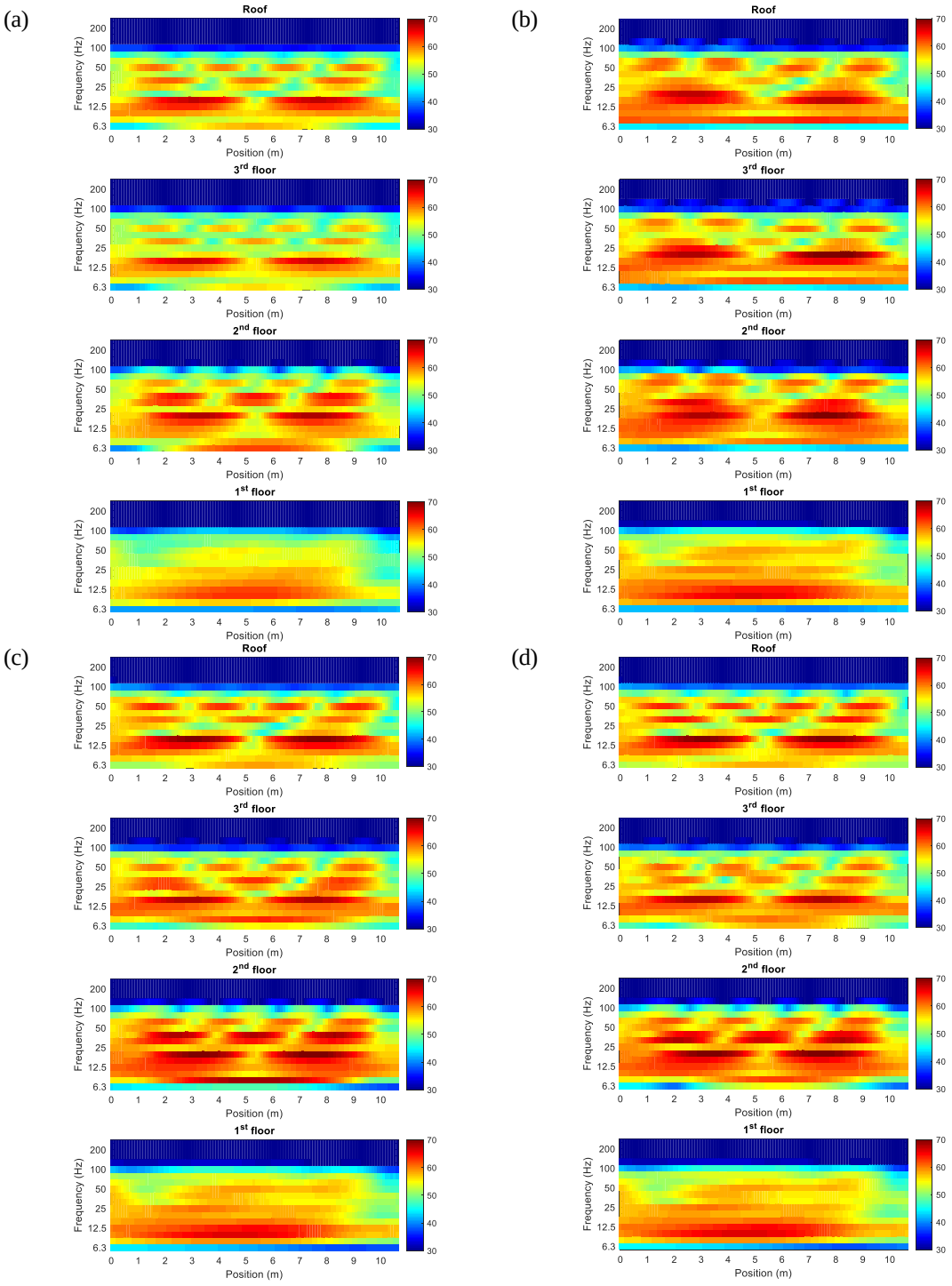


Figure 7. Slab velocity level (dB ref. 50 nm/s) for 100 m long train; (a) without wall, (b) concrete wall, (c) brick wall and (d) equivalent lightweight partition.



Figure 8. Velocity level (dB ref. 50 nm/s) for 100 m long train; at (a) one-quarter, (b) middle, (c) three-quarter, of the slab length and (d) space averaged, (left) Spectrum and (right) global value over the frequency range.

4.2 Ground-borne noise levels

Preliminary results were obtained in terms of ground-borne noise levels. Figure 9 presents the ground-borne noise levels in dB(A) over the investigated frequency range (one-third octave bands from 6.3 to 250 Hz) at a height of 1.3 m in the different rooms and for the different cases considered. Depending on the frequency, the pressure distribution across the room differs. Figure 10 shows the pressure distribution in the building rooms for the case without wall and for the case with a concrete wall at the one-third octave band of 50 Hz. These preliminary results need more in-depth analysis in order to reach any guidance with respect to measurements. A corner position could be an interesting option since it is easily identifiable and usably available for measurement in furnished room, and is expected to be an overestimate of the space average ground-borne noise level.

5. CONCLUSION

In the first part of this work, the effect of using tabulated transfer function to evaluate building floor vibration velocity was investigated. Due to these observations, tabulated transfer function must be used with caution, particularly when issued from measured point to point transfer function. It is more accurate to use a building correction factor C_b measured in situ. If impossible, a security margin of 6 dB should be considered when using tabulated transfer functions in the case of buildings located near the railway track (about 10 m).

In a second part of this paper, vibration velocity of building floors was investigated without and with several types of walls. For lightweight wall, it appears of interest to evaluate the velocity level at the centre of the room (in the present case at one-quarter of the slab length) but to also investigate the center of the slab and if not taking a margin into account (margin of about 3 dB). For heavyweight wall, the evaluation of the velocity level at the centre of the room appears appropriate.

Finally, concerning ground-borne noise inside building, the analysis of the preliminary results requires more work in order to determine general guidelines for preferable measurement positions.

Measurements are planned before the summer in a building to investigate in-situ the floor vibration velocity level distribution as well as the ground-borne noise level distribution.

6. ACKNOWLEDGMENTS

The authors gratefully acknowledge the financial support of this study by the CSTB Research & Innovation department.

7. REFERENCES

[1] P. Jean, C. Guigou-Carter, M. Villot: “A 2D ½ BEM model for ground structure interaction,” *Building Acoustics*, 11(3), pp. 157-163, 2004.

[2] P. Jean: “A 2.75D model for the prediction of noise inside buildings due to train traffic,” *Acta Acustica united with Acustica*, 104, pp. 1009-1018, 2018.

[3] RIVAS project: *Deliverable D1.6 Definition of appropriate procedures to predict exposure in buildings and estimate annoyance*, FP7 European project under grant agreement 265754, 2012 https://uic.org/projects-99/article/rivas

[4] SILVASTAR project: *Deliverable D1.1 State of the art and concept of the vibration prediction tool*, H2020 Collaborative Projects S2R-OC-CCA-01-2020: Noise and Vibration under grant agreement 101015442, 2021 https://www.silvarstar.eu/

[5] XP ISO/TS 14837-31, *Mechanical vibration - Ground-borne noise and vibration arising from rail systems - Part 31: guideline on field measurements for the evaluation of human exposure in buildings*, 2018.

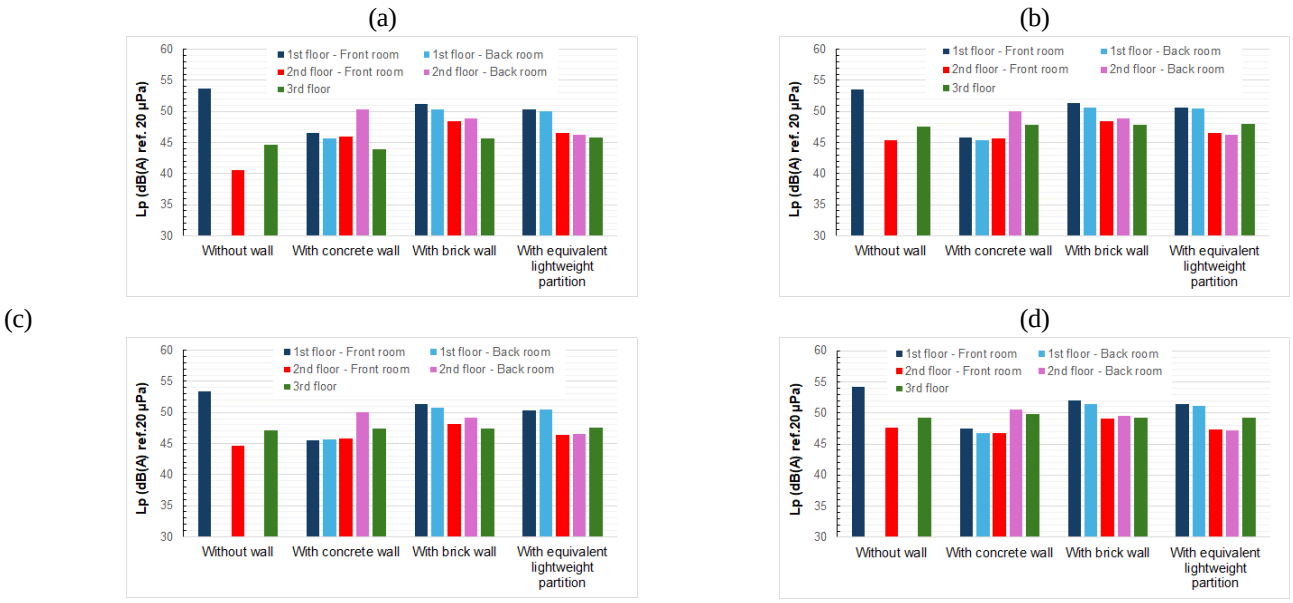


Figure 9. Ground-borne noise level (dB(A) ref. 20µPa) for 100 m long train; at (a) middle, (b) one-third, (c) two-third, of the different rooms at a height of 1.3 m and (d) space averaged.

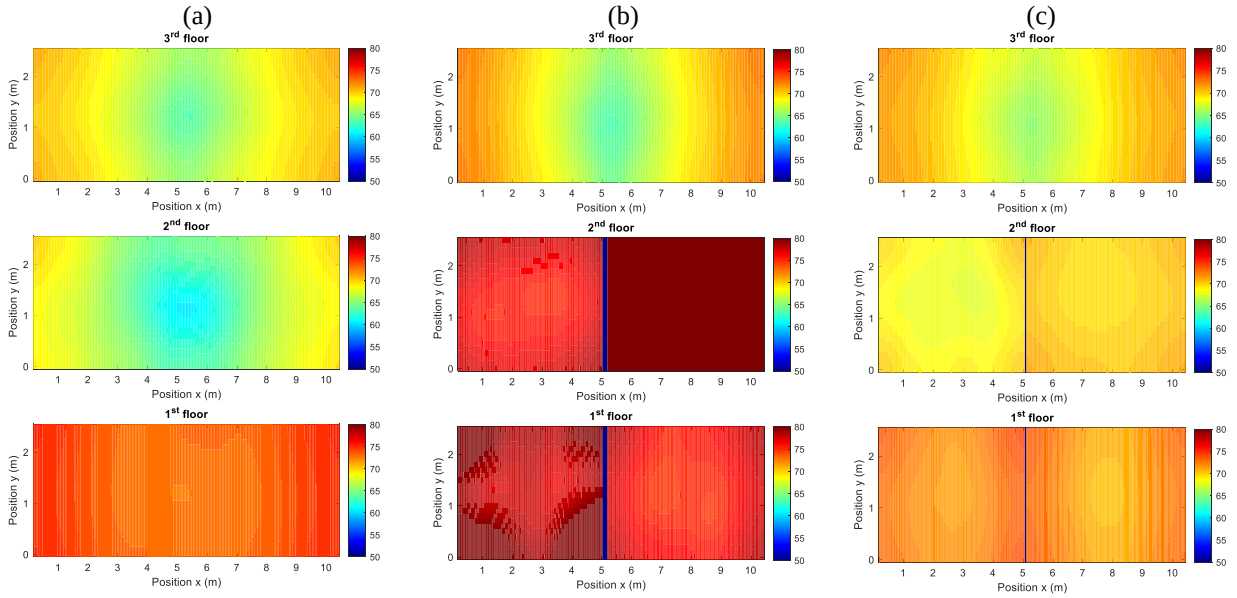


Figure 10. Ground-borne noise level (dB ref. 20µPa) distribution in the rooms for 100 m long train at the one-third octave band of 50 Hz; (a) without wall, (b) with concrete wall, and (c) with brick wall.

DOI: 10.61782/fa.2025.0562

FORUM ACUSTICUM EURONOISE 2025

METHODOLOGY FOR ASSESSING STRUCTURAL NOISE ANNOYANCE IN BUILDINGS CAUSED BY RAIL TRAFFIC. COMPARATIVE ANALYSIS BETWEEN PORTUGAL AND SPAIN

Sónia Antunes[1*] **Jorge Patrício**[1]
[1] National Civil Engineering Laboratory, Lisbon, Portugal

ABSTRACT

In recent years, the development of new construction materials and the publication of standards associated with new construction processes and evaluations have made it possible to construct buildings with high acoustic comfort. Alongside the construction of buildings with high sound insulation requirements, other aspects, such as structural noise, are becoming more important. This paper presents the evolution of the vibration and structural noise (ground-borne noise) descriptors in environmental impact studies derived from rail traffic in Portugal. However, these criteria are not regulated, but good practice guidelines are implemented by the management entities in order to contribute to the reduction of annoyance and, consequently, complaints from the nearby residents. In this context, a comparative analysis is carried out between the criteria used to assess low-frequency noise annoyance in two neighboring countries (Portugal and Spain), to encourage the drafting of possible Portuguese regulations in this area.

Keywords: *railway vibration, structural noise, comfort inside buildings*

1. INTRODUCTION

Noise regulations in Portugal is established by Decree-Law no. 9/2007 of 17 January, which approved the *Regulamento Geral do Ruído* (RGR) [1] . This law aims to prevent and control noise pollution, safeguarding public health and the population's well-being. Criteria are defined for assessing various noise sources likely to cause annoyance, including noise from transport infrastructures. To this end, maximum sound levels are established for outdoor environmental noise, depending on the time of day and the type of land use classification of the area. Regarding noise levels inside buildings, the only reference is to the minimum value (equal to 27 dB(A)), above which the annoyance assessment criterion applies. This regulation also does not specify any criteria for vibration levels inside buildings, and penalties to be considered when the sources being assessed have low-frequency components. Currently, in Portugal, there is still no legal obligation to comply with standards or regulations regarding vibrations that don't have the potential to cause damage to buildings, like explosions, even if they cause annoyance to occupants inside buildings.

The minimum acoustic performance criteria that buildings must meet to ensure user comfort and quality of life are established in the *Regulamento dos Requisitos Acústicos de Edifícios* [2], approved by Decree-Law No. 129/2002. This regulation applies to seven main building categories, namely: residential, mixed-use, and hotel buildings; commercial, industrial, or service buildings; educational institutions; hospitals; sports centers; passenger transport stations; and auditoriums. The criteria are defined based on sound insulation values for airborne and impact sound transmission, reverberation time, and noise levels associated with technical equipment and installations. Only in the latter case are values given for sound levels inside rooms where more noise-sensitive activities can take place. The noise sources should derive from the operation of equipment and installations inside the building and located in adjacent rooms. In this context, maximum permissible sound levels are established as follows: 27 dB(A) in bedrooms and living areas of residential buildings, 37 dB(A) in spaces where concentration and leisure activities take place (e.g., commercial, industrial, or service buildings), 30 dB(A) in hospital wards and libraries within educational institutions. These values apply under the

[*] ***Corresponding author***: *santunes@lnec.pt*
Copyright: *©2025 First author et al. This is an open-access article distributed under the terms of the Creative Commons Attribution 3.0 Unported License, which permits unrestricted use, distribution, and reproduction in any medium, provided the original author and source are credited.*

assumption of continuous operation of noise sources. Additionally, penalties are imposed when noise sources exhibit tonal components, with an added correction of +3 dB(A).

In Spain, the central administration is responsible for establishing legislation at the national level; however, the implementation and enforcement of these regulations fall under the jurisdiction of the autonomous communities. Consequently, most autonomous communities have developed their own regulatory frameworks in this domain, leading to slight variations in the indices used and the corresponding limit values. This study will therefore examine the noise and vibration assessment criteria established by the autonomous communities of Madrid and Barcelona, as well as those implemented by the city of Valencia.

2. CRITERIA USED IN PORTUGAL

Even though Portugal might not have specific regulations for ground-borne vibration and noise from rail traffic, the EU Directive 2016/797 (also known as the Railway Safety Directive) provides a framework to ensure that the levels of vibration and noise generated by rail operations do not cause annoyance. It's critical for rail operators to consider these environmental impacts, and ensure that mitigation measures are implemented if necessary, particularly in areas with sensitive uses (residential, healthcare, or industrial zones). In this context, the authors published in 2019 a methodological action guide for minimising the occurrence of potential noise and vibration annoyance situations inside homes derived from the operation of the Lisbon metro. This document indicates the criteria related to vibrations and ground-borne noise limit values inside buildings for the different phases of a railway infrastructure project (construction and operation), which are explained below (exploration phase):

2.1 Ground-borne noise

To predict ground-borne noise levels in exposed dwellings, it is recommended that, for each individual metro train passage, the vibration velocity values (RMS) be analysed within one-third-octave frequency bands ranging from 16 Hz to 250 Hz:

2.1.1 Underground track

- be less than 0.02 mm/s in the most unfavourable situations where the vibrational reduction index from the slab in question to the surrounding walls (*Kij*) are very low and the transmission between elements is very high. This case occurs when the construction solutions are very heavy and most of the connections considered are rigid;

- between 0.02 - 0.025 mm/s, in intermediate situations where vibrational reduction index of the slab in question to the surrounding walls (*Kij*) already has some relevance, so there is less vibration transmission than in the previous case are medium values. This case corresponds to the most common situations.
- between 0.025 - 0.03 mm/s, in the more favorable situations where vibrational reduction of the slab in question to the surrounding walls (*Kij*) are very high, and the transmission between elements is very low. This case will occur when the constructive solutions of the walls are lightweight.

It is acceptable to assume an average value of 0.025 mm/s, representing most situations. As an alternative option, bearing in mind that low-frequency noise is somewhat complex from the point of view of human perception, a noise limit value of 27 dB(A) can be considered, calculated for the third-octave frequency bands between 16 Hz and 250 Hz), which approximately corresponds to the response of 10 per cent of the most sensitive individuals [3].

2.1.2 Surface track

For the purpose of predicting ground borne noise that may be established in compartments of dwellings and/or other buildings of sensitive use, taking into account the specificity of the situation under analysis (noise and vibrations induced by the movement of railway traffic), it is recommended that the vibration velocity values (RMS) of the horizontal partition element (floor), vertical or horizontal component, if more relevant, integrated in the one-third-octave frequency bands between 16 Hz and 250 Hz, should be less than 0.05 mm/s. Bearing in mind that the difference between the limit values for vibration velocity between the vertical and horizontal directions correspond roughly in terms of L_{Aeq} sound level (with A weighting in each third-octave frequency band between 16 Hz and 250 Hz) is approximately 9 - 10 dB, a value of L_{Aeq} = 36 dB [16-250 Hz] is recommended for ground-borne noise indoors.

This criterion is more permissive than the one recommended for tunnelled tracks, as, there is a masking effect from airborne noise coming directly from the infrastructure.

2.2 Vibration (perception)

2.2.1 Underground track

The following criteria are recommended to assess annoyance induced by continuous or intermittent vibrations inside buildings.
1. Average effective vibration velocity value of less than 0.28 mm/s;
2. Application of the ISO 2831-2 base curve (1989 version) [4], with the multiplicative factors corresponding to intermittent vibrations for residential buildings. In this case, the spectrum of vibration velocity values (RMS), in one-third-octave bands, must be less than 0.14 mm/s, for central frequencies between 8 and 80 Hz (period 8 pm-8 am), this limit increasing to 0.4 mm/s at 2 Hz, and 0.8 mm/s at 1 Hz. For the daytime period (8 am-8 pm), the vibration velocity value, vef < 0.20 mm/s, assumed for central frequency bands between 8 and 80 Hz, and increases to 0.56 mm/s for 2 Hz, and 1.12 mm/s for 1 Hz. These values are valid for the vertical or horizontal component of the velocity, if the latter is the most significant.

2.2.2 Surface track

For the perception of vibrations inside buildings, the reference values shown in Table 1 are recommended in terms of the vibration velocity values (RMS). In this table, the vibration can be considered Perceptible during the infrastructure's operating day (08-20h) and Null during the complementary period of operation.

Table 1 - Limit values for the perception of continuous vibration inside buildings

v_{rms} (mm/s)	Sensation
$v_{rms} < 0{,}11$	Null
$0{,}11 < v_{rms} < 0{,}28$	Perceptible, bearable for short duration
$0{,}28 < v_{rms} < 1{,}10$	Clear, annoying, may affect working conditions
$v_{rms} > 1{,}10$	Very clear, very annoying, reducing working conditions

The ISO 2631-2 base curve (1989 version) can be also applied, with the multiplicative factors corresponding to intermittent vibrations for residential buildings. In this case, the spectrum of vibration velocity values (RMS) in one-third-octave bands must be less than 0.14 mm/s for centre frequencies between 8 and 80 Hz (period 20h-08h), a limit that increases to 0.4 mm/s at 2 Hz and 0.8 mm/s at 1 Hz. For the daytime period (08-20h), the effective vibration value, vef < 0.20 mm/s, assumed for centre frequency bands between 8 and 80 Hz, increases to 0.56 mm/s for 2 Hz, and 1.12 mm/s for 1 Hz. The lower value shown (0.11 mm/s) is considered the perception threshold. Although the criterion recommended for the night period (more restrictive) includes verification of the daytime criterion, in terms of corrective measures, there may be cases of operations management in which such differentiation may be applicable.

3 . CRITERIA USED IN SOME SPANISH MUNICIPALITIES

In 2003, the National Noise Law (*Ley 37/2003*) was published and developed into Royal Decree 1513/2005 [5] (on about the assessment and management of environmental noise), and Royal Decree 1367/2007 of October 19 (on acoustic zoning, quality objectives and acoustic emissions) [6]. With the updating of the European Directive on the assessment and management of environmental noise, the Royal Decree 1513/2005 has undergone some changes, specifically in its Annex II (Order PCI/1319/2018 of December 7 and Order PCM/80/2022 of February 7) and Annex III (Order PCM/542/2021 of May 31).
The aforementioned regulatory sets out the acoustic quality levels (equivalent SPLs) that ought to be met inside buildings depending on their use, as shown in Table 2. Where the indices L_d, L_e and L_n refer to the A-weighted, equivalent continuous sound level for daytime period (12 hours), evening period (4 hours) and night-time period (8 hours).
Regarding transmission between adjacent locations, without noise transmission between the emitter and the receiver through the external environment, the values indicated in Table 3 apply, depending on the type of use of the receiving location. These limit values are applied when the noise source relates to commercial, industrial activities, installations, sports or leisure establishments. The descriptor used to assess noise is the noise index $L_{keq,T}$, which corresponds to the A-weighted, equivalent continuous sound level, ($L_{Aeq,T}$), with, at least, an integration time of 5 seconds ($L_{kAeq,\ 5s}$). This value should be corrected for the presence of emergence of tonal components, low-frequency components and impulsive noise. The limits are met when the values of the acoustic indices, after assessing the existence of low-frequency components, do not exceed in any case more than 5 dB(A), the application limit values indicated in Table 3.

Table 2 - Acoustic quality objectives inside buildings, depending on their use

Building Type	Local	Ld and Le	Ln
Dwellings	Living areas	45	35
	Bedrooms	40	30
Hospitals	Living areas	45	35
	Bedrooms	40	30
Educational and Cultural Centres	Classrooms	40	40
	Libraries	35	35

Table 3 - The limits of sound levels transmitted to acoustically adjacent locations by any installation, establishment, activity or behavior (Real Royal Decree 1367/2007)

Building Use	Local	$L_{k,d}$ / $L_{k,e}$ Day/ Evening	$L_{k,n}$ Night
Dwellings	Living areas	40	30
	Bedrooms	35	25
Hospitals	Living areas	40	30
	Bedrooms	35	25
Educational and Cultural	Classrooms	35	35
	Libraries	30	30
Offices		35	35

For the assessment of low frequency noise, a detailed evaluation of the noise is carried out, introducing the appropriate corrections (Table 4) according to the following methodology:

a) Simultaneous measurement of the sound pressure level with C and A weighting.

b) Calculation of the difference between the values obtained (L_f), corrected for background noise;

c) Determining the presence or absence of low-frequency components, and the value of the correction (K_f) to be introduced, according to the values in Table 4.

Table 4 - Correction values (K_f) to be added in case of the presence of low-frequency components

$L_f = L_{Ceq,Ti} - L_{Aeq,Ti}$ (dB)	K_f (dB)
$L_f > 10$	0
$10 < L_f <= 15$	3
$L_f > 15$	6

However, the legislation only indicates the use of the above-mentioned correction factor (K_f) when dealing with noise sources located inside the building or in adjoining buildings. However, in view of the problem presented, assessing ground-borne noise annoyance in buildings caused by rail traffic, it was also decided in this work to incorporate this criterion.

Regarding the quality criteria for vibrations inside buildings, the values in Table 5 apply depending on the type of building use; the L_{aw} index refers to the vibration level according to the W_m weighting curve defined in the ISO 2631-2: 2003 standard. When assessing this criterion, the maximum RMS acceleration value with slow time constant and W_m frequency weighted is used (defined as Maximum Transient Vibration Value in ISO 2631-1: 1997). However, for transient vibrations, the W_m weighting is not used (because of the slow response of the lowest one-third-octave filters relative to the slow time constant). It is only limited to the case of stationary vibrations.

Table 5 - Acoustic quality objectives for vibrations transmitted to interior spaces

Building Type	Vibration Index L_{aw} dB re. 10^{-6} m/s^2	mm/s^2
Dwellings	75	5.6
Hospitals	72	4.0
Educational and Cultural centers	72	4.0

In the case of the community of Madrid and according to the *Ordenanza de Protección contra la Contaminación Acústica y Térmica* (2021 version), the acoustic quality objectives inside buildings are identical to those shown in Table 2 (noise). In the case of sound level measurements and for acoustic sources in the building (or adjacent buildings), the values from Table 6 are applied. The limits are met when the values of the acoustic indices, after assessing the existence of low-frequency components (Table 4), do not exceed in any case more than 5 dB(A), the application limit values indicated in Table 6.

For vibrations inside buildings, the values in Table 5 apply in addition to the limits imposed on four new building uses: hostels (78 dB/7,9mm/s2), offices (84 dB/15,8 mm/s^2), shops and warehouses (90 dB/31,6 mm/s^2), and industry (97 dB/70,8 mm/s^2).

Table 6 - The limits of sound levels transmitted to acoustically adjacent locations by any installation, establishment, activity or behavior (community of Madrid)

Building Use	Local	$L_{kAeq,5s}$ Day/ Evening	$L_{kAeq,5s}$ Night
Dwellings	Living areas	35	30
	Bedrooms	30	25
Hospitals	Living areas	40	30
	Bedrooms	30	25
Cultural	Cinemas, theaters	30	30
Educational	Classrooms	35	35
	Libraries	30	30
Offices	--------	35	35
Commerce	---------	50	50
Industrie	-----	55	55

In the case of the city of Valencia, the Municipal Ordinance for Protection against Acoustic Contamination, approved in February 2023, states criteria for sound levels inside buildings derived from airborne and structural transmission. Regarding airborne transmission, the most stringent values are for residential buildings (55 dB(A) during the day and evening, 45 dB(A) at night), and for hospitals and schools (45 dB(A) during the day and evening, and 35 dB(A) at night). These higher permissible values are related to the microphone position that should be placed in the window opening at the plane of the exterior facade and orientated towards the sound source. (windows open). The values for structural transmission are presented in Table 6. Also, when low-frequency components are detected in the noise measurement process, a detailed evaluation of the noise is carried out, introducing the appropriate corrections (identical to Table 4 correction values).
Like in Madrid, the values in Table 5 are also used as quality objectives for vibrations applicable to the interior habitable space of buildings intended for housing, residential, hospital, educational, or cultural uses.

Table 7. Assessment levels inside buildings, derived from structural transmission (city of Valencia)

Building Use	Local	Day/Evening dB(A)	Night dB(A)
Dwellings	Living areas	40	35
	Bedrooms	40	30
Hospitals	Living areas	45	35
	Bedrooms	40	30
Cultural	Concert halls	35	35
	Libraries	35	35
	Museums	45	45
	Exhibitions	45	45
Educacional	Classrooms	40	35
	Libraries	35	35
Offices	--------	40	40
Commerce	---------	45	45

For the autonomous region of Catalonia, Decree 176/2009, approving Law 16/2002 about protection against noise pollution, sets out the objectives for noise quality inside buildings intended for residential, hospital, educational and cultural use, identical to the ones shown in Table 2. About admissible sound levels for acoustically adjacent locations by any installation, establishment, activity or behaviors, values similar to those shown in Table 6 apply, except that in this case, the index used is the A-weighted equivalent continuous sound pressure level, corresponding to the daytime (7 am to 9 pm), evening (9 pm to 11 pm), and night-time (11 pm to 7am) periods.

Regarding the low-frequency assessment, the procedure differs slightly from the previous one. Thus, if the difference between simultaneous measurement of the sound pressure level with C and A-weighting is greater than 20 dB, a detailed assessment of low frequency components carried out, according to the following procedure:

a) Obtaining the low-frequency audible level, which is calculated for each third-octave band between 20 and 160 Hz, from the difference between the measured value of each one third octave band (unweighted) and the human hearing threshold published in ISO 226:2003.
b) Obtaining the L_B value, corresponding to the energetic sum of the values corresponding to the one-

third-octave bands between 20Hz and 160Hz, and whose difference obtained in a) is greater than zero.
c) Determining the presence or absence of low-frequency components and the correction parameter K_f by applying the criteria in Table 8.

Table 8 - Correction values to be added in the presence of low-frequency components

L_B (dB)	K_f (dB)
L_B< 25 dB	0
25<=L_B<=35	3
L_B>35	6

For vibrations, and like in the city of Valencia city, the values in Table 5 are applied, corresponding to quality objectives applicable to the interior habitable space of buildings intended for housing, residential, hospital, educational, or cultural uses.

3. CASE STUDIES

3.1 Case 01

The building under evaluation is a semi-detached house, with a basement, ground floor, and first floor. The metro tunnel is located at a depth of approximately 20 m from the ground surface. The sound environment outside the residence is characterized mainly by road traffic noise and air traffic noise. Inside the house, given the sound insulation against airborne sounds provided by the walls and windows (made up of double glazing), the noise from the external sound environment is almost imperceptible. Three 01 dB Symphonie measurement systems were used (located on the railway platform, tunnel wall structure and inside the residence) and a Pulse measurement system from Bruel & Kjaer (located inside the residence) to which one microphone (GRAS 40AF microphone) and accelerometers (IMI 626A04 and PCB, model 393A03) were connected. Inside the residence, measurements were taken on the ground floor (living room, labeled as S and nº of measurement) and on the 1st floor (bedroom, labeled as Q). All measurements taken inside the house were accompanied by simultaneous and synchronized measurements of the metro train passages with the accelerometers placed on the railway platform, and in the tunnel wall structure. Tables 9, 10 and 11 present the results of vibration measurements taken on the ground floor. Tables 9 and 10 refer to individual passages of metro trains. In contrast, Table 11 shows the results obtained in three measurements, each lasting 30 minutes, with the noise levels already corrected from residual sound values.

Table 9 – Vibration values for single metro train passages in the living room (ground floor)

Nº Mes.	L_a dB	L_{aw} dB	MTVV dB	v_{rms} (mm/s) [1-80 Hz]	v_{rms} (mm/s) [16-250Hz]	ISO 2831-2
S1	73	56	**77**	0,024	0,022	Pass
S2	77	61	**81**	0,036	**0,035**	Pass
S3	77	59	**80**	0,03	**0,03**	Pass
S4	78	61	**82**	0,06	**0,057**	Pass
S5	74	57	**78**	0,028	**0,027**	Pass
S6	71	56	74	0,026	0,025	Pass

Table 10 - Vibration values and noise levels for single metro train passages in the living room (ground floor)

Nº Mes.	L_a dB	L_{aw} dB	MTVV dB	v_{rms} (mm/s) [1-80 Hz]	v_{rms} (mm/s) [16-250Hz]	ISO 2831-2	L_{Aeq} [16-250Hz	L_f /L_B
S7	76	60	**79**	0,028	**0,028**	Pass	30	16/14
S8	74	56	**77**	0.019	0,019	Pass	27	26/13
S9	76	59	**80**	0,025	0,025	Pass	25	30/13
S10	77	60	**81**	0,028	**0,028**	Pass	26	28/10
S11	75	57	**79**	0,022	0,022	Pass	30	26/18
S12	68	60	72	0,011	0,011	Pass	24	27/11
S13	72	58	**75**	0,016	0,016	Pass	33	20/11
S14	75	57	**79**	0,022	0,022	Pass	30	26/18
S15	80	60	**77**	0,029	**0,029**	Pass	28	28/13
S16	74	61	**77**	0,021	0,021	Pass	23	29/10
S17	82	68	**85**	0,046	**0,046**	Pass	28	33/14
S18	77	59	**80**	0,029	**0,029**	Pass	26	30/13
S19	75,8	60	**79**	0,028	**0,028**	Pass	38	16/14

Table 11- Vibration values and noise levels for 30 minutes measurements (ground floor)

Period / nº passages	L_a dB	L_{aw} dB	MTVV dB	v_{rms} (mm/s) [1-80 Hz]	v_{rms} (mm/s) [16-250Hz]]	ISO 2831-2	L_{Aeq} [16-250Hz]
6h30-7h00/5	59	42	45	0,006	0,0062	Pass	19
8h30-9h/10	66	49	70	0,009	0,0089	Pass	26
13h-13h30/11	66	49	70	0,010	0,010	Pass	21

The tables above show the results for vibration acceleration level (L_a), W_m weighted vibration acceleration level (L_{aw}), Maximum Transient Vibration Value (MTVV, calculated by multiplying 1.5 by the RMS acceleration value), and RMS velocity value (v_{rms}, in mm/s), for frequencies between 1 and 80 Hz (v_{rms} (mm/s) [1-80 Hz] and for frequencies between 16 and

250 Hz, (v_{rms} (mm/s) [16-250 Hz]). The column labeled as ISO 2831-2, presents the results of applying the base curve (1989 version) of this standard, with the multiplicative factors corresponding to intermittent vibrations for residential buildings. Tables 10 and 11 also show the A-weighted sound equivalent levels (L_{Aeq}), measured during single metro train passages (for the definition of the duration of each passage, -10dB rule was used in relation to the maximum value). These levels refer to the frequencies between 16-250 Hz. The results of the calculations for assessing the existence of low-frequency components are also shown, namely the Lf values (Royal Decree 1513/2005) and the L_B value (Catalonia, Decree 176/2009). Table 12 refers to the measurement results for the bedroom on the first floor of the house. The labels for each column have the same meaning that the previous tables.

Table 12- Vibration values and noise levels for single metro train passages in bedroom (first floor)

Nº Mes.	L_a dB	L_{aw} dB	MTVV dB	v_{rms} (mm/s) [1-80 Hz]	v_{rms} (mm/s) [16-250Hz]	ISO 2831-2	L_{Aeq} [16-250Hz	L_f /L_B
Q1	65	47	67	0,007	0,006	Pass	17	30/4
Q2	69	52	72	0,011	0,011	Pass	18	31/ 3
Q3	70	53	73	0,013	0,013	Pass	19	30/7
Q4	65	48	69	0,007	0,007	Pass	17	30/3
Q5	71	53	**75**	0,013	0,013	Pass	21	30/9
Q6	68	60	71	0,012	0,012	Pass	20	30/8
Q7	72	54	**76**	0,015	0,015	Pass	22	28/10
Q8	85	67	**88**	0,064	**0,064**	Pass	27	34/11
Q9	80	63	**84**	0,038	**0,038**	Pass	26	33/12

3.2 Case 02

The measurements were taken on the first floor of a 4-storey urban building with a reinforced concrete structure. The vibration levels of the metro single metro train passages were measured in the center of the floor and on two side walls. The microphone was placed in the center of the room. Two measurement chains were used, each consisting of a real-time analyser with two channels, brand 01dB, model Symphonie, to which the respective microphone (GRAS 40 AF) and accelerometers (PCB model 393B04) were connected, and which carried out simultaneous measurements in 3 different directions. The ground-borne noise derived from each metro train passage was clearly audible, standing out from the residual sound. Table 13 refers to vibration and noise levels for single metro train passages in the living room (first floor)

Table 13- Vibration values and noise levels for single metro train passages in the living room (first floor)

Nº Mes.	L_a dB	L_{aw} dB	MTVV dB	v_{rms} (mm/s) [1-80 Hz]	v_{rms} (mm/s) [16-250Hz]	ISO 2831-2 [Hz]	L_{Aeq} [16-250 Hz	L_f /L_B
1	97	78	**100**	0,22	**0,22**	[20]	48	25/26
2	98	79	**101**	0,21	**0,21**	[40, 50]	47	25/26
3	98	79	**102**	0,25	**0,25**	[40, 50]	50	25/26
4	97	78	**101**	0,23	**0,24**	[40, 50]	50	25/26
5	96	77	**100**	0,20	**0,20**	[50]	48	24/26
6	97	78	**101**	0,23	**0,23**	[40, 50]	48	25/26
7	96	77	**100**	0,20	**0,20**	[50 Hz]	48	24/26
8	98	78	**101**	0,24	**0,24**	[40, 50]	50	25/26
9	97	78	**101**	0,23	**0,23**	[40, 50]	49	26/26
10	97	77	**100**	0,21	**0,21**	[40, 50]	48	25/36

4. COMPARATIVE ANALYSIS

4.1 Vibration

The bold values in the MTVV column of Tables 9,10,12, and 13 correspond to acceleration vibration levels that exceed the threshold values established in the Spanish criteria for assessing vibrations in residential buildings (as specified in Table 5). Similarly, the bold values in the v_{RMS} (mm/s) [1-80 Hz] column denote metro train passages where the measured vibration velocity surpasses the general threshold outlined in the Portuguese criteria (v_{RMS}=0.28 mm/s). However, as none of the recorded measurements exceed this limit, no bold values appear in the referenced tables. Furthermore, the values in the ISO 2631-2 column indicate a "PASS" when the measured values for each third-octave band remain below the thresholds established in the ISO 2631-2:1989 standard. If a threshold is exceeded, the corresponding frequency band is specified. Consequently, only the metro train passages listed in Table 13 (passages 1-10) fail to comply with the vibration assessment criteria applicable in Portugal. The comparison of results, particularly for Case Study 1 (as presented in Tables 8, 9, and 11), suggests a higher sensitivity of the criterion employed in Spain concerning the assessment of vibrations.

4.2 Ground-borne noise

According to Spanish regulations, the assessment of railway traffic noise inside residential spaces requires a minimum of three series of measurements. Each series must comprise multiple measurements (at least 3), with a minimum duration of five minutes per measurement. Furthermore, the time interval between consecutive

measurement series must exceed five minutes. The final noise level assessment is determined as the energy average of the three series. Based on the values presented in Table 10, the resulting noise level is 23 dB(A).

In the context of noise assessment and the comparative study, additional considerations were incorporated that are not explicitly specified in Spanish regulations. Specifically, the evaluation included the assessment of sound levels generated by an individual passage of a metro train, categorized as noise resulting from an activity, as outlined in Tables 3, 6, and 7. To achieve this, three series of measurements were conducted, each lasting longer than five seconds. The maximum recorded value from each series was retained, and the presence of low-frequency components was analyzed. The results of this assessment are presented in Table 14. The bold values in the v_{RMS} (mm/s) [16-250 Hz] column denote metro train passages where the measured vibration velocity surpasses the general threshold outlined in the Portuguese criteria for ground-borne noise. Similarly, the bold values for the L_{Aeq} columns (Real Decreto and Barcelona) indicate that the admissible sound levels are exceeded, considering the most critical situations for residential buildings during the night (equal to 30 and 25 dB(A), or 35 and 30 dB(A) in the case of the city of Valencia).

Table 14- Assessment of noise levels for individual metro trains passages

Nº Mes./ Table	v_{rms} (mm/s) [16-250 Hz]	L_{Aeq} [16-250 Hz]	L_{Aeq} Real Decreto	L_{Aeq} Barcelona
S7/9	**0,028**	30	**36**	30
S11/9	0,022	30	**36**	30
S13/9	0,016	33	**39**	33
S17/9	**0,046**	28	**34**	28
Q3/11	0,013	19	25	19
Q5/11	0,013	21	**27**	21
Q8/11	**0,064**	27	**33**	**27**
3/12	**0,25**	50	**56**	**53**
4/12	**0,24**	50	**56**	**53**
8/12	**0,24**	50	**56**	**53**

Regarding the assessment of sound levels, only the evaluation of individual metro train passages yields values exceeding the established criteria. Additionally, a greater degree of harmonization is observed between the two countries in this context.

5. CONCLUSIONS

The evaluation of vibration and ground-borne noise based on measurements presents significant challenges due to the small amplitudes involved and the presence of residual vibration and noise in the surrounding environment. However, the analysis of the two case studies provided insights into the higher sensitivity of the criterion applied in Spain for vibration assessment, which classifies vibrations based on the type of building use.

Regarding ground-borne noise, harmonization of results between the two countries is achieved only when individual pass-by values and criteria related to activity operation are considered. Additionally, differences in the criteria for evaluating low-frequency components in Spain have a direct impact on the final assessment outcomes. Nevertheless, it is important to emphasize that in both case studies, residents reported significant annoyance due to ground-borne noise.

6. REFERENCES

[1] Portugal. (2007). *Decree-Law No. 9/2007 of January 17 – General Noise Regulations*. Diário da República. https://dre.pt.

[2] Portugal. (2008). *Decree-Law No. 96/2008 of June 9 – Building Acoustics Code*. Diário da República. https://dre.pt.

[3] Waddington, D.; Woodcock, J.; Smith, M.; Janssen, S.; Waye, K., "CargoVibes: Human response to vibration due to freight rail traffic", in International Journal of Rail Transportation, Volume 3 (4), (2015), pp. 233-248, 2015

[4] ISO, "*ISO 2631-2:1989: Mechanical vibration and shock – Evaluation of human exposure to whole-body vibration – Part 2: Vibration in buildings (60 Hz to 100 Hz), 1989*.

[5] Spain. (2005). *Decree 1513/2005, of December 16, regulating the assessment and control of environmental noise*. Official State Gazette. https://www.boe.es

[6] Spain. (2007). *Royal Decree No. 1367/2007 of October 19 – Regulation on the assessment and control of environmental noise*. Official State Gazette (BOE), 255, 37666-37676. https://www.boe.es.

DOI: 10.61782/fa.2025.0182

FORUM ACUSTICUM EURONOISE 2025

BUILDING BASE ISOLATION DESIGN: QUANTIFICATION OF VIBRATION TRANSMISSION USING POWER FLOW ANALYSIS

Hamid Masoumi[1*] **James Talbot**[2]
[1] CDM Stravitec , Overijse, Belgium
[2] Department of Engineering, University of Cambridge, UK

ABSTRACT

This paper reports on ongoing work aimed at developing practical guidance for designing BBI solutions. This includes examining the mechanisms by which ground-borne vibrations from railway activities are transmitted into buildings, in particular, the soil-structure interaction (coupling loss), the role of the isolation system and the influence of structural elements within the building using power flow analysis. Power flow analysis provides valuable insight into the vibration transmission through the system, offering an effective basis for isolation design. This analysis requires estimating the mobility of the substructure (foundation and ground), the isolation system and that of the superstructure. The paper presents a series of experimental measurements of these essential parameters, made at various stages of construction in a recent BBI project. The mobility of the substructure was measured using hammer impact, and vibration levels due to train passages were recorded both at the beginning of construction, before the construction of the superstructure and after the completion of the building. Since the mobility of the superstructure cannot be measured directly, this was estimated by numerical simulation. The characteristics of the isolation system were determined by laboratory tests under loading conditions representative of the operating state of the building.

Keywords: *Ground-borne vibration, Ground-borne noise, Building base isolation, Power flow analysis*

**Corresponding author*: h.masoumi@cdm-stravitec.com.
Copyright: *©2025 Masoumi et al. This is an open-access article distributed under the terms of the Creative Commons Attribution 3.0 Unported License, which permits unrestricted use, distribution, and reproduction in any medium, provided the original author and source are credited.*

1. INTRODUCTION

Buildings, especially those near railway or subway networks, can be subjected to ground-borne vibrations that result in unacceptable levels of structure-borne noise and vibration for the occupants of the building. In order to protect a building from such disturbance, it is necessary to decouple the building from the surrounding sources at the foundation level or on the columns or walls in an upper level by introducing a building base (vibration) isolation solution.

A true assessment of any isolation solution requires comparing noise or vibration levels inside the building with and without the isolation system. This indicator is known as the insertion loss. In practice, once a building is isolated, the non-isolated condition is unavailable, making the true insertion loss unmeasurable.

Today, the performance of a Building Base Isolation (BBI) system is often defined solely in terms of transmission loss, where vibration levels are typically measured above and below the isolation 'cut' in the completed isolated building. However, these measurements do not accurately reflect true isolation performance as they focus on the forced response of a limited section of a complex structure. Furthermore, in an isolated building, increased vibration in the foundation (substructure) may lead to an inaccurate assessment of isolation performance compared to a non-isolated building [1]. Transmission loss and insertion loss indicate the same performance only when the building acts as a SDOF mass-spring system.

A comprehensive study of vibration transmission between the ground and a building was conducted by Edirisinghe and Talbot [2]. They investigated the fully coupled three-dimensional behavior of a tunnel–foundation–building system, analysing the effects of

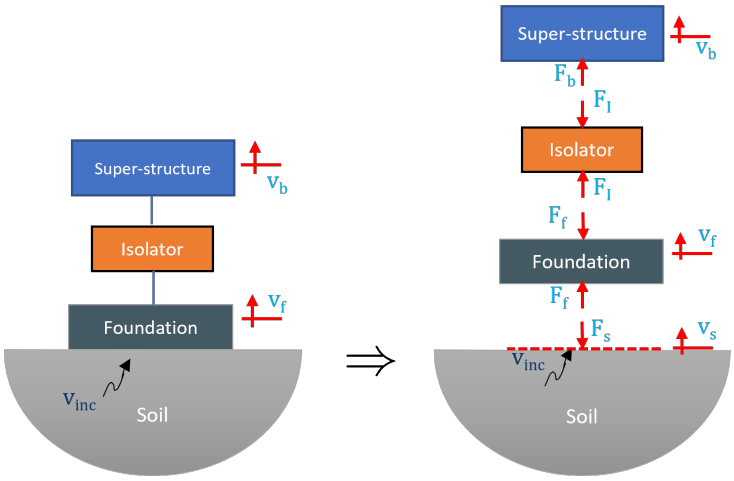


Figure 1. A general overview of the ground-foundation-building interaction.

the source location (the tunnel) relative to the building, the foundation configuration and the flexibility of the building structure. The results showed that simplified models, which capture the fundamental soil-structure interaction (SSI) of the system without including tunnel interaction, can provide sufficiently accurate predictions of vibration transmission through the building.

Using numerical modelling and experimental measurements, Kuo et al. [3] studied the coupling loss of a building subjected to railway-induced vibrations. Their field measurements and numerical studies also showed that a simplified SSI model, which does not include the track or tunnel, provides a sufficiently accurate estimation for the purposes of design. Additionally, their results showed that ground conditions significantly influence coupling loss, whereas the building geometry and foundation type have a more limited impact.

Disregarding the effect of any source-building interaction, the vibration transmission through the system can therefore be decomposed into three main parts: (1) vibration transmission from the ground to the building foundation, (2) vibration transmission through the isolation system and (3) vibration transmission through the building floors above the vibration cut.

One approach to quantifying the vibration transmission process between the different domains (the substructure, the isolator and the superstructure) is to evaluate the vibration energy flux using structural power flow analysis [1,4]. In this paper, theoretical expressions of this analysis are first presented, and the essential parameters governing the interaction between the domains are described. A recent building base isolation project is then used to illustrate how these quantities may be derived from experimental in-situ measurements and then used to estimate the power flow into the building.

1.1 Application of structural power in Building Base Isolation

Focusing on vibration levels at the ground-building interface accounts for transmission at only one location and in one direction. In contrast, power flow analysis can provide a global measure of isolation performance by evaluating the vibrational power at multiple locations and in several directions, leading to a more accurate evaluation of the transmissibility process.

Figure 1 shows the two main coupled domains with the intermediate isolation system, where the substructure (the foundation) has been excited by an incident wave $\mathbf{v}_{\text{inc}}$. The interaction force between the domains depends not only on the excitation but also on the dynamic characteristics of each domain, which can be represented by the mobilities of the coupled domains.

To analyse vibrational/structural power transmission through a building, we need to determine the power in terms of the interaction forces (F) and velocities (v) at each domain's interface. Based on the domain decomposition shown in Fig. 1 for the isolated building, these can be expressed in terms of the 'free' velocities of either the foundation or the soil, that is, the velocities measured at the interface between either the foundation and the future

superstructure before the superstructure is constructed, or the velocities measured on the ground surface before the future foundation is constructed (Fig. 2):

$$\begin{aligned} \mathbf{v}_\mathrm{f} &= \mathbf{v}_\mathrm{f,free} - \mathbf{Y}_\mathrm{f} \cdot \mathbf{F}_\mathrm{f} \\ \mathbf{v}_\mathrm{b} &= \mathbf{Y}_\mathrm{b} \cdot \mathbf{F}_\mathrm{b} \\ \mathbf{v}_\mathrm{b} - \mathbf{v}_\mathrm{f} &= \mathbf{Y}_\mathrm{I} \cdot \mathbf{F}_\mathrm{I} \end{aligned} \tag{1}$$

where, $\mathbf{v}_\mathrm{f,free}$ is the foundation's free vibration, and $\mathbf{Y}_\mathrm{f}$, $\mathbf{Y}_\mathrm{b}$, and $\mathbf{Y}_\mathrm{I}$ are the mobility of the foundation, the building and the isolator, respectively.

Since the mobility of the superstructure cannot be measured directly, it is estimated through numerical simulation. In contrast, the mobility of the substructure (the foundation-soil system) can be obtained via either numerical simulation or measurement using a conventional hammer impact test. For a complex substructure, an averaged mobility can serve as a representative value for varying mobilities at different points. The mobility of the isolation system is defined by the bearing dynamic stiffness, which is determined through laboratory tests under load conditions representative of the building's operational state.

Since the isolator is assumed to be massless, $\mathbf{F}_\mathrm{b} = \mathbf{F}_\mathrm{f} = \mathbf{F}_\mathrm{I}$, and the interaction forces and velocity responses can be obtained from Eqn. 1 as follows:

$$\begin{aligned} \mathbf{F}_\mathrm{I} &= \|\mathbf{Y}_\mathrm{b} + \mathbf{Y}_\mathrm{I} + \mathbf{Y}_\mathrm{f}\|^{-1} \cdot \mathbf{v}_\mathrm{f,free} \\ \mathbf{v}_\mathrm{b} &= \|\mathbf{Y}_\mathrm{b}\| \cdot \|\mathbf{Y}_\mathrm{b} + \mathbf{Y}_\mathrm{I} + \mathbf{Y}_\mathrm{f}\|^{-1} \cdot \mathbf{v}_\mathrm{f,free} \\ \mathbf{v}_\mathrm{f} &= \|\mathbf{Y}_\mathrm{b} + \mathbf{Y}_\mathrm{I}\| \cdot \|\mathbf{Y}_\mathrm{b} + \mathbf{Y}_\mathrm{I} + \mathbf{Y}_\mathrm{f}\|^{-1} \cdot \mathbf{v}_\mathrm{f,free} \end{aligned} \tag{2}$$

For the non-isolated case, the free velocity of the foundation can be expressed in terms of the free-field velocity measured on the ground surface before the future foundation is constructed (Fig. 2):

$$\mathbf{v}_\mathrm{f,free} = \|\mathbf{Y}_\mathrm{f}\| \cdot \|\mathbf{Y}_\mathrm{f} + \mathbf{Y}_\mathrm{soil}\|^{-1} \cdot \mathbf{v}_\mathrm{inc} \tag{3}$$

The transmitted vibrational power to the foundation, and that transmitted through the building's columns and floors, is given by:

$$\begin{aligned} \Pi_\mathrm{f} &= \frac{1}{2}\Re\left\{\mathbf{F}_\mathrm{f}^\mathrm{H} \cdot \mathbf{v}_\mathrm{f}\right\} \\ \Pi_\mathrm{b} &= \frac{1}{2}\Re\left\{\mathbf{F}_\mathrm{b}^\mathrm{H} \cdot \mathbf{v}_\mathrm{b}\right\} \end{aligned} \tag{4}$$

where the superscript "H" denotes to the Hermitian transpose operation.

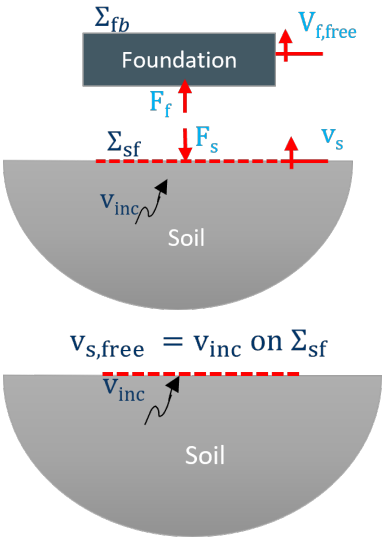


Figure 2. An overview of (bottom) the ground free vibration and (top) the free foundation vibration.

Introducing Eqn. 2 to Eqn. 4, the transmitted power can be written in terms of the measurable free vibration velocity and the mobilities:

$$\Pi_\mathrm{b} = \frac{1}{2}\Re\left\{\mathbf{v}_\mathrm{f,free}^\mathrm{H} . \mathcal{H}^{-\mathrm{H}} . \mathbf{v}_\mathrm{f,free}\right\} \tag{5}$$

with

$$\mathcal{H}^{-\mathrm{H}} = \|\mathbf{Y}_\mathrm{b} + \mathbf{Y}_\mathrm{I} + \mathbf{Y}_\mathrm{f}\|^{-\mathrm{H}} . \|\mathbf{Y}_\mathrm{b}\| . \|\mathbf{Y}_\mathrm{b} + \mathbf{Y}_\mathrm{I} + \mathbf{Y}_\mathrm{f}\|^{-1} \tag{6}$$

It is worth noting that, since the mobility of the foundation is independent of that of the superstructure, the total mobility is often approximated as the sum of the individual mobilities, i.e., $\|\mathbf{Y}_\mathrm{b} + \mathbf{Y}_\mathrm{I} + \mathbf{Y}_\mathrm{f}\|^2 \approx \|\mathbf{Y}_\mathrm{b} + \mathbf{Y}_\mathrm{I}\|^2 + \|\mathbf{Y}_\mathrm{f}\|^2$. This approximation neglects the phase interaction between the mobility terms but does not introduce significant errors in the calculation under the assumption of weak coupling.

1.2 Application in SSI impact and coupling loss estimation

Power flow analysis is helping to further our understanding of SSI and its significance in the response of buildings to ground-borne vibration. By analysing the mean vibrational power input to a building, it is clear that SSI must

be accounted for to avoid over-predicting building vibration levels. The constraining of the soil by foundation and building structures, and the radiation damping provided by the soil to the building, all act to limit vibration levels in the building to below those predicted when SSI is neglected.

SSI should therefore be accounted for in any assessment of building base isolation. However, there is growing evidence that this may be achieved by using either simplified models or limited site measurements to estimate the coupling loss introduced by constructing a building and its foundation [2].

1.3 Application in building isolation performance evaluation

The isolation performance of a BBI system can be defined in terms of power-flow insertion gain as the ratio of the power transmitted by the isolator to the superstructure to that transmitted by a rigid connection for the non-isolated building [1]:

$$\mathrm{PFIG}\,[\mathrm{dB}] = 10\,\log_{10}\left(\frac{\Pi_{\mathrm{b,\,iso}}}{\Pi_{\mathrm{b,\,non\text{-}iso}}}\right) \tag{7}$$

where $\Pi_{\mathrm{b,\,iso}}$ and $\Pi_{\mathrm{b,\,non\text{-}iso}}$ are the total mean power flows entering an isolated and non-isolated building, respectively.

The power flow transmitted through the non-isolated building can be determined by setting the mobility of the isolator to zero in Eqn. 5, ensuring a rigid contact between the foundation and the building.

In the frequency range from 16 to 250 Hz, BIOVIB [5, 6] proposed an approximation to the PFIG formulation and justified a new performance indicator that may be more easily evaluated via in-situ measurements. Assuming that the vibration transmission is dominated by vertical vibration, and that the isolator mobility is large compared to that of the foundation, this is expressed in terms of the transmission loss (TL) through the isolator and the mobilities of the building and foundation:

$$\mathrm{PFIG}\,[\mathrm{dB}] \approx \mathrm{TL} + 10\,\log_{10}\left(\frac{\|\mathbf{Y}_\mathrm{b} + \mathbf{Y}_\mathrm{f}\|^2}{\|\mathbf{Y}_\mathrm{b}\|^2}\right) \tag{8}$$

The first term of Eqn. 8, the transmission loss, is defined as the ratio of the vibrational input power to that transmitted to the isolated building:

$$\mathrm{TL}\,[\mathrm{dB}] = 10\,\log_{10}\left(\frac{\Pi_{\mathrm{b,\,iso}}}{\Pi_{\mathrm{f,\,iso}}}\right) \tag{9}$$

This approximation offers the advantage that the vibrational power transmission into an isolated building can be obtained either through in-situ measurements or from the mobilities of the isolator and the building:

$$\mathrm{TL}\,[\mathrm{dB}] = 10\,\log_{10}\left(\frac{\|\mathbf{Y}_\mathrm{b}\|^2}{\|\mathbf{Y}_\mathrm{b} + \mathbf{Y}_\mathrm{I}\|^2}\right) \tag{10}$$

The application of this performance indicator (Eqn. 8) within the framework of the BIOVIB project has been validated through laboratory and in-situ measurements [7, 8].

2. CASE STUDY: PERFORMANCE ASSESSMENT OF AN ISOLATED BUILDING

In the following, a hybrid experimental-numerical methodology is used to determine the parameters necessary for assessing the performance of an isolated building by means of power flow analysis. The proposed methodology has four steps:

1. Determine the mobility of the building (superstructure) using numerical calculation, such as Finite Element Analysis (FEA) in the frequency domain.

2. Determine the isolator mobility based on the dynamic characteristics of the bearings, $\mathbf{Y}_\mathrm{I} = |i\omega/K^*_{\mathrm{iso}}|$. The complex dynamic stiffness of the isolation bearing ($K^*_{\mathrm{iso}} = K_{\mathrm{iso}}(1 + i\eta)$) and the bearing loss factor η are defined under the specific bearing design load by a dynamic test following the procedure described in ISO 4664-1 [9].

3. Determine the substructure mobility through an in-situ hammer impact test at the bearing locations before installing the building (superstructure), following the measurement procedure described in ISO 7626 [10].

4. Measure train pass-bys at the substructure (i.e., the free vibration of the foundation) before the building (superstructure) is installed, following the measurement procedure described in ISO 14837-31 [11].

5. Measure train pass-bys on the substructure below the vibration isolation system and on the floors above it, following the measurement procedure described in ISO 14837-31 [11].

Given that the quality of the rail-wheel contact surface (a crucial factor in the induced vibrations) may degrade over time, the measured free vibration levels of the foundation or soil should be normalised using a reference vibration level recorded at a point near the source, before calculating the contact force in the completed building using Eqn. 2.

This methodology is examined for the real case study of a two-story building constructed on footings adjacent a railway station in Barcelona. The building is isolated on elastomeric bearings on top of the foundation footings.

2.1 Mobility of the building (super-structure)

To determine the mobility of the building, a Finite Element (FE) model of the superstructure is developed. Since the building structure exhibits a repeated section along its length, a section of building perpendicular to the track with three supports is modelled (Fig. 3). A unit force is applied at each support, and the building response — both at the same support and at the other supports — is calculated to enable the assembly of the building's $N \times N$ mobility matrix, $Y_{b,ij} = v_{b,j}/F_{b,i}$, where N represents the number of bearing locations.

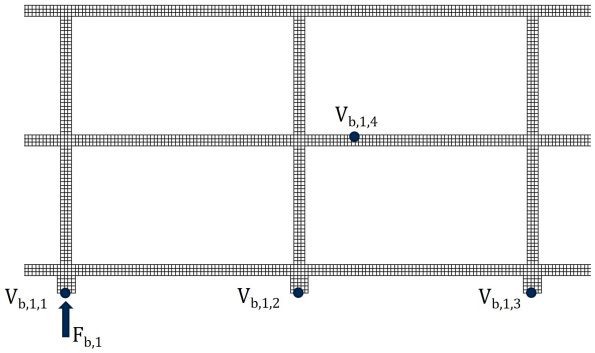


Figure 3. 2D - Finite Element modeling of the building.

Figure 4 shows the direct mobility (the diagonal terms) at each isolator location. Despite the peaks and troughs caused by the bending modes of the structure, the building mobility is primarily dominated by the mass effect, expressed as $Y_b \approx |1/\omega M_b|$.

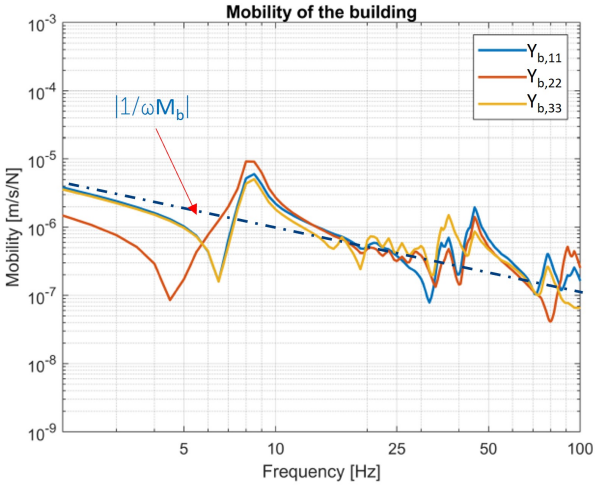


Figure 4. The mobility of the building calculated by FEA.

2.2 Mobility of the foundation (sub-structure)

In the second step, an in-situ measurement campaign is carried out to obtain the foundation mobility using an instrumented hammer, following the measurement procedure described in ISO 7626 [10]. At each bearing location, the mobility of substructure is obtained by applying a hammer impact at each bearing location and measuring the substructure response at the impact location as well as at the other supports. The mobility of the substructure is then assembled as an $N \times N$ matrix, $Y_{f,ij} = v_{f,j}/F_{f,i}$.

In this case study, since the footings are similar, the mobility has been measured only at one of the footings, and only the direct mobility is taken into account. The cross-mobility between the horizontal and vertical foundation responses has been found to be negligible relative to the direct mobility, as illustrated in Fig. 5.

The building is isolated using steel reinforced rubber bearings (type Stravibase VHS) installed between the concrete distribution beams of the superstructure and the footings, as shown in Fig. 6. The measured dynamic stiffness, including the loss factor of the bearings (under the design load), has been used to determine the mobility of isolator at each support. The isolation bearings are designed to exhibit a rigid-body resonance frequency of 10 Hz under the Acoustic design load (in an equivalent SDOF system). Figure 7 shows the averaged vertical mobility of the foundation, as well as that of the building and isolator at each

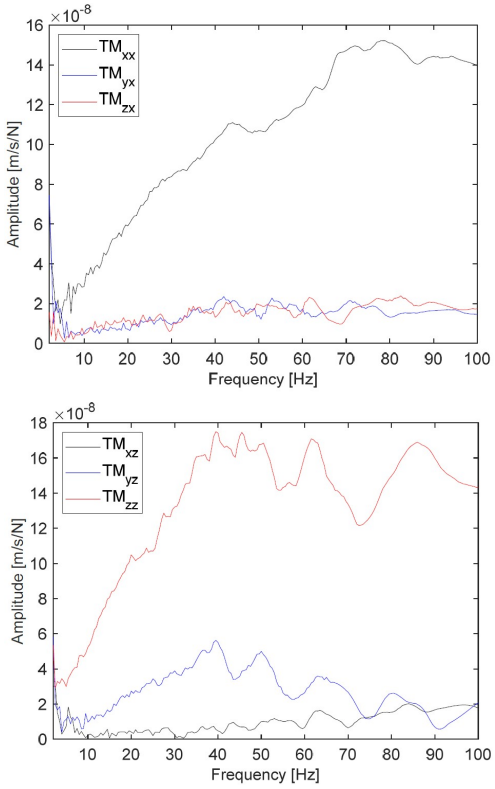


Figure 5. (Top) The three components of the foundation mobility measured under horizontal impact; (Bottom) The three components of the foundation mobility measured under vertical impact.



Figure 6. The isolation bearing, type Stravibase VHS, installed between the concrete distribution beams and the footings.

bearing location. The comparison clearly shows that, at frequencies above 30 Hz, the building and isolator mobilities dictate the foundation-isolator-building behavior that governs the transmission mechanism.

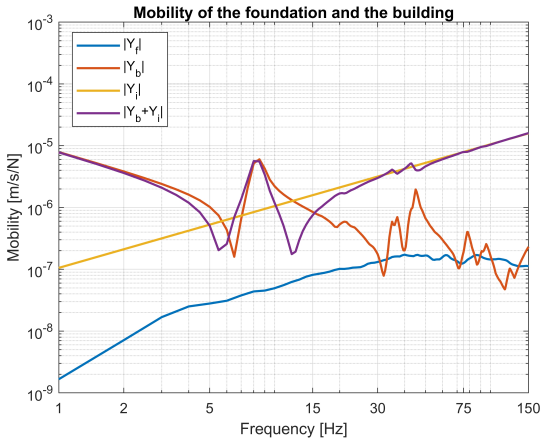


Figure 7. The average measured vertical mobility of the foundation (blue line) compared with the calculated mobility of the building superstructure (red line) and the measured isolator mobility (orange line).

2.3 The building and foundation responses due to train pass-bys

Train pass-bys were measured at different stages of construction, following the measurement procedure described in ISO 14837-31 [11]:

1. After the foundation construction and before the building superstructure installation, on the foundation, to measure the foundation's free vibration.

2. After the building construction, to measure the isolated building response at both the substructure and superstructure levels.

In the first phase, train pass-bys were measured on top of the foundation. The vibration level on the free foundation is used, to evaluate the coupling loss considered in the early-stage vibration study, and to apply any final adjustments to the isolation design before installation, if required.

In the second phase, the building and foundation vibration levels were measured after the building was completed and furnished, once the bearings had received their intended design load, for which their performance was optimized.

During each phase, train pass-bys were recorded simultaneously at a reference point near the railway, to normalize the building's performance, making it independent of any changes in the source strength.

Figure 8 displays the spectra of the train pass-by vibrations measured on the foundation before the installation of superstructure and those measured at the end of construction on the ground floor (above the vibration cut) and on top of the foundation (below the vibration cut).

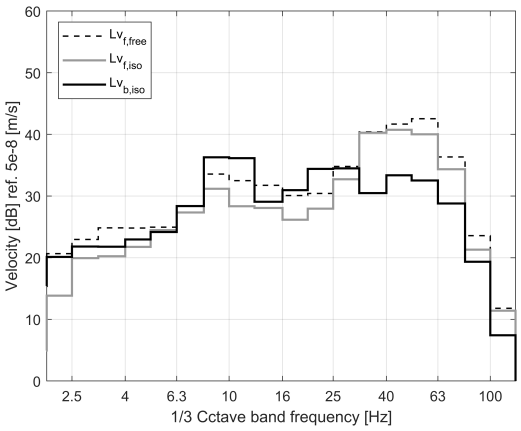


Figure 8. The average train pass-by vibrations measured on top of the free foundation (dashed line), and those measured after completion of the building at the foundation (grey line) and on the ground floor (black line).

A comparison is presented in Fig. 9 between the estimated power flow transmitted to the non-isolated building (i.e., on rigid supports) and that of the building supported by the designed isolation bearings. The power flow is calculated using Eqn. 4, while the interaction force is obtained from Eqn. 2 using the measured foundation free vibration $v_{f,free}$. Since the non-isolated building is not physically available, Equation 2 has also been used to estimate the building vibration for the non-isolated case.

In Fig. 10, the direct PFIG, defined in Eqn. 7, is compared with the performance indicator established by BIOVIB (Eqn. 8). Despite a reasonable correspondence

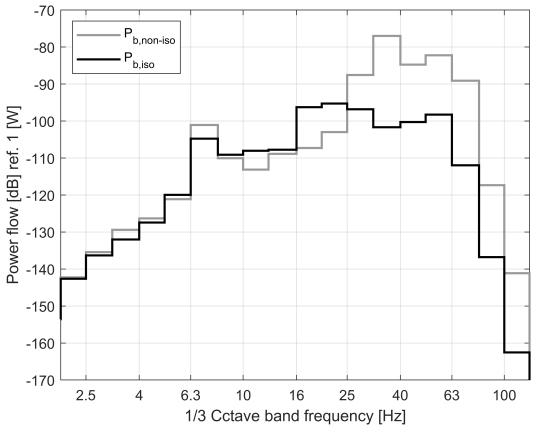


Figure 9. The power flow transmitted through the non-isolated building (gray line) and isolated building (black line).

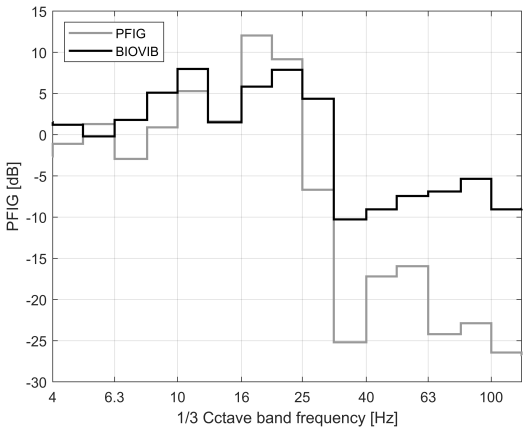


Figure 10. The power flow transmitted through the non-isolated building (gray line) and isolated building (black line).

at frequencies below 25 Hz, reflecting the isolation system's resonance around 10 Hz and the dominant bending modes of the building floors at 20–25 Hz, at higher frequencies, the direct PFIG indicates a higher level of isolation than the BIOVIB indicator. This discrepancy appears to be due to an overestimated vibration level for the non-isolated building, calculated (rather than measured) using Eqn. 5, which may be due to an inaccurate estimation of the building mobility at higher frequencies.

3. CONCLUSIONS

This paper has illustrated the use of power flow analysis for quantifying the vibration transmission into a building, as an effective basis for isolation design. The analysis is based on a hybrid approach that estimates the mobility of the substructure (foundation and ground) and isolation system via measurement, and that of the superstructure via calculation (Finite Element Analysis). The work is part of ongoing research aimed at developing practical guidance for designing building base isolation solutions.

4. REFERENCES

[1] J. Talbot and H. Hunt, "On the performance of base-isolated buildings," *Building Acoustics*, vol. 7, no. 3, p. 163–178, 2000.

[2] T. Edirisinghe and J. Talbot, "The significance of soil–structure interaction in the response of buildings to ground-borne vibration from underground railways," *Journal of Sound and Vibration*, vol. 597, p. 118812, 2025.

[3] K. Kuo, M. Papadopoulos, G. Lombaert, and G. Degrande, "The coupling loss of a building subject to railway induced vibrations: Numerical modelling and experimental measurements," *Journal of Sound and Vibration*, vol. 442, pp. 459–481, 2019.

[4] T. Edirisinghe and J. Talbot, "Some observations on the transmission of ground-borne vibration into base-isolated buildings," in *Proceedings of ISMA2022: International Conference on Noise Vibration Engineering*, (Leuven, Belgium), 2022.

[5] BIOVIB, *Building Isolation against Outdoor Vibration*. EUROSTARS -VLAIO projects - CDM Stravitec and ACOUPHEN, 2017-2019.

[6] M. Villot, B. Trévisan, L. Grau, and P. Jean, "Indirect method for evaluating the in-situ performance of building base isolation," *Acta Acustica*, vol. 105, p. 630–637, 2019.

[7] H. Masoumi, B. Veelhaver, M. Papadopoulos, F. Augusztinovicz, and P. Carels, "Evaluation of bbi performance indicator in a full-scale test bench," in *Proceedings of the 13th International Workshop on Railway Noise, volume 150 of Notes on Numerical Fluid Mechanics and Multidisciplinary Design*, (Cham, Switzerland), pp. 267–274, 2021.

[8] H. Masoumi, B. Noori, J. Cardona, and P. Carels, "Assessment of building performance against train induced vibrations by a hybrid experimental-numerical methodology," in *Noise and Vibration Mitigation for Rail Transportation Systems*, (Singapore), pp. 731–739, Springer Nature, Singapore, November 2024.

[9] I. 4664-1:2022, "Rubber, vulcanized or thermoplastic – determination of dynamic properties – part 1: General guidance.,"

[10] I. 7626-5:2019, "Mechanical vibration and shock — experimental determination of mechanical mobility part 5: Measurements using impact excitation with an exciter which is not attached to the structure,"

[11] I. 14837-31:2017, "Mechanical vibration — ground-borne noise and vibration arising from rail systems, part 31: Guideline on field measurements for the evaluation of human exposure in buildings,"

DOI: 10.61782/fa.2025.0568

FORUM ACUSTICUM EURONOISE 2025

MITIGATING GROUND-BORNE VIBRATIONS WITH A BOX-IN-BOX SOLUTION: FEASIBILITY AND CHALLENGES IN A REAL CASE STUDY

Iñigo Arana Goenaga[1], Pere Vicenç Rodríguez Sorribes[2], Albert Isnardo Iglesias[2], Sérgio Fernando Frasson Quaresma[1], Hamid Masoumi[1]*

[1] CDM Stravitec, Overijse, Belgium

[2] ICR, Barcelona, Spain

ABSTRACT

When addressing ground-borne vibration issues, such as those caused by railways, the state-of-the-art for new building projects typically includes various Building Base Isolation (BBI) solutions. However, some projects face constraints that complicate the implementation of such systems. Specifically, when isolation measures are introduced late in the planning phase, a Box-in-Box (BiB) isolation system can be a practical alternative to achieve the required vibration reduction. This paper discusses the mitigation of ground-borne vibrations in a building near a metro line using a BiB system. It emphasizes the importance of detailed design and rigorous quality control during construction to ensure the system's success. The case study also demonstrates the feasibility of BiB systems as a practical alternative to BBI in constrained situations, while offering recommendations on decoupling details to achieve promised performance in vibration isolation projects. This study highlights challenges posed by the acoustic bridges, which led to performance deficiencies in some areas. In contrast, sections where decoupling measures were carefully followed achieved the expected performance, as verified through in-situ measurements.

Keywords: *Ground-borne noise and vibration, Building Base (vibration) isolation, Box-In-Box*

***Corresponding author**: h.masoumi@cdm-stravitec.com.*

***Copyright**: ©2025 Masoumi et al. This is an open-access article distributed under the terms of the Creative Commons Attribution 3.0 Unported License, which permits unrestricted use, distribution, and reproduction in any medium, provided the original author and source are credited.*

1. INTRODUCTION

Buildings located near railway infrastructure are often subjected to ground-borne vibration (GBV), which is generated by passing trains and transmitted through the soil to the building structure. Train-induced vibrations can cause discomfort for habitant due to both floor vibrations and re-radiated (structural) noise inside the rooms. This requires a decoupling and mitigation strategy either between the surrounding ground and the building foundation, or inside the building between the building's main structural element and the sensitive spaces. Such an approach demands a multi-disciplinary effort, involving a comprehensive understanding of the railway infrastructure and the train types and speeds (as the source of vibration), on the dynamic characteristics of the ground (as the vibration propagation path), the building structural dynamics (for vibration response), and acoustics of the sensitive spaces (as the receivers), [1].

Two primary strategies used for ground-borne vibrations mitigation in buildings are:

- Building Base Isolation (BBI): This method involves isolating the entire building by decoupling it from the ground at the foundation level or at least at one storey below the sensitive spaces. BBI effectively mitigates low-frequency ground-borne vibrations using elastomeric bearings or structural coil springs. Once BBI is implemented at a certain level, the entire structure above the vibration cut remains decoupled from the incoming ground-borne vibrations.
- Box-in-Box (BiB) Solutions: This technique in-

Table 1. Comparison between BBI and BiB solutions for building vibration isolation.

	BBI (Building Base Isolation)	**BiB (Box-in-Box)**
Primary Function	Reduces vibration transmission through the entire building (superstructure) above the vibration cut.	Creates an acoustically isolated space within the building by decoupling its floors, walls, and ceilings.
Efficiency Range	Highly effective in mitigating low-frequency ground-borne vibrations (e.g., from railway traffic).	Optimized for controlling high-frequency vibrations, including both airborne and structure-borne noise within the building.
Structural Adaptation & Design Challenges	The serviceability of the building, must be carefully checked under all load conditions; performance improves with increased stiffness of both the superstructure and substructure.	Effectiveness is enhanced by incorporating an independent "floating" space within the building, requires a detailed design for decoupling the floor, walls, and ceiling.
Installation challenges	Easy installation on a flat, clean surface in a protected area against water inundation, with possible fire protection requirements, for placing BBI bearings.	Precise execution is required to prevent conflicts between new elements and the existing non-isolated structure, ensuring the avoidance of acoustic bridges.
Suitability	Ideal for isolating the entire buildings with a high number of vibration-sensitive spaces, especially those in close proximity to railway infrastructure.	Best suited for buildings with a limited number of sensitive spaces, where both internal and environmental (external) noise and vibration sources need to be controlled between different areas.
Impact on Occupants	Significantly reduces both ground-borne noise and perceptible vibrations for occupants.	Effectively minimizes both vibration and noise transmission into and out of sensitive environments.

volves creating an independent, locally isolated space within the building by incorporating isolated floors, walls, and ceilings. A conventional BiB is effective particularly in controlling high-frequency noise and vibration in specific sensitive areas, such as recording studios, rehearsal rooms, cinemas, or laboratories. However, achieving higher performance against low-frequency ground-borne vibrations (GBV) may require a low-frequency isolation system combined with heavy floating floors, walls and suspended ceilings.

Table 1 presents a comparison of key characteristics and critical aspects of BBI (Building Base Isolation) and BiB (Box-in-Box) solutions for building vibration isolation:

Although Building Base Isolation (BBI) is often considered a more practical solution for mitigating train- induced vibrations, as it provides a one-time payment system to isolate the entire building at once, some projects face constraints that complicate its implementation. These challenges include the retrofitting and restoration of existing (older) buildings or cases where isolation systems are introduced late in the planning phase. In such situations, the Box-in-Box (BiB) system can serve as an effective alterna-

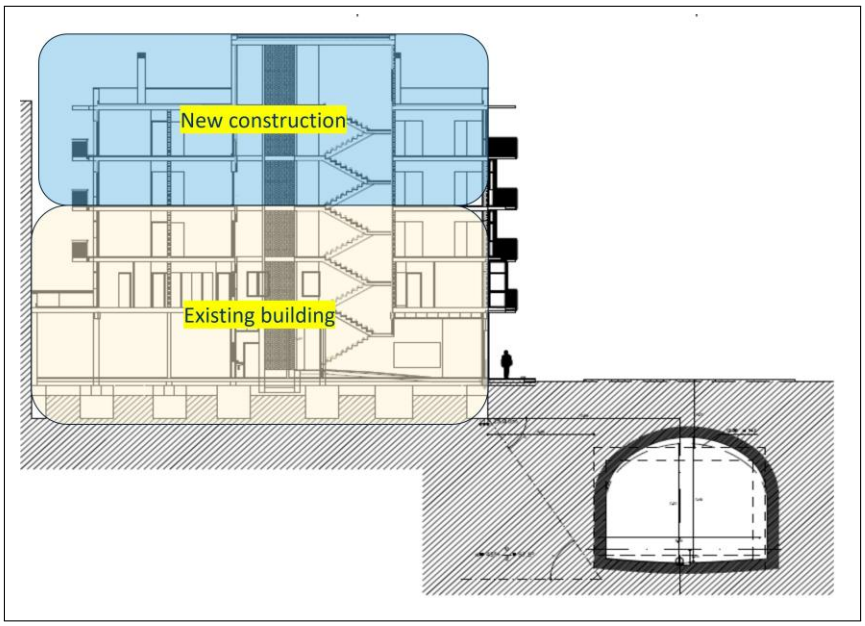


Figure 1. General overview of the building and the metro tunnel.

tive to achieve the required noise and vibration reduction.

While BiB is a viable solution, its effectiveness depends largely on high-quality installation and precise execution during construction. This case study highlights challenges which resulted in performance deficiencies in certain areas, emphasizing the critical role of execution accuracy. This paper explores the mitigation of ground-borne vibrations in a building located near a metro line through the application of a BiB system. It presents both pre- and post-construction vibration measurements, analyses the system's overall performance, and examines the key installation challenges encountered during the process.

For the evaluation of vibrations inside a building in Spain, the vibration measurement is processed according to Decree 176/2009, Annex 7 "Immission of vibrations into the interiors of buildings." The limit levels of immission established in this Annex are shown in Tab. 2, based on the building's use. The vibration levels are presented in terms of weighted acceleration level according to ISO 2631, [2].

2. CASE STUDY: ISOLATION OF NEW STORIES ON AN EXISTING BUILDING

The case study involves a residential building with a ground floor and two upper floors. The project aims to add two additional floors on top of the existing structure, resulting in a building with a ground floor and four upper floors.

Table 2. Vibration Limit Values.

Building Use	L_{aw} [dB]
Dwelling and Residential	75
Healthcare	72
Educational or Cultural	72

The building is located adjacent to a metro tunnel, which is very close to the surface (at a depth of 4 meters) and situated 6 meters away from the building's edge.

Following the vibration study and on-site measurements, the maximum recorded vibration levels on the second floor ranged between 70 and 73 dB. Although these levels are below the legal limit of 75 dB for residential buildings, as stipulated by law, the vibrations are perceptible and could cause discomfort to future occupants.

Given that structural modifications and the addition of floors could amplify vibrations due to floor resonance, potentially exceeding the limit on the upper floors. To prevent these potential risks, based on the results of the vibration study, the acoustic consultant has proposed implementing a vibration isolation system from the third floor



Figure 2. Box-in-Box solution .

upwards. The system involves using Stravitec SEB elastomeric bearings at 12 Hz on top of the third floor to isolate the new structure from the existing one.

However, in practice, the proposed BBI isolation system was introduced late in the construction planning, and instead, a Box-in-Box (BiB) isolation system was proposed to achieve the required vibration reduction.

Figure 2 illustrates a general overview of the proposed Box-in-Box system, where the base slabs are decoupled using a concrete floating floor, 80 mm thick, on elastomeric bearings at 12 Hz (Fig. 3). Additionally, the structural walls are decoupled using elastomeric strips and double gypsum with an intermediate mineral wool layer.

3. VALIDATION OF VIBRATION LEVEL

Vibration level validation was conducted in the building at the completion of construction, following the addition of two floors, to assess compliance with current regulations on vibrations from the nearby metro line L1. The objective of the study was to determine whether the renovated building, now consisting of a ground floor and four upper floors (following the addition of two floors on top of the existing structure), meets the vibration standards set by Decreto 176/2009 due to the passage of passenger trains on the adjacent metro line L1.

Since the apartments are in their final construction

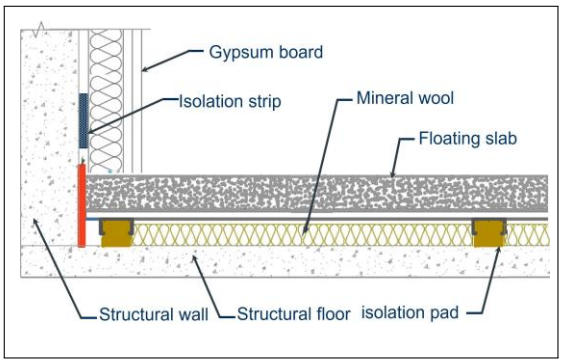


Figure 3. Section of the floating floor and the structural wall decoupling.

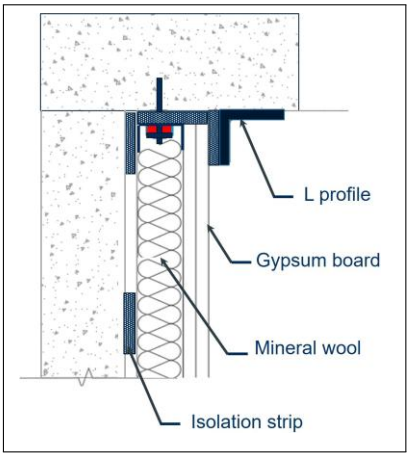


Figure 4. Section of the floating floor and the structural wall decoupling.

stage, with finished walls, floors, doors, and windows, vibration measurements have been carried out at four control points: three in the bedroom and two in the living room of the apartment closest to the metro line. These measurements were taken on each of the three floors with residential units (PL2, PL3, and PL4, as shown in Fig. 5).

A summary of the vibration measurement results is presented in Tab. 3. While the majority of measurement points across different floors of the building show compliance with current vibration regulations, one critical location— a bedroom on the third floor closest to the metro line—exhibits vibration levels exceeding the permissible limit. This non-compliance raised concerns regarding potential discomfort for occupants and regulatory adherence,

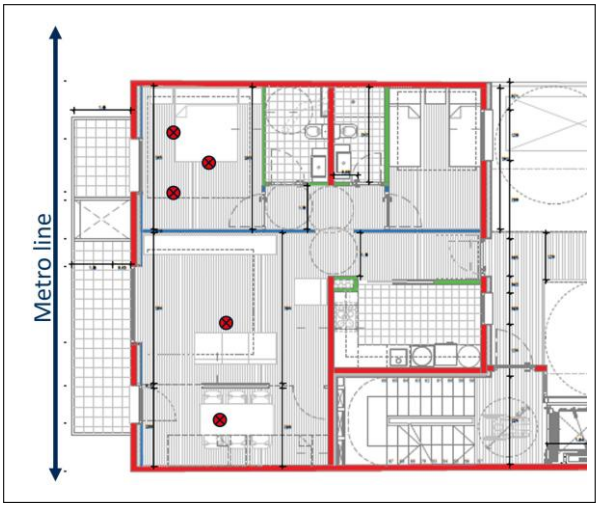


Figure 5. Measurement points in the apartment closest to the metro line.

Table 3. Vibration levels at different floor levels.

Measurement Point	Background L_{aw} [dB]	Maximum L_{aw} [dB]
PL2 Bedroom	44.6	71.1
PL3 Bedroom	49.2	76.3
PL4 Bedroom	51.7	71.1
PL2 Living Room	44.7	73.4

necessitating a more detailed investigation.

To further assess the issue, a follow-up measurement campaign was conducted within the affected bedroom, with vibration levels recorded at four distinct points, as illustrated in Fig. 6. The results of this secondary assessment, presented in Tab. 4, indicate that while three of the measured positions remained within acceptable limits, one location continued to exceed the regulatory threshold of 75 dB.

Following this assessment, a technical inspection of the building's structural elements was carried out to identify possible causes of the elevated vibration levels. The investigation revealed the presence of a mortar bridge beneath the balcony door frame, which was likely facilitating the transmission of vibrations from the structural floor (non-isolated part) to the bedroom floating floor (see Fig. 7). This rigid connection was suspected to be a significant contributing factor to the non-compliant vibration levels in the affected area.

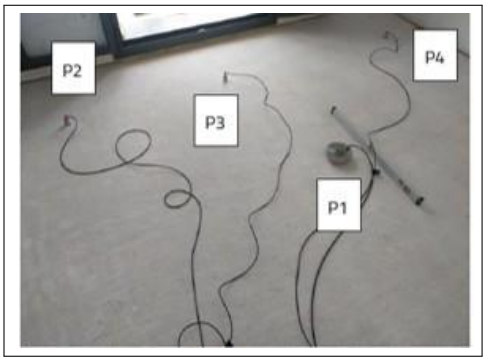


Figure 6. Measurement points in critical bedroom.



Figure 7. Acoustic bridges in critical room.

To address the identified issue, a series of corrective measures were implemented to eliminate the acoustic bridges beneath the balcony door frame. These measures involved removing the rigid connections and ensuring that no direct pathways remained for vibration transmission. Special attention was given to the interface between the door frame and the floating floor to prevent any residual mechanical coupling that could compromise the effectiveness of the isolation.

Figure 8 provides a detailed illustration of the corrective measures undertaken. Following the modifications, a repeat measurement campaign was conducted at the same four positions within the affected bedroom to verify the effectiveness of the intervention. The updated results, presented in Tab. 5, confirm that vibration levels at all measurement points now fall below the legal limit of 75 dB, ensuring compliance with current regulations.

These findings indicate that the applied mitigation measures successfully addressed the excessive vibration issue, restoring the acoustic performance of the space and minimizing potential discomfort for future occupants.



Figure 8. Removing the acoustic bridges before the final assessment.

Table 4. Vibration levels at different points in the critical bedroom.

Measurement Point	Background L_{aw} [dB]	Maximum L_{aw} [dB]
P1 Bedroom	46.2	76.4
P2 Bedroom	42.9	69.8
P3 Bedroom	43.9	72.1
P4 Bedroom	41.2	63.5

Table 5. Vibration levels at the critical bedroom after removing the acoustic bridges.

Measurement Point	Background L_{aw} [dB]	Maximum L_{aw} [dB]
P1 Bedroom	51.4	74.7
P2 Bedroom	46.5	69.1
P3 Bedroom	47.8	68.8
P4 Bedroom	45.0	63.2

4. GUIDANCE AND RECOMMENDATION

The successful implementation of a Box-in-Box (BiB) system for vibration mitigation requires careful planning, precise execution, and thorough quality control at every stage of construction. Based on the findings of this study, the following key recommendations should be considered for future projects involving BiB systems in vibration-sensitive environments:

- Isolation Efficiency at low frequency: While BiB systems are generally effective for high-frequency isolation, their performance at lower frequencies—such as those typically generated by railway traffic—can be highly sensitive to the flexibility of both the floating floor and the substructure, which exhibit multiple vibration modes within the 25-30 Hz range.

  In predicting isolation performance, it is essential to consider the mobility of both the base slab and the floating floor, as their dynamic interaction can lead to practical performance deviations from those predicted by a single-degree-of-freedom (SDOF) model. This effect can result in lower vibration reduction in spaces with larger spans compared to those with shorter spans, where structural flexibility of the structural floor plays a more significant role.

- Quality Control and Inspection During Construction: Proper execution is critical to achieving the expected vibration reduction. Special attention should be given to junctions between walls, floors, and ceilings to prevent rigid connections that could bypass the isolation system.

  Frequent inspections should be conducted at key milestones, such as after the installation of the floating floor and before closing walls, to identify and rectify potential acoustic bridges before they compromise system performance.

- Effective Communication Between Architects and Contractors: Successful BiB implementation requires clear coordination and communication between the architects, acousticians, and contractors throughout the project. The architect should provide detailed construction drawings and specifications highlighting vibration isolation requirements, verified by acoustical consultant of the project. The Contractor must be fully informed of BiB system sensitivities, especially regarding structural decoupling and the avoidance of rigid connections. Regular coordination meetings should be held to review and address potential challenges, and ensure compliance with the intended design.

5. REFERENCES

[1] J. P. Talbot, "Base Isolation of buildings for control of ground-borne vibration," *Handbook of Noise and Vibration Control*, John Wiley & Sons, Hoboken, p. 1470-1478, 2007.

[2] ISO 2631-2:2003 "Mechanical vibration and shock — Evaluation of human exposure to whole-body vibration. Part 2: Vibration in buildings (1 Hz to 80 Hz)".

DOI: 10.61782/fa.2025.0445

FORUM ACUSTICUM EURONOISE 2025

IMPACT NOISE HORIZONTALLY WITH 80 MM CONCRETE SLAB AND UPPER 80 MM POLYSTYRENE SPLITTED WITH CONTINUOUS POLYSTYRENE BENEATH

Bernt Mikal Larsen[1*]
[1] Multiconsult Norway, Fjellgata 6, 4612 Kristiansand, Norway

ABSTRACT

Measurement of impact noise horizontally for slab on ground has been done between different rooms in a residence building. The construction is with vinyl coating fastened with adhesive Casco Proff Extra on concrete. The thickness of the splitted concrete slab is 80 mm on 3 mm continuous thick tar coating. In administration part of the building the upper layer of 80 mm polystyrene is splitted, and the two lower layers of polystyrene beneath (total thickness 160 mm) are continuous. Corrected for the damping of the flooring (2 dB for vinyl coating with adhesive) and to receiving room volume of 100 m^3, the measurement shows 62 dB horizontally for impact noise without any flooring on the concrete. Between living room and common room the situation is with splitted concrete slab, continuous 3 mm thick tar coating and all three layers of polystyrene splitted and $L'_{n,w}$ sideways of 53-55 dB. The comparison shows that continuous tar coating does not transmit significantly impact noise horizontally or limits impact noise through the polystyrene, but that the transmission to neighbor room is through continuous layers of polystyrene.

Keywords: *impact noise, concrete slab, splitted polystyrene, continuous tar coating*

[*] ***Corresponding author***: *bernt.mikal.larsen@multiconsult.no.*
Copyright: *©2025 First author et al. This is an open-access article distributed under the terms of the Creative Commons Attribution 3.0 Unported License, which permits unrestricted use, distribution, and reproduction in any medium, provided the original author and source are credited.*

1. INTRODUCTION

Few studies have been made in field on impact noise horizontally with concrete slab on ground and layers of polystyrene beneath [1]. This paper shows impact noise levels with splitted concrete slab and upper layer of polystyrene splitted as well as the case with splitted concrete slabs and all layers of polystyrene splitted. For all situations there is a continuous 3 mm tar coating between the concrete slab and the upper layer of polystyrene.

2. METHOD AND MEASUREMENTS

The impact noise levels were measured with tapping machine Norsonic 211 in finished building. The measurement with concrete slab and upper layer of polystyrene splitted was done in administration part of a healthcare building, while the measurement with both concrete and all layers of polystyrene splitted was done between living room and neighbor room. The results are given for bare concrete slab, corrected for damping effect of floor coating and to receiving room volume of 100 m^3. Above the concrete slab, there was vinyl coating fastened with adhesive. The damping effect of vinyl coating with adhesive is assumed to be 2 dB, as for tiles fastened to concrete with adhesive. The frequency spectrum is also given in figures for both measurements. The results are compared with paper from year 2021 [2].

3. CONCRETE SLAB AND UPPER LAYER OF POLYSTYRENE SPLITTED

The construction was as follows in the administration, where the concrete and upper layer of polystyrene were both splitted:

- Vinyl coating fastened with CascoProff Extra adhesive

- 80 mm concrete (splitted)
- 3 mm continuous tar coating
- 80 mm EPS (polystyrene splitted)
- 2 x 80 mm continuous EPS (polystyrene)

The measured $L'_{n,w}$ for this configuration was 56 dB. Corrected for floor coating and to receiving room volume of 100 m^3, the $L'_{n,w}$ is 62 dB. When only concrete slab is split with plastic film below the concrete, results from 2021 [2], showed $L'_{n,w}$ of 66 dB, which shows a reduction of 4 dB by splitting the upper layer of polystyrene and still with continuous film/coating between concrete and polystyrene. The measured result shows very good correspondance with given values in paper from 2021 [2] with similar configuration, where values of $L'_{n,w}$ for similar configuration was 58-61 dB. Difference in results could be explained by the 3 mm tar coating below the concrete for results presented here, and thin plastic film between layers of polystyrene in the measurements presented year 2021. The measurements from 2021 [2] show lower values in the highest frequencies due to a coating with much better damping effect above the concrete slab.

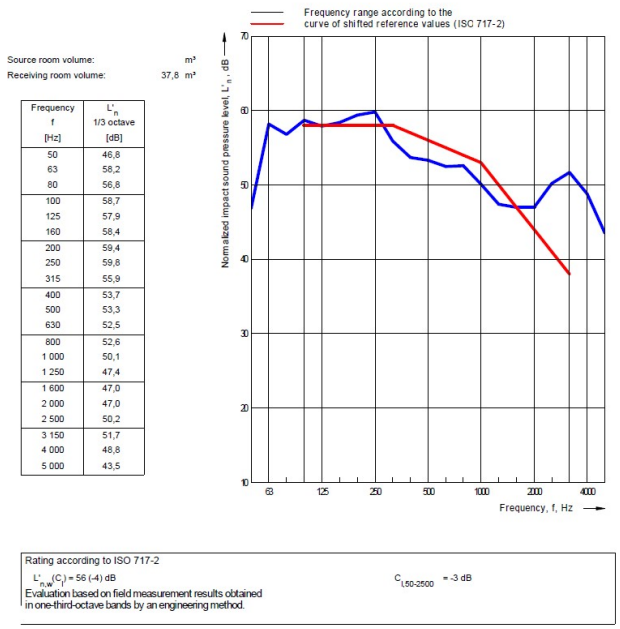


Figure 1. Impact noise level for slab on ground, with concrete and upper layer of polystyrene splitted

The reason for limited reduction in the higher frequencies is due to continuous layers of polystyrene and due to limited damping effect of vinyl coating fastened with adhesive to the concrete slab. The 3 mm continuous tar coating transfers impact noise in the frequency range from 315 to 630 Hz, in a similar way like connection points across concrete for a situation not properly splitted.

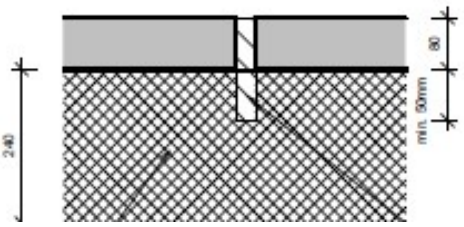


Figure 2. Splitting of concrete and polystyrene in administration part of healthcare building

The figure shows the splitted 80 mm concrete with 3 mm continuous tar coating below and splitted upper layer of polystyrene.

4. CONCRETE SLAB AND ALL LAYERS OF POLYSTYRENE SPLITTED

Between living room and neighbor room both the concrete slab and all three layers of polystyrene were splitted. The construction was as follows:

- Vinyl coating fastened with CascoProff Extra adhesive
- 80 mm splitted concrete slab
- 3 mm continuous tar coating
- 3 x 80 mm EPS (polystyrene) splitted

The measured $L'_{n,w}$ for this configuration was 48 dB. Corrected for floor coating and to receiving room volume of 100 m^3, the $L_{n,w}$ is 55 dB. The results shows very good correspondance with given values in paper from 2021 with similar configuration. There is a significant reduction of impact levels in the high frequency range due to the splitting of all layers of polystyrene. The detailed result is shown below in figure 3.

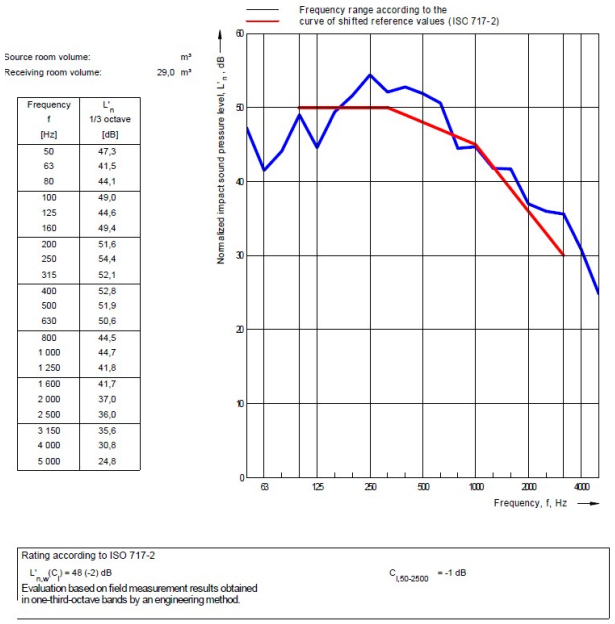


Figure 3. Impact noise level for slab on ground, with concrete and all layers of polystyrene splitted.

The result shows significant reduction in the whole frequency range, compared with the situation where only concrete slab and upper layer of polystyrene are splitted. At frequency 500 Hz the level is almost similar. From comparison of the two measurements, the continuous tar coating is seen to transmit significant impact noise in the frequency range from 315 to 630 Hz. Outside that range, the impact noise levels are at least 10-15 dB lower when the construction is splitted down to the ground. The splitting for results in figure 3 is shown below in figure 4. Comparison with similar splitting and plastic film between layers of polystyrene in [2] proves that the high levels in frequency range 315-630 Hz are transmitted through the continuous 3 mm tar coating below the concrete.

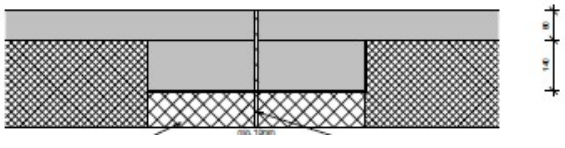


Figure 4. Splitting between living rooms.

There was also a measurement with splitting of concrete and all layers of polystyrene, but with continuous pipes of plastic for water and heating in the first and second layer of polystyrene. The result of this measurement is given in figure 5.

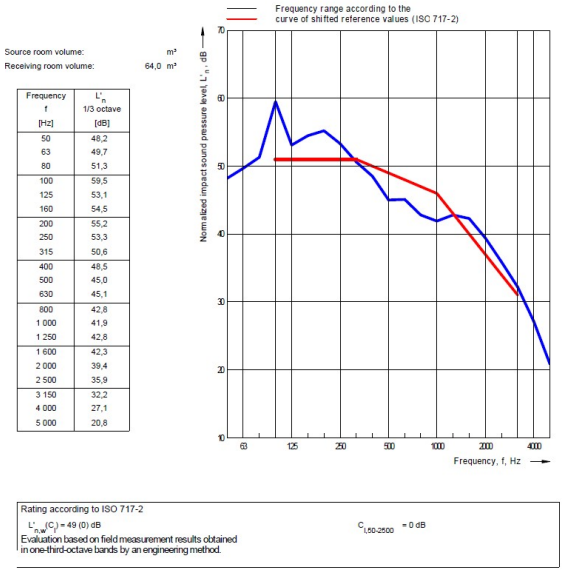


Figure 5. Impact noise level for slab on ground, with concrete and all layers of polystyrene splitted. Water pipes of plastic are continuous 5 cm down in upper layer of polystyrene, while heating pipes of plastic are continuous in the second layer of polystyrene.

The result in figure 5 corrected to 100 m3 is $L'_{n,w}$ of 53 dB, and shows that continuous pipes in the polystyrene will not increase horizontally impact noise.

5. CONCLUSION

The measurements done for concrete slab with 3 mm tar coating below the concrete and splitted upper layer of polystyrene shows very good correspondance with similar measurements in 2021 [2]. With splitting of concrete and upper layer of polystyrene, $L'_{n,w}$ is 62 dB compared with 58-61 dB from the measurements in 2021. The difference of 1-4 dB is supposed to be due to transmission through continuous tar coating and because earlier measurements had plastic film between splitted and continuous layers of polystyrene. When concrete and all layers of polystyrene are splitted (but with continuous tar coating and continuous

pipes of plastic in the polystyrene), $L'_{n,w}$ horizontally is 53-55 dB, which is similar with measurements summarized in [2] with continuous foundation below the layers of polystyrene. The correspondance with earlier measurements confirms that it seems to be correct with 2 dB damping effect of vinyl coating fastened to concrete slab with adhesive. The situation with continuous tar coating below the concrete and continuous foundation below all layers of polystyrene both give the same value of sideways $L'_{n,w}$.

5.1 Effect of continuous tar coating below the concrete

The measurements show that with polystyrene splitted to the ground, a continuous 3 mm tar coating (and continuous pipes for water and heating) seems not to limit achieved $L'_{n,w}$ of 53-55 dB compared with earlier results for similar configuration [2] when there is continuous foundation below splitted layers of polystyrene. It seems that the dominating impact noise horizontally is through the continuous layers of polystyrene. In Norway the need for continuous tar coating is critical in areas with radon gas. The measurements show that such a solution may be used to achieve good results for impact noise. The continuous tar coating below the concrete is not thought to limit single-value of horizontally impact noise, because reduction from 62 to 53-55 dB is achieved only by splitting more layers of polystyrene. Because the impact noise level is similar (1-4 dB difference) with only concrete slab and upper layer of polystyrene splitted with earlier experience [2], there is no reason to assume that continuous 3 mm tar coating transfers significant impact noise sideways. It seems that the tar coating transfers impact noise in the frequency range from 315 to 630 Hz, by comparing figure 1 and 3. This is confirmed by comparing the levels in figure 1 with earlier measurements where concrete and first layer of polystyrene are both splitted and a with a plastic film below the upper layer of polystyrene which shows lower levels in the range 315-630 Hz. From earlier measurements with all layers splitted to the ground [2] and $L'_{n,w}$ 46 dB, a continuous tar coating below the concrete seems to give 7-9 dB higher value sideways than with all layers splitted.

5.2 Meaning for future projects

The experience shows that it is possible to achieve limits in Norwegian rules with a continuous tar coating below concrete slab, which may be necessary due to radon gas from the ground. With splitting of layers of polystyrene and proper floor coating, this kind of solution may both give low impact noise levels, and good sound insulation between apartments. The achieved R'_w for the situation with concrete slab and all three layers of polystyrene splitted was 64 dB. The sideways $L'_{n,w}$ with concrete splitted, continuous 3 mm tar coating and upper layer of polystyrene splitted corresponds very well with earlier measurements and experience.

6. SUMMARIZING POEM

Impact noise to the side is transmitted
Even though flooring on top is splitted
Below the concrete a continuous tar coating
On upper splitted polystyrene is floating
The result for splitted polystyrene was like expected
Effect of continuous tar coating – to be neglected

Continuous polystyrene gives impact high
Measurements show we cannot deny
The reduction is big for the impact sound
When polystyrene is splitted to ground

7. ACKNOWLEDGMENTS

May I give my biggest acknowledgements to Kristiansand kommune, who allowed me to present results from measurements in their building with valuable information on impact levels from slab on ground.

8. REFERENCES

[1] John LoVerde and Wayland Dong, Measurement of Lateral impact noise isolation, *24th International Congress on Sound and Vibration (2017)*.

[2] Bernt Mikal Larsen, “Impact sound pressure values – Field measurements for different configurations of concrete slabs on ground”, *Internoise21, Washington DC*

DOI:

Main theme: A03 Building Acoustics

Session A03.05 Structure -borne sound and noise from building services

Chair(s): U. Schanda, C. Hoeller, M. Garai

DOI: 10.61782/fa.2025.0699

FORUM ACUSTICUM EURONOISE 2025

PREPARATORY WORK TOWARD EXPERIMENTAL ESTIMATION OF WATER EXCITATION TERMS IN WASTEWATER SYSTEMS

Yohko Aoki[1*] **Sven Öhler**[1] **Bernd Kaltbeitzel**[1]
[1] Fraunhofer Institute for Building Physics IBP, Department Acoustics, Stuttgart, Germany

ABSTRACT[*]

Structure-borne sound generated by wastewater pipe systems often dominates noise emissions from sanitary installations in buildings. This paper presents a preparatory investigation aimed at estimation of the water excitation terms by the inverse method. The experimental setup followed EN 14366-1:2023 and the vibration response of the pipe was quantified in terms of the blocked force at the wall fixing points. Noise from wastewater systems is generated by turbulent annular flow and the impact of water at the inlets, tees, and bends. These excitation terms were estimated through a methodical, stepwise approach. First, a customized impact-free inlet was installed to the pipe to eliminate water inlet effects, and thus the annular flow served as the primary excitation source in a straight pipe configuration. Subsequently, the impact of the flow turning elements was evaluated. The numerical model of the drainpipe was then introduced and experimentally verified. Using this model, the inverse method was tested to indirectly identify the applied force acting on the pipe. These presented results serve as the essential basis toward the development of a mathematical model of the stochastic water loads applied to the pipes.

Keywords: *drain pipe, structure-borne noise, EN 14366-1*

1. INTRODUCTION

Wastewater noise is often a problem in adjacent rooms in buildings. When water flows through the pipe, running water induces the pipe vibrations. Due to the connection of the pipe system to the installation wall with fixing elements, like pipe clamps, the vibrations are led into the building structure, and consequently, radiated as airborne sound.

Knowledge of flow induced force magnitudes and its predominant frequency is crucial for designing acoustically optimized drainpipes. The drainpipe system is generally not designed to be fully filled with water, to minimize the risk of backflow or overflow. Instead, the flowing water adheres to the inner walls of the pipe, creating a thin film of water with small air bubbles, while air continuously flows through the central region of the pipe. This type of axial two-phase flow pattern is classified as annular flow [2]. The turbulent annular flow causes the unsteady random wall pressure fluctuation. Furthermore, geometrical discontinuities at flow-turning pipe elements such as bends, inlets and tees also have a substantial impact [3]. Finally, the pressure fluctuation on the wall and impact at flow-turning elements causes vibrations on the pipe wall and the system itself.

Simulation of two-phase gas-liquid flow in pipes requires considerable computational efforts due to its great complexity, and thus a large degree is still not characterized by modern-day fluid dynamic models [4]. It is also difficult to experimentally identify the stochastic water excitation terms by transducers. Numerous attempts were made to numerically and experimentally determine the force excitation at the bend and discontinuing element of the pipe [5], however, yet comprehensive analytical model of the water excitation is not available.

On the other hand, the vibration response of the pipe can be conveniently measured [6]. Under these circumstances, indirect methods are preferred, where the input of a system, i.e. water excitation, is reconstructed from its output by inverting the model of a mechanical system. Considering that the water flow is primarily influenced by the internal geometry of the pipe and the friction factor of the inner wall, while the interaction to the pipe vibration is relatively weak, the water excitation term remains unchanged for pipes with comparable geometries and friction factors. Thus, the identified water excitation is applicable to other pipe systems with similar inner geometries and friction

[*]***Corresponding author***: yohko.aoki@ibp.fraunhofer.de
Copyright: *©2025 First author et al. This is an open-access article distributed under the terms of the Creative Commons Attribution 3.0 Unported License, which permits unrestricted use, distribution, and reproduction in any medium, provided the original author and source are credited.*

factors, such as the same pipe configuration but are constructed from new materials like biopolymers or recycled polymers.

A key objective of this study is to establish a methodology for identifying the excitation water force for adapting the excitation model to changes in pipe geometry. This paper presents preparatory work to develop a mathematical model of the stochastic water loads applied to the pipe, using both the experimental responses of the pipe system and a computational dynamical model. First, the experimental setup designed to separate each water excitation term is described, followed by a discussion of the measured results. The numerical model of the drainpipe system is then introduced and experimentally verified. Finally, the inverse method was applied to this numerical model with the measured response to identify the applied point force.

2. PHYSICAL ARRANGEMENT

Figure 1 shows the setup of wastewater systems at the Fraunhofer Institute for Building Physics IBP in Stuttgart. The pipe is made of PP-MD (polypropylene with mineral additives, density 1.7 kg/m^3) with the outer diameter of 110 mm, and the wall thickness of 3.2 mm. The steel pipe clamps with rubber inserts connect the pipe to the installation wall with M10 screws.

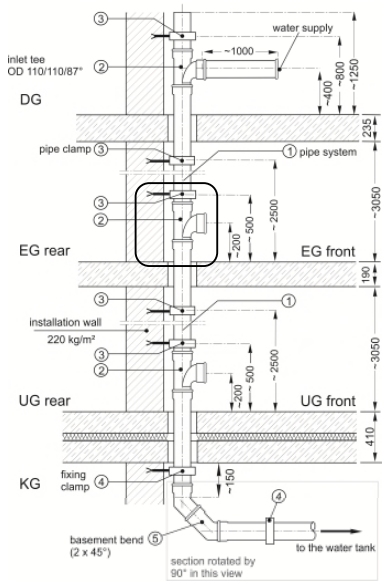


Figure 1: Test facility with the standard wastewater system set-up at Fraunhofer IBP, Stuttgart for measurements according to EN 14366-1:2003 [1].

The structure-borne and air-borne noise measurements are performed according to EN 14366-1:2003 [1]. The test facility is specially designed for measuring very low sound levels and can be used to test all types of domestic installations under practical conditions. The installation wall in the test facility has a surface density of 220 kg/m² and thus corresponds to the lightest single-shell solid wall permitted for mounting sanitary installations according to the German Standard DIN 4109 without special proof of suitability. These wall properties also comply with the specifications of EN 14366-1:2003 [1].

2.1 Blocked Force

Since wastewater systems are connected to the installation wall solely through six clamping points, the vibration response of the pipe was assessed in terms of the forces at these contact points. The contact force between the *i*-th pipe clamp and the installation wall was measured using a force transducer placed between the wall and the clamp (see Fig. 2). Two accelerometers were positioned on the wall near each fixing screw to measure the wall velocity. With this configuration, the power transmitted from the pipe system to the wall via the clamp can be quantified as the real part of the cross-power spectrum of the contact force and the velocity.

The RMS values of the blocked force level at *i*-th clamp position, expressed in dB reference to 10^{-6} N, was indirectly determined using the measured *i*-th installed power, $L_{Ws,i}$, and the pre-determined mobility of the test wall, Y_R [7].

$$L_{Fb,i} \sim L_{Ws,i} - 10 \log_{10} \mathrm{Re}\left\{\frac{Y_{R,i}}{Y_0}\right\} \quad (1)$$

where Y_0 = 1 m/sN, the reference value of mobility. The installed power L_{Ws} is expressed in decibels relative to the reference nominal power W_0 = 10^{-12} Nm/s. The blocked force on the installation wall can be used as an input to estimate the structure borne noise in the adjacent rooms [7].



Figure 2. A force transducer and two accelerometers on the installation wall.

2.2 Separation of Excitation Sources

As shown in Fig. 1, the standard pipe system extends four floors. The system consists of the straight pipes with the water inlet in the attic ('DG' in Fig. 1), two tees (closed with a lid) situated on the ground and the underground floors ('EG' and 'UG'), and the bend with 2 x 45-degree angle in the basement ('KG').

The excitation sources of this pipe are separated into the following four components: (1) turbulent water flow on the pipe wall, (2) impact force at the water inlet, (3) waterfall at the tee on EG and UG, and (4) waterfall on the basement bend. It is assumed that the air-borne noise generated by the system doesn't influence vibrations of the pipe. To effectively isolate each excitation source, the pipe setup needs to be modified from the standard arrangement.

2.2.1 Tees and basement bend

To eliminate the effects of the tees, each tee can be replaced with straight cylindrical pipes of the equivalent length. Similarly, the basement bend can be decoupled from the system and replaced by a bend with a larger diameter than that of the pipe system, to ensure no physical contact between the bend and the upper drainpipe. A thin waterproof membrane loosely covers the lower end of the drainpipe system to prevent splashing water falling onto the bend (see Fig. 3).

The flow impacting the disconnected basement bend generates noise, which may be comparable to or exceed the excitation caused by the turbulent water flow. To suppress airborne noise from the bend, the bend is covered by mass-loaded pipe insulation. The laboratory measurements indicated that the vibration caused by the airborne noise from the insulated bend is at least 10 dB lower than that caused by the turbulent annular flow.



Figure 3: The decoupled basement bend covered by mass-loaded pipe insulation with the loose waterproof membrane cover.

2.2.2 Impact-free inlet for laboratory testing

The impact-free inlet (see Fig. 4) was designed for the laboratory tests presented in this paper to eliminate the effects of water hammer caused by the water inlet. This inlet consists of a thin metal pipe with a closed-end short cylinder. The metal pipe is inserted into the cylinder and welded to its bottom cap. Near the welded edge, three rectangular openings are formed, each measuring 10 mm by 20 mm with rounded corners. The total opening area exceeds 600 mm², which is larger than the inner cross-sectional area of the metal pipe (560 mm²), ensuring smooth water flow from the metal pipe to the cylinder. Finally, the cylinder with the metal pipe is inserted into the drainpipe to a depth of 325 mm from the top and is carefully positioned at the center of the drainpipe. This impact free inlet was first fixed to the 20 mm wooded board, and the board was fixed to a separate wall section via 25 mm of elastomeric material, made of polyurethane foam. The inlet has no direct contact to the main drainpipe to prevent the structure borne excitation from the flow conditioner to the drainpipe.

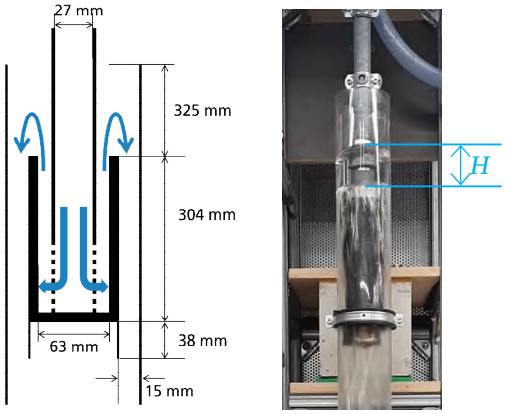


Figure 4: (a) The design of the impact-free inlet, (b) photo the impact-free inlet during operation.

Initially, water flows through the metal pipe and then flows into the cylinder through the side openings. In the cylinder, water runs upward, and then spills over from the upper opening of the cylinder. Finally, water moves into the gap between drainpipe and the cylinder. To prevent water from flowing to the back side of the bottom cap and dripping off, the outer wall of the cylinder is vertically extended by 38 mm using a thin metal sheet.

The flow conditioner begins functioning at a flow rate of 0.7 l/s and operates stably above 1.0 l/s. At flow rates below 0.7 l/s, water tends to flow along the cylinder wall rather than the drainpipe wall. Additionally, due to the constraints of the inner pipe's size, the maximum achievable flow rate

is limited to 3.0 l/s. Therefore, in this study, the water flow rates examined are 1.0 l/s, 1.5 l/s, 2.0 l/s, and 3.0 l/s, while the common flow rates of 0.5 l/s and 4.0 l/s [1] were not included in the measurements.

2.3 Water Velocity

When the volume flow rate exceeds approximately 1.0 l/s, the upward water in the cylinder flows beyond the top edge of the cylinder and fills the drainpipe above. The surface of the filled water is softly rippled due to the upward water flow underneath, but the height remains relatively constant over time. Table 1 summarizes the measured filled heights from the upper edge of the cylinder, shown as H in Fig. 4 (b). Starting from this upper surface, the flow continues to accelerate due to gravity until it reaches a terminal point, where the gravitational force is equal to the wall shear stress. The velocity at this point is referred to as the terminal velocity. According to [8], the terminal velocity of the annular flow, v_t, and the vertical distance required to achieve terminal conditions, d_t, are respectively expressed by the following formulas:

$$v_t = \left(\frac{1}{n^2}\frac{1}{\pi^{\frac{4}{3}}}\right)^{0.3}\left(\frac{Q_w}{D}\right)^{0.4} \quad (2)$$

$$d_t = \frac{1.42}{g}v_t^2 \quad (3)$$

where Q_w is the volume flow rate, D is the inner diameter of the drainpipe, and g = 9.81 m/s^2. The coefficient n is related to the surface roughness suggested by Manning and was set to 0.007 in this study [8]. The predicted values for each flow rate are summarized in Table 1.

Table 1. The terminal velocity v_t, the terminal distance d_t, and the filled height H with reference to the flow rate.

Flow rate	v_t [m/s]	d_t [m]	H [m]
1.0 l/s	3.89	2.2	0.02
1.5 l/s	4.31	2.7	0.04
2.0 l/s	4.63	3.1	0.075
3.0 l/s	5.12	3.8	0.13

The terminal point, at which the flow reaches terminal velocity, should be measured from the upper surface of the filled water, where the vertical velocity of the water is zero. As the filled water prevents air from being drawn in or released from the pipe, the water in the narrow gap between the cylinder and the drainpipe flows without air, at least partly. In this region, the acceleration of the flow is zero, i.e., constant velocity due to mass conservation law. Therefore, total the length of the cylinder with the extended cover, 342 mm, should be added to the distance calculated by Eqn. (3). The terminal point is explicitly shown in the Fig. 5 for each flow rate. These heights are valid for the pipe system using the impact free inlet, but not for the standard pipe setting.

It must be noted that terminal conditions are strongly influenced by the surface roughness of the pipe, n, which depends not only on the material, but also on manufacturing process and the environmental factors. The applied value n = 0.007 is appropriate for the very smooth surface. When the actual surface roughness is higher than the applied value in this paper, the terminal velocity decreases and thus the flow reaches the terminal condition at higher position than drawn in the Fig. 5. Therefore, the presented values in Table 1 should be regarded as the upper limit rather than definitive values. Nevertheless, this estimation indicates that the flow velocity is rather constant in the underground section, while the flow continues to accelerate on the ground floor.

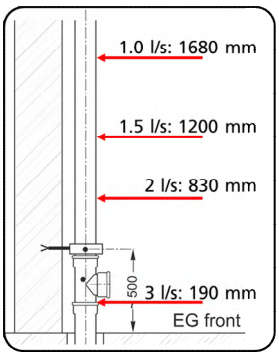


Figure 5: The magnified view of Fig. 1 around the ground floor with the position reaching terminal velocity for each flow rate.

3. EXPERIMENTS

Three different pipe arrangements were tested with four different flow rates. The 1st configuration is the standard model (shown in Fig. 1) with all flow turning elements, while the straight drainpipe, the 2nd configuration, is composed of the straight cylindrical components only. The water runs into the pipe from the impact free inlet, and the bend is disconnected. Under this configuration, the straight pipe is excited only by the annular turbulent flow. The 3rd model is composed of the straight pipe with a tee on the ground floor.

3.1 Straight Pipe

Figure 6 shows the blocked force of the straight pipe at four clamp positions on EG and UG with the flow rate of 2.0 l/s, which empirically exhibited the highest repeatability.

For all cases, the blocked force keeps decreasing with minor oscillations as frequency rises. In the absence of additional pipe components, the blocked force values at all four clamp positions were comparable. Particularly, the forces measured at clamps on the underground floor (green and black curves) overlaps quite well across the entire frequency range. The red curve shows slightly lower values than these two overlapping curves, while the blue curve was again slightly below the red curve. It comes from the fact that the flow reached the terminal velocity near the ground level of the ground floor. According to Fig. 1, the 2.0 l/s flow reaches the terminal velocity at around 300 mm above the lower clamp position on the ground floor. Therefore, the speed of the annular flow in the pipe was constant over the vertical direction in the underground floor, while the flow still accelerates in the upper section of the ground floor.
The sharp drop of the red curve around 2 kHz may come from the weak contact of the accelerometer on the wall with the surface coating. It is expected that the red line remains between the blue and black lines.

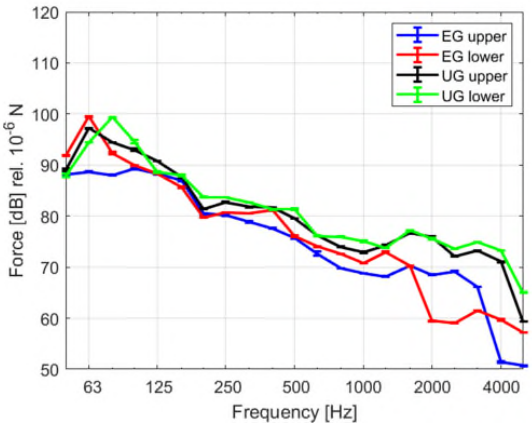


Figure 6: The blocked force of the straight pipe (#2) on four clamp positions on EG and UG with the flow rates of 2.0 l/s.

3.2 Maximum Achievable Reduction

Four plots in Fig. 7 visualizes the difference between the blocked force of the standard pipe (#1) and that of the straight pipe (#2) at four clamp positions. The difference of the blocked forces reaches even above 15 dB at every position, because the standard pipe has additional excitation sources to the straight pipe, such as an inlet, tees and a bend. The difference highlights the potential for maximum achievable reduction by optimizing the geometry of these flow-turning elements, to the point where the excitation forces are theoretically reduced to zero. Although this is not feasible, Fig. 7 represents the upper limit of possible reduction.
The difference varies with the flow rate and frequency, but in general is more prominent at the low flow rate and low frequency. Above 2 kHz, the difference is diminishing. It indicates that the annular flow dominates the vibration of the pipe, or at least the annular flow is comparable with other excitation sources.

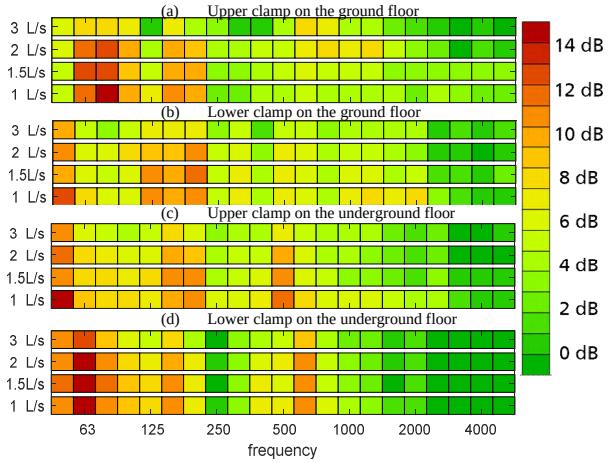


Figure 7: The difference between the blocked force of the standard pipe (#1) and that of the straight pipe (#2), measured on the upper (a, c) and lower (b, d) clamps on the EG (a, b) and UG (c, d) with different volume flow rates.

3.3 Effect of the Tee

Figure 8 shows the difference between the blocked force of the straight pipe with (#3) and without (#2) the tee on the ground floor. The effect is most prominent in plot (b): the blocked force at the clamp located only 300 mm above the tee. The peak appears around 1.5 kHz, and the effect is stronger with low flow rate. The effect also clearly visible in Plot (c): the adjacent clamp located approximately 1000 mm away from the tee in the downstream. The affected frequency range becomes broader, particularly towards lower frequency. It indicates that the effect of the tee is not only the local impact, but also the flow distortion toward downstream. When water flows through the pipes with the tee, the tee is partially filled with water, and thus the water movement around the circular perimeter of the tee is not uniform. Finally, the tee causes the flow disruption.
On the other hand, the tee effect is only fairly visible at the first clamp, which is located approximately 2 m above the tee. The effect is similar to that of the nearest clamp, but much lower amplitude, because the impact propagates

along the pipe with energy loss. On the furthest clamp in plot (d), the effect of the impact is merely visible. Only broadband effect is slightly visible at the lowest flow rate of 1 l/s. It indicates that the length necessary for the flow to stabilize again after the tee disruption varies with the flow rate. It probably comes the different film layer thickness. Theoretically, the layer thickness at the terminal velocity depends on the flow rate [8] and reaches 1 mm (1 l/s) to 2 mm (3 l/s). With low flow rate, this thin film does not fully coat the entire inner surface of the pipe; instead, it only partially covers it. When the water layer is thicker, the effect of the disruption can be quickly recovered.

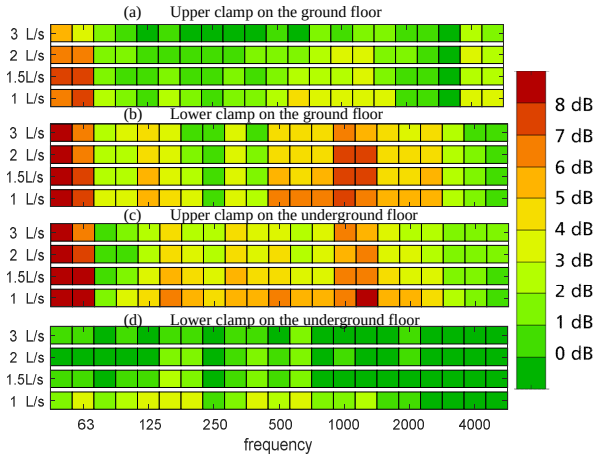


Figure 8: The difference between the blocked force of the straight pipe (#2) and that of the straight pipe with the tee on EG (#3) in dB, measured on the upper (a, c) and lower (b, d) clamps on the EG (a, b) and UG (c, d) with different volume flow rates.

4. NUMERICAL MODEL

In addition to the experiments, a detailed numerical model of a drainpipe was built by the commercial Finite Element (FE) software COMSOL (version 6.3) to simulate vibration due to structural excitation. However, direct measurement or CFD simulation of the random dynamic loads generated by the turbulent flow within the pipe is very challenging [4]. Therefore, it is necessary to indirectly identify the random dynamic loads from the measured blocked force with the aid of the numerical model.

The identification of stochastic loads applied to dynamical systems using uncertain computational models with experimental data is a classic but still active topic [9]. This problem is challenging, because the inverse method often amplifies both numerical model uncertainties and experimental data uncertainties, resulting in inaccurate solutions. Therefore, numerous papers have been published focused on robust identification methods to suppress the impact of uncertainties. Nevertheless, the final reconstructed load heavily relies on the quality of the numerical model. A FE approach is a promising solution to construct a reliable detailed model of the dynamic system. However, it is computationally extremely complex to model all the details of the drainpipe. Furthermore, even a finely constructed numerical model cannot reproduce exactly the real behavior of a structure due to limitations of the model itself.

Therefore, the following simplifications were applied to the model to keep a balance between simulation accuracy and computational efficiency: (1) The pipe structure is modelled by shell elements, while the screw is modelled by solid elements. (2) The pipe is fixed to the impervious rigid wall. Although the mobility of the installation wall affects the measured results particularly at low frequency, they are essentially not related to the acoustic performance of the drainpipe. (3) Air-borne noise, both the noise in the pipe and the radiated sound from the pipe the room, is ignored. (4) the pipe clamp with the rubber inlay is modelled by the single layer shell with the equivalent damping of two layers.

4.1 Experimental Verification

The developed FE model should be verified with reference to the experimental data obtained from the actual structure to assess its predictive capability. Instead of stochastic water excitation, the deterministic point force generated by a small inertia shaker was applied to the pipe. The shaker was attached to the pipe on 300 mm above the ground on the 1st floor (‘DG’ in Fig. 1) via the 2 mm thick steel clamp and was oriented normal to the wall (see Fig. 9). The shaker was driven by the band limited pink noise, and the exerted force was measured by the force transducer attached between the shaker and the pipe clamp.

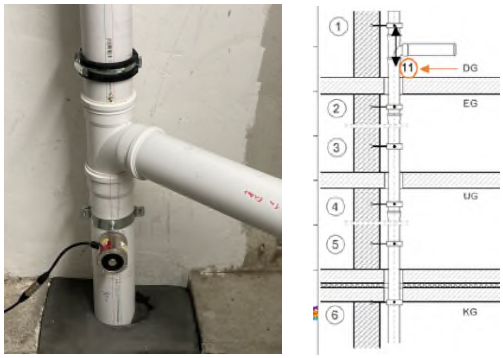


Figure 9: The configuration of the pipe with the attached shaker.

The measured exerted force by the shaker was used as input force in the FE model. The material parameters of the pipe are summarized in Table 2, while the geometrical parameters are visualized in Fig. 1. The Young's modulus of elesticity and the loss factor of the pipe were experimentally identified by the modal analysis using a 2 m long pipe piece. The vibrations of the pipe were simulated in 1/24th octave band frequency resolution between 44 Hz and 1.4 kHz, which are respectively the lower and the upper frequency limits of the octave band, centered at 62.5 Hz and 1 kHz.

Figure 10 compares the measured (black) and simulated (red) blocked forces at the lower clamp on the ground floor. Although some discrepancies are observed, particularly at low frequencies below 100 Hz, the overall agreement is substantial in terms of both amplitude and peak frequencies. The narrowband spectra show that most peaks and dips are accurately represented by the simulation, although minor shifts in peak frequencies are noticeable.

Table 2. Material parameters of the drainpipe systems used in the FE model

Parameter	Pipe	Clamp
E-modulus	3.92 GPa	200 GPa
Poisson ratio	0.3	0.3
Density	1700 kg/m^3	7850 kg/m^3
Loss factor	0.055	0.1

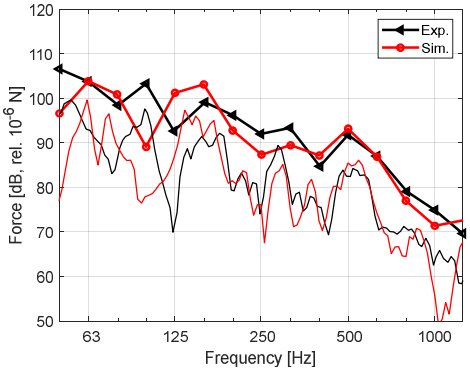


Figure 10: Comparison of the measured (black) and the simulated (red) blocked force at the lower clamp on EG.

4.2 Inverse Determination of the Point Force

As the simplest case study for the verification of the inverse method, the pipe system in the previous section is considered. The applied point force is identified through an inverse analysis using the FE model and the measured blocked forces. The accuracy of the identified primary force can be readily assessed by comparing it to the measured primary force.

The blocked force at i-th clamp position, f_{bl}^i, can be expressed as follows:

$$f_{bl}^i(\omega) = H^i(\omega) f_p(\omega) \tag{4}$$

where H^i is the transfer function between the point force and the i-th blocked force, and f_p is the point excitation force. The transfer functions of the FE model can be easily obtained from the simulation results with trivial primary force, such as, f_p = 1 N. Solving Eqn. (4) under the given boundary condition, e.g. the measured blocked force, leads to the unknown point force, f_p. The Least Square Method (LSM) is used to compute the frequency-dependent point force, f_p, by minimizing the sum of the differences between the measured and simulated blocked forces.

$$\epsilon = \sum_{i=1}^{6} \left| f_{bl,\,m}^i(\omega) - H_s^i(\omega) f_p(\omega) \right|^2 \tag{5}$$

where the subscript m and s denotes "measured" and "simulated", respectively.

This is a straightforward approach without any advanced methods to enhance its robustness against uncertainties. As shown in Fig. 11, the predicted point force (blue curve) doesn't align well with the measured applied force, though the simulated values fluctuate around the measured values. Both numerical model uncertainties in H^i and experimental data uncertainties of $f_{bl,m}$, result in inaccurate prediction of the primary force.

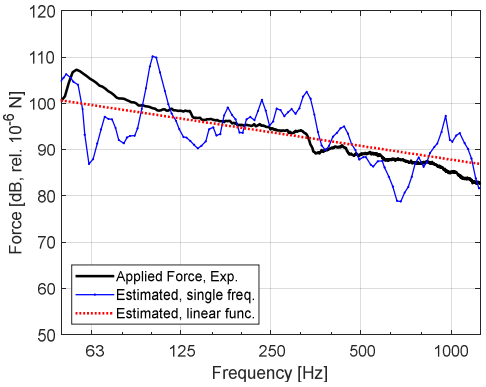


Figure 11: Comparison of the measured excitation force by the shaker (black), and the estimated point force by the direct inverse method without (blue with dots) and with the predefined excitation function (red dotted).

To improve the prediction accuracy, additional constraints must be imposed on the model. Assuming that the primary force is a linear function in double logarithmic scale,

$$f_p(\omega) = b \cdot \omega^a \tag{6}$$

the coefficient *a* and *b* can be estimated by the LMS method. The estimated point force was plotted by the red dotted line in Fig. 11. The agreement was significantly improved. The gradient of the predicted force in double logarithmic scale was -2.96 dB per octave, which is very similar to the pink noise characteristics. This case study proves that the inverse method can predict the input excitation terms using the FE model of the drainpipe and the measured blocked forces, but additional constraints are crucial for reliable results.

5. CONCLUSIONS

This paper presented preparatory work to develop a mathematical model of the stochastic water loads applied to the pipes.

Through experiments, the impact of each excitation source was separately investigated, and their contributions were quantified. The excitation terms generated by water flow within the drainpipe was separated by using the impact-free inlet as well as the decoupled or replaced flow turning elements. The analysis highlighted the significance of annular flow at high frequencies, while flow turning elements have significant influence at low frequency. Their effect is more prominent with low flow rates.

The three-dimensional finite element (FE) model of the drainpipe was developed and demonstrated a good agreement with measured blocked forces. Using this FE model, the inverse method was tested to identify the point force acting on the pipe. By incorporating additional constraints, the primary force was predicted with high accuracy. This approach emphasizes the importance of additional constraints to improve the accuracy of the results. Although the point force itself is considered deterministic rather than stochastic, this study verified the applicability of the inverse method with the measured blocked force and the developed FE model.

Future work will focus on the development of a mathematical model of the stochastic water loads applied to the pipe using both experimental responses of the pipe system and a computational dynamical model of it. The water excitation and structural response are regarded as a stochastic process and should be described in the form of a power spectrum density (PSD). To derive appropriate additional conditions for the inverse method, it is essential to measure the homogeneous flow velocity, because these parameters are known to influence the turbulence, the impact force, and its peak frequency [2]. Additional measurements are planned to assess the effect of other flow turning elements.

6. ACKNOWLEDGMENTS

We acknowledge financial support from The Federal Institute for Research on Building, Urban Affairs and Spatial Development (BBSR) Germany under grant number 10.08.18.7-24.60. We also extend our appreciation to Gebr. Ostendorf Kunststoffe GmbH, REHAU Industries SE & Co. KG and Wavin Technology & Innovation B.V., Wienerberger AG, for their support.

7. REFERENCES

[1] EN 14366-1: 2003: *Laboratory measurement of airborne and structure-borne sound from service equipment –Part 1: Application rules for waste water installations*, 2023.

[2] C. Monette, M.J. Pettigrew: “Fluidelastic instability of flexible tubes subjected to two-phase internal flow”, *Journal of Fluids and Structures*, Vol. 19, Issue 7, pp. 943-956, 2004.

[3] Y. Aoki, A. Filand, S. Öhler, and B. Kaltbeitzel: “Experimental Investigation of the Governing Vibration Excitation Mechanism in Wastewater Pipe Systems”, in *Proc. of DAGA 2023* (Hamburg, Germany), 2023.

[4] B. Song, C. Plana, et al.: “Phase-field simulation of core-annular pipe flow”, *Int. J. of Multiphase Flow*, Vol. 117, pp. 14-24, 2019.

[5] J. L. Riverin, E. de Langre, M. J. Pettigrew: “Fluctuating forces caused by internal two-phase flow on bends and tees”, *J. of Sound and Vibration* 298 (4-5), pp. 1088–1098, 2006

[6] B. Kaltbeitzel S. Öhler. “Latest results on the characterization of wastewater pipes according to the draft EN 14366, In: *Proc. of Euronoise 2021* (Madeira, Portugal), 2021.

[7] EN 12354-5: *Building acoustics - Estimation of acoustic performance of buildings from the performance of elements - Part 5: Sounds levels due to the service equipment*, 2023

[8] J. Swaffield, G. Wright, I. McDougall: *Transient Free Surface Flows in Building Drainage Systems*, 2015.

[9] J. Sanchez, H. Benaroya: “Review of force reconstruction techniques”, *J. of Sound and Vibration*, Vol. 333, Issue 14, 2999-3018, 2014.

DOI: 10.61782/fa.2025.0401

FORUM ACUSTICUM EURONOISE 2025

FH-IPTOOLS: PREDICTING WASTEWATER NOISE IN TIMBER CONSTRUCTIONS - A PROJECT INTRODUCTION

Tobias Kruse[1*] **Andreas Mayr**[1] **Ulrich Schanda**[1]
Fabian Schöpfer[1]
[1] Rosenheim Technical University of Applied Sciences, Germany

ABSTRACT

The research project FH-IPTOOLS is a joint project between Rosenheim Technincal University of Applied Sciences (THRo) and the University of Applied Sciences Döpfer (HSD) in collaboration with industrial partners and timber construction associations. The aim is to develop prediction tools for sound insulation, focusing on acoustic comfort and the perception of noise from technical service equipment. The project focuses on wastewater systems in timber and lightweight constructions.
Concepts need to be developed to ensure that acoustic comfort is taken into account in the design process. HSD is working on the psychoacoustic aspects. Signal detection theory will be used to formulate suitable evaluation methods to assess noise from building service equipment. Listening tests and field measurements will be used to develop criteria for sound insulation in timber construction to improve acoustic comfort.
As part of the project, structure-borne sound characterisation will be carried out at THRo on a reception plate test rig. Therefore a reception plate with similar properties to timber frame constructions will be used. The aim is to develop methods for the direct measurement of structure-borne sound power in timber and lightweight constructions, while also determining airborne sound power. Initial results will be presented in the paper.

Keywords: *Structure-borne sound, Source characterisation, building acoustics, psychoacoustics*

**Corresponding author*: tobias.kruse@th-rosenheim.de.
Copyright: *©2025 Tobias Kruse et al. This is an open-access article distributed under the terms of the Creative Commons Attribution 3.0 Unported License, which permits unrestricted use, distribution, and reproduction in any medium, provided the original author and source are credited.*

1. INTRODUCTION

Timber constructions are in the focus of the transition towards sustainable and energy-efficient buildings. Sound insulation is a key issue, as it is crucial for the acceptance and perceived quality of timber buildings. However, regulatory uncertainties and the lack of planning tools hinder the reliable prediction of acoustic comfort, particularly with regard to noise from building service installations, such as wastewater systems. These systems can exhibit an increased disturbance potential in timber and lightweight structures. The latest revision of DIN EN ISO 12354-5 [1] provides prediction methods for estimating the sound pressure levels in receiving rooms due to service equipment. In most cases however, the source input data required for such predictions are not available. In addition, predictions are not suitable to describe the subjective perception of disturbance experienced by occupants.

2. PROJECT INTRODUCTION

The research project FH-IPTOOLS (”Research in Timber Construction for Engineering-Based and Psychoacoustically Validated Planning and Advisory Tools for Sound Insulation”) is a joint initiative between THRO and HSD in close cooperation with renowned industry partners. The primary objective is to develop engineering-relevant and psychoacoustically validated methods that enable a reliable prediction and optimisation of acoustic comfort in timber and lightweight buildings. The project covers the whole acoustic transmission chain. This starts with the sound source (with a focus on wastewater systems), then energy transmission into the building structure, propagation within the building, and finally perception and assessment by the occupants. Building acoustics measurements

are carried out under real building conditions to compare with the applicable normative requirements, while simultaneous binaural recordings are performed for listening tests aiming psychoacoustic evaluation.

2.1 Project targets

HSD is focusing on the development of psychoacoustically based assessment methods. These methods reliably predict the subjective perception of acoustic comfort by building occupants. Technical and psychoacoustic parameters are combined to establish an evidence-based prediction model that provides realistic and reliable estimates of the expected acoustic quality. In collaboration with partners from industry, legally robust and practice-oriented tools for prediction and consultancy that can be used by construction companies, designers and users are developed. These tools aim to contribute to the acceptance and quality of sustainable timber buildings. THRo focuses on the characterisation of wastewater systems specifically for the application in timber constructions. This includes the use of methods introduced in EN 15657:2009-10 [2]. New measurement techniques for the indirect determination of the structure-borne sound power under installed building conditions will be developed. ISO 20270:2019 [3] already provides methods for the indirect measurement of the installed source power and these may also be applicable within building environments. However, the associated measurement effort is considerably great compared to conventional building acoustics measurements. For prediction purposes, a technically simplified method with acceptable uncertainties is derived from the existing procedure. Also, the project will identify and quantify the acoustic optimisation potential of wastewater systems in timber frame buildings.

3. TEST RIG

To determine the spatially averaged vibration velocity on the surfaces of conventional timber frame building elements is a challenging task. Structural inhomogeneities, caused by stiffening timber frames and multilayer claddings, lead to significant fluctuations in the spatial distributions of velocity levels [4–6]. Therefore, in an initial methodological development phase, an idealised receiving structure is employed. This structure is intended to exhibit vibro-acoustic characteristics comparable to those of typical timber frame constructions. The driving-point mobility of such an idealised reception plate



Figure 1: Test Rig showing the 15 mm perspex reception plate coated with a highly reflective surface layer (silver-grey) in combination with a 3D Laser Scanning Vibrometer.

should lie within a similar order of timber frame structures. For this purpose a 15 mm thick perspex plate was chosen. The objective is, that the installed power of building service equipment, due to similar structural properties, will be in comparable range one either the 15 mm thick perspex plate or any typical timber-frame structure. The perspex reception plate is mounted at the reception plate test rig at THRo and is coated with a highly reflective surface layer to enable measurement of vibration velocities using a 3D laser doppler vibrometer (see Figure 1). In accordance with the support requirements for reception plates with high mobility, as defined in [2], the perspex reception plate is currently mounted on a fully elastic support and has no direct contact with adjacent structural elements. Investigations of lightweight reception plates made from a perforated steel sheet [7] showed, that boundary conditions significantly influence the damping loss factor of a plate. The perspex plate is joined (cold welded) perpendicularly at two positions across its width, as the material is not available in the required dimensions of 3.7 m × 2.18 m and a thickness of 15 mm.

4. FIRST RESULTS

To enable the characterisation of structure-borne sound sources in accordance with EN ISO 15657:2019-10 [2], the properties of the receiving structure must be well de-

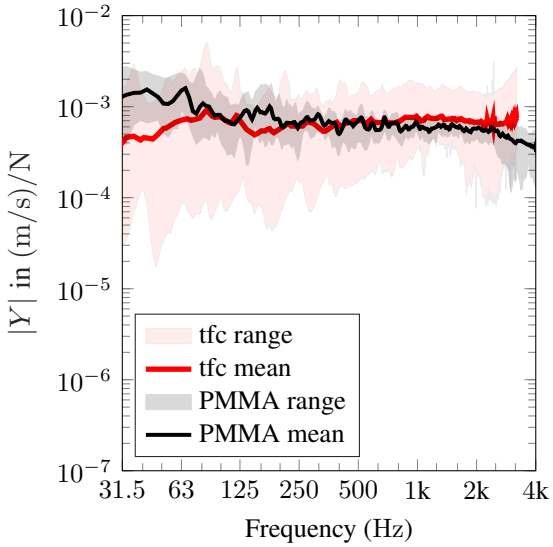


Figure 2: Magnitude of the point mobility from the perspex reception plate (PMMA) and timber frame construction (tfc). Shaded areas represent the envelopes of all measurement points (range).

fined. It is essential to ensure that the joints in the plate do not exert any significant influence on the spatial distribution of velocity levels. A series of measurement-based investigations have been carried out to characterise the perspex reception plate. This includes the determination of the longitudinal wave velocity, the velocity level distribution with point excitation and the loss factor of the plate.

4.1 Mobilities of reception structures

Figure 2 shows the arithmetic mean of driving-point mobilities of typical timber frame walls (tfc) in black and the perspex (PMMA) reception plate in red. The shaded areas represent the envelopes of the individual measurement points for the perspex plate and the range of mobilities across 20 measurements on different timber wall specimen which is in the order of $10^{-3}\,(\mathrm{m/s})/\mathrm{N}$ [8, 9]. The mobility behaviour of timber frame walls typically shows a decreasing mobility characteristic in the low frequency range, corresponding to that of an infinite beam, and a flat mobility characteristic in the higher frequency range, similar to that of an infinite plate. In the transition zone the mobility increases [6, 8]. This transition is also evident in the trend of the averaged mobilities considering the envelope in particular.

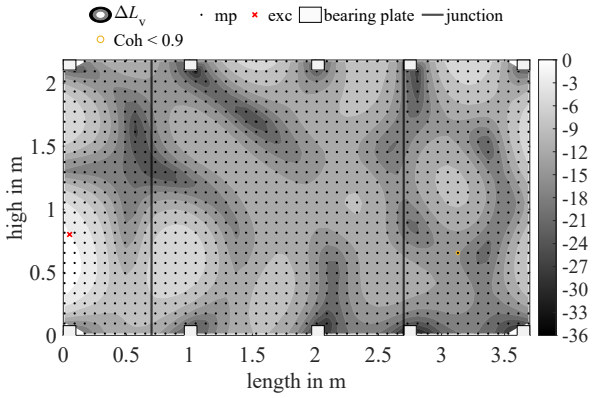
The averaged mobility values of the PMMA plate were determined at a distance of $0.87\,\mathrm{m}$ from the edge, with vertical increments of $10\,\mathrm{cm}$. This area corresponds to potential mounting positions of pipe clamps used in the wastewater systems under investigation. The PMMA mobility curves show a relatively flat frequency response, indicating high material damping and exhibit significantly less scatter compared to the timber structures. The decreasing trend in the PMMA mobility between $31.5\,\mathrm{Hz}$ and $100\,\mathrm{Hz}$ is investigated as it differs from the typical behaviour of timber-frame walls in this frequency range. Nevertheless, the magnitude of the mobilities of both receiving structures is of the same order, allowing for meaningful comparison.

4.2 Contour plots from measured velocity levels

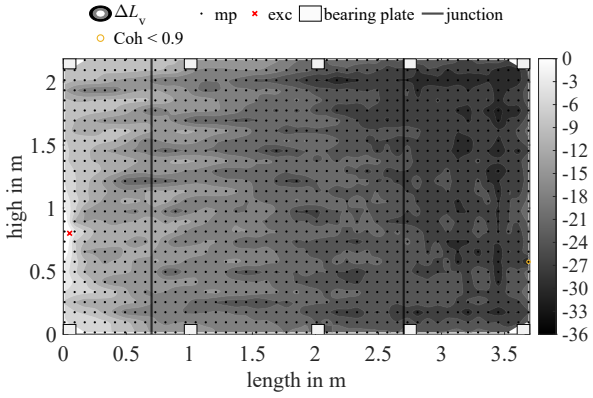
The velocity level distribution was measured by exciting the (PMMA) plate on the backside using point excitation with an electrodynamic shaker. The vibration velocities on the plate surface were measured on a grid with a resolution of $8\,\mathrm{cm} \times 8\,\mathrm{cm}$. The contour plots shown in Figure 3 correspond to the one-third octave bands at $31.5\,\mathrm{Hz}$, $1250\,\mathrm{Hz}$ and $3150\,\mathrm{Hz}$, respectively. These are normalised to the velocity level at the excitation point. The colour gradation is shown in steps of $3\,\mathrm{dB}$. Measurement points with a mean arithmetic coherence < 0.9 in the one-third octave band are marked with a yellow circle and measurement points with a signal-to-noise ratio (SNR) $\leq 10\,\mathrm{dB}$ are marked with a purple dot.
In Figure 3a, distinct vibration antinodes and nodal lines are visible, indicating modal shapes within the $31.5\,\mathrm{Hz}$ band, with differences reaching up to approximately $18\,\mathrm{dB}$. In contrast, Figure 3b and Figure 3c show no identifiable modal patterns. But here, a clear decay in velocity level with increasing distance from the excitation point is observed. The decay is up to $20\,\mathrm{dB}$ in the $1250\,\mathrm{Hz}$ one-third octave band and up to $36\,\mathrm{dB}$ in the $3150\,\mathrm{Hz}$ one-third octave band. At the cold welded junction (shown with a gray line in Figure 3), there is no significant drop in velocity level due to the continuous adhesive bonding. It is therefore assumed, that the receiving plate, consisting of three bonded elements, can be considered as a homogeneous structure up to approximately $3150\,\mathrm{Hz}$.

5. CONCLUSION

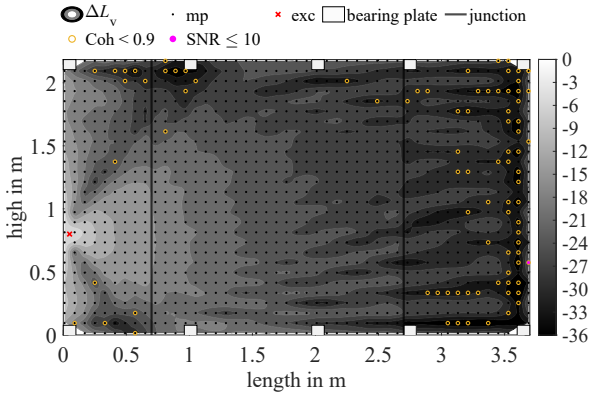
The project will be conducted over the next three years. It will generate further insights and identify optimisation potentials specifically in the area of wastewater noise in



(a) 31.5 Hz



(b) 1250 Hz



(c) 3150 Hz

Figure 3: Contour plot of velocity level across the perspex plate for selected one-third-octave bands. Levels are normalized to the velocity at the excitation point. Legend entries: $\Delta L_\mathrm{v} = L_\mathrm{v,mp} - L_\mathrm{v,exc}$, shading in 3 dB steps; mp: measuring point; exc: excitation point.

timber buildings. At the start of the project, fundamental investigations to characterise the idealised reception plate as a substitute for timber frame constructions are carried out. The results obtained so far are promising and indicate that the selected perspex receiving structure is suitable. It exhibits similar and more homogeneous properties compared to conventional timber stud wall constructions.

6. OUTLOOK

Further measurements and evaluations will be carried out to characterise the reception plate in more detail. The determination of the loss factor will be extended by additional methods, such as the power injection method, in order to investigate the influence of boundary conditions on the dynamic behaviour of the plate. In addition, suitable buildings for acoustic measurements and binaural recordings for listening tests will be selected and carried out in cooperation with industry partners. Surveys conducted in collaboration with timber construction associations will provide an overview of the currently prevailing installation conditions for wastewater systems in timber buildings.

7. ACKNOWLEDGMENT

The research project (FH-IPTOOLS, ref.no.: 13FH076KA2) is funded by the German Federal Ministry of Education and Research and the state of Bavaria as part of the funding programme ”Forschung an HAW”. Also thanks to Müller-BBM VibroAkustik Systeme GmbH for their support in measurement technology at THRo.

8. REFERENCES

[1] DIN EN 12354-5:2023-08, “Bauakustik – berechnung der akustischen eigenschaften von gebäuden aus den bauteileigenschaften: Teil 5: Installationsgeräusche;.”

[2] EN 15657-1:2009-10, “Acoustic properties of building elements and of buildings – Laboratory measurement of airborne and structure-borne sound from building equipment: Part 1: Simplified cases where the equipment mobilities are much higher than the receiver mobilities, taking whirlpool baths as an example.”

[3] ISO 20270:2019, “Acoustics - characterization of sources of structure-borne sound and vibration: Indirect measurement of blocked forces.”

[4] J. Weinzierl, T. Kruse, A. R. Mayr, F. Schöpfer, and U. Schanda, "Leistungsvergleich gebäudeähnlicher strukturen bei in-plane und out-of-plane anregung," in *Fortschritte der Akustik - DAGA* (Deutsche Gesellschaft für Akustik e.V., ed.), 2022.

[5] F. Schöpfer, C. Hopkins, A. R. Mayr, and U. Schanda, "Structure-borne sound propagation across a double leaf timber-frame wall," in *Proceedings of ICSV22*, 2015.

[6] F. Schöpfer, *Vibroacoustics of timber-frame structures excited by structure-borne sound sources*. Dissertation, University of Liverpool, Liverpool, 2019.

[7] T. Kruse, F. Schöpfer, U. Schanda, A. R. Mayr, and M. Dehm, "Experience with the high mobility reception plate for source characterization according to en 15657," in *Proceedings of Inter-Noise 2024*, 2024.

[8] A. R. Mayr, *Vibro-acoustic sources in lightweight buildings*. Berlin: Logos Verlag, 2009.

[9] F. Schöpfer, A. R. Mayr, U. Schanda, S. Öhler, and J. Scheck, "Geräusche gebäudetechnischer anlagen – bestimmung von eingangsdaten und berechnung der schallübertragung im gebäude," in *Bauphysik-Kalender 2025* (N. A. Fouad, ed.), pp. 469–500, Berlin: Ernst & Sohn, 2025.

DOI: 10.61782/fa.2025.0413



FORUM ACUSTICUM
EURONOISE 2025

FROM CLASSIFICATION TO PREDICTION: APPLYING EN 14366-1 TO FRESHWATER SYSTEMS

Lukas Däuble[1*] **Jochen Scheck**[1] **Berndt Zeitler**[1]
[1] Stuttgart University of Applied Sciences, 70174 Stuttgart, Germany

ABSTRACT

Sound emission of and transmission in plumbing systems are currently standardized with different approaches for waste water and fresh water applications. While EN 14366 provides characterization methods for waste water systems that deliver essential input data for the prediction of sound levels in buildings, DIN EN ISO 3822 focuses solely on the classification of individual water appliances, which are the predominant acoustic sources in fresh water installations. However, the methodology outlined in DIN EN ISO 3822 exhibits significant limitations, leading to inconsistencies between different laboratories and focusing solely on classification rather than prediction purposes. This research explores the potential application of EN 14366-1 characterization methods to freshwater systems by experimentally investigating complete installations – including appliances, pipes, and pipe clamps – to assess the necessity of developing a new standard that characterizes entire systems based on the approach used in EN 14366-1.

Keywords: *building acoustics, freshwater, structure-borne sound transmission, sanitary installations, pipe noise*

1. INTRODUCTION

Noise from building equipment is a topic that has been addressed intensely in the last two decades. Numerous case studies on various types of sources to determine the acoustic properties have been performed and led to the development of the test standard EN 15657 in 2009 that has been revised in 2017 to account for all installation conditions [1]. The results according to EN 15657 serve as input data for predictions of the sound propagation in buildings according to EN 12354-5 [2] that was recently revised. The general methods in EN 15657 have been implemented in EN 14366-1 [3] for testing wastewater pipes. While experience with this new standard is gained by numerous laboratories, a current work item of CEN/TC 126 WG7 aims to develop a second part: 14366-2 for water supply installations. The idea is to keep the methods and test facilities the same as for waste water systems and include installations with different components, not only different appliances (e.g. taps or valves), but also different piping configurations and mounting elements. Previously, only the appliances like taps and valves in water supply systems were characterized by EN ISO 3822 which exhibits significant limitations [4]. However, this method only allows the appliances to be categorized into sound classes without delivering input data for predictions. This paper aims to demonstrate the suitability of the methods from EN 14366-1 for the characterization of fresh water pipe systems.

2. TEST SETUP

For the here shown investigations, first, a fresh water system from previous publications [5,6] is used, for which the blocked force has already been determined using the reception plate method by EN 15657. This freshwater system consists of a 1-inch galvanized steel pipe connected to the building via 2 pipe clamps. The test setup on the reception plate is shown in figure 1. The internal noise source of the pipe system is the installation noise standard (INS) by EN ISO 3822, which is a reference source used to characterize appliances like taps and valves. The system is driven by a water supply pump with a controlled flow pressure of 3 bar, leading to a flow rate of 16.4 l/min, mainly determined by the INS. This short pipe section is

[*] ***Corresponding author***: *lukas.daeuble@hft-stuttgart.de*
Copyright: *©2025 Daeuble et al. This is an open-access article distributed under the terms of the Creative Commons Attribution 3.0 Unported License, which permits unrestricted use, distribution, and reproduction in any medium, provided the original author and source are credited.*

installed on the 2nd floor of an installation test stand shown in figure 3.



Figure 1. Short pipe section from previous investigations on the reception plate [5,6], the same pipe system is investigated in the installation test stand. Blue arrows depict the water flow direction.

In a second step, the system is exchanged for a longer pipe system running through several floors of the installation test stand. This longer pipe is expected to be more building-like than the short pipe section and follows the configuration in EN 14366-1 for testing waste water pipe systems. Schematic sketches of the test setups are shown in figure 2.

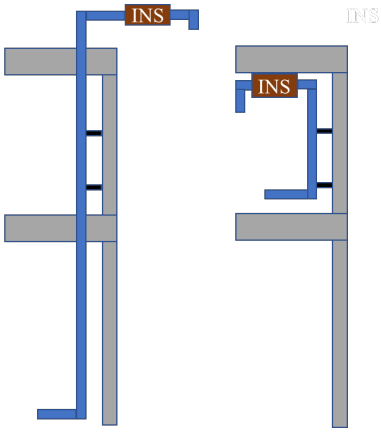


Figure 2. Schematic setup of the pipe systems in the building-like test stand, left: long pipe over several storeys, right: short pipe section within one storey.

3. APPLICATION OF EN 14366-1 TO FRESHWATER PIPES

The concept behind EN 14366-1 is to use a structure-borne sound power substitution method in order to determine the blocked force. Therefore, a calibration source with known power input is needed.

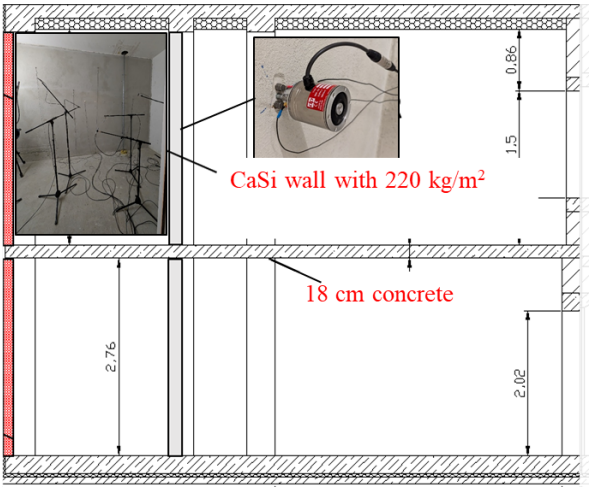


Figure 3. Cross section of the installation test stand. The mean sound pressure level and wall velocity level are measured in the sending room side. The calibration source is mounted on the test wall on the receiving room side.

In this investigation the calibration source is an inertial shaker that is screwed into the threading of the metal expansion anchors in the wall used to mount the pipe clamps of the fresh water pipe. The shaker force is measured via a force transducer while simultaneously the velocity at the contact point is measured via accelerometers. From the cross product of force and velocity at the contact point, the structure-borne sound power of the calibration source is determined. By comparing the response for shaker excitation (mean wall velocity and airborne sound power in the room) to the response for the fresh water pipe system, the source data (blocked force, airborne sound power) of the fresh water pipe system is determined. The wall velocity is captured simultaneously with 6 accelerometers on the test wall and the sound pressure level with 6 microphones in the test room, as shown in figure 3.

Note: So far, the EN 14366-1 (and EN 15657) methods are restricted to stationary excitation. For the characterization of sources with transient excitation (here e.g. closing of a water tap), a new method is explored in [7].

3.1 Structure-borne sound characterization

To determine the structure-borne sound power of the fresh water pipe system, it is assumed that the structure-borne

sound power of any source is proportional to the squared mean plate velocity [1]. This leads to the following relation between the structure-borne sound power and mean squared velocity for the source (pipe system) and the calibration source (shaker).

$$\frac{W_{source}}{\langle v^2_{source} \rangle} = \frac{W_{cal}}{\langle v^2_{cal} \rangle} \qquad (1)$$

As can be seen in figure 4, the mean wall velocity is well above background noise in the investigated frequency range and so is the mean sound pressure level (not shown).

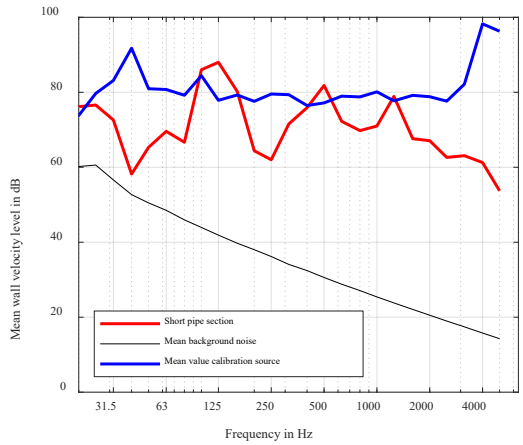


Figure 4. Mean velocity levels on the test wall with the calibration source (blue), with the short pipe section (red) and without excitation (black).

For several contact points j, expressed in levels[1] and rearranged to the structure-borne power of the source, equation (1) becomes:

$$L_{Ws} = 10\lg\left(\sum_j 10^{\frac{L_{Ws,cal,j}}{10}}\right) + L_{\langle v \rangle} - 10\lg\left(\sum_j 10^{\frac{L_{\langle v \rangle,cal,j}}{10}}\right) \qquad (2)$$

As can be seen by comparing figure 4 and 5, the difference of structure-borne power levels and wall velocity levels between calibration source and test specimen are equal.

[1] For the calculation of levels, the reference values of EN 14366-1 and EN 15657 are used.

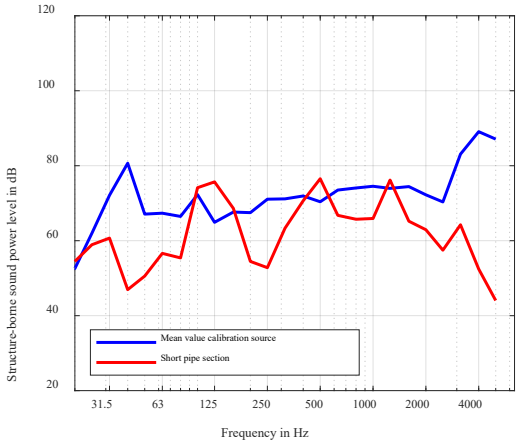


Figure 5. Structure-borne sound power levels of the calibration source (blue) and the short pipe section (red)

Assuming a force source condition, where the receiver mobility Y_R is much lower than the source mobility Y_S, the blocked force level $L_{Fb,eq}$ is calculated using the real part of the equivalent receiver mobility $Y_{R,low,eq}$:

$$L_{Fb,eq} \approx L_{Ws} - 10\lg\left(\frac{\mathrm{Re}(Y_{R,low,eq})}{Y_0}\right) \mathrm{dB} \qquad (3)$$

The blocked force is independent of the receiving structure and is used as input data for predictions in heavyweight building situations using EN 12354-5, which has already been shown in [6]. For the short pipe section, the blocked force is shown in figure 6.

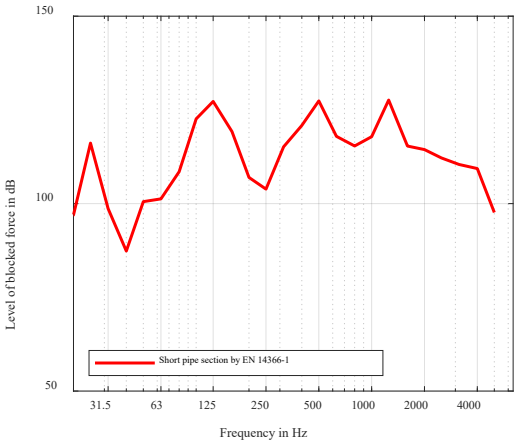


Figure 6. Blocked force of the short pipe section determined according to EN 14366-1

3.2 Airborne sound characterization

To determine the airborne sound power of the test specimen, first the mean total sound pressure level $L_{p,total}$ is measured in the test room. With the reverberation time and the volume of the test room, the normalized total sound pressure level $L_{n,total}$ is calculated.

$$L_{n,total} = L_{p,total} - 10\lg(T_R) + 10\lg\left(\frac{0{,}16V}{10}\right) \quad (4)$$

The total airborne sound power $L_{Wa,total}$ in the test room is:

$$L_{Wa,total} = L_{n,total} + 4\ \text{dB} \quad (5)$$

Since the fresh water system is a combined structure-borne and airborne sound source, the total airborne sound power in the room $L_{Wa,total}$ is a combination of direct radiation of airborne sound by the pipe L_{Wa} together with the airborne sound radiation of the wall $L_{Wa,struc}$ due to structure-borne excitation of the wall at the pipe contacts. Therefore, the airborne sound power of the pipe system itself can be separated using:

$$L_{Wa} = 10\lg\left(10^{\frac{L_{Wa,total}}{10}} - 10^{\frac{L_{Wa,struc}}{10}}\right) \quad (6)$$

To determine the airborne sound due to structure-borne excitation $L_{Wa,struc}$, the structure-borne sound power level of the calibration source $L_{Ws,cal}$ is compared to the structure-borne sound power level L_{Ws} of the test specimen. With the difference between those two and the radiated airborne sound power level $L_{Wa,struc,cal}$ radiated by the structure-borne excitation of the calibration source, calculated using equations (4) and (5), the radiated airborne sound power level of the wall $L_{Wa,struc}$ can be determined:

$$L_{Wa,struc} = 10\lg\left(\sum_j 10^{\frac{L_{Wa,struc,cal,j}}{10}}\right) + L_{Ws} - 10\lg\left(\sum_j 10^{\frac{L_{Ws,cal,j}}{10}}\right) \quad (7)$$

The separation according to equation (6) is only applicable if $L_{Wa,total}$ is greater than $L_{Wa,struc}$. As seen in figure 7, the radiation of the wall due to structure-borne excitation is dominant up to 600 Hz. This is already a hint that for the prediction of the sound transmission in a real building, airborne sound radiation of the pipe is negligible compared to structure-borne sound transmission.

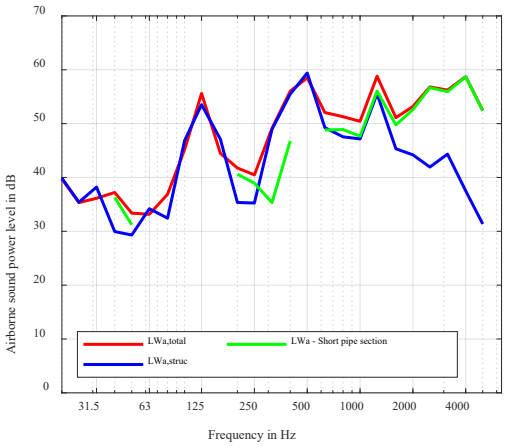


Figure 7. Separation of total airborne sound power (red) of the short pipe section into shares of wall (blue) and pipe (green).

It should be noted that for the short pipe section, the airborne sound in the room is influenced by the noise of water running out of the pipe system and into and through a drainage pipe without any connection to the wall. The radiation by the fresh water pipe itself could then be even lower than shown here.

3.3 Source mobility

To assess the validity of the force source condition, the equivalent source mobility Y_S is determined according to EN 14366-1 indirectly from the equivalent free velocity $v_{f,eq}$ of the contact points when the pipe is disconnected from the test wall and the beforehand measured equivalent blocked force of the pipe system:

$$|Y_{S,eq}|^2 = 10^{\frac{L_{vf,eq} - L_{Fb,eq}}{10}} \cdot 10^{-6} \quad (8)$$

The equivalent free velocity level of the pipe can be calculated by energetically summing up the free velocity levels at each contact point:

$$L_{vf,eq} = 10\lg\left(\sum_j 10^{\frac{L_{vf,j}}{10}}\right) \quad (9)$$

For comparison, the source mobility has also been determined directly by impact hammer excitation at each contact point while keeping the accelerometer at the same position as for the free velocity measurement , see figure 8. The equivalent magnitude of source mobility is then the

arithmetic average of the measured mobilities at each contact point.

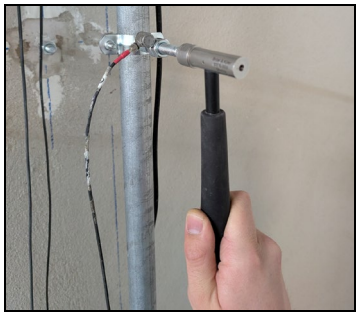


Figure 8. Direct measurement of source mobility at a contact point (threaded rod) of the pipe system.

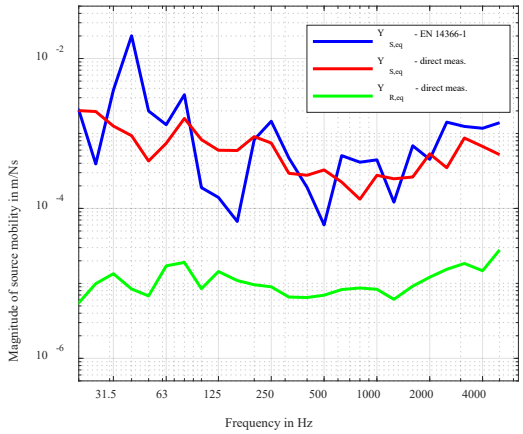


Figure 9. Mean mobility of the test wall (green) and the short pipe section (red) directly measured and the equal mobility of the short pipe section by the standardized method (blue).

Figure 9 shows the measured mobilities of source and receiver together with the source mobility determined by the EN 14366-1 method. Because the source mobility is much higher than the receiver mobility, the force source condition holds true, even though the agreement between the source mobility methods is not perfect.

4. PREDIICTION

With the blocked force from equation (3), predictions of the normalized sound pressure level in a receiving room due to structure-borne excitation of the fresh water pipe system can be made according to DIN EN 12354-5 [2] using

$$L'_{ne,s} = L'_n + L_{Fb,eq} - L_{Fb,eq,stm} \quad (10)$$

where L'_n is the apparent impact sound pressure level of the wall caused by the ISO tapping machine and $L_{Fb,eq,stm}$ is the blocked force of the ISO tapping machine. The apparent impact sound pressure level L'_n can either be calculated using EN 12354-2 [9] or measured using the normalized spatial average transmission function $D_{TF,av,n}$ from ISO 10848-1 [8]. The determination of L'_n using transfer functions has been implemented in the recently published EN 17823 [10] and can be calculated according to

$$L'_n = D_{TF,av,n} + L_{Ws,stm} \quad (11)$$

where $L_{Ws,stm}$ is the structure-borne sound power of the ISO tapping machine calculated using its blocked force $L_{Fb,eq,stm}$ and the equivalent mobility of the test wall $Y_{R,low,eq}$:

$$L_{Ws,stm} = L_{Fb,eq,stm} + 10\lg\left(\mathrm{Re}\left\{\frac{Y_{R,low,eq}}{Y_0}\right\}\right) \quad (12)$$

The normalized spatial average transfer function $D_{TF,av,n}$ by ISO 10848-1 is determined from the spatial average transfer function $D_{TF,av}$ which is the energetical average of the transfer functions $D_{TF,k}$ between structure-borne sound power and sound pressure level in the test room for each excitation position k:

$$D_{TF,k} = L_{p,cal,k} - L_{Ws,cal,k} \quad (13)$$

$$D_{TF,av} = 10\,lg\left(\sum_j 10^{\frac{D_{TF,j}}{10}}\right) \quad (14)$$

$$D_{TF,av,n} = D_{TF,av} + 10\,lg\left(\frac{A}{A_0}\right) \quad (15)$$

It should be noted that, since a force source condition is assumed for equation (12), the same evaluations could be made using directly measured forces instead of using the structure-borne sound power W_s of the calibration source. Since the mobility of the test wall still has to be determined to check if the force source condition holds true, no measurement effort can be saved.

The apparent impact sound pressure level of the test wall in the installation test stand using the two methods are shown in figure 10.

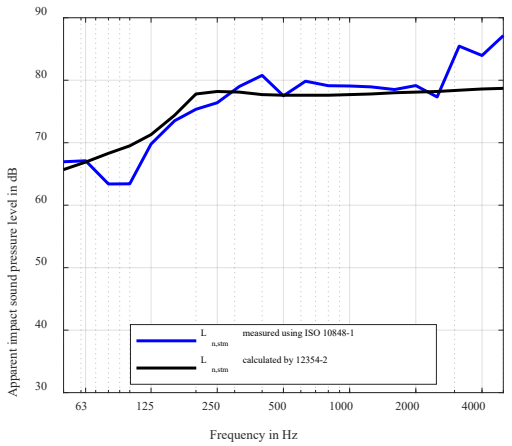


Figure 10. Apparent impact sound pressure level calculated by EN 12354-2 and measured using transfer functions from ISO 10848-1.

EN 14366-1 already uses a similar approach with transfer functions for the determination of the radiated airborne sound power of the wall due to structure-borne excitation $L_{Wa,struc}$ of the fresh water pipe system, compare equations (4), (5) and (7). The main difference is the determination of the average transfer function $D_{TF,av}$. While the ISO 10848-1 averages the transfer functions themselves (see equation (14)), EN 14366-1 sums the power input at all contact points and the mean sound pressure levels caused by each power input. The average transfer function EN 14366-1 implicitly uses is:

$$D_{TF,av,EN14366} = 10\lg\left(\sum_j 10^{\frac{L_{p,cal,j}}{10}}\right) - 10\lg\left(\sum_j 10^{\frac{L_{Ws,cal,j}}{10}}\right) \quad (16)$$

If the power input is the same for each contact point the two methods deliver the same results. If the power input at any contact point is much higher than at other contact points, which is easily possible for impact hammer excitation, the resulting average transfer function from equation (16) is dominated by the result of that point. For the investigations made here, there are only minor differences caused by the inconsistent determination of average transfer functions, because the shaker delivers nearly identical structure-borne excitation at each contact point and the individual transfer functions of each point also only show small deviations.

The predicted normalized sound pressure levels in the receiving room of the installation test stand using equation (10) with calculated and by ISO 10848-1 determined apparent impact sound pressure levels are shown in figure 11. The by EN 14366-1 predicted normalized sound pressure levels $L_{n,struc} = L_{Wa,struc} - 4$ dB, compare equation (5), shows small deviations to the prediction with the transfer function from ISO 10848-1, which is only due to the different averaging, see equations (13) (14) and (16). The measured and predicted sound pressure level in the receiving room is in good agreement for all prediction methods.

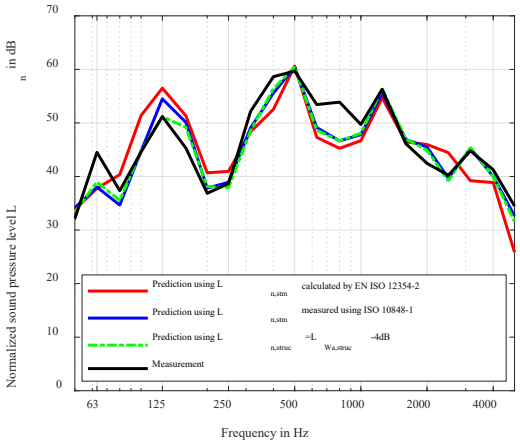


Figure 11. Normalized sound pressure level in the receiving room caused by the short pipe section excited by the INS.

5. COMPARISONS

To validate the blocked force determined by EN 14366-1 a comparison with the results on the reception plate by EN 15657 [5] is made in figure 12. The results show good agreement between the two methods from 50 Hz upwards. This shows, that the EN 14366-1 method is suitable to characterize fresh water pipe systems as structure-borne sound sources.

For the long pipe section, the blocked force of the pipe system is much lower than for the short pipe section. Such large differences were not expected, since in previous studies on the reception plate [5], only minor variations of the blocked force with respect to the pipe geometry were found.

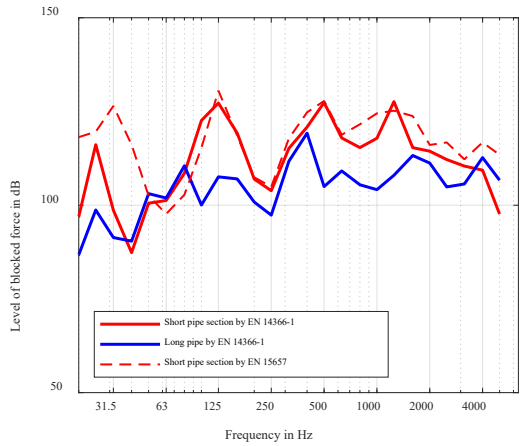


Figure 12. Blocked force of the long pipe (blue) and the short pipe section (red) by EN 14366-1 method in comparison with the blocked force of the short pipe section on the reception plate by EN 15657 (red dashed).

In the previous investigations on the reception plate [5], it has been shown that the insertion loss is independent of the excitation of the pipe but dependent on the specific combination of pipe and pipe clamp. To verify these results, the long pipe system is mounted with pipe clamps with a rubber inlay. The influence of the pipe clamp inlay on the blocked force is shown in following figure.

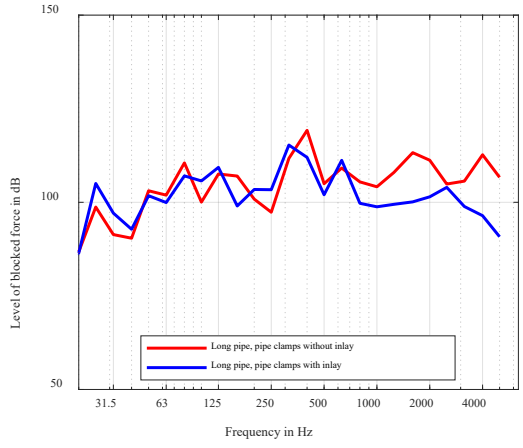


Figure 13. Effect of a rubber inlay in the pipe clamps of the long pipe.

The effect of the inlay in the pipe clamp on the blocked force is limited to the high frequency range above 600 Hz, except for the 3150 Hz 3rd-octave band. Below 600 Hz, the resilient inlay has only a minor effect. The difference in blocked force level will lead to the same difference in sound pressure level in the receiving room, which effectively is the insertion loss, displayed in figure 14. To evaluate the validity of this result, the insertion loss determined on the reception plate for the small pipe section with the same pipe clamps [5] is also shown.

The insertion loss of the pipe clamps determined via the EN 14366-1 methods for the long pipe system show the same trend as for the short pipe section characterized on the reception plate. This approves the expectation from previous investigations that the insertion loss of pipe clamps has a minor dependency of the geometry of the pipe but is heavily dependent on the combination of pipe and pipe clamp.

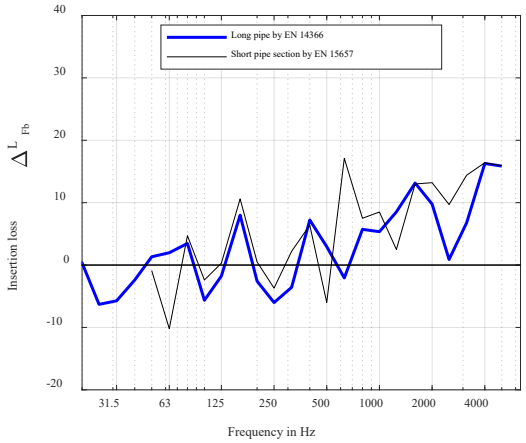


Figure 14. Insertion loss of the pipe clamp with a resilient inlay determined by the blocked force for the long pipe system by EN 14366-1 and for the short pipe section by EN 15657 at the reception plate.

6. CONCLUSIONS

It was shown that the methods of EN 14366-1 are in principle suitable for characterizing fresh water pipe systems. The blocked forces determined for the short pipe section according to EN 14366-1 are in good agreement with the results from measurements on the reception plate method according to EN 15657. The airborne sound power can also be determined in accordance with EN 14366-1, however the valid frequency range is limited here as the structure-borne sound component dominates up to 600 Hz.

The source quantities free velocity and mobility can also be determined using the methods in EN 14366-1.

The blocked force for the long pipe is significantly lower than for the short pipe section, which was not expected from previous investigations. This indicates that the pipe length has a relevant effect that has to be investigated in further detail. The consequence so far is that a laboratory test set-up needs to be as building-like as possible which requires an installation over more than one storey as for waste water pipe systems.

7. ACKNOWLEDGMENTS

The authors are grateful to the Federal Ministry of Education and Research (BMBF) and fischerwerke GmbH & Co. KG for their support (Grant number: 13FH172KA0).

8. REFERENCES

[1] EN 15657:2017: Acoustics – Measurement of structure-borne sound power of noise sources in buildings using a reception plate method.

[2] EN 12354-5:2023: Building Acoustics – Estimation of acoustic performance of buildings from the performance of elements – Part 5: Sound pressure levels from building services.

[3] EN 14366-1:2023: Laboratory measurement of airborne and structure-borne sound from service equipment – Part 1: Application rules for waste water installations.

[4] H.M. Fischer: Describing Noise of Water Appliances by ISO 3822: What happens really?, *Proc. CFA/DAGA '04 Stasbourg*, 165-166, 2004.

[5] L. Däuble, J. Scheck and B. Zeitler: Insertion loss of pipe clamps: Quantity for prediction or manufacturer's advertising?, Internoise 2024 Nantes, France.

[6] J. Scheck, L. Däuble and B. Zeitler: Freshwater pipes as structure-borne sound sources: laboratory measurement and prediction, Forum Acusticum 2023 Torino, Italy.

[7] A. Rieger, L. Däuble, J. Scheck, B. Zeitler and C. Höller: Experimental study on using transient excitation signals in the prediction of sound pressure levels from building services according to EN 12354-5 and EN 15657, DAS-DAGA 2025 Copenhagen, Denmark.

[8] ISO 10848-1:2017: Acoustics – Laboratory and field measurement of flanking transmission for airborne, impact and building service equipment sound between adjoining rooms - Part1: Frame document.

[9] EN 12354-2:2017: Building acoustics – Estimation of acoustic performance of buildings from the performance of elements – Part 2: Impact sound insulation between rooms.

[10] EN 17823:2024: Acoustic properties of building elements and of buildings – Laboratory measurement of the impact sound insulation of stairs and stair isolating elements.

DOI: 10.61782/fa.2025.0657

FORUM ACUSTICUM EURONOISE 2025

ON-SITE APPLICATION OF NOISE REDUCTION TECHNOLOGIES FOR BATHROOM DRAINAGE IN APARTMENT BUILDINGS

Guk-Gon SONG[1*] **Jin-Yun CHUNG**[1] **A-Hyeon JO**[1]
[1] Korea Conformity Laboratories, Republic of Korea

ABSTRACT

In Korea, most apartment bathrooms use an under-slab-piping method, causing drainage to occur through the ceiling of the lower floor when the upper floor bathroom is used, inevitably leading to drainage noise issues. Especially in older apartment buildings, noise reduction measures have not been considered, resulting in significant harm to residents.

This study aims to apply noise reduction technology to older apartment buildings vulnerable to bathroom drainage noise and verify its effectiveness. The target site is an apartment built in 1997, with an exclusive area of 84 m². The existing PVC drainage pipes, asbestos slate ceiling material, and wooden doors were replaced with low-noise PVC pipes, sound-absorbing ABS ceiling material, and ABS doors.

The noise reduction performance was evaluated at maximum noise levels during toilet, sink, and bathtub drainage. Measurement results in the main bathroom showed a reduction of 22.9 dB(A) for toilet drainage noise and 16.6 dB(A) for sink drainage noise. In the family bathroom, reductions were 10.1 dB(A) for toilet drainage noise, 5.9 dB(A) for sink drainage noise, and 12.0 dB(A) for bathtub drainage noise. Applying this technology is expected to reduce living noise issues between neighbors in apartment buildings.

Keywords: *drainage noise, bathroom noise, apartment building, noise reduction*

[*]***Corresponding author***: *gsong@kcl.re.kr*
Copyright: *©2025 Guk-Gon SONG et al. This is an open-access article distributed under the terms of the Creative Commons Attribution 3.0 Unported License, which permits unrestricted use, distribution, and reproduction in any medium, provided the original author and source are credited.*

1. INTRODUCTION

According to the 2023 KOSIS survey, approximately 80% of Koreans reside in multi-unit housing such as apartments, villas, and studio flats [1]. Multi-unit housing is vulnerable to noise transmitted from neighbors due to shared walls, floors, and ceilings between adjacent units. In particular, floor impact noise caused by children running or adults walking has intensified conflicts between households, becoming a significant social issue. However, survey results on living noises in apartment buildings revealed that in the main bedroom, more respondents reported being affected by drainage noise from bathrooms rather than floor impact noise [2]. Unlike the living room, where the family gathers and spends time together, the main bedroom is used as a space for rest and sleep. As a result, background noise in the main bedroom is lower compared to other spaces, making individuals more sensitive to even small noises. Since floor impact noises, such as children running, mainly occur in living rooms or hallways, they are evaluated as being relatively less sensitive. On the other hand, bathroom drainage noises, which occur more frequently in main bedroom, are analyzed to have a higher sensitivity level. In particular, the method of installing drainage pipes beneath the slab in multi-unit housing is commonly used, which is believed to cause significant noise-related issues.

This study applied technologies designed to reduce bathroom drainage noise in multi-unit housing and evaluated their effectiveness on-site.

2. DRAINAGE NOISE REDUCTION TECHNOLOGIES

Technologies for reducing bathroom drainage noise in apartment buildings include low-noise piping, sound-absorbing ceiling boards, and high-soundproof doors.

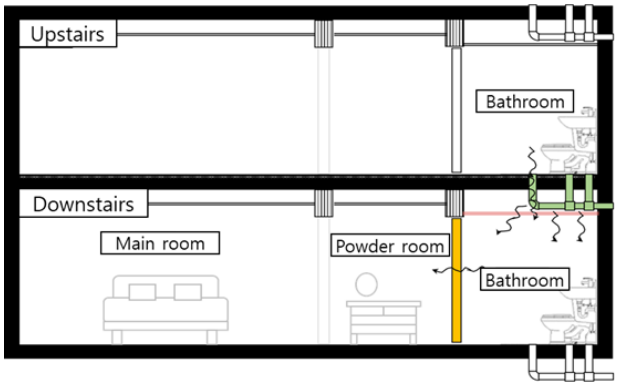


Figure 1. Section and drainage noise transmission path.

2.1 Low noise piping

Low-noise piping is designed with two or three layered structures to reduce internal noise through vibration isolation and sound insulation, while also preventing the transmission of noise externally. This technology has the greatest impact on reducing drainage noise and demonstrates highly effective noise reduction capabilities. The sound insulation performance of the piping can be evaluated in laboratories using ISO [3] and KS [4] standard test methods.

2.2 Sound absorbing ceiling board

Sound-absorbing ceiling materials are a technology designed to reduce the transmission of noise, generated by drainage pipes installed beneath the slab, to the interior of the downstairs bathroom. Typically, PVC, SMC, or ABS ceiling materials are used, with PU foam sound-absorbing material attached to the upper side of the ceiling material, aiming to reduce noise through absorption within the ceiling. This technology is expected to be particularly effective in narrow spaces within the frequency range of 500 Hz or higher, where the effects of sound absorption are more noticeable. Laboratory measurements can be conducted according to ISO 10140-2 standard [5].

2.3 High-soundproof door

High-soundproof doors can reduce the transmission of bathroom noise to the master bedroom. They are effective not only in minimizing noise caused by upstairs neighbors using their bathrooms, but also in decreasing the noise from family members within the same unit, making it less audible in the master bedroom. Generally, doors used indoors do not have high air-tightness or soundproofing performance. By enhancing the soundproofing performance of the door itself and improving the air-tightness of the door set, the soundproofing effect can be increased. The soundproofing performance of the door set can be evaluated using ISO 10140-2 test method [5].

3. ON-SITE APPLICATION

To verify the effectiveness of noise reduction technologies for bathroom drainage noise in actual multi-unit housing settings, these technologies were applied on-site. The target site was an apartment built in 1997, approximately 28 years old, with an exclusive area of 84 m² and a layout featuring one bathroom adjacent to the master bedroom and another to the living room. While the main focus of this study was noise reduction in the master bedroom bathroom, the same technologies were applied to the living room bathroom for comparison purposes.
The applied technologies included low-noise piping, sound-absorbing ceiling materials, and high-soundproof doors. Additionally, the walls, floor tiles, and sanitary fixtures were all reconstructed.

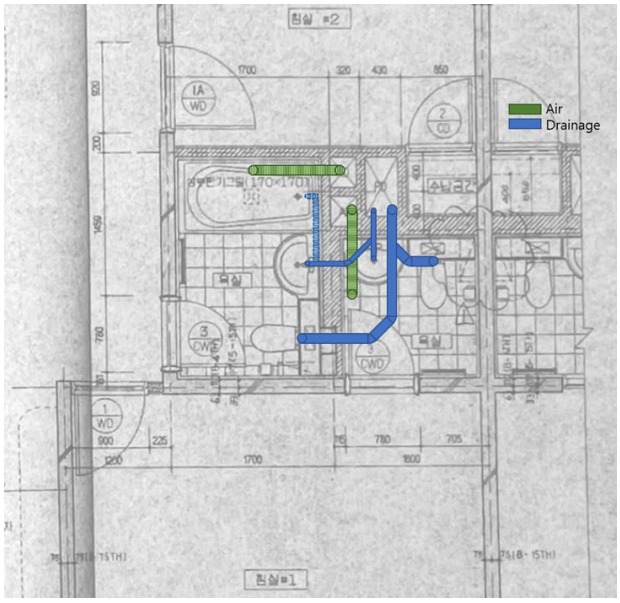


Figure 2. Plan of apartment noise reduction technology applied.



Figure 3. Images of bathroom before noise reduction technology application.



Figure 4. Images of bathroom after noise reduction technology application and measurement.

4. MEASUREMENT AND ASSESSMENT

4.1 Measurement method

The measurement of drainage noise followed the test methods outlined in KS F 2871 [4]. Noise levels were measured at the central point inside the downstairs bathroom and at a location 1 m in front of the bathroom door outside. During the whole drainage time, noise was measured after filling 6L of water into the flush toilet, 6L into the washbasin, and 60L into the bathtub. Both the equivalent noise level (L_{eq}) and the maximum noise level (L_{max}) were measured using the Fast time characteristic. Three measurement data were averaged.

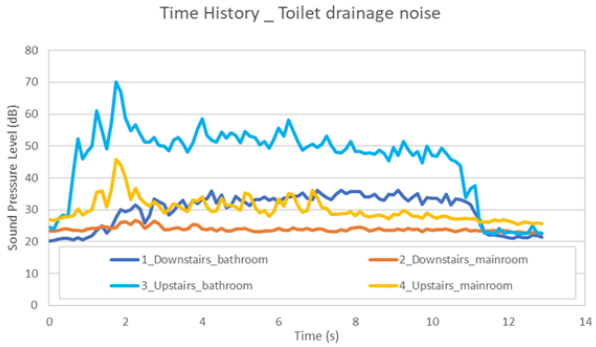


Figure 5. Time history graph of bathroom toilet drainage noise measurement after technologies application.

4.2 Measurement before and after application

To evaluate the noise reduction performance of drainage noise mitigation technologies, measurements were taken before and after the application of the technologies. To ensure comparability, the measurement locations and conditions were kept identical, and measurements were repeated three times under the same conditions. The arithmetic mean of the results was then compared. The noise reduction effects were evaluated for each sanitary fixture, including the toilet, sink, and bathtub.

Based on Figure 5, the noise was measured by identifying the time when noise occurred relative to the background noise, including the time during which the drainage process was ongoing.

4.3 Noise reduction

Changes in noise levels due to drainage time delays were anticipated, so the noise reduction performance was evaluated using the maximum noise level.

The toilet drainage noise from the bathroom adjacent to the master bedroom was reduced by 22.9 dB, from 59.8 dB to 36.9 dB, while the sink drainage noise decreased by 16.6 dB, from 49.1 dB to 32.5 dB. In the shared bathroom adjacent to the living room, the toilet drainage noise was reduced by 10.1 dB, from 45.5 dB to 35.4 dB, while the sink noise decreased by 5.9 dB, from 43.0 dB to 37.1 dB, and the bathtub noise was reduced by 12.0 dB, from 50.5 dB to 38.5 dB.

As shown in Figure 1, the drainage pipes of the living room bathroom were constructed to merge with the ceiling space

of the master bedroom bathroom and meet the vertical pipes in the pipe duct (PD) space. Since the internal pipe length in the living room bathroom ceiling is shorter, the noise level was measured to be relatively lower than in the master bedroom bathroom, and the noise reduction effect due to the applied technology was also less significant.

Table 1. Maximum sound pressure level of bathroom drainage noise.

Room	Fixture	L_{Amax} (dB)	L_{Amax} (dB)	ΔL_{Amax} (dB)
Main bathroom	Toilet	59.8	36.9	22.9
	Sink	49.1	32.5	16.6
Public bathroom	Toilet	45.5	35.4	10.1
	Sink	43.0	37.1	5.9
	Bathtub	50.5	38.5	12.0

5. CONCLUSION AND DISCUSSION

5.1 Conclusion

This study aimed to verify the effectiveness of technologies applied on-site to reduce toilet drainage noise in apartment buildings. It assessed the current drainage noise condition in an apartment building approximately 28 years after completion, and applied technologies such as low-noise pipes, sound-absorbing ceiling materials, and high-soundproof doors. To verify the effectiveness of these technologies, noise was measured before and after construction for each drainage fixture, confirming the noise reduction performance of the technologies.

As a result of the application, maximum noise levels showed reductions of 22.9 dB for toilet noise and 16.6 dB for sink noise in the master bedroom bathroom, and reductions of 10.1 dB for toilet noise, 5.9 dB for sink noise, and 12.0 dB for bathtub noise in the shared bathroom adjacent to the living room. Following the application of these technologies, all drainage conditions presented low noise levels of under 40 dB. Particularly, the drainage noise reduction effect was significant in the master bedroom bathroom, where the piping from the shared bathroom and the master bedroom bathroom merged and connected to the pipe duct (PD).

5.2 Discussion

This study aimed to verify the field performance of noise reduction technologies, specifically targeting aging apartment buildings. While the significance of confirming the performance of technologies validated in existing experimental facilities and applying them on-site was acknowledged, the study was limited to results from a single site, making generalization difficult. Therefore, it is necessary to obtain additional field data to enhance the reliability of the findings. Furthermore, the testing methods for measuring drainage noise on-site require review and discussion.

6. ACKNOWLEDGMENTS

This work is supported by the Korea Agency for Infrastructure Technology Advancement (KAIA) grant funded by the Ministry of Land, Infrastructure and Transport (Grant RS-2022-00144050).

7. REFERENCES

[1] KOSIS (Statistics Korea, Population Census), Jul. 29th 2024.

[2] A.-H. Jo, G.-G. Song and J.-Y. Chung, "Survey of perceived living noise in apartment buildings", Trans. Korea Soc. Noise Vib. Eng., Vol. 35, no. 1, pp. 88-98, 2025.

[3] ISO 15665:2023, “Acoustics – Acoustic insulation for pipes, valves and flanges”, 2023.

[4] KS 2871:2021, “Standard test method of drainage noise in apartment bathroom”, 2021.

[5] ISO 10140-2:2021, “Acoustics – Laboratory measurement of sound insulation of building elements – part 2: Measurement of airborne sound insulation”, 2021.

[6] J.-Y. Jeon, H.-I. Jo, S.-M. Kim and H.-S. Yang, “Subjective and objective evaluation of water-supply and drainage noises in apartment buildings by using a head-mounted display”, Applied Acoustics, Vol. 148, pp.289-299, 2019.

DOI:

Main theme: A03 Building Acoustics

Session A03.07 Acoustics of wooden buildings

Chair(s): S. Schoenwald, M. Fuente

DOI: 10.61782/fa.2025.0461

FORUM ACUSTICUM EURONOISE 2025

IMPROVEMENT OF THE AIRBORNE AND IMPACT SOUND INSULATION OF A TIMBER STUD WALL

Jochen Scheck[1,2*] **Ulrike Schüttler**[3] **Christoph Fichtel**[2] **Berndt Zeitler**[1]
[1] Stuttgart University of Applied Sciences, 70174 Stuttgart, Germany
[2] STEP GmbH, 71364 Winnenden, Germany
[3] IngenieurGruppe Bauen, 76133 Karlsruhe, Germany

ABSTRACT

The airborne and impact sound insulation in wooden buildings is often poor, in particular at low frequencies. For a German manufacturer of prefabricated houses, the sound insulation of a separating wall was investigated and improved in the laboratory. By constructive measures such as using a planning filled with silica sand that provides a high internal damping and the partial separation of the wooden studs a considerable improvement of the airborne sound insulation could be achieved. In a next step the impact sound insulation of a standard wooden stair was successfully optimized by isolation measures at the contacts of stair and wall.

Keywords: *building acoustics, separating wall, laboratory tests, airborne sound insulation, impact sound insulation.*

1. INTRODUCTION

Wooden buildings are gaining popularity, also in Germany. The use of renewable raw materials, lower costs and shorter construction times are advantageous in comparison to heavyweight constructions made of concrete and bricks. However, the airborne and impact sound insulation is often poor, in particular at low frequencies which can cause complaints by inhabitants. The construction of the separating wall in-between residential units plays an important role for the total sound transmission. Within the scope of a master thesis [1], the sound insulation of a separating wall of the German manufacturer Keitel-Haus GmbH was investigated and improved in the laboratory of STEP GmbH.

2. TEST STAND

The airborne and impact sound insulation of the separating wall was measured in the test stand of STEP GmbH that was constructed in 2001 with the main purpose of testing lightweight and heavyweight stairs (Figure 1).

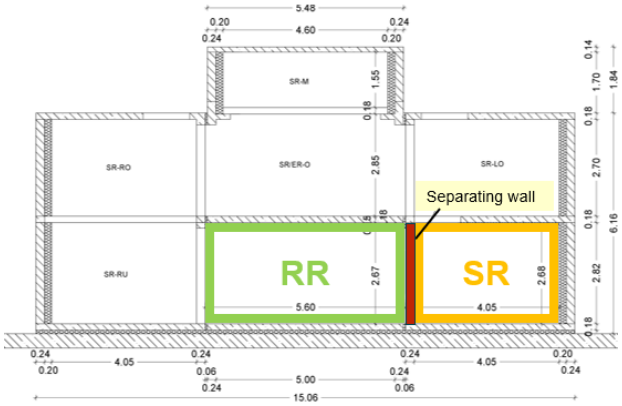


Figure 1. Test stand with sending and receiving room used for the investigations.

The test stand is in accordance with EN ISO 10140-5 [2]. Flanking transmission is avoided by structural linings and the reverberation time in the rooms was conditioned by using absorbers to be within 1s ≤ T ≤ 2s in the frequency range between 50 Hz – 5 kHz.

[*] ***Corresponding author**: jochen.scheck@hft-stuttgart.de*
***Copyright**: ©2025 First author et al. This is an open-access article distributed under the terms of the Creative Commons Attribution 3.0 Unported License, which permits unrestricted use, distribution, and reproduction in any medium, provided the original author and source are credited.*

3. BASIC CONSTRUCTION

The frame construction of the timber stud wall consisted of studs, sills and frames with a depth of 200 mm made of wood (Figure 2). The studs were mainly arranged in a grid of 62.5 cm. Individual areas of the wall had a smaller stud spacing for the later planned connection of a staircase. The compartments were filled with mineral wool.



Figure 2. Frame construction of the timber stud wall.

Figure 3 shows the basic construction chosen for the investigations. For this construction, the planking of the timber stud wall consisted of coarse chipboard (OSB) with a thickness of 12 mm and a mass per unit area of 7.4 kg/m^2, which was screwed to the studs, sill and frame. Additionally, gypsum plasterboard fire protection boards (GKF) with a thickness of 12.5 mm and a mass per unit area of 10.2 kg/m^2 [3] were used, which were screwed onto the OSB plate.

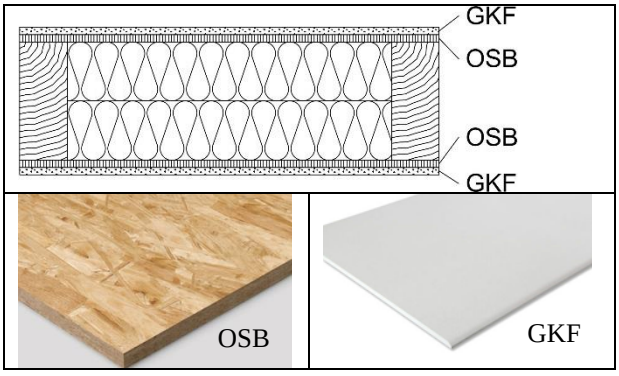


Figure 3. Basic construction of the timber stud wall with OSB and GKF planking.

4. AIRBORNE SOUND INSULATION OF THE BASIC CONSTRUCTION

The airborne sound insulation was determined according to EN ISO 10140-2 [4]:

$$R = L_1 - L_2 + 10\,lg\,S/A \qquad (1)$$

L_1: averaged sound pressure level in sending room [dB]
L_2: averaged sound pressure level in receiving room [dB]
S: wall area [m^2]
A: equivalent absorption area in receiving room [m^2]

The single number value and spectrum adaptation terms were evaluated according to ISO 717-1 [5]. In the following the spectrum adaptation value $C_{50\text{-}5000}$ that accounts for the low frequency sound transmission down to 50 Hz is also given as in [6].

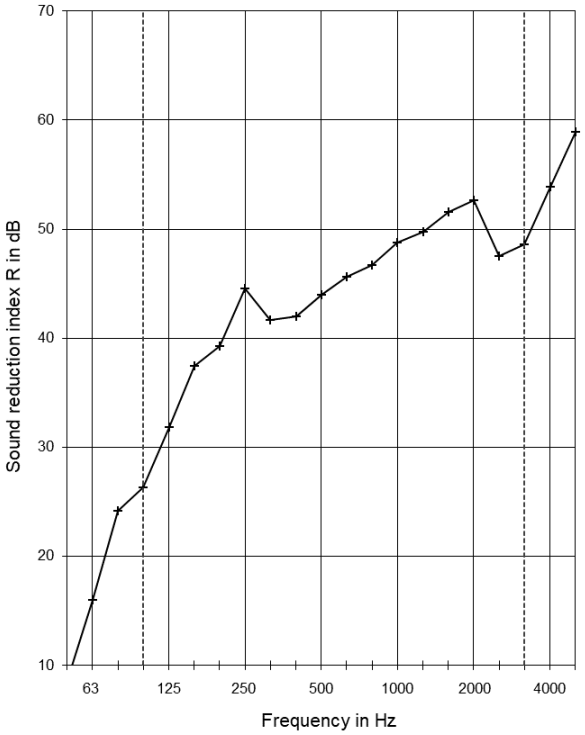


Figure 4. Sound reduction index of the basic construction of the timber stud wall with OSB and GKF cladding; R_w ($C_{50\text{-}5000}$) = 47.8 (-3) dB.

The basic construction achieved a weighted sound reduction index of **R_w ($C_{50\text{-}5000}$) = 47.8 (-3) dB**.

Figure 4 shows the frequency-dependent sound reduction index. Below 200 Hz a strong decrease is visible. An improvement of the sound insulation, particularly in the low-frequency range, was the aim of the design modifications.

5. VARIATION OF THE CLADDING

The cladding of a timber stud wall is known to have a significant influence on the sound reduction index, which is why the optimization of the wall construction was initially started here. In order to improve sound insulation, [6] recommends the use of multi-layer, flexible planking with a high mass per unit area.

Two commercially available additional layers named "Silentboard GKF" [7] and "Phonestar ST Tri" [8] were used. Both layers have a thickness of 12,5 mm and a mass per unit area of 17.5 kg/m^2. They were inserted in-between the OSB and GKF layers, the connection was screwed (Figure 5, Figure 6).

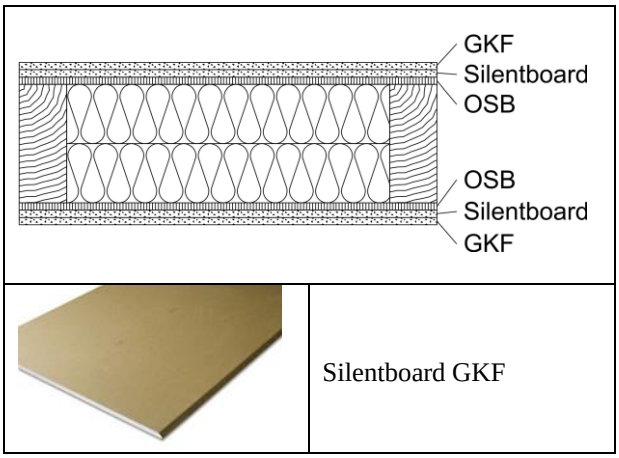


Figure 5. Timber stud wall with an additional layer "Silentboard GKF" [7], a gypsum board recommended for exceptional sound insulation in drywalling.

In Figure 7 are compared the sound reduction indices of the basic construction and with the additional layers.
With the Silentboard a weighted sound reduction index of **R_w ($C_{50\text{-}5000}$) = 50.6 (-1) dB** and thus an improvement of the basic construction by ΔR_w = 2,8 dB is achieved.

With the Phonestar a weighted sound reduction index of **R_w ($C_{50\text{-}5000}$) = 55,7 (-3)** and thus an improvement of the basic construction by ΔR_w = 7.9 dB is achieved.

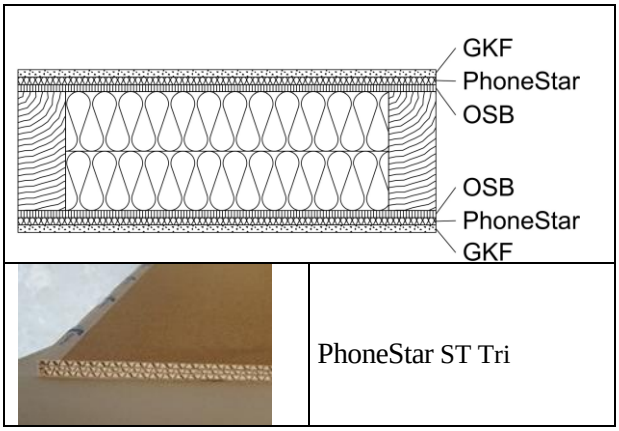


Figure 6. Timber stud wall with an additional layer "PhoneStar ST Tri" [8], a three-layer corrugated board filled with fine, loose quartz sand.

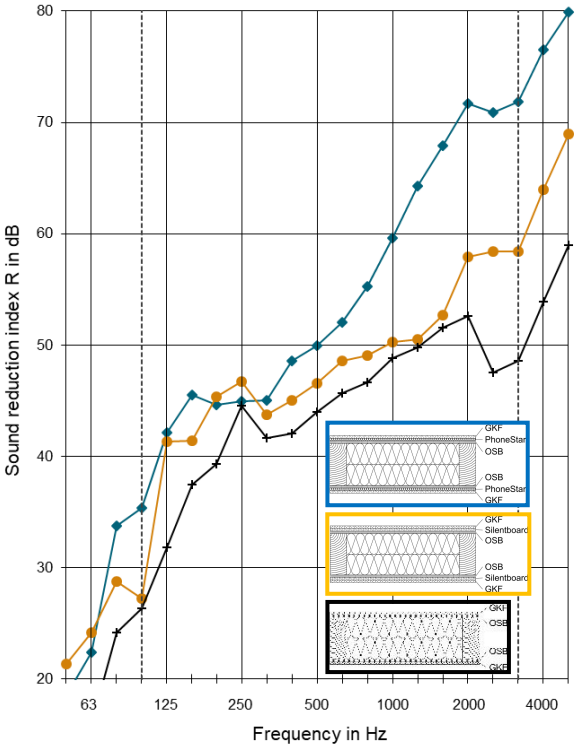


Figure 7. Sound reduction index of the wall with different claddings:

Table 1: Single number values for the frequency spectra in figure 7.

OSB + GKF	R_w ($C_{50\text{-}5000}$) = 47.8 (-3) dB
OSB + Silentboard + GKF	R_w ($C_{50\text{-}5000}$) = 50,6 (-1) dB
OSB + Phonestar + GKF	R_w ($C_{50\text{-}5000}$) = 55,7 (-3) dB

The performance of the Phonestar is clearly better. At low frequencies up to 200 Hz the improvement is about 10 dB. Above 250 Hz the increase of the sound insulation is much steeper than with the Silentboard. It is assumed that this is mainly due to high internal damping caused by the loose sand in the panels. Due to the better performance PhoneStar ST Tri was used for the further investigations.

6. SEPARATION OF THE WOODEN STUDS

The planking of the two sides of the wall is coupled via studs, sills and frames. According to [6], improvements in sound insulation can be achieved by separating the two wall shells. In order to achieve a solution that is as practical as possible, the studs were separated, while the sill and frame remained continuous (Figure 8). In this way, complete decoupling of the two wall shells is not achieved, but the wall can be manufactured, transported and assembled in one piece. This meets the prefabricated house industry's desire for a high degree of prefabrication. As before, the wall with separate studs was cladded with OSB, PhoneStar ST Tri and GKF (Figure 9).



Figure 8. Timber stud wall with separated studs and continuous sill and frame.

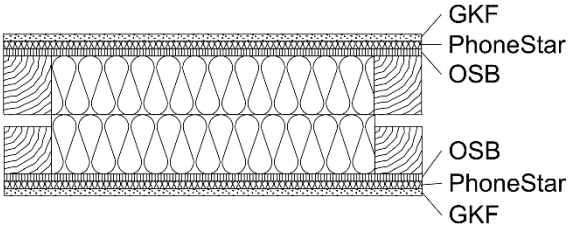


Figure 9. Timber stud wall with separated studs and cladding with OSB, Phonestar ST Tri and GKF.

In Figure 10 are compared the sound reduction indices of the basic construction, with the additional layer Silentboard and without and with separated studs.

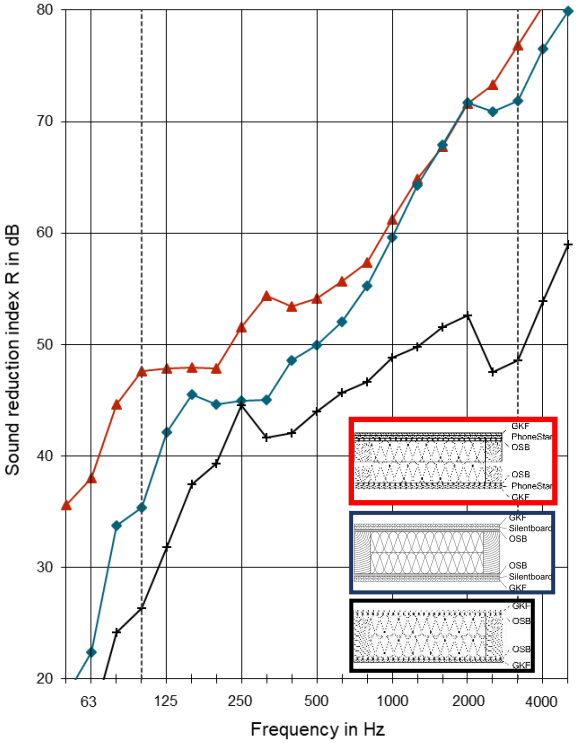


Figure 10. Sound reduction index of the wall with different claddings:

The separation of the studs leads to a significant improvement of the sound insulation below 1 kHz and especially in the low frequency range where the improvement of the previous construction is about 10 dB.
With the separated studs a weighted sound reduction index of **R_w ($C_{50\text{-}5000}$) = 60,4 (-1) dB** and thus an improvement of the basic construction by ΔR_w = 12.6 dB

is achieved. According to the German standard DIN 4109-5 the "increased" requirement in multi-family houses is $R_w \geq 56$ dB. This value is met by far even when the spectrum adaptation term is added. In a building of course flanking transmission has to be taken into account. Calculations and a measurement in a real building [1] indicate that with this wall construction and so far used flanking element constructions the targeted value is still met with safety.

Table 2: Single number values for the frequency spectra in figure 10.

OSB + GKF	R_w ($C_{50\text{-}5000}$) = 47.8 (-3) dB
OSB + Phonestar + GKF	R_w ($C_{50\text{-}5000}$) = 55,7 (-3) dB
OSB + Phonestar + GKF; separated studs	R_w ($C_{50\text{-}5000}$) = 60,4 (-1) dB

7. IMPACT SOUND INSULATION

On the optimized wall construction with OSB, PhoneStar ST Tri and GKF cladding on both sides and with separated studs (Figure 9) a quarter-spiral wooden staircase with stringboard was installed in the test stand (Figure 11). A side wall was also added here, which was bolted to the partition wall. In the original state, the stair stringboard was rigidly bolted to the partition and side wall and had no distance to them.



Figure 11. Wooden staircase with stringboard connected to the optimized wall construction with separated studs (Figure 9) and optimized corner support.

Based on this standard construction used so far, the screw connections to the wall were loosened and the staircase was moved away from the wall. Statically, a corner support was then required, which was screwed to the side wall, as shown in Figure 11. In addition, an elastomer isolating element was placed under the corner support to decouple the stair string board and rubber sleeves were used to decouple the screws for connecting the stair to the corner support.

The impact sound insulation was determined according to EN ISO 10140-3 [9]:

$$L_n = L_i + 10\ lg\ A/A_0 \quad (1)$$

L_i: averaged sound pressure level in receiving room [dB]
A: equivalent absorption area in receiving room [m²]
A_0: reference absorption area, $A_0 = 10$ m²

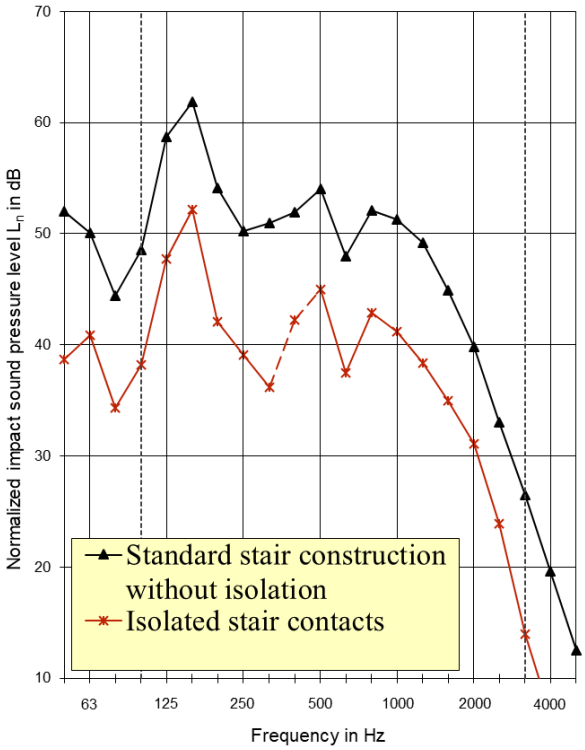


Figure 12. Normalized impact sound pressure level of the stair attached to the optimized wall:

The single number value and spectrum adaptation terms were evaluated according to ISO 717-2 [10]. In the following the spectrum adaptation value $C_{I,50\text{-}2500}$ that

accounts for the low frequency sound transmission down to 50 Hz is also given as in [6].

Table 3: Single number values for the frequency spectra in figure 12.

Standard stair configuration without isolation	$L_{n,w}$ ($C_{I,50\text{-}2500}$) = 51.2 (0) dB
Optimized stair configuration with isolated wall contact	$L_{n,w}$ ($C_{I,50\text{-}2500}$) = 41.2 (0) dB

The results for the two stair configurations are shown in Figure 12.
The isolation of the stair leads to a significant improvement of the normalized impact sound pressure level in the whole frequency range and especially in the low frequency range where the improvement is about 10 dB. For the non-isolated stair a weighted normalized impact sound pressure level of **$L_{n,w}$ ($C_{I,50\text{-}2500}$) = 51.2 (0) dB** is obtained.
With the isolated stair contacts a weighted normalized impact sound pressure level of **$L_{n,w}$ ($C_{I,50\text{-}2500}$) = 41.2 (0) dB** and thus an improvement by $\Delta L_{n,w}$ = 10 dB is achieved. According to the German standard DIN 4109-5 the "increased" requirement in multi-family houses is $L_{n,w} \leq 47$ dB. This value is met by far even when the spectrum adaptation term is added. Again, in a building situation flanking transmission has to be considered but it is unlikely that this will dramatically worsen the laboratory value.

8. SUMMARY

The airborne sound insulation of a timber stud wall was to be determined and optimized by constructive measures, for which measurements were carried out in a test stand. Starting from a basic wall construction and a weighted sound reduction of R_w ($C_{50\text{-}5000}$) = 47.8 (-3) dB the final value achieved was R_w ($C_{50\text{-}5000}$) = 60,4 (-1) dB. The significant improvement was obtained by adding an additional cladding - a three-layer corrugated board filled with fine, loose quartz sand - and a separation of the wall studs.
In a second step the impact sound insulation of a standard wooden staircase attached to the optimized wall was improved by isolation measures at the stair-wall contacts from $L_{n,w}$ ($C_{I,50\text{-}2500}$) = 51.2 (0) dB to $L_{n,w}$ ($C_{I,50\text{-}2500}$) = 41.2 (0) dB. The constructive modifications are highly effective in the low frequency range that is mainly problematic in wooden buildings.

9. ACKNOWLEDGMENTS

The authors gratefully acknowledge the financial support by the manufacturer Keitel-Haus GmbH.

10. REFERENCES

[1] Schüttler, U. Untersuchung der Luft- und Trittschalldämmung von Holzständerwänden im Prüfstand. Masterarbeit KIT, Karlsruhe, 2023.

[2] ISO 10140-5:2021: Acoustics - Laboratory measurement of sound insulation of building elements - Part 5: Requirements for test facilities and equipment.

[3] Knauf Gips KG. Feuerschutzplatte Knauf Piano GKF. Wirtschaftliche Gipsplatte für Brand- und Schallschutzsysteme im Trockenbau. K713E.de Technisches Blatt. 03/2023.

[4] ISO 10140-3:2021: Acoustics - Laboratory measurement of sound insulation of building elements - Part 2: Measurement of airborne sound insulation.

[5] ISO 717-1:2020: Acoustics - Rating of sound insulation in buildings and of building elements - Part 1: Airborne sound insulation.

[6] Blödt, A.; Rabold, A.; Halstenberg, M.; Ecker, T.; Huber, A.; Huissel, L.; Löffler, S.; Scheuerpflug, M. Schallschutz im Holzbau – Grundlagen und Vorbemessung. holzbau handbuch, REIHE 3, TEIL 3, FOLGE 1. Holzbau Deutschland-Institut e.V., 2019.

[7] Knauf Gips KG. Knauf Silentboard-Systeme. Schallschutz mit hochwertigem Trockenbau. SIB01.de Technische Broschüre. 01/2018.

[8] Wolf Bavaria GmbH. PhoneStar ST Tri. Technische Daten. 01.10.2020.

[9] ISO 10140-3:2021: Acoustics - Laboratory measurement of sound insulation of building elements - Part 3: Measurement of impact sound insulation.

[10] ISO 717-2:2020: Acoustics - Rating of sound insulation in buildings and of building elements - Part 2: Impact sound insulation.

DOI: 10.61782/fa.2025.0787

FORUM ACUSTICUM EURONOISE 2025

SOUND INSULATION PERFORMANCE OF TIMBER FLOORS WITH ELASTICALLY MOUNTED AND SUSPENDED LAYERS

Jesse Lietzén[1*] **Lauri Talus**[1] **Alina Lahdensivu**[1]
Aitor Lopetegi[2] **Ander Aldalur**[2]
[1] AINS Group, Department of Acoustical Engineering, Finland
[2] AMC Mecanocaucho, Spain

ABSTRACT

Massive timber buildings are often equipped with concrete or cement screed floors to increase the mass of the structures and to improve the sound insulation between rooms. However, the use of concrete is more and more often seen as an unfavourable option due to the increasing need to decrease the carbon dioxide emissions of the construction sector. A recent field study performed in a mock-up CLT-framed building showed that the sound insulation can drastically be improved without concrete by mounting the upper layers of the floor and the suspended ceiling elastically to the load-bearing timber slabs. In comparison with the conventional screed solution, the vertical airborne and impact sound insulation was improved with the elastically mounted floor up to 13 and 20 dB in terms of the single-number quantities $D_{nT,w}$ and $L'_{nT,w}$. This study aims to investigate the sound insulation performance of the conventional and elastically supported floors by conducting computational assessments which were compared with the field measurement results. Furthermore, the assessments were broadened to study the sound insulation between rooms in the horizontal direction. These computations based on FEM and parametric models reveal the superior performance of the elastically mounted floor both in horizontal and vertical directions.

Keywords: *timber floor, elastic mounting, suspended ceiling, sound insulation, finite element method*

[*] ***Corresponding author***: *jesse.lietzen@ains.fi*
Copyright: *©2025 Lietzén et al. This is an open-access article distributed under the terms of the Creative Commons Attribution 3.0 Unported License, which permits unrestricted use, distribution, and reproduction in any medium, provided the original author and source are credited.*

1. INTRODUCTION

Massive timber such as cross-laminated-timber (CLT) is a typically applied load-bearing frame solution in different timber building types. When timber apartment buildings with high sound insulation requirements are considered, the frame is usually partly decoupled and supported with elastic bearings and partly covered with sound insulating structural layers such as elastically suspended ceilings. The reason for these solutions is to avoid flanking sound transmission between adjacent rooms.

One conventionally applied solution to improve sound insulation performance of massive timber buildings is to pour concrete or cement screed on the massive timber floors. This increases the mass of the floors, but on the other hand, the use of concrete or cement increases the carbon dioxide emissions of the building.

An alternative solution to improve sound insulation is to cover the massive timber floors with elastically attached building board layers. A recent field study performed in a CLT framed mock-up building showed that the sound insulation of the building can be improved in comparison with the conventional concrete solution [1]. Based on the study, the improvement of sound insulation in vertical direction due to the elastically mounted floor was up to 23 and 36 dB in terms of the single-number quantities (SNQ) $D_{nT,w}$ and $L'_{nT,w}$.

The purpose of this paper is to further compare the sound insulation of CLT floors with cement screed, and elastically mounted floor. In the first part, the sound insulation of the floors was computationally assessed in vertical direction. Second part of the study involved application of the results to predict the horizontal sound insulation between two adjacent rooms in an imaginary CLT framed building. The computational assessments were performed with the finite element method and with parametric calculation models.

2. MATERIALS AND METHODS

2.1 Studied floors

2.1.1 Floor assemblies

The sound insulation of five timber floors F0–F4 was studied. In all the cases, the load-bearing structure was a 140 mm thick 5-layered CLT slab, which also acted as the reference floor F0. The rest of the studied floors had either a cement screed (F1–F2) or an elastically mounted floor (F3–F4) as floor toppings. Two of the studied floors (F2 and F4) had also elastically suspended ceilings installed below the CLT slab. None of the floors had floor coverings in the study. Briefly, the studied floors were:

- F0: CLT 140 mm
- F1: Screed 50 mm + underlayment 3 mm + F0
- F2: F1 + elastically suspended ceiling
- F3: Elastically mounted floor + F0
- F4: F3 + elastically suspended ceiling

The study aimed to compare the sound insulation performance of the floors F1 and F3 (Fig. 1). Floors F1 and F2 were equipped with the cement screed on the CLT slab. An elastic underlayment of thickness 3 mm (a bitumen-based product with dynamic stiffness 120 MN/m^3) was installed below the screed. Floors F3 and F4 had an elastically mounted floor topped with 18 mm OSB and two 12,5 mm Fermacell fibre gypsum boards. The elastic floor mounts (AMC Mecanocaucho Akustik+Sylomer® 25 Floor Mount) were installed between the CLT slab and the 50 mm timber battens in a 500/600 mm spacing. The space between the CLT slab and the elastically mounted floor was filled with 75 mm thick glass wool.
Floors F2 and F4 were equipped with a suspended ceiling. Two 13 mm thick plasterboards were hanged from the CLT slab with elastic elastomer hangers (AMC Mecanocaucho Akustik+Sylomer® 15 Type B) which were installed in a 500/1200 mm spacing and attached to metal frames (spacing c/c 1200 mm) for the plasterboard installation. The air gap between the gypsum boards and the CLT slab was 100 mm including 75 mm of glass wool.

2.1.2 Measurements

Airborne and impact sound insulation of the floor assemblies F0, F1 and F3 has previously been measured in a timber mock-up building [1]. The measurement results for the floors have been presented in Tab. 1 in SNQs, in a case where the main flanking sound transmission routes were covered with sound insulating wall linings.

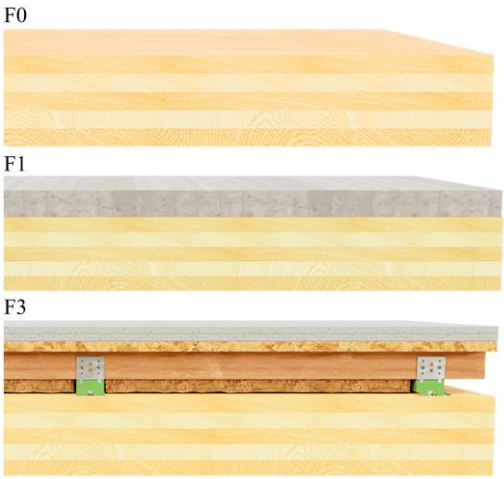


Figure 1. Studied floor assemblies F0, F1 and F3.

Table 1. Airborne and impact sound insulation of the floors F0, F1 and F3 measured in vertical direction in a timber mock-up building [1].

Floor	$D_{nT,w}$	$L'_{nT,w}$
F0: CLT 140 mm	39 dB	86 dB
F1: Screed 50 mm + underlayment 3 mm + F0	49 dB	70 dB
F3: Elastically mounted floor + F0	62 dB	50 dB

The measurements were performed in the field in the vertical direction in a three-story high timber building. In the measurement situation, the source room (V = 51 m^3) was located on the second floor and the receiving room (V = 26 m^3) on the ground floor. The area of the measured floor structures was 9,5 m^2. However, it must be noted that the flanking structures were not equivalent with each other in different measurement arrangements.
The measurement results clearly indicate a superior performance of the elastically suspended floor (F3) compared to the screed floor (F1) in vertical direction. In terms of $D_{nT,w}$ and $L'_{nT,w}$, the improvement of sound insulation of the elastically mounted floor was 23 and 36 dB whereas the effect of the screed floor on the sound insulation was only 10 and 16 dB, respectively.
The sound insulation performance of the floor solutions was not compared in a horizontal direction, although the effectiveness of the elastically mounted floor in this respect has previously been shown [2]. Because of this, the effect of the solutions on the horizontal sound insulation was studied computationally in this paper.

2.2 Sound insulation between adjacent rooms

In a complete building, the sound insulation between adjacent rooms depends on the room properties and flanking sound transmission between rooms. Thus, the effect of the studied floors on the horizontal sound insulation cannot directly be explained by the performance of the floors. To study further how the floors influence the horizontal sound insulation between rooms, a flanking transmission analysis was carried out for an imaginary timber building setup.

In the analysis, airborne and impact sound insulation between two rooms (Fig. 2) was computationally determined applying the methods presented in the parts 1 and 2 of the ISO 12354 [3,4] and the computational results for the floors based on the methods presented in Section 2.3. All the load-bearing structures surrounding the studied rooms were 140 mm thick CLT plates and the T- and X-junctions between the CLTs were rigid. The dimensions of the adjacent rooms were 3 m x 2.8 m x 3.8 m of which the area of the wall separating the rooms was 3 x 2.8 m^2.

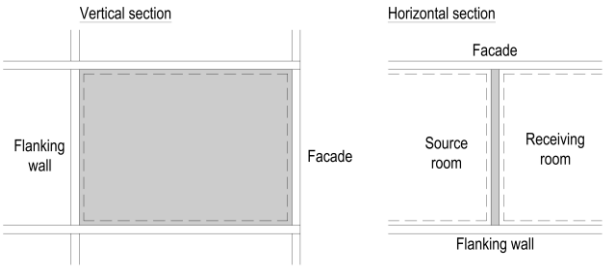


Figure 2. Flanking sound transmission setup. Rooms were surrounded with 140 mm thick CLT plates with rigid junctions. The grey areas represent the wall separating the rooms, and the dashed lines illustrate the ceilings, wall linings and floor coverings.

Sound insulation between the rooms was determined in six different cases: for the floors F0, F1, and F3 with two different partition walls. The studied walls were:

- A: 2 plasterboards 13 mm + steel frame 45 mm and mineral wool + air gap 27 mm + steel frame 45 mm and mineral wool + 3 plasterboards 13 mm
- B: CLT 140 mm + air gap 30 mm + 45 mm and mineral wool + 2 plasterboards 13 mm

In all the cases, except for the case with the floor F0, the other indirect flanking transmission routes were covered with wall linings (the same CLT lining as in wall B), or suspended ceilings (see floors F2 and F4, in Section 2.1).

2.3 Simulation procedures and model descriptions

The sound insulation of floors F0, F1 and F3 was examined using a similar approach as in a previous study [5], in which the benefits of an elastically suspended ceiling was investigated. Similarly to the previous study, both parametric calculation models as well as the finite element method were used to examine the impact and airborne sound insulation of the floors.

The analytical models were used to analyse the frequency range 250–5000 Hz, whereas the FE-model was used in the low frequencies between 50–200 Hz 1/3-octave bands.

In addition to floors F0, F1 and F3 the aforementioned calculation methods were used to examine the partitions and other flanking constructions of the CLT building setup described in Section 2.2.

2.3.1 Material properties

The material properties used in the calculation of sound insulation have been presented in Tab. 2.

Table 2. Applied elastic material properties.

Material	ρ [kg/m^3]	E [MPa]	ν [-]	η_s [-]
CLT	510	4600*	0.28	0.02
Screed	2200	30000	0.20	0.01
Fermacell	1270	3800	0.28	0.01
OSB	490	2210	0.28	0.01
Plasterboard	710	3100	0.28	0.01

* Equivalent isotropic value based on the ref. [6].

The static airflow resistivity of the glass wool was 10000 Pa·s/m^2. Spring constant and structural loss factors of the elastic floor mounts and the elastic hangers were 122990 N/m and 0.07 and 29960 N/m and 0.07, respectively.

The CLT plate and the floor topping of floor F3 were modelled as equivalent isotropic plates in an approach similar to the one used in [6]. The bending stiffnesses of the structure in the different main directions B_x and B_y were first determined, and the equivalent bending stiffness was:

$$B_{eq} = \sqrt{B_x B_y} \tag{1}$$

From the equivalent bending stiffness, the equivalent Young's modulus can then be determined from:

$$E_{eq} = \frac{B_{eq}}{I} \tag{2}$$

where E_{eq} is the equivalent Young's modulus, and I is the second moment of area.

2.3.2 Finite element method

The FE-modelling of floors F0, F1 and F3 was carried out using COMSOL Multiphysics 6.2. The same finite element model was used for both airborne and impact sound insulation, with the only difference being the type of excitation used. The model was a fully coupled analysis with two-way acoustic-structural interaction between the structural and acoustical parts of the model, and it was built to correspond to laboratory conditions. The CLT was simple supported and the other structural parts were connected to the CLT but otherwise the boundary conditions were free. The geometries of the FE-models of the floors F1 and F3 are presented in Fig. 3.

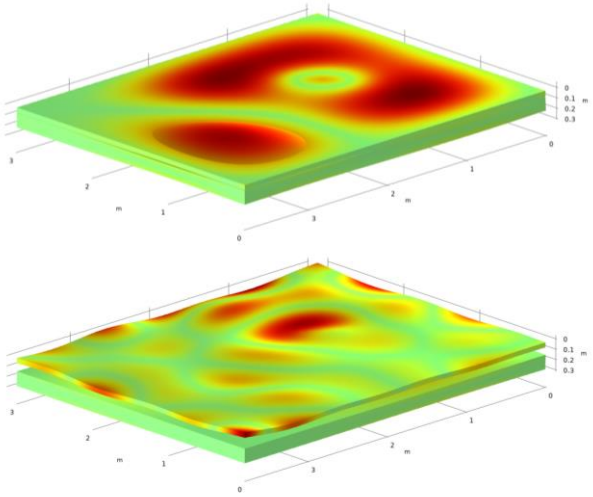


Figure 3. The FE-models of the floors F1 (above) and F3 (below) presenting the floor displacements at 100 Hz during the impact excitation.

The governing equation of motion for the structural parts of the model was:

$$\nabla \cdot \boldsymbol{S} = -\rho\omega^2\mathbf{u} \tag{3}$$

where $\boldsymbol{S}$ is the second Piola-Kirchhoff stress tensor, ρ is the material density, ω is the angular frequency and $\mathbf{u}$ is the displacement vector [7]. The acoustical domains were governed by the Helmholtz equation:

$$\nabla \cdot \left(-\frac{1}{\rho_0}\nabla p\right) - \frac{\omega^2 p}{\rho_0 c_0} = 0 \tag{4}$$

where p is the time harmonic sound pressure, ρ_0 is the density of air and c_0 is the speed of sound in air [8].

The sound absorbing materials in the air cavities of the suspended ceiling and the floor topping of floor F3 were modelled using the modified Champoux-Allard equivalent fluid model [8, 9].

The elastic floor mounts and ceiling hangers were modelled as spring-damper components as in [5, 10, 11]. The use of spring-damper components as a substitute for a full 3D-model of an elastic ceiling mount was previously found to yield good results [5]. The spring-damper components were given a spring coefficient k and loss factor corresponding to the pre-loaded state of the elastic mount. The natural frequency f_0 of the ceiling hangers was 9,5 Hz and the mass per hanger was 8,4 kg. The natural frequency of the floor mounts was 16 Hz and the mass per mount was 12,2 kg.

To solve the radiated sound power, a half-infinite acoustic domain representing the receiving airspace was modelled on the receiving side of the floor constructions. The fully absorptive boundary condition of the half-infinite domain was achieved using perfectly matched layers.

The mesh of the FE-model was built using hexahedral quadratic elements. The mesh was frequency dependent with the element size being a fifth of the wavelength of sound according to [8].

The airborne sound insulation of the floor constructions was assessed by applying a diffuse sound field excitation modelled after [12]. The excitation applied on the surface of the floor construction was a sum of N plane waves evenly distributed over a half-sphere with random phase. The FE-model was then used to determine the radiated sound power. Then the sound reduction index of the floor construction was determined from:

$$R = 10\log\left(\frac{P_{dif}}{P_{rad}}\right) \tag{5}$$

where P_{dif} is the sound power generated by the diffuse field excitation on the sending side of the structure and P_{rad} is the radiated sound power on the receiving side.

The impact sound insulation of the floors was determined using an ISO tapping machine excitation modelled as a series of point forces on the floor surface after [13]. Again, the sound power radiated by the structure was solved from the FE-model. The normalized impact sound pressure level was then determined from:

$$L_n = \log\left(\frac{P_{rad}}{P_0}\right) + 10\log\left(\frac{A_{ref}}{A_0}\right) \tag{6}$$

where P_0 is the reference sound power 10^{-12} W, and A_{ref} and A_0 are the reference sound absorption areas 4 and 10 m^2.

2.3.3 Parametric models

The airborne and impact sound insulation of the were examined in the mid and high frequency range with parametric calculation tools developed by AINS Group.
The airborne sound insulation of the floor constructions was examined with a tool that combines a number of different calculation models based on statistical energy analysis, lumped mechanical models and forced transmission approaches. The calculation method is based on Refs. [3, 14–18].
The impact sound insulation of the floor structures was calculated using a method based on Refs. [4, 19–23]. In addition to the features of the airborne sound insulation model, the impact sound insulation model takes into account the force interaction of the ISO tapping machine and the floor surface.

3. RESULTS

3.1 Sound insulation of the floor assemblies

Simulated sound reduction index R and normalised impact sound pressure level L_n of floors F0, F1 and F3 are presented together with the measured standardised level difference D_{nT} and standardised impact sound pressure level L'_{nT} results in Fig. 4 and Fig. 5. Thus, discrepancies between the results are partly explained by the differing quantities.
Fig. 4. shows that the calculated sound reduction index correlates well with the measured level difference. The effect of the bare CLT slab (F0) accumulates to the results of F1 between 80 and 400 Hz in both the measured and simulated results. Having an elastically mounted floor (F3), the effect of the CLT slab is no longer displayed.
The correlation between the simulated and measured impact sound pressure levels is weaker than for airborne sound yet acceptable (Fig. 5). The calculation result for F0 seems to have shifted to lower frequencies compared to the measured result. The effect of the CLT slab can be seen also on the other simulated results.
Calculation results underestimate the sound insulation of floor F3 on low frequencies below 250 Hz. The resonance frequencies of floor F3 are shifted higher by 1/3 octave on the simulated results compared to measurements.

3.2 Sound insulation between adjacent rooms

The predicted total sound insulation between rooms and all flanking transmission paths between rooms are presented in Fig. 6 and Fig. 7 for all examined cases.

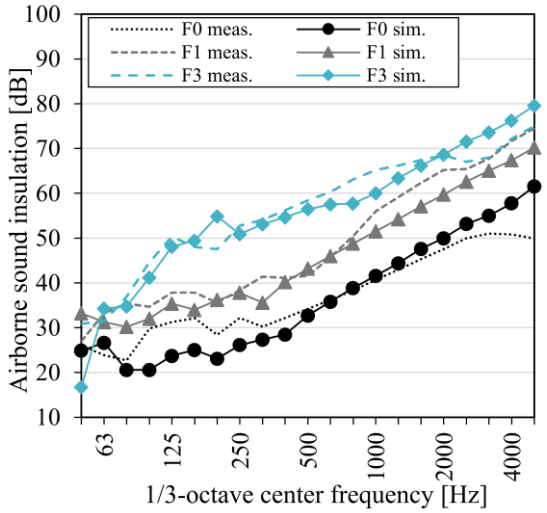


Figure 4. Measured standardised sound level difference D_{nT} and simulated sound reduction index R of floors F0, F1 and F3.

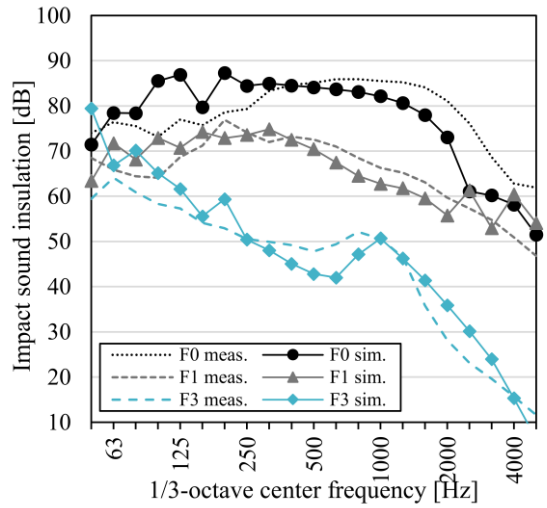


Figure 5. Measured standardised impact sound pressure level L'_{nT} and simulated normalised impact sound pressure level L_n of floors F0, F1 and F3.

In case of the horizontal airborne sound insulation, the main limiting factor is the flanking path Ff through the floor structures (see Fig. 6). Covering the floor with the screed (F1) (and other flanking paths with the linings) improves the horizontal airborne sound insulation. However, the total sound insulation is still limited due to the flanking sound transmission via the floor-to-floor route. In case of the floor F3, the limiting factor is the sound reduction index of the wall itself.

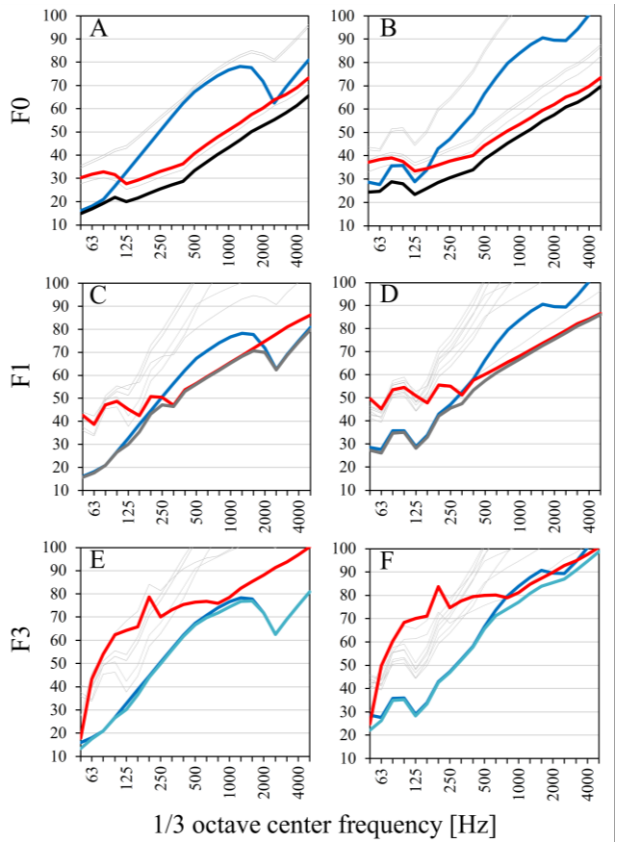


Figure 6. Airborne sound insulation (D_{nT} [dB]) between rooms. Dark blue line denotes the direct path Dd of wall A or B, red line indicates flanking path through floor, light grey lines indicate other flanking paths, and bold line denotes the total sound insulation. A. floor F0, wall A, B. floor F0, wall B, C. floor F1, wall A, D. floor F1, wall B, E. floor F3, wall A, F. floor F3, wall B. On figures A and B, the flanking elements are bare CLT. Figures C-F have linings and suspended ceiling on flanking structures.

The horizontal impact sound insulation is determined mostly by the impact sound insulation of the floor structure (see Fig. 7). For elastically mounted floor F3 the total impact sound insulation is a combination of different flanking paths: path Fd from floor to wall below 500 Hz and path Ff from floor to floor above 500 Hz. In case of the floor F1, a soft floor covering should be applied to reach reasonable impact sound insulation between rooms.
The results show that by applying the elastically mounted floor, better sound insulation can be achieved also between rooms.

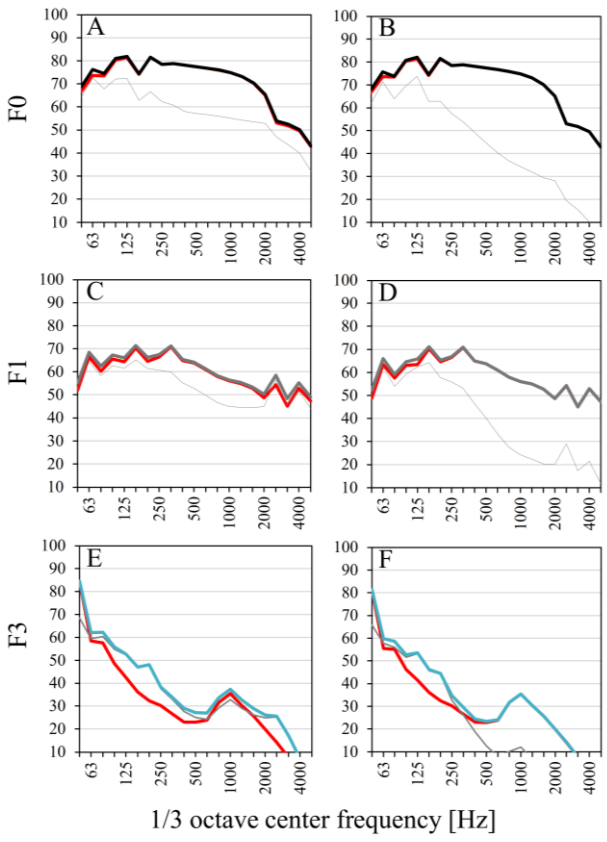


Figure 7. Impact sound insulation (L'_{nT} [dB]) between rooms. Dark blue line denotes the sound insulation of wall A or B, red line indicates flanking path through floor, light grey lines indicate other flanking paths, and bold line denotes the total sound insulation. A. floor F0, wall A, B. floor F0, wall B, C. floor F1, wall A, D. floor F1, wall B, E. floor F3, wall A, F. floor F3, wall B. On figures A and B, the flanking elements are bare CLT. Figures C-F have linings and suspended ceiling on flanking structures.

The total horizontal sound insulation results that were presented in the Figs. 6 and 7 are repeated in Figs. 8 and 9. The corresponding SNQs are presented in Tab. 3.

Table 3. Predicted single-number quantities.

Floor, wall	$D_{nT,w}$ (C, $C_{50-3150}$)	$L'_{nT,w}$ (C_I, $C_{I,50-2500}$)
F0, A	37 (-1, -2) dB	76 (-2, -1) dB
F0, B	42 (-2, -2) dB	76 (-2, -1) dB
F1, A	54 (-3, -7) dB	64 (-1, -1) dB
F1, B	55 (-4, -5) dB	63 (-1, -1) dB
F3, A	56 (-4, -9) dB	41 (2, 29) dB
F3, B	56 (-5, -5) dB	40 (2, 26) dB

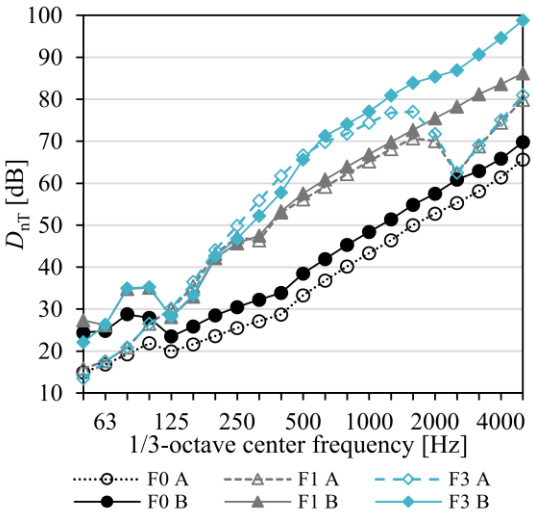


Figure 8. Standardised level difference between rooms for walls A and B.

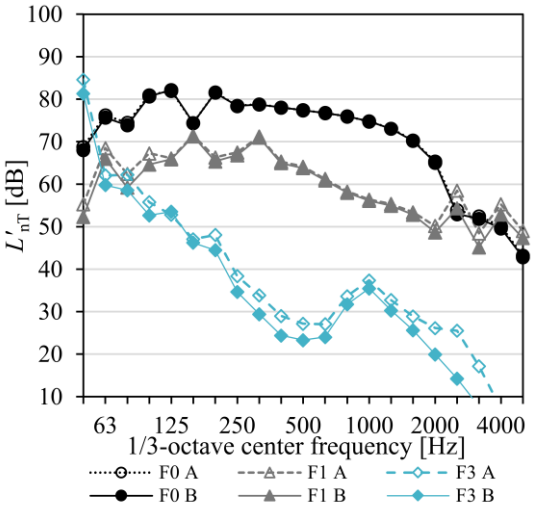


Figure 9. Standardised impact sound pressure level between rooms for floors F0, F1 and F3. The weak results for the floor F3 at 50 Hz cumulate from the simulation result (see Fig. 5), and are likely to underestimate the performance of the solution at this frequency band.

The standardized level difference $D_{nT,w}$ is significantly higher when using sound insulating linings on room surfaces. Compared to the reference case F0 with no linings, the airborne sound insulation is improved by 13–17 dB with floor F1 and 16–19 dB with floor F3. The standardized impact sound pressure level $L'_{nT,w}$ is improved by 12–13 dB with floor F1 and 35 – 36 dB with floor F3.

4. DISCUSSION

In the first part of this study (3.1) the airborne and impact sound insulation of floors F0, F1 and F3 were examined with FEM and parametric calculation methods. The calculation results were then compared to vertical field measurement results acquired in [1] (Figs. 3 and 4). The agreement between the simulated and measured results was good apart from the 50 Hz 1/3-octave band for floor F3, where a significant increase in the impact sound pressure level can be seen in the simulation result. The spectrum adaptation term $C_{I,50-2500}$ for structure F3 is determined by the divergent 50 Hz result and has a significant effect on the single-number quantities. From Figs. 3 and 4 the same decrease in sound insulation is not visible in the corresponding measurement results.

The discrepancy in the lower frequencies for F3 could be due to the boundary conditions in the FE-model. The results of [2] indicate the building boards of the elastically mounted floor were connected to the partition wall. This causes the floor assemblies to not perform as intended and affects the measured sound insulation. The building boards of the elastically mounted floor in F3 were modelled in FEM as freely supported, which differs from the *in-situ* conditions.

Floor construction F1 seems to perform better at low frequencies, which could be due to F1 not being a conventional screed floor. Typically, the cement screed is cast on top of a protective layer, and sometimes additional connectors are used to make the joint between CLT and screed stiffer. In this case, however, the underlay was a elastic bitumen-based product, which lead to the screed working as a floating floor structure rather than a compound structure. Therefore, floor F1 might have better sound insulation qualities than a conventional CLT-screed compound floor.

The CLT was modelled in FEM as a ~10 m^2 plate, whereas the CLT in the ADIVBois mock-up connected to the surrounding structures. Therefore, the total losses of the CLT were higher than in a laboratory setting, and the sound energy was spread to a wider area instead of being completely transmitted to the room below.

The sound insulation between rooms in the mock-up building, including flanking transmission, was investigated in [25] with both measurements and predictions using ISO 12354 [3, 4]. It was found that the agreement between measurement and prediction was reasonable. However, there was rather significant uncertainty in the measured vertical impact sound insulation, especially at low frequencies. Additionally, the accuracy of the predictions in [25] was worse at lower frequencies.

The horizontal sound insulation between rooms was also investigated in [25], but no comparison was done between different floor structures. Horizontal sound insulation between rooms with floors F1 and F3 was compared in Figs. 7 and 8. Fig 7 shows that the horizontal airborne sound insulation is greatly improved with the use of wall linings, floor toppings and suspended ceilings. It is also worth noting that F3 performs better than the screed solution F1.

The horizontal impact sound insulation is also significantly improved with the use of either the screed floor or the elastically mounted floor (Fig. 9). However, the elastically mounted floor again performs better than the screed floor in most of the building acoustics frequency range. The weaker apparent impact sound insulation at 50 Hz is due to the calculated impact sound insulation of floor structure F3, which was discussed above.

The elastically mounted linings effectively reduce flanking transmission via the load bearing CLT frame. According to calculation results in Figs. 5 and 6 the joints of the CLT frame can be rigid, when wall linings, suspended ceiling and floor are connected elastically. This solution is essentially a room-in-room solution, where the choice of partition wall becomes the limiting factor for horizontal airborne sound insulation.

Horizontal impact sound insulation is dependent on both the partition wall and the floor assembly. Since all impact sound is transmitted via the floor, it's the most important element. However, the performance of the floor may be superseded by a particularly weak wall structure, causing sound to be transmitted via the floor-wall path instead of the floor-floor path. An example could be a bare CLT partition rigidly connected to the load bearing floor structure. On the other hand, a completely rigid CLT frame could be a functional choice when using elastically connected lining structures. Having a rigid load bearing frame is beneficial for example for the bracing of a building.

5. CONCLUSIONS

The horizontal sound insulation in a CLT framed building was investigated with sound insulation predictions using the ISO 12354 method. The airborne and impact sound insulation of the individual building elements were determined using both the finite element method as well as parametric methods. The calculated sound insulation of the building elements was compared to field measurements with good agreement. Larger discrepancies were found in the low frequency range, which could be due to differences between calculation assumptions and *in-situ* conditions as well as measurement uncertainties.

According to the calculation results the horizontal sound insulation between rooms can be significantly improved with elastically attached linings on room surfaces. Additionally, it was found that using an elastically mounted lightweight floor topping was a superior solution when compared to a cement screed floor.

REFERENCES

[1] Institut technologique FCBA "Measures acoustiques entre deux locaux d'un bâtiment d'étude en bois" Rapport d'essais no. 403/22/0690/A-1-v1 du 13/12/23. 163 p., 2023. (in French)

[2] J-L. Kouyoumji, A. Lopetegi, and A. Aldalur: "Wooden multistorey acoustic test facility for vibration reduction indices measurement on different junctions of floor decking used to reduce flanking transmissions" *INTER-NOISE and NOISE-CON Congress and Conference Proc.* (Nantes, France) pp. 3199–3210, 2024.

[3] ISO 12354-1:2017 "Building acoustics. Estimation of acoustic performance of buildings from the performance of elements. Part 1: Airborne sound insulation between rooms" Brussels, European Committee of Standardisation, 2017.

[4] ISO 12354-2:2017 "Building acoustics. Estimation of acoustic performance of buildings from the performance of elements. Part 2: Impact sound insulation between rooms" Brussels, European Committee of Standardisation, 2017.

[5] J. Lietzén, V. Kovalainen, L. Talus, M. Kylliäinen, A. Lopetegi, and A. Aldalur: "Sound insulation of suspended ceilings: a FEM-based comparison of suspension systems" *Proc. of Forum Acusticum* (Turin, Italy), 2023.

[6] C. Churchill, B. Nusser, C. Lux: "Calculating the equivalent elastic moduli and their influence on modelling the sound insulation of softwood cross laminated timber (CLT)," *Applied Acoustics*, Vol. 205, 2023.

[7] COMSOL: *Structural Mechanics Module User's Guide*, 2023.

[8] COMSOL: *Acoustics Module User's Guide*, 2023.

[9] J.F. Allard and Y. Champoux: "New empirical equations for sound propagation in rigid frame fibrous materials," *Journal of the Acoustical Society of America*, Vol. 91, No. 6, pp. 3254–3258, 2000.

[10] M. Kohrmann, M. Buchschmid, G. Müller, R. Völtl, U. Schanda: ”Numerical models for the prediction of vibro-acoustical characteristics of light-weighted ceilings,” in *Proc. of the Inter-Noise* (Innsbruck, Austria), No. 710, 2013.

[11] M. Korhmann: *Numerical Methods for the Vibro-Acoustic Assessment of Timber Floor Constructions*. Technische Universität München, Dissertation, Germany, 2017.

[12] B. Rafaely: “Spatial-temporal correlation of a diffuse sound field,” *Journal of the Acoustical Society of America*, Vol. 107, No. 6, pp. 3254–3258, 2000.

[13] V. Wittstock: “On the spectral shape of the sound generated by standard tapping machines,” *Acta Acustica united with Acustica*, Vol. 98, No. 2, pp. 301–308, 2012.

[14] B.H. Sharp: “Prediction methods for the sound transmission of building elements,” *Noise Control Engineering Journal*, Vol. 11, pp.53–63, 1978.

[15] E.C. Sewell: “Transmission of reverberant sound through a single leaf partition surrounded by an infinite rigid baffle,” *Journal of Sound and Vibration*, Vol. 12, pp.21–32, 1970.

[16] J. Kristensen and J.H. Rindel: *Bygningsakustik – teori og praksis.* Glostrup: Statens Byggeforskningsinstitut, SBI-anvisning 166, 1989.

[17] V. Hongisto: *Monikerroksisen seinärakenteen ilmaääneneristävyyden ennustemalli*. Helsinki, Työterveyslaitos, Työympäristötutkimuksen raporttisarja 2, 2003.

[18] P. Virjonen and V. Hongisto: ”Joustavarankaisen levyrakenneseinän äänenläpäisy,” *in Proc. of the Akustiikkapäivät* (Vaasa, Finland by Akustinen Seura ry), 2009.

[19] J. Brunskog and P. Hammer: ”The interaction between the ISO tapping machine and lightweight floors,” *Acta Acustica united with Acustica*, Vol. 89, pp. 296–308, 2003.

[20] J.H. Rindel: *Sound Insulation in Buildings*. CRC Press, 2018.

[21] C. Hopkins: *Sound Insulation*. Oxford: Butterworth-Heinemann, 2007.

[22] L. Cremer, M. Heckl, B.A.T Petersson: *Structure-borne sound, structural vibrations and sound radiation at audio frequencies*. Berlin: Springer-Verlag, 2005.

[23] S. Gudmundsson: *Sound insulation improvement of floating floors. A study of parameters*. Lund University of Technology, Department of Building Acoustics, Report TVBA-3017, 1984.

[24] C. Guigou-Carter, N. Balanant, and J-L. Kouyoumji: “Building acoustic performance prediction – Feedback from Adivbois CLT building mockup” *INTER-NOISE and NOISE-CON Congress and Conference Proc.* (Glasgow, Scotland) pp. 3537–3548, 2022.

DOI: 10.61782/fa.2025.0458

FORUM ACUSTICUM EURONOISE 2025

IMPACT SOUND INSULATION OF CLT FLOORS: EVALUATION OF SMALL SCALE SPECIMENS AND CORRELATION WITH LARGE SCALE SYSTEMS

Maro Puljizevic[1*] **Tadej Poljansek**[1] **Milan Grasic**[1]
[1] Knauf Insulation, Trata 32, 4220 Skofja Loka, Slovenia

ABSTRACT

CLT has emerged as widely adopted material due to its versatility and environmental benefits. However, achieving suitable impact sound insulation for CLT floor systems is challenging. Laboratory tests of impact sound insulation present an invaluable source of information for design teams, but they are time consuming due to required sample size (10-20 m^2) and complexity of installation. Performing impact sound insulation tests on small samples offers operational advantages and provides an attractive testing option for comparative purposes and design decisions. This study provides a systematic analysis of impact sound insulation measurements conducted on a variety of small scale and large scale specimens utilizing CLT reference floor. Unlike concrete reference floors, CLT exhibits significant contribution of airborne sound component induced by the tapping machine. This phenomenon necessitates careful consideration when employing small-scale specimens for impact sound insulation analysis. Study highlights the advantages and limitations of conducting impact sound insulation tests on small scale specimens, emphasizing their practicality for comparative analyses and design decision-making. Furthermore, it points to certain constraints when extrapolating these findings to large-scale systems, offering insights into refining testing protocols for CLT-based constructions.

Keywords: *cross-laminated timber, impact sound insulation, sample size, small scale.*

[*] ***Corresponding author***: *maro.puljizevic@knaufinsulation.com*
Copyright: *©2025 First author et al. This is an open-access article distributed under the terms of the Creative Commons Attribution 3.0 Unported License, which permits unrestricted use, distribution, and reproduction in any medium, provided the original author and source are credited.*

1. INTRODUCTION

Alongside the airborne sound insulation, impact sound forms one of the cornerstones for acoustic requirements throughout the world. The robust information of impact sound levels for floor constructions is indispensable for all the parties involved in the acoustic design process. Whether in the form of laboratory test reports, published data for common building systems or computer simulations.

Compared to the substantial data available for standard monolithic floors, information concerning lightweight floors, particularly cross-laminated timber (CLT) floors, is limited. The latter is of particular importance considering relatively poor impact sound insulation performance of the basic CLT floor elements themselves; necessitating certain upgrades by means of complex floor coverings and/or suspended ceilings.

Laboratory testing, in accordance with ISO 10140-3:2021 [1], provides a reliable means to determine floor impact sound levels. However, such tests are inherently complex due to the required sample size and installation procedure.

While Bet et al. [2] previously explored the implications of sample size reduction in impact sound tests on heavyweight concrete floors, similar studies are lacking for CLT floors.

This work aims to fill this void by assessing the efficacy and reliability of small scale impact sound tests on basic CLT floor.

The discussion will commence with an overview of impact sound insulation test method, followed by an experimental investigation employing tapping machine on a variety of small scale and large scale floor coverings built on top of the CLT reference floor (without the ceiling). Concluding

remarks will summarize the main findings of the experimental investigation and the analysis of correlations between different sample sizes.

2. IMPACT SOUND INSULATION TEST METHOD

ISO 10140-3:2021 [1] details the procedure for impact sound insulation measurements and refers to other parts of ISO 10140 where appropriate.

Accordingly, the size of the test opening for floors shall be between 10 m^2 and 20 m^2, with the shorter edge length not less than 2,3 m.

Annex H of ISO 10140-1:2021 [3] introduces the concept of testing on small specimens, the minimum size of which is 650 mm x 350 mm. However, the latter procedure is introduced only for floor coverings of Category I, which include flexible coverings (plastics, rubber, cork, matting or combinations thereof).

On the other hand, typical complex floor systems built on CLT would be generally classified as Category II floors, with the requirement for specimen size of at least 10 m^2.

Therefore, the current standard does not make a provision for the testing of small samples for floor systems and/or floor coverings typically built on the basic CLT slab.

As described, the concept of tests on small specimens is indeed rooted in the ISO 10140 test standard for certain floor coverings but one of the main obstacles remains the requirement that the airborne sound transmission from the source to the receiving room is at least 10 dB below the level of the transmitted impact sound in each frequency band.

The latter requirement is particularly constraining for small samples built on basic CLT floor, as relatively low airborne sound insulation of CLT will be the limiting factor.

Regardless of the small scale build-up (and its potentially high airborne sound insulation), airborne sound component produced by the tapping machine in the source room will inevitably propagate through the basic CLT element alone.

Therefore, the measured impact sound should be corrected according to ISO 10140-4 [4].

If the condition

$$L_i - (L_{TS} - D) \geq 10\ \text{dB} \qquad (1)$$

is valid in all one-third octave bands, a correction of airborne sound transmission is not necessary.

For

$$L_i - (L_{TS} - D) \leq 3\ \text{dB} \qquad (2)$$

sound transmission is dominated by airborne sound and impact sound insulation cannot be measured correctly.

L_i is the sound pressure level generated by the tapping machine in the receiving room;
L_{TS} is the sound pressure level generated by the tapping machine in the source room;
D is the sound pressure level difference between the source and receiving room with the loudspeaker on.

3. EXPERIMENTAL INVESTIGATION

Impact sound insulation tests were carried in accordance with ISO 10140-3:2021 [1] on ten pairs of small and large scale floor samples (all without the ceiling), built on top of the basic 5-ply 140 mm CLT installed between vertically adjacent source and receiving room (V = 58 m^3).

3.1 Test samples and materials

Size of large scale sample was 15,6 m^2 and that of small scale samples around 0,54 m^2 (ca 900 x 600 mm).

Four 900 x 600 mm samples were installed for each floor type, all of them large enough to support the whole tapping machine. Number of tapping machine positions was the same as the number of small scale samples (four).

Details of tested floor systems are provided in Tab. 1, listed from top to bottom layers (from walking surface to the structural CLT slab).

Floor systems were tested with and/or without the backfill. Where used, backfill was installed directly on top of CLT.

Floor numberings in Tab. 1 are done according to the following principle: F1 – floor one without the backfill, F1B – floor one with the backfill.

Table 1. Tested floor systems.

Floor No.	Build-up
F1 / F1B	Dry screed (Backfill) CLT
F2	Dry screed PE membrane CLT
F3	Dry screed EPS CLT
F4 / F4B	Dry screed EPS PE membrane (Backfill) CLT
F5 / F5B	Dry screed GMW (Backfill) CLT
F6 / F6B	Dry screed RMW (Backfill) CLT

Density (ρ), thickness (d) and dynamic stiffness (s') of used materials are listed in Tab. 2

Table 2. Material properties.

Material	ρ (kg/m^3)	d (mm)	s' (MN/m^3)
Backfill	1750	60	-
GMW (glass mineral wool)	50	40	6
RMW (rock mineral wool)	100	40	25
EPS	-	40	-
PE membrane	-	5	-
Dry screed	1280	18	-

Fig. 1 and Fig. 2 illustrate the typical testing arrangement for small scale samples. Where used, backfill was installed inside the wooden frame and laid on top of a thin layer of geotextile.

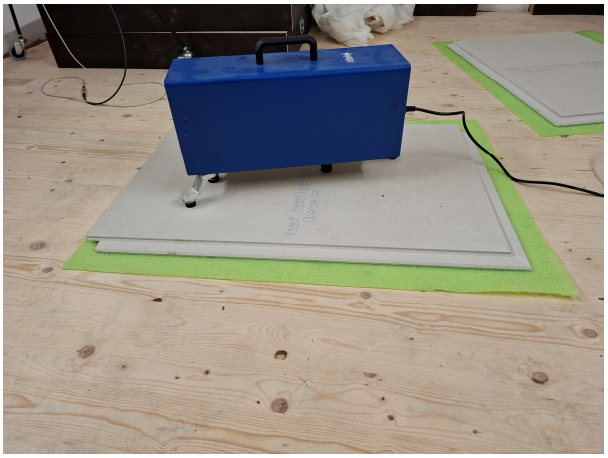


Figure 1. Test sample F2 (small scale).

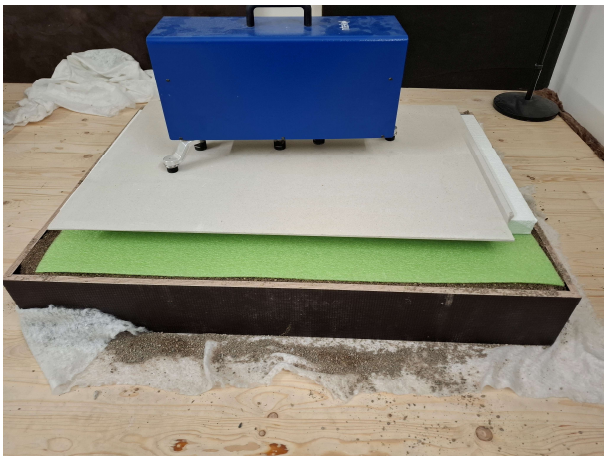


Figure 2. Test sample F4B (small scale).

3.2 Airborne sound component and testing limits

One-third octave sound reduction index (R) of basic 140 mm CLT floor is given in Fig. 3, with the corresponding single-number rating R_w 39 dB.

Such relatively low airborne sound insulation will have a determining influence on the frequency limit up to which the impact sound insulation can be measured correctly.

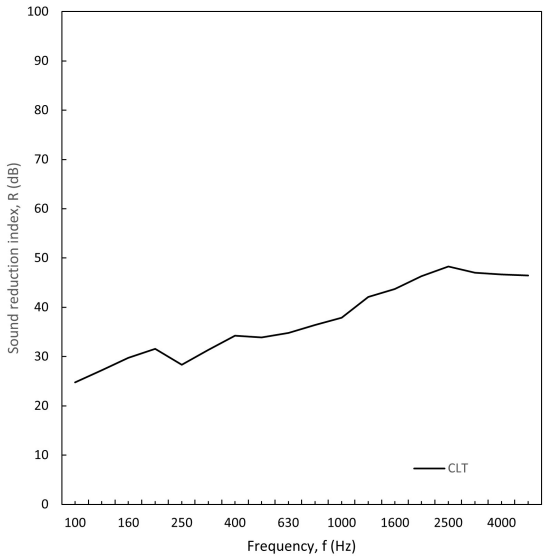


Figure 3. Airborne sound insulation of basic 140 mm CLT floor.

Sound pressure level generated by the tapping machine in the source room was measured for all the test samples.

There were minor differences observed between the sample sizes or due to the backfill. Fig. 4 illustrates the latter levels for basic CLT (solid line) and all the tested floors (shaded area).

Measured sound pressure levels in the source room were of a similar trend for all the tested floors, with relatively minor changes in the absolute values. Contribution of the top layer (dry screed) seems to be predominant, with no significant influence caused by the floors size, subsequent floor layers or backfill.

Equivalent A-weighted sound pressure level in the source room for all the test samples amounted between 93 and 95 dB(A).

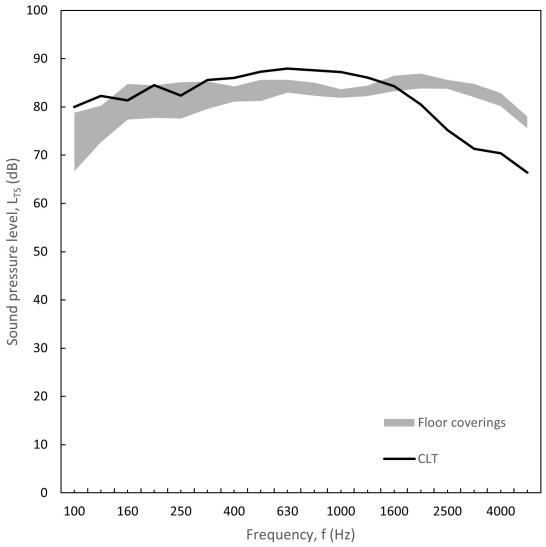


Figure 4. Sound pressure level (L_{TS}) generated by the tapping machine in the source room.

Sound pressure level generated by the tapping machine in the source room (93-95 dB(A)) will be attenuated only by the basic CLT floor (R_w 39 dB) for all the small scale samples, and by the entire floor build-up for every corresponding large scale sample.

Such constraint is the limiting factor for correct measurement of high performing floors, where airborne component will dominate on certain frequencies.

For example, Fig. 5 illustrates the normalized impact sound pressure levels (L_n) for floors F6 and F6B (small and large scale), with black-filled markers added to the frequencies where the result is dominated by the airborne sound and impact sound insulation cannot be measured correctly (result of equation (2) is $\leq$ 3 dB).

It can be noticed that such limitations can occur for small scale samples, as well as for high performing large scale samples.

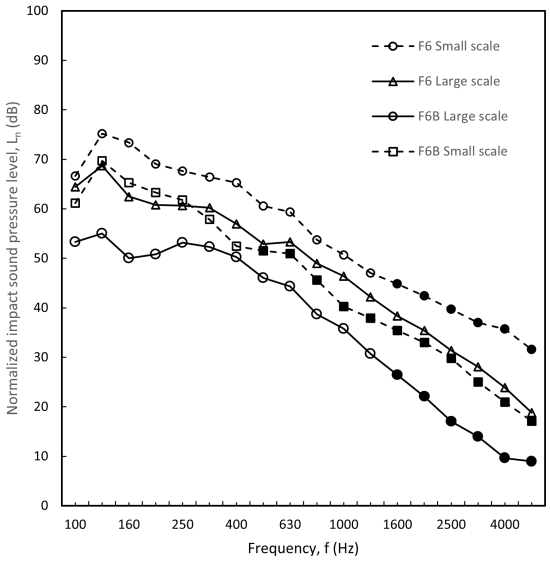


Figure 5. Limit of measurement precision for floors F6 and F6B.

Corresponding single-number ratings for airborne and impact sound insulation are provided in Tab. 3, together with the limiting frequency (f_l) where contribution of the airborne sound from source room starts to dominate and impact sound insulation cannot be measured correctly.

Prefixes *s* and *l* added to floor numberings indicate small and large samples.

Despite the fact that impact sound insulation cannot be measured correctly in the entire frequency range, single-number weighted normalized impact sound pressure level ($L_{n,w}$) can be determined as the unfavorable deviations from the ISO 717-2:2000 [5] reference curve occur below f_l.

Limit of frequencies where unfavorable deviations occur can be denoted as f_2. Therefore, as long as $f_l > f_2$, $L_{n,w}$ can be correctly evaluated.

Table 3. Test results – Floors F6 and F6B.

Floor No.	$L_{n,w}$ (dB)	R_w (dB)	f_l (Hz)	f_2 (Hz)
F6s	63	39	1600	315
F6l	56	51	-	-
F6Bs	56	39	500	250
F6Bl	46	58	1600	315

This analogy has been used to list all test results in the following chapter and indicate whether the evaluation of $L_{n,w}$ was accurate.

3.3 Test results

Complete overview of test results for all ten floors, in both sizes (together with the basic CLT), is presented in Tab. 4.

It should be noted that R_w value for all the small scale tests represents the airborne sound insulation of basic CLT (R_w 39 dB).

Table 4. Test results.

Floor No.	$L_{n,w}$ (dB)	R_w (dB)	f_l (Hz)	f_2 (Hz)
CLT	88	39	-	-
F1s	80	39	-	-
F1l	75	44	-	-
F1Bs	63	39	1600	315
F1Bl	61	54	-	-
F2s	72	39	-	-
F2l	67	47	-	-
F3s	71	39	-	-
F3l	66	48	-	-
F4s	70	39	-	-
F4l	64	49	-	-
F4Bs	61	39	800	250
F4Bl	54	57	-	-
F5s	58	39	800	250
F5l	54	52	-	-
F5Bs	53	39	400	250
F5Bl	42	58	1000	315
F6s	63	39	1600	315
F6l	56	51	-	-
F6Bs	56	39	500	250
F6Bl	46	58	1600	315

Fig. 6 illustrates a comparison of two impact sound insulation curves (floor F5), for a typical case where large scale test was not affected by the airborne component, while small scale test had a limitation already at 800 Hz. Black-filled markers are added to the frequencies where the result is dominated by the airborne sound and impact sound insulation cannot be measured correctly.

Regardless of the obvious limitations in accurately measuring the complete spectrum of impact sound for F5s, $L_{n,w}$ is determined only by the values up to 250 Hz; where airborne component was not an issue (shaded area in Fig. 6).

In other words, the unfavorable deviations from the ISO 717-2:2000 [5] reference value for floor F5s occur only between 100 and 250 Hz. Other values are not relevant for single-number evaluation.

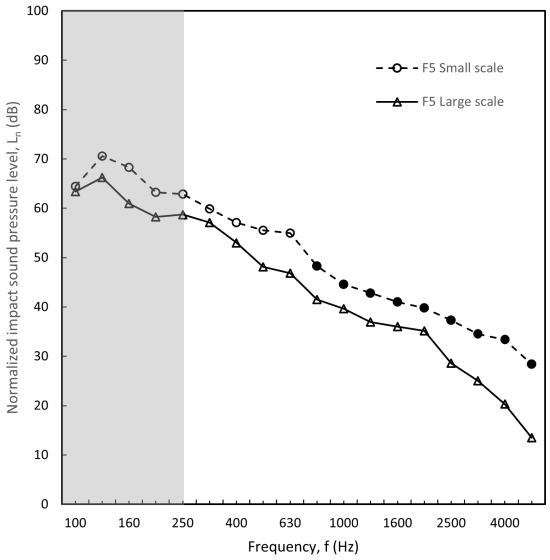


Figure 6. Impact sound insulation for floor F5 (small and large).

3.4 Analysis

Considering the results in Tab. 4, condition $f_1 > f_2$ was valid for all the floors where airborne sound component was influencing the results.

Therefore, despite the latter shortcoming the single-number $L_{n,w}$ rating could be accurately evaluated for all the tested floors.

Difference (in dB) between the $L_{n,w}$ for small scale and large scale tests is given in Tab. 5. Results for small scale tests are constantly higher than those for large scale. Hence, all the values in Tab. 5 are positive.

Table 5. Difference between $L_{n,w}$ for small scale and large scale tests.

Floor No.	$L_{n,w}$ small – $L_{n,w}$ large (dB)
F1	5
F1B	2
F2	5
F3	5
F4	6
F4B	7
F5	4
F5B	11
F6	7
F6B	10

It is indicative that differences in $L_{n,w}$ between small scale and large scale tests ($\Delta L_{n,w}$) are higher for better performing floors (floors with lower $L_{n,w}$). This trend is indicated in Fig. 7.

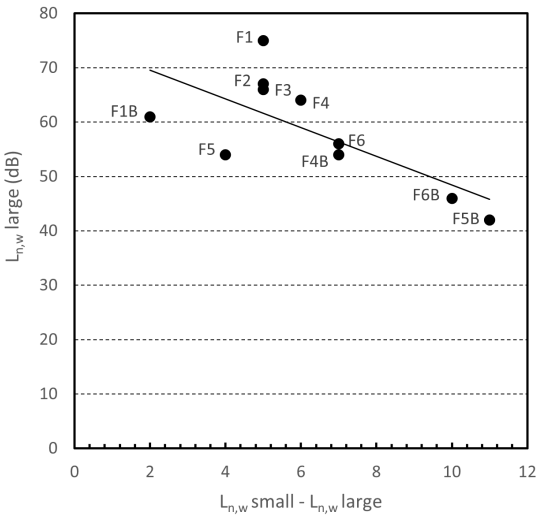


Figure 7. $\Delta L_{n,w}$ in relation to floor's $L_{n,w}$.

Finally, correlation between single-number $L_{n,w}$ ratings for small scale and large scale tests is illustrated in Fig. 8 (with an $R^2 = 0.95$).

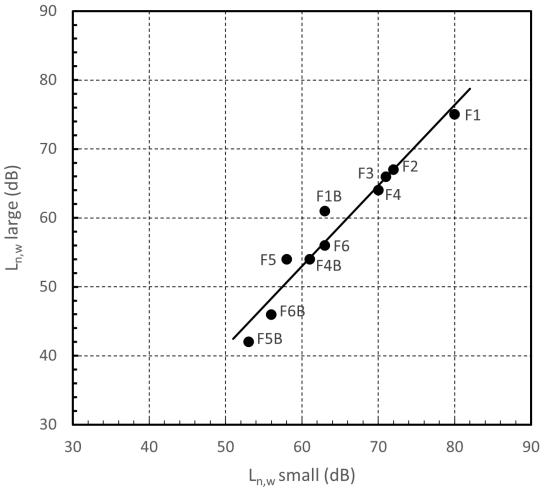


Figure 8. Correlation between $L_{n,w}$ for small scale and large scale tests.

4. CONCLUSIONS

This study provides a detailed correlation analysis of impact sound insulation tests conducted on a variety of small scale and large scale samples, built on the 140 mm CLT reference floor.

For all the small scale samples, sound pressure level generated by the tapping machine in the source room is attenuated only by the basic CLT floor (R_w 39 dB).

Such particularity of the sound propagating mechanism presents the limiting factor for accurate measurements of impact sound insulation in the standard frequency range (100-3150 Hz). Airborne component turned out to be dominant for eight out of twenty tested floors. Six of them being small scale and two large scale.

Notwithstanding the latter shortcoming, single-number weighted normalized impact sound pressure level ($L_{n,w}$) could be accurately determined as the latter value is driven primarily by floor's low frequency response.

For all eight floors influenced by the airborne component, the unfavorable deviations from the ISO 717-2:2000 [5] reference value occurred only between 100 and 315 Hz. Values on other frequencies were not relevant for single-number evaluation.

The latter frequency range was always well below the limiting frequency of the airborne component. So long as this condition is fulfilled, single-number rating can be accurately determined.

Consequently, single-number ratings could be accurately evaluated for all the tested floors and good correlation between $L_{n,w}$ of small scale and large scale tests established (see Fig. 8).

To conclude, this study demonstrated that it is possible to perform impact sound insulation tests on small samples built on CLT floor and accurately estimate the expected single-number $L_{n,w}$ for equivalent large scale samples. The established relationship presents useful tool for comparative analyses and design decision-making.

5. REFERENCES

[1] ISO 10140-3:2021, Acoustics – Laboratory measurements of sound insulation of building elements. Part 3: Measurement of impact sound insulation.

[2] K. Bet, R. Heissler, M. Oliveira, F. Pacheco, J. Patricio: "Influence of sample size on impact noise test results", in *Proc. of InterNoise 2019* (Madrid, Spain).

[3] ISO 10140-1:2021, Acoustics – Laboratory measurements of sound insulation of building elements. Part 1: Application rules for specific products.

[4] ISO 10140-4:2021, Acoustics – Laboratory measurements of sound insulation of building elements. Part 4: Measurement procedures and requirements.

[5] ISO 717-2:2020, Acoustics – Rating of sound insulation in buildings and of building elements. Part 2: Impact sound insulation.

DOI: 10.61782/fa.2025.0469

FORUM ACUSTICUM EURONOISE 2025

INFLUENCE OF GRAVEL ON FLANKING TRANSMISSION IN CLT BUILDINGS

Arne Dijckmans[1*] **Charlotte Crispin**[1]

[1] Buildwise, Belgium

ABSTRACT

Gravel layers are sometimes used to improve the airborne and impact sound insulation of Cross Laminated Timber (CLT) floor constructions. The gravel increases the mass and damping of the bare CLT floor and will also improve the efficiency of a floating floor. It is generally assumed that additions like linings and floating floors do not influence the vibration damping in junctions. While this is usually a reasonable assumption, the effect of the gravel on the vibration damping in CLT junctions cannot be neglected. This paper presents laboratory measurement results for the vibration reduction index of a rigid CLT junction with and without gravel. The influence of the gravel layer on the flanking transmission paths is investigated by means of the simplified SEA model of ISO 12354. SEA simulations, incorporating the effect of the gravel layer, are validated with in situ measurements.

Keywords: *sound insulation, flanking transmission, vibration reduction index, gravel layer, wooden buildings*

1. INTRODUCTION

Due to its relatively low weight and high stiffness, the acoustic performance of bare Cross Laminated Timber (CLT) constructions is limited and acoustic linings are generally necessary to achieve the required sound insulation. A well-established method to improve the impact sound insulation of CLT floors is to increase its mass, e.g. by applying a gravel ballast layer beneath the floating floor [1, 2]. The gravel adds mass that reduces the amplitude of vibrations and shifts the mass-spring-mass-resonance frequency of the floating floor to lower frequencies. In addition to the mass effect, the gravel can enhance energy dissipation, thereby reducing the radiated sound power.

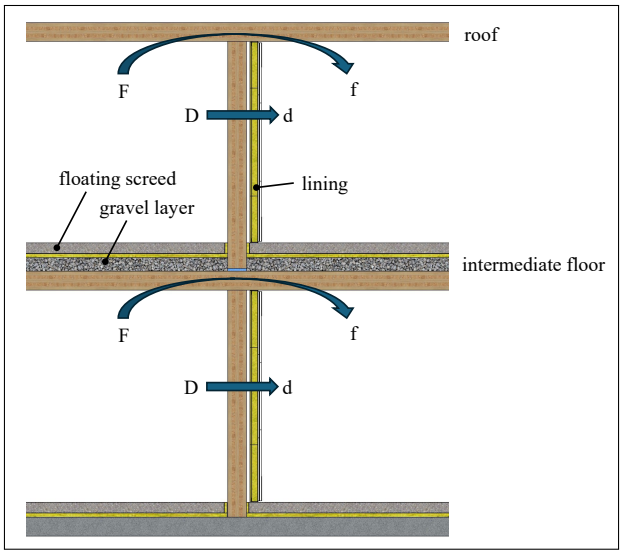


Figure 1. Application of gravel layers in a CLT building

While the influence of gravel layers on the direct airborne and impact sound insulation has been extensively investigated in literature, the effect on flanking transmission is unclear. The vibration transmission across junctions is characterized by the vibration reduction index K_{ij}, which is generally measured on bare junctions according to ISO 10848 [4]. This property can then be used in statistical energy analysis (SEA) calculations,

**Corresponding author*: arne.dijckmans@buildwise.be.

Copyright: *©2025 Arne Dijckmans et al. This is an open-access article distributed under the terms of the Creative Commons Attribution 3.0 Unported License, which permits unrestricted use, distribution, and reproduction in any medium, provided the original author and source are credited.*

e.g. following ISO 12354 [5], where it is assumed that linings and floating floors do not influence K_{ij}. This assumption seems not valid for CLT junctions loaded with a gravel layer. In situ measurements in CLT apartment buildings with such floors have systematically indicated significantly higher airborne sound insulation values at intermediate floors than at the top floor (Figure 1). The observed differences cannot be entirely explained by the variation in K_{ij} of T- and cross junctions, which is on average 3 dB for heavy rigid junctions.

In this paper, the effect of a gravel layer on the flanking transmission across junctions of CLT walls and floors is investigated by means of laboratory K_{ij}-measurements (section 2) and simulations of *in situ* airborne sound insulation according to ISO 12354-1 (section 3).

2. LABORATORY MEASUREMENTS

2.1 CLT mockup

A full-scale mockup of a CLT junction was realised at the acoustics laboratory of Buildwise to measure the vibration reduction index of a reference junction without gravel, a junction with a 2.5 cm gravel layer and a junction with a 5 cm gravel layer. The horizontal L-junction consists of a 5-ply CLT-floor with thickness 14 cm and dimensions 4.93 m × 2.25 m and a 5-ply CLT wall with thickness 12 cm and dimensions 3.94 m × 2.40 m. The density of the CLT floor and wall is approximately 485 kg/m^3 and 470 kg/m^3 respectively. The wall was placed between two transmission chambers of the acoustics laboratory with the top 0.6 m of the panel protruding from the chambers. The floor panel was placed on one side on the wall panel and on the other side on concrete blocks resting on the concrete ceiling of the transmission chambers. To ensure maximum contact between the floor and the wall, a very thin layer of plaster was used to level out the slight roughness and non-flatness of the wood.

Wooden boards were screwed into the CLT floor around the perimeter to create a box to hold the gravel (Figure 2). The CLT floor was covered with a gravel layer with an average thickness of 5 cm (Figure 3). A plastic foil was placed beneath the gravel to avoid the CLT panel getting wet because the gravel was still damp when placed on the floor. However, the gravel was completely dry at the moment of the measurements. Afterwards, half of the gravel was removed and the remaining gravel was levelled to a thickness of approximately 2.5 cm. Finally,



Figure 2. Reference junction without gravel



Figure 3. Junction with 5 cm gravel

the vibration reduction index of the reference junction with box but without gravel was measured.

The gravel has a density of approximately 1080 kg/m^3, as measured in dry condition after the K_{ij}-measurements, and the size of the round aggregates varies widely with pebbles up to 7 cm. The mass loading of the gravel layer is approximately 600 kg (54 kg/m^2) and 300 kg (27 kg/m^2) for the 5 cm and 2.5 cm thick gravel layer respectively.

2.2 Measurement procedure

The vibration reduction index K_{ij} between the floor and the wall was measured according to the ISO 10848 standards series [4]. The velocity level of both panels was measured simultaneously using eight accelerometers on each panel. The accelerometers were glued to the bottom

side of the floor panel and to the outer side of the wall panel. Each panel was excited at three different locations using hammer excitation over an area of approximately $1\,\mathrm{m}^2$. The floor was excited at the underside, also for the reference measurement. The same accelerometer and excitation positions were used for the three junctions.

To limit the effect of parastic airborne noise generated by the sound radiation from the excited element [3], mineral wool was placed in the cavity below the floor element to cover the part of the wall extruding the transmission chambers (Figure 3).

The structural reverberation time T_s of each panel was measured using hammer excitation for four source positions and eight receiver positions. The integrated impulse response method with backward integration of the squared impulse response was used. Measurements not fulfilling the requirement $BT_s < 4$ (with B the frequency bandwidth), which are influenced by the filter and detector, are discarded.

At low frequencies, the measurement results are influenced by the modal behaviour of the junction, with low modal overlap factors (< 1) and low mode counts (< 5) up till approximately $400\,\mathrm{Hz}$. This means that the measured K_{ij}-values might not be relevant and might not be situation-invariant in this frequency range. Although one thus has to be careful when using the K_{ij} as input to ISO 12354, relative differences between the different measurements are relevant.

2.3 Measurement results

2.3.1 Loss factor

Figure 4 compares the loss factor η for the floor without and with gravel, calculated from the measured structural reverberation time. The loss factor of the CLT floor without gravel has a relatively constant value of $2.5 - 3\%$ up till $1250\,\mathrm{Hz}$ and decreases slightly at higher frequencies. For the floor with $2.5\,\mathrm{cm}$ gravel, the loss factor is significantly larger than the unloaded floor from $100\,\mathrm{Hz}$ upwards. For the floor with $5\,\mathrm{cm}$ gravel, the loss factor is larger from $160\,\mathrm{Hz}$ upwards and peaks between $400\,\mathrm{Hz}$ and $1000\,\mathrm{Hz}$.

At mid frequencies, where the loss factor is maximal, it was difficult to accurately measure the structural reverberation times of the floor panel, as indicated by the large standard uncertainty. Furthermore, a lot of measurements showed a very low reverberation time for which the condition $BT_s < 4$ was not met and ringing of the band pass filters influenced the measurements. The loss factor is thus probably an underestimation of the actual damping. When the measurement results with $BT_s < 4$ are not discarded, higher loss factors are obtained (Figure 4, dashed lines).

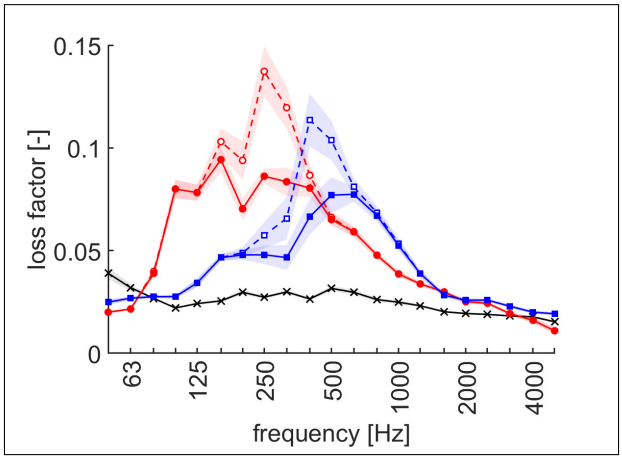


Figure 4. Loss factor of CLT floor without gravel (×), with $2.5\,\mathrm{cm}$ gravel (●) and $5\,\mathrm{cm}$ gravel (■). The shaded areas show the standard uncertainty. The dashed lines show the average values when measurements with $BT_s < 4$ are not discarded.

2.3.2 Velocity levels

The gravel layer has a significant influence on the vibro-acoustic behaviour of the CLT floor panels (Figure 5). The velocity levels L_v of the floors with gravel show a pronounced dip at mid frequencies, both when the floor and the wall are excited. For the $5\,\mathrm{cm}$ gravel layer the dip is observed around $315 - 400\,\mathrm{Hz}$, for the $2.5\,\mathrm{cm}$ gravel layer around $200 - 250\,\mathrm{Hz}$ (not shown for brevity). Furthermore, the dip in velocity level strongly depends on the accelerometer position, indicated by the large spread in this frequency range. The gravel layer thus limits the vibration of the CLT floor, especially at mid frequencies. This effects seems to be linked to a resonance phenomenon in the gravel layer, for which the resonance frequency depends on the thickness of the gravel layer.

The dip in L_v leads to a pronounced peak in velocity level difference $D_{\mathrm{v},ij}$ from wall to floor (Figure 6b). At high frequencies, $D_{\mathrm{v},ij}$ is not influenced by the gravel. When the floor is excited, the lower vibration energy in the floor panel due to the gravel layer also leads to a dip in the wall velocity level. Although it could be expected that $D_{\mathrm{v},ij}$ from floor to wall is independent of the gravel layer,

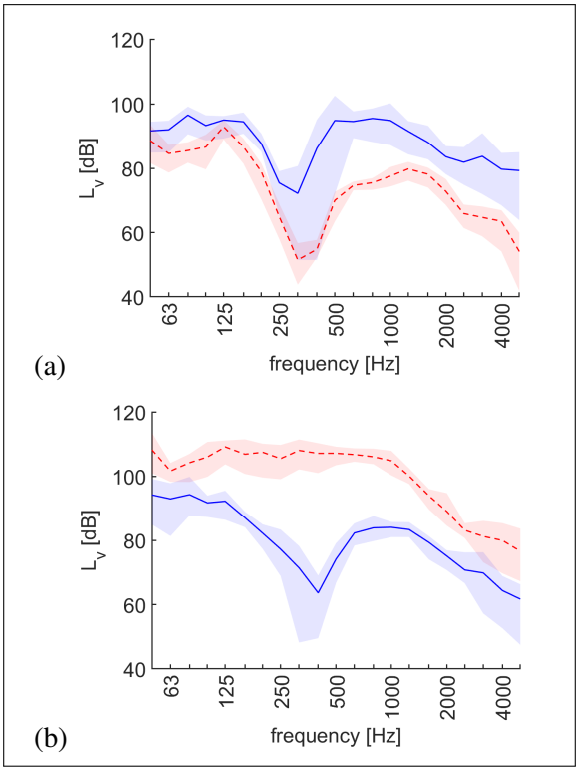


Figure 5. CLT junction with 5 cm gravel. Average velocity levels of floor (—) and wall (– –) for 1 source position on (a) floor and (b) wall. The shaded areas show the spread over 8 accelerometer positions.

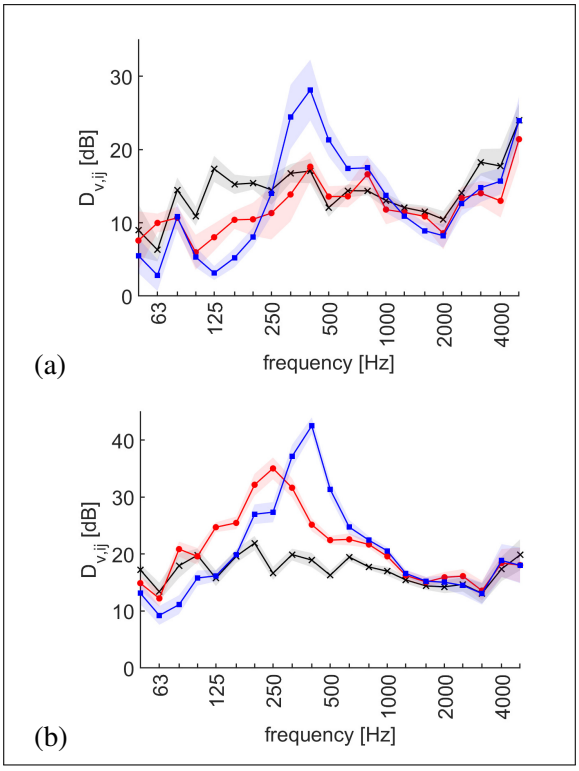


Figure 6. Velocity level difference for excitation of (a) floor and (b) wall for the CLT junction without gravel (×), with 2.5 cm gravel (●) and 5 cm gravel (■). The shaded areas show the standard uncertainty.

this is not the case at low and mid frequencies, especially for the 5 cm gravel layer (Figure 6a).

To further investigate the effect of the gravel layer on the vibration transmission across the junction, the difference in $D_{\mathrm{v},ij}$ in both directions is checked. According to SEA theory, $D_{\mathrm{v},ij}$ can be deduced from the coupling loss factor η_{ij} following:

$$D_{\mathrm{v},ij} = 10\lg\frac{\eta_j}{\eta_{ij}} - 10\lg\frac{m_i}{m_j} \tag{1}$$

where η_j is the total loss factor of element j and m_i and m_j are the mass of element i and j respectively. Using the consistency relationship, the following equality can be deduced for the difference in $D_{\mathrm{v},ij}$ normalized to the loss factor:

$$\Delta = D_{\mathrm{v},ji} - D_{\mathrm{v},ij} + 10\lg\frac{\eta_j}{\eta_i} = 20\lg\frac{m_i}{m_j} + 10\lg\frac{n_j}{n_i} \tag{2}$$

where n_i and n_j is the modal density of element i and j respectively. This normalized difference is thus only dependent on the ratio of element mass and modal density.

For the reference junction, there is a good agreement between measured values and SEA estimations in a broad frequency range, except at low frequencies where the SEA assumptions of high modal overlap and high mode count are not met, and at high frequencies where in-plane wave propagation becomes important (Figure 7). Above 500 Hz, the measurement results for the junctions with gravel also agree well with the predicted value, indicating that the gravel layer does not influence the vibration transmission across the junction in this frequency range. Below 500 Hz, the measurements show significantly higher values. This can partly be explained by the activation of the mass of the gravel layer. By including the mass of the gravel layer in the term m_i in Eqn. (2), the predicted difference is larger and agrees

better with the measured values, although there is still a large undestimation.

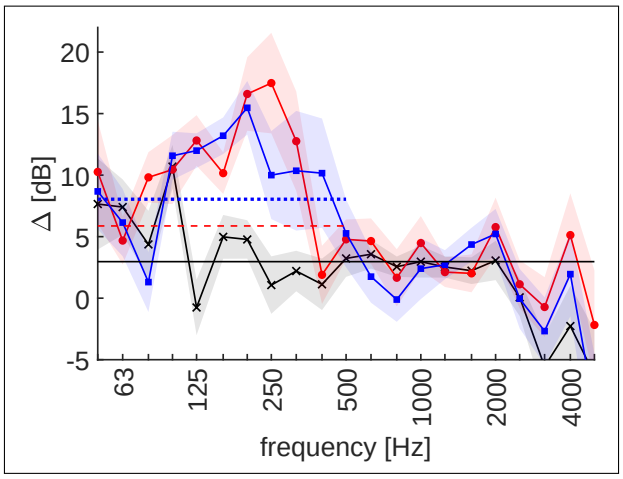


Figure 7. Difference $D_{\mathrm{v},ji}$- $D_{\mathrm{v},ij}$ normalized to the loss factors for the CLT junction without gravel (×), with 2.5 cm gravel (●) and 5 cm gravel (■). The measured values are compared with SEA predictions with $m_i = m_{\mathrm{CLT}}$ (—), $m_i = m_{\mathrm{CLT}} + m_{2.5\,\mathrm{cm\,gravel}}$ (– –), $m_i = m_{\mathrm{CLT}} + m_{5\,\mathrm{cm\,gravel}}$ (· · ·). The shaded areas show the standard uncertainty.

2.3.3 *Vibration reduction index*

The CLT wall panel is considered a type A element according to ISO 10848-1. Because the structural reverberation time of the floor panels with gravel is primarily determined by the gravel and not by the connected elements, they are considered to be a type B element. As an advantage, this eliminates the large uncertainty in the structural reverberation time measurements of the floor panels with gravel. To have a fair comparison between the K_{ij}-values of the unloaded and loaded junctions, the floor panel of the reference junction is also considered a type B element.

For a junction composed of both type A and type B elements, the vibration reduction index is determined by:

$$K_{ij} = \frac{D_{v,ij} + D_{v,ji}}{2} + 10\lg\frac{l_{ij}}{\sqrt{a_i a_j}} \tag{3}$$

with

$$a = \frac{2.2\pi^2 S}{T_s c_0}\sqrt{\frac{f_{\mathrm{ref}}}{f}} \tag{4}$$

for type A elements, and

$$a = S/l_0 \tag{5}$$

for type B elements. S is the surface area of the element, $c_0 = 343\,\mathrm{m/s}$ is the speed of sound in air, $f_{\mathrm{ref}} = 1000\,\mathrm{Hz}$ and $l_0 = 1\,\mathrm{m}$.

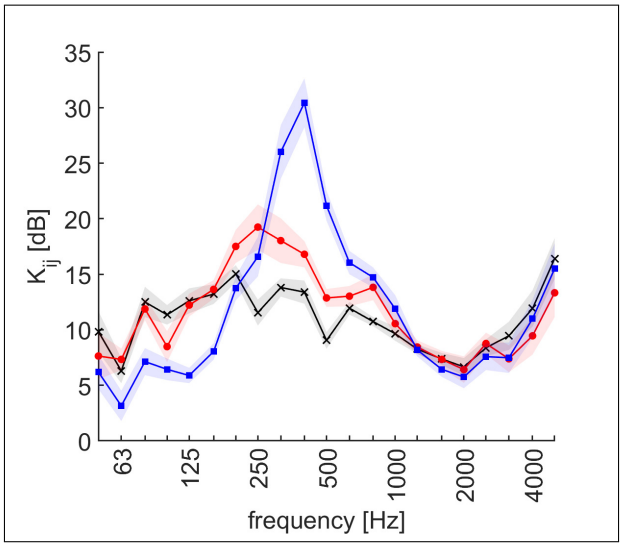


Figure 8. Vibration reduction index of the CLT junction without gravel (×), with 2.5 cm gravel (●) and 5 cm gravel (■). The shaded areas show the standard uncertainty.

The vibration reduction index of the reference junction is relatively independent of frequency, with an average value of 11.7 dB between 200 Hz and 1250 Hz (Figure 8). At high frequencies, the vibration reduction index drops, with a minimum value of approximately 7 dB at 2000 Hz. In this frequency range, the vibration reduction is strongly influenced by the connection details. Previous measurements without plaster layer showed no dip at high frequencies due to a non-perfect contact, while screws or angle brackets further reduced the K_{ij} at high frequencies.

The gravel layer does not influence the K_{ij} at high frequencies, with variations that are within the repeatability limits of the measurement procedure. At mid frequencies, a peak can be observed in the K_{ij}-values for the junctions with gravel layer, which is related to the dip in floor velocity levels. The 5 cm gravel layer significantly increases K_{ij} between 250 Hz and 500 Hz, with a peak

value of 31.5 dB at 400 Hz, i.e. 15 dB above the K_{ij} of the reference junction. The effect of the 2.5 cm gravel layer is less pronounced, but the K_{ij} is still approximately 5 dB higher in the 250 Hz octave band compared to the reference junction. At low frequencies, where global modes of the junction are important, the influence of the 2.5 cm gravel layer is negligible, but the 5 cm gravel layer reduces K_{ij} on average with 5 dB up to 160 Hz. As noted earlier, it is difficult to extrapolate these results because the SEA assumptions of the measurement method are not met at low frequencies.

3. IN SITU SOUND INSULATION

3.1 Prediction model

The airborne sound insulation between two rooms can be estimated from the element and junction properties following the standard ISO 12354-1 [5]. The SEA-based model incorporates the direct transmission path (with sound reduction index R_{Dd}) and the first order flanking transmission paths. The flanking sound reduction index R_{ij} for the transmission path between element i in the source room and element j in the receiving rooms is estimated from:

$$R_{ij} = \frac{R_{i,\mathrm{situ}}}{2} + \Delta R_{i,\mathrm{situ}} + \frac{R_{j,\mathrm{situ}}}{2} + \Delta R_{j,\mathrm{situ}} + \overline{D_{v,ij,\mathrm{situ}}} + 10\lg\frac{S_s}{\sqrt{S_i S_j}} \quad (6)$$

where R_{situ} is the *in situ* value of the sound reduction index, S_s is the area of the separating element between the rooms and $\overline{D_{v,ij,\mathrm{situ}}}$ is the *in situ* direction-averaged junction velocity level difference, which can be determined from:

$$\overline{D_{v,ij,\mathrm{situ}}} = K_{ij} - 10\lg\frac{l_{ij,\mathrm{situ}}}{\sqrt{a_{i,\mathrm{situ}} a_{j,\mathrm{situ}}}}. \quad (7)$$

For junctions composed of both type A and type B elements, the *in situ* equivalent absorption of the type B element can be taken equal to the element area:

$$a_{i,\mathrm{situ}} = S_{i,\mathrm{situ}}/l_0 \quad (8)$$

Because of the limited information available on the structural reverberation time of CLT panels *in situ*, the equivalent absorption length of the type A elements is also taken equal to the element area S in this paper, following the assumption of the simplified model in ISO 12354-1.

The *in situ* value of the sound reduction index of the CLT floor with gravel is estimated with the transfer matrix method (TMM), using an equivalent orthotropic plate model for the CLT and the measured loss factors for the CLT floors with gravel. Because the loss factor for the floors is significantly increased due to the gravel, the sound reduction index is also larger in a broad frequency range. Above the critical frequencies of the CLT panel, the improvement can be estimated from:

$$R_{\mathrm{situ}} = R_{\mathrm{ref}} + 10\lg\frac{\eta_{\mathrm{gravel}}}{\eta_{\mathrm{ref}}}. \quad (9)$$

For example, the predicted global sound reduction index $R_A = R_w + C$ of a 14 cm CLT floor increases from 35.2 dB to 37.4 dB due to the additional structural damping of the 5 cm gravel layer.

The vibration reduction index K_{ij} is not measured for all types of junctions with CLT floors loaded with gravel. Therefore, the vibration reduction index $K_{ij,\mathrm{gravel}}$ of the junction path between a CLT floor with gravel and another element is estimated from the vibration reduction index $K_{ij,0}$ of the equivalent junction without gravel,

$$K_{ij,\mathrm{gravel}} = K_{ij,0} + \Delta K_{ij,\mathrm{gravel}}. \quad (10)$$

The improvement $\Delta K_{ij,\mathrm{gravel}}$ due to the gravel layer is estimated from the improvement measured in the laboratory for the L-junction. For the transmission between two floors, the improvement $\Delta K_{ij,\mathrm{gravel}}$ is only added once to $K_{ij,0}$.

3.2 Theoretical example

As an example, the horizontal sound insulation between two rooms (with depth 3.0 m) is calculated, either disregarding the effect of the gravel or taking into account its effect on R_{situ} and K_{ij}. The separating wall with dimensions 4.0 m × 2.6 m consists of a 10 cm CLT panel and an acoustic lining. The 14 cm CLT floor and ceiling run across the separating wall. The $K_{ij,0}$ of the CLT junctions is estimated following Annex F3.2 of ISO 12354-1 [5]. A floating screed is placed on top of a 2.5 cm or 5 cm gravel layer on both the floor and the ceiling panels. Flanking transmission across the side walls is limited due to the application of a structural break at the junction with the separating wall.

The sound insulation between the rooms is dominated by the flanking transmission via the ceiling, more specifically the Ff path from ceiling to ceiling (Table 1). Only at low frequencies, the transmission through the

separating wall is the dominant path (Figure 9). When the effect of the gravel is disregarded, a global sound insulation $D_A = D_{nT,w} + C = 48.5\,\text{dB}$ is predicted. The predicted sound insulation increases to $D_A = 52.5\,\text{dB}$ and $50.9\,\text{dB}$ due to the effect of the $2.5\,\text{cm}$ and $5\,\text{cm}$ gravel layer, respectively, of which approximately $2\,\text{dB}$ can be attributed to the increase in R_{situ}. The additional improvement is related to the increase in K_{ij} between $250\,\text{Hz}$ and $1000\,\text{Hz}$. The improvement in D_A is smaller for the $5\,\text{cm}$ gravel layer due to the reduction in K_{ij} at lower frequencies.

Table 1. Sound reduction indices R_A

Path	reference (no gravel)	2.5 cm gravel	5 cm gravel
Direct - Dd	60.1 dB	60.1 dB	60.1 dB
Ceiling - Ff	49.7 dB	54.6 dB	52.6 dB
Ceiling - Fd	56.3 dB	60.0 dB	58.1 dB
Ceiling - Df	80.4 dB	84.0 dB	76.1 dB
Total	48.5 dB	52.5 dB	50.9 dB

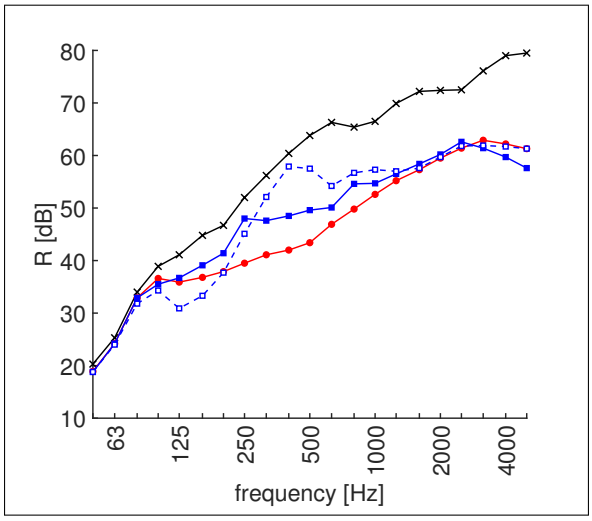


Figure 9. Sound insulation between two rooms according to ISO 12354-1 ($\times\ R_{Dd}$, $\bullet\ R'_{\text{ref}}$, $\blacksquare\ R'_{2.5\,\text{cm gravel}}$, $\square\ R'_{5\,\text{cm gravel}}$)

3.3 Case study

The prediction model is applied to a case study of a CLT apartment building. The intermediate floors consist of a $22\,\text{cm}$ CLT panel, a $9\,\text{cm}$ gravel layer and a floating screed. The ceiling of the top floor consists of a $22\,\text{cm}$ CLT panel. Above the ceiling is an empty plenum with a variable height ($60 - 170\,\text{mm}$) to create a slope for the flat roof which consists of an OSB plate, a stiff thermal insulation plate and a ballast layer. The walls consist of a $12\,\text{cm}$ CLT panel with an acoustic lining on both sides (2 gypsum boards on $50\,\text{mm}$ metal studs and a $50\,\text{mm}$ mineral wool filling). An elastic joint is inserted between the floor panels at the junctions with the separating walls between dwellings.

The sound insulation between the living room and a bedroom of two neighbouring dwellings was measured on an intermediate floor and on the top floor of the building. The sound insulation on the top floor is significantly lower with a difference in D_A of $7\,\text{dB}$ (Figure 10).

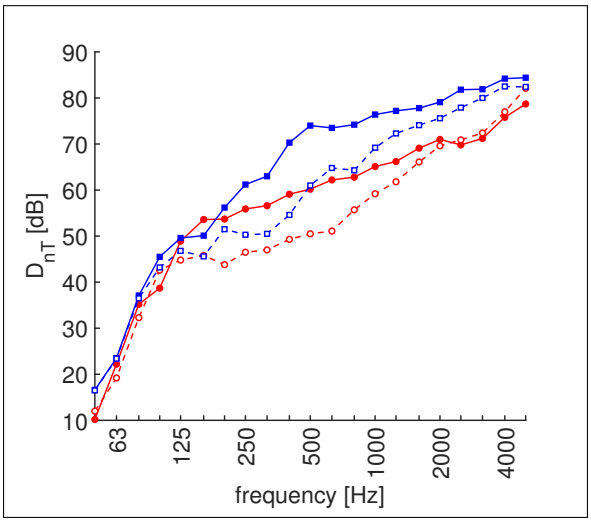


Figure 10. Case study: measured ($\bullet$) and simulated ($\blacksquare$) sound insulation between two rooms on the intermediate (—) and top (– –) floor.

For the predictions, the following assumptions have been made for the vibration reduction indices:

- The $K_{ij,0}$-value of the cross junctions is estimated from K_{ij}-measurements in a mock-up with a similar junction without gravel. The mock-up values have been reduced at mid and high frequencies to account for two effects: the loading

of the elastic layer *in situ*, which will decrease its effect [6], and the mechanical coupling present in the apartment building to assure lateral stability.

- The $K_{ij,0}$-value of the T-junction on the top floor is estimated to be 3 dB lower than the $K_{ij,0}$-value of the cross junction.
- The average $\Delta K_{ij,\text{gravel}}$-value of the laboratory measurements with 2.5 cm and 5 cm is applied. Below 200 Hz, no effect is taken into account ($\Delta K_{ij,\text{gravel}} = 0$).

The simulations indicate that the Ff path from ceiling to ceiling is the dominant transmission path in the entire frequency range of interest ($\geq$ 100 Hz), both on the intermediate floor and on the top floor, despite the elastic joint between the ceiling plates.

Although the sound insulation is globally overestimated by the model, the relative difference between intermediate and top floor is well predicted. The model difference of 7 dB in D_A-value is partly due to the difference between T- and cross junction (3 dB), partly due to the effect of the gravel layer on R_{situ} (1.5 dB) and partly due to the effect of the gravel layer on K_{ij} (2.5 dB). The overestimation may be attributed to several factors, like an overestimation of the sound insulation R by the TMM, an overestimation of the vibration reduction index $K_{ij,0}$, or the presence of other transmission paths not taken into account in the model. On the top floor, indirect airborne transmission via the plenum in the roof could e.g. further reduce the sound insulation.

4. CONCLUSIONS

While gravel layers are primarily used to improve the airborne and impact sound insulation of CLT floors, the gravel layer also influences the flanking transmission across the floor junctions in two ways. First, the gravel layer significantly increases the loss factor of the floor, and thus also the sound reduction index of the floor, especially above its critical frequency. The global improvement in $R_{A,\text{situ}}$ of typical CLT floors is estimated to be 2 dB based on TMM simulations. Second, the vibro-acoustic behaviour of the junction, as characterized by the vibration reduction index K_{ij}, is changed. The measured K_{ij}-values show a pronounced peak at mid frequencies, linked to a resonance phenomenon in the gravel layer. Simulations with the SEA-based model of ISO 12354 indicate that for situations where flanking transmission across the ceiling is dominant, the gravel layer can improve the global sound insulation with up to 5 dB. Case studies learn that care should be taken with sound transmission across ceilings at the top floor where this positive effect of gravel layers is not present, while flanking transmission across the top T-junctions is already larger than across intermediate cross junctions.

5. ACKNOWLEDGMENTS

The results presented in this paper have been obtained within the frame of the projects "STABBS II" (Standards for acoustic better buildings II). The authors are grateful for the financial support from the Federal Public Service Economy of Belgium.

6. REFERENCES

[1] C. Guigou-Carter, N. Balanant, and J.-L. Kouyoumji. Apparent wood elements and acoustic performance - Feedback from Adivbois CLT building mockup. In *Proc. of InterNoise22* , pages 3513–3524, Glasgow, Scotland, 2022.

[2] A. Homb, C. Guigou-Carter, and A. Rabold. Impact sound insulation of cross-laminated timber/massive wood floor constructions: Collection of laboratory measurements and result evaluation. *Building Ac*, 24(1):35–52, 2017.

[3] C. Crispin, V. Pettoni Possenti, A. Dijckmans, and L. Barbaresi. Improving the accuracy of vibration reduction index measurements: Assessing and correcting parasitic airborne noise effects. *Available at SSRN*: http://dx.doi.org/10.2139/ssrn.5168683, 2025.

[4] ISO 10848-1:2017 *Acoustics – Laboratory and field measurement of flanking transmission for airborne, impact and building service equipment sound between adjoining rooms – Part 1: Frame document*

[5] ISO 12354-1:2017 *Building acoustics – Estimation of acoustic performance of buildings from the performance of elements – Part 1: Airborne sound insulation between rooms*

[6] V. Pettoni Possenti, C. Crispin, A. Dijckmans, and L. Barbaresi. Load effects in flanking transmission of CLT structures with resilient interlayer. In *Proc. of Forum Acusticum Euronoise*, Málaga, Spain, 2025.

DOI: 10.61782/fa.2025.0694



FORUM ACUSTICUM
EURONOISE 2025

PREDICTION OF FLANKING SOUND TRANSMISSION ACROSS PERIODIC CROSS-LAMINATED TIMBER JUNCTIONS WITH AREA COUPLINGS

Stijn Moons [1,2*] **Reinhilde Lanoye**[2] **Edwin P.B. Reynders**[1]

[1] Department of Civil Engineering, KU Leuven, Kasteelpark Arenberg 40, 3001 Leuven, Belgium
[2] CDM Stravitec, Reutenbeek 9/11, 3090 Overijse, Belgium

ABSTRACT

Cross-laminated timber (CLT) has gained popularity as a lightweight, carbon-neutral material for load-bearing walls and floors. However, its poor acoustic performance poses a crucial challenge to its further adoption. A critical factor is flanking sound, where vibrational energy is transmitted between two walls across a common junction. Typically, this transmission is analyzed with models based on plate or shell theory, but their accuracy at high frequencies is limited the ratio of wavelength to wall thickness is not large. While full-scale finite element analysis is possible, its computational cost at high frequencies is prohibitive as very fine element meshes are required. In the current study, an approach is presented which exploits the spatial periodicity often exhibited by CLT junctions. This allows the use of Bloch-Floquet analysis of the junction itself and the connected walls, leading to diffuse transmission coefficients between all wave types in the junction. The junction is treated as an elastic solid as opposed to the conventional thin shell modelling which results in a line coupling. Statistical Energy Analysis (SEA) is employed to compute the vibration reduction indices of the junction from these coefficients. The prediction model is applied to rigidly connected CLT junctions.

Keywords: *cross-laminated timber, flanking sound transmission, statistical energy analysis, periodic finite element method.*

**Corresponding author*: *stijn.moons@kuleuven.be.*

***Copyright**: ©2025 Moons et al. This is an open-access article distributed under the terms of the Creative Commons Attribution 3.0 Unported License, which permits unrestricted use, distribution, and reproduction in any medium, provided the original author and source are credited.*

1. INTRODUCTION

Cross-laminated timber (CLT) has gained popularity as an alternative to more carbon-intensive materials for load-bearing structures such as concrete. However, its further adoption is hindered by a generally poor acoustic performance. Especially structure-borne sound poses a problem due to the low weight and relatively high stiffness of CLT, with flanking sound transmission often dominating the overall sound transmission. In this transmission mechanism, vibration energy is exchanged between connected walls across their common junction. As a result, CLT junctions are often designed to mitigate flanking sound transmission with solutions such as resilient interlayers or pads between a wall and the floor beneath it. While these solutions are often effective, a better, deeper understanding of the vibration transmission is required to optimize their design. Computationally efficient prediction models are important tools in the further development of vibration reducing solutions and CLT junctions in general, because of the large variation in transmission paths.

In a recent publication [1], an analytical prediction model for continuous CLT junctions was presented within a Statistical Energy Analysis (SEA) framework [2]. The CLT walls are modelled as directly connected homogeneous thin plates [3, 4]. While the broadband predictions are quite accurate, thickness effects are absent in this model, leading to prediction deviations in the high-frequency range. Numerical modelling with volumetric finite elements allows to take high-frequency thickness effects into account as well as the layered nature of CLT panels. While full-scale modelling of a building junction

is possible, the computation time is a limiting factor, especially at high frequencies where fine element meshes are required. Exploiting the spatial periodicity of the CLT junctions, it is possible to model only a repeated unit cell deterministically with the finite element method and apply Bloch-Floquet analysis to each connected wall as well as to the junction itself. The resulting approach is often termed as the periodic finite element method (pFEM). In this article, a prediction model for the vibration reduction index K_{ij} of CLT junctions is presented where the connected walls and the junction itself are modelled with a pFEM approach. The vibrational energy transmission is analysed in a SEA framework. Section 2 describes the general principles behind the prediction model. The model is validated with experimental laboratory measurements on a rigid CLT X-junction in Section 3.

2. THEORETICAL FRAMEWORK OF THE PREDICTION MODEL

Fig. 1 contains a schematic representation of the type of system that is being considered. The junction is connected to a total of n walls via area couplings. The assembly is spatially periodic in the global x-direction and the corresponding unit cell length is denoted as l_x. Each wall j is also spatially periodic in its local y-direction, with corresponding unit cell width $l_{\mathrm{y},j}$. In what follows, displacements $\mathbf{u}_j$ are expressed in the local coordinate system of wall j, unless stated otherwise. The subscript j is omitted for notational simplicity wherever possible.

Free plane waves in the periodic structure adhere to the Bloch-Floquet theorem, such that the displacements $\mathbf{u}(\mathbf{x},\mathbf{n})$, expressed in the local coordinate system of a wall, in any cell with position $\mathbf{n} = (n_\mathrm{x}, n_\mathrm{y})$ relative to the reference cell of the wall satisfy

$$\mathbf{u}(\mathbf{x},\mathbf{n}) = \mathbf{u}(\mathbf{x})\,\mathrm{e}^{-\mathrm{i}\epsilon_\mathrm{x}-\mathrm{i}\epsilon_\mathrm{y}}, \qquad (1)$$

for coordinates $\mathbf{x} = (x, y)$ within the reference unit cell. The factors ϵ_x and ϵ_y are the phase constants corresponding to a given wave [5]. Unit cells of the walls and junction itself are modelled deterministically with volumetric finite elements, allowing to compute the unit cell stiffness and mass matrices $\mathbf{K}$ and $\mathbf{M}$ of each component.

Figures 2 and 3 illustrate the unit cell for a connected wall and the junction beam with interfaces between connected elements indicated in grey. The nodes and corresponding degrees of freedom in the finite element model of each wall can be distributed into separate groups related to their position within the unit cell: left bottom (LB), right bottom (RB), bottom (B), left (L), right (R), left top (LT), right top (RT), top (T) and internal (I). By imposing Bloch boundary conditions on the unit cell with phase constants in the local x- and y-direction on the degrees of freedom as in equation (1), the system can be reduced by matrix $\mathbf{R}$ with $\mathbf{u}_\mathrm{full} = \mathbf{R}\mathbf{u}_\mathrm{red}$ to a system with only degrees of freedom LB, B, L and I. For free wave propagation, the equations of motions of a wall lead to the

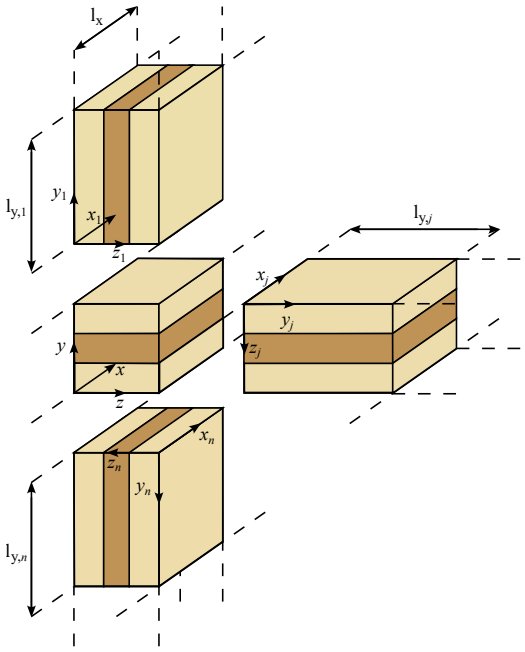


Figure 1. Exploded view of a T-junction with indication of the local coordinate systems of each element.

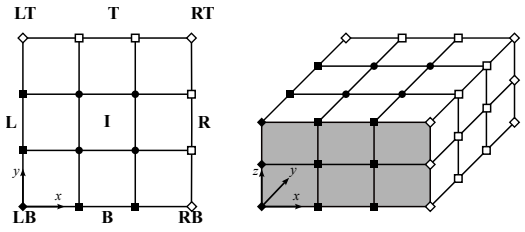


Figure 2. Unit cell of a wall with separate node labels.

following eigenvalue problem solved for eigenfrequencies ω and displacement eigenvectors $\boldsymbol{\phi}$, corresponding to the reduced degrees of freedom for displacements $\mathbf{u}_{\mathrm{red}}$:

$$\mathbf{R}^{\mathrm{H}}\left(\mathbf{K}-\omega^{2}\left(\epsilon_{\mathrm{x}},\epsilon_{\mathrm{y}}\right)\mathbf{M}\right)\mathbf{R}\boldsymbol{\phi}\left(\epsilon_{\mathrm{x}},\epsilon_{\mathrm{y}}\right)=0. \tag{2}$$

Similarly, the junction beam degrees of freedom are divided into: left (L), right (R), sleeve (S), left sleeve (LS), right sleeve (RS) and internal (I), which can be reduced to LS, L, S and I for an imposed ϵ_{x}.

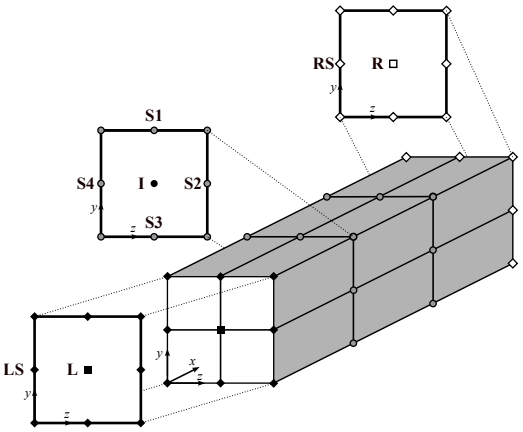


Figure 3. Unit cell of the junction beam with separate node labels.

The vibration transmission of the junction is analysed in a Statistical Energy Analysis (SEA) framework [2] with subsystems corresponding to free propagating wave types in a given connected element. In further derivations, the subscripts m and n are used to denote given source and receiver subsystems, respectively, such that a source subsystem m corresponds to wave type s in wall i and a receiver subsystem n to wave type t in wall j. The subsystems in all walls are assumed to be diffuse. Following a modal approach, this implies that each mode resonating within a given frequency band $\Delta\omega$, corresponding to a wave type with imposed phase constants ϵ_{x} and ϵ_{y}, has the same energy density e [6].

In order to study the energy exchange across the junction, the power balance of the overall SEA system is expressed in function of the subsystem energies E_m, input powers W_m, total loss factors η_m and coupling loss factors η_{mn} between subsystems m and n:

$$\begin{bmatrix}-\eta_1 & \eta_{21} & \eta_{31} & \dots\\ \eta_{12} & -\eta_2 & \eta_{32} & \dots\\ \eta_{13} & \eta_{23} & -\eta_3 & \dots\\ \dots & \dots & \dots & \dots\end{bmatrix}\begin{bmatrix}E_1\\E_2\\E_3\\\dots\end{bmatrix}=\begin{bmatrix}-W_1/\omega\\-W_2/\omega\\-W_3/\omega\\\dots\end{bmatrix}. \tag{3}$$

This system is solved for the subsystem energies E_m at each frequency of interest. The total number of subsystems and, therefore, the size of the SEA system may differ in function of frequency, as higher order wave types can cut on within the frequency range of interest. The system requires the computation of η_{mn}, η_m and W_m in function of frequency, where

$$\eta_m=\eta_{\mathrm{d},m}+\sum_{m=1}^{M}\eta_{mn}, \tag{4}$$

where $\eta_{\mathrm{d},m}$ is the equivalent internal loss factor of the subsystem. For laminates with layers with identical damping properties such as CLT, this value is equal to the material internal loss factor if edge radiation and damping are negligible.

The input power W_m per source subsystem m is derived in accordance with [7]; in the special case where the wall is excited on its top surface by a point load $\mathbf{F}$. This load is exerted in the z-direction at location $\mathbf{x}_0$ in a unit cell with position $\mathbf{n}_0$ relative to the reference unit cell. For a given surface traction $\mathbf{t}\left(\mathbf{x},\mathbf{n}\right)$, the resulting complex amplitude $a_m\left(\epsilon_{\mathrm{x}},\epsilon_{\mathrm{y}}\right)$ for a given subsystem is given by

$$a_m\left(\epsilon_{\mathrm{x}},\epsilon_{\mathrm{y}}\right)=\frac{\iint_A\boldsymbol{\phi}_m^{\mathrm{H}}\left(\mathbf{x},\mathbf{n}\right)\mathbf{t}\left(\mathbf{x},\mathbf{n}\right)\mathrm{d}X\mathrm{d}Y}{N_{\mathrm{x}}N_{\mathrm{y}}\left(\left(1+\mathrm{i}\eta_{\mathrm{d},m}\right)\omega_m^2-\omega^2\right)}, \tag{5}$$

where X and Y are the coordinates in the global coordinate system of the wall, which can also be indicated by $(\mathbf{x},\mathbf{n})$, A is the total surface area of the wall, N_{x} and N_{y} the number of unit cells in their respective dimensions and ω_m the eigenfrequency for subsystem m for an imposed phase constant combination. In the special case of an external point load, the traction corresponds to a spatial Dirac impulse with $\mathbf{t}=\mathbf{F}\delta\left(\mathbf{x}-\mathbf{x}_0\right)$ for an excitation location $(\mathbf{x}_0,\mathbf{n}_0)$. As a result, equation (6) can be simplified to

$$a_m\left(\epsilon_{\mathrm{x}},\epsilon_{\mathrm{y}}\right)=\frac{\boldsymbol{\phi}_m^{\mathrm{H}}\left(\mathbf{x}_0,\mathbf{n}_0\right)\mathbf{F}\left(\mathbf{x}_0,\mathbf{n}_0\right)}{N_{\mathrm{x}}N_{\mathrm{y}}\left(\left(1+\mathrm{i}\eta_{\mathrm{d},m}\right)\omega_m^2-\omega^2\right)}. \tag{6}$$

This amplitude is always a scalar and is computed for every source subsystem for the wave with phase constants

(ϵ_x, ϵ_y). The input power $W_m(\epsilon_x, \epsilon_y)$ for subsystem m for a point load excitation is given by

$$W_m(\epsilon_x, \epsilon_y) = \frac{1}{2}\mathrm{Re}\left\{\mathrm{i}\omega \mathbf{F}^{\mathrm{T}}(\mathbf{x}_0, \mathbf{n}_0)\, \mathbf{u}_m^*(\mathbf{x}_0, \mathbf{n}_0)\right\}, \quad (7)$$

where

$$\mathbf{u}_m(\mathbf{x}_0, \mathbf{n}_0) = a_m(\epsilon_x, \epsilon_y)\, \boldsymbol{\phi}_m(\mathbf{x}_0, \mathbf{n}_0). \quad (8)$$

The total subsystem input power per frequency band is obtained by summing the contribution of any (ϵ_x, ϵ_y) combination where its eigenfrequency ω_m lies within the frequency band of interest $\Delta\omega$. Born-Von Kárman (also termed periodic) boundary conditions are applied on the full wall to take the finite wall size into account, where the movement at opposite edges is continuous, such that the wave motion in the wall is spatially periodic. This enables the resonating modes in the wall to be composed of purely travelling waves in opposite directions. The range of imposed phase constants can be limited to the Brillouin zone of $[-\pi, \pi]$ [5]. For orthotropic structures such as CLT walls, this can be limited to $[0, \pi]$ due to symmetry.

The coupling loss factors η_{mn} between subsystems m and n are defined as

$$\eta_{mn} = \frac{W_{mn}}{\omega E_m}, \quad (9)$$

where W_{mn} is the power transmitted across the junction from m to n and $E_m = eV_iN_m$ with volume V_i of wall i and N_m the number of modes resonating in the frequency band of interest. The intensity in the local y-direction for a single resonating mode is $ec_{\mathrm{gy},m}$ with $c_{\mathrm{gy},m}$ the y-component of the group velocity. The transmitted power $W_{mn}(\epsilon_x, \epsilon_y)$ for imposed phase constants is given by

$$W_{mn}(\epsilon_x, \epsilon_y) = \tau_{mn}(\epsilon_x, \epsilon_y)\, S_{ij} e_m c_{\mathrm{gy},m}(\epsilon_x, \epsilon_y), \quad (10)$$

where S_{ij} is the area of the interface between the wall and the junction, and $\tau_{mn}(\epsilon_x, \epsilon_y)$ the transmission coefficient for an incident wave in subsystem m and transmitted or reflected wave to subsystem n. The total transmitted power W_{mn} in a frequency band is obtained by summing the contributions of each mode with resonance frequency within this frequency band, analogous to the input power.

The procedure to determine the transmission coefficients $\tau_{mn}(\epsilon_x, \epsilon_y)$ is a generalization of the approach of [3]. An incident wave of wave type s in source plate i with imposed phase constant ϵ_x and an arbitrary displacement amplitude impinges on the junction. Given that all system components exhibit the same spatial periodicity along the x-axis, all reflected and transmitted waves have the same phase constant. Additionally, the analysis is conducted at a frequency corresponding to the eigenfrequency of the incident wave. The interface forces of the unit cells of the different components, indicated in grey in Figures 2 and 3, should be in equilibrium, such that for the forces in global coordinates

$$\mathbf{f}_{\mathrm{jun}} + \mathbf{f}_{\mathrm{inc}} + \sum_{j=1}^{n} \mathbf{f}_j = \mathbf{0}, \quad (11)$$

where $\mathbf{f}_{\mathrm{jun}}$ represents the interface forces of the junction, $\mathbf{f}_{\mathrm{inc}}$ the interface forces of the incident wave in wall i, and $\mathbf{f}_j$ the interface forces of the outgoing waves in wall j. The forces in the walls for outgoing wave motion can be related to the interface displacements by exploiting the two-dimensional spatial periodicity. This leads to the dynamic stiffness matrix of wall j for outgoing wave motion, denoted as $\mathbf{D}_j(\epsilon_x, \omega)$. Furthermore, in the junction itself, the forces and displacements at the interface degrees of freedom can be coupled via a junction dynamic stiffness matrix $\mathbf{D}_{\mathrm{jun}}(\epsilon_x, \omega)$ by exploiting the one-dimensional spatial periodicity. As a result, one has that

$$\mathbf{D}_{\mathrm{jun}}\mathbf{u} + \mathbf{f}_{\mathrm{inc}} + \sum_{j, j\neq i} \mathbf{D}_j\mathbf{u} + \mathbf{D}_i(\mathbf{u} - \mathbf{u}_{\mathrm{inc}}) = \mathbf{0}, \quad (12)$$

where all displacements $\mathbf{u}$ are expressed in global coordinates. Note that $\mathbf{u}_{\mathrm{inc}}$ represents the displacements at the interface due to the incident wave motion only, which can be obtained by only considering one wavetype propagating in the $-y$-direction with fixed wave amplitude, so it is uniquely determined.

The procedure to derive the interface dynamic stiffness matrices $\mathbf{D}_j(\epsilon_x, \omega)$ follows that of [8]. The dynamic stiffness matrix of the unit cell $\mathbf{D} = \mathbf{K} - \omega^2\mathbf{M}$ is reduced to degrees of freedom LB and B by imposing ϵ_x, ω and solving ϵ_y from equation (2). This leads to an eigenvalue problem with $2N$ solutions in function of ϵ_y with eigenvectors composed of the modal displacements $\boldsymbol{\phi}_{\mathrm{u}}$ and forces $\boldsymbol{\phi}_{\mathrm{f}}$ at these degrees of freedom for all potential outgoing waves. The total interface displacements and forces $\mathbf{u}_j$ and $\mathbf{f}_j$ of wall j are computed from these eigen-

vectors as

$$\mathbf{u}_j = \sum_{n=1}^{N} a_n \boldsymbol{\phi}_{\mathrm{u}} = \mathbf{Q}\mathbf{a}, \tag{13}$$

$$\mathbf{f}_j = \sum_{n=1}^{N} a_n \boldsymbol{\phi}_{\mathrm{f}} = \mathbf{P}\mathbf{a}, \tag{14}$$

where $\mathbf{a}$ is a set of a priori unknown amplitudes. Given that $\mathbf{f}_j = \mathbf{D}_j \mathbf{u}_j$,

$$\mathbf{D}_j\left(\epsilon_{\mathrm{x}}, \omega\right) = \mathbf{P}\mathbf{Q}^{-1}. \tag{15}$$

Note that only N eigensolutions are taken into account, corresponding to outgoing waves propagating or decaying in the local $+y$-direction of the wall. For the junction beam, a similar procedure is followed to determine $\mathbf{D}_{\mathrm{jun}}$, exploiting the one-dimensional spatial periodicity along the x-axis. Solving equation (12) for the interface displacements $\mathbf{u}$ allows to determine the power related to each outgoing wavetype t in receiver wall j by decomposition of the wall edge displacements $\mathbf{u}_j$ within the full set of interface displacements $\mathbf{u}$ as in equations (13) and (14). The corresponding transmitted power per subsystem is given by

$$W_{mn}\left(\epsilon_{\mathrm{x}}, \epsilon_{\mathrm{y}}\right) := \frac{1}{2}\mathrm{Re}\left\{\mathbf{f}_{mn}^{\mathrm{T}} \mathbf{u}_{mn}^{*}\right\}. \tag{16}$$

The definition of incident wave power $W_{\mathrm{inc}}\left(\epsilon_{\mathrm{x}}, \epsilon_{\mathrm{y}}\right)$ is analogous. The transmission coefficients $\tau_{mn}\left(\epsilon_{\mathrm{x}}, \epsilon_{\mathrm{y}}\right)$ required in equation (10) are defined as

$$\tau_{mn}\left(\epsilon_{\mathrm{x}}, \epsilon_{\mathrm{y}}\right) := \frac{W_{mn}\left(\epsilon_{\mathrm{x}}, \epsilon_{\mathrm{y}}\right)}{W_{\mathrm{inc}}\left(\epsilon_{\mathrm{x}}, \epsilon_{\mathrm{y}}\right)}. \tag{17}$$

Finally, the measurement formula for the vibration reduction index K_{ij} between connected walls i and j following ISO 12354-1 [9] is given by

$$K_{ij} = \frac{\sum_{s,t} D_{\mathrm{vz},ij}^{st} + \sum_{s,t} D_{\mathrm{vz},ji}^{ts}}{2} + 10\log\frac{l_{ij}}{\sqrt{a_{\mathrm{eq},i} a_{\mathrm{eq},j}}}, \tag{18}$$

where l_{ij} is the junction length, $a_{\mathrm{eq},i}$ and $a_{\mathrm{eq},j}$ the equivalent absorption lengths of the walls and $D_{\mathrm{vz},ij}^{st}$ the transverse velocity level differences between the subsystems, defined as

$$D_{\mathrm{vz},ij}^{st} := 10\log\frac{< v_{mz}^2 >}{< v_{nz}^2 >} = 10\log\frac{E_{mz} m_j}{E_{nz} m_i}, \tag{19}$$

where $< v_{mz}^2 >$ denotes the surface-averaged squared velocity of subsystem m in the local z-direction, E_{mz} is the subsystem energy for the local z-components and m_i and m_j are the total masses of wall i and j, respectively. At resonance, the subsystem energy is given by

$$E_m = \frac{1}{4}\left|a_m\right|^2 \boldsymbol{\phi}_m^{\mathrm{H}} \left(\mathbf{K} + \omega_m^2 \mathbf{M}\right) \boldsymbol{\phi}_m, \tag{20}$$

for an amplitude a_m such that $\mathbf{u}_m = a_m \boldsymbol{\phi}_m$. Equation (3) is solved for the total band-averaged subsystem energies per subsystem E_m. The transverse subsystem energy E_{mz} can be computed by only taking the z-components of $\boldsymbol{\phi}_m$ into account. Both $E_{mz}\left(\epsilon_{\mathrm{x}}, \epsilon_{\mathrm{y}}\right)$ and $E_m\left(\epsilon_{\mathrm{x}}, \epsilon_{\mathrm{y}}\right)$ are calculated with equation (20) for each phase constant combination, after which their values are band-averaged in the same way as the input power. The subsystem energies resulting from equation (3) are then multiplied by the ratio E_{mz}/E_m per frequency band for each subsystem. In this way, all contributions to the transverse wave motion and therefore, the sound radiation, are taken into account in equation (18) for K_{ij}.

3. RESULTS AND DISCUSSION

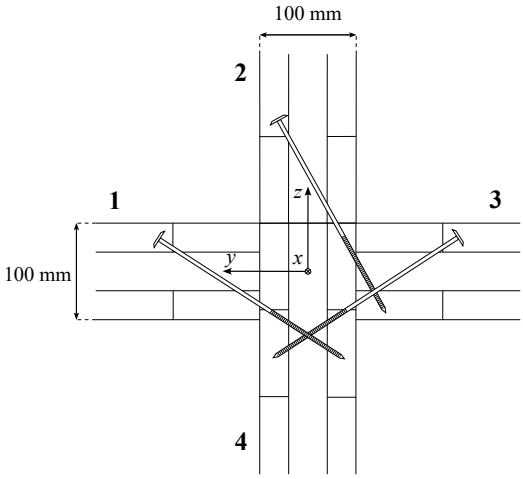


Figure 4. Configuration of the junction with screw positions.

The prediction model is validated with laboratory measurements of the vibration reduction index K_{ij} for a CLT X-junction consisting of 4 walls [11, 12]. Each wall is a 3-ply cross-laminated timber panel with a layer stacking of [0 π/2 0] relative to the global $x-$axis. The material properties of a single timber layer of strength class C24 are summarized in Table 1. Each layer has

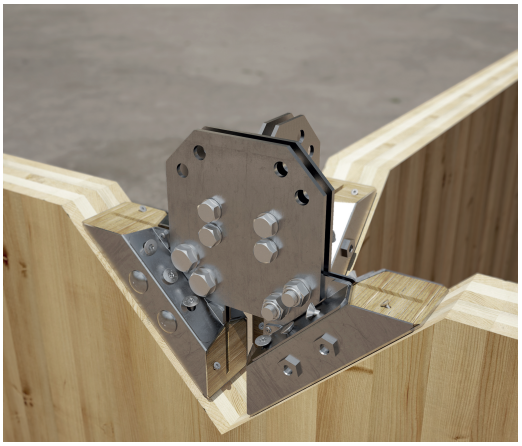


Figure 5. Rotationally stiff X-RAD connector [10].

Table 1. Mechanical properties of timber of strength class C24 [13].

ρ [kg/m^3]	E_x [MPa]	E_y [MPa]	G_xy [MPa]	ν_yx [-]
450	11 000	367	690	0.014

an assumed internal loss factor of 0.02. The structural wall connections are obtained either by screws or more rotationally stiff connectors, displayed in Figure 5. Figure 4 illustrates the junction configuration including the screw positions.

The vibration reduction indices are predicted with the pFEM model detailed in the previous section, where the panels are modelled with 8-node solid volume elements, with each timber layer modelled separately. Due to the homogeneity of the CLT in the lateral directions of each wall, the unit cell can be taken arbitrarily small to reduce computation time. The junction beam is also considered as a CLT volume with a lateral dimensions corresponding to the thicknesses of the connected walls. In this example, the screws or the other connector are not modelled explicitly, but in this prediction framework this is a future possibility. Additionally, predictions with an analytical wave approach model for thin homogeneous plates, directly connected along a massless line connection [1]. This requires the mechanical properties for an homogeneous plate equivalent to the CLT panel. They are determined with the modified gamma method [14], imposing static equivalence between the transverse bending stiffness of the separate layers and an equivalent single-layer

Table 2. Mechanical properties for an equivalent single-layer CLT panel.

ρ [kg/m^3]	E_x [MPa]	E_y [MPa]	G_xy [MPa]	ν_yx [-]
450	7 533	768	690	0.149

panel, summarized in Table 2. For both models, equivalent absorption lengths $a_{\mathrm{eq},j}$ were determined from the experimentally determined structural reverberation times $T_{\mathrm{s},j}$:

$$a_{\mathrm{eq},j} = \frac{2.2\pi^2 S_j}{T_{\mathrm{s},j} c_0 \sqrt{f/f_\mathrm{ref}}}, \tag{21}$$

where $c_0 = 343\,\mathrm{m/s}$, $f_\mathrm{ref} = 1000\,\mathrm{Hz}$ and S_j the surface area of wall j. As another reference for comparison, the empirical K_{ij} formulae from Annex F of ISO 12354-1 [9] for rigid CLT junctions were applied for the transmission paths as follows

$$K_{12} = 18.8 + 3.3\log\left(\frac{f}{f_\mathrm{k}}\right), \tag{22}$$

$$K_{13} = 23 + 3.3\log\left(\frac{f}{f_\mathrm{k}}\right), \tag{23}$$

$$K_{24} = 10 - 3.3\log\left(\frac{f}{f_\mathrm{k}}\right) + 10M, \tag{24}$$

where $f_\mathrm{k} = 500\,\mathrm{Hz}$ and $M = \log\left(m"_{\perp,j}/m"_j\right)$ for surface masses $m"_j$ and $m"_{\perp,j}$ for wall j and the wall perpendicular to it. Figures 6 up to 7 display the predicted values alongside the measured values for the corner transmission paths, the coplanar transmission path and the continuous coplanar transmission path. Prediction results are illustrated by black lines; coloured lines indicate experimental values, with red lines for the rotationally stiff connector in Figure 5 and blue lines for the screwed junction in Figure 4.

While the global frequency trend established by the empirical formulae from the international standard is more or less correct with the exception of path $2-4$, they are a clear oversimplification of the actual K_{ij} as the material and geometric parameters and connection type are not taken into account, leading to deviations of over 5 dB in most 1/3 octave bands.

Both prediction models showcase a correct frequency trend with generally closer correspondence to K_{ij} for either experimental configuration than the empirical formulae. As noted in [1], the analytical prediction model typ-

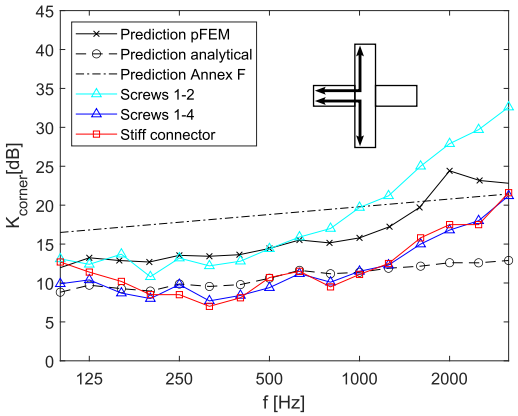


Figure 6. Vibration reduction index for the corner transmission paths in the CLT X-junction.

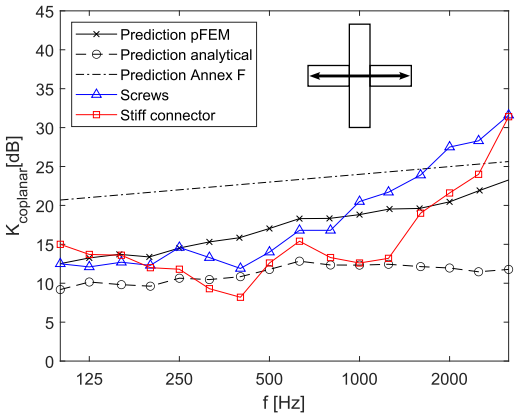


Figure 7. Vibration reduction index for the interrupted coplanar transmission path in the CLT X-junction.

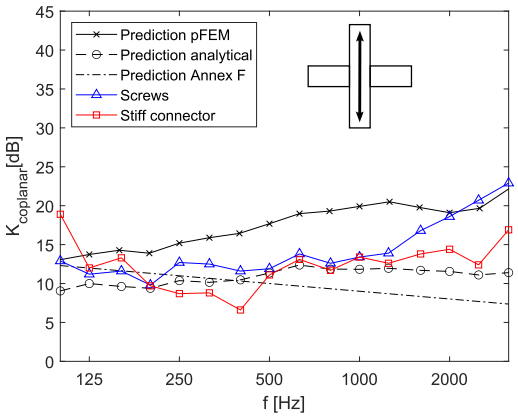


Figure 8. Vibration reduction index for the uninterrupted coplanar transmission path in the CLT X-junction.

ically offers a lower limit for K_{ij} due to the assumption of a rotationally stiff line connection. Therefore, it corresponds most closely to the results for stiffer connection types such as the X-RAD and the screwed junction for transmission path 1-4 which, unlike path 1-2, has a direct screw connection. Notably, the predictions are less accurate in the high-frequency range, where the thin plate assumption is typically invalid due to the small wavelengths compared to the wall thickness. As a result, the high-frequency K_{ij} increase is underestimated for each transmission path. Due to the inclusion of thickness effects, the new pFEM prediction model performs better in the high-frequency range. In general, the predicted K_{ij} values are several dB higher than the analytical model. One potential reason for this is the layered finite element modelling of the CLT walls, while homogenized single-layer values are used for the thin plate model which are not necessarily fully equivalent. Additionally, the junction itself has a mass and volume unlike the line connection in the analytical model, which could lead to a globally less stiff connection. While the thin plate model corresponds more closely to the stiffly connected transmission paths such as corner path 1-4 for the screws, the opposite holds for the pFEM model with the exception of the high-frequency range. Most notably, K_{24} across continuous coplanar transmission path 2-4 is better represented by the thin plate model, although the pFEM predictions are still relatively accurate. Note that the pFEM prediction results can be improved by explicitly including the screws

or X-RAD connector in the finite element model. Similarly, it is possible to implement flexible connectors (e.g. resilient pads) in future work, which allows for much design freedom and detail when modelling various building junctions. In general, the difference between the pFEM K_{ij} predictions and the experimental values lie beneath 5 dB for most 1/3 octave bands, with especially good correspondence to K_{ij} for connections with lower rotational stiffness. For example, the pFEM predictions of K_{12} differ less than 2 dB from the experimental results for the screw connection up to 1000 Hz.

4. CONCLUSIONS

The presented work introduces a prediction model for the vibration reduction index K_{ij} across CLT junctions with spatial periodicity along the junction direction, constructing finite element models for a repeated unit cell and applying Bloch analysis. The prediction model is validated with rigid X-junctions consisting of 3-ply CLT walls, connected by screws or more rotationally stiff modular connectors. The predicted values are quite accurate with differences with experimental results beneath 5 dB in most 1/3 octave bands and even lower for less rigid connections. Due to the large modelling freedom in this framework, it is possible to further improve the predictions by including resilient or stiff elements (e.g. resilient pads and screws, respectively) in future work.

5. ACKNOWLEDGMENTS

The research was funded by a Baekeland fellowship (HBC.2022.0712) from Flanders Innovation & Entrepreneurship (VLAIO).

6. REFERENCES

[1] S. Moons, R. Lanoye, and E. Reynders, "Prediction of flanking sound transmission through cross-laminated timber junctions with resilient interlayers," *Applied Acoustics*, vol. 228, January 2025.

[2] R. Craik, *Sound transmission through buildings using statistical energy analysis*. Aldershot, UK: Gower, 1996.

[3] R. Langley and K. Heron, "Elastic wave transmission through plate/beam junctions," *Journal of Sound and Vibration*, vol. 143, no. 2, pp. 241–253, 1990.

[4] I. Bosmans, P. Mees, and G. Vermeir, "Structure-borne sound transmission between thin orthotropic plates: analytical solutions," *Journal of Sound and Vibration*, vol. 191, pp. 75–90, May 1996.

[5] L. Brillouin, *Wave propagation in periodic structures*. New York City, NY,: Dover Publications, 2 ed., 1953.

[6] R. Lyon, "Needed: a new definition of diffusion," *Journal of the Acoustical Society of America*, vol. 56, pp. 1300–1302, October 1974.

[7] V. Cotoni, R. Langley, and P. Shorter, "A statistical energy analysis subsystem formulation using finite element and periodic structure theory," *Journal of Sound and Vibration*, vol. 318, pp. 1077–1108, 2008.

[8] R. Langley and V. Cotoni, "The direct field boundary impedance of two-dimensional periodic structures with application to high frequency vibration prediction," *The Journal of the Acoustical Society of America*, vol. 127, pp. 2118–2128, 2010.

[9] International Organization for Standardization, *Building acoustics — Estimation of acoustic performance of buildings from the performance of elements — Part 1: Airborne sound insulation between rooms*. Geneva, Switzerland, 2017.

[10] Rothoblaas, "X-RAD:X-RAD connection system." `https://www.rothoblaas.com/products/fastening/brackets-and-plates/x-rad/x-rad`.

[11] "Flanksound project," tech. rep., Rothoblaas, Bolzano, Italy, November 2016.

[12] F. Morandi, S. De Cesaris, M. Garai, and L. Barbaresi, "Measurement of flanking transmission for the characterisation and classification of cross laminated timber junctions," *Applied Acoustics*, vol. 141, pp. 213–222, July 2018.

[13] Austrian Institute of Construction Engineering, "European technical assessment eta-14/0349," Technical assessment ETA-14/0349, Austrian Institute of Construction Engineering, Vienna, Austria, 2020.

[14] J. Zhou, Y. Hei Chui, M. Gong, and L. Hu, "Elastic properties of full-size mass timber panels: Characterization using modal testing and comparison with model predictions," *Composites Part B: Engineering*, vol. 112, pp. 203–212, March 2017.

DOI: 10.61782/fa.2025.0378



FORUM ACUSTICUM
EURONOISE 2025

EXPERIMENTAL MODAL ANALYSIS OF A CROSS-LAMINATED TIMBER L-JUNCTION WITH A VIEW TOWARDS PREDICTING FLANKING SOUND TRANSMISSION

Sven Vallely[1,2*] **Antonio Esposito**[1] **Stefan Schoenwald**[1]
[1]Laboratory for Acoustics / Noise Control, Empa, Switzerland
[2]Department of Civil Engineering – Structural Mechanics Section, KU Leuven, Belgium

ABSTRACT

The trend towards engineered wood and, as a result, lightweight constructions has led to noise and vibration design challenges. One such challenge that is currently an active research topic is flanking sound transmission through connected building elements. Mass timber buildings are typically formed by connecting cross-laminated timber panels, whereby the type and number of joints used to form a connection can vary depending on the design and purpose of the building. The variety of connector types and implementations poses challenges for the prediction process. Moreover, the connection of the simpler panel subsystems gives rise to emergent behaviour, resulting in a complex dynamic system. As a first step, to better predict flanking sound transmission and to correctly simulate the junction mechanics in vibroacoustic numerical models, it is important to understand the emergent dynamic behaviour due to the connection of these structural elements. This contribution presents a detailed experimental modal analysis of a scaled cross-laminated timber L-junction structure. The mock-up is considered representative of a cross-section that would be encountered in the practice. The experimental modal analysis examines three different L-junction configurations to deduce the contribution of both the brackets and the resulting contacting panel interfaces to the system's dynamic behaviour.

Keywords: *CLT, modal analysis, connection, FEM, acoustics*

**Corresponding author*: *sven.vallely@empa.ch.*

***Copyright**: ©2025 This is an open-access article distributed under the terms of the Creative Commons Attribution 3.0 Unported License, which permits unrestricted use, distribution, and reproduction in any medium, provided the original author and source are credited.*

1. INTRODUCTION

Due to its lightweight yet stiff nature, Cross-Laminated Timber (CLT) is a popular structural element choice for the construction of mass timber buildings. While this property is generally beneficial, it poses vibration serviceability and acoustic design challenges.

One approach to help address these challenges is the development of methods and models to characterise and predict the behaviour of CLT structures. This has been considered at several scales, from individual elements [1–3] to operational mid-rise structures [4, 5]. While each modelling scale has its own challenges, modelling at a junction scale has a unique challenge since, here, not just material properties play a crucial role but also the intricate dynamics of the connections [6].

This contribution takes an experimental approach to considering the role of connection dynamics with the view of developing models to accurately predict flanking sound transmission across CLT elements. An experiment was designed with the intent to isolate and determine the contributions of the connectors and contact between plate interfaces on the modal response of a system. To achieve this, three structurally isolated L-junction configurations were investigated: (1) An L-junction connection with two standard steel angle brackets and contact between plate interfaces; (2) The same L-junction connection as (1), but with a 3 mm gap between the plate interfaces; (3) The same L-junction as (1), but with no angle brackets.

2. BACKGROUND AND THEORY

In order to compare and correlate the experimentally fitted modes, a shape-based index, namely the Modal Assurance Criterion (MAC), is chosen. The MAC has diverse appli-

cations not just for mode pairing, but also for for eigenmode error analysis [7]. Such an example is the use of the AutoMAC to check against spatial aliasing. For assessing MAC (and AutoMAC) indices, values of 0.9 or greater are considered to be well-correlated eigenmode pairs and values of 0.1 or less are considered to be uncorrelated eigenmode pairs for the purpose of this contribution. Further discussion of the benefits, limitations, and interpretation of this shape-based index can be found in Refs. [7, 8].

3. MATERIALS AND METHODS

3.1 Experimental set-up

The experimental set-up involved vibration measurements of three CLT L-junction configurations. The L-junction configurations were each formed by connecting two 3-ply CLT plates denominated as CLT060C1 and CLT100A1, respectively. The geometrical properties of the plates are presented in Table 1.

Table 1. Geometrical properties of the experimentally investigated plates. Namely length a, width b, individual layer thickness t_i, and lay-up.

Plate ID	a (m)	b (m)	t_i (mm)	Lay-up (°)
CLT100A1	2.87	1.14	[30/40/30]	[90/0/90]
CLT060C1	1.52		[20/20/20]	

A schematic of the L-junction formed by the two plates and the three different configurations is presented in Fig. 1. The three different configurations of the L-junctions were formed by using different joining methods to connect the two plates along their respective short edges, labeled as DA in Fig. 1. The configurations are designated as follows. 0G2B is the case for using two brackets (2B) and contact, that is, a 0 mm gap (0G) between the plates when forming their connection. 3G2B is the case for using two brackets (2B) and no contact, that is, a 3 mm gap (3G) between the plates when forming their connection. 0G0B is the case for using no brackets (0B) and contact, that is, a 0 mm gap (0G) between the plates when forming their connection.

The brackets used to form the connection for configs. 0G2B and 3G2B were standard steel angle brackets with product number. The brackets had global dimensions of $90 \times 90 \times 65 \times 2.5$ mm and were offset 150 mm from the long edge of the plate and fastened with 8 wood screws per bracket. The screws had a thread length of 40 mm and an

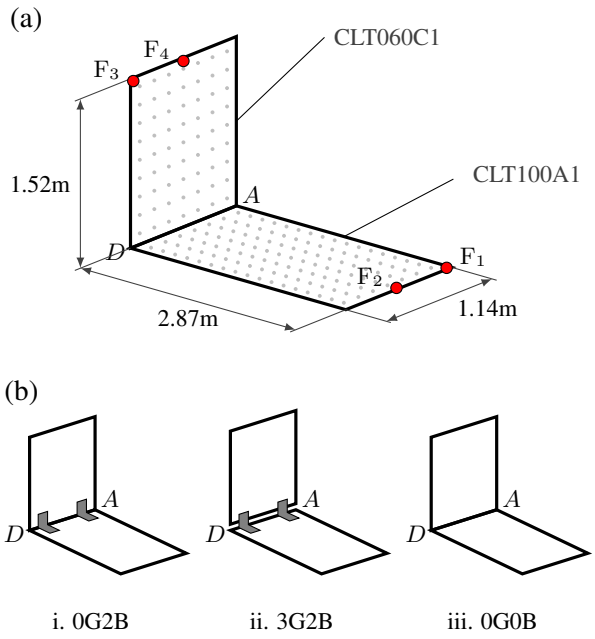


Figure 1. Schematic of the experimental set-up. (a) Schematic of the experimental set-up indicating planar dimensions, approximate measurement grid, and locations of the excitation positions. (b) Schematics of the different joining methods used to connect the two CLT plates along edge DA.

outer thread diameter of approximately 5 mm. An image of an individual bracket is presented in Fig. 3b along with the fixing point locations.

The test structure was supported on four air cushions near the corners of plate CLT100A1 in order to simulate free boundary conditions. The air cushions enabled the test object to be structurally isolated from the ambient environment while minimising the constraint effects of the supports on vibroacoustic behaviour of the system, thereby approximating free boundary conditions.

For the measurement of the vibrational response of the system, a Polytec PSV-400 Laser Doppler Vibrometer measured the normal velocities of the top-side surfaces of plates CLT060C1 and CLT100A1. The measurement grids on plates CLT060C1 and CLT100A1 were 7×9 and 7×17 Cartesian point grids, respectively. These Cartesian point grids corresponded to a spatial resolution of approximately 18 cm. The approximate measurement grids are depicted in Fig. 1a.

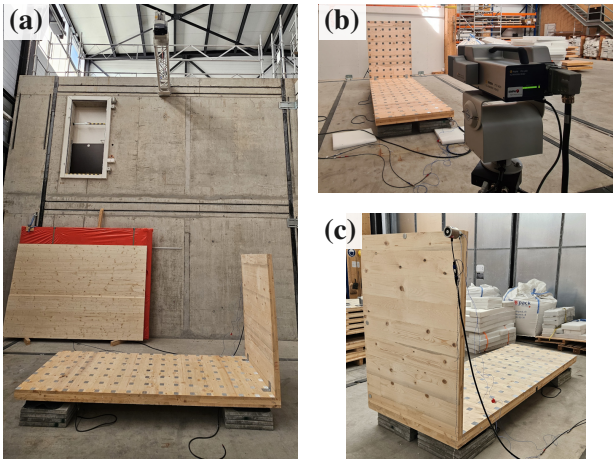


Figure 2. Images of the general experimental set-up: Configuration 0G2B is shown. (a) Acquisition of the normal surface velocities on plate CLT100A1. (b) Acquisition of the normal surface velocities on plate CLT060C1. (c) Rear view with shaker attached.

Four different excitation points were considered, two per plate, with one being approximately on a corner of the plate at the free end, and one being in the middle of the short edge of the plate. The locations of the excitation points are depicted in Fig. 1a. At the excitation points, an impedance head was attached to which a shaker was then attached. The velocity response surface was measured for each excitation point with a swept sine excitation. The transfer mobilites were then calculated based on the measured response surfaces with respect to the force signal of the impedance head. A frequency range from 0 Hz to 800 Hz with a resolution of 62.5 mHz was considered. For each measurement point, the measurements were repeated 5 times for each point, and a complex average was taken.

An overall view of the experimental set-up is presented in Fig. 2, which shows the 0G2B configuration. The 3G2B and 0G0B configurations required slight modification to the structure for safety reasons due to the reduced stability of the connection. For config. 3G2B, plate CLT060C1 was supported from behind with two air cushions. Images of the modification made for config. 3G2B are presented in Fig. 3. For config. 0G0B, guiding cross-bars at the front and back sides were constructed to ensure that plate CLT060C1 did not tip or slide away from its location. CLT060C1 was decoupled from the cross-bars with soft elastic interlayers to ensure that the cross-bars did not influence the vibroacoustic response of the system. The Images of the additional modifications made for config. 0G0B are presented in Fig. 4. It should be stated that the L-junction was constructed so that CLT060C1 was supported as much as possible by CLT100A1 and structurally isolated from the frame which acted as a secondary support.

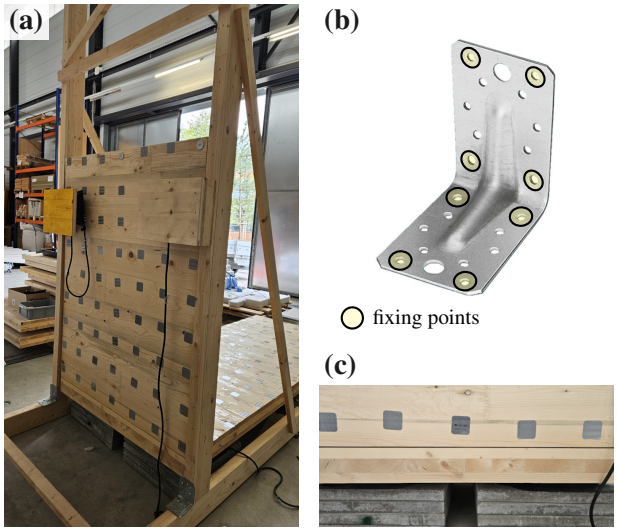


Figure 3. Images of the 3G2B configuration. (a) Rear view of the supporting frame for plate CLT060C1. (b) The angle bracket used to form the connection (also used with config. 0G2B). (c) Close-up view of the 3 mm gap between plate edges.

The measurements for the modal analysis were conducted as part of a broader investigation into flanking sound transmission. See Ref. [9] for details on other excitation points and investigations in the mid- to high-frequency range.

3.2 Modal Parameter Estimation

The experimental modal parameters presented in this contribution were fitted as part of an Experimental Modal Analysis (EMA) using the combined measurement data obtained with the procedure discussed in Sec. 3.1. Further details of the EMA method can found in Ref. [8].

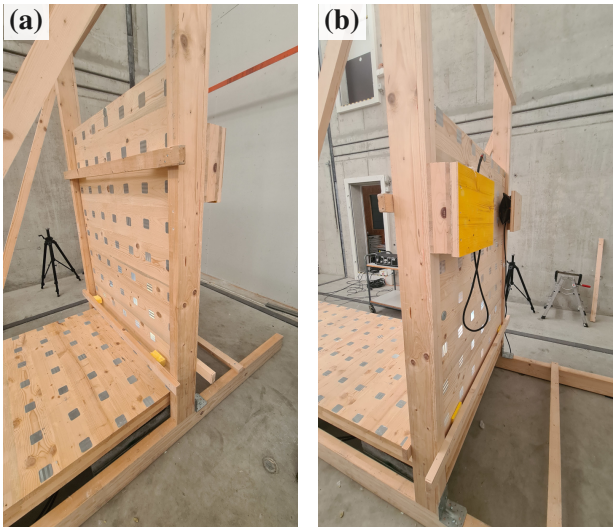


Figure 4. Images of the 0G0B configuration. (a) Front view of the supporting frame for plate CLT060C1. (b) Rear view of the supporting frame for plate CLT060C1.

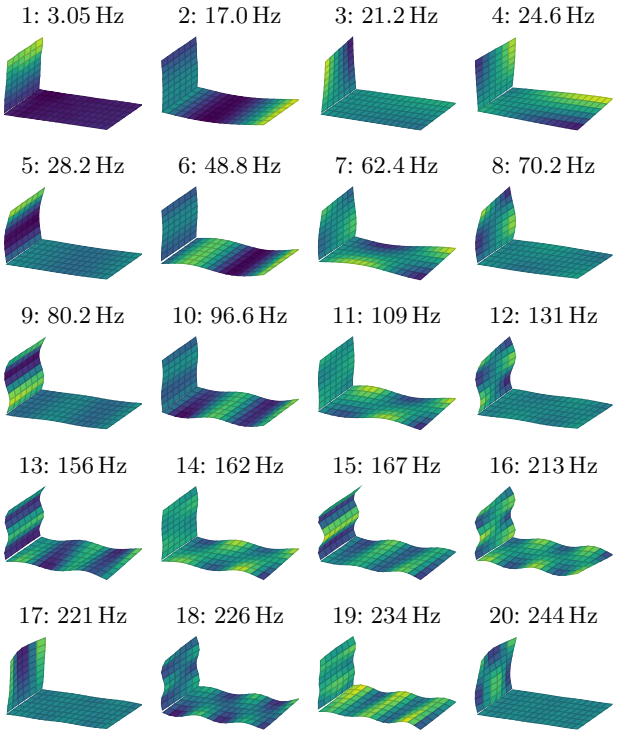


Figure 5. The first twenty identified eigenmodes with their experimental eigenfrequencies for 0G2B.

4. RESULTS AND DISCUSSION

4.1 Modal Parameter Estimation

The EMAs of each of the configurations were able to fit 20 modes for the 0G2B and 3G2B configurations and 18 modes for the 0G0B configuration. The fitted eigenmodes and their associated eigenfrequencies are presented in Figs. 5 to 7. The AutoMAC matrices of the respective eigenmodes are presented in Figs. 8 to 10. The eigenmodes, as expected, correlate exactly with themselves, i.e. $MAC_{i,j} = 1 \quad \forall i = j$ and the off-diagonal terms are mostly zero or uncorrelated, i.e. $MAC_{i,j} < 0.10 \quad \forall i \neq j$. This indicates that the mode parameter estimation is valid and that the eigenmodes contain a sufficient number of degrees of freedom to prevent spatial aliasing. A corollary of this is that the measurement grid is adequate for the identified modes.

There is, however, one pair of modes where the spatial resolution appears to be inadequate. For config. 3G2B, $MAC_{19,20} = 0.65$, indicating a moderate correlation between the modes. Visually comparing eigenmodes 19 and 20 in Fig. 6 confirms this moderate correlation and indicates a potential spatial aliasing. For config. 0G0B, a moderate correlation between modes is also found, with $MAC_{1,6} = 0.50$. Comparing these modes in Fig. 7, there appears to be an adequate spatial resolution to resolve the modes, therefore, the mild correlation is more likely due to coherent noise as a result of non-linearities at the connection caused by the rigid body motion of mode 1. For the remaining non-zero off-diagonal values in Figs. 8 to 10, it is expected that the values would be zero or much closer to zero if the MAC were to be calculated with mass normalised eigenmodes.

4.2 Auto-Comparison and Auto-Correlation of the Experimental Configurations

Considering the identified eigenmodes in Figs. 5 to 7, three different types of modes have been identified by measuring the normal surface velocities of the structure, that is; rigid body modes, torsional modes, and bending modes. The rigid body modes are modes 1 for configs. 0G2B and 3G2B, and modes 1 to 3 for config. 0G0B. The rigid body modes occur at frequencies approximately an order of magnitude lower than the fundamental bending and torsional modes for the 0G2B and 0G0B configura-

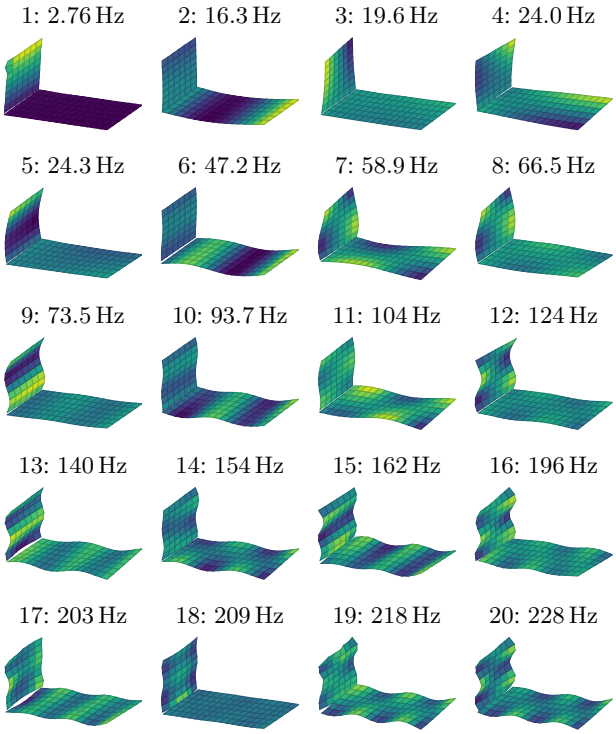


Figure 6. The first twenty identified eigenmodes with their experimental eigenfrequencies for 3G2B.

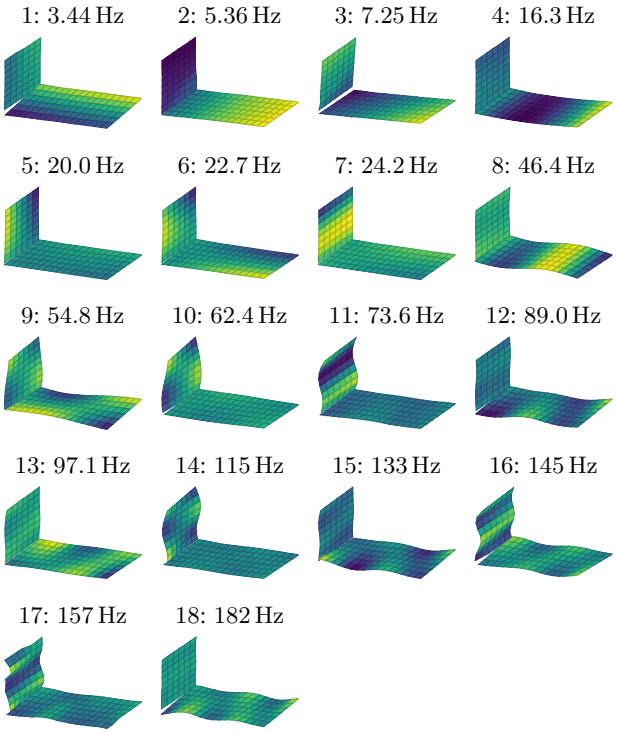


Figure 7. The first twenty identified eigenmodes with their experimental eigenfrequencies for 0G0B.

tions. These rigid body modes are associated with the deformation of the angle bracket and, in conjunction, can potentially provide valuable information for structural identification of the stiffness and damping properties of the connection. The three rigid body modes identified for config. 0G0B have higher eigenfrequencies than those of configs. 0G2B and 3G2B with the steel angle brackets. This result, at a surface level, indicates that the connection is stiffer for 0G0B; however, this additional stiffness is likely due plate CLT060C1 interacting with its supporting structure than with the joining method or, rather, lack there of. A quick visual comparison between the different configurations indicates that the torsional and bending modes do not appear to be influenced by, or at most, negligibly influenced by the supporting structure.

Considering the torsional and bending modes across Figs. 5 to 7, there appears to be cases where the individual plate modes are uncoupled, and other cases where the individual plate modes couple. An example of uncoupled individual plate modes are modes 2 and 5 in Fig. 5. On the other hand, an example of coupled individual plate modes are 13 and 15. What is particularly interesting about these coupled modes, is that they are composed of the same two individual plate modes when considering the plates as individual structural subsystems; however, considering their AutoMAC values, $AutoMAC_{13,15} = 0.05$ (cf. Fig 8), the two modes can be considered uncorrelated. The connection of these two subsystem gives rise to emergent behaviour, whereby they are coupled and moving in phase with respect to each other for mode 13, and coupled and moving out of phase with respect to each other for mode 15, resulting in an approximately 7 % shift in the eigenfrequency. This result of identifying coupling and non-coupling modes could potentially open new possibilities for addressing low-frequency flanking sound transmission. While not a standalone noise control solution, the identification of coupling modes during the design phase of a building could potentially allow for an approach to address problem frequencies for flanking sound transmission without adding additional mass to the structure. For example, by changing of aspect ratios of elements to minimise coupling across the connection, or changing the connec-

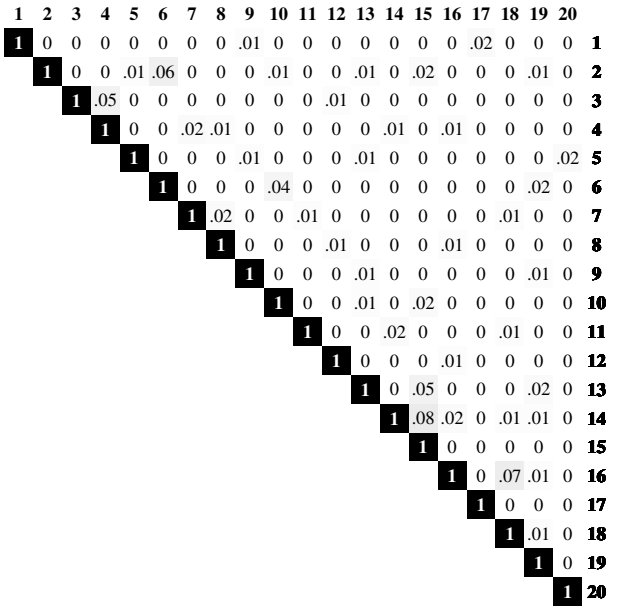


Figure 8. AutoMAC matrix for 0G2B. The colourmap is a linear scale from white ($MAC = 0$) to black ($MAC = 1$).

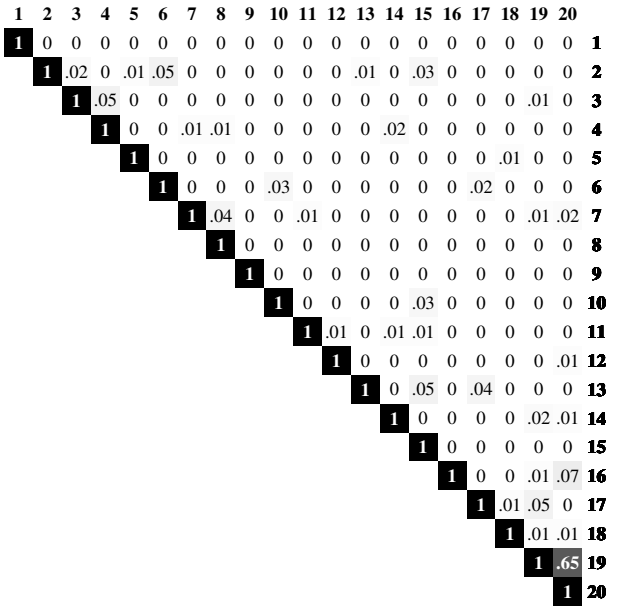


Figure 9. AutoMAC matrix for 3G2B. The colourmap is a linear scale from white ($MAC = 0$) to black ($MAC = 1$).

tion itself.

4.3 Cross-Comparison and Cross-Correlation of the Experimental Configurations

The MAC matrix is computed for each of the three considered experimental configurations against each other in Figs. 11 to 13.

For Fig. 11, where config. 3G2B is compared against config. 0G2B, it can be seen that the eigenmodes of both of the configurations occur in the same order and are well correlated up to the 12$^{\text{th}}$ mode, that is $MAC_{i,j} > 0.9 \quad \forall i = j \in \{1, ..., 12\} : i, j \in \mathbb{N}$. Considering the eigenfrequencies of these well-correlated mode pairs in Figs. 5 and 6, it can be seen that the eigenfrequencies for config. 0G2B are approximately 5 % higher than those of config. 3G2B. This result implies an overall global increase in stiffness of the structure to the effect of approximately 25 % due to the contact at the plate interfaces. This stiffening is even seen when when a resonance of one plate occurs uncoupled from the other, for example with modes 2 and 4. After the 12$^{\text{th}}$ mode, the eigenmode pairs are less well correlated. These results indicate that the brackets most important for coupling of the junction at lower frequencies, but the contact starts to have a greater influence on the response of the system as the frequency range increases.

For Fig. 12, where config. 0G0B is compared against config. 0G2B, it can be seen that the eigenmodes the configurations differ more than with the 3G2B-0G2B case. The modes do not occur in the same order, but this is largely due to the identification of the additional rigid body modes in the 0G0B case. Otherwise, it can be said that the significantly correlated eigenmode pairs occur in the same order. Their are 5 well-correlated mode pairs, that is, the mode pairs with indices $i, j \in \{\{4, 2\}, \{5, 3\}, \{8, 6\}, \{9, 7\}\}$. A general observation that can be made, is that the correlation between mode pairs is generally good for uncoupled plate modes.

Considering Fig. 11 where config. 0G0B is compared against config. 3G2B, it can be seen that the correlation between systems improves, with 8 well-correlated eigenmode pairs. The well-correlated pairs have indices $i, j \in \{\{4, 2\}, \{5, 3\}, \{6, 4\}, \{7, 5\}, \{8, 6\}, \{9, 7\}, \{10, 8\}, \{11, 9\}\}$. As with the case for Fig. 12, the correlation between mode pairs is good for uncoupled plate modes, but the correlation drops off once coupled plate modes start occurring. This implies that for the first several modes

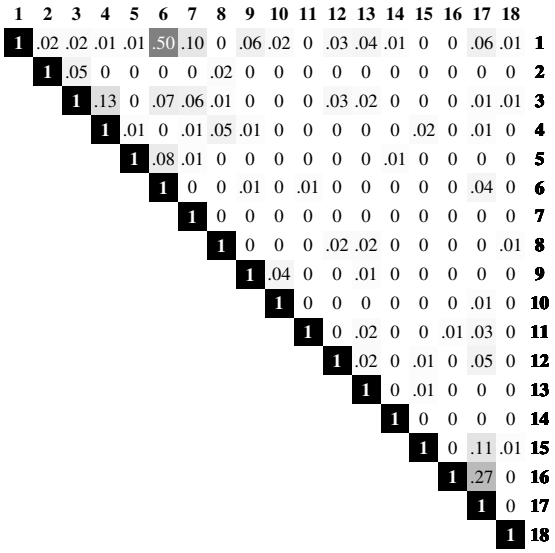


Figure 10. AutoMAC matrix for 0G0B. The colourmap is a linear scale from white ($MAC = 0$) to black ($MAC = 1$).

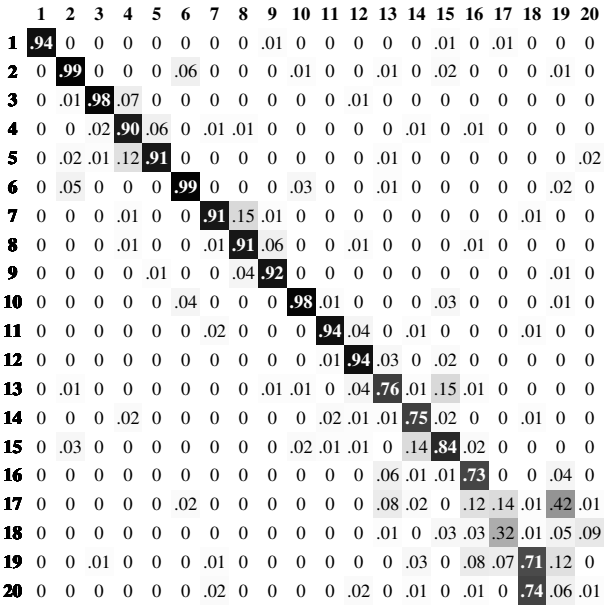


Figure 11. MAC matrix of 3G2B (vertical axis) against 0G2B (horizontal axis) eigenmodes. The colourmap is a linear scale from white ($MAC = 0$) to black ($MAC = 1$).

where the plate subsystems are generally resonating independent of each other, the type of connection doesn't appear to play a large role in influencing the eigenmodes, but does play a moderate role in influencing the global stiffness of the system. However, once the modes of the plate subsystems start coupling, the connection type starts to change the behaviour of the system.

5. SUMMARY AND CONCLUSION

This contribution compares and correlates experimentally estimated modal parameters for three CLT L-junction configurations with the goal of better understanding the behaviour at element interfaces for predicting flanking sound transmission. Each configuration used the same two CLT plates, but the plates in each configuration were connected with slightly different joining methods. The first method involved using two commercially available steel angle brackets supporting one plate resting on top of the other. The second configuration was the top plate supported solely by the angle brackets, thus eliminating any contact between the plates. The third configuration was just the top plate resting on the top plate without angle brackets. These three experimental configurations allowed for the components that form the connection between a typical L-junction, for example, the surface contact between two connected elements and their joining mechanism, to be analysed in a deductive manner.

The analysis identified three different types of modes, namely rigid body, torsional, and bending modes that contribute to the normal response of the L-junction structure. It was found that rigid body modes with the angle brackets could be potentially used for structural identification purposes of the connection. For the first several bending and torsional modes, where the modal density was relatively low, the resonances of the plate subsystems did not couple with each other. In this region, the type of connection did not have a large influence on the eigenmodes. This implies that for the first several bending and torsional modes, aside from moderate changes in the stiffness of the system, the type of connection does not grossly influence the system's structural response. However, for higher frequencies, the modes of the subsystems start to couple, and the simpler plate subsystems give rise to emergent behaviour. That is, a system formed from the connection of simpler subsystems behaves in a way that is more complex than the individual subsystems would behave on their own. This emergent behaviour is, at first, mostly due to the brackets,

	1	2	3	4	5	6	7	8	9	10	11	12	13	14	15	16	17	18	19	20
1	0	.01	0	**.48**	0	0	.04	0	0	.01	.04	.01	0	0	0	.01	0	.03	0	0
2	.01	0	0	0	0	.02	0	0	0	.01	0	0	0	0	.01	0	0	0	0	0
3	.16	.12	0	.08	.01	.01	0	0	0	.04	.01	.01	.01	0	.01	0	0	0	.04	0
4	0	**.98**	.01	0	0	.05	0	0	0	.01	0	0	.01	0	.02	0	0	0	.01	0
5	0	0	**.96**	.05	0	0	0	0	0	0	0	.01	0	0	0	0	0	0	0	0
6	0	.01	.05	**.84**	.11	0	.01	0	0	0	0	0	0	.01	0	0	0	0	0	0
7	.01	.03	0	.19	**.80**	.01	0	0	0	0	0	0	0	0	0	0	0	0	0	.02
8	0	.05	0	0	.01	**.96**	.02	0	0	.02	0	0	.01	0	0	0	0	0	.02	0
9	0	0	.01	.03	0	.01	**.91**	.04	.01	0	0	0	0	.02	0	0	0	0	0	0
10	0	0	.01	.01	0	0	.01	**.88**	.10	0	0	0	0	0	0	.02	0	.01	0	0
11	0	0	0	.01	0	0	.03	.05	**.88**	0	.01	0	0	0	0	0	0	0	0	0
12	0	0	0	0	0	.04	.05	0	0	**.69**	.21	0	0	.01	.01	.01	0	.02	0	0
13	0	0	0	0	0	.02	.06	0	0	.15	**.72**	0	0	0	.01	.01	0	.01	.01	0
14	0	0	0	0	0	0	0	.02	0	0	0	**.85**	.02	.01	.02	0	0	0	0	0
15	0	.02	0	.01	0	0	0	0	0	.06	.17	0	.33	.20	.01	.01	0	0	0	0
16	0	0	0	0	0	0	0	0	.01	0	.01	.10	.34	.23	.14	.02	0	.02	0	0
17	0	.01	0	.04	0	0	.01	0	.03	.02	0	.05	.21	.02	.34	.16	0	0	.01	0
18	0	0	0	0	0	.01	.01	0	0	0	0	0	.19	.17	0	.25	.01	.22	.01	0

Figure 12. MAC matrix of 0G0B (vertical axis) against 0G2B (horizontal axis) eigenmodes. The colourmap is a linear scale from white ($MAC = 0$) to black ($MAC = 1$).

	1	2	3	4	5	6	7	8	9	10	11	12	13	14	15	16	17	18	19	20
1	0	.01	0	**.47**	.04	0	.03	.01	0	.01	.04	.01	0	0	0	0	0	0	.04	0
2	.03	0	0	0	0	.02	0	0	0	.01	0	0	0	0	.01	0	0	0	0	0
3	.11	.13	0	.06	.03	0	0	0	0	.04	.01	0	0	0	0	.01	.05	0	.02	0
4	0	**.99**	.03	0	0	.05	0	0	0	0	0	0	.01	0	.03	0	0	0	0	0
5	0	0	**.97**	.04	0	0	.01	0	0	0	0	0	0	0	0	0	0	0	0	0
6	0	.01	.08	**.97**	0	0	.01	0	0	0	0	0	0	.01	0	0	0	0	0	0
7	0	.02	0	.02	**.96**	0	0	.01	0	0	0	0	0	0	0	0	0	.01	0	0
8	0	.05	0	.01	0	**.98**	.01	0	0	.02	.01	0	0	0	0	0	.02	0	0	0
9	0	.01	0	.02	0	0	**.92**	0	0	0	0	.01	0	.01	0	0	0	0	0	.01
10	0	0	.01	.02	0	0	.14	**.91**	0	0	0	.01	0	.01	0	0	0	0	0	0
11	0	0	0	.01	0	0	.01	0	**.96**	.01	.01	0	.01	0	0	0	0	0	0	0
12	0	0	0	0	0	.04	.02	.01	0	**.76**	.17	0	0	0	.01	.01	0	0	.02	.01
13	0	0	0	0	0	.02	.03	.01	0	.10	**.79**	0	0	0	.01	.01	.01	0	.02	0
14	0	0	0	0	0	0	0	.02	0	.01	.05	**.84**	0	.02	0	.01	0	0	.01	.02
15	0	.02	0	.01	0	0	0	0	0	.04	.11	.01	.28	**.39**	0	0	0	0	.02	0
16	0	0	0	0	0	0	0	0	.01	0	0	.06	**.60**	.24	.04	0	.03	.02	.01	0
17	0	.01	0	.04	0	0	.01	.01	.03	.03	0	.01	.35	0	.28	.05	.08	.10	0	0
18	0	0	0	0	0	.01	.01	0	0	0	0	0	.02	.20	.01	.29	.04	0	.16	.06

Figure 13. MAC matrix of 0G0B (vertical axis) against 3G2B (horizontal axis) eigenmodes. The colourmap is a linear scale from white ($MAC = 0$) to black ($MAC = 1$).

but as the frequency range increases, the contact between the elements starts to have an increasingly larger influence on the response of the system.

Further, this contribution highlights the potential for new measures in addressing flanking sound transmission performance in the low-frequency range. While the effect of the emergent system behaviour due to the coupling of modes from simpler panel subsystems and their direct influence on flanking sound transmission requires further investigation, these modes, once identified, can be shifted or even partially avoided. This could be accomplished without adding additional mass to the structure, such as by carefully selecting element aspect ratios in the design phase or changing the types of connectors themselves. This could even potentially be done remedially with other available measures, such as changing the stiffness of plates, but potentially at the expense of negatively influencing the radiation efficiency of the structure at higher frequencies.

The results of this contribution could be used as a basis for updating or validating a numerical model, such as in Ref. [9].

6. ACKNOWLEDGMENTS

The presented results were developed within the framework of the cooperative project “Schallschutz im Holzbau” between Lignum and Empa.

7. FUNDING

The authors gratefully acknowledge the financial support of the cooperative research project by the Swiss Federal Office for Environment (FOEN) as part of the “Aktionsplan Holz”.

8. REFERENCES

[1] C. E. Churchill, B. Nusser, and C. Lux, “Calculating the equivalent elastic moduli and their influence on modelling the sound insulation of softwood cross laminated timber (clt),” *Applied Acoustics*, vol. 205, 2023.

[2] S. Vallely and S. Schoenwald, “An efficient analytical method to obtain the homogenised frequency-independent elastic material properties of cross-laminated timber elements,” *Journal of Sound and Vibration*, vol. 546, p. 117424, 2023.

[3] J. Lietzén, V. Kovalainen, M. Kylliäinen, and S. Pajunen, "Computational prediction of impact sound insulation of a full-scale timber floor applying a fem simulation procedure," *Engineering Structures*, vol. 310, p. 118130, 2024.

[4] A. Aloisio, D. Pasca, R. Tomasi, and M. Fragiacomo, "Dynamic identification and model updating of an eight-storey clt building," *Engineering Structures*, vol. 213, p. 110593, 2020.

[5] B. Kurent, B. Brank, and W. K. Ao, "Model updating of seven-storey cross-laminated timber building designed on frequency-response-functions-based modal testing," *Structure and infrastructure Engineering*, vol. 19, no. 2, pp. 178–196, 2023.

[6] S. Moons, R. Lanoye, and E. P. Reynders, "Prediction of flanking sound transmission through cross-laminated timber junctions with resilient interlayers," *Applied Acoustics*, vol. 228, p. 110317, 2025.

[7] R. J. Allemang, "The modal assurance criterion–twenty years of use and abuse," *Sound and vibration*, vol. 37, no. 8, pp. 14–23, 2003.

[8] S. Vallely and S. Schoenwald, "Higher-order modal parameter estimation and verification of cross-laminated timber plates for structural-acoustic analyses," *Acta Acustica*, vol. 8, p. 52, 2024.

[9] A. Esposito, S. Vallely, and S. Schoenwald, "Modelling cross-laminated timber plate connections: A numerical investigation on flanking sound transmission through angle brackets," in *Proceedings of Forum Acusticum*, 2025.

DOI: 10.61782/fa.2025.0525



FORUM ACUSTICUM
EURONOISE 2025

LOAD EFFECTS IN FLANKING TRANSMISSION OF CLT STRUCTURES WITH RESILIENT INTERLAYER

Vincenzo Pettoni Possenti[1*] **Charlotte Crispin**[2] **Arne Dijckmans**[2] **Luca Barbaresi**[1]

[1] Department of Industrial Engineering, University of Bologna, Italy
[2] Buildwise, Belgium

ABSTRACT

With the increasing construction of Cross Laminated Timber (CLT) buildings, the demand for enhanced acoustic performance is also rising. To improve the sound insulation, resilient interlayers are inserted in the structure, which decreases the flanking transmission. These interlayers are generally placed between the floor and the wall and are under a static load, which depends on the relative floor. Interlayers are usually viscoelastic materials with non-linear behaviour. This is why the vibroacoustic behaviour under different loading conditions is investigated in this paper. Through a full-scale mockup, the vibration reduction index K_{ij} of some resilient material with different elastic modulus is measured by placing various static loads over the junction to evaluate different performances.

The results reveal significant differences depending on the load applied to the junction. In particular, in the mid-high frequencies, the higher the load, the lower the K_{ij} due to the increase in the dynamic stiffness of the resilient layer in the compression. This supports the importance of choosing the proper resilient material in the design step and carrying out laboratory measurements of K_{ij} with the test conditions as close as possible to the actual conditions of use.

Keywords: *cross laminated timber - resilient interlayer - flanking transmission*

1. INTRODUCTION

Obtaining good acoustic comfort also requires consideration of flanking transmission in addition to wall, floor and façade sound insulation. Wooden buildings like CLT (Cross Laminated Timber) have high radiation efficiency and low mass, which makes them particularly challenging to solve in terms of sound insulation. Engineered cross laminated timber (CLT) constructions permit the reduction of the acoustic vibrations transmitted into the structure by inserting resilient strips, usually elastomers, between the floor and wall [1] [2] [3].

CLT, in the past, was mainly used for small buildings with a few storeys, but today, it is also used for large buildings up to 18 storeys. The resilient strips under the supporting walls are, therefore, subjected to large loads, particularly on the lower floors. Also, the load on the resilient strip varies depending on the floor it is located on due to the weight of the upper floors.

Nilsson et al. [4] give an in-depth overview of the current literature on vibration reduction index, in particular on CLT, and analyse the effects of loading in junctions with resilient strips and fastening systems by comparing in-situ measurements of junctions in the first floors (higher load) with junctions with similar boundary conditions in the upper floors (lower load). The effects of loading on vibration reduction index were also studied by Crispin et al. [5], but for lightweight masonry constructions.

Schoenwald et al. [6] show that the vibration reduction index of junctions without resilient interlayers and with a fastening system is influenced to a considerable amount when

[*] ***Corresponding author***: vincenzo.pettoni2@unibo.it
Copyright: *©2025 First author et al. This is an open-access article distributed under the terms of the Creative Commons Attribution 3.0 Unported License, which permits unrestricted use, distribution, and reproduction in any medium, provided the original author and source are credited.*

the weight of the first storey is added, while the effect on the K_{ij} decreases significantly when additional storeys are added.

In the standard ISO 10848-1 (under revision) [7] for measuring the vibration reduction index K_{ij} there is no standardised methodology for measuring structures with resilient strips.

Also measuring the properties of elastomers in the dynamic regime under high loads with equipment is not easy, and there is a lack of suitable instrumentation [8]. Currently, there is the standard ISO 4664-1, also known as DMA, of which it is difficult to find ready-built machines that can perform analyses with high loads. This standard is designed for measurements at frequencies up to 200 Hz and applies to samples with a form factor of *h:d=1:1.5*, where h is the height of the sample and d is the diameter of the cylindrical sample. The results obtained are influenced by this form factor. The deformation considered is only 10%. Another standard is ISO 9052-1, which, however, is only intended for loads similar to a screed.

In this article, experimental measurements were carried out in the laboratory to see the effects of loading on the vibroacoustic properties of CLT junctions with resilient strips and without a fastening system. First by measuring the characteristics, such as the elastic modulus, of certain elastomers and then by measuring the K_{ij} after inserting them into a mockup junction.

2. BACKGROUND THEORY

Cross-laminated timber (CLT) structures are classified as Type A and therefore the descriptor for expressing the insulation effectiveness at the passage of acoustic vibrations through the junction is the vibration reduction index K_{ij} defined in ISO 10848-1 as:

$$K_{ij} = \overline{D_{v,ij}} + 10lg\left(\frac{l_{ij}}{\sqrt{a_i a_j}}\right) \quad \text{[dB]} \qquad (1)$$

with

$\overline{D_{v,ij}}$ [dB]: direction-averaged velocity level difference between elements i and j;

l_{ij} [m]: junction length between elements i and j;

a_i, a_j [m]: equivalent absorption lengths of elements i and j.

3. METHOD

3.1 Compressive elastic modulus

The compressive modulus of elasticity was measured according to ISO 844 [9] with the specifications of the EAD 042232-00-0503 [10]. In this EAD, the compressive elastic modulus is defined as:

$$E_c = \frac{\sigma_{15}-\sigma_5}{\varepsilon_{15}-\varepsilon_5} \quad \text{[MPa]} \qquad (2)$$

with

σ_{15} [MPa]: compressive stress at 15% strain (ε_{15});

σ_5 [MPa]: compressive stress at 5% strain (ε_5).

The samples had square dimensions of 50x50mm² and a thickness of 6mm. Five unlubricated samples of each material were tested. The tests were carried out using an INSTRON 8023 hydraulic press with steel plates and a compression speed of 0.01mm/s. This test was conducted under static conditions.

3.2 Vibration reduction index

A full-scale mockup of a horizontal L-junction (Figure 1) was built in the laboratories of Buildwise in Belgium. The floor is a 0.14m thick 5-ply CLT panel (panel i) with a width of 2.25m and a length of 4.93m. The wall is a 0.12m thick 5-ply CLT panel (panel ii) with a width of 2.4m and a length of 3.94m. The mockup is inside a warehouse, with the floor (panel i) supported on one side by three columns of cellular concrete blocks (height approx. 0.6m) and on the other side by panel i. Only the top 0.6m of the wall (panel i) is visible in the warehouse as it is inserted between two transmission chambers normally used for laboratory sound insulation tests. Three source points and eight receiver points were chosen for each panel. A hammer was used as the source. The velocity levels of the panels were measured using accelerometers placed at the receiver points and glued to the panel's surface with a two-component glue. Panel dimensions, source and receiver positions are compliant with ISO 10848-1. The structural reverberation time of the panels was determined from the impulse response of a hammer.

First, the vibration reduction index K_{ij} was measured for the rigid junction (without resilient strip), with panel ii just placed on panel i. Next, measurements were made by placing resilient materials in the junction between the two panels. Several resilient strips were tested, each with an equivalent length to the junction, i.e., 2.2m, width 0.08m and uncompressed thickness of 0.006m. In this case, a load is applied on the resilient material equivalent to the self-weight of the structure and thus half the weight of the floor, corresponding to 377kg and, therefore, a pressure on the resilient material of 0.021MPa.

Next, measurements were made by varying the load applied to the junction. To do this, starting with one, then two and then three reinforced concrete blocks were placed on the floor slab right above the junction (Figure 1, right). The concrete blocks were placed vertically and have a

Table 1. Measured configuration for vibration reduction index.

Configuration	Resilient interlayer	Number of concrete blocks	Pressure on the junction [MPa]	Deformation of the resilient interlayer	$K_{ij,high}$ [dB] (average 1250-5000HZ)
Conf.rigid_0	no	0	0.014	-	22.2
Conf.rigid_1	no	1	0.027	-	20.6
Conf.rigid_2	no	2	0.040	-	16.8
Conf.rigid_3	no	3	0.053	-	15.5
Conf.A_0	A	0	0.021	10%	35.8
Conf.A_1	A	1	0.040	19%	33.4
Conf.A_2	A	2	0.060	28%	32.5
Conf.A_3	A	3	0.079	35%	31.8
Conf.B_0	B	0	0.021	4%	34.6
Conf.B_1	B	1	0.040	5%	30.3
Conf.B_2	B	2	0.060	7%	28.5
Conf.B_3	B	3	0.079	9%	27.5
Conf.C_0	C	0	0.021	< 2%	29.4
Conf.C_1	C	1	0.040	< 2%	26.5
Conf.C_2	C	2	0.060	< 2%	25.3
Conf.C_3	C	3	0.079	< 2%	24.1

parallelepiped shape with dimensions: height 1m, width 0.25m and length 0.6m. Each block weighs 346kg, which in total, with the weight of the structure, becomes a pressure on the resilient material of 0.040MPa for one block, 0.060MPa for two blocks, and 0.079MPa for three blocks (assuming that the load is evenly distributed). The configuration with one block has the block placed in the centre of the junction, while the configuration with two blocks has them placed at the extremes of the junction.

All measurements were carried out within 10 minutes of the resilient material being loaded in an attempt to have approximately the same creep effects given by the loading time. All configurations are without a fastening system.

The maximum weight applied (3 blocks) to the junction is approximately 1000kg (without the self-weight of panel i). In a real service condition, we would also have other weights bearing down on the junction. For example, considering the partitions (an upper CLT wall, insulation, lining), the floating floor (floor, screed, floor finish), a ceiling, and the residential loads of normal use that would weigh on a floor with dimensions like those of the mockup, we would have an addition of approximately 2000kg on the junction. This would correspond to a pressure of 0.13MPa on the resilient strip. This load would only be that of a single storey and thus the typical load for the upper storey, in lower storeys the loads can be considerably higher as all the weights of the individual storeys are added together in load-bearing wall structures such as CLT.

4. RESULTS

Three different resilient materials (with different shore) were tested, two expanded EPDM (A and B) and one extruded polyurethane (C). Materials A (Figure 2), B (Figure 3) and C (Figure 4) were measured in compression to determine the compressive elastic modulus in static conditions. The typical non-linear behaviour of elastomers is recognisable in the graphs comparing pressure and deformation.

The summary of the configurations tested for the vibration reduction index K_{ij} has been schematised in Table 1. The measurement results are shown in Figure 5 to Figure 8.



Figure 1. Horizontal L-junction CLT mockup. On the left without extra weight. On the right with three concrete blocks.

5. DISCUSSION

It is desirable to use elastomers with low deformations and within their elastic range in building structures in order to have greater predictability of behaviour and to limit permanent deformations and structural stresses. Figure 2 to Figure 4 show the linear regression from 5% to 15% strain as in (2) to find the elastic modulus of the respective materials, indicated as the angular coefficient in the graph formula.

Figure 2 shows that for elastomer A, a pressure of 0.021MPa corresponds to a deformation of 10% (equivalent to 0.6mm), while for a pressure of 0.040MPa there is a deformation of 19% (1.14mm), with 0.060MPa it is 28% (1.68mm), and with 0.079MPa it is 35% (2.1mm). For elastomer B (Figure 3), there is a deformation of 4% (0.24mm) at a pressure of 0.021MPa, 5% (0.3mm) at 0.040MPa, 7% (0.42mm) at 0.060MPa, 9% (0.54mm) at 0.079MPa. For elastomer C (Figure 4), all loads applied in the K_{ij} tests are under 2% deformation. In Table 1 there is a summary of the relative deformation.

During the K_{ij} tests, we are within the elastic range of 5-15% deformation for elastomer A without concrete blocks and almost with one block; for elastomer B with one, two and three blocks; and for elastomer C we are significantly outside this elastic range. Although the weights are added by linear steps of 0.02MPa this is not reflected in a direct correlation of the K_{ij} measurements. There are different behaviours between the static regime (ISO 844) and the dynamic regime (ISO 10848-1).

It should be pointed out that the compressive elastic modulus measurements, following the roughness requirements of the standard ISO 844, were carried out with steel plates which produce different friction compared to wood and elastomer.

Figure 5 shows the measured results of the vibration reduction index K_{ij} of the rigid configurations without interlayer. It can be observed that there are differences in adding load to the junction. This is because adding weight will smooth out any possible gaps between panel i and panel ii caused by the roughness of the wood and the concavities in panel i. It seems that above a certain load (in this case from the second block), almost any imperfections in the contact surface between the two panels are smoothed out, resulting in a large decrease in the junction insulation. Beyond this threshold, the effects of further loading diminish drastically, as already seen in [6].

For configurations with the interlayer, the effects of the load are seen above the 400Hz band (Figure 6, Figure 7, and Figure 8). In general, as the load increases, the junction insulation decreases.

Below 125Hz, the vibration of the panels is determined by global modes, i.e. the two panels of the mockup behave as a single system and the resilient interlayer is not effective. From 160Hz local plate modes appear and the two panels operate as two subsystems. The two panels are effectively decoupled by the resilient interlayer, which is reflected in the sudden increase of the K_{ij} at this frequency (Figure 6, Figure 7, and Figure 8). Around the 250Hz band, there is an insulation gap due to parasitic airborne noise that is emitted from

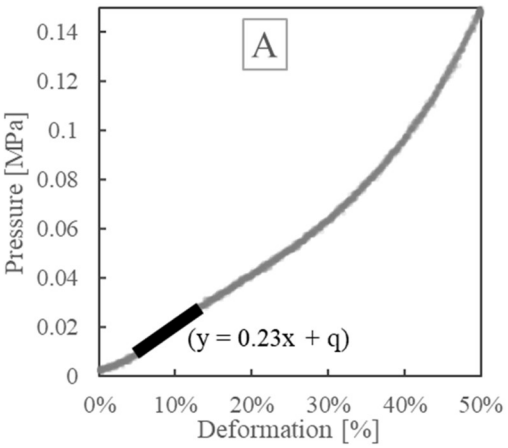


Figure 2. Compressive elastic modulus of interlayer A.

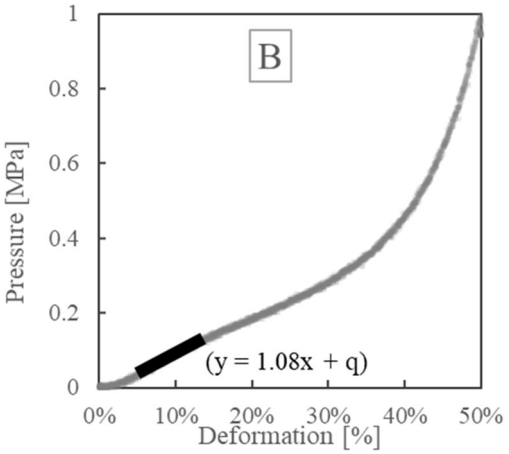


Figure 3. Compressive elastic modulus of interlayer B.

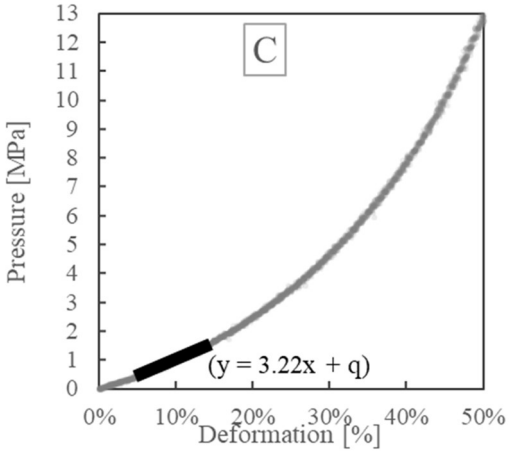


Figure 4. Compressive elastic modulus of interlayer C.

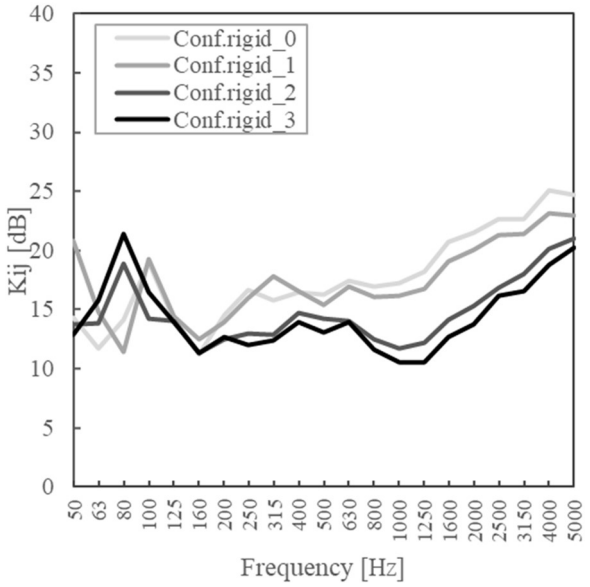


Figure 5. Vibration reduction index K_{ij} of the rigid configuration of the junction (no interlayer).

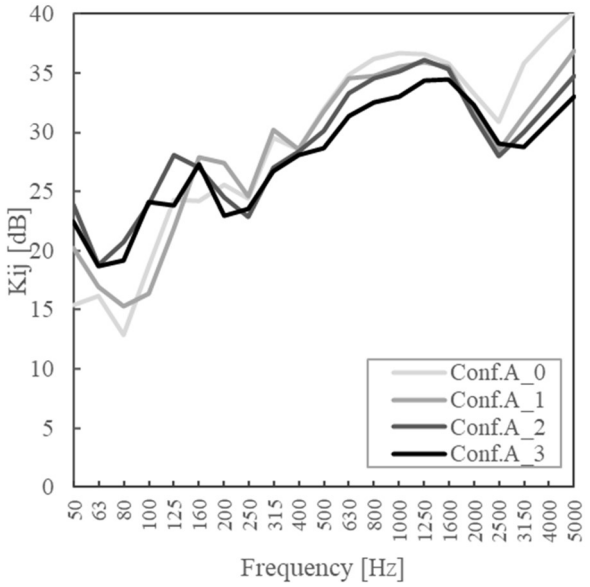


Figure 6. Vibration reduction index K_{ij} of the junction with resilient interlayer A.

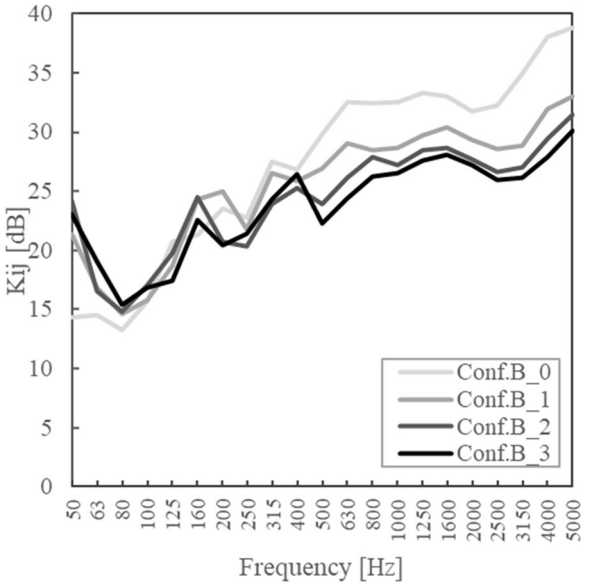


Figure 7. Vibration reduction index K_{ij} of the junction with resilient interlayer B.

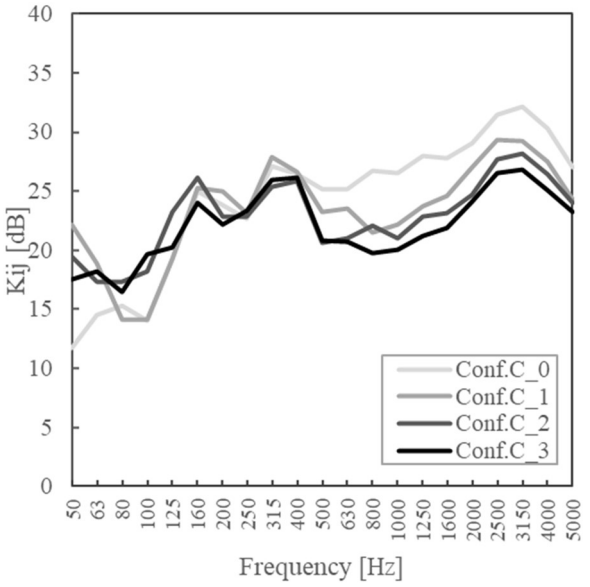


Figure 8. Vibration reduction index K_{ij} of the junction with resilient interlayer C.

the source panel and passes through the air to re-enter the receiving panel [11].

In elastomers A and B (Figure 6, Figure 7), a dip is observed in the frequency range of 2500-3150Hz for the K_{ij} values. This dip is attributed to the thickness resonance of the resilient interlayer [11]. The resonance frequency, which depends on the elastic modulus of the resilient interlayer, increases as the load on the resilient material rises.

To compare the different configurations with a single index, it is possible to use the division made by Hopkins [12] of $K_{ij,high}$ for the frequency range 1250-5000Hz, whose values for the tested configurations are summarised in the Table 1. This range is designed for isotropic homogeneous structures, whereas CLT is orthotropic and composed of several cross-layers. Indeed, the measurements shown in this article do not have a linear behaviour in this range. However, it was decided to use this method for coherence with the scientific literature and to have a curve comparison number. The difference of the unique index $K_{ij,high}$ between the configuration without added load and with loads is then made to have an easy indication of how much the performance is varying.

The difference between the $K_{ij,high}$ of the rigid configuration (Conf.rigid_0) and that with one block (Conf.rigid_1) is 1.6dB, adding a second block (Conf.rigid_2) loses another 3.9dB (5.4dB compared to Conf.rigid_0), while with three blocks (Conf.rigid_3) another 1.2dB (6.7dB compared to Conf.rigid_0) is lost.

Elastomer A comparing the configuration without added loads (Conf.A_0) with that with one block (Conf.A_1) loses 2.4dB, with two (Conf.A_2) another 0.9dB (3.3dB relative to Conf.A_0), with three (Conf.A_3) a further 1.1dB (2.3dB relative to Conf.A_0). The dynamic stiffness of the resilient strip increases significantly due to the loading and related thickness loss, reducing performance.

Elastomer B comparing the configuration without added loads (Conf.B_0) with the one block configuration (Conf.B_1) loses 3.3dB, with two (Conf.B_2) a further 1.4dB (4.6dB over Conf.B_0), with three (Conf.B_3) a further 0.8dB (5.5dB over Conf.B_0).

Elastomer C comparing the configuration with no added load (Conf.C_0) with the one block configuration (Conf.C_1) loses 3.8dB, with two (Conf.C_2) another 1dB (4.9dB relative to Conf.D_0), with three (Conf.C_3) a further 1.3dB (6.2dB relative to Conf.C_0).

For elastomers B and C, the most significant changes occur with the addition of the first block, as any gaps or lack of contact at the wood-elastomer interface are eliminated.

6. CONCLUSION

This article discusses the fact that the vibration reduction index, K_{ij}, of junctions with resilient interlayers is influenced by the load applied to the junction (for example, in this article, up to 7dB). Elastomers, usually used as resilient strips, do not have linear pressure-deformation behaviour. It is, therefore, difficult to make exact predictions of their behaviour in the dynamic regime under the design loads without measuring the appropriate conditions.

An important point to consider is the fact that in-situ measurements of K_{ij} are often performed during the construction phase when linings are not yet present. The linings (including the floating screed) can have a significant influence on the masses involved, especially for lightweight CLT structures. The measurement that is taken is, therefore, biased by a different load condition than the one that will be found when the building is finished (and foreseen in the design phase for the correct choice of resilient material based on its optimal load range) encountering the problems noted in this article. It is, therefore, important to find a method for predicting the effects to correct in situ measurements.

A method would also need to be found to measure a parameter in a dynamic regime under the right design load. One idea could be the dynamic stiffness, but the current ISO 9052-1 standard does not allow measurement under loads other than those typical of a screed (8±0.5kg on a 200x200mm², so in the range of 0.002MPa). Another possible standard could be the ISO 4664-1, but this standard is not meant for different loads and for measuring frequencies above 200Hz.

As loads in CLT buildings vary greatly, for example, between the first floors and the upper floors, there is a need to conduct K_{ij} measurements in the laboratory with the right design load to avoid overestimating the junction insulation.

It is therefore planned in the current revision of ISO 10848-1 to include a common standardised procedure for measuring the K_{ij} of structures with resilient interlayers.

It has to be said that in a real CLT building there will always be a fastening system in the junction. It is expected that the differences with varying load for such junctions are smaller as the performance of the junction is obviously lower.

7. ACKNOWLEDGMENTS

The results presented in this paper have been obtained within the frame of the projects "STABBS II" (Standards for acoustic better buildings II). The authors are grateful for the financial support from the Federal Public Service Economy of Belgium.

8. REFERENCES

[1] S. Mecking, T. Kruse and U. Schanda, "Measurement and calculation of sound transmission across junctions of solid timber

building elements," in *EuroNoise*, Maastricht, 2015.

[2] F. Morandi, S. De Cesaris, M. Garai and L. Barbaresi, "Measurement of flanking transmission for the characterisation and classification of cross laminated timber junctions," *Applied Acoustics,* no. 141, pp. 213-222, 2018.

[3] L. Barbaresi, P. Brugnara, V. Pettoni Possenti, A. Speranza and L. Sestigiani, "ON THE LABORATORY STUDY OF JUNCTION IN FLANKING TRANSMISSION IN TIMBER BUILDINGS," in *Forum Acusticum*, Torino, 2023.

[4] E. Nilsson, S. Ménard, D. Bard and K. Hagberg, "Effects of Building Height on the Sound Transmission in Cross-Laminated Timber Buildings—Vibration Reduction Index.," *Buildings,* vol. 13.12, no. 2943, 2023.

[5] C. Crispin, B. Ingelaere and G. Vermeir, "Innovative building systems to improve the acoustical quality in lightweight masonry constructions: Application of resilient joints at junctions-PART 1: analysis of the experimental results," in *Euronoise*, Paris, 2008.

[6] S. Schoenwald, B. Zeitler, I. Sabourin and F. King, "Sound insulation performance of Cross Laminated Timber Building Systems," in *Internoise*, Innsbruck, 2013.

[7] *EN ISO 10848-1:2017. Acoustics - Laboratory and field measurement of flanking transmission for airborne, impact and building service equipment sound between adjoining rooms.*

[8] H. Masoumi, S. Guns, R. Lanoye and P. Carels, "ELASTOMERIC MATERIAL TESTING AND STANDARDS IN BUILDING," in *30th International Congress on Sound and Vibration*, Amsterdam, 2024.

[9] *EN ISO 844:2021. Rigid cellular plastics — Determination of compression properties.*

[10] *EAD 042232-00-0503. Flexible interlayer for the reduction of flanking sound and vibration transmission. EOTA.*

[11] C. Crispin, V. Pettoni Possenti, A. Dijckmans and L. Barbaresi, "Improving the Accuracy of Vibration Reduction Index Measurements: Assessing and Correcting Parasitic Airborne Noise Effects.," *Available at SSRN 5168683,* vol. (PREPRINT), 2025.

[12] C. Hopkins, Sound Insulation, 1st ed., London, UK: Routledge, 2007.

DOI: 10.61782/fa.2025.0578

FORUM ACUSTICUM EURONOISE 2025

MODELLING CROSS-LAMINATED TIMBER PLATE CONNECTIONS: A NUMERICAL INVESTIGATION ON FLANKING SOUND TRANSMISSION THROUGH ANGLE BRACKETS

Antonio Esposito[1*] **Sven Vallely**[1,2] **Stefan Schoenwald**[1]

[1] Laboratory for Acoustics/Noise Control, Empa, Switzerland
[2] Department of Civil Engineering – Structural Mechanics Section, KU Leuven, Belgium

ABSTRACT

In recent years, interest has grown in numerical models to predict flanking sound transmission through Cross-Laminated Timber (CLT) junctions. The panels are typically connected with screwed metal brackets, which are differently shaped depending on the junction geometry and structural requirements. To predict the Vibration Reduction Index K_{ij}, available models rely either on empirical formulae or simplified junctions with idealized connection. In this contribution, a numerical investigation on the dynamics of a CLT L-junction is presented, starting from a detailed representation of an angle bracket. This was modelled in FEM and validated with vibrometry measurements. It was then integrated into the model of a CLT L-junction mock-up and compared to experimental datasets from two different configurations, where CLT plates were either in direct contact or separated by an air gap. Validation in the modal domain showed a good agreement of the model with both experimental configurations. The comparison with experimental K_{ij} showed a better correlation with the latter configuration, whereas larger deviations were observed above 1 kHz in the former case. This provided some insights on the modelling of bracket fastening and highlighted the need of introducing constraint conditions at the interface between CLT plates to simulate the effects of direct contact.

*__Corresponding author__: antonio.esposito@empa.ch.

__Copyright__: ©2025 Antonio Esposito et al. This is an open-access article distributed under the terms of the Creative Commons Attribution 3.0 Unported License, which permits unrestricted use, distribution, and reproduction in any medium, provided the original author and source are credited.

Keywords: *Cross-Laminated Timber, Flanking Sound Transmission, Vibration Reduction Index, Finite Element Method.*

1. INTRODUCTION

The use of Cross-Laminated Timber (CLT) has become well established in the construction industry due to its proven benefits in terms of structural efficiency, cost-effectiveness and environmental sustainability. CLT plates are often employed as load-bearing elements, due to their orthotropy and high strength-to-weight ratio. On the other hand, this feature causes significant structure-borne sound power flow across their junctions [1]. CLT plates are usually connected with screwed metal brackets, especially for specific types like L-, T- or X- junctions [2]. Given the above, the numerical modelling of flanking vibration transmission mechanisms in CLT junctions has received particular attention, with the aim of predicting the Vibration Reduction Index K_{ij}, as defined in the ISO 12354-1:2017 [3] and the ISO 10848-1:2017 [4] standards. The computation of this quantity becomes critical since the interface between CLT plates is, in most cases, both punctual, due to fasteners, and linear, due to the contact between plates [2]. Existing predictive approaches rely either on empirical or analytical models. In particular, the ISO 12354:2017-1 standard [3] provides empirical formulae, based on laboratory measurements, to compute K_{ij} for T- and X- CLT junctions. Nevertheless, such relationships are considered valid only within a limited range of area mass density ratios between the elements. In addition to empirical models, various analytical or numerical

approaches for modelling CLT junctions can be found in the literature. Among others, Salvalaggio et al. [5] investigated the impact of sound-insulated joints on the dynamics of CLT structures. In their study, plate joints with steel fasteners were modelled as linear interface elements and angle brackets as nodal linear springs, whose stiffnesses were retrieved from a model updating process. In a recent work, Moons et al. [6] proposed an efficient analytical wave approach to predict K_{ij} through CLT junctions with and without resilient interlayers. Their model without interlayers showed deviations against experiments below 5 dB in 1/3 octave bands up to 2000 Hz. In this latter case, CLT plates were modeled as semi-infinite, assuming ideal rigid connections. In the context of the research project "Schallschutz im Holzbau", conducted in a cooperation between Lignum (Swiss Forestry Association) and Empa, the dynamic behavior of metal angle brackets was analyzed with the aim of investigating the effects of point connections between plates on CLT junctions. A steel angle bracket has been modelled in FEM and validated with laser doppler vibrometry measurements in the modal domain. It has been then integrated in a global FEM model of a CLT L-junction mock-up. The numerical K_{ij} was computed and compared against the experimental K_{ij} obtained by measuring two different setups, in which plates, connected with two angle brackets, were either in direct contact or separated by a 3 mm air gap. Based on the above, an alternative approach is proposed herein, for the dynamic characterization of CLT junction components. This may constitute a preliminary stage of a bottom-up procedure for setting up broadband versatile FEM models, which could possibly account for the effects of a change in the number and position of connectors in the junction. Please note that the graphs presented in this updated version of the paper are revised with respect to that initially submitted for the conference.

2. THEORY AND BACKGROUND

In the following subsections, the basic principles of FEM modal and harmonic analyses, conducted on the proposed models, are outlined. Furthermore, the theoretical background underlying the Vibration Reduction Index K_{ij} is summarized, since it was calculated and referred to as a validation of the numerical model of the L-junction.

2.1 Modal analysis

For an undamped multi-degree of freedom system, the equation of motion for free vibration is written as [7]:

$$[\mathbf{M}]\{\ddot{\mathbf{x}}\} + [\mathbf{K}]\{\mathbf{x}\} = 0 \tag{1}$$

where $\{\ddot{\mathbf{x}}\}$ is the nodal acceleration vector, $\{\mathbf{x}\}$ is the nodal displacement vector, $[\mathbf{M}]$ is the mass matrix and $[\mathbf{K}]$ is the stiffness matrix of the system. Assuming the displacement field solution of Eqn. (1) to be harmonic, the natural frequencies and the eigenvectors of the system can be calculated by solving the corresponding eigenvalue problem.

2.2 Harmonic analysis

When a damped system is excited by an external harmonic force $\{\mathbf{F}\}$, Eqn. (1) becomes [7]:

$$[\mathbf{M}]\{\ddot{\mathbf{x}}\} + [\mathbf{C}]\{\dot{\mathbf{x}}\} + [\mathbf{K}]\{\mathbf{x}\} = \{\mathbf{F}\} \tag{2}$$

where $\{\mathbf{F}\}$ is the external harmonic forcing vector and $[\mathbf{C}]$ is the structural damping matrix of the system.

2.3 Vibration Reduction Index K_{ij}

In order to predict the flanking sound transmission across a junction between building elements, the ISO 12354-1:2017 standard [3] introduces the Vibration Reduction Index K_{ij}. This quantity represents, analogously to the Sound Reduction Index, the attenuation of structure-borne sound at a junction. It is based on Statistical Energy Analysis simplifications on power transmission. It is frequency-dependent, expressed in decibels and defined as:

$$K_{ij} = \overline{Dv,_{ij}} + 10lg\left(\frac{l_{ij}}{\sqrt{a_i a_j}}\right). \tag{3}$$

where $\overline{Dv,_{ij}}$ is the direction-averaged velocity level difference between two elements, l_{ij} is the junction length and $a_{i,j}$ are the equivalent absorption lengths of the elements i and j. These are defined as [4]:

$$a = \frac{2.2\pi^2 S}{c_0 T_s}\sqrt{\frac{f_{ref}}{f}} \tag{4}$$

where T_s is the structural reverberation time of the element, S is the surface area of the element, f is the centre band frequency, f_{ref}, equal to 1000 Hz, is the reference frequency and c_0 is the speed of sound in air.

3. NUMERICAL MODELLING AND VALIDATION OF A STEEL ANGLE BRACKET

In the following subsections, the FEM model of a single steel angle bracket is described. The numerical and experimental setups are described and the validation of the FEM model in the modal domain is presented.

3.1 FEM model setup

An angle bracket was numerically modelled in Ansys Mechanical (Release 2024, R2) and its geometry was reproduced starting from that of a commercially available galvanized steel bracket (Fig. 1). The bracket is modelled as an elastic isotropic shell element and discretised by using 2 mm quadratic triangular mesh elements (Fig. 1), with a total number of 90546 degrees of freedom (DOFs). Elasticity parameters for DX51D galvanized steel are drawn from [8] and listed in Tab. 1.

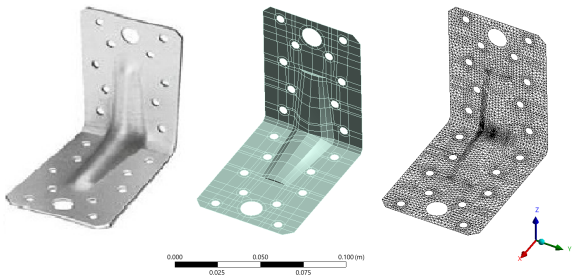


Figure 1. Left-hand side: commercial sample of the analyzed galvanized steel angle bracket. Center: CAD geometry of the bracket sample. Right-hand side: meshed geometry with 2 mm quadratic triangular elements.

Table 1. Elastic constants of DX51D galvanized steel [8].

Mass density, ρ [kgm^{-3}]	Elastic modulus, E [GPa]	Poisson's ratio, ν [-]
7830	210	0.30

A FE modal analysis is performed on the bracket, which is assumed to be in free boundary conditions. Numerical results in terms of eigenfrequencies and modeshapes are reported in the subsection 3.2 and compared to experimental data for validation in the modal domain.

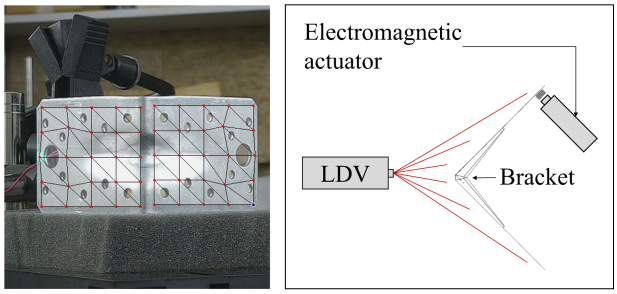


Figure 2. Setup of the experiment on a steel angle bracket. Left-hand side: laser vibrometer measurement grid. Right-hand side: schematic of the measurement setup.

3.2 Vibration measurements and validation in the modal domain

Vibration measurements on the steel angle bracket were carried out with a Laser Doppler Vibrometer. In order to ensure repeatability of the results, tests were performed on three different samples of the same bracket model. To replicate the free boundary conditions during measurements, brackets were resting on a layer of melamine foam. As visible in Fig. 2, they were excited at a corner position with an electromagnetic actuator to minimize possible alterations on mass and stiffness due to the use of a mechanical shaker. A grid of measurement points was set over the surface of the bracket to measure surface velocities (Fig. 2). Where possible, most of the points were evenly spaced on a 13 mm modular grid. The frequency range was from 0 Hz to 6.4 kHz with a spectral resolution of 500 mHz. Ten measurements were averaged at each point and point mobility was exported for each sample. As visible in Fig. 3a, the frequency response functions measured at a corner point were compared. The natural frequencies of the bracket were identified by the peaks of the mobility functions. At the corresponding frequencies, the measured modeshapes showed a good agreement with the numerical results (Fig. 3b and Fig. 3c). Furthermore, the percentage error between numerical and experimental eigenfrequencies was consistently below 5%, except for one eigenmode occurring at 3395.2 Hz, showing a 5.3% error against experimental data. Given the above, the FEM model of the steel angle bracket was considered validated.

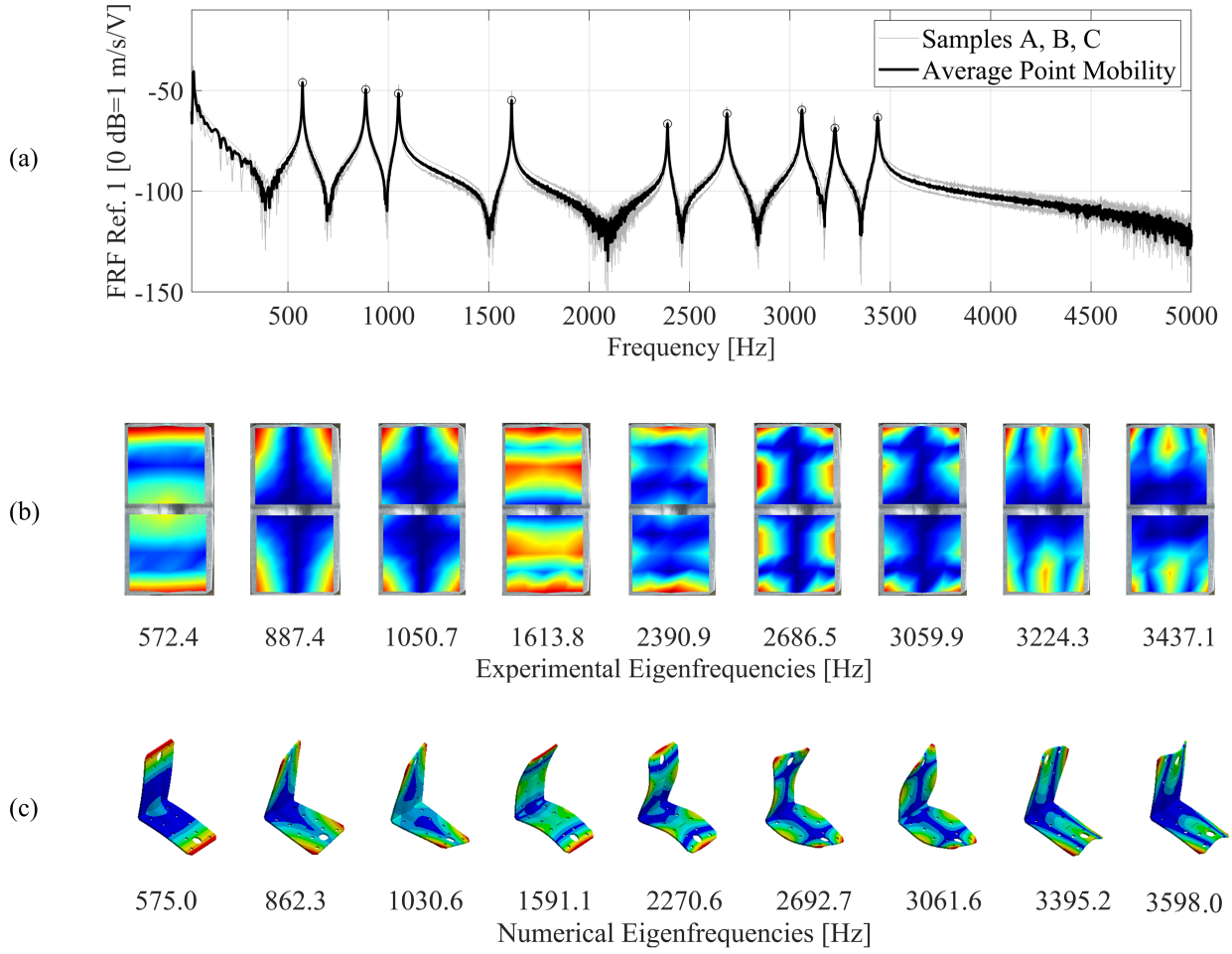


Figure 3. (a) Point Mobility response functions measured on three samples of the same angle bracket model (in gray). The average mobility is represented in black. Abscissas of circled peaks identify the eigenfrequencies of the bracket. (b) Measured modeshapes of the bracket and corresponding eigenfrequencies. (c) FEM modeshapes of the bracket and corresponding eigenfrequencies.

4. NUMERICAL MODELLING OF AN L-JUNCTION MOCK-UP

Once validated against experimental data, the FE model of the bracket was integrated into the numerical model of a CLT L-junction mock up. The latter was validated against laser vibrometry measurements in the modal domain. In the following subsections, the numerical model is described and the setup from two different experimental configurations is reported.

4.1 FEM model setup

A mock-up of a CLT L-junction has been modelled in FEM. Two CLT plates (henceforth referred to as CLT100A1 and CLT060C1) were connected along their short edge with two steel angle brackets (Fig. 4). Brackets were modelled as isotropic shells and meshed according to what mentioned in subsection 3.1. CLT plates were represented as two-dimensional orthotropic shells where the [90/0/90] orientation of the plies was implicitly modelled in a layer-wise representation. The plates were discretised

using 4 cm quadratic triangular mesh elements (Fig. 4b). Physical connections at bracket-plate interface required a specific modelling approach. Multi Point Constraint (MPC) rigid joints were defined to tie nodal displacements at the edges of the bracket screw holes to the nodes defined on the adjacent plates, lying in correspondence of the hole edges projected from the bracket onto the plate surface. With MPC formulation, individual degrees of freedom defined along these edges were eliminated and forced to have the same solution as a single node placed at the origin of the joint reference system (Fig. 4c). Along the contact edge between the two plates, no constraint condition was introduced. Geometrical and mechanical properties of the plates are reported in Tab. 2. Elastic orthotropic parameters of CLT plates were obtained using a numerical parameter estimation based on vibration measurements conducted on the same plates individually. From the same set of measurements, frequency independent structural loss factors were obtained by applying the Power Injection Method (PIM) [1]. The description of the aforementioned procedures is based on the methods applied in [9] for material property derivation. Modal and full harmonic structural dynamic analyses were conducted for the L-junction system. In the former case, eigenfrequencies and mode-shapes of the first fifteen modes were used for calculation of the Percentage Error (PE) and Modal Assurance Criterion (MAC) against experimental data for validation in the modal domain. The PE index provides the relative difference between numerical and experimental eigenfrequencies, expressed in percentage. The MAC index is defined as a squared linear regression correlation coefficient (ranging from 0 to 1) between numerical and experimental eigenvectors. The plates were excited by a transverse harmonic force at three different nodal positions for each plate, as depicted in Fig. 4a. The force amplitude was set as 1 N. The normal surface velocities were acquired as a function of frequency. The surface velocity response of the nodes were then mapped using two-dimensional linear interpolation to the grid measurement points used for the measurements with a laser vibrometer, as described in subsection 4.2. A logarithmic solution interval was defined for the full harmonic analysis, ranging from 200 Hz to 3150 Hz with 575 frequency steps.

Table 2. Geometrical and mechanical properties of CLT100A1 and CLT060C1 plates. Parameters are referred to the reference system of each plate, in which the z-axis is parallel to the plate thickness and the x-axis is perpendicular to the fibers of the top plies.

Property	Units	Plate ID	
		CLT100A1	CLT060C1
Length	m	2.87	1.52
Width	m	..... 1.14	
Thickness	m	0.10	0.06
Density, ρ	kgm^{-3}	462.00	452.00
Loss Factor, η	-	0.014	0.0083
Elastic Moduli			
E_x	GPa	12.70	11.50
E_y	GPa	0.42	0.38
E_z	GPa	0.42	0.38
Poisson's Ratios			
ν_{xy}	-	..... 0.10	
ν_{yz}	-	..... 0.30	
ν_{xz}	-	..... 0.10	
Shear Moduli			
G_{xy}	GPa	0.79	0.72
G_{yz}	GPa	0.16	0.14
G_{xz}	GPa	0.79	0.72

4.2 Experimental setup

The numerical setup described in subsection 4.1 was replicated experimentally in the lightweight facility at Empa (Fig. 5a). CLT100A1 and CLT060C1 plates were connected with two steel angle brackets, each of which was fixed with four wood screws to the plates (Fig. 5a). In order to isolate the dynamic effects of bracket fastening onto CLT plates in the junction, two different configurations were setup: in the first, plates were touching each other along the common edge (configuration A in Fig. 5b); in the second, a 3 mm air gap was left between the plates, in order to ensure structural coupling to be exclusively due to bracket fastening (configuration B in Fig. 5c). In order to emulate the free boundary conditions, the system was resting on four air jacks, located close to the corners of the CLT100A1 plate, the internal air pressure of which has been kept constant during the measurements. Each plate was dynamically excited with an inertial shaker emitting

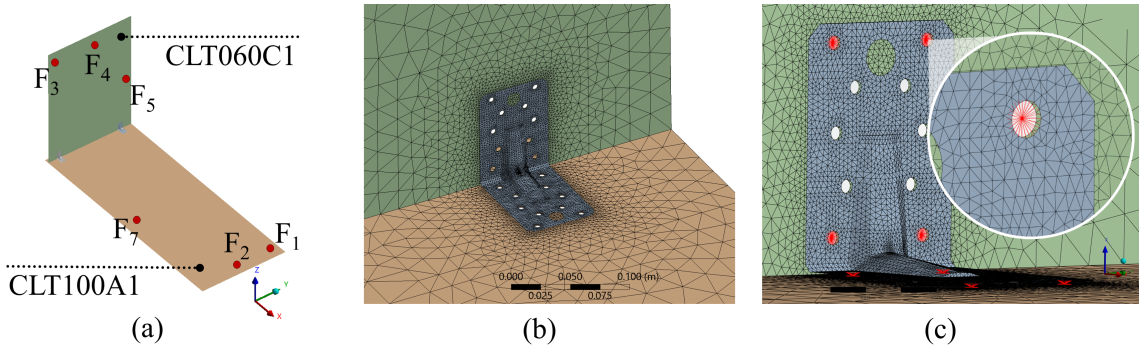


Figure 4. (a) Drawing of the FEM geometry of the L-junction. Excitation points F1 to F7 are highlighted with red dots. (b) Close-up on mesh elements: bracket was modelled with 2 mm triangular elements. Gradual size transition to the 4 cm plate mesh was guaranteed. (c) Close-up on the MPC joints defined at the screw positions.

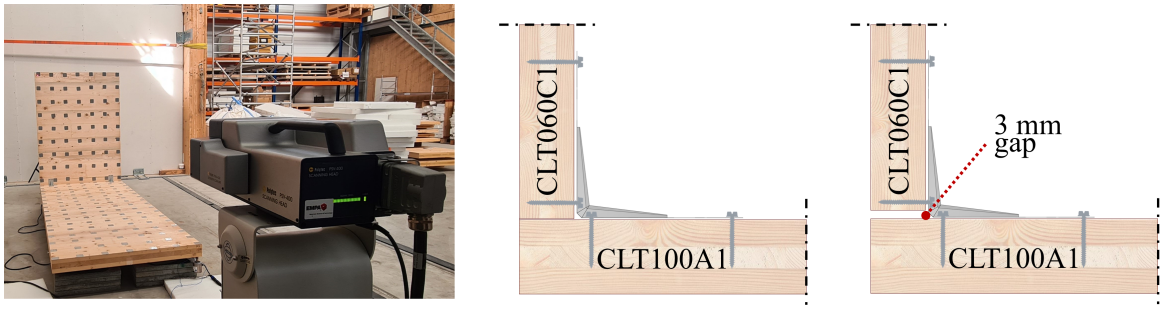


Figure 5. (a) Picture of the CLT L-junction mock-up during the laser doppler vibrometry measurements. (b) Schematization of the configuration A with plates in direct contact. (c) Schematization of the configuration B with a 3 mm air gap between plates.

a sine sweep signal. For each plate, three different excitation positions were set up, according to the schematization of the numerical model depicted in Fig. 4a. Normal surface velocities were acquired with a Polytec PSV-400 scanning vibrometer pointing normally to the plates, over a 17×7 points regular grid for the CLT100A1 plate, and over a 9×7 points grid for the CLT060C1 plate. Results were exported within the 1 Hz-5.8 kHz frequency range with a resolution of 62.5 mHz.

5. RESULTS AND DISCUSSION

5.1 FEM model validation in the modal domain

Results from the FEM modal analysis described in subsection 4.1 were compared for validation to the first fifteen bending and torsional eigenmodes of both experimental configurations, in terms of eigenfrequency PE and MAC. It should be noted that the first rigid-body mode of the junction, occurring below 10 Hz, has not been considered in this analysis. As visible from Fig. 6, a good correlation against both experimental datasets is observable. In particular, PE values were found to be below 10% and, as visible in Fig. 6a, configuration A was stiffer than configuration B, as expected. The minimum MAC value was found to be 0.7 among all modes of both configurations (Fig. 6b,c). This reveals that, in the low-frequency range, edge contact between CLT plates does not significantly affect the modal behaviour of the system. Furthermore, assuming rigid multi-point constraint at screw holes was sufficient to ensure good correlation with experimental data and no further contact modelling is needed at low frequencies.

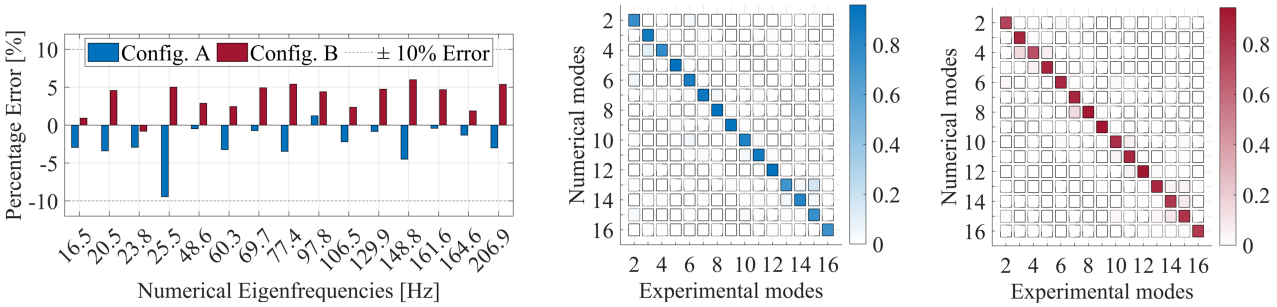


Figure 6. (a) Percentage error of numerical against experimental eigenfrequencies from configurations A and B. (b,c) Modal Assurance Criterion of numerical against experimental eigenmodes from configuration A (b) and configuration B (c).

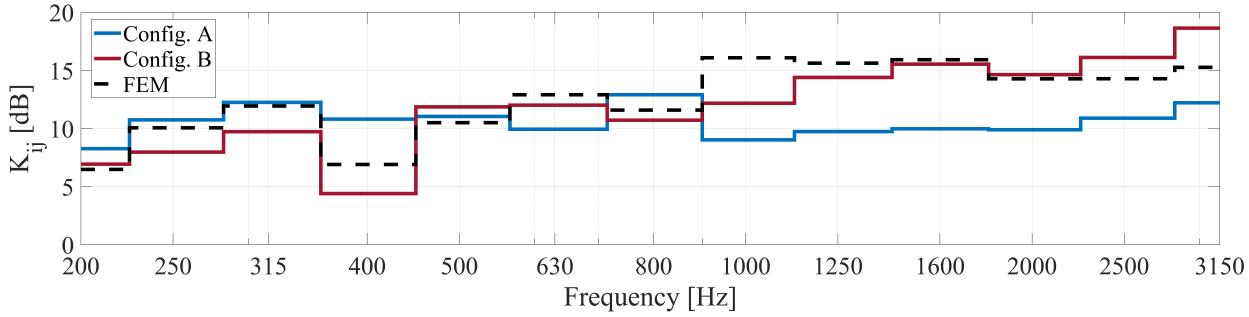


Figure 7. Comparison of numerical and experimental K_{ij} from configurations A and B in one-third octave bands.

5.2 Calculation of the Vibration Reduction Index K_{ij}

As an outcome of the FEM full harmonic analysis, the numerical Vibration Reduction Index K_{ij} was computed and compared to the K_{ij} from configurations A and B in the 200 Hz-3150 Hz frequency range, as shown in Fig. 7. Numerical data show an average deviation of 3.2 dB and a maximum deviation of 7.1 dB at 1 kHz from the experimental K_{ij} of the configuration A, in which the plates were in contact. In addition, the deviation between numerical and experimental single-number K_{ij} was calculated in the mid-frequency (250 Hz - 1 kHz) and high-frequency (1.25 kHz - 3.15 kHz) ranges, as defined in [4]. In the former case, the deviation was equal to 0.5 dB, whilst in the high frequency range it was found to be 4.5 dB. Analysing the overall trend, it appears that the FEM model underestimates the mechanical coupling between the CLT plates above 1 kHz. This can be attributable to possible effects of friction and pre-stress due to the direct contact between the plates in the configuration A, which are neglected in the numerical model. Such effects may be accounted for by introducing non-linear contact conditions or contact stiffness values at the nodes along the common edge between the two plates. These stiffness values may be retrieved from parameter estimation procedures based on curve fitting algorithms against experimental data. As visible in Fig. 7, there is a better agreement between numerical data and K_{ij} from configuration B, in which the plates were separated by an air gap. In particular, the overall trend of numerical K_{ij} is consistent with experimental data over the entire frequency range. An average deviation of 1.7 dB is observed, which almost halves the 3.2 dB mean deviation from the configuration A in the same frequency range. The maximum deviation from configura-

tion B was found to be equal to 3.9 dB at the 1 kHz third octave band. Furthermore, the deviations between numerical and experimental single-number K_{ij} in the mid and high-frequency ranges are respectively equal to 1.6 dB and 0.8 dB. This confirms that the effects of direct contact between plates plays a major role at high frequencies. As a result, it can be stated that the modelling of the bracket with screws can be considered acceptable, although still subject to possible improvements. For example, the use of rigid MPC joints at screw locations could possibly overconstrain the connections at some third octave frequency bands. On this basis, stiffnesses of the screw fastening may be obtained from further experimental investigations and introduced into the model.

6. CONCLUSIONS

This contribution presents a numerical investigation for the prediction of flanking sound transmission across a CLT L-junction, starting from the detailed representation of a commercially available angle bracket. This was modelled in FEM, validated with vibrometry measurements and integrated into a global FEM model of an L-junction mock-up. The numerical K_{ij} was compared with the experimental counterpart from measurements on two different configurations, in which plates were either in contact or separated by an air gap. The analysis provided useful insights on how to model the bracket fastening and the line connections between CLT plates. In particular, the comparison of the numerical K_{ij} with that from the experimental setup in which plates were in direct contact highlighted that the contact forces between plates play a major role and need to be included in numerical models, possibly by means of nodal stiffness values. These can be retrieved from further investigations on experimental data, conceivably with parameter estimation algorithms. A better agreement was observed from the comparison of numerical data against the K_{ij} from the configuration in which plates were separated by a gap. This suggested that modelling the bracket fastening with multi-nodal rigid joints can be partially acceptable, but still subject to possible improvements, e.g. by including nodal stiffnesses along the screw hole edge interfaces in order to reduce coupling overestimation.

7. ACKNOWLEDGMENTS

The presented results were developed within the framework of the cooperative project ”Schallschutz im Holzbau” between Lignum and Empa. The project was funded by the Swiss Federal Office for the Environment (FOEN) as part of the Aktionsplan Holz. We gratefully acknowledge this financial support.

8. REFERENCES

[1] L. Cremer and M. Heckl, *Structure-Borne Sound: Structural Vibrations and Sound Radiation at Audio Frequencies*. Berlin, Germany: Springer Science & Business Media, 2013.

[2] F. Morandi, S. De Cesaris, M. Garai, and L. Barbaresi, “Measurement of flanking transmission for the characterisation and classification of cross laminated timber junctions,” *Applied Acoustics*, vol. 141, p. 213 – 222, 2018.

[3] International Organization for Standardization, *ISO 12354-1:2017 Building acoustics — Estimation of acoustic performance of buildings from the performance of elements*, 2017.

[4] International Organization for Standardization, *ISO 10848-1:2017 Acoustics — Laboratory and field measurement of flanking transmission for airborne, impact and building service equipment sound between adjoining rooms - Part 1: Frame document*, 2017.

[5] M. Salvalaggio, F. Lorenzoni, and M. R. Valluzzi, “Impact of sound-insulated joints in the dynamic behavior of cross-laminated timber structures,” *Journal of Building Engineering*, vol. 91, p. 109525, 2024.

[6] S. Moons, R. Lanoye, and E. P. Reynders, “Prediction of flanking sound transmission through cross laminated timber junctions with resilient interlayers,” *Applied Acoustics*, vol. 228, p. 110317, 2025.

[7] S. V. Modak, *Analytical and Experimental Modal Analysis*. Boca Raton, USA: CRC Press Taylor & Francis Group, 2023.

[8] R. Vasile, S. G. Racz, and O. Bologa, “Experimental and numerical investigations of the steel sheets formability with hydroforming,” in *Proc. of MATEC Web of Conferences CoSME’16*, p. 02016, 2017.

[9] S. Vallely and S. Schoenwald, “Frequency-independent homogenised elastic and damping constants of cross-laminated timber,” in *Proc. of Forum Acusticum 2023*, (Turin, Italy), pp. 1297–1304, 2023.

DOI: 10.61782/fa.2025.0838

FORUM ACUSTICUM EURONOISE 2025

SUGGESTION FOR A ROUND ROBIN TEST ON THE MEASUREMENT OF VIBRATION REDUCTION INDICES ON CLT JUNCTIONS

Fabian Schöpfer[1*] **Ulrich Schanda**[1] **Camille Chateauvieux-Hellwig**[1]

[1] Rosenheim Technical University of Applied Sciences, Germany

ABSTRACT

Prediction methods for sound insulation require input data for the vibration reduction indices. For heavy buildings, ISO 12354-1 provides methods based on the mass ratio of elements. The same holds for solid timber. However, these data are based on a small number of measurements in buildings without the effect of additional loads or elastic interlayers, highlighting the essential need for additional measured data. ISO 10848-1 [1] describes methods to measure the vibration reduction index. But there is room for interpretation of the guidelines given in this standard. For example previous research showed that the choice of sampling points is crucial [2]. To quantify the measurement uncertainty, this paper suggests a concept for a round robin test for discussion. This could be carried out in the laboratory at the Technical University of Applied Sciences in Rosenheim. This laboratory provides a mock-up that allows to set up either a L-junction or a T-junction formed by CLT (cross laminated timber) panels that can be reconfigured quickly with an overhead crane. The possibility to apply additional loads which can be monitored and controlled with load cells as well as the application of elastic interlayers is given. The mock-up can stay in place to have enough time for several institutions to measure.

Keywords: *vibration reduction index, inter-laboratory test, measurement methods*

**Corresponding author*: *fabian.schoepfer@th-rosenheim.de.*

***Copyright**: ©2025 Schöpfer et al. This is an open-access article distributed under the terms of the Creative Commons Attribution 3.0 Unported License, which permits unrestricted use, distribution, and reproduction in any medium, provided the original author and source are credited.*

1. INTRODUCTION

The standard ISO 10848 was first publised in 1999 with the title *Acoustics - Labaratory measurement of the flanking transmission of airborne and impact noise between adjoining rooms - Part 1 : Frame document* [3]. The scope of this standard was to describe measurement procedures to determine the characteristics of one or more building elements in terms of flanking transmission. These characteristics can be used as input data for the prediction methods given in the EN 12354 series. Measured data is particularly needed for junctions formed by timber elements. Hence this standard was used widely to gather data that can be used for prediction. Almost two decades after the publication of ISO 10848, Timpte et al. [4] collected data across Europe from six institutions with more than 200 datasets of vibration reduction indices of cross-laminated-timber (CLT) junctions. It was found that there is a significant deviation between vibration reductions indices measured at various institutes for similar junction configurations. These deviations include parameters related to the mock-up, such as the CLT element itself, construction details of the junction, the choice of optional resilient interlayers or additional loads but also parameters related to the measurement procedure and the processing of data.

The intention of this paper is to initiate an inter-laboratory test (round-robin test) on the measurement procedure including the processing of data to determine vibration reduction indices. This suggested test would not consider all parameters related to the mock-up or the CLT elements itself. It is aimed to consider one specific mock-up formed by CLT elements that will stay in place in one laboratory with different people visiting this laboratory to measure the vibration reduction index according to ISO 10848. However, this standard is currently under revision by ISO/TC 43/SC 2/WG 18 where the measurements pro-

cedure and the processing of data is considered. The suggested inter-laboratory test will include the application of the current standard in comparison with the proposed revision by WG 18.

2. INTER-LABORATORY TEST

Deviations caused by material properties or details on the construction of the junction will not be considered. Only one mock-up with a single set of CLT elements should be part of the inter-laboratory test. The suggested approach is therefore identical with the *measurement situation B* in combination with section 5.6.2 described in [5]. Following this approach the so-called *in-situ* standard deviation can be obtained.

Although the identical CLT elements will be used in the test, it is aimed to consider not only one fixed junction configuration. Each team should measure the vibration reduction index for a set of junctions formed by the same CLT elements, such as an L-junction and a T-junction with the corresponding different transmission paths. It is also aimed to consider different loads on the junction. In addition a junction configuration with an elastic interlayer should also be considered and could easily be implemented in the test procedure.

This requires a careful documentation and monitoring during the reassembly of the considered junction configurations. To ensure identical configurations, parameters such as tightening torques of screws or a measurement, respectively a monitoring of the applied load is required. In addition parameters such as temperature, humidity and moisture will need to be monitored.

3. SUGGESTED TEST FACILITY

For the suggested inter-laboratory test on the measurement of vibration reduction indices of CLT junctions, the laboratory at Rosenheim Technical University of Applied Sciences can be made available. This laboratory offers a mock-up that was already well investigated. This included a statistical study on the vibration field and the corresponding sampling to determine the plate energy [2]. Figure 1 shows the bottom of the junction with the dimensions given in Figure 2. It is possible to configure either a L-junction or a T-junction. Three CLT elements, two wall and one floor element is already in place. A reconfiguration of junctions is possible with an overhead crane.

To apply additional loads on the junction a construction with steel girders is installed. This can be seen in the section drawing in Figure 2 as well as in the photo in Figure 3. These Figures also indicate the two load cells that are installed to monitor the applied load. This mock-up can stay in place for several months in order to allow various teams to come and perform the measurements.

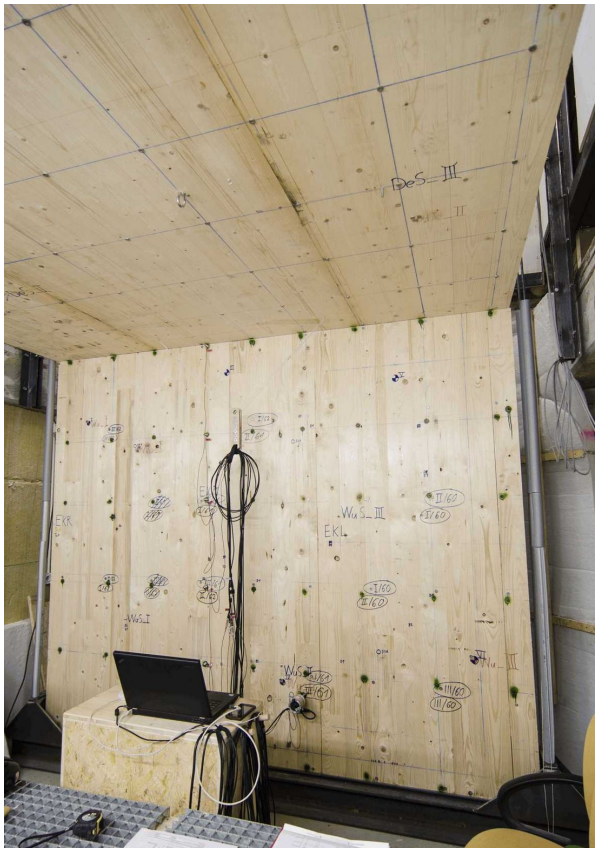


Figure 1. Bottom view of the junction mock-up.

4. CONSIDERATIONS ON THE TYPE OF AVERAGING LEVEL DIFFERENCES

In the course of the round robin test, measurements could as well be compared when applying different calculation approaches of averaging, especially the averaging of results from different excitation positions as discussed in the revision of ISO 10848.

In the current standard of ISO 10848 the velocity level difference $D_{v,ij}$ is calculated using the arithmetic mean of the $D_{v,ij,m}$ for $m = 1 \ldots M$ excitation positions (see equation (2)). Using the familiar physical approach from

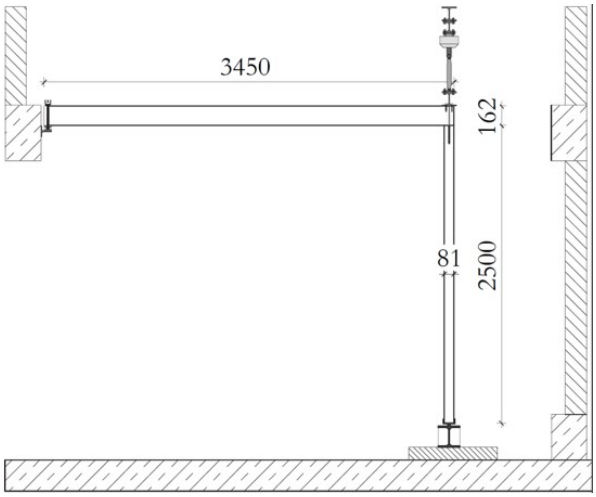


Figure 2. Section of a L-junction configuration indicating the dimensions of the elements. The width of the wall and floor elements not shown in this section is three metres.

EN ISO 10140-4 using transmission coefficients

$$\tau_{ij,m} = \frac{\overline{v_{j,m}^2}}{\overline{v_{i,m}^2}} \tag{1}$$

as the ratio of the mean squared velocity of the receiving element j and the exited element i respectively, the current definition of $D_{v,ij}$ is based on the geometric mean of the transmission coefficients for different excitation positions according to the following derivation.

$$\begin{aligned} D_{v,ij} &= \frac{1}{M}\sum D_{v,ij,m} \\ &= \frac{1}{M}\sum \left(L_{v,i,m} - L_{v,j,m}\right) \\ &= \frac{1}{M}\sum 10\lg\left(\frac{\overline{v_{i,m}^2}}{\overline{v_{j,m}^2}}\right) \\ &= \frac{1}{M}\sum -10\lg\left(\tau_{ij,m}\right) \\ &= -10\frac{1}{M}\lg\left(\prod \tau_{ij,m}\right) \\ &= -10\lg\left(\sqrt[M]{\prod \tau_{ij,m}}\right) \end{aligned} \tag{2}$$

A comparison using the arithmetic mean

$$D_{v,ij} = -10\lg\left(\frac{1}{M}\sum \tau_{ij,m}\right) \tag{3}$$



Figure 3. Top of the L-junction shown in the section drawing in Figure 2. Steel girders to apply a load on the junction. Between the two horizontal girders load cells are in place to measure the force.

or the harmonic mean

$$D_{v,ij} = 10\lg\left(\frac{1}{M}\sum \frac{1}{\tau_{ij,m}}\right) \tag{4}$$

might be evaluated with the measurement results. This would enable to derive the standard deviation using different calculation approaches for the determination of the vibration reduction index.

5. SUMMARY AND OUTLOOK

The measurement of vibration reduction indices is crucial for the application of the the prediction methods given in EN 12354. However previous research [4] showed that there can be great uncertainty in the measured values. This is not only due to deviations in the material parameters or construction details but also due to the measurement procedure and the processing of data. The suggested inter-laboratory test would enable to identify the *in-situ* standard deviation due to the measurement procedure given in ISO 10848. As this standard is currently under revision, both the current procedure as well as the proposed revision could be considered. For the inter-laboratory test the facilities at Rosenheim Technical University of Applied Sciences can be used. In advance repeatability measurements according to the *measurement situation C* in section 5.3.2 [5] would be carried out and compared with corresponding standard deviations from other laboratory setups. Furthermore the possibility to extend the measurement procedure to include the determination of the structure-borne reverberation time should be discussed with potential measurement teams before.

6. REFERENCES

[1] ISO 10848-1:2017, "Acoustics – Laboratory and field measurement of flanking transmission for airborne, impact and building service equipment sound between adjoining rooms – Part 1: Frame document."

[2] S. Mecking, M. Scheibengraber, T. Kruse, U. Schanda, and U. Wellisch, "Experimentally based statistical analysis of the vibrational energy of clt building elements," in *Proc. of ICSV24*, (London, UK), 2017.

[3] ISO/DIS 10848-1:1999, "Acoustics - Labaratory measurement of the flanking transmission of airborne and impact noise between adjoining rooms - Part 1 : Frame document."

[4] A. Timpte, S. Mecking, U. Schanda, and A. Rabold, "Vibration reduction indices of CLT junctions," in *Proc. of ICSV24*, (London, UK), 2017.

[5] EN ISO 12999-1:2020, "Acoustics - Determination and application of measurement uncertainties in building - Part 1: Sound insulation."

DOI: 10.61782/fa.2025.0283

FORUM ACUSTICUM EURONOISE 2025

DETAILED ANALYSIS OF DIFFERENT SOFTWARE FOR SOUND INSULATION CALCULATIONS OF VARIOUS STRUCTURES

Klas Hagberg[1,2*] **Erik Nilsson**[2] **Delphine Bard**[2]
[1] Engineering Acoustics, Luleå Technical University, Sweden
[2] Acouwood AB, Malmö, Sweden

ABSTRACT

Easily accessible engineering software to calculate the airborne and impact sound insulation of structural components are a shortage, which hinders the development of new efficient building systems and the inclusion of new environmentally friendly building materials. There are some good possibilities today to calculate field values using commercial programs following the series ISO 12354. However, these standards need to be fed with lab measurements or calculations of each product combination, and all possible product combinations can never be measured. Therefore, calculation tools for various floor and wall configurations are the key for the future development of new building systems and the verification of new materials in the structural components. Few software are available to calculate sound insulation for walls and floors in buildings. Stora Enso offers the CLT software "Calculatis", Marshall Day Acoustics provides "INSUL 10" and the company Sonusoft provides the software "Acoulatis". The three software have slightly different approaches, and so is their capability to calculate various wall and floor structures for CLT. In this paper, a detailed comparative analysis between the software is carried out, based on CLT combinations. The results presented also include comparisons to measured lab values in third octaves, single numbers, and spectrum adaptation terms.

Keywords: *sound insulation, building acoustic predictions, impact sound, airborne sound, calculations, software.*

[*] ***Corresponding author***: klas.hagberg@acouwood.com.

Copyright: *©2025 First author et al. This is an open-access article distributed under the terms of the Creative Commons Attribution 3.0 Unported License, which permits unrestricted use, distribution, and reproduction in any medium, provided the original author and source are credited.*

1. INTRODUCTION

To promote a sustainable development of future buildings with acoustically optimized building components (such as floor structures and wall structures), various calculation tools must become available to acousticians globally, but also used! To some extent acousticians are lacking helpful engineering prediction tools, especially when it comes to wooden buildings. However, acousticians show a tendency to avoid calculations and base the acoustic design in buildings by using comparable available measured data and local national tools. That is a big problem for the industry in general since this approach limits the possible material combinations when designing the building components and in addition, it creates non-scientific and unnecessary high margins to the actual requirements. Hence, the lack of prediction tools creates costly solutions due to these excessive margins usually used to make sure not to fail in the final building. Luckily, at least three different engineering tools are available to optimize the building parts, e.g., walls and floors. One software is limited to CLT structures, and two are more comprehensive.

- Acoulatis – CLT and concrete structures, and lightweight frame walls. Online software for purchase, accessible via web browsers [1].
- INSUL 10 – CLT structures and layups with other materials. Software requiring dongle [2].
- Calculatis – CLT structures based on StoraEnso CLT panels. Free online software [3].

While other tools are available that address specific transmission paths of walls and floors, such as flanking transmission following ISO 12354-1 and ISO 12354-2 [4,5], this paper concentrates on a comparative analysis of the three engineering tools aimed to calculate laboratory values, mentioned above.

2. METHOD

Some typical floor and wall buildups commonly used in the European market have been arbitrarily chosen to calculate and evaluate with the different software mentioned in section 1. The calculations are then compared with laboratory values if available. We did not have laboratory values for the exact buildup of some instances and for those, we just compare the calculated values or in some cases the values were recalculated based on field measurements of sound insulation values and the vibration reduction index, following ISO 16283-1, ISO 16283-2, and ISO 10848-1 [6,7,8].

Material data, such as dynamic stiffness, elasticity modules, and other important material characteristics vary between the construction elements. In this paper, we have done our best to use the same material data for each element, such as density, in each software. However, some material data cannot be varied in all software (for example the dynamic stiffness in INSUL and the elasticity modules in Calculatis).

2.1 Calculated wall configurations

Firstly, three bare CLT walls were calculated to compare the basic model in detail, see Figure 1. The CLT walls have a mean density of approximately 470 kg/m^3.

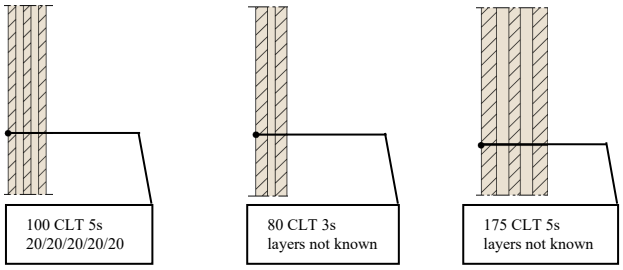


Figure 1. Bare CLT walls compared (calculation 01, 02 and 03).

Additionally, some typical "European" wall configurations are selected for modelling. They are primarily selected since data from lab measurements were accessible, which is considered valuable for the comparison. However, few walls are still selected since they represent a common configuration, but no measurements from lab are available to our knowledge. All wall configurations are shown in Figures 2, 3 and 4. The walls are then modelled in the three software and the results are compared and analyzed in third octaves from 50-5000 Hz (see section 3.1). The following wall combinations are included (apart from the bare CLT walls):

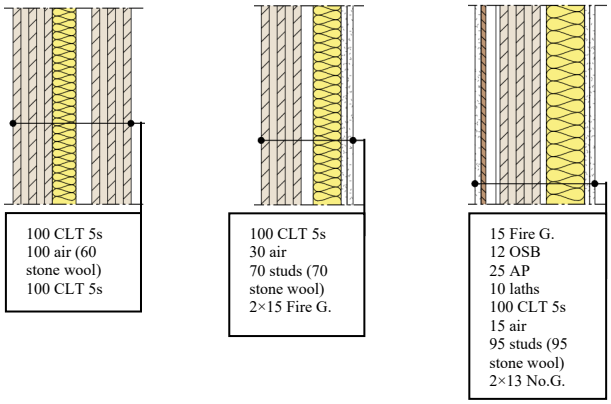


Figure 2. Wall configurations 04 to 06 with 100 CLT C5s (calculation 04, 05 and 06). Fire G. = fire gypsum; AP = acoustic profile; No.G. = Normal Gypsum

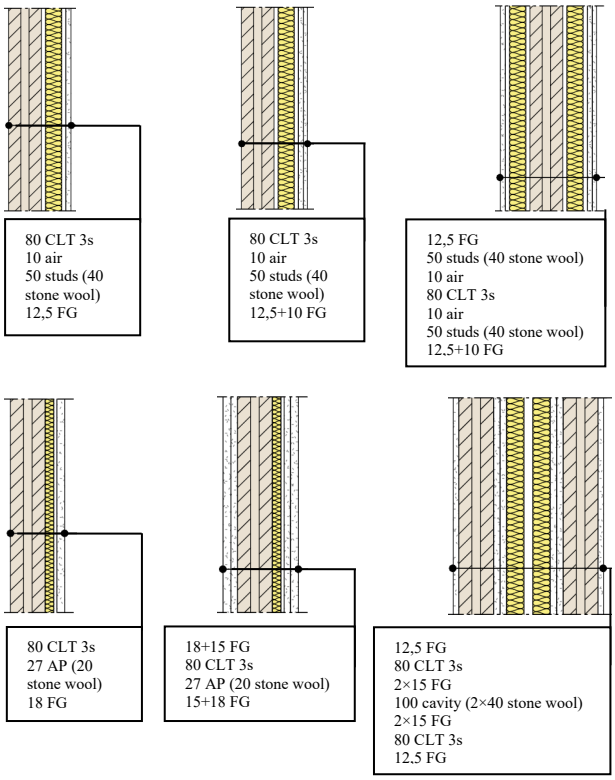


Figure 3. Wall configurations 07 to 12 with 80 CLT C3s (calculation no 07 to 12). FG. = Fibre gypsum; AP = acoustic profile.

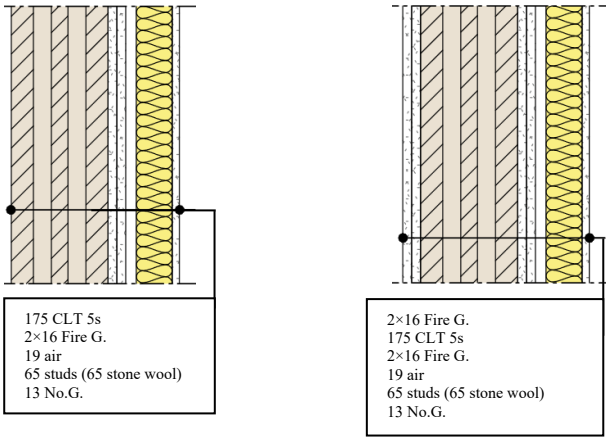


Figure 4. Wall configurations 13 and 14 with 175 CLT C5s (calculation 13 and 14). Fire G. = Fire gypsum; No.G. = Normal Gypsum

2.2 Calculated floor configurations

For the floor structures, calculations were carried out with some different thicknesses of the CLT plates and common material combinations (CLT 140, 180 and one example from a floor buildup typically used in volume elements). However, the possible combinations are close to infinity, implying that a rather small number of available floor constructions have been selected. Nevertheless, they represent some typical floor combinations, frequently used in Europe even if the manufacturers can vary from what is displayed in Figures 5 to 8.

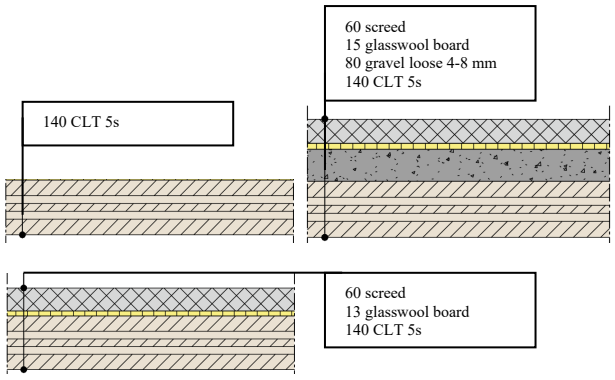


Figure 5. Floor configurations 01 to 03 with 140 CLT L5s (calculation 01 to 03).

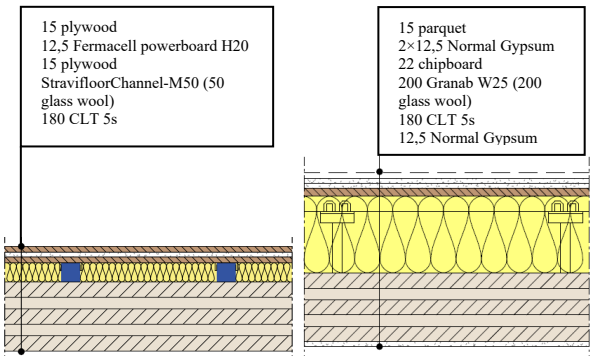


Figure 6. Floor configurations 04 to 05 with raised floor on 180 CLT L5s (calculation 04 to 05).

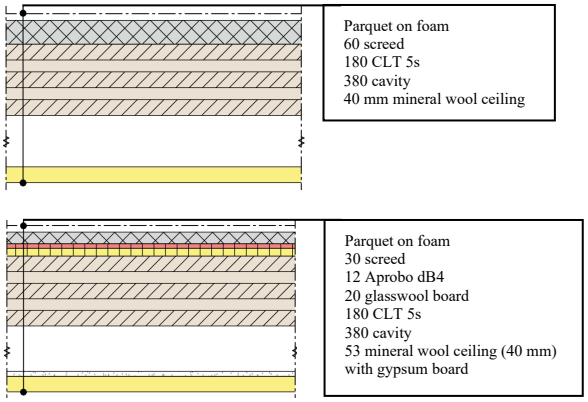


Figure 7. Floor configurations 06 to 07 with screed on 180 CLT L5s (calculation 06 to 07).

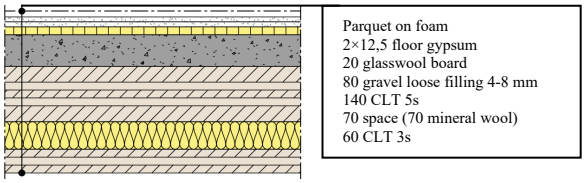


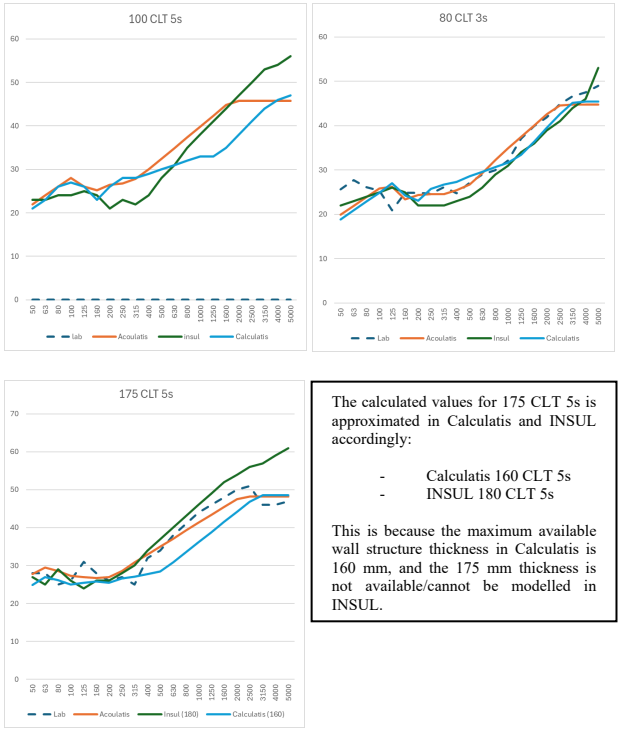
Figure 8. Floor configuration 08 (typical CLT volume elements, calculation no 08).

3. RESULTS

In this section, the results from all the different wall and floor configurations are shown. The results are shown in the same order as displayed in section 2.

3.1 Results from wall calculations

Below are the calculated results and they follow the same order as in section 2.1. In Figures 9 to 13, the results are shown in third octaves and the corresponding single number values are shown in Table 1 to Table 5 immediately after the corresponding figure with third octave band levels.



The calculated values for 175 CLT 5s is approximated in Calculatis and INSUL accordingly:

- Calculatis 160 CLT 5s
- INSUL 180 CLT 5s

This is because the maximum available wall structure thickness in Calculatis is 160 mm, and the 175 mm thickness is not available/cannot be modelled in INSUL.

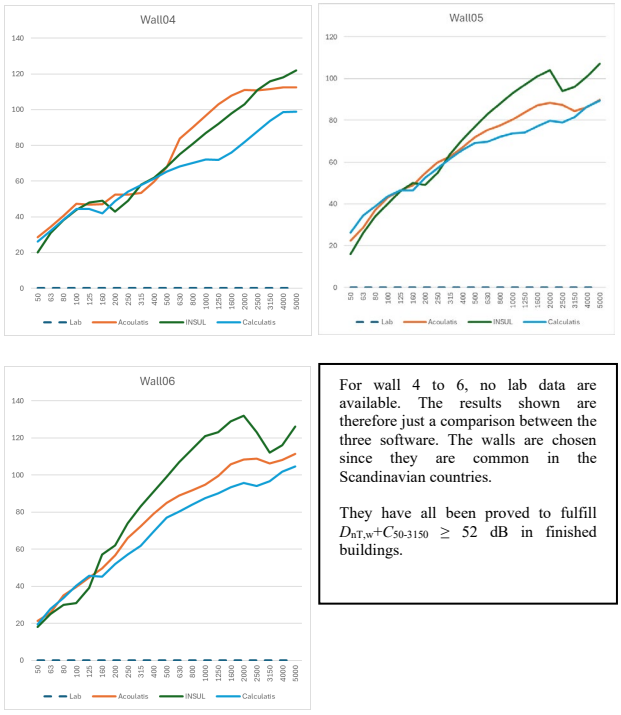
Figure 9. Bare CLT walls, calculated and measured values in 1/3rd octave bands.

Table 1. Corresponding single number values for Figure 9.

	Lab	Acoulatis	INSUL 10	Calculatis
	R_w (C, $C_{50\text{-}3150}$)			
100 C5s	--	37 (-1,-1)	33 (-1,-1)	34 (-1,-1)
80 C3s	33 (-1,-1)	33 (-1,-1)	30 (0,0)	33 (-1,-1)
175 C5s	39 (-2,-2)	39 (-1,-1)	40 (-1,-1)	35 (-1,-1)

The CLT models in INSUL 10 and Calculatis differ, since identical panels from Stora Enso exhibit different results for the 80 and 100 mm CLT plates depending on software. In reality, the panels are identical and therefore the results should be identical. For the 175 mm CLT, the differences are partly explained by the fact that 175 CLT cannot be modelled exactly in Calculatis and INSUL. The selections are fixed to specific panels. Therefore, the thickness of the CLT slab must be approximated to a thickness as close as possible to 175, that is 180 mm in INSUL and 160 mm in Calculatis.

Figure 10 shows the results from calculations of three common dwelling partition wall combinations in Scandinavia, with buildup according to Figure 2.



For wall 4 to 6, no lab data are available. The results shown are therefore just a comparison between the three software. The walls are chosen since they are common in the Scandinavian countries.

They have all been proved to fulfill $D_{nT,w}+C_{50\text{-}3150} \geq 52$ dB in finished buildings.

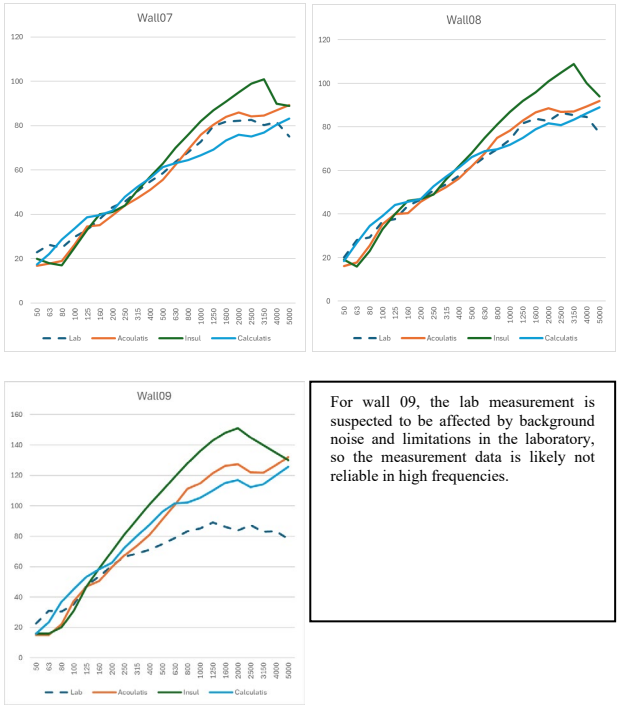
Figure 10. Three different wall configurations calculated, as described in Figure 2. No corresponding lab measurement data is available.

Table 2. Corresponding single number values for Figure 10.

	Lab	Acoulatis	INSUL 10	Calculatis
	R_w (C, $C_{50\text{-}3150}$)			
Calc. 04	--	65 (-2,-4)	65 (-4,-7)	64 (-3,-5)
Calc. 05	--	66 (-3,-10)	67 (-3,-13)	68 (-3,-7)
Calc. 06	--	70 (-6,-19)	72(-12,-19)	67 (-3,-9)

All three software can model the walls in Figure 10 without specific adaptations or additional assumptions. Still the results differ and INSUL generally result in higher values in

high frequencies and slightly lower values in low frequencies, ending up in larger negative values for the *C*-corrections compared to the other two software.
Figures 11 and 12 show the results from calculations of wall 07 to wall 09 (Figure 11) and wall 10 to wall 12 (Figure 12). Their buildups are shown in Figure 3 and CLT 80 3s is the base element. They might represent partitions for some high protection office spaces or in some countries for dwellings (wall 09 and wall 12).



For wall 09, the lab measurement is suspected to be affected by background noise and limitations in the laboratory, so the measurement data is likely not reliable in high frequencies.

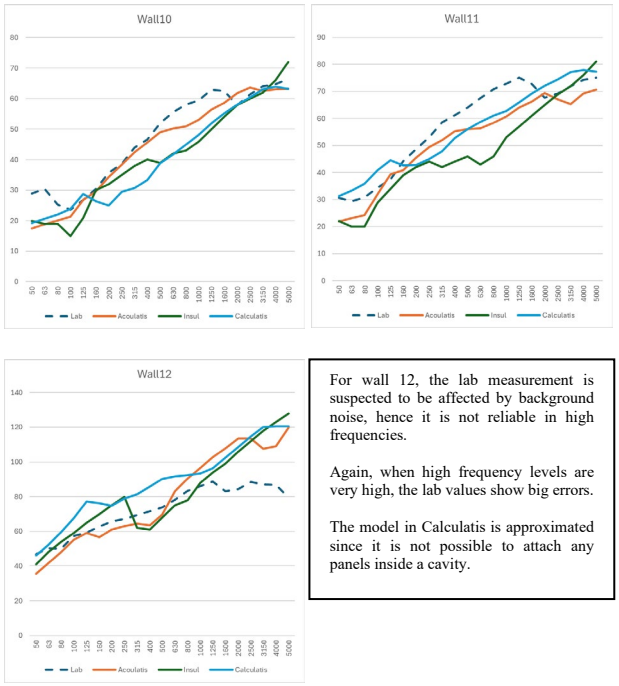
Figure 11. Three different wall configurations calculated, described in Figure 3.

Table 3. Corresponding single number values for Figure 11.

	Lab	Acoulatis	INSUL 10	Calculatis
	R_w (C, $C_{50\text{-}3150}$)			
Calc. 07	56 (-3,-5)	54 (-3,-7)	55 (-3,-9)	58 (-2,-6)
Calc. 08	61 (-2,-6)	60 (-2,-10)	61 (-2,-12)	64 (-3,-9)
Calc. 09	71 (-8,-13)	71 (-6,-23)	72(-12,-24)	77 (-5,-23)

There is generally a good agreement between the software calculations and corresponding laboratory data, except for wall 09, that has extremely good sound insulation in high frequencies compared to the laboratory measurement. For this wall, the calculated values should be more reliable than the laboratory measurement due to max values that can possibly be measured in a lab.

In Figure 12, the results for walls 10 to 12 are shown.



For wall 12, the lab measurement is suspected to be affected by background noise, hence it is not reliable in high frequencies.

Again, when high frequency levels are very high, the lab values show big errors.

The model in Calculatis is approximated since it is not possible to attach any panels inside a cavity.

Figure 12. Three different wall configurations calculated, described in Figure 3.

Table 4. Corresponding single number values for Figure 12.

	Lab	Acoulatis	INSUL 10	Calculatis
	R_w (C, $C_{50\text{-}3150}$)			
Calc. 10	49 (-2,-3)	48 (-3,-4)	43 (-3,-3)	41 (-1,-2)
Calc. 11	62 (-3,-5)	58 (-2,-6)	50 (-1,-3)	58 (-1,-2)
Calc. 12	78 (-1,-3)	74 (-2,-4) 5	75 (-2,-3)	91 (-2,-9)

Finally, in Figure 13 the results from two walls based on 175 CLT 5s are shown with buildups as described in Figure 4.

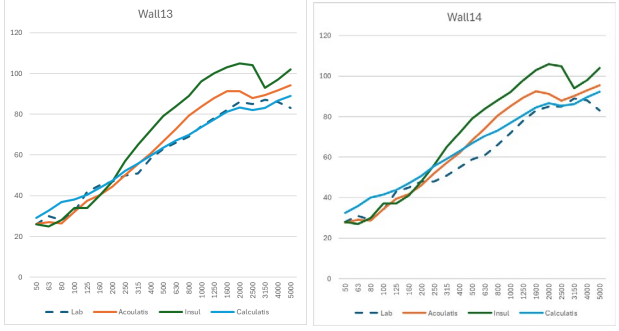


Figure 13. Two different wall configurations calculated, described in Figure 4.

Table 5. Corresponding single number values for Figure 13.

	Lab	Acoulatis	INSUL 10	Calculatis
	R_w (C, $C_{50\text{-}3150}$)			
Calc. 13	61 (-3,-6)	60 (-3,-6)	61 (-4,-7)	62 (-2,-3)
Calc. 14	60 (-2,-4)	61 (-3,-5)	63 (-4,-7)	66 (-3,-4)

These configurations are rather similar, the difference is that calculation 13 emanates from visible wood on one side while calculation 14 is supplied with two extra layers of plasterboards directly attached to the CLT on the opposite side of the cavity. The results indicate that the low frequency performance improves with the extra layers, however the weighted sound reduction index is not really affected. Calculatis shows bigger differences since plasterboards inside the cavity cannot be included in the model.

3.2 Results from floor calculations

Below are the calculated results shown for airborne and impact sound insulation, following the same order as in section 2.2. In Figures 14 to 16, third octaves values are shown and in addition, the corresponding single numbers are shown in tables immediately after the figure with third octave band levels.
INSUL cannot include gravel in its floor configurations and thus, it was modelled as cement / render. Furthermore, INSUL does not include impact boards on CLT for impact noise. Therefore, insulated panels were used instead for the impact sound calculations. The approximations are shown for floors 02 and 03 in Figure 14.

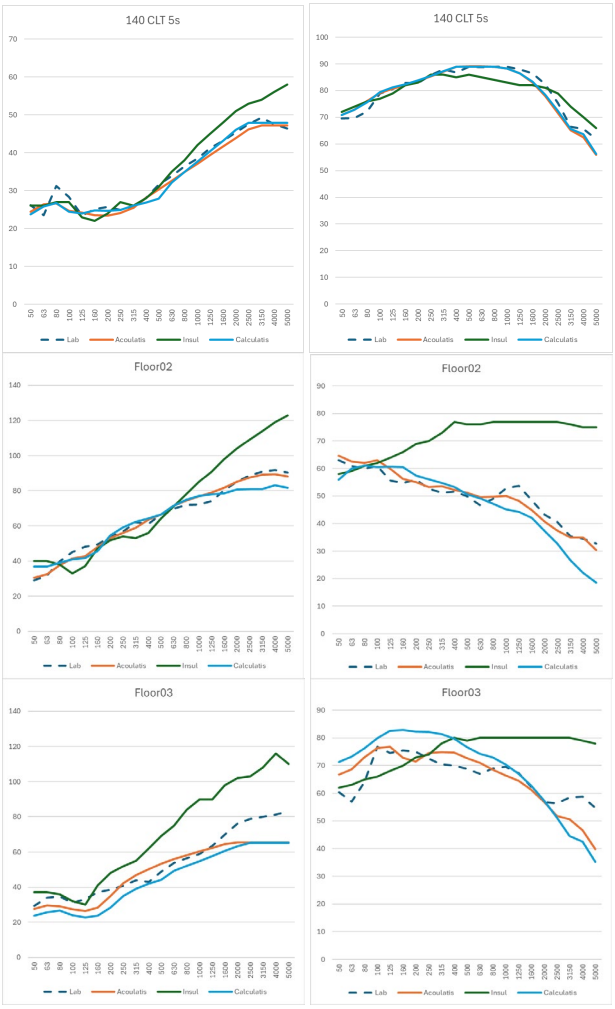


Figure 14. Three different floor configurations calculated, described in Figure 5.

Table 6. Corresponding single number values for airborne sound reduction related to Figure 14.

	Lab	Acoulatis	INSUL 10	Calculatis
	R_w (C, $C_{50\text{-}3150}$)			
CLT 140 5s	36 (-1,-1)	35 (-1,-1)	36 (-1,-1)	35 (-1,-1)
Calc. 02	68 (-2,-6)	66 (-2,-5)	62 (-1,-4)	67 (-4,-5)
Calc. 03	52 (-2,-2)	51 (-4,-4)	59 (-,-)	45 (-3,-3)

Table 7. Corresponding single number values for impact sound levels related to Figure 14.

	Lab	Acoulatis	INSUL 10	Calculatis
	$L_{n,w}$ (C_I, $C_{I,50\text{-}2500}$)			
CLT 140 5s	88 (-5,-5)	87 (-4,-4)	84 (-7,-7)	87 (-4,-4)
Calc. 02	53 (-3,1)	52 (0,3)	81(-11,-11)	52 (0,2)
Calc. 03	70 (-2,-1)	70 (-1,0)	86(-12,-12)	76 (0,0)

In Figure 15, results from calculations of two different combinations of raised floors are shown and compared to the lab values.

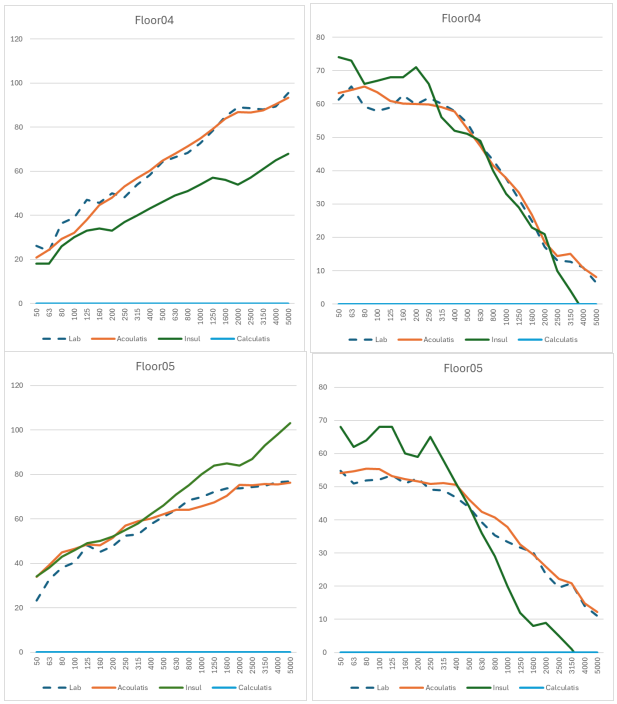


Figure 15. Two different raised floor configurations calculated, described in Figure 6.

Table 8. Corresponding single number values for airborne sound reduction related to Figure 15.

	Lab	Acoulatis	INSUL 10	Calculatis
	R_w (C, $C_{50\text{-}3150}$)			
Calc. 04	63 (-2,-6)	62 (-4,-8)	49 (-2,-3)	--
Calc. 05	63 (-2,-5)	65 (-1,-2)	67 (-1,-3)	--

Table 9. Corresponding single number values for impact sound levels related to Figure 15.

	Lab	Acoulatis	INSUL 10	Calculatis
	$L_{n,w}$ (C_I, $C_{I,50\text{-}2500}$)			
Calc. 04	54 (0,2)	54 (0,3)	66 (0,1)	--
Calc. 05	45 (0,2)	46 (0,2)	56 (1,4)	--

There are no results to present for Calculatis since raised floors cannot be modelled in that software. For INSUL, the floor in calc. 4 is replaced by Stravifloor w/HR50 and in calc. 5 with Mason EAFM Mount (explaining the deviation) since there are only a limited number of raised floors available in INSUL.

In Figure 16, results from calculations of two different combinations with screed and suspended absorbing ceilings are shown and compared to the lab values.

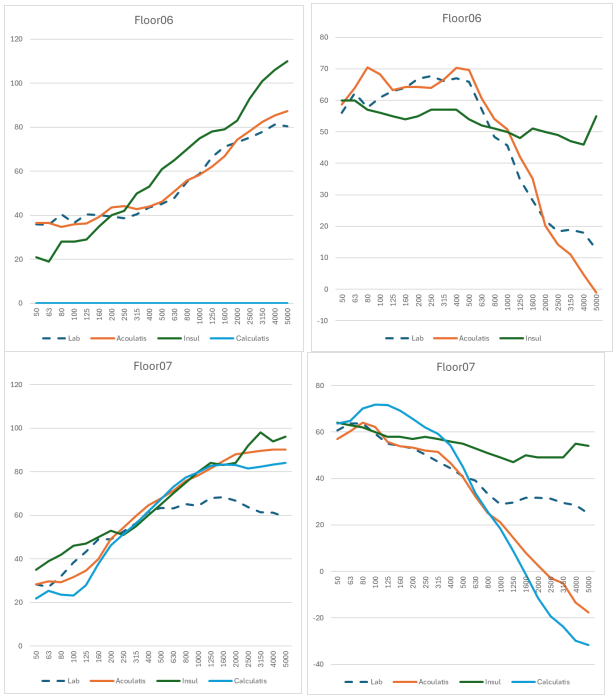


Figure 16. Two different screed floor configurations (including ceilings) calculated, described in Figure 7.

Table 10. Corresponding single number values for airborne sound reduction related to Figure 16.

	Lab	Acoulatis	INSUL 10	Calculatis
	R_w (C, $C_{50\text{-}3150}$)			
Calc. 06	51 (-1,-1)	53 (-1,-2)	54 (-2,-5)	--
Calc. 07	62 (-2,-5)	61 (-5,-6)	66 (-1,-3)	56 (-7,-8)

Table 11. Corresponding single number values for impact sound levels related to Figure 16.

	Lab	Acoulatis	INSUL 10	Calculatis
	$L_{n,w}$ (C_I, $C_{I,50\text{-}2500}$)			
Calc. 06	54 (0,2)	54 (0,3)	56 (-5,-3)	--
Calc. 07	47 (1,7)	48 (2,5)	56 (-4,0)	60 (2,3)

Calculatis has no option to model screed directly on the CLT slab and the results are therefore missing for Floor 06. For Floor 07 the ceiling is approximated with a 13 mm normal gypsum board in INSUL and Calculatis since they don't have that product available, contradictory to Acoulatis. The impact board is modelled as one single 30 mm impact board (dynamic stiffness 10 MN/m^3). For

INSUL the impact board is simulated by an insulated panel, as is the ceiling.

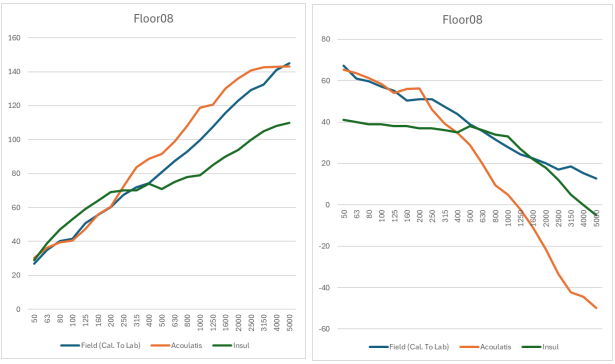


Figure 17. One type of volume element floor calculated, as described in Figure 8.

Table 12. Corresponding single number values for airborne sound reduction related to Figure 17.

	Field (re-calc.to lab)	Acoulatis	INSUL 10	Calculatis
	R_w (C, $C_{50\text{-}3150}$)			
Calc. 08	74 (-5,-11)	73 (-6,-9)	77 (-1,-10)	--

Table 13. Corresponding single number values for impact sound levels connected to Figure 17.

	Field (re-calc.to lab)	Acoulatis	INSUL 10	Calculatis
	$L_{n,w}$ (C_I, $C_{I,50\text{-}2500}$)			
Calc. 08	45 (1,9)	47 (1,7)	33 (-1,1)	--

Calculatis cannot model double CLT floors, that is why it is not included in the comparison. Furthermore the "lab value" is recalculated based on field measurements, hence not measured in lab. For the INSUL values, the impact board and the gravel are approximated by an insulated panel and sand/cement render respectively.

4. DISCUSSION AND CONCLUSION

Developing engineering software for building acoustic calculations demands a high degree of flexibility to accommodate the wide variety of floor and wall constructions encountered for future sustainable buildings. Seamless integration of new products must be possible as they become available. In parallel, developers should continuously seek and incorporate new data into the calculation model. Regular updates are essential, otherwise, the credibility and relevance of the software can quickly diminish. Engineering-based calculation models are fundamental to the future of acoustic design. Without reliable calculation tools, acousticians must rely on standard assemblies or informed guesses, which limit innovation and the ability to design novel solutions tailored to specific projects. Measurements remain crucial and calculation models must be validated against them. However, it is not feasible to measure every possible combination. Therefore, well-calibrated and frequently updated software models are a more practical and scalable solution. This paper highlights that many material options and construction variants for CLT are still missing from existing engineering software tools, like INSUL and Calculatis. As a result, modelling certain combinations may involve a high degree of uncertainty, underscoring the need for continuous development and data integration. Furthermore, for CLT structures, this paper shows that Acoulatis predicts with the highest accuracy for all wall and floor variants combined, of course pre assuming that we can rely on the measured values.

5. REFERENCES

[1] Sonusoft. Acoulatis – The acoustic prediction model for future buildings. www.sonusoft.com/acoulatis

[2] INSUL 10.0.4. Predicting sound insulation. www.insul.co.nz

[3] Stora Enso. Calculatis. https://calculatis.storaenso.com

[4] ISO 12354-1. Building acoustics - Estimation of acoustic performance of buildings from the performance of elements. Part 1: Airborne sound insulation between rooms. ISO: Geneva, Switzerland, 2017.

[5] ISO 12354-2. Building acoustics - Estimation of acoustic performance of buildings from the performance of elements. Part 2: Impact sound insulation between rooms. ISO: Geneva, Switzerland, 2017.

[6] ISO 16283-1. Acoustics - Field measurement of sound insulation in buildings and of building elements. Part 1: Airborne sound insulation. ISO: Geneva, Switzerland, 2014.

[7] ISO 16283-2. Acoustics - Field measurement of sound insulation in buildings and of building elements. Part 2: Impact sound insulation. ISO: Geneva, Switzerland, 2020.

[8] ISO 10848-1. Acoustics - Laboratory and field measurement of flanking transmission for airborne, impact and building service equipment sound between adjoining rooms. Part 1: Frame document, 2017.

DOI: 10.61782/fa.2025.0725

FORUM ACUSTICUM EURONOISE 2025

RAINFALL SOUND INSULATION OF (LIGHTWEIGHT) WOODEN ROOF CONSTRUCTIONS

Alexander Stenitzer[1*] **Bernd Nusser**[1] **Christian Lux**[1]
Herbert Müllner[2]
[1] Holzforschung Austria, Department of Building Physics, Vienna, Austria
[2] Staatliche Versuchsanstalt TGM, Vienna, Austria

ABSTRACT

Rain can lead to increased noise levels in the building, especially in lightweight structures with metal roofs. To evaluate the rainfall sound insulation of roofs in the laboratory, the heavy rain simulation method according to EN ISO 10140-5:2021 Annex H is used. In this study, the rainfall sound insulation of timber roofs was determined, optimised and compared with the corresponding airborne sound insulation. The paper first presents the development of the test stand to measure both airborne and rainfall sound insulation on the same test element. The results of the measurements on different types of timber roofs are then discussed. In addition to the substructure of the roofs (exposed rafters, cross-laminated timber) and the roofing itself (concrete tiles, sheet metal, FPO membrane), the type of insulation placed on the substructure (PUR/EPS/mineral wool/wood fibre) was varied. The article shows that the roof covering has the most significant influence on the rainfall sound insulation and that there is only a limited correlation between the airborne sound insulation and the rainfall sound insulation of the roofs studied.

Keywords: *artificial rain, laboratory measurements, lightweight roof, rain noise, rain sound intensity*

[*] ***Corresponding author***: *a.stenitzer@holzforschung.at*
Copyright: *©2025 First author et al. This is an open-access article distributed under the terms of the Creative Commons Attribution 3.0 Unported License, which permits unrestricted use, distribution, and reproduction in any medium, provided the original author and source are credited.*

1. INTRODUCTION

In general, timber roofs can be divided into a) structures insulated between rafters and b) structures insulated on top of the roof. Roofs with the insulation on top are robust constructions in terms of thermal and moisture insulation, as the supporting structure is always in the warm zone and is therefore protected from condensation. From the building acoustics point of view, however, insulated roofs have disadvantages, especially around rain noise protection.
For this reason, Holzforschung Austria (HFA), together with the Technologisches Gewerbemuseum (TGM) and partners from industry, carried out the research project "Schutz.aufs.Dach", in which the airborne sound insulation as well as the rainfall sound insulation of roofs with insulation mounted on top was investigated [1]. The test setup for achieving this research objective was integrated into the large-scale test stand of the Akustik Center Austria (ACA) [2] and is presented in the following. Furthermore, the validation of the airborne sound measurements of the new implemented test stand configuration is presented. In the main part of the paper, individual constructive influences on the airborne and rainfall sound insulation of roofs are discussed.

1.1 Sound insulation requirements

The minimum requirements for the airborne sound insulation of roofs (in Austria) essentially correspond to those for external walls, although also installations such as roof windows must be considered. This means that the weighted sound reduction index of $R_w \geq 48$ dB must be achieved for opaque building elements and $R'_{res,w} \geq 43$ dB must be achieved for all external building elements including windows [3].

Similarly to the weighted sound reduction index R_w, there is also a normatively defined Single-Number Quantity (SNQ) for rainfall sound insulation, the A-weighted sound intensity level L_{IA}, which can currently only be used to compare components. In contrast to airborne noise, there are no minimum requirements for the rain sound insulation of building components. Rather, the purpose of the rain sound measurements is (according to EN ISO 10140-1:2021 Annex H) a) to assess the noise in the room under the test object, b) to design components for adequate rainfall sound insulation, c) to compare the rainfall sound insulation of components. Due to the increased use of attics as living space, as well as the increase in storm events with heavy rainfall [4], special requirements for bedrooms could be useful. The World Health Organization (WHO) itself states that a sound level of less than 30 dB(A) should prevail in bedrooms for healthy, restful sleep [5]. This is often significantly exceeded by many roof constructions during rain events.

2. MATERIALS

In the course of the work, exposed rafter roofs and cross-laminated timber (CLT) roofs are discussed. The focus of the project was the variation of the roof insulation materials, whereby the influence of the roofing was also investigated. Table 1 shows the construction details presented in this paper. In addition to the load-bearing structure (roof type), the various design influences are illustrated either for the CLT or the exposed rafter roof.

Table 1. Variations of the different layers of the discussed roofs. (s'...dynamic stiffness in MN/m³)

Layer	Variation
Roof type	CLT (120 mm) Esposed rafters
Insulation (on top)	MW: Mineral wool (s‘ = 1 MN/m³) WF: Wood fibre (s‘ = 16 MN/m³) PUR: Polyurethan (s‘ = 18 MN/m³) EPS: expanded polystyrol (s‘ = 46 MN/m³)
Roof covering	Sheet metal (Aluminium) Concrete tiles
Other	Influence of screwing Additional weight Structural mat

Underhead or double-thread screws were always used to screw the counter-battening in place. As a result of the reduced pressure of the counter-battening on the roof deck, significantly better sound insulation values can be achieved compared to a screw connection using part-threaded screw [6, 7]. Further details of the designs can be found in the final report [1].

3. METHODS

The building acoustics measurements were all performed at the ACA, with both airborne sound and rain noise measurements performed in the larger (XL) of the two test benches. The test opening for roof measurements in the XL-test stand has a surface area of 10.3 m² with an inclination of 5°. The volume underneath is approximately 150 m³. To achieve the highest possible maximum sound insulation of the test stand, the test component mask was made of reinforced concrete and acoustically equipped with additional facing layers. The performance of the airborne and rain sound measurements on the same test specimen is described below.

3.1 Airborne sound reduction

In order to validate the airborne sound measurements in the newly established XL-test stand, similar roof constructions were tested for their airborne sound insulation in the standard test stand (M-test stand, test opening: 19.8 m², volume of the receiving room: 54 m³, see also [8]) and in the ventilation test rig of the ACA (XL-test stand, test opening: 10.3 m², volume of the receiving room: 153 m³). The sound insulation values of two constructions, their deviations and the standard uncertainty according to EN ISO 12999-1:2021 are shown and discussed in section 4.1.

3.2 Sound intensity level of artificial rainfall noise

A test facility for determining rainfall noise has been installed in the source room of the XL-test stand. The 5° inclined test surface ensures that water can drain off. The test facility for generating artificial rainfall consists of the above-mentioned component mask, the irrigation system itself including a water supply system and a positioning system. The development as well as a detailed description of the artificial irrigation is to be found in [9]. To produce artificial rain drops, a tank with a perforated bottom according to EN ISO 10140-5:2021 Annex H was used. Figure 1 shows the tank placed in the positioning system described. This allows the test specimen to be easily moved to three different positions as required in EN ISO 10140-1:2021 Annex K.

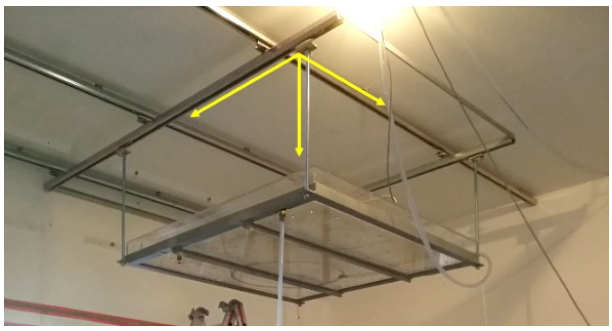


Figure 1. Water tank with perforated bottom to produce artificial rain in a positioning system with guide rails.

Prior to each measurement, the system was calibrated to ensure that the precipitation rate of 40 mm/h (heavy rain) was maintained over the measurement period (see [9). The sound intensity levels L_I in the receiving area are to be used for the evaluation of the rainfall sound insulation. The A-weighted intensity sum level L_{IA} from 100 Hz to 5000 Hz is the SNQ and must be specified to one decimal place.

4. RESULTS & DISCUSSION

The following graphs show the frequency-dependent results of the airborne sound measurements (R) and the rain sound measurements (L_I). In addition, for the airborne sound measurements, the insertion values R_w including the spectrum adaption terms for the extended frequency range $R_w + C_{50\text{-}5000}$ and $R_w + C_{tr,50\text{-}5000}$ are given in dB in the legend (according to EN ISO 717-1). For rain measurements, the SNQs L_{IA} in dB(A) are rounded to one decimal place in the legend (according to EN ISO 10140-1:2021 Annex K).

4.1 Validation of the airborne sound reduction index

As mentioned above, the first step was to carry out comparative measurements on the M- and XL-test stands. Figure 2 compares the sound reduction indices of a 120 mm CLT-roof (left) and a flat roof element (OSB – rafters, insulated - OSB) (right) in the two test stands. From a constructional point of view, the components in the test benches differ not only in area (M: 4230 mm × 5240 mm; XL: 4705 mm × 2350 mm), but also only minimally in the arrangement of the elements (CLT-roof) and in the spacing between the rafters (flat roof).
In addition to the sound reduction index of the components, the maximum airborne sound insulation of the XL-test stand is also given. As it is much higher for these two elements, the influence of it can be ruled out. The deviations lie mostly within the normative standard uncertainty, as can be seen in the lower part of the figure. However, in individual one-third octave bands, especially in the low and medium frequencies, this is also clearly exceeded. In the case of the flat roof element, the sound insulation value is shifted by one one-third octave band.

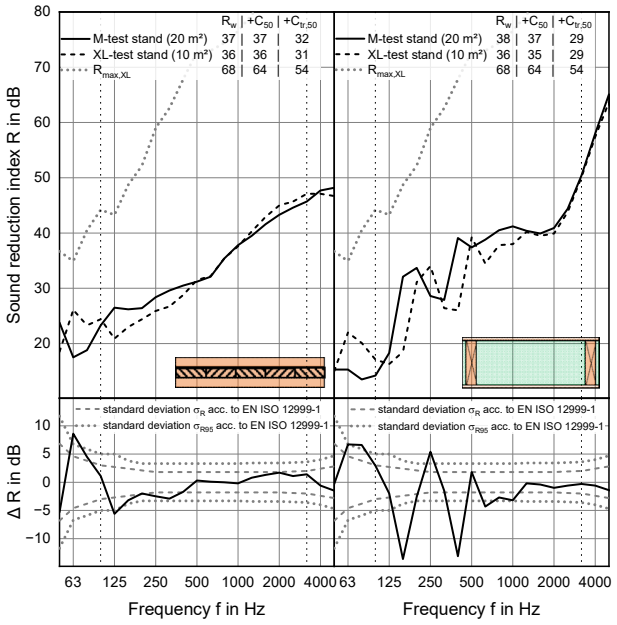


Figure 2. Comparison of the sound reduction index of a CLT element (left) and a flat roof element (right) in the two test stands at the ACA with different test openings. The differences and the standard uncertainty according to EN ISO 12999-1:2021 are shown in the lower part of the figure.

One reason for the deviations is to be found in the eigenfrequencies of the structures, as shown by the simulated velocity levels for point excitation in Figure 3. The FEM-simulations of the eigenmodes were performed using the software COMSOL 6.3. For the two flat roof elements, the eigenfrequencies are shifted to the same extent as the sound reduction indices. Due to the clear differences in the eigenfrequencies and its dependence on the element size, the different sound reduction indices in these one-third octave bands can be explained.
Only the frequency range below 100 Hz cannot be explained by the simulation, as no eigenmodes for the flat roofs occur below 125 Hz. In the authors' opinion, the size of the test opening, which is only 2350 mm in one direction

in the XL-test stand, also plays a role here, as sound transmission for low frequencies below 100 Hz is only possible to a limited extent.

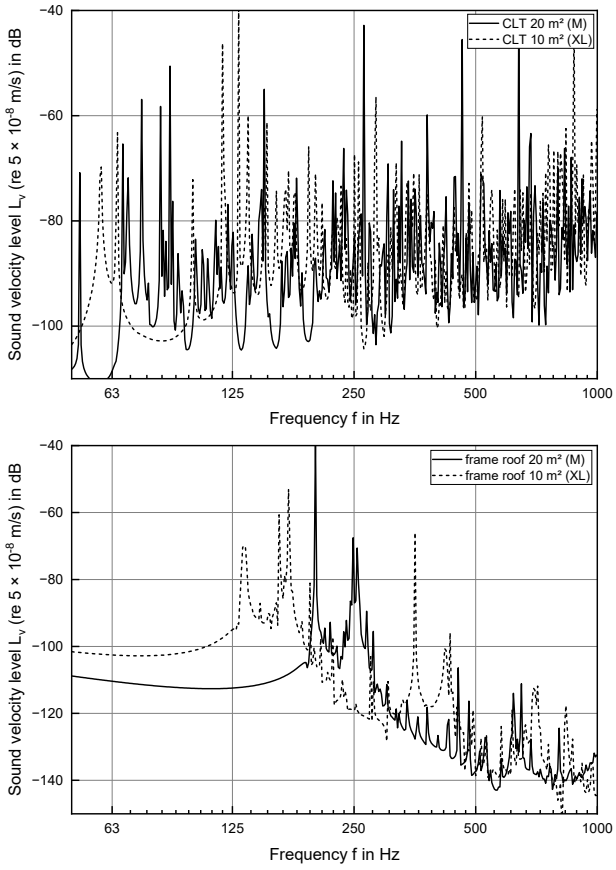


Figure 3. Comparison of the sound velocity levels of CLT elements (top) and flat roof elements (bottom) in the two test stands at the ACA with different test openings.

The large deviations beyond the standard deviation according to EN ISO 12999-1:2021 are no longer detectable in the case of practical roof constructions including roofing as well as insulation. With the explainable differences in the eigenfrequencies, as well as the approximation of the sound insulation values of structures including roofing (see project report [1]), the suitability of the XL-test stand could be ensured. However, the dependence on the test size should be considered as the simulations and comparative measurements have shown.

4.2 Influence of construction details

4.2.1 Influence of the structural roof

Figure 4 illustrates the influence of the structural roof on the airborne and rainfall sound insulation of a roof with WF or PUR insulation and sheet metal covering. As can be seen, the use of a CLT- instead of an exposed rafter roof results in a higher airborne and rainfall sound insulation over almost the entire frequency range. For the roofs with rigid foam insulation, the differences in airborne sound attenuation are even more pronounced than for the fibre insulation.
The sound intensity levels in the graph on the right also show the more favourable influence of the CLT-roof on rainfall sound insulation. The intensity levels in individual one-third octave bands differ much more from each other than the sound reduction indices in the left graph. A continuous parallel shift can be seen. This is also reflected in the SNQs in the legends. After the choice of roof covering (see section 4.2.3), the supporting structure has the greatest influence on the rain attenuation of the roof.

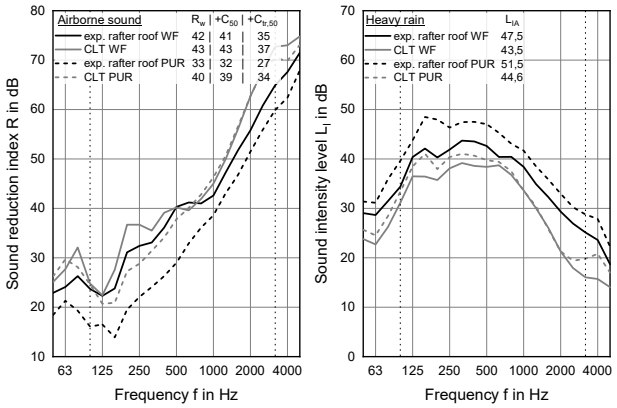


Figure 4. Influence of the load-bearing structure (exposed rafters/CLT) with roof insulation (PUR/WF) and sheet metal covering on the airborne sound insulation (left) and the rainfall sound insulation (right).

4.2.2 Influence of the insulation material type

Figure 5 shows the influence of the type of insulation on the airborne sound reduction index (left) and the rainfall sound insulation (right) of an exposed rafter roof with sheet metal covering. As can be seen, the rigid foam (PUR/EPS) and fibrous (MW/WF) insulation materials behave very differently in terms of airborne sound reduction. However, the differences within these groups of insulation materials

are small, with the WF achieving slightly higher sound insulation values in the frequency range below 160 Hz than the MW. Similarly, with EPS slightly higher sound insulation values are achieved than with PUR.
Looking at the rainfall sound insulation (right), we can see that the groups of insulation materials do not differ as clearly as in the case of airborne sound insulation. In any case, the highest levels are achieved with PUR, followed by EPS, MW and finally WF with the lowest levels due to higher mass. A similar picture can be seen for insulation layers with a thickness of 260 mm instead of 200 mm (data not shown), where the advantage of the wood fibre insulation is even clearer. Below 125 Hz, unexpectedly MW, PUR and EPS produce almost the same rain noise levels.

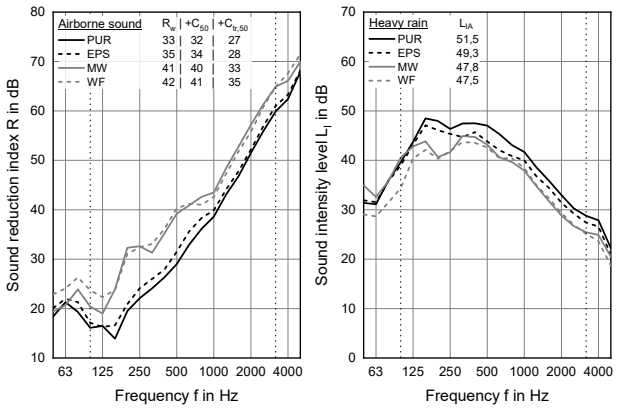


Figure 5. Influence of the insulation material (PUR/EPS/MW/WF) on the airborne sound insulation (left) and the rainfall sound insulation (right) of an exposed rafter roof with sheet metal covering.

If we look only at the SNQs L_{IA} from the rain noise measurement, we see a slightly different picture to that of the R_w-values. The L_{IA}-values of the roofs with fibre insulation materials are very close to each other, whereas the roof with EPS insulation material tends to be closer to the fibre-insulated roofs than the PUR roof as for the airborne sound insulation.

4.2.3 Influence of the roof covering

Figure 6 shows the difference in the roof covering by means of a CLT-roof with MW insulation. The roofing options are concrete tiles, a sheet metal (aluminium), and an FPO roofing membrane. As can be seen, in the mid-frequency range, a higher airborne sound insulation is achieved with a concrete roof than with sheet metal covering. However, in the frequency range below 100 Hz, the roofs with sheet metal covering have higher sound insulation values than those with concrete tiles. This was also observed in [9].
Calculated, the mass-spring-mass-resonance frequency of the concrete tiles on the MW at a CLT-roof (without consideration of the screws) is $f_0 = 31$ Hz, which may explain the lower sound insulation compared to the sheet metal covering. In the higher frequency range, the sound insulation values of the concrete tiles and sheet metal covering approach each other. With FPO a clearly different behaviour can be observed. Due to reduced mass, the airborne sound insulation is very low at low frequencies but rises very steeply due to the absorption properties of the MW underneath and the low stiffness of the FPO itself. Above 250 Hz, this element has the highest sound insulation.
The same variation was also carried out with PUR insulation (data not shown), where the FPO roofing showed the lowest sound insulation above the resonance frequency of the concrete tiles on PUR due to the low absorption properties of the foam insulation. In the case of the PUR insulation, the sheet metal covering also exceeded the sound insulation values of the concrete tiles variant in the frequency range above 1250 Hz, which can be attributed to the higher airtightness of the sheet metal covering.

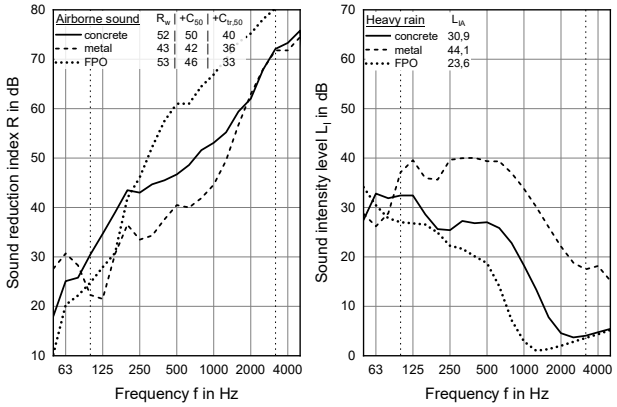


Figure 6. Influence of the covering (aluminium sheet, concrete block, FPO) on the airborne sound insulation (left) and the rainfall sound insulation (right) of a BSP roof with mineral wool roof insulation.

The rainfall sound insulation values in the graph on the right show that the concrete tiles produce significantly lower sound intensity levels than the sheet metal covering

over almost the entire frequency range. The FPO variants again behave differently depending on the insulation material. While the lowest sound intensity levels are achieved with a soft MW insulation with a FPO membrane, a much stiffer PUR insulation with a FPO membrane produces the highest rain sound intensity levels, as the variant with a sheet metal covering (data not shown).
The significant differences in the air and rainfall sound insulation provided by the different roof coverings are also illustrated by the SNQs in the legends. The choice of roof covering in combination with the insulation material has the greatest influence on the rain attenuation of the roof.

4.2.4 Influence of screwing of the counter-battening

To investigate the influence of the acoustical bridge caused by the underhead or double-thread screws on the air and rainfall sound insulation, the counter-battening was not screwed to the supporting structure during a comparative measurement but was simply laid loose on the insulation material.
Figure 7 shows the influence of the screw connection on the air and rainfall sound insulation of a CLT-roof with 200 mm WF insulation and concrete tiles. As can be seen, the screwing does not influence the airborne sound insulation up to 400 Hz, but it clearly does above 400 Hz. The drop in the slope of the sound reduction index due to the acoustical bridge is clearly visible. However, these differences do not show up in the SNQs of the airborne sound insulation.

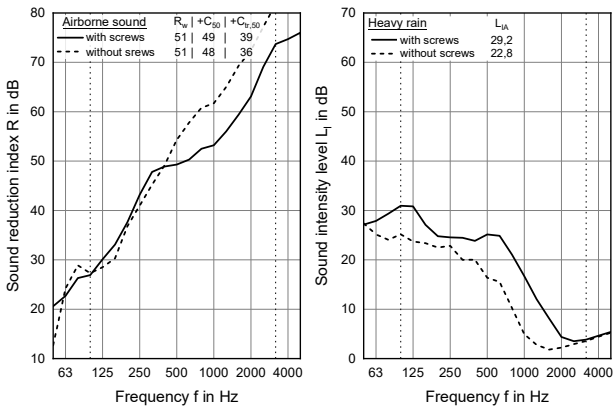


Figure 7. Influence of the screwing of the counter-battening on the airborne sound insulation (left) and the rainfall sound insulation (right) of a CLT-roof with WF insulation and concrete tiles.

Looking at the sound intensity levels in the right-hand graph; the bolted joint has a very significant effect on the rainfall sound insulation over the entire frequency range. This can also be seen from the significant difference in the L_{IA}-values in the legend.

4.2.5 Structural mat / additional weighting

Figure 8 (left) shows the effect of a structured mat underneath the sheet metal covering on the rainfall sound insulation of an exposed rafter roof with a 200 mm EPS insulation. As can be seen, the mat has a positive effect on the rainfall sound insulation above 1000 Hz. The same applies to the airborne sound insulation, which is not shown here, although the structural mat has no effect on sound insulation in the more relevant frequency range below 1000 Hz. The SNQs in the legends therefore hardly differ.
A variant to effectively reduce the rain sound intensity levels is shown in Figure 8 on the right-hand side. Two layers of gypsum board (12.5 mm) have been placed on top of the structural exposed rafter roof to increase its mass. This not only increases the rainfall sound insulation shown, but also the airborne sound insulation, which is not shown here.

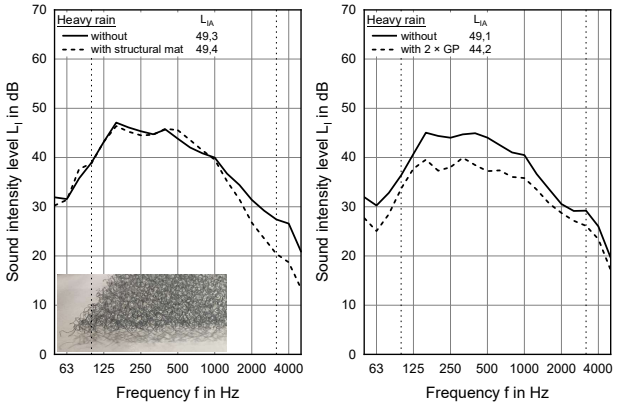


Figure 8. Effect of a structural mat beneath the roofing (left) and additional weight (2 × 12.5 mm Gypsum board) (right) on an exposed rafter roof with EPS insulation and sheet metal covering.

4.3 Correlation of Single-Number Quantities

Figure 9 shows the relationship between the SNQs R_w and L_{IA} of the air and rainfall sound insulation measurements of the investigated roof constructions with sheet metal covering and concrete tiles. As can be seen, the L_{IA}-values of the roofs differ significantly depending on the roofing,

even though their R_w-values are very similar. From the R_w-value of a roof, therefore, it is not possible to conclude on its L_{IA}-value. At the very least, a distinction must be made between the different types of roofing, with only a weak correlation between the R_w- and L_{IA}-values for roofing with concrete tiles. For sheet metal covering, the relationship between air and rainfall sound insulation shown in [10] is more likely to be present. In addition to the regression lines, the graph also shows the standard errors of the regression SER and the coefficients of determination R^2 for both roofing types. The given coefficient of determination for the sheet metal covering indicates a strong correlation between the R_w- and L_{IA}-values. In contrast, the R^2 for the (very few) concrete-covered roofs illustrates the rather low correlation between the R_w- and L_{IA}- values.
Also shown in the graph are the prediction bands, which have a 95 % probability of containing new measured values for the same roofing. Due to the relatively wide prediction bands, a practical prediction of the L_{IA}-value based on the R_w-value is only possible to a limited extent, also for the variants with sheet metal covering.

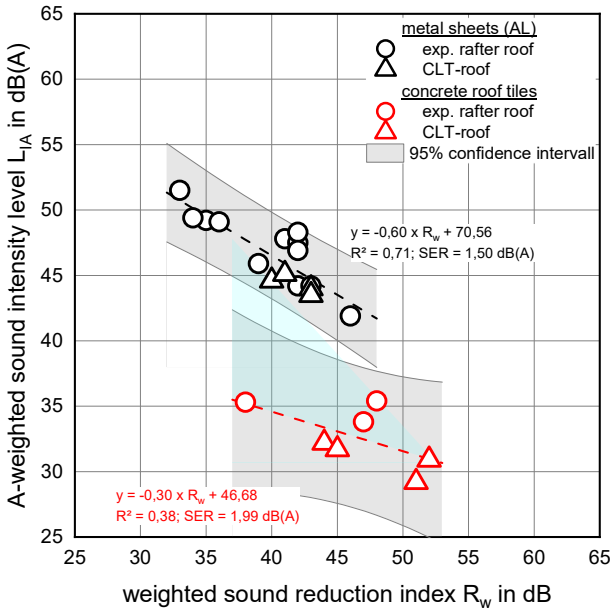


Figure 9. Relationship between the airborne sound insulation (R_w) and the rainfall sound insulation (L_{IA}) of the investigated roofs with concrete tiles and sheet metal coverings. The graphs include linear regressions lines, the standard errors of the regressions SER and the coefficients of determination R^2 for the different coverings.

5. SUMMARY & OUTLOOK

5.1 Airborne and rain noise measurements

As shown, the results of the airborne sound measurements on CLT-roofs in the developed test stand (test opening 10.3 m²) are comparable with those in the standard test stand (test opening 19.8 m²). The deviations found are mostly within the standard deviation according to EN ISO 12999-1:2021, but in some cases they are higher. The reasons for this are mainly due to the different component sizes and the resulting different natural frequencies, what was shown by FEM-simulations. The test openings for frequencies below 100 Hz are also not to be underestimated. In any case, the largest differences can be explained; the suitability of the XL-test stand for airborne sound measurements was shown.
In [9] it was shown that heavy rain according to EN ISO 10140-1:2021 Appendix K can be well realised with a water tank with a perforated bottom according to EN ISO 10140-5:2021 Appendix H. It is important to accurately calibrate the rainwater system and to continuously check the precipitation rate.

5.2 Influence of construction details

The investigations carried out have provided an in-depth look at the air and rainfall sound insulation of lightweight roof constructions. As can be seen, there is only a limited correlation between the SNQs of air and rainfall sound insulation.
It has been shown that the rain sound intensity levels are mainly determined by the covering, although factors such as the roof insulation and the supporting structure can also play a decisive role, especially in combination with the covering. High A-weighted sound intensity sum levels up to 50 dB(A) are achieved, particularly with sheet metal covering. The maximum sound pressure level of 30 dB(A) at night recommended by the WHO [5] will be exceeded by such roofs with heavy rain and may be perceived as annoying by occupants [11].
At present, it is not known to what extent the L_{IA}-values correlates with the subjective perception of rainfall sound insulation, or to what extent roof installations and "ancillary areas" (e.g. the surrounds of roof installations or attics) influence the rainfall sound insulation of roofs. These issues must be addressed in a further research project.

6. ACKNOWLEDGEMENTS

The authors would like to thank the Österreichische Forschungsförderungsgesellschaft mbH (FFG) and all

project partners (Fachverband der Holzindustrie Österreich, Austrotherm GmbH, Holzwerk Gebr. SCHNEIDER GmbH, Ing. Werner Linhart, Saint-Gobain ISOVER Austria GmbH, Schallfresser GmbH, Steinbacher Dämmstoff GmbH, Zimmerei Eberl e.U.) for supporting the project "Schutz.aufs.Dach".

7. REFERENCES

[1] B. Nusser, A. Stenitzer, C. Lux, H. Müllner: *Schutz.aufs.Dach - Schallschutz aufdachgedämmter Dächer in Holzbauweise*. Final report F50610. Holzforschung Austria (Ed.). Vienna, Austria. 2023.

[2] F. Dolezal, M. Neusser.; M. Teibinger, "Akustik Center Austria - neue Prüf- und Forschungskompetenz für Holzkonstruktionen in Österreich mit Fokus auf tiefe Frequenzen", in *Proc. of DAGA 2016*. Deutsche Gesellschaft für Akustik e.V. (Ed.). Aachen, Germany. pp. 413-414. 2016.

[3] OIB-Richtlinie 5: Schallschutz. Österreichisches Institut für Bautechnik (Ed.). 2023.

[4] APCC: *Österreichischer Special Report. Gesundheit, Demographie und Klimawandel (ASR18)*. Final report, in cooperation with W. Haas, H. Moshammer, R. Mutturak, H. Formayer, C. Matulla, E. Striessnig et al. Verlag der Österreichischen Akademie der Wissenschaften (Pb.). Vienna, Austria. 2018.

[5] World Health Organization: "Fact sheets – Noise". 2010. https://www.who.int/europe/news-room/fact-sheets/item/noise [checked on: 07.04.2025].

[6] E. Sälzer, J. Maack: *Schallschutz von geneigten Dächern und Dachflächenfenstern.* Final report. ITA Ingenieurgesellschaft für technische Akustik MBH Beratende Ingenieure VBI (Ed.). Stuttgart, Germany. 2008.

[7] F. Holtz, J. Hessinger, A. Rabold et al.: "Schallschutz - Wände und Dächer", in *Informationsdienst Holz.* no. 3/3/4. 2004.

[8] B. Nusser, C. Lux, H. Müllner: "Luftschalldämmung von Dächern in Holzbauweise – Einfluss von Konstruktionsdetails", in *Proc. of DAGA 2021.* Deutsche Gesellschaft für Akustik e.V. (Ed.). Vienna, Austria. pp 155-156. 2021.

[9] A. Rabold, W. Jehl: "Einfluss unterschiedlicher Dachdeckungen auf die Schalldämmung von Steildächern", in *Bauphysik,* vol. 32, no 5, pp 327-329. 2010

[10] A. Rabold, C. Châteauvieux-Hellwig: "Flach- oder steil geneigt? – Schalldämmung von Steil- und Pultdächern", in *Holzbau - die neue quadriga*, no. 1, pp. 21-24. 2021.

[11] M. F. M. Idris, M. M. Musa, S. M. Ayob: "Noise Generated by Raindrop on Metal Deck Roof Profiles – It's Effect towards People Activities", in *Procedia - Social and Behavioral Sciences,* vol. 36, pp. 485-492. 2012.

DOI: 10.61782/fa.2025.0067

FORUM ACUSTICUM EURONOISE 2025

ACOUSTIC COMFORT OF LIGHTWEIGHT TIMBER WALLS: CORRELATION BETWEEN SUBJECTIVE EVALUATIONS AND OBJECTIVE MEASUREMENTS

Federica Morandi[1*] **Alice Speranza**[2] **Paola Brugnara**[2]
Francesca Cappelletti[3] **Andrea Gasparella**[1]
[1] Faculty of Engineering, Free University of Bozen-Bolzano, Italy
[2] Rotho Blaas GmbH, Cortaccia (BZ), Italy
[3] Department of Architecture and Arts, Iuav University of Venice, Italy

ABSTRACT

Sound insulation of timber frame walls has been the object of several studies over the past 30 years. Most concerns about acoustic comfort of lightweight partitions is their poor sound insulation at low frequencies, in contrast with a high sound insulation performance at higher frequencies usually exceeding the one of traditional heavy weight structures. These characteristics are usually considered of great concern because it has been established that perceived sound insulation is strongly affected by the perception of low frequencies. This study investigates comfort levels experienced by subjects that are asked to listen to audio tracks that reproduce noises through several lightweight timber frame walls with different sound insulation properties, previously tested in laboratory conditions, and to rate the perceived annoyance. This information is then correlated to the single number ratings associated to the measurement and to the spectral adaptation constants that can be added. The results show that (i) users express different annoyance ratings for walls having the same single number rating but different spectra; (ii) the use of the spectral adaptation constants C and C_{tr} improves the correlation between single number rating and annoyance; (iii) subjects can consistently evaluate annoyance upon multiple administration of the same tracks.

Keywords: *airborne sound insulation, acoustic comfort, listening tests, spectral adaptation constants.*

1. INTRODUCTION

The development of multi storey timber construction brought the attention to the sound insulation properties of lightweight assemblies. It is well established that timber structures, due to the low density of wood in relation to its stiffness, provide good sound insulation properties at high frequencies, while poor performance in the low frequency ranges, as typical of double walls [1]. Achieving good sound insulation levels at low frequencies is of great importance in attaining good acoustic comfort performance even if it may be difficult to correlate that to the actual evaluation from the occupants, particularly in this specific frequency range. Recent literature started to investigate which metrics (including low-frequency correction terms) are most closely related to the subjective evaluation of acoustic comfort [2-3]. In this study, subjective evaluations on comfort are compared to the objective sound insulation measurements of lightweight timber construction, with the aim to gain a deeper understanding on (i) the correlation between subjective evaluation and airborne sound insulation indices (ii) the identification of spectral adaptation constants that improve such correlation and (iii) the evaluation of the reliability of the responses upon multiple administrations.

[*] ***Corresponding author***: federica.morandi@unibz.it.
Copyright: *©2025 First author et al. This is an open-access article distributed under the terms of the Creative Commons Attribution 3.0 Unported License, which permits unrestricted use, distribution, and reproduction in any medium, provided the original author and source are credited.*

2. METHODOLOGY

2.1 Characterization of the sound reduction index of timber frame walls

A measurement campaign on timber frame walls has been conducted at the Building Envelope Lab of the Free University of Bozen-Bolzano, Italy. The measurement campaign encompassed different configurations, including three kinds of linings: (i) gypsum board plates directly fixed to the timber frame wall, (ii) gypsum board plates fixed to wood studs screwed to the structure, and (iii) completely decoupled drywall with stainless steel C profiles. Membranes and damping profiles were also tested as improvement measures that positively affect the performance whilst minimally increasing the wall thickness. Measurements were conducted both using the EN ISO 10140-4 standard [4] and by additional testing according to the EN 16283-1 standard [5].

The base timber frame wall analyzed for this study consists of timber studs (60x140 mm, 600 mm spacing), mineral wool (140 mm, 70 kg/m^3), OSB (15 mm, 550 kg/m^3). Among the wall elements tested, 6 construction solutions were selected, exhibiting different sound insulation properties:

- **Wall #1**: Timber frame wall.
- **Wall #2**: Timber frame wall. On the emitting and receiving sides: timber studs (40x60 mm, 600 mm spacing), mineral wool (40 mm, 38 kg/m^3), 1x gypsum board (12.5 mm, 720 kg/m^3).
- **Wall #3**: Timber frame wall. On the emitting side: closed cell polyethylene strip (3 mm, 25 kg/m^3), timber studs (40x60 mm, 600 mm spacing), mineral wool (40 mm, 38 kg/m^3), 1x gypsum board (12.5 mm, 720 kg/m^3).
- **Wall #4**: Timber frame wall. On the emitting and receiving side: timber studs (40x60 mm, 600 mm spacing), closed cell polyethylene strip (3 mm, 25 kg/m^3), mineral wool (40 mm, 38 kg/m^3), 1x gypsum board (12.5 mm, 720 kg/m^3).
- **Wall #5**: Timber frame wall. On the emitting and receiving side: closed cell polyethylene strip (3 mm, 25 kg/m^3), timber studs (40x60 mm, 600 mm spacing), mineral wool (40 mm, 38 kg/m^3), soundproofing bitumen sheet (5 kg/m^2), 1x gypsum board (12.5 mm, 720 kg/m^3).
- **Wall #6**: Timber frame wall. On the emitting and receiving side: 10 mm airgap, C-profiles (50 mm), mineral wool (40 mm, 38 kg/m^3), 1x gypsum board (12.5 mm, 720 kg/m^3).

The single number rating for airborne sound insulation was calculated together with the relevant spectral adaptation constants: C, $C_{50\text{-}3150}$, $C_{50\text{-}5000}$, $C_{100\text{-}5000}$, C_{tr}, $C_{tr,50\text{-}3150}$, $C_{tr,50\text{-}5000}$, $C_{tr,100\text{-}5000}$. An overview of the results of the sound reduction index measurements is presented in Figure 1, while the relevant features and single number ratings are listed in Table 1.

Table 1. Characteristics of the walls selected for the listening tests.

#	m' (kg/m^2)	R_w (dB)	C (dB)	C_{tr} (dB)
1	24.3	41	-3	-8
2	49.5	49	-4	-10
3	37.0	49	-4	-10
4	49.7	53	-5	-11
5	59.7	57	-4	-12
6	49.1	62	-7	-15

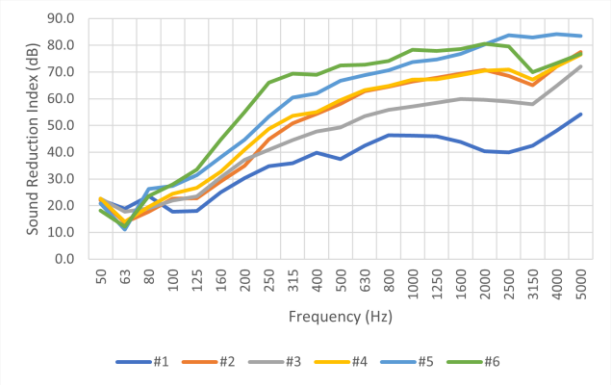


Figure 1. Sound reduction index of the 6 walls used as reference for the listening tests.

The R_w of the chosen walls ranges from 41 dB (wall #1) to 62 dB (wall #6), covering a wide range of conditions. Walls identified as #2 and #3 have the same R_w but a different spectral response, as seen in Figure 1. Other walls are characterized by different R_w and different spectral responses.

To understand how much the different frequency-dependent sound insulation performance affects comfort, and to understand which metric and spectral adaptation

term most closely matches the comfort votes expressed, listening tests were performed.

2.2 Listening tests design

A full factorial design was used in which subjects listened to 16 audio tracks and rated the perceived annoyance. The audio tracks were generated from two baseline signals, a traffic noise and a speech noise, both lasting 40 seconds. Traffic noise was chosen to mimic the response to façade sound insulation, while speech was used to evaluate the annoyance of airborne sound from adjacent environments.
The baseline signals were equalized (in terms of dBA) and filtered based on the spectra recorded when measuring sound insulation properties of the walls. Repeated tests were performed on tracks 3 and 5, to verify if the responses were consistent upon multiple administration, thus testing the repeatability of the results. As such, 8 tracks were created for both speech and traffic audio files. These audio files underwent a low pass filtering (30 Hz, slope 6 dB/oct) and a high pass filtering (16 kHz, slope 6 dB/oct), and 2 seconds of fade in and fade out effects were added.

The listening test was structured in 5 steps:

- **Part I: Introduction.** Subjects were informed about the scope of the test and signed privacy disclosure. Personal data (age, gender, living context, first language, and self-reported hearing impairment) were collected to check whether they influenced the responses.
- **Part II: Pretest A**. To allow subjects to get familiar with the audio tracks, they were fed a short portion (20 s) of three audio tracks, among those that would be tested afterwards, in the following order: the louder, the fainter, and in intermediate one. They were not asked to report any evaluation.
- **Part III: Test A** (traffic noise, 8 tracks). Listeners had to listed to 8 audio tracks, whose order was randomized. They could listen again to the tracks, if thew wanted. After each listening, they were asked to evaluate the annoyance on a digital questionnaire.
- **Part IV: Pretest B**. Same as Part II, with speech noise.
- **Part V: Test B** (speech noise, 8 tracks). Same as Part III, with speech noise.

Before starting the listening tests, subjects were given the following context: “When the sound is playing, imagine you are alone at home in an apartment building in complete peace. You are reading a magazine or a book or browsing the internet and you start hearing noises from outside/the apartment upstairs.”
The annoyance rating was introduced by the following question: “How much does the sound disturb, annoy, or bother you?” The evaluation scale was a modified version of the ISO/TS 15666 [6] annoyance scale: instead of having 11 points, the neutral point was removed resulting in 10 points, ranging from 1 (“Not at all”) to 10 (“Extremely”). If they could not hear the sound, they were asked to leave the questionnaire blank (“zero” votes in the analysis of the results).

2.3 Test environment and measurement equipment

Tests were carried out in a room located in an unoccupied area of an office building, with dimensions 3.30 x 4.50 x 3.18 m. Tests were administered during 5 working days, between 18.03.24 and 22.03.34, from 8 am to 1 pm.
The overall duration of the test was approximately 30 min for each participant. Circumaural closed-back headphones ATH-M70x and a Zoom F8 sound card were used for the reproduction of audio tracks. During the tests, environmental conditions were monitored as illustrated in Figure 2.

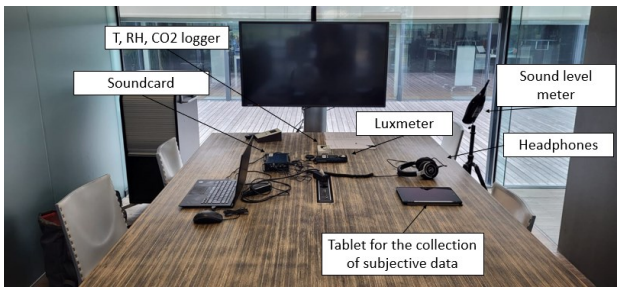


Figure 2. Test environment and equipment.

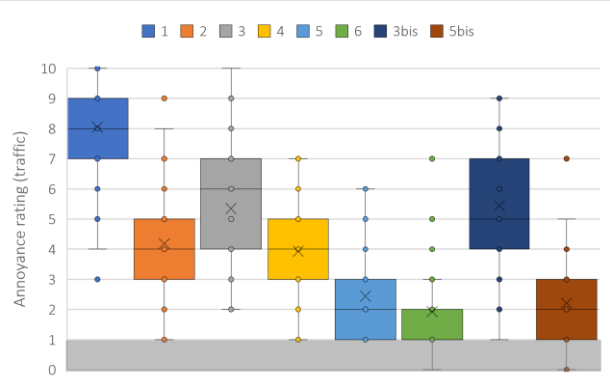
Sound pressure level was monitored close to the subject (h = 1.20 m) using a B&K 2270 sound level meter; illuminance on the desk was measured with a Konika Minolta T-10A illuminance meter, while temperature, relative humidity and CO_2 concentration were monitored using a HOBO MX1102 logger located on the desk. Subjective responses were collected using a tablet.

3. RESULTS

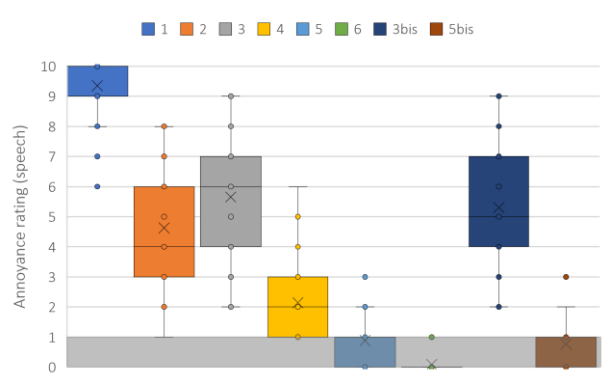
3.1 Overview of participants profiles

The test was completed by 43 participants, whose profiles are summarized below:

- **Age:** 40% between 21 and 30 years, 44% between 31 and 40 years, 16% between 41 and 50 years
- **Gender**: 49% females, 51% males
- **Living context**: 12% countryside, 67% small village, 21% city
- **First language**: 81% Italian, 9% Spanish, 7% German, 2% French
- **Hearing impairment**: none



(a) Traffic noise



(b) Speech noise

Figure 3. Annoyance rating for the 8 audio tracks related to traffic (a) and speech noise (b).

The environmental conditions monitored during the tests, expressed in terms of average and standard deviation, displayed a sound pressure level of (37.2 ± 1.1) dBA, an illuminance of (1460 ± 860) lx, a temperature of (23.9 ± 1.2) °C, a relative humidity of (35 ± 4) % and a CO2 concentration of (550 ± 110) ppm.

3.2 Annoyance ratings

The distribution of annoyance responses is represented in Figure 3a for traffic noise and Figure 3b for speech noise.

In Figure 3, the "zero" vote in the annoyance scale, shaded in grey, was associated with subjects who could not hear the track. For speech noise, many subjects could not detect tracks #5 and #6, filtered by spectra characterized by high sound insulation values at mid-high frequencies.

Significant differences in the annoyance rating is evident between walls #2 and #3, characterized by the same R_w, a sound transmission curve dominated by low frequency and a different energy content over the whole frequency range. Wilcoxon rank sum tests were conducted to check whether the distribution of votes related to tracks 2 and 3 were had significantly different medians. The test results confirmed that the distributions have different medians at the 5% significance level, both for speech and traffic noise.

The repeated response to tracks 3 and 5, aimed at evaluating the consistency of the answers of the subjects, confirmed the ability of subjects to evaluate consistently their annoyance, both for traffic noise and for speech noise.

3.3 Spectral adaptation constants

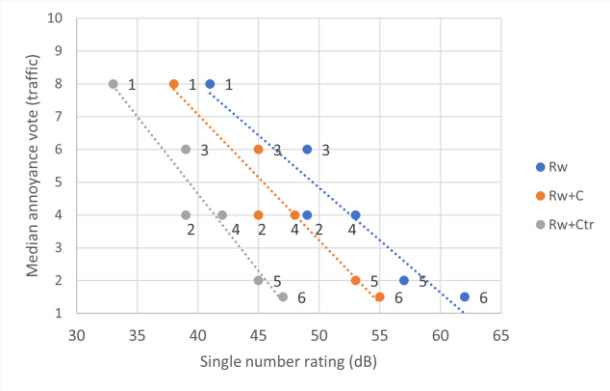
To evaluate which spectral adaptation constant is better suited to describe the relation between single number rating and annoyance level, regression analysis was performed between the median annoyance vote expressed by the subjects and the single number rating with different spectral adaptation constants. The R^2 of each correlation is reported in Table 2.

Table 2. R^2 of the correlations between single number rating and annoyance level.

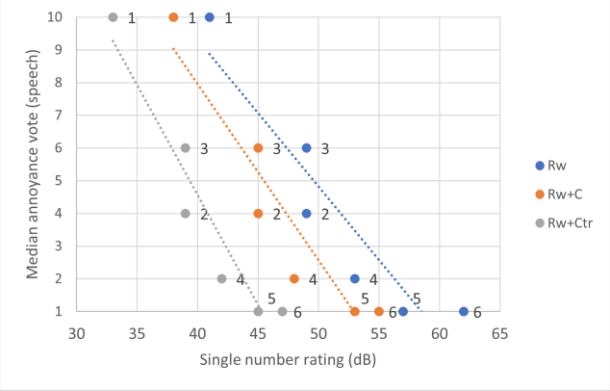
	Traffic noise	Speech noise
R_w	0.91	0.86
$R_w + C$	0.93	0.89
$R_w + C_{tr}$	0.93	0.91
$R_w + C_{50\text{-}3150}$	0.78	0.89

$R_w + C_{50\text{-}5000}$	0.78	0.89
$R_w + C_{100\text{-}5000}$	0.93	0.89
$R_w + C_{tr,\ 50\text{-}3150}$	0.06	0.14
$R_w + C_{tr,\ 50\text{-}5000}$	0.06	0.14
$R_w + C_{tr,\ 100\text{-}5000}$	0.93	0.91

The results show that the spectral adaptation constants C and C_{tr} help improve the explained variance of the correlation, while spectral adaptation constants evaluated in different frequency ranges do not necessarily do so. Correlations with C_{tr} evaluated over the ranges 50-3150 Hz and 50-5000 Hz display extremely low R^2 values, as these spectral adaptation constants tend to flatten the differences among the single number ratings. In Figure 4, the correlations between single number rating and annoyance are reported for R_w, $R_w + C$ and $R_w + C_{tr}$.



(a) Traffic noise



(b) Speech noise

Figure 4. Correlations between single number rating and annoyance for traffic (a) and speech noise (b).

It should be noted that the median value of 1.5 (Figure 4a) is estimated as the average between two numbers occupying the central position in the distribution as, for that specific case, there is an even number of occurrences.

3.4 Personal factors affecting the response

Finally, the categorical variables collected related to personal information (age range, gender, living context and first language) were used to run an ANOVA and check whether there was a significant impact of any of those features on the expression of votes. In detail, the living context might have been relevant in the evaluation of the traffic-related annoyance, while the first language might have had an impact on the evaluation of the speech noise. Statistical analysis showed that, at a significance level of 5%, none of the categorical variables listed above was significant, neither for the traffic noise nor for the speech noise.

4. DISCUSSION

The main outcomes of the presented research can be summarized as follows:

- Subjects were able to coherently rate annoyance in a proportional manner with respect to the airborne sound insulation provided by the walls and the interquartile range spans 2 or 3 votes.
- Speech noise is generally attributed higher annoyance levels compared to traffic noise.
- Both for speech and traffic noise, subjects rated wall #3 as more annoying compared to wall #2. The two walls have the same R_w but different spectra; this suggests that additional considerations should be performed when evaluating the perceptual relevance of sound insulation indices.
- Repeated exposure to the same audio track returned consistent results for both speech and traffic noise.
- The spectral adaptation constants C and C_{tr} improve the correlation between R_w and median annoyance vote, confirming the relevance that they have in relation to the expression of subjective ratings.
- The slope of the regressions for speech is steeper compared to traffic noise, indicating a much more limited range for acceptability of such conditions.
- Age, gender, living context and first language were not significantly impacting the distribution of votes, neither for speech nor for traffic noise.

Some limitations might have affected the results presented above, namely:

- Spectral filtering might be considered a suboptimal solution to perform listening tests, compared to recordings.
- Specific features of the original audio signals might have led to a visual and/or acoustic mismatch between the sound scene and the room where the tests took place.
- Tests were performed in a quiet environment; nevertheless, impulsive background noises might have affected the results for the softer tracks.
- The number of participants was relevant, but the limited variability of the personal data might have not allowed specific features to emerge.

5. CONCLUSIONS

The present study aimed at testing the perceptual effects of noise propagating through lightweight timber walls. To this aim, experimental measures of airborne sound insulation were performed on timber frame walls; a few of them were selected, and the amplitude spectra of the recorded signals was used to filter traffic and speech noise and perform listening tests. The results showed that there is a significant correlation between single number rating and annoyance, which is further improved if spectral adaptation constants are used. Nevertheless, walls having the same R_w were rated differently and the signal rated as more annoying was characterized by lower R values in the frequency range. Correlation between single number rating and annoyance was steeper for speech noise compared to traffic noise, indicating narrower acceptability ranges for that sound type.

Further work will be devoted to improving the experiment setup from the side of signal generation and reproduction, to expand the sample to study in detail the effect of personal factors, and to enlarge the number of descriptors used to characterize the listening experience.

6. ACKNOWLEDGMENTS

The research activity related to the measurement of sound insulation of timber frame walls was funded by Rotho Blaas GmbH and by the BIGWOOD project (Interreg Italia-Austria V-A, BIGWOOD, ITAT1081). The authors gratefully acknowledge the Rotho Blaas staff who took care of the accurate mounting of the test configurations and who participated in the listening tests.

7. REFERENCES

[1] Cost Action FP0702 - Net-Acoustics for Timber based Lightweight Buildings and Elements. Final Report. Available online (last viewed on April 19th, 2022): https://www.cost.eu/ac0tions/FP0702/.

[2] N.-G. Vardaxis, D. Bard. Review of acoustic comfort evaluation in dwellings: Part III—airborne sound data associated with subjective responses in laboratory tests. Building Acoustics 25(4), 289–305, 2018.

[3] V. Hongisto, P. Virjonen, H. Maula, P. Saarinen, J. Radun. Impact sound insulation of floating floors: A psychoacoustic experiment linking standard objective rating and subjective perception. Building and Environment 184, 107225, 2020.

[4] EN ISO 10140-4:2021. Acoustics - Laboratory measurement of sound insulation of building elements - Part 4: Measurement procedures and requirements. European Committee for Standardization, Brussels, 2021.

[5] EN ISO 16283-1:2014/A1:2017. Acoustics - Field measurement of sound insulation in buildings and of building elements - Part 1: Airborne sound insulation. European Committee for Standardization, Brussels, 2017.

[6] ISO/TS 15666:2021. Acoustics — Assessment of noise annoyance by means of social and socio-acoustic surveys. International Organization for Standardization, Geneva, 2021.

DOI: 10.61782/fa.2025.0477

FORUM ACUSTICUM EURONOISE 2025

Initial Results of the Research Project Sound and Vibration Protection for Long Span Timber Floors

Martin Schneider[1] **Johannes Ruf**[2] **Michaela Marxt**[1]
Berndt Zeitler[1]
[1] University of Applied Sciences Stuttgart, Germany
[2] University of Applied Sciences Biberach, Germany

ABSTRACT

Long-span timber floors are usually designed with regard to the permissible deflection and/or position of the first natural frequency due to the serviceability requirements. Increasing the mass of the construction is often required to ensure sufficient impact sound insulation. In this research project, sound insulation and vibration measurements are carried out on floors, both during construction (without floating floors) and after completion. The focus is on the low-frequency airborne and impact sound transmission of the ceilings. In addition to classic building acoustics measurements, the influence of boundary conditions on the eigenmodes is to be clarified with the help of modal analyses of the floors. Inital results of the research project are reported here.

Keywords: *long-span timber floors, low frequencies, sound transmission, mode shapes.*

1. INTRODUCTION

Aesthetically designed and ecologically sustainable buildings are increasingly in demand. This requires the selection of construction methods and materials that are orientated towards these and future needs. Looking at CO_2 emissions in Germany, for example, the construction sector is responsible for a large percentage of these emissions. In order to reduce these CO_2 emissions, sustainable alternatives to CO_2 and energy-intensive building materials are being sought in the construction sector. Timber buildings are a viable solution due to their lower environmental impact. Lightweight construction has many positive aspects such as lighter foundations, lower transportation weight, storage of CO_2, etc., but other aspects such as the vibration behaviour of timber floors and sound insulation must also be considered. It is therefore essential to investigate the vibration behaviour and sound insulation in the low-frequency range of long-span floors in more detail.

2. PROJECT PRESENTATION

The "SchwallBe" project aims to investigate the vibration and sound behaviour of long-span timber and timber-concrete composite floors (TCC). The aim of the project is to refine the design methodology for the assessment of vibrations in long-span timber floors. Empirical studies have repeatedly shown that wooden floors exhibit better vibration properties under real conditions than predicted by calculations. This study deals with the analysis of constructed buildings to determine their actual vibration and sound insulation behaviour. In particular, it is investigated whether the measured first resonance frequency is higher in practice than expected by calculation using the existing prediction method due to boundary conditions.
This research project is a co-operation between Biberach University of Applied Sciences (HBC) and Stuttgart University of Applied Sciences (HFT). In Biberach, the main focus is on the design methodology for the evaluation of vibrations in long span wooden floors, while in Stuttgart the acoustic properties are being investigated, particularly in the low-frequency range. The project runs from May 2024 to December 2026. The analysed floors are mainly located in Germany, Switzerland and Austria. The research project is an EFRE project and is financially supported by the European Union and the state of Baden-Württemberg. This article only refers to the area of acoustics.

*Corresponding author: martin.schneider@hft-stuttgart.de
Copyright: ©2025 Martin Schneider et al. This is an open-access article distributed under the terms of the Creative Commons Attribution 3.0 Unported License, which permits unrestricted use, distribution, and reproduction in any medium, provided the original author and source are credited.

3. TASK IN BUILDING ACOUSTICS

The requirements for airborne and impact sound insulation are specified in building regulations in DIN 4109-1 [1]. The weighted apparent building sound reduction index R'_w and the weighted apparent normalized impact sound pressure level $L'_{n,w}$ are the characteristic requirement values. These values cover the building acoustics frequency range of 100 Hz - 3150 Hz. There are no requirements for frequencies below 100 Hz (hereinafter referred to as "low frequencies"). However, studies (e.g. Holzbauhandbuch [2]) show that the subjective perception or the level of annoyance caused by the impact sound level of people walking does not correspond particularly well with the weighted standard impact sound pressure level. However, if the spectrum adaptaion term $C_{I,50\text{-}2500}$ is considered, there is a good correlation between the measured value, the impact sound level of the person walking and the subjectively perceived annoyance of the impact sound. In Germany, the proof of sound insulation required by building regulations is provided by calculation in accordance with DIN 4109-2 [3] with single-number quantities (SNQ) without taking the low frequencies into account.
As part of this research project, measurement data for airborne and impact sound insulation is to be determined for buildings with long-span timber floors. In particular, the frequencies in the frequency range between 20 Hz and 200 Hz are to be analysed separately, as very little data is currently available for this frequency range. In addition to the influence of the supporting structure (mass timber, timber-concrete composite, ribbed floors, etc.), the influence of mass per unit area, the influence of the resonance frequency of the screed and a possible influence of the support conditions on sound transmission in the low frequency range will be analysed.

4. MEASUREMENT PROCEDURES

Measurements are carried out both after construction of the supporting structure (timber floor) and after completion of the building (occupied). Measurements of the airborne and impact sound reduction in the receiving room are not possible before the building is finished, as the transmission via the door openings determines the overall transmission. However, by means of structure-borne sound measurements on the bare floor, it is possible to determine the velocity levels when excited with the standardised ISO tapping machine or with the ISO rubber ball. These measured values can then be used to estimate SNQs according to ISO 717-2: the weighted apparent normalized impact sound pressure level when excited with the tapping machine or the maximum level when the floor is excited with the rubber ball.
The airborne and impact sound insulation in the completed buildings is carried out in accordance with DIN EN ISO 16283-1 [4] and -2 [5]. The frequency range is extended to low frequencies of up to 20 Hz. For the airborne sound measurements, a subwoofer is used in addition to the usual dodecahedron to excite the low frequencies.
Binaural recordings are also made in the receiving room when walking on the floors, as well as during excitation with the standard tapping machine and the rubber ball. An evaluation of these measurements with regard to annoyance is planned.

5. ANALYSED BUILDINGS

5.1 Building description

The long-span timber floors with spans of over 7 metres are mainly found in school buildings as well as in office and workshop buildings. Spans of over 7 metres have not yet been investigated in residential buildings. The measured values are compared with the sound insulation requirements for classrooms and office buildings. In Germany and some other European countries, the apparent weighted sound insulation index R'_w or the weighted normalized impact sound pressure level $L'_{n,w}$ are used as SNQs. In Switzerland and other countries, reverberation time related parameters: the weighted standardized sound level difference $D_{nT,w}$ or the weighted apparent standardized impact sound pressure level $L'_{nT,w}$ are used as the required quantities.
The floor constructions analysed are mainly mass timber floors (with bulk filler), timber-concrete composite floors, timber beam floors, modular floors, etc.. Some of the measurements are carried out on the bare floor, while others are carried out on floors with a heavy screed.

5.2 Results of the analysed floors with airborne and impact sound measurements

The following Table 1 shows the component description and measured SNQ of the floors where airborne and impact sound measurements were carried out.

Table 1. Component description and determined weighted apparent sound reduction indices and weighted apparent impact sound pressure levels of the floors.

Nr.	Construction	R'_w dB	L'_{nw} dB	$L'_{nw} + C_{I50\text{-}2500}$dB	$L'_{nT,w}$ dB
D204	5 mm Linoleum flooring 60 mm cement screed 30 mm impact sound insulation board 60 mm Liapor weighting (20 kg/m²) 120 mm cross-laminated timber floor with glulam beams	52 53	61 61	62 62	54 54
D306	2 mm linoleum covering with 3 mm levelling adhesive 74 mm calcium sulphate flowing screed 22/20 mm impact sound insulation board 10 mm EPS insulation 30 mm calcium sulphate board 190 mm hollow floor system 120 mm concrete topping 200 mm glulam timber C24, partly as acoustic element	60 59	48 52	49 52	40 44
D205	5 mm linoleum flooring on 40 mm dry screed 22/20 mm impact sound insulation board 60 mm bulk filler 90 mm modular floor CLT plate 3-layer 50 mm mineral fibre boards 120 mm modular ceiling CLT plate 5-layer	57 55	55 56	58 58	48 48
D101	10 mm carpet floor covering 40 mm raised floor panel 600 mm x 600 mm 80 mm cavity floor with system floor supports 5 mm PU insulation boards 30 mm GF carrier board, 2-ply 30 mm impact sound insulation board 60 mm honeycomb fill 300 mm cross-laminated timber floor	52	45	53	42
D102	15 mm parquet flooring 70 mm cement screed 30 mm impact sound insulation 60 mm chippings fill 280 mm CLT	60	48	53	41
D203	7 mm linoleum flooring 70 mm cement screed 30 mm impact sound insulation 80 mm glulam board 60 mm chippings fill 400 mm glulam timber	66	56	60	48

5.3 Detailed Results for floor #D204

Construction measurement D204 is presented below as an example. This school building is a timber construction, with the separating floors consisting of timber beams with cross laminated timber (CLT) and floating screed, the exterior walls of timber stud walls and the interior walls of metal stud walls with plasterboard.

DIN 4109-1 specifies the following minimum requirements for the airborne sound insulation of floors between classrooms for schools: weighted apparent sound reduction index $R'_w \geq 55$ dB, weighted normalized impact sound pressure level $L'_{n,w} \leq 53$ dB. The floor construction has a span of 7.5 m, with CLT-elements with a thickness of 120 mm laid on glulam beams (spacing of 3000 mm). A bulk filler of 90 kg/m² was planned on these. However, at the insistence of the building contractors, a lighter bulk filler

with only 20 kg/m² was used. The floating screed with 60 mm was applied on an insulation layer with s' = 16 MN/m³. The floor covering (5 mm linoleum) was also present in the measurement. The measurements were carried out in two pairs of classrooms of different sizes, one above the other. Figure 1 shows the frequency curve of the sound reduction index for one measurement. Here the drop in the sound reduction curve at 125 Hz is presumably caused by the mass-spring-mass resonance of the floating screed. $R'_w = 52$ dB / 53 dB are determined as SNQs for the weighted apparent sound reduction index.
This means that the required values are not achieved. The weighted apparent normalized impact sound pressure level of $L'_{n,w} = 61$ dB measured in both pairs of rooms also does not fulfill the minimum requirement of DIN 4109-1. For the maximum A-weighted impact sound level $L'_{iA,Fmax}$ when excited with a rubber ball in accordance with DIN EN ISO 16283-2, measured values of $L'_{iA,Fmax,50\ -\ 630\ Hz} = 47$ and 52 dB are determined. Due to the low surface mass of the mass timber floor in combination with the reduced mass of the fill, the available data results in a resonance frequency of approx. 100 Hz with relatively high impact sound levels in the frequency range from 100 Hz to 500 Hz.

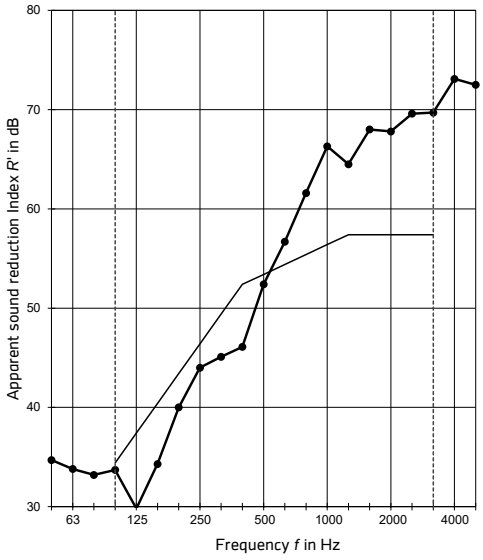


Figure 1. Measured sound reduction index of the analysed floor construction D204.

The following figure 2 shows the measured impact sound pressure level by the tapping machine and the maximum sound pressure level due to the impact of the rubber ball for two different floors in the building.

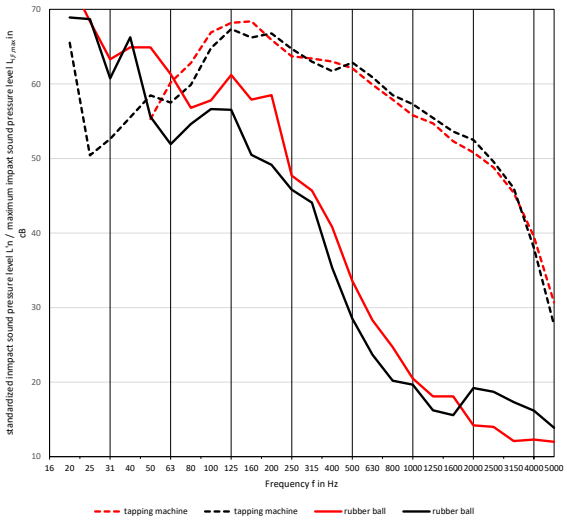


Figure 2. Measured sound pressure level due to excitation by tapping machine (solid lines) and rubber ball (dashed lines).

In the frequency curves from the measurements, at 125 Hz a local maximum can be recognised for both excitation with the tapping machine and with the rubber ball. However, while the level decreases towards lower frequencies with the hammer excitation, the level continues to increase towards lower frequencies with the rubber ball. The relatively large reverberation time correction of the measured impact sound level is particularly striking. With a room volume of approx. 200 m³ and a reverberation time of T = 0.5 s, which is common in classrooms today, a correction of 7.5 dB results due to the reference to an equivalent absorption area of $A_0 = 10$ m². This correction results in a very high weighted apparent normalized impact sound pressure level of $L'_{n,w} = 61$ dB (weighted apparent standardized impact sound level $L'_{nT,w} = 54$ dB).
Although the minimum requirements stipulated by the building authorities are clearly not met, the teaching staff rated the sound insulation as very good. Presumably, particularly in primary schools, the background noise levels present during lessons are higher than the impact noise from the classrooms above.

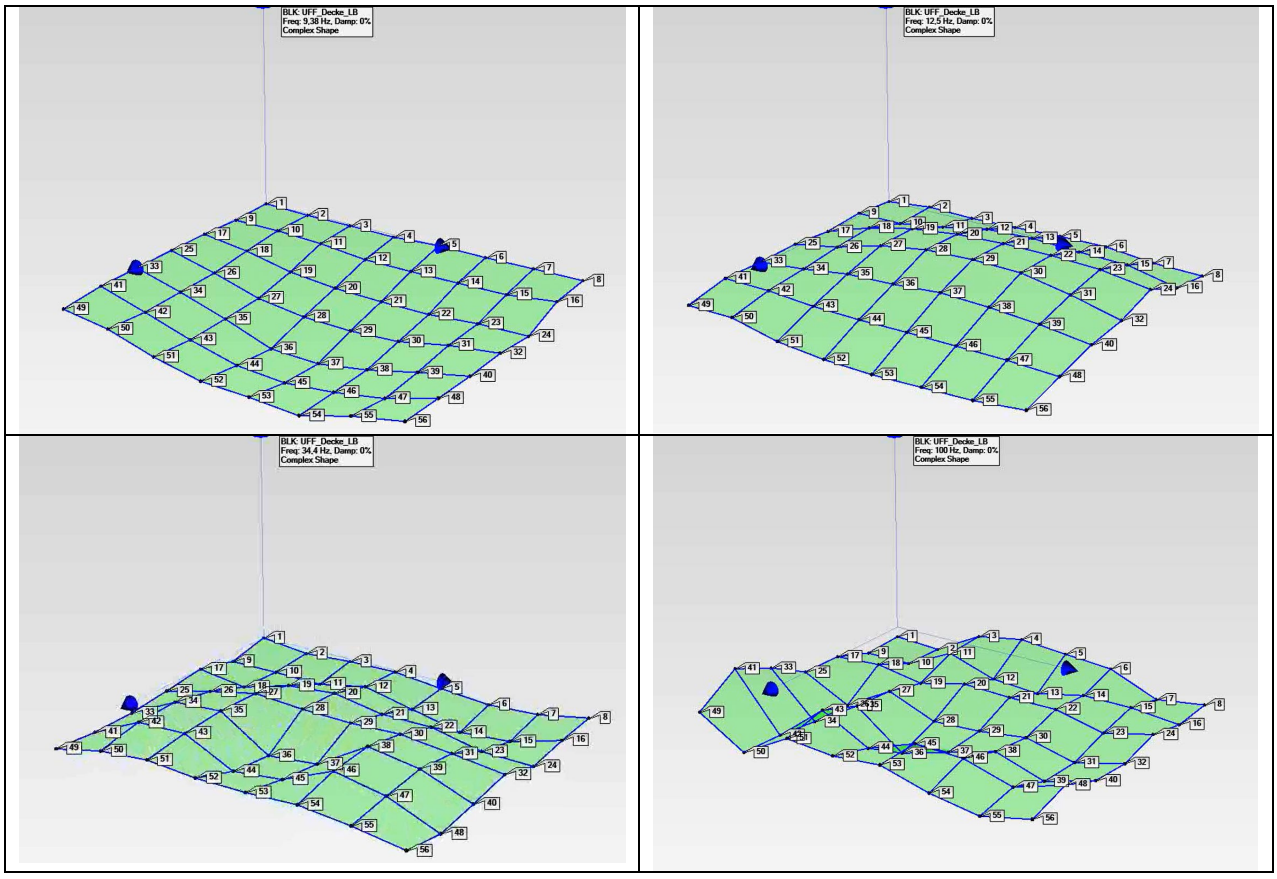
5.4 Modal Analysis

In addition to the building acoustics measurements, measurements of the vibration modes are also carried out on this object. Furthermore, the natural vibrations and eigenmodes of the solid floor are measured in selected

buildings with the reciprocal roving hammer technique. The force F is measured using an impulse hammer, which is used to excite corresponding points in a fixed grid. The acceleration is measured at a point slightly outside the center of the field. The transfer function acceleration/force is formed for each of the measuring points from the force applied and the resulting acceleration. Using the modal analysis software ME'scope, the vibrations are analysed, the first natural frequencies of the floor are determined and the corresponding vibration images are created. Due to the rough grid, it is only possible to visualise the first natural vibration modes. Even at a frequency of approx. 50 Hz, it is usually no longer possible to clearly recognize the vibration patterns of the floor.

The transfer function for the floor #D204 is determined in a grid of 1 m x 1 m at 56 points on one half of the floor (but over the entire span direction). The following Table 2 shows the maximum acceleration at different resonance frequencies.

Table 2. Measured maximum deflection of the analysed half of the floor for f = 9.4 Hz (top left) f = 12.5 Hz (top right), 34.4 Hz (bottom left) f = 100 Hz (bottom right).



The first natural frequency of the floor at 9.4 Hz is clearly recognisable and distinct in Table 2 (top left half ceiling). The second natural frequency shows a pronounced oscillation transverse to the direction of tension. Moving to higher frequencies and higher mode orders, it becomes increasingly difficult to identify the individual modes. At significantly higher frequencies (f = 100 Hz Table 2 bottom right), the modes can no longer be identified. However, it can be seen that the edges in particular experience a large acceleration. This is due to the fact that the screed slab is now decoupled from the floor slab because of the mass-spring-mass resonance. As the edges of the screed are free, they show a relatively large acceleration in the area of the resonance frequency and above, in contrast to the edges of the bare floor.

6. CALCULATION OF THE SOUND INSULATION OF TIMBER FLOORS

In Germany, airborne and impact sound insulation is verified in accordance with DIN 4109-2. However, there is currently no calculation method for calculating the direct airborne and impact sound insulation of timber floors. It is still unclear to what extent findings from solid construction can be transferred to timber construction e.g. dependence of the equivalent standard impact sound level on the mass per unit area, impact sound reduction of screeds can be described by resonance frequency. Furthermore, there are major differences between elementised load-bearing structures such as beam or ribbed floors and more homogenised structures such as timber-concrete composite floors. Here, reference is made to table values in the component catalogue for timber and lightweight construction (DIN 4109-33 [6]) or in other publications such as "Holzbauhandbuch" [2]. These table values come from laboratory measurements in accordance with ISO 10140, whereby the dimensions of the floors in the laboratories are generally only 4 - 5 metres. It is unclear to what extent this measurement data can be transferred to floors with spans of over 7 meters.

Due to the large number of new load-bearing structures (modular floors, timber-concrete composite elements on glulam beams, timber beam or timber ribbed floors, etc.) and different additional layers to the load-bearing structure (suspended ceilings, floating screeds, suspended or acoustic ceilings), it is usually difficult, if not impossible, to calculate or estimate the expected sound insulation from the values in the standard. Planners then rely on their experience or plan appropriate safety measures, usually in conjunction with an increased use of materials.

The modal analyses carried out can be used to visualise the vibration pattern of the floors. Particularly in the edge areas of the floor, it is then possible to draw conclusions about the boundary condition (hinged or nevertheless restrained to a certain extent). Initial results show, on the one hand, large deflections in mass timber floors in the area of the panel joints and, on the other hand, an influence of non-load-bearing partition walls on the vibration behaviour. An additional evaluation with the determined transfer functions with regard to the boundary conditions is planned here, as has already been successfully carried out with a bending beam [7].

7. SUMMARY

In the project described, the sound and vibration properties of long-span timber floors were and are still being measured in realised buildings. When possible, these properties are compared with mathematical approaches and the results of verification procedures. The first results of the vibration analyses will be presented at the WCTE 2025 (World Conference on Timber Engineering) in Brisbane [8]. The first results regarding the sound insulation of the analysed floor constructions are presented here. Most of the tested floors meet or even highly exceed the minimum requirements for airborne sound insulation. However, in one case, the requirements are not achieved due to the incorrectly carried out back filler, in another case due to the cavity floor used.

A different picture emerges for impact sound insulation. Here, many floors don't come close to meeting the minimum requirements. The reason for this is actually that the single number quantity, $L'_{nw,}$ prescribed in the DIN 4109 is not suited for large class rooms. It normalises to a reference absorption area of 10 m², which is much higher for the investigated and most class rooms. It should be replaced by the standardized impact sound level $L'_{nT,w}$, which is normalised toT = 0.5 s reverberation time common in class rooms.

With the visualisation of the vibration shapes using modal analysis, it was possible to clarify the initial effects with regard to the boundary conditions. Further measurements still to be carried out will provide the basis for calculating the acoustic properties in the low frequency range.

8. ACKNOWLEDGMENTS

The research project is an EFRE-project and is financially supported by the European Union and the state of Baden-Württemberg.

Kofinanziert von der Europäischen Union

Baden-Württemberg

9. REFERENCES

[1] DIN 4109-1:2018-01: Schallschutz im Hochbau – Teil 1: Mindestanforderungen.

[2] A. Blödt, A. Rabold, M. Halstenberg: holzbau handbuch, Reihe 3: Bauphysik, Teil 3: Schallschutz, Folge 1: Schallschutz im Holzbau – Grundlagen und Vorbemessung

[3] DIN 4109-2:2018-01: Schallschutz im Hochbau – Teil 2: Rechnerische Nachweise der Erfüllung der Anforderungen

[4] ISO 16283-1:2018: Acoustics - Field measurement of sound insulation in buildings and of building elements - Part 1: Airborne sound insulation (ISO 16283-1:2014 + Amd 1:2017)

[5] ISO 16283-2:2020: Acoustics - Field measurement of sound insulation in buildings and of building elements - Part 2: Impact sound insulation

[6] DIN 4109-33:2016-07 Schallschutz im Hochbau – Teil 33: Daten für die rechnerischen Nachweise des Schallschutzes (Bauteilkatalog) – Holz-, Leicht- und Trockenbau

[7] B. Zeitler, S. Reinhold, M. Schneider, H. Häfner: et al.: On identifying boundary conditions of a beam DAS DAGA2025 (to be published)

[8] J. Ruf, P. Hamm, M. Schneider: Comparison of the calculated and measured vibration behavior of long span timber floors, World Conference on Timber Engineering, 2025 Brisbane, Australia (to be published)

DOI:

Main theme: A03 Building Acoustics

Session A03.08 Reducing neighbour noise by acoustic retrofit in housing

Chair(s): B. Rasmussen, T. Carrascal

DOI: 10.61782/fa.2025.0463

FORUM ACUSTICUM EURONOISE 2025

IMPROVING SOUND INSULATION OF OLD TIMBER FLOOR CONSTRUCTIONS 1917/1937 IN MULTI-STOREY HOUSING – FIELD CASE STUDY & PERSPECTIVES

Birgit Rasmussen [1*]
[1] BUILD – Department of the Built Environment, Aalborg University, 2450 Copenhagen SV, Denmark

ABSTRACT

In Denmark, the first national requirements for sound insulation in housing were published in 1961. Most complaints about neighbour noises are from people in multi-storey housing (MSH) and relate to impact sound from both children and adults, although also annoyance due to airborne sounds are common. A mapping of the housing stock timeline and construction types showed that more than half of the MSH dwellings were built before 1961 and that most housing is brick-built with timber floor constructions.
In a project investigating air particle transfer vertically between dwellings, we had the opportunity to make a case study with test of airborne and impact sound insulation before and after mounting a new independent ceiling below the existing construction.
Measurements were made for eight floor constructions in housing built 1917/1937. The acoustic classification standard DS 490 has six classes A-F with Class C being the building code requirement for new housing. Before renovation, the airborne sound classes were D-E and impact sound F. After mounting of new ceilings, R'_w values were improved ~6 dB and $L'_{n,w}$ ~12 dB, implying that all results became Class C, thus complying with limits for new-build. The paper will describe experiences from the case study and the perspectives concerning preparation of acoustic regulations for renovated dwellings and mandatory acoustic labelling.

Keywords: *apartments, sound insulation improvement, old timber floors, acoustic labelling, building regulations.*

[*] ***Corresponding author**: bira@build.aau.dk.*
***Copyright**: ©2025 Birgit Rasmussen. This is an open-access article distributed under the terms of the Creative Commons Attribution 3.0 Unported License, which permits unrestricted use, distribution, and reproduction in any medium, provided the original author and source are credited.*

1. INTRODUCTION

Most countries in Europe have acoustic regulations for various types of buildings, including housing. This paper deals with airborne and impact sound insulation between dwellings in multi-storey housing (MSH) and the need for improvements, especially for old housing. The results for a field case study with renovated timber floor constructions in housing from 1917 and 1937 are described. Information about the Danish requirements is found in Table 1.
Sound insulation requirements for 35 countries in Europe are found in [1]. Several countries also have acoustic classification schemes (ACS), and national regulations often refer to or correspond to a specific class in a national ACS. Information about acoustic classification schemes and sound insulation descriptors in 14 countries in Europe are described in [2]. Several ACS have none or too few classes for old housing.
Both requirements and acoustic classes relate to peoples everyday life, because neighbour noise often is a significant problem in multi-storey housing (MSH), cf. [3] and [4], both based on a social media analysis of over 700 comments to two newspaper articles about neighbour noise and acoustic labelling of dwellings. The housing stock in Denmark and the case study results are described in the following Sections of the paper.

Table 1. Sound insulation main requirements [(1)] in the Danish building regulations for walls/floors between dwellings constructed in the period from 1961 until now.

Period	Housing type	Airborne sound insulation [(1)]	Impact sound insulation [(1)]
1961[(2)] –2008	Multi-storey [(3)]	$R'_w \geq 52$ dB (horizontal) $R'_w \geq 53$ dB (vertical)	$L'_{n,w} \leq 58$ dB
Since 2008	Multi-storey and row housing	$R'_w \geq 55$ dB	$L'_{n,w} \leq 53$ dB

Note 1: Limit values until 1982 are estimated by converting to the descriptors R'_w and $L'_{n,w}$ applied in the current Danish building code.

Note 2: Before 1961, there were no general national building regulations.

Note 3: For terraced housing (row housing), the limit values were: $R'_w \geq 55$ dB from 1966 and $L'_{n,w} \leq 53$ dB from 1977.

2. MULTI-STOREY HOUSING IN DK AND THE NEED FOR IMPROVED SOUND INSULATION

In Table 2 is found an overview of classes in the current Danish classification scheme, DS 490:2018 [5], which has six classes A-F covering the Danish housing stock. The table provides simple explanations of the intended application of classes for new and old housing, see [5],[6]. It also indicates the occupants' expected evaluation of the sound insulation.

In Figure 1 is found overview of the Danish ,multi-storey housing stock with construction types in different time periods, number of dwellings and estimated acoustic performance. More information is found in [6],[7],[8],[9]. Detailed construction guidelines for new housing are found in [10] and guidelines for improvement of existing housing are found in [7].

.

Table 2. Occupants' expected satisfaction for different sound classes according to DS 490:2018 [5]. Summary based on information in DS 490.

Sound insulation between dwellings Main class criteria A-F in DS 490:2018		
Class	Airborne	Impact
A	$R'_w + C_{50\text{-}3150} \geq 63$ dB	$L'_{n,w} \leq 43$ dB and $L'_{n,w} + C_{I,50\text{-}2500} \leq 43$ dB
B	$R'_w + C_{50\text{-}3150} \geq 58$ dB	$L'_{n,w} \leq 48$ dB and $L'_{n,w} + C_{I,50\text{-}2500} \leq 48$ dB
C	$R'_w \geq 55$ dB	$L'_{n,w} \leq 53$ dB
D	$R'_w \geq 50$ dB	$L'_{n,w} \leq 58$ dB
E	$R'_w \geq 45$ dB	$L'_{n,w} \leq 63$ dB
F	$R'_w \geq 40$ dB	$L'_{n,w} \leq 68$ dB
Reference: DS 490:2018 "Lydklassifikation af boliger" (Sound classification of dwellings)		

Characteristics of DS 490 sound classes for dwellings and occupants' estimated evaluation Information from DS 490:2018		
Sound class descriptions	Good or very good	Poor
Excellent acoustic conditions. Occupants will be disturbed only occasionally by sound or noise.	> 90 %	
Significant improvement compared to minimum in class C. Occupants may be disturbed sometimes.	70-85 %	< 10 %
Sound class intended as the minimum for new buildings.	50-65 %	< 20 %
Sound class intended for older buildings with less satisfactory acoustic conditions.	30-45 %	25-40 %
Sound class intended for older buildings with unsatisfactory acoustic conditions.	10-25 %	45-60 %
Sound class intended for older buildings with clearly unsatisfactory acoustic conditions.	< 5 %	65-80 %
Note: Within each sound class the percentage of satisfied or dissatisfied occupants may depend on the type of criterion. The grouping is mainly based on the subjective assessments of airborne and impact sound from adjacent dwellings.		

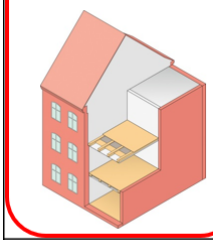
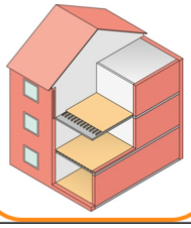
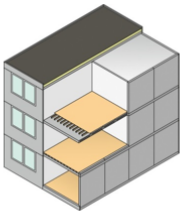
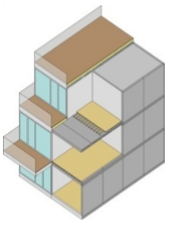
Building type E1	Building type E2	Building type E3	Building type NEW
Old brick-built buildings with timber floor constructions Period: ~ 1850 to 1930/1950 No. of dwellings in Danmark: ~ 500.000	Brick-built buildings with thin in-situ concrete slabs and wooden floors Period: ~ 1930 to 1960 No. of dwellings in Danmark: Up to ~ 100.000	Concrete elements with wooden floors Period: ~ 1960 to 2009 No. of dwellings in Danmark: ~ 400.000	Concrete elements with wooden floors Period: ~ 2010 to 2024ff No. of dwellings in Danmark: ~ 160.000 (incl. 2024)
			
Regulations: None	Regulations: None	Regulations: BR1961-BR1995	Regulations: From BR2008
Estimated performance: R'_w ~ 42-50 dB $L'_{n,w}$ ~ 63-75 dB	Estimated performance: R'_w ~ 45-53 dB $L'_{n,w}$ ~ 58-67 dB	Estimated performance: $R'_w \geq$ 52-53 dB $L'_{n,w} \leq$ 58 dB	Estimated performance: $R'_w \geq$ 55 dB $L'_{n,w} \leq$ 53 dB
Acoustic classification DS 490:2007: None DS 490:2018: Class F	Acoustic classification DS 490:2007: None DS 490:2018: Class E	Acoustic classification DS 490:2007: Class D DS 490:2018: Class D	Acoustic classification DS 490:2007: Class C DS 490:2018: Class C

Figure 1. Overview multi-storey housing stock in Denmark, number of dwellings and construction types in various time periods. Building regulations, estimated acoustic performance and expected acoustic classes indicated. More information about constructions is found in [6], [7], [8].

The housing stock in Denmark consists of about 2.8 mio dwellings [11], of these almost 1.2 mio dwellings in multi-storey (MS) housing, 450.000 row houses and most others single-family houses. In Figure 2 is found a diagram with number of MS dwellings according to construction year, and with the estimated acoustic class F, E, D, C according to DS 490:2018 [5], shown for various time periods. A Danish Health and Morbidity Survey in 2017 showed that about 36 % of people in multi-storey housing are slightly or very annoyed by neighbour noise, while for row/double housing only 12 %, see [12], [13]. The disturbing/annoying neighbour noises include for example footsteps, voices/shouting/arguments, playing/jumping children, parties, barking dogs, see e.g. [3], [9], [14], and for many people, the implications are sleep disturbances and strong negative influence on own "freedom" and activities. The result is adverse influence on quality of life.

In many old dwellings, people experience an almost total lack of privacy, since they hear, what they don't want to hear, which reminds them that even one's own ordinary activities being a part of a normal life are no longer possible without involuntarily "informing" the neighbours, [3], [9].

The relevant sound insulation improvement solutions depend on the actual performance of the existing building, the wishes/goals for the future acoustic conditions and the resources available for the upgrading. For the Danish multi-storey housing stock, the highest need is for building types E1 (almost half of Danish dwellings) and E2, cf. Figure 1 and Figure 2. The main principles for improvement of sound insulation of dwellings are indicated in Figure 3.

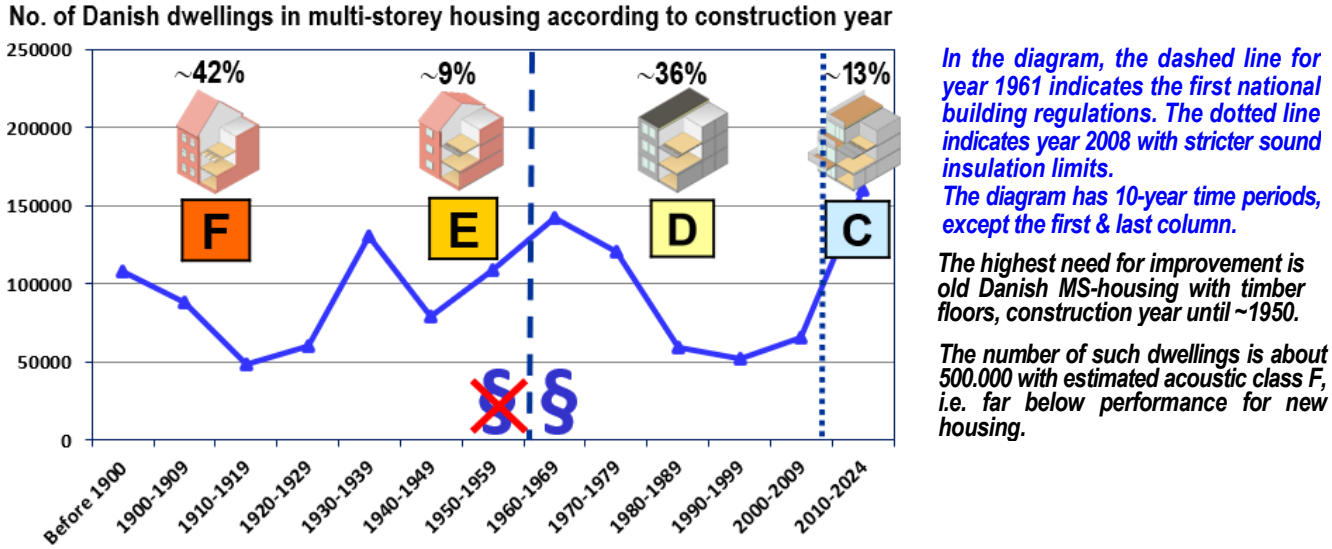


Figure 2. No. of Danish dwellings 1900-2024 in multi-storey housing according to construction year [11]. Estimated acoustic classes F, E, D, C according to DS 490:2018 [5] are indicated.



Figure 3. Left: Main principles for improvement of sound insulation in existing housing: New ceilings, wall linings, floors, see red lines. Right: A 10-page folder [9] has been published with indications of construction solutions for housing from different time periods. Detailed construction guidelines are found in [7].

3. CASE STUDY PROCEDURE AND TEST RESULTS

A case study about improvement of airborne and impact sound insulation for timber floor constructions was conducted for eight floors in two housing blocks in Copenhagen – as a supplement to a research project about air particle transfer through timber floor constructions in the same apartments.
We contacted several housing associations in the Copenhagen area, explaining the relevant construction type, purposes of project and asking about potential apartments appropriate for the case study. After inspection and evaluation, it was decided to make the renovation for eight floor constructions, four of them in apartments in 2200 CPH N (AKB, Guldbergsgade GBG, construction year 1917), and the other four in 2300 CPH S (AAB, Kirkegårdsvej KGV and Tycho Brahes Allé TBA, construction year 1937). In all cases, the occupants had made complaints about neighbour noises.
The existing timber floor constructions had a height ~27 cm, and the height of the ceiling to be installed below is ~12 cm. The ceiling consists of two gypsum plates fixed to steel profiles mounted from wall to wall and with mineral wool in the spacing above the gypsum plates, cf. Figure 4. For further details, see manufacturers' instructions. The room height in all rooms was 270 cm, and it was possible to install the ceilings without severe obstacles.

Field tests were carried out using the standardized methods [15], [16] as prescribed in the building regulations. The field tests were carried out by Rambøll [17], [18]. The project results are described in [19], section 2.
Floor areas S and room volumes V in GBG, 2200 CPH N, were 15-30 m^2, and 38-85 m^3. For KGV and TBA, 2300 CPH S, floor areas S were 14-19 m^2, and room volumes 36-51 m^3.



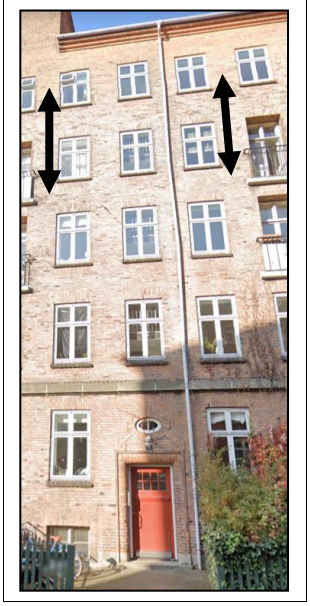
Figure 4. Timber floor constructions. The left drawing shows the original construction, the drawing to the right includes a new self-supporting ceiling. The drawings are from https://gi.dk/byggeteknisk-viden/.

The test results for GBG (CPH 2200 N) are found in [17], [19] and summarizwd in Table 3 below. The improvements in sound insulation values and classes are shown in the two last columns. The test results for CPH 2300 S were similar and also reached Class C after renovation. The results are found in [18] and in [19], Section 2.

Table 3. Test results for airborne and impact sound insulation between floor 3 and 4 before and after mounting new ceilings in GBG, rooms on 3rd floor, two rooms in each apartment (denoted Room1 and Room2). In total four constructions tested.

Address: AKB, Guldbergsgade, 2200 Copenhagen N. Construction year 1917.							
Test results airborne sound insulation R'_w between 3rd and 4th floor before and after mounting of new ceilings in rooms on 3rd floor. Test results before are in brackets.							
Test No. & direction		Source room	Receiving room	R'_w dB	Acoustic class	**Before / After**	
						$\Delta R'_w$ dB	**Acoustic class**
1	↑	GBGth3 Room2	GBGth4 Room2	57 (50)	C (D)	**+ 7**	**D → C**
2	↑	GBGth3 Room1	GBGth4 Room1	56 (49)	C (E)	**+ 7**	**E → C**
3	↑	GBGtv3 Room2	GBGtv4 Room2	56 (51)	C (D)	**+ 5**	**D → C**
4	↑	GBGtv3 Room1	GBGtv4 Room1	57 (49)	C (E)	**+ 8**	**E → C**
Test results impact sound $L'_{n,w}$ between 4th and 3rd floor before and after mounting of new ceilings in rooms on 3rd floor. Test results before are in brackets.							
Test No. & direction		Source room	Receiving room	$L'_{n,w}$ dB	Acoustic class	**Before / After**	
						$\Delta L'_{n,w}$ dB	**Acoustic class**
5	↓	GBGth4 Room2	GBGth3 Room2	53 (64)	C (F)	**– 11**	**F → C**
6	↓	GBGth4 Room1	GBGth3 Room1	53 (64)	C (F)	**– 11**	**F → C**
7	↓	GBGtv4 Room2	GBGtv3 Room2	52 (65)	C (F)	**– 13**	**E → C**
8	↓	GBGtv4 Room1	GBGtv3 Room1	52 (66)	C (F)	**– 14**	**F → C**

Apartments 3rd & 4th floor



It must be noted that the project included only investigation of timber floor constructions, i.e. vertical tests of airborne and impact sound insulation, but not all the other tests requested for a complete classification of an apartment or building according to DS 490 [5]. These tests are for example sound insulation tests between rooms in other directions, façade sound insulation, service equipment noise and reverberation time in stairwells.

Results GBG 121, 2200 CPH N (construction year 1917).
Results due to new ceilings in the apartments:
The airborne sound insulation changed from Class D/E to C.
The impact sound insulation changed from Class F to C.
For all renovated constructions, Class C is obtained, which is the building code requirement for new-build.

Results KGV & TBA, 2300 CPH S (construction year 1937)
Results due to new ceilings in the apartments:
The airborne sound insulation changed from Class D/E to C.
The impact sound insulation changed from Class E/F to C.
For all renovated constructions, Class C is obtained, which is the building code requirement for new-build.

Summary of results for all eight renovated constructions
It was a positive surprise that all timber floor constructions renovated with a new ceiling obtained acoustic class C for both airborne and impact sound insulation. It was not on beforehand a goal to reach Class C, since it was expected that flanking transmission through the walls might reduce significantly the effect of the new ceilings. The goal was mainly to observe how far we could get.
The big question is of course whether similar results could be expected for other multi-storey housing with similar constructions? A wider project is necessary to investigate variants of the housing type E1 and also to get experience with type E2 (cf. Fig. 1) with completely different construction materials and with a lower room height, typically 250 cm.

Experiences from the project process
Starting, carrying out and completing all the activities related to the renovation project depended completely on the initiatives from and active collaboration with the housing association managers and the occupants. Thus, we are grateful to all those involved during the project period, which due to Covid-19 restrictions became longer and more complicated than expected on beforehand. However, even before the mounting of new ceilings, some occupants moved, since they had found other apartments and they had already suffered from neighbour noise for a long period and didn't know how and when the renovation would end. Moving seems to be a typical way to cope with the neighbour noise situation, cf. [3] and [4], but it requires a lot of resources in more ways (expenses, find a new place, moving).

4. ACOUSTIC REGULATIONS FOR NEW AND RENOVATED HOUSING

Sound insulation requirements for New-build in 35 countries in Europe are found in [1]. Specific requirements for renovated housing are often not clear or renovation not well-defined. The increasing building costs in general and the more recent challenge to use biogenic materials (to reduce building constructions' negative influence on climate changes) is a challenge. since the building industry has very little experience with use of lightweight materials to be applied and how to fulfil sound insulation requirements and at the same time reducing costs. Since stability of constructions and fire protection *must* be complied with, reducing other performances are considered. Consequently, acoustic requirements have got "critical" attention for more reasons, one of them being uncertainty about how to design with new materials (and fulfil requirements), another one the fact that sound insulation is not visible, and parts of the building industry consider sound insulation as luxury and not something needed for wellbeing or health.
However, typical reasons for acoustic regulations are *health* related. For example, in the current DIN 4109-1 [20], the introduction refers to health protection of occupants in housing, including also confidentiality during normal speech and protection against unreasonable disturbance. It is also stated that it *cannot* be expected that noise from outside or from neighbouring apartments will no longer be perceived or found annoying, even if the requirements laid down in the standard are met. For more information about the long story behind the current DIN 4109 series of standards and the importance for building acoustics in Germany, see [21].
In Denmark, the background and development until 1994 of acoustic regulations for housing are described in [22] and current regulations indicated in e.g. [23]. Again, as in Germany, the word health is predominant in the beginning of the regulations chapter. The situation is probably similar in many other countries.
Concerning disturbing neighbour noises, results from research projects agree that impact sound (footsteps) annoy most people, see e.g. [24],[25],[26]. Several disturbing neighbour noises are listed in [27], which also – based on a representative national survey – reports examples of potential adverse health effects of neighbour noise in multi-story housing. A strong association is found between self-reported neighbour noise annoyance and perceived stress, poor mental health, fatigue, sleeping problems, sleep quality (getting enough sleep to feel rested), see [27]. In fact the DIN 4109-1 introduction refers to the EU No 305/2011 [28] stating that construction works must be designed and built in such a way that noise perceived by the occupants or people nearby

is kept to a level that will not threaten their health and will allow them to sleep, rest and work in satisfactory conditions.
Public knowledge and awareness about how to describe acoustic performance for housing seems limited. Some countries have included acoustic quality test certificate layouts in their acoustic classification schemes, cf. DAGA 103, [29]-[30], and ÖNORM B 8115-5 [31]. However, the actual quantitative use of such certificates has not been investigated.
Some people believe that fulfilling regulations means that you cannot hear neighbours or at least not get disturbed. That is not the reality, cf. e.g. the DIN 4109-1 introduction. In Table 2 about DS 490, expected percentages of people finding classes good or very good and poor These statements help understanding the need for both higher classes, but also for lower classes, which are needed. to be able to classify before renovation and decide the gap to current regulations. ISO/TS 19488 [32] and some national schemes have lower classes, cf. [2].
Regulations are useful, but must be supported by enforcement and knowledge about design, planning, workmanship and inspection. The Danish regulations require documentation [33] uploaded as a condition for getting a permit for use. We don't have statistics for fulfilment in reality, but in several cases things go wrong. Four severe cases are described in [23]. Reasons are either lack of respect for regulations and/or lack of knowledge in parts of the whole process. Some mistakes have been well-known for decades. European collaboration about constructions, mistakes and enforcement should be strengthened to learn from other countries. Experiences from ~30 countries are found in the COST TU0901 e-books [34]-[35], but need follow-up due to many new materials and practices.

5. CONCLUSIONS AND PERSPECTIVES

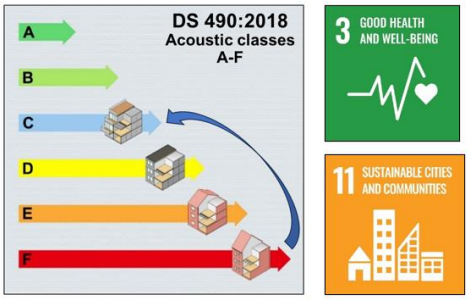
A case study about improvement of airborne and impact sound insulation R'_w and $L'_{n,w}$ for eight timber floor constructions in two old housing blocks 1917/1937 was conducted. New self-supporting ceilings were installed below the existing timber floors. The test results were very promising, since all results for the renovated constructions reached Class C, which is the requirement for New-build.
WHO and EEA have published several reports about influence of noise on health, e.g. [36]-[39]. Unfortunately, they don't deal with neighbour noise, since the focus is mainly traffic noise. However, they highlight sleep as a necessity for good health due to the restorative and consolidating effects of sleep. In the WHO-report [36], the health risks due to sleep disturbances are emphasized: "*Sleep disturbance is one of the most serious effects of environmental noise, causing both immediate effects and next-day and long-term effects on mental and cardiovascular health".* Sleep disturbance is also a typical neighbour noise problem, and it seems likely that the health risks are the same as for traffic noise.

Neighbour noise is potentially experienced 24h/7d, implying a need for more awareness, both for renovation of housing and New-build. In addition to the results of the case study, the following recommendations could be given:

- Regulations needed for renovated housing.
- Enforcement of regulations should always be respected to ensure fulfilment of requirements.
- Subjective (verbal) descriptions of classes could be included in more national acoustic classification schemes or in other ways to create more public awareness about the adverse influence of neighbour noise in housing and enhance consumer rights.
- Enhance consumer rights concerning access to acoustic quality. Occupants of dwellings should have "open access" to acoustic performance.
- Mandatory labelling [40] should be introduced as soon as possible, starting with New-build.
- Information about acoustic performance/class for dwellings should be mandatory in advertisements – as for energy.

Based on findings and quoted literature, it's hopefully obvious that sound insulation in housing is strongly related to health and quality of life. It's not just a question about comfort/luxury, but it's about protection from noise annoyances in everyday life. Proper regulations and enforcement would support healthy life for people and sustainable cities, cf. UN SDGs 3 and 11 [41].

Figure 5. The six acoustic classes A-F in DS 490 [5] and the improvement from F to C in the case study.



A strong recommendation is found in a Danish guideline from 1992: *"It should be ensured that renovation of homes also includes a decision on acoustic conditions, so that one is not subsequently left with a large housing stock that appears to have been thoroughly renovated, but is still acoustic slum."* The same reminder is unfortunately still highly relevant and included in the most recent version [7] from 2014.

6. ACKNOWLEDGMENTS

The author wants to thank the managers in the housing associations AKB and AAB and the occupants for great help and cooperation during the project period. Also, thanks to Rambøll for doing the field tests of sound insulation and being flexible about test dates.
Funding: The case study is a part of a project funded the Danish National Building Fund (Landsbyggefonden).

7. REFERENCES

[1] Rasmussen B. (2019) *Sound insulation between dwellings – Comparison of national requirements in Europe and interaction with acoustic classification schemes*. Proceedings of ICA 2019, 23rd International Congress on Acoustics, Sept. 2019, Aachen, Germany. Deutsche Gesellschaft für Akustik (DEGA e.V.). https://doi.org/10.18154/RWTH-CONV-239983.

[2] Rasmussen, B. (2022). *Acoustic classification of dwellings – A growing diversity of sound insulation descriptors in national schemes in Europe*. In *ICA 2022 Proceedings of the 24th International Congress on Acoustics* (Paper 981, pp. 199-206).

[3] Şentop Dümen A, Rasmussen B. (2025). Neighbour noise in multi-storey housing: Public experiences, attitudes and the need for acoustic labelling to ensure consumer protection. Build. Acoust. 2025;32(1):25-49. DOI: 10.1177/1351010X24131180

[4] Şentop Dümen A, Rasmussen B. (2025). Emotions elicited by neighbour noise and coping process: A social media research based on two newspaper articles. Build. Environ. (269) 2025,112432. DOI: 10.1016/j.buildenv.2024.112432

[5] DS 490:2018. *Lydklassifikation af boliger*. (Sound classification of dwellings). Danish Standards, Denmark.

[6] Rasmussen, B. *Encouraging acoustic renovation of housing in Denmark by extending acoustic classification with two lower classes E and F for old housing*. In J. Yong Jeon (Ed.), Proceedings of 2020 International Congress on Noise Control Engineering: INTER-NOISE 2020 The Korean Society of Noise and Vibration Engineering, Seoul, Korea. 2020.

[7] Rasmussen, B. & Petersen, C.M. (2014). *Lydisolering mellem boliger - eksisterende byggeri.* (Sound insulation between dwellings – existing housing). SBi guideline 243. Danish Building Research Institute, Aalborg University, Denmark.

[8] Rasmussen, B. & Hoffmeyer, D. (2015). *Lydisolation mellem boliger i etagebyggeri – Kortlægning og forbedringsmuligheder* (Sound insulation between dwellings in multi-storey housing - Mapping and possibilities for improvements). Copenhagen, SBi Report No. 2015:27.

[9] Rasmussen, B. (2021). *Lydisolering mod nabostøj i etageboligbyggeri - GOD PRAKSIS* (Sound insulation against neighbour noise in multi-storey housing – GOOD PRACTICE). BUILD, Aalborg University, Denmark. https://www.nabostoej.aau.dk

[10] Rasmussen, B., Petersen, C.M. & Hoffmeyer, D. (2011). *Lydisolering mellem boliger - nybyggeri* (Sound insulation between dwellings – new housing). SBi guideline 237. Danish Building Research Institute, Aalborg University, Denmark.

[11] Statistics Denmark (2025). https://www.statbank.dk/20064

[12] Rasmussen B & Ekholm O (2019). *Is noise annoyance from neighbours in multi-storey housing associated with fatigue and sleeping problems?* ICA 2019 proceedings, Paper 1521. DOI: 10.18154/RWTH-CONV-239984

[13] Jensen HAR, Rasmussen B, Ekholm O. (2019), *Neighbour noise annoyance is associated with various mental and physical health symptoms: Results from a nationwide study among individuals living in multi-storey housing*. BMC Public Health 2019;19,1-10. (1508). https://doi.org/10.1186/s12889-019-7893-8

[14] Grimwood, C.J. *Complaints about Poor Sound Insulation between Dwellings in England and Wales*. Applied Acoustics, Vol. 52, No. 3/4, pp. 211-223, 1997.

[15] EN ISO 16283, Acoustics – Measurement of sound insulation in buildings and of building elements – Part 1: Field measurements of airborne sound insulation between rooms, 2014. – Part 2: Field measurements of airborne sound insulation of facade elements and facades, 2020. – Part 3: Field measurements of impact sound insulation of building elements, 2016.

[16] EN ISO 717:2020, Acoustics – Rating of sound insulation in buildings and of buildings elements. – Part 1: Airborne sound insulation. – Part 2: Impact sound insulation.

[17] Rambøll (2022). Sound insulation field test reports (in Danish): Rambøll No. 1100048238. BUILD No. 130190-L1&L2. Sound insulation GBG 2200 CPH N before renovation (L1). Sound insulation GBG 2200 CPH N after renovation (L2).

[18] Rambøll (2022). Sound insulation field test reports (in Danish): Rambøll No. 1100048238. BUILD No. 130190-L3&L4. Sound insulation KGV&TBA 2300 S before renovation (L3). Sound insulation KGV&TBA 2300 S after renovation (L4).

[19] Afshari, A., Johnston, C. J., & Rasmussen, B. (2024). *Etablering af underlofter til forsøg med lyd- og røg/lugt-isolering mellem boliger* (in Danish). Department of the Built Environment, Aalborg University, BUILD Report 2024:13.

[20] DIN 4109-1:2018-01 Schallschutz im Hochbau – Teil 1 Mindestanforderungen (Sound insulation in buildings - Part 1: Minimum requirements).

[21] Martin Schneider & Heinz-Martin Fischer (2023). *German Standard DIN 4109 (Sound Insulation in Buildings) in the Context of Technical, Scientific and Social Developments*. Proceedings of Forum Acusticum 2023 : 10th Convention of EAA (pp. 2849-2856). European Acoustics Association - EAA. https://doi.org/10.61782/fa.2023.0065

[22] Rasmussen, B. & Rindel, J. H. (1994). *Lydforhold i boliger - 'State-of-the-art'* (Acoustic conditions in dwellings - 'State-of-the-art'). Bygge- og Boligstyrelsen, Copenhagen, Denmark. https://vbn.aau.dk/en/publications/lydforhold-i-boliger-state-of-the-art

[23] Rasmussen, B., & Petersen, C. M. (2024). *Compliance procedures for sound insulation between dwellings in new housing – Rules according to Danish regulations & Experiences from practice*. In T. Lokki (Ed.), *Proceedings of the Baltic-Nordic Acoustics Meeting 2024* Article 56.

[24] Fredrik Ljunggren, Christian Simmons (2022). Correlation between sound insulation and occupants' perception – Proposal of alternative single number rating of impact sound, Part III. Applied Acoustics, 197: 108955. DOI: 10.1016/j.apacoust.2022.108955

[25] DIBK (2016), *Lydforhold i boliger. Evaluering av byggtekniske krav til lydforhold*, (In Norwegian). Doc. 127762-RIA-RAP-001. National Office of Building Technology and Administration, Oslo, Norway. https://www.dibk.no/globalassets/byggeregler/tek10-til-tek17/rapporter/lydforhold-i-boliger_samlerapport_sintef_toi_multiconsult_mars-2016.pdf

[26] Løvstad A, Rindel JH, Høsøien CO, Milford I, Klaebo R. (2017). *Perceived sound quality in dwellings in Norway.* 12th ICBEN Congress on Noise as a Public Health Problem, Zürich. https://www.icben.org/2017/ICBEN%202017%20Papers/SubjectArea06_L%C3%B8vstad_0619_3814.pdf

[27] Rasmussen, B., & Ekholm, O. (2021). *Neighbour noise in multi-storey housing - Annoyance and potential health effects*. Proceedings of INTER-NOISE 2021 (Vol. 263(4), pp. 2783-2792). Article #2228 Institute of Noise Control Engineering. https://doi.org/10.3397/IN-2021-2228.

[28] EU (2011). Regulation (EU) No 305/2011 of the European parliament and of the council. Harmonised conditions for the marketing of construction products. https://eur-lex.europa.eu/legal-content/EN/TXT/PDF/?uri=CELEX:32011R0305

[29] DEGA-Richtlinie 103-1:2024-09. Schallschutz im Wohnungsbau - Teil 1: Schallschutzklassen und erhöhter Schallschutz. DEGA, Berlin. https://www.dega-akustik.de/fileadmin/dega-akustik.de/publikationen/DEGA-Richtlinie_103-1.pdf

[30] Entwurf DEGA-Richtlinie 103-2:2024-09. Schallschutz im Wohnungs--bau Teil 2: Schallschutzausweis. DEGA, Berlin. https://www.dega-akustik.de/fileadmin/dega-akustik.de/publikationen/DEGA-Richtlinie_103-2_2024-09_Entwurf.pdf

[31] ÖNORM B 8115-5:2021, *Schallschutz und Raumakustik im Hochbau - Teil 5: Klassifizierung.* (Sound insulation and room acoustics in building construction – Part 5: Classification). ÖNORM, Austria.

[32] ISO/TS 19488:2021. Acoustic classification of dwellings. ISO, Geneva, Switzerland. https://www.iso.org/standard/77742.html

[33] Danish Authority of Social Services and Housing (2023). *Dokumentation af bygningsreglementets tekniske bestemmelser i forbindelse med færdigmelding af byggeriet* (Documentation of the building regulations' technical provisions in connection with the completion notification of the building). https://bygningsreglementet.dk/Administrative-bestemmelser/BRV/Dokumentationsvejledning.

[34] Rasmussen B. and Machimbarrena M. (editors), *COST Action TU0901 – Building acoustics throughout Europe. Volume 1: Towards a common framework in building acoustics throughout Europe*. DiScript Preimpresion. 2014. http://www.costtu0901.eu/tu0901-e-books.html.

[35] Rasmussen, B., Machimbarrena, M., & Fausti, P. (red.) (2014). *COST Action TU0901 – Building acoustics throughout Europe. Volume 2: Housing and construction types country by country*. DiScript Preimpresion, S. L. http://www.costtu0901.eu/tu0901-e-books.html

[36] WHO (2009). *Night noise guidelines for Europe.* World Health Organization Regional Office for Europe, Copenhagen. https://iris.who.int/handle/10665/326486

[37] European Environment Agency. Good practice guide on noise exposure and potential health effects. EEA Technical report No.11/2010. https://www.eea.europa.eu/publications/good-practice-guide-on-noise

[38] WHO (2018). *Environmental noise guidelines for the European Region.* Copenhagen: World Health Organization. http://www.euro.who.int/en/publications/abstracts/environmental-noise-guidelines-for-the-european-region-2018

[39] European Environment Agency (2020). *Noise in Europe 2020.* EEA Report No. 22/2019. Luxembourg: Publications Office of the European Union, 2020. https://doi.org/10.2800/686249

[40] Rasmussen, B. (2024). *Could mandatory open access to sound insulation performance in housing promote "visibility" of acoustic quality?* Internoise 2024 Proceedings, 10238-10245. Nantes. INCE. DOI: 10.3397/IN_2024_4470.x

[41] UN SDG goals (2025). SDGs 3 and No. 11, "Good health and wellbeing" and "Sustainable cities and communities". Links: https://sdgs.un.org/goals, SDGs 3 & 11.

DOI: 10.61782/fa.2025.0075

FORUM ACUSTICUM EURONOISE 2025

ACOUSTIC INSULATION IN PLASTERBOARD SYSTEMS WITH MINERAL WOOL

Paula Belenguer Rubio[1] **Penélope González de la Peña**[2]
[1] Técnico Saint-Gobain CITAV
[2] Responsable Saint-Gobain CITAV
[3] Saint-Gobain España, Príncipe de Vergara, 132, 28002 Madrid, España

ABSTRACT

One of the most important features in plasterboard systems with mineral wool (MW) is the acoustic insulation they provide between different rooms, with minimal space and weight requirements.

When designing this type of system, there are several factors that can influence the acoustic insulation: the number and type of boards, the spacing between the profiles, the bracing of the structure, the thickness of the system... But are they all equally important? What is the influence of the density of mineral wool in this type of system?

The paper analyses the acoustic behavior of plasterboard systems with mineral wool, and the influence of system parameters on acoustic insulation, in order to help designers to configure systems to reduce the noise between neighbors through acoustic retrofitting in residential buildings.

Keywords: *plasterboard, mineral wool, acoustic insulation,*

1. INTRODUCTION

Acoustic insulation is nowadays one of the most important features in today's building systems. Acoustic independence between rooms is one of the main requirements of internal partitions in order to guarantee the well-being of all users.

2. LIGHT VS HEAVY CONSTRUCTION

It is important to distinguish between massive and light construction systems. First ones mentioned consist of a massive structure of walls, and second ones mentioned consist of a structure of pillars and beams, including light façade systems, wood and glass structures, etc.

Massive systems work with the mass of the element. The thicker the construction element, the better acoustic insulation. However, the stiffness of the material implies a variation in the critical frequency.

Nevertheless, in lightweight systems, particularly in gypsum plasterboard (GP) partition systems, consisting of a plasterboard layer, followed by a cavity and closed again by another plasterboard layer, it is the width of the cavity that has the greater impact on the increase in acoustic insulation, as well as the mass of the plasterboard layers.

Paula Belenguer Rubio: *paula.belenguer@saint-gobain.com*
Copyright: *©2025 First author et al. This is an open-access article distributed under the terms of the Creative Commons Attribution 3.0 Unported License, which permits unrestricted use, distribution, and reproduction in any medium, provided the original author and source are credited.**

3. OPERATION OF LIGHT WEIGHT SYSTEMS

This performance is due to the fact that these systems operate as a mass-spring-mass system. The graph shows three different zones (Figure 1):

- **First zone**: The two "masses" oscillate in phase, and behave as a single-layer system.
- **Second zone**: The "masses" oscillate at the highest amplitude, where the resonance frequency is perceived.
- **Third zone**: The two "masses" oscillate independently, where the isolation is greater than in a single-layer wall.

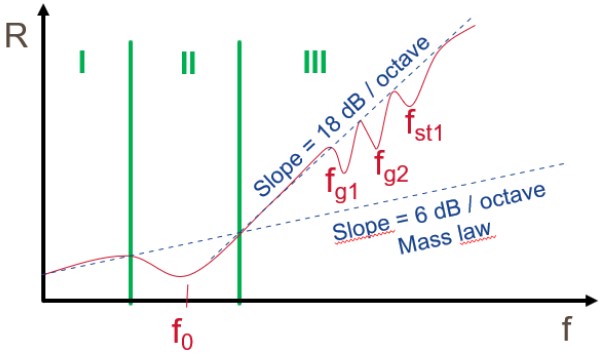


Figure 1. Operation of plasterboard systems

4. PARAMETERS INFLUENCING THE PLASTERBOARD SYSTEMS

It is also possible to optimize the acoustic performance of these systems by adding or modifying elements of their composition.

There are several parameters that influence the acoustic insulation performance of a plasterboard system:

- Insulation in the cavity and the thickness of the insulation, usually mineral wool (MW).
- Cavity width.
- Number of plasterboards.
- Distance between profiles.
- Type of profiles.
- Bracing of the structures.
- Total thickness of the system.
- Installation conditions.

However, there are aspects that are sometimes considered to be influential but are not, such as the density of the mineral wool.

5. CAVITY INSULATION AND MINERAL WOOL THICKNESS

Based on tests on the same system, 2 Placo® BA15 + M150 + 2 Placo® BA15 with 600 mm modulation between profiles, an increase in acoustic insulation can be perceived (Figure 2) by increasing the thickness of the mineral wool in the cavity:

- 0 mm MW: 47 dBA. (Figure 3)
- 65 mm MW: 52 dBA. (Figure 4)
- 150 mm MW: 53 dBA. (Figure 5)

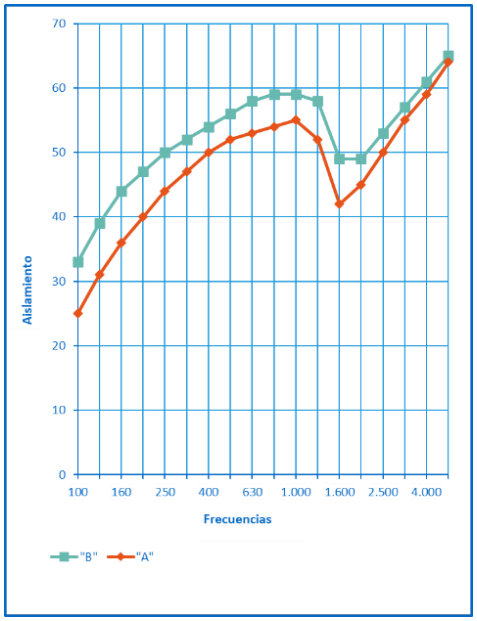


Figure 2. Comparison between systems:

2 Placo® BA15 + M150 (MW 0 mm) + 2 Placo® BA15 with 600 mm modulation (sample A)
2 Placo® BA15 + M150 (MW 150 mm) + 2 Placo® BA15 with 600 mm modulation (sample B)

frec. (Hz(	R(dB)	R(dB)
50	12	
63	8	11
80	17	
100	25	
125	31	28
160	36	
200	40	
250	44	43
315	47	
400	50	
500	52	52
630	53	
800	54	
1000	55	54
1250	52	
1600	42	
2000	45	45
2500	50	
3150	55	
4000	59	58
5000	64	

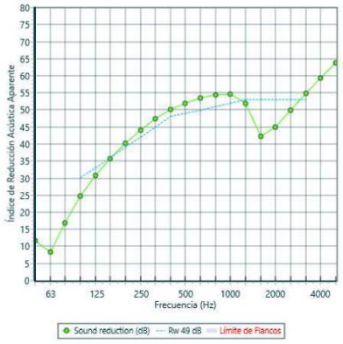


Figure 3. Simulation results from system 2 Placo® BA15 + M150 (MW 0 mm) + 2 Placo® BA15

frec. (Hz(	R(dB)	R(dB)
50	11	
63	14	14
80	23	
100	31	
125	37	34
160	42	
200	46	
250	49	48
315	52	
400	54	
500	56	56
630	58	
800	59	
1000	59	59
1250	58	
1600	49	
2000	49	50
2500	53	
3150	57	
4000	61	60
5000	65	

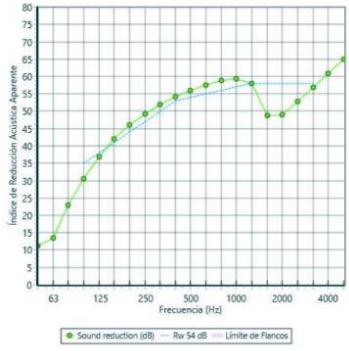


Figure 4. Simulation results from system 2 Placo® BA15 + M150 (MW 65 mm) + 2 Placo® BA15

frec. (Hz(	R(dB)	R(dB)
50	12	
63	15	15
80	24	
100	33	
125	39	36
160	44	
200	47	
250	50	50
315	52	
400	54	
500	56	56
630	58	
800	59	
1000	59	59
1250	58	
1600	49	
2000	49	50
2500	53	
3150	57	
4000	61	60
5000	65	

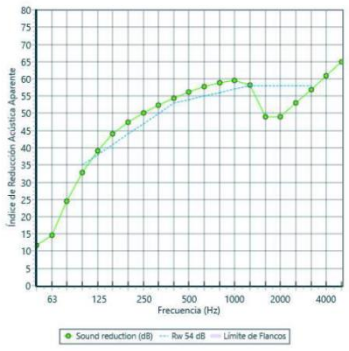


Figure 5. Simulation results from system 2 Placo® BA15 + M150 (MW 150 mm) + 2 Placo® BA15

Furthermore, it is observed that the inclusion of insulation in the plasterboard system cavity, with an air flow resistance of at least 5 kPa·s/m^2, achieves optimization of this system, as the resonance frequency is outside the range of interest for these systems, as well as reducing the loss of coincidence frequency in the overall computation of the system.

6. CAVITY WIDTH

Enlarging the cavity allows the thickness of the internal MW to be increased, giving the following results (Figure 6):

- M48 (MW): 47 dBA. (Figure 7)
- M70 (MW): 50 dBA. (Figure 8)
- M100 (MW): 52 dBA. (Figure 9)

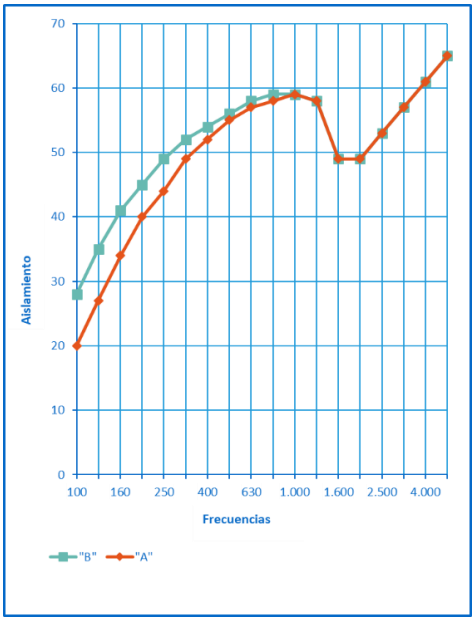


Figure 6. Comparison between systems:

2 Placo® BA15 + M48 (MW) + 2 Placo® BA15 with 600 mm modulation (sample A)
2 Placo® BA15 + M100 (MW) + 2 Placo® BA15 with 600 mm modulation (sample B)

Figure 7. Simulation results from system 2 Placo® BA15 + M48 (MW) + 2 Placo® BA15

frec. (Hz(	R(dB)	R(dB)
50	20	
63	14	16
80	16	
100	24	
125	31	28
160	38	
200	43	
250	47	46
315	50	
400	53	
500	55	55
630	57	
800	59	
1000	59	59
1250	58	
1600	49	
2000	49	50
2500	53	
3150	57	
4000	61	60
5000	65	

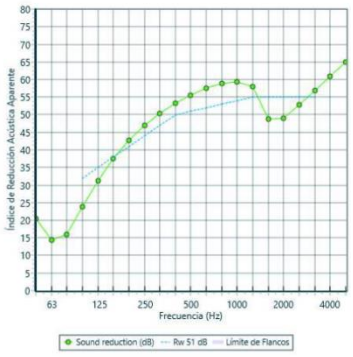


Figure 8. Simulation results from system 2 Placo® BA15 + M70 (MW) + 2 Placo® BA15

frec. (Hz(	R(dB)	R(dB)
50	15	
63	13	15
80	19	
100	28	
125	35	32
160	41	
200	45	
250	49	48
315	52	
400	54	
500	56	56
630	58	
800	59	
1000	59	59
1250	58	
1600	49	
2000	49	50
2500	53	
3150	57	
4000	61	60
5000	65	

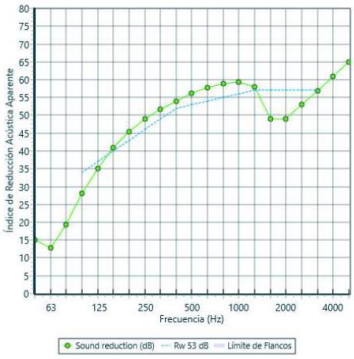
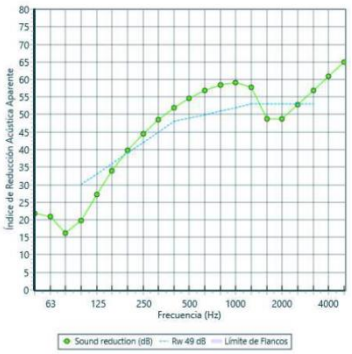


Figure 9. Simulation results from system 2 Placo® BA15 + M100 (MW) + 2 Placo® BA15

For conventional systems up to about 100 mm cavity thickness, the insulation effect is approximately a 1 dB increase for every 1 cm of mineral wool included (although it can be seen that this is not linear).

frec. (Hz(	R(dB)	R(dB)
50	22	
63	21	19
80	16	
100	20	
125	27	24
160	34	
200	40	
250	44	43
315	49	
400	52	
500	55	54
630	57	
800	58	
1000	59	58
1250	58	
1600	49	
2000	49	50
2500	53	
3150	57	
4000	61	60
5000	65	



7. MINERAL WOOL DENSITY

One characteristic of mineral wool that is often confusing is the influence of mineral wool density on plasterboard systems.

The Spanish standard UNE-EN 13162:2012+A1:2015 “Thermal insulation products for building applications” does not consider density as a performance characteristic for products manufactured under these conditions.

8. NUMBER OF PLASTERBOARDS

In self-supporting plasterboard framing systems, an increase in the surface mass of the mass-spring-mass system implies an improvement in the acoustic insulation performance. Therefore, increasing the number of boards will provide better acoustic insulation results. (Figure 10) (Figure 11) (Figure 7).

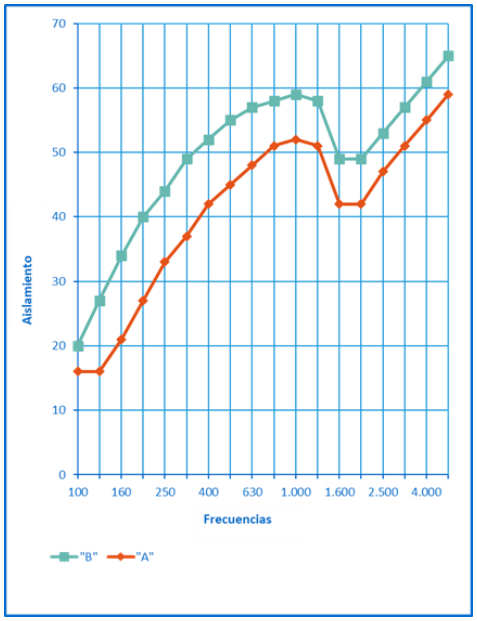


Figure 10. Comparison between systems:

Placo® BA15 + M48 (MW) + Placo® BA15 with 600 mm modulation (sample A)
2 Placo® BA15 + M48 (MW) + 2 Placo® BA15 with 600 mm modulation (sample B)

frec. (Hz(	R(dB)	R(dB)
50	18	
63	18	18
80	18	
100	16	
125	16	17
160	21	
200	27	
250	33	31
315	37	
400	42	
500	45	44
630	48	
800	51	
1000	52	51
1250	51	
1600	42	
2000	42	43
2500	47	
3150	51	
4000	55	54
5000	59	

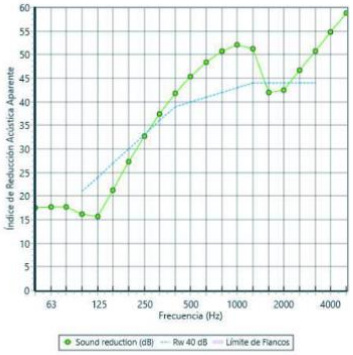


Figure 11. Simulation results from Placo® system BA15 + M48 (MW) + Placo® BA15 (38 dBA)

The increase in boards mass increases the overall acoustic insulation value by approximately 9 dBA in a plasterboard partition system by adding one layer of plasterboard on each side of the system.

9. TYPE OF PLASTERBOARDS

There are boards with improved acoustic performance. In the case of Saint-Gobain, changing from a plasterboard Placo® BA to a plasterboard Placo® PPH allows greater acoustic insulation to be obtained, specifically of 3 dBA in the solution tested (Figure 12) (Figure 13) (Figure 14).

Therefore, there may be situations in the project where this change could be an important aspect.

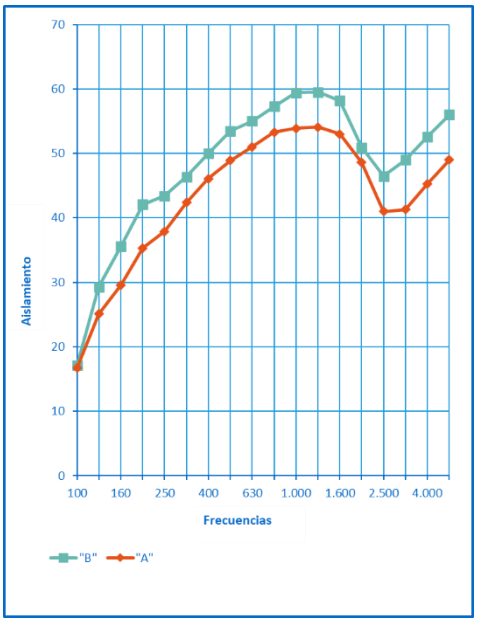
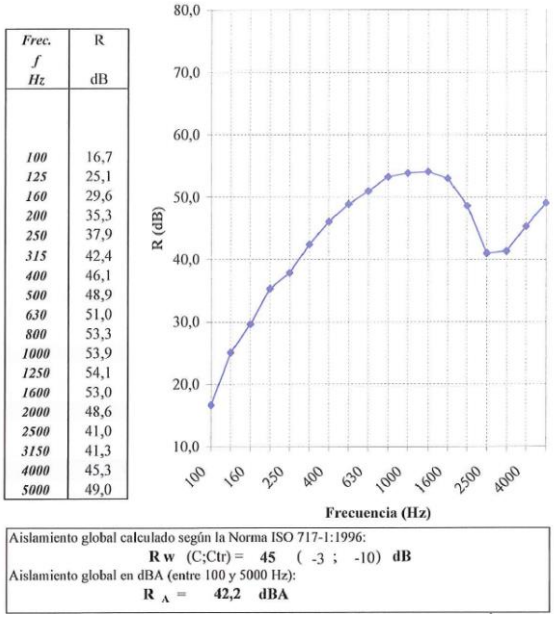


Figure 12. Comparison between systems:

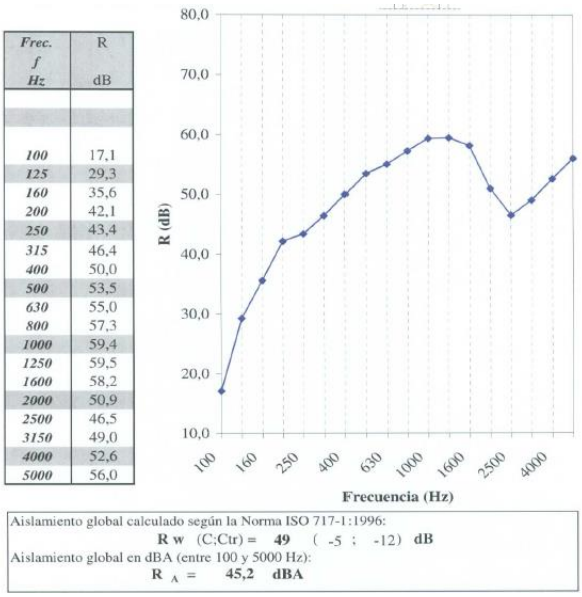
Placo® BA15 + M48 (MW) + Placo® BA15 with 600 mm modulation (sample A)
Placo® PPH15 + M48 (MW) + Placo® PPH15 with 600 mm modulation (sample B)



Frec. f Hz	R dB
100	16,7
125	25,1
160	29,6
200	35,3
250	37,9
315	42,4
400	46,1
500	48,9
630	51,0
800	53,3
1000	53,9
1250	54,1
1600	53,0
2000	48,6
2500	41,0
3150	41,3
4000	45,3
5000	49,0

Aislamiento global calculado según la Norma ISO 717-1:1996:
R w (C;Ctr) = 45 (-3 ; -10) dB
Aislamiento global en dBA (entre 100 y 5000 Hz):
R_A = 42,2 dBA

Figure 13. Test results from Placo® system BA15 + M48 (MW) + Placo® BA15 (CTA 116/07/AER-1)



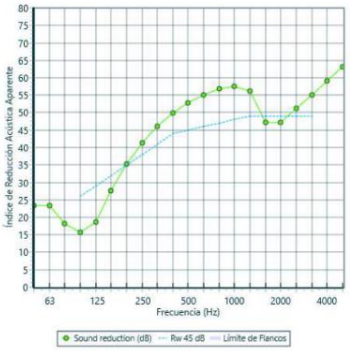
Frec. f Hz	R dB
100	17,1
125	29,3
160	35,6
200	42,1
250	43,4
315	46,4
400	50,0
500	53,5
630	55,0
800	57,3
1000	59,4
1250	59,5
1600	58,2
2000	50,9
2500	46,5
3150	49,0
4000	52,6
5000	56,0

Aislamiento global calculado según la Norma ISO 717-1:1996:
R w (C;Ctr) = 49 (-5 ; -12) dB
Aislamiento global en dBA (entre 100 y 5000 Hz):
R_A = 45,2 dBA

Figure 14. Test results from Placo® system PPH15 + M48 (MW) + Placo® PPH15 (CTA 213/09/AER)

The Placo® BA15 has a density of 653 kg/m^3, while the Placo® PPH15 has a density of 966 kg/m^3. The increase in the plasterboard density also means an improvement in acoustic insulation, so the type of board used can improve the results.

frec. (Hz(	R(dB)	R(dB)
50	23	
63	23	21
80	18	
100	16	
125	19	19
160	28	
200	35	
250	41	39
315	46	
400	50	
500	53	52
630	55	
800	57	
1000	57	57
1250	56	
1600	47	
2000	47	48
2500	51	
3150	55	
4000	59	58
5000	63	



10. PROFILE SPACING

A profile spacing of less than 500 mm can reduce the acoustic insulation of the system by 4-5 dB. In Spain, due to the dimensions of the GP, the profile spacing is set at 400 mm and 600 mm, and a decrease in acoustic insulation is observed in structures with modulation every 400 mm (Figure 15) (Figure 16) (Figure 7).

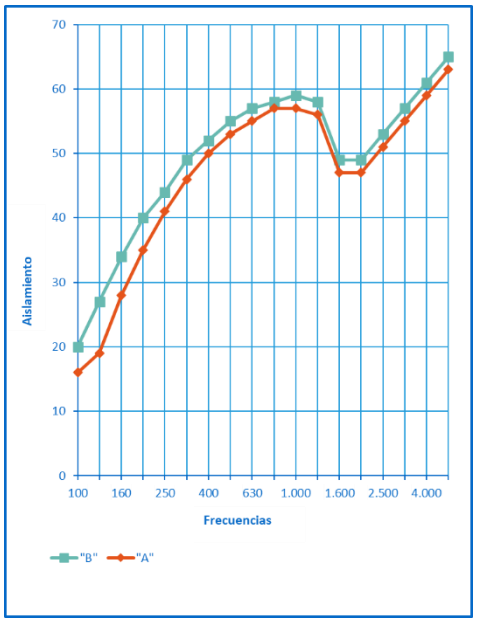


Figure 15. Comparison between systems:

2 Placo® BA15 + M48 (MW) + 2 Placo® BA15 with 400 mm modulation (sample A)

2 Placo® BA15 + M48 (MW) + 2 Placo® BA15 with 600 mm modulation (sample B)

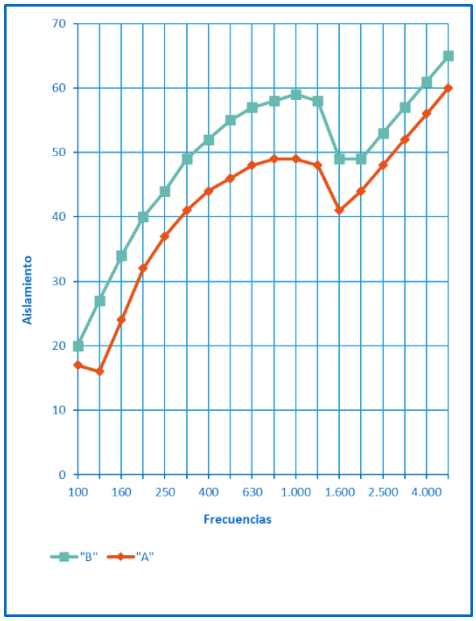


Figure 16. Simulation results from system 2 Placo® BA15 + M48 (MW) + 2 Placo® BA15 with 400 mm modulation (42 dBA)

Approximation between profiles provides more stable systems that achieve greater mechanical heights, but the system is stiffer, reducing the acoustic performance by approximately 5 dBA.

11. TYPE OF PROFILES

If we compare two systems that change the composition of their profiles, one based on the metal profiles of the plasterboard partition and wall systems, and the other based on wooden profiles, we obtain the following results (Figure 17) (Figure 18) (Figure 7):

Figure 17. Comparison between systems:

2 Placo® BA15 + 48 mm wooden profile (MW) + 2 Placo® BA15 with 600 mm modulation (sample A)
2 Placo® BA15 + M48 (MW) + 2 Placo® BA15 with 600 mm modulation (sample B)

frec. (Hz(	R(dB)	R(dB)
50	23	
63	24	22
80	19	
100	17	
125	16	18
160	24	
200	32	
250	37	35
315	41	
400	44	
500	46	45
630	48	
800	49	
1000	49	49
1250	48	
1600	41	
2000	44	43
2500	48	
3150	52	
4000	56	55
5000	60	

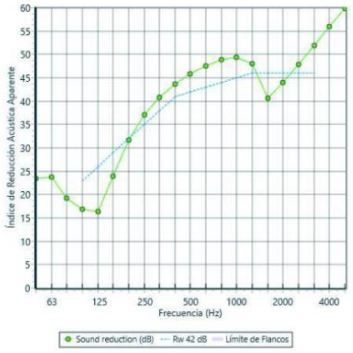


Figure 18. Simulation results from system 2 Placo® BA15 + 48 mm wooden structure (MW) + 2 Placo® BA15 with 400 mm modulation (40 dBA)

The metal profiles of plasterboard systems provide better acoustic insulation than wooden profiles, giving an improvement of up to 8 dBA. It also moves the resonance

frequency to a lower frequency, out of the range of interest.

12. BRACING OF STRUCTURES

In double-structured systems, the use of unbraced structures can lead to a significant improvement in acoustic insulation (Figure 19) (Figure 20) (Figure 21).

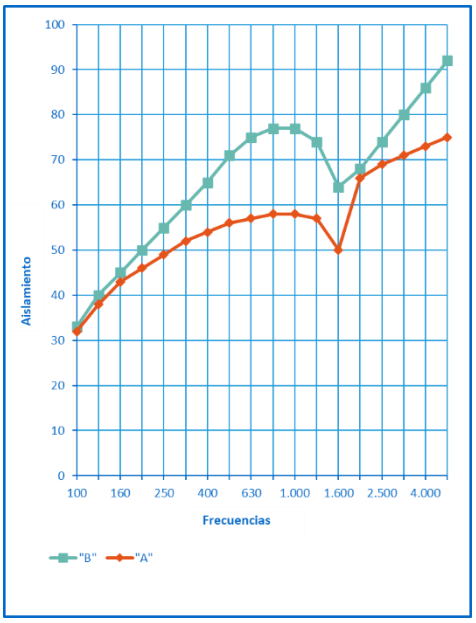


Figure 19. Comparison between systems:

2 Placo® BA15 + M48 (MW) + M48 (MW) + 2 Placo® BA15 with braced structures (sample A)
2 Placo® BA15 + M48 (MW) + M48 (MW) + 2 Placo® BA15 with non-braced structures (sample B)

frec. (Hz(	R(dB)	R(dB)
50	18	
63	16	18
80	24	
100	32	
125	38	35
160	43	
200	46	
250	49	49
315	52	
400	54	
500	56	55
630	57	
800	58	
1000	58	58
1250	57	
1600	50	
2000	66	55
2500	69	
3150	71	
4000	73	72
5000	75	

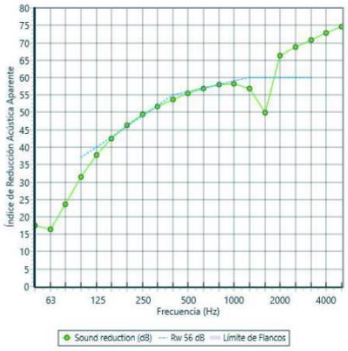


Figure 20. Simulation results from system 2 Placo® BA15 + M48 (MW) + M48 (MW) + 2 Placo® BA15 with braced structures (55 dBA)

frec. (Hz(	R(dB)	R(dB)
50	15	
63	19	18
80	26	
100	33	
125	40	37
160	45	
200	50	
250	55	54
315	60	
400	65	
500	71	68
630	75	
800	77	
1000	77	76
1250	74	
1600	64	
2000	68	67
2500	74	
3150	80	
4000	86	83
5000	92	

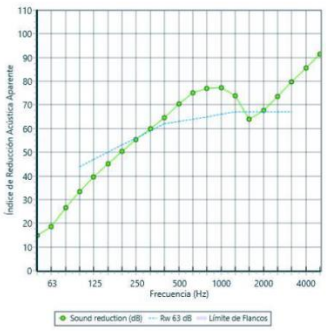


Figure 21. Simulation results from system 2 Placo® BA15 + M48 (MW) + M48 (MW) + 2 Placo® BA15 with non-braced structures (60 dBA)

Bracing between structures provides systems that reach a higher mechanical height, but as in the previous point, the system is stiffened, reducing the acoustic performance. The acoustic insulation can be reduced by approximately 5 dBA.

13. TOTAL THICKNESS OF THE SYSTEM

On the basis of each of the characteristics studied, it can be seen that increasing the overall thickness of the system brings with it a number of aspects that generally improve the acoustic performance of the system:

- Cavity width and thickness of MW in the cavity: It is observed that in systems with cavity widths up to 100 mm, there is an increase of 1 dB for every 1 cm of MW included. In addition, the inclusion of MW in the cavity means that the

resonance frequency is outside the range of interest for these systems, as well as the coincidence frequency for both layers. The difference between including or not including MW in the cavity can make a difference of about 8 dB.

- Number of boards: Increasing the plasterboard mass increases the overall sound insulation value of a plasterboard partition system by approximately 9 dBA by adding one layer of board on each side of the system.

14. INSTALLATION

Finally, it is important to mention that the quality of the construction will have a great influence on the effectiveness of the acoustic insulation of the solution, with differences ranging from 2 to 15 dB.

Acoustic bridges must be taken into account, and it is recommended that an elastic band be installed in the junction of the profiles with the support structure, as well as at the junction between the systems, in order to avoid the transmission of noise between rooms.

15. CONCLUSION

As a manufacturer of plasterboard systems, we can specify the following points based on the acoustic requirements of the project:

- Fill the air cavity of the systems with mineral wool.
- Increase the number of boards to achieve better acoustic performance.
- Use the appropriate board for improved acoustic performance.
- Use double non-braced systems for partition walls between apartments, hotel rooms, etc.
- Pay attention to the performance characteristics of each product and the complete system in each case.

16. REFERENCES

[1] Acoustic simulations made by INSUL.
[2] UNE 102043 "Montaje de los sistemas constructivos con placas de yeso laminado (PYL): Tabiques, trasdosados y techos. Definiciones, aplicaciones y recomendaciones".
[3] UNE-EN 13162:2012+A1:2015 “Thermal insulation products for building applications”

DOI: 10.61782/fa.2025.0481

FORUM ACUSTICUM EURONOISE 2025

IN-SITU EVALUATION OF CONCRETE INTERLAYER ADHESION BY VIBRATION IN GARAJE FLOORS

David Caballol Bartolomé[1*] **Álvaro Pérez Raposo** [1] **Francisco Gil Carrillo**[2]

[1] Architectural Acoustics Research Group, Universidad Politécnica de Madrid, Spain.
[2] Department of Architectural Constructions and Assessment, Universidad Politécnica de Madrid, Spain

ABSTRACT

A new practice in the construction of garage floors of residential and office buildings in Spain, is to build the concrete slab in two steps: one thick layer at the beginning of the work (≈ 12-35 cm) and a second thin layer (≈ 8 cm) at the end of it. This procedure creates a cold joint between the two layers that may eventually get loose or even split and produce noise when driving over it.
We have designed a nondestructive test to perform in situ measurements to determine the level of fixation of two layers of any concrete slab that causes noise emission problems.
The test is independent of the characteristics of the slab thanks to statistical tools applied to the data.
Vibration induced by a source, the passage of a car, was measured at several locations, with loose and well-fixed layers. The vibration was recorded with a vibrometer. The test can be applied, and the results are compatible with the known state of the slab: we obtain 77.0% sensitivity and 54.5% specificity, while there are only 1.0% false positives and no false negatives. The only drawback of the test is its high number of undecidable cases, which amounts to 24.1%.

Keywords: *Concrete layers bond, Non-destructive test, Accelerometer, In-situ test.*

[*] ***Corresponding author***: *david.caballol@upm.es.*
Copyright: *©2025 First author et al. This is an open-access article distributed under the terms of the Creative Commons Attribution 3.0 Unported License, which permits unrestricted use, distribution, and reproduction in any medium, provided the original author and source are credited.*

1. INTRODUCTION

Traditionally, basement floors were constructed as a single layer concrete slab, which was then polished. However, the work done on this slab often ruined the final construction treatment, which had to be repaired at the end. As a time-saving alternative, the basement floors are constructed in two layers. A first thick layer is made at the beginning, which is the support for all the works during the construction. A second thin layer is applied a few days before the inauguration of the building in order to finish the garage floor without deterioration.
However, this solution has a disadvantage in the form of a cold joint between the concrete layers. Because they are applied at different times and work has been done on top of the first layer, dirt or other debris can accumulate on top of it and weaken the joint with the second layer.
Numerous studies have been conducted about pavement health and vibration [1-6]; however, these studies do not align with the particular problem described above.
We evaluate this problem by performing a non-destructive test on the slab using vibration data.

2. METHODOLOGY

Two experimental procedures were carried out in the study, each designed for a specific purpose in relation to the evaluation of adhesion between concrete layers through vibration measurement:

2.1 Laboratory Measurements:

This first procedure is focused on evaluating the ability of vibration measurements to discern the bond state between two layers of material (concrete and MDF).

In a controlled laboratory environment, based on the facilities described in Annex A of ISO 16251-1 [7], an experimental setup was created where a concrete slab was used as the bottom layer and an MDF (medium density fiberboard) as the top layer. The two layers were bonded together with a material that simulates adhesive (gypsum), and different levels of fixation were varied between them. Vibrations were generated using a standard tapping machine and measured with a vibrometer.
This approach provided consistent and repeatable data, demonstrating that it was possible to detect differences in bonding between the layers depending on the percentage of surface area covered by the adhesive.

2.2 In-situ measurements:

The study measures vibrations in a real building's basement floors. The building, located in Madrid, was constructed between 2016 and 2017 and delivered in May 2017. A few months after the building's completion, variable noises were noticed coming from the garage floor when vehicles passed. All procedures were carried out in accordance with ISO 2631 [8].
To ensure reality's representativeness, measurements were obtained as a light vehicle (Land Rover Discovery Model HSE Sd6) traversed the pavement. The 2249-kilogram vehicle was driven at 20 kilometers per hour (the garage's maximum speed) and vibration levels were measured. The driver started moving from a certain distance to ensure the correct speed at the moment of passing in front of the accelerometer. Data acquisition began when the vehicle started moving and ended when it was far enough away for the vibration to stabilize. A time-dependent vibration history between 1 Hz and 80 Hz was obtained for each pass. The measurements were obtained using a triaxial accelerometer attached to the pavement with a wax disc. The accelerometer was positioned to allow the vehicle to pass through the central roadway. The vibrations were measured in three directions: *Z* axis, vertical; *Y* axis, parallel to the line of pillars inside the garage; and *X* axis, perpendicular to the previous one. The accelerometer was positioned 1.5 m from the nearest parking space. The accelerometer was always positioned away from cracks or defects in the pavement.
The following conditions were fulfilled in all cases:

- The standard vehicle moved forward at data acquisition, staying >1.4 m from the accelerometer.
- Vibration measurements were taken at least 60 seconds apart.
- Vehicles must be in motion forward at the time of data acquisition. Maintain 1.4 meters from the accelerometer and ensure parallel alignment with the Y-axis.
- At least 60 seconds separated each measurement to mitigate the impact of prior vibrations.
- If there was a small unevenness in the pavement that would
cause the vehicle to ‘‘jump’’ even slightly, the measurement was
discarded.
- Measurements were excluded if the pattern vehicle made contact with a manhole or drain.
- At measurement time, the pattern vehicle was the sole vehicle in the garage.

The operator stayed 1.5 meters from the accelerometer. This allowed them to qualitatively classify the vibrations by the sensation under their feet and the noise generated by movement of the vehicle.
The procedure was replicated 108 times at locations across the floors -2 and -1, so that together they represent a complete study of their surface.

3. DATA ANALYSIS AND RESULTS

3.1 Laboratory results

In the laboratory, the acceleration in the X, Y, and Z axes was measured as the response variables.
The acceleration values for a duration of one second are integrated into a single value by means of the r.m.s., resulting in a value for each second.
The vibration magnitude of the tapping machine is approximately 10^{-4} m²/s² when it is deactivated, and it fluctuates between 10^{-2} and 1 m²/s² when it is activated. This indicates that the ambient vibration is negligible in comparison to that induced by the tapping machine.

Since the vibration source is stationary, we can reduce each measurement to a unique value representing an average of the vibration. We have taken the r.m.s. value of each one. In the following we study this single value of each measurement in order to find out the role of the other variables: location of the tapping machine, location of the accelerometer and percentage of fixed surface area (figure 1).

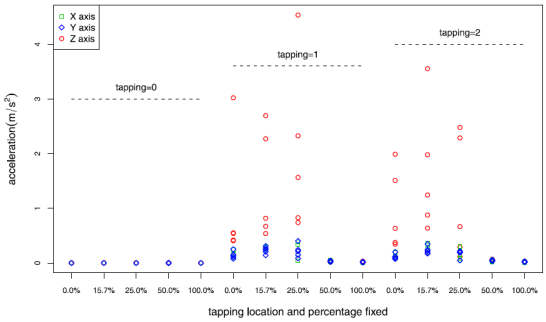


Figure 1. The r.m.s. value of each measurement in the laboratory.

In figure 1, we can see that there is a significant difference in the acceleration values in the Z axis versus those in either X or Y axes, which are significantly lower.
Moving forward, we will exclusively measure acceleration in the Z-axis because it is more sensitive to the effects of the tapping machine.
We can also observe that the percentage of fixed surface area plays an important role when it gets to 50% or higher, in which case the vibration is about 2 orders of magnitude lower than percentages of 25% or below. However, in this figure we do not appreciate differences among 0%, 15.7% or 25% of fixed surface area, nor do we appreciate differences among 50% and 100%.
Given the wide range of acceleration values, it is advisable to use the logarithmic scale for these measurements. To ensure consistency and accuracy in our analysis, it is necessary to establish a reference point for the data. Rather than selecting a single reference value for all data points, we have opted to utilize an average value as a reference point. This approach enables a direct comparison of results from laboratory tests with those obtained from measurements in actual buildings.

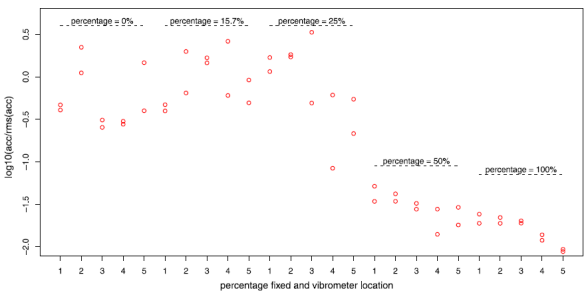


Figure 2. The r.m.s. value of the acceleration in the *Z* direction of measurements in the laboratory.

The results suggest that the recorded acceleration can distinguish between the low percentages (0, 15.7 and 25%) and the high ones (50 and 100%) but not among each of these groups

3.2 Test proposal

We propose a test to classify the degree of fixation between the two layers using vibrational data from an accelerometer. The test will categorize fixation as either low or high. The test will proceed as follows:

- Measure the vertical vibration induced, for instance, by the passage of a car, on the concrete slab. A sample of measurements in different locations is needed, both in locations suspected of abnormal fixation and locations suspected of good fixation between the layers

- Reduce the measurement at each location to a single number, such as the root mean square of the series or the maximum value.

- Compute a suitable average of all the representative values and then compute the decimal logarithm of the representative acceleration in each location relative to the average. The status of the slab layers should be classified using the following criterion:

  Low fixation: locations with a logarithm higher than −0.5.

  Uncertain: locations with a logarithm between −0.5 and −1.0.

  High fixation: locations with a logarithm lower than −1.0.

We use this criterion with data obtained in the garage of an actual building so as to check its validity. In situ results

3.3 In situ results

Figure 3 illustrates four of the 108 recordings obtained in the Madrid building, which exemplify the primary characteristics of all the measurements. Each graph in the figure distinctly captures the passage of the car. Additionally, it is observed that vertical acceleration consistently exceeds the horizontal ones in all cases.

Consequently, from this point on, we will focus exclusively on vertical acceleration.

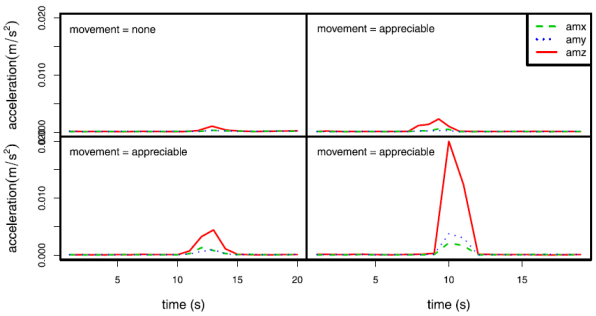


Figure 3. r.m.s. acceleration, with 1 s integration, taken along the passage of the car.

3.4 Test application

Figure 4 illustrates the maximum vertical acceleration of each series, as it relates to the qualitative classification of the movement of the top layer of the pavement. The vertical acceleration is plotted as the logarithm of the value relative to the mean value of all of them.

After applying the criterion defined in Section 3.2 to the data shown in Figure 4, the following results were obtained:

- Seven out of 108 data points, representing 6.5% of the total, have a logarithm lower than −1.0. These data points must be classified as locations where the layers are highly fixed. Only one of these seven locations does not fit into this category.
- 75 of the data, or 69.4%, have a logarithm higher than −0.5, indicating a low fixation of the layers. In this case, all the locations are classified accordingly by the operator, including the 19 locations where a test core was taken, according to EN13863-2 [9], resulting in completely separated layers.
- 26 of the data, 24.1%, cannot be clearly classified by our criterion, as their measurement lies within the uncertain range.

These numbers, though not very impressive, say our criterion may be useful as a first approximation in determining, with a very simple and non-destructive test, the status of the concrete slab in different locations of a garage.

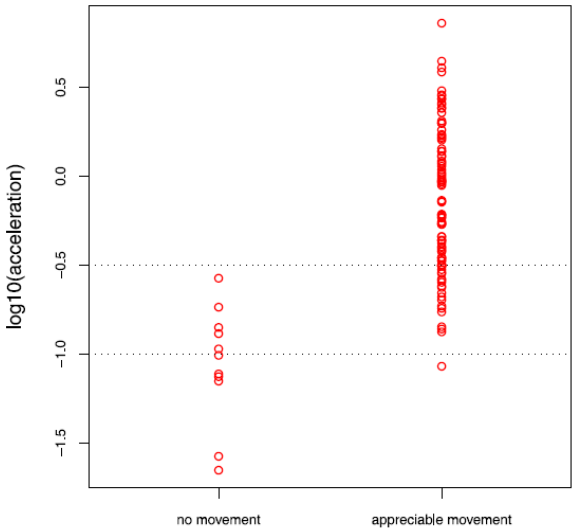


Figure 4. Maximum value of the vertical acceleration in each of the 108 recordings.

4. CONCLUSION

We have proposed a non-destructive test to check the level of fixation of the thin top layer of a concrete slab to the underlying layer using a vibrometer.

We applied our test to data measured in a real building with known fixing problems in the concrete slab of the garage floors.

We measured the vibration past a car in 108 locations within the garage and applied the test previously described.

We found quite a good predictive power of our test, for it classified 82 out of 108 cases, and only one of them was wrongly classified, that is 75.0% where correctly classified.

On the other hand, 26 of the 108 cases were not classified at all, that is a 24.1% of undecidable cases.

As a future work the test should be improved especially by narrowing the interval of undecidable cases.

We are currently extending the study by using the standardized impact machine as an exciter on real building garage floors. We hope to be able to present new results soon.

5. REFERENCES

[1] Z. Ye, Y. Wei, B. Yang, L. Wang, Performance testing of micro-electromechanical acceleration

sensors for pavement vibration monitoring, Micromachines 14 (1), 2023.

[2] Z. Ye, Y. Lu, L. Wang, Investigating the pavement vibration response for roadway service condition evaluation, Adv. Civ. Eng. 2018 (2018)

[3] Z. Li, Y. Aliakseyeu, Q. Zhang, A. Bubulis, V. Minchenya, J. Shi, A. Romanov, A. Khadasevich, I. Charnabai, Georadar vibration-acoustic technology for express control of road pavement strength and results of its application, J. Meas. Eng. 7 (1) 20-33, (2019)

[4] P. Liu, F. Otto, D. Wang, M. Oeser, H. Balck, Measurement and evaluation on deterioration of asphalt pavements by geophones, Measurement 109, 223-232, (2017)

[5] J. Zhang, X. Weng, B. Yang, Y. Li, J. Liu, L. Jiang, Bonding characteristics of grouting layer in prefabricated cement concrete pavement, Constr. Build. Mater. 145, 528-537, (2017)

[6] Y. Zhang, J. Roesler, S. Dahal, Predicting transverse crack properties in continuously reinforced concrete pavement, Constr. Build. Mater. 364, (2023)

[7] ISO 16251-1:2014, Acoustics. Laboratory Measurement of the Reduction of Transmitted Impact Noise By Floor Coverings on a Small Floor Mock-Up. Part 1: Heavyweight Compact Floor, International Organization for Standardization, Geneva, Switzerland, 2014.

[8] ISO 2631-2:2011, Mechanical Vibration and Shock. Evaluation of Human Exposure to Whole-Body Vibration–Part 2: Vibration in Buildings (1 Hz to 80 Hz), International Organization for Standardization, Geneva, Switzerland, 2011.

[9] EN 13863-2:2003, Concrete Pavements – Part 2: Test Method for the Determination of the Bond Between Two Layers, European Committee for Standardization, Bruxelles, Belgium, 2003.

DOI: 10.61782/fa.2025.0618

FORUM ACUSTICUM EURONOISE 2025

NOISE REDUCTION MAT PERFORMANCE OF APARTMENT HOUSES ACCORDING TO SLAB CONDITIONS

Jinyun Chung[1*] **Gokgon Song**[1]
Ahhyun Cho[2] **Seojin Jeong**[2]
[1] Korea Conformity Laboratories, Cheongju-Si, Republic of Korea
[2] Yonsei University, Seoul-Si, Republic of Korea

ABSTRACT

The floor impact sound problem, which is a living noise that can easily occur in apartment houses, is serious. In particular, Korea has a unique panel heating system called 'Ondol', which installs heating pipes on concrete slabs. Because of this heating system, Korea has a culture of taking off shoes in the living room, and this is the cause of floor impact sound problems. Reduction mats, which are widely used to solve floor impact sound in Korea, are made of various thicknesses and materials. Requirements for confirming the noise performance of the floor impact sound reduction mat are presented in the relevant standard (ISO 10140-5). The base floor is presented as a homogeneous reinforced concrete slab with a thickness of 100 to 160 mm. But, there is a big difference in floor mat noise performance between slabs including ondol structure and single slabs. Most floor in Korea are structures in which an ondol layer is installed on 210mm slab. In this study, the mat reduction performance according to the presence or absence of an ondol layer and the slab thickness was compared. However, the evaluation method used ISO 16283-2's general single number quality (SNQ) to confirm the light & heavy-weight impact sound reduction performance. Through this, it is intended to provide noise performance that can be referred to when consumers select floor mats.

Keywords: *floor impact sound, resilient layer, slab thickness, finishing material, floor mat*

[*] ***Corresponding author***: *jinyun97@kcl.re.kr.*

Copyright: *©2025 First author et al. This is an open-access article distributed under the terms of the Creative Commons Attribution 3.0 Unported License, which permits unrestricted use, distribution, and reproduction in any medium, provided the original author and source are credited.*

1. INTRODUCTION

Korea is a world-class country with a population density of 516 people per square kilometer. It ranks first among OECD countries. For that reason, there are many apartments where many people can live together in a narrow area. However, in co-living apartments, living noise between neighbors, especially floor impact sound problems, occurs very seriously. In addition, since Korea uses a panel heating method called ondol on concrete slabs, they live without shoes indoors. Since there are no shoes or slippers that can buffer, the floor impact sound problem becomes more serious. In Korea, it is mandatory to install a resilient material between slab ondol heating to reduce floor impact sound. Even with these efforts, the floor impact sound is the most serious cause of civil complaints in Korea.

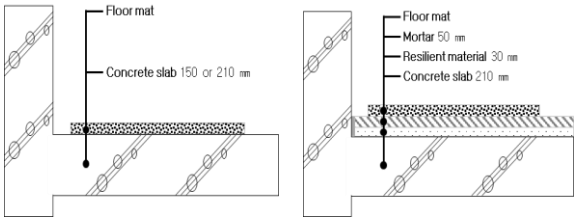
Houses with children use floor mats of various thicknesses and materials to reduce floor impact sounds. Noise performance measurement conditions for floor mats are provided in ISO 10140-5. The test slab is presented in homogeneous reinforced concrete with a thickness of 100 to 160 mm. However, the floor structure in Korea is different from the slab conditions and composition suggested by ISO because the minimum thickness is 210mm and a resilient layer must be installed to reduce floor impact sound.

The purpose of this study is to examine how these differences in floor structure affect the performance of floor mats, and to provide noise reduction performance according to conditions that consumers can refer to when choosing a floor mat

2. MEASUREMENT OVERVIEW

For the floor mat used in the experiment, 12 mats currently used in the market in Korea were selected. There are a total of 12 mats used, 6 inexpensive polyethylene-based products, 3 ethylene vinyl acetate products with excellent stability, and 3 polyurethane products with excellent eco-friendliness. In addition, in order to compare the noise reduction performance of the mat according to the thickness, an experiment was conducted on mats with different thicknesses for each material.

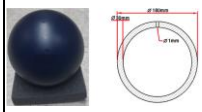
The section of the floor structure used in the experiment is shown in Figure 1. It is a floor structure without a Resilient layer with a thickness of 150 and 210 mm of concrete slab and a slab with a Resilient layer of 210 mm. The Resilient layer is a 'Ondol' structure on the slab, consisting of 'Concrete slab 210 mm + Resilient material (Expanded poly-styrene) 30 mm + Mortar 50 mm'. The measurement equipment used is shown in **Table 1**.



(a) Without resilient layer (b) With resilient layer

Figure 1. Section of test structures.

Table 1. Measurement system.

Measurement system	Products	
Real Time Analyzer	PAK MK Ⅱ (12 channel), Müller-BBM, Germany	
Microphone	46AE(1/2“), GRAS, Denmark	
Light-weight Impact Sound Source	Tapping Machine, 01dB, France	
Heavy-weight Impact Sound Source	Rubber Ball, RION, Japan	

3. MEASUREMENT AND EVALUATION METHOD OF FINISHING MATERIAL

Currently, an evaluation method for evaluating the performance of the floor finishing material is presented in ISO 717-2. However, only the light-weight impact sound single number index (ΔL_w) for the reduction performance of the upper floor coverings is defined, and there is no separate method for evaluating the weight impact sound. In the case of the existing light-weight impact sound reduction evaluation method that can evaluate finishing materials, it is difficult for users to judge performance by looking at figures because the calculation results are difficult for ordinary residents to feel. In this study, we evaluated the insertion loss by confirming the light & heavy-weight impact sound reduction performance and comparing the common single number quality (SNQ) of ISO 16283-2, which is easy to understand when users install floor mat. This method is already widely used as a method of evaluating the floor impact sound of foam mat products. Equations (1) and (2) show how to reduce light-weight and heavy-weight impact sound insertion losses.

$$\Delta L_{Lw}(dB) = L_{without\ covering} - L_{with\ covering} \quad (1)$$

Where, $\Delta L_{Lw}(dB)$: Light-weight impact sound insertion loss due to finishing materials

$L_{without\ covering}$: Floor impact sound level before finishing installation, standardized impact sound pressure level ($L'_{nT,W}$)

$L_{with\ covering}$: Floor impact sound level after finishing installation, standardized impact sound pressure level ($L'_{nT,W}$)

$$\Delta L_{Hw}(dB) = L_{without\ covering} - L_{with\ covering} \quad (2)$$

Where, $\Delta L_{Hw}(dB)$: Heavy-weight impact sound insertion loss due to finishing materials

$L_{without\ covering}$: Floor impact sound level before finishing installation, standardized impact sound pressure level ($L'_{iA,Fmax}$)

$L_{with\ covering}$: Floor impact sound level after finishing installation, standardized impact sound pressure level ($L'_{iA,Fmax}$)

4. RESULTS OF MAT REDUCTION PERFORMANCE

4.1 Acoustic characteristic of floor mat

Figure 2 shows the noise reduction performance of floor mat. As a result of comparing the floor mat by material, the reduction performance of PE products is the best, followed by PU and EVA. In all materials, as the thickness increases, the reduction performance is also excellent. In particular, in the case of heavy-weight floor impact sound, the effect of thickness appears significantly.

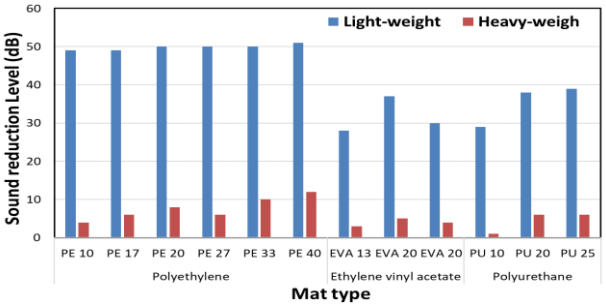
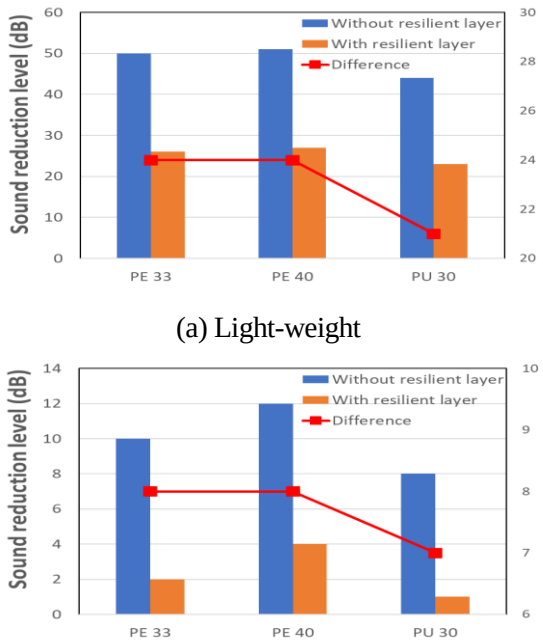


Figure 2. Sound reduction level of floor mat.

4.2 Installation of resilient layer on slab

Korea uses 'Ondol', a panel heating system, on the top of the slab in apartment houses. However, the current International Standard (ISO 10140-5) evaluates the floor impact sound reduction performance under the condition that the installation of a resilient layer on the top of the slab is not considered. Therefore, when floor mat is installed to reduce floor impact sound, on-site reduction performance in Korea may differ from results measured by international standards. Among the 12 types of mats reviewed in 4.1, three representative mats with excellent performance and high use (33 mm PE, 40 mm PE, and 30 mm PU) mat were selected. The floor impact sound reduction performance was compared according to the presence or absence of a resilient layer considering the 'ondol' structure in Korea. As shown in Figure 3, depending on the presence or absence of a resilient layer, there is a difference between 21 and 24 dB for the lightweight impact sound and 7-8 dB for the weight impact sound. Through this, if mat reduction performance is measured on the slab before installing the resilient layer as an ISO international standard measurement method, the noise performance of mat may be overestimated compared to the actual living performance in Korea. A separate evaluation method different from the ISO standard is required for floors where additional layers are installed on the slab, as in Korea.



(a) Light-weight

(b) Heavy-weight

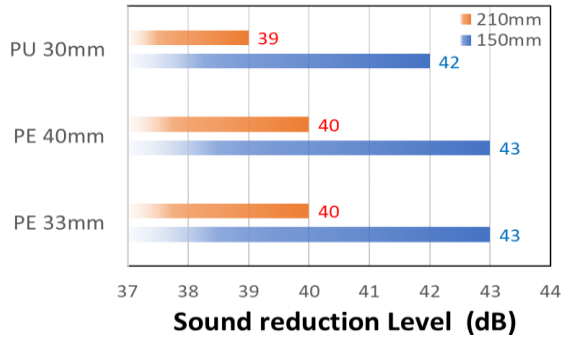
Figure 3. Reduction performance by resilient layer.

4.3 Slab thickness

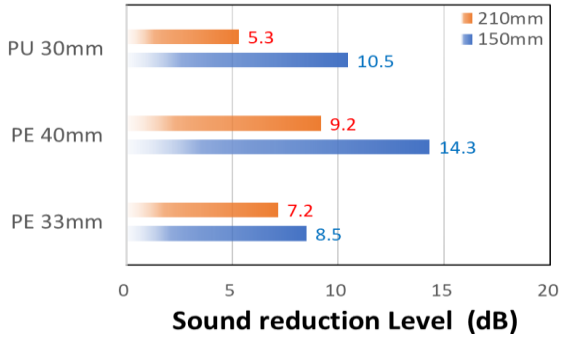
In ISO 10140-5, the reduction performance measurement condition of floor finishing material is 100-160mm in slab thickness, but the minimum slab thickness is 210mm in Korean apartments. This means that evaluating the performance of the finishing material according to ISO measurement conditions is different from the field conditions in Korea. Therefore, it is necessary to examine the possibility that the floor impact sound reduction performance of floor mat will vary according to the change in slab thickness.

The experiment was conducted on the floor mat used in 4.2. Two types of slabs, 150 and 210 mm, were compared, and the reduction performance of the mat was examined in slabs without a resilient layer.

As a result of the measurement, the reduction performance of the mat is evaluated higher by 150mm slab than 210mm. When the slab thickness increases from 150mm to 210mm, the light-weight impact sound decreases by 3dB in all three mats, and the heavy-weight impact sound decreases by 1.3dB to 5.1dB.

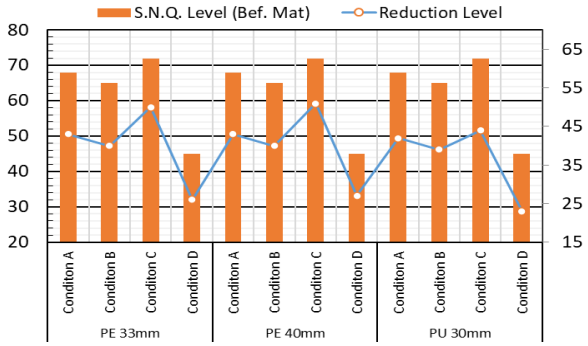


(a) Light-weight

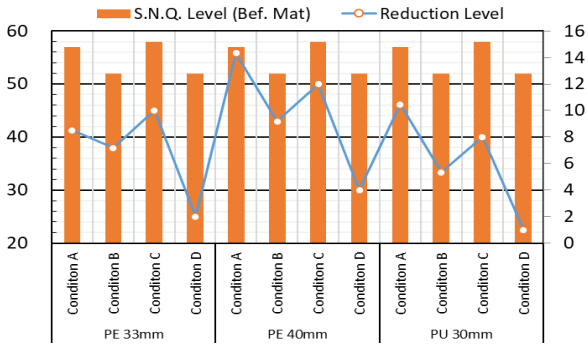


(b) Heavy-weight

Figure 4. Reduction performance with slab thickness.



(a) Light-weight



(b) Heavy-weight

Figure 4. Relationship between SNQ and reduction level.

5. RESULTS

The reduction performance of floor mat varies depending on the conditions of the slab. Slab conditions are not significantly affected by finishing materials such as fly-wood that do not have high sound insulation performance, but finishing materials with high sound insulation performance such as floor mat are affected by slab thickness and the presence or absence of a resilient layer. In the case of floor mats with excellent reduction performance, the reduction performance tends to decrease when the slab thickness becomes thicker or when a resilient layer is installed. Figure 5 is the result of comparing the reduction level of floor mat with the performance before mat installation (SNQ). It can be seen that the reduction performance of the finishing material tends to be excellent when the reduction performance is measured under poor performance conditions. Therefore, in evaluating the performance of the finishing material, it is necessary to clearly present conditions such as the thickness and composition of the slab.

6. ACKNOWLEDGMENTS

This work is supported by the Korea Agency for Infrastructure Technology Advancement (KAIA) grant funded by the Ministry of Land, Infrastructure and Transport (Grant RS-2022-00144050)

7. REFERENCES

[1] ISO 10140-5:2021, “Acoustic – Laboratory measurement of sound insulation of building elements – Part 5: Requirements for test facilities and equipment”.

[2] ISO 16283-2:2020, “Acoustic – Field measurement of sound insulation in buildings and of building elements – Part 2: Impact sound insulation”.

[3] ISO 717-2:2020, “Acoustic – Rating of sound insulation in buildings and of building elements – Part 2: Impact sound insulation”.

DOI: 10.61782/fa.2025.0213

FORUM ACUSTICUM EURONOISE 2025

COMUNICATION BETWEEN CAREGIVERS AND CHILDREN REGARDING INTER-FLOOR NOISE IN MULTI-FAMILY HOUSING: A KOREAN STUDY

Miji Kwon[1] **Wonyoung Yang**[2 *]
[1] Department of Speech-Language Pathology, Gwangju University, Gwangju, South Korea
[2] Division of Architecture, Gwangju University, Gwangju, South Korea

ABSTRACT

Inter-floor noise in multi-family housing has become a significant source of social conflict leading to neighborly conflicts and legal disputes, with children's footsteps and running and resulting noise being major sources. This study examined whether caregivers' communication skills with children could help mitigate inter-floor noise problems caused by children in Korean multi-family housing. An online survey was conducted among 323 caregivers (119 male, 204 female) with minor children, using a 7-point Likert scale across three components: the Highly Sensitive Person Scale (27 items), neighbor communication survey (15 items), and inter-floor noise-related questions (5 items). Results indicated that female caregivers, more sensitive caregivers, and those with better neighbor communication skills were more proactive in conveying noise reduction messages to their children. The findings suggest that sensitive caregivers are more likely to recognize and address inter-floor noise issues with their children, while those with better neighbor communication skills demonstrate improved social consideration. The study concludes that caregivers in multi-family housing should actively engage in communication with their children about inter-floor noise to reduce disturbances through effective parent-child interactions

Keywords: *inter-floor noise, multi-family housing, caregiver-child communication, sensitive caregivers*

[*] ***Corresponding author***: *wyyang@gwangju.ac.kr*
Copyright: *©2025 First author et al. This is an open-access article distributed under the terms of the Creative Commons Attribution 3.0 Unported License, which permits unrestricted use, distribution, and reproduction in any medium, provided the original author and source are credited.*

1. INTRODUCTION

Inter-floor noise remains a significant source of conflict in multi-family housing environments, particularly in dense urban settings [1], with children's footsteps and running and resulting noise being major sources [2]. Despite increasing awareness of this issue, to the best of our knowledge, no research has been found examining the relationship between caregiver communication and children's behavior causing inter-floor noise. This study investigates the communication patterns between caregivers and minor children regarding inter-floor noise, focusing on how caregiver sensitivity, neighbor communication quality, gender, and family composition influence these interactions. Understanding these dynamics is essential for developing effective interventions to reduce noise-related conflicts and improve community relations in residential settings, ultimately enhancing quality of life for families living in multi-unit dwellings.

2. METHOD

2.1 Participations and procedure

The subjects of this study were 323 primary caregivers (119 male, 204 female) raising minor children aged under eighteen. We developed a questionnaire on communication between primary caregivers and their children regarding noise between floors, distributed it online, and collected responses. This study was conducted after receiving prior approval from the Institutional Review Board (IRB) of Gwangju University.

2.2 Research tools

This study aimed to examine the characteristics of communication between caregivers and minor children

regarding inter-floor noise. The survey used in this study consisted of 27 items from the Highly Sensitive Person Scale (HSPS) [3], 15 items on communication between neighbors (NC) [4], and 5 items related to inter-floor noise communication between children and caregivers. After composing the entire survey, we consulted two experts and finalized the questionnaire. Each survey item was structured on a 7-point Likert scale (1 point - "not at all" to 7 points - "very much so"). The five items related to inter-floor noise communication are shown in Table 1.

Table 1. Items for the inter-floor noise-related questions

No	Questionnaire items
1	I explain to my child in advance about situations that could cause inter-floor noise
2	I inform my child that their actions causing inter-floor noise can harm our family and neighbors.
3	I give warnings when my child engages in behavior that causes inter-floor noise.
4	I stop my child when they engage in behavior that causes inter-floor noise.
5	I discuss with my child about conflicts with neighbors caused by inter-floor noise.

2.3 Data Collection and Processing

For this study, a questionnaire was created that could be distributed and collected online. It was distributed to general adults in the form of a URL address. The questionnaire specified the purpose of the research and the contact information of the research director, and included notifications about research ethics and consent to participate. Statistical analyses were performed using Minitab 22.1

3. RESULTS

Table 1 lists the main effects of the ANOVA. HSPS, NC, gender, no of family and no of age ≤ 18 significantly affected inter-floor noise-related questions scores. In terms of the Highly Sensitive Person Scale (HSPS), there was a significant difference ($F = 3.38$, $p < 0.05$) among the three sensitivity groups, with the high sensitivity group ($M = 5.70$) scoring significantly higher than the low sensitivity group ($M = 5.35$), while the medium sensitivity group ($M = 5.54$) did not differ significantly from either extreme.

Regarding neighbor communication (NC), a highly significant difference was observed ($F = 18.01$, $p < 0.001$) between the high ($M = 5.75$) and low ($M = 5.31$) groups. Similarly, gender showed a significant effect ($F = 5.07$, $p < 0.05$), with females ($M = 5.66$) reporting higher scores than males ($M = 5.40$).

The number of family members also yielded significant differences ($F = 2.50$, $p < 0.05$). Notably, households with five members showed the highest mean score ($M = 6.39$), which was significantly different from single-person households ($M = 3.47$). Families with two to four members and those with six or more members showed intermediate values that did not differ significantly from each other.

Finally, the number of family members under 18 years of age also demonstrated significant differences ($F = 3.24$, $p < 0.05$). Households with one child under 18 reported the highest scores ($M = 5.87$), significantly differing from households with three children under 18 ($M = 5.01$), while households with two children ($M = 5.72$) showed intermediate scores that were significantly different from those with three children but not from those with one child.

Table 2. Results of ANOVA (means that do not share a letter are significantly different; A > B > C)

Factor		F P	N	Mean	Group
HSPS	High	3.38 <0.05	113	5.70	A
	Medium		132	5.54	AB
	Low		78	5.35	B
NC	High	18.01 <0.001	136	5.75	A
	Low		187	5.31	B
Gender	F	5.07 <0.05	204	5.66	A
	M		119	5.40	B
No of family	1	2.50 <0.05	1	3.47	B
	2		1	5.65	AB
	3		107	5.63	AB
	4		174	5.78	AB
	5		31	6.39	A
	>6		9	6.27	AB
No of age ≤ 18	1	3.24 <0.05	128	5.87	A
	2		164	5.72	AB
	3		31	5.01	C

4. DISCUSSION AND SUMMARY

This study examined communication patterns between caregivers and children regarding inter-floor noise. Key findings reveal that highly sensitive caregivers, those with better neighbor communication skills, and female caregivers demonstrate more effective noise-related

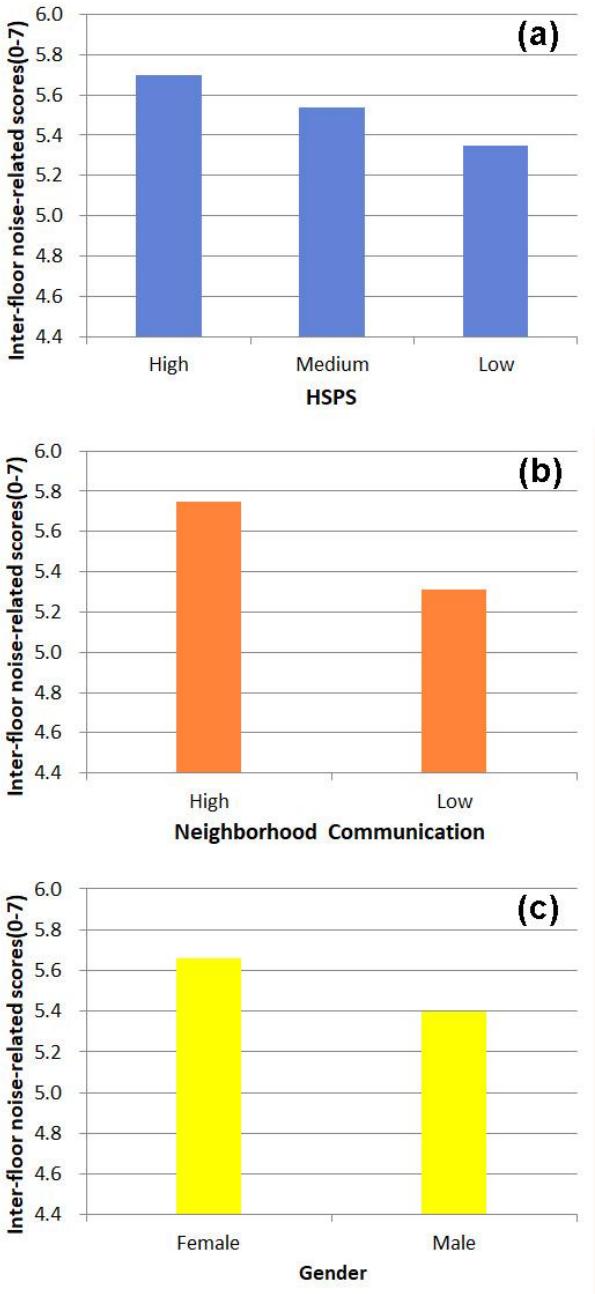


Figure 1. Inter-floor noise-related question scores according to HSPS, NC, and gender (a) HSPS, (b) Neighborhood Communication, (c) gender.

communication with children. Family composition significantly impacts communication patterns, with five-member households showing the highest levels of noise awareness communication, while families with fewer children under 18 reported more focused communication. These findings suggest that personal sensitivity, social communication skills, gender dynamics, and family structure all influence how caregivers address noise issues with children. Results highlight the importance of targeted interventions and education programs to improve noise management in multi-family housing environments. Future research should focus on longitudinal studies to assess the sustained impact of these implementation strategies and explore cultural variations in caregiver-child communication regarding environmental behavioral constraints.

5. ACKNOWLEDGMENTS

We gratefully acknowledge the contributions of all the respondents in our online survey.
This study was supported by the Basic Science Research Program of the National Research Foundation (NRF) [Grant No. RS-2023-00280485], funded by the Ministry of Science and ICT, Republic of Korea. This study was also conducted with research funds provided by Gwangju University in 2025.

6. REFERENCES

[1] Yang, W., *Comparing self-generated noise reduction efforts and tolerance of neighbours' noise in multi-residential buildings.* Journal of Building Engineering, 2024. **98**: p. 111495.

[2] Lee, J.-s., *A study of a new multi-story home model for reducing floor noise in Korea - Focused on service design framework and selective auditory attention -.* Journal of Communication Design, 2016. **57**: p. 510-519.

[3] Yang, W. and M. Kwon, *Cut-off scores for sensitivity interpretation of the Korean Highly Sensitive Person Scale.* Plos one, 2024. **19**(9): p. e0309904.

[4] Yang, W. and M. Kwon, *Face-to-face interpersonal communication between neighbors in high-density urban housing: A cross-sectional survey in South Korea.* Journal of Asian Architecture and Building Engineering, 2025. Under Review.

DOI:

Main theme: A03 Building Acoustics

Session A03.09 Acoustic and thermal retrofit of office building stock in EU

Chair(s): M. Rychtáriková, V. Chmelík

DOI: 10.61782/fa.2025.0095

FORUM ACUSTICUM EURONOISE 2025

ActaReBuild MSCA-DN PROJECT - ACOUSTIC AND THERMAL RETROFIT OF OFFICE BUILDING STOCK IN EU

Vojtech Chmelik[1*] **Monika Rychtarikova**[1,2]

[1] Department of Materials Engineering and Physics, Faculty of Civil Engineering, STU Bratislava, Slovakia

[2] Department of Architecture, KU Leuven, Campus Brussels and Ghent, Belgium

ABSTRACT

MSCA Doctoral Network projects are essential in fostering international collaboration and developing interdisciplinary, innovative solutions. The Horizon MSCA-DN project "ActaReBuild" advances sustainable retrofitting solutions for office buildings in Europe.

The unique feature of this project is that it addresses both the acoustic and thermal performance of buildings in their conversion to other uses.

The project consists of ten Individual Research Projects performed by ten Doctoral Candidates (DCs) under joint PhD supervision.

Research within "ActaReBuild" includes developing innovative materials such as customisable mycelium bio-composites, recycled plastic composites, bio-based materials optimised for acoustic and thermal performance and metamaterials. It addresses novel solutions to improve low-frequency airborne sound insulation in lightweight constructions and refines descriptors for airborne sound insulation of facades, addressing spectral and temporal noise features. In the framework of the project, advanced measurement techniques for remote in-situ measurements for building facades are developed. It explores the balance between airtightness, energy efficiency, and acoustic performance and application on biotic materials for lightweight building envelopes, which significantly reduce embodied carbon and support circular economy principles.

Keywords: *building retrofit, acoustics, thermal physics, MSCA-DN*

1. INTRODUCTION

ActaReBuild project is MSCA – DN (Doctoral Network). The scheme aims to train 10 highly skilled doctoral candidates, fostering their creativity, enhancing their innovative abilities, and boosting their employability for the future [1]. Candidates are enrolled in joint PhD programmes and are supervised by joint supervisory committees. The ActaReBuild project started on 1st September 2022 and is a 4-year project funded under the Horizon Europe scheme.

2. BACKGROUND

Recent European research initiatives have focused on mitigating climate change by implementing energy-efficient building retrofits to achieve near-zero energy use and reduce urban heat islands [2-3]. Although these projects have achieved notable advancements in material and energy efficiency, acoustic performance is often overlooked. Long utilised in construction, recent advancements in bio-composites have enhanced traditional biomaterials like wood, straw, and mud [4-7]. A promising method utilizes mycelium-based composites made from agricultural waste, offering the potential for excellent acoustic absorption while replacing non-renewable materials [8]. A well-known example of sustainable material reuse involves incorporating

[*] ***Corresponding author***: *vojtech.chmelik@stuba.sk.*

Copyright: *©2025 Chmelik et al. This is an open-access article distributed under the terms of the Creative Commons Attribution 3.0 Unported License, which permits unrestricted use, distribution, and reproduction in any medium, provided the original author and source are credited.*

rubber or plastic to create various products that dampen vibrations in floating floor systems [9], and there is also a possibility of using such material in the concrete industry [10-12]. However, the acoustic and thermal performance of materials like granulated plastic and glass [13] requires more research.

In addition to material innovation, phase change materials (PCMs) aid in passive thermal regulation by stabilising indoor temperatures and lowering energy usage [14]. Acoustic metamaterials, designed for targeted sound insulation, show potential for lightweight partition systems; however, they are still largely overlooked in extensive building retrofits [15]. Another developing technology is ethylene tetrafluoroethylene (ETFE) cushion systems, commonly utilised in lightweight façade and roofing applications for their transparency and energy efficiency [16]. Despite this, the acoustic properties of large ETFE structures are still not adequately characterised since conventional room-based tests [17] are inappropriate for them. Advanced in-situ measurement techniques, such as surface impedance measurement with intensity probes or laser Doppler vibrometry (LDV), provide potential solutions [18-19].

Acoustic assessment methodologies also require refinement. Existing sound insulation descriptors, such as Single Number Quantities (SNQs) defined in ISO 717 [20], are often not sufficient for evaluating modern lightweight and hybrid materials, particularly at low frequencies [21]. Furthermore, Life Cycle Analysis (LCA) is increasingly recognized as essential for assessing the sustainability of construction materials, with studies indicating that substituting traditional materials with bio-based alternatives, such as timber, can halve the embodied carbon footprint [22]. However, guidelines for incorporating these materials into large-scale retrofit projects remain underdeveloped.

3. FOCUS OF THE PROJECT AND RECENT FINDINGS

So far, the following results have been obtained. Research, where myco-materials were developed using Pleurotus Ostreatus mycelium grown in various natural substrates, was performed. The materials have undergone testing for compression and tensile strength as well as thermal conductivity. The study highlights the potential of agricultural residues for sustainable construction, with sugarcane bagasse composites exceeding other samples in strength and insulation. While drying and autoclaving are still CO2-intensive, solar drying could reduce the environmental impact. Despite challenges in scaling, mycelium's ability to bind waste materials makes this method economically attractive [23]. Another study has been performed which examined the degree of accuracy on the tortuosity of a porous material using ultrasound transmission measurements. Compared to pulse measurements, the method shows improvement in signal quality. Subsequently, various configurations of tilt angle and transducer spacing were examined, and the results obtained were comparable to other studies dealing with the characterization of tortuosity [24].

Experiments on the performance of a novel bio-based material in terms of sound transmission, sound absorption coefficients as well as thermal properties were conducted. The results showed improvement in monitored parameters in comparison with conventional materials. Several ideas of possible use were concluded [25-27].

The experiments on the acoustic performance of recycled material in the form of loose plastic granules – ethylene-vinyl acetate, polyethene, and polystyrene – were performed. The measurements showed the possible alternative to conventional materials while addressing the waste disposal challenge [28]. Furthermore, the waste material was used to fill cavity resonators. Because of their sound absorption performance, they could be used as an alternative to fibrous materials, although only in exterior applications such as noise barriers [29].

Another part of the project's research focuses on applying PCMs in building construction. The results of the investigations involve composite components that are created by impregnating a highly porous material with two different paraffinic PCMs. The findings emphasize calcium silicate panels as a possible host material for PCMs [30].

A comparative study of various methods for calculating the transmission loss of double panels with the application of metamaterial, demonstrating the broader applicability of the transfer-matrix method in predicting transmission loss, was conducted [31]. The following research was aimed at the possibility of improving the sound transmission loss of a metamaterial unit comprising a membrane with a centre mass used for sound insulation of heat pumps in residential buildings [32].

The use of the LDV method for estimating sound power, as well as the exploitation of the Nyquist-Shannon sampling theorem for pressure estimation criterion in flat plates, are shown in the next study [33].

The assessment of the life cycle of materials is another topic of interest in the framework of the project. The research published in [34] emphasizes the possibility of converting fibrous agricultural resources into insulation products that require less energy. It also investigates innovative methods such as electrospinning and additive manufacturing for bio-

based applications composites. The further study provides a foundational basis for developing methodologies to influence local policies that promote sustainable strategies [35].

The study related to the relevance of various listening test methodologies for evaluating the influence of façade sound insulation on the perception of outdoor noises was also presented [36]. Another study recommends better incorporating all aspects of noise annoyance in future listening test experiments based on the overview of the methodology and sound stimuli used in previous studies [37].

Two experiments on the relation between sound insulation performance and airtightness of constructive solutions were also conducted [38-39].

Another important topic addressed in the project is the life cycle of constructions based on ETFE foils/cushions. The published study on this topic assesses the environmental impact of ETFE foil's End-of-Life scenarios using LCA, emphasizing recycling as the preferred option while considering incineration if transportation emissions are too high [40]. A different study Analyzes uniaxial hysteresis tests on ETFE foil, revealing 33 years of wind load history, supporting material reduction, and validating the method while recommending bi-axial tests for accuracy [41].

4. REFERENCES

[1] ACT-REBUILD Project, "Home," *actarebuild.eu*. [Online]. Available: https://actarebuild.eu. [Accessed: Apr. 7, 2025].

[2] RECO2ST Project, "Home," *reco2st.eu*. [Online]. Available: https://reco2st.eu. [Accessed: Apr. 7, 2025].

[3] COOL TOWNS Project, "Home," *cooltowns.eu*. [Online]. Available: https://www.cooltowns.eu. [Accessed: Apr. 7, 2025].

[4] L. Chen, Y. Zhang, Z. Chen, Y. Dong, Z. Jiang, J. Hua, and P. S. Yap, "Biomaterials technology and policies in the building sector: a review," *Environmental Chemistry Letters*, vol. 22, no. 2, pp. 715–750, 2024.

[5] J. T. Aladejana, Z. Wu, M. Fan, and Y. Xie, "Key advances in development of straw fibre bio-composite boards: An overview," *Materials Research Express, vol.* 7, no. 1, p. 012005, 2020.

[6] C. Moletti, P. Aversa, A. E. Losini, G. Dotelli, M. Woloszyn, and V. A. M. Luprano, "Hygrothermal behaviour of hemp-lime walls: the effect of binder carbonation over time," *Building and Environment*, vol. 233, 2023. doi: 10.1016/j.buildenv.2023.110129

[7] D. Alemu, M. Tafesse, and A. K. Mondal, "Mycelium-Based Composite: The Future Sustainable Biomaterial," *International Journal of Biomaterials*, vol. 2022, 2022. doi: 10.1155/2022/8401528

[8] P. Stamets, *The role of mushrooms in nature: Culturing mushroom mycelium on agar media*, Hong Kong: Ten Speed Press, 2000.

[9] European Commission, "Smart Resource Efficient Modular Building – ISOBIO," CORDIS, 2019. [Online]. Available: https://cordis.europa.eu/project/id/821366

[10] M. Maaroufi *et al.*, "Characterisation of EPS lightweight concrete microstructure by X-ray tomography with consideration of thermal variations," *Construction and Building Materials*, vol. 178, 2018. doi: 10.1016/j.conbuildmat.2018.05.142

[11] S. I. Basha, M. R. Ali, S. U. Al-Dulaijan, and M. Maslehuddin, "Mechanical and thermal properties of lightweight recycled plastic aggregate concrete," *Journal of Building Engineering*, vol. 32, p. 101710, 2020.

[12] A. Poonyakan, M. Rachakornkij, M. Wecharatana, and W. Smittakorn, "Potential use of plastic wastes for low thermal conductivity concrete," *Materials*, vol. 11, no. 10, p. 1938, 2018.

[13] F. Asdrubali, S. Schiavoni, and K. V. Horoshenkov, "A review of sustainable materials for acoustic applications," *Building Acoustics*, vol. 19, no. 4, pp. 283–312, 2012.

[14] J. Čurpek and M. Čekon, "Climate response of a BiPV façade system enhanced with latent PCM-based thermal energy storage," *Renewable Energy*, vol. 152, pp. 368–380, 2020.

[15] F. Cui, Z. He, J. Li, L. Zhang, and B. Assouar, "Acoustic metamaterials: Recent advances and future perspectives," *Advanced Functional Materials*, vol. 31, no. 29, p. 2101748, 2021. doi: 10.1002/adfm.202101748L.

[16] C. Maywald, "Sustainability–The Art of Modern Architecture," *Procedia Engineering*, vol. 155, pp. 238–248, 2016. doi: 10.1016/j.proeng.2016.08.025

[17] *ISO 10140-1:2021. Acoustics — Laboratory measurement of sound insulation of building elements.*

Part 1: Application rules for specific products, International Organization for Standardization, 2021.

[18] N. B. Roozen, Q. Leclere, D. Urbán, L. Kritly, and C. Glorieux, "Assessment of the sound reduction index of building elements by near field excitation through an array of loudspeakers and structural response measurements by laser Doppler vibrometry," *Applied Acoustics*, vol. 140, pp. 225–235, 2018.

[19] D. Urbán *et al.*, "Vibrometry assessment of the external thermal composite insulation systems influence on the façade airborne sound insulation," *Applied Sciences*, vol. 8, no. 5, p. 703, 2018.

[20] *ISO 717-1:2020. Acoustics — Rating of sound insulation in buildings and of building elements. Part 1: Airborne sound insulation*, International Organization for Standardization, 2020.

[21] B. Rasmussen and M. Machimbarrena, COST Action TU0901 – *Building acoustics throughout Europe. Volume 1: Towards a common framework in building acoustics throughout Europe*, 2014.

[22] C. Monticelli and A. Zanelli, "Life Cycle Design and Efficiency Principles for Membrane Architecture: Towards a New Set of Eco-design Strategies," *Procedia Engineering*, vol. 155, pp. 416–425, 2016.

[23] T. S. Gomez *et al.*, "Development of a myco-material based on textile and agro-industrial waste for thermal insulation," in *E3S Web of Conferences*, vol. 546, p. 03003, 2024.

[24] T. S. Gomez *et al.*, "Extraction of tortuosity of melamine foam from ultrasonic transmission measurements: experimental improvement," in *Proc. ISMA 2024 - International Conference on Noise and Vibration Engineering and USD 2024*, pp. 313–322, 2024.

[25] J. J. Garcia and E. A. Piana, "Exploring bio-recycled residues: Innovating sustainable building materials for acoustic retro-fitting," in *Proc. Int. Congress on Sound and Vibration*, 2024.

[26] J. J. Garcia, D. Tonetti, and E. A. Piana, "Sound reduction index of cardboard panels featuring a honeycomb paper core," in *Proc. Int. Congress on Sound and Vibration*, 2024.

[27] J. J. Garcia, D. Tonetti, and E. A. Piana, "Assessing the sound insulation and thermal performance of a partition based on recycled materials as a sustainable retrofitting solution for buildings," in *E3S Web of Conferences*, vol. 546, p. 03002, 2024.

[28] J. Potocar, D. Jun, S. Unčík, C. Glorieux, and M. Rychtáriková, "Acoustic properties of Helmholtz resonator filled with granulated polymer waste material," in *INTER-NOISE and NOISE-CON Congress and Conference Proceedings*, vol. 270, no. 2, pp. 9297–9304, Oct. 2024.

[29] J. Potočár, S. Unčík, C. Glorieux, and M. Rychtarikova, "Sound-absorbing properties of granulated plastic waste materials," in *Acoustics 2024 High Tatras*, Štrbské Pleso, Vysoké Tatry, Slovakia, pp. 93–96, Jun. 12–14, 2024.

[30] R. Cottone *et al.*, "Investigation of phase change material impregnation in a highly porous structure," in *Proc. Int. Assoc. of Building Physics*, pp. 455–460, Springer, Singapore, 2025.

[31] R. Zeng, E. Deckers, C. Glorieux, D. Urbán, and B. Chmielewski, "Wall-applicable metamaterial: mitigating resonance dip for enhanced sound transmission loss," in *INTER-NOISE and NOISE-CON Congress and Conference Proceedings*, vol. 270, no. 4, pp. 7144–7155, Oct. 2024.

[32] R. Zeng *et al.,* "Locally resonant metamaterial wall targeting tonal noise arising from heat pumps in residential buildings," in *Proc. ISMA 2024 - International Conference on Noise and Vibration Engineering*, pp. 2652–2661, Nov. 2024.

[33] A. Singh, V. Jandak, D. Urban, and O. Jiricek, "Experimental verification of sound power determination methods based on radiation matrix," in *INTER-NOISE and NOISE-CON Congress and Conference Proceedings*, vol. 270, no. 1, pp. 10183–10192, Oct. 2024.

[34] I. Nuvolari-Duodo *et al.,* "Integrated climate change mitigation and public health protection strategies: The case of the city of Bologna, Italy," *Int. J. Environ. Res. Public Health*, vol. 21, no. 11, p. 1457, 2024.

[35] I. Nuvolari-Duodo, M. Dolcini, M. Buffoli, A. Rebecchi, G. Dall'Ò, C. Monticelli, C. Vertua, A. Brambilla, and S. Capolongo, "Integrated climate change mitigation and public health protection strategies: The case of the city of Bologna, Italy," *Int. J. Environ. Res. Public Health*, vol. 21, no. 11, p. 1457, 2024.

[36] M. Geluykens, H. Müllner, V. Chmelík, and M. Rychtáriková, "Listening test methodology for building acoustic issues," in *Fortschritte der Akustik - DAGA* 2024, pp. 263–266, 2024.

[37] M. Geluykens, H. Muellner, V. Chmelik, and M. Rychtarikova, "Airborne sound insulation and noise annoyance: Implications of listening test methodology," in *Proc. Forum Acusticum 2023*, pp. 155–162, Sep. 2023.

[38] A. Elsaei *et al*., "Airtightness/airborne sound insulation study in accredited sound insulation facilities," 2023.

[39] A. Elasei, M. Machimbarrena, A. Meiss, and I. Poza-Casado, "Exploring the correlation between airtightness and acoustic performance in building systems within certified sound insulation lab," in *Proc. 30th Int. Congress on Sound and Vibration*, 2023.

[40] K. Solanki, T. Balster, C. Monticelli, M. Á. Padilla Marcos, and C. Maywald, "Closing the loop: the influence of recycling of ETFE foils within the life cycle assessment (LCA) approach," in *Proc. 6th Int. Conf. on Energy & Environment: Engineering and Economics*, pp. 504–509, 2024.

[41] K. Solanki, T. Balster, C. Maywald, C. Monticelli, and M. Á. Padilla Marcos, "Evaluation of the wind load history of environmentally exposed ETFE foils," in *Proc. IASS 2024 Symposium*, pp. 1–6, 2024.

DOI: 10.61782/fa.2025.0598

FORUM ACUSTICUM EURONOISE 2025

MYCELIUM COMPOSITES COMBINING DIFFERENT WASTE SOURCES FOR SUSTAINABLE ACOUSTIC SOLUTIONS

Tomas Simon Gomez[1,2*] **Luis Miguel Garcia**[3] **Nelson Escobar**[3]
Maria de los Angeles Navacerrada[4] **Christ Glorieux**[1]

[1] KU Leuven, Department of Physics and Astronomy, Laboratory for Acoustics - Soft Matter and Bio-physics, Celestijnenlaan 200D, 3001, Heverlee, Belgium

[2] University of Brescia, Department of Mechanical and Industrial Engineering, Via Branze 38, 25123, Brescia, Italy

[3] Escuela de Ingeniería Universidad Pontificia Bolivariana, Circular 1 #70-01, 050031 , Medellín, Colombia

[4] Grupo de Acústica Arquitectónica, Escuela Técnica Superior de Arquitectura, Universidad Politécnica de Madrid, Avda Juan de Herrera 4, 28040, Madrid, Spain

ABSTRACT

Mycelium is a biological material that consists of filamentous fungi, forming intricate networks of hyphal micro-filaments that naturally bind organic matter. This unique way of growing offers promising potential for developing innovative materials, including acoustic absorbers. A lot of variety is possible, since mycomaterial properties are highly dependent on the substrate used.

The presented research reports on the development and acoustic characterization of mycelium composites derived from diverse substrates. These include the fungal strain Pleurotus Pulmonarius, combined with leaves and grass clippings with textile waste. 3 distinct material combinations were made. For each material combination, the density and porosity were obtained by the gas pycnometer method. The sound absorption of the samples was determined using an impedance tube, in compliance with the ISO-10534-2 standard, spanning frequencies from 200 Hz to 5000 Hz. The microstructure of the samples was characterized by Scanning electron microscopy (SEM). The mycomaterials exhibited sound absorption values exceeding 50% across frequencies ranging from 1500 Hz to 4000 Hz.

Keywords: m*ycelium-based composites, sound absorption, sustainable materials, bio-composites, ActaReBuild*

[1]****Corresponding author**: tomas.gomez@kuleuven.be*

***Copyright**: ©2025 First author et al. This is an open-access article distributed under the terms of the Creative Commons Attribution 3.0 Unported License, which permits unrestricted use, distribution, and reproduction in any medium, provided the original author and source are credited.*

1. INTRODUCTION

Mycelium-based composites (MBC) have gained interest as viable alternatives to conventional synthetic materials in construction, packaging, and acoustic and thermal applications. These biocomposites are compostable and derived from renewable or waste resources. They also exhibit promising functional characteristics, including thermal insulation and sound absorption [1], [2]. Recent studies highlight the versatility of mycelium materials, demonstrating their potential to porous absorbers in acoustic solutions. For instance, mycelium-grown substrates such as agricultural waste, spent coffee grounds, and paper industry byproducts have achieved sound absorption coefficients comparable to traditional materials like polyurethane and extruded polystyrene [3], [4]. The acoustic performance of these composites is closely tied to their microstructure, which can be tailored through substrate selection, fungal species, and processing methods [5], [6], [7]. Despite these advances,

gaps remain in understanding how specific waste streams, particularly urban biowaste (e.g., leaves, grass clippings) combined with textile waste, influence the acoustic and physical properties of mycelium composites. While prior research has explored lignocellulosic substrates like sawdust and straw [8], [9], [10], [11], the integration of textile waste into mycelium matrices requires further investigation. Textile processing methods (e.g., grinding, stripping) may significantly alter composite porosity, density, and hyphal adhesion, thereby impacting acoustic efficiency.

This study addresses these gaps by developing and characterizing mycelium composites derived from leaves, grass clippings, and recycled textiles (ground, stripped, and combined forms) using Pleurotus pulmonarius. Through impedance tube testing, helium pycnometry, and scanning electron microscopy (SEM), we evaluate how textile treatment methods affect the composites' sound absorption, density, and microstructure.

2. MATERIALS AND METHODS

2.1 Sample Preparation

The production of the composite samples was based on solid-state fermentation of Pleurotus pulmonarius cultivated on lignocellulosic and textile-based substrates. This was carried out in Medellín, Colombia, under controlled environmental conditions to eliminate the influence of external weather fluctuations.

Agro-industrial and textile residues were selected as the main substrate components, a mixture of grass cuttings and dry leaves sourced from the organic waste disposal system of Universidad Pontificia Bolivariana were used as the primary lignocellulosic materials. Additionally, recycled textile fibres were provided by a local textile recycling company and pre-processed into fine ground material and textile strips prior to use. By varying the textile processing method across samples, this study aims to evaluate its influence on the structural and acoustic properties of the resulting composites.

Preliminary treatment of the substrates included the removal of any non-organic contaminants from the grass and leaf mixture.

In order to reduce the microbial load, an autoclaving step was conducted, at 120 °C and 15 psi for 45 minutes. Excess moisture was subsequently removed from the substrates.

Each mixture was placed into sterile trays measuring and inoculated with Pleurotus pulmonarius grain spawn, with an amount corresponding to a 20 percent of the total substrate dry weight. The trays were covered with sterilized polyethylene bags to limit light exposure, then incubated at 21 °C with 50 percent relative humidity for 45 days to facilitate mycelial colonization.

Throughout the incubation period, mycelial growth was monitored. Any fruiting bodies that emerged were removed to maintain focus on vegetative mycelium development. Upon completion of the cultivation phase, the samples were removed from the bags and dehydrated in a convection oven at 65 °C for 24 hours. This post-processing step deactivated the fungal metabolism. After deactivation the samples had a thickness of 2 cm.

Table 1 shows the different sample compositions. The substrate composition consisted of 70 percent lignocellulosic material and 30 percent recycled textile by weight; with these different sample configurations the effect of the textile processing method on the structure and acoustic capabilities of the developed materials is being evaluated.

Fig. 1 to 3 show developed samples, Fig 1. Ground Textile (GT), Fig 2. Striped Textile (ST), Fig 3. Combined Textile (CT), Respectively.

Table 1. Sample composition

Sample	Composition
GT	70% lignocellulosic composite - 30% ground textile
ST	70% lignocellulosic composite - 30% striped textile
CT	70% lignocellulosic composite - 15% ground textile - 15% stripped textile

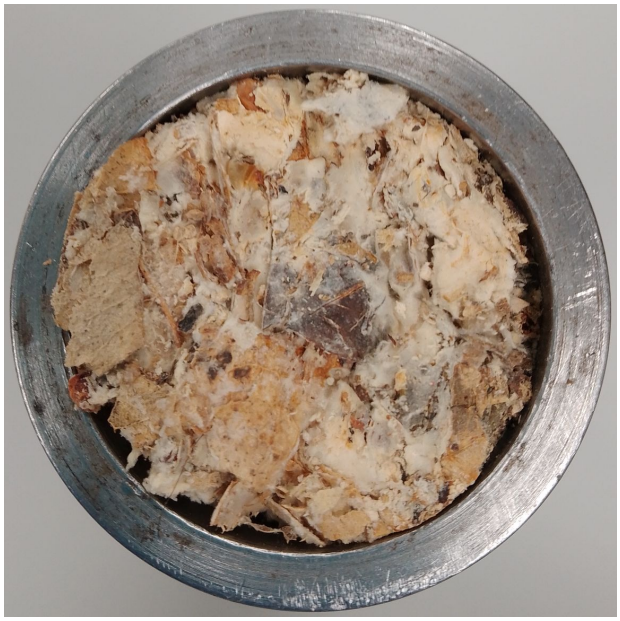


Figure 1. Ground Textile mycelium sample (GT)



Figure 2. Striped Textile mycelium sample (ST)

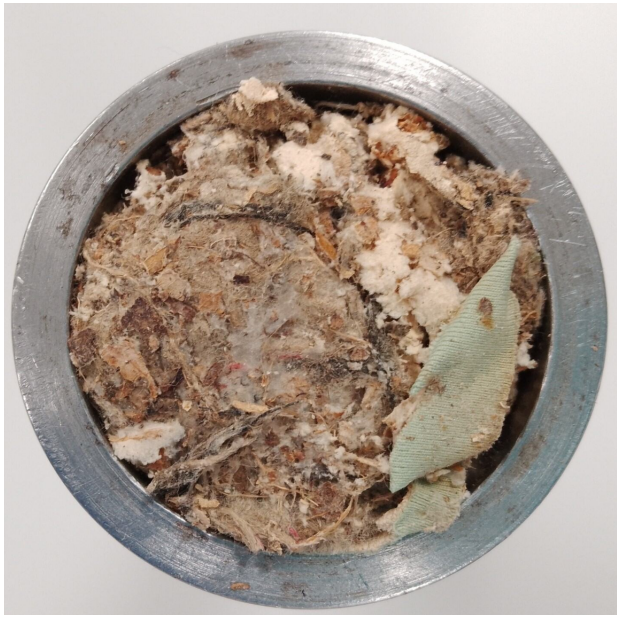


Figure 3. Combined Textile sample (CT)

2.2 Sample characterization

Following the cultivation of the mycelium-based composites, a series of physical and acoustic characterization procedures were conducted to evaluate their suitability as sound-absorbing materials.

2.2.1 Density and Porosity Analysis

The physical characterization of the mycelium composites included the determination of their bulk density and open porosity. The bulk density was calculated as the ratio between the oven-dried mass and the geometric volume of the samples. To obtain the true (skeletal) density of the solid phase, a helium gas pycnometry was performed using an AcuPyc II 1345 pycnometer, in accordance with ASTM D923. Each measurement included 50 purges and measurement cycles to ensure accuracy and stability of the results. Open porosity (ϕ) was then calculated using:

$$\phi = 1 - \frac{\rho_{Bulk}}{\rho_{Real}} \quad (1)$$

2.2.2 Sound absorption coefficient

The sound absorption spectra of the mycelium composites were determined using the impedance tube method, following the guidelines established in ISO

10534-2. Measurements were conducted using a custom-built impedance tube setup equipped with two Behringer ECM8000 condenser microphones. Pink noise was generated within the tube to simulate plane wave propagation under normal incidence conditions, the frequency range of the analysis went from 200 Hz to 5000 Hz. Cylindrical samples with a 38 mm diameter were cut to fit the inner diameter of the impedance tube, ensuring airtight contact with the tube walls. Each test was repeated three times per sample type to assess experimental variability. The resulting absorption coefficient curves were analyzed to compare the acoustic behavior of the different substrate combinations and to identify trends associated with material composition and structure.

2.2.3 Scanning Electron Microcopy

Scanning Electron Microscopy (SEM) was employed to investigate the internal microstructure and hyphal network formation within the mycelium composites. Prior to imaging, small cross-sectional fragments of each sample were cut and coated with a thin layer of gold. SEM imaging was carried out at an accelerating voltage of 15 kV.

3. RESULTS AND DISCUSSION

The physical properties of the mycelium composites are presented in Table 2. Density values ranged from 1.05 to 1.08 g/cm³,. Bulk density values, as measured via helium gas pycnometry, varied between 0.13 and 0.15 g/cm³ depending on the textile waste used.

Calculated porosity values ranged from 86% to 88%. The GT sample showed the highest porosity, while ST and CT had slightly lower porosities. These small differences suggest that the processing method of the textile component may have a subtle effect on the internal structure of the resulting composites.

Table 1. Density and porosity of leaves and grass cuttings based mycelium composites with different textiles.

Sample	Real Density (g/cm^3)	Bulk Density (g/cm^3)	Porosity (%)
GT	1.08	0.13	88
CT	1.06	0.15	86
ST	1.05	0.15	86

Examination of the acoustic performance (Figure 4) of the composites showed a typical trend for porous materials: the sound absorption increased with frequency. However, notable distinctions were observed among the different textile treatments. The GT sample demonstrated the highest absorption coefficients, particularly in the mid to high frequency range (1000–4000 Hz). In comparison, both ST and CT exhibited similar absorption, with slightly lower performance, especially at higher frequencies, whilst having greater absorption at low frequencies.

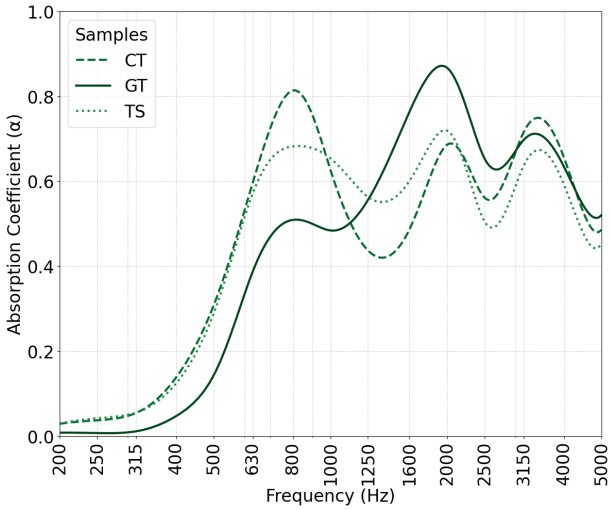


Figure 4. Sound absorption coefficient of mycelium based composites.

These differences in acoustic performance are further supported by the density and porosity results and SEM imaging, which revealed variations in the internal structures of the composites. The GT sample displayed a porous network, while ST showed a more compact and layered micro-structure with lower porosity.

The SEM images revealed key differences in the internal structure of the based mycelium composites, which help contextualize the observed acoustic and physical properties.

The GT (Ground Textile) sample (Fig 5) presents a highly irregular and open structure. The fibres are fragmented and loosely packed, creating an interconnected network with visible voids. This morphology is consistent with its higher porosity and lower bulk density. The open and tortuous structure increases the surface area available for interaction with sound waves, supporting the superior acoustic

performance observed. Fig. 6 and Fig. 7 show how mycelium does not grow over the textile fibers.

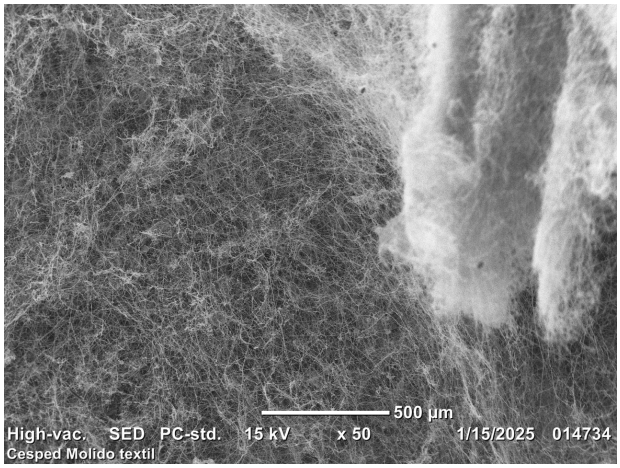


Figure 5. SEM image of the GT (Ground Textile) sample at 50× magnification, showing a fragmented and loosely packed fiber network with high porosity and open structure.

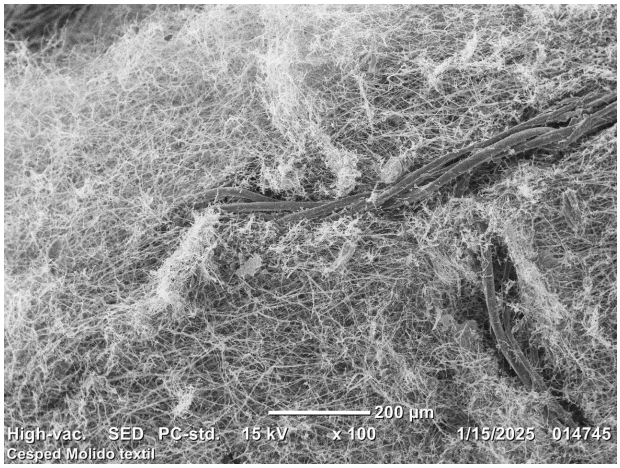


Figure 6. SEM image of the GT sample at 100× magnification. Exposed textile fibers remain largely uncovered by mycelium, suggesting limited adhesion or colonization.

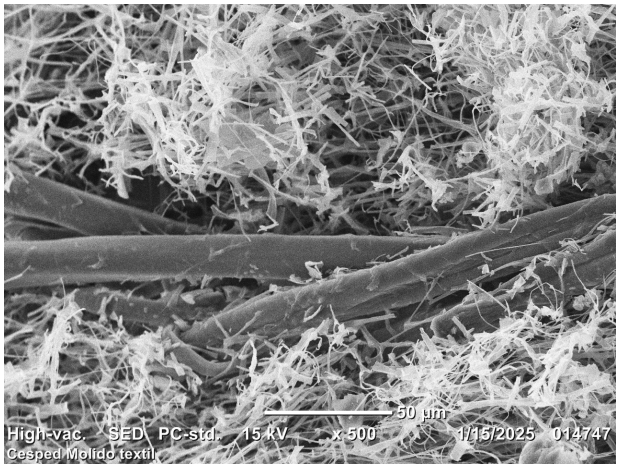


Figure 7. SEM image of the GT sample at 500× magnification. The mycelium grows around but not across the textile fibers, maintaining distinct fiber contours.

Composites with textile strips (Figs 8–10) show a more compact microstructure. Large woven threads and continuous regions of dense material are visible. At higher magnification (Fig 9), the textile structure exhibits a low porosity, compared to the GT sample.

The mycelial coverage is extensive in both samples, but the distributions of pores differ. In the GT composite, the broken-down textile allows the mycelium to colonize a fragmented, aerated matrix. In CT and ST, the woven structure may limit the internal pathway for sound wave dissipation.

These findings align with the fact that finer textile processing in GT likely facilitates better air-flow and energy dissipation, whereas the denser structure in CT and ST may restrict sound penetration to some extent, resulting in a somewhat lower absorption performance at higher frequencies.

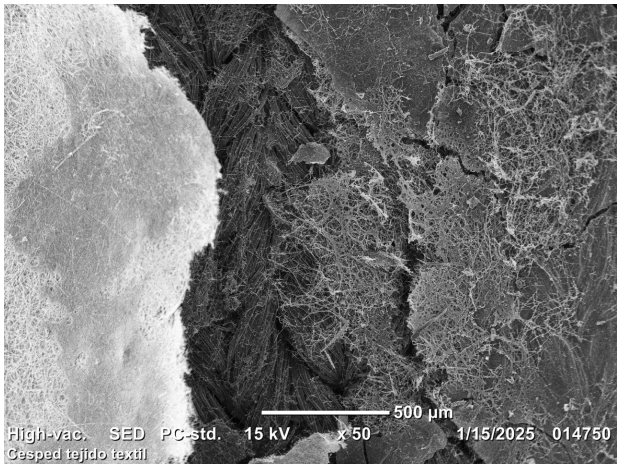


Figure 8. SEM image of the ST sample at lower magnification (50×), highlighting a more continuous and layered surface with reduced structural openness compared to GT.

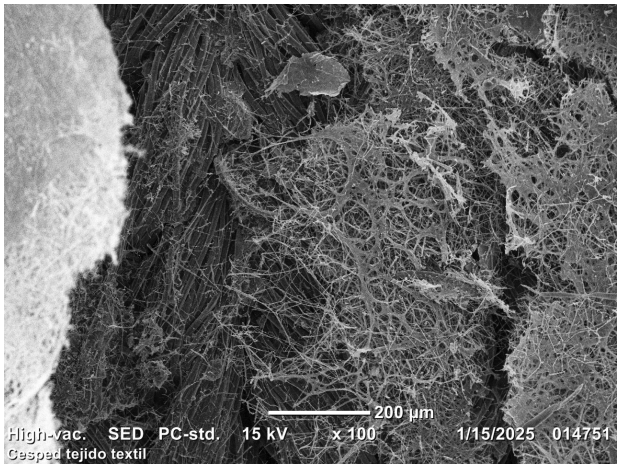


Figure 9. SEM image of the ST (Textile Strip) sample at 100× magnification. Large textile bundles and a more compact structure are clearly visible.

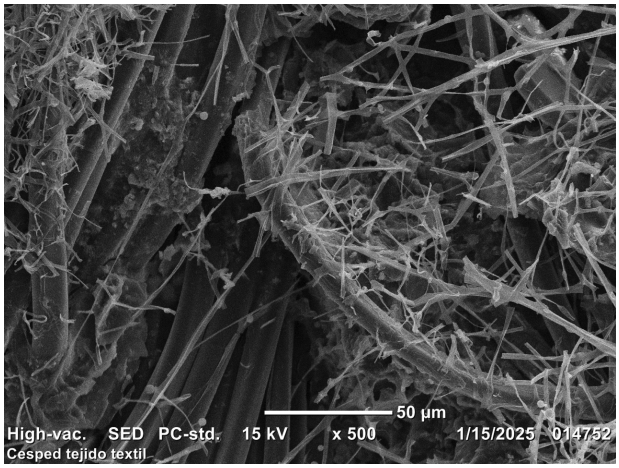


Figure 10. Higher magnification SEM image (500×) of the ST sample, revealing limited porosity and dense fiber regions surrounded by mycelial growth.

4. CONCLUSIONS

This study explored the development and characterization of mycelium-based composites using leaves and grass clippings combined with different forms of textile waste. The influence of textile processing was examined through physical measurements, acoustic absorption testing, and scanning electron microscopy (SEM).

All based composites exhibited high porosity and relatively low bulk density, confirming their potential as lightweight, bio-based acoustic materials. Among the samples, the GT (Ground Textile) formulation showed the most favorable acoustic performance, particularly in the mid-to-high frequency range. This correlated with its lower bulk density and microstructural features observed under SEM, which revealed a more open, irregular internal network with greater void content. In contrast, CS and CT samples presented slightly denser structures, with larger, more continuous fibre zones and moderately reduced sound absorption.

These results suggest that substrate processing plays a critical role in defining the physical and functional behavior of mycelium composites. Loose fibres appear to enhance porosity and acoustic absorption by promoting a more penetrable internal structure for sound wave dissipation. Overall, the findings provide preliminary support for the viability of mycomaterials as sustainable alternatives for acoustic applications, with

potentially adjustable properties through substrate formulation.

5. ACKNOWLEDGMENT

This project has received funding from the European Union's Horizon Europe research & innovation programme under the HORIZON-MSCA-2021-DN-01 grant agreement No. 101072598 – "ActaReBuild".

6. REFERENCES

[1] W. Sun, M. Tajvidi, C. Howell, and C. Hunt, "Insight into mycelium-lignocellulosic bio-composites: Essential factors and properties," Composites Part A-Applied Science And Manufacturing, vol. 161, 2022.

[2] T. S. Gomez, M. Rychtarikova, R. Armstrong, and E. Piana, "Acoustic Applications Of Bio-Mycelium Composites, Current Trends And Opportunities: A Systematic Literature Review," in Proceedings of the 29th International Congress on Sound and Vibration, (Prague, Czechia), 2023.

[3] H. Muñoz et al., "Applicability of Paper and Pulp Industry Waste for Manufacturing Mycelium-Based Materials for Thermoacoustic Insulation," Sustainability (Switzerland), vol. 16, no. 18, 2024.

[4] N. Walter and B. Gürsoy, "A Study on the Sound Absorption Properties of Mycelium-Based Composites Cultivated on Waste Paper-Based Substrates," Biomimetics, vol. 7, no. 3, p. 100, 2022.

[5] E. D. Gezer and S. Kuştaş, "Acoustic and Thermal Properties of Mycelium-based Insulation Materials Produced from Desilicated Wheat Straw-Part B," BioResources, vol. 19, no. 1, pp. 1348–1364, 2024.

[6] C. Dognini, S. Basu, P. Piana, and E. Gobbi, "Variation Of The Acoustic Characteristics Of Mycelium-Based Biomaterials With Time," in Proceedings of the 29th International Congress on Sound and Vibration, (Prague, Czechia), 2023.

[7] D.-G. Barta, I. Simion, A.-E. Tiuc, and O. Vasile, "Mycelium-Based Composites as a Sustainable Solution for Waste Management and Circular Economy," Materials, vol. 17, no. 2, 2024.

[8] W. Sun, S. H. Strässle Zúñiga, V. Philippe, L. Rinaldi, and T. Abitbol, "Mycelium-Bound composites from agro-industrial waste for broadband acoustic absorption," Materials and Design, vol. 250, 2025 .

[9] P. Jinanukul et al., "Comparative Evaluation of Mechanical and Physical Properties of Mycelium Composite Boards Made from Lentinus sajor-caju with Various Ratios of Corn Husk and Sawdust," Journal of Fungi, vol. 10, no. 9, 2024.

[10] C. Kohphaisansombat et al., "Fabrication of mycelium (oyster mushroom)-based composites derived from spent coffee grounds with pineapple fibre reinforcement," Mycology, vol. 15, no. 4, pp. 665–682, 2024.

[11] T. Anto, R. C. Rajendran, P. K. Muraleedharan, and E. Jayamani, "Effect of Borax-Boric Acid Treatment on Fire Resistance, Thermal Stability, Acoustic, and Mechanical Properties of Mycelium Bio Composites," Applied Science and Engineering Progress, vol. 17, 2024.

DOI: 10.61782/fa.2025.0383



FORUM ACUSTICUM
EURONOISE 2025

EXPLORATION OF USE OF MEMBRANE-TYPE METAMATERIAL LAYER FOR APPLICATION IN BUILDING ACOUSTICS

Rui ZENG[1,2,3*] **Elke DECKERS**[1,4] **Christ GLORIEUX**[5]
Daniel URBAN[2,6] **Bartosz CHMIELEWSKI**[3]
[1] Department of Mechanical Engineering, KU Leuven, Belgium
[2] Department of Materials Engineering and Physics, STU Bratislava, Slovakia
[3] KFB Acoustics Sp. z o. o., Oławska 8, 55-040 Domasław, Poland
[4] Flanders Make @ KU Leuven, Diepenbeek, Belgium
[5] Department of Physics and Astronomy, KU Leuven, Belgium
[6] Faculty of Civil end Environmental Engineering, TU Wien, Austria

ABSTRACT

This study investigates the sound transmission loss (STL) and absorption performance of a membrane-type metamaterial layer through a series of controlled experiments. Measurements were conducted in an impedance tube to independently characterize the STL and absorption properties of the metamaterial layer. Based on the results from numerical simulations and impedance tube measurements, a larger-scale prototype layer was designed and tested in a transmission room configuration, for verifying the potential for application as part of acoustic insulation solutions in retrofitting applications.

Keywords: *membrane-type acoustic metamaterials, sound transmission loss, architectural acoustics, impedance tube measurement, transmission chamber test*

1. INTRODUCTION

Low-frequency noise insulation presents a significant challenge in building acoustics, particularly in lightweight structures where traditional solutions often fall short in performance. Due to its long wavelength, low-frequency sound can efficiently propagate through walls, making it difficult to attenuate using conventional porous absorbers. Increasing mass is an effective way to improve sound insulation, but in many applications, especially in retrofitting, adding substantial weight is neither practical nor desirable.

In retrofitting applications, where modifications to existing structures are constrained by space, weight, and cost, improving low-frequency sound insulation is particularly challenging. Common strategies involve adding additional panels, integrating resilient layers for decoupling, or incorporating insulation boards. While these approaches can enhance sound insulation in certain frequency ranges, they may also introduce resonance effects that degrade performance in others [1].

Acoustic metamaterials have been explored as a complementary solution to conventional sound insulation approaches by utilizing locally resonant mechanisms to enhance STL in targeted frequency bands [2–5]. Among them, membrane-type metamaterials have attracted increasing attention due to their ability to achieve strong low-frequency sound insulation with limited added mass. These metamaterials typically consist of a tensioned membrane with an attached mass, forming a resonant system that blocks sound transmission at specific frequencies [6]. Despite extensive studies on the fundamental properties of membrane-type metamaterials, their large-scale application in building acoustics remains unexplored. Most existing research has focused on numerical modeling and small-scale impedance tube measurements, with limited investigations into their performance

*Corresponding author: rui.zeng@kfb-acoustics.com.
Copyright: ©2025 First author et al. This is an open-access article distributed under the terms of the Creative Commons Attribution 3.0 Unported License, which permits unrestricted use, distribution, and reproduction in any medium, provided the original author and source are credited.

in configurations relevant to architectural acoustics.

This study investigates the sound transmission loss and absorption performance of a membrane-type metamaterial layer through a series of controlled experiments. The primary objectives are:

- To evaluate the STL and absorption properties of the metamaterial layer through impedance tube experiments.
- To compare numerical simulations with experimental results.
- To assess the effectiveness of a scaled-up prototype for practical building applications.

These studies lay the groundwork for future research and fine-tuning of metamaterial designs for practical applications.

2. EXPERIMENTAL AND NUMERICAL METHODS

2.1 Membrane Material

A commercially available black rubber sheet with a nominal thickness of $1\,\mathrm{mm}$ was used for the membrane, selected for its accessibility rather than specific mechanical properties, as detailed parameter measurements were not available. The density of the rubber was estimated through simple mass and volume measurements, yielding a value of $1590\,\mathrm{kg\,m^{-3}}$ with an uncertainty of $40\,\mathrm{kg\,m^{-3}}$.

2.2 Impedance Tube Measurements

The impedance tube (see Fig. 1), custom-made by KFB Acoustics for studying this case, has an internal acoustic passage diameter $102\,\mathrm{mm}$. A sample holder with steel rings was designed to clamp the membrane, with the membrane's outer diameter being $122.5\,\mathrm{mm}$.

The membrane samples for the impedance tube, as shown in Fig. 2, were manually cut and bonded to two steel rings on each side for structural support, ensuring a fixed boundary condition for the impedance tube experiments. The edges of the ring-rubber-ring sample were polished smooth, and slight unevenness was introduced during manual fabrication. The pretension in the membrane was assumed to be small, as the manual stretching process aimed only at flattening the membrane without inducing significant pre-stress. Additionally, modified samples were prepared by attaching one or two identical cylindrical steel masses ($1.85\,\mathrm{g}$ each, $10\,\mathrm{mm}$ diameter, $3\,\mathrm{mm}$

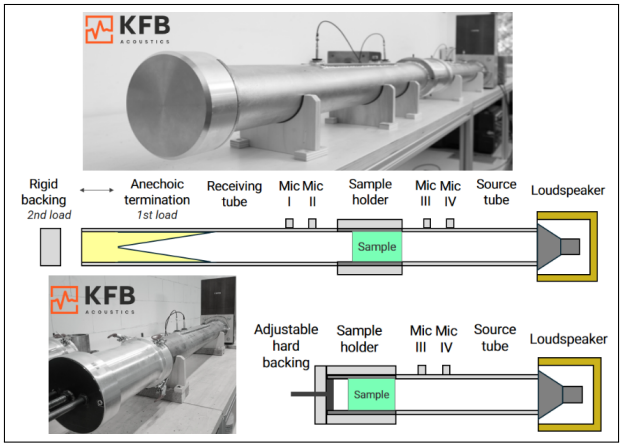


Figure 1. Impedance tube set-up for sound transmission loss and absorption measurements.

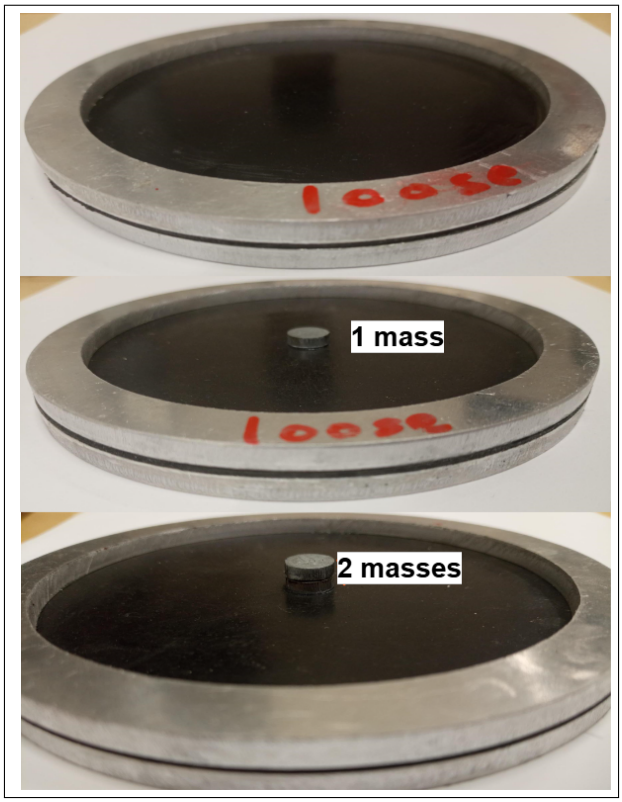


Figure 2. Membrane samples using the same $1\,\mathrm{mm}$ rubber: (1) plain membrane, (2) with one central mass ($10\,\mathrm{mm}$ diameter, $3\,\mathrm{mm}$ thick), (3) with two stacked masses (total $6\,\mathrm{mm}$). Edges clamped with steel rings.

thickness) at the membrane center. Two such masses were stacked in the two-mass configuration, resulting in a total thickness of 6 mm.

The test frequency range spanned from 50 Hz to 1600 Hz. White noise was used as the excitation source, with its level carefully adjusted to avoid nonlinear effects and prevent structural vibrations of the tube or mounting components. Each experiment was repeated three times for the sake of checking consistency.

For the STL measurements, a four-microphone configuration was employed, with an anechoic termination to minimize reflections, following ASTM E2611 [7]. Absorption measurements utilized a two-microphone setup with a rigid backing, in accordance with ISO 10534 [8]. The rigid backing distance from the sample was adjustable to explore different resonance conditions by varying the air gap between the membrane and the backing. In this study, two air gap configurations were tested, with the rigid backing positioned to create an 50 mm air gap and an 100 mm air gap.

Prior to testing, a reference measurement was conducted with an empty tube. The results confirmed that the presence of the steel rings did not introduce significant effects on measurements within the selected frequency range.

2.3 Impedance Tube Simulation

Numerical simulations were conducted using the finite element method (FEM) in COMSOL Multiphysics [9] to analyze the sound transmission loss and absorption performance of the membrane-type resonator. The simulation follows the impedance tube approach in [10] with modified material parameters and implementation. Specifically, incident wave excitation and non-reflecting boundaries were replaced by port-based plane wave excitation and termination, ensuring accurate sound power calculations. Additionally, the membrane was modeled with the Shell Module to capture its flexural motion. The tube was assumed to be rigid, and the membrane edges were set to fixed, consistent with the experimental setup.

Two simulation configurations, as illustrated in Fig. 3, were implemented to correspond with the experimental setups:

- Sound Transmission Loss Simulation: The impedance tube was modeled as a cylindrical waveguide with an internal diameter of 102 mm, matching the actual acoustic passage in the experiment. The STL was obtained by calculating the ratio of incident to transmitted acoustic power at the respective ports.
- Absorption Simulation: A rigid backing was introduced at a controlled distance behind the membrane to investigate absorption characteristics. The absorption coefficient was determined by subtracting the ratio of reflected to incident acoustic power from one at the input port.

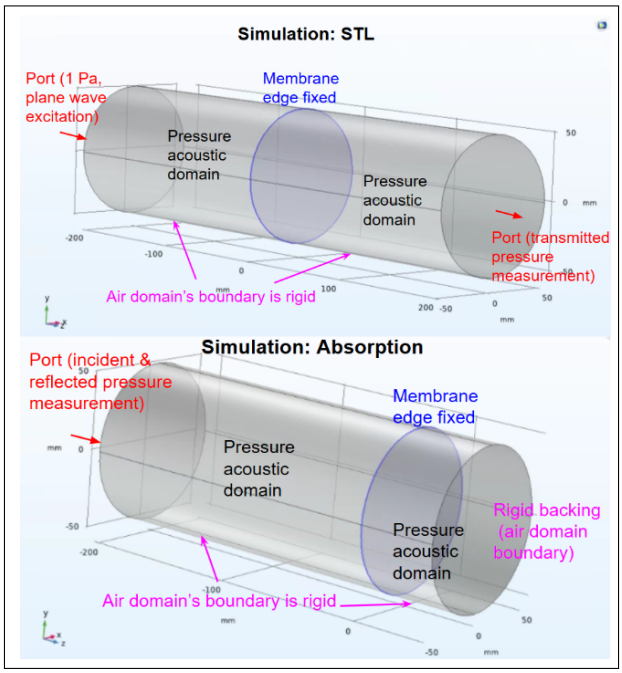


Figure 3. Schematic of the simulation setup of the impedance tube.

The computational domain was discretized using free tetrahedral elements with normal resolution, following built-in mesh size calibration for general physics applications. The number of degrees of freedom in the simulation ranged from approximately 2977 to 3033, depending on the configuration.

Since the exact viscoelastic properties of the rubber membrane were unknown, the material parameters in the simulation were taken from [11], which measured a similar type of rubber. However, these measured values have significant uncertainties, meaning the chosen parameters are only rough estimates. As a result, any differences between the simulation and experiment may be partly due to inaccuracies in the material properties.

2.4 Transmission Chamber Test

The transmission loss measurements were conducted in the V1 Laboratory test stand at the Acoustic Research and Innovation Centre (KFB Acoustics, Poland), designed for measuring airborne sound insulation of vertical partitions and components according to ISO 10140 with standardized window openings. The experimental facility is shown in Fig. 4.

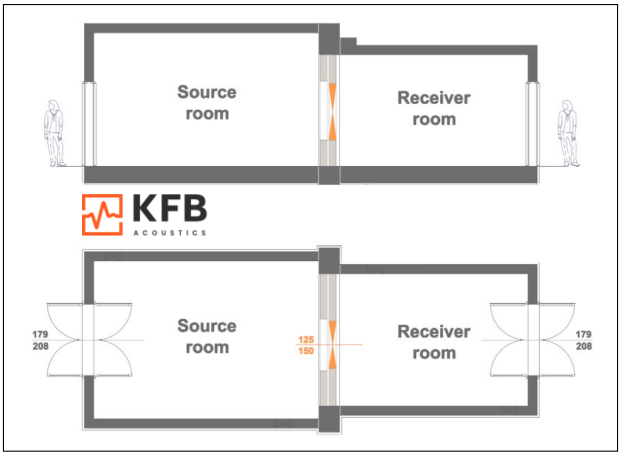


Figure 4. Experimental facility for the transmission chamber test.

Seven configurations were examined:
(1) Steel: a 1.5 mm thick steel plate
(2) Rubber: a 1 mm thick rubber layer
(3) Rubber–Air Gap–Steel: a 1 mm rubber layer with a 50 mm air gap and a steel plate
(4) Membrane Metamaterial: a 1 mm rubber layer supported by a perforated 1.5 mm steel frame with circular cutouts (102 mm diameter, 30 mm spacing)
(5) Membrane Metamaterial–Air Gap–Steel: the metamaterial with a 50 mm air gap and steel plate
(6) Metamaterial + Mass: the metamaterial with a central steel mass in each unit cell
(7) Metamaterial + Mass–Air Gap–Steel: the metamaterial with masses, plus a 50 mm air gap and steel plate.

All samples were mounted in a wooden frame to maintain consistent boundary conditions. As shown in Fig. 5, configuration (6)—a metamaterial with central masses—serves as a representative example of the tested samples, which were assembled within a standardized test window (1250 mm × 1500 mm).

Measurements were conducted following standardized procedures to evaluate the STL of large-scale samples. Two measurement approaches were employed to ensure both standardized evaluation and high-resolution analysis:

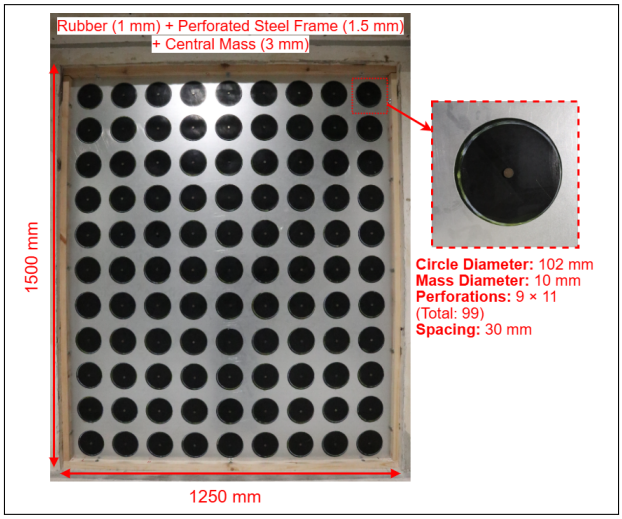


Figure 5. Configuration (6): membrane-type metamaterial consisting of a 1 mm-thick rubber layer and a perforated 1.5 mm-thick steel frame (9 × 11 circular cutouts, 102 mm diameter, 30 mm spacing), with a central steel mass (10 mm diameter, 3 mm thick) in each unit cell.

- Method 1 (ISO 10140 [12]): A calibrated omnidirectional loudspeaker generated white noise. Reverberation time (RT60) as measured via the interrupted noise method at six microphone positions. The STL measurements were performed using the Norsonic Nor850 Measurement System with a rotating boom for spatial averaging. Additionally, microphone signals were split: one for 1/3-octave band processing, the other recorded for finer-resolution post-processing.
- Method 2 (ISO 18233 [13]): A custom logarithmic sine sweep (40 Hz–2000 Hz, 10 s duration + 5 s silence) was used as excitation, played from the same loudspeaker. The signal was played and recorded using the Head Acoustic SQuadriga III module. Measurements were conducted with fixed loudspeaker and microphone positions to maintain time-invariance. The STL was computed based on the difference in impulse responses measured in the source and receiving rooms, while RT60 was de-

rived using the Schroeder integral method. This method enables post-processing in both 1/3-octave bands and finer resolution (every 5 Hz).

3. RESULTS AND DISCUSSION

3.1 STL and Absorption in Impedance Tube

Impedance tube measurements for STL and absorption (Fig. 6, Fig. 7) provide insights into membrane acoustic performance.

As observed in Fig. 6, even the plain rubber sample exhibits a notable STL peak around 200 Hz, reaching approximately 14 dB. This peak can be attributed to the lowest vibrational mode induced by the fixed boundary conditions at the sample's edges. Apart from its resonance, the overall STL trend increases with frequency, which aligns with the expected mass-law trend of a single material layer.

Introducing a small steel mass at the membrane center modifies the vibrational response, leading to a shift of the main STL peak toward lower frequencies. The STL magnitude at resonance is also enhanced, indicating improved low-frequency isolation. Using two masses amplifies this effect, showing that localized mass can tune the membrane's resonance behavior, as also reported in literature [14].

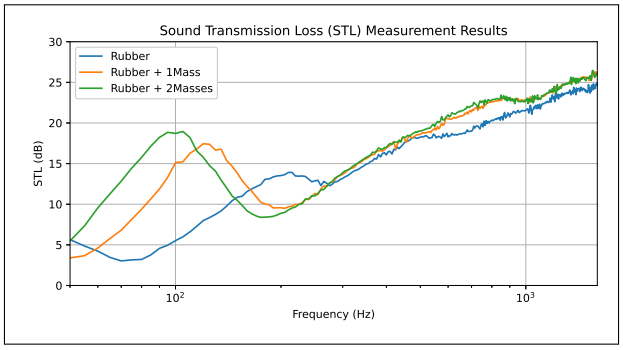


Figure 6. Impedance tube measurement for sound transmission loss of three rubber samples.

The absorption coefficients of the samples, measured under different air gap configurations (50 mm and 100 mm), are presented in Fig. 7. The plain rubber membrane exhibits multiple absorption peaks, with the first low-frequency peak becoming more pronounced and shifting to lower frequencies as the air gap increases, suggesting a significant membrane-cavity interaction, with the membrane as mass and the air cavity as a spring. The second peak corresponds to the membrane's structural mode, which is less affected by the air gap.

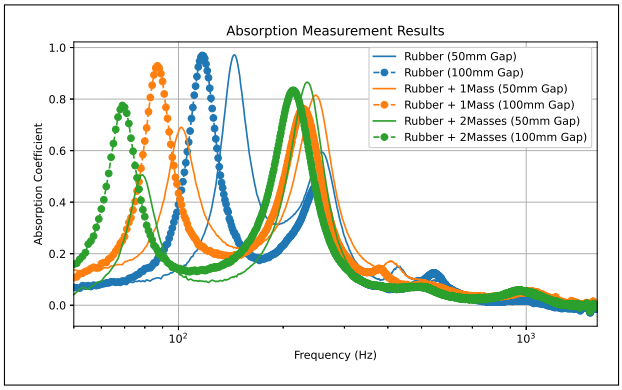


Figure 7. Impedance tube measurement for absorption of three rubber samples under different air gap configurations.

When a single steel mass is added, the first absorption peaks move to lower frequencies, similar to the trend seen in the STL results. This suggests that the added mass changes the membrane's resonance, affecting how it interacts with the backing cavity. With two masses, the resonance shifts further to lower frequencies, although the absorption amplitude becomes smaller.

To further validate the impedance tube results, another rubber sample without added mass was tested, and its STL and absorption performance were compared with simulations, as shown in Fig. 8 and Fig. 9. Due to the differences in experimental setups—STL measured for the membrane alone and absorption measured with a 50 mm air gap and a rigid backing—the two cannot be directly compared. However, both experimental and simulated results revealed a complementary relationship between STL and absorption.

In the STL results, the simulation captures the first and second resonance peaks observed experimentally, while the absorption simulation identifies three primary peaks, aligning well with the measurements. The main STL peak and absorption peaks appear in similar frequency regions, confirming that the numerical model accurately represents the essential resonance behavior of the membrane.

This complementary relationship is reflected in the resonance characteristics: STL peaks correspond to absorption dips, as strong resonance blocks sound transmis-

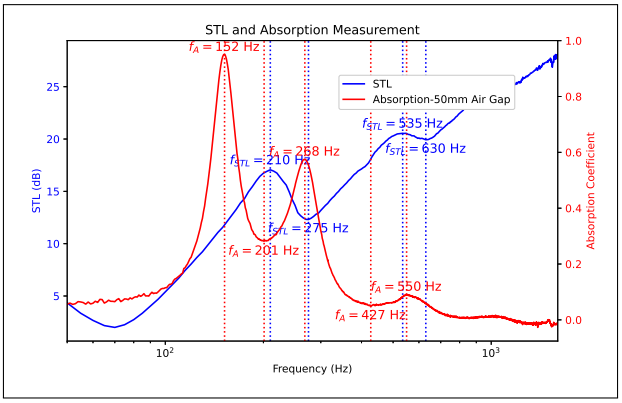


Figure 8. Measured sound transmission loss (STL) and absorption coefficient of a rubber sample without added mass. Peaks and dips are marked to indicate resonance behaviors.

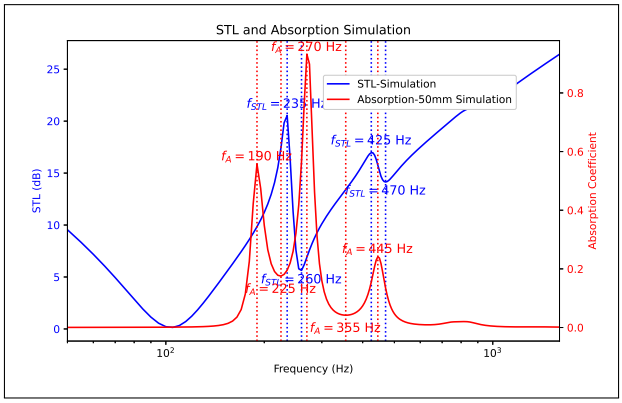


Figure 9. Simulated STL and absorption coefficient of a rubber sample without added mass. Marked peaks and dips highlight resonance effects captured in the model.

sion but increases reflection, reducing energy dissipation. Conversely, absorption peaks occur when the membrane couples more effectively with the backing cavity, enhancing energy dissipation and reducing STL. However, in the STL experiment, the membrane vibrates without the rigid backing, so while STL and absorption show a complementary trend, their peaks and dips don't always align.

It is further important to recognize that the precise values of STL and absorption in the simulation are highly dependent on the assumed material parameters. Factors such as mass per unit area, elastic properties, pre-stress conditions, and damping characteristics can all impact the frequency and amplitude of the response. Though not detailed here, these factors are relevant for future model refinement.

3.2 STL Results in the Transmission Chamber

Figures 10 and 11 show STL measurements in 1/3-octave bands from the transmission chamber, obtained using the Norsonic analyzer for both single-layer and double-layer configurations, with the single value Rw included.

In the single-layer case (Figure 10), the steel panel shows the highest STL across the full frequency range, following the expected mass law behavior. In contrast, the much lighter rubber panel exhibits significantly lower STL. A dip around 80 Hz for both steel and rubber may result from the coupling of the room and sample. It should be noted that results below 100 Hz are presented for informational purposes only, as they fall outside the effective measurement range of the laboratory setup, where uncertainties in the data may arise. The membrane metamaterial (rubber bonded to a perforated steel frame) improves the STL over plain rubber, performing better above 160 Hz. The dip observed around 80 Hz for steel and rubber appears shifted in the metamaterial, likely due to changes in resonance behavior. Adding a central mass to the membrane further enhances the STL below 200 Hz, indicating a local resonance mechanism.

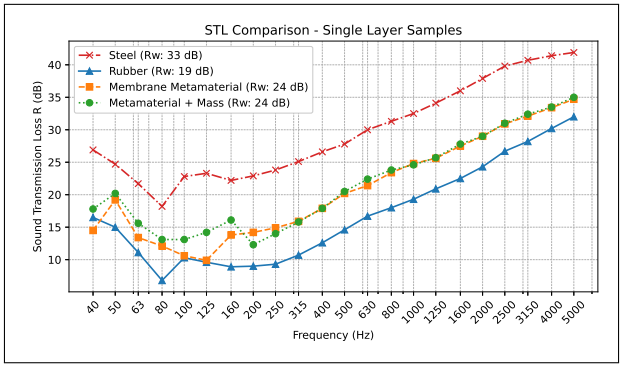


Figure 10. STL of single-layer samples measured using the Norsonic analyzer.

The double-layer samples (Figure 11) represent a more realistic wall structure, consisting of a decoupled cavity between a front rubber layer and a steel panel. Compared to single-layer configurations, the rubber–air–steel structure already achieves higher STL in the

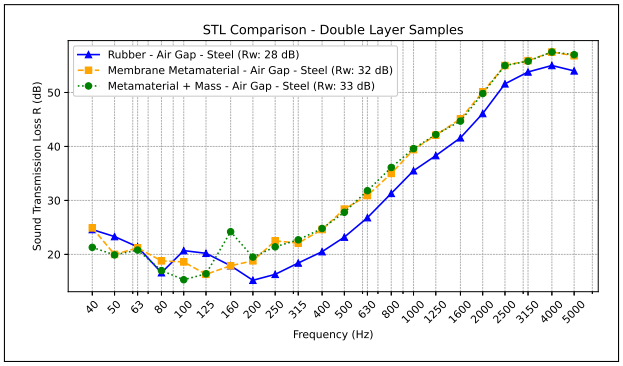


Figure 11. STL of double-layer samples measured using the Norsonic analyzer.

mid-to-high frequency range due to added mass and decoupling. However, a low-frequency dip appears around 200 Hz, resulting from the mass-spring-mass resonance, within the range predicted by a typical resonance calculation (e.g., [[1]]).

Replacing the rubber layer with a membrane metamaterial, the 200 Hz dip of the rubber–air–steel configuration becomes less noticeable. The overall STL improves in the mid-to-high frequency range, due to increased surface density. More significantly, the metamaterial introduces an STL enhancement around 250 Hz, attributed to local resonance effects. Adding a central mass shifts the resonance to around 160 Hz, improving the STL by about 6 dB compared to the rubber–air–steel configuration at this frequency.

The low-frequency STL enhancement observed in the transmission chamber is consistent with impedance tube measurements. In both setups, adding a central mass shifts the dominant resonance toward lower frequencies and increases STL, though the resonance peaks appear at different frequencies due to boundary conditions and interactions with the surrounding frame and air cavity.

This confirms that locally resonant metamaterials can improve sound insulation in both idealized tube and realistic large-scale wall applications.

To complement the standardized ISO 10140 measurements, two alternative methods—noise recording and swept-sine signal excitation—were used to extract the level difference between the source and receiver rooms at finer frequency resolution. The level difference improvement, shown in 1/3-octave bands (Figure 12) and at finer frequency resolution (Figure 13), quantifies the increased isolation achieved by the metamaterial samples compared to the rubber reference.

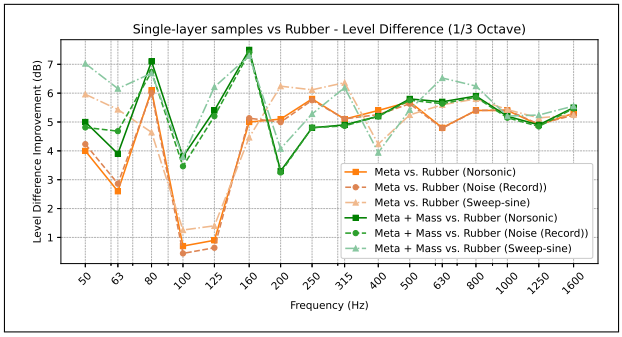


Figure 12. Effect of single-layer metamaterial samples on sound pressure level difference between source and receiving rooms, compared to the rubber reference, in 1/3-octave bands using three methods.

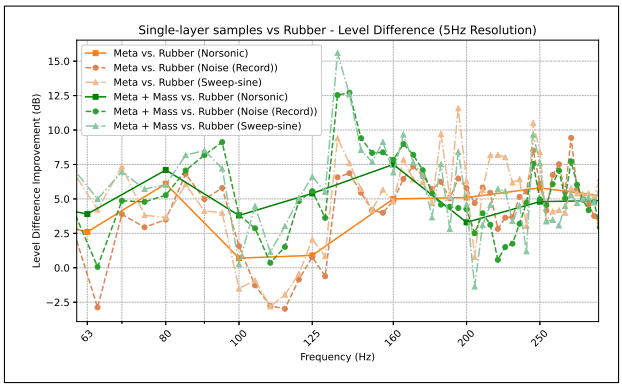


Figure 13. Level difference improvement (60–300 Hz) of single-layer metamaterials over rubber, 5 Hz resolution.

In 1/3-octave bands, all methods show similar trends. The noise recording data aligns well with Norsonic data, while swept-sine shows greater deviation. At finer resolution (5 Hz), swept-sine reveals sharper low-frequency peaks, suggesting better sensitivity to local resonance, although small mismatches due to timing, filtering, or noise remain.

Given the current stage of development, the ISO 10140 method provides the most stable and interpretable data for comparison across configurations and is therefore used as the primary dataset in this study.

4. CONCLUSION

This study investigated the sound insulation performance of a membrane-type acoustic metamaterial layer through a combination of numerical simulations, impedance tube measurements, and scaled-up transmission chamber tests. The results confirm the presence of low-frequency STL enhancement due to local resonance effects, particularly when central masses are added to the membrane. These effects were consistently observed across both small and large experimental configurations, demonstrating the metamaterial's potential for application in lightweight and retrofittable wall systems.

Despite the promising results, several limitations remain. Variations in sample fabrication, limited control over membrane pretension, and measurement uncertainties—especially in fine-resolution methods—may affect the accuracy of the results. Additionally, material parameter uncertainties in simulations restrict direct quantitative comparisons.

Future work will focus on improving sample consistency, refining structural designs to better control resonance frequencies, and implementing higher-precision measurement workflows. These developments aim to further explore and optimize the practical application of membrane-type metamaterials in building acoustics.

5. ACKNOWLEDGMENTS

This project has received funding from the European Union's Horizon Europe research & innovation programme under the HORIZON-MSCA-2021-DN-01 grant agreement No. 101072598 –"ActaReBuild".

6. REFERENCES

[1] R. Zeng, E. Deckers, C. Glorieux, D. Urbán, and B. Chmielewski, "Wall-applicable metamaterial: mitigating resonance dip for enhanced sound transmission loss," in *Proc. INTER-NOISE and NOISE-CON*, pp. 7144–7155, 2024.

[2] N. B. Roozen, D. Urban, E. A. Piana, and C. Glorieux, "On the use of dynamic vibration absorbers to counteract the loss of sound insulation due to mass-spring-mass resonance effects in external thermal insulation composite systems," *Applied Acoustics*, vol. 178, p. 107999, 2021.

[3] G. Ji and J. Huber, "Recent progress in acoustic metamaterials and active piezoelectric acoustic metamaterials: a review," *Appl. Mater. Today*, vol. 26, p. 101260, 2022.

[4] Y. Zhang, J. Zhang, Y. Li, D. Yao, Y. Zhao, Y. Ai, W. Pan, and J. Li, "Research progress on thin-walled sound insulation metamaterial structures," in *Acoustics*, vol. 6, pp. 298–330, 2024.

[5] A. Arjunan, A. Baroutaji, J. Robinson, A. Vance, and A. Arafat, "Acoustic metamaterials for sound absorption and insulation in buildings," *Build. Environ.*, p. 111250, 2024.

[6] C. Wang, L. Cai, M. Gao, L. Jin, L. Sun, X. Tang, G. Shi, X. Zheng, and C. Guo, "Manufacturing of membrane acoustical metamaterials for low frequency noise reduction and control: a review," *Mech. Adv. Mater. Struct.*, vol. 31, no. 25, pp. 7008–7023, 2024.

[7] "Standard test method for measurement of normal incidence sound transmission of acoustical materials based on the transfer matrix method," Tech. Rep. ASTM E2611-19, ASTM International, 2019.

[8] "Acoustics — determination of sound absorption coefficient and impedance in impedance tubes — part 2: Transfer-function method," Tech. Rep. ISO 10534-2, International Organization for Standardization, 1998.

[9] COMSOL AB, *COMSOL Multiphysics® v. 6.1*, 2022.

[10] R. Zeng, E. Deckers, C. Glorieux, D. Urbán, and B. Chmielewski, "Locally resonant metamaterial wall targeting tonal noise arising from heat pumps in residential buildings," in *Proc. ISMA 2024—Int. Conf. on Noise and Vibration Eng.*, pp. 2652–2661, 2024.

[11] A. Dobrucki, R. Bolejko, P. Nieradka, and A. Klimek, "Generalized oberst beam method for measuring viscoelastic parameters of layered composite components," *Arch. Mech.*, vol. 75, no. 1-2, pp. 27–52, 2023.

[12] "Acoustics — laboratory measurement of sound insulation of building elements," Tech. Rep. ISO 10140-2:2010, International Organization for Standardization, 2010.

[13] "Acoustics — application of new measurement methods in building and room acoustics," Tech. Rep. ISO 18233:2006, International Organization for Standardization, 2006.

[14] C. J. Naify, C.-M. Chang, G. McKnight, and S. Nutt, "Transmission loss and dynamic response of membrane-type locally resonant acoustic metamaterials," *J. Appl. Phys.*, vol. 108, no. 11, 2010.

DOI: 10.61782/fa.2025.0321



FORUM ACUSTICUM
EURONOISE 2025

EFFECT OF LOAD PLATE MASS ON DYNAMIC STIFFNESS DETERMINATION

Daniel Urban[1,2*] **Maximilian Neusser**[1]

[1] Research Division for Building Physics, Institute of Material Technology, Building Physics, and Building Ecology, Faculty of Civil Engineering, Technische Unviersität Wien, Karlsplatz 13, A-1040 Vienna
[2] Department of Materials Engineering and Physics, Faculty of Civil Engineering, STU Bratislava, Radlinského 2766/11, 810 05 Bratislava, Slovakia

ABSTRACT

This study investigates the effect of load plate mass on the dynamic stiffness determination of resilient materials used in acoustic applications, specifically through the single mass method outlined in ISO 9052-1. The standard method, primarily designed for materials under floating floor conditions, may not be applicable for acoustic material stiffness determination in constructions used in cavity dampening solutions (e.g. wall linings) or heavy machinery foundations, due to differing load conditions. The study aims to assess how varying load plate masses influence the apparent dynamic stiffness of several resilient materials, including EPS, mineral wool, wood fibre, and foamed polyurethane elastomers. Experiments were conducted using load plates with total mass range from 0.868 kg to 7.665 kg . The results show a significant reduction in dynamic stiffness when the material is subjected to lower loads. Notably, for lighter load plates, nonlinearities and contact disruptions between the load plate and the material were observed, impacting the accuracy of dynamic stiffness measurements following the ISO 9052-1 measurement procedure. This study highlights the importance of considering load conditions when interpreting dynamic stiffness values in acoustic applications, especially in structures like double walls, where load and deformation conditions differ from those prescribed in ISO 9052-1.

Keywords: *dynamic stiffness, load plate mass effect, experiment, case study).*

1. INTRODUCTION

The ISO 9052-1 standard [1] is frequently employed in building acoustics to determine the dynamic stiffness of resilient materials. Originally, this method was specifically designed for evaluating materials used beneath floating screeds, particularly those with smooth surfaces laid in a continuous layer. However, the applicability of this standard is limited to materials subjected to compressive loads between 0.4 kPa and 4 kPa. It is therefore unsuitable for materials experiencing lower loads, such as those found in wall cavities, or higher loads, such as in machinery foundations. Despite these specified limitations, dynamic stiffness values obtained using the ISO 9052-1 method are often referenced in studies analysing the sound insulation performance of lightweight wall systems to often used to predict the mass-spring-mass resonance frequency, even though the materials in such constructions are subjected to markedly different loading and boundary conditions. This inconsistency prompted us to investigate the extent to which variations in compressive loading influence the dynamic stiffness of resilient materials. Understanding this relationship is particularly relevant when examining how loose-form resilient materials contribute to a wall's

*Corresponding author: daniel.urban@tuwien.ac.at.
Copyright: ©2025 First author et al. This is an open-access article distributed under the terms of the Creative Commons Attribution 3.0 Unported License, which permits unrestricted use, distribution, and reproduction in any medium, provided the original author and source are credited.

acoustic behaviour. This need has been repeatedly emphasized in cases of studying the stiffness of loose form materials implemented in double [2–4] walls, but also in the case of research related to the stiffness of ETICS [5]. Building upon findings reported in previous studies [6, 7], we hypothesized that resilient materials exhibit reduced stiffness under lower loads. The mechanical behaviour of elastic, soft, and porous materials is often complex and subject to varying interpretations. Their apparent stiffness is influenced not only by the degree of compression or applied load [8], but also by the boundary conditions under which the material is installed [9, 10]. In particular, the material's response is affected by factors such as the sealing of contact surfaces, the geometric dimensions of the resilient layer, and the compliance or stiffness of the applied load mass. These variables can significantly alter the measured stiffness, complicating the evaluation of the material's performance in real-world applications. This study highlights the importance of considering load conditions when interpreting dynamic stiffness values in acoustic applications, especially in structures like sandwich panels, where load and deformation conditions differ from those prescribed in ISO 9052-1. The case study focusing on how the mass of the load plate affects the measured dynamic stiffness of commonly used resilient materials is presented in this paper.

2. CASE STUDY DESCRIPTION

2.1 Materials under test

A case study was conducted with the objective of comparing commonly utilized resilient materials frequently encountered in practical applications. The investigation accounted for the assumption that material stiffness would decrease under reduced loading conditions. The materials selected for evaluation were as follows:

All test samples had a lateral edge dimension of 0.20 m, except for the PU elastomer sample, which measured 0.10 m. Testing procedures were conducted in accordance with ISO 9052-1, with minor deviations: no plaster intermediary layer was applied between the steel plate and the material sample (goal was to simulate boundary conditions similar to conditions applied in dry building processes), and the interface between the test base and material was not sealed. These deviations are not expected to significantly influence the experimental outcome, as the primary aim was not the precise quantification of dynamic stiffness, but rather to examine the influence of varying load magnitudes on relative stiffness variation, particularly in the context of resonance response behaviour.

Table 1. Thicknesses of individual resilient materials.

Material	thickness in m
EPS	0.04
XPS	0.04
Light MW	0.02
Heavy MW	0.01
Wood Fibre Board	0.01
PU Elastomer	0.025



Figure 1. Example of a measurement setup - measurement of a sample marked Light MW.

2.2 Measurement setup and procedure

Three types of loading plates were employed in the testing. Two plates had dimensions of height × 0.20 m × 0.20 m and masses of m_{lp1}= 7.665 kg and m_{lp2}= 1.263 kg, respectively. The third plate had dimensions of height × 0.19 m × 0.19 m and a mass of m_{lp3}= 0.868 kg see (Fig. 1). The motivation behind this variation of unequal surface dimension case was to assess the effect of localized deflection in the damping material at the periphery of the load plate on

the measured dynamic stiffness. A logarithmic frequency sweep signal was applied to excite the specimens using a shaker, and the resulting data were extrapolated to a zero-force amplitude condition. Excitation was provided by a TIRAvib 50018 shaker driven by a TIRA E60 analog power amplifier. The dynamic response was captured using a Dytran 3055B2 accelerometer and a Dytran 1051V1 force sensor, with data acquisition handled via NI 9234 hardware. Data analysis was performed using an automated routine developed in MATLAB.

3. RESULTS

A series of dynamic stiffness measurements were performed for selected resilent materials that can be encountered in practice in horizontal and vertical building structures. The measurements were performed using three different load plates as explained in the previous chapter. Apparent dynamic stiffness was determined by extrapolation to zero excitation force in agreement to standard [1] (see Fig. 3). Individual resulting dynamic stiffness values are presented in Tab. 2.

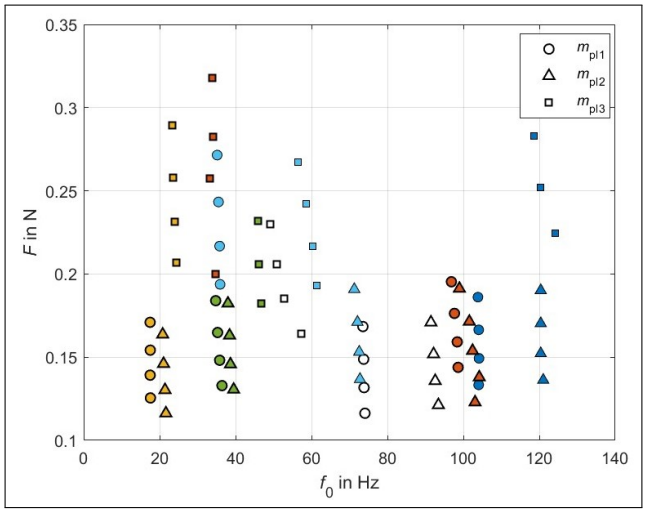


Figure 2. Measured resonance frequencies for three load plate variants and individual material types. Markers sequentially indicate the specific load plate used during the experiment: ○ - m_{lp1}; △ - m_{lp2}; □ - m_{lp3}. Materials are color coded - EPS (white); XPS (dark blue); Light MW (yellow); Heavy MW (green); Wood Fibre Board (red); PU Elastomer (light blue).

First of all, it should be noted that the use of a low-mass load plate can be associated with several problems. The first is the self-resonance of the load plate. The used load plates had their first natural resonance frequency in free boundary conditions (steel plates only) at frequencies $f_{0,\mathrm{m,lp1}}$=1942 Hz, $f_{0,\mathrm{m,lp2}}$=331 Hz and $f_{0,\mathrm{m,lp3}}$=367 Hz. Therefore, it is important to have the assumed resonance of the measuring system under strict control when evaluating selected materials. As was shown in the experiments, the effect of reducing the load had such a significant effect on the reduction of stiffness that resonance phenomena always occurred in the region below 130Hz.

Here, a second important note was opened: the assumption is that individual materials will show significantly lower stiffness when loaded by a light plate. This is related to the compression of the tested samples due to the pull. Zhou has already addressed this issue [6].

The third complication is the bouncing of the plate with a low mass. Of course, applying a thin layer of plaster could have helped slightly here to achieve a better connection of the load plate and the individual layers. However, since the aim was to test the samples under conditions that can be encountered in dry construction processes as well as in applications in vertical structures (e.g. wall cavities, double walls), plaster was not additionally applied. The aforementioned bouncing of the load plate was already evident at low excitation values in the materials Wood fibre boards, EPS and XPS. This was of course also reflected in the results themselves. Table Tab. 2 presents a significant decrease in stiffness recorded in all samples by reducing the load mass. However, the unsystematic behaviour of the resonance response was evident precisely in the mentioned relatively stiffer materials

The PU Elastomer sample had smaller area dimensions than each of the load plates. In this case, the effect of the load on the resulting actual stiffness of the resilient material was clearly demonstrated. The dynamic stiffness, depending on the type of load plate, decreased from 43.56 MN/m^3 to 18.94 MN/m^3. The loading effect effect was of course also evident in the MW type fibrous materials. In this case, load plates 1 and 2 had the same area dimensions as the area of the damping pad. Here, the actual stiffness decreased from 2.37 to 0.71 MN/m^3 and from 12.5 to 2.29 MN/m^3, respectively. Since load plates 2 and 3 have the same mass per unit area (24 kg/m^2) but different contact areas, we could expect slight differences in the determined results of the actual dynamic stiffness in this case. In both cases, MWs showed a slight increase in stiffness by applying m_{lp3} (3 to 28 %). This can be explained by the effect of increased flow resistivity on the resulting actual stiffness

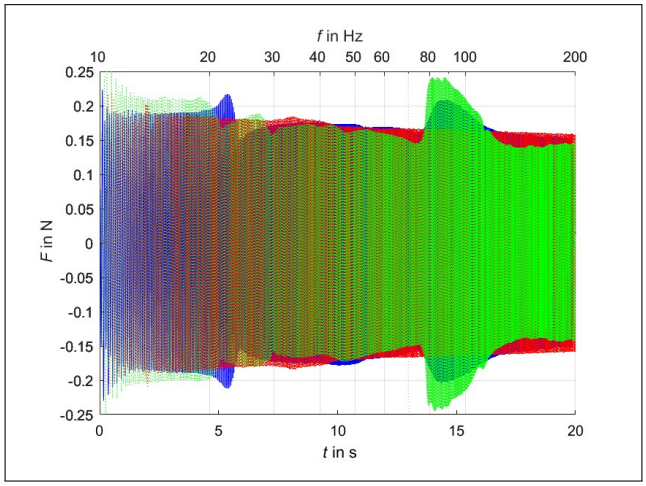


Figure 3. Example of a time record of force during logarithmic sweep excitation. Tested material XPS. Load plate type applied was color coded - m_{lp1} (red); m_{lp2} (blue); m_{lp3} (green);

of the sample as well as local overpressure of the sample at the edge of the light load plate. A similar effect can also be observed for the XPS sample. However, this result must be taken with a "grain of salt" since the XPS had a lattice texture on the surface.

Table 2. Determined dynamic stiffness depending on the load.

Material	s' in MN/m^3		
Load plate	m_{lp1}	m_{lp2}	m_{lp3}
EPS	42.78	11.95	5.52
XPS	82.81	18.63	19.82
Light MW	2.37	0.71	0.91
Heavy MW	12.5	2.29	2.36
Wood Fibre Board	81.61	14.84	1.21
PU Elastomer	43.56	29.35	18.94

4. CONCLUSIONS

This study investigated the effect of the weight of the load plate on the determination of the dynamic stiffness of soft materials used in acoustic applications, in particular according to the method defined by ISO 9052-1. The results showed that reducing the weight of the load plate leads to a significant decrease in the measured dynamic stiffness. This effect was particularly pronounced for materials with higher elasticity. However, this was due to the occurrence of nonlinearity associated with the interruption of contact between the plate and the material. This is very important, for example, for accurate prediction of $f_{\text{m-s-m}}$, which plays a role in evaluating the low-frequency performance of building elements.

Especially in vertical structures such as wall cladding or double walls, the materials are not exposed to the same load as in floor structures. Therefore, it is necessary to develop or recommend a measuring set-up that can accurately determine the actual stiffness of these materials. This set-up must: - eliminate the effect of the shaker pressure, which can affect the accuracy of the measurement, - ensure permanent contact between the load plate and the damping material even without the use of a gypsum layer.

The obtained results show that current measurement methods can distort dynamic stiffness values, especially under low load conditions, thus underlining the need to develop a more suitable variation of measurement techniques for soft structural elements loaded by low mass in various applications.

5. ACKNOWLEDGMENTS

The authors acknowledge the financial support from the AUSTRIAN SCIENCE FUND (FWF), grant number I 5503-N, (Engineered wood composites with enhanced impact sound insulation performance to improve human wellbeing), the support of all project partners of the research project "Schall.Holz.Bau II" and the project "NÖ Wirtschafts- und Tourismusfonds" in the funding track "Kooperation" under the number WST3-F2- 525823/007-2018. Author DU acknowledges support by the Slovak national grant VEGA 1/0205/22, KEGA 033STU-4/2024 by funding from the European Union's Horizon Europe research and innovation programme under the HORIZON-MSCA-2021-DN-01 grant agreement No. 101072598 – "ActaReBuild".

6. REFERENCES

[1] "ISO 9052-1:1989. Acoustics — determination of dynamic stiffnesspart 1: Materials used under floating floors in dwellings," 1989.

[2] M. Neusser, F. Dolezal, M. Wurm, H. Müllner, and T. Bednar, "Evaluation of the acoustic and environmental performance of different wall structures with particular emphasis on straw," *Journal of Building Engineering*, vol. 66, p. 105922, 2023.

[3] M. Neusser, D. Urban, F. Dolezal, and H. Müllner, "The influence of different material properties of straw on the building acoustic performance of lightweight wall constructions," *Cellulose*, vol. 5, pp. 3–7, 2023.

[4] M. Neusser, D. Urban, and H. Müllner, "Acoustic performance and measurement challenges of loose blown-in insulation materials in wall constructions: A focus on straw," *Building Acoustics - Accepted for publication*, 2025.

[5] H. Bietz and V. Wittstock, "Investigations to determine the dynamic stiffness of elastic insulating materials," in *Proc., Euronoise*, 2018.

[6] J. Zhou, P. Zhao, and B. Z. Yang, "Apparent impact sound insulation performance of continuous floating concrete toppings on mass timber slab floors," *Journal of Architectural Engineering*, vol. 30, no. 4, p. 04024035, 2024.

[7] I. L. Ver, "Measurement of dynamic stiffness and loss factor of elastic mounts as a function of frequency and static load," *Noise Control Engineering*, vol. 3, no. 3, pp. 37–42, 1974.

[8] A. Schiavi, C. Guglielmone, and P. Miglietta, "Effect and importance of static-load on airflow resistivity determination and its consequences on dynamic stiffness," *Applied Acoustics*, vol. 72, no. 9, pp. 705–710, 2011.

[9] C. Crispin, C. Mertens, and J. Medved, "Measurement of the dynamic stiffness of porous materials taking into account their airflow resistivity," *Building Acoustics*, vol. 21, no. 3, pp. 221–233, 2014.

[10] M. Schmelzer, V. Wittstock, H. Bietz, and S. Brezas, "On the influence of the air flow resistivity on the measurement of the dynamic stiffness of underlays for floating floors," *Acta Acustica*, vol. 5, p. 13, 2021.

DOI: 10.61782/fa.2025.0358

FORUM ACUSTICUM EURONOISE 2025

EVALUATING RECYCLED PET FILAMENTS AS A SUSTAINABLE SOUND ABSORBING MATERIAL FOR BUILDING RETROFITTING

Joaquin Garcia[12*] **Diego Tonetti**[1] **Edoardo Alessio Piana**[1] **Ondrej Jiricek**[2]
[1] Applied Acoustics Laboratory, University of Brescia, via Branze 38, Brescia, Italy.
[2] Czech Technical University in Prague, Jugoslávských partyzánů 1580/3, Prague, Cechia.

ABSTRACT

The development of sound absorbers made from PET fibres from recycled PET bottles presents a cheap and attractive solution for building retrofit applications. PET fibres of about 2-4 mm width are processed into a structure through random compaction and heat treatment, resulting in a sample that retains its shape. The normal incidence sound absorption coefficient of the samples was derived through measurements in an impedance tube, exhibiting potential effectiveness as a sound absorber. An innovative application of this material is the creation of transparent devices. This unique feature allows for sound attenuation without sacrificing natural light infiltration, addressing the common conflict between acoustic treatment and daylight access in architectural design. These items can serve as transparent partitions, sound absorbers, or design gadgets for lighting in areas near windows. Furthermore, using recycled PET fibres not only contributes to waste reduction but also promotes sustainability in construction, aligning the research's aim with contemporary environmental goals. By offering functional aesthetic solutions that enhance both acoustic comfort and visual appeal, these PET fibre-based sound absorbers hold potential for improving the habitability of retrofitted spaces.

Keywords: *Recycled materials, sound absorption, PET, building retrofitting*

**Corresponding author*: jorge.garcia@unibs.it.
Copyright: *©2025 Garcia et al. This is an open-access article distributed under the terms of the Creative Commons Attribution 3.0 Unported License, which permits unrestricted use, distribution, and reproduction in any medium, provided the original author and source are credited.*

1. INTRODUCTION

The polymerisation process yields polyethylene terephthalate (PET), which involves two main chemical reactions: 1) esterification Reaction: this involves the reaction between terephthalic acid and ethylene glycol; 2) trans-esterification Reaction: The latter process involves the reaction between ethylene glycol and dimethyl terephthalate. In both processes, the resulting product is PET in the form of a molten, viscous mass. This can then be spun into fibres or extruded and moulded into various shapes. Commonly used for beverage packaging, polyethylene terephthalate (PET) bottles have found interesting applications. Their unique material properties, such as lightweight, durability, and ease of manipulation, make them suitable for acoustic applications. Mainly, researchers have explored the use of PET bottles in constructing sound-absorbing panels, resonators, and diffusers. These applications leverage the inherent characteristics of PET to enhance sound quality and control noise reflection in different environments. There may be some environmental advantages to using PET bottles in acoustics. For example, recycled PET bottles are used to make PET felt acoustic panels, which helps keep plastic trash out of landfills. This recycling method reduces the total environmental impact by using less water and energy compared to producing new fabric materials. The current manuscript explores the idea of using a material made from PET bottles that uses even less energy. PET felt panels also emit fewer volatile organic compounds (VOCs), which improves the quality of the air indoors. These panels' resilience and recyclability contribute to their sustainability and support a circular economy. Several studies have demonstrated the effectiveness of PET bottles in acoustic applications. One study investigated the acoustic properties of rigid polyurethane foam mixed with shred-

ded PET bottle waste, finding that the composite material exhibited improved sound absorption properties [1]. Another study highlighted the use of PET felt acoustic panels, which are made from recycled PET bottles and offer enhanced acoustic performance along with environmental benefits [2]. Additionally, research has shown that PET bottle-based materials can be used to create effective sound diffusers. A study explored the use of PET bottles filled with different materials to create Helmholtz resonators, which were found to significantly improve sound absorption at specific frequencies [3]. Another investigation focused on the use of PET bottles in HVAC systems as Helmholtz resonators, demonstrating their potential to reduce annoyance from ventilation ducts [4]. These examples underscore the potential of PET bottles in creating sustainable acoustic solutions.

2. MATERIALS AND SAMPLES

The samples were prepared starting from plastic PET bottles fraied using a tool developed in the Applied Acoustics Laboratory (Figure 1). In this way, it was possible to obtain long PET filaments that were 0.5 mm thick and 4 mm wide.

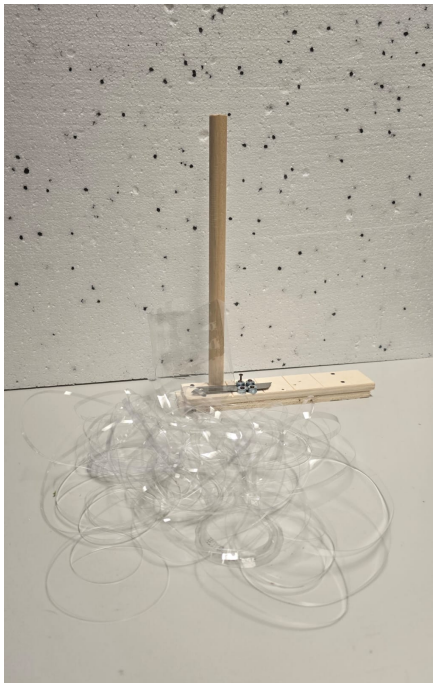


Figure 1. Tool used to obtain the PET filaments.

The filaments were placed inside the sample holder, an aluminium tube with a diameter of 46 mm and a length of 100 mm. Given the stiffness of the PET filaments, they cannot remain in place inside the tube because they tend to regain the original shape. For this reason, the PET filaments and the sample holder were placed inside an air fryer for 5 minutes at a temperature of about 80 °C. As shown in Figure 2, at the end of the thermal treatment, the sample could easily keep the desired dimensions and was ready to be tested in the impedance tube.



Figure 2. Example of a sample after thermal treatment and a 100 mm sample ready to be tested in the impedance tube.

3. EXPERIMENTAL SETUP

3.1 Impedance tube measurements

We tested the sample in a four-microphone impedance tube in accordance with the ASTM E2611 standard [5]. The applied technique allows the determination of the sound pressure and particle velocity at either side of the sample and thus its transfer matrix. As standard results, the normal incidence sound absorption, and the Transmission Loss (TL) of the sample are available at the end of the testing procedure. Nonetheless, the available results

can be extended to other quantities, like the wave number, the speed of sound in the material, the surface impedance, and the characteristic impedance (inside the material). For the preliminary study presented in the current manuscript, only the sound absorption and the TL will be presented and discussed.

At one endpoint of the tube, a loudspeaker generates a wide-band white noise test signal. The tube mounts the sample for testing in its central section, sandwiched between two pairs of microphones. You can equip the tube's second endpoint with either anechoic or reflecting termination, enabling you to conduct tests with two distinct boundary conditions. Being able to compare signals from four microphones helps to separate the sound wave into the parts that are coming in and bouncing back on both sides of the sample. The custom-made impedance tube consists of two segments of length 1200 mm and internal diameter 45 mm. The corresponding cross-section allows keeping the plane-wave assumption valid up to about 3800 Hz. The source endpoint features a loudspeaker of 100 mm enclosed in a sealed volume, while the second endpoint can be connected to a rigid reflective termination or to an anechoic termination. The microphone ports for high-frequency measurements are spaced 45 mm apart; the ports for low-frequency measurements are spaced 500 mm. The sample can be placed in a separate segment of tube of the most appropriate length, which can subsequently be installed between the two measurement sections described above. Four BSWA Type MPA416 microphones housed in o-ring-equipped ports have been used. The diaphragm of the microphones is recessed with respect to the side wall of the tube. We connect the transducers to an OROS Type OR36 analyser, which measures the complex transfer functions between the microphones. During the measurements, the coherence function is also monitored to check that the signal-to-noise ratio is high enough over all the frequency range of interest. The white noise employed as a test signal is generated by the analyser itself.

For symmetric samples, only a single boundary condition for the tube termination is necessary. To avoid strong standing waves, we decided to apply a soft end boundary condition (as much absorbing as possible) in the case at hand. The standard procedure adopted in the laboratory implies switching the microphones positions to correct the transfer functions for amplitude and phase mismatches. This time a new calibration system was developed and tested so that all the necessary corrections between the reference microphone and the other three can be computed only once, avoiding having to repeat the measurement four times. The part of the tube representing the calibration section of the tube was 3D printed using a Bambu Lab A1 Mini with a Bambu PLA filament (Figure 3). The calibration device is placed in the central section of the tube, as in the sample case.

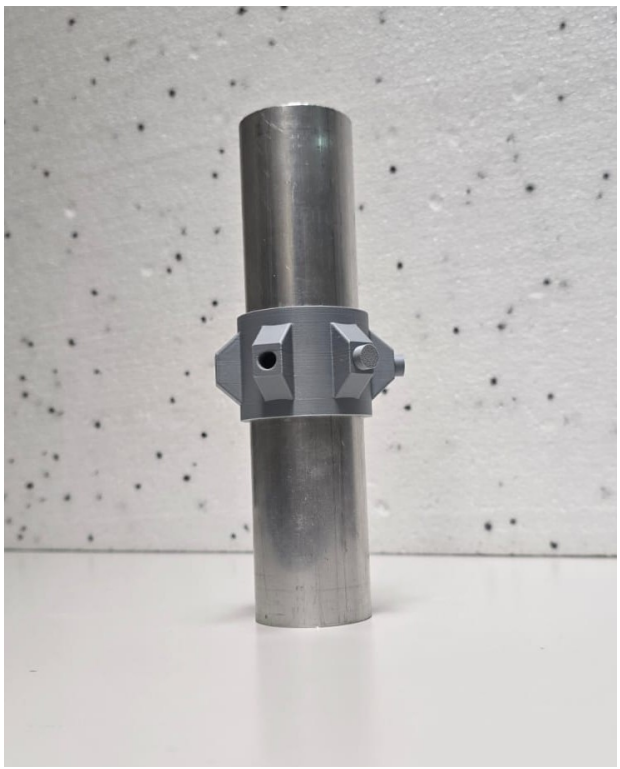


Figure 3. Calibration device.

4. RESULTS AND DISCUSSION

Figure 4 shows the normal incidence sound absorption coefficient for the tested sample. A sample inside a four-microphone impedance tube behaves like a 1/4 wavelength resonator. This means that at room temperature, for a 100 mm thick sample, an absorption resonance should occur at around 850 Hz. In the case at hand, the absorption coefficient curve shows a maximum at 610 Hz, meaning that the celerity of the sound wave is slowed down by the tortuosity of the material. As a matter of fact, the speed of sound in the material has an asymptotic behaviour, with a maximum celerity of 244 m/s (Figure 5). This allows us to determine also the tortuosity of the sample, which results in being around 2.

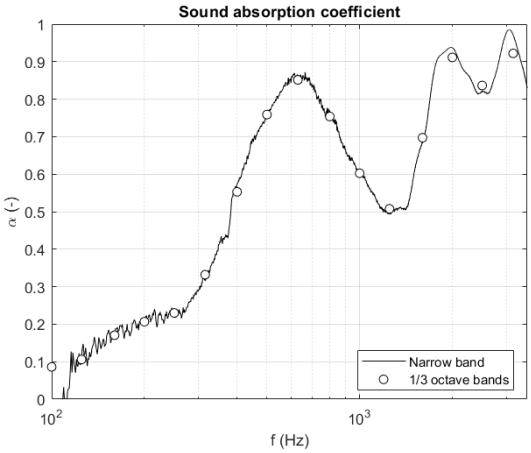


Figure 4. Normal incidence sound absorption coefficient.

The sound absorption graph shows good values also above 600 Hz, with a decrease of the coefficient around 1250 Hz ($\alpha = 0.5$) and then a sudden increase to values of 0.92, 0.84 and 0.92 for the 2000 Hz, 2500 Hz and 3150 Hz 1/3-rd octave frequency bands.

Finally, Figure 6 shows the TL values. The sample is so porous and light that the resulting insulation is lower than 6 dB in the investigated frequency range. for this reason, if the PET filaments must be used as soundproofing material, it would be necessary to improve the mass per unit area and lower the porosity.

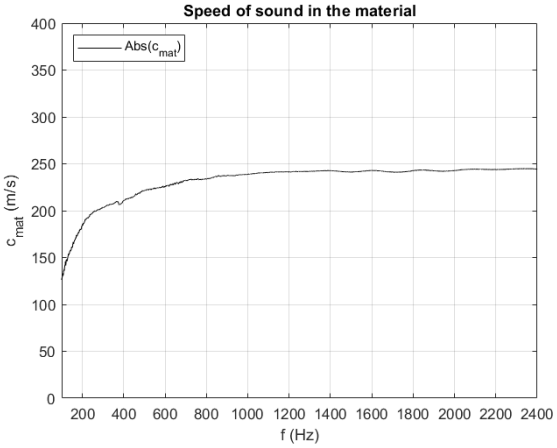


Figure 5. Speed of sound

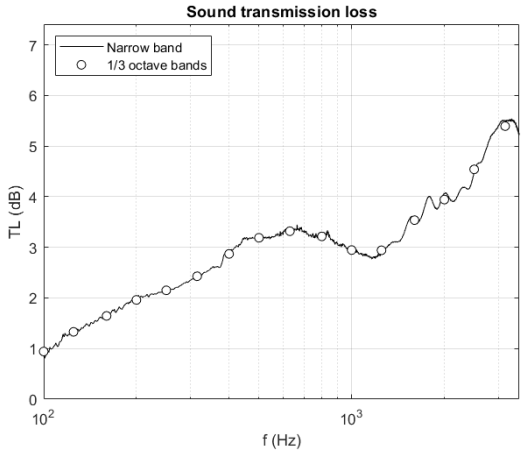


Figure 6. Transmission loss

5. CONCLUSIONS

The experimental analysis of PET filaments from plastic bottles using a four-microphone impedance tube has yielded interesting results regarding their acoustic properties. The findings indicate that PET filaments exhibit excellent sound absorption capabilities, making them a promising material for applications requiring effective noise reduction in confined spaces. The advantage of this type of material is that since it is transparent it allows the light to come through so it can be a potential solution for making windows less reflective. However, the sound insulation performance of PET filaments was found to be suboptimal, suggesting that while they can absorb sound efficiently, they are less effective at preventing sound transmission.

These results highlight the potential of PET filaments in environments where sound absorption is critical without sacrificing natural light infiltration, such as in acoustic panels for correction of rooms placed close to windows. Nevertheless, for applications where sound insulation is equally important, further modifications or alternative materials may be necessary to achieve the desired acoustic performance. Future research should focus on enhancing the sound insulation properties of PET filaments or exploring composite materials that can offer a balanced combination of sound absorption and insulation.

6. ACKNOWLEDGMENTS

This project has received funding from the European Union's Horizon Europe research & innovation pro-

gramme under the HORIZON-MSCA-2021-DN-01 grant agreement No. 101072598 – "ActaReBuild".

7. REFERENCES

[1] C. G. Thottumkal, "Acoustic properties of rigid polyurethane foam mixed with PET bottle wastes," *Int. J. Multidiscip. Res.*, 2022.

[2] S. Yilmazer, T. Keseci, and E. Fasllija, "Objective and subjective assessment of PET felt recycled panels as an acoustic treatment in the meeting rooms," *INTER-NOISE and NOISE-CON Congress and Conference Proceedings*, vol. 270, no. 11, pp. 485–494, 2024.

[3] M. Monteiro, C. Stari, C. Cabeza, and A. C. Marti, "A bottle of tea as a universal Helmholtz resonator," *The Physics Teacher*, vol. 56, no. 9, pp. 644–645, 2018.

[4] S. Dogra, P. Gulia, and A. Gupta, "Noise isolation in building HVAC system using recyclable plastic bottles," *Proceedings of the Institution of Mechanical Engineers, Part C: Journal of Mechanical Engineering Science*, vol. 238, no. 8, pp. 3327 – 3337, 2024.

[5] American Society for Testing and Materials, "ASTM E2611 – Standard Test Method for Normal Incidence Determination of Porous Material Acoustical Properties Based on the Transfer Matrix Method," 2017.

DOI: 10.61782/fa.2025.0183

FORUM ACUSTICUM EURONOISE 2025

BUILDING ENVELOPE ASSESSMENT OF AIRTIGHTNESS USING AN ACOUSTIC CAMERA: A CASE STUDY IN VALLADOLID, SPAIN

Ahmed Elsaei[1,3*] **Maria Machimbarrena**[2] **Alberto Meiss**[1]
Sergio Herguedas[4]
[1] Dpto. Construcciones Arquitectónicas I.T. y M.M.C.T.E, E.T.S. de Arquitectura, Universidad de Valladolid, Spain
[2] Dpto. Física Aplicada, Universidad de Valladolid, Spain
[3] Architecture, Built Environment and Construction Engineering Department (ABC), Politecnico di Milano, Italy
[4] HEAD acústicas GmbH, 08940 Carnella de Llobregat, Barcelona, Spain

ABSTRACT

Assessment of the building envelope quality in terms of airtightness and sound insulation is a critical factor to properly design an optimal retrofitting action plan. Therefore, the development of reliable and non-destructive measurement techniques for assessing these factors pre- and post-retrofitting is a crucial milestone, impacting costs, precision, and time efficiency. This study explores the use of an acoustic camera in evaluating airtightness performance in residential buildings. A measurement campaign was conducted across two houses in Valladolid, Spain, integrating blower door tests, smoke generator, and acoustic camera methods to assess air leakage and its interplay with sound transmission. The main goal of this research case study is to better understand the interplay between airtightness and acoustic performance within a real building façade.

Keywords: *building retrofitting, airtightness, sound insulation, acoustic camera.*

[*] ***Corresponding author***: *ahmedelsaei@uva.es*
Copyright: *©2025 Ahmed Elsaei et al. This is an open-access article distributed under the terms of the Creative Commons Attribution 3.0 Unported License, which permits unrestricted use, distribution, and reproduction in any medium, provided the original author and source are credited.*

1. INTRODUCTION

One of the main goals of building retrofitting is to improve a building's energy performance. Air infiltration is widely recognized as a major cause of energy loss, typically occurring through façade cracks or construction defects. According to recent European studies, air leakage may account for 30–50% of the total energy consumption in the building sector [1]. Therefore, addressing infiltration points is essential during the renovation process. Accurately identifying the location of these cracks and quantifying their impact is critical to planning effective retrofitting strategies, and post-retrofit evaluations help determine the success of such interventions. Currently, no single method exists that can both quantify and localize air infiltration in building envelopes. Traditional methods such as the blower door (fan pressurization) test are commonly used to estimate the volume of air leakage under an artificial pressure difference [2]. However, this method cannot pinpoint the specific locations of leaks, often requiring additional tools like smoke generators or tracer gases [3]. These combinations are not only time-consuming and costly but also require technical expertise for proper setup and analysis.

In recent years, research has increasingly focused on alternative, non-invasive methods to assess airtightness. One promising approach is the use of acoustic-based methods, which are generally quicker, non-destructive, and potentially more precise. For instance, [4] and [5] used sound pressure level measurements in building acoustic frequency range to assess airtightness and conclude an empirical equation. However, significant

research efforts have been devoted to leak detection and localization, spanning from early work by [6] to recent contributions by [7] and [8]. These efforts have evolved from utilizing basic acoustic equipment to employing modern acoustic cameras and advanced beamforming techniques. Acoustic cameras, based on beamforming technology, offer the added advantage of visualizing leak locations in real time. However, while promising for detection, these methods face challenges in quantifying the infiltration rate. This quantification might be achieved by studying the interplay between sound transmission characteristics and airflow behavior through openings. Although previous studies highlight the complexity of this relationship [9], [10], [11], advances in acoustic technology may pave the way toward a practical solution. To explore this potential further, experimental campaigns must be conducted to test modern tools like acoustic cameras in real-world settings. The present study aims to contribute to this effort by demonstrating the effectiveness of acoustic methods in evaluating airtightness. Our work follows the direction of earlier studies and contributes modestly to ongoing efforts aimed at improving diagnostic tools for building envelope assessment.

2. METHODOLOGY

The method consisted in using an acoustic camera as measurement device to identify the potential air leak points, assuming that air leaks, under special conditions, should produce sound. Although the type of sound produced at air leak points could be different depending on the physical origin (forced air or real sound) the position of the air leak points should be coincident.

2.1 Overview

The measurement campaign was conducted in two occupied residential buildings located in Valladolid, Spain. These buildings were selected to represent typical Spanish multi-family housing stock, with conventional building envelopes and standard terrace window installations.

House 1 was a two-story family home in a residential compound. This unit served as a baseline scenario, without any specialized ventilation features as shown in Fig.1 and Fig.2. **House 2**, was a second floor of typical apartment in a mid-high residential building in Valladolid City, as depicted in Fig.3, featured micro-ventilation openings integrated into its terrace window frames. Both houses underwent a full testing sequence including pressurization, depressurization, and sound transmission analysis using both sides of the façade internally and externally. For House no.2 the measurements were performed with the micro-ventilation openings in both open and closed positions to study their impact. A smoke generator test was also performed in both houses to visually confirm major leakage points identified acoustically.

2.2 Equipment

The experimental campaign employed three main types of equipment: a blower door and an omnidirectional sound source as “exciting devices” and an acoustic camera as measurement device. Additionally, a portable smoke generator was used to visualize air leaks.

The blower door system used combined with a DG-700 digital pressure gauge as shown in Fig.4. This system allowed for controlled pressurization and depressurization of the interior space by creating artificial pressure differentials of 50 Pa and 80 Pa, thereby forcing air infiltration through leaks and enabling airflow quantification through the envelope which could then be localized using the acoustic camera.

An omnidirectional sound source, as depicted in Fig.2, was also used during the measurement campaign to try to identify airborne sound leakage paths. This device emitted broadband white noise within a range of 40 Hz to 16 kHz and was placed strategically inside or outside the dwellings depending on the test configuration. The noise served as a reference signal to help determine the extent and location of sound transmission paths through the façade.

To localize potential leakage paths and visualize sound transmission, the HEAD VISOR 7500ff acoustic camera was utilized shown in 3 and a schematic drawing of it illustrated in Fig.5. This high-resolution beamforming system consists of a 56-microphone spiral array paired with three synchronized industrial cameras. The system operates over a wide frequency range from 300 Hz to 20 kHz, offering both real-time and post-processed visualization of sound sources. The portable smoke generator was used to release non-toxic visible smoke into the interior space during pressurization / depressurization. Leakage paths were identified by observing smoke escaping through façade discontinuities from the exterior / interior. This method provided a qualitative visual reference to complement the acoustic recordings.

2.3 Measurement procedure

In both houses the same measurement protocol was followed to ensure comparability between test cases. For House 2, the measurement protocol was performed twice to analyze the impact of window micro-ventilation

features: first with window micro ventilations closed and then with window micro ventilations open. This enabled a comparative analysis of acoustic and airflow behavior under varying boundary conditions, offering insight into how these small architectural features influence both airtightness and sound insulation

The measurement protocol was the following:

The Acoustic Camera (AC) was placed outside the house in front of the terrace window (as in Fig.1 and Fig.3) and measurements were made under different excitation conditions:

- No forced excitation: This set up was chose to assess environmental noise and thus establish baseline acoustic conditions. These preliminary recordings helped identify uncontrollable ambient noise sources—such as birds, street traffic, or nearby recreational areas—and allowed later to filter them out during analysis. In each configuration, at least two or three random baseline recordings were performed to improve the robustness of the dataset.
- Blower door mounted to force air in/out potential leak paths: the blower door was installed in the main entrance of the apartment to enable full control over the internal pressure. Blower door tests were then conducted in both pressurization and depressurization modes at pressure differentials of 50 Pa and 80 Pa. During each steady-state phase, the acoustic camera recorded for 30 seconds to capture noise emissions through the façade.
- Omnidirectional speaker placed inside the house and activated to emit white noise, simulating real-world sound transmission while the acoustic camera recorded also for 30 seconds to capture noise emissions through the façade.

Additionally, for House 1 the measurements related to the blower door tests were repeated placing the acoustic camera inside the house to assess the influence of directionality on leak detection and source visualization.



Figure 1. House 1 Terrace Window. AC outside



Figure 2. House 1. Sound source inside. AC outside



Figure 3. House 2 Façade. AC outside.



Figure 4. Blower Door setup – House 1



Figure 5. Microphone arrays and the camera setup

3. RESULTS

All the images shown in this section correspond to a specific moment within a preselected short time period (2 to 3 seconds) and within a selected limited frequency range. The acoustic camera software allows to analyze the video recording filtering both according to a selected frequency range and to a selected time period. Results shown have consistently been observed over time and over different frequency ranges as it will be explained hereinafter.

3.1 SPL peaks spots within House 1

Fig.6 and Fig.7 show persistent SPL peaks in the same position (upper right section of the terrace window frame), in different moments and under blower door pressurization 50 Pa conditions. This position is also seen when performing the smoke generator test integrated with blower door as shown in Fig.8. These SPL peaks points were found across multiple frequency bands and are shown for the following intervals: 580–715 Hz and 1647–1829 Hz. Due to its position on the edge of the window frame, these spots are preliminary identified as potential air leakage spots.

On the other hand, when using the sound source as an excitation signal, a sound peak is detected close to the previous location across the frequency band of 1016–1211 Hz as shown in Fig.9. Due to its position slightly away from the frame edge and directly on the window (curtains behind the sound peak shown in figure 10), it is not considered a potential air leakage spot but rather an external sound reflection or glass vibration.

When the tests were performed with the blower door under depressurization conditions (50 Pa and 80 Pa) and the acoustic camera was placed inside the house, SPL peaks were detected exactly between window frames 1 and 2, as shown in Fig.10 and Fig.11, notably in higher frequency band: 4833–5695 Hz. Other sound peaks have been identified within different time periods and across different frequency bands as summarized in Tab.1. All these spots shown in Tab.1 are potential air leakage spots due to their position.

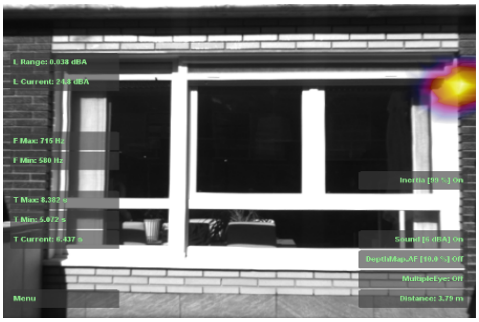


Figure 6. SPL peak located in upper right window frame in House 1. (50 Pa pressurization. AC outside)

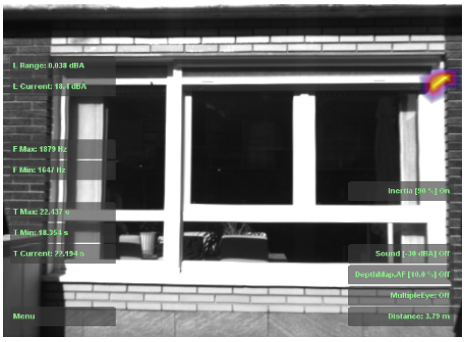


Figure 7. SPL peak located in in upper right window in House 1 (50 Pa pressurization. AC outside)



Figure 8. Visual identification of air leakage locations in House 1 using smoke generator



Figure 9. SPL peak located on the glass (curtain behind), close to the right side of the window frame in House 1. (Sound source inside. AC outside.)

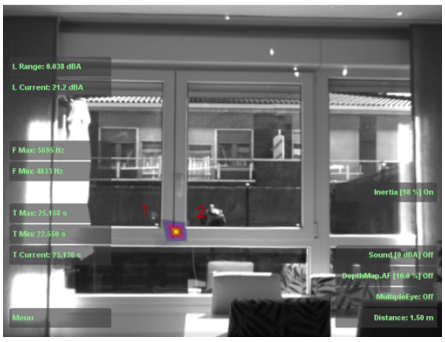


Figure 10. SPL peak located between adjacent window frames in House 1. (50 Pa depressurization. AC inside)

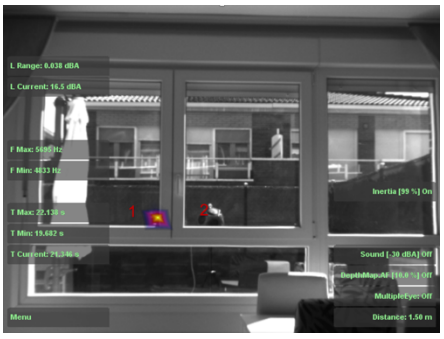
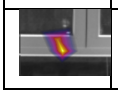
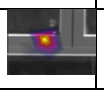
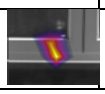
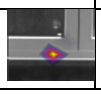


Figure 11. SPL peak located between adjacent window frames in House 1 (80 Pa depressurization. AC inside)

Table 1. SPL peaks near window frames 1 and 2 during blower door depressurization of 50 Pa and 80 Pa, across multiple frequency bands in House 1. (AC inside)

50 Pa	80 Pa	50 Pa	80 Pa	50 Pa	80 Pa
1759 – 2143 Hz	1759 – 2143 Hz	2169 - 2750 Hz	2169 - 2750 Hz	2699 - 3836 Hz	2699 - 3836 Hz
					

3.2 SPL peaks spots within House 2

The evaluation of House No. 2 focused on verifying and analyzing air leakage detected visually via smoke generator. Fig.12 shows two key locations where fog was observed to come out when the fog generator was used inside the house. Fig.13 identifies the upper frame area as position A and the lower frame zone between adjacent window segments as position B. In fact, position B corresponds to the position of a small open/close micro-ventilation opening.

Both air leaks have been consistently detected by the acoustic camera independently of the type of excitation used (pressurization/depressurization at 50/80 Pa or loudspeaker). The leaks are seen at specific frequencies which need to be identified among the full data set. For example, sound pressure level peaks were consistently identified at position A in the frequency band of 1412 - 2120 Hz and at position B in the 1000 - 1841 Hz band. Some of these findings are summarized in Tab.2 and Tab.3, which compile results across various test conditions. Similar images are found at different moments within the full recording periods.

When the sound source is used as excitation signal, a SLP peak is also observed at the same location but at a higher frequency band of 3387 - 4112 Hz as shown in Fig.14.

As mentioned earlier, in some of the acoustic camera tests conducted in House 2, the micro-ventilation feature on the window was intentionally left open. As it can be seen in Tab.4, the SPL values increase in all cases when the micro-ventilation is open, as it was expected.



Figure 12. Visual identification of air leakage locations in House 2 using smoke detection



Figure 13. Positions A and B (micro-ventilation)



Figure 14. SPL peak at Position A in House 2. (Sound source inside. AC outside.)

Table 2. SPL peaks at Position A. Frequency range 1412 - 2120 Hz. Various testing conditions. AC outside

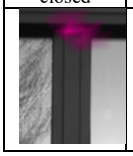
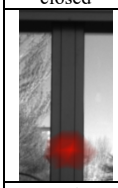
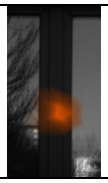
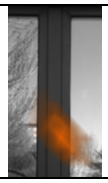
50 Pa Press Microvent closed	50 Pa Press Microvent open	Speaker Inside Microvent closed	Speaker Inside– Microvent open	80 Pa Press. Microvent open
				

Table 3. SPL peaks at Position B. Frequency range 1000 - 1841 Hz. Various test conditions. AC outside.

50 Pa Press Microvent closed	50 Pa Press Microvent open	Speaker Inside Microvent closed	Speaker Inside– Microvent open	80 Pa Press. Microvent open
				
37.2 dBA	41.2 dBA	42.3 dBA	46.5 dBA	34.1 dBA

4. DISCUSSION

4.1 House 1

The results from House 1 can be used to discriminate whether a SPL peak corresponds or not to an air leakage path. To support this type of classification, we refer to the study by Schiricke et al. [12], which introduced the Acoustic Assessment Score (ASS). This score ranges from 0 to 3 and is used to assess the likelihood that a detected peak corresponds to a real leakage point—helping distinguish between unlikely and likely leakage sources. In this case study three different SPL peaks spots have been identified:

The SPL peaks shown in Fig.6 and Fig.7 (upper right corner of the window façade) is located on the edge of the frame and aligns with the smoke generator results, strongly supporting the conclusion that, at this location, there is an air leakage path.

On the contrary, the SPL peak observed in Figure 10 is located over the glass. Since the glass was visually inspected and confirmed to be intact with no cracks or defects, this signal is likely the result of structure-borne sound or vibration rather than air leakage.

Lastly, another SPL peak zone was consistently identified under depressurization conditions, at a location which was not observed with the smoke generator. This is around the lower edge of the frame, near the junction of both frames. This SPL peak zone was detected very consistently at middle frequencies as shown in Tab.1, but it was more precisely spotted at higher frequencies as shown in Fig.10 and Fig.11. According to its position, it is very likely an air leak path. If we assume this is a crack or infiltration path, it is likely very narrow—possibly too thin to be detected by the smoke method and better detected at higher frequencies. This suggests that the acoustic method is particularly sensitive to small or layered cracks that may not be visible using smoke or fog-based techniques. Lower frequency bands (as shown in Tab.1) also detected the signal, but with less accurate localization.

4.2 House 2

In this house, the analysis focused on validating the leakage locations identified by the smoke generator method using the acoustic camera. The two-leakage points A and B detected with the smoke were confirmed across multiple frequency bands. Additionally, the consistency of such detections within specific frequency ranges suggests a potential link to the type or characteristics of the cracks when analyzing the sound spectral properties at these locations. This needs to be further explored.

Concerning the effect of the window micro-ventilation system whether in open or closed configuration, the results shown in Tab.3 indicate that, even when the feature is closed, there is measurable sound transmission with relatively high sound power. This suggests that air leakage may still occur through the micro-ventilation component even when it is closed. While the system appears to function as intended, the observed sound peaks while not activating it and the difference in sound power between closed ad open cases should be taken into account when evaluating the need for potential renovation or design improvement.

Overall, the acoustic data aligned well with the visual smoke-based observations while offering a more detailed and frequency-sensitive picture of infiltration behaviour, reinforcing the value of acoustic camera data both as confirmatory and diagnostic tool in complex façade assessments.

4.3 General insights

The combined findings from House 1 and House 2 strongly support the feasibility and added value of using acoustic cameras for airtightness evaluation. In both case study, the acoustic camera successfully detected leakage spots confirmed by smoke and, in some cases, it was possible to identify additional narrow leak paths which were visually undetectable with smoke. This detection was observed at high-frequency bands which most likely can provide information about the thin and narrow nature of the leak path. Overall, the findings confirm that acoustic imaging can complement or even exceed traditional air leakage localization methods, especially when visual cues are weak or absent.

The results further emphasize that it is not possible to identify all leakage points in a single acoustic image, as leakage signatures appear at different locations depending on the frequency band. Therefore, it is necessary to have a multi frequency band visualization, where the sound peaks are distributed across the façade, varying between lower and higher frequencies. This observation aligns also with findings reported by Schiricke et al. [12], confirming that a sequence of images across third-octave or narrow-band frequency bands is necessary to detect all potential leakage areas. Therefore, comprehensive leakage visualization requires multi-frequency acoustic analysis to account for the variability in spectral responses caused by differences in geometry, crack size, and flow behavior.

4.4 Further research

Finally, these findings support the work of Schiricke et al. [12], who demonstrated that acoustic cameras could detect small leakage points that are often missed by traditional tools such as blower door tests, smoke generators, or gas tracer methods. However, Kölsch and colleagues highlighted that additional knowledge is still required to reliably distinguish between true leak sources, reflected signals, and airborne sound transmission, especially in complex real-world settings. This remains an open research question and presents a critical avenue for further development.

Therefore, one of the key ongoing tasks in our study is to analyze the spectral characteristics of each confirmed leakage point, with the goal of establishing acoustic signatures or spectral patterns that may correlate with leak size, type, or severity. This spectral approach could form the basis for developing more automated or semi-automated leakage classification tools using acoustic data. As also discussed by Schiricke et al. [12], the spectral fingerprint of a leak may offer valuable diagnostic insight, and future work will aim to explore this potential in depth.

5. CONCLUSIONS

House 1 demonstrated the potential ability of the acoustic camera to show sound pressure peaks that could correspond to subtle air leaks where the smoke testing failed to produce a visual cue. The existence of the sound peak at relatively high frequencies and between the frames most likely corresponds to a fine or narrow leak. This highlights a key advantage: acoustic tools offer higher sensitivity to narrow or complex leakage paths, especially in the mid to high frequency range. House 2 provided an opportunity to evaluate the influence of micro-ventilation features. The integration of multiple source types (blower door and speaker) revealed consistent detection at smoke-identified positions.

Overall, this study shows the potential use of acoustic beamforming as a complementary, or in some cases with further research as independent, tool to traditional diagnostic techniques. Their ability to visualize, localize, and interpret leak behavior in real time provides a user-friendly and highly effective solution for both researchers and practitioners. Importantly, the integration of sound-frequency analysis with pressure-based testing opens the door to more detailed diagnostics that could evolve into hybrid quantification models in the future. Our findings confirm that single-frequency images are insufficient for capturing all leakage paths. A multi-frequency approach is necessary to visualize the full range of leakage behavior.

6. ACKNOWLEDGMENTS

This project has received funding from the European Union's Horizon Europe research & innovation programme under the HORIZON-MSCA-2021-DN-01 grant agreement No. 101072598 – "ActaReBuild". We would also like to express our gratitude to the homeowners for their support and flexibility throughout the testing process

7. REFERENCES

[1] J. Fernández-Agüera, J. J. Sendra, and S. Domínguez, "Protocols for measuring the airtightness of multi-dwelling units in Southern Europe," *Procedia Eng*, vol. 21, pp. 98–105, 2011.

[2] ISO, "ISO 9972. Thermal performance of buildings. Determination of air permeability of buildings. Fan pressurization method (ISO 9972:2015)," 2015. [Online]. Available: https://www.iso.org/standard/55718.html

[3] I. Poza Casado, "Airtightness performance of the building envelope of dwellings in Spain. Characterisation and energy impact of air infiltration," 2021.

[4] V. Iordache and T. Catalina, "Acoustic approach for building air permeability estimation," *Build Environ*, vol. 57, pp. 18–27, Nov. 2012, doi: 10.1016/j.buildenv.2012.04.008.

[5] T. Sonoda and F. Peterson, "A Sonic Method for Building Air-Leakage Measurements*," 1986.

[6] D. N. Keast, "Acoustic location of infiltration openings in buildings," 1978. [Online]. Available: https://www.aivc.org/resource/acoustic-location-infiltration-openings-buildings

[7] B. Schiricke and B. Kölsch, "Acoustic method for measurement of airtightness-field testing on three different existing office buildings in Germany," 2023. [Online]. Available: https://www.researchgate.net/publication/374913643

[8] G. Raman, K. Chelliah, M. Prakash, and R. T. Muehleisen, "Detection and quantification of building air infiltration using remote acoustic methods," *INTERNOISE 2014 - 43rd International Congress on Noise Control Engineering: Improving the World Through Noise Control*, no. January, 2014.

[9] M. Ringger and P. Hartmann, "Evaluation of an acoustical method for detecting air leaks," *Air Infiltration Review*, vol. 11, no. 1, 1989, [Online]. Available: https://www.aivc.org/resource/use-acoustic-intensimetry-size-air-leakage-cracks-0

[10] M. H. Sherman and M. P. Modera, "Signal attenuation due to cavity leakage," *J Acoust Soc Am*, vol. 84, no. 6, pp. 2163–2169, Dec. 1988, doi: 10.1121/1.397062.

[11] T. Sonoda and F. Peterson, "A sonic method for building air-leakage measurements," *Appl Energy*, vol. 22, no. 3, pp. 205–224, Jan. 1986, doi: 10.1016/0306-2619(86)90003-6.

[12] B. Schiricke, M. Diel, and B. Kölsch, "Field Testing of an Acoustic Method for Locating Air Leakages in Building Envelopes," *Buildings 2024, Vol. 14, Page 1159*, vol. 14, no. 4, p. 1159, Apr. 2024, doi: 10.3390/BUILDINGS14041159.

DOI: 10.61782/fa.2025.0293



FORUM ACUSTICUM
EURONOISE 2025

DEVELOPMENT OF ACOUSTIC RESONATORS USING RECYCLED PLASTICS

Juraj Potočár[1,2] **Maroa Maaroufi**[3,4] **Stanislav Unčík**[2]
Christ Glorieux[5] **Monika Rychtarikova**[1,2]
[1] KU Leuven, Department of Architecture, Campus Brussels and Ghent, Belgium
[2] STU Bratislava, Faculty of Civil Engineering, Department of Materials Engineering and Physics, Slovakia
[3] Université Paris-Saclay, ENS Paris-Saclay, CNRS, LMT – Laboratoire de Mécanique et Technologie, 91190 Gif-sur-Yvette, France
[4] EPF-Ecole d'Ingénieurs, 55 Avenue du Président Wilson, Cachan 94230, France
[5] KU Leuven, Department of Physics and Astronomy, Laboratory of Soft Matter and Biophysics – Acoustics, Heverlee, Belgium

ABSTRACT

In this contribution, we discuss preliminary research results obtained within the framework of one of the ten individual research projects of the EU-MSCA-DN, "ActaReBuild", which focuses on the development of acoustic resonators based on lightweight concrete using recycled aggregates. In particular, we examine using loose granules of flo-pak plastic as material to fill and absorb sound in the resonator cavity. The sound absorption of the granules was measured in a reverberant room and compared with the sound absorption properties of melamine foam, a common porous material of the same thickness. Also the absorption of a wooden resonator (1) filled with melamine and (2) filled with loose plastics was determined and compared to that of (3) an empty resonator. The results show that adding granules in the cavity leads to an increase in resonance frequency, likely due to their closed pores reducing the effective cavity volume and increasing stiffness. Also broadening of the absorption peak is observed.

Keywords: *resonator, waste plastics, sound absorption*

[*] ***Corresponding author***: *juraj.potocar@kuleuven.be*
Copyright: *©2025 Juraj Potočár et al. This is an open-access article distributed under the terms of the Creative Commons Attribution 3.0 Unported License, which permits unrestricted use, distribution, and reproduction in any medium, provided the original author and source are credited.*

1. INTRODUCTION

In architectural acoustics, sound absorption plays a key role in regulating the reverberation time, reducing noise levels from sound sources in the room, and improving the overall acoustic quality of a space. By reducing echoes, flutter echoes, and standing waves, sound absorption ensures clarity, comfort, and functionality in various environments, such as auditoriums, offices, classrooms, and recording studios.

In situations when sound containing mid and high-frequencies needs to be absorbed, the usage of porous absorbers is convenient. Typically, the lowest absorbed frequency is the one for which a quarter wavelength corresponds with the distance between the most protruding porous material and the rigid wall behind. In practice, this makes the use of porous materials as absorbers impractical or even impossible for bass frequencies, and the use of resonators becomes necessary. One of the possibilities is the use of a cavity resonator.

Empty Helmholtz resonators exhibit a sharp absorption peak, of which the (typically low) frequency depends on the dimensions of the neck and cavity. The absorption is a consequence of viscous loss effects of the air velocity oscillations in and near the neck. By inserting porous materials, preferably near the neck, additional sound energy is absorbed, broadening the absorption peak.

Besides conventional fibrous and foam-based materials, recycled polymer waste is gaining attention as a promising option for sound absorption. These materials are typically

processed into granular form, influenced by factors such as grain size, and internal structure. These variables can significantly affect the acoustic performance across specific frequency ranges. A classification framework for granular absorbents - such as vermiculite, perlite, granulated rubber, and nitrile foam - was introduced by Voronina and Horoshenkov [1]. Studies show that granules obtained from recycled products like tires and cables offer favorable properties for the development of tailored acoustic solutions. Further evidence of the acoustic viability of recycled rubber granulate comes from Swift and Horoshenkov [2], who demonstrated that rubber crumb not only supports broadband absorption but can also be modeled effectively using a semi-empirical approach that captures both viscous and thermal losses in porous structures. Their findings underline the impact of grain shape, flow resistivity, and packing density on absorption characteristics, especially within mid- to high-frequency ranges.

Notably, plastic granulated materials showed effectiveness in providing relatively wide-band sound absorption [3-5]. By adjusting parameters such as granule size and material thickness, one can fine-tune the absorption peak to align with target frequencies. Research by Bumanis et al. on recycled expanded polystyrene granules revealed efficient sound absorption in the range of 600–700 Hz [6].

Although flo-pak granules - EPS-based loose-fill foam products - have been previously evaluated in terms of their mechanical performance [7], their acoustic behavior has not yet been comprehensively studied. In this work, we consider the use of this type of granules in a way to dissipate acoustic energy in the resonator's cavity, compared to foam material - melamine.

2. METHODS

2.1 Samples preparation

Two resonators were used for measurement, made of MDF (medium-density fibreboard) plates. Each of them had internal dimensions of 100x100x7 cm^3 (Figure 1). The thickness of the perforated plate t = 9 mm, with holes at an axial distance of 20 cm and a hole diameter of 25 mm.

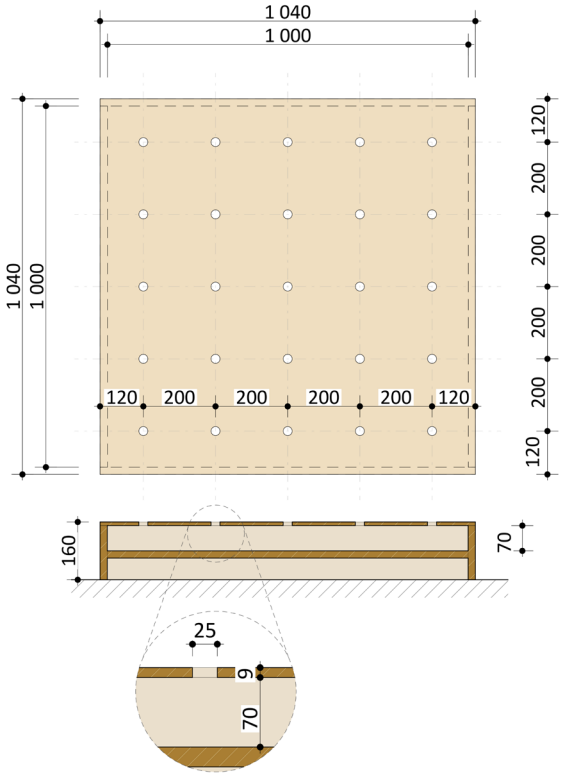


Figure 1. Dimensions of the used resonator (in millimeters)

Two types of porous materials were characterized. The melamine foam (Figure 2a) was used for reference as a well-known open-cell, lightweight foam with a density of approximately 7-11 kg/m³. Melamine foam is widely known for its excellent sound absorption capabilities due to its fine, interconnected pore structure, which enhances sound wave dissipation. The foam used in the study had a dimension of 100x100 cm2 and a thickness of 50 mm.

The sample of main interest consisted of flo-pak granules. The granules have sizes around 10x20x30 mm3, and a variety of different shapes (“S-shape”, “8-shape”). The bulk mass density was 4 kg/m³. This type of loose-fill packaging material is commonly used for cushioning and protecting items in boxes during shipping and handling. Granules are made from both expanded PS (EPS) and extruded PS (XPS). It is a lightweight, rigid, and versatile material. Although this material is often made of recyclable PS and can be reused, it rarely happens, and most of it ends up in landfills or incinerators. For this reason, we found it interesting to look for possibilities of reuse in a new context, i.e. as an absorber in acoustic applications.



Figure 2. Detailed view of investigated materials: Left: melamine foam (cylinder cut out of the 50mm thick panel. Right: Selection of flo-pak granules from the 50 mm loose stack

2.2 Reverberant room measurements

The spectrum of the sound absorption coefficient per 1/3 octave band was determined inspired by the conventional ISO 354 method in the reverberant room. While the reverberant room is suitable for ISO 354 measurements (197 m3), due to practical constraints, the sample surface size (2 m²) was lower than the required size (10-12 m2) Measurements were performed by means of impulse response with exponential sweep signal (duration of 23.8 seconds) generated in the room through an omnidirectional loudspeaker. The acoustic absorption of a flo-pak granules (Fig. 4) layer of about 50mm thickness was characterized both in loose form and as cavity-filling material under a 9 mm thick perforated plate with 25 mm diameter holes arranged on a cubic grid with 20 cm interspacing. The melamine reference layer had a thickness of 50 mm and was tested loose and in the cavity configuration. Also, the empty cavity configuration was characterized. The average of measured sound absorption was based on 18 measurements – 6 microphone positions for each of 3 sound source positions.

The temperature, relative humidity, and atmospheric pressure were carefully controlled during the measurement procedure, and taken into account in the analysis.

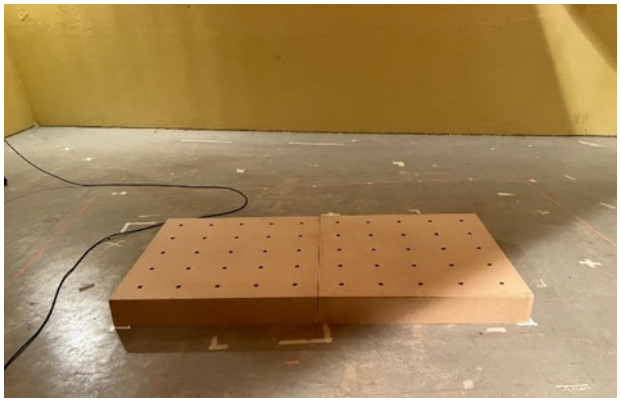


Figure 4. Two adjacent wooden resonators placed in the reverberant room

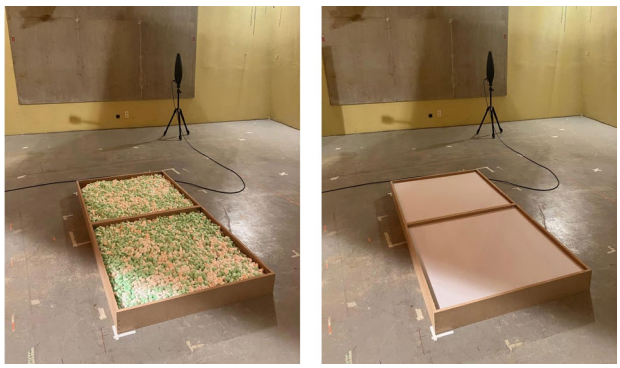


Figure 5. Open resonators with flo-pak granules (left) and melamine foam (right)

3. RESULTS AND DISCUSSION

The sound absorption (α) spectra of the open resonators with porous materials are presented in Figure 5. Melamine foam shows the typical behavior of foam or fibrous porous material, with low α values at low frequencies (α=0.17 at 125 Hz), followed by a gradual increase with increasing frequency, reaching 100% absorption at frequencies of 630 Hz and higher. As expected, due to its much lower porosity and large pores, the absorption of the flo-pak granule layer is substantially lower than the one of the equally thick melamine. Nevertheless, the absorption values between 0.2 and 0.8 across the audio range give the potential for using recycled flo-pak granules for acoustic absorption applications. The weakly pronounced maximum around 1250 Hz, combined with a speed of sound of 340 m/s of the air in the large pores, corresponds with a quarter

wavelength of 7 mm, a bit more than 5mm, the nominal thickness of the flo-pack layer.

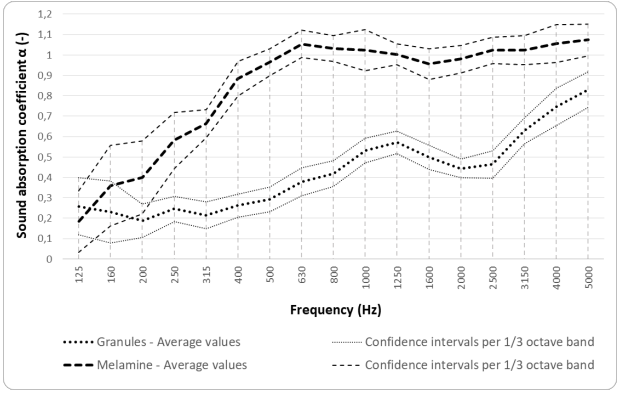


Figure 6. Sound absorption spectrum of a 50 mm layer of melamine foam (dashed line), and flo-pak granules (dotted line)

The α spectra of the perforated panel resonator with different filling conditions are presented in Figure 6. Combining the dimensions of the resonator (Figure 1), its resonance frequency can be calculated as [8]:

$$f_r = \frac{c}{2\pi}\sqrt{\frac{A_{perf}}{A_{panel}.d_{cavity}.t_{eff}}}$$

where c is the speed of sound in air (340 m/s) and teff = t + 2δr = 0,02325 m with $\delta = 0.85(1 - 1.47\varepsilon^{1/2} + 0{,}47\varepsilon^{3/2}) = 0{,}57$. $\varepsilon = A_{perforation}/A_{panel}$ denotes the porosity of the plate. The calculated value of the resonance frequency (140 Hz) is consistent with the sound absorption peak (α=0.55) of the empty resonator in the 160 Hz 1/3 octave band.

Compared to the empty cavity, filling the resonator with flo-pak granules induces a shift towards the 200 Hz-250 Hz 1/3 octave bands, in accordance with the effect of a reduction of the free cavity volume due to the granules. The absorbing function is similar to the one of the empty resonator (α=0.57), but it acts across a wider frequency range.

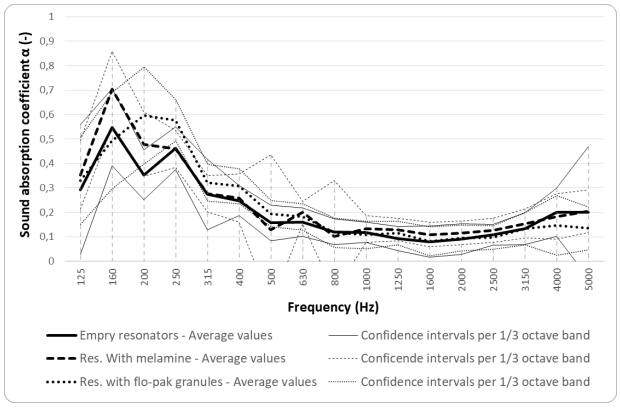


Figure 7. Sound absorption spectrum of the perforated panel resonator with different cavity filling conditions: melamine foam (dashed line), flo-pak granules (dotted line), and empty (solid line)

4. CONCLUSIONS

This study explored the potential of recycled plastics in acoustic resonators, focusing on flo-pak granules as cavity fillings and comparing them to melamine foam. The results confirm that granule filling influences the resonator performance, increasing the resonance frequency (as a consequence of the reduced free volume) and broadening the absorption peak.

As expected, also filling the resonator cavity with melamine increased damping. Still, the overall absorption remained relatively low, possibly due to insufficient perforation or improper placement of melamine (2 cm gap between the melamine and perforation).

The sample dimensions were smaller than the standardized sizes required by ISO norms, which may have influenced the absorption measurements by reducing the overall impact of the material on the acoustic environment. While these recycled materials offer promising applications for sound absorption, challenges remain in optimizing their performance. Future research will focus on refining cavity-filling configurations, analyzing the dynamic stiffness of granules, and conducting larger-scale measurements to assess their viability in real-world noise mitigation solutions.

5. ACKNOWLEDGEMENTS

This project has received funding from the European Union's Horizon Europe research & innovation programme

under the HORIZON-MSCA-2021-DN-01 grant agreement No. 101072598 – "ActaReBuild"

6. REFERENCES

[1] N. N. Voronina, K. V. Horoshenkov. A new empirical model for the acoustic properties of loose granular media. Applied Acoustics 64.4, 2003

[2] M. J. Swift, P. Bris, and K. V. Horoshenkov: "Acoustic absorption in re-cycled rubber granulate," Applied Acoustics, vol. 57, no. 3, pp. 203–212, 1999.

[3] R. Maderuelo-Sanz R. et al. Acoustical performance of porous absorber made from recycled rubber and polyurethane resin. Latin American Journal of solids structures 10(3), 2013

[4] A. Biskupicova, et al. Sound absorbing properties of recycled polymers. Akustika 35 2020

[5] Z. Hong, L. Bo, H. Guangsu, H. Jia. A novel composite sound absorber with recycled rubber particles. Journal of Sound and Vibration 304, 2007

[6] G. Bumanis, et al. Thermal and sound insulation properties of recycled expanded polystyrene granule and gypsum composites. Recycling 8.1, 2023

[7] P. D. Tatarka and R. L. Cunningham: "Properties of protective loose‐fill foams," Journal of Applied Polymer Science, vol. 67, no. 7, pp. 1157−1176, 1998.

[8] S. N. Rschevkin. Gestaltung von Resonanzschallschallschluckern und deren Verwendung fur die Nachhallregelung und Schallabsorption. Hochfrequenztechnik und Electrokustik 67.4, 1959

DOI: 10.61782/fa.2025.0748

FORUM ACUSTICUM EURONOISE 2025

RETHINKING MATERIAL CYCLES: COMBINING MYCELIUM AND PAPER WASTE FOR THE DEVELOPMENT OF SOUND ABSORBERS.

Anna Maria Kubiak[1,2*] **Tomas Simon Gomez**[3,4] **Christ Glorieux**[3]
Maria de los Angeles Navacerrada[5] **Nadia Vasileva Nicheva**[2] **David Sanz-Arauz**[2]
[1] TU Wien, Karlsplatz 13, 1040, Vienna, Austria
[2] Department of Construction and Architectural Technology, Escuela Técnica Superior de Arquitectura, Universidad Politécnica de Madrid, Av Juan de Herrera 4, 28040, Madrid, Spain
[3] KU Leuven, Department of Physics and Astronomy, Laboratory for Acoustics - Soft Matter and Bio-physics, Celestijnenlaan 200D, 3001, Heverlee, Belgium
[4] University of Brescia, Department of Mechanical and Industrial Engineering, Via Branze 38, 25123, Brescia, Italy
[5] Grupo de Acústica Arquitectónica, Escuela Técnica Superior de Arquitectura, Universidad Politécnica de Madrid, Av Juan de Herrera 4, 28040, Madrid, Spain

ABSTRACT

Due to different environmental challenges, using sustainable materials has become increasingly important. Mycelium-based materials show promising potential in many applications within architecture, such as sustainable acoustic absorbers. Here we present results on the acoustic and thermal performance of mycelium panels that use paper waste as substrate for the growth of Pleurotus Ostreatus. Regarding the substrate choice, the potential application of the widely accessible residue material in combination with acoustic application was examined. Mycelium-based materials show a sustainable life cycle, which is amplified by using residual materials as a base. The panels were created using different growing times and mixtures of inoculated and non-inoculated substrate and dried in convection ovens to deactivate the fungi and remove the moisture excess. Samples were tested using an in-situ method with a Pressure-Particle velocity probe (PU probe). The acoustic absorption turns out to be highly dependent on the processing method, growing time and mixture use, though overall maximum absorption is found around 1kHz. The thermal conductivity was found to be around 0.07 W/(m.K).

[*] ***Corresponding author***: *anna-maria.kubiak@hotmail.com*
Copyright: *©2025 Anna Kubiak et al. This is an open-access article distributed under the terms of the Creative Commons Attribution 3.0 Unported License, which permits unrestricted use, distribution, and reproduction in any medium, provided the original author and source are credited.*

Keywords: *mycelium based composites, sound absorption, sustainable materials, bio-composites, ActaReBuild*

1. INTRODUCTION

The increasing urgency of environmental challenges has led to a growing interest in developing sustainable and functional materials. Mycelium-based composites have emerged as a particularly promising class of biomaterials due to their biodegradability, renewability, and ability to repurpose waste. Formed from the filamentous root structure of fungi, mycelium can bind together various lignocellulosic substrates into lightweight, insulating, and biodegradable composites. Their potential as an alternative to conventional, resource-intensive construction materials positions them at the forefront of sustainable innovation in architecture and design [1].

Among the various applications of mycelium-based materials, acoustic conditioning is gaining traction. Mycelium panels have shown significant sound absorption capabilities, particularly in the mid-frequency range around 1kHz, making them suitable for use in interior environments seeking eco-friendly acoustic solutions. The structure of the mycelium network, combined with the porosity of the substrate, contributes to these properties. Traditional acoustic materials such as fiberglass and polystyrene often come with health or environmental drawbacks, thus supporting the application of mycelium as a safer, greener alternative [1].

Most fungal strains used for the development of mycelium composites are saprotrophic Basidiomycota, thus, nutrient-rich lignocellulosic materials such as wood, hemp, straw, or cotton are effective substrates for mycelium growth [2]. Paper waste, an abundantly available lignocellulosic material, was chosen as the substrate for this research. Cultivating mycelium on paper waste has substantial potential to be a cheap and sustainable solution. Paper waste follows a complex life cycle, typically beginning as virgin fiber harvested from trees and processed into paper products for packaging, printing, or hygiene purposes. After use, a part of this material enters recycling streams, while the rest, especially low-grade or contaminated paper, ends up in landfills or incinerators, contributing to carbon emissions. Even when recycled, paper fibers degrade in quality, eventually becoming unsuitable for further reuse and becoming a waste burden. Repurposing this terminal-stage paper waste as a substrate for mycelium growth presents a sustainable alternative that intercepts the material before disposal. Rich in cellulose, this waste becomes a nutrient source for fungal colonization. Using waste cardboard and paper not only diverts significant volumes of material from landfills but also enhances the circular economy by transforming low-value residues into high-performance biomaterials [3]. Moreover, this approach reduces the environmental footprint of the material production process and opens up possibilities for decentralized, local manufacturing of building materials.

The fabrication of mycelium composites requires careful control of several variables, including substrate composition, moisture levels, pH, temperature, and sterilization procedures. Failure to optimize these conditions can result in contamination, uneven growth, or insufficient binding strength. Research has shown that substrates rich in cellulose and hemicellulose, like paper products, can support fungal growth, especially when paired with fungi such as Pleurotus Ostreatus [1], [3].

Recent studies have also highlighted the role of processing variables such as growing time and the use of mixed inoculated and non-inoculated substrate batches. These parameters significantly affect the mechanical and acoustic properties of the final composites [2]. For instance, longer growth periods typically lead to denser mycelial networks [4], while different substrate blends can influence porosity and structural cohesion. Post-growth treatments like oven-drying are critical to halting fungal activity and stabilizing the material [3], [5].

This paper investigates the performance of mycelium panels grown on wastepaper substrates in combination with fungal species Pleurotus Ostreatus, emphasizing their acoustic absorption and thermal conductivity and the influence of different parameters. Section 2 defines the methodology followed to develop the mycelium composites and the techniques used for its characterization, section 3 includes the results and discussion on the materials performance.

2. MATERIALS AND METHODS

2.1 Materials and sample preparation

Shredded paper and Pleurotus Ostreatus spawn were acquired from the Universidad Politécnica de Madrid recycling center and by a local provider in Spain, respectively.

The general procedure for the development of the mycelium composite consisted in different stages: sterilization of the substrate, inoculation and mixing, cultivation and a drying process.

Paper was introduced into a pot with water taking it to the boiling point for approximately two hours to reduce potential contamination. After cooling, mycelium spawn and the sterilized substrate were mixed in a food processor, avoiding paper paste lumps and distributing the mycelium spawn in the substrate, resulting in a looser and lighter texture. The mix was filled into 3D printed square molds, of 15 x 15 x 4 cm^3, with small openings on four sides allowing for airflow, promoting uniform growth. The samples were placed inside a curing chamber, which kept the humidity at relative 90%, and the temperature at 22°C. Upon reaching the desired growth time, the samples were dehydrated in a convection oven at a temperature of 40˚C until reaching constant weight. Fig. 1 shows a generalized procedure on the mycelium composite development process.

Three different mycelium composite types were developed. In all cases the amount of mycelium spawn, substrate and the total mass of the mixture before drying were kept constant at 68.5% for paper waste and 31.5% mycelium spawn and 0.4 kg for the total mass of the composite, corresponding to a density of 0.44 g/cm^3.

The main variable was the incubation time, Group A was let to grow for 4 days, group B for 14 days and group C 19 days. Fig. 2 shows a diagram of the compositions and growing time for each sample group.

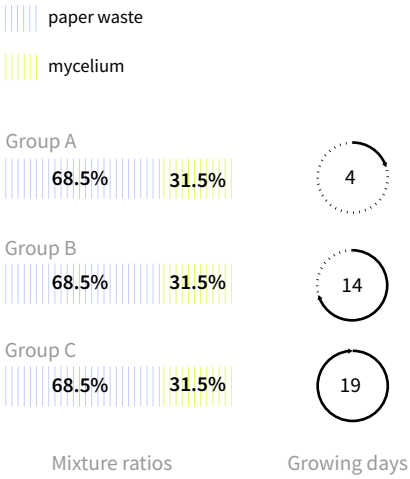


Figure 1. Generalized paper-based mycelium composite developing process.

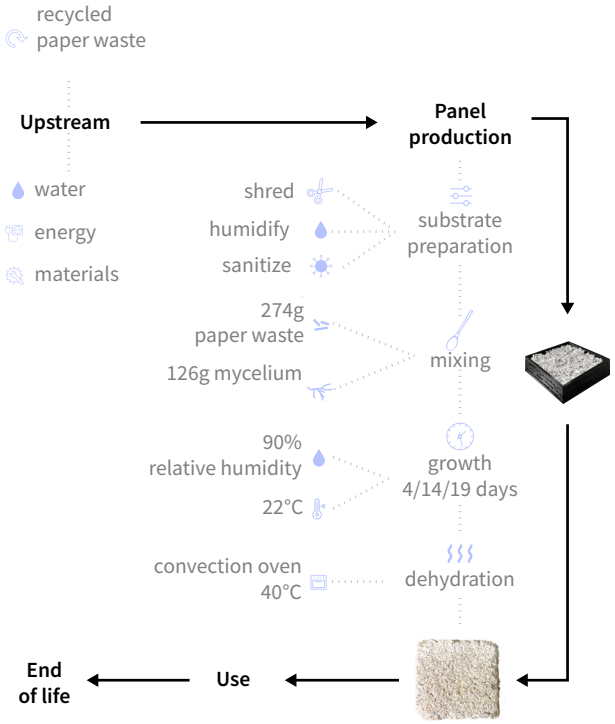


Figure 2. Mixture ratio and growing times for different paper-based mycelium composites.

2.2 Sound absorption coefficient

A Microflown Technologies' PU impedance gun (In-situ sound absorption testing setup), was employed to perform sound absorption measurements. This equipment includes a spherical loudspeaker along with a combined pressure and particle velocity sensor (PU probe). The measurements were conducted across a frequency range of 500 Hz to 8 kHz. During the tests, the loudspeaker generated broadband noise, and the PU probe simultaneously captured pressure and velocity data. The plane wave model was selected for calculating the sound absorption coefficient in this study, owing to its minimal sensitivity to variations in the measurement environment and the distance between the probe and sample surface, as well as its alignment with results from the impedance tube method [6]. Atmospheric conditions (pressure and temperature) were integrated into the model. While reflections from surrounding objects could theoretically influence outcomes, their effect was negligible in practice due to the proximity between the sample and the PU probe. Nevertheless, prior to measurements, the impedance gun was calibrated under free-field conditions to minimize interference. The absorption coefficient was determined as the average of three measurements conducted at the sample's. center.

2.3 Thermal conductivity

The thermal conductivity of the samples was measured using the heat flow meter method. A heat flow meter model HFM 436 Lambda was used, samples were placed between two heated plates, set at different temperatures. A calibrated heat flux transducer measured the heat flow through the sample, following EN ISO 12667 standard. The thermal conductivity was measured at 5-degree intervals over the temperature range of 15°C to 35°C.

3. RESULTS AND DISCUSSION

Once the growing and drying of the mycelium based composites was finished, the density of the samples was calculated, Table 1, shows the results by each composite group.

Table 1. Density of Mycelium composites after drying for the different sample types.

Sample	Density(kg/m³)
A	318 ± 21
B	240 ± 18
C	257 ± 51

The average results for sound absorption coefficient on each sample type and standard deviations are shown in Fig 3. Typical porous materials behaviour is observed for all samples, with the sound absorption being low at low frequencies. Towards higher frequencies, the three groups showed a similar particularity, with a first peak around 1 kHz, and a considerable dip around 2.5kHz. There are also some systematic differences between the different sample groups. Group C shows as an offset from the other curves, thus might be due to a reduced porosity, given the longer cultivation time, the mycelium had more time to grow over the porous network of the samples.
It is expected that the first absorption peak would be related to a particle velocity maxima associated with the thickness of the sample. It was observed that the first absorption peak was obtained around 1 kHz instead of 1.7 kHz, suggesting that this material has a high tortuosity which would slow down acoustic waves, effectively making the path of the wave larger.

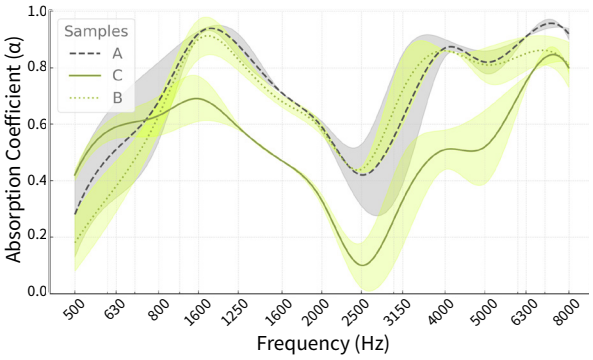


Figure 3. Sound absorption coefficient for different paper based mycelium composite samples.

Figure 4 shows the thermal conductivity for the developed samples in the range of temperatures from 15 to 35 in steps of 5. It is observed that the as temperature increases so does the thermal conductivity, aside from that, by a small margin, group B has a increased performance compared to the other types of samples, with group C showing the higher thermal conductivity consistently thorough the temperature range.
As heat transport is strongly influenced by the porosity and density of a material, the differences in thermal conductivity between group C and the others could be associated with a decreased porosity as shown in table 1, the densities of sample group C and B are comparable, and regardless of that it shows higher thermal conductivity.

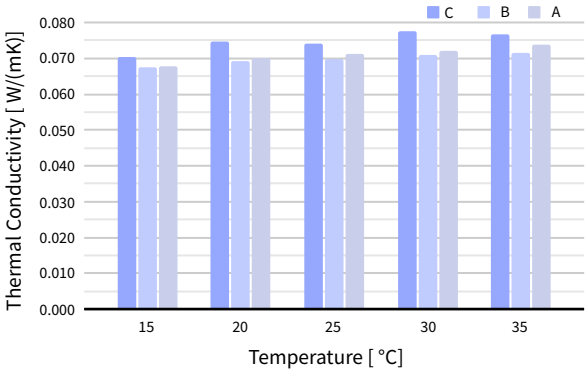


Figure 4. Thermal conductivity in function of temperature for different the developed mycelium composites.

Table 2 shows the average thermal conductivity of the samples after testing them at temperatures ranging from 15-35°C. All types of samples showed low variance in thermal conductivity among the different temperatures.

Table 2. Thermal conductivity for mycelium composites.

Sample	Thermal conductivity (W/m·K)
A	0.071 ± 0.002
B	0.070 ± 0.002
C	0.075 ± 0.003

Thermal conductivity performance shows more insulating capabilities that other mycelium based materials and are close to 0.06 W/(m·K), below which the material could be considered thermally insulating. Thus if the fabrication method is slightly improved it could position the material as a potential replacement for mineral-based wools for instance in vertical partition walls.

4. CONCLUSIONS

This study confirms that paper-based mycelium composites are also effective as absorbing materials, particularly in the mid-frequency range. The findings emphasize the importance of substrate selection and growth duration in tuning both acoustic and thermal performance. The peak absorption around 1 kHz in a 4 cm thick sample suggests a surprisingly high tortuosity which should be confirmed on a later stage by direct characterization.

Among the three sample types, those with longer incubation time, hence higher colonization, showed lower sound absorption coefficient.These insights support the continued development of mycelium-based composites as low-impact alternatives to synthetic insulation materials. Future work should explore optimized mold geometries, thicker sample configurations for low-frequency performance, and quantitative modeling using Johnson-Champoux-Allard frameworks to further refine acoustic predictions.

5. ACKNOWLEDGMENTS

This project has received funding from the European Union's Horizon Europe research & innovation programme under the HORIZON-MSCA-2021-DN-01 grant agreement No. 101072598 – "ActaReBuild".

6. REFERENCES

[1] M. A. Shakir and M. I. Ahmad, "Bioproduct advances: insight into failure factors in mycelium composite fabrication," Biofuels Bioprod Bioref, vol. 18, no. 5, pp. 1739–1754, 2024.

[2] T. S. Gomez, M. Rychtarikova, R. Armstrong, E. Piana, and C. Glorieux, "Acoustic Applications Of Bio-Mycelium Composites, Current Trends And Opportunities: A Systematic Literature Review," presented at the Proceedings of the International Congress on Sound and Vibration, (Prague Czechia), 2023.

[3] N. Walter and B. Gürsoy, "A Study on the Sound Absorption Properties of Mycelium-Based Composites Cultivated on Waste Paper-Based Substrates," Biomimetics, vol. 7, no. 3, p. 100, 2022

[4] C. Dognini, S. Basu, P. Piana, and E. Gobbi, "Variation Of The Acoustic Characteristics Of Mycelium-Based Biomaterials With Time," in Proceedings of the 29th International Congress on Sound and Vibration, (Prague Czechia), 2023.

[5] H. Le Ferrand, "Critical review of mycelium-bound product development to identify barriers to entry and paths to overcome them," Journal of Cleaner Production, vol. 450, p. 141859, 2024.

[6] A. Pedrero, M. Á. Navacerrada, D. De La Prida, L. Iglesias, and A. Díaz-Chyla, "On the accuracy of the sound absorption measurement with an impedance gun," Applied Acoustics, vol. 158, p. 107039, 2020.

[7] T. S. Gomez et al., "Development of a myco-material based on textile and agro-industrial waste for thermal insulation," E3S Web Conf., vol. 546, p. 03003, 2024

DOI:

Main theme: A03 Building Acoustics

Session A03.10 Acoustic consultancy projects and BIM

Chair(s): C. C. Mastino, A. Díaz

DOI: 10.61782/fa.2025.0440

FORUM ACUSTICUM EURONOISE 2025

IFC OPEN BIM FOR NOISE EMISSION EVALUATION OF THE HVAC SYSTEMS

Costantino Carlo Mastino[1*] **Antonino Di Bella**[2] **Juozas Vaičiūnas**[3]
Possidente Raffaello[1] **Mohsen Zavari**[1] **Manuela Piga**[1]
[1] D.I.C.A.AR., University of Cagliari, Italy
[2] DII, University of Padova, Italy
[3] KTU, Kaunas University of Technology, Lithuania

ABSTRACT

The European Community has introduced several directives and initiatives to promote the digitalization of buildings, aiming to improve enviromental efficiency and reduce carbon emissions. The obligation of BIM (Building Information Modeling) in Europe is regulated by Directive 2014/24/EU on public procurement, which promotes the use of BIM to improve efficiency and transparency in public projects. In several European countries the law require the use of open and interoperable formats, such as IFC (Industry Foundation Classes), to ensure of read the data for many years. The evaluation of noise emitted by HVAC (Heating, Ventilation, and Air Conditioning) systems using BIM models in open IFC format represents an innovative and precise approach. BIM models allow the integration of acoustic data directly into the project, facilitating noise analysis at different stages. The use of the IFC format ensures interoperability between different software, enhancing collaboration among professionals. This approach helps identify and mitigate noise sources, optimizing the acoustic comfort of buildings and complying with current regulations. In summary, the integration of IFC-BIM in HVAC noise evaluation offers an efficient and collaborative solution. This work analyzes all the information managed by the IFC format on HVAC system noise emission, highlighting deficiencies and proposing improvements.

[*]***Corresponding author***: mastino@unica.it.
Copyright: *©2025 First author et al. This is an open-access article distributed under the terms of the Creative Commons Attribution 3.0 Unported License, which permits unrestricted use, distribution, and reproduction in any medium, provided the original author and source are credited.*

Keywords: *BIM HVAC, IFC, MEP, Noise emission.*

1. INTRODUCTION

Building Information Modeling (BIM) for buildings, and particularly Mechanical, Electrical, and Plumbing (MEP) is a methodology that enables the design, management, and maintenance of a building's technical systems in an integrated and collaborative manner. At the European level, the adoption of BIM is regulated by various standards, including in Italy the BIM Decree (DM 560/2017) and its subsequent amendments, which make the use of BIM mandatory for public works above a certain amount. The Ministerial Decree 560/2017, known as the BIM Decree, establishes the methods and timelines for the progressive introduction of electronic modeling methods and tools for construction and infra-structure in Italy. The obligation to adopt BIM in public procurement was introduced gradually from 2019 to 2025. The decree also defines EIR (Employer's Information Requirements), known in Italy as "Capitolato informativo", interoperable platforms, and open formats. The main objective is to improve the efficiency, transparency, and quality of public construction projects. The latest Public Procurement Code, updated with Legislative Decree 36/2023, confirms the obligation to use BIM for a wide range of public projects starting from 2025. This obligation applies to new construction projects and interventions on existing buildings with an estimated project value exceeding 2 million euros, and for cultural heritage with a threshold of 5.538 million euros. The code also provides technical incentives for the use of BIM procedures and promotes the adoption of interoperable platforms and open formats such as IFC and OpenBIM. The

goal is to improve the efficiency, transparency, and quality of public construction projects. **Figure 1** provides an overview of the regulations and strategies adopted by various European countries for the adoption of BIM procedures at the governmental level. Among the most active nations on this issue is Lithuania, where the obligation to use Building Information Modeling (BIM) methods was established starting from January 1, 2021. This obligation applies to high-value construction projects in the public sector, with the aim of improving efficiency and resource management.



Figure 1. Countries of the European Community

In Lithuania, the adoption of BIM is promoted through various initiatives and regulations. The Lithuanian government has recognized the importance of BIM to improve the efficiency and quality of construction projects. In 2018, the Ministry of Environment introduced guidelines for the implementation of BIM in public projects, encouraging the use of this methodology for all new construction projects funded with public funds. Additionally, Lithuania follows international and Europe-an standards, such as the ISO 19650 series[1–6], which provides a framework for managing information related to construction and civil engineering works using BIM. These standards help ensure interoperability and consistency of information among the various stakeholders involved in projects. The adoption of BIM in Lithuania is seen as a crucial step to modernize the construction sector, improve transparency, and reduce project costs and completion times. Other non-European Union countries have also contributed to the development of BIM. The United Kingdom has been one of the pioneers in adopting BIM. The main regulation is PAS 1192, which has been replaced by international standards ISO 19650. Since 2016, the use of BIM has been mandatory for all public projects, with the goal of achieving BIM Level 2 maturity. The "Digital Built Britain" program aims to bring the construction sector to BIM Level 3 maturity by 2025. In Singapore [7,8], the government actively promotes the use of Building Information Modeling (BIM) in the construction sector. Since July 1, 2015, all projects with a gross floor area of 5,000 m² or more must be submitted in BIM format. The Singapore BIM Guide provides detailed guidelines for BIM implementation [9], covering modeling and collaboration specifications and procedures. Additionally, the country has introduced Integrated Digital Delivery (IDD) to integrate digital technologies throughout the construction lifecycle. In the United States, BIM is widely used, with mandates for public projects in many states. In Canada, BIM is rapidly gaining ground, with national standards under development. The United Arab Emirates has adopted BIM to improve efficiency in their ambitious construction projects. In Australia, BIM is used for infrastructure and building projects, with national guidelines pro-moting its adoption. In China [10] and Japan [10,11], BIM is also widely adopted to im-prove efficiency and quality in construction projects. An open and interoperable BIM format is essential to ensure collaboration among the various project stakeholders. The Industry Foundation Classes (IFC) format [12,13], standardized by buildingSMART In-ternational, is one of the most widely used for interoperability between different software platforms. IFC allows data exchange between different BIM platforms, ensuring that all information is accessible and usable by all project participants.

2. DATA STRUCTURE IN THE IFC FORMAT FOR HVAC SYSTEMS

The authors can submit for the EAA FA2025 Conference either a short paper from 2 to 4 pages or a long paper of maximum 8 pages, all written in English, and not previously published. Each length indicated is intended as overall and includes figures, tables, references and acknowledgments.

The Industry Foundation Classes (IFC) format is an open standard for data representation in Building Information Modeling (BIM), which facilitates interoperability between different software applications in the construction sector. Within IFC, HVAC (Heating, Ventilation, and Air Conditioning) systems are represented through a series of specific entities that describe components and equipment used for environmental control in buildings. HVAC entities in the IFC format are included in the IfcHvacDomain subschema, which defines the fundamental concepts for

interoperability in the HVAC domain. This schema includes entities that represent both the segments and fittings of distribution systems (such as ducts and pipes) and the equipment typically used in building services, such as boilers, chillers, fans, and pumps. It also considers vibration isolation associated with these components. Examples of HVAC entities in the IFC format include:

- IfcAirTerminal: represents air terminals such as diffusers or grilles.
- IfcBoiler: represents a boiler used for heating.
- IfcChiller: represents a chiller for cooling water.
- IfcFan: represents a fan used for air movement.
- IfcPump: represents a pump for fluid circulation.

These entities can have detailed properties such as location, dimensions, manufacturer, operational status, and other relevant parameters. Managing acoustic properties in the IFC format is essential for evaluating and controlling the sound performance of buildings. One of the main properties used is AcousticRating, which indicates the sound transmission resistance of a given object through a standardized index. This property is often specified according to national building codes and provides an indicative value of the element's acoustic insulation capacity. AcousticRating can be applied to various entities in the IFC format, including:

- IfcWall: to evaluate the acoustic insulation of walls.
- IfcSlab: to determine the acoustic performance of slabs.
- IfcDoor: to analyze sound transmission through doors.
- IfcWindow: to evaluate the acoustic insulation of windows.

Integrating these acoustic variables into the BIM model allows professionals to simulate and analyze the acoustic performance of buildings during the design and subsequent phases, helping to ensure acoustic comfort and compliance with current regulations. Additionally, the use of open standards like IFC facilitates the integration of acoustic information with other aspects of building design, promoting a holistic and multidisciplinary approach in the design and construction process. In the Figure 2 is show the entity in IFC space

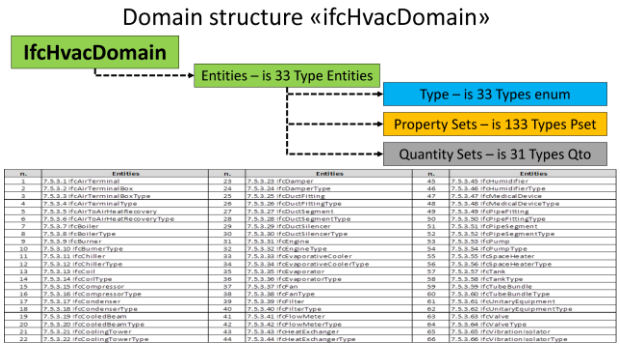


Figure 2. Entity into IFC format

3. DATA FLOW FOR DESIGN AND CHECK WITH THE PHONOMETER

The workflow with Building Information Modeling (BIM) tools for acoustic design and instrumental noise verification allows for an integrated and multidisciplinary approach to designing acoustic comfort in buildings. The process develops in several stages, each supported by interconnected digital tools. Figure 3 shows the workflow from the initial modeling phase to the verification of results. The initial phase involves the architectural modeling of the building in BIM software such as Revit, Archicad, or Allplan, where building elements (walls, floors, fixtures) and systems (HVAC, water, electrical) are inserted. BIM objects must be equipped with relevant acoustic properties, such as Rw (sound insulation index), Ln,w (impact noise), DnT,w (apparent sound insulation), and surface mass. These properties can be added manually or imported from standardized digital dictionaries like the bSDD (buildingSMART Data Dictionary) [14] or manufacturer databases. Subsequently, the model is exported in IFC format to be analyzed with acoustic simulation software such as CATT-Acoustic, Odeon, Insul, or SoundPLAN, GEAR [15]. These tools allow for the simulation of sound propagation in indoor environments and insulation between rooms, considering materials, geometries, volumes, and sound sources. At this stage, the project can be optimized, for example, by modifying stratifications, adding suspended ceilings, sound-absorbing panels, or acoustic barriers. After construction, in-situ instrumental verification is carried out by competent technicians with sound level meters and standardized sound sources. The detected data (such as sound pressure levels, reverberation times, or insulation indices) are compared with the design values. The results can be inserted into the BIM model through parametric properties, creating an acoustic as-built. Finally, all

documentation (technical reports, graphs, measurements) can be attached to the BIM model as informational objects, making the project consultable, traceable, and updatable over time. This workflow allows for the design of buildings compliant with regulations (such as UNI 11367 [16] or ISO 12354 [17–22]), improves the quality of acoustic comfort, and reduces the risk of disputes.

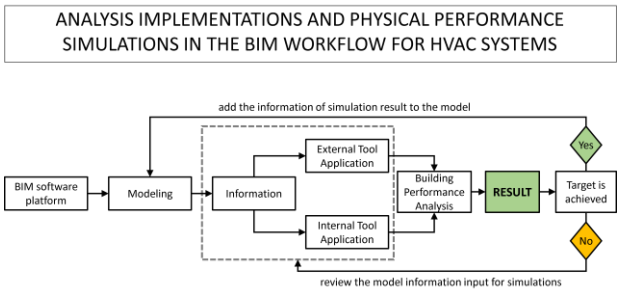


Figure 3. Entity in to IFC format

The IFC data structure does not contain all the necessary information for acoustic calculation. The default property sets contain only a few very limited parameters. To address this, it is necessary to define a bSDD [14] at the standard level for acoustic calculation and verification, within which all the variables present in the various technical standards used are included. Figure 4 shows the workflow that can be followed in the modeling phase and in the code checking phase for the verification of acoustic parameters

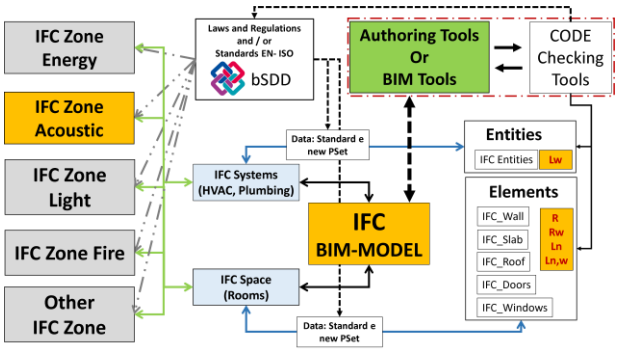


Figure 4. Entity in to IFC format

4. CONCLUSION

In conclusion, the integration between BIM modeling and acoustic design represents a significant breakthrough for the construction sector. The use of digital tools allows for a more precise, coordinated, and informed approach, capable of improving both design quality and environmental comfort. The interoperability between software, data traceability, and the ability to anticipate acoustic issues from the early stages of the project provide tangible benefits for designers, companies, and clients. The synergy between technologies and skills promotes a holistic vision of the building, where sound is considered an integral part of well-being. Investing in acoustic design through BIM is not only a technical choice but also a cultural and sustainable one. In a context increasingly focused on quality of life and energy efficiency, acoustic comfort becomes an essential requirement. Today, digitalization offers all the tools to achieve it effectively. It is up to us to use them to their fullest potential.

5. ACKNOWLEDGMENTS

This work has been developed within the framework of the project e.INS- Ecosystem of Innovation for Next Generation Sardinia (cod. ECS 00000038) funded by the Italian Ministry for Research and Education (MUR) under the National Recovery and Resilience Plan (NRRP) - MISSION 4 COMPONENT 2, "From research to business" INVESTMENT 1.5, "Creation and strengthening of Ecosystems of innovation" and construction of "Territorial R&D Leaders. And The “NEST- Network 4 Energy Sustainable Transition” funded by the Italian Ministry of University and Research under the Next-Generation EU Programme (National Recovery and Resilience Plan)

6. REFERENCES

[1] ISO, 2018, “ISO 19650-1 - Organization and Digitization of Information about Buildings and Civil Engineering Works, Including Building Information Modelling (BIM) — Information Management Using Building Information modellingPart 1: Concepts and Principles.” [Online]. Available: 1.

[2] 2018, “ISO 19650-2 -Organization and Digitization of Information about Buildings and Civil Engineering Works, Including Building Information Modelling (BIM) — Information Management Using Building Information modellingPart 2: Delivery Phase of the Assets.”

[3] 2020, “ISO 19650-3 - Organization and Digitization of Information about Buildings and Civil Engineering Works, Including Building Information Modelling (BIM) — Information

Management Using Building Information modellingPart 3: Operational Phase of the Assets."
[4] 2022, "ISO 19650-4 - Organization and Digitization of Information about Buildings and Civil Engineering Works, Including Building Information Modelling (BIM) — Information Management Using Building Information modellingPart 4: Information Exchange."
[5] 2020, "ISO 19650-5 - Organization and Digitization of Information about Buildings and Civil Engineering Works, Including Building Information Modelling (BIM) — Information Management Using Building Information modellingPart 5: Security-Minded Approach to Information Management."
[6] 2025, "ISO 19650-6 - Organization and Digitization of Information about Buildings and Civil Engineering Works, Including Building Information Modelling (BIM) — Information Management Using Building Information modellingPart 6: Health and Safety Information."
[7] Liao, L., Teo, E. A. L., Chang, R., and Zhao, X., 2020, "Diffusion of Building Information Modeling in Building Projects and Firms in Singapore," Sustainability, **12**(18), p. 7762. https://doi.org/10.3390/su12187762.
[8] Liao, L., Teo, E. A. L., and Chang, R., 2019, "Reducing Critical Hindrances to Building Information Modeling Implementation: The Case of the Singapore Construction Industry," Applied Sciences, **9**(18), p. 3833. https://doi.org/10.3390/app9183833.
[9] 2013, "Singapore BIM Guide Version 2." [Online]. Available: https://www.corenet.gov.sg/media/586132/Singapore-BIM-Guide_V2.pdf.
[10] Liu, B., Wang, M., Zhang, Y., Liu, R., and Wang, A., 2017, "Review and Prospect of BIM Policy in China," IOP Conf. Ser.: Mater. Sci. Eng., **245**, p. 022021. https://doi.org/10.1088/1757-899X/245/2/022021.
[11] Rui, S., Makanae, K., Fujiu, M., and Morisaki, Y., 2024, "SWOT-AHP Analysis of BIM Technology Utilization in the Japanese Construction Industry," Buildings, **14**(11), p. 3549. https://doi.org/10.3390/buildings14113549.
[12] Mastino, C. C., Baccoli, R., Frattolillo, A., Marini, M., and Bella, A. D., "The Building Information Model and the IFC Standard: Analysis of the Characteristics Necessary for the Acoustic and Energy Simulation of Buildings," p. 8.
[13] 2018, "ISO 16739-1:2018 Industry Foundation Classes (IFC) for Data Sharing in the Construction and Facility Management Industries -- Part 1: Data Schema."
[14] BuildingSMART International, "buildingSMART Data Dictionary (bSDD) - Https://Www.Buildingsmart.Org/Users/Services/Buildingsmart-Data-Dictionary/." [Online]. Available: https://www.buildingsmart.org/users/services/buildingsmart-data-dictionary/.
[15] Marini, M., Baccoli, R., Mastino, C. C., Da Pos, V., and Tóth, Z., 2015, "A New Computational Model: G.E.A.R. Graphical Expert Analytical Relations," *Proceedings of BSA 2015, the Second IBPSA-Italy Conference on "Building Simulation Applications,"* bu,press - Bozen-Bolzano University Press Free University of Bozen-Bolzano, Bolzano, pp. 305–312. [Online]. Available: http://www.ibpsa.org/proceedings/BSA2015/9788860460745_38.pdf.
[16] 2010, "UNI 11367:2010 - Acoustics in buildings - Acoustic classification of residential units - Field evaluation and verification (in Italian)."
[17] 2017, "ISO 12354-1:2017 Building Acoustics -- Estimation of Acoustic Performance of Buildings from the Performance of Elements -- Part 1: Airborne Sound Insulation between Rooms."
[18] 2017, "ISO 12354-2:2017 Building Acoustics -- Estimation of Acoustic Performance of Buildings from the Performance of Elements -- Part 2: Impact Sound Insulation between Rooms."
[19] 2017, "ISO 12354-3:2017 Building Acoustics -- Estimation of Acoustic Performance of Buildings from the Performance of Elements -- Part 3: Airborne Sound Insulation against Outdoor Sound."
[20] 2017, "ISO 12354-4:2017 Building Acoustics -- Estimation of Acoustic Performance of Buildings from the Performance of Elements — Part 4: Transmission of Indoor Sound to the Outside."
[21] 2009, "EN 12354-5:2009 Building Acoustics - Estimation of Acoustic Performance of Building from the Performance of Elements - Part 5: Sounds Levels Due to the Service Equipment."
[22] 2003, "EN 12354-6:2003 Building Acoustics - Estimation of Acoustic Performance of Buildings from the Performance of Elements - Part 6: Sound Absorption in Enclosed Spaces."

DOI: 10.61782/fa.2025.0184



FORUM ACUSTICUM
EURONOISE 2025

BUILDING INFORMATION MODELING: EXAMPLE OF USE IDS FILE AND bSDD DATA BASE FOR ACOUSTIC EVALUATION

Costantino Carlo Mastino[1*] **Antonino Di Bella**[2] **Anna Sygulska**[3]
Raffaello Possidente[1] **Andrea Frattolillo**[1] **Mohsen Zavari**[1] **Valerio Da Pos**[4]
[1] DICAAR, University of Cagliari, Italy
[2] DII, University of Padova, Italy
[3] Poznan University of Technology, Poland
[4] Cadline Software srl, Padova, Italy

ABSTRACT

The obligation of BIM (Building Information Modeling) in Europe is regulated by Directive 2014/24/EU on public procurement, promoting its use to improve efficiency and transparency in public projects. In Italy, the New Procurement Code (Legislative Decree 36/2023) mandates BIM for public works above a specific value starting January 1, 2025. In contrast, Poland does not currently mandate BIM, with its implementation driven by the private sector voluntarily. However, the Ministry of Infrastructure and Construction in Poland is working to integrate BIM into public procurement contracts to achieve significant savings for the State Treasury. The use of BIM is growing, with many technical standards requiring open and interoperable formats like IFC (Industry Foundation Classes) defined by an ISO standard to ensure collaboration among stakeholders. This work analyses the information managed by the IFC format for acoustic purposes with an automated verification approach through an IDS (Information Delivery Specification) file. Additionally, it defines the main variables provided by reference standards and not present by default in the IFC file through the use of the bSDD (building SMART Data Dictionary), where all variables should be described in geometric and physical terms.

Keywords: *BIM, bSDD, IDS, BIM Validation.*

[*] ***Corresponding author***: *mastino@unica.it.*
Copyright: *©2025 First author et al. This is an open-access article distributed under the terms of the Creative Commons Attribution 3.0 Unported License, which permits unrestricted use, distribution, and reproduction in any medium, provided the original author and source are credited.*

1. INTRODUCTION

The Building Information Modeling (BIM) is a digital process that involves the creation and management of digital representations of the physical and functional characteristics of buildings. BIM integrates multidisciplinary data to produce a digital model that covers the entire lifecycle of a building, from design and construction to operation [1,2]. This approach enhances collaboration, visualization, and resource management, enabling more informed decision-making and greater efficiency. The integration of BIM with open interoperable formats such as IFC [3], IDS [4], and bSDD [5] provides a powerful tool for managing construction projects, improving collaboration, efficiency, and the quality of information. Specifically, for building acoustic assessments, these tools ensure that acoustic requirements are met, improving the comfort and quality of life for occupants. The Open BIM IFC format (Industry Foundation Classes) [3] is an open and standardized file format for exchanging BIM models. Developed by buildingSMART [6], IFC enables interoperability between different BIM software tools, ensuring that data can be shared without loss or distortion [7–9]. IFC facilitates collaboration among various project stakeholders by allowing them to consistently input, extract, update, or modify model information [10,11]. Checks on the IFC format can be carried out using another data format called IDS (Information Delivery Specification) [4,10]. IDS is a standard that defines the specific data required for a BIM project. An IDS file ensures that all parties involved understand what information must be provided and how it should be structured. In particular, IDS helps standardize data, improve interoperability, and perform automatic compliance checks, reducing errors throughout the different

project phases. All acoustic and non-acoustic parameters, including those not defined within the IFC file, can be included using the bSDD (buildingSMART Data Dictionary) [5]. bSDD is a library of standardized concepts and attributes — for example, a bSDD can be created for all parameters from ISO 12354 [12–17] or ISO 16283 [18–20], which can then be used to manage the acoustic requirements of buildings. Using bSDD, it is possible to clearly define acoustic requirements, classify objects and materials for sound insulation, and integrate this information into BIM models. This approach allows for automatic control and validation of acoustic data, ensuring that the requirements are properly implemented [21–29].

2. MAIN FEATURES OF IDS AND BSDD FORMATS

Below is an overview of the main features of the IDS (Information Delivery Specification) and bSDD (buildingSMART Data Dictionary) formats, which is necessary to introduce the use of these formats in digital processes based on the open BIM IFC data format [21,22,30,31].

2.1 Information Delivery Specification (IDS)

The IDS format is a standard developed by buildingSMART to define information requirements in a form that can be interpreted by both humans and computers. It implements the following key features:

- Clear specifications: Allows for detailing which information must be provided in a BIM model, specifying objects, properties, values, and units of measurement.
- Automated validation: Facilitates the automatic verification of IFC model compliance with defined requirements, improving quality control and data consistency.
- dìIFC integration: Designed to work in synergy with the Industry Foundation Classes (IFC) format, the open standard for BIM model exchange.

In other words, this open data format allows for the definition of requirements and specifications for the project that designers can use to develop their work. The same IDS file will later be used, at the end of the project or during an intermediate or subsequent phase, to verify that the required specifications have been implemented in the model.

2.2 buildingSMART Data Dictionary (bSDD)

The bSDD "database" is a collection of interconnected data dictionaries that provide definitions of terms used to describe the built environment. In practice, within the bSDD it is possible to define all the variables required for acoustic calculations according to ISO 12354, as well as all the variables needed for acoustic classification of buildings according to ISO/TS 19488 [32]. The bSDD includes the following main features:

- Centralized library: Provides an online repository of classes (terms) and properties, including allowed values, units, and translations, promoting terminological consistency.
- Interoperability: Facilitates the integration of existing national and international standards, improving compatibility across different systems and software.
- Open access: Offers a free service accessible by all software solutions, allowing for easy use and integration.

he bSDD is a library based on the IFD ISO 12006-3 standard [33]. The IFD (International Framework for Dictionaries) is a system developed by buildingSMART to facilitate data interoperability in the construction sector. It is a framework that allows the creation, management, and use of standardized data dictionaries to describe the built environment. The IFD focuses on creating an ontology of common concepts and terminologies that can be shared among different software and BIM applications [34].

2.3 IDS and bSDD

In summary, IDS focuses on defining and verifying the information requirements in BIM models, and the same file can be used to communicate to designers which parameters are required within the BIM model. The same IDS file can then be used once a specific project phase is completed to check if it contains all the specified data. bSDD, unlike the IDS format, provides a standardized dictionary of terms and properties to describe the built environment, supporting interoperability and data consistency within the construction sector. Within a bSDD, various rules or variables can be standardized, such as acoustic standards for design and/or on-site verification, to be used automatically by tools. The use of bSDD allows for the implementation of any regulation, technical standard, or requirement in BIM processes without needing to modify the IFC data format. Once defined, the bSDD is published on the buildingSMART International website and, after being validated, is accessible to all operators who request its use.

3. USE OF IDS AND BSDD FORMATS IN BIM PROCESSES FOR ACOUSTICS

The bSDD can be used, either alone or in conjunction with the IDS format, to manage the acoustic requirements of buildings in various ways. Definition of acoustic requirements: The bSDD allows for the clear definition of acoustic requirements using standardized and shared terms. This ensures that all project participants have a uniform understanding of the acoustic specifications. Meanwhile, the IDS file can be used to verify the presence or absence of parameters and/or information regarding acoustic aspects.

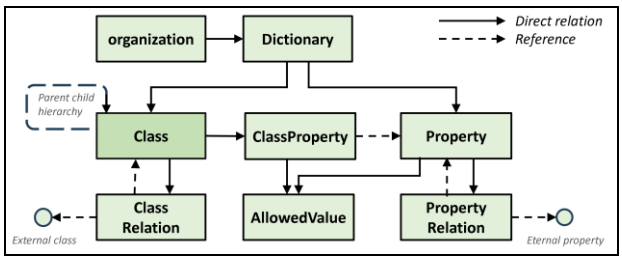


Figure 1. bSDD organization - https://technical.buildingsmart.org/services/bsdd/data-structure

In Figure 1, the following are represented:

- **Classification of objects**
  Objects and materials used for acoustic insulation can be classified in the bSDD. This facilitates the selection of appropriate materials and the verification of their acoustic properties.
- **Integration into BIM models**
  The bSDD can be integrated into BIM (Building Information Modeling) models, allowing acoustic requirements to be directly associated with the elements of the model. This helps ensure that acoustic specifications are met during design and construction.
- **Control and validation**
  By using the bSDD, automatic control and validation of acoustic data can be performed. This reduces communication errors and ensures that acoustic requirements are properly implemented.
- **Extension of property sets or new Psets**
  The bSDD allows the extension of property sets to include specific requirements, such as acoustic ones. This enables the dictionary to be tailored to the particular needs of a project.

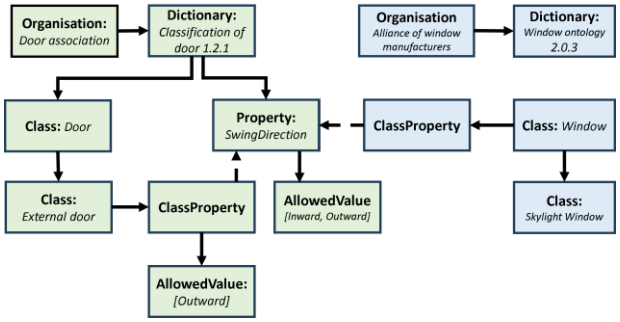


Figure 2. Example demonstrating the usage of the above concepts [4,5]

The bSDD is a service to facilitate the distribution of data dictionaries (read below about what those are) published by independent organisations. The diagram Figure 1 and Figure 2 shows the simplified data model behind the bSDD.

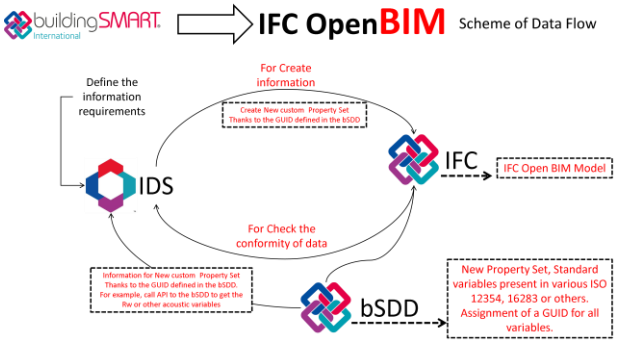


Figure 3. Flow of information for acoustic goals

In Figure 3, the information flow that the various data follow is shown. In particular, it can be observed that the definition and use of one or more bSDD allows, in a standardized way, to define all those variables that are not present in the default property sets provided by the IFC standard. In fact, when a bSDD is created for any purpose, such as project calculation or acoustic tests, a GUID is assigned to the various variables, which allows these to be included in new customized property sets without losing the reference to the standard.

4. CONCLUSIONS

In this work, the procedures that need to be followed for various acoustic issues when using open BIM models have been analyzed. The use of these models created by

buildingSMART International is essential for obtaining standardized calculations and projects within a digital project. The use of the IDS format together with the bSDD dictionary format allows for acoustic issues to fill the information gap that the default IFC open format presented. With the analysis carried out in this work, it has evolved to show how the data flow and various information can be defined within a design or verification process that relies on the use of open BIM models thanks to the open IDS and bSDD formats

5. ACKNOWLEDGMENTS

This work has been developed within the framework of the project e.INS- Ecosystem of Innovation for Next Generation Sardinia (cod. ECS 00000038) funded by the Italian Ministry for Research and Education (MUR) under the National Recovery and Resilience Plan (NRRP) - MISSION 4 COMPONENT 2, "From research to business" INVESTMENT 1.5, "Creation and strengthening of Ecosystems of innovation" and construction of "Territorial R&D Leaders. And The “NEST- Network 4 Energy Sustainable Transition” funded by the Italian Ministry of University and Research under the Next-Generation EU Programme (National Recovery and Resilience Plan)

6. REFERENCES

1. Mastino, C.C.; Baccoli, R.; Frattolillo, A.; Marini, M.; Salaris, C. Acoustic Insulation And Building Information Modeling: A Model Of Calculation For The Code Checking In The Forecast Phase And Of Measurement The Performances.; Rome, Italy; pp. 205–212.
2. Mastino, C.C.; Di Bella, A.; Semprini, G.; Frattolillo, A.; Marini, M.; Da Pos, V. BIM APPLICATION IN DESIGN AND EVALUATION ACOUSTIC PERFORMANCES OF BUILDINGS. In Proceedings of the 25th International Congress on Sound and Vibration; International Institute of Acoustics and Vibration, IIAV: Hiroshima, July 8 2018; Vol. 7, pp. 4241–4248.
3. ISO 16739-1:2018 Industry Foundation Classes (IFC) for Data Sharing in the Construction and Facility Management Industries -- Part 1: Data Schema 2018.
4. BuildingSMART International Information Delivery Specification IDS - Https://Technical.Buildingsmart.Org/Projects/Information-Delivery-Specification-Ids/ 2023.
5. BuildingSMART International buildingSMART Data Dictionary (bSDD) - Https://Www.Buildingsmart.Org/Users/Services/Buildingsmart-Data-Dictionary/.
6. buildingSMART Specification, Http://Www.Buildingsmart-Tech.Org/Specifications.
7. Hernández, J.; Martín Lerones, P.; Bonsma, P.; van Delft, A.; Deighton, R.; Braun, J.-D. An IFC Interoperability Framework for Self-Inspection Process in Buildings. *Buildings* **2018**, *8*, 32, doi:10.3390/buildings8020032.
8. Muller, M.F.; Esmanioto, F.; Huber, N.; Loures, E.R.; Canciglieri, O. A Systematic Literature Review of Interoperability in the Green Building Information Modeling Lifecycle. *Journal of Cleaner Production* **2019**, *223*, 397–412, doi:10.1016/j.jclepro.2019.03.114.
9. Utkucu, D.; Sözer, H. Interoperability and Data Exchange within BIM Platform to Evaluate Building Energy Performance and Indoor Comfort. *Automation in Construction* **2020**, *116*, 103225, doi:10.1016/j.autcon.2020.103225.
10. MASTINO, Costantino Carlo; DI BELLA, Antonino; SYGULSKA, Anna; FRATTOLILLO, Andrea; RICCIU, Roberto; BACCOLI, Roberto; SOLINAS, Elisa On the Use Open BIM Procedures for Acoustic Problems of the Buildings: The New IDS Standard for the Design and Verification Stages.; Institute of Noise Control Engineering: Nantes, 2024; pp. 10068–10074.
11. ISO 19650-4 - Organization and Digitization of Information about Buildings and Civil Engineering Works, Including Building Information Modelling (BIM) — Information Management Using Building Information modellingPart 4: Information Exchange 2022.
12. ISO 12354-1:2017 Building Acoustics -- Estimation of Acoustic Performance of Buildings from the Performance of Elements -- Part 1: Airborne Sound Insulation between Rooms 2017.
13. ISO 12354-2:2017 Building Acoustics -- Estimation of Acoustic Performance of Buildings from the Performance of Elements -- Part 2: Impact Sound Insulation between Rooms 2017.
14. ISO 12354-3:2017 Building Acoustics -- Estimation of Acoustic Performance of Buildings from the Performance of Elements -- Part 3: Airborne Sound Insulation against Outdoor Sound 2017.
15. ISO 12354-4:2017 Building Acoustics --Estimation of Acoustic Performance of Buildings from the

Performance of Elements — Part 4: Transmission of Indoor Sound to the Outside 2017.
16. EN 12354-5:2009 Building Acoustics - Estimation of Acoustic Performance of Building from the Performance of Elements - Part 5: Sounds Levels Due to the Service Equipment 2009.
17. EN 12354-6:2003 Building Acoustics - Estimation of Acoustic Performance of Buildings from the Performance of Elements - Part 6: Sound Absorption in Enclosed Spaces 2003.
18. ISO 16283-1:2014 Acoustics -- Field Measurement of Sound Insulation in Buildings and of Building Elements -- Part 1: Airborne Sound Insulation 2014.
19. ISO 16283-2:2018 Acoustics -- Field Measurement of Sound Insulation in Buildings and of Building Elements -- Part 2: Impact Sound Insulation 2018.
20. ISO 16283-3:2016 Acoustics -- Field Measurement of Sound Insulation in Buildings and of Building Elements -- Part 3: Façade Sound Insulation 2016.
21. Cooperative Research Centre for Construction *Adopting BIM for Facilities Management: Solutions for Managing the Sydney Opera House*; CRC for Construction Innovation: Brisbane, Qld., 2008; ISBN 978-0-9775282-2-6.
22. Asl, M.R.; Bergin, M.; Menter, A.; Yan, W. BIM-Based Parametric Building Energy Performance Multi-Objective Optimization.; Newcastle upon Tyne, UK, 2014; pp. 455–464.
23. Calquin, D.A.L. Automated Building Data Exchange between BIM and BPS Supporting Building Environmental Assessment Methods (BEAM). **2017**, 5.
24. Czmoch, I.; Pękala, A. Traditional Design versus BIM Based Design. *Procedia Engineering* **2014**, *91*, 210–215, doi:10.1016/j.proeng.2014.12.048.
25. ISO ISO 19650-1 - Organization and Digitization of Information about Buildings and Civil Engineering Works, Including Building Information Modelling (BIM) — Information Management Using Building Information modellingPart 1: Concepts and Principles 2018.
26. Guignone, G.; Calmon, J.L.; Vieira, D.; Bravo, A. BIM and LCA Integration Methodologies: A Critical Analysis and Proposed Guidelines. *Journal of Building Engineering* **2023**, *73*, 106780, doi:10.1016/j.jobe.2023.106780.
27. Marini, M.; Mastino, C.C.; Baccoli, R.; Frattolillo, A. BIM AND PLANT SYSTEMS: A SPECIFIC ASSESSMENT. *Energy Procedia* **2018**, *148*, 623–630, doi:10.1016/j.egypro.2018.08.150.
28. Mastino, C.C.; Concu, G.; Baccoli, R.; Frattolillo, A.; Di Bella, A. Methods for Acoustic Classification in Buildings: An Example of Application of BIM Procedures on Wooden Buildings. In Proceedings of the INTER-NOISE and NOISE-CON Congress and Conference Proceedings; Institute of Noise Control Engineering: Madrid, Spain, 19/06 2019; pp. 7018-7029 (12).
29. Mastino, C.C.; Di Bella, A.; Semprini, G.; Frattolillo, A.; Marini, M.; Da Pos, V. BIM Application in Design and Evaluation Acoustic Performances of Buildings.; ICSV25 Local Committee in Hiroshima, 2018; Vol. 7, pp. 4241–4248.
30. Abd, A.M.; Khamees, A.S.; Liu, J. As Built Case Studies for BIM as Conflicts Detection and Documentation Tool. *Cogent Engineering* **2017**, *4*, 1411865, doi:10.1080/23311916.2017.1411865.
31. Habibi, S. The Promise of BIM for Improving Building Performance. *Energy and Buildings* **2017**, 24.
32. ISO/TS 19488:2021 Acoustics — Acoustic Classification of Dwellings 2021.
33. ISO ISO 12006-3:2022 Building Construction — Organization of Information about Construction Works 2022.
34. Gerrish, T.; Ruikar, K.; Cook, M.; Johnson, M.; Phillip, M.; Lowry, C. BIM Application to Building Energy Performance Visualisation and Management: Challenges and Potential. *Energy and Buildings* **2017**, *144*, 218–228, doi:10.1016/j.enbuild.2017.03.032.

DOI: 10.61782/fa.2025.0059

FORUM ACUSTICUM EURONOISE 2025

ACOUSTIC CALCULATIONS AND WORKFLOW BASED ON LIST OF ACOUSTICALLY DISTINGUISHABLE SPACES

Andor T. Fürjes
aQrate Acoustics Ltd., Csákvár (HU)

ABSTRACT

Acoustic consulting often requires to make decisions and do calculations based on simplified data, such as list of rooms to support other relevant fields involved in the design of buildings. In general, a list of rooms contains a summary of data sheet for each room. For acoustic calculations basic geometry (floor area, height), comfort category, number and type of noise sources, exposure to adjacent disturbances, sound absorbing surfaces and objects etc. are useful. The paper provides an overview on what types of acoustically important aspects can be derived from such simple descriptions, using database relations, including room acoustics, sound isolation, MEP noise and electroacoustics. The aim is to create a simple to use integrated tool to increase efficiency and accuracy of the work of acousticians.

Keywords: *room list, architectural acoustic calculations, workflow optimization, room acoustics.*

1. INTRODUCTION

The design process is similar for solving any engineering problem: establishing requirements, assessing constraints, selecting solutions (materials, build-ups, details) to meet requirements, checking compliance by calculation, documenting the results (Figure 1).
It is no different in acoustics practice.
The author's own experience is that most of the time spent on design is spent searching for and organizing data, and that with no other solution at hand, this process is supported almost exclusively by his own collection of technical literature and Excel templates and MatLab routines.

*Corresponding author: furjes.andor@aqrate.hu
Copyright: ©2025 First author et al. This is an open-access article distributed under the terms of the Creative Commons Attribution 3.0 Unported License, which permits unrestricted use, distribution, and reproduction in any medium, provided the original author and source are credited.

Moreover, the vast majority of tasks do not require complex calculations, while thoroughness requires that attention be paid to every room and structure of the planned facility.

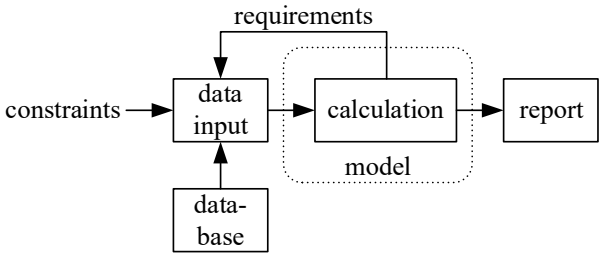


Figure 1. Generic design process.

According to the popular saying, a job can be done quickly, accurately and cheaply, but typically only two of the three aspects can be met.
The aim of the study is to find a more optimal workflow to support acoustic design, by developing a bespoke database-driven approach for generic situations.
Examples are given for room acoustic problems, but other disciplines of acoustics (e.g. sound isolation, MEP noise and isolation, electroacoustics, etc.) can be applied similarly.

2. KEY ELEMENTS OF THE WORKFLOW

The key to optimize design workflow is to a) find a repeatable and algorithmic representation of the problem and b) a scheme that requires minimum effort in calculations.

2.1 Data input: Room Schedules

The author found, that lists of acoustically distinguishable spaces (or room schedules) are the most effective interface to other engineering disciplines in terms of understanding, communicating and to specify generic architectural acoustic problems. With the appropriate support of databases, it can be the center of an efficient workflow in acoustics (Figure 2). A tabular representation of the most important data is easy to input, maintain, import, export or process further. Moreover, most related data (e.g. set of requirements, material properties) are also given in tabular formats anyway.

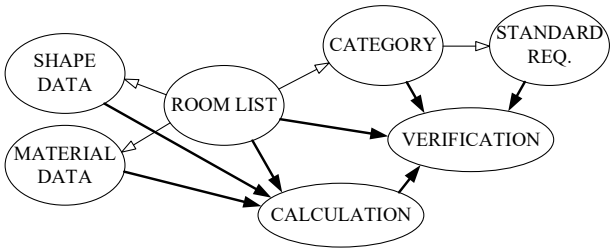


Figure 2. A room schedule (or room list) supported by appropriate databases can be the center of an efficient workflow (hollow arrow: reference, solid arrow: data).

2.2 Calculation Model: Accuracy vs. Complexity

The next question is then to find the minimum number of data, that are sufficient to describe each room in the list to meet the required accuracy of the set of specifications.
Generally speaking, the more effort (input data, complexity and quantity of calculation etc.) is put into a calculation model, the more it should approximate reality. Accuracy of a proper model is surely an asymptotic function of efforts, while the required resources will stay monotonically increasing (Figure 3).

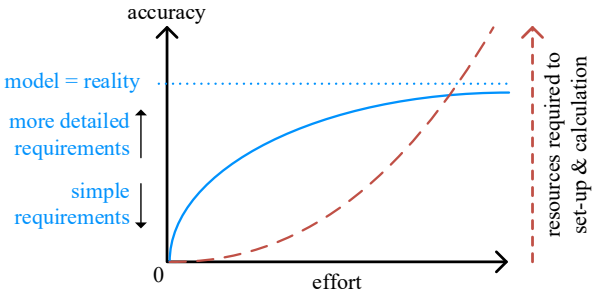


Figure 3. Generic hypothetical functions of accuracy and required resources vs. efforts put into a model.

2.3 Formulating Criteria: Generalization

From a purely engineering point of view, it is rather unfortunate, that still there is no unified and consensual set of metrics and thresholds in regulatory and standard documents yet. A generalization of requirements is therefore necessary in order to be able to adapt different regulatory schemes within the same project.

2.4 Databases: Generalization, Uncertainties

No calculation model is of much use, if there are no reliable databases of sound sources and materials. An acoustic calculation requires at least sound absorption data.
Sound absorption data in form of sound absorption coefficients or sound absorbing power are usually available in various forms (tabular, graphical) for surfaces meant for acoustic treatments in 1/1 or 1/3 octave resolution between 100Hz and 5kHz. Properties of generic ("non-acoustic") types of surfaces or objects are often found in literature, but more often can be estimated only. This resolution and dataset are acceptable, if the aim is to ensure a minimum quantity of absorption to meet usual acoustic requirement metrics. A metric for uncertainty would be nice, though.

2.5 Reporting

As soon as all the data and results are at hand, generating reports can be automated as well:
- summaries of requirements
- calculation results in the required details (tabular or graphic)
- bill of quantities.

3. ROOM ACOUSTIC CRITERIA

On a basic level, setting up room acoustic criteria should be an easy task, if there are any local regulations. The task is cumbersome, however, as soon as the situation is beyond the scope of local regulation or there are other types of standards to be considered.
The reason is, that room acoustic quality is expressed in many different ways with seemingly few consensual conclusions.

3.1 Acoustics Parameters vs. Input Data

Room acoustic criteria should be sorted in the order of complexity with respect to efforts (input data required, calculation complexity etc.) needed for verification.
An informative overview of the most common room acoustic parameters and the minimum required data for their estimation is shown in Table 1 (using [1], [2] and [3]). Important distinctions are around consideration of shape

(V/S ratio or different derivations of mean path lengths between reflections), effects of distance and directivity on early-late energy ratios.
As one can see, a fairly small amount of input data can be sufficient to estimate relevant quality descriptors.
Please note, that since standard measurements of room acoustic descriptors assume omnidirectional sources and receivers, directivity considers only the type of mounting (free, on or near wall, on or near corners etc.).
The next leap in calculation efforts is when mean path length and source-receiver distances are calculated in more detail. Nevertheless, requirements related to spatial deviations are rather rare and neglected in most room acoustic specifications.

Table 1. Overview of estimations of room acoustic descriptors with respect to input data required.

calculated parameter			required or considered input data										
			V	S_{total}	$S_{treatment}$	α	mpf	L, W, H	shape	T_{60}	Q_S	d_{S-R}	Q_R
sound absorption		A	-	-	X	X	-	-	-	-	-	-	-
sound absorption coefficient		α	-	X	X	X	-	-	-	-	-	-	-
reverberation time	Sabine	T_{60}	X	X	X	X	-	-	-	-	-	-	-
	Eyring	T_{60}	X	X	X	X	X	-	-	-	-	-	-
	Fitzroy	T_{60}	X	X	X	X	-	X	-	-	-	-	-
	Kuttruff	T_{60}	X	X	X	X	X	-	X	-	-	-	-
	Fürjes	T_x	-	X	X	X	X	-	X	-	X	X	-
total level	Sabine	L	X	X	X	X	-	-	-	-	X	X	-
	Barron	L	X	X	X	X	-	-	-	X	X	X	-
	Rychtárikova	L	X	X	X	X	X	-	-	-	X	X	-
	Fürjes	L	-	X	X	X	X	-	X	-	X	X	-
early-late level	Barron	L_{te}	X	X	X	X	-	-	-	X	X	X	-
	Fürjes	L_{te}	-	X	X	X	X	-	X	-	X	X	X
gain	Sabine	G	X	X	X	X	-	-	-	-	X	X	-
	Barron	G	X	X	X	X	-	-	-	X	X	X	-
	Fürjes	G	-	X	X	X	X	-	X	-	X	X	X
clarity	Barron	C_{te}	X	X	X	X	-	-	-	X	X	X	-
	Fürjes	C_{te}	-	X	X	X	X	-	X	-	X	X	X
early-decay time	Fürjes	EDT_{10}	-	X	X	X	X	-	X	-	X	X	X

3.2 Mean of Frequencies

Acoustic parameters depend on frequency. Single value requirements use arithmetic means, direct weights or tolerances with allowed deviances across frequency bands.
For room acoustic parameters, the 'mean' value in most cases means the arithmetic mean of values at different frequency bands. Usually, 1/1 octave bands, namely 250 Hz, 500 Hz, 1 kHz and 2 kHz bands are considered.
The author denotes $m1$ if 500 Hz, $m2$ if 500 Hz and 1 kHz, $m3$ if 500 Hz, 1 kHz and 2 kHz and $m4$ if all the four octave bands are used. Please note, that notation might change from standard to standard and using arithmetic means might be just a formal habit with no physical meaning (e.g. summing decay times or energy ratios).
Unfortunately, if different standards need to be applied at the same time, a conflicting definition of 'mean' cannot be resolved, because neither type of mean is more inclusive than the other. On the other hand, measured results show low deviation of different means (e.g. $m2$ vs. $m4$).
Definition of a mean requires flagging considered frequency bands and the type of calculation (arithmetic mean, harmonic mean, power mean), in the form like $\{m_{31.5Hz} \dots m_{8kHz}; m_{type}\}$ for each parameter type.

3.3 Mean Sound Absorption (A_m)

A requirement of minimum of sound absorption represents the aim to reduce noise levels within the rooms. A general form based on formulas found in standards (e.g. [4], [5]) could be

$$A_m \geq \frac{a_A}{[1+b_A \cdot log_{10}(H/H_0)]} \cdot V + c_A \cdot S + d_A \cdot S_f \quad (1)$$

where A_m is the mean sound absorption requirement, V is the volume of the room, S is the total surface area of the room, H is the height of the room, $H_0 = 1m$, S_f is the floor area in the room and $\{a_A; b_A; c_A; d_A\}$ are parameters depending on the category of the room.
The above formulation considers only architectural surfaces (i.e. not air absorption, not furniture or occupants), meaning that c_A is actually the average absorption coefficient $\bar{\alpha}_{arch}$ of architectural boundaries.
For example, a requirement of MSZ2080 (see [6]) of $A_m/V \geq 0.20\frac{m^2}{m^3}$ of corridors with max. 3.2 m height can be translated to $\{0.20; 0; 0; 0\}$ terms. Similarly, a $\alpha_{m2} \geq 0.30$ requirement is translated as $\{0; 0; 0.30; 0\}$ or a DIN18041:B2 $h > 2.5m$ situation $A/V \geq [4.8 + 4.69lg(h/1m)]^{-1}$ is translated to $\{0.208; 0.977; 0; 0\}$ terms.

3.4 Mean Reverberation Time (T_m)

A maximum reverberation time or maximum length of sound level decay requirement is a simple tool to limit detrimental effects caused by late or ongoing reflections. Also, it is a very illustrative descriptor to both non-professionals and musicians.
As an overall ruler, a limited reverberation time will also limit other quality descriptors in favor of higher early/late energy ratios. That explains most correlations found with other parameters.
Please note, that while definitions of T_{60} rely on the *length* of sound decay, estimations except given in [3] approximate

the *slope* of the decay only, which are not the same. The difference in these is significant only when the early/late energy ratio is affected by directivity or local reflections at either the source or receiver side.

Using formulas found in standards (e.g. [4], [7]), one may use the general formula of setting maximum mean reverberation time requirement as

$$T_m \leq a_T \cdot log_{10}(V/V_0) + b_T \cdot (V/V_0)^{c_T} + d_T \quad (2)$$

where T_m is the mean reverberation time requirement, V is the volume of the room, $V_0 = 1m^3$, and $\{a_T; b_T; c_T; d_T\}$ are parameters depending on the category of the room. For example, a DIN18041:A2 requirement is described by $\{0.37; 0; 0; -0.14\}$. In addition, these forms also come with a minimum and maximum of V or T_m.

To the author's knowledge, both the parameters and the formulas used in standards are empirically chosen with no direct physical explanation.

A minimum mean reverberation time requirement can be added where an acoustic source needs support from reverberation in the room.

3.5 Reverberation Time Frequency-Dependence

Requirements controlling frequency dependence of reverberation time have usually the same mission, but differ significantly from standard to standard (Figure 4). The aim of using tolerances is to keep deviation from a mean reverberation time to a reasonable minimum as a function of frequency, while allowing longer reverberation at low frequencies to support moderately loud operation and to avoid excessive high frequency attenuation overall.

Frequency dependent specifications can be absolute (e.g. [8], [9], [10]) or adjusted to the mean reverberation time by a ratio (e.g. [4], [11]) or a difference (e.g. [7]).

For the sake of simplicity, tolerances can be considered at 1/1 octave bands only. This way, a tolerance requires values to specify minimum and maximum for each frequency band, and a flag if is related to the mean value.

3.6 Considering Room Conditions

Conditions of occupancy (in percentage) and furnishing ("yes" or "no") must be clearly stated in a definition of room acoustic criteria, because these have significant effect on their interpretation.

Atmospheric conditions are usually not mentioned in standards of room acoustics. This is important however to set for frequency dependent tolerances, because deviations in temperature or relative humidity can cause room acoustic parameters to change noticeably (>5%) at 2 kHz and higher frequencies (see [12]).

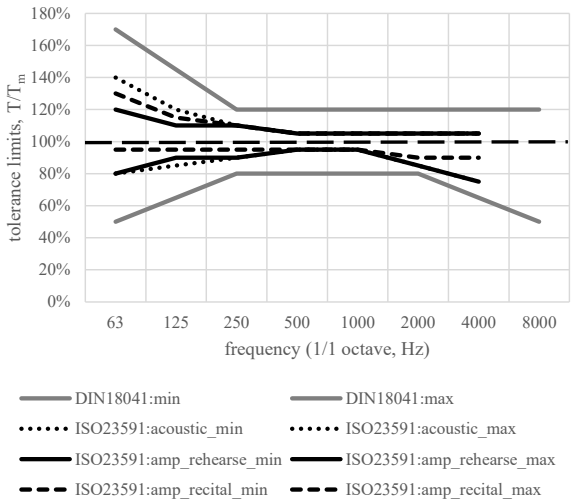


Figure 4. Mean-related frequency-dependent tolerances of reverberation times are different.

3.7 Additional Criteria

Additional technical parameters can be used to refine expectation of room acoustic qualities.

Loudness of reverberation can be expressed as the actual reverberating sound level relative to the free-field sound level of a sound source. This is called Gain, defined in [13], given in dB, used in [11]. Frequency dependence is not considered.

The ratio of early/late energy portions of an impulse response in dB correlates to perception of clarity (see [13]). Minimum mean speech clarity like $C_{50,m3}$ (see [14]) uses early-late time limit of $t_e = 50ms$. Frequency dependence is not considered.

Perceivable acoustic parameters change also from position to position within a room. Parameters discussed so far assume a spatial average, though requirement standards usually are not explicit in this respect or refer to definition standards. Spatial decay rate is an important issue for open spaces with multiple simultaneous activities. By using distance-dependent estimations of room acoustic effects, requirements like $D_{A,S}$ (in-situ attenuation of speech) or $D_{2,S}$ (spatial decay rate of speech) of [9] can be calculated. Frequency dependence is not considered, A-weighting is used.

Calculation of sound level requires the sound power level L_w of the source and its directivity factor Q, or if Q is not of concern, the free-field sound level at a reference distance to be known. For example, $L_{p,A,S,4m}$ (A-weighted sound

pressure level of speech at 4 m) of [ISO22955] is defined by a reference sound level at 1 m distance for octave bands.
Preferred ratios of dimensions can be used to avoid unfavorable situations, like e.g. uneven frequency response at low frequencies due to modal behavior (see [11], [7], [15]). A generic form of these requirements can be:

$$sign(a_R \cdot L + b_R \cdot W + c_R \cdot H) = d_R, \quad (3)$$

where for example equality of [11] $L/H = 2.36\,W/H - 1.38$ can be translated to $\{1; -2.36; 1.38; 0\}$ or unequality of [7] $1.1 \cdot W/H \leq L/H$ can be translated to $\{1; -1.1; 0; 1\}$.
In cases, where room conditions require to define occupancy and the number N of occupants is known, ratios of N/S_f or N/V can by added to the set of requirements, because occupants have a significant effect on room acoustics.

4. CALCULATION FORMULAS

4.1 Main Dimensions

For box-shaped rooms, main dimensions of L, W and H can be read from drawings and volume V, surface S, floor area S_f can be calculated easily.
Dimension-related criteria can be verified directly.
The mean path length between reflections in a box-shaped volume is

$$\bar{l}_{stat} = 4\,V/S, \quad (4)$$

which can be derived in different ways (e.g. [1]), even using mirror image sources (i.e. not assuming diffuse reflections). This suggests, that multiple different reflection paths can be approximated by a single repeating reflection with length $\bar{l}_{stat}$ and $\bar{l}_{stat}/c$ average time, when c is the speed of propagation.
Room schedules often present only floor area S_f and height H. With no further information, an estimation of $L = W = \sqrt{S_f}$ can be used as a worst-case scenario, because a square floor area has the highest V/S ratio and longest $\bar{l}_{stat}$ estimation of box-shaped geometries.

4.2 Room Shape

The author found, that formulas can be rewritten meaningfully when normalizing the mean path length $\bar{l}_{stat}$ and source-receiver distance r by $\sqrt{S}$:

$$\bar{l}_n = \bar{l}_{stat}/\sqrt{S} = 4\sqrt{V^2/S^3} \quad (5a)$$

$$r_n = r/\sqrt{S} \quad (5b)$$

The importance lies in the fact, that $\bar{l}_n$ depends only on the shape of the room, but not its dimensions, like a shape factor.
If the room is not rectangular or absorption is extremely irregular (e.g. open ceiling), estimation of $\bar{l}_{stat}$ or $\bar{l}_n$ requires more complex calculations.
This is where using prepared simple convex volumetric shape-models can help. Using only a specification like $\{L_1; W_1; H_1; L_2; W_2; H_2; X_1; X_2\}$ (see Figure 5) can describe most typical situations convincingly, without the need to build 3D room acoustic models. Values of X_1 and X_2 can be additional sizes or the number of segments approximating continuous arcs.
Shape-models are then useful also to generate valid source and receiver positions and from that, valid source-receiver distances and effects of source directivity can be considered as well.

4.3 Sound Level

The sound level L_p consists of the direct sound and the sum of reflections.
Classic theory suggests, that the sum level of reflections is constant across the room:

$$L_p = L_w + 10 \cdot log_{10}\left[\frac{Q_{SR}}{4\pi \cdot r^2} + \frac{4}{A}\right], \quad (6)$$

where L_w is the sound power level of the source, r is the distance, Q_{SR} is the directivity factor for the given source-receiver constellation and A is the total sound absorption of the room.
A is simply the sum of A_S absorption of boundaries, A_O absorption of objects and A_V absorption of the volume:

$$A = A_S + A_O + A_V. \quad (7a)$$

Absorption of boundaries A_S can be calculated as

$$A_S = -ln(1 - \bar{\alpha}) \cdot S, \quad (7b)$$

using the Eyring-formula, and

$$\bar{\alpha} = \alpha_0 \cdot (S - \sum S_i) + \sum \alpha_i \cdot S_i \quad (7d)$$

where $\bar{\alpha}$ is the average sound absorption coefficient of surfaces, α_i is the sound absorption coefficient of the material with surface S_i and α_0 is the sound absorption coefficient of the default (untreated) surface. Obviously, condition $S \geq \sum S_i$ must be preserved.
Absorption of free-standing objects is

$$A_O = \sum A_j \cdot n_j, \quad (7c)$$

Where A_j is the sound absorption and n_j is the quantity.
Absorption of the volume is

$$A_V = 4 \cdot m \cdot V, \quad (7d)$$

where m is the sound absorption of the air.
Room schedules include references to material databases and quantities S_i and n_j. Material databases contain frequency-dependent properties α_0, α_i and A_j. Absorption of air can be calculated from standards, but must be converted from single-frequency values to 1/1 octave band values beforehand (see [12]).

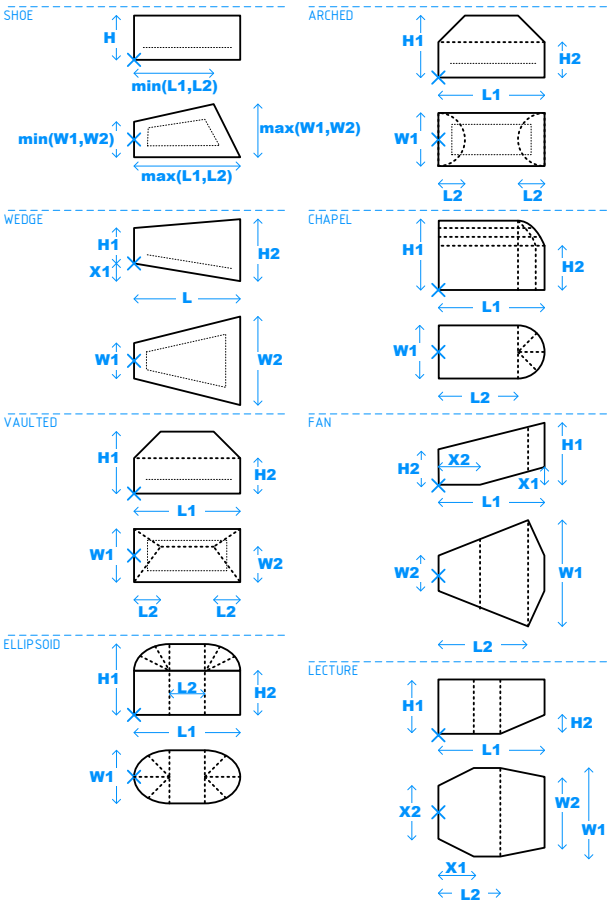


Figure 5. Typical convex room shapes for fast entry and calculation of shape-dependent parameters.

More recent approximations follow the experience (see [2]), that sound level of reflection is not constant across the room, but decrease with distance. Classic theory in (6) still can be used for worst-case approximation of noise levels.
Revised approximation of sound level, considering shape-factor (see [3]) is

$$L_p = L_w + 10 \cdot log_{10}\left[\frac{Q_{RS} \cdot e^{-m \cdot r}}{4\pi \cdot r_n^2} + \frac{4 \cdot (1-\alpha^*)^{r_n/\bar{l}_n+1}}{\alpha^*}\right] - 10 \cdot log_{10} S, \quad (8)$$

where $e^{-m \cdot r}$ is the sound absorption of the air to the direct sound, and the total average sound absorption α^* includes sound absorptions of surface, objects and air.
It is important to see, that according to Eq. (8), reverberating sound level depends more on absorption α^*, shape r_n/l_n and total surface area S, than volume V.
Equation (8) has been tested and found following measured tendencies well (see [3]) and can be completed by adding Waterhouse-correction $C_W = 10 \cdot log_{10}(1 + 2\,\lambda/\bar{l})$ at low frequencies and small rooms when necessary.

4.4 Reverberation Time as Decay Rate

Classic theory suggests, that reverberation time governed by reverberating volume and absorbing power:

$$T_{60,stat} = 24 \cdot ln(10) \cdot \frac{V}{A}, \quad (9a)$$

which can be rewritten in the form

$$T_{60,stat} = 6 \cdot ln(10) \cdot \frac{\bar{l}}{c} \cdot \frac{1}{\bar{\alpha} + [A_O/(4 \cdot V) + m] \cdot \bar{l}}. \quad (9b)$$

The latter form reflects, that temporal rate of decay depends on the average time $\bar{l}/c$ spent between reflections the average energy loss α^* during each cycle, as

$$\alpha^* = \bar{\alpha} + [A_O/(4 \cdot V) + m] \cdot \bar{l}. \quad (10)$$

If $\alpha^* > 1$, $\alpha^* = 1$ must be used.
It is important to note, that $T_{60,stat}$ is not the length, but the rate of decay of reverberation. This is why it is valid to consider it constant across the volume of the room, as long mean path length and characteristic absorbing properties are seen constant across the volume of the room.

4.5 Reverberation Time as Measured

At any point in a room, the response is a sum of the direct sound and the sound coming from reflections. When the source is visible to the receiver, direct sound always arrives first, reflected sound follows. Energy-time response (ETC) can be converted to the energy decay curve (EDC), which is the ratio of remaining energy of the response and the total energy of the response (see Figure 6).
When reverberation time T_{60} is defined as a length of the response where EDC drops below -60 dB, it can be calculated as

$$T_{60} = \frac{60dB + EDC_{t_{0+}}}{60dB} \cdot T_{60,stat} \quad (11a)$$

where $EDC_{t_{0+}}$ is the first drop in EDC

$$EDC_{t_{0+}} = -10 \cdot log_{10}\left[1 + 10^{DRR/10}\right] \quad (11b)$$

and DRR is the ratio of the direct sound and the reflected sound

$$DRR = 10 \cdot log_{10}\left[\frac{Q_{SR} \cdot \alpha^*}{16\pi \cdot r_n^2 \cdot e^{m \cdot r \cdot (1-\alpha^*)^{r_n/l_n+1}}}\right]. \quad (11c)$$

Measured reverberation time according to [13] is a linear regression of the EDC between two points. For example, reverberation time T_{20} from the of EDC -5 dB and -25 dB points can be approximated as

$$T_{20} \approx \frac{(25dB + EDC_{t_{0+}}) \cdot (15dB - EDC_{t_{0+}})}{25 \cdot 15\ \mathrm{dB}^2} \cdot T_{60,stat} \quad (12)$$

assuming that $EDC_{t_{0+}} > -25$ dB (i.e. response contains enough reverberant energy).

This approach explains, how different reverberation time definitions relate to each other (see Figure 7) and agrees well with measured tendencies.

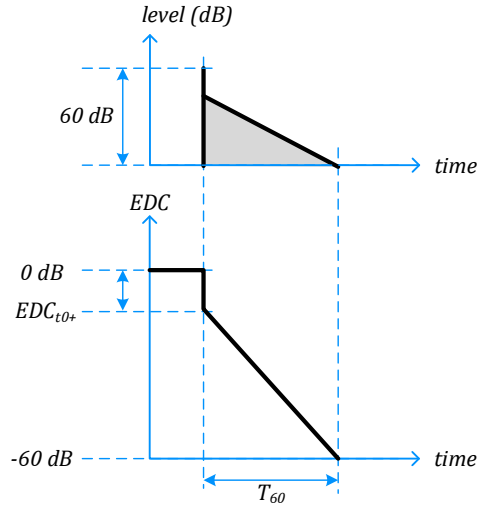


Figure 6. The simplest form of response shown as energy time curve (ETC) and energy decay curve (EDC).

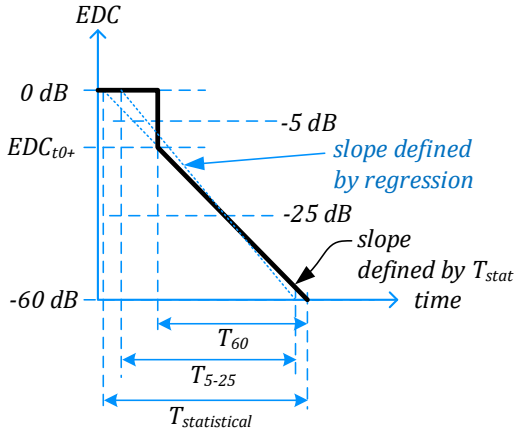


Figure 7. Comparing different reverberation times.

4.6 Early Decay Time as Measured

In a similar manner, early-decay time EDT_{10} can be approximated, when $EDC_{t_{0+}} > -10$ dB as

$$EDT_{10} \approx \frac{(10dB+EDC_{t_{0+}})\cdot(10dB-EDC_{t_{0+}})}{10\cdot 10\ \mathrm{dB}^2}\cdot T_{60,stat} \quad (13)$$

assuming that $EDC_{t_{0+}} > -10$ dB. This condition explains also, why evaluation of EDT_{10} can be ambiguous when DRR is high.

4.7 Early-Late Ratios

Early-late ratios can be taken directly from EDC at any given early-late t_e time limit from the onset of the direct sound (t_{0+} point):

$$C_{t_e} = 10\cdot log_{10}\left(10^{-EDC_{t_e}/10}-1\right), \quad (14a)$$

where

$$EDC_{t_e} = EDC_{t_{0+}} - \frac{t_e}{T_{60,stat}}60\mathrm{dB}. \quad (14b)$$

4.8 Parameters Considering SNR

Certain standards use speech transmission index (STI) in order to specify speech clarity requirements. STI is not a room acoustic measure, but a parameter for electroacoustic transmission, as it is developed to consider signal to noise ratios (SNR) and possible distortions along the transmission, with many correction options for perceptual masking or non-native speaker issues for example. If STI is applied assuming linear transmission, without perceptual corrections, an STI requirement will implicitly call for a minimum signal-to-noise ratio as well.

Without considering SNR, measurement results show STI to correlate many of the room acoustic parameters fairly well (see [17]). The tendency is, that STI correlate early-late ratios directly within ± 0.05 error, while reverberation time allows a 'worst case' STI estimate:

$$STI_{C_{80}} \approx 0.022\cdot C_{80,m4} + 0.53, \quad (15a)$$

$$STI_{EDT_{10}} \approx -0.165\cdot ln\left(EDT_{10,m4}\right) + 0.594, \quad (15b)$$

$$STI_{T_{20}} \geq -0.2\cdot ln\left(T_{20,m4}\right) + 0.55. \quad (15c)$$

When SNR must be considered, a better option is to calculate useful-to-detrimental ratio

$$U_{50} = 10\cdot log_{10}[E_0^{50}/(E_{50}^{\infty}+E_N)] \quad (16a)$$

or

$$U_{50} = C_{t_e} - 10\cdot log_{10}\left[1+\frac{10^{-SNR/10}}{10^{-EDC_{t_e}/10}}\right], \quad (16b)$$

where $SNR = L_p - L_N$ and $t_e = 0.05s$.

According to [16]

$$STI \approx 0.114\cdot U_{50} - 0.54 \quad (16c)$$

is a good estimate.

4.9 Application

Figure 8 shows an example of graphic report of calculation results of T_{20} reverberation time when applying the "lecture" shape. Setting up and running similar calculations can happen in real time for all listed parameters. Most of the work is done by checking input data and setting up requirements. More advanced calculation methods (low order image sources, diffuse radiosity) for better precision can also happen in seconds, but can be run in batch mode, after setting up the room schedule.

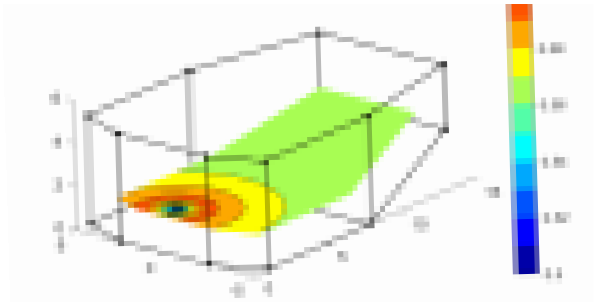


Figure 8. Calculation example: reverberation time T_{20} in a "lecture" shape with dimensions {15;10;5;8;7;2;1;5} and {0.40;0.10;0.50} absorption coefficients on the floor, walls and ceiling respectively, from one omni source

5. SUMMARY

It is important in acoustic engineering practice to be efficient and thorough at the same time, in order to fulfill the ever-growing number of acoustic requirements. Calculation schemes, however are not scalable: one either uses oversimplistic statistical formulas in spreadsheets with minor efforts or creates acoustic models with disproportionate efforts required. Diverse formulation of requirements in different standards and recommendations is also a problem.
The paper suggests to use room schedules, which can be used to generate simple models for calculations. Room schedules are usually available from architectural data, but even the cost of manual data input or its maintenance should not be a problem in most cases.
Most relevant acoustic requirements can be verified using revised formulas without the computation cost of conventional acoustic modelling. Results can be used to generate reports in any required format from graphical representations to simple spreadsheets of bill of quantities.
The next step is to interface to more advanced calculation methods and add functionalities of other fields of acoustics (noise, sound isolation, PA). Also, simple algorithms can suggest solutions or indicate weaknesses automatically.

6. REFERENCES

[1] H. Kuttruff "Room acoustics" ISBN 0-230-87637-7

[2] L. Nijs, M. Rychtárikova, "Calculating the Optimum Reverberation Time and Absorption Coefficient for Good Speech Intelligibility in Classroom Design Using U50", 2011, *Acta Acustica united with Acustica*, Vol. 97 (2011) pp93-102

[3] A. T. Fürjes: "Comparing Derivation from the Revised Theory of Sound Level Distribution in Rooms to Measurement Results", *DAGA 2023* pp. 1307-1310

[4] DIN 18041 "Hörsamkeit in Räumen – Anforderungen, Empfehlungen und Hinwiese für die Planung", 2016

[5] ÖNORM B 8115-3 "Sound insulation and room acoustics in building construction - Part 3: Architectural acoustics", 2005

[6] MSZ 2080, "Acoustics. Specifications and recommendations for room acoustic design", 2020

[7] EBU Tech. 3276 "Listening conditions for the assessment of sound programme material: monohpnic and two-channel stereophonic", 1998.

[8] ANSI S12.60-2010/Part1 "Acoustical Performance Criteria, Design Requirements, and Guidelines for Schools, Part 1: Permanent Schools", 2010

[9] ISO 22955 "Acoustics -. Acoustic quality of open office spaces"

[10] IEC. 60268-13, "Sound System Equipment–Part 13: Listening Tests on Loudspeakers" *International Electrotechnical Commission*, 1998

[11] ISO 23591 "Acoustic quality criteria for music rehearsal rooms and spaces"

[12] J. H. Rindel "Air Attenuation in Octave Bands and How to Normalize Measurements to a Standard Atmosphere" *Applied Sciences,* 2024, 14, 10139

[13] ISO 3382-1 "Acoustics – Measurement of room acoustics parameters – Part1: Performance spaces"

[14] UNI 11532-2:2020, "Caratteristiche acustiche interne di ambienti confinati – Metodi di progettazione e technice di valutazione – Parte 2: Settore scolastico"

[15] J. H. Rindel, "Searching the musical rehearsal room", *BNAM Proceedings*, May 2020

[16] Y. Choi "Comparison of Two Types of Combined Measures, STI and U50, for Predicting Speech Intelligibility in Classrooms", *Archives of Acoustics*, vol. 42, no. 3, pp. 527-532, 2017

[17] A. Fürjes, A. Nagy "Tales of more than One Thousand and One Measurements (STI vs. room acoustic parameters – a study on extensive measurement data)", research report, DOI:10.13140/RG.2.2.15781.01760, 2023

DOI: 10.61782/fa.2025.0492



FORUM ACUSTICUM
EURONOISE 2025

INTRODUCTION OF A GRASSHOPPER WORKFLOW FOR THE INTEGRATION OF THE ACOUSTIC ANALYSIS IN A MULTI-DOMAIN BIM MODEL

Andrea Gerbotto[1*] **Louena Shtrepi**[1] **Fabio Favoino**[1] **Arianna Astolfi**[1]
[1] Department of Energy, Politecnico di Torino, Italy

ABSTRACT

The growing demand for sustainable, energy-efficient buildings underscores the need for integrated modelling and simulation tools that support informed decision-making during early design stages. Among these, simulation of building physics performance, mainly acoustic analysis, has emerged as a critical focus area. Addressing multi-domain perspectives poses challenges, primarily due to interoperability issues and the varied data management approaches across specialised tools. This paper presents a workflow for integrating acoustic performance calculations within a BIM (Building Information Modeling) model. It details the development of an acoustic assessment tool in Grasshopper, utilising Rhino.Inside Revit, for preliminary evaluations of facade acoustic insulation. The tool supports the selection of transparent and opaque elements while accounting for potential conflicts with other performance criteria, such as thermal and lighting properties. Developed as part of the iclimabuilt project, this workflow aims to advance decision-making through seamless interoperability, enhancing efficiency, sustainability, and architectural performance outcomes.

Keywords: *BIM, BPS, facade insulation*

1. INTRODUCTION

A multidomain simulation workflow was developed, integrating Rhino.Inside® Revit to connect the BIM tool Revit with the Building Performance Simulation (BPS) tools in Grasshopper within Rhino. Specifically, 'Honeybee' was utilised for energy and daylighting simulations via EnergyPlus and Radiance engines. The interoperability between BIM and BPS was enhanced through the use of Python scripts, ensuring the accurate linkage of geometry and material performance parameters between Revit and Grasshopper. Additionally, the workflow was extended to incorporate acoustic analysis for façade sound insulation and the 'Bombyx' tool for Life Cycle Assessment (LCA). This expansion enabled a more comprehensive evaluation, including occupant comfort and the embodied energy of materials, which complemented the assessment of operational energy for cooling, heating, and lighting.

2. DEVELOPMENT OF THE RHINO.INSIDE REVIT SIMULATION WORKFLOW

A comprehensive analysis of the current workflow involving BIM models, either within authoring software or through external IFC-compliant tools, has been conducted to define the integration of acoustic simulations into the multi-domain workflow. This analysis demonstrates that there is great potential in integrating building and room acoustics into architectural models to make more informed decisions about acoustic characteristics in the design phases of a building; however, several challenges have so far prevented such large-scale integration [1].

Most studies focus on reverberation time calculations and, in some cases, impulse response and auralization, with a specific emphasis on environments such as auditoriums and classrooms. Some contributions have explored the connection between BIM and acoustic software:

*__Corresponding author__: andrea.gerbotto@polito.it.
__Copyright__: ©2025 First author et al. This is an open-access article distributed under the terms of the Creative Commons Attribution 3.0 Unported License, which permits unrestricted use, distribution, and reproduction in any medium, provided the original author and source are credited.

- Kim, Coffeen, and Sanguinetti [2] linked Revit with EASE to enhance collaboration between acousticians and architects;
- Mastino et al. [3] developed a workflow for integrating acoustic assessments into BIM processes;
- More recently, McGinley et al. [4] proposed an OpenBIM workflow to improve collaboration between designers and acoustic consultants, while Starowicz and Zielinski [5] analyzed the potential of Artificial Intelligence in acoustic design.

The findings suggest that although partial approaches exist, fully interoperable tools between BIM and acoustic analysis software are still lacking. A major obstacle is the absence of a structured acoustic ontology within the IFC standard [6], which hinders the full integration of acoustic analysis into BIM models.

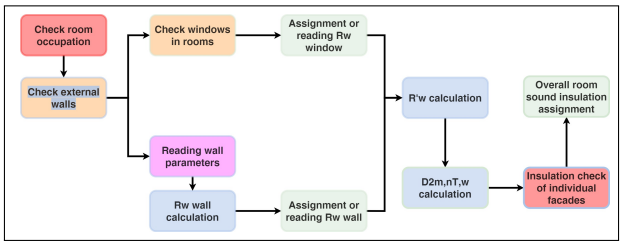


Figure 1. Rhino.Inside Grasshopper workflow.

2.1 Airborne sound insulation against outdoor noise

The workflow has been developed to calculate the standardised level difference of the façades of the occupied rooms $D_{2m,nT,w}$ as:

$$D_{2m,nT,w} = R'_w + \Delta L_{fs} + 10\log\left(\frac{C_{sab}V}{T_0 S}\right) \quad (1)$$

where:

- R'_w is the apparent sound reduction index of the façade;
- ΔL_{fs} is the level difference due to façade shape, in dB;
- C_{sab} is the Sabine constant, $C_{sab} = 0.16$ s/m;
- V is the volume of the receiving room, in m^3;
- S is the total area of the façade as seen from the inside, the sum of the area of all the façade elements, in m^2;
- T_0 is the reference reverberation time, $T_0 = 0.5$ s.

The volume and surfaces can be derived from the model, while ΔL_{fs} must be manually defined for each façade, as specified in Table C.1 (EN ISO 12354-3, Annex C).

The apparent sound reduction index R'_w of the façade is the sum of the sound reduction index R_w of the façade and a contribution due to the flanking transmissions of the surrounding elements. This contribution usually is negligible; however, if rigid components, such as concrete or brick, are connected to other rigid elements within the receiving room, such as floors or partition walls, flanking transmission can contribute to the overall sound transmission; so, in cases with rigid elements, flanking transmission can be incorporated globally by reducing the sound reduction index subtracting 2 dB (EN ISO 12354-3).

The sound reduction index of the façade, then, is the average of the sound reduction indexes of the elements composing it, mainly walls and windows, because it's possible to have different distributions of windows, with different areas and sound reduction indexes, in the façades, it's convenient, in the implemented workflow, to calculate an average sound reduction index and a total area of the windows of the single façade.

2.2 Model geometry

It has been considered, as a case study, a typical 4-floor office building constructed with a concrete structure and brick walls (Figure 2), featuring an additional external layer of high-density insulating mineral wool. From each office room, it has been derived, thanks to Rhino.Inside components, all the geometric inputs needed for the analysis, in particular:

- the volume $[m^3]$ of each room;
- the surface $[m^2]$ of each external wall;
- the dimensions $[m]$ of each window in the external walls of the considered rooms;
- the thickness $[m]$ of the layers of the wall stratigraphy.

2.3 Acoustic parameters

Due to the insufficient implementation of acoustic ontology in the IFC schema, it has been necessary to define some shared parameters in the Revit project to correctly insert acoustic parameters into the model, which can be queried for analysis, updated, or compiled at the end.

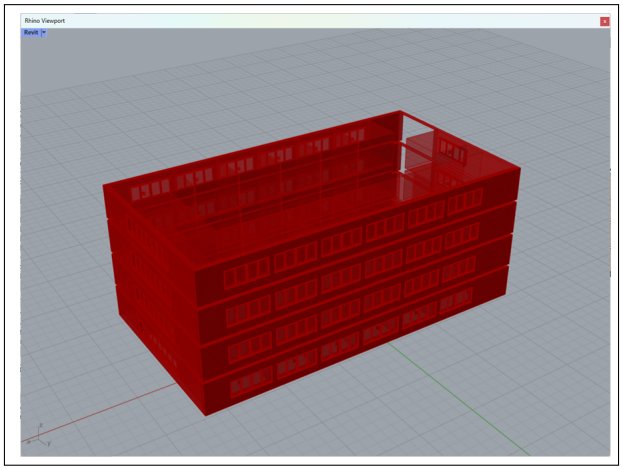


Figure 2. BIM model analysed.

This shared parameters could be of two different types:

- Type parameters, which define common properties shared by all instances of a specific type;
- Instance parameters, which represent unique properties of individual occurrences.

2.3.1 Input parameters

As input parameters, it is necessary to define the **Sound Reduction Index** of the elements involved, specified as a type parameter, because it is derived solely from the stratigraphy or the specific construction type of the element. In particular, while the sound reduction index of the windows is usually derived from facility testing and certified due to the standardised way they are produced, for the walls, it could be defined from facility testing in very specific conditions or, more often, derived from semiempirical formulas, like the ones suggested in the EN ISO 12354-1, where it's also defined how to calculate the ΔR_w due to additional layers, like wall linings or thermal insulation systems. Other necessary parameters are mainly instance parameters because they are specific for each element, like the **Occupancy** of each room, the **Façade Shape Factor**, potentially different for each external wall, or the **Flanking**, defined by the type of connections between external and internal walls.

2.3.2 Output parameters

As output parameters, it has been necessary to define a Sound Insulation parameter for each room into which to insert the calculation results and permit the automatic validation of the model according to EIR specifications in the IDS file.

Table 1. Input parameters.

Parameter	Typology	Data type
Sound Reduction Index	Type	integer
Façade Shape Factor	Instance	integer
Flanking	Instance	boolean
Occupancy	Instance	text

Table 2. Output parameters.

Parameter	Typology	Data type
Sound Reduction Index	Type	integer
Sound Insulation	Instance	integer

2.4 Outputs

Given the input parameters, the workflow calculates the standardised level difference of the façades ($D_{2m,nT,w}$), with a graphic and intuitive preview of the results to highlight those that need improvement, by changing the Sound Reduction Index of the windows or defining a new typology that could be selected from a database and instantly update the model (Figure 3).

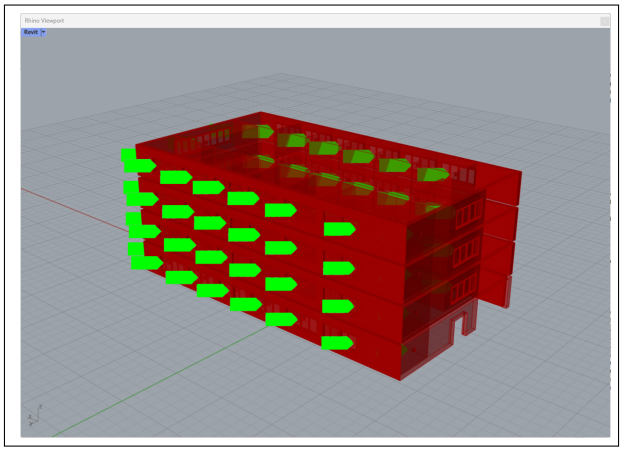


Figure 3. Façade insulation verified.

It is possible to export schedules or views from Revit

with all the correct data directly in the right families and instances (Figure 4) and, defined the proper PSets according to EIR specifications, it is possible to export an IFC that can be validated with the IDS file.

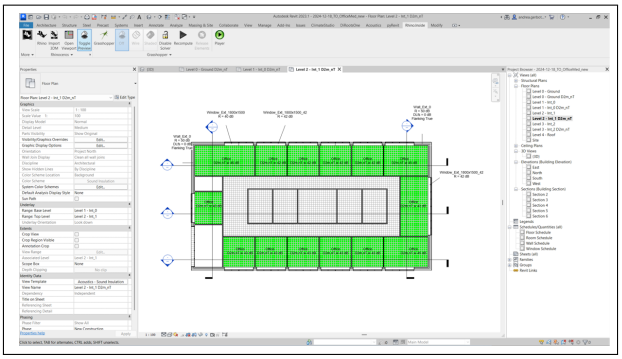


Figure 4. Floor plan with parameters.

3. CONCLUSIONS

This paper presented a novel workflow for integrating acoustic performance evaluation within a BIM-based multi-domain simulation framework. By leveraging Rhino.Inside Revit and Grasshopper, the approach ensures seamless interoperability between geometric and simulation tools, allowing for early-stage acoustic analysis alongside other performance criteria such as energy and daylighting. The proposed method enables the automated extraction of key geometrical and material parameters from BIM models, ensuring accurate and efficient façade sound insulation assessments.

The results demonstrate that incorporating acoustic analysis within the BIM workflow enhances decision-making by providing designers with immediate feedback on the acoustic performance of façade elements. The automated parameter integration and visualization capabilities further facilitate optimization, reducing manual errors and improving efficiency in the early design phase.

Some limitations remain. Certain parameters, such as the façade shape factor and flanking transmission contributions, still require manual input, which may introduce variability and reduce automation. Additionally, the Sound Reduction Index for walls often needs to be calculated externally using different theoretical models better suited to specific conditions, limiting full automation in material property assignment.

Future developments will focus on expanding the workflow to include more advanced room acoustics simulations and improving the implementation of curtain walls, given their widespread use in both new buildings and renovations, particularly in office and multifunctional spaces.

4. ACKNOWLEDGMENTS

The experimental activities presented in this paper were carried out as part of the H2020 project “iclimabuilt—Functional and advanced insulating and energy harvesting/storage materials across climate adaptive building envelopes” (Grant Agreement no. 952886).

5. REFERENCES

[1] L. Shtrepi, F. Aletta, L. Aspöck, A. Astolfi, J. Fels, M. Hornikx, K. Jambrošić, C.-H. Jeong, E. Kahle, J. Llorca-Bofí, J. H. Rindel, M. Rychtáriková, S. Torresin, and M. Vorländer, “Ten questions concerning Architectural Acoustics,” *Building and Environment*, vol. 265, p. 112012, Nov. 2024.

[2] S. Kim, R. C. Coffeen, and P. Sanguinetti, “Interoperability Building Information Modeling and acoustical analysis software - A demonstration of a performing arts hall design process,” *Proceedings of Meetings on Acoustics*, vol. 19, p. 015136, May 2013.

[3] C. C. Mastino, R. Baccoli, A. Frattolino, M. Marini, and C. Salaris, “Acoustic Insulation And Building Information Modeling: A Model Of Calculation For The Code Checking In The Forecast Phase And Of Measurement The Performances,” *Proceedings of Building Simulation 2019: 16th Conference of IBPSA*, vol. 16, pp. 205–212, 2019.

[4] T. P. McGinley, T. Vestergaard, C.-H. Jeong, and F. Pind, “An OpenBIM workflow to support collaboration between Acoustic Engineers and Architects,” *J. Phys.: Conf. Ser.*, vol. 2069, p. 012164, Nov. 2021.

[5] A. Starowicz and M. Zieliński, “Sustainable Acoustics: The Impact of AI on Acoustics Design and Noise Management,” *ts*, Oct. 2024.

[6] D. Utkucu and R. Sacks, “Generation of acoustic ontology for a holistic building performance domain,” *Proceedings of the 2023 European Conference on Computing in Construction and the 40th International CIB W78 Conference*, vol. 4, 2023.

DOI:

Main theme: A03 Building Acoustics

Session A03.11/A05.11 Heat pump sounds in residential settings: challenges and solutions

Chair(s): J. Harvie-Clark, C. Reichl, G. Fusaro

DOI: 10.61782/fa.2025.0542

FORUM ACUSTICUM EURONOISE 2025

MACHINE LEARNING-BASED PREDICTION OF AIR SOURCE HEAT PUMP NOISE ANNOYANCE

Volkan Acun[1*] **Simone Graetzer**[1] **Antonio J. Torija Martinez**[1]
[1] Acoustics Research Centre, University of Salford, United Kingdom

ABSTRACT

Air Source Heat Pumps (ASHPs) are pivotal in decarbonising domestic heating and air conditioning, yet noise emissions remain a significant barrier to their wider adoption. This paper presents a machine learning-based approach to predicting annoyance caused by ASHP noise emissions to address the complexity of human perception of noise by integrating psychoacoustic metrics, emotional responses, and demographic factors. Seven predictive models were evaluated, including tree-based methods (Gradient Boosting and Random Forest) and traditional regression approaches (Support Vector Machine, Lasso, Linear Regression, Ridge, and ElasticNet). Among these, the Gradient Boosting method demonstrated superior performance (test R^2 = 0.846, RMSE = 0.910) compared to linear methods, highlighting the non-linear nature of annoyance response. Feature importance analysis revealed emotional responses (Arousal and Valence) as the dominant predictors, collectively accounting for 92.3% of the model's predictive capability, while Zwicker's Psychoacoustic Annoyance (PA) and Tonality showed moderate correlations with these emotional factors, suggesting indirect influence and mediation effect. Despite limitations in available training data that did not allow full implementation of neural network approaches, the current model provides a robust foundation for predicting annoyance caused by ASHP noise emissions and highlighting the impact of subjective perception

[*] ***Corresponding author***: v.acun@salford.ac.uk
Copyright: *©2025 Acun et al. This is an open-access article distributed under the terms of the Creative Commons Attribution 3.0 Unported License, which permits unrestricted use, distribution, and reproduction in any medium, provided the original author and source are credited.*

Keywords: *noise perception, air source heat pumps, noise annoyance, machine learning, regression*

1. INTRODUCTION

Switching from fossil fuels to renewable options is key for reducing carbon emissions in domestic heating and air conditioning around the globe. In Europe, buildings are the largest consumers of energy. Most of these buildings waste energy. They account for 36% of greenhouse gas emissions and 40% of total energy use [1]. One way to tackle this issue is by replacing old fossil fuel heating systems with energy-efficient options like air source heat pumps (ASHPs).

ASHPs are easy to maintain and cost-efficient. The thermal energy produced by an ASHP can be well over 100% of the amount of energy they use[2]. However, noise emissions from these units have raised concerns among the public. The spectrum of the ASHP noise varies depending on the operating condition of the unit. Low-frequency content dominates the ASHP signal, but it also typically includes both narrowband and tonal components [3], with becoming particularly more tonal in the low-frequency region. These components can significantly contribute to the annoyance caused by noise emissions.

The most common policy around ASHP noise emissions is regulating the A-weighted sound pressure levels. In addition, some countries, such as Germany, Finland, and the Netherlands, included tonal penalties in their noise assessment regulations to address the annoyance that could be caused by the tonal character of the signal [4]. These policies, in general, fell short of including the human perception of ASHP noise and solely relied on objective measures. People's subjective responses should

be used alongside the A-weighted sound pressure level-based measurement to ensure best practice in the policy.

This paper presents the preliminary results of a more extensive study to incorporate Machine Learning (ML) based models to predict the noise annoyance caused by ASHP noise emissions. This paper aims to investigate which acoustics and non-acoustic factors and ML methods are most suitable for developing a robust model that accurately predicts noise annoyance caused by ASHP noise emissions. By incorporating additional data from diverse datasets in the future, this research aims to develop a fast and accessible tool for supporting decision-making based on relevant acoustic and non-acoustic metrics. This will facilitate effective planning and placement of ASHP units to minimise noise impact on communities.

2. METHODS

The data used for this study were gathered through a listening test conducted at the Acoustics Research Centre of the University of Salford. This listening test was concerned with human perception of ASHP noise at various source distances, background noise levels, and under different loads. It consisted of two parts, each examining different aspects of the ASHP noise under different background noise levels and source distances. The first part of the experiment considered people's reactions to continuous ASHP noise. In contrast, the second part concerned the response to transient ASHP noise. However, the scope of this study does not include the investigation of the responses to continuous and transient noise, source distances or the effect of different background noise levels. Instead, the focus is on understanding how the subjective response and psychoacoustic character of ASHP noise affects perception and how it can be used to develop an ML-based prediction model. Therefore, only a brief overview of the experimental procedure is provided.

2.1 Audio Stimuli

The audio stimuli used in this experiment were based on recordings conducted as part of the IAE HPT Annex 51[4][5]. These recordings had a sampling rate of 96 kHz and were calibrated to the original levels based on a 94 dB(A) 1 kHz calibration tone.

Two recordings were selected from this original recording dataset and trimmed into shorter segments of two different lengths for two distinct parts of the experiment (20 s for Part 1 and 60 s for Part 2). Responses to both parts of the experiment were used in this ML implementation. The sound levels (L_{Aeq20s} and L_{Aeq60s}) of these excerpts were calibrated in the Listening Room of the University of Salford's Acoustics Labs to ASHP-receiver distance attenuation target levels (36.5 dB(A) at 15 m, 40 dB(A) at 10 m, and 46 dB(A) at 5 m).

In addition, ambient background noise is added to the ASHP signal. Instead of a soundscape recording, a shaped pink noise is used as the ambient background noise. To achieve this, pink noise is filtered to represent a typical traffic noise spectrum based on the filter curve detailed in the BS EN ISO 717-2020 [7]. The shaped-pink noise was then calibrated to 39.5 dB(A) and 31.5 to represent the ambient daytime and nighttime background noise levels of a typical rural area [8].

Lastly, these stimuli were propagated indoors through a partially open window (0.05 m^2) following a filter curve provided by [9]. A total of 114 audio stimuli were used for parts one (84 stimuli) and two (30 stimuli). The participants were pseudo-randomly presented with half of the stimuli (57 stimuli) from the stimulus sets for each part of the experiment. Additionally, three control stimuli (2 stimuli for Part 1 and 1 stimulus for Part 2), which only included the shaped pink noise as ambient background noise, were presented to each participant.

2.2 Experimental Procedure

Listening tests were conducted in the University of Salford's Listening Room following ethical approval (Ref: 2024-0145-228). Participants listened to 60 audio stimuli across two parts (Part 1: 42 audio stimuli + 2 control stimuli; Part 2: 15 Audio stimuli and one control stimulus), with responses submitted via a custom Python GUI. The playback system included a Motu 4Pre interface, Genelec 8030A loudspeaker, and 7020B subwoofer, with participants seated 2 m from the source.

Each session lasted approximately 70 minutes and included breaks between parts. Before starting, participants completed consent forms, demographic questions, and the NoiSeQ noise sensitivity scale. After each stimulus, they rated Valence and Arousal on a 9-point Self-Assessment Manikin (SAM) scale, reflecting pleasantness and alertness. Annoyance was rated using a 0–10 scale (0 – "Not Annoying at All," 10 – "Extremely Annoying") adapted from ISO/TS 15666:2021 [10].

In Part 2, participants responded to two temporal points per stimulus to capture perceptual changes, resulting in 75 total responses per participant.

2.3 Participants

The dataset used for research consisted of 50 volunteers that participated in the experiment: 35 male (70%) and 15 female (30%), aged between 19 and 57 years (mean = 32.1, SD = 8.95). Nearly half of the participants reported having expertise in audio or music (n= 24, 48%), while just over half stated they had no previous experience (n= 26, 52%). Most participants lacked expertise in environmental noise or urban planning (n=40, 80%). In terms of housing, 18 participants resided in apartments (36%), nine in terraced houses (18%), six in semi-detached houses (12%), five in detached houses (10%), and the rest lived in student accommodation or shared housing.

2.4 Data Analysis

ArtemiS Suite 15.6 is used to calculate the sound quality metrics (SQM) of the audio stimuli, including Loudness, Sharpness, Roughness, Fluctuation Strength, and Tonality. Loudness and Sharpness metrics are calculated according to DIN 45631/A1[11] standard, while ECMA 418-2(1st)/(2nd) [12] is used for calculating Roughness, Tonality and Fluctuation Strength.

In addition to SQM, Zwicker's Psychoacoustic Annoyance (PA)model [13] is calculated using the formula:

$$PA = N_5\left(1 + \sqrt{w_S^2 + w_{FR}^2}\right) \tag{1}$$

Where:

- N5 percentile loudness in Sone

$$w_S = \left(\frac{S}{\text{acum}} - 1.75\right) \cdot 0.25 \log\left(\frac{N_5}{\text{sone}} + 10\right) \quad \text{for} \quad S > 1.75\ \text{acum} \tag{2}$$

- describing the effect of Sharpness in S and

$$w_{\text{FR}} = \frac{2.18}{(N_5/\text{sone})^{0.4}}\left(0.4 \cdot \frac{F}{\text{vacil}} + 0.6 \cdot \frac{R}{\text{asper}}\right) \tag{3}$$

- describing Roughness R and Fluctuation F.

To quantify the application of ML methods to predict annoyance from ASHP noise emissions, Python 3.13.1 was used with relevant data analysis and visualisation libraries, including scikit-learn, statsmodels, matplotlib, and seaborn.

As previously mentioned, the dataset used for this experiment consisted of responses from 50 participants, each submitting a total of 75 responses, resulting in 3750 data points. Because of this relatively small sample size, ANN-based models were not considered in the prediction model. Instead, the study employed a range of ML-based linear regression models, including Ridge, Lasso, Elastic Net and Linear; tree-based models, including Random Forest and Gradient Boosting; and Support Vector Machine regression (SVR). These models were selected to compare performance across different regression approaches, balancing interpretability and prediction accuracy.

To optimise the hyperparameters of these models, GridSearchCV from the scikit-learn library was employed. This tool is commonly used for tuning the hyperparameters for ML algorithms by automating the process of finding the optimal combination of hyperparameters by exploring a predefined grid of parameter values and evaluating each combination using cross-validation [14]

To ensure the robustness of the results, 5-fold cross-validation (k=5) was used. This method partitions the dataset into five subsets, using each one for validation while the remaining four subsets are used for training. The use of cross-validation helps mitigate overfitting and provides a more reliable estimate of model performance, particularly given the relatively limited sample size in this study.

3. RESULTS AND DISCUSSION

The main focus of developing this prediction model was to incorporate the subjective response and psychoacoustic characteristics of ASHP noise using SQM. Performances of different feature combinations are compared across the previously listed regression and tree-based ML methods to determine which features to include in addition to the subjective response variables of Valence and Arousal and the SQM.

Table 1: Comparison of VIF values for training features that include Psychoacoustic Annoyance (PA) and Sound Quality Metrics (SQM)

Variance Inflation Factor (VIF) values:		
Feature	SQM as Predictors	PA as a Predictor
Tonality	8.673	8.456
Valence	8.08	6.161
Arousal	13.668	5.751
Age	12.258	10.231
PA	NA	10.539
Loudness	27.238	NA
Roughness	23.52	NA
Sharpness	27.557	NA
Fluctuation	4.618	NA

Multicollinearity analysis was conducted as part of the model comparisons, which revealed substantial interdependence among the original SQM. VIF values for Loudness (27.238), Sharpness (27.557), and Roughness (23.52) in the initial model exceeded recommended thresholds, indicating problematic collinearity (Table 1). When these metrics were replaced with the composite Psychoacoustic Annoyance (PA) parameter, the model's multicollinearity was substantially reduced. The PA-inclusive model demonstrated improved VIF values across predictor variables, with Arousal showing the most dramatic reduction (from 13.668 to 5.751). Although PA exhibited a VIF (10.539) value right at the cutoff value, it remains considerably lower than the metrics it replaced. The replacement of individual sound quality metrics with PA not only addresses multicollinearity concerns but also provides a more compact model while preserving essential psychoacoustic information. A-weighted sound levels are not included in this model, as they provided extreme VIF values and did not significantly contribute to the predictive power in any of the tested models.

The only demographic variable included in the models was Age. While other demographic variables were initially considered, such as gender and noise sensitivity data from NoiSeQ responses, they either produced extremely high VIF values (e.g. NoiSeQ VIF = 32.780 when used alongside the final features) or were found to not meaningfully contribute to the model based on correlation and feature importance analysis.

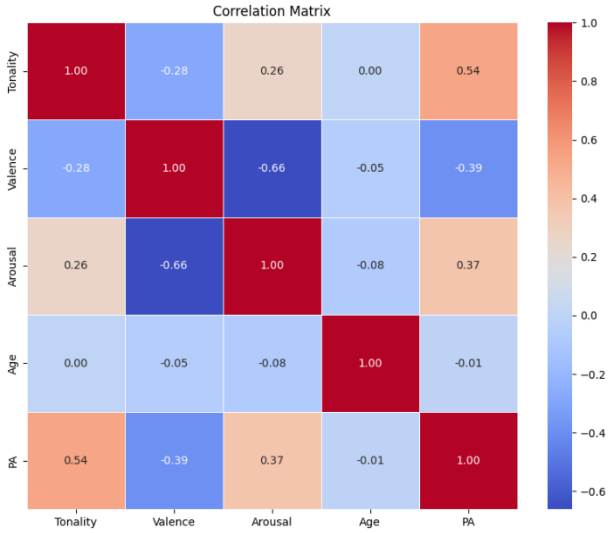


Figure 1: Heatmap representing the correlation matrix between the final set of predictor variables.

Figure 1 shows the correlation matrix between the final set of predictor variables used in the model comparison, providing further justification for the variable selection strategy explained in the VIF analysis. PA and Tonality are the strongest predictors in the matrix. The moderate correlation between PA and subjective response variables (Valence: -0.30, Arousal: 0.37) indicates that while PA effectively consolidates the SQM, it remains sufficiently distinct from other subjective response variables. Age shows the weakest correlation among all the predictors. It is kept as an independent factor in the model since a correlation matrix only captures the linear relationships, while models like Gradient Boosting and Random Forest can capture non-linear patterns and interaction effects that may not be evident in a correlation matrix.

A comprehensive evaluation of predictive models was conducted to identify the optimal approach for estimating acoustic responses. Performance metrics, including R^2, Mean Absolute Error (MAE), Mean Squared Error (MSE), and Roost Mean Squared Error (RMSE), were calculated for training and test datasets across seven distinct modelling techniques (Table 2). Among all the models compared, the Random Forest achieved the highest training R^2 (0.917), suggesting excellent data fitting; however, the slightly lower test performance (R^2 = 0.834) indicated potential overfitting. Linear models (SVR, Lasso, Linear Regression,

Table 2: Comparison of train and test performance of different models.

Model	Train R^2	Test R^2	Train MAE	Test MAE	Train MSE	Test MSE	Train RMSE	Test RMSE
Gradient Boost	0.902	0.846	0.543	0.677	0.525	0.829	0.725	0.910
Random Forest	0.917	0.834	0.500	0.703	0.447	0.889	0.668	0.943
SVR	0.758	0.757	0.875	0.877	1.298	1.301	1.139	1.140
Lasso	0.751	0.750	0.892	0.892	1.339	1.341	1.157	1.158
Linear Regression	0.754	0.753	0.888	0.889	1.321	1.326	1.149	1.151
Ridge	0.754	0.753	0.888	0.889	1.321	1.325	1.150	1.151
ElasticNet	0.753	0.752	0.890	0.891	1.330	1.331	1.153	1.154

Ridge, and ElasticNet) exhibited comparable performance patterns, with test R^2 values ranging from 0.750 to 0.757, substantially lower than the ensemble methods. The consistency between training and test metrics for these linear models, particularly SVR (training $R^2 = 0.758$, test $R^2 = 0.757$), suggests stable performance despite lower overall accuracy. A significant performance gap between tree-based ensemble methods and linear models was observed, with approximately 10% improvement in explained variance and almost 20% reduction in prediction error, highlighting important non-linear relationships in the data.

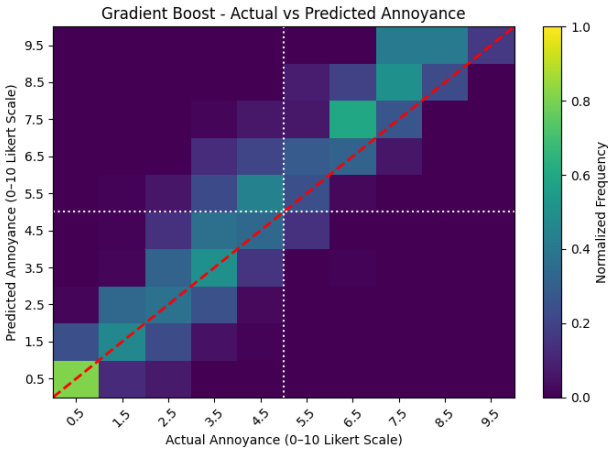


Figure 2: Heatmap showing the normalised frequency of predicted vs annoyance ratings for the Gradient Boost model. Each cell's colour represents the proportion of test samples falling into the corresponding (actual, predicted) bin. The red dashed line diagonal represents the perfect prediction.

The consistency between training and test metrics for these linear models, particularly SVR (training $R^2 = 0.758$, test $R^2 = 0.757$), suggests stable performance despite lower overall accuracy.

Among the models compared, the Gradient Boosting model demonstrated the best balance between predictive accuracy and generalisation. It achieved the highest test R^2 (0.846) while maintaining the lowest test error metrics (MAE = 0.677, RMSE = 0.910), indicating superior performance on unseen data and capturing potentially non-linear relationships. While Random Forest showed a slightly better prediction power over the training data, as it showed evidence of overfitting, the Gradient Boosting model was chosen to be used. In addition, the Gradient Boost method effectively handles multicollinearity. Based on the VIF values shown in Table 01, this is a requirement of the model, as both PA and Age are at the critical thresholds for multicollinearity.

Figure 2 illustrates the predictive performance of the model by comparing the actual and predicted values. The heatmap demonstrates a strong linear relationship between predicted and actual Annoyance values. Overall, the model aligns strongly with the prediction diagonal (red dashed line) but shows some deviation and mild underprediction for higher annoyance values.

Finally, feature importance scores were computed for the Gradient Boost model to understand the relative contribution of each predictor. The highest feature importance scores were observed for Arousal (0.550) and Valence (0.373), which accounted for 92.3% of the predictive power, which are also affected by the ASHP noise. Feature importance scores show that Age contributed

0.0659, while PA (0.0078) and Tonality (0.0026) had minimal impact. While these results indicate that psychoacoustic factors and tonality have a minimal direct impact on this model, their role in shaping the primary predictors should not be overlooked. When these results are considered with the insights from the correlation matrix (Figure 1), it shows that PA and Tonality are moderately correlated with Arousal and Valence, which are the most influential features. This indicates a potential mediating effect, where PA and Tonality influence the prediction indirectly via Arousal and Valence. This emphasises the importance of gaining a deeper understanding of the subjective responses to ASHP noise emissions and considering the soundscape approach.

4. LIMITATIONS AND FUTURE WORK

The main aim of this research was to create a robust ML-based prediction model and leverage ANN models. At the time of writing this paper, this is only partially achieved due to the lack of access to relevant datasets. The first step in future work will be supplementing this research with further data from similar acoustic studies. This will allow the development of more sophisticated ANN-based models capable of capturing the complex non-linear relationships observed in the Gradient Boost implementation. The significant performance gap between ensemble and linear models suggests that deep learning approaches offer additional predictive power with sufficient training data.

Future iterations of the model can also include temporal dynamics ASHP operation cycles. While the dataset from this study included different operating conditions and transient events, possibly due to sample size limitations, they were not found to be significant in any of the top-performing models. The temporal dynamics of SMQ and PA should also be further investigated. Incorporating time-varying acoustic features could better represent real-world ASHP operational conditions.

5. CONCLUSION

This study investigated the prediction of Annoyance responses to Air Source Heat Pump (ASHP) noise using machine learning (ML) approaches. The comparison of various regression models demonstrated that tree-based models, particularly Gradient Boosting, outperformed linear regression techniques. This superior performance highlights complex non-linear relationships in the perception of annoyance that simpler models fail to capture adequately. The PA is implemented as a composite metric to address multicollinearity issues present in the original SQM, resulting in a more compact and robust model.

Feature importance analysis revealed that emotional responses, specifically Arousal (0.550) and Valence (0.373), were the dominant predictors of annoyance, collectively accounting for over 92% of the model's predictive power. While PA and Tonality showed minimal direct contributions, their moderate correlations with the primary predictors suggest an indirect influence through emotional responses. This finding underscores the complex interplay between objective acoustic parameters and subjective emotional responses, supporting the adoption of soundscape approaches in noise annoyance research. The observed relationships emphasise the necessity of considering both acoustic and non-acoustic factors when evaluating and mitigating ASHP noise impacts.

The successful development of this predictive model represents a significant step toward practical applications in sustainable urban development. Despite limitations in available training data, the model demonstrates considerable potential for real-world implementation. Future work will focus on expanding the dataset to enable more sophisticated neural network implementations and incorporating temporal variations in acoustic features. The ultimate goal remains the integration of these predictive capabilities into accessible tools for optimal ASHP placement, thereby supporting the widespread adoption of this sustainable technology while minimising community noise impacts. This balanced approach could substantially contribute to meeting climate goals without compromising acoustic comfort in residential environments.

6. ACKNOWLEDGEMENTS

This study was supported by the University of Salford's Pump Prime Funding and the Future Homes Project, which is funded through the Innovation Accelerator programme by Innovate UK (Project No. 10054845).

7. REFERENCES

[1] European Commission, "European Green Deal: Commission proposes to boost renovation and decarbonisation of buildings," European Commission. Accessed: Dec. 04, 2024. [Online]. Available: https://ec.europa.eu/commission/presscorner/detail/en/ip_21_6683

[2] Natural Resources Canada, "Heating and Cooling With a Heat Pump," Natural Resources Canada. Accessed: Oct. 04, 2024. [Online]. Available: https://natural-resources.canada.ca/energy-efficiency/energy-star-canada/about/energy-star-announcements/publications/heating-and-cooling-heat-pump/6817

[3] P. Brandstätt, M. Krämer, and B. Kaltbeitzel, "Noise and Vibration Characteristics of Outdoor Heat Pumps," 2024.

[4] R. Fumagalli *et al.*, "Acoustic Signatures of Heat Pumps Final Report – Part 4 1.2 Regulations - Countries overview," Heat Pump Centre, 2020.

[5] C. H. Kasess, C. Reichl, H. Waubke, and P. Majdak, "Perception Rating of the Acoustic Emissions of Heat Pumps," in *Forum Acusticum*, Lyon, France, Dec. 2020, pp. 2453–2458. doi: 10.48465/fa.2020.0363.

[6] C. Reichl, "IEA HPT Annex 51: Acoustic Signatures of Heat Pumps – Final Report," Heat Pump Centre, HPT-AN51-1, 2020.

[7] *BS EN ISO 717-1:2020 Acoustics. Rating of sound insulation in buildings and of building elements - Airborne sound insulation*, 2020.

[8] C. Skinner and Grimwood, Colin, "The National Noise Incidence Study 2000/2001 (United Kingdom): Volume 1 - Noise Levels," BRE Environment, United Kingdom, 206344f, 2000.

[9] T. Waters-Fuller and D. Lurcock, "NANR116: 'Open/Closed Window Research' Sound Insulation Through Ventilated Domestic Windows," The Building Performance Centre, School of the Built Environment, Napier University, Apr. 2007.

[10] International Organization for Standardization, *PD ISO-TS 15666-2021- Acoustics — Assessment of noise annoyance by means of social and socio-acoustic surveys*, 2021.

[11] *DIN 45631/A1:2010-03 - Calculation of loudness level and loudness from the sound spectrum - Zwicker method - Amendment 1: Calculation of the loudness of time-variant sound*, 2010. [Online]. Available: https://doi.org/10.31030/1555185

[12] *ECMA-418-2, Psychoacoustic metrics for ITT equipment Part 2 (models based on human perception)*, 2022.

[13] E. Zwicker and H. Fastl, *Psychoacoustics: Facts and Models*. Berlin: Springer, 2006.

[14] "3.2. Tuning the hyper-parameters of an estimator," scikit-learn. Accessed: Apr. 07, 2025. [Online]. Available: https://scikit-learn/stable/modules/grid_search.html

DOI: 10.61782/fa.2025.0191

FORUM ACUSTICUM EURONOISE 2025

CHARACTERISATION AND CONTROL OF AERO-ACOUSTICAL INFLOW NOISE SOURCES OF THE EVAPORATOR FAN IN HEAT PUMPS

Frieder Lörcher* **Sandra Hub**

ZIEHL-ABEGG SE, 74653 Künzelsau, Germany

ABSTRACT

Recent heat pump fans are nowadays often optimized towards a very low self-noise level. Still less effort is expended in the field of additional noise sources generated by spatially and temporally inhomogeneous inflow to the fan, in particular the tonal unsteady loading noise and the broadband turbulence ingestion noise, which depend mainly on the upstream installation conditions and are therefore called “inflow noise”. It is shown for a state-of-the art air-to-water heat pump with 12 kW rated capacity and an evaporator heat exchanger in L-form that the inflow noise exceeds the self-noise of the fan given by the fan supplier. The conclusion is that the optimisation potential considering the inflow noise is more promising than considering a further self-noise optimisation of the fan.
For the considered device, the inflow noise is analysed and characterized along with the causal inhomogeneous inflow conditions to the fan. Both numerical and experimental results are presented. Some optimizing approaches to reduce the inflow noise are investigated, considering both the fan design and installation arrangement. The A-rated total noise emission can be reduced, but, more important, the annoying tonal character of the noise can be attenuated significantly.

Keywords: *heat-pumps, fans, fan-noise, installation noise, aeroacoustics, tonality*

*__Corresponding author__: frieder.loercher@ziehl-abegg.de
__Copyright__: ©2025 ZIEHL-ABEGG SE. This is an open-access article distributed under the terms of the Creative Commons Attribution 3.0 Unported License, which permits unrestricted use, distribution, and reproduction in any medium, provided the original author and source are credited.

1. INTRODUCTION

Heat pumps have become established as efficient and environmentally friendly solutions for the heating and cooling of buildings. Despite their numerous advantages, the noise emitted by the outdoor units (evaporators) poses a significant challenge - particularly in residential areas where low sound levels are required. A substantial proportion of this noise arises from aeroacoustic phenomena associated with the operation of the evaporator fans.
The analysis and control of these noise sources are essential for improving acoustic comfort and enhancing the acceptance of heat pump systems. In recent years, fan researchers and manufacturers have made considerable progress in reducing the sound power levels of their products. However, the focus of such development work is often limited to the fan's intrinsic noise under laboratory conditions, as for example the tip gap noise [2] or stall-related noise [3]. When integrated into actual heat pump systems, significantly higher noise levels are frequently observed. Installation effects of fans in heat pumps concerning efficiency have been investigated in [4]. In [5], the installation fan noise induced by upstream located heat exchangers is investigated.
This study focuses on the mechanisms responsible for the additional aeroacoustic noise (installation noise) generated by evaporator fans in heat pumps, which go beyond the fan's self-noise. These mechanisms are categorised into two principal types: tonal and broadband installation noise. Based on numerical simulations and experimental measurements carried out on a specific evaporator configuration from the publicly funded collaborative "WarmHome" project [1], models for these noise sources are presented, along with strategies for their mitigation.

2. EVAPORATOR AND REFERENCE FAN IN THE WARMHOME PROJECT

In the WarmHome project, a specifically designed L-shaped evaporator heat exchanger with dimensions Width x Depth x Height = 1070 mm x 315 mm x 1200 mm is used to enable particularly compact integration into the heat pump's installation space. The L-shaped geometry induces a deflection of the airflow within the outdoor unit, resulting in more inhomogeneous inflow conditions at the evaporator fan. These installation-specific conditions form the basis for the aeroacoustic effects investigated in this study. A sample of the heat exchanger mounted in a wooden mock-up of the airside of the evaporator is shown in Figure 1.

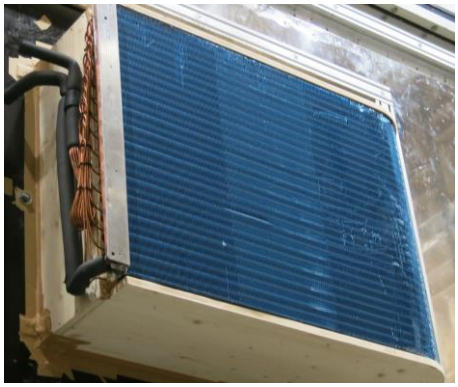


Figure 1. The L-shaped evaporator heat exchanger mounted in the test chamber.

To investigate the relevant noise generation mechanisms and possible optimization approaches, a reference fan was selected that reflects the current state of the art. The chosen axial fan is the commercial fan ZIEHL-ABEGG FPowlet [6] with rotor diameter of 630 mm, 3 impeller blades and a maximum rotation speed of 770 rpm. It is suitable for an operating point of 5000 m³/h at 17 Pa at rotation speed 475 rpm and features low self-noise emission levels. The total sound power of the self-noise given in the data sheet at the nominal operating point is 49 dB(A). This makes it a suitable match for the air-to-water heat pump with a heating capacity of 12 kW to be developed within the project, using the selected evaporator heat exchanger. A model of the fan is shown in Figure 2. The with aerodynamic parts are made of glass fibre reinforced polypropylene

The combination of the L-shaped heat exchanger and the reference fan represents the system under acoustic investigation. This system and variations of it were analysed both experimentally under controlled conditions in a free-field environment and numerically using Lattice-Boltzmann simulation methods.



Figure 2. Reference fan FP063.

3. EXPERIMENTAL SETUP

Aeroacoustic experiments are performed in the ZIEHL-ABEGG anechoic facility with experimental fan testing according to ISO 5801 [7]. The test rig consists of two large anechoic rooms separated by a partition wall. The fan or evaporator unit were attached und integrated with in the partition wall between an upstream and a downstream plenum. Both the inlet plenum (Figure 3) and the outlet plenum have non-reflective walls down to 100 Hz and have dimensions of 9 m x 9 m x 9 m.. Using this experimental setup, the baseline evaporator configuration, the baseline fan and variations thereof are analysed. The volume flow rate Q_V, the static pressure rise Δp_{stat} between the plenums and the shaft input power P_1 are recorded for different duty points, as well as the A-rated specific sound power levels L_W5 and L_W6 on the suction and pressure side, respectively, with the hull surface method. To obtain the total sound power level, the two sound power levels can be summed up using the logarithmic summation rules for level quantities.



Figure 3. Inlet plenum of the anechoic test facility with fan mounted in separation wall.

In addition to the sound power levels, a narrow band spectral decomposition of the emitted sound can be

obtained using the recorded sound signals of the 2 x 12 microphones used for sound analysis.

4. NUMERICAL METHOD

4.1 Numerical Setup

For deeper insight to flow phenomena, numerical simulations using the commercial PowerFLOWsolver 5.5a based on the Lattice-Boltzmann Method (LBM) are performed. The LBM is naturally transient and compressible providing a direct insight into hydrodynamic mechanisms responsible for the acoustic sources but also into acoustic propagation. The LBM tracks the time and space evolution of a truncated particle distribution function on a lattice grid. The particle distribution evolution is driven to the equilibrium by the so-called collision operator. The discrete Lattice-Boltzmann equations are solved with 19 discrete velocities for the third order truncation of the particle distribution function, which has been shown sufficient to recover the compressible Navier-Stokes equations for a perfect gas at low Mach number in isothermal conditions [8]. In PowerFLOW, a single relaxation time is used, which is related to the dimensionless laminar kinematic viscosity [9]. This relaxation time is replaced by an effective turbulent relaxation time that is derived from a systematic Renormalization Group procedure detailed in [10]. It captures the large structures in the anechoic room but also the small turbulent scales that develop along the wall surfaces in a Large Eddy Simulation manner. The particular extension developed for rotating machines can be found in Pérot et al. [11]. The computational domain includes the two coupled anechoic rooms as shown in Figure 4.

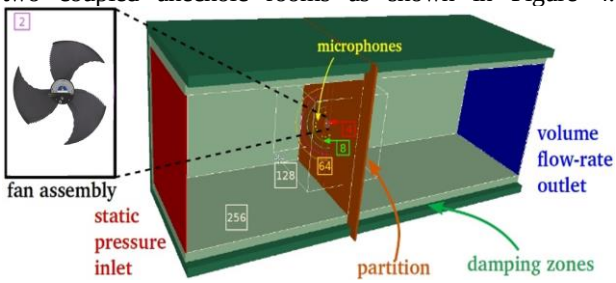


Figure 4. Computational domain and refinement volume definitions. Numbers in squares provide the mesh size in mm for the outlined refinement

The square cross section of the simulation volume has a width of 10 m and the upstream and downstream plenums are also 30 m and 20 m long, respectively. The atmospheric pressure p = 101325 Pa is imposed on the left red surface, while the volume flowrate Qv is imposed on the downstream blue surface. The convergent inlet nozzle and detailed geometry of the fan impeller are considered. Only the motor and its shaft are discarded in the numerical setup. The mesh resolution in the domain is defined through successive embedded volumes, outlined in Figure 4, the mesh size being decreased by a factor of 2 between them. The resolution around the fan blades and the inlet nozzle wall is 0.5 mm. The volume around the fan is defined as a rotating volume at a rotational speed. Extended logarithmic wall functions to account for adverse and favourable pressure gradients [12] are applied on all wall surfaces. The total numerical domain counts 98 million cells and 7 million surface elements. Simulations are performed for several flow rates. First, the setup is initialized in two steps from pre-converged flow obtained from simulations with coarser meshes without the highest resolved refinement regions (50 revolutions computed on the mesh with maximum resolution of 2 mm and subsequently, 25 revolutions computed on the mesh with maximum resolution of 1 mm). Then, the finest mesh is used for performance prediction. The convergence is obtained after 2 fan revolutions on the finest mesh, and data are acquired for 5 fan revolutions. Static pressure is recorded at the exact locations of the microphones in the experiments. In addition, some cross-sections including the one at mid-blade height (midspan) and blade surface are recorded at high frequency sampling for frequency analysis.

4.2 Ingestion Turbulence Modelling

The modelling of the turbulence generated by the heat exchanger is crucial to get a good prediction of the installation noise for the installed condition. Three variants have been considered: Treatment of the heat exchanger as porous block; the same with modelled cooling liquid tubes downstream of the porous block and the use of a turbulent seeding with data obtained from a highly resolved simulation of a small heat exchanger segment. The latter is quite complex, and as the version with the modelled tubes gave similar results, it was applied for the present study.

4.3 Quality of numerical results

The numerical model presented above is validated through the comparison of performances with experimental measurements acquired on the certified ISO 5801 ZIEHL-ABEGG facilities. In Figure 7, a simulated sound power spectra comparison of the fan alone and the fan in installation situation is shown. The results must be seen in

comparison with the experimentally measured ones in Figure 6. At least the trend between the two, and thus the installation sound, is captured well by the simulations.

5. CHARACTERISATION OF INSTALLATION NOISE

5.1 Decomposition to Self-Noise and Installation Noise

The overall sound level of an evaporator fan in a heat pump primarily consists of two components: the self-noise of the fan and the installation noise, which arises from the specific integration of the fan into the device. Additional aerodynamic noise sources may also contribute, such as protective grille noise, but these are not considered in this study. Installation noise can be calculated as the difference between the total sound level in the installed condition and the isolated self-noise of the fan, typically determined under laboratory conditions. This approach applies to both overall sound power levels and their spectral representation.

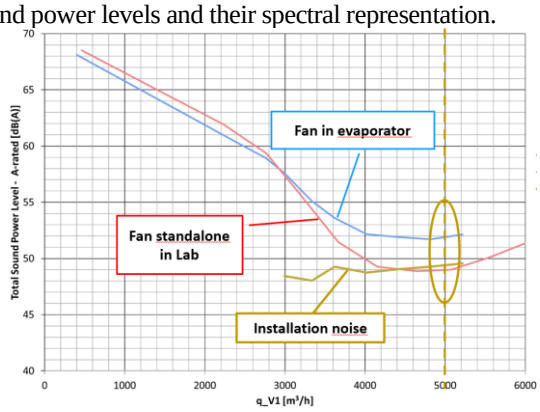


Figure 5. Decomposition of the fan noise in the evaporator installation condition

Figure 5 shows A-weighted overall sound power levels based on experimental measurements of the standalone fan and the fan installed within the evaporator for constant rotation speed and varying airflow Q_V (varying device resistance). The figure also includes the computed difference between both conditions (note that the subtraction must be performed using de-logarithmised sound power values). This difference is referred to as the inflow noise component associated with the heat exchanger measurement. It reaches a magnitude comparable to the fan's self-noise. At the highlighted operating point—corresponding to the nominal design point of the heat pump of Q_V=5000 m³/h—the installation noise component is even slightly higher than the fan's self-noise.

In typical heat pump applications, installation noise can significantly exceed the fan's self-noise—especially when an already acoustically optimised fan is used, as the optimisation typically focuses on the fan's self-noise emission. Consequently, the targeted reduction of installation noise represents a particularly promising strategy and an important measure for improving the overall acoustic performance of the system.

5.2 Spectral Analysis of Installation Noise and Tonality

The subtraction method for determining installation noise, as described in the previous section, can also be applied to sound power spectra, i.e. the frequency-resolved representation of sound power levels. Figure 6 shows a spectral comparison between the self-noise of the reference fan and the total noise measured in the installed configuration within the evaporator at the nominal operating point of Q_V= 5000 m³/h. The abscissa indicates the dimensionless frequency, expressed as multiples of the blade passing frequency (BPF), which is defined as the product of the number of blades and the rotational frequency of the impeller.

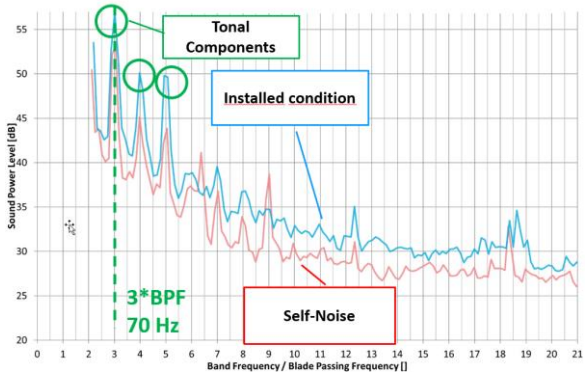


Figure 6. Total sound and self-noise (exp.)

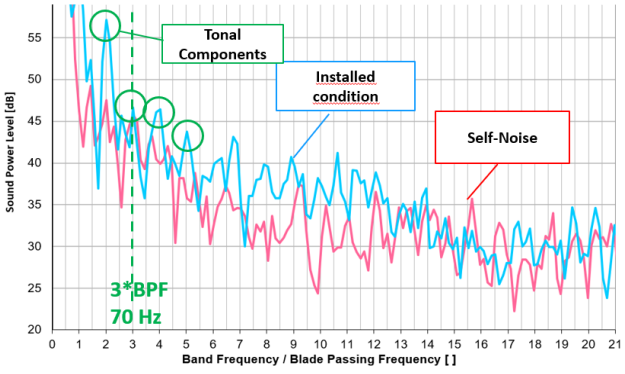


Figure 7. Total sound and self-noise (sim.)

The figure clearly reveals that tonal components are amplified at integer multiples of the BPF, and that the broadband noise level also increases in the installed condition. Figure 8 illustrates the resulting installation noise—i.e. the difference between total and self-noise—along with the self-noise spectrum for comparison. While both exhibit similar overall sound power levels, the installation noise in the current configuration shows a significantly more tonal character. This is a common observation in heat pump noise measurements, and it results in a perceptibly more tonal quality of the sound emission, as also evident in Figure 6.

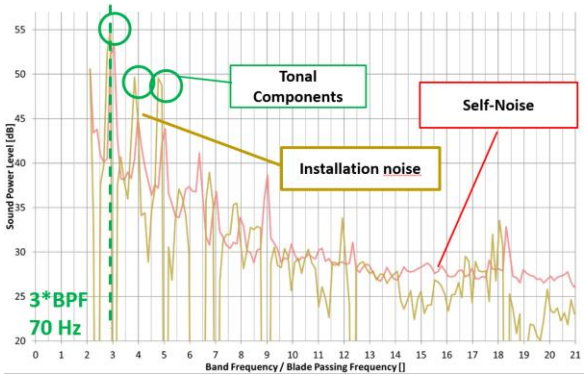


Figure 8. Spectral decomposition of installation noise and self-noise

Tonal sound components are generally perceived as more annoying. Therefore, standard [13] defines a concept of a tonality penalty, which adds a level adjustment in (dB) in cases where prominent tonal peaks occur in the noise spectrum. This approach is increasingly applied in the heat pump industry. According to Figure 6, the self-noise of the fan does not justify any tonality penalty, whereas the total noise measured in the installation condition results in a penalty of +2 dB. Consequently, from an acoustic design perspective, the tonal component of the installation noise should be a key area for system-level optimisation.

5.3 Generation Mechanisms

Installation noise can be divided into two main components:

- **Tonal components**, which appear as narrowband peaks in the frequency spectrum
- **Broadband components**, which manifest as a spectrally distributed sound power over a wide frequency range

These two types of noise result from distinct underlying physical mechanisms. A brief description of these is provided to better support the optimisation strategies discussed in later sections.

5.3.1 Generation Mechanisms of Tonal Installation Noise

Tonal noise components are typically caused by **unsteady aerodynamic loading**, which arises from time-averaged asymmetric inflow conditions. These may be induced by skewed or one-sided inflow, transitions from rectangular ducts, inflow grilles, bends, or obstructions in the intake region. Such features create a non-rotationally symmetric pressure field at the fan inlet, through which the rotor blades pass periodically. The resulting sound radiation occurs at discrete frequencies, often at multiples of the blade passing frequency (e.g. 3×BPF ≈ 70 Hz), and significantly contributes to the perceived tonality of the total sound.

5.3.2 Generation Mechanisms of Broadband Installation Noise

Broadband noise components primarily originate from the **interaction between the fan and turbulent structures** in the inflow, which are inherently unsteady and time-varying. Due to the stochastic distribution of their size, intensity, and form, the resulting sound has a broadband spectral character. These turbulent structures may arise from sharp flow deflections, abrupt geometry changes, structural elements such as struts, flow separations at the heat exchanger, or large stationary vortices.

The interaction with these turbulence-induced structures results in broadband pressure fluctuations at the blade surfaces, which are converted into acoustic emissions. The frequency content of this noise is related to the characteristic scale of the vortices—larger vortices generally lead to lower-frequency components. While this type of noise typically has less impact on the fan's aerodynamic performance, it can significantly contribute to the radiated sound power.

Notably, mechanisms that generate tonal noise—such as time-averaged inhomogeneous inflow fields—can also induce **secondary broadband noise components**, due to the additional generation of turbulence in the vicinity of the rotor.

6. OPTIMIZATION APPROACHES CONCERNING THE TONAL INSTALLATION NOISE

Three optimization approaches specifically aiming at the reduction of tonal installation noise by homogenising the inflow have been tested and are briefly described in this section.

6.1 Optimization of component arrangement

This is often the most cost-effective approach to reduce tonal—and potentially also broadband—installation noise, as it requires no additional components. Instead, the existing elements, particularly the fan, are arranged within the heat pump to achieve the most symmetrical inflow conditions possible at the fan inlet.
Figure 9 shows a visualisation of the time-averaged inflow velocity field—specifically, the circumferential velocity component VT—on a plane upstream of the fan impeller. The reference evaporator configuration, as analysed in Section 5, serves as the basis. A pronounced asymmetry in the inflow distribution can be observed, which is likely caused by the L-shaped geometry of the heat exchanger.

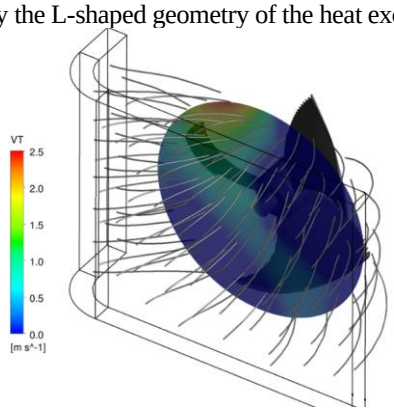


Figure 9. Time-averaged fan inflow velocity VT (reference configuration, simulation)

Shifting the fan approximately 10 cm towards the short branch of the L-shaped heat exchanger results in a more homogeneous inflow distribution, as shown in Figure 10.

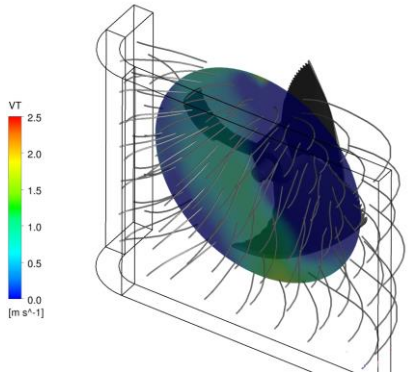


Figure 10. Time-averaged fan inflow velocity VT (optimized configuration, simulation)

The corresponding sound power spectrum, in comparison with the reference configuration, is presented in Figure 11. A substantial reduction in tonal components can be observed. According to [13], no tonal penalty is applicable in the optimised configuration—representing a significant acoustic improvement, even though the A-weighted total sound power level (not shown) remains nearly unchanged. In conclusion, careful spatial arrangement of components—particularly to achieve the most symmetrical and undisturbed fan inflow possible—proves highly effective in reducing the tonal content of heat pump noise emissions.

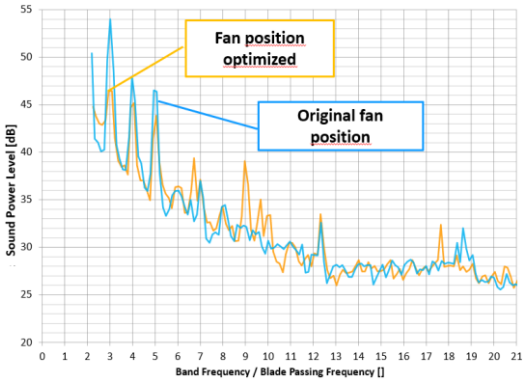


Figure 11. Spectral decomposition of the total noise (fan position optimization)

6.2 Use smooth flow-guiding wall elements

The flow-guiding elements depicted illustrated in Figure 12 were designed to reduce tonal noise by promoting a smoother and more symmetrical inflow distribution to the fan—primarily through the suppression of so-called corner vortices, potentially also reducing inflow turbulence and associated broadband noise. Previous investigations on a planar heat exchanger demonstrated that the implementation of four such elements, realised as 3D-printed parts and placed in each of the four corners, resulted in a significant reduction in installation noise tonality. In the present configuration, however, only a marginal improvement was achieved, and the tonal penalty could not be eliminated. This underlines that the effectiveness of such measures is highly case-specific. Therefore, the potential benefits of flow-conditioning elements should always be assessed through numerical simulations or prototype testing.

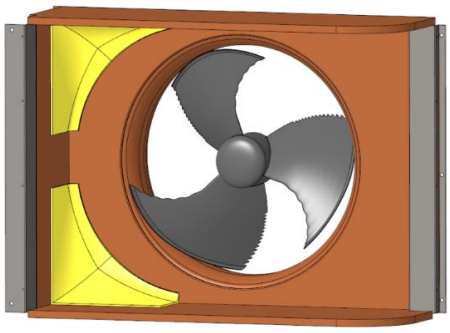


Figure 12. Flow-guiding wall elements (CAD, yellow)

6.3 Use of an inflow grid

To homogenise the inflow to the fan and reduce tonal as well as low-frequency broadband noise associated with large-scale vortical structures, inflow grids represent a promising solution. Figure 13 shows the CAD model of an inflow grid investigated in the present study.

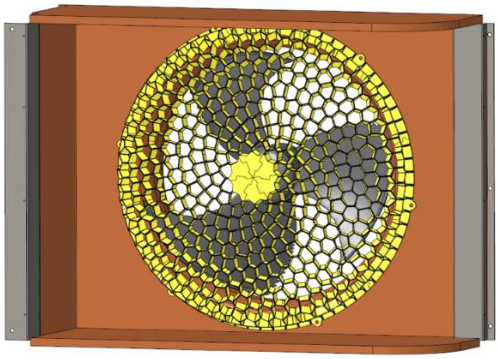


Figure 13. Inflow grid (CAD, yellow)

The corresponding comparison of the sound power spectra is shown in Figure 14. Similar to the optimised fan position (note: in this case, the fan position is not optimised), the tonal components are noticeably reduced, resulting in the elimination of the tonality penalty. In contrast to Figure 11, a broadband reduction in sound power is observed in the low-frequency range—likely due to the smoothing of large-scale vortical structures by the inflow grid. However, at higher frequencies, the installation noise increases, as the grid itself generates fine-scale turbulence. As a consequence, the A-weighted total sound power level is elevated when the inflow grid is used, making this approach less favourable than fan position optimisation in the present configuration.

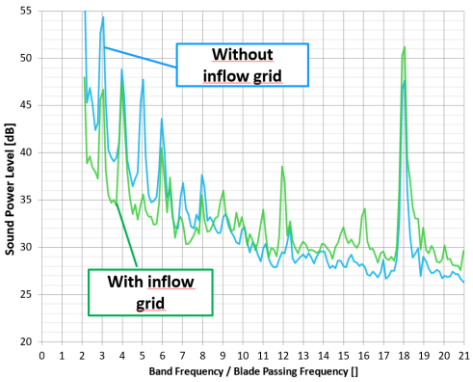


Figure 14. Spectral decomposition of the total noise with and without inflow grid

7. OPTIMIZATION APPROACHES CONCERNING THE BROADBAND INSTALLATION NOISE

In this section, some results concerning optimisation approaches with respect to broadband installation noise are briefly given in Tab. 1. The measures, located at the impeller blades, aim at reducing the emitted sound power when flow inhomogeneities as vortices collide with the blades. So in principle, they are also suitable to reduce tonal noise, but in practise, the effectiveness is more given for smaller vortical structures and thus higher frequencies where broadband noise dominates.

Table 1. Investigates measures at impeller blades to reduce sound emissions.

Description	Photograph	Best Results
Slotted Leading edge region		Tonality +-0 dB Broadband -1 dB(A) Efficiency -1%
Porous leading Edge Region		Tonality +-0 dB Broadband +2 dB(A) Efficiency -1%

8. CONCLUSIONS

An investigation of the aeroacoustic installation noise of an evaporator fan in a 12-kW air-to-water heat pump, featuring an L-shaped heat exchanger, is presented in the present work. While modern axial fans often exhibit low self-noise in standardised laboratory conditions, significantly higher noise levels can be observed once integrated into the system. The analysis revealed that the installation noise—arising from the upstream flow conditions—can exceed the fan's self-noise and substantially contribute to the perceived tonality of the emitted sound.

A combination of experimental and numerical methods, including Lattice-Boltzmann simulations and measurements in a certified anechoic facility, enabled a decomposition of self-noise and installation noise. The spectral analysis confirmed that tonal components are amplified due to asymmetric and broadband components due to turbulent inflow, both being strongly influenced by the geometric integration of the fan within the heat exchanger housing.

Three optimisation strategies were tested to reduce tonal components of installation noise: (1) optimised fan positioning, (2) flow-guiding elements, and (3) inflow grids. Among these, shifting the fan towards the short branch of the L-shaped evaporator yielded the most significant acoustic improvement, effectively eliminating tonal penalties without increasing the overall sound power level. While flow-guiding elements and inflow grids showed some positive effects, their performance was highly case-dependent and, in the case of the inflow grid, introduced additional high-frequency noise.

The findings highlight that system-level integration and spatial arrangement of components play a critical role in the aeroacoustic performance of heat pump fans. Future work should focus on the automated optimisation of inflow conditions using simulation-driven design and on establishing robust guidelines for low-noise fan integration in compact heat pump units.

9. ACKNOWLEDGMENTS

This work has been supported by the Federal Ministry for Economic Affairs and Energy (BMWi) in the frame of the collaborative Project “WarmHome” [1].

10. REFERENCES

[1] Collaborative Project “WarmHome”, Grant Number (“Förderkennzeichen”) 03EN4065E, funded by the Federal Ministry for Economic Affairs and Energy (BMWi), Weblink: EnArgus

[2] T. Zhu, and T.H. Carolus: “Axial fan tip clearance noise: Experiments, Lattice–Boltzmann simulations, and mitigation measures”, *Int. J. of Aeroacoustics*, vol. 17.1-2, pp. 159–183, 2018.

[3] F. Lörcher, S. Hub, S. Moreau and M. Sanjosé: “Investigations concerning the flow stabilization of backward curved centrifugal impellers at low flow rate”, *Int. J. of Turbomachinery, Propulsion and Power*, vol. 7(4), 37, 2022, **https://doi.org/10.3390/ijtpp7040037**.

[4] F. Lörcher, “CFD-Based Fan Optimizations considering the System Integration in a Heat Pump”, in *Proc. of Fan 2015 Conf., (Lyon, France)*, 2015.

[5] S. Becker and F. Czwielong: Funding project “Installationseffekte Axial*”*, Grant Number (“Förderkennzeichen”) IGF 20659 N Abschlussbericht (final report), Funded by the BMWi, 2023.

[6] Commercial Reference Fan of size 630 mm *FPowlet-FP063-6IA.BD.V3P1*, manufacturer ZIEHL-ABEGG SE, weblink: Detail - FPowlet - FP063-6IA.BD.V3P1

[7] ISO 5801:2017, “*Industrial Fans: Performance Testing Using Standardised Airways*.”, 2017

[8] S. Chen and G. D. Doolen: *Annual Review of Fluid mechanics* 30:329-364 ISSN 00664189, 1545-4479, 1998.

[9] S. Marié: *Etude de la méthode Boltzmann sur Réseau pour les simulations en aéroacoustique*, Ph.D. thesis Université Pierre et Marie Curie – Paris VI, 2008.

[10] H. Chen, O. Filippova, J. Hoch, K. Molvig, R. Shock, C. Teixeira and R. Zhang: *Physica A: Statistical Mechanics and its Applications*, 362:158-167 ISSN 03784371, 2006.

[11] F. Pérot, M.S. Kim, S. Moreau, M. Henner and D. Neal, “Direct Aeroacoustics Prediction of a Low-Speed Axial Fan”, in *Proc. of 16th AIAA/CEAS Aeroacoustics Conf. (Stockholm, Sweden)*, 2010.

[12] E. Fares: – *Computers and Fluids* 35: 940-950 ISSN 00457930, 2006.

[13] DIN45681:2005-04,“*Acoustics-Determination of tonal components of noise and determination of a tone adjustment for the assessment of noise emissions*.”, 2005

DOI: 10.61782/fa.2025.0460



FORUM ACUSTICUM
EURONOISE 2025

IMPROVE HEAT PUMP PLACEMENT CONSIDERING FREQUENCY RESOLVED ACOUSTIC DIRECTIVITY DATA: CREATION OF AN OPEN DATABASE

Reichl Christoph[1*] **Bessac Francois**[2] **Klein Georg**[1]
Stöckl Luisa[1] **Czuka Martin**[1]
[1] Center for Energy, AIT Austrian Institute of Technology, Vienna, Austria
[2] CETIAT, Villeurbanne, France

ABSTRACT

Heat pumps are becoming increasingly popular due to their efficiency, carbon neutrality and use of renewable energy resources. Air-to-water heat pumps are often chosen because of their low cost and ease of installation. However, optimal placement to minimise acoustic emissions is mandatory for a barrier-free deployment. At present, the assessment of noise propagation for outdoor units suffers from a lack of information on the frequency content, and particularly the directivity of the sound source. During heat pump certification, standardised test procedures using the sound intensity measurement technique provide frequency-resolved partial sound power levels for the five different surfaces surrounding the heat pump. This gives the basic directivity information needed for optimised placement recommendations. In the framework of IEA HPT Annex 63, an anonymous database has been designed that combines dimensions, operating conditions and a generic description of each of the 5 sides (fan(s), heat exchanger, blind sides) with their corresponding frequency spectrums. Initially, about 30 heat pumps measured at CETIAT and AIT will be included in the database and a first exploitation will be presented. The database will be enriched by the authors during the year 2025 with the possibility of contributions from other interested laboratories during this period.

*__Corresponding author__: christoph.reichl@ait.ac.at.
__Copyright__: ©2025 Reichl Christoph et al. This is an open-access article distributed under the terms of the Creative Commons Attribution 3.0 Unported License, which permits unrestricted use, distribution, and reproduction in any medium, provided the original author and source are credited.

Keywords: air-to-water heat pumps, acoustics, directivity, database

1. INTRODUCTION

For many potential future users of heat pumps, noise remains one of the main reasons for their reluctance to switch to this method of energy production: noise to themselves, but more importantly, noise to their neighbours. The most reliable acoustic data available to end users is that obtained through certification. This is because the values displayed are verified by independent third party laboratories that follow a certification protocol based on international measurement standards. The certified value is the overall sound power level in $dB(A)$, which is already very valuable information. However, the laboratories all measure the sound power level spectrum in third octaves, which is not publicly available. This is a gap in the acoustic description of heat pumps, which may be missed by acousticians who want to implement noise attenuation measures, or optimise the placement of outdoor units. Another missing piece of data is the directivity of the units; this data can be very useful in a predictive calculation of the positioning of the outdoor unit in a dense urban environment. The noise requirements are such that the intelligent use of radiation directivity can become a parameter to be exploited. This data is not generally available, including from manufacturers, and is not directly part of the certification process. The EN 12102-1 standard authorises several acoustic measurement methods, the two most commonly used being the reverberation chamber and intensimetry. The latter, which measures the sound power

level per surface, ultimately provides information on the directivity of the unit. Admittedly, it is a bit crude, but it is very interesting, because it gives the sound power level per surface for each 1/3 octave frequency. It is this level of directivity that is the constitutive idea of the database that we propose in the framework of IEA HPT Annex 51 [1] and IEA HPT Annex 63 [2] to build and make available to stakeholders in the field.

2. DATABASE CONSTRUCTION

The database is provided as an *Excel* sheet starting with anonymous results from two certification laboratories on outdoor heat pump units (sometimes reversible), see Fig. 1. It consists of a header part (lines 1-8 with the header in line 6, the items in line 7 and their corresponding units in line 8), and several blocks of data each consisting of 6 consecutive lines (e.g. lines 9-14 for entry 1, named *A06*, lines 15-20 for entry 2, named *B01* in the example given in Fig. 1).

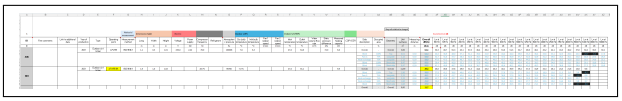


Figure 1. Overview of header line and two entries in the database

Most of the entries are free entries, only some of the fields contain formulas and are calculated automatically. Notes can (and should) be added to the fields to clarify specialities. Some items in line 6 contain notes detailing its usage. No field is mandatory but it is intended to include as much information as possible allowing for various ways of database exploitation, e.g. depending on the laboratory in charge of the measurements not all frequencies are reported, compressor frequencies have been recorded or fan speeds might be available. During discussions in the Task 2 meetings of IEA HPT Annex 63 several additional fields have been added (e.g. Coefficient of Performance, COP), which might be interesting for special analysis routes.

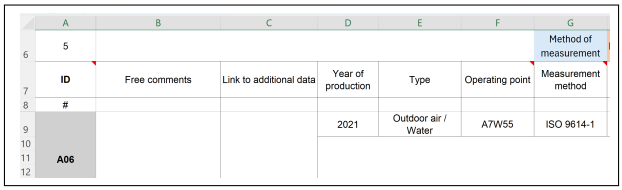
From left to right, content per block is organized in the following sections:

- leading part, *col. A-G*
- dimensioning, electrics & refrigerant, *col. H-N*
- boundary conditions & fan speeds, *col. O-Y*
- geometric description, *col. Z-AD*
- acoustic data description, *col. AE-AZ*

These blocks are described in detail in the following subsections.

2.1 Leading part - general information

The leading part (see Fig. 2 first assigns an unique identifier (*col. A*), which is constructed using a capital letter followed by two numbers. The letter is used to differentiate the contributing sources (e.g. laboratories) to the database. A field for free comments is presented in *col. B*, links to additional data should be given in *col. C*. All additional data should be made available as *zip*- or *7z*-archives with their names beginning with the identifier given in *col. A* followed by the dash symbol, e.g. *A06-waves.zip*. A detailed description should be placed in a *readme.txt*-file inside the corresponding archive. The leading part concludes with the year of production (*col. D*) and the type (*col. E*) of the unit as well as the point, which the unit was operating in (*col. F*). This operating point of the unit includes the temperature conditions on the ambient air, for example 7(6) °C , and on the water, for example 47-55 °C , summarized in the abbreviation *A7W55*.



	A	B	C	D	E	F	G
6	5						Method of measurement
7	ID	Free comments	Link to additional data	Year of production	Type	Operating point	Measurement method
8	#						
9	A06			2021	Outdoor air / Water	A7W55	ISO 9614-1
10							
11							
12							

Figure 2. Leading part of the database

Finally the leading part includes the measurement method in *col. G*. It is highly recommended to use data acquired utilizing either the ISO 9614-1:1993(en) Acoustics — Determination of sound power levels of noise sources using sound intensity — Part 1: Measurement at discrete points or the ISO 9614-2:1996(en) Acoustics — Determination of sound power levels of noise sources using sound intensity — Part 2: Measurement by scanning.

2.2 Dimensioning, electrics and refrigerant

First, in *col. H-J* the unit dimensions (see Fig. 3 in m are provided (length, width, height). This is followed by the necessary voltage supply to operate the unit (*col. K*) in V

and the power supplied to the unit *col. L* in kW. The compressor frequency in Hz is provided in *col. M* and the refrigerant entered in *col. N* using the ASHRAE 23-2022 standard [3], e.g. R290 for propane.

	H	I	J	K	L	M	N
	Dimensions of **unit**			Electric			
	Long	Width	Height	Voltage	Power supply	Compressor frequency	Refrigerant
	m	m	m	V	kW	Hz	
	1,1	0,5	1,01	230,0	2,42	78,0	

Figure 3. Dimensioning, electrics and refrigerant section of the database

2.3 Boundary conditions & fan speeds

The atmospheric pressure during the measurements is given in Pa in *col. O*, followed by the data characterising the outdoor unit. This includes the dry (*col. P*) and wet (*col. Q*) bulb temperatures in °C as well as the fan speeds in turns/minute (rpm) for up to two fans in (*col. R* and *col. S*), see Fig. 4. The boundary conditions for the indoor unit are the inlet (*col. T*) and outlet (*col. U*) temperature of the water given in °C , the water volume flow rate (*col. V*) given in m^3/h, the static pressure difference (*col. W*) in kPa and the measured heating capacity (*col. X*) in kW. Finally a field for the Coefficient of Performance (COP) is included in *col. Y*.

	O	P	Q	R	S	T	U	V	W	X	Y
		Outdoor (AIR)				Indoor (WATER)					
	Atmospheric pressure	Dry bulb temperature	Wet bulb temperature	Fan 1 rotation speed	Fan 2 rotation speed	Inlet temperature	Outlet temperature	Water volume flow rate	Static pressure difference	Measured heating capacity	COP / EER
	Pa	°C	°C	tr/min	tr/min	°C	°C	m³/h	kPa	kW	-
	100008	7,6	6,3			47,0	54,9		72,0	6,6	

Figure 4. Boundary conditions & fan speed section of the database

2.4 Geometric description

From here on the single data line (see Fig. 5, line 9) expands to 6 lines (lines 9-14). The unit is expected to consist of five faces (top, two long sides and two short sides). Each of these five faces is then described with the following options in *col. Z* (see Fig. 5, lines 10-14. For a better post processing workflow (avoiding typing errors and ambiguities), these options are made available via a dropdown menu.

- presence of fan (1 or 2), e.g. Fan x1, Fan x2;
- presence of a heat exchanger;
- ... or none of these elements, then the surface is described as "blind".

For the *fan* and *heat exchanger* elements, the proportion of surface area occupied by these elements is briefly described in *col. AA*, with four possible surface proportions: 25, 50, 75, or 100 %.

	A	Z	AA	AB	AC	AD
6	5					
7	ID	Side description	Occupied area	Geometry	Unit surfaces	Measuring distance
8	#	-	%		m^2	m
9	A06	Overall	-	Overall	3,69	
10		Blind	100%	Top	0,51	0,50
11		Fan x1	75%	Long side	1,12	0,50
12		Heat exchanger	75%	Long side	1,12	0,50
13		Blind	100%	Short side	0,47	0,50
14		Blind	100%	Short side	0,47	0,50
15	B01	Overall	-	Overall	11,59	
16		Blind	100%	Top	1,98	0,50
17		Fan x1	75%	Long side	3,13	0,50
18		Heat exchanger	75%	Long side	3,13	0,50
19		Heat exchanger	50%	Short side	1,68	0,50
20		Blind	100%	Short side	1,68	0,50

Figure 5. Geometric description including the unit and the distance of measurements

The grey cells in *col. AB* and *col. AC* should not be altered. The unit surfaces in *col. AC* in m^2 are extracted using the data in *col. H*-*col. J*, the overall unit surface is calculated and presented in the above the 5 unit surfaces in m^2. Finally, *col. AD* shows the distance between the surfaces and the measurement probe in m.

2.5 Acoustic data description

Six spectrums are required, one for the sound power level of the unit, as it is given as official result. The five other are partial sound power levels for each side (long side, short side, top side). Data are given in 1/3 octave bands, at least between 100 Hz and 5000 Hz, but the bands 50-63-80 Hz and 6300-8000-10000 Hz bands can be provided.

The acoustic data (see Fig. 6) consists of the (calculated) sound power level spectra of each face (*col. AE*), as well as the spectrum of the entire unit (*col. AF*-*col. AZ*). The sound power level corresponds to the fictitious surface located a few dozen centimetres from the actual surface of the machine which is given by the measurement distance for each face (*col. AD*).

The third octave band spectra data (blue values, *col. AF-col. AZ*) are entered in dB into the database for each of the five faces (e.g. into lines 10-14) allowing for a full set of 21 times 5 equals 105 entries. Black fields mark negative sound levels from intensity measurements (sound oriented from outside to the unit rather from being radiated from the unit to the outside and thus coming in to the mesh).

For each frequency band (100 Hz up to 10000 Hz), an overall sound level in dB is calculated automatically and presented in the first line (e.g. line 9) of the entry (above the data of the five sides). Out of these frequency resolved data, an overall *A-weighted* sound power level in $dB(A)$ is calculated and given in *col. AE*. Note, that the entry in the first line in *col. AE* (e.g. field *AE9*) will typically be the one reported on a certification label.

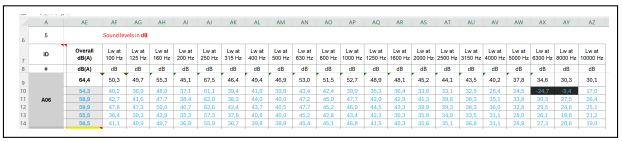


Figure 6. Acoustic data description using frequency resolved spectra

3. CONTRIBUTING TO THE DATABASE

Other parties than CETIAT and AIT, both inside and outside of the IEA HPT Annex 63 consortium are invited to contribute to the database. The template can be downloaded from the IEA HPT Annex 63 website following `https://heatpumpingtechnologies.org/annex63/database`. [4]. For further questions related to the format and usage of the database template, please contact `christoph.reichl@ait.at` (AIT) or `francois.bessac@cetiat.fr` (CETIAT). It is intended to initially expand the database till end of the first quarter of 2026.

4. EXAMPLE EXPLOITATION

A first exploitative analysis is done on the 27 available data sets (see Fig. 7). It focuses on the overall directivity based on the *max-min* of data from each side. The *max-min 5 sides* average corresponds to average of the *max-min* for the 5 sides (4 lateral + top), whereas the *max-min horizontal* average only includes the data for the 4 lateral sides, excluding the top. Then, *max-min vertical long side* and *max-min vertical short side* considers lateral sides and top side, either on the long side, or on the short side, respectively.

For the sake of readability, calculation & results are given based on the data transformed in octave bands, from 125 to 4000 Hz band. The overall directivity given by *max-min* (dark blue bars) shows, that it falls between 5 to almost 10 dB, the highest values being at higher frequencies. This means, that compared to the overall spectrum, a difference from ± 2.5 to almost $\pm 5\,dB$ can be extracted, depending on the location of the hearing point and on the frequency. The consideration of *max-min vertical* directivity is smaller, especially for the short side (light blue bar).

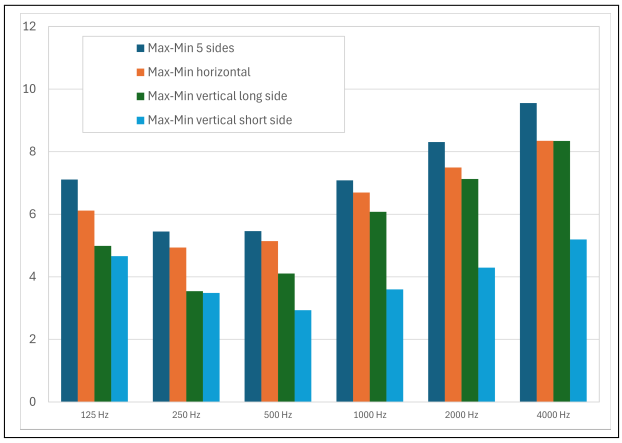


Figure 7. Max-Min directivity, averaged on the 27 data sets.

There are 16 results for lateral fan(s) units and 11 with top fan(s) units in the data set (see Fig. 8). When analysing the results considering the location of fan(s), the *max-min horizontal* average on all sides shows a bigger influence of the fan(s) located on the lateral side (orange bars). The overall directivity is then higher, especially at low and high frequencies, with a general envelope between 5.5 and almost 9 dB.

This is also the case when considering the vertical directivity (see Fig. 9), the top fan(s) configuration (dark green bars) being then smaller than the lateral fan(s) (orange bars) configuration.

5. CONCLUSION AND OUTLOOK

In the framework of IEA HPT Annex 63, a database consisting of frequency resolved acoustic directivity data to

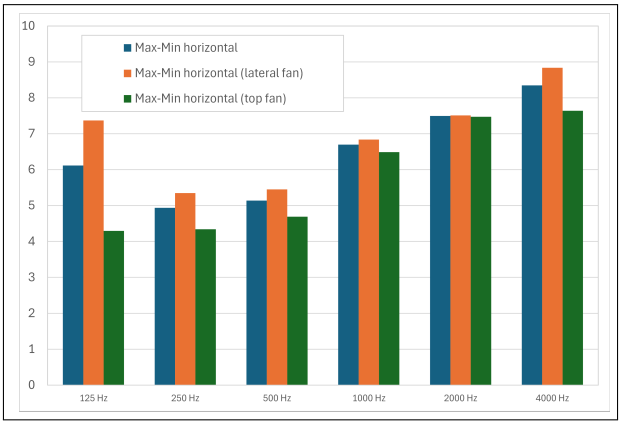


Figure 8. Max-Min directivity, on 5 sides, all data, and considering the location of fan(s).

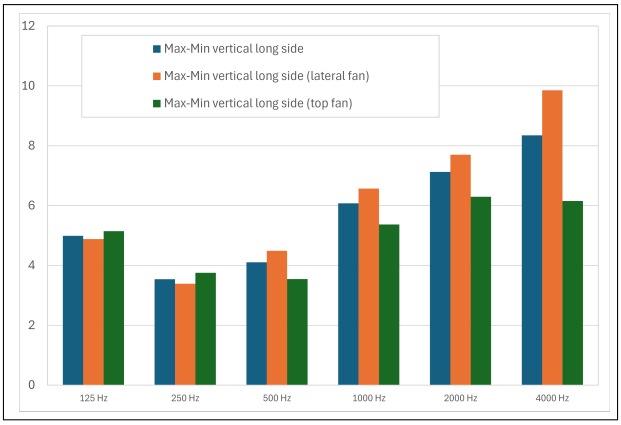


Figure 9. Max-Min horizontal directivity, all data, and considering the location of fan(s).

improve heat pump placement has been constructed. An initial set of 27 datasets from the laboratories of CETIAT, France and AIT, Austria consisting of a leading part, comments, dimensions, boundary conditions, geometric descriptions and acoustic data have been implemented. Both, the initial database and the template for contributing to the database are available for download on the IEA HPT Annex 63 website [4].

Although priority is currently being given to the collection of data measured according to the ISO 9614 protocol, additional content for measurements (e.g. more detailed data on dome measurements, wave files with raw acoustics, images) could be implemented, as well as (depending on request), inclusion of sound pressure level measurements is intended. These updated, will also be accessible through the database website.

An initial exploitation of the data base is presented based on *max-min* averages. The overall directivity falls between 5 to almost 10 dB with higher values extracted at elevated frequencies. These results, compared to the overall spectrum, to a difference from ± 2.5 to almost $\pm 5\,dB$.

It is intended to expand the database till the first quarter of 2026 with both entries from CETIAT and AIT and other parties. Further work with the data base will include expanded analysis on the directivity as well as utilization of the frequency content of the presented measurements.

6. ACKNOWLEDGMENTS

We want to express our gratitude to the consortium of IEA HPT Annex 63, especially to the contributors to Task 2 *Urban Acoustics Impact of Heat Pumps*. This work was funded in the framework of the Austrian FFG IEA cooperation project IEA HPT Annex 63, *Placement Impact on Heat Pump Acoustics* [2].

CETIAT thanks its industrial members for supporting its participation and work in the IEA HPT Annex 63.

7. REFERENCES

[1] IEA HPT Annex 51, "Acoustic Signatures of Heat Pumps." https://heatpumpingtechnologies.org/annex51/, 2024. Accessed: 2025-04-10.

[2] IEA HPT Annex 63, "Placement Impact on Heat Pump Acoustics." https://heatpumpingtechnologies.org/annex63/, 2024. Accessed: 2025-04-10.

[3] ASHRAE, "ANSI/ASHRAE 34-2022, Designation and Safety Classification of Refrigerants." https://www.ashrae.org/technical-resources/standards-and-guidelines/ashrae-refrigerant-designations, 2022. Accessed: 2025-04-10.

[4] IEA HPT Annex 63, "IEA HPT Annex 63 database." https://heatpumpingtechnologies.org/annex63/database, 2024. Accessed: 2025-04-10.

DOI: 10.61782/fa.2025.0883



FORUM ACUSTICUM
EURONOISE 2025

THE ROLE OF MEASUREMENT LOCATIONS IN LOW-FREQUENCY NOISE ASSESSMENT

Luka Čurović[1*] **Jurij Prezelj**[1]
[1] Faculty of Mechanical Engineering, University of Ljubljana, Slovenia

ABSTRACT

With the increasing use of heat pumps as a sustainable solution for heating and cooling, their acoustic impact on the environment has become of crucial importance. Heat pumps are acoustically complex sources that can be controlled by smart algorithms and have specific low-frequency characteristics that differ from well-studied sources. An accurate noise assessment of heat pumps requires careful consideration of the measurement locations, as these have a direct influence on the characterization of noise emissions and their potential impact on the environment. In this study, the influence of the measurement locations on the low-frequency noise levels is investigated, including the positions in front of the façade, on the façade and in the free field. A loudspeaker and a custom-built low-frequency sound source are used to generate the low-frequency sound. The results show significant differences in the measured sound pressure levels depending on the position of the receiving point in relation to the low-frequency sound source. By emphasizing the importance of selecting appropriate measurement locations, this work is intended to assist acoustics professionals and policy makers in establishing robust standards for the assessment of heat pump noise.

Keywords: *low-frequency sound, frequency weighting,facade, microphone position, environmental noise*

**Corresponding author*: luka.curovic@fs.uni-lj.si.
***Copyright**: ©2025 L.Čurovič and J.Prezelj This is an open-access article distributed under the terms of the Creative Commons Attribution 3.0 Unported License, which permits unrestricted use, distribution, and reproduction in any medium, provided the original author and source are credited.*

1. INTRODUCTION

Sound levels are often assessed in dwellings, at the most exposed façade where the sound field is determined by reflections and diffraction. To ensure reproducibility and comparability of results, guidelines such as ISO 1996-2 [1] or ISO 16283-3 [2] suggests a +3 dB correction when the microphone is located between 0.5 and 2 m from a reflecting surface, and up to + 6 dB (with default value of +5,7 dB) correction when the microphone is placed directly on the surface. However, factors such as the source-receiver geometry, the nature of the noise source (e.g., point source vs. line source), the composition of the façade materials, and the presence of other reflective or scattering surfaces can influence the actual reflection contribution. Research has indicated that in many practical measurement situations, the +3 dB and +6 dB approximations might not be appropriate, with some studies suggesting smaller correction values. Furthermore, the source-façade distance (D) and the microphone-façade distance (d) have been identified as important parameters influencing the reflection effects [3–11]. Given the potential for discrepancies between standardized corrections and real-world measurements, ongoing research is essential to refine the guidelines for noise assessment near building façades. This includes investigating the accuracy of existing correction factors for new sound sources such as heat pumps, which are becoming an integral part of the built environment. Heat pumps are acoustically complex sources that can be controlled by intelligent algorithms, differ from well-studied sources by their specific frequency and operational characteristics and are often placed in locations where the resulting sound field is affected by multiple reflections or where the receiver is in the near sound field. An accurate noise assessment of heat

pumps requires careful consideration of the measurement locations, as these have a direct influence on the characterization of noise emissions and their potential impact on the environment. The aim of this study is to carry out an initial experimental investigation of the influence of the measurement locations on the measured low-frequency sound levels. A loudspeaker producing 125 Hz octave band noise is used to perform measurements in an otherwise anechoic room and a custom-made sound source emitting a 50 Hz tone is used to perform measurements in the real environment. The acoustic measurements include the positions in front of the façade, on the façade and in the free field. The analysis of the measured sound levels should provide initial insights into the correction factors for façade measurements of low-frequency sound and their dependence on relevant parameters.

2. METHODOLOGY

In the experimental study, two low-frequency sound sources were used and the signals were recorded with class 1 sound level analyzers, which were checked with a sound calibrator before and after the measurements. The measurements were carried out in an anechoic chamber and in a real environment. To gain an initial insight, various incidence configurations and different microphone positions were investigated.

2.1 Measurements performed in an anechoic environment

The signals were recorded using Norsonic 140 Class 1 sound analyzers with a 1/2-inch preamplifiers type 1209 and a Nor1225 free-field microphones. The preamplifier and microphone were connected to the analyzer via a cable. A windscreen was not used. The source was a B&K HP 1001 loudspeaker driven by a B&K type 4205 generator. The loudspeaker was used to generate a wide band signal (white noise) in the frequency range from 100 Hz to 100 kHz and a 125 Hz octave band noise. The sound power level was set to 95 dB. The microphone locations included positions on the facade and in the free field. For the free-field position, the microphone was placed in front of the wall of the room made of pyramid-shaped glass wool elements. For the position on the facade, the microphone was mounted against a painted 20 mm chipboard panel. In both cases, the microphone was directed towards the sound source at an 90^0 degree angle of incidence. Two series of measurements were performed with different microphone and source positions to simulate normal (0^0) and parallel (90^0) incidence:

a) For the first configuration, the loudspeaker was placed at a distance of 2 m in front of the microphone.

b) For the 90^0 incidence, the loudspeaker and the microphone were placed in the same horizontal plane. The distance between the loudspeaker and the receiver was 1.55 m. The measurement setup with the loudspeaker and the free field microphone is shown in Fig. 1

In both series, the signals (125 Hz octave band and 100 Hz – 10 kHz white noise) were first recorded with the microphone at the facade position. Then the plate was removed, and free-field measurements were made. Each recording was at least 3 minutes long.

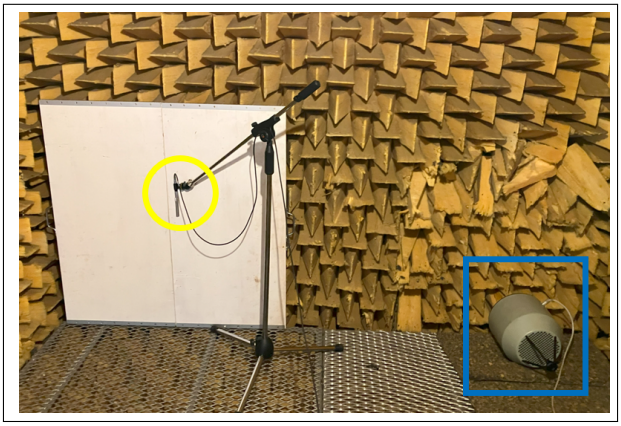


Figure 1. The 90^0 incidence measurement setup in the anechoic room with the loudspeaker (blue square) and the facade microphone (yellow circle).

2.2 Measurements performed in the real environment

The measurements were carried out on a two-storey house. The south façade (S façade) of the house is made of brick and has two windows and a door. The length of the S façade is 13.5 m, and the maximum height is around 8 m. The ground in front of the S façade is an acoustically hard. The western part of the brick façade (W façade) has 4 windows, is 15 m long and 7 m high. The ground in front of the façade consists of grass (soft ground).

The signals were recorded with two Norsonic 140 Class 1 sound analyzers and the windscreen was used. The sound source was a loudspeaker connected to an electrical transformer and housed in a square wooden box measuring 500 mm x 500 mm x 500 mm. The source emitted a

very intrusive 50 Hz tonal sound. The emission characteristics of the source was determined by measurements at a distance of 2 m and at a height of 2 m from the surfaces of the box in four directions. The equivalent continuous A-weighted sound pressure level ($L_{\mathrm{Aeq,T=2min}}$) was in the range of 55.9 dB(A) to 56.9 dB(A). The equivalent continuous C-weighted sound pressure level ($L_{\mathrm{Ceq,T=2min}}$) was in the range of 83.1 dB(C) to 83.5 dB(C). The equivalent continuous sound pressure level in the 50 Hz one-third octave band ($L_{\mathrm{eq,50Hz,T=2min}}$) was in the range of 84.7 dB to 83.3 dB. Based on the emission measurements, the source was considered omnidirectional. At a distance of 4 m from the source, $L_{\mathrm{Aeq,T=2}}$ min, $L_{\mathrm{Ceq,T=2min}}$ and $L_{\mathrm{eq,50Hz,T=2min}}$ min were reduced by 5.5 dB(A), 6 dB(C) and 6 dB respectively, so that the source was considered to be a point source.

The microphone locations included positions on the façade (façade position), near a façade (near position) and in the free field. Three series of measurements were carried out with different microphone and source positions:

a) In the first series, the interference pattern expected due to façade reflections was investigated. The sound source was placed on the ground at a distance of 12.4 m from the S façade. One microphone was placed on the façade at a height of 3.6 m relative to the source height. The distance of the second microphone to the source was varied at 2 m, 4 m, 9.2 m and 10.8 m.

b) In the second series, the influence of the distance between the facade and the source was tested. The source were initially positioned on the ground at a distance D = 15.1 m from the S façade. One microphone was placed on the façade at a height of 3.6 m relative to the source height. The position of the second microphone was varied. It was placed in the free field (10 m from the source and 5 m from the SW edge of the house) and in the near field, where strong interference effects are expected, at 1.7 m and 3.2 m from the façade. The measurements were repeated, only this time the source was placed at a distance D = 10.0 m from the S façade and the second (free field) microphone at a distance of 10 m from the source.

c) In the third series, the influence of the angle of incidence was investigated. The source was placed on the ground at a distance of 0.3 m from the W façade. The microphones were placed at a distance of 4.5 m on the same horizontal plane to simulate the 90^0 incidence. One microphone was placed on the façade and the other microphone in the free field (2.8 m from the SW edge of the house). The measurement setup with the loudspeaker and the free field microphone is shown in Fig. 2.

For each series and each microphone–source configuration, the source signal was averaged for at least 10 minutes. All unwanted sound events and removable residual noise signals were removed. The recordings included distant low-amplitude background noise sources, such as birdsong and distant road noise, which could not be excluded.



Figure 2. The 90^0 incidence measurement setup with the loudspeaker (blue square) and the free field microphone (yellow circle).

3. RESULTS AND DISCUSSION

3.1 Measurements performed in an anechoic environment

The measurement results for both series include A- and C-weighted levels (Tables 1 and 2) and 1/1-octave frequency analysis in the 16 Hz – 20000 Hz range (Figure 3). The integration time interval was 3 minutes long.

At normal (0^0) incidence, the expected difference between the levels at the facade and free field positions is about 6 dB, assuming perfect reflection, and should be less otherwise [4, 12]. At normal incidence, the L_{Aeq} values at the façade for both sources were about 6 dB(A) higher than in the free field, which is to be expected if perfect reflection is assumed. The difference in L_{Ceq} values was 2.2 dB(C) and 6 dB(A) for the 125 Hz octave band and the broadband signal respectively. The same trend was observed for the $L_{\mathrm{eq,125Hz}}$ level, emphasising that L_{Aeq} cannot always be used to evaluate the difference between façade and free field when the level difference comes from

Table 1. $L_{\mathrm{Aeq,T=3min}}$ and $L_{\mathrm{Ceq,T=3min}}$ levels in the anechoic room for normal (0^0) and parallel incidence (90^0) for the 125 Hz octave band source.

0^0	Facade	Free-field
L_{Aeq}	59.4	53.6
L_{Ceq}	72.3	70.1
90^0	Facade	Free-field
L_{Aeq}	56.1	56.8
L_{Ceq}	71.5	73.7

Table 2. $L_{\mathrm{Aeq,T=3min}}$ and $L_{\mathrm{Ceq,T=3min}}$ levels in the anechoic room for normal and parallel incidence for the wide band 100 Hz - 10 kHz source.

0^0	Facade	Free-field
L_{Aeq}	86.2	80.8
L_{Ceq}	86.0	80.5
90^0	Facade	Free-field
L_{Aeq}	78.9	73.4
L_{Ceq}	79.5	75.3

low frequencies.

At 90^0 incidence the expected difference between the facade and free field levels should be close to 0 dB. However, the measurement results indicate that the levels in the free field can be even greater than the levels at the façade, as observed in the case of the 125 Hz octave band source. The difference between the A-weighted façade and free-field levels for the low-frequency source was positive (+0.7 dB), while the difference between the $L_{\mathrm{eq,125Hz}}$ levels was negative (-2.5 dB). L_{Ceq} followed the $L_{\mathrm{eq,125Hz}}$ trend. The level differences for the broadband noise source, to which the high frequencies make a significant contribution, are probably largely determined by their directivity pattern.

3.2 Measurements performed in the real environment

Fig.4 shows a typical one-third octave band spectrum in the range 20 Hz – 20 kHz, measured at a distance of 2 m from the source. The spectrum is characterized by a pronounced tone at 50 Hz. The results therefore include A-weighted (L_{Aeq}), C-weighted levels (L_{Ceq}) and one-third octave band levels in the 50 Hz band $L_{\mathrm{eq,50Hz}}$.

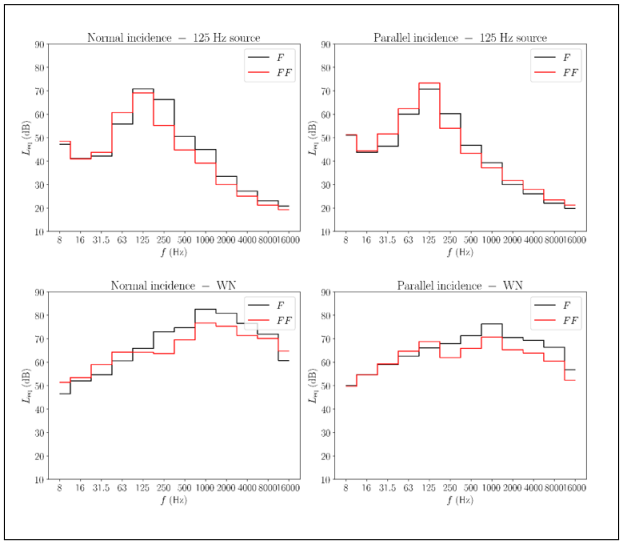


Figure 3. Octave band sound pressure level spectra, measured in an anechoic room for the low-frequency 125 Hz octave band sound source for (a) normal and (b) 90^0 incidence and for the wide band sound source for (c) normal and (d) 90^0 incidence.

3.2.1 Interference pattern

The levels $L_{\mathrm{Aeq,T=10min}}$, $L_{\mathrm{Ceq,T=10min}}$ and $L_{\mathrm{eq,50Hz,T=10min}}$ as a function of distance from the source are shown in Fig. 5. The distance between the source and the facade is 12.4 m. The measured values are shown as dots. The dashed prediction curves represent the sound attenuation due to the geometric spreading for a point source.

L_{Ceq} and $L_{\mathrm{eq,50Hz}}$ points far from the source and are located near and on the façade deviate significantly from the prediction curve. The levels at a distance of 3.2 m from the façade are similar to the façade levels and the levels at a distance of 1.7 m from the façade are significantly lower, which is in good agreement with the theoretical analysis of the sound fields at the boundaries. The L_{Aeq} levels show less variation near and at the façade and the interference pattern is not clear.

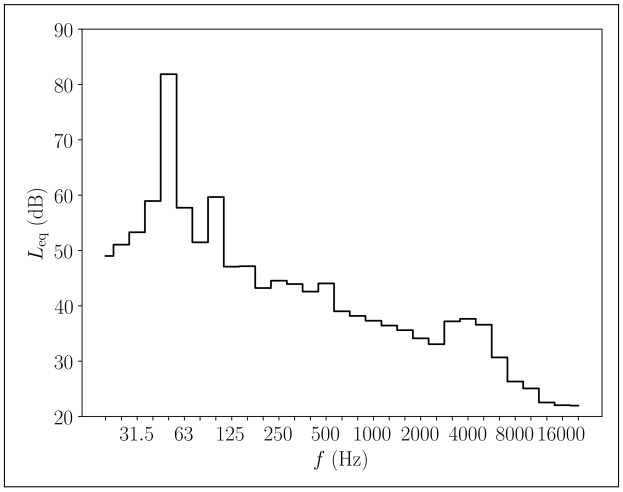


Figure 4. Third-octave band sound pressure level spectrum in the range 20 Hz – 20 kHz, measured at a distance of 2 m from the source.

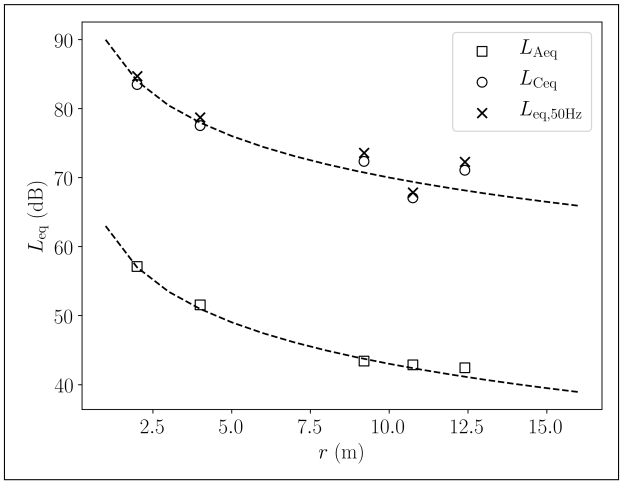


Figure 5. The levels $L_{Aeq,T=10min}$, $L_{Ceq,T=10min}$ and $L_{eq,50Hz,T=10min}$ as a function of distance from the source

3.2.2 *Source-facade distance*

The levels $L_{Aeq,T=10min}$, $L_{Ceq,T=10min}$ and $L_{eq,50Hz,T=10min}$ and the distance between source and microphone (r) in the near field (1.7 and 3.2 m from the façade), at the façade and in the free field when the source was placed at a distance of D = 15.1 m and D= 10 from the façade are shown in Tables 3 and 4 respectively.

Table 3. $L_{Aeq,T=10min}$, $L_{Ceq,T=10min}$ and $L_{eq,50Hz,T=10min}$ at source – facade distance D = 15.1 m and different microphone positions. NF (3.2 m) = near field (3.2 m from facade), NF (1.7 m) = near field (1.7 m from facade), F = facade, FF= free-field

r (m)	$L_{eq,50Hz}$	L_{Aeq}	L_{Ceq}	Position
11.9	68.0	42.9	67.1	NF (3.2 m)
13.4	63.8	43.4	63.5	NF (1.7 m)
15.1	68.5	42.6	67.6	F
15.1	64.6	42.5	63.2	FF

The $L_{eq,50Hz}$ was highest at the façade and at the near-field position at 3.2 m from the façade. The $L_{eq,50Hz}$ was lower at the free-field and near-field positions (1.7 m from the façade). As expected, L_{Ceq} reflects the trend at 50 Hz, while L_{Aeq} values are consistent across all positions. The L_{Aeq} values do not follow the interference pattern. This behaviour is very consistent at both distances between source and facade. The L_{Ceq} and $L_{eq,50Hz}$ level differences between the façade and free-field positions are uniform at around 4 dB.

Table 4. $L_{Aeq,T=10min}$, $L_{Ceq,T=10min}$ and $L_{eq,50Hz,T=10min}$ at source – facade distance D = 10.0 m and different microphone positions. NF (3.2 m) = near field (3.2 m from facade), NF (1.7 m) = near field (1.7 m from facade), F = facade, FF= free-field

r (m)	$L_{eq,50Hz}$	L_{Aeq}	L_{Ceq}	Position
6.8	73.3	46.0	72.1	NF (3.2 m)
8.3	67.4	44.4	66.8	NF (1.7 m)
10	73.3	45.2	72.2	F
10	69.4	44.4	68.3	FF

3.2.3 *90^0 incidence*

The levels $L_{Aeq,T=10min}$, $L_{Ceq,T=10min}$ and $L_{eq,50Hz,T=10min}$ at the façade and in the free field are shown in Table 5 respectively.

The free-field $L_{eq,50Hz}$ and L_{Ceq} values were slightly

Table 5. $L_{\mathrm{Aeq,T=10min}}$, $L_{\mathrm{Ceq,T=10min}}$ and $L_{\mathrm{eq,50Hz,T=2min}}$ at façade and free field positions for the 90^0 incidence configuration in the real environment. F = facade, FF= free-field.

Position	$L_{\mathrm{eq,50Hz}}$	L_{Aeq}	L_{Ceq}
F	79.5	52.0	78.3
FF	80.3	51.6	79.2

higher than the façade values, while L_{Aeq} showed the opposite trend. The differences were not considered significant, however the higher low frequency level in the free field was also observed in the anechoic room. A default facade correction would probably not be justified in such cases, as the façade seems to have only a very small influence on the measured values.

4. CONCLUSION

The evaluation of the difference between façade and free-field sound pressure levels is a complex task, even when a simple low-frequency sound sources is investigated. In this study, the A-, C-weighted, octave and one-third octave band sound pressure levels in front of the façade, on the façade and in the free field were experimentally investigated in order to gain initial insights into the façade correction factors for low-frequency noise. The experiments were carried out in a controlled environment (anechoic room) and in a real environment.

In the anechoic room, a 125 Hz octave band sound signal was used to determine the difference between L_{Aeq}, L_{Ceq} and $L_{\mathrm{eq,125Hz}}$ levels at the façade and the free-field microphone positions at normal and 90^0 incidences. The results showed that the characterization of the façade correction in the anechoic room using A-weighted levels was only successful at normal incidence using a wide band white noise signal with sufficient energy in the high frequency range. For the low-frequency 125 Hz octave band source, C-weighted and band levels were better suited to characterize the effect of sound reflection and angle of incidence on the resulting sound field. At 90^0 incidence, the measurement results showed that the free-field levels can be even greater than the façade levels when a 125 Hz octave band source was used.

A custom-built source emitting a 50 Hz tone was then used to conduct field experiments in a real environment. Three series of measurements were carried out to investigate the interference pattern, the effect of the distance between the source and the façade and the façade corrections for 90^0 incidences of low-frequency tonal sound at 50 Hz. The L_{Ceq} and $L_{\mathrm{eq,50Hz}}$ values were closely correlated and could be attributed to the interference patterns, the effects of the angle of incidence and the lower reflection characteristics associated with low-frequency sound. One of the test results is also that low-frequency sound levels could be underestimated if the standard façade factor (5.7 dB(A) or 6 dB(A)) is used to correct the A-weighted sound pressure levels measured at the façade at large angles of incidence.

5. ACKNOWLEDGMENTS

The authors acknowledge the financial support from the Slovenian Research Agency (research fundings No. P2-0401 and No. V2-24025).

6. REFERENCES

[1] "ISO 1996-2:2017 Acoustics - Description, measurement and assessment of environmental noise - Part 2: Determination of sound pressure levels," standard, International Organization for Standardization, Geneva, CH, 2017.

[2] "ISO 16283-3:2016 Acoustics - Field measurement of sound insulation in buildings and of building elements, url=https://www.iso.org/standard/59748.html, volume = 2016, address = Geneva, CH, institution = International Organization for Standardization," standard, 2016.

[3] F. Hall, M. Papakyriakou, and J. Quirt, "Comparison of outdoor microphone locations for measuring sound insulation of building facades," *Journal of Sound and Vibration*, vol. 92, p. 559–567, Feb. 1984.

[4] J. D. Quirt, "Sound fields near exterior building surfaces," *The Journal of the Acoustical Society of America*, vol. 77, p. 557–566, Feb. 1985.

[5] G. Memoli, M. Paviotti, S. Kephalopoulos, and G. Licitra, "Testing the acoustical corrections for reflections on a façade," *Applied Acoustics*, vol. 69, p. 479–495, June 2008.

[6] A. Jagniatinskis and B. Fiks, "Assessment of environmental noise from long-term window microphone measurements," *Applied Acoustics*, vol. 76, p. 377–385, Feb. 2014.

[7] M. Mateus, J. Dias Carrilho, and M. Gameiro da Silva, "An experimental analysis of the correction factors adopted on environmental noise measurements performed with window-mounted microphones," *Applied Acoustics*, vol. 87, p. 212–218, Jan. 2015.

[8] D. Montes González, J. Barrigón Morillas, and G. Rey Gozalo, "The influence of microphone location on the results of urban noise measurements," *Applied Acoustics*, vol. 90, p. 64–73, Apr. 2015.

[9] R. Flores, C. Asensio, P. Gagliardi, and G. Licitra, "Study of the correction factors for aircraft noise façade measurements," *Applied Acoustics*, vol. 145, p. 399–407, Feb. 2019.

[10] D. Montes González, J. M. Barrigón Morillas, G. Rey Gozalo, and P. Atanasio Moraga, "Microphone position and noise exposure assessment of building façades," *Applied Acoustics*, vol. 160, p. 107157, Mar. 2020.

[11] A. Zagubień and K. Wolniewicz, "Impact of measuring microphone location on the result of environmental noise assessment," *Applied Acoustics*, vol. 172, p. 107662, Jan. 2021.

[12] R. V. Waterhouse, "Interference patterns in reverberant sound fields," *The Journal of the Acoustical Society of America*, vol. 27, p. 247–258, Mar. 1955.

DOI: 10.61782/fa.2025.0483

FORUM ACUSTICUM EURONOISE 2025

IN-SITU TRANSFER PATH ANALYSIS OF A ROOF MOUNTED AIR SOURCE HEAT PUMP

L Barton* **J Hargreaves**[1] **V Acun**[1]
A Torija Martinez[1] **S Graetzer**[1] **D Waddington**[1]
[1] Future Homes Project, Acoustic Research Centre,
University of Salford, United Kingdom

ABSTRACT

To combat carbon emissions and move towards Net Zero, many EU countries have begun phasing out fossil fuel domestic heating in favour of air source heat pumps. The UK government has set a target of installing 600,000 air source heat pumps per year from 2028.Though restrictive installation guidelines for air source heat pumps have been revised, this does not negate the issue of suitable unit placement for retrofit in existing UK housing stock. In many cases, the existing homes are attached, terraced homes with little outdoor space to accommodate a heat pump. An option is to mount the heat pump in the attic space, by attaching to the roof. This provides a reasonable alternative to using up potentially limited outdoor space and may utilise unused interior space. This approach presents its own challenges, however, notably the potential for structure-borne noise transmission to the dwelling and adjoining homes, due to the attachment to the roof, and potentially airborne noise transmission, due to the proximity of bedrooms etc. With the aim of better understanding – and therefore mitigating – these potential issues, this paper explores the benefits of in-situ Transfer Path Analysis – a method normally employed for vehicles and mechanical structures – for this application.

1. INTRODUCTION

As retrofit becomes a realistic prospect for the development of net-zero heating in domestic homes using Air Source Heat Pumps (ASHPs), suggestions for options of ASHP placement within the loft space of homes has become a popular idea. Due to the comparatively large existing housing stock in the UK, retrofit is necessary to meet the UK government targets for becoming carbon neutral. Many of these houses have limited outdoor space, or have close borders to neighboring dwellings, which creates challenges for external ASHP placement when considering existing noise and boundary regulations. As roof mounting an ASHP is a relatively new concept, especially in the UK, a method for the determination of structure and air-borne noise transmission is required for the analysis of the acoustic impact of the system. This paper proposes an in-situ methodology for the characterization of structural transmission paths of a roof-mounted ASHP. Using a Transfer Path Analysis (TPA) [1] approach, which is commonly applied to all manner of structural problems and applications, such as in vehicles [2] and buildings [3]. The blocked forces are measured at the frame from to which the ASHP is attached, with excitation by a pair of shakers within the ASHP external case at the mounting positions. Noise predictions are made for response positions at remote accelerometers on the adjacent roof structure, remote microphones in the loft space, and microphones in the bedroom and the bedroom below.

2. THEORY

The methodology proposed in this paper is based on the in-situ TPA method [4]. This involves the characterisation of a coupled structure in terms of a source and receiver, with an interface. The blocked forces are the for which is

*Corresponding author: L.S.Barton1@salford.ac.uk
Copyright: ©2025 L Barton et al. This is an open-access article distributed under the terms of the Creative Commons Attribution 3.0 Unported License, which permits unrestricted use, distribution, and reproduction in any medium, provided the original author and source are credited.

needed to constrain the velocity of the device under test to zero [5].
The method does not require the separation of source and receiver and, as no assumption is required for the behaviour of the receiver structure, the in-situ method is most likely more reliable than the previous TPA approaches. Another advantage of the in-situ approach is that the operational blocked forces are independent of the receiver structure, meaning that they remain valid for different assemblies by re-measuring or modelling the transfer function for a different assembly [6].

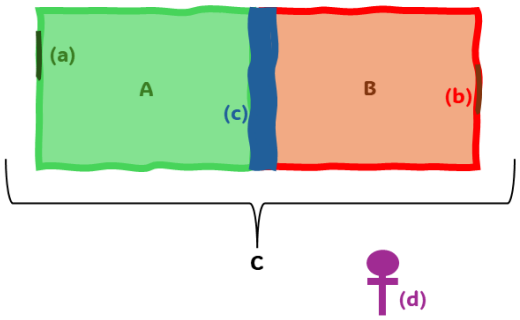


Figure 1. Schematic diagram illustrating the source (A), receiver (B), and couple assembly (C).

Figure 1 illustrates an arbitrary source- receiver assembly, where in this case the source 'A' is the ASHP, and the receiver 'B' is the frame attached to the roof. The responses (d) are remote accelerometers on other structural roof beams, and microphones in the loft space and the bedroom below the ASHP. The blocked forces are calculated by:

$$\dot{\bar{f}}_{A,c} = \boldsymbol{Y}_{C,cc}^{-1} \dot{\boldsymbol{v}}_{C,c} \quad (1)$$

Where $\boldsymbol{Y}_{C,cc}^{-1}$ is an inverted matrix of mobilities, measured using a force hammer at the accelerometer positions on the frame. These excitations were made either side of the accelerometers and were averaged due to a lack of access for direct excitation. $\dot{\boldsymbol{v}}_{C,c}$ is a vector of operational mobilities, measured when the source (in this case, a pair of shakers) is running, and is the transfer function between the shaker voltage and the acceleration measured at the frame accelerometers.
The predicted pressure is then given by:

$$\dot{\boldsymbol{P}}_{C,d} = \boldsymbol{H}_{C,db} \dot{\bar{\boldsymbol{F}}}_{A,c} \quad (2)$$

In this paper, the transfer functions used for $\boldsymbol{H}_{C,db}$ are referred to as $\boldsymbol{H}_{pf}$, as they are the acoustic transfer function between the response and the hammer excitation, as pressure due to force. For the remote validation measurements, these are acceleration due to force, but for consistency the transfer function name remains the same.

3. METHODOLOGY

The experiment was conducted in Energy House 2.0, a climatic chamber at The University of Salford. The facility consists of two climatic chambers, which can produce a multitude of environmental conditions and temperatures. The HVAC system of the chamber was deactivated during the course of this measurement.



Figure 2: The Future Home at Salford University's Energy House 2.0

The ASHP is mounted in the loft space of a detached brick house, as shown in **Figure 2.** The roof frame where the ASHP attaches to the rafters was instrumented with 15 accelerometers; 5 on each of the 3 accessible sides, which are shown in **Figure 3** and **Figure 4**.

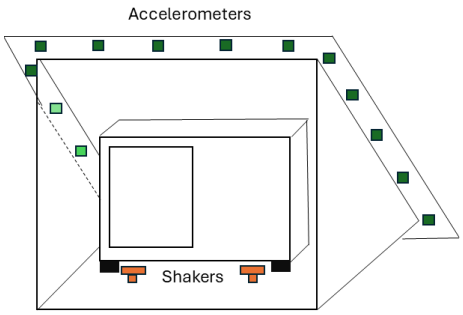


Figure 3. Diagram of ASHP in housing, with accelerometers and shakers shown.

Due to access limitations, only three sides of the frame were accessible for measurement. However, the rear side of the frame does not have a beam and does not appear to be rigidly connected to the ASHP housing.



Figure 4. Photograph of accelerometers

The ASHP was enclosed in plastic housing, with a hatch for access inside. The external roof above the ASHP had a large vent for airflow. Due to logistical restrictions, it was not possible to use the ASHP as an operational source during this measurement. Instead, two small shakers were mounted next to the connecting feet at the base of the ASHP inside the plastic casing, shown **in Figure 5.**



Figure 5. Photograph of one of the shakers

The shakers were measured in various operational combinations using both pink and white noise, and a voltage reference was taken from the supplying noise source. Two accelerometers were attached to struts in the loft space as remote validation points. These were vertical beams attached to the floor and ceiling, and not directly in contact with the ASHP housing. Three microphones were located in the loft space as illustrated in **Figure 6**.



Figure 6. Diagram of microphone placement

A further four microphones were located in the bedroom immediately below the ASHP, as shown in **Figure 7**. These were located to the left side of the room near the window directly below the ASHP, in the centre of the room, at the right hand side of the room near the door, and at a position just above the pillow area of the bed.



Figure 7. Microphones in bedroom

A modal hammer was used to make excitations either side of the accelerometers and averaged using the finite difference approach to measure the Frequency Response Functions (FRFs) for the interface. A voltage reference was used to measure the shakers.

4. RESULTS

For the results presented here, both shakers were operational using a pink noise signal, as this most resembled the ASHP noise. Firstly, the raw data is shown in terms of Power Spectral Density (PSD) to establish that the signal is sufficiently above the background noise.

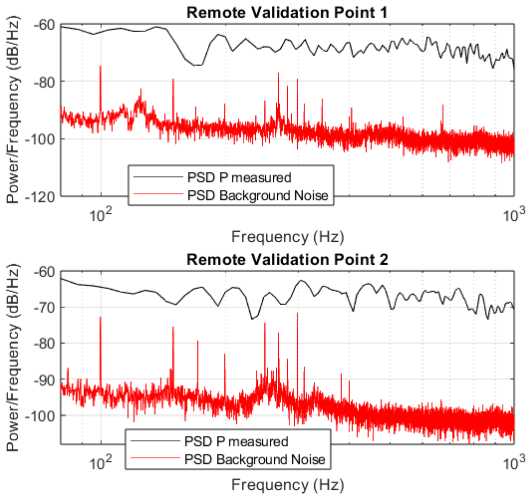


Figure 8. PSD of measured acceleration, in black, and background noise, in red, for remote validation points 1 and 2, from 80 Hz to 1kHz.

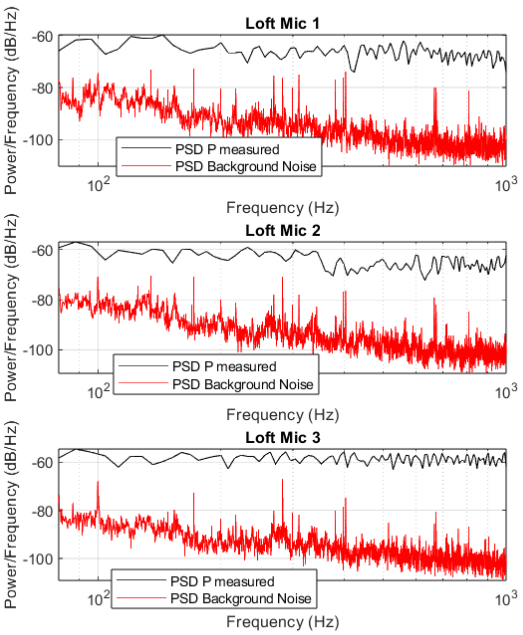


Figure 9. PSD of measured pressure in black, and background noise, in red, for loft microphones, from 80 Hz to 1kHz.

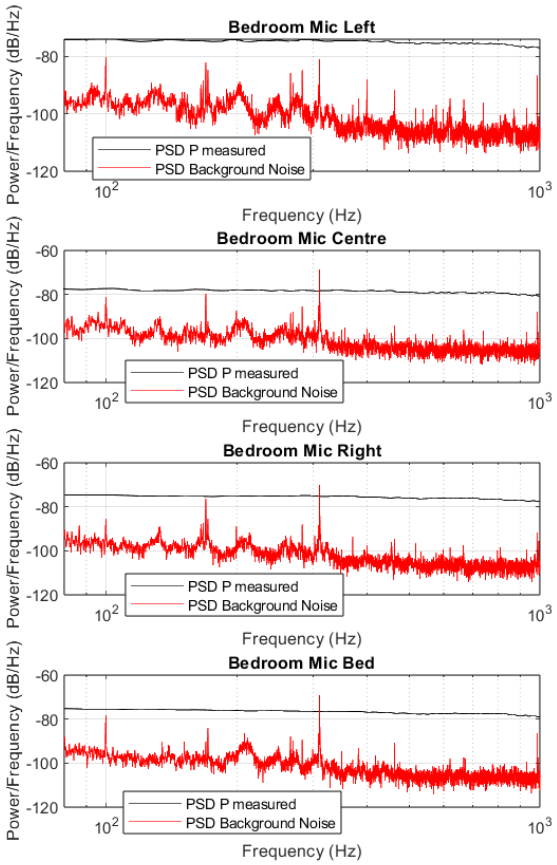


Figure 10. PSD of measured pressure in black, and background noise, in red, for bedroom microphones, from 80 Hz to 1kHz.

Seen in **Figure 10,** there are some erroneous peaks visible in the background noise spectra in three of the bedroom mics, at around 310Hz, which are a higher in magnitude than the measured as seen in **Figure 10**. This could be due to some interfering noise being present during the background noise recording, due to another system in the house such as ventilation, which was outside of operational control during the experiment. The measured signal is out of the noise floor for the remote validation accelerometers and the loft microphones at this frequency range, as seen in **Figure 8** and **Figure 9.**

Using Equations 1&2, predictions at the response positions due to excitation by both shakers are presented here.

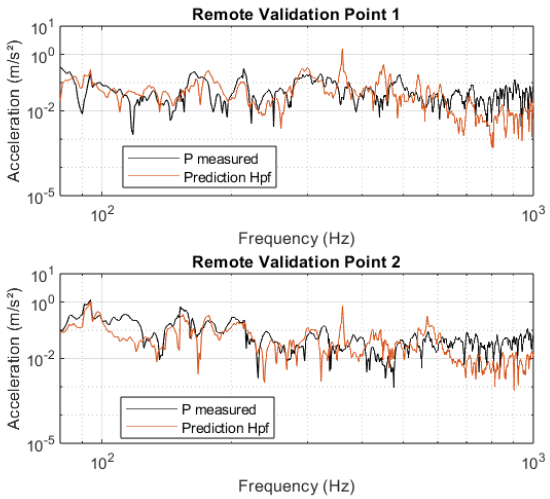


Figure 11. Predicted acceleration at remote validation points using the Hpf transfer function, compared to the measured acceleration, from 80 Hz to 1kHz.

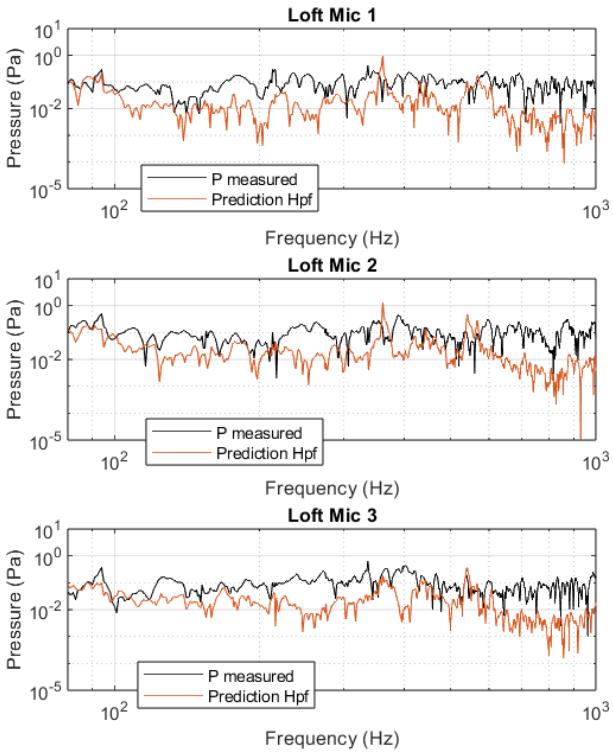


Figure 12. Predicted pressure at loft microphones using the Hpf transfer function, compared to the measured acceleration, from 80 Hz to 1kHz.

At the remote validation accelerometers, which were mounted on wooden roof struts in the loft room, there is relatively close agreement between the measurement and prediction across the measured frequency range, though both positions have an over prediction at around 361 Hz, as shown in **Figure 11.**
There is less overall agreement for the predictions to the loft microphone positions, shown in **Figure 12.** Again, an overprediction is seen at 361 Hz in Loft Mic 1 & 2, as with the remote validation sensors.

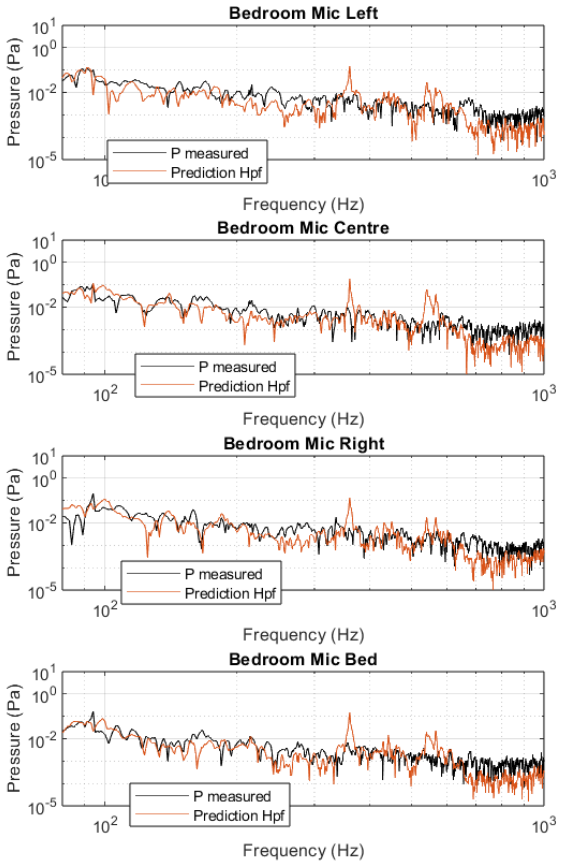


Figure 13. Predicted pressure at bedroom microphone using the Hpf transfer function, compared to the measured pressure, from 80 Hz to 1kHz.

As seen in the remote validation accelerometers and two of the loft microphones, the erroneous peak in the prediction is also present in the bedroom microphone predictions, seen in **Figure 13.**

5. DISCUSSION

The predictions have mixed accuracy. The remote validation accelerometers and the bedroom microphone predictions, both appear to have higher accuracy than the microphones in the loft. This may be due to the different frequency content of airborne and structural excitations within this frequency range. The loft space also has its own acoustic behaviour which may be contributory, and does not have the reassurance lent by laboratory conditions.
The results may be improved by refining the data, using methods such as singular value discarding, to remove noise. Although further analysis is required to be confident of the results, the blocked forces approach can be applied to the measurement of structure- and air-borne noise from a roof mounted ASHP.

6. CONCLUDING REMARKS AND FURTHER WORK

The in-situ TPA approach using blocked forces, which is commonly used in automotive engineering, has been used to evaluate vibroacoustic transfer paths in a home with a roof-mounted ASHP. Following this initial data analysis, there are further steps to be taken. Additional data measured using a volume velocity source will be used to make further blocked forces predictions, treating the entire loft room as the source. This may give clarity to some of the errors in predictions shown in this paper.
If logistics allow, it would be beneficial to repeat the measurement with the ASHP running, to provide verification that the dynamic behaviour and spectral content of the shakers is sufficient to emulate the operational state of the ASHP. Though every care was taken to reduce and mitigate interfering noise from other systems running in the house, any further experiments would take further steps to ensure minimal background noise from processes such as ventilation.
A further condition which may be desirable is to fully instrument around the aperture in which the ASHP hangs, as though the rear quarter of the frame does not appear to be coupled to the ASHP housing, it would be beneficial to ensure this and work towards a more complete interface characterisation.

7. ACKNOWLEDGMENTS

This work was carried out as part of the Future Homes Project, funded by UKRI.

8. REFERENCES

[1] A. T. Moorhouse, "On the characteristic power of structure-borne sound sources," *J Sound Vib*, vol. 248, no. 3, pp. 441–459, Nov. 2001, doi: 10.1006/JSVI.2001.3797.

[2] A. S. Elliot and A. T. Moorhouse, "A Quarter Vehicle Transfer Path Analysis by In-Situ Measurement," *INTER-NOISE and NOISE-CON Congress and Conference Proceedings*, vol. 244, no. 1, pp. 807–813, 2012.

[3] J. Y. Jeon, H. Lim, and B. K. Lee, "Transfer path analysis of floor impact noise and vibration in a multi-story building." [Online]. Available: https://www.researchgate.net/publication/281871601

[4] D. Zabel, T. Alber, M. Sturm, and A. T. Moorhouse, "Internal transfer path analysis based on in-situ blocked forces and transmissibility functions," *Proceedings of 24 International Congress on Sound and Vibration (ICSV24)*, no. July, 2017.

[5] L. Barton, "Decomposed Vibro-acoustic Frequency Response Functions for the Prediction of Radiated Sound," University of Salford, 2023.

[6] A. Elliott, "Characterisation Of Structure Borne Sound Sources In-Situ," University Of Salford, Greater Manchester, 2009.

DOI: 10.61782/fa.2025.0774

FORUM ACUSTICUM EURONOISE 2025

SIMULATION-BASED ANALYSIS OF THE SOUND EMISSIONS OF DECENTRAL AIR-TO-WATER HEAT PUMPS IN RENOVATED MULTI-FAMILY BUILDINGS

William Monteleone[1*] **Fabian Ochs**[1]
[1] Unit for Energy Efficient Building, University of Innsbruck, Austria

ABSTRACT

To decarbonize Europe's building stock by 2050, renovation rates must rise, and fossil-based heating systems must be phased out. Heat pumps (HPs) are central to this effort, but their installation in multi-family buildings presents challenges like space limitations, noise, and invasive infrastructure work. As part of the "PhaseOut" research project, seven multi-family buildings in Vienna will undergo renovations. Each will use a centralized, speed-controlled monobloc air-to-water HP for space heating. The feasibility of decentralized, façade-integrated mini-split air-to-water HPs for domestic hot water will also be explored. To support this, 3D simulation models of a single façade-integrated HP will be created using COMSOL and CadnaA, a commercial acoustic modeling tool. Both platforms will then be used to assess the acoustic impact of multiple HP units installed on façades, highlighting differences in modeling approaches. Simulations in CadnaA will also evaluate the environmental sound pressure levels on the renovation site. Preliminary findings show that sound emissions from decentralized HP units remain within legal limits at the property boundary. However, while tools like CadnaA effectively estimate sound levels across broad areas, they struggle to model near-field acoustics and complex interactions from multiple noise sources with high precision.

Keywords: *Heat pumps; renovation; multi-family buildings; sound emissions; simulation*

[*] ***Corresponding author***: *william.monteleone@uibk.ac.at*
Copyright: *©2025 Monteleone et al. This is an open-access article distributed under the terms of the Creative Commons Attribution 3.0 Unported License, which permits unrestricted use, distribution, and reproduction in any medium, provided the original author and source are credited.*

1. INTRODUCTION

In nearly-zero energy buildings (nZEBs) a combination of adequate insulation of the building and efficient heat pump (HP) based hydronic systems is required [1,2] to reach the goal of the European Union of a fully decarbonised building stock by 2050 [3]. For existing multi-family buildings, the energy performance of the building envelope can be improved fast and reliably by means of serial prefabricated retrofit solutions [4]. In prefabricated renovation solutions, most of the work can be performed off-site to reduce the installation time and disruption to the building tenants. Moreover, decentral air-source heat pumps can be efficiently integrated in prefabricated façade elements, thereby reducing the amount of disruptive and cost-intensive installation work within the flat, as shown in [5] and [6]. For prefabricated façades with integrated building services, an integral design and analysis approach which unites building physics, thermodynamics and architecture is required [7]. However, one of the main concerns for the extensive acceptance of HPs in residential buildings is noise [8] and the actual legislative framework in Europe does not accurately consider the relationship between HP placement and its operational state [9,10], as frequently the sound power level reported in technical datasheets is not measured at full capacity. Within the Austrian research project PhaseOut [11], seven identical social housing multi-family buildings in Vienna, with each six flats, will be renovated. In two of them, a silent façade-integrated mini-split HP for flatwise domestic hot water (DHW) preparation, installed in a prefabricated timber frame façade, will be installed, while space heating (SH) will be provided by two external monobloc air-to-water HPs. First, the analysis will focus on the comparison between a 3D COMSOL [12] simulation model of the sound propagation around a single façade-integrated

mini-split HP and a 3D simulation model developed within the environment of the commercial software of CadnaA [13]. Then a 3D simulation will be performed in both simulation programs considering the sound emissions of three façade-integrated HPs to evaluate the modelling of interference patterns. Finally, simulations within the software environment will assess the sound propagation on the whole renovation site (i.e. for all seven buildings) and the resulting sound pressure level considering only the decentral DHW HPs will be compared with the limits imposed by the existing regulations. Based on the simulation results, recommendations are made for the creation of a reduced-order simulation model for the pre-design of HP systems.

2. RENOVATION CONCEPT

The mini-split HP concept developed within the research project "PhaseOut" is depicted schematically in Figure 1. The system combines a façade-integrated outdoor unit including the evaporator and four parallel axial fans with an indoor unit housing the compressor, the condenser and the expansion valve. The HP indoor unit is in turn connected hydraulically with a compact 120 Litres hot water storage for the delivery of the DHW demand. The nominal HP heating capacity corresponds to 1.5 kW (A2W55) at an airflow rate of 350 m^3/h. A 2.73 x 2.73 m timber frame test façade was built to measure the HP performance under real operating conditions and installed in a so-called PASSYS test cell [14] at the University of Innsbruck, as shown in Figure 2. The outdoor unit of the mini-split air-to-water HP is integrated in a 120 x 60 x 20 cm niche within the test façade (see lower casing in Figure 2). The back side of the outdoor unit is further insulated towards the inside with a 5 cm aerogel layer (see also Figure 1). A vapour barrier is inserted between the prefabricated façade and the existing wall. Seven three-storey multi-family houses will be renovated in Vienna, Austria. Each building consists of six flats (see also Figure 3), with an average flat size of 55 m^2. SH in the flats is provided currently mainly by decentral gas boilers or electric ovens, while DHW is either supplied by electric boilers or by the same gas-fired boiler used for SH, if existing.

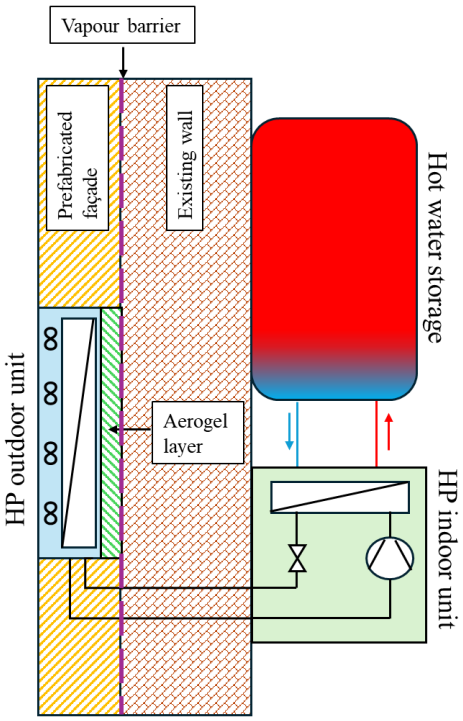


Figure 1. Schematic drawing of the developed façade-integrated air-source mini-split-type HP.



Figure 2. Outdoor unit of a façade-integrated mini split air-to-water heat pump for domestic hot water installed at the University of Innsbruck.

Figure 4 gives an aerial overview of the seven buildings subjected to renovation as well as an indication of the property limit (red dotted line), which is crucial for the evaluation of the sound emissions. Each of the seven buildings will undergo deep renovation to achieve a heating demand of 25 kWh/(m^2 y). Buildings 1 and 4 will be equipped with two centralised speed-controlled air-to-water HPs with a nominal thermal capacity of 5.3 kW each (A2W35) supplying low-temperature water to a water-to-water speed-controlled 7.2 kW (W15W55) booster HP in each flat for SH and DHW preparation. For buildings 2 and 7 the SH demand will be covered by two centralised air-to-water HPs, identical to those in buildings 1 and 4, while DHW preparation will be provided through the developed façade-integrated mini-split air-to-water HP on the south-east façade (see Figure 1, Figure 2 and Figure 3). Buildings 3, 5 and 6 will feature instead a fully centralised system with two monobloc 5.3 kW speed-controlled air-to-water HPs identical to those in the other buildings, one for SH and one for DHW.

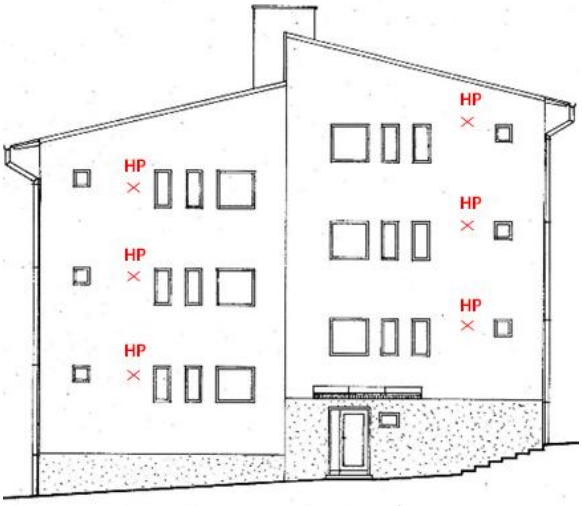


Figure 3. Drawing of the east façade of one of the three-storey buildings subjected to renovation in Vienna within the research project "PhaseOut" with indication of the possible position of the façade-integrated DHW HP.



Figure 4. Aerial view of all seven buildings on the renovation site located in Vienna with indication of the property limit (dotted red line).

3. REGULATORY FRAMEWORK

In Austria, environmental noise propagation is assessed based on ÖNORM S 5021, ÖAL Guideline No. 6 (Austrian Noise Abatement Association), and relevant Federal Province regulations. ÖNORM S 5021:2017 establishes planning values for noise emissions, considering both location (zone) and time of day.
For urban residential areas, the reference sound pressure levels are:

- 55 dB(A) from 6 a.m. to 7 p.m.
- 50 dB(A) from 7 p.m. to 10 p.m.
- 45 dB(A) from 10 p.m. to 6 a.m.

According to ÖNORM S 5021 and ÖAL Guideline No. 6, a continuously operating system (e.g., heat pumps) is deemed non-intrusive if the sound pressure level at the property boundary remains below the base level. This base level is generally approximated as 10 dB lower than the permitted assessment level [15]. Therefore, in the absence of more detailed in-situ measurements, the critical conditions are expected to occur at night and a maximum sound pressure

level of 35 dB(A) must not be exceeded at the site boundary.

4. METHODOLOGY

For the simulations model in COMSOL, the measured sound power level of the outdoor unit of the mini-split HP shown in Figure 5 (described also in [16]) was used as a base for the definition of the properties of the sound source.

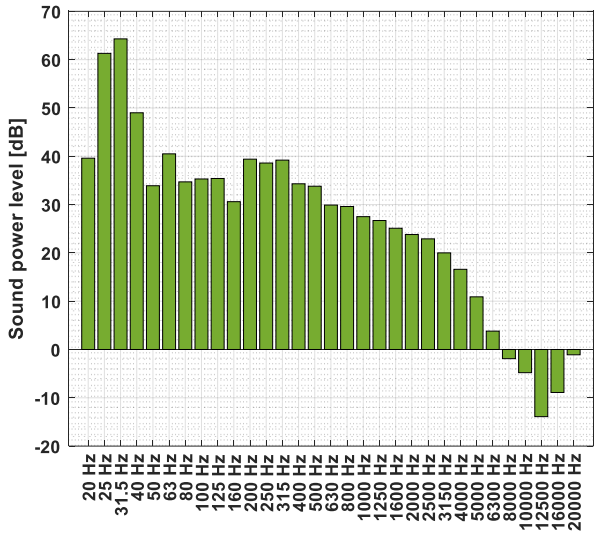


Figure 5. Measured sound power level spectrum of the outdoor unit of the façade-integrated mini-split HP.

The analysis is performed at 125 Hz for sake of manuscript length, but the same methodology can be applied to the remaining frequencies in the spectrum.

A first simulation is performed with a single homogeneous sound source, while a second one is performed for three identical sound sources, with a distance of 3 m between one source and the next one. The sound source is placed at a height of 5 m above ground level and the sound pressure level is evaluated on a horizontal plane orthogonal to the sound source(s).

In the CadnaA simulation model the sound source is modelled as a two-dimensional object with the frontal dimensions of the mini-split HP together with the building façade on which it is installed. The sound pressure level L_r in every point of the domain and for each frequency is calculated according to Eqn. (1):

$$L_r = L_w + L_z + K_0 - 20 \log r - C \ / \ [dB] \quad (1)$$

Where L_w is the sound power level of the sound source, L_z the eventual correction for low-frequency tonalities, K_0 the adjustment value for the position of the HP, r the distance from the sound source and C a constant correlating sound power level and sound pressure level, depending on the sound propagation pattern (e.g. hemispherical or spherical). In Table 1 a summary of the applied boundary conditions (BC) for the CadnaA simulations can be found. For the sake of simplicity, it was decided to discard the influence of low-frequency tonalities for the current analysis. The absorption coefficient of the building façade at 125 Hz $\alpha_{f,125}$ is assumed to be equal to 0.05 and the ground absorption coefficient $\alpha_{g,125}$ corresponds to 0.25.

Table 1. Summary of selected boundary conditions for the CadnaA simulations.

BC	Value
L_z	0 dB
K_0	+ 3 dB (façade installation)
C	8 dB (hemispherical propagation)
$\alpha_{f,125}$	0.05
$\alpha_{g,125}$	0.25 [17]

In the COMSOL simulations, an air volume of 10 m x 10 m x 10 m is defined for the calculation of the sound pressure level (see Figure 6), which includes a fictitious building façade (highlighted in Figure 6) and the ground. The HP is modelled as a cavity in the air volume and a sound pressure is applied to its front surface. The assigned sound pressure is derived by the measurement of the sound power level shown in Figure 5. An impedance boundary condition is assigned to the building façade and to the ground, with absorption coefficients equal to those presented in Table 1. The remaining surfaces are assumed to be open boundaries. The pressure field within the air domain is solved by the software by means of the Helmholtz equation, shown in Eqn. (2), which applies if no monopole or dipole domain sources are assumed. It is also assumed that the background pressure is zero, so the total sound pressure is equal to the scattered pressure.

$$\nabla \cdot \left(-\frac{\nabla p_t}{\rho_a} \right) - \frac{k^2 p_t}{\rho_a} = 0 \qquad (2)$$

Where p_t is the total sound pressure in [Pa], ρ_a the density of air in [kg/m^3] and k the wave number in [1/m]. To minimize the computational effort of the model, a hybrid FEM-BEM (Finite Element Method – Boundary Element Method) approach was used, with all the surfaces except the façade and the ground acting as a BEM-FEM boundary.

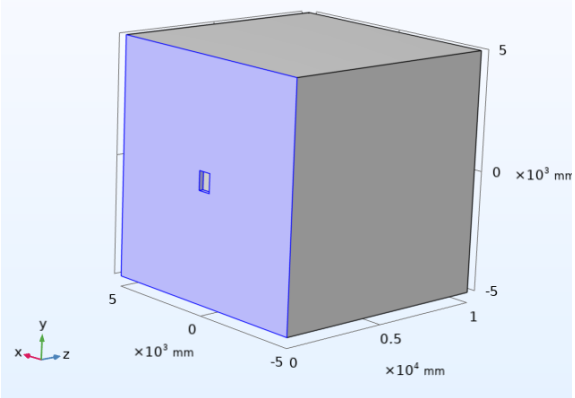


Figure 6. Depiction of the control volume of air assumed in COMSOL. The façade of the building is highlighted, and it is possible to see the HP cavity.

Finally, to calculate the sound emissions due to the DHW HPs around the renovation site, a model in CadnaA was built replicating the location and assuming a total of six façade- integrated heat pumps (e.g. one for each flat) on the east-southeast façade of building 2 and six heat pumps on the east-northeast façade of building 7 (see also Figure 3). To check the compliance with the regulations at night, fictitious receivers have been placed at the property boundary at a height of 2 m. The HPs have been modelled in this a case as one-dimensional sound sources.

5. RESULTS

The sound pressure level on a 2D plane perpendicular to the sound source is depicted in Figure 7 and Figure 8 for the CadnaA and COMSOL simulations respectively. In Figure 7, ideal receivers on the same plane of the sound source can be scene at distances between 0.5 m and 5 m from the sound source. Compared to CadnaA, the COMSOL simulation in Figure 8 is able to represent in a more detailed the sound propagation pattern caused by a two-dimensional sound source, as the sound propagation deviates from a purely hemispherical pattern for distances higher than about 2.5 m. Evaluating the sound pressure level at 125 Hz on a line perpendicular to the sound source yields the diagram in Figure 9. Below 1 m distance from the sound source a similar decay in the sound pressure level can be observed in both CadnaA and COMSOL simulations. Between 1 m and 2.5 m the COMSOL simulations slightly overestimate the sound pressure level compared to CadnaA and for distances higher than 3 m from the sound source, the profiles deviate.

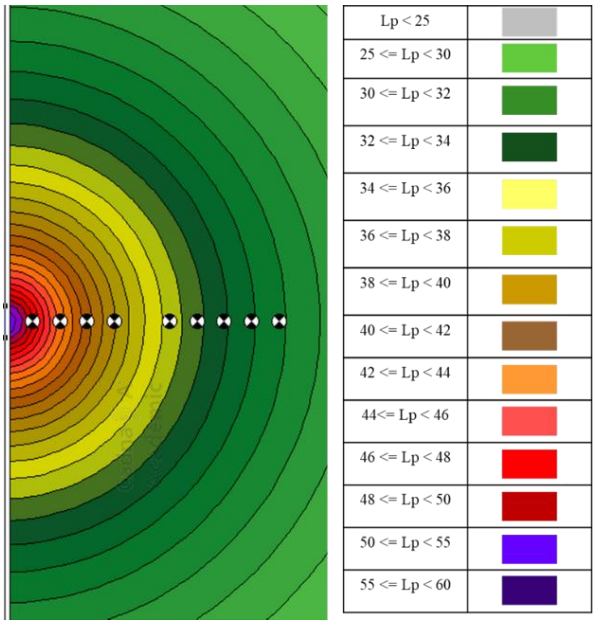


Figure 7. 2D plane of the overall sound pressure level in dB generated by a single HP in CadnaA.

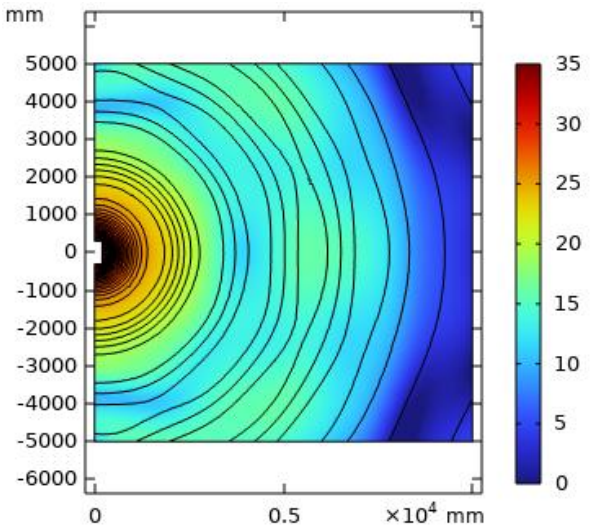


Figure 8. 2D plane of the sound pressure level in dB at 125 Hz generated by a single HP in COMSOL.

The differences between the two simulation tools are more clearly visible if three operating HPs are considered, as shown in Figure 10 and Figure 11. While near (within 1 m of) the sound source the sound pressure levels exhibit similar behaviour, as the distance from the HPs grows, the COMSOL simulation is able to reproduce the constructive and destructive interference patterns caused by the simultaneous sound emission of the three HPs and the reflections from ground a façade, while the sound pressure level in CadnaA assumes a more homogenous behaviour.

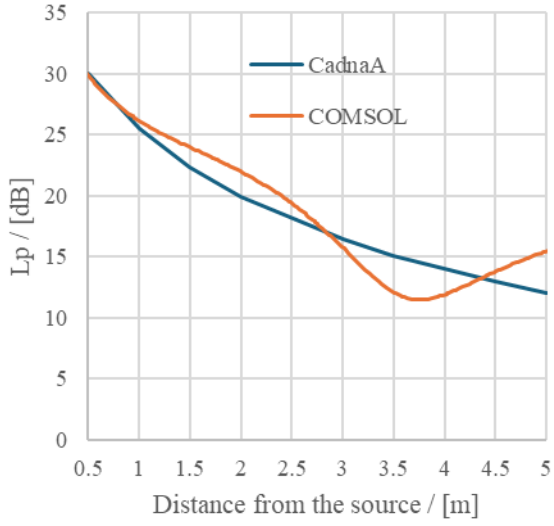


Figure 9. Comparison between CadnaA and COMSOL of the sound pressure level at 125 Hz with a single HP on a line perpendicular to the sound source.

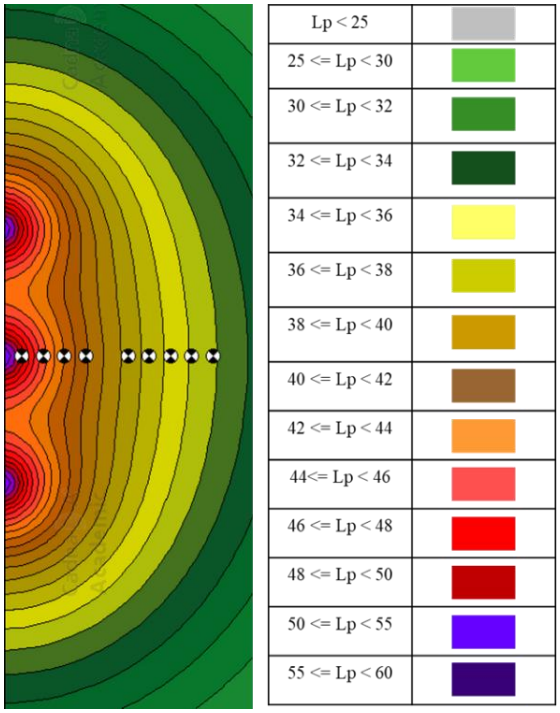


Figure 10. 2D plane of the overall sound pressure level in dB generated by three HPs in CadnaA.

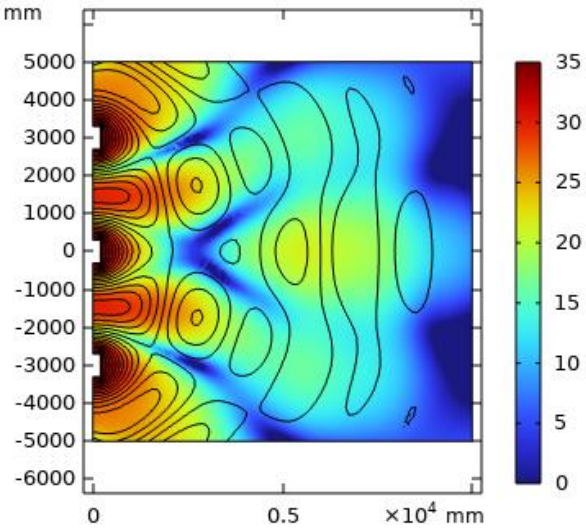


Figure 11. 2D plane of the sound pressure

level in dB at 125 Hz generated by three HPs in COMSOL.

As a result, the sound pressure level on a line perpendicular to the central HP in Figure 12 shows large deviations between the CadnaA and the COMSOL model for normal distances from the sound sources higher than 1 m.
Reflections in the COMSOL model contribute therefore first to a reduction in the sound pressure level from 1 m to 2.5 m, with a minimum around 5 dB and then to an increase from 2.5 m to 5 m.

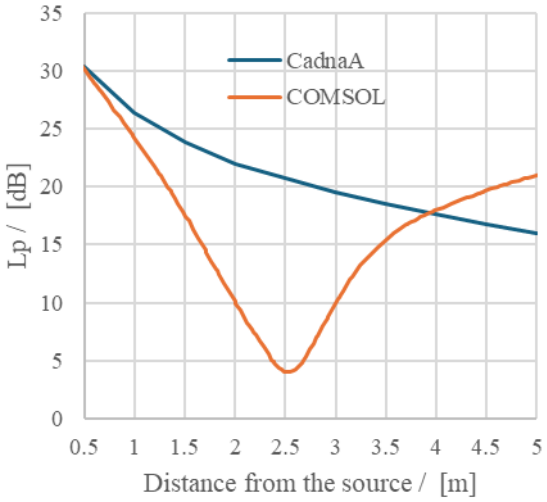


Figure 12. Comparison between CadnaA and COMSOL of the sound pressure level at 125 Hz with three HPs on a line perpendicular to the central HP.

In Figure 13 the simulated sound pressure level at 2 m height on the renovation site described in section 2 is observed considering the simultaneous operation of the twelve DHW HPs, six for building 2 and six for building 7. During night, the most critical property boundaries are therefore for building 2 the points exactly in front of the façade where the HPs are installed and for building 7 also the points southeast of the building. The maximum overall sound pressure level (considering only the DHW HPs) at the property boundaries near building 2 corresponds to 20.4 dB(A), while a maximum value of 29.3 dB(A) is observed near building 7 where the distance between sound sources and property boundary is at its minimum. In both cases, therefore, the regulatory limit is met.

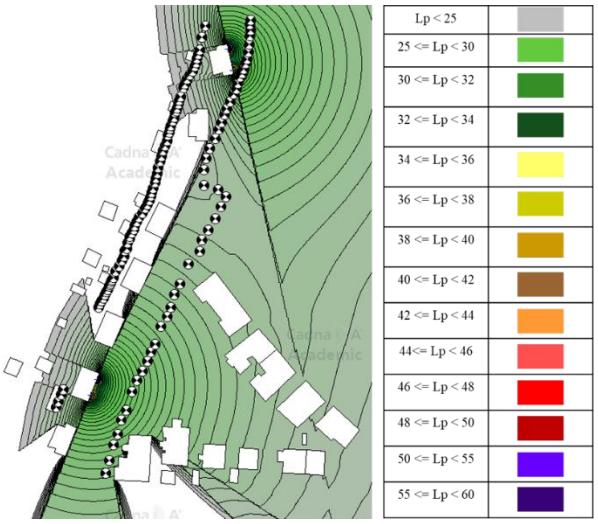


Figure 13. CadnaA simulation of the sound pressure level at the renovation site considering only the decentral DHW HPs. Ideal receivers are placed on the property boundary.

6. CONCLUSIONS

As part of the PhaseOut research project, seven multi-family buildings will undergo deep renovation. In two of these buildings, domestic hot water (DHW) will be supplied using compact, façade-integrated mini-split air-to-water heat pumps (HPs). This study evaluated the sound pressure levels around the renovation sites using the software CadnaA, specifically considering the nighttime operation of the DHW heat pumps alone.
Simulation results show that the sound pressure level at the property boundary remains below regulatory limits (e.g., 35 dB(A)) even at the shortest distance between the HPs and the boundary, where a value of 29.3 dB(A) was observed.
Additionally, the sound propagation characteristics of a single HP and of three HPs were analysed using two simulation models developed in CadnaA and COMSOL. Both models exhibited similar sound pressure level decay within 1 meter of the sound source. However, when simulating three simultaneous sound sources, significant deviations—up to approximately 15 dB—were observed at greater distances. This discrepancy is attributed to COMSOL's more accurate representation of wave phenomena, in contrast to the more uniform sound propagation observed in CadnaA.
These findings suggest that geometric acoustic simulation tools like CadnaA are more suitable for evaluating HP

installations over larger domains. However, for detailed assessment of sound propagation at short distances—especially in scenarios where HPs are installed close to property boundaries—FEM-based physical models like those in COMSOL offer greater precision.
To validate these results, future measurements will be conducted using a mock-up of a prefabricated timber façade integrated with an integrated mini-split HP. Furthermore, the effect of directional sound sources will be incorporated into the simulation models, and the results will be compared with in-situ measurements.

7. ACKNOWLEDGMENTS

This work has been part of the research projects "PhaseOut" (FFG-Nr. 999895470) funded by the FFG (Austrian Research Promotion Agency) in the "Stadt der Zukunft" program and of the "IEA HPT Annex 63".
Our thanks go to the project partners Drexel und Weiss, Rothbacher, Kulmer Holzbau and Nussmüller Architects.

8. REFERENCES

[1] G. Aruta, F. Ascione, N. Bianco, T. Iovane, M. Mastellone, G. Maria Mauro, Optimizing the energy transition of social housing to renewable nearly zero-energy community: The goal of sustainability, Energy Build 282 (2023) 112798. https://doi.org/10.1016/j.enbuild.2023.112798.

[2] IEA, The Future of Heat Pumps, The Future of Heat Pumps (2022). https://doi.org/10.1787/2bd71107-en.

[3] European Parliament, Directive (EU) 2024/1275 of the European Parliament and of the Council of 24 April 2024 on the energy performance of buildings (recast), 2024. http://data.europa.eu/eli/dir/2024/1275/oj.

[4] L. Lihtmaa, T. Kalamees, Emerging renovation strategies and technical solutions for mass-construction of residential districts built after World War II in Europe, Energy Strategy Reviews 51 (2024). https://doi.org/10.1016/j.esr.2023.101282.

[5] G. Dermentzis, F. Ochs, D. Siegele, W. Feist, Renovation with an innovative compact heating and ventilation system integrated into the façade – An in-situ monitoring case study, Energy Build 165 (2018) 451–463. https://doi.org/10.1016/j.enbuild.2017.12.054.

[6] D. Siegele, F. Ochs, W. Feist, Novel speed-controlled exhaust-air to supply-air heat pump combined with a ventilation system, Appl Therm Eng 162 (2019). https://doi.org/10.1016/j.applthermaleng.2019.114230.

[7] G. Malacarne, G.P. Monizza, J. Ratajczak, D. Krause, C. Benedetti, D.T. Matt, Prefabricated Timber Façade for the Energy Refurbishment of the Italian Building Stock: The Ri.Fa.Re. Project, Energy Procedia 96 (2016) 788–799. https://doi.org/10.1016/j.egypro.2016.09.141.

[8] M. Torjussen, Sound from domestic air source heat pumps: a case study, in: Proceedings of the Institute of Acoustics, Institute of Acoustics, 2020. https://doi.org/10.25144/13323.

[9] C. Reichl, Annex 51: Acoustic Signatures of Heat Pumps - Final Report, 2021. https://heatpumpingtechnologies.org.

[10] E. Langerova, J. Kralicek, M. Kucera, Air-to-water heat pump noise in residential settings: A comprehensive review, Renewable and Sustainable Energy Reviews 207 (2025). https://doi.org/10.1016/j.rser.2024.114968.

[11] FFG (Austrian Research Promotion Agency), PhaseOut - Wärmepumpentechnologien in der Bestandssanierung, (2024). https://projekte.ffg.at/projekt/4499093 (accessed July 17, 2024).

[12] COMSOL Inc., COMSOL Multiphysics 6.0, (2022). https://www.comsol.com/comsol-multiphysics.

[13] DataKustik GmbH, CadnaA, (2025). https://www.datakustik.com/products/cadnaa/cadnaa (accessed January 26, 2025).

[14] E. Hahne, R. Pfluger, Improvements on PASSYS test cells, Solar Energy 58 (1996) 239–246. https://doi.org/10.1016/S0038-092X(96)00080-1.

[15] C. Reichl, HPT IEA Annex 51 - Acoustic Signatures of Heat Pumps - Executive Summary, 2021. https://heatpumpingtechnologies.org/annex51/.

[16] W. Monteleone, F. Ochs, G. Dermentzis, S. Breuss, Simulation-assisted design of a silent façade-integrated R290 mini-split heat pump, Appl Therm Eng 243 (2024) 122520. https://doi.org/10.1016/j.applthermaleng.2024.122520.

[17] G.W.C. Kaye, E.J. Evans, The sound-absorbing properties of some common out-door materials, Proceedings of the Physical Society 52 (1940) 371–379. https://doi.org/10.1088/0959-5309/52/3/307.

DOI: 10.61782/fa.2025.0032

FORUM ACUSTICUM EURONOISE 2025

A RISK-BASED FRAMEWORK FOR ACOUSTIC ASSESSMENT OF ASHPS - FROM DOMESTIC TO COMMERCIAL APPLICATIONS

Jack Harvie-Clark[1*] **James Hill**[1] **Nicholas Dobinson**[1] **Richard Hinton**[1]
[1] Apex Acoustics Ltd, Gateshead, UK

ABSTRACT

Air Source Heat Pumps (ASHPs) are critical for decarbonising building heating across Europe, but their widespread deployment may be hindered by inefficient, inconsistent acoustic assessment methodologies. Through detailed acoustic modelling of realistic scenarios, we demonstrate that the UK's national calculation methodology for permitted development rights (MCS 020) can consistently predict sound levels 5-7 dB higher than calculations to ISO 9613-2. We propose a hierarchical assessment framework where evaluation complexity aligns with installation risk: from simplified MCS-based screening for domestic and commercial installations to more detailed evaluation where necessary. Our analysis addresses both domestic and non-domestic contexts, examining specific challenges around source characterisation, operational patterns, and cumulative impacts. For non-domestic installations, we identify particular issues regarding low-frequency emissions and night-time operation. Critical areas for further research include validation of propagation models, systematic post-installation studies, and standardised approaches to character corrections in the absence of data at the design stage. This framework could significantly reduce barriers to ASHP adoption by making assessments more efficient and consistent while ensuring appropriate acoustic protection as deployment scales up to meet decarbonisation targets.

Keywords: ***ASHP, acoustics, noise, planning.***

[*] ***Corresponding author***: *jhc@apexacoustics.co.uk.*
Copyright: *©2025 Jack Harvie-Clark et al. This is an open-access article distributed under the terms of the Creative Commons Attribution 3.0 Unported License, which permits unrestricted use, distribution, and reproduction in any medium, provided the original author and source are credited.*

1. INTRODUCTION

This paper critically examines current acoustic assessment methodologies for Air Source Heat Pumps (ASHPs) in the UK and proposes a risk-based framework to streamline evaluation while maintaining appropriate sound protection. First, we analyse the limitations of existing assessment approaches by comparing predicted sound levels using different methodologies. Then, we propose a hierarchical framework where assessment detail aligns with installation complexity and risk. Finally, we identify key areas requiring further research to support the proposed framework, with the goal of reducing obstacles to wider ASHP adoption while maintaining community sound protection. This approach addresses both domestic and commercial installations, recognising their distinct acoustic challenges while seeking consistent principles for assessment.

1.1 Background

Air source heat pumps (ASHPs) play a crucial role in decarbonising heating across all building sectors. Their successful integration into our built environment necessitates addressing sound emissions, which vary significantly between domestic and commercial installations. While domestic installations typically involve units of 3-16 kW heat output capacity mounted at ground level, commercial installations can be orders of magnitude larger and are often mounted on rooftops or in service yards, presenting distinct acoustic challenges.

1.2 Current planning regime

For domestic units the Microgeneration Certification Scheme 020 standard (MCS 020) [1] provides a simplified assessment framework that enables Permitted Development Rights (PDR), which therefore avoids the planning process. However, PDR do not apply to all domestic installations, and if the proposed installation does not comply with MCS

020 then full planning permission is required. Non-domestic installations typically require planning permission and are usually assessed using BS 4142 [2], though this standard was not specifically developed for heat pump applications, but industrial and commercial sound sources in general.

1.3 Opportunity to simplify the acoustic assessment

Through comprehensive acoustic modelling of realistic scenarios, we have previously demonstrated [3] that the MCS 020 method can consistently predict sound levels 5 -7 dB higher than ISO 9613-2 [4] calculations. This potentially inherent conservatism in the MCS methodology presents an opportunity for streamlining the planning process. For full planning applications, current reliance on BS 4142 introduces specific challenges around background sound level determination and character corrections that cannot be reliably predicted at design stage; in addition, different local planning authorities have different standards for noise impact assessments using BS 4142. These uncertainties introduce additional risk to the acoustic assessment and may also mean inconsistencies between practitioners. Our analysis indicates that a more structured, hierarchical approach to assessment could benefit both sectors.

1.4 More work is needed!

While this paper proposes a framework for determining an appropriate assessment methodology based on risk of adverse outcomes, this would require the consent of planning authorities to become a practical reality. Critical areas for further research are identified, including validation of propagation models and systematic post-installation studies, to inform future standards and ensure a suitable balance between facilitating ASHP adoption and community sound management.

1.5 Considerations for acoustic planning

To undertake the acoustic design for a new sound source, it is necessary to consider three distinct aspects of the sound:

- Source characterisation
- Propagation model
- Impact assessment

These aspects are considered in turn. See section 3 for a description of sound propagation modelling (the differences between those methods used in MCS 020 and typically adopted in BS 4142), and section 4 for a description of sound impact assessment methods.

2. CHARACTERISATION OF THE SOUND SOURCE

2.1 Sound power level

To comply with European Directive 813/2013 [5], ASHPs sold in the UK must declare their rated sound power level. The various EN Standards required to describe how the heat pump should be mounted in the laboratory, the environmental conditions, the water flow and return conditions, are described in [3, 5]. However, the heating load point is described in the EU Directive itself and has some ambiguity within it; manufacturers believe that the sound power test carried out at around 40 % of full load is compliant with the EU Directive, and therefore this is what they do to declare the ErP Sound Power Level, SWL, on the product label.

As there is no other description of the load point, a “full load” test does not have a formal definition and is not standardised. However, in other countries there appears to be data available for both the ErP sound power and “full load” or “maximum” sound power, such as in the German heat pump association’s online calculator [6]. A sample of data from the German website suggests that the maximum sound power may be up to 15 dB more than the ErP sound power, or it may have the same value. The sample data suggests that at sound power levels below 60 dBA the maximum sound power diverges more significantly from the ErP sound power. A discrepancy between the ErP stated sound power and actual maximum sound power introduces uncertainty into the assessment which is impossible to quantify if the data is not available.

For commercial units, source characterisation presents additional challenges. While domestic units must declare their ErP sound power level, commercial units often come with limited acoustic data. Manufacturers may report sound pressure levels at specified distances rather than sound power tests undertaken according to recognised standards.

The operating conditions under which acoustic data is measured may not reflect real-world operation. Literature describing in-situ measurements and comparison with manufacturer’s laboratory test data suggests discrepancies can be significant.

2.2 Tonality

Some countries include a penalty for tonality in the assessment at design stage, as can be seen on the German heat pump association website. The information on the German website indicates a “surcharge” (penalty) for tonality, K_T. The accompanying information notes indicate that a penalty shall be set at 3 or 6 dB, depending on the

degree of conspicuity. The tonal quality of a sound can also be determined by measurement (DIN 45681, draft edition May 1992).
Note that DIN 45681 [7] can only be applied in-situ for the determination of tones. Current practical methods for assessing tonality are hotly debated – three methods are described in BS 4142, with the preferred being the subjective method. This is not possible at the design stage without full auralisation of the sound – which requires directional information of the sound source, and an auralisation of the background sound. Our random sampling of manufacturers and models in the German database has not revealed any units that have a K_T (tonality) penalty.
There is no standardised information available from suppliers in the UK that indicates tonality of ASHP units. It has been mentioned previously [8] that including a characterisation for tonality may facilitate consistency in assessments, but this information is not currently available.
While it is currently not possible to carry out a representative tonality assessment at the design stage, new methods are currently being proposed [9]. Practitioners must often make assumptions about character corrections without having the detailed spectral data that would inform a more nuanced assessment. The MCS 020 procedure does not take account of tonality.

2.3 Low frequency sound

When spectral data is provided, it typically excludes frequencies in and below the 63 Hz octave band, yet low frequency sound can be significant for both small and particularly for larger units. The laboratory standards disregard all sound below the 100 Hz third octave band, as laboratories are typically not big enough to reliably measure at lower frequencies.
Some countries have anomalies, such as the Netherlands; the in-situ standard for ASHPs includes a low frequency criterion, but the information is not available at design stage to assess for this outcome. Where design stage assessment differs from in-situ assessment this introduces a risk for the designers, who respond by taking a prudent approach. This potentially hinders the rollout of ASHPs unnecessarily, as it can entail an unnecessary constraint where there are little or low levels of sound character.

2.4 Directionality

Directional characteristics are also not required to be measured according to the standards. There is only one facility in the UK for measuring the sound power of ASHPs, at BSRIA. Laboratory measurements require a thermo-acoustic chamber, which may be either a reverberation room or a (semi or full) anechoic chamber. Directional sound is only possible to measure in an anechoic chamber, while the facility at BSRIA is a reverberation room.
Many laboratories across Europe are starting to measure the directional characteristics of ASHPs [10]; this necessitates recording both temporal and spatial characteristics of the sound, i.e. the quantity of data recorded is many orders of magnitude greater than for a simple sound power characterisation. Methods to use this data and predict in-situ impacts will also need to be developed, such methods are currently the demise of research institutions and significant project effort.

2.5 Operating conditions and background variations

In operation, the ASHP output is modulated to match the load. The main sources of noise, the compressor and fan, have their speeds and load adjusted, typically to optimise energy efficiency for a given output demand. The background sound level generally varies throughout the nighttime period, typically being lowest in the early hours of the morning. Many manufacturers provide a “low noise mode” for places where there are separate daytime and nighttime noise level limits. While low noise mode operation may reduce the thermal efficiency, its adverse effect is likely to be much less than provision of an acoustic enclosure, for example, or other forms of mitigation.
A “worst case scenario” approach to assessment is typical; under MCS 020 there a single noise level threshold for daytime and nighttime, with no opportunity to use a low noise mode of operation in the nighttime. A more sophisticated assessment under BS 4142 can accommodate different noise emissions in different time periods.

2.6 A common practitioners’ mistake

Practitioners should be wary of manufacturer's data that presents "sound level at 1 m" without accompanying sound power data. While superficially attractive for calculations, such metrics can lead to significant errors. These values typically represent measurements averaged over a control surface 1 m from the unit's dimensions, according to the laboratory test standards such as ISO 3744, ISO 3745, and ISO 3746. This is quite different from the way that practitioners often use this data – assuming a point source of sound, and a simple 20*log(r) to account for attenuation due to distance. Using these data in point-source propagation calculations systematically underestimates the source sound power level, as the total sound energy is

always actually distributed over a larger measurement surface area than assumed in this calculation.
Only declared sound power levels, measured according to recognised standards, provide a reliable basis for acoustic calculations. When manufacturers present sound pressure levels at a stated distance, the unit dimensions and measurement methodology must be clearly stated to enable calculation of sound power level. A variety of reputable manufacturers appear to present data as sound levels at 1 m that encourages acousticians to make this mistake, by using an image with a "measurement location" indicated at a distance of 1 m from the unit.

3. SOUND PROPAGATION MODELS

When calculating the sound propagation and impact from an installation, a variety of models are available to the practitioner. Through systematic comparison of these models, we demonstrate that simpler approaches can provide inherently conservative results that may be sufficient for many scenarios. If a simple calculation demonstrates a robust case for a sufficiently low sound impact, there is no need to expend additional effort on more sophisticated modelling methods. However, simple models have risks in both directions – in simplifying the calculation of sound propagation, simple models need to be used with caution in situations that are beyond the scope of their simplifying assumptions. It can take a greater level of expertise to know when a simpler model is appropriate.

3.1 MCS 020 sound propagation model

As MCS 020 is applied by people with no acoustics expertise, it is based on three simple input data:

- Distance between source and assessment position, rounded down to tabulated integer values
- Number of reflecting planes (one, two or three)
- Barrier attenuation (either 0, 5 or 10 dB)

These data are used to calculate the sound propagation to the receptor location. The approach simplifies the same concepts used in ISO 9613 but treats reflecting surfaces and barriers differently. In MCS 020, each reflecting plane conceptually constrains the sound propagation to half the previously available space (solid angle), adding 3 dB to the calculated level. Our modelling has shown [3] that this in particular can consistently lead to higher predicted levels than the application of ISO 9613-2.

3.2 ISO 9613-2: 2024

A method identified in BS 4142 for calculating sound propagation outdoors is BS ISO 9613-2; this standard is typically applied using specialist software and expertise. The standard accounts for reflecting surfaces by calculating additional sound propagation paths for specular reflections to the receiver location. Our analysis demonstrates that this can result in predicted levels 5 - 7 dB lower than MCS calculations for equivalent scenarios.
While much more comprehensive than the MCS 020 model, ISO 9613 still has limitations when applied to the specific context of ASHP sound assessment. The standard was designed for sound propagation over longer distances and in open environments, rather than the close proximity and complex geometries often encountered around ASHP installations. The standard's assumptions about ground effects and meteorological conditions might also not be entirely suitable for the constrained urban morphologies where ASHPs are typically located.
ISO 9613 does not include wave-based sound propagation effects on tonal content, which can influence the perceived impact. There is a common misconception that ISO 9613 is "3D" modelling, as the model appears to have three dimensions. However, it is described as "2.5 D" [12], as it treats the height dimension differently to the horizontal plane .
For commercial installations, particularly those mounted on rooftops, ISO 9613-2 presents additional challenges. Rooftop installations often involve multiple units in close proximity, making it crucial to accurately model their cumulative impact. The typical lack of information about source directivity means that the manner of modelling the ASHP can become critical for determining barrier heights, for example.

4. SOUND IMPACT ASSESSMENT

The sound impact from a development is considered within the planning regime as part of the assessment of its environmental impact. In England this is guided by the National Planning Policy Framework (NPPF) [13]. The NPPF emphasises the need to avoid noise giving rise to significant adverse impacts on health and quality of life, and minimising any adverse effects. Further government guidance on noise is provided on the Planning Practice Guidance website [14].
The most common way that planning authorities assess noise impacts from building services plant is by applying British Standard BS 4142: 2019, "Methods for rating and assessing industrial and commercial sound." [2]. This

standard provides a method for calculating a rating level that can be compared to background sound levels to determine the likely significance of the impact, depending on the context. Historically, the application of BS 4142 has been subject to varying interpretations. To address this and promote consistency, the Association of Noise Consultants (ANC) published additional guidance in the form of a Technical Note to BS 4142:2014+A1:2019. [15].

If the planning regime fails to sufficiently protect people from noise, there is statutory nuisance legislation that can be invoked under Part III of the Environmental Protection Act 1990 (EPA) [16]. A local authority has a legal obligation to investigate noise nuisance complaints under the EPA. This duty is entirely separate from its function as a planning authority, although in practice, the same environmental health or public protection officers within the local authority often handle both planning applications and nuisance complaints. In addition to complaining to the local authority, aggrieved parties can also take legal action through the courts based on private nuisance.

Under statutory nuisance legislation, there are no fixed noise levels that automatically constitute a nuisance. Instead, the judgement is made based on whether the noise is "unreasonable". Factors considered include the duration, frequency, loudness, and character of the noise, as well as the time of day and local context.

Planning seeks to achieve a high level of amenity for communities; sound impacts should be well below the threshold for a noise to be considered a statutory nuisance. Compliance with BS 4142 is typically used by local planning authorities to not just prevent a statutory nuisance, but in order to protect local amenity and quality of life.

4.1 MCS 020 assessment

The MCS 020 calculation includes a much-simplified sound propagation model, and has a fixed absolute impact limit of 37 dBA based on the declared (ErP) ASHP sound power level. This simple criterion takes no account of sound character such as tonality or low frequency content, and any intermittency during different phases of operation (e.g. during defrosting). The standard was developed specifically for domestic installations under Permitted Development Rights (PDR).

4.2 BS 4142 assessment

BS 4142 describes a process for assessing the impact of industrial or commercial sound at a receptor location – it is not designed to be used for prediction of future sound sources, although this is a common application. It is frequently used for assessment of domestic installations, despite its title "..assessment of industrial or commercial sound", suggesting that a domestic installation would fall outside of its scope.

4.2.1 Background sound levels

For new residential developments, particularly if comprising many dwellings, background levels must be predicted rather than measured. There is little experience within the acoustics industry of predicting background sound levels in new residential developments that may themselves have a significant impact on the background sound environment, for example.

In locations with low background sound levels (e.g. below 30 – 35 dBA), achieving rating levels below background may preclude viable installations, which may not be necessary to preserve quality of life for residents.

According to the National Noise Incidence Study, the percentage of dwellings exposed to background, $L_{A90,\ T}$ levels above 40 dBA is:

- 20 % of dwellings at night ($L_{A90,\ 8\ hr}$)
- 70 % of dwellings during the day ($L_{A90,\ 16\ hr}$)

In Scotland, many local authorities specify absolute limits for plant noise impact, typically adopting thresholds of NR 35 for daytime operation, and NR 25 for nighttime, internally, with open windows. It is standard practice to assume a 10 dB attenuation through the open windows, which means levels of (approximately) NR 45 daytime and NR 35 nighttime externally. NR 35 is likely to be marginally higher than 37 dBA, depending on the frequency content. This approach is not common in England, but can expedite an assessment and reduce its cost burden by omitting the background sound survey. Where the ambient sound environment is louder, and a higher sound impact may be acceptable, a dual approach can enable those assessments that benefit from a more nuanced assessment to proceed without excessive, unnecessary mitigation.

4.2.2 Character corrections

BS 4142 contains detailed guidance on decibel penalties that may be attributed to the character of sound at a receptor location – see section 2, characterisation of the sound source, for discussion of the challenges in predicting character corrections at the design stage.

In practice the background is not stationery in either time or space around a receptor location, which can make assigning character corrections contentious where sounds exist, and a challenging task at the design stage.

4.2.3 Commercial installation considerations

For commercial installation, night-time operation usually drives the acoustic design due to lower environmental background sound levels. Although buildings may only be occupied during daytime hours, frost protection operation or building pre-heating may occur during normally quiet periods of the night. The cumulative impact of multiple units may need appropriate assessment.

4.2.4 Rating level thresholds

Currently local authorities take various approaches to setting sound impact limits relative to background sound levels: some permit rating levels 5 dB above background, while others require the rating level to be 10 dB below background, although meeting the background sound level is more common. The more stringent limits are likely to be a significant obstacle to the roll-out of ASHPs.

5. PRAGMATIC APPLICATION OF ASSESSMENT METHODS

We propose a hierarchical, risk-based framework for assessment that could streamline the planning process while maintaining acoustic protection. A standardised, industry-accepted approach could itself reduce costs and risks associated with proposed installations.

5.1 Step 1: Enable a fixed level threshold for planning

Where an installation requiring planning permission can demonstrate compliance with the 37 dBA threshold from MCS 020, this could be considered sufficient evidence of acceptable acoustic impact. This approach could significantly reduce assessment costs for domestic installations that fall outside permitted development, as well as non-domestic installations that are low-risk due to the low sound level impact. The approach of using fixed threshold levels is proven to be successful across Scotland and much of Europe, where daytime thresholds are generally significantly higher than 37 dBA.

5.2 Step 2: Allow the MCS 020 sound propagation model

To minimise the cost of the acoustic assessment, the simplest assessment of sound transmission is embodied in the MCS 020 sound transmission model. Where an assessment uses the MCS 020 sound transmission model and threshold, it is compliant with PDR requirements. Although there is currently nothing preventing planning authorities from approving this method for planning applications, it could be positively affirmed as being sufficient, given its demonstrated prudence in comparison with more detailing sound propagation modelling.

5.3 Step 3: Permit more detailed sound propagation assessment

Where a simple sound transmission model indicates a marginal failure to comply with the identified criterion, permitting more detailed modelling of sound propagation would be appropriate. However, there are a variety of models, and many model parameters that practitioners may consider to various extents. It is suggested that industry-standard guidelines for modelling ASHP sound propagation with ISO 9613-2 are developed by consensus, to help achieve consistency.
This route could avoid the additional resources associated with a background sound survey while benefiting from more sophisticated treatment of barriers and reflecting surfaces.

5.4 Step 4: Predetermine higher thresholds in higher background sound environments

Where background sound levels are higher, it can be unnecessary to mitigate the sound impact to the threshold level that is considered suitable everywhere – i.e. a higher impact can be acceptable according to BS 4142.
A consensus on rating level margins could expedite assessments and reduce risks and delays with a process of agreeing rating level thresholds compared with background sound levels on a case-by-case basis, as can happen currently.
A BS 4142 assessment also requires an assessment of tonality, intermittency, impulsiveness, and any other features that may attract a rating penalty. In the absence of this information at design stage, a consensus could be developed to agree rating penalties for these features.

5.5 Step 5: Full BS 4142 assessment

Beyond the features of step 4, a full BS 4142 assessment also includes consideration of context, on a case by case basis. Although practitioners regularly carrying out these assessments, there is no assurance of consistency; consultants working for developers and public protection officers may take different views of appropriate penalties between each other as well as amongst themselves. This is the current state for all assessments that fall outside the scope of MCS 020 and PDR.

6. FURTHER OPPORTUNITIES TO FACILITATE ASHP ROLLOUT, AND FURTHER WORK

6.1 Enable further acoustic assessment options under PDR

The first four steps of assessment could be adopted in MCS 020. This could enable some of those properties that currently marginally fail the "noise test" (i.e. just fail to comply with the current scope of MCS 020) to benefit from a more detailed acoustic evaluation, while still avoiding a full planning application. A more detailed assessment would need to be undertaken by a suitably competent person; while MCS 020 is designed to be undertaken by an installer with no specialist acoustics knowledge, a more nuanced a sophisticated assessment would require commensurate accountability, which would be based on a greater level of expertise and experience. It would be prudent to investigate the real-world evidence base discussed below first, to help establish the case for this option.

6.2 Extend PDR

Currently PDR apply to domestic installations only, where there may be a maximum of two units per dwelling. Permitted development rights could be extended to non-domestic properties, with prior approval being required if necessary as a safeguard against potential adverse effects from cumulative impact, for example. This could reduce the planning barriers to ASHP uptake.

6.3 Daytime / Night-time thresholds

The single threshold in the UK that applies at all times of day and night is similar to the nighttime limit in other European countries, where a higher daytime limit is also used. It is standard practice in some European countries to design to different daytime and nighttime sound level thresholds, and to use a reduced sound power mode at night if this is necessary for acoustic compliance.

Discussions with installers during recent research indicated little appetite for this approach, in part amid concerns that residents may adjust the settings on their appliances. Currently installers need not waste time with sites that present challenges, but for wider roll out the more acoustically challenging sites will also need solutions. Enabling higher sound levels during the daytime is one option that could facilitate installations for sites that might otherwise be problematic, and accepting quiet mode operation with associated drop in thermal performance at nighttime.

6.4 Real world evidence base

Currently there appear to be relatively few noise complaints compared with the numbers of installations. However, there is little information about real-world sound impact from installations that are designed with the MCS 020 method. Building further confidence in this approach, and considering potential changes to the threshold levels requires systematic post-installation studies comparing predicted and measured levels, alongside documentation of planning outcomes where MCS compliance has been used as evidence.

Field measurements comparing predicted and actual sound levels are needed to validate both MCS 020 and ISO 9613 predictions. These studies should also examine real installations across different mounting arrangements, particularly investigating the effectiveness of different barriers and the influence of reflecting planes, and the potential effectiveness of sound absorption on nearby surfaces. This also requires a methodology for measuring the sound of an ASHP installation in-situ, which is not a simple task.

This evidence base would help to determine if the current threshold is appropriate, too permissive or too restrictive, and could support a future revision.

6.5 Cumulative impact considerations

Previous research [17] has investigated the potential for cumulative sound impact from multiple domestic ASHPs in high-density residential areas. The study focused on worst-case scenarios in terraced and semi-detached housing, representing the majority of the UK's housing stock. Even under conservative assumptions with all units operating simultaneously at maximum permissible MCS sound levels, the increase in overall sound levels was found to be modest. The cumulative effect typically resulted in increases of up to 2-3 dB at dwelling facades compared to a single unit, with larger increases occurring in garden areas and places where absolute levels remained low.

These findings have important implications for our proposed assessment framework. Where a Step 1 assessment demonstrates compliance for individual installations, cumulative impact is unlikely to be significant even in high-density deployments. Therefore planning conditions requiring the impact to be many decibels below the background, to prevent cumulative impact, are considered unnecessary, and could hinder the roll-out of ASHPs.

7. CONCLUSIONS

The evidence presented strongly supports adopting a proportionate framework for ASHP acoustic assessment. Using MCS 020 as an initial screening tool, with options for detailed modelling in borderline cases, or assessment against a higher background sound level, could significantly reduce obstacles to installation while maintaining appropriate acoustic protection. Success relies on planning authorities agreeing clear guidance on:

- Criteria for selecting appropriate assessment steps
- Documentation requirements proportionate to installation complexity
- Treatment of cumulative impacts
- Standardised approaches to character corrections where detailed data is unavailable

The evidence from the further work proposed would help refine assessment methodologies and support wider adoption of ASHPs whilst maintaining appropriate acoustic protection. This is particularly important as the scale of heat pump deployment increases to meet decarbonisation targets. Implementing this risk-based framework would remove unnecessary barriers to heat pump adoption while ensuring communities remain protected from inappropriate noise impacts.

8. ACKNOWLEDGEMENTS

No financial assistance was given to create this paper; the work is supported by Apex Acoustics Ltd, to enable this activity. We are grateful to the contributions from our many collaborators.

9. REFERENCES

[1] MCS Charitable Foundation, Microgeneration Installation Standard: MCS 020 Version 1.3 (2019)

[2] BS 4142: 2014 + A1: 2019, Methods for rating and assessing industrial and commercial sound

[3] Harvie-Clark, J; Dobinson, N; *et al*, Planning for Sound from ASHPs: Options, Risks and Opportunities, Proc. IOA Vol 46. Pt 2. 2024.

[4] BS ISO 9613-2, Acoustics — Attenuation of sound during propagation outdoors. Part 2: Engineering method for the prediction of sound pressure levels outdoors.

[5] European Directive 813/2013

[6] German heat pump association online calculator, available: www.waermepumpe.de/schallrechner/

[7] DIN 45681:2005-03 Acoustics - Determination of tonal components of noise and determination of a tone adjustment for the assessment of noise immissions

[8] Torjussen, M; Harvie-Clark, J; *et al*, Noise from ASHPs – What Do We Know? Proc. IOA Vol. 45 Pt. 3. 2023

[9] Torjussen, M *et al*. Predicting BS 4142 Character Corrections at the Planning Stage. Proc. IOA Vol 45. Pt. 3. 2023

[10] Stürenburg, L; Braren, H; *et al*. Recordings of an Air-to-Water Heat Pump. Institute for Hearing Technology and Acoustics, RWTH Aachen University, Germany. September 2024.

[11] Editor Reichl, C; Acoustic Signatures of Heat Pumps, Final Report –Technology Collaboration Programme on Heat Pumping Technologies (HPT TCP), Annex 51.

[12] W, Wei; Harvie-Clark, J; *et al*, Predicting Sound Levels Behind Buildings - How Many Reflections Should I Use? Proc. IOA Vol. 37. Pt. 2. 2015

[13] National Planning Policy Framework (NPPF), .gov.uk, December 2023

[14] Planning Practice Guidance -Noise, .gov.uk, July 2019

[15] Technical Note to BS 4142:2014+A1:2019, Association of Noise Consultants, March 2020

[16] Environmental Protection Act 1990, Part III. Statutory nuisances

[17] Hill, J; Harvie-Clark, J. ASHP cumulative noise impact – noise modelling study. Report 11520.3D, 30th July 2024, Apex Acoustics Ltd. Available from NESTA.

DOI:

Main theme: A03 Building Acoustics

Session A03.12 Ventilation noise in dwellings: challenges, measurements, and solutions

Chair(s): J. Harvie-Clark, C. Reichl, G. Fusaro

DOI: 10.61782/fa.2025.0763

FORUM ACUSTICUM EURONOISE 2025

SCALABILITY OF VENTILATION AND NOISE INSULATION METHODS FOR ASSESSING A FULL-SCALE METAWINDOW

Gioia Fusaro[1*] **Luca Barbaresi**[1] **Massimo Garai**[1]
[1] Department of Industrial Engineering, University of Bologna, Italy

ABSTRACT

Natural ventilation in homes often compromises indoor acoustic comfort by allowing outdoor noise to enter. Recent advancements in acoustic metamaterials (AMMs) have enabled the development of innovative solutions, such as integrating AMMs into windows, to provide effective natural ventilation while maintaining sound insulation. However, European standards for evaluating façade insulation properties primarily focus on closed systems, limiting their applicability to AMM-based windows (AMWs). This study addresses this gap by using the ISO 10140 measurement method to evaluate a full-scale acoustic metawindow (AMW) capable of simultaneous noise insulation and ventilation when open. The sound reduction index (R) was used to measure its noise insulation performance, showing an R in between 13 and 34 dB in the 100-3150 Hz frequency range combined with a more elevated flow rate than the AMW unit. Indeed, additionally, laboratory tests on airflow performance (adapted ISO 9972) across a pressure range of 10-80 Pa demonstrated that the metamaterial acoustic filter does not significantly affect airflow, making this solution versatile and practical. These findings underscore the potential of the AMW for multi-domain comfort with a more sustainable approach and scalable technology.

Keywords: *Acoustic metamaterials, Outdoor noise, Ventilation, Indoor Environmental Comfort, Environmental noise.*

[*] ***Corresponding author***: *gioia.fusaro@unibo.it*
Copyright: *©2025 First author et al. This is an open-access article distributed under the terms of the Creative Commons Attribution 3.0 Unported License, which permits unrestricted use, distribution, and reproduction in any medium, provided the original author and source are credited.*

1. INTRODUCTION

Traditionally, sound insulation and façade ventilation in buildings have been managed separately [1]. Standard windows allow for natural ventilation and an outside view but force users to choose between noise control and airflow, affecting overall Indoor Environmental Quality (IEQ) [2]. Researchers have explored various solutions, such as mechanical ventilation and passive or active noise control systems [3–5]. Passive approaches, like microperforated panels (MPPs) and acoustic metamaterials (AMMs), are particularly advantageous because they require minimal energy and can be integrated into windows, enhancing durability [2].

Acoustic metamaterials used for noise and ventilation management are typically duct-like structures with embedded resonant elements, such as metasurfaces, metamaterial cages, and labyrinthine designs [2]. Originally developed for mechanical applications, such as soundproofing in engines, these structures are now being adapted for building use. However, there are three key challenges in developing metamaterial-based ventilated soundproof windows [2,6]: i) the need for scalable metamaterial modules, ii) a consistent multi-physical analysis approach that aligns both numerical and experimental results, and iii) the absence of standardised methods for assessing sound insulation in open windows.

More details can be found in the comprehensive paper [7].

For these reasons, a numerical and experimental study was run respectively for assessing the acoustic and the ventilation performance of an AMM-based window (AMW) at its full scale (0.8x1.2 m). Previously, an AMW unit was developed and assessed, but its dimensions were relatively small (0.4x0.4 m). This new prototype allows to prove the scalability of the AMM technology towards a more ergonomic and user-friendly design. FEM models were modelled to represent the experimental boundary conditions. ISO 10140 configuration was used to experimentally assess the acoustic performance in a diffuse sound field [6,8–10], while the ISO 9972 [31]) evaluates the ventilation capacity.

2. METHOD

The methodology follows the approach in [3], combining numerical and experimental techniques to assess the Acoustic Metawindow (AMW). First, the Finite Element Method (FEM) is used to simulate measurement configurations and validate the numerical model against laboratory boundary conditions, including source positioning, direction, and edge effects. Then, an experimental method is applied: the ISO 10140 test in a diffuse sound field [6,8–10] to measure the sound reduction index for the prototype (R_w). Additionally, the blower door test (ISO 9972 [31]) evaluates the ventilation capacity while maintaining acoustic insulation.

The AMW prototype measures 0.8 × 1.2 × 0.17 m and integrates an Acoustic Metamaterial (AMM) system within its frame. Key acoustic parameters—specific impedance ($Z_{1,2}$) and refractive index ($n_{1,2}$)—are considered for different regions of the AMW. Variations in the refractive index create an out-of-phase effect on sound waves passing through the AMM unit cell, independent of the angle of incidence. The prototype consists of 5-mm thick laser-cut plexiglass panels for the indoor and outdoor surfaces, with AMM unit cells 3D-printed in polylactic acid (PLA) using fused deposition modeling (FDM). The AMW slides within the wall, allowing two configurations: fully open (duct opening of 0.075 × 0.13 m) and half-open (0.075 × 0.06 m). Before experiments, FEM analysis is performed to optimize the test setup.

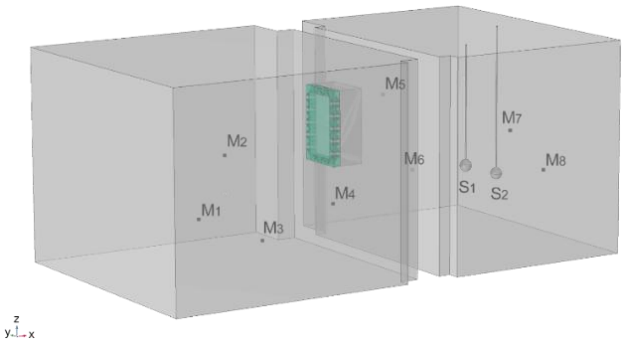


Figure 1. Numerical model of the coupled chambers test setup. S1 and S2 are the two omnidirectional sources, while M1- M8 represent one of the two microphones' positions.

Following ISO 10140, the specimen is installed in a partition between two coupled reverberation rooms to assess airborne sound insulation. ISO 10140-1 [8] defines the test element, while ISO 10140-2 [6] describes the façade opening. A sound source in one room generates noise, and sound pressure levels are recorded in both the source and receiving rooms. Sealant ensures airtightness around the structural window edges.

To address the challenges of having a coherent numerical model, a study was conducted using simulations with the Finite Element Method (FEM). The numerical model is characterised by an air density of 1.215 kg/m³ and a sound speed in air of 343 m/s at 20°C. A 1 Pa sound wave was directed at the test specimen using two omnidirectional sound sources (S1 and S2) across a frequency range of 100-5000 Hz. The simulation replicated two connected reverberation rooms (116 m³ total volume), separated by a 0.4 m partition containing the AMW test sample. The setup involved a coupled room geometrical configuration with a hole in the dividing wall of dimension 0.8x1.2 m. This hole represents the configuration without the AMW, while in the other configuration investigated in this study, the AMW would be placed instead. The receivers of the numerical analysis were placed at multiple points following the indications of to ISO 10140 [6] to calculate sound insertion loss. The sound insulation performance was determined using insertion loss (IL), calculated as:

$$IL_{AMW} = SPL_{noAMW} - SPL_{AMW}\ (dB) \qquad (1)$$

Where SPL_{noAMW} and SPL_{AMW} are respectively the average of SPL measured in the numerical model without and with the AMW unit.

Additionally, a numerical ventilation analysis was conducted using FEM with the k-ε turbulence model to evaluate pressure drop (ΔP) at different airflow velocities (0.5–1.132 m/s). The inlet surface, which represents the outdoor conditions, is used to define the flow, with the maximum wind velocity set according to Asfour and Gadi's criteria [11], based on a height of 20 m above the ground and a room height of 3 m. The model assumed no-slip conditions in a 3D air-filled domain, focusing on natural ventilation at low Mach numbers to reduce noise interference. The outlet pressure was set at 101.325 Pa, with refined meshing in turbulence-prone regions. A stationary solver performed CFD analysis based on pressure and velocity components. The geometric boundaries are the same as the acoustic FEM model, consistent with the 3 m room height assumption in the Asfour and Gadi criteria [11]. For the mesh size in this 3D study, the maximum element size is 0.115 m, and the minimum element size is 0.0144 m, with finer mesh in regions expected to experience turbulence, particularly near corners within the AMW structure. The study is performed using a stationary solver, with the CFD analysis depending on pressure (p) and velocity (u, and velocity components u,

v, and w). To analyse the flow velocity (v) the parameter was assessed as the average throughout the openings on the AMW. The pressure difference defining different flow rates per person was calculated considering the area of the receiving room (20 m²) able to host a maximum of three occupants. The flow rate per person was determined by the Blower Door Test method, which is pre-set by default to a Δp value for three people in the same room, with a gradual gradient from q10 to q80 (ISO 9972) [12].

3. RESULTS

3.1 Acoustic results

The comparison between experimental and numerical IL values in Figure 2 shows a reasonable agreement in the general trend, with both datasets capturing the main characteristics of the AMW's acoustic performance. However, some discrepancies are noticeable, particularly in the frequency range between 200 and 500 Hz. The numerical IL curve underestimates the experimental IL at certain frequencies and overestimates it at others, possibly due to model assumptions. One key factor could be the rigid wall assumption in the numerical model, which does not account for real-world material absorption and edge diffraction effects. Additionally, the sound field conditions in the experimental setup may differ slightly from the idealised conditions assumed in the FEM simulation, contributing to observed deviations. Improving the numerical model by incorporating realistic boundary conditions and absorption properties could enhance accuracy.

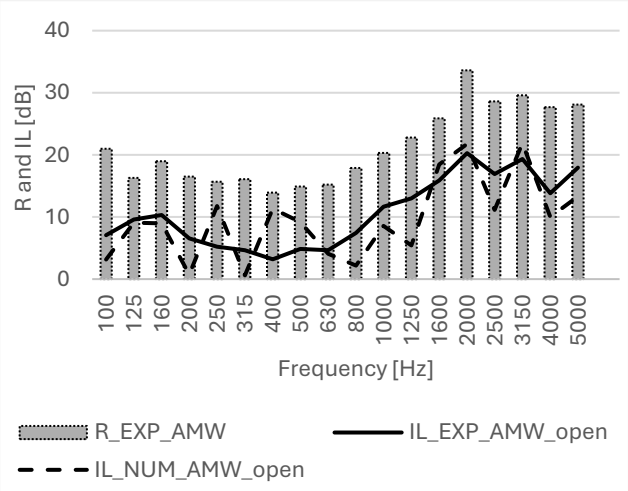


Figure 2. Comparison of the IL in a diffuse sound field calculated experimentally and numerically by subtracting a) the SPL with the fully open AMW from b) the SPL without the AMW in the wall opening.

R values on the other hand, result capturing the noise reduction index in a more realistic indoor acoustic setup.

3.2 CFD results

Building on a previous study [3], numerical analysis in the ventilation domain was carried out using computational fluid dynamics (CFD). The flow velocity and flow rate comparisons between experimental and numerical results in Figure 3 exhibit good agreement, with numerical results generally following the same trend as the experimental data. However, numerical results tend to slightly overpredict airflow velocity and flow rate, particularly at higher flow rates per person (q50 and q80). This discrepancy may be attributed to the k-ε turbulence model's limitations, particularly in capturing near-wall viscous effects and small-scale flow structures. Despite these minor differences, the overall similarity between the experimental and numerical results validates the CFD model's effectiveness in capturing airflow characteristics. Compared to the previous AMW unit model, the flow rate performance of the scaled AMW is higher (see Figure 3) while keeping a perceivable noise attenuation.

While both numerical and experimental analyses show similar trends, refinements in boundary conditions, material properties, and turbulence modeling could improve accuracy, particularly for the IL calculation in the low-frequency range and the airflow simulation at higher velocities. Future work should consider incorporating more complex wall absorption characteristics and refining turbulence models to better represent real-world airflow conditions.

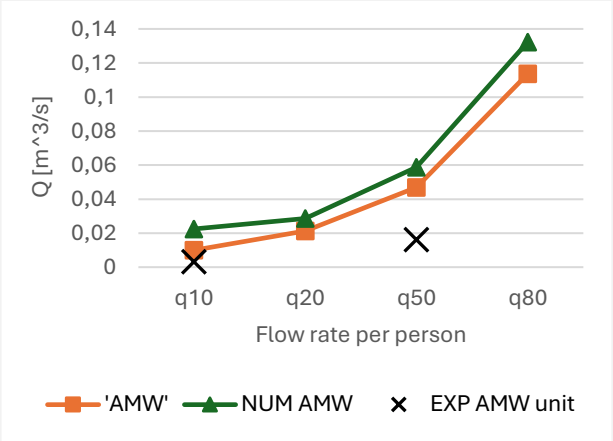


Figure 3. Comparison of different airflow rates of the AMW from Experimental and Numerical analysis.

4. CONCLUSIONS

This study demonstrates the potential of Acoustic Metawindows (AMWs) to provide both effective natural ventilation and significant noise insulation through a scalable technology and a sustainable design. Through a combination of experimental and numerical analyses, the AMW achieved an IL of 23 dB and R of 34 dB in the 100–3150 Hz range. Additionally, airflow testing confirmed that the integrated acoustic metamaterial does not significantly impede ventilation, ensuring a balance between acoustic and indoor environmental comfort. Moreover, the flowrate performance of the scaled-up AMW model is improved compared to unit one.

Numerical simulations using the Finite Element Method (FEM) and Computational Fluid Dynamics (CFD) largely aligned with experimental results, validating the modelling approach. However, minor discrepancies in low-frequency sound insulation and airflow predictions highlight the need for further refinement in boundary conditions, material properties, and turbulence modeling.

The findings underscore the viability of AMWs as a scalable, energy-efficient solution for sustainable building design. Future work should focus on optimizing material properties, refining numerical models, and exploring long-term durability in real-world applications. The integration of standardized testing methods for open-window configurations will be crucial in advancing the adoption of AMW technology in building acoustics and ventilation strategies.

5. ACKNOWLEDGMENTS

This research was funded by the Italian Ministry of University and Research, within the project PRIN 2022, Grant No. 2022RA785R: “METAWAVE - New METAmaterial Window for simultaneous Acoustic, Ventilation and Energy performance”.



6. REFERENCES

[1] J. Harvie-Clark, A. Chilton, N. Conlan, D. Trew, Assessing noise with provisions for ventilation and overheating in dwellings, J. Build. Serv. Eng. Res. Technol. 40 (2019) 263–273. https://doi.org/10.1177/0143624418824232.

[2] C. Rubino, S. Liuzzi, G. Fusaro, F. Martellotta, C. Scrosati, M. Garai, Balancing ventilation and sound insulation in windows by means of metamaterials A review of the state of art.pdf, Build. Environ. 275 (2025). https://doi.org/https://doi.org/10.1016/j.buildenv.2025.112780.

[3] G. Fusaro, L. Barbaresi, P. Guidorzi, M. Garai, Investigation of the sound insulation and natural ventilation performance of a metamaterial-based open window, Build. Environ. 266 (2024) 112140. https://doi.org/10.1016/j.buildenv.2024.112140.

[4] G. Fusaro, S. D’Auria, D. D’Orazio, Multiphysical numerical analysis for acoustic metamaterials in ventilated ducts, in: Internoise 2023, Chiba, Japan, 2023: pp. 7–8. https://doi.org/https://doi.org/10.3397/IN_2023_0699.

[5] B. Lam, C. Shi, D. Shi, W.S. Gan, Active control of sound through full-sized open windows, Build. Environ. 141 (2018) 16–27. https://doi.org/https://doi.org/10.1016/j.buildenv.2018.05.042.

[6] ISO 10140-2 : 2021 Acoustics – Laboratory measurement of sound insulation of building elements, Measurement of airborne sound insulation, 2021.

[7] G. Fusaro, L. Barbaresi, M. Garai, Experimental validation of a full-scale acoustic metamaterial-based window a multi-domain approach, Build. Environ. (n.d.).

[8] ISO 10140-1 : 2021 Acoustics – Laboratory measurement of sound insulation of building elements, Application rules for specific products, 2021.

[9] ISO 10140-4 : 2021 Acoustics – Laboratory measurement of sound insulation of building elements, Measurement procedures and requirements, 2021.

[10] ISO 10140-5 : 2021 Acoustics – Laboratory measurement of sound insulation of building elements, Requirements for test facilities and equipment, 2021.

[11] O.S. Asfour, M.B. Gadi, A comparison between CFD and Network models for predicting wind-driven ventilation in buildings, Build. Environ. 42 (2007) 4079–4085. https://doi.org/10.1016/j.buildenv.2006.11.021.

[12] EN ISO 9972 : 2015, Thermal performance of buildings — Determination of air permeability of buildings — Fan pressurization method, 2015.

DOI: 10.61782/fa.2025.0771

FORUM ACUSTICUM EURONOISE 2025

A SILENCER DESIGN FOR A MECHANICAL HEAT RECOVERY UNIT

Darragh Mullally[1*] **John Kennedy**[1]
[1] Department of Mechanical and Manufacturing Engineering, Trinity College Dublin, Ireland

ABSTRACT

Modern homes require energy efficient airtight designs using controlled ventilation systems to retain the heat energy. Mechanical Ventilation Heat Recovery (MVHR) units help to maintain air circulation between the building and the outdoors, while not compromising energy efficiency. A significant challenge to implementation and continuous use of these devices is the noise emission. Noise from MVHRs can cause indoor noise levels to exceed the recommended levels, with respect to the Noise Rating (NR) guidelines. The noise has a frequency content below 500 Hz, which many conventional sound absorbers struggle to attenuate without large space requirements. This research develops a compact silencer suitable for a domestic MVHR unit with a large duct diameter. The design consists of stacked Helmholtz resonators with embedded necks and relatively large cavity volumes. The proposed design achieved >8dB transmission loss for frequencies 250 Hz, 300 Hz and 350 Hz. These were compared with data from an MVHR and the NR guideline and was found to reduce the MVHR SPL to below NR35 for the octave bands 250 Hz and 500 Hz.

Keywords: Transmission Loss, MVHR, Helmholtz Resonators, 3D Printing

1. INTRODUCTION

Mechanical Ventilation and Heat Recovery systems (MVHR) are devices that ventilate rooms and buildings, while recovering heat energy from outgoing air. In modern homes that are highly insulated and airtight, this technology is essential to maintain good indoor air quality [1]. The main challenge to further adoption and continuous use of MVHR are the noise emissions from the fans. It has been reported that a significant portion of MVHR users either rarely or never use their systems and cite noise as the cause [2, 3]. The noise emissions typically exist below 500 Hz [2, 4]. Some manufacturers provide noise emission data on their systems, for example the unit considered in this work is the Air Cycle 1.3+, which has a reported sound power level of 45.4 dB and 46.8 dB at 250 Hz and 500 Hz respectively [5]. Data were taken at the maximum possible flow rate for the unit. With regards to guidelines, the Noise Rating standard for dwellings should be within NR35. Other guidelines suggest a lower SPL for dwellings [6]. In residential buildings, research indicates that due to relatively lower background noise, noise from ventilation systems is more noticeable [2, 3].

There are many ways to address the noise emissions of MVHRs, either at the source (fan blades, DC motor) or applying an acoustic treatment downstream from the source. Suitable designs from literature used to achieve low frequency attenuation in ventilated systems include space-coiled channels [7], singular or double Helmholtz resonators [8, 9] and adaptive resonators [10]. MVHRs available on the market typically have duct diameters >5 inches (127 mm) [5], which is much larger than the experiment setups seen in the cited works. Further more, while research has been done to study the effects of flow on transmission loss [11], no work has been found on application in real MVHR systems.

In this paper, an acoustic treatment for a large circular duct is proposed. The design utilizes Helmholtz resonators with embedded necks, and can be manufactured with a desktop 3D printer at a low cost. The objective is to achieve high attenuate at specific frequencies with minimal resources. Hence, a basic analytical approach is taken for the design rather than a detailed FEM combined with an optimisation scheme.

*__Corresponding author__: mullalda@tcd.ie.
__Copyright__: ©2025 Darragh Mullally et al. This is an open-access article distributed under the terms of the Creative Commons Attribution 3.0 Unported License, which permits unrestricted use, distribution, and reproduction in any medium, provided the original author and source are credited.

2. THEORY

The goal of the design is to attenuate the tonal noise of the fan at specified frequencies, which are characteristic of the blade pass frequency. The resonance frequency of a Helmholtz resonator is expressed as:

$$f_0 = \frac{c_0}{2\pi}\sqrt{\frac{S_n}{V(l_n+\delta)}} \tag{1}$$

Where c_0 is the speed of sound in air, S_n is the area of the neck cross section, V is the volume of the cavity, l_n is the neck length and δ is the end correction length. The many different formulations of the δ exist in the literature, mainly for resonators with cylindrical cavities. For a cylindrical neck and cuboid cavity, Catapane *et al* derived an expression for the end correction length [12]. Given in Eq 2 , where $\xi = 2r_n/d_c$, d_c is the cavity width.

$$\delta = (-5.98\xi^3 + 14.8\xi^2 - 9.75\xi + 3.60)l_n\xi \tag{2}$$

Solving Eq 1 for a resonance at 300 Hz and a cavity volume of 125000 mm^3 yields different combinations of r_n and l_n (neck radius and length). The chosen values are list in Table 1. Although there are more sophisticated methods to maximize the magnitude and bandwidth of the transmission loss, the low cost of this design approach may be more relevant for industrial settings. The drawback to this analytical approach is that while target frequencies can be easily attained there, the expected transmission loss is not estimated. A parametric investigation of 3D printed structures allows for empirical refinement of the design at low cost.

3. EXPERIMENTAL SETUP

The transmission loss experiment setup is shown in Fig 1 in accordance with ASTM E2611-09, using the two-load method. The loudspeaker has a frequency range of 10 Hz - 1400 Hz, and is enclosed in a foam filled box. Four GRAS 40PL-10 microphones were used, they have a frequency range of 50 Hz - 5000 Hz (±1.5dB). The microphones were connected to a National Instruments USB-4431 analogue I/O device.

The setup is designed for large samples with an inner radius of 63.5 mm, with mounting screws 106 mm from the centre. This leaves 42.5 mm of width for the acoustic treatment. For every sample and configuration, the tests were performed 3 times to test the repeatability of the results. The frequency resolution of the calculated spectra

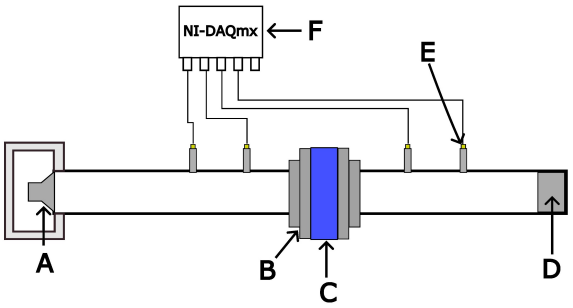


Figure 1. Experiment Setup. (A) Enclosed Loudspeaker, (B) Gaskets, (C) Sample, (D) Anechoic Termination, (E) Microphones, (F) Data Acquisition System

was 2.4 Hz, with a sampling rate of 40 kHz. The measurement duration was 30 seconds, then the termination is changed, and another 30 second measurement was taken. Each of the resonator rings described in Section 4 were tested alone before being stacked together for broadband attenuation.

4. DESIGN AND MANUFACTURING

The goal of the resonator is to attenuate transmission noise while being compact and sub wavelength. Since the operating frequencies are between 250 Hz - 350 Hz, the sub-wavelength constraint is easily satisfied. For compactness, the overall thickness was arbitrarily constrained to 40 mm which was considered representative of a real system. Eq 1 was solved for the specified frequencies, returning a set of radius and length values, given in Table 1. The length L is determined by the volume of the embedded neck in Eq 3, where W is the width of the resonator, S is the arc length and V_n is the volume of the neck, with the wall included. $R_1 = 63.5$mm and $R_2 = 100$mm

$$L = \frac{V_c + V_n}{WS} \tag{3}$$

The Helmholtz Resonator rings were manufactured with a Prusa i3 MK3 printer, using PLA filament and a 0.4 mm nozzle. The printer settings were as follows: 0.2 mm layer height, 205°C and 65°C nozzle and bed temperature respectively. The lower nozzle temperature helped to eliminate stringing while maintaining layer adhesion.

The resonators are asymmetric, this deviation from the model, where the neck and cavity are assumed to be

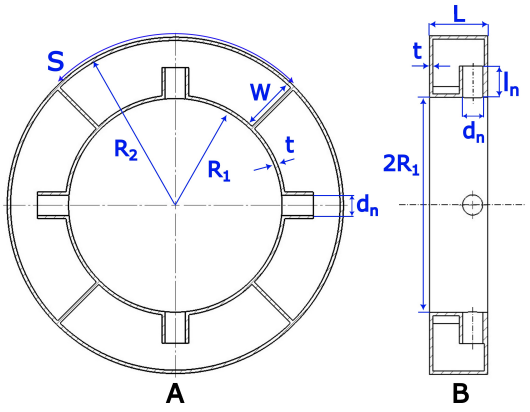


Figure 2. Cross section view of the 300 Hz ring, with dimensions provided in Table 1.

Frequency (Hz)	r_n	l_n	W	L	t
250	5.5	25.5	32.5	36.5	2
300	6	18.8	32.5	35	2
350	5.5	14	32.5	31.5	2

Table 1. Dimensions of resonator rings, dimensions are all in millimeters

concentric, was made to improve the manufacturability. In this configuration, there is no overhang underneath the neck (see Fig 2B), hence no internal supports are required. From the literature, the effect of the asymmetry on the transmission loss should be negligible [11]. The print time for each ring was 14h 30m, using 194 g of PLA, with an estimated cost of €3.8 per unit (estimated cost of PLA is €20/kg).

5. RESULTS AND DISCUSSION

Figure 3 shows the transmission loss of individual resonator rings, and the broadband attenuation when they are all stacked together in the transmission loss tube. The designs achieve transmission loss values at the target frequencies between 8dB and 11 dB. The transmission loss of the stacked configuration provides an increased transmission loss at 358 Hz, from 11 dB to 13 dB. The largest deviation between the calculated and measured resonance frequency is 4%, which is acceptable.

Applying this design to a real MVHR system will be the subject of future work. However the expected performance can be evaluated with a known MVHR and a comparison with the Noise Rating Curves. Provided that the tonal noise emission of the fan aligns with the chosen frequency values this design provides approximately 9 dB attenuation in each of the 250 Hz and 500 Hz octave bands. Figure 4 shows the curve for NR25 and NR35. The data available for the Air Cycle 1.3+ is used to calculate the total sound pressure level, direct plus reverberant, in a domestic bedroom. Reverberation time measurements were made in a domestic bedroom to accurately estimate the sound field in the room for a MVHR unit installed in one wall far from a corner or ceiling. It shows that without acoustic treatment, the SPL in the room would be unacceptable for a private dwelling. The noise reduction from the resonator ring is applied, using the experimentally determined values of 9 dB at 250 Hz and 500 Hz. The SPL reduces from 42 dB to 33 dB at 250 Hz. For 500 Hz, the SPL reduces from 44 dB to 35 dB. This means that the MVHR unit will not exceed the NR35 curve for the bedroom which may be deemed acceptable. The figure also shows that for further improvements additional attenuation will be required for the 1 kHz octave band. It is suggested that acoustic foam could be applied in combination with the designed resonator to provide this attenuation.

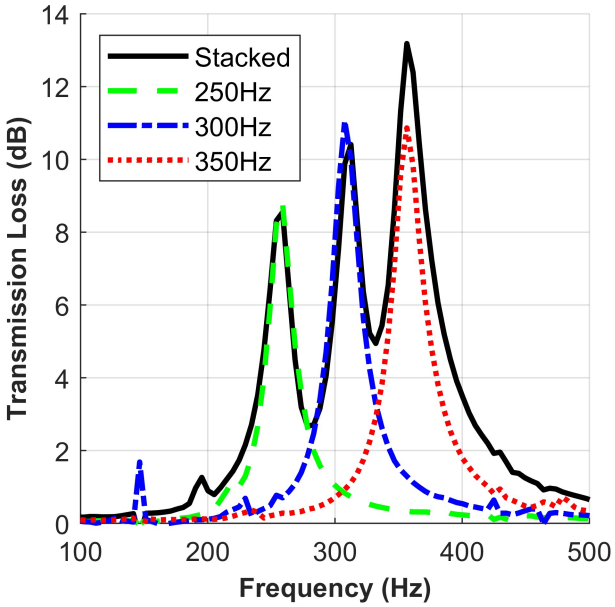


Figure 3. Broadband and tonal transmission loss with 3 resonator rings stacked together. Dashed lines represent individual performance

6. CONCLUSION

In this work, a 3D printed silencer for a circular duct MVHR was designed and tested. The design approach used basic analytical expressions for a Helmholtz resonator, to define the geometries. Three rings with four Helmholtz resonators with embedded necks were manufactured and tested for transmission loss in a 127 mm tube. The individual rings successfully achieved tonal transmission loss ranging from 8 to 13 dB. The maximum error between the target and measured resonance frequency was 4%, which is acceptable for this application. Applying the noise reduction to a MVHR unit in a domestic bedroom room would reduce the SPL below the NR35 curve, which is deemed acceptable. Future work will include applying the design to a real MVHR, by attenuating the measured noise from the system.

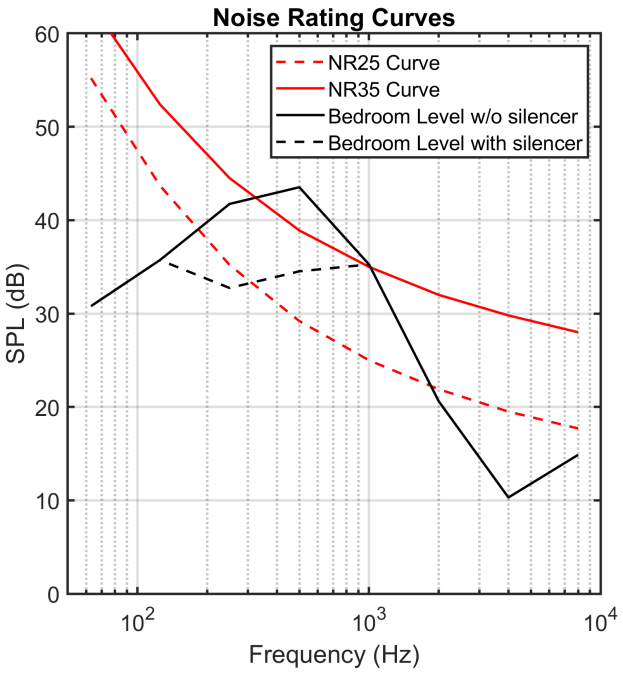


Figure 4. Noise Rating curves for bedroom with a AirCycle 1.3+ present

7. REFERENCES

[1] S. G. Howieson, A. Lawson, C. McSharry, G. Morris, E. McKenzie, and J. Jackson, "Domestic ventilation rates, indoor humidity and dust mite allergens: are our homes causing the asthma pandemic?," *Building Services Engineering Research and Technology*, vol. 24, pp. 137–147, Aug. 2003.

[2] M. Baborska-Narozny and F. Stevenson, "Mechanical ventilation in housing: understanding in-use issues," *Proceedings of the Institution of Civil Engineers - Engineering Sustainability*, vol. 170, pp. 33–46, Feb. 2017.

[3] J. Harvie-Clark, N. Conlan, W. Wei, and M. Siddall, "How loud is too loud? noise from domestic mechanical ventilation systems," *International Journal of Ventilation*, vol. 18, pp. 303–312, Oct. 2019.

[4] T. Carrascal García, A. Romero Fernández, and B. Casla Herguedas, "Applying Spanish Acoustic Regulations to mechanical ventilation with heat recovery systems. Case study.," *INTER-NOISE and NOISE-CON Congress and Conference Proceedings*, vol. 265, pp. 2271–2280, Feb. 2023.

[5] "AirCycle 1.3 Digital Range," product Brochure, Brookvent Ltd, 38-39 Fitzwilliam Square, Dublin 2 D02 NX53, Ireland, 2019.

[6] B. Rasmussen and M. Machimbarrena, "COST Action TU0901: Integrating and Harmonizing Sound Insulation Aspects in Sustainable Urban Housing Constructions," *European Cooperation of Science and Technology*, vol. Volume 1, 2014.

[7] S. Du, D. Zhang, X. Sun, X. Chen, and G. Zhang, "Model analysis and experiment study for effects of thermal viscous and fluid flow on ventilated acoustic metamaterials labyrinth," *Scientific Reports*, vol. 14, p. 27200, Nov. 2024. Publisher: Nature Publishing Group.

[8] C. Bricault, Y. Meng, and S. Goudé, "Optimization of a silencer design using an helmholtz resonators array in grazing incident waves for broadband noise reduction," *Applied Acoustics*, vol. 201, p. 109090, Dec. 2022.

[9] I. Han, I. Lee, and G. Yoon, "Studies on Dual Helmholtz Resonators and Asymmetric Waveguides for Ventilated Soundproofing," *Sensors*, vol. 24, p. 1432, Jan. 2024. Number: 5 Publisher: Multidisciplinary Digital Publishing Institute.

[10] S. J. Estève and M. E. Johnson, "Adaptive Helmholtz resonators and passive vibration absorbers for cylinder interior noise control," *Journal of Sound and Vibration*, vol. 288, pp. 1105–1130, Dec. 2005.

[11] Z. Lu, W. Pan, and Y. Guan, "Numerical studies of transmission loss performances of asymmetric Helmholtz resonators in the presence of a grazing flow," *Journal of Low Frequency Noise, Vibration and Active Control*, vol. 38, pp. 244–254, June 2019.

[12] G. Catapane, D. Magliacano, G. Petrone, A. Casaburo, F. Franco, and S. De Rosa, "Semi-analytical estimation of Helmholtz resonators' tuning frequency for scalable neck-cavity geometric couplings," *CEAS Aeronautical Journal*, vol. 13, pp. 797–808, July 2022.

DOI: 10.61782/fa.2025.0363

FORUM ACUSTICUM EURONOISE 2025

EVALUATION OF ACOUSTIC PERFORMANCE IN SMART VENTILATED WINDOWS WITH INTEGRATED HEAT STORAGE

Andrea Gerbotto[1*] **Louena Shtrepi**[1] **Fabio Favoino**[1] **Arianna Astolfi**[1]
[1] Department of Energy, Politecnico di Torino, Italy

ABSTRACT

Windows are essential façade components that balance multiple functions, including daylighting, natural ventilation, and thermal regulation. However, conventional windows often suffer from significant energy losses and inadequate air exchange, even with regular ventilation. To address these challenges, the iclimabuilt project has developed a smart, ventilated window that integrates advanced technologies, including PCM (phase-change material) heat storage, triple glazing with air-filled chambers for enhanced thermal insulation, and 3D-printed components for noise reduction and air purification. These innovations minimise energy losses, improve thermal management, and promote occupant health and well-being.

This study focuses on evaluating the acoustic performance of the three operational modes of the fans integrated into the window of a Living Lab environment. Noise measurements were conducted in accordance with EN ISO 16032:24, both with and without an acoustic filter installed in the PCM box and air filtration unit. Data were collected from three microphone positions: a corner and two reverberant field points. The analysis reveals that the noise levels generated by the fans are in the 35–45 dB range, exceeding standard limits. Moreover, the findings highlight the need to further optimise noise control strategies in smart window design while maintaining their energy efficiency and indoor air quality benefits.

Keywords: *ventilation noise, ventilated window, smart window*

**Corresponding author*: andrea.gerbotto@polito.it.
Copyright: *©2025 Gerbotto et al. This is an open-access article distributed under the terms of the Creative Commons Attribution 3.0 Unported License, which permits unrestricted use, distribution, and reproduction in any medium, provided the original author and source are credited.*

1. INTRODUCTION

The integrated assessment of acoustic conditions, ventilation, and overheating prevention is essential to ensure that residential developments provide a balanced indoor environmental quality (IEQ) [1]. Neglecting any of these aspects may lead to housing that fails to meet occupants' overall comfort and well-being.

Windows and other ventilation openings constitute the primary interfaces between the indoor and outdoor environments and have been the subject of increasing research and development [2]. However, this connection poses a significant challenge for natural ventilation, as it creates a trade-off between fresh air intake and external noise intrusion. This conflict often prevents naturally ventilated buildings from complying with background noise limits established by acoustic standards, building regulations, and rating protocols. In response, extensive research has focused on developing solutions that enable ventilation without compromising façade sound insulation [3, 4].

Over recent decades, double-glazed windows have been enhanced to provide excellent sound insulation when closed. However, they restrict natural ventilation, increasing reliance on mechanical ventilation and leading to higher energy consumption. To address this issue, windows with integrated mechanical ventilation have been introduced. These systems allow for a reduced opening area without diminishing the air exchange rate, significantly improving acoustic comfort and energy efficiency [5]. Despite their advantages, integrated mechanical ventilation systems introduce a continuous noise source within the room. This internal noise must be accurately measured and, if necessary, mitigated to ensure overall acoustic comfort.

2. METHODOLOGY

2.1 Test case

The Test Case is a smart, ventilated heat-harvesting window that consists of a ventilated window with additional functions supporting ventilation, thermal management, and improved air quality in indoor spaces, which sound reduction index has been measured in [6].



Figure 1. The Test Case; PCM-Air exchanger (blue); outer bottom vent (green); Air Filtration Unit (red)

The smart window is composed of the following main sub-components (figure 1):

- Triple-glazed window unit with a ventilated exterior chamber, Air-filled interior chamber, NIR absorbing layer, and omniphobic coating;
- Upper box – PCM-Air exchanger unit which hosts:
  - One axial fans per unit;
  - A stack of five plates filled with Phase Change Material;
  - One 3D printed acoustic absorbers, each consisted of one casing (H130 mm x W130 mm x T100 mm) with nine panels (approx. H120 mm x W120 mm x T3 mm);
- Lower box – Indoor Air Filtration Unit which includes:
  - One 3D printed CO_2 absorber consisted of one casing (H130 mm x W130 mm x T425 mm) with twenty five electro-spun membranes;
  - One 3D printed acoustic absorbers, each consisted of one casing (H130 mm x W130 mm x T100 mm) with nine panels (approx. H120 mm x W120 mm x T3 mm);
  - Ventilator for air circulation.

2.2 Operational modes

The outer cavity of the TGU can be activated using electrical fans, with an airflow path from the outside (with an outer bottom vent integrated into the framing system) to the inside (with an inner top vent integrated into the framing system) to provide the indoor environment with primary ventilation air at a temperature level closer to the indoor required temperature, in heating dominated conditions (Supply Air, SA, operation mode).

In cooling dominated conditions instead the TGU outer cavity ventilation is used with an airflow path from the outside to the outside (with an outer top vent integrated into the framing system), to reduce the g-value (total solar energy transmittance) of the TGU by removing unwanted solar gains absorbed within the glass layers (Outdoor Air Curtain, OAC, operation mode), while a fan-assisted vents provide primary ventilation bypass within the top part of the framing system.

In order to reduce the differences between the air temperature entering the room through the glazing ventilation and the thermal comfort conditions inside the building, the air from the glazing ventilation is conveyed to a PCM to

Air heat exchanger before being delivered to the indoor environment.

Finally, the TGU can also be used as a conventional TGU, in conditions in which solar radiation is not very high and in which ventilation is not needed, by switching off the fans and closing all the vents included in the system (Thermal Buffer, TB, operation mode).

2.2.1 *Supply Air throught the window*

To assess the noise generated by the fan in the bottom box, the system was operated in Supply Air window mode. In this configuration, external forced air enters through the bottom outdoor inlet, flows through the window cavity, and is directed to the PCM-Air heat exchanger by the fan located in the bottom box.

2.2.2 *Supply Air direct*

To evaluate the noise produced by the fan in the PCM box, the system was set to Supply Air direct mode. In this setup, external forced air is drawn in through the top outdoor inlet and directly supplied to the PCM-Air heat exchanger by the fan installed in the PCM box.

In both configurations (figure 2), the fan speed, which can be continuously adjusted with a potentiometer from 0 to 100, was set to either 30% or 100%.

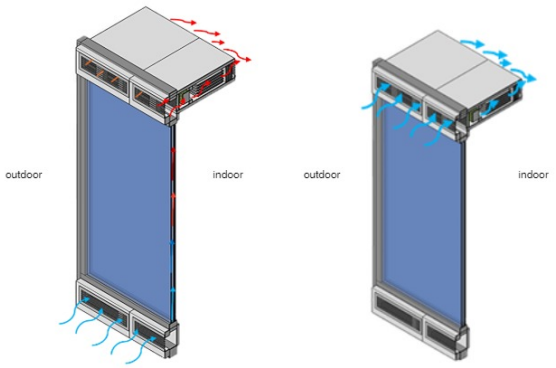


Figure 2. The two considered operational modes

2.2.3 *Air filtration*

For improving indoor air quality and wellbeing, the Test Case features CO_2 capturing filters. The 3D printed component design consists of a Light-Weight PLA-based casing with a customisable number of incisions to integrate

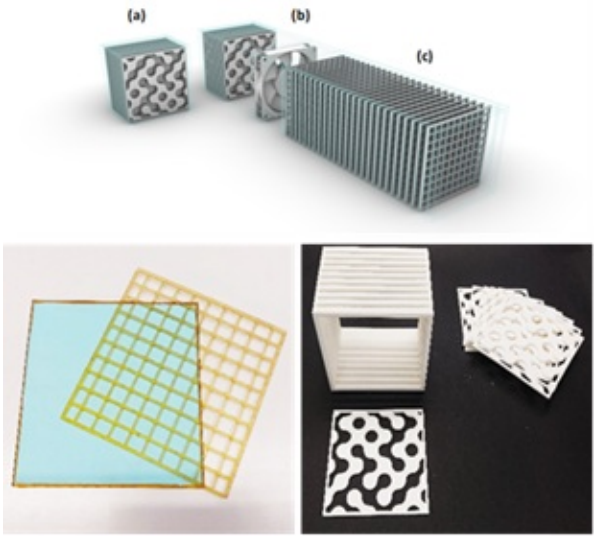


Figure 3. Design of 3D printed air-filtration unit and collateral acoustic components (top); functional panel with CO_2 absorptive properties made of (a) a High HDT photocurable resin-based frame and (b) an electro-spun MOFs/PAN polymer membrane (bottom-left); functional component with acoustic properties based on thermoplastic with foaming agents (bottom-right)

resin-based frames with MOFs/PAN layers of electro-spun CO2 Capturing Membranes and a fan for air circulation. Additionally, an acoustic absorber was integrated in the assembly to reduce the noise of the fan (figure 3).

For all the configurations considered, the air flow rates generated by the fans were measured (table 1).

Table 1. Volumetric flow measurements

Mode	Velocity [%]	Q_{max} $[m^3/h]$
SA_{window}	30	12.68
SA_{window}	100	29.23
SA_{direct}	30	30.53
SA_{direct}	100	35.70
$Air filtration$	100	4.45



Figure 4. Fixed microphone positions

2.3 Test equipment and method

The sound pressure level, L_i, from the service equipment is measured in a fixed position i as the linear (Z weighted) spectrum in one-third-octave-bands during the operation time of the service equipment under test.

For each measurement it is determined the equivalent continuous sound pressure level, $L_{Zeq,i}$, over a period of $t = 30$ seconds. The sound pressure levels taken in the three positions are then used to calculate the average sound pressure levels L_{Aeq} in one-third-octave bands. These average sound pressure levels are then corrected for background noise, measured over $t = 30$ seconds in the same positions before and after the operation time.

The background noise-corrected average sound pressure levels $L_{Aeq,corr}$ in one-third-octave bands are then used to calculate the standardized average sound pressure levels $L_{Aeq,corr,nT}$ to a reference reverberation time as:

$$L_{corr,nT} = L_{corr} - 10\log\left(\frac{T}{T_0}\right) \quad (1)$$

where:

- T is the measured reverberation time in seconds;
- T_0 is the reference reverberation time 0.5 seconds.

2.3.1 Filter

The acoustic performance is evaluated by measuring the insertion loss (IL), calculated by the difference between the sound pressure level (SPL) in the room with and without the filter applied. Therefore, the IL of the filter is calculated as

$$IL_{filter} = SPL_{wout} - SPL_w \quad (2)$$

where:

- SPL_{wout} is the A-weighted SPL measured without the filter, in dB;
- SPL_w is the A-weighted SPL measured with the filter, in dB.

2.4 Measurements

The Test Case was installed on the south-oriented vertical façade in the Living Lab at Politecnico di Torino (Torino, Italy), a single office room of approximately 10 m^2 floor area.

Three different conditions of the test room have been defined, and, for each condition, three measurement positions, one in a selected corner of the room and two positions in the reverberant sound field (figure 4), have been used to characterize the room acoustically, according to EN ISO 16032:2024. For each measurement position, three repetitions were performed. Figure 5 and figure 6 present the equivalent sound pressure levels (L_{Aeq}) of the background noise and the L_{Aeq} for fan speeds of 100% and 30% for the two operational SA modes (through the window and direct), while figure 7 presents that of air filtration box. These curves have been adjusted for background noise and the room's reverberation time (figure 8), measured using the impulse response method in the 100 Hz to 5 kHz one-third-octave bands.

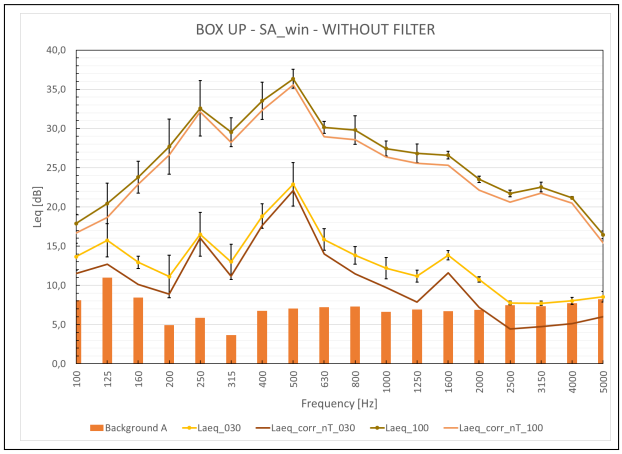


Figure 5. Supply Air window

3. RESULTS AND DISCUSSION

It can be observed that the background noise remains relatively low (< 15 dB for each third octave band) and has a

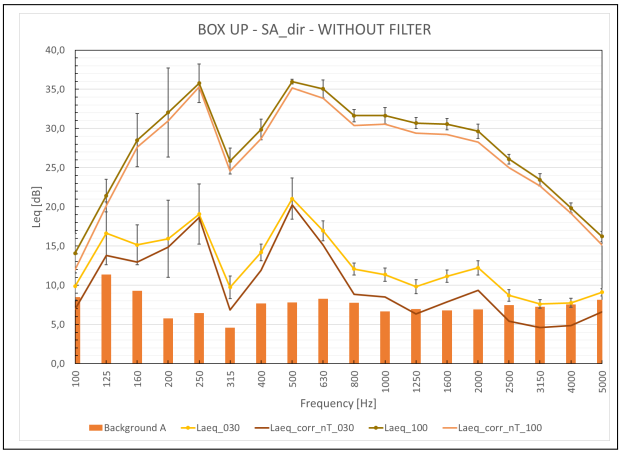


Figure 6. Supply Air direct

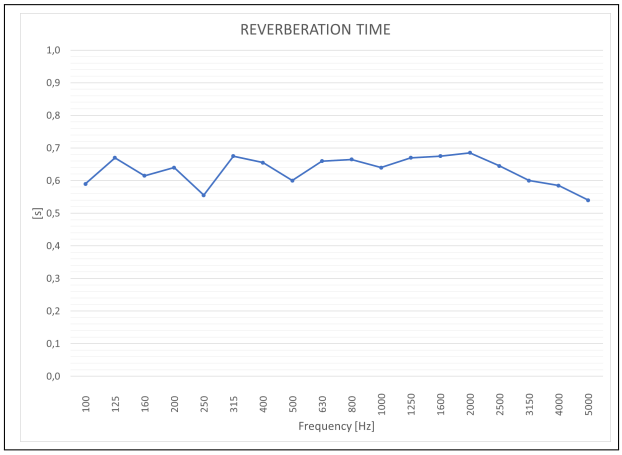


Figure 8. Reverberation Time

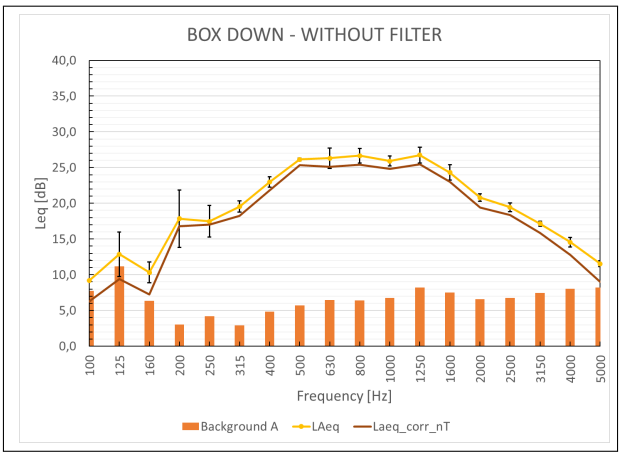


Figure 7. Air filtration

Table 2. Measurements results

Mode	$L_{A,back}$	L_{Aeq}	$L_{Aeq,nT}$
SA_{win} 100 %	20.8 dB	41.6 dB	40.7 dB
SA_{win} 30 %	20.8 dB	27.9 dB	26.3 dB
SA_{dir} 100 %	21.1 dB	43.4 dB	42.4 dB
SA_{dir} 30 %	21.1 dB	27.3 dB	25.7 dB
$Airfil$ 100 %	20.6 dB	35.1 dB	33.9 dB

lot of influence in the low-speed condition. The correction for the background noise and the reverberation time standardisation minimally impacts the results for the condition with the fan speed at 100%, this leads to a limited difference between the two curves, L_{Aeq} and $L_{Aeq,corr,nT}$. Thus the test room could be considered appropriate for evaluating the noise produced only by the fans and the effects of the acoustic filters.

Both the fan in the lower box and the one in the PCM box have two peaks at 250 Hz and 500 Hz, which amplify as the speed increases and which are responsible for exceeding the 30 dB(A) threshold indicated in literature as critical for living spaces, particularly bedrooms [7]. The path through the window in the SA_{win} mode filtered the frequencies above 630 Hz and below the 250 Hz and amplify the range between 315 Hz and 500 Hz, probably due to a resonance in the PCM box, also found in the measurement of the sound reduction index of the test case in [6].

The tested filter, designed as a series of panels with staggered incisions to hinder the transmission of sound with labyrinthine channels to increase the distance sound must travel, enhancing phase cancellation, reveals a frequency-dependent behavior, indicative of a filter optimised for mid-to-high frequency performance. At mid and low frequencies (100–1250 Hz), the insertion loss fluctuates between -1.6 dB and +1.4 dB, with a minimum observed at 1000 Hz. These results suggest limited attenuation capacity in the lower frequency range, likely due to the relatively long wavelengths and reduced interaction with the filter geometry. Above 1250 Hz, the filter demonstrates more attenuation, reaching up to +2.0 dB at 5000 Hz. This indicates enhanced interaction with shorter wavelengths.

Overall, the filter exhibits modest insertion loss across the full spectrum and needs some improvements, as try-

ing to implement helmholtz resonators or using layered impedance transitions to improve energy dissipation.

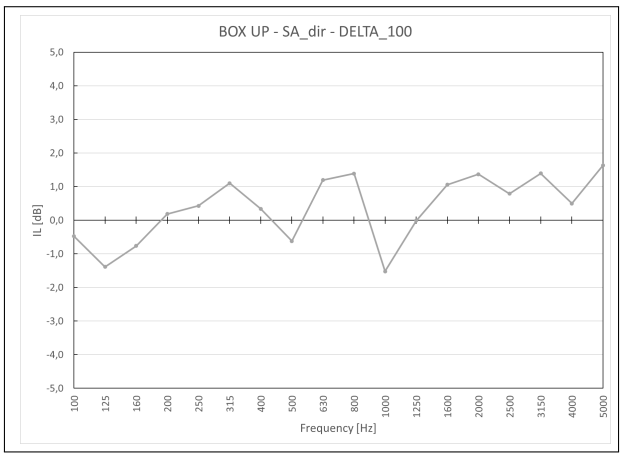


Figure 9. Insertion Loss

4. CONCLUSION

This study presented an experimental evaluation of the acoustic performance of a smart, ventilated window system with integrated phase-change material (PCM) and air purification modules. The results demonstrated that the noise levels generated by the fans in all operational modes exceed recommended indoor background noise limits for residential or office environments, particularly at full-speed operation. While the integrated acoustic treatments provided measurable insertion losses, their effectiveness was not sufficient to reduce fan noise to acceptable levels.

The findings highlight a key challenge in balancing acoustic comfort with advanced functionalities such as heat recovery and indoor air quality control. Future developments should focus on optimising fan design and speed control, improving the acoustic performance of integrated absorptive materials. A holistic design approach is essential to ensure that smart façade components can meet the increasingly stringent performance criteria for indoor environmental quality in low-energy buildings.

5. ACKNOWLEDGMENTS

The experimental activities presented in this paper were carried out as part of the H2020 project "iclimabuilt—Functional and advanced insulating and energy harvesting/storage materials across climate adaptive building envelopes" (Grant Agreement no. 952886). We gratefully acknowledge the support Anna Karatza and Vaia Tsiokou (BIOG3D, Greece) provided for generously sharing detailed design information, which was instrumental in developing this study, Asmaa Ali (Rubitherm GmbH, Germany) and Gianni Cassera (BGTec Sp. z o.o., Poland) for the preparation of the mock-ups.

6. REFERENCES

[1] J. Harvie-Clark, A. Chilton, N. Conlan, and D. Trew, "Assessing noise with provisions for ventilation and overheating in dwellings," *Building Services Engineering Research and Technology*, vol. 40, pp. 263–273, May 2019.

[2] F. Favoino, R. C. Loonen, M. Michael, G. De Michele, and S. Avesani, *Advanced fenestration—technologies, performance and building integration*. 2021.

[3] S. Torresin, R. Albatici, F. Aletta, F. Babich, T. Oberman, and J. Kang, "Acoustic Design Criteria in Naturally Ventilated Residential Buildings: New Research Perspectives by Applying the Indoor Soundscape Approach," *Applied Sciences*, vol. 9, p. 5401, Dec. 2019. MAG ID: 2994653179.

[4] C. Rubino, S. Liuzzi, G. Fusaro, F. Martellotta, C. Scrosati, and M. Garai, "Balancing ventilation and sound insulation in windows by means of metamaterials: A review of the state of the art," *Building and Environment*, vol. 275, p. 112780, May 2025.

[5] L. Du, S.-K. Lau, S. E. Lee, and M. K. Danzer, "Experimental study on noise reduction and ventilation performances of sound-proofed ventilation window," *Building and Environment*, vol. 181, p. 107105, Aug. 2020.

[6] L. Shtrepi, A. Gerbotto, F. Favoino, and A. Astolfi, "Sound insulation characterisation of innovative natural ventilated façade in the context of living lab installations," *inter noise*, vol. 270, pp. 10094–10102, Oct. 2024.

[7] J. Harvie-Clark, N. Conlan, W. Wei, and M. Siddall, "How loud is too loud? noise from domestic mechanical ventilation systems," *International Journal of Ventilation*, vol. 18, pp. 303–312, Oct. 2019.

DOI:

Main theme: A04 Education, Public Outreach and History in Acoustics

Session A04.01 Education, Public outreach and history in acoustics - General

Chair(s): M. Pàmies-Vilà, N. Campillo-Davo

DOI: 10.61782/fa.2025.0892

FORUM ACUSTICUM EURONOISE 2025

THE TEACHING OF ACOUSTICS AT THE HIGHER TECHNICAL SCHOOL OF ARCHITECTURE OF MADRID IN 1855

Alexander Díaz-Chyla[1*]
[1] Grupo de Investigación de Acústica Arquitectónica, Universidad Politécnica de Madrid, Spain

ABSTRACT

The Madrid "Escuela Especial Preparatoria de Arquitectura" was created in 1844, with a holistic educational model, which required the reinforcement of technical training to achieve an appropriate balance with the artistic part of the curriculum. In 1848, with the creation of the Preparatory School for Civil Engineers, Mining Engineers and Architects, the scientific-technical training for architectural studies was reinforced. In 1855 a new curriculum was approved for the Architecture degree program, which among its novelties introduced the subject: Notions of acoustics, optics and hygiene applied to architecture. This communication shows the program of this subject, 170 years after the beginning of teaching acoustics in the Higher Technical School of Architecture of Madrid.

Keywords: *History, Architecture, Education in acoustics, Teaching.*

1. INTRODUCTION

The Higher Technical School of Architecture of Madrid is the school of architecture of the Universidad Politécnica de Madrid (Spain) and was created in 1844 under the name of Escuela Especial de Arquitectura de Madrid, being the oldest school of architecture in Spain. Its origins date back to the 18th century.

In Spain, the Royal Academy of the Three Noble Arts (painting, sculpture and architecture) was founded in 1744. In 1752, the Royal Academy of Fine Arts of San Fernando was created. It organized the regulated teaching of architectural studies in that year and its statutes were approved in 1757. Since then, it has been responsible for awarding the title of architect, replacing the old system of guilds [1], [2], [3], [4], [5].

Given the evidence of the lack of technical knowledge of architecture students and their disadvantage compared to engineers, in 1844 the "Escuela Especial Preparatoria de Arquitectura" was created because of the transformation of the teachings of the Royal Academy of Fine Arts of San Fernando, which in 1848 was established as an independent institution understood as a School for the Application of Arts. This Preparatory School was created for the special studies of Architects, Civil Engineers and Mining Engineers, as they all shared a similar scientific background. The duration of studies at the Preparatory School was two years and it was abolished in 1855.

The architecture degree lasted four years and previously required an entrance exam and two years at the Preparatory School. With the Moyano Law of Public Instruction (1857), the School of Architecture came under the university regime as the Higher School of Architecture, dependent on the Central University (currently the Complutense University), and became responsible for awarding the official title of architect.

2. THE NEEDS OF ARCHITECTURE AND THEORETICAL ACOUSTICS IN THE EARLY 19TH CENTURY

Before the 20th century and the development of modern acoustics, there was very little connection between the theoretical knowledge of acoustics and the needs of architects in the design of venues [6]. Architects at that time could not rely on scientific support for their designs.

[*] ***Corresponding author***: alexander.diazr@upm.es.
Copyright: *©2025 First author et al. This is an open-access article distributed under the terms of the Creative Commons Attribution 3.0 Unported License, which permits unrestricted use, distribution, and reproduction in any medium, provided the original author and source are credited.*

The evolution of venues design was slow and gradual, with small architectural milestones throughout history. The Roman architect Vitruvius Polion, author of *De Arquitectura* [7], exhaustively described aspects of the design of theatres and their acoustics, one of his aims being to ensure good vision and hearing for the spectators. The architects of the Renaissance and Baroque periods would place the actors on stages elevated above the lower plane of the audience. In 1580 the first permanent theatre designed by Andrea Palladio, the Teatro Olimpico, was built in Vicenza. It is a covered theatre, the stage in the configuration of the ancient Roman theatres and the audience area was in the shape of a semi-ellipse. In 1628 the Farnese theatre was inaugurated in Parma with a U-shaped audience area. The first Italian opera house in the shape of a horseshoe with overlapping boxes on five levels was built in Venice in 1654, initiating a typology that remained unchanged for almost two centuries, being the most common in the design of theatres in the 18th and 19th centuries.

In the 18th century, musical events took place in different venues, such as palaces, masonic lodges, public gardens and ballrooms. Initial venues, sponsored by royalty or nobility were small. As the acoustic power level of the new musical instruments increased and in response to the demand of larger audiences, concert halls dimensions increased. The new need for larger venues in view of the interest in paid music meant that the audience had to be able to see and hear. During the 18th century, the Italian theatrical model became generalized with different floorplan geometries: elliptical, circular, bell-shaped. In central and northern Europe, concert halls evolved from churches and the rectangular floor plans of ballrooms.

During this period, architects continued designing spaces for music, and the first treatises on the topic appeared, specifying technical solutions that had previously worked and were repeated by designers. Two architects who influenced theatre architecture in their countries were the Frenchman Pierre Patte who in 1782 wrote the book Essai sur l'Architecture théatrale [8], and the Englishman George Saunders who in 1790 wrote A Treatise on Theatres, [9]. In 1880, the architect Jean Louis Charles Garnier, designer of the Paris Opera House, [10] expressed his disappointment at not finding any help from the theoretical knowledge of acoustics.

Today, in the subjective ranking of the acoustic quality of opera houses and auditoriums carried out by conductors and acousticians, many of the considered as best halls were built before any scientific knowledge of the behavior of sound in a venue was applied, such as: Teatro La Scala, Milan, 1778; Teatro San Carlo, Naples, 1737; Grosser Musikvereinsaal, Vienna, 1870; Opera Garnier, Paris, 1875; Concertgebouw, Amsterdam,1888; Carnegie Hall, N York, 1891; Teatro Colón, Buenos Aires, 1908, etc.

Throughout the 19th century, the study of acoustics as a science and its dissemination through books and technical journals began. In 1862 Hermann Helmholtz [11] wrote a treaty on acoustics and hearing, and in 1877 Lord Rayleigh (John William Strutt) [12] published The Theory of Sound, considered the beginning of modern acoustic theory. They established acoustics as a science where observation, experimentation and a mathematical basis led to significant advances. Room acoustics as a scientific discipline can be considered to begin with the work of W.C. Sabine at Harvard University at the end of the 19th century with his experimental work on reverberation time in rooms [6].

3. THE 1855 ACADEMIC CURRICULUM

After becoming independent from the Royal Academy of Fine Arts of San Fernando, the new "Escuela Especial Preparatoria de Arquitectura" adopted a holistic educational model, where it was necessary to reinforce the technical background in order to achieve an appropriate balance with the artistic side. With a model similar to that followed in France, the Preparatory School for Civil Engineers, Mining Engineers and Architects was created in 1848, which improved the scientific-technical training for architectural studies with a two-year plan. Table 1 shows the subjects taken at the Preparatory School. Table 2 shows the subjects of the academic curriculum of the Civil Engineering and Architecture courses.

Table 1. Preparatory School subjects

	Subjects
First Year	- Differential and integral calculus. - Geometry. - Graphical constructions. - Physics and chemistry. - Landscape drawing. - Architectural drawing.
Second Year	- Rational mechanics - Applications of descriptive geometry. - Graphical constructions. - Topography and Geodesy. - Topographical drawing. - Architectural drawing.

Table 2. Comparison between the academic curriculum of the degrees of Civil Engineering (1849) and Architecture (1850).

Civil Engineering	Architecture
First year	
Applied mechanics	Industrial mechanics
Stereotomy	Mineralogy and mineral chemistry
Mineralogy	Extension of stereotomy
Graphical and practical exercises	Graphic exercises and architectural drawing
Second year	
Constructions, part one	General construction theory
Machines	Road construction
Geology	Practical resolution of construction problems
Drawing and practice	Architectural drafting
Third year	
Constructions, part two	General theory of art and decoration.
Civil architecture	Use of water.
Administrative law, Part I	Analysis of ancient and modern buildings.
Drawing and practice	Composition exercises.
Fourth year	
Constructions, Part III	Legal architecture
Water supply	Art practice
Administrative law, Part II	Composition
Drawing and practice	Composition exercises

The disappearance of the Preparatory School in 1855 brought another reorganization of teaching at the School of Architecture. In the same year, a new curriculum was approved in which the architecture degree became a six-year course. Among its changes, it introduced the subject: Notions of acoustics, optics and hygiene applied to architecture. In this subject, the teaching of these three subjects, especially hygiene, began. Table 3 shows the subjects of the 1855 curriculum at the "Escuela Especial Preparatoria de Arquitectura".

In order to gain access to architecture studies, students were required to have a certificate of having successfully passed physics and chemistry in an official center or to take an exam in these subjects at the School of Architecture. They then had to pass entrance exams. Classes were held for six hours a day from 15 September to 30 June.

Table 3. 1855 academic curriculum, Escuela Especial Preparatoria de Arquitectura

	Subjects
First Year	- Integral and differential calculus - Topography - Descriptive geometry - Topographical drawing - Architectural drawing
Second Year	- Rational mechanics. - Industrial mechanics. Part I. - Applications of descriptive geometry to shadows - Gnomonic perspective - Mineralogy - Chemistry applied to architectural uses -Analysis, manipulation and manufacture of materials - Architectural drawing
Third year	- Industrial mechanics Part II: Hydraulics; Mechanics applied to construction - Stereotomy, wood and iron; graphic works of this subject - Architectural drawing
Fourth year	- Civil construction - Hydraulics - Staking out and uprights - Acoustics, optics and hygiene applied to architecture - Theory of art and composition - Elements of composition and 3rd order projects
Fifth year	- History of architecture -Analysis of ancient and modern buildings - Composition
Sixth year	- Legal aspects - Composition

4. ACOUSTICS, OPTICS AND HYGIENE APPLIED TO ARCHITECTURE

The following is the curriculum of the subject which was a pioneer in the teaching of acoustics at Spanish universities. The course consisted of sixteen lessons divided into two blocks: Block I (lessons I to XII) on acoustics and optics and Block II (lessons XII to XVI) on hygiene and health applied to civil constructions. The acoustics and optics program follows the book written in 1848 by Theodore Lachèz [13], a 19th-century French architect, known for his contributions in these fields. His influence extended to the educational field, where he wrote about the teaching of architecture and evaluated institutions such as the *École Impériale et Spéciale des Beaux-Arts* and the *École Centrale d'Architecture* [14].

Lesson I	Laws of acoustics and general considerations on some of the phenomena to which it refers.
-Acoustics and music -Sound -Propagation, reflections and modifications -The voice -Air, vehicle and instrument of sound -Echoes, resonance, sonority	
Lesson II	Optics, light and distance
-The intensity of light is inversely proportional to the square of the distance	
Lesson III	Classification of theatres
-Theatres and amphitheaters among the ancients and in modern times -Needs they have to satisfy -Differences which characterize them -Their special purposes -Wise acoustic arrangements -Sound vessels -Velarium	
Lesson IV	Modern Theatres and amphitheaters
-Different purposes -Characteristic differences with ancient monuments	
Lesson V	Defects of theatres and amphitheaters, resulting from the non-observance of the laws of acoustics
-Local or general resonances -Echoes -Suppression of sounds or their destroyed intensity -Denomination of vaults, ceilings, niches, semicircles, coffers -Effects of wooden stands, carpets and upholstery -Harmful air volumes in amphitheaters, auditoriums and concert halls	
Lesson VI	Defects resulting from the non-observance of the best optical considerations
-Light poorly distributed and hurting the eyesight -Absorbed by dark colored walls -Chandeliers, steps and handrails poorly arranged -Inconvenience of direct light coming from the south	
Lesson VII	Favorable acoustic conditions for theatres and amphitheaters according to their use
-Speech and chant -Conditions of their sound propagation -Triangular and parabolic amphitheaters. -Particular inclination of the tiers according to a curve -Harmful vibrations of the tiers -Desired modifications in performance halls -Pulpits -Concert halls	
Lesson VIII	Conditions of optics, light and distance
-Conditions of optics, light and distance -Light distribution -Rooms for scenic effects and meeting rooms -Historical theatres -Congress of Deputies	
Lesson IX	Investigation for the most suitable shape for amphitheaters.
-Circle and half circle; Segment or quarter circle -Point of view or place of the scene -Enclosures proportional to the number of spectators -Special circumstances for amphitheaters -Respective position of audience for viewing objects	
Lesson X	Classification of amphitheaters and public assembly halls into five categories
-Rooms satisfying optical conditions -Rooms satisfying acoustic conditions -Mixed music halls for simultaneous seeing and hearing -Demonstrations and experiments	
Lesson XI	Some observations on the inclination of the stands used today in existing halls and amphitheaters

-Poorly used space -Arbitrary inclination of the tiers. -Parallel visual rays instead of rays converging towards the point of view	
Lesson XII	Research and determination of the curve, according to which the benches or floor of public halls and amphitheaters should be laid
-Point of view or proscenium -Average height of the audience -Abscissae and ordinates of the stands -Width and height of seats -Variable vertical distance between successive rows of listeners	

5. CONCLUSIONS

The political and social changes throughout the convulsive 19th century in Spain had an influence on education and, in particular, on the teaching of architecture. It was necessary to go with its *zeitgeist* in terms of progress, social welfare, economic development and, with criteria of technological development that were more pragmatic than artistic. From 1844 to the present day there have been at least 15 academic curriculums until the most recent one in 2010, adapted to the European Higher Education Plan, and an attempt has been made to seek a balance between artistic and scientific-technical subjects.

The teaching of some notions of acoustics at the Higher Technical School of Architecture of Madrid has been changing according to the different study plans; it has never been taught as an independent subject.

For example: it was taught in the 1855 and 1858 curriculum, but then eliminated in the 1864, 1885 and 1932 ones. In the 1875 and 1896 curriculum, it was included under the subject Applications of the physical-natural sciences to Architecture (together with concepts such as ventilation, heating and building services). In 1914 it was offered in the subject of optics and acoustics, as well as in the 1956 curriculum for electrical engineering and acoustics. It was in 1957 when the subject of Acoustics and building services was created, evolving in the curriculum of 1964, 1975 and 1996 within the subject of Building Physics, where it ended up having a marginal presence. In the current plan, curriculum 2010, a series of fundamentals classes are given within the subjects of Physics and Environmental Conditioning and Habitability, and it's also offered as an elective subject, Experimental Workshop in Architectural Acoustics, with 6 ECTS credits.

At present, scientific-technical subjects in architectural studies in Spain continue to represent an important percentage of the subjects on the academic curriculum (they have a greater weight than in other European countries), as the Spanish architect assumes among his competencies some aspects of civil engineering in relation to buildings, which must be preserved as opposed to the figure of an architect who is merely a designer.

In Spain, the architect has a regulated qualification with professional attributions and the curriculum of this qualification have been adapted to the regulatory body of the country. For this reason, some subjects have been modified over the years and new technical subjects have been introduced according to the new requirements of urban planning, construction and building services. Spanish legislation establishes that buildings, including their services, must meet basic safety (structural, fire, usability and accessibility) and habitability (hygiene, health and environmental protection; noise protection; energy saving and thermal insulation) requirements, with the responsibility lying on the architect.

6. REFERENCES

[1] P. Navascués Palacio, "La Escuela de Arquitectura de Madrid (1844-1914)," in *Escuela Técnica Superior de Arquitectura de Madrid. Memoria 1991-1993*, Madrid, Instituto Juan de Herrera, 1994.

[2] P. Navascués Palacio, *Summa Artis. Historia general del arte, vol. 35.2, Arquitectura española 1808-1914*, Madrid, Espasa Calpe, 1993.

[3] J. Vidaurre Jofré, "Panorama histórico de la enseñanza de la Arquitectura en España desde 1845 a 1971," in *Ideología y Enseñanza de la Arquitectura en España Contemporánea*, A. Fernández Alba, Coord., Madrid, Tucar Ed., 1975.

[4] M. Prieto González, *Aprendiendo a ser arquitectos. Creación y desarrollo de la Escuela de Arquitectura de Madrid (1844-1914)*, Madrid, Consejo Superior de Investigaciones Científicas, 2004.

[5] M. Á. Baldellou and A. Capitel, *Summa Artis. Historia general del arte, vol. 40, Arquitectura española del siglo XX*, Madrid, Espasa Calpe, 1996.

[6] A. Díaz-Chyla and D. de la Prida, "The relevance of the collaboration between W. C. Sabine and architects for the early development of room acoustics," in *XII Congreso Ibérico de Acústica*, Faro, 2024.

[7] V. Polion, *De Architectura*, J. Ortiz y Sanz, Trad., Madrid, Imprenta Real, 1787; *The Ten Books on Architecture*, M. H. Morgan, Trans., New York, Dover Publications, 1960.

[8] P. Patte, *Essai sur l´Architecture théatrale, ou de l´Ordonnance la plus avantageuse à une salle de Spectacles, relativement aux principes de l´Optique et de l´Acoustique*, Paris, Chez Moutard, 1782.

[9] G. Saunders, *A Treatise on Theatres*, London, I. & J. Taylor, 1790.

[10] J. L. C. Garnier, *Le nouveau Opéra de Paris*, vol. 1-2, Paris, Ducher et Cie, 1876–1880.

[11] L. Helmholtz, *Über die Tonempfindungen als physiologische Grundlage für die Musiktheorie* (*On the Sensations of Tone as a Physiological Basis for the Theory of Music*), 1862.

[12] J. W. Strutt, *The Theory of Sound*, 1877.

[13] T. Lachez, *Acoustique et optique de salles de réunions publiques, théatres et amphithéâtres*, Paris, 1848.

[14] T. Lachèz, *Enseignement de l'architecture. L'École impériale et spéciale des beaux-arts, section d'architecture, l'École centrale d'architecture et ses parallèles, avec son modèle cité, l'École impériale centrale des arts et manufactures*, Paris, A. Lévy fils, 1868.

DOI: 10.61782/fa.2025.0093

FORUM ACUSTICUM EURONOISE 2025

ACOUSTICS IN MUSIC EDUCATION: EMPOWERING MUSIC TEACHERS AS STEM AMBASSADORS

Montserrat Pàmies-Vilà*
Department of Music Acoustics – Wiener Klangstil
mdw – University of Music and Performing Arts Vienna, Austria

ABSTRACT

Whether formally at music universities or informally in everyday conversations, it is common for acousticians to discuss acoustics-related topics with musicians or music educators. While few University programmes offer joint studies in acoustics and music, many conservatories and music universities require music students to take courses in acoustics and/or organology. At the University of Music and Performing Arts Vienna, for instance, students in both music and music education programmes can enrol in musical acoustics courses. At a time when STEM education (Science, Technology, Engineering, Mathematics – or STEAM when including the Arts) gains increasing importance, music educators have a key role to play at the intersection of music and science. They can make a difference by stimulating their pupils' curiosity about musical instruments and the science of sound, while strengthening critical thinking. To provide music educators with the necessary tools, the acoustics lecture should not only cover essential acoustic concepts, but also include strategies for conveying this knowledge. This paper proposes practical examples and discusses their applicability beyond the acoustics laboratory. This approach not only motivates future teachers while learning acoustics, but also expands their pedagogical resources for introducing STEM concepts into their music classes.

Keywords: *Music acoustics, Music education, STEM, Interdisciplinary education*

**Corresponding author*: *pamies-vila@mdw.ac.at.*
***Copyright**: ©2025 Pàmies-Vilà. This is an open-access article distributed under the terms of the Creative Commons Attribution 3.0 Unported License, which permits unrestricted use, distribution, and reproduction in any medium, provided the original author and source are credited.*

1. INTRODUCTION

Music education and the teaching of musical instruments take place in a variety of contexts and learning and teaching situations. Whether in collective or individual lessons, in schools, institutions and private lessons, or even via online tools, the fundamental aim remains the transmission and development of musical skills and an appreciation of the art of music.

Music educators may be employed in general schools (primary or secondary) or in music schools. In general schools, the music educator teaches general musical concepts to a group of pupils. In music schools, both group lessons and individual instrumental teaching take place. The background of music educators can vary depending on how much they have specialized in one instrument. Some teachers may have studied music education at university, others may have specialized in the performance and/or pedagogy of a particular instrument, and in many cases they may be trained professional musicians who also teach their instrument. At the University of Music and Performing Arts Vienna, for example, bachelor's and master's degree programs are offered for music students who wish to teach at the secondary school level (Lehramtsstudium Musikerziehung), for music students who wish to teach an instrument (or singing) at music schools (Musikpädagogik), and for music students who wish to study instrumental performance (among other programs such as Tonmeister, composition, theatre, film...). For all these study programs, music students —many of whom might become music educators— can take courses on music acoustics at the Department of Music Acoustics – Wiener Klangstil.

In recent years, lots of studies have explored the application of technology-enhanced learning (TEL) in music [1], with examples ranging from computer- or

smartphone-aided gamification tools [2] and sensoric-aided tools [3], to renderings in virtual reality [4,5]. Some studies have also addressed the challenges of preparing music educators for such digital tools [6], and examined the intersection of technology and gender in music education [7]. In parallel, many studies have highlighted the importance of music in STEM (Science, Technology, Engingeering and Mathematics), proposing methods to include music in STEM lessons [8], and proposing ways to give music a place in the 'A' of STEAM (Science, Technology, Engingeering, Arts and Mathemathics) [9, 10]. Yet only a few studies have reflected on the importance of STEM and STEAM in music teacher training [11] or have analyzed the role of acoustics in music education [12, 13].

Musicians and music educators are a very particular audience for a lecture on acoustics. They have a range of prior knowledge, including great practical knowledge of their instrument(s) and great musical skills, but also common misconceptions and beliefs about general acoustics and about the sound production in musical instruments (such as the influence of playing gestures on the produced sound). The acoustics lecture can be seen not only as a place for musicians to learn about the acoustics of their instruments, while reinforcing their critical thinking about their beliefs, but also to learn strategies for transferring acoustical concepts to their pupils. Since acoustics itself is a very interdisciplinary field, the concepts that may arise in the music lecture can be very diverse, ranging from physics and mathematical concepts to electronics, aeroacoustics, psychoacoustics, and more [9]. The current article concentrates on examples that refer to the physics of sound and showcases some exercises that the acoustics educator can use to engage with musicians and future music educators and provide them tools to become STEM ambassadors.

2. TEACHING ACOUSTICS TO (FUTURE) MUSIC EDUCATORS

In a conversation with Gordon Ramsey (Loyola University Chicago), who has recently published on the importance of acoustics and music in STEAM education [9], we shared our views on how to engage students in learning physics through acoustics and music. One of the many pieces of advice he gave me was to always think about the visual memory. "Anything you might say or have written on your slides may not last, but if you show them, it may last", were Ramsey's words. How to activate the (long-term) visual memory could therefore be seen as a motivation for the acoustics educator when preparing a lecture. Ramsey suggested preparing in-class labs and demonstrations and showing examples of the phenomena described. As an acoustics educator in a music university, I agreed and emphasized the importance of using descriptive physics. When preparing a lecture with a focus on descriptive acoustics, one can consider any topic in the field [14], while focusing on the concepts and the relationships between the physical variables, with the goal of introducing certain vocabulary, making connections between concepts, and helping students develop a deeper understanding of how physics principles apply to their instruments.

With these thoughts in mind, I have dedicated this year's lecture preparation to the question "How can I teach acoustics in a way that motivates my students (musicians and music teachers alike) to incorporate acoustics into their teaching?". The first step was to assess the current teaching situation of my students and the age of their pupils. I am currently teaching two courses on music acoustics where I meet musicians of all instruments, some specializing in performance and others in music pedagogy or education. Of the enrolled students, 15 completed a short questionnaire during the first lecture. Most of the students (11/15) are currently teaching an instrument to young pupils in private lessons, and some of them already have experience as music teachers in general secondary schools and/or teaching an instrument in music schools. The ages of their pupils were between 6 and 18 years old, with one student also teaching adults. The rest of the students (4/15) reported that they had no previous or current teaching experience.

Then I rethought the lectures to see how I could add transferable value to the demonstrations I usually show in class. So I would spend more time in class "showing how to show". For example, after we have learned what standing waves look like on a string, and they have identified nodes and anti-nodes in an in-class demonstration of a vibrating string (using a shaker and a tight elastic band), I would say to them, "I know this is some equipment that may not be available in your teaching situation, but let's try to find the similarities on a guitar". Then we would try to relate what they had just learned about standing waves to playing natural harmonics on the guitar (also known as flageolets), a technique most musicians have heard of or played themselves. If there are guitarists or violin-family players in the lecture, I encourage them to demonstrate the technique and explain what they are doing. They would claim that they touch the string lightly in a certain position

to play a given harmonic (Figure 1). Then, the abstraction we do together is to relate the position of the finger with the positions of the nodes of the standing wave. They quickly understand that the finger dampens the standing waves that do not have a node in that position. During this demonstration there is often an aha moment when they see the symmetry of the standing wave, i.e., when they realize that the natural harmonics can be played both near the bridge and near the fingerboard/fretboard. I use this moment to emphasize that they could show this effect to talk about the acoustics of the vibrating string when teaching flageolets (especially for guitar and violin teachers). If they do not teach flageolets, there is usually a guitar available in every general and music school that they can use as non-guitarists to talk about the fundamental frequency and the overtones. Then we look for the positions of the nodes of the standing waves together and find out that many guitars may have fret markers or side dots that show these positions on the fretboard (Figure 1).

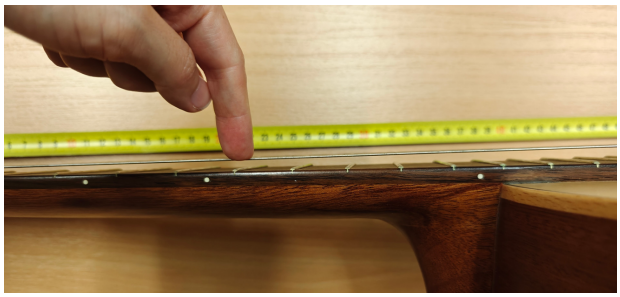


Figure 1. Classical guitar with side dots placed slightly left from the positions of 1/2, 1/3 and 1/4 on the string (from right to left). The finger is placed lightly touching the string on the fret that corresponds to 1/3 of the string.

Finding an equivalent for flageolets in wind instruments is not straightforward. The first association might be the registers: woodwind instruments can play certain notes, and they can be overblown either at an octave above or a quint-above-the-octave above the fundamental frequency that would correspond to the fingered position. Yet, according to my experience with musicians, while flageolets might be introduced very early on in the description of the string motion, standing waves in wind instruments require more careful treatment. It is common to describe the boundary conditions of wind instruments as closed or open [15]. One exercise with accessible materials (instruments) to do with musicians is to play a similar air-column length on two different instruments and discuss about the pitch of the resulting sound. From the acoustics point of view, an easy example is to compare a clarinet and a recorder. I would, first of all, ask them if they know why the recorder plays higher notes than the clarinet. They would usually reply: because the recorder is shorter. After introducing the concepts of open and closed tubes, I would ask two students to play the same length on a B-clarinet and on a soprano recorder. The recorder plays its whole length (C_5) and the clarinet plays a written D_4, sounding C_4. The first open tonehole of the clarinet is marked in red in Figure 2. The students can play the two notes and compare their interval: the flute plays one octave above the clarinet, although a similar air-column length is used. We then talk about the differences in wavelength that result in this difference in frequency. And they can finally complete the correct answer to the question of why the clarinet plays lower notes. Here, again, I would encourage teachers (clarinet teachers or anyone who might have an available clarinet at their school) to demonstrate this phenomenon to their pupils. To support the observations and shared discussions, I would show them a representation of the wavelengths of both instruments (Figure 3). If the group is interested in knowing more, one can also calculate the true length of the instrument for these frequencies according to the wavelength that is given by the frequency and the speed of sound and even introduce more advanced concepts like the end correction.



Figure 2. Comparison of the total length of a soprano recorder (sounding C_5) to the corresponding length on a clarinet (written D_4, sounding C_4). The first open tonehole on the clarinet for this demonstration is marked with an arrow.

Other examples that can be explored in the acoustics lecture while considering the transfer to the demonstration in a music lecture are collected in Table 1. These examples show some of the many useful acoustics demon-

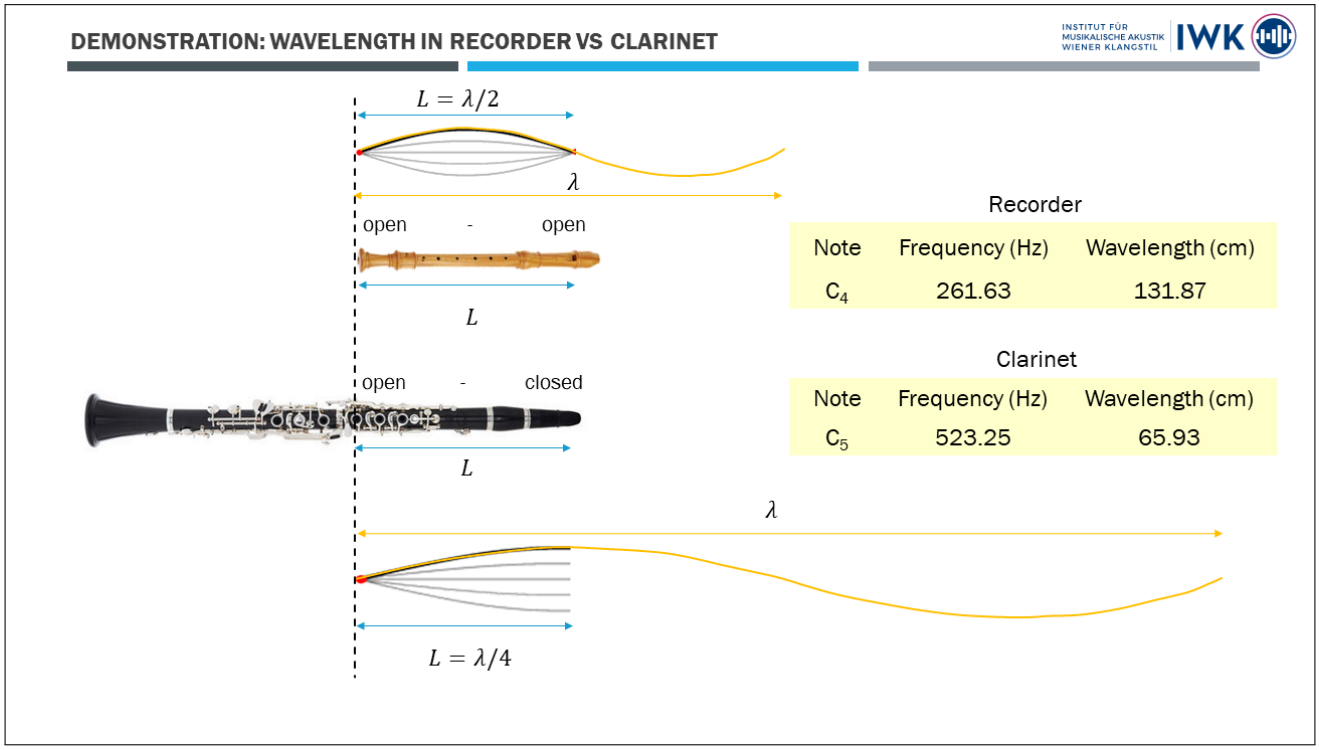


Figure 3. Comparison of the total length of a soprano recorder (sounding C_5) to the corresponding note on a clarinet (written D_4, sounding C_4)

.

strations that can be explored with musicians and music teachers either in a general acoustics lecture, in a lecture on string instruments, or in a lecture on wind instruments (from top to bottom). The paper would be too long if I were to explain the exact procedure in the acoustics lecture for all six examples, as it may be similar to the two demonstrations explained above. In all cases, I would support the use of these demonstrations outside the acoustics lecture by adding sentences like "try this at home" or "try this with your pupils", and I would ask them later if they have tried it (they claim they do!). This collection is by no means complete, but rather an inicial list of examples that the acoustics educator might consider incorporating, while presenting them as transferable demonstrations for a music lecture, and observe if the students engagement in the lecture increases, as well as their willingness to continue talking about acoustics with their pupils.

3. CONCLUSIVE REMARKS

This paper suggests that music educators have an important role to play in promoting STEM-related concepts in their music teaching through acoustics. By integrating acoustics into their teaching practices, music educators increase the interdisciplinarity of their teaching approach, not only to enhance their students' understanding of musical instruments and the science of sound, but also to stimulate curiosity and critical thinking. In doing so, they can inspire their pupils to explore the intersection of arts and sciences, which would contribute to the broader STEAM framework. This interdisciplinary approach not only enriches music education, but also positions the music educator as a valuable contributor to science literacy and as a facilitator of knowledge and awareness of the science of sound.

The examples chosen for this paper demonstrate how practical demonstrations can be made transferable from the acoustics lecture to the music lecture. The paper pro-

Table 1. Proposed use of material that might be accessible or made available in a music school and how to introduce it both in the acoustics lecture (focusing on string and wind instruments) and the music lecture, followed by the related descriptive physics.

Accessible material	Action in the acoustics lecture	Action in the music lecture	Descriptive physics
Slinky spring	Demonstrate pressure disturbance travelling and reflecting	When talking about sound production, use a slinky to represent the particles of air	Sound waves travel when air particles get compressed and decompressed, but the air particles themselves do not move forward
Tuning fork	Press the foot piece of the tuning fork against a table or the sound box of a guitar	When talking about the role of a sound boxes, press the foot piece against a table or a guitar	The table or sound box can make the vibrations of the tuning fork audible. The table or sound box shares more surface with the surrounding air than the tuning fork.
Guitar or violin	Demonstrate natural harmonics (lightly press finger on 1/2, 1/3, 1/4 of string). Demonstrate symmetry. Make standing waves 'visible'.	When teaching about flageolet (natural harmonics) introduce the concept of standing wave and its nodes.	The string vibration is the sum of the modes that are multiples of the fundamental frequency. These frequencies are all present in the string: the finger in the flageolet dampens the frequencies that do not have a node in this position.
Piece of paper	Blow above the paper and see how it raises; discuss Bernoulli principle. Mention plane sustain in air.	When teaching a reed woodwind instrument, introduce the Bernoulli principle to demonstrate the functioning of the reed. The paper mimics the reed.	If the particles of air gain velocity, they have less air pressure. If there are differences in pressure, objects might move (from the part where there is more pressure to the part where there is less pressure).
Clarinet and recorder	Play D in Bb-clarinet (sounding C) and C in soprano recorder, show that although similar air-column length, the clarinet plays one octave below. Discuss about their wavelengths.	Introduce the concept of open-closed and open-open tubes, by demonstrating that the clarinet can reach one octave lower than the flute.	The clarinet has a reed that creates differences in pressure at the beginning of the instrument, while the end of the instrument is open to atmospheric pressure. The flute has an air stream that moves in and out of the tube at almost atmospheric pressure.

poses to use these examples in the acoustics lecture, while including descriptive physics that links the concepts necessary to describe (some aspect of) sound production on string and wind instruments. The aim is to use accessible tools (e.g. instruments found in schools and music schools) to make acoustics engaging and relevant in different teaching contexts.

Further pedagogical development would require a thorough evaluation of the impact of the proposed action, including a follow-up with the music teachers to discuss the challenges they face in introducing acoustic concepts into their teaching practice. In addition, future research could explore other instrument families and acoustic concepts, as well as the relationship between music and other STEM disciplines, such as mathematics or electronics. For example, the mathematical principles underlying musical scales and intervals could be explored and made transferable to the music classroom [9]. Similarly, engineering concepts could be introduced by exploring the role of electronics in sound synthesis and amplification. These interdisciplinary pedagogical approaches would still need to take into account the possibilities of future music teachers in their teaching environment.

One of the main barriers to STEM education in general schools is known to be inadequate teacher preparation and a lack of interdisciplinarity [16]. This paper serves as a call to action for institutions to prioritize acoustics education in music performance and music teacher training programs, ensuring that educators are well equipped to inspire future learners at this unique intersection of STEM and arts disciplines.

4. ACKNOWLEDGMENTS

I would like to thank past and present colleagues at the Department of Music Acoustics - Wiener Klangstil, from whom I have learned about teaching acoustics to musicians and integrating demonstrations into the acoustics lecture (V. Chatziioannou, W. Goebl, A. Hofmann, A. Mayer, W. Kausel, G. Widholm). Thanks to Gordon Ramsey for the discussions on involving music students in the physics lecture. This research was funded in part by the Austrian Science Fund (FWF) [10.55776/T1295].

5. REFERENCES

[1] A. Acquilino and G. Scavone, "Current state and future directions of technologies for music instrument pedagogy," *Frontiers in Psychology*, vol. 13, p. 835609, 2022.

[2] K. I. C. H. Weatherly, B. Wright, and E. Y. Lee, "Digital game–based learning in music education: A systematic review between 2011 and 2023," *Research Studies in Music Education*, p. 1321103X241270819, 2024.

[3] J. Van Der Linden, E. Schoonderwaldt, J. Bird, and R. Johnson, "Musicjacket—combining motion capture and vibrotactile feedback to teach violin bowing," *IEEE Transactions on Instrumentation and Measurement*, vol. 60, no. 1, pp. 104–113, 2010.

[4] S. Serafin, A. Adjorlu, N. Nilsson, L. Thomsen, and R. Nordahl, "Considerations on the use of virtual and augmented reality technologies in music education," in *2017 IEEE virtual reality workshop on K-12 embodied learning through virtual & augmented reality (KELVAR)*, pp. 1–4, IEEE, 2017.

[5] S. Yu, Q. Liu, M. C. Johnson-Glenberg, M. Han, J. Ma, S. Ba, and L. Wu, "Promoting musical instrument learning in virtual reality environment: Effects of embodiment and visual cues," *Computers & Education*, vol. 198, p. 104764, 2023.

[6] Y. Ma and C. Wang, "Empowering music education with technology: a bibliometric perspective," *Humanities and Social Sciences Communications*, vol. 12, no. 1, pp. 1–14, 2025.

[7] V. Armstrong, *Technology and the Gendering of Music Education*. Ashgate, 2011.

[8] F. Abrahams, "A framework to integrate music into a stem curriculum," in *ICERI2018 Proceedings*, pp. 10453–10460, IATED, 2018.

[9] G. P. Ramsey, "Integrating science, technology, engineering, and math (stem) and music: Putting the arts in science, technology, engineering, arts, and math (steam) through acoustics," *The Journal of the Acoustical Society of America*, vol. 152, no. 2, pp. 1106–1111, 2022.

[10] D. Maier-Zucchino, "Sound of science: Music as a means for equity in stem educationn," Master's thesis, University of Chicago, 2021.

[11] D. Liu, "Potential impact of steam education on the outcomes of music teacher training," *Scientific Journal of Polonia University*, vol. 66, no. 5, pp. 94–102, 2024.

[12] L. Gomez-Agustina and M. S. Reigersberg, "Do performance musicians need acoustic education?," in *24th International Congress on Sound and Vibration*, vol. 8, pp. 5743–5750, International Institute of Acoustics and Vibration (IIAV), 2017.

[13] C. B. Goates, J. K. Whiting, M. L. Berardi, K. L. Gee, and T. B. Neilsen, "The sound of steam: Acoustics as the bridge between the arts and stem," in *Proceedings of Meetings on Acoustics*, vol. 26, AIP Publishing, 2016.

[14] B. E. Anderson, K. L. Gee, and T. B. Neilsen, "Teaching the descriptive physics of string instruments at the undergraduate level," in *Proceedings of Meetings on Acoustics*, vol. 26, AIP Publishing, 2016.

[15] T. D. Rossing, *The Science of Sound*. San Francisco, CA: Addison-Wesley, 3rd ed., 2001.

[16] J. A. Ejiwale, "Barriers to successful implementation of stem education," *Journal of Education and Learning (EduLearn)*, vol. 7, no. 2, pp. 63–74, 2013.

DOI: 10.61782/fa.2025.0417

FORUM ACUSTICUM
EURONOISE 2025

FROM SOUNDS TO ARCHITECTURAL DESIGN: ACOUSMATIC SPACES

Ayca Sentop Dumen[1*] **Yagdir Celiker-Cenger**[2]
[1] Department of Civil and Environmental Engineering, Norwegian University of Science and Technology, Norway
[2] Department of Architecture, Ozyegin University, Turkey

ABSTRACT

Acousmatic sounds are those that one hears without identifying their origin. Originating from musique concrète of Pierre Schaeffer, acousmatic music detaches the sounds from the individuals, instruments, and visual elements, to focus on the act of 'pure listening'. Implementing this notion on architecture, one can generate acousmatic spaces by detaching sounds from visual references of a space and re-compose them to design an experience.
A 10-day workshop was conducted that questioned the sound environment's potential in design by introducing it as the main element for design ideation while introducing acoustics as a building physics subject. 20 students of Faculty of Architecture in Istanbul Bilgi University participated in this workshop. Through a sequence of listening exercises, soundwalks, seminars and discussions, the students were trained about the main concepts of acoustics, structure-form-sound-perception continuum. A re-design problem was given that started with a blind walk for enabling 'pure listening' and data was collected with soundscape assessment questionnaires and voice recordings. A spatial narrative was created by 'sketching' sounds (sound-editing) and used in the regeneration of the spatial structures. The study showed that introducing systematic steps and experience-based teaching can encourage students to utilize auditory information in design and enable active learning in acoustics.

Keywords: *Acoustic education, Design education, Soundscape, Acousmatic music, Architecture*

[*]***Corresponding author***: *ayca.s.dumen@ntnu.no*
Copyright: *©2025 Ayca Sentop-Dumen & Yagdir Celiker-Cenger. This is an open-access article distributed under the terms of the Creative Commons Attribution 3.0 Unported License, which permits unrestricted use, distribution, and reproduction in any medium, provided the original author and source are credited.*

1. INTRODUCTION

The word "acousmatic" roots back to the ancient Greek word "acousma" which means "the object of hearing" and "akousmatikoi" which described the pupils of Pythagoras who listened the class while a curtain hindered the sound originator to avoid distraction. In 20th century the term "acousmatic" was adopted (initially by Jérôme Peignot and Pierre Schaeffer, later evolved by François Bayle) to describe the sounds that one hears without identifying its origin [1]. The framework for acousmatics comes from "musique concrète" and "reduced listening" pioneered by Pierre Schaeffer - *not to be confused with R. Murray Schafer, known for his contributions to soundscape studies.*

Musique concrète emerged as an experimental composing method using recorded sound "objects" and organizing them by implementing 3 main techniques: (1) transformation of time, (2) transformation of texture and timbre and, (3) spatialisation [2]. Fascinated by the recording technologies, Schaeffer believed that there existed a domain "beyond the sounds" through recording "the noises of things" [2]. This approach emphasized the abstraction of sound, thus enabling its use as a raw material for musical and spatial composition.

Recording technology not just offered the new method of music making but also allowed a new definition of listening. The sounds were disengaged from the origin, striped from indicative and communicative signs and they were no longer a "placeholder for some other thing" which Schaffer theorized as "reduced listening" [3]. By adopting this approach, one could focus on the musical characteristics of a sound or combination of sounds within a composition rather than identifying their source or the action that produced them [4].

Stemming from these fundaments, acousmatic music detaches the sounds from the individuals, instruments, and visual elements, to focus on the act of "pure listening". "Often taken by surprise, sometimes uncertain, we discover that much of what we thought we could hear was in reality merely seen, and explained, by the context." [1; p.66]. Acousmatic sound directs attention to sound characteristics that are typically overlooked when sight is present, as these visual cues tend to emphasize certain elements while masking others [5]. One challenge is that invisibility of the source initially evokes curiosity and intensifies causal listening, although this can be overcome through repetitive hearing [1, 5]. Therefore, acousmatic sounds challenge the listener to shift from conventional listening habits and requires them to focus on the sonic properties rather than their origin or cause.

Inspired by these notions, this study explores application of "acousmatics" in acoustic education as a way to stimulate spatial and soundscape design. In a workshop, students were engaged in a blind walk. They navigated in a building with their eyes closed, took recordings of sounds and defined their perception through a set of questions. This exercise in acousmatic perception aimed to detach the sounds from the space and allow them to reimagine the built environment as a composition of auditory elements rather than predefined spatial functions. The collected sounds were then used to compose new soundscapes, which were later translated into structural and spatial forms—creating a visual entity that emerged from a designed sound experience. In this sense this study aims to introduce a reverse design method to acoustics and spatial design. This paper presents the methodology and the results of this workshop.

2. METHODS

2.1 Preparation and development of the workshop methodology

A 10-days workshop was organized in 2019 summer in Istanbul Bilgi University. The workshop was planned with "learning-by-doing" approach and separated into three parts: (a) novice soundwalk, (b) training and (c) trained (blind) soundwalk.

The initial part of the study benefited from the methods and experiences of a former workshop study which investigated design methods for soundscape interventions [6]. In this previous workshop, students got engaged in a soundwalk, listened the acoustic response of the environment to the spatial sounds as well as self-generated sounds, and analysed their perception through the soundscape assessment forms. The assessment form and reading cards were prepared in line with ISO 12913-2:2018 and ISO 12913-3:2019 [7, 8] and benefited from [9 - 14]. Reading cards were used to evaluate the effect of acoustics during ensemble readings. Acknowledging the role of visual representation in design thinking, the study proposed techniques for audio-visual representation, namely: sound infogram, sound collage with recordings, and abstract sound-model with audio and visual elements. After this representation stage, students were encouraged to work with sound files, as well as sketches, texts and diagram for proposing a design intervention (further explained in [6]).

The current study used the sound evaluation form for the first soundwalk and an adjusted version for the second, i.e. blind walk (Figure 1). A challenge associated with acousmatic sounds was mentioned as the likelihood of the listener's attention shifting to the source due to curiosity. Instead of conflicting with this curiosity, we allowed students to first question the space characteristics through rating items of (a) socio-spatial environment, (b) spatial configuration, and (c) localisation inside the space, before moving to the questions related to soundscape quality.

Audio-visual representation techniques were applied although simplified for the purpose of the current study. An infogram consisting of only the radar chart of studied zone, sound collage with recordings, and sound-model with only visual representation was aimed for the first stage while students were intended to work with sound files, physical models and a videoclip in the second stage.

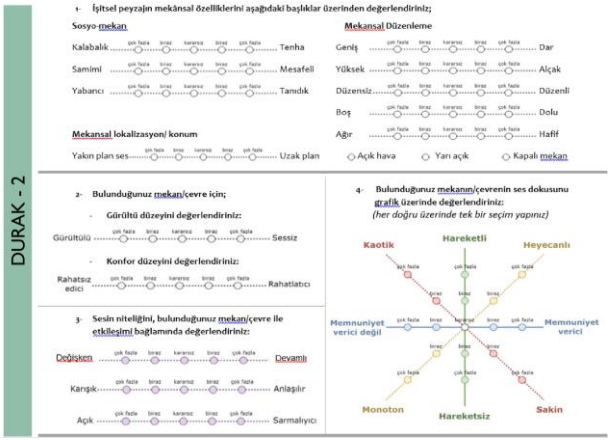


Figure 1. Assessment forms for blind walk

2.2 Workshop process

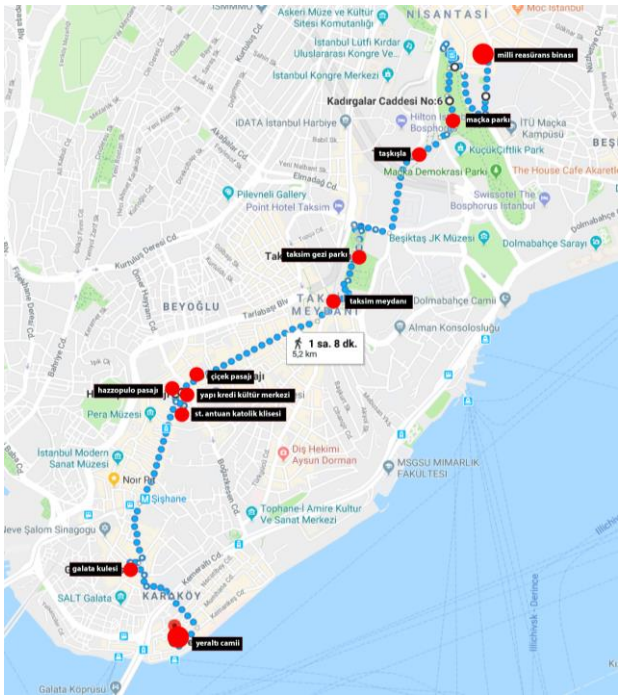
20 students participated to this workshop (15 female and 5 male). The majority had completed first year and had little or no knowledge on acoustics.

2.2.1 Novice soundwalk

Route: The novice soundwalk route was a central 5,2 km long walking route in Istanbul in the axis of Maçka – Taksim – Karaköy (Figure 2). 11 evaluation stops were predefined which would offer variety in terms of spatial, architectural and sound attributes. 4 open areas included both natural and urban soundscapes (Maçka Park, Gezi Park, Taksim Square, Galata Square). 3 passages constituted narrow urban corridors and courtyards which hosted both transit and leisure (café) activities (Milli Reasürans Passage, Çiçek [Flower] Passage, Hazzapulo Passage). 4 indoor spaces represented different architectural periods and had different spatial ratios (Taşkışla - ITU Architecture Faculty, Yapı Kredi Culture and Arts Centre, Church of St. Anthony of Padua, Yeraltı [Underground] Mosque).

Soundwalk procedure: A group walk was conducted on the route lead by instructors. Students were instructed to listen to the sounds and take recordings. In each stop they listened to their environment for approximately 3 minutes and filled the soundscape evaluation form. To understand the acoustic environment, they were instructed to use self-generated sounds (claps, footsteps) and do ensemble readings (4 students read the given texts while others listened). Afterwards instructors explained the historical background, architectural form and its effect on acoustics.

Audio-visual representation: On the following day, students discussed their experiences and the affective quality responses of all participants were averaged for each stop. Later the students were separated in 4 groups and assigned with one of the stops on the route. They were guided to experiment with the audio-visual representation techniques by preparing (1) a sound collage of maximum 1-minute using Adobe Premiere, (2) a graphical expression (poster) and (3) a physical model of sound-structure interaction. The students had little acoustical knowledge at this point and the aim of this study was to initiate questioning rather than proposing design solutions, while mastering representation techniques and tools. This activity continued for one and a half day.



(a)



(b)



(c)

Figure 2. Novice soundwalk; (a) route map, (b) ensemble reading at Yapi Kredi Culture and Arts Centre, (c) ensemble reading at passage

2.2.2 Training soundwalks and teaching

Theoretical knowledge was developed with seminars on basics of architectural acoustics, spatial design for sounds and interactive structures. An emphasize was given on on-foot learning. Two training soundwalks were conducted with approximately 1 hour duration.

- A soundwalk took place within the Istanbul Bilgi University campus, featuring multiple indoor and outdoor stops. This route encouraged students to perceive their familiar surroundings from a fresh perspective. Along the way, they were introduced to fundamental acoustical concepts and engaged in discussions on the relationship between sound, space, and human interaction.
- The second soundwalk involved a visit to Dialogue in the Dark [15], an exhibition where visually impaired guides lead visitors through a completely dark environment. The experience allowed participants to navigate solely through non-visual senses, deepening their awareness of sound and spatial perception.

2.2.3 Trained soundwalk – blind walk

Route: The trained soundwalk was conducted inside Istanbul Naval Museum in Besiktas (Figure 3). This building consisted of a heritage wing from 1897 and a newly built modern wing from 2013 [16]. Two separate routes were defined in two wings. The route in new wing was characterized by volumetric spaces and ended in a narrower glass bridge that connected the two wings. The route in heritage wing consisted of small- and moderate-size rooms distributed in 3 floors and an installation with water sound. Each route included 4 evaluation stops.

Procedure: Students were separated in groups of two. In each route one completed the walk blind (with eyes-covered) while the other acted as their guide and asked the affective quality assessment questions. They implemented the methods they practiced during the novice soundwalk (self-generated sounds, listening). They simultaneously took recording of the whole route.

Reverse design: Students were given the task of redesigning the route that they walked blindly. They were asked to design an "aural experience" and the form, structure and elements for it.

Students worked individually in this phase. They were encouraged to start with a sound collage of the route by using Adobe Premiere and go through the sound recordings, and their responses to affective quality questions. After familiarization process, they started to "design + compose" the spatial sounds by manipulating the sound texture and adding / subtracting sound elements. These were converted into a physical model where this sonic experience would occur. Students were asked to think about the acoustic principles and sound elements in relation to architectural form and socio-spatial environment.

The method for model making was defined as infilling within a 30x30 wooden frame, and students were free to use multiple frames if needed. For the submission students made a stop-motion video that combined the sound file with the corresponding vistas of their model.

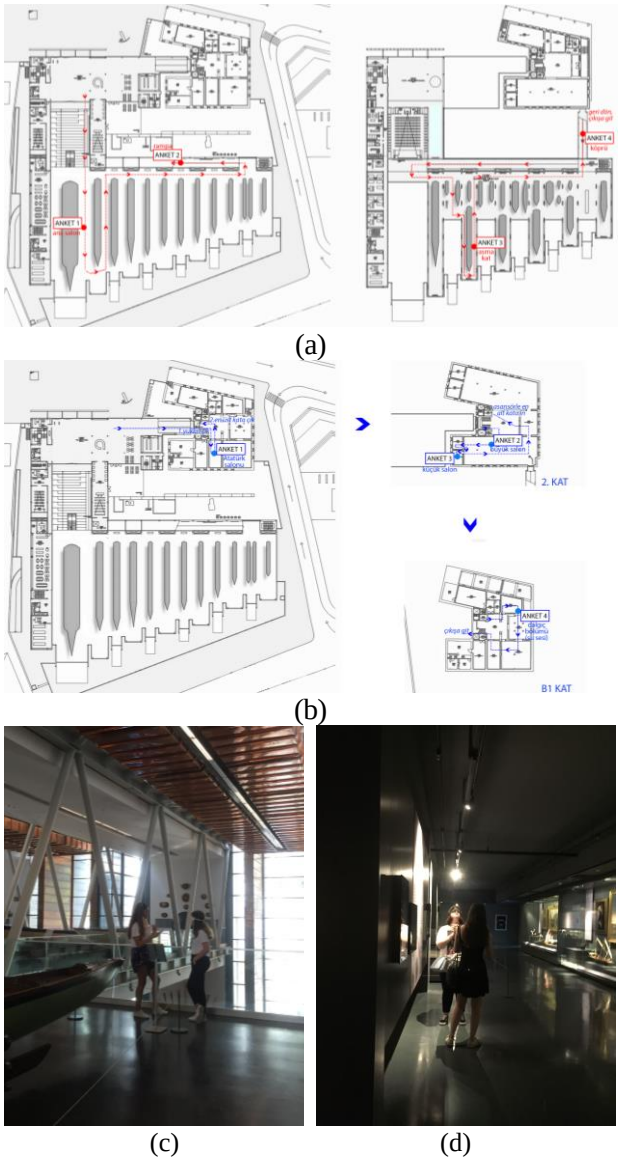


Figure 3. Trained soundwalk; (a,c) route in the new wing, (b,d) route in the heritage wing

3. RESULTS

3.1 Representation of acoustic environments (novice walk)

The first study involved a representation task, and the outcomes included a short sound collage, a poster and a model for four selected spaces.

All four-student-works reflected alterations and contrasts that emerged in the sound environment. When the contrast was not evident, students chose to extend the frame of the study. This was the case for two spaces (2nd and 3rd group) where students included street in addition to the assigned space. Both of them shared similar affective qualities rated as monotonous, uneventful and calm.

1. Çiçek [Flower] Passage
Affective quality: Eventful, exciting, chaotic
Represented elements: The alteration in strength of emotions (colourful spheres), user density (red line), sound level (blue line), reverberation time (green line), location of echo (arrow) (Fig. 4).

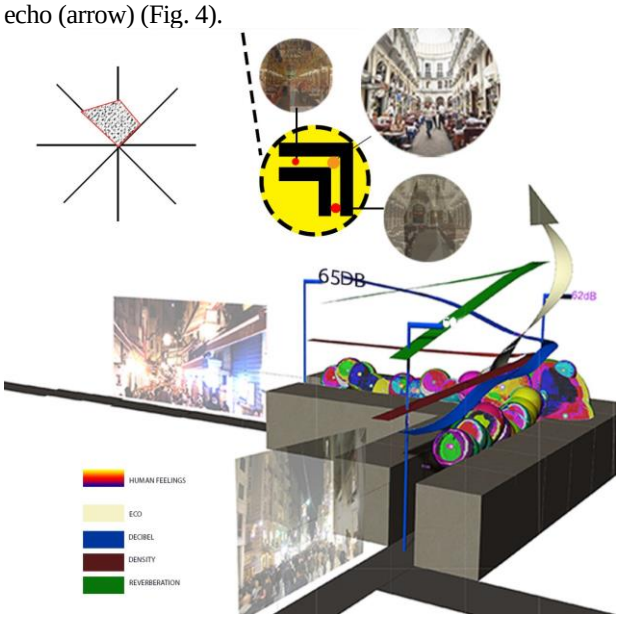


Figure 4. Graphic expression of sound environment in Çiçek [Flower] Passage

This work shows the perception of gradual alteration in sound environment in response to this transition space. The midpoint (corner) corresponds to largest volume which is depicted as climax for emotions along with the reverberation and echo perception (based on hand claps).

2. Church of St. Anthony of Padua
Affective quality: Uneventful, calm, (a little) monotonous
Represented elements: Sound levels (bar heights), variety (colourful vs. blue), envelopment (tangled forms vs. straight forms), transmissibility (forms bending over courtyard boundaries but not over church boundaries) (Fig. 5)

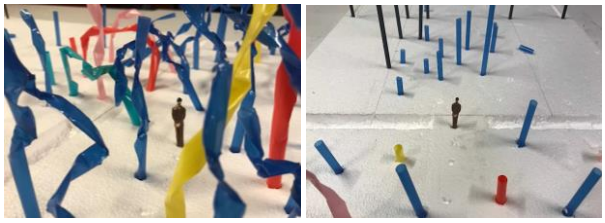


Figure 5. Physical model of sound environment in Church of St. Anthony of Padua

This work shows three different sound zones separated by borders. The two graving on ground shows borders of courtyard (Fig. 5 left) and church (Fig. 5 right). While preparing this work students commented on their observation that although the sound environment was very calm, any single event sounded "bigger" (long reverberation time) and they expressed these events with tall blue bars separated from each other.

3. Yeraltı [Underground] Mosque
Affective quality: Monotonous, uneventful, calm, (a little) pleasant
Represented elements: Temporal and level characteristics (outdoor sounds: rhythmic red line at top vs indoor sounds: continuous beige line at bottom with few movements), sound texture (onomatopoeic words) (Fig. 6)

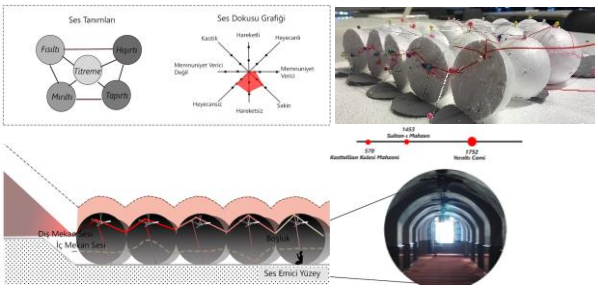


Figure 6. Graphic expression and physical model of sound environment in Yeraltı[Underground] Mosque

Originally built as an underground cellar, this is an unusual space consisting of repetitive domes, low ceiling, massive load bearing columns that create visual and acoustic barrier,

and absorption due to carpet. Students' physical model shows the negative space (void as mass). Their choice of onomatopoeic words (*fısıltı*: whisper, *hışırtı*: rustle, *tapırtı*: tapping, *mırıltı*: murmur) implies perception of soft, subtle and continuous sounds and a non-intrusive environment.

4. Yapı Kredi Culture and Arts Centre
Affective quality: Pleasant, calm, (a little) uneventful
Represented elements: Reflection and absorption of sound by different materials (lines) (Fig. 7)

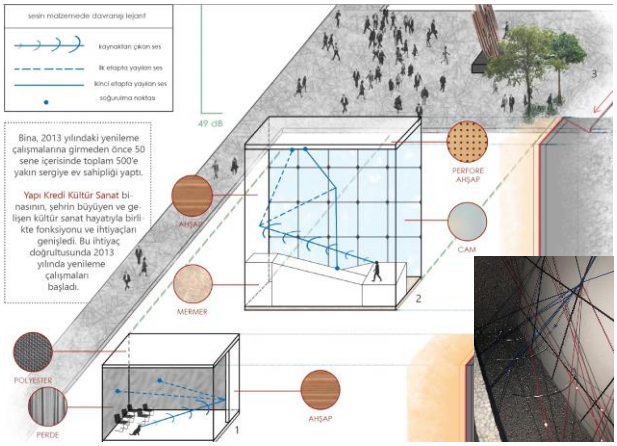


Figure 7. Graphic expression and physical model of sound environment in Yapı Kredi

This group focused on sound reflection from surfaces. They compared circulation area which was characterised by its high ceiling, glass and stone surfaces, with the seminar room which contained absorptive surfaces.

3.2 Reverse design (trained / blind walk)

The second study involved a reverse design task, and the outcome was a stop-motion video which combined the sound file and the physical model prepared by the students. 15 of the students submitted their final work. 11 of them were able to complete the final video in time, two students submitted a sound file and a photo of the model, and two students submitted only a sound file.

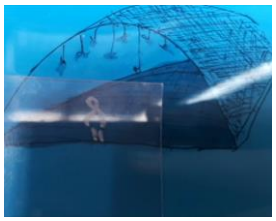
Students presented their work to the instructors and their peers at the end of the workshop. Due to the absence of students' own verbal descriptions at this stage (contrary to the first study where students' intentions were explicit in posters), the results presented in this chapter include mainly our observations on outcomes and process.

3.2.1 Observations on the design works

Students' instinct of searching for contrasts and comparisons was also evident in the second study (design works) as many of the works offered richness in designed sound experience. Students adjusted the sound characteristics (temporal, frequency, levels), added directivity and spatialization (using left-right channels, dynamic levels, reverb and echo), and through introducing new sounds (spatial, environmental, self-generated, musical and other "effect" sounds). This was reflected in the architectural geometry with changing size, ratio, form and sound elements as well as open / semi-open areas to enable city, and/or nature sounds. This shows that designing "experience" output as a starting point, encourages students to form dynamic spaces (Fig. 8 and 9).



(a)



(b)



(c)

Figure 8. Screenshots from one of the videos with a rich space and sound configuration



Figure 9. A study in which a parallel was drawn between the visually reflective tubular form and sounds distorted through delayed repetition

Most designs also included movement at Z axis (stairs / ramps) (Fig. 10). This might be an attempt of creating different "sound vista"s. However, it is also possible that this was induced by the vestibular sense of the movement pattern during the blind walk, or by the model-making method which involved filling in a wooden frame.

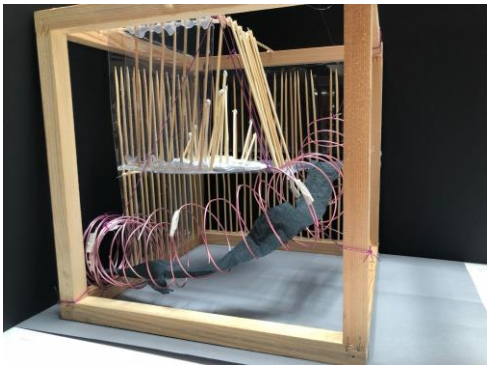
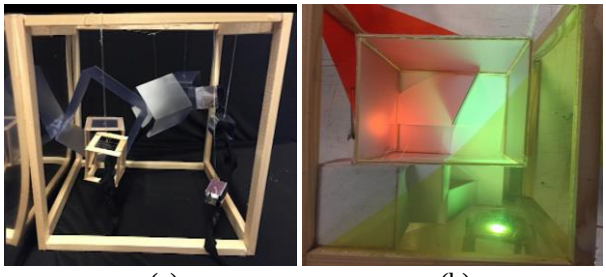


Figure 10. A route where a ramp forms a transition zone between the outdoor sounds and indoor sounds as well as between street level and upper level. The large and reverberant indoor space hosts an inner structure with contrasting sound characteristics

When the studies are analyzed together, a distinction emerges between two approaches to user movement within designed spaces. Some allow for free navigation, enabling users to explore the space openly, while others establish a continuous, predetermined route that guides movement in a specific direction. The intentionality behind these choices needs further examination in future studies (Fig. 11).



(a) (b)

Figure 11. Two approaches to user movement. (a) restricted, (b) free navigation *(the image shows top view)*

There was a clear tendency to include music, even though it was not the main element in most studies. Musical elements can serve as immediate cues for conveying emotion. This should be critically examined in future studies to encourage students to explore alternative means of emotional expression and search spatial sounds.

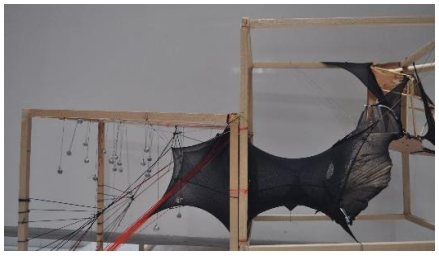


Figure 12. A study where student used spatial sounds very minimally and created a more-deliberately designed sound file composed with sound effects

3.2.2 Observations on the blind walk process

The blind walk received strong interest, and students were generally positive about this experience. The training soundwalk in "Dialogue in the Dark" was helpful for preparing students to navigate in space in the lack of their visual sense (with a guide) and focus on their audio environment. Nevertheless, one student reported being uncomfortable of walking while eyes were covered and that this sense influenced their final work (Fig. 13). This comment and the observed tendency of movement at Z axis (see section 3.2.1) suggest that while blind walk helps to omit visual input, vestibular sense might continue to intervene with the perception.



Figure 13. Student work that reflected discomfort during the blind walk. The sound file included eerie elements such as squeaks and screams, while the spatial model featured vertiginous, torsional surfaces

The implementation of the soundscape assessment forms not only systematized the evaluation but also it directed the

attention to the experience of acousmatic sounds. Furthermore, the voice record of the guide who read the questions on the form and the reading texts was used as a "sound object" in many of the sound collages.

Many students expressed their curiosity about the space. This confirms the challenge associated with acousmatic sounds, as the listener's attention is likely to shift away from the sound upon first contact. Repetitive listening of recordings is found useful for reframing sounds as objects of redesign.

3.2.3 Observations on the design process

The physical model fed from the sound file, demonstrating an example of reverse design, where students first crafted the sound environment and then derived the spatial form from it. This approach highlights the potential of sound as a generative tool in design, encouraging a deeper understanding of the relationship between auditory and spatial experiences. Additionally, it offers a method of acoustic learning where students not only analyse their own perceptions but also design a soundscape and search for forms elements to materialise it.

The two-stage study (novice + trained) helped students to familiarize with listening to spaces, discovering acoustics through self-produced sounds and assessment of soundscape quality as well as representation tools and techniques. This helped the students to focus less on mastering the techniques and more on the activity itself in this second part of the study.

4. CONCLUSION

Inspired by the acousmatic music, this workshop explored its implementation in a design study. Acousmatics suggests renouncing the instrument and traditional musical frameworks, focusing instead on sound itself and its inherent musical "potential" [1]. In this workshop study, students listened to the space without visual cues, stripped the sounds of their origins and spatial context, and explored their potential in designing an aural experience. This provided an alternative way of engaging with sound, moving beyond traditional acoustic design. The designed/composed sound was converted into a spatial form thus exemplifying a reverse design method for architecture and soundscape.

During the 10-day workshop, students were trained in attentive listening and developed a deeper understanding of the acoustic environment. The acoustic training primarily occurred through on-foot experiences and learning-by-doing. This approach fostered an intuitive understanding of how sound interacts with space, offering insights for architectural and acoustic education.

5. ACKNOWLEDGMENTS

This study was conducted in Istanbul Bilgi University.

6. REFERENCES

[1] P. Schaeffer. *Treatise on Musical Objects : An Essay Across Disciplines.* (C. North & J. Dack, Trans.). University of California Press, 2017.
[2] M. Battier. "What the GRM brought to music: from musique concrète to acousmatic music". *Organised Sound*, 12(3), pp. 189-202, 2007. DOI: 10.1017/S1355771807001902
[3] B. Kane. "L'Objet Sonore Maintenant: Pierre Schaeffer, sound objects and the phenomenological reduction". *Organised Sound*, 12(1), pp. 15-24, 2007. DOI:10.1017/S135577180700163X
[4] L. Landy. "Chapter 2. Work discussions across sound-based creativity". *Experiencing Organised Sounds*. Routledge, 2023.
[5] M. Chion, "Chapter 5. the three listening modes" in The sound studies reader, *The Sound Studies Reader* (ed. J. Sterne). Routledge, 2012.
[6] A. Sentop Dumen & M. Koyaz. "*A study on audio visual representation and thinking for designing acoustic environments".* 24th International Congress on Acoustics, Gyeongju, 2022.
[7] ISO, "ISO/TS 12913-3:2019 Acoustics -Soundscape, Part 3: Data analysis." 2019.
[8] ISO, "ISO/TS 12913-2:2018 Acoustics -Soundscape, Part 2: Data collection and reporting requirements." 2018.
[9] Ö. Axelsson, M. E. Nilsson, and B. Berglund, "A principal components model of soundscape perception," *J Acoust Soc Am*, vol. 128, no. 5, pp. 2836–2846, Nov. 2010, DOI: 10.1121/1.3493436.
[10] A. Özçevik. An Approach on the Evaluation of Urban Acoustical Comfort with the Soundscape Concept. Istanbul, 2012. [in Turkish]
[11] A. Özçevik and Z. Yüksel Can, "A Study on the Documentation and Analysis of the Urban Acoustical Environment in Terms of Soundscape," *Megaron*, vol. 7, no. 2, pp. 129–142, 2012.
[12] W. J. Davies *et al.*, "Perception of soundscapes: An interdisciplinary approach," *Applied Acoustics*, vol. 74, no. 2, pp. 224–231, Feb. 2013, DOI: 10.1016/j.apacoust.2012.05.010.
[21] S. Bahalı, Urban Soundscape Research in The Route Of Gezi Park – Tünel Square. Istanbul Technical University, Istanbul, 2015. [in Turkish]
[13] S. Bahalı and N. Tamer-Bayazıt, "Soundscape research on the Gezi Park –Tunel Square route," *Applied Acoustics*, vol. 116, pp. 260–270, Jan. 2017, DOI: 10.1016/j.apacoust.2016.10.002.
[14] E. Thompson, *The Soundscape of Modernity: Architectural Acoustics and the Culture of Listening in America, 1900-1933*. The MIT Press, 2004.
[15] Diyalog Muzesi Istanbul. Dialogue in the Dark. Accessed on 1.4.2025. URL: https://www.istanbuldiyalogmuzesi.org/en/dialogue-in-the-dark/
[16] Turkish Museums. Istanbul Naval Museum. Accessed on 1.4.2025. URL: https://www.turkishmuseums.com/museum/detail/22321-istanbul-naval-museum/22321/4

DOI: 10.61782/fa.2025.0079

FORUM ACUSTICUM EURONOISE 2025

ACOUSTIC MULTI-COMPONENT MONITORING OF ECOSYSTEMS: TRAINING FOR MANGROVES' CONSERVATION IN AFRICA

Clotilde Fátima Nhancale[1*] **Zaira Valgi Macheve**[2] **Aura Rapino**[3]
Augusto Júnior Nhampossa[4] **Marta Polizzi**[5] **Pier Francesco Moretti**[6]
[1*] Centre for Functional Ecology, Department of Life Sciences, University of Coimbra, Portugal
[2] Natural History Museum, Maputo, Mozambique
[3] Department of Environmental Biology, University of Rome "La Sapienza", Rome, Italy
[4] Associação NATURA Moçambique, Maputo, Mozambique
[5] UNESCO Chair of Management of Conservation Areas, CUAS, Villach, Austria
[6] CNR-Department of Earth System Sciences and Environmental Technologies, National research Council of Italy, P.le A. Moro 7, 00185 Rome, Italy

ABSTRACT

Mangrove ecosystems are critical habitats that provide a diversity of ecological services. Societal and economic sustainability of populations living with mangroves rely on health of those ecosystems, through fishing activities and extraction of firewood, material to build houses, furniture and fishing gear. A knowledge-based support to policy decisions and identification of appropriate interventions for conservation and restoration of ecosystems is needed, including education and training of young generations. We describe the experience of a training course for the installation and management of an observing station for the monitoring of the soundscape. For the first time, a system for monitoring the acoustic field in air, soil, and water has been installed in Inhaca (Mozambique) to provide clues on the mangroves' ecosystems. The potential of operational acoustic measurements, as well as protocols for training and managing observing stations for conservation and protection of the environment, are provided. By integrating acoustic measurements into conservation efforts, the station not only advances ecological monitoring but also acts as a key resource for local communities and schools, fostering environmental education and empowering stakeholders in the protection and sustainable management of mangroves. The experience highlights both the potential and challenges of leveraging soundscape data for environmental stewardship.

Keywords: *mangroves, ecosystem, bioacoustics, education, conservation.*

[*] ***Corresponding author**: clonhancale92@gmail.com*
***Copyright**: ©2025 Nhancale, C. et al. This is an open-access article distributed under the terms of the Creative Commons Attribution 3.0 Unported License, which permits unrestricted use, distribution, and reproduction in any medium, provided the original author and source are credited.*

1. INTRODUCTION

Mangroves are intertidal habitats, occurring in the sub-tropics along sheltered and shallow-water coastlines [1]. There are important ecosystems that provide goods and services for coastal environments, communities and society as a whole [2-4]. Above the water, the mangrove trees and canopy provide an important habitat for a wide range of species, including birds, insects, mammals and reptiles. Below the water, the mangrove roots are overgrown by epibionts such as tunicates, sponges, algae, and bivalves [1]. Despite being among the most productive ecosystems, mangrove forests have historically been undervalued, and their area has been reduced due to poor management and increasing demand for coastal lands for development [3; 5]. Thus, it has been a high priority for the global community to arrest mangrove loss and restore degraded mangrove ecosystems, and the Knowledge-based approach has been an important support to policy decisions and the identification of appropriate interventions for the conservation and restoration of these ecosystems.

Education and training programs of mangrove ecosystems are held worldwide, to understand all the aspects of the

structure and function of mangroves, as well as their bio-geographical affinities and their conservation and management, which is important to have a considerable knowledge of the species composition and ecology [1-2]. These educational programs are to guide and equip the local communities with the basic technical know-how and skills for conserving, managing and rehabilitating mangroves in their areas.

In Mozambique, the Sapienza - University of Rome, in collaboration with Eduardo Mondlane University, launches an annual Intensive Summer School Course "ManGrowth - Preservation of Ecosystems for Sustainable Development." The course is promoted and funded by the Italian Agency for Development Cooperation, as part of the ManGrowth Project (Preservation of Ecosystems for Sustainable Development – AID 012432/01/2), which focused on the importance of mangrove forests as an essential ecosystem to promote the sustainable development of coastal areas, the mitigation of the effects of climate change and the conservation of animal and plant species that are linked to them by their life cycle.
In this context, as part of the technical training and capacity building for young researchers, two low-cost bioacoustics stations were installed. Sounds from the air, soil, and water were recorded to monitor the soundscape made by the living organisms that occur in the mangrove ecosystems and their behavior due to the floatation of tides and day season into the mangrove. The use of bioacoustics as a biomonitoring tool allows us to understand what the ecosystem's dynamics can tell about the habitat's health, which may aid in monitoring the success or progress of ecosystems restoration and conservation [6-8].

2. THE TRAINING APPROACH

The training course was focused on soundscape ecology. Soundscape ecology is the integration of geophysical, biological and anthropogenic sounds that fill an ecosystem and which vary over space and time [9]. It has recently emerged as an interdisciplinary scientific field that investigates the acoustic field in relation to ecological processes. In this context, the training course tested in mangrove ecosystems an innovative instrumental set-up aimed to use multi-component observing stations of the biosphere for the identification of emergent properties of the status of the ecosystems.
The design and development of the training course was mainly guided by a "learning by doing" approach. Frontal teaching on fundamentals of acoustics, signal treatment, specifications and calibration of instrumentation, concepts of measure, sensitivity and bits were provided. Students were involved from the beginning in a co-decision process for the identification of locations for the observing stations and the adjustment of the parameters of the instrumentation. Students were also divided into sub-groups for the responsibilities of recharging the batteries, inspection of the functioning of the instrumentation, data analysis.



Figure 1. Training session on the field: first concepts of bioacoustics and instrumentation used (Photo by Enrico Nicosia).

Every day, an early morning briefing and a post-dinner reflection meeting were implemented to plan activities and further developments. The duration of the course was a whole week and was included in a one-month summer school (see the acknowledgements for further details), with a final report to be delivered [10], and an extension of 4 more days for the collection of additional data.

3. THE EXPERIENCE IN INHACA

3.1 Study Area

Inhaca Island (Mozambique) is a 40 km² island with diverse ecosystems, including coastal forests, mangroves, and seagrass meadows. Two bioacoustics monitoring stations were set up: one near the Inhaca Marine Biology Station and another at Ponta Rasa. The island experiences a tropical climate with distinct wet and dry seasons. Inhaca has semidiurnal tides, crucial for both ecosystem dynamics and study design. Stations were installed during low tide to ensure accessibility and reduce equipment damage.

3.2 Equipment and Setup

To ensure effective acoustic monitoring that captured the full range of environmental sounds, the recording system was designed with a combination of hydrophones and

microphones, strategically positioned in air, water, soil, and intertidal zones. At the core of the setup was the Zoom P4 PodTrak recorder, powered by reliable power banks to maintain continuous operation in the field [10].



Figure 2. Study area: this is an overview of the second station at Ponta Rasa, which was very close to a channel with continuous water flow from the sea to the internal areas (Photo by Augusto Nhampossa).

Special attention was given to installation to minimize environmental interference. Microphones were shielded to reduce wind noise, while hydrophones were carefully anchored to ensure constant submersion. Additionally, all equipment was securely mounted to prevent accidental disturbances that could affect data quality.



Figure 3. Setup of the acoustic stations: cables needed to be accurately positioned in order to avoid contact with water or movements that could give biased sounds in the recordings (Photo by Enrico Nicosia).

3.3 Data Collection

Recordings were conducted from October 1–8, 2024. Data were collected in segments of 3h22min53sec, and a further selection or shorter time intervals allowed a smooth processing for later analysis [10].



Figure 4. Hydrophone hung on the roots in order to be outside of the water with the low tide and submerged with the high tide (Photo by Enrico Nicosia).



Figure 5. Recorder: as inputs, we used one microphone for air and three hydrophones for water and soil (Photo by Aura Rapino).

3.4 Challenges and Solutions

Several environmental factors posed challenges during the study. The muddy terrain made installation difficult, requiring careful planning and teamwork to position the equipment properly. Ensuring a stable power supply was also crucial, and the use of power banks provided a reliable solution for uninterrupted monitoring and silent generators [10].

Wind interference was another challenge, necessitating adjustments to microphone shielding to reduce background noise. The placement of hydrophones required particular attention as well, as maintaining continuous submersion was essential for accurate data collection. Additionally, managing the large volume of data was a key consideration, with daily recordings reaching approximately 30 GB, making efficient segmentation necessary to facilitate analysis [10].



Figure 6. Microphone hung on a higher branch in order to record air sounds, covered to avoid disturbance from wind and rain (Photo by Enrico Nicosia).

3.5 Recommendations

For future monitoring efforts, conducting a preliminary site assessment can help identify potential challenges and optimize equipment placement. Ensuring secure installations is also essential to minimize environmental and human disturbances. Combining acoustic monitoring with additional sensors, such as anemometers, thermometers and camera traps, can provide a more comprehensive understanding of environmental dynamics. Ultimately, bioacoustics monitoring proves to be a cost-effective and valuable tool for mangrove conservation, offering critical data for assessing ecosystem changes and informing management strategies.

4. CONCLUSIONS

This study highlights the feasibility of monitoring mangrove ecosystems using accessible and cost-effective acoustic techniques. By capturing variations in soundscapes, passive acoustic monitoring provides valuable insights into biodiversity, habitat health, and ecosystem dynamics. However, to fully harness its potential, future research should focus on refining methodologies, expanding monitoring efforts, and establishing standardized protocols for long-term ecosystem assessments.

One key avenue for development is the identification of reliable acoustic indicators that reflect the state of the ecosystem. Distinctive sounds produced by organisms such as crabs, shrimps, fish, and insects, as well as abiotic elements like bubbles and water flow, could serve as bioacoustics markers for assessing habitat quality and ecological changes. Creating archives of reference signals would be instrumental in building a comparative framework, enabling researchers to detect shifts in species composition, human-induced disturbances, or natural seasonal variations.

Mozambique, with its vast coastal and wetland habitats, presents a significant territorial opportunity for expanding acoustic monitoring beyond the initial study site. Establishing a network of monitoring stations across key mangrove regions could provide large-scale, long-term datasets, supporting conservation strategies at both national and regional levels. Scaling these efforts across other African coastal ecosystems could contribute to a continent-wide initiative aimed at protecting critical biodiversity hotspots using non-invasive, technology-driven approaches.

Beyond scientific applications, fostering community engagement is essential for the success and sustainability of bioacoustics monitoring. Training a new generation of “guardians” and citizen scientists—including local fishers, students, and conservationists—can promote widespread participation in data collection and habitat protection. Educational programs, field workshops, and accessible training materials could empower local communities to take an active role in conservation, bridging the gap between research and real-world impact.

The integration of social media and web platforms could further enhance outreach and collaboration. By sharing acoustic recordings and findings through digital platforms, or common devices such as mobile phones, researchers can engage a wider audience, increase public awareness, and facilitate knowledge exchange between scientists, conservationists, and the general public.

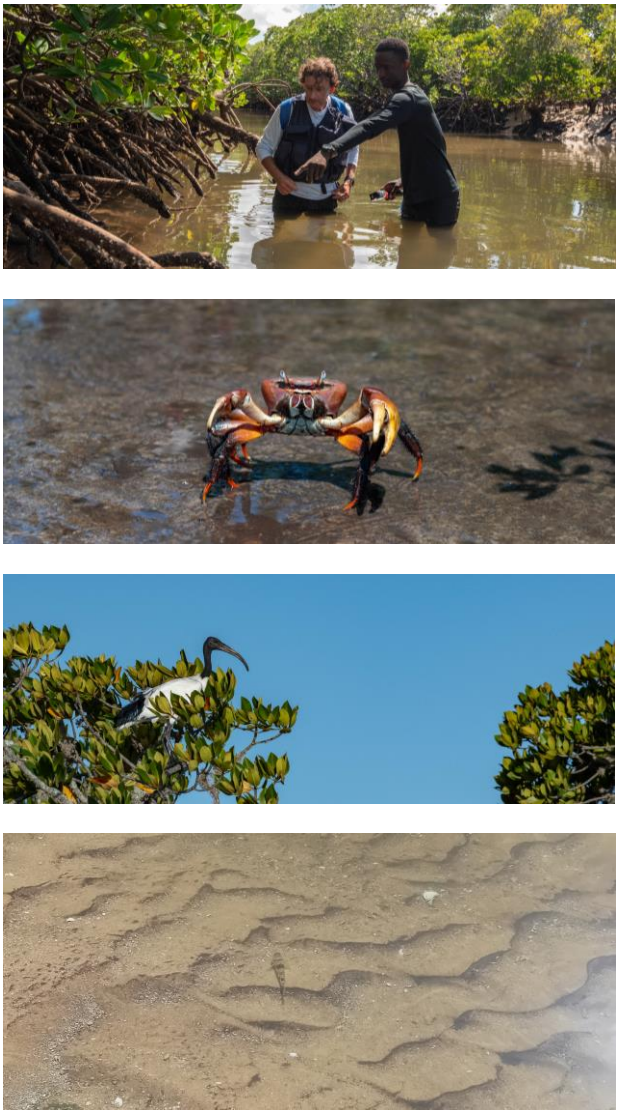


Figure 7. During the field stations, different species where observed in the ecosystem. From top to bottom: crabs, birds, fish (Pictures by Enrico Nicosia and Pier Francesco Moretti).

Open-access databases for bioacoustics data sharing could also help create global repositories of environmental sounds, supporting comparative studies and collaborative research initiatives. Furthermore, the user-friendly, low-cost nature of this system makes it easy to handle and accessible for widespread implementation, ensuring that local communities and researchers can adopt it with minimal technical barriers. Strengthening methodologies, expanding research networks, and engaging local communities will ensure that these efforts contribute to the long-term sustainability of coastal environments. This study serves as a foundation for future bioacoustics monitoring initiatives, demonstrating the potential of soundscape analysis in environmental conservation.

In conclusion, bioacoustics has the potential to become a powerful tool for mangrove conservation, blending science, technology, and community participation. Strengthening methodologies, expanding monitoring networks, and integrating digital tools can significantly enhance our ability to assess and protect these critical ecosystems for future generations.

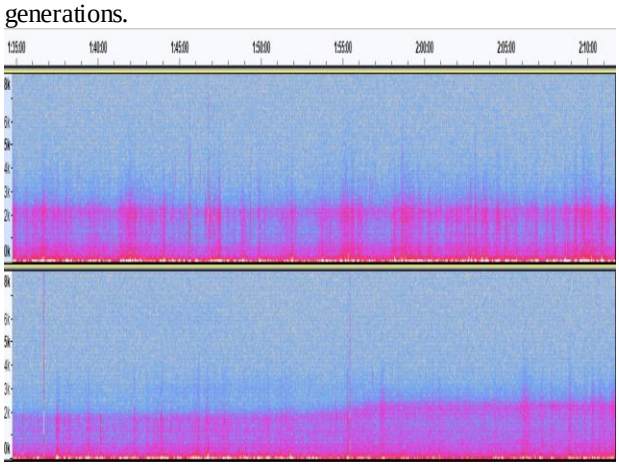


Figure 8. Spectrograms of two selections of approximately 35 minutes of data from the hydrophone hanging on the roots (partially in air and partially in water). Low and high tide cycles are clearly visible, as well as differences in the intensity and variety of sounds, that needs further analysis. Spectrograms are obtained through Audacity® ver. 3.6.4 [11], white and reddish colors refer to more powerful signals.

5. ACKNOWLEDGMENTS

This research was conducted within the framework of the ManGrowth Project (Preservation of Ecosystems for Sustainable Development – AID 012432/01/2), funded by the Italian Agency for Development Cooperation. We extend our gratitude to *Sapienza* University of Rome, Eduardo Mondlane University (UEM), and the National Research Council of Italy (CNR) for their valuable contributions and institutional support.

We also thank Paolo Ramoni as the project coordinator of ManGrowth: without him all of this wouldn't be possible.

6. REFERENCES

[1] I. Nagelkerken, S.J.N Blaber, S. Bouillon, P. Green, M. Haywood, L.G. Kirton, J.O. Meynecke, J. Pawlik, H.M. Penrose, A. Sasekumar, & P.J. Somerfield: "The habitat function of mangroves for terrestrial and marine fauna: A review," Aquatic Botany, vol. 89, no. 2, pp. 155–185, 2008. https://doi.org/10.1016/j.aquabot.2007.12.007

[2] J.P. Alappatt: "Chapter 5 - Structure and species diversity of mangrove ecosystem," In Biodiversity and Climate Change Adaptation in Tropical Islands (pp. 127–144), Elsevier Inc., 2018. https://doi.org/10.1016/B978-0-12-813064-3.00005-3

[3] R. Chevallier, R.: Balancing Development and Coastal Conservation - Mangroves in Mozambique, 2013.

[4] P. Erftemeijer, M. de Boer & L. Hilarides: The state of mangroves in the Western Indian Ocean, 2022

[5] UNEP/USAID/WIO: "Guidelines on Mangrove Ecosystem Restoration for the Western Indian Ocean Region," United Nations Environment Programme/Nairobi Convention Secretariat, 2020. https://www.unep.org/resources/report/guidelines-seagrass-ecosystem-restoration

[6] C.W. Maina: "Bioacoustic approaches to biodiversity monitoring and conservation in Kenya," in *2015 IST-Africa Conference, IST-Africa 2015, May*, 2015. https://doi.org/10.1109/ISTAFRICA.2015.7190558

[7] W. Penar, A. Magiera, & C. Klocek: "Applications of bioacoustics in animal ecology," *Ecological Complexity*, vol. 43, 2020. https://doi.org/10.1016/j.ecocom.2020.100847

[8] A.K.H.A. Rahim, C.L. Puan, M. Zakaria, N. Jamaludin, & N.S.A. Wahaf: "Diel Soundscape Patterns As a Potential Indicator of Mangrove Health in Peninsular Malaysia," *Malaysian Forester*, vol. 87, no. 1, pp. 118–136, 2024.

[9] B.C. Pijanowski, L.J. Villanueva-Rivera, S. Dumyahn, A. Farina, B. Krause, B. Napoletano, S. Gage, and N. Pieretti: "Soundscape Ecology: The Science of Sound in Landscapes", *BioScience*, vol. 61, pp. 203-216, 2011.

[10] A. Nhampossa, A. Rapino, C. Nhancale, M. Polizzi, L. Scepi, Z. Macheve, and P.F. Moretti: "Exploring the potential of a bioacoustic monitoring station in the mangrove ecosystem of Inhaca", in *Proc. of the Summer School ManGrowth 2023: Ecology and conservation* (Inhaca, Mozambique), in press.

[11] Audacity Development Team, Audacity, 2010. http://audacity.sourceforge.net

DOI:

Main theme: A04 Education, Public Outreach and History in Acoustics

Session A04.02 Online resources and simulations for teaching and learning acoustics

Chair(s): A. Ernoult, M. Pàmies-Vilà, L. Aspöck

DOI: 10.61782/fa.2025.0586

FORUM ACUSTICUM EURONOISE 2025

MOOCs FOR INTRODUCTORY COURSES IN ACOUSTICS AT THE UNIVERSITY OF LE MANS: ASSESSMENT AND PROSPECTS

Jean-Pierre Dalmont
Laboratoire d'Acoustique LAUM UMR CNRS, Le Mans Université, France

ABSTRACT

The University of Le Mans and its acoustic laboratory have initiated a series of MOOCs in French (Massive Open Online Courses) for an introduction to acoustics. The first, " Les bases de l'acoustique - la voix dans tous ses états ", is aimed primarily at high school students and physics teachers. Open since 2018, it has more than 20,000 registered students and has been used in particular in several speech therapy schools. The second, " Théorie pour un son – l'acoustique au service musicien ", is aimed at musicians and the curious with the aim of creating a generation of acoustically informed musicians. Each chapter begins with a video scenario and offers animations, interactive resources, expert interviews, activities with Audacity and quizzes. Opened in 2024, it has already attracted more than 5,000 registered students. Le Mans University is now working on developing a MOOC on the construction and physics of musical instruments. In collaboration with Itemm (Institut Technologique Européen des Métiers de la Musique), this evolving MOOC, after providing the basics of instrument physics, will detail a certain number of instruments, including the voice. The opening is planned for 2026.

Keywords: *Education, Massive Open Online Courses, Musical acoustics.*

*Corresponding author: jean-pierre.dalmont@univ-lemans.fr

***Copyright**: ©2025 First author et al. This is an open-access article distributed under the terms of the Creative Commons Attribution 3.0 Unported License, which permits unrestricted use, distribution, and reproduction in any medium, provided the original author and source are credited.*

1. INTRODUCTION

MOOCs, i.e. Massive Online Open Courses, are a tool for disseminating knowledge that has become considerably widespread since 2008. The basis of the MOOCs are short videos completed by some written documents. Other resources are usually proposed such as quiz to test knowledge, exercises to put the lessons into practice and discussion forums to interact with the teaching team and other students. Le Mans University made 2 MOOCs which are still available and started to work on third one. These MOOCs are briefly presented below.

2. FIRST MOOC

This MOOC, "Les bases de l'acoustique - la voix dans tous ses états" was and is still dedicated to high school students. It was designed based on the official baccalaureate acoustics program and is proposed on the French MOOC platform "France Université Numérique" (FUN). It contains 5 lessons and the total time investment needed is evaluated to 10 hours. Each lesson starts with a video putting the subject into context and contains experiments and exercises. First lesson is about waves and their speed. It is asked to the student to measure the speed of sound with their phone and give the result on a forum. Second lesson is about sound analysis and signal processing. Using the software Audacity, it is asked to measure the frequency of whistling and vowels. At the end it is asked, using processing tools to transform the vowel [a] into the vowel [i]. Third lesson is about modes of simple resonators such as string and tubes and finally the fourth lesson is devoted to signal digitization.
This MOOC opened first on spring 2018 for 6 weeks. There were important exchanges in the forums and the teaching team was solicited quite a lot. All these exchanges led to important modifications for the second session of winter 2018. Between 2018 and 2021 there were two sessions per year. During the period we observed an important decrease

of the use of the forums and despite a still positive evaluation of the MOOC, the teaching team was no longer in demand. So, we decided to leave it open almost permanently.
Over the years this MOOC had more than 20,000 registrations. However, it didn't it did not completely reach its target since most of high school students in France do not know what is a MOOC. They go much more naturally to platforms such as YouTube. The audience was more teachers, retired people working in the sound domain and curious people. We noticed that the MOOC has been included by some speech therapy schools in their teaching program.

3. SECOND MOOC

The idea for this MOOC entitled "Théorie pour un son – l'acoustique au service musicien" comes from an observation: most of the musicians we met have very little basic knowledge of acoustics. This is a real handicap whether in terms of hearing risk prevention, room acoustics, basics of harmony and the question of temperaments and auditory perception in general. We have therefore designed an introductory MOOC on acoustics for musicians to try to fill these gaps by introducing very little mathematics. This MOOC contains 7 lessons and the total time investment needed is evaluated to 12 hours. As for the previous, each lesson starts with a video putting the subject into context followed by an expert interview. It contains also animations, practical works, exercises, and JAVA applets which can be found independently on JPQ.fr. In the first lesson students are invited to discover the spectrogram with audacity and to make the link with the musical score. Second lesson is about room acoustics and third about decibel scale and the summation of sources and masking. In this lesson is also discussed the question of auditive risks. In the fourth lesson the link between frequency and pitch is explained so that musicians can have an informed use of the tuner. The fifth lesson delves deeper into the subject and addresses the dual perception of pitch: tonal pitch related to frequency and resulting from a counting process and spectral pitch related to the center of gravity of the spectrum and resulting from cochlear tonotopy. Lesson 6, according to Helmholtz, give the physical basis of harmony and discuss the question of tuning and temperament. Finally Lesson 7 addresses the issue of timbre.
This MOOC is open since 2024 and has already been followed by more than 5000 students. As the previous one it has forums but these are almost not used by the users. This is a bit disappointing but this shows that despite a high satisfaction rate, interaction with teachers and other students is not sought.

4. THIRD MOOC

As discussed above, most musicians know very little about acoustics but they also know very little about the making and functioning of their instruments. To try to fill this gap Le Mans Université and the school for instrument making and repair Itemm (Institut Technologique Européen des Métiers de la Musique) join their forces to build a MOOC about making and physics of musical instruments. Firsts lessons will describe the different elements that make up a musical instrument and then the physics of these different elements: exciter, resonator and "radiator". The following courses will deal with specific instruments: piano, voice, guitar, violin and its family, clarinet, flutes, saxophone and oboe, brass, percussions, etc. The MOOC is scheduled to open in 2026, but the different instruments will be covered gradually. For each instrument, the building will be first detailed. Different aspects of their operation will be explained. Our aim is that musicians will find answers about their instruments.
.

5. CONCLUSION

MOOCs are knowledge dissemination tools that can be both rigorous and user-friendly. They allow for the implementation of different learning methods. They are also a way for universities to develop their reputation in their fields of excellence. Our experience at the University of Le Mans, however, has allowed us to identify two limitations to this tool. First, MOOCs are insufficiently known among young people, who are nevertheless the main target audience. We have indeed noted that the very concept of MOOC is unknown to the majority of students, including those in master's programs. Furthermore, one of the advantages of MOOCs is the possibility of having remote interaction with a teaching team, which implies that they can only be open for limited periods. However, our experience has shown that this interaction is not sought by students, which led us to open our MOOCs permanently.

6. REFERENCES

https://www.fun-mooc.fr/fr/cours/les-bases-de-lacoustique-la-voix-dans-tous-ses-etats/
https://www.fun-mooc.fr/fr/cours/theories-pour-un-son-lacoustique-au-service-du-musicien/

DOI: 10.61782/fa.2025.0488



FORUM ACUSTICUM
EURONOISE 2025

INTERACTIVE SIMULATION APPS FOR TEACHING ACOUSTICAL PHENOMENA AND VIBRATION EFFECTS.

Marcus Maeder[1] **Michael Buba**[1*] **Mert Dogu**[1]
Mihály Tamás Bárány[2] **Tabea Breitkreutz**[3] **Louis Heggemann**[3]
Luis Enrique Roca Paz[4] **Simon Kersten**[2] **Johannes D. Schmid**[1]

[1] Chair of Vibroacoustics of Vehicles and Machines,
Technical University of Munich, 85748 Garching b. Muenchen, Germany
[2] Institute for Hearing Technology and Acoustics,
RWTH Aachen University, 52074 Aachen, Germany
[3] Hochschule Mittweida, 09648 Mittweida, Germany
[4] Erich-Thienhaus Institut, HfM Detmold, 32756 Detmold, Germany

ABSTRACT

Teaching acoustical phenomena, such as the propagation of acoustic waves through different environments, poses many comprehensional challenges for pupils and students due to their abstract nature. Therefore, technical aids play a crucial role in teaching by making acoustics comprehensible and understandable while ensuring learning success. To overcome these difficulties, we present interactive simulation apps that visualize acoustic phenomena and vibrations in essential application areas. These apps enable students to validate the results of hands-on experiments by numerical simulations. The visualization and adaptation of simulation parameters facilitate understanding the underlying physical principles. The interactive apps were initially developed at the Technical University of Munich and employ the numerical software COMSOL MULTIPHYSICS to visualize acoustic phenomena in various fields. During an interdisciplinary cooperation project of the German Acoustical Society (DEGA), students from several universities worked together to create apps related to their respective areas of study, such as noise control, hearing acoustics, room acoustics, and musical acoustics. The apps can be accessed by students and lecturers via the website of the Chair of Vibroacoustics of Vehicles and Machines at the Technical University of Munich (https://apps.vib.ed.tum.de). They are freely available for academic use without license requirements and provide an opportunity to explore acoustical phenomena.

Keywords: *Interactive simulation, acoustic apps, teaching*

**Corresponding author*: michael.buba@tum.de.

Copyright: *©2025 Maeder et al. This is an open-access article distributed under the terms of the Creative Commons Attribution 3.0 Unported License, which permits unrestricted use, distribution, and reproduction in any medium, provided the original author and source are credited.*

1. INTRODUCTION

The 'junge DEGA' group unites young acousticians in Germany to establish a network and promote professional exchange. As part of this group, a collaborative German university project was initiated to develop interactive acoustics apps for teaching acoustics. The students contributed with the expertise of their supervising institutes, resulting in apps for various sub-areas of acoustics. Based on the existing acoustics apps, which have been developed by the Chair of Vibroacoustic of Vehicles and Machines at the Technical University of Munich [1–4] using the software COMSOL MULTIPHYSICS [5], new apps have been developed to illustrate phenomena in the areas of vibroacoustic, hearing acoustics and musical acoustics. They can be accessed via the website https://apps.vib.ed.tum.de.

2. BACKGROUND INFORMATION

The study of acoustic phenomena, e.g., the knowledge about sound propagation, is associated with some diffi-

culties due to the abstractness of acoustic wave visibility. Certain technical aids help ensure effective knowledge transfer between lecturers and students in the context of school and university teaching. This includes collaborative working and learning in teams, mutual feedback, and the use of active learning methods [6]. The visualization of the phenomena, in combination with practical application, significantly increase understanding of acoustics [7]. The acquisition of expensive measuring instruments and limited access to anechoic chambers restrict the possibility of conducting experiments in teaching. For this reason, interactive learning apps aim to conduct experiments using digital devices. Over time, many different apps were developed to explain acoustic phenomena [8]. The complexity of the problems restricts these tools since they can be resolved only analytically. The multiphysics software COMSOL MULTIPHYSICS allows users to solve problems described by differential equations. Individual geometries and boundary conditions can be modified according to the user's needs. The simulations are calculated on a server and made available to the user via a browser.

3. NEWLY DEVELOPED ACOUSTICS APPS

In the following section, a brief introduction is given to the four apps developed as part of the cooperation project. The interdisciplinary research of the participating institutes resulted in apps dealing with vibroacoustics, musical acoustics, psychoacoustics, and noise reduction.

3.1 Comparison of a Schroeder-diffuser and a meta-surface-based Schröder-diffuser

Mert Dogu, Technical University of Munich

The objective of the app is to compare the Schroeder-diffuser to the meta-surface based Schroeder-diffuser and to illustrate the calculation of the scattering coefficient in the frequency domain. The selected Schroeder-diffuser is based on the primitive root sequence with seven as an odd prime number, which yields a diffuser with six cavities. The study is conducted in two dimensions to reduce the degrees of freedom and, therefore, the computational effort of the simulation. In the case of the Schroeder diffuser, two cases are considered: (1) a single diffuser recessed in an infinite baffle; (2) an array of three adjacent diffusers with a total of 18 cavities recessed in an infinite baffle. For both diffusers, the depths and widths of the indentations can be varied to show the different influences of the geometry. The app offers the possibility to vary the depths and widths of the Schroeder-diffusor and the metasurface-based Schroeder-diffusor to demonstrate different geometrical influences on the sound pressure field. The simulation visualizes the sound pressure and sound pressure level in the room depending on various angles of incidence, varying from $-80°$ to $80°$ per octave band. A visual radiation pattern of the sound pressure displaying the directional characteristic shows the radiation's effect depending on the incidence angle, which can be seen in Figure 1.

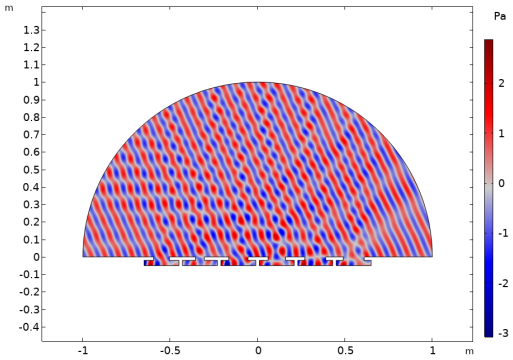


Figure 1. Visualization of the sound pressure field around a meta-surface-based Schroeder-diffuser.

3.2 Simulation of a 'Head-related transfer function'

Mihály Tamás Bárány, RWTH Aachen University

The app calculates the head-related transfer function (HRTF) for a three-dimensional scanned geometry of a human head and torso. Two different simulations are carried out using the Boundary Element Method (BEM), one for the left and one for the right ear so that the differences in sound perception between the two ears can be illustrated. Instead of determining the HRTF by calculating the sound pressure at the entrances of the ear canals for sound sources at certain positions around the head, which would correspond to a measurement setup, the reciprocity principle was applied. In this case, the entrances of the ear canals were each assigned a sound particle velocity in the normal direction, and then the sound pressure was evaluated at positions around the head. This reciprocal approach leads to the same transfer functions as with sources around the head but reduces the number of simulations to only two per frequency. The HRTFs displayed in the app are referenced to the sound pressure measured at the center of the head as if the head is not present. Accordingly, a value of $0\,\mathrm{dB}$ indicates that the body has no influence

on the sound pressure at the ears at a given frequency, while negative dB values indicate shadowing and positive dB values indicate amplification effects, e.g. due to pinna resonances. According to the reciprocity principle, the sound pressure values of the BEM simulation are normalized by the analytically calculated sound pressure of a point source located in the center of the head and whose sound flux corresponds to the sound flux at the ear canal entrances [9].
The app includes three sliders that can be used to adjust the azimuth and elevation angles as well as the distance of the sound source. The selected position is also displayed in a separate window together with the model geometry. In addition to the frequency response, a polar diagram, directivity diagrams and balloon diagrams help to visualize the spatial properties of the HRTF. The polar diagrams show the directivity in the horizontal plane for a given frequency along a circle centered at the center of the head with a radius of one meter.

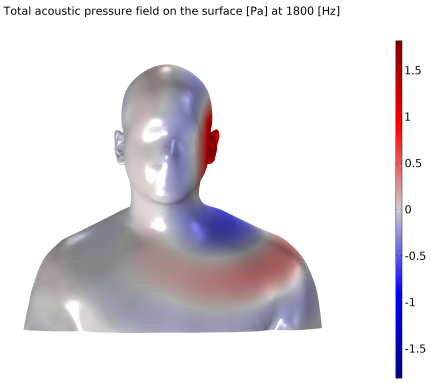


Figure 2. Visualization of the sound pressure field with a sound source in the left ear channel.

3.3 Numcerical simulation of a noise barrier
Tabea Breitkreutz, Louis Heggemann, Hochschule Mittweida, University of Applied Sciences

This app calculates the sound propagation from a sound source along a noise barrier. It shows how sound waves are refracted, absorbed, or reflected at the barrier. The calculation is realized by using the finite element method. A two-dimensional simulation environment was chosen for the display due to the reduced computational effort compared to a three-dimensional calculation domain. The user can change the geometrical properties of the computation domain as well as individually adapt the parameters of temperature and density. The sound absorption coefficient can be entered into the user interface and is incorporated into the model. This app computes numerically the acoustic effectiveness of sound barriers that are used, e.g., to protect neighbors from roadway noise. Analytical approaches calculating noise reduction by noise barriers are delivered by Maekawa [10]. The reference formulas by Kurze [11] and calculation results are displayed in the sidebar. The app shows the cross-section of a sound barrier (see Figure 3), which can be further adjusted in height and thickness using the sliders in a sidebar. Here, the acoustic phenomena of diffraction, refraction, and reflection can be sufficiently well recognized and explained.

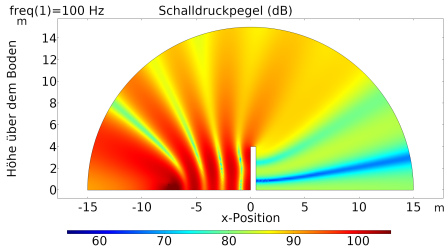


Figure 3. Representation of the sound pressure level at a frequency of 100 Hz, with all sound absorption coefficients set to zero.

3.4 Numerical simulation of the comb filter effect
Luis Enrique Roca Paz, HfM Detmold

The comb filter effect is an acoustic phenomenon that occurs when the same signal arrives at different times at the receiver. This effect is caused by sound reflections from hard surfaces, from multiple sources generating the same tone, or electronically through delay effects and latency. The transfer function between the loudspeakers and the microphones represents the frequency response of the receiver at a specific position and illustrates the effect of comb filtering (see Figure 4). [12]
By using this app, users can explore the influence of various parameters related to the comb filtering effect and observe changes in frequency response in real-time, which helps them to deepen their understanding. The application is also integrated into the learning platform wiki.audio [13, 14]. Wiki.audio is a free online encyclopedia that can be used by pedagogues and audio enthusiasts to easily and intuitively understand various topics in audio technology.

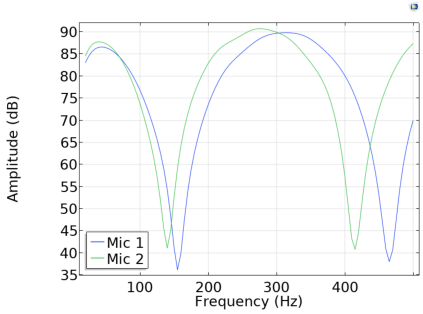


Figure 4. Transfer function of two microphones at a distance of 0.5 meters.

4. OUTLOOK

Students developed acoustic simulation apps using the software COMSOL MULTIPHYSICS during this collaboration project. The apps are related to the research areas of the participating institutes and are intended for use in teaching. For most of the students involved in the project, developing their app was their first experience working with numerical simulation, allowing them to gain many new insights. Through regular meetings and mutual support, they also gained insights into other areas of acoustics.

5. ACKNOWLEDGMENTS

We would like to thank DEGA for financially supporting the project. We would also like to thank the professors from the involved institutes, namely Prof. Dr.-Ing. Steffen Marburg, Prof. Dr. rer. nat. Michael Vorländer, Prof. Dr.-Ing. Janina Fels, Prof. Dr.-Ing. Jörn Hübelt and Prof. Dr.-Ing. Malte Kob, as well as Prof. Stefan Sentpali from the Acoustics Teaching Committee of the DEGA.

6. REFERENCES

[1] L. Moheit, J. Schmid, J. Schmid, M. Eser, and S. Marburg, "Acoustics Apps: Interactive simulations for digital teaching and learning of acoustics," *J. Acoust. Soc. Am.*, vol. 149, no. 2, p. 1175, 2021.

[2] L. Moheit, M. Maeder, and S. Marburg, "Interaktive Akustik-Apps – Akustik 'klickbar' machen in Schule, Studium und Beruf," in *Fortschritte der Akustik – DAGA 2018, 44. Jahrestagung für Akustik, München, S. 834–835.*, 2018.

[3] J. Schmid, J. Schmid, L. Moheit, and S. Marburg, "Interaktive Akustik-App zur Visualisierung akustischer und strukturdynamischer Effekte an Musikinstrumenten," in *Fortschritte der Akustik – DAGA 2019, 45. Jahrestagung für Akustik, Rostock, S. 268-270.*, 2019.

[4] M. Buba, S. Kersten, J. Schmid, M. Barany, T. Breitkreutz, M. Dogu, Y. Heggemann, and L. Paz, "Kooperationsprojekt der jungen DEGA: Entwicklung interaktiver Akustik-Apps für die Lehre in der Akustik," in *Fortschritte der Akustik – DAGA 2024, 50. Jahrestagung für Akustik, Hannover, S. 814-817.*, 2024.

[5] COMSOL, Inc., "Combfilter," 2020. `http://www.comsol.com/comsol-server` [Accessed: 03/24/2025].

[6] A. Chickering and Z. Gamson, "Seven Principles for Good Practice in Undergraduate Education," *AAHE Bulletin*, pp. 3–7, 1987.

[7] P. Goeser, W. Johnson, F. Hamza-Lup, and D. Schaefer, "VIEW – A virtual interactive web-based learning environment for engineering," *Advances in Engineering Education*, vol. 2, no. 3, pp. 1–24, 2011.

[8] F. Taddei, B. Rüth, C. Karpfinger, and G. Müller, "Interactive Web Apps for Visualizations in Mathematics and Engineering," *PAMM*, vol. 18, no. 1, 2018.

[9] B. Katz, "Boundary element method calculation of individual head-related transfer function. I. Rigid model calculation," *J. Acoust. Soc. Am.*, vol. 110, no. 5, pp. 2440–2448, 2001.

[10] Z. Maekawa, "Noise reduction by screens," *Appl. Acoust.*, vol. 1, no. 3, pp. 157–173, 1968.

[11] U. Kurze and G. Anderson, "Sound attenuation by barriers," *Applied Acoustics*, vol. 4, no. 1, pp. 35–53, 1971.

[12] M. Christensen, "Comb Filters and Periodic Signals," in *Introduction to Audio Processing*, Springer, Cham, 2019.

[13] Wiki.audio, "Combfilter," 2025. `https://wiki.audio/En/0050` [Accessed: 03/24/2025].

[14] L. Paz, L. Jäger, and M. Kob, "Interactive comb filter effect demonstration," in *Fortschritte der Akustik – DAGA 2024, 50. Jahrestagung für Akustik, Hannover, S. 829-830.*, 2024.

DOI: 10.61782/fa.2025.0658



FORUM ACUSTICUM
EURONOISE 2025

OPEN EDUCATIONAL RESOURCES FOR ACOUSTICS AND AUDIO SIGNAL PROCESSING USING JUPYTER NOTEBOOKS AND PYFAR

Fabian Brinkmann[1*] **Marco Berzborn**[2,9] **Anne Heimes**[2]
Anton Hoyer[1] **Xenofon Karakonstantis**[3] **Simon Kersten**[2]
Tim Lübeck[4] **Pascal Palenda**[2] **Cristobal Andrade**[5]
Johannes M. Arend[6] **Nara Hahn**[7] **Tobias Jüterbock**[1]
Nils Meyer-Kahlen[6] **Artur Paskiewicz**[1] **Sebastian J. Schlecht**[5]
Frank Schultz[8] **Stefan Weinzierl**[1]

[1] Audio Communication Group, Technische Universität Berlin
[2] Institute for Hearing Technology and Acoustics, RWTH Aachen University
[3] Audiological Solutions, Oticon, Smørum
[4] Institute of Computer and Communication Technology, TH Köln - University of Applied Sciences
[5] Multimedia Communications and Signal Processing, Friedrich-Alexander-Universität Erlangen
[6] Acoustics Lab, Department of Information and Communications Engineering, Aalto University
[7] Institute of Sound and Vibration Research, University of Southampton
[8] Institute of Communications Engineering, Universität Rostock
[9] German Institutes of Textile and Fiber Research, Denkendorf

ABSTRACT

Many universities offer courses on acoustics and audio signal processing, often with overlapping content. Nevertheless, the lectures and teaching material have typically been developed independently. We present a growing collection of programming exercises in the form of Jupyter notebooks that allow to interactively write and execute code including in-line graphical output such as figures. They can also contain text, equations, and multimedia content. Solutions can optionally be checked automatically using the `nbgrader` package, making notebooks a suitable tool for code-related assignments. Our notebooks are hosted on pyfar.org and are often based on the Python packages for acoustics research (pyfar). Pyfar provides functions for signal processing tasks, as well as for reading, writing, and visualizing audio data. By providing such functionality, it allows the content of the notebooks to focus on core concepts and didactics. Solutions to all exercises will be made available to teachers upon request. We hope that this initiative will foster cross-university collaboration, reduce the workload for educators, improve the quality of assignments through peer review, harmonize the content and didactics of courses across universities, and increase the number of available assignments. We will present sample assignments, the infrastructure behind the collection, and how to contribute.

Keywords: (virtual) acoustics, audio signal processing, open educational resources, python, jupyter notebook

1. INTRODUCTION

Academic teaching is integral to scientific and societal progress because it supports to educate the next generation of researchers and developers for universities and companies. Thus, the quality of education in terms of didactics and content is crucial. However, the conditions for achiev-

*Corresponding author: info@pyfar.org.
Copyright: ©2025 The pyfar developers. This is an open-access article distributed under the terms of the Creative Commons Attribution 3.0 Unported License, which permits unrestricted use, distribution, and reproduction in any medium, provided the original author and source are credited.

ing this goal at the university level are often far from optimal. Depending on the country and the university, newly assigned lecturers frequently must develop their lectures and teaching materials under time pressure due to parallel tasks, such as setting up a new research group and raising funds for future projects. Doctoral students and postdoctoral researchers are also often involved in teaching but face their own challenges—first and foremost the need to complete their scientific work before the end of their mostly fixed-term contracts. In addition, undergraduate students involved in teaching are still in the process of internalizing the concepts and topics being taught and are therefore qualified for limited conceptual contributions.

Cross-university efforts to collaborate on teaching materials could address some of these challenges and potentially improve teaching quality through a collaborative peer review process. Although collaboration and peer review are common in research, we are aware of only a few examples in teaching. One example is the Massive Open Online Course (MOOC) on communication acoustics organized by T9, the nine technical universities in Germany [1,2]. However, this course is not free of charge. A second example is the Acoustics Courseware (acoucou) project [3], which is currently being developed by educational and industrial partners. It aims to provide open educational materials for different levels of expertise. Further, in the field of signal processing and communication acoustics, Spors et al. [4] discussed the open education resources workflow for their courses [1]. Some of these courses are heavily forked. Peer reviews are incorporated, but mostly only within the group of the initial developers. Active outside collaboration is on a very low level, currently.

Integrating programming exercises into lectures is generally advantageous, as it is an important method in engineering or more general in all algorithmic- and data-related tasks. An explicit and dedicated training on this skill will help students to cope with their future challenges in the natural sciences and engineering. Rather than introducing algorithms only in formal notation, actively implementing these often facilitates a deeper understanding of the core concepts behind the particular methods. Hence, solving analytical problems shall be accompanied by solving problems through implementation as this equivalently trains these different skills. Thus, the integration of programming assignments into lectures follows *constructive alignment*, which aims at an "alignment between the intended learning outcomes of the course, the teaching/learning activities and the assessment tasks" [5, p. 95]. At the time of writing, none of the above mentioned projects offers programming assignments in Python that could be integrated into existing or projected lectures. In the following, we propose our initiative to provide such material. By that, we aim at supporting and improving educational collaboration and material.

[1] `https://github.com/spatialaudio/signals-and-systems-exercises`

2. PYFAR OPEN EDUCATIONAL RESOURCES

The pyfar open educational resources, freely available at `pyfar.org`, provide Python-based programming assignments in the form of Jupyter notebooks [2] developed by different institutes from different countries. In the following, we introduce the scope and concepts of the pyfar open educational resources. For detailed technical instructions on how to obtain and contribute assignments, we refer the reader to the open educational resources and contributing section at `pyfar.org`.

2.1 Scope

The pyfar open educational resources are intended to provide programming assignments for acoustics and audio signal processing. At the time of writing, the majority of the assignments focused on virtual acoustics covering topics such as the

- creation of virtual sources using using head-related transfer functions,
- estimation of interaural cues from head-related transfer functions,
- interpolation of head-related transfer functions using local and global interpolation approaches,
- creation of virtual moving sources using vector base amplitude panning,
- creation and rendering of sound scenes using Ambisonics en- and decoding,
- extraction of sound-field parameters (direction of arrival, diffuseness) from microphone array recordings,
- parametric audio rendering such as the spatial decomposition method, and

[2] `https://jupyter.org/`

- room acoustic simulation using image sources and feedback delay networks.

However, we also welcome and encourage submissions from other areas of acoustics including but not limited to audio signal processing, basics of (technical) acoustics, and the measurement of acoustic properties (transfer functions of linear & time-invariant systems, room acoustic parameters, etc.). Many assignments actively use pyfar functionality, but this is not a strict requirement. For assignments focusing on more basic signal processing, such as introducing the Fourier transform or finding the onset of an impulse response, it may be more appropriate to use low-level Python, `numpy`[3] and `scipy`[4] functionality, and pyfar could serve as a reference implementation against which students can compare their own solutions. On the other hand, high-level assignments that aim to introduce more complex algorithms or audio signal processing, such as measuring an impulse response, may benefit from using pyfar functionality directly to hide some complexity in favor of a clearer and shorter presentation of the required processing blocks.

2.2 Concept

Figure 1 illustrates the concept and technical realization of the pyfar open educational resources. The notebooks initially contain the assignments and their solutions. These notebooks are stored in a private (non-public) git repository to prevent an uncontrolled circulation of the solutions. This is important for teachers who grade assignments as part of their course work. Lecturers will be granted access to the private repository, and thereby the solutions, after having proven that they are teaching a course in acoustics or signal processing. The same holds for teachers who want to contribute an assignment (cf. Section 2.3 for details). Solution-free assignments are made available on the open educational resources section at pyfar.org. They can be accessed by students and interested teachers. The `nbgrader`[5] package is utilized to remove the solutions from the notebooks hosted in the private repository before they are published.

2.3 Requirements

Before an assignment is added to the pyfar open educational resources, it is peer reviewed within the pyfar community to ensure that it meets our imposed requirements. First and foremost, the assignment and its solution should be correct, clear, self-contained, and provide at least one scientifically qualified reference for further reading. Apart from that, a few formalities need to be followed to make the assignments more accessible, such as adding author's contact details, stating the required skills, and providing an estimated time in which the assignment shall be completed. Importantly, the notebook must use `nbgrader` to ensure that the solution can be removed automatically. As an additional benefit, `nbgrader` can be used to automatically grade the students' solution, which could further reduce the lecturer's workload. However, this requires well-defined problems suitable for automatic grading and code blocks that test the solutions. Such tests typically require more design effort. Therefore, we leave the use of this functionality up to the lecturer, as it may not be appropriate for all types of assignments. A sample assignment is

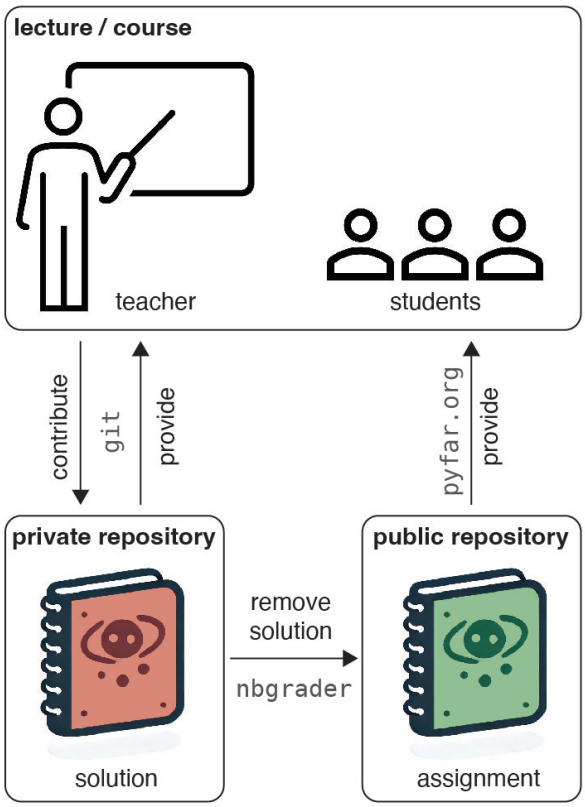


Figure 1. Proposed workflow for providing course materials using the pyfar open educational resources.

[3] `https://numpy.org/`
[4] `https://scipy.org/`
[5] `https://nbgrader.readthedocs.io`

provided to help contributing teachers follow these rules.

2.4 Example

Figure 2 shows a short excerpt from the basic *pyfar challenge* assignment. Like all assignments, it begins with a brief introduction and lists the requirements, the estimated time to complete the task, and the required dependencies. The positions where code has to be added are marked with the comment `#YOUR CODE HERE` and an error will be raised if the block is executed without adding any code. These blocks are automatically generated using `nbgrader` after deleting the solutions.

This specific example might work best as an ungraded assignment at the beginning of a course to familiarize students with Jupyter notebooks, Python, and pyfar. Other assignments could be used in different ways: An assignment could be shown to the class by the lecturer and solved collaboratively during the course. It could also be distributed within a dedicated tutorial to be solved by (groups of) students; or it could be part of the graded course work.

3. CONCLUSION

We introduced the pyfar open educational resources containing programming assignments for teaching (virtual) acoustics and audio signal processing. The assignments are collaboratively developed, maintained, and peer reviewed across different institutes and countries. This may help to improve the quality of teaching and simultaneously reduce the workload of lecturers. The assignments are freely available from `pyfar.org`. At the time of writing, assignments mostly covered topics in virtual acoustics, but we warmly welcome contributions from all other areas of acoustics.

4. REFERENCES

[1] S. Möller, J. Ahrens, E. Altinsoy, J. Fels, G. Müller, G. Reimers, B. Seeber, M. Vorländer, and S. Weinzier, "Konzeption eines MOOC der TU9 zum Thema Communication Acoustics," in *Fortschritte der Akustik – DAGA 2016*, (Aachen, Germany), pp. 527–529, Mar. 2016.

[2] T9, "Communication Acoustics (edX)." `https://www.mooc-list.com/course/communication-acoustics-edx`, 2016. (accessed 2025-03-24).

[3] Acoucou and KFB Acoustics, "Acoucou. Acoustic Courseware." `http://acoucou.com`, 2025. (accessed 2025-03-24).

[4] S. Spors, F. Schultz, V. Erbes, and M. Schröder, "Concept and Realization of Open Educational Resources using Jupyter," in *Fortschritte der Akustik – DAGA 2020*, (Hannover (Remote)), pp. 531–534, March 2020.

[5] J. Biggs and C. Tang, *Teaching for Quality Learning at University*. New York, NY, USA: McGraw-Hill, 4 ed., 2011.

pyfar challenge

The pyfar developers pyfar.org Contact: info@pyfar.org

This assignment will familiarize you with some of the basic pyfar functionality. For help visit the pyfar documentation

Audience: People, who are new to pyfar.

Requirements: No previous knowledge required. Minimal numpy skills are advantageous.

Duration: 45 Minutes

Dependencies `pip install pyfar>=0.7 sounddevice ipympl ipykernel`

```
[ ]: import pyfar as pf
     import numpy as np
     import sounddevice as sd
     import matplotlib.pyplot as plt
     %matplotlib ipympl
```

1. pyfar Signals

pyfar Signal objects store audio data that can be converted between the time and frequency domain. They also contain useful meta data such as the sampling rate or the frequencies at which the spectrum is available. See their documentation for more information

Generate a Signal with a sampling rate of 48 kHz and the time data `[0, 2, 0, 0]`.

```
[ ]: # YOUR CODE HERE
     raise NotImplementedError
```

Inspect your Signal by printing the sampling rate, time data, the times at which the data is available, and the number of samples.

```
[ ]: # YOUR CODE HERE
     raise NotImplementedError
```

Figure 2. Example for an assignment in the form of a Jupyter notebook.

DOI: 10.61782/fa.2025.0143



FORUM ACUSTICUM
EURONOISE 2025

APPLICATION OF ROOM ACOUSTICS SIMULATION SOFTWARE IN UNIVERSITY TEACHING

Lukas Aspöck* **Pascal Palenda** **Janina Fels** **Michael Vorländer**

Institute for Hearing Technology and Acoustics, RWTH Aachen University, Germany

ABSTRACT

Room acoustics simulation software has become an established tool for researchers and consultants. Although such software applications are often regarded as expert tools, they can be effectively integrated into university courses focused on room acoustics and simulation techniques. At RWTH Aachen University, the RAVEN software environment — a C++-based simulation that utilises a hybrid approach that combines the image source model with an efficient ray tracing algorithm — was initiated over 15 years ago. Today, RAVEN is employed in various teaching and research activities and features multiple interfaces, including a MATLAB interface that enables script-based configuration of simulations. Its integration with the 3D modelling software SketchUp creates an interactive environment where students can immediately experience the effects of changes to room designs. This interface allows students to quickly access their first room simulation and auralization, facilitating the incorporation of the software into courses. Currently, it is used in block courses, laboratory sessions, and as a demonstration tool during lectures — not only in Aachen but also at several other universities worldwide. This work summarizes the challenges and opportunities associated with the application of RAVEN in an educational context.

Keywords: *room acoustics, education, simulation, auralization, teaching*

**Corresponding author*: las@akustik.rwth-aachen.de.

Copyright: *©2025 Lukas Aspöck et al. This is an open-access article distributed under the terms of the Creative Commons Attribution 3.0 Unported License, which permits unrestricted use, distribution, and reproduction in any medium, provided the original author and source are credited.*

1. INTRODUCTION

As nowadays, most people spend the majority of their time indoors, room acoustics is of particular relevance in many locations, e.g., in classrooms, in workplace environments or in restaurants. For this reason, the traditional field of room acoustics is even today a part of almost every lecture series related to acoustics. It is popular as it contains concepts which are rather easy to grasp (such as specular reflections or the reverberation time), phenomena which are well-defined and understood such as rooms modes, but also less intuitive and more complex aspects such as the spatial perception of sound in rooms or the description of diffuse sound fields, which are also the topic of current research.

In typical environments we experience in our daily lives, the room acoustics can vary substantially. For the sole purpose of demonstrating the role of absorption, volume and reverberation time, the use of simulations and the tool of auralization in the context of acoustics courses is an effective approach to teach students about room acoustics.

While many (commercial) tools for room acoustic modelling exist since the 1990s [1], many of these tools are (understandably) designed for use by experts and do not have interfaces that allow them to be quickly learned and used in courses. This work introduces the room acoustic simulation software RAVEN [2] and how it is applied in university teaching.

2. THE SOFTWARE ENVIRONMENT RAVEN

The RAVEN (Room Acoustics for Virtual ENvironments) software modules were originally initiated by the Institute of Technical Acoustics at RWTH Aachen University by Dirk Schröder and supervised by Michael Vorländer around the year 2005. The main simulation concept

is based on a hybrid model including the image source model for the specular reflections and a ray tracing algorithm for the diffuse and later part of the room impulse responses. The ray tracing algorithm is extended by a diffuse rain model efficiently determining the amount of scattered energy projected to the receiver. The underlying models have already been developed and elaborated in earlier research projects, successively by Vorländer and Heinz under guidance by Heinrich Kuttruff [3–6] and by Schmitz under guidance of Michael Vorländer [7]. The most comprehensive documentation of the main software library is included in Dirk Schröder's PhD thesis [8].
After its initial phase, in which the base functionality for a GA-based room simulation was implemented, the software was extended with various interfaces and integrated in (VR) applications [9, 10]. The efficient implementation of the room simulation and the synthesis of binaural room impulse responses makes it possible to render auralizations in real-time. A MATLAB interface allows script-based configuration and operation of simulations, making it a convenient tool for researchers - a Python-based interface is currently in preparation. At the moment, the software is not an open-source project, but freely available for academic, non-commercial purposes.

2.1 The SketchUp interface

A plug-in for the 3D modelling software *SketchUp* was created with the intention of providing an easy-to-learn user interface to control a room acoustic simulation and efficiently modify the simulated scene (positions, geometry, boundary conditions). The plug-in's interface, integrated into the *SketchUp* environment, is shown in Fig. 1. By transferring all acoustically relevant information from SketchUp to a C++ application, running in the background, room acoustic parameters and reflection paths can be efficient visualised [11] while the user is able to modify the scene within *SketchUp*. Additionally, room impulse responses for defined positions can be exported, or directly applied for auralizations, either for the static situation, or interactively while the receiver position is moving or the scene is modified [12].
This interface, supported by a basic documentation and a tutorial, makes the RAVEN software suitable for application in university courses, also by students without a background in computer science, engineering or acoustics.

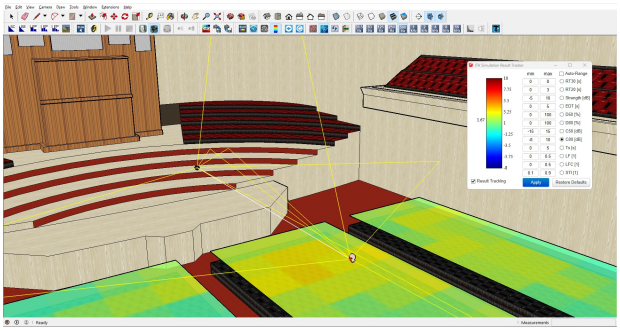


Figure 1. *SketchUp* interface of RAVEN - a simulated concert hall with visualized room acoustic parameters (here: C80) and first order reflection paths.

2.2 Tutorials and examples

Both, for MATLAB as well as for the SketchUp interface of RAVEN, tutorial procedures have been created in English language. The MATLAB tutorial, which is provided in the software's documentation folder, is complemented by various example scripts in the git-repository of the ITA-Toolbox [13] (www.ita-toolbox.org). As the MATLAB interface is mainly intended for researchers, who can be considered as expert users and who typically spend a longer period of time working with the software, the MATLAB interface is rarely used in courses, but frequently applied as a tool in final thesis projects (inside and outside of RWTH Aachen University).
The tutorial document [14] for the SketchUp interface currently includes 17 sections, starting with general information on the involved tools and a very brief introduction of 3D modelling in SketchUp. The main part of the tutorial explains the required steps to start, control a evaluate simulations and auralizations. Completing the tutorial takes around 45 to 120 minutes, depending on the previous experience of the user with SketchUp and room acoustics simulation. The steps of the tutorial also have been recorded and published on *YouTube* [15]. RAVEN's SketchUp tutorial is complemented by a short exercise, which includes the task to run and adjust a simulation of a typical concert hall.

3. APPLICATION IN UNIVERSITY COURSES

Today, RAVEN is used in academic courses related to room acoustics, virtual acoustics and/or auralization at various universities. In these courses, the contents related

to the application of RAVEN range from just demonstrating room simulations and auralizations (by following the tutorial), to specific exercise tasks and project-style group assignments, e.g., the design of a concert hall, theatre or a rehearsal space.

3.1 RAVEN at RWTH Aachen University

For a period of around 10 years, the RAVEN software has regularly been part of two courses at the Institute for Hearing Technology and Acoustics. The first one is a laboratory course on *Acoustic Virtual Reality*, where each semester eight students from electrical engineering learn about the concepts of room acoustic and corresponding geometrical acoustics-based simulation and auralizations. As part of one out of eight experimental session of the course, the students first have to investigate the difference between RAVEN's hybrid simulation model to a previously implemented simplified image-source model [16], before they are asked to investigate the stochastic error of the simulation and its dependence on the number of ray tracing particles. In a final step, the students have to check the impact of an occupied seating area in contrast to an empty concert hall.
The second teaching activity is a one-week block course on room acoustics, which is attended by 30-40 students from architecture, electrical engineering and sound engineering. In this course, students learn about the fundamentals on room acoustics, related regulations as well as measurement and simulation techniques until on the third day. Afterwards they form (if possible) interdisciplinary project groups to design (performance) spaces, where room acoustics are of critical relevance. The project scenarios are usually adapted examples from past editions of the ASA student design competition (Newman Student Award Fund). During the block course, the students are provided with the RAVEN software and can use it to design and improve the acoustics of the designed venue. The application of RAVEN for their projects is complemented by other tools such as equation-based approaches (implemented in spreadsheets) or by web-based applications (e.g., the *amray* Raytracing Sketchpad [17]) which can easily be accessed by the students, supporting their design decisions.
In addition to these courses, the software has also been applied at RWTH Aachen University in seminar work of architecture and electrical engineering students, as a demonstration tool in lectures and laboratory tours, and in numerous final thesis projects (BSc & MSc).

3.2 RAVEN used by other universities

In recent years, RAVEN has been also integrated in or been part of courses in Australia (the University of Sydney), in the UK (University of Edinburgh), in Spain (Universitat Politècnica de Catalunya) and on a regular basis at the Slovak University of Technology in Bratislava. At TU Berlin, HS Düsseldorf and HfM Detmold (all in Germany), the software is also frequently applied in final thesis projects. During the EAA Summer School 2023 (part of Forum Acusticum 2023 in Turino, Italy), the software was integrated in the course on Auralization.
At the Slovak University of Technology in Bratislava, RAVEN is used as a tool in a yearly course for around 15 students from architecture and civil engineering - these students work in larger groups with the task to design rooms in various types of buildings such as music schools, primary schools, university buildings and concert halls. Rooms of these buildings are evaluated with respect to room acoustic parameters required in the corresponding standards and recommendations, and compared to good practice example projects. In some cases, students with a focus on building services or building technology are asked to conduct a parametric study (working in smaller groups) to investigate the influence of various factors on room acoustic parameters, e.g., the influence of volume vs. average sound absorption coefficient and shape, etc.

4. SUMMARY

This work introduced the room acoustic simulation software RAVEN and summarized how it is applied in teaching activities. In general, it is a challenge to implement software, which is not only intended as a research tool, but can also be used in teaching, not only as a tool to demonstrate and explain room acoustics (and its simulation), but also during hands-on exercises in which the students can learn how to run room simulations in a short amount of time and directly use for short studies and projects.
When teaching courses that involve the use of the software, it is essential to ensure that despite a quick and rather short introduction to the software, the students learn how to use the simulation correctly. They need to be made aware of uncertainties, the limits of the simulations and possible errors in the simulation results.
After years of application, based on positive experiences and feedback, the additional effort for specifically creating interfaces and documentation can be considered as worthwhile. However, similarly to other software solutions that

have been in use for many years, the frequently changing staff at the university and dependencies on third party software packages and operating systems are challenges that need to be tackled on an ongoing basis to ensure that the software can continue to be used in teaching.

5. ACKNOWLEDGMENTS

The authors would like thank the developers of RAVEN, especially Dirk Schröder, Sönke Pelzer and Ralf Schallenberg for remarkable efforts during the implementation of the main parts of the RAVEN software and the SketchUp interface. Thanks also to Vojtech Chmelík from the Slovak University of Technology in Bratislava for providing details on the usage of RAVEN in their courses.

6. REFERENCES

[1] L. Savioja and U. P. Svensson, "Overview of geometrical room acoustic modeling techniques," *J. Acoust. Soc. Am.*, vol. 138, pp. 708–730, Aug. 2015.

[2] D. Schröder and M. Vorländer, "RAVEN: A real-time framework for the auralization of interactive virtual environments," in *Forum Acusticum*, pp. 1541–1546, Aalborg Denmark, 2011.

[3] M. Vorländer, "Simulation of the transient and steady-state sound propagation in rooms using a new combined ray-tracing/image-source algorithm," *J. Acoust. Soc. Am.*, vol. 86, pp. 172–178, July 1989.

[4] H. Kuttruff, "Digital simulation of concert hall acoustics and its applications," *Acoustic Bulletin*, vol. 16, no. 5, pp. 5–8, 1991.

[5] R. Heinz, "Binaural room simulation based on an image source model with addition of statistical methods to include the diffuse sound scattering of walls and to predict the reverberant tail," *Applied Acoustics*, vol. 38, no. 2-4, pp. 145 – 159, 1993.

[6] K. H. Kuttruff, "Auralization of impulse responses modeled on the basis of ray-tracing results," *J. Audio Eng. Soc*, vol. 41, no. 11, pp. 876–880, 1993.

[7] O. Schmitz, "Betrachtung der Simulationsalgorithmen eines raumakustischen Simulationssystems," in *Fortschritte der Akustik – DAGA 1997*, (Kiel, Germany), pp. 519–520, 1997.

[8] D. Schröder, *Physically based real-time auralization of interactive virtual environments*. PhD thesis, RWTH Aachen, Aachen, Germany, 2011.

[9] T. Lentz, D. Schröder, M. Vorländer, and I. Assenmacher, "Virtual reality system with integrated sound field simulation and reproduction," *EURASIP Journal of Advances in Signal Processing*, pp. 1–19, 2007.

[10] F. Wefers, J. Stienen, S. Pelzer, and M. Vorländer, "Interactive acoustic virtual environments using distributed room acoustic simulations," in *Proc. of the EAA Joint Symposium on Auralization and Ambisonics*, (Berlin, Germany), pp. 48–55, Apr. 2014.

[11] S. Pelzer, L. Aspöck, D. Schröder, and M. Vorländer, "Integrating real-time room acoustics simulation into a cad modeling software to enhance the architectural design process," *Building Acoustics*, vol. 4, pp. 113–138, Apr. 2014.

[12] L. Aspöck, S. Pelzer, F. Wefers, and M. Vorländer, "A real-time auralization plugin for architectural design and education," in *Proc. of the EAA Joint Symposium on Auralization and Ambisonics*, (Berlin, Germany), pp. 156–161, Apr. 2014.

[13] M. Berzborn, R. Bomhardt, J. Klein, J.-G. Richter, and M. Vorländer, "The ITA-Toolbox: An open source MATLAB toolbox for acoustic measurements and signal processing," in *Fortschritte der Akustik – DAGA 2017*, (Kiel, Germany), pp. 222–225, Mar. 2017.

[14] Institute for Hearing Technology and Acoustics, RWTH Aachen University, "Tutorial: RAVEN SketchUp Interfaces (last access: 2025-04-06)." `https://rwth-aachen.sciebo.de/s/1vbs9JC0U8Cmsct`.

[15] Institute for Hearing Technology and Acoustics, RWTH Aachen University, "YouTube video of the RAVEN SketchUp Interface Tutorial (last access: 2025-04-06)." `https://www.youtube.com/watch?v=P27z3PWBNpM`.

[16] J. B. Allen and D. A. Berkley, "Image method for efficiently simulating small-room acoustics," *J. Acoust. Soc. Am.*, vol. 65, pp. 943–950, Apr. 1979.

[17] Melcher, Andreas, "amray - The Raytracing Sketchpad (last access: 2025-04-06)." `https://amcoustics.com/tools/amray`.

DOI:

Main theme: A04 Education, Public Outreach and History in Acoustics

Session A04.05 Yesterday, today and tomorrow of research in acoustics

Chair(s): W. A. Montano Rodríguez, N. Campillo-Davo

DOI: 10.61782/fa.2025.0113

FORUM ACUSTICUM EURONOISE 2025

AL-ÁNDALUS. SPREADING ACOUSTIC KNOWLEDGE FROM SPAIN TO WESTERN EUROPE

Walter A. Montano Rodríguez[1*]

[1] Acoustics Measurements, Laboratory, ARQUICUST. Gualeguaychú, Argentina

ABSTRACT

During the Early Middle Ages, while in Western Europe science was almost forbidden, in al-Ándalus scientific knowledge flourished, not only for translating Greek philosophers into Arabic, but also for being free to practice art and technology. The first transference from there was the ten digits numeral system adopted in the 11th century, and the milestone is the translation from Arabic to Latin of Euclid's Elements book. In those years the study of sound waves was embedded in music or mathematics, it was not a separate discipline, then to understand their achievements in acoustics a closer look at their writings is needed, of which the few that survived are in the library of *El Escorial*. In al-Ándalus, there were several schools of music, and some of the teachers were craftsmen who made musical instruments, many of them required skills and acoustic knowledge to be designed. The list of scientific contributions made by Moorish Spain to the West is almost endless, and this paper will focus on how they interpreted the translations of the Greeks and their learning and development of the sound wave physics, which became part of the acoustical knowledge.

Keywords: *history of science, al-Ándalus, acoustics, music.*

1. INTRODUCTION

The Iberian Peninsula was militarily occupied by the Muslims in 711, who later introduced, in addition to their religion, the practice and theory of knowledge that the Arabs philosophers had, some of it taken from the writings of the Greek philosophers, whose reading was forbidden in Western Europe. This article only mentions that the study of ancient Greek philosophy was forbidden in Western Europe, it will not go deeper, nor will it comment on the political and/or religious situations that motivated such prohibitions for centuries, a period that until a few years ago was pejoratively called the "Dark Ages," which is now known as the "Early Middle Ages," a historical interval that spans from the fall of the Roman Empire to the 10th century. These occupied territories took the name of al-Ándalus, being Córdoba the city that stood out in the arts and sciences, which sheltered libraries with documents brought from Turkey, Persia, and the rest of the Arab world, among them the translated writings of the Greek philosophers in Arabic.

Regardless of the coexistence between Christianity, Judaism and Islam, which certainly did not have social and/or economic equality in those occupied territories [1], here it will be highlighted those areas in which sound and music were developed in al-Ándalus as a means of cultural expression and human knowledge.

This article is a meta-analysis based on firsthand secondary sources (free available from the Internet), and it is part of a side research started later in 2022, which is conducted by the author who is publishing the history of the acoustics in Spain, in the Acoustics Journal of the *Spanish Acoustical Society*.

2. SOUND AS A PART OF MUSIC INSIDE OF THE QUADRIVIUM

The *Quadrivium* comprised arithmetic, geometry, astronomy and music, and this article is focused on highlighting the scientific contributions that were made in al-Ándalus, in the field of wave phenomena from music, because in the Early Middle Ages physics, and much less acoustics, were not individualized as knowledge since its

[*] ***Corresponding author***: *wmontano@arquicust.com*

Copyright: *©2025 Walter A. Montano Rodríguez. This is an open-access article distributed under the terms of the Creative Commons Attribution 3.0 Unported License, which permits unrestricted use, distribution, and reproduction in any medium, provided the original author and source are credited.*

theoretical content is embedded in the texts of practical and/or theoretical music written by the Arabs, it is not possible to pinpoint a right place of their theories, and here is shared a summary of what could be unearthed from the main music's treatises known in al-Ándalus, by the most prominent thinkers who subsequently were spread in Western Europe, which ultimately shaped the science that prevailed in the Renaissance and the Enlightenment.

All Arabs books and manuscripts on music include writings which in modern words we could identify as behavior of waves, some translated from Greek texts (and corrected or expanded) and many others elucidated by the Arabs themselves. Those writings were brought mostly from Persia and Turkey to al-Ándalus, as books and treatises written in Arabic were gradually translated into Latin – mostly at Toledo– first spread them from al-Ándalus to Bath and Oxford (in England), and later to France and the rest of medieval Europe.

Certainly, the Arabic thinkers analyzed here, using craft techniques of "trial and error" applied to improve the loudness of musical instruments, accumulated basic knowledge of musical acoustics (in modern words) that is revealed in their writings, i.e., they did not describe a section on physics, but rather the explanation of wave physics is deeply inserted in their musical treatises.

3. MUSIC AND SOUND TREATISES IN AL-ÁNDALUS

One of the firsts books which highlight the Arab legacy on Western culture, was published in 1875 under the title "The intellectual development of Europe," where is discussed the crucial role that Arab scholar played in the preservation and translation of ancient knowledge, protecting many Greeks and Romans texts (mostly at Egyptians, Persians and Turkish libraries) that might have otherwise been lost [2]. This book emphasizes that the Arab world not only preserved those texts but also expanded upon them, making significant contributions to various fields, and discusses the influence of Arab music on European culture.

Also, it highlights how Arab musical traditions and instruments significantly impacted on Western European music, during the Early Middle Ages and beyond. Arab instruments such as the lute ('ud in Arabic), the guitar (qitār), and the rebec (rabāb) were introduced and became integral to European musical development. Besides, it notes that the transmission of these musical elements occurred through cultural exchanges between Iberian Peninsula and other regions which enriched European music, contributing to its diversity and evolution [2].

In the opinion of the author of this article, four are the most important personalities who would be highlighted as the main thinkers of the Arab world in producing philosophical treatises on music and sound (which was used in al-Ándalus), in chronological order they are: Ziryab, al- Kindī, al-Fārābī, and Avicenna.

3.1 Ziryab and the school of music at Córdoba, the first in Europe

Abulhasán Ali ben Nafi (789–857), nicknamed Ziryab, was born in Baghdad. He arrived in al-Ándalus circa 822 and settled in Córdoba city, where he started a revolutionary age of several cultural changes. Among dozens of contributions, he made significant ones in the field of sound physics, particularly musical theory domain and instruments design.

According to the Royal Academy of History of Spain[1], his major contributions were in the art of music: "He made some modifications in the construction technique of the lute, adding a fifth string and reducing its weight with thinner woods with better resonance" [6]. He improved the sound quality of the lute and some other chordophone instruments by using new materials, not only for their frames or bodies, but also for the strings.

He created around 850 in Córdoba, what is considered the first school of music in the world, which was revolutionary both in its time and today, because it was open, did not depend on any religion, and people of both sexes studied.

From some sources [7] [8] [9] it is possible to outline that his direct contributions to acoustics may not be easy to pinpoint, his innovations in designing musical instruments and performance techniques likely had implications for sound production and perception; he concentrated on the theory of composition, chords, rhythms, etc., so that music were pleasant to hear for the human mind.

Regarding musical acoustics, it is credited that Zyrab improved the *nuba* (*nawba*) style, by introducing a structured suite based on modal principles, distinct rhythmic cycles within movements that feature tempo acceleration, and integration of instrumental and vocal elements. Then, these can be understood as a move towards structured musical sequences within a modal framework. Acoustically, the nuba results in a musical form with a defined harmonic color, rhythmic complexity, dynamic contrast, and a rich timbral environment.

His emphasis on the quality of sound and the nuances of musical expression suggests an understanding of basic

[1] In 1738, thanks to the enlightened action of various eighteenth-century personalities, the *Royal Academy of History of Spain* was founded.

acoustic principles; for example, the lengthening of the neck of the lute contributed to the improvement of other stringed instruments, it's likely that Ziryab's modifications were informed by an understanding of acoustic principles, such as string tension, resonance, and sound projection.
While specific details about Ziryab's direct contributions to the field of sound physics and musical notation, may be limited due to historical context, his innovations in musical theory and instrument design had an impact on the understanding and appreciation of waves behavior.

3.2 Works of al-Kindī

According to the Stanford Encyclopedia of Philosophy, *Abu Yusuf Ya'qub ibn Ishaq al-Kindī* (800–873 C.E.) was the first self-identified philosopher in the Arabic tradition (and one of the most prolific writers), and the first to translate Aristotle into Arab. Although he initially borrowed ideas from the Greeks on music and wave physics, he developed, deepened and went beyond what they contributed, improving the theory of sound and its perception.
As it is cited in [3], contrary to the Greeks, he proposed that sound is a form of wave motion "similar to how waves form when you throw a pebble into a pond;" al-Kindī theorized that when an object vibrates, it causes the air around it to also vibrate, and these vibrations spread outwards in a spherical pattern, forming waves of compressed and rarefied air. He recognized that air acts as the medium for these sound waves, transmitting them from the source to our ears. Al-Kindī's theories were remarkably accurate for its time (considering technological limitations), he also theorized that when these sound waves reach our ears, they cause our eardrums to vibrate; then, those vibrations are then translated into signals that our brains interpret as sound [3].
A brief summary of his works on music theory (he wrote at least seven treatises) is presented in [4], where is described how al-Kindī found a scientific approach as well, because one of his aims was "to find a logical explanation of the peculiarities of sound grouping;" he also observed "how harmony is produced by the arrangement of specific notes." Al-Kindī "noticed that each note carries a precise pitch and that those notes with a very high or a very low pitch do not fit in a harmonious manner." Then, he concluded that it is necessary to create an explanation on how to establish a pitch, a revolutionary thought at that time, formalizing the use of the notes by alphabetic names which opened the scientific description of musical instruments by means of the instrumental tablature, the basis of manufacturing instruments, and centuries later this was the most important tool for the tempered system.
Links between music and mathematics are deeply analyzed in [5], where it is explained that al-Kindī reached a blend of scientific observation and mathematical reasoning, when he explored the relationship between the pitch of a sound and the length of the string that produces it. By the available means of his time, he meticulously calculated the precise mathematical ratios that correspond to different musical intervals, developing a system for tuning musical instruments, particularly the 'ud (the lute), being a pioneering acoustical tool, because he came up with his own ideas. It is important to mention that he used for all mathematical reasoning the Hindu numeral system.
Al-Kindī's thoughts on sound physics (music) were accurate for the 9th century, and it laid the foundation for later medieval philosophers to further develop the understanding of acoustics. While he didn't have sophisticated tools that we have today to study sound waves, his logical reasoning and observations led him to a groundbreaking discovery.

3.3 "The great book of music" of al-Fārābī

Perhaps the most relevant and influential treatise on sound and music from the Arab world, was written by *Abū Naṣr Muḥammad ibn al-Faraj al-Fārābī* (870–950 C.E.) titled *Kitāb al-Mūsīqā al-Kabīr* (The great book of music), which the only surviving copy is in custody at *El Escorial* (part of the Spanish National Library–BNE). There are three other musical treatises in other European libraries.
It is important to highlight that al-Fārābī for the Arab world is considered as "The second thinker," being Aristotle the first one. He wrote extensively on music theory, exploring the mathematical and physical principles underlying musical sounds.
According to [10] [11] al-Fārābī writings are being reviewed and revisited, in order to make a distinction among what he borrowed from the Greeks, what he corrected and what are his own contribution to the field of music and sound, because the fact that he gave detailed information about instruments and surpassed the Greeks in the field of sound physics gave him a place in the history of music [11].
Al-Fārābī's work on the physics of sound built upon the knowledge of earlier Greek philosophers like Aristotle, but he is the thinker least influenced by the ideas about music and sound of Pythagoras or Plato [11]. Criticizing the Pythagorean concept of music, he discussed the distinction between practical and theoretical music and emphasized the importance of understanding the physical foundations of sound, because he recognized the significance of sound as a

physical phenomenon; then, he recognized the significance of a sensory foundation for theoretical music.

According to a philosophy of music research on al- Fārābī's work [12], he discusses the relationship between practice and theory of music, and also between the composition and performance of music, and the justification that he gives about that in modern words could be said to belong to psychoacoustics, since "the fact that theories come after sensory experience in the temporal sense does not render reason completely useless or trivial in musical analysis" [12]; then, he expanded on his analysis, including distinctions between sensation, imagination, and reasoning in classical theories of the soul in the study of music (as Greeks did it).

As a music theorist, al-Fārābī conceptualized that music brings together many aural experiences, because tones, melodies, and intervals are indeed dependent on sensation and imagination, meaning that both the inductive method (melody has rational principles), and the deductive method (taking the principles to the individual melodies), both have to be used. This last statement has a deep meaning to human knowledge: It was one of the first times that it was proposed to have the reasoning of the Scientific Method.

While not explicitly focusing on modern physics, his insights into propagation and nature of sound were significant for his time. A few key points on the physics of al-Fārābī's on sound: He realized that sound originates from vibrations, whether produced by the human voice, musical instruments, or natural phenomena. He described how these vibrations travel through the air, creating sound waves. He understood that a medium, such as air or water, is necessary for the transmission of sound, he explained that the denser the medium, the faster sound travels.

While al-Fārābī's contributions to acoustics are significant, it's important to note that his work primarily focused on the theoretical aspects of music rather than practical acoustics or physics of sound. However, his exploration of the nature of sound and its relationship to the human psyche laid the groundwork for future developments.

As a general summary of al-Fārābī's work, he examines the production and perception of sound, contributing to the understanding of the underlying principles of music, writing extensively on music theory, including the physical properties of sound, the mathematical relationships between notes, and the psychological effects of music.

Al-Fārābī left a lasting legacy in the field by moving away from mystical explanations of music and focusing (in modern words) on the physical principles that govern sound.

3.4 Ibn Sina (Avicenna) and his "Book of healing"

Abū 'Alī al-Husayn ibn 'Abd Allāh ibn Sīnā (980–1037 C.E.) or Avicenna, highly influenced by al-Fārābī's, he made significant contributions to the understanding of sound propagation and acoustics, Avicenna works on the nature of sound and its transmission through different mediums helped to lay the foundation for many developments in acoustics. His writings on music theory, such as the *Kitāb al-Shifā'* ("Book of Healing" or "The physics of the healing" for some translators), explored the relationship between music, mathematics, and the natural world [13], and it is a comprehensive encyclopedia which covers a vast range of subjects [14] [15], including medicine, philosophy, astronomy, music and physics.

He discussed the mathematical principles underlying musical scales and intervals, as well as the physiological and psychological effects of music on the human body. It's important to note that Avicenna's primary focus was on music theory and its philosophical implications on human behavior (following the al-Fārābī's work). His insights into sound propagation, including reflection and refraction, were likely integrated within his broader understanding of acoustics and their relation to music and human experience.

Avicenna describes sound as a form of vibration that travels through the air, explaining that sound is produced when an object moves and creates a disturbance in the surrounding medium, typically air, then, sound waves propagate through different media, highlighting that the speed and quality of sound can vary depending on the medium it travels through, such as air, water, or solid materials; all of his explanations were primarily qualitative rather than quantitative.

Avicenna also discusses the phenomena of sound reflection (echoes) and refraction (bending of sound waves), demonstrating his understanding of how sound waves interact with different surfaces and materials, providing a framework to understand that sound as a wave-like disturbance.

Avicenna was interested in movement phenomena and its measurement; he based his analysis on two concepts: rapidity and slowness. As cited in [16] he distinguished between the speed of light and of sound: "Thunder can be seen and heard. Thunder (lightning) is seen at one time, but heard at another, after it (the sound) has moved in the air and gradually reached the hearing." In other words, he established the difference in the speeds of the two forms of movement of matter.

It's important to note that much of Avicenna's work on sound is linked to his philosophical and musical investigations. He explored the relationship between sound, music, and the human soul, considering how music can

evoke emotions and affect the human body (In modern words: a journey between musical acoustics and psychoacoustics), and while his explanations may differ from modern scientific concepts.
Avicenna's work played a significant role in the history of acoustics.

4. EARLIEST WESTERN PHILOSOPHERS WHO USED TRANSLATED ARABIC TEXTS

As cited in [17], the first known translation of philosophical manuscripts from Arab to Latin were made by Adelard of Bath, an English philosopher, during the 12th century introducing ancient Greek texts which had only existed in Arabic form to Western Europe. Among his translations, the most influential work was of Euclid's Elements (text used for eight centuries), and the second is the introduction of the Hindu ten digits numeral system and the zero.
Roger Bacon (1214–1292) is the most prominent philosopher and thinker in disseminating the contributions of the Greeks, which he made known through his great philosophical works with translations into Latin that were made in al-Ándalus, or by translating himself directly from Arabic. Concerning the interpretation of the texts that he translated into Latin, they were not always correct, Bacon himself shared an anecdote about the misinterpretations of the translations: "When I lectured on this in my classes but did not know how to explain it, as was required, my Spanish students derided me. I later learned from them that [the name] was not Arabic, as all the doctors believe, but Spanish, and [the plant] is seed of henbane" [18].
Based on al-Kindī's treatises on Hindu-Arabic numerical notation, Roger Bacon is one of the first to promote its use to leave aside the Roman one (which used letters), saying that it is good for science and academic learning. As cited in [19], Roger Bacon along Robert Grosseteste (1175–1253), based mostly on al-Fārābī's work, they were the first to conceptualize the importance of practice and experimental actions in science, merging the mathematical method with the experimental one, thus beginning the qualitative method in scientific research centuries before Francis Bacon.
Concerning sound physics [20], Bacon applied the term "algorithm"[2] to explain the step-by-step resolution of mathematical problems with algebra (to elucidate sound refraction and other matters), and the result obtained through these procedures he identified as *secundum computistas* (computed afterwards).
Although Greeks wrote about a grammar in music, later improved by Arabs, it was Roger Bacon who gave it a scientific form by incorporating mathematical logic, initiating the idea of meter and rhythm in music in Western Europe, saying that sound is part of music (reinforcing the Quadrivium); at the same time, it can be established that Roger Bacon in the 13th century is the first philosopher who grants the study of sound the entity of a scientific nature.
Among several of his contributions, Roger Bacon formalized the study of sound waves by stating that they do not propagate like a ray because do not have a linear pathway, but he did conceptualize that sound "can be studied as the path of a ray" [20] [21]. *Note*: Roger Bacon use the word "species" to describe rays.

5. DISCUSSION

It is well known that in the Early Middle Ages in Western Europe, the reading of Greek philosophers was forbidden (it was considered as pagan literature), then their writings were completely unknown; the opposite happened in Arab culture. Henry G. Farmer, a renowned researcher on Arabian music, in 1930 stated that the musical treatises of Greeks thinkers were well known among Islamic intellectual circles, and this familiarity was expressed in many of their writings, since Arab thinkers borrowed some ideas from the Greeks, but this does not take away from the originality of their contributions to scientific knowledge, and "al-Fārābī's treatment of physical and physiological principles of sound and music, is certainly an advance on that of Greeks" [22].
The Moorish culture were not mere transmitters of Greek heritage, but rather refiners and creators, who considerably contributed to the foundations of the later Western science, because scholars from European regions went to al-Ándalus (Spain) to study or seek books at Toledo's libraries, then they disseminated to the West the knowledge kept there.
Arabs' theories were accurate in those years and laid the foundation for later thinkers and philosophers of Western Europe (those that emerged in the Renaissance and the Enlightenment) to further develop our understanding of sound waves and acoustics. While they didn't have sophisticated tools that we have today to study sound waves. Their logical reasoning and observations led them to groundbreaking discoveries in the acoustics field. Therefore, it is important to understand that the concept of

[2] Word derived from Al-Khwarizmi, the Arab thinker who introduced the idea of solving arithmetic problems by methodical, step-by-step approach.

waves they had was not understood in the same way then, as it is now.

For some researchers it might seem that many of the contributions made by Ziryab, al-Kindī, al-Fārābī, and Avicenna, they are more focused on musical acoustics than on the physics of waves themselves, but it is important (once more) not to forget that until the Enlightenment sound itself was part of the music, not an individual entity.

All the sources consulted for writing this article agree on one thing: al-Fārābī was the first to give a scientific explanation of sound and to draw up rules for the construction of musical instruments, and "Fārābī made a valuable contribution to physiological acoustics which was not touched by the Greeks" [23]

As mentioned in this article, manuscripts translated from Greek-Arabic and Arabic-Latin are being revisited, not only to better decide how these texts were originally written, but also to find out what contributions were made by Arab philosophers; also, many are being translated directly into English from Arab [24]. Therefore, in the coming years it will be possible to update what is known about the contributions of the Arabs to the science and knowledge.

The way of interpreting the teachings that the Moors had in al-Ándalus had a great impact on the Iberian populations, because when, in the 13th century, the first kingdom of the future Spain could be formed, in order to establish its political power, King Alfonso X *El Sabio* (The Wise) created the first Spanish university in 1254 at Salamanca, which was also the first university that was not dependent on the Catholic Church, like the other three at that time, and also the first to have a Chair of Music [25].

6. CONCLUSION

Unlike the study of medicine, law, astronomy, and other disciplines, that were individualized in the Early Middle Ages, sound and wave physics were not studied separately (acoustics did not even exist as a field of knowledge). Since the study of sound and the behavior of elastic waves were not independent matters during those years, in the texts written by Arabs philosophers these theories are embedded and deeply rooted in their musical treatises, and to a lesser extent in medical ones (those who studied the curative use of music), perhaps for this reason an in-depth study and analysis of those writings is still pending.

Although not strictly "acoustics" in the modern sense, works of these Arabs scholars were an exploration of the physical manifestations of sound, and in essence, advanced the understanding of sound and acoustics by:

- Applying mathematical principles to music theory.
- Exploring the physical and psychological effects of music.
- Systematizing musical knowledge and practice.
- Contributing to the development of musical instruments.

The purpose of this article is to begin this discussion because **ultimately music is part of the creation of sounds**, and also, in a way, to recognize the contributions of those Arab thinkers whose works on music were translated in al-Andalus (from Arab into Latin), and whose ideas spread from Spain to Western Europe through European scholar's sway, leading to the Renaissance and the Enlightenment.

Acknowledgement. The author wants to thank to Prof. Eng. Federico Miyara (University of Rosario, Argentina), his review and comments on this article.

Disclaimer. The author has no feelings against any religion or culture; this article was written under the sole agenda of History of Science. Research and the writing of this paper were not funded and were done in the author's free time.

7. REFERENCES

[1] Darío Fernández-Morera: *The Myth of the Andalusian Paradise: Muslims, Christians and Jews under Islamic Rule in Medieval Spain*, ISI Books, 2016.

[2] John William Draper: *The Intellectual Development of Europe*, George Bell and Sons, 1875.

[3] Stephanie Schewe: *Al-Kindī und die Wirkung der Musik. 'Das Buch der Chordophone von den einsaitigen bis zu den zehnsaitigen' (Kitāb al-muṣawwitāt al-watariyya min ḏāt al-watar al-wāḥid ilā ḏāt al-ʿašarat al-autār)*. Institute for the History of Arabic-Islamic Science, 2018.

[4] Martin Nick: Al Kindi. The great Arab philosopher. *Al Shindagah Journal*. Al Habtoor Group, Sep/Oct 2005.

[5] Cris Forster: *Part IV: Arabian, Persian, and Turkish Music*. Section 11.45. Chapter 11: World tunings musical mathematics on the art and science of acoustic instruments. The Chrysalis Foundation, 2000–2025.

[6] RAH: Ziryab. Músico, cantor, poeta, gastrónomo y esteta. *Royal Academy of History of Spain* website.

[7] Epstein, Joel: *The Language of the Heart: A musical, fantastical journey through a land of magic*. Juwal publications, May 24, 2019

[8] Dris, Youcef: *Ziryab, le maître de l'Andalousie: Histoire de musique arabe*. 07/07/2021. Ed. Primento.

[9] Reynolds, Dwight F.: *The Biography of ʿAlī ibn Nāfiʿ, Known as Ziryāb*. Medieval Arab Music and Musicians, pp. 307–335. 13 Dec 2021. Brill

[10] Tercan, Nurfer (2020) Al-Farabi's philosophy of music. *International Scientific Conference students and young scientists "FARABI WORLD."*

[11] Turabi, A. H.: *Fârâbî's views and works in the field of music. The adventure of thought from East to West: The Golden Age of Islamic thought*. F. Terkan and Ş. Korkut, Ankara: Elis Yayınları, 2005.

[12] Hafız, Muharrem (2024) al-Fārābī's Philosophy of Music. Meshk Journal of Religious Music. Istambul university Press, 2024

[13] Murmura, Michael E.: *The Metaphysics of the Book of Healing by Avicenna*. Birgham Young University press. Provo, Utah, 2005.

[14] Bertolacci, Amos: *"Avicenna's Kitāb al-Šifāʾ (Book of the Cure/Healing): The Manuscripts Preserved in Turkey and Their Significance."* in The Reception of the Classical Arabic Philosophy in the Ottoman Empire, ed. J. Jabbour, Mélanges de l'Université Saint-Joseph, 67, pp. 265-304, 2017-2018.

[15] Avicenna: *The physics of the healing. Books I & II*. A parallel English-Arabic text translated, introduced, and annotated by Jon McGinnis. Brigham Young University, 2009.

[16] Sadykov, Abid S.: A forerunner of modern science. Avicenna. The UNESCO Courier. Paris, 1980.

[17] New world encyclopedia: *Adelard Of Bath*, 2023.

[18] Polloni, Nicola: Disentangling Roger Bacon's criticism of medieval translations. *Early Thirteenth-Century English Franciscan Thought* (pp.261-282). De Gruyter, 2021.

[19] Crombie, A. C.: *Robert Grosseteste and the origins of experimental science 1100–1700*. Oxford, 1953.

[20] Bacon, Roger: *Capitulum II. Multiplicationis specierum. Pars secunda*. Opus Majus Volume II.

[21] Kedar, Yael: Sound is not made of rays. Roger Bacon's rejection of heavenly music. *The Philosophy and Science of Roger Bacon*. Routledge Ed., 2021.

[22] Farmer, Henry George: *Historical facts for the Arabian musical influence*. Studies in the music of the Middle Ages. London, 1930.

[23] Ahmad, Khwaja Jamil: Hundred great Muslims. Library of Islam. Kazi Publication Chicago. Second Ed., 1987.

[24] L'Université Saint-Joseph: *The Reception of Classical Arabic Philosophy in the Ottoman Empire*. Proceedings of the Workshop Held by the International Associated Laboratory "Philosophie dans l'aire ottomane", 2014.

[25] Montano, Walter: *Music studies in 1254 at the University of Salamanca. an al-Ándalus legacy*. Forum Acusticum 2025. 11th Convention of the European Acoustics Association, Málaga, 2025.

DOI: 10.61782/fa.2025.0596

FORUM ACUSTICUM EURONOISE 2025

MUSIC STUDIES IN 1254 AT THE UNIVERSITY OF SALAMANCA. AN AL-ÁNDALUS LEGACY

Walter A. Montano Rodríguez[1*]
[1] Acoustics Measurements, Laboratory, ARQUICUST. Gualeguaychú, Argentina

ABSTRACT

The first university in Spain, the fourth in Europe, was founded in Salamanca in 1254, and among the persons mentioned in its Royal Charter to teach, one of them was an "organo teacher" ("maestro en organo") this was a uniqueness because in the 13th century music was taught only in churches and monasteries. Its existence is not a coincidence, because this novel university replicated the way of learning in al-Ándalus, where music was taught and played outside religious life. That fact was worldwide known in 1720 when *The history of Spain* was published and since then, some have debated whether it was a "chair of music" and whether the "organo teacher" taught theory. Considering that in the Quadrivium the physics of sound was not independent, it could be inferred that principles of acoustics was taught there in 1254. In this paper it will be demonstrated that it is not a semantic question of interpreting words, but of interpreting them in the historical context that was written, then it can be assured that it was a professorship, and by the counterfactual in this chair of music was taught the theory of sound/music, just as it was done in al-Ándalus.

Keywords: *history of science, al-Ándalus, acoustics, music, University of Salamanca.*

1. INTRODUCTION

Spain was built with the fusion of kingdoms and crowns that existed in the Iberian Peninsula, and one of them organized in the early 13th century was that of Castile, (*Castle* in English, named for the large number of castles in that region), which, to ensure its linguistic and political identity, King Alfonso X *El Sabio* (The Wise) created in 1254 at Salamanca city the first Spanish university, being the fourth in Europe.

Contrary to the rest of the European kingdoms of that time, authorities, universities, institutions and the Vatican itself, which used Latin as a cultured language for official written and oral communication and also for teaching, Alfonso X "through the work of his *scriptorium* and the dissemination of documents from his chancellery, left this prominent position to Castilian" [1] (Castilian as a language of Castile); hence the use of Castilian language[1] in the first-born University of Salamanca. This decision is evidenced by a copy of the original manuscript of the Royal Charter, which is written entirely in Castilian language.

The first history of the University of Salamanca was written by Pedro Chacon in 1569, which mentions also the "maestro en organo" [2], but according to an in-depth analysis of his manuscript published in 1990 [3], the text was biased and tendentious, perhaps to please the authorities (who were in power in the year this manuscript was written), making it an unreliable source of information. Another book discarded as a source was published in 1855 by Mariano Soriano Fuertes [4], mainly because his investigation relied on *Virgilius Cordobensis* (a.k.a. Virgilio), an apocryphal writer, who supposedly wrote about the creation of the Chair of Music at University of Salamanca, and other issues linked to this matter, as if he had been contemporary [5].

Since it is necessary to increase the importance of this Chair of Music at the University of Salamanca in 1254, the author proposes this discussion, because ultimately music is the creation of sound. This article is a meta-analysis based on

[*] ***Corresponding author***: *wmontano@arquicust.com*
Copyright: *©2025 Walter A. Montano Rodríguez. This is an open-access article distributed under the terms of the Creative Commons Attribution 3.0 Unported License, which permits unrestricted use, distribution, and reproduction in any medium, provided the original author and source are credited.*

[1] Centuries later "Castilian" language gradually changes its name to "Spanish" language. After the creation of the Royal Spanish Academy (RAE) in 1713, contributes to the standardization and promotion of the term "Spanish" instead of Castilian. The RAE is Spain's official royal institution with a mission to ensure the stability of the Spanish language.

primary sources (old, digitalized manuscripts available on the Internet), and it is part of a side research started later in 2022, which is conducted by the author who is publishing the history of the acoustics in Spain, in the Acoustics Journal of the *Spanish Acoustical Society*.

2. THE HERITAGE OF AL-ÁNDALUS ON THE CREATION OF THE UNIVERSITY OF SALAMANCA

In the 13th century, part of the Iberian Peninsula was still occupied by Moors, where in al-Ándalus they cultivated (among other arts) the music. In Córdoba city was created around 850 what is considered the first school of music in western world, where they taught theory and practice, which was revolutionary both in its time and today, because it was open, did not depend on any religion, and people of both sexes studied [6]. Later, other teaching centers similar to this music school existed in some other cities such as Malaga, Murcia, Seville, and Toledo (the latter had already been reconquered by the Iberians in the 11th century).

It is important to highlight that in al-Ándalus learning and practice of medicine, law, music and other disciplines were open, considering that the knowledge of the Greeks philosophers through Arabs translations were of usual reading. Unlike the rest of Europe, where Greeks writing was banned, in the Iberian Peninsula it was commonly read by the ruling class.

In the 13th century, the city of Toledo was annexed to the Kingdom of Castile, which had a school for translating manuscripts from Arabic to Latin (and probably to Castilian as well), which was of great relevance to the future University of Salamanca. Another city occupied was Murcia where Abu Bakr Muhammad ibn Ahmad al-Raquti (?), a renowned Muslim scholar who born in al-Ándalus, Alfonso X distinguished for his abilities in music, mathematics and other disciplines, so kept him to teach in the schools (Murcia, Sevilla and Salamanca) founded in his kingdom [6].

As for the study and teaching of the physics of waves and sound, in the Middle Ages these were integrated into music as part of the Quadrivium, they did not exist as separate entities. In al-Ándalus, music played a very important role in society, it was seriously studied with the advances introduced by Arab thinkers who improved and deepened the contributions that the Greeks had made in this field. Although not explicitly focused on modern physics, Arab and Moorish scholars explored the physical nature of sound, its propagation, and its relationship to musical intervals.

The contributions of Moorish scholars in al-Andalus to the study of sound waves and music were part of a broader intellectual tradition that extended beyond the Iberian Peninsula. This knowledge, accumulated over four centuries, gradually spread from al-Andalus to the rest of Western Europe. A summary of these historical facts is presented in another article by the author [7].

3. 1254: THE ROYAL CHARTER OF THE SALAMANCA UNIVERSITY AND THE "MAESTRO EN ORGANO" (TEACHER IN MUSIC)

The germ of this university dates back to 1218, which began as *Studium generale* (higher studies), and king Alfonso X El Sabio (The Wise) elevated them to the category of university studies on 1254, through a Decree which is known as "Carta Magna de la fundación de la Universidad de Salamanca" (Royal Charter of the foundation of the University of Salamanca).

The original manuscript of the Royal Charter is lost and the oldest handwritten copy of it is from 1401 and is preserved into the archives of the University of Salamanca [8]. The manuscript is written in square Gothic script (see Fig 1) and vocals has no accent marks (diacritics)[2].



Figure 1. Image extracted from the Royal Charter copy from 1401. Paragraph where "maestro de organo" is mentioned. All rights are reserved, Universidad de Salamanca®

Regarding the people who would teach at this university, they are mentioned as "maestros" ("teachers") [8]:

> *De los maestros mando e tengo por bien que ayan vn maestro en leys […] Otrosi mando que ayan vn maestro en decretos […] Otrosi mando que ayan dos maestros en decretales […] Otrosi tengo por bien que ayan dos maestros en lógica […] Otrosi mando e tengo por bien que ayan dos maestros en lo gramatica […] Otrosi mando e tengo por bien que ayan dos maestros en fisica […]* ***Ot si mando y tengo por bien q' ayan bn maestro en organo y yo q'le enqina m'rs cada Anio***.

Among them, the last one is stated as "maestro en organo" (music teacher). Fig 1 shows the paragraph where the Royal Charter refers to "maestro en organo," and it is written (in

[2] First written Spanish texts using diacritics to indicate the tonic syllable, date from the mid-16th century.

old Castilian language) that: "Another thing I do order, and it is good that there is a teacher of music, and I give him fifty maravedis each year."
It is important to note that the word "organo" was written without an accent on the first letter "o," firstly because the Castilian script (writing) was still developing at the time and the accent on vowels was not yet in use, and secondly (and more importantly) because "maestro en organo" refers to the teaching of music and not to the learning of the organ (to be more precise, "the pipe organ"). This statement will be demonstrated later.
The existence of a chair of music at this university is not a coincidence, and there are two very important reasons that justify that fact: In his youth, Alfonso X received theoretical and practical training in music from the people of al-Ándalus; and throughout his adult life, he distinguished himself as a musician, composer and protector of music [8].
Alfonso X is considered one of the composers who contributed the most songs to the *Cantigas de Santa María* (Songs of Holy Mary), a collection of 420 poems with musical notation –written between 1270 and 1282– that is one of the most important compilations of monodic songs in medieval literature. Of a troubadour and paraliturgical nature, it differs from the openly profane themes of the troubadours of the rest of Western Europe and from the sacred music of the 13th century [9].

4. MISTAKE IN MANY REFERENCES FOR USING THE WORD "ORGANO" ACCENTED

The author of this article considers a mistake to write in Spanish about the history of the University of Salamanca without considering the historical context of the 13th century, and there are countless references where the word "organo" is written with an accent on the first letter "o," resulting in "órgano," being this a mistake.
Writing the word "órgano" (with accent mark) instead of "organo" (without accent) changes the original meaning of the function of the music teacher at the University of Salamanca in 1254, and also because someone who uses this incorrect reference to translate it into another language will unknowingly misinterpret that "it was a teacher who taught how to play the pipe organ."
In section 7, the fact that singing and music were taught as a science in this Chair of Music could be demonstrated by a document from 1256 on the organization of the University of Salamanca.

5. FIRST CHRONICLE IN CASTILIAN ABOUT THE "MAESTRO EN ORGANO"

Although the history of the University of Salamanca was written in 1569, this manuscript was stored away for almost 300 years, and it was around 1840 that it was recovered from an archive in the Vatican.
Although the "maestro en organo" is briefly mentioned by Francisco de Salinas, in a prologue of his Treatise of music published in 1577, the first book which summarizes the creation of the University of Salamanca was published in 1720 by the Jesuit scholar Juan de Ferreras y García, co-founder of the Royal Spanish Academy, refers to the Royal Charter for the foundation of the University of Salamanca in his encyclopedia "The History of Spain," transcribing instead of literally copying the 1401 text as "instituyendo ... una Cathedra de Musica" (establishing … a Chair of Music) [10]. This change introduced in the original text is interesting for two reasons: **(a)** He categorizes the function of "teacher" at the level of a professorship, and **(b)** he assumes that "organo" refers to the teaching of music.

6. EARLY REFERENCES IN OTHER LANGUAGES TO THE "MAESTRO EN ORGANO"

The author of this article, after three years of searching the Internet, has not found any direct or indirect references published before 1720 about this music teacher at the University of Salamanca, in other language than Spanish[3]. Below are the first references available on the Internet to this Chair of Music.

6.1 First reference published in French

"The History of Spain" encyclopedia was translated and published in French in 1751 by Ferreras, so, following the original form written by himself, that phrase was translated as "Chaire de musique" (Chair of music) [11].

6.2 First reference published in German

In 1767, in a book published in German, which summarizes the history of Europe "according to what is reflected in proven news," it does not mention the source of information but surely it is the Ferreras' encyclopedia. The phrase "Cathedra de Musica" was written as "lehrstuhl der musik" (teacher of music) [12], that is, it maintains the semantics of what was written into Spanish in the 1720 encyclopedia following the meaning that music was taught in a chair.

[3] The reader should consider that search engines do not display all documents available on the Internet.

6.3 First reference published in English

As far as an English reference is concerned, of the publications available on the Internet, the first is from 1800, and it is cited in a British encyclopedia as follows: "In Spain, music was early included in the circle of sciences. The professorship of music at Salamanca was founded by Alfonzo the Wise, K. of Castile [13], in which it makes it clear that it was a chair for the teaching of music in a university field of knowledge as a science.

7. IN 1254 MUSIC WAS TAUGHT AS SCIENCE IN THE UNIVERSIT OF SALAMANCA

After the Royal Charter was published, Alfonso X wrote a codex containing laws for this new Kingdom, originally named as *Libro de las Leyes* (Book of Laws) now is identified as *Siete Partidas* (Seven Records), which contain several regulations for the University of Salamanca that reflect the medieval view of education and the importance of this university in that social milieu.

According to a comparative analysis between what is written in the Siete Partidas and the Royal Charter, indicates that they differ since the lexicon in the Siete Partidas "is closer to the Bologna model or reality than Salamanca's" [14]. One of the most reliable transcriptions of the Siete Partidas, is published by the Royal Spanish Academy [15], because this document keeps the original ancient scripts and spelling.

Regarding the legislation on the University of Salamanca, the main content is in *Segunda Partida* (Second Record) under the title "De los estudios en que se aprenden los saberes e de los maestros e de los escolares" (On the studies in which knowledge is learned and of teachers and students), and some other regulations are scattered in the other six Records.

In the following, the number of the page is mentioned where the references to the "maestro" and also to the music and the science in the Siete Partidas can be found in [15], then the sentence in old Castilian, and next its translation in English:

- On page 66: "E otrosy en musica que es saber de los ***sones*** que es menester para los cantos de santa Iglesia." The word "sones" is purposely highlighted, because it is the Latin word "sonus" in Castilian language. "And others, in music, which is the knowledge of sounds that is necessary for the songs of the holy church."
- On page 200: "Ley .x. que los maestros no deuen vender la çiençia por precio." "Law 10. Teachers shall not sell science for money."
- On page 500: "Estudio es ayuntamiento de maestros & de escolares que es fecho en algun logar & con voluntad & con entendimiento de aprender los saberes (…) es a que dizen estudio general en que ay maestros de las artes assi como de gramatica & de la logica & de rretorica & de arismetica & de geometria & de musica & de astrologia." "Study is the conjunction of teachers and scholars that is done in some place and with the will and understanding to learn knowledge (...) general study is in which there are teachers of the arts as well as grammar, logic, rhetoric, arithmetic, geometry, music and astrology."
- On page 905: "& los maestros a los disçipulos a que muestran su çiensçia" "And the teachers to the disciples to whom they show their science."
- On page 947: "mismo dezimos que seria si le diesse en salario a algund su maestro que le mostrasse ciencia" "We say the same thing would happen if a salary were given to a teacher who shows his science."
- On page 983: "& los otros maestros de las çiençias que han salarios çiertos cada año del rey o del comun de alguna çibdad o villa" "and the other teachers of the sciences who have received certain salaries each year from the king or the common people of some city or village."

In the Siete Partidas, instead of referring to the "maestro en organo," it is written as "maestro de música" (music teacher), which is very important since it gives a more direct clue that the function of that teacher in 1254 was to teach music.

Regarding the use of the word "science" to identify the pedagogical functions of teachers in the Siete Partidas, it shall be noted that the meaning it had in the 13th century does not have the same meaning today, since in Latin the word *scientia* means knowledge.

Then, at this point, it urges us to ask a rhetorical question:

Can we say that in 1254 the presence of a "maestro en organo" (teacher of music) was equivalent to a professorship?

It can be observed that there is a lot of information about the "maestro en organo" inside the Siete Partidas: Alfonso X thought music and sound as science. A complete analysis of the university's studies on music in the *Siete Partidas* are in [16] [17].

8. DISCUSSION ABOUT WHAT THE STUDY COULD HAVE INCLUDED IN THIS CHAIR OF MUSIC

As was indicated in the Introduction, it is necessary to increase the importance of this Chair of Music at the University of Salamanca, and because there are no written documents for the first 200 years of this institution, the author will use some additional investigations.

A few researchers have made interdisciplinary studies among Arab philology, musicology, medieval linguistics, and comparative literature [9] [18], that is said about the chair of music are inferences based on documents of that time, such as the Siete Partidas, the Cantigas de Santa María, and other sources of information also from that era. So, in order to put some general context involving the teaching of music in 1254, to find what kinds of topics that would have been involved.

8.1 Organum, the polyphonic chant

Polyphonic chant, also known as *organum*, was a complex musical form that developed in the 12th century, and "by 'maestro en organo' probably organum in the sense of the science of discant was meant" [19]. The word organum was also used to refer to the teaching of this kind of chant, for this reason it is inferred that "organo" could be associated to teach music. Additionally, the Cantigas de Santa María often feature complex polyphonic arrangements, indicating a knowledge of harmony.

8.2 Quadrivium: Music and arithmetic

Cantigas de Santa María offer a way (by the contrafactual) to understand what could be teaching in the chair of music in 1254. They are a collection of secular poems with musical notation, showcasing a sophisticated understanding of music theory. The use of mensural notation, which precisely indicates rhythmic values, suggests an awareness of intricate musical structures, and the knowledge to link the theoretical aspects of arithmetic with musical sounds, meaning the mathematical foundations of sound and its relationships between musical intervals.

8.3 The science of sound

Continuing with the tradition inherited from al-Ándalus, the "maestro en organo" taught the behavior of sound embedded in music [7], because their ideas could have influenced the thinking of music theorists in Salamanca, even if they were not explicitly articulated in the same terms. Then, it could be inferred that this chair of music would include the study of: Sound physics, understanding how sound is produced and transmitted; the theory of musical intervals and consonances; the study of musical notation and the principles of musical composition. It's highly probable that the study of sound (sones) were incorporated, albeit in a more rudimentary form than we understand today.

9. CONCLUSION

We are able to say that in 1254 the University of Salamanca had a chair of music, the first in the world, with a professor called as "maestro en organo." This historical fact is justified by hermeneutics, understood as a general theory of the understanding of texts, with the intention of giving a systematic approach to the translation of ancient texts, consisting in reading the manuscripts as they were intended at the time of their writing and understanding them in their real social context and cultural environment.

It is also clear that in order to understand this historical event of 1254, the "maestro en organo" cannot be analyzed as isolated data, as mentioned in the Royal Charter, but rather it is necessary to refer to the Siete Partidas to better understand his academic role as a professor who could be dedicated to: Teaching music, polyphonic singing, playing instruments.

It's important to remember that medieval music education was very different from modern music education, the focus was on understanding the underlying principles of music, rather than developing performance skills. In essence, the teaching of music by the "maestro en organo" in 1254 at the University of Salamanca would have been a blend of theoretical understanding, arithmetic, and secular/religious music.

In the Middle Ages, when music in Western Europe was taught only in churches and monasteries, the creation of a chair of music with one professorship at the University of Salamanca in 1254 is revolutionary.

The contributions of the Arabs thinkers whose works on music were translated in al-Ándalus (from Arab to Latin), and whose ideas spread from Spain to Western Europe, leading to the Renaissance and the Enlightenment. They played an important role in the creation of this Chair of Music at the University of Salamanca.

Finally, the "maestro en organo" in modern words could be identified like a "chair of musical acoustics," because ultimately music is part of the creation of sounds.

Acknowledgement. The author wants to thank to Prof. Eng. Federico Miyara (University of Rosario, Argentina), for reviewing and his comments to this article.

Disclaimer. The author has no feelings against any religion or culture; this article was written under the sole agenda of History of Science. Research and the writing of this paper were not funded and were done in the author's free time.

10. REFERENCES

[1] Provencio Garrigós, Herminia; Martínez Egido, José Joaquín: *La época alfonsí y los inicios de la prosa castellana*. Biblioteca Virtual Miguel de Cervantes, (n.d.).

[2] Chacón, Pedro: La primera historia de una universidad: la «Historia de la Universidad de Salamanca», 1569.

[3] Carabias Torres, Ana María: *Historia de la Universidad de Salamanca» hecha por el maestro Pedro Chacón*. Edición y estudio al cuidado de Ana María Carabias Torres. Salamanca, 1990.

[4] Soriano Fuertes, Mariano: *Historia de la música española: desde la venida de los fenicios hasta el año de 1850*. Barcelona, 1855.

[5] Farmer, Henry George: *Historical facts for the Arabian musical influence*. Studies in the music of the Middle Ages. London, 1930.

[6] Farmer, Henry George: *A history of Arabian music to the XIIIth century*. Luzac & co. 1929

[7] Montano, Walter: *al-Ándalus. Spreading acoustic knowledge from Spain to Western Europe*. 11th Convention of the European Acoustics Association. Málaga, 2025.

[8] Documentos Reales: *Enrique III, rey de Castilla y León, confirma la carta abierta otorgada a la Universidad de Salamanca por Alfonso X en Toledo el 8 de mayo de 1254*. Archivo de la Universidad de Salamanca.

[9] Mettmann, Walter: *Alfonso el Sabio, Cantigas de Santa Maria*. 4 vols., Coímbra 1959–1972.

[10] Ferreras, Juan de: *Historia de España*. Parte sexta, contiene los sucesos de el syglo XIII, 170.

[11] Ferreras, Juan de: Histoire générale d'Espagne, traduite de l'Espagnol de Jean de Ferreras. Tome quatrieme. France, 1751.

[12] Theil, Erster: Der gegenwärtige Zustand von Europa, worin die natürliche und politische Beschaffenheit der Europäischen Reiche und Staaten aus bewährten Nachrichten beschrieben wird von M. E. Tozen, Dedentlichen Lehrer der Geschichte auf der Herzoglich- Mecklen burgischen Univerſität zu Büßow, 1767.

[13] Johnson, W. M: The new imperial encyclopaedia, or, Dictionary of the sciences and arts. Volume III. London, 1800.

[14] García y García, Antonio: La enseñanza universitaria en las Partidas. *Glossae*. Revista de historia del derecho europeo 2 (1989-90). Instituto de Derecho Común, Universidad de Murcia.

[15] *Siete Partidas*. Edición de textos alfonsíes en REAL ACADEMIA ESPAÑOLA: Banco de datos (CORDE) [en línea]. Corpus diacrónico del español. [7 de marzo 2006]

[16] Van Scoy, Herbert A.: *Alfonso X, Educator*. South Atlantic Bulletin Vol. 24, No. 1 pp. 4-6 (3 pages). Published By: South Atlantic Modern Language Association, 1958.

[17] Turner, Daymond: *The university in the "Siete Partidas."* Romance Notes Vol. 11, No. 2 pp. 447-451. Ed. University of North Carolina, 1969.

[18] Carpenter, Nan Cooke: *Music in the medieval and renaissance universities*. Ed. Norman, University of Oklahoma Press, 1958.

[19] Angles, Higini: Hispanic musical culture from the 6th to the 14th century. *The Musical Quarterly*, Vol. XXVI N° 4, pp. 494-528. Oct 1940.

DOI: 10.61782/fa.2025.0002

FORUM ACUSTICUM EURONOISE 2025

20 YEARS OF RESEARCH ON ACOUSTICS AND VIBRATIONS AT MIGUEL HERNANDEZ UNIVERSITY OF ELCHE

Ramon Peral-Orts[1] **Nuria Campillo-Davo**[1*] **Hector Campello-Vicente**[1]
Miguel Fabra-Rodriguez[1] **David Abellan-Lopez**[1] **David Clar-Garcia**[1] **Emilio Velasco-Sanchez**[1]
[1] Engineering Research Institute of Elche (I3E), Miguel Hernandez University of Elche, Elche, Spain

ABSTRACT

The Miguel Hernandez University of Elche (UMH) is a public and young university located in Alicante province, in the southeast of Spain, founded in December 1996 and which started its academic activities in the course 1997/1998. In the earliest beginnings of the UMH, a very small group of researchers of the Mechanical Engineering teaching area had the motivation of creating a working line focused on research on acoustics and vibrations. That fact led, in 2005, to the foundation of the Acoustic Engineering and Vibrations Laboratory of the UMH (LIAV-UMH). Since then, the members of the LIAV-UMH group focus their research lines mainly in the field of sound emissions and vibrations of road traffic and environmental acoustics, which results have naturally led to the knowledge transfer and collaboration with different entities and companies. In the current year, 2025, the LIAV-UMH celebrates its 20 years of research. This is why this paper summarizes the scientific trajectory followed by the group from its creation to the present days, showing the different working lines, developed research projects and knowledge transfer activities.

Keywords: *vehicle noise, tyre road noise, traffic noise prediction model, warning sound, metasurface.*

[*] ***Corresponding author***: *ncampillo@umh.es*
Copyright: *©2025 First author et al. This is an open-access article distributed under the terms of the Creative Commons Attribution 3.0 Unported License, which permits unrestricted use, distribution, and reproduction in any medium, provided the original author and source are credited.*

1. INTRODUCTION

Noise pollution has been perceived throughout the history of civilisations as a nuisance that reduces the quality of life of people exposed to high noise levels. Noise exposure may lead to negative consequences that might vary from difficulties for holding a conversation, to sleep problems and disturbances in the performance of activities that require concentration, or even variations in the nervous system. In the last decades, different policies have been developed to control and reduce environmental noise. In this respect, the European Commission's Green Paper on 'Future Noise Policy' was a first step towards a common noise policy in the European Union [1]. Subsequently, in 2002, the publication of the European Directive 2002/49 on Assessment and Management of Environmental Noise [2], provided the main legislative framework to address noise reduction in Europe. The Directive established a common approach to avoid and prevent exposure to environmental noise through noise mapping and action plans. However, almost two decades after its publication, it was shown that noise from road traffic was still the noise source that affected the largest number of people [3]. This is still the case today, as reported in the European Environment Agency's latest publication [4] on exposure to transport noise in the European Union, which highlights the fact that the number of people exposed to high levels of road traffic noise remains high and is likely to increase in the coming years. Thus, it is estimated that about 113 million people are affected by traffic noise levels of at least 55 dB(A) over extended day-evening-night periods (Lden). This emphasises the need to designate and protect more quiet zones both in cities and in areas outside cities.

The motivation for environmental awareness has always been one of the main concerns of the group of the Acoustic

Engineering and Vibrations Laboratory of the UMH (LIAV-UMH), and what led the team to start research in environmental acoustics and noise and vibration control. In that context, the LIAV-UMH group began its work in 2005. Currently, the group is integrated by a team of seven researchers and several collaborators. All the members of the group are professors and lecturers of the Mechanical Engineering Teaching Area of the Department of Mechanical Engineering and Energy of the UMH, and their lines of work have been oriented towards acoustic engineering and applied vibrations, as well as offering a practical approach to the transfer and provision of services to companies and public and private entities.

The work of the group members is currently framed within the University Institute for Engineering Research of Elche (I3E - https://i3e.umh.es/en/), within the research lines of the Energy and Mechanics Unit. This article mainly describes the research trajectory of the group, focusing on the priority lines of research.

2. FIRST STEPS: TOWARDS STUDYING ROAD TRAFFIC NOISE AND VIBRATION CONTROL

Strategic noise maps are the tool that allows the global assessment of noise exposure of the population in a given area. In this sense, the beginnings of the group coincided with a period when the study of noise mapping was a trending topic.

In this line, one of the first works of the group that received public funding (Generalitat Valenciana, GV05/100, 2005-2006), focused on the development of a prediction model of night-time traffic noise based on the vehicles' sound directivity. The research also allowed the study of the horizontal sound directivity of vehicles travelling at high speed [5] (2009). To this end, work was carried out to establish a methodology capable of providing information on the sound distribution of a noise source in its main plane of emission, based on the proposal of different configurations of microphone arrays [6] -a linear antenna with uniformly distributed microphones (ULA) and a linear antenna with proportionally distributed microphones (PROP)-, in different orientations with respect to the vehicle's driving line. The results of this work yielded very interesting conclusions and led to the registration of a patent for an acoustic speedometer system [7].

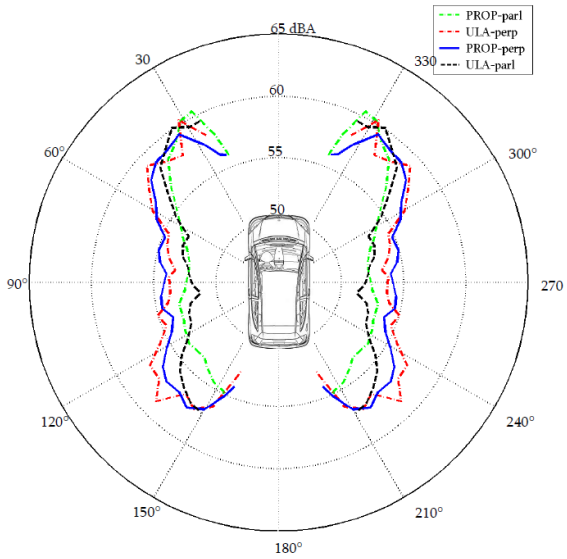


Figure 1. Polar plot of the sound level obtained with each of the proposed antennas [5].

During this first period, members of the group also collaborated in a much larger project (Generalitat Valenciana, GVEMP06/011, 2006), which included other researchers, for the construction of a drum-type tyre testing machine, Fig. 2. The machine allows to perform load/speed tests for new and retreaded passenger car and commercial vehicle tyres according to UNECE regulations 30, 54, 108 and 109, and rolling resistance tests according to ISO 28580.



Figure 2. Tyre testing facility at the UMH.

3. TYRE/ROAD NOISE AS A FOCUS OF ATTENTION IN VEHICLES

The results obtained in that first stage on the sound directivity of vehicles led the group in the subsequent years to open one of its main current lines of work: the study of tyre/road noise. Initially, work was carried out on the development of new measurement methodologies to assess tyre/road noise, the novelty of which laid in the evaluation of sound emission through a standardised engineering method (ISO 3744), to determine the sound power level in the tyre/pavement interaction [8], Fig. 3.

In a first phase, two methodologies were designed for evaluation on track [9] (2013): Alternative Coast-By (A-CB) [10] and Alternative CPX (A-CPX) [11], inspired by the traditional CB and CPX methodologies, but with the result of obtaining the sound power level of the set of sources formed by the four tyres of a vehicle rolling on a pavement (A-CB), and the sound power level of the interaction of a single tyre rolling on the pavement (A-CPX). One of the conclusions drawn from this phase of work was that the tyre/road sound power level of a complete vehicle can be calculated from the energetic sum of the tyre/road sound power level of each individual tyre that comprises a vehicle [12].

At the time when the group had the tyre testing facility in operation, two analogous methodologies were developed for the study of tyre/road noise on a drum testing machine [13] (2018): Alternative Drum methodology (A-DR) [14,15] and Alternative CPX Drum methodology (A-CPX-DR) [16].

4. THE INCORPORATION OF ELECTRIC VEHICLES INTO ROAD TRAFFIC

In parallel to the line related to tyre/road noise, the group also began another of its major fields of work: the study of the effect generated by the inclusion of electric vehicles in noise maps. At this point, in the early years work was carried out on adapting the NMPB-Routes 2008 road traffic noise prediction model to the presence of electric vehicles [17] (2014). The group's work was collected in different publications - some of them of relevant impact [18] - where, among other conclusions, it was possible to gather that the noise emitted by an electric vehicle can be compared with that emitted by an internal combustion vehicle without mechanical noise, when both circulate at speeds above 50km/h.

The study of the NVH (Noise, Vibration and Harshness) of electric vehicles was a very important topic in the early period of the introduction of electric vehicles into vehicle fleets - and it remains so today. That led to the group's participation in the COST Action TU1105 'NVH analysis techniques for design and optimisation of electric vehicles' (European Union, Cost Action TU1105, 2012-2016). As a result of the joint efforts of the members of the Action consortium, a comprehensive catalogue of NVH-related technologies for electric and hybrid vehicles was compiled [19].

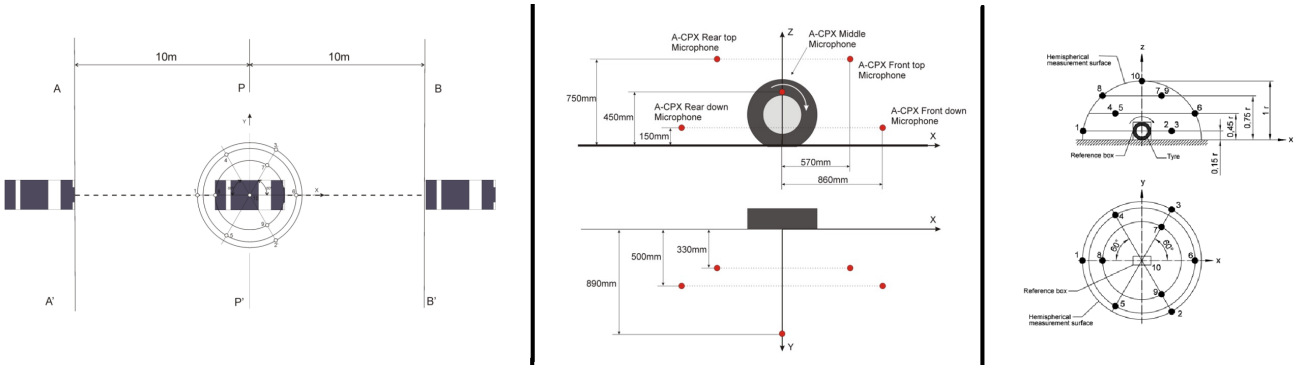


Figure 3. Configurations of the alternative methodologies designed by the LIAV-UMH group for evaluation of sound power level of tyre/road noise [9,13]. Left: A-CB tests. Center: A-CPX. Right: A-DR.

5. WARNING SOUNDS: PEDESTRIANS AT POTENTIAL RISK

The experience that the group was acquiring in the NVH of alternative vehicles was focused on the study of their acoustic detectability. In this field, the group had the opportunity to work on different projects. Among them, one of the most noteworthy was the collaboration with ONCE (Spanish National Organisation for the Blind), in a project (Generalitat Valenciana, GV/2017/004, 2017-2019) whose objective was to improve the detection, localisation and identification of the warning sounds of electric vehicles through the perception of blind people. To this end, the emotional response of the test volunteers to different warning sounds was studied, as well as the detectability of these sounds through the analysis of detection times.

More recently, the work carried out in the group has focused mainly on the development of numerical models of mechanical systems that can help to improve the sound detectability of alternative vehicles [20] (2023). In this field, the modelling of the noise generated by a tyre either when it impacts against the ground in free fall or when it impacts against elements external to the vehicle, such as a speed bump or a pothole in the pavement, has been studied. The model developed by the group is solved in two steps: a dynamic analysis of the contact of the tyre with the element against which it impacts, through FEM modelling; and a subsequent BEM analysis of the sound field generated in the environment, based on the vibration of the tyre surface as a sound source.

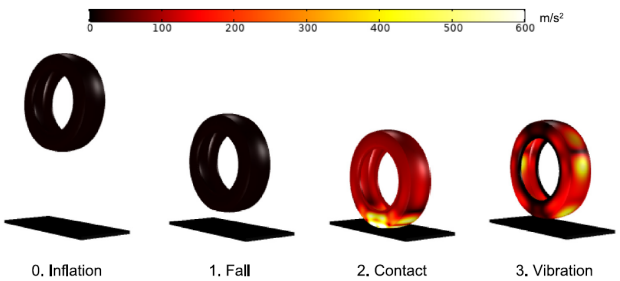


Figure 4. Phases of a transient analysis in a FEM simulation of a tyre impacting a flat, rigid, and reflective surface [20,21].

6. CURRENT RESEARCH IN THE GROUP

The experience accumulated by the group to date has allowed us to identify the need for further research into aspects related to the detectability of electric and hybrid vehicles in particularly sensitive environments in low-speed traffic conditions. To this end, the group is currently exploring the potential that metasurfaces may provide for this solution (Generalitat Valenciana, CIGE/2022/1, 2023-2024). The term 'rolling metasurface' was coined by the team [22] to refer to a surface pavement design modified in its geometry, which confers different properties to those provided by its original textural characteristics (micro, mega and macro texture), and which is capable of generating controlled sound emission and propagation when a tyre circulates on this pavement. Previous work in this line [23], has led the team to continue investigating this proposal.

Finally, the group is also currently exploring the sound directivity capabilities of a low height stepped directional acoustic barrier (SDAB) system. The aim of the design of this barrier is to create an interference to sound propagation in the transverse direction, but at the same time to allow sound transmission at a certain angle in both horizontal and vertical planes [24].

7. CONCLUSIONS

The LIAV-UMH group has focused its work over the last 20 years in the field of applied acoustics and vibrations, especially in the area of vehicle acoustics, with the development of methodologies and characterisation of the sound emission of conventional vehicles, as well as electric and hybrid vehicles; the study of tyre/road noise; environmental acoustics, with the improvement of traffic noise prediction models, development of noise maps and experimental studies of traffic noise emission sources; acoustic studies of sound sources, with special attention to studies on the control of noise measurement installations in MOTs; development of vibration behaviour models for road and rail vehicles; among many others. This article covers only part of the group's work, the most closely related to its research work.

The group's research strategy for the coming years will continue to focus on the search for solutions to improve urban environments in terms of noise emissions. To this end, the group intends to continue collaborating with institutions and entities, both public and private, national and international, with the ultimate aim of achieving results

with a social impact that can be transferred and implemented in practice.

8. ACKNOWLEDGMENTS

The members of the LIAV-UMH research group would like to thank all the people who, in one way or another, have contributed to the development of the group: from students and scholarship holders, members of other UMH research groups, colleagues from other Spanish and international universities with whom they have worked together, and companies and public institutions with which they have collaborated.

9. REFERENCES

[1] European Comission. *Future Noise Policy – European Commission Green Paper*. Brussels, 1996.

[2] European Parliament and Council of the European Union. *Directive 2002/49/EC of the European Parliament and of the Council of 25 June 2002 relating to the assessment and management of environmental noise*. Luxembourg, 2002.

[3] European Environment Agency. *Road traffic remains biggest source of noise pollution in Europe*. 2017.

[4] European Environment Agency. *Environmental Noise in Europe – 2020*. EEA Report No 22/2019. Luxembourg: Publications Office of the European Union, 2020.

[5] R. Peral-Orts: "(Horizontal sound directivity of a motor vehicle travelling at high speed) Directividad sonora horizontal de un vehículo automóvil circulando a alta velocidad". *Doctoral thesis*. Miguel Hernandez University of Elche. 2009.

[6] R. Peral-Orts, E. Velasco-Sanchez, N. Campillo-Davo, H. Campello-Vicente: "Using microphone arrays to detect moving vehicle velocity", *Archives of Acoustics*, vol. 38, no. 3, pp. 407-415, 2013.

[7] R. Peral-Orts, E. Velasco-Sanchez, N. Campillo-Davo, and H. Campello-Vicente. Patent nº. P200930283. Sound kinemometer. Spain. 17/01/2013. Miguel Hernandez University of Elche. Patent in operation by PROINTER.

[8] N. Campillo-Davo, R. Peral-Orts, H. Campello-Vicente, D. Clar-Garcia, and E. Velasco-Sanchez, "Compilation of some novel approaches for rolling noise evaluation in vehicles", in *Proc. of the Internoise 2019 Conference*, (Madrid, Spain), 2019.

[9] N. Campillo-Davo: "(Experimental modelization of tyre/road noise in type approval test) Modelización experimental del ruido de rodadura en ensayo de homologación de neumáticos". *Doctoral thesis*. Miguel Hernandez University of Elche. 2013.

[10] N. Campillo-Davo, R. Peral-Orts, E. Velasco-Sanchez, H. Campello-Vicente: "An experimental procedure to obtain sound power level of tyre/road noise under Coast-By conditions", *Applied Acoustics*, vol. 74, pp. 718–27, 2013.

[11] N. Campillo-Davo, R. Peral-Orts, H. Campello-Vicente, E. Velasco-Sanchez: "An alternative close-proximity test to evaluate sound power level emitted by a rolling tyre", *Applied Acoustics*, vol. 143, pp. 7-18, 2019.

[12] N. Campillo-Davo, R. Peral-Orts, H. Campello-Vicente, E. Velasco-Sanchez: "A methodology for the extrapolation of coast-by noise of tyres from sound power level measurements", *Applied Acoustics*, vol. 159, nº 107077, 2020.

[13] D. Clar-Garcia: "(Laboratory test methodology for the measurement of tire rolling noise) Metodología de ensayo en laboratorio para la medición del ruido de rodadura de neumáticos". *Doctoral thesis*. Miguel Hernandez University of Elche. 2018.

[14] D. Clar-Garcia, E. Velasco-Sanchez, N. Campillo-Davo, E. Campello-Vicente, "A new methodology to assess sound power level of tyre/road noise under laboratory controlled conditions in drum test facilities", *Applied Acoustics*, vol. 110, pp. 23-32, 2016.

[15] D. Clar-Garcia, E. Velasco-Sanchez, M. Sanchez-Lozano, H. Campello-Vicente: "An alternative Drum test method to UNECE Regulation 117 for measuring tyre/road noise under laboratory controlled conditions", *Applied Acoustics*, vol. 151, pp 113-123, 2019.

[16] D. Clar-Garcia, H. Campello-Vicente, N. Campillo-Davo, M. Sanchez-Lozano, E. Velasco-Sanchez: "A New CPX Drum Test to Obtain Sound Pressure Levels of Tyre Noise for Type Approval", *Acoustics*, vol. 6(3), pp. 579-592, 2024.

[17] H. Campello-Vicente: "(Adaptation of the road traffic noise prediction model NMPB-Routes 2008 to the

presence of electric vehicles) Adaptación del modelo de predicción de ruido de tráfico rodado NMPB-Routes 2008 a la presencia de vehículos eléctricos". *Doctoral thesis*. Miguel Hernandez University of Elche. 2014.

[18] H. Campello-Vicente, R. Peral-Orts, N. Campillo-Davo, and E. Velasco-Sanchez: "The effect of electric vehicles on urban noise maps", *Applied Acoustics*, vol. 116, pp. 59-64, 2017.

[19] N. Campillo-Davo, and Ahmed Rassili (eds.): "NVH Analysis Techniques for Design and Optimization of Hybrid and Electric Vehicles". Aachen: Shaker Verlag, 2016.

[20] M. Fabra-Rodriguez: "(Numerical modelling of mechanical systems for the improvement of noise detectability of silent vehicles) Modelos numéricos de sistemas mecánicos para la mejora de la detectabilidad sonora de los vehículos silenciosos". *Doctoral thesis*. Miguel Hernandez University of Elche. 2023.

[21] M. Fabra-Rodriguez, R. Peral-Orts, D. Abellan-Lopez, H. Campello-Vicente, and N. Campillo-Davo: "Numerical sound prediction model to study tyre impact noise", *Applied Acoustics,* vol. 206, nº. 109325, 2023.

[22] S. Nuñez-Andres, N. Campillo-Davo, M. Fabra-Rodriguez, D. Abellan-Lopez, H. Campello-Vicente, R. Peral-Orts, "Estudio del campo sonoro inducido por geometrías tridimensionales sobre una superficie reflectante," In *Proc. of the TECNIACUSTICA 2023 Conference,* (Cuenca, Spain), pp. 125-131, 2023.

[23] M. Fabra-Rodriguez, D. Abellan-Lopez, F.J. Simon-Portillo, H. Campello-Vicente, N. Campillo-Davo, and R. Peral-Orts: "Numerical model for vibro-acoustics análisis of tyre-road noise generation caused by speed bumps," *Applied Acoustics,* vol. 216, nº. 109830, pp. 1-7, 2024.

[24] N. Campillo-Davo, M. Fabra-Rodriguez, H. Campello-Vicente, D. Abellan-Lopez, E.M. Mora-Saura, D. Clar-Garcia, and R. Peral-Orts: "Numerical study of a stepped directional barrier for urban noise control", in *Proc. of Forum Acusticum Euronoise 2025 Conference*, (Malaga, Spain), 2025.

DOI: 10.61782/fa.2025.0717

FORUM ACUSTICUM EURONOISE 2025

PSYCHOACOUSTICS, THE LONG WAY TO BE CONSIDERED INTO INTERNATIONAL STANDARDS

Klaus Genuit[1*]
[1] HEAD-Genuit-Foundation, Herzogenrath, Germany

ABSTRACT

For several decades the A-weighted sound pressure level has been used for the evaluation of sound. But sound character is determined by the spectral composition and the temporal patterns. For this reason, the discipline of psychoacoustics has established itself, which can provide more differentiated analyses describing the sound character. With the help of psychoacoustics parameters such as loudness, sharpness, tonality, roughness, fluctuation and impulsiveness, the auditory impression of sound events can be viewed in a more differentiated way than just with the A-weighted sound pressure level. The first standards were developed for stationary loudness DIN 45632 and ISO 523. In the meantime, we have standards by ECMA-418-2 describing different psychoacoustical parameters based on a hearing model like tonality, roughness and fluctuation strength. The international standard ISO 12913 "Soundscape" describes this relationship of perceived sound quality considering the context.

Keywords: *psychoacoustics, standardization, soundscape*

1. INTRODUCTION

The noise nuisance of the population has increased in recent years, despite numerous measures to reduce the noise emissions of individual noise sources. According to the German Federal Environment Agency (UBA), more than 50% of the population is affected by traffic noise [1]. Although psychoacoustics was introduced by ZWICKER [2] in the middle of the last century, first with the parameter loudness, the A-weighted sound pressure level still dominates all legal regulations with respect to noise measurements. The advantage of the A-weighted SPL is the option to calculate with these data. If you know the level of two sources, a calculation of the superposition is possible. It is not possible to predict the psychoacoustical parameters by superposition of different sound sources, the time signal is necessary. The absence of standardization for a long time was another disadvantage of the introduction. It has been a long way to overcome this handicap.

2. WHAT IS NOISE

Noise is caused by the perception of humans and describes the effect of sounds. Consequently, noise cannot be measured with sound level meters, but sound only becomes noise if it is undesirable for those affected or is likely to affect them psychologically, physically, socially or economically [3]. Noise represents a negatively assessed sound immission, i.e. it does not exist without the perceiving subject. This understanding is also shared by the DEGA (German Acoustical Society) Noise Working Group (ALD) and explains that noise is an evaluative term and therefore cannot be measured with physical devices alone [4]. Consequently, a physically unambiguously describable sound event can certainly lead to different auditory events. The context, the attitude of the exposed person to the source of the noise or to its originators, as well as the experience and expectations of the noise exposure, influence the perception and assessment of sounds. According to this understanding, noise cannot be validly determined based on an A-weighted sound pressure level alone, as is suggested by terms such as "noise measurement" and "noise map". A so-called "noise map" is so far only a map that shows sound pressure levels based on calculated data. A sound pressure level map is certainly necessary for the discussion of noise exposure, but it is not sufficient for the valid determination of nuisance caused by noise, i.e. in the context of noise [5].

3. PSYCHOACOUTSICS

Usually when noise effects are considered with respect to well-being and health, A-weighted sound pressure level indicators are analyzed. However, several decades ago researchers started to use measurement methods to quantify auditory sensations in more detail. Later the soundscape pioneer SCHAFER [6] described acoustics and

[*] ***Corresponding author***: *klaus.genuit@head-genuit-stiftung.de*
Copyright: *©2025 First author et al. This is an open-access article distributed under the terms of the Creative Commons Attribution 3.0 Unported License, which permits unrestricted use, distribution, and reproduction in any medium, provided the original author and source are credited.*

psychoacoustics as the cornerstones to understanding the physical properties of sound and the way sound is perceived. This approach emphasized that all aspects of soundscape are related to perception. Psychoacoustic data are considered for a more comprehensive evaluation of acoustic environments that goes beyond the simplified use of sound level indicators. Moreover, a key consideration is that acoustic environments are perceived binaurally by humans. Thus, measurement equipment that collects spatial information about the acoustic environments is increasingly being applied in soundscape investigations and consequently is suggested in soundscape standards. Following the soundscape concept, all measurements and analyses must reflect the way soundscape is perceived by people in the appropriate context. This insight led to an increase in research and applications of psychoacoustic measurements to understand the effects of acoustic environments on humans in more detail. Psychoacoustics deals with the description of the relationship between physical stimuli and the auditory perceptions they evoke. Experimentally observed relationships between stimuli and sensations result in mathematical descriptions and psychoacoustic models. This makes it possible to make statements about the acoustic properties of sounds and their perception. An extended assessment of environmental noise to predict noise pollution can be carried out by considering psychoacoustic characteristics of environmental noise. The most important psychoacoustical parameters are:

3.1 Loudness:

Consideration of distribution of critical bands and masking properties in the hearing, DIN 45631/A1, ISO 532-1. Studies [7] have shown that the 5% percentile loudness (N5) correlates highly with the perceived total loudness valid in cases of unsteady sounds, since the mean value of time varying loudness compared with the subjectively evaluated loudness provides a value, which is too low, the 5% percentile loudness (N5) has to be used with respect to the perceived overall loudness. Experiments have shown that the perception of loudness correlates better with the psychoacoustic parameter loudness than with the A-weighted sound pressure level [7]. Thus, the representative singular value, which considers human cognitive stimulus integration, is based less on a mean value than on the loudness peaks of the function of loudness over time. Basically, loudness depends on the spectral distribution, considers the level-dependent loudness perception of different tones and the duration as well as simultaneous-, pre- and post-masking properties of the human ear.

3.2 Sharpness:

Weighted first moment of distribution of critical band rates of specific loudness, relationship of high-frequency spectral components to total loudness, DIN 45692. The sharpness parameter covers the aspect that sounds with energetic focus in the high frequency range are perceived as sharp, which often leads to increased annoyance independent on level.

3.3 Roughness & Fluctuation:

Time structure of the sound signal, modulation factor and level difference determine roughness & fluctuation, amplitude- and frequency modulation, DIN 38455, ECMA 418-2 [8] (ECMA develops and publishes international standards for the information and communication industry). Roughness or fluctuation, deal with sensations that are evoked in sounds due to special temporal structures caused by modulation of tones or different tones in one frequency group.

3.4 Tonality:

Products emit tonally perceived noises due not only to pure tones but also to narrow noise bands, and to same-vicinity combinations of pure tones and narrow elevated noise bands, ECMA 418-2. The psychoacoustic parameters behave (almost) orthogonally, i.e. one psychoacoustic parameter can vary whereas another parameter remains constant. There is a gain in information compared to the sound pressure level and more differentiated statements about the characteristics and potential reactions of the listener become possible.

4. STANDARDIZATION OF PSYCHOACOUSTIC

Psychoacoustics will be more and more established: automotive field, office and appliance equipment, environmental noise and soundscape. The first standards within psychoacoustics were the loudness standards from stationary sound represented by the recommendation ISO 532-A and ISO 532-B (1966) “Method calculating loudness level”. ISO 532-A is based on octave spectrum in accordance with STEVENS [9], ISO 532-B is based on third octave spectrum in accordance with ZWICKER [10]. These recommendations became an ISO standard in 1975. This early introduction of the loudness standard has had some disadvantages: 1. the calculation was very complicate, 2. two standards instead of one, 3. the discussion that loudness is correct and A-weighted level is wrong has prevented a quick acceptance of this new approach, 4. ISO-

532 was only valid for stationary sounds but in reality around 80% of daily sounds are time-variant. In 1996 the German Institute for Standardization (DIN) initiated a new working group "Psychoacoustical Measurement Technique" to standardize the time-variant loudness, sharpness and binaural measurement system (artificial head). The first result was the DIN 45692 (2009) for "Sharpness" which standardized a modified VON BISMARK sharpness [11] with a different weighting function. Informative was the AURES sharpness [12] mentioned which has a dependence on loudness. One year later the new time variant loudness DIN 45631/A1 was published 2010 based on the ZWICKER method. Parallel the ISO working group WG9 has started in 2007 to review the ISO 532 stationary loudness. In the meantime, another approach was established, the US ANSI S3.4-2007 "Procedure for the computation of steady sounds" in accordance with GLASBERG & MOORE loudness [13] using 40 equivalent rectangular bands instead of the 24 frequency groups by ZWICKER. The ANSI loudness was based on the new ISO 226 from 2003 (Equal Loudness Curves) whereas the ZWICKER loudness was based on the older ISO 226 from 1987. These differences led to a lengthy controversial discussion about which loudness should now be standardized. Unfortunately, the two calculation methods led to different results depending on the signal. It was questioned whether ISO 229 from 2003 is really better or more correct than the old ISO 229 from 1987 or whether it would be better to revise ISO 226 again. Finally, after many years, it was agreed to develop three new standards: ISO 532-1 (2017) according to the ZWICKER method for stationary as well as time-variant noises, ISO 532-2 as stationary loudness according to MOORE & GLASBERG [14] and later in 2023 ISO 532-3 for time-variant signals according to the MOORE & GLASBERG & SCHLITTENLACHER method [15]. In 2008, the first efforts were again made at DIN to standardize roughness. In the meantime, various software solutions were available for calculating roughness, but they yielded extremely different results. While the calculation of the roughness of pure, modulated sine tones was still quite uniform, large differences were revealed for broadband signals. Narrowband signals can cause roughness, but broadband noise cannot. Therefore, the calculation algorithm had to recognize whether the partial roughness occurring in the individual frequency groups correlates with each other or not. Numerous listening experiments with typical everyday noises also showed a large dispersion in terms of the assessment of roughness, even among experts. It was not until 2024 that DIN 38455 Roughness was published. In the field of office equipment manufacturers ECMA, the demand for the calculation of tonality and roughness came earlier, so that psychoacoustic parameters were standardized in parallel with ECMA-418-2 as early as 2022 based on SOTTEK's hearing model [16]. In addition to tonality, roughness has also been defined, and the fluctuation strength will also be standardized 2025.

5. SOUNDSCAPE

Psychoacoustics, sound quality and cognition provide information on how humans perceive and interpret their surrounding world. With psychoacoustics alone it is only possible to describe the sound character. Psychoacoustics can analyze in detail the acoustic composition of a soundscape and the signal properties that elicit specific auditory sensations; however, a comprehensive interpretation of the results requires feedback from the listeners. Whereas the perceived sound quality depends on the context how people experience the sound situation. While the overall noise measured at a specific location can be analyzed in terms of several acoustical parameters, the annoyance or pleasantness level of a complex soundscape composed of several sound sources cannot be determined solely from the values obtained through such analyses. Even if the acoustic contribution of a single sound source to the overall noise does not appear significant in a physical sense, the influence of this sound source on the soundscape can be relevant perceptually [17]. In 2008 a new working group WG54 at ISO started the development of the soundscape standard which was the basis of the first standard ISO 12913. The definition was part of ISO 12913-1 (2014): Soundscape is the acoustic environment as perceived or experienced and/or understood by a person or people, in context. Two major components like pleasantness and eventfulness describe soundscape. This concept allows considering sound quality aspects beyond noise annoyance, a good soundscape quality is not simply identical to the absence of annoyance. Judgments cannot be fully understood by only considering acoustical quantities, since contextual parameters and interactivity are relevant for assessment of a soundscape as well. The ISO/TS 12913-2 (2018) "Data collection and reporting requirements" is the first standard requesting normative the use of binaural measurement as the judgment of acoustical environment is multidimensional, the effects of superposition of several sound sources is not easy to predict and the human hearing is able to select a single sound source among others. Whereas ISO/TS 12913-3 (2019) "Data analysis" recommends the application of psychoacoustical

parameters. The ISO/TS 12913-4 "Design and intervention" is under development.

6. SUMMARY

It is astonishing that for many decades, the complexity of sounds and the perception by humans has only been described with a simple A-weighted sound pressure level measurement. Neither the temporal structures nor the spectral distributions are considered. For over 100 years, scientific investigations have been carried out within psychoacoustics, and for over 60 years there have been efforts to standardize these findings. Difficulties arose due to different scientific approaches, limited practical application and initially technically difficult implementations. In the meantime, standards are available for almost all relevant psychoacoustic parameters, unfortunately within different standardization committees such as ISO, DIN, ANSI, ECMA. However, with the standard for Soundscape ISO 12913, for the first time, the implementation of normative binaural measurement technology and informative use of psychoacoustics has been carried out. A long way! Psychological and cognitive aspects of sound are not physically measurable. The question is: How to measure sound? Very accurate with highest precision using a calibrated A-weighted sound pressure level meter class 1 or correct like the human hearing with consideration of context? A complete overview with respect to soundscape is given in [17].

7. REFERENCES

[1] Umweltbundesamt, 2022: https://www.umweltbundesamt.de/themen/laerm/laermwirkungen/laermbelaestigung

[2] E. Zwicker, „Über psychologische und methodische Grundlagen der Lautheit", *Acustica 8*, pp. 237–258, 1958

[3] R. Guski, „Lärm. Wirkungen unerwünschter Geräusche, *Hans Huber*, Bern, 1987

[4] ALD Arbeitsring Lärm der Deutschen Gesellschaft für Akustik (DEGA) Germany, https://www.ald-laerm.de/publikationen/laermlexikon/laerm

[5] K. Genuit, A. Fiebig, "Kritische Betrachtung zum Thema „Lärm"-Messung. Erweiterung von Lärmprognosen durch die Psychoakustik", *Zeitschrift für Lärmbekämpfung*, Nr. 1, 2014

[6] R.M. Schafer, "The Soundscape: Our Sonic Environment and the Tuning of the World". *Destiny Books*, 1994

[7] H. Fastl, E. Zwicker, „Psychoacoustics", *Springer Berlin Heidelberg*, 2007

[8] ECMA International - European association for standardizing information and communication systems, Genf

[9] S. S. Stevens, "Calculation of Loudness", *Journal of the Acoustical Society of America*, 33, pp. 1577-1585, 1961

[10] E. Zwicker, "A procedure for calculating loudness", *Acustica,* 10, 1960

[11] G. von Bismarck, "Sharpness as an attribute of the timbre of steady sounds", *Acustica*, Vol. 20, pp. 159-172, 1974

[12] W. Aures, "Berechnungsverfahren für den Wohlklang beliebiger Schallsignale. Ein Beitrag zur gehörrichtigen Schallanalyse", *Dissertation*, München, 1984

[13] B.R. Glasberg, B.C.J. Moore, "Prediction of absolute thresholds and equal-loudness contours using a modified loudness model". *J. Acoust. Soc. Am. 120*, pp. 585–588., 2006

[14] B.C.J. Moore, B.R. Glasberg, "A Revision of Zwicker's Loudness Model", *Acta Acustica,* Vol. 82, pp. 335-345, 1996

[15] B.C.J. Moore, B.R. Glasberg, A. Varathanathan, J. Schlittenlacher, "A Loudness Model for Time-Varying Sounds Incorporating Binaural Inhibition", *Trends in Hearing*, https://doi.org/10.1177/2331216516682698

[16] R. Sottek, "Loudness models applied to technical sounds", *Noise-Con*, Baltimore Maryland, USA, 2010

[17] B. Schulte-Fortkamp, A. Fiebig et.al., "Soundscapes: Humans and Their Acoustics Environment", *Springer,* (2023)

DOI: 10.61782/fa.2025.0012

FORUM ACUSTICUM EURONOISE 2025

A HISTORICAL OVERVIEW OF HIGINI ARAU'S PROPOSAL FOR CALCULATING REVERBERATION TIME (1988)

Julián Álvarez[1*] **Ramon Graus**[2] **Helena Martín-Nieva**[3]

[1] Department of Physics, Universitat Politècnica de Catalunya, Spain
[2] Department of Theory and History of Architecture, Universitat Politècnica de Catalunya, Spain
[3] Department of Human Sciences, Universidad de La Rioja, Spain

ABSTRACT

In 1988, Barcelona physicist Higini Arau-Puchades published in international journal *Acustica* an alternative to Sabine's classical formula for reverberation time (T). Arau's formula resulted from a process of reflection that began in 1985, when Arau came into contact with Lothar Cremer during the acoustic renovation of the Palau de la Música Catalana in Barcelona, which architect Oscar Tusquets was restoring. Arau proposed a formula that considered the non-uniform distribution of absorbing material in a concert hall. Consequently, the decay rate of sound was quantified in the three directions X, Y and Z. Of course, Arau went on to use his formula in the auditorium designs that he undertook in the 1990s. He developed it in a second paper published in 1998, while his first paper cut a path in the scientific field. During the 2000s, several articles comparing Arau's work with other known formulae led to his formula being incorporated in the statistical calculation section of some of the most highly regarded computer programs on international acoustic design. We aim to analyse the impact of Arau's proposal in international academic publications to date.

Keywords: *architectural acoustics, reverberation time, non-diffuse field, Higini Arau-Puchades, Lothar Cremer.*

[*] ***Corresponding author**: julian.alvarez@upc.edu.*
***Copyright**: ©2025 Álvarez et al. This is an open-access article distributed under the terms of the Creative Commons Attribution 3.0 Unported License, which permits unrestricted use, distribution, and reproduction in any medium, provided the original author and source are credited.*

1. REVERBERATION TIME IN ROOMS WITH UNIFORM DISTRIBUTION OF ABSORPTION

1.1 Sabine (1900)

US physicist Wallace C. Sabine (1868-1919) published his studies on reverberation time in seven issues of the periodical *The American Architect and Building News*, between April and June 1900 [1-7]. He had started to research this area in 1895, when Harvard University asked him for advice on how to correct severe acoustic problems in the lecture room of Fogg Art Museum [1, p. 3], which architect Richard Morris Hunt had designed in a semi-circular shape, like old Greek theatres.

In these first articles, which combined experimental measurement of the phenomenon with its physical and mathematical analysis, Sabine formulated a hyperbolic law where the reverberation time in a space would be inversely proportional to its average absorption coefficient [2].

In turn, we owe to US physicist William S. Franklin (1863-1930) the mathematical workings that demonstrated the definitive form of Sabine's equation (1) for calculating reverberation time in 1903 [8]:

$$T = \frac{0.161V}{\sum_i S_i \alpha_i + 4mV} \tag{1}$$

In the framework of statistical theory, the equation (1) provided a global value for the behaviour of sound over time in a particular space that would enable comparisons with other rooms that are known for their acoustics.

1.2 Eyring (1930)

When Sabine had passed away, the publication of his *Collected Papers*, in 1922, spread his legacy worldwide [9]. However, it was soon shown that his equation (1) was suitable for "live" rooms, but not as appropriate for rooms that had a high level of absorption surfaces, such as those of radio stations. US physicist Carl F. Eyring (1889-1951), who worked for Bell Telephone Laboratories, drew up a general theory [10] that could be applied to all types of rooms and was formulated as follows:

$$T = \frac{0.161V}{-S\ln(1-\bar{\alpha}) + 4mV} \tag{2}$$

2. REVERBERATION TIME IN ROOMS WITH NON-UNIFORM DISTRIBUTION OF ABSORPTION: TAKING X, Y, Z INTO ACCOUNT

2.1 Bagenal (1942)

Hope Bagenal (1888-1979), a British architect specialised in acoustics, had grasped back in 1942 the difficulties of assessing reverberation time in rooms when the distribution of absorbent material was not uniform. Without a clear theory, he merely pointed out that: "Another factor also enters into reverberation design. It applies in practice specially to studios and small halls. Reverberation in rectangular rooms really consists of three sets of inter-reflections set up between the three pairs of parallel opposite surfaces. It is important that these three reverberation times should be roughly of equal length and blend into one smooth tone." [11, pp. 113–115].

2.2 Fitzroy (1959)

Shortly afterwards, US acoustic engineer Dariel Fitzroy (1898-1977) noted deviations from the formulae of Sabine (1) and Eyring (2) when they were applied in rooms where the absorption is nonuniformly distributed. Supported by a large number of measurements in rooms of these characteristics, and without seeming to be aware of Bagenal's opinion, he stated that "…the sound field may tend to settle into a pattern of simultaneous oscillation along a rectangular room's three major axes—the vertical, the transverse, and the longitudinal. […] In its simplest case, a rectangular room, we are presented with three sets of parallel boundaries. If the energy oscillates simultaneously between each pair of boundaries—the author is aware that this is highly speculative—the average absorption in each pair would control the sound wave excursions between that specific pair during the 60-db decay period." [12, p. 893]. From his measurements, he inferred an equation (3), without mathematical proof, that brought the estimated reverberation time closer to the measured values in rooms of these characteristics:

$$T = \left(\frac{S_x}{S}\right)\left(\frac{0.161V}{-S\ln(1-\bar{\alpha}_x) + 4mV}\right) + \left(\frac{S_y}{S}\right)\left(\frac{0.161V}{-S\ln(1-\bar{\alpha}_y) + 4mV}\right) + \left(\frac{S_z}{S}\right)\left(\frac{0.161V}{-S\ln(1-\bar{\alpha}_z) + 4mV}\right) \tag{3}$$

2.3 Cremer (1978)

German acoustic consultant Lothar Cremer (1905-1990), in his book *Die wissenschaftlichen Grundlagen der Raumakustik* (1978) with Helmut A. Müller (1930-2015), translated into English as *Principles and applications of room acoustics* (1982), dedicated the chapter "Refinements of the reverberation formulae based on geometric considerations" to reflections on how to assess the impact on reverberation time of a non-uniform distribution of the absorbent material in a room. He recommended dividing "…the total surface area first into several large 'principal surfaces', which can be regarded as encountered by the sound rays one after the other ('in series'); and to subdivide these large surfaces into smaller areas with different absorption, which can be regarded as encountered side by side ('in parallel'). The smaller subdivisions are first averaged arithmetically, to determine the mean absorption coefficients for each of the principal surfaces. Those values are then transformed to the corresponding absorption exponents, and are averaged arithmetically…" [13, p. 235].

2.4 Arau-Puchades (1988)

Thirty years after Fitzroy, Higini Arau-Puchades (b.1946), a Spanish physicist specialised in acoustics, was also concerned about cases of non-diffuse fields. Between 1982 and 1989, when he was director of the Laboratori General d'Assaigs i Investigacions [General Laboratory for Testing and Research], he advised on acoustic improvements for the Palau de la Música Catalana, the most important concert hall in Barcelona, designed by architect Lluís Domènech i Montaner in 1905 [14]. The refurbishment was led by architects Oscar Tusquets and Lluís Clotet. There, Arau-Puchades worked with Lothar Cremer who, from 1973, had collaborated on the design of many concert halls in Spain [15].



Figure 1. From right to left, Higini Arau-Puchades, Lothar Cremer and Oscar Tusquets at the Palau de la Música Catalana of Barcelona. Photo: Pau Barceló (1985), Centre de Documentació de l'Orfeó Català.

The Palau de la Música Catalana was a masterpiece of *Catalan Modernisme* (Art Nouveau). Its ceiling was covered in ceramic tiles, the side walls were formed of a type of glass curtain wall and work could only be done on the absorption of the stalls area. This was a prototypical example of sound propagation in a non-diffuse field, which could not be modified as it was a listed building.

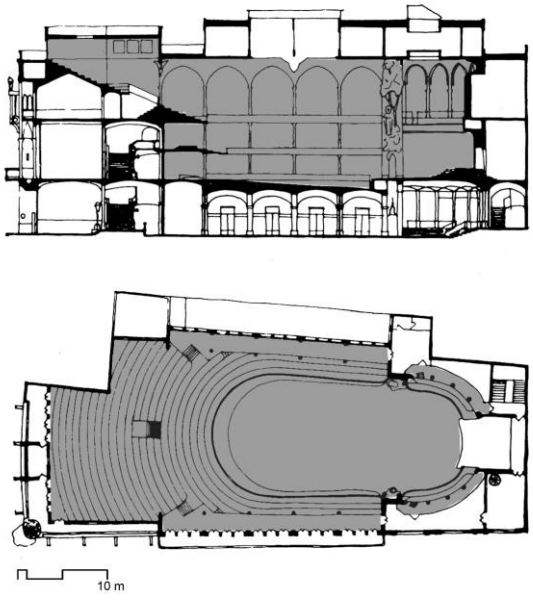


Figure 2. First floor plan and cross-section of the Palau de la Música Catalana (1905-1908).

From conversations between Arau-Puchades and Cremer, Arau-Puchades's dissatisfaction with classic formulae for determining reverberation time in a non-diffuse field began to emerge. As Higini Arau-Puchades explained to a journalist, first he tried an approach to the problem that he showed to Cremer, who "responded to the theory, saying that his calculations were focused on a linear reverberation curve from top to bottom and that in no case did this linearity occur. Stimulated by the problem, Arau averaged the absorption coefficients so that 'now I can calculate all the decays of the reverberation curve'." [16].

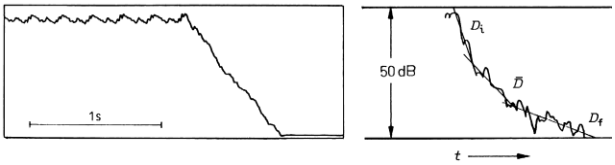


Figure 3. Left, sound decay in a diffuse field, right, sound decay in a non-diffuse field [17, p. 54].

In May 1986, Higini Arau-Puchades presented his theory to the specialised journal *Acustica*. The article was published in the March issue of 1988 under the title "An improved reverberation formula" [18].
Returning to Fitzroy's approach (3), Arau-Puchades proposed that the varying degree of reflectivity of the pairs of walls that make up a room could be broken down using the following convention:

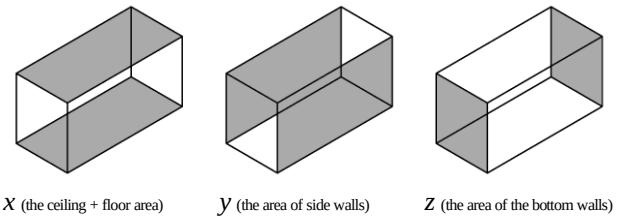


Figure 4. Pairs of parallel surfaces according to Arau-Puchades [18].

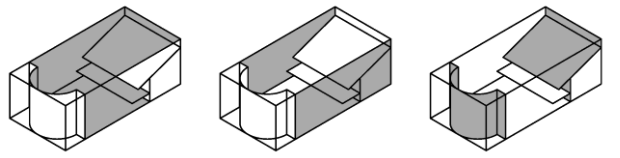
Arau-Puchades considered that the reverberation time of a room with non-uniform absorption would be equal to the area-weighted geometrical mean of the reverberation periods in each one of the directions considered [18, p. 166]. Therefore, in his theory, Arau-Puchades proposed the coexistence of simultaneity (three parallel walls at the same time) and sequentiality (reflections occur on each wall, one after the other).

$$T = \left(\frac{0.161V}{-S\ln(1-\bar{\alpha}_x)+4mV}\right)^{x/S}\left(\frac{0.161V}{-S\ln(1-\bar{\alpha}_y)+4mV}\right)^{y/S} \cdot \left(\frac{0.161V}{-S\ln(1-\bar{\alpha}_z)+4mV}\right)^{z/S} \quad (4)$$

In addition, we know that Lothar Cremer stressed in conversations with Higini Arau-Puchades "that all theories that try to demonstrate the non-diffuse case should be able to calculate the reverberation time T and EDT, the Early Decay Time" [19, p. 4]. In fact, Arau-Puchades's mathematical approach allows this aspect to be obtained using a log-normal distribution [18, pp. 166–170].

In the same article, Arau-Puchades described the application of his formula to various rooms and compared the results with the predictions of Sabine (1) and Eyring (2) and with some real measurements. This was a generalisable theory that was close to the results of Sabine and Eyring in rooms with a uniform distribution of absorption. In addition, to demonstrate its suitability, Arau-Puchades used the experimental data of Koesten [20] and Mehta & Mulholland [21] to support his proposal.

If we go back to the example of the Palau de la Música Catalana, the pairs of walls were broken down according to Figure 5. Table 1 shows the calculation of the absorption coefficient values and Table 2 compares the estimated and measured results.



x (the ceiling + floor area) *y* (the area of side walls) *z* (the area of the bottom walls and upper stalls)

Figure 5. Allocation of surfaces in the study on the Palau de la Música Catalana, Barcelona [18].

Table 1. Dimensional ratios and absorption coefficients of the Palau de la Música Catalana, Barcelona [18, p. 171].

Dimensions	Percentage area	Absorption coefficients		
		$\bar{\alpha}_t$ (energy)	$\bar{\alpha}_i$ (decay)	$\bar{\alpha}_{av}$ (whole energy average)
Ratio: Non rectangular form	$\frac{x}{S} = 0.407$	$\bar{\alpha}_x = 0.250$	$\bar{\alpha}_x = 0.287$	$\bar{\alpha}_{av} = 0.385$
V = 10,352	$\frac{y}{S} = 0.296$	$\bar{\alpha}_y = 0.543$	$\bar{\alpha}_y = 0.784$	
S = 2,438	$\frac{z}{S} = 0.297$	$\bar{\alpha}_z = 0.413$	$\bar{\alpha}_z = 0.532$	

Table 2. Comparison of estimations of reverberation time according to various formulae and the experimental measurements of the Palau de la Música Catalana, Barcelona [18, p. 173].

Eyring (2)	Fitzroy (3)	Arau-Puchades (4)	Experimental
1.37 s	1.57 s	1.44 s	1.47 s

Ten years later, in 1998, Arau-Puchades revisited his article of 1988 with the aim of expanding his results to a general theory of acoustic values of rooms [22]. Its development was based on ideas proposed by Mike Barron, characterised for the case of non-uniform distribution of absorption [23].

3. INTERNATIONAL IMPACT OF ARAU-PUCHADES'S FORMULA

3.1 Use in Arau Acústica for the design of concert halls

The following are notable among the early collaborations of Higini Arau-Puchades, now with his office Arau Acústica and with architects designing concert halls using his method: the Auditori Enric Granados in Lleida (1983-1995) and the Teatre-Auditori de Sant Cugat (1989-1994), both by the firm Artigues & Sanabria; L'Auditori of Barcelona (1987-1999) and Kursaal in San Sebastián (1990-1999), both by architect Rafael Moneo; and the reconstruction of the Gran Teatre del Liceu of Barcelona (1994-1999), with architects Ignasi de Solà-Morales, Lluís Dilmé and Xavier Fabré. These early works catapulted him to consultancy on over 200 auditoriums in Spain and over twenty in other countries, including the refurbishment of the Teatro alla Scala of Milan (2002-2004) and the Tonhalle of St. Gallen, with Bosshard Vaquer Architekten (2009-2010), or the new Filharmonia im. Mieczysława Karłowicza in Szczecin (2007-2014), with Barozzi Veiga [14].

Considering the great demand for collaboration, Higini Arau-Puchades and Lluís Jutglar, a professor at the Universitat de Barcelona, developed their own software for acoustic verification of rooms, which formed part of the firm's unpublished know-how [14].

In addition, Arau-Puchades widely disseminated his equation (4) through his handbook, the *ABC de la acústica arquitectónica* (1999). This is one of the most widespread handbooks on acoustics in Spanish. Beyond the didactic needs of the book, he dedicated 17 pages to showing chronologically the scientific contributions of Sabine's formula to his proposal. He included critical commentaries on the formulae of Sabine, Eyring, Norris, Millington, Sette, Fitzroy, Gomperts, Kosten, Pujolle, Kuttruff and

Wernly, and on computer approaches with ray tracing [24, pp. 227–242].

3.2 Implementation of Arau-Puchades's equation in international professional software

In fact, the publication of Arau-Puchades's equation (4) coincided with the development of the first computer programs that aimed to simulate the behaviour of sound in its three dimensions. Furthermore, Arau-Puchades's formula began to be compared favourably with other statistical methods and the results achieved with these computer simulations. An article published in 2000 by Brazilian engineer Sylvio R. Bistafa and Canadian researcher John S. Bradley [25] was fundamental for the successful dissemination of Arau-Puchades's proposal. Table 3 shows the results of this study, in which seven equations that assessed absorption in a different way were compared with real laboratory measurements. Arau-Puchades's formula had the lowest errors at all frequencies.

Table 3. Overall average relative errors of the analytical predictions of reverberation time for ten sound-absorbing configurations in the simulated classroom, according to Bistafa and Bradley [25, p. 1727].

	Overall average relative error (%)		
	Frequency bands included in the averages		
	1 kHz	500 Hz–2 kHz	125 Hz–4 kHz
Sabine (1)	38.8	31.6	21.5
Eyring (2)	42.6	35.7	24.7
Millington	36.1	30.4	21.1
Cremer	26.7	23.9	17.4
Kuttruff	68.0	63.5	49.3
Fitzroy (3)	92.0	95.8	65.7
Arau-Puchades (4)	22.9	22.7	16.7

The same article compared these statistical results with those obtained from two computer programs, RAYNOISE 3.0 of LMS Numerical Technologies NV (Leuven, Belgium) and ODEON 2.6 of the Department of Acoustic Technology at the Danmarks Tekniske Universitet (Lyngby, Denmark). Reading the article prompted the developers of ODEON software to incorporate Arau-Puchades's formula in their program, probably already in version 5.0 of 2001[1]. Of course, over time, the ray-tracing and wave-based algorithms have improved considerably, but at that time the formula played a notable role in the adjustment of this parameter.

Other researchers have incorporated Arau-Puchades's formula in more specific software such as WINRT60 1.0. This is a program for calculating reverberation time designed by Tor Erik Vigran, professor of the Norges teknisk-naturvitenskapelige universitet (NTNU), in 2006. Using this program, it was possible to calculate the reverberation time of a room using formulae by Sabine (1), Eyring (2) and Arau-Puchades (4) [26]. Likewise, in 2015, STRUTT by Arup incorporated the Arau-Puchades equation in its v5.15.12 [27]. This is a plug-in for MICROSOFT EXCEL that includes a large number of functions for acoustic calculations.

3.3 A proposal with a long history

A simple bibliometric approach shows that the article "An improved reverberation formula" [18] has been cited 40 times in articles indexed in the Web of Science, 64 times in Scopus and 138 times in Google Scholar[2]. The Figure 6 indicates that interest in the model proposed by Arau-Puchades increased notably from the year 2000.

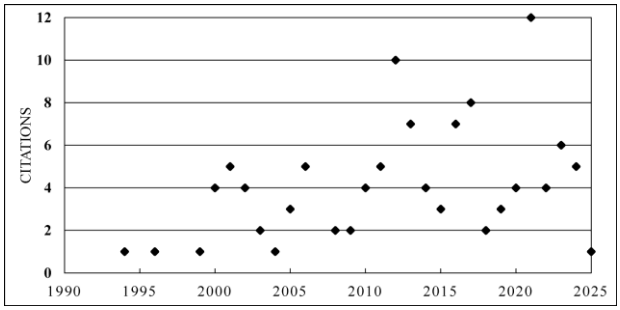


Figure 6. Number of citations per year of "An improved reverberation formula" [18], as recorded in Google Scholar on 23 March 2025.

As noted above, the study by Bistafa and Bradley of 2000 [25] showed that Arau-Puchades's model (4) obtained the lowest relative errors compared to the reverberation time measured in the laboratory. A similar result was obtained by French researchers Joël Ducourneau and Vincent Planeau in 2003. They concluded that, among all the models studied, which included Sabine (1), Eyring (2), Millington, Pujolle, Arau-Puchades (4) and Fitzroy (3), "The Arau-Puchades's model, which is adapted to non-

[1] Claus Lynge Christensen, personal communication (e-mail), December 27, 2024.

[2] Consulted: March 23, 2025.

uniformly distributed absorption, is the closest to the experimental results (maximal relative error <20%)" [28, p. 853].

After these two articles, numerous researchers have shown interest in Arau-Puchades's model, which has been incorporated in some handbooks such as *Sound insulation* by Carl Hopkins (2007) [29, p. 42], *Building acoustics* by Erik Tor Vigran (2008) [30, p. 122], and *Acústica de salas: projeto e modelagem* by Eric Brandão (2018) [31, p. 461].

4. CONCLUSIONS

Finally, we might wonder about the opportunity at the end of the 1980s [32, pp. 390–391] to propose a new model for calculating reverberation time at a time in which new room acoustic parameters were being developed, such as *Deutlichkeit* [D50, definition] (1953), Early Decay Time [EDT] (1970), Clarity [C80] (1974) and G-Strength (1976) [33-35]. However, considering that many of these parameters continue to be governed by reverberation time [36], it makes sense to have as accurate statistical models as possible.

In fact, the model proposed by Higini Arau-Puchades aimed to respond to the need to improve the prediction of reverberation time in a non-diffuse field and took these new parameters into account. The same model enabled determination of the Early Decay Time, as had been suggested by Lothar Cremer.

Nevertheless, it was not an easy model to apply. As we have seen in the case of the Palau de la Música Catalana, the acoustic consultant had to select with criteria the pairs of surfaces that would be assigned to the directions X, Y and Z. For this reason, whoever applies the model must know how the equation works to be able to understand the results that are obtained.

5. ACKNOWLEDGMENTS

This paper is part of the R&D grant PID2022-138760NB-C21, funded by MICIU/AEI/10.13039/501100011033/ and ERDF/EU.

Lucille Banham with her usual care and rigour has translated the original text from Spanish to English.

6. REFERENCES

[1] W. C. Sabine, "Architectural acoustics, I: Introduction," *The American Architect and Building News*, vol. LXVIII, no. 1267, pp. 3–5, Apr. 1900.

[2] W. C. Sabine, "Architectural acoustics, II: Reverberation: Absorbing power of wall-surfaces," *The American Architect and Building News*, vol. LXVIII, no. 1269, pp. 19–22, Apr. 1900.

[3] W. C. Sabine, "Architectural acoustics, III: Reverberation: Approximate solution," *The American Architect and Building News*, vol. LXVIII, no. 1271, pp. 35–37, May 1900.

[4] W. C. Sabine, "Architectural acoustics, IV: Reverberation: Rate of decay of residual sound," *The American Architect and Building News*, vol. LXVIII, no. 1272, pp. 43–45, May 1900.

[5] W. C. Sabine, "Architectural acoustics, V: Reverberation: Exact solution," *The American Architect and Building News*, vol. LXVIII, no. 1274, pp. 59–61, May 1900.

[6] W. C. Sabine, "Architectural acoustics, VI: Reverberation: The absorbing power of an audience, and other data," *The American Architect and Building News*, vol. LXVIII, no. 1276, pp. 75–76, Jun. 1900.

[7] W. C. Sabine, "Architectural acoustics, VII: Reverberation: Calculation in advance of construction," *The American Architect and Building News*, vol. LXVIII, no. 1277, pp. 83–84, Jun. 1900.

[8] W. S. Franklin, "Derivation of equation of decaying sound in a room and definition of open window equivalent of absorbing power," *Physical Review (Series I)*, vol. 16, no. 6, pp. 372–374, Jun. 1903, doi: 10.1103/PhysRevSeriesI.16.372.

[9] W. C. Sabine, *Collected papers on acoustics*. Cambridge, MA, London: Harvard University Press, 1922.

[10] C. F. Eyring, "Reverberation time in 'dead' rooms," *J Acoust Soc Am*, vol. 1, no. 2A, pp. 217–241, Jan. 1930, doi: 10.1121/1.1915175.

[11] H. Bagenal, *Practical acoustics and planning against noise*. London: Methuen & Co.Ltd., 1942.

[12] D. Fitzroy, "Reverberation formula which seems to be more accurate with nonuniform distribution of absorption," *J Acoust Soc Am*, vol. 31, no. 7, pp. 893–897, Jul. 1959, doi: 10.1121/1.1907814.

[13] L. Cremer and H. A. Müller, *Principles and applications of room acoustics: vol. 1*. London: Applied Science, 1982.

[14] J. Álvarez, R. Graus, and H. Martín-Nieva, "Higini Arau y la acústica de salas: el camino hacia su reconocimiento internacional," in *Redes Transnacionales de la Arquitectura Española (1976-2006): 1.er seminario RETRANSLATES*, Barcelona: Iniciativa Digital Politècnica, 2025, pp. 20–21. doi: 10.5821/ebook-9791387613174.

[15] G. Vallejo Ortega and J. I. Sánchez Rivera, "Lothar Cremer in Spain: his influence on the architect García de Paredes," in *INTER-NOISE 2012, New York, August 19-22*, New York: Institute of Noise Control Engineering, 2012.

[16] J. Guerrero Martín, S. Fondevila, L. Bonet Mojica, and A. Mallofré, "El físico Arau y su teoría de la reverberación," *La Vanguardia*, Barcelona, p. 26, Jan. 21, 1989.

[17] H. Arau-Puchades, "Aproximació científica a un problema formal: contribució acústica al disseny arquitectònic: En record al prof. Eng. Lothar Cremer," *Revista de Física*, no. 7, pp. 50–57, 1994.

[18] H. Arau-Puchades, "An improved reverberation formula," *Acustica*, vol. 65, no. 4, pp. 163–180, Mar. 1988.

[19] H. Arau-Puchades, "Revisión del tiempo de reverberación: El método de cálculo, la precisión predictiva y la Ley," in *TecniAcustica'10: León, octubre 2010*, León: Sociedad Española de Acústica, 2010, pp. 1–16.

[20] C. W. Kosten, "International comparison measurements in the reverberation room," *Acustica*, vol. 10, no. 5/6, pp. 400–411, 1960.

[21] M. L. Mehta and K. A. Mulholland, "Effect of non-uniform distribution of absorption on reverberation time," *J Sound Vib*, vol. 46, no. 2, pp. 209–224, May 1976, doi: 10.1016/0022-460X(76)90438-7.

[22] H. Arau-Puchades, "General theory of the energy relations in halls with asymmetrical absorption," *Building Acoustics*, vol. 5, no. 3, pp. 163–183, Sep. 1998, doi: 10.1177/1351010X9800500302.

[23] M. Barron and L.-J. Lee, "Energy relations in concert auditoriums, I," *J Acoust Soc Am*, vol. 84, no. 2, pp. 618–628, Aug. 1988, doi: 10.1121/1.396840.

[24] H. Arau-Puchades, *ABC de la acústica arquitectónica*. Barcelona: Ceac, 1999.

[25] S. R. Bistafa and J. S. Bradley, "Predicting reverberation times in a simulated classroom," *J Acoust Soc Am*, vol. 108, no. 4, pp. 1721–1731, Oct. 2000, doi: 10.1121/1.1310191.

[26] T. E. Vigran, *Manual for WinRT60, version 1.0*. Trondheim: Gray literature, 2006.

[27] "Strutt Revision History," Strutt Acoustics. Accessed: Mar. 27, 2025. [Online]. Available: https://strutt.arup.com/help/

[28] J. Ducourneau and V. Planeau, "The average absorption coefficient for enclosed spaces with non uniformly distributed absorption," *Applied Acoustics*, vol. 64, no. 9, pp. 845–862, Sep. 2003, doi: 10.1016/S0003-682X(03)00047-1.

[29] C. Hopkins, *Sound insulation*. Oxford: Butterworth-Heinemann, 2007.

[30] T. E. Vigran, *Building acoustics*. London, New York: Taylor & Francis, 2008.

[31] E. Brandão, *Acústica de salas: Projeto e modelagem*. São Paulo: Blucher, 2016.

[32] R. T. Beyer, *Sounds of our times: Two hundred years of acoustics*. New York: Springer, 1999.

[33] J. S. Bradley, "The evolution of newer auditorium acoustics measures," *Canadian Acoustics*, vol. 18, no. 4, pp. 13–23, Oct. 1990.

[34] M. Barron, "The development of concert hall design–A 111 year experience," *Proc. of the Institute of Acoustics*, vol. 28, no. 1, p. [1-14], 2006.

[35] R. Lacatis, A. Giménez, A. Barba Sevillano, S. Cerdá, J. Romero, and R. Cibrián, "Historical and chronological evolution of the concert hall acoustics parameters," in *Proc. of Acoustics'08: Paris, June 29-July 4, 2008*, Paris: SFA, 2008, pp. 4377–4382.

[36] M. Skålevik, "Reverberation time–The mother of all room acoustic parameters," in *Proc. of 20th International Congress on Acoustics, ICA 2010: 23-27 August 2010, Sydney*, Sydney: International Commission for Acoustics, 2010, pp. 1–5.

DOI: 10.61782/fa.2025.0412



FORUM ACUSTICUM
EURONOISE 2025

FROM ACOUSTIC TESTING AND MODELING TOWARDS MULTI-PHYSICAL DIGITAL TWINS: USE CASES AND DEMONSTRATORS

Lucas Van Belle[1,2*] **Dionysios Panagiotopoulos**[1,2] **Vanessa Cool**[1,2]
Hervé Denayer[1,2] **Claus Claeys**[1,2] **Wim Desmet**[1,2] **Bert Pluymers**[1,2]
Konstantinos Gryllias[1,2] **Frank Naets**[1,2] **Elke Deckers**[2,3]

[1] Department of Mechanical Engineering, KU Leuven, Belgium
[2] Flanders Make@KU Leuven, Belgium
[3] Department of Mechanical Engineering, Campus Diepenbeek, KU Leuven, Belgium

ABSTRACT

In the past decades, noise has gained growing significance. Also in mechanical engineering, increasingly complex mecha(tro)nic systems are emerging which have to perform optimally while satisfying ever more stringent noise regulations and customer expectations. Nowadays, electrification and transition to greener technologies and materials leads to novel noise sources and problems, posing significant engineering challenges.

With increasing computation power over the past decades, also rapid technological evolutions have unfolded in acoustics: from testing to numerical modeling and simulation, from mono- to multi-physical simulation, from offline to real-time online simulations, … Thanks to these evolutions, noise is evolving from an attribute to quantify and control towards an integrated design parameter for the entire lifetime of systems, enabled by reduced order modeling, innovative signal processing techniques, novel emerging vibro-acoustic solutions and optimization. Moreover, combining fast multi-physical models with acoustic measurements has opened the door to a variety of novel developments including auralization, virtual sensing, real-time state/parameter estimation and prognostics.

This paper gives an overview of the dynamics (noise, vibration & motion) research at the KU Leuven Mechanical Engineering Department, in the LMSD research group.

Keywords: *testing, modeling, multi-physics, digital twins*

1. INTRODUCTION

In the past decades, the field of noise, vibration and harshness (NVH) engineering has expanded and evolved. With the growing awareness of the negative impact of noise on human health, the increasingly stringent noise legislation and ever more demanding customer expectations, noise has not only changed from an (unwanted) byproduct to a key product differentiator, but also to a key quantity which is accounted for and exploited at every life phase of a product. At the same time, mechanical engineering systems have evolved to mechatronic systems. These are not only more complex to design, model and analyze, but also create the opportunity for built-in sensorization and continuous data streams between products and virtual counterparts.

Together with this evolution, the LMSD System Dynamics research group at KU Leuven grew from the Noise & Vibrations research group which in its turn started over 5 decades ago as the MOD – Modal analysis research group. The research at LMSD spans a broad spectrum from methodologies, over theoretical foundations, to various application domains: by understanding, monitoring and controlling the dynamics (motion-vibration-acoustics) of mecha(tro)nic systems, LMSD aims at creating added value

[*] ***Corresponding author***: *lucas.vanbelle@kuleuven.be*
Copyright: *©2025 Lucas Van Belle et al. This is an open-access article distributed under the terms of the Creative Commons Attribution 3.0 Unported License, which permits unrestricted use, distribution, and reproduction in any medium, provided the original author and source are credited.*

during every phase (design, manufacturing, and operations) in their lifetime. Having built out dedicated in-house testing and validation platforms, as well as software toolchains, the research group closely co-innovates together with world-wide research and industry partners and, in doing so, actively cross-fertilizes between applied and industrial research[1][2] [1]. Furthermore, to create scientific as well as societal impact, LMSD regularly brings its latest developments closer to the wide public[3,4].

The rest of this paper presents several recent developments and (industrial) use cases in acoustics research at LMSD. After describing progress in acoustic testing and modeling in Sections 2 and 3, Section 4 discusses advanced techniques for (vibro-)acoustic measurement and analysis. Novel (vibro-)acoustic solutions are the topic of Section 5. Section 6 discusses how models and measurements come together in Digital Twins and add value, and Section 7 provides an outlook on how this digitally connected concept can be elevated to close the loop across all life phases of products. Section 8 summarizes the main conclusions.

2. ACOUSTIC TESTING

With the change from analog to digital, the increase in computing power, and the downscaling of circuits, acoustic measurement devices have become more portable, precise and versatile in the past decades (Fig. 1). Along with that digital (r)evolution, acoustic testing nowadays comprises far more than sound pressure recording, covering a broad spectrum ranging from characterization and (model) updating/validation (Section 3) to condition monitoring (Section 4), sensing and digital twinning (Section 6).



Figure 1. Historical collection of LMSD's vibro-acoustic measurement systems.

[1] https://www.mech.kuleuven.be/en/mod/Projects
[2] https://www.youtube.com/watch?v=gQBgfSLdwJg
[3] https://www.linkedin.com/showcase/lmsd-kuleuven
[4] https://www.youtube.com/@lmsd-kuleuven

Standard (vibro-)acoustic measurement techniques rely on controlled environments, for which simple analytical models can relate sound pressure measurements to the quantities of interest. However, these idealized environments are often not representative for the final application. Over the years, various non-standard test rigs have been developed to enable the characterization of (vibro-)acoustic properties in more representative environments (Fig. 2), often relying on virtual counterparts (Section 6).

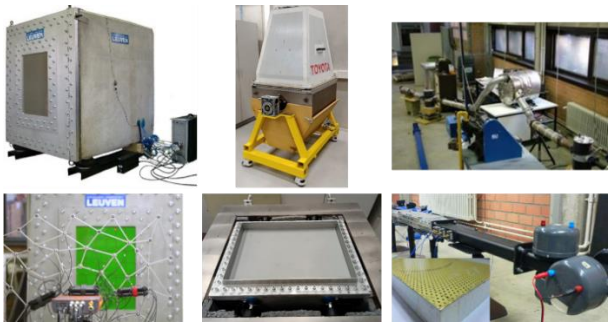


Figure 2. (left, center) Non-standard test-rigs for (vibro-)acoustic transmission, absorption & radiation, (right) modular infrastructure for characterization of (flow-)acoustic properties of duct systems.

These test rigs are augmented with various measurement systems, including sound intensity probes, acoustic arrays, acoustic camera, (scanning) laser doppler vibrometers (SLDV), ... Furthermore, digital counterparts of these test rigs have been created using different modeling strategies (Section 3), which not only enables updating models of tested components, but also allows gaining additional insights via model-measurement combinations (Section 6).

SLDVs have especially gained interest as they enable full-field characterization, not only useful for (source) localization (Fig. 3), but also for analyzing structural wave phenomena in novel materials (Section 5). Recently, also camera-based measurements have gained interest in vibro-acoustics. In contrast to conventional acoustic sensors, cameras allow directly observing the structure-borne noise source. Methods were developed to predict full-field acoustic radiation of vibrating surfaces independently of the acoustic environment (Fig. 4) by leveraging camera measurements with acoustic models (see also Section 6). These techniques especially also hold promise for vibro-acoustic problems involving transient behavior and moving systems.

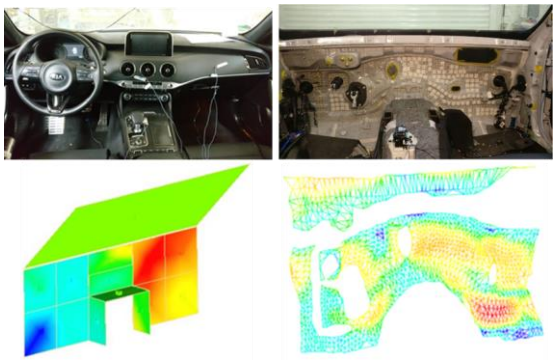


Figure 3. (left) Sound intensity, (right) SLDV-based vibration field measurements of a car firewall [2].

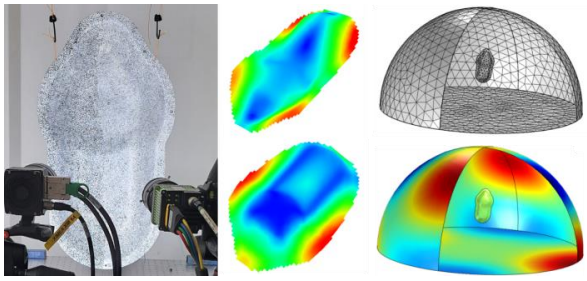


Figure 4. (left & center) Camera-based vibration field measurement, (right) combined measurement-model based acoustic radiation estimation [3].

In particular with the rise of novel emerging materials and structures such as metamaterials (Section 5), which exhibit non-conventional acoustic wave propagation behavior, dedicated acoustic test setups and routines have been developed (Fig. 5) that enable characterizing their performance already early in design process, without need for full 3D simulation, design, manufacturing and testing.

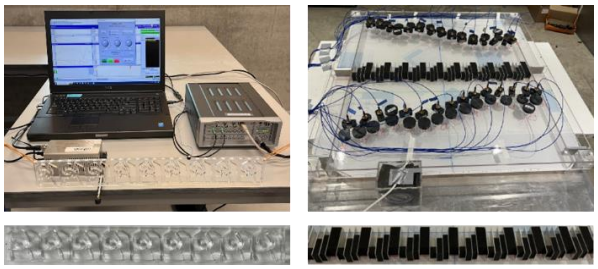


Figure 5. (left) Hammer impact-based method to validate the Sound Transmission Loss (STL) of 2D structures [4], (right) 2D rectangular waveguide for angle-dependent transmission, reflection and absorption coefficient characterization [5].

3. ACOUSTIC MODELING

In the past decades, element-based numerical techniques such as the Finite Element Method (FEM) and Boundary Element Method (BEM) have become industry standard for solving large and complex (vibro)-acoustic problems (Fig. 6a). With increasing frequency, element sizes must decrease, which drives up computation cost of element-based techniques, limiting their application mostly to lower frequencies. Although high-frequency techniques such as Statistical Energy Analysis (SEA) exist, a mid-frequency gap persisted and drove the search for mid-frequency methods[5]. In particular, at LMSD, the Wave Based Method (WBM) for (vibro)acoustics was developed, which is an indirect Trefftz approach. It partitions the (interior/exterior) problem in large convex subdomains, approximating the solution with wave functions, being exact solutions of the governing equation [6]. Although mainly suitable for problems with limited geometrical complexity, WBM was shown to be more efficient than FEM and BEM for said problems. Hybrids with FEM (Fig. 6b), BEM and SEA were developed to combine the best of several worlds. Later, to allow ensuring geometrical exactness - which element based techniques typically lose - isogeometric analysis (IGA)-based FEM and BEM have been proposed [7,8], using Non-Uniform Rational B-splines (NURBS) to represent the geometry and discretize the wave equation (Fig. 6c) instead of polynomials in classical FEM or BEM.

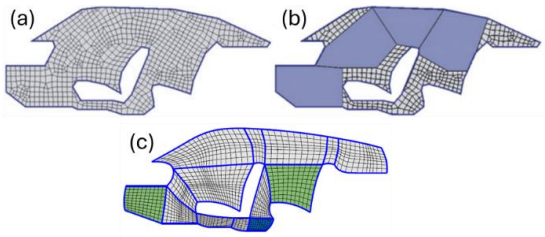


Figure 6. Numerical modeling methods in acoustics: (a) FEM, (b) WBM and hybrid WB-FEM for mid-frequency analysis [6], (c) IGA FEM [7].

Performing a frequency sweep either with FEM or BEM can induce high computation costs (solution time, memory). Such costs can be alleviated, by so-called Model Order Reduction (MOR) techniques, where the structure of the system and the repetitiveness of the procedure are exploited to provide a fast yet accurate solution. Specifically, in case of affine systems (e.g. regular vibro-acoustic FE models), it is possible to split the calculation in an expensive offline part and a cheap online part. In the offline part a reduction

[5] https://www.youtube.com/watch?v=m9OHmurazTA

basis is computed and the system matrices are projected on this basis. The different MOR strategies typically differ in the way the reduction bases are computed. Common techniques are POD, reduced basis method, rational Krylov approximation, … When combined with exterior acoustics, boundary treatments, and time-domain solution procedures, particular attention has gone to preserve stability (Fig. 7) [9]. Compared to FEM, MOR for BEM is more challenging as the frequency is non-affinely involved in the system matrices. To enable the application of MOR, the system needs to be approximated through an affine expression [10].

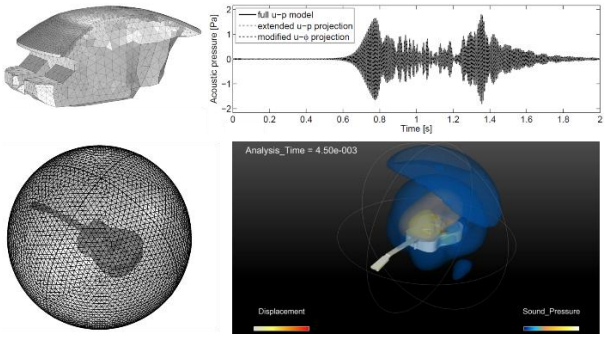


Figure 7. MOR for time stable, efficient FE time-domain simulations for interior/exterior acoustics [9].

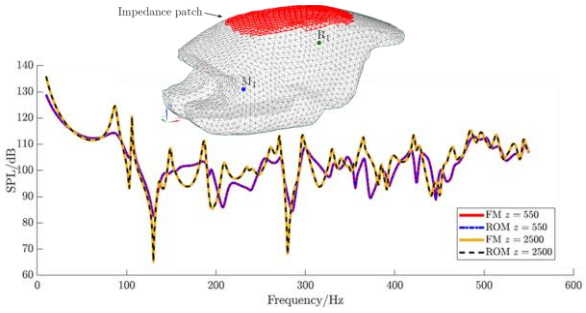


Figure 8. pMOR for acoustic BEM. Interior acoustic treatment modeled with impedance patch [10].

Following the same logic as in conventional MOR for FEM and BEM, it is possible to increase the number of parameters to include e.g. material, source position, shape … which has led to parametric MOR (pMOR) techniques, for instance by sampling information from the parameter space beforehand (Fig. 8) [10]. Doing so, pMOR allows fast transitions among different design configurations, either for design or fast inverse parameter estimation (Section 6). Recently, time-stable MOR routines for vibro-acoustic models including frequency-dependent admittance relations, porous and poro-elastic layers, and PMLs have also been developed [11].

Another avenue on the rise is the use of Machine Learning (ML), not only for MOR, but also to accelerate and improve acoustic model generation. E.g. in absence of CAD data, techniques have been developed to enable creating geometrically accurate acoustic meshes using photo-grammetry (Fig. 9). The latter allows for a high degree of customization of acoustic predictions, but also for improved immersion when considering also the receiver and sound perception in the acoustic problem for e.g. auralization [12].

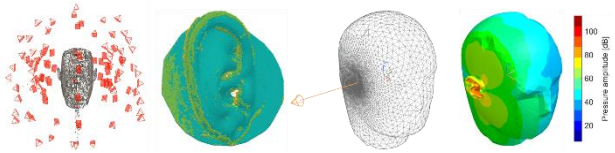


Figure 9. Dummy head ear scans are fed to DNNs trained on point cloud denoising for numerical Head-Related Transfer Function (HRTF) prediction [12].

4. (VIBRO)ACOUSTIC MONITORING AND DETECTION

In many industrial applications including manufacturing, power generation and transportation, rotating machinery plays a pivotal role. As continuously operating drivetrains predisposes their rotating components (e.g. gears, bearings …) to a risk of failure, condition monitoring for accurate and on-time fault detection has grown indispensable.

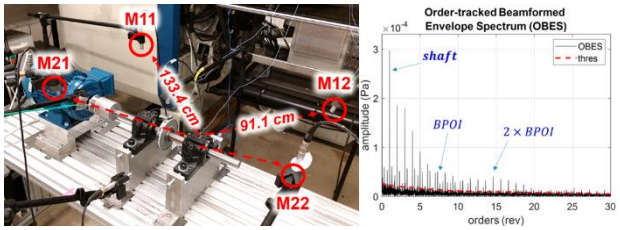


Figure 10. (left) In-house modular drivetrain test setup for bearings & gears diagnostics instrumented with accelerometers and microphones, (right) tracked spectrum of a damaged bearing [13].

While vibration sensors have been historically used for fault detection, recent work has focused on also harnessing the integratory capability of microphones to capture the global, overall acoustic signature of the entire drivetrain with limited and non-contact sensors. Several dedicated setups for drivetrain components have been built and instrumented at LMSD to develop and validate novel advanced signal processing techniques for vibro-acoustics based condition monitoring (Fig. 10) [13].

On the other hand, also nondestructive testing (NDT) has been a topic of extensive research lately with the goal of detecting defects in complex composite parts and assemblies in a limited inspection time. Classical NDT often relies on thermal imaging techniques and ultrasound. At LMSD, the use of vibro-acoustic signals to detect and identify damage is researched (e.g. loose bolt detection with MUSIC[6], Fig. 11). Combining vibro-acoustic information originating from defects with accurate numerical models enables enhancing the detection of such defects (Section 6), while lowering the required number of sensors [14].

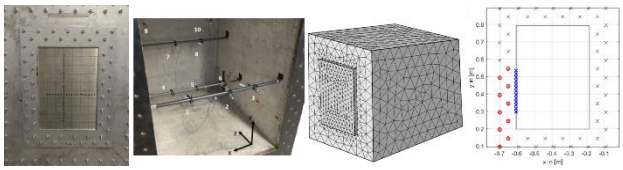


Figure 11. Structural damage (loose bolt) detection of assembly using acoustic measurements (with/ without combination with numerical model) [14].

5. INNOVATIVE VIBRO-ACOUSTIC SOLUTIONS

As classical passive solutions to increase sound insulation and/or absorption rely on adding mass and/or volume, they are less suitable for low frequencies. With the advent of more powerful controllers, active noise control gained a lot of interest in the 90s for low-frequency noise abatement [15]. Two decades later, (vibro-)acoustic metamaterials emerged and have meanwhile shown great potential as lightweight and compact solutions for high noise and vibration attenuation in targeted frequency ranges called “stop bands” [16], enabled by sub-wavelength added resonant inclusions on or in a (flexible)host structure.

To characterize, design and optimize the performance of (vibro-)acoustic metamaterials, a complete toolchain has been developed at LMSD[7] which enables covering all relevant physics, as well as translation from idealized infinite periodic structure theory to more complex, practically realizable solutions (Fig. 12) [17]. Their versatility and effectiveness in treating vibration, acoustic radiation and transmission problems has been proven through a variety of demonstrators, ranging from academic to industrial application (Fig. 13) [16, 18, 19].

Nowadays, metamaterials research at LMSD is expanding towards (mass-)manufacturability (e.g. injection molding) and variability, (topology-optimized [4]) multi-functional metastructures[8] and phase gradient acoustic metamaterials (Fig. 5) [5], as well as active (piezoelectric) metamaterials.

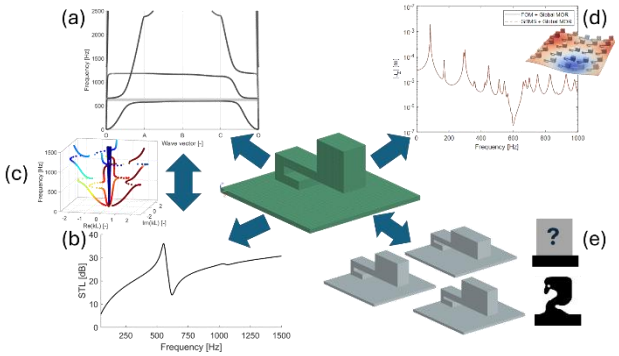


Figure 12. Unit cell modeling developments: (a) fast dispersion curve predictions, (b) periodic structure STL computations, (c) wave mode contributions to STL, (d) finite structure forced response computations, (e) design/topology optimization.

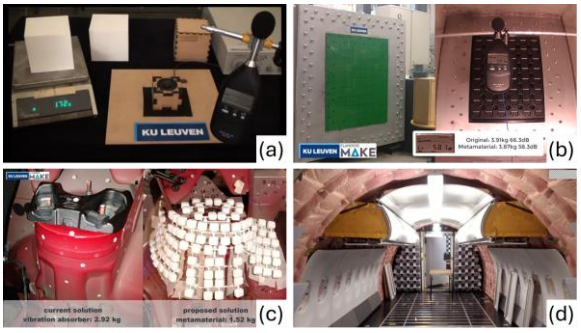


Figure 13. (a) 3D printed metamaterial enclosure[9], (b) lightweight thermoformed metamaterial panel[10], (c) 3D printed metamaterial patches on the rear shock tower of a vehicle[11], (d) laser cut add-on to aircraft fuselage panels [19].

6. VIBRO-ACOUSTIC DIGITAL TWINNING

Leveraging increasingly fast yet accurate (vibro-)acoustic models together with measurement data, enables creating digital twins[12], which are not only continuously updated

[6] https://www.youtube.com/watch?v=H0nFtsJ4HYM
[7] https://www.youtube.com/watch?v=DPbPjo3du5Q
[8] https://www.youtube.com/watch?v=jFNa8gOn-eo
[9] https://www.youtube.com/watch?v=JUi3qK32mf0
[10] https://www.youtube.com/watch?v=GWHeiEnx4ks
[11] https://www.youtube.com/watch?v=MdHVCnvj9x0
[12] https://www.youtube.com/watch?v=_d1oMRVlvMA

with reality, but provide insight in difficult to measure or unmeasurable quantities. Deploying the developed modeling strategies and in-house available test rigs and physical assets at LMSD, in the past years, a Digital Twin Experience Center has been established (Fig. 14).

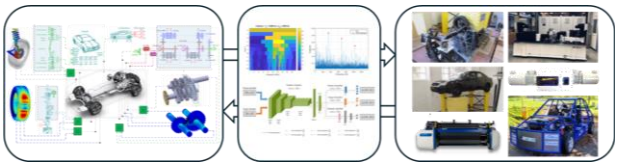


Figure 14. digital twins at LMSD: (left) modeling & simulation platforms for component and system dynamics, (center) estimation, signal processing & ML, (right) full-scale mechatronic systems.

Setting up digital twins for NVH requires digitizing the full chain from source/inputs, over path to receiver. Hence, multi-physical and multi-domain simulation frameworks have been set up, combining e.g. multibody simulation, 1D and 3D simulations, electromagnetic simulations and vibro-acoustic simulations (Fig. 15) [20].

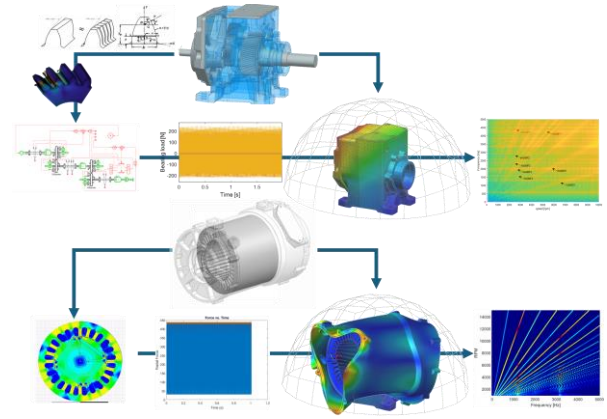


Figure 15. Multi-physical simulation workflow for (top) gearbox and (bottom) e-motor noise [20].

Through combining dedicated test-setups & physics-based (digital) counterparts, these digital twins enable amongst others experimental model-based input and parameter estimation of vibro-acoustic systems[13] as well as optimizing sensor selection and placement: e.g. for operational load estimation (Fig. 16), for source localization in complex environments, for acoustic material identification in reverberant environments [22], for acoustic material characterization under various flow conditions, … In particular acoustic virtual sensing[14], model-based augmented sensing of input forces, acoustic pressure and intensity with numerical models (Fig. 17), but also experimental modal models for e.g. virtual acoustic measurements in exterior vibro-acoustic problems (Fig. 18) have been developed and demonstrated.

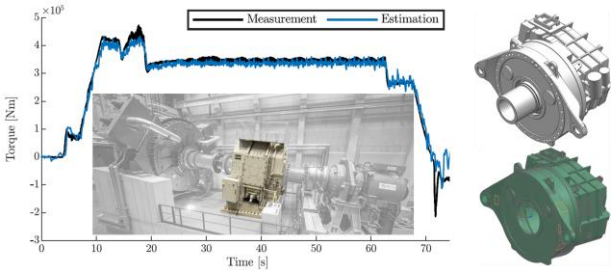


Figure 16. Virtual torque sensing of ZF wind turbine gearbox tested on the 4MW drivetrain testing infrastructure at Center for Wind Power Drives [21].

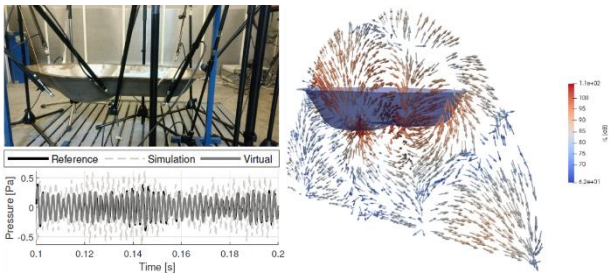


Figure 17. (top left) Measurement setup in in-house semi-anechoic room, (bottom left) measured, simulated and estimated sound pressure, (right) sound intensity field estimation [23].

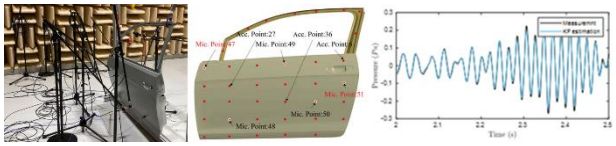


Figure 18. (left) Operational vibro-acoustic measurements, (center) experimental model, (right) measured and estimated sound pressure [24].

7. THE FUTURE

Building models and validating products requires accurate data. In the current Industry4.0 era, data is becoming increasingly abundant: during every life phase of a product,

[13] https://www.youtube.com/watch?v=1dW2g6tYsgI

[14] https://www.youtube.com/watch?v=fx6-yIMkN6s

digital information (digitized knowledge, simulation models, test data, production data, etc.) is generated, from early concept design, over detailed design and analysis, virtual and physical prototyping, product validation, commissioning, production and assembly, quality control, to the operational product in-use phase, and even the end-of-life (re-use, re-cycling, re-manufacturing) phases. Digital twins allow collecting and comprehensively managing all digital information linked to a unique product in all its different life phases, and to generate unprecedented added value by digitally connecting these phases in a closed loop, coined by KU Leuven as the "infinity loop" (Fig. 19). As such, the amount of available information and knowledge per product substantially increases, and more optimized and effective decisions can be taken.

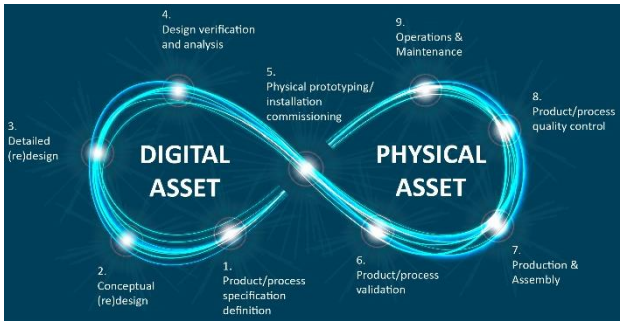


Figure 19. Enabled by digital twins, the infinity loop digitally connects all life phases in a closed loop.

From a vibro-acoustic point of view, this opens the door to various scenarios, such as for example (i) improved product validation since individual variations in part geometry or (mis-)alignment can be propagated to update nominal design models and hence take the effect of off-design into account, (ii) more accurate operational estimation, as these updated vibro-acoustic models allow for better estimates of transfer functions and thus better estimation of loads or states of the mecha(tro)nic system, and (iii) better next-generation designs as operational and end-of-life information can be fed-back to the designers, and many more scenarios.

8. CONCLUSIONS

In line with the increasing importance of quieter living and working environments, acoustic modeling and testing procedures keep improving, and innovative NVH solutions keep getting closer to widespread application. Noise and vibrations are omnipresent, and with the advent of (vibro-acoustic) digital twins, capabilities to both control NVH as well as harness its value at every life phase of the product lifecycle are ever expanding, thereby enabling the development of high-tech products, processes and systems, while at the same time accounting for the health of people and the well-being of society, for a sustainable environment and energy supply, and for safe and comfortable mobility.

9. ACKNOWLEDGMENTS

Internal Funds KU Leuven are gratefully acknowledged for their support. The Research Foundation – Flanders (FWO) is also gratefully acknowledged for its support through the fellowships of L. Van Belle (no. 1254325N) and Vanessa Cool (no. 1213925N) and research grants and fellowships no. G0F9922N, G0AA125N, G066725N, 12E2823N, 1SHCW24N and 1S63423N. The work is also partially supported by VLAIO (Flemish Innovation & Entrepreneurship) and by Flanders Make, the strategic research centre for the manufacturing industry. Resources and services used in part of this work were provided by the VSC (Flemish Supercomputer Center), funded by the FWO and the Flemish Government. Finally, the European Union is gratefully acknowledged for their support of the GECKO (GA 101073106), VAMOR (GA 101119903), GAPNOISE (GA 101073014), INNOVA (GA 101073037), MOIRA (GA 955681), ACTAREBUILD (GA 101072598), METAVISION (GA 101072515), METRAMAT (GA 101119917), VOLTCAR (GA 101096557) and GIANTS (GA 101138220) projects. Views and opinions expressed are however those of the authors only and do not necessarily reflect those of the European Union. The European Union cannot be held responsible for them.

10. REFERENCES

[1] C. Claeys, B. Pluymers, H. Van Der Auweraer & W. Desmet (2018). Dual-Desk PhD researchers. *Proc. of the UIIN Conference 2018*.

[2] K. J. Chang, N. G. R. de Melo Filho, L. Van Belle, C. Claeys & W. Desmet (2019). A study on the application of locally resonant acoustic metamaterial for reducing a vehicle's engine noise. *Proc. of INTERNOISE 2019*, Vol. 259, No. 9, pp. 102-113.

[3] F. S. Egner, W. Desmet & E. Deckers (2023). Full-field Camera Measurements for Structural and Vibro-acoustic System Analysis.

[4] V. Cool, C. Claeys, H. Denayer, F. Naets & E. Deckers (2024). Experimental validation of a topology optimized 2D sandwich panel for sound transmission minimization. *Mech. Syst. Signal Process.*, 211, 111197.

[5] Z. Zhang, H. Denayer, C. Claeys, W. Desmet & E. Deckers (2021). Angle-dependent reflection, transmission and absorption coefficients measurement using a 2D waveguide. *Appl. Acoust.*, 177, 107946.

[6] E. Deckers, O. Atak, L. Coox, R. D'Amico, H. Devriendt, S. Jonckheere, ... & W. Desmet (2014). The wave based method: An overview of 15 years of research. *Wave Motion*, 51(4), 550-565.

[7] L. Coox, E. Deckers, D. Vandepitte & W. Desmet (2016). A performance study of NURBS-based isogeometric analysis for interior two-dimensional time-harmonic acoustics. *Comput. Methods Appl. Mech. Eng.*, 305, 441-467.

[8] E. O. Inci, L. Coox, O. Atak, E. Deckers & W. Desmet (2020). Applications of an isogeometric indirect boundary element method and the importance of accurate geometrical representation in acoustic problems. *Eng. Anal. Boundary Elem.*, 110, 124-136.

[9] A. van de Walle, F. Naets, E. Deckers & W. Desmet (2017). Stability-preserving model order reduction for time-domain simulation of vibro-acoustic FE models. *Int. J. Numer. Methods Eng.*, 109(6), 889-912.

[10] D. Panagiotopoulos, W. Desmet & E. Deckers (2022). Parametric model order reduction for acoustic boundary element method systems through a multiparameter Krylov subspaces recycling strategy. *Int. J. Numer. Methods Eng.*, 123(22), 5546-5569.

[11] Y. Cai, S. van Ophem, W. Desmet & E. Deckers (2024). Model order reduction of time-domain vibro-acoustic finite element simulations with poroelastic materials. *Comput. Methods Appl. Mech. Eng.*, 426, 116980.

[12] F. Di Giusto, S. van Ophem, W. Desmet & E. Deckers (2023). Analysis of laser scanning and photogrammetric scanning accuracy on the numerical determination of Head-Related Transfer Functions of a dummy head. *Acta Acust.*, 7, 53.

[13] A.M. Mauricio, H. Denayer, & K. Gryllias. (2023). Beamformed Envelope Spectrum Of Acoustic Signals For Bearing Diagnostics Under Varying Speed Conditions. *Proc. of NOVEM 2023*, paper 7B-4-036.

[14] P. Becht, E. Deckers, C. Claeys, B. Pluymers & W. Desmet (2019). Loose bolt detection in a complex assembly using a vibro-acoustic sensor array. *Mech. Syst. Signal Process.*, 130, 433-451.

[15] L. de Oliveira, K. Janssens, P. Gajdatsy, H. Van der Auweraer, P. Varoto, P. Sas, W. Desmet (2009). Active sound quality control of engine induced cavity noise. *Mech. Syst. Signal Process.*, 23 (2), 476-488.

[16] C. Claeys, E. Deckers, B. Pluymers & W. Desmet (2016). A lightweight vibro-acoustic metamaterial demonstrator: Numerical and experimental investigation. *Mech. Syst. Signal Process*, 70, 853-880.

[17] V. Cool, E. Deckers, L. Van Belle & C. Claeys (2024). A guide to numerical dispersion curve calculations: Explanation, interpretation and basic Matlab code. *Mech. Syst. Signal Process.*, 215, 111393.

[18] L. Van Belle, L. Sangiuliano, N. G. R. de Melo Filho, M. Clasing Villanueva, R. F. Boukadia, S. Ahsani ... & W. Desmet (2021). Vibro-acoustic metamaterials for improved interior NVH performance in vehicles. *Future Interior Concepts*, 31-51.

[19] F. A. Pires, R. F. Boukadia, M. Wandel, C. Thomas, E. Deckers, W. Desmet & C. Claeys (2025). Novel resonator concept for improved performance of locally resonant based metamaterials. *Thin-Walled Struct.*, 209, 112866.

[20] H. Wang, L. Van Belle & F Naets (2024) Model based noise and vibration analysis framework of electric vehicle e-motor and gearbox. *Proc. of ISMA2024.*

[21] J. Bosmans, S. Gallas, V. Smeets, M. Kirchner, L. Geens, J. Croes & W. Desmet (2025). Experimental validation of virtual torque sensing for wind turbine gearboxes based on strain measurements. *Wind Energy*, 28(2), e2955.

[22] D. Panagiotopoulos & E. Deckers (2023). Inverse impedance identification using an efficient BEM strategy. *In Proc. of Forum Acusticum 2023*.

[23] S. van Ophem, E. Deckers & W. Desmet (2019). Model based virtual intensity measurements for exterior vibro-acoustic radiation. *Mech. Syst. Signal Process.*, 134, 106315.

[24] J. Staiger, S. van Ophem, J. Troge, & F. Naets (2024). Virtual measurements for exterior vibro-acoustic problems using experimental modal models. *Mech. Syst. Signal Process.*, 209, 111110.

DOI:

Main theme: A05 Environmental Acoustics

Session A05.01 Environmental acoustics - General

Chair(s): J. Picaut, M. Pawelczyk, M. Arana

DOI: 10.61782/fa.2025.0187

FORUM ACUSTICUM EURONOISE 2025

NOISE SOURCE ANALYSIS THROUGH ENVIRONMENTAL NOISE MEASUREMENTS

Omar Odeh[1*] **Dr. Maria Bite**[2] **Dr. Dénes Kocsis**[3]
[1]Doctoral School of Informatics, University of Debrecen, Debrecen, Hungary
[2]CEO, Noise and Vibration Expert, Vibrocomp Ltd., Budapest, Hungary
[3]Department of Environmental Engineering, Faculty of Engineering, University of Debrecen, Debrecen, Hungary

ABSTRACT

Exposure to excessive noise is linked to significant adverse effects on human health, including stress, sleep disturbances, and reduced quality of life, particularly in residential areas near commercial or industrial zones. This study focuses on analyzing the noise components emitted by various sources located on the rooftop of a hypermarket. The aim was to measure and identify the noise levels generated by the operating machinery, such as air-conditioning systems, cooling units, rooftop ventilation, transformers and compressors, which could impact the nearby environment, particularly the residential buildings located in front of the examined hypermarket.

Field noise surveys were carried out in the summer period during daytime and night-time to measure noise levels under operational conditions. These measurements were followed by thorough frequency spectra investigations utilizing Fast Fourier Transform (FFT) analysis, which helped identify the most significant noise contributors. While the study provided clear insights into the operational noise impacts during the summer, winter-specific noise sources, such as boilers were excluded due to seasonal constraints.

The findings serve as a foundation for further mitigation measures, including re-evaluation during winter operation to address potential regulatory noise exceedances and noise complaints.

[*]***Corresponding author***: omarrodehh@gmail.com.
Copyright: *©2025 First author et al. This is an open-access article distributed under the terms of the Creative Commons Attribution 3.0 Unported License, which permits unrestricted use, distribution, and reproduction in any medium, provided the original author and source are credited.*

Keywords: *noise measurements, environmental noise, spectra analysis, noise exposure, case study*

1. INTRODUCTION

Exposure to high noise levels can cause mental and physical adverse health effects [1]. It is linked with long-term risks of cardiovascular illnesses [2], such as heart attacks or hypertension. Moreover, excessive prolonged noise exposure affects work and educational environments, overall cognition, communication, and it weakens our attention [3-4]. Noise from industry increases the probability of residents nearby to suffer from mental illnesses [5]. Therefore, different mitigation measures to reduce the hazard caused by industrial noise were evaluated by many researchers [6]. For instance, sound absorption and insulation enclosures were designed to reduce the noise emissions of transformers [7], noise reduction of around 20 dBA was obtained by building noise barriers around a metallurgical factory [8], and acoustic metamaterials that could be used to increase the sound insulation performance for a better acoustic building design [9]. However, implementing noise reduction measures usually demand significant manpower and financial resources [6]. Therefore, this study utilized the Fast Fourier Transform (FFT) method through environmental noise measurements to analyze the spectral emissions of various equipment. The results were compared with the spectral emissions at the sensitive receptor to identify the most significant noise contributors. The findings are expected to provide a basis for further mitigation measures to reduce noise levels from the major contributors.

2. MATERIALS AND METHODS

2.1 Problem Overview

Residents of a dwelling situated across the street from a hypermarket were disturbed by the noise generated from the machines operating both within the hypermarket, and on its rooftop, despite the presence of a 3-m noise barrier. The study was limited to identifying the most contributing noise sources to the reported annoyance rather than to evaluate compliance with regulatory limits. Figure 1 below illustrates the location of the study area.

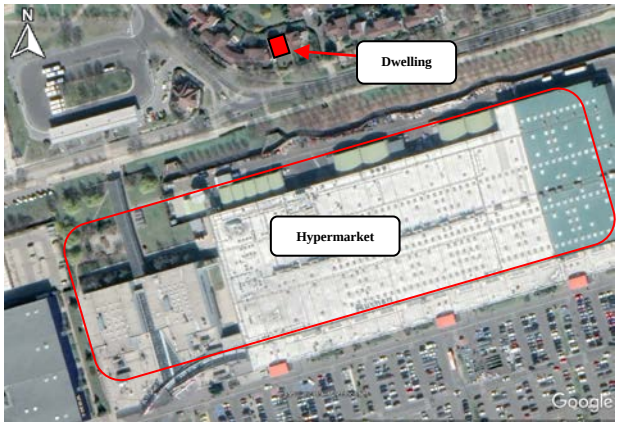


Figure 1. Study Area Overview.

2.2 Methodology

To assess the noise levels and identify the dominant noise sources accurately, two Class 1 Sound Level Meters (SLM) were utilized. One SLM was positioned at 2 meters from the façade of the Dwelling, referred to as Sensitive Receptor (SR) and at a height of 1.5 m from the ground level, according to ISO 1996 series [10-11], to measure the noise levels experienced by the residents, while the second SLM was placed around the machinery operating within the Hypermarket boundary, such as air-conditioning systems, cooling units, rooftop ventilation, transformers and compressors. This simultaneous measurement at both locations was conducted during daytime and nighttime and allowed for direct correlation between the noise contributions of specific machinery and their impact on the residential area. Fast Fourier Transform (FFT) function was enabled during the measurements to provide a full overview of the spectrum at both locations for further analysis.

Additionally, the study took place during the summer period. Therefore, winter-specific noise sources, such as boilers were excluded due to seasonal constraints.
Table 1 summarizes the description of each measurement point depicted in Figure 2 below.

Table 1. Measurement Points Description.

MP ID.	Noise Source Description	Operation (Day/Night)*
R0	Cooling Unit 1	I/I
R1	Transformer 1	C/C
R2	IT Equipment Noise 1	C/-
R3	Exhaust Chimney 1	C/-
R4	Exhaust Chimney 2	C/C
R5	Outdoor AC Unit	C/-
R6	Air Conditioner 1	C/-
R7	Air Conditioner 2	C/-
R8	Exhaust Chimney 3	C/C
R9	Cooling Unit 2	C/-
R11	IT Equipment Noise 2	C/-
R12	IT Room Ventilation	C/-
R13/R14	Cooling Unit 3	C/C
R15/R16	Cooling Unit 4	C/-
R17	Waste Collection Area	C/C
R18	Manual Pallet Truck	C/-
R19	Ice Maker Outdoor Unit	C/C
R20/R33	Transformer 2	C/C
R21	Press Machine	I/-
R22/R34	Air Cooler	I/I
R23	Cooling Unit 5	I/-
R24	Air Conditioner 3	C/C
R25	Fans	C/C
R26/R39	Exhaust Chimney 4&5	C/C
R27	Rooftop Fresh Air Fan 1	C/C
R28	Rooftop Fresh Air Fan 2	C/C
R30/R37	Pumps	C/C
R31	Exhaust Chimney 6	I/I
R40/R41	Compressor Venting	I/I
R42/R43	IT Equipment Noise 3	C/C

*C = Continuous, I = Intermittent



Figure 2. Measurement Point Locations.

Then, the results obtained from all measurement points were plotted in charts utilizing FFT analysis and compared with the results obtained at the Sensitive Receptor (SR) during both daytime and nighttime to identify any correlations in the measured spectra. In all charts, the right Y-axis represents the noise levels (dB) of the machinery and the left Y axis represents the noise levels (dB) at SR, while the X-axis accounts for the frequency in Hz.

3. RESULTS AND DISCUSSION

The present section highlights the measurement processing step utilizing FFT analysis. It is to be noted that if no correlation was identified, the measurement point was excluded. Therefore, the following sources were identified as potential contributors:

- Transformers
- Cooling Units (Chillers)
- Pumps
- Air Cooler
- Ice Maker Outdoor Unit

3.1 Transformers

Two transformers were identified in the study area: Transformer 1 (R1), located 170 m from SR, and Transformer 2 (R20/R33), located 85 m from SR, both operating continuously. It was observed that both transformers correlate with the nighttime spectrum measured at SR, with Transformer 2 having a higher contribution due to its closer proximity and higher noise levels. Figure 3 and Figure 4 below illustrates the FFT analysis charts for both transformers.

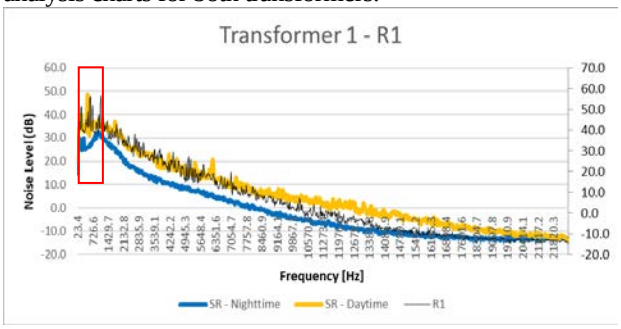


Figure 3. Transformer 1 (R1) FFT Chart.

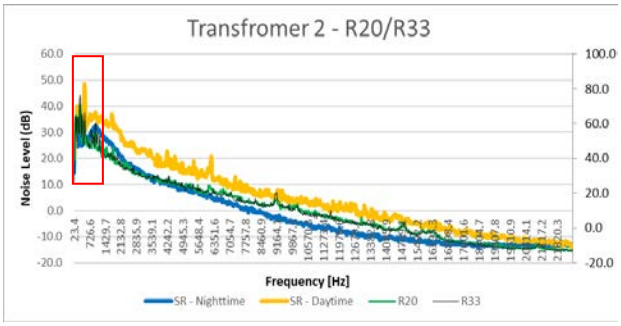


Figure 4. Transformer 2 (R20/R33) FFT Chart.

3.2 Cooling Units (Chillers)

Although five different Chillers were examined, only Cooling Unit 5 (R23), which has intermittent operations during daytime, showed significant correlation with the daytime noise spectrum observed at SR in the low and mid-frequency ranges, due to the following reasons:

a) It is the closest Chiller at 90 m distance from SR.
b) It is positioned on the rooftop of the Hypermarket, above the existing noise barrier.
c) It is oriented perpendicularly to SR.

The FFT analysis showed that in the low and mid-frequency ranges, e.g. 492 Hz, 750 Hz, 1000 Hz, and up to 7200 Hz, the Chiller's spectrum precisely with the peaks identified in the daytime spectrum at SR. However, the peak observed in the high-frequency range (around 15k Hz) in the Chiller's spectrum did not have an impact at SR, due to its rapid attenuation with distance compared to lower frequency. As a result, it was no longer detectable at SR. Figure 5 below depicts the FFT analysis chart for Cooling Unit 5.

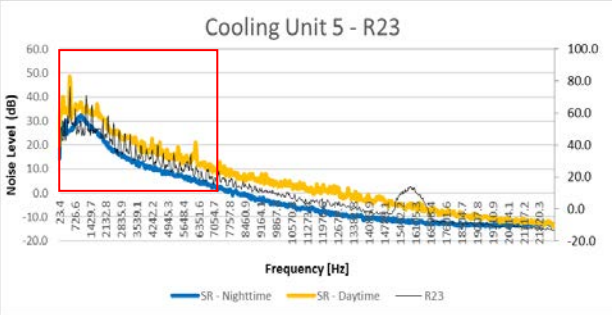


Figure 5. Cooling Unit 5 (R23) FFT Chart.

3.3 Pumps

Two measurements were conducted to analyze the spectrum of the Pumps, R30 and R37, which operate continuously during the day and night. The FFT analysis showed a weak correlation observed during nighttime only at 492 Hz. However, they are located 140 m from SR. Therefore, it was concluded that they are not a main contributor to the annoyance observed at SR. Figure 6 presents the FFT analysis chart for Pumps.

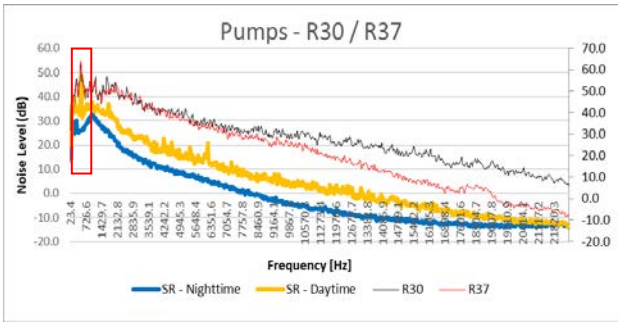


Figure 6. Pumps FFT Chart.

3.4 Air Cooler

Air Cooler, located 112 m from SR, was also evaluated. Two measurement were conducted around the unit, R22 and R34, to analyze its spectrum. Although the Air Cooler's noise was detectable at SR, both measurement indicated weak correlation during its intermittent operations in both daytime and nighttime. Therefore, it did not contribute to the reported annoyance, which can be linked to the characteristics of the noise source, as it lacked tonal or narrowband components. Figure 7 below depicts the FFT analysis chart for the Air Cooler.

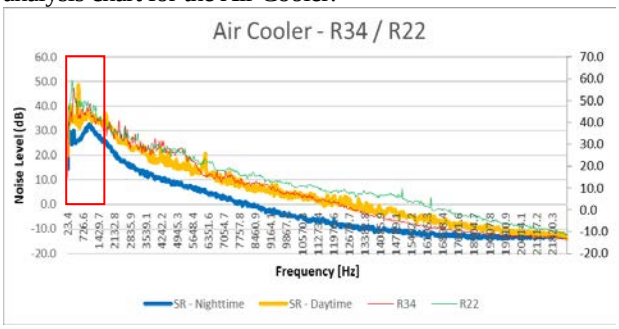


Figure 7. Air Cooler FFT Chart.

3.5 Ice Maker Outdoor Unit

The Ice Maker Outdoor Unit (R19) spectrum showed a weak correlation with the spectrum recorder at SR during nighttime. Despite being 85 m from SR, it was observed that its noise level at 1 m is not high enough to reach SR, especially that it is located behind the noise barrier. Therefore, it can be concluded that the correlation is due to another equipment which has similar characteristics, which in this case is Transformer 2. Figure 8 below depicts the FFT analysis chart for the Ice Maker Outdoor Unit.

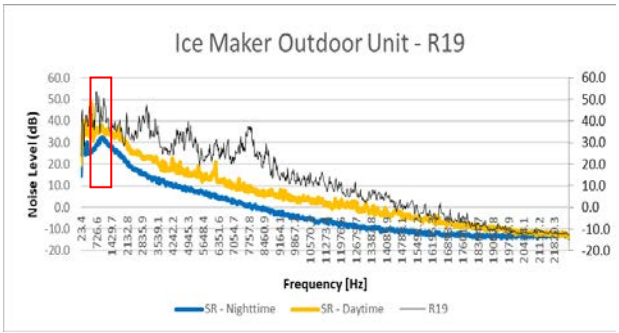


Figure 8. Ice Maker Outdoor Unit FFT Chart.

4. CONCLUSION

This study aimed to analyze the primary noise sources contributing to the disturbance reported by the residents of a dwelling located in front of a Hypermarket. A comprehensive noise measurement campaign was carried out to identify the most significant noise contributors operating within and on the rooftop of the Hypermarket utilizing FFT analysis. The results depicted that during daytime, the most significant contributor is Cooling Unit 5 (Chiller). This conclusion was based on the high correlation between its spectrum and the spectrum recorded at SR, its distance from SR, its high noise levels., and its position on the rooftop above the noise barrier, oriented perpendicularly to SR. However, its operation is intermittent and limited daytime.

During nighttime, it was observed that both Transformer 1 and Transformer 2, correlate with the measured spectrum at SR. Among them, Transformer 2 is more likely to be the primary contributor, due to its higher noise levels being significantly closer to the dwelling.

Other equipment, such as Ice Maker Outdoor Unit, Pumps, and Air Cooler, were also considered as potential contributors. However, the FFT analysis showed a weak correlation with SR. Additionally, site conditions, including their location and distance from SR, indicating that these source are either not detectable or had a negligible effect on the recorded noise levels at SR during both daytime and nighttime.

5. REFERENCES

[1] Hume, K., & Ahtamad, M. (2013). Physiological responses to and subjective estimates of soundscape elements. Applied Acoustics, 74(2), 275-281.

[2] World Health Organization. (2018). Environmental noise guidelines for the European region. World Health Organization. Regional Office for Europe, Copenhagen.

[3] Thompson, R., Smith, R. B., Karim, Y. B., et al. (2022). Noise pollution and human cognition: An updated systematic review and meta-analysis of recent evidence. Environment International, 158, 106905.

[4] Śliwińska-Kowalska, M., & Zaborowski, K. (2017). WHO environmental noise guidelines for the European region: A systematic review on environmental noise and permanent hearing loss and tinnitus. International Journal of Environmental Research and Public Health, 14(10), 1139.

[5] Ihinegbu, C., Nwosu, I., & Nnamchi, H. (2020). Residents' perception of the consequences of industrial activities in Ilupeju, Southwestern Nigeria. Journal of Human Behavior in the Social Environment, 30(8), 951–970.

[6] Wang, Y., Xie, J., Mun Lee, H., & Pueh Lee, H. (2025). Industrial noise reduction measures based on the Italian prioritisation index, Journal of Building Engineering, 111642.

[7] Fan, X., Li, L., Zhao, L., He, H., Zhang, D., Ren, Z., & Zhang, Y. (2020). Environmental noise pollution control of substation by passive vibration and acoustic reduction strategies, Applied Acoustics, 107305.

[8] Butorina, I., Butorina, M., Kuklin, D., & Shashurin, A. (2022). Innovative Approaches to Noise Reduction in Metallurgy, The Bulletin Tabbin Institute for Metallurgical Studies (TIMS), 110(1), pp. 68-80.

[9] Arjunan, A., Baroutaji, A., Robinson, J., Vance, A., & Arafat, A. (2024). Acoustic metamaterials for sound absorption and insulation in buildings, Building and Environment, 111250.

[10] ISO 1996-1:2016 – Acoustics — Description, measurement and assessment of environmental noise — Part 1: Basic quantities and assessment procedures

[11] ISO 1996-2:2017 – Acoustics — Description, measurement and assessment of environmental noise — Part 2: Determination of sound pressure levels

DOI: 10.61782/fa.2025.0640

FORUM ACUSTICUM EURONOISE 2025

OBTAINING NOISE LEVELS FROM PROJECTED OVERPRESSURE LEVELS GENERATED BY BLASTING OPERATIONS

Max Glisser[1*] **Betsabé Vásquez**[1]
[1] Gerard Ingeniería Acústica SpA, Villaseca 21 Oficina 1105 - Ñuñoa – Santiago – Chile

ABSTRACT

The overpressure levels generated by blasting generally increase with greater charge mass and decrease with greater distance from the blast site. Scaling methods are often used to determine the relationship between charge mass, distance and peak blast overpressure levels. The overpressure levels were calculated using a cube root scaling equation, taking into account constants that respond to the type of terrain of the blasting site. However, these peak overpressure levels are obtained as a global level in dBL. Therefore, this research gathers background information to provide a more comprehensive understanding of the noise caused by blasting and to advance its analysis. The results can be used for evaluations that require various weightings such as A, C and Z.

Keywords: *noise, blasting, mining*

1. INTRODUCTION

To determine the noise coming from a blasting at a given receiver we use an equation and constants that provide a single value of overpressure level. However, in some cases we need the noise level in different descriptors and/or weightings. For example, when evaluating fauna impact thresholds may be specified in dBA or dBZ. [1]
In Chile, the technical document "Evaluation criteria in the SEIA: Evaluation of noise impacts on native fauna" [1], has brought renewed attention to the assessment of noise effects on native wildlife.

This technical document establishes impact threshold for groups of vertebrate animals, i.e., amphibians, reptiles, birds and mammals, thresholds that are determined based on the species (or group) being evaluated, the type of noise source (continuous, impulsive or intermittent) and the associated adverse effects (physiological and behavioral). The thresholds are weighted using different curves such as A and C.
According to current legislation [2], it is required to study the impact of noise generated by blasting on all objects of protection. In the case of fauna, the object of protection is the relevant habitat for nesting, reproduction, or feeding, which must be located within the project's noise influence area (Guide for the Description of Soil, Flora and Fauna Components of Terrestrial Ecosystems in the SEIA, 2015) [3].
Therefore, this presents the challenge of predicting the noise levels generated by blasting at different weightings and distances in order to determine the impact area and assess compliance with the proposed thresholds.

2. ASSESSMENT OF IMPULSIVE NOISE ON WILDLIFE

For the specific case of impulsive noise, there are thresholds for birds and mammals, which are indicated below:

Table 1. References for the determining of reference thresholds for evaluating the noise impact on terrestrial fauna. Avifauna.

Effect description	Effect Type	Source Type	Threshold	Reference
Increased alertness and vigilance	Behavio-ral	Impulsive (military or blasting)	80 dBA max 63 dBA average	(Shannon et al., 2016) [4] [5] [6]
Direct	Physio-	Single	140 dBA	(Dooling

* ***Max Glisser***: mglisser@gmail.com.
Copyright: *©2025 First author et al. This is an open-access article distributed under the terms of the Creative Commons Attribution 3.0 Unported License, which permits unrestricted use, distribution, and reproduction in any medium, provided the original author and source are credited.*

Effect description	Effect Type	Source Type	Threshold	Reference
hearing damage	logical	impulse (blasting)	max	& Popper, 2007) [7]

Table 2. References for the determining of reference thresholds for evaluating the noise impact on terrestrial fauna. Mammals.

Effect description	Effect Type	Source Type	Threshold	Reference
Increased alertness and vigilance	Behavio-ral/ Physio-logical	Impulsive (military)	85 dBZ average	(Shannon et al., 2016) [4]

In the case of avifauna, the thresholds are presented with the frequency weighting filter A, or dBA. Additionally, "max" refers to the maximum Sound Pressure Level (SPL) recorded during the measurement period, it is sub understood, of the event or blasting, given the short duration that these have, while one of them is indicated not maximum SPL, but average, not indicating the integration time or "averaging".

On the other hand, for mammals a single threshold applies to both behavioral and physiological effects and it based on an unweighted frequency measurement or dBZ and an average value, without specifying the integration time. However, due to the impulsive nature of the source, it can be inferred that the integration time is short.

3. SOUND PROPAGATION EQUATION

The accurate estimation of ground vibration and airblast levels is a complex task. The blasting process is highly non-linear and the variability of most rock types also contributes to the difficulty in accurate predictions of the environmental outcomes. The random character of the blasting outcomes suggests the need for probability distributions to describe strictly the range of possible ground vibration and airblast levels. [8]
In the absence of either field data or the opportunity to conduct blasting trials in the region of interest, it is possible to estimate likely ground vibration and airblast levels using simple charge weight scaling laws. Such laws incorporate the charge weight per delay and the distance from the blast to the monitoring location. Two site parameters are assumed and these influence the peak level and the rate of decay for the levels.
Airblast levels have been commonly estimated using the following cube root scaling formula:

$$P = K_a \left(\frac{R}{Q^{1/3}} \right)^{\alpha} \quad (1)$$

Where:
P = pressure, in kilopascals.
Q = explosives charge mass, in kilograms (charge mass per delay, (MIC)).
R = distance from charge, in meters.
Ka = site constant.
α = site constant.

For unconfined surface charges, in situations that are not affected by meteorological conditions, a good estimate may be obtained by using a site exponent (α) of -1.45, ((which corresponds to an attenuation rate of 8.6 dBL with doubling of distance), and a site constant (Ka) of 516.
For confined blasthole charges, when using a site exponent (α) of -1.45, the site constant (Ka) is commonly in the range 10 to 100.

Airblast is proportional to the cube root of the charge mass. This limits the effectiveness of charge mass reduction as a method of reducing airblast levels; other factors are often more important, especially for confined blasthole charges. In unfavorable meteorological conditions, it is common for airblast levels to be increased by up to 20 dBL due to the combined effects of an increase with altitude of temperature (an inversion) and/or wind velocity (windshear). Effective assessment of meteorological reinforcement requires accurate measurement of temperature, wind speed, and wind direction, generally at heights up to 1000 m above the ground.

4. FREQUENCY SPECTRUM OF BLASTING EVENT

In March 2019 Journal of Vibroengineering article Vibroacoustic measurements and analysis of blasting works by Józef Pyra and Maciej Kłaczyński of AGH University of Science and Technology in Kraków, Poland, sound spectra of measurements made during blasting events are shown. [9]
The investigation was conducted near one of the largest military training camps in Poland within a built-up area.

The study focused on the impact range of explosive charges during detonation, including structural vibrations, overpressure (AB) and acoustic waves (AW). During the measurements, three series of ANFO-type explosive material were detonated, with the following masses: series I - 150 kg, series II - 300 kg and series III - 450 kg. In all cases, the explosive charges were detonated on the surface.
Measurements were taken simultaneously at two points located at the nearest positions in the direction of propagation. At each station, a full set of equipment was used to measure ground vibration intensity, overpressure and noise level (acoustic waves). The distance from the blasting site to measurement point No. 1 (town 1) was approximately 7.5 km, and to measurement point No. 2 (town 2) was approximately 6.5 km.
The following figure shows the spectrum of the maximum unweighted sound pressure level for the explosion event, along with the background noise level at the same location, corresponding to point No. 2.

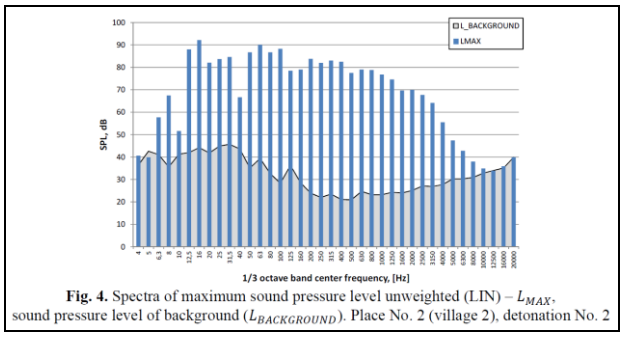


Fig. 4. Spectra of maximum sound pressure level unweighted (LIN) – L_{MAX}, sound pressure level of background ($L_{BACKGROUND}$). Place No. 2 (village 2), detonation No. 2

Figure 1. Spectrum of the maximum sound pressure level of the blasting event and background noise in dBZ.

The following table presents the spectrum in numerical form. Additionally, weighting is applied to obtain values in dBA and dBC.

Table 3. Maximum sound pressure level of the blasting event in spectral weightings Z, A and C.

Frequency Hz	Lmax dBZ	Lmax dBA	Lmax dBC
6,3	57,0	-28,4	35,7
8	67,0	-10,8	49,3
10	52,0	-18,4	37,7
12,5	88,0	24,6	76,8
16	92,0	35,3	83,5
20	82,0	31,5	75,8
25	84,0	39,3	79,6
31,5	85,0	45,6	82,0
40	62,0	27,4	60,0
50	86,0	55,8	84,7
63	90,0	63,8	89,2
80	86,0	63,5	85,5
100	88,0	68,9	87,7
125	78,0	61,9	77,8
160	79,0	65,6	78,9
200	84,0	73,1	84,0
250	82,0	73,4	82,0
315	83,0	76,4	83,0
400	83,0	78,2	83,0
500	77,0	73,8	77,0
630	79,0	77,1	79,0
800	79,0	78,2	79,0
1000	77,0	77,0	77,0
1250	75,0	75,6	75,0
1600	70,0	71,0	69,9
2000	70,0	71,2	69,8
2500	67,0	68,3	66,7
3150	64,0	65,2	63,5
4000	55,0	56,0	54,2
5000	47,0	47,5	45,7
6300	43,0	42,9	41,0
8000	38,0	36,9	35,0
10000	35,0	32,5	30,6
12500	34,0	29,7	27,8
16000	36,0	29,4	27,5
20000	40,0	30,7	28,8
Global	**98,2**	**86,4**	**95,9**

The following figure graphically represents the spectra considering the three indicated weightings .

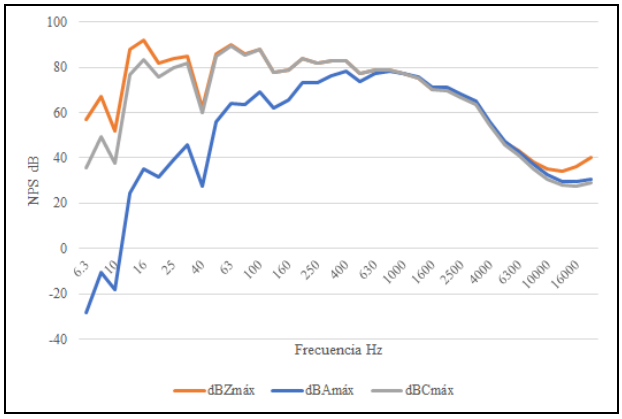


Figure 2. Maximum blasting event sound pressure level spectrum in dBZ, dBA and dBC.

5. ADJUSTMENT FOR OBTAINING NPS, FROM OVERPRESSURE LEVELS IN dBL PEAK

As specified, the results of the projections using the given equation are expressed in terms of overpressure in linear dB, or dBL. In this regard, AS 2187.2-2006 states: "... if a sound level meter measures an airblast level of 115 dBL, the same meter would measure approximately 90 dBA for the same event.

The frequency content of the particular airblast time history will determine the relative levels between the dBL and dBA readings.

This same correlation was found and reported in the document "Prediction and Control of Air overpressure from blasting in Hong Kong". Appendix A, "Analysis of dBA v/s dBL measurements Choi Wan Road and Jordan Valley" records and compares in detail a total of 137 blasting events in dBA and dBL. [10]

In consideration of the above, this correlation is already applied as a factor or correction to obtain the results from the projections. That is, overpressure in dBL is used to estimated sound pressure levels with dBA weighting. Then using a known spectrum from the data above, the levels can be determined at any scale (A, C, Z, etc.), using the following procedure:

(i) Perform the overpressure projection using Equation (1), with the result expressed in dBL peak;

ii) Apply the correction subtracting 25 to the overpressure level result, obtaining the value expressed in dBA;

Considering the blast spectrum presented in chapter 4, this time, between 20 Hz and 20 kHz and applying the A-weighting curve, the results are summarized in the following table:

Table 4. Frequency response of blasting in 1/3 octave bands in dBA.

Frecuency	Lp dBA	Frecuency	Lp dBA
20	31,5	**800**	78,2
25	39,3	**1000**	77,0
31.5	45,6	**1250**	75,6
40	27,4	**1600**	71,0
50	55,8	**2000**	71,2
63	63,8	**2500**	68,3
80	63,5	**3150**	65,2
100	68,9	**4000**	56,0
125	61,9	**5000**	47,5
160	65,6	**6300**	42,9
200	73,1	**8000**	36,9
250	73,4	**10000**	32,5
315	76,4	**12500**	29,7
400	78,2	**16000**	29,4
500	73,8	**20000**	30,7
630	77,1	**Global**	86,4

iii) Express the result in 1/3 octave frequency bands by adjusting the spectrum to the global dBA value obtained in ii). From there, convert it to any other desired weighting.

6. CONCLUSIONS

With the proposed methodology, sound pressure level values can be derived from overpressure levels using any spectral weighting, such as dBZ, dBA and dBC. Therefore, these values can be compared with impact thresholds using different weighting curves.

There is limited information on impact thresholds for blasting noise on reptiles and amphibians. It is important to continue the researching for information maximum acceptable limits for impulsive noise, especially for species where such data are not yet available.

Finally, it would be beneficial to have more noise measurements with spectral information from blasting events and to assess the noise generated in the fauna through empirical results. However, an alternative for

making projections is to follow the steps outlined in this work.

7. REFERENCE

[1] SEA. “Criterio de Evaluación En El SEIA: Evaluación de Impactos Por Ruido Sobre Fauna Nativa”, 2022.

[2] SEA. “Guía Para La Predicción y Evaluación de Impactos Por Ruido y Vibración En El SEIA”, 2019.

[3] SEA. “Guía Para La Descripción de Los Componentes Suelo, Flora y Fauna de Ecosistemas Terrestres En El SEIA2, 2015.

[4] Graeme Shannon. “A synthesis of two decades of research documenting the effects of noise on wildlife”, 1Department of Fish, Wildlife, and Conservation Biology, Colorado State University, Fort Collins, CO 80523, U.S.A., 2016.

[5] Conomy, J. T., Dubovsky, J. A., Collazo, J. A. & Fleming, W. J. (1998). Do black ducks and wood ducks habituate to aircraft disturbance? The Journal of Wildlife Management 62, 1998.

[6] Goudie, R. & Jones, I. L. (2004). Dose-response relationships of harlequin duck behaviour to noise from low-level military jet over-flights in central Labrador. Environmental Conservation 31, 2004.

[7] Robert J. Dooling and Arthur N. Popper. “The Effects of Highway Noise on Birds”, The California Department of Transportation Division of Environmental Analysis1120 N Street Sacramento, CA 94274, 2007

[8] Standards Australia. “Australian Standard AS 2187.2:2006 Explosives - Storage and Use - Use of Explosives – Victoria”, 2006.

[9] Pyra J, Kłaczyński M. “Vibroacoustic measurements and analysis of blasting works. Journal of Vibroengineering”, 2019.

[10] Richards AB. “Prediction and Control of Air Overpressure from Blasting in Hong Kong. Government of the Hong Kong Special Administrative Region”, 2008.

DOI: 10.61782/fa.2025.0372

FORUM ACUSTICUM EURONOISE 2025

EXPERIMENTAL ASSESSMENT OF OUTDOOR LEISURE NOISE: SAMPLING METHODOLOGY AND ANNOYANCE INDICATORS

Antonio Hidalgo[1*] **Alberto Hernandez**[1]
[1] Centro de Estudio y Control de Ruido SL (CECOR), Valladolid, España

ABSTRACT

Leisure noise is a significant environmental issue across Europe, particularly in Mediterranean countries where outdoor leisure activities are more prevalent and widespread. These regions experience higher levels of outdoor gatherings, music events, and nightlife activities, which contribute substantially to noise pollution in both urban and suburban areas. Although this type of noise is within the scope of Directive 2002/49/EC of the European Parliament and of the Council of 25 June 2002 [1], the directive does not impose specific obligations for controlling leisure noise, leaving a gap in its practical application. Additionally, there are no established standards or universally accepted methodologies for the accurate assessment of this noise type. This lack of regulation creates challenges for policymakers and urban planners attempting to mitigate its impact on communities.

In this paper, a comprehensive guideline is proposed to address these limitations. The guideline focuses on key aspects such as spatial and temporal sampling strategies, the processing of noise measurements, and the selection of appropriate indicators to evaluate noise annoyance effectively. By providing a structured approach, the proposed methodology aims to improve the accuracy and consistency of leisure noise assessments, facilitating better decision-making and promoting healthier, quieter environments.

Keywords: *Leisure noise Acoustic measurements Noise assessment Environmental noise Noise limits*

[*] ***Corresponding author***: *antoniohidalgo@cecorsl.com*
Copyright: *©2025 Antonio Hidalgo et al. This is an open-access article distributed under the terms of the Creative Commons Attribution 3.0 Unported License, which permits unrestricted use, distribution, and reproduction in any medium, provided the original author and source are credited.*

1. INTRODUCTION

The problem of noise derived from leisure activities in Spain and Europe has specific characteristics and increasing relevance. This noise is closely linked to nighttime and evening leisure activities in bars, terraces, nightclubs, and restaurants, affecting the quality of life of residents by disturbing rest, concentration, and even auditory health.

Leisure noise, particularly in densely populated or tourist areas, causes significant discomfort and an increase in neighborhood complaints. In many Spanish cities (Madrid, Barcelona, Vitoria, Valencia, Málaga, Ibiza, Alicante, Murcia, Logroño, Badajoz, Benidorm, Ciudad Real, etc.), studies based on acoustic measurements have identified notable differences between noise levels during weekdays and weekends, showing an alarming increase during the weekend nighttime period.

European environmental noise legislation, with its main regulation being Directive 2002/49/EC [1], while not excluding leisure noise as an acoustic pollutant, does not explicitly address it as it does with sources such as road, rail, and air traffic, and industry. For example, there is an obligation to carry out Strategic Noise Maps and Action Plans against noise in major cities for the previously mentioned sources, but not for leisure noise. In Spain, strategies such as the designation of Special Acoustic Protection Zones (ZPAE), Acoustically Saturated Zones (ZAS), or Special Acoustic Situations Zones (ZSAE) have been developed. However, leisure noise is not included in the Strategic Noise Maps, and it is often a point of contention whenever a Strategic Noise Map is approved in Spanish cities.

Nighttime leisure noise presents technical challenges for its assessment, such as the absence of valid empirical models for its implementation in acoustic prediction, the difficulty in measuring it representatively, and the impact of factors such as seasonality and tourist density. This article aims to provide a baseline methodology for assessing leisure noise through in situ measurements.

The proposed methodology provides the indicators that best represent the impact of leisure noise, as well as the procedures for the temporal and spatial sampling of measurements. Efforts have been made to draw a parallel with the international standards ISO 1996-1 [2] and 1996-2 [3] (*Acoustics — Description, measurement and assessment of environmental noise*) which provide guidelines for environmental noise measurement, focusing on noise from industry and infrastructure. This article presents the instructions for the experimental assessment of leisure noise.

The recommendations in this work are guidelines; however, the applicable legislation must be taken into account, as it may impose more restrictive conditions in certain aspects.

2. MOTIVATIONS

Leisure noise has many peculiarities and characteristics that differ from other environmental noises such as industrial noise and infrastructure noise. These differences are particularly related to their variability in time and space. There are numerous leisure noise measurements conducted in various studies of cities; however, as mentioned, there is no uniformly accepted methodology.

The behavior over time of leisure noise can be classified as fluctuating sound according to the classification made by ISO 1996-1 [2] (3.4.5). The variation in leisure noise occurs in the short term (in minutes), medium term (different hours of the day with very high variability), and long term (days with high sound emission, such as weekends or differentiated periods like summer and winter). The evaluation method must account for this temporal variation and already indicates that measurement periods should be long, with repeated intervals across the week and over several weeks. Additionally, the selected indicator for measurement should reflect the concentration of emission over short periods of time, especially during the night. Evaluation over periods of several hours (day, evening or night) could attenuate the emission that occurs during shorter periods, typically between 1 and 3 hours.

Regarding spatial variability, it can also be very high, as the typical area for this type of noise is the city center. It is possible to have a high noise level on a street with a high concentration of activities or people, which can decrease drastically just a few meters away on an adjacent street. Since these measurements involve long recording times, it will be necessary to optimize the number of measurement points, as each one will incur high costs.

In conclusion, the high variability of leisure noise over time and space makes it necessary to have a thorough understanding before proposing a spatial or temporary sampling method for its assessment. It may even be necessary to evolve in successive measurement campaigns, expanding points and measurement time based on previous experiences.

The figure below shows the evolution of the 1-hour equivalent level throughout the days of the week in a beachfront leisure area in summertime. The equivalent levels are over 70 dB(A) in the worst night period. There is a clear increase in levels between 1:00 AM and 6:00 AM, with a more pronounced rise on the weekend. The levels during the daytime period are stabilized between 60-65 dB(A).

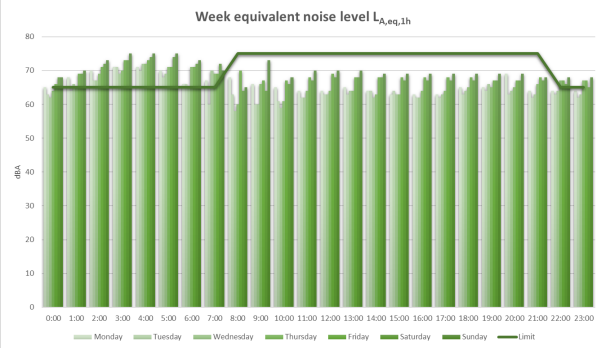


Figure 1. Noise level ($L_{A,eq,1h}$) for one week.

Another special characteristic of leisure noise is that the noise measurements themselves can change the behavior of people or the activities that are intended to be measured. Therefore, measurements with the sonometer at street level over a short period of time should be avoided, as could be done in industrial or infrastructure measurements.

3. ANNOYANCE INDICATORS

3.1 Time-weighted and frequency-weighted sound pressure level

The frequency behavior of leisure noise is broadband, with no low-frequency components or high impulsivity. Therefore, measurements with A-weighting and FAST time weighting are valid.

The appropriate frequency range for the assessment of leisure noise is between 20 Hz and 10,000 Hz. In addition to providing the overall value, it is recommended to perform measurements in third-octave bands or at least in octave bands.

3.2 Noise descriptors

The most appropriate indicator to estimate the annoyance of leisure noise is the equivalent continuous sound pressure level. The reference time interval to process the equivalent noise level is the day, evening, and night reference periods (in dependence of each country), but it is not sufficient. At least during the nighttime period, it should be accompanied by the evaluation of the continuous level over 1 hour. Shorter evaluation periods may not be suitable due to their low representativeness for this type of fluctuating noise. The assessment over a 1-hour period during the night is appropriate for determining the potential sleep disturbance caused by leisure noise.
The maximum level should be recorded in each measurement period ($L_{F,max}$) for each sampling day.
N percent exceedance level, ($L_{N,T}$) are very useful from a technical perspective to determine the behavior of the noise throughout the measurement period, but they are difficult to interpret for non-technical people and are not practical for setting emission limits.

4. MEASUREMENT PROCEDURE

To select appropriate observation and measurement time intervals, it may be necessary to conduct survey measurements over relatively long periods.

4.1 Time intervals, time sampling

About the long-term time interval, leisure noise can exhibit periodic behavior both during the week and throughout the year. During the week, it is common for high noise levels to occur on weekends (from Friday to Sunday). Throughout the year, noise levels typically increase during summer periods, when leisure activities take place outdoors. This is added to the fact that during hot weather, it is more common to have windows open in residences, which increases the noise impact. Therefore, in the long term, measurements should be evaluated as day-week averages, ensuring that high noise level events are repeated for at least three consecutive weeks.

4.2 Spatial sampling

Measurements should preferably be conducted in outdoor spaces, although indoor spaces may be monitored for specific purposes.
At least one measurement point should be placed on each of the streets affected by leisure noise, in the area where the highest impact is expected. For streets longer than 100 meters, a second measurement point should be installed.

4.3 Microphone location

The measurement points should preferably be located at a height of 4 meters. Measurement stations can be placed on balconies, windows (exterior part), or façades, taking into account potential corrections for reflections.
Locations on streetlights or electricity poles may also be acceptable, provided that the anchoring element does not transmit noise or vibrations to the measurement equipment.
In all cases, the equipment should be positioned in such a way that it is not visible from the leisure areas, either by the users or by the staff of the establishments, to avoid altering the behavior of the business owners or users.
In the case of indoor measurements, it must be ensured that the measurement space is not occupied during the measurements. It must also be ensured that the noise coming from the outside is predominant.

4.4 Instrumentation

Depending on the purpose of the measurements, the following types can be established.
Measurements aimed at establishing corrective measures or delineating special action zones by local authorities:
• Class 1 sound level meters according to IEC 61672-1, calibrated before and after each measurement.
• Class 1 acoustic calibrator to verify the proper functioning of the equipment.
Control measurements carried out directly by the local authorities or regulatory bodies may use Class 2 sound level meters according to IEC 61672-1 [4].
For measurements in octave or one-third-octave bands, the class 1 and class 2 instrumentation systems shall meet the requirements of a class 1 or class 2 filter, respectively, specified in IEC 61260:1995.
In all cases, microphones should be protected with windshields and weatherproof kits to prevent wind disturbances and damage from rain.

4.5 Weather conditions

The weather conditions shall be representative of the noise exposure situation under consideration, and it should be registered on the measurement period.

4.6 Other parameters to be controlled.

The noise assessment should include a list of the leisure activities present in the area with at least the following information:

- Name of the activity.
- Type of activity (pub, restaurant...).
- Operating hours.

- Venue capacity.
- Terrace capacity.

Alternatively, other parameters can be monitored, such as the occupancy level of the area being measured. There are person-counting systems supported by Artificial Intelligence that allow the establishment of an occupancy level for terraces or public streets, which can be related to the recorded noise levels.

4.7 Residual sound

The measurements must be corrected for the presence of residual sound (total sound remaining at a given position in a given situation when the specific sounds under consideration are suppressed) with levels similar to those of the leisure activity itself. These levels can be evaluated during the hours of the day when leisure activity decreases, such as in the early hours of the morning. The type of noise may change, with leisure activity being predominant at night, while traffic noise tends to be higher during the day.

5. EVALUATION OF THE MEASUREMENT RESULT

5.1 Correction factors

If the residual sound pressure level is 10 dB or more below the measured sound pressure level, make no corrections.
If the residual sound pressure level is 3 dB or less below the measured sound pressure level, no corrections are allowed. The measurement uncertainty is then large. The results may, however, still be reported and may be useful for determining an upper boundary to the sound pressure level of the source under test.
For cases when the residual sound pressure level is within a range from 3 dB to 10 dB below the measured sound pressure level it should be corrected according to ISO 1996-2 method.
Regarding meteorological corrections, measurements taken in conditions of rain or winds exceeding 5 m/s should be discarded.
Corrections for reflections may be applied in the case of measurements taken near façades, subtracting 3 dB(A) from the average level obtained.

5.2 Noise limits

The competent authorities (usually local authorities) should establish limits for each of the equivalent level parameters for the day, evening, and night periods for leisure activities, as well as for the 1-hour equivalent level parameter for night period.

In the case of equivalent levels, the limits can be the same as the acoustic quality objectives for the designated area. For the 1-hour equivalent level, the limit can be set at 5 dB(A) above the nighttime acoustic quality objective.
Exceedance ranges can be established to determine the types of actions to be taken in each case. For example,

- Exceedances between 0-5 dB(A) may involve implementing zonal plans for the gradual reduction of noise and controlling emissions.
- Exceedances between 10-15 dB(A) may require immediate actions such as time restrictions or limiting terrace areas.
- Exceedances above 15 dB(A) may result in the establishment of Acoustically Saturated Zones with the application of corrective measures, including the closure of establishments.

6. INFORMATION TO BE RECORDED AND REPORTED

For measurements, the following information shall, if relevant, be recorded and reported:
a) time, day and place for measurements.
b) instrumentation and its calibration.
c) measured and, if relevant, corrected sound pressure levels ($L_{A,eqT}$), A-weighted and, optionally, in frequency bands.
d) estimate of the measurement uncertainty together with the coverage probability.
e) information on residual sound pressure levels during the measurements.
f) time intervals for the measurements.
g) thorough description of the measurement site, including ground cover and condition, and locations including height above ground, of microphone.
h) description of the operating conditions, including the list of leisure activities in the area with is main operating description.
i) description of the meteorological conditions, including wind speed, wind direction, cloud cover, temperature, barometric pressure, humidity and presence of precipitation and location of wind and temperature sensors.

7. ACKNOWLEDGMENTS

This work is the result of the intense efforts of CECOR, in collaboration with numerous public administrations, primarily local authorities, in the fight against leisure noise. Special emphasis is placed on the support of CECOR's technicians. Acknowledgements to the University of

Alicante, and in particular to Mr. Jaime Ramis, for his involvement and support in this work.

8. REFERENCES

[1] Directive 2002/49/EC of the European Parliament and of the Council of 25 June 2002 relating to the assessment and management of environmental noise. Official Journal of the European Union, L 189/12.

[2] ISO 1996-1:2016. (2016). Acoustics – Description and measurement of environmental noise – Part 1: Basic quantities and procedures. International Organization for Standardization.

[3] ISO 1996-2:2017. (2017). Acoustics – Description and measurement of environmental noise – Part 2: Acquisition of data pertinent to land use. International Organization for Standardization.

[4] IEC 61672-1, Electroacoustics — Sound level meters — Part 1: Specifications

DOI: 10.61782/fa.2025.0687

FORUM ACUSTICUM EURONOISE 2025

PRACTICAL NOISE IMMISSION MODELING FOR CONCERTS IN STADIUMS: SANTIAGO BERNABÉU - REAL MADRID (SPAIN)

Viloria-Yzquier, Camila Valentina[1*] **García-Calderón, Eugenio**[2]
San Millán-Castillo, Roberto[1]

[1] Universidad Rey Juan Carlos-Departamento de Teoría de la Señal y Comunicaciones - EIF, Spain
[2] Ingeniería Acústica García-Calderón (IAG), Spain

ABSTRACT

The recent controversy surrounding the cancellation of future concerts at the Santiago Bernabéu Stadium, affecting approximately 250,000 attendees, many of whom came to Madrid from other cities, has generated intense debate. Neighbors in the area claim that "it is a sports stadium, not a space for musical events", and express their complaints regarding the noise generated at these events. With the firm belief that it is possible to address residents' concerns about the development of noise-producing activities in a city, new regulations have been introduced to correct deficiencies in these activities [1]. This project evaluates the impact of these recreational activities on the quality of life of nearby residents and determines whether they follow legally established noise levels. To accomplish this, data collected from in situ measurements will form the basis for simulating the noise affecting residents, verifying the model's accuracy, and suggesting potential solutions.

Keywords: *noise immission, noise modeling, concerts, stadiums*

1. INTRODUCTION

On December 14, 1947, the Santiago Bernabéu Stadium was officially opened with a friendly soccer match as the new Real Madrid Stadium. Today, almost 80 years later, Real Madrid´s president Florentino Pérez claims that "We are in the final phase of meeting the great challenge that Real Madrid set itself five years ago: that the Bernabéu stands as a universal avant-garde icon and an architectural emblem of Madrid. It is the most iconic stadium in world football" [2]. Addressing the impact of the stadium's latest renovations.

In addition to providing a new aesthetic, the renovation also increased the stadium's capacity to 80,000 people and opened the door to new events such as recurring concerts. In 2024 alone, the stadium held more than 15 major concerts, each drawing around 65,000 attendees [3], the maximum allowed for these events. However, it is important to remember that Bernabéu is located in Chamartín District, a predominantly residential area, which is also an environmentally protected zone [4]. These events disturb the lives of local residents because noise affects their well-being and causes significant annoyance.

In the past, sound systems engineering for musical events focused on sound quality in the audience. There has been an increase in these events in stadiums along with complaints from nearby residential neighbors. Some novel and recent methodologies have contributed to addressing this major concern, linking complex loudspeaker systems to outdoor environmental propagation and working with detailed data of sound systems, stadiums, and surroundings for open-air events, as in [5,6]. The current prediction tools do not provide right-away models to fill this gap. Environmental classical noise sources, such as road and train radiation, which are decorrelated, are significantly different from those of sound systems, which

*__Corresponding author__: cv.viloria.2020@alumnos.urjc.es.
__Copyright__: ©2025 Viloria-Yzquier, Camila et al. This is an open-access article distributed under the terms of the Creative Commons Attribution 3.0 Unported License, which permits unrestricted use, distribution, and reproduction in any medium, provided the original author and source are credited.

are coherent and highly directional acoustic sources [6]. There is a significant need to plan the environmental impact of these modern scenarios and reach the expected immision noise levels that comply with local regulations [6, 7].

However, some stadiums can be considered semi-closed rooms. Hence, the walls of the stadium do not behave as acoustic barriers, as in open-air events, and there is remarkable acoustic leakage through the walls. Real Madrid's stadium is located in a dwelling area and brings environmental conflict with its dwellers. This leads to a significant lack of relevant data regarding sound systems and building of insights.

This study proposes a practical methodology for modeling noise immision for concerts in semi-closed stadiums with sparse data and moderate resources but with accurate field measurements performed at the neighbors' façades.

The remainder of this paper is organized as follows: Section 2 explains the materials and methods, Section 3 discusses the results, Section 4 suggests mitigation solutions, and Section 5 presents the conclusions.

2. MATERIALS AND METHODS

This paper proposes a practical methodology that can contribute to predicting and finding solutions to highly complex problems. We work on a particular case: Real Madrid's stadium. However, the same approach can be applied to similar stadiums and musical events. Sparse data are a major drawback in these cases because it is common to encounter conflicts with victinity residential buildings and even non-compliant noise radiation according to local regulations. Hence, obtaining insights from stadiums such as loudspeaker setups and construction plans is rare. Our approach consists of the following steps.

1. **Field noise measurements**. We used noise measurements at keypoints/receivers to assess the scenario and obtain valuable data for modeling.

2. **Noise immision modeling**. We modeled the scenario using public data from the stadium and its surroundings, along with sound acoustical assumptions.

3. **Validation of the model**. We made measurements and modeling meet ends and provided a tool to evaluate current and future scenarios.

4. **Analysis of results**. We provided stakeholders with solutions to consider a range of challenges.

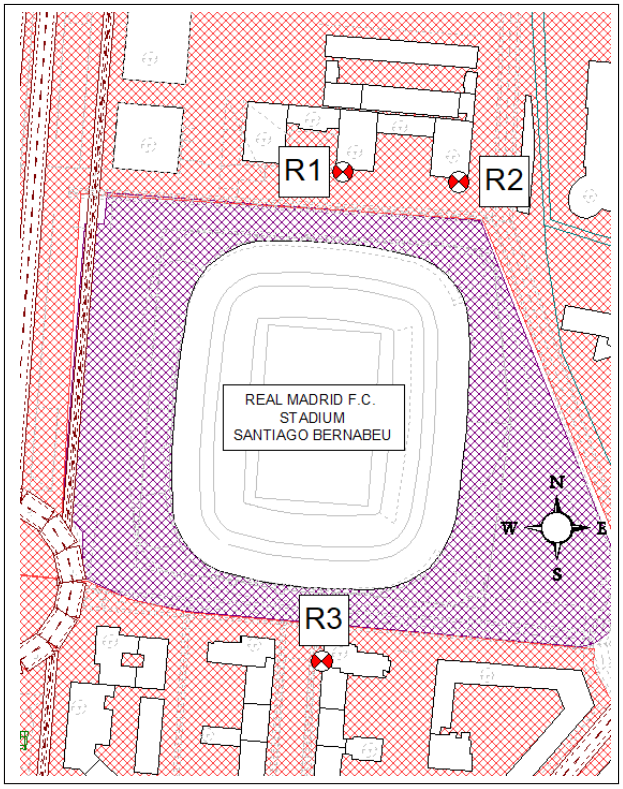


Figure 1. Location of the three receivers situated on the northern and southern sides of the stadium and the areas' land use (The red being residential and purple being recreational).

2.1 Field noise measurements

A noise monitoring campaign was conducted in the outdoor environment on 20th July 2024, the day when Karol G's concert took place. Measurements were taken every 5 s, including the indices required by RD1367/2007 [8] and the local law [1] (L_{Aeq}, L_{Ceq}, L_{AIeq}, and the spectrum in one-third octaves from 20 Hz to 10 kHz). The recordings covered the periods before, during, and after the concerts, allowing for the analysis of noise from activity (music) and noise without activity (no music).

Measurements were performed using 01 dB sound level meters, type SOLO, Class 1 equipped with third-octave filters compliant with the IEC 61672-1 Class 1



Figure 2. View of the microphone on the façade from a house in the vicinity of the stadium.

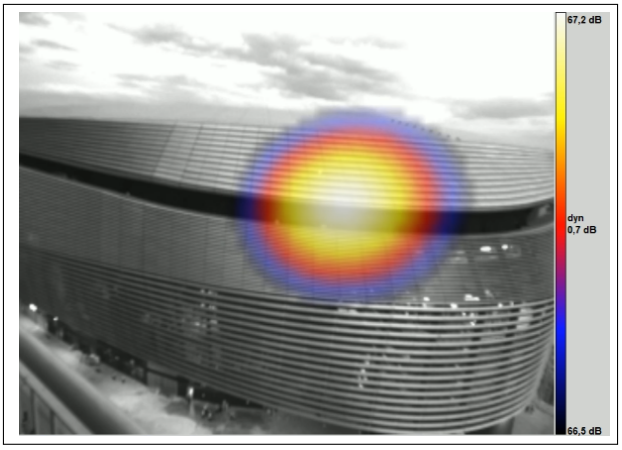


Figure 3. Visualization of the noise radiated from the stadium with an acoustic camera (Soundcam 2 Cae Systems).

standard [9]. A Rion NC74 sound calibrator that meets the IEC 60942 Class 1 standard [10] was used before and after the measurement campaign. All measuring instruments, including sound level meters and acoustic calibrators, have type approval and periodic verification in accordance with the Spanish law (ITC 155/2020 order) [11]. The measurements were performed simultaneously in multiple homes surrounding the Santiago Bernabéu Stadium.

For each sound level meter, the measurement microphone was placed outdoors, 2 m from the façade, using a telescopic pole and microphone extension cable. This positioning minimized the sound reflected by the façade. Each unit was located in one apartment; therefore, we were able to obtain the variability of sound levels at different heights from the street floor. The exact location is not detailed enough to maintain confidentiality and to comply with the Data Protection Act. Fig. 1 shows the locations of all receivers, that is, measurement points, from the stadium; the upper receivers R1 and R2 are on the northern side of the stadium and receiver R3 is located on the southern side.

2.2 Noise inmission modeling

The acoustic modeling was performed with Cadna A (Version 2025, DatakustiK), one of the leading softwares for calculation, presentation, assessment and prediction of environmental noise. Some software configurations worth highlighting: CNOSSOS-EU [12] is the propagation model for estimating L_{Aeq} for the moments of maximum noise impact according to the required limits. The stadium noise was modeled using horizontal surface sources for the ceiling and vertical surface sources for façades. These sources had different assigned values for the northern, southern, eastern, and western sides, and their values were specifically adjusted to those measured with sound level meters. The sound powers of these surface sources were adjusted in the frequency domain at the receivers.

We also incorporated traffic data assigned to each of the surrounding roads, setting up their average daily traffic densities (MDTD). The evaluation of traffic noise is based on the ambient noise scenario in the vicinity of buildings when there are no concerts, thus observing a large difference in levels between the two scenarios: 1) when only traffic noise was present, and 2) when there was only concert music.

Table 1. Model's Validation comparing the measurements results with the prediction value obtained by the model, L_{Aeq} dBA.

	Measurements L_{Aeq} dBA	Model L_{Aeq} dBA	Deviation (dBA)
R1	80	78,2	-1,8
R2	77,6	77,5	-0,1
R3	72,3	72,4	-0,1

2.3 Validation of the model

The validation consisted of comparing the prediction of the outdoor propagation model with the measurements us-

ing the same source and evaluation points. The sound levels of the noise sources involved in the model were conveniently adjusted to fit the measurements. Eventually, the deviations between both L_{Aeq} values were adequate to provide a valuable predictive model (less than 2 dBA), as shown in Tab. 1, thus validating the model. In Fig. 4 and Fig. 5, we observe the spectrum on both the north and south sides of the stadium.

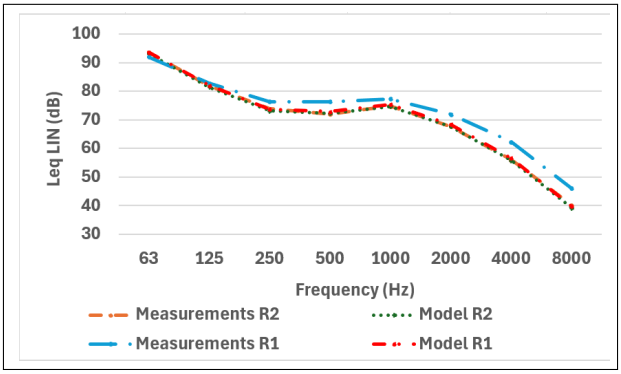


Figure 4. Spectra of measured and simulated levels in the northern side (Reveiver R1 and R2).

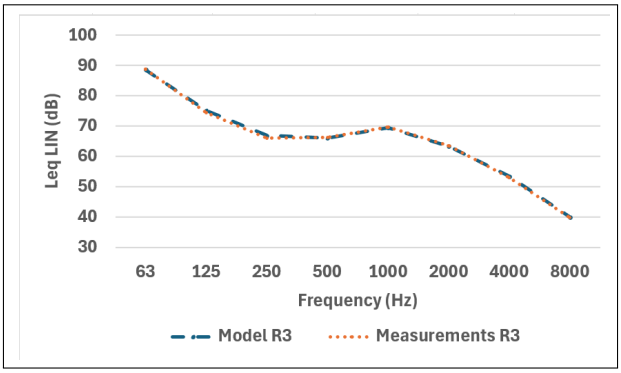


Figure 5. Spectra of measured and simulated levels in the southern side (Receiver R3).

During this project, we faced certain limitations, including a lack of access to the stadium or its construction plans, which restricted our ability to study sound propagation inside and near façade openings where sound leaks. The modeling was performed using surface sources with three validation receivers placed at different heights.

3. RESULTS

To assess compliance with noise regulations during the concert, land use in this area must be considered. Most of the study area is considered residential by the Madrid City Council, except for the area where the stadium is located, which is considered recreational and has its own limits. Fig. 1 shows the purple area, which is the recreational zone, and the red area, which is the residential zone. Since 1997, the stadium's surroundings have been declared an environmental protection area by the Madrid City Council, meaning that the limits should be restricted to 5 dB more than the rest of the acoustic areas [4]. This indicates that it is a noise-sensitive area owing to the amount of activities currently taking place and is considered a noise-saturated area.

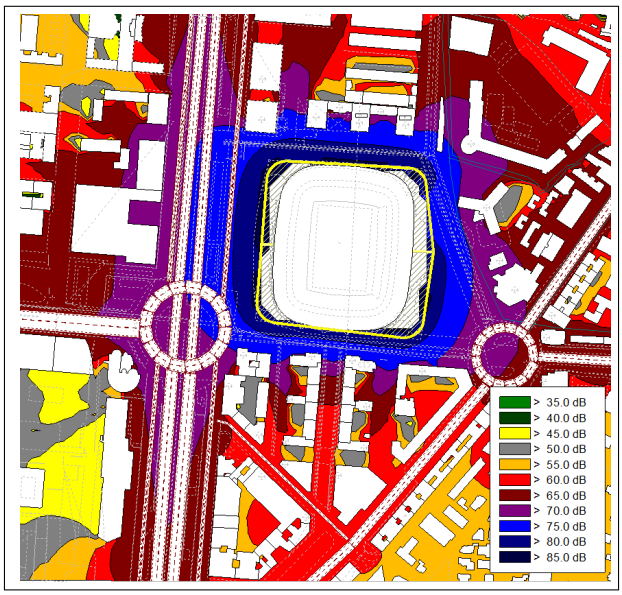


Figure 6. Global horizontal noise map of the area, including traffic and concert noise at 21 m height.

After simulating the noise map of the area shown in Fig. 6 shows how the problem impacts the whole neighborhood, not just the ones closest to the source, putting everyone at risk. Noise limits are exceeded in residential areas, at least within a 500-meter radius of the stadium center in the evening, and at night, they are exceeded at distances greater than 1 km. The "front line" buildings surrounding the stadium are receiving more than 70 dBA or 75 dBA, as seen in purple and blue on the map in Fig. 7. The area shown in red has noise levels higher than 60

dBA, which is the majority of the area whose levels exceed the legal limits established by law.

The simulated value is $L_{Aeq,5s}$, but we must consider 6 dB extra, owing to tonal and low-frequency components (there were no impulsivity components) in accordance with Article 15 of the Madrid ordinance [1], for the evaluation of $L_{Aeq,5s}$, which becomes $L_{Keq,5s}$. This can be observed in Tab. 2, as well as the extent to which the noise levels were exceeded at the receiver points compared with the limits in the evening and at night, when the concert took place. As can be observed, none of the points complies with regulations.It is worth mentioning that the current legislation establishes maximum noise emission limits because it is scientifically proven that exceeding these levels directly affects the health of people exposed to these noises.

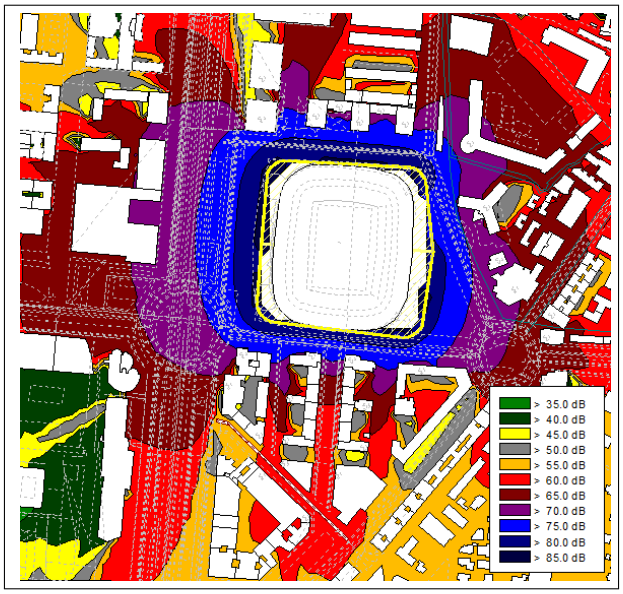


Figure 7. Horizontal noise map: ONLY concert noise at 21 m height.

In addition to modeling the concert, a simulation was conducted only in the area on concert days, considering the traffic of nearby streets. The streets surrounding the stadium, Rafael Salgado and Padre Damian Streets, and Concha Espina Avenue are not simulated, as traffic suffers a cut off during concerts. However, large avenues, such as Paseo de la Castellana, have constant traffic that contributes to global noise levels. As mentioned previously, we simulated roads in the area setting in Cadna A,

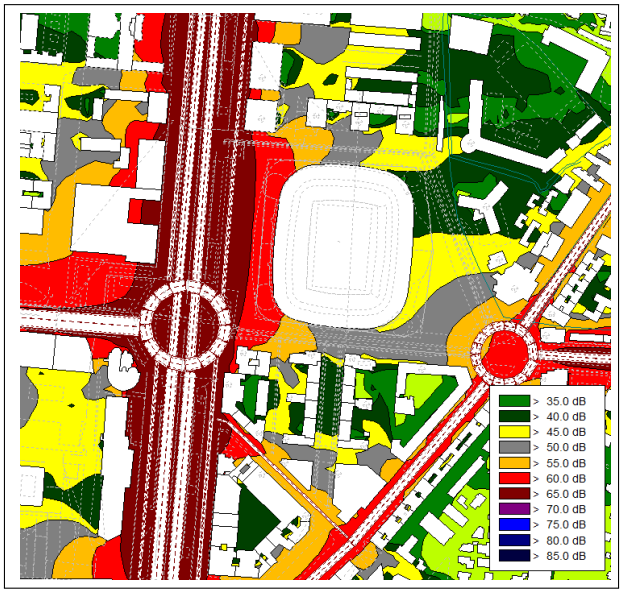


Figure 8. Horizontal noise map: ONLY traffic noise at 21 m height.

each with its traffic limit and MDTD capacity, to obtain the sound levels produced by them. As a result, we observed that Fig. 7 and Fig. 8, where we can clearly see a difference in the noise levels in the area.

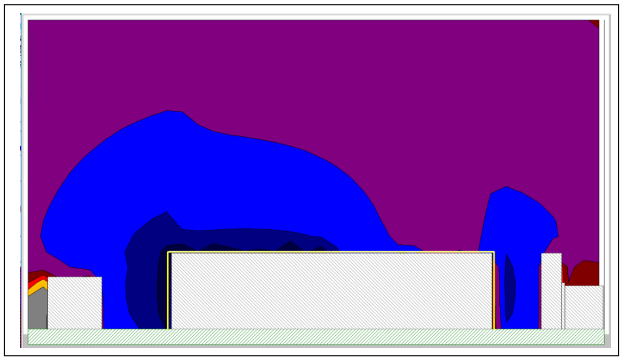


Figure 9. Vertical noise map during the concert.

In Fig. 7 we can observe how the front row of buildings functions as a barrier, reducing the noise observed in the vertical noise map in Fig. 9, which is a longitudinal cut along the z-axis perpendicular to the floor that crosses the stadium from North to South. Noise propagation from the middle of the stadium is shown in the middle of Fig. 9, towards the residential buildings located North and South

Table 2. Comparison of measured levels with legally authorized limits and the degree to which they were exceeded, both in the evening and at night.

Receiver	Measurements L_{KAeq} (dBA)	Limits Evening/Night (dBA)	Exceedance (Evening, dBA)	Exceedance (Night, dBA)	Compliant?
R1	80 + 6 = 86	55 / 45	31	41	No
R2	77,6 + 6 = 84	55 / 45	29	39	No
R3	72,3 + 6 = 78	55 / 45	23	33	No

(right and left sides of the figure). In Fig. 9 we observe that most of the acoustic energy is radiated by the vertical façades and roof of the stadium.

Although we do not know the exact speaker configuration at the concert, we do know that the stage was located near the southern side, facing North. Hence, northern sound sources are more powerful than southern ones. Furthermore, the "front line" buildings act as acoustic barriers for more distant buildings, as shown in Fig. 9 we can see the gray area behind the building on the right, showing lower noise levels. However, horizontal maps have shown that noise from the stadium spreads through the streets perpendicular to the stadium, affecting most of the neighborhood.

In Fig. 8, just modeling with traffic noise, there are many more green areas, indicating noise levels of approximately 35 dBA; however, we can also observe yellow, gray, and orange areas, indicating meaningful noise levels between 45 dBA and 55 dBA. Tab. 3 shows a comparison of the sound levels reaching receivers R1, R2, and R3, modeling concert, and traffic, separately. With no concert, the receivers do not exceed the limits, whereas when simulating a concert, traffic noise barely affects the level received by the receivers.

Table 3. Comparison of traffic noise and concert sound pressure levels, L_{Aeq} dBA, during the concert by the prediction software.

	R1 L_{Aeq} dBA	R2 L_{Aeq} dBA	R3 L_{Aeq} dBA
Concert	78,2	77,5	72,4
Traffic	52,8	45,3	43,1

4. NOISE MITIGATION PROPOSAL

Looking at Fig. 4 and Fig. 5, we can observe that the problem is focused on low frequencies. The 63 Hz and 125 Hz bands have the highest levels, whereas the 8 kHz band has the lowest levels. Low-frequency noise causes vibrations that can cause discomfort among neighbors, thereby increasing their perception of noise (window vibrations).

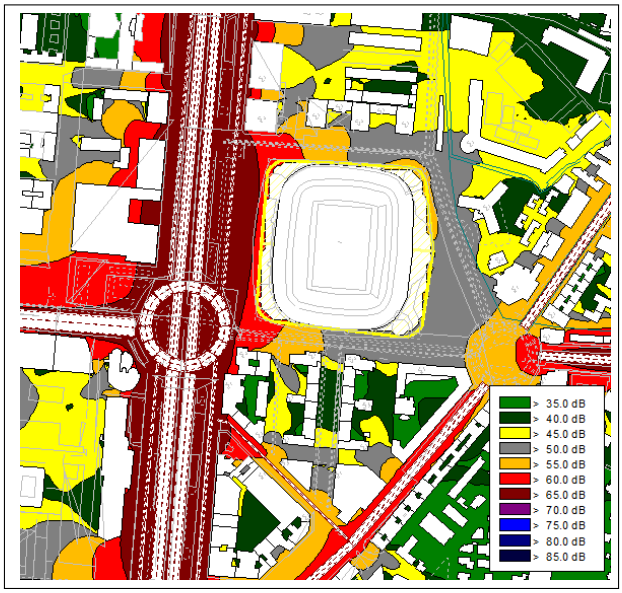


Figure 10. Noise map including corrective measures on the façades of the stadium and roof at 21 m height.

To lower the sound level of the show was first considered. In another concert (Aventura), after months of complaints from neighbors about noise, a test was conducted during the event. It was found that this could not solve the problem; it only frustrated the attendees, who claimed that "they could not hear the music properly." Therefore, it is necessary to provide solutions that reduce the noise

Table 4. Levels at the receivers after the proposed mitigation solutions and its compliance in the evening and at night.

	L_{Aeq} dBA	Evening Compliance	Night Compliance
R1	54,6	Yes	No
R2	51,8	Yes	No
R3	45,8	Yes	No

level approximately by about 30-40 dBA. After modeling several mitigation options, Fig. 10 shows the results of the simulation of an adequate solution. By acting homogeneously on the façades of the stadium, we obtained a decrease of 30 dBA, setting-up 30 dB transmission losses on the vertical surface sources. The same procedure was used on the roof, but the sound power was lowered 10 dB, setting-up 10 dB transmission losses on the horizontal surface sources.

In Tab. 4, the levels obtained at the receivers after applying the aforementioned modifications can be observed. As shown, these levels manage to comply with legal limits in the evening; however, at night, they are still noncompliant. Since it may be difficult to further increase façades' attenuation to comply with the more restrictive nighttime limits, we suggest considering modifying the schedule of the next stadium concerts that will take place during the evening hours.

5. CONCLUSION

In short, the noise levels generated by concerts in the stadium exceed what is permitted and healthy, and it is not a situation that can be sustained. A series of on-site measurements were taken at Karol G's concert, allowing for the creation and validation of a model in which the measurements and predictions match. Noise limits are exceeded in residential areas, at within a 500-meter radius of the stadium center in the evening and even more at night. As a problem that affects both the well-being and the inconvenience in the daily lives of the residents of the area, an improvement in the insulation of façades of the stadium by approximately 30 dB and the consideration of a new concert schedule are proposed to avoid exceeding these levels. This model can be used to directly incorporate the attenuation values obtained from façades and immediately obtain the expected emission values from nearby homes.

We encountered several limitations in accessing detailed information on the stadium's structure, which would be interesting to have more in order to create a simulation that better fits the existing openings and façade, as well as the sound insulation characteristics of the roof. It would also be useful to obtain the information necessary to simulate the transmission of the electroacoustic system during a concert, to consider the diffraction of linear arrays, and to gain a better understanding of how sound is transmitted from the inside of the stadium to the outdoor environment.

6. REFERENCES

[1] Ayuntamiento de Madrid, "Ordenanza de protección contra la contaminación acústica y térmica," 2011.

[2] "El Santiago Bernabéu cumple 77 años," *Real Madrid*, Dec 2024.

[3] B. F. Sebastián, "El breve paso de los conciertos por el nuevo Santiago Bernabéu: Los artistas que se quedan en 'fuera de juego'," *elconfidencial.com*, Sep 2024.

[4] Ayuntamiento de Madrid, "Zonas ambientalmente protegidas. Distrito de Chamartín: Acuerdo del Pleno de 25 de abril de 1997," 1997.

[5] M. Christner, J. Schaal, D. Zollitsch, E. Shabalina, and D. Belcher, "Far-field noise prediction for open-air events. part 1: Background and propagation models," in *Audio Engineering Society Convention 142*, Audio Engineering Society, 2017.

[6] T. G. Stefan Feistel, Janosch Blaul and A. Nicht, "Sound inmission modeling of open-air sound systems," *AES Convention Paper*, 2024.

[7] J. L. Sánchez Ayuso and J. García Ruiz, "Acoustic problems in the new Atlético de Madrid Club Stadium: A change for the worse," in *INTER-NOISE and NOISE-CON Congress and Conference Proceedings*, vol. 259, pp. 7581–7591, Institute of Noise Control Engineering, 2019.

[8] M. de la Presidencia BOE núm. 254, "Real Decreto 1367/2007, de 19 de octubre, por el que se desarrolla la Ley 37/2003, de 17 de noviembre, del ruido, en lo referente a zonificación acústica, objetivos de calidad y emisiones acústicas," 2007.

[9] International Electrotechnical Commission, "Electroacoustics – Sound level meters – Part 1: Specifications," *International Standard*, no. IEC 61672-1:2002, 2002.

[10] International Electrotechnical Commission, "Electroacoustics – Sound calibrators," *International Standard*, no. IEC 60942.

[11] Ministerio de Industria, Comercio y Turismo, "Orden ICT/155/2020, de 7 de febrero, por la que se regula el control metrológico del Estado de determinados instrumentos de medida," 2020.

[12] A.-L. F. Kephalopoulos S, Paviotti M, "Common noise assessment methods in Europe (cnossos-eu)," *Publications Office of the European Union*, 2012.

DOI: 10.61782/fa.2025.0215

FORUM ACUSTICUM EURONOISE 2025

COMPARATIVE ANALYSIS BETWEEN CNOSSOS-EU AND INTERIM METHODS

Miguel Ausejo Prieto[1*] **Rubén García Morales**[1] **Ignacio Soto Molina**[2,3]

[1] Eurocontrol, S.A. Grupo APAVE, Spain.
[2] Ministerio para la Transición Ecológica y el Reto Demográfico (SGPC-MITECO), Spain.
[3]Centro de Investigación del Transporte, TRANSyT, Universidad Politécnica de Madrid, Spain

ABSTRACT

According to Order PCI/1319/2018, Spain has replaced the interim calculation methods with a common calculation methodology developed by the European Commission through the project "Common noise assessment methods in Europe (CNOSSOS-EU)".

The establishment of the common European calculation method CNOSSOS-EU in noise mapping projects implies the replacement of the previously used calculation methodologies (interim methods) for this new methodology.

It is therefore necessary to compare these calculation methods, in order to evaluate the traceability of the Strategic Noise Maps of different rounds, assess the real effectiveness of the Noise Action Plans and compare simulations carried out using different methodologies.

This paper presents a comparative analysis of the interim calculation methods and the CNOSSOS-EU calculation method. For this purpose, 45 different scenarios were analysed in pairs using both calculation methods, with more than 12 variables studied, for road, railway and industrial noise.

Pairs of sound power level data (when comparable) and mainly pairs of LAeq levels were compared, resulting in more than 1,800 pairs of data analysed.

Keywords: *environmental noise, noise mapping, CNOSSOS-EU, interim methods, comparative study.*

[*]***Corresponding author***: mausejo@eurocontrol.es
Copyright: *©2025 M. Ausejo et al. This is an open-access article distributed under the terms of the Creative Commons Attribution 3.0 Unported License, which permits unrestricted use, distribution, and reproduction in any medium, provided the original author and source are credited.*

1. INTRODUCTION

According to Directive 2002/49/EC of the European Parliament and of the Council of 25 June 2002, the use of common assessment methods was recommended across all Member States of the European Union. This Directive was transposed into national legislation through Royal Decree 1513/2005 of 16 December, which implements Law 37/2003 of 17 November on Noise, specifically regarding acoustic zoning, quality objectives, and noise emissions.

The common assessment methods outlined in the aforementioned legislation—known as interim calculation methods—include the following, depending on the noise source:

- The French national calculation method, NMPB – Routes – 96 (SETRA-CERTU-LCPC-CSTB), designated as the reference method for road traffic noise.
- The Dutch national calculation method SRM II (Reken- en Meetvoorschrift Railverkeerslawaai'96), designated as the reference method for railway traffic noise.
- The ISO 9613-2 method, designated as the reference method for industrial noise.
- The ECAC.CEAC Doc. 29 method, designated as the reference method for aircraft noise.

In 2008, the European Commission initiated the development of a unified methodological framework for noise assessment through the project Common Noise Assessment Methods in Europe (CNOSSOS-EU), led by the Joint Research Centre (JRC), the scientific service of the European Commission.

As a result of this initiative, Commission Directive (EU) 2015/996 was adopted, establishing common noise assessment methods pursuant to Directive 2002/49/EC.

This Directive replaced Annex II of Directive 2002/49/EC with the updated methodology and was required to be transposed into the legal frameworks of Member States by no later than 31 December 2018.

Spain transposed Directive (EU) 2015/996 through Order PCI/1319/2018 of 7 December, amending Annex II of Royal Decree 1513/2005 of 16 December, which implements Law 37/2003 of 17 November on Noise, in relation to the assessment of environmental noise.

Under this regulation, the previous calculation methods for noise indices were replaced by a unified calculation methodology developed by the European Commission through the CNOSSOS-EU project. The use of this methodology has been mandatory for all Member States since 31 December 2018.

Subsequently, the European Commission conducted a revision of this common calculation methodology, addressing several aspects including new formulations for diffraction in sound propagation and approaches for evaluating population exposure to noise on building façades. These updates were incorporated into Annex II of the Environmental Noise Directive via Commission Delegated Directive (EU) 2021/1226 of 21 December 2020, which amended Directive 2002/49/EC to align with scientific and technical progress. This Directive was transposed into national law through Order PCM/80/2022 of 7 February, which amends Annex II of Royal Decree 1513/2005 of 16 December, concerning the assessment and management of environmental noise.

The establishment of the European CNOSSOS-EU common calculation method for noise mapping tasks marks the replacement of previously used interim methods for this new standardized methodology. Consequently, a comparative analysis between the interim calculation methods and the CNOSSOS-EU method is presented in this study through a comprehensive examination of 45 noise scenarios.

By identifying systematic variations in noise predictions, we seek to provide insights into how the methodological shift affects environmental noise assessments and regulatory compliance.

2. METHODOLOGY

To conduct a robust comparative analysis, a set of 45 noise scenarios was designed, divided into road traffic (17 scenarios), railway (12 scenarios), and industrial noise sources (16 scenarios). Each scenario was modeled using both CNOSSOS-EU and interim models, keeping environmental, topographical, and source parameters consistent with receptor grids placed at varying distances and heights to capture sound propagation effects under different environmental conditions.

2.1 Road Traffic Noise

Several hypotheses have been proposed to assess how sound power and sound pressure levels vary based on the Average Daily Intensity, the percentage of heavy vehicles, and speed.

Different values of Average Daily Intensity were considered: high (which constitute major roadways), medium, and low (which do not constitute major roadways). For each scenario in which the traffic value was set, other variables (percentage of heavy vehicles, speeds, etc.) were varied to assess the variation in both methods.

The percentage distribution of heavy vehicles, as well as the speed, has been varied for probable scenarios and to determine actual ranges of comparable cases.

Free field, urban settings and noise barriers have been included to assess the effects of diffraction and obstacles.

The study considers different road types, traffic compositions, and surface materials. Key parameters analyzed include:

- Traffic volume (light and heavy vehicles).
- Vehicle speeds (urban vs. highway conditions).
- Pavement type (reflective vs. absorbent materials).

2.2 Railway Noise

As in the case of road noise, for railway noise, a series of variables have been established and others varied for each case study to assess their effect on both methods.

The most critical aspect was determining similar rolling stock, as both methods differ significantly in the definition of noise sources and the track parameters considered in each.

Different types of trains have been considered, analyzing not only the sound pressure levels of the receivers, but also evaluating the vertical meshes to compare the different radiation of the source and the propagation between methods.

Noise emissions from railway operations depend on train characteristics and track conditions. The study accounts for:

- Train types (high-speed, freight, regional).
- Track configurations (ballast, slab track).
- Speed variations and train frequency.
- Barrier effects and terrain interactions.

2.3 Industrial Noise

In order to compare methods for industrial noise sources, point, linear, and surface sources were analyzed. Setting the same sound power level (Lw) for each method enabled comparability between methods.

Particular attention was paid to analyzing vertical and horizontal diffraction, for which urban environments with more complex obstacles were modeled to analyze differences in propagation.

Key factors evaluated are:

- Source height and spatial distribution of noise emissions.
- Influence of obstacles (buildings).
- Ground absorption and terrain effects.

2.4 Ground absorption

Finally, different noise sources were analyzed comparing ground absorption (absorbent ground and reflective ground) as a variable.

Results were statistically analyzed to quantify differences in power level estimations and equivalent continuous sound levels (LAeq), as shown in **Table 1.**

Table 1. Summary table of all the cases considered and the pairs of data analyzed.

		Power Data Pairs	Pressure Data Pairs	# Cases
Road Traffic	Free field	18	288	6
	Agglomerations	6	96	4
	Noise barriers	0	96	2
Railway Traffic	Free field	21	336	7
	Agglomerations	12	96	4
	Noise barriers	0	96	2
Industrial Noise	Free field	0	192	4
	Agglomerations	0	144	6
	Noise barriers	0	192	4
Ground Absorption	Various	0	288	6
		57	**1824**	**45**

3. RESULTS AND DISCUSSION

3.1 Road Traffic Noise

3.1.1 Percentage of Heavy Vehicles:

Variation of the percentage of heavy vehicles has a more pronounced effect on the sound power level in the interim method (NMPB – Routes – 96) compared to CNOSSOS-EU.

3.1.2 Vehicle Speed:

Speed variations impact the sound power level more significantly in the CNOSSOS-EU method.

3.1.3 Receiver Height and Distance:

The greatest differences in sound pressure levels are observed at lower heights and distances beyond 25 m from the source, with the interim method producing levels typically over 5 dB(A) higher.

3.1.4 Obstacles (Buildings and Barriers):

Obstacles reduce discrepancies at low heights and shielded positions, though the interim method still results in higher levels.

Summary: Overall, the interim method produces higher road traffic noise levels under the studied variables and conditions.

3.2 Railway Traffic Noise

3.2.1 High-Speed Trains:

The interim method (SRM II) delivers higher sound pressure levels than CNOSSOS-EU, with differences ranging from 4 to over 6 dB(A).

3.2.2 Other Train Types:

For medium-distance, suburban, and freight trains, CNOSSOS-EU estimates levels between 0.1 and 3.5 dB(A) higher than the interim method.

3.2.3 Vertical Propagation:

CNOSSOS-EU shows notable differences in vertical propagation due to its inclusion of directivity effects.

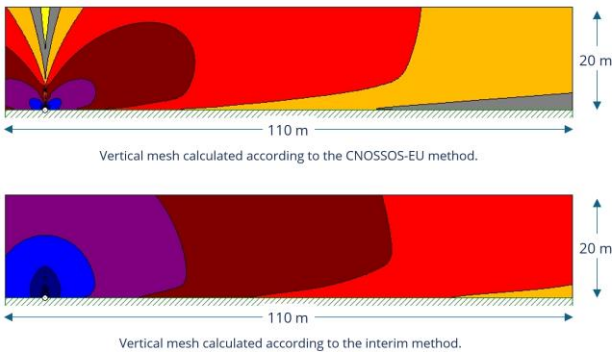


Figure 1. Comparison of vertical propagation for different methods for railway traffic noise.

3.2.4 Obstacles:

The presence of buildings or barriers reduces differences at shielded receivers, although variations persist.

Summary: Generally, the interim method produces higher values. However, direct comparisons are complex due to differing input data and modeling formulations.

3.3 Industrial Noise

3.3.1 Point, Line, and Vertical Surface Sources:

Sound pressure levels estimated using the interim method (ISO 9613-2) are consistently about 1 dB(A) higher across different distances and heights.

3.3.2 Surface Sources:

The interim method again produces higher levels, particularly at low heights and long distances, with differences exceeding 3.5 dB(A).

3.3.3 Noise Barriers:

In shielded scenarios, the interim method estimates sound pressure levels 4–5 dB(A) higher than CNOSSOS-EU.

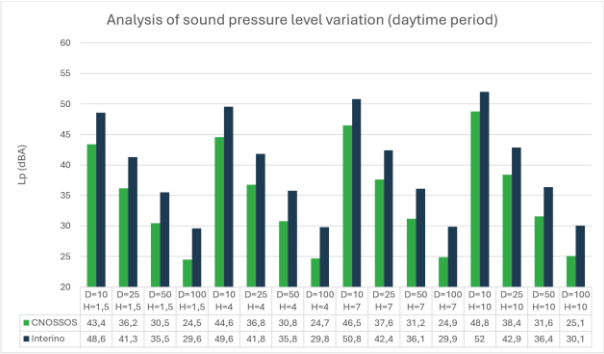


Figure 2. Comparative analysis of sound pressure levels for a point source of industrial noise with an acoustic barrier (*CNOSSOS-EU in green and interim in blue*).

3.3.4 Obstacles and Diffraction:

Without Lateral Diffraction: CNOSSOS-EU predicts higher levels (~6 dB(A)) at shielded positions.

With Lateral Diffraction: The interim method shows higher levels (~5 dB(A)).

With Combined Vertical and Horizontal Diffraction: The interim method estimates levels ~7.5 dB(A) higher.

3.3.5 Vertical Propagation Differences:

CNOSSOS-EU introduces a vertical propagation component for point sources, absent in the interim method.

Summary: Variability in results for industrial noise prevents broad generalization. Nevertheless, significant discrepancies exist, especially in complex propagation scenarios involving multiple obstacles.

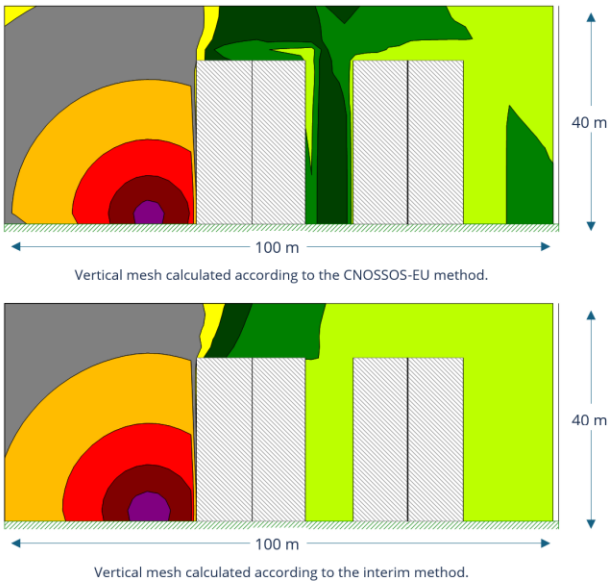


Figure 3. Comparison of the diffraction effect for both methods with industrial noise sources**.**

3.4 Ground Absorption

CNOSSOS-EU is more sensitive to ground absorption variations, leading to greater differences in sound pressure levels. With reflective ground, propagation differences between methods are reduced.

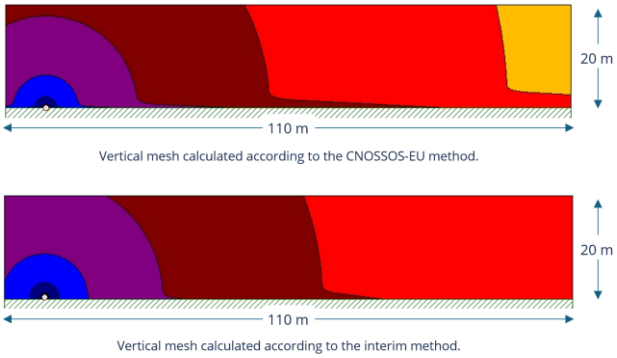


Figure 4. Comparison of methods for road traffic noise in reflective terrain.

4. CONCLUSIONS

This study highlights systematic differences between the CNOSSOS-EU and Interim methods for environmental noise assessment. The main findings are:

- Comparison between methods is not immediate and can be complex since, in addition to differences in the input parameters, the output variables of the parametric equations can also yield different indicators.
- Road traffic noise and industrial noise are more easily comparable, as the power level indices are comparable.
- The comparison is especially sensitive when it is made between railway noise indicators, as there are significant methodological differences between the two methods.
- The Interim method generally predicts higher LAeq values, particularly in road traffic and railway noise scenarios. These differences can be up to 5 dBA.
- The sound pressure level using the interim method may, in general terms, be higher than that used by CNOSSOS for railway noise from high-speed trains. However, for medium-distance trains and freight trains, the opposite may be true.
- Vertical propagation for rail traffic noise is very different between methods.
- Regarding industrial noise, there is large variability when comparing methods. Significant differences are found when comparing scenarios with many obstacles and vertical and horizontal diffraction.
- The transition to CNOSSOS-EU may affect regulatory compliance and noise action plans, requiring careful evaluation of historical and future noise maps.
- The change in ground absorption has a greater impact on the sound pressure levels predicted using the CNOSSOS-EU method. With reflective ground, there is less difference in propagation between the two methods.
- Further research is needed to assess the impact of these differences on long-term noise exposure assessments and public health policies.

This analysis was focused on direct comparisons of comparable pressure levels and power levels across methods; it did not analyze population allocation methodologies or noise-exposed population calculations, which could be the subject of future research.

5. ACKNOWLEDGMENTS

This research was developed within a project funded by the Center for Studies and Experimentation of Public Works (CEDEX) and the Spanish Ministry for Ecological Transition and the Demographic Challenge.

The authors would like to thank ADIF (Spanish railway infrastructure manager) for the consultations carried out to correctly characterize and compare rolling stock across methods.

6. REFERENCES

[1] ADIF, 2022. *Guía para la aplicación del método CNOSSOS-EU en la modelización del ruido producido por las circulaciones ferroviarias en las infraestructuras de ADIF y ADIF AV*.

[2] Ausejo, M.; Simón, L.; García, R.; Sánchez, D. *Estudio de sensibilidad de los datos de distribución de categorías de tráfico en el método CNOSSOS-EU.* Tecniacústica 2022, Elche, España.

[3] Ausejo, M; García, R.; Vas, D.; Rojas, R. M.; Simón, L. *Influencia de la resolución del terreno en simulaciones acústicas con pantallas de ruido.* Tecniacústica 2024, Faro, Portugal.

[4] CEDEX: Servicio de Publicaciones. (2025). Guía técnica para la aplicación del método común europeo de evaluación del ruido ambiental (CNOSSOS-EU) en los estudios de ruido en España. R-25 (Soto-Molina, I., Ausejo Prieto, M., García Morales, R., Simón Otegui, L., González García, M. Á., Soriano Pastor, C., Cachón de Mesa, J., & Querol Herrá, R., Autores). Centro de Publicaciones, Secretaría General Técnica, Ministerio de Transportes y Movilidad Sostenible. ISBN: 978-84-7790-675-9.

[5] CIRCABC (Communication and Information Resource Centre for Administrations, Businesses and Citizens) de la Comisión Europea. Appendix 10: Guide for Mapping Existing National Road Methods to the CNOSSOS-EU Road Source Method.

[6] CIRCABC (Communication and Information Resource Centre for Administrations, Businesses and Citizens) de la Comisión Europea. Develop and Implement Harmonised Noise Assessment Methods. Process Applied to Establish CNOSSOS-EU/National Method Equivalence for Road Source data.

[7] EPA Research. Report No. 382. Transitioning to Strategic Noise Mapping under CNOSSOS-EU (Noise Adapt).

[8] European Commission Working Group Assessment of Exposure to Noise (WG-AEN). Good Practice Guide for Strategic Noise Mapping and the Production of Associated Data on Noise Exposure.

[9] European Commission, "CNOSSOS-EU: Common Noise Assessment Methods in Europe," Technical Report, 2018.

[10] J. Doe and A. Smith, "Comparative analysis of noise models," Journal of Environmental Acoustics, vol. 15, no. 3, pp. 200-215, 2019.

[11] Kephalopoulos, S., Paviotti, M., & Anfosso-Lédée, F. (2012). Common noise assessment methods in Europe (CNOSSOS-EU), 180-p.

[12] Kephalopoulos, S., Paviotti, M., Anfosso-Lédée, F., Van Maercke, D., Shilton, S., & Jones, N. (2014). Advances in the development of common noise assessment methods in Europe: The CNOSSOS-EU framework for strategic environmental noise mapping. Science of the Total Environment, 482, 400-410.

[13] MITERD-CEDEX. Guía básica de recomendaciones para la aplicación de los métodos comunes de evaluación del ruido en Europa (CNOSSOS-EU). Recomendaciones para su aplicación a la evaluación del ruido de fuentes industriales, carreteras, ferrocarriles y aglomeraciones. 2022.

[14] S. Shilton, N. Jones, A. Stimac, and M. Ausejo. Improving consistency through quality control with a large strategic noise mapping project. Internoise 2013. Innsbruck, Austria.

[15] Sakamoto, S. (2020). Road traffic noise prediction model “ASJ RTN-Model 2018": Report of the Research Committee on Road Traffic Noise. Acoustical Science and Technology, 41(3), 529-589.

[16] Soto-Molina, I., Ausejo Prieto, M., & Arce Ruiz, R. M. (2025). Enhancing noise assessment accuracy: FEM as an advanced complement to CNOSSOS-EU. Noise & Vibration Worldwide, 09574565251319271.

DOI: 10.61782/fa.2025.0600

FORUM ACUSTICUM EURONOISE 2025

NEED OF A NATIONAL NOISE STRATEGY IN SPAIN ANDAPPROACH TO DEVELOP IT.

Miguel Ángel González García[1*] **Ignacio Soto Molina**[1]
Carlos Soriano Pastor[1]
[1] Ministerio para la Transición Ecológica y el Reto Demográfico, España

ABSTRACT

The last decade made us awareness of the importance of environmental noise as cause of disease and life quality loss for the population. Since the entry into force of END and Spanish legislation on noise progress has been made, especially in noise evaluation, even with difficulties. Nevertheless, reaching objectives of noise reduction nowadays on the table (ZPAP) seems a difficult goal.

To afford this challenge it is needed a correct overview of noise problems at a macro scale and a strategic approach of what the causes are and the possible ways to work to solve it effectively. This work reviews why this strategical vision is needed, what are the works in course for developing it and which could be, at the State level, the main axes that guide the action of the different administrations to address environmental noise.

Keywords: *Environmental noise,Public health,Noise management,Strategic approach,National noise strategy*



[*] ***Corresponding author***: maggarcia@miteco.es
Copyright: *©2025 González García, M. et al. This is an open-access article distributed under the terms of the Creative Commons Attribution 3.0 Unported License, which permits unrestricted use, distribution, and reproduction in any medium, provided the original author and source are credited.*

1. INTRODUCTION

The impact of noise on health is a key concern for several international bodies. The World Health Organization (WHO) has published guidelines recommending safe noise levels to protect public health, as noise exposure has been linked to sleep disturbances, cardiovascular diseases, and other health problems. Additionally, global institutions like the World Bank and the United Nations Environment Programme (UNEP) have incorporated noise pollution into their sustainable development agendas.

Within the framework of the United Nations Sustainable Development Goals (SDGs), noise pollution is directly related to SDG 3 (Good Health and Well-being) and SDG 11 (Sustainable Cities and Communities). Reducing noise not only minimizes non-communicable diseases but also enhances the overall quality of urban life by creating healthier, more livable environments.

At the European level, Directive 2002/49/EC plays a central role by establishing a common framework for the evaluation and management of environmental noise. This directive requires member states to develop strategic noise maps for urban areas, major transport infrastructures, and densely populated regions, along with comprehensive action plans aimed at reducing noise levels.

In addition to the Directive, the European Green Deal and its Zero Pollution Action Plan integrate noise management into broader sustainability strategies. These initiatives aim to transition the EU towards a sustainable, climate-neutral economy, with noise reduction being a key element in improving both environmental quality and public health.

The European Environment Agency (EEA) plays a pivotal role in tracking and assessing noise pollution across Europe. The report, “Environmental Noise in Europe —

2020," illustrates that noise exposure remains a significant issue, affecting millions of people.

Despite the importance of the problem, we are far from achieving a sound environment aligned with what, according to science, would be adequate for citizens. Some challenges for more progress on this path are:

- A complete picture of the problem is lacking. Based on the best possible technical approach, it would shed light on the true severity of this form of pollution. This work can help administrations and the public better understand the significance of noise pollution for the country's society and economy.
- Despite the existence of long-standing regulations, their application is not always efficient or easy, and there is a significant gap in their implementation.
- This form of pollution has generally been considered a local problem, to be addressed locally. However, this has not led to an improvement in the situation and does not always help address the issue in a coherent and appropriate manner.
- Many times there are no comprehensive policies that are sustained over time.

2. WHY IS A NOISE STRATEGY NECESSARY IN SPAIN?

In Spain, a noise strategy is needed, as the current approach to assessing noise pollution only provides a partial view of its impact on both citizens' quality of life and terrestrial habitats. While strategic noise maps are developed for urban areas with more than 100,000 inhabitants and significant noise sources—such as busy roads, railways, and airports, as defined by the Environmental Noise Directive—this methodology leaves many areas and sources unexamined. For example, while higher noise levels (Lden > 70) are reasonably well represented in current noise maps, initial estimates indicate that, at medium noise levels (Lden 55-70), approximately 50% of the exposed population is not adequately studied. This significant data gap underscores the limitations of the existing framework.

Spain's National Information System on Noise Pollution (SICA) currently only reports data from a limited number of urban agglomerations and infrastructure, including 64 large cities, 21,000 km of main roads, 1,800 km of major railways, and 13 major airports. Consequently, numerous small municipalities and diverse noise sources—from industrial activities, wind farms, and port facilities to local disturbances from leisure activities, neighborhood events, urban services, and construction noise—remain unassessed. This narrow focus means that a large segment of the population and numerous sensitive receptors in the natural environment are not considered in current assessments.

The Environmental Noise Directive's approach, which determines study areas based on noise sources rather than the distribution of affected receptors, results in many affected communities and natural habitats being overlooked. While the European Environment Agency has made efforts to use statistical methods to fill the gaps, these methods can be significantly biased due to a lack of comprehensive data and do not yet identify all areas requiring corrective action.

For these reasons, the Ministry for the Ecological Transition and the Demographic Challenge (MITECO) emphasizes the urgent need for a comprehensive noise strategy. A comprehensive assessment of noise pollution is essential to clearly understand the various problems, analyze the potential impacts on public health and natural environments, and develop synoptic documents that facilitate access to this information for monitoring and evaluating the effectiveness of policies. MITECO is developing global noise models for key sources, especially road traffic, which has the greatest impact on environmental acoustic quality, in addition to promoting assessment methodologies for other noise sources. This strategy would ensure the identification and addressing of all affected areas, thus protecting both the health of the population and the integrity of natural habitats.

3. STRATEGY OBJECTIVES

The National Noise Strategy aims to serve as a benchmark document that not only meets the regulatory requirements set by the European Union but also identifies national priorities and establishes effective measurement indicators to assess progress. This strategy is designed to guide specific policies for mitigating noise across various economic sectors and social environments, ultimately protecting public health, preserving the acoustic quality of natural surroundings, and enhancing the overall well-being of Spanish society. In doing so, it aligns with international commitments and promotes a more livable and healthy environment for current and future generations. The objectives pursued are the following:

- Analyze the information generated, identifying the needs for action to improve current noise pollution levels and reduce its adverse effects on health and the

environment. To this end, the most appropriate tools will be used for this analysis (SWOT).

- Identify those elements with the greatest potential to improve the noise environment but that may still be less developed, such as Quiet Zones, Soundscapes, or Sound Reserves, etc.
- Identify the strategic axes and lines of work that can help gradually improve the noise environment.
- Identify the stakeholders with the greatest responsibility for improving the noise environment to increase the positive impact of the actions that this document may lead to.
- Set achievable objectives for the different strategic axes/lines and define policies and actions that will help the Competent Authorities make progress in reducing noise pollution problems.
- Assess the potential costs and impact of such policies and actions, as well as the best way to implement them.
- Establish formulas to keep the diagnosis of noise pollution in Spain up-to-date, in the simplest and easiest way possible, to evaluate trends and identify potential emerging problems in noise pollution, and to monitor the implementation of the Strategy.

Together, these objectives and guiding principles provide a robust framework for the National Noise Strategy, laying the groundwork for comprehensive actions that protect public health, sustain natural environments, and contribute to the overall quality of life in Spain.

4. METHODOLOGY FOR STRATEGY DEVELOPMENT

4.1 General Methodology

The methodology for developing the National Noise Strategy is structured around a comprehensive index that ensures a thorough analysis of all aspects of environmental noise and its impacts.

The process begins with the justification and objectives of the Strategy. This initial phase examines the nature of environmental noise, its causes, and its effects on both public health and the environment. It also identifies potential for improvement and highlights the need for a strategic approach to noise management.

The Strategy's development is then based on a review of the national, European, and international legal context for noise management. This involves analyzing previous approaches to environmental noise in Spain, examining the international and European frameworks that have influenced current practices, and considering how Spanish national, regional, and local regulations interact with broader environmental policies. This phase also explores the relationship between noise pollution and other environmental issues to identify potential synergies with existing plans and strategies.

The next step is a detailed diagnosis of the current situation. This assessment employs a multifaceted methodological approach that includes both quantitative and qualitative analyses. Quantitative methods involve the collection and processing of noise level data from various sources, the application of standardized noise modeling techniques, such as CNOSSOS-EU, and the use of Geographic Information Systems to assess noise exposure in different population segments and sensitive natural areas.

Complementary semi-quantitative and qualitative approaches help fill data gaps and provide insight into public perception, regulatory compliance, and the effectiveness of existing noise management tools.

Particular attention is paid to assessing significant noise sources—from road traffic, rail, and air transport to industrial activities, port operations, and even local events—allowing for a comprehensive evaluation of both modelable and non-modelable noise sources.

Once the current status has been diagnosed, the synthesis of the findings identifies key needs and challenges that need to be addressed.

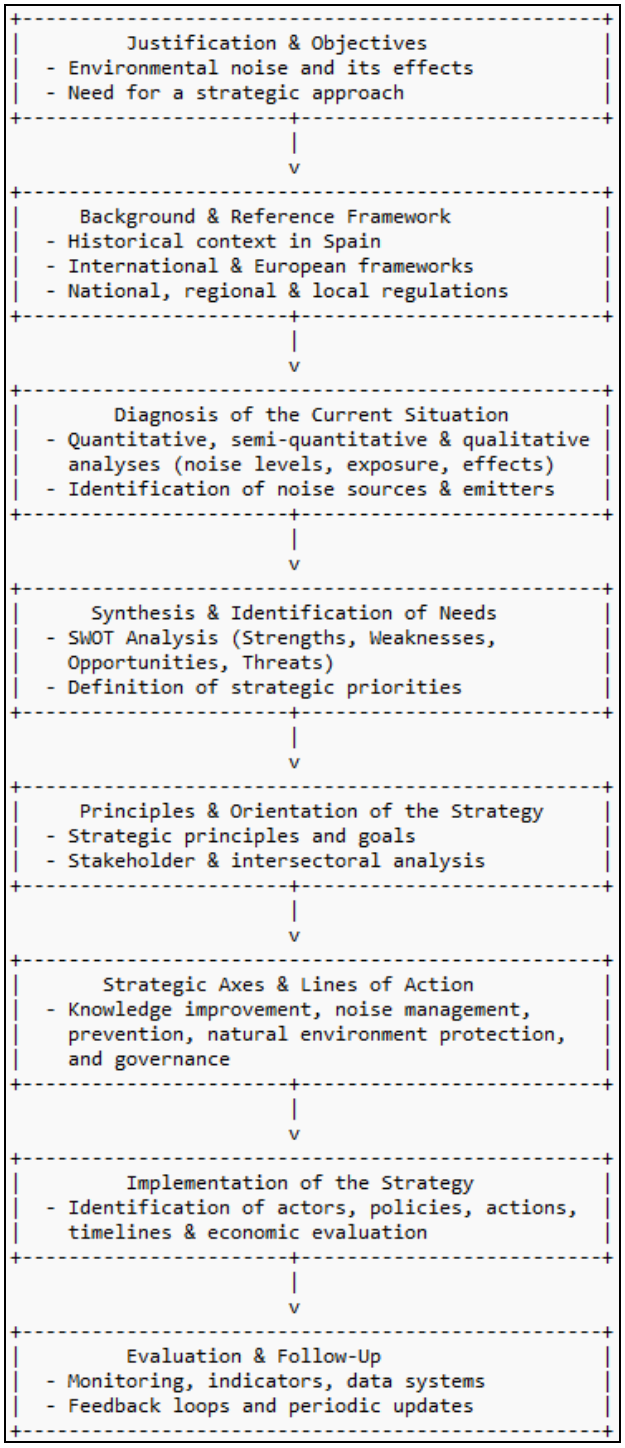


Figure 1. Methodological diagram.

This summary lays the groundwork for defining the Strategy's principles and strategic directions. It includes an analysis of the strengths, weaknesses, opportunities, and threats (SWOT analysis) related to noise management in Spain, as well as an assessment of how various sectors, such as urban planning, environmental protection, and public health, can be integrated into a coherent strategic framework.

The Strategy will define the strategic axes and lines of action. These include improving citizen knowledge and awareness, noise management in different sectors, preventing noise pollution, improving the quality of the acoustic environment, and improving intervention and regulation tools. Each strategic axis is detailed in terms of specific actions, such as capacity building, intersectoral cooperation, and the development of clear policy objectives.

The Strategy's implementation will be planned through a detailed roadmap that identifies key stakeholders, defines specific policies and actions, sets measurable objectives, and includes an economic evaluation of the proposed interventions. This stage also addresses the need for planning, programming, and periodic reviews to ensure the Strategy maintains its effectiveness over time.

Finally, the methodology incorporates an evaluation and monitoring phase. This phase is designed to periodically update the noise pollution assessment, monitor the effectiveness of the implemented measures using defined indicators, and ensure the availability of robust information systems and data sources. This continuous feedback loop is essential for adapting the Strategy to new challenges and technological advances.

Overall, the methodology for developing the National Noise Strategy is an integrated and iterative process. It combines historical analysis, rigorous data collection and modeling, strategic planning, and ongoing evaluation to create a robust framework aimed at significantly reducing noise pollution and its impacts in Spain, while ensuring the necessary participation of all involved authorities and the public through appropriate public consultations and information periods.

4.2 Considered Noise Sources in Diagnosis

To effectively analyze noise pollution within this Strategy and achieve an accurate diagnosis, it is essential to systematically identify and understand the sources responsible for this type of contamination. These noise sources vary greatly in their characteristics, and their contribution to the overall environmental problem differs significantly. Below, the characteristics of some of the most important sources are described.

Road traffic is recognized as the primary source of noise pollution in urban and suburban areas, affecting a large proportion of the population. The noise from road traffic primarily results from the contact between tires and pavement, compounded by engine noise and, to a lesser extent, the use of braking systems. Similarly, rail transport is an important contributor, particularly in urban areas. Trains—especially high-speed ones—generate noise due to the contact between wheels and tracks, as well as aerodynamic noise at high speeds. In urban contexts, the passage of trains at level crossings or in proximity to residential areas can adversely affect quality of life, and noise from freight trains can also cause significant issues in the surrounding environment.

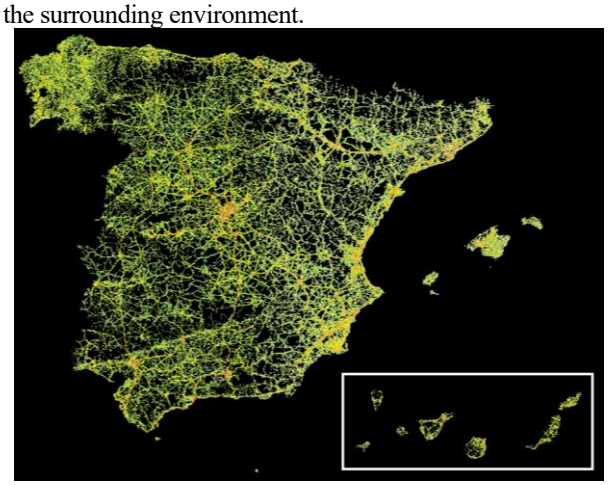


Figure 2. First version of the supra-strategic road map of Spain.

Aviation is another significant source of noise, especially near airports where takeoffs and landings create high noise levels that impact both nearby residents and sensitive natural areas. In a similar vein, maritime transport and port activities are major contributors to noise pollution, even though they are not mandated to conduct noise evaluations and action plans under the Environmental Noise Directive. Operations such as loading and unloading, the movement of heavy machinery, and the vessel traffic within ports generate substantial noise, particularly in port cities.

The industrial sector also plays a key role. Industries contribute to noise not only through manufacturing processes but also via logistics and transportation operations. Noise generated by machinery, material handling, and the movement of vehicles during loading and unloading creates significant issues in industrial areas adjacent to residential zones. Additionally, industrial noise affects rural areas where facilities such as farms, food processing plants, and other agro-industrial activities are located.

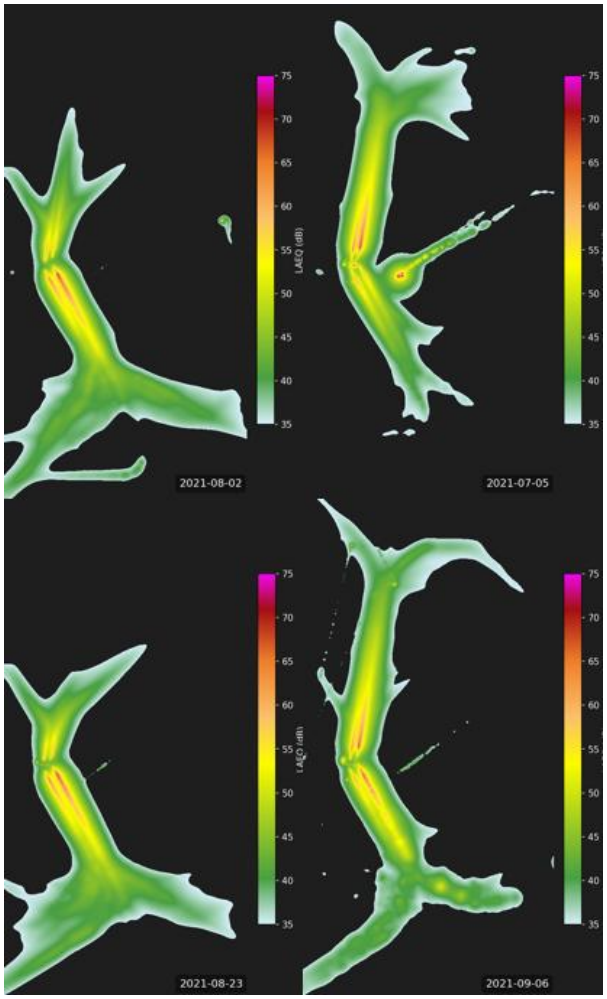


Figure 3. Noise footprints of aeronautical operations on different evaluation days.

The leisure and hospitality sector is a notable source of urban noise, especially in tourist and residential areas with a high density of bars, nightclubs, and restaurants.

Construction, though typically a temporary activity, produces significant noise impact—especially in urban areas where building and renovation projects are continuously underway. These construction activities, which may last for months or even years, can greatly affect residents' quality of life. Moreover, the construction of infrastructures such as roads or rail stations contributes to noise pollution both during the construction phase and in subsequent operational phases.

Other significant noise sources include local festivities and public events like popular celebrations, which generate temporary yet intense increases in noise levels.

Other sources, such as wind turbines—despite being a renewable and sustainable energy source—can emit significant noise in the areas where they are installed, particularly in rural and mountainous regions.

Based on the diagnosis, a framework of noise sources will be established for consideration in the National Noise Strategy. As said before, for each type of emitter, different methodological approaches will be applied to diagnose their importance and significance, depending on the available information and possible work methodologies. These approaches include a quantitative method, a semi-quantitative method, a qualitative approach at the level of territorial administrative entities, a large-scale analysis, and a normative and management analysis, along with a category for those sources not analyzed.

The quantitative approach involves evaluating the noise generated by all identifiable entities from available cartographic data. This process entails identifying the study entities, processing the available information, characterizing the necessary parameters for strategic input into noise calculation software, generating a calculation model using source data and lidar-derived digital terrain models that include building data, and calculating noise levels using base maps from the National Geographic Institute and tools like CEREMA-FR's Noise Modelling based on the CNOSSOS-EU methodology. The results from this approach will later be used to assess noise exposure and its effects.

In contrast, the semi-quantitative approach employs a mixed methodology by calculating noise levels for typical cases and extrapolating the results. This method starts with approximating the territorial distribution of each type of emitter using available cartographic products, classifying groups of similar emitters into synthetic types, and characterizing the noise each type produces. Noise calculations will then be performed for specific cases or by using available data from such cases (e.g., strategic noise maps of urban agglomerations, environmental procedures), potentially utilizing more tailored methods (such as ISO-9613), before extrapolating these analyses to the broader territory using Geographic Information Systems. The outcomes will again be used to evaluate noise exposure and its subsequent effects.

A qualitative approach will also be undertaken at the level of territorial administrative entities, analyzing the significance of each type of source based solely on statistical data and the most disaggregated local or regional data available. This analysis will be extrapolated to the entire set of territorial entities and will include an examination of existing management tools and the need for improvements. Additionally, a large-scale state-level analysis will be conducted to assess the overall importance of these noise sources and evaluate the effectiveness of current management tools, potentially supplemented by expert opinions, communications, or relevant literature.

Finally, a normative and management analysis will examine the current regulatory framework and the possible need for additional instruments, focusing on preserving acoustic quality against the noise generated by these sources. For some types, it may be possible to consider the definition of "tolerable limits" for noise pollution.

It is important to note that the list of noise sources included in this framework is not intended to be an exhaustive catalog of all possible sources of environmental noise in urban, rural, and natural areas. Instead, it aims to provide a sufficiently comprehensive approximation that covers the primary contributors to noise pollution for the current Strategy, grouping them into basic typologies that facilitate systematic analysis and diagnosis.

4.3 Main Lines of Action

To structure the National Noise Strategy in Spain and maximize the effectiveness of interventions on acoustic pollution, the main strategic axes need to be a identified, for instance trough a SWOT analysis.

These axes will serve to orient the Strategy according to both challenges and opportunities, strengthening capabilities in critical areas and improving coordination among administrations and other stakeholders.

Preliminary, with the work already done, the following lines of action can be advanced:

- Improvement of Knowledge, Dissemination, and Awareness, emphasizes the need to expand understanding of noise pollution and its impacts on health. It also focuses on training professionals in the sector and raising public awareness about the importance of this issue.
- Management of Acoustic Pollution, advocates for the effective handling of the main sources of noise. This includes addressing major transport infrastructures, industrial and urban activities, and temporary noise emitters, while also targeting interventions in urban spaces to enhance the overall sound environment.
- Prevention of Pollution and Improvement of the Acoustic Environment, is centered on preserving acoustic quality in areas with low pollution levels and preventing noise in urban settings and new constructions. This axis also encompasses efforts to

improve sound quality in urban areas and in indoor environments, such as residential buildings and workplaces.

- Noise, Biodiversity, and the Natural Environment, underlines the critical importance of preserving biodiversity and natural ecosystems as part of an integrated approach to combating acoustic pollution. It includes managing noise in rural areas, natural settings, and the marine environment to protect vulnerable species and ecosystems.
- Improvement of Management and Intervention Tools, focuses on strengthening the tools necessary for effective governance and compliance. This involves ensuring adherence to regulatory obligations, enhancing the regulatory framework, managing conflicts related to noise, and promoting cross-sector policies that foster synergies and collaboration among various administrations.

Together, these strategic axes will guide the implementation of measures in the areas of management, prevention, knowledge, and regulation of acoustic pollution. They establish a comprehensive framework that contributes to the effective reduction of noise exposure in Spain.

5. EXPECTED RESULTS AND BENEFITS OF THE STRATEGY

The expected results and benefits of the National Noise Strategy are multifaceted, touching on public health, quality of life, environmental protection, and economic gains.

By effectively reducing noise levels, the Strategy is anticipated to lead to significant improvements in public health, lowering the incidence of noise-related issues such as sleep disturbances, cardiovascular problems, and stress. This reduction in noise exposure will enhance urban livability, creating quieter, more harmonious communities that support overall well-being and productivity.

In addition to health benefits, the Strategy aims to preserve and improve the acoustic quality of both natural and urban environments. This will help protect biodiversity and ensure that natural habitats, particularly in rural, coastal, and marine areas, remain less disturbed by excessive noise.

The strengthened regulatory framework and enhanced monitoring tools resulting from the Strategy will facilitate better compliance with European directives and more efficient enforcement of noise standards, leading to a more coordinated and effective noise management system.

Economically, the Strategy is expected to yield benefits by reducing healthcare costs associated with noise-induced conditions and minimizing social costs related to stress and reduced quality of life. Moreover, improved urban planning and intersectoral coordination can lead to increased property values and a boost in tourism, while encouraging innovation in noise reduction technologies that can spur new business opportunities.

Finally, the Strategy's focus on improving knowledge, dissemination, and public engagement will foster greater awareness and participation among citizens and stakeholders, ensuring that noise management becomes a shared responsibility across communities and administrations.

6. CONLUSION

The National Noise Strategy will present a comprehensive framework to address the multiple challenges posed by noise pollution in Spain. Through a systematic and integrative approach, the Strategy will address not only the assessment and monitoring of noise sources, but also the development of effective mitigation measures in various sectors, from urban transport and industrial activities to leisure events and natural habitats.

The analysis underpinning this Strategy highlights the need for a detailed diagnosis that encompasses both modelable and non-modelable noise sources, ensuring that the data-driven approach captures the full magnitude of environmental noise and its impact on public health and biodiversity. By integrating robust methodologies, including quantitative, semi-quantitative, and qualitative assessments, the Strategy lays a solid foundation for informed decision-making and policymaking. The strategic axes, ranging from improving public knowledge and awareness to improving noise management, prevention, and regulatory frameworks, guide the plan toward the creation of a cohesive and adaptive system for noise control.

The emphasis on cross-sector collaboration and inter-administrative coordination further strengthens the potential for achieving tangible improvements in both urban acoustic environments and natural ecosystems. Ultimately, the expected outcomes of implementing the Strategy include policies and tools aimed at achieving significant reductions in noise exposure, improvements in public health and well-being, the preservation of acoustic quality in natural areas, and economic benefits through reduced healthcare costs and improved urban livability.

This Strategy will establishes a forward-looking agenda that supports the goal of ensuring a healthier, more sustainable, and acoustically harmonious environment for present and future generations.

7. REFERENCES

[1] Council of Europe. (1950). *European Convention on Human Rights*. Retrieved from https://www.coe.int/en/web/human-rights-convention

[2] European Commission. (2021). *EU Action Plan: 'Towards Zero Pollution for Air, Water and Soil'*. https://environment.ec.europa.eu/strategy/zero-pollution-action-plan_en

[3] European Environment Agency. (2020). *Environmental noise in Europe — 2020 (EEA Report No. 22/2019)*. https://www.eea.europa.eu/en/analysis/publications/environmental-noise-in-europe

[4] European Parliament & Council of the European Union. (2002). *Directive 2002/49/EC of the European Parliament and of the Council of 25 June 2002 on the assessment and management of environmental noise*. Official Journal of the European Communities, L 183, 1–7. Retrieved from https://eur-lex.europa.eu

[5] United Nations Environment Programme. (n.d.). UNEP. Retrieved from https://www.unep.org

[6] United Nations. (1948). *Universal Declaration of Human Rights*. Retrieved from https://www.un.org/en/universal-declaration-human-rights

[7] World Bank. (n.d.). World Bank. Retrieved from https://www.worldbank.org

[8] World Health Organization. (2018). *Environmental noise guidelines for the European Region*. https://www.who.int/europe/publications/i/item/9789289053563

DOI: 10.61782/fa.2025.0696

FORUM ACUSTICUM EURONOISE 2025

PRELIMINARY EVALUATION OF A LOW-COST DEVICE FOR BINAURAL RECORDING AND SOUNDSCAPE MONITORING

Juan Miguel Navarro Ruiz[1*] **Massimiliano Masullo**[2]
[1] Research Group in Advanced Telecommunications (GRITA),
UCAM Universidad Católica de Murcia, 30107 Guadalupe, Spain
[2] Department of Architecture and Industrial Design,
Università degli Studi della Campania "Luigi Vanvitelli", 81031 Aversa, Italy

ABSTRACT

The growing interest in soundscape analysis has highlighted the need for accessible tools capable of capturing and processing audio with high spatial sound fidelity. This study presents a low-cost device designed for binaural recording and soundscape monitoring. The device employs a microphone array to capture sound signals and subsequently applies signal processing techniques to synthesize a binaural output.

A preliminary evaluation was conducted to assess the device's performance in a controlled urban environment characterized by road traffic noise. The evaluation compared recordings obtained with the prototype device against reference recordings captured using in-ear microphones in an artificial head and worn by human. Key metrics, including spatial accuracy, and psychoacoustic parameters, were analyzed to determine the device's suitability for soundscape studies.

Results suggest that the proposed device provides an effective approximation of binaural audio, with certain limitations inherent to its low-cost design. These findings support the potential of the device as a scalable solution for soundscape monitoring, particularly in applications where traditional binaural equipment may be cost-prohibitive. Future work will focus on refining the signal processing algorithms and expanding the evaluation to diverse soundscapes.

*__Corresponding author__: *jmnavarror@ucam.edu.*
__Copyright__: *©2025 Navarro JM and Masullo M This is an open-access article distributed under the terms of the Creative Commons Attribution 3.0 Unported License, which permits unrestricted use, distribution, and reproduction in any medium, provided the original author and source are credited.*

Keywords: *soundscapes, binaural, traffic noise, IoT, monitoring*

1. INTRODUCTION

The study of soundscapes has emerged as a crucial area in acoustic research, particularly in the context of urban planning, environmental monitoring, and public health. Soundscape analysis aims to understand how people perceive and interact with their acoustic environment, providing valuable insights to design more sustainable and livable urban spaces [1, 2]. A fundamental aspect of soundscape studies is the ecological capture of spatial auditory information, which requires high-fidelity binaural recordings. These recordings preserve the spatial cues necessary for human auditory perception, including interaural level and time differences, which are essential for evaluating the subjective experience of sound environments [3].

Traditional binaural recording techniques employ artificial heads, binaural headsets or in-ear binaural microphones worn by human subjects. These devices offer high spatial sound accuracy but are often expensive, equipment and/or human resources, limiting their widespread use in large-scale or long-term soundscape monitoring [4, 5]. Additionally, logistical challenges arise when deploying multiple binaural recording units in diverse environments, further restricting their applicability. To address these limitations, recent advancements in the Internet of Things (IoT) and digital signal processing have facilitated the development of alternative low-cost solutions. Even though low-cost IoT solutions have made significant progress in the soundscape monitoring field, challenges are still open in capturing perceptually accurate data. One approach has focused on integrating low-cost acoustic sensors with

AI-based analysis for urban soundscape research, but the system relies on monaural recording and does not incorporate psychoacoustic parameter extraction [6]. Another initiative has introduced a FIWARE-based wireless acoustic sensor network designed for urban sound classification, utilizing machine learning models; however, it lacks binaural capabilities and the ability to assess perceptual sound attributes [7]. A different solution has explored a multipurpose IoT sensor for biologging and soundscape applications, offering flexibility in data collection but still relying on monaural recording without advanced psychoacoustic analysis [8]. While these efforts contribute to the accessibility and scalability of soundscape monitoring, they also reveal gaps in binaural recording and perceptual sound analysis, highlighting the need for enhanced solutions that improve fidelity and psychoacoustic processing.

In this study, a preliminary evaluation of a low-cost IoT device designed for binaural recording and soundscape monitoring is presented. The proposed system employs a microphone array to capture sound signals and implements signal processing algorithms to synthesize binaural output [9], [10]. A controlled experiment was conducted in an urban environment dominated by road traffic noise to assess the device's performance against a reference system consisting of human-worn binaural headphones. Key performance metrics, including including spatial accuracy, and psychoacoustic parameters, were analyzed to determine the suitability of the proposed device for soundscape research.

The remainder of this paper is structured as follows: Section 2 describes the materials and methods, including the system architecture, experimental setup, and evaluation methodology. Section 3 presents the results and discussion, highlighting the device's performance in comparison with the reference system. Finally, Section 4 concludes the study and outlines potential directions for future work.

2. MATERIALS AND METHODS

The following section provides a comprehensive description of the methodology employed in this study. In the first part, the evaluated device is described in terms of its hardware and software components. Subsequently, the experimental setup is presented, detailing the environment and reference system used for evaluation. The third part outlines the data collection procedure, including the recording protocols and evaluation criteria. Finally, data processing and analysis methods are described, emphasizing the techniques used to assess the performance of the device.

2.1 Description of the Device

The low-cost IoT device was designed to approximate the spatial fidelity of conventional binaural recording systems. The system is structured into two main components: the audio acquisition subsystem and the processing core, which together facilitate real-time data capture, processing, and transmission.

The audio acquisition is based on a Sony PlayStation Eye camera, which features a four-microphone array. This array captures sound with 16-bit depth at a sampling rate of 16 kHz, offering a signal-to-noise ratio of 90 dB. The array configuration is specifically designed to replicate spatial hearing characteristics, with an inter-microphone distance of approximately 62 mm and reversed polarity in the central microphones to enhance spatial audio capture. Calibration procedures were conducted in a semi-anechoic chamber comparing the results with those of a Rion NL-05 sound level meter to ensure reliable and accurate measurements.

The processing core is based on a Raspberry Pi 3 Model B, which serves as the central processing and control unit. This platform is equipped with a 1.2 GHz 64-bit quad-core ARMv8 CPU, 1 GB of RAM, four USB ports, and integrated 802.11n Wireless LAN.

The system captures audio in configurable time-window segments and utilizes a signal processing pipeline to synthesize binaural output. The stages of the pipeline are shown in Fig. 1.

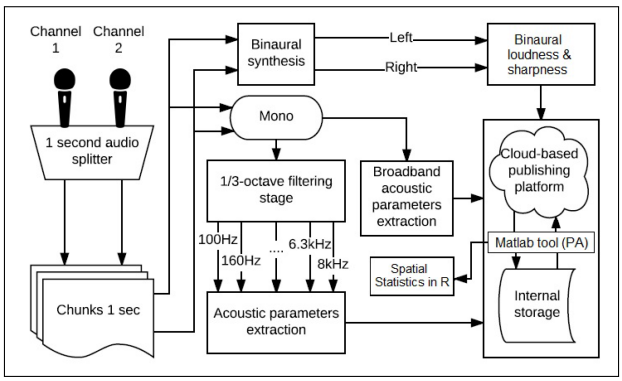


Figure 1. Diagram of the signal processing pipeline to synthesize binaural output. [9]

The system estimates the direction of incoming

sounds using time-frequency domain analysis, employing the Short-Term Fourier Transform and assuming sparsity of audio sources to calculate the Direction-Of-Arrival (DOA). Based on the estimated DOA, the system applies Head-Related Transfer Functions (HRTFs) to synthesize binaural audio. The selected HRTF corresponds to the estimated azimuth, ensuring an accurate spatial representation. The device computes objective psychoacoustic metrics, following Zwicker's and Moore's loudness models. The processed data, including acoustic parameters and raw recordings, are stored locally on the Raspberry Pi and transmitted to a cloud platform for further analysis and archiving.

The entire processing pipeline is implemented in Python, using the Advanced Linux Sound Architecture (ALSA) for audio acquisition. The modular software architecture allows independent operations of each processing stage, enhancing robustness and facilitating updates or modifications. The system periodically uploads processed data to an IoT cloud platform, enabling real-time monitoring and remote data retrieval.

2.2 Experimental Setup

As a preliminary experiment, the performance of the proposed device was evaluated in an indoor environment, specifically an open-plan office of the Universidad Católica de Murcia, Spain. This setting is characterized by stable and consistent acoustic conditions, with predominant noise sources originating from vocal interactions among staff members. The environment was chosen due to its relevance in soundscape studies, as speech-related acoustic fields are common in office and educational settings, making it an ideal scenario to assess the device's performance in capturing binaural audio under realistic indoor conditions. The recording area was situated at the center of the right-hand row of desks within the open-plan office, which is composed of three parallel rows of desks. This positioning was chosen to minimize reflections from nearby furniture and maintain consistency throughout the data collection process.

To assess the accuracy of the proposed device, the recordings were compared against two reference systems. The first reference system consisted of a Roland CS-10EM binaural headphones connected to a Zoom H4n Pro 4-channel digital recorder. The Roland CS-10EM headphones, featuring built-in omnidirectional microphones, were placed in the listener's ear canals. The second reference system consists of the a OKM II Classic Binaural Microphones mounted on a Soundman Dummy Head, also connected to a Zoom H4n Pro. The Zoom H4n Pro recorder provided high-quality audio capture with 24-bit/96 kHz resolution, ensuring accurate documentation of the acoustic environment.

Each recording session lasted 10 minutes, ensuring adequate signal representation for analysis. Both systems were synchronized to ensure simultaneous recording sessions under identical acoustic conditions. Synchronization was achieved using a common time reference and initiating recordings simultaneously to eliminate temporal discrepancies between datasets. Calibration procedures were performed before the experiments to ensure that the signal levels recorded by both systems were comparable, thereby minimizing potential bias due to differences in microphone sensitivity or frequency response.

The experimental setup was designed to allow both the proposed device and the reference system to capture the same acoustic events from identical spatial perspectives. This approach enabled a direct comparison between the binaural outputs of the low-cost device and the reference microphones, focusing on spatial accuracy and perceptual fidelity.

2.3 Data Processing and Analysis

All recorded signals were processed and analyzed using MATLAB. The analysis workflow included signal segmentation, feature extraction, and statistical comparison between the proposed device and the reference system. The 10-minute recording session was segmented into 10-second windows, and for each window, several key performance metrics were calculated, followed by the extraction of statistical descriptors from the entire session.

Spatial accuracy was assessed by comparing the interaural level differences (ILD) in dB, the interaural time differences (ITD) in ms, and the interaural cross-correlation (IACC). Perceptual fidelity was evaluated through an objective analysis of psychoacoustic metrics, including loudness (LO) in sone, sharpness (SH) in acum, roughness (RO) in asper, and fluctuation strength (FS) in vacil, using MATLAB's psychoacoustic modeling tools.

3. RESULTS AND DISCUSSION

This section presents the preliminary results obtained from the evaluation of the proposed low-cost binaural recording device analyzing a single 10-minute recording session, with particular emphasis on a detailed examination of a 10-second window within that session to assess

the suitability of the system. The performance of the device was compared with two reference systems consisting of human-worn binaural microphones and a dummy head equipped with binaural microphones. Moreover, to evaluate the impact of the binaural synthesis algorithm on the recorded signals, the results include the metrics calculated both before (denoted as pre in tables and figures) and after (denoted as post in tables and figures) the signal processing implemented in the device. The results are presented in terms of average values, highlighting the comparative performance of the proposed device relative to the reference system.

Tab. 1 presents the spatial accuracy metrics obtained for the open-plan office environment, including values recorded before and after the signal processing applied in the device.

Table 1. Spatial accuracy analysis metrics for the open-plan office

Capture	ILD (dB)	ITD (ms)	IACC
Device (pre)	-0.18	0.0000	0.97
Device (post)	3.24	-0.5000	0.24
Dummy	0.88	-0.5575	0.50
Human-worn	0.28	-0.5568	0.36

The proposed device demonstrated significant changes in spatial accuracy after the binaural synthesis process. Notably, the ILD increased from -0.18 dB to 3.24 dB, indicating an adjustment in interaural level representation. Similarly, the ITD shifted from 0 ms to -0.5 ms, suggesting an alteration in the interaural time alignment. The IACC also decreased from 0.97 to 0.24, reflecting a reduction in spatial coherence after processing.

When compared with the reference systems, the device's post-processed ITD was closer to the values observed in the dummy and human-worn setups. However, the ILD values remained less consistent, highlighting a limitation in accurately reproducing level-based spatial cues. The reduction in IACC after processing indicates a potential loss of spatial coherence, which could affect the perceptual quality of the binaural output.

These findings suggest that, while the proposed system is capable of approximating spatial cues, improvements in the signal processing algorithm and microphone array configuration are necessary to enhance spatial fidelity, particularly regarding ILD accuracy and spatial coherence.

Tab. 2 presents the perceptual fidelity analysis metrics obtained for the open-plan office environment, including values recorded before and after the signal processing applied in the device.

Table 2. Perceptual fidelity analysis metrics for the open-plan office

Recording	LO (sone)	SH (acum)	RO (asper)	FS (vacil)
Device (pre)	16.32	1.10	0.08	0.16
Device (post)	12.79	1.07	0.10	0.04
Dummy	13.36	1.11	0.10	0.16
Human-worn	8.50	1.15	0.07	0.08

The analysis revealed that the proposed device's loudness decreased from 16.32 sone to 12.79 sone, aligning more closely with the dummy reference, 13.36 sone, but remaining notably higher than the human-worn microphones, 8.50 sone. Sharpness values remained relatively consistent across all setups, with a slight decrease after processing. Moreover, sharpness values around 1 acum show a balanced sound, with a certain brightness, characteristic of a speech signal.

Roughness showed a small increase from 0.08 asper to 0.10 asper, which corresponds with the dummy reference value but is slightly higher than the human-worn system, 0.07 asper. Fluctuation strength exhibited a more pronounced reduction from 0.16 vacil to 0.04 vacil, diverging from both the dummy and human-worn references, which recorded values of 0.16 and 0.08 vacil, respectively.

These results suggest that the proposed device, after binaural synthesis, more accurately replicates loudness and roughness when compared to the dummy reference. However, the reduced fluctuation strength indicates a potential loss in the dynamic variability of the signal, which could impact the perceived naturalness of the soundscape. Adjustments in the signal processing algorithm could help preserve fluctuation cues while maintaining perceptual fidelity.

To further analyze the frequency response of the proposed device and the effect of the binaural synthesis algorithm, the specific loudness versus frequency for a representative 10-second recording is examined. Fig. 2 shows the specific loudness spectra for both the device, before a) and after processing b), and the reference systems, dummy head c) and human-worn binaural microphones d).

In terms of frequency distribution, both device graphs, Fig. 2a and Fig. 2b, display a concentration of loud-

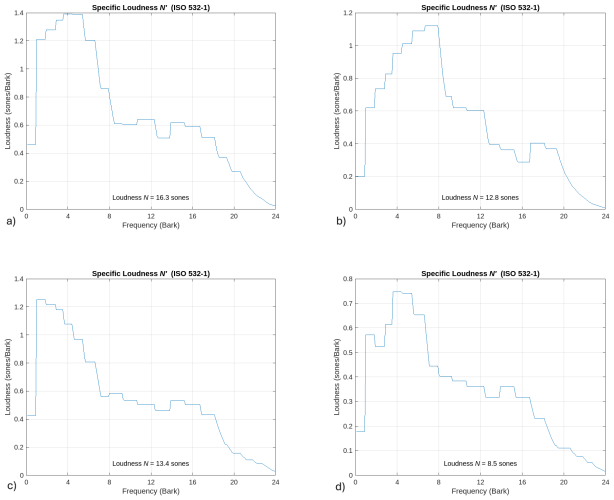


Figure 2. Specific loudness versus frequency for an example of 10 second-recording. a) Device (pre) b) Device (post) c) Dummy d) Human-worn

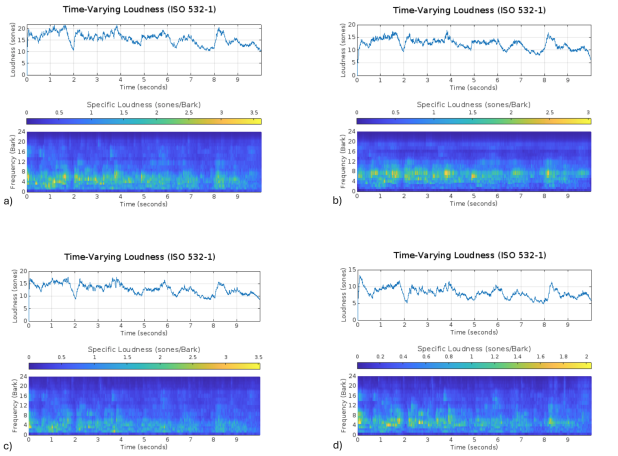


Figure 3. Time-varying loudness for an example of 10 second-recording. a) Device (pre) b) Device (post) c) Dummy d) Human-worn

ness predominantly in the low-to-mid frequency range (0-8 Bark), followed by a gradual decline up to approximately 16 Bark. This pattern is consistent with the human-worn microphone response, Fig. 2d, though with generally lower peak values. In contrast, the dummy head response in Fig. 2c shows a concentration in the lower frequencies, which also exhibits a more uniform distribution across the mid-frequency range, maintaining higher levels up to 16 Bark before decreasing.

Overall, the specific loudness analysis indicates that while the binaural synthesis algorithm can adjust the overall intensity, it does not fully compensate for spectral discrepancies inherent to the device's hardware configuration. Future improvements could include the integration of higher-bandwidth microphones to better capture high-frequency content and enhance perceptual accuracy.

To assess the dynamic behavior of the proposed device, the time-varying loudness for a representative 10-second recording is analyzed. Fig. 3 shows the time-varying loudness (ISO 532-1) for both the device, before and after processing, and the reference systems. The graphs illustrate the variation of loudness over time and its distribution across frequency bands.

Overall, the pattern of level variations, in the time-domain representation in Fig. 3 is similar across the four recordings, indicating that despite differences in loudness values, the temporal dynamics of the sound are consistently captured by both the proposed device and the reference systems. In Fig. 3a, the device's pre-processed signal exhibits noticeable fluctuations in loudness, with values ranging between approximately 10 and 20 sones. After processing, Figure 3b, the device shows a reduction in overall loudness variation, stabilizing around 12 to 18 sones. This decrease suggests that the binaural synthesis algorithm reduces the intensity dynamics, potentially due to signal averaging or noise reduction mechanisms. Comparatively, the dummy head recording, Fig. 3c, presents a loudness range similar to the post-processed device, with values between 10 and 18 sones. On the other hand, the human-worn microphone setup, Fig. 3d, exhibits consistently lower loudness values, ranging from 8 to 15 sones.

The spectrograms in Fig. 3 reveal that the loudness distribution across frequency bands differs notably between the device and both reference systems. Both the pre-processed and post-processed device signals show dominant loudness contributions concentrated in the lower frequency range (below 8 Bark), whereas both reference systems (dummy head and human-worn) exhibit a more evenly distributed loudness profile, particularly across mid-to-high frequencies. This discrepancy can be attributed to the limited frequency response of the PS3 Eye microphones, which do not capture higher frequencies as effectively as the reference binaural microphones. Consequently, the device may not fully replicate the time-varying perceptual attributes of the soundscape, especially

in scenarios with prominent high-frequency components.

In summary, the time-varying loudness analysis indicates that while the binaural synthesis algorithm smooths the loudness profile, it does not fully compensate for the hardware limitations of the proposed device. Further improvements could involve using higher-bandwidth microphones to capture a more accurate representation of dynamic acoustic environments.

4. CONCLUSIONS

This study evaluated a low-cost IoT device for binaural recording and soundscape monitoring in an indoor environment with vocal noise. The device demonstrated reasonable spatial cue approximation, showing potential as a cost-effective alternative for soundscape studies. However, differences in interaural cues and psychoacoustic metrics indicate areas for improvement.

The spatial accuracy analysis showed that after processing, the device achieved interaural time differences similar to reference systems, but interaural level differences remained inconsistent. This suggests limitations in reproducing level-based spatial cues. The reduced interaural cross-correlation after processing indicates a possible loss of spatial coherence, affecting binaural output quality.

After processing, the device's psychoacoustic metrics were closer to the dummy head, especially for sharpness and loudness. However, discrepancies were noted in roughness and fluctuation strength, likely due to the PS3 Eye microphone's limited frequency bandwidth, which may hinder accurate high-frequency representation.

The time-varying loudness analysis showed consistent temporal dynamics across the signals, though the device's processed signal displayed reduced variability, likely due to the synthesis algorithm. The device signals concentrated loudness in lower frequencies, while reference systems had a more even distribution, particularly at higher frequencies.

Despite some limitations, the device demonstrates the potential for affordable binaural recording, useful for soundscape monitoring. Future work should improve spatial accuracy, loudness estimation, and frequency capture, focusing on diverse environments and refining algorithms for better accuracy.

5. ACKNOWLEDGMENTS

This work is the result of the stay 22208/EE/23 funded by the Fundación Séneca - Science and Technology Agency of the Region of Murcia, under the Regional Program for Mobility, International Collaboration, and Knowledge Exchange "Jiménez de la Espada" (Action Plan 2023).

6. REFERENCES

[1] J. Kang, "Soundscape in city and built environment: current developments and design potentials," *City and Built Environment*, vol. 1, no. 1, p. 1, 2023.

[2] A. Fiebig and B. Schulte-Fortkamp, "How to put soundscape into practice," in *Soundscapes: Humans and Their Acoustic Environment*, pp. 313–330, Springer, 2023.

[3] M. Yang and M. Masullo, "Combining binaural psychoacoustic characteristics for emotional evaluations of acoustic environments," *Applied Acoustics*, vol. 210, p. 109433, 2023.

[4] G. Brambilla and A. Fiebig, "Measurements and techniques in soundscape research," in *Soundscapes: humans and their acoustic environment*, pp. 185–214, Springer, 2023.

[5] O. Acosta, L. Hermida, M. Herrera, C. Montenegro, E. Gaona, M. Bejarano, K. Gordillo, I. Pavón, and C. Asensio, "Remote binaural system (rbs) for noise acoustic monitoring," *Journal of Sensor and Actuator Networks*, vol. 12, no. 4, p. 63, 2023.

[6] J. Wang, C. Li, Y. Lin, C. Weng, and Y. Jiao, "Smart soundscape sensing: A low-cost and integrated sensing system for urban soundscape ecology research," *Environmental Technology & Innovation*, vol. 29, p. 102965, 2023.

[7] P. Arce, D. Salvo, G. Piñero, and A. Gonzalez, "Fiware based low-cost wireless acoustic sensor network for monitoring and classification of urban soundscape," *Computer Networks*, vol. 196, p. 108199, 2021.

[8] D. Vasconcelos and N. J. Nunes, "A low-cost multipurpose iot sensor for biologging and soundscape activities," *Sensors*, vol. 22, no. 19, p. 7100, 2022.

[9] J. E. Noriega-Linares, A. Rodriguez-Mayol, M. Cobos, J. Segura-García, S. Felici-Castell, and J. M.

Navarro, "A wireless acoustic array system for binaural loudness evaluation in cities," *IEEE Sensors Journal*, vol. 17, no. 21, pp. 7043–7052, 2017.

[10] J. Segura-Garcia, J. M. Navarro-Ruiz, J. J. Perez-Solano, J. Montoya-Belmonte, S. Felici-Castell, M. Cobos, and A. M. Torres-Aranda, "Spatio-temporal analysis of urban acoustic environments with binaural psycho-acoustical considerations for iot-based applications," *Sensors*, vol. 18, no. 3, p. 690, 2018.

DOI: 10.61782/fa.2025.0146

FORUM ACUSTICUM EURONOISE 2025

ASSESSING ACOUSTIC DYNAMICS IN ALPINE ECOSYSTEMS: THE NIVOLET PASS CASE STUDY

Giorgia Guagliumi[1*] **Fabio Angelini**[1] **Roberto Benocci**[1]
Giovanni Zambon[1]
[1] Dept. of Earth and Environmental Sciences, Università degli Studi di Milano-Bicocca, Milano

ABSTRACT

Alpine ecosystems, among the most vulnerable to climate change and anthropogenic disturbances, remain underexplored in their acoustic dimensions despite their crucial role in supporting biodiversity and ecological processes. These environments also attract significant human activity, becoming hotspots of interaction between natural and anthropogenic dynamics. This study investigates the acoustic impact of road traffic noise along the SP50 provincial road, from Lake Serrù to Savoia Refuge, in Gran Paradiso National Park (Italy).

Acoustic levels were monitored using class 1 sound level meters, with measurements conducted during periods of both road closure and peak tourist activity. The recorded data were analyzed to assess sound pressure variations in relation to traffic flow and other local sources. Simultaneously, vehicle density was quantified to establish correlations between traffic patterns and acoustic conditions. The findings demonstrate the significant influence of anthropogenic noise on the acoustic environment, highlighting the need for informed noise management strategies.

By situating these results within the European frameworks for noise management and biodiversity conservation, the study underscores the critical role of acoustic monitoring in guiding targeted conservation strategies. This research highlights the importance of integrating noise control measures with ecosystem management to mitigate human impacts and ensure the sustainable preservation of fragile alpine environments.

Keywords: *protected areas, traffic noise, alpine ecosystems, acoustic monitoring, biodiversity conservation.*

1. INTRODUCTION

In recent decades, noise pollution has been recognised as a major environmental stressor with documented effects on a wide range of terrestrial and aquatic ecosystems [1,2]. While anthropogenic noise is typically associated with urban and industrial environments, recent studies have highlighted its increasing impact on protected natural areas, including alpine ecosystems [3,4]. Seasonal road reopening and tourism-related activities in high altitude environments can generate sound pressure levels significantly above natural background levels, altering the soundscape and influencing wildlife behaviour [5].

Alpine ecosystems are characterised by abundant species richness and a remarkable degree of endemism [6]. However, they are particularly vulnerable to anthropogenic pressures, including land-use change [7] and climate change [8]. In the European Alps, climate change is particularly pronounced, leading to increased air temperatures, earlier snowmelt [9], shifts of alpine flora and fauna to higher elevations, and phenological changes in several taxa [10]. In this context, noise management policies have increasingly focused on the protection of ecologically sensitive areas. The European Directive 2002/49/EC on environmental noise management emphasises the need to preserve natural soundscapes [11]. This Directive introduces the concept of quiet areas both within and outside urban agglomerations, recognising their ecological importance. In Italy, Legislative Decree No. 194 of August 19, 2005, Article 4, Paragraph 10-bis [12], defines quiet areas as ecologically valuable locations where minimizing anthropogenic noise is

[*]***Corresponding author***: g.guagliumi@campus.unimib.it.
Copyright: *©2025 First author et al. This is an open-access article distributed under the terms of the Creative Commons Attribution 3.0 Unported License, which permits unrestricted use, distribution, and reproduction in any medium, provided the original author and source are credited.*

essential for biodiversity conservation. According to the Ministry of Ecological Transition (MiTE), these areas are situated far from significant anthropogenic sources, maintaining sound pressure levels well below those permitted in urban and residential zones. The natural soundscape of these regions varies significantly, ranging from deep quiet (as low as 25 dBA in remote snowfields during winter) to higher levels (exceeding 70 dBA) near waterfalls in summer. Given this variability, the impact of anthropogenic noise should be assessed on a case-by-case basis, using the site-specific natural ambient sound levels as reference points [13].

At the same time, mountain tourism is an important socio-economic sector, often developing in highly sensitive ecological contexts. Local communities and park authorities face the complex challenge of balancing the promotion of tourism with the preservation of acoustic quality in protected areas. This task is further complicated by the limited availability of empirical data on soundscapes in high-altitude environments subject to seasonal tourist influx.

The Gran Paradiso National Park stands out for its commitment to conservation and environmental protection, particularly in the Nivolet Pass, a high altitude area (~2,500 m) of exceptional ecological value. This plateau, characterised by wetlands and peat bogs, is an important habitat for numerous alpine species. Efforts to mitigate anthropogenic impacts in this area have led to a number of conservation initiatives and public awareness campaigns.

The aim of this study is to assess noise levels on the Nivolet Pass during periods of varying traffic intensity (July, August and September) compared to road closure days, which serve as a reference for natural background noise. The measured noise levels are also compared with existing legal limits and stricter limits proposed for designated “quiet areas”. The results provide critical insights into the effectiveness of current traffic management policies and offer guidance for future interventions aimed at preserving the natural acoustic environment while ensuring sustainable tourism practices within the protected area.

2. MATERIALS AND METHODS

2.1 Study Area

The study area is located in the heart of the Graian Alps, on the border between the Orco Valley (Piedmont) and the Valsavarenche (Aosta Valley), within the Gran Paradiso National Park (PNGP), Italy's first protected area established in 1922.

The site extends around Nivolet Pass, at an altitude of 2,612 m a.s.l., and represents a landscape of significant natural and ecological value. Access to the Pass is provided by Provincial Road SP50, which branches off from State Road SS460 of Ceresole Reale (TO) and extends for approximately 20 km, with an elevation gain of over 1,000 meters. The road runs alongside two artificial reservoirs, Lake Serrù and Lake Agnel, both used for hydroelectric power generation (Fig. 1).

During winter and spring, the road is closed to vehicular traffic due to safety concerns related to snow and ice. The seasonal closure is regulated by an ordinance issued by the Metropolitan City of Turin, prohibiting traffic from October 15 to May 15, subject to extensions due to adverse weather conditions or delays in snow removal operations.

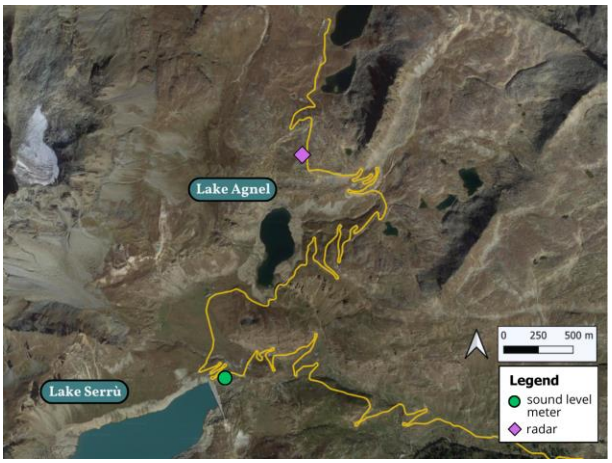


Figure 1. Geographic location of the measurement sites, showing the positions of the sound level and the radar used for monitoring.

2.1.1 Sound sources

The primary contributors to the soundscape in the study area can be categorized as anthropogenic and natural sources. The dominant anthropogenic noise source is road traffic on Provincial Road SP50, which present a peak of vehicular activity during summer, including private cars, motorcycles, heavy vehicles, and shuttle buses operating as seasonal public transport. Other human activities, such as hiking and cycling, also contribute to anthropogenic noise,

particularly in the vicinity of mountain refuges, including Chivasso and Savoia Refuges.

The main natural sources include:

- Geophonies: Wind, which is frequent due to the high altitude and local topography, plays a significant role in shaping the natural acoustic environment.
- Hydrological elements: Flowing water from streams, waterfalls, and alpine lakes contributes to the overall soundscape.
- Wildlife: The presence of species such as chamois, marmots, and various birds, including raptors and passerines, enriches the natural acoustic environment.

2.2 Acoustic Monitoring Plan and Monitoring sites

The acoustic monitoring plan follows national and international regulations on environmental noise management and the protection of ecologically sensitive areas. The study area is part of the Natura 2000 network, including Special Areas of Conservation (SACs) and Special Protection Areas (SPAs), established by Directive 92/43/EEC [14].

Classified as Class I in the Acoustic Classification Plan (PCA), the area is subject to strict noise limits to protect human health and wildlife: I. 50 dB(A) for the day period (06:00-22:00); II. 40 dB(A) for the night period (22:00-06:00). For transport infrastructure, PCA limits do not apply within designated noise buffer zones, as defined by Presidential Decree no. 142/2004 [15]. The SP50, under the jurisdiction of the Metropolitan City of Turin, is a class Cb road with a speed limit of 40 km/h. In the study area, the relevant noise limits are as follows: for Zone A, with a width of 100 meters, the limits are 70 dB during the day and 60 dB at night; for Zone B, with a width of 150 meters, the limits are 65 dB during the day and 55 dB at night.

The monitoring sites were selected to ensure representativeness in terms of major noise sources and proximity to sensitive habitats. A Class 1 sound level meter (Fig. 2a) was placed near the parking area of Lake Serrù, adjacent to the SP50 but outside the parking lot to avoid interference from vehicle movements. The meter was placed next to a small shelter to minimise wind effects and maintain data quality. A traffic radar (Fig. 2b), provided and managed by the PNGP, was installed at Nivolet Pass. This location was chosen because vehicle passages could not be effectively distinguished at the Lake Serrù parking area, where movements within the lot would have compromised data accuracy.



Figure 2. Positioning of the sound level meter (a) and the traffic radar (b).

2.3 Data analysis

The analysis of sound emissions was conducted through a four-month acoustic monitoring campaign, divided into different time blocks based on traffic regulations and seasonal characteristics of the study area. The monitoring periods were defined as follows: during the road open period (July–September), data were analyzed on a monthly basis to capture variations in tourist flows, which significantly influence the acoustic environment. Conversely, during the closing period (October) the collected data served as a reference to determine background noise levels. In this case measurements were taken over three representative days (28–30 October), chosen one week after the road closure to allow the soundscape to stabilise under typical environmental conditions. These days were characterised by favourable meteorological conditions and stable day and night noise levels.

To ensure the reliability and robustness of the results, the dataset underwent a filtering process to exclude periods with hourly precipitation exceeding 0.2 mm, in accordance with the guidelines of D.M. 16/03/98 [16] and UNI EN ISO 1996-1:2017 [17].

For each monitored month, the hourly equivalent noise levels (Leq) were analysed to assess the acoustic impact of road opening. Weekly daytime (06:00–22:00) and nighttime (22:00–06:00) LAeq values were calculated

and visualised using histograms to illustrate their temporal variations. These values were compared with the legal limits for secondary extra-urban roads [15] and estimated thresholds for quiet areas [12].

To further investigate noise trends, the average hourly noise levels were calculated for each monitored month, using the acquired hourly data. The results were graphically represented through three different curves, each corresponding to a different month, illustrating the hourly noise trends throughout the day. Each graph included four data series, representing different day types: weekdays, Saturdays, holidays, and a reference trend corresponding to the background noise levels recorded during road closure.

The effect of road opening on sound levels was assessed through a comparative analysis between the noise levels recorded during the period when the road was open and the background noise levels measured when the road was closed. Data were classified by time period (day/night) and day type: weekdays, Saturdays, holidays and special event days when the road was closed for outdoor activities such as cycling, fitwalking and Nordic walking. For each condition, the mean equivalent noise levels were calculated and compared with the background noise to obtain the Leq differences. The results were aggregated on a weekly basis, with averages calculated for each day category, maintaining the distinction between day and night

3. RESULTS

The results provide an overview of the hourly equivalent levels (Leq) recorded during the monitoring period corresponding to the opening of the road (Fig. 3). There are clear differences between months and times of day, with pronounced peaks during the day. The highest Leq values were observed in July, due to the increased presence of tourists, which led to an increase in vehicle activity and consequently high noise levels. In the following months, August and September, the hourly Leq values showed a progressive decrease, coinciding with a reduction in the traffic flow rate. This decrease was accompanied by a more uniform Leq distribution and overall lower mean values, consistent with the decrease in tourist presence and related activities.

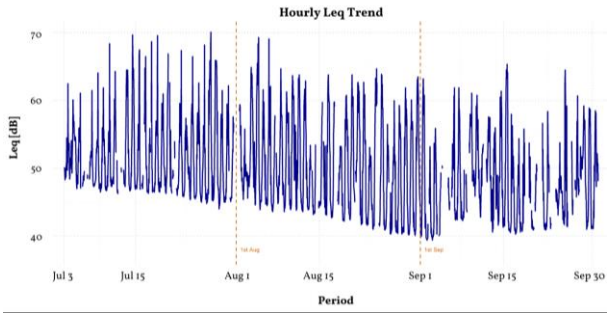
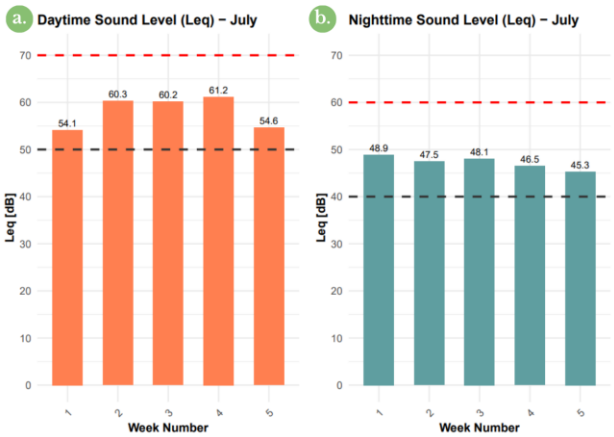


Figure 3. Trend of hourly equivalent levels (Leq) during the opening phase of the SP50, with the transition between consecutive months highlighted in orange.

The analysis of the phonometric data collected during the road opening period focused on equivalent noise levels, distinguishing between daytime (LAeq) and nighttime (LAeq) values. The results (Fig. 4) show weekly average LAeq values [dB] for both periods, plotted against the consecutive week numbers within each month. Daytime equivalent noise levels were consistently higher than nighttime values by more than 10 dB, a difference attributable to anthropogenic activities and increased vehicle traffic flow rate. Each histogram contains two dashed reference lines: the red dashed line represents the legal noise exposure limits for secondary extra-urban roads (category Cb) established by [15]; the black dashed line indicates the limits proposed for quiet areas by [12].



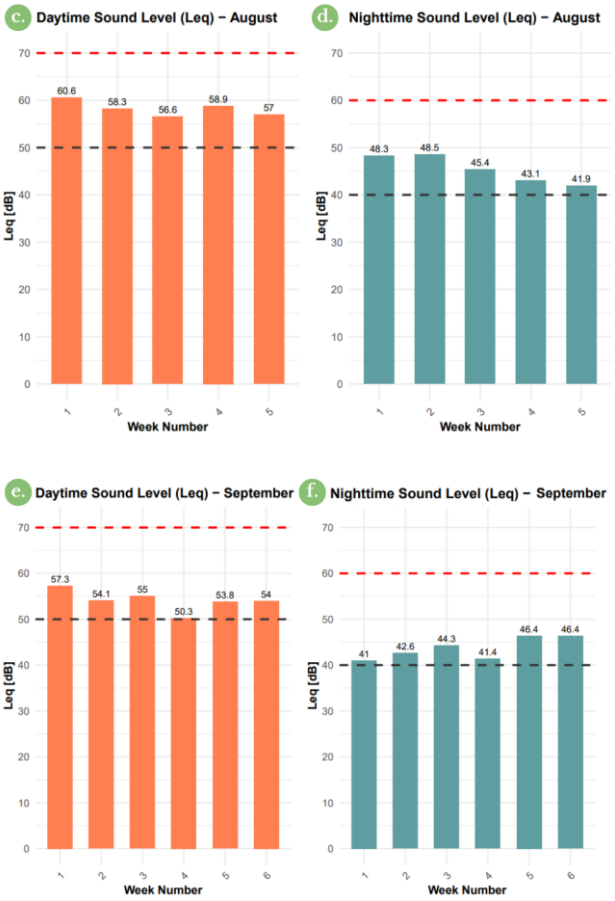
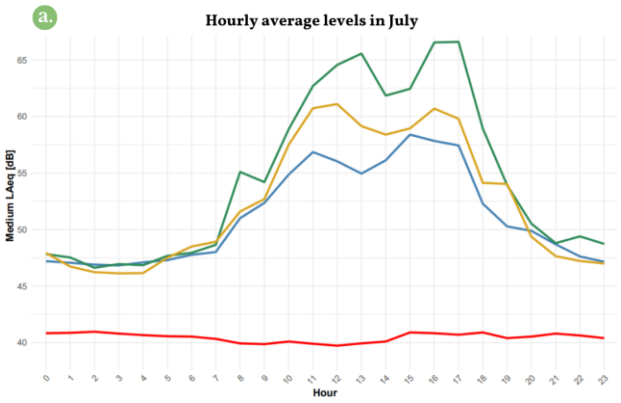


Figure 4. Weekly trend of daytime LAeq levels (in orange) and nighttime LAeq levels (in blue) [dB] for the months of July (a-b), August (c-d), and September (e-f). The red and black dashed lines indicate the regulatory limits and the hypothesized limits for quiet areas, respectively.

A temporal analysis revealed that July recorded the highest LAeq values, reaching 61.2 dB during the daytime and 51.7 dB at night (Fig. 4a-b), in line with the seasonal increase in tourist presence, which generates higher traffic intensity. In August and September, a progressive decrease in LAeq levels was observed, with values reaching 56.6 dB during the daytime and 41.9 dB at night in August, and 50.3 dB during the daytime and 41.0 dB at night in September (Fig. 4c-f), reflecting the reduction in visitor numbers and associated activities. Regarding regulatory limits, LAeq values remained within the thresholds defined for secondary extra-urban roads (70 dB during the daytime and 60 dB at night). However, systematic exceedances of the estimated limits for quiet areas were observed, with values surpassing the proposed thresholds of 50 dB during the daytime and 40 dB at night.

Hourly average levels were calculated for each monitoring month (July, August, September) based on the data collected. In July (Fig. 5a), noise peaks on weekdays were mainly recorded in the late morning (around 11:00, 56.9 dB) and afternoon (15:00, 58.4 dB). On Saturdays, higher noise levels were observed compared to weekdays, with several peaks distributed between 08:00 (55.1 dB) and 17:00 (66.6 dB), indicating more intense and variable traffic. On holidays, noise levels were generally lower, but significant peaks were recorded around 11:00 (60.7 dB) and 16:00 (60.7 dB), followed by a sharp decline in the following hours. In August (Fig. 5b), weekday noise patterns were similar to those in July, but with slightly earlier peaks, particularly between 11:00 (59.3 dB) and 12:00 (60.2 dB), and a gradual decline after 14:00. On Saturdays, peaks were recorded mainly at 11:00 (62.5 dB), 12:00 (62.5 dB) and 15:00 (62.6 dB), with greater variability in the evening hours compared to July, with a notable increase from 22:00 onwards (49.6 dB). On holidays, noise levels increased significantly from 08:00 (49.9 dB), with the highest peak at 14:00 (62.8 dB). In September (Fig. 5c), weekday peaks were concentrated between 12:00 (54.1 dB) and 15:00 (52.5 dB), followed by a slight decrease after 16:00. On Saturdays peaks were recorded at 11:00 (57.8 dB), 13:00 (59.1 dB) and midnight (42.7 dB), suggesting the influence of evening events or specific social activities. On holidays the noise patterns were similar to those in July, with peaks between 11:00 (60 dB) and 15:00 (58.5 dB), followed by a relative stabilisation in the evening hours.



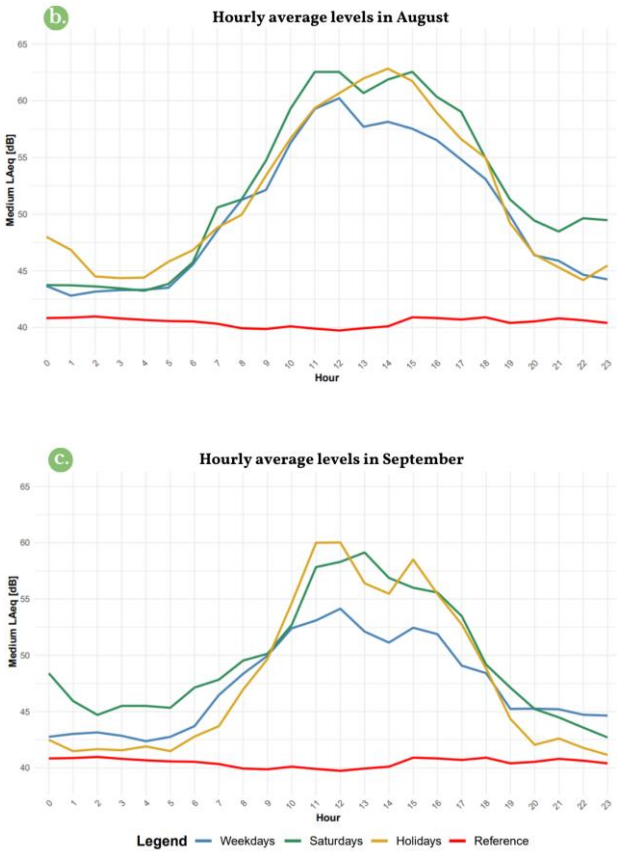


Figure 5. Hourly average Leq trends across different months, categorized by day type, as a function of the time of day: (a) July, (b) August, (c) September.

Finally, the difference (Δ) between the monthly mean levels for each category and the ambient background noise was calculated for both day and night periods to assess the increase in sound levels due to the road opening (Fig. 6). July showed the highest increase in sound pressure for both the daytime (21 dB) and nighttime periods (7.4 dB). On weekdays, daytime levels were highest in July (15.7 dB) and August (16.1 dB), while nighttime levels were highest in July (6.6 dB). Significant increases in daytime noise levels were observed on holidays and Saturdays, with average Δ values of 21 dB and 19.1 dB for Saturdays in July and August, and 18.6 dB and 18.1 dB for holidays in the same months. In sharp contrast, special event days showed a significant reduction in noise levels, with a decrease of 9.4 dB during the day and 3.8 dB at night. These events, marked by road closures to motorised traffic, resulted in a considerable drop in noise emissions.

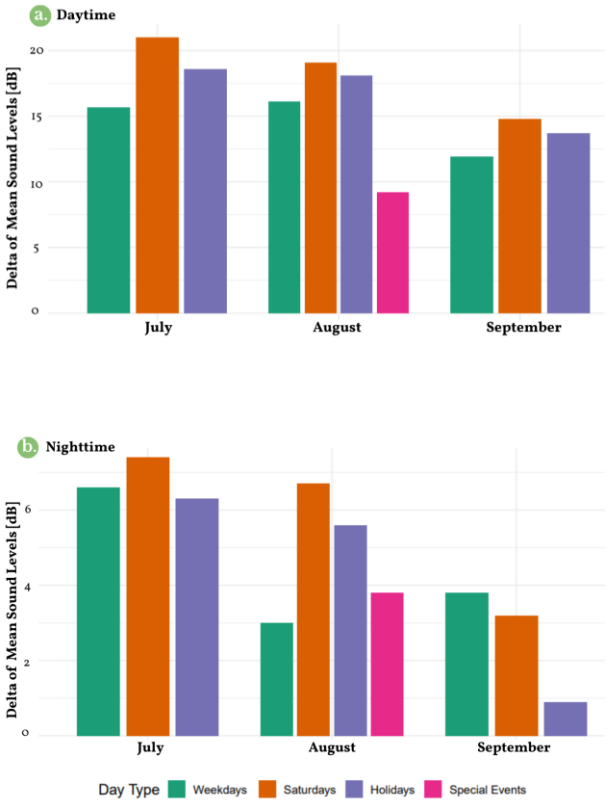


Figure 6. Difference in average daytime (a) and nighttime (b) noise levels (delta), categorized by day type.

4. DISCUSSION

This study provides a preliminary assessment of the acoustic environment at Nivolet Pass during the road opening period, revealing significant temporal variations in noise levels influenced by the seasonal dynamics of tourism and vehicular activity, and by the road closure. Such patterns are characteristic of protected areas with seasonal access [18].

The highest equivalent noise levels (Leq) were recorded in July, coinciding with the peak tourist influx and increase in traffic. This is in line with previous studies showing a direct correlation between road traffic density and environmental noise [19, 20]. The subsequent decline in Leq values in August and September reflects the progressive decrease in visitor numbers, further

highlighting the role of anthropogenic pressure as a primary driver of changes in the soundscape.

Daytime noise levels exceeded nighttime levels by more than 10 dB, a discrepancy attributed to motorised traffic and human activity during the diurnal hours, consistent with observations in other natural and semi-natural areas [21]. While the recorded noise levels were within the legal limits for secondary extra-urban roads (Presidential Decree no. 142/2004), they often exceeded the proposed thresholds for quiet areas (Legislative Decree no. 194/2005). This suggests that, despite legal compliance, the acoustic environment may still be compromised in terms of ecological and recreational expectations.

Temporal analysis of hourly Leq patterns further clarifies the impact of human activity on noise dynamics. In July, peak levels were observed in the late morning and afternoon on weekdays, with values of 56.9 dB at 11:00, 58.4 dB at 15:00, and 57.4 dB at 17:00. On Saturdays, more intense and prolonged noise events were recorded at 11:00 (62.7 dB), 12:00 (64.6 dB), and 16:00 (66.6 dB), due to increased recreational activity. Noise levels on holidays were lower overall, but still showed pronounced peaks around 13:00 (59.2 dB) and at 16:00 (60.7 dB), reinforcing the hypothesis that weekend and holiday tourism has a significant impact on the acoustic environment [13, 22]. A similar trend was observed in August and September, although with reduced intensity, reflecting the seasonal decrease in visitors.

Analysis of the monthly mean sound pressure levels and their deviation from the background noise (Δ) further highlights the influence of road accessibility on the dynamics of the soundscape. July showed the most pronounced Δ values, with marked differences between day and night, especially during Saturdays (21 dB during the day and 7.4 dB at night) and holidays (18.6 dB during the day and 6.3 dB at night). These findings are consistent with previous research showing that increased human presence in protected areas increases ambient noise, potentially disrupting wildlife communication and visitor experience [18]. In particular, during the special event days, when motorised traffic was restricted, noise levels decreased significantly and approached background conditions. This highlights the effectiveness of traffic management strategies in reducing noise pollution and maintaining soundscape quality in protected areas.

5. CONCLUSIONS

The results of this study show how seasonal tourism and vehicular traffic shape the acoustic landscape of Nivolet Pass, with significant differences in noise levels between months and times of day. While the levels recorded are in line with the current legal limits for secondary roads outside urban areas, they often exceed the limits recommendetions for quiet areas. This discrepancy highlights the inadequacy of the current legal limits to take into account the specific environmental context of SP50, which crosses sensitive habitats and is home to species of high conservation value.

A particularly important aspect that emerged from the analysis concerns the special days of experimental mobility management, when the road was closed to motorised traffic and reserved for outdoor activities (such as cycling and Nordic walking). On these days, noise levels were significantly reduced, with a Δ of 9.2 dB during the day and 3.8 dB at night, demonstrating the effectiveness of these initiatives in reducing acoustic impact and improving environmental quality.

The next phase of the project will involve detailed analysis of the data obtained through the expansion of the monitoring network, which has included the installation of additional acoustic detection stations and the introduction of low-cost recording devices for soundscape analysis. This analysis phase will provide a deeper understanding of the ecological impact of anthropogenic noise and help design more targeted noise management strategies for sensitive areas. The results of this analysis will be fundamental in optimising conservation policies, promoting a balance between environmental protection and sustainable access to protected areas.

6. REFERENCES

[1] G. Shannon, M. F. McKenna, L. M. Angeloni, K. R. Crooks, K. M. Fristrup, E. Brown, ... & G. Wittemyer: "A synthesis of two decades of research documenting the effects of noise on wildlife," *Biological Reviews*, vol. 91, no. 4, pp. 982–1005, 2016.

[2] H. Brumm and H. Slabbekoorn: "Acoustic communication in noise," *Advances in the Study of Behavior*, vol. 35, pp. 151–209, 2005.

[3] R. T. Buxton, M. F. McKenna, D. Mennitt, K. Fristrup, K. Crooks, L. Angeloni, and G. Wittemyer:

"Noise pollution is pervasive in US protected areas," *Science*, vol. 356, no. 6337, pp. 531–533, 2017.

[4] C. D. Francis and J. R. Barber: "A framework for understanding noise impacts on wildlife: an urgent conservation priority," *Frontiers in Ecology and the Environment*, vol. 11, no. 6, pp. 305–313, 2013.

[5] W. Halfwerk and H. Slabbekoorn: "Pollution going multimodal: the complex impact of the human-altered sensory environment on animal perception and performance," *Biology Letters*, vol. 11, no. 4, p. 20141051, 2015.

[6] C. Rahbek, M. K. Borregaard, R. K. Colwell, B. O. Dalsgaard, B. G. Holt, N. Morueta-Holme, ... & J. Fjeldså: "Humboldt's enigma: What causes global patterns of mountain biodiversity?," *Science*, vol. 365, no. 6458, pp. 1108–1113, 2019.

[7] M. Brambilla, F. Casale, V. Bergero, G. Bogliani, G. M. Crovetto, R. Falco, ... & I. Negri: "Glorious past, uncertain present, bad future? Assessing effects of land-use changes on habitat suitability for a threatened farmland bird species," *Biological Conservation*, vol. 143, no. 11, pp. 2770–2778, 2010.

[8] D. Araújo, M. B. Errea, and M. P. Martinez-Rica: "Exposure of global mountain systems to climate warming during the 21st century," *Global Environmental Change*, vol. 17, pp. 420–428, 2007.

[9] A. Serrurier, P. Zdroik, R. Isler, T. Kornienko, E. Peris-Morente, T. Sattler, and J. N. Pradervand: "Mountain is calling–decrypting the vocal phenology of an alpine bird species using passive acoustic monitoring," *Ibis*, vol. 166, no. 4, pp. 1338–1353, 2024.

[10] Y. Vitasse, S. Ursenbacher, G. Klein, T. Bohnenstengel, Y. Chittaro, A. Delestrade, C. Monnerat, M. Rebetez, C. Rixen, N. Strebel, B. R. Schmidt, S. Wipf, T. Wohlgemuth, N. G. Yoccoz, and J. Lenoir: "Phenological and elevational shifts of plants, animals and fungi under climate change in the European Alps," *Biological Reviews*, vol. 96, pp. 1816–1835, 2021.

[11] F. Aletta, J. Kang, and Ö. Axelsson: "Soundscape descriptors and a conceptual framework for developing predictive soundscape models," *Landscape and Urban Planning*, vol. 149, pp. 65–74, 2016.

[12] Legislative Decree No. 194/2005 (Italy), "Article 4, Paragraph 10-bis", 2005.

[13] C. Tibone, M. Masoero, F. Berlier, G. Tabozzi, D. Crea, C. Tartin, G. Agnesod: "Seasonal Variability of the Acoustic Climate of Ski Resorts in the Aosta Valley Territory," *Environments*, vol. 7, no. 3, p. 18, 2020.

[14] Habitat Directive 92/43/EEC (European Union), "Conservation of natural habitats and of wild fauna and flora," 1992.

[15] Presidential Decree No. 142/04 (Italy), "Provisions for the containment and prevention of noise pollution from road traffic, in accordance with Article 11 of Law No. 447/1995," 2004.

[16] Ministerial Decree No. 16/03/1998 (Italy), "Technical standards for the determination of exposure limits to noise." 1998.

[17] UNI EN ISO 1996-1:2017 (Italy), "Acoustics – Description and measurement of environmental sound – Part 1: Determination of sound pressure levels." 2017.

[18] R. T. Buxton, M. F. McKenna, D. Mennitt, K. Fristrup, K. Crooks, L. Angeloni, and G. Wittemyer: "Noise pollution is pervasive in US protected areas," *Science*, vol. 356, no. 6337, pp. 531–533, 2017.

[19] E. M. Salomons and M. B. Pont: "Urban traffic noise and the relation to urban density, form, and traffic elasticity," *Landscape and Urban Planning*, vol. 108, no. 1, pp. 2–16, 2012.

[20] D. A. Jiménez-Uribe, D. Daniels, Á. González-Álvarez, and A. M. Vélez-Pereira: "Influence of vehicular traffic on environmental noise spectrum in the tourist route of Santa Marta City," *Energy Reports*, vol. 6, pp. 818–824, 2020.

[21] R. T. Buxton, M. F. McKenna, D. Mennitt, E. Brown, K. Fristrup, K. R. Crooks, ... & G. Wittemyer: "Anthropogenic noise in US national parks–Sources and spatial extent," *Frontiers in Ecology and the Environment*, vol. 17, no. 10, pp. 559–564, 2019.

[22] G. Agnesod, C. Tibone, C. Tartin, D. Crea, and F. Berlier: "High naturalness alpine areas acoustical characterization in Aosta Valley," in *Proc. of the International Euronoise Congress*, 2006.

DOI: 10.61782/fa.2025.0355



FORUM ACUSTICUM
EURONOISE 2025

EVALUATING BACKGROUND NOISE CRITERIA FOR ESTIMATING OUTDOOR-TO-INDOOR LEVELS VIA A STATISTICAL LEARNING MODELLING FRAMEWORK

Michail Evangelos Terzakis[1*] **Cédric Van hoorickx**[1] **Maarten Hornikx**[1]
Faridah Naim[2] **Daniela Fecht**[3] **Anna L. Hansell**[4,5] **John Gulliver**[6]
[1] Building Acoustics Group, Department of the Built Environment, Eindhoven University of Technology, Eindhoven, The Netherlands
[2] School of Health Sciences, Universiti Sains Malaysia, Kubang Kerian, Malaysia
[3] School of Public Health, Imperial College London, London, The United Kingdom
[4] The National Institute for Health Research (NIHR), Leicester Biomedical Research Centre (BRC), Leicester General Hospital, Leicester, The United Kingdom
[5] The National Institute of Health Research (NIHR) Health Protection Research Unit (HPRU) in Environmental Exposures and Health, University of Leicester, Leicester, The United Kingdom
[6] Population Health Research Institute, City St George's, University of London, London, The United Kingdom

ABSTRACT

Urban noise exposure has shown significant negative associations with health effects, largely based on outdoor assessments. As most people spend the majority of time indoors, especially at night, assessments should include the attenuation of outdoor noise exposure to estimate indoor noise exposure for developing epidemiological evidence on health-related noise effects. In this study, a prediction modelling framework is defined for estimating the outdoor-to-indoor level differences for three time periods (day, evening, and night) via statistical learning models, employing synchronised and unsupervised outdoor and indoor noise exposure measurements from 49 locations in Greater London, UK. The study evaluates which background noise criteria expressed via percentile indicators (L_{A90}, L_{A95}, and L_{A99}) under two conditions are most effective. In the analysis, stronger correlations between the equivalent outdoor-to-indoor level differences and outdoor levels were obtained after applying the more stringent condition. Particularly, stronger night-time relationships (r = 0.66–0.76) were obtained compared to daytime (r = 0.55–0.63) and evening (r = 0.43–0.55) relationships. Regarding the modelling validation, the lowest RMSE was observed in the night-time models (RMSE = 2.0–2.8dB(A)), followed by the day-time (RMSE = 2.9–3.0dB(A)) and evening (RMSE = 2.5–4.0dB(A)) models. The study's findings support the value of random forest models in estimating outdoor-to-indoor level differences, executing errors mostly below the just perceptible level difference (3dB(A)).

Keywords: *outdoor-to-indoor, noise exposure, statistical learning, attenuation.*

*__Corresponding author__: m.e.terzakis@tue.nl.

__Copyright__: ©2025 Terzakis et al. This is an open-access article distributed under the terms of the Creative Commons Attribution 3.0 Unported License, which permits unrestricted use, distribution, and reproduction in any medium, provided the original author and source are credited.

1. INTRODUCTION

The impact of noise exposure on human health has shown significant negative associations with a range of non-auditory health effects effects, including annoyance, sleep disturbance, reduced quality of life, and cardio-metabolic outcomes [1, 2]. The consequences of chronic noise exposure in childhood may manifest in adverse outcomes in later life [2]. Furthermore, the impact of noise exposure,

associated with the indirect accumulation of measurement of noise exposure in human organisms [3], underscores the importance of expressing noise exposure via objective noise indicators for exploring exposure-response relationships [2].

In urban noise exposure studies, outdoor noise exposure levels are usually employed as a basis for analyses in contrast to the utilisation of indoor levels [2]. This suggests the potential for a systematic risk of bias in the identification of exposure-response relationships. This is particularly salient in relation to vulnerable groups whose activities are predominantly confined to indoor environments. Hence, statistical prediction models have been developed with the purpose of estimating outdoor-to-indoor level differences based on outdoor levels as well as parameters related to outdoor environment, indoor environment, and building façade characteristics. This has been done via both supervised [4] and unsupervised [5] measurement approaches. These models allow for a more precise estimation of attenuation levels in comparison to a single-valued attenuation factor (e.g., [4–7]).

Focusing on the incorporation of unsupervised noise measurements in the estimation of outdoor-to-indoor level differences, a recent methodology has been proposed [5]. In this methodology, the L_{A99} percentile indicator has been applied for the estimation of background noise levels, while two defined background noise conditions (6dB(A) and 10dB(A)) verify the incorporation of the proper indoor (and their respective outdoor) noise levels.

The objective of this study was to establish attenuation levels for use in the adjustment of outdoor noise levels to facilitate the prediction of indoor noise exposure levels. First, the impact of indoor background noise levels on the relationship between the outdoor-to-indoor level differences and outdoor levels was investigated via experimental data from 49 dwellings in Greater London, UK. Second, statistical learning models (random forest), were developed for predicting the outdoor-to-indoor attenuation levels with respect to outdoor levels and predictors related to outdoor and indoor environment as well as façde characteristics.

2. METHODOLOGY

In this section, the principal methodologies are presented, corresponding to the dataset processing and the prediction modelling. For a comprehensive overview of the study design, including the detailed procedure of the noise exposure assessment, the reader is directed to [8].

2.1 Data Processing

Following the capturing of outdoor and indoor noise exposure levels [8], the A-weighted equivalent noise indicator was used for the assessment of outdoor ($L_{\text{Aeq,Out}}$), indoor ($L_{\text{Aeq,In}}$), and outdoor-to-indoor noise exposure levels ($L_{\text{Aeq,Out-In}}$) for day-time (07:00-19:00), evening (19:00-23:00), and night-time (23:00−07:00) period based on an integration time of 1-minute and a time-period of 1-hour.

Since noise exposure measurements were conducted via an unsupervised approach, a data processing procedure was employed for capturing the representative outdoor-to-indoor levels. Particularly, noise exposure (i.e. full bandwidth) measurements, where indoor levels exceeded outdoor levels, were excluded. Then, the spectral characteristics of both outdoor and indoor exposure levels were evaluated in 1/3-octave bands (50Hz–5kHz). Consequently, measurements for which the indoor spectral levels were determined to exceed those of the outdoors were excluded. In order to reduce the impact of indoor background noise on the identification of the appropriate outdoor-to-indoor level differences, some percentile noise indicators were selected to express the background noise levels. These correspond to $L_{\text{A99,In}}$, $L_{\text{A95,In}}$, and $L_{\text{A90,In}}$. Finally, two background noise conditions (6dB(A) and 10dB(A)) were defined associated to the minimum level difference between the equivalent indoor levels and the background noise levels (i.e., $L_{\text{Aeq,In}} - L_{\text{AN,In}}$). Differences lower than the two conditional levels indicate a significant effect of the indoor background noise, and therefore they were excluded.

2.2 Prediction Modeling

Initially, the relationship between outdoor levels and outdoor-to-indoor level differences per time-period (day, evening, and night), background noise indicator (L_{A90}, L_{A95}, and L_{A99}) and condition (6dB(A) and 10dB(A)) was verified via a simple regression model, using the R^2 metric and Pearson correlation coefficient (r). For explaining the percentage of unexplained variance in the estimation of the outdoor-to-indoor level difference, random forest (RF) models were developed. Numerical predictors associated to the outdoor noise levels ($L_{\text{Aeq,Out}}$), the room volume (RV), the window size (WS) and the window numbers (WN), as well as to the categorical variables associated to the window type (WT), the room type (RT), the building type (BT), and the site type (ST) were applied. In all the models, the datasets were split into 70% for training and 30% for testing. The random forest models were ap-

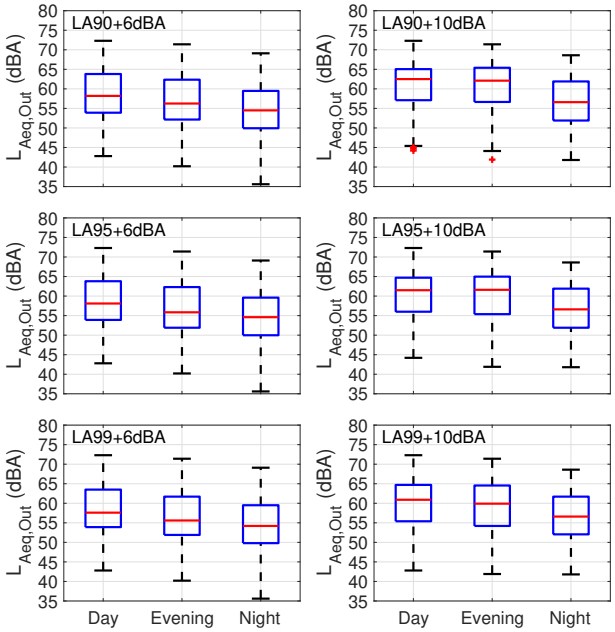


Figure 1. Outdoor levels per time period, background noise indicator and condition.

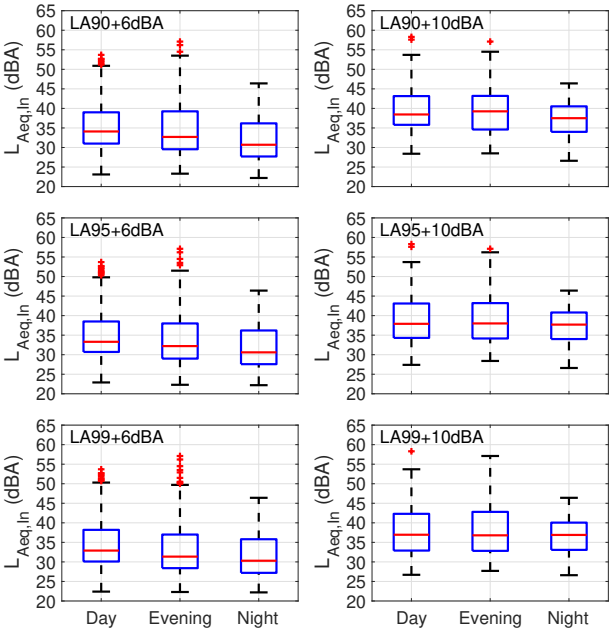


Figure 2. Indoor levels per time period, background noise indicator and condition.

plied via the *ranger* package [9] in RStudio software. All the models were tuned via three (hyper)parameters: the number of trees (n_{tr}), the number of variables (n_{v}) used at each split (m_{tr}), and the complexity of trees (c_{t}). The number of trees was chosen to range from 70 to 1200 trees with a step of 10 trees. The number of split-variables used to tune the models ranged from 2 to 8 variables with a step of 1 variable. Regarding the complexity of tree parameter (tree nodes), the number of nodes ranged from 1 node to 15 nodes with a step of 1 node. Moreover, the (normalized) importance of each predictor per model was evaluated. Finally, the error between predicted and observed $L_{\text{Aeq,Out-In}}$ levels was verified via the root-mean-squared error (RMSE) metric [10].

3. RESULTS

3.1 Assessment of Noise Exposure Levels

First, the outdoor, indoor, and outdoor-to-indoor noise exposure levels were assessed per time period, background noise indicator and condition, and the results are presented in Fig. 1, Fig. 2 and Fig. 3, respectively.

As seen from Fig. 1 and Fig. 2, the median outdoor and indoor exposure levels based on the 6dB(A) background noise condition are lower than the corresponding

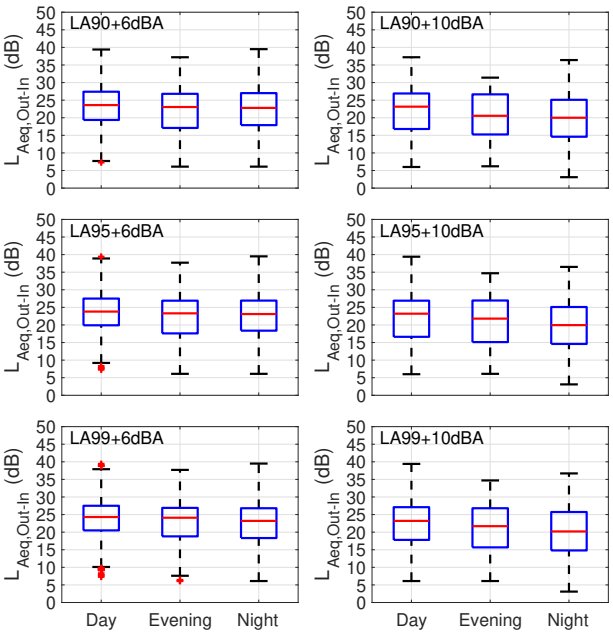


Figure 3. Outdoor-to-indoor levels per time period, background noise indicator and condition.

levels based on the 10dB(A) background noise condition for all time periods and background noise indicators. Fur-

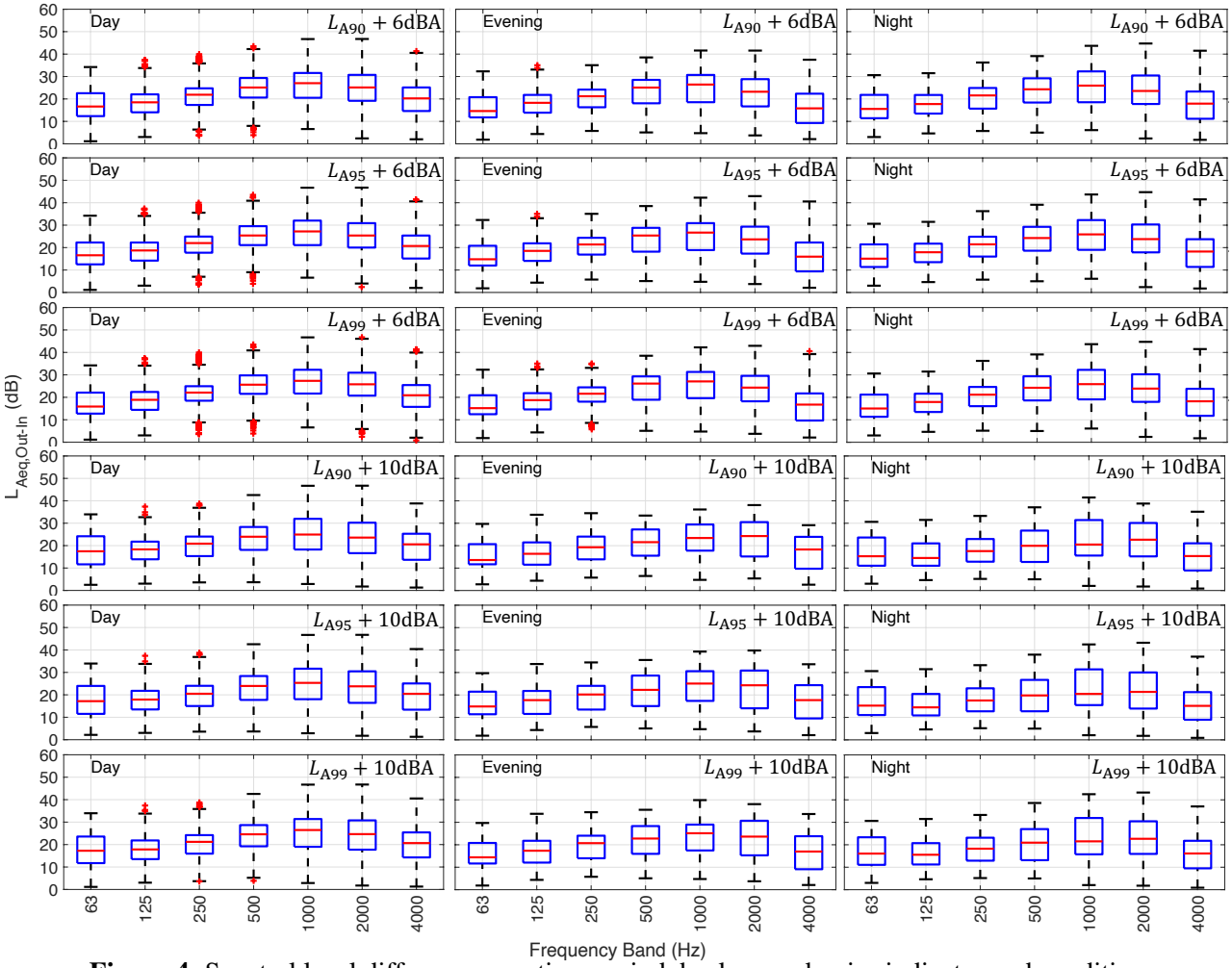


Figure 4. Spectral level differences per time period, background noise indicator and condition.

thermore, the median day-time outdoor and indoor levels are generally higher than evening and night-time levels across the background noise conditions and indicators.

Opposite to Fig. 1 and Fig. 2, the median outdoor-to-indoor levels in Fig. 3 presented a downward trend by increasing the background noise condition across the background noise indicators and exposure periods. The decline in outdoor-to-indoor levels in the transition to stringent background noise conditions is associated with the higher transmission of energy affected less by the indoor background noise. Consequently, the stringent background noise condition is responsible for the presence of broader IQR (interquartile range) across the time periods and background noise indicators.

Focusing on the median average spectral outdoor-to-indoor levels per 1/1-octave bands in Fig. 4, it can be seen that levels based on the 10dB(A) condition present less outliers compared to the levels based on the 6dB(A) condition. Furthermore, the stringent background condition presents broader IQR at most frequency bands across the time periods and background noise indicators.

3.2 Relationship between $L_{Aeq,Out}$ and $L_{Aeq,Out-In}$

For exploring the relationship between outdoor and outdoor-to-indoor levels, simple regression models per background noise indicator and condition were executed. In Fig. 5, the scatter plots between the $L_{Aeq,Out}$ and $L_{Aeq,Out-In}$ are presented, while in Tab. 1, the R^2 and Pearson correlation coefficient (r) are summarized.

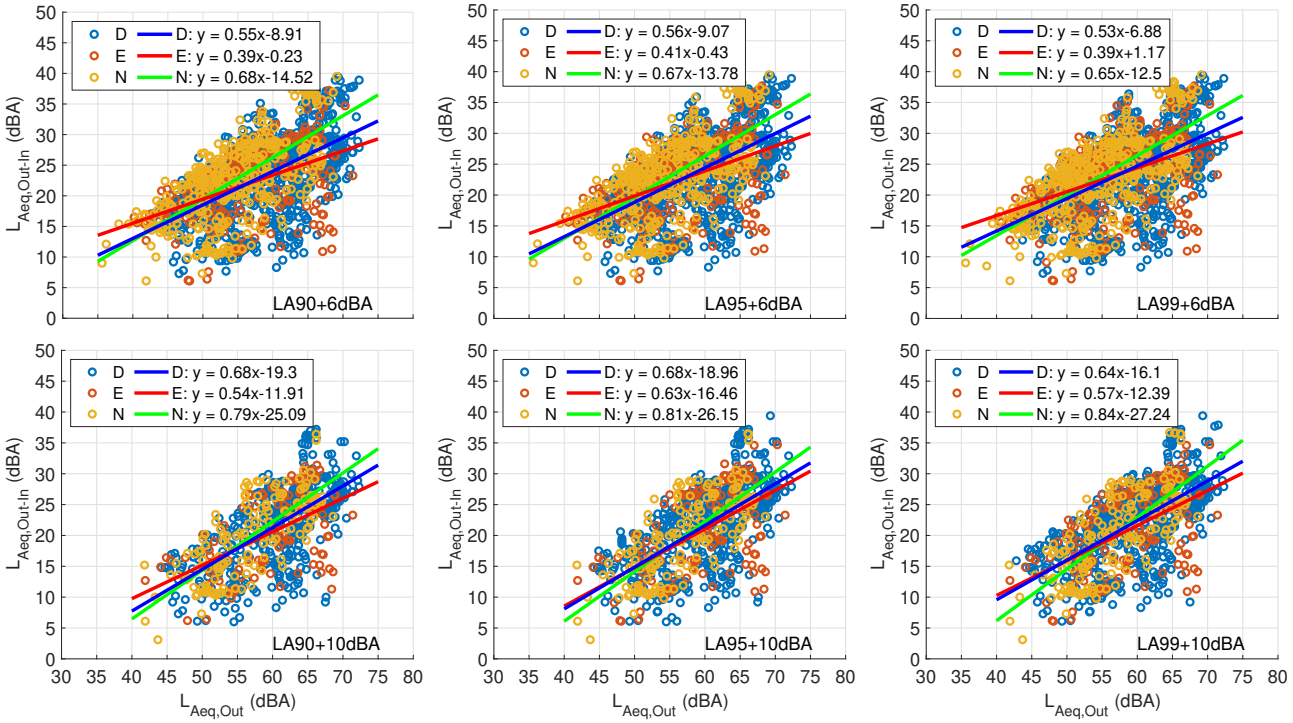


Figure 5. Relationship between outdoor and outdoor-to-indoor levels per time period and setting.

Table 1. Diagnostics per explored relationship.

Model	BGN: 6dB(A)		BGN: 10dB(A)	
	R^2	r	R^2	r
$L_{Aeq,LA90,D}$	0.34	0.58	0.40	0.63
$L_{Aeq,LA95,D}$	0.34	0.58	0.39	0.62
$L_{Aeq,LA99,D}$	0.31	0.55	0.39	0.62
$L_{Aeq,LA90,E}$	0.20	0.44	0.27	0.52
$L_{Aeq,LA95,E}$	0.20	0.45	0.30	0.55
$L_{Aeq,LA99,E}$	0.19	0.43	0.27	0.52
$L_{Aeq,LA90,N}$	0.44	0.66	0.57	0.76
$L_{Aeq,LA95,N}$	0.44	0.66	0.57	0.75
$L_{Aeq,LA99,N}$	0.44	0.66	0.56	0.75

Green cells: Moderate, Blue cells: Strong

As seen from Fig. 5 and focusing on Tab. 1, an increase in background noise from 6dB(A) to 10dB(A) resulted in stronger correlations, indicating the inclusion of less affected indoor background noise levels. In particular, the correlation coefficient exhibited an increase from moderate to strong for day-time exposure. For evening exposure, the correlation coefficient increased, yet it maintained a moderate correlation degree. Regarding night-time exposure, the correlation coefficient exhibited an increase, and therefore it continued to demonstrate a strong degree. As the indoor background levels exhibited less significant variations at night-time stronger correlations were obtained in comparison to the day-time and evening time periods. By comparing r and R^2 with respect to the type of background noise indicator, it can be seen that there were no significant differences among them across the time periods and background noise conditions. Hence, it can be suggested that for a single response relationship, the background noise indicator is less important than the background condition.

3.3 Prediction Modelling

Following the tuned RF models, the importance of each predictor in the estimated response ($L_{\text{Aeq,Out-In}}$) was identified via the normalized importance and the results are presented in Fig. 6.

As seen from Fig. 6, the $L_{\text{Aeq,Out}}$ emerges as the most important predictor across all models, explaining the majority of the variance in the estimation of the outdoor-to-indoor levels. For the 6dB(A)-based models, the RV, WS, and BT predictors mostly accounted for more than 40% of the variance across noise conditions and time periods. In contrast, the ST and WT predictors for the day-time and

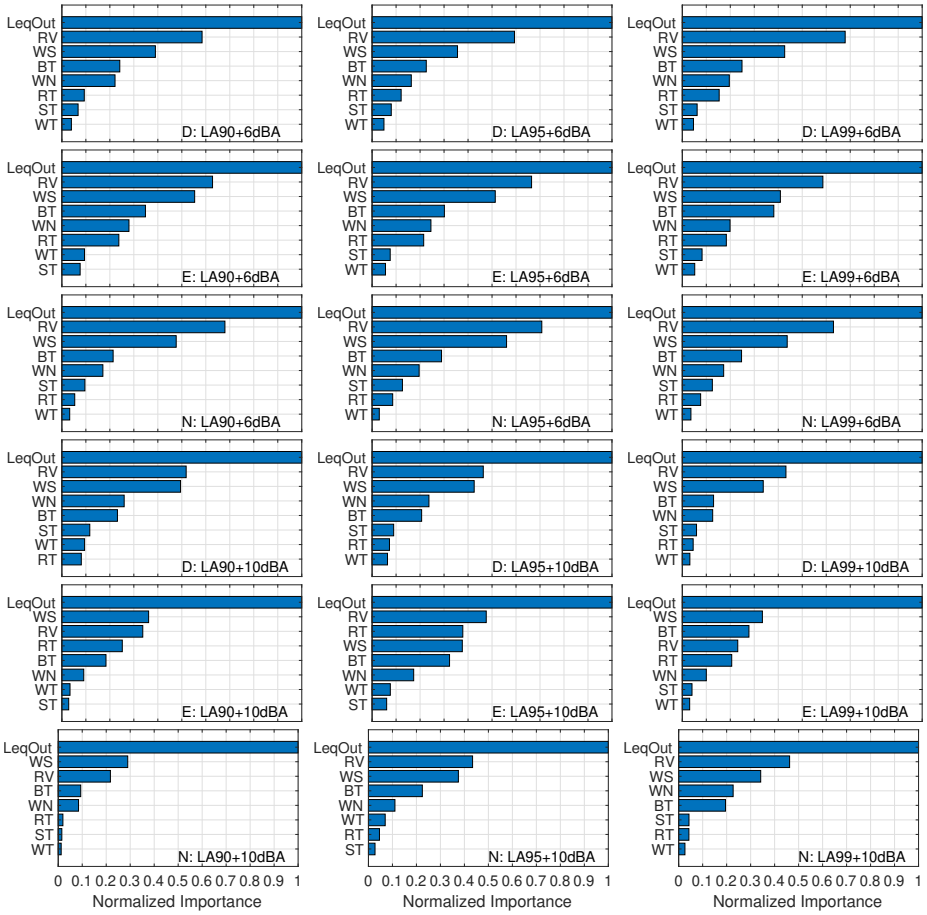


Figure 6. Importance of predictors in models per time period, background noise indicator, and condition.

evening models as well as the RT and WT predictors for the night-time models explained less than the 10% of variance. In the 10dB(A) models, the RV and WS predictors accounted for most of 40% of variance for the day-time models. For evening models, the WS and RV predictors in the L_{A90} model, the WS, RV, BT, and RT predictors in the L_{A95} model, and the WS in the L_{A99} model accounted for more than 30% of variance. For night-time models, the RV and WS predictors primarily accounted for a greater of 30% variance across the background noise indicators. Finally, in all the time period models, the ST and WT predictors explained less than the 10% of variance.

For validating the performance of the developed models, the test datasets were employed and the observed outdoor-to-indoor levels were compared with the estimated levels. The performance of models based on the training and test datasets, is presented in Tab. 2.

Table 2. Modelling performance.

Model	BGN: 6dB(A)				BGN: 10dB(A)			
	Train Dataset		Test Dataset		Train Dataset		Test Dataset	
	RMSE	R^2	RMSE	R^2	RMSE	R^2	RMSE	R^2
$L_{\text{Aeq,LA90,D}}$	3.09	0.76	2.91	0.77	3.12	0.77	2.98	0.79
$L_{\text{Aeq,LA95,D}}$	2.77	0.80	2.97	0.77	3.25	0.77	2.64	0.83
$L_{\text{Aeq,LA99,D}}$	2.75	0.79	2.91	0.78	2.85	0.80	2.99	0.80
$L_{\text{Aeq,LA90,E}}$	3.41	0.71	2.53	0.83	4.08	0.59	4.00	0.61
$L_{\text{Aeq,LA95,E}}$	3.12	0.76	2.74	0.81	3.89	0.77	3.65	0.77
$L_{\text{Aeq,LA99,E}}$	3.36	0.71	2.94	0.76	3.90	0.66	3.42	0.76
$L_{\text{Aeq,LA90,N}}$	2.12	0.90	2.38	0.89	2.99	0.79	2.00	0.90
$L_{\text{Aeq,LA95,N}}$	1.93	0.92	2.28	0.89	2.87	0.82	2.22	0.88
$L_{\text{Aeq,LA99,N}}$	2.26	0.88	2.01	0.92	2.28	0.88	2.83	0.84

Green cells: RMSE≤3dB(A), Blue cells: RMSE>3dB(A)

As illustrated in Tab. 2 and with particular attention to the test dataset, night-time models exhibited the lowest RMSE levels, followed by day-time models across the background noise indicators and conditions. In the

case of the evening models, a greater degree of variation was exhibited, with RMSE levels exceeding 3dB(A) for the more stringent background condition across all background noise indicators. In consideration of the less stringent background condition, RMSE levels lower than 3dB(A) were obtained in the evening models and across the background noise indicators.

3.4 Single-Valued Attenuation Factors

Focusing on the single-valued attenuation factors, the estimated factors were compared to the observed ones and the results are presented in Fig. 7.

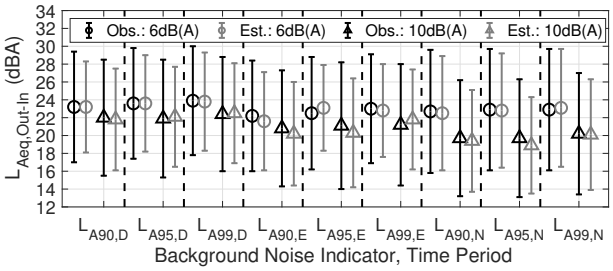


Figure 7. Single-valued attenuation factors per time period, background noise indicator and condition.

As Fig. 7 illustrates, the outdoor-to-indoor attenuation factors for the 6dB-based models are higher than those for 10dB-based models. These differences are more pronounced in the case of night-time noise exposure than of day-time and evening exposure, presenting mean differences up to 4dB(A). Regarding the background noise indicator, mean differences up to 2dB(A) were detected for evening and day-time periods.

4. DISCUSSION

4.1 Noise Assessment

The incorporation of methodologies for the identification of appropriate noise exposure levels, associated with the transmission of noise exposure from outdoors to indoors, could be characterised as important, especially when noise exposure measurements are conducted via an unsupervised approach. The assessment of the relationship between the outdoor and outdoor-to-indoor levels revealed a stronger correlation by increasing the background noise condition from 6dB(A) to 10dB(A) across the time periods and background noise indicators. Consequently, a decrease in the median/mean outdoor-to-indoor levels and an increase in their interquartile ranges across the time periods and background noise indicators was obtained. Consequently, this is associated with the further minimization of noise levels affected by background levels, and therefore with the inclusion of noise levels related to higher transmission of energy. Our results demonstrate analogous trends to those previously depicted in [5]. Focusing on the type of background noise indicator for mitigating indoor background noise levels, it was observed that there were no significant differences in the outdoor-to-indoor levels between the background noise indicators used.

Various outdoor-to-indoor attenuation factors have been reported for closed windows, ranging from 25dB(A) to 32dB(A) [4,6,7,11]. These factors are contingent upon the characteristics of the measurement locations and the measurement methodology employed. In our study, analogous outcomes were obtained, particularly in the context of the 6dB(A) background noise condition, wherein the attenuation factor approximates 23dB(A) across the majority of the background noise indicators and time-periods. However, in the case of the 10dB(A) background noise condition, the outdoor-to-indoor level differences exhibited more pronounced fluctuations in terms of the time period, as opposed to the background noise indicators. Specifically, outdoor-to-indoor level differences of approximately 22dB(A) for day-time, 21dB(A) for evening, and 20dB(A) for night-time were obtained. This indicates the significant impact of the variations in indoor background noise levels and characteristics across the different time periods. Day-time outdoor and indoor levels reach higher levels in relation to the evening and night-time ones from various indoor and outdoor sound sources. Night-time exposure presents less level variations in both environments as well as lower indoor background noise levels, indicating a more representative period for exploring the noise propagation from outdoors to indoors.

4.2 Prediction Modeling

Regarding the performance of the prediction models, almost similar diagnostics were obtained across the different models. In order to gain a deeper understanding of the performance of the prediction models, the RMSE is interpreted by the ability of healthy ear to detect changes in broadband noise [12]. In this context, noise level differences of 3dB(A) and 5dB(A) are associated with just and clearly perceptible differences, respectively [12]. The majority of the day-time and night-time models are subjected to RMSEs that are up to the just perceptible level dif-

ference (3dB(A)), in contrast to the evening-time models where the RMSEs are up to the clearly perceptible level difference (5dB(A)). Regarding the background noise indicators, their performance presented similar diagnostic characteristics with respect to the time period. It is important to note that the number of predictors employed in this study was limited. Incorporating a greater number of measurements and predictors might lead to a more comprehensive dataset based on detailed built environment characteristics.

5. CONCLUSIONS

In this study, a methodology to derive outdoor-to-indoor noise attenuation levels for day, evening, and nigh time exposure was developed, utilising unsupervised outdoor and indoor noise exposure measurements with information related to building characteristics in random forest (regression) modelling. This method minimizes the presence of dominant indoor noise sources and background noise levels, considering the equivalent spectral characteristics of noise measurements. Across the various used background noise indicators, similar results were obtained. Finally, the attenuation factors obtained in the present study have been generated from UK data, reflecting localized noise sources and the characteristics of the built environment.

6. ACKNOWLEDGMENTS

This research was funded by the European Union's Horizon 2020 research and innovation program under grant agreement No. 874724, Equal-Life Project, part of the European Human Exposome network.

7. REFERENCES

[1] I. van Kamp, S. Simon, H. Notley, C. Baliatsas, and E. van Kempen, "Evidence Relating to Environmental Noise Exposure and Annoyance, Sleep Disturbance, Cardio-Vascular and Metabolic Health Outcomes in the Context of IGCB (N): A Scoping Review of New Evidence," *International Journal of Environmental Research and Public Health*, vol. 17, p. 3016, 4 2020.

[2] M. E. Terzakis, M. Dohmen, I. van Kamp, and M. Hornikx, "Noise Indicators Relating to Non-Auditory Health Effects in Children—A Systematic Literature Review," *International Journal of Environmental Research and Public Health*, vol. 19, p. 15633, 11 2022.

[3] W. Babisch, H. Ising, and Gallacher JE, "Health status as a potential effect modifier of the relation between noise annoyance and incidence of ischaemic heart disease," *Occupational and Environmental Medicine*, vol. 60, 10 2003.

[4] B. Locher, A. Piquerez, M. Habermacher, M. Ragettli, M. Röösli, M. Brink, C. Cajochen, D. Vienneau, M. Foraster, U. Müller, and J. Wunderli, "Differences between Outdoor and Indoor Sound Levels for Open, Tilted, and Closed Windows," *International Journal of Environmental Research and Public Health*, vol. 15, 1 2018.

[5] M. Terzakis, C. Van hoorickx, M. Hornikx, F. Naim, A. Hansell, and J. Gulliver, "Estimation of Low Frequency Outdoor-to-indoor Noise Attenuation Factors Based on Night-time Noise Exposure," in *30th International Congress on Sound and Vibration (ICSV)*, (Amsterdam, The Netherlands), pp. 1–8, 2024.

[6] WHO, "Environmental noise guidelines for the European region," *World Health Organization*, 2018.

[7] S. Pirrera, E. De Valck, and R. Cluydts, "Nocturnal road traffic noise assessment and sleep research: The usefulness of different timeframes and in- and outdoor noise measurements," *Applied Acoustics*, vol. 72, pp. 677–683, 9 2011.

[8] F. Naim, D. Fecht, A. Hansell, and J. Gulliver, "Assessment of residential exposure to aircraft, road traffic and railway noise in London: Relationship of indoor and outdoor noise," in *Euronoise, 2018*, (Crete, Greece), pp. 2905–2912, 2018.

[9] M. N. Wright and A. Ziegler, "ranger : A Fast Implementation of Random Forests for High Dimensional Data in C++ and R," *Journal of Statistical Software*, vol. 77, no. 1, 2017.

[10] E. Bartz and T. Beielstein, *Hyperparameter tuning and optimization applications. In: Hyperparameter tuning for machine and deep learning with R: a practical guide.* Springer, 2023.

[11] F. Scamoni and C. Scrosati, "The facade sound insulation and its classification," in *Forum Acusticum, Kraków, Poland*, 2014.

[12] E. Murphy and E. A. King, "Principles of Environmental Noise," in *Environmental Noise Pollution*, pp. 9–49, Elsevier, 2014.

DOI: 10.61782/fa.2025.0911



FORUM ACUSTICUM
EURONOISE 2025

TOWARDS THE WORLDS LARGEST NOISE COMPLAINT DATABASE

Eoin A King[1*] **Enda Murphy**[2] **Thomas Messerer**[3] **Theo Messerer**[3]

[1] Mechanical Engineering and Ryan Institute, University of Galway, Ireland
[2] University College Dublin, Ireland
[3] Silencio Network LLC, USA

ABSTRACT

Silencio is a community-driven platform tackling the escalating issue of noise pollution across the world. Through its free application, Silencio aims to become the world's largest citizen science initiative dedicated to combating noise pollution. Users contribute hyper-local noise data and are incentivized with 'noise coins', redeemable for goods, services, and environmental initiatives within the platform. As of April 2025, Silencio has collected 35 billion data points from over 1 million sensors across 180 countries. A key feature allows users to log noise complaints, transforming crowd-sourced data into actionable insights for governments and urban planners. This paper explores the noise complaints dataset, analysing patterns in timing, location, and the types of noise most likely to prompt complaints. We believe this represents the world's largest noise complaint database.

Keywords: Noise**,** complaints, citizen science.

1. INTRODUCTION

Silencio is a community-driven platform tackling urban noise pollution through a free smartphone application (app) that aspires to be the largest citizen science project in the world [1]. By leveraging blockchain technology, it enables users worldwide to contribute real-time noise data by transforming their smartphones into anonymous noise monitoring devices that record decibel levels, creating a detailed global noise map. Users are incentivized through 'noise coins' which can be redeemed for goods, services, and environmental initiatives within the platform, allowing them to generate passive income while improving urban living conditions. By utilizing blockchain technology, the system enables users to maintain full control over their data and receive equitable compensation for their contributions. The economic model incorporates a revenue-sharing mechanism, whereby a substantial fraction of commercialization proceeds are returned to the data-generating community, aiming to establish a sustainable and equitable web3 data economy.

With an innovative tokenomics model, Silencio fosters a sustainable and engaging ecosystem where participants actively combat noise pollution while benefiting from their contributions. By collecting accurate, real-time data, the platform empowers governments, city planners, and industries to make informed decisions, leading to more effective noise control strategies and enhanced quality of life for urban residents.

As of April 2025, there are over 1 million devices on the Silencio Network, across 180 countries. In the month of February 2025 alone, there were 600,000 hours measured across 51.9 million measurement uploads, 400,0000 check-ins and 125,000 new users. Since its inception in 2023, Silencio has become the largest decentralized noise intelligence network in the world.

1.1 Silencio App

1.1.1 Street Level Explorer

Silencio uses a data pipeline to continuously stream information from their database for user interaction. This

[*] ***Corresponding author***: *eoin.king@universityofgalway.ie*

Copyright: *©2025 King et al. This is an open-access article distributed under the terms of the Creative Commons Attribution 3.0 Unported License, which permits unrestricted use, distribution, and reproduction in any medium, provided the original author and source are credited.*

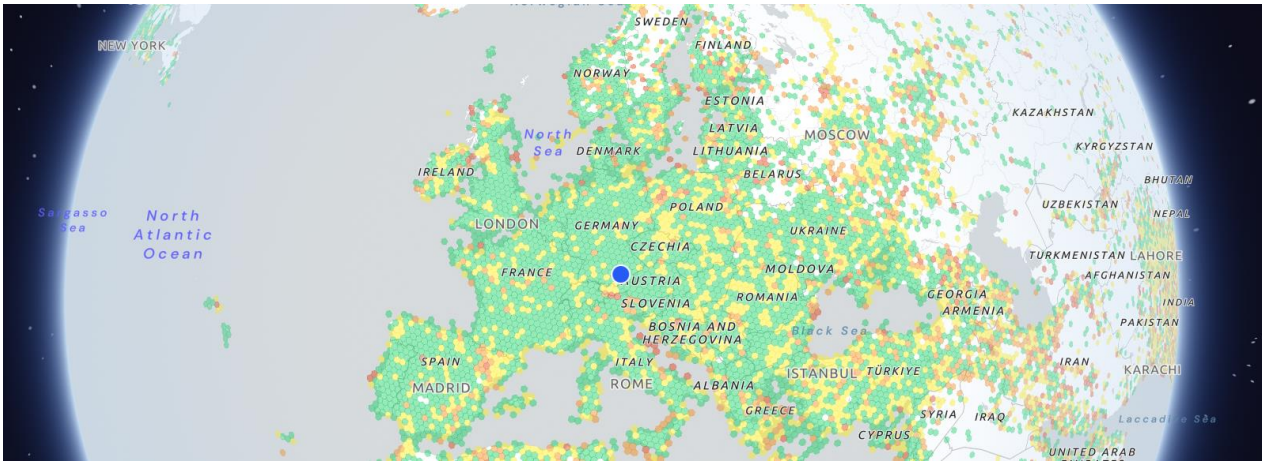


Figure 1. The Silencio Steet Level Explorer

pipeline systematically processes hexagons at multiple resolutions, ranging from 3 - 13, depending on geographic location. It then recalculates and updates the average noise levels in each hexagon. Overall results are displayed on a map that users can explore from a broad overview (Figure 1) to the street level (for examples a street level map for the city of Malaga is displayed in Figure 2). These maps are developed from real noise measurement data, uploaded by users of the Silencio App.

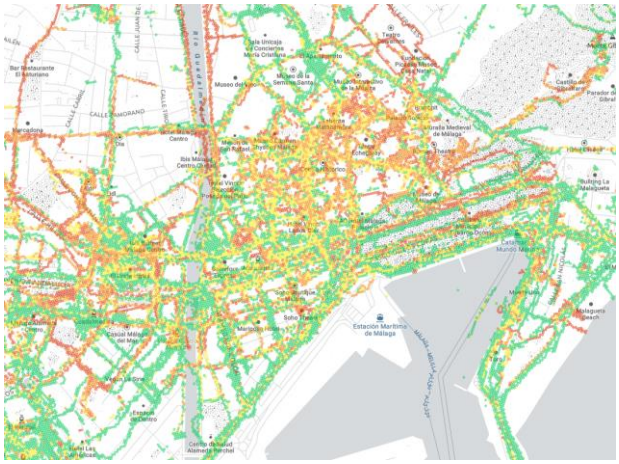


Figure 2. Results from Malaga, Spain

1.1.2 Venue Check in Explorer

Silencio also lets users check in at venues and measure and report noise levels in real-time using their mobile devices. The app verifies the user's location to ensure noise levels are accurately associated with the corresponding venue. The app first records a 15 second noise measurement. After that, users answer a series of questions about their environment, such as whether they are indoors or outdoors, how easy it is to have a conversation, and how crowded the venue is. These measurements are then aggregated and displayed on a map for easy visualization. Users can view the number of check-ins and the average noise level at each venue, all of which are displayed on the map for easy reference.

1.1.3 Noise Complaints

The app also allows users to log noise complaints when they encounter excessive noise in their area. Complaints can be reported at any location or venue, making it easy for users to highlight problematic areas. Each complaint is recorded and displayed on the map, with clusters indicating areas with higher noise levels based on the zoom level. This visual representation helps users and city officials quickly identify noise hotspots. By collecting and analyzing this data, cities can gain valuable insights into noise pollution trends, enabling them to implement better urban planning strategies and public health initiatives to create quieter, more livable spaces.

1.1.4 Noise Coins

Silencio harnesses blockchain technology to build a global community of users contributing to a real-time noise map. By turning their smartphones into anonymous noise monitoring devices, users help collect decibel measurements, creating a detailed worldwide picture of noise levels. In return for their contributions, users can earn passive income while also helping to improve urban soundscapes. With an innovative tokenomics model, Silencio fosters a sustainable and engaging ecosystem where participants are rewarded for their efforts in reducing noise pollution and enhancing overall quality of life.

Central to the Silencio ecosystem is the $SLC token, powered by the Blocksound Foundation, which is used for rewarding contributors, transactions, staking, and governance across the network. The network allows contributors to earn $SLC tokens as a reward for their data contributions, ensuring that every user is a stakeholder in the network's success.

2. NOISE COMPLAINT DATABASE

For this paper we focus on the noise complaint database acquired through the Silencio App. As of March 2025, Silencio users have logged over 150,000 noise complaints all across the world. Complaints are logged for over 180 countries.

Table 1 presents the top 10 countries by noise complaint logged on the Silencio App.

Table 1. Top 10 countries by noise complaint logged.

Country	Number of Complaints
Nigeria	50,400
Philippines	16,509
India	10,553
Bangladesh	9,994
Indonesia	9,759
Pakistan	7,028
United States	6,362
Brazil	3,922
Turkey	2,421
Vietnam	1,922

Figure 3 presents the geographical spread of noise complaints over Europe, while Figure 4 presents results from Nigeria.

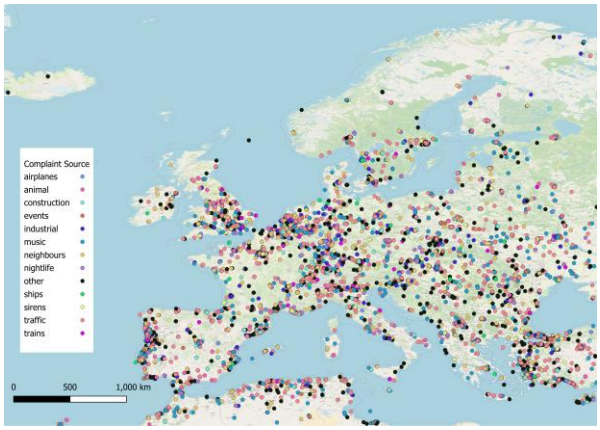


Figure 3. Noise complaints from the European Region.

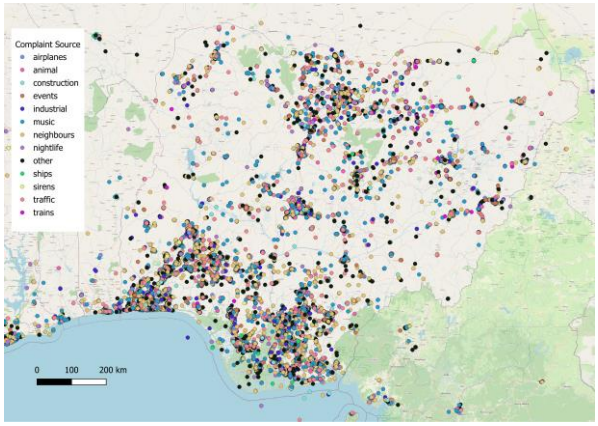


Figure 4. Noise complaints from Nigeria

2.1 Results Analysis

Figure 5 presents the source of noise by category logged. It is evident that road traffic noise is the number one source of noise complaints logged, contributing to over 35,000 noise complaints.

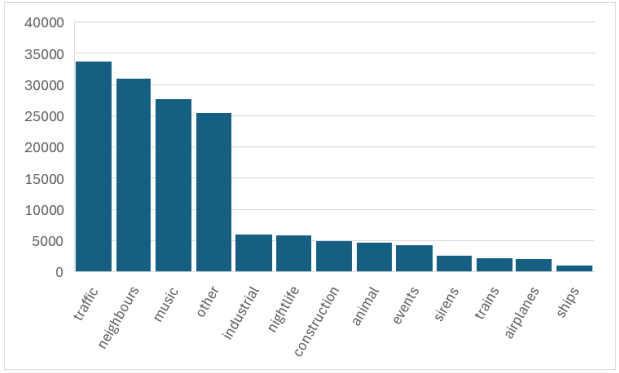


Figure 5. Number of complaints by source type.

Users are also asked to describe how the noise affecting them is impacting their well-being. They can choose from various options, including "uncomfortable," "annoyed," "disruption of relaxation," "anxious," "difficulty sleeping," "increased stress," or "angry." The results, shown in Figure 5, reveal that the most common response fell under the "other" category, suggesting a range of additional disturbances not explicitly listed. The second most frequently reported impact was feeling "uncomfortable," followed closely by "annoyed."

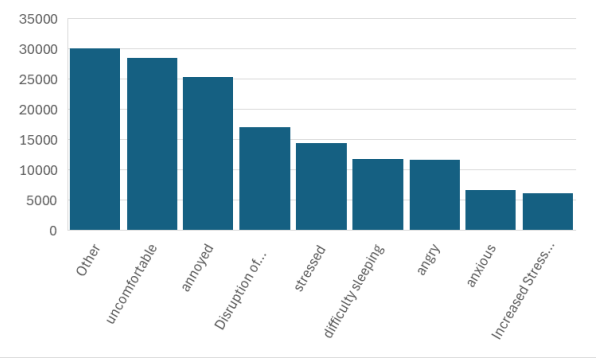


Figure 5. Number of complaints by effect induced.

3. DISCUSION

The Silencio noise complaint database builds on previous research [2-4] that explored the use of smartphones as noise meters, offering valuable insights into global noise pollution and its effects. With over 150,000 complaints across 180 countries, the data highlights the widespread nature of noise disturbances and the need for targeted mitigation strategies.

A key finding is the concentration of complaints in specific regions, with Nigeria reporting the highest number. The dominance of road traffic noise aligns with global urban trends, emphasizing the impact of transportation infrastructure on acoustic environments. Beyond identifying noise sources, the reported effects, such as discomfort, annoyance, difficulty sleeping, and increased stress, underscore the serious implications of noise pollution on well-being and public health.

Silencio's blockchain-based model enables large-scale, community-driven data collection, providing valuable insights for urban planners, policymakers, and researchers.

As this database continues to grow, its potential to drive meaningful changes becomes even greater. By refining data collection methods and integrating advanced analytics, we can uncover deeper patterns in noise pollution and its long-term effects on public health. Future efforts could involve collaborations with city governments, environmental agencies, and urban developers to create smarter noise management policies and real-time response systems. Additionally, integrating Silencio's data with other environmental datasets, such as air quality and traffic patterns, could provide a more holistic view of urban livability. For example, previous research has considered combining air and noise into one index to assist with urban planning [5]. Ultimately, this expanding database has the potential to become a powerful tool for shaping quieter, healthier, and more sustainable cities worldwide.

4. ACKNOWLEDGMENTS

The authors gratefully acknowledge the Silencio team for sharing noise complaint data.

5. REFERENCES

[1] https://www.silencio.network/

[2] E. Murphy, E.A. King, Testing the accuracy of smartphones and sound level meter applications for measuring environmental noise, Applied Acoustics 106, 16-22, January 2016.

[3] E. Murphy, E.A. King, Smartphone-based noise mapping: Integrating sound level meter app data into the strategic noise mapping process, Science of The Total Environment, 562, 852-859, August 2016.

[4] C.A. Kardous, P.B. Shaw, Evaluation of smartphone sound measurement applications, J Acoust Soc Am, 135, 2014.

[5] E.A. King, E.P. Bourdeau, X.Y.K. Zheng, F. Pilla, A combined assessment of air and noise pollution on the High Line, New York City, Transportation Research Part D: Transport and Environment, 42, 91-103, January 2016

DOI: 10.61782/fa.2025.0151

FORUM ACUSTICUM EURONOISE 2025

ASSESSMENT AND ANALYSIS OF VIBRATION IMPACTS FROM UNDERGROUND RAILWAY TUNNELLING AND EXCAVATION IN SYDNEY, AUSTRALIA

Aaron Miller[1] **Jeffrey Parnell**[2,3*] **Vyshakh Ajith Menon**[1] **David Hanson**[1]
[1] Acoustic Studio, Sydney, Australia
[2] University of Technology, Sydney, Australia
[3] Sydney Metro, Sydney, Australia

ABSTRACT

The NSW Government is building, operating and maintaining a network of four metro rail lines, 46 stations and 113km of new metro rail in Sydney, Australia. Whilst there have been geographical challenges with the new alignments, Sydney's high strength sandstone bedrock has provided a very stable substrate in which to tunnel. This has meant that measurable and perceptible levels of vibration can be propagated to significant distances. Contemporary understanding of tunnelling impacts is mostly underpinned by overseas experiences with respect to peak particle velocity (PPV). Moreover, this is generally limited to the relatively short setback distances applicable to structural damage concerns. This study presents PPVs, A-weighted ground-borne RMS vibration levels and one-third octave band spectra from tunnel boring and cross-passage excavation activities at various offset distances out to 300m that may be applicable to ground-borne noise or sensitive equipment concerns. This data will likely inform future predictions of tunnelling projects in Sydney and may be applicable to other regions both domestically and internationally. It also highlights uncertainties in predictions, ground conditions and the practicalities of contemporary tunnelling processes.

Keywords: *vibration, tunnelling, geology, propagation, prediction.*

[*] ***Corresponding author***: *jeffrey.parnell@uts.edu.au.*
Copyright: *©2025 Miller et al. This is an open-access article distributed under the terms of the Creative Commons Attribution 3.0 Unported License, which permits unrestricted use, distribution, and reproduction in any medium, provided the original author and source are credited.*

1. INTRODUCTION

Sydney is the largest city in Australia and is the capital of the State of New South Wales with a population of over 5.6 million (2025). Being a harbour city, it has geographical constraints that have historically resulted in the city expanding parabolically westward from the coastline. Whilst this is not an unusual configuration, it has occurred in a short space of time with Sydney only being declared a city in 1842. The delivery of large infrastructure brings significant challenges of whether this can be accommodated on the surface, or needs to be underground, and as is common in most international cities, the preference is for underground public transport, particularly in high density CBD environments.

1.1 Project Description

Sydney Metro is building, operating and maintaining a network of four metro rail lines, 46 stations and 113km of new metro rail, some of which is underground. The metro program includes the operational M1 Metro North West & Bankstown Line, and three projects under construction: Sydney Metro Southwest (upgrade of the existing rail line between Sydenham and Bankstown to metro standard), Sydney Metro West (24km of new twin tunnels between Westmead and the Sydney CBD) and Sydney Metro - Western Sydney Airport (23km, including 9.8km of twin tunnel between St Marys and Bradfield City Centre).
Geologically, Sydney sits on a large sedimentary feature known as the Sydney Basin. The metro rail corridors are dominated by Triassic-Age Hawkesbury Sandstone and Ashfield Shale. There are some instances of Quaternary Age alluvial/fluvial sediments comprising sand, silt and clay, but these are minor in the tunnel sections. Of most interest is the Hawkesbury Sandstone which is a very high

strength medium to coarse grained quartz sandstone. Its high compressive strength is characteristic of Sydney's large vertical coastal cliffs, and it was used extensively in the 19th and early 20th Century in the building of significant Government buildings and churches. It is therefore an excellent material in which to tunnel and is very stable. However, this also makes it quite efficient at transmitting vibration energy. The Ashfield Shale which comprises claystone, mudstone, siltstone, laminites, and fine-grained lithic sandstone has a much lower compressive strength and is more prone to weathering. Consequently, it is not as efficient in the propagation of vibration energy.

1.2 Impact Assessment

Following initial geotechnical and civil engineering concept designs, but prior to any infrastructure project being approved, a number of studies are undertaken to confirm the project viability and to assess likely environmental impacts from construction and operation. This includes noise exposure to surrounding residents, and potential building damage from tunnelling. Where Planning Approvals are granted, they will be subject to meeting certain noise and vibration objectives. In NSW, Australia these objectives are articulated in various policies, guidelines and Standards including BS7385.2 [2] which provides guidance on building damage from vibration, DIN 4150.3 [3] which makes recommendations for protection of structurally unsound heritage buildings, BS6472 [4] which discusses the impact of vibration on humans and is referenced in the NSW Environment Protection Authority's (EPA) Assessing Vibration: A Technical Guideline [5] and the Vibration Criterion (VC) Curves [6] which provide guidance for sensitive equipment. In regard to Ground Borne Noise (GBN) impacts, the NSW EPA's Interim Construction Noise Guideline [7] provides guidance.

1.3 Excavation Considerations

Excavation of an underground railway is primarily undertaken through three separate activities:

- Excavating the fixed diameter mainline tunnel using tunnel boring machines.
- Mining of irregular shaped underground infrastructure such as station and crossover caverns using road headers.
- Use of percussive methods to excavate the cross passages between the twin mainline tunnels, and for some minor cavern excavation works.

These tunnelling works can generate significant amounts of vibration that can propagate through the ground and into nearby buildings. This vibration has the potential to impact sensitive receivers in two ways:

1. Higher frequency vibrations (approximately 20 Hz to 250 Hz) will propagate through the ground, and into buildings. These will result in building elements vibrating and acting like loudspeakers, creating an audible rumble. This is known as 'ground-borne noise'.
2. Lower frequency vibrations (typically <20 Hz) can also induce cosmetic damage into buildings at high amplitudes, be felt (rather than heard) by building occupants to the extent that they disturb or annoy at moderate-to-low amplitudes, or interfere with the operations of sensitive equipment at very low amplitudes.

Tunnel depth will vary along an alignment being largely a function of changing surface topography as shown in the example given in Figure 1 where it varies from around 10m depth down to more than 90m below ground level. The intervening material along with coverage and specifically the slant distance from a tunnel to the foundations of a sensitive receiver are also important factors in the propagation of vibration.

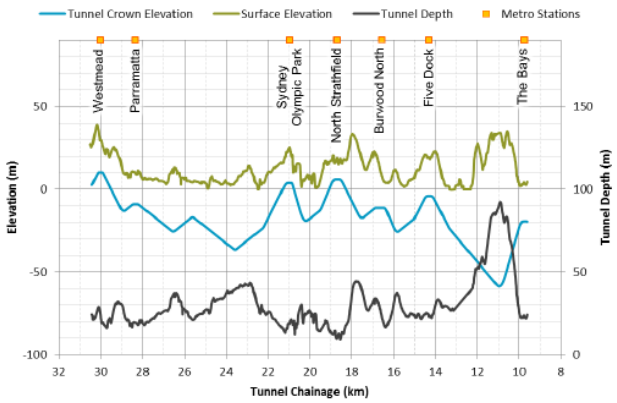


Figure 1. Tunnel depths and existing ground elevation on Sydney Metro West. [1]

1.4 Tunnel Excavating Techniques and Equipment

There are three main excavation techniques associated with rail tunnelling and one ancillary technique that can result in significant vibration. Firstly, is the use of a Tunnel Boring Machine (TBM) that effectively drills through the substrate to provide the mainline rail tunnel. Secondly, is the use of road headers (typically associated with larger diameter road tunnels) to excavate larger irregular shaped caverns for crossovers and underground stations, and for pedestrian and ventilation adits. Thirdly, there is the use of hydraulic rock

hammering often used to provide interconnecting cross passages between twin rail tunnels. Lastly, and ancillary to the three other excavating techniques is the need to insert rock bolts in unsupported spaces to improve stability. A brief discussion of these techniques and equipment is provided below.

1.4.1 Tunnel Boring Machines

TBMs are designed to excavate through sandstone and shale and are in the order of 1250 tonnes and 165m long. The operations include:

1. The cutterhead at the front of the TBM spins and as it does, high-steel alloy steel discs extend out to the rock surface and crush the material in its path.
2. Crushed rock is scooped into the machine's head and onto a conveyor belt.
3. The conveyor moves rock through the machine and out of the tunnel behind it.
4. Concrete ring segments are delivered to the ring building area.
5. Concrete ring segments are fixed onto the tunnel wall carved out by the TBM using a vacuum lifting device.
6. When completed, the ring is connected to the previously built ring.
7. The gap between the concrete ring and the rock is filled with grout – this helps keep water out of the tunnel.

A total of six concrete segments make up one concrete tunnel ring. Once the TBM finishes building the fully lined tunnel, it breaks through a rock wall to arrive at its destination where it is then retrieved.

1.4.2 Road Headers

Road Headers used on Sydney Metro projects are typically in the order of 120 tonnes. They are used for a large range of excavation work such as for the new Pyrmont Metro Station where they will excavate a future station cavern. This will eventually measure 18m high, 24 m wide and 170m long, requiring the removal of 151,000 tonnes of material from the site over a 2 year period. Unlike the TBMs which move along the alignment at a steady rate in one direction, road headers can work in specific areas for long periods of time, increasing the exposure time and fatigue of affected residents and buildings.

1.4.3 Rock Hammering

Hydraulic hammering refers to the highly percussive impact excavation methods that are sometime used underground to excavate or remove small areas of rock.

1.4.4 Rock Bolting

The drilling and subsequent installation of anchors or rock bolts into excavated caverns and passages can result in a more intermittent vibration pattern that can be perceived on the surface.

1.5 Approvals and Operating Constraints

Planning approvals usually allow tunnelling activities to occur 24 hours per day, seven days per week, primarily in order to reduce project timelines, noting that TBMs and road headers are expected to excavate approximately 200m per week and 20-40m per week, respectively. In practice, however, TBMs and road headers produce vibration approximately 50% of the time (as the other 50% of the time is spent erecting tunnel lining and support structures) and will have breaks of days or weeks to undertake maintenance.

TBMs and road headers cannot be replaced with alternative, less vibration-intensive equipment, and there are no reasonable and feasible path or receiver controls that will reduce the vibration levels. Consequently, assessments of ground-borne noise and vibration impacts from these activities are limited to ensuring that vibration will be below structural damage thresholds, and then quantifying the ground-borne noise and vibration levels that the surrounding community / sensitive equipment will be exposed to, as well as the duration (which is usually in the order of days rather than weeks or months). These impacts and their duration then determine the extent to which community consultation is undertaken, and in extreme cases, the extent to which temporary alternative accommodation will be provided.

Other excavation activities using hydraulic hammers, like cross passage excavation and minor cavern works, do not necessarily need to occur 24 hours per day, seven days per week, and can therefore be restricted to standard construction hours as a means of mitigating their impacts.

Whilst potential building damage is rarely a concern, perception of vibration or ground-borne noise is usually expected as a TBM both approaches and then departs. Figure 2 provides an example showing that a residential receiver with a 20m slant distance from the nearest tunnel alignment will likely experience internal ground-borne noise levels greater than the 35 dB(A) night-time ground-borne noise management level (NML) objective [7] for around five days if the TBM is transiting at 20m/day. The maximum ground-borne noise level is expected to peak at around 50 dB(A).

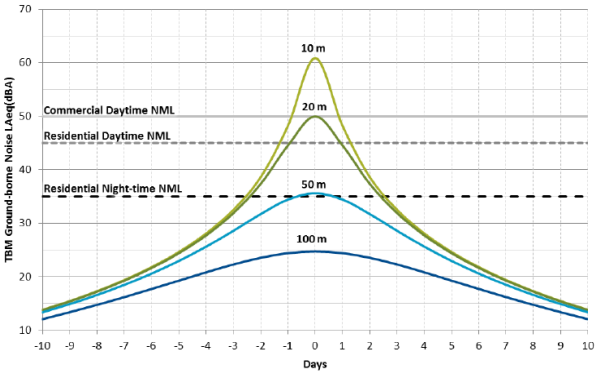


Figure 2. Example of TBM Ground Borne Noise levels (where progress ~ 20m/day). [1]

2. CURRENT PREDICTION METHODOLOGIES

The assessments for recent projects in Sydney typically use similar approaches to predict the ground-borne noise and vibration impacts as summarised below:

- PPVs and A-weighted ground-borne noise levels are presented as single curves with respect to distance. These appear to be based on the datasets provided in Speakman and Lyons, Hiller and Karantonis [8-10] as well as unpublished internal databases. These are usually based on Hawkesbury Sandstone.
- Human comfort is assessed in one of two ways:
  - The PPVs are used as a screening assessment, or
  - Estimated Vibration Dose Values (eVDVs) are predicted based on the PPV vs distance curves, incorporating assumptions regarding crest factors, dominant frequencies and how often the equipment is used within a daytime or night-time period.
- The duration of these impacts is assessed based on a combination of the PPV and ground-borne noise vs distance curves, and typical progress rates per day.
- Parameters like coupling loss, internal amplification and floor-to-floor attenuation are conservatively assumed and generically applied across every building included in the assessment.

2.1 Limitations of Current Methodologies

The current prediction methodologies tend to be generic in nature, mostly as a consequence of there being insufficient data available in the literature to perform any kind of detailed assessment. Moreover, there is currently no mechanism for assessing vibration impacts against the VC curves. For example, this would be limited to assuming a crest factor to convert a PPV at a specific distance to a maximum one-third octave band velocity level. This generic approach tends towards conservatism, which can lead to the over-specification of community consultation measures and the provision of temporary respite accommodation. This can be problematic, particularly with multi-storey buildings with large footprints. In such a scenario, a generic assessment might indicate that all occupants of such a building require temporary alternative accommodation due to excessive annoyance. In reality, only the lower floor apartments might require this level of respite because this building may have a much higher coupling loss than the assessment assumed, which would result in a much lower impact to the upper floors and other ends of the building.

Capturing one-third octave band spectra and associated waveforms at various offset distances would allow for more detailed assessments to be undertaken when necessary because:

- It provides a mechanism to assess vibrations against VC curves.
- It can be used in conjunction with other parameters such as coupling loss, internal amplification, floor-to-floor attenuation and vibration to noise transfer functions that are published in terms of one-third octave bands in sources such as the Federal Transit Administration manual [13], RIVAS Project [12] and Transit Cooperative Research Program [13] or data sourced locally, such as Karantonis et al. [14].
- Calculations of eVDVs can be improved by validating the assumptions around crest factors and dominant frequencies or going further and calculating weighted RMS or weighted RMQ accelerations at various distances directly.

There are also additional opportunities for improving generic assessments. Hiller [9] notes that "*in general terms, the vibration increases as the strength of the ground through which the tunnel is bored increases*", this is also demonstrated in Rallu et al. [15]. ITA [16] also suggests that reducing thrust may also reduce vibrations. This presents two opportunities:

- Capturing data covering different rock types may allow for less conservative predictions on rock types that are softer than Hawkesbury Sandstone.
- Capturing different thrust conditions and quantifying their differences may allow for specific thrust conditions to be specified as mitigation measures.

Finally, capturing long-term monitoring data allows for the impacts and durations to be quantified based on actual

progress rates, rather than the typical progress rates used in these generic assessments.

3. STUDY OBJECTIVE AND SCOPE

This paper provides a small sample of the results of monitoring that has been undertaken to address these shortfalls identified in Section 2.1. Monitoring is ongoing, but the possibilities of quantifying and presenting this are practically endless. This paper focuses on the opportunities to improve the generic assessments, and provides one-third octave band spectra from two sites, at which very robust datasets were able to be collected.

3.1 Methodology

Attended monitoring has been undertaken across the Sydney basin using a consistent approach using 10 V/g or 1V/g accelerometers (Wilcoxon 731-207 and PCB 393A03, respectively). External monitoring utilised small ferrous stakes driven into the earth, and magnetically mounting the accelerometers to these stakes. At most locations, vibration has only been measured in the vertical direction. Rallu et al. [15] notes that vibrations at the surface are similar in all three spatial directions, which has been confirmed in our monitoring at the small number of locations at which triaxial vibrations were measured. Vibration on or inside buildings has been undertaken by mounting the accelerometers using beeswax.

The attended monitoring has typically involved setting up one location to continuously monitor vibration, and then measuring at numerous other locations to triangulate the location of the TBM from the surface. The continuous monitor is able to capture changes in vibration emissions due to (what is believed to be) changes in thrust.

Data have been recorded using National Instruments cDAQ units incorporating sampling rates of 2048 Hz, with anti-aliasing filters providing unfiltered data up to 800 Hz. The waveforms have been processed to calculate LZeq and LZSmax one-third octave band spectra, overall LZeq, LAeq, LZSmax and LASmax levels, PPVs, Wb and Wg weighted RMS and RMQ levels, and crest factors (PPV / LZeq) all at 1s intervals.

3.2 Location Details

The geographic spread of locations across the Sydney basin at which monitoring, and the subsequent analysis has been completed (at the time of writing) is shown in Figure 3. Details about the monitoring are provided in Table 1, rock types are based on those described by Willan [17].



Figure 3. Aerial View of Measurement Locations.

Table 1. Locations, rock types, and activities measured at each location.

Location	Rock Type	Activity
Luddenham	Sandstone, shale and thin coal seams	TBM
St Marys	Silt and clay	TBM
Sydney Olympic Park	Silt and clay	TBM
North Strathfield	Clay shale and sandy shale	TBM
Five Dock	Hawkesbury Sandstone	TBM, Cross-passage hammering
Leichhardt	Hawkesbury Sandstone	TBM, Cross-passage hammering

4. RESULTS

The measurement results are presented in terms of PPVs in Figures 4a/4b, and ground-borne vibration levels in Figures 5a/5b. Figures 4a/4b and Figures 5a/5b also include typical curves (shown in black solid, dashed and dotted lines) that have been used at EIS and construction vibration management plan stage on Sydney projects and are based on Hawkesbury Sandstone. The curves on Figures 5a/5b are ground-borne noise curves to which 27 dB has been added (based on the formula from Kurzweil, [18].

The maximum one-third octave band levels and corresponding dominant frequencies for three of these datasets are provided in Figures 6a/6b. Figures 7 and 8 are effectively a summary of the velocity spectra measured for TBMs at St. Marys and Five Dock West respectively, whilst Figure 9 graphically presents Cross Passage hammering in Five Dock. The VC curves (from IEST) [19], which have evolved from those described in [6] as described in Miller [20] are overlaid on these spectra as black dashed lines.

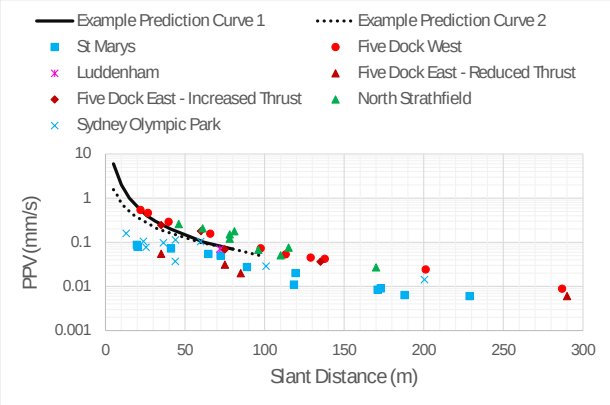


Figure 4a. PPV vs Distance: TBM.

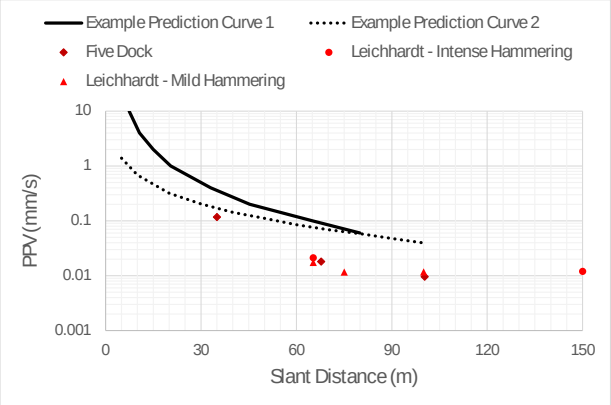


Figure 4b. PPV vs Distance: Cross Passage Hammering

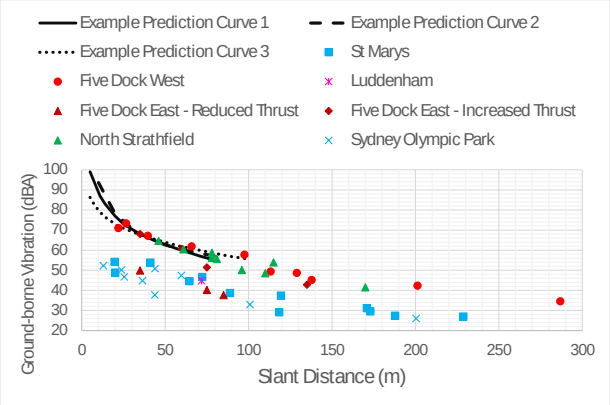


Figure 5a. A-weighted Ground-borne Vibration vs Distance: TBM.

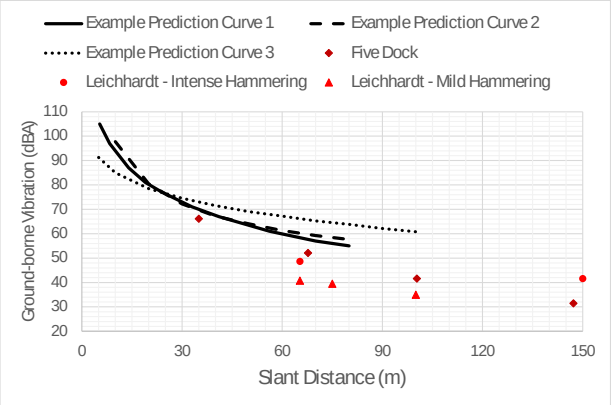


Figure 5b. A-weighted Ground-borne Vibration vs Distance: Cross Passage Hammering

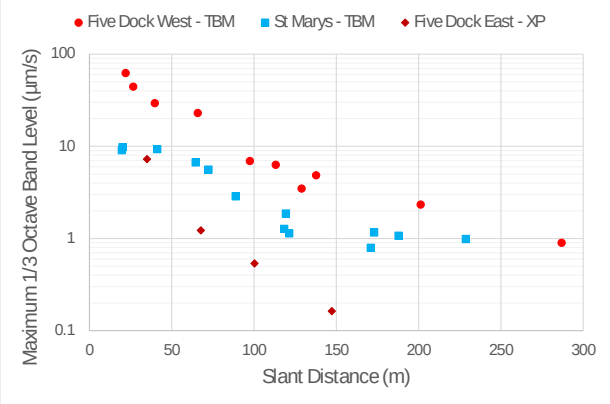


Figure 6a. Maximum One-third Octave Band level vs Distance

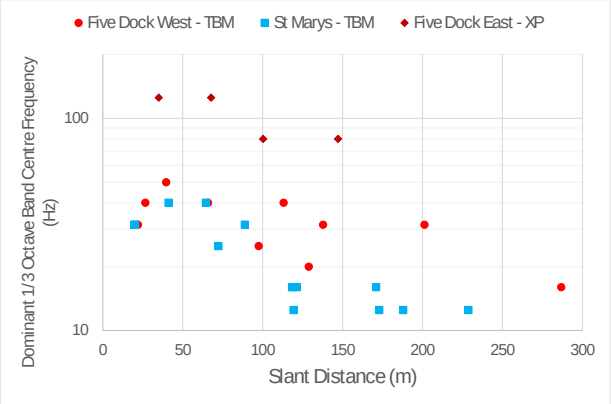


Figure 6b. Dominant One-third Octave Band Centre Frequency vs Distance

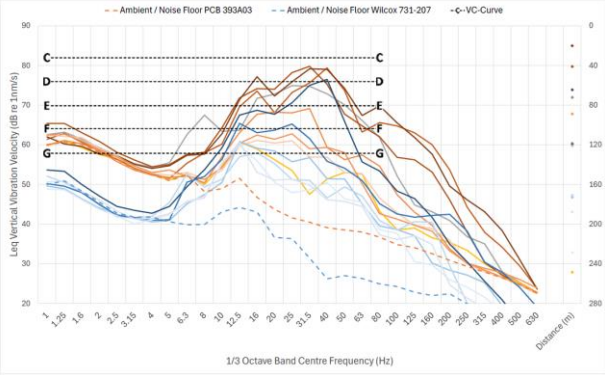


Figure 7. One-third octave spectra of TBM at St. Marys.

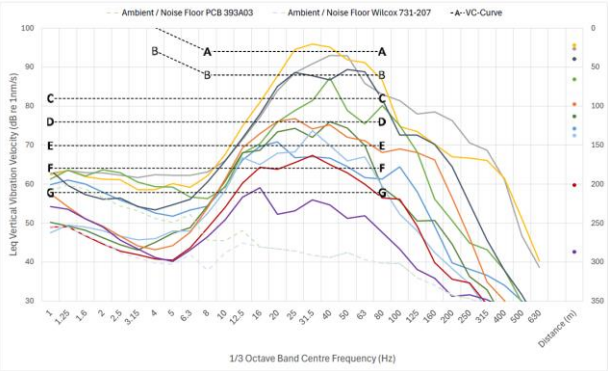


Figure 8. One-third octave spectra of TBM at Five Dock West.

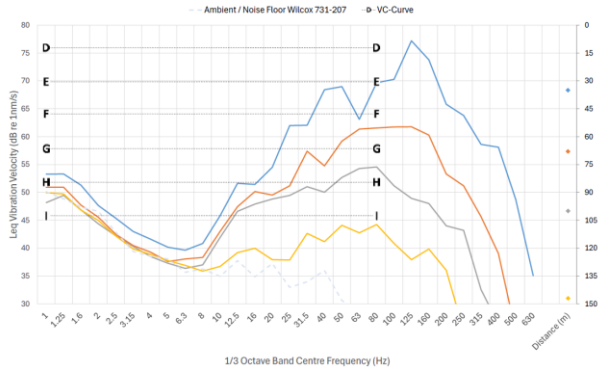


Figure 9. One-third octave spectra of Cross Passage Hammering at Five Dock.

5. DISCUSSION

It can be observed from Figures 4a and 5a that the TBM PPV's and A-weighted ground-borne vibration levels can, in practice, be significantly lower than those typically predicted. There are two possible explanations for this:

- Changing the thrust of the TBM appears to be able to significantly reduce vibration levels, particularly at shorter slant distances. This is evident when comparing the 'increased thrust' and 'reduced thrust' values at Five Dock East. This was also very clearly evident when reviewing the spectra versus time at individual locations where 'continuous' monitoring was undertaken at Five Dock East.
- Operating the TBM in different rock types appears to significantly influence the vibration levels as evidenced by comparison of vibration levels measured at St. Marys, in silt and clay, compared to levels measured at Five Dock West, in Hawkesbury Sandstone.

It is not clear which of these is the dominant contributing factor. At Five Dock East, it may not have been a change in thrust that changed the vibration levels, but rather the TBM may have temporarily encountered different rock. Conversely, the TBM at St. Marys may have been operating at reduced thrust settings in comparison to the TBM at Five Dock West. More information is needed from the tunnelling contractors to understand this.

The measured vibration levels for cross-passage hammering shown in Figures 4b and 5b are generally significantly lower than the prediction curves with some variation in the intensity of hammering also observed, particularly at high frequencies. Whilst this did not increase the PPVs significantly, it did produce large increases in A-weighted ground-borne vibration levels. Again, it is unclear if the lower levels or variations in intensity are due to a different rock type, different hammer, or hammering technique. Understanding this might allow for ground-borne noise mitigation measures, in the form of restricting how hammers are used, to be implemented where tunnelling works occur near noise-sensitive receivers. More cross passage hammering data is needed in different rock types.

6. FUTURE WORK

The authors intend to continue building and subsequently publishing this dataset for widespread use. This will include calculations of weighted RMS and weighted RMQ at various offset distances to assist with human comfort calculations.

7. CONCLUSIONS

Vibration monitoring that uses sensitive accelerometers to capture one-third octave spectra and waveforms has been undertaken at multiple locations, covering a cross-section of the bedrock found in the Sydney basin. The purpose of the monitoring is to construct a database that can be referred to by those undertaking ground-borne noise and vibration predictions of tunnelling activities, to improve the current prediction methods. The dataset presented in this paper will facilitate vibration predictions with respect to sensitive equipment (VC curves). Monitoring is ongoing, and the dataset will continue to improve. Collaboration with the tunnelling contractors will be essential in understanding the large variations in measured levels.

8. ACKNOWLEDGMENTS

The authors acknowledge the support of Sydney Metro in undertaking the research that forms the basis of this paper. However, any opinions expressed are those of the authors and do not necessarily reflect those of Sydney Metro, Transport for NSW or the NSW State Government.

9. REFERENCES

[1] Sydney Metro. *Sydney Metro West Environmental Impact Statement – Concept and Stage 1. Westmead to The Bays and CBD*. Sydney Metro 2020.

[2] British Standards. *BS 7385-2:1993: Evaluation and measurement for vibration in buildings - Guide to damage levels from groundborne vibration*. BSI 1993.

[3] Deutsches Institut für Normung. *DIN 4150-3:2016 Vibration in buildings - Part 3: Effects on structures*. DIN 2016.

[4] British Standards. *BS 6472–1992. Evaluation of human exposure to vibration in buildings (1–80 Hz)*. BSI 1992.

[5] NSW EPA. *Assessing Vibration: A technical guideline*. EPA 2006.

[6] C.G. Gordon. Generic Vibration Criteria for Vibration-Sensitive Equipment. *Proc. Cur. Dev. in Vib. Control for Optomech. Sys.* Denver. 1999.

[7] NSW EPA. *Interim Construction Noise Guideline*. EPA 2009.

[8] C. Speakman and S. Lyons. Tunnelling induced ground-borne noise modelling. *Proc. of Acoustics 2009*. Adelaide. 2009.

[9] D. Hiller. The prediction and mitigation of vibration impacts of tunnelling. *Proc. of Acoustics 2011*. Gold Coast, Australia. AAS 2011.

[10] P. Karantonis, M. Tabacchi, S. Pareek, J. McMahon and M. Knezevic. Ground-borne Noise & Vibration Results from recent Tunnelling & Construction Projects *Proc. Acoustics 2018*. Adelaide. 2018.

[11] Federal Transit Administration. *Transit Noise and Vibration Impact Assessment Manual Report N0. 0123*. Washington, USA. FTA 2018.

[12] M. Villot, C. Guigou, P. Jean and N. Picard. *Procedures to predict exposure in buildings and estimate annoyance*. Railway Induced Vibration Abatement Solutions (RIVAS). 2012.

[13] Transit Cooperative Research Program. *Ground-Borne Noise and Vibration in Buildings Caused by Rail Transit.* Nat. Acad. Sci., Eng and Med. 2009.

[14] P. Karantonis, C. Weber and H. Puckeridge. Ground-Borne Noise and Vibration Propagation Measurements and Prediction Validations from an Australian Railway Tunnel Project. *Proc 13th Int. Workshop on Railway Noise*. Ghent, Belgium. 377 – 84. 2021

[15] A. Rallu, N. Berthoz, S. Charlemagne and D. Branque. Vibrations induced by tunnel boring machine in urban areas: In situ measurements and methodology of analysis. *J. Rock Mech. and Geotech. Eng.* 130-145. 2023.

[16] International Tunnelling Association Working Group 14. *Recommendations and Guidelines for Tunnel Boring Machines.* Lausanne. ITA 2000.

[17] T. L.Willan. *Geological Map of the Sydney District.* NSW Department of Mines, Sydney, NSW, Australia. 1925.

[18] L. G. Kurzweil. Ground-borne Noise and Vibration from Underground Rail Systems. *J. Sound and Vib.* 66(3), 363-370. 1979.

[19] Institute of Environmental Sciences and Technology. *IEST-RP-NANO201.1 Measuring and Reporting Vibrations in Advanced-Technology Facilities.*. IEST 2024.

[20] A. Miller. Vibration Criterion Curves – Part 1: Evolution and Interpretation. *Proc. Of Acoustics 2024*. Gold Coast. 2024

DOI: 10.61782/fa.2025.0443

FORUM ACUSTICUM EURONOISE 2025

IMMISSION DIRECTIVITY IN THE FREQUENCY DOMAIN

Jure Murovec[1*] **Luka Čurović**[1] **Anže Železnik**[1] **Jurij Prezelj**[1]
[1] Laboratory for Pumps, Compressors and Technical Acoustics LEDSTA, Faculty of Mechanical Engineering, University of Ljubljana, Slovenia

ABSTRACT

The spatial domain has proven to be a crucial element in the measurement of environmental noise and allows for better identification and classification of noise sources. This paper presents spectral immission directivity, an extension of the concept of immission directivity into the frequency domain, which improves the spatial representation of noise at different frequencies. The proposed methodology combines spectral and spatial insights and provides a comprehensive view of the acoustic environment. Theoretical simulations were performed and validated by measurements in an anechoic chamber, confirming the reliability and precision of the approach. The integration of spectral immission directivity into existing noise measurement systems is seamless and requires no significant changes, and it improves their ability to localize and characterize noise sources. This advance reduces reliance on complex post-processing algorithms and promotes more efficient, accurate and cost-effective noise monitoring strategies. By enriching environmental noise assessments with spectral-spatial data, this research paves the way for innovative approaches to noise assessment and management.

Keywords: *Environmental noise measurements, Immission directivity, Sound source localization, Microphone array, Spatial filtering*

[*] ***Corresponding author***: *jure.murovec@fs.uni-lj.si.*
Copyright: *©2025 Jure Murovec et al. This is an open-access article distributed under the terms of the Creative Commons Attribution 3.0 Unported License, which permits unrestricted use, distribution, and reproduction in any medium, provided the original author and source are credited.*

1. INTRODUCTION

Noise pollution in urban areas is a significant but often overlooked environmental problem, largely due to inadequate measurement methods and impact assessments. Noise is defined as unwanted or disturbing sound and is constantly perceived by the auditory system, making it inherently intrusive. Urban areas, with their dense population and industrial activity, face particular challenges in managing noise levels. Apart from the effects on human health - which are associated with sleep disturbance, cardiovascular disease and cognitive impairment, noise pollution also has economic costs, such as healthcare expenditure, property devaluation and lost productivity. In addition, it disrupts ecosystems and affects biodiversity on land and in the sea [1-3]. Tackling noise pollution presents significant technical challenges, with the most effective strategy being to reduce noise pollution at the source itself. However, many noise sources, such as industrial plants, ports, railways, airports and construction sites, are constantly in operation and cannot be easily mitigated. The simultaneous activity of multiple sources makes accurate assessment difficult, as environmental noise is inherently dynamic and varies in time, frequency and space. Effective assessment requires sophisticated measurement and modeling techniques [4-6].

Noise propagation modeling, combined with sound power assessments, helps estimate individual contributions to overall noise levels. However, these models depend on extensive input data, including operating times, source geometries, and terrain characteristics, and are subject to uncertainties from variations in software tools and standards. Consequently, noise modeling primarily serves to extrapolate data from limited measurement points (MPs) to broader areas, a method supported by numerous studies [7-9]. Long-term measurements are crucial for accurate assessments, allowing the identification of dominant noise sources and enabling targeted reduction strategies.

However, manual post-processing, such as listening to recordings, is time-consuming and costly.

Recent advances in noise research have led to the development of the immission directivity (ID), a concept that can be seamlessly integrated into existing legally compliant noise measurement methods. By combining ID with standardized approaches, noise monitoring technologies can be further improved. ID is compatible with calibrated Type 1 noise level meters, ensuring traceability to SI units and enabling accurate assessments of environmental noise [10-12].

Using a small microphone array, ID identifies the most dominant noise source at each measurement integration time based on its location and direction relative to the MP. The inclusion of this spatial dimension in equivalent sound pressure level measurements has proven valuable in analyzing acoustic environments and distinguishing individual noise sources. Since traditional noise source identification is based on frequency analysis, combining spatial and spectral data is a logical next step. This paper presents Spectral Immission Directivity (SID), a novel approach that has emerged from our recent research and improves the analysis of environmental noise by incorporating spatial and frequency data. By mapping the directional distribution of different frequency components around the MP, SID improves the identification and classification of noise sources, especially in complex environments with multiple overlapping sources [13].

In addition to human-generated noise from traffic, industry and construction, SID can also be used to analyze biological sounds such as bird calls, insect activity and wildlife vocalizations, making it valuable for both urban and ecological studies. Its applications extend to urban planning, building design, traffic noise studies, public health research and biodiversity monitoring, supporting targeted noise mitigation strategies. In addition, SID can be seamlessly integrated into existing regulatory compliant methodologies and can serve as a key component in classification models and smart city monitoring networks.

To validate this approach, 16 hours of in-situ pilot measurements were conducted in a multi-source noise environment, demonstrating the ability of the SID's to distinguish and identify different noise sources and their contribution to the overall noise level. This study aims to use SID to transform the assessment of environmental noise, making it more accurate and effective.

2. METHODOLOGY

In this study, we performed in-situ measurements as a case study to evaluate the SID approach and analyze its performance in a real-world environment. We used a dedicated microphone array and the Delay, Subtract, and Sum (DSS) algorithm [12] to determine the direction of arrival (DOA) and spectral characteristics of the noise sources. Using SID, we identified the number of individual noise sources, analyzed their contribution to the overall noise level, examined their frequency characteristics, and determined the times at which they were present.

2.1 Equipment

The experimental setup for this research included specialized measuring devices and software tools for data acquisition. The Behringer UMC404HD ADC USB audio interface, which operates at a high sampling frequency of 192 kHz, was used to capture audio signals. A horizontal microphone array consisting of four Behringer ECM8000 measurement microphones arranged in a circle with a diameter of 27 mm was used. The DSS method was applied to the signals from the array. This configuration provided a computationally efficient system capable of capturing DOA over the frequency range of most environmental noise sources (100 Hz to 6300 Hz, in 1/3 octave bands) and operating with an integration time of 125 ms. The user interfaces and data acquisition programs were developed using LabVIEW 2023, while the processing of the measurement data and the generation of the figures was performed in MATLAB R2024a. This combination of hardware and software ensures accurate data acquisition and analysis.

2.2 Spectral immission directivity

ID, first introduced in 2018, is a ground-breaking concept in environmental acoustics that aims to address the challenges of understanding and quantifying the contributions of different noise sources to the overall noise level at a given MP. It captures both the spatial and temporal dynamics of noise and provides a detailed representation of how sound energy from different directions affects an acoustic environment. By incorporating both the direction of arrival (DOA) and the sound pressure level (SPL) of noise sources, ID serves as a valuable tool for analyzing complex soundscapes found in urban or industrial environments.

Building on the foundational principles of ID, a derived concept known as SID was developed. SID extends ID by

integrating a 1/3-octave frequency analysis alongside the spatial distribution of noise sources around the MP. This extension enables a more comprehensive understanding of the acoustic environment and provides deeper insights into the frequency-specific contributions of the different noise sources. By combining spectral and spatial data, SID is a powerful tool for the assessment of environmental noise and contributes to the development of more effective noise mitigation strategies and the design of the urban soundscape.

To simplify the SID pattern, it can be reduced to a two-dimensional spatial problem by disregarding the elevation angle. This approach is feasible because environmental noise sources such as traffic, industrial plants and wind turbines are usually located at a certain distance from the MP, so that the propagating sound waves can be approximated as parallel to the ground. As a result, the A-weighted equivalent sound pressure level $L_{A,eq,T,fi}$ at a specific frequency can be defined by Eq. (1).

$$L_{A,eq,T,f_i} = 10 * \log\left[\frac{1}{T}\int_0^T\int_0^{2\pi} 10^{\frac{L_{p,A}(t,f_i,\varphi)}{10}} d\varphi dt\right] \quad (1)$$

Where $L_{p,A}(t,f_i,\varphi)$ stands for A-weighted instantaneous sound pressure level for the frequency f_i as a function of time t and direction φ. $L_{A,eq,T,fi}$ can be defined as the sum of a specific frequency of all noise sources that are present in the vicinity of the MP in the time interval T (from directions between 0 to 2π). To obtain the total A-weighted equivalent sound pressure level, we use the logarithmic summation of all $L_{A,eq,T,fi}$ for I number of frequency bands described with Eq. (2).

$$L_{A,eq,T} = 10 * \log\int_0^{f_I} 10^{\frac{L_{A,eq,T,f_i}}{10}} \quad (2)$$

At each point in time, the levels of the individual frequencies are assigned to a single direction — the most dominant — as the DSS algorithm only identifies the strongest source. By extending the measurement duration and sequentially activating different noise sources, unique ID patterns are generated for each frequency. The aggregation of these patterns forms the SID. As shown in the results section, analyzing the ID on a frequency basis helps significantly to identify the main noise sources, understand their contribution to the overall noise level and determine their spectral characteristics.

The frequency resolution can be chosen according to need. However, in this study, a 1/3-octave spectral analysis was chosen in line with standard practice to limit the amount of data and improve conceptual clarity. Regardless of whether a narrowband frequency analysis is used, the underlying method for calculating the SID remains unchanged.

In discrete form, Eq. (1) and Eq. (2) can be rewritten as Eq. (3) and Eq. (4), where N represents the measurement duration in terms of integration time count. I corresponds to the number of frequency bands, which was set to 19 in this study. The spatial resolution for DOA determination at the immission point was fixed at 6° on the horizontal plane, resulting in $M = 60$ observed angles.

$$L_{A,eq,T_N,f_i} = 10 * \log\left[\frac{1}{T_N}\sum_{n=1}^{N}\sum_{m=1}^{M} 10^{\frac{L_{p,A}(t_n,f_i,\varphi_m)}{10}}\right] \quad (3)$$

$$L_{A,eq,T_N} = 10 * \log\sum_{i=1}^{I} 10^{\frac{L_{A,eq,T_N,f_i}}{10}} \quad (4)$$

2.3 Measurement location

The MP was placed near a large cement plant, its stone quarry and an industrial area. The location of the main sources of noise can be seen in Fig. 1. Otherwise, there are several small villages in the vicinity of the MP where agriculture is practised.



Figure 1. MP and surrounding noise sources.

3. RESULTS

The in-situ measurements were carried out on a working day from 15:00 to 7:00. Fig. 2 shows the recorded data and the dynamics of the acoustic scene during the measurement. It can be clearly seen that the dominant direction (Fig. 2.b) was quite stationary during the night when the overall sound pressure level (Fig. 2.a) was lower. Spectrogram and spectrum (Fig. 2.c and Fig. 2.d) are also shown, which is a typical representation of noise measurement data. Even with only 16 hours of data, no direct conclusions about the noise sources can be drawn from Fig. 2. The data must be condensed to a level that is easier to interpret and clearer.

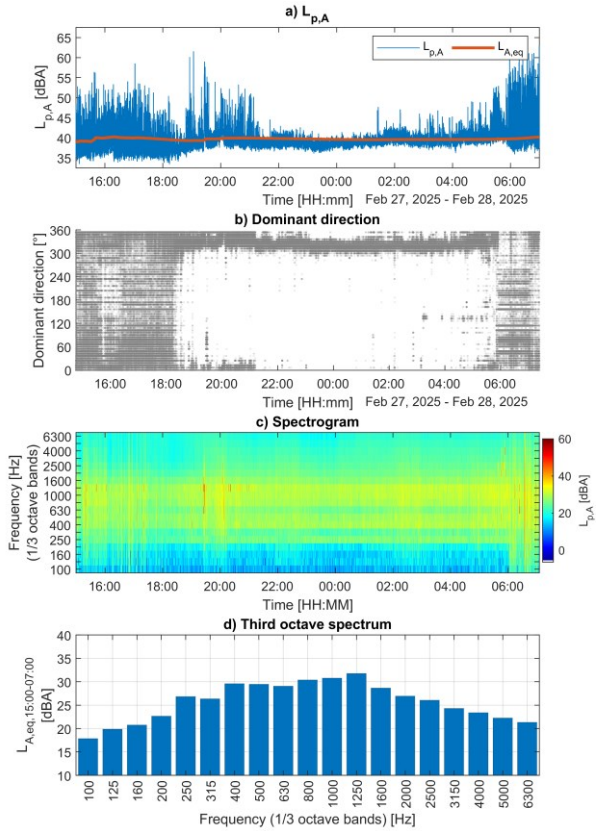


Figure 2. Noise measurement data.

To get a clearer picture of the contribution of the different noise sources around the MP, we use the ID pattern as shown in Fig. 3. The polar diagram shows how $L_{A,eq}$ is spatially distributed. We can notice that most of the sound energy comes from the southeast direction, but some other directions are also notable.

To get a better understanding of the different noise sources, Fig. 4 shows the comparison of the dominant direction distribution and the ID. It can be seen that the noise source in the southeast direction (approx. 330°) had a lower SPL at the MP than the noise sources in the directions 6°-30°, 72°-90°, 102°, 114° and 156°, as the contribution of the noise source in the southeast direction to the total $L_{A,eq}$ was not much higher compared to the other sources, although it was the most dominant noise source for most of the measurement.

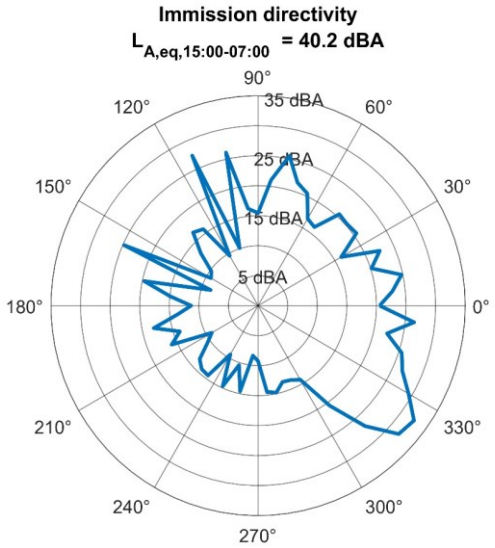


Figure 3. Imission directivity.

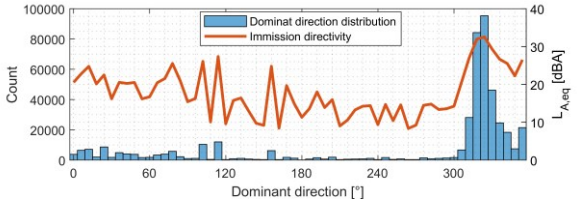


Figure 4. Dominant direction distribution around the MP.

Fig. 5 shows the SID of the measurement performed. The approximate spectrum and the dominant frequency bands of the main noise source are clearly recognisable. The sources in the directions 102°, 114° and 156° show a rather broadband spectrum, while the sources in the directions 72°-90° and 6°-30° show peaks in certain frequency bands.

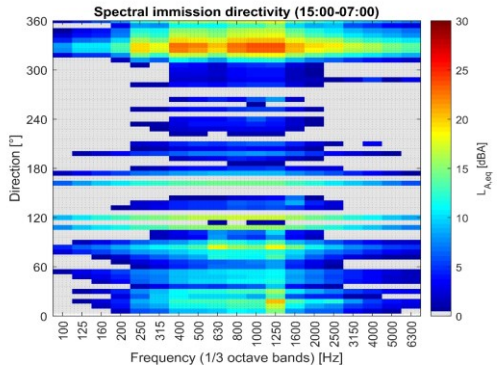


Figure 5. Spectral immission directivity.

To better represent the spatial-temporal dynamics of the acquired noise data, IDs for 1-hour intervals were calculated and can be seen in Fig. 6. A shift from a multiple noise source operation to a single noise source operation can clearly be observed as IDs between 15:00 and 19:00 display a more spatially even distribution of $L_{A,eq}$ around the MP and then a transition at 19:00 , when a noise source at 78° starts to dominate alongside the noise sources east of the MP. While some sources at 342°-24° are still present between 21:00 and 23:00, they completely stop operating thoughout the night. The dominance of this noise source ends at 5:00 when noise sources from other directions start to appear and by 7:00 they start to dominate.

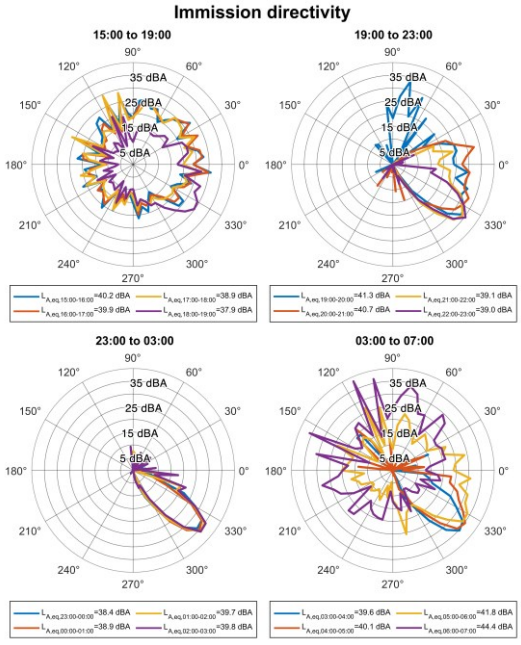


Figure 6. Hourly imission directivity.

SID allows us to examine 1-hour data in more detail by analysing the spatial-frequency content of the measurement. In Fig. 7, we can observe a noise source at 18° with a prominent peak at 1250 Hz in the frequency band from 15:00 to 17:00.

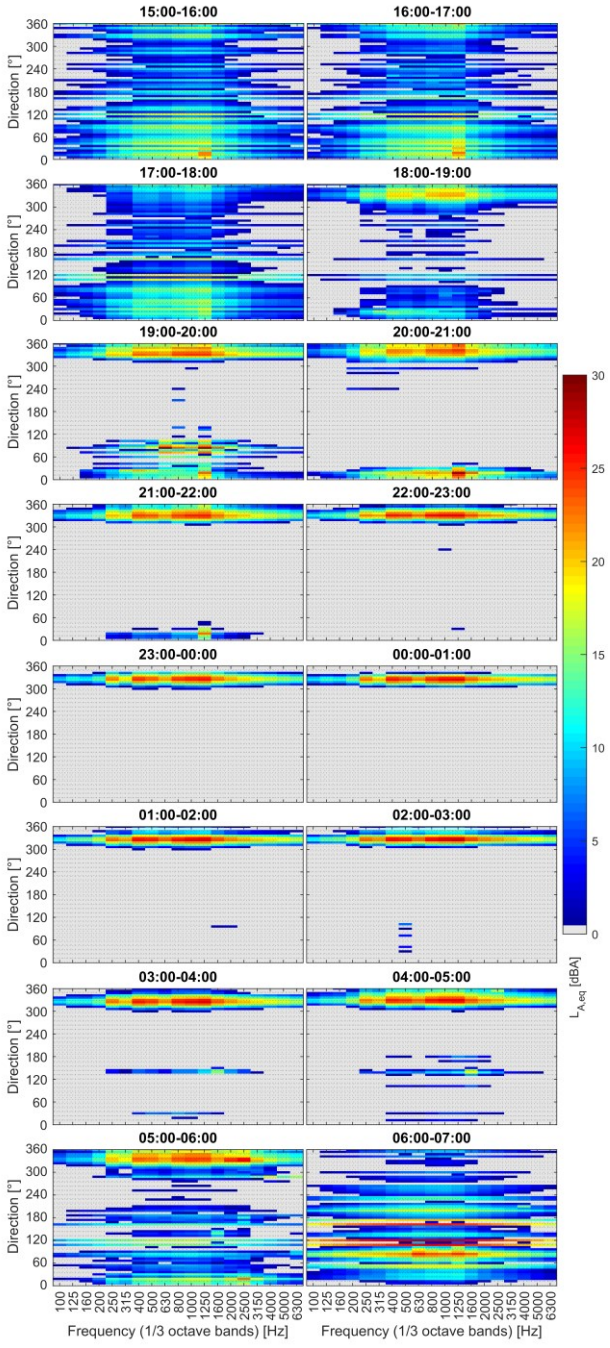


Figure 7. Hourly spectral imission directivity.

It is obvious that the operation of the source stopped between 17:00 and 19:00 and then continued until 22:00. Another noise source occurred between 19:00 and 20:00 with peaks at 630 Hz and 1250 Hz in a direction of about 78°. Looking at the data in the morning, especially between 6:00 and 7:00, noise with broadband frequency content and higher amplitudes can be observed in the directions of 102°, 114° and 156°.

If we filter the data spatially, we can calculate $L_{A,eq}$ of the 1/3-octave spectra for specific noise sources (their direction/location relative to the MP). Fig. 8 shows the results for six noise sources together with the total $L_{A,eq}$ (from 0° to 360°). It can be seen that the main noise source contributing the most to the total noise level is between 312° and 360°. The sources at 102°, 114° and 156° have broadband frequency components (influenced by the A-weighting) that could belong to an impulse noise source. The source at 6° - 30° had a peak in the frequency band of 1250 Hz, while the source at 72° - 90° had an additional peak in the frequency band of 630 Hz.

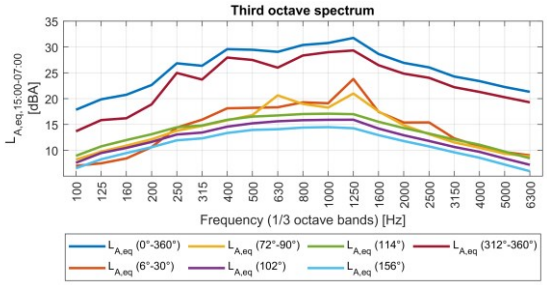


Figure 7. 1/3-octave spectrums of selected directions.

4. DISCUSSION

Pilot measurements were carried out on site to validate and evaluate the usability of the SID. Several noise sources were identified during the analysis, one of which accounts for the largest share of the total noise level. As shown in the ID polar diagram (Fig. 3), the industrial area proved to be the main noise source. A further analysis with the SID (Fig. 7) showed that the noise emissions from the industrial area have a broadband frequency spectrum that is most pronounced in the evening and at night (19:00–06:00).

In certain cases, certain frequency components can cause greater disturbance, especially when people are at home. This effect is more pronounced at lower frequencies, which are better able to penetrate into people's homes. In addition, it is widely recognized that tonal noise is a significant contributor to noise annoyance. The use of SID facilitates the rapid identification of such noise sources and increases the efficiency of noise monitoring and mitigation efforts.

One such noise source, presumably a heat exchanger, was detected between 19:00 and 20:00 at an angle of 78°. This source showed clear peaks at 630 Hz and 1250 Hz within the 1/3-octave frequency bands (Fig. 7). Another conspicuous noise source associated with stone quarry activities was detected in an 18° direction and occurred from 15:00 to 17:00 and again from 19:00 to 22:00. This source had strong tonal characteristics, as shown in Fig. 7.

In addition, three separate noise sources with broadband spectral characteristics were identified in the morning hours (06:00-07:00) in the directions 102°, 114° and 156°. These sources also appeared between 15:00 and 19:00. As these directions coincide with residential areas in nearby villages, it is plausible that these noise sources originate from human activities and may represent impulsive noise events.

These results highlight the effectiveness of SID in accurately identifying and characterizing complex noise environments, thereby supporting more targeted noise mitigation strategies.

5. CONCLUSION

The results of this study show the usefulness and efficiency of the SID for the measurement of environmental noise. A key advantage of SID is its ability to provide a comprehensive overview of the acoustic environment at a glance, allowing for quick identification of dominant noise sources without the need for extensive post-processing. In addition, SID offers flexibility in data analysis as measurements can be analyzed in real time or retrospectively, providing valuable insights for both immediate assessments and in-depth post-measurement evaluations. This capability significantly increases the efficiency of environmental noise assessments and facilitates targeted noise mitigation measures.

To further validate and extend the applicability of SID, future work will focus on conducting longer measurement campaigns in more diverse acoustic environments. This will include the investigation of biological sounds, which will provide additional insights into the effects of natural and anthropogenic noise sources. In addition, efforts will be made to expand the frequency range of the microphone

array's frequency range will be extended to capture and analyze a wider range of noise sources. These planned improvements will increase the versatility of SID and make it a more robust tool for environmental and industrial noise monitoring.

6. ACKNOWLEDGMENTS

The authors acknowledge the financial support by The Slovenian Research and Innovation Agency (ARIS) - funding no. Z7-60185.

7. REFERENCES

[1] Mucci, N., Traversini, V., Lorini, C., De Sio, S., Galea, R. P., Bonaccorsi, G., & Arcangeli, G. (2020). Urban noise and psychological distress: A systematic review. International journal of environmental research and public health, 17(18), 6621. https://doi.org/10.3390/ijerph17186621

[2] Stanovská, M., Tomášková, H., Šlachtová, H., Potužníková, D., & Argalášová, L. U. (2024). Health impact of environmental and industrial noise-a narrative review. Medycyna Pracy. Workers' Health and Safety, 75(5), 425-431. https://doi.org/10.13075/mp.5893.01491

[3] Smith, M. G., Cordoza, M., & Basner, M. (2022). Environmental noise and effects on sleep: an update to the WHO systematic review and meta-analysis. Environmental health perspectives, 130(7), 076001. https://doi.org/10.1289/EHP10197

[4] González, David Montes, Juan Miguel Barrigón Morillas, and Guillermo Rey-Gozalo. "Effects of noise on pedestrians in urban environments where road traffic is the main source of sound." Science of the total environment 857 (2023): 159406). https://doi.org/10.1016/j.scitotenv.2022.159406

[5] Bocanegra, Johan Augusto, et al. "A novel approach to port noise characterization using an acoustic camera." Science of The Total Environment 808 (2022): 151903. https://doi.org/10.1016/j.scitotenv.2021.151903

[6] Ganić, Emir, Fiona Rajé, and Nico van Oosten. "New perspectives on spatial and temporal aspects of aircraft noise: Dynamic noise maps for Heathrow airport." Journal of Transport Geography 106 (2023): 103527. https://doi.org/10.1016/j.jtrangeo.2022.103527

[7] Ibili, Fidelma, et al. "Traffic noise models and noise guidelines: A review." Noise & Vibration Worldwide 53.1-2 (2022): 65-79. https://doi.org/10.1177/09574565211052693

[8] J. Prezelj, J. Murovec, Traffic noise modelling and measurement: Inter-laboratory comparison, Applied Acoustics 127, 160-168 (2017). https://doi.org/10.1016/j.apacoust.2017.06.010

[9] Aumond, Pierre, et al. "Global sensitivity analysis for road traffic noise modelling." Applied acoustics 176 (2021): 107899. https://doi.org/10.1016/j.apacoust.2020.107899

[10] Murovec, J., Prezelj, J., Čurović, L., & Novaković, T. (2018). Microphone array based automated environmental noise measurement system. Applied Acoustics, 141, 106-114. https://doi.org/10.1016/j.apacoust.2018.07.004

[11] Prezelj, J., Čurović, L., Novaković, T., & Murovec, J. (2022). A novel approach to localization of environmental noise sources: Sub-windowing for time domain beamforming. Applied Acoustics, 195, 108836. https://doi.org/10.1016/j.apacoust.2022.108836

[12] Murovec, J., Čurović, L., Železnik, A., & Prezelj, J. (2023). Automated identification and assessment of environmental noise sources. Heliyon, 9(1). https://doi.org/10.1016/j.heliyon.2023.e12846

[13] Čurović, L., Jeram, S., Murovec, J., Novaković, T., Rupnik, K., & Prezelj, J. (2021). Impact of COVID-19 on environmental noise emitted from the port. Science of The Total Environment, 756, 144147. https://doi.org/10.1016/j.scitotenv.2020.144147

DOI:

Main theme: A05 Environmental Acoustics

Session A05.03 Environmental noise perception

Chair(s): T. Van Renterghem, A. Barros

DOI: 10.61782/fa.2025.0549

FORUM ACUSTICUM EURONOISE 2025

MEASUREMENT OF THE SOUND FIELD OVER A GREEN ROOF USING SIMULTANEOUS SOUND PRESSURE RECORDINGS

Julián Álvarez Chaia [1], **Aleix Alva**[2], and **Ana M. Lacasta**[3]

[1]Departament de Física, EPSEB, Universitat Politècnica de Catalunya, Av. Dr. Marañón 44, 08028, Barcelona, Catalonia, Spain
[2]Departament de Tecnologia de l'Arquitectura, ETSAB, Universitat Politècnica de Catalunya, Av. Diagonal 649-651, 08028, Barcelona, Catalonia, Spain
[3]Departament de Tecnologia de l'Arquitectura, EPSEB, Universitat Politècnica de Catalunya, Av. Dr. Marañón 44, 08028, Barcelona, Catalonia, Spain

ABSTRACT

Green roofs provide a distinct acoustic environment with reduced sound pressure levels (SPL) compared to conventional roofs. These levels arise from a combination of direct sound, diffraction, reflection, and absorption effects—strongly influenced by measurement height. Simultaneous SPL measurements at eight heights were carried out to examine how roof geometry and materials affect SPL through absorption and diffraction. Results show that SPL decreases with decreasing measurement height, particularly when greenery covers wall parapets, highlighting the role of vertical surfaces in shaping rooftop soundscapes.

Keywords: *green roofs, sound absorption, soundscape, height dependency of SPL, sound diffraction* .

1. INTRODUCTION

Urban noise pollution is a widespread source of discomfort, with potential medical implications [1]. Among other benefits, urban greenery contributes to noise reduction and improves acoustic comfort [2]. To achieve these effects, densely built cities with limited space for ground vegetation, such as Barcelona, must integrate greenery into the architectural envelope. This study examines the acoustic effects of a semi-intensive green roof comprising $350\,\mathrm{m}^2$ of horizontal vegetation and $200\,\mathrm{m}^2$ of vertical greenery, located primarily along the walls of the roof parapet; and of a conventional roof with no vegetation. The conventional roof refers to a typical Mediterranean solution with ceramic tiles.

A preliminary study at the same location [3] explored differences in soundscape between the two aforementioned roofs. That study, along with subsequent field observations, led to the hypothesis that noise reduction exhibited a marked dependence on height, meriting further investigation. Subjective experience suggested a substantial change in perceived sound when standing versus sitting: from an open, noisy soundscape—where multiple urban sources were clearly identifiable—to a rooftop soundscape characterised by significantly lower sound levels. This contrast, though still present, was less pronounced on the conventional roof.

The soundscape of green roofs has been the subject of numerous studies [4]. In addition, the acoustic absorption properties of green roofs and green walls have been analysed both in laboratory [5] and in situ [6], confirming the expected good sound absorption behaviour due to both, substrate and vegetation.

The experienced sound field results from a combination of direct, diffracted, and reflected components.

***Corresponding author**: julian.alvarez@upc.edu*
***Copyright**: ©2025 Álvarez et al. This is an open-access article distributed under the terms of the Creative Commons Attribution 3.0 Unported License, which permits unrestricted use, distribution, and reproduction in any medium, provided the original author and source are credited*

While previous models describe insertion loss behind sound barriers due to diffraction [7] [8], the geometric and absorptive particularities of the green roof—such as the highly absorbent wall parapet/barrier walls and substrate—warrant specific analysis. This experimental study investigates the dependence of SPL on both height and distance to the parapet, with a focus on the diffracted field within the acoustic shadow cast by the roof's parapet walls.

2. MATERIALS AND METHODS

2.1 Roofs under analysis

The selected roofs are located in a peripheral district, with a sparse population, approximately 500 m from an extensive green zone along the Besòs river. The immediate environment consists of a noisy, heavily motorised industrial park. The green and conventional roofs are separated by about 100 m and are part of the same industrial complex. The green roof, beneath its soil, water-proofing and drainage layers, features a thin roof system, while the conventional roof has a standard roofing solution. The dimensions of the green roof are $37 \times 13\,\mathrm{m}^2$ with a height 20 m, while the conventional roof measures $27 \times 6\,\mathrm{m}^2$ with a height of 12 m.

Figure 1 shows the floor plans of the two roofs, indicating the locations of the microphone arrays and their respective planes. Figure 2 shows a photo collage featuring five key scenes from the study.

2.2 In-situ sound absorption coefficient

Acoustic absorption measurements were conducted in situ using an impedance gun from Microflown Technologies [9–11]. This device consists of a spherical loudspeaker and a PU probe that simultaneously detects acoustic pressure and particle velocity. White noise is generated by the loudspeaker, placed 23 cm from the probe. The probe is positioned near the surface to be measured, as shown in the bottom-right image of Figure 2. The absorption coefficient is obtained from the impedance, that is, the complex ratio between acoustic pressure and particle velocity. The frequency range analysed spans from 200 Hz to 8000 Hz, and the results are presented in third-octave bands.

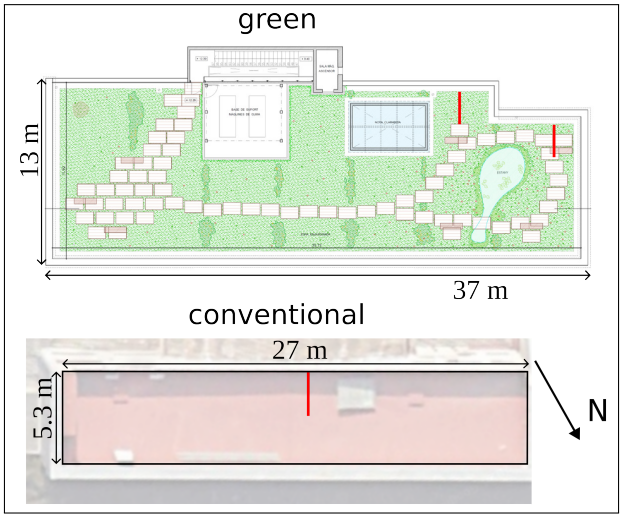


Figure 1: Floor plans of the green (top) and conventional (bottom) roofs. The red stripes indicate the locations and planes of the microphone arrays.

2.3 8-Microphone Array

A special arrangement of eight microphones was used to simultaneously measure sound variation at different heights and distances from the wall, as the background noise was highly variable. The microphone configuration was employed both vertically, with a fixed distance to the wall, and horizontally, with a fixed distance to the floor. These configurations are shown in the diagram of Figure 3. The measurements were recorded using 8 free-field Roga MI-17 microphones and a Rion DA-40 8-channel data recorder, and processed with the Rion AS-70 waveform analysis software.

3. RESULTS AND DISCUSSION

3.1 Acoustic absorption

The acoustic absorption coefficient is determined following the procedure described in Section 2.2, in different areas of the green roof. The results obtained for two representative areas of the roof are shown in Figure 4. The results are presented in third-octave bands between 200 Hz and 8000 Hz. In both cases, relatively high absorption coefficients are observed, with values approaching 1 for frequencies above 2500 Hz in the area with the most vegeta-



Figure 2: Photo collage of five key scenes. Left: vertical array of microphones in front of a conventional wall parapet. Middle top: vertical array of microphones in front of a photovoltaic glass of width 0.02 m. Middle bottom: horizontal array of microphones along a vegetated zone. Right top: acoustic camera facing a conventional wall parapet. Right bottom: impedance gun measuring absorption of a vegetated surface.

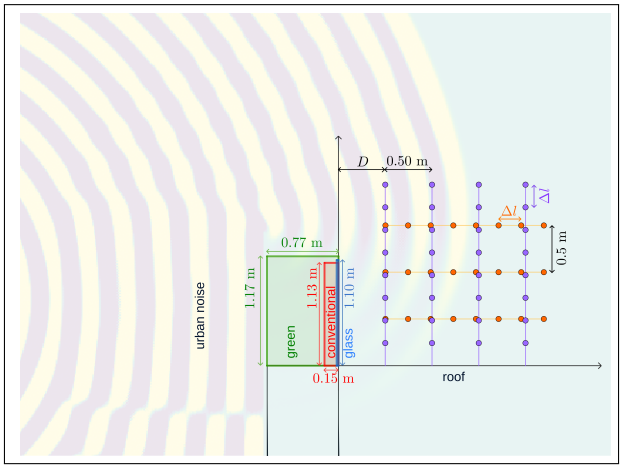


Figure 3: Diagram of wall parapets and microphone array positions (arrays are dots connected by lines). Two types of parapets are shown on the green roof: one wide and vegetated (green in the figure), and another thin, made of photovoltaic glass (blue in the figure). The wall parapet of the conventional roof is shown in red. Vertical microphone array positions are indicated in violet, while horizontal arrays are shown in red. The spacing between microphones in each array is Δl =24.2 cm, with recordings within a given array being simultaneous. The background wavefront represents sound propagation, depicted artistically from a 2D sound-wave simulation using Python Matplotlib. The distance D between the wall parapet and the first microphone of a horizontal array is 50.2 cm for the green roof and 54.2 cm for the conventional roof. For vertical arrays, the first microphone is located 50.0 cm from the parapet.

tion (right image).

3.2 Acoustic camera

We use an acoustic camera to localise the sources of noise in order to characterise the incident sound field. The equipment used was the SevenBel Sound Scanner with the P132 sensor, capable of measuring down to 250 Hz. Figure 5 shows three images of the three wall parapets.

3.3 Sound pressure levels

Figure 6 shows the results for three different fixed heights, where in each case the sound is recorded simultaneously by the eight microphones located at 8 distances from the barrier. The sound levels remain approximately constant with height while changing the distance. Figure 7 displays the A-weighted equivalent continuous sound level for measurements taken at three different positions, with simultaneous measurements from eight microphones at varying heights above the ground. The three graphs correspond to the three barriers analysed. For a fixed distance, the difference in sound level with height exhibits different behaviour in each case. The difference between the maximum height, h =1.94 m, and the lowest height, h =0.25 m, is 10 dB(A) in the green roof-green wall configuration, 6 dB(A) in the green roof-glass wall configuration, and 2 dB (A) in the conventional roof-brick wall configuration.

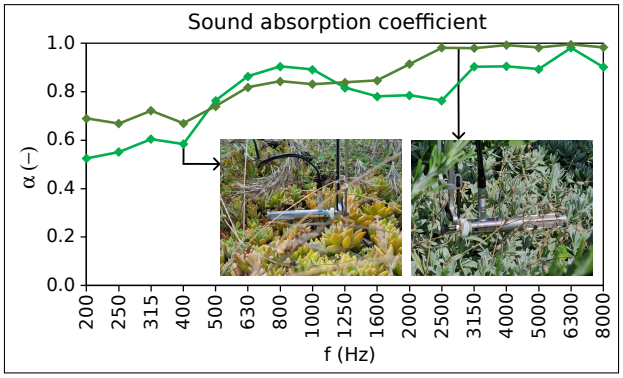


Figure 4: Acoustic absorption coefficients as a function of frequency measured with the impedance gun. Light green represents absorption coefficients for low vegetation, such as Sedum, and dark green for intermediate vegetation, such as leaf plants.

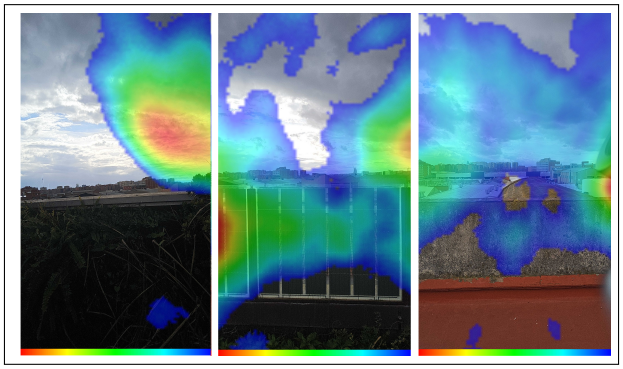


Figure 5: Acoustic camera measurements. From left to right: green roof with green barrier; green roof with glass barrier; conventional wall with brick barrier. The optical image is overlaid with a sound level map, where blue and red represent lower and higher sound levels, respectively. The dynamic range is 3dB. In the left image the sound source is perceived to be slightly higher than the noise source. In the centre image, the two original noise sources are perceived but are out of the frame. The same happens at the conventional wall

3.4 Noise level dependency on the frequency

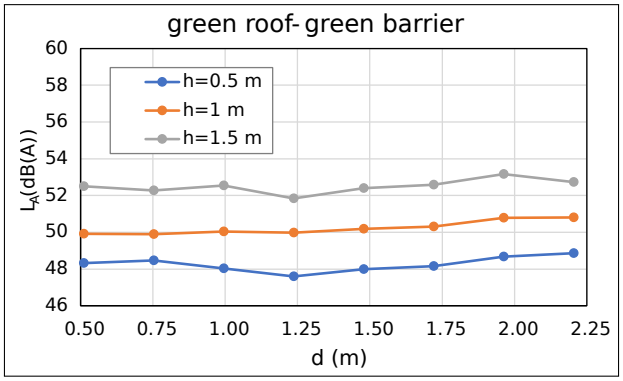
To understand which frequency bands contribute to the overall decrease in sound level, sound levels in third-octave bands between 50 Hz and 10.000 Hz are analysed for eight different heights at a distance of d=1.0 m from the wall in the three roof-barrier configurations (Figure 8). Additionally, for each configuration, the variation in noise levels in some selected third-octave bands with respect to height is plotted in Figure 9.

The spectrum of the conventional roof (Figure 8 c) does not depend on the height of the receiver, and the noise level decreases monotonically with frequency. The green-green case (Figure 8 a) exhibits a behaviour similar to the conventional one at low frequencies, while at medium and high frequencies the curves diverge, clearly decreasing the sound level. Low frequencies at different heights appear to have similar values of L_p, but as the frequency increases, so does the difference between the sound levels at difference heights. The green-glass roof (Figure 8 b) displays intermediate behaviour between the two previous ones. To illustrate this, a closer look at the variations in different third-octave frequency bands for a selected position, as a function of height, is provided in Figure 9. At low frequencies, the level decreases slightly with height across all three configurations. In contrast, at higher frequencies (from 500 Hz onward), the level increases with height. This increase is greater for the green-green roof and modest for the conventional one.

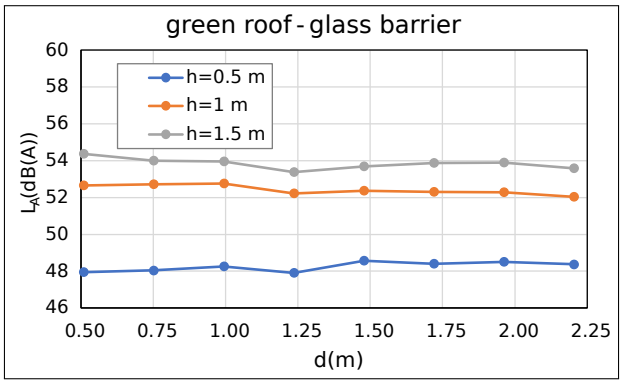
The difference in sound levels for eight different heights in the 125 Hz and 1000 Hz third-octave bands, for two selected distances d=1 m and d=2 m, is shown in Figure 10. For each position, the difference in level of each microphone is determined in relation to the highest microphone, which is taken as the reference level.

In all three cases, the 125 Hz band increases at lower heights, contrary to expectations based on diffraction models. This behaviour could be explained by the low absorption at low frequencies in both the green roof and conventional configurations, allowing the sound to reflect off the barrier walls and the floor at these heights. In the case of the 1000 Hz band, which behaves similarly to the 500 Hz, 2000 Hz, and 4000 Hz bands, the difference between roof-barrier configurations is much clearer.

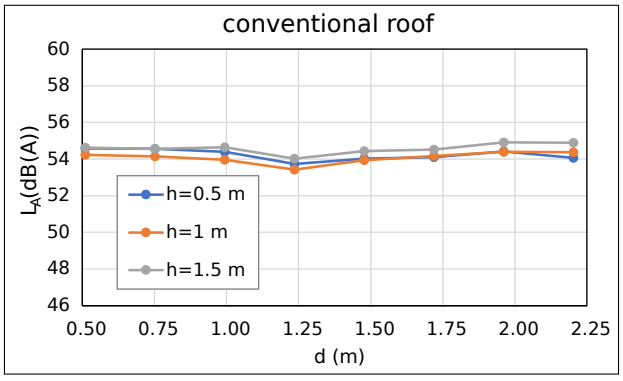
The difference between the reference level (highest microphone) and the lowest microphones ranges from 14 – 16 dB in the green roof-green barrier configuration. The same measurement on the glass barrier shows a difference of 10 – 12 dB between the extremes. In both



(a)

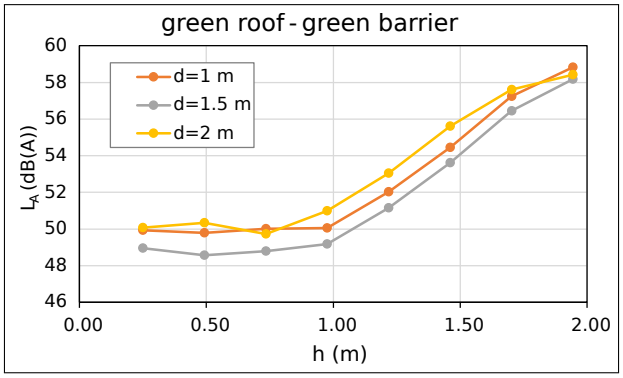


(b)

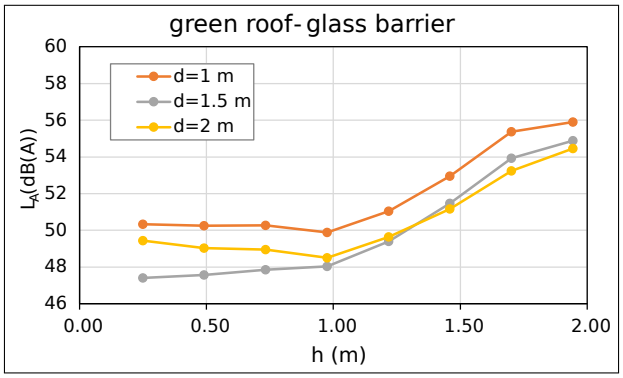


(c)

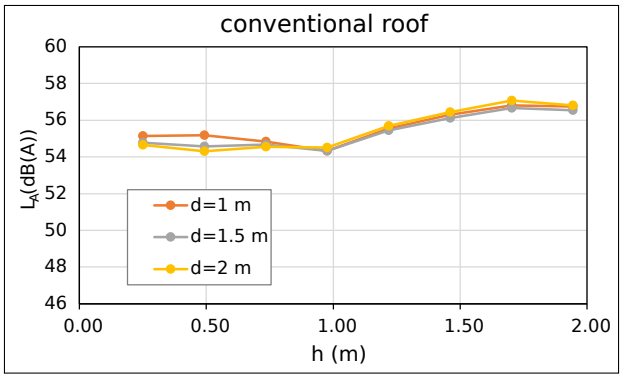
Figure 6: L_A vs d. Panels (a), (b), and (c) show the A-weighted sound pressure level, L_A, as a function of distance to the wall, for three different fixed heights h. The measurements are performed at the green roof-green barrier case (a), the green roof-glass barrier case (b), and the conventional roof (c).



(a)

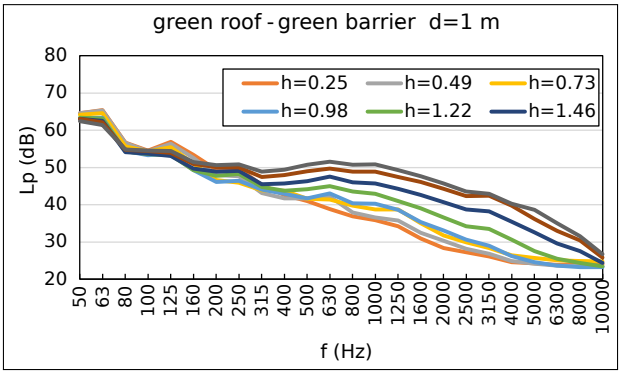


(b)

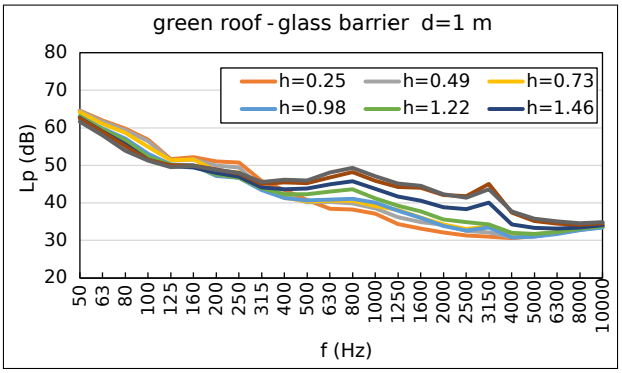


(c)

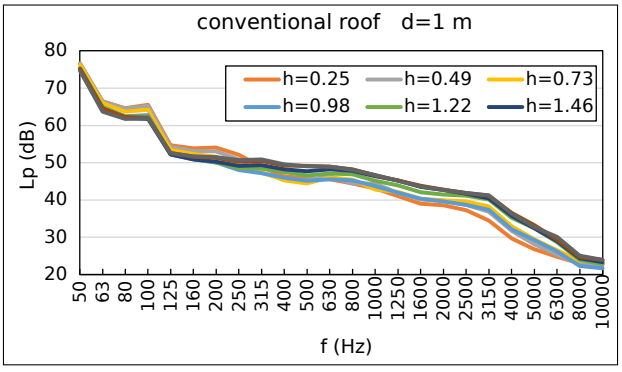
Figure 7: L_A vs h. Panels (a), (b), and (c) show the A-weighted sound pressure level, L_A, as a function of height, for three different fixed distances d from the wall. The measurements are performed at the green roof-green barrier case (a), the green roof-glass barrier case (b), and the conventional roof (c).



(a)



(b)



(c)

Figure 8: Panels (a), (b), and (c) show the sound pressure level, L_p, in third-octave bands as a function of frequency, for a fixed distance d=1 m from the wall. The measurements are taken at different heights for the green roof-green barrier case (a), the green roof-glass barrier case (b), and the conventional roof (c).

cases, the trend is relatively linear. Finally, the conventional roof-brick wall configuration shows differences of $4-5$ dB between the highest and lowest microphones.

From these measurements, it can be inferred that the L_A level differences presented in Section 3.2 are mainly driven by medium and high frequencies, from 500 Hz to 4000 Hz, as also evident from the graphs in Figure 8.

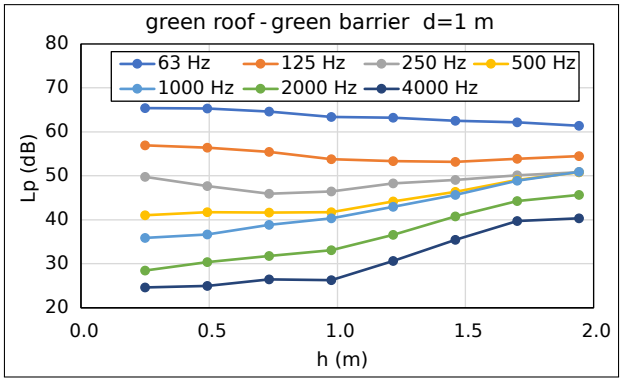
4. CONCLUSIONS

Three different cases were analysed: a green roof with a green wall parapet, a green roof with a glass barrier, and a conventional roof with a brick parapet. The green roof with a green barrier exhibited the largest difference in sound levels between the highest measurement point and the lowest, with level differences of up to 15 dB in medium to high frequencies, from the 500 Hz band up to 4000 Hz. The glass barrier showed a similar behaviour but with smaller differences, up to 10 dB. The conventional roof showed a maximum difference of 5 dB. This comparison is shown in Figure 10 (b).

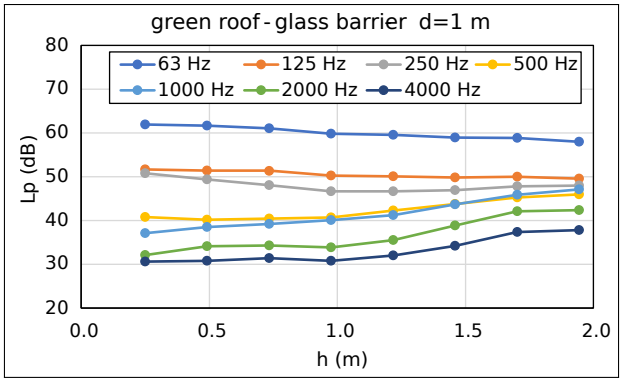
This contrasting behaviour was also observed when measuring the A-weighted global sound levels. In this case, the green roof with a green wall parapet exhibited differences of 10 dB(A), the green roof with a glass barrier 6 dB(A), and the conventional roof with a brick parapet 2 dB(A).

Much smaller variations between roofs were observed at low frequencies ($125-250$ Hz), as shown in Figure 10 (a). The three configurations show similar behaviour, reaching 4 dB as the measurement height decreases. Therefore, the trend is reversed at higher frequencies. The effect of internal sound reflections inside the roof is hypothesised, as there is low absorption coefficients of the walls and plants at low frequencies, along with the possibility of additional inter-reflections of sound inside the roof walls.

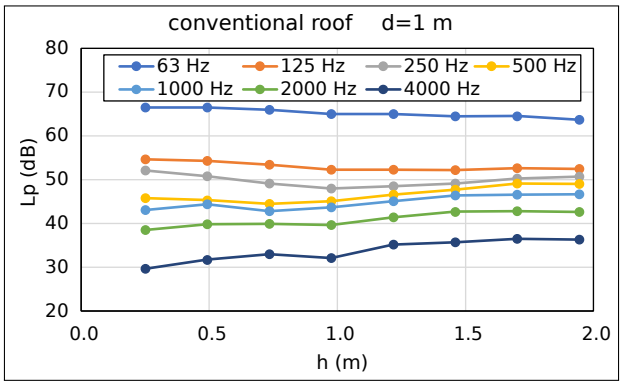
The hypothesis is confirmed: greenery on the roof, particularly when covering wall parapets, results in a reduction of overall sound levels with decreasing measurement height. Future work will involve numerical modelling of diffraction, absorption and reflection to better understand and predict the mechanisms shaping rooftop soundscapes.



(a)

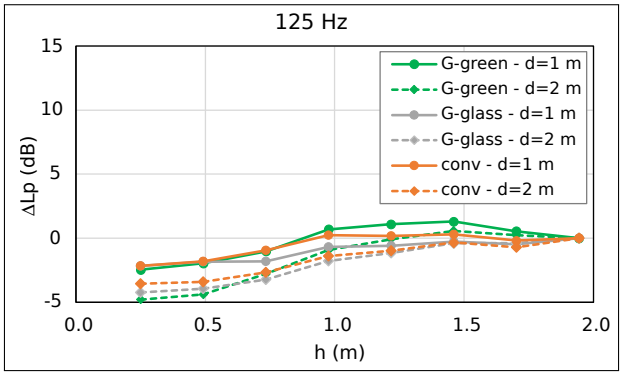


(b)

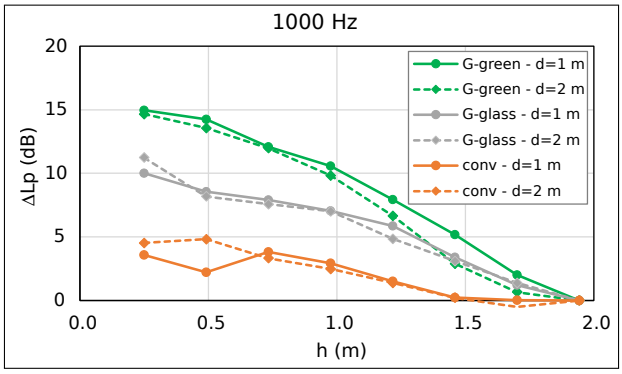


(c)

Figure 9: Panels (a), (b), and (c) show the sound pressure level, L_p, in different third-octave bands (63 Hz-4000 Hz) as a function of height, for a fixed distance d=1 m from the wall. The measurements are taken at varying heights for the green roof-green barrier case (a), the green roof-glass barrier case (b), and the conventional roof (c).



(a)



(b)

Figure 10: ΔL_p vs h. Panels (a) and (b) show the variation of the sound pressure levels with height ΔL_p, for two different distances of the microphone array to the wall in each of the roof-barrier configurations. ΔL_p represents the difference between the value at the higher microphone and each of the other microphones.The 125 Hz band case is represented in panel (a) and the 1000 Hz band in panel (b)

5. ACKNOWLEDGEMENTS

We would like to thank Núria Castelló and Urbaser for their help and support. This work was partially funded by MICIU/ AEI/10.13039/501100011033 through the project PID2020-117530RB-I00.

6. REFERENCES

[1] "European commission, european noise directive 2002/49/ec of the european parliament and of the council, of 25 june 2002, relating to the assessment and management of environmental noise," (2002).

[2] T. Van Renterghem, M. Hornikx, J. Forssen, and D. Botteldooren, "The potential of building envelope greening to achieve quietness," *Building and Environment*, vol. 61, pp. 34–44, 2013.

[3] A. Alva and A. M. Lacasta, "Cubiertas verdes en barcelona: Un paisaje sonoro particular dentro de la ciudad," *In Tecniacústica 2024: 55 Congreso Español de Acústica; XIII Encuentro Ibérico de Acústica*, 2024.

[4] T. Van Renterghem and D. Botteldooren, "In-situ measurements of sound propagating over extensive green roofs," *Building and environment*, vol. 46, no. 3, pp. 729–738, 2011.

[5] A. Tadeu, J. Carrilho, A. Cortês, F. Ferreira, and J. Almeida, "Acoustic absorption, scattering, and diffusion provided by green roof systems," *Building and Environment*, vol. 262, p. 111778, 2024.

[6] V. Oquendo-Di Cosola, M. Á. Navacerrada, L. Ruiz-García, and F. Olivieri, "Evaluating the acoustic absorption of modular vegetation systems: Laboratory and field assessments using an impedance gun," *Buildings*, vol. 15, no. 3, p. 389, 2025.

[7] Z. Maekawa, "Noise reduction by screens," *Applied acoustics*, vol. 1, no. 3, pp. 157–173, 1968.

[8] K. Li and H. Wong, "A review of commonly used analytical and empirical formulae for predicting sound diffracted by a thin screen," *Applied Acoustics*, vol. 66, no. 1, pp. 45–76, 2005.

[9] M. Navacerrada, M. Barbero-Barrera, R. Fort, D. de la Prida, J. Núñez, and T. Gómez, "Application of acoustic impedance gun to non-destructively monitor stone damage," *Construction and Building Materials*, vol. 323, p. 126510, 2022.

[10] E. Tijs, D. Fernandez Comesana, and D. Garcia Escribano, "Caracterización de absorbentes acústicos in-situ mediante sonda pu," 2011.

[11] M. Li, W. van Keulen, E. Tijs, M. van de Ven, and A. Molenaar, "Sound absorption measurement of road surface with in situ technology," *Applied Acoustics*, vol. 88, pp. 12–21, 2015.

DOI: 10.61782/fa.2025.0667

FORUM ACUSTICUM EURONOISE 2025

REDUCING THE TRAFFIC INDUCED ANNOYANCE BY PUBLIC PARTICIPATION; INTERACTION BETWEEN QUESTIONNAIRES, MODEL CALCULATIONS, AND MEASUREMENTS

Wim van Keulen[1*]
[1] VANKEULEN advies, Schijndel, the Netherlands

ABSTRACT

Commissioned by a major province in the Netherlands, VANKEULEN advies conducted a study into the annoyance aspects of a main 2-laned road. In 2019, a study was conducted into the complaints and the possible solution(s). Due to its complexity, a step-by-step approach was chosen at the time to quantify the problem based on the path: source - transfer – receiver.
To this end, the first 'subjective' and 'objective' measurements were carried out in 2019. The subjective measurements consisted of a survey among residents, the objective of several measurements on the existing road surface and expansion joints. In addition, noise calculations were carried out. After the application of noise reduction measures (noise barrier, low-noise joints and asphalt), the survey and measurements were repeated in 2022. In this way, the partial effects and the total effect (subjective and objective) of the measures could be determined.
The total noise reduction amounted to 12 – 15 dB(A). The overall nuisance decreased by approximately 50%. At the same time, a significant majority indicated that the overall environmental quality improved. However, the overall appreciation for the high impact of the two measures is surprisingly low.

Keywords: *traffic noise, public participation, noise barriers, low noise pavement, environmental quality*

[*] ***Corresponding author***: *info@vankeulenadvies.nl.*
Copyright: *©2025 First author et al. This is an open-access article distributed under the terms of the Creative Commons Attribution 3.0 Unported License, which permits unrestricted use, distribution, and reproduction in any medium, provided the original author and source are credited.*

1. INTRODUCTION

On behalf of the Province of South Holland, VANKEULEN Advies conducted a study on noise annoyance associated with the N210 near Rotterdam a road section where numerous complaints were reported to road management authorities in recent years. Significant noise disturbance was documented among residents living along the N210.
In 2019, a global study was initiated to analyse complaints and investigate potential mitigation strategies. Due to the complexity of the issue, a phased approach was adopted, adhering to the framework of **source–transmission–receiver**. Both subjective and objective measurements were conducted in 2019 and repeated in 2022. The subjective assessment involved a survey of residents on both sides of the roadway, while the objective evaluation comprised various assessments of the existing road surface and expansion joints.
Additionally, noise modelling calculations were performed to determine the optimal height for a potential noise barrier and assess its effectiveness. Subsequently, the following noise-reduction measures were implemented:

- 2021: Installation of a noise barrier close to the road, measuring 1.40 meters in height, consisting of a concrete barrier topped with noise-absorbing panels.
- 2022: Application of a noise-reducing thin surface layer.

The follow-up study replicated the pre-measurement assessments to evaluate the individual and cumulative effects (both subjective and objective) of the implemented measures. The total noise reduction at the façades of adjacent residences (relevant for regulatory compliance) and the net noise reduction (relevant for nuisance reduction) were systematically assessed.

2. QUESTIONAIRE

2.1 Questionnaire Design

The questionnaire in 2022 was largely based on the initial survey conducted in 2019. However, in 2022, the primary objective shifted from determining the extent of annoyance to evaluating the reduction of annoyance. The questionnaire was conducted among residents of two sides of the road during September 19 and 22, 2022, concurrently with the noise level measurements. A total of 47 valid replies were collected, of which 24 completed electronically and 23 via postal mail. Statistical analysis indicated no significant differences between the response methods. For comparative analysis, the results were categorised by roadside (south and north) and expressed as percentages.

2.4 Indoor Noise Perception

Tab. 1 presents the results for noise barriers under conditions of closed and open windows.

Table 1. Improvement in Indoor Traffic Noise Due to Noise Barriers [%].

	Closed Windows	Open Windows
High	20	4
Moderate	43	46

Approximately half of the respondents experienced an improvement due to the new noise barrier. Tab. 2 presents the results for quieter asphalt under conditions of closed and open windows.

Table 2. Improvement in Indoor Traffic Noise Due to Quieter Asphalt [%].

	Closed Windows	Open Windows
High	15	7
Moderate	43	48

More than half of the respondents reported improvements due to this measure. Furthermore, the results suggest that the perceived positive effect of quieter asphalt was slightly greater than that of the noise barrier.

2.5 Outdoor Noise Perception

Tab. 3 presents the results for the noise barrier and quieter asphalt in outdoor environments, respectively. The findings indicate a relatively limited impact of the measures in outdoor spaces, except on the north side of the roadway, where the noise barrier had a more pronounced effect.

Table 3. Improvement in Outdoor Traffic Noise [%].

	Noise Barrier	Quieter Asphalt
High	4	9
Moderate	24	39

The quieter asphalt was generally perceived as more effective than the noise barrier.

2.6 Perceived Traffic Noise Annoyance

Tab. 4 presents the results regarding the reduction in traffic noise annoyance due to the noise barrier and quieter asphalt, respectively.

Table 4. Reduction in Traffic Noise Annoyance [%].

	Noise Barrier	Quieter Asphalt
High	9	11
Moderate	37	53

The noise annoyance was reduced by 46% due to the noise barriers, whereas quieter asphalt led to a 64% reduction. Again, the positive effect of quieter asphalt on reducing annoyance was larger.

2.7 Changes in Traffic Noise Characteristics

Tab. 5 presents the results regarding improvements in the perceptual characteristics ("colour") of traffic noise.

Table 5. Improvement in Traffic Noise Perception [%].

	Noise Barrier	Quieter Asphalt
much	13	28
Moderate	49	47

These findings indicate a greater perceived improvement in noise characteristics than the reduction in noise annoyance presented in Tab. 4.

2.8 Overall Improvement

Tab. 6 presents the average improvement in traffic noise perception across different environments.
The average reported improvement in noise perception was 2.3. In summary, while annoyance levels decreased slightly due to the implemented measures, the overall acoustic environment improved for most respondents. However, overall appreciation for the two measures remained relatively low.

Table 6. Average Improvement in Traffic Noise Perception [sca1e 1–5].

Inside	Outside	Area	Total
2.6	2.2	2.1	2.3

3. MONITORING

3.1 Immisions

Monitoring stations were installed at two residential locations, one at the north side and one at the south side. During September 19–22, 2022, concurrent with the survey, noise levels at the two locations were continuously recorded over the course of a workweek. The monitoring results were categorised into daytime, evening, and nighttime periods. These measurements provide insight into the variation of the equivalent continuous sound level (L_{Aeq}) over different short time periods (every 5 minutes). Microphones were positioned at the façades of the residences at both side of the road: northside: 2 m high and southside: 5 m high. These measurement heights correspond to the upper floors where noise-sensitive rooms are located. The monitoring results were compared with those from 2019 to identify relevant differences and potential causes.

3.2 Results

During monitoring, construction activities were ongoing in the vicinity of a patrol station. These activities significantly impacted some measurements (>10 dB(A)); however, these intervals were readily identifiable and accounted for in the analysis. Additionally, the central bus lane had not yet been opened, which led to a slight increase in the influence of bus traffic. However, this effect was found to be minimal. Fig. 1 illustrates the monitoring data obtained from the two locations.

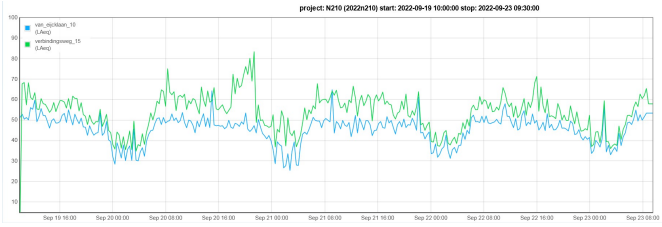


Figure 1. Results of the full monitoring at the two locations.

Tab. 7 provides an overview of the average noise levels for each period. The data have been rounded to the nearest whole number and adjusted for prescribed façade reflection (-3 dB(A)).

Table 7. Average Noise Levels per Time Period [dB(A)].

Location	Day	Evening	Night
North	47	43	34
South	55	49	38

The measured values at south side were higher than those on the north side, primarily due to its closer proximity to the road.

4. NEW ROAD PAVEMENT

4.1 Noise Measurement

A SPB measurement [1] was conducted on September 22, 2022. Tab. 8 presents the measured SPB values for light motor vehicles, along with the strict Dutch reference values.

Table 8. Measured SPB-levels [dB(A)].

Speed	SPB level	reference
50 km/h	63.6	71.0

The noise reduction at the SPB measurement point is approximately 7 dB(A). CPX measurements [2] were conducted on September 11, 2022. Tab. 9 presents the measured CPX values for light motor vehicles.

Table 9. Measured CPX-levels [dB(A)].

Direction	CPX level
East	87.8
West	86.9

By using the calibration relationship between the SPB and CPX measurements conducted in this study, the CPX values were converted into an average SPB level of the entire section as presented in Tab. 10.

Table 10. Average Noise Reductions of the new pavement [dB(A)].

Direction	Noise Reduction
East	7.4
West	8.3

The average initial noise reduction for light motor vehicles travelling at 50 km/h is approximately 8 dB(A). The new expansion joints are not audible and, therefore, not measurable.

5. COMPARISON WITH THE 2019 SITUATION

5.1 Representativeness for the Considered Area

Considering the relatively simple acoustic environment and the symmetry around the road, the results obtained for the two monitoring locations can be generalised to all residences in the vicinity of the road except for a small number of houses located directly behind the petrol station. In this specific area, the full benefit of the quieter road surface is observed, but the influence of the newly constructed noise barrier is minimal.

5.5 Reduction of the immission

Tab 11. shows the average noise immission levels as measured in 2019 and 2022, respectively.

Table 11. Average Noise Immission Levels [dB(A)].

Location	2019	2022	Reduction
North	62	47	14 ± 3
South	68	55	12 ± 3

5.2 Effect of Road Pavement

By comparing noise emissions before and after repaving, the net effect of the new pavement has been quantified (see Tab. 12).

Table 12. Average Noise Reductions before and after Repaving [dB(A)].

Situation	Noise Reduction
Before Reconstruction	1.1
After Reconstruction	7.8

The new pavement results in an approximate noise reduction of 7 dB(A) compared to the previous pavement, which is acoustically equivalent to a fourfold reduction in traffic volume.

5.3 Effect of Noise Barriers

The absolute shielding effect of noise barriers is not easily quantifiable, as it depends on the relative position of the receiver, the noise source, and the barrier. This is because noise barriers primarily attenuate sound via diffraction rather than absorption. When the receiver is located within the acoustic shadow of the barrier, noise attenuation is maximal. However, when the road is directly visible from the receiver's position, the noise attenuation is minimal. The absorptive panels installed on the noise barriers are designed exclusively to prevent reflections that may affect positions on the opposite side of the road. The effect of a noise barrier can be accurately calculated using the Dutch Noise Calculation Method. This method was applied to the two measurement locations based on the actual geometry and placement of the implemented noise barriers (see Tab. 13).

Table 13. Average Noise Reductions before and after Construction of the Barriers [dB(A)].

Situation	Noise Reduction
North	8.5
South	5.5

5.4 Net Subjective and Objective Effect of the Measures

From the data presented in Tab. 12 and Tab. 13 it is evident that the overall noise reduction due to the implemented measures ranged from 12 to 15 dB(A). Notably, the results exhibit a high degree of similarity to those presented in Tab. 11 and in this section. However, as can be seen in Tab. 6, despite the substantial improvements in noise levels and environmental quality, the perceived appreciation of these measures is relatively low.

6. CONCLUSIONS

Based on the findings derived from the questionnaire responses, as well as the noise emission and immission measurements, it can be concluded that, despite achieving a substantial overall noise reduction (>10 dB(A)), the subjective evaluations provided by the residents were only moderately favourable. Furthermore, the research indicates that the level of public participation did not meet anticipated expectations.

7. REFERENCES

[1] ISO 11819-1, "Acoustics -- Measurement of the influence of road surfaces on traffic noise -- Part 1: Statistical Pass-By method", 1997.

[2] ISO 11819-2, "Acoustics -- Measurement of the influence of road surfaces on traffic noise -- Part 2: The close-proximity method", 2017.

DOI: 10.61782/fa.2025.0854

FORUM ACUSTICUM EURONOISE 2025

THE ALLEVIATING ROLE OF RESIDENTIAL GREEN ON ROAD TRAFFIC NOISE ANNOYANCE: INSIGHTS FROM THE RESTORE PROJECT

Claudia Kawai[1*] **Javier Dopico**[1] **Beat Schäffer**[1]
María García-Martín[2] **Natalia Kolecka**[2] **Silvia Tobias**[2]
Danielle Vienneau[3,4] **Martin Röösli**[3,4] **Mark Brink**[5]
Jean Marc Wunderli[1]

[1] Empa, Swiss Federal Laboratories for Materials Science and Technology, Dübendorf, Switzerland
[2] Swiss Federal Institute for Forest, Snow and Landscape Research (WSL), Birmensdorf, Switzerland
[3] Swiss Tropical and Public Health Institute (Swiss TPH), Allschwil, Switzerland
[4] Faculty of Science, University of Basel, Basel, Switzerland
[5] Federal Office for the Environment (FOEN), Bern, Switzerland

ABSTRACT*

Long-term exposure to noise is linked to various adverse effects on human health. Growing evidence suggests that residential green spaces can positively influence a wide range of health outcomes. Noise annoyance is a key factor examined in the literature in this context. We present findings from two large-scale studies conducted in Switzerland (combined n = 3,340 participants), one in the city of Zurich and one nationwide. Road traffic noise annoyance data was collected and regressed on exposure to (a) road traffic noise and (b) residential green around participants' home location. Higher exposure-response curves were found for the nationwide sample compared to the Zurich sample. Importantly, more residential green was associated with lower annoyance at comparable road traffic noise exposure. These findings highlight the positive, mitigating influence of natural green on negative noise-induced outcomes.

Keywords: *noise, annoyance, residential green, NDVI, exposure–response curve*

1. INTRODUCTION

Noise has demonstrable detrimental effects on human health. Long-term exposure to transportation noise from road traffic, as one of the most prominent noise sources, has been associated with noise annoyance, sleep disturbance, increased risk of cardio-vascular diseases, hypertension, and depression [1-2]. As a countermeasure to the negative impact of noise, the beneficial role of nature on human health has come into focus in recent years. Access to nature has shown to reduce noise annoyance, perceived stress, blood pressure, and stress hormone concentration short-term [3-5]. Long-term effects of living in green neighborhoods have also been shown, protective effects on mental and physical health [6-7].

The Swiss project RESTORE (www.restore-project.ch) investigated the positive influence of green spaces in conjunction with the negative influence of noise on stress

* ***Corresponding author***: claudia.kawai@empa.ch.
Copyright: *©2025 C. Kawai et al. This is an open-access article distributed under the terms of the Creative Commons Attribution 3.0 Unported License, which permits unrestricted use, distribution, and reproduction in any medium, provided the original author and source are credited.*

restoration. The present contribution reports data from two RESTORE surveys: one conducted in the city of Zurich and one nationwide across Switzerland. Road traffic noise (RTN) annoyance is analyzed in dependence of RTN exposure (L_{den}) as well as residential green (normalized difference vegetation index NDVI) to gauge if and by how much natural environments may mitigate the negative impact of noise.

2. METHOD

The two surveys were conducted between the years 2021–2022 in Switzerland. The Zurich (ZH) survey collected data only from residents of the city of Zurich, while the Swiss (CH) survey was conducted nationwide. Both surveys followed a stratified sampling approach to cover an ample range of RTN exposure and degree of residential green. Areas with increased exposure to aircraft and railway noise were excluded to avoid mixing different noise sources that may disparately impact health outcomes [8]. RTN annoyance data was collected using the ICBEN 11-point numerical scale (annoyance ratings from 0–10) [9].

2.1 Participants & Exposure Data

Annoyance data from 1,111 (ZH) plus 2,229 (CH) respondents were analyzed (combined n = 3,340). Gender was balanced in both samples, and the mean age was 51.4 (SD±16.1) years. For each respondent, individual RTN exposure (L_{den}, modelled in sonBASE 2015 [10]) and NDVI (300 m Euclidean buffer, years 2019-2021 [11]) were linked to the annoyance response via a residential unit identifier.

2.2 Statistical Analysis

Annoyance data were transformed into 'highly annoyed' (HA) by setting all ratings ≥ 8 to 1 and all others to 0. The binary HA data then served as the dependent variable for a generalized linear model using a logit link function to predict pHA (probability 'highly annoyed'), in which L_{den} and NDVI were included as predictors, see Eqn. (1).

$$\text{logit}(p\text{HA}) = \beta_0 + \beta_1 \cdot L_{den} + \beta_2 \cdot NDVI \qquad (1)$$

Two separate regression models were fitted following Eqn. (1), one with the CH survey data ('CH model') and one with the ZH survey data ('ZH model').

3. RESULTS

Model coefficients for the CH model and the ZH model are given in Tab. 1. Both models revealed L_{den} to be significantly associated with pHA (p < .001), with ORs of 1.15, meaning for every 1 dB increase in L_{den} the odds of a HA response increase by 15%.

Table 1. Log-odds coefficients (coef.), odds ratios (OR) with their 95% confidence interval (CI), and p-values for the CH and ZH models following Eqn. (1).

Parameter	Coef.	OR	CI OR	p
CH Model				
Intercept	-8.3008	-	-	**< .001**
L_{den}	0.1368	1.15	[1.13; 1.16]	**< .001**
NDVI	-1.3611	0.26	[0.10; 0.67]	**.006**
ZH Model				
Intercept	-9.7014	0.00	[0.00; 0.00]	**< .001**
L_{den}	0.1431	1.15	[1.12; 1.19]	**< .001**
NDVI	-0.8904	0.41	[0.07; 2.33]	.314

Fig. 1 displays the relationship of noise exposure and residential green with the outcome of pHA to RTN for both samples. The ZH exposure-response curves are shifted downwards on the y-axis compared to CH (also visible with the lower intercept in the CH Model). Given that the slopes (β_1) for L_{den} are very similar for both models, this shift signifies that, at comparable L_{den} values, the overall pHA is lower in ZH than in CH.

Concerning NDVI, the negative log-odds coefficient β_2 indicates a protective effect of residential green against RTN annoyance. This association is statistically significant in the CH model with an OR of 0.26 (i.e., 74% decreased odds of a HA response per 1-unit increase in NDVI). In the ZH model, the confidence interval around the OR for NDVI is large and not statistically significant.

To gauge the size of the protective effect of NDVI, the equivalent sound pressure level change (ΔL) between the 5th and 95th percentile NDVI (i.e., for areas with little vs. much green) can be calculated as the shift along the x-axis between the two curves. Inserting the respective model coefficients and solving Eqn. (1) for L_{den} results in a ΔL of ca. 4 dB for CH, and ca. 3 dB for ZH in terms of magnitude of a protective effect of residential green against RTN annoyance.

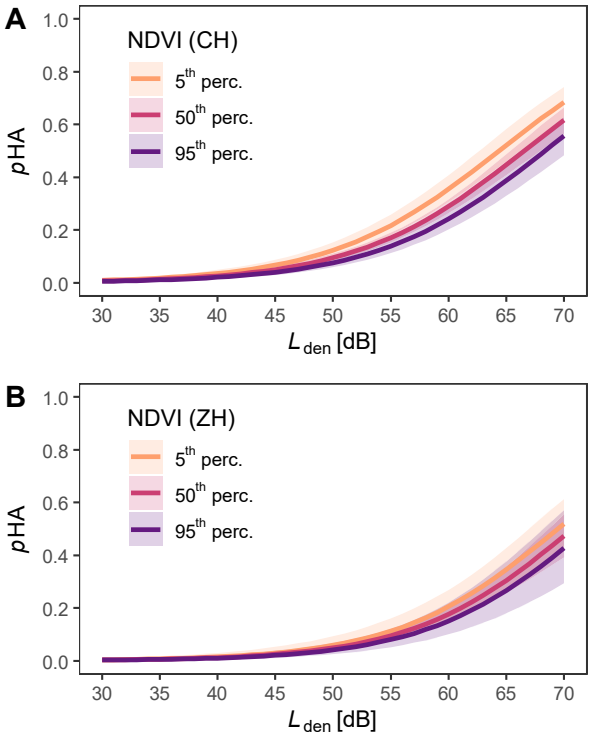


Figure 1. Exposure-response curves after Eqn. (1) for the CH sample (A) and the ZH sample (B).

4. DISCUSSION

The data reported here, collected in two stratified Swiss surveys, contribute evidence towards the mitigating effect of residential green on RTN annoyance. For the nationwide sample, an increase in residential green (as measured by NDVI) was associated with decreased probabilities of being 'highly annoyed' by RTN. Comparing residents in areas with little (5th percentile) versus much green (95th percentile) in the CH sample, an equivalent level reduction of RTN of 4 dB was found. This also indicates that, at the same RTN exposure, 'highly annoyed' reactions are less likely when the neighborhood is greener. While the results for the ZH sample go in the same direction, the protective effect of residential green was smaller and not significant ($\Delta L \approx 3$ dB).

The finding that the Zurich sample, covering the most populated city in Switzerland, showed a smaller protective effect for NDVI compared to the nationwide sample could indicate that there might be some differences in other qualities of residential green (e.g., biodiversity, openness) between the metropolitan ZH area and the heterogeneous CH area that NDVI alone cannot entirely explain.

In general, the magnitude of the protective effect of residential green on noise annoyance found here, while corroborative, falls short of those reported in the literature, with reported values of 6 dB [12] and 10 dB [13]. Possible reasons for this discrepancy might relate to the green metric used, which differs between studies in this research field, as well as other manifold methodological differences (e.g., different NDVI buffer sizes, context of the questions, etc.).

In conclusion, our results demonstrate that natural green in residential areas can help to decrease the negative impact of road traffic noise on the population.

5. FUNDING

This work was supported by the Swiss National Science Foundation (SNF) Sinergia [grant number CRSII5_193847 / 1, 2020] and the Federal Office for the Environment (FOEN, Assignment No. 5211.02161.100.01; Contract No. 22.0001.PJ/7E3987669).

6. REFERENCES

[1] M. Basner, W. Babisch, A. Davis, M. Brink, C. Clark, S. Janssen and S. Stansfeld, "Auditory and non-auditory effects of noise on health," *The Lancet*, vol. 383, no. 9925, pp. 1325–1332, Apr. 2014, doi: 10.1016/S0140-6736(13)61613-X.

[2] K. Sivakumaran, J.A. Ritonja, H. Waseem, L., AlShenaibar, E. Morgan, S. A. Ahmadi, A. Denning, D. S. Michaud, R. L. Morgan, "Impact of Noise Exposure on Risk of Developing Stress-Related Health Effects Related to the Cardiovascular System: A Systematic Review and Meta-Analysis," *Noise Health*, vol. 24, no. 114, pp. 107–129, Jul. 2022, doi: 10.4103/nah.nah_83_21.

[3] T. Hartig, G. W. Evans, L. D. Jamner, D. S. Davis, and T. Gärling, "Tracking restoration in natural and urban field settings," *J. Environ. Psychol.*, vol. 23, no. 2, pp. 109–123, Jun. 2003, doi: 10.1016/S0272-4944(02)00109-3.

[4] B.-J. Park, Y. Tsunetsugu, T. Kasetani, H. Hirano, T. Kagawa, M. Sato, and Y. Miyazaki, "Physiological Effects of Shinrin-yoku (Taking in the Atmosphere of the Forest)—Using Salivary Cortisol and Cerebral Activity as Indicators—," *J. Physiol. Anthropol.*, vol. 26, no. 2, pp. 123–128, 2007, doi: 10.2114/jpa2.26.123.

[5] C. Kawai, F. Georgiou, R. Pieren, S. Tobias, P. Mavros, and B. Schäffer, "Investigating effect chains from cognitive and noise-induced short-term stress build-up to restoration in an urban or nature setting using 360° VR," *J. Environ. Psychol.*, vol. 100, p. 102466, Dec. 2024, doi: 10.1016/j.jenvp.2024.102466.

[6] B. Wicki, B. Schäffer, J. M. Wunderli, T. J. Müller, C. Pervilhac, M. Röösli, and D. Vienneau, "Suicide and Transportation Noise: A Prospective Cohort Study from Switzerland," *Environ. Health Perspect.*, vol. 131, no. 3, p. 037013, Mar. 2023, doi: 10.1289/EHP11587.

[7] D. Vienneau, K. de Hoogh, D. Faeh, M. Kaufmann, J. M. Wunderli, M. Röösli, and SNC Study Group, "More than clean air and tranquillity: residential green is independently associated with decreasing mortality," *Environ. Int.*, vol. 108, pp. 176–184, 2017.

[8] J. Dopico, B. Schäffer, M. Brink, M. Röösli, D. Vienneau, T. M. Binz, S. Tobias, N. Bauer, J. M. Wunderli: "How do road traffic noise and residential greenness correlate with noise annoyance and long-term stress? protocol and pilot study for a large field survey with a cross-sectional design. Article No. 3203.," *International Journal of Environmental Research and Public Health*, vol. 20, 19 pp., 2023.

[9] ISO, *Acoustics — Assessment of noise annoyance by means of social and socio-acoustic surveys (ISO/TS 15666)*, 2nd ed. Geneva, Switzerland: International Organisation for Standardization (ISO), 2021.

[10] FOEN, "Lärmbelastung der Schweiz. Ergebnisse des nationalen Lärmmonitorings sonBASE, Stand 2015 [Noise pollution in Switzerland. Results of the national noise monitoring sonBASE, 2015]," Federal Office for the Environment, Bern, Nr. 1820, 2018. Accessed: Jul. 04, 2024. [Online]. Available: https://www.bafu.admin.ch/bafu/de/home/themen/thema-laerm/laerm--publikationen/publikationen-laerm/laermbelastung-in-der-schweiz-sonbase.html

[11] M. Drusch, U. Del Bello, S. Carlier, O. Colin, V. Fernandez, F. Gascon, B. Hoersch, C. Isola, P. Laberinti, and P. Martimort, "Sentinel-2: ESA's optical high-resolution mission for GMES operational services," *Remote Sens. Environ.*, vol. 120, pp. 25–36, 2012.

[12] B. Schäffer, M. Brink, F. Schlatter, D. Vienneau, and J. M. Wunderli, "Residential green is associated with reduced annoyance to road traffic and railway noise but increased annoyance to aircraft noise exposure," *Environ. Int.*, vol. 143, p. 105885, Oct. 2020, doi: 10.1016/j.envint.2020.105885.

[13] T. Van Renterghem, "Towards explaining the positive effect of vegetation on the perception of environmental noise," *Urban For. Urban Green.*, vol. 40, pp. 133–144, Apr. 2019, doi: 10.1016/j.ufug.2018.03.007.

DOI: 10.61782/fa.2025.0205

FORUM ACUSTICUM EURONOISE 2025

CLUSTERING INDIVIDUALS BASED ON PERFORMANCE IN AUDIO-VISUAL TESTING

Timothy Van Renterghem
Ghent University, Department of Information Technology, WAVES research group, Technologiepark 126, Gent-Zwijnaarde B 9052, Belgium

ABSTRACT

Audio-visual interactions play a crucial role in shaping individuals' perception of their surroundings and have been proposed as an effective strategy for improving environmental noise perception. However, the relative influence of visual and auditory inputs, as well as the degree of audio-visual integration, will vary across individuals. To investigate these influences, a dataset of 196 valid participations in an audio-visual performance test was collected under controlled laboratory conditions. Using Uniform Manifold Approximation and Projection (UMAP) for dimensionality reduction and k-means clustering, three distinct participant groups were identified based on six relative performance indicators. These clusters were categorized as *visual-first responders* (cluster A), *balanced integrators* (cluster B) and *visually dominated* individuals (cluster C). Visual-first responders and the visually dominated group show hardly any audio-visual integration in the audio-visual acuity test, while the balanced integrators clearly do. Notably, clusters A and C, accounting for 68% of the test population, are expected to benefit most from noise annoyance mitigation strategies that incorporate green window views.

Keywords: *environmental noise perception, psycho-acoustics, audio-visual integration.*

1. INTRODUCTION

The concept of enhancing environmental noise perception through audio-visual interactions is gaining increasing attention. A key example is the ability of visual vegetation in a window view to mitigate noise annoyance, a phenomenon convincingly demonstrated by multiple studies [1-5]. In these, contrasting vegetation views are typically compared at fixed sound exposure levels to ensure fair comparisons. While much of the focus has been on the quantity of greenery, recent controlled virtual reality research [5] suggests that the aesthetic quality of urban vegetation is a key factor in noise annoyance mitigation. Specifically, visually appealing greenery may encourage prolonged viewing, which in turn enhances cognitive restoration and stress reduction—two critical mechanisms counteracting the negative effects of environmental noise exposure.

Beyond exposure levels and green-related (or potentially non-green) contextual factors, individual characteristics also play a role. People process auditory and visual information differently, and the extent to which these inputs are integrated can vary widely. Research indicates that differences in audio-visual processing are shaped by cognitive abilities, personality traits, attentional capacities, and neural processing styles [6]. While green window views have shown a broad, positive effect across large-scale studies, it is crucial to investigate for whom these effects are most pronounced and whether certain subpopulations benefit less. This study takes an initial step in that direction by analyzing data from an audio-visual acuity test.

2. AUDIO-VISUAL PERFORMANCE TEST

The audio-visual dominance/acuity test used in this work is based on an object recognition task proposed in Ref. [7] and implemented in Ref. [8]. In front of a computer screen with headphones, participants were randomly presented with two

Corresponding author: timothy.vanrenterghem@ugent.be
Copyright: *©2025 Timothy Van Renterghem et al. This is an open-access article distributed under the terms of the Creative Commons Attribution 3.0 Unported License, which permits unrestricted use, distribution, and reproduction in any medium, provided the original author and source are credited.*

objects, indicated as A and B (see Fig. 1), and were asked to correctly classify these objects as fast as possible by pressing the left or down arrow key, corresponding to object A and B, respectively.
Objects were defined by visual features alone, auditory features alone or in combination. The visual part of the object consisted of a circle deforming into an ellipse, either horizontally (object A) or vertically (object B). The auditory part was of a pure tone of 540Hz (object A) or 560Hz (object B).

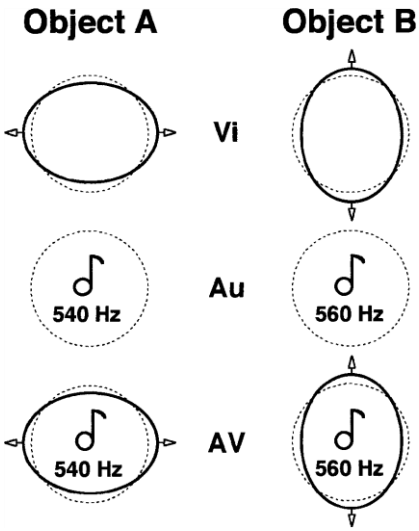


Figure 1. Illustration of the audio-visual objects used in the acuity test.

After each trial, the accuracy of the response was recorded. If correct, the reaction time was also saved. After initial practice trials, each participant completed 72 trials, consisting of 6 repetitions of audio-only (Au), visual only (Vi), and the audio-visual (AV) representations for both objects A and B. This enabled calculating the average accuracy and reaction times for audio-only, video-only, and audio-visual cues, finally leading to 6 parameters describing the audio-visual acuity of the test persons.

3. RESULTS

3.1 Data set

The performance test was held as a part of other audio-visual experiments [5][9], operated in 3 batches. In total, 218 valid audio-visual acuity tests were taken. As an additional criterion, participants with accuracies of less than 33% on both the Au, Vi and AV challenges were removed as these participants might not have understood the task well or might have pressed the keys randomly. In total, 196 datapoints were finally retained for further analysis.
The age of the participants was inclined towards younger people and students, but not restricted to this group. The average ages were 32.9 years (SD=standard deviation=13.9), 27.6 years (SD=12.9) and 29.6 years (SD=11.9) over the 3 batches. Overall, there were slightly more female than male participants (56%, 61% and 45% in each of the batches, respectively). In Table 1, the overall performance on the acuity test is summarized.

Table 1. Overall performance of the test panel with relation to the audio-visual acuity test.

	Mean	SD
N	196	
Acuity test : Correctness Audio only (%)	74%	24%
Acuity test : Correctness Audio-Visual (%)	87%	18%
Acuity test : Correctness Visual only (%)	86%	17%
Acuity test : Reaction time Audio only (ms)	810	150
Acuity test : Reaction time Audio-Visual (ms)	680	140
Acuity test : Reaction time Visual only (ms)	710	130

3.2 Cluster analysis

3.2.1 Relative acuity indicators

In order to identify distinct groups based on the 6-dimensional parameter space, clustering analysis was performed. To rule out the fact that some persons will generally perform better in the tests, regardless of the presentation modality, both the correctness scores ("corr") and reaction times ("rt") are considered in a relative way per test person. Following parameters were therefore defined for subsequent analysis: "corr_AV-A", "corr_AV-V", "rt_A-AV", "rt_V-AV", "corr_V-A", and "rt_A-V". Based on the average responses, positive values are expected for these relative parameters.

3.2.2 Optimized clustering

Uniform Manifold Approximation and Projection (UMAP) [10] was applied for dimensionality reduction, preserving both local and global structure, followed by k-means clustering to identify patterns in the data. Key UMAP parameters, such as the number of neighbors and minimal distance, were tuned for optimal embedding.
The 2D representation obtained via UMAP (see Fig. 2) was clustered using k-means, with the optimal number of clusters determined iteratively through the elbow method and silhouette analysis. The best clustering performance was achieved with 3 clusters, yielding the highest silhouette score (0.68) and the lowest Davies-Bouldin Index (0.69). In

theory, silhouette scores range from -1 (poor clustering) to 1 (perfect clustering), while a Davies-Bouldin Index of 0 indicates ideal, well-separated clusters, with values above 1 suggesting poor clustering. Visual inspection of Fig. 2 already suggested the presence of 3 clusters. Without using UMAP, the silhouette score was 0.42, while the Davies-Bouldin Index increased to 1.20, highlighting UMAP's effectiveness in enhancing pattern discovery while reducing noise and redundancy, finally leading to a better clustering performance.

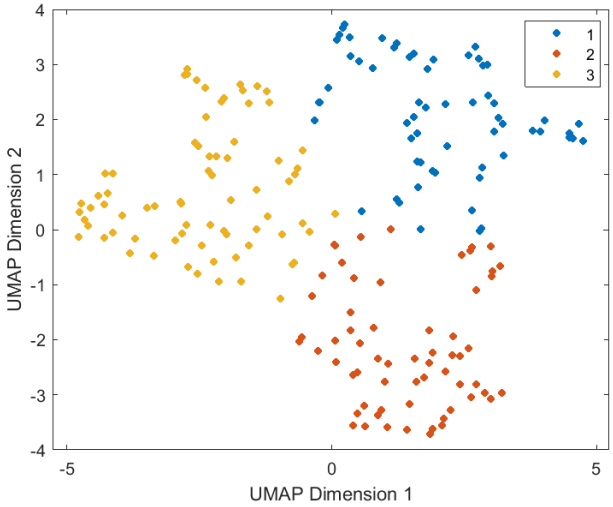


Figure 2. Clustering results in a 2-dimensional UMAP space, the latter being a reduction from a 6-dimensional parameter space.

3.2.3 Cluster centroids

Table 2 shows the cluster centroids after transforming back to the original 6-parameter space. This table should be jointly analyzed with Table 3, indicating which cluster centroids give rise to statistically significantly different means of the relative acuity parameters.

The clustering resulted in groups of roughly equal size, reinforcing the robustness of the classification. Combined with strong clustering performance metrics (see Section 3.2.2), statistically significant differences were observed across the six indicators, further supporting the existence of three distinct groups in how people process audio-visual information.

Table 2. Average values for the relative parameters in the identified clusters.

	cluster A	cluster B	cluster C
n	61	62	73
corr_AV-A (%)	4.1%	3.3%	28.5%
corr_AV-V (%)	3.0%	0.7%	-0.1%
rt_A-AV (ms)	173	63	174
rt_V-AV (ms)	9	97	15
corr_V-A (%)	1.1%	2.6%	28.6%
rt_A-V (ms)	164	-34	159

Table 3. p-values of two-sample t-tests analyzing the means between each cluster pair for the relative performance parameters. "*" means statistically significant at the 5% level, "**" at the 1% level, and "***" at the 0.1% level.

	cluster A-B	cluster A-C	cluster B-C
corr_AV-A (%)	0.483	<1E-10 ***	<1E-10 ***
corr_AV-V (%)	0.030 *	0.017 *	0.522
rt_A-AV (ms)	<1E-10 ***	0.965	<1E-10 ***
rt_V-AV (ms)	<1E-10 ***	0.487	<1E-10 ***
corr_V-A (%)	0.302	<1E-10 ***	<1E-10 ***
rt_A-V (ms)	<1E-10 ***	0.724	<1E-10 ***

4. DISCUSSION

4.1 Single modality analysis

Clusters A and C process visual information much faster than cluster B. In Cluster C, in contrast to cluster A, this also leads to a strong accuracy gain. Notably, Cluster B even leads to faster reaction times for audio only relative to visual only, but also here, similar to cluster A, accuracy gains are very minor.

Persons belonging to cluster C can be called *visually dominated*, as the correctness is much higher (29%) and responses are much faster (159 ms) for visual only compared to audio only inputs. Cluster B could be called the *balanced cluster*. Unimodal audio-input even leads to slightly faster reactions (-34 ms) to the challenges in the performance test but with nearly no accuracy gains (3%). So both modalities have a similar reliability and reaction time. When comparing to the other clusters, this group seems better in processing audio information and its description might tend towards audio dominance. However, audio dominance is clearly not reached, as the speeding up in case of audio only inputs is very limited, while visual

input is still slightly more accurate. So this means that he visual dimension is still important.
Cluster A positions somewhere in between clusters B and C. Similar to cluster C, reactions to audio only are much faster (164 ms), and similar to cluster A, unimodal audio and visual inputs lead to more or less the same correctness (1%). This group is therefore called *visual-first responders*.

4.2 Audio-visual integration analysis

In cluster A and C, audio-visual integration is limited. Audio-visual inputs, relative to visual only, hardly lead to a decrease in reaction time (only 9 ms and 15 ms difference on average), while correctness gains are very limited or non-existent (3% and -0.1%, respectively). Although the correctness gain is limited, in cluster A it is nevertheless statistically significantly different from the other clusters. These characteristics align with the concept of modality appropriateness [11], which posits that the dominant modality (in this case, visual information) becomes the primary source of information for decision making.
Note that for cluster A, visual information only increases processing speed but not accuracy relative to audio only. In cluster C, both speeding up and a strong increase in accuracy is obtained when comparing unimodal cues, leading to true visual dominance. Regarding audio-visual integration, both seem to follow the race model [12] but with a very weak redundant multi-sensory gain.
In cluster B there is a significant reaction time decrease for combined audio-visual cues relative to visual only information, but without accuracy gains. Audio-visual exposure significantly enhances visual processing. This can be explained since both audio and visual information are reliable inputs, with audio slightly faster and visually slightly more accurate. But also relative to audio-only, reaction to the audio-visual stimulus is significantly faster. Strong audio-visual integration is thus observed in this cluster, suggesting co-activation [13].

4.3 Relation to environmental noise perception

The cluster descriptions allow hypothesizing how audio-visual interactions influence environmental noise perception, particularly in relation to the green window view concept discussed in the Introduction.
Since vision dominates environmental processing in Clusters A and C, individuals in these groups are likely to benefit most from an attractive visual element, such as vegetation, which shifts auditory cues—and their associated disturbance—into the background. Auditory information integration remains minimal when both auditory and visual inputs are present. In Cluster C, the visually dominated group, the strongest effects could be expected, as visual input not only enhances the speed of scene evaluation but also contributes to a more accurate mental representation of the surroundings.
Together, Clusters A and C account for 68% of the test population in this work, aligning with the findings in Refs. [1-5], which demonstrated that the positive effects of green window view holds overall for the populations surveyed.
In contrast, the balanced audio-visual integration group (Cluster B) is expected to benefit less from an attractive window view. Here, environmental sounds are likely to carry equal weight to the visual scene and may even elicit faster responses. As a result, auditory information is less likely to be suppressed in favor of appealing visuals, leading to a weaker mitigation effect on noise annoyance.

5. CONCLUSIONS

Performance indicators from an audio-visual acuity test suggest that individual responses to green window views as a noise annoyance mitigation strategy are likely to be influenced by personal characteristics, forming three distinct clusters. It is hypothesized that the *visually dominated* group (Cluster C) and the *visual-first* responders (Cluster A) - together comprising 68% of the test population - stand to gain the most from this strategy. In contrast, Cluster B, consisting of more proficient listeners who integrate both auditory and visual information to a similar extent (the *balanced* group), may experience less benefits, if any.

6. ACKNOWLEDGMENTS

The author is grateful to master thesis students Elin Vermandere, Maarten Lauwereys and Amber Lippens for guiding the test panels through the audio-visual acuity tests that complemented other audio-visual perception experiments.

7. REFERENCES

[1] H. Li, C. Chau, and S. Tang: “Can surrounding greenery reduce noise annoyance at home?” *Science of the Total Environment*, vol. 408, pp. 4376–4384, 2010.

[2] T. Van Renterghem and D. Botteldooren: “View on outdoor vegetation reduces noise annoyance for dwellers near busy roads,” *Landscape and Urban Planning*, vol. 148, pp. 203–215, 2016.

[3] T. Leung, J. Xu, C. Chau, S. Tang, and P.-C. L. Pun-Cheng: "The effects of neighborhood views containing multiple environmental features on road traffic noise perception at dwellings," *Journal of the Acoustical Society of America*, vol. 141, pp. 2399–2407, 2017.

[4] B. Schäffer, M. Brink, F. Schlatter, D. Vienneau, and J.-M. Wunderli: "Residential green is associated with reduced annoyance to road traffic and railway noise but increased annoyance to aircraft noise exposure," *Environment International*, vol. 143, 105885, 2020.

[5] T. Van Renterghem, E. Vermandere, and M. Lauwereys: "Road traffic noise annoyance mitigation by green window view: optimizing green quantity and quality," *Urban Forestry and Urban Greening*, vol. 88, 128072, 2023.

[6] R. A. Stevenson and M. T. Wallace: "Individual differences in the multisensory temporal binding window predict susceptibility to audiovisual illusions," *Journal of Experimental Psychology: Human Perception and Performance*, vol. 39, pp. 884–898, 2013.

[7] M. Giard and F. Peronnet: "Auditory-Visual Integration during Multimodal Object Recognition in Humans: A Behavioral and Electrophysiological Study," *Journal of Cognitive Neuroscience*, vol. 11, pp. 473–490, 1999.

[8] J. De Winne, P. Devos, M. Leman, and D. Botteldooren: "With no attention specifically directed to it, rhythmic sound does not automatically facilitate visual task performance," *Frontiers in Psychology*, vol. 13, 894366, 2022.

[9] T. Van Renterghem and A. Lippens: "The audio-visual incongruency asymmetry. Natural sounds in an urban visual setting are more relaxing than urban sounds in visual nature," *Urban Forestry and Urban Greening*, vol. 101, 128514, 2024.

[10] L. McInnes, J. Healy, N. Saul, and L. Großberger: "UMAP: Uniform Manifold Approximation and Projection," *Journal of Open Source Software*, vol. 3, 861, 2018.

[11] R. B. Welch and D. H. Warren: "Immediate perceptual response to intersensory discrepancy," *Psychological Bulletin*, vol. 88, pp. 638–667, 1980.

[12] D. H. Raab: "Statistical facilitation of simple reaction times," *Transactions of the New York Academy of Sciences*, vol. 24, pp. 574–590, 1962.

[13] J. Miller: "Divided attention: Evidence for coactivation with redundant signals," *Cognitive Psychology*, vol. 14, pp. 247–279, 1982.

DOI: 10.61782/fa.2025.0391

FORUM ACUSTICUM EURONOISE 2025

EXPLORING SOUNDSCAPE PERCEPTION THROUGH THE ITALIAN LANGUAGE: A STUDY ON DESCRIPTIVE WORDS FOR NOISE AND SOUND

Melissa Ferretti[1*] **Davide Chiarella**[1] **Alessandra Cinini**[1] **Paola Cutugno**[1]

[1] Istituto di Linguistica Computazionale "Antonio Zampolli", Consiglio Nazionale delle Ricerche, Italy

ABSTRACT

This study investigates the linguistic description of soundscapes in seven port and hinterland areas in Italy, focusing on the perceptual aspects of remembered or heard sounds. Adjectives associated with the Italian nouns "rumore" (*noise*) and "suono" (*sound*) were extracted from large linguistic corpora and presented in a linguistic-acoustic questionnaire, allowing participants to select those most descriptive of the sounds they perceived.

Through the analysis of responses, a four-point scale was constructed, ranging from "silenzioso" (*silent*) to "molto rumoroso" (*very noisy*), with significant adjectives identified for each level. This scale offers a structured framework to interpret and classify soundscapes, linking linguistic descriptors to specific acoustic environments and sound sources.

The findings highlight the importance of integrating linguistic and perceptual approaches to capture the subjective and cultural dimensions of soundscapes. By offering a language-specific perspective, this research aims to support a deeper understanding of auditory perceptions and inform urban and environmental planning in culturally sensitive ways.

Keywords: *sound perception, linguistic analysis, subjective survey, port noise, sound characterisation*

[*] ***Corresponding author***: *melissa.ferretti@cnr.it.*

Copyright: *©2025 Melissa Ferretti et al. This is an open-access article distributed under the terms of the Creative Commons Attribution 3.0 Unported License, which permits unrestricted use, distribution, and reproduction in any medium, provided the original author and source are credited.*

1. INTRODUCTION

Sound perception is a multidisciplinary field encompassing medicine, ecology, and architecture. Traditional quantitative methods, such as equivalent sound levels (Leq, LAeq), often fail to capture the emotional and subjective responses elicited by sounds [1]. Psychoacoustics highlights that noise perception is shaped not only by the physical intensity of sound but also by individual interpretations and psychological factors, thus underscoring the importance of adopting a qualitative approach to the study of sound [2].

Language plays a critical role in this process, providing a framework through which sensory experiences are articulated and understood [3]. The words we use to describe sound shape our perceptions of it, reflecting both cultural norms and personal experiences. This understanding is essential for addressing broader issues related to well-being, health, and the environment, particularly in urban areas, where the interplay of these factors significantly impacts the quality of life.

The European Landscape Convention (2000) [4] marked a pivotal moment in recognizing how collective perception shapes the identity of a place. Well before the Convention, attention to environmental perception had already extended beyond the visual to include the auditory dimension. In the 1960s, Michael Southworth and R. Murray Schafer [5, 6] introduced the concept of soundscape, emphasizing that sounds, like visual elements, play a fundamental role in defining spatial experiences.

Despite the growing recognition of the importance of auditory perception, there remains a gap in systematic studies focused on the language used to describe sound.

Understanding the semantics of sound-related terms can provide deeper insights into how we interpret our acoustic environment. This need is particularly evident in multicultural research contexts, where translating sound

perception terms requires sensitivity to cultural nuances for accurate conceptual understanding.

For example, the translation of *quiet areas* into Italian as *zone silenziose* led to restrictive interpretations of noise regulations, distorting the original intent of European legislation. Our study examined linguistic and cultural variations in sound perception through Italian and French corpora, identifying adjectives linked to "rumore" (*noise*) and "suono" (*sound*) in Italian and "bruit" and "son" in French. This analysis revealed how cultural differences shape perceptions of the soundscape.

By analyzing terms within their linguistic context, we gain a more nuanced understanding of sound experiences, helping to avoid misinterpretations and fostering respect for cultural diversity. This study underscores the importance of a culturally informed approach in international research, ensuring that sound perception is represented accurately across different languages and contexts.

Despite advances in sound perception research [7, 8, 9], there is still much to explore regarding the language used to describe sound environments. Our study focused on adjectives associated with noisy and quiet spaces, aiming to provide insights into the terminology that characterizes these environments.

2. METHODOLOGY

This study, part of a cross-border cooperation project between Italy and France [10], aims to enhance the sustainability of commercial ports and their logistics platforms, addressing high noise pollution levels in areas between ports and logistics hubs. These zones, often marked by intense freight and vehicle traffic, present significant acoustic challenges affecting the environment and local quality of life.

The project's primary goal was to create a joint strategy to reduce noise pollution by optimizing traffic flows and minimizing the acoustic impact of logistics activities. Efficient traffic management not only promotes environmental sustainability but also improves livability for nearby communities.

Beyond logistics, the project also focused on the perceptual dimension of the soundscape. Understanding how local populations perceive port and logistics sounds is crucial for supporting policymakers in planning and balancing economic development with community well-being.

Language plays a key role in this context. It reflects the experiences and cultures of communities, shaping perceptions of the soundscape. This study investigates noise perception in port and hinterland areas, combining subjective questionnaire data with objective sound recordings.

The research involved multiple phases: identifying areas of interest, recording characteristic sounds, selecting descriptive adjectives for the questionnaire, and administering it across seven pilot areas.

2.1 Study areas

The study areas include seven locations in different pilot territories: Livorno and Lucca in Tuscany (Italy), Sassari and Porto Torres in Sardinia (Italy), Genoa in Liguria (Italy) and Toulon and La Seyne-sur-Mer in the Var region (France). Each area within the port or retro-port contexts represents a distinct environment shaped by social, economic and natural activities, ranging from industrial sounds to rural noises and port-specific acoustics. The study also includes areas further away from the port, such as Lucca and Sassari. Although these areas are geographically distant, they are significantly affected by port activities, as they serve as key hubs for the traffic and processing of goods. For example, the paper mill districts on the outskirts of Lucca and the industrial area of Sassari highlight how these regions remain closely connected to Livorno and Porto Torres, respectively, contributing to the distinctive soundscape of each territory.

2.2 Recordings

The noise associated with port and hinterland infrastructures is a complex form of acoustic pollution. The noise includes typical port sounds, such as ships and machinery, and noises from surrounding areas, like cranes and road and rail traffic. To capture this complexity, the sounds characteristic of the locations were recorded on-site, and locations that best represented the acoustic profile of each area were carefully selected. For example, we recorded road traffic in Lucca and Toulon to capture the distinct soundscapes of each location.

Up to four sound level meters were used to measure psychoacoustic parameters, while two digital recorders captured 16-bit audio at 44,100 Hz. The recordings were brief, typically lasting a few minutes for constant noises and up to several dozen minutes for more variable sounds. The data analysis involved creating spectrograms and extracting key acoustic events, from which we selected 10-second normalized sound samples. These samples, consisting of sounds like seagulls, crickets, cranes, boarding and disembarking operations, chainsaws, forklifts, level crossings, ship sirens, vehicle traffic, and rail traffic, were later included in the questionnaire.

2.3 Adjectives

This study adopted an approach based on large textual corpora to explore the cultural and linguistic nuances of Italian and French. The primary objective was to collect many authentic examples, an essential condition for developing reliable statistical models that accurately reflect the linguistic peculiarities of both languages. The use of large-scale corpora, as suggested by Sinclair [11], enables a more accurate analysis of lexical distribution and grammatical structures within a given context.

In particular, several linguistic web corpora were used: vast digital archives consisting of texts extracted from various online sources, including journalistic articles, literary works, social media posts, blogs, and other written content. The use of these corpora allowed for an examination of how the language is effectively used by speakers, thus providing a solid empirical basis for linguistic analysis. The methodology adopted aligns with the perspective of Biber et al. [12], who argue that corpora represent a fundamental resource for quantitative linguistic analysis.

The corpora employed underwent a tokenization process, which involves dividing the text into basic linguistic units (words or sentences), followed by lemmatization to normalize each term to its base form (for example, the verb "went" became "go"). Additionally, grammatical annotation assigned each term its corresponding morphosyntactic category, such as verb, noun, or adjective. These operations are essential to ensuring a high-level linguistic analysis, as highlighted by McEnery and Hardie [13].

Incorporating morphosyntactic information into the corpora enabled the extraction of a targeted sample of adjectives and nouns linked to the lemmas "suono"-"son" (*sound*) and "rumore"-"bruit" (*noise)*. Further statistical and linguistic analyses explored these terms, focusing on the most frequent collocations and examining how the two lemmas behave in different usage contexts. This approach follows the perspective of Stubbs [14], who emphasizes the importance of collocations in lexical meaning analysis.

The statistical investigations focused mainly on the data extracted from various linguistic corpora. The analysis of these corpora included absolute frequency, relative frequency, and lemma dispersion. We examined the adjectives from the corpora to determine usage trends and discrepancies. We subsequently applied a reduction process based on linguistic and statistical criteria to streamline the initial set of adjectives. The process included eliminating adjectives with low co-occurrence, normalizing through synonymy and polysemy, and filtering out less relevant elements using linguistic rules. This approach is consistent with the methodologies commonly used in computational linguistics, as highlighted by Kilgarriff and Grefenstette [16].

For Italian, the analysis also included a comparison with data from a preliminary questionnaire administered to a group of students at the University of Pavia [15]. This questionnaire provided additional insights into adjective usage, subsequently compared with the corpus data to examine possible discrepancies and trends specific to the Italian language.

2.4 Questionnaire

The online questionnaire explored participants' acoustic perceptions through three sections. The first collected demographic data, including gender, age, origin, and hearing ability, and allowed participants to select a relevant investigation area, which determined the audio recordings they would hear later.

In the second section, participants described a street in their chosen area, providing personal impressions of its soundscape by selecting adjectives from a predefined set.

The third section involved listening to recordings from pilot locations, identifying the dominant sound source, and selecting adjectives from the same linguistic sets categorized into Evaluation, Strength/Type, and Space/Time, requiring at least one choice per group.

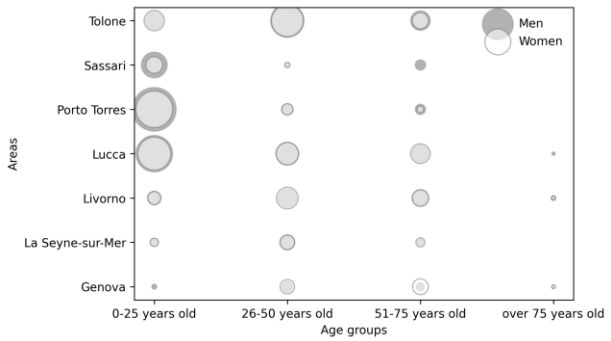


Figure 1. Age groups and areas with gender distinction

The respondent sample, shown in Figure 1, represented the areas under study and ensured demographic diversity. The sample included 46% women and 54% men, with 50% under 25, 32% between 26 and 50, and 18% over 50. Regarding education, 35% had completed high school, 31% secondary school, 9% held a bachelor's degree, and 12% had a master's or higher. A combined 13% had a doctoral degree, vocational training, or only primary school education. Regarding hearing ability, 52% rated their

hearing as excellent, 37% as good, and 11% reported a lower level of hearing, with 1% of this group using a hearing aid. This diversity provided a representative group for sound perception experiences.

3. RESULTS

This study was conducted on both Italian and French. So far, we have discussed findings related to both languages; however, in the following section, we will focus specifically on the results obtained for Italian.

3.1 Initial observations and analysis

In the first section of the survey, participants rated the soundscape of a street of their choice, using a five-point scale ranging from *very quiet* to *very noisy*. They then identified the most relevant sound source from categories including vehicular traffic, railway, airport, port activities, industrial noise, neighbourhood sounds, human activity (daytime or nighttime), and natural or atmospheric elements.

After classifying the street according to these scales, participants selected at least one adjective from a predefined list.

We initially decided to create word sets based on these classifications. As a result, five documents were compiled for noise, one for each noise level and, in the same way, ten for sound sources. A TF-IDF (Term Frequency-Inverse Document Frequency) analysis was conducted, followed by NMF decomposition.

Regarding the first question, we divided the data into five topics, aligning with the five response options. The analysis revealed a clear association between each topic and a specific noise level, identifying distinctive linguistic patterns for each category. We selected only the words with the highest weights, which represented 50% of the total weight, to highlight key descriptors for each noise level.

For *quiet* or *very quiet* places, adjectives like “naturale” (*natural*), “rilassante” (*relaxing*), “sopportabile” (*bearable*), and “innocuo” (*harmless*) suggest a positive and reassuring perception, often linked to natural or domestic settings. In *very quiet* places, words like “soffuso” (*soft*) and “leggero” (*light*) indicate subtle, almost imperceptible sounds that contribute to a peaceful sense of isolation. In *quiet* places, terms like “gradito” (*pleasant*) and “avvolgente” (*enveloping*) reflect a contained and comfortable soundscape.

Conversely, *noisy* and *very noisy* places are associated with adjectives like “eccessivo” (*excessive*), “fastidioso” (*annoying*), and “insopportabile” (*unbearable*), highlighting a persistent disturbance that negatively affects well-being. Terms like “artificiale” (*artificial*), “urbano” (*urban*), and “motore” (*engine*) emphasize a human-made soundscape, often linked to traffic and industry, distancing it from nature. In *very noisy* places, words such as “nocivo” (*harmful*) and “insostenibile” (*unsustainable*) suggest potential health risks.

Overall, these adjectives show that quieter places are perceived as spaces of relaxation and well-being, whereas noisier ones evoke artificiality and discomfort.

We also analyzed the responses regarding the dominant sound source to see if there were correlations between the adjectives used and the identified sources. The results show that each topic aligns with one of the response options, demonstrating a strong correspondence between specific sound sources - such as vehicular traffic, industrial activity, or natural elements - and the adjectives used to describe them.

To better understand the impact of traffic, we analyzed adjectives associated with categories like vehicular, railway, aircraft, and port traffic, identifying distinguishing features for each type of traffic. This analysis highlights variations in perceived noise intensity and the distinctive acoustic traits of different traffic types.

For airport traffic, adjectives such as “crescente” (*rising*), “potente” (*powerful*), “ritmico” (*rhythmic*), “insopportabile” (*unbearable*), and “assordante” (*deafening*) emphasize not only its high volume but also its disruptive and cyclical nature, evoking tension and discomfort.

“Ferroviario” (*railway*) and “ferroso” (*ferrous*) define railway traffic, along with “rumoroso” (*noisy*), “costante” (*constant*), and “artificiale” (*artificial*). These suggest a recognizable but less distinct identity, blending with other urban sounds like vehicular traffic.

Vehicular traffic is associated with a broad range of terms, from “caotico” (*chaotic*), “fastidioso” (*annoying*), and “persistente” (*persistent*) to “quotidiano” (*daily*), “continuo” (*continuous*), and “cittadino” (*urban*). This reflects its omnipresence in city life - both integrated into routines and perceived as intrusive.

Port traffic presents a complex soundscape, combining industrial and natural elements. Adjectives like “marittimo” (*maritime*), “profondo” (*deep*), “chiassoso” (*boisterous*), and “minaccioso” (*threatening*) suggest an intense yet variable acoustic environment.

We then considered the responses identifying natural and atmospheric elements, daytime or nighttime human activity, and the neighbourhood as the primary sources of the evaluated area. Common adjectives, such as “ambientale” (*environmental*), “vivo” (*lively*), “acceptable” (*acceptable*), and “allegro” (*cheerful*), indicate an impact perceived as

predominantly positive or tolerable, suggesting a sense of belonging to the daily context. However, the adjectives associated with each source provide insight into how listeners experience these sources in distinct ways.

Natural and atmospheric elements are described by terms like "naturale" (*natural*), "rilassante" (*relaxing*), and "piacevole" (*pleasant*), evoking a harmonious and calming atmosphere, in stark contrast to urban sources. Words like "avvolgente" (*enveloping*) and "magnetico" (*magnetic*) suggest that these sounds are not only pleasant but also engaging.

For human activity, adjectives such as "notturno" (*night*), "lavorativo" (*working*), and "caotico" (*chaotic*) paint a lively yet ambivalent picture, where some sounds are perceived as intrusive, while others like "colorato" (*colourful*), "divertente" (*fun*), and "festoso" (*festive*) contribute to an enriching social dimension.

Finally, the neighbourhood is associated with adjectives like "domestico" (*domestic*), "tollerabile" (*tolerable*), and "quotidiano" (*everyday*), indicating that neighbourhood sounds are part of daily life, perceived as manageable and non-invasive, creating a sense of familiarity and intimacy.

Overall, the analysis highlighted how each sound source contributes to creating a unique *acoustic footprint*, reflecting the complex interaction between sound, environment, and human perception.

3.2 Creating a vocabulary associated with the value scale: very quiet - very noisy

The previous analysis identified key adjectives for each noise type, focusing on those with the most significant weight in their respective classes.

Next, we aimed to create a vocabulary linked to the scale from *very quiet* to *very noisy*. We focused on identifying adjectives that specifically characterize each noise class. To do this, we analyzed the distribution of adjectives, concentrating on those not overly spread out across multiple groups. We regarded adjectives as specific if they appeared in at most two contiguous classes, reflecting a stronger association with the noise type.

3.2.1 Analysis for identifying significant adjectives by noise class

In 824 Italian questionnaires, participants provided 3,337 adjectives describing the overall soundscape of a road they had selected. On average, participants provided four adjectives for location, with a standard deviation of 6.3 and a mode of 1. The data showed that, generally, participants used only one adjective to describe the sound characteristics, with more adjectives used when the area was considered *very noisy*. Interestingly, only 3% of respondents labelled the area as *very quiet*, and just 3% of adjectives were assigned to this category, making it impossible to identify representative adjectives for *very quiet*. Thus, the analysis focused on identifying significant adjectives for four of the five noise classes.

Out of the 312 adjectives initially proposed, participants selected 261 at least once. After excluding 40 adjectives with infrequent usage, we retained 221 adjectives for further analysis.

Table 1. List of adjectives identified for noise classes

Classes	Adjectives
Silenzioso[1]	Delicato, rilassante, simpatico, tranquillo, usuale
Né silenzioso, né rumoroso[2]	Allegro, banale, bianco, breve, casalingo, casuale, ciclico, discreto, distante, distinto, elettrico, familiare, lento, lieve, limitato, magnetico, marittimo, melodico, meraviglioso, monotono, noioso, normale, occasionale, percettibile, perenne, periodico, potente, sintetico, statico, tenue, tollerabile, udibile
Rumoroso[3]	ansioso, continuo, eccessivo, elettromagnetico, frustrante, inaccettabile, incessante, innaturale, logorante, martellante, metropolitano, percepibile, prolungato, rumoroso, snervante
Molto rumoroso[4]	assordante, insostenibile, roboante

For each adjective, we calculated its relative frequency in each class. We then used these frequencies to compute a

[1] Quiet: gentle, relaxing, sympathetic, peaceful, usual

[2] Neither quiet nor noisy: cheerful, dull, white, brief, homely, casual, cyclical, discrete, distant, distinct, electric, familiar, slow, slight, limited, magnetic, maritime, melodic, wonderful, monotonous, boring, normal, occasional, perceptible, perennial, periodic, powerful, synthetic, static, tenuous, tolerable, audible

[3] Noisy: anxious, continuous, excessive, electromagnetic, frustrating, unacceptable, incessant, unnatural, wearing out, pounding, metropolitan, perceptible, prolonged, noisy, unnerving

[4] Very noisy: deafening, unsustainable, bombastic

weighted average noise index, reflecting the adjective association with different noise levels.
The index is calculated by multiplying the relative frequency of each adjective in a class by the corresponding noise level of that class and then summing these values. This method allows adjectives to be assigned a noise value between 1 (very quiet) and 5 (very noisy) based on how they appear across the different classes. A standard deviation threshold of 0.7, validated by TF-IDF analysis, ensured the selection of the most significant adjectives for each class. The final list includes 55 adjectives, mostly with positive connotations for quiet environments and negative ones for noisy areas. The *neither quiet nor noisy* class was more complex, containing positive and negative adjectives, demonstrating how sound perception depends on noise intensity, context, personal expectations, and emotional experiences. For instance, environments in this category could be described as dull or cheerful, showing that emotional and contextual factors shape sound perception beyond simple decibel measurements.

3.2.2 Analysis of the sounds presented based on the noise scale

In the second part of the questionnaire, participants listened to audio recordings and matched them with adjectives from the first part. We then compared the adjectives assigned to vehicular traffic, railway traffic, and natural elements in the first part with those selected for recorded sounds of traffic, trains, crickets, and seagulls.
The first set of adjectives describes a remembered soundscape with a known source, while the second refers to listened audio recordings with unspecified sources. This distinction reveals how different conditions influence descriptions. Adjectives for remembered soundscapes tend to be broader and influenced by visual elements or personal memories, "gioioso" (*joyful*), "soave" (*sweet*), "magnetico" (*magnetic*), "lento" (*slow*), "atmosferico" (*atmospheric*), "leggero" (*light*), "piacevole" (*pleasant*), for natural elements which integrate an overall mental vision of the soundscape. In contrast, adjectives for heard sounds are more specific, focusing on the perceived characteristics; for example, "breve" (*brief*), "contenuto" (*contained*), "crescente" (*increasing*), "inconfondibile" (*unmistakable*) for crickets and seagulls, indicate how the participants tried to describe concrete and observable properties.
The memory of railway traffic emphasizes general and constant aspects, such as "costante" (*continuous*) and "artificiale" (*artificial*). Terms like "ferroviario" (*railway*) and "ferroso" (*metallic*) highlight its mechanical and metallic nature, while "rumoroso" (*noisy*) reflects a more generic negative perception. In contrast, direct listening elicits a broader and more detailed range of descriptions "breve" (*brief*) and "contenuto" (*contained*), "crescente" (*increasing*), "cigolante" (*squeaky*), "secco" (*dry*), and "brusco" (*abrupt*)). Spatial and temporal terms like "vicino" (*near*), "distante" (*distant*), "circostante" (*surrounding*), and "diurno" (*daytime*) demonstrate how listening engages multiple perceptual dimensions.
A similar trend appears for road traffic. Heard traffic sounds are associated with intensity and spatiality, with adjectives like "atmosferico" (*atmospheric*), "avvolgente" (*enveloping*), "basso" (*low*), and "circostante" (*surrounding*) emphasizing their immersive quality. In contrast, remembered traffic is more influenced by prior knowledge, leading to adjectives such as "nocivo" (*harmful*), "indesiderato" (*undesirable*), "confusionario" (*confusing*), "lavorativo" (*working*), "persistente" (*persistent*), and "innaturale" (*unnatural*), reflecting a broader consideration of its impact beyond sound. Notably, 43% of participants misattributed the vehicular sound to natural or animal sources, influencing their lexical choices and leading to terms such as "naturale" (*natural*), "atmosferico" (*atmospheric*), "avvolgente" (*enveloping*), and "soffuso" (*muffled*), which evoke a sense of tranquility. When, however, the source "traffic" is known, the adjectives become predominantly negative, such as "nocivo" (*harmful*), "dannoso" (*damaging*) and "fastidioso" (*annoying*). That suggests that the perception of sound and the language used to describe it depend not only on the acoustic experience but also on expectations and knowledge of the source.
Subsequently, we applied the classification obtained to position the sounds along a scale ranging from *quiet* to *very noisy*.
Before conducting the analysis, several preprocessing steps were applied. First, since the number of adjectives associated with the different noise classes was uneven, a normalization of the classes was performed, assigning each a weight proportional to the reciprocal of the number of adjectives present, then normalized relative to the total sum of the reciprocals. Second, the adjectives, divided into three distinct groups (Evaluation, Strength/Type, and Space/Time), were weighted to account for differences in size: smaller groups received lower weights, while larger groups were assigned greater weights. Finally, we halved the weight of adjectives belonging to multiple groups to prevent overestimation.
This classification placed seagulls and crickets in the *quiet* category, traffic and railway crossings as *neutral*, and industrial sounds (e.g., crane, chainsaw, ship siren) in the *noisy* category.

A deeper analysis shows that while seagulls and crickets evoke calm, some participants perceive them as "assordante" (*deafening*) in specific contexts. Traffic sometimes appears "rilassante" (*relaxing*) due to misidentification with natural sounds. Noisy sounds, such as trains and cranes, are described as "assordante" (*deafening*) and "incessante" (*incessant*), while workplace sounds like forklifts seem more tolerable.

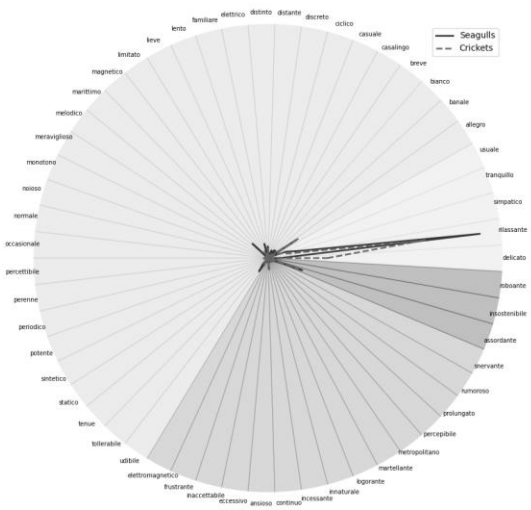


Figure 2. Sounds classified as *quiet* based on adjectives from the *quiet*-to-*very noisy* scale.

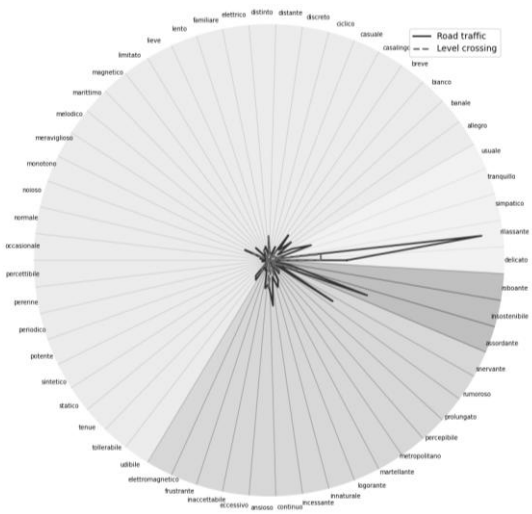


Figure 3. Sounds classified as *neither quiet nor noisy* based on adjectives from the *quiet*-to-*very noisy* scale.

The ship siren and loading/unloading sounds are strongly associated with "marittimo" (*maritime*), reflecting their port context.

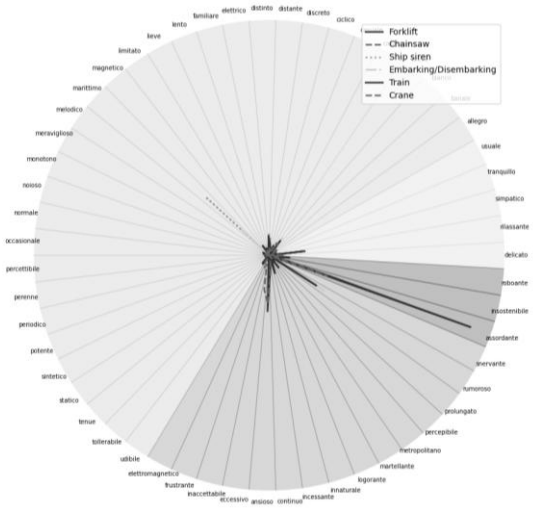


Figure 4. Sounds classified *noisy* based on adjectives from the *quiet*-to-*very noisy* scale.

4. CONCLUSIONS

The study addressed the issue of sound perception in port and hinterland environments, with particular attention to the linguistic description of soundscapes perceived as noisy or quiet. The research stemmed from the need to understand how describing the acoustic characteristics of specific areas requires measurable data, such as decibel levels and qualitative impressions that emerge exclusively through linguistic descriptors. The study adopted a methodological approach that combined questionnaires, linguistic analyses, and audio recordings.

When interpreting the results, it becomes clear that the linguistic descriptors used by participants offer a rich and nuanced representation of sound perception, emphasizing both the degree of noisiness and the emotional and contextual qualities associated with sounds. This variety of adjectives reflects a complex interaction between the physical characteristics of sound and the environmental and social contexts of the analyzed areas.

These observations find a theoretical framework in the concept of soundscape [5, 6], which emphasizes how the sounds of a place, much like visual elements, play a role in defining our experience of space, creating a multisensory dimension that influences both perception and the meaning attributed to landscapes.

A critical aspect that emerged is the role of source awareness: when participants were aware of the sound source, their descriptions often included evaluative and contextual elements, whereas when the source was unknown, they focused more on purely acoustic characteristics. This result reinforces the idea that sound perception is a complex process influenced both by direct experience and by the mental construction of context.
Previous research, such as Raimbault [17], has shown that knowledge of a sound source influences its perceived quality, supporting these findings.
Future research could further explore the role of familiarity and cultural context in the perception and description of the soundscape.
The relevance of this study to the fields lies in its methodological and applicative implications. The main conclusion is that combining qualitative and quantitative approaches offers a more complete understanding of the soundscape, addressing the limitations of relying solely on physical noise measurements. These findings can contribute to developing more perceptually and emotionally sensitive acoustic policies, emphasizing language as a key tool for capturing the complexity of sound perception.

5. REFERENCES

[1] P. Lercher1, B. Schulte-Fortkamp, "Soundscape of European cities and landscapes." in *Proc. of the Final conference of Soundscape-COST-TD0804-project,* (Merano, Italy), 2013.

[2] K. Genuit: "Status of psychoacoustics in noise analysis" *Journal of the Acoustical Society of America*, vol. 137, pp. 2291–2291, 2015.

[3] D. Dubois: "10. From psychophysics to semiophysics: Categories as acts of meaning. A case study from olfaction and audition, back to colors" *Speaking of colors and odors*, pp. 167–184, 2007.

[4] Council of Europe: *European Landscape Convention*. Florence, 2000. Available at: https://www.coe.int/en/web/conventions/full-list?module=treaty-detail&treatynum=176.

[5] M. F. Southworth: "The Sonic Environment of Cities" *Environment and Behavior*, vol. 1, no. B, pp. 49 - 70, 1969.

[6] R. M. Schafer, "The Soundscape: Our Sonic Environment and the Tuning of the World", 1993.

[7] Ö. Axelsson, M. Nilsson, and B. Berglund: "A principal components model of soundscape perception" *The Journal of the Acoustical Society of America*, vol. 128, no. 5, pp. 2836-2846, 2010.

[8] D. Dubois, C. Guastavino, and M. Raimbault: "A cognitive approach to urban soundscapes: Using verbal data to access everyday life auditory categories" *Acustica united with Acustica*, vol. 92, pp. 865-874, 2006.

[9] M. Chudalla, F. Strigari, D. Ackermann, S. Boehm, Sandra, A. Fiebig, H. Horn, A. Karakantas, A. Oehme, S. Pourpart, M. Schuck, and S. Weinzierl: "Psychoacoustic parameters in noise assessment – A research within the BMDV Network of Experts" *Transportation Research Procedia*, vol. 72, pp. 2479–2486, 2023.

[10] Interreg Maritime: *TRIPLO - TRasporti e collegamenti Innovativi e sostenibili tra Porti e piattaforme Logistiche.* Available at: https://interreg-maritime.eu/web/triplo.

[11] J. Sinclair: *Corpus, Concordance, Collocation.* Oxford: Oxford University Press, 1991.

[12] D. Biber, S. Conrad, and R. Reppen: *Corpus Linguistics: Investigating Language Structure and Use.* Cambridge: Cambridge University Press, 1998.

[13] T. McEnery, and A.D. Hardie: *Corpus Linguistics: Method, Theory and Practice.* Cambridge: Cambridge University Press, 2011.

[14] M. Stubbs: *Words and Phrases: Corpus Studies of Lexical Semantics.* Oxford: Wiley-Blackwell, 2001.

[15] A. Cerniglia, D. Chiarella, P. Cutugno, L. Marconi, A. Magrini, G. Di Feo, M. Ferretti, "Questionnaire analysis to define the most suitable survey for port-noise investigation" in *Proceedings of the 26th International Congress on Sound and Vibration,* (Montreal, Canada), 2019.

[16] A. Kilgarriff, and G. Grefenstette: "Introduction to the Special Issue on the Web as Corpus" *Computational Linguistics*, vol. 29, pp. 333-347, 2003.

[17] M. Raimbault: "Qualitative judgements of urban soundscapes: Questionning questionnaires and semantic scales" *Acta Acustica United With Acustica*, vol. 92, pp. 929-937, 2006.

DOI: 10.61782/fa.2025.0690

FORUM ACUSTICUM EURONOISE 2025

KEY ASPECTS FOR SURVEY DATA PROCESSING AND STATISTICAL ANALYSIS WHEN MODELLING EXPOSURE-ANNOYANCE RELATIONSHIPS

Mark Brink[1*] Beat Schäffer[1] Dirk Schreckenberg[2]
[1] Swiss Federal Office for the Environment, CH-3003 Bern, Switzerland
[2] Empa, CH-8600 Dübendorf, Switzerland
[3] ZEUS GmbH, D-58095 Hagen, Germany

ABSTRACT

In the context of (classical) noise annoyance surveys, the main product of interest is usually exposure-response relationships to inform health risk assessments or policy makers. Surveys conducted for this purpose are becoming increasingly complex, raising the question of what the key aspects in terms of data processing and statistical analysis are, that allow valid and representative exposure-response functions to be derived from the data collected. In this talk we will look at relevant decisions at different stages of analysis and illustrate their impact, in parts using data from the NORAH and SiRENE noise annoyance surveys as examples. The focus is on the necessary data processing and statistical considerations when aiming at statistically sound predictions of the percentage of 'highly annoyed' (%HA) as a function of noise exposure, alongside potential further predictors. The paper touches on the issues of (a) the explanatory or predictive approach related to variable selection and modelling, (b) the use of survey weights or not, (c) the proper handling of cases with low or missing exposure values in survey samples, (d) population-averaged vs. subject-specific responses and (e) the treatment of non-focal predictors when plotting exposure-response curves.

Keywords: noise annoyance, exposure-response relationship, statistical modelling

[*] ***Corresponding author***: *mark.brink @bafu.admin.ch.*
Copyright: *©2025 Mark Brink et al. This is an open-access article distributed under the terms of the Creative Commons Attribution 3.0 Unported License, which permits unrestricted use, distribution, and reproduction in any medium, provided the original author and source are credited.*

1. STARTING POINT

Annoyance is one of the most widespread immediate and long-term effects of transportation noise exposure, and this outcome has always played a pivotal role in informing policy, carrying out environmental impact assessments, or setting noise limits. All these goals require solid and valid exposure-response functions, which are derived from the data of so-called socioacoustic surveys. Most common statistical techniques to derive these functions are generalized linear (mixed) models. Corresponding model parameters are used to predict the outcome (mostly, the percentage highly annoyed, %HA) for a given level of noise exposure, which can be visualized in exposure-response curves (i.e., graphical representations of the exposure-effect relationship). Even though statistical analyses are *the* crucial part in the processing of data from socio-acoustic studies to derive exposure-response relationships, the steps to arrive there are usually hardly questioned out of habit – although there are various important decisions to be made regarding how to proceed in each particular case. While the things that are usually decided during the planning/conceptualization phase of a survey, such as sampling strategy, stratification, the way the questionnaires are presented, survey mode, response scales used etc., are of course crucial factors for the final result (cf. for example [1, 2]), the focus of this conference talk is basically on what happens *after* data collection. The talk covers the following points:

(1) The decision for an either explanatory or predictive approach related to variable selection and modelling

(2) Whether to use survey weights in the data prior to inferential statistical modelling
(3) The proper handling of low and missing exposure values in survey samples (censoring vs. truncation)
(4) The choice of modelling population-averaged or subject-specific exposure-response relationships (in the case of longitudinal surveys)
(5) The treatment of non-focal predictor variables when plotting exposure-response curves.

The present short paper is a brief preview of the conference talk. Our thoughts on the above topics will be consolidated in a journal paper containing a more extensive discussion and detailed recommendations.

2. BRIEF ROUNDUP OF COVERED POINTS

2.1 Aspect #1: Purpose of an annoyance survey: Explanation versus prediction

We argue that the distinction between predictive and explanatory approach is key when analysing data from socioacoustic surveys. Is the goal of the study to obtain, from amongst a large collection of variables, a set which best predicts the outcome variable? Or is the goal to estimate the association between a risk factor (i.e., exposure or treatment variable) and the outcome? Indeed, this principal decision should be taken even before designing a survey as it affects every aspect of model construction and evaluation thereafter. Just look back at your own career: you will find introductory texts from term papers to theses to maybe even the first peer-reviewed articles later on, where your research goals were rather vaguely described, perhaps in the sense of "by this research we aim at a *better understanding* of the association between x and y" or "this research wants to *examine* the factors that influence x"... things of that sort (by the way, we are no exception). A very basic question that should be answered before the set-up of any noise study (and even more so before the analysis begins) is whether the research pursues a *descriptive* goal (summarizing characteristics), a *predictive* goal (forecast effects [of noise, and maybe additional variables]), or, whether the goal is *explanatory* (unravel causal mechanisms). Various statisticians have pointed out the importance of this distinction [e.g. 3]. When it comes to environmental impact assessments, the explanatory ("risk factor") approach is perhaps the least cumbersome because it leads to more easily interpretable exposure-effect curves.

2.2 Aspect #2: Should one use survey weights?

In response to a request from a colleague, we deal with the question of whether case weighting may have an advantage in socio-acoustic surveys or not. For purely descriptive purposes, where the aim is to achieve the highest possible representativeness for the population, the weighting of sample data is widely accepted. For analytical conclusions about model parameters, however, there is a wide range of opinions about the role of sample weights among statisticians. We concluded that it is better to avoid weighting and stick to the original data when inferential statistical questions are in the foreground. The disadvantage of weighting is that it moves the data away from what has actually been empirically observed. And experience shows that the more data have been processed, the more difficult it becomes to understand what they represent. Also, results based on a weighted data set can be more difficult to interpret or communicate to stakeholders, especially if the weighting factors are complex or not well known.

2.3 Aspect #3: How to handle cases with low and missing exposure values?

Standard uncertainties in noise exposure assessments are larger at lower exposure levels than in the vicinity of infrastructure (roads, railways, airports) where the respective noise levels are higher. For some of the receiver points in a sample, the noise levels may even fall outside the calculation grid and thus are completely missing. This is often the case in socio-acoustic surveys, in which several noise sources are examined simultaneously in the same sample, but where not all noise sources are present at each receiver. Further, modelled exposure values may be so low that they may not actually be perceptible in "real life" with other ambient sound sources [4]. This raises the question of how low the bottom of an exposure-response function should be for a particular noise source and whether cases with very low or missing exposure values should be a) included in the analysis, b) replaced by a specified value (censoring), or c) excluded from the analysis altogether (truncation). In the talk, we discuss these alternatives and come to a fairly clear judgment, namely, that the inclusion of essentially unexposed cases has the potential to bias the resulting exposure-response curve. We therefore recommend that, given the weaknesses in exposure estimation at low exposure levels, cases with exposure levels below some 30 to 40 dB (L_{den} or L_{Day}) should be excluded from the analysis. This may limit the number

of cases available, but will lead to better, i.e. more representative %HA predictions, especially at higher exposure levels.

2.4 Aspect #4: GEE vs GLMM modelling

The primary product one usually has in mind when carrying out socio-acoustic surveys are noise exposure-response relationships which are important for predicting the effects of noise on individuals and populations. In the case of %HA-research, such relationships can be derived from independent (this means: non-nested and non-hierarchical) or, – admittedly – less often, repeated binary observations ("repeated measures"; e.g. in laboratory listening studies/experiments). As long as the binary observations are independent, a "standard" logistic regression analysis is applied, which yields so-called population-averaged exposure-response relationships that are directly applicable in risk assessment on the population level. However, if data from repeated binary observations are collected, one needs to account for the correlation of the data within individuals. Possible approaches to do so are generalized linear mixed models (GLMM) [5] or generalized estimating equations (GEE), [6]. We thoroughly discuss the two options of deriving exposure-response relationships in longitudinal or repeated measures studies, namely, the population average versus subject-specific prediction, that can be achieved with the GEE and GLMM modelling approaches, respectively.

2.5 Aspect # 5: Treatment of non-focal predictor variables when plotting exposure-response curves

For most use cases, socioacoustic surveys are carried out to describe or indeed, predict the association between some amount of noise exposure and a corresponding health effect. The minimum set of variables that is needed for this is an exposure variable, here L_{den}, and an effect variable, here HA. However, most survey designs are more complex, and modelling involves additional variables such as level-2 variables in hierarchical (multilevel) designs and/or additional covariates and/or confounders. Regardless of the number of predictors in the model, one can just use two dimensions to describe the relationship between exposure and effect in a graphically simple (two-dimensional) exposure-response plot with the so-called *focal term* (e.g. L_{den}) on the x-axis and the outcome on the y-axis. This requires all *non-focal terms* (non-focal predictors in the model) to be fixed (kept constant) at a certain value. For continuous predictors, this is often (but not necessarily) the sample mean. If categorical variables with multiple levels are involved, e.g. "gender", or "school", it is not immediately evident how to "average" over them, especially when the group sizes are different. We show in detail which methods of marginalization of non-focal predictors are possible when it comes to draw exposure-response curves for %HA (or similar outcomes). We will particularly shed light on *empirical average* and *estimated marginal means* prediction.

Of course, we cannot – for all the aspects mentioned above – give an unequivocal recommendation in every case for or against a specific way of action. However, we believe it is important that our peers from the field of noise effects research are aware of the issues and pitfalls we raise in the talk, and that they can overcome them by making well-informed decisions. We hope that our soon to be published full paper on the topic will prove to be a useful resource for this decision-making process.

3. REFERENCES

[1] Brink M, Schreckenberg D, Vienneau D, et al. Effects of Scale, Question Location, Order of Response Alternatives, and Season on Self-Reported Noise Annoyance Using ICBEN Scales: A Field Experiment. *Int J Environ Res Public Health*2016 Nov 23;13(11).

[2] Gjestland T. Measuring Community Response to Noise—Factors Affecting the Results of Annoyance Surveys. *International Journal of Environmental Research and Public Health*2024;21(4):420.

[3] Shmueli G. To Explain or to Predict. *Statistical Science*2010;25(3):289-310.

[4] Mestre VE. Describing the uncertainty associated with low aircraft noise level data derived from noise models: implications for noise effects studies. *Internoise 2010*; Lisbon2010.

[5] Stiratelli R, Laird N, Ware JH. Random-effects model for serial observations with binary response. *Biometrics* 1984;40:961–71.

[6] Liang K-Y, Zeger SL. Longitudinal data analysis using generalized linear models. *Biometrika*1986;73(1):13-22.

DOI: 10.61782/fa.2025.0393

FORUM ACUSTICUM EURONOISE 2025

EXPLORING THE ACOUSTIC ENVIRONMENTS OF BARCELONA'S SUPERBLOCKS: PERCEPTIONS FROM SOUNDWALKS

Aline Ramos Esperidião[2],[1*] **Andrea Potenza**[3] **Ester Vidaña-Vila**[1] **Marc Freixes**[1]
Antonella Radicchi[4] **Alfredo Iarozinski Neto**[2] **Rosa Ma. Alsina-Pagès**[1]
[1] Human Environment Research (HER), La Salle Campus Barcelona – Ramon Llull University, Spain
[2] Department of Civil Engineering (PPGEC), Federal University of Technology – Parana, Brazil
[3] Department of Earth and Environmental Sciences, University of Milano – Bicocca, Italy
[4] Order of Architects – Florence, Italy

ABSTRACT

The Superblock proposal in Barcelona is a strategy for urban intervention that aims to promote lower traffic density, increased green spaces and quiet areas, thereby improving the health and well-being of citizens. Consequently, it can serve as a valuable case study for testing tools for soundscape assessment, as it provides a unique acoustic environment. To evaluate it, soundwalks were conducted in the Poblenou, Sant Gervasi, and Sant Antoni Superblocks. This study examined the similarities among these three locations in terms of how people perceive the quietness and sounds in each area. Subjective data were obtained through questionnaires with a 5-point Likert scale and multiple-choice questions. The results showed that Sant Gervasi and Sant Antoni Superblocks were not considered quiet areas by the participants, although birds and vegetation contributed positively to the sense of quietness in the first location. In Poblenou, the quietest point is related to the promotion of social interaction. The findings of this study can be used to plan new superblocks and analyze their effectiveness in promoting a better acoustic environment in the city.

Keywords: *urban soundscape, environmental noise perception, citizen science, urban planning*

*__Corresponding author__: aline.ramos@ext.salle.url.edu.
__Copyright__: ©2025 Esperidião et al. This is an open-access article distributed under the terms of the Creative Commons Attribution 3.0 Unported License, which permits unrestricted use, distribution, and reproduction in any medium, provided the original author and source are credited.

1. INTRODUCTION

Proposals to rethink urban environments based on enhancing proximity relations have been extensively discussed across various fields of study. Notably, global cities such as Paris, Milan, and Barcelona are striving to place citizens at the center of urban planning [1]. Furthermore, it not only aims to alleviate the negative impacts of urban congestion but also seeks to foster a healthier environment for residents.

These cities are promoting active mobility and reducing reliance on private vehicles through measures aimed at mitigating air and noise pollution. This approach aligns with the implementation of the "proximity city" concept, which seeks to create more accessible and sustainable urban spaces put all citizens at the centre [2].

In Barcelona, the Superblock proposal represents a comprehensive urban intervention strategy designed to reduce traffic density, enhance green spaces, and create quieter zones [3, 4]. The superblock is a spatial unit consisting of nine blocks, forming a square of (400x400) m, delineated by a network of primary roads that connect various origins and destinations throughout the city. When this unit is replicated within the urban framework, its dimensions are adapted to accommodate the morphological and functional characteristics of the existing city [5].

This approach maximizes the availability of public space, which is currently dominated by vehicular traffic, while simultaneously ensuring the system's functionality and organization. By prioritizing pedestrian accessibility and promoting active forms of mobility, the Superblock approach encourages community engagement and social

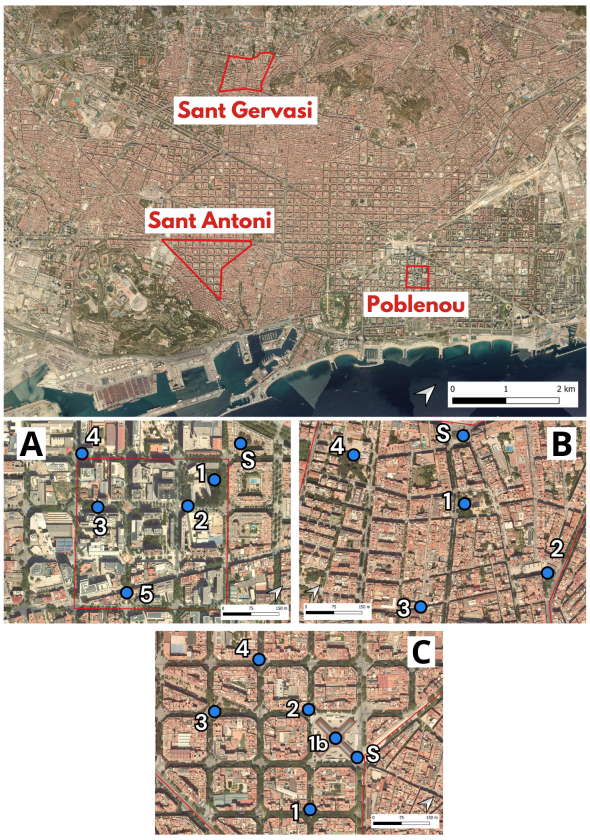


Figure 1. Three Superblocks analyzed (above) and the three soundwalks stops: A) Poblenou B) Sant Gervasi C) Sant Antoni.

interaction [3, 4]. The boundaries of the Superblock are defined by the primary roads, where through and connecting traffic is permitted to travel at a maximum speed of 50 km/h. In contrast, the interior roads (intervias) of the superblock form a local network with speed limits of 10 or 20 km/h, facilitating shared urban uses [4, 5].

The initial three superblocks were implemented between 2016 and 2019 in the neighbourhoods of Poblenou, Sant Antoni, and Horta. These interventions yielded benefits such as improved opportunities for rest, reduced noise levels, and decreased air pollution [4]. Consequently, these areas became quieter, fostering enhanced interactions among residents [3]. Over the years, other superblocks have been implemented in neighborhoods such as Sant Gervasi, Hostafrancs and Sagrada Familia [4]. This strategy is intended to enhance the overall well-being of citizens, contributing to health benefits [3,6] and a more sustainable and livable urban landscape [7].

In this context, the proposal of superblocks aligns with the necessity to enhance soundscapes through an understanding of the perceived acoustic environment. The purpose of quiet areas is to safeguard human health against noise annoyance and sleep disturbances—psychological factors that cannot be quantified using physical measuring instruments [8]. Only an assessment of how people perceive a quiet area can provide these insights. Considering that, superblocks may be a valuable source of information for the assessment of the sound environment, as they foster a distinct acoustic setting within the city.

For this purpose, were performed soundwalks, a conventional method for data collection in soundscape research, which offers a qualitative overview of typical methodological approaches in this field [9]. Therefore, the aim of this study is to examine the similarities among Poblenou, Sant Gervasi and Sant Antoni Superblocks in



Figure 2. Three Soundwalks (from left to right): A) Poblenou - participants listening to the soundwalk instructions at Ada Byron Square (point S); B) Sant Gervasi - acoustic measurements being taken at *Jardins de Vil·la Florida* (point 1); C) Sant Antoni - intersection of Parlament and Comte Borrell Streets, both pedestrianized (point 1).

terms of how people perceive the quietness and sounds in each area.

2. METHODOLOGY

To evaluate each location, one soundwalk was conducted in each Superblock: Poblenou, Sant Gervasi and Sant Antoni (Figures 1 and 2). The structure of the soundwalks was detailed in each starting point (S), with an introduction to the activity in the field and a description of its purpose. Each soundwalk was designed to cover a length of 1.3 to 1.7 km. Each route was predefined incorporating 4 to 5 quiet areas. Participants were guided along the designated route, making stops at the identified quiet areas. At these locations, they were encouraged to engage in active listening to the surrounding environment for a duration of 1 to 3 minutes in silence. After listening, the soundwalk participants were requested to assess their experiences using a questionnaire that included open entry, multiple choice and 5-point Likert scale questions, to measure different aspects of the acoustic environment.

In total, a sample of 21 participants voluntarily participated in three soundwalks: 12 at Poblenou, 7 at Sant Gervasi and 2 at Sant Antoni. The participants were asked to evaluate the soundscape and express their perceptions using Hush City App [10]. Respondents answered questions concerning about what people were doing around, and evaluated the overall quality, cleanliness, maintenance, security and accessibility of each point. Related to acoustic environment, respondents answered the questions shown in Table 1 and L_{eq} values were collected at each stop via smartphone through the App. The subjective data collected were analyzed through descriptive statistical analyzes and qualitative data analyzes.

2.1 Poblenou Superblock

The first soundwalk was conducted in the Poblenou neighborhood, which has undergone significant transformation in recent decades, evolving from an industrial zone into a residential and commercial district, while still retaining several areas of undeveloped land [11]. In September 2016, the Poblenou Superblock was established within the perimeter formed by Badajoz, Pallars, Llacuna, and Tànger streets [4]. The soundwalk was conducted in the fall of 2019 (27 September) at 3:00 pm.

The proposal involves a guided walk through the Poblenou Superblock, with stops at five listening points, beginning at Ada Byron Square (point S), a quiet area situated near the first street of the Superblock.

Point 1 is located within the Superblock, in a green space between the Can Framis Museum and a roadway. Point 2 is positioned between this museum and the Flor de Maig School. This street has been pedestrianized, converting it into a public space for community use.

Point 3 is situated in an office area where enhancements have been made, including resurfacing the ground and installing benches and tables, attracting office workers during lunch breaks. Point 4 is found in the border of the Superblock, adjacent to a busy road where traffic noise dominates the soundscape. Finally, point 5 is near one of the access points to the Superblock, where road traffic noise remains a significant presence.

Table 1. Variables and questions used in this research.

Variables	Questions
Participant emotional status	What prompted you to record this sound?
Quietness of the soundscape	Rate how quiet the soundscape is in this location
Sense of quietness	Sounds that contribute positively to your sense of quietness
Social interaction	Do the sounds promote social interaction?
Conversations	Do the sounds encourage you to have conversations here?

2.2 Sant Gervasi Superblock

Sant Gervasi is a residential neighborhood known for its green spaces, such as *Parc de la Tamarita* and *Jardins de Vil·la Florida*. The soundwalk was conducted in the spring of 2021 (29 April) at 4:00 pm. The starting point (S) is located at the center of Bonanova Square, where Sant Gervasi de Cassoles Street begins, characterized as a semi-pedestrianized thoroughfare. Point 1 is situated in the park between Muntaner Street and Sant Gervasi de Cassoles Street, known as *Jardins de Vil·la Florida*.

Point 2 is positioned at the center of the square adjacent to the Mercat de Sant Gervasi, specifically in Frederic Soler Square. Point 3 is located at the intersection of Sant Marius Street (semi-pedestrianized) and Muntaner Street.

The path to point 4 extends outside the Superblock, traversing primarily through usual streets, such as Mandri Street. Point 4 is found in a highly regarded tranquil area of the neighborhood, known as Can Altimira Gardens.

2.3 Sant Antoni Superblock

Sant Antoni is a neighborhood of the Eixample district, close to the old city centre, and famous for its market which has recently been renovated [5]. The work carried out in this Superblock is the result of a dialogue process with local residents, merchants, and community organizations that began in February 2017 [4]. The soundwalk was conducted in the fall, on 17 November 2020 at 4:30 pm.

The starting point (S) is located in the final section of Ronda Sant Antoni, near the Sant Antoni Market, one of the largest markets in the city. Point 1 is situated at the intersection of Parlament Street (pedestrianized) and Comte Borrell Street (also pedestrianized). Point 1b is inside of Sant Antoni Market.

Point 2 is positioned in the center of the Superblock, at the crossing of Tamarit St. and Comte Borrell St. Point 3 is in a pedestrianized area, yet close to a road with traffic, located at the intersection of Tamarit St. and Calabria St., marking one of the borders of the Superblock.

The route to point 4 extends outside the Superblock, passing through "normal" streets; however, point 4 is back within the Superblock, at the intersection of Viladomat Street and Floridablanca Street.

3. RESULTS

3.1 Poblenou Superblock

Participants were asked what activities the other people present at the location were doing, with the majority of responses indicating "passing through" or "talking", and, in point 1, "relaxing" was highlighted.

In Poblenou Superblock (PB), when asked what prompted them to record the sound (Table 2), points 1, 2, and 3 were primarily characterized by the participants as associated with "comfort", "calm" and "interest". In contrast, point 4 was predominantly characterized by "disgust", "irritation", and "distraction", while point 5 was identified with "distraction", "disgust" and "interest".

Therefore, points 1 and 2, identified as the quietest, were more closely associated with promoting social interaction and encouraging conversations (Figure 3). Conversely, points 4 and 5, which were less quiet, showed a weaker correlation with these factors.

Regarding sounds that positively contribute to a sense of quietness (Figure 4), "bird songs" at point 2, "leaves moved by wind" at points 1, 3, and 5, and "speech" at points 4 and 5 were particularly notable, although the latter were considered the least quiet among them.

Furthermore, participants evaluated how quiet each point was on a scale from 1 to 5, where 5 represents "very quiet". It was observed that points 1 and 2 exhibited the highest average scores (3.5 and 4.2, respectively), whereas point 4 was the least quiet, with an average score of 2, as confirmed by L_{eq} smartphone measurements (Figure 5).

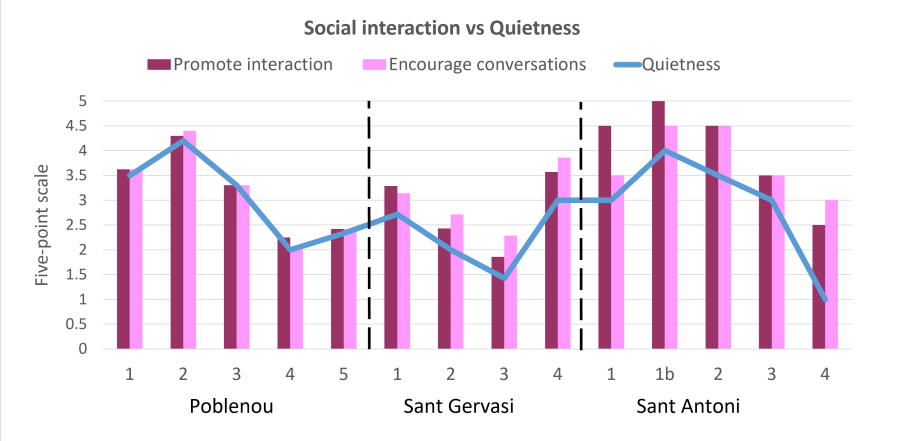


Figure 3. Answers to: To what extent do the sounds in this location promote social interaction and encourage conversations? - graph counting answer occurrance and plotted to get a 100 percentage on each bar.

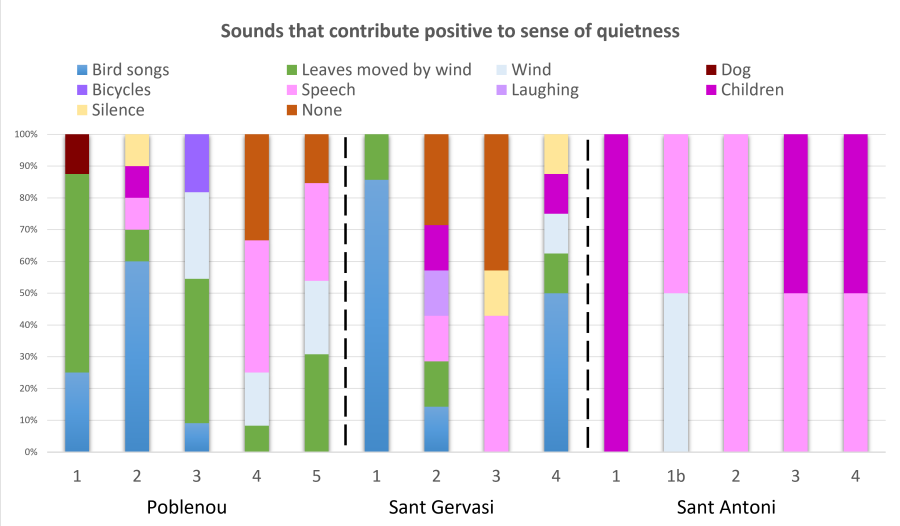


Figure 4. Answers to: Sounds that contribute positively to the sense of quietness - graph counting answer occurrence and plotted to get a 100 percentage on each bar.

Therefore, it was observed that in Poblenou Superblock, the sense of quietness is associated with green spaces (such as point 1), and pedestrianization of the street (point 2) has also contributed to a quieter environment, encouraging social interaction. However, points 4 and 5, characterized by higher traffic noise, caused feelings of irritation and disgust among the participants.

3.2 Sant Gervasi Superblock

In Sant Gervasi (SG), responses indicated that individuals were passing through, talking, and relaxing, but other activities also emerged, such as recreation, playing, and reading. When asked what prompted them to record the sound (Table 2), point 1 was characterized by feelings of distraction, comfort, and calm. Point 1 is located in *Jardins de Vil·la Florida*, recognized as one of the more

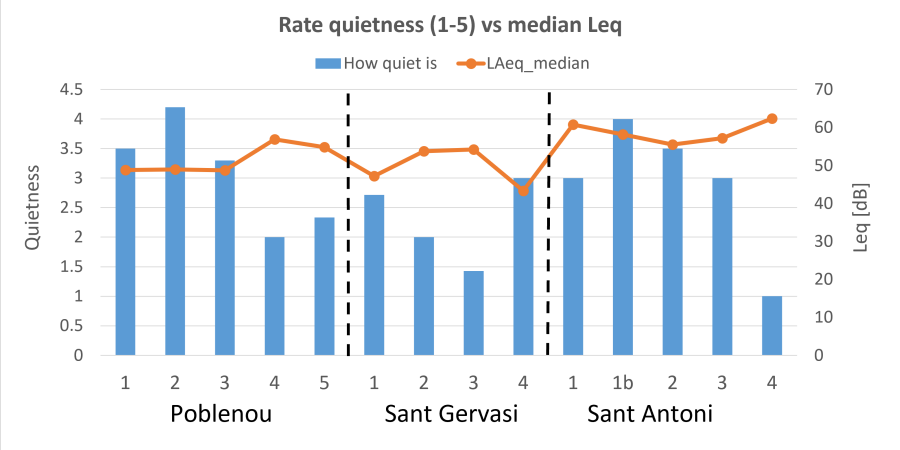


Figure 5. Answers to: mean Rate the quietness (1-5) vs median L_{eq} measured by smartphones.

tranquil areas in the neighborhood.

Point 2 also revealed distraction, along with irritation, which is interesting since this stop is located in a small square with a small park with a children's playground, adjacent to a market (Frederic Soler Square).

Point 3 was associated with irritation, anxiety, and distraction. This point marks the intersection of "quiet" area with a broader street that features ample pedestrian walkways. This segment of the Superblock has seen fewer interventions compared to others, but is home to several stores, bars, and restaurants. Point 4, a green space characterized by silence and tall trees, featuring a small bridge for crossing and recreational activities (Can Altimira Gardens), was primarily linked to distraction and enjoyment.

Participants evaluated the quietness of each point (Figure 5) on a scale from 1 to 5, with the highest score being 3 at point 4 and the lowest score of 1.43 at point 3, indicating that this area was not considered quiet by the participants.

Regarding the promotion of social interaction and encouragement of conversations (Figure 3), point 4 stood out compared to the others.

Finally, bird songs positively contributed to the sense of quietness (Figure 4) at points 1 and 4, while the sound of leaves moving in the wind was noted at points 1, 2, and 4. Speech was particularly prominent at point 3, and children were also mentioned at points 2 and 4.

Therefore, in Sant Gervasi Superblock the sense of quietness is associated with green spaces (point 1 and 4). However, points 2 and 3, characterized by closed proximity to trafficked roads caused feelings of distraction and disgust among the participants. On the other hand, bird songs and moved vegetation produces positive sensation to people.

3.3 Sant Antoni Superblock

In Sant Antoni (SA), responses also indicated that individuals were passing through, talking, or relaxing. The Sant Antoni Superblock is situated in a highly commercial area of Barcelona (Eixample) and encompasses one of the largest markets in the city. When asked what prompted them to record the sound (Table 2), point 1 was associated with feelings of comfort, pleasure, surprise, and fun. Point 1b was characterized by calmness, nostalgia, and comfort, probably related to the market. Point 2 elicited feelings of comfort, calm, distraction, and pleasure. This area features a spacious environment adjacent to the market, while still accommodating local residents in terms of traffic flow.

Point 3 was associated with pleasure, irritation, and calm. This point is designated as a pedestrianized zone; however, it remains in close proximity to a roadway with vehicular traffic. While point 4 was primarily associated with disgust, distraction, and irritation, which involves interventions on two of the four surrounding streets to improve accessibility for pedestrians. Although Calabria Street continues to experience traffic and is not pedestrianized, this area has been adapted for urban life in a calming manner. It predominantly hosts conventional retail outlets and features a large square for public use.

The participants evaluated how quiet each point was

(Figure 5) on a scale from 1 to 5. Points 1 and 3 had an average score of 3, with point 1b recording the highest average score of 4, followed by point 2 with an average of 3.5. The lowest value was observed at point 4, with an average score of 1, indicating that the area was not quiet. Furthermore, it was observed that points 1, 1b and 2 were more closely associated with promoting social interaction, while points 1b and 2 were related to encouraging conversations (Figure 3).

Table 2. Participants' results to the question: What prompted you to record this sound?

Location	Stop	Emotional status
PB	1	Calm (5), Comfort (4), Interest (2)
PB	2	Comfort (6), Calm (6), Interest (3)
PB	3	Comfort (4), Calm (3), Interest (3), Disgust (2)
PB	4	Disgust (5), Distraction (4)
PB	5	Distraction (5), Interest (2), Disgust (2)
SG	1	Comfort (3), Distraction (3), Calm (2)
SG	2	Distraction (4), Disgust (1)
SG	3	Distraction (2), Disgust (1)
SG	4	Calm (4), Distraction (3), Comfort (2)
SA	1	Comfort (1)
SA	1b	Calm (2), Comfort (1)
SA	2	Comfort (2), Calm (1), Distraction (1)
SA	3	Calm (1)
SA	4	Disgust (2), Distraction (1)

Regarding sounds that positively contribute to a sense of quietness, children were notably present at points 1, 2, and 3, while speech (people talking) was significant at points 1b, 2, and 3 (Figure 4).

Although numerous streets are pedestrianized, the Superblock does not conform to the traditional shape associated with such developments and is primarily concentrated around Comte Borrell Street and the Sant Antoni Market.

3.4 Discussion

Although the L_{eq} values are similar between the Superblocks (with Sant Antoni's being slightly higher), it is observed that Sant Gervasi was perceived as the least quiet by the participants, although birds and the sound of leaves moving in the wind contributed positively to the sense of quietness. This result was unexpected, considering that two of the four points are located in green areas, which are generally presumed to be quieter. However, this result could be partially explained by the presence of an adjoining road to the park at point 2 that may have caused "distraction" and "disgust" feelings. This relation is also evident in the fourth points of Poblenou and Sant Gervasi which are located at the edge of the Superblock and are exposed to traffic. This relation is observed in [12] where a significant relationship is reported between L_{eq} and the perceived annoyance of traffic noise.

However, there are some cases where, even if the L_{eq} values were similar to those points or slightly inferior, the soundscape of the stop was perceived as positive using adjectives such as "comfort", "calm" and "interest"; it is the case of points 1 to 3 of Poblenou, 1 in Sant Gervasi and 1 to 3 in Sant Antoni. This relation was also found by [13], underlying the differences between objective measure and people's perceptions and the role played by other sound sources (birds and leaves) and visual pleasantness.

In the case of Sant Antoni Superblock, no biophonies or geophonies were assessed as positive contributors to the sense of quietness. This may be due to the absence of parks in the area, but also to the low number of participants; for this reason, another soundwalk will take place in Sant Antoni to better assess its soundscape. It was also observed that the quieter points were more conducive to promoting social interaction and encouraging conversations. Furthermore, the presence of people talking did not negatively influence the sense of quietness.

4. CONCLUSIONS

This study examined the similarities among these three locations in terms of how people perceive the quietness and sounds in each area. The findings of this study can be used to plan new superblocks and analyze their effectiveness in promoting a better acoustic environment in the city.

The results underscore the importance of understanding the perceptions of individuals of acoustic environments, providing essential information for planning new superblocks and promoting improved acoustic conditions within the city. Assessment while participants were still at the specific location allowed them to better express their perceptions of the acoustic environment. Furthermore, understanding citizens' perceptions of the soundscape allows for a more accurate comprehension of the acoustic environment.

As a limitation of the research, there were few participants in the soundwalk conducted in Sant Antoni Superblock, once it was a pilot study of the route. Nevertheless, the validity of the data is corroborated by the acoustic measurements collected. Further studies could reapply soundwalks in the Superblocks to conduct comparative analyzes over time.

5. ACKNOWLEDGMENTS

The authors would like to thank the Departament de Recerca i Universitats (Generalitat de Catalunya) under Grant Ref. 2021-SGR-01396 for the funding of HER (Human-Environment Research) research group. Also, this study was financed in part by the Coordenação de Aperfeiçoamento de Pessoal de Nível Superior - Brasil (CAPES) - Finance Code 001.

6. REFERENCES

[1] F. Alberti and A. Radicchi, "The proximity city: a comparative analysis between paris, barcelona and milan," *TECHNE-Journal of Technology for Architecture and Environment*, pp. 69–77, 2022.

[2] F. Alberti and A. Radicchi, "From the neighbourhood unit to the 15-minute city. past and recent urban models for post-covid cities," in *Urban and Transit Planning: City Planning: Urbanization and Circular Development*, pp. 159–170, Springer, 2023.

[3] M. Nieuwenhuijsen, A. de Nazelle, M. C. Pradas, C. Daher, A. M. Dzhambov, C. Echave, S. Gössling, T. Iungman, H. Khreis, N. Kirby, *et al.*, "The superblock model: A review of an innovative urban model for sustainability, liveability, health and wellbeing," *Environmental research*, p. 118550, 2024.

[4] Ajuntament de Barcelona, "Superilles," 2025. Available at: `https://ajuntament.barcelona.cat/superilles/ca`, Accessed on: 19-03-2025.

[5] S. Rueda, "Superblocks for the design of new cities and renovation of existing ones: Barcelona's case," *Integrating human health into urban and transport planning: A framework*, pp. 135–153, 2019.

[6] N. Mueller, D. Rojas-Rueda, H. Khreis, M. Cirach, D. Andrés, J. Ballester, X. Bartoll, C. Daher, A. Deluca, C. Echave, *et al.*, "Changing the urban design of cities for health: The superblock model," *Environment international*, vol. 134, p. 105132, 2020.

[7] J. Scudellari, L. Staricco, and E. Vitale Brovarone, "Implementing the supermanzana approach in barcelona. critical issues at local and urban level," *Journal of Urban Design*, vol. 25, no. 6, pp. 675–696, 2020.

[8] G. Licitra, M. Van den Berg, and P. De Vos, "Good practice guide on quiet areas," *European Environmental Agency, EAA Technical Report*, no. 4, p. 2014, 2014.

[9] F. Aletta, C. Guattari, L. Evangelisti, F. Asdrubali, T. Oberman, and J. Kang, "Exploring the compatibility of "method a" and "method b" data collection protocols reported in the iso/ts 12913-2: 2018 for urban soundscape via a soundwalk," *Applied Acoustics*, vol. 155, pp. 190–203, 2019.

[10] A. Radicchi, "The hush city app," in *Proc Inv Places, Int Conf Sound, Urbanism Sense of Place*, 2017.

[11] R. M. Alsina-Pagès, G. J. Ginovart-Panisello, M. Freixes, and A. Radicchi, "A soundwalk in the heart of poblenou superblock in barcelona: Preliminary study of the acoustic events," *Noise Mapping*, vol. 8, no. 1, pp. 207–216, 2021.

[12] K. H. Evensen, R. K. Raanaas, and A. Fyhri, "Soundscape and perceived suitability for recreation in an urban designated quiet zone," *Urban forestry & urban greening*, vol. 20, pp. 243–248, 2016.

[13] S. Mancini, A. Mascolo, G. Graziuso, and C. Guarnaccia, "Soundwalk, questionnaires and noise measurements in a university campus: A soundscape study," *Sustainability*, vol. 13, no. 2, p. 841, 2021.

DOI:

Main theme: A05 Environmental Acoustics

Session A05.04 Wind turbine noise

Chair(s): J. Picaut, M. Arana

DOI: 10.61782/fa.2025.0641



FORUM ACUSTICUM
EURONOISE 2025

OFF-COUSTICS: PREDICTING THE UNDERWATER ACOUSTIC FOOTPRINT OF OFFSHORE WIND TURBINES

Esteban Ferrer[1*] **Laura Botero-Bolívar**[1] **Oscar A. Marino**[1]
Martín de Frutos[1] **David Huergo**[2] **Abbas Balout**[1]
Eduardo Jané[1] **Himpu Marbona**[1] **Gonzalo Rubio**[1]
[1] ETSIAE-UPM-School of Aeronautics, Universidad Politécnica de Madrid,
Plaza Cardenal Cisneros 3, E-28040 Madrid, Spain

ABSTRACT

The growing demand for offshore wind energy has driven a rapid increase in wind turbine size and the development of large-scale wind farms, often comprising more than 100 turbines. However, the environmental impact of underwater noise emissions remains largely unaddressed. The Off-coustic project (ERC Consolidator Grant Ref. 101086075) develops numerical methods and experiments by integrating wind turbine noise prediction techniques to predict the wind turbine acoustic footprint.

Here, we present an approach to calculating the transmission of aerodynamic noise into underwater acoustics, taking into account the air-water impedance and the penetration angle (governed by Snell's law). Our calculations show that aerodynamic noise from offshore wind farms may affect marine life. In addition, we present the capabilities of our solver, HORSES3D, to simulate wind turbines in offshore environments. This solver will soon be capable of simulating acoustics in offshore environments.

Keywords: *Wind turbine Noise, Offshore energy, Underwater noise, Marine life, high order discontinuous Galerkin*

**Corresponding author*: *esteban.ferrer@upm.es.*
***Copyright**: ©2025 Ferrer et al. This is an open-access article distributed under the terms of the Creative Commons Attribution 3.0 Unported License, which permits unrestricted use, distribution, and reproduction in any medium, provided the original author and source are credited.*

1. INTRODUCTION

The rapid expansion of offshore wind energy has led to large-scale wind farms with more than 150 turbines (1). Although turbine designs prioritise power output (2; 3; 4), their acoustic emissions remain largely unexamined. Aerodynamic noise from the blade trailing edge and blade-turbulence interactions is well studied for onshore turbines, but remains unexplored offshore. Aerodynamic noise scales with rotor diameter (D^5) and aggregates between turbines ($\sim 20\log_{10}(N)$) (5; 6). Although prior research focused on mechanical noise (7; 8; 9; 10; 11; 12), the transmission of aerodynamic noise in water is still poorly understood. Governed by Snell's law, only sound waves within $\sim 13°$ of normal refract into water, with further attenuation due to impedance differences. However, offshore wind farms can generate detectable underwater noise, raising concerns for marine species dependent on sound (13; 14; 15; 16).

In response to this emerging environmental challenge, the *Off-coustic* project introduces a novel methodology that merges advanced aerodynamic noise prediction techniques. This framework enables estimation of the underwater noise levels generated by large offshore turbines and their assemblies. By quantifying the acoustic footprint and comparing it with the auditory thresholds of diverse marine species, our approach offers insights into the environmental impacts of offshore wind energy and paves the way for noise-mitigating design strategies.

2. ACOUSTIC UNDERWATER FOOTPRINT OF AEROACOUSTIC NOISE

2.1 Acoustic analysis

Aerodynamic noise is the dominant noise source in modern wind turbines, generated by the turbulent interaction of flow with blades (17). This noise comprises two main components: leading edge noise (LE) from the impingement of atmospheric turbulence on the blade front and trailing edge noise (TE) from the interaction of the turbulent boundary layer with the finite trailing edge. Due to the wide range of turbulent scales—from hundreds of metres in the atmosphere to millimetres along the blade—this noise exhibits a broadband spectrum that can affect marine species with different hearing thresholds.

The turbine blade is divided into n segments, each modelled as a two-dimensional airfoil. For each segment, LE and TE noise are computed as uncorrelated sources using Amiet theory (18; 19) (with corrections for finite chord effects (20)). The overall blade noise is obtained by summing the contributions from all segments and applying a Doppler correction to account for the motion relative to the observer. The transmission of sound from air to water is governed by Snell's law, which confines the effective propagation to a narrow cone (approximately 13°relative to normal); see figure 1a. In addition, we account for the transmission loss across the air-water interface (due to the change in media), which is 29.5 dB. Underwater propagation is modelled via cylindrical spreading, while atmospheric attenuation (21; 22). Finally, for a wind farm consisting of N turbines, the overall noise level scales as $10\log_{10}(N)$ when each turbine is considered an uncorrelated noise source. This framework provides a concise method for predicting aerodynamic noise emissions and their potential impact on marine life.

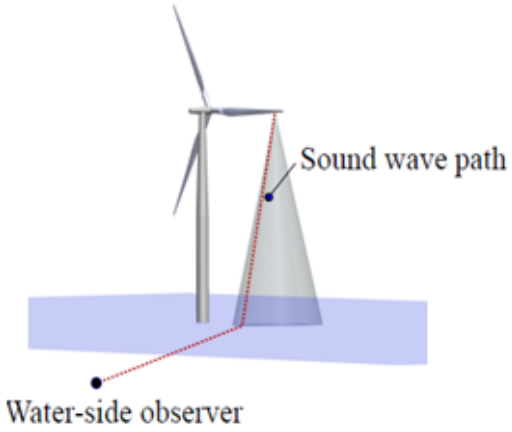
We consider the IEA 22 MW (5). The IEA 22 MW offshore wind turbine represents a significant advancement in turbine design for large-scale energy production. It features a hub height of 170 m and a massive rotor diameter of 284 m, which enables it to capture more wind energy even at relatively low wind speeds. The turbine is designed to operate at a nominal wind velocity of 11.78 m/s, with a rotor angular velocity of 7.1 rpm. This results in a high blade tip speed of 102.0 m/s, ensuring efficient aerodynamic performance. In addition, the turbine employs a blade pitch of 6.6°, which is crucial for optimising power output and reducing aerodynamic loads.

Figure 1 shows the far-field aerodynamic noise spectra generated by a single wind turbine and groups of 100 and 150 wind turbines for each case, compared to the hearing thresholds of various functional hearing groups, i.e., low-, mid-, and high-frequency cetaceans and pinnipeds (14; 23; 24). The figure shows that aerodynamic noise from the three wind turbines affects the low-frequency hearing group even when considering only a single wind turbine. When considering farms, the figure shows that a group of 100 turbines causes a general increase in the amplitude of aerodynamic noise spectra, with a footprint underwater of 25 dB louder than the hearing threshold of some marine animals, for the 22 MW wind turbine. In these cases, the aerodynamic noise of offshore farms is much larger than the hearing threshold of several groups of marine species, which can potentially mask the natural sound present in the environment. Further details of the methodology and analysis of other turbines can be found in our paper (25).

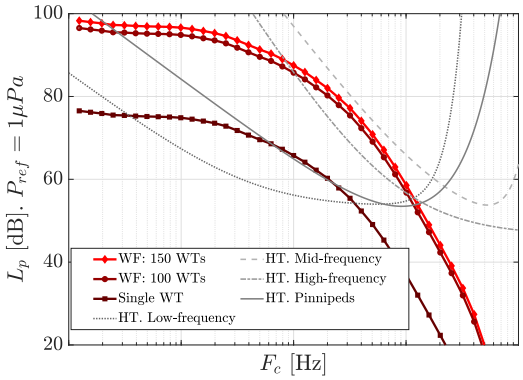
2.2 Simulations using the high order solver HORSES3D

Having identified a potential problem, our aim is to develop accurate tools that allow deeper studies. We are currently developing the open source solution HORSES3D (26; 27; 28) at the ETSIAE-UPM School of Aeronautics in Madrid, and available on Github (`https://github.com/loganoz/horses3d`). This solver is a high-order discontinuous Galerkin (DG) tool capable of addressing a wide array of flow applications. These applications encompass compressible flows, incompressible flows, multiphase flows, and aeroacoustics, see Figure 2. Furthermore, HORSES3D is equipped to manage body-fitted, immersed boundaries, and actuator lines.

One of the main advantages of DG methods is their ability to accurately capture high-order spatial and temporal variations of the solution, which makes them particularly suitable for simulating flows with sharp gradients and complex flow phenomena. DG methods also exhibit good numerical stability and conservation properties because of the local nature of the approximation and the use of fluxes at the interfaces of the elements. In HORSES3D, rotating turbine blades can be modelled using either actuator line methods or sliding meshes, while the air-water interface is captured using a robust Cahn-Hilliard formulation; see figure 3. Additional components, such as tower, nacelle, and platform, can be incorporated through immersed boundary techniques(29; 30; 31; 32; 33), offering exceptional flexibility. We include a robust local p-adaptation based on reinforcement learning to enhance ac-



(a) Sketch of wind turbine with Snell's cone for air and water: cone of 13° angle with respect to the air-water interface normal vector, that encompasses acoustic waves that penetrate underwater.



(b) IEA 22 MW wind turbine. One-third octave far-field noise spectra for a Water observer (10 m deep) at 100 m downwind of the turbine. Overlaid are hearing threshold of marine animals. WT: wind turbine; WF: wind farm with 100 and 150 WTs; HT: hearing threshold. Color scales from 20-100 dB in figure (d).

Figure 1: Acoustic analysis to quantify the underwater acoustic footprint of offshore wind turbines.

curacy at an affordable cost. Finally, we demonstrate the solver's capabilities through large eddy simulations of offshore wind turbines to soon provide a characterisation of their noise emissions and underwater footprint.

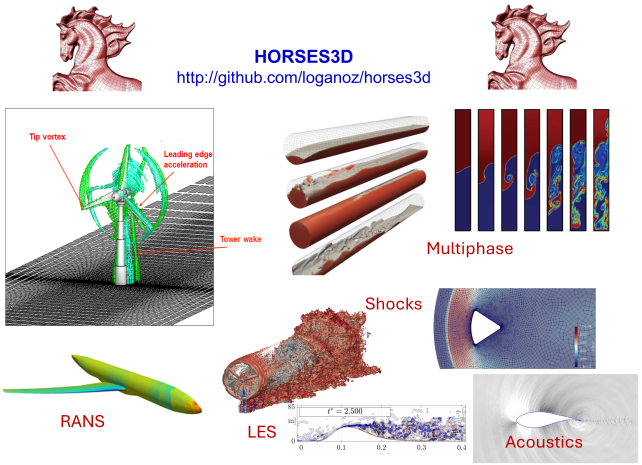


Figure 2: Summary of HORSES3D features (Ferrer et al. 2023).

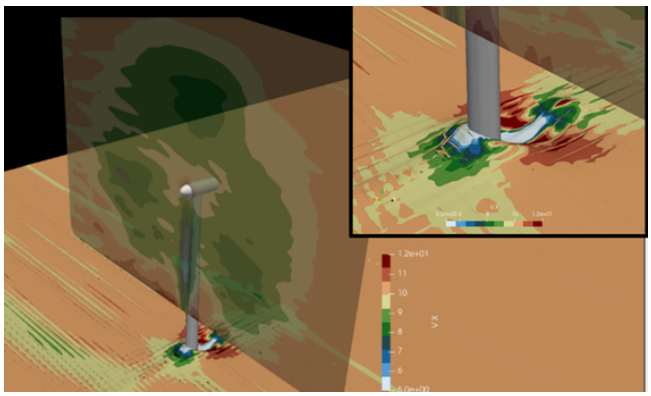


Figure 3: Example of offshore wind turbine simulated with actuator lines and free-surface using a Cahn-Hilliard formulation.

3. CONCLUSIONS

Achieving sustainable offshore energy means addressing environmental impacts, particularly the underwater noise of wind turbines, which can harm marine life. Traditional designs often focus on energy output while overlooking aerodynamic noise transmission into water.

We introduce a methodology that integrates noise models, offering manufacturers and policy makers a versatile tool for predicting underwater noise in both low- and high-fidelity scenarios. For the first time, we quantify the acoustic footprint of a 22 MW turbine and scale emissions to wind farms of 100–150 turbines, confirming that

aerodynamic noise—especially from trailing edges—is a significant environmental challenge.

Furthermore, our ongoing development of the HORSES3D solver will advance underwater acoustic predictions for offshore wind turbines, filling a current gap in capabilities.

4. ACKNOWLEDGMENTS

This research has received funding from the European Union (ERC, Off-coustics, project number 101086075). Views and opinions expressed are, however, those of the authors only and do not necessarily reflect those of the European Union or the European Research Council. Neither the European Union nor the granting authority can be held responsible for them.

5. REFERENCES

[1] Ørsted, "Hornsea 1 offshore wind farm." https://orsted.co.uk/energy-solutions/offshore-wind/our-wind-farms/hornsea1, 2024. Accessed: 2024-10-01.

[2] N. Akhtar, B. Geyer, and C. Schrum, "Larger wind turbines as a solution to reduce environmental impacts," *Nature Scientific Reports*, vol. 14, no. 1, p. 6608, 2024.

[3] P. Sherman, X. Chen, and M. McElroy, "Offshore wind: An opportunity for cost-competitive decarbonization of china's energy economy," *Science Advances*, vol. 6, no. 8, p. eaax9571, 2020.

[4] B. Desalegn, D. Gebeyehu, B. Tamrat, T. Tadiwose, and A. Lata, "Onshore versus offshore wind power trends and recent study practices in modeling of wind turbines' life-cycle impact assessments," *Cleaner Engineering and Technology*, vol. 17, p. 100691, 2023.

[5] F. Zahle, A. Barlas, K. Lønbæk, P. Bortolotti, D. Zalkind, L. Wang, C. Labuschagne, L. Sethuraman, and G. Barter, "Definition of the IEA wind 22-megawatt offshore reference wind turbine," *Technical University of Denmark*, 2024.

[6] Mingyang-Wind-Power, "Myse 22mw from mingyang wind power," 2024.

[7] J. Tougaard, L. Hermannsen, and P. T. Madsen, "How loud is the underwater noise from operating offshore wind turbines?," *The Journal of the Acoustical Society of America*, vol. 148, pp. 2885–2893, 11 2020.

[8] C. Hooper, J. Nedwell, D. J. Nedwell, M. J. Langworthy, and M. D. Howell, "Assessment of sub-sea acoustic noise and vibration from offshore wind turbines and its impact on marine wildlife; initial measurements of underwater noise during construction of offshore windfarms, and comparison with background noise," 2003.

[9] P. T. Madsen, M. Wahlberg, J. Tougaard, K. Lucke, and P. Tyack, "Wind turbine underwater noise and marine mammals: implications of current knowledge and data needs," *Marine ecology progress series*, vol. 309, pp. 279–295, 2006.

[10] M. Marini, R. Baccoli, C. C. Mastino, A. D. Bella, C. Bernardini, and M. Masullo, "Assessment of the noise generated by wind turbines at low frequencies," *Journal of Energy Resources Technology, Transactions of the ASME*, vol. 139, 9 2017.

[11] F. Thomsen and R. Kafemann, "Effects of offshore wind farm noise on marine mammals and fish," 2006.

[12] J. Tougaard, O. D. Henriksen, and L. A. Miller, "Underwater noise from three types of offshore wind turbines: Estimation of impact zones for harbor porpoises and harbor seals," *The Journal of the Acoustical Society of America*, vol. 125, pp. 3766–3773, 6 2009.

[13] T. Götz, G. Hastie, L. Hatch, O. Raustein, B. Southall, M. Tasker, F. Thomsen, J. Campbell, and B. Fredheim, "Overview of the impacts of anthropogenic underwater sound in the marine environment," tech. rep., OSPAR Commission, 2009.

[14] C. Erbe, C. Reichmuth, K. Cunningham, K. Lucke, and R. Dooling, "Communication masking in marine mammals: A review and research strategy," *Marine Pollution Bulletin*, vol. 103, pp. 15–38, 2 2016.

[15] U. Stöber and F. Thomsen, "How could operational underwater sound from future offshore wind turbines impact marine life?," *The Journal of the Acoustical Society of America*, vol. 149, pp. 1791–1795, 3 2021.

[16] J. N. Daly and J. Harrison, "The marine mammal protection act: A regulatory approach to identifying and minimizing acoustic-related impacts on marine mammals," in *The Effects of Noise on Aquatic Life*, pp. 537–539, Springer New York, 2012.

[17] S. Oerlemans, P. Sijtsma, and B. Méndez López, "Location and quantification of noise sources on a wind

turbine," *Journal of Sound and Vibration*, vol. 299, no. 4, pp. 869–883, 2007.

[18] R. Amiet, "Acoustic radiation from an airfoil in a turbulent stream," *Journal of Sound and Vibration*, vol. 41, no. 4, pp. 407–420, 1975.

[19] R. Amiet, "Noise due to turbulent flow past a trailing edge," *Journal of Sound and Vibration*, vol. 47, no. 3, pp. 387–393, 1976.

[20] M. Roger and S. Moreau, "Back-scattering correction and further extensions of Amiet's trailing-edge noise model. part 1: theory," *Journal of Sound and Vibration*, vol. 286, no. 3, pp. 477–506, 2005.

[21] C. H. Hansen, C. J. Doolan, and K. L. Hansen, "Wind farm noise: measurement, assessment, and control," *John Wiley & Sons*, 2017.

[22] ANSI/ASA, "Ansi/asa s1. 26-2014: Methods for calculation of the absorption of sound by the atmosphere," 2014.

[23] C. Carter, B. Wilson, and M. Burrows, *Tidal energy underwater noise and marine mammals*. PhD thesis, University of Aberdeen and the University of the Highlands and Islands, 2013.

[24] J. Tougaard, "Thresholds for noise induced hearing loss in marine mammals," *Journal of Aeroacoustics Society of America*, vol. 118, pp. 3154–3163, 2021.

[25] L. B. Bolívar, O. A. M. Sánchez, M. de Frutos, and E. Ferrer, "On the prediction of underwater aerodynamic noise of offshore wind turbines," 2025.

[26] E. Ferrer, G. Rubio, G. Ntoukas, W. Laskowski, O. Mariño, S. Colombo, A. Mateo-Gabín, H. Marbona, F. Manrique de Lara, D. Huergo, J. Manzanero, A. Rueda-Ramírez, D. Kopriva, and E. Valero, "Horses3d: A high-order discontinuous galerkin solver for flow simulations and multi-physics applications," *Computer Physics Communications*, vol. 287, p. 108700, 2023.

[27] L. Botero-Bolívar, O. A. Marino, C. H. Venner, L. D. de Santana, and E. Ferrer, "Low-cost wind turbine aeroacoustic predictions using actuator lines," *Renewable Energy*, vol. 227, p. 120476, 2024.

[28] O. A. Marino, R. Sanz, S. Colombo, A. Sivaramakrishnan, and E. Ferrer, "Modelling wind turbines via actuator lines in high-order h/p solvers," 2024.

[29] J. Kou, S. Joshi, A. H. de Mendoza, K. Puri, C. Hirsch, and E. Ferrer, "Immersed boundary method for high-order flux reconstruction based on volume penalization," *Journal of Computational Physics*, vol. 448, p. 110721, 2022.

[30] J. Kou, A. H. de Mendoza, S. Joshi, S. Le Clainche, and E. Ferrer, "Eigensolution analysis of immersed boundary method based on volume penalization: Applications to high-order schemes," *Journal of Computational Physics*, vol. 449, p. 110817, 2022.

[31] S. Colombo, G. Rubio, J. Kou, E. Valero, R. Codina, and E. Ferrer, "A high-order immersed boundary method to approximate flow problems in domains with curved boundaries," *Journal of Computational Physics*, vol. 528, p. 113807, 2025.

[32] J. Kou and E. Ferrer, "A combined volume penalization / selective frequency damping approach for immersed boundary methods applied to high-order schemes," *Journal of Computational Physics*, vol. 472, p. 111678, 2023.

[33] J. Núñez, D. Huergo, D. Lodares, S. Shrestha, J. Guerra, J. Florenciano, E. Ferrer, and E. Valero, "Implementation of immersed boundaries via volume penalization in the industrial aeronautical computational fluid dynamics solver coda," *Engineering with Computers*, February 2025.

DOI: 10.61782/fa.2025.0528



FORUM ACUSTICUM
EURONOISE 2025

LONG-TERM WIND FARM NOISE ASSESSMENT OVER DIFFERENT METEOROLOGICAL CONDITIONS

Dr. Krispian Lowe[1*] **Mikel Amatriain**[2] **Sylvia Broneske**[3]

[1] RWE Renewables UK, Reading, UK
[2] RWE Renewables Iberia, Zaragoza, Spain
[3] RWE Renewables UK, Swindon, UK

ABSTRACT

Recently European Court of Auditors (ECA) recommended introducing EU noise-reduction targets and noise limits in the Environmental Noise Directive. The ECA approach would be aligning the noise exposure reporting thresholds, as closely as possible, with the guideline levels in the 2022 update report by the World Health Organization (WHO) in urban areas. WHO Guidelines provide guideline L_{den} and L_{night} levels for specific noise sources. For wind turbines, they provide a guideline level of 45 dB L_{den} with no L_{night} guideline determined. For long term assessment relevant factors must be defined, as the calculation method for yearly L_{den} may be affected by different meteorological conditions, operational states of the turbines, relative position of the source and receptor, background noise and masking levels or applicable daily night-time and short time limits. The determination of how to determine compliance with an L_{den} will be explored.

The present work's aim is the identification of the environmental parameters necessary for sound propagation and the reasonable evaluation time for long term wind farm noise assessment. A detailed knowledge and understanding of the emission and propagation characteristics can allow an optimised noise levels and energy yield, which can be achieved by adapting the operation of the turbine.

Keywords: *long-term, wind, turbine, farm, noise*

[*] ***Corresponding author***: *Krispian.Lowe@rwe.com*
Copyright: *©2025 First author et al. This is an open-access article distributed under the terms of the Creative Commons Attribution 3.0 Unported License, which permits unrestricted use, distribution, and reproduction in any medium, provided the original author and source are credited.*

1. INTRODUCTION

European Union Directive 2002/49/EC (END) [1] was published to define a common approach intended to avoid, prevent or reduce on a prioritised basis the harmful effects, including annoyance, owing to exposure to environmental noise. Noise indicators L_{den} and L_{night} were selected for the preparation and revision of strategic noise mapping. Day-evening-night level L_{den} in decibels (dB) is defined by the A-weighted long-term average sound level as defined in ISO 1996-2:1987 [2] and the updated to ISO 1996-2:2017 [3]. The equation for the day-evening-night weighted sound pressure level, L_{den}, for the equivalent continuous sound pressure level for day-time, L_{day}, evening-time, $L_{evening}$, and night-time, L_{night}, with the weightings of 0 dB, 5 dB and 10 dB, respectively, is shown in the equation below [4]. The time, in hours, for the day-time, t_{day}, evening-time, $t_{evening}$, and night-time, t_{night}, are normally 12, 4 and 8 hours, respectively. These times may vary for different countries[1].

$$L_{den} = 10\,log_{10}\left[\frac{t_{day}10^{0.1L_{day}} + t_{evening}10^{0.1(5+L_{evening})} + t_{night}10^{0.1(10+L_{night})}}{24}\right] \quad (1)$$

European Environment Agency collects official noise data reported every five years by EEA member countries under the Environmental Noise Directive (END) with last available noise country fact sheets of 2021, including road, rail, aviation and industry sound sources.

The WHO Regional Office for Europe developed environmental noise guidelines for the European Region in 2018 [5], proposing an updated set of public health recommendations on exposure to environmental noise. The

[1] The typical values are day-time of 0700 to 1900, evening time of 1900 to 2300 and night-time 2300 to 0700.

guidelines presented recommendations on reducing noise levels for road, railway, aircraft, wind turbine and leisure noise sources.

A compendium of WHO and other UN guidance on health and environment update of 2022 refers to L_{den} and L_{night} indicators for noise monitoring and exposure assessment adding $L_{Aeq,T}$ for measuring leisure noise exposure. For average noise exposure, sound pressure levels <45 dB L_{den} for wind turbine noise are recommended. There is not any reference for night noise exposure or $L_{Aeq,T}$ for wind turbine noise.

Recently, the European Court of Auditors (ECA) [6], published a special report about Urban pollution in the EU, giving the recommendation of prioritising actions against noise pollution to The European Commission, to assess the feasibility of introducing EU noise-reduction targets in the Environmental Noise Directive and aligning the noise exposure reporting thresholds as closely as possible with those recommended by the World Health Organization with a target implementation date of 2029. The referred indicators are L_{den} and L_{night} without any reference to $L_{Aeq,T}$ levels. The noise sources are focused on road, aircraft and railway noise.

1.1 World Health Organisation 2018

World Health Organisation (WHO): Regional Office for Europe (ROE) provided Environmental Guidelines for the European Region for the following noise sources: Road Traffic, Railway, Aircraft, Wind Turbines and Leisure Activities. The recommended level for wind turbine noise is an L_{den} value of 45 dB. This latest report works in conjunction with WHO 1999 [7] and WHO 2009 [8] where those guidelines levels also apply, in particular 45 $L_{Aeq,8hour}$ outside a bedroom with a wind open, and 40 dB $L_{night,outside}$, respectively.

The wind turbine guideline level was given a **conditional** recommendation and would require substantial debate amongst stakeholders, since the quality of the evidence used to derive the rating was **low quality.** It was marked as **low quality** owing to heterogeneity, inconsistency and imprecision. No guidelines for L_{night} were produced since the evidence consisted of study limitations, inconsistent results and imprecision.

The WHO themselves state that the L_{den} and L_{night} is a poor acoustic measure for wind turbines in section 3.4.2.3, an excerpt is quoted below:

"*Even though correlations between noise indicators tend to be high (especially between L_{Aeq}-like indicators) and conversions between indicators do not normally influence the correlations between the noise indicator and a particular health effect, important assumptions remain when exposure to wind turbine noise in L_{den} is converted from original sound pressure level values. The conversion requires, as variable, the statistical distribution of annual wind speed at a particular height, which depends on the type of wind turbine and meteorological conditions at a particular geographical location. Such input variables may not be directly applicable for use in other sites. They are sometimes used without specific validation for a particular area, however, because of practical limitations or lack of data and resources. This can lead to increased uncertainty in the assessment of the relationship between wind turbine noise exposure and health outcomes.*".

"*Based on all these factors, it may be concluded that the acoustical description of **wind turbine noise by means of L_{den} or L_{night} may be a poor characterization of wind turbine noise** and may limit the ability to observe associations between wind turbine noise and health outcomes.*"

It is important to note that the WHO does not provide methodology, procedure or detailed information on how to predict, measure and assess an L_{den} for wind turbines.

1.2 Compendium of WHO and other UN guidance on Health and Environment 2022 update

The compendium of WHO and other UN guidance on Health and Environment report, Chapter 11, provides a short summary of the guideline levels to achieve for a range of sources such as: road traffic noise, railway noise, aircraft, wind turbine, leisure sources [9]. The compendium states an average level of less than 45 dB L_{den} is recommended. There is no other guidance or other information provided for wind turbines in the compendium document.

1.3 Special report 02/2025

The European Court of Auditors (ECA) provides a review of the European Green Deal and the Zero Pollution Action Plan to reduce air and excessive noise on human health with respect to the END [6]. The special report found that there are no EU limit values or reduction targets for noise, and provides recommendations for limits for road, rail and aircraft. There is no mention of wind turbines in the report; however, the ECA special report should assess the feasibility of aligning the reporting thresholds as closely as

possible with those recommended by the WHO by 2029. Therefore, wind turbine levels could be passed through without careful consideration.

2. REGULATION ON LONG-TERM ASSESSMENT

The application of the calculation and enforcement of short-term and long-term sound levels from wind turbines varies from country to country owing to noise prediction, noise modelling, legislative frameworks and evidence at the time of the law and/or supplementary guidance creation. Countries such as Spain, Lithuania and Poland may have stated annual limit, but have short-term $L_{Aeq,T}$ levels that are more stringent. . Therefore, in practice, the annual levels are not generally calculated or assessed.

2.1 Netherlands

The Netherlands had a law to assess the annual levels for 47 dB L_{den} and 41 dB L_{night} [10]. The Law seta out the source level for which measurements should be done according to the method in the law or NEN-EN-IEC 61400-11 (2002). These methods determine the sound power level of the wind turbine per wind speed bin at hub height from cut-in to rated power. For sound power levels at wind speeds greater than the rated power, then the sound power level at the rated power can be used for these higher wind speeds.

The wind speed distribution for day, evening and night from a long-term wind statistics should be obtained from KNMI[2]. The annual average sound power level per octave band is calculated for each period of day. The predicted immission level is then determined from subtracting following attenuation terms: geometric divergence, atmospheric attenuation[3], reflecting objects, screening, vegetation, industrial, ground, housing and meteorological corrections. It should be noted that though the propagation methods and parameters are similar to ISO 9613-2:1996 [11] and ISO 9613-2:2024 [12], but the ground attenuation is less in the Netherlands Law. The immission level is then modified for each turbine-receptor based on the relative bearing, owing to the long-term meteorological effects. However, this only comes into effect at a distance 10 times the combined receptor and source heights. Once the immission has been calculated for each period, it is combined into the L_{den}. The receptor height is 5 m.

Compliance with the limits is determined by a sound power level measurement, since it is not possible to measure an annual level at a receptor location. This is owing to the influence of the dominant background noise on measurements at receptors [10].

The ruling on Dutch wind farms means that law cannot be applied, but a temporary bridging scheme is in place until new rules are in place [13]. The publication of the new draft law and consultation period were in October 2023 to November 2023, whilst the new law will come into force in 2025 or 2026 [13].

2.2 Norway

The guideline for noise is specified in T-1442/2021 as an L_{den} of 45 dB [14]. The prediction of the immission level is according to NORD2000, assuming that the turbines are operating 100 per cent of the time, and the sound power level at wind speed of 8 m/s, at 10 m standardised height, shall be used. There are no set parameters for NORD2000 calculations and it is dependent on the experience of the practitioner; however, the following parameters are typically used:

- Receptor height of 4 m,
- Ground is a uniform class D [4],
- Temperature of 10 degrees Celsius and relative humidity of 70 per cent, and
- Wind speeds at 10 m standardized height.

3. FACTORS AFFECTING LONG-TERM ASSESSMENTS

3.1 Source Sound Power Levels

The sound power level of a turbine should be determined using the IEC 61400-11:2012+AMD1:2018 CSV [15], where the sound power level is determined with respect to hub height wind speeds and third octave frequency. The wind speed bins are centred on the integer and half integer. The sound level index should be expressed as an $L_{Aeq,T}$. Depending on the regulatory context, further treatment of the measured sound power levels should be used, or the warranted levels - usually issued by the manufacturer - or declared sound power levels using IEC TS 61400-14:2005 [16]. A comparison of different representations of sound power levels are shown in Institute of Acoustics (IOA)

[2] www.windenergie.nl

[3] 10 degrees Celsius and 80 per cent relative humidity

[4] 2000 kPas/m2 - Normal uncompacted ground (forest floors, pasture field)

Good Practice Guide (GPG) Supplementary Guidance Note (SGN) 3 [17].

The sound power level should be declared between cut-in to cut-out wind speeds. If the sound power level is not declared for wind speeds above the rated power wind speed, then the rated power sound power level should be used. If the sound power level is unknown for wind speeds between cut-in and the 68 per cent of the rated capacity[5], then care should be taken in extrapolating these data. An example is given in Figure 1. Any omission of sound power levels, at wind speeds where the turbine can generate, will reduce the calculated annual average sound power level.

A larger rotor size for the same rated power would increase the swept area, energy yield and capacity factor[6]. Increasing the energy yield would typically involve shifting the power curve, and sound power level curve, to lower wind speeds. This would increase the L_{den} and L_{night} values, but maximum sound power level, L_{WA}, would remain the same. Increasing the rotor size does not necessarily increase the sound power level, owing to the tip speed being the limiting speed.

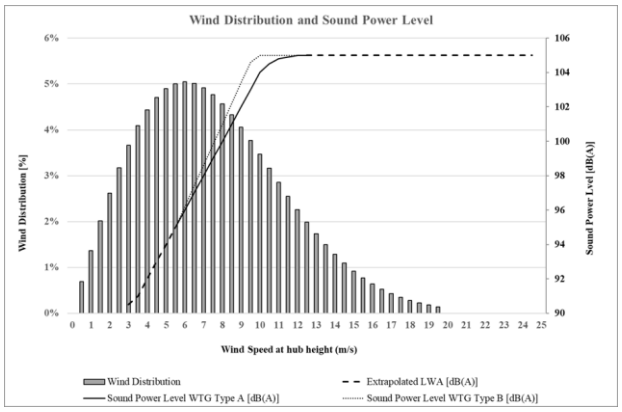


Figure 1. showing an example of sound power level (right y-axis), for Turbine Type A, with respect to hub height wind speed (x-axis) showing the solid black line as the declared sound power level and the dashed black line is the extrapolated level. Turbine Type B is shown as dotted lines. The wind distribution percentage of occurrence (left y-axis) at hub height wind speeds. The maximum sound power level for Turbine Type A and B is 105 dB(A), whilst the average sound power level is 100.8 dB(A) and 101.3 dB(A), respectively. If the wind speed distribution is the same for day, evening and night, then the Lden value would be 107.2 dB and 107.7 dB for turbines Type A and B, respectively.

[5] 0.8 times the 85 per cent of the maximum power as per section 5 in IEC 61400-11.

[6] Capacity factor is the actual or predicted energy yield divided by the maximum potential energy yield.

3.2 Wind Speed

The wind speed for calculating the annual average should be measured at the same resolution as the sound power level measurements. The introduction of binning data to a lower resolution or interpolating to a higher resolution, will introduce systematic errors and additional uncertainty. The wind speed should be measured at hub height or at points above and below the proposed hub height. Therefore, care should be taken to ensure that the correct wind speeds are used with the correct hub heights for all turbines. Typically, wind turbines with a lower hub height will see lower wind speeds compared to turbines with a higher hub height. When converting wind speeds from one height to another, wind shear must be taken into account, guidance is provided within IEC 61400-11 [15], IEC 61400-11-2 [18] and the IOA GPG [19] and the IOA GPG SGN 4 [20]. When using wind speed measurements with lower anemometers on a mast, care should be taken to account for the mast wind shadow. When using a LiDAR, data quality and signal to noise must be considered, either by filtering, infilling or omitting some data.

Each site will have its own wind speed and wind direction distributions. In the case of wind measurements, a metrological mast and/or LiDAR should follow to the IEC 61400-50 series, and a robust long-term wind catalogue can be used. Wind speed measurements conducted on the development site may be limited to 1 or 2 years. These "shorter" measurements could be correlated with longer-term wind measurements from a national or international wind catalogue. Wind speed distribution will vary year by year; therefore, the annual average sound power level of the turbine will vary year by year. The wind speed distribution can be approximated to a Weibull distribution. The wind speed distributions and power curves are used to calculate representative wind energy yield(s). The calculated energy yield should be considered as the greatest values. In real-life power output is likely to be slightly below these values due to downtimes: maintenance, grid outages, sector managements and others (see section 3.4).

Wind speed distribution should be grouped for the day-time, evening-time and night-time periods. These time periods may vary for different countries or regions, and that

the hour change to and from summer-time should also be taken into account. Therefore, the average sound power level, for a period of day, per octave band, $L_{W,period,j}$, Eqn (2), is the logarithmic sum between cut-in and cut-out wind winds speeds for the frequency of occurrence of the wind speed bin, V_i, for the corresponding sound power level per octave and wind speed bin, $L_{W,i,j}$,

$$L_{W,period,j} = 10\log_{10}\left[\sum_{i=v_{cut-in}}^{v_{cut-out}} V_i 10^{(0.1L_{W,i,j})}\right] \quad (2)$$

The sum of V_i may not equal 1 owing to wind speeds outside of the cut-in and cut-out region.

For simple flat sites it may be appropriate to use a single point for the entire wind farm, but for larger wind farms or those with complex terrain, multiple wind speed measurement locations may be needed. In addition, when a wind turbine is downwind of another turbine, the wind speed may be lower. Determining the "mean" sound power level from the arithmetic mean wind speed is an incorrect method this is owing to 1) the wind speed distribution follows a Weibull distribution rather than a Gaussian distribution, and 2) the annual average is based on weighted logarithmic average.

3.3 Wind Direction

Wind direction will have an effect at the receptor location owing to the shadow zone for the upwind and close to cross wind positions [19 and references within]. The prevailing wind direction may change owing to the season and time of day, in particular for regions in coastal or areas close to large bodies of water. Treatment of the effect of wind direction on the sound propagation is discussed further in ISO 9613-2:2024 Annex C [12] and the IOA GPG section 4.4 [19].

The distribution of wind directions is important for the siting of wind turbines in a wind farm. A wind rose shows probability of a wind from a certain sector. In addition, the wind speed distributions can be different for these wind direction sectors.

Higher wind speeds may be associated with the prevailing wind directions, whilst lower wind speeds in for non-prevailing wind directions. The wind direction may vary across the site, especial for site with complex terrain and inter- and intra-wind farm turbulence.

When assessing the directional effects, it is prudent to create an attenuation matrix of wind speed, wind direction and period for each receptor turbine pair.

According to the IEC TS 61400-14, the apparent sound power level shall be declared by combining the mean sound power level and the confidence level. Aerodynamic sound theories and experiments have demonstrated that the sound pressure levels in the crosswind direction are lower than those in the up- or downwind direction [21] [22]. There is no definition of emission directivity in the manufacturer's sound power declaration.

3.4 Turbine Operation

The operation of the turbines on a wind farm will affect the annual average owing to, but not limited to, the following:

- Availability of the turbine, where turbines are subject to maintenance, expected levels of stoppages owing to faults and grid outages. The availability of a wind farm will not be 100 per cent but expected to be greater than 95 per cent.
- The wind farm may be constrained by the grid restriction based on capacity load, where the wind farm may have to run a reduced power mode or shutdown owing to oversupply or other restrictions by the grid operator.
- Individual turbines operate in curtailed modes or shut down at specified wind speeds, wind directions and time of day owing to turbine wakes, turbulence from the terrain, noise mitigation, bat and bird protection, shadow flicker, intra-wind farm grid constraint, loading, etc.

These operational constraints may be known for the development under assessment but may be unknown for neighbouring wind farms that are not under the operator's control. Assuming that the wind farm will be operational 100 per cent of the time would often lead to an over estimation of the annual average.

3.5 Propagation

The depending on the propagation model (NORD2000, ISO 9613-2 etc) some of the attenuation parameters may vary over the year. The predicted levels according to ISO 9613-2 is for downwind conditions under a moderate ground-based temperature inversion, such as commonly occur on clear and calm nights.

Geometric divergence should be the same irrespective of the time and date. However, the parameters for atmospheric absorption and ground attenuation will vary. Ambient temperature, temperature gradient, relative humidity and atmospheric pressure will change throughout the day and through each season. Wind farms coexist with agricultural activities and the ground factor may change over the course of the year depending on the land use. For example, there may be crops in the summer, bare ground in winter and spring, frozen, snow or flooded during the winter. Therefore, full evaluation of temperature, relative humidity and ground conditions should be used; however, a pragmatic approach could be to use the average values.

If turbine rotors are obscured by landforms relative to the receptor location, the screening attenuation for that turbine at the receptor, is limited to 3 dB according to ISO 9613-2:2024 Annex D or 2 dB according to the IOA GPG Section 3[7] . Where there is a concave ground occurs between the source and the receptor, then an additional 3 dB can be added to the contribution of that turbine at that receptor according to ISO 9613-2:2024 and IOA GPG Section 3. However, it should be noted that the calculation of the mean propagation height and the trigger criteria are different in ISO 9613-2 and the IOA GPG.

3.6 Receptor locations

The receptor location for the predicted levels should be carefully selected. Country specific requirements such as prediction on the façade closest to the wind farm or in free field conditions should be used. Care also needs to be taken, as national legislation could mandate the precise location for measurements, such as in Germany, where the immission level should be measured 0.5 m in front of the open window, outside, of the most affected room in need of protection, such as bedrooms [23].

4. MEASUREMENT AND ENFORCEMENT

Measurement of an annual average at receptor locations will be impracticable owing to the effect of background noise, road, rail, aircraft, industry or other anthropogenic sources. Therefore, it may be impracticable to determine the specific sound level of the wind farm or wind turbine at receptor locations, owing to the unknown contribution of the other sounds. Also, the presence of measurement equipment in at receptor locations, may have a disruptive effect on inhabitants of the dwelling and affect their subjective response to the source of noise.

To implement long-term (annual) immission measurements at several receptor positions around a wind farm, during the development and operation, would increase the cost of energy production and the security of supply, owing to the number and complexity of the measurements and precision instrumentation needed for the task. In addition, a clear description of uncertainties in any methodology should be calculated and stated.

In shorter term measurements, assessed against L_{Aeq}, L_{A50}, L_{A90} indices, it is a proper approach to perform shutdowns and logarithmically subtract the shutdown levels from the total levels, to give the specific sound pressure level owing to the source [18] [24]. However, it is impracticable to have regular shutdowns, over a year, for the wind farm, since this will impede the generation of electricity. In addition, neighbouring wind farms that were stopped for various reasons throughout the year would provide an incorrect picture of the cumulative noise exposure.

The Netherlands and Norway, where the L_{den} index is used, state that measurements at receptor locations are impracticable. They sate that compliance is assessed with sound power level measurements with a prediction of immission levels at receptor locations [10] [14]. Therefore, given the multiple meteorological effects on propagation it is more logical to use receptor measurements to compare to L_{Aeq}, L_{A50}, L_{A90} or other similar indices for sound level limits, rather than attempt to measure an annual average.

The annual average sound level indicators may not reflect the neighbours experience of sound at their dwelling. For example, the character or level of the sound that may occur under specific conditions that may cause a complaint. Would a complaint be resolved if the annual average was compiled with?

There are some challenges with showing compliance with the annual limit under the following circumstances:

- The nature of the annual average implies that the short-term immission level would be greater than the annual average limit. Therefore, if a

[7] If the landform is close to the receptor, then a reduction of 10 dB can be used.

limit was X dB L_{night}, then the source could remain at X+3 dB $L_{Aeq,T}$ for 50 per cent of the year, and then shutdown for the rest of the year and meet the limit.

- If the annual average is calculated from the operational data , would the wind turbine(s) or wind farm have to cease operating, or the operator would be subject to penalties, if they reach the annual limit before the 12 months? Would it be a fixed 12 months or a rolling 12 months?

5. SUMMARY

The EU Directive 2002/49/EC aims to mitigate harmful effects of environmental noise using indicators like L_{den} and L_{night} for strategic noise mapping. The WHO European Region issued noise guidelines in 2018, recommending guideline levels for various noise sources including wind turbines. However, the WHO guidelines levels in 1999 and 2009 are still extant. The WHO guidelines level was given a **conditional** recommendation and still requires substantial debate, since the quality of evidence used to derive this guideline level was **low quality**. In addition, the WHO 2018 report states that the L_{den} and L_{night} is a poor acoustic measure for wind turbines.

A 2022 guidance update references L_{den} and L_{night} for noise monitoring, recommending L_{den} < 45 dB for wind turbine noise, with no L_{night} or $L_{Aeq,T}$ reference for wind turbines. The ECA recommended prioritising noise pollution actions and assessing EU noise-reduction targets within the END. These targets should align with WHO recommendations by 2029, focusing on indicators L_{den} and L_{night} for road, aircraft, and railway noise.

The Netherlands has set annual sound limits at 47 dB L_{den} and 41 dB L_{night}, assessing turbine sound power levels with NEN-EN-IEC 61400-11 and KNMI wind statistics for immission predictions. Currently, a temporary bridging scheme is active whilst the Netherland's wind farm laws are under review, with new regulations anticipated by 2025 or 2026. Norwegian guideline T-1442/2021 sets a 45 dB L_{den} limit for noise prediction using NORD2000, with turbines assumed to operate continuously. Sound power level is based on 8 m/s wind speed at 10 m height. Norway and Netherlands calculate the L_{den} in different ways and therefore a direct comparison is not advised. Both countries do not recommend receptor measurements for the determination of the annual levels, but a sound power level measurement with a prediction to the receptor is required to determine compliance.

Sound power levels must be declared from cut-in to cut-out wind speeds, using rated levels if not specified above rated speeds. Extrapolation outside of measured levels requires caution to avoid reducing the annual average sound power level. The resolution of wind speed measurements for calculating annual averages shall be the same as the sound power levels, avoiding errors from binning or interpolating. Measurement of wind speeds should be at hub height or appropriate heights, considering wind shear to convert between heights, guided by IEC standards and good practice guides.

Wind direction affects the immission at receptor locations, especially in shadow zones, with variations owing to season and time, notably near coasts and large water bodies. Wind direction distribution, illustrated by wind roses, is crucial for turbine siting in farms, with differing wind speed distributions across these sectors.

Prediction of annual levels at the receptor will have to take account the wind statistics, meteorological conditions, operational conditions and variations in the propagation attenuation over the year and lifetime of the wind farm. Assuming the turbines are operating at full rated capacity would be an overestimation of the annual averages. Annual average sound levels may not reflect the neighbours' experience, as long-term averages often miss short-term variations, character and specific disruptive conditions.

Measuring annual average sound levels at receptor locations are impactable owing to background noise and the presence of measurement equipment, which may disrupt inhabitants and affect their response to wind farm noise. Long-term immission measurements around a wind farm increase costs and complexity, requiring precision and clear methodology, whilst trying to minimise uncertainties in the result.

Challenges in meeting annual sound limits include potentially exceeding short-term immission levels and needing shutdowns to comply. Questions arise about operations ceasing and penalties if limits are reached, whether on a fixed or rolling 12-month basis.

6. REFERENCES

[1] European Parliament and of the Council, Directive 2002/49/EC of the European Parliament and of the

Council of 25 June 2002 relating to the assessment and management of environmental noise, EUR-Lex, 2002.

[2] ISO, "Acoustics — Description and measurement of environmental noise Part 2: Acquisition of data pertinent to land use," ISO, Geneva, 1987.

[3] ISO, "Acoustics - Description, measurement and assessment of environmental noise - Part 2: Determination of sound pressure levels," ISO, Geneva, 2017.

[4] ISO, "Acoustics - Description, measurement and assessment of environmental noise - Part 1: Basic quantities and assessment procedures," IOA, Geneva, 2016.

[5] World Health Organization (WHO):ROfe, "Environmental Noise Guidelines for the European Region," World Health Organization, Copenhagen, 2018.

[6] European Court of Auditors, "Special report: Urban pollution in the EU - Cities have cleaner air but are still too noisy," Publications Office of the European Union, Luxembourg, 2025.

[7] World Health Organisation (WHO), "Guidelines for Community Noise," WHO, Geneva, 1999.

[8] World Health Organisation (WHO, "Night Noise Guidelines for Europe," WHO Regional Office for Europe, Copenhagen, 2009.

[9] World Health Organization, "Compendium of WHO and other UN guidance on health and environment 2022 update," Geneva, 2022.

[10] Secretary of State for Infrastructure and the Environment, "General rules for environmental management establishments (calculation and measurement of noise impact of wind turbines)," STAATSCOURANT, The Hague, 2010.

[11] ISO, "Acoustics - Attenuation of sound during propagation outdoors - Part2: General method of calculation," ISO, Geneva, 1996.

[12] ISO, "Acoustics — Attenuation of sound during propagation outdoors — Part 2: Engineering method for the prediction of sound pressure levels outdoors," ISO, Geneva, 2024.

[13] IPLO, "Environmental impact assessment and new general environmental rules for wind farms," Living Environment Information Point, [Online]. Available: https://iplo.nl/regelgeving/regels-voor-activiteiten/gevolgen-nevele-arrest/mer-nieuwe-regels-windparken/. [Accessed 05 03 2025].

[14] Milø-direktoratet, "Guidelines on the teatment of noise in land-use planning," Oslo, 2021.

[15] IEC, "Wind Turbines - Part 11: Acoustic Noise Measurement Techniques," IEC, Geneva, 2012.

[16] IEC, "Wind Turbines - Part 14: Declaration of apparent sound power level and tonality values," IEC, Geneva, 2005.

[17] Institute of Acoustics, "SUPPLEMENTARY GUIDANCE NOTE 3: SOUND POWER LEVEL DATA," IOA UK, St. Albans, 2014.

[18] IEC, "Wind Energy Generation Systems - Part 11-2: Acoustics noise measurement techniques - Measurement of wind turbine sound characteristics in receptor position," IEC, Geneva, 2024.

[19] Institute of Acoustics, "A Good Practice Guide to the Application of ETSU-R-97 for the Assessment and Rating of Wind Turbine Noise," Institute of Acoustics, St. Albans, 2013.

[20] Institute of Acoustics, "Supplementary Guidance Note 4: Wind Shear," IOA, St Albans, 2014.

[21] S. Oerlemans and J. G. Schepers, "Prediction of wind turbine noise and validation against experiement," National Aerospace Laboratory NLR, Amsterdam, 2009.

[22] C. Rautmann, "Numerical Simulation Concept for Low-Noise Wind Turbine Rotors," Deutsches Zentrum fuer Luft- und Raumfahrt, 2017.

[23] Sechste Allgemeine Verwaltungsvorschrift zum Bundes- Immissionsschutzgesetz (Technische Anleitung zum Schutz gegen Lärm - TA Lärm, 01.06.2017).

[24] Institute of Acoustics, "Supplementary Guidance Note 5: Post Completion Measurements," Institute of Acoustics, St. Albans, 2014.

DOI: 10.61782/fa.2025.0614

FORUM ACUSTICUM EURONOISE 2025

OPTIMIZING ELECTRICITY PRODUCTION IN WIND FARMS WITH NOISE MITIGATION STRATEGIES

Álvaro Grilo[1*]
[1] INERCO Acústica, S.L., Tomas Alba Edison, 2, 41092 Sevilla, Spain

ABSTRACT

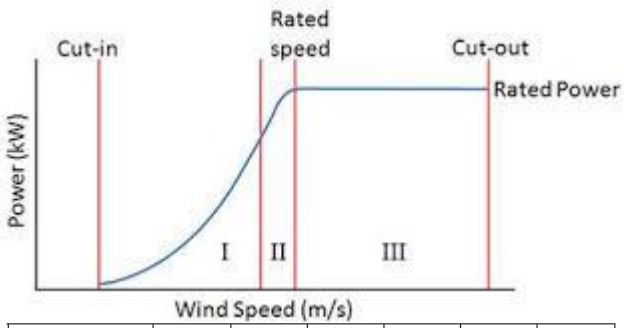
Wind power will be key to achieve the European Renewable Energy targets and making the EU carbon-neutral by 2050. Wind farms can cover several square kilometers of land and the permitting processes must consider the legitimate concerns of citizens regarding the environmental noise impact. In order to increase local acceptance of wind farm projects, a noise mitigation strategy should be available in cases where the noise standards are exceeded. A validated noise prediction model with monitored data will permit to verity the compliance of the noise regulations with best precision and limit the production of the wind turbines only when it is strictly required. This paper shows a methodology for the optimization of the electricity production of a wind farm, considering different noise calculation standards during the design of noise mitigation strategies.

Keywords: *wind farm, noise mitigation, low noise operation, CNOSSOS, ISO9613*

1. INTRODUCTION

Wind energy production constitutes a fundamental pillar of the energy sector, compensating for the energy deficit of the system through the development of alternative renewable energies, which have rapidly developed worldwide in recent decades. In Europe, wind farm capacity exceeds 270 GW, covering the wind energy almost a quarter of the demand in Spain [1].

From an acoustical point of view, wind turbines are a noisy source whose sound power level increases with their electrical power and depends on wind speed. When the wind turbine starts operating (usually at wind speeds between 4 and 30 meters at hub height), the sound power increases gradually until it reaches a stationary level as can be seen in Figure 1.



U_s m/s	4	5	6	7	8	9
Lw dB(A)	97.9	100.9	104.2	106.1	107.0	106.9

Figure 1. Evolution of electrical production and example of associated acoustic power (Lw) for a 3 MW wind turbine, according to wind speed [2][3]

Given these particular emission characteristics, the evaluation of the acoustic impact of wind farms requires a specific methodology regarding the development of prediction models and acoustic monitoring. Some countries, such as Australia or New Zealand, have developed methodological guidelines for the acoustic study of wind farms. Additionally, there are different studies and recommendations that refer to the need to adapt acoustic prediction models that were not designed for elevated sources:

- Studies [4] have demonstrated the deviations derived from the use of the ISO 9613-2 standard, so the selection of the calculation standard and input parameters must be carefully analyzed.
- The Institute of Acoustics [6] already established correction factors associated with visibility criteria

[*] ***Corresponding author***: agrilo@inerco.com
Copyright: *©2025 First author et al. This is an open-access article distributed under the terms of the Creative Commons Attribution 3.0 Unported License, which permits unrestricted use, distribution, and reproduction in any medium, provided the original author and source are credited.*

or average height calculated independently for each receiver.

- Other authors [7] recommend the validation of the prediction models to ensure their suitability for the evaluation of wind farms, with the value of ground absorption (G) being one of the key parameters that determines the representativeness of noise predictions.

In the present study, an update of the validation of a noise prediction model under different calculation standards and different values of acoustic impedance has been carried out for a case study, in order to maximize the precision of the model and the optimization of the electrical production.

2. METHODOLOGY

The present study has developed the workflow described in to verify the effectiveness of the mitigation plan for an operating wind farm:

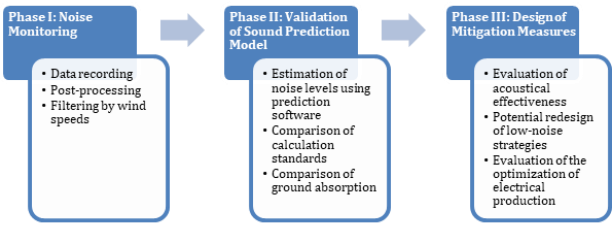


Figure 2. Workflow of the present study

In the phase of monitoring the noise of the wind farm, an in-situ acoustic testing campaign was carried out in accordance with ISO 1996-2 (under favorable conditions), with the aim of obtaining sufficient and representative sound records of the wind farm's operation at different wind speeds. The noise campaign was conducted over more than seven (7) days for a total of 368 hours of measurement and a database with more than 20,000 noise-meteorology-operation records of the park. The variation of sound levels with the wind speed was represented was obtained using the binned method, as described at in the Ontario Wind Farm Acoustic Measurement and Evaluation Guide [11], for each measurement position and period (day/night).

The acoustic testing campaign was carried out in two buildings (see Figure 3) located in the vicinity of the eastern area of the wind farm, with dominant westerly winds (predominant in the area).

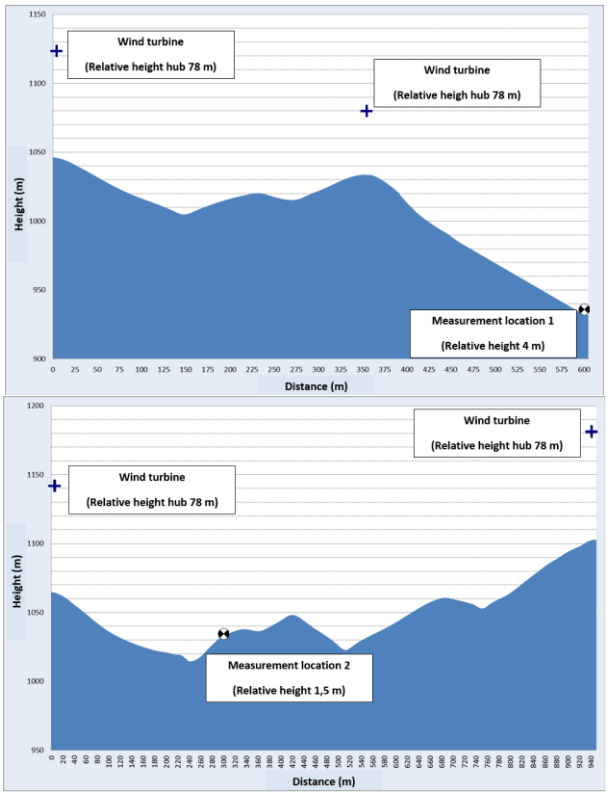


Figure 3. Elevation Profiles of Measurement Positions (Position 1 – up, Position 2 – down)

The noise prediction models were developed using the CadnaA acoustic software from Datakustik, for simulating the noise levels at the monitoring points according to the following calculation standards:

- ISO 9613-2:2024 "Acoustics — Attenuation of sound during propagation outdoors Part 2: Engineering method for the prediction of sound pressure levels outdoors" [12].
- CONCAWE-report 4/81, "The propagation of noise from petroleum and petro-chemical complexes to neighboring communities" [13]
- The Nordic sound prediction model NORD2000 [14]
- Common Noise Assessment Methods (CNOSSOS-EU) [15].

The ground absorption parameter has been configured for different scenarios including hard (G=0) and mixed ground (0,5) according to various European recommendations [16] as well as considering an absorption map based on land uses or covers established in the EAA Corine Land Cover (CLC) database [18]. The G absorption coefficient was established based on the different land use categories established in CORINE and following recommendations from previous studies [19], resulting an average G value for the study area of 0.71. More technical details about the developed noise campaign and prediction models can be found in [21] .

3. STUDY CASE

The wind farm under study is located in an extensive area situated between small towns, in a region with a marked rural-natural character dominated by crops, as well as scattered groves and scrubland. Especially during the nighttime period, human influence is practically nonexistent, and sound levels are mainly influenced by natural noise and the operation of the wind turbines.

The wind farm has more than 50 wind turbines and an installed capacity of over 100 MW. The wind turbine model under study develops an electrical power of 2 MW and has a rotor diameter of 90 meters and a total hub height of 78 meters. The wind turbines under study have a sound emission power provided by the manufacturer in accordance with IEC 61400-11, reaching a maximum power (106 dBA) at wind speeds above 6 m/s. This model can operate under low-noise configurations that can be used as corrective measures in the management of the wind farm to avoid exceeding the limit levels established by current regulations (45 dBA). Table 1 specifies the noise attenuation of the available low-noise modes for a hub height of 78 meters, in accordance with IEC 61400-14, with a reduction range of 1,4-4,8 dBA. Since noise attenuation relies on reducing the blade speed, implementing low-noise modes results in decreased electrical production from the wind turbine

Wind Speed W10 (m/s)	Noise Attenuation of Low-Noise Modes				
	NRS01	NRS02	NRS03	NRS04	NRS 05
5	0,5	0	0	0	0
6	4,4	3,9	3,2	2,4	1,4
7 – 10	4,8	4,3	3,6	2,8	1,8
dBA					

Table 1. Reduction of sound power level of low-noise mode compared to the normal operation (Source: Wind turbine manufacturer)

In the wind farm under study, low-noise operating modes were implemented, designed using a sound prediction model based on the CONCAWE standard with an absorption value of G=0.5 (developed prior to this study and validated with discrete noise records) to not exceed a sound level of 45 dBA during nighttime. This strategy is implemented exclusively during nighttime, from 5 m/s at measurement point 1 and from 6 m/s at measurement point 2.

4. RESULTS AND DISCUSION

4.1 Noise monitoring

Figure 4 below presents the wind bin analysis derived from the noise campaign data, after filtering and post-processing for the two measurement positions. The central line indicates the arithmetic mean of the sample records, and the upper (red) and lower (green) lines show the result of adding or subtracting the standard deviation value, respectively. In addition, tables with the arithmetic mean of the total noise (expressed as $L_Aeq_{1\ min}$) and the standard deviation for each analyzed wind window are included.

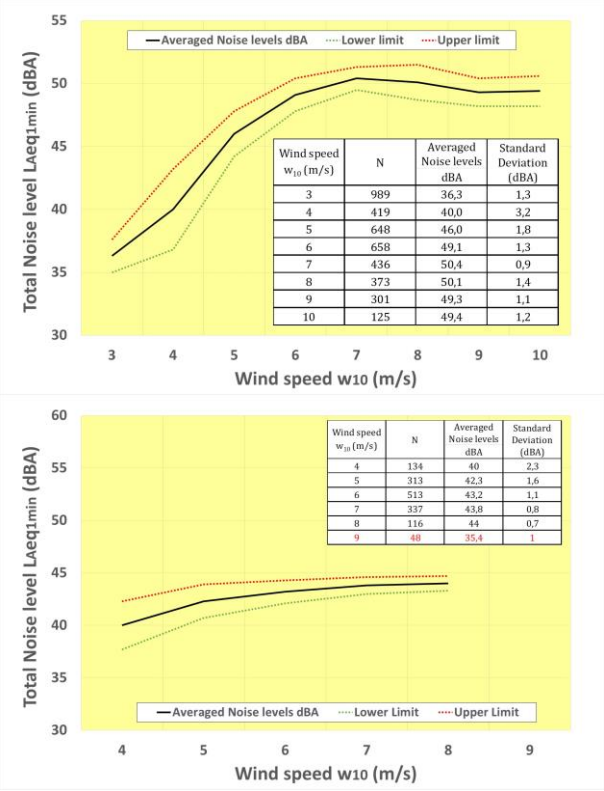
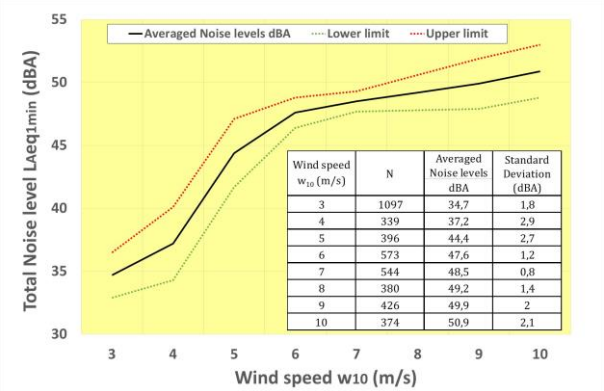


Figure 4. Monitored noise levels at measurement position 1 (Day – up, Night – down)



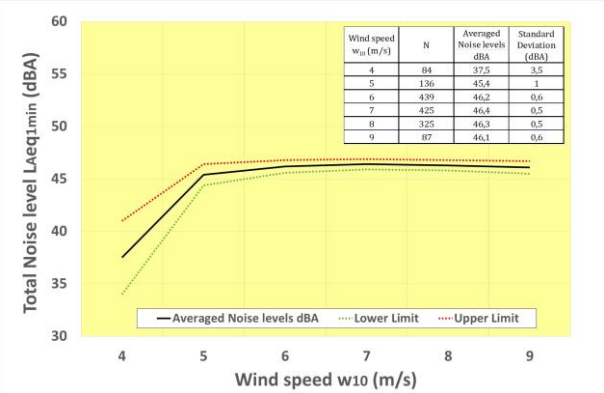


Figure 5. Monitored noise levels at measurement position 2 (Day – up, Night – down)

This analysis provides highly valuable information about the most probable average value, as well as the dispersion of samples within that interval. Generally, the variation of arithmetic averages increases with wind speed during the daytime period. During the nighttime period, the moment when mitigation measures come into operation is more clearly identified to achieve the regulatory compliance of 45 dBA: for measurement point 1 at 5 m/s (42.3 dBA) and for measurement point 2 at 6 m/s (46.2 dBA).

4.2 Noise predictions

Table 2 shows the average deviations (simulated value minus measured noise levels) for each calculation standards considering the different G values considered. The analysis of the results has revealed the following for the case study:

- All calculation standards predict conservative estimations (around 3 dBA) for hard ground, with CONCAWE showing significantly higher deviations of up to 7 dBA.

Table 2. Average deviation of noise calculations according to ground absorption for all studied cases

Calculation Standard	Average Deviation (dBA) (Predicted – Monitored)		
	Absorption G=0	Absorption G=0.5	Absorption G=CLC (0,71)
CONCAWE	6,9	2,7	2,7
NORD2000	2,6	1,9	1,5
ISO9613	2,8	-0,1	-1,2
CNOSSOS	2,7	1,0	0,3

- As the ground absorption value increases, the prediction models reduce deviations from monitored levels, without underestimations except in the case of the ISO 9613 standard (-1,2 dBA deviation). These results are in line with the recommendation not to use values above 0.5 with this standard, confirming the recommendation of the Institute of Acoustics [6] and other references [12].
- CONCAWE and NORD2000 overestimate monitored sound levels for all considered scenarios, although in the case of the NORD2000 standard, the smallest deviations are obtained with porous absorption values (deviations of 1.5 dBA for G values of 0.71).
- For the case study, the ISO9613 and CNOSSOS standards are the most accurate (below 0.5 dBA) for absorption values of 0.5 and 0.7 respectively. In the case of the CNOSSOS method, there are no underestimations in any studied scenarios.
- The results obtained for the ISO9613-2 standard are explained by other authors [22] considering the topography and the distance of the receivers vary. The ISO 9613-2 model with hard terrain has been used in other studies as a conservative model [24] with deviations ranging between 1.5 and 2.7 dBA depending on the degree of terrain irregularity. These data are in line with the deviations found of 2,8 dBA for hard terrain in the case study. The consideration of mixed terrain (0.5 or CLC) results in slight underestimations (0.1 dBA in the case of G=0.5) and -1.2 dBA in the case of absorption based on land uses.

Additionally, it is relevant to identify how the G absorption value affects the range of average deviations found for each calculation model. The CONCAWE model presents the

greatest range of variation (4.2 dBA) followed by the ISO9613 model (4.0 dBA) and CNOSSOS (2.4 dBA). The NORD2000 model is confirmed as the standard with the least variations regarding terrain attenuation (1.1 dBA). It is observed that the CNOSSOS-EU model has a lower tendency to underestimation compared to the ISO9613 model as the acoustic impedance of the terrain increases, in line with previous studies in which CNOSSOS-EU predicts higher levels than ISO 9613 [28]. These results differ from other previous studies for this case study [21], although such deviations might be explained by the different versions of the standards used and their implementation in the simulation software itself.

The NORD2000 model presents overestimations of the monitored level in the range of 1.5-2.6 dBA, being the most accurate model that uses land use covers based on CLC, making this database relevant for absorption evaluation with this standard, in line with Kokowski et al. [29] .

Finally, it is noteworthy that the CONCAWE model obtains predictions with overestimations of monitored levels, especially considering hard terrain (6.9 dBA), and in the case study, it should only be used from a conservative point of view with porous terrain absorption values and/or prior validation through acoustic tests.

The following Figure 6 graphically represent the deviation of each noise prediction model based on the G value.

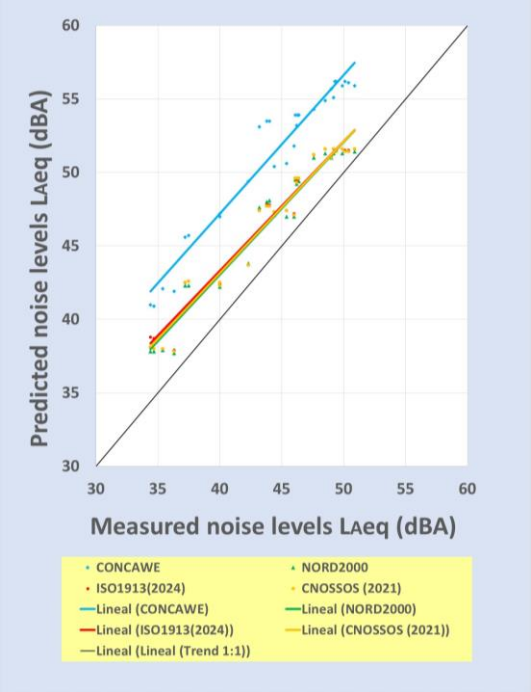


Figure 6. Comparative Analysis Between Monitoring and Sound Prediction for hard ground (G=0)

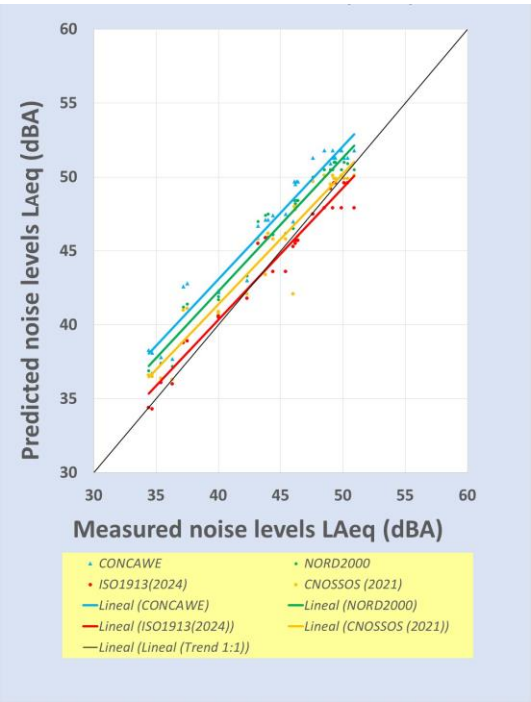


Figure 7. Comparative Analysis Between Monitoring and Sound Prediction for mixed ground (G=0,5)

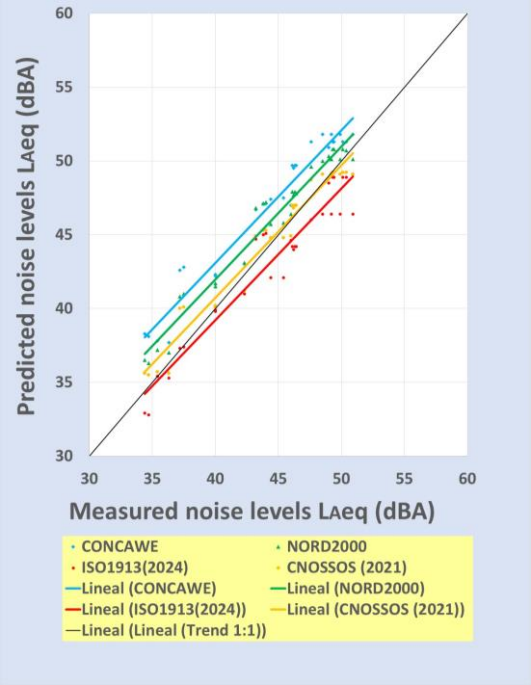


Figure 8. Comparative Analysis Between Monitoring and Sound Prediction for porous ground (G=0,71 - CLC)

4.3 Noise reduction of Mitigation Plan

Figure 9 compares the total noise with and without the implementation of low-noise modes in order to evaluate the effectiveness of the Noise Mitigation Plan strategy.

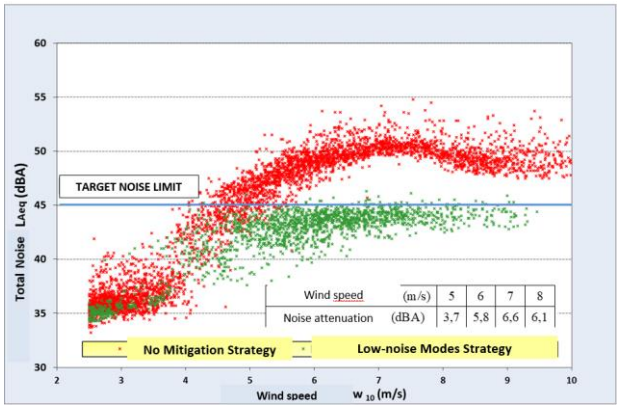


Figure 9. Total noise ($L_A$eq) during the night period and target sound level with the application of low-noise strategies at measurement position 1

The results demonstrate the effectiveness of the proposed corrective measures for reducing sound levels, especially at measurement point 1, where the average reduction is 6.2 dBA for the maximum emission of the wind turbine. At measurement point 2, the average acoustic attenuation is around 2.9 dBA and deviates by about 2 dBA from the expected sound levels. These deviations could be explained by insufficient model validation or could be associated with the implementation of low-noise strategies and the deviations found when they come into operation [30] .

Once the noise attenuation of the low-noise is confirmed, the next step is to consider the impact of the precision of the noise prediction in the design of the mitigation plan, especially during the early permitting phase when all studies are based on simulations. For this purpose, new noise reduction strategies were designed using the most accurate models (ISO9613 for G=0.5 and CNOSSOS for G=0.7) and compared against the original reduction strategy at measurement position 2. The following graph shows the accumulated electrical power as a function of wind speed for the four wind turbines with the highest contribution at that location.

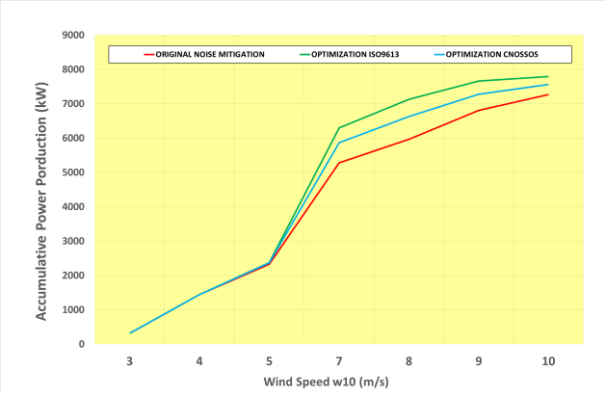


Figure 10. Accumulated electrical power (kW) for the four wind turbines with the highest contribution according to different prediction models

The results show that more accurate prediction models could lead to improvements in the electrical production of these wind turbines by up to 12% in the case of the ISO9613 standard and up to 7% in the case of the CNOSSOS model for these four wind turbines and for that wind direction. The real optimization of electrical production will evidently depend on each case study, including the frequency and distribution of wind speeds and directions, but undoubtedly, the use of more accurate sound

prediction models validated with in-situ monitoring data will potentially allow designing a noise reduction strategy that optimizes the installation's production.

5. CONCLUSIONS

This study has developed a specific system for assessing the acoustic impact of wind farms, using a prediction and acoustic monitoring method, which has been validated in a practical case with complex topography. According to the results obtained for the case under study, the following can be confirmed:

- The prediction model according to CNOSSOS-EU with a ground absorption value G equal to 0,7 and the ISO9613 standard G=0,5 are the calculation standards with the least deviations from the monitored values.
- The results of the monitoring campaigns have shown that the design of low-noise strategies with prediction models is effective for managing the noise generated by wind turbines.
- The use of more accurate and validated prediction models potentially allows for the selective optimization of wind turbine electrical production, ensuring regulatory compliance.

The application of this methodology has allowed to estimate the noise immission level of the wind farm under study with a high degree of precision (average deviation less than 0,5 dBA) and would allow optimizing the electrical production of the four wind turbines with the highest contribution in a range of between 7 and 12%.

In the future, it is recommended to compare the conclusions derived from this study by expanding the validation cases under different variables (topography, distances, height and power of wind turbines, and land uses) as well as verifying the real optimization of production of a wind farm by evaluating long-term averages that consider different wind speeds and directions.

6. REFERENCES

[1] AEE (2024). Anuario 2024. Asociación Empresarial Eólica, 152 pages.

[2] Tonin, R. (2012). «Sources of Wind Turbine Noise and Sound Propagation», Acoust. Aust., 40, 20-27.

[3] Evans, T., Cooper, J., y Lenchine, V. (2013). Wind Turbine Control Methods - National Instruments. From http://www.ni.com/white-paper/8189/en/

[4] Cooper, J., Evans, T., y Najera, L. (2012). «Comparison of compliance results obtained from the various wind farm standards used in Australia», Acoust. Aust., 40, 37-44.

[5] Delaire, C., Griffin, D., y Walsh, D. (2011). «Comparison of predicted wind farm noise emission and measured post- construction noise levels at the Portland Wind Energy Project in Victoria, Australia», Proc. 4 th Int. Meet. Wind Turbine Noise. Rome, Italy, 1-24.

[6] Institute of Acoustics (2013). A Good Practice Guide to the Application of ETSU-R-97 for the Assessment and Rating of Wind Turbine Noise 40 pages.

[7] Chiles, S. (2010). «NZS 6808 :2010 Acoustics – Wind farm noise», New Zeal. Acoust., 23, 20-22.

[8] Dickinson, P. J. (2009). «Nonsense on s tilts», Acoust. Aust. 2009. Adelaide, Aust., Adelaide, 8.

[9] Tickell, C. (2006). «Wind Farm Noise Assessment in Australia and Model Comparison», Can. Acoust., 34, 37-44.

[10] Rosão, V., Leonardo, R., & Santos, P. (2021). Necessary adjustments in ISO 9613-2 and CNOSSOS (industries) methods for noise forecasting in Wind Farms. Proceedings of Euronoise 2021. https://documentacion.sea-acustica.es/publicaciones/Madeira21/ID214.pdf

[11] Ontario Ministry of the Environment (2008). Noise Guidelines for Wind Farms 20 pages.

[12] ISO (2024). International Standard ISO 9613-2:2024 - Acoustics — Attenuation of sound during propagation outdoors — Part 2: Engineering method for the prediction of sound pressure levels outdoors Edition 2, 2024-01

[13] Manning, C. J. (1981). The propagation of noise from petroleum and petrochemical complexes to neighboring communities Technology. Recuperado a partir de http://www.concawe.be/Content/Default.asp?PageID=569

[14] Plovsing, B. (Delta A. and V. (2010). Proposal for Nordtest Method: Nord2000 – Prediction of Outdoor Sound Propagation 1-176 pages. DOI: AV1106/07

[15] European Commission. (2015). Commission Directive (EU) 2015/996 of 19 May 2015 establishing common noise assessment methods according to Directive 2002/49/EC of the European Parliament and of the Council. Official Journal of the European Union, L 168, 1-823 and further modifications.

[16] European Commission Working Group Assessment of Exposure to Noise (2007). Position Paper: Good Practice Guide for Strategic Noise Mapping and the Production of Associated Data on Noise Exposure 129 pages.

[17] R. Nota et al. (2005). HARMONOISE - Engineering method for road traffic and railway noise after validation and fine-tuning.

[18] EAA (2006). Corine Land Cover — Copernicus Land Monitoring Services, from http://land.copernicus.eu/pan-european/corine-land-cover

[19] AMEC Environment & Infrastructure (2012). Provision of Second Round Noise Maps for Northern Ireland. 3D modelling report 89 pages.

[20] Northern Ireland EPA (2009). Guidance Note for Strategic Noise Mapping 126 pages.

[21] Grilo, Álvaro. (2024). Design, Monitoring, and Validation of Noise Mitigation Strategies in Wind Farms. Proceedings of the Ibero-American Congress on Acoustics, Santiago de Chile, 2024.

[22] Cooper, J., y Evans, T. (2013). «Accuracy of noise predictions for wind farms», Proc. 5 th Int. Meet. Wind Turbine Noise. Denver, US., 17.

[23] Öhlund, O., y Larsson, C. (2013). «Sound propagation from wind turbines under various weather conditions», Proc. 5 th Int. Meet. Wind Turbine Noise. Denver, US., 13.

[24] Siponen, D., Napoli, C. Di, Eurasto, R., Uosukainen, S., y Nykänen, H. (2013). «The new good-practice-guide to help assessment of wind turbine noise in Finland», Proc. 5 th Int. Meet. Wind Turbine Noise. Denver, US., 10.

[25] Teague, P., Leonard, A., Engineers, V., y Town, K. (2011). «Prediction, Validation, Assessment & Compliance of Wind Farm Noise in Australia», Proc. 4 th Int. Meet. Wind Turbine Noise. Rome, Italy, 19.

[26] Søndergaard, B. (2012). «Noise from Wind Turbines Measurement and prediction including low frequency noise», Jt. Balt. Acoust. Meet., BNAM2012, Odense, Denmark, 8.

[27] Evans, T., y Cooper, J. (2012). «Comparison of predicted and measured wind farm noise levels and implications for assessments of new wind farms», Acoust. Aust., 40, 28-36.

[28] King, E. A., & Ní Bhraonáin, L. (2022). Evaluating the potential impact of noise annoyance from Offshore Wind Turbines in Ireland. Proceedings of the 10th Convention of the European Acoustics Association Forum Acusticum 2023, 3101–3106. DOI: 10.61782/fa.2023.0634

[29] Kokowski, P., Libiszewski, P., Kaczmarek, T., Gałuszka, M., Pękala, P., & Gjaestland, T. (2024). On-line wind farm noise control. Proceedings of the 10th Convention of the European Acoustics Association Forum Acusticum 2023. DOI: 10.61782/fa.2023.1292

[30] Evans, T., y Cooper, J. (2011). «Comparison of predicted and measured wind farm noise levels and implications for assessments of new wind farms», Acoust. Aust. 2011, Gold Coast, Aust., 1-8.

DOI: 10.61782/fa.2025.0606

FORUM ACUSTICUM EURONOISE 2025

NOISE AND VIBRATION MEASUREMENTS EMITTED BY WIND TOWERS

Gino Iannace [1*] **Luca Fredianelli** [2] **Andac Akbaba** [1]

Giuseppe Ciaburro [3] **Francesco Artuso** [4]

[1] Department of Architecture and Industrial Design, University of Campania L. Vanvitelli, Italy
[2] Institute for Chemical-Physical Processes, National Council of Research, Pisa, Italy
[3] Faculty of Engineering and Informatics, Department of Engineering, Pegaso University, Naples, Italy
[4] University of Pisa, Physics Department, Pisa, Italy

ABSTRACT

Wind turbines are a valid alternative to produce electricity in place of hydrocarbons, in this way it is possible to achieve the objectives set by the energy transition and limit the effects of greenhouse gas emissions. One of the problems that limit the spread of wind turbines are the effects of the impact on the environment. The problems identified are those of flicker shadow, noise and visual impact. The biggest problem is that due to noise. In fact, people who live near wind turbines complain about the negative effects of noise. This paper reports noise measurements carried out in proximity to wind turbines in different wind speed conditions.

Keywords: *wind turbines, acoustic measurements, wind speed, noise, annoyance.*

1. INTRODUCTION

Wind energy contributes significantly to reducing the use of fossil fuels in electricity production and is a valid contribution to the reduction of greenhouse gas emissions. Today, wind energy is spreading to achieve the goals of the energy transition. The first windmills were built in the Middle East around 600 AD and later spread to the countries of Northern Europe. The first wind towers for the transformation of wind energy into electricity were built in the United States in the 1950s and then spread in the 1970s, following the oil crisis. The areas with the greatest presence of wind farms are Asia (China and India), Northern Europe and the United States. In Italy the first wind towers were installed in 1990, but only from 1996 onwards has there been a significant number of plants connected to the electricity grid. In fact, in Italy in 2001 there were only 81 wind farms installed, with a total power of 664 MW (3% of the electricity produced from renewable sources). In 2015 there were 2,734 plants, with a power of approximately 10,000 MW (18% of the electricity produced from renewable sources). In Italy, due to the morphology, the areas with the greatest presence of towers are those in the south, where the average wind speed during the year exceeds 5 m/s. Many wind farms have been built near homes, creating problems for people living in those areas. Compared to other sources of noise (for example, airplanes, railways, etc.), the degree of annoyance of the noise emitted by wind turbines is the one that generates the greatest disturbance in the population. The noise due to the operation of wind turbines is potentially capable of causing sleep disturbances and other pathologies. The reason for these disturbances is due to the particular noise emitted that modulates over time, the type of noise concentrated in the medium - low frequencies and the fact that the towers are over 100 meters high, and the sight of these objects is not accepted by the populations living near the wind farms.

[*] ***Corresponding author***: gino.iannace@unicampania.it.
Copyright: *©2025 First author et al. This is an open-access article distributed under the terms of the Creative Commons Attribution 3.0 Unported License, which permits unrestricted use, distribution, and reproduction in any medium, provided the original author and source are credited.*

Usually, the noise emitted by a wind turbine is broadband and concentrated in the frequency range between 300 Hz and 2,000 Hz, in the range in which the human ear is most sensitive and therefore the individual feels greater discomfort [1-2]. The types of noise produced are aerodynamic noise due to the rotation of the blades and mechanical noise inside the nacelle, due to the electromechanical components (generator, gear multiplier, cooling systems and other components) [3-4]. Aerodynamic noise is a very complex phenomenon and is due to the turbulence of the air generated by the rotation of the blades and the compression effect of the air on the tubular tower. Another possible discomfort that can be generated is that of the "flicker shadow", or the intermittent effect of the shadow, which occurs when the wind tower is placed between the sun and the observer. The effect of the intermittence of the shadow caused by the rotation of the blades is visible to the observer for over 300 meters from the tower. This phenomenon does not occur when the blades do not rotate. Furthermore, one of the problems that arises in the design phase of wind farms is the theoretical estimate of the acoustic impact generated by the operation of the towers [5-8]. The estimate of the noise produced is performed in accordance with the ISO 9613:2-20024 standard, but in the verification phase the numerical model underestimates the measured value of the sound pressure level [9]. Wind turbines, even if they are complex systems, are considered point sources of sound, since the source-receiver distance is considered sufficiently large compared to the dimensions of the towers. For the determination of environmental noise levels, the ISO 9613-2:2024 standard provides a theoretical method to evaluate the sound attenuation, with the source-receiver distance, in propagation in open-air. The standard provides for the calculation of the equivalent noise level “filtered A”, assuming meteorological conditions favorable to the propagation of sound, through the application of the following simplified relationship:

$$Lp = Lw - 20\,Log\,(d) - 11$$

Where d, is the distance in meters between the sound source (tower) and the receiver as the distance increases the sound pressure level Lp decreases. Furthermore, over time the rotating parts of the towers wear out with a consequent increase in the sound level emitted compared to the initial conditions. This condition has not yet been fully examined, but the effects of mechanical wear and the consequent increase in noise are a problem that needs to be analyzed.

2. ACOUSTIC MEASUREMENTS

The acoustic measurements were carried out with a sound level meter configured to acquire the equivalent sound level of the linear sound, A-weighted, of the statistical levels with a Fast constant time. The sound level meter was installed at a height of 1.70 m from the ground and more than 1.0 m from any vertical surfaces [10]. The wind turbines subject to acoustic measurements have a nominal power of 3 and 4 MW, with a total tower height equal to 100 m and a blade length equal to 60 m. The acoustic measurements were taken with the wind turbines are on (ambiental noise) and off (background noise), to evaluate, with the same wind speed, the noise contribution caused by the operating wind towers. in the condition in which the sound levels were acquired inside an house with open windows. The measured sound levels are reported as a function of time and a table indicating the value of the equivalent sound level LeqA in dBA, the statical sound level L95 in dBA and the wind speed in the condition in which the wind farms are in operation or are turned off. For wind speeds of about 9 m/s, when the towers are in operation compared to when they are turned off it is possible to notice a difference in the measured sound levels. This difference denotes that for this wind speed the towers in operation generate annoyance in the populations living in the vicinity of the wind farms. Table 1 shows the acoustic measurements when the wind speed is below 9 m/s. While Figure 1 shows the time history of the measured sound level (dBA) inside home when the wind speed is below 9 m/s.

Table 1. Acoustic measurements when the wind speed is below 9 m/s

Activities	Leq (dBA)	L95 (dBA)	Average wind speed (m/s)
Towers on Measurements 1	38.5	37.0	9.0
Towers off Measurements 2	25.0	21.5	9.0
Towers on Measurements 3	37.0	35.5	8.8

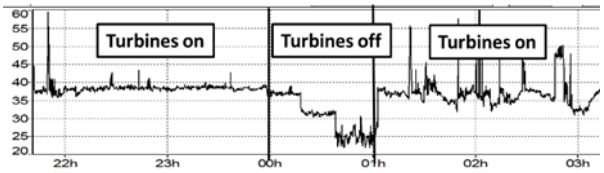


Figure 1. Time history of the measured equivalent sound level (dBA) inside home when the wind speed is below 9 m/s.

Table 2 and Figure 2 instead show the sound levels when the wind speed exceeds 12 m/s. It is noted that for the tower in operation or when it is turned off no differences in the sound level are detected. For these wind speeds the towers in operation do not generate annoyance. The wind's noise covers the noise emitted by the towers.

Table 2 Acoustic measurements when the wind speed between 12 m/s and 25 m/s.

Activities	LeqA dBA	L95 dBA	Average wind speed, m/s
Towers on measurement 1	40.5	37.0	12.0
Towers off measurement 2	40.5	36.0	15.0
Towers on measurement 3	39.0	36.5	14.2
Towers on measurement 4	45.0	37.5	14.4
Towers on measurement 5	51.0	47.0	21.3
Towers off measurement 6	54.0	47.5	23.1
Towers off measurement 7	52.5	48.5	24.4

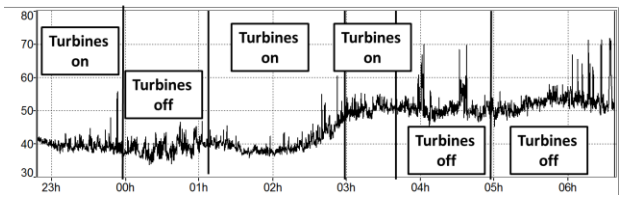


Figure 2. Time history of the measured equivalent sound level (dBA) inside home when wind speed is in the range between 12 m/s and 25 m/s.

The following are the results of measurements of noise generated by wind towers and the relative wind speed near the microphone, carried out outside a house. The distance from tower to home is 200 meters; the wind tower is 70 m height; the nominal power is 200 kW. The measurements are performed with a sound level meter and the equivalent sound levels have been grouped in function of the wind speed range (from 1 m/s to 5 m/s). The values of the ambient noise level (active source) are shown in solid line, while the background noise (source off) are shown in dashed line. Figure 3 shows the sound trends in the daytime period; Figure 4 shows the sound trends in the night period. The wind speed varies between 1 m/s to 5 m/s. For wind speed values above 5 m/s the measured sound level values are meaningless.

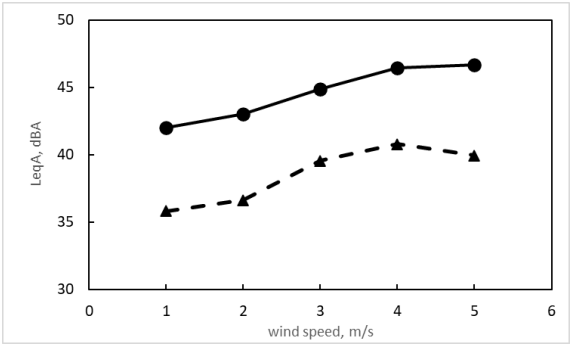


Figure 3. Sound level trends in the daytime period.

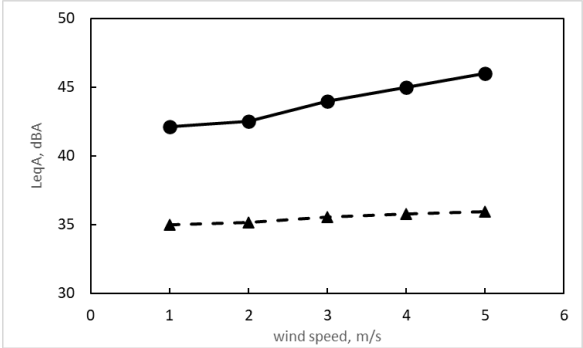


Figure 4. Sound level trends in the night period

The background noise during the day is higher than the night one due to the presence of human activities. While the environmental noise (tower in operation) increased with the increase of the wind speed as expected. It should be noted that the noise levels when the source is active do not change between the night and day periods. The noise of the wind tower is a stationary sound source, for each interval of the wind speed considered.

3. CONCLUSIONS

This paper reports the results of acoustic measurements performed near wind towers. The effects of wind on phonometric measurements have been analyzed. For measurements inside houses, it has been noted that the effects of noise disturbance are due to wind speeds up to 9 m/s. For higher wind speeds, the wind noise covers the noise emitted by the wind towers. Furthermore, the values of acoustic measurements performed outside a house are reported for different wind speeds both when the wind tower is in operation and when it is off. It is possible to note that as the wind speed increases, the effect of the wind tower emission increases.

4. ACKNOWLEDGMENTS

This research was financially supported by the European Union – Next Generation EU, the Ministry of University and Research (MUR) as part of the PRIN 2022 project 20223LMSZN, COMBINE "Sustainable condition monitoring of wind turbines using acoustic signals and machine learning techniques" and as part of the PON 2014-2020 "Research and Innovation" resources – Green/Innovation Action – DM MUR 1061/2022.

5. REFERENCES

[1] D. Bowdler, L. Leventhall. "Wind turbine noise". Multi-science Publishing Co. Ltd., 2011.

[2] G. Iannace. "Effects of noise from wind turbines inside home". Wind Engineering, 40 (1), 25-30, 2016.

[3] R. Makarewicz "Is a wind turbine a point source? (L)". Journal of Acoustical Society of America, 129 (2), 580-581, 2011

[4] G. Iannace, A. Trematerra and I. Lombardi. "Effects of nightlife noise in a city center". Noise Mapping, 8(1), 228-235, 2021.

[5] A. Trematerra. "Evaluation of noise when a disturbing sound source cannot be off". Noise & Vibration Worldwide 47, 2016, doi 10.1177/0957456516683012

[6] G. Iannace, A. Trematerra, U. Berardi. "Assessment of the noise produced by wind farms with the acoustically analogous techniques without stopping the noise source". Wind Engineering, 43(2), 201–209, 2019.

[7] S. Sukaj, G. Iannace, G. Ciaburro, F. Iannace. "Wind Turbines Noise: Predictions and Measurements". Romanian Journal of Acoustics and Vibration, 18(2), 69–75. 2022.

[8] G. Iannace, U. Berardi, G. Ciaburro, D. D'Orazio, A. Trematerra. "Mini-wind turbine noise measured inside near-by houses" Canadian Acoustics - Acoustique Canadienne, 48(3), 18–2, 2020.

[9] ISO 9613-2:2024, Acoustics - Attenuation of sound during propagation outdoors - Part 2: General method of calculation.

[10] G. Iannace, U. Berardi, G. Ciaburro, A. Trematerra "Wind turbines noise measurements inside homes". In Proceedings of Internoise Conference, Madrid 16-19 June 2019

DOI: 10.61782/fa.2025.0971

FORUM ACUSTICUM EURONOISE 2025

WIND TURBINE DIRECTIONAL TONALITY

Mikel Amatriain[1*] **Miguel Arana**[2]
[1] RWE Renewables Iberia, Zaragoza, Spain
[2] Sciences Department, Public University of Navarre, Pamplona, Spain

ABSTRACT

Knowledge of the emission patterns (directivity) of modern wind turbines improves the prediction of noise levels at receptors over medium and long distance. Tonality is usually attributed as a penalty or character correction factor in most regulations. In some of them, the penalty, up to 6 dB, is equivalent to quadrupling the power of the wind turbine. To predict the impact caused to residents near wind farms, it is desirable to know precisely both the directivity of the wind turbines and the potential tonality.

The present work shows the results of the tonality around a wind turbine and not only for the downwind conditions of the IEC standard. It was carried out for different wind speeds. The aim of this work is to contribute to the improvement of the prediction of wind farm nuisance.

Keywords: *Directivity, Tonality, Wind, Turbine*

1. INTRODUCTION

Part 11 of the IEC 61400 standard [1] outlines a structured methodology designed to ensure consistent and precise measurement and analysis of acoustic emissions from wind turbines. This section of the standard offers procedures for characterizing the noise emissions of a wind turbine by considering it as a point source situated at the rotor center.
Standard measurements are typically conducted at a designated reference location to determine the turbine's acoustic profile. However, to gain further insight into the directional tonality of emissions, supplementary measurement positions can be used. These additional measurement locations, while not commonly applied in traditional IEC testing protocols, provide valuable data concerning the directional characteristics of wind turbine noise.
By incorporating a greater number of measurement positions, this paper seeks to explore the tonal directivity of a wind turbine, offering a comprehensive analysis that extends beyond standard practices.

2. METHODOLOGY

The reference position for the measurements is specified as the downwind location, situated at a distance equal to the hub height plus rotor radius from the rotor center. As optional measurement locations, positions at upwind and downwind angles of ±60° are also considered at the same distance.

In both the downwind and upwind positions, similar sound pressure levels are anticipated, whereas greater variations are expected at the crosswind positions, as suggested by aerodynamic sound theories and empirical studies [2-5]. The directionality of the predominant aerodynamic sound source is primarily attributed to trailing edge noise; however, variations in mechanical and electrical noise can arise depending on the wind turbine's cooling system configuration or whether the power electronics are housed inside or outside the tower. Some setups may also include additional cooling systems. To evaluate the impact of these components, supplementary measurement locations may be necessary [6].

This setup aims to provide a comprehensive array of measurement points to capture a detailed acoustic profile of the wind turbine from multiple directional perspectives. By

[*] ***Corresponding author***: *Mikel.Amatriain@rwe.com*
Copyright: *©2025 First author et al. This is an open-access article distributed under the terms of the Creative Commons Attribution 3.0 Unported License, which permits unrestricted use, distribution, and reproduction in any medium, provided the original author and source are credited.*

using these positions, both aerodynamic and mechanical noise characteristics can be thoroughly analyzed.

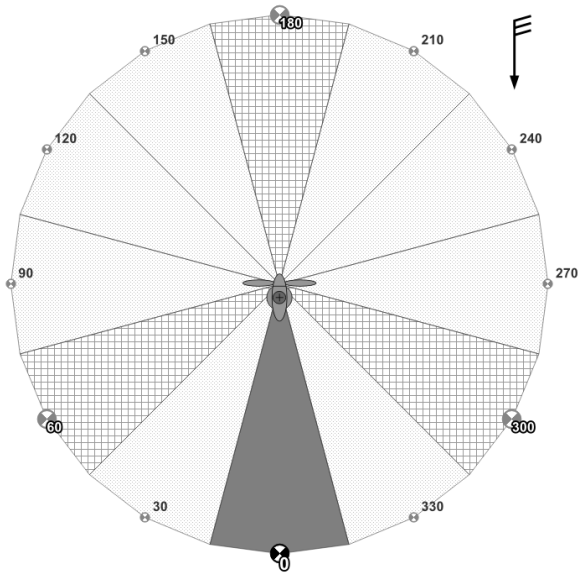


Figure 1. Plan Standard pattern for microphone measurement positions (plan view). Measurement positions for reference (0º), optional locations (60º, 180º and 300º) and complementary locations in 30º sectors.

3. TONAL AUDIBILITY

The IEC 61400-11 standard provides clear definitions and descriptions for terms related to the tonality and tonal audibility of the noise generated by wind turbines. Specifically, Section 9.5 of the standard outlines the procedure for assessing tonality across varying wind speeds through narrowband analysis.

According to this procedure, the tonality should be represented for each wind speed bin, using increments of 0.5 m/s. This approach ensures a detailed examination of tonal characteristics over a spectrum of operating conditions, thereby providing a comprehensive understanding of the noise emissions from wind turbines.

3.1 Fixed positions with board positioned on the ground

Measurements are conducted using a microphone positioned on a measurement board placed at ground level. This setup is designed to reduce wind noise impacting the microphone and minimize the influence of varying ground types on acoustic data. All measurements are synchronized with data from both the turbine and mast anemometers to ensure accurate correlation. The reference wind speed for analysis is derived from the turbine's electrical power output.

For each wind speed bin, ten measurements were selected for analysis. In this study, a sampling frequency of 25,600 samples per second was employed, resulting in data matrices with dimensions of 256,000 x 10 cells for each set of conditions. Although the wind speeds varied from 6 to 13 m/s, the results presented will focus specifically on the wind speed bins of 6 and 11 m/s.

The algorithm outlined by the standard is straightforward, though it allows flexibility in narrowband spectral resolution, accepting values between 1 and 2 Hz. The results obtained using both resolutions are practically identical [7]. In the analysis, ten measurement records each lasting 10 seconds are utilized for a given wind speed. The overall tonal audibility is confirmed if at least six out of ten narrowband spectra exhibit an identified tone originating from the same source. Tones identified in different spectra are considered to have the same origin if they fall within an interval of ±25% of the critical band centered at their frequency. Tones of the same origin are treated and reported as one tone.

Tables 1 to 19 detail the methodology employed by the implemented program in Matlab [8] for tone detection and audibility analysis. Utilizing the Fast Fourier Transform (FFT) of the ten input signals, the program computes sound levels, energy, and bandwidth for resolutions of 1 and 2 Hz. It identifies local maxima of the signals but selects only those whose levels surpass the critical band average by more than 6 dB (excluding the maximum line and its two adjacent ones) as potential tones. The *findTones()* function then locates these tones.

The signal lines are categorized as 'masking,' 'tones,' or 'neither' using the L_{70} and L_{pn} criteria (sound pressure level of masking noise within a critical band). The process concludes with the determination of tonality (the difference between the tone level and the masking noise level) and audibility, which includes a frequency-dependent correction to account for the human ear's response to tones at varying frequencies.

Table 1. Tone identification for 60° position and wind speed of 11 m/s with 1 Hz resolution.

f_c,[1] Hz	Identification of spectra with a tone at this line									
112	0	0	1	1	0	0	0	0	0	0
113	0	1	0	0	1	1	1	1	0	0
115	1	0	0	0	0	0	0	0	1	0
116	0	0	0	0	0	0	0	0	0	1
223	0	0	0	1	0	0	0	0	0	0
224	0	0	1	0	0	0	0	0	0	0
225	0	1	0	0	1	0	0	0	0	0
227	0	0	0	0	0	1	1	0	0	0
229	0	0	0	0	0	0	0	0	1	0
230	1	0	0	0	0	0	0	1	0	0
231	0	0	0	0	0	0	0	0	0	1

Table 2. Tone identification for 60° position and wind speed of 11 m/s with 2 Hz resolution.

f_c, Hz	Identification of spectra with a tone at this line									
112	0	0	1	1	0	0	0	0	0	0
114	0	1	0	0	1	1	1	1	0	0
116	1	0	0	0	0	0	0	0	1	1
224	0	0	1	1	0	0	0	0	0	0
226	0	1	0	0	1	0	0	0	0	0
228	0	0	0	0	0	1	1	0	0	0
230	1	0	0	0	0	0	0	1	1	0
232	0	0	0	0	0	0	0	0	0	1

Only tones that are present in at least six of the ten analyzed spectra and have an average audibility, $\Delta L_{a,j,k}$,[2] of equal to or greater than -3 dB are presented. A tone is considered audible if its tonal audibility exceeds 0 dB.

Table 3. Average tone and average audibility for each register, tone at 113 Hz, 1 Hz resolution.

f_c Hz	Aver. Tonal (dB) $\Delta L_{tn,j,11}$	Aver Audib. (dB) $\Delta L_{a,j,11}$	N in 10	fc in 10	Tone Y/N
112	0,44	2,45	10	2	Y
113	**0,44**	**2,45**	**10**	**5**	**Y**
115	0,44	2,45	10	2	Y
116	0,44	2,45	10	1	Y

[1] f_c centre frequency of critical band

[2] $\Delta L_{a,k}$ difference between the tonality and the audibility criterion in each wind speed bin, where k is the centre value of the wind speed bin

Table 4. Average tone and average audibility for each register, tone at 227 Hz, 1 Hz resolution.

f_c, Hz	Aver. Tonal (dB) $\Delta L_{tn,j,11}$	Aver Audib. (dB) $\Delta L_{a,j,11}$	N in 10	f_c in 10	Tone Y/N
223	-3,53	-1,47	10	1	Y
224	-3,53	-1,47	10	1	Y
225	-3,53	-1,47	10	2	Y
227	**-3,53**	**-1,47**	**10**	**2**	**Y**
229	-3,53	-1,47	10	1	Y
230	-3,53	-1,47	10	2	Y
231	-3,53	-1,47	10	1	Y

Table 5. Average tone and average audibility for each register, tone at f_c = 114 Hz, 2 Hz resolution.

f_c, Hz	Aver. Tonal (dB) $\Delta L_{tn,11}$	Aver Audib. (dB) $\Delta L_{a,11}$	N in 10	f_c in 10	Tone Y/N
112	1,62	3,63	10	2	Y
114	**1,62**	**3,63**	**10**	**5**	**Y**
116	1,62	3,63	10	3	Y

Table 6. Average tone and average audibility for each register, tone at 228 Hz, 2 Hz resolution.

f_c, Hz	Aver. Tonal (dB) $\Delta L_{tn,j,11}$	Aver Audib. (dB) $\Delta L_{a,j,11}$	N in 10	f_c in 10	Tone Y/N
224	-3,02	-0,97	10	2	Y
226	-3,02	-0,97	10	2	Y
228	**-3,02**	**-0,97**	**10**	**2**	**Y**
230	-3,02	-0,97	10	3	Y
232	-3,02	-0,97	10	1	Y

At this wind speed, 11 m/s, only one audible tone is identified at a frequency of 113 Hz (or 114 Hz when using a 2 Hz resolution). Reporting these frequencies is justified, as they correspond to the maximum number of records with a tone present at that frequency, totaling five for both scenarios.

Furthermore, a secondary tonal presence at 227 Hz aligns with the frequency of 2 * f_c, suggesting a mechanical origin, likely related to the slow axis of the nacelle.

Table 7. Tone identification for 300° position and wind speed of 11 m/s with 1 Hz resolution.

f_c, Hz	Identification of spectra with a tone at this line									
110	0	0	0	0	0	0	0	0	0	1
111	0	0	0	0	0	0	0	1	1	0
115	1	0	0	1	0	1	1	0	0	0
116	0	1	0	0	1	0	0	0	0	0
117	0	0	1	0	0	0	0	0	0	0
5179	0	0	0	0	0	0	0	1	0	0
5181	0	0	0	0	0	0	0	0	1	0
5196	0	0	0	0	0	1	0	0	0	0
5216	0	0	0	1	0	0	0	0	0	0
5229	0	0	0	0	0	0	1	0	0	0
5404	0	0	0	0	0	0	0	0	0	1

Table 8. Tone identification for 300° position and wind speed of 11 m/s with 2 Hz resolution.

f_c, Hz	Identification of spectra with a tone at this line									
110	0	0	0	0	0	0	0	0	0	1
112	0	0	0	0	0	0	0	1	1	0
114	1	0	0	0	0	0	0	0	0	0
116	0	1	0	1	1	1	1	0	0	0
118	0	0	1	0	0	0	0	0	0	0
5180	0	0	0	0	0	0	0	1	0	0
5182	0	0	0	0	0	0	0	0	1	0
5196	0	0	0	0	0	1	0	0	0	0
5216	0	0	0	1	0	0	0	0	0	0
5230	0	0	0	0	0	0	1	0	0	0
5404	0	0	0	0	0	0	0	0	0	1

Table 9. Average tone and average audibility for each register, tone at 115 Hz, 1 Hz resolution.

f_c, Hz	Aver. Tonal (dB) $\Delta L_{tn,j,11}$	Aver Audib. (dB) $\Delta L_{a,j,11}$	N in 10	f_c in 10	Tone Y/N
110	2,75	4,76	10	1	Y
111	2,75	4,76	10	2	Y
115	**2,75**	**4,76**	**10**	**4**	**Y**
116	2,75	4,76	10	2	Y
117	2,75	4,76	10	1	Y

Table 10. Average tone and average audibility for each register, tone can`t be clearly locate, 1 Hz resolution.

f_c, Hz	Aver. Tonal (dB) $\Delta L_{tn,j,11}$	Aver Audib. (dB) $\Delta L_{a,j,11}$	N in 10	f_c in 10	Tone Y/N
5179	-3,53	-1,47	6	1	Y
5181	-3,53	-1,47	6	1	Y
5196	-3,53	-1,47	6	1	Y
5216	-3,53	-1,47	6	1	Y
5229	-3,53	-1,47	6	1	Y
5404	-3,53	-1,47	7	1	Y

Table 11. Average tone and average audibility for each register, tone at 113 Hz, 2 Hz resolution.

f_c, Hz	Aver. Tonal (dB) $\Delta L_{tn,11}$	Aver Audib. (dB) $\Delta L_{a,11}$	N in 10	f_c in 10	Tone Y/N
110	2,69	4,70	10	1	Y
112	2,69	4,70	10	2	Y
114	2,69	4,70	10	1	Y
116	**2,69**	**4,70**	**10**	**5**	**Y**
118	2,69	4,70	10	1	Y

Table 12. Average tone and average audibility for each register, tone at 228 Hz, 2 Hz resolution.

f_c, Hz	Aver. Tonal (dB) $\Delta L_{tn,j,11}$	Aver Audib. (dB) $\Delta L_{a,j,11}$	N in 10	f_c in 10	Tone Y/N
5180	-4,78	-0,24	6	1	Y
5182	-4,78	-0,24	6	1	Y
5196	-4,78	-0,24	6	1	Y
5216	-4,78	-0,24	7	1	Y
5230	-4,78	-0,24	7	1	Y
5404	-4,78	-0,24	7	1	Y

The tonal noise identified in the high-frequency range is attributed to background noise from bird songs and is not considered a tonal component originating from the wind turbine. To accurately assess this background noise, narrowband spectra should be utilized to isolate and analyze these frequencies.

Table 13. Tone identification for 60° position and wind speed of 6 m/s with 2 Hz resolution.

f_c, Hz	Identification of spectra with a tone at this line									
220	0	0	1	1	1	0	0	0	0	0
222	0	0	0	0	0	1	0	0	0	0
224	0	1	0	0	0		1	0	0	0
226	1	0	0	0	0	0	0	0	0	0
242	0	0	0	0	0	0	0	0	1	0
246	0	0	0	0	0	0	0	0	0	1

Two different critical bands are identified very close one to each other. One with centre frequency at 220 and the other at around 250 Hz.

Table 14. Average tone and average audibility for each register, tone at 220 Hz, 2 Hz resolution.

f_c, Hz	Aver. Tonal (dB) $\Delta L_{tn,j,6}$	Aver Audib. (dB) $\Delta L_{a,j,6}$	N in 10	f_c in 10	Tone Y/N
220	0,34	2,4	9	3	Y
222	0,34	2,4	9	1	Y
224	0,34	2,4	9	2	Y
226	0,34	2,4	9	1	Y

For low wind speed only at 60 degree position two critical band are obtained, at 220 Hz centre frequency.

Table 15. Average tone and average audibility for each register, tone at 242-246 Hz, 2 Hz resolution.

f_c, Hz	Aver. Tonal (dB) $\Delta L_{tn,j,6}$	Aver Audib. (dB) $\Delta L_{a,j,6}$	N in 10	f_c in 10	Tone Y/N
242	0,31	2,36	10	1	Y
246	0,31	2,36	10	1	Y

The highest tone audibility is found in the range of 220 Hz and 246 Hz, with $\Delta L_{a,6}$ ==2.4 dB. This results is lower than the maximum tone at 11 m/s $L_{a,11}$=3.63 dB at f_c=114 Hz.

Table 16. Tone identification for 300° position and wind speed of 6 m/s with 2 Hz resolution.

f_c, Hz	Identification of spectra with a tone at this line									
140	0	0	0	0	0	1	1	1	0	0
144	0	0	0	0	1	0	0	0	0	0
154	0	0	1	0	0	0	0	0	0	0
164	1	0	0	0	0	0	0	0	0	0
224	0	0	0	1	0	0	0	0	0	0
228	0	0	0	0	0	0	0	0	0	0
232	0	0	1	0	0	0	0	0	0	1
250	1	1	0	0	0	1	1	1	1	0

In the case of 300º position three different critical bands are identified.

Table 17. Average tone and average audibility for each register, tone around 150 Hz, 2 Hz resolution.

f_c, Hz	Aver. Tonal (dB) $\Delta L_{tn,j,6}$	Aver Audib. (dB) $\Delta L_{a,j,6}$	N in 10	f_c in 10	Tone Y/N
140	-0,94	1,08	6	3	Y
144	-0,94	1,08	6	1	Y
154	-0,94	1,08	6	1	Y
164	-0,94	1,08	6	1	Y

Table 18. Average tone and average audibility for each register, tone around 228 Hz, 2 Hz resolution.

f_c, Hz	Aver. Tonal (dB) $\Delta L_{tn,j,6}$	Aver Audib. (dB) $\Delta L_{a,j,6}$	N in 10	f_c in 10	Tone Y/N
224	2,21	4,28	10	1	Y
228	2,21	4,28	10	1	Y
232	2,21	4,28	10	1	Y

Table 19. Average tone and average audibility for each register, tone around 250 Hz, 2 Hz resolution.

f_c, Hz	Aver. Tonal (dB) $\Delta L_{tn,j,6}$	Aver Audib. (dB) $\Delta L_{a,j,6}$	N in 10	f_c in 10	Tone Y/N
250	**2,29**	**4,36**	**9**	**6**	**Y**

The highest average audibility for low wind, 6 m/s at hub height, is found at f_c=250 Hz with $\Delta L_{a,6}$ =4.36 dB, similar to the audibility of $\Delta L_{a,11}$=4.76 dB resulted at 11 m/s for the same position but at different central frequency f_c=114 Hz.

3.2 Short time complementary positions

Short-time measurements were conducted around the wind turbine. All measurements were performed using a tripod set at a height of 1.5 meters. Events not associated with the wind turbine source under investigation are excluded from the analysis.

Measurements are carried out with an emphasis on minimizing wind noise at the microphone. A temporary mast-mounted anemometer serves as a reference to ensure accuracy, with measurements discarded if wind speeds exceed 5 m/s at 3 meters above ground level. Consistent with the IEC standard, the reference wind speed is derived from the turbine's electrical power output.

In parallel with the IEC methodology test, additional logs were obtained using a moving tripod, maintaining a distance of hub height plus rotor radius. The testing was extended up to the 180-degree position (upwind) in 30-degree increments relative to the yaw orientation, ranging from 0 degrees (downwind) to 180 degrees (upwind). These measurements incorporated A-weighted spectra, including FFT analysis with a sound level meter integrated at a 1.465 Hz resolution, alongside third-octave band recordings. These positions were synchronized with recordings from the fixed ground-mounted board and turbine data to ensure comprehensive analysis.

The reference condition for measurements is established during middle-range turbine operation, which corresponds to 30% to 60% of the rated power. This operational range represents wind speeds at hub height between 6 and 11 m/s, effectively minimizing background noise levels and wind-induced distortion. All measurements are conducted under conditions where wind speeds remain below 5 m/s, as monitored by a temporary meteorological pole synchronized with the system.

Short-time complementary measurement positions focus on the frequency range of 20 Hz to 1500 Hz. These efforts aim to minimize background noise effects while identifying frequencies detectable from standard positions.

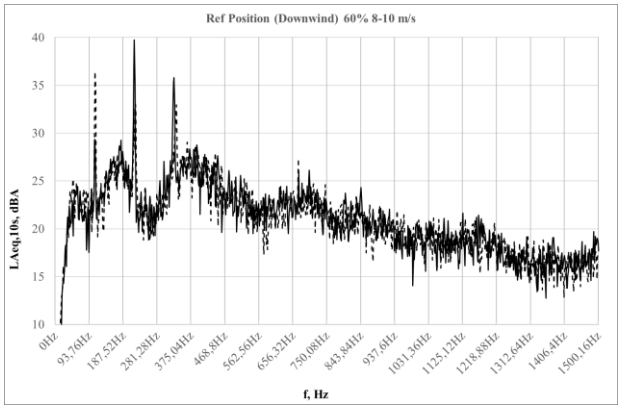


Figure 2. A-weighted FFT-spectra for reference position at 60% of capacity.

The FFT-spectra analysis reveals similar tonal components to those identified in the board-positioned measurements, specifically at frequencies of 110 Hz, 218 Hz, and 328 Hz. These complementary positions are strategically employed to corroborate findings from automated audio extraction analysis, ensuring consistency and accuracy in the detection and characterization of tonal components.

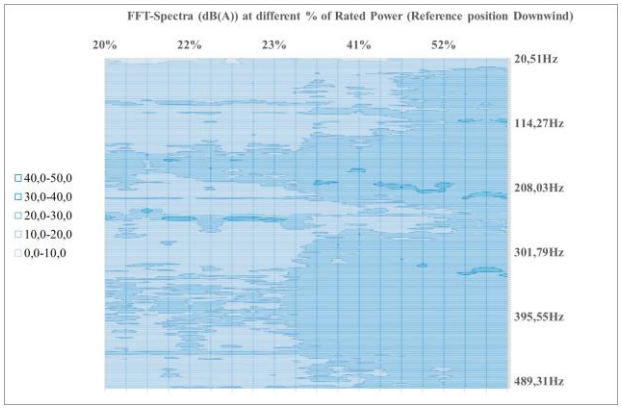


Figure 3. FFT-spectra change at different operational conditions 20 to 60% of active power output at downwind reference position.

Selected spectra from the same location are grouped and organized according to output power and derived wind speed. In Figure 4, the tones identified per the IEC standard exhibit a frequency shift from f_c = 83 Hz to 114 Hz, emerging at higher power ratings. Additionally, this shift reveals three harmonics at frequencies of 2 * f_c and 3 * f_c.

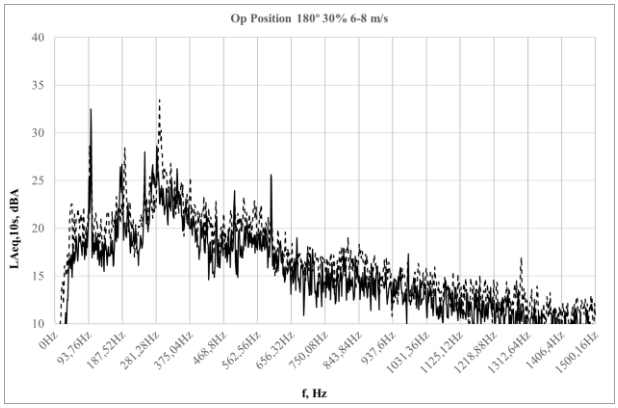


Figure 4. A-weighted spectra for upwind position at 30% of capacity.

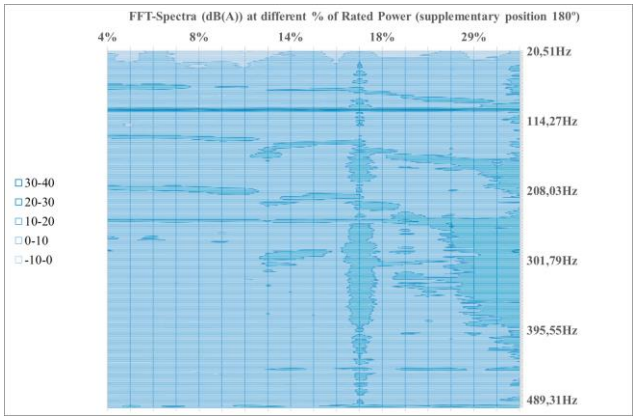


Figure 5. FFT-spectra change at different operational conditions 5 to 30% of active power output at 180 position (upwind).

The results from the upwind position indicate an increase in the tonal component at 100 Hz. The origin of this tone is electrical and aligns with the behavior typically observed in transformers. The tonality at 100 Hz remains stable across all operational rates, whereas the predominant tone at 113 Hz, identified at the IEC-positioned measurements, varies according to the wind turbine's rotary speed.

The sources and locations of the two tonal components are distinct. However, under specific operational conditions, they can converge at the same frequency, leading to enhanced audibility and perception of the tones.

4. CONCLUSIONS

The IEC 61400-11 standard specifies the measurement position to be in the downwind condition. It assumes an apparent sound power level from a point source located at the rotor center, with emissions in the downwind direction analogous to those of the wind turbine.

Experimental noise measurements around a modern wind turbine have been carried out to explore the tonal directivity associated with the turbine.

The primary noise source of a modern wind turbine is attributed to the blades. Specifically, it is recognized that the main emissions originate from the last third of the blade. Additionally, the trailing edge noise exhibits a non-omnidirectional directivity, varying with different wind speeds, rotor speeds, and pitch angles.

Mechanical and electrical components can contribute to the tonal characteristics of a wind turbine. These components tend to be more audible at lower wind speeds, as emissions from the rotor decrease and background noise is minimal.

The noise emitted by the wind turbine was measured in the absence of other external sources such as other wind turbines, industrial noise, or traffic noise. Some bird songs have been identified in the recordings, contributing primarily in the 4-5 kHz range. These contributions do not affect the results, which focus on the frequency range of 20 to 1500 Hz.

The automated audio analysis from fixed positions (with board positioned on the ground) shows good correlation with the short term moving positions (tripod at 1.5 meter).

Ideally, reference measurements and all complementary measurements should be performed simultaneously, adhering to the methodology outlined in the IEC standard. Utilizing synchronized parallel measurements conducted over short periods at 1.5 meters above ground level demonstrates excellent correlation, particularly when the maximum wind speed is controlled and limited. The ground effect, in general, must be considered and corrected to ensure measurement accuracy.

This technique offers increased flexibility while maintaining reference positions downwind, enabling the investigation of tonal components whose origins may not be readily apparent from a fixed position.

Certain components of wind turbines can contribute to overall sound levels and, particularly, to tonal components, which may not originate from the hub height. These components may have directivity characteristics that might alter test results, as they deviate from the assumption that emissions are centered at the rotor location.

When noise sources are situated close to ground level, the topography of the terrain significantly influences sound propagation. The selection of test conditions, including the IEC-specified downwind positions, can alter results, especially concerning components close to ground level.

The use of optional and complementary measurement positions reveals significant differences in audibility assessments. These variations can even alter the dominant tonal frequency observed in the analysis.

Further investigations should involve additional measurements across different turbine types. Measurements at higher wind speeds are preferable, with devices positioned on the ground, and simultaneous assessments conducted in various optional or complementary locations. The variability in wind direction presents a challenge for these tests. Effective synchronization of non-acoustic data aids in filtering results when necessary. However, ideally, stable conditions are preferred, allowing measurements to cover different wind speeds within a shorter period of time and enabling precise repositioning.

5. REFERENCES

[1] IEC, *Wind turbines - Part 11: Acoustic noise measurement techniques (IEC Standard No. 61400-11:2012+AMD1:2018 CSV)*, 2018.

[2] S. Oerlemans and S. J. G., “Prediction of Wind Turbine Noise and Validation against Experiment,” *International Journal of Aeroacoustics*, pp. 555-584, 2009.

[3] Y. Okada, K. Yoshihisa, K. Higashi and N. Nishimura, “Radiation characteristics of noise generated from a wind turbine,” in *Acoustical Science and Technology, 2015, Volume 36, Issue 5, Pages 419-427*, Japan, 2015.

[4] C. Rautmann, Numerical Simulation Concept for Low-Noise Wind Turbine Rotors, Brunswick: DLR Institut für Aerodynamik und Strömungstechnik > Technische Akustik, 2017.

[5] O. Saldaña, R. C. and A. Plaza, "A directivity correction for accurate semi-empirical wind turbine noise prediction," in *TORQUE 2024*, Florence, 2024.

[6] M. Arana, J. Machín and ·. R. San Martín, "Measurement and Analysis of Mechanical Noise in Wind Turbines," *Australian Acoustical Society*, vol. 43, p. 295–302, 2015.

[7] M. Arana, R. San Martin, A. Ezcurra, A. Valencia and E. Llorente, "An efficient algorithm for the evaluation of tonality and the determination of the tonal frequency according to IEC 61400-11," in *INTER-NOISE 48th International Congress and Exhibition on Noise Control Engineering*, Madrid, 2019.

[8] T. MathWorks, “MATLAB version 24.2.0 (R2024b),” 2024. [Online]. Available: https://www.mathworks.com.

DOI:

Main theme: A05 Environmental Acoustics

Session A05.05 Urban sound planning

Chair(s): L. Estévez-Mauriz, T. Maag

DOI: 10.61782/fa.2025.0425

FORUM ACUSTICUM EURONOISE 2025

GUIDELINES FOR AN INSTITUTIONAL PROPOSAL FOR THE CREATION OF A NOISE AND VIBRATION OBSERVATORY IN URUGUAY

Luis Marisquirena[1*] **Elizabeth González**[2] **Pablo Gianoli**[3]
[1 2 3] Facultad de Ingeniería, UDELAR, Uruguay

ABSTRACT

Concern about noise pollution and the consequences of exposure to noise and vibration is of worldwide relevance. Organizations such as the World Health Organization have dedicated spaces to visualize these problems of exposure to noise and vibration. So much so that they describe noise pollution as the first environmental nuisance in developed countries and as a threat to public health. In Europe, noise pollution is the second most harmful environmental factor. There are multiple studies where it is demonstrated the link of diseases with exposure to noise and vibration, such as heart disease, emotional pathologies, digestive disorders, among others.

Keywords: *Observatory, Noise, Vibrations*

1. INTRODUCTION

What is a Noise and Vibration Observatory?
The Noise and Vibration Observatory operates as a tool that, from the processing of environmental information on noise and vibration, generates knowledge and guidelines for action so that, jointly, the population and the authorities become aware and act to mitigate the effects on the welfare and public health of exposure to noise pollution caused by noise and vibration. It will supervise, together with the Government and the University, the operation of an equipment calibration laboratory.

The information processed will be used to develop communications of interest to the population as well as to support actions in defense of citizens and to seek changes in legislation to improve their welfare and health conditions.

2. GENERAL OBJECTIVE OF THE NOISE AND VIBRATION OBSERVATORY

To manage the environmental information on Noise and Vibrations, making it available for actions for the benefit of the population.
This Observatory is aimed to carry out actions such as:
- Working together with the Institutions that already carry out some of the tasks related to environmental noise pollution, for the collection of information on Noise and Vibrations. The compilation will include records of measurements, reports related to the subject, description of actions developed from detected problems related to noise and vibrations, etc.
- The development of local information through the promotion of inter-institutional and intra-institutional research related to the consequences of noise and vibration exposure. Developing local databases with historical and new information obtained. Processing information with inter-institutional data cross-checking.
- The analysis of current regulations, proceeding to their assessment, the follow-up of policies related to noise and vibration, and their evaluation with respect to international regulations and environmental agreements entered into by Uruguay. Reviewing the regulations, particularly those related to construction (buildings, traffic routes) regarding

[*] ***Corresponding author***: luismarisquirena@gmail.com
Copyright: *©2025 First author et al. This is an open-access article distributed under the terms of the Creative Commons Attribution 3.0 Unported License, which permits unrestricted use, distribution, and reproduction in any medium, provided the original author and source are credited.*

noise and vibration. Updating the regulations in response to environmental commitments acquired. Proposing adjustments for its updating and seeking consensus to unify noise and vibration regulations in the country.
- Registering and analyzing the social problems associated with noise and vibrations (Noise Pollution).
- Proposing a noise and vibration monitoring network with fixed and mobile stations. Registering and processing data. Elaboration of reports. Generation of proposals for noise attenuation solutions. Elaboration of the "MAP OF NOISE AND VIBRATION ALERTS". Analyzing the information to be made public on noise and vibration. Maintaining public information channels and managing their operation. Evaluating the realization of mass participatory mapping for noise and vibration. Maintenance of technical and information processing equipment. Maintenance of an operational Noise and Vibration Control Center where the Noise and Vibration Alerts Map is displayed centrally in addition to being able to visualize specific selected points. Developing noise and vibration simulation models.
- Giving general guidelines for the installation in the country of a certification laboratory for noise and vibration measurement equipment. This laboratory will depend on public institutions with competences for this task.
- Supporting the actions of the municipalities in their competence as environmental police. Reviewing specific regulations and evaluation of problems. Generating actions and designing a system, with specific equipment and resources, for the automatic control of deviations from the regulations and subsequent derivation of the information to the offices with competence to apply sanctions.
- Analyzing specific noise pollution problems and proposing possible solutions.
- Systematizing information related to noise and vibration from the register of complaints. Statistical treatment of information.
- Promoting the relationship with other organisms related to noise and vibration problems. Facilitating the generation of agreements for the exchange of information and homogenization of information to be made public.
- Promote the formation of a National Noise and Vibration Honorary Advisory Council (CCOHNARVI) that will function as a consultative body. The National Noise and Vibration Honorary Advisory Council should have the participation of at least three national referents in noise and vibration issues and in parallel maintain communication with the main actors linked to the subject such as the Ministry of Environment, the Congress of Mayors, the UDELAR (Faculty of Engineering, Faculty of Architecture, Faculty of Social Sciences, Faculty of Information and Communication, etc.), the Neighborhood Ombudsman, Social and Business Organizations.
- To carry out the management for the realization of training and communication instances such as Congresses, Forums, Informative Talks, etc. to spread and raise awareness about the noise and vibration problems and to elaborate possible actions to mitigate the impacts of these problems.
- It will supervise, together with the National Government and the University, the operation of a calibration laboratory for equipment related to noise and vibration measurements.

3. SPECIFIC LINES OF WORK

- Centralizing information on noise and vibration.
- Managing the network of noise and vibration records.
- Processing available information and information generated from new records.
- Updating available tools (acoustic map, regulations). Definition of homogeneous noise and vibration zones. Strategic map. Support environmental police tasks. Noise and vibration laboratory.
- Raising awareness of noise and vibration problems. Periodic reporting. Preparing information for public disclosure. Developing the concept of co-responsibility.
- Evaluating the development of collaborative noise and vibration maps adjusting them with the records of fixed and mobile networks.
- Developing noise and vibration simulation models.
- Coordinating the supervision of the equipment calibration laboratory.

4. INSTITUTIONAL INTEGRATION

General aspects of the integration of the observatory in an Institution are shown:
- Dependency relationship: 2nd or 3rd institutional level.
- Unit modality with allocation of resources

4.1 MINIMUM HUMAN RESOURCES:

- 1 engineer specialized in Acoustics and Vibrations.
- 2 assistant engineers
- 1 electronics technician with knowledge in telecommunications.
- Transversal supports from institutional dependencies linked to noise and vibrations.

4.2 EQUIPMENT:

- Sound level meter network reviewing and complementing other existing networks and adapting mobile recording equipment.
- Seismograph network to be considered and vibration equipment to be acquired.
- Data transmission and reception at headquarters. Maintenance and operation of recording networks. Noise and Vibration Control Center.
- Processing software and appropriate hardware. Data backup units.
- Availability of transportation for recording, maintenance and supervision of the networks.

5. ENVIRONMENTAL POLICE

To the extent that it falls within the purview of the Institution that hosts the Observatory, support the environmental police tasks that will continue to be carried out as before. The observatory will support these offices.

6. INFORMATION TO BE COLLECTED AND ORGANIZED ON NOISE AND VIBRATIONS

- Compilation of information within public institutions: City Halls, Faculty of Sciences, Faculty of Engineering, Neighborhood Ombudsman, etc.
- Information on noise and vibration regulations: National norms and departmental norms. Compilation.
- Records of the existing sound level meter network in Uruguay.
- Compilation of data on complaints or inspections related to noise and vibration.
- Acoustic map of Montevideo. Departmental acoustic maps.
- Proposals for updating regulations. Feasibility of unification of regulations.
- Compilation of other available information
- Experiences from Uruguay
- Experiences outside Uruguay
- International regulations. Agreements and commitments.
- Equipment certification. Certification laboratory.

7. EQUIPMENT FOR NOISE AND VIBRATION RECORDING NETWORKS TO BE INSTALLED

7.1 Recording networks with sound level meters.

The Municipality of Montevideo has a network of fixed sound level meters that should be updated and maintained. Verify the existence of other networks in the country. Implement the installation of equipment to develop a recording network with sound level meters. It is proposed, based on this existing network, to acquire equipment for fixed installations and mobile noise recording to complement the existing network and meet the specific needs of the Observatory. Analyze the network, adapting it to obtain data of homogeneous quality in the fixed network compared to the mobile equipment.

7.2 Seismograph recording networks

There is a network of seismographs operated by the Faculty of Sciences. It is proposed to acquire equipment for fixed installations and mobile vibration recordings to complement the existing network and meet specific needs of the Observatory.

7.3 Recording networks oriented to monitoring.

Evaluate international experiences of recording and monitoring networks for noise, especially associated with construction and traffic. The facilities have noise recording equipment and cameras to identify noise sources.

7.4 Network complements to be installed.

- Hardware and software for network data storage and transmission.
- Implement the noise and vibration monitoring network based on the knowledge generated in the development of other data recording and transmission networks.

8. MINIMUM SOFTWARE AND HARDWARE FOR THE NOISE AND VIBRATION OBSERVATORY.

- The use of free software is suggested as far as possible.
- Mapping in the existing geographic systems of Ministries and Municipalities. Implement the warning map. Improvements to be proposed in the existing systems.

Linkage for the reception of information from mobile telephone equipment.
- Use for dissemination the existing channels already established for environmental issues in both the Ministries and the Intendancies. Improve and expand communication channels.
- Two fixed equipment and one laptop for information management.
- All the equipment will have the software installed.
- They will have features that will allow storing and processing all available information and making adequate backups.
- One of the fixed equipment will be the main equipment and will receive the information from the sound level meter and seismograph networks. The other equipment will function as a backup. All the information is backed up in the institutional servers.

9. NOISE AND VIBRATION HONORARY ADVISORY COUNCIL

- The Noise and Vibration Observatory, together with other institutions, shall promote the creation of an Honorary Advisory Council on Noise and Vibration, which shall have at least three members, who are referents in Uruguay on noise and vibration issues. It will act in consultation with the rest of the actors linked to noise and vibration issues: Ministry of Environment, Congress of Mayors, UDELAR (Faculties of Medicine, Engineering, Social Sciences, Psychology, Architecture, Information and Communication), Neighborhood Ombudsman, associations of transport companies, events (discos, parties, music, dances, ...).
- Functioning as a forum to raise and discuss general issues of social scope related to noise and vibrations.
- Resolutions of an orientation nature that may or may not be taken later at a normative level.
- Contribute to raising awareness on noise and vibration issues and the generation of strategies to address this problem with general consensus.

10. EXPERIENCES IN URUGUAY TO BE TAKEN INTO ACCOUNT BY THE NOISE AND VIBRATION OBSERVATORY

OAN: National Environmental Observatory. It depends on the Ministry of Environment. Among the environmental issues it could integrate noise and vibrations.

MOVES PROJECT: Noise studies were carried out as part of this project.
NOISE MONITORING: Municipality of Montevideo (Grafana) There is a fixed network of sound level meters that theoretically measure 24/7 but have some updating problems. There is historical information that should be evaluated.
NEIGHBORHOOD OMBUDSMAN: Compilation of complaints related to noise and vibrations.
ELECTRICAL AND MECHANICAL INSTALLATIONS SERVICE: Municipality of Montevideo. History of noise nuisance complaints. History of seismograph measurements in tasks related to construction using explosives.
FACULTY OF SCIENCES: Geophysical Observatory of Uruguay.
NATIONAL EMERGENCY SYSTEM: Record of earthquakes in Uruguay.

11. NOISE AND VIBRATION OBSERVATORY. EXPERIENCES OUTSIDE URUGUAY.

There are similar experiences in the world. In some cases, they are already implemented and in development; in other cases, only some aspects of the proposal have been implemented.
As examples we have the City Grenoble with Accoucite [1] of Paris with Bruitparif [2] , , in Cordoba (Argentina) the Noise Observatory of Cordoba [3], in Australia the Australian Observatory of Acoustics [4], Ecodes in Barcelona [5] , and experiences in some cities of Colombia [6] and in Santiago de Chile [7].

12. RELEVANT ROLE FOR DEVELOPMENT IN LATIN AMERICA

Some experiences have been reported, mainly in Europe, of noise observatories. In the case of Latin America, being able to set up a noise and vibration observatory such as the one proposed will be a milestone to support the development of those partial experiences already underway and to encourage the installation of other observatories in Latin American countries.
The possibility of having local noise and vibration measurements makes it possible to develop policies to improve the quality of life of the inhabitants of Latin America. The possibility of having own indicators for Latin America favors a more effective measurement of development projects that include improvements in noise and vibration impacts. It also makes possible, to the extent

that it is possible to maintain continuity, the existence of time series of values to weigh improvements due to implemented policies.

13. ASPECTS OF NOISE POLICY.

In the case of Uruguay, regulations originate from different agencies at the two higher levels of government. The initiative may come from these levels of government or from other agencies. There are laws, decrees, regulatory decrees that cover the whole country. There are local regulations that originate from departmental governments.
At the national level, through the Ministries of the Environment, Labor and Social Security and the Ministry of Health, there are regulations and the authority to oversee the regulations. At the departmental government level, there are regulations and the authority to oversee them.
The regulations also include the international conventions signed by Uruguay at the ILO or the WHO that are related to noise and vibration control.
A review of the existing regulations shows that in many cases they are outdated, the values are difficult to adequately control and there are differences between the requirements of the departmental governments.

14. URUGUAYAN REGULATIONS

In the case of Uruguay there are national and departmental regulations.

14.1 NATIONAL REGULATIONS

Law No. 17852. Prevention, surveillance and correction of noise pollution.
Decree N° 143/012
Noise and vibration regulations are included in the regulatory compendium on occupational health and safety. [8]

14.2 DEPARTMENTAL GOVERNMENT REGULATIONS

Each departmental government has its own regulations in addition to the national regulations they must comply with. [9] .

15. RECOMMENDATIONS.

It is advisable to set up a Noise and Vibration Observatory in Uruguay to centralize existing and new information generated from field work on noise and vibration.

This Observatory will become a national reference point on this subject, making the information available for its use with different scopes, from the elaboration of regulations to the dissemination for educational purposes.

The existence of a reference center of this type in the country will serve as a bridge to establish exchange agreements with other similar centers around the world.

16. REFERENCES

[1] ACCOUCITE: Grenoble (France). https://www.acoucite.org/observatoire/reseau-de-mesures/reseau-permanent-de-mesure/

[2] BRUITPARIF: Paris (France). https://www.bruitparif.fr

[3] CORDOBA NOISE OBSERVATORY https://reporteruido.cial.faudi.unc.edu.ar

[4] THE AUSTRALIAN ACOUSTIC OBSERVATORY https://acousticobservatory.org/

[5] ECODES – BARCELONA https://ecodes.org/

[6] VALLE DE ABURRA – COLOMBIA https://www.metropol.gov.co

[7] SANTIAGO DE CHILE – CHILE https://ruido.mma.gob.cl/mapas-de-ruido/

[8] Noise and vibration regulations are included in the regulatory compendium on occupational health and safety. https://www.gub.uy/ministerio-trabajo-seguridad-social/politicas-y-gestion/normas-comprendidas-ultimo-compendio-normativo-materia-salud-seguridad-trabajo

[9] Normativa https://www.fing.edu.uy/imfia/grupos/contaminacion-acustica/archivos/03%20Cuaderno%203%20Normativa.pdf

DOI: 10.61782/fa.2025.0193

FORUM ACUSTICUM EURONOISE 2025

CHARACTERISTICS DETERMINING THE ATTRACTIVENESS OF URBAN GREEN SPACES: INSIGHTS FROM THE RESTORE PROJECT

Jean Marc Wunderli[1*] **Claudia Kawai**[1] **Javier Dopico**[1]
Martin Röösli[2,3] **Danielle Vienneau**[2,3] **Mark Brink**[4]
Silvia Tobias[5] **Beat Schäffer**[1]

[1] Empa, Swiss Federal Laboratories for Materials Science and Technology, Dübendorf, Switzerland
[2] Swiss Tropical and Public Health Institute (Swiss TPH), Allschwil, Switzerland
[3] Faculty of Science, University of Basel, Basel, Switzerland
[4] Federal Office for the Environment (FOEN), Bern, Switzerland
[5] Swiss Federal Institute for Forest, Snow and Landscape Research (WSL), Birmensdorf, Switzerland

ABSTRACT

Literature provides strong evidence that nature can potentially alleviate negative mental as well as physiological health effects of excessive traffic noise exposure. As green spaces (GSs) not only help mitigating negative noise impact, but also improve public health in general, GS planning has become an important task for cities. We conducted a field study in the city of Zurich, Switzerland, to investigate which characteristics of GSs determine their attractiveness. In three waves in the summer periods of 2022 and 2023, 1,129 participants filled out an online questionnaire that included a participatory geographical information system approach to specify and characterize their most visited GS. Interestingly, while the distance to the nearest GS was important for how frequently residents visited GSs spaces, 64% of the participants still did not indicate their closest GS as their most visited one. We found that large GSs, which in general exhibit lower traffic noise exposure, attract more visitors than small ones. Water bodies were also identified as attractive. Our study highlights the relevance of these features for city planners and urbanists when planning, designing and/or maintaining urban GSs.

Keywords: *green space, urban planning, attractiveness, visits, traffic noise*

[*] ***Corresponding author***: *jean-marc.wunderli@empa.ch.*
Copyright: *©2025 J.M. Wunderli et al. This is an open-access article distributed under the terms of the Creative Commons Attribution 3.0 Unported License, which permits unrestricted use, distribution, and reproduction in any medium, provided the original author and source are credited.*

1. INTRODUCTION

Urban areas are continuously expanding. As urbanization increases, permanent noise-related activities within these areas also rise. In Europe, a large proportion of the population in urban areas is currently exposed to harmful environmental noise, particularly from road traffic [1]. With rising demand of mobility, exposure of the population and corresponding undesirable health outcomes are likely to aggravate. Environmental resources, specifically green spaces (GSs), have been identified as potential elements to alleviate the adverse noise-induced health impacts. However, urban densification not only entails an increase in noise pollution, but usually also a loss of GSs.

One of the goals of the RESTORE project (Restorative potential of green spaces in noise polluted environments; www.restore-project.ch) was to determine how frequently GSs are used and what features make them attractive.

2. METHODS

The concept and methodology of the survey (i.e., noise and green exposure assessment, stratification to identify study areas, participant selection and inclusion/exclusion criteria, recruitment, etc.) follows the study protocol by Dopico et al. [2]. In the following, we give a short methodological overview of this cross-sectional study.

The survey was conducted in a stratified population sample across the municipality of the city of Zurich, Switzerland, according to varying levels of road traffic noise exposure and the degree of access to GSs at home.

The city of Zurich has 139 publicly accessible GSs. All GSs were characterized by size, modelled road traffic noise exposure, type (i.e., bathing area, botanic garden, cemetery, meadow, miscellaneous, playground, sports complex, urban forest and urban park) and the presence of natural water bodies (stream, river or lake: with vs. without). In addition, 156 audio and video recordings of five minutes length were taken in 48 GSs close to the sampling areas, to characterize landscape and soundscape in more detail.

A total of 7,368 potential participants were randomly selected within the stratified sample and contacted with an invitation letter, followed by a reminder letter in case of no response by the specified deadline, in three waves in the summer periods of 2022 and 2023.

The participants filled in an online survey in German covering, among others, questions about noise annoyance and leisure time activities, where participants were asked about the main reason for GS visits. In addition, they were asked to pinpoint a location in their most visited GS on a map. The participants were also presented the ISO 12913-2 soundscape assessment scale [3], to retrospectively describe the soundscape in their most visited GS. The soundscape variables Pleasantness and Eventfulness were derived according to ISO 12913-3 [4].

Each participant was assigned an anonymized identification number, and a building code was linked to each identification number, enabling the merging of survey and geospatial data, which were extracted from public sources. Data from public sources comprised (i) modelled road traffic noise exposure data (L_{den}) across the city of Zurich for façade points of all buildings for the year 2020 to quantify the noise situation at home, (ii) road traffic noise exposure data for the day (L_{day}) from sonBASE, the Swiss-wide noise data base, for the year 2015 to quantify the noise exposure of the GSs, (iii) location (as polygons) and properties of public GSs, and (iv), quantification of greenness around participant's dwellings (within a 300 m euclidean buffer) with the mean value of the satellite-derived Normalized Difference Vegetation Index (NDVI).

A total of 1,129 participants across Zurich took part in the online survey (response rate of 15.3%). From those, 282 participants were excluded due to wrong or missing indication of their preferred GSs location or due to missing data (either L_{den} or questionnaire data). The final sample comprised 847 participants. Figure 1 shows a density heat map of the home locations of the study participants, as well as the locations of publicly accessible GSs and water bodies.

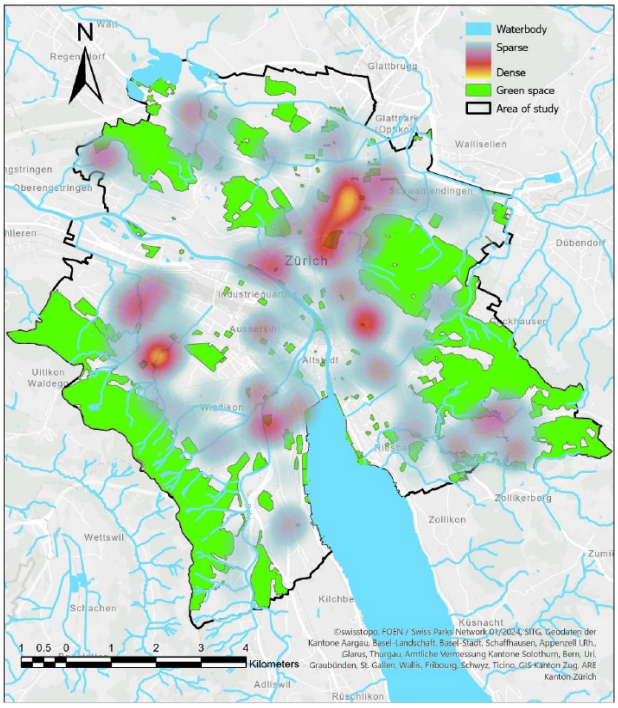


Figure 1. Density heat map of the city of Zurich showing the home locations of the study participants.

Two outcome variables were explored by means of negative binomial regression models analysis:

a) The **frequency of visits**, which reflects the individual perspective and is based on the question how often participants visit their most frequented GS.
b) The **number of visitors of a specific GS**, which serves as an indicator of attractiveness by reflecting the number of visits a GS generates.

As predictor variables, the characteristics of the home environment (L_{den}, NDVI, gardens), individual factors (noise annoyance, perceived free time) as well as GS characteristics (L_{day}, size, water bodies, soundscape variables Eventfulness and Pleasantness) were explored.

3. RESULTS

A share of 68% of the participants reported to visit their most frequented GS at least once a week, confirming the importance of public GSs in their daily routine. Urban forests and parks as well as GSs close to water bodies were visited very frequently and seem to be specifically attractive. Interestingly, 64% of the participants did not indicate their closest GS as their most visited one. In total, 91 GSs were selected by the participants, while 48 GSs remained unvisited in this study. An explorative analysis comparing the properties of visited vs. non-visited GSs showed that visited GSs tended to be substantially larger than the non-visited ones. In addition, visited GSs had considerably lower noise exposure, with a median L_{day} of 44 dBA and of 57 dBA for visited compared to non-visited GSs, respectively. This raises the question which factor is more relevant for people to visit a GS; low noise exposure or the size of the GS.

The statistical analysis revealed the following associations:

The individuals' frequency of visits to GSs significantly increased with (i) increasing greenness (NDVI) at home, (ii) increasing road traffic noise annoyance at home (particularly for females), (iii) increasing perceived free time (particularly for males), (iv) decreasing distance from home to the most visited GSs, and (v) increasing individually perceived eventfulness of the GS's soundscape.

The finding about the soundscape variables should be interpreted with caution. All GSs exhibited neutral to pleasant and medium eventful soundscapes. The fact that pleasantness did not show any significant associations might be attributable to the small variability of pleasantness scores in the dataset. On the other hand, the positive association with eventfulness could be a coincidence, as the sound recordings revealed that positively connoted events like bird song or human voices were present in some locations, while in others negatively connoted events like individual vehicle pass-bys dominated.

The attractiveness of urban GSs, as measured by the number of visitors (our study sample only), was found to increase with (i) increasing size, and (ii) when water bodies are present. Here, one should note that size and noise exposure were negatively correlated, i.e., the importance of (large) size indicates also the importance of (low) road traffic noise exposure.

4. CONCLUSION

This cross-sectional study investigated the determinants for the frequency of GS visits in an urban environment in the municipality of Zurich, Switzerland. It also assessed the attractiveness of GS by the number of visitors they received from the study sample. The size of GSs and the presence of water bodies emerged as the main attributes to attract visitors. The visited GSs were generally also rather quiet.

Our study highlights the relevance of these features for city planners and urbanists when planning, designing and/or maintaining urban GSs.

5. REFERENCES

[1] European Environment Agency (EEA) (2020). Environmental noise in Europe — 2020. Luxembourg, Publications Office of the European Union. 2020.

[2] Dopico, J., Schäffer, B., Brink, M., Röösli, M., Vienneau, D., Binz, T. M., Wunderli, J. M.: "How do road traffic noise and residential greenness correlate with noise annoyance and long-term stress? Protocol and pilot study for a large field survey with a cross-sectional design." *International Journal of Environmental Research and Public Health*, 20(4), 3203 (2023).

[3] ISO/TS 12913-2. "*Acoustics—Soundscape—Part 2: Data collection and reporting requirements.*" International Organisation for Standardization. (2018)

[4] ISO/TS 12913-3:2019, "*Acoustics—Soundscape—Part 3: Data analysis.*" International Organization for Standardization. (2019)

DOI: 10.61782/fa.2025.0599

FORUM ACUSTICUM EURONOISE 2025

NECESSARY STEPS TO ADVANCE RESEARCH ON HEALTHY URBAN SOUND PLANNING

Timo Haselhoff[1*] **Susanne Moebus**[1]
[1] Institute for Urban Public Health, University Hospital Essen, Essen, Germany

ABSTRACT

The acoustic environment (AE) matters for human health and well-being. Decades of research revealed noise pollution to be a major disease burden. Well-established mitigation strategies like speed limits or noise barriers exist. Beyond noise, field and laboratory studies suggest salutogenic properties of the AE. However, for a more comprehensive understanding of the relationship between human health and the AE beyond noise, i.a., population-based epidemiological studies are necessary.
However comprehensive studies are missing, and robust strategies for health-promoting urban sound planning are scarce. Currently, several factors limit research in this area. A major factor is the difficulty in quantifying acoustic properties that may reflect the salutogenic properties of AEs on a population-level. This is particularly important, as such studies are needed to investigate health issues of defined populations in real-life settings. While various methods (e.g. the soundscape approach by DIN ISO 12913) aim to assess the "acoustic quality" of an AE and provide valuable insights, they do not provide the spatially high-resolution exposure data needed. Here, we outline requirements necessary to advance research at the population-level. We discuss and demonstrate approaches in AE research that show promise in meeting these requirements and could guide urban planning towards healthier AEs.

Keywords: *Public Health, Urban Planning, Soundscape, Epidemiology*

[*]***Corresponding author***: *timo.haselhoff@uk-essen.de*
Copyright: *©2025 First author et al. This is an open-access article distributed under the terms of the Creative Commons Attribution 3.0 Unported License, which permits unrestricted use, distribution, and reproduction in any medium, provided the original author and source are credited.*

1. INTRODUCTION

In recent decades, significant efforts were undertaken to investigate the link between the urban acoustic environment (AE) and human health. Among other definitions, the AE can be defined as “the sound from all sound sources as modified by the environment” [1]. While the link between environmental noise exposure and adverse health effects (e.g. cardiovascular disease or mental health) is well established [2], an increasing number of studies focusses on the potential beneficial effects that high quality AEs may provide [3]. For example, using laboratory settings, studies found that uneventful and more pleasant sounds were linked to a greater reduction in heart rate [4], that stress recovery was facilitated by sounds from nature [5] or that biophonic AEs have a favourable impact on the functional connectivity of the human brain [6]. In addition to laboratory studies, several field studies investigated the impact of natural sounds on different human health dimensions and found, e.g., associations with decreased pain, lower stress or enhanced cognitive performance [7]. However, so far, studies are missing that take into account a broad spectrum of urban neighbourhoods as well as population based studies. The lack of population based studies highlights a substantial research gap. These studies are essential to investigate patterns, causes and effects of health issues of defined population (groups) in real-life settings [8]. By addressing this gap, we can better identify which acoustic properties benefit human health and well-being in order to develop robust measures for health-promoting urban sound planning. Currently, a significant challenge in this area of research is obtaining the high-resolution spatial exposure data required for population based studies. Below, we will discuss reasons behind this challenge. We will focus on issues regarding definitions, operationalisations and measurements of exposure, as well as the difficulty of linking findings to urban planning.

2. THE CONCEPT OF EXPOSURE

In general, prerequisites to plan healthy urban AEs are insights into how the AE and human health are related. Here, the embedding into the framework of epidemiology is appealing, as it is concerned with the distribution, patterns and determinants of health and disease [8]. Following epidemiological basics, the determination of exposure and outcome is fundamental to gain such insights. Since the measurement of health outcomes on a population-level is a well-established research field, we will not address the challenges associated with defining and measuring outcomes here. Rather we want to focus on the challenges in defining and measuring the exposure (e.g. natural sounds) on a high spatial resolution, and how this complicates population based studies at the time.

2.1 Defining the exposure

One criterion to define the exposure is that it is derived from a research question, which reasonably connects it to a health outcome [8]. While the question of a reasonable connection is rather philosophical [8], there are multiple theories and studies on the relations between the AE and human health that can legitimize an investigation (e.g. stress reduction through biophonic sounds). Furthermore, the construct of the exposure needs to be clearly defined. Regarding the example above, questions such as whether biophonic sounds include human sounds, dog barks, or leaves rustling in the wind need to be answered. However, other constructs such as "(high) acoustic/sound-(scape) quality" or "fidelity" are frequently used but often only vaguely defined or have varying definitions. Acoustic and sound-(scape) quality are often used interchangeably, but lack a uniform definition. Kang and Schulte-Fortkamp [9] define "environments of high acoustic quality [as those] where one can postulate that type 1 restorative effects could occur", while soundscape quality may be defined as "warm-hearted, lively and peaceful, therefore noisy but enjoyable" [10] or solely by survey responses [11]. In addition to the latter being problematic from a measurement theory point of view, because the construct is not defined a priori [12], vague definitions of constructs complicate their operationalisation, and thus a valid measurement [12]. For example, biophonic sounds are often operationalized by the amplitude of a recording between 2 and 8 kHz, also allowing other sound sources in this frequency range to be considered biophonic. Besides physical-acoustic measures, constructs derived from the AE are also often operationalised by sound source classes or questionnaires.

Regarding the literature, there are also differences on which level the AE is operationalized as exposure. Hypotheses concern settings (e.g. urban vs. rural AEs), complex mixtures (e.g. pleasant sounds) as well as single agents (e.g. birdsongs) of exposures [8]. Neither of which are generally weaker approaches to assess exposures, but it underlines that there are most likely multiple relevant exposures that need to be considered, if we want to assess the relation between the AE and human health.

In summary, many theories in the field of AE have gathered sufficient evidence to warrant further investigation on population-level. However, the definitions and operationalisations of some constructs from the AE are often too vague, which can hinder interpretation, comparability and generisability of results.

2.2 Measuring the exposure

When it comes to measuring the operationalized constructs of the AE (e.g. urban soundscapes, pleasant sounds, biophonic sounds), the most widely used approaches include the use of acoustic indices and surveys using questionnaires. In the following, we will shortly describe each approach, followed by an evaluation of their respective challenges to assess the exposure on a high-resolution spatial level.

2.2.1 Acoustic indices

We refer to acoustic indices as those, which represent physical-acoustic properties of an AE. An elaborate example to illustrate the construct, operationalization and measurement of an exposure through an acoustic index is environmental noise. Among other definitions, the one from the European Directive 2002/49/EC is probably the most widely used. Here, environmental noise is defined as "unwanted or harmful outdoor sound created by human activities, including noise emitted by means of transport, road traffic, rail traffic, air traffic, and from sites of industrial activity". The operationalisation is the A-weighted long-term average sound level and the exposure measures are derived from strategic noise maps, which model the a-weighted sound pressure level (SPL).

Beyond SPL, there is a plethora of acoustic indices that are designed to measure constructs in relation to, e.g., human perception of acoustic phenomena (e.g. from psychoacoustics) or specific sound sources (e.g. from ecoacoustics). Some examples are measures for psychoacoustic annoyance (as a combination of loudness, sharpness, roughness and fluctuation strength) [13] or biophonic activity (measured e.g. by the normalized difference soundscape index) [14].

However, unlike to SPLs, methods to derive exposure levels for these indices on a population-level are not established to this date. Acoustic measurements could provide the necessary exposure data, but are complex and costly, especially on a larger scale. In contrast to strategic noise maps, no models are yet established from which high-resolution exposure data could be derived. In addition, research into the performance of certain acoustic indices and their relations with exposure constructs (e.g. natural sounds) in the urban environment is a relatively new field of study. Still, there are significant developments in recent years that explore the relation between acoustic indices and, e.g., human perception in the urban environment [15, 16].
Drawing from the example of strategic noise maps, which utilise traffic estimates and the built environment to predict SPL, similar information could be used to create sound maps for additional acoustic indices (see Fig. 1), as their relations to the built environment are getting increasingly more evident. Additionally, these relationships provide insights necessary for urban sound planning.

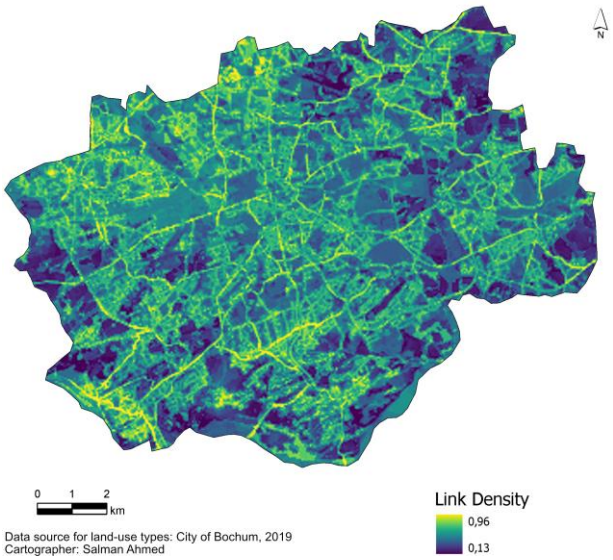


Figure 1. Exemplary presentation of preliminary results for exposure assessment of an acoustic index. Here, acoustic dominance, operationalised by the acoustic index link density, is shown using a prediction model based on land use types. The area depicted is Bochum, Germany.

2.2.2 Questionnaires

In recent years, the use of questionnaires has emerged as a popular method to investigate the urban AE. Among the various questionnaires deployed, one of the most frequently applied is from the DIN ISO 12913 [1]. Here, e.g., the construct of perceived acoustic pleasantness, operationalised as a combination of multiple human answers on a 5-point Likert scale, is investigated. In addition, the context (e.g. the built environment, socioeconomic factors) plays a crucial role here, as it influences the rating of the respondents and should always be considered[1].
Regarding the exposure measurement on population-level, the application of questionnaires on the AE represents a highly feasible approach, as questionnaires are an established method for population surveys. Such surveys could also gather additional person-related variables, offering insights into the contextual factors influencing AE perception or even individuals' health. However, this approach is not without challenges. Existing questionnaires are primarily designed for in-situ applications, which poses difficulties when adapting them for population surveys[2]. Here, the reliance on context also raises the question of whether people can be effectively queried about their responses to hypothetical or memorized acoustic scenarios (e.g. the perception of the AE at home for the last month). Currently, the research field lacks widely established questionnaires for population surveys [18].
In addition, the insights required for healthy urban sound planning regarding the interplay between the built environment and the perceived AE would need to be gathered through additional surveys or similar methods.

2.2.3 Additional considerations

In addition to the method specific challenges, there are general factors that need to be considered in exposure assessment, namely the intensity duration, and timing [9]. For example, the mitigating effects of being indoors might be important for the intensity of the exposure to the outside AE. This might also be important for the duration of exposure if we expect an isolation from the outdoor AE. Furthermore, the place of stay needs to be considered, as the exposure may vary from being at home, being outside or at work. Even the place at home might matter, if the exposure

[1] An issue that arises here concerns whether the operationalization measures the acoustic pleasantness of the AE specifically, or rather the overall pleasantness of the investigated place, as recent research suggests [17], but this question remains open to future debate.
[2] Due to its high expenditure on time and personnel we do not consider in-situ measurements (e.g. soundwalks) a feasible option for assessing exposure on a population-level.

differs across rooms. Also the timing might be important. For instance, the recommendations for SPLs are lower at night than at daytime.

3. CONCLUSION

There remain multiple challenges that need to be addressed to assess exposure to the AE on a population-level. For acoustic indices, their functionality and effectiveness in reflecting relevant constructs in the urban environment in relation to humans needs to be further investigated. For example, it is necessary to investigate whether and which indices could represent biophonic sounds in the urban environment. In addition, models need to be developed to predict relevant indices at high spatial resolution.
For the questionnaire approach, instruments need to be developed that measure perceived constructs of the AE for non in-situ situations. Furthermore, the challenges of context dependency need to be addressed and methods to relate results to the built environment need to be established.

4. REFERENCES

[1] DIN ISO/TS 12913-1: "Soundscape Definition and conceptual framework", ISO/TS 12913-1:2018, 2018.

[2] European Environmental Agency: Environmental noise in Europe: 2020. Luxembourg: EEA, 2019.

[3] B. Schulte-Fortkamp, A. Fiebig, J. A. Sisneros, A. N. Popper and R. R. Fay: Soundscapes: humans and their acoustic environment, Berlin/Heidelberg: Springer, 2023.

[4] O. Medvedev, D. Shepherd and M. J. Hautus: "The restorative potential of soundscapes: A physiological investigation", Applied Acoustics, 96, 20-26, 2015.

[5] M. Annerstedt, P. Jönsson, M. Wallergård, G. Johansson, B. Karlson, P. Grahn, ... and P. Währborg: "Inducing physiological stress recovery with sounds of nature in a virtual reality forest—Results from a pilot study", Physiology & behavior, 118, 240-250, 2013.

[6] E. Stobbe, C.G. Forlim, and S. Kühn: "Impact of exposure to natural versus urban soundscapes on brain functional connectivity, BOLD entropy and behaviour", Environmental Research, 244, 117788, 2024.

[7] R.T. Buxton, A.L. Pearson, C. Allou, K. Fristrup and G. Wittemyer: "A synthesis of health benefits of natural sounds and their distribution in national parks", Proceedings of the National Academy of Sciences, 118(14), e2013097118, 2021.

[8] K. J. Rothman, S. Greenland, and T.L. Lash: Modern epidemiology (Vol. 3), Philadelphia: Wolters Kluwer Health/Lippincott Williams & Wilkins, 2008.

[9] J. Kang and B. Schulte-Fortkamp: Soundscape and the built environment. Boca Raton, FL, USA: CRC press, 2016.

[10] C. Guastavino: "The ideal urban soundscape: Investigating the sound quality of French cities", Acta Acustica united with Acustica, 92(6), 945-951, 2006.

[11] Ö., Axelsson: "How to measure soundscape quality", in Proceedings of the Euronoise 2015 conference, 1477-1481, 2015.

[12] E. E. Roskam: "Operationalization, a superfluous concept", Quality and Quantity, 23, 237-275, 1989.

[13] H. Fastl, and E. Zwicker: Psychoacoustics: facts and models, Berlin/Heidelberg: Springer Science & Business Media, 2007.

[14] E. P. Kasten, S.H. Gage, J. Fox and W. Joo: "The remote environmental assessment laboratory's acoustic library: An archive for studying soundscape ecology", Ecological informatics, 12, 50-67, 2012.

[15] B.T. Lawrence, J. Hornberg, K. Schröer, D. Djeudeu, T. Haselhoff, S. Ahmed, ... and D. Gruehn: "Linking ecoacoustic indices to psychoacoustic perception of the urban acoustic environment", Ecological Indicators, 155, 111023, 2023.

[16] M.S. Engel, A. Fiebig, C. Pfaffenbach, and J. Fels: "A review of the use of psychoacoustic indicators on soundscape studies" Current Pollution Reports, 1-20, 2021.

[17] C. Kawai, F. Georgiou, R. Pieren, and B. Schäffer, B., "An investigation into the audio-visual characteristics of restorative spaces using VR", in INTER-NOISE and NOISE-CON Congress and Conference Proceedings 270, 11, 921-928, 2024.

[18] A. Magrini, G. Di Feo, and A. Cerniglia: "Acoustic quality of the external environment: indications on questionnaire structure for investigating subjective perception", Journal of Otorhinolaryngology, Hearing and Balance Medicine, 4(1), 4, 2023.

DOI: 10.61782/fa.2025.0292

FORUM ACUSTICUM EURONOISE 2025

DEVELOPMENT OF A TOOL FOR NOISE MANAGEMENT IN LEZs

José Ignacio Riesco[1*] **Saray Herrero** [1] **Lidia García** [1]
Ramón Díez [1] **Ruth Paredes** [1] **Ana Esther Espinel** [1] **Marco Lora** [1]
Audiotec Ingeniería Acústica S.A., 4 JuaneloTorriano St., 47151, Boecillo (Valladolid), Spain

ABSTRACT

Audiotec is part of a consortium that is carrying out an R&D project with the overall objective of developing a comprehensive and accessible prototype to assist decision-makers in the fight against climate change and air pollution in the task of defining and assessing the economic, social and environmental impact of Low Emission Zones (LEZs) in urban areas.

Audiotec's role in the project is the development of a non-standardized tool for environmental noise prediction in LEZs using geographic information systems (GIS).

The developed tool, which is easy to use, allows to quickly predict the evolution of acoustic indices and health indicators in LEZs, as well as to analyze the acoustic impact in these areas in different alternative scenarios, varying the mobility parameters.

The developed prototype presented here allows municipal technicians to manage LEZs through the use of commonly used free software, with the consequent saving of resources.

Keywords: Low Emission Zones, acoustic module, noise map.

1. INTRODUCTION

The Spanish Law on Climate Change and Energy Transition defines a LEZ as 'an area delimited by a public administration, in the exercise of its powers, within its territory, of a continuous nature, and in which restrictions on access, circulation and parking of vehicles are applied to improve air quality and mitigate greenhouse gas emissions, according to the classification of vehicles by their level of emissions in accordance with the provisions of the General Vehicle Regulations in force'.

Low Emission Zones are a mobility management tool that helps to promote a modal shift in cities towards more sustainable modes of transport, as well as the adoption of low-emission alternative vehicles, such as electric cars.

Spanish municipalities are currently in the process of implementing LEZs, and there is a need for public administrations to have tools that facilitate the definition of their boundaries and perimeter, the analysis of emission reductions, and access to information on public health, as well as economic and social aspects.

In this context, in 2024, an R&D project was proposed in collaboration with several companies, with the overall objective of developing a comprehensive and accessible prototype that would assist decision-makers in the fight against climate change and air pollution by facilitating the task of defining and evaluating the economic, social, and environmental impacts of Low Emission Zones (LEZs) in urban areas. The aim was to promote more effective and sustainable management of urban mobility, in line with the objectives of reducing pollutant emissions and improving air quality, as established in regulatory frameworks at all levels (local, regional, national, and European). At the same time, it aimed to provide additional benefits for the locality and its citizens, such as reducing noise pollution, improving health and quality of life, promoting alternative forms of mobility (sustainable mobility), and creating healthier and more livable urban spaces; see Fig. 1.

- To analyze and diagnose the starting point by calculating the current balance of carbon and pollutant emissions in the municipality through the integration of data from public and private sources. Among other sources of information, noise maps are used to

***Corresponding author**: idi@audiotec.es*
***Copyright:** ©2025 First author et al. This is an open-access article distributed under the terms of the Creative Commons Attribution 3.0 Unported License, which permits unrestricted use, distribution, and reproduction in any medium, provided the original author and source are credited.*

identify not only sources of noise pollution but also atmospheric pollution, as these often overlap.

- Design the LEZ by defining its area, extension and perimeter, as well as the number of LEZs in the city being studied.
- Evaluate and visualize the potential impacts and changes that the LEZ causes in the carbon balance and pollutant emissions in the municipality (CO, NO, NO2, O3, PM10, PM2.5, SO2).
- Quantify other impacts and benefits (economic, social and environmental) that the defined LEZ could potentially produce.
- Evaluate the different options (scenarios) by calculating indicators that enable quantitative comparison and support informed decision-making.
- Export the results for the scenario identified as optimal.

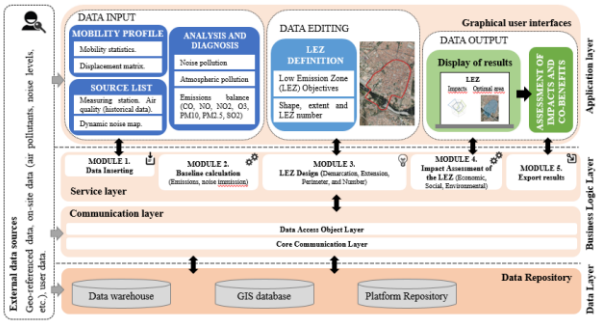


Figure 1. Conceptual framework and functional modules of the platform prototype

Audiotec's role in this R&D project has focused on the development of the acoustic module of the platform.

2. NEED FOR THE DEVELOPED TOOL

Currently, municipalities with more than 100.000 inhabitants are required to update and approve the strategic noise maps for their territory, along with the corresponding action plans.

Strategic noise maps are a valuable tool for assessing the acoustic environment of a municipality with respect to environmental noise and for developing, based on the graphical and statistical results they provide, well-founded action plans to address noise pollution. However, updating these maps requires considerable effort and the use of specialized software for environmental noise prediction, which makes it challenging for government technicians to perform frequent updates.

In this context, Audiotec has developed a module for the acoustic assessment of LEZs with the following objectives:

- To thoroughly research and analyze the specific characteristics and needs of the city regarding the implementation and management of Low Emission Zones (LEZ), considering environmental noise as a key factor.
- Design and develop an automated, intuitive, and easily accessible prototype that enables decision-makers (consultants, urban planners, politicians, etc.) to visualize and analyze the 'noise' variable when defining the area and impact of the LEZ.
- Develop algorithms and models to assess the potential impact of implementing or expanding of an LEZ in terms of noise reduction.
- Integrate Geographic Information Systems (GIS) based calculation capabilities, up-to-date databases and public information sources on noise and mobility to ensure the accuracy and reliability of the data used in developing of the acoustic module.
- Conduct a pilot test to validate the results in collaboration with local authorities and other relevant stakeholders to ensure the practical utility, acceptability, and adaptability of the acoustic module in various urban contexts.

3. DESCRIPTION OF ACOUSTIC MODULE

This is a prototype developed to assess and compare the acoustic impact of various traffic management measures in Low Emission Zones (LEZ). The tool allows users to edit and update the parameters related to traffic in the different streets within the LEZ. Using an intuitive interface in QGIS, users can select a specific road by name and modify key data such as traffic volume, speed, and road surface type. These changes are applied to a new layer that duplicates the original, ensuring that the previous data is preserved and enabling direct comparisons.

Additionally, the tool includes a feature that allows for the calculation of noise levels that receptors will experience after the implementation of the new conditions. As a result, a new receptor layer is generated with the updated values, facilitating the analysis of the acoustic impact of the introduced changes; see Fig. 2.

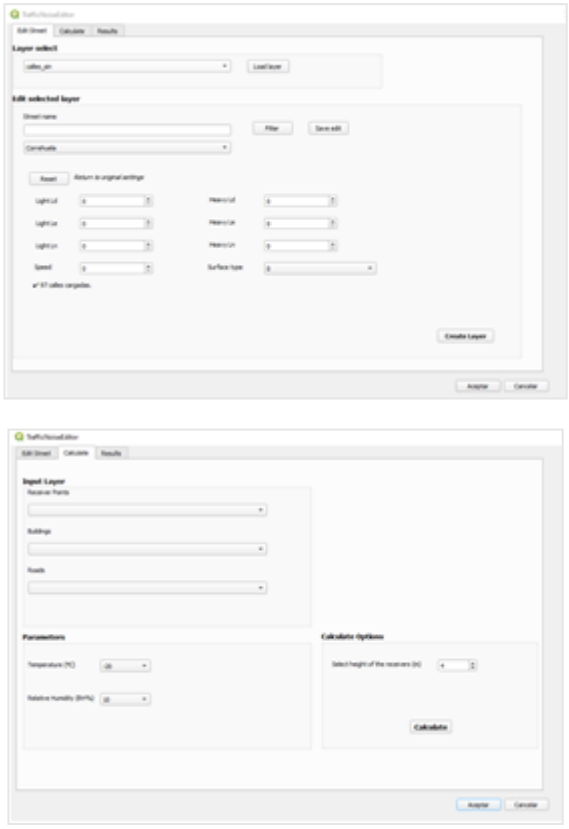


Figure 2. Prototype Model.

It should be noted that these calculations do not account for factors such as the topography of the terrain or the acoustic absorption properties of various urban elements. Furthermore, the search radius for assigning values to receptors is limited to 50 meters. However, in the context of Low Emission Zones, where the analysis focuses on small areas, this approach is sufficiently valid to support decision-making. These simplifications enable faster processing times and dynamic visualization of the effects of the proposed measures, facilitating a quick and effective assessment of their impact on urban noise pollution.

In addition, the tool has been designed with an adaptive approach that allows it to be adapted to the specific characteristics of each city. This enables it to be configured to accommodate different types of road infrastructure, analysis criteria, and local regulations, offering a flexible solution for planning noise mitigation strategies in LEZ environments.

As a prototype, the tool is in the initial development phase and can be refined and adapted in the future based on emerging needs and methodological advancements.

Being developed in QGIS environment, this tool leverages the full range of benefits offered by this open-source software, including its visualization and geospatial analysis capabilities. Users can overlay multiple layers of information, perform spatial queries, and combine results with other environmental or urban data available within the project. This enables a more comprehensive interpretation of the impact of the measures implemented and facilitates the integration of acoustic variables into urban planning processes. Furthermore, as part of the QGIS ecosystem, the tool is compatible with a wide variety of data formats and can be easily adapted to meet the specific needs of each city, ensuring its applicability across diverse urban contexts.

One of the key advantages of this tool is its accessibility for users who are not familiar with the QGIS environment. Thanks to its intuitive interface, no advanced knowledge of geospatial editing methods is required to modify traffic parameters. Users can quickly make adjustments through the integrated questionnaire, enabling them to incorporate changes such as traffic volume, speed, or pavement type with ease. This ease of use broadens the tool's accessibility to a wider audience, including urban planners, local authorities, and other non-technical users, empowering them to make informed decisions without the need for specialized GIS expertise.

4. PROTOTYPE VALIDATION PILOT TEST.

In 2023, Audiotec was responsible for updating the fourth-phase of the strategic noise map and action plan in the city of Salamanca, a municipality in Castilla y León (Spain) with a population of over 140,000 inhabitants.

During the duration of the Noise Action Plans, the Low Emission Zone is expected to be implemented.

The Low Emission Zone, expected to have a highly beneficial impact on environmental noise, is designed as a ring system, given that Salamanca is a radial city with its epicenter at Plaza Mayor, the city's geographic and cultural hub.

The first of the rings encompasses an area of approximately 600 000 m², which is being fully pedestrianized. It merges

areas that previously contained intermediate corridors and adds new streets and squares that were once designated for unrestricted motor vehicle movement. All access points to this area will be monitored by cameras equipped with license plate recognition.



Figure 3. Pedestrian area.

The second perimeter shares its northern boundary with the first and spans approximately 1 500 000 m²; it encompasses the entire first ring road of the city, along with both banks of the River Tormes. This area includes all the monuments that contributed to Salamanca being designated a UNESCO World Heritage City, making it essential to protect the health of its inhabitants.



Figure 4. Low Emission Zone (ZLE) area.

The Low Emission Zone (LEZ) of Salamanca has been selected to test and validate the developed acoustic module. This decision is based on the availability of sufficient cartographic and demographic data to feed the model, as well as the existence of previous results obtained using the commercial software CadnaA. A comparison was then made between the model generated with CadnaA and the prototype acoustic tool developed.

The analyzed area of the LEZ has a population of 14 665 inhabitants. The evaluation enables the analysis of differences in the estimation of environmental noise impact and health indicators for the population, as well as the verification of the prototype's usefulness in the acoustic management of these areas. It is important to note that the prototype is not intended to be standardized software, but rather an analytical tool whose results should be interpreted relatively, rather than absolutely. Its goal is to provide an accessible tool for municipal technicians responsible for managing Low Emission Zones (LEZ), enabling them to evaluate alternative scenarios using free and commonly available software.

4.1 Analysis of acoustic receivers in façades

When comparing the estimated values at the receptors on the façades of both models for a typical building in the LEZ, it can be observed that the model generated with CadnaA presents slightly higher noise levels on certain façades, particularly in areas with greater exposure to traffic.

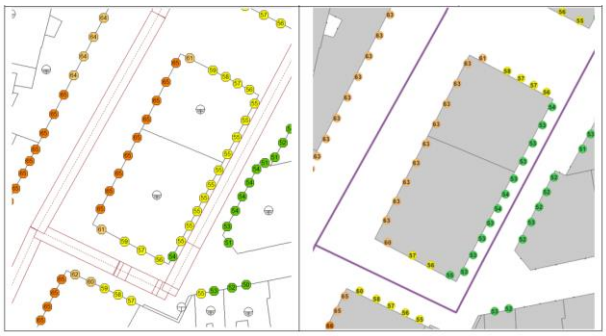


Figure 5. Noise levels in facade. CadnaA model on the left and GIS model on the right.

The maximum difference between the two models is approximately 2 dBA.

The following graphs display the distribution of the percentage of receivers as a function of the acoustic index value within the range of 55 to 69 dBA for three time periods (day, evening, and night) in the analyzed LEZ. Each graph compares the values obtained using the

commercial software CadnaA with those from the developed acoustic prototype, see Fig.6.

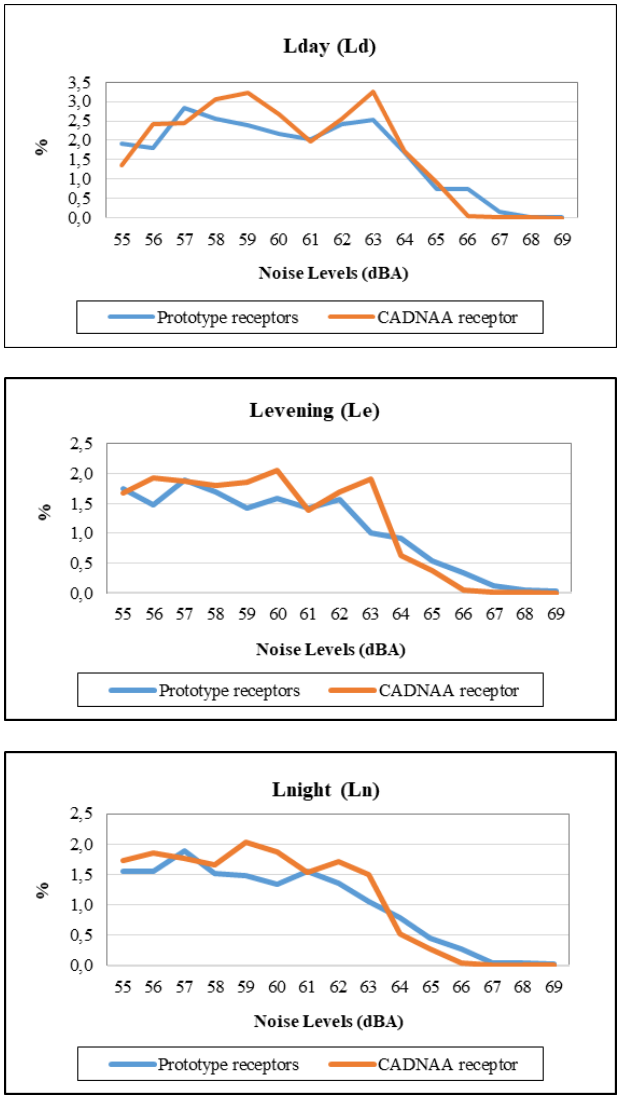


Figure 6. Distribution of the percentage of receptors across three time periods (day, evening, and night) in the analyzed Low Emission Zone (LEZ).

In all three time periods, the distribution of the percentage of receptors is similar in both models.
It is observed that the maximum number of receptors occurs at intermediate values, followed by a gradual decrease as the noise level increases.

The developed acoustic prototype shows significant agreement with the results obtained using CadnaA, with differences falling within an acceptable range for decision-making in the management of the LEZ.

4.2 Analysis of the population impacted by environmental noise

In the evaluated Low Emission Zone (LEZ), the results for the number of people and the percentage of the population exposed to noise, as estimated by both methods, have been compared across the different acoustic indicators, see Table 1:

Table 1. Population exposed to noise.

Acoustic Indicator	CadnaA		Prototype	
	Number of people	% population	Number of people	% population
Ld > 65 dBA	215	1.47%	374	2.56%
Le > 65 dBA	229	1.57%	371	2.53%
Ln > 55 dBA	2596	17.70%	2538	17.31%

The results indicate that, although the values estimated by both methods are similar, the prototype estimates a higher number of people affected during the daytime (Ld) and evening (Le) periods compared to the CadnaA software, while the differences are smaller during the nighttime (Ln) periods.

The Ln indicator has been chosen as the reference to study the distribution of people by ranks and the percentages of the population exposed to noise. The results obtained are as follows, see Table 2:

Table 2. Population exposed to noise based on the Ln indicator.

Nighttime noise level range (Ln, dBA)	CadnaA		Prototype	
	Number of people	% population	Number of people	% population
50 < Ln ≤ 55	2897	19.75%	2550	17.39%
55 < Ln ≤ 60	2433	16.60%	2238	15.26%
60 < Ln ≤ 65	163	1.10%	300	2.05%
Ln > 65	0	0%	0	0%

It is observed that both models provide similar estimates; however, the acoustic tool prototype, compared to CadnaA, predicts lower impairment in the 50-55 dBA

and 55-60 dBA ranges, but higher impairment in the 60-65 dBA range.

4.3 Analysis of health indicators related to environmental noise

In addition to acoustic information, the prototype enables the calculation of health indicators related to noise exposure. The results obtained are presented below, see Table 3:

Table 3. Population exposed to noise according to health indicator.

Health Indicator	CadnaA		Prototype	
	Number of people	% population	Number of people	% population
Nxy_ECI	180	0.82%	180	0.82%
Nxy_MI	1385	6.28%	1341	6.08%
Nxy_AGS	287	1.30%	275	1.25%

The estimated values of the health indicators obtained using the prototype are very similar to those obtained using CadnaA.

5. CONCLUSIONS

As part of an R&D project aimed at developing a comprehensive and accessible prototype to assist decision-makers in defining and assessing the economic, social, and environmental impacts of Low Emission Zones (LEZs) in urban areas, Audiotec has developed a module that enables the assessment of environmental noise in LEZs.

The acoustic module has been developed based on the Common Noise Assessment Methods in Europe (CNOSSOS-EU) for road traffic noise, although certain simplifications have been made to the methodology to enhance its agility and operational efficiency, as well as to expand its use to operators working with open-source software.

A pilot test has been conducted to validate the module in the LEZ of the city of Salamanca by comparing the results obtained from the acoustic module with those estimated in the municipality's strategic noise map. The differences between the two methods are not significant, and it can be concluded that the developed acoustic module provides reliable information.

The acoustic module offers several advantages over standard commercial programs for environmental noise prediction, including reduced processing times, ease of use, strong dynamic visualization capabilities for the effects of proposed measures, and quick, effective evaluation of noise-related health indicators and the impact of noise pollution in LEZ.

6. REFERENCES

[1] GIDAHATARI. Modelamiento de Ruido Urbano con opeNoise. < http://gidahatari.com/ihes/modelamiento-de-ruido-urbano-con-openoise> [Consulta: Septiembre 2017]

[2] DIDAC, D.; MARTINEZ, J.; LLIMPE, C. E. (2017). Comparación de mapas de ruido obtenidos con software libre (opeNoise v0.3.1) Y COMERCIAL (Predictor-LimA v11.10). LA CORUÑA

[3] I. Soto et al. “Análisis comparativo de softwares de simulación de ruido ambiental: comparación entre una solución comercial y una de código abierto”, (Cuenca, España), 2023.

[4] UMRAE - Lab-STICC, “Noise Modelling software Scientific production,” 2022.

[5] P. Aumond et al., “Strategic noise mapping in France to 2023: Coupling a national database with the open source software NoiseModelling,” 2022.

[6] J. Fogola et al. “Openoise: A free and open source project for environmental noise assessment”. Arpa Piemonte – Environmental Protection Agency for the Piedmont Region, Italy, 2023.

[7] SOTO, I; SEGUÉS, F; ARCE, R. "Sensitivity analysis in the calculation of the exposed population in the strategic noise maps of the Fourth Phase, according to the methods proposed by Delegated Directive (EU) 2021/1226 for the distribution of population in receptors." National Congress on Environmental Impact Assessment, Madrid 2022.

[8] Order PCI/1319/2018, of December 7, which amends Annex II of Royal Decree 1513/2005, of December 16, which implements Law 37/2003, of November 17, on noise, regarding the assessment of environmental noise.

[9] Order PCM/542/2021, of May 31, which amends Annex III of Royal Decree 1513/2005, of December

16, which implements Law 37/2003, of November 17, on noise, regarding the assessment and management of environmental noise.

[10] SOTO, I and ARCE, R. “Critical analysis of the application of Order PCM/542/2021, of May 31, which amends Annex III of Royal Decree 1513/2005, of December 16, which implements Law 37/2003, of November 17, on noise, regarding the assessment and management of environmental noise in the fourth phase of the Environmental Noise Directive”. 53rd Spanish Congress on Acoustics and XII Iberian Congress on Acoustics, 2022.

[11] Ministry for Ecological Transition and the Demographic Challenge: "Basic guide with recommendations for the application of the CNOSSOS-EU method”, 2025.

[12] Strategic Noise Map of Salamanca (4th phase)

[13] Action Plan for Noise Pollution in the Municipality of Salamanca (4th Phase)

DOI: 10.61782/fa.2025.0800



FORUM ACUSTICUM
EURONOISE 2025

SOUNDSCAPE EVALUATION OF RESIDENTIAL OUTDOOR SPACES BASED ON A SUBJECTIVE QUESTIONNAIRE AND OBJECTIVE ACOUSTICAL MEASURES

Manuel Isenegger[1*] **Thomas Steiner**[2] **Gregor Heini**[1]
Lél Bartha[1] **Ulrike Sturm**[2] **Armin Taghipour**[1]
[1] Institute of Electrical Engineering
[2] Institute of Sociocultural Community Development
Lucerne University of Applied Sciences and Arts, Switzerland

ABSTRACT

With the increasing attention to soundscape concepts in noise policy discussions and the recent integration into legislation in some regions, there is a growing need for objective measures to assess soundscape quality. In a project funded by the Swiss Federal Office for the Environment, various acoustical, room-acoustical, and psychoacoustical parameters identified through acoustic literature, as well as preliminary research and measurements, were used to evaluate soundscape quality. These parameters include, among others, L_{Aeq}, RT60, STIPA, sharpness, loudness, tonality, and fluctuation strength. Additionally, environmental factors such as nearby noise sources, greenery, and spatial morphology were documented. Measurements were conducted in four residential outdoor spaces in Switzerland and compared to subjective evaluations obtained from a small group of participants at the same locations. This paper presents the measurement results and subjective evaluations, along with a statistical analysis comparing the two datasets. Based on the findings, a method for the objective assessment of soundscapes is proposed, and recommendations for improving soundscape quality are discussed.

Keywords: *Soundscape quality, Soundscape Evaluation, Soundscape indices, ISO 12913*

*__Corresponding author__: manuel.isenegger@hslu.ch.
__Copyright__: ©2025 Manuel Isenegger et al. This is an open-access article distributed under the terms of the Creative Commons Attribution 3.0 Unported License, which permits unrestricted use, distribution, and reproduction in any medium, provided the original author and source are credited.

1. INTRODUCTION

According to the ISO 12913-1 standard, a soundscape is an ”acoustic environment as perceived or experienced and/or understood by a person or people, in context” [1]. This definition entails the inclusion of holistic principles and subjective views of the people experiencing the soundscape [2, 3]. For legislative purposes, objective, simple and reproducible methods to assess the quality of soundscapes are needed, however. Different researchers have thus proposed objective evaluation methods, a review of which can be found in [4]. The ISO/TS 12913-2 and 12913-3 standards [5, 6] propose a number of methods for the collection and analysis of soundscape studies, investigations and applications. Different, more recent efforts aim for a simplification of soundscape evaluation by providing single number indices [7, 8].

The Swiss Federal Council proposed an amendment to the Environmental Protection Act (EPA), according to which, among other things, the planning of additional residential housing in noise-polluted areas should also include the provision of open spaces/quiet areas for recreation and measures to ensure an acoustically appropriate quality of living. These requirements need to be specified and objectified. As part of a study for the Swiss Federal Office for the Environment FOEN, the physical and perceived soundscape qualities of urban residential courtyards at four locations in Switzerland were investigated by the authors. The goal of the study is to provide insights for the as of yet not clearly defined minimum requirements and guideline values in the context of soundscape design in view of aforementioned changes to the Environmental Protection Act. This interdisciplinary project aimed to de-

velop an objective evaluation method for soundscape assessment and classification. Both acoustic measurement methods and qualitative survey methods of soundscape perception were tested and compiled into suitable sets of methods. These were tested on four case studies - different residential courtyards in four Swiss cities. Subsequently, the acoustic and qualitative results were checked for consistency and initial findings were derived.

2. METHODS

2.1 Selection of objects

The aim of the object selection was to achieve heterogeneity in the survey of the soundscape quality of different recreational spaces in housing areas. The main parameters for the selection were their noise situation, proportion of greenery, and character as a publicly used space. All objects are surrounded by residential buildings. The soundscapes are located in four different cities in Switzerland (see Tab. 1).

Table 1: Selection of soundscapes

No.	Object	City
1	Erlenmatt Ost	Basel
2	Park Humboldtstrasse	Bern
3	Himmelrich 3	Luzern
4	Zwicky-Areal	Zürich

2.2 Acoustical measurements

Measurement variables were chosen according to results found in the scientific and normative literature, linking them to subjectively perceived soundscape quality [4, 5, 9, 10]. The main data acquisition methods included the measurement of sound pressure level (*SPL*), reverberation time (*RT60*), speech transmission index (*STI*) and room impulse responses (RIR). Binaural audio recordings were made and used for the extraction of psychoacoustic metrics. Additional metrics were extracted from the RIRs and audio files, recorded by the sound level measurement device. Measurement methods were adapted according to the findings of a preliminary study [11]. This includes the measurement of sound pressure level during different times of the day, a high number of measurement repetitions for reverberation time measurements and the possible division of the soundscape into sub-spaces with different acoustical characteristics. A complete list of the measured and calculated variables can be found in Tab. 2.

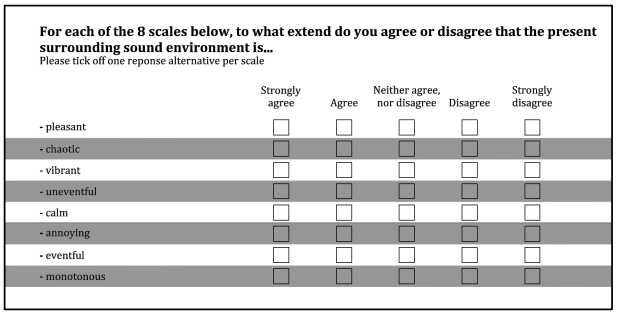


Figure 1: Questionnaire related to the perceived soundscape quality according to ISO/TS 12913-2 [5]

2.3 Subjective Survey

Soundscapes are inextricably linked to their uses and users. However, a mere description of uses and users is not sufficient for describing how soundscapes are perceived. It is the meaning which respondents (users) attribute to uses and other users that provides clues to how the soundscape is perceived.

Based on results of previous research ([25] and ISO/TS 12913-2 [5]), the following procedure was designed for the survey in the four soundscapes.

1. Questionnaire survey on the perception of the soundscape with the following questions:
   - Opening question: what do you hear? (Please indicate in descending order of clarity) the various sound sources that you can identify (e.g., “children,” “airplane,” “birds,” ... maximum of 8).
   - Three statements regarding the perception of sounds and soundscape, rated on a 5-point scale: It’s loud here / it’s acoustically pleasant here / the sounds fit the surroundings.
   - How do you perceive the soundscape? (ISO/TS 12913-2 dimensions [5]; see Fig. 1).
2. On-site focus group discussion on perception of the soundscape, guided by the following questions:
   - What do you like about this place? Why?
   - What is the quality of stay of this place? What defines it?
   - How would you rate the ”room acoustics” of this courtyard?

Table 2: Acoustical measurement variables with measurement/calculation method

Variable	Method	Ref.
SPL with different time and frequency-weightings, as well as percentiles	4 measurements of 15 minutes between 08:00 and 18:30 hours per area	[12]
RT60 (T30)	1 measurement with 10-12 repetitions per area	[13]
STI	1 measurement distances 1m/4m 8 repetitions per measurement	[14]
RIR	1 measurement distances 1m/4m	[15]
Sharpness	Evaluation of 4 binaural audio recordings of 15 minutes between 08:00 and 18:30 hours	[16] [17]
Loudness	See *Sharpness*	[18]
Harshness	See *Sharpness*	[19]
Tonality	See *Sharpness*	[20]
Mel Frequency Cepstral Coefficients (*MFCC*)	Evaluation of the audio recordings from the *SPL* measurements	[21]
Spectral Slope	See (*MFCC*)	[22]
Time Frequency Second Derivative (*TFSD*)	See (*MFCC*)	[4]
Echo criterion	Evaluation with RIR-measurements	[23]
Percentage of green/blue	Calculation of green/blue from views of typical seating locations	[24]

- What sounds/soundscape would you typically expect in this place?
- Would you want to live here? Why/why not?

3. Questions regarding additional assessment positions:

   - What has changed in the sounds/soundscape compared to the center of the courtyard?

Note: Evaluating audio recordings without direct spatial reference at other times of day has not proven effective. For spaces characterized by different areas, this survey should be conducted separately for each area.

3. RESULTS

3.1 Acoustical measurements

Tab. 3 shows average values across all measurements, positions and measurement repetitions of the four soundscapes. The averaged L_{Aeq} values are significantly lower in Basel and Bern, while the *RT60* measurement shows similar values across objects. The median values of the *STI* measurements at a distance of 1 meter are above limit A (high speech intelligibility, complex messages, unfamiliar words) for 3 objects. Depending on the room and measurement position, the values fluctuate between the F (Good quality PA systems, complex messages, familiar context) and A ratings (see Fig.2). At a distance of 4 meters, the median value in Basel remains at level D, while the values of the other objects drop to level H (normal lower limit for VA systems, simple messages, familiar context).

Table 3: Averaged results of the measurements

Parameter	Basel	Bern	Luzern	Zürich
L_{Aeq} [dB]	50.02	53.39	61.90	58.51
RT60 [s]	1.29	1.44	1.35	1.24
STI 1m	0.88	0.77	0.73	0.71
STI 4m	0.65	0.47	0.51	0.45
Percentage of Green	21.9%	64.9%	14.6%	15.8%

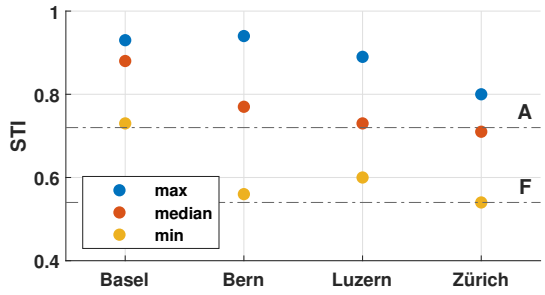


Figure 2: Measured *STI* values at 1 m distance

3.2 Subjective Survey

Mean ratings of the ISO items are shown in Fig. 3 for the four locations investigated in this study.

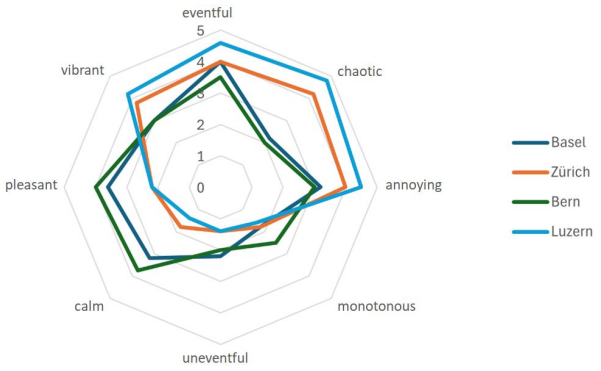


Figure 3: Survey results of soundscape perception according to ISO/TS 12913-2.

The following indications for the planning of soundscapes can be derived from the case studies:

- Greenery and proximity to nature (also sounds of nature) is associated with a more positive perception of the soundscape.
- Attractive utilization options and high-quality design can improve the quality of stay.
- The above positive criteria can only partially compensate for high-level noise pollution.
- A variety of possible uses and the presence of other people play a decisive role in whether people feel comfortable or not.
- Identification with the space, its uses, and people present fosters a positive soundscape perception.

3.3 Comparison of acoustical and subjective data

A post hoc correlational analysis was conducted to investigate the extent of the association between quantifiable subjective perception indications and objective data. A few examples are shown in the following.

3.3.1 Percentage of green

Tab. 4 shows correlations between *Percentage of green* and the subjective quantitative items (translated from German). Strong associations are observable: courtyards with more greenery were perceived as more pleasant, calming, and less noisy or annoying. A saturation of the positive greenery effect can be observed in Fig. 4.

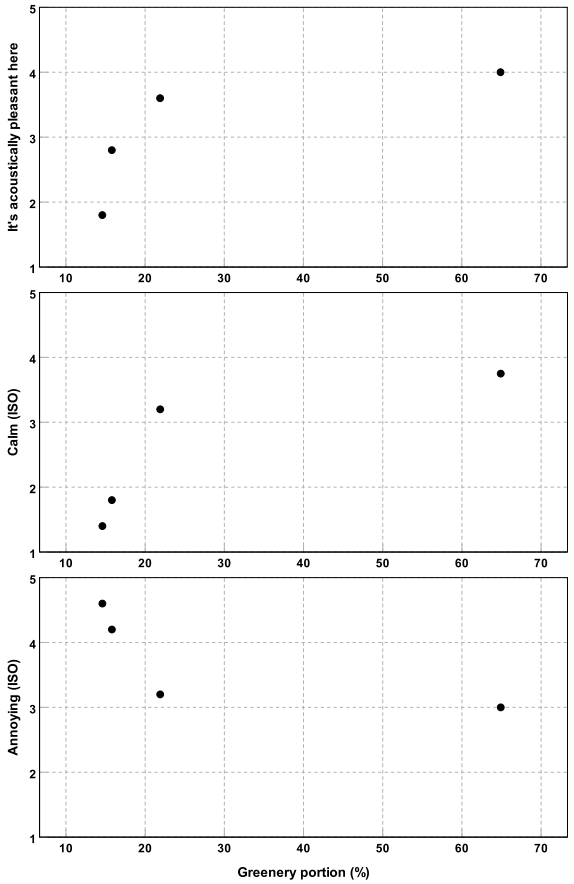


Figure 4: Mean subjective ratings for the items *It's acoustically pleasant here*, *Calm (ISO)*, and *Annoying (ISO)* as a function of *Percentage of green*.

Table 4: Correlations between *Percentage of green* and *STI* and the subjective ratings. Significant ($p < 0.05$) and highly significant correlations ($p < 0.01$) are marked with * and **, respectively.

	Green (%)		*STI*	
	r	p	r	p
It's loud here	-.585**	.008	-.863**	.000
It's acoustically pleasent here	.555*	.014	.741**	.000
The sounds fit the surroundings	.253	.295	.090	.714
eventful (ISO)	-.303	.208	-.578**	.010
chaotic (ISO)	-.626**	.004	-.884**	.000
annoying (ISO)	-.575**	.010	-.786**	.000
monotonous (ISO)	.495*	.031	.420	.074
uneventful (ISO)	.233	.338	.409	.082
calm (ISO)	.611**	.005	.772**	.000
pleasent (ISO)	.522*	.022	.660**	.002
vibrant (ISO)	-.335	.162	-.503*	.028

3.3.2 STI

Correlations between the *STI* and the subjective quantitative items are presented in Tab. 4. Courtyards with high *STI* values (at 1 m) were rated more positively (see also Fig. 5). This was also the case for *STI* values measured at a distance of 4 m (not shown here).

3.3.3 RT60

The potential correlation between *RT60* and the subjective ratings was examined, but no such relationship was observed in the cases investigated in this study. Instead, the subjective evaluations appeared to be more strongly influenced by the *Percentage of green*, *STI*, and *SPL* than by *RT60*. This finding warrants further investigation, as it contrasts with previous results and recommendations reported in the literature [7, 10, 11].

3.3.4 Subjective methods

It was investigated whether the first three quantitative items (*It's loud here*, *It's acoustically pleasant here*, and *The sounds fit the surroundings*) are correlated with the ISO items. Tab. 5 shows that most items were significantly correlated, and in a reasonable and interpretable direction. Several items exhibited significant and strong correlations. Notably, this was not the case for the item *The sounds fit the surroundings*. The authors suggest that this item may represent a distinct dimension in soundscape assessment or may capture a novel factor in the context of factor analysis.

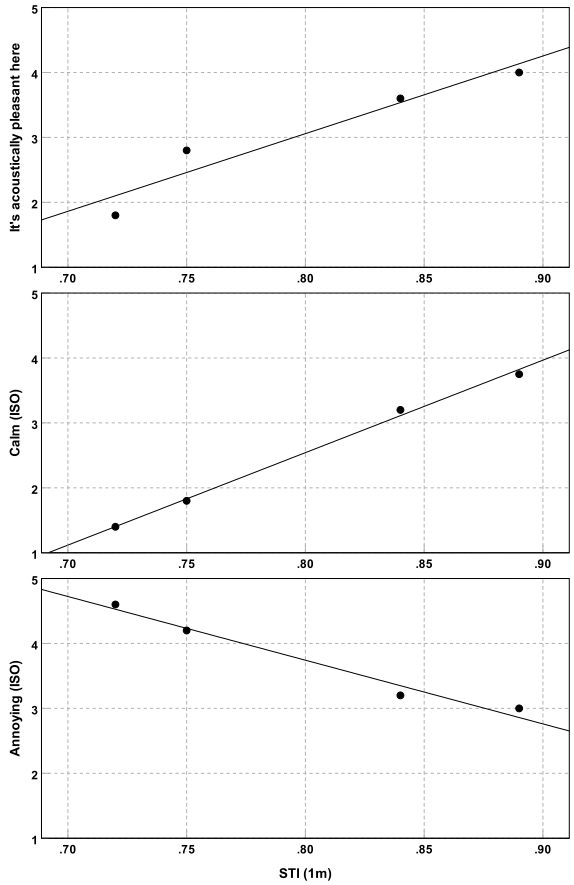


Figure 5: Mean subjective ratings for the items *It's acoustically pleasant here*, *Calm (ISO)*, and *Annoying (ISO)* as a function of *STI*.

Table 5: Correlations between the subjective items *It's loud here*, *It's acoustically pleasant here*, and *The sounds fit the surroundings*, and the ISO items. Significant ($p < 0.05$) and highly significant correlations ($p < 0.01$) are marked with * and **, respectively.

	It's loud		Acoustically pleasant		Sounds fit	
	r	p	r	p	r	p
It's loud here	1					
It's acoustically pleasant here	-.737**	.000	1			
The sounds fit the surrounding	-.011	.965	.323	.177	1	
eventful (ISO)	.658**	.002	-.663**	.002	-.158	.519
chaotic (ISO)	.803**	.000	-.763**	.000	-.208	.392
annoying (ISO)	.735**	.000	-.823**	.000	-.414	.078
monotonous (ISO)	-.230	.344	.153	.532	-.043	.862
uneventful (ISO)	-.420	.073	.374	.114	.171	.484
calm (ISO)	-.720**	.001	.875**	.000	.312	.193
pleasent (ISO)	-.696**	.001	.821**	.000	.402	.088
vibrant (ISO)	.588**	.008	-.394	.095	-.037	.881

4. DISCUSSION

4.1 Proposal for new evaluation method

Research into the perception of soundscapes requires the human perspective. The survey by a selected group of test subjects, who adopted the perspective of users, has provided results that, together with the measurement results, provide comprehensible interpretations. In particular, the separation into individual perception of the sound situation and a dialogue-based consideration in the group led to differentiated results and the integration of different perspectives. A strong agreement was observed between the objective measurement results and the subjective quantitative ratings across the different methods and items.

4.2 Limitations and further research

The sample size of objects (4) and participants (a maximum of 5 per room) in this study's subjective survey is limited. A larger sample size would enable more reliable statistical analyses, allowing the tendencies observed in this study to be verified.

5. CONCLUSIONS

This study investigated a combination of objective (acoustical) measurement methods and a subjective evaluation (including qualitative and quantitative items and focus group discussion) to assess soundscape quality in the vicinity of residential housing complexes. Four objects were investigated in this case study, representing various courtyards. The results emphasize the need for both objective and subjective evaluations. Acoustical data (e.g. *SPL*, *STI*) combined with non-acoustical parameters (e.g. *percentage of green*, natural elements) and qualitative descriptions (e.g., usage, design) were shown to provide provide a multi-disciplinary description of soundscapes, enabling evaluation. The quantitative survey data showed statistical correlations with the acoustical data to some degree. It was not possible to further simplify the evaluation using e.g. a point-based or traffic light system. Developing such a system would require a systematic investigation of all relevant factors, based on a substantially larger dataset and analysis using multi-factorial models. Furthermore, it remains uncertain whether an objective evaluation of soundscapes is achievable, as subjective, holistic and descriptive factors appear essential for a comprehensive assessment.

6. ACKNOWLEDGMENTS

This study was funded by the Swiss Federal Office for the Environment (FOEN) and authors' employer, The Lucerne University of Applied Sciences and Arts. The authors are grateful to the test subjects for their valuable contributions. Furthermore, the authors would like to thank Silvio Emmenegger, Mario Rölli, Mauro Ronchetti, Nadja Hutmacher, and Sandra Hollenstein for their contributions in the project.

7. REFERENCES

[1] ISO 12913-1:2014, "Acoustics - Soundscape – Part 1: Definition and Conceptual Framework," standard, International Organization for Standardization: Geneva, Switzerland, 2014.

[2] B. Schulte-Fortkamp and P. Jordan, "Soundscape: The holistic understanding of acoustic environments," in *Soundscapes: Humans and Their Acoustic Environment*, pp. 49–79, Springer, 2023.

[3] A. Taghipour, A. Gisladottir, F. Aletta, M. Bürgin, M. Rezaei, and U. Sturm, "Improved acoustics for semi-enclosed spaces in the proximity of residential buildings," in *Proc. of Inter-noise 2022*, (Glasgow, UK), 2022.

[4] M. Lionello, F. Aletta, and J. Kang, "A systematic review of prediction models for the experience of urban soundscapes," *Applied Acoustics*, vol. 170, p. 107479, 2020.

[5] ISO/TS 12913-2:2018, "Acoustics - Soundscape – Part 2: Data Collection and Reporting Requirements," standard, International Organization for Standardization: Geneva, Switzerland, 2018.

[6] ISO/TS 12913-3:2019, "Acoustics - Soundscape – Part 3: Data analysis," standard, International Organization for Standardization: Geneva, Switzerland, 2019.

[7] B. W. Hohmann, "Beurteilung der Klangqualität von Innenhöfen, Plätzen und Pärken als Erholungsorten im Siedlungsraum," tech. rep., Cercle Bruit Schweiz/Suisse, 2023.

[8] A. Mitchell, F. Aletta, T. Oberman, and J. Kang, "Soundscape perception indices (spis): Developing context-dependent single value scores of multidimensional soundscape perceptual quality," *The Journal of the Acoustical Society of America*, vol. 156, no. 6, pp. 3694–3706, 2024.

[9] R. Pheasant, K. Horoshenkov, and G. Watts, "Tranquillity rating prediction tool (trapt) acoust," *Bull*, vol. 35, pp. 18–24, 2010.

[10] A. Taghipour, S. Athari, A. Gisladottir, T. Sievers, and K. Eggenschwiler, "Room acoustical parameters as predictors of acoustic comfort in outdoor spaces of housing complexes," *Front. Psychol.*, vol. 11, p. 344, 2020.

[11] G. Heini, M. Isenegger, L. Bartha, T. Steiner, U. Sturm, and A. Taghipour, "Could acoustical, room acoustical, and psycho-
acoustical measures be utilized to quantify the soundscape quality of residential outdoor spaces?," in *30th International Congress on Sound and Vibration, ICSV 2024*, International Institute of Acoustics and Vibration (IIAV), 2024.

[12] ISO 1996-1:2016, "Acoustics - description, measurement and assessment of environmental noise – part 1: Basic quantities and assessment procedures," standard, International Organization for Standardization: Geneva, Switzerland, 2016.

[13] ISO 3382-2:2008, "Acoustics – Measurement of room acoustic parameters – Part 2: Reverberation time in ordinary rooms," standard, International Organization for Standardization: Geneva, Switzerland, 2008.

[14] IEC 60268-16, "Sound system equipment – part 16: Objective rating of speech intelligibility by speech transmission index," standard, International Electrotechnical Commission: Geneva, Switzerland, 2011.

[15] A. Farina, "Advancements in impulse response measurements by sine sweeps," in *Audio engineering society convention 122*, Audio Engineering Society, 2007.

[16] DIN 45692:2009-08, "Messtechnische Simulation der Hörempfindung Schärfe," standard, DIN, the German Institute for Standardisation: Berlin, Deutschland, 2009.

[17] ISO 532-1:2017, "Acoustics — Methods for calculating loudnessPart 1: Zwicker method," standard, International Organization for Standardization: Geneva, Switzerland, 2017.

[18] DIN 45631/A1:2010-03, "Berechnung des Lautstärkepegels und der Lautheit aus dem Geräuschspektrum - Verfahren nach E. Zwicker - Änderung 1: Berechnung der Lautheit zeitvarianter Geräusche," standard, DIN, the German Institute for Standardisation: Berlin, Deutschland, 2010.

[19] DIN 38455:2024-11, "Berechnung der Hörempfindung Rauigkeit," standard, DIN, the German Institute for Standardisation: Berlin, Deutschland, 2024.

[20] ECMA-74, "Measurement of Airborne Noise emitted by Information Technology and Telecommunications

Equipment," standard, ECMA international, Rue du Rhône 114, CH-1204 Geneva, Switzerland, 2022.

[21] A. Noviyanti, A. S. Sudarsono, and D. Kusumaningrum, "Urban soundscape prediction based on acoustic ecology and mfcc parameters," in *AIP Conference Proceedings*, vol. 2187, AIP Publishing, 2019.

[22] D. Botteldooren, B. De Coensel, and T. De Muer, "The temporal structure of urban soundscapes," *Journal of sound and vibration*, vol. 292, no. 1-2, pp. 105–123, 2006.

[23] K. W. Dietsch L., "Ein objektives Kriterium zur Erfassung von Echostörungen bei Musik- und Sprachdarbietungen," tech. rep., Technische Universität Dresden, Sektion Informationstechnik, Deutsche Demokratische Republik, 1985.

[24] R. Pheasant, K. Horoshenkov, G. Watts, and B. Barrett, "The acoustic and visual factors influencing the construction of tranquil space in urban and rural environments tranquil spaces-quiet places?," *The Journal of the Acoustical Society of America*, vol. 123, no. 3, pp. 1446–1457, 2008.

[25] U. Sturm, M. Bürgin, and A. Schubert, *Stadtklang – Wege zu einer hörenswerten Stadt 2 – Band 2: Klangraumgestaltung von Aussenräumen*. Zurich, Switzerland: vdf Hochschulverlag AG, 2019.

DOI: 10.61782/fa.2025.0037



FORUM ACUSTICUM
EURONOISE 2025

A SPATIAL PROCESSING FRAMEWORK FOR MAPPING AREAS BENEFITING FROM URBAN MORPHOLOGY AND BUILDING DESIGN IN AIRPORT REGIONS

Gustaf Wuite[1,2*] **Martijn Lugten**[1,2] **Rodrigo Vassallo**[1,2]
Arjan van Timmeren[1]
[1] Department of Urbanism, TU Delft, Netherlands
[2] AMS Institute for Advanced Metropolitan Solutions, Amsterdam

ABSTRACT

In many places, ongoing urban expansion, in conjunction with higher traffic volumes, have reduced or dissolved the separation between environmental noise zones. This is specifically the case near airports, with conflicting land-use demands for housing and flight operations. Apart from zoning, aircraft noise plays no role in urban design and form studies. Serving as tall noise barriers, recent studies in a designated test street demonstrated the potential of buildings as noise barriers for reducing aircraft noise in urban contexts. Correlating sound shielding levels with the elevation angle of passing aircraft, results from the test street environment were used for mapping shielding potential areas on a regional scale. This study introduces a spatial framework combining aircraft trajectory, and land-use, geo-data to determine such areas using a geo-spatial processing methodology in QGIS. It is applied the Amsterdam Schiphol airport region as case study.The methodology determines areas affected by noise from passing aircraft at elevation angles identified as most indicative for leveraging optimal shielding by buildings. The subsequent map layers can aid urban planners in decision-making processes for further exploring the potential of urban design for mitigating aircraft noise in urban airport regions, serving further tool development for livable and healthier neighborhood design.

*Corresponding author: f.g.e.wuite@tudelft.nl.

Copyright: ©2025 Gustaf Wuite et al. This is an open-access article distributed under the terms of the Creative Commons Attribution 3.0 Unported License, which permits unrestricted use, distribution, and reproduction in any medium, provided the original author and source are credited.

Keywords: *urban design, aircraft noise, noise mapping*

1. INTRODUCTION

Prolonged exposure to aircraft noise is associated with various health risks, both physical and psychological. For example, communities close to airports report higher cardiovascular hospital admission rates [1], and worse sleep quality [2], and have an increased risk of high blood pressure [3]. Compared to other traffic noise sources, aircraft noise is perceived as more annoying, at similar L_{DEN} noise levels. To mitigate and minimize aircraft noise effects, land use planning and management constitutes a priority of the International Civil Aviation Organization's "Balanced Approach" for noise reduction around airports [4]. A consequence of this approach is a strict regulation of housing developments through environmental zoning in the proximity to flight paths, depending on air traffic movements. The boundary conditions for land use and planning are defined by noise contours, generated computationally based on standardized methods, such as Doc29, INM (Integrated Noise Model), or national equivalents such as NRM (Netherlands Regional Model) in the Netherlands. For the case of Schiphol International Airport in the Netherlands, this amounts to a total area of 203 km^2 in which new housing projects and urban area (transformation) development is mostly prohibited (LIB 4), and or, an even greater surface of 384 km^2 where area development and housing expansion is strictly regulated (LIB 5) (See Fig. 1) [5]. This has resulted in so-called 'noise landscapes' around many airports, referring to land-use patterns and spatial typologies unique for airport regions. To

compromise computational overhead and model complexity, aircraft noise prediction methods rely on various assumptions for describing source, atmospheric and surface conditions. One of these assumptions is that the ground below a receiver position comprises flat surfaces, thus omitting the reflections and diffraction of sound waves in the built environment [6]. Although this approach seems acceptable valid under flat-field conditions based on annual aggregations, this is not the case for urban contexts.

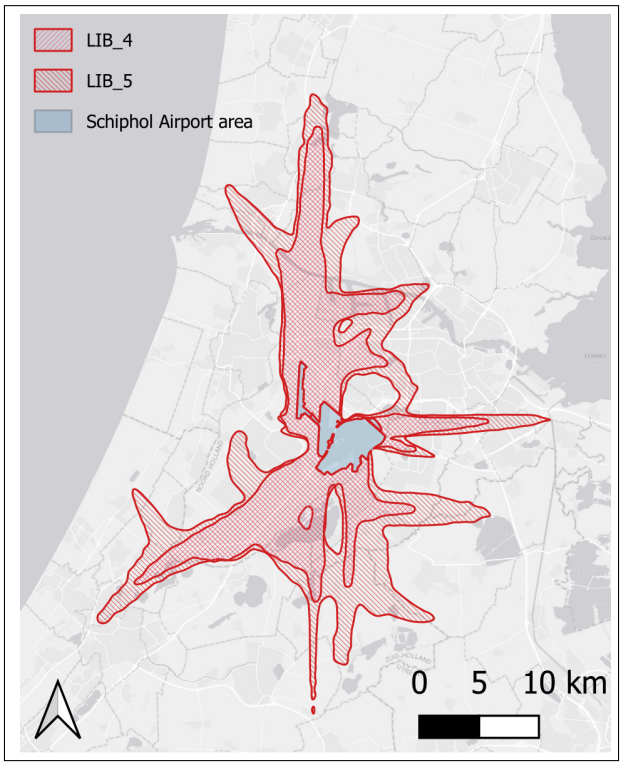


Figure 1. Areas of noise sensitive building restrictions and consideration between noise and external safety around Schiphol airport, Netherlands

Buildings, when placed parallel along flight paths, can function as noise barriers, reducing noise levels on the facade shielded from direct incident noise. This effect was investigated at the Urban Comfort Lab (abbr. UCLab) from 2022-2024, with a full-scale measurement facility consisting of 120 shipping containers arranged to recreate the urban form of three different courtyard configurations. Long-term measurements were conducted, and recorded a mean A-weighted sound exposure level (abbr. ASEL) reduction of 8.1 dB(A) between exposed and shielded building sides for two-story courtyards [7]. The addition of a slanted roof on the exposed side to reduce courtyard noise reflection effects, and a building inset on the shielded side to reduce diffraction levels, further increased the mean ASEL difference to 11.6 dB(A). These ASEL differences were measured for flights passing the facility at a mean elevation angle at closest point of passing of 37 degrees (abbr. °), with a standard deviation of $\pm 7°$.

While these findings demonstrate the potential of the use of buildings to reduce local sound levels, the integration of these effects into land use management and planning is lacking. Despite demonstrating the potential of low-rise urban canyons for aircraft noise reduction for a single test site consisting of three canyons, the potential of the UCLab results at regional scale largely remain unclear. Also, such cross-scale extrapolation at full scale of airport operations would allow for further examination of the impact of this approach, compared to the existing spatial zoning regime and described aircraft noise prediction methods. Assuming similar noise reductions for the range of elevation angles passing the UCLab, this study proposes a first assessment entailing the integration of the built environment into the strategic noise planning in airport regions.

This study presents a methodology for mapping the number of daily flyovers at elevation angles recorded in the UCLab for regions around airports using QGIS and historical ADS-B aircraft positional data as input. The methodology is then applied to a test case of Schiphol airport, for flights departing and arriving in January 2023. Finally, an exploration into the integration of the generated maps in land use planning is conducted.

The objectives of this study are defined as follows:

1. Design of a methodology that maps aircraft flyovers at defined elevation angles for airport regions.
2. Application of the methodology to aircraft arriving and departing from Schiphol airport in January 2023.
3. Examining the spatial consequences of the method in comparison with e.g. existing noise zoning and land-side aircraft noise mitigation schemes.

2. METHODOLOGY

Based on the study conducted by Lugten et al. [7], one can expect courtyard ASEL shielding effects between 8.1

dB(A) and 11.6 dB(A) for flights passing at a mean elevation angle of 37° at closest point of passing , with a standard deviation of ±7°. Within this elevation angle range, it is assumed urban canyon morphologies similar to UCLab can yield equivalent noise reduction levels between exposed and shielded building facades. This elevation angle range of 30° and 44° can be extrapolated along flight paths. The measured ASEL differences are assumed independent of ground distance [8]. Results depend accordingly on the altitude of the aircraft (see Fig 2), leading to ground areas parallel to the flight path. The areas increase in width and in distance from the ground flight path with increasing aircraft altitude. Within these two boundaries, the method presented in this paper assumes that the urban geometry akin the UCLab design is applicable and will yield comparable noise shielding effects.

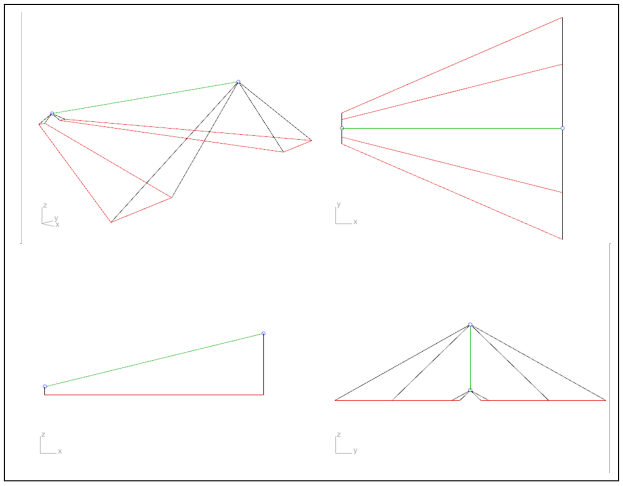


Figure 2. Flight path following a straight ascent (green) and applicable areas for noise-adaptive building (red) in perspective view (top left), top view (top right), side view (bottom right), and under flight path (bottom right)

For spatial mapping purposes, the open-source geospatial software QGIS (version 3.34) was used to create the processing framework. The methodology is generated in the graphical modeler environment, using native processing algorithms and processing scripts created using the QGIS Python Console. A graphical overview of the input, processing steps, relevant parameters, and output is shown in Figure 3. The input data is of format line .shp data. The line data contain z (altitude) variables of all vertices of each flight. The line data are fed into the model and split up into vertices. Vertices with an altitude between 50 and 1500 meters are extracted. 50 meters as a lower threshold is defined to remove flight points on the runways. The higher threshold is set to reduce computational overhead, under the assumption that aircraft passing at an altitude of 1500 m and higher do not lead to high noise exposure. Subsequently, variable width buffers are calculated for maximum and minimum elevation angles, with the width defined as altitude/tan(elevation angle). Differences between the lower and upper boundary elevation angle buffers are generated per feature and intersected with a flat end buffer., leading to ground areas parallel to the flight paths in which the aircraft passes at an elevation angle between 30° and 44°. The resulting area for a single flight is displayed in Fig. 4

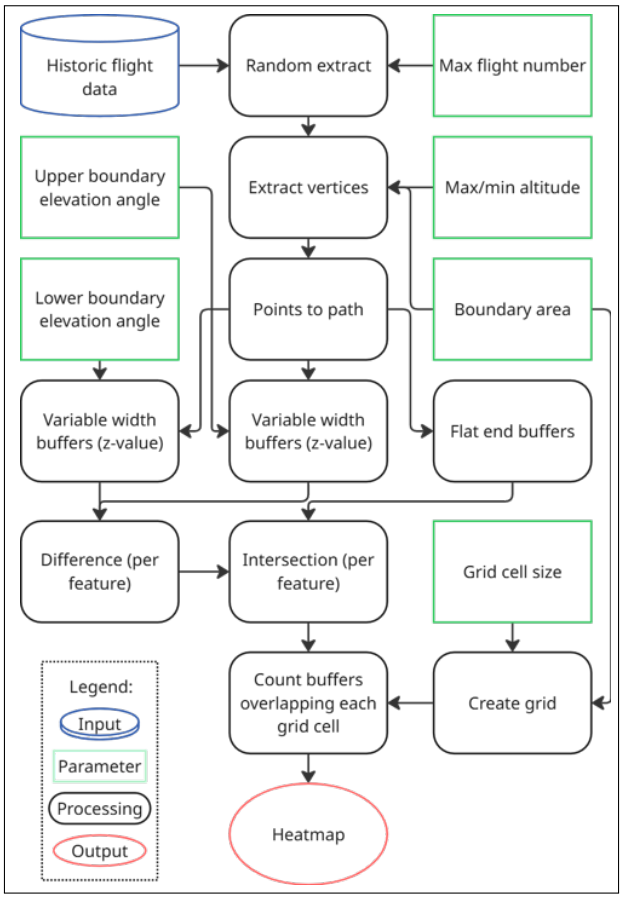


Figure 3. Geo-processing flowchart of the developed spatial framework

To map the number of flights passing locations on the

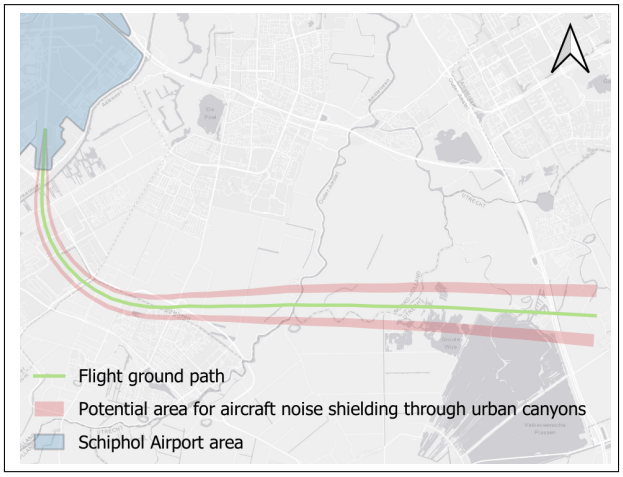


Figure 4. Flight path (green) of Flight KLM831 departing from Schiphol Airport (blue) to an altitude of 1500m on Jan 1st 2023 and altitude-dependent potential area (red)



Figure 5. Grid cell map layer displaying the number of flights passing at an elevation angle range between 30° - 44 °

ground at the defined elevation angles, a hexgrid of 200m x 200m is generated within a predefined boundary area around Schiphol airport, based on the extent of the LIB 5 layer. For each grid cell, the amount of buffers overlapping the cell are counted, creating an index of the total flights passing at an angle between 30° and 44° at closest ground distance between flight path and grid cell. The index is divided by the amount of days of the period of analysis, yielding the number of flights per day to identify areas with high daily flyover rates at elevation angles suitable for noise shielding through urban canyons. Fig 5 shows an example output of the processing methodology. Grid cells recording less than 4 flights per day are removed from the dataset for legibility.

3. AMSTERDAM SCHIPHOL AIRPORT

To test the methodology's applicability, the processing framework was applied to the region surrounding Amsterdam Schiphol airport, in the Netherlands. The line input data consist of all flights departing and arriving from Schiphol airport during January 2023, based on ADS-B radar data retrieved from Casper flight data portal, provided by the airport authority. For processing capacity reasons, for the case study presented in this paper a only half of the data was used, based on randomized selection, resulting in a total of 15545 flights. For data processing a laptop computer was used (11th Gen Intel(R) Core(TM) i7-1185G7 @ 3.00GHz with 16GB RAM), requiring a runtime of 13 hours. Figure 6 shows the resulting grid layer for the area surrounding Schiphol airport. The main arrival and departure routes are visible. Arrivals can be distinguished from departures, characterized by straighter and narrower surface boundaries due to fixed arrival trajectories. In contrast, climb rates are steeper for departures compared to arrivals, resulting in 'shorter' areas per flight path, which are also more curved and less fixed.

4. GEO-SPATIAL AND LAND-USE ANALYSES

Apart from the area plots, the density maps presented in the previous section can be combined with other spatial datasets, e.g. related to the spatial distribution of complaints, building stock and facade insulation data, and/or planned location for housing development or urban retrofitting.

For example, Figure 7 combines the density grid with residential land use and planned residential areas layers and with Dutch Spatial Legislation for Airport Land-side Management layers LIB 4 and LIB 5 [**?**]. Within LIB 4, housing projects and urban area (transformation) development is mostly prohibited. In LIB 5, area development and housing expansion is strictly regulated. These maps indicate which areas might benefit from the findings as introduced in this article. One such (illustrative) exam-

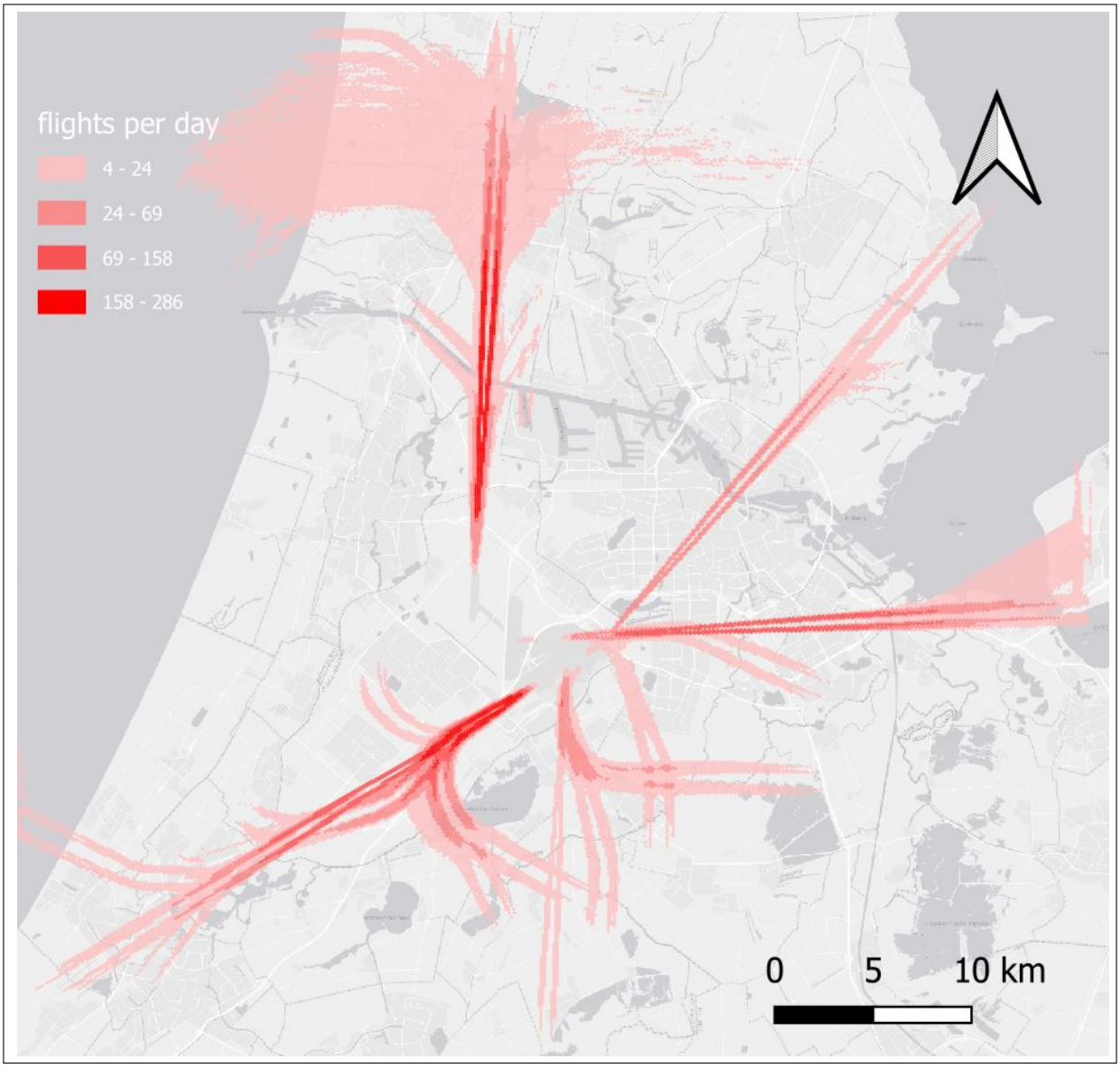


Figure 6. Number of flights passing at an elevation angle range between 30° and 44° per grid cell for flights to and from Schiphol airport in January 2023

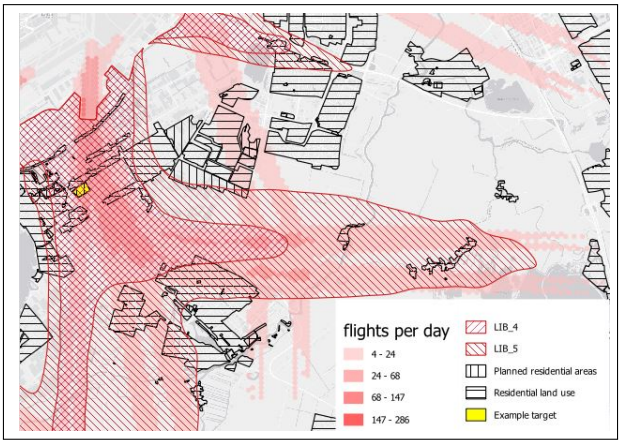


Figure 7. Overlay of spatial processing output, LIB 4 and LIB 5 zones, (planned) residential land use and spatial processing output, with high potential example target

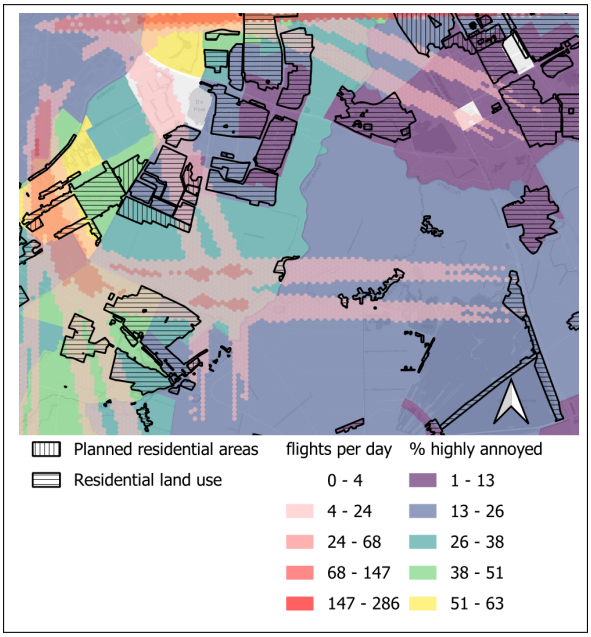


Figure 8. Overlay of spatial processing output, (planned) residential land use areas, and percentage of inhabitants highly annoyed by aircraft noise per neighborhood

ple area is highlighted in Figure 7, indicating a planned residential development in the LIB 4 zone, with a high frequency of flyovers within the elevation range allowing the use of urban form for noise shielding. Thereby these maps could aid spatial planners, urban designers - but also airport and governmental authorities - in determining for which locations additional 'urban and architectural form' oriented measured could be investigated and considered. To further pinpoint areas of heightened interest, grid density maps can be combined with noise annoyance data. Figure 8 shows flight paths and the percentage of highly annoyed inhabitants by aircraft noise per neighborhood. Neighborhood shape files are sourced from the Dutch national Geo-registry [9], the noise annoyance per neighborhood is sourced from the RIVM open StatLine data portal [10] . Although higher noise levels largely coincide with higher noise annoyance, it is advisable to take into account both where data allows.

5. CONCLUSIONS

In this article a spatial analysis framework is presented, aimed at identifying areas in which building and urban design interventions may contribute to aircraft noise attenuation in urban contexts. Using aircraft flight data, the framework generates a grid overlay to extrapolate small-scale findings to the mesoscale airport regions. The method calculates the number of aircraft passing at elevation angles fitting the conditions for building-induced shielding effects between 8.1 dB(A) and 11.6 dB(A) derived from in-situ measurements in a test canyon for each grid cell. This added layer of spatial information presents areas which meet similar conditions, based on cross-scalar spatial extrapolation of measurement results. The outcomes are useful for e.g. identifying where urban design might be of further interest for aircraft noise mitigation in existing and planned housing and area developments around airports. The method takes into account e.g. aforementioned elevation angles, derived from flight data obtained for a test location in which extensive measurements were carried out. Factors including variations of atmospheric refraction over longer distances were omitted for this method. Sound shielding variances arising from weather variables could be studied as part of future research. While this methodology delivers robust results for the analyzed area and time-frame, extended aggregation for the time period of a full representative year is envisioned. This time-frame will allow for more accurate representation of the flight distribution arriving to, and departing, from Schiphol airport.

6. REFERENCES

[1] A. W. Correia, J. L. Peters, J. I. Levy, S. Melly, and F. Dominici, "Residential exposure to aircraft noise and hospital admissions for cardiovascular diseases: multi-airport retrospective study," *Bmj*, vol. 347, 2013.

[2] R. van Poll, M. Reedijk, J. Hoekstra, W. Swart, J. van de Kassteele, and D. Houthuijs, "Relaties vliegtuiggeluid–hinder en slaapverstoring 2020. civiele en militaire vliegvelden in nederland," 2023.

[3] W. H. Organization *et al.*, "Burden of disease from environmental noise: Quantification of healthy life years lost in europe," in *Burden of disease from environmental noise: Quantification of healthy life years lost in Europe*, 2011.

[4] I. C. A. Organization, *Guidance on the balanced approach to aircraft noise management*. International civil aviation organization, 2004.

[5] "wetten.nl - Regeling - Luchthavenindelingbesluit Schiphol - BWBR0014329 — wetten.overheid.nl." https://wetten.overheid.nl/BWBR0014329/2024-01-01. [Accessed 07-04-2025].

[6] H. Van der Wal, P. Vogel, and F. Wubben, "Voorschrift voor de berekening van de lden en lnight geluidbelasting in db (a) ten gevolge van vliegverkeer van en naar de luchthaven schiphol; part 1: Berekeningsvoorschrift," *National Aerospace Laboratory*, 2001.

[7] M. Lugten, G. Wuite, Z. Peng, and M. Tenpierik, "Assessing the influence of street canyon shape on aircraft noise: Results from measurements in courtyards near amsterdam schiphol airport," *Building and Environment*, vol. 255, p. 111400, 2024.

[8] G. Wuite, M. Lugten, and M. Tenpierik, "Determining causes of variance in ground-level aircraft noise: Combining in-situ noise and weather measurements with spatial aircraft data," in *Forum Acusticum 2023: 10th Convention of the European Acoustics Association*, pp. 5481–5488, Politecnico di Torino, 2023.

[9] "Nationaal georegister — nationaalgeoregister.nl." https://nationaalgeoregister.nl/geonetwork/srv/dut/catalog.search#/metadata/caeb52a3-cbaa-4e9b-a23e-d4dc0335b506. [Accessed 07-04-2025].

[10] "CBS Dataportaal — statline.rivm.nl." https://statline.rivm.nl/portal.html?_la=nl&_catalog=RIVM&tableId=50090NED&_theme=94. [Accessed 07-04-2025].

DOI: 10.61782/fa.2025.0347

FORUM ACUSTICUM EURONOISE 2025

ENHANCING URBAN ACOUSTIC COMFORT: THE ROLE OF FREE SURFACES, GREEN SPACES AND WATER BODIES IN MITIGATING ROAD TRAFFIC NOISE

Costanza Vittoria Fiorini[*1] **Vincenzo Battistini**[2] **Momisch Calanna**[2] **Luca Quaranta**[2] **Claudia Guattari**[3] **Anna Tarsitano**[2] **Andrea Vallati**[1]

[1] DIAEE Dipartimento di Ingegneria Astronautica, Elettrica ed Energetica, Università di Roma "Sapienza", Via Eudossiana 18, 00184, Roma,

[2] Diapason Ingegneria srl , Viale Pola, 6, 00198 Roma

[3] Dipartimento di Filosofia Comunicazione e Spettacolo, Università degli Studi Roma TRE, Via Ostiense, 234, 00146 Roma

ABSTRACT

This study examines the role of urban free surfaces—parks, trees, water bodies and open squares—in mitigating road traffic noise in adjacent buildings. Case studies focused on built-up areas near roads with defined traffic levels, including aligned frontages, widened streets and urban courtyards with corner buildings.

Free surfaces were analyzed using parameters such as the green-to-paved surface ratio, grass-to-tree vegetation ratio, tree height, and percentages of green areas, paved areas and water bodies. Noise level measurements (LAeq), were taken at different times of the day and under various weather conditions, to understand the acoustic contributions of these surfaces. Qualitative data and measurements enabled the verification of parameter distributions (e.g., green-to-paved surface ratio, grass-to-tree ratio, vegetation height) in relation to LAeq, considering seasonal features and surrounding building heights. Multivariate regression identified linear relationships between factors. Finally, an average dynamic absorption coefficient was estimated for open spaces, treating them as equivalent absorbing areas. This coefficient, influenced by seasonal and meteorological variations, allows modeling of open spaces as acoustically active surfaces. It also provides a basis for designing optimal configurations, offering practical recommendations for urban planners and policymakers to improve acoustic comfort in urban environments.

Keywords: *road traffic noise, urban design, acoustic measurement, acoustic absorption, multivariate regression model, optimization algorithm*

1. INTRODUCTION

Acoustic absorption in urban spaces is a crucial topic for improving the quality of life in densely populated cities. With the increase in urban noise, mainly due to traffic and other human activities, it is essential to develop effective strategies to reduce noise pollution and enhance the acoustic environment. The importance of developing quiet areas within urban environments is addressed at the European directive level by the European Directive 2002/49/EC "European Directive relating to the assessment and management of environmental noise".

In this context, urban design should not be limited to considering noise indicators, but must also integrate human perception into the definition of the acoustic landscape. Aspects such as acoustic quality, the type of predominant sounds, and acoustic contrast with the surrounding environment are indeed decisive, as well as thermal and visual comfort [1].Greenery, in city landscape or building envelopes, helps mitigate the

[*] ***Corresponding author***: costanzavittoria.fiorini@uniroma1.it

Copyright: *©2025 First author et al. This is an open-access article distributed under the terms of the Creative Commons Attribution 3.0 Unported License, which permits unrestricted use, distribution, and reproduction in any medium, provided the original author and source are credited.*

urban heat island [2], with trees and hedges reducing peak temperatures by up to 7 K and green roofs by up to 3 K. Alongside thermal control, greenery components and water bodies contribute to citizens' mental balance and noise mitigation. Water bodies like lakes and rivers can cool urban areas by evaporation: 1 kg of water can lower the temperature of 2000 m³ of air by 1 K. Water surfaces are generally cooler than built environments, reducing air temperature through convection. Passive systems such as pools and fountains are commonly used in public spaces for both decoration and climate regulation [3, 4]. There is growing interest in the relationships between acoustics and urban planning, particularly in how factors such as urban density, morphology, land use, street distribution, the surrounding street environment and green spaces influence sound dynamics [5, 6]. [7,8] developed models to characterize urban sound environments, focusing on selecting key variables that aid in decision-making for the effective characterization of environmental urban noise. Some studies have shown that sound fields in urban squares surrounded by reflective façades present a uniform reverberation time (RT), while the initial decay time (EDT) is low in the near field and increases rapidly with distance, approaching the RT. Sound pressure level (SPL) attenuation is generally smaller with geometric boundaries compared to diffuse ones, unless the height/width ratio is high [9, 10]. Adding absorptive materials to façades or the ground can increase sound attenuation by 2-4 dB. Reducing building height or creating spaces between buildings can further provide sound attenuation [10]. Directives promoting urban acoustic design face the challenge of integrating acoustic planning with urban design. This process requires the support of specialized technicians and adequate time for accurate calculations, which are often difficult to manage during the preliminary design phases. For detailed analyses, the UNI 9613-2 standard is used to calculate the ground effect attenuation (Agr) for a specific octave band. Agr is determined by summing the attenuations of the three regions involved in the sound path—source (As), receiver (Ar), and intermediate (Am)—based on the ground factors of the corresponding terrain (Gs, Gr, Gm) and the source (hs) and receiver (hr) heights. Ground factors range from G = 0 for reflective surfaces (pavement, concrete, water) to G = 1 for highly absorptive surfaces (agricultural soil, sand, earth), while for mixed terrain, $0 < G < 1$, depending on the fraction of porous ground.

This work purposes a data-driven optimization framework, implemented in Python, developed to determine the optimal distribution of urban surfaces (green areas, paved areas and water bodies) to achieve a target equivalent sound absorption coefficient (α_eff) for a given available area. The workflow is based on Leq measurements conducted in urban spaces with different geometric configurations and various horizontal surface treatments, and consists of three key steps: data preprocessing, regression modeling, and constrained optimization.

2. METHODOLOGY

2.1 Selection of Study Sites

Three urban configurations were chosen for consideration: Aligned Frontages, Widened Streets, and Courtyards (Fig. 1). For each of these, 15 study sites were identified across the neighborhoods of Rome's EUR and Parioli districts (Fig.2). This selection ensured that the buildings were from the same construction period, and therefore had similar construction techniques and materials. The buildings facing the chosen open spaces are also of comparable height, ranging from 5 to 6 stories. the focus of this phase is to account for and compare the effects of the planimetric configuration of the buildings on the open spaces between them, rather than different aspect ratios. The selected sites are also similar in terms of building density, typology and traffic volumes.

2.2 Measurement Campaign

The case study employed Brüel & Kjær 2250 sound level meter to measure and collect data on the environmental SPL of selec ted urban areas. SPL was measured on working days in February 2025. To ensure consistent traffic conditions, measurements were carried out during three time intervals: 8:00–10:00, 12:00–14:00, and 16:00–18:00. Sound pressure levels were recorded at a height of 1.5 meters, corresponding to the average ear level of a standing person. At each measurement point, 15-minute recordings were performed. The weather during the measurement was stable, sunny, with a temperature of 15-20°C and a wind speed of 3 m/s.

2.3 Data Collection and Processing

The sound pressure levels measured at each receiver point were normalized with respect to the same traffic volumes to obtain comparable results. The actual Lw was adjusted to 74 dB, which corresponds, according to

the ROUTES NMPB 96 model, to 86 light vehicles and 8 heavy vehicles passing at a speed of 50 km/h. This reference Lw′ was chosen since it reflects average traffic volumes across the dataset, and ensures a balanced comparison without biasing results toward high or low traffic intensity scenarios. To adjust Lp accordingly, the general relationship between sound power level and free-field sound pressure level was used.

$$Lp=Lw-10\log(S)+DI-A \quad (1)$$

where S is the area over which the sound energy is distributed, DI is the directivity, and A is the attenuation in the propagation path from source to receiver, which accounts for atmospheric absorption, ground effect, presence of barriers, and additional types of attenuation such as vegetation, industrial sites and densely built-up areas.



Figure 1. (a) Widened Street-Tipo1, (b) Aligned Frontages-Tipo2, (c) Courtyards-Tipo 3.



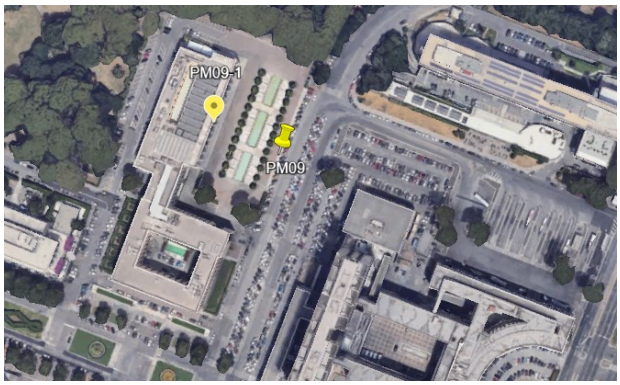


Figure 2. Measurement points in EUR

If the propagation type, the distance of the measurement point from the source, the directivity, and the environment remain constant, we can assume:

$$Lp'=Lp+(Lw'-Lw) \quad (2)$$

Where Lw'=74 dB (3)

Having identified paved area, green area and water body area as predictive variables, it was necessary to recognize and assess the extent of these surfaces in each urban space examined. The spaces were analyzed by defining the study area as the space bounded by the streets (5.5 m width for each traffic flow direction) and the fronts of the buildings facing it (Fig 1). To determine the area occupied by trees, an average was considered for each tree between the area of the trunk and the area of the canopy.

3. RESULTS: ACOUSTIC ANALYSIS OF FREE SURFACES

3.1 Influence of Urban Configuration and Surface Composition on Noise Levels

Figures 3, 4, and 5 demonstrate the effect of green, paved, and water surface treatments on the frequency distribution of noise for the selected urban configurations. In Widened Streets, all surface types showed similar performance at frequencies up to 63 Hz, but differences emerged at higher frequencies. Green areas performed poorly at lower frequencies, while paved surfaces began to outperform green ones around 630 Hz.

Table 1. Measurements results.

		Point	Lw	Light vehicles	Heavy vehicles	Leq	L1	L5	L10	L50	L90	L95
TIPO2	greenery	1	74	86	8	60.08	71.7	66.9	64.5	54.3	48.7	47.1
TIPO2	pavement	2	71.4	70	3	62.5	69.4	65	63.7	59.4	54.9	54
TIPO1	greenery	3	70	69	1	61.9	71.2	67.9	65.3	57.2	52	50.5
TIPO1	pavement	4	72	90	3	60.8	70.5	64.7	63.3	53.5	47.8	46.8
TIPO3	greenery	6	73.6	99	6	58	66.9	62.7	61.1	55.4	49.7	48.8
TIPO3	greenery	7	77	120	19	61.3	70	66.1	64.4	58.4	53.6	52.4
TIPO3	pavement	8	78.3	316	16	64.7	75.2	67.5	65.4	60.8	57.5	56.8
TIPO1	water	9	76	77	17	57	64.7	62	60.6	54.6	50.8	50.1
TIPO2	water	10	77.3	153	19	65.1	72.2	69.5	68.2	63.7	59.2	58.1

Table 2. Analysis of free spaces treatments and Leq normalized results (Lp) with respect to Lw' = 74 dB.

		Green-Paved Ratio	Grass-Tree Ratio	Tree Height (m)	Green Area	Paved Area	Water Body	Green Area (%)	Paved Area (%)	Water Body (%)	Open Space (m²)	Lw (dB)	Lp (dB)
TIPO1	3	2.00	0.3	3	5054.09	2523.91	0	67	33	0	7578	74	65.9
TIPO1	4	0.16	0.5	3	2108.53	13010.67	0	14	86	0	15119.2	74	62.8
TIPO1	9	0.37	0.4	3	2519.88	6813.34	1316.12	24	64	12	10649.34	74	55
TIPO2	1	10	10	3	3952	0.00001	0	100	0	0	3952	74	60.08
TIPO2	2	0	0	0	0	2084	0	0	100	0	2084	74	65.1
TIPO2	10	0.82	10	3	4852	5923	28625	12	15	73	39400	74	61.8
TIPO3	6	8.95	1	3	23594.37	2635.55	0	90	10	0	26229.92	74	58.4
TIPO3	7	4.76	0.7	3	13711.22	2882.05	0	83	17	0	16593.27	74	58.3
TIPO3	8	0	0	0	0	13390.73	0	0	100	0	13390.73	74	60.4

Water bodies provided the best acoustic benefits starting at 160 Hz. In Aligned Frontages, green spaces improved acoustic performance from 63 Hz to 1000 Hz due to the sound-absorbing properties of vegetation, but water bodies had mixed effects. They offered some benefits at lower frequencies but worsened at higher frequencies, likely due to reflection and scattering. In Courtyards, paved surfaces performed better than green areas, with a 6.45 dB higher Leq in paved areas, likely due to the reflective properties of paved surfaces that help distribute sound evenly. In general, a trend can be observed in the influence of surface treatments on

acoustic performance of various urban settings: green areas offer sound absorption, water bodies excel at mid-to-high frequencies but can cause issues at lower and higher ones, and paved surfaces provide stable acoustic performance, particularly in courtyard environments. Urban designers should consider these factors when planning for desired acoustic outcomes.In the analysis of urban spaces, sound level fluctuations, evaluated between L90 and L5 (Table 1), varied depending on the surface type and traffic volumes. The smallest fluctuations were observed in Type 1 areas with water, while the highest occurred in Type 1 areas with green surfaces and pavement. These differences may be linked to the urban space configuration, as traffic volumes were similar, indicating the layout's influence on acoustics. For Type 2 areas, water features caused the least fluctuation, followed by pavement and green surfaces. However, the result is less reliable due to the traffic volume being double in the water scenario compared to the others. In Type 3 areas, fluctuations remained stable regardless of traffic volume. Notably, fluctuations in pavement areas with 300 vehicles were slightly lower than in green areas with 150 vehicles, suggesting that surface type is more influential than traffic volume on acoustic variation.

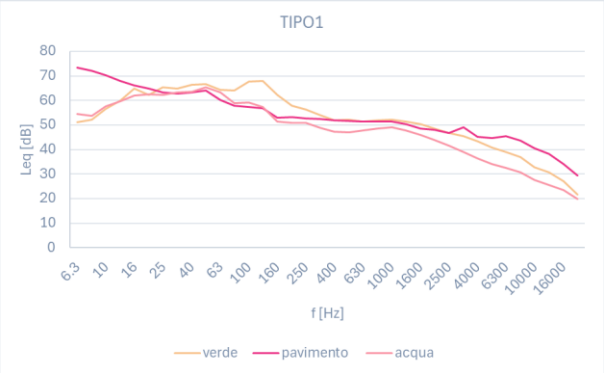


Figure 3. Widened Street.

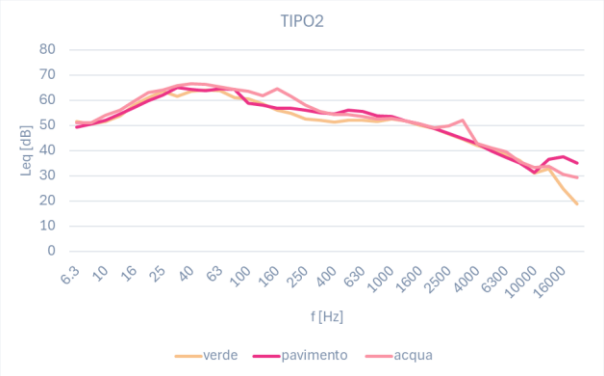


Figure 4. Aligned Frontages.

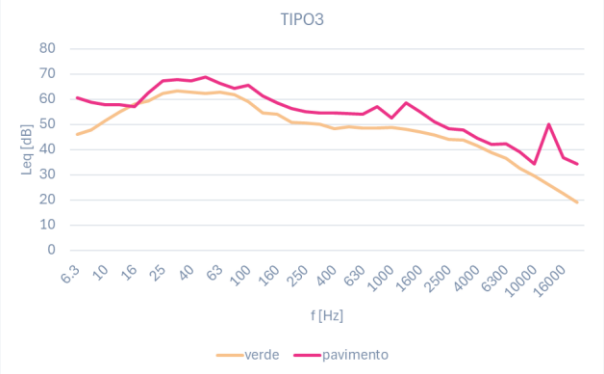


Figure 5. Courtyards.

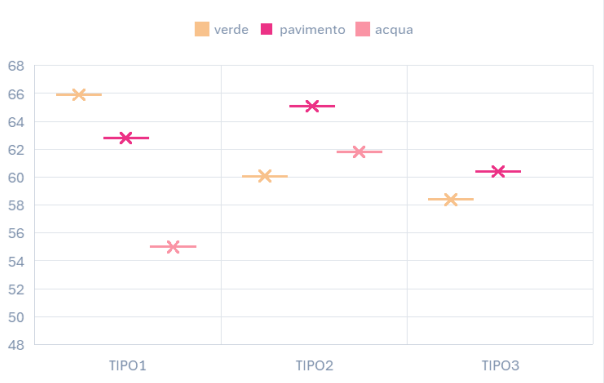


Figure 6. Treatments and urban layouts influence on Leq.

The analysis of global noise levels (Leq) in identical urban configurations with varying surface treatments

(Fig. 6) revealed that in Widened Streets, water was the most effective treatment, followed by pavement and green surfaces. For Alignments, green surfaces performed best, with pavement and water following. In Courtyards, green surfaces also provided the best noise reduction, with pavement in second place. As a whole, water proved more effective in type 1 configurations than in type 2, suggesting that water sources contribute to better noise management. Pavement in type 1 yielded the best results, followed by type 2 and type 3, indicating that the materials used in type 1 are more efficient in reducing noise. Greenery performed best in type 3, with a decline in effectiveness in types 2 and 1. The ideal configuration was type 1 with water, while type 3 with pavement was the least favorable, possibly due to high traffic volume, which requires further normalization specified below.

3.2 Estimation of the Absorption Coefficient: Multivariate Regression and Linear Relationships

Having conducted several measurements in urban spaces containing open areas of various sizes, and having Leq data for comparable traffic volumes, it is possible to estimate an average absorption coefficient for an open space by treating it as an equivalent absorbing area. This approach is useful for modeling open spaces as acoustically active surfaces with a simplified overall behavior. Acoustic and surface data are loaded in Python from a CSV file, containing measured sound pressure levels (L_p_meas), source power levels (L_W), and surface percentages. The effective absorption coefficient (α_eff) is computed as:

$$\alpha\text{eff} = S\text{eq}/(\%A\text{green} + \%A\text{paved} + \%A\text{water}) \quad (4)$$

where Seq represents the equivalent absorbing surface area derived from acoustic measurements

$$S\text{eq} = 10\text{^}((LW - Lp,\text{meas})/10) \quad (5)$$

A first-order polynomial regression (Ordinary Least Squares, OLS) is fitted to correlate α_eff with the three surface types. The model includes an intercept term to ensure physical interpretability, as there is always a contribution from the geometry of the surrounding environment and atmospheric conditions. The models obtained for the Widened Streets, Aligned Frontages and Courtyards configurations are reported in Eq. (6), Eq. (7), and Eq. (8), respectively, where GA = Green Area, PA = Paved Area, and WA = Water Body Area. Table 3 provides the distribution of surface treatments, the absorption coefficients calculated using Eq. (4) and Eq. (5), and those obtained by applying the models developed for Widened Streets.

$$\alpha\text{eff} = 0.000455 * 1 + 0.001461 * \text{GA (\%)} + -0.000654 * \text{PA (\%)} + 0.044671 * \text{WA (\%)} \quad (6)$$

$$\alpha\text{eff} = 0.000050 * 1 + 0.002657 * \text{GA (\%)} + 0.000626 * \text{PA (\%)} + 0.001747 * \text{WA (\%)} \quad (7)$$

$$\alpha\text{eff} = 0.000032 * 1 + 0.003972 * \text{GA (\%)} + 0.002599 * \text{PA (\%)} + -0.003357 * \text{WA (\%)} \quad (8)$$

Table 3. Comparison between α_eff calculated by acoustic equation and polynomial regression for Widened Streets (TIPO1).

	Green Area (%)	Paved Area (%)	Water Body (%)	α eff	α eff predicted
0	67	33	0	0.06	0.08
1	14	86	0	0.13	-0.04
2	24	64	12	0.79	0.53
3	20	69	11	0.40	0.48
4	26	69	5	0.25	0.22
5	45	50	5	0.28	0.26
6	30	60	10	0.48	0.45
7	20	69	11	0.40	0.48
8	26	69	5	0.25	0.22
9	50	45	5	0.20	0.27
10	15	80	5	0.11	0.19
11	35	55	10	0.52	0.46
12	10	85	5	0.10	0.18
13	40	50	10	0.35	0.47
14	5	90	5	0.08	0.17

Model significance is verified via summary statistics such as R-squared, p-value, correlation matrices and Variance Inflation Factor (VIF) (Tab.4, Tab.5).
The model for Typology 1 (Eq. 6) demonstrates a good explanatory capacity ($R^2 = 0.722$), with variable x_3 significantly contributing to sound absorption ($\beta = 0.0447$, $p < 0.001$). However, the presence of multicollinearity (Cond. No. = 6.94×10^{18}) suggests caution in interpreting the coefficients of x_1 and x_2, which are not statistically

significant. The multicollinearity analysis revealed a strong inverse correlation between green areas and paved surfaces ($r = -0.87$), further confirmed by VIF values > 10.
The model for Typology 2 (Eq. 7) shows an excellent fit to the data and is statistically significant overall. The p-values indicate that all variables are significant.
The model for Typology 3 (Eq. 8) explains 65.8% of the variability in α_eff and is globally significant ($R^2 = 0.658$, $p = 0.0005$), with x_1 and x_2 positively influencing α_eff ($p < 0.001$). However, the presence of multicollinearity (Cond. No. = 2.34×10^{18}) and non-normal residuals suggests caution in interpretation and highlights the need for improvements, such as handling multicollinearity through Ridge Regression techniques and increasing the sample size.

Table 4. α_eff prediction accuracy.

	average Δ (eff-eff_predicted)	average α_eff_predicted
TIPO 1	0.082	0.294
TIPO 2	0.012	0.164
TIPO 3	0.026	0.293

Table 5. Statistical results.

	Variable	**Std Err**	**t-value**	**p-value**
TIPO 1	const	6.62E-05	6.867	<0.001
	x1	0.001	1.049	0.315
	x2	0.001	-0.749	0.469
	x3	0.008	5.946	<0.001
TIPO 2	const	1.70E-05	1.889	0.080
	x1	0	17.708	<0.001
	x2	0	11.572	<0.001
	x3	0.002	-1.752	0.102
TIPO 3	const	1.71E-06	29.45	0.001
	x1	8.77E-05	30.29	0.001
	x2	8.34E-05	7.51	0.001
	x3	0	8.85	0.001

3.3 Constrained optimization tool

A nonlinear optimization problem is solved to find the surface distribution that, given the total available area (A1) and a desired target value of *α_eff,* minimizes the squared error between predicted and target *α_eff*:

$$\text{minimize}(\alpha\text{pred} - \alpha\text{target})$$

subject to constraints:

$$A\text{green} + A\text{paved} + A\text{water} = A\text{total}$$

Bounds ensure each surface percentage lies within [0,Atotal]. The solver uses an initial guess of equal distribution (33% per surface).
The algorithm returns the optimal surface percentages (e.g., 45% green, 30% paved, 25% water) or reports convergence failure. The results of TYPE 2 appear to be evenly distributed among the treatment types (Tab. 6). Keeping the study area unchanged but imposing α_eff = 0.6, the optimization yields 64.4% Green Area and 35.6% Water Body.

4. CONCLUSIONS

The analysis was automated through a Python script that combines regression modeling and constrained optimization. Acoustic data were processed to compute an effective absorption coefficient (α_eff) for each studied area, which was then correlated with surface compositions using first-order polynomial regression (OLS), providing a characteristic polynomial for each urban configuration. An optimization routine was implemented to determine the optimal surface distribution to achieve a target α_eff under area constraints, offering a scalable tool for urban noise mitigation design to mitigate the impact of urban noise on receivers, in terms of sound pressure levels at building façades.

Table 6. Example of optimization algorithm application.

	Green Area (%)	**Paved Area (%)**	**Water Body (%)**
	A1=100, α=0.3		
TIPO1	46	48	5.9
TIPO2	33.3	33.3	33.3
TIPO3	51.7	43	5.3

Summary of findings

- Configuration-specific α_eff integrates empirical acoustic measurements with surface composition.
- First-order polynomial terms prevent overfitting while effectively capturing linear relationships.
- The developed design tool provides practical, actionable recommendations and implications for urban planning.

Limitations and future research directions

- Besides area extension in widened streets and courtyards, aspect ratio and maximum source distance should also be considered.
- The linearity between α_eff and surface ratios is likely due to the limited number of samples; a greater number of experimental Lp will allow for extensions to higher-order terms, capturing nonlinear effects.
- The simplified method for α_eff proved valid for fixed-distance data; for greater flexibility with variable distances, the full physical approach including source geometry and directivity will be implemented.
- Increasing the sample size and refining the regression model will improve statistical robustness; future developments will include frequency-domain analysis and economic constraints in optimization.

5. ACKNOWLEDGMENTS

The authors thank Andrea Lucio Posteraro, graduate student in Building Engineering-Architecture at Sapienza University, for conducting the measurement campaign.

Funded by the European Union NextGenerationEU

The work of C.V. Fiorini was funded by the European Union-Next Generation EU under the PNRR (National Recovery and Resilience Plan – NEST "Network 4 Energy Sustainable Transition" – PE2 NEST Spoke 8 – B53C22004070006).

6. REFERENCES

[1] Morillas, Juan & Rey Gozalo, Guillermo & Mg, David & Moraga, Pedro & Vílchez-Gómez, Rosendo. (2018). Noise Pollution and Urban Planning. Current Pollution Reports. 4. 1-12. 10.1007/s40726-018-0095-7.

[2] Manteghi, G., bin Limit, Hasanuddin, Remaz, Dilshan, 2015. Water bodies an urban microclimate: a review. Mod. Appl. Sci. 9 (6), 10.

[3] M. Santamouris, L. Ding, F. Fiorito, P. Oldfield, P. Osmond, R. Paolini, D. Prasad, A. Synnefa, Passive and active cooling for the outdoor built environment – Analysis and assessment of the cooling potential of mitigation technologies. Solar Energy, 2017, 154, 14–33. http://dx.doi.org/10.1016/j. solener.2016.12.006

[4] Dayi Lai, Wenyu Liu, Tingting Gan, Kuixing Liu, Qingyan Chen, A review of mitigating strategies to improve the thermal environment and thermal comfort in urban outdoor spaces. Science of the Total Environment, 2019, 661, 337–353. https://doi.org/10.1016/j.scitotenv.2019.01.062

[5] WangB,KangJ.Effects ofurban morphology on the traffic noise distribution through noise mapping: a comparative study between UKand China. Appl Acoust. 2011;72:556–68.

[6] Primus Francesco. Morfologia urbana e rumore. Tesi Di Laurea Magistrale (Relatori Shtrepi Louena, Astolfi Arianna), Politecnico di Torino. (2021)

[7] Torija AJ, Genaro N, Ruiz DP, Ramos-Ridao A, Zamorano M, Requena I. Priorization of acoustic variables: environmental decision support for the physical characterization of urban sound en vironments. Build Environ. 2010;45:1477–89.

[8] Spatial Analysis of Noise Contour Maps Based on Traffic Speed Using Predictor-LimA Software

[9] Kang, J. (2005). Numerical modeling of the sound fields in urban squares.. *The Journal of the Acoustical Society of America*, 117 6, 3695-706 . https://doi.org/10.1121/1.1904483.

[10] Valle, F., Veres, E., Brodbeck, M., Xiaoru, Z., & Zannin, P. (2021). Acoustic Behavior and Design of Large Urban Spaces – Canyon and Tunnel. *Revista Nacional de Gerenciamento de Cidades*. https://doi.org/10.17271/2318847297220212962.

DOI: 10.61782/fa.2025.0181

FORUM ACUSTICUM EURONOISE 2025

BRINGING SOUNDSCAPE AURALIZATIONS TO THE URBAN CITY PLANNING

Josep Llorca-Bofí[1, 2*] **Hou Hin Au-Yeung**[1] **Moritz Lippold**[3] **Christa Reicher**[3,4]
[1] Fraunhofer- Institute for Building Physics, 70569 Stuttgart, Germany
[2] Architectural Representation Department, Universitat Politècnica de Catalunya, 08028 Barcelona
[3] Reicher Haase Assoziierte, 52066 Aachen
[4] Institute of Urbanism, RWTH Aachen University, 52062 Aachen

ABSTRACT

The use of city-scale big data in urban planning practices has grown significantly over the past few decades, revolutionizing the way cities are designed and managed. This trend holds the promise of creating urban environments that better account for the perceptions, needs, and complex interactions of people with the built environment. However, despite these advancements, there remains a lack of comprehensive frameworks for incorporating the auralization of urban soundscapes into city-scale big data systems. The integration of soundscape auralization is critical, as it offers the potential to address the acoustic dimension of urban life, enabling more informed and human-centered urban sound planning. In this regard, soundscape auralization frameworks are expected to play a pivotal role in facilitating data-driven decision-making processes that enhance the auditory quality of urban spaces. This contribution aims to address the challenges associated with achieving such integration, outlining a structured workflow for creating soundscape digital twins—virtual representations of urban acoustic environments. The contribution will also highlight that these digital twins could serve as powerful tools for simulating and evaluating soundscapes, ultimately supporting urban planners in designing cities that are not only functional but also acoustically pleasant.

Keywords: *soundscape, auralization, urban, acoustics.*

[*] ***Corresponding author***: *josep.llorca-bofi@fraunhofer.de*
Copyright: *©2025 First author et al. This is an open-access article distributed under the terms of the Creative Commons Attribution 3.0 Unported License, which permits unrestricted use, distribution, and reproduction in any medium, provided the original author and source are credited.*

1. INTRODUCTION AND SIMULATION WORKFLOW

As urban challenges become more complex, innovation alone is insufficient; strong partners are needed for comprehensive support and diverse perspectives. The Fraunhofer Institute for Building Physics in Stuttgart has established the Urban and Architectural Acoustics research group (UAA) to accelerate innovation in urban acoustic challenges. By uniting research institutions and demonstration environments under one partner, it aims to improve solutions for society's sound and noise issues.
Noise mapping is a well-established practice in acoustic urban planning, calculating noise levels based on sound source models, propagation effects, and receiver positions. However, this method is limited to frequency band levels, lacking temporal and spectral information, which affects qualitative sound properties evaluated through psychoacoustic parameters. Auralization and physically-based simulation can enhance urban soundscape analysis beyond classical noise mapping. By integrating auralization technology with visual representations of urban spaces, a plausible virtual environment can be created. In this chapter we present the simulation workflow used by the UAA group and in chapter 2 we discuss several challenges and opportunities of soundscape auralizations in urban planning.

1.1 Auralization signal chain

An auralization usually consists of separated simulation models for sources, propagation, and receivers [1]. Virtual Acoustics (VA) is a physics-based auralization framework developed at the Institute for Hearing Technology and Acoustics (IHTA) at the RWTH Aachen university [2] and is intended to be used by the UAA group.

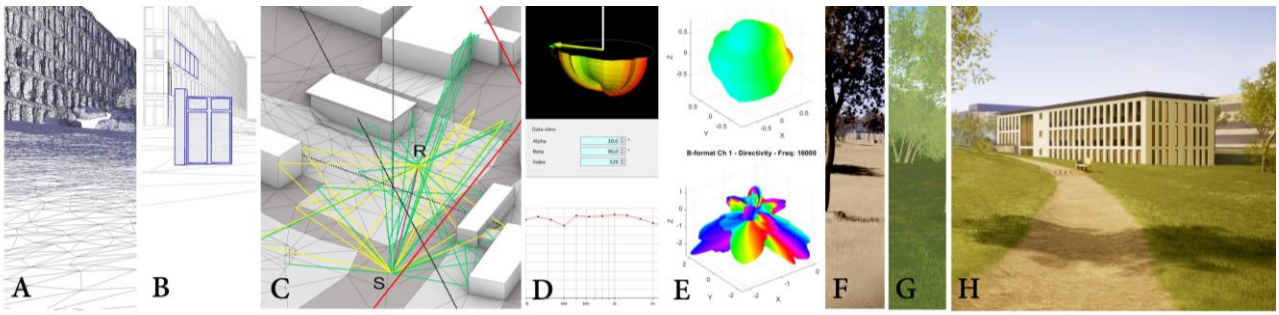


Figure 1. Soundscape auralization workflow example: A) photogrammetry; B) visual geometry; C) acoustic geometry and sound propagation paths; D) sound source directivity characterization; E) 1st HOA receiver characterization; F) light sources and shadows calculation; G) visual materials definition; H) Final audio-visual model of IHTApark [5].

In general, VA allows the acoustic rendering of virtual scenes purely based on synthesized data using physics-based models. It follows a server-client architecture with bindings to various technologies like Matlab (The MathWorks, Portola Valley, CA), Python (Python Software Foundation, Wilmington, DE), Unity (Unity Technologies, San Francisco, CA), or Unreal Engine (UE). Using a purpose-built plugin, UE connects to an instance of VA. During execution, all sound source information is forwarded. VA then handles the auralization including propagation effects according to the selected renderers, as well as the reproduction via an audio interface (Figure 1).

The sound propagation model applies effects to the raw input signal from the source model. For outdoor auralization, it involves two steps: simulating geometric sound paths connecting source and receiver, and deriving acoustic parameters for each path, including spreading loss, propagation delay, and air attenuation. These parameters, called auralization parameters, control digital signal processing during auralization. The consideration of propagation effects and sound path simulation depends on the detail level needed for the scenario. For a car pass-by in an open field, considering solely direct sound and ground reflection may suffice, while urban scenarios require additional effects like reflections and scattering, especially in dynamic situations where movement can occlude direct sound.

1.2 Visualization framework

The basic paradigm of visual simulation of architectural and urban scenes includes four interconnected prerequisites: geometry, materials, light sources and viewers. The approach to construct the model is highly modular. The modular setup allows for the independent modification of each module under certain variables, independent from the rest of the modules, which makes the models versatile. The visualization includes the following elements: geometry, or ways to represent and process surfaces; an imaging or processing acquisition, ways to reproduce the visual—or material—characteristics of objects; rendering, algorithms to reproduce light rays; and animation, ways to represent and manipulate motion, as described by Foley et al. [4]. Further details on the visualization workflow can be found under Llorca-Bofí et al [5].

1.3 Digital twin scenario for validation

To test and develop the simulation workflow, an immersive environment was created over the last years. The IHTApark digital twin, an accurate virtual recreation of the small park behind IHTA in RWTH Aachen, was chosen for this purpose. Combined with VA and the UE VA plugin, the IHTApark project serves as a template for complex audiovisual environments [5]. The park was monitored with audio recordings across multiple weather conditions and visually recreated in Unreal Engine (UE) for presentation on monitors and in VR. The templates made use of VA for auralization and simulated sound propagation in IHTApark with a simplified acoustic model. Further validation of these urban digital twins is planned by the UAA group soon.

2. SELECTED CHALLENGES AND OPPORTUNITIES

2.1 Weather changes

One major problem in auralizing complex urban scenarios is creating ambience - the diffuse background representing the sound floor for the acoustic scene. Omitting realistic ambience leads to a sterile impression. A hybrid approach with spatially recorded background sounds appears promising. Llorca-Bofí et al. [6] explored the influence of weather changes on psychoacoustic parameters (Figure 2). To address improving spatial diffusivity and accounting for weather-dependent variations in outdoor auralizations, we collected and characterized background sounds from the urban scenario IHTApark regarding acoustic parameters and weather conditions. Results indicate that sharpness and roughness correlate highly with relative humidity and cloudiness, while tonality relates to surface wetness. In contrast, loudness correlates with fewer and weaker weather indicators. Thus, it is important to use background sounds in virtual soundscapes, given that the temporal and spectral content affect the soundscape evaluation as well.

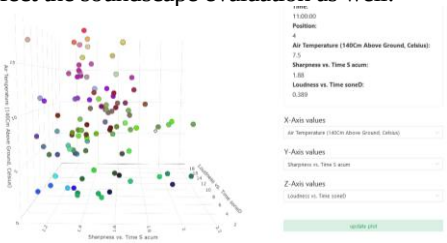


Figure 2. A web application to explore a dataset of ambient noise recordings made at IHTA Park. It can be interactively explored here: https://paad-group.github.io/IHTApark-ambient-recordings/

2.2 Auralization for citizen science

The use of such digital twins in citizen science is a promising field. They can be used to collect assessments of urban design variations across questionnaires to citizens using streaming technologies. In [2] the authors validated the plausibility of such tests comparing virtual reality and web-based listening experiments. For such noise perception experiments, the results are promising, showing minimal differences in questionnaire ratings between VR and streaming reproduction. Visual quality ratings suffered mildly in the consumer setup, but auralization quality was rated similarly positive in both cases. Even for lower feeling of presence in the consumer setup, the subjects' attention remained similarly high despite having lower sense of presence in the consumer setup. Finally, accessibility and quality ratings indicate equally promising results.

2.3 Neural networks training of urban soundscapes

Recent advances in machine learning (ML) and artificial intelligence (AI) have enabled predictive models that capture nonlinear interactions between environmental parameters and psychoacoustic features. Specifically, neural networks are powerful tools for modeling these complex relationships. The authors explored the performance of Back-Propagation networks in predicting psychoacoustic features from urban meteorological inputs using a soundscape database as training data (Figure 3) [7]. The networks' predictive potential suggests that synthetic soundscapes could be generated for various urban situations. These synthetic soundscapes could preserve the physical and psychoacoustic properties from the training data while streamlining the time-consuming modeling process of soundscape environments.

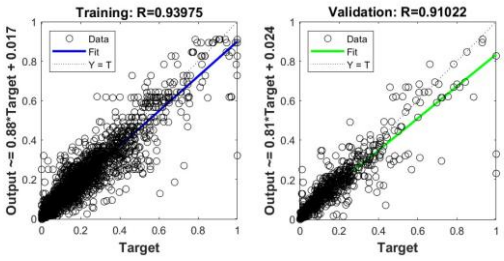


Figure 3. Back-propagation network performance prediction of psychoacoustic indicators based on weather indicators. The dataset is part of the urban background soundscapes dataset, using 80 % as training data and the resting 20% as validation dataset.

2.4 Integrating sustainability measures with noise simulations in urban planning

Towns and cities have to strike a balance between the needs of society and individuals, which tend to clash and coincide with one another. Acoustic urban design has to deal with an unrestrained demand for mobility, increasing urban density and many other factors, together with all other sustainable challenges that cities face. For this reason, today it is even more important to look at the future of acoustic urban design integrated to sustainability measures. The integration of acoustic data together with sustainability data in urban planning simulation is key to tackle those challenges. Available acoustic measurements, air pollution reduction index, resilience to climate change and other data for green

facades at the Fraunhofer-IBP makes the urban planning simulations and optimizations possible (Figure 4).



Figure 4. Measurements of the integrated database of acoustic and other sustainability indicators, available at https://imcom2.hoki.ibp.fraunhofer.de/attribute/index.php

2.5 Soundscape planning at the micro, meso and macro levels



Figure 5. Urban planning concept fort he „Gräselberg – Auf den Eichen“ urbanization area, in Germany, by Reicher-Haase Assoziierte.

The use of auralization techniques might be implemented at different scales in the urban design process, this is for example, to check the impact of the U-shaped buildings as sound barriers for the highway noise, or to assess the impact of the façade manterials to reduce noise on the inner courtyards (See Figure 5). However, since auralization techniques aim to render the soundscape at the receiver position, it is important to mention that the renderings will be perceived from the human point of view, this is, as a pedestrian or dwelling inhabitant. In order to assess the impact of the near sounds as well as the far-away ones, the physically-based auralization techniques previously presented are necessary.

3. DISCUSSION AND CONCLUSION

In this manuscript a workflow to integrate soundscape auralization in urban planning was presented and selected challenges were discussed, in particular, the effects of varying weather conditions, the opportunities of urban soundscape auralization for citizen science, the use of neural networks to agilize the simulation processes, and the integration of sustainable data of facades and buildings, into the acoustic simulations to achieve a multidisciplinary urban planning. Further work at the UAA group will be published in future steps.

4. ACKNOWLEDGMENTS

The authors acknowledge the support from J. Heck, G. Atay and T. Waldvögel, Y. Liu and Prof. J. Beetz. This work was funded by the Fraunhofer Gesellschaft; by the Spanish Ministry of Science under the code J-03040 by MICIU/AEI/10.13039/501100011033; and the European Union NextGenerationEU/PRTR.

5. REFERENCES

[1] Vorländer, M. (2020) Auralization. Springer.

[2] Schäfer, P., et al. (2024). “Virtual acoustics - A real-time auralization framework for scientific research,” At: https://doi.org/10.5281/zenodo.13788752

[3] Rehman, R., et al. (2025) Comparison of Virtual Reality and Web-Based Listening Experiments on the Perception in Complex Auralized Environments. *J. Acous. Soc. Am.* 157, no. 3. Doi: https://doi.org/10.1121/10.0036147.

[4] Foley, J. D. (1996). Computer graphics. Wesley.

[5] Llorca-Bofí, J. et al. (2022) Urban Sound Auralization and Visualization Framework—Case Study at IHTApark. *Sustainability*, *14*, 2026. Doi: https://doi.org/10.3390/su14042026

[6] Llorca-Bofí, J. et al., (2024). Urban background sounds under various weather conditions categorized for virtual acoustics. *J. of Env. Man.* 371, 123081. Doi: https://doi.org/10.1016/j.jenvman.2024.123081

[7] Yuan, L., and Llorca-Bofí, J. (2025). Neural network-based psychoacoustic prediction of urban background soundscapes under different weather conditions. *Under review*.

DOI:

Main theme: A05 Environmental Acoustics

Session A05.06 Recent advances in noise mitigation methods

Chair(s): P. Bellucci, G. Licitra

DOI: 10.61782/fa.2025.0873

FORUM ACUSTICUM EURONOISE 2025

THE LIFE SILENT PROJECT: ADVANCING SUSTAINABLE SOLUTIONS TO MITIGATE NOISE IN URBAN ENVIRONMENTS

Patrizia Bellucci[1*] **Francesc Ciarallo**[1] **Massimo Garai**[2]
Gaetano Licitra[3] **Tina Onorato**[1] **Filippo Giammaria Praticò**[4]
[1] ANAS S.p.A, Research and Development Unit, Via Pianciani 16, 00185 Rome, Italy
[2] Department of Industrial Engineering – University of Bologna
Viale Risorgimento 2 – 40136 Bologna, Italy
[3] ARPAT – Environmental Protection Agency of Tuscany Region
Via V. Veneto, 27 - 56127 Pisa, Italy
[4] DIIES Department
Via Graziella Feo di Vito, SNC, 89124 Reggio Calabria, Italy

ABSTRACT

In this paper an overview of the LIFE SILENT Project and its preliminary results is presented. The project aims to develop and implement sustainable solutions for mitigating noise in complex urban scenarios affected by the coexistence of multiple and diverse noise sources, typically from road and railway traffic, in proximity to densely populated areas. In such contexts, conventional noise mitigation solutions, such as noise barriers, are often unsuitable due to their impact on nearby receivers. However, high noise barriers can reduce visibility, hinder air circulation, and alter the microclimate, potentially leading to social opposition.
To address these challenges, at-source solutions are recommended. For roads, low-noise pavements are proposed, while railways are encouraged to adopt measures such as dampers, rail grinding, and silent brakes. However, these solutions are often limited by issues such as durability and high implementation and installation costs. The LIFE SILENT Project seeks to overcome these challenges by developing and testing innovative solutions, including low-noise pavements and low-height noise barriers incorporating metamaterials, designed to deliver enhanced environmental performance and improved durability.
Finally, to facilitate the coordinated implementation of these solutions by infrastructure owners and managers, the project aims to define a dedicated management procedure.

Keywords: *low-noise pavements, low-height noise barriers, metamaterials, innovative mitigation measures, management procedures.*

1. INTRODUCTION

Urban areas are frequently affected by noise pollution stemming from various simultaneous sources, predominantly road and railway infrastructures. Commonly adopted solutions, such as noise barriers or extensive structural installations, can significantly impact the local environment. These intrusive methods often disrupt visibility, impede airflow, alter microclimates, and negatively influence the overall urban aesthetics, consequently leading to dissatisfaction and opposition among local communities.
In response to such issues, more effective strategies aim to mitigate noise directly at the source. Approaches like low-noise pavements and vibration dampers, rail grinding, and silent braking systems for railways, are

[*] ***Corresponding author***: p.bellucci@stradeanas.it.
Copyright: *©2025 P. Bellucci et al. This is an open-access article distributed under the terms of the Creative Commons Attribution 3.0 Unported License, which permits unrestricted use, distribution, and reproduction in any medium, provided the original author and source are credited.*

promising but can face challenges related to durability or substantial implementation costs.
Consequently, it is essential to explore sustainable and less intrusive noise-mitigation techniques that balance effectiveness with minimal environmental and social impact. To this end, the LIFE SILENT project aims to develop and test advanced, durable, and environmentally friendly solutions, and to provide comprehensive guidelines to transport infrastructure owners for managing noise mitigation measures in a synergistic way.

2. THE LIFE SILENT PROJECT

The LIFE SILENT project [1] specifically aims to address three key areas:

- sustainable Low-Noise Pavements (LNP);
- compact Low-Height Noise Barriers (LHNBs);
- and coordinated implementation strategies.

The idea of developing and exploring these three areas stems from the following considerations.

Low-noise pavements. Despite the effectiveness of traditional low-noise pavements in reducing noise (approximately 3-5 dB), existing solutions often face durability and sustainability issues. Projects like PERSUADE, LIFE NEREIDE [2][3], LIFE C-LOW-N, LIFE E-VIA, LIFE SNEAK, and IASNAF [4] have advanced research in this area. Particularly notable is the project IASNAF, demonstrating the effectiveness of functionalized cellulose fibres in enhancing pavement durability. However, most studies remain limited to laboratory conditions. LIFE SILENT aims to overcome these limitations by validating durable, sustainable pavements using recycled and eco-friendly materials in real-world settings, improving durability, reducing CO2 emissions, costs, and health impacts, while maintaining optimal acoustic performance.

Low-height noise barriers. Low-Height Noise Barriers have gained popularity as cost-effective solutions, providing noise reductions between 5 and 10 dB [5][6][7]. Typically installed directly onto rail infrastructure, LHNBs eliminate the need for costly foundations, making them economically advantageous and visually appealing. Studies, including numerical simulations and scale-model tests, have demonstrated the effectiveness of LHNBs through optimized designs developed using boundary element methods (BEM) [6]. However, real-world trials have reported noise attenuation ranging from 1.5 to 5 dB(A) [8][9][10][11], primarily limited by multiple sound reflections between LHNB surfaces and train bodies. The LIFE SILENT project aims to address this limitation by integrating metamaterials to enhance LHNBs' sound-absorbing properties, thereby reducing multiple reflections and providing improved durability over time.



Figure 1. LHNB built by Kraiburg STRAIL in San Cugat (Spain).

Noise mitigation synergistic procedures. Effective noise management in complex urban environments, impacted by multiple noise sources, needs coordinated actions among diverse infrastructure stakeholders, as mandated by European and Italian regulations (DPCM 29/11/2000, Directive 2002/49/CE [7], Legislative Decree 42/2017). However, the absence of detailed operational guidelines has hindered effective implementation. LIFE SILENT addresses this gap by developing practical methodologies to facilitate integrated, collaborative solutions across different transportation entities, ensuring sustainable, comprehensive, and regulatory-compliant noise mitigation strategies.

2.1 Project's objectives

Following the previous considerations, the LIFE SILENT project sets out three main goals aimed at innovative noise mitigation strategies.
Firstly, it seeks to enhance road pavement durability and resistance while reducing costs by integrating cellulose fibres derived from recycled waste materials like textiles, paper, and cardboard into bitumen mixtures. This

approach aims to improve fatigue performance, extending pavement lifespan.

Secondly, the project aims to design and implement advanced Low-Height Noise Barriers (LHNB) by using metamaterial technology and a significant proportion (approximately 85%) of recycled materials. These materials will be specifically designed to maximize acoustic absorption and durability, overcoming the limitations of traditional fibrous components, which degrade rapidly. Particular attention will be given to sustainability, ease of maintenance, and structural integrity.

Lastly, LIFE SILENT will establish comprehensive guidelines and procedures for the management and implementation of noise mitigation measures, especially in complex and environmentally sensitive contexts. This will ensure efficient implementation and consistent performance of noise solutions in different scenarios.

3. METHODOLOGY

The methodology adopted by the LIFE SILENT project involves a systematic, multi-phase approach structured into five sequential stages (Figure 2). Initially, the innovative solutions are conceptualized and developed. Then, these solutions are designed and implemented in a dedicated pilot area. Following installation, rigorous impact monitoring and performance evaluation are conducted. The sustainability of the proposed interventions is then thoroughly assessed. Finally, the developed prototypes undergo a formal certification process to confirm their compliance with relevant standards and their effectiveness in real-world conditions [1].

3.1 Development of innovative solutions

The initial phase of the LIFE SILENT project is structured around three core activities:

- Defining procedures and guidelines to support the synergistic implementation of noise mitigation measures.
- Development and design of the innovative LNP:
- Development and design of the LHNB.

The first core activity involves identifying methodologies and preparing guidelines to implement synergistic noise mitigation measures in challenging environmental contexts. This entails the analysis of complex scenarios and existing conditions to ensure effective integration of noise mitigation solutions.

The design and characterization of the innovative low-noise pavements is based on previous findings from the IASNAF project. This approach involves developing a sustainable asphalt mixture incorporating cellulose fibres obtained from recycled textiles, paper, and cardboard. Through iterative laboratory tests and subsequent real-world trials, the project aims to optimize pavement formulations, enhancing durability by approximately 20% compared to current state-of-the-art options, without compromising acoustic and safety performance. This strategy is expected to reduce long-term costs and significantly lower environmental impacts by decreasing reliance on virgin materials and minimizing landfill waste.

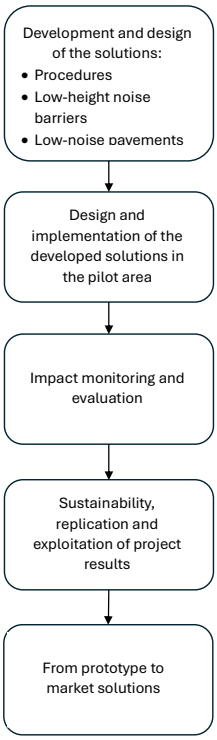


Figure 2. Flow-chart of the main steps of the project.

Lastly, the LIFE SILENT project targets the development and characterization of advanced Low-Height Noise Barriers. Insights from prior research, particularly the experiences from the Kraiburg STRAIL prototype, guide the selection of suitable recycled materials evaluated against EN 15804 standards. Additionally, metamaterials will be employed to significantly improve acoustic absorption characteristics, surpassing traditional fibrous materials in

both performance and durability. Ensuring structural integrity, safety, and ease of maintenance is also a critical component of this barrier design phase, supplemented by fatigue testing and innovative acoustic performance assessment methodologies.

3.2 Implementation of the developed solutions in the pilot area

The innovative solutions developed and tested through initial laboratory testing will subsequently be implemented at a real-world pilot site located in a densely populated urban area (Muratella, Rome, Italy), characterized by proximity to both road and railway infrastructures (see Figure 3). Specifically situated within Rome's XI District, the selected area is crossed by the Rome-Fiumicino Airport railway line and the A91 motorway. This predominantly residential zone includes buildings typically comprising three to four floors, primarily positioned on the northern side of the roadway. Approximately 170 buildings, housing a population of nearly 19,769 residents, students, hospital personnel, and patients, are exposed to noise levels exceeding 55 dB(A) Lden.



Figure 3. View of the pilot area (Muratella, Rome) crossed by the A91 Motorway and the railway line Rome – Fiumicino Airport.

Prior to the full-scale implementation, comprehensive baseline measurements will be conducted to accurately assess subsequent improvements resulting from the new low-noise pavement and low-height noise barrier. This assessment will involve a detailed measurement campaign designed to calibrate the noise propagation model and refine strategies for effective noise mitigation.

The campaign includes five distinct measurement procedures:

- Road vehicle noise emissions measured following ISO standard 11819, with both Close Proximity and Statistical Pass-By methods, including the backing board approach, to assess the influence of pavement characteristics on noise generation.
- Noise level recordings at sensitive receiver locations based on the Italian decree DM 16/03/1998, essential for validating the acoustic propagation model.
- Ex-ante evaluation of the effectiveness of LHNBs using the methodology specifically developed within the project.
- Assessment of pavement surface texture and mechanical impedance following standards UNI CEN 13036-1 and UNI EN ISO 7626-5.
- Preliminary evaluations of community noise annoyance through psychoacoustic methodologies and social surveys aligned with guidelines established in the LIFE NEREiDE project.

The collected data are then used to calibrate an acoustic model that simulates various acoustic scenarios, offering insights into total noise exposure and identifying individual noise source contributions. The measurement results will guide the project's design phase, integrating newly established management procedures to harmonize and optimize noise mitigation efforts by road and rail infrastructure authorities.

To mitigate noise impact, a 200-meter LHNB will be installed adjacent to the railway tracks, primarily targeting sensitive areas on the southern side. The barrier's design prioritizes easy maintenance and structural stability while minimizing visual disruption and preserving views for residents and train passengers.

Additionally, a 1.9 km section of newly formulated low-noise pavement will be implemented on the A91 motorway. Its design will consider urban-specific factors such as road safety, geometric layout, and logistical considerations related to asphalt production and application processes.

The design phase will focus on optimizing asphalt mixtures, refining material compositions and proportions, improving supply chain efficiency, and implementing rigorous quality control measures. Environmental protection will also be a

key priority, achieved through reduced toxic emissions, and strict adherence to safety standards.

3.3 Performance assessment of the implemented solutions

A comprehensive monitoring campaign will be conducted to assess the acoustic effectiveness and long-term performance of the implemented noise mitigation solutions. Specifically, the acoustic durability of the new low-noise pavement will be evaluated through four measurement sessions scheduled at intervals of 3, 6, 12, and 18 months after the laying of the new mixtures. To accurately characterize the pavement durability, data on rolling noise emissions, traffic volume, and weather conditions will be collected even beyond the project's duration of 60 months. The performance assessment for the pavement will also include Statistical Pass-By noise measurements, Close Proximity evaluations, and non-acoustic indicators such as surface texture, frictional properties, and mechanical impedance. These combined data sets will feed fatigue test validation and provide essential inputs for Life Cycle Assessment (LCA) and Life Cycle Cost (LCC) analyses.
The effectiveness of the installed low-height noise barriers will similarly be evaluated through targeted acoustic measurements conducted according to the methodology developed specifically within this project. Additionally, regular visual inspections and periodic testing of the barriers will be performed to monitor structural integrity and material durability.
Further impact assessments will involve detailed measurements of noise levels at sensitive receiver locations, according to the Italian decree DM 16/03/1998. Additionally, psychoacoustic studies and structured social surveys will measure public perception and evaluate community acceptance and response to the implemented noise mitigation strategies.
Finally, the established procedures for managing noise mitigation actions will be continuously evaluated to monitor their effectiveness and efficiency, from the initial strategy formulation to the practical implementation phase. This evaluation will systematically identify potential challenges, recommend corrective actions, and refine the methodology based on feedback from citizens, stakeholders, and public institutions involved in the process.

3.4 Sustainability analysis of the newly developed solutions

The sustainability of the LIFE SILENT approach will be assessed with a focus on the solutions implemented in the pilot area, ensuring a comprehensive analysis of their long-term effectiveness. In addition to the traditional environmental, social, and economic dimensions, the assessment will also consider technical aspects.
The technical evaluation will be performed using standardized methodologies and protocols. Specifically, EN 1794-1/2 will be employed to assess the non-acoustic performance of road traffic noise-reducing devices, while EN 14389 will be used to evaluate their long-term non-acoustic performance. In the railway sector, the non-acoustic performance of noise barriers and related devices will be analysed according to EN 16727-1/2/3.
The assessment of environmental, social, and economic impacts across the life cycle of each technology will be conducted using the Life Cycle Sustainability Assessment (LCSA) framework. This integrated approach combines Life Cycle Assessment (LCA), Social Life Cycle Assessment (S-LCA), and Life Cycle Costing (LCC), in alignment with ISO EN 14040/14044, EN 15804, and the UNEP/SETAC Guidelines for Social Life Cycle Assessment of Products.
The LCSA methodology follows a structured four-stage process: (i) definition of objectives and scope; (ii) inventory compilation; (iii) impact assessment; and (iv) interpretation of results. Additionally, public perception of both conventional and the newly developed noise mitigation technologies will be analysed through a mixed-methods approach, incorporating qualitative and quantitative data collection techniques, such as structured surveys and in-depth interviews.
By integrating technical, environmental, social, and economic considerations, this comprehensive approach ensures a robust sustainability evaluation of the project's solutions. A Multi-Criteria Decision Making (MCDM) framework will be applied to compare the LIFE SILENT noise reduction solutions against an Optimal Hypothetical Ideal Solution (OHIS), which will serve as a reference benchmark. The final assessment will generate an Overall Sustainability Index (OSI), ranging from 0 to 1, quantifying the proximity of the LIFE SILENT solutions to the OHIS.

3.5 Prototypes certification

To ensure the validation of the developed technologies and enhance their market potential, both the newly designed low-noise pavement and the low-height noise barriers will undergo Environmental Product Declaration (EPD) certification. This certification process aims to support the deployment of environmentally sustainable technologies by providing technology developers, manufacturers, and investors with independent third-party verification of their

environmental performance. Achieving EPD certification will attest the reliability of the LIFE SILENT solutions, fostering greater confidence among potential stakeholders and accelerating their adoption and large-scale implementation.

4. EXPECTED OUTCOMES AND IMPACTS

The expected outcomes and impacts of the project are classified into three main domains: low-noise pavements, low-height noise barriers, and advanced methodologies for the management and implementation of noise mitigation measures in complex environmental settings.

4.1 Low-noise pavements

The adoption of low-noise pavement technologies is expected to bring substantial environmental and functional improvements to road infrastructure. One of the main advantages is a projected 4 dB reduction in noise levels, achieved through modifications in surface texture, optimized aggregate gradation, and the incorporation of crumb rubber. This is designed to meet EU Green Public Procurement Criteria, ensuring CPX noise levels around 86±1 dB(A) at 50 km/h.

Beyond noise reduction, the durability of these pavements is anticipated to improve by 20% compared to conventional solutions, thanks to the integration of functionalized cellulose fibres. This enhancement not only extends the pavement's lifespan but also contributes to sustainability by lowering the carbon footprint by 17%, which translates to an annual reduction of approximately 420 tons of CO_2 per kilometre. Additionally, the use of 16 tons of recycled materials per kilometre aligns with circular economy principles.

The implementation of these mixture is also expected to reduce volatile organic compounds (VOC) and polycyclic aromatic hydrocarbons (PAH) emissions, leading to better air quality in road-adjacent areas. From an economic perspective, the extended lifespan of the pavement is projected to result in a 14% cost reduction, reinforcing the technology's role in promoting sustainable and cost-efficient road infrastructure.

4.2 Low-height noise barriers

The Low-Height Noise Barrier represents an innovative solution that integrates environmental sustainability, social acceptance, acoustic efficiency, durability, and cost-effectiveness into a novel design paradigm. Composed of 85% recycled rubber, the LHNB is strategically developed to enhance the circular economy, significantly reducing the environmental impact associated with traditional noise barriers. Due to its low-profile design (0.5 meters in height), it is anticipated to achieve twice the level of public acceptance compared to conventional barriers, primarily due to its minimal visual intrusion into the surrounding landscape.

Despite its compact dimensions, the LHNB employs metamaterial technology to enhance sound absorption and an estimated noise reduction of 5 dB. Engineered for a service life exceeding 15 years, the barrier is also linked to the development of a novel acoustic testing methodology, currently under refinement, with the potential to serve as a future standardization framework.

From a structural perspective, the LHNB is designed for ease of installation and maintenance, benefiting from its lightweight composition and modular assembly. To ensure long-term reliability, the barrier will be subjected to comprehensive fatigue resistance testing, assessing its ability to withstand mechanical stress and environmental degradation.

Economically, the LHNB is projected to deliver a 30% improvement in the benefit-cost ratio compared to conventional barriers, positioning it as a pioneering solution in noise mitigation that effectively addresses spatial, aesthetic, and economic constraints while maintaining superior performance standards.

4.3 Advanced methodologies for the management and implementation of noise mitigation measures

The LIFE SILENT project is also dedicated to developing a systematic methodology for the coordination and implementation of diverse noise mitigation strategies, including low-noise pavements and low-height noise barriers, to optimize their effectiveness. This approach is designed to facilitate collaboration among key stakeholders, such as public transport operators and infrastructure managers, ensuring that their interventions align with broader urban planning frameworks. By fostering coherent and integrated action plans, the initiative aims to enhance noise reduction in urban and suburban environments, contributing to a more sustainable acoustic landscape.

A key component of the project is the development of guidelines to facilitate compliance with legislative requirements, particularly those related to the formulation of Action Plans under European Directive 2002/49/EC. These guidelines are expected to benefit all designated agglomerations covered by the Directive, as well as other European cities seeking to implement more effective noise mitigation strategies.

For infrastructure owners, the project provides clear and structured implementation frameworks, facilitating cost-effective planning, construction, and maintenance of noise-reducing devices. It is estimated that this methodology could lead to a 50% reduction in costs for adjacent infrastructure development, significantly improving the economic feasibility of noise control interventions.

In the pilot area of Muratella (Italy), the project seeks to substantially reduce noise exposure for approximately 19,769 residents, including vulnerable groups in hospitals and schools. This will be achieved through the deployment of 1.9 km of low-noise pavement and a 200-meter low-height noise barrier, with the objective of reducing the annoyed population by 12%, equivalent to 2,464 individuals.

Furthermore, the project emphasizes community engagement and social acceptance, incorporating co-design methodologies that actively involve residents in the planning and design of mitigation measures. By fostering public participation, the initiative enhances community support for noise reduction solutions, ensuring their long-term success and integration into the urban landscape.

5. CONCLUSIONS

The LIFE SILENT project represents a significant step forward in the development and implementation of innovative noise mitigation strategies that address both environmental and societal challenges associated with urban noise pollution. By integrating low-noise pavements, low-height noise barriers, and a coordinated management approach, the project provides a comprehensive and sustainable framework for reducing noise exposure in complex urban environments.

The project's findings demonstrate that low-noise pavements, incorporating recycled and eco-friendly materials, can effectively reduce noise emissions while enhancing durability and sustainability. Similarly, the low-height noise barriers, using metamaterial technology, have shown promising noise attenuation capabilities while maintaining a low visual and spatial footprint, ensuring higher public acceptance. Additionally, the development of standardized methodologies for noise mitigation planning and implementation will facilitate more effective collaboration among stakeholders, enhancing the feasibility of large-scale adoption.

The pilot implementation in Muratella, Italy, highlights the potential impact of these solutions, with an expected 12% reduction in noise-exposed people and significant cost savings for infrastructure owners. The systematic evaluation process, including acoustic performance assessments, environmental impact analyses, and stakeholder engagement strategies, further ensures the long-term viability and replicability of these interventions across various urban settings.

Moving forward, the project's methodological approach and technological advancements will provide a blueprint for future noise reduction policies and urban planning strategies. The integration of sustainable materials, advanced acoustic engineering, and participatory design principles sets a new benchmark for noise mitigation efforts, fostering greener, more liveable urban environments.

By bridging scientific innovation, regulatory compliance, and public engagement, the LIFE SILENT project offers a scalable and transferable model for tackling urban noise pollution, reinforcing its potential as a pioneering initiative in sustainable infrastructure development.

6. ACKNOWLEDGMENTS

Funded by the European Union. Views and opinions expressed are, however, those of the authors only and do not necessarily reflect those of the European Union or CINEA. Neither the European Union nor the granting authority can be held responsible for them.

7. REFERENCES

[1] P. Bellucci, F. Ciarallo, M. Garai, G. Licitra, F.G. Praticò, "The LIFE SILENT Project's approach to sustainable noise mitigation", *Proc. of Internoise 2024,* Nantes (France), 25-29 August 2024.

[2] G. Licitra, M. Cerchiai, C. Chiari, E. Ascari "Life Nereide: innovative monitoring activities on implementation urban sites", *Proceedings of 24th International Congress on Sound and Vibration*, ICSV (2017).

[3] F. Lo Castro, S. Iarossi, M. De Luca, M. Bernardini, G. Brambilla, G. Licitra, "Life NEREiDE project: preliminary evaluation of road traffic noise after new pavement laying". In: *Proceedings of INTER-NOISE and NOISE-CON Congress*, 19, 4999-5997, Madrid, Spain, 2019.

[4] P. Bellucci, P. Bernardinetti, G. Chidichimo, G. Meli, F.G. Praticò, C. Sartori, "Cellulose fibres for better performing road pavements", *Roads and*

airports surface characteristics, 2023, CRC Press, ISBN 97811003429258.

[5] K. Horoshenkov, D. C. Hothersall, S. E. Mercy, "Scale modelling of sound propagation in a city street canyon". *Journal of Sound and Vibration*, 223, 795–819, 1999.

[6] M. Baulac, J. Defrance, P. Jean, "Optimization of low-height noise protections in urban areas", In *Proc. of Forum Acusticum 2005*, pp. 1075–1080, Budapest, Hungary, Aug.-Sep. 2005.

[7] L. Ding, T. Van Renterghem, D. Botteldooren, "Estimating the effect of semi-transparent low-height road traffic noise barriers with ultra-weak formulation", *Acta Acustica united with Acustica*, 97, 391–402, 2011.

[8] Directive 2002/49/EC of the European Parliament and of the Council of 25 June 2002 relating to the assessment and management of environmental noise

[9] Deutsche Bahn. https://gruen.deutschebahn.com/en/measures/noise-reduction.

[10] E. Nieuwenhuizen, N. Yntema, "The effect of close proximity, low-height barriers on railway noise", in *Proceedings of Euronoise 2018*, Crete, Greece, May 2018.

[11] P. Fernandez, I. Diez, J. L. Eguiguren, I. Aspuru. "Noise barriers customized to abate non-conventional noise sources", in *Proc. of Inter-noise 2013*, Innsbruck, Austria, Sept. 2013.

[12] Kraiburg Strail GmbH. "Expert's report on the application of a mini sound protection wall made of fibre-reinforced hard rubber mats under fatigue stress on railway lines of Deutsche Bahn", June 2017.

[13] C. Praticò F.G., Fedele R., Road pavement macrotexture estimation at the design stage (2023) *Construction and Building Materials*, 364, art. no. 129911, DOI: 10.1016/j.conbuildmat.2022.129911.

[14] Praticò F.G., Fedele R., Pellicano G., Pavement FRFs and noise: A theoretical and experimental investigation (2021) *Construction and Building Materials*, 294, art. no. 123487, DOI: 10.1016/j.conbuildmat.2021.123487.

[15] G. Licitra, M. Cerchiai, L. Teti, E. Ascari, L. Fredianelli. Durability and variability of the acoustical performance of rubberized road surfaces. *Applied Acoustics*, 94, 20-28, 2015. 10.1016/j.apacoust.2015.02.001.

[16] D. Landi, M. Marconi, E. Bocci, M. Germani. Comparative life cycle assessment of standard, cellulose-reinforced and end of life tires fiber-reinforced hot mix asphalt mixtures. *J. Cleaner Production*, 248, 119295, 2020. 10.1016/J.JCLEPRO.2019.119295.

[17] A. Jolibois, J. Defrance, H. Koreneff, P. Jean, D. Duhamel, V.W. Sparrow. In situ measurement of the acoustic performance of a full scale tramway low-height noise barrier prototype. *Applied Acoustics*, 94, 57-68, 2015.

[18] Cummer S., Christensen J., Alù, A. Controlling sound with acoustic metamaterials. *Nature Reviews Materials*. 1, 16001, 2016.

[19] Jiménez N., Huang W., Romero-García V., Pagneux V., Groby J.-P. Ultra-thin metamaterial for perfect and quasi-omnidirectional sound absorption. *Appl. Phys. Lett.*, 109, 121902, 2016.

[20] G. Fusaro, L. Barbaresi, M. Cingolani, M. Garai, E. Idà, A. Prato, A. Schiavi. Investigation of the impact of additive manufacturing techniques on the acoustic performance of a coiled-up resonator. *J. Acoustical Soc. America*, 153(5), 2921–2931, 2023. DOI: 10.1121/10.0019474.

[21] P. Guidorzi, M. Garai. Repeatability of the European standardized method for measuring sound reflection and sound insulation of noise barriers. *Environments*, 10, 139, 2023. DOI: 10.3390/environments10080139.

[22] European Commission, Directorate-General for Environment, Kantor, E., Klebba, M., Richer, C. et al. Assessment of potential health benefits of noise abatement measures in the EU – Phenomena project, Publications Office, 2021. https://data.europa.eu/doi/10.2779/24566.

DOI: 10.61782/fa.2025.0189

FORUM ACUSTICUM EURONOISE 2025

CHALLENGES IN PRODUCING INNOVATIVE LOW-NOISE ASPHALT MIXTURES WITH RECYCLED MATERIALS AND ADDITIVES: INSIGHTS FROM LIFE SILENTPROJECT

Massimiliano Diamantini[1*] **Patrizia Bellucci**[1] **Giuseppe Chidichimo**[2] **Filippo Praticò**[3]

[1] ANAS S.p.A., Research & Development Department, Via Luigi Pianciani, 16, 00185, Rome, Italy
[2] University of Calabria, TEBAID Consortium, Via P. Bucci, 15D, 87036, Rende (Cs), Italy
[3] Department of Information Engineering, Infrastructure and Sustainable Energy, University Mediterranea di Reggio Calabria, Via dell'Università, 25, 89124, Reggio Calabria, Italy

ABSTRACT

This paper discusses the challenges encountered during the LIFE SILENT project in producing innovative asphalt mixtures designed to develop low-noise, sustainable, and eco-friendly pavements for urban environments. The project's aim to integrate recycled materials and innovative additives into asphalt production revealed several technical and operational issues that required careful consideration and adaptation of traditional processes.

Key challenges included ensuring the proper integration of unconventional materials into the mixture, managing their physical characteristics to prevent compaction issues, and adjusting production parameters, such as the order of ingredient introduction, mixing time, and temperature.

This study provides an overview of the lessons learned during the experimental phase, focusing on the technical adjustments and pre-treatments required to overcome production obstacles. By addressing these challenges, the research offers valuable insights into the potential for scaling up the production of innovative low-noise pavements that combine environmental sustainability with improved performance.

Keywords: *Asphalt Plant, Waste Reuse, Low Noise Pavement.*

1. INTRODUCTION

The LIFE SILENT project represents a significant endeavor to advance the development of sustainable, low-noise pavements for urban environments. This research focuses on the integration of recycled materials and innovative additives into asphalt mixtures, aiming at both addressing environmental concerns and enhancing pavement performance. The experimental project revealed a series of technical and operational challenges in adapting traditional asphalt production processes to accommodate these novel materials. Specifically, the introduction of crumb rubber and other additives needs a thorough re-evaluation of mixture design and production parameters. This paper outlines the key challenges encountered during the production processes of asphalts, including material handling, mixture homogeneity, and environmental compliance, and discusses the innovative solutions developed to overcome these obstacles. Ultimately, the insights gained from this project contribute to the broader goal of fostering sustainable urban infrastructure through the adoption of advanced asphalt technologies. This paper is divided into three sections: the first section (Section 2) provides a literature

[*] ***Corresponding author***: m.diamantini@stradeanas.it
Copyright: *©2025 Diamantini et al. This is an open-access article distributed under the terms of the Creative Commons Attribution 3.0 Unported License, which permits unrestricted use, distribution, and reproduction in any medium, provided the original author and source are credited.*

review related to the plants' structure and the obstacles that emerge during the production phase of the asphalts. The second one (Section 3) provides a critical review of the problems encountered with the use of innovative materials. In the last section (Section 4), some conclusions are drawn.

2. LITERATURE REVIEW

One of the goals of the LIFE SILENT project is to design, manufacture, and test new asphalt mixtures. This new mix formulation includes bitumen, coarse aggregate, filler, and additives, such as crumb rubber and fibers. The production of such a mixture is associated with a few potential risks that can occur at any stage of the production process, including the mixing stage within the production facility, which could significantly compromise the expected performance of the mixture. For this reason, it is essential for designers and producers to be aware of the critical issues that may arise in asphalt plants so that they can address them effectively, not only to prevent performance decline but also to avoid project delays and increases in production costs.

An asphalt plant is a facility designed to produce asphalt mixtures and it typically consists of a dryer drum, conveyor belts, cold feed bins, a hot elevator, storage silos (for filler and powder additives), tanks for storing hot bitumen and liquid additives, pumps, pneumatic and screw conveyors, and control systems. The operational process of each asphalt plant necessitates input materials, such as aggregates (e.g., crushed stones, gravel, sand, and filler), bitumen, and other raw materials that are transformed into asphalt concrete at the end of the production process [1].

The coarse aggregates in various sizes and types are previously stored in the hoppers. Filler, additives and bitumen are stored in tanks and silos.

In any Asphalt Plant, based on the recipe, the control system selects the hoppers, and aggregates are properly dried in the Dryer Drum.

There are two main types of asphalt plants: batch or discontinuous and continuous. A batch plant, whose schematic representation is shown in Figure 1, produces asphalt mixtures in discrete batches, making it suitable for small and medium-sized projects. In contrast, a continuous plant, as shown in Figure 2, produces asphalt mixtures without interruption. The key difference between continuous and batch plants lies in their production method. Batch plants produce asphalt in discrete batches, where materials are loaded, and the binder is injected directly into the mixer. This type of machinery offers high control over the mixture quality and allows for frequent changes in the asphalt recipe.

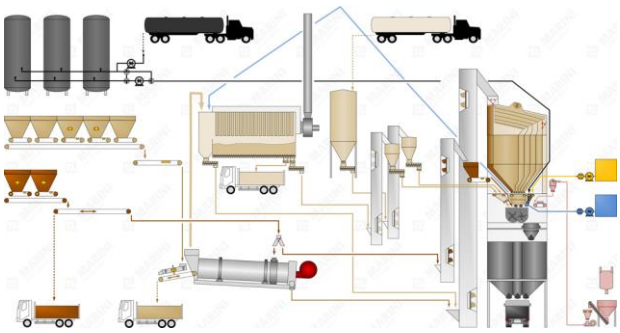


Figure 1. Schematic representation of a Discontinuous Plant (source: Schema di un impianto discontinuo per asfalto - Marini Makina A.Ş.).

In contrast, continuous plants produce asphalt continuously at high rates, without interruption, as the materials are processed within the dryer drum.

The coarse aggregates, bitumen, filler and other aggregates are mixed in the last part of the Dryer Drum.

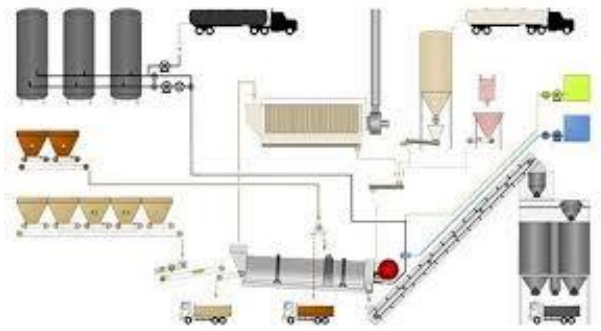


Figure 2. Schematic representation of a Continuous Plant (source: Schema di un impianto discontinuo per asfalto - Marini Makina A.Ş.).

The control systems used in modern facilities are very important because they play an important role in the efficiency of the entire production process: controlling and monitoring the final temperature of the coarse aggregates and asphalt, ensuring the accurate proportioning of materials, controlling the production

rate, and ensuring the safety of the process. The Emission Control Systems (filters, scrubbers, dust collectors) collect and capture dust and any type of emission.

In recent years, to improve the performance of asphalt mixtures, crumb rubber has been added to hot mix asphalt [2]. Crumb rubber, recycled from end-of-life tires (ELTs), has a powder-like consistency and can be incorporated into the mixture using different technologies, including the wet and dry methods. In the wet method, the rubber is added directly to the bitumen, modifying the base binder and resulting in a more resistant and durable asphalt mixture [3].

On the other hand, with the dry method, crumb rubber is added directly to the asphalt mixture during production at the asphalt plant.

One of the main goals of the LIFE SILENT project is to develop a new sustainable, eco-friendly bituminous conglomerate and to improve its durability by preventing fractures and increasing load distribution, mechanical properties and shear resistance. A key part of this project is the design and testing of a new asphalt formulation incorporating fibers derived from waste materials, such as recycled cardboard. These materials are properly treated. The chemical treatment of the fibers makes them suitable for mixing with bitumen to produce the bituminous conglomerate and enables the formation of strong bonds between the fibers [4]. Furthermore, to reduce energy consumption and improve environmental performance, special chemical additives will be used to help maintain the fluidity of bitumen at lower temperatures [5][6][7][8][9].

3. PROBLEMS ENCOUNTERED

Any commercial asphalt plant utilizing innovative materials such as crumb rubber and fibers is facing adjustment challenges. Some of the difficulties related to the use of ELTs, fibers, and additives were addressed within the LIFE SILENT project. This project developed a mixture containing these elements, in addition to the standard asphalt constituents, to be produced using the dry method at a traditional discontinuous asphalt plant.

The introduction of rubber powder and other innovative components into the mixer represents a significant challenge, as traditional plants were not specifically designed for these materials. This is due to the following characteristics of these materials:

- Crumb rubber and fibers are low-density ($<<1 g/cm^3$), are made of low-cost waste materials, and have a powder-like consistency.
- There is a number of liquid additives that were used.

During the production of asphalt, additives and fibers must be inserted into the mixer at different times to prevent them from reacting exclusively with each other. Different methods were investigated for liquid additives, including 1) the use of a dedicated line composed of tank, pipeline, and pump. 2) the use of the existing bitumen line, combining additives and bitumen.

As mentioned above, ELTs and treated fibers, characterized by a powdery consistency, could create problems in the asphalt plant.

The problems that could arise include the following:

- The materials could compact inside their respective feed pipes and create blockages that would reduce or block their regular flow.
- Given their consistency, they might not flow when discharged from the special weighing device into the mixer.

One solution that could be applied for addressing these issues is to form the powder materials into pellets. The palletization process, although offering advantages in terms of handling and dosing powdery materials such as ELTs and fibers, can present several disadvantages from the economic and chemical points of view, implying a new experimental campaign in the laboratory. The traditional palletization process often involves moistening the material to facilitate pellet formation; however, this process could be incompatible with the characteristics of fibers. Consequently, a palletization method for fibers that does not require the addition of moisture could be investigated. Collaboration with the plant owner is crucial to ensure that the developed solutions are practical and applicable to the real-world context, with the aim of overcoming the limitations of palletization methods, which can involve additional costs and operational complexities. The introduction of powder-like materials, using manual or automated feeding systems without compressed air, represents a potential solution, for example, using biodegradable bags.

Another important, eco-friendly and cost-effective advantage of the LIFE SILENT mixture could be linked to lower mixing temperatures (WMA). Lowering the

mixture temperature involves lowering the heating temperature of coarse aggregates, one of the most energy-intensive steps in asphalt production (cf. ANAS RUFAS project) and results in a reduction of emissions from the asphalt plant's chimney and a decrease in perceived bad odors.
The last parameter that requires control is the mixing time, owing to the quantity of components in the bitumen conglomerate mixture, to achieve homogeneous asphalt. Mixing time is defined as the duration needed to thoroughly blend the heated aggregates, bitumen, and any added additives within the asphalt plant's mixer.
The mixing time must be appropriate for the specific asphalt mix being prepared. An insufficient mixing time will result in a non-homogeneous final product, while excessive mixing can lead to asphalt overheating and significantly reduced product quality.
The WMA developed in the LIFE SILENT project, as previously detailed, incorporates rubber powder and fibers in addition to hot aggregates, filler, and modified bitumen. Achieving a uniform distribution of these various elements within the mixture has fundamental importance. The rubber powder must not clump or concentrate in localized areas, and the fibers must be distributed homogeneously, as they are essential for enhancing the mechanical properties of the asphalt.

4. CONCLUSION AND OUTLOOKS

The LIFE SILENT project has the aim of demonstrating the feasibility and potential of producing innovative, low-noise asphalt mixtures utilizing recycled materials and advanced additives. However, the experimental phase highlighted several critical challenges that must be addressed for successful large-scale implementation. The need for precise material handling, particularly with powder-like substances and reactive chemicals necessitates the development of tailored production methodologies. Furthermore, optimizing mixing parameters, such as temperature and time, is essential to ensure mixture homogeneity and environmental compliance.
The exploration of alternative palletization techniques and manual feeding systems, as well as the adoption of warm mix asphalt (WMA) technologies, has shown promise in mitigating these challenges. By documenting these findings and the solutions developed, this research provides valuable guidance for future projects aiming to integrate sustainable practices into asphalt production. The successful application of these technologies holds the potential to significantly reduce the environmental impact of urban pavements while enhancing their performance and longevity.

5. REFERENCES

[1] E-MAK Innovation and reliability, official website, What is Asphalt Plant? | E_MAK BLOG (last accessed on March 19, 2025).

[2] L. G. Picado-Santos, S. D. Capitão, J. M. C. Neves: "Crumb rubber asphalt mixtures: A literature review", *Construction and Building Materials*, vol. 24, 2020.

[3] ECOPNEUS, official website, Characteristics and performances - Ecopneus (last accessed on March 19, 2025).

[4] Bellucci, P., Bernardinetti,P., Chidichimo, G., Meli, G., Praticò, F., Sartori, C., "Cellulose fibres for better performing road pavements", *Roads and Airports Pavement Surface Characteristics*. CRC Press, 768-777, 2023

[5] Praticò, F., Perri, G., "A look at sustainability challenges in road pavement design and construction: the project Silent", in proceedings of International Conference CrossMED (Landscapes Across the Mediterranean) 11*th* – 13*th* December 2024

[6] ECOPNEUS, official website, "Strati di usura con polverino da Pneumatici Fuori Uso per pavimentazioni stradali della viabilità urbana. Manuale Tecnico (last accessed on March 25, 2025).

[7] Superior Asphalt LC, official website, What is Warm Mix Asphalt? A Guide to Asphalt (last access on March 25, 2025)

[8] Praticò F.G., Perri G., De Rose M., Vaiana R., "Comparing bio-binders, rubberised asphalts, and traditional pavement technologies", (2023) Construction and Building Materials, 400, art. no. 132813, DOI: 10.1016/j.conbuildmat.2023.132813.

[9] Praticò F.G., Vaiana R., Gallelli V. "Transport and traffic management by micro simulation models: Operational use and performance of roundabouts" (2012) WIT Transactions on the Built Environment, 128, pp. 383 - 394, DOI: 10.2495/UT120331

DOI: 10.61782/fa.2025.0433

FORUM ACUSTICUM EURONOISE 2025

HOW SUSTAINABLE ARE INNOVATIVE NOISE MITIGATION ROAD PAVEMENTS? AN LCA APPROACH

Alessandra Altobello[1] **Francesco Valerio Catania**[1] **Martina Busti**[1]
Chiara Ravagnan[1] **Almona Tani**[1*]
[1] Italferr SpA – Gruppo Ferrovie dello Stato Italiane, via V. G. Galati 71 - 00155 Rome (Italy)

ABSTRACT

The use of innovative materials is being experimented in asphalt mixtures to improve acoustic performance of road pavements with the aim of mitigating noise as one of the impacts generated by road infrastructures. However, further investigation is required to evaluate their sustainability.
To this end, as part of the LIFE SILENT project- aimed at developing innovative and sustainable solutions for mitigating road and railway noise- a comparative Life Cycle Assessment (LCA) has been conducted to assess the environmental impacts of asphalt mixtures incorporating recycled and innovative components.
The LCA has considered multiple processes involved in the application of asphalt mixtures, from raw material extraction and transportation to manufacturing and laying, as each of these contributes to the overall impact. The study compares 8 alternatives of asphalt mixtures, that differ from each other for the presence of traditional or innovative materials, such as crumb rubber. The latter enhances the acoustic performance of the paved surface and could provide environmental benefits, being a secondary raw material.
This approach enables standardized assessments at system level, offering the opportunity to compare the impacts of either different flows within the same process or different product alternatives, to identify and promote more sustainable practices.

Keywords: *life cycle assessment, asphalt mixtures, environmental impacts, acoustic performance*

[*] ***Corresponding author***: *a.tani@italferr.it*
Copyright: *©2025 Altobello et al. This is an open-access article distributed under the terms of the Creative Commons Attribution 3.0 Unported License, which permits unrestricted use, distribution, and reproduction in any medium, provided the original author and source are credited.*

1. INTRODUCTION

Asphalt mixtures are essential materials in modern infrastructures, widely used in the construction of roads and other surfaces. These mixtures are composed of a variety of materials, including aggregates, bitumen, and, increasingly, recycled and innovative components, such as the ones used for the road pavements developed in the LIFE SILENT project that are the focus of this paper.
The production and application of asphalt mixtures involves multiple and various processes, from raw material extraction and transportation to manufacturing and construction. Each of these stages contributes to the overall impact of asphalt, making its environmental life cycle assessment (LCA) a highly complex task.
A comprehensive LCA is based on extensive and detailed data collection and analysis and often requires the definition of assumptions for calculations; therefore, changes in material composition and processes for asphalt mixture production involve significant variability in LCA outcomes. Therefore, a life cycle thinking (LCT) method represents a powerful tool to compare product alternatives and have a detailed understanding of generated impacts.

2. THEORETICAL FRAMEWORK AND RESEARCH GOAL

Sustainability assessment methodologies in road infrastructure design and construction have been extensively addressed and rated by the scientific literature [1-3], highlighting their capacity to innovate existing procedures and approaches. While the importance of sustainability is nowadays recognized in all aspects of life [4], the significant weight of road infrastructures in destabilizing the environment has stimulated strategic and proactive approaches towards the adoption of low-emissions and energy saving

solutions starting from the phases of infrastructures design [5-7]. In particular, the application of a life cycle assessment (LCA) to road pavement industry has been receiving considerable attention by practitioners and policy makers for the recognised ability of this methodology to assess the performance of materials and products throughout their life cycle [8-10], considering both their technical and environmental characteristics.
In this context, this work contributes to the existing studies focused on the potential of innovative materials in asphalt mixtures to help alleviating the environmental burden of road pavements [11-13]. The comparison of multiple additives through the LCA approach has been helpful to assess the consequences and to highlight the hotspots of incorporating innovative solutions into asphalt mix production, contributing in particular to the assessment of the use of crumb rubber in asphalt mixtures [14-18].
Crumb rubber is a recycled material obtained from end-of-life tires (ELT) through mechanical shredding and grinding processes. It can be used as an additive in asphalt mixtures to enhance performance characteristics such as durability, flexibility, and above all noise reduction. By incorporating crumb rubber into asphalt, the material, besides improving the mechanical properties of road surfaces, contributes to the overall asphalt's sustainability, by reducing tire waste and minimizing the demand for virgin raw materials. The LCA approach inquires further in the environmental impacts of its production, including the energy-intensive chipping process, to fully assess its benefits.
Against this framework, the goal of the paper is to assess the sustainability of innovative and low-noise road solutions developed in the LIFE SILENT project through an LCA study. In particular, the paper aims to contribute to the assessment of environmental impacts, paying attention to the analysis of hotspots generated by incorporating innovative solutions into asphalt mix production.

3. METHODOLOGICAL APPROACH

For the purposes of this study, the LCA work breakdown structure of the analysis conducted, aligned with international sectorial standards, consists in the following steps:

A) Scope definition;
B) Base assumption and Inventory analysis (LCI);
C) Selection of impact categories and Impact assessment for the selected impacts (LCIA);
D) Results interpretation.

A) SCOPE

Comparative LCA analysis constitutes a useful and adaptable tool for identifying and promoting more sustainable practices; this applies also to asphalt mixture design and production as required by CAM Strade - the ministerial decree nr. 279/2024 indicating the Minimum Environmental Criteria for the design, construction, and maintenance of road infrastructures. The scope of the LCA analysis reported in this paper is to present and compare LCA results for 8 alternatives of closed asphalt mixtures, which are listed and described in the table below.

Table 1. Description of the 8 asphalt mixture alternatives.

Type	Description
A	This traditional asphalt type, developed by ANAS and used as a reference scenario in the LIFE SILENT project, includes bitumen and stone aggregates. Its composition contains a slightly higher percentage of bitumen and a lower percentage of aggregates in comparison to type B.
B	This traditional asphalt type, developed according to regulatory standards in the LIFE SILENT project, includes bitumen and stone aggregates, and is used as a reference scenario together with type A.
2	This new asphalt type, developed within the LIFE SILENT project, includes bitumen, stone aggregates, crumb rubber, warm mix asphalt additives, and treated cellulose fibre. Its composition contains the highest percentage of warm mix asphalt additives, compared to all other new types.
4	This new asphalt type, developed within the LIFE SILENT project, includes bitumen, stone aggregates, crumb rubber, additives for warm mix asphalt and cellulose fibre. Its composition contains the same percentage of additives for warm mix asphalt as types 5 and 6, and lower percentage compared to types 2, 7 and 8.

5	This new asphalt type, developed within the LIFE SILENT project, includes bitumen, stone aggregates, crumb rubber and additives for warm mix asphalt. Its composition contains the same percentage of additives for warm mix asphalt as types 4 and 6, and a lower percentage compared to types 2, 7 and 8.
6	This new asphalt type, developed in the LIFE SILENT project, includes bitumen, stone aggregates, crumb rubber, hot asphalt additives and treated cellulose fibre. Its composition contains the same percentage of additives for warm mix asphalt as types 4 and 5, and a lower percentage compared to types 2, 7 and 8.
7	This new asphalt type, developed in the LIFE SILENT project, includes bitumen, stone aggregates, crumb rubber, hot asphalt additives and treated cellulose fibre. Its composition contains a higher percentage of hot asphalt additives compared to types 4, 5 and 6, but a lower percentage compared to type 2. Also, the amount of treated cellulose fibre is lower than in mixtures 2 and 6.
8	This new asphalt type, developed in the LIFE SILENT project, includes bitumen, stone aggregates, crumb rubber, hot asphalt additives and treated cellulose fibre. Its composition contains a higher percentage of hot asphalt additives compared to types 4, 5 and 6, but a lower percentage compared to type 2. In addition, the amount of treated cellulose fibre is lower than in types 2 and 6. It differs from all other new types by the lower amount of crumb rubber.

B) BASE ASSUMPTION AND INVENTORY ANALYSIS

Determining raw material inputs, energy requirements, and other fundamental data is a critical step in conducting comprehensive and close-to-reality LCA studies.
The baseline assumptions and the inventory analysis are described in the following:
The *declared unit* is one square meter of pavement.

The *system boundary* is *"Cradle-to-Gate"* with declared modules of life stages A1 to A5 (see table below). The setting of calculation follows the Allocation Cut Off System model in line with regulatory standards [19-21] and PCRs [22-23], and meets the requirements set by EN 15804+A2:2019 in compliance with the end-of-waste criteria [24].

Table 2. Life cycle stages [22].

Product Stage			Construction process stage		Use Stage	End of life Stage	Benefits and loads beyond the system boundary
A1	A2	A3	A4	A5	B1-B7	C1-C4	D
Raw materials supply	Transport	Manufacturing	Transport	Construction-Installation	Modules not declared		

Geographical aspects were considered those as representative as possible of the life cycle processes of the mixtures analysed.
Data Quality is assured using the most recent available datasets and internationally recognized database. The software employed for the assessment is OpenLCA, which allows for a detailed evaluation of the environmental impacts associated with asphalt mixture production and installation through the use of Ecoinvent 3.10 and other specifically selected datasets.
Necessary data from the production, transportation and installation processes are collected using the best available datasets, including both primary and secondary data collection, such as:

- consultations and data exchange with industry specialists: for material and other input selection and *quantity estimation*;
- sectorial scientific literature: utilized when direct access to experts' data was not available;
- official database "Ecoinvent 3.10 – 15804 Unit process Cut-off", and publicly available LCA studies: for supplementary data and validation.

Besides, the baseline assumptions on material inputs are established for LCA calculations. While specific input

quantities are not detailed in this paragraph, the association of calculation inputs with relevant environmental datasets is provided to introduce the assumptions of the analysis.
The following table summarizes the inputs considered in the model along with their corresponding data sources used later for the impact assessment.

Table 3. Datasets used for each life cycle stage.

Life Cycle Stage	Data source
A1	LCI by Eurobitume, 2012 [25] LCI by Ortega et al., 2023 [26] Ecoinvent 3.10 [27]
A2	Ecoinvent 3.10 [27]
A3	
A4	
A5	

Additionally, assumptions regarding energy consumption and transportation distances are made based on the best available data sources. The energy consumption associated with the manufacturing of asphalt mixture production process is derived from technical plant sheets provided by LIFE SILENT partners.
Similarly, transportation distances for materials and finished products were estimated based on discussions with sector experts, aiming to the most realistic representation of logistics and supply and transport chain.

C) SELECTION OF IMPACT CATEGORIES AND IMPACT ASSESSMENT

The methodology adopted for identifying the environmental Impact Categories, and relative KPIs, consists of a literature review carried out as a joint work of the project partners and consolidated in specific meetings. For the literature review were considered, among others, European and international standards, scientific journals and research projects' reports, as well as FS Group internal documents. The initial list of KPIs resulted from the literature review was further refined through desk analysis and validated in a workshop held with the project partners, in order to cover all the life cycle phases of the solutions developed in the project. This process has been critical to confirm the reliability of the methodology and refine its reproducibility.
Impact Categories and indicators used for this LCA study are listed in the following table. The choice of KPIs started from the EN 15804+A2 (EF v3.1) standard, which has a high relevance being among the main standards of the LCA and found to be recurring as a source also in other documents of the literature reviewed.
In addition to the 14 indicators of the most known 7 Environmental Impact Categories, the table lists also:
• 6 indicators for the 5 additional Environmental Categories;
• 5 indicators for the category Outgoing Flows;
• 10 indicators for the category Consumption of Resources;
• 3 indicators for the Waste category.
This makes a total of 15 impact categories and 38 indicators used for the LCA of the LIFE SILENT project asphalt mixtures.

Table 4. Impact Categories and KPIs used for LCA.

Impact category	Indicator (Acronym)	Unit of measure
Environmental		
Abiotic depletion potential	ADP - fossil resources (ADPF)	MJ
	ADP - non-fossil resources (mineral and metal) (ADPE)	kg Sb eq.
Acidification Potential	AP, Accumulated Exceedance (AP)	Mol H+ eq
Ozone depletion Potential	Depletion potential of the stratospheric ozone layer (ODP)	kg CFC 11 eq.
Eutrophication potential	EP – freshwater	kg P eq.
	EP - marine	kg N eq.
	EP - terrestrial	mol N eq.
Global Warming Potential	GWP - biogenic	kg CO2 eq.
	GWP - fossil fuels	kg CO2 eq.
	GWP - land use and land use change	kg CO2 eq.
	GWP - total	kg CO2 eq.
	GWP except emissions and uptake of biogenic carbon (GWP-GHG)	kg CO2 eq.
Photochemical Ozone Creation Potential	POCP	kg NMVOC eq.
Water Depletion potential	Water (user) deprivation potential (WDP)	m3 world eq. deprived
Ecosystem Potential Toxicity	Potential Comparative Toxic Unit for ecosystems (freshwater) (ETP-fw)	CTUe
Additional environmental impacts		
Human Toxicity Potential	Potential Comparative Toxic Unit for humans - cancer effects (HTP-c)	CTUh
	Potential Comparative Toxic Unit for humans - non-cancer effects (HTP-nc)	CTUh
Ionizing radiation	Potential Human exposure efficiency relative to U235 (IRP)	kBq U235 eq.
Particulate Matter emissions	Potential incidence of disease due to PM emissions (PM)	Disease Incidence
Soil Quality Potential	Potential Soil quality index (SQP)	Adimensional
Outgoing flow (energy and other materials)		
Outgoing Flows	Components for re-use (CRU)	kg

	Exported electrical energy (EEE)	MJ
	Exported thermal energy (EET)	MJ
	Materials for energy recovery (MER)	kg
	Materials for recycling (MFR)	kg
Consumption of resources		
Consumption of Resources	Total use of non-renewable primary energy resources (PENRT)	MJ
	Total use of renewable primary energy resources 8 PERT)	MJ
	Use of net fresh water (FW)	m3
	Use of non renewable primary energy resources used as energy carrier (PENRE)	MJ
	Use of non renewable primary energy resources used as raw materials (PENRM)	MJ
	Use of non renewable secondary fuels (NRSF)	MJ
	Use of renewable primary energy resources used as energy carrier (PERE)	MJ
	Use of renewable primary energy resources used as raw materials (PERM)	MJ
	Use of renewable secondary fuels (RSF)	MJ
	Use of secondary materials (SM)	kg
Waste		
Waste	Hazardous waste disposed (HWD)	kg
	Non hazardous waste disposed (NHWD)	kg
	Radioactive waste disposed (RWD)	kg

D) RESULTS INTERPRETATION

This paragraph summarizes the results of the comparative LCA of innovative and complex asphalt mixtures, evaluating their environmental performances against standard ones. Due to the extensive amount of data reported for each mixture, the complete set of results of the LCA study conducted with OpenLCA are available from the authors upon reasonable request.
A specific focus on Global Warming Potential (GWP-total) is provided here for a clearer understanding of the carbon footprint associated with the different alternatives. GWP is one of the most significant impact categories since all the indicators show similar trends, therefore it can be used as a key indicator for assessing the overall sustainability of asphalt mixtures.

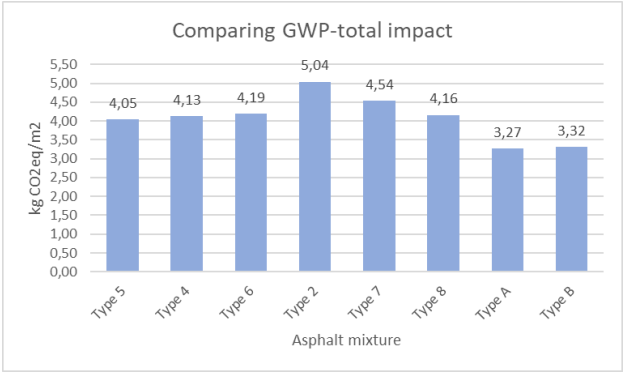


Figure 1. GWP-total for the 8 asphalt mixture alternatives.

The above graph shows the impact in terms of GWP-total. It highlights that the innovative LIFE SILENT mixtures could have higher carbon impact compared to traditional ones, with type 5 and 8 mixtures having the lower impact and type 2 the highest.
The higher impact of these mixtures may be attributed to the greater variety of materials and processes which leads to a higher number of assumptions, also increasing the level of uncertainty. It is worth noting that when the LCA for preliminary assessment was conducted, project data was not fully available therefore secondary data has been used as well [13].
Furthermore, the below graph illustrates the contribution of each life cycle phase to the total impact across the A1-A5 life stages, using average data. The results show consistent trends among all the mixtures.

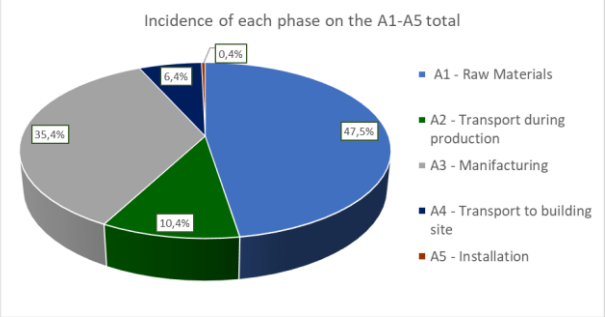


Figure 2. Contribution of each life cycle phase to the total impact.

4. CONCLUSIONS AND WAY FORWARD

The findings provide valuable insights into key impact areas and highlight opportunities for further improvements of the sustainability of the asphalt mixtures proposed within the LIFE SILENT project.
The incorporation of recycled materials, such as crumb rubber and cellulose fibres from recycled cardboard offers notable environmental and economic benefits, which adds to the aim of improved acoustic performance. By replacing virgin aggregates with the right amount of recycled materials, the demand for raw material extraction is reduced, leading to lower environmental impacts. Additionally, recycling minimizes waste generation and landfill disposal, contributing to a more circular and sustainable approach to asphalt production.
To improve the accuracy and reliability of LCA studies on the LIFE SILENT asphalt mixtures, future research should focus on refining critical parameters and assumptions, particularly by collecting more detailed and reliable data on:

- production temperature and its corresponding energy consumption;
- raw material transportation and packaging;
- Crumb rubber and cellulose fibres production, assessing its processing and potential optimizations;
- proportion of primary and secondary materials, including the presence and typology of chemical additives.

Along with the abovementioned points, a scenario comparison is presented to evaluate the potential impact of the LIFE SILENT mixtures production choices, again in terms of GWP-total.
The following graph illustrates how GHG emissions vary when reducing packaging (i.e., avoiding the use of big bags) and cutting off waste impact from the crumb rubber production. According to the LCA results this can lower GHG emission of about 10 % on average.

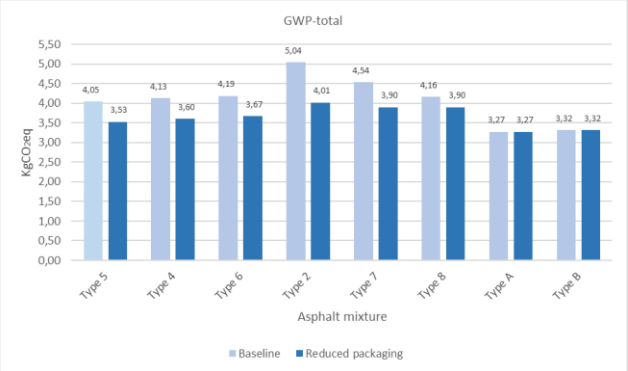


Figure 3. GWP-total in the scenario comparison.

Another graph shows the potential benefit of using higher amounts of crumb rubber by replacing virgin aggregates. The results illustrated in the graph below show that variations in crumb rubber content can improve the mixtures' impacts.

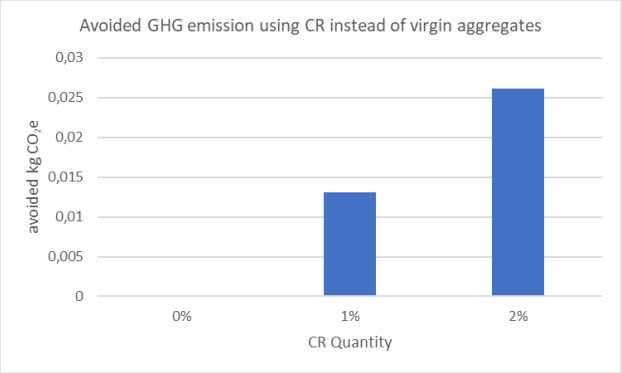


Figure 4. Avoided GHG emissions for different crumb rubber contents.

Additional sensitivity analyses can be conducted on materials' selection. For instance, bitumen, which represents another significant environmental impact, can be the subject of further analysis. While this study assumes the use of virgin bitumen (with SBS), incorporating recycled bitumen could significantly reduce resource depletion and environmental impacts, further contributing to the sustainability of the LIFE SILENT asphalt mixtures.
Together with bitumen, chemical additives also contribute to the overall impact of LIFE SILENT mixtures, despite being used to reduce production temperatures. In future studies, it will be crucial to assess

the benefits of lower temperatures against the environmental impact of these chemical products.
Although the improvement opportunities identified in an LCA study can be numerous, the participation of other academia, industry and design experts is essential to identify additional optimization scenarios and to validate the abovementioned ones.

5. ACKNOWLEDGMENTS

The research has been developed as part of the LIFE SILENT project (Sustainable Innovations for Long-life Environmental Noise Technologies), funded by the European Climate, Infrastructure and Environment Executive Agency under the LIFE Project Grants (LIFE22-ENV-IT-LIFE SILENT).

6. REFERENCES

[1] G.B Suprayoga, M. Bakker, P. Witte, and T. Spit: "A systematic review of indicators to assess the sustainability of road infrastructure projects", *European Transportation Research Review*, Vol. 12, No.19, 2020.

[2] C. Kapatsa, N. Kavishe, S.L. Zulu, and G. Maro: "Sustainability assessment indicators of road infrastructure projects: a systematic literature review", *Journal of Engineering, Design and Technology*, 2024.

[3] R.A. Mehraban, L. Tsantilis, P.P. Riviera, and E. Santagata: "Comprehensive Analysis of Sustainability Rating Systems for Road Infrastructure.", *Infrastructures*, Vol. 10, No.1, 2025.

[4] P. Horton and B. P. Horton: "Re-defining Sustainability: Living in Harmony with Life on Earth", *One Earth*, Vol. 1, No. 1, pp. 86-94, 2019.

[5] F. Praticò, R. Fedele, P.G. Briante, G. Pellicano and G. Colicchio: "Innovative Technologies and Materials for more Sustainable Transportation Infrastructures", Extra n. 6/2019, 10.14633/AHR198, 2019.

[6] N. Liu, Y. Wang, Q. Bai, Y. Liu, P. Wang, S. Xue, Q. Yu and Q. Li: "Road life-cycle carbon dioxide emissions and emission reduction technologies: A review", *Journal of Traffic and Transportation Engineering*, Vol. 9, No. 4, pp. 532-555, 2022.

[7] A. Tafida, W.S. Alaloul, N.A.B.W. Zawawi, M.A. Musarat and A.S. Abubakar: "A Review of Eco-Friendly Road Infrastructure Innovations for Sustainable Transportation", *Infrastructures*, Vol. 9, 2024.

[8] R. Yang, H. Ozer, S. Kang and I. Al-Qadi, "Environmental impacts of producing asphalt mixtures with varying degrees of recycled asphalt materials", in *Proceedings International Symposium on Pavement LCA* 2014, Davis, California, USA. October 14-16, 2014.

[9] B. Awuzie, and A. Ngowi: "Sustainability performance of infrastructure projects: the case for life cycle sustainability assessment methodology", *Journal of Construction Project Management and Innovation*, Vol. 8, No. 1, 2018.

[10] A. Alhjouj, A. Bonoli and M. Zamorano: "A Critical Perspective and Inclusive Analysis of Sustainable Road Infrastructure Literature", *Applied Sciences*, Vol.12, No. 24, 2022.

[11] M. Ohiduzzaman, O. Sirin, E. Kassem and J.L. Rochat: "State-of-the-Art Review on Sustainable Design and Construction of Quieter Pavements—Part 1: Traffic Noise Measurement and Abatement Techniques" *Sustainability*, Vol. 8, No. 8, 2016.

[12] W. Hu, X. Shu, B. Huang: "Sustainability innovations in transportation infrastructure: An overview of the special volume on sustainable road paving", *Journal of Cleaner Production*, Vol. 235, pp. 369-377, 2019.

[13] F.G. Praticò, G. Perri, M. De Rose and R. Vaiana: "Comparing bio-binders, rubberised asphalts, and traditional pavement technologies", *Construction and Building Materials*, Vol. 400, 2023.

[14] MR. Pouranian and M. Shishehbor, "Sustainability Assessment of Green Asphalt Mixtures: A Review" *Environments*, Vol. 6, No. 6, 2019.

[15] M. Puccini, P. Leandri, A.L. Tasca, L. Pistonesi and M. Losa: "Improving the Environmental Sustainability of Low Noise Pavements: Comparative Life Cycle Assessment of Reclaimed Asphalt and Crumb Rubber Based Warm Mix Technologies", *Coatings*, Vol. 9, No.5, 2019.

[16] D. Landi, M. Marconi, E. Bocci and M. Germani: "Comparative life cycle assessment of standard, cellulose-reinforced and end of life tires fiber-reinforced hot mix asphalt mixtures", *Journal of Cleaner Production*, Vol. 248, 2020.

[17] M.S. Siverio Lima, C. Makoundou, C. Sangiorgi and F. Gschösser: "Life Cycle Assessment of Innovative Asphalt Mixtures Made with Crumb Rubber for Impact-Absorbing Pavements", *Sustainability*, Vol. 14, No. 22, 2022.

[18] F.R. Apaza, V. Fernández Vázquez, S.E. Paje, F. Gulisano, V. Gagliardi, L. Saiz Rodríguez and J. Gallego Medina: "Towards Sustainable Road Pavements: Sound Absorption in Rubber-Modified Asphalt Mixtures.", *Infrastructures*, Vol. 9, No. 4, 2024.
[19] UNI EN ISO 14040:2021.
[20] UNI EN ISO 14044:2021.
[21] UNI EN 15804:2021.
[22] EPD International, PCR: "Asphalt Mixtures: UN CPC 1533 & 3794", Version 1.03, 2019.
[23] TII Publications, PCR: "Complementary Product Category Rules for Bituminous Mixtures (c-PCR Bituminous Mixtures) DN-PAV-03077", 2024.
[24] D. Ioannidou, C. Foster, A. Symeonidis A., J. Müller, G. Bourgault, D. FitzGerald and R. Moreno Ruiz: "Documentation for the 'Allocation, cut-off, EN15804' system model" (2021.10.01), Ecoinvent, 2021.
[25] European Bitumen Association, "Life Cycle inventory: Bitumen", Eurobitume 2012, 2nd Edition, (Brussels, Belgium), pp. 000–060, 2012.
[26] J. Los Santos-Ortega, E. Fraile-Garcìa and J. Ferreiro-Cabello: "Methodology for the environmental analysis of mortar doped with crumb rubber from end-of-life tires", *Construction and Building Materials*, Vol. 399, pp. 5-6, 2023.
[27] EcoInvent v3.10, Available on https://ecoquery.ecoinvent.org/3.10/cutoff/ .

DOI: 10.61782/fa.2025.0353

FORUM ACUSTICUM EURONOISE 2025

EUROPEAN PROJECTS FOR NOISE QUALITY IN FLORENCE

First author Arnaldo Melloni[1] **Second author** Gessica Pecchioni[1], **Third author** Raffaella Bellomini[2]

[1] Municipality of Florence
[2]Vie en.ro.se.Ingegneria srl, Florence Italy

ABSTRACT

The city of Florence has promoted and participated in numerous European projects (LIFE and HORIZON 2020) on the topic of environmental noise in cities. Over the last 10 years, the topics of quiet areas, sound-absorbing asphalt, noise produced by tramways and roadside noise control methods have been addressed. The presentation will illustrate the main results obtained and the practical applications in urban areas.

Keywords: European projects, cities, environmental noise

1. INTRODUCTION

The municipality of Florence programs and plans activities for the control of environmental noise using the tools provided for by European directives: strategic noise map and action plan. The main activities are concentrated on the reorganization of city mobility, with the creation of a tram system spread throughout the urban area. The reorganization of private and public mobility is being developed around the tram system, favoring cycle and pedestrian mobility. The goal is to make the city more sustainable, reducing air and noise pollution. The European projects that the municipality of Florence uses to experiment with innovative and replicable activities in the field of sustainability fit into this general framework. Below are presented the results of some European projects on the topic of environmental noise containment and the positive effects on the territory of our city.

*Corresponding author: first.author@email.ad.

Copyright: ©2025 First author et al. This is an open-access article distributed under the terms of the Creative Commons Attribution 3.0 Unported License, which permits unrestricted use, distribution, and reproduction in any medium, provided the original author and source are credited.

2. LIFE HUSH

The H.U.S.H. project moves from the evidence that harmonization of noise action planning methods is needed, not only in Italy but also in all the European countries where a former Legislation about noise planning was present at the moment of END Directive adoption. Among particular project's objectives, one is to define a new development system (procedures and database) for action planning, by testing it in two pilot cases, in the city of Florence. In each selected area a qualitative analysis phase besides a quantitative standard analysis phase is carried out, by means of surveys on sensitive areas, hotspots and quiet areas, as well as through inquiries about people's opinion regarding the disturb perception. In this paper methodological approach for the collection of non-acoustic data, procedures adopted for sample selection, methods for building up and analysis of questionnaires, in the frame of a participatory planning approach, are described. The results of non-acoustic surveys already carried out on a significant sample of people are reported. Expected outcomes are a collection of information that can be used to plan the actions and the community involvements.

3. LIFE QUADMAP

Quadmap Project has met the challenge of defining a methodology to select, analyse and manage QuieTUrban Areas (QUAs) which has been tested in 10 Pilot Areas located in Florence (6 schoolyards), Bilbao (a square and a green corridor) and Rotterdam (2 public parks). The methodology is thoroughly illustrated in the Guidelines which can be considered one of the Project's main final. The methodology proposed by the QUADMAP Project is based on a new definition of QUA. END definition: "quiet area in an agglomeration" shall mean an area, delimited by the competent authority, for instance, which is not exposed to a value of Lden or of another appropriate noise indicator greater than a certain value set by the Member State, from any noise source. QUADMAP definition: a QUA is an

urban area whose current or future use and function require a specific acoustic environment, which contributes to the well-being of the population. The QUADMAP project focused on the problem of noise in urban areas, not only considering the legal limits on noise pollution and taking into account that noise is one (and not the only one) of the sources of pollution that cause discomfort. The main objective of the QUADMAP project was to develop a harmonized methodology for the selection, evaluation (combining quantitative and qualitative parameters) and management (noise attenuation, increase in usability of the areas and user satisfaction) of the Areas Urbane Quiete (QUA), with the aim of overcoming the regulatory and procedural impasse. These objectives were achieved, leaving each responsible entity free to produce its own Action Plan, evaluating and addressing both territorial specificities and political priorities. The validated results of the project facilitated urban planners to apply standard procedures for the identification, delimitation and prioritization of QUAs. A significant part of the project was dedicated to the development and testing of methods for determining the relative weight of concomitant sources of discomfort, considering various factors and acoustic indicators. • Another important topic was the systematic use of soundscape analysis in qualitative acoustic analysis and in the general collection of stakeholders' opinions on the present and desired characteristics of the selected QUA.

4. LIFE E-VIA

Reduce noise on the streets of highly populated urban areas through the implementation of a mitigation measure aimed at optimizing road surfaces and electric vehicle tyres. Three road surfaces (and one test area), at least 5 different electricvehicles (including tires specially designed for electric vehicles) will be tested; The holistic soundscape approach will be used to evaluate the performance of EV vs ICEV in the new scenario (also qualitative evaluation). Awareness campaign: 20,000 people reached. The estimate was based on the experience of previous LIFE projects and on the various initiatives that are expected to be organized during the project. Noise level reduction: noise level reduction Lden and Lnight -5dB (A). The estimate of noise exposure is made taking as reference the side of the road of the receptors. 5 dB (A) reduction compared to the current situation. Improvement of the soundscape: acoustic perception and comfort of an optimized asphalt compared to the standard one. The estimate of the improvement in perception will be verified based on the questionnaires that will be collected. Number of people benefited from noise reduction: 2000 people. The estimate is based on the evaluation of the number of residents in a buffer of 50 m from the road axis.

5. LIFE SNEAK

The general objective is to reduce noise from roads in densely populated urban areas, where noise and vibrations from trams and road traffic overlap, using low noise/vibration surfaces and retrofitting solutions with life cycle costs comparable to those of standard surfaces. The following solutions will be tested in the pilot area: Sound- absorbing asphalt, sound-absorbing panels, miniskirts and mixture of water and oil on the tram to reduce squeel noise when cornering. Furthermore, the psychoacoustic parameters will be evaluated to evaluate the annoyance of citizens before and after the interventions. A contribution will be made to Directive 996/2015/EC regarding the noise assessment method (CNOSSOS).

6. HORIZON NEMO PROJECT

NEMO aims to create a complete (and therefore replicable) solution through which new systems are integrated into existing infrastructures to empirically measure the emissions and noise emitted by individual vehicles. The new measurement systems, together with the implementation of new mitigation solutions, form a comprehensive and modular approach to improve air quality and reduce noise impact in EU cities. Thanks to standardization, the systems will represent a tool for applying limitations to polluting media in low-emission zones and other sensitive areas. The first dimension of the project includes a new and advanced autonomous remote sensing system that identifies noisy and polluting vehicles in existing traffic and makes this information available for possible tolling or access systems. The system can be fully integrated into the road/rail infrastructure and will have the tools to communicate with the existing data structure of both vehicle/train operators and road/rail authorities. The second dimension develops a holistic solution to mitigate noise and emissions from passing vehicles. This integral approach involves the optimization of road structures, green barriers, photocatalytic materials and

the collection of microplastics in the pores of the asphalt layer.

7. CONCLUSION

The description of the activities and results obtained thanks to the European project aims to provide an example of how the experimental and replicable activities carried out thanks to this funding can offer innovative and effective operational tools for the planning and programming activities of the Local societies. In particular, they can contribute to the drafting of Noise Mappings and Action Plans within which medium and long-term strategies for the containment of environmental noise are defined - even punctually.

DOI: 10.61782/fa.2025.0543

FORUM ACUSTICUM EURONOISE 2025

MANAGING ENVIRONMENTAL NOISE BY BRINGING TOGETHER CONTINUOUS MONITORING AND SIMULATION MODELS

Luis Conde Santos[1*] **André Carvalho**[2] **Jorge Preto**[1]
Paulo Valério[1] **Cristina Leão**[1] **Guilherme Covas**[2]
[1] dBwave.i - Acoustic Engineering, SA, Oeiras, Portugal
[2] Instituto de Soldadura e Qualidade, Oeiras, Portugal

ABSTRACT

Assessment of environmental noise is commonly done by either performing measurements, long or short-term, or by calculating noise by means of acoustic models. These methods, although satisfactory for long-term planning or for noise limit compliance assessment, may not be suitable as a basis for an environmental noise management and control system, especially if one wants to be able to act upon the noise sources almost in real time. This paper addresses the implementation of environmental noise management systems based on continuous monitoring together with simulation models, which seek to combine real-time information from monitoring stations, installed close to the noisy activity, with information from an acoustic model that allows to predict sound levels at a distance, typically near sensitive receivers. Monitoring data is processed and made available by a digital platform, with the capacity to detect and classify noises, and that can generate alarms in quasi-real time, making it possible to take immediate action to reduce noise emission. The monitoring data is fed into the acoustic model to adjust noise sources emission for a best-fit with the measured levels. Examples of application are presented, namely the case of a racetrack and the case of a construction site.

Keywords: *Environmental Noise, Noise Management, Permanent Monitoring, Digital Platform.*

[*] ***Corresponding author***: luis.conde@dbwave.pt.
Copyright: *©2025 Luis Conde Santos et al. This is an open-access article distributed under the terms of the Creative Commons Attribution 3.0 Unported License, which permits unrestricted use, distribution, and reproduction in any medium, provided the original author and source are credited.*

1. INTRODUCTION

A common method for assessing environmental noise generated by a noisy activity is to carry out noise measurements near potentially affected sensitive receptors, which can be carried out by sampling or continuously over several days (e.g. 48 hours). Another method is by developing an acoustic model of the noisy activity (e.g. a factory) and its surroundings and use it to calculate noise levels at the sensitive receptors and, in a more comprehensive way, noise maps throughout the surroundings. These methods, although applicable in many cases, have some limitations as a basis for an environmental noise management and control system, and are even totally inadequate in situations where there is great variability or unpredictability in the noise emitted by the activity and/or where there is a need for real-time monitoring of the noise of the activity.

In fact, in the context of rapid changes in society and the technologies at its disposal, the methods and technologies used in the assessment and management of environmental noise have evolved slowly, failing to keep up with the real paradigm shifts that have been occurring around them. dBwave, an acoustic engineering company of the ISQ Group, seeking to address this type of issues, has developed and has been applying continuous noise monitoring methodologies, for more or less extended periods (from 48 hours to several weeks), with manual analysis of the recordings in post-processing, methodologies that are currently insufficient, consuming a lot of time, not allowing remote access to the data during monitoring, nor any real-time control of the activity or noisy source that is being monitored and that are only identified a posteriori.

2. MIRA – AN INTELLIGENT PLATFORM FOR ENVIRONMENTAL NOISE MONITORING

To respond to the afore-mentioned challenges, dBwave and ISQ joined efforts to develop an innovative solution, named MIRA, which focuses on continuous, unaccompanied noise monitoring, by means of type 1 sound level meters which communicate with an integrated digital platform with automations to identify specific sounds or noises, as well as the generation of alerts and daily reports of measurements made. MIRA aggregates different modules, all interconnected by a robust architecture, which allows the integration and centralization of several existing technologies, as well as new ones developed with innovative and differentiating characteristics. It thus seeks to respond to the needs identified in the market, in sectors such as industry, construction, transport infrastructures, municipalities and musical and sports performances [1].

MIRA platform is designed to allow flexibility, performance, scalability and ease of use, with the main focus on the ability to scale depending on the traffic that is occurring at the time. For this purpose, a cloud service is used that allows flexibility of the contracted computing capacities according to the need of the moment. This aspect is critical because it allows us to guarantee great security in the quality and responsiveness of the service, but also control the associated costs, since these are directly related to the number of equipment/work to be carried out at any given time.
Figure 1 illustrates the various existing modules and how they communicate with each other.

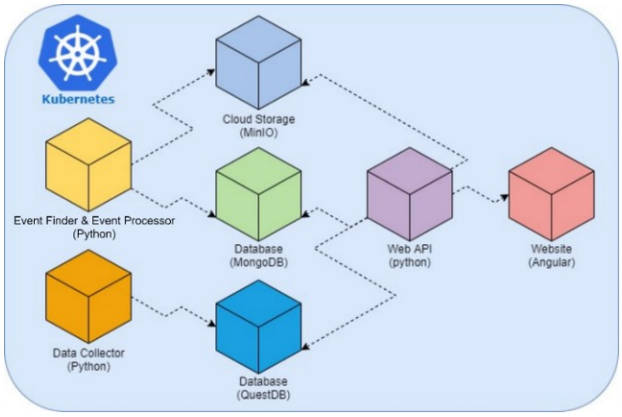


Figure 1. MIRA Architecture Schematic.

3. NOISE MANAGEMENT WITH PERMANENT MONITORING AND SIMULATION MODELS

As far as we know, the first time the approach to environmental noise management with the integration of noise mapping and monitoring techniques was proposed, goes back to 1999 [2]. Since than substantial developments have taken place, such as the technique of Dynamic Noise Mapping, extensively addressed in the European project LIFE DYNAMAP [3].

One of the areas in which permanent monitoring and noise simulation models have long been combined is that of noise management and monitoring systems around airports [4]. For example, in Portugal, Noise Monitoring Systems (in continuous operation) are installed with the aim of monitoring and controlling noise levels, with a special focus on those generated by aircraft, at Humberto Delgado, Francisco Sá Carneiro, Faro and Madeira airports. Simulations/forecasts are also carried out, through the regular preparation of Noise Maps, which are integral elements of the noise monitoring reports of these airports. Real data associated with aircraft movements in the reference periods (flight tracking technology) are used, allowing greater accuracy of the results obtained.

This paper addresses environmental noise management systems based on permanent monitoring and simulation models, in which it is sought to combine real-time information from monitoring stations, installed near the noisy activity, with information from an acoustic model that allows predicting sound levels at a distance, typically near sensitive receivers. The monitoring data is processed and made available by a digital platform, with the capacity to detect and classify noise, feeding the acoustic model for assigning sound power to the noise sources present.

4. EXAMPLES OF APPLICATION

4.1 Environmental noise management of a Racetrack

4.1.1 Background

In the specific case of motorsport tracks, as in other situations (airports, industries) the problem generally arises that, although the objective is to control and limit noise near sensitive receptors, in practice it is not possible to control the noise generated by the racetrack based on monitoring near these receptors. In fact, there are almost always other sources of noise present, such as road, air, rail traffic, animal noise, etc., and it is not possible to attribute the

noises monitored at these points to the specific noise of the racetrack alone. On the other hand, the high number of sensitive receivers to be analyzed could make it unfeasible to install permanent monitoring equipment in all of them.

In this context, many automotive circuits have implemented Noise Management Plans, often based on the imposition of limits on the noise emission of vehicles and their control, either through static tests (at 50 cm and 45º from the exhaust), or drive-by tests (20 m from the track) [5], as well as monitoring systems, such as the Circuit de Spa-Francorchamps, in Belgium[1], using one or more trackside monitoring points and others near potentially more affected sensitive receivers, then seeking to correlate the noise recordings near the sensitive receivers with the trackside recordings, thus seeking to rule out noise that does not originate from circuit activity. In other cases, the approach is to monitor the noise inside the circuit, near the track, and calculate the relationship between the sound level near the source and the sound level near the sensitive receivers, which in practice can be done with an acoustic model of the circuit and its surroundings [6].

Some noise indicators have been developed for automobile circuits such as the Lap Equivalent Level (LEL) and the Race Equivalent Level (REL), the first defined as the L_{Aeq} of the noise received at a given point due to a lap of the track by a single vehicle, and the second as the L_{Aeq} of the noise received at a given point due to the set of vehicles during a race [7].

4.1.2 The Estoril Racetrack

Inaugurated on June 16, 1972, the Estoril Circuit has had some layout changes throughout its history, and the track currently has the following main technical characteristics:

- Runway length (centerline): 4,182.7 m
- Ideal Length of the Route: 4,140.4 m
- Runway Width: between 10 and 18 m
- Total turns: 13
- Longest Straight (Finish Line): 985.7 m

[1] Webpage of the Spa-Francorchamps circuit: http://www.francorchamps-acoustique.be/index.aspx



Figure 2. Example of preliminary noise measurements for the development of the acoustic model, during a classics race.

4.1.3 Elements of the noise management system

This case study refers to the environmental noise management and control system implemented at the Estoril Circuit. The system is intended to control the noise emission of all private and corporate events (i.e., other than official sports competitions and respective training), and is essentially based on the following elements:

Event planning and emission control procedures:

- Pre-setting the maximum noise emission levels of vehicles for each event, as well as the maximum number of vehicles that may circulate simultaneously on the track, and previously inform the organizers of these events;
- Systematic pass/fail inspection of all vehicles, before the start of the event, according to a standard procedure (noise level measured at 50 cm and 45 º from the exhaust pipe outlet, at 3/4 of the maximum engine speed);
- Planning of the events for each month in such a way as to avoid concentration of noisiest events in the same month and try to mix them with less noisy events (e.g. alternating track days for motorcycles and for electric cars).

Environmental noise monitoring network, consisting of:

- 3 permanent continuous monitoring stations for ambient noise, weatherproof, consisting of type 1 sound level meters, duly approved in Portugal and subject to annual metrological control, installed within the limits of the circuit, strategically placed to determine the noise emission of the various sections of the circuit;
- Integrated digital platform, MIRA, which receives, stores, and processes the data transmitted by the monitoring stations, namely relevant noise indicators for environmental noise assessment (L_{Aeq}, L_d, L_{den} and

others, including analyses in 1/3 octave), with capacity to generate reports, make information available via the web to those responsible for the circuit, as well as detect specific characteristics of the noise, such as exceeding pre-programmed thresholds and generating alarms for the user.

Acoustic simulation model of the circuit and the surrounding area, developed based on 3D cartographic information, including the digital terrain model, buildings and other obstacles, as well as the layout of the track, which constitutes the specific noise source, divided into a number of segments according to their characteristic sound emission levels. The model allows relating the following variables, involved in the activity of the circuit:

- Maximum permitted noise levels within 0,5 m of vehicle exhaust, taking into account the number of simultaneous vehicles on the track;
- Noise emitted by each segment of the runway, based on the developed acoustic simulation model;
- Noise levels measured at the 3 permanent monitoring stations;
- Specific and background noise levels in the most critical sensitive receivers, to verify the noise nuisance criterion of the Portuguese Noise Regulations.

The environmental noise management and control system includes the preparation of monthly reports with the results of permanent monitoring at the 3 points, respective detailed analysis, identification and individualized calculation of the noise generated in private and corporate events, estimation of the acoustic impact at sensitive receivers, with evaluation of the applicable legal criteria (maximum exposure and nuisance) for a monthly evaluation period. Also, an annual report is produced, synthesizing and systematizing the information from the monthly reports, and making an annual assessment of noise emissions, control and monitoring measures implemented, and evaluation of the applicable criteria.

4.1.4 Noise monitoring network

Monitoring stations have been installed at the following points:

- PM1: "Airton Senna Parabolic" Curve
- PM2: Finish line (Stand B)
- PM3: “Chicane” Curve

Location and example of results are depicted in the next figures.



Figure 3. Location of the monitoring points.

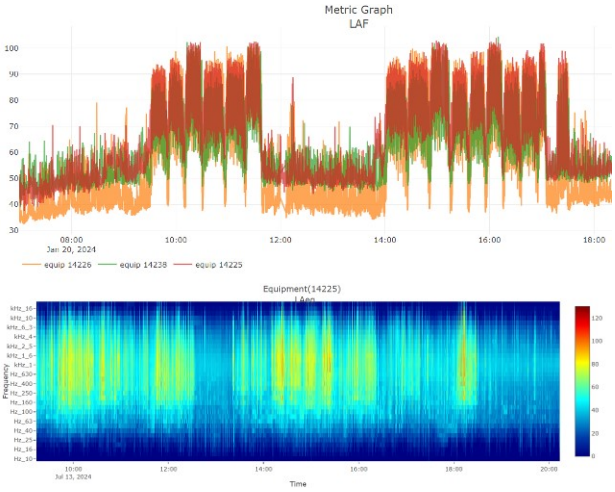


Figure 4. Examples of records on MIRA platform.

4.1.5 Acoustic Model

The acoustic model developed for the Estoril Circuit and surrounding area is shown in the following figure. The model was developed using CadnaA software and is used to calculate the specific noise of the events recorded each month, next to the defined sensitive receptors. For this purpose, the sound power emitted by each segment of the track is optimized for a best-fit between measured and calculated sound levels at the receivers, thus obtaining a model which is calibrated by continuous monitoring.

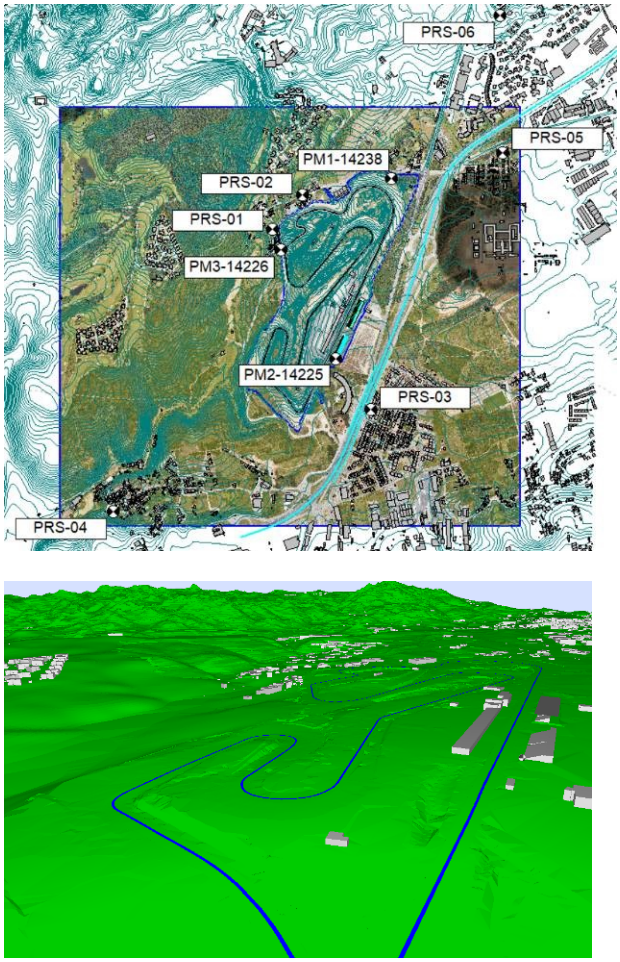


Figure 5. Images of the acoustic model, seen in plan (above) and in 3D view (below).

4.1.6 Evaluation procedure

Taking into account the assumptions of the circuit noise management system, the following compliance assessment procedure has been defined:

- Monitoring of L_d values (L_{Aeq} of the daytime period) for the days with private/corporate events that occurred in the month and calculation of the respective logarithmic average;
- Monitoring of L_d values on days with no activity in the circuit, as a reference for residual noise, and calculation of the respective logarithmic average;
- Extrapolation of the residual noise values obtained above to the closest sensitive receptors or with sound environment characteristics similar to the monitoring points (the so called "image points" according to Procedure 2 of Note 8 of the Practical Guide for Environmental Noise Measurements, published by the Portuguese Environment Agency (APA));
- Calibration of the model to adjust, at the monitoring points, with the values of the logarithmic mean of the L_d values recorded during the private/corporate events;
- Calculation of the specific noise by the model, at points representative of the areas with sensitive use in the circuit envelope;
- Definition of the limits to be applied to the differential of the nuisance criterion, taking into account the quotient between the number of days in the month with private events and the total number of days in the month (for example, in a given month in which there are private events in 9 out of 30 days, the regulatory quotient q = 30% is calculated, so correction regarding the duration of the activity will be D = 2, the regulatory limit to be considered is then 5+2 = 7 dB(A), in the daytime);
- Analysis of the results to verify the criteria of nuisance and of maximum exposure.

4.1.7 Noise control procedures

Within the scope of the noise management system, control procedures have been implemented for private/corporate events which, since its entry into operation in January 2024, have been adjusted according to the results obtained with monitoring. The main procedures currently in force are the following:

Prior Inspection of Vehicles:

All vehicles participating in private events are subject to systematic inspection prior to the start of the event, by

measuring 50 cm from the exhaust, at 3/4 of the maximum engine speed and with the sound measured at a 45-degree angle to the tailpipe outlet. Purely electric vehicles (which do not have exhaust) are excluded.

The emission limit set for most private events has been 100 dB(A), and any vehicle that fails this inspection is prohibited from entering the track. The limits are announced in advance to the promoters of the events, and in the future there may be greater or lesser restrictions on emission levels, as is the case in other international circuits [5], taking into account aspects such as:

- Maximum number of vehicles on the track at the same time;
- Number of events scheduled for the month (in a month with many scheduled events, it may be necessary to restrict emissions further, at least in some of them);
- Event schedules;
- Vehicle and event type in question.

The results of all emission measurements are presented as an annex to the monthly report.

Generation of automatic alarms for the motorsport marshals:

Taking into account the experience of several months of monitoring, and the identification of some of the most critical points, an alarm was programmed for one of the monitoring stations, with the following trigger configuration: LAeq (5 min) > 85 dB(A). Thus, if this alarm is triggered during a race, the responsible marshal is notified and, depending on the conditions of the race/event, will act accordingly: for example, by forcing a reduction in speed in the most critical area of the track, through the use of signal flags.

Opening hours

The Estoril Circuit only operates during the day – typically not occupying the full period. In addition and depending on possible noise management needs of private events, schedules may be adjusted for some events (e.g. noisier events).

4.2 Noise management of a large construction project

4.2.1 Background

Construction noise can affect the physical and mental health of construction workers as well as of the people in the surrounding area and has been reported as one of the main reasons for complaints and disputes that cause delays and cost overruns for construction projects. Several studies have been conducted in the subject of construction noise management, and a comprehensive investigation of the current state of the art in this area was presented in the article by Mir et al. [8].

4.2.2 The Ruby line of Porto metro

The Ruby Line (H) of the Porto Metro is a line under construction that will connect Casa da Música, in Porto, to Santo Ovídio, in Vila Nova de Gaia.
Line features

- The new line will add 6.3 kilometers to the Metro do Porto network, with buried sections, on the surface and on viaduct;
- The project is funded by the Recovery and Resilience Plan (RRP);
- The investment is around 379.5 million euros;
- The work involves the construction of tunnels, 8 stations, 5 ventilation and/or emergency wells, a connection branch at both ends of the line (for the injection and removal of vehicles and track to carry out the reversal of vehicles, viaducts, a new bridge over Douro river and reformulation of the urban space (including roads).

Social, economic and environmental impact

- The Ruby Line will bring social, economic and environmental benefits quantified at 1.7 billion euros

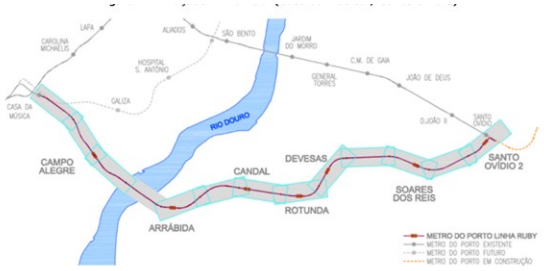


Figure 6. Simplified plan of the Ruby line.

The project was subjected to an Environmental Impact Assessment procedure, which laid out a set of requirements relative to noise and vibration planning and management

during the construction phase. With respect to noise, a management plan was established with the following main steps:

- Identify the sensitive receivers potentially affected and the noise requirements and limits applicable to the project;
- Survey ambient noise levels before construction begins at a number of points nearby the various construction sites involved in the project;
- List all relevant noise sources and noisy activities that will be present on the sites, for each scenario of the construction process, and develop an acoustic model to simulate the various scenarios and the expected noise levels in the nearby sensitive receivers, including residential building façades;
- Propose and implement noise mitigation measures at the source (e.g. less noisy machines, acoustic enclosures), at the propagation path (e.g. noise barriers) or at the receivers (e.g. façade insulation);
- Install continuous noise monitoring stations, at over 20 points and throughout the entire duration of the construction works, connected to a web platform, with capacity of sending automatic exceedance alarms to the various parties involved and information to help identifying the related sources and, also, correlate them to the acoustic model of the site – this enables, works in the first place, to check if the exceedance is related to the construction and, if yes, provide information to quickly take action and correct the exceedance;
- Provide regular noise reports, during the various construction phases and for all construction sites.

4.2.3 Acoustic simulations for various sites and scenarios

For each site, a comprehensive study was carried out before starting the construction works, including a characterization of the construction process, with its successive phases, each involving its specific noise sources, with corresponding sound power levels and working times, and topographic changes (excavations), and, for each phase, simulations were carried out with the acoustic model to check for compliance with noise limits and to test noise abatement measures.

For example, for a typical metro station construction, the following phases were simulated:

- Demolitions, Affected Services and Excavations;
- Excavation of the Tunnel + Coatings
- Internal Structures;
- Urban Insertion and Landscaping

The figures below illustrate the acoustic simulations of two of the construction sites, at a particular phase of the construction process.

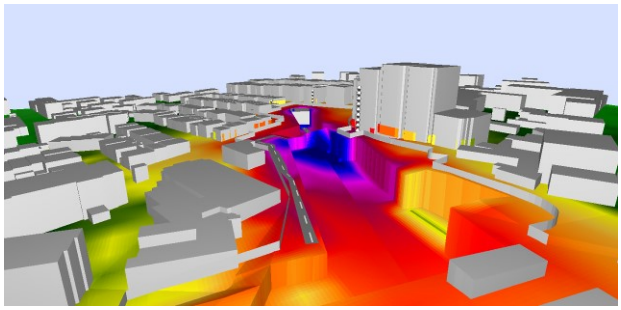


Figure 7. 3D noise map for the Santo Ovidio station.

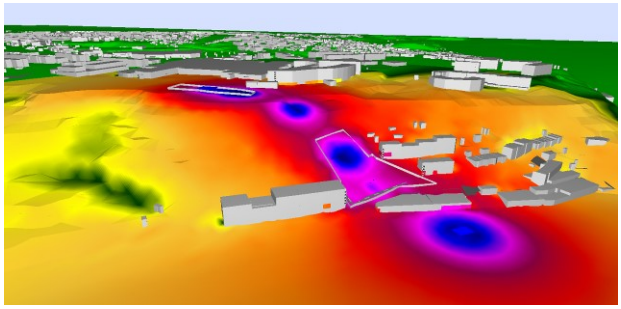


Figure 8. 3D noise map for the south bank side of the bridge over Douro river.

4.2.4 Noise monitoring

At the time of writing this paper, the construction works haver recently started, and the first 3 monitoring stations have just been installed – it is planned that over 20 will need to be working simultaneously, distributed by various sites, as the construction works proceed.

These monitoring stations are being connected to MIRA platform, for automatic reporting and alarm generation. Source detection and correlation with the acoustic simulation models of each site is envisaged and is expected to be tested in the near future.

Next figure shows photos of the noise monitoring stations already installed on site.



Figure 9. Photos of noise monitoring on one of the construction sites.

5. CONCLUSIONS

In this communication, the problem of implementing environmental noise management systems based on permanent monitoring and simulation models was presented, in which it is sought to combine real-time information, from monitoring stations installed next to or within the noisy activity, with an acoustic model that allows predicting sound levels at a distance, typically next to sensitive receptors. The integrated digital platform MIRA, developed by dBwave, which allows the management, communication, registration and analysis of environmental noise monitoring networks, was briefly described and its application was illustrated, together with a simulation model, in the development of an environmental noise management and control system for a racetrack and for a construction site. These were analysed in more or less detail, describing the constituent elements of the system, with emphasis on the monitoring network and the simulation model, as well as describing the procedures for evaluating and controlling the noise generated by the noisy activities. In the case of the circuit, from the experience of 15 months of operation of the system, it can be concluded that it has proved to be very useful, functional and adaptable to different conditions and needs, making it an effective tool in the management and control of circuit noise. In the case of the construction site, although the monitoring part of the project has just started, the almost one year experience with the development and practical application of the simulation models has been proven very useful, helping in the definition and adoption of abatement measures, in the approval and licensing of the construction sites by the authorities and, also, in the acceptance of the unavoidable nuisances by the affected population.

6. REFERENCES

[1] Conde Santos, L., Carvalho, A., Melo, A., Covas, G., Leão, C. & Figueiredo, J. "Projeto MIRA – Desenvolvimento de uma Plataforma Inteligente de Monitorização de Ruído Ambiental" (in Portuguese), in *Proceedings of the 54th Spanish Congress on Acoustics Tecniacustica and 13th Iberian Congress on Acoustics,* (Cuenca, Spain), pp. 846-851, 2023.

[2] Manvell et al, "Managing Urban Noise in Cities – An Integrated Approach to Mapping, Monitoring, Evaluation and Improvement", *Proceedings of INTER-NOISE 1999* (Fort Lauderdale, USA), 1999.

[3] Bellucci, P., Peruzzi, L. & Zambon, G. (2016). "LIFE DYNAMAP - an overview of the project after two years working". *INTER-NOISE 2016*, (Hamburg, Germany), pp. 6338-6349, 2016.

[4] "A review of aviation noise metrics and measurement", *Published by ICCAN (Independent Commission on Civil Aviation Noise)*, 2020.

[5] "Noise Management Plan relating to Brands Hatch Racing Circuit 2022/23". *Published by Motor Sport Vision Limited and Sevenoaks District Counc*il (Sevenoaks, UK), 2022.

[6] Magrini, A, Cerniglia, A., Lenti, M. & Cattani, L., "Noise evaluation in a race-track: measurements, software analyses and need of continuous monitoring. Comparison among the results.", *Proceedings of ICSV14, 14th International Congress on Sound and Vibration* (Cairns, Australia), 2007.

[7] Pascale, A., Mancini, S., Coelho, M. & Guarnaccia, C., "Acoustic Indicators for Motor Race Noise: Definition, Validation, and Tests in Simulated and Real Races", *Applied Acoustics*, 2 Volume 200 (2022), 109071.

[8] Mir, M., Nasirzadeh, F., Lee, S., Cabrera, D., Mills, A., "Construction noise management: A systematic review and directions for future research", *Applied Acoustics*, Volume 197 (2022), 108936.

DOI: 10.61782/fa.2025.0536

FORUM ACUSTICUM EURONOISE 2025

LOW-HEIGHT NOISE BARRIERS FOR RAILWAYS: MEASUREMENT STANDARDIZATION AND METAMATERIALS APPLICATION FOR NOISE REDUCTION

Domenico De Salvio* **Paolo Guidorzi** **Massimo Garai**
Department of Industrial Engineering, University of Bologna, Italy

ABSTRACT

The present work is part of a LIFE project to develop a measurement standard to assess the acoustic performance of low-height noise barriers for railways. Low-height noise barriers (LHNB) present a cost-effective and space-efficient solution to mitigate railway noise, especially in urban and densely populated areas. However, the lack of standardized methods to evaluate their performance challenges their effective implementation. This project addresses these challenges by developing a robust measurement protocol for real-world railway operating conditions. Additionally, the study explores innovative strategies to enhance the absorption performance of these barriers through the integration of metamaterials. Metamaterials, with their ability to achieve tailored acoustic properties, offer promising solutions for maximizing noise attenuation while maintaining compact barrier designs. The research investigates advanced geometrical configurations by combining different resonators to optimize sound absorption across a broad frequency spectrum (100-5000 Hz). Preliminary results indicate significant improvements in noise reduction performance, validating the potential of metamaterial-enhanced barriers. The outcomes of this project will provide critical insights into sustainable noise management for railways, contributing to quieter and more livable urban environments while supporting European Union policy objectives on environmental noise reduction.

Keywords: *noise mitigation, low-height noise barrier, measurements, metamaterials, resonators.*

1. INTRODUCTION

Railway noise pollution is a growing concern, especially in urban areas where proximity to tracks worsens its impact. Sources include rolling noise, aerodynamic noise, and structural vibrations [1]. Long-term exposure is linked to health issues such as sleep disturbances and cardiovascular diseases [2].

Traditional noise barriers are effective but have spatial, financial, and aesthetic drawbacks. Low-height noise barriers (LHNBs) offer a cost-effective alternative for urban settings, though their acoustic performance lacks standardized evaluation methods [3]. Unlike full-height barriers, LHNBs reduce noise differently, focusing on source-level mitigation.

Within a LIFE project, this study aims to develop a standardized measurement protocol for assessing LHNB effectiveness under real-world conditions and integrate metamaterials to enhance noise absorption while maintaining compact designs. Metamaterials, with tailored acoustic properties, optimize sound absorption across 100–5000 Hz [4].

By advancing evaluation methodologies and leveraging innovative materials, this research supports sustainable railway noise management, aiding policymakers and engineers in implementing effective, space-efficient solutions aligned with EU environmental noise directives [5].

2. THE STANDARDIZATION OF THE MEASUREMENT METHOD

Currently, a method for measuring the acoustic performance of low-height noise barriers does not exist. A study is

*Corresponding author: domenico.desalvio2@unibo.it
Copyright: ©2025 First author et al. This is an open-access article distributed under the terms of the Creative Commons Attribution 3.0 Unported License, which permits unrestricted use, distribution, and reproduction in any medium, provided the original author and source are credited.

currently in progress aimed at adapting the European standard EN 1793-6 (also known as "Adrienne") [6], which defines the standard measurement method for measuring sound insulation of highway and railway noise barriers [7], to low-height noise barriers as well.



Figure 1. Insertion Loss: a) measurement of impulse response with the barrier, no obstacles nearby; b) measurement of free-field impulse response; c) setup with reflective surface simulating train body; d) measurement of impulse response with barrier and reflective surface.

The EN 1793-6 standard was conceived for sound insulation measurements on barriers with appropriate dimensions, usually at least 3-4 m high. Two sets of impulse responses are measured using a sound source (positioned on the sound source side at the height of 2 m from the ground and 1 m from the noise barrier) and a 9-microphone grid (positioned on the other side of the barrier at the height of 2 m from the ground and 0.25 m from the noise barrier): one set is measured with the barrier interposed and one in free-field, at the exact relative distances, as described in detail in [6] and [8]. An MLS signal was used to measure impulse response [9]. By selecting data from the two measurement sets and by performing the logarithmic ratio of the transmitted power spectra to the free-field power spectra, the so-called Sound Insulation Index can be obtained averaged over all 9 microphones [6].

This method can be adapted to measure the Insertion Loss of LHNBs. However, as shown in Figure 1, the small size of the barrier and the reduced height on the ground of the microphone and the sound source pose a challenge: the sound reflection on the ground disrupts the measurement. It can be partially reduced using an ultra-directive microphone; however, the low barrier height shortens the data analysis selection window in the time domain and, consequently, a minimum valid frequency analysis of 400 Hz. Figure 1 shows the measurement setup: the microphone and sound source are placed 0.4 m from the noise barrier, both at a height above the ground of 0.21 m. The noise barrier had a height of 0.56 m and a thickness (at the height of the microphone and sound source) of 0.12 m. Figure 1 a) shows the barrier measurement configuration, and Figure 1 b) shows the free-field measurement. Figure 1 c) shows a measurement setup that involves placing the barrier near a highly reflective surface to simulate the train facade, visible in the graphical mock-up in Figure 1 d), in which the sound source is placed in the position corresponding to a train wheel.

3. INTEGRATION OF METAMATERIALS FOR ENHANCED ABSORPTION

As an LHNB is installed close to the track, reducing the rail-wheel noise bouncing between the train body and the noise barrier is essential. Otherwise, it overcomes the LHNB, reducing its efficacy. The proposed metamaterial solution integrates Helmholtz resonators and Fabry-Pérot channels onto the surface of an existing LHNB manufactured by Kraiburg Strail to enhance its absorption performance across a broad frequency spectrum. The design is tailored to achieve an absorption coefficient of at least 0.8 over the 100–5000 Hz range, despite railway noise energy being most concentrated between 500–4000 Hz, as indicated by EN 16272-3-2 [10].

Neck-embedded Helmholtz resonators are incorporated into the barrier surface to address the lower frequency range (100–1700 Hz). These resonators trap and dissipate low-frequency energy by exploiting localized resonance effects [11]. Beyond 1700 Hz, Fabry-Pérot channels enhance absorption at higher frequencies by leveraging quarter-wavelength resonance phenomena [12]. Combining these two metamaterial elements ensures broadband noise attenuation while maintaining a compact barrier profile.

Given the geometrical constraints imposed by the low-height Strail barrier, both perfect and imperfect coupling mechanisms have been exploited to maximize performance. The design carefully balances the interaction between resonators and Fabry-Pérot channels to achieve optimal impedance matching with the incident sound waves, thereby enhancing absorption efficiency across the entire target spectrum. The structural integration of these elements does not compromise the mechanical integrity of the barrier, making it a viable solution for real-world railway applications. The metasurface covering the barrier is subdivided into different bricks, each related to a given frequency range.

The acoustic performance of each individual metamaterial brick composing the total barrier surface has been

assessed under normal incidence conditions using an impedance tube [13]. These laboratory tests provide precise absorption coefficient measurements, allowing fine-tuning resonator geometries to optimize real-world performance.

4. RESULTS AND REMARKS

4.1 Measurements of Insertion Loss

The first results from the adaptation of the Adrienne method to LHNBs in the measurement configurations shown in Figure 1, are shown in Figure 2; here, the test barrier is placed away from nearby obstacles (Figure 1 a) and b)) and near a reflective surface, to simulate the reflecting body of the train (Figure 1 c) and d)). The measurements in the two configurations are similar at mid and high frequencies, showing good repeatability of the measurement method, while they differ somewhat at lower frequencies. Studies are underway to reduce soil's effect further and to evaluate the intrinsic effectiveness of the LHNB better.

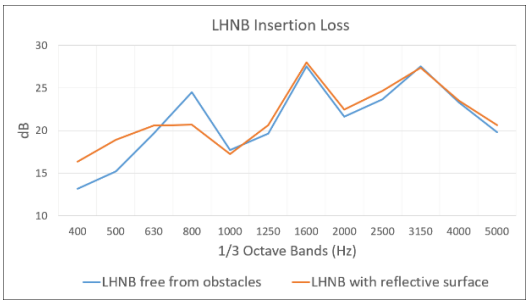


Figure 2. Insertion Loss measurement of the low-height noise barrier shown in Figure 1.

4.2 Metamaterial optimization

This section shows the main results for three "bricks" (sound absorbing units) incorporating imperfect and perfect coupled neck-embedded Helmholtz resonators (NEHR) and a Fabry-Pérot (FP) channel brick. Figure 3 shows the results of brick 1, composed of FP channels. The resonance peaks of the FP channels bricks are designed to keep them away from each other due to the low porosity of the brick (only 6 channels for each brick). The optimal results for FP channels are obtained for high porosity values [14].

Figure 4 shows the results of bricks brick 2, tuned in the 150-220 Hz frequency range and composed by 9 imperfect NEHRs (top), brick 5 tuned in the 550-1050 Hz range and composed by 20 perfect NEHRs (bottom). The imperfect coupling of the NEHRs in brick 2 allows this design to achieve a high absorption performance regardless of the geometrical constraints of the surface.

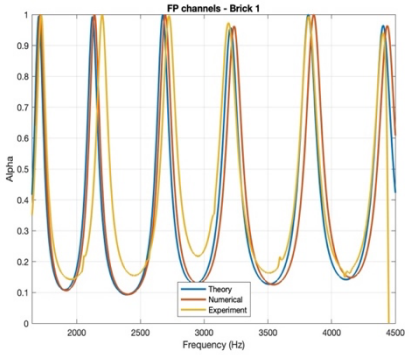


Figure 3. Results for brick 1, including perfect FP channels.

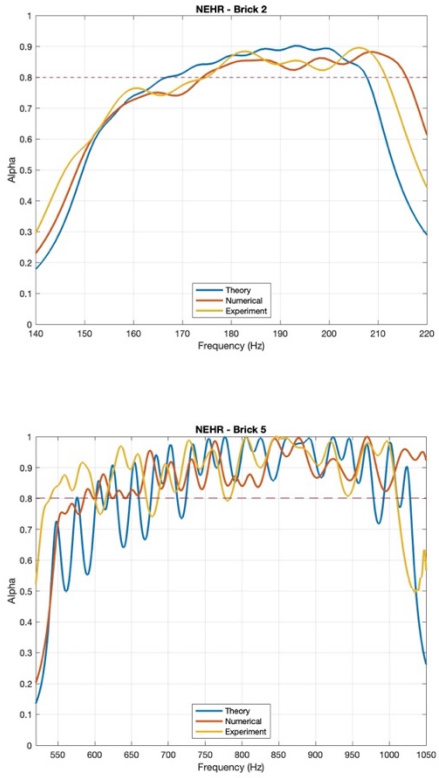


Figure 4. Results for brick 2, including 9 imperfect NEHRs (top) and brick 5, including 20 perfect NEHRs (bottom).

5. CONCLUSIONS

This study highlights the importance of standardizing measurement protocols for low-height railway noise barriers

and explores the potential of metamaterials to enhance their performance. By establishing a reliable assessment framework and leveraging advanced acoustic materials, the project contributes to more effective noise reduction solutions. The integration of metamaterials represents a breakthrough in sustainable urban noise management, supporting European Union initiatives for quieter and more livable urban environments.

FUNDING

The project is co-funded by the European Union under the LIFE 2021-2027 *Environment and Climate Action Program*.





REFERENCES

[1] Thompson, D. (2008). *Railway noise and vibration: mechanisms, modelling and means of control*. Elsevier.

[2] Basner, M., Babisch, W., Davis, A., Brink, M., Clark, C., Janssen, S., & Stansfeld, S. (2014). Auditory and non-auditory effects of noise on health. *The lancet*, *383*(9925), 1325-1332.

[3] De Coensel, B., Botteldooren, D., De Muer, T., Berglund, B., Nilsson, M. E., & Lercher, P. (2009). A model for the perception of environmental sound based on notice-events. *The Journal of the Acoustical Society of America*, *126*(2), 656-665.

[4] Ma, G., & Sheng, P. (2016). Acoustic metamaterials: From local resonances to broad horizons. *Science advances*, *2*(2), e1501595.

[5] European Environment Agency. (2020). *Environmental noise in Europe — 2020. EEA Report No 22/2019*.

[6] EN 1793-6:2018/A1:2021: Road traffic noise reducing devices - Test method for determining the acoustic performance - Part 6: Intrinsic characteristics - In situ values of airborne sound insulation under direct sound field conditions.

[7] Garai M., Guidorzi P., *In situ measurements of the intrinsic characteristics of the acoustic barriers installed along a new high speed railway line*, Noise Control Eng. J., ***56*(5)**, (2008), pp. 342-355.

[8] Guidorzi P., Garai M., *Repeatability of the European Standardized Method for Measuring Sound Reflection and Sound Insulation of Noise Barriers*, Environments, ***10*(8)** (2023), 139.

[9] Borish, J.; Angell, J. B. *An Efficient Algorithm for Measuring the Impulse Response Using Pseudorandom Noise*. J. Audio Eng. Soc., **31** (1983), pp. 478-488.

[10] EN 16272-3-2 (2023) - Railway applications - Infrastructure - Noise barriers and related devices acting on airborne sound propagation - Test method for determining the acoustic performance - Part 3-2: Normalized railway noise spectrum and single number ratings for direct field applications.

[11] Huang, S., Fang, X., Wang, X., Assouar, B., Cheng, Q., & Li, Y. (2019). Acoustic perfect absorbers via Helmholtz resonators with embedded apertures. *The Journal of the Acoustical Society of America*, *145*(1), 254-262.

[12] Liu, C., Yang, Z., Liu, X., Wu, J. H., & Ma, F. (2023). Ultra-broadband acoustic absorption with inhomogeneous high-order Fabry–Pérot resonances. *APL Materials*, *11*(10).

[13] ISO 10534-2 (2023). Acoustics–Determination of Acoustic Properties in Impedance Tubes–Part 2: Two-microphone Technique for Normal Sound Absorption Coefficient and Normal Surface Impedance.

[14] Yang, M., Chen, S., Fu, C., & Sheng, P. (2017). Optimal sound-absorbing structures. *Materials Horizons*, ***4*(4)**, 673-680.

DOI: 10.61782/fa.2025.0130

FORUM ACUSTICUM EURONOISE 2025

ANALYSIS OF COMPLEX SCENARIOS IN THE NOISE MITIGATION OF MAIN INFRASTRUCTURES IN ITALY IN LIFE SILENT PROJECT

Mauro Cerchiai [1] **Matteo Bolognese** [1] **Andrea Panci** [1]
Davide Vatteroni [1] **Diego Palazzuoli** [1] **Gaetano Licitra** [1*]
[1] Environmental Protection Agency of Tuscany Region (ARPAT), Via del Ponte alle Mosse 211, 50144, Florence (FI), Italy.

ABSTRACT

Transportation infrastructures are responsible for most noise exposure in Europe. The Europe Environmental Noise Directive prescribes a cycle of noise mapping, citizen involvement, and action plans to reduce annoyance and sleep disturbance. In Italy, national regulation shares with END the aim to reduce noise, but is more focused on the definition, and respect, of noise limits rather than considering noise effects on citizens. In the case of multiple noise sources acting in the same area (complex acoustics scenario), Italian regulation asks transportation infrastructure managers to cooperate and share the mitigation costs. In these cases, without an integrated mitigation plan, acting on one source can lead to higher costs or, at worst, an increase in exposure. However, the regulation does not provide practical guidelines on how to manage this process, thus very little progress has been made in mitigating noise in those complex scenarios. The Life SILENT project aims to address this problem by developing a methodology for highlighting conflicts in complex scenarios and solving them, reducing total citizen exposure while minimizing costs and considering EU requests at the same time. The present work will describe a preliminary study conducted with this intent.

Keywords: *concurrent infrastructures, railway noise, road noise.*

[*] ***Corresponding author***: *g.licitra@arpat.toscana.it.*
Copyright: *©2025 Mauro Cerchiai et al. This is an open-access article distributed under the terms of the Creative Commons Attribution 3.0 Unported License, which permits unrestricted use, distribution, and reproduction in any medium, provided the original author and source are credited.*

1. INTRODUCTION

Environmental noise is a significant health concern in Europe, identified as the second most critical environmental stressor in six European countries, according to the WHO's 2018 "Environmental Noise Guidelines for the European Region" [1]. Approximately 20% of the European population resides in areas where noise levels pose health risks, leading to substantial economic costs due to non-productive workdays, healthcare system burdens, and decreased property values [1].

The Environmental Noise Directive (END) provides essential tools, such as Action Plans, to develop effective noise reduction measures by integrating local and regional actions as per Member States' regulations [2].

Despite the establishment of national noise limits, challenges persist in implementing these Action Plans effectively considering also national legal framework. Fragmented responsibilities and a decentralized approach often delay noise mapping and Action Plan execution. Additionally, the absence of common guidelines for prioritizing interventions hampers the development of uniform methods, leaving decisions to local authorities based on health impact assessments and public consultations [2].

While there is a growing body of research on health impact indicators for prioritizing interventions, the mitigation of multiple noise sources in complex scenarios, particularly outside urban areas, remains underexplored. There is a notable lack of interventions and pilot projects that provide practical, verified examples for infrastructure managers.

In Italy, the Ministerial Decree 29/11/2000 (DM 2000) establishes that in case of limits exceeding due to concurrent infrastructures, the operators must proceed to a joint execution of the noise remediation actions. This scenario is likely to be spotted in the case of parallel infrastructures e.g. a highway that runs parallel to a railway

line, very common along the Italian costal lines. However, this approach was never applied to real cases, also considering END requirements, due to a lack in the definition of accountability and the procedure to be followed.
The SILENT Project (Sustainable Innovations for Long-life Environmental Noise Technologies) [3] aims to address these issues by developing mitigation proposals for population exposure to noise in complex scenarios involving road and rail sources. This project will explore the current state of Remediation Plans, identify critical issues, and propose regulatory measures to establish measurable and replicable intervention procedures in complex acoustics scenarios.
The first step towards this goal is to experiment with a simple case study to understand the critical points to be solved.
In the present paper, the case study of Italy, Fano (PU) will be presented.

2. METHODS

The test site of Fano covers a total area of 0,9 km^2 with a total resident population of 621 inhabitants. The site was selected due to exceeding noise limits caused by the combined effect of road and railway sources. The two infrastructures run parallel for all the length of the test site as shown in Fig. 1.

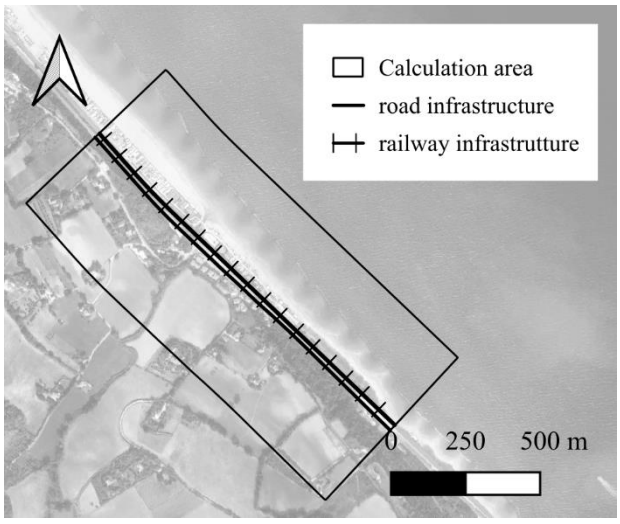


Figure 1. The test site of Fano.

According to the Italian law, when a regulatory limit exceedance is attributable to multiple sources, the relative responsibilities will be assigned by the calculation of the priority index (P_i) defined by DM 2000. The calculation starts by partitioning the total area of interest into several smaller areas in which the noise limits are uniform, the noise level does not change more than 3 dB (A), and the population distribution is the same. To obtain those A_i, the intersection between isophone areas (Figure 1), Census areas (Figure 2), and noise limits (Figure 3) must be done. In this way the priority index can be calculated as follows:

$$P_i = \sum R_i \, (L_i - L_i^*) \qquad (1)$$

Where R_i indicates the number of resident inhabitants in the area A_i. The A_i are the areas in which the values L_i and the limit L^*_i are constant. For each A_i, the value R_i is obtained by multiplying the surface by the population density provided by the corresponding census area.
In order evaluate relative responsibility in the case of concurrent infrastructures it is of pivotal importance to have homogenous noise exposure data.
GIS approach is mandatory in order to obtain the priority index Pi.
The first step is to obtain the required geospatial and traffic input data:

- Terrain model [4],
- Buildings layer (with heights),
- Census areas [5] (Fig. 2),
- Infrastructures' map,
- Traffic data.

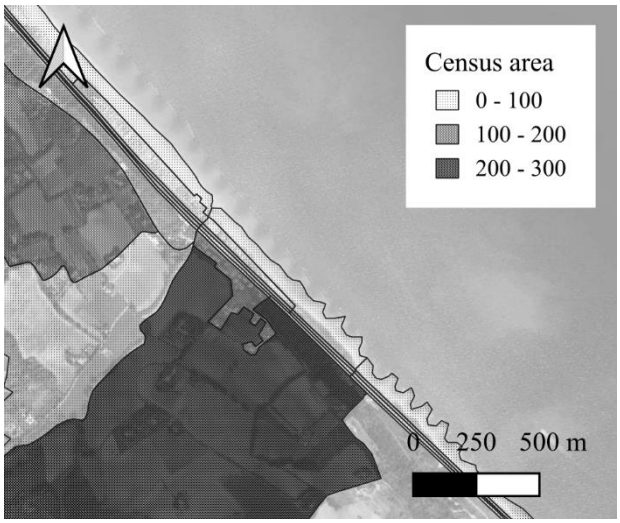


Figure 2. Number of residents per census areas in the test site of Fano.

Usually, all geospatial input information is provided by national or local authorities by open-data services. The unavailability of shared data can represent a significant issue in the process of identifying priority indices and subsequently undertaking shared acoustic mitigation paths.
The test site in Fano represents a case study in order to define a possible approach to overcome such problems.
The **building profiles**, lacking in public open data database, were extracted from OSM [6] and the height was extrapolated comparing the DTM and the Digital surface Model (DSM) provided by [4]. **Infrastructures' maps** and **traffic data** were provided by operators of the two infrastructures. This source of data is preferred to the OSM or other web service providers because it is more accurate in terms of number and exact location of the road lanes and railway lines.
ISTAT, the Italian National Institute of Statistics, provides **census areas** in shapefile (*.shp)* file format for all the municipalities with the number of people for different areas. From such information local population density can be computed. Finally, to calculate the required value R_i noise levels must be computed and compared with noise limits (Fig. 3).

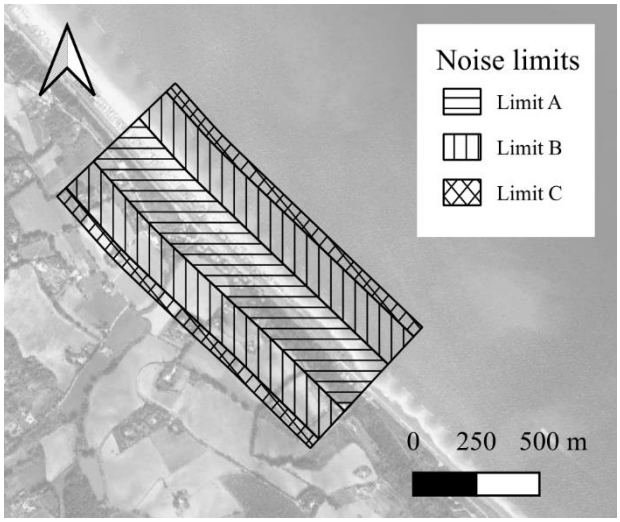


Figure 3. Noise limits for the test site of Fano.

With this aim, geographical and traffic data were used as input for commercial acoustic simulation software. The software allows us to calculate a noise map in accordance with the CNOSSOS-EU framework.

3. RESULTS

The present section will report the results for the test site of Fano. Noise simulation software produced a noise map for each infrastructure. In Fig. 4 the noise levels for the road infrastructure are reported as an example. The maximum calculated L_i overall is 79 dB (A), and the maximum for road and railways is 73 dB (A) and 79 dB (A) respectively.

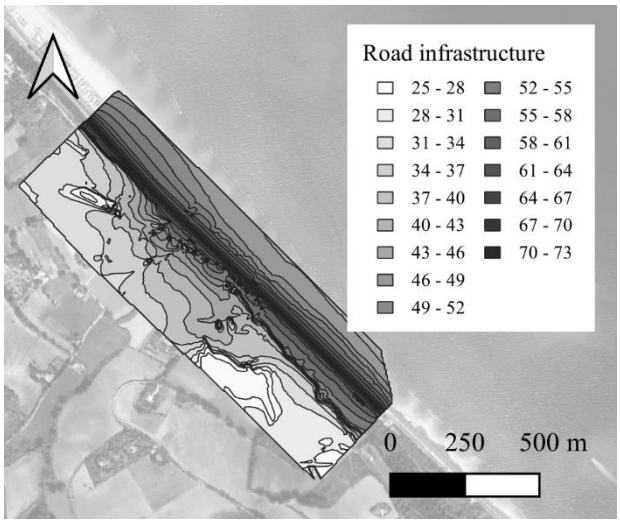


Figure 4. Noise isophones in dB (A) in the test site of Fano for the road infrastructure.

Those maps were then used to obtain the final A_i reported in Fig. 5 with the corresponding P_i value for the railway infrastructure. The results in terms of P_i for the test site of Fano are presented in Tab. 1.

Table 1. P_i calculated for the day (06-22) and night periods (22-06).

Source	P_i Day	P_i Night
Road	153	395
Railway	739	8564

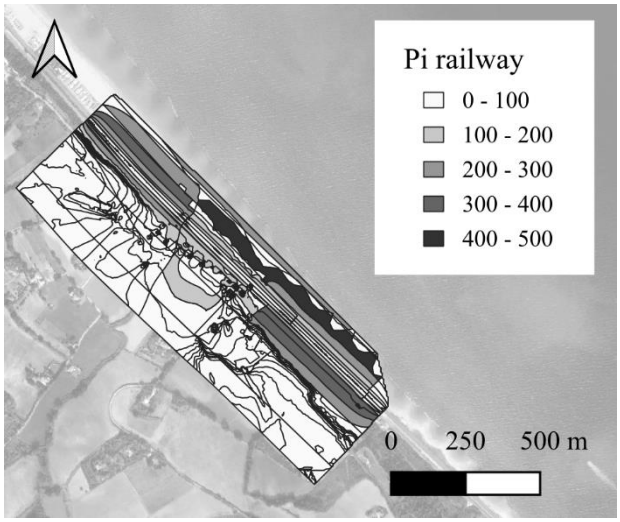


Figure 5. Priority values for the test site of Fano for railway infrastructure.

4. DISCUSSION

The results presented in Tab. 1 show that railway noise has higher priority both in the day and night period. The difference is more important during the night compared to the day, with a P_i for the railway almost 22 times bigger than the road one. This behavior can be ascribed to two independent causes: at night road traffic decreases consistently but railway traffic remains unchanged. At the same time noise limits L^*_i decrease by 10 dB (A) in the night period.

For the Italian regulation, both infrastructures would be remediated but they will be scheduled in different cycles of remediation plans due to the great difference in the priority levels. This causes an inefficient resolution of the concurrency, non-optimized spending and, in the worst case, an increase in population exposure. This could be the case of a noise barrier installed between the infrastructures to remediate the railway. The barrier, while remediating railway noise, will lead to an increase of almost 3 dB (A) of road noise due to unwanted reflection.

5. CONCLUSION

As we showed in this paper, Italian Regulation, especially the noise indices proposed, are not sufficient to resolve a (simple scenario with concurrent infrastructures like the case study of Fano (PU), where the two infrastructure runs parallel with no buildings in between and very few buildings in the calculation area, meaning little population affected by the traffic noise. The results underline the need for a different approach towards the resolution of complex scenarios. The Life SILENT Project will develop and test new indicators to better evaluate the concurrency and support the future remediation plan with more accurate and relevant information.

6. REFERENCES

[1] World Health Organization: *Environmental noise guidelines for the European Region* ISBN 978 92 890 5356 3 WHO/EURO:2018-3287-43046-60243, 2018 http://www.euro.who.int/en/publications/abstracts/environmental-noise-guidelines-for-the-european-region-2018 Accessed 01 April 2025

[2] World Health Organization: *Burden of disease from environmental noise: Quantification of healthy life years lost in Europe.* ISBN: 978 92 890 0229 5, 2011. https://www.who.int/publications/i/item/9789289002295 Accessed 01 April 2025

[3] LIFE SILENT Project, "Sustainable Innovations for Long-life Environmental Noise Technologies" LIFE 2022-ENV-IT-LIFESILENT https://www.stradeanas.it/it/life-silent Accessed 01 April 2025

[4] Italian Ministry of the Environment and Energy Security, PST data base. https://sim.mase.gov.it/portalediaccesso/mappe/#/viewer/new Accessed 01 April 2025

[5] National Institute of Statistics INSTAT, https://www.istat.it/notizia/basi-territoriali-e-variabili-censuarie/ Accessed 01 April 2025

[6] OpenStreetMap contributors. (n.d.). OpenStreetMap. https://www.openstreetmap.org Accessed 01 April 2025

Funded by the European Union. Views and opinions expressed are however those of the authors only and do not necessarily reflect those of the European Union or CINEA. Neither the European Union nor the granting authority can be held responsible for them

DOI: 10.61782/fa.2025.0943

FORUM ACUSTICUM EURONOISE 2025

USING MICROPHONES IN OUTDOOR PASS-BY NOISE TESTING FOR VEHICLE SPEED MEASUREMENT

Fabio Lo Castro1* **Maria Luisa Ariza Alvarez[1]** **Massimiliano De Luca1**
Sergio Iarossi[1]
[1] CNR-INM Sezione Acustica e Sensoristica O.M. Corbino, Rome Italy

ABSTRACT

In environmental noise pollution assessments, the Statistical Pass-By method (SPB, ISO 11819-1) is employed to evaluate different road surfaces based on their influence on traffic noise. It requires measuring the speed of heavy and light vehicles, with an error of less than 2.5 %, as they pass in front of and perpendicular to a Class I microphone, positioned 7.5 meters from the center of the road lane, along with the speedometer readings and the corresponding sound pressure levels (SPL). In this paper, we focus on evaluating the feasibility of using one or more microphones, instead of a speedometer and a video camera, to enhance performance in speed measurement, vehicle classification, vehicle counting, and sound pressure level (SPL) detection. The soundtracks used were recorded during the SPB measurements conducted along Highway A91 in Rome, Italy.

Keywords: *traffic noise, vehicle speed, road monitoring, sound measurement, microphone detection.*

1. INTRODUCTION

The accurate estimation of vehicle speed is a fundamental component of traffic management, urban monitoring, and road safety technologies. Traditionally, speed measurement has relied on radar, laser sensors, and video-based systems. However, these technologies often involve high costs [1]. In this context, passive acoustic sensing using microphones has emerged as a cost-effective and scalable alternative for vehicle speed estimation.

According to the Statistical Pass-By (SPB) method, which requires the use of microphones to measure sound pressure levels, a relevant question arises: can these microphones also be used to estimate vehicle speed through acoustic signal analysis? Specifically, two methodological approaches are investigated: a frequency-domain analysis, which exploits variations in the spectral components of recorded signals, and a time-domain analysis, which relies on signal amplitude and the time delay of signal arrival at multiple microphones to infer speed. The accuracy and error margins of both methods are evaluated and compared

Recent studies have demonstrated the potential of acoustic signal processing for vehicle speed estimation. For instance, a Doppler-based method employing spectrogram seam tracking was proposed to estimate vehicle speed from engine harmonics, achieving an average error between 0 and 10 km/h, with reduced accuracy at lower speeds (10–30 km/h) due to weaker Doppler shifts [2]. Similarly, multi-microphone arrays were utilized to enhance accuracy in dense traffic conditions [3].

Other studies, explored variations in noise levels as an indirect speed indicator, reporting errors of up to 17% at 50 km/h, improving to 8% at 120 km/h; however, it was concluded that the method does not meet the precision requirements of ISO 11819-1 [4].

[1]**Corresponding author**: *fabio.locastro@cnr.it.*
***Copyright**: ©2025 Fabio Lo Castro et al. This is an open-access article distributed under the terms of the Creative Commons Attribution 3.0 Unported License, which permits unrestricted use, distribution, and reproduction in any medium, provided the original author and source are credited.*

In parallel, Doppler-shift techniques and various correlation-based methods within microphone arrays were reviewed to estimate traffic parameters [Borkar and Malik], while a high-resolution spectral method (AR-z spectrum) was proposed to detect harmonic signals in noisy environments, enhancing the identification of vehicular acoustic features [5].

The primary objective of this study is to determine which of the two proposed methodologies, frequency-based or time-domain analysis, yields the lowest error rate in speed estimation. To validate the accuracy of the proposed approach, simultaneous speed measurements were obtained using a laser-based sensor, providing a reliable reference for direct comparison with the results derived from acoustic signal analysis.

2. MATERIALS AND METHODS

2.1 Sound source description and models

The object of investigation is the speed of a vehicle as it passes in front of one or more microphones, as illustrated in Figure 1. The vehicle is assumed to have multiple acoustic sources. In the case of an internal combustion engine (ICE) vehicle, the primary sources of noise include the engine, typically located at the front of the vehicle, the exhaust system at the rear, tire and wheel noise from four or more contact points, and aerodynamic noise

The ICE vehicles dominate at lower speeds, but as speed increases beyond 40 km/h [6], road and tire noise (caused by rolling resistance, road surface texture, and tread pattern) becomes more prominent. Aerodynamic noise is considered significant when speeds exceed 100 km/h [7-8].
The spectrum of the ICE noise exhibits a fundamental frequency, f_0 (Eqn. 1) in the frequency range of 50 to 150 Hz [9], which is proportional to the number of cylinders, N, the firing frequency and its harmonics. These components are influenced by the engine's revolutions per minute (RPM) and the transmission gear ratios.

$$f_0 = \frac{N}{2}\left(\frac{RPM}{60}\right) \quad (1)$$

The Exhaust System Noise, due to the turbulent exhaust gas flow and muffler design, has a frequency range of 50 Hz to 3 kHz. The road/tire/wheel noise generates broadband noise starting from 125 Hz to 4 kHz, but is predominant at frequencies ranging from 500 to 2 kHz [10]. In electric vehicles, the electric motor noise is in the range of 1 kHz to 10 kHz [11]. It is quieter than an IC engine, but at speeds higher than 50 km/h the whole noise is comparable, if they mount the same tire size and model, due mainly to road/tire noise. Wind and Aerodynamic Noise Sources due to the Airflow around the vehicle, mirrors, and body gaps are in the frequency range of 500 Hz to 5 kHz. [12].
The model used to simulate the vehicle noise source is, as a first approximation, a moving monopole source with broadband noise attributed to tire–road interaction. This modeling choice is justified by the fact that not all recorded vehicle sounds in this study originate from ICE vehicles. Moreover, in some ICE vehicles, engine noise is significantly reduced due to improved acoustic insulation and vibration-damping engine mounts [13].

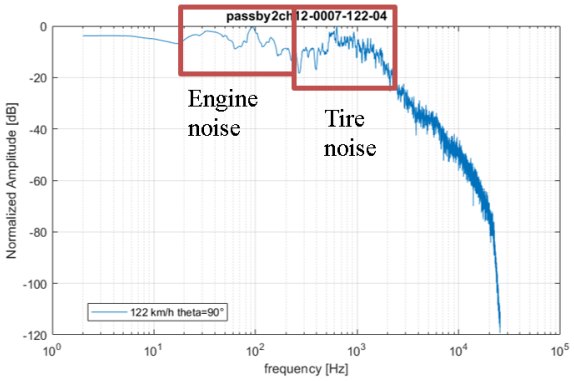


Figure 1. Example of a pass-by passenger vehicle normalized noise spectrum versus time.

2.2 Measurement set-up

Acoustic and speed measurements were conducted on the A91 highway in Rome, Italy, following the ISO 11819-1:2023 standard requirements. The highway consists of two lanes in each direction. For this study, two additional microphones were used for multisensor, located as illustrated in Figure 2.
Microphone M3 was placed 7.5 m from the centerline of the slow lane at a height of 3.0 m, while M1 and M2 were positioned 6.45 m from the centerline, also at 3.0 m in height. The distance between M3 and M1 (d_{13}) was 2.2 m, and the distance between M1 and M2 (d_1) was 1.9 m.
The microphones used were ½" Class I omnidirectional condenser microphones. Data acquisition was performed with a Sinus Apollo system, featuring four simultaneous acquisition channels, set to a sampling rate of 51,200 ksps.

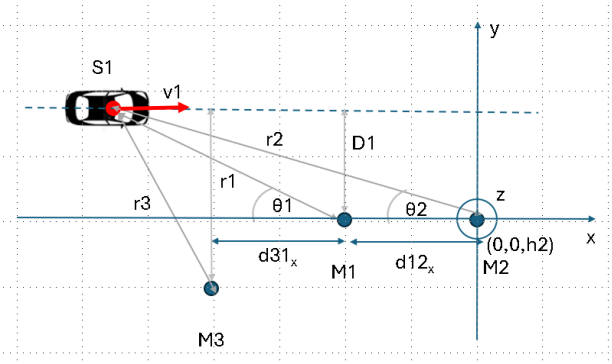




Figure 2. Measurement site and microphone positions; geometry of the problem, top view.

Vehicle speed was recorded using a SODI Scientifica KV Laser Statistic Analyzer, which provides an accuracy of ±1 km/h. This ensured precise speed measurements, allowing a reliable synchronization between noise levels and vehicle velocity, as required by the Statistical Pass-By (SPB) method.

The measurement site, located near the Smart Pole of the ANAS Smart Road project (PON-IR 2014-2020), was selected based on an inspection that ensured compliance with ISO 11819-1:2023 requirements. Particular attention was given to minimizing interferences from obstacles such as guardrails and road barriers, as their presence can alter sound measurements.

Tests were conducted at night when traffic density was lower, reducing the overlap of multiple sound sources and allowing a single vehicle pass-by. This also helped in ensuring that vehicles passed at a constant speed, preventing unwanted variations in noise levels and frequencies.

2.3 **Analysis methods**

In this study, both frequency-domain and time-domain analyses are employed for vehicle speed estimation. A single microphone (M3) is used for time- and frequency-domain analysis, leveraging sound pressure level (SPL) and the Doppler effect to estimate vehicle speed. Additionally, two microphones (M1 and M2) are utilized for time difference of arrival (TDOA) analysis to determine speed based on acoustic wave propagation delay. The inclusion of a third microphone (M3) enhances accuracy by precisely calculating the vehicle's distance from the microphones rather than relying on assumptions.

2.2.1 *Frequency-based analysis*

This approach utilizes variations in the spectral components of the acquired acoustic signal to infer vehicle speed, employing signal processing techniques.

Doppler shift and harmonic extraction

When a vehicle is moving relative to a fixed microphone position, the sound captured by the microphone presents changes in frequency content due to a Doppler effect. As the vehicle approaches, the sound is compressed, increasing its frequency; conversely, as it moves away, the frequency decreases. The frequency shift, $\Delta f = f(t) - f_0$, is measured in the spectrogram, generated by Short-Time Fourier Transform (STFT) or by the instantaneous phase (IF), obtained as the time derivative of the phase of the complex spectrum of the signal [14-15]. The source speed is estimated, as shown in Eqn. 2, based on the difference between the maximum and minimum detected harmonic's frequency.

$$|v_v| \cos(\theta) = \left(\frac{f_a - f_d}{f_a + f_d}\right) \qquad (2)$$

Where: f_a and f_d are the frequencies during vehicle's approaching and departure the CPA; θ is the vehicle's approach angle; v_v is the vehicle's constant speed.

The frequency variation respect to f_o usually is less the 11% at the maximum highway speed.

.

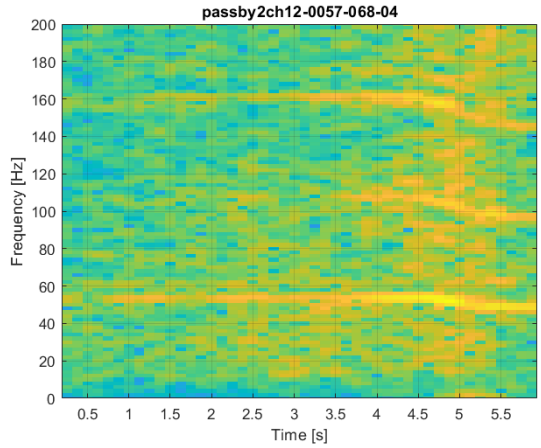


Figure 3. Example of a vehicle sonogram calculated using the STFT. The frequency variation of the engine harmonics due to the Doppler effect is observed.

To improve accuracy, engine harmonics are tracked, and spectral interpolation techniques are applied to refine signal variations [2].

2.2.2 *Time-Domain analysis*

In the time-domain analysis, two approaches were employed for vehicle speed estimation: one based on the measurement of sound pressure level over time, and the other on the time delay between signal arrivals at multiple microphones. In the first approach, the narrowing of the sound pressure level curve correlated with vehicle speed is used to estimate the speed. In the second method, correlation techniques combined with maximum likelihood estimation are applied to determine the time delay, which is then used to calculate the speed.

One microphone narrow envelope technique

This method relies on the observation that the sound pressure envelope of a passing vehicle exhibits a narrowing effect as vehicle speed increases [16]. This approach, which uses a single microphone, offers a low-cost and easy-to-deploy solution for traffic speed monitoring using minimal equipment, without requiring inter-sensor synchronization.

During the pass-by, the recorded acoustic signal shows a bell-shaped envelope centered around the vehicle's closest point of approach (CPA) (Figure 4). As the vehicle moves faster, the duration of this envelope shortens, resulting in a steeper and narrower profile.

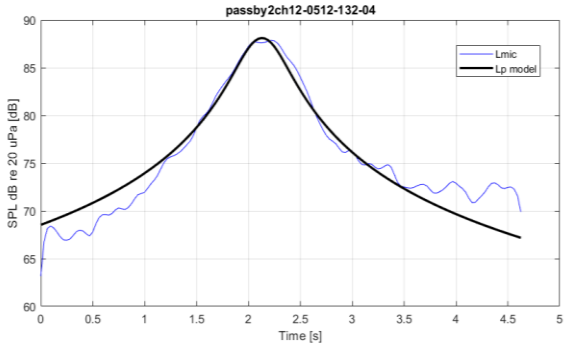


Figure 4. Sound pressure level recorded, Lmic, recorded at the microphone and curve modelled.

The sound pressure level, L_p, at the microphone can be written as:

$$L_p(t, v_0) = L_w - 8 - 20log_{10}(r(t, v_0)) + ID - A + n \quad (3)$$

Where: L_w is the sound power level of the vehicle; *r(t)* is the distance between the vehicle and the microphone changing in time; *ID* is the directivity index; *A* is the attenuation along the path; and *n* is the unwanted noise.

The distance between the microphone and the vehicle, which depends on time t and the vehicle's speed, v0, assumed constant during the measurement, can be expressed as:

$$r(t; v_0) = \sqrt{D^2 + \left(v_0(t - t_{CPA})\right)^2} \quad (4)$$

Where D is the perpendicular distance from the microphone when the vehicle is at the CPA at the time, t_{CPA}.

To mitigate the impact of variations in the distance between the vehicle and the microphone, amplitude normalization techniques and band-pass filtering are employed to eliminate low and high-frequency noise.

The signal has been analyzed in three frequency bands: (50–200) Hz, (500–3000) Hz, and (3000–8000) Hz, each corresponding to different sound sources as described in Paragraph 2.1. For each band, one or two sources were considered, located either at the center or at the front and rear of the vehicle, with corresponding modifications applied to Equation 4.

To determine the speed, v0, the vehicle speed v that minimizes the mean square error between the processed

recorded sound pressure level, $y(t)$, and the model $L_p(t,v)$ is calculated as follows:

$$\underset{v}{\text{Arg min}}\left(\frac{1}{T}\sum_{t=0}^{T}\left(y(t)-L_p(t,v)\right)^2\right) \quad (5)$$

The results obtained for each band have been averaged.

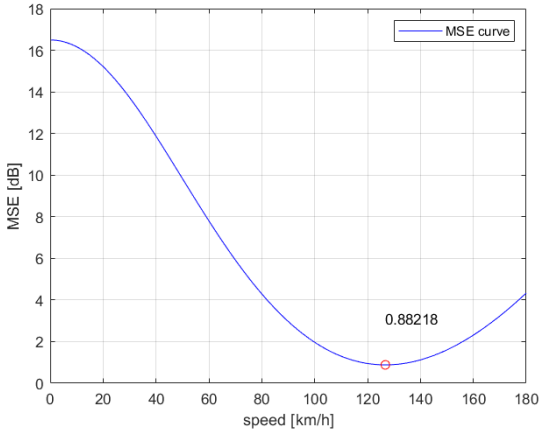


Figure 5. Curve of the mean square error of the Time Difference of Arrival (TDOA) estimation

Two-microphone technique and the Time Difference of Arrival (TDOA) estimation

In this method, at least two microphones are required to measure the TDOA, $\Delta\tau$, of the acoustic wave generated by the vehicle, positioned at a known distance, d. It is given by:

$$\Delta\tau(t) = \frac{r_2(t) - r_1(t)}{c} \quad (6)$$

Where r_1 and r_2 are the unknown vehicle distances from each of the two microphones, and c is the speed of sound. $\Delta\tau$ also represents the time delay between the acoustic signals received at each microphone. The received signals, $y_1(t)$ and $y_2(t)$, can be modelled as:

$$y_1(t) = h_1(t) * s(t) + n_1(t) \quad (7)$$
$$y_2(t) = h_2(t) * s(t-\tau) + n_2(t)$$

Were $s(t)$ is the source acoustic signal; $h_1(t)$ and $h_2(t)$ are the impulse responses from the instantaneous position of the moving vehicle and each microphone; $n_1(t)$ and $n_2(t)$ represent the unwanted signals, which also contain uncorrelated noise; τ is the delay of the second signal relative to the first signal, which is assumed to be the reference and not delayed. If the positions of the microphones are not sufficiently close to each other, the impulse responses cannot be simplified to an amplitude difference between the received signals.

Signal processing techniques are employed to identify similarities between signals captured by microphones, detecting the temporal offset between them. The maximum likelihood technique is applied, constructing a correlation matrix between microphone signals to identify the delay that maximizes correlation.

Due to the motion of the vehicle, the sound source is non-stationary, and thus the signal is also non-stationary. In this condition, the Least Mean Square (LMS) algorithm can be used to find the delay. However, if the process is considered quasi-stationary over a short time interval, this allows for the application of the Fourier transform, thereby enabling the use of the cross-correlation function, $R(t)$, defined as the product of the transformed signals [17], to estimate the delay

$$\underset{t}{\arg\max}\ (R_{ss}(t-\tau)) \quad (8)$$

By substituting Eqn. 4 into Eqn. 6 for each distance, r_1 and r_2, the vehicle speed can be determined. [3]. As the vehicle approaches the CPA, the values of τ change rapidly, and the FFT-based correlation may fail. In this condition, it is useful to apply a fitting function. We use the logistic tanh function (Figure 6) to model the delay behavior:

$$\tau(t) = a\tanh\left(b(t-c)\right) \quad (9)$$

Where a represents the delay when the vehicle is far from the microphone, c is the time corresponding to the CPA, and b is the slope of the curve, which is proportional to the vehicle speed.

$$v = b * D \quad \left[\frac{m}{s}\right] \quad (10)$$

Where, D is the perpendicular distance from the vehicle to the microphones at the CPA.

This method has proven particularly useful in dense traffic environments, where tracking individual vehicles may be unfeasible. Passive sound detection using a microphone array has been shown to capture the overall acoustic pattern of traffic across multiple reference points [18].

By applying cross-correlation algorithms to the collected signal, the average vehicle speed within specific lanes can be estimated. Unlike Doppler-based methods, passive detection does not rely on a single vehicle's emitted signal but rather on the overall acoustic pattern of traffic, increasing its applicability in complex urban conditions.

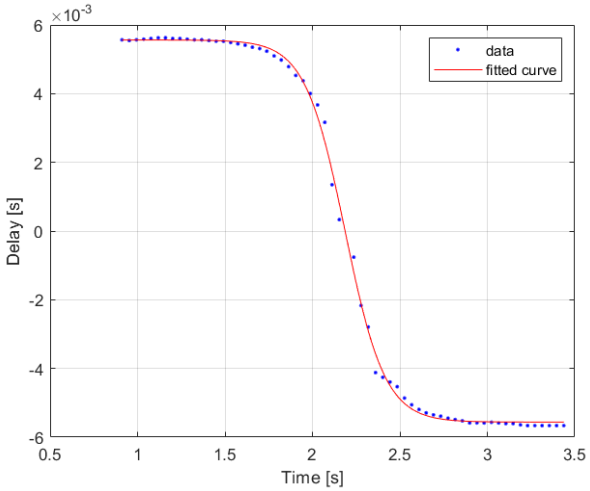


Figure 6. Signal time difference of wave arrival (blue dotted), and the fitting function.

3. RESULTS AND DISCUSSION

For speed calculation and accuracy evaluation, over 400 valid events were recorded, and the measured speeds were associated with these events. The distribution of the vehicle speed is shown in Figure 7. In each pass-by, only one vehicle was present, no vehicles in the other 3 lanes, and the difference between the maximum level during pass-by and the minimum before another pass-by was greater than 6 dB.

The classification was based only on vehicle type (passenger or heavy vehicles), without distinguishing between EVs and ICE vehicles.

Applying the different signal processing techniques, explained in the previous paragraph, to the recorded audio signals to estimate the vehicle speed, the results are summarized in Table 1 and Table 2.

Considering the increasing number of microphones from one to three, there is little improvement in the spread of the measured values from 10.0 km/h to 8.6 km/h. If it is considered the same number of two microphones, the method based on TDOA exhibits a better standard deviation from 8.9 km/h to 8 km/h.

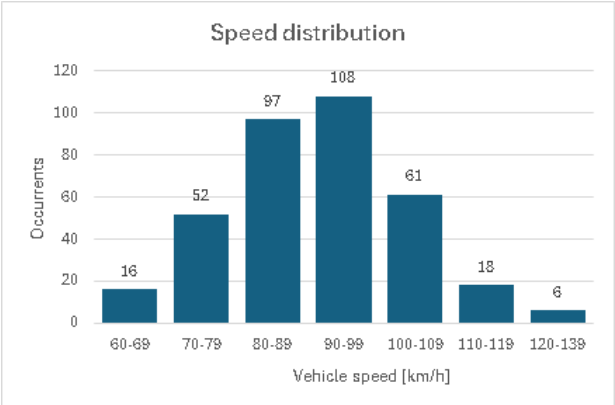


Figure 7. Vehicle speed distribution, measured with laser instrumentation.

The values at the extremes of the tables are not considered reliable due to the limited number of measured velocity cases in those ranges.

Table 1. Speed error estimation with the three methods based on the SPL envelope.

	1-Mic		2-Mic		3-Mic	
Speed	**Mean**	**Std**	**Mean**	**Std**	**Mean**	**Std**
[km/h]	**[km/h]**	**[km/h]**	**[km/h]**	**[km/h]**	**[km/h]**	**[km/h]**
50-59	17.0	n.d.	14.1	n.d.	10.4	n.d.
60-69	5.7	9.0	7.7	11.1	9.6	11.7
70-79	1.4	8.9	5.0	9.2	7.6	11.0
80-89	0.1	9.9	4.7	11.0	5.9	10.3
90-99	-2.9	10.7	3.2	10.1	5.0	10.1
100-109	-1.4	9.9	0.3	8.8	3.0	9.6
110-119	-2.7	10.0	-4.7	10.3	-3.9	9.5
120-129	-14.2	12.8	6.0	7.3	0.5	8.1
130-139	-16.1	0.0	0.0	0.0	-2.7	2.7
Global	-0.9	10.0	3.1	8.9	4.5	8.6

Only 10 samples have been tested with the Doppler effect method, and without an autonomous algorithm. The algorithm is under development.

Table 2. Speed error estimation with the methods based on the Doppler effect (1-Mic) and TDOA (2-Mic)

	1-Mic		2-Mic	
Speed	**Mean**	**Std**	**Mean**	**Std**
[km/h]	**[km/h]**	**[km/h]**	**[km/h]**	**[km/h]**
50-59	n.d	n.d.	n.d.	n.d.
60-69	-1.6	n.d.	6.7	9.0
70-79	-12	n.d.	7.3	9.6
80-89	5.9	n.d.	5.6	9.4
90-99	3.3	n.d.	3.0	7.5
100-109	-3.3	n.d.	2.5	7.0
110-119	8.8	n.d.	-0.8	7.3
120-129	14.3	n.d.	-6.6	13.2
130-139	-3.7	n.d.	-4.9	4.9
Global	0.5	7.7	4.1	8.0

The high standard deviation observed in the speed evaluation is primarily attributed to limitations in the automatic processing. In the case of the SPL envelope-based methods, the model often fails to align accurately with the measured signal when the envelope's peak is flat rather than sharply defined, as assumed by the model. For the TDOA method, the error arises near the point of inversion of the time difference of arrival, where the fitting procedure may fail due to a limited number of data points or inaccuracies in their evaluation.

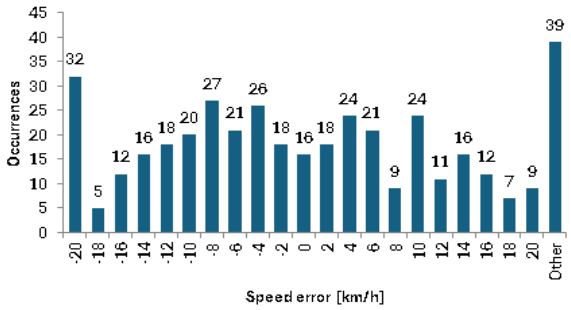


Figure 8. 1-Mic SPL envelope-based speed estimation method distribution error.

The distributions of the speed estimation error for the 1-mic SPL envelope-based and 2-mic TDOA are shown in Figure 8 and Figure 9. Although the standard deviation is higher for the first method, the failure rate, labeled as 'Other' in the figures, is lower than that of the second method, suggesting greater robustness.

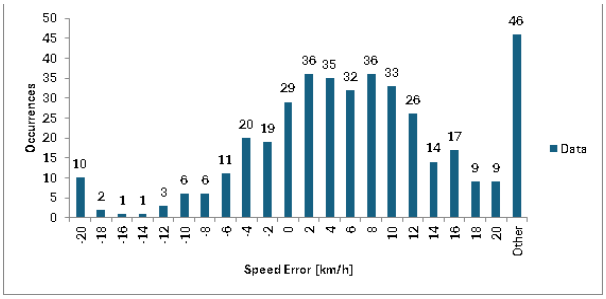


Figure 9. 2-Mic TDOA speed estimation method distribution error.

The other 2-mic method shows the same robustness, while the 3-mic method is the least robust method, with 61/401 fails.

4. CONCLUSIONS

In this study, a database of acoustic events, recorded during measurement sessions conducted in accordance with the ISO 11819-1 standard, was first established. Each event, corresponding to a single vehicle pass-by, was classified by vehicle type, either as a passenger vehicle or a heavy truck. This database was subsequently used to evaluate five elementary methods for estimating vehicle speed based on the pass-by sound generated by the vehicle itself. Four of these methods operate in the time domain, while one is based on frequency-domain analysis.

The uncertainty associated with the estimated values remains relatively high compared to other methods reported in the literature. This is primarily due to occasional failures in automatic processing, where the model fitting does not adequately match the measured data. Further studies are currently underway to address these issues and enhance the performance of the proposed algorithms

5. ACKNOWLEDGMENTS

This research was funded by the European Commission Executive Agency for Small and Medium-Sized Enterprises LIFE program (LIFE22-ENV-IT-LIFE SILENT - 101114310).

The authors declare no conflict of interest. The funders had no role in the design of the study, in the collection, analysis, or interpretation of data, in the writing of the manuscript, and in the decision to publish the results.

6. REFERENCES

[1] F. Lo Castro, M.L Ariza Alvarez, M. De Luca, S. IAROSSI, P*roc INTER-NOISE 2024, Nantes, France*, Pages 7999 - 8999, pp. 8386-8397(12), DOI: https://doi.org/10.3397/IN_2024_4086

[2] S. Barnwal, R. Barnwal, R. Hegde, R. Singh, & B. Raj. (n.d.). Doppler-based speed estimation of vehicles using a passive sensor. *Proc. of an Unspecified Conf. or Journal.*

[3] F. Pérez-González, R. López-Valcarce, & C. Mosquera. (1998). Road vehicle speed estimation from a two-microphone array. *Proc. IEEE Int. Conf. on Acoust., Speech, and Signal Process. (ICASSP)*, 2, 1321–1324.

[4] V. Rosão, E. Conceição, & L. Házyóvá. (2010). Method to determine the speed of vehicles by means of noise levels variation. *Proc. INTERNOISE 2010 Conf., Lisbon, Portugal.*

[5] H. Ding & B. F. Chao. (2015). Detecting harmonic signals in a noisy time-series: The z-domain autoregressive (AR-z) spectrum. *Geophys. J. Int., 201(3)*, 1287–1296. https://doi.org/10.1093/gji/ggv077

[6] Kephalopoulos S, Paviotti M, Anfosso-Lédée F. Common Noise Assessment Methods in Europe (CNOSSOS-EU). *EUR 25379 EN. Luxembourg (Luxembourg): Publications Office of the European Union;* 2012. JRC72550

[7] Beckenbauer, TRoad Traffic Noise. In: Müller, G., Möser, M. (eds) *Handbook of Engineering Acoustics. Springer, Berlin, Heidelberg 2013*. https://doi.org/10.1007/978-3-540-69460-1_15

[8] A. Lorea, V. Castelluccio, A. Costelli and M. Masoero, A Wind-Tunnel Method for Evaluating the Aerodynamic Noise of Cars, *SAE Transactions Vol. 95, Section 1 (1986)*, pp. 1096-1105.

[9] T. Priede, Origins of automotive vehicle noise, *Journal of Sound and Vibration,V. 15, I. 1,1971*, pp. 61-73, ISSN 0022-460X, doi.org/10.1016/0022-460X(71)90360-9

[10] K. Iwao, I. Yamazaki A study on the mechanism of tire/road noise, *JSAE Review Volume 17, Issue 2*, April 1996, Pages 139-144

[11] Bao Meng, Chen Enwei, ,Lu Yimin, ,Liu Zhengshi, Liu Shuai, Vibration and noise analysis for a motor of pure electric vehicle, *Advanced Materials Research, ISSN: 1662-8985, Vols. 915-916*, pp 98-102.https://doi.org/10.4028/www.scientific.net/AMR.915-916.98

[12] George, A. and Callister, J., "Aerodynamic Noise of Ground Vehicles," *SAE Technical Paper 911027*, 1991, https://doi.org/10.4271/911027

[13] Somashekarappa M, A noise reduction technique in internal combustion engines: A multidisciplinary approach, *World Journal of Advanced Research and Reviews, 2020, 05(03)*, 170–179

[14] Toshihiko Abe, Harmonics tracking and pitch extraction based on instantaneous frequency *Conference Paper in Acoustics, Speech, and Signal Processing, 1988. ICASSP-88., 1988 International Conference on · June 1995* DOI: 10.1109/ICASSP.1995.479804 · Source: IEEE Xplore

[15] Toshihiko Abe, Harmonics Estimation Based on Instantaneous Frequency and Its Application to Pitch Determination of Speech. *IEICE Transactions on Information and Systems · September 1995*

[16] Cevher, V., Chellappa, R., & McClellan, J. H. (2009). Vehicle speed estimation using acoustic wave patterns. *IEEE Transactions on Signal Processing, 57(1)*, 30–47. https://doi.org/10.1109/TSP.2008.2005752

[17] C. Knapp and G. Carter, "The generalized correlation method for estimation of time delay," *IEEE Transactions on Acoustics, Speech, and Signal Processing, vol. 24, no. 4, pp*. 320-327, August 1976, https://doi.org/10.1109/TASSP.1976.1162830

[18] P. Borkar & L. G. Malik. (2013). Review on vehicular speed, density estimation, and classification using acoustic signals. *Int. J. for Traffic and Transport Eng., 3(3)*, 331–343. https://doi.org/10.7708/ijtte.2013.3(3).08

DOI: 10.61782/fa.2025.0515

FORUM ACUSTICUM EURONOISE 2025

LCA APPROACH TO EVALUATE THE SUSTAINABILITY OF INNOVATIVE LOW-HEIGHT NOISE BARRIERS

Marco Montesi[1] **Antonio Tranzi**[1] **Marco Fantozzi**[1]
Massimo Garai[2]
Cosimo Micheletti[3]
[1] Rete Ferroviaria Italiana SPA, Roma, Italy
[2] Alma Mater Studiorum Università di Bologna, Bologna, Italy
[3] Mopi SRL, Pisa, Italy

ABSTRACT

As part of the LIFE SILENT project[1] (focused on developing innovative and eco-friendly solutions for noise mitigation in road and railway contexts - innovative materials and advanced technologies are being explored to design Low-Height Noise Barriers (LHNB) with enhanced acoustic properties and a significantly reduced environmental impact. For this scope a comparative Life Cycle Assessment (LCA) was conducted to evaluate the environmental impacts of different typologies of LHNBs.
The LCA focused on the production phase ("from cradle to gate") of three LHNB solutions, analysing their material composition and overall environmental performance. Solution 1, the STRAILastic barrier, incorporates recycled rubber, which significantly reduces its Global Warming Potential (GWP) compared to barriers made mainly of virgin materials. Solution 2, composed primarily of reinforced concrete and recycled rubber, and Solution 3, including steel, aluminium, and PET foam which both exhibit higher environmental impacts due to the predominant use of high-emission materials such as concrete and aluminium.
The study highlights the crucial role of integrating recycled materials in reducing environmental impacts and underscores the need to optimize designs to minimize the use of high-impact components. This standardized LCA approach provides a comprehensive framework for assessing and fostering sustainable practices in noise mitigation infrastructure.

Keywords: *Life Cycle Assessment, Low-Height Noise Barriers, Environmental Impacts, Recycled materials, Acustic performance*

1. INTRODUCTION

The aim of this study is to design an innovative Low Height Noise Barrier (LHNB) made from recycled materials, with improved acoustic properties thanks to the implementation of metamaterial technology. Furthermore, the last step of this work package is to test a new LHNB prototype in a controlled test environment (laboratory or similar) and characterise its acoustic performance.
As the metamaterial technology is applicable to any material, it is essential to start with a material capable of guaranteeing the best environmental sustainability. In turn, this can be demonstrated by evaluating the most important Key Performance Indicators (KPIs) of the environmental impact of any material. This evaluation must be done in a systematic way, following a standardized method in order to ensure an objective and accurate understanding, based on objective data. Several methods of this kind exist, but the most widely accepted are reducible to the Life Cycle Assessment method (LCA) codified in some international standards [[1],[2],[3],[4]]. LCA is a quantitative approach that follows a systematic method to study and compare the impacts of products and systems throughout their life cycle.

*Corresponding author: m.montesi@rfi.it.
Copyright: ©2025 First author et al. This is an open-access article distributed under the terms of the Creative Commons Attribution 3.0 Unported License, which permits unrestricted use, distribution, and reproduction in any medium, provided the original author and source are credited.
[1] Co-funded by European Union (LIFE22-ENV-IT-LIFE-SILENT/101114310).

In the current study the GWP (Global Warming Potential) category is quantitatively evaluated, also considering the EU "net zero" objectives, aimed at urgently reducing greenhouse gas emissions.
Therefore, the objective of this study is to demonstrate, through a comparative Life Cycle Analysis (LCA) focused on the production phase (A1-A2-A3) and based on sustainability criteria, that the selected low-height noise barrier (Strailastic msw360), thanks to the use of recyclable materials, is capable to minimize the GWP environmental impact compared to the other low-height noise barriers available on the market. Moreover, this highlights important sustainability considerations in the design and implementation of the analysed products.
Through the application of the Life Cycle Assessment (LCA) methodology in the "*from cradle to gate*" phase, we were able to assess the impact of the different components of the barriers, identifying the solutions that most effectively minimize environmental impacts.
From the preliminary sustainability assessment conducted on the Strail LHNB, compared to two other types of LHNB, it emerges that the LHNB supplied by Strail represents the solution that most effectively minimizes environmental impacts.
The presence of recycled rubber in the composition of the Strail barrier has contributed significantly to reducing the overall environmental impact compared to the exclusive use of virgin materials. This highlights the positive potential of recycling and reusing materials to mitigate environmental impact, while also providing a sustainable solution for waste management.

2. OBJECTIVES AND SUCCESS CRITERIA

The LCA methodology allows the quantification of the impacts of a product or process, and in this study, it will be used to evaluate, analyse and compare the impacts of the Strail low-height noise barrier with two other low-height noise barriers currently available on the market [5].
LCA is a quantitative approach that follows a systematic method, regulated by international ISO standards [[1],[2],[3],[4]], to study and compare the impacts of products and systems throughout their life cycle. It is essential to have a quantitative sustainability assessment tool in order to ensure an objective and accurate understanding, based on objective data.
According to the current ISO reference standard regulations, an LCA study consists of the following phases, which will be further detailed in the following sections.

1. Goal and scope definition: preliminary phase where the study's objectives, declared unit, boundaries of the system studied and assumptions are defined;
2. Inventory analysis: quantification of input and output flows for all analysed processes;
3. Impact assessment: aggregation of inventory results, with scientific models, into a number of potential environmental impacts;
4. Interpretation: analysis of the results obtained in order to draw conclusions.

The four steps of a life cycle analysis are interrelated, making the whole process iterative (**Errore. L'origine riferimento non è stata trovata.**). Each phase is based on the results obtained in the previous phase, thereby promoting the completeness and coherence of the study. If there is a need to integrate further information in a previous step or to revise the initial settings, any changes are also carried over to the subsequent levels of the analysis.

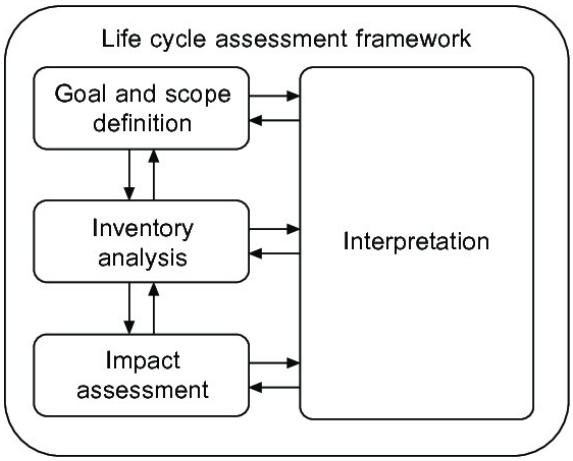


Figure 1. LCA phases according to ISO 14040/14044

Life cycle analysis approaches provide various perspectives for assessing the environmental impact of a product or system over time. These include the assessment of the entire life cycle, from production to disposal (Cradle to Grave), adopting circular practices that allow for the complete reuse of materials (Cradle to Cradle), and focusing on the initial stages of the life cycle until the product is ready for use (Cradle to Gate). These approaches offer complementary perspectives for understanding and addressing the challenges related to the sustainability of products and industrial processes.

The success of this study is demonstrated by the successful completion of the LCA analysis of the Strail low-height noise barrier and two main competitors.

3. GOAL AND SCOPE DEFINITION

The LCA analysis in question focuses on assessing the environmental impacts of the Strail low-height noise barrier, compared to two competing products currently available on the market. In this study, the life cycle analysis was conducted 'from cradle to gate', considering all stages of the product life cycle from the production of raw materials to the manufacture of the noise barriers. This approach allowed us to comprehensively evaluate the environmental impact of different types of noise barriers until they are ready for installation.
In the comparative study of the three LHNBs, it is important to note that the analysis focused exclusively on the materials constituting the sound-insulating part of the barriers themselves. Support and anchoring structures of the barriers, which may include elements such as steel and reinforced concrete, as well as packaging and packing processes, were deliberately excluded from the assessment.

Declared unity
The unit declared examined, against which all the quantitative input and output data collected in the study are calculated, is the production of 1 linear meter of noise barrier.

System boundaries
The modules for which the environmental impact of barriers is quantified in this study are the following:

- A1: Procurement of raw materials for barriers production;
- A2: Transportation of raw materials for barriers making;
- A3: Processing of raw materials to obtain the barriers.

Data quality and Impact Assessment Methodology
The study uses generic secondary data from the Environmental Footprint 3.1 databases [6], which is part of the broader Ecoinvent 3.10 database [7]. The data, representing the period 2020-2023, reflect both European and global contexts. Impact assessments are conducted using OpenLCA 2.0.0, applying the "Environmental Footprint (Mid-point indicator)" method to evaluate Global Warming Potential (GWP) as a key performance indicator (KPI).

4. INVENTORY ANALYSIS

Inventory analysis is the most crucial phase of an LCA study. It involves collecting data to quantify the inflows and outflows from the system during its life cycle in relation to the declared unit. Inputs include the use of natural resources, materials, and energy while Outputs include emissions to air, water and soil associated with the system and the generated waste.
Once the processing is complete, the sum of inputs and outputs for each unit process yields the "inventory," which is a catalogue of all mass and energy flows entering and leaving the system.
The environmental impacts of the secondary data used in the analysis are automatically counted by selecting the material to be modelled from the databases used, which already contain all the information from its supply chain, from raw materials extraction to production.
Below are all the technical specifications considered in the inventory analysis of the barriers considered.
The Strail Barrier will be identified as “Solution 1”, while the other two barriers will be referred to as “Solution 2” and “Solution 3”.

4.1 Solution 1: STRALastic_mSW 360

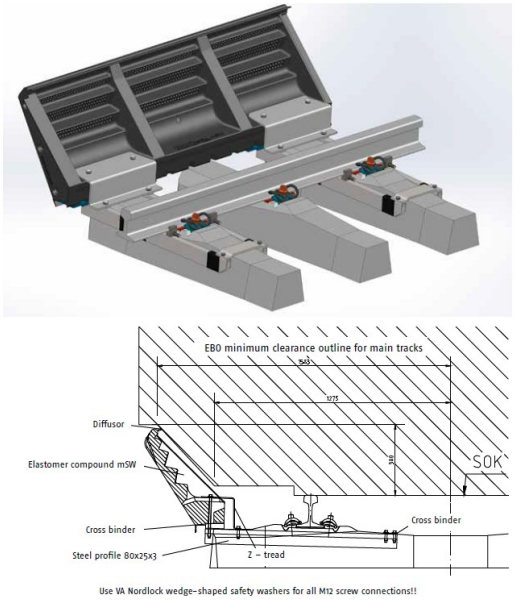


Figure 2. STRAILastic_Msw 360

Barrier Module: length 1.8 m, height 0.53 m and thickness 0.30 m.

Weight of recycled material 61,564 kg per 1,8m of length (data provided by Strail), which is approximately 34,202 kg/m.
Weight of virgin material 58,605 kg per 1,8m of length (data provided by Strail), which is approximately 32,558 kg/m [8].
The processes used are summarized in the following Table.

Table 1. Processes Used in STRAILastic_mSW 360 Low Height Noise Barrier Definition

	Database	Process	Amount [kg/m]
Recycled Material	Strail Self Calculation	Buffering meal retreading (Waste tire industries)	3,801
	Strail Self Calculation	Rework STRAIL shredded & broken (old used panels)	4,881
	Strail Self Calculation	Roughing Rubber meal (waste tire industry)	4,881
	Strail Self Calculation	Rubber granules (waste tire industry)	20,641
Virgin Material	Ecoinvent 3.10	Grinding sulphur Sodium silicate production, spray powder, 80%	1,318
	Ecoinvent 3.10	Stearic acid Chloropropionic acid	0,133
	Ecoinvent 3.10	MBTS 2-methyl-2-butanol production	0,079
	Ecoinvent 3.10	ZBEC market for dithiocarbamatePro-compound	0,052
	Ecoinvent 3.10	Plasticizer oil Softener rubber production	1,929
	Ecoinvent 3.10	Latex latex production	0,502
	Ecoinvent 3.10	New rubber layer (DP 1350x2,5) market for seal, natural rubber based	11,772
	Ecoinvent 3.10	New rubber layer (DP high light protection 3,0x960D300DPU) market for synthetic rubber	16,772

4.2 Solution 2

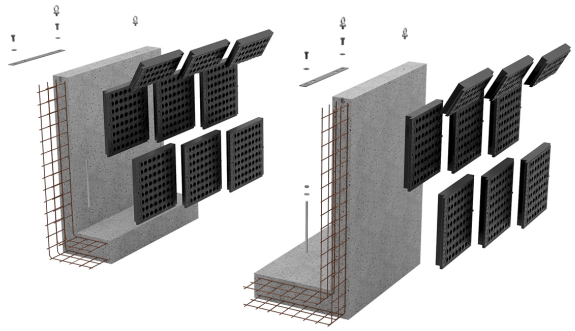


Figure 3. Representative image of Solution 2

Barrier Module: length 1,0 m, height 0,67 m and thickness 0,20 m.
Assuming that the thickness of this barrier is made up of 0,15 m of reinforced concrete and 0,05 m of recycled rubber, we have:
Volume of reinforced concrete = 1,0 m × 0,67 m × 0,15 m = 0,1005 m^3
Weight of reinforced concrete = Density of concrete (average 1400 kg/m^3) × Volume ≈ 140,07 kg (assuming a weight of 14 kg for steel and 6 kg for construction timber)
Volume of recycled rubber per meter = 1,0 m × 0,67 m × 0,05 m = 0,0335 m^3
Weight of recycled rubber per meter = Density of recycled rubber (average 800 kg/m^3) × Volume ≈ 26,8 kg
The processes used are summarized in the following Table.

Table 2. Processes Used in the definition of solution 2

Database	Process	Amount [kg/m]
Ecoinvent 3.10	Recycled Rubber - market for waste rubber, unspecified	26,8
Environmental Footprint 3.1	Concrete C20/25 (Ready-mix concrete), production mix, at plant, technology mix, C20/25	140,07
Environmental Footprint 3.1	Reinforced steel (wire), production mix, at plant, EAF route, wire	14,0
Environmental Footprint 3.1	Solid construction timber (softwood) (EN15804 A1-A3), production mix, at plant, technology mix, 529 kg/m3 at 15% moisture	6,0

4.3 Solution 3



Figure 4. Representative image of Solution 3

Barrier Module: length 2,04 m, height 1,04 m and thickness 0,24 m.
Total module weight 150 kg.
Therefore, the weight per meter of barrier is about 75 kg/m.
It is assumed:
Steel weight ≈ 40,0 kg
Aluminium weight ≈ 25,0 kg

PET foam weight ≈ 10,0 kgnot modify headers, footers or page numbers in your submission. These will be added electronically at a later stage, when the publications are assembled.
The processes used are summarized in the following Table.

Table 3. Processes Used in the definition of solution 3

Database	Process	Amount [kg/m]
Environmental Footprint 3.1	Reinforced steel (wire), production mix, at plant, EAF route, wire	40,0
Environmental Footprint 3.1	Aluminium foil , single route, at plant, primary production, 2.7 g/cm3 - EU-28+EFTA	25,0
Environmental Footprint 3.1	Polyurethane rigid foam, production mix, at plant, from methylene diisocyanate (MDI) and polyols, 18- 53 kg/m3 - EU-28+EFTA	10,0

5. IMPACT ASSESSMENT

Impact assessment is the phase where the inputs and outputs, reported in the inventory, are translated into potential environmental impacts. The environment is a complex system of physical, chemical and biological factors, living and non-living elements, and relationships in which all the organisms that inhabit the planet are immersed, where any variation of one of these components affects the whole system. Therefore, to study such a complex reality, the LCA methodology involves the compartmentalization of the entire environmental system into a limited number of impact categories.
Each impact category is determined by a different reference unit that allows quantifying the impact following classification and characterization operations.

Classification
The classification is a qualitative step in which emissions from modelled elementary flows, collected in the inventory, are associated with the impact categories according to the potential environmental effects. It answers the question "what does this emission contribute to"?

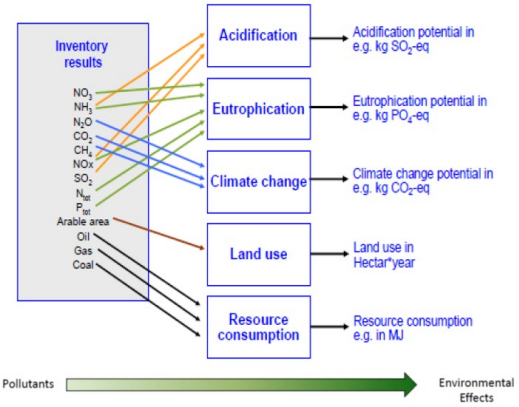


Figure 5. Example of classification of some substances (JRC Scientific and Technical Reports) [9]

Characterization
Characterization allows quantifying the contribution of different elementary flows within an impact category. It answers the question "how much does this emission contribute to the impact compared to the others?". The environmental impacts assessment was carried out through the *"Environmental Footprint (Mid-point indicator)"* impact assessment method. In the current study, we will consider only the GWP (Global Warming Potential, reference unit kg CO_2 eq.) category, also considering the EU "net zero" objectives, aimed at urgently reducing greenhouse gas emissions.

We will examine the results of the LCA analysis conducted on different types of noise barriers. Through a critical and in-depth analysis of these results, we will provide a clear and informative view of the environmental impact of the available options and the contribution of specific materials that compose them.
At the end of our research, we aim to conduct an in-depth comparative analysis of the different solutions examined to identify the most sustainable and least impactful from an environmental point of view. Through this process, we aim to provide a comprehensive and objective assessment of the options available, allowing for an informed and conscious choice in line with sustainability principles.

5.1 Results of the STRAILastic_mSW 360 Analysis (Solution 1)

The results obtained from the LCA analysis for the Strail barrier are represented through the following bar chart that shows the LCA modelling process of the barrier with the respective contributions of the materials that compose it.

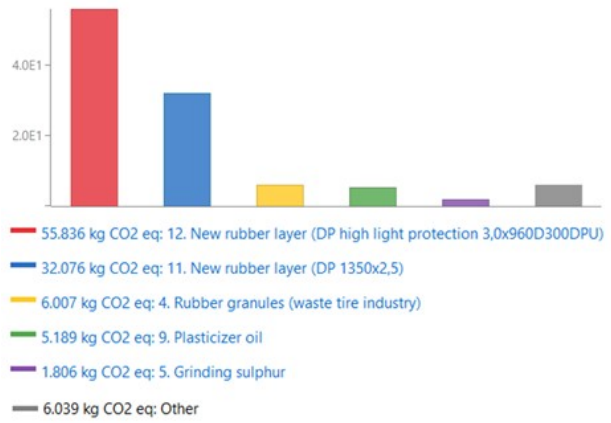


Figure 6. GWP Contribution of the materials composing the "Solution 1: Strail" (OpenLCA)

Based on the results of the LCA analysis conducted on the Solution 1 Strail barrier, composed of a combination of recycled rubber and virgin rubber, it is evident that the significantly more impactful components in terms of Global Warming Potential (GWP) are those related to the production of virgin rubber. These results unequivocally underline the importance of recycling and reusing materials in the design and production of infrastructure such as noise barriers.

5.2 Results of the SOLUTION 2 analysis

The results obtained from the LCA analysis for the Solution 2 are represented through the following bar chart that shows the LCA modelling process of the barrier with the respective contributions of the materials that compose it.

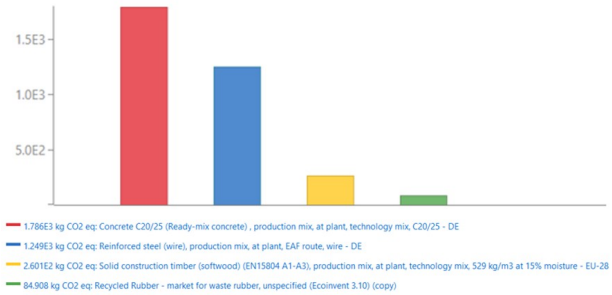


Figure 7. GWP Contribution of the materials composing the "Solution 2" (OpenLCA)

Based on the results of the LCA analysis conducted on the "Solution 2", composed mainly of reinforced concrete with a reduced percentage of recycled rubber, it is clear that the most impactful component in terms of Global Warming Potential (GWP) is the reinforced concrete. It is important to note that despite the use of recycled material, the substantial presence of reinforced concrete has a significant impact on the overall environmental impact of the barrier.

5.3 Results of the SOLUTION 3 analysis

The results obtained from the LCA analysis for the Strail barrier are represented through the following bar chart that shows the LCA modelling process of the barrier with the respective contributions of the materials that compose it.

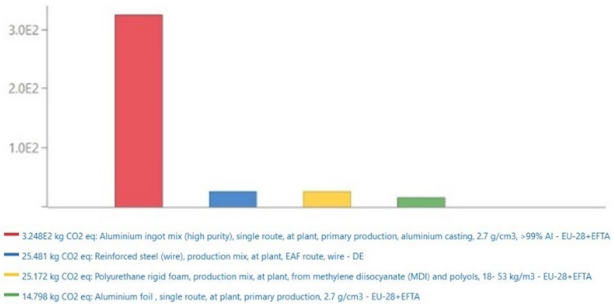
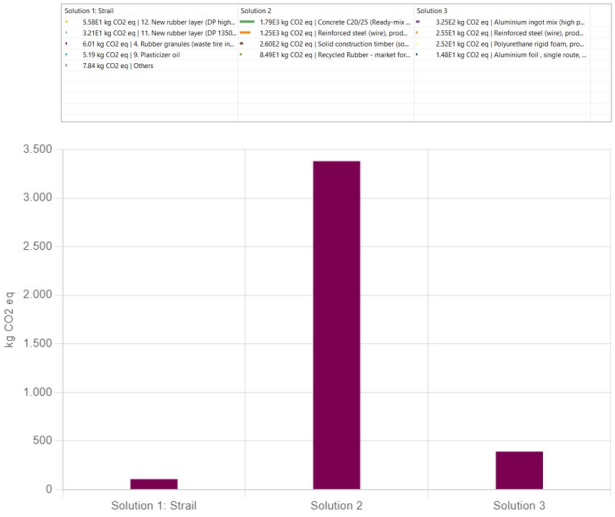


Figure 8. GWP Contribution of the materials composing the "Solution 3" (OpenLCA)

Based on the results of the LCA analysis conducted on the "Solution 3", composed of steel, aluminum and PET foam, it reveals that aluminum has the most significant impact in terms of Global Warming Potential (GWP), while steel and PET foam have very similar CO2 equivalent quantities.

5.4 Results of Comparative Analysis

After examining the impacts associated with the Global Warming Potential (GWP) component of the three low-height noise barriers, the results of our comparative analysis are presented in Figure 14 to identify the solution that best fits the environmental sustainability criteria defined by this indicator.



6. CONCLUSIONS AND RECOMMENDATIONS

In conclusion, this study provided an in-depth analysis of the environmental impact of different types of noise barriers, highlighting important sustainability considerations in their design and implementation.

Through the application of the Life Cycle Assessment (LCA) methodology in the "*from cradle to gate*" phase, we were able to assess the impact of the different components of the barriers, identifying the solutions that most effectively minimize environmental impacts.

From the preliminary sustainability assessment conducted on the three solutions of noise barriers, the LHNB supplied by Strail represents the solution that most effectively minimizes environmental impacts.

The presence of recycled rubber in the composition of the Solution 1 Strail barrier has contributed significantly to reducing the overall environmental impact compared to the exclusive use of virgin materials. This highlights the positive potential of recycling and reusing materials to mitigate environmental impact, while also providing a sustainable solution for waste management.

Although the use of recycled materials is essential, it is necessary to consider the overall contribution of predominant high-emission materials (such as reinforced concrete in the Solution 2 and aluminium in the Solution 3) that can contribute significantly to the overall environmental impact. This highlights the importance of considering not only the presence of recycled materials, but also the overall composition and relative amount of each material within the final product when assessing environmental impact. The high impact of these materials underscores the importance of carefully examining alternatives during the design process to reduce the overall environmental impact of these barriers. This may include identifying substitute materials or optimizing the design to reduce the use of high-emission materials.

This study represents a significant step towards a deeper understanding of the environmental implications associated with LHNBs, providing a solid basis for future development in the design of more sustainable barriers. We are confident that the results and conclusions drawn can influence and guide informed and responsible decisions in the context of environmental sustainability, thus contributing to promoting positive progress towards a future characterized by greater environmental respect and fairness for future generations.

7. ACKNOWLEDGMENTS

Funded by the European Union. Views and opinions expressed are, however, those of the authors only and do not necessarily reflect those of the European Union or CINEA. Neither the European Union nor the granting authority can be held responsible for them.

8. REFERENCES

[1] UNI EN ISO 14025 (2010): requirements and guidelines for type III environmental labeling.

[2] UNI EN ISO 14040 (2006): general description of LCA concepts.

[3] UNI EN ISO 14044 (2006): incorporates the previous ISO 14041, 14042 and 14043. It defines the guidelines and provides practical information useful to the LCA operator.

[4] UNI EN 15804: Development framework regulation for the product category "construction product" and subsequent update to EN 15804:2012+A2:2019/AC:2021.

[5] UIC International Union of Raylways (2012): Rail Dampers, Acoustic Rail Grinding, Low Height Noise Barrier: https://img3.uic.org/IMG/pdf/2012_dampers_grinding_lowbarriers.pdf

[6] Environmental Footprint v. 3.1 - https://nexus.openlca.org/database/Environmental%20Footprints

[7] Ecoinvent v. 3.10 - https://ecoquery.ecoinvent.org/3.10/cutoff/search

[8] Strail: https://www.strail.de/en/strailastic-sound-protection/

[9] Simone Manfredi and Rana Pant – Joint Research Centre (JRC), Insitute for Environment and Sustainability (IES), Sustainability Assessment Unit (2011): Supporting Environmentally Sound Decision for Construction and Demolition (C&D) Waste Management: https://op.europa.eu/en/publication-detail/-/publication/5a4330e8-aed4-4bf6-8d92-8cb6ad7cceda/language-en

DOI: 10.61782/fa.2025.0519

FORUM ACUSTICUM EURONOISE 2025

LIFE SILENT: IMPLEMENTATION OF THE SOLUTIONS DEVELOPED IN THE PILOT SITE

Cinzia Giangrande[1*] **Marco Fantozzi**[1] **Simone Relandini**[1]
Laura Peruzzi[2]
[1] Rete Ferroviaria Italiana S.p.A., Rome, Italy
[2] ANAS S.p.A., Rome, Italy

ABSTRACT

This paper shows LIFE SILENT project – WP5, a European Community co-financed project which aims to find sustainable and eco-compatible solutions to reduce noise in complex urban situations, where different noise sources are present (especially roads and railways) in densely inhabited areas. The described activities are related to the project phase of developed solutions and to the following implementation in the test site which has been identified between the city of Rome and its international airport: a major highway and a primary railway are located very close to each other, and a hospital is just between them. The solutions which are been chosen are "at source" mitigation: a noise-reducing asphalt for the highway and a Low Height Noise Barrier (LHNB) for the railway. They will be further adapted to the specifics of the test site.
Nowadays, a noise measurement campaign has been completed, in order to identify the current sound levels at various receivers.

Keywords: *noise, railway, roads, mitigation.*

1. INTRODUCTION

According to the World Health Organization, 20% of the European population is exposed to noise levels above 65 dB(A) during the day [1]. Reducing noise levels is particularly complex in urban environments, where various noise sources coexist. In such contexts, noise mitigation generally excludes the use of solutions that could interfere with the urban context, such as traditional noise barriers, for many reasons, such as the proximity of receptors to the noise source, visual impact, etc.
To achieve these goals, the LIFE SILENT project [2][3] involves the development of innovative and sustainable noise-reducing pavements for road infrastructure and low-height noise barriers (LHNB) for railway infrastructure and testing in a test site, in order to provide transport infrastructure managers with information to support the dissemination of these technological solutions.

2. INNOVATIVE SOLUTIONS

Regarding noise-reducing pavements, during the LIFE SILENT project, the solution developed in the IASNAF [4] project will be optimized. It consists of a sustainable low-noise mixture enriched with functionalized cellulose fibers of plant origin, by replacing them with waste materials (packaging and textiles) to make the process more sustainable.
As for the low-height noise barrier (Fig. 1), it will be made with recycled materials appropriately shaped based on recent results in the field of metamaterials to achieve better sound-absorbing performance and greater durability. The proposed solution, thanks to its reduced height, will provide significant landscape integration, thus reducing the visual impact usually attributed to traditional noise barriers while maintaining acoustic effectiveness to be quantified based on boundary conditions.



Figure 1. Example of a low-height noise barrier (LHNB).

[*] ***Corresponding author***: c.giangrande@rfi.it
Copyright: *©2025 First author et al. This is an open-access article distributed under the terms of the Creative Commons Attribution 3.0 Unported License, which permits unrestricted use, distribution, and reproduction in any medium, provided the original author and source are credited.*

3. TEST SITE

The solutions developed and tested in the laboratory will be implemented in a test site located in a densely populated area (Muratella, Rome, Italy), which includes both roads and railways at close distance (see Fig. 2).



Figure 2. LIFE SILENT project test site.

Specifically, the identified area, which has about 150,000 inhabitants, is crossed by the Roma-Fiumicino airport railway line managed by RFI and the A91 highway managed by ANAS. The railway line is characterized by passenger traffic of over 70,000 trains/year with a maximum speed of 110 km/h, while the A91 highway is characterized by traffic flow of about 72,000 vehicles/day.
The pilot area mainly consists of residential buildings with 3-4 floors above ground at a short distance from the railway and highway. Additionally, there is the San Giovanni Battista hospital (see Fig. 3), located between the A91 highway and railway line.



Figure 3. San Giovanni Battista Hospital (aerial view).

According to the European Environmental Noise Directive 2002/49/EC (END), both infrastructures in the area must be acoustically mapped every five years and an Action Plan must be drawn up to define strategies and solutions to mitigate noise levels at receptors. The RFI Noise Remediation Plan (updated 2018), which also incorporates Action Plans, currently provides for two noise barriers in the investigation area measuring 385 and 704 meters long and 4 and 5 meters high along the railway line.
The mitigation measures provided by ANAS's Action Plan include noise-reducing pavement for an extension of 1.9 km and direct interventions at receptors. Additionally, there is already a 3-meter high noise barrier along the highway on the north side.

4. IMPLEMENTATION OF DEVELOPED SOLUTIONS

Prior to implementing developed solutions in the identified pilot site, some ex-ante evaluations will be carried out to set reference values against which to evaluate overall performance of new pavement and noise attenuation introduced by LHNB.
Specifically:

- Acoustic measurements of road pavements using Statistical Pass-by (SPB) [5] and Close Proximity (CPX) [6] techniques based on ISO 11819 standard to evaluate influence of existing pavement on traffic noise and calibrate source model. This evaluation will be carried out using Urban Pass-By Method developed within LIFE NEREiDE [7] project;
- Noise level measurements at receptors according to DM 16/03/1998 to calibrate propagation model;
- Texture and mechanical impedance measurements of road surface according to UNI CEN 13036-1 [8] and UNI EN ISO 7626-5 [9];
- Annoyance measurements of exposed population according to guidelines developed within LIFE NEREiDE project through psychoacoustic and social surveys. Zwicker descriptors defined by ISO 532-1 [10] and DIN 45692 [11] will be evaluated to determine psychological and physiological response of exposed population in terms of annoyance.

Based on inputs from measurement campaign, acoustic model will be calibrated and various scenarios simulated to map overall noise level and contributions from individual noise sources.
To facilitate monitoring of road section and make results robust and reliable over long term, pilot area has been equipped with DYNAMAP system [12], an automatic system capable of continuously measuring noise levels

and providing real-time acoustic maps developed within LIFE Dynamap project.
The sensor has been installed on a vertical road sign pole close to the A91 motorway and in proximity to the San Giovanni Battista Hospital (see Fig. 4).



Figure 4. Dynamap sensor installation.

Then follows a design phase supervised by road and railway infrastructure managers to ensure appropriate safety standards during which developed solutions will be adapted to specific test site requirements. A co-design approach will also be promoted to ensure citizen participation in development of these solutions for easier acceptance.

Finally, noise-reducing pavement will be laid along a highway section measuring 1.9 km and low-height noise barrier (LHNB) will be installed along a railway section measuring 200 m.

5. CONCLUSIONS

Preliminary activities are currently underway for developing identified innovative solutions and planning field activities for LIFE SILENT project.

5.1 Measurements of road pavements

Measurements using the Statistical Pass-By Method were carried out in January and February 2025, in a site close to the San Giovanni Battista Hospital near a Smart Pole of the Anas Smart Road project (see Fig. 5).
Measurements of the acoustic emission due to tyre/pavement interaction by means of Close-ProXimity (CPX) method, instead, were organized on 2-3 July 2024. The CPX measurements were carried out in the slow and fast lanes of both carriageways, eastbound towards Rome centre and westbound towards Fiumicino.



Figure 5. Statistical Pass-By set-up measurement.

For each road section investigated, at least three acquisition runs were carried out at the reference speed of 80 km/h.
On the road sections investigated there were different porous pavements, called in this report Ante Operam 1 (AO1), Ante Operam 2 (AO2) and Ante Operam 3 (AO3). Fig. 6 shows the instrumented vehicle used in the measurements.



Figure 6. CPX instrumented vehicle

In Table 1 the results obtained for the road sections investigated are shown. The reported LCPX values

represent the spatial average value over the section considered. For each of the investigated pavements, both the average LCPX level value for each run and the final average over all acquired runs are reported.

Table 1. Results obtained for the investigated pavements at the reference speed of 80 km/h.

Pavement	Lane	speed [km/h]	Run	East Direction		West direction	
				L_{CPX} for run [dB(A]	L_{CPX} (Average) [dB(A]	L_{CPX} for run [dB(A]	L_{CPX} (Average) [dB(A]
AO1	Slow	80	1	99.4	99.4 ± 1.0	99.6	99.8 ± 1.0
			2	99.1		99.8	
			3	99.8		100.0	
			4	99.4		96.0	
AO2	Slow	80	1	96.4	96.2 ± 1.2	96.1	96.0 ± 1.0
			2	95.5		96.0	
			3	96.3		101.5	
			4	96.5		101.6	
AO3	Slow	80	1	100.7	100.5 ± 1.1	101.4	101.5 ± 1.0
			2	100.6		97.8	
			3	100.7		98.1	
			4	99.9		98.1	
AO1	Fast	80	1	98.2	98.2 ± 1.0	95.7	98.0 ± 1.0
			2	98.2		95.6	
			3	98.2		95.7	
AO2	Fast	80	1	95.1	95.2 ± 1.0	102.3	95.7 ± 1.0
			2	95.3		102.1	
			3	95.1		102.2	
AO3	Fast	80	1	100.5	100.3 ± 1.0	99.6	102.2 ± 1.0
			2	100.1		99.8	
			3	100.3		100.0	

During data processing, the LCPX level was corrected for the reference air temperature and for the rubber hardness of the reference tyre as specified by the technical standards.
In addiction, at the same time, measurements of the road texture using a triangulation point profile sensor complaint with the requirements of ISO 13473 standards were carried out.
The texture measurements instead concerned only the slow lanes of both carriageways. Table 2 shows the results in terms of the MPD (Mean Profile Depth) indicator in the slow lane for the two directions analysed.

Table 2. Results obtained in terms of indicator MPD (Mean Profile Depth) for the investigated pavements.

Pavement	Direction	Lane	MPD
AO1	East	Slow	2.05 ± 0.32 mm
AO2	East	Slow	0.59 ± 0.10 mm
AO3	East	Slow	1.89 ± 0.17 mm
AO1	West	Slow	2.03 ± 0.22 mm
AO2	West	Slow	0.56 ± 0.09 mm
AO3	West	Slow	0.59 ± 0.12 mm

In a second stage, also texture and mechanical impedance measurements of road surface will be carried out to exploit the construction site built for the new pavement implementation.

5.2 Noise level measurements at receivers

Beside noise measurement at receptors to calibrate propagation model, a monitoring campaign has been organized in order to detect railway and road noise contribution.
The noise measurements were made according to the Decree of the Ministry of the Environment dated March 16, 1998, "Techniques for the detection and measurement of noise pollution."
"PR" measurement locations (Reference Points) for the characterization of source noise were positioned, in free-field conditions, close to the railway and road line. "PS" measurement locations (Significant Points) were placed at the receivers, in particular at the most exposed façade to railway noise, at the middle position between the two sources railway and highway and at a receiver affected only by road noise.
In Fig. 7 a map extract with the indication of the measurement locations is shown.



Figure 7. Measurement locations

Some pictures of the measurement campaign are shown in Fig. 8.
the results of the measurements are reported In Table 3.

Table 3. Noise measurements at reiceves results

Measurement Location	Leq,A [dBA] Day	Leq,A [dBA] Night
PR-1	63.2	55.4
PR-2	61.5	53.8
PR-3	61.4	57.3
PS-1	62.9	57.4
PS-2	58.9	55.0

PS-3	-	-
PS-4	65.2	61.8

at measurement location PS-3, individual train pass-bys could not be distinguished because of building ventilation and extraction system with predominant noise. Similarly, results at the measurement point PS-4 are affected by the presence of Via della Magliana close to the A91 motorway.



Figure 8. Measurements at receivers.

5.3 Annoyance measurements of exposed population

A questionnaire will be distributed and submitted to people present at a meeting with the president of the Municipality. Furthermore, on the same day it will be also distributed to families thanks to teachers of the school "I.C. Santa Beatrice - Plesso Santa Beatrice".

6. REFERENCES

[1] https://www.who.int/europe/news-room/fact-sheets/item/noise

[2] Project 101114310 – LIFE 2022-ENV-IT-LIFESILENT

[3] https://www.rfi.it/it/innovazione-e-ricerca/progetti/life-silent---sustainableinnovations-for-longlife-environmental.html

[4] Bellucci P., Bernardinetti P., Chidichimo G., Meli G., Praticò F. e Sartori C., *"Cellulose fibres for better performing road pavements", in "Atti del Convegno SURF 2022, The 9th Symposium on pavement surface characteristics"* (Milan, Italy) September 12/14, 2022.

[5] UNI EN ISO 11819-1:2004, Acustica - Misurazione dell'influenza delle superfici stradali sul rumore da traffico- Metodo statistico applicato al traffico passante.

[6] ISO/CD 11819-2:2011, Acoustics - Measurement of the influence of road surfaces on traffic noise - Part 2: The close-proximity method.

[7] LIFE15 ENV/IT/000268

[8] UNI EN 13036-1:2010, Caratteristiche superficiali delle pavimentazioni stradali ed aeroportuali - Metodi di prova - Parte 1: Misurazione della profondità della macrotessitura della superficie della pavimentazione tramite tecnica volumetrica ad impronta.

[9] ISO 7626-5:2019, Mechanical vibration and shock - Experimental determination of mechanical mobility - Part 5: Measurements using impact excitation with an exciter which is not attached to the structure.

[10] ISO 532-1:2017,Acoustics Methods for calculating loudness, Part 1: Zwicker method.

[11] DIN 45692, Measurement technique for the simulation of the auditory sensation of sharpness.

[12] https://life-dynamap.eu/it/

DOI: 10.61782/fa.2025.0349



FORUM ACUSTICUM
EURONOISE 2025

ENVIRONMENTAL NOISE REDUCTION USING GEOMETRIC GROUND SHAPING: RESULTS FROM SCALE MODEL EXPERIMENTS

Tom Shaked[1*] **Simon Fishkin**[1] **Alon Hauptman**[2]
Nir Fink[2]

[1] School of Architecture, Architectural Robotics and Construction Automation Lab, Ariel University, Ariel 40700, Israel.

[2] Department of Communication Disorders, Acoustics and Noise Research Lab in the Name of Laurent Levy, Ariel University, Ariel 40700, Israel

ABSTRACT

Noise pollution is a significant environmental and public health challenge, particularly near urban infrastructure such as highways and airports. Traditional mitigation methods, such as vertical barriers, often disrupt landscapes and ecosystems. Ground shaping, an innovative approach that modifies terrain to reduce noise propagation, remains largely unexplored despite its promising potential. Building on prior research that simulated its effectiveness, this study empirically evaluates the noise reduction performance of specific ground shapes. Using a 1:500 scale model in a controlled acoustic environment, a robotic arm was used to create precise three-dimensional ground forms. These forms were positioned between a noise source emitting broadband noise (100–16,000 Hz) at 65 dB SPL and a miniature microphone at a scaled distance equivalent to 425 meters. Results demonstrate that ground shapes reduce noise to varying degrees, with specific geometries achieving an average reduction of over 2.5 dB and a maximum exceeding 7.5 dB. These findings highlight the potential of ground shaping as a sustainable alternative to traditional noise mitigation, offering empirical support for its integration into urban and environmental planning while enhancing public health and minimizing ecological disruption.

*__Corresponding author__: tomsha@ariel.ac.il.

__Copyright__: ©2025 Tom Shaked et al. *This is an open-access article distributed under the terms of the Creative Commons Attribution 3.0 Unported License, which permits unrestricted use, distribution, and reproduction in any medium, provided the original author and source are credited.*

Keywords: *urban noise, ground forming, noise mitigation, robotic earthmoving, acoustics*

1. INTRODUCTION

Ground shaping, though potentially effective for noise reduction, has yet to be experimentally validated. Schiphol Airport in the Netherlands implemented a landscape design plan to combat noise through ground shaping, but its effectiveness remains largely unquantified due to the lack of specific experimental research [1]. Additionally, noise monitoring studies have highlighted the significant impact of aircraft noise on nearby communities [2].

Environmental acoustics software—such as SoundPLAN, CadnaA, TNM, Predictor-LimA, and IMMI—use standardized models (e.g., ISO 9613, CNOSSOS-EU, TNM) to predict noise levels and assess mitigation strategies like vertical barriers [3, 4]. While widely used in urban planning, these tools are not well-suited to simulate non-standard interventions like ground shaping, and often rely on idealized input data. As such, empirical measurements remain essential to capture site-specific effects and validate model assumptions.

This research aims to fill that gap by using robotic earthmoving and scale models to experimentally evaluate the noise reduction effectiveness of different ground forms in high-noise environments. Rather than relying solely on simulations, we focus on direct measurement to explore the acoustic potential of terrain shaping under controlled but realistic conditions.

1.1 Rationale

Ground forming involves reshaping terrain to influence environmental factors. This study aims to empirically evaluate its effectiveness in reducing urban noise levels near airports. It addresses a significant gap in current noise mitigation strategies by systematically exploring the relationship between ground shapes and noise reduction. The goal is to generate insights into terrain acoustics and contribute to the broader field of environmental acoustics, architecture, landscape design, and robotic earthmoving.

1.2 Novelty

Unlike traditional vertical noise barriers, ground forming offers a sustainable, landscape-friendly alternative that can simultaneously reduce noise and enhance urban spaces. This research employs robotic earthmoving to create specific ground shapes in a lab environment, allowing for precise experimental control and repeatability. By bridging simulation and reality, the study aims to enhance the reliability of noise reduction models and contribute valuable insights to environmental noise management.

2. STATE OF THE ART

This section reviews the current knowledge of environmental noise, urban noise mitigation methods, and the role of robotic earthmoving in noise reduction. The subsections focus on the challenges posed by noise pollution, existing mitigation strategies, and innovations using terrain shaping.

2.1 Environmental and Urban Noise

Environmental noise is a significant public health issue, contributing to a range of adverse health effects, including cardiovascular diseases, cognitive impairment, and sleep disturbance [5]. Long-term exposure to environmental noise is associated with increased risks of ischemic heart disease, hypertension, and mental health issues [6]. The World Health Organization (WHO) guidelines recommend road traffic noise levels not exceeding 53 dB Lden (day-evening-night average) to avoid adverse health effects, or 45 dB Lnight to prevent sleep disturbance [7].

Recent studies highlight the increasing issue of urban noise pollution and its impact on public health. Studies show that exposure to noise levels exceeding the WHO guidelines for road traffic noise has significant adverse effects. Despite the recognition of these risks, few studies explore outdoor noise reduction techniques beyond traditional barriers, especially in environments near airports and highways.

2.2 Urban Noise Mitigation Methods

Traditional mitigation techniques have predominantly focused on reducing indoor noise levels, with some outdoor solutions, like the use of vertical barriers, being common. These barriers are generally effective in reducing noise from road traffic, but they often disrupt the landscape, negatively impacting local ecosystems and human activities [7–9]. In urban settings, the deployment of vertical barriers often presents challenges, such as limiting land use and not integrating seamlessly into the landscape [10].

However, these approaches have been shown to reduce noise, with mixed effectiveness depending on design and context. Additionally, low-frequency noise from aircraft remains a major challenge for standard noise barriers [11]. A key problem with vertical barriers is that they limit land use and do not integrate well into the surrounding environment. Urban planners are now seeking alternatives that reduce noise while maintaining the aesthetic and environmental value of urban landscapes.

2.3 Robotic Earthmoving and Terrain Modification

Advancements in robotic earthmoving technology have significantly improved our ability to create precise and repeatable terrain modifications [12]. These robots have been employed in various soil manipulation tasks, including leveling, shifting, and piling [13]. The development of autonomous systems and mobile robotic platforms for earthworks has opened up new possibilities for large-scale, highly accurate terrain reshaping [14].

Recent research has demonstrated the use of robotic technologies for autonomous terrain manipulation. These technologies enable precise shaping of the landscape in a repeatable manner, allowing for highly controlled experimental testing [15]. Robotics in earthmoving allows researchers to produce ground shapes that can be tested for noise mitigation capabilities, ensuring accuracy and precision in experiments.

2.4 Recent Innovations in Noise Mitigation Using Ground Shaping

In addition to traditional vertical barriers, recent innovations have explored terrain modifications as a means to mitigate noise in outdoor environments. Previous studies

have shown that certain terrain shapes, like concave and convex forms, can significantly alter the propagation of sound waves, creating acoustic shadows that reduce noise exposure [16, 17]. These studies found that mounds with varying heights could reduce noise by up to 28 dB under ideal conditions, with larger terrain shapes achieving better results.

These studies demonstrated that altering the ground shape could help reduce the reflection of sound waves, with notable reductions in noise levels. Despite promising simulation results, there is a lack of empirical data validating these simulations in real-world settings.

2.5 Research Gaps

While simulation studies have made significant progress in predicting the potential benefits of terrain shaping for noise reduction, there is a lack of empirical validation in actual field environments. Key gaps in the research include: (1) a lack of direct comparisons between different ground shapes and their effectiveness in noise reduction across a range of frequencies; (2) insufficient exploration of how robotic technologies can be employed to create accurate ground forms for testing; and (3) limited understanding of how terrain modification can be effectively integrated into urban planning and landscape design. This research aims to fill these gaps by conducting scale model experiments with controlled acoustic conditions and robotic earthmoving technology, providing empirical data to validate the effectiveness of ground shaping for noise reduction.

3. OBJECTIVES AND SIGNIFICANCE

This study aims to empirically evaluate the effectiveness of ground shapes in reducing noise levels using scale model experiments that simulate real-world urban noise conditions. The key objectives include: (1) identifying the most effective ground forms for reducing noise in scale models; (2) analyzing the potential for applying these findings to full-scale outdoor scenarios; and (3) exploring how scale models and robotic technologies can advance our understanding of terrain-acoustic interactions.

The expected significance of this work lies in the development of more sustainable and integrated noise reduction strategies. By providing empirical validation for terrain shaping, the research offers a potential alternative to conventional vertical barriers—one that can be better integrated into urban planning and landscape design, with implications for future environmental policy.

4. METHODOLOGY

This section describes the experimental approach used to assess the effectiveness of different ground shapes in reducing noise. It covers the scale model setup, the robotic earthmoving process, and how noise attenuation is measured.

4.1 Experimental Setup

The experimental setup (seen in Fig. 1) uses a 1:500 scale model to replicate urban noise conditions, allowing controlled experimentation while maintaining key real-world acoustic interactions [18]. Ground shapes, including convex, concave, tri-convex, and random, were created using robotic earthmoving technology (see Fig. 2). Noise is generated using a speaker, and its attenuation along the shaped ground is measured using a high-precision microphone. This setup allows for controlled, repeatable experiments to assess the impact of different ground shapes on noise propagation.

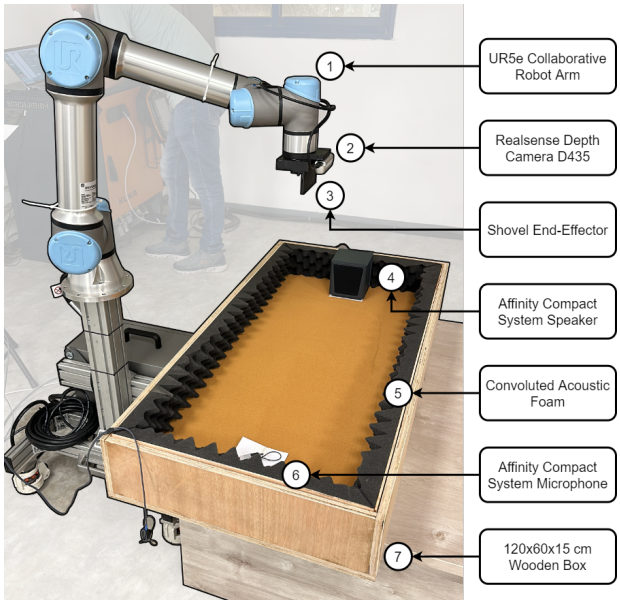


Figure 1: The experimental setup: (1) UR5e robot, (2) Intel RealSense D435 depth camera for 3D scans, (3) a custom 10×5 cm shovel for robotic earthmoving, (4) Interacoustics Affinity speaker (noise source), (5) convoluted acoustic foam , (6) Interacoustics Affinity microphone for noise measurement, and (7) a 120×60×15 cm box for the terrain model.

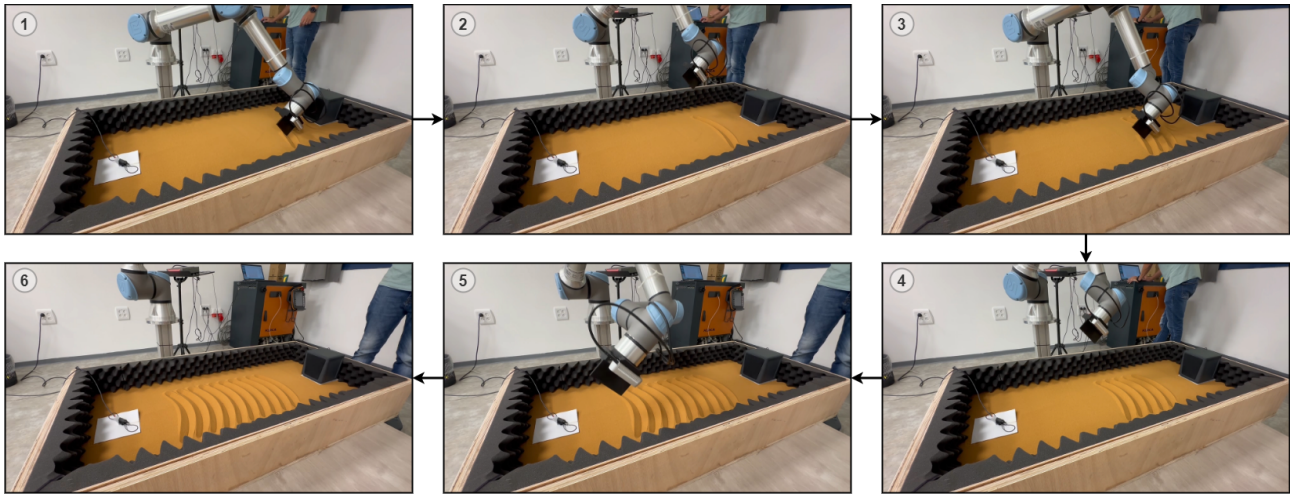


Figure 2: The robotic earthmoving process displayed on the Convex toolpath.

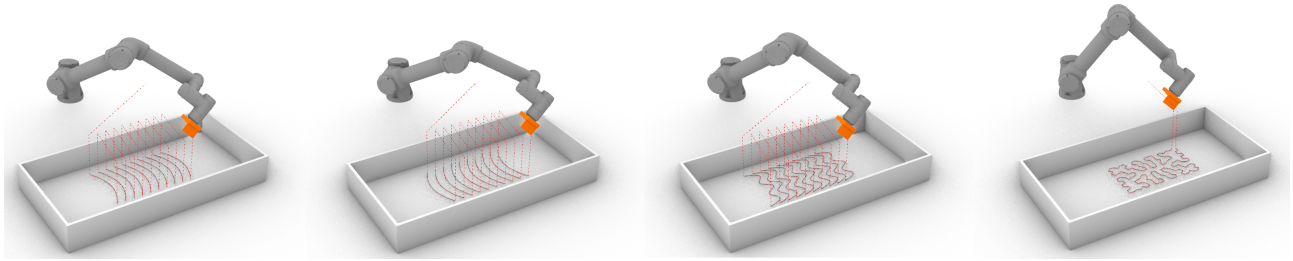


Figure 3: The robotic toolpaths designed for shaping ground forms (left to right): (a) Convex, (b) Concave, (c) Tri-Convex, (d) Random.



Figure 4: The resulting ground shapes (left to right): (a) Convex, (b) Concave, (c) Tri-Convex, (d) Random.

4.2 Robotic Earthmoving

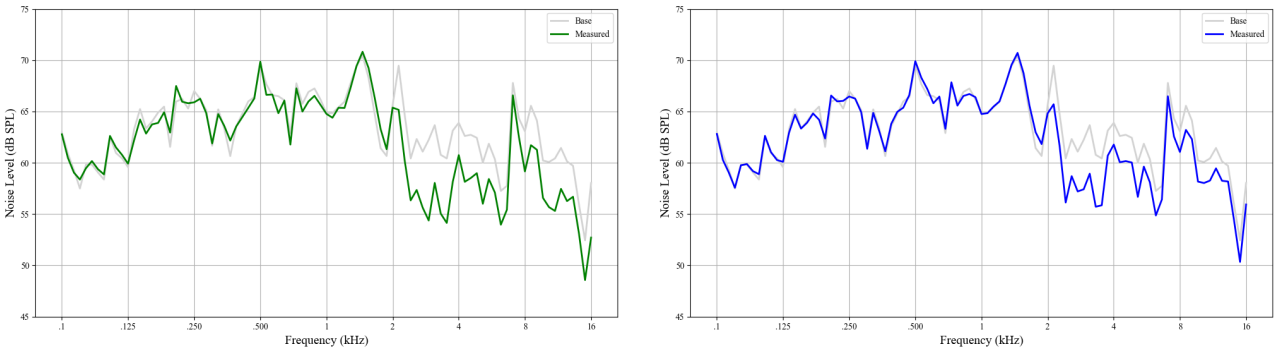
The robot was pre-programmed to produce each of the four geometries, following toolpaths corresponding to each shape (see Figs. 3–4). The terrain, consisting of sifted dry sand, was leveled using a custom tool before creating the next shape. To eliminate any other noise, all non-essential electronic equipment in the lab was turned off during measurements.

4.3 Noise Measurements

Each terrain geometry underwent five consecutive noise measurements to minimize variability and ensure robust data. The microphone was manually positioned at one end of the box, maintaining a fixed 85 cm distance from the speaker. An initial noise measurement, referred to as 'Base' in the graph, was performed on a leveled ground surface to provide a controlled baseline for comparison.

(a) Convex

(b) Concave



(c) Tri-Convex

(d) Random

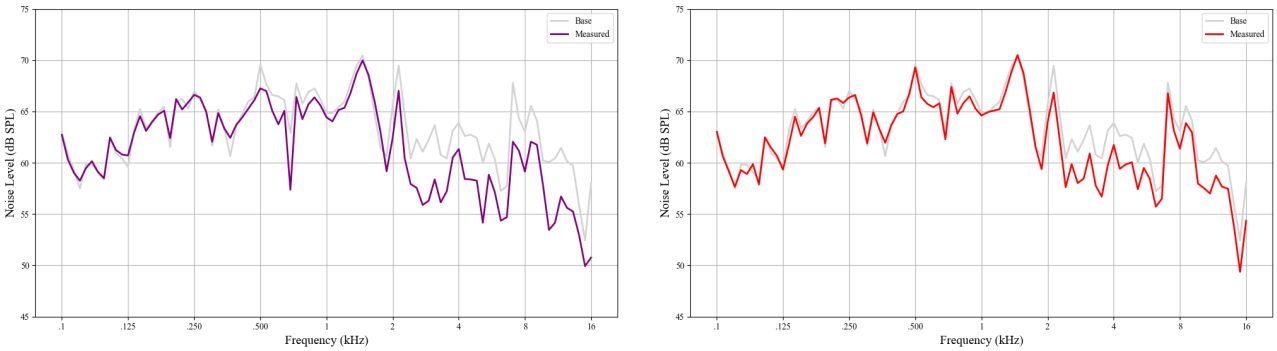


Figure 5: Noise attenuation for each tested ground shape compared to the 'Base' measurement (gray). Each plot illustrates the frequency-dependent noise reduction achieved by the specific terrain configuration.

5. RESULTS

All tested ground shapes showed a measurable reduction in noise level compared to the base especially for frequencies higher than 2kHz, with some proving more effective than others (see Table 1 and Figs. 5 and 6). Among the tested geometries, the concave shape achieved the greatest maximum reduction, with a 7.86 dB decrease in noise levels. The tri-convex shape followed closely with a maximum reduction of 7.27 dB, while convex and random shapes exhibited lower peak reductions of 5.06 dB and 3.77 dB, respectively.

The average attenuation values were calculated within the measurable frequency range of the setup (400–16,000 Hz). On average, the tri-convex shape reduced noise by 2.61 dB, followed by concave (2.37 dB), convex (1.55 dB), and random (1.55 dB). These results suggest that terrain shaping influences noise propagation, with the tri-convex shape providing the most consistent noise reduction, while the concave shape exhibited peak attenuation.

Table 1: Noise reduction summary for the tested ground shapes, showing the attenuation (Δ dB) relative to the base measurement.

Shape	Avg Δ (dB)	Max Δ (dB)
Convex	1.55	5.06
Concave	2.37	**7.86**
Tri-Convex	**2.61**	7.27
Random	1.55	3.77

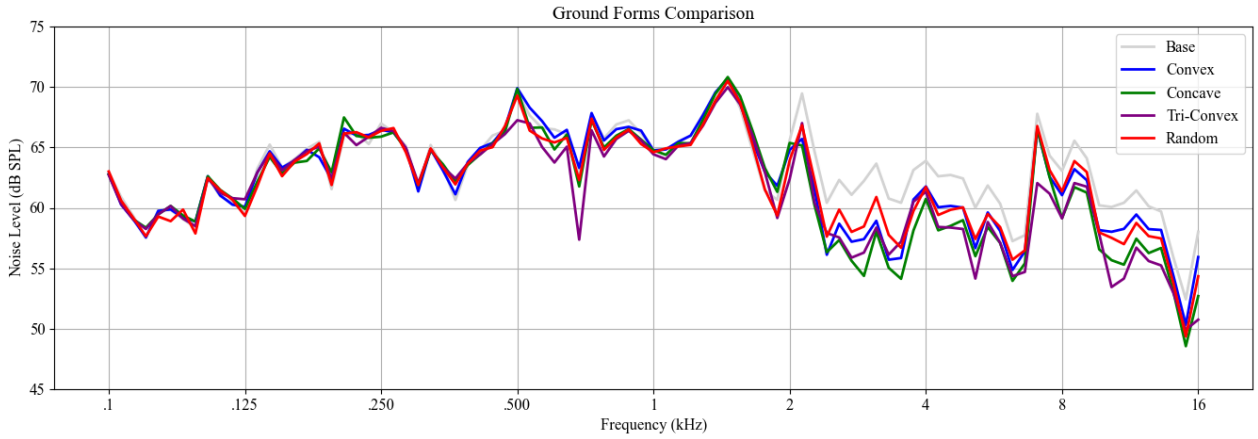


Figure 6: Comparison of noise attenuation across all tested ground shapes. The graph presents the frequency-dependent reductions in noise level relative to the 'Base' measurement, highlighting variations in attenuation effectiveness among the different geometries.

6. CONCLUSIONS

This study addresses a crucial gap in understanding how terrain modifications can mitigate urban noise. By using advanced robotic technologies to shape ground forms and validate their effectiveness through scale model experiments, the research offers a new approach to noise reduction.

While the findings provide valuable insights, three limitations should be noted: (1) the speaker–microphone distance constrains the measurement of frequencies below 400 Hz, as the corresponding wavelengths do not complete a full cycle within the setup; (2) the Sound-Level-Meter captures frequencies only up to 16,000 Hz, excluding higher frequencies that may be relevant in real-world conditions; and (3) although the tested ground shapes demonstrated measurable noise reduction, further exploration of alternative geometries—including variations in height and spacing—could enhance attenuation.

Future work will address these limitations by broadening the frequency range of analysis, scaling up experiments, and testing a wider range of geometric configurations. Nevertheless, the presented findings already demonstrate the potential of robotic earthmoving to precisely manipulate terrain for noise control. These insights may influence urban planning practices and environmental policies, offering a sustainable, landscape-integrated alternative to traditional noise barriers.

7. REFERENCES

[1] H+N+S Landscape Architects, "Land art park buitenschot," 2024. Accessed: 2025-03-12.

[2] A. Vidović, I. Štimac, and R. Zečević-Tadić, "Aircraft noise monitoring in function of flight safety and aircraft model determination," *Journal of advanced transportation*, vol. 2017, no. 1, p. 2850860, 2017.

[3] A. Balderrama, D. Arztmann, and J.-U. Schulz, "Review of commercial software tools for facade acoustics," *ce/papers*, vol. 4, no. 6, pp. 465–472, 2021.

[4] D. F. REMIGI, K. MATOGA, and S. MANISKOSA, "Gis: an essential tool for noise mapping," *International Journal of Innovations in Engineering Research and Technology*, vol. 6, no. 9, pp. 1–5.

[5] World Health Organization, "Environmental noise guidelines for the european region," 2019.

[6] S. Khomenko, M. Cirach, J. Barrera-Gómez, E. Pereira-Barboza, T. Iungman, N. Mueller, M. Foraster, C. Tonne, M. Thondoo, C. Jephcote, *et al.*, "Impact of road traffic noise on annoyance and preventable mortality in european cities: A health impact assessment," *Environment international*, vol. 162, p. 107160, 2022.

[7] M. Brink, B. Schäffer, R. Pieren, and J. M. Wunderli, "Conversion between noise exposure indicators

leq24h, lday, levening, lnight, ldn and lden: Principles and practical guidance," *International Journal of Hygiene and Environmental Health*, vol. 221, no. 1, pp. 54–63, 2018.

[8] B. Peters, "Integrating acoustic simulation in architectural design workflows: the fabpod meeting room prototype," *Simulation*, vol. 91, no. 9, pp. 787–808, 2015.

[9] S. Tashakkor, A. Chamani, M. A. Nadoushan, and M. Moshtaghie, "Acoustics in urban parks: Does the structure of narrow urban parks matter in designing a calmer urban landscape?," *Frontiers of Earth Science*, vol. 14, pp. 512–521, 2020.

[10] J. M. B. Morillas, G. R. Gozalo, D. M. González, P. A. Moraga, and R. Vílchez-Gómez, "Noise pollution and urban planning," *Current Pollution Reports*, vol. 4, no. 3, pp. 208–219, 2018.

[11] C. Bosschaart, A. Eisses, and F. van der Eerden, "A barrier for low frequency noise from starting aircraft: comparison between numerical and scale model results," in *INTER-NOISE and NOISE-CON Congress and Conference Proceedings*, vol. 2010, pp. 1305–1314, Institute of Noise Control Engineering, 2010.

[12] K. L. Bar-Sinai, T. Shaked, and A. Sprecher, "Informing grounds: A theoretical framework and iterative process for robotic groundscaping of remote sites," in *Ubiquity and autonomy-proceedings of the 39th annual conference of the association for computer aided design in architecture (ACADIA). CUMINCAD, Austin, TX, USA*, pp. 258–265, 2019.

[13] Y. Miron, C. Ross, Y. Goldfracht, C. Tessler, and D. Di Castro, "Towards autonomous grading in the real world," in *2022 IEEE/RSJ International Conference on Intelligent Robots and Systems (IROS)*, pp. 11940–11946, IEEE, 2022.

[14] T. Shaked and A. Degani, "Shepherd: A fabrication-oriented tool for simulation and control of mobile robotic platforms for collaborative earthworks," in *Proc. 41th Annu. Conf. Assoc. Comput. Aided Design Archit., Realignments, Toward Crit. Comput.(ACADIA)*, pp. 480–489, 2021.

[15] T. Shaked, K. L. Bar-Sinai, A. Meles-Braverman, O. Elmakis, and A. Degani, "Aggregate-forming planner for autonomous earth-moving," *IEEE Access*, vol. 11, pp. 118841–118848, 2023.

[16] K. L. Bar-Sinai, T. Shaked, E. S. Fettahoglu, J. Krimm, and B. Boucsein, "Embedding acoustic analysis in landscape architecture design processes: A case study of munich airport," *Buildings*, vol. 13, no. 1, p. 143, 2023.

[17] K. L. Bar-Sinai, T. Shaked, E. S. Fettahoglu, J. Krimm, E. Pestriakova, L. Kniazeva, S. Friedberg, and B. Boucsein, "Toward acoustic landscapes: A digital design workflow for embedding noise reduction in ground-forming," *Journal of Digital Landscape Architecture*, pp. 273–283, 2023.

[18] R. I. Emori and D. J. Schuring, *Scale Models in Engineering: Fundamentals and Applications*. Elsevier, 2013.

DOI:

Main theme: A05 Environmental Acoustics

Session A05.07 Outdoor sound propagation

Chair(s): L. Godinho, P. Amado Mendes

DOI: 10.61782/fa.2025.0764

FORUM ACUSTICUM EURONOISE 2025

SELF-SHIELDING WINDOWS : SCALE MODEL MEASUREMENTS AND NUMERICAL SIMULATIONS

Timothy Van Renterghem* **Pieter Thomas**
Ghent University, Department of Information Technology, WAVES research group, Technologiepark 126, Gent-Zwijnaarde B 9052, Belgium

ABSTRACT

The concept of self-shielding windows is introduced as an innovative approach to mitigate sound exposure in urban environments at the most exposed façade. Unlike conventional windows aligned parallel to the building façade, this study examines the sound pressure level exposure at windows oriented obliquely toward the sky. This configuration forces sound from street-level sources to diffract around convex elements before reaching the windows, resulting in reduced sound exposure. Additionally, these façade geometries promote a diffuse sound field within the street canyon, diminishing the influence of specular reflections from opposing façades. However, reflections and scattering from nearby elements may offset these benefits by increasing exposure levels. To elucidate the significance of these physical phenomena, scale model experiments were conducted with simplified triangular façade elements at varying angles and story heights. Especially at the higher stories, significant noise reduction was measured. The experimental findings were further validated by 3D full-wave numerical simulations, reinforcing confidence in both the accuracy of the scale model measurements and the reliability of the numerical predictions for optimizing façade elements.

Keywords: *urban sound propagation, street acoustics, environmental noise, building envelope design, scale model.*

1. INTRODUCTION

Street acoustics play a central role in urban sound propagation studies. Three main strategies can help limit noise exposure during propagation in streets: introducing absorption, implementing screening, or promoting diffusivity.
Since building materials are typically rigid or nearly so, achieving significant absorption with common materials is challenging. However, building envelope greening, such as non-ground-based green walls [1], is worth considering. The use of low-height screens has been shown effective [2][3], though they generally shield only a limited area. To maximize their noise-mitigating potential, incorporating some degree of absorption is recommended [3].
Promoting diffuse reflection is another effective approach. Studies have demonstrated its benefits for both longitudinal and cross-sectional sound propagation in streets [4][5]. Balconies along façades contribute to this effect [6][7]. With well-designed parapets, balconies can also provide direct shielding of the façade, though this differs from common practice, which often leaves gaps between the vertical and horizontal surfaces. Additionally, balconies enhance diffuse reflection. Due to their typical dimensions, they interact with lower-frequency sounds, which are more dominant in surface transport noise spectra.

2. SELF-SHIELDING WINDOWS

The concept of self-shielding windows is introduced here as an innovative approach to reduce noise exposure. Unlike conventional windows, which are aligned parallel to the building façade, these windows are oriented obliquely toward the sky. This configuration forces street-level sound to diffract around convex façade elements before reaching the windows, effectively reducing noise exposure. Additionally, these façade geometries enhance the diffusion

*Corresponding author: timothy.vanrenterghem@ugent.be
Copyright: ©2025 Timothy Van Renterghem et al. This is an open-access article distributed under the terms of the Creative Commons Attribution 3.0 Unported License, which permits unrestricted use, distribution, and reproduction in any medium, provided the original author and source are credited.

of sound within the street canyon, thereby minimizing the impact of specular reflections from opposing façades.
This concept was first introduced in Ref. [8] based on full-wave sound propagation simulations using a 2D approach, but validated with real-life sound measurements in street canyons [9]. It emerged from an exploration of both conventional and more inventive façade and street profiles to reduce road traffic noise exposure.
However, further studies on this specific building envelope geometry are needed to better understand the underlying physical mechanisms. Similar to the effects observed near balconies, reflections and scattering from higher-positioned elements could potentially offset the noise reduction benefits by increasing exposure levels. Therefore, further optimizations may be necessary to assess its feasibility for practical implementation

3. SCALE MODEL STUDY

3.1 Street geometry

A simple scale model of a street (length of 2450 mm) consisting of smooth plywood panels, with façade height of 910 mm and the distance between opposing façades of either 977 mm (no façade elements, perfectly rectangular cross-section) or 990 mm (with façade elements). Note that there is a slightly different street width in the reference situation for practical reasons. Foam blocks are used to terminate the street avoiding diffraction at its edges (see Fig. 1).

3.2 Sound source

The sound source (tweeter) is located in a strongly acoustically insulated box, hung below the bottom of the panel representing the street surface (see Fig. 1). The connection between the loudspeaker box and the street is by a cylindrical opening with diameter 10 mm. This setup should prevent all flanking transmissions. White noise sequences (of 30 seconds) were emitted by the tweeter with repetitions.

3.3 Microphones

Five type-1 ½ inch microphones were used for simultaneous measurements, one at the first floor at the left façade (only in the flat façade case, see Fig. 1), and 4 on top of each other along the right façade, all flush mounted. Given the execution of the measurements in a semi-anechoic room and having full control over the loudspeaker and its amplitude, high signal-to-noise ratios are obtained in this experiment.

3.4 Scale factor

Assuming a scale factor of 15, and taking into account the flat frequency range of a ½ inch microphone, the maximum sound frequency to be reached at full scale is 1330 Hz. Note that the scale model measurements are mainly intended for validation purposes, at least in this low frequency range. Nevertheless, the peak of road traffic rolling noise at moderate urban vehicle speeds is believed to be captured.



Figure 1. Scale model setup showing the surface sound source at street level, and the street canyon in absence of façade elements. In this work, focus is on the 4 flush mounted microphones along the right facade.

3.5 Façade elements

Isosceles triangular facade elements with external angles of 60°, 45° and 30° were used. In Fig. 2, the 60° outer angle configuration is shown, with triangles at both facades, and 4 microphones flush mounted at the elements' faces directed towards the sky, along the right façade.



Figure 2. Scale model showing a single configuration of 24 self-shielding façade elements (with 60° outer angles). Four microphones are visible along the right façade centrally positioned in the upwardly directed faces.

4. NUMERICAL SIMULATIONS

4.1 The 3D FDTD method

The explicit pressure-velocity finite-difference time-domain (FDTD) method is used, with staggered-in-place and staggered-in-time update schemes, modelling linear sound propagation in absence of air absorption. Acoustic pressures are located in the center of each computational cell, the particle velocities on the faces that border the cell. A lowest-order spatial and temporal discretization is used here. Perfectly matched layers (PML) are used to simulate an unbounded atmosphere where needed. All other surfaces are considered rigid. The interested reader is referred to Ref. [10] for a justification of these model choices.

For simplicity, the sound source is modelled as a point source in the centre of the first grid cell above the street surface. The receivers are similarly positioned in the centres of the first cells next to the flat façade or directly near the oblique face of the triangular elements. Although this involves reflections not present in the experimental scale model given the flush mounted microphones and the construction of a surface source, when comparing configurations in a relative way, as will be done here, such effects are expected to largely level out.

Grid spacing was equal to 5 mm, with a time step of 8.49 µs, leading to a Courant number equal to 1, ensuring numerical stability while minimizing computational cost and phase errors [10]. Optimized PMLs of 40 cells thick ensure near perfect reflection free boundaries. When imposing a limit of 10 computational cells per wavelength, the 1/3 octave band frequency of 6.3 kHz can be attained (scale model frequencies). Along the street length, a stretch of 2 m is modelled. Although there is a fine discretization in the model relative to the wave length, staircase effects cannot be excluded in case of oblique surfaces [11] which are prominent in this work.

4.2 Mirror source method

The FDTD simulations are accompanied with the mirror source method (see e.g. Ref. [4]), at least for the flat façade geometry. With this method, including higher frequencies comes naturally. Relevant parameters such as the number of mirror sources are increased until sound pressure level differences (see further) converged.

This technique is mainly used to assess the effect of small deviations from the exact positioning (but manually measured) of sources and receivers in the scale model.

5. RESULTS

5.1 Validation case 1 : Level differences between stories along flat façade

Figure 3 shows the differences in 1/3 octave band levels between the 4th floor and first floor microphone, in case of fully flat facades, along the right facade. The bunch of thin colored lines show mirror source simulations using a large number of combinations using small deviations on geometrical parameters such as street width and heights of the microphones.

The microphone capsule surface covers multiple FDTD grid cells, leading to significant variations in the actual exposure. To stabilize results, averaging over a receiver zones of 1.5 times the microphone diameter was performed. To some extent, this procedure also accounts for small deviations in exact positioning.

Starting from 400 Hz on, the scale model measurements, FDTD simulations and the mirror source approach are in good agreement. At high frequencies, small variations in exact positioning lead to strong level differences.

The peak at 315 Hz is almost perfectly predicted by the FDTD model. This peak is much more moderate with the mirror source model, potentially pointing at being related to diffraction of sound which is not modelled with the latter.

Note that the strong level difference peak at the 160 Hz 1/3 octave band only appears in the measurements, and might indicate a deficiency of the measurement setup (of unknown nature). When scaling up to real sound frequencies (so near 10 Hz at full scale), however, its relevance if very minor in environmental noise sources.

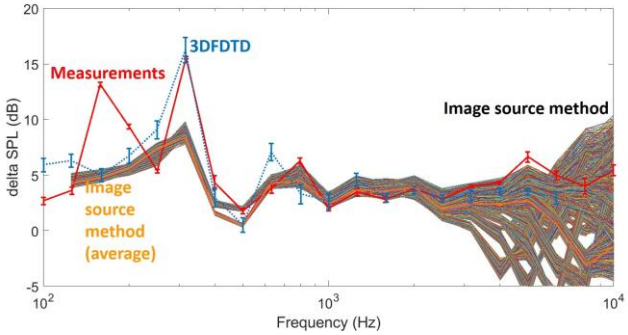


Figure 3. Measurements and simulations of the sound pressure level difference between the 4th and first floor microphone, for the flat façade case.

5.2 Validation case 2 : Self-shielding window insertion losses

In Fig. 4, measured and predicted insertion loss spectra are presented. The 3D full wave simulations are in adequate agreement with the measurements and give confidence on both the measurements performed and the numerical simulations.

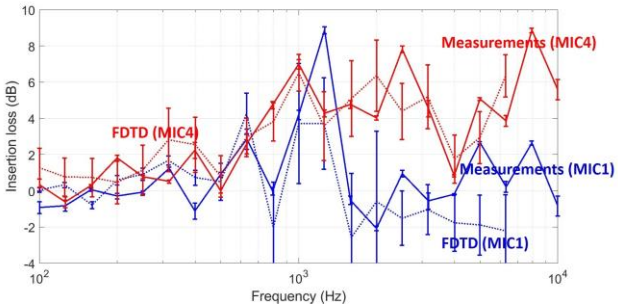


Figure 4. Measurements (full lines) and FDTD simulations (dashed lines) of the insertion losses at the 4th (MIC4) and first (MIC1) floor due to inclusion of 24 triangular elements (with 45° outer angles). The total length of the errorbars equals two times the standard deviation.

Note that simulating the insertion losses involves shifts in interference patterns, making it hard to correctly model the amplitude of these peaks. Further note that the microphones were placed in the middle of the oblique face pointing upwards, so microphone height relative to the street surface is not exactly the same as in the flat façade configuration. Another difference is that the street width in the flat façade situation is slightly lower than in the configuration including triangular façade elements. The large errorbars on the simulations further show that small shifts in receiver position can lead to large differences in insertion loss.

5.3 Element shape

In Fig. 5, insertion loss spectra with different outer angles are shown at the 4th floor, where effects are largest. A 60° outer angle involves smaller façade elements, and consequently, the position of the window pane stays closer to the flat façade configuration. At scale model sound frequencies between 10 kHz and 20 kHz (660 Hz and 1330 Hz at full scale), level reductions exceeding 8 dB (30°), between 6 dB and 8 dB (45°) and between 2 dB and 4 dB (60°) are measured.

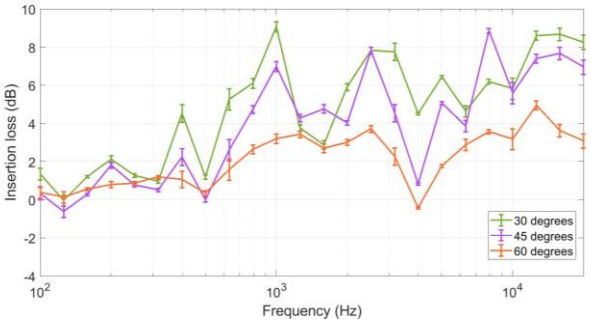


Figure 5. Measurements of the insertion losses at the 4th floor due to inclusion of 24 triangular elements with different outer angles.

5.4 Number of elements

Compared to the influence of the outer angles of the façade elements as discussed in Section 5.3, the effect of the number of elements is limited as becomes clear in Fig. 6. The neighboring columns of elements at the right façade (12 elements relative to 4 elements) hardly influence the insertion loss along the central column where the microphones were placed. This means that for the current setup scattering by these side elements do not influence the exposure levels.

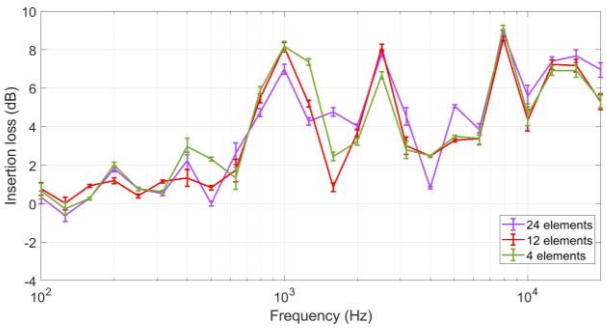


Figure 6. Measurements of the insertion losses at the 4th floor due to inclusion of an increasing number of triangular elements (45°). The case with 24 elements is the one shown in Fig. 2, “12 elements” only has elements along the right façade (with the left façade fully flat), and “4 elements” means a single column of elements on the right facade (with the left façade fully flat).

In the higher sound frequency range (above 10 kHz, at scale), the presence of elements along the left façade leads to a small increase in insertion loss, likely by limiting specular sound paths reaching the upper microphone.

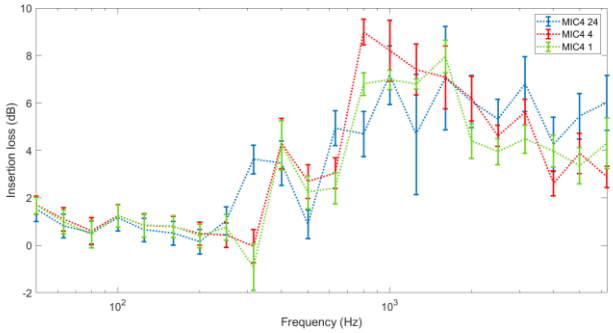


Figure 7. Simulated insertion losses with FDTD at the 4th floor due to inclusion of an increasing number of triangular elements (30°). The case with 24 elements is the one shown in Fig. 2, "4 elements" means a single column of elements at the right façade only (left façade fully flat), and "1 element" means a single element at the right façade (where the microphone is located) with the left façade fully flat.

Analysis of Figs. 7 and 8 indicate different behavior at the 4th floor (top floor) and second floor microphone with relation to the number of façade elements. At the top floor microphone, no elements are present above. Above 2 kHz (130 Hz at full scale) 24 elements lead to the highest insertion losses overall. Preventing specular reflections from the left façade leads to a significant reduction in exposure levels as can be concluded when comparing 24 elements to 4 elements.

Using 4 elements gives a slightly higher insertion loss than when only using a single element, although given the peaky behavior, this does not hold for any frequency. This might point at a second order effect where also specular reflections from the right façade are prevented. Overall, given that many reflections contribute to the sound pressure level at the higher stories, a large number of façade elements seems beneficial.

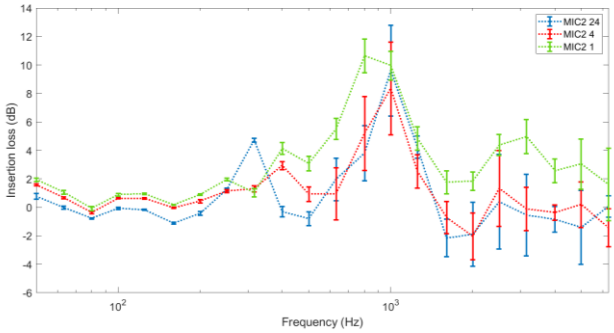


Figure 8. See caption of Fig. 7, but now for the microphone at the second floor.

At the lower stories (here second floor), a single element is clearly the optimum, only allowing for direct shielding. Note that the effect is quite pronounced since an outer angle of 30° leads to rather large façade elements. When having 2 elements on top and one below (so 4 elements in a single column along the right facade), multiple scattering and reflections tend to limit the insertion loss. Adding elements to the left façade (24 elements) does not impact the insertion losses relative to 4 elements.

6. CONCLUSIONS AND OUTLOOK

The concept of self-shielding windows presents a promising noise mitigation solution for the most exposed façades in urban streets. This approach is particularly effective at higher floors, where it can achieve substantial noise reduction compared to fully flat façades. Notably, the greatest improvements occur in key frequency ranges associated with common transport noise sources.

The design of individual elements plays a crucial role in achieving significant noise reduction, as demonstrated by studying triangular elements with varying angles in the current work. At higher stories, interactions with other elements help reduce the intensity of specular sound paths, enhancing overall effectiveness. At lower stories, these interactions mitigate insertion losses due to scattering and reflections from higher positioned elements

Scale model measurements, combined with full-wave 3D numerical simulations, confirm that the simulations accurately capture the underlying physics. Moreover, they validate the precision of the measurements, which is an equally challenging task. Predicting insertion losses in such environments is particularly complex, as pronounced interference shifts create a highly variable spectral response, making it very difficult to fully model their magnitudes.

The numerical model enables further optimizations without the need for labor-intensive scale model measurements. Continued research is required to enhance the architectural quality of the simplified triangular façade elements used in this study while considering cost-effectiveness and the potential integration of thermal performance.

7. ACKNOWLEDGMENTS

The authors are grateful to master thesis students Jules Bastiaensen and Joren Goeteyn for initiating the practical work on the scale model.

8. REFERENCES

[1] T. Van Renterghem, M. Hornikx, J. Forssen, and D. Botteldooren: "The potential of building envelope greening to achieve quietness," *Building and Environment*, 61, pp. 34-44, 2013.

[2] P. Thorsson: "Optimisation of low-height noise barriers using the equivalent sources method," *Acta Acustica united with Acustica*, 86, pp. 811-820, 2000.

[3] T. Van Renterghem, M. Hornikx, Y. Smyrnova, P. Jean, J. Kang, D. Botteldooren, and J. Defrance: "Road traffic noise reduction by vegetated low noise barriers in urban streets," in *Proc. of the 9th European conf. on noise control*, (Prague, Czech Republic), 2012.

[4] J. Kang: "Sound propagation in street canyons: Comparison between diffusely and geometrically reflecting boundaries," *Journal of the Acoustical Society of America*, 107, pp. 1394-1404, 2000.

[5] H. Onaga, and J. Rindel: "Acoustic characteristics of urban streets in relation to scattering caused by building facades," *Applied Acoustics*, 68, pp. 310-325, 2007.

[6] D. Hothersall, K. Horoshenkov, and S. Mercy: "Numerical modelling of the sound field near a tall building with balconies near a road," *Journal of Sound and Vibration*, 198, pp. 507-515, 1996.

[7] P. J. Lee, Y. H. Kim, J. Y. Jeon, and K. D. Song: "Effects of apartment building facade and balcony design on the reduction of exterior noise," *Building and Environment*, 42, pp. 3517-3528, 2007.

[8] G. Echevarria-Sanchez, T. Van Renterghem, P. Thomas, and D. Botteldooren: "The effect of street canyon design on traffic noise exposure along roads," *Building and Environment*, 97, pp. 96-110, 2016.

[9] P. Thomas, T. Van Renterghem, E. De Boeck, L. Dragonetti, and D. Botteldooren: "Reverberation-based urban street sound level prediction," *Journal of the Acoustical Society of America*, 133, pp. 3929-3939, 2013.

[10] T. Van Renterghem: "Efficient outdoor sound propagation modeling with the finite-difference time-domain (FDTD) method: a review," *International Journal of Aeroacoustics*, 13, pp. 385-404, 2014.

[11] J. Häggblad, and O. Runborg: "Accuracy of staircase approximations in finite-difference methods for wave propagation," *Numerische Mathematik*, 128, pp. 741-771, 2014.

DOI: 10.61782/fa.2025.0691

FORUM ACUSTICUM EURONOISE 2025

PREDICTING THE EFFECTS OF GROUND IMPEDANCE IN LONG-RANGE LOW-FREQUENCY PROPAGATION WITH THE SEMI-ANALYTIC FINITE-ELEMENT (SAFE) METHOD.

Rafael Castro Mota[1,2*] **Paul Williams**[3] **Ray Kirby**[4] **Stefan Jacob**[1,2]
[1] Physikalisch-Technische Bundesanstalt, Braunschweig, Germany
[2] Technische Universität Braunschweig, Braunschweig, Germany
[3] University of Technology Sydney, Sydney, Australia
[4] RMIT University, Melbourne, Australia

ABSTRACT

The outdoor propagation of infrasound can be impacted by atmospheric conditions, such as temperature inversions and winds, that channel sound into acoustic waveguides allowing for efficient long-range propagation. For near ground acoustic waveguides, ground impedance can also play an important role. In this study, the Semi-Analytic Finite Element (SAFE) method is used to predict the acoustic field generated by a point source emitting into a stratified, range independent atmosphere with a logarithmic wind profile. We study the influence of ground impedance by setting two cases with different ground boundary conditions: a fully reflective ground condition, mimicking sea propagation; and an impedance ground boundary condition, mimicking a sandy landscape. We found a significant contrast in the two test cases for the near-ground acoustic waveguides, especially for a particular near-ground acoustic mode. Thus, ground impedance should be included in predictions

Keywords: *low-frequency sound, outdoor propagation, normal-mode methods*

[*]***Corresponding author***: *rafael.castro-mota@ptb.de*
Copyright: *©2025 First author et al. This is an open-access article distributed under the terms of the Creative Commons Attribution 3.0 Unported License, which permits unrestricted use, distribution, and reproduction in any medium, provided the original author and source are credited.*

1. INTRODUCTION

The outdoor propagation of infrasound can be impacted by atmospheric conditions, such as temperature inversions and winds. By refracting sound downwards, acoustic energy gets channeled into acoustic waveguides, reducing geometric spreading. Lower frequencies, notably infrasound, which experience decreased atmospheric damping, can travel efficiently inside these ducts, leading to increased sound pressure levels down-range of an emitter. For highly refracting conditions, near-ground waveguides can be dominant features in the acoustic field and, due to their interaction with the ground, be influenced by the acoustic behavior of this surface.

Large energy converters such as wind turbines and biogas power plants are possible emitters in the lower frequency spectrum and, when installed next to populated areas, raise concerns regarding exposure levels and annoyance. Accurate prediction of the noise levels at these locations is important and depends on a good understanding of the influence of the ground surface on the acoustic field.
Numerical predictions for the outdoor propagation of sound tend to either be heavy, due to large domain size, or rely on approximations, to reduce computational costs. The semi analytical finite-element (SAFE) method has been introduced by Kirby as an alternative to PEs to model outdoor sound propagation for range-independent domains [1], [2]. The procedure translates the acoustic field into a set of vertical atmospheric acoustic modes, propagating in the down-range direction. The method was originally introduced by Waxler [3] with numerical solutions for modes based on

an approximate wave equation. Using the SAFE method enables the solution of the exact governing equations with arbitrary atmospheric profiles while being able to accommodate a range-independent Ingard-Myers impedance boundary condition at the ground level [2]. The SAFE method has been tested against analytic solutions [1] and validated against test cases computed with the direct numerical computations of the Linearized Euler Equations [4]. It has also been shown to be particularly efficient for highly refracting atmospheres, requiring a limited number of modes for accurate near-ground far-field predictions [5].

In this study, the Semi-Analytic Finite-Element (SAFE) method is used to predict the acoustic field generated by a point source emitting into a stratified, range-independent atmosphere with a logarithmic wind profile. We study the influence of ground impedance by setting two cases with different ground boundary conditions: a fully reflective ground condition, mimicking sea propagation; and an impedance ground boundary condition, mimicking a sandy landscape. In the downwind direction, we found a significant contrast for the near-ground acoustic waveguides while the acoustic field at higher altitudes is significantly less affected. We conclude that ground impedance should be included in near-ground predictions as it plays an important part in both amplitude and distribution of sound pressure levels.

2. SAFE METHOD

The SAFE method is derived and discussed with more extent in [1], [2]. A short description is given here.

The method starts with an accurate pressure equation for acoustic waves propagating in stratified, range-independent atmospheres for frequencies above the Brunt-Väisälä limit, nominally 0.05 Hz (from [6], Eq. 2.58).

$$\left[\frac{1}{c^2}D_t^3 - D_t\left(\frac{\partial^2}{\partial x^2}+\frac{\partial^2}{\partial z^2}+2\tilde{g}\,\frac{\partial}{\partial z}+\tilde{g}^2-\frac{2\tilde{g}}{c}\frac{\partial c}{\partial z}\right)+ 2\frac{\partial u_0}{\partial z}\frac{\partial}{\partial x}\left(\tilde{g}+\frac{\partial}{\partial z}\right)+\left(2\tilde{g}+\frac{1}{\rho}\frac{\partial \rho_0}{\partial z}\right)D_t\left(\tilde{g}+\frac{\partial}{\partial z}\right)\right]p' = \rho D_t^2 Q, \quad (1)$$

where p' is the acoustic pressure, ρ' is the acoustic density, u_0 is the background velocity in the range direction (x), $\tilde{g}$ is the acceleration of gravity divided by the speed of sound squared ($\tilde{g} = \frac{g}{c^2}$), Q is a mass source, $D_t = (\frac{\partial}{\partial t} + u_0\frac{\partial}{\partial t})$, x denotes the range coordinate, z the height coordinate and t denotes time. This two-dimensional equation results from assuming a stratified atmosphere in a linearized two-dimensional Euler equation

$$\begin{cases} \frac{d\rho'}{dt} + (V'\cdot\nabla)\rho_0 + \rho_0\nabla\cdot V' + \rho'\nabla\cdot V_0 = \rho_0 Q \\ \frac{dV'}{dt} + (V'\cdot\nabla)V_0 + \frac{1}{\rho_0}\nabla p' - \frac{\rho'\nabla p_0}{\rho} = F \\ \frac{ds'}{dt} + (V'\cdot\nabla)s_0 = 0 \end{cases}, \quad (2)$$

with F being a force source, (ρ_0, p_0, V_0) being quantities related to the background field, namely, density, pressure and velocity, and (ρ', p', V') the same quantities for the acoustic field.

The pressure field may be expressed as a sum of range propagating vertical modes, following the Ansatz

$$p'(x,z,t) = \sum_{n=1}^{\infty} A_n p_n(z) e^{iwt - ik_0\gamma_n x}, \quad (3)$$

where A is the complex mode amplitude, p_n are the mode shapes, k_0 is the reference wave number and γ_n are the eigenvalues associated with the mode shapes. Equation 1 then turns into an eigenvalue problem in the height coordinate

$$+k^2[1-\gamma M]^3 p' + [1+\gamma M]\left\{\left(\tilde{g}^2 - \frac{2\tilde{g}}{c}\frac{\partial c}{\partial z}\right) + 2\tilde{g}\frac{\partial}{\partial z} + \frac{\partial^2}{\partial z^2} - k_0^2\gamma^2\right\}p' + 2\gamma\frac{\partial M}{\partial z}\left(\tilde{g}+\frac{\partial}{\partial z}\right)p' - \left[2\tilde{g} + \frac{1}{\rho}\frac{\rho}{\partial z}\right][1-\gamma M]\left(\tilde{g}+\frac{\partial}{\partial z}\right)p' = 0, \quad (4)$$

with M being the Mach number [4,5].
Equation 4 can be solved using the finite-element method and an eigen solver. The ground impedance ($\tilde{Z}$) is set on the finite-element approximation by following the steps in [2] and using the Ingard-Myers boundary condition expressed as a function of purely acoustic pressure.

$$\frac{\partial p'(0)}{\partial z} = \left[\frac{ik_0}{\tilde{Z}}(1-\gamma M_0)^2 + \tilde{g}_0\right]p'(0), \quad (4)$$

For the test cases shown here, we use an in-house FE solver, based on quadratic elements and the *eig* function from the scientific Python package *numpy*. More details about the method and the weak formulation of the eigenvalue problem are available in Refs [1], [2].

The modes' amplitudes are computed by employing a vertical mode matching scheme that was derived to mimic

a harmonic point source. Details about the mode matching can again be found in Refs [1], [2].

3. RESULTS

We computed two cases with the same atmospheric conditions: $u_0 = 2.33 \cdot \ln(1 + 2.3z), v_0 = 0,$ $t_0 = 293.15\,K,$ $\rho_0 = 1.23\,Kg/m^3,$ and $p_0 = 1\,atm;$ and different ground impedances, namely: a fully reflective ground surface ($\tilde{Z} = \infty$), mimicking sea propagation; and an impedance ground boundary condition ($\tilde{Z} = 38.79 - 38.41i$), mimicking a sandy landscape. For both test cases, the acoustic field was excited via a 10 Hz point source placed at the origin of the range coordinate and at height of 100m.

Figures 1.a) and 1.b) show a normalized pressure contour plot for both scenarios. The acoustic pressure has been normalized with the maximum recorded acoustic pressure for each. Downwind from the source, the plots show significant differences close to the ground, whereby the lower-altitude acoustic waveguide visible in Figure 1.a) is not evident in Figure 1.b). Below 250m, the remaining acoustic features related to atmospheric ducting are visible in both plots, having more contrast in Figure 1.a). For higher altitudes, both plots are qualitatively very similar. In the upwind direction, the acoustic field seems to not have been significantly affected by the difference in ground impedance.

The acoustic transmission, at the heights of, respectively, 1.8m and 500m, is plotted in Figures 1.c) and 1.d), along a range extending from -5km to 20km. At each height, the results for the two ground impedances are presented with the maximum recorded acoustic pressure being used as a reference. In Figure 1.c), the transmission recorded at 1.8m is evidently affected by the addiction of a ground-impedance, with a clear alteration in the downwind near-ground ducted pattern, being starker for the fully reflective ground surface. The acoustic field appears as more dampened for the sandy landscape scenario. Figure 1.d) indicates a quantitively similar transmission between both scenarios at an altitude of 500 m. At both heights, results in the upwind direction are similar.

Having noted a more prevalent effect on the near-ground acoustic field of the ground impedance change, five modes have been selected. These are modes that are important to the far-field (low dampening) and concentrate at least 15 per cent of their energy (signal energy) below 250 m. Figures 1.c) and 1.d) show that while these modes are not sufficient for an accurate prediction, at 500m, they provide good results for the near-ground far field, where the field is more affected by the change in impedance.

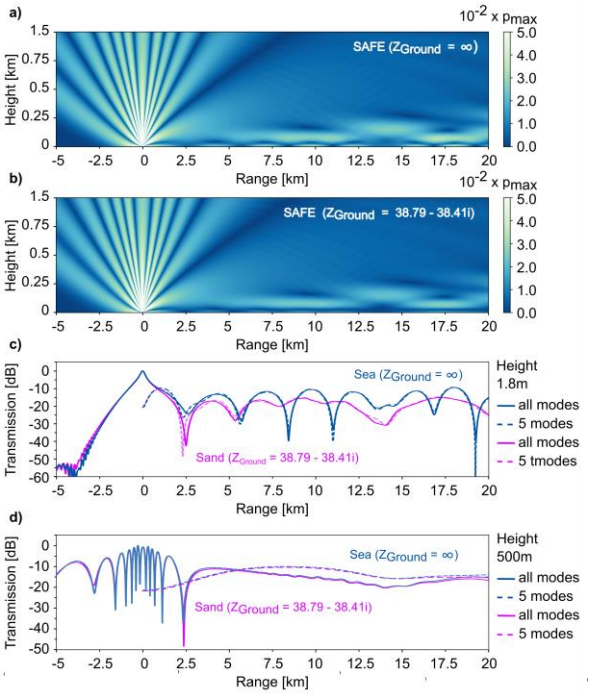


Figure 1. Normalized pressure contours of a point source radiating sound at 10 Hz in a atmosphere with a logarithmic wind profile and constant temperature and pressure for a) a fully reflective sea surface and b) a sandy landscape ($\tilde{Z} = 38.79 - 38.41i$). Transmission Loss along a horizontal line at a height of c) 1.8 m, d) 500m.

With the near-ground far-field prediction reduced to five propagating modes, a mode decay plot for each of the two cases is shown, respectively, in Figures 2.a) and 2.b). The modes have been paired up by how close their real parts are and given a numbering. Comparing the two figures, mode 5 seems to have been, by far, the most affected by the change in ground impedance. By looking at Figure 1.c), where the real and imaginary parts have been plotted for each case, one can check that the energy of the mode is highly concentrated near the ground and that the overall modal shape has not been severely altered. The respective eigenvalues of 0.972860-0.000996j (sand) and 0.971968-

1.205441e-06j (sea) also show that the phase-speed of the mode (real part), has almost been retained, with the attenuation of the mode (imaginary part) having been significantly increased.

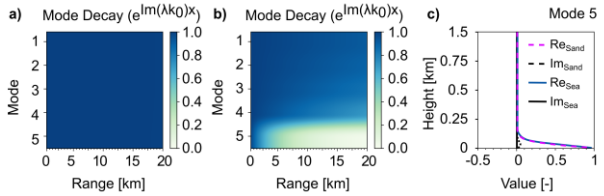


Figure 2. Modal decay plot for a) sea and b) sandy surface and a logarithmic wind profile. c) The real and imaginary parts for the 5th mode in the sea and sand surface test cases.

4. FINAL COMMENTS AND CONCLUSIONS

The purpose of this paper was to dwell into the influence of ground acoustic impedance for acoustic propagation in a highly refracting atmosphere. We did this by comparing the results of the SAFE method in two different test scenarios, each with the same atmosphere with a logarithmic wind profile and a different ground impedance: the 1st variation mimicking propagation along a fully reflective sea surface and the 2nd along a sandy landscape. Downwind from the source, the computations showed a significant change in the near-ground acoustic field, indicating a strong dampening of acoustic modes closer to the ground. Apart from the near-ground field, the acoustic field below 250m seems less sensitive to the change, with the same patterns in the contour plots being visible. Upwind from the source, we speculate that the upward refracting effect of the atmosphere contributed to a clear insensitivity to the change in ground impedance. The results for the higher altitudes in both directions presented themselves as almost unchanged. By reducing the modal base down to five modes, we deciphered that one mode was particularly affected by the change in ground impedance. We conclude that, in the context of highly refracting atmospheres, ground impedance plays a bigger role in near-ground predictions and that a limited number of modes, with most of its energy near the ground, experience noticeable changes. This result appears to indicate that there might be a reduction in complexity for predicting acoustic in highly-refracting atmospheres with ground impedances jumps by focusing the analysis on the more affected modes.

5. ACKNOWLEDGMENTS

This research is funded by the Deutsche Forschungsgemeinschaft (DFG, German Research Foundation) – JA 3325/2-1“

6. REFERENCES

[1] R. Kirby, “Atmospheric sound propagation in a stratified moving media: Application of the semi analytic finite element method,” *J. Acoust. Soc. Am.*, vol. 148, no. 6, pp. 3737–3750, Dec. 2020, doi: 10.1121/10.0002912.

[2] R. Kirby, “Atmospheric sound propagation in a moving fluid above an impedance plane: Application of the semi-analytic finite element method,” *J. Acoust. Soc. Am.*, vol. 149, no. 2, pp. 1285–1295, Feb. 2021, doi: 10.1121/10.0003567.

[3] R. Waxler, J. Assink, and D. Velea, “Modal expansions for infrasound propagation and their implications for ground-to-ground propagation,” *J. Acoust. Soc. Am.*, vol. 141, no. 2, pp. 1290–1307, Feb. 2017, doi: 10.1121/1.4976067.

[4] R. MOTA, R. KIRBY, P. WILLIAMS, and S. JACOB, “Efficient modeling of atmospheric infrasound propagation with the Semi-Analytical-Finite-Element (SAFE) method,” *INTER-NOISE NOISE-CON Congr. Conf. Proc.*, vol. 270, pp. 2711–2718, Oct. 2024, doi: 10.3397/IN_2024_3223.

[5] R. Castro Mota, R. Kirby, P. Williams, and S. Jacob, “Modelling Low-Frequency Sound Propagation in a Ducted Atmosphere Using a Semi-Analytic Finite-Element Method,” in *Proceedings of Acoustics 2024*, Gold Coast, Australia, Nov. 2024.

[6] V. Ostashev and D. Wilson, *Acoustics in Moving Inhomogeneous Media, Taylor & Francis (2015).*, 2nd ed. Taylor & Francis, 2015. [Online]. Available: https://doi.org/10.1201/b18922

DOI: 10.61782/fa.2025.0462



FORUM ACUSTICUM
EURONOISE 2025

IMPROVEMENTS IN MEASURING ACOUSTIC IMPEDANCE OF OUTDOOR GROUND SURFACES

Andreas Fuchs **Manfred Haider**
AIT Austrian Institute of Technology GmbH, Transportation Infrastructure Technologies.

ABSTRACT

The acoustic impedance of a ground surface has an influence on sound propagation over long distances and therefore needs to be known to predict the sound imissions for residents suffering from transport noise. In the Commission Directive (EU) 2015/996 (CNOSSOS-EU) as well as in more detailed methods (e.g. NORD2000), a classification of flow resistivity is given for various ground surfaces. In Nordtest NT ACOU 104:1999 a suitable measurement method for measuring ground surface absorption is described. In this work, the setup of NT ACOU 104 is combined with modern approaches to signal processing and analysis. Quarterly measurements were carried out at eight locations in which the impulse responses between the loudspeaker and microphones were measured. In analyzing the measurements, the ground surface's effective flow resisitivty was calculated using least-squares optimization, and various impedance models were investigated for appropriability. The performance of the different impedance models was evaluated by predicting the sound pressure of a third additionally measured microphone position.

Keywords: *acoustic impedance, ground surface, measurement*

1. INTRODUCTION

The study of the interaction between airborne sound and a surface has many applications, e.g. noise abatement in machines or room acoustics. Especially for understanding outdoor sound propagation the interaction with the ground surface must be well understood.

In the Commission Directive (EU) 2015/996 (CNOSSOS-EU) the ground surface is categorized in eight categories, where the acoustic absorption properties of the ground are mainly linked to its porosity [1]. The eight categories of CNOSSOS-EU extend the seven *impedance classes* of the HARMONOISE model [2], which is considered overall to be more elaborate and in complex and more realistic situations superior to the NMPB 2008 model [3], which is the basis for CNOSSOS-EU. Table 1 lists the eight categories of ground surfaces. In CNOSSOS-EU a factor G is used, which controls the amount of absorption of the surface. In the sound propagation model HARMONOISE as well as in the similar NORD2000 [4], the ground impedance class is expressed by a effective flow resistivity σ_e, which is used as an input factor for calculating the surface impedance with the empirical Delany-Bazley model. HARMONOISE and NORD2000 only use seven classes and make no distinction between the classes G and H. [1]

For the determination of the effective flow resistivity NORD2000 refers to the Nordtest method NT ACOU 104 [5], which devides the acoustic impedance of ground surfaces into twelve flow resistivity classes using the Delany-Bazley impedance model. For many research questions, a precise prediction of outdoor sound propagation is mandatory, if a reliable determination of the acoustic ground surface for the NORD2000 or HARMONOISE models is necessary. As the latest version of NT ACOU 104 dates back to 1999, more modern approaches to signal processing and analysis are examined in this paper.

*Corresponding author: andreas.fuchs@ait.ac.at.
Copyright: ©2025 Andreas Fuchs et al. This is an open-access article distributed under the terms of the Creative Commons Attribution 3.0 Unported License, which permits unrestricted use, distribution, and reproduction in any medium, provided the original author and source are credited.

[1] For a hard surface HARMONOISE suggests a flow resistivity of 200 000 kPa s m^{-2} whereas NORD2000 suggests a flow resistivity of 20 000 kPa s m^{-2}.

Table 1: Ground impedance classes with factor G (CNOSSOS-EU) and effective flow resistivity σ_e (HARMONOISE).

	Description	G	σ_e (kPa s m^{-2})
A	Very soft (snow or moss-like)	1	12.5
B	Soft forest floor (short, dense heather-like or thick moss)	1	31.5
C	Uncompacted, loose ground (forest floors, pasture field)	1	80
D	Normal uncompacted ground (forest floors, pasture field)	1	200
E	Compacted field and gravel	0.7	500
F	Compacted dense ground (gravel road, parking lot)	0.3	2000
G	Hard surfaces (mostly normal asphalt, concrete)	0	20 000
H	Very hard and dense surfaces (dense asphalt, concrete, water)	0	200 000

2. MEASUREMENT OF GROUND SURFACE IMPEDANCE

This section gives a short summary of the NT ACOU 104 test method. Afterwards, the studied alterations are presented.

2.1 NT ACOU 104

The nordtest method NT ACOU 104 measures the level difference in third-octave bands between two microphones above a ground surface [5]. The set-up of the microphones and loudspeaker is shown in Fig. 1. The test signal shall consist of a broadband random or pseudo random noise and the time-averaged sound pressure level over at least 15 seconds is recorded for each third-octave band j in the frequency range from 200 Hz to 2500 Hz. The measured level difference

$$\Delta L_{i,j}^{\mathrm{M}} = L_{\mathrm{eq},i,j,\mathrm{top}} - L_{\mathrm{eq},i,j,\mathrm{bottom}} \qquad (1)$$

is recorded and averaged over four independent measurements i of an adjacent piece of identical ground to calculate ΔL_j^{M}.

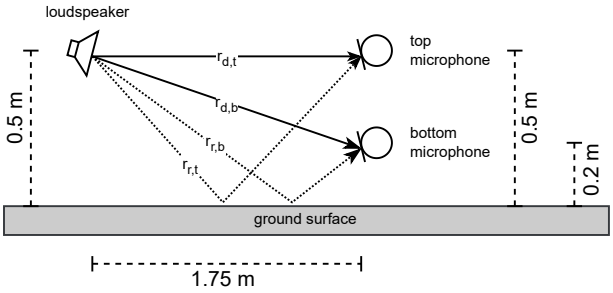


Figure 1: Measurement set-up according to NT ACOU 104.

This measured and averaged level difference ΔL_j^{M} is compared to precalculated level differences $\Delta L_j^{\mathrm{C}}(x)$ for distinct classes of flow resistivity, where the class with the smallest linear error is selected as flow resistivity. For a general parameter x, which might be multi-dimensional, this minimization can be written as:

$$\min_x E(x), \quad E(x) = \sum_j \left|\Delta L_j^{\mathrm{M}} - \Delta L_j^{\mathrm{C}}(x)\right| \qquad (2)$$

In NT ACOU 104, values are given in tables for $\Delta L_j^{\mathrm{C}}(x)$ for twelve different flow resistivity classes for a single-layer Delany-Bazley impedance model, as well as for a porous layer above a rigid surface with 0.05 m, 0.1 m and 0.15 m thickness for high and low temperatures. For measurements to be valid, the standard deviation between the repeated measurements for each third-octave band $s_{\mathrm{D},j}$ shall not exceed 4 dB. Also, the error E should be less than 15 dB. In an informative annex in NT ACOU 104 the use of a different impedance model is described.

2.2 Proposed adaptions to NT ACOU 104

The following adaptions to NT ACOU 104 are proposed and presented in this section:

- record impulse responses with time windowing,
- always solve the minimization problem for continuous values,
- examine different impedance models
- validate best fit with third microphone position.

2.2.1 Record impulse responses and use time-windowing

Recording broadband noise is sensitive to disturbing noise sources, wind noise and the surrounding area. For the in-situ measurement of the intrinsic characteristics of sound

reflection of noise barriers under direct sound field conditions (as described in EN 1793-5 [6]), impulse responses are used to measure the reflection index of noise barriers and the measurements can be performed along a highway under normal operation. If a Maximum-Length-Sequence (MLS) is used as test signal for NT ACOU 104 to calculate the impulse responses, this technically still classifies as a pseudo random test signal. This adds robustness against disturbing noise sources for the measurements. However, another advantage of impulse responses is the possibility to perform time filtering to suppress unwanted reflections. Beside the calculation of an impulse response, we propose the use of the Adrienne time-window from EN 1793-5 [6] with a length of the flat top (main part) of 10 ms and total window length of 14.8 ms. Therefore, a third-octave band level can be calculated for a impulse response $h(t)$, a time window $w_\mathrm{A}(t)$ and the Fourier transform $\mathcal{F}$ with

$$L_j = 10\log\left(\int_{\Delta f_j} |\mathcal{F}[h(t)w_\mathrm{A}(t)]|^2\right) \tag{3}$$

for the third-octave frequency bands j with a width of Δf_j. Figure 2 shows the measured impulse response for the top microphone over grass (green line) as well as the proposed Adrienne time window (orange line). At around 5.1 ms the first peak of the direct path is visible, whereas at 6 ms the first peak of the reflected component can be distinguished. The time window is long enough to include the whole impulse response of the loudspeaker for both components.

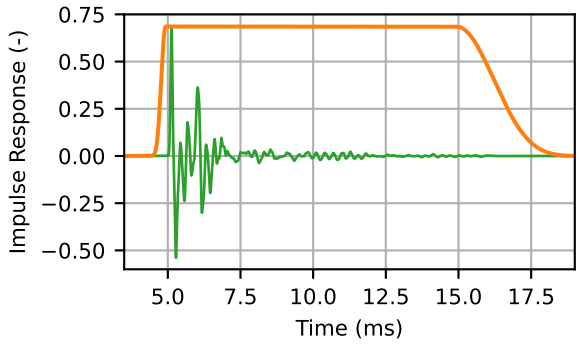


Figure 2: Impulse response (green) and Adrienne time window (orange).

2.2.2 *Solving the minimization problem for continuous values*

Instead of a table look-up from NT ACOU 104 we suggest solving the minimization problem for continuous values of the required impedance parameter(s). This can be achieved with the underlying Weyl-Van der Pol equation, which is able to predict the sound pressure p from a point source above a locally reacting ground as a superposition of the sound pressure from the direct path p_d and the reflected path (p_r), which is multiplied with the *spherical reflection coefficient* Q [7]:

$$p = p_\mathrm{d} + Qp_\mathrm{r} = \frac{\mathrm{e}^{\mathrm{i}kr_d}}{4\pi r_d} + Q\frac{\mathrm{e}^{\mathrm{i}kr_r}}{4\pi r_r}, \tag{4a}$$

$$Q = R_\mathrm{p} + (1-R_\mathrm{p})(1+\mathrm{i}\sqrt{\pi}w\mathrm{e}^{-w^2}\,\mathrm{erf}(-\mathrm{i}w)), \tag{4b}$$

$$w = \frac{1+\mathrm{i}}{2}\sqrt{kr_r}(\cos(\theta)+Z^{-1}), \tag{4c}$$

$$R_\mathrm{p} = \frac{\cos(\theta)-Z^{-1}}{\cos(\theta)+Z^{-1}} \tag{4d}$$

and R_p as the plane wave reflection coefficient of the locally reacting ground surface, r_d and r_r as the distance between source and receiver position for the direct and reflected path respectively, the wave number k, the incident angle θ and the normalized impedance of the ground Z. If the Delany-Bazley impedance model is used, then the impedance is calculated with [5]

$$Z = 1 + 9.08\left(\frac{f}{\sigma_\mathrm{e}}\right)^{-0.75} + i11.9\left(\frac{f}{\sigma_\mathrm{e}}\right)^{-0.73}. \tag{5}$$

The predicted sound pressure levels must be calculated in third-octave bands for both microphone positions for comparison with the measurement data. Afterwards, the minimization in Eqn. (2) can be solved for continuous values of the required impedance parameter.

2.2.3 *Examination of different impedance models*

Including the Annex D, NT ACOU 104 suggests the use of three different impedance models: Delany-Bazley, Delany-Bazley with an additional porous layer above a rigid surface and the variable porosity model. Among the commonly used impedance models models [8], [9], we studied the following ones by using the respective model in the plane wave reflection coefficient in Eqn. (4d):

Delany-Bazley The semi-empirical Delany-Bazley [8] model given in Eqn. (5) with the parameter effective flow resistivity σ_e.

Variable Porosity The variable porosity model considers an increasing porosity with increasing depth as approximation with two parameters (effective flow resistivity σ_e and effective rate of change of porosity α_e) and uses the heat capacity ratio γ [7]:

$$Z = \frac{1+\mathrm{i}}{\sqrt{\pi\gamma\rho_0}}\sqrt{\frac{\sigma_\mathrm{e}}{f}} + \frac{\mathrm{i}c_0\alpha_\mathrm{e}}{8\pi\gamma f}. \tag{6}$$

Zwikker-Kosten The phenomenological model from Zwikker-Kosten uses the three parameters flow resistivity σ, porosity Ω and structure factor K [7]:

$$Z = \frac{\sqrt{K}}{\Omega}\left(1 + \frac{\mathrm{i}\Omega\sigma}{2\pi f\rho_0 K}\right). \tag{7}$$

Taraldsen Taraldsen transformed the phenomenological model from Zwicker-Kosten to a one-parameter model (effective flow resistivity σ_e) [7]:

$$Z = \left[\sqrt{\gamma}\frac{\Omega}{\sqrt{T}}\left(1 + \frac{f*}{f}\right)\right]^{-1} \tag{8a}$$

$$f* = \frac{1}{2\pi\rho_0}\frac{\Omega}{\sqrt{T}}\sigma_\mathrm{e} \tag{8b}$$

$$\frac{\Omega}{\sqrt{T}} = 100\left(10^{X/10}\right) \tag{8c}$$

$$X = \frac{1}{19.76}\Big[-10\log(\sigma_\mathrm{e}) + 404.55 + \sqrt{546.166 + [9.35 - 10\log(\sigma_\mathrm{e})]^2}\Big]. \tag{8d}$$

Slit-pore The slit-pore model is based on the simulation of the internal structure of the absorber with interconnected slits and pores. For the impedance of the ground, the assumption of identically wound slit-like pores is used with the three parameters flow resistivity σ, porosity Ω and tortuosity T [8] and uses the Prandtl number Pr:

$$Z = \frac{1}{\rho_0 c_0}\sqrt{\frac{T}{\Omega^2}\frac{\rho(\lambda)}{C(\lambda)}} \tag{9a}$$

$$\rho(\lambda) = \frac{\rho_0}{G_S(\lambda)} \tag{9b}$$

$$C(\lambda) = \frac{1}{\gamma P_0}\left[\gamma - (\gamma-1)G_S(\lambda\sqrt{Pr})\right] \tag{9c}$$

$$G_S(\lambda) = 1 - \frac{\tanh(\lambda\sqrt{-\mathrm{i}})}{\lambda\sqrt{-\mathrm{i}}} \tag{9d}$$

$$\lambda = \sqrt{\frac{6\rho_0\pi f T}{\Omega\sigma}} \tag{9e}$$

For the Delany-Bazley, the Zwikker-Kosten as well as for the slit-pore model also the respective layered model is considered, where the impedance is calculated with

$$Z = Z_\mathrm{n}\coth(-ikd) \tag{10}$$

with the layer thickness d of the porous material over a rigid surface. Z_n is the impedance of the according impedance model (Eqn. (5), (7) or (9a) respectively).

2.2.4 *Validate best fit with third microphone position*

For validation purposes, we propose to measure a third microphone position between the top and bottom microphone in the set-up of NT ACOU 104 (see Fig. 1), which is 35 cm above the ground. The *validation* level difference $\Delta L^\mathrm{M}_{\mathrm{v},j}$ is calculated from the difference from the validation to the bottom microphone via Eqn. (4a) and Eqn. (1). This gives the advantage of new independent measurement data on an identical test specimen with minimal extra effort. The *validation error* E_v is then similar to Eqn. (2)

$$E_\mathrm{v} = \sum_j \left|\Delta L^\mathrm{M}_{\mathrm{v},j} - \Delta L^\mathrm{C}_{\mathrm{v},j}(x)\right|. \tag{11}$$

Figure 3 shows the level difference ΔL_j for the standard set-up from NT ACOU 104 (top to bottom microphone) as well as as the level difference from the additional proposed validation microphone to the bottom microphone $\Delta L_{\mathrm{v},j}$. The computed level difference values are calculated for a flow resistivity class of 400 kPa s m^{-2},

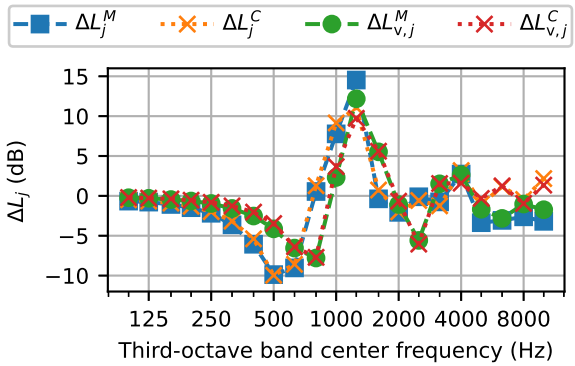


Figure 3: Measured ($^\mathrm{M}$) and computed ($^\mathrm{C}$) level difference between the top and bottom microphone (ΔL_j) and additional validation microphone and bottom ($\Delta L_{\mathrm{v},j}$).

which was calculated for a minimum error of E (Eqn. (2)). For the additional validation microphone the third-octave band values of the level difference $\Delta L_{\mathrm{v},j}$ are different to ΔL_j due to the changed geometry. Nevertheless, the computed values are quite close to the measured values for a frequency range from 100 Hz to 4000 Hz. This gives the ability to validate the obtained value of $\sigma_\mathrm{e} = 400\,\mathrm{kPa\,s\,m^{-2}}$ for a microphone and geometry, which was not included in the calculation of the value.

3. MEASUREMENTS

The analysis presented in this paper is based on measurements which were performed to study the ground surface absorption of earth berms for calculating sound propagation alongside highways. Therefore, measurements were performed on flat and inclined surfaces, although NT ACOU 104 suggests only to perform measurements on a flat surface. For the measurements on the slope, the set-up according to NT ACOU 104 is rotated with respect to the inclination. Measurements were performed on two sites, with multiple measurement positions for each site:

Site A: 2 measurement positions on level ground and 4 measurement positions on tilted surfaces with angles ±16° and ±35°. [2]

Site B: 2 measurement positions on tilted surfaces with angles 35° and 38°.

The measurements were performed repeatedly on the same spots on a quarter year basis from Q4 2023 until Q3 2024. Although, all measurements sites can be considered covered with grass, the ground was much more compacted in Q4 2023. In Q1 2024 and Q3 2024 very similar conditions could be found with low length grass, where in Q2 2024 the measurements were performed on a hot day with high grass. The measurement sites are less than 30 km apart from each other. Figure 4 to Fig. 7 show pictures of the measurement sites. As this study did not focus on performing measurements, the variation of the measurement sites is limited. Nevertheless, the data set spans over four of the seven impedance classes of HARMONOISE (classes B - E from Tab. 1).

For the measurements a MLS signal was used as test signal with a length of two seconds, which was repeated

[2] For a positive angle the loudspeaker is below the microphone and emits sound upwards the slope, whereas for a negative angle the loudspeaker is placed above the microphones.



Figure 4: Picture of measurement site A Q4 2023.



Figure 5: Picture of measurement site A Q2 2024.



Figure 6: Picture of measurement site B Q4 2023.



Figure 7: Picture of measurement site B Q2 2024.

30 times. Therefore, it is possible to calculate a two second long impulse response for each microphone, which was averaged 30 times.

4. RESULTS AND DISCUSSION

In this section the proposed adaptions to NT ACOU 104 from section 2.2 are evaluated.

4.1 Solving the minimization problem

The minimization problem in Eqn. (2) is solved using a curve-fitting algorithm. This gives the ability to calculate continuous values for the impedance model parameters, especially a continuous value for the effective flow resisitivty for the Delany-Bazley model instead of the 12 classes according to NT ACOU 104. Figure 8 shows a box plot of the error E from Eqn. (2) and validation error E_v from Eqn. (11) for all obtained measurements, if the effective flow resisitivty, which minimizes E, is determined with a table lookup as in NT ACOU 104 or if a continuous value is calculated. This value is then used to calculate the validation error E_v by using it to predict the level difference. Afterwards, the predicted level difference is compared to the measured level difference between the validation and bottom microphone and the validation error E_v calculated. As expected, the errors are smaller for the fitting approach compared to the table lookup method. However, the improvement can be seen even better for the validation error E_v, where the mean error is decreased by about 2 dB.

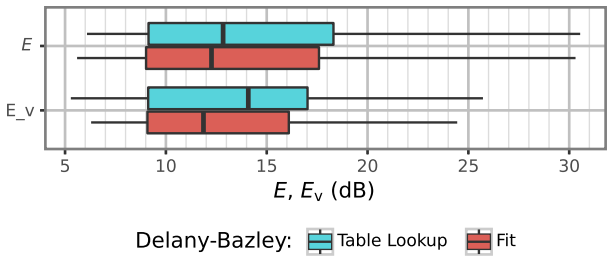


Figure 8: Comparison of the error between the measured and computed level difference for the standard set-up (E) and the validation set-up (E_v) for all obtained measurements (Delany-Bazley model).

4.2 Impulse Responses

For all performed measurements the effective flow resistivity σ_e was determined according to the Delany-Bazley model by running a curve fitting algorithm on the error function $E(x)$ (Eqn. (2)) for two specific test cases:

Noise The $L_{\mathrm{eq},j}$ values are calculated with time filters on the recorded signal and averaged over 60 s.

Impulse Response Instead of the $L_{\mathrm{eq},j}$, the L_j from Eqn. (3) are used as third-octave band levels and are calculated by deconvoluting the recorded signal to obtain the impulse response.

Figure 9 compares the effective flow resistivity σ_e for the two test cases, where no significant deviations are visible. For one measurement the deviation is 6 %, for all other measurements the deviation is less than 5 %, Also, for more than half of the 27 data points the deviation is less than 1 kPa s m^{-2}.

In the standard deviations between the four measurements for each measurement position no significant difference can be found, as the mean difference between the standard deviation for the *noise* and *impulse response* test case for each measurement position for all third-octave bands is smaller than 0.1 dB. As the measurements were performed without external noise sources, the main benefit of the impulse response calculation can not be shown. Nevertheless, the results are similar and there is no apparent downside to using impulse responses.

4.3 Impedance Models

The error E as well as the validation error E_v can also be used to compare different impedance models. Figure 10

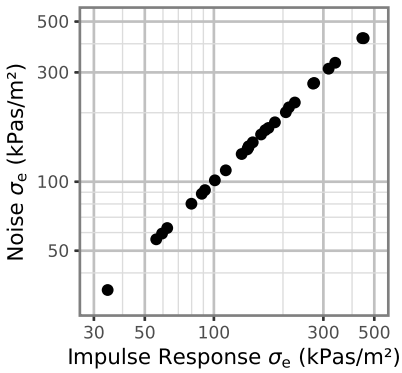


Figure 9: Estimated effective flow resistivity σ_e with the Delany-Bazley impedance model by directly processing the noise signal or calculating impulse responses.

shows box plots, where the range of the occurring errors for all obtained measurements is visible with respect to the impedance model. Again, the validation error E_v is calculated by using the obtained impedance model parameters, which result from minimizing the error E for the top to bottom microphone set-up, for predicting and comparing the level difference of the validation to bottom microphone set-up. The impedance models are ordered by increasing number of parameters from top to bottom. For the one-parameter Taraldsen model it was not possible to find a good fit. All the other newly considered models performed similar or better than the Delany-Bazley model. Especially, the variable porosity model (except for a few outliers) and also the phenomenological model from Zwikker-Kosten show promising results pushing the mean of the errors in the dataset closer to 10 dB than the Delany-Bazley model. However, the Delany-Bazley model shows a quite reasonable performance considering its simplicity. The respective layer variants of the models show small improvements, but might not be applicable for the performed measurements. The validation error E_v is in the same range as E except for the Taraldsen impedance model, which supports the assumption that the fit of the these models can be generalized and can be used for sound propagation calculations.

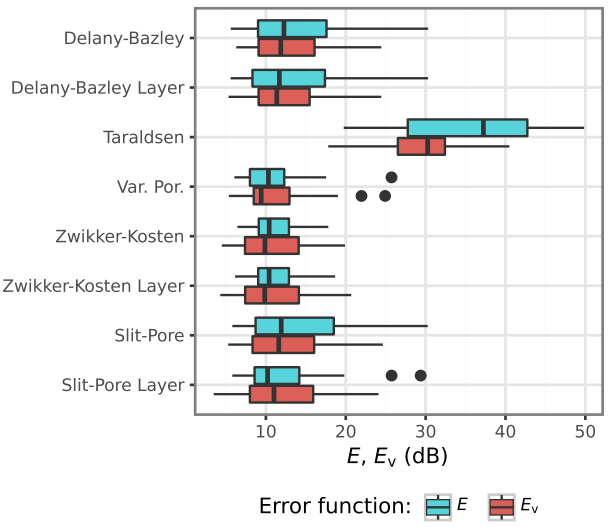


Figure 10: Comparison of error E and validation error E_v of the impedance models for all obtained measurements.

4.4 Influence of Angle

In contrast to NT ACOU 104, measurements were also performed on tilted surfaces. No significant influence of the angle of the surface on the error and the validation error could be found, which means the fit to the standard set-up and the validation set-up works for tilted surfaces as well as for flat ground. Nevertheless, the obtained values for the flow resistivity are quite different for the different angles. Figure 11 shows the estimated effective flow resis-

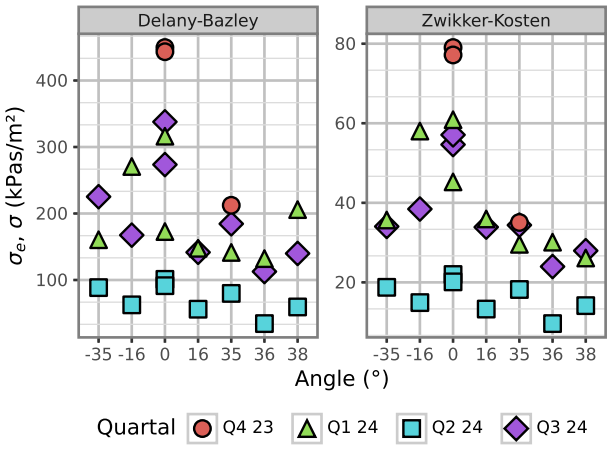


Figure 11: Estimated (effective) flow resistivity for the Delany-Bazley (σ_e) and the Zwikker-Kosten (σ) model for all obtained measurements.

tivity σ_e for the Delany-Bazley impedance model as well as the flow resistivity σ for the Zwikker-Kosten model for all measurements for the different surface angles for the repeated measurements. It can be seen, that the flow resistivity is significantly lower in Q2 2024, which may be attributed to a drier ground. This can also be attributed to the porosity Ω in the Zwikker-Kosten model, which is significantly higher in Q2 2024 than for the other quarters. For Q4 2023 not all measurements were performed. Nevertheless, the respective highest values for the flow resistivity were measured in this quarter, which get close to class E according to the HARMONOISE classification (compacted field). For the measurements, which were not performed in Q2 2024, it can be seen that for the non flat measurements the estimated flow resistivity is lower. This may be attributed to a less compacted ground on the earth berm. It should be noted, that the measurements at 36° and 38° inclination were performed at a different site, which might have different sound absorbing characteristics.

5. SUMMARY AND OUTLOOK

In this paper, adaptions to the standard NT ACOU 104 for measuring ground surface absorption were presented. The measurements were obtained on grass covered earth berms. The use of a third microphone for validation provides valuable insight into how well the estimated parameters can actually describe the acoustic properties of the ground surface. Because the extra effort seems reasonable compared to the information gain, we recommend the use of an extra microphone position. Also, no significant difference in the analysis with impulse responses to the previous method could be found. As the measurement with impulse responses is generally seen as more robust, we encourage their use instead of evaluating noise signals.

Depending on the application, the use of a fitting algorithm to determine a continuous parameter as well as other impedance models, might improve sound propagation over long distances. Nevertheless, this must be supported by the underlying sound propagation calculation method and must be evaluated in further research. Also, the measurement on inclined surfaces showed promising results over short distances due to the low validation error. However, further research is encouraged to evaluate if for larger propagation paths it is more beneficial to use values obtained from the inclined plane than from the flat surface.

6. ACKNOWLEDGMENTS

This report is based on parts of the research project carried out at the request of the Federal Ministry for Digital and Transport, represented by the Federal Highway and Transport Research Institute, under research project No. 02.0455/2022. The author is solely responsible for the content.

7. REFERENCES

[1] Commission Directive (EU) 2015/996 of 19 May 2015 establishing common noise assessment methods according to Directive 2002/49/EC of the European Parliament and of the Council (CNOSSOS-EU), 2015.

[2] R. Nota, R. Barelds, and D. van Maercke, *Technical Report HAR32TR-040922-DGMR20, Harmonoise WP 3 Engineering method for road traffic and railway noise after validation and fine-tuning. Deliverable 18*, 2005.

[3] S. Kephalopoulos et al., "Advances in the development of common noise assessment methods in Europe: The CNOSSOS-EU framework for strategic environmental noise mapping," *Science of The Total Environment*, vol. 482-483, pp. 400–410, 2014.

[4] NORD 2000, *Comprehensive Outdoor Sound Propagation Model. Part 1: Propagation in an Atmosphere without Significant Refraction.* DELTA - Danish Electronics, Light & Acoustics, Denmark, 2001.

[5] NT ACOU 104, *Ground surfaces: Determination of the acoustic impedance - nordtest method*. Nordtest, Finland, 1999.

[6] EN 1793-5, *Road traffic noise reducing devices – Test method for determining the acoustic performance – Part 5: Intrinsic characteristics – In situ values of sound reflection under direct sound field conditions*, 2016.

[7] K. Attenborough and T. van Renterghem, *Predicting Outdoor Sound*. USA: CRC Press, 2nd ed., 2021.

[8] K. Attenborough, I. Bashir, and S. Taherzadeh, "Outdoor ground impedance models," *The Journal of the Acoustical Society of America*, vol. 129, pp. 2806–2819, 05 2011.

[9] K. Attenborough, "Outdoor ground impedance models," in *Euronoise Maastricht*, 2015.

DOI: 10.61782/fa.2025.0147



FORUM ACUSTICUM
EURONOISE 2025

ASSESSING FOREST ACOUSTICS: A COMPARISON OF IN-SITU AND SCALE MODEL ACOUSTIC IMPULSE RESPONSES

Sinuo Feng[1*] **Francis Stevens**[1] **Andrew Chadwick**[1]

[1] AudioLab, School of Physics, Engineering and Technology, University of York, UK

ABSTRACT

Acoustic impulse responses (IRs) can be used for the analysis of a space's acoustic properties and for convolution based auralisation (which has many applications, including in music production and sound design). However, the vast majority of impulse responses are recorded indoors, typically in musical performance spaces. As a result there are relatively few IRs available recorded in outdoor conditions. This paper presents an analysis of IRs recorded in a forest environment, comparing in-situ results with those recorded using a scale model. The in-situ recordings were measured in mono and B-format, and are analysed in terms of reverberation parameters and spatial characteristics. A 1:10 scale model of the forest environment was then constructed and measured. This work aims to contribute to the understanding of sound propagation in a forest environment (particularly in terms of the acoustic effect of tree trunks of different diameters at different positions relative to the listener, which previous studies have determined to be of particular importance) and to assess the suitability of scale modelling in this context. The resultant impulse responses are available online.

Keywords: *forest acoustics, acoustic impulse response measurement, scale model*

1. INTRODUCTION

An understanding of the acoustic properties of forest environments is of great importance to many fields, including noise propagation, soundscape evaluation, and sound design [1, 2]. There is existing literature focussing on different aspects of forest acoustics, but work remains to be done in developing a full understanding of how the different physical characteristics of a forest (the layout, number of trees, tree trunk diameters, bark material) combine and result in a particular acoustic. This work investigates the acoustics of a forest environment, by assessing in-situ impulse responses and scale model measurements, and aims to answer the following questions:

1. What are the acoustic properties of tree trunks in a forest environment?
2. Is a scale model a good approach to studying forest acoustics?

The structure of this paper is as follows: Section 2 presents a review of relevant prior research; Section 3 presents the method of impulse response recording used in the forest and the scale model; Section 4 presents the analysis and comparison of the impulse responses from both environments; and Section 5 concludes the paper, considering the above questions.

2. BACKGROUND

This section presents a brief review of the relevant existing literature, include material on the study, analysis, and modelling of forest acoustics, and acoustic scale modelling.

2.1 Forest acoustics

Sound attenuation by vegetation has been investigated since at least 1946, when Eyring investigated the acoustic properties of a Panamanian jungle [3]. It has been proposed that trees can be used as noise barriers near sources such as highways and railroad tracks [4,5]. The form and layout of a forest have been indicated as important properties in determining sound attenuation [6, 7]. This is related to the interaction of various acoustic phenomena in a forest environment. Noise attenuation can occur due to sound energy absorption and scattering effects by branches, foliage, and shrubbery [5, 8]. The effect of sound propagation in a forest environment has been shown to be highly frequency dependent [9]. A relatively small sound attenuation in a frequency range between 1 and 2 kHz was observed by Fricke, and a similar reduction in attenuation was found by Kragh, typically between 500 Hz and 2 kHz [7, 10].

Previous IR measurement work has been conducted in a forest environment, where Shelley et al. conducted a study at Koli

*__Corresponding author__: sinuo.feng@york.ac.uk.

__Copyright__: ©2025 Sinuo Feng et al. This is an open-access article distributed under the terms of the Creative Commons Attribution 3.0 Unported License, which permits unrestricted use, distribution, and reproduction in any medium, provided the original author and source are credited.

National Park in Finland using a B-format microphone and a single speaker [11]. This method followed ISO 3382 IR measurement procedure (designed for indoor measurement) [12]. The analysis of acoustic parameters, including reverberation time (T30) and clarity (C50) was conducted, and a reverberation time of between 1.3s and 1.7s was found in the 1 kHz octave band. Previous studies have indicated that tree trunks are a key factor in sound scattering above 1 kHz in a forest environment [9, 13–15]. Chobeau determined that the scattering caused by tree trunks is dependent on the apparent diameter of the trunk and the relationship between the diameter and the frequencies present in the incident sound [16]. Generally, tree trunks scatter sound frequencies with wavelengths equal to or smaller than their diameters [9].

Previous studies in modelling forest acoustics have considered tree trunks as the key factor in sound propagation. *Treeverb*, a digital reverberator, simulates acoustic reverberation in a forest environment, modelling the scattering of acoustic waves among trees in a simplified forest model [17]. Fig. 1 shows a simple example of a forest modelled in this way, where T1, T2, and T3 are the interconnected tree-nodes, S is the source and R is the receiver. In this work an image-source model, along with Morse's solution to the acoustic scattering from a cylinder [18], was used to generate IRs. In [19] a similar approach was used to model forest acoustics, using a set of waveguides to connect the tree nodes (extending the scattering delay network approach in [20]).

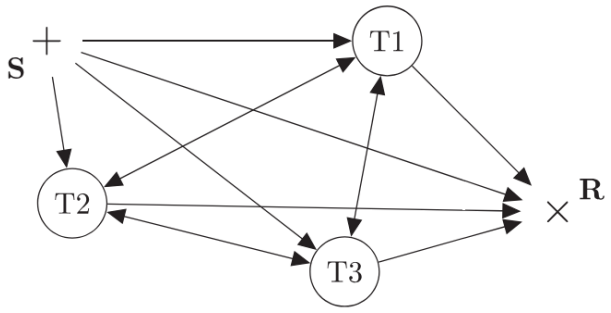


Figure 1. An example of a simplified model of a forest, consisting of three tree-nodes, T1, T2, T3, a source, S, and a receiver, R. From [19].

2.2 Scale modelling

Acoustic scale modelling was first used in the design of concert halls and opera theatres in the 1930s [21]. This method allows for the prediction of the acoustic properties of a full-scale space as it captures complex wave effects such as diffusion, diffraction, and ground interference [22, 23]. The model scale factor (k) determines the relationship between the scale frequency (f_{scale}) and the corresponding full scale frequency (f_{real}) [24]:

$$f_{\text{scale}} = k \times f_{\text{real}} \tag{1}$$

When determining the scale factor there is a trade-off between the capability of the available recording equipment [25], the space available, and the increased air absorption at higher frequencies [26]. When constructing a scale model, the materials used should closely approximate sound absorption coefficients (SACs) at the scaled frequencies [27].

Scale modelling has previously been used to study sound propagation in outdoor spaces. Cox et al. studied the acoustic properties of Stonehenge using an acoustic scale model [23]. This research used a scale factor of 12, and IR measurement and analysis were conducted in accordance with ISO 3382 [12]. The Exponential Sine Sweep (ESS) method was used with frequencies ranging from 800 Hz to 96 kHz. Four compact tweeters, arranged in a square configuration, and an ultrasonic microphone were used to approximate an omnidirectional source and receiver. The model stones were designed and constructed to minimise sound absorption (given the typically low SAC of stone), and unvarnished Medium Density Fibreboard (MDF) was used to model the ground, to match the SACs of grassland in a true scale frequency range of 125 Hz to 1 kHz. The scale modelling work presented in this paper draws on Cox et al.'s approach.

3. METHODOLOGY

This section covers the methods of IR measurement used in the real forest (Section 3.1), the design and construction of the scale model (Section 3.2), and the scale model IR measurement (Section 3.3).

3.1 Forest IR Measurement

The chosen measurement site was in Wheldrake Woods, c. 8 miles south-east of York [28]. Fig. 2 shows the chosen environment. The trees are all the same species (*Abies Grandis*), and consist primarily of tall, straight, trunks with no large branches. The ground surface is relatively flat with no additional low vegetation.

Two source and two receiver positions were selected for measurement. Source *S1* was placed with clear sight lines to Receivers *R1* and *R2*. *S2* was placed with a tree obstructing its view of both receivers. Each position was at least 1m away from the nearest tree. The positions and diameters of the trees within an area of 20m $\times$ 20m around the sources and receivers were measured, the layout of which is shown in Fig. 3. The size of the surveyed area was determined by the maximum scale model size, as discussed in Sections 3.2 and 3.3.

The IRs were measured with the ESS method, using a Genelec 8130A loudspeaker to reproduce a sine sweep of 15s duration with a frequency range of 60 Hz - 20 kHz ($f_s = 48\,\text{kHz}$). Recordings were made using two microphones: an Earthworks M30 omnidirectional measurement microphone (mono), and a



Figure 2. The forest environment considered in this study. The measurement setup can be seen: an Earthworks M30 omnidirectional measurement microphone and a Genelec 8130A loudspeaker.

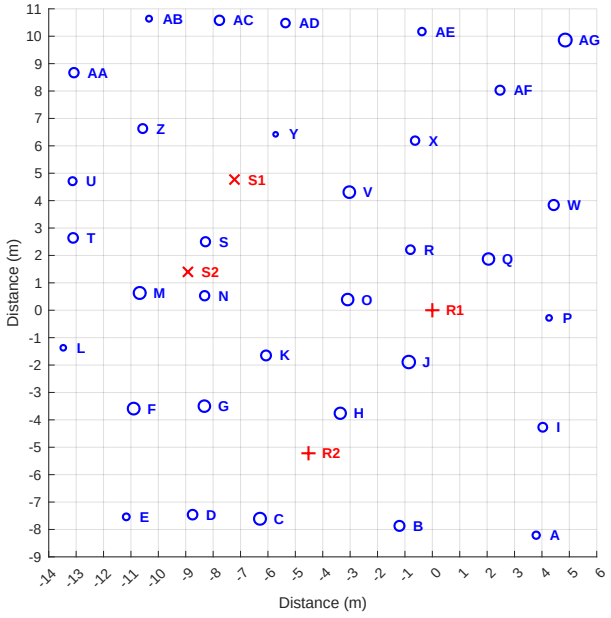


Figure 3. Diagram of the layout of the forest environment, showing source, receiver, and tree positions. Within the measurement area there were 33 trees with diameters ranging between 0.17m to 0.47m.

Soundfield ST450 MkII (B-Format). The speaker and microphones were placed at a height of 1.5m. For each source position, four measurements were made: first recording a sweep with the speaker facing *R1*, then three further recordings with the speaker rotated clockwise 90° each time. These four orientations were then averaged to approximate an omnidirectional source [11].

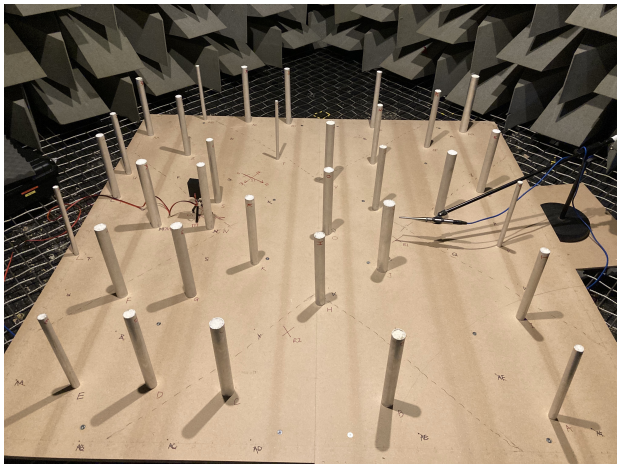


Figure 4. A picture of the forest scale model setup in the anechoic chamber, formed by 33 aluminium tubes (filled with plaster) and an MDF board. Here source and receiver are at position S2R1.

3.2 Design of the scale model

The scale model was constructed with a scale factor of 10. This was determined by the maximum usable area of the anechoic chamber in which the recording took place, and the microphone in use (an Earthworks M30) having a flat response up to 30 kHz. This allowed for useful measurement up to $f_{real} = 3\,\text{kHz}$, and the use of available materials with SACs appropriate to this scale.

Aluminium tubes were used to model the trees, due to their smooth surface which is reflective at high frequencies. To avoid capturing the resonant frequencies of the tubes, each was filled with plaster. The tubes were chosen from available diameters, resulting in some minor error (maximum 6.85%).

In this experiment, the height of each tube was 40cm. This was chosen as it is more than twice height of the source/receiver in the scale model (15cm). Unvarnished MDF was used to model the ground, as in [23].

To construct the scale model, a square MDF board (with side length of 2.1m) was mounted to the floor of the anechoic chamber. Dowels were then used to attach the model trees in their correct positions. The final forest scale model setup is shown in Fig. 4.

3.3 Scale Model IR Measurement

A Peerless OC20SC14-04 tweeter with a diameter of 33.2mm, and a frequency response from 750 Hz to 38 kHz was used as the source in the scale model measurements, with the Earthworks M30 used to record the signals produced. A 15s duration ESS ($f_s = 96\,\text{kHz}$) was used with a frequency range from 1 kHz to 30 kHz, allowing for IR analysis of octave bands from 125 Hz to 2 kHz at full scale. For each source/receiver pair, 16 recordings were made: four speaker orientations (as in the in-situ measurement), each recorded four times (in an attempt to improve the signal-to-noise ratio [23]). These 16 takes were then averaged and equalised for the speaker's response using an inverse filter based on a free-field measurement of the speaker.

4. EVALUATION

This section presents analysis of the IRs measured in-situ and using the scale model. This includes ISO 3382 analysis and spatial analysis of the B-format recordings. The full sets of recorded IRs are available online [29, 30].

4.1 Forest IR Analysis

Fig. 5 shows the reverberation time (T30) results for the four forest IRs. They each show a similar trend, with a pronounced peak across the 500 Hz, 1 kHz, and 2 kHz octave bands, where the values are above 1.5s. These results are partly due to the measured tree trunk diameters (ranging between 0.17m and 0.47m), which correspond to wavelengths from 735.6 Hz to 2072.5 Hz, this is an expected result given the importance of tree trunk reflections identified in the literature [9, 13–16].

Ground interference is likely to have an impact below 500 Hz [13,31], resulting in constructive and destructive interference in the 125 Hz, 250 Hz, and 500 Hz octave bands [32]. Low-frequency wind noise in the recordings may result in overestimation of reverberation time, particularly for the 125 Hz octave band. The significant drop in reverberation time for the 4 kHz and 8 kHz octave bands is due to the open nature of the forest and absorption by tree bark [19, 33].

Fig. 6 shows a comparison of Definition (D50) results for the four forest IRs. D50 values are generally above 80%, suggesting significant sound attenuation at high frequencies and good speech intelligibility. A reduction in D50 is observed for the 1 kHz and 2 kHz octave bands of each IR, due to the increased reverberant energy. At position S2R1, the source is occluded by *Tree O*, and at position S2R2, the source is occluded by *Tree N*. Without a clear line of sight between source and receiver there is no true direct sound present in the IR, resulting in a decrease in D50 [34]. This is particularly evident in the results for S2R1.

Fig. 7 shows a waveform plot of the S1R2 IR. Alongside the IR, red lines indicate the timings of reflections from the tree trunks in the environment (calculated using the forest layout data). It can be seen that a number of strong early reflections in the IR line up with these predicted timings, confirming the impact that tree trunks have on a forest's acoustic properties.

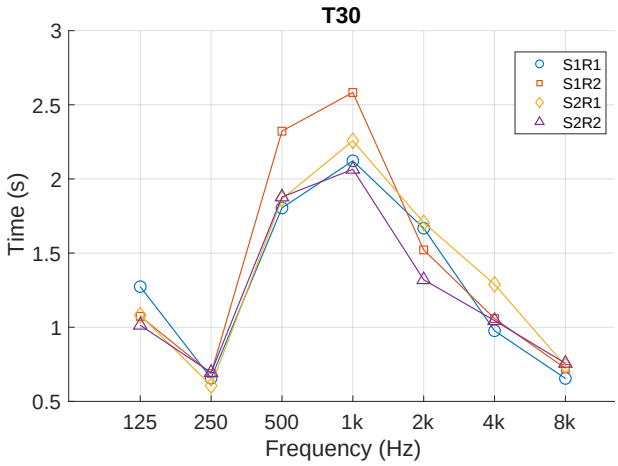


Figure 5. Reverberation time (T30) results for the four forest IRs.

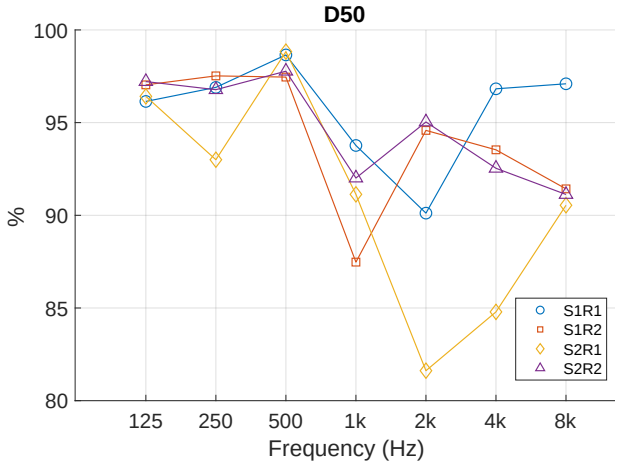


Figure 6. Definition (D50) results for the four forest IRs.

The spatial information captured in the B-format IRs can be evaluated by spatial impulse response rendering (SIRR) analysis. Here the signals are divided into discrete time frames, and then a short-time Fourier transform (STFT) is performed on each channel. A instantaneous intensity vector **I** vector can then be estimated according to:

$$\mathbf{I}(\omega) = \frac{\sqrt{2}}{Z_0}\Re\{W^*(\omega)U(\omega)\} \tag{2}$$

where U(ω) is vector [X(ω), Y(ω), Z(ω)], Z_0 is the char-

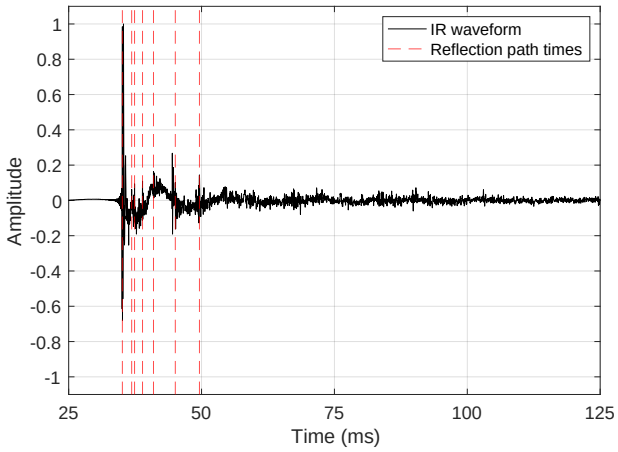


Figure 7. Waveform plot of the S1R2 IR recorded in the forest. The red lines indicate the timing of first-order reflections from nearby trees.

acteristic acoustic impedance of air, and $*$ denotes the complex conjugate [35].

Fig. 8 shows a SIRR plot for the IR at position S1R2. Only the horizontal plane is considered in this SIRR analysis, due to the open nature of the forest environment precluding significant directional information in the vertical plane [36]. The arrows indicate the direction of arrival of sound in each frequency bin for each frame. An arrow pointing to the right corresponds to a sound arriving straight-on to the microphone (0°); an arrow pointing down corresponds to a sound coming from the right to the microphone (90°). These arrows are overlaid on a spectrogram of W-channel of the IR, allowing for concurrent analysis of the magnitude and direction of arriving acoustic energy.

The SIRR plot shows a strong direct sound followed by a set of early reflections coming from different directions. At certain points in time, clusters of arrows can be found pointing in the same direction. These indicate reflections from particular tree trunks, and a summary of the first-order reflections (with suggestions of the particular trees contributing to them) is given in Table 1. This analysis could be continued to include further reflection paths; previous work has shown the importance of reflections of up to third-order in outdoor environments [36].

4.2 Scale Model IR Analysis

The scale model IRs were interpolated to be 10 times longer, in order to conduct analysis at true scale. Fig. 9 shows the waveform plot of the IR recorded at position S1R2 in the scale model. As before, red lines indicate the estimated reflection path times calculated using the forest layout data. The results show that the reflections indicated in the waveform align well with the potential reflections indicated in the actual layout, and the error range

Table 1. Details of the first-order reflections identified in the SIRR analysis in Fig. 8.

Timing	Direction of arrival	Frequency	Relevant Tree(s)
12-16ms	0°	0-5 kHz	*K*, *S*, *H*, *N*, *O*
20-22ms	315°	1-5 kHz	*M*
22-26ms	45°	1-4 kHz	*V*, *Y*
28-30ms	225°	2-5 kHz	*C*

is small. The waveform shows a strong direct sound followed by clusters of early reflections, which is similar to the IR recorded in the real forest (as shown Fig. 7).

Fig. 11 shows the early decay time (EDT) results for the four scale model IRs, which can be compared with Fig. 10 (which shows the EDT results for the in-situ forest IRs). EDT was chosen for comparison here as it has previously been shown to be useful when comparing scale model and real-world IRs [23]. EDT results in the scale model show generally low values due to the limited number of model trees and the anechoic environment. Although a similar trend can be found in both results: higher EDT values in the 250 Hz octave band than at 500 Hz, then a general increase for higher bands.

Spectral plots of the IRs are shown in Fig. 12 (in-situ) and Fig. 13 (scale model). Results were calculated by filtering the IRs into one-third octave bands and then calculating the dBFS values (decibels relative to full scale) for each band. There are similarities in the spectra, with a decrease in magnitude centred around the 250 Hz band, and an increase above this range.

The spectrum of the forest shows another small decrease in response of 2 to 4 dB around 800 Hz, and the results from the scale model show a similar reduction at positions S1R2 and S2R1. In the case where the source and receiver are obstructed by a tree, the frequencies are greatly pronounced below 800 Hz in the real forest. For these receiver positions in the scale model, the magnitudes are higher at the tree-obstructed (*S2*) position below this frequency. Above 250 Hz, the scale model magnitudes are generally higher than in the real forest.

5. CONCLUSION

This paper has presented the measurement and analysis of IRs recorded in a forest environment, comparing in-situ IRs with those recorded using a scale model. The questions posed in Section 1 will now be considered:

1. What are the acoustic properties of tree trunks in a forest environment?
2. Is a scale model a good approach to studying forest acoustics?

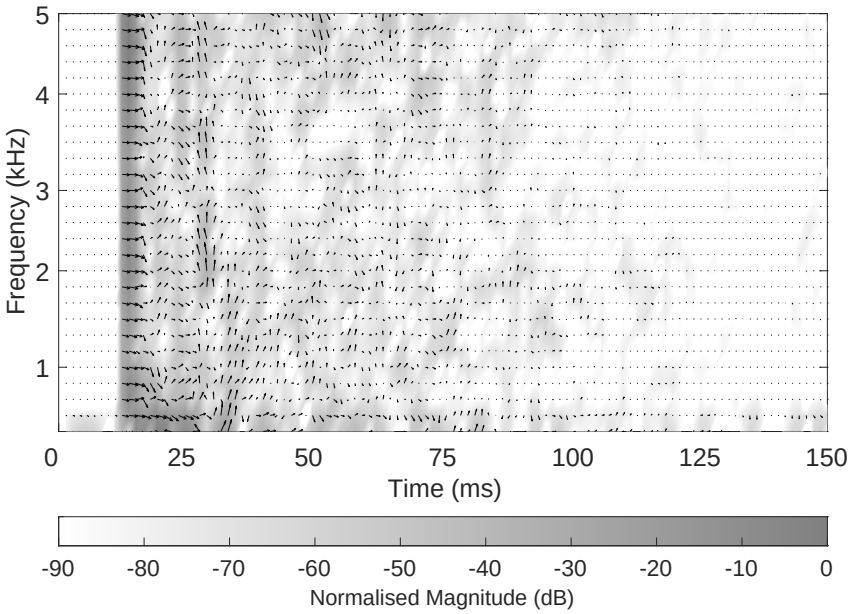


Figure 8. SIRR analysis plot of the B-format IR reorded at position S1R2 in the forest, where a spectrogram of the IR's W-channel is overlaid with arrows representing the direction of sound arrival (in the horizontal plane) in different frequency bins for each time frame.

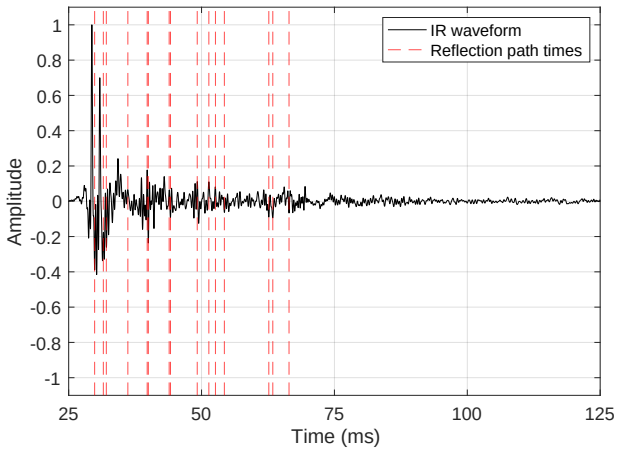


Figure 9. Waveform plot of impulse response recorded at position S1R2 in the scale model. The red lines indicate the estimated timing of early reflections.

The presented IR analysis has demonstrated the impact that tree trunks have on the acoustic of a forest environment. The presence of tree trunks results in strong early reflections (as shown by the SIRR analysis results), and can occlude sound paths reducing the acoustical clarity (as shown by the D50 results), and can increase reverberation time in 1 kHz and 2 kHz octave bands (as shown by the T30 results). The results presented here are limited by the small number of source and receiver positions, and the area of the forest environment surveyed and measured.

The results from the scale modelling work indicate that this may be a useful approach to the study of forest acoustics, as there are similarities between the scale model and in-situ results presented in the evaluation. That said, there are still a number of unanswered questions that bear consideration. There is further work to be done in assessing the appropriateness of the materials used in the scale model, and whether they correctly represent the full scale acoustic behaviour. The scale model used here is also limited to 33 trees in a 20m $\times$ 20m area (as determined by the chosen scale factor and model size limitations). Further work investigating the effect of the scale factor on the results, and the impact of the number of modelled trees, should be conducted.

6. REFERENCES

[1] C. Hansen and K. Hansen, "Recent advances in wind turbine noise research," in *Acoustics*, vol. 2, p. 13, MDPI, 2020.

[2] F. Wind. `https://www.forestwind.com.au/`.

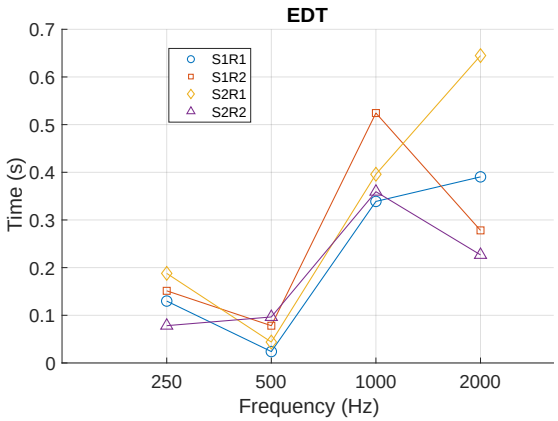


Figure 10. Early decay time (EDT) of four forest IRs at octave bands ranging from 125 Hz to 2 kHz.

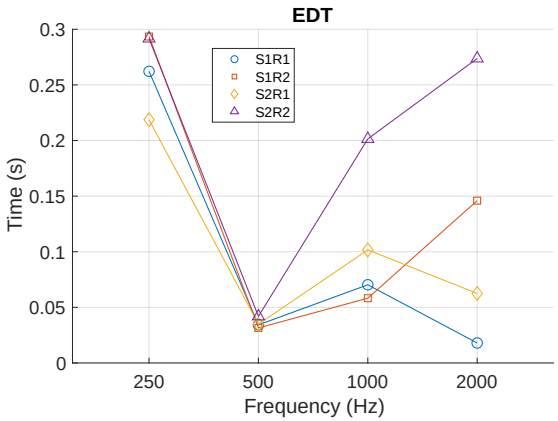


Figure 11. Early decay time (EDT) of four scale model IRs at octave bands ranging from 250 Hz to 2 kHz.

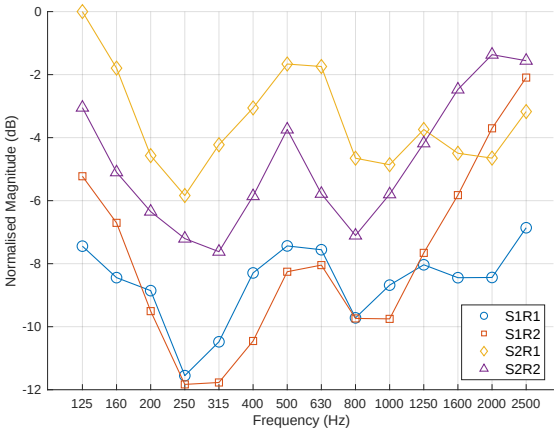


Figure 12. Spectral plots (1/3 octave bands) of the four in-situ IRs.

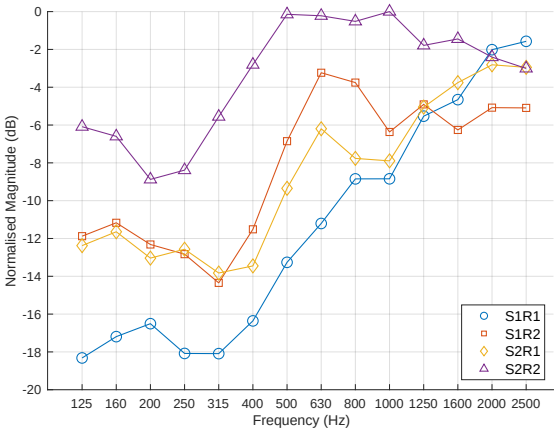


Figure 13. Spectral plots (1/3 octave bands) of the four scale model IRs.

[3] C. F. Eyring, "Jungle acoustics," *The Journal of the Acoustical Society of America*, vol. 18, no. 2, pp. 257–270, 1946.

[4] T. Embleton, "Sound propagation in homogeneous deciduous and evergreen woods," *The Journal of the Acoustical Society of America*, vol. 35, no. 8, pp. 1119–1125, 1963.

[5] D. Aylor, "Noise reduction by vegetation and ground," *The Journal of the Acoustical Society of America*, vol. 51, no. 1B, pp. 197–205, 1972.

[6] D. I. Cook and D. F. Van Haverbeke, "Trees and shrubs for noise abatement," *[s.l.]*, 1971.

[7] F. Fricke, "Sound attenuation in forests," *Journal of Sound and Vibration*, vol. 92, no. 1, pp. 149–158, 1984.

[8] C.-F. Fang and D.-L. Ling, "Investigation of the noise reduction provided by tree belts," *Landscape and urban planning*, vol. 63, no. 4, pp. 187–195, 2003.

[9] R. Bullen and F. Fricke, "Sound propagation through vegetation," *Journal of sound and Vibration*, vol. 80, no. 1, pp. 11–23, 1982.

[10] J. Kragh, "Road traffic noise attenuation by belts of trees," *Journal of Sound and Vibration*, vol. 74, no. 2, pp. 235–241, 1981.

[11] S. B. Shelley, D. T. Murphy, and A. J. Chadwick, "B-format acoustic impulse response measurement and analysis in the forest at koli national park, finland," in *Proceedings of the 16th International Conference on Digital Audio Effects (DAFx13)*, pp. 351–355, York, 2013.

[12] ISO3382-1, *3382, Acoustics–Measurement of room acoustic parameters–Part 1: Performance spaces, 2009*. ISO, 2009.

[13] M. A. Price, K. Attenborough, and N. W. Heap, "Sound attenuation through trees: Measurements and models," *The Journal of the Acoustical Society of America*, vol. 84, no. 5, pp. 1836–1844, 1988.

[14] H. Sakai, S. Shibata, and Y. Ando, "Orthogonal acoustical factors of a sound field in a bamboo forest," *The Journal of the Acoustical Society of America*, vol. 109, no. 6, pp. 2824–2830, 2001.

[15] M. Padgham, "Reverberation and frequency attenuation in forests—implications for acoustic communication in animals," *The Journal of the Acoustical Society of America*, vol. 115, no. 1, pp. 402–410, 2004.

[16] P. Chobeau, *Modeling of sound propagation in forests using the transmission line matrix method*. PhD thesis, Université du Maine, 2014.

[17] K. Spratt and J. S. Abel, "A digital reverberator modeled after the scattering of acoustic waves by trees in a forest," in *Audio Engineering Society Convention 125*, Audio Engineering Society, 2008.

[18] P. M. Morse, A. S. of America, and A. I. of Physics, *Vibration and sound*, vol. 2. McGraw-Hill New York, 1948.

[19] F. Stevens, D. T. Murphy, L. Savioja, and V. Välimäki, "Modeling sparsely reflecting outdoor acoustic scenes using the waveguide web," *IEEE/ACM Transactions on Audio, Speech, and Language Processing*, vol. 25, no. 8, pp. 1566–1578, 2017.

[20] E. De Sena, H. Hacıhabiboğlu, Z. Cvetković, and J. O. Smith, "Efficient synthesis of room acoustics via scattering delay networks," *IEEE/ACM Transactions on Audio, Speech, and Language Processing*, vol. 23, no. 9, pp. 1478–1492, 2015.

[21] F. Spandöck, "Akustische modellversuche," *Annalen der Physik*, vol. 412, no. 4, pp. 345–360, 1934.

[22] J. Y. Jeon, J. K. Ryu, Y. H. Kim, and S.-i. Sato, "Influence of absorption properties of materials on the accuracy of simulated acoustical measures in 1: 10 scale model test," *Applied Acoustics*, vol. 70, no. 4, pp. 615–625, 2009.

[23] T. J. Cox, B. M. Fazenda, and S. E. Greaney, "Using scale modelling to assess the prehistoric acoustics of stonehenge," *Journal of Archaeological Science*, vol. 122, p. 105218, 2020.

[24] J. H. Rindel, "Modelling in auditorium acoustics. from ripple tank and scale models to computer simulations," *Revista de Acústica*, vol. 33, no. 3-4, pp. 31–35, 2002.

[25] M. Ismail and D. Oldham, "A scale model investigation of sound reflection from building façades," *Applied Acoustics*, vol. 66, no. 2, pp. 123–147, 2005.

[26] J.-D. Polack, X. Meynial, G. Dodd, and A. H. Marshall, "The midas system for all scale room acoustics measurements," in *Audio Engineering Society Conference: 11th International Conference: Test & Measurement*, Audio Engineering Society, 1992.

[27] A. Burd, "Acoustic modelling-design tool or research project? chapter 7 in "auditorium acoustics" r. mackenzie," 1975.

[28] "Wheldrake Woods - Forestry England." https://www.forestryengland.uk/wheldrake-woods.

[29] S. Feng and F. Stevens, "Abies grandis forest, wheldrake wood - openair." `https://www.openair.hosted.york.ac.uk/?page_id=1293`.

[30] S. Feng and F. Stevens, "Forest scale model - openair." `https://www.openair.hosted.york.ac.uk/?page_id=1323`.

[31] H.-S. Yang, J. Kang, C. Cheal, T. V. Renterghem, and D. Botteldooren, "Quantifying scattered sound energy from a single tree by means of reverberation time," *The Journal of the Acoustical Society of America*, vol. 134, no. 1, pp. 264–274, 2013.

[32] K. B. Rasmussen, "How to take absorptive surfaces into account when designing outdoor sound reinforcement systems," in *Audio Engineering Society Convention 100*, Audio Engineering Society, 1996.

[33] F. Stevens, "Source localisation using early reflection information," Master's thesis, University of York, 2015.

[34] C. Cooper, "The sound of debate in georgian england: Auralising the house of commons," *Parliamentary History*, vol. 38, no. 1, pp. 60–73, 2019.

[35] J. Merimaa and V. Pulkki, "Spatial impulse response rendering i: Analysis and synthesis," *Journal of the Audio Engineering Society*, vol. 53, no. 12, pp. 1115–1127, 2005.

[36] F. Stevens and D. T. Murphy, "Acoustic source localisation in an urban environment using early reflection information," *Proc. EuroNoise 2015*, pp. 257–262, 2015.

DOI: 10.61782/fa.2025.0511

FORUM ACUSTICUM EURONOISE 2025

KEY UPDATES IN ISO 9613-2:2024 – WHAT'S NEW IN OUTDOOR NOISE PREDICTION STANDARDS

Omar Odeh[1*] **Aiham Khayyat**[2] **Dr. Dénes Kocsis**[3]
[1]Doctoral School of Informatics, University of Debrecen, Debrecen, Hungary
[2]Suhail Metal Formings, Street 10, Small and Medium Industrial Zone, Ar-Rayyan, Qatar
[3]Department of Environmental Engineering, Faculty of Engineering, University of Debrecen, Debrecen, Hungary

ABSTRACT

ISO 9613-2:2024 standard, titled "Acoustics — Attenuation of sound during propagation outdoors — Part 2: Engineering method for the prediction of sound pressure levels outdoors", which is a governing standard for outdoor sound propagation calculations, was recently revised with significant enhancements to improve the accuracy, consistency, and applicability of noise prediction models. The revision refines key parameters, such as meteorological corrections, ground effects, and source characterization, along with improved formulas for attenuation due to atmospheric absorption, updated guidance for terrain and obstacle modeling, and expanded methodologies for complex source configurations.

The new features were evaluated in this paper by presenting examples from a commercial noise mapping software that has already adapted the new revision, assessing their impact on noise modeling practice compared to the previous version, ISO 9613-2:1996. The paper also highlights how the updates align with advancements in measurement technologies and software tools. By summarizing these amendments, it offers valuable insights for acousticians, engineers, and regulatory authorities integrating the revised standard.

Keywords: *ISO standards, environmental noise, noise propagation, noise modeling, review study.*

[*]***Corresponding author***: *omarrodehh@gmail.com.*
Copyright: *©2025 First author et al. This is an open-access article distributed under the terms of the Creative Commons Attribution 3.0 Unported License, which permits unrestricted use, distribution, and reproduction in any medium, provided the original author and source are credited.*

1. INTRODUCTION

Modeling of outdoor sound propagation poses a critical aspect to urban and rural tranquility, environmental noise assessment, regulatory compliance, and civil planning, as urban acoustics are defined by different noise sources, environmental factors affecting noise propagation and a complex geometry with a high number of surfaces and materials [1].

ISO 9613-2:2024 standard, titled "Acoustics — Attenuation of sound during propagation outdoors — Part 2: Engineering method for the prediction of sound pressure levels outdoors", offers an engineering method for predicting sound attenuation in open environments to estimate noise levels from noise sources ranging from industrial facilities to transportation networks and urban development [2-3]. Since its release in 1996, ISO 9613-2 has been in wide use by acousticians. However, due to the latest advancements in computational noise modeling, environmental acoustics, and noise prediction methods, it went through a revision and was updated in 2024. ISO 9613-2:2024 introduced new correction factors, and refined existing formulas to provide more accuracy in noise modeling of various environmental conditions.

In the 1996 version of ISO 9613-2, sound attenuation was taken into account mainly for ground effect, atmospheric absorption, geometrical divergence, reflections, and diffraction [2]. However, research in outdoor sound propagation revealed some limitations in the use of these calculations, especially with respect to ground effect modeling, multi-edge diffraction, and reflections from curved surfaces [4-5]. One of the newly added features in the 2024 revision addresses these gaps by introducing a ground effect correction factor (K_{geo}), improved screening calculations, and refined directivity correction (D_c) for

chimney stacks. Furthermore, the revision includes a comprehensive approach to calculate the foliage attenuation as an alternative to the simplified empirical method of ISO 9613-2:1996.

This study compares ISO 9613-2:1996 and ISO 9613-2:2024 by highlighting the influence of these changes on environmental noise mapping. The methodology section summarizes the main computational changes implemented in the 2024 version and the corresponding scientific literature. Finally, the results section presents the effect of these updates utilizing a commercial noise mapping software which implemented ISO 9613-2:2024, in the form of noise maps. By linking the theory behind the updates in the standard with relevant practical examples, this study describes how ISO 9613-2:2024 improves the accuracy of outdoor noise predictions, and make it a more effective tool for acousticians, urban planners, and policymakers.

2. MATERIALS AND METHODS

As mentioned earlier, the purpose of this study is to compare ISO 9613-2:1996 and ISO 9613-2:2024 standards as they pertain to advancements in outdoor noise propagation modeling.

The comparison is made following an organized approach beginning with a review of ISO 9613-2 revised methodology, which is primarily based on octave band calculations to predict outdoor sound levels taking into account the influence of ground effect, atmospheric absorption geometrical divergence, reflections, and screening by obstacles [2-3]. ISO 9613-2:2024 implements some clarifications adopted from ISO 17534-3 standard, titled “Acoustics — Software for the calculation of sound outdoors — Part 3: Recommendations for quality assured implementation of ISO 9613-2 in software according to ISO 17534-1”, which includes improved screening calculations [6]. The mathematical refinements studied in this paper are; K_{geo}, a geometric correction factor that eliminates ground effect attenuation (A_{gr}) under certain height conditions, A_{bar}, barrier attenuation, A_{curv}, which considers additional attenuation from curved surfaces and is part of the attenuation due to miscellaneous other effects (A_{misc}), foliage attenuation, A_{fol}, and chimney stacks directivity factor, D_c.

2.1 Ground Effect Correction Factor

K_{geo} factor in the 2024 revision directly addresses the need for ground interactions with the sound waves, which depends on the ground surface and source-receiver geometry, given by the following formula:

$$K_{geo} = \frac{d_p^2 + (h_S - h_R)^2}{d_p^2 + (h_S + h_R)^2} \quad (1)$$

where,

d_p: the source to receiver distance projected on the horizontal plane, expressed in meters;

h_S: the height of the source above ground, expressed in meters;

h_R: the height of the receiver above ground, expressed in meters.

This new factor led to the need of revising the existing formula to calculate A_{gr} in dB as follows:

$$A_{gr} = 10 \log[1 + (10^{\frac{-A'_{gr}}{10}} + 1) \times K_{geo}] \quad (2)$$

$$A'_{gr} = A_S + A_R + A_m \quad (3)$$

where,

A_S: the source region, stretching over a distance from the source towards the receiver of $30\,h_S$, with a maximum distance of d_p;

A_R: the receiver region, stretching over a distance from the receiver back towards the source of $30\,h_R$, with a maximum distance of d_p;

A_m: a middle region, stretching over the distance between the source and receiver regions. If $d_p < (30\,h_S + 30\,h_R)$, the source and receiver regions will overlap, and there is no middle region.

In summary, K_{geo} eliminates the ground effect if the source and receiver heights are much larger compared to the distance between them, which was confirmed by research that highlighted the need of this factor to increase the modeling accuracy due to the inconsistencies of ground reflection in previous methods [7].

2.2 Improved Screening Calculations

As mentioned earlier, the updated version of the standard expands the screening effect extensively. This effect varies depending on the height of the noise measurement and the distances between the sound source and the screen or barrier [8], this has been done by improving the calculation of the barrier attenuation (A_{bar}) which is determined by (Z_{min}) the minimum difference between the paths of the direct sound as if there were no barrier and diffracted path above the barriers. This is particularly helpful in multi-edge diffraction settings like urban environments.

Furthermore, ISO 9613-2:2024 implements the reflection condition recommended in ISO 17534-3. The barrier

attenuation (A_{bar}) in dB, which represents the sound attenuation due to a barrier is considered be equal to the diffraction attenuation of the barrier for each octave band (D_z) if the ground effect (A_{gr}) attenuation is larger than zero.

$$A_{bar} = D_z \; if \; A_{gr} > 0 \tag{4}$$

2.3 Reflection of Cylindrical Surfaces

ISO 9613-2:2024 now sheds light on two major parts; the first focusing on planar reflections, while the second deals with curved structures as in chimney stacks, storage tanks or silos. A reflection model for cylindrical surfaces was introduced to calculate additional attenuation based on the radius and the angle of incidence.

Curved surfaces in sound wave interactions emphasize the imperfection of the existing models in urban scenarios. For example, curved architectural elements can lead to unplanned sound concentration [9], requiring design interventions to achieve noise free distribution.

New refinements in diffraction and screening calculations have also been introduced. The complex barriers or multi-screen situations [10] lead to underestimation of noise reduction when using a single diffraction edge model as screening attenuation in ISO 9613-2:1996. It further improves this by introducing side screening factors that include diffraction across multiple edges, resulting in more accurate attenuation estimation. Figure 1 illustrates how sound rays are expected to reflect from a cylinder considering all dimensions in projection are parallel to the axis [4].

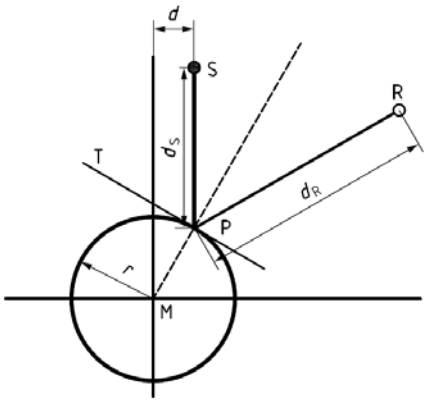


Figure 1. Reflection of sound ray at a cylinder.

The introduction of an additional attenuation term (A_{curv}) also includes reflections from cylindrical surfaces in dB, where A_{curv} can be defined as:

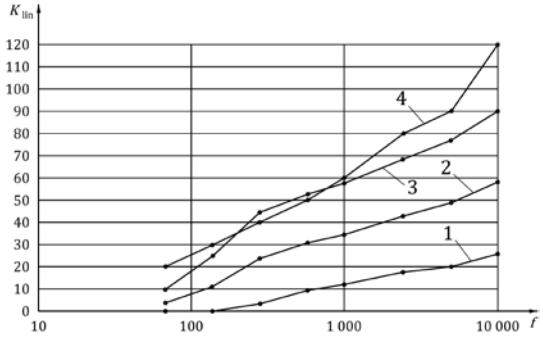
$$A_{curv} = 10\log[1+\frac{2d_s d_R}{r(d_s+d_R)}(1-k^2)^{\frac{-1}{2}}] \tag{5}$$

$$k = \frac{d}{r} \tag{6}$$

where,
M: center-point;
S: point source;
R: receiver;
R: radius, expressed in meters;
P: point of reflection;
T: tangent in point of reflection;
d_S: source-receiver distance, expressed in meters;
d_R point of reflection-receiver distance, expressed in meters;
d: distance of the straight line defined by the incident ray from the center-point, expressed in meterts.

2.4 Attenuation of Foliage

The 2024 revision provides a more comprehensive foliage attenuation (A_{fol}) method, whereas the 1996 edition included only a simple empirical correction for tree belts or vegetation. The new method includes five forestry parameters, namely stem diameter (D), basal area (G), standing stock (V), horizontal structuring (S), and low height foliage (Z). Vegetation density, thickness and structural parameters were found to have a significant impact on sound attenuation in urban and suburban areas [11], which makes this update consistent with these findings. In addition, the frequency dependent attenuation factor (K_{lin}) is introduced in the new method to improve prediction under different environmental conditions. Figure 2 below highlights the typical ranges of K_{lin} as specified in ISO 9613-2:2024 [3].



Key

K_{lin}	attenuation factor, expressed in decibels per kilometre
f	frequency, expressed in hertz
1	light forest
2	normal forest
3	dense forest
4	attenuation with simplified method A.2.2 for 20 m ≤ d_f ≤ 200 m

Figure 2. Typical K_{lin} factors for different forestall parameters.

2.5 Directivity of Chimney Stack

Finally, the directivity correction of chimney stacks (D_c) is introduced. In ISO 9613-2:1996, chimney stacks were modeled as point sources, with the assumption of an omnidirectional radiation pattern. Nevertheless, the update indicates that industrial stacks have strong directional characteristics and hence a correction factor is required to account for the receiver level calculations. This correction is now embedded in the 2024 update and defined as D_c, which is a function of the opening geometry and radiation characteristics which depends on the frequency. Chimney stack directivity correction (D_c) is now included in the calculation of the receiver level for the equivalent continuous downwind octave band source sound pressure level at a receiver location.

This study evaluates the methodological improvements in outdoor noise prediction using practical simulations of a commercial noise mapping software, i.e. SoundPLAN. The impact of these updates is illustrated with figures and examples through the next section.

3. RESULTS

The present section summarizes the findings of noise modeling utilizing both ISO 9613-2:2024 and ISO 9613-2:2024. The results are presented in the form of noise maps.

3.1 Ground Effect Correction Factor

To evaluate the effect of K_{geo} on environmental noise propagation, two cases were assessed assuming a fully reflective ground (G=0), and noise maps highlighting the difference between 1996 and 2024 versions results were generated. In Figure 3, a point source was placed at a height of 50 m above ground level and a vertical cross-sectional grid noise map was generated to reflect the difference in noise levels between both versions. In a close distance at the same height of the source, a 3 dB difference was observed, which can be related to the fact that K_{geo} removes ground effect if the source and receiver heights are much larger compared to the distance between them. However, in Figure 4, the source was positioned at 2 m above ground level and therefore the difference between both versions is negligible.

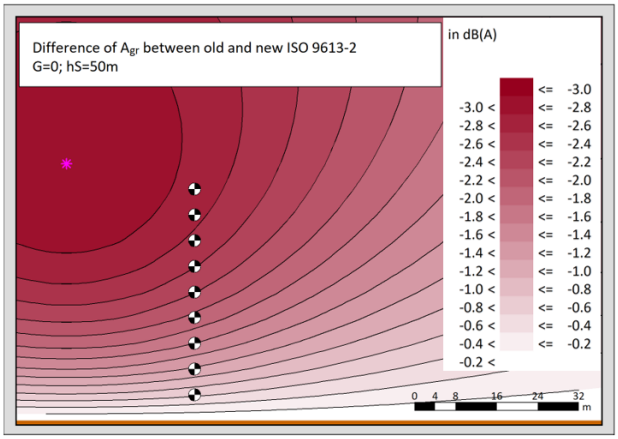


Figure 3. Difference of A_{gr} between 1996 and 2024 ISO 9613-2. Source height 50 m above ground level.

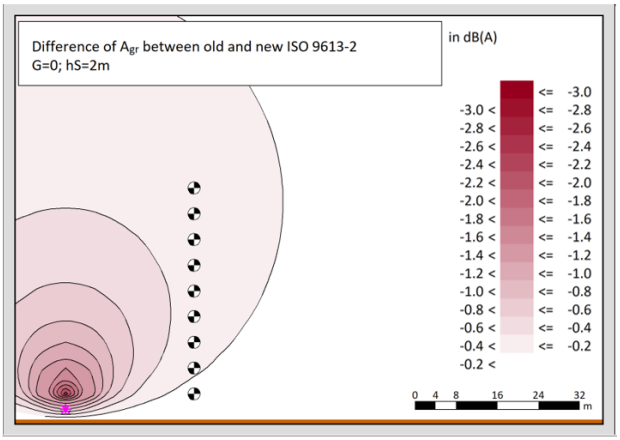


Figure 4. Difference of A_{gr} between 1996 and 2024 ISO 9613-2. Source height 2 m above ground level.

3.2 Reflection of Cylindrical Surfaces

Figure 5 and Figure 6 below show the difference in sound ray reflections at polygons and cylinders for 1/1 octave bands from 63 Hz to 8000 Hz.

In ISO 9613-2:1996, A_{curv} was not defined. Therefore, cylindrical surfaces were modelled as polygons. However, after defining A_{curv} in ISO 9613-2:2024, cylinder objects are now introduced in the mapping software, to account for more reflection points of sound rays. It can be noticed that cylinders have continuous reflections for all frequencies, while polygon objects have minimal reflections on examined frequencies until 500 Hz and straight line reflections due to the multi-edge polygon from 1000 Hz reaching 8000 Hz.

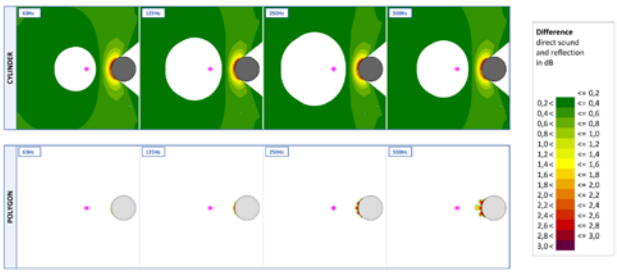


Figure 5. Difference between direct sound and reflection for 1/1 octave bands from 63 Hz to 500 Hz at polygon and cylinder objects.

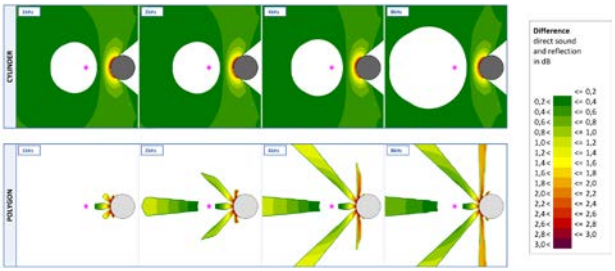


Figure 6. Difference between direct sound and reflection for 1/1 octave bands from 1 kHz to 8 kHz at polygon and cylinder objects.

3.3 Directivity of Chimney Stack

Chimney stacks and other vertical upward-facing open objects' sound is modelled as a point source in the center of the opening assuming omnidirectional radiation. However, ISO 9613-2:2024 indicates that a frequency-dependent directivity correction factor (D_c) shall be considered in noise modeling based on tables resulted from measurements conducted on large industrial chimneys [3].

Figure 7 illustrates how sound waves propagate at 125 Hz and 4000 Hz after implementing the chimney stack directivity correction D_c. This implementation is expected to increase precision and accuracy of noise modeling when compared in-situ sound propagation of chimney stacks.

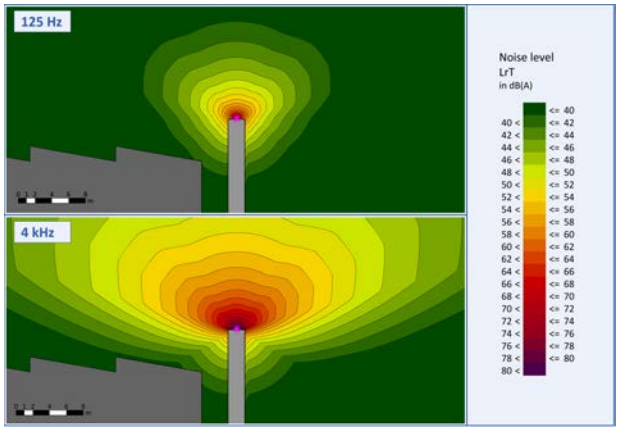


Figure 7. Sound propagation for a chimney stack (radius 1m) implementing directivity correction at 125 Hz and 4 kHz.

In summary, ISO 9613-2:2024 significantly enhances the accuracy of outdoor noise modeling by introducing key refinements that are directly applicable to environmental noise assessments. In practical tools like SoundPLAN, visualizations of parameters such as A_{curv} and K_{geo} illustrate

how curved surfaces influence noise propagation and how source and receiver heights affect ground attenuation. These advancements are expected to improve noise mapping overall and enhance the precision of environmental noise evaluations in particular.

4. CONCLUSION

The differences between ISO 9613-2:1996 and ISO 9613-2:2024 are substantial in terms of the modeling of sound propagation. The standard's predictive accuracy is improved through introduction of K_{geo} for ground effects, A_{curv} for cylindrical reflections, refined screening calculations and expanded foliage attenuation model. These changes are shown to be practical for the implementation in noise mapping software, which show that they result in more accurate noise assessments and better mitigation strategies. This revision ensures that ISO 9613-2 continues to be a reliable outdoor noise prediction standard for urban planners, environmental engineers, and regulatory agencies alike.

5. REFERENCES

[1] Attenborough, K., Li, K. M., & Horoshenkov, K. (2007). Predicting outdoor sound (1st ed.). CRC Press. https://doi.org/10.1201/9781482295023

[2] ISO 9613-2:1996 - Acoustics — Attenuation of sound during propagation outdoors — Part 2: Engineering method for the prediction of sound pressure levels outdoors.

[3] ISO 9613-2:2024 — Acoustics — Attenuation of sound during propagation outdoors — Part 2: Engineering method for the prediction of sound pressure levels outdoors.

[4] Bérengier, M., Gauvreau, B., Blanc-Benon, P., & Juvé, D. (2003). Outdoor sound propagation: A short review on analytical and numerical approaches. Acta Acustica united with Acustica, 89, 980–991.

[5] Vercammen, M. L. S. (2012). Sound concentration caused by curved surfaces (Doctoral dissertation, Technische Universiteit Eindhoven). Technische Universiteit Eindhoven. https://doi:10.6100/IR732483

[6] ISO 17534-3:2015 — Acoustics — Software for the calculation of sound outdoors — Part 3: Recommendations for quality assured implementation of ISO 9613-2 in software according to ISO 17534-1.

[7] De Jong, B. A., Moerkerken, A., & van der Toorn, J. D. (1983). Propagation of sound over grassland and over an earth barrier. Journal of Sound and Vibration, 86(1), 23–46. https://doi.org/10.1016/0022-460X(83)90941-0

[8] Montes González, D., Barrigón Morillas, J. M., Godinho, L., & Amado-Mendes, P. (2018). Acoustic screening effect on building façades due to parking lines in urban environments: Effects in noise mapping. Applied Acoustics, 130, 1–14. https://doi.org/10.1016/j.apacoust.2017.08.023

[9] Cairoli, M. (2020). Ancient shapes for modern architectural and acoustic design: Large interiors formed by curved surfaces. Applied Acoustics, 170, 107497. https://doi.org/10.1016/j.apacoust.2020.107497

[10] Menounou, P., Salagas, S., & Nikolaou, P. (2025). Empirical formulas for the prediction of the diffraction field around rigid, absorbing, single or multiple wedges. Applied Acoustics, 233, 110592. https://doi.org/10.1016/j.apacoust.2025.110592

[11] Attal, E., & Dauchez, N. (2025). Acoustic performance of foliage based on green systems at normal incidence. Applied Acoustics, 234, 110591. https://doi.org/10.1016/j

DOI:

Main theme: A05 Environmental Acoustics

Session A05.08 Advances in noise mapping

Chair(s): E. Murphy, D. Manvell

DOI: 10.61782/fa.2025.0617

FORUM ACUSTICUM EURONOISE 2025

NOISE POLLUTION IN SPAIN: TOWARDS A COMPREHENSIVE ASSESSMENT

Ignacio Soto-Molina[1,2*] **Miguel Ángel González García**[1]
Carlos Soriano Pastor[1] **Rosa María Arce Ruiz**[2]

[1] Ministerio para la Transición Ecológica y el Reto Demográfico (SGPC-MITECO), Madrid, España
[2] Centro de Investigación del Transporte, TRANSyT, Universidad Politécnica de Madrid, España

ABSTRACT

This research addresses the lack of a comprehensive view of noise pollution in Spain, which affects both citizens' quality of life and the preservation of terrestrial habitats. Strategic Noise Maps (SNMs), developed under the Environmental Noise Directive (END), currently cover only agglomerations with more than 100,000 inhabitants and major infrastructure (roads, railways, and airports). Consequently, large areas of the territory, smaller municipalities, and other significant sources, such as industry, ports, leisure activities, and events, are ignored, resulting in information gaps. This work highlights the need for an integrated diagnosis of noise produced by all sources, regardless of whether or not they are within the scope of the END, and shows progress in the development of a methodology for an integrated diagnosis of road noise, covering all sources of road traffic noise in Spain. Furthermore, it proposes analyzing the effects of noise pollution on human health and the loss of terrestrial habitat quality, with the goal of generating concise information for society. Through this assessment, the aim is to establish a solid foundation for the implementation of policies and measures to reduce noise levels, thus ensuring effective protection against noise pollution in Spain.

Keywords: *Noise pollution, Strategic Noise Maps, Noise assessment, Spanish strategy against noise*

**Corresponding author*: isoto@miteco.es.

Copyright: *©2025 Soto-Molina et al. This is an open-access article distributed under the terms of the Creative Commons Attribution 3.0 Unported License, which permits unrestricted use, distribution, and reproduction in any medium, provided the original author and source are credited.*

1. INTRODUCTION

In Spain, there is no comprehensive understanding of the existing noise pollution issues affecting both the quality of life for citizens and the habitats for terrestrial wildlife [1, 2]. Strategic Noise Maps, prepared by various Competent Authorities, offer insights into the noise situation in urban agglomerations with over 100,000 inhabitants and near major sources (significant noise emitters) as defined by the Environmental Noise Directive (END). This includes roads with more than 3,000,000 vehicles per year, railways with more than 30,000 traffic per year, and airports with more than 50,000 operations per year. However, areas likely impacted by sources that do not meet these thresholds, as well as other types of noise sources, are often not adequately studied [3, 4]. These data may not, therefore, be included in the National Information System on Noise Pollution (SICA) [1] . According to the information available on SICA, Spain only reports to the European Commission strategic noise mapping data for 64 agglomerations with more than 100,000 inhabitants, 21,000 km of major roads, 1,800 km of major railways, and 13 major airports.

This means, studies for 87 cities with populations between 50,000 and 100,000; 613 cities with populations between 10,000 and 50,000; 2,381 cities with populations between 1,000 and 10,000; and 4,986 towns with fewer than 1,000 inhabitants [2] have not been included in the strategic noise mapping.

Furthermore, derived from the consultation of the

[1] https://sicaweb.cedex.es/
[2] https://www.ine.es

transport network cartography of the National Geographic Information Center of Spain [3], excluded from the END scope are 154,000 km of roads, 21,770 km of railways, and 1,136 air facilities, including aerodromes, heliports, and hydro-aerodromes.

Regarding industrial sources, a significant number of 9,067 industrial facilities registered in the Spanish State Registry of Emissions and Polluting Sources (PRTR) [4], and 1,345 wind farms deploying over 22,000 wind turbines are not included in the SICA. Also, according to the Spanish public body Puertos del Estado [5], 49 major state port facilities are also out of the scope of END.

Lastly, local disturbances from sources such as leisure noise, neighborhood activities, urban service noise, recreational events, and construction noise are also overlooked in the SICA, and have an important effect on health [5].

From what has been discussed so far, it can be deduced that the Environmental Noise Directive suffers from "original sin." By determining the study areas based on noise sources, rather than sensitive receptors, it leaves a large part of the human population and sensitive receptors in the natural environment outside its scope.

This lack of a comprehensive perspective on noise pollution has led organizations such as the European Environment Agency (EEA) to attempt to assess noise problems globally [6], using gap-filling statistical methods [7]. However, these estimates can be significantly biased due to the lack of comprehensive data, and they do not address the problem, as they still fail to identify areas affected by noise that require corrective action.

For these reasons, the Spanish Ministry for Ecological Transition and the Demographic Challenge (MITECO) asserts the need for a comprehensive assessment of noise pollution problems. This assessment is crucial for establishing an initial understanding of noise-related issues, analyzing the potential human health impacts of noise pollution, and how it correlates with the degradation of natural terrestrial habitats. Providing synthesized information on noise pollution in Spain could be made publicly accessible through synoptic documents that would support monitoring and evaluating the effectiveness of policies aimed at mitigating noise pollution.

The aforementioned diagnosis is currently in the development phase, with the MITECO team working on global noise models for roads, aeronautical noise, and railways, and advancing evaluation methodologies for the remaining sources (industry, leisure activities, works and other). In this communication, we focus on the global road noise model. It is considered one of the most important because, globally, road traffic has the greatest impact on the acoustic quality of the environment [8].

2. OBJETIVES

Thus, the objectives of the global analysis of road noise in Spain are as follows:

General Objective: To comprehensively assess road traffic noise pollution across Spain, including areas not covered by the Strategic Noise Maps established under the Environmental Noise Directive (END), in order to provide a complete understanding of the issue, enhance the knowledge base on the health and environmental impacts of noise, and support policy-making through accessible and nationally consistent tools.

Specific Objectives

- To identify and quantify the acoustic impact of road traffic in areas not included in the END, such as municipalities with fewer than 100,000 inhabitants, rural environments, and low-traffic interurban roads.
- To fill the existing data gaps in the National Information System on Noise Pollution (SICA), by incorporating information on road segments, environmental conditions, and population exposure.
- To estimate the number of people potentially exposed to harmful noise levels in areas not currently addressed by strategic noise mapping.
- To evaluate the impact of road traffic noise on the acoustic quality of terrestrial habitats, particularly in protected areas such as the Natura 2000 protected areas network.
- To develop a transparent and reproducible nationwide modeling methodology, integrating open data and open-source technologies.
- To provide a solid technical foundation for the design and implementation of public policies such as the National Noise Strategy, ensuring effective, equitable, and consistent noise protection throughout the Spanish territory.

[3] https://centrodedescargas.cnig.es/CentroDescargas/redes-transporte

[4] https://prtr-es.es

[5] https://www.puertos.es

3. MAIN REFERENCE WORKS

Few studies address noise impact assessment using national-scale models. Countries implementing systemic environmental noise management models typically incorporate advanced statistical methodologies and large-scale data approaches to effectively quantify the impacts of noise pollution [7].

However, several relevant reference works, platforms, and tools have contributed to the development of comprehensive noise assessments at the national and international levels. These resources provide methodological guidance, technical capabilities, and strategic perspectives applicable to the Spanish context.

Notable progress has been made in the Fourth Round of the END implementation in France, where a national database, PlaMADE, was adopted [9]. This database compiles essential data for the development of large-scale noise maps through automated processes using open-source modeling tools [10]. This method not only improves the efficiency of data processing but also provides a more comprehensive national overview of noise pollution, helping competent authorities develop informed noise reduction strategies.

The U.S. National Transportation Noise Map [6], developed by the Volpe National Transportation Systems Center, provides a large-scale visualization of noise exposure from transportation sources across the United States. It serves as a reference for national modeling using open datasets, integrating road, rail, and airborne noise data with demographic information. Similarly, the U.S. National Park Service Noise Map provides large-scale maps of existing acoustic conditions across the country, as well as a map of natural conditions, calculated from long term measurements of sound in national parks as well as urban and rural areas across the country [7].

As for open and collaborative tools, the *Noise Map Tool* [8] is an interactive dashboard that visualizes global noise pollution generated by aircraft and other modes of transportation. It compiles real-time aircraft positions and performs noise simulations to estimate hourly noise exposure near airports. Developed and maintained by Nawar Halabi, it exemplifies the potential of data-driven, web-based noise assessment platforms.

From a computational perspective, some works have highlighted the importance super-computing for noise assessments. For example, the work of Ming Cai et al. [11] presents methodologies for modeling urban traffic noise in complex 3D building environments using high-performance computing, which has implications for model refinement in dense urban areas. Also, the noise maps of major infrastructures in France from the Fourth Phase, previously mentioned, have been produced using supercomputing systems [10].

Together, these references, among others, lay the foundation for the national assessment of road noise pollution in Spain. They highlight the integration of standardized assessment frameworks (CNOSSOS-EU), the use of massive data, environmental considerations, and advanced computing as pillars of modern noise assessments.

4. METODOLOGY

The methodology outlined in the following sections focuses on the development, calculation, and calibration of a large-scale road traffic noise model in Spain. Much work remains to be done in the evaluation of results for the exposed population and impacts on the natural environment, aspects not addressed in this paper.

4.1 Geographical Scope of Study

The study area is the entire national territory. The calculation area is the entire territory located within 1,500 meters of any road axis (streets, roads, highways, and motorways) mapped in the National Geographic Institute's transport network database and considered capable of supporting road traffic.

Regarding distance calculation, in Stylianos Kephalopoulos et al. (2014) [3], a calculation distance of less than 800 meters is recommended. However, since that publication, the CNOSSOS-EU method has been corrected [12]. The propagation method is based on the ISO 9613-2 standard [13, 14], which does not establish a distance limit. The CEDEX CNOSSOS-EU technical application guide [15] establishes calculation distances greater than 2,000 meters for average daily traffic intensities greater than 300,000 vehicles. Since the propagation method is based on spherical divergence and attenuation and corrections due to atmospheric and environmental conditions, a 1,500 meters source-receiver distance is considered adequate for the purpose of this study.

[6] https://maps.dot.gov/BTS/NationalTransportationNoiseMap/
[7] https://www.nps.gov/subjects/sound/soundmap.htm
[8] https://noise-map.com

4.2 Software and Hardware Tools

NoiseModelling software [16] (NM) is used. *NoiseModelling* is a free and open-source tool designed to calculate noise maps in urban areas, as well as road, railway, and industrial source maps. As stated on its GitHub repository [9], it can be freely used for research, education, or by experts for professional use. NM has been used in various academic and institutional settings [10]. Of note is the creation of the French Government's strategic road noise maps, corresponding to the Fourth Round of END, through the creation of a national database, which feeds the NM software and allows for periodic updates of these maps [10]. The version of *NoiseModelling* used in this study was 4.0.5. According to the developers, this software reasonably complies with the ISO 17534-4:2020 standard checks for the application of the CNOSSOS-EU method.

The noise simulations were carried out using a high-performance workstation equipped with an Intel® Xeon® w9-3475X processor running at 2.21 GHz and 512 GB of installed RAM (fully usable). This equipment was provided to MITECO by the Center for Studies and Experimentation of Public Works (CEDEX) [11], Spain.

4.3 Data Sources for Acoustic Environment Modelling

The following data sources were used to design the acoustic environment, all from the official cartography of the Spanish National Geographic Information Center (CNIG) [12]:

Road transport network mapping, which includes all types of roads with traffic, from residential streets to major thoroughfares.

National Topographic Database (BTN), from which information on buildings, both residential and other types, is extracted.

Digital Terrain Model (DTM), at a scale of 1:25,000, used to obtain the topography.

Digital Building Surface Model (MDSnE2.5 2nd Coverage), used for automatic building height assignment.

4.4 Traffic Data and Emission Power Assignment

In CNOSSOS-EU method, the emission power of roads is obtained from their traffic intensity, pavement conditions and vehicle type distribution. The traffic intensity of main roads was obtained from the massive data provided by the Ministry of Transport and Sustainable Mobility [13]. This source offers traffic information for the main national roads and many sections of regional and provincial roads [14].

For the remaining roads for which traffic data are unavailable, the assignment was carried out according to the recommendations of the *Good Practice Guide for Strategic Noise Mapping and the Production of Associated Data on Noise Exposure* [17]. All roads have been assigned the CNOSSOS-EU reference pavement.

4.5 Calculation Process

The simulation process involved dividing the calculation area into 1,058 subdomains, each corresponding to one of the 25,000-scale sheets of the national topographic database. For each subdomain, specific layers were generated, including roads, buildings, a digital terrain model (DTM), and receptors. The calculations were launched by piloting the *NoiseModelling* software using scripts, as indicated in the official documentation [15]. However, it was also necessary to develop additional Python scripts to automatically generate and execute the corresponding software commands for batch processing.

Due to computational capacity constraints, the density of receptors was limited by applying a triangulation with a maximum mesh size of 2,500 m^2, which corresponds to a maximum spacing of 50 m between receptors. This triangulation was performed using the Delaunay algorithm implemented in the *NoiseModelling* software, which enables the refinement of receptor density in acoustically sensitive areas (e.g., near buildings), while reducing density in free-field zones. This approach optimizes the computational load without compromising accuracy in critical regions [18]. The evaluation periods, reflection order, meteorological conditions, and probable propagation conditions are those recommended in the CEDEX CNOSSOS-EU guide [15].

[9] https://github.com/Universite-Gustave-Eiffel/NoiseModelling

[10] https://noisemodelling.readthedocs.io/en/latest/Scientific_production_list.html

[11] https://www.cedex.es

[12] https://centrodedescargas.cnig.es

[13] https://www.transportes.gob.es/ministerio/proyectos-singulares/estudios-de-movilidad-con-big-data/opendata-movilidad

[14] https://mapas.fomento.gob.es/VisorHermes

[15] https://noisemodelling.readthedocs.io/en/latest/Get_Started_Script.html

After the simulation, the results were transformed into raster format by applying interpolation over the irregular triangular network, enabling spatial visualization and analysis of the acoustic indicators.

4.6 Calibration Procedure

The Strategic Noise Maps (SNM) of the Fourth Round of the Noise Directive (END) of the official agglomerations of A Coruña, Santander, Bilbao, Pamplona, Salamanca, Roquetas de Mar, Madrid, Barcelonès, Vallès Occidental I and II, Sevilla and Valencia were used for the calibration process.

A total of 8,696,039 point pairs were generated, each representing a spatial match between the simulated noise levels and the official SNM data. These point pairs were used to extract and compare values of the calculated noise levels and the reference data. A linear regression model was then applied to fit the simulated results to the official values. This linear transformation was applied to the raster layers of calculated noise levels.

5. RESULTS

5.1 Calculated Noise Map

Table 1 summarizes the descriptive statistics for the initial calculated road traffic noise simulation (LAEQ data), compared to the reference values (LAEQ_Ref) obtained from those points with values above 30 dB, resulting in a total of 8,696,039 valid records.

Table 1: Descriptive statistics of LAEQ and LAEQ_Ref (only values $>$ 30 dB)

Statistic	LAEQ_Ref (dB)	LAEQ (dB)
Mean	56.17	59.75
Median	57.00	58.98
Std. Dev	10.60	11.85
Min	31.00	30.00
Max	101.00	96.80

As observed, the uncalibrated model tends to overestimate sound levels, with LAEQ values on average 3.6 dB higher than the references. Figure 1a shows the histogram of LAEQ distribution, with a peak between 55 and 60 dB, slightly shifted to the right of the LAEQ_Ref distribution.

The correlation between LAEQ and LAEQ_Ref was 0.575, and the linear regression model yielded the following equation:

$$\begin{aligned} L_{AEQ} &= 23.6350 + 0.6429 \cdot L_{AEQ_{\text{Ref}}}, \\ R^2 &= 0.331 \end{aligned} \tag{1}$$

This indicates a moderate association, with only 33.1% of the variance explained by the reference values, and a slope significantly less than 1, suggesting a proportional underresponse of the calculated indicator relative to the reference. The weak association also indicates that there is no real linear correlation between the two variables. Noise data depend on a set of highly heterogeneous variables, and small variations in the input data can significantly alter the model's output [19].

5.2 Calibrated Noise Map

To correct the overestimation observed in the initial model, a calibration process was carried out using a linear regression adjustment. This yielded a calibrated indicator, LAEQ_Cal, which was subsequently used to replace the original values.

The calibration reduced the average estimated levels, bringing them closer to the reference values, as shown in Table 2.

Table 2: Descriptive statistics of LAEQ_Cal and LAEQ_Ref (only values $>$ 30 dB)

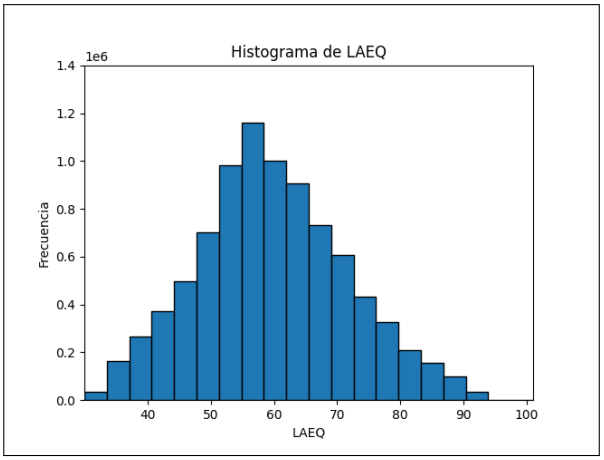
Statistic	LAEQ_Ref (dB)	LAEQ_Cal (dB)
Mean	56.17	54.22
Median	57.00	53.51
Std. Dev	10.60	10.41
Min	31.00	30.00
Max	101.00	86.68

Although LAEQ_Cal tends to slightly underestimate the reference values, the bias has been significantly reduced. The histogram in Figure 1b illustrates a shift of the distribution toward lower values compared to the original LAEQ.

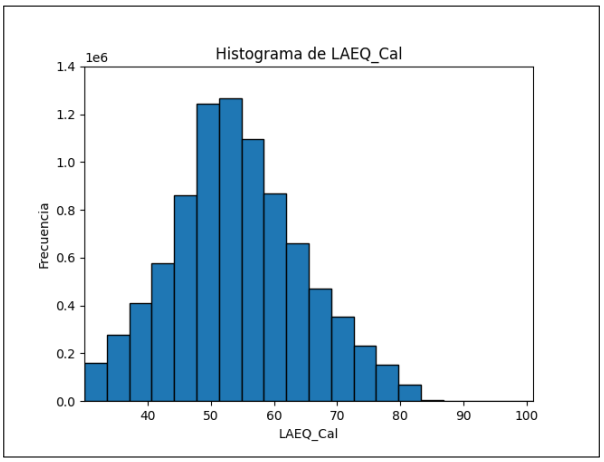
The adjusted regression model is:

$$\begin{aligned} L_{AEQ_{\text{Cal}}} &= 22.0235 + 0.5732 \cdot L_{AEQ_{\text{Ref}}}, \\ R^2 &= 0.340 \end{aligned} \tag{2}$$

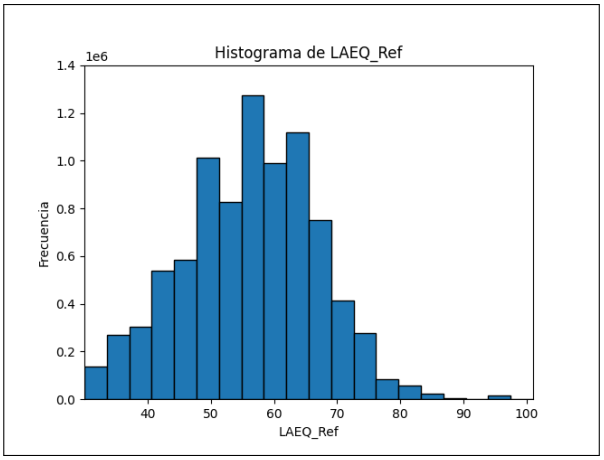
With a slightly improved R^2 and points correlation (from 0.575 to 0.583), the calibration enhances the consistency between calculated and reference values.



(a) Histogram of LAEQ (original calculated values).



(b) Histogram of LAEQ_Cal (after calibration).



(c) Histogram of LAEQ_Ref (reference values).

Figure 1: Comparison of LAEQ distributions before and after calibration, and reference values.

6. DISCUSSION

In the creation of a road noise map for Spain, significant differences were observed when compared to official strategic noise maps. Understanding these discrepancies is important for interpreting the data accurately and grasping the wider implications associated with noise pollution assessment and management.

One of the primary factors contributing to the difference between the calculated noise map from this work and the reference maps is the use of lower-precision source cartography, particularly regarding the digital terrain model employed. The DTM used in this study was less precise as a consequence of attempting to cover a larger calculation area within computational limitations. This inaccuracy inevitably leads to an underrepresentation of terrain-induced attenuation effects that are integral to interpreting noise propagation. According to Renterghem et al. [5], inaccuracies in urban noise mapping frequently stem from adjustments made to reflect the topographic characteristics of the area under consideration. The lack of rigorous terrain models can result in an inadequate reflection of real-world conditions, which is essential for properly modeling the effects of topography.

Furthermore, the absence of noise barriers in the calculated map remains another significant area leading to discrepancies. Noise barriers have a significant impact on reducing the levels of road traffic noise in adjacent areas, and their omission results in an overestimation of noise levels in shielded zones. Studies show that effective noise barriers can yield a reduction of up to 10 dB in sound pressure levels, indicating their importance in comprehensive noise assessments, as highlighted by Morley et al. [20]. Without these barriers, the calculated map fails to capture the corrective measures already implemented, leading to an overestimation of noise in some areas.

The varying mesh sizes utilized in the calculations create another layer of complexity affecting the outcomes. The calculated map's larger receiver mesh size leads to interpolation of results derived from the reference maps. When mapping noise on a larger scale, finer resolutions can capture localized variations that a coarser grid may overlook, thus leading to different noise exposure estimations. Differences in mesh size can substantially affect estimations, particularly when significant noise barriers or other mitigating factors spatially coalesce, as discussed by Hauge et al. [21].

Traffic data constitute another relevant difference. The current approach relies on data derived from sources

other than official reference maps and, in some cases, applies generic traffic volume assignments based on road characterization. Reference maps are expected to employ more rigorous methodologies, likely integrating real-world traffic data that reflect precise traffic conditions. Consequently, this variation can lead to misalignment in the noise levels associated with particular roads, as variations in traffic flow and speed contribute significantly to the overall noise profile [19]. Moreover, the software implementing the CNOSSOS-EU standard demonstrates a substantial influence on the results obtained from the noise mapping procedure. Different software tools designed to comply with CNOSSOS-EU may yield variations in results, with discrepancies noted to exceed 5 dB in some studies, as indicated by Khan et al. [22].

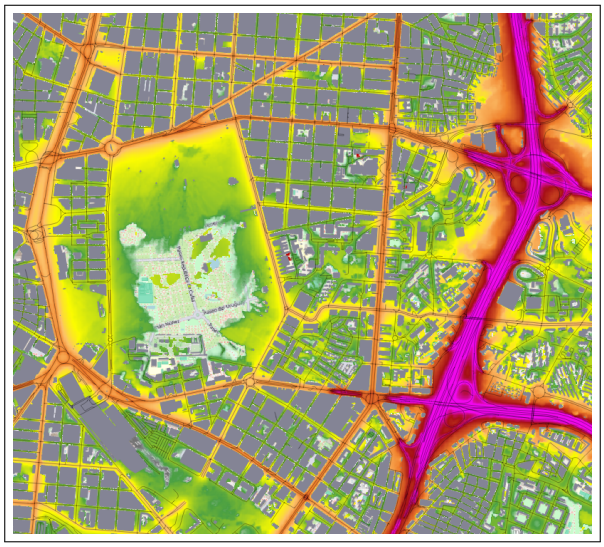


Figure 2: Overview of calculated road noise map for Spain.

The variability found is due to the accuracy of the traffic data, the precision of the design of the propagation environment, the use of different software, the availability of information such as noise barriers, etc. The multiple factors that influence the results of the noise assessment, in this case traffic noise, and the need to standardize methodologies are highlighted.

7. CONCLUSIONS

Despite the observed disparities, it is considered that the main objective of generating a noise map that encompasses all road traffic sources in Spain, regardless of whether they fall within the scope of the END, has been achieved. The objective was to provide a large-scale assessment, and it is generally considered acceptable within the limitations of the approaches adopted. The analysis performed presents significant, but at the same time reasonable and acceptable, discrepancies compared to the reference strategic noise maps.

8. FUTURE STEPS

Looking ahead, much work remains to be done to achieve a comprehensive view of noise pollution in Spain. Some of the most significant work already underway relates to large-scale studies of aeronautical, railway, and industrial noise. In addition, the methodology for studying other sources outside the scope of END and CNOSSOS-EU is currently being designed, such as noise from leisure activities, neighborhood activities, and events, which often cause significant disturbance to the population. The work already underway toward a comprehensive noise assessment in Spain is exciting.

9. REFERENCES

[1] C. I. Merchan, L. Diaz-Balteiro, and M. Solino, "Noise pollution in national parks: Soundscape and economic valuation," *Landscape and Urban Planning*, vol. 123, pp. 1–9, 2014.

[2] I. Soto-Molina and R. M. Arce Ruiz, "Estimación de la afección por ruido de carreteras en los espacios de la Red Natura 2000 en la España peninsular, y determinación preliminar de superficies con potencial para la declaración de reservas de sonidos de origen natural," in *Tecniacústica 2023*, (Cuenca, España), Sociedad Española de Acústica (SEA), 2023.

[3] S. Kephalopoulos, M. Paviotti, F. Anfosso-Lédée, D. Maercke, S. Shilton, and N. Jones, "Advances in the development of common noise assessment methods in Europe: the CNOSSOS-EU framework for strategic environmental noise mapping," *Science of the Total Environment*, vol. 482-483, pp. 400–410, 2014.

[4] Y. Shen, K. Hoogh, O. Schmitz, J. Gulliver, D. Karssenberg, R. Vermeulen, and G. Hoek, "Europe-wide road traffic noise modelling using a harmonized methodological framework (CNOSSOS-EU)," *EGUsphere*, 2023.

[5] T. Renterghem, V. Bescond, L. Dekoninck, and D. Botteldooren, "Advanced noise indicator mapping relying on a city microphone network," *Sensors*, vol. 23, no. 13, p. 5865, 2023.

[6] EEA, "Environmental noiseNoise in Europe — 2020," Tech. Rep. EEA Report 22/2019, European Environment Agency, 2020.

[7] EEA, "Noise indicators under the Environmental Noise Directive 2021: Methodology for estimating missing data," Tech. Rep. ETC/ATNI Report 06/2021, European Topic Centre on Air Pollution, Transport, Noise and Industrial Pollution (ETC/ATNI), July 2021. Prepared by Jaume Fons-Esteve (UAB), Francisco Domingues (UAB), and Maria José Ramos (UAB).

[8] A. Recio, R. Carmona, C. Linares, C. Ortíz, J. R. Banegas, and J. Díaz, "Efectos del ruido urbano sobre la salud: estudios de análisis de series temporales realizados en madrid," *Instituto de Salud Carlos III, Escuela Nacional de Sanidad*, 2016.

[9] P. Aumond, S. Cariou, O. Chiello, D. Ecotière, A. Bellec, D. Maltete, C. Marconot, N. Fortin, S. Palominos, G. Petit, and J. Picaut, "Couplage entre la base de données nationale PlaMADE et l'outil open-source NoiseModelling pour la réalisation de cartes de bruit stratégiques," 04 2022.

[10] P. Aumond, S. Cariou, O. Chiello, D. Écotière, A. Bellec, D. Maltete, and J. Picaut, "Strategic noise mapping in France to 2023: Coupling a national database with the open-source model NoiseModelling," in *Inter-Noise and Noise-Con Congress and Conference Proceedings*, vol. 265, pp. 2617–2624, 2023.

[11] M. Cai, Y. Yao, and H. Wang, "Urban traffic noise maps under 3d complex building environments on a supercomputer," *Journal of Advanced Transportation*, vol. 2018, no. 1, p. 7031418, 2018.

[12] A. Kok and A. van Beek, "Amendments for CNOSSOS-EU: Description of issues and proposed solutions," tech. rep., Rijksinstituut voor Volksgezondheid en Milieu (RIVM), 2019.

[13] International Standardization Organization, "ISO 9613-1:1993. Attenuation of sound during propagation outdoors Part 1: Calculation of the absorption of sound by the atmosphere," 1993.

[14] K. Larsson, "Updated road traffic noise emission models in Sweden," in *INTER-NOISE and NOISE-CON Congress and Conference Proceedings*, vol. 253, (Hamburg, Germany), pp. 7180–7191, Institute of Noise Control Engineering, 2016.

[15] I. Soto-Molina, M. Ausejo Prieto, R. García Morales, L. Simón Otegui, M. González García, C. Soriano Pastor, J. Cachón de Mesa, and R. Querol Herrá, *Guía técnica para la aplicación del método común europeo de evaluación del ruido ambiental (CNOSSOS-EU) en los estudios de ruido en España. R-25*. Servicio de Publicaciones del CEDEX, 2025.

[16] E. Bocher, G. Guillaume, J. Picaut, G. Petit, and N. Fortin, "Noisemodelling: An open source GIS based tool to produce environmental noise maps," *ISPRS International Journal of Geo-Information*, vol. 8, no. 3, 2019.

[17] European Commission Working Group Assessment of Exposure to Noise (WG-AEN), "Good practice guide for strategic noise mapping and the production of associated data on noise exposure." Position Paper, Final Draft, Version 2, January 2006. 13th January 2006.

[18] I. Soto-Molina, L. Simón Otegui, M. Ausejo Prieto, and R. M. Arce Ruiz, "Análisis comparativo de softwares de simulación de ruido ambiental: Comparación entre una solución comercial y una de código abierto," in *Tecniacústica 2023*, (Cuenca, España), Sociedad Española de Acústica (SEA), 2023.

[19] M. Ausejo Prieto, M. Recuero López, C. Asensio Rivera, I. Pavón García, and R. Pagán Muñoz, "Study of uncertainty in noise mapping," 2010.

[20] D. Morley, K. Hoogh, D. Fecht, F. Fabbri, M. Bell, P. Goodman, and J. Gulliver, "International scale implementation of the CNOSSOS-EU road traffic noise prediction model for epidemiological studies," *Environmental Pollution*, vol. 206, pp. 332–341, 2015.

[21] L. Hauge, K. Evensen, and H. Olsen, "How to ensure reliable noise calculations with CNOSSOS-EU," in *Inter-Noise and Noise-Con Congress and Conference Proceedings*, vol. 268, pp. 4430–4437, 2023.

[22] J. Khan, E. Thysell, C. Backalarz, P. Finne, O. Hertel, and S. Jensen, "Performance evaluation of Nord2000, RTN-96 and CNOSSOS-EU against noise measurements in Central Jutland, Denmark," *Acoustics*, vol. 5, no. 4, pp. 1099–1122, 2023.

DOI: 10.61782/fa.2025.0753

FORUM ACUSTICUM EURONOISE 2025

ROAD TRAFFIC NOISE MODELLING NEAR HIGHWAY STREET USING THE CNOSSOS-EU METHOD

Karam Waleed Katw[1*], Béla Tóthmérész[2], Dénes Kocsis[3]
[1] Department of Environmental Engineering, Faculty of Engineering, University of Debrecen, Debrecen, Hungary
[2] Juhász-Nagy Pál Doctoral School, University of Debrecen, Debrecen, Hungary

ABSTRACT

Environmental noise is a damaging environmental factor in the cities. Acoustic barriers are commonly used to mitigate highway traffic noise. Nevertheless, they adversely affect the visual aesthetics of the metropolitan environment. We investigated how a certain type of noise barrier application decreased the nearby traffic noise at a designated location. The CNOSSOS-EU calculation method was used to evaluate the road traffic noise. The noise mapping software IMMI facilitated the investigation. The results showed that the noise barrier effectively reduces noise levels at the receptor side where the population exposure was computed. Our findings indicate that, in the absence of a noise barrier, an additional 114 individuals were exposed to noise levels exceeding 50–55 dB(A) during the day (L_{day}), while an additional 175 individuals experienced noise levels exceeding 45–50 dB(A) at night (L_{night}), compared to the scenario where the barrier was in place. This impacts both future population exposure estimates and the execution of urban noise management plans.

Keywords: *noise pollution, road traffic noise, CNOSSOS-EU method.*

1 INTRODUCTION

The term "noise" refers to an unwanted or unpleasant sound [1]. Urban noise constitutes a global issue that has been thoroughly researched internationally [2]. Currently, noise pollution in cities is seen as a public health issue [3]. The World Health Organisation [4] defines environmental noise as noise that is released from all sources and encompasses all types of noise, including that from roads, trains, aeroplanes, factories, public works projects, and even residential areas, except for noise at the industrial workplace. The adverse health effects are usually non-auditory, as the noise levels often do not exceed 85 dB for extended durations. In terms of magnitude, road traffic, air traffic, railway, and industrial noise constitute the four principal causes of environmental noise disturbance in metropolitan settings [5]. Road traffic noise has become the most extensively studied source because of its widespread occurrence and significant level of disruption. In this regard, it is estimated that almost 50% of the European Union's population is subjected to road traffic noise levels that are deemed detrimental to their health and general well-being [6]. The population affected by road traffic noise greatly exceeds that affected by rail, aeroplane, and industrial noise. This is due to the extensive road network, which significantly surpasses all other sources of noise. The existing mitigations seem inadequate in achieving the objectives established by the zero-pollution strategy, and the effectiveness of their implementation is insufficient. Several studies have compared and analysed effective measures, all of which agree that implementing mitigation at the source produces the most favourable outcomes [7]. An effective mitigation should be proven against other potential alternatives and assessed based on cost-benefit analysis. Different approaches can be adopted for dealing with issues regarding road traffic noise, focusing on any of the following phases: source generation, environmental propagation, and reception [8]. At the initial stage, the concept is to interpose physical obstacles, such as acoustic barriers, between the sound source and the receivers. Acoustic barriers are a conventional method employed in noise reduction; by being positioned along the path of sound propagation, they have emerged as a prevalent

[*] ***Corresponding author***: karamjihad91@gmail.com.

Copyright: *©2025 KARAM WALEED KATW et al. This is an open-access article distributed under the terms of the Creative Commons Attribution 3.0 Unported License, which permits unrestricted use, distribution , and reproduction in any medium, provided the original author and source are credited.*

approach to address the issue [9]. Research on the effectiveness of various configurations of acoustic barriers provides insight into their ability to reduce sound intensity [10]. An important factor in noise attenuation is the barrier edge's height and shape, which have been thoroughly studied. Indeed, the quantity of barriers and their distance from each other directly impact the performance of the acoustic barrier. For instance, the implementation of parallel barriers is often used to reduce noise in locations close to a road; nonetheless, their efficacy may be inferior when compared to a singular barrier [11]. The opposite acoustic barrier reduces the nearby acoustic barrier's attenuation by reflecting multiple waves [10], [11]. The CNOSSOS-EU calculating technique was approved by the European Commission in 2009 in compliance with Directive 2002/49/EC's article 6.2. The legal foundation for the implementation of future rounds of strategic noise mapping was established in 2015 with the publication of Commission Directive (EU) 2015/996, which mandates that all EU MS switch from their previous nationally based methods to the CNOSSOS-EU standardised method for the 2022 round of strategic noise mapping. Europe is the inaugural region for creating an urban noise mapping and developing the technical underpinnings for such maps [12]. The European Noise Directive advises using computational methods over in-situ measurements for the construction of noise maps whenever feasible [13],[14]. The traffic noise computation models are utilised to compute the noise map [15], which is then conjoined with GIS, and the evaluation of noise pollution relies on L_{den} and L_{night}. This study investigates the impact of road noise barriers on sound levels near a major roadway and identifies the noise levels that reach buildings and the population in the Kismacs district of Debrecen (Hungary). The evaluation focuses on a recently built noise barrier designed to reduce road traffic noise in this district, as a significant increase in traffic is forecasted for this road section due to industrial developments.

2 MATERIALS AND METHODS

2.1 Average Daily Traffic

The source of average daily traffic (ADT) data is Hungarian Public Roads, which is used to estimate the traffic volume for each road section. The road type, the road's county-specific location, the number of the studied section, and the border sections of the examined section are used to assign a specific code number to the cross-sectional traffic data so that the ADT data can be accessed. To create the comprehensive traffic data needed for the noise maps, the raw traffic count data from Hungarian Public Roads was categorised and systematised into acoustic groups. For both road directions, the hourly vehicle traffic data for each lane was added up and then combined for the specified time of day (day and night). The data analysis results were converted into information that the noise mapping software could process.

Table 1. Average hourly distribution statistics by acoustic vehicle category (unit: vehicle/hour) for the section (D: day, N: night)

Time	Cat. 1	Cat. 2	Cat. 3	Cat. 4a	Cat. 4b
2021 D	770.58	12.70	27.27	1.55	1.55
2021 N	148.71	2.73	6.47	0.34	0.34

2.2 IMMI noise mapping program

This program, which originated in Germany, provides numerous opportunities in various domains of noise mapping. The CNOSSOS-EU method was used for the calculations of noise levels within the software, depending on the provided traffic data and other parameters. For each category of acoustic vehicles, IMMI software models noise sources as road sections with a specific average speed and flow rate per hour. The average speed is subsequently computed, and the IMMI software is employed to determine the sound power level for each road section and time interval. In this work, the noise levels were computed for a grid size of 20 m x 20 m in the examined area. Performing individual model runs for every measurement point using “hourly distribution data as input” was shown to be the most appropriate approach for processing the data analysis results. The determination of category-specific average speeds was carried out considering the characteristics of different road sections and traffic lights. A precise calibration of certain parameters is necessary to calculate the transmission of sound from the source to the receivers. The meteorological conditions used in the model closely matched the characteristics observed during the

measurements. The road and building network are sourced from OpenStreetMap, while the road gradient data is collected from the STRM digital elevation model [16]. In the model, the traffic flow for the research area was selected as continuous fluid flow, while the reference surface was chosen as the characteristic of the road surface, the building's height: ground level—3 metres; the roof's height—2 metres.

The base map designates road No. 33 as a line source. The source lines were positioned in the middle of each lane of the road while utilising "CNOSSOS-EU" calculating methods. The buildings near the measurement point were individually modelled based on the Debrecen urban development plan (satellite images allow for the input of additional details, like the height of the buildings).

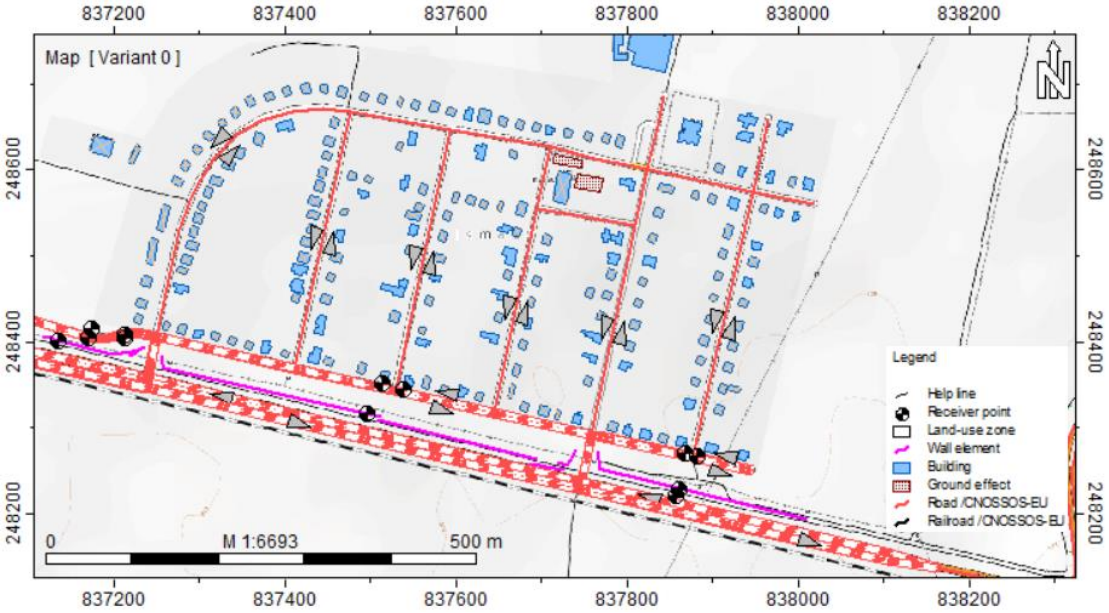


Fig. 1. Base map of the study area under investigation.

3 RESULTS AND DISCUSSION

3.1 Population exposure estimation

During the noise mapping technique, average hourly values for both day and night across the survey period were used as a percentage for each hour of the ADT data. The IMMI noise mapping tool is applicable for several parameters, allowing for the creation of thematic maps. Each of these thematic maps illustrates the population residing in certain residential structures, as ascertained by the IMMI program by examining the parameters of the buildings. This map can be used to analyse how many people are directly impacted by the noise burden that the specified road segment causes. The software can also perform intricate calculations on the involvement topic, allowing it to ascertain the number of people who are impacted by noise exposure ranges at a specific distance from the source. The program analysis determines that the noise pollution from the investigated area affects approximately 427 residents in the modelled area, which is immediately adjacent to the analysed section (Fig. 2).

For the day case (Fig. 3), most residents fall within the 45-to-50 decibel range, with approximately 216 people belonging to this category. The highest load range is 55–60 dB, affecting 14 individuals. For the night case (Fig. 5), most of the residents fall within the 35-to-40 decibel range, with approximately 183 people belonging to this category. The highest load range, which affects two individuals, is between 50 and 55 dB. It is important to observe that more people belong to smaller load categories due to the presence of condominiums that can house more residents at a distance from the roadway compared to those situated near it.

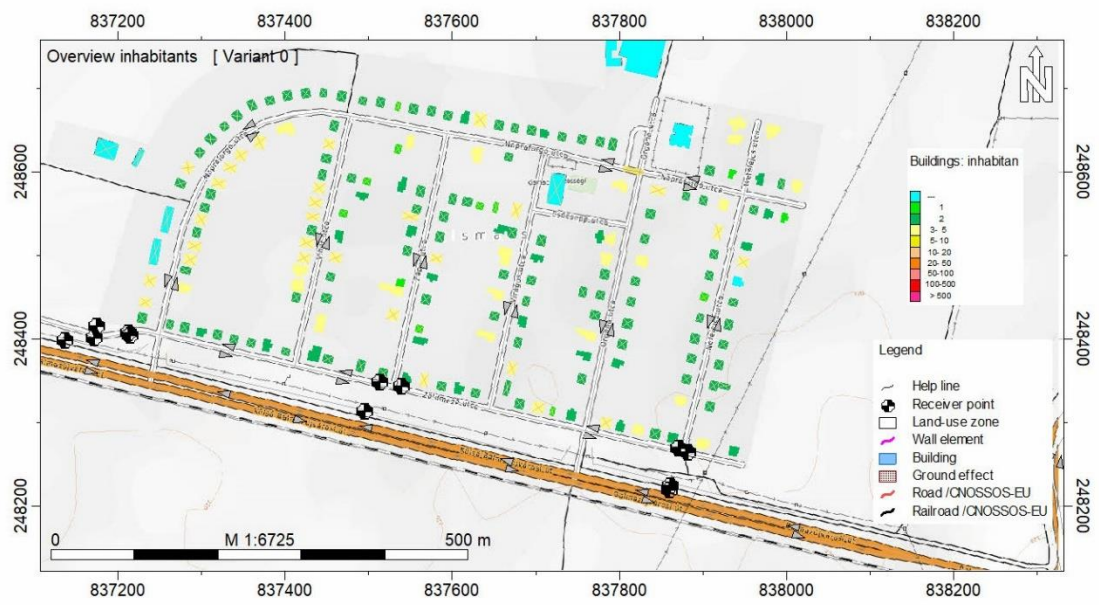


Fig. 2. Number of people living in the near vicinity of the investigated area.

3.2 The efficiency of the acoustic barrier

The efficiency of the existing barrier from the receptor side was evaluated in the investigated area in Kismacs City. The IMMI software was used to calculate the difference that would occur if the current acoustic barrier did not exist. For the noise mapping process, the average hourly distribution results from the ADT (from Hungarian Public Roads) data were used. The comparison was conducted between the simulation results at the receptor side of the barrier, based on the traffic ADT data in scenario one, and the results after the removal of the existing barrier in scenario two. The substantial associations between noise levels and the traffic volume are anticipated, given that road traffic was the primary noise source in the study area.

Fig. 3 details the results of the population exposure assessment for the Kismacs district of Debrecen using L_{day} values and the CNOSSOS-EU model. For the day case, the result indicates that the no-barrier case, as opposed to the barrier case, would expose an additional 114 people to decibel levels of road traffic that are >50-55 dB(A) $L_{day,}$ since most residents fall into this category. For the noise level >60-65, the no-barrier case would expose an additional 62 people to this highest load range level of noise. This conclusion implies that the noise barrier could significantly decrease the population's exposure to noise levels from road traffic in the investigated area. Figure 4 provides a graphic representation of these discrepancies.

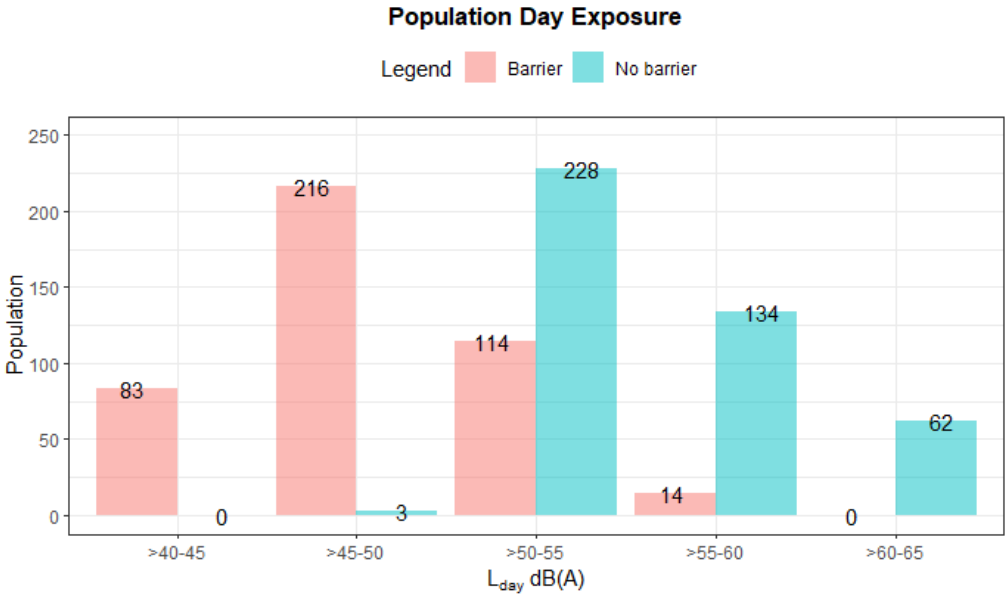
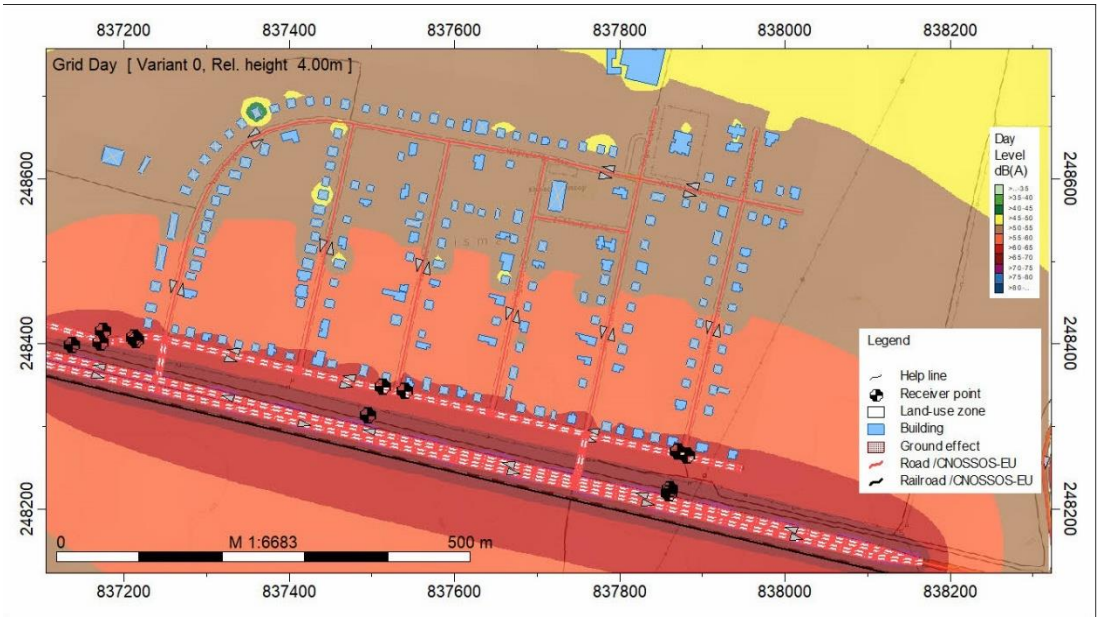


Fig. 3. Population exposure (L_{day}) in the Kismacs district of Debrecen —no barrier/barrier.



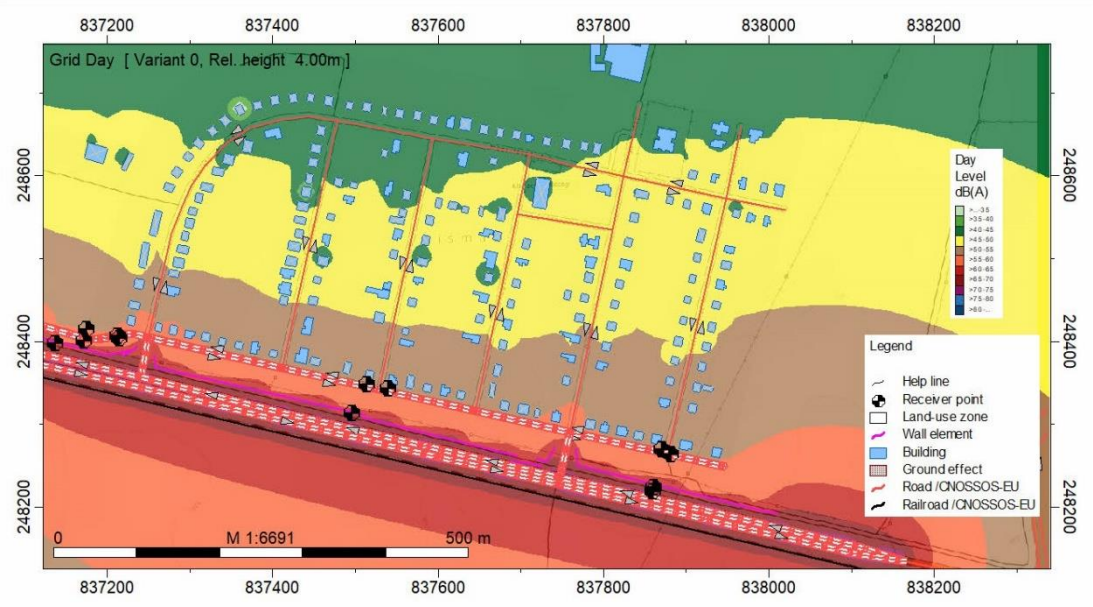


Fig. 4. A graphic representation of the daytime noise variation at the building façade in the Kismacs district of Debrecen —no barrier/barrier.

Fig. 5 details the results of the population exposure assessment for the Kismacs district of Debrecen using L_{night} values and the CNOSSOS-EU model. The result indicates that the no-barrier case, as opposed to the barrier case, would expose an additional 175 people to decibel levels of road traffic that are >45-50 dB(A) $L_{night,}$ since most residents fall into this category. For the noise level >50–55, the no-barrier case would expose an additional 119 people to this highest load range level of noise. Like the day (L_{day}) measurement, the barrier modelling case also successfully reduces the road traffic noise levels that the population experiences in the investigated area. Figure 6 provides a graphic representation of these discrepancies.

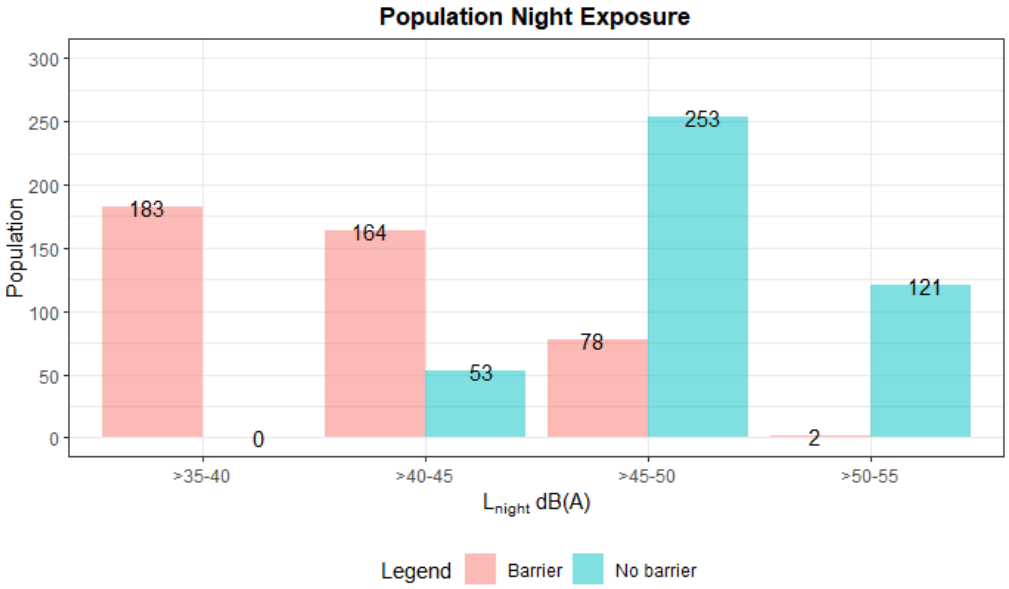
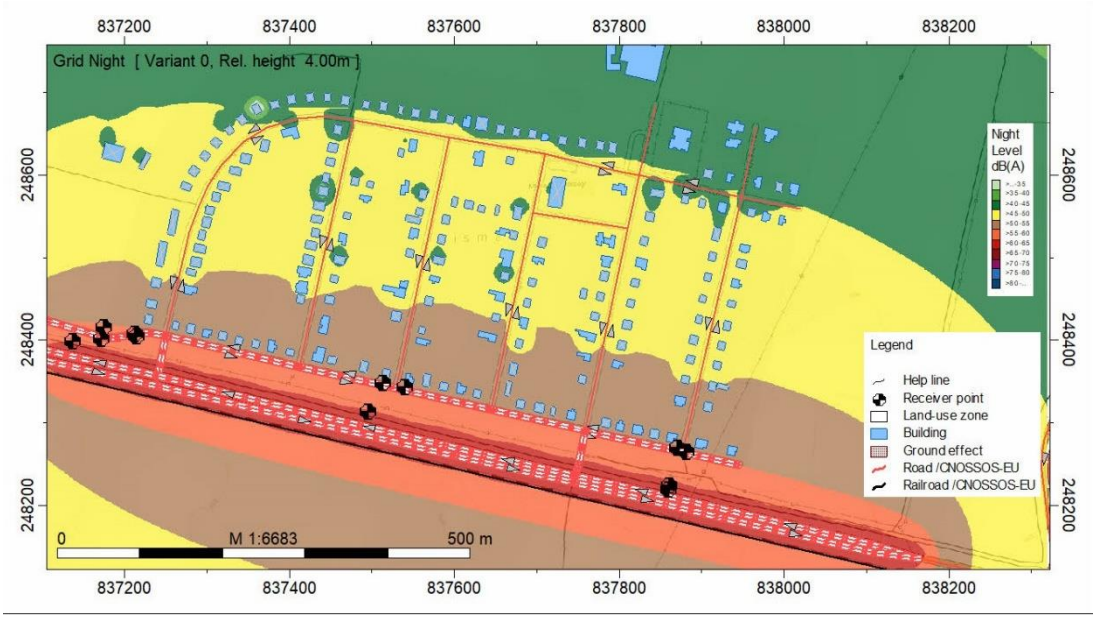


Fig. 5. Population exposure (L_{night}) in the Kismacs district of Debrecen —no barrier/barrier.



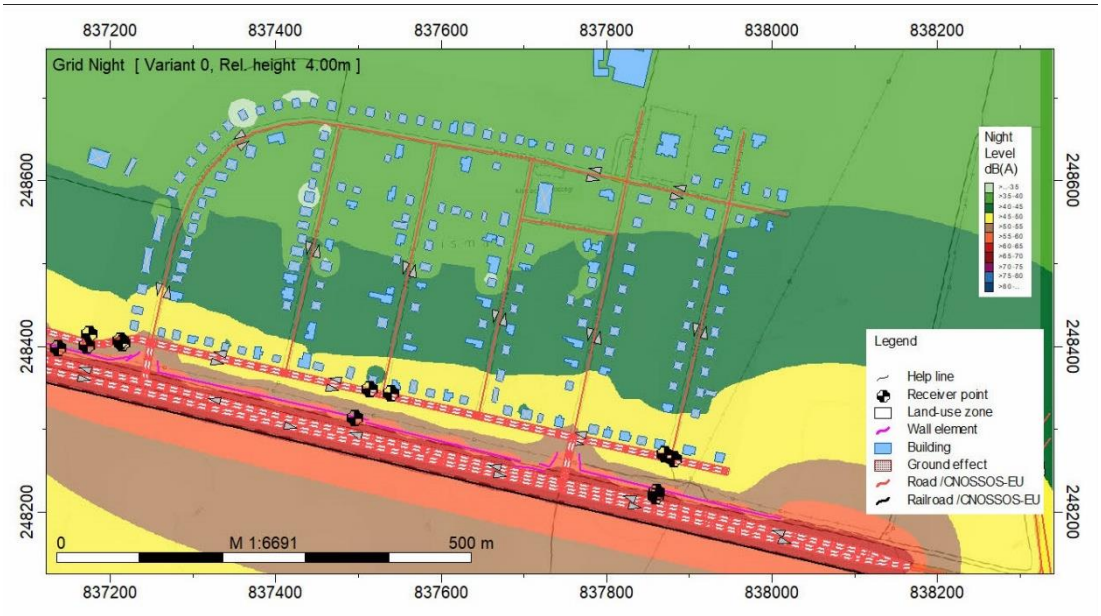


Fig. 6. A graphic representation of the nighttime noise variation at the building façade in the Kismacs district of Debrecen —no barrier/barrier.

4 CONCLUSIONS

The implementation of noise barriers as part of strategies to mitigate environmental noise is a prevalent method of controlling road noise. This study examined the concurrent impact of a particular noise barrier installation on proximal road noise at a designated location. The calculation of population exposure for the investigated area was estimated using the IMMI software tool in accordance with CNOSSOS-EU methodologies. Most populations expected to be exposed to road traffic noise levels exceeding 45-50 dB(A) L_{day} (approximately 216 persons) and 35-40 dB(A) L_{night} (approximately 183 persons) belong to this category. A comparison was performed between the simulation results at the noise barrier's receptor side, derived from the average hourly traffic data in scenario one, and the results after the removal of the existing barrier at each measurement point in scenario two. The software's elimination of the existing barrier revealed that an additional 114 people were exposed to noise levels >50-55 dB(A) $L_{day,}$ and an additional 175 people were exposed to noise levels >45-50 dB(A) L_{night} when no barrier was used, compared to the barrier case that was used. This study revealed that noise barriers can effectively diminish noise levels at the receptor sides of the barriers. With appropriate design, noise barriers can serve as effective tools for reducing noise exposure, as this study has also demonstrated. The conducting modelling could also be suitable for predicting future changes through appropriate traffic forecasting.

5 REFERENCES

[1] M. E. Héroux et al., “WHO environmental noise guidelines for the European Region,” Euronoise 2015, pp. 2589–2593, 2015.

[2] E. C. da Paz, A. M. C. Ferreira, and P. H. T. Zannin, “Comparative study of the perception of urban noise,” Rev. Saude Publica, vol. 39, no. 3, pp. 467–472, 2005, doi: 10.1590/s0034-89102005000300019.

[3] World Health Organization, “Burden of Disease from Environmental Noise,” p. 128, 2011.

[4] World Health Organization, “Guideline for Community Noise,” Ecotoxicol. Environ. Saf., 1999.

[5] European Environment Agency, “The NOISE Observation & Information Service for Europe,”

2017.

[6] K. V. Weyde et al., “Nocturnal road traffic noise exposure and children’s sleep duration and sleep problems,” Int. J. Environ. Res. Public Health, vol. 14, no. 5, pp. 5–7, 2017, doi: 10.3390/ijerph14050491.

[7] K. E. Salomons E, Fons Estevez J, Zeisl Y, Klebba M, Richer C, Oosten N, Blanes Guardia N, Kubota U, “Assessment of potential health benefits of noise abatement measures in the EU: Phenomena project,” Publ. Off. Eur. Union, Luxemb., 2021.

[8] G. Watts, “Barrier designs to reduce road traffic noise,” Proc. Inst. Civ. Eng. Transp., vol. 153, no. 2, pp. 79–86, 2002, doi: 10.1680/tran.2002.153.2.79.

[9] L. Chen, W. Zhao, X. Yuan, and B. Zhou, “Study on the Optimization of the Distribution of Absorbing Material on a Noise Barrier,” Acoust. Aust., vol. 46, no. 1, pp. 119–130, 2018, doi: 10.1007/s40857-017-0123-6.

[10] C. Yang, J. Pan, and L. Cheng, “A mechanism study of sound wave-trapping barriers,” J. Acoust. Soc. Am., vol. 134, no. 3, pp. 1960–1969, 2013, doi: 10.1121/1.4816542.

[11] Z. B. Wang and Y. S. Choy, “This is the Pre-Published Version . Tunable parallel barriers using Helmholtz resonator,” pp. 1–34, 2018.

[12] Z. Lan and M. Cai, “Dynamic traffic noise maps based on noise monitoring and traffic speed data,” Transp. Res. Part D Transp. Environ., vol. 94, no. March, p. 102796, 2021, doi: 10.1016/j.trd.2021.102796.

[13] European Commission, “Directive 2002/49/EC of the European Parliament and of the Council of 25 June 2002, relating to the assessment and management of environmental noise,” Off. J. Eur. Communities, vol. 189, no. 25, 2002.

[14] J. M. Barrigón Morillas, D. Montes González, V. Gómez Escobar, G. Rey Gozalo, and R. Vílchez-Gómez, “A proposal for producing calculated noise mapping defining the sound power levels of roads by street stratification,” Environ. Pollut., vol. 270, 2021, doi: 10.1016/j.envpol.2020.116080.

[15] E. Murphy, E. A. King, and H. J. Rice, “Estimating human exposure to transport noise in central Dublin, Ireland,” Environ. Int., vol. 35, no. 2, pp. 298–302, 2009, doi: 10.1016/j.envint.2008.07.026.

[16] B. Rabus, M. Eineder, A. Roth, and R. Bamler, “The shuttle radar topography mission - A new class of digital elevation models acquired by spaceborne radar,” ISPRS J. Photogramm. Remote Sens., vol. 57, no. 4, pp. 241–262, 2003, doi: 10.1016/S0924-2716(02)00124-7.

DOI: 10.61782/fa.2025.0439

FORUM ACUSTICUM EURONOISE 2025

IDENTIFYING NOISE ACTION PLAN PRIORITY LOCATIONS IN IRELAND

Simon Shilton[1*] **Tony Dolan**[2]
[1] Acustica (EU) Ltd, Dublin, Ireland
[2] Environmental Protection Agency, Wexford, Ireland

ABSTRACT

The Environmental Protection Agency (EPA) in Ireland published a guidance note for noise action planning in 2009, to support the Local Authorities designated as Action Planning Authorities (APAs) under the Environmental Noise Regulations (ENR). An update to the guidance note was published in June 2018, in support of the Round 3 noise action plans (NAPs). Ahead of the Round 4 NAPs, the EPA extensively revised the draft guidance note; aligning with the 2018 Regulations, implementing the revisions to the Environmental Noise Directive (END), including Annex II (CNOSSOS-EU as amended) and Annex III (harmful effects). The noise action plans are to be drawn up on the basis of the results of the strategic noise mapping. As there are no statutory noise limit values in Ireland, the EPA developed other relevant criteria for identifying priorities, and the most important areas, exposed to road and railway noise to be addressed within the NAPs. The paper provides an overview of the methodology developed to identify priority important areas (PIA) to be assessed by APAs during implementation of the Round 4 NAPs. The methodology uses a combination of GIS analysis, and localised decision making within the APA to provide a nationally consistent, and locally responsive approach.

Keywords: *environmental noise, action plan, priority actions, noise planning, environmental noise directive*

[*] ***Corresponding author***: *simon.shilton@acustica.ie*
Copyright: *©2025 Simon Shilton et al. This is an open-access article distributed under the terms of the Creative Commons Attribution 3.0 Unported License, which permits unrestricted use, distribution, and reproduction in any medium, provided the original author and source are credited.*

1. INTRODUCTION

Environmental noise is the second biggest environmental cause of health problems in the EU, after air pollution (the fine particulate matter in air), according to the World Health Organisation (WHO), and the European Environment Agency (EEA). Prolonged exposure to noise can lead to serious illnesses including: cardiovascular diseases; reduced cognitive performance in children; severe annoyance, which is a form of stress; and sleep disturbance.

The Environmental Noise Directive (END) is the main pan-European regulatory framework established to manage environmental noise, through harmonised procedures to assess levels of noise exposure, assess the impact on human health, and prepare noise action plans. The END is transposed into Irish law through the European Communities (Environmental Noise) Regulations 2018 (amended) (the Regulations) [1].

The Environmental Protection Agency (EPA) is the designated national authority for the purposes of the Regulations and is to exercise general supervision over the functions and actions of noise mapping bodies and action planning authorities, and to provide guidance or advice, where necessary.

The EPA has developed guidance for strategic noise mapping in 2009, 2011 and fully revised for Round 4 using the CNOSSOS-EU assessment methods between 2022 and 2024 [2]. The EPA also developed guidance on noise action planning published in July 2009 [3], with updated sections published for round 3 in June 2018 [4]. The guidance was revised for Round 4 and the draft guidance was issued to the Action Planning Authorities (APA) in December 2024 [5].

As there are no statutory noise limit values in Ireland, the EPA developed other relevant criteria for identifying priorities, and the most important areas, exposed to road and railway noise to be addressed within the noise action plans (NAPs).

The 2009 guidance on noise action planning recommended the use of a noise score matrix to help Action Planning Authorities (APAs) identify priority locations. During the revision of the NAP guidance for Round 4 the matrix approach was reviewed and a revised methodology developed to identify priority important areas (PIAs) to be assessed by APAs during implementation of the Round 4 NAPs.

2. REQUIREMENTS

The Regulations defines an "action plan" as a plan designed for the purpose of managing noise issues and their effects, including noise reduction if necessary. Local Authorities are designated as Action Planning Authorities (APA) under the Regulations, and have a statutory responsibility to make noise action plans, consult with the public, and report to the EPA on all action taken under each action plan in the previous 12 months.

The aims and objectives of the Directive state that the adoption of action plans, based upon noise-mapping results, should be concerned with:

"preventing and reducing environmental noise where necessary and particularly where exposure levels can induce harmful effects on human health and to preserving environmental noise quality where it is good."

Under the Regulations, Action Planning Authorities (APAs) are to determine the measures to be included within the noise action plans, and:

"Each action plan or revision of an action plan shall address priorities which—

(i) may be identified on the basis of exceedances of any relevant noise limit value or other relevant criteria established by the Agency in accordance with subparagraph (3), and

(ii) shall, in the first instance, address the most important area or areas, as the case may be, established by strategic noise mapping."

The noise actions plans are to be drawn up on the basis of the results of the strategic noise mapping of major roads, major railways, major airports and agglomerations as defined in the Regulations, which has previously been completed by the designated Noise Mapping Bodies (NMBs). The strategic noise maps provide graphical and statistical data on the exposure of people, dwellings and areas to noise.

The Regulations require that *"priorities"* and *"the most important area or areas"* are to be addressed.

Additionally, the EPA recommended that noise action plans have regard to Policy Objective 65 from the National Planning Framework 2040, which states:

"Promote the pro-active management of noise where it is likely to have significant adverse impacts on health and quality of life and support the aims of the Environmental Noise Regulations through national planning guidance and Noise Action Plans."

In May 2021 the EU launched the Zero Pollution Action Plan (ZPAP) with a vision for 2050 that air, water and soil pollution is reduced to levels no longer harmful to health and natural ecosystems. The targets set to be achieved by 2030 include *"reducing the share of people chronically disturbed by transport noise by 30%",* compared to 2017.

In support of ZPAP, the EU PHENOMENA project was undertaken to identify cost-effective noise mitigation measures which may help competent authorities to achieve noise reductions across large parts of the exposed population.

The previous version of the EPA guidance notes on noise action planning, from 2009 to 2018, focused noise mitigation measures on locations exposed to high levels of noise, however in the context of the ZPAP it was determined that a different approach would be required to help support APAs actions to reduce the overall health effects of environmental noise. The aim of the revised approach recommends the identification of Priority Important Areas (PIAs). This approach is to support the aspirations of ZPAP by providing for noise reductions to larger numbers of exposed residents.

3. RATIONALE

The objective of the Regulations is to:

"avoid, prevent or reduce on a prioritised basis the harmful effects, including annoyance, due to exposure to environmental noise". Where environmental noise is *"unwanted or harmful outdoor sound created by human activities"*.

The results of the strategic noise mapping provide information on the assessed noise levels at all noise sensitive properties within the assessment area, along with an estimate of the number of inhabitants.

The NMBs *"shall calculate the harmful effects in accordance with the Second Schedule"* of the Regulations. Meanwhile, the APAs *"shall estimate the expected reduction in the harmful effects of noise exposure to the population as a result of the mitigation measures contained in their Noise Action Plans"*. The Second Schedule of the Regulations sets out a mandatory assessment of the harmful

effects of environmental noise using the dose-response relationships set out in Commission Directive (EU) 2020/367 [6] and transposed under S.I. 663/2021 [7], replacing Annex III of the END.

The European Commission, on its Environmental Noise Directive webpage, outlines that the harmful effects assessment methods in *'Annex III of the Environmental Noise Directive describes the methods for calculating the burden of disease caused by exposure to specific noise levels. The methods include dose-effect relations for a set of health endpoints such as cardiovascular disease, annoyance and sleep disturbance. Annex III was revised in 2020 following the latest scientific review of the health effects of noise that is being performed by the WHO.'* Box 2 'Impact of the Guidelines at EU level' in the joint WHO and EEA briefing [9] provides details on the where Annex III originated from and its links to WHO guidelines [10].

The results of the strategic noise mapping, including the harmful effects, may then be used to identify important areas [IAs] where long term noise exposure to noise from transport infrastructure is likely to produce negative health effects on the exposed population. This would be all areas exposed above the outdoor noise levels set out within WHO guidelines [10-12].

The main purpose of the WHO guidelines is to provide recommendations for protecting human health from exposure to environmental noise originating from various sources. They provide public health advice underpinned by evidence, which is essential to drive policy action that will help to protect communities from the adverse effects of noise. The WHO ENG 2018 guidelines reviewed the pertinent literature in order to incorporate significant research undertaken in the area of environmental noise and health since the *Community Noise Guidelines* (1999) [11] and *Night Noise Guidelines for Europe* (2011) [12] were issued. The significant health impacts of noise are most likely to be underestimated, with WHO evidence demonstrating effects from noise levels below the thresholds that countries report against under the Environmental Noise Directive.

The WHO Environmental Noise Guidelines (ENG 2018) formulated recommendations based on the available evidence, and exposure values based on a relevant risk increase of adverse health effects. Thus, the 2018 guideline values define an exposure level at which effects certainly occur. Furthermore, the WHO developed dose-response relationships for the assessment of health effects due to chronic long-term exposure to environmental noise from roads, railways and aircraft. These dose-response relationships have subsequently been adopted by the EU as Annex III of the END as set out in the Second Schedule of the Regulations, which sets out methodologies to be used for the assessment of three harmful effects:

- Ischaemic heart disease due to road traffic noise, and
- High annoyance and high sleep disturbance due to road, railway and aircraft noise.

The WHO definition of health is *"a state of complete mental, physical and social well-being"*. In addition, noise annoyance in this field means a feeling of displeasure, nuisance, disturbance or irritation caused by a specific sound, and in the context of the WHO guidelines and END it refers to long-term (chronic) noise annoyance, rather than just a temporary irritation. The WHO acknowledge that there are uncertainties in the quantification of health impacts from a range of factors, including: in their own recommendations; the modelling of noise exposure; transferability of exposure response functions to locations beyond where they were studied. However, they concluded that the recommended values provide an acceptable estimate of the average response to certain noise levels in Europe.

4. OVERVIEW OF METHODOLOGY

Following consultation with the NMBs and APAs the EPA developed relevant criteria for action plan priorities, recommended as a three-step approach to identify one or more of these priorities due to exposure to noise from roads and railways:

- **Step 1: Important Areas (IA)** – these are locations exposed to environmental noise which may be harmful to human health, such as high annoyance, above the relevant thresholds with reference to the WHO 2018 guidelines on road and railway noise;
- **Step 2: Most Important Areas (MIA)** – these locations are a sub-set of Important Areas where the health effects are highest, typically through a product of noise exposure levels and the number of people exposed to noise;
- **Step 3: Priority Important Areas (PIA)** – where appropriate and relevant to the individual local authority between 5 and 10 MIAs, or groups of similarly affected MIAs, which are identified by the APAs as those which will be addressed during the implementation of the Noise Action Plan (NAP).

5. IDENTIFYING MOST IMPORTANT AREAS (MIAs) – ROADS AND RAILWAYS

The END requires that:
"The measures within the plans are at the discretion of the competent authorities, but should notably ***address priorities*** *which may be identified by the* ***exceeding of any relevant limit value or by other criteria*** *chosen by the Member States and* ***apply in particular to the most important areas*** *as established by strategic noise mapping."*
As there are no statutory noise limit values in Ireland, the EPA has developed other relevant criteria for identifying priorities, and the most important areas, exposed to road and railway noise to be addressed within the noise action plans.
While the below method sounds complex, it can be automated in a few steps within modern GIS (geographical information system) software, resulting in a graphical map which effectively shows the relative number of people highly annoyed due to noise, as shown in Figure 1 below.

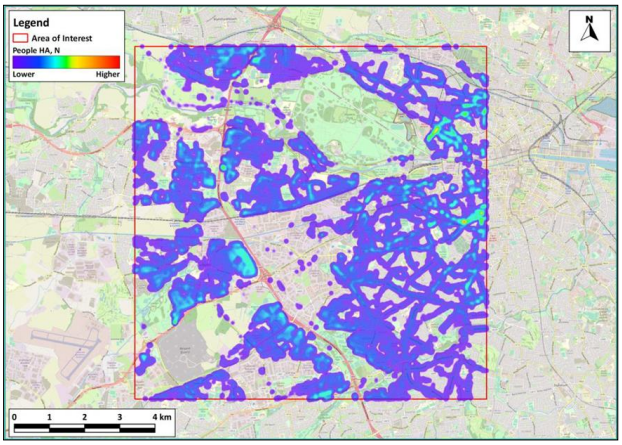


Figure 1. Heat map of density of people highly annoyed due to road traffic noise above 53 dB L_{den}

The results of the strategic noise mapping include noise levels calculated around the facades of noise sensitive buildings, and an estimate of the number of dwellings and people in dwellings within each residential building.
The assignment of population to the calculated noise levels is set out within Annex II of the END (CNOSSOS-EU) and provides building level statistics across the assessment area. Following the method in Annex II of the END, the harmful effects due to noise may also be statistically assessed at the centre point of each building location. For example, the number of people highly annoyed, due to road traffic noise.

It is important to note that this is a statistical approach across the whole population covered by the noise maps and should not be considered to be an accurate assessment of the possible health effects at any specific building. The WHO recommended dose-response curves were derived from meta-analysis of a large number of studies and are considered representative across the overall population within the study.
The point dataset of the number of people highly annoyed is then interpolated to generate a raster heatmap, using a quadratic weighted circular neighbourhood around each point. The heatmap process only includes important areas above the WHO guideline levels, and is generated on a 100 metre radius, which generates 100 m^2 raster cells.
From the heatmap it is then possible to identify the most important areas (MIAs), which are those IAs with the largest concentration of people highly annoyed due to noise. This aims to identify locations where noise mitigation measures may have a positive effect on the quality of life for a large number of people. Using a criterion of 15 or more people highly annoyed per 100 m^2, the MIAs (delineated as polygons) for an example area are shown in Figure 2 below.

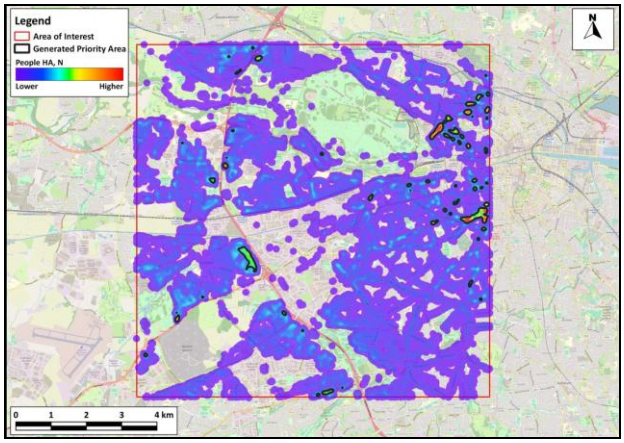


Figure 2. Most Important Areas (MIAs) highlighted (15 people per 100 m^2 criterion)

The criterion of 15 or more people per 100 m^2 has been found to be appropriate in the main urban areas within agglomerations. For edge of urban, or rural, locations it may be found that very few MIAs are identified based on this criterion. In this situation it is recommended that the criterion is reduced to 10, or even 7.5, in order to ideally identify at least 15 to 20 MIAs within the region covered by strategic noise mapping.

The recommended process aims to identify areas with high levels of health impact, due to both noise exposure levels and population density. This is designed to support aims of the EU Zero Pollution Action Plan and provide noise reduction, and associated reductions in health effects, for groups of the population.
It is accepted that this may result in some locations with similar or even higher noise exposure levels and lower levels of population density not being identified as MIAs. It is within the discretion of the APAs to identify specific locations with ongoing noise problems as MIAs, or PIAs, if the automated process does not identify them, but this alternative method of designating PIAs must be backed up with well-grounded evidence in order that comparisons can be made at a Regional/National Level.

6. IDENTIFYING PRIORITY IMPORTANT AREAS (PIAs) – ROADS AND RAILWAYS

The recommended process described in Section 5.2 above is expected to identify a range of most important areas (MIAs), and there are likely to be more identified than it would be possible to address within the current noise action plan lifecycle. It is therefore the task of each Local Authority to select their Priority Important Areas (PIAs), informed by the list of most import areas.
The MIAs are described as areas within the map, and the GIS may be used to develop a series of statistics about each of these MIAs, for example:

- Noise source identifying the Most Important Area, i.e., railways or roads
- Area (m^2)
- Total population
- Number of people highly annoyed (HA)
- Number of people highly sleep disturbed (HSD)
- Population increased risk to ischaemic heart disease (IHD)
- Number of dwellings
- Population noise exposure above END threshold values:
    - road traffic noise exposure in 5 dB bands (L_{den} 55 - >75 dB, L_{night} 50 – >70 dB)
    - railway noise exposure in 5 dB bands (L_{den} 55 - >75 dB, L_{night} 50 – >70 dB).

When considering the selection of PIAs to address under the action plan, it is recommended that the APAs consider the following aspects for each of the MIAs:

- Number of people exposed to noise, and the health effects
- Level of noise exposure
- Potential for grouping adjacent MIAs into a larger PIA
- The main source of transport noise
- Competent body to carry out any proposed mitigation measures
- History of complaints
- Planned road maintenance and resurfacing programme
- Planned speed or traffic calming measures
- Planned nearby developments
- Existing noise reduction measures
- Proposed noise reduction measures
- Options available for noise reduction measures, if available

Based upon all the information available, where necessary, it is recommended that APAs identify at least 5 and up to 10 Priority Important Areas (PIAs) which will be included within the noise action plan, with a plan to undertake an assessment of noise mitigation measures for each PIA within the life cycle of the noise action plan (e.g.: 2024-2028, 2028-33, 2033-38).
The selection of the PIAs from the MIAs is be documented within the NAP, including a rationale for each PIA selected.
The PIAs selected within Limerick Agglomeration are shown in Figure 3, which illustrates how adjacent MIAs exposed to the same source have been clustered into a single PIA.

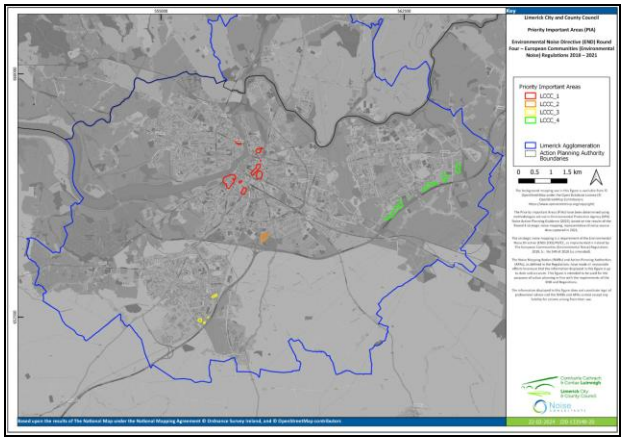


Figure 3. Limerick Agglomeration –Priority Important Areas (PIAs) - LCCC_1: Limerick City; LCCC_2: John Carew Park; LCCC_3: Ballycummin; LCCC_4: Monaleen/Castletroy

7. ASSESSMENT OF NOISE MITIGAITON MEASURES

Following adoption of the NAP, for each of the Priority Important Areas, an assessment of cost-effective noise mitigation measures is undertaken during implementation of the NAP. It is recommended that this assessment includes:

- noise monitoring to confirm exposure levels;
- noise modelling calculations of practical noise mitigation measures, and
- cost-benefit analysis based on estimated costs of implementing and maintaining mitigation works, and monetised benefit to health of noise reduction.

It is recommended that the most cost-effective noise mitigation measures, or combination of measures, are proposed to the relevant departments, organisations and fund holders to be incorporated within their future work plans as robust proposals for cost-effective noise mitigation measures.

8. CONCLUSIONS

The Environmental Protection Agency in Ireland is to exercise general supervision over the functions and actions of noise mapping bodies and action planning authorities, and to provide guidance or advice, where necessary.

The EPA has developed a revised draft guidance note on noise action planning for Round 4 of the END implementation.

As there are no statutory noise limit values in Ireland, the EPA developed other relevant criteria for identifying priorities, and the most important areas, exposed to road and railway noise to be addressed within the noise action plans.

The recommended approach identifies Important Areas (IA) as areas exposed above the relevant thresholds with reference to the WHO 2018 guidelines on road and railway noise.

The recommended approach then identifies Most Important Areas (MIA) on the basis of interpolating a building point dataset of the number of people highly annoyed to generate a raster heatmap, using a quadratic weighted circular neighbourhood around each point.

From the heatmap it is then possible to identify the most important areas (MIAs), which are those IAs with the largest concentration of people highly annoyed due to noise. This aims to identify locations where noise mitigation measures may have a positive effect on the quality of life for a large number of people. Using a criterion of 15 or more people highly annoyed per 100 m^2.

The criterion of 15 or more people per 100 m2 has been found to be appropriate in the main urban areas within agglomerations. For edge of urban, or rural, locations it may be found that very few MIAs are identified based on this criterion. In this situation it is recommended that the criterion is reduced to 10, or even 7.5, in order to ideally identify at least 15 to 20 MIAs within the region covered by strategic noise mapping.

The Action Planning Authorities should then propose 5 to 10 MIAs to be the Priority Important Areas (PIA) to be assessed during the implementation of the noise action. The recommended approach to assessment of each PIA includes noise monitoring, review of noise mitigation measures, and cost-benefit assessment, with the aim to develop robust proposals for cost-effective noise mitigation measures. The recommended process aims to identify areas with high levels of health impact, due to both noise exposure levels and population density. This is designed to support aims of the EU Zero Pollution Action Plan and provide noise reduction, and associated reductions in health effects, for groups of the population.

In late 2024, a number of pilot acoustic design studies were undertaken to look at validating some of the identified PIAs. It is hoped that any lessons learned from these initial pilot studies can be shared with other APAs in 2025.

9. ACKNOWLEDGMENTS

This work has been undertaken with the support of the Environmental Protection Agency, and assistance from Dublin City Council and Noise Consultants Limited.

10. REFERENCES

[1] S.I. No. 549/2018 - European Communities (Environmental Noise) Regulations 2018.

[2] Guidance Note for Strategic Noise Mapping, Environmental Protection Agency, Version 1 2009, Version 2 August 2011, and Version 3 January 2025.

[3] Guidance Note for Noise Action Planning, Environmental Protection Agency, July 2009.

[4] Guidance Note for Noise Action Planning, Updated sections, Environmental Protection Agency, June 2018.

[5] Draft Guidance Note for Local Authorities on the preparation of Noise Action Plans, Environmental Protection Agency, December 2024.

[6] Commission Directive (EU) 2020/367 of 4 March 2020 amending Annex III to Directive 2002/49/EC of the European Parliament and of the Council as regards the establishment of assessment methods for harmful effects of environmental noise, OJ L 67, 5.3.2020, p. 132–136.

[7] S.I. No. 663/2021 - European Communities (Environmental Noise) (Amendment) Regulations 2021.

[8] European Commission, Environmental Noise Directive website, available at: https://environment.ec.europa.eu/topics/noise/environmental-noise-directive_en

[9] Uptake and impact of the WHO Environmental noise guidelines for the European Region: experiences from Member States, WHO, June 2023.

[10] Environmental noise guidelines for the European Region, WHO, January 2019.

[11] Community Noise Guidelines, WHO, 1999.

[12] Night Noise Guidelines for Europe, WHO, 2009.

DOI: 10.61782/fa.2025.0718

FORUM ACUSTICUM EURONOISE 2025

QUALITY ASSURANCE AND MODELING LIMITATIONS IN NOISE EMISSION CONTROL USING ISO 9613-2 AND ISO 17534

Jochen Schaal * **Dieter Zollitsch**[1]
[1] SoundPLAN GmbH, Etzwiesenberg 15, 71522 Backnang (Germany)

ABSTRACT

The calculation of noise emissions according to ISO 9613-2 is an established method for estimating sound propagation and serves as the foundation for noise emission control. However, the standard offers limited capabilities for modeling complex acoustic scenarios, particularly in accounting for sound transmission through obstacles such as walls and other semi-transparent objects.
Users of simulation software like SoundPLAN often aim for more detailed modeling to accurately represent specific properties of walls or other obstacles. These requirements go beyond the standardized assumptions of ISO 9613-2 and necessitate adaptations to the official calculation methods in the simulation software.
ISO 17534 provides an important framework for software quality assurance by ensuring transparency and comparability of the software products used. However, advanced modeling and calculation approaches, such as those for sound transmission, can compromise the comparability of results if standardized procedures are not established.
This contribution highlights the challenges and opportunities in modeling sound transmission through obstacles, the limitations of ISO 9613-2 in this context, and the role of ISO 17534 in ensuring the quality and validity of simulation results.

Keywords: *sound transmission, ISO 9613-2, quality assurance, A-QNS.*

* ***Corresponding author***: *jochen.schaal@soundplan.de.*
Copyright: *©2025 Jochen Schaal et al. This is an open-access article distributed under the terms of the Creative Commons Attribution 3.0 Unported License, which permits unrestricted use, distribution, and reproduction in any medium, provided the original author and source are credited.*

1. INTRODUCTION

In the area of noise prediction, software developers are confronted with a conflict between the requirements of quality assurance and the wishes of the users. On the one hand, the quality assurance process, in accordance with standards such as ISO 17534, requires that software solutions comply with standardized test tasks for specific regulations, such as ISO 9613-2, and deliver comparable results within a specified tolerance range. This ensures transparency, comparability, and consistency between different software products in terms of the calculated noise levels.
On the other hand, users are increasingly demanding more detailed and specific modeling that goes beyond the capabilities of existing standards. This includes, for example, the precise consideration of transmission through walls, reflections on slanted surfaces, the simulation of horizontal obstacles such as the roofs of gas stations, or the consideration of tunnel openings. These extensions, however, go beyond the scope of the standards defined in official test tasks and therefore fall outside the scope of standards-based quality assurance.
For software developers, this necessitates a delicate balance: there is the requirement to ensure compliance with standards and the comparability of results. At the same time, the commitment to meeting the practical needs of the users in order to enable realistic and practice-oriented simulations is essential. One approach is to develop optional, well-documented extensions that provide users with additional options without compromising standards-compliant quality assurance.

2. QUALITY ASSURANCE OF SOFTWARE FOR CALCULATING SOUND

The quality assurance of simulation software such as SoundPLAN does not entail the testing or validation of the quality or accuracy of official guidelines, including

ISO 9613-2 and similar standards. As a software developer, it is incumbent upon us to acknowledge the validity of the assumptions inherent in these standards. Any interrogation of these assumptions must therefore be confined to the standardization process. Once published, however, they are binding and are considered the established standard.

Instead, quality assurance focuses on ensuring that different software products with the same input scenarios produce identical results within a defined range of variations. This approach fosters the principles of comparability and consistency among various software solutions. This procedure is specified in ISO/TR 17534 Parts 1 and 2 and provides clear requirements for the verification and validation of calculation results.

For software developers, the existence of official test tasks for the calculation methods to be implemented constitutes a significant advantage. These are typically either provided directly by the creators of the guidelines or developed by specific committees.

Examples are the official test tasks for the German RLS-19, Schall 03 or the Scandinavian NORD2000, which are provided by the respective guideline authorities. Another possibility is test tasks developed by expert committees, as described in ISO/TR 17534 Parts 3 and 4 for ISO 9613-2:1996 and CNOSSOS-EU. In addition, the German Federal Environmental Agency (Umweltbundesamt) provides specific test tasks, e.g. for BUB - the German version of CNOSSOS-EU. Such standardized test tasks make implementation and quality assurance much easier, as they create a uniform basis for validating and comparing software solutions.

However, if no official tests are available, the need to resort to in-house testing arises. This means a lot of extra work, as these test scenarios must be developed and ideally checked by hand to ensure that the implementation is correct. This additional work is not only time-consuming but also carries the risk that the results are less comparable due to the lack of external reference values. In addition, there is always a risk that the same "errors of reasoning" or interpretations that were made when the rules and regulations were translated into software code will be made when the test items are developed internally, especially if this is done by the same person. Therefore, this should always be done by different people, further increasing the effort.

The A-QNS (Association for the Quality Assurance of Noise Propagation Software) was founded to ensure the quality, comparability and transparency of software products for sound immission prediction. The initiative arose from the growing need to establish binding standards and test procedures for the standard-compliant implementation of calculation methods such as ISO 9613-2, CNOSSOS-EU, RLS19 or Schall 03. The main reasons for its establishment were:

1. Ensure standards compliance:
   with the increasing number of sound calculation software products, the challenge has been to ensure that all programs implement the calculation guidelines correctly and consistently. A-QNS ensures that software products use the same input data to produce comparable results.
2. Promotion of transparency:
   in approval procedures, environmental impact assessments and other official processes, it is essential that the calculation results are comprehensible and trustworthy. The A-QNS provides an objective basis for the evaluation of software solutions through tests and certificates.
3. Development of test tasks:
   many standards and guidelines do not contain complete test tasks for software validation. The A-QNS is working on the creation of such tasks in order to be able to test software products independently. Examples include the validation of the acoustic reference model K1 according to RVS 04.02.11-2021 and ÖAL No. 28-2021.
4. Independent quality assurance:
   the establishment of an independent association has created a central body that performs quality assurance impartially and independently of individual software vendors.
5. Cooperation and standardization:
   The association promotes cooperation between software developers, users, authorities and standardization bodies in order to support the further development and standardization of calculation methods and test procedures.

The foundation of the A-QNS was therefore an important step towards creating a reliable basis for the development and testing of software in an increasingly complex technical and regulatory environment. The aim is to increase both user confidence and the acceptance of calculation results in legal and planning contexts.

3. MODELING BEYOND THE LIMITS OF THE STANDARD

Users of simulation software such as SoundPLAN often require more detailed modeling that goes beyond the standardized assumptions of ISO 9613-2:2024. The focus is on specific properties such as the transmission of sound through walls or other obstacles. There is also a desire for more detailed simulation of obstacles, for example to accurately account for reflections from slanted surfaces such as roofs or inclined walls. Another common simulation request concerns horizontal obstacles such as gas station roofs, bridges, or similar structures. This is where the ISO 9613-2:2024 guideline has its limitations, as it only takes into account diffraction above and to the side of objects but does not take into account underside diffraction. Reflections from such horizontal surfaces are also not considered in this standard, although they may play a role in practice.

To meet these partially justified user requirements, it is necessary to adapt the official calculation methods in the simulation software. However, this means that the calculated results are, strictly speaking, outside the calculation standard used and the scope of official quality assurance, since such extensions can be implemented differently by software developers.

4. EXTENSION EXAMPLE - TRANSMISSION THROUGH WALLS

A recurrent request received by software developers involves the extension of the calculation methodology for sound transmission through shielding objects such as walls. This subject is of particular pertinence to mobile noise control solutions in scenarios such as moving construction sites, temporary events, machine enclosures, noise protection cabins, room partitions, and demolition work. These applications necessitate the development of advanced models capable of accurately assessing sound transmission through a diverse range of often temporary obstacles. The existing calculation methods are often found to be insufficient and require further development of the methodology to achieve more realistic and reliable results.

To illustrate this point, this paper demonstrates the integration of this user requirement into the ISO 9613-2:2024 standard. It is important to acknowledge that ISO 9613-2:2024 calculates three paths from the source to the receiver when a screen edge intersects the line of sight between the two objects. These paths include the direct path over the screen edge and the path that goes around both sides of the screen (horizontal extension). The calculated barrier attenuation, D_z, is frequency-dependent and is largely determined by the difference between the direct sound path and the detour via the shielding edge (z).

$$D_z = 10lg\left[1 + \left(2 + \left(\frac{C_2}{\lambda}\right)C_3 z\right)K_{met}\right] dB \quad for\ z > z_{min} \quad (1)$$

For the lateral detours, K_{met} is set to one in the formula. In the subsequent step, the attenuation due to a barrier, including possible corrections (A_{bar}) for the three paths is calculated separately based on D_z. This results in a combined A_{bar} through energetic summation. To take the transmission of a wall into account, D_z of the vertical sound path must be adjusted. The calculation of the lateral paths around the obstacle and the basic procedure remains unchanged. Three different cases must be considered.

a) The line of sight between the source and receiver is not interrupted.
b) The line of sight between the source and receiver is interrupted by several screens.
c) The line of sight between the source and receiver is interrupted by one screen.

In the proposed extension of ISO 9613-2:2024 implemented in SoundPLAN$_{noise}$, all three cases are considered and treated accordingly. This paper focuses on case c), with a screen that intersects the line of sight, which is the most relevant in practice. The following calculation steps are necessary:

1. Determination of a rubber band (connection between source and receiver) across the screen without taking into account the sound transmission. This results geometrically in z>0, d_{ss} and d_{sr} and finally the diffraction reduction, in this case called $D_{z,No,TL}$.
2. Determination of a multipath through the base of the screen, with z_{TL}, $d_{ss,TL}$ and $d_{sr,TL}$. Where z_{TL} takes values less than zero when the base point is below the line of sight. This results in the new diffraction reduction for the base point $D_{z,TL}$.
3. Considering the sound reduction index (R), the two diffraction reductions are then energetically combined to give the final D_z.

$$D_z = -10\log\left(10^{\left(-\frac{D_{z,No,TL}}{10}\right)} + 10^{\left(-\frac{D_{z,TL}-R}{10}\right)}\right) \quad (2)$$

This adjustment reduces D_z and takes into account the additional energy reaching the receiver through the screen. The calculation is performed for each frequency band and only minimally interferes with the basic ISO 9613-2:2024 procedure by adjusting D_z.

5. REAL APPLICATION: BUILDING SERVICES ON THE ROOF WITH ACOUSTIC BLINDS

Noise-intensive building services located on the roofs of buildings often cannot be completely enclosed due to the need for ventilation. In inner-city areas, this often leads to considerable noise pollution for residents and the surrounding area. In such cases, acoustic louvers are often used to reduce the noise sufficiently while ensuring air circulation at the same time. However, their acoustic performance is limited, particularly at low frequencies, where the low mass of the materials reduces their effectiveness. This type of noise control highlights the need for accurate modelling in order to more realistically estimate and optimize the sound insulation effect.

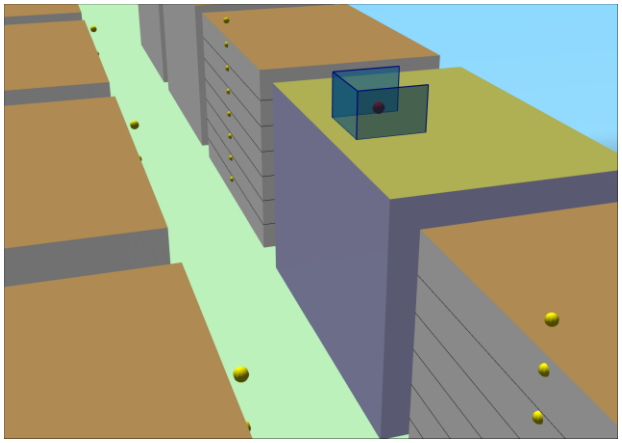


Figure 1. 3D-view of the acoustic model with the acoustic louvers around the noise source.

For the sound source, a spectrum from the literature was used that realistically describes the characteristic emissions for the application under consideration. In our example, a typical product with the following sound transmission loss was used for the acoustic louvers.

Table 1. Spectral sound transmission loss of the considered acoustic louvers.

Frequency [Hz]	125	250	500	1000	2000	4000
STL [dB]	5,0	8,0	9,0	12,0	9,0	7,0

As expected, the 'solid' wall variant with unlimited sound insulation (in accordance with the guidelines) results in significantly lower levels in the surrounding area than the variant with no wall. On the opposite façade, there is a reduction of between 8 and 19 dB, depending on the floor.

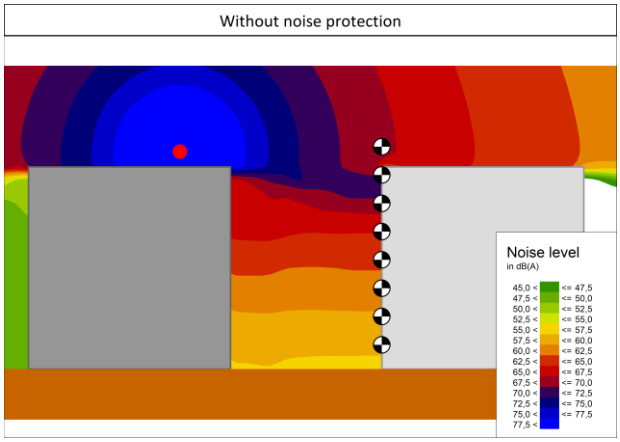


Figure 2. Noise dispersion in the cross-section without acoustic louvers.

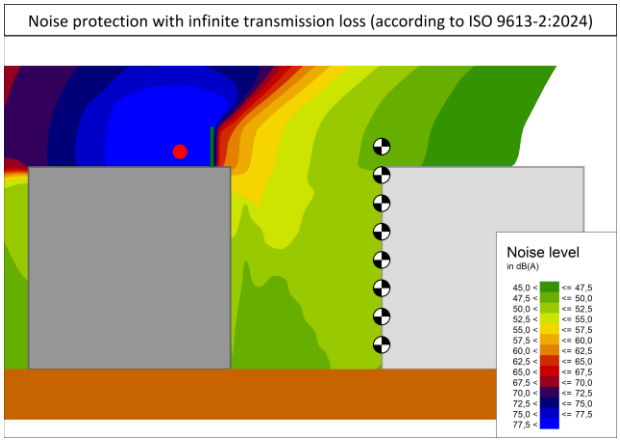


Figure 3. Noise dispersion in the cross-section with acoustic louvers (infinite transmission loss assumed).

The next variant was calculated using a wall with the real sound insulation of the acoustic louvers and the adapted algorithms. The resulting level reduction is only between 5 and 14 dB.

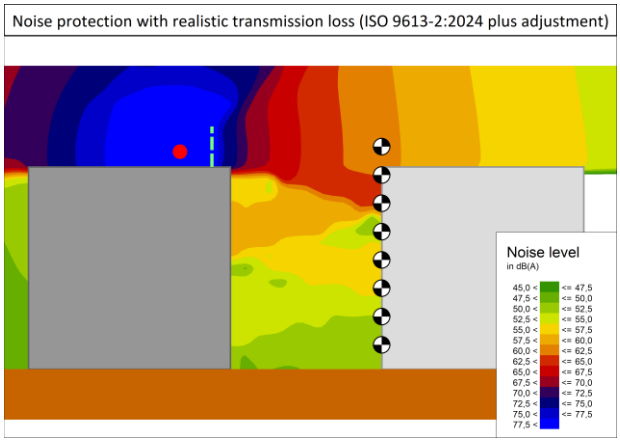


Figure 4. Noise dispersion in the cross-section with acoustic louvers (realistic transmission loss according to Table 1).

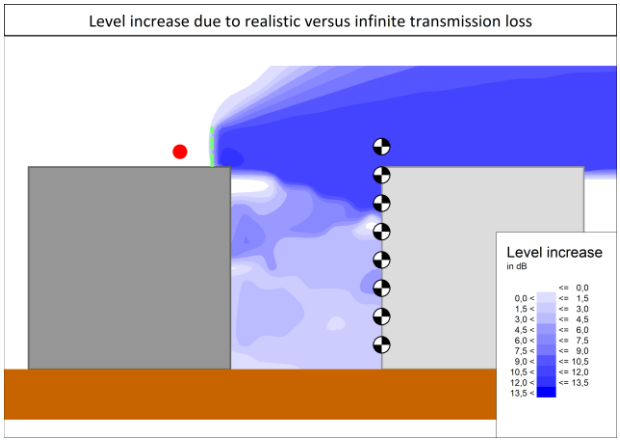


Figure 5. Noise level increase in the cross-section resulting from the realistic transmission loss of the acoustic louvers.

At some points, the passage of sound through the louvers will increase the level by up to 12 dB compared to a wall without a passage, while at other points it will be virtually 0 dB. The effect is highly dependent on height, as reflections play a significant role in this geometric situation. Above the roof, where there are no reflections, the reduction due to the semi-transparent wall is approximately 7 dB, which is roughly equivalent to the average sound reduction of the acoustic blinds.

The implemented extension of ISO 9613-2 in SoundPLANnoise allow for a more accurate modelling of the real acoustic conditions and emphasizes the importance of realistic sound insulation parameters in the simulation of special situations.

6. REAL APPLICATION: TEMPORARY NOISE PROTECTION MEASURES DURING CONSTRUCTION WORK

Construction work in urban areas often causes considerable noise pollution for residents and the surrounding area. Temporary noise barriers or curtains, which can be installed quickly, are an effective way of reducing noise. In the situation studied, work is carried out with a hammer drill on scaffolding attached to an external facade at a height of 11 m. The grey floorboards of the scaffolding are shown in the figure but were not considered in the noise simulation.

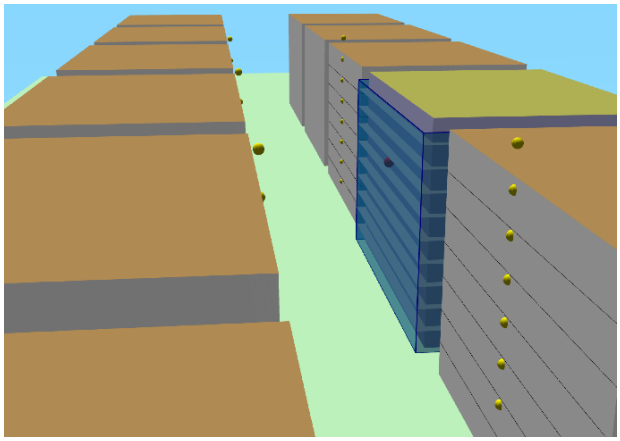


Figure 6. 3D-view of the acoustic model with the noise protection curtain around the scaffoldings.

The product CISILENT Typ L of Calenberg Ingenieure was used as sound insulation curtain. This mobile curtain has excellent acoustic properties, making it particularly suitable for temporary applications such as construction sites and events. Its sound absorbing and insulating properties offer an effective reduction of noise pollution in various application scenarios.

Table 2. Sound transmission loss of the sound insulation curtain.

Frequency [Hz]	125	250	500	1000	2000	4000
STL [dB]	13,2	15,5	17,6	19,0	20,0	24,0

At a computation height of 4 m above ground, there are large reductions of around 20 dB in the relevant area (e.g. road canyon). This result is to be expected, as the algorithm quickly reaches the maximum diffraction limit of 20 dB defined in the guideline due to the large extra path length.

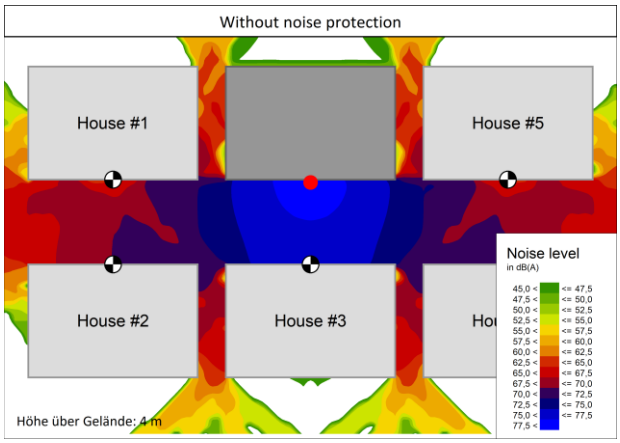


Figure 7. Noise dispersion without sound insulation curtains.

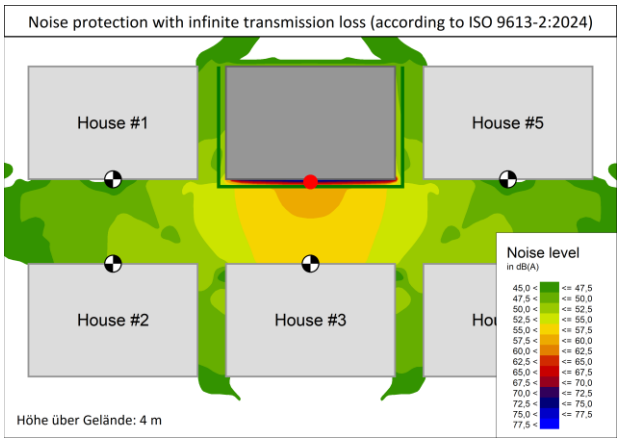


Figure 8. Noise dispersion with sound insulation curtains (infinite transmission loss assumed).

Additionally, there is a slight correction of the levels due to other sound paths, such as reflections and lateral paths. These effects contribute to the level reductions deviating slightly from the theoretical maximum but remain within the limits of the modelled calculation methodology. By adapting the ISO 9613-2:2024 algorithms in SoundPLAN$_{noise}$ to the real sound insulation, the following picture emerges. The level reduction is now about 19 dB. This result correlates very well with the real sound insulation of the noise barrier, considering that additional effects such as reflections and diffracted sound paths can occur.

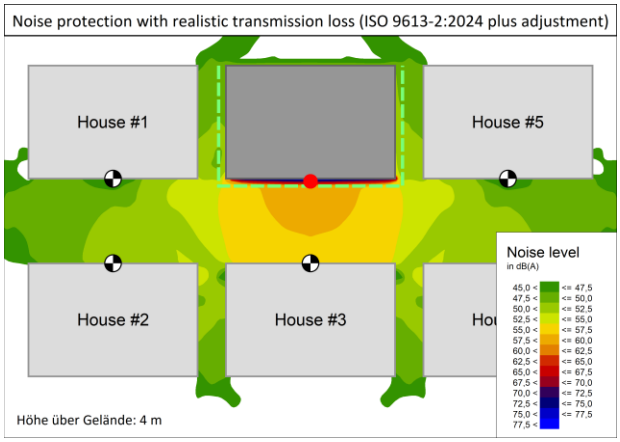


Figure 9. Noise dispersion with sound insulation curtains (realistic transmission loss according to Table 2).

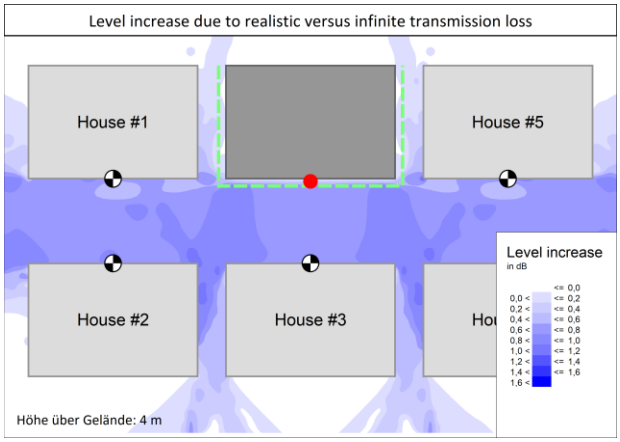


Figure 10. Noise level increase resulting from the realistic transmission loss of the sound insulation curtains.

The proposed adaptation of ISO 9613-2:2024 allows also in this case a more accurate modelling of the real acoustic conditions. In this case, however, the change in predicted results is rather small, around 1 dB, and has very little impact on the results. This is due to the high sound attenuation of the product used, which is close to the maximum diffraction limit of 20 dB.

7. CONCLUSION

The tested extension of ISO 9613-2:2024 by an additional term for the consideration of the sound insulation of walls leads to qualitatively meaningful results. It should only be used by the assessor/acoustician on a case-by-case basis, as the changes in the results are only relevant if the sound insulation is below the maximum diffraction limit of 20 dB. In such cases, a result can be calculated that is a much better estimation of the reality, as otherwise the level reduction would be overestimated by the assessor and complaints could later be made due to excessive noise pollution. Despite the successful extension of ISO 9613-2:2024 in SoundPLAN$_{noise}$ to include an additional term to account for sound insulation, comparability between different software products remains a key challenge. To address this issue from a quality assurance perspective, the following actions are critical:

1. Transparent quality assurance by the software developer:
   the software developer should clearly document which internal and external quality assurance measures are performed. This information should be openly available to users and should include an overview of the test tasks performed.
2. Documentation by assessors:
   assessors should document the software used in their reports, including the version number and quality checks performed. If the calculation settings differ from those recommended by the software developer, it should be noted.
3. Declaration of standard deviations:
   if objects or methods are used in the calculation models that exceed the limits of the standards, this should be clearly indicated and justified in the documentation of the results by both the software developers and the expert.

In addition, software developers should work together to fill gaps in existing standards and to address user requirements in a unified approach. This could be done through committees such as ISO/TC 43/SC 1/WG 56 or the A-QNS group. A revision of the propagation guidelines could also be used to make progress. However, it has been shown that such committees often work slowly and have to deal with conflicting interests, which makes quick innovations difficult. Regardless, it is essential that all interested parties have access to relevant information and documentation to ensure fair competition, transparency and comparability.

8. REFERENCES

[1] ISO 9613-2:2024 – Acoustics – Attenuation of sound during propagation outdoors – Part 2: Engineering method for the prediction of sound pressure levels outdoors

[2] SoundPLAN$_{noise}$ 9.1 Handbook, March 2025, SoundPLAN GmbH, Etzwiesenberg 15, 71522 Backnang, Germany

[3] A-QNS "Verband zur Förderung der Qualitätssicherung von Software zur Berechnung von Schall e.V": https://a-qns.de/en/home-english/, April 2025

DOI: 10.61782/fa.2025.0220

FORUM ACUSTICUM EURONOISE 2025

COMPARATIVE ANALYSIS OF STRATEGIC NOISE MAPS: USING HEAT MAPS TO FIND WHY TWO CNOSSOS-EU IMPLEMENTATIONS (INOISE AND CADNAA) DIFFER

Andrés L. Peña[1*]

[1] Calpe Institute of Technology, S.L., C/Severo Ochoa, 4, Málaga, Spain

ABSTRACT

Strategic noise maps are the tool to assess the population noise exposure, perform cost-benefit studies of the available measures to be adopted to abate that exposure as part of the noise action plans, and evaluate the effective improvement achieved after its implementation. CNOSSOS-EU is the homogenized calculation method for sound propagation outdoors in Europe, existing several applications implementing it. CNOSSOS-EU includes quality controls every application must fulfil, so no important deviations are expected in the results obtained when using different applications. However, such deviations exist and can be sensitive in some cases. The objective of this study is to present a method to detect where the disparities between both applications are more relevant: a heat map of the deviations obtained at the same grid point results, and an example of application in a real case scenario.

Two of these applications have been chosen, iNoise and CadnaA, to calculate the same strategic noise map of the population area of Santa Rosalía-Maqueda, Málaga. The different approaches in data processing and calculation method implementation of these applications are compared, the detected deviations in the outcomes obtained for both sound propagation and population noise exposure are analyzed, and the causes are inferred.

[*] ***Corresponding author***: andres@caltech.es.

Copyright: *©2025 Andrés L. Peña. This is an open-access article distributed under the terms of the Creative Commons Attribution 3.0 Unported License, which permits unrestricted use, distribution, and reproduction in any medium, provided the original author and source are credited.*

Keywords: *Strategic noise maps, CNOSSOS-EU, population noise exposure, comparative analysis.*

1. INTRODUCTION

Noise mapping is the presentation of data on an existing or predicted noise situation in terms of a noise indicator, indicating breaches of any relevant limit value in force, the number of people affected in a certain area, or the number of dwellings exposed to certain values of a noise indicator in a certain area [1]. "Strategic" refers to maps designed for the global assessment of noise exposure in a given area due to different noise sources, or for overall predictions for such an area.

CNOSSOS-EU has become the homogenized calculation method for sound propagation outdoors in Europe, being the mandatory calculation method in most European states, starting from December 31, 2018 [2].

This method is paired with strict quality requirements and quality assurance methods defined in the ISO 17534 series, "to ensure, to indicate, and to verify the degree of conformity of a software program with a consistently implementable calculation method/procedure" [3]. Thus, given a certain dataset, any implementation of the CNOSSOS-EU should lead to the same results, this been checked by dozens of tests cases [4]. However, such deviations have been noted [5], and can be of statistical significance, even when assessing the sound power of sources [6].

Two different modelling software suites are compared in this study, DataKustik CadnaA® [7] and DGMR iNoise® [8], in the real case scenario of Santa Rosalía-Maqueda, a town area with a main through road and residential streets,

being roads the only noise source considered. The comparison focuses on propagation differences detected. CadnaA was selected due to having access to a full working educational licence, and iNoise due to having access to a full commercial licence.

2. OBJECTIVES

The objectives are to compare the results obtained by both modelling implementations, minimizing the differences between the models loaded. To achieve this, minimal and unavoidable optimisations were applied to both models.
The author has no commercial or whatsoever interest in any of the two CNOSSOS-EU implementations used in this work, nor recommends the usage of one above the other.
Conclusions are applicable only to this case scenario, as no additional scenarios were checked for correlation.

3. METHODOLOGY

3.1 Data pre-processing

Data was gathered and pre-processed in QGis. Sources used were:

- Terrain digital model → MDT02 layer, 2nd coverage (2015 – up-to-date), with 2m grid spacing, Centro Nacional de Información Geográfica [10]
- Buildings → from Oficina Virtual del Catastro: layer CONSTRU for heights, and INSPIRE layer A.ES.SGDC.BU for layout, current use, construction date, number of dwellings (1 = single dwelling, 2 or more = multiple dwellings) and current status [11]
- Roads → OpenStreetMap project [12]
- Traffic flows and speeds → Plan for traffic flows from Junta de Andalucía, and WG-AEN [13] tool 2.5 where no data was available
- Population → DEGA (Datos Geoespaciales de Andalucía [14], evenly distributed between the buildings located in each data cell, but considering the volume of each building

The information was pre-processed and formatted for each software in QGis and then imported at CadnaA and iNoise.

3.2 Import process

Huge differences between CadnaA and iNoise data import interfaces were noted. While iNoise import/export process is clear, user-friendly and versatile, CadnaA has a completely different approach with a powerful but complex import interface but limiting the model data that can be exported.
As CadnaA allows a model to be calculated with several methods, item types have fields not used by CNOSSOS-EU (i.e., road width). As iNoise models are assigned to a calculation method at creation, the interface is adapted to it, and no unnecessary fields are shown.
Buildings and roads were directly imported and not simplified to minimise the differences between the models of each software. Height lines had to be minimally simplified, as CadnaA was unable to generate a 3D view if this step was avoided, and such a view is required to check for modelling errors. Terrain resolution has been proved to have minimal to no impact in the results [15].
CadnaA's tool to adapt the terrain digital model to avoid burial of roads in several points. While iNoise lacks such tool, these burials were avoided by rising all roads by 0,01m, which is trivial with its mass editing interface.
Road slopes were calculated at QGis, as CadnaA offers no direct option to export its calculated slopes and iNoise has no tool for calculating them.
Sound power levels of roads calculated by both applications were compared with almost no deviations between them, as Table 1 shows. Absence of integrity, duplicities and geometric errors were checked by iNoise for both items and terrain (CadnaA has no equivalent tool).

Table 1. Sound power estimation differences for roads by CadnaA and iNoise (dBA).

	$L_{w,d}$	$L_{w,e}$	$L_{w,n}$
Max, abs	0,450	0,450	0,660
Mean	0,026	0,005	0,101
Median	0,010	0,000	0,050

iNoise building item type has fields for designated use (i.e. residential, educational, industrial…) and dwelling type (no dwellings, single dwelling or multiple dwellings), while population data is managed with the address point item type. Address points are linked to residential buildings.
CadnaA building item type has a "residential" Boolean field and a population field, but there is no way to mark single or multiple dwellings.

3.3 Grid calculation

The calculation grid points were spaced by 2m in both dimensions, a high density, to better asses the differences in propagation obtained by both applications. Both models were not optimised for calculation but to minimise differences, so no conclusions can be made about

performance nor efficiency of both applications, even when they both were run on the same server. Partial views of grid results are shown in Figure 1 (CadnaA) and Figure 2 (iNoise).

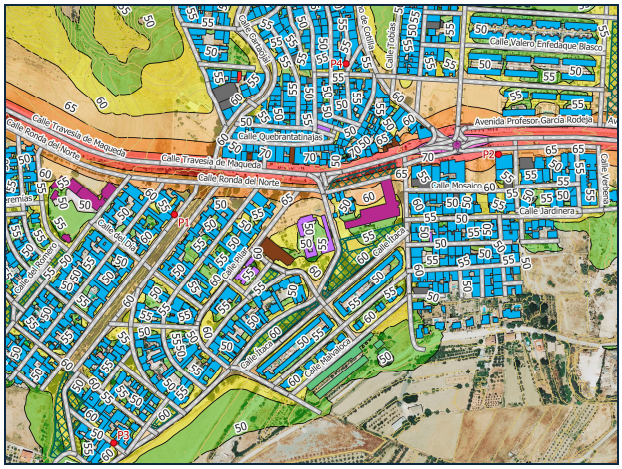


Figure 1. CadnaA grid results (L_{den})

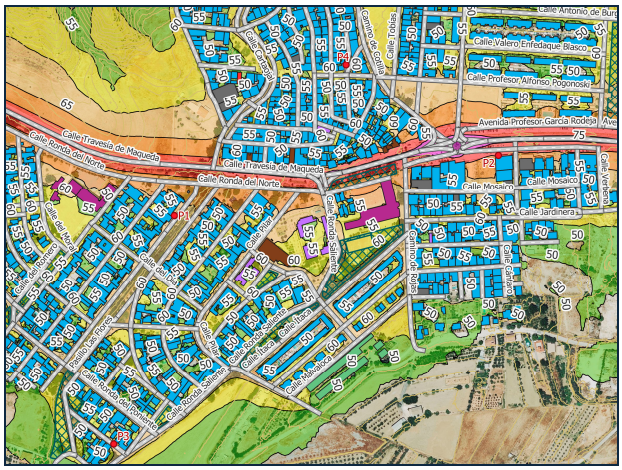


Figure 2. CadnaA grid results (L_{den})

3.4 Population exposure calculation

CNOSSOS-EU include methods 1 (most exposed), 2a (length) and 2b (median value) for population exposure calculation [16].

Unlike iNoise, CadnaA requires grid to be calculated prior to obtain population exposure, and by using the building evaluator item type. The façade exposure calculation method to be used can be chosen, but there is no option to use different methods for both single and multi-dwelling buildings.

iNoise has a tool to automatically mass add receivers at façades, which are calculated independently of the grid. These receivers are linked to the buildings, and the population exposure calculation may consider, if selected, different methods for façades of single and multi-dwelling residential buildings.

These radically different approaches to façade calculation might be behind the deviations detected in population exposure between both applications.

4. RESULTS

4.1 Grid results

As noted before, sound power of roads was estimated with minimal or no differences between both applications. However, sound propagated further according to iNoise compared to CadnaA. Grid point results were compared one by one, excluding those CadnaA and iNoise excluded (i.e., points located inside buildings). A statistical analysis (Table 2) of the deviations was carried out with the 72.388 grid points calculated by both applications. For each point, the iNoise result was subtracted from the CandaA result.

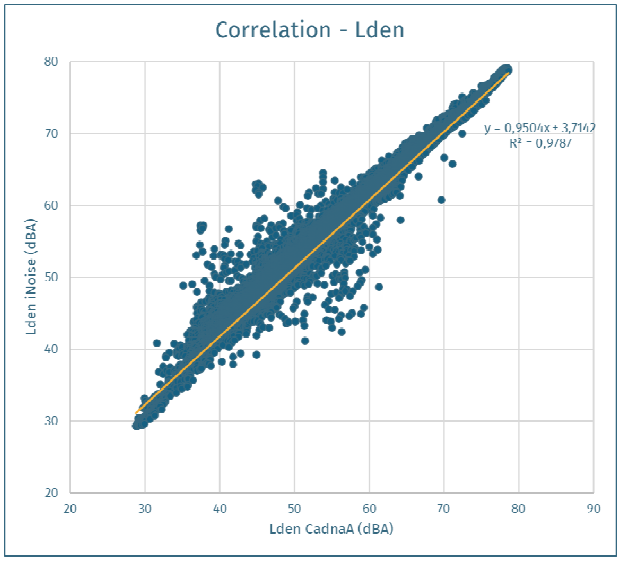


Figure 3. Linear correlation of grid points results

Considering L_{den}, CadnaA deviates >3dBA from iNoise in 105 points (0.15%), while the opposite happens in 3,769 points (5.21%). So, the difference at 68,514 points (94.65%) is in the (-3, 3) interval. A total of 43,530

points (60.13%) are in the (-1, 1) interval. Figure 3 shows linear correlation for L_{den} grid point results, with a Pearson r correlation coefficient higher than 0.97. A histogram for the same data is presented at Figure 4.

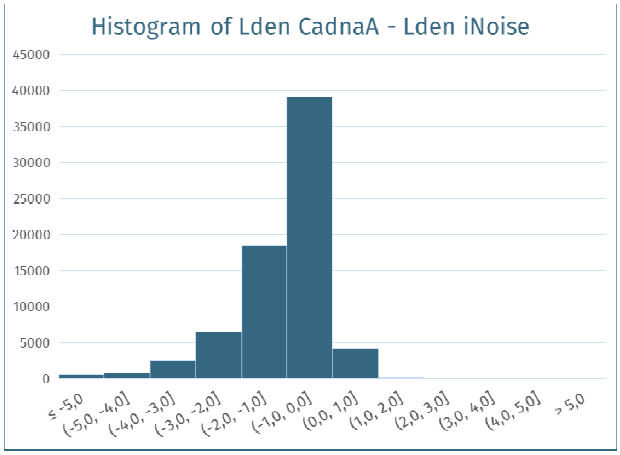


Figure 4. Histogram of L_{den} CadnaA - iNoise

To visualise the areas where the differences were located, the calculated differences were represented as a GIS layer, represented as a heat map as seen in Figure 5. Cold dots mean a higher value was calculated by CadnaA, and the warm areas are those where iNoise is the one estimating a higher result. This map allows examining not only the differences between the results, but how they are located, and may be the reason behind it.

Parameter	L_d	L_e	L_n	L_{den}
Max diff	14.03	14.16	14.04	13.97
Min diff	-19.29	-19.66	-20.08	-19.84
Mean	-0.95	-1.03	-1.04	-1.02
Median	-0.73	-0.78	-0.77	-0.76
Typ.Dev.	1.15	1.13	1.14	1.14
Variance	1.32	1.27	1.31	1.29

Table 2. Statistical analysis (CadnaA - iNoise)

The highest deviations are located 1) close to buildings, and 2) in complex terrain areas. Thus, obstacles as buildings or changes in terrain seem to have a lesser impact in iNoise than in CadnaA, as levels behind or next to obstacles tend to be higher in iNoise. Flat, open areas have almost equivalent results in both applications.

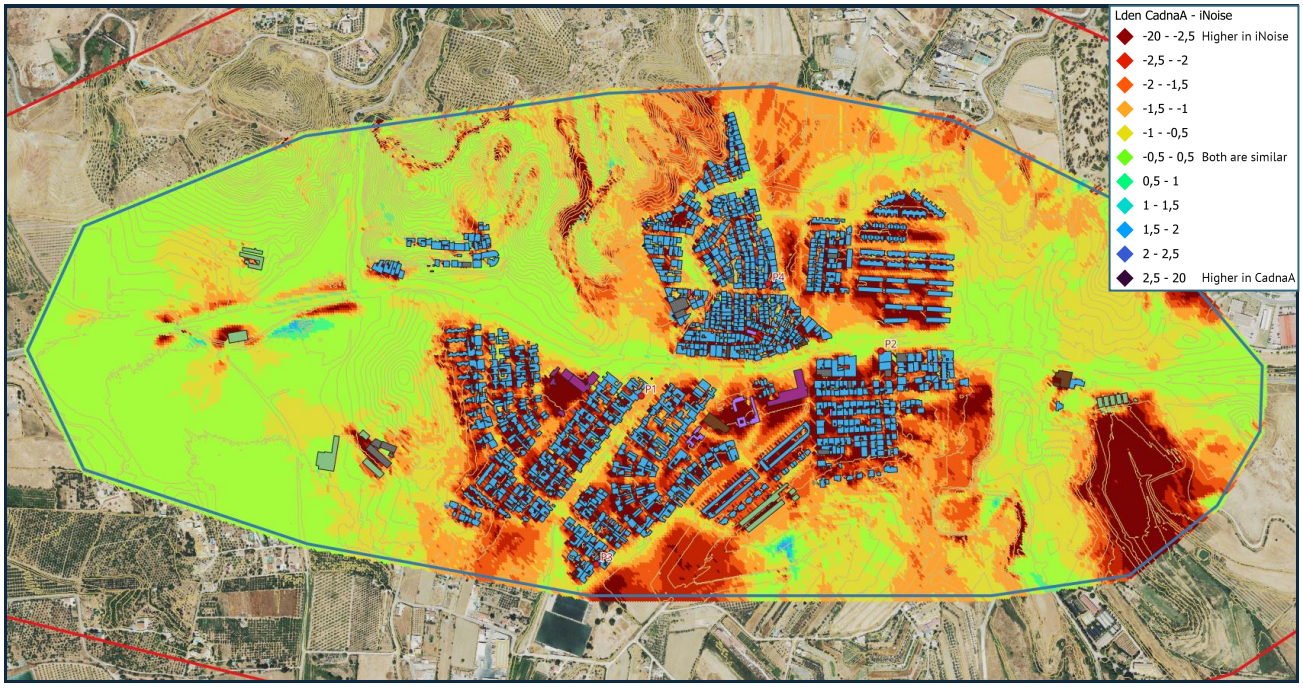


Figure 5. Heat map of L_{den} CadnaA - iNoise

4.2 Population exposure

Noteworthily, deviations in population exposure between both applications were detected to be in the opposite direction: CadnaA obtains higher exposure levels than iNoise, as seen at the Figure 6, with more people considered to be in the higher isophonic ranges.
Day, evening and night exposure levels follow the same trend, so for brevity only L_{den} exposure is shown here.
As stated before, the radically different approaches between both applications to assess population exposure might be the reason of these deviations: independent façade receivers in iNoise vs grid results with building evaluators in CadnaA, and the usage of different calculation methods for single and multi-dwelling façades in iNoise vs a single method for all dwelling types in CadnaA.

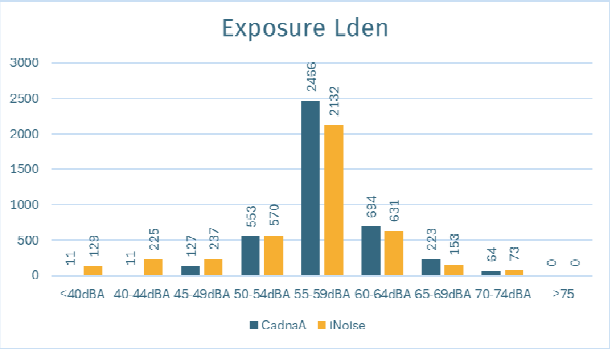


Figure 6. L_{den} exposure levels

5. DISCUSSION

The ISO 17534 is a huge step in harmonising the results obtained by diverse implementations of sound propagation modelling implementations in general, and the CNOSSOS-EU method in particular. These quality tests are a crucial advance in noise modelling across Europe. However, the question on disparities in the results obtained by different applications still remains, as several studies on the matter keep reaching to the same conclusions: fulfilling the test cases considered by the ISO 17534 quality controls is not enough to always achieve consistent results with different CNOSSOS-EU implementations [5][6].
While the ISO 17534 quality control focuses on propagation, reflections, diffractions, abatement, terrain, obstacles, etc., sometimes the divergence in results have other causes: disparities in data importing and management flows, model tools and optimisers, data item implementation, terrain model triangulation algorithms, software licence limitations, grid design and requirements, optional methods or parameters considered, and other hard to homogenise nor reconcile software design decisions taken by the developers of these applications.
No unique and definitive solution can be proposed here, but suggestions and wishes.
Adding implementation directives to the current test cases should improve the homogenisation of CNOSSOS-EU implementation and reliability.
Moving model information between applications should not be this hard. A data exchange file format for acoustic modelling would be of high interest for administrations, the main client for noise maps, and would help to ascertain deviations between implementations with more ease.
While acoustic modelling has had remarkable progression in the last 20 years, and CNOSSOS marked a critical step in the best direction, there is still a fascinating road ahead.

6. CONCLUSIONS

iNoise® and CadnaA® are fully valid implementations of the CNOSSOS-EU method, as they are certified to fulfil all ISO 17534 requirements, as many other solutions available.
While these conclusions are only applicable to this case scenario, deviations in results were found, which was not surprising as this is a recurrent situation every time the results of two or more implementations for the same model are compared.
While statistical analysis provides conclusions on the importance and relevance of deviations in results obtained by several implementations of CNOSSOS-EU, heat maps offer insight on the reasons behind those deviations.
For the case scenario of this study, iNoise calculated a higher propagation of sound than CadnaA, and according to the heat map, the cause of these deviations might be in how each application deal with obstacles and terrain. On the other hand, CadnaA considered population exposure to be higher than iNoise, and in this case the reason behind it might be CadnaA has no option to employ different calculation methods for single and multiple dwellings.

7. ACKNOWLEDGMENTS

The author would like to thank Jordi García and DGMR for their support with iNoise, and Cástor Rodriguez and DataKustik for the same with CadnaA. Alfonso Corz has been crucial and supportive during the whole process. Enrique Nava sparked the idea of representing in a map the differences that should not exist between the results of both

models. Eva García-Escobar, Óliver Peña, Carmen Escobar, Sandra Escobar, Ana Belén Olmo and Elena Olmo helped to gather invaluable field information. Also, a special nod goes to Elena Díaz, who suggested this article should be written.

8. REFERENCES

[1] Directive 2002/49/EC of the European Parliament and of the Council of 25 June 2002 relating to the assessment and management of environmental noise.

[2] Commission Directive (EU) 2015/996 of 19 May 2015 establishing common noise assessment methods according to Directive 2002/49/EC of the European Parliament and of the Council.

[3] ISO 17534-1:2015; Acoustics — Software for the calculation of sound outdoors. Part 1: Quality requirements and quality assurance.

[4] W. Probst, "Quality assurance methods demonstrated with the calculation of sound propagation with ISO 9613-2 and with CNOSSOS-EU", in *Proc. of the 23rd International Congress on Acoustics* (Aachen, Germany), pp. 1616-1623, 2019.

[5] I. Soto Molina, L. Simón Ortega, M. Ausejo Prieto, R.M. Arce Ruíz, "Análisis comparativo de softwares de simulación de ruido ambiental: comparación entre una solución comercial y una de código abierto", in *Proc. of the 54º Congreso Español de Acústica TecniAcústica 2023* (Cuenca, Spain), 2024.

[6] J. Grijota, R. Gey, M. Tomás, J.L. Cueto, "Análisis del cálculo de la potencia acústica lineal Lw' en diferentes softwares comerciales para el modelo de ferrocarriles de CNOSSOS EU", in *Proc. of the XIII Congreso Ibérico de Acústica y 55º Congreso Español de Acústica TecniAcústica 2024* (Faro, Portugal), pp. 281-288, 2024.

[7] DataKustik CadnaA®, sound propagation modelling software implementing CNOSSOS-EU method, https://www.datakustik.com/products/cadnaa/cadnaa

[8] DGMR iNoise®, sound propagation modelling software implementing CNOSSOS-EU method, https://dgmrsoftware.com/products/inoise/

[9] QGis, spatial visualization tool, https://qgis.org/

[10] MDT02 2ª cobertura (2015-actualidad), CNIG, https://centrodedescargas.cnig.es/CentroDescargas/modelo-digital-terreno-mdt02-segunda-cobertura

[11] Oficina Virtual del Catastro – sede electrónica, https://www.sedecatastro.gob.es/

[12] OpenStreetMap (OSM), free, open map database, https://www.openstreetmap.org/

[13] Good Practice Guide for Strategic Noise Mapping and the Production of Associated Data on Noise Exposure, version 2, 13th January 2006. European Commission Working Group Assessment of Exposure to Noise (WG-AEN).

[14] DEGA, datos geoespaciales de Andalucía, https://www.juntadeandalucia.es/institutodeestadisticaycartografia/dega/distribucion-espacial-de-la-poblacion-en-andalucia

[15] M. Ausejo, R. García, D. Vas, R.M. Rojas, L. Simón, "Influencia de la resolución del terreno en simulaciones acústicas con pantallas de ruido", in *Proc. of the XIII Congreso Ibérico de Acústica y 55º Congreso Español de Acústica TecniAcústica 2024* (Faro, Portugal), pp. 111-120, 2024.

[16] E. Hartog van Banda, "The three methods of calculating population exposure according to CNOSSOS-EU", in *Proc. of the Inter-Noise 2022* (Glasgow, Scotland), 2022.

DOI: 10.61782/fa.2025.0266

FORUM ACUSTICUM EURONOISE 2025

DEFRA'S NOISE MODELLING SYSTEM: A NEW APPROACH TO NATIONWIDE MODELLING IN SUPPORT OF RESEARCH AND EVIDENCE

James Trow[1*] **Hilary Notley**[2]
[1] Noise Consultants Limited, Warrington, United Kingdom
[2] Department for Environment, Food & Rural Affairs, London, United Kingdom

ABSTRACT

The United Kingdom Department for Environment, Food and Rural Affairs (Defra) commissioned the design and build of an environmental noise modelling system (NMS). The NMS has been developed to support Defra in preparing its environmental noise evidence base by preparing national road and railway noise models. Since its development in 2022, the NMS has successfully delivered national coverage noise models, noise maps and population exposure statistics for all public road and railways sources in England, Wales and Scotland. This paper provides an overview of the design of the NMS, the specific design choices made in its development, and how these design choices feature in models and noise exposure data can be used to support the development of re-search and evidence.

Keywords: *noise mapping, research, Defra noise modelling system (NMS)*

1. BACKGROUND

The UK Department for Environment, Food and Rural Affairs (Defra) commissioned the design and build of an environmental noise modelling system (NMS) in 2021. From inception, Defra has overseen the development of its NMS to ensure that it is capable of transforming the way in which Government can both understand the scale of impact of noise from road and railway sources across England, but also work with stakeholders to integrate their own data sources, provide access to the underlying noise model and results, and ingest and integrate other data sources to support research and develop evidence.

This paper focusses on how design choices in the NMS's development can be used to support the development of research and evidence.

2. NMS DESIGN OBJECTIVES AND REQUIREMENTS

The core functional requirement of the NMS is to deliver Defra's regulatory requirements by producing strategic noise models, maps and exposure datasets for relevant road and railway sources in England, along with preparing analysis to fulfil the requirements of the Environmental Noise (England) Regulations 2006 (as amended) [1], the Defra 25-year Environment Plan [2], and the Public Health Outcomes Framework [3].

These requirements set a design requirement for the NMS to deliver a national noise model and associated noise exposure dataset for England with all public roads and railway including in the noise model. An example noise model within England using the NMS is presented in Figure 1.

Copyright: *©2025 J. Trow et al. This is an open-access article distributed under the terms of the Creative Commons Attribution 3.0 Unported License, which permits unrestricted use, distribution, and reproduction in any medium, provided the original author and source are credited.*

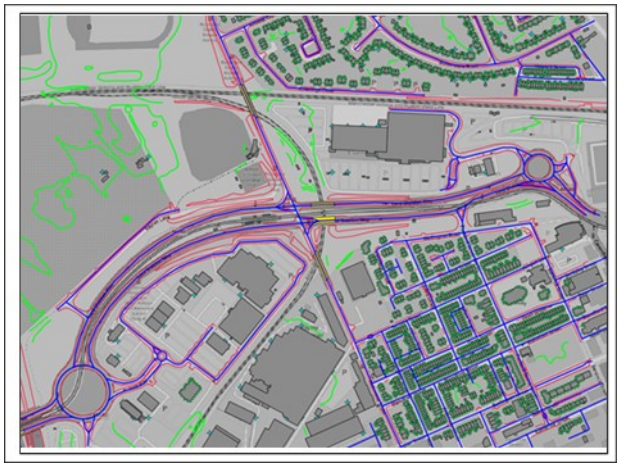


Figure 1. Noise model example highlighting road and railway sources, propagation model and façade receivers

The noise models delivered within the NMS are produced in line with the requirements of the adapted assessment methods based on the Calculation of Road Traffic Noise (CRTN), Calculation of Railway Noise (CRN), and CNOSSOS-EU. A design objective for the NMS is to deliver these requirements through automated processes wherever possible.

The wider design requirement for the NMS is to allow future users across the public sector to access the noise model through the NMS using open data standards.

For Defra, a key requirement of the NMS is to utilise and integrate noise exposure datasets produced from its model to support research and evidence building. It is this requirement which has driven design choices in how data is stored, processed and managed within the NMS, along with how national calculations and the NMS's noise calculation engine have been designed and configured.

3. CONCEPTUAL DESIGN

The NMS is designed as a web accessible cloud computing service hosted in Microsoft Azure. It has been designed to connect a series of components secured behind a web application firewall. The design of the NMS has taken a 'decoupled' approach which utilizes existing commercial products with 'ground up' development in areas such as its database design and Extract Transform Load (ETL) tools.

At the heart of the NMS is a Postgres geospatial database served on Azure CosmosDB. The database has been designed to store noise models and noise exposure datasets alongside each other. In support of Defra's requirements, the NMS has been designed to deliver automated processes whereby selected input datasets are transformed into noise model datasets using Feature Manipulation Engine (FME) software running bespoke ETL tools.

The models are stored in a manner which conforms to its system's open data standards which have been developed in parallel with the NMS. The parallel development of the database alongside the open data standards has highlighted where and how relationships between the datasets held within the NMS can be established and where these relationships can be extended to external data sources.

A core principle in the conceptual design has been to retain internal and external relationships in the noise source, propagation, receiver and noise exposure results datasets. To achieve this the design concept has relied on retaining identifiers through the calculation process which has required developments to the NMS's calculation engine, which utilises LimA calculation cores.

The high-level design of the NMS and its components is presented in Figure 2.

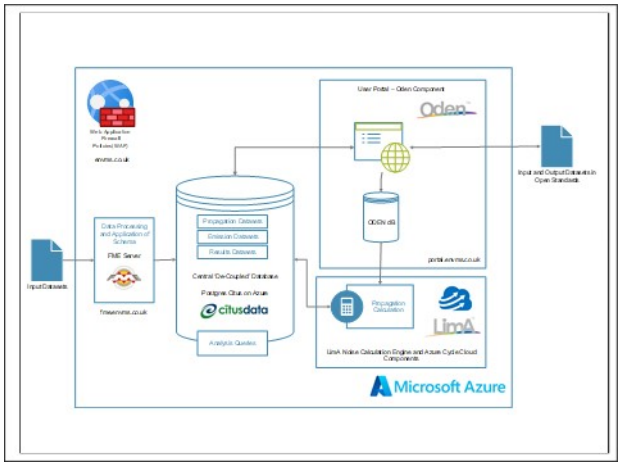


Figure 2. High Level Design of the NMS, its associated components and indicative data flows

4. DESIGN CHOICES AND FEATURES

In developing the NMS, specific design choices were made as part of the data and database architecture to support and facilitate the use of Defra's noise model and exposure

datasets to support research and evidence building. Three key design choices with this end use in mind are discussed.

4.1 Statistical Relational Modelling

A key design choice has been to develop a relational dataset which allows receptor datasets (buildings and noise calculation points) to be joined directly to results datasets stored in the NMS with wider external relational information to facilitate integration with wider Government statistics and data.

Each receptor at a building is provided with its own ID which is linked to each building. Each residential dwelling is pre-computed with population estimates. Each receptor is fed into the NMS's calculation engine with the results provided back to the database with reference to the receptor.

Each building is marked with relevant external identifiers that allows it to be assigned to various statistical geographies as defined by the UK Office for National Statistics. These geographies include Output Areas, Lower Super Output Areas, Ward Code, and Local Authority District Codes. Health Geographics are also assigned [4].

Using the CNOSSOS-EU 2a method for consistency, the database has been designed to allow noise exposure values for a range of metrics to be assigned to each building in 1 dB bands which are stored within the NMS as a dataset.
The retention of relational identifiers with Government statistical geometries within the NMS data model facilitates wider Government statistics to be joined to noise exposure datasets.

To support this, an end user tool referred as the 'Joint Statistics Tool' (JST) has been developed and is hosted within the NMS itself. This tool has been developed so that statistical data can be proportioned to a building level based on population estimates. This approach allows population noise exposure in 1 dB bands as held at building level to be considered based on the likelihood of that population falling into other statistical categories. An example is presented in Figure 3 which indicates how a general health statistic can be joined to noise exposure.

4.2 Source Apportionment

The NMS data model has been developed so that road and railway noise levels at each façade receptor and each grid calculation point can be revealed. This logic can be extended to incorporate noise exposure levels from industry and airport sources allowing the contributions from each noise source at location to be understood.

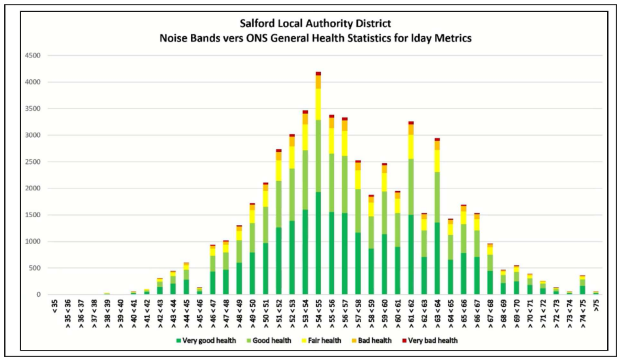


Figure 3. Example of an external statistic joined to noise exposure at building level

For road and railway sources, the concept of source apportionment has been further extended. Developments to the NMS's calculation core allows the contribution from individual road and railway sources to be understood with the contribution from each segment presented in order of its contribution to the overall noise exposure level by noise metric. This logic allows for noise emission parameters within the model to be presented alongside each contribution to provide an end user with an understanding of model inputs alongside their contribution to noise impacts. This is again achieved by retaining and reporting noise level contributions by source identifiers held in the model as stored in the central database by retaining these identifiers through the calculation process.

An example output from the NMS's source apportionment tool is presented in Figure 4.

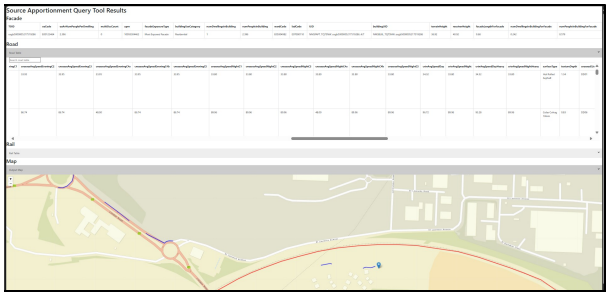


Figure 4. Example output from the NMS's source apportionment tool

4.3 Octave Bands

CNOSSOS-EU requires calculations to be carried out in octave bands. A key design choice has been to retain calculated octave band noise levels for each metric as part of the road and railway noise calculations. The NMS's database design and results tables allow octave band data to be stored for overall levels and as part of the source apportionment logic. Octave band results datasets are stored for façade receivers and noise grids.

Example road traffic noise maps calculated at the 1kHz and 250Hz octave band centre frequencies are presented in Figures 5 and 6 respectively.

Retention of octave band data allows the source and propagation characteristics to be captured over large areas and at discrete receptors opening up the potential to consider exposure relationships based on the character of the noise received.

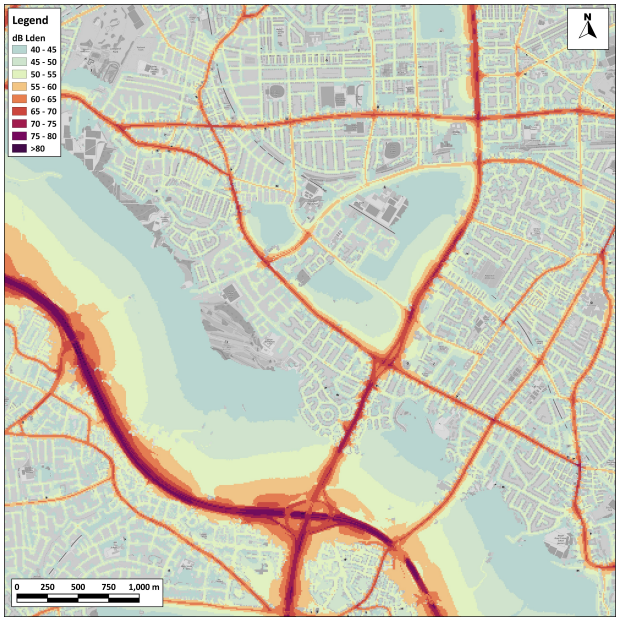


Figure 5. Road traffic noise maps (L_{den}) based on calculated levels at 1kHz

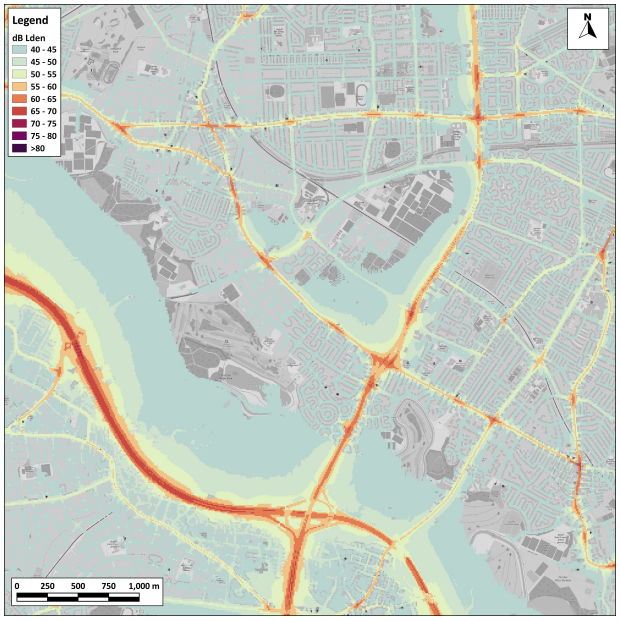


Figure 6. Road traffic noise maps (L_{den}) based on calculated levels at 250 Hz

5. OPPORTUNITIES FOR EVIDENCE AND RESEARCH

Section 4 of this paper highlights three key design choices within the NMS which provide opportunities for evidence building and research.

5.1 Inequalities in noise exposure

The NMS's Joint Statistics Tool provide opportunities for Defra to utilise its national noise exposure dataset to explore inequalities in noise exposure to individual transportation sources and/or combined transportation noise.

Using the JST, external datasets held by UK ONS as prepared using outputs from the 2021 Census [5], can be considered against exposure to environmental noise facilitating research and evidence generation exploring inequalities against a range of socio-economic and socio-demographic factors.

5.1.1 Socio-economic Factors

The National Statistics Socio-economic Classification (NS-SEC) is a standard classification which the UK ONS use to assign information such as occupations, employment status and history in statistical geographics across the UK [6]. ONS datasets also provide information that describe other

information such tenure of household and area-level income deprivation.

This data is held across a range of statistical geographies however through the JST this can be reconciled to building level allowing population and household noise exposure in 1 dB bands to be considered alongside statistical descriptions representing the likelihood that the population at each building falls into a particular socio-economic classification.

When considered and enumerated at regional and/or national level, the JST provides Defra with the opportunity to consider whether inequalities in noise exposure exist with respect to:

- Employment and Unemployment;
- Occupation;
- Household Income;
- Property Values;
- Household Tenure and Type;
- Income Deprivation; and
- Education.

5.1.2 Socio-demographic factors

The same techniques available in the JST provide opportunities to consider noise exposure against socio-demographic factors, namely ethnic group and household composition. The data model therefore provides Defra with the ability to consider whether there are systematic differences in exposure to environmental noise and different groups of people.

5.2 Mixed Source Environments

The NMS provides a national picture of exposure to transportation noise sources. In agglomerations, this is supplemented with exposure to industrial noise. This data is held in a standardised and consistent manner. The main evidence base for the effects of environmental noise still focuses on source-specific impacts and does not incorporate combined exposure to effects of multiple noise sources and/or other pollutants. The NMS and its data model provides opportunities to consider the effects of noise in mixed source environments. The national coverage of the exposure datasets provides further consideration to be given to the combined effects of other pollutants.

Defra carry out regular nationally representative social surveys on attitudes to different aspects of the environment and the work that Defra is responsible for [7]. These surveys include questions on people's response to different noise sources experienced whilst at home. Combining these results with outputs from the NMS provides the opportunity to look at exposure-response relationships at a national level.

5.3 Outcome Mapping

With noise exposure metrics stored alongside population at building level, the data model developed for the NMS provide opportunities to explore how harmful effects due to exposure to environmental noise can be mapped by calculating the number of people highly annoyed, highly sleep disturbed and/or at risk of health outcomes using odds ratios (OR) at building level and enumerating this information into zones, clusters, or within statistical and/or health reporting geographies to geographically map and identify burden through metrics such as Disability Adjusted Life Years (DALY).

The ability to store temporal data allows trends to be tracked over time.

5.4 Impacts on Biodiversity

Ecological research now deals increasingly with the effect of noise pollution on biodiversity [8]. Although habitats are not specific receptors in Defra's model, the national coverage of its noise exposure maps and grids cover biodiversity sites such as:

- Ramsar;
- Special Protection Areas (SPA);
- Sites of Specific Scientific Interest (SSSI); and
- Special Areas of Conservation.

These sites are designated in England as important for wildlife and other factors such as geology. Defra's datasets allow noise exposure to be considered across these areas, with octave band exposure datasets providing the ability for road and railway noise exposure to be considered using different frequency weightings and/or at specific frequencies which may best reflect the hearing characteristics of different species.

5.5 Tranquility Mapping

Outputs from the NMS have already been used by Welsh Government and Natural Resources Wales as part of the development of national tranquility maps [9]. National road and railway noise maps have been combined with other

datasets and rulesets to calculate tranquility indices as presented in Figure 7.

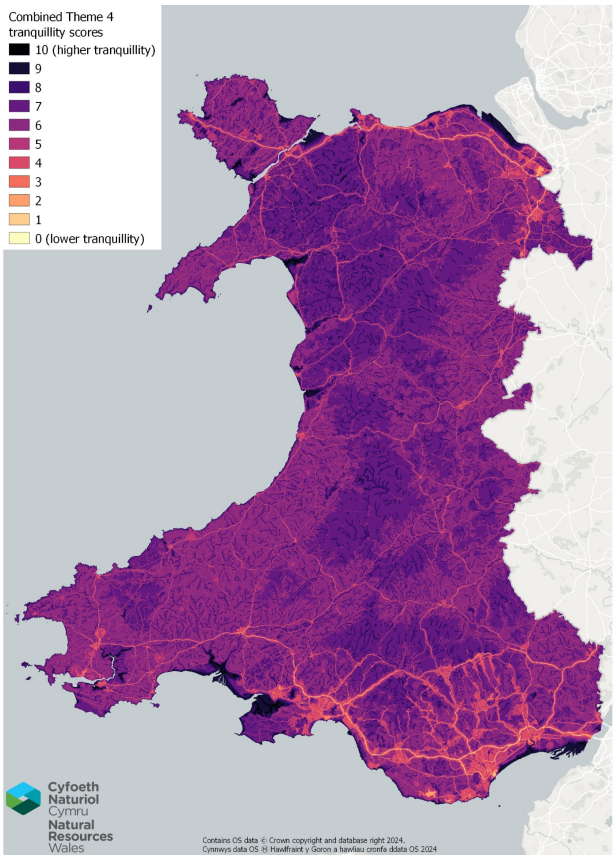


Figure 7. Tranquility map in Wales developed in part using NMS road and railway noise level grid outputs.

6. CONCLUSION

The development of the NMS has met the aims and objectives set out by Defra at the start of the project and even exceeded the expectations of many in the industry, It is the recipient of a number of awards for innovation from professional, government and non-governmental organisations. The NMS provides a solid foundation for building an evidence base over many years, with the flexibility to incorporate future datasets, not only related to noise modelling, but also wider environmental impacts or those associated with the broader built environment.

The above examples all show how the model and its outputs can be used to better understand the impact of environmental noise on the population. The data has also been used to enhance other indicators used widely in UK policy-making. The English Indices of Deprivation measure relative levels of deprivation in neighbourhoods in England [10]. In the next release, for the first time ever, environmental noise exposure to transportation sources will be one of the indices included in this composite measure. This would not have been possible had the NMS not covered all public roads and railway and the whole population of England.

7. ACKNOWLEDGMENTS

The development of the NMS has been a team effort. Defra would like to acknowledge the contributions from Noise Consultants Ltd, Acustica Ltd, Mott MacDonalds, NGIS, Stapelfeldt, M+P and ISVR

8. REFERENCES

[1] HM Government, *The Environmental Noise (England) (Amendment) Regulations 2018* (2018).

[2] HM Government, *A Green Future: Our 25 Year Plan to Improve the Environment* (2018).

[3] https://www.gov.uk/government/collections/public-health-outcomes-framework (accessed 28 March 2025)

[4] https://www.ons.gov.uk/methodology/geography/ukgeographies (accessed 4 April 2025)

[5] https://www.ons.gov.uk/census (accessed 4 April 2025)

[6] https://www.ons.gov.uk/methodology/classificationsandstandards/otherclassifications/thenationalstatisticssocioeconomicclassificationnssecrebasedonsoc2010 (accessed 4 April 2025)

[7] HM Government, Survey on Attitudes to the Environment (2021), https://randd.defra.gov.uk/ProjectDetails?ProjectId=20907 (Accessed 4 April 2025).

[8] R. Sordello, O. Ratel, F. Flamerie De Lachapelle, C. Leger, A. Dambry and S. Vanpeene: "Evidence of the impact of noise pollution on biodiversity: a systematic map," *Environmental Evidence*, 9, Article Number 20, 2020.

[9] https://storymaps.arcgis.com/stories/865c1876d9f64280a3dfc6e2769a46a5 (Accessed 4 April 2025)

[10] https://www.gov.uk/government/collections/english
-indices-of-deprivation (Accessed 4 April 2025)

DOI: 10.61782/fa.2025.0207

FORUM ACUSTICUM EURONOISE 2025

CNOSSOS ENVIRONMENTAL NOISE ANALYSIS ASSISTED BY CLOUD-BASED MODEL REFINEMENT AND CALCULATION

Dipl.-Ing. Hartmut Stapelfeldt [1] **Dr. Isabelle Naegelen** [2]

[1] Stapelfeldt Ingenieurgesellschaft mbH, D 44141 Dortmund, Germany
[2] LE GOUVERNEMENT DU GRAND-DUCHÉ DE LUXEMBOURG
Ministère de l'Environnement, du Climat et de la Biodiversité
Administration de l'environnement, Luxemburg

ABSTRACT

The environmental noise modelling system (NMS), DEFRA's approach for Great Britain, already showed the feasibility of cloud-based CNOSSOS noise mapping within Great Britain (GB). Using external resources for Environmental Noise Directive (END) [1] analysis in a "Software as a Service" (SaaS) concept appears to be economically viable. Ideally, noise mapping shall be based on standardized initial data. Over the years a few attempts have been made but with little success (QSI, CityGML etc.) as data providers do not take care of niche interests. In smaller scale projects than NMS, users might prefer to refine their model as part of an automated cloud process rather than manipulating data locally. Luxembourg's road and railway model for END 2022 activities represent an interesting collection of acoustic modelling aspects that require refinement, among others railway usage (XLS) provided by the national rail authority. This paper will present macro applications in context of 2022 END calculations as well as the status of cloud-based model refinement and calculation.

*Corresponding author: Hartmut.Stapelfeldt@stapelfeldt.de
Copyright: ©Hartmut Stapelfeldt et al. This is an open-access article distributed under the terms of the Creative Commons Attribution 3.0 Unported License, which permits unrestricted use, distribution, and reproduction in any medium, provided the original author and source are credited.

Keywords: *noise mapping, model refinement, cloud-service (SaaS)*

1. INTRODUCTION

Noise mapping and action planning or rather most of environmental noise analysis are common practice over many years. In most of the past the necessary software tools were provided as desktop solutions. With the increase in calculation demands and model size, the remote cluster- or cloud-based calculation, hereinafter called cloud-processing, is getting more relevant.
Calculation software requires model data provision to be canonical (e.g. CityGML QSI, NMS open standard…) or to follow the standard of the respective calculation software. Cloud processing speeds up noise map calculation. The remaining bottleneck is the significant manual interaction for initial model refinement. The authority or the consultant in charge has to compile subject related model data from several suppliers with differing data structures and content rules. Experiences show that the 3 aspects also vary over the time.
The concept promoted in this paper aims at reducing the manual work of model data refinement by making use of cloud-based model processing.

Any manual refinement approach has to consider:

- That the amount of involved data is huge
- Manual work of "Windows style" interactive refinement of graphic features and related attribute information is tedious and prone to human error.

- Expert knowledge remains with the individual engineer who fulfils the task of refinement
- Quality assessment is difficult as extra protocols need to be kept in parallel to the actual work
- Last minute provision of new/extra model data produces stress and the need for instantly available extra workforce

The aspects listed above are the reason why LimA, from Stapelfeldt Ingenieurgesellschaft GmbH SIG, focusses on the use of macros and workflows. This concept has driven SIG's development strategy right from its start in 1992. The concept is also followed in DEFRA's Noise Modelling System [2], where Feature Manipulation Engine (FME) tools are used to undertake refinements that are highly automized. The actual noise calculation in Microsoft's Azure Cloud uses LimA modules.
SIG has already significant experience with remote calculation services based on LimA's calculation cores for a number of years. Based on this we want to take a next step in cloud-processing:
"Why not uploading initial raw data and create a refined model in a Software-as-a-Service (SaaS) concept?"
Long standing experience allows SIG to provide useful macro tools from which a user can select intended model check and refinement steps. Alternatively, he can write his own macros for customized purposes and send them along with the raw data for external processing.
The potential user group may work on medium size model data, still practical to handle via FTP services.

2. REMOTE MODEL REFINEMENT

The final responsibility for model data will always stay with the users. This includes an insight into the original data to identify the required steps of refinement as well as a check of refinement results by the service before any noise calculation is initiated. In the following text LimA's feature types or attribute names are indicated by e.g. "<HIN>".

2.1 Principle steps of the process

Fig. 1. provides an overview of processing steps in remote refinement, which can be described as:

- All initial model data required in the process is available in SHAPE format.
- A CSV-file is filled in that describes the complete task
- Optional substitutes for general background data, such as object definitions or macros by own configurations
- All files are stored in a fixed structure of sub-directories underneath a main project directory
    - FILE_IN Initial model data
    - FILE_OUT Refined model data as result of processing
    - JOB_DEF CSV file with task description
    - PRJ_CONF Files adapted to project needs instead of background defaults
- Main project directory is zipped
- Initiate remote processing by invoking a small dialogue on desktop
- SIG cluster registers and orchestrates the process below:
    - Relevant server is chosen and, if running in the cloud outside SIG cluster is intended, is registered in LimA's remote licensing.
    - Decision on "cluster or cloud" is internal, but with respect to user restriction
    - Data package is sent onto relevant server
- Relevant server
    - Sends acknowledgement to user's FTP
    - Expands data package
    - Interprets CSV and performs workflow
    - Packs results and sends to user's FTP

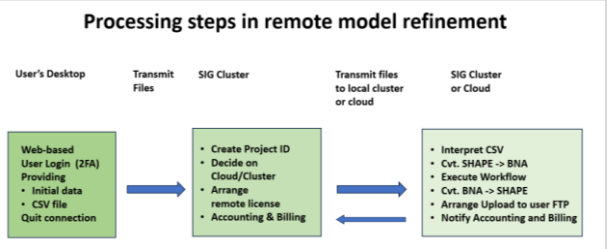


Figure 1. CSV file with task description

A CSV file (Tab. 1.) contains all instructions for model data refinement. It consists of lines covering different steps. Each line starts with a specific keyword or blank in case of identical keywords. Information provided covers:

- FTP for client/service communication
- Project identifier
- Restrictions for use of CPU(s) to limit financial risk in case of human definition during the task
- Restrict use of cloud beyond SIG cluster to be in line with potential restrictions
- Define object definition set, reflecting national and regulatory demands
- Define extra variables for sue in macros
- Repetitive definition for model file treatment
    - File name
    - Conversion rule SHAPE to LimA file

- Repetitive definition of applicable macros with potential list of parameters
- Conversion rule for LimA to SHAPE

Table 1. CSV file defining refinement task

Keyword	Comment	File, macro or key	parameters	param	param	param
User_FTP	FTP adress for I/O	X-Y-Z				
PRJ_ID	Project ID is internally combined with user key for unique storage	PRJ_01				
Runtime_limit	defines max CPU time in (s)		3600			
Allow_cloud	Allow use of cloud		No			
Object_DEF	Object definition	ODF_CNO.BIF				
Variable_DEF	Define variables and content for potential use in macros	User	NN	ModiX	-A-	
Info	*New file / new subject*					
File	Terrain.SHP					
CVT_to_BNA	Terrain_Def_IMP.L39					
Info	*Parameter explanation*		*(m) Pitch*			
MAKRO		smooth_obj.mak	2,0			
Info	*Filter by value*		*Attribute*	*Min_val*	*Increme*	*Tolerance*
MAKRO		Filter_Val.mak	GEL	-10	1	0.1
CVT_to_SHP	Terrain_Def_EXP.L39					

3. EXAMPLES OF MODEL REFINEMENT

As contractor of Administration de l'environnement, Luxemburg, SIG took over the task of creating END-conformal noise maps. This included checks and refinements of initially provided model data in cooperation with Kramer Schalltechnik GmbH, Germany.
The task aims at achieving several aspects:

- Ensure valid attribute content by translation tables, syntax checks and default settings
- Simplify model data to reduce memory consumption and speed up calculation
- Fix geometry in case of geometric conflicts or inaccuracies
- Merge traffic data to road or rail networks

Some examples of automated macro processing are now addressed with respect to the Luxembourg model, which may indicate the potential of macro-based data refinement in cloud processing.

3.1 Terrain simplification

Luxemburg has a challenging terrain model. To support its usability by other software tools it was decided to work with a contour line increment of 2.5 m.
Terrain model simplification by smoothing helps to reduce model size. In the project, smoothing with a tolerance of only 1 m already brought down data volume to half. In general, LimA may work with larger tolerances as this is automatically decreased while neighbouring contours come into short distance. Fig. 2 compares project contour lines before and after smoothing.

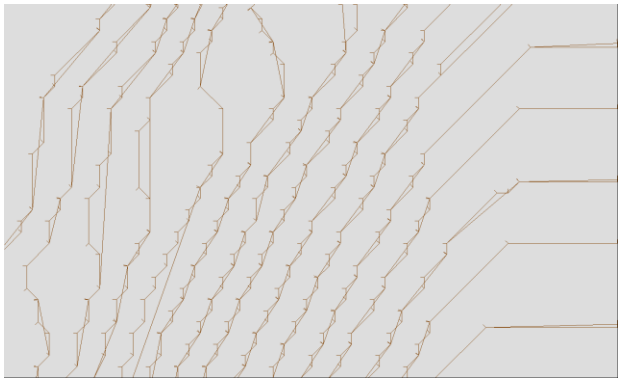


Figure 2. Detailed and smoothed terrain

3.2 Terrain refinement

The terrain model is retrieved from Lidar/radar scan data which takes bridges as terrain level information as seen in Fig. 3.
Therefore, terrain needs to be reshaped by erasing contours within necessary distance to the bridge and then establish a <GBO> break-line on the edge of this region.

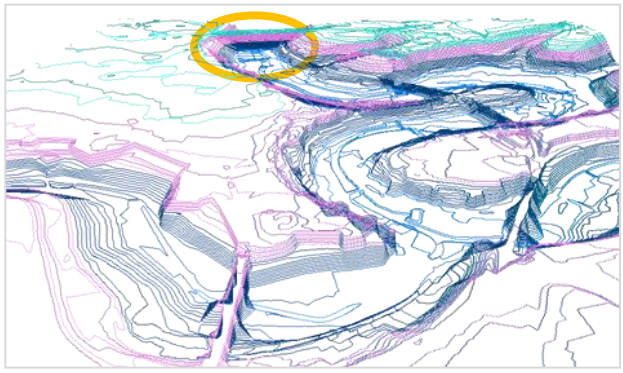


Figure 3. Initial terrain model takes bridges as terrain

Fig. 4 shows the bridge marked in orange in Fig. 3 as green surface and axis in orange. Next to it a <GBO> object with short vertex distances is generated that adjusts itself to the terrain nearby using the remaining contour lines.

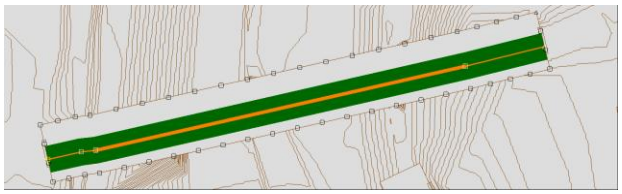


Figure 4. Bridge and clipped terrain

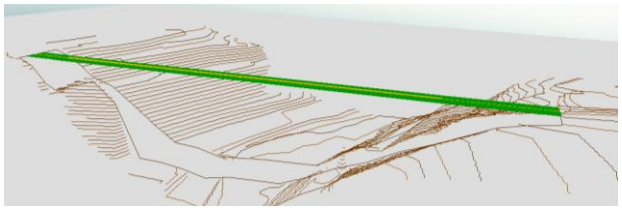


Figure 5. Bridge & clipped and substituted terrain

Original length of bridge axis (fat orange line in Fig. 4.) is extended (slim orange line), following the road centreline until terrain levels represent climb rates reasonable for road traffic. The issue of too short bridge objects seems to have a systematic background as it occurs regularly – maybe the digitized length of road axes are related to the edge of the support constructions at the end of bridges. Fig. 5. shows the resulting 3D model.

3.3 Ground cover

Gound cover polygons (<TOP>) were reduced by two strategies:

- Ignore hard surface areas and make hard ground default
- Simply geometry by smoothing, but keep adjacent polygon vertexes adjacent

3.4 Roads

Traffic data for the road network was provided by Luxemburg "Administration des ponts et chaussées" based on a simulation model which allows estimates for smaller roads in agglomerates. Traffic data is linked to the road network. As mapping also has to cover silent areas, the complete road-net is processed for the two agglomerations of AggloLux and AggloSud. The initial work was undertaken by Kramer Schalltechnik GmbH, and LimA macros are finally used for QA/plausibility checks and for filling up estimated ADT (average daily traffic) for roads that still miss traffic data.
This estimate for residential roads identifies the road-related number of inhabitants. Working upwards from dead-end roads or "half way" split positions up to roads with known traffic, traffic increase is calculated along the shortest connection. Initial values for average daily car movements per inhabitant are adjusted to some further condition.
Fig. 6 shows the result for additionally estimated traffic (slim lines) and the initially provided traffic (fat lines). Colours given per emission in 5 dB steps.



Figure 6. Road net mix of basic and estimated traffic (map: © wmts1.geoportail.lu/opendata)

3.5 Rail

For 2022 END mapping, CFL (Société Nationale des Chemins de Fer Luxembourgeois) provided rail traffic information for an update of the existing rail net model in the form of several XLS files. In order to make data available for macro processing, files were merged into a single CSV file. Content covers:

- Sector index for stretch of relevant railway track
- Client ID, i.e. company running the train service
- Time of service to associate with periods (DEN)
- Locomotive type/Traction
- Number of axles
- Number of trains per year
- Average total weight per train
- Average total length per train

In addition to this, a 2nd file gives a translation table that helps to link CFL train descriptors to CNOSSOS train configurations and assignment to passenger or freight trains. Per track section information is directly integrated into the customized macro:

- Track construction
- Admitted speed

In LimA rail tracks (<CRA>) are objects with all track building information as well as admitted speed and IDs of "train-service"-configurations that are running on the track. Separate "train-services" (<CTN>) are defined as the

combination of vehicle types, technical speed limit and flow per period. Information in the CSV file is used to:

- Create <CTN> train-service objects for each unique train configuration (traction, vehicle types & numbers, daily frequency of service, max. speed)
- Update <CRA> object with respect to train-services running on a specific section of the rail track.
- Calculate track emission per height and per period

3.6 Some hints on other typical project experiences

Further typical tasks within this and other projects include:

- Adjust bridge and noise barrier geometries as these. may be provided by different institutions without proper alignment of geometry (Fig. 7.)
- "Terrain Construction Lines" (<TCL> objects) help to automatically reshape rough or old terrain model next to roads given in 3D (Fig. 8.)
- Organize multipart residential buildings, using attribute <MPRT> to group building parts belonging to the same building and avoid building parts with relative low volume from blocking facades of parts with most inhabitants. When calculating the number of inhabitants per valid façade point this is accounted for (Fig. 10.). Macros also fix geometry conflicts and merge/simplify building parts (Fig. 9.).
- Recognize major roads (ADT 8200 vehicles/day) when roads are represented by separate tracks with individual traffic data
- Recognize anchor points in roundabouts/crossings
- Define average road climb rates along stretches of road

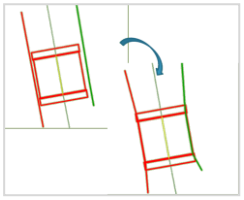


Figure 7. Refinement of bridge and barrier

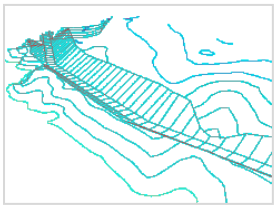


Figure 8. Reconstruction of terrain

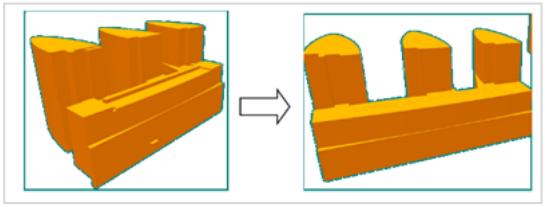


Figure 9. Merging and simplifying of multipart buildings (© GeoBasis-DE / BKG (2018)

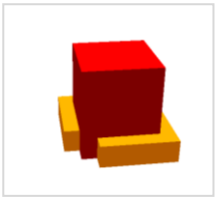


Figure 10. Blocking facades of multipart building

4. CALCULATION AND POST-PROCESSING

For the refined Luxembourg model of ~2600 km², CNOSSOS calculations were performed for road and rail. Road noise calculation took on average 0.65 h/km² of CPU time. As calculation was organized separately per ~100 communities, this includes some overlapping processing.



Figure 11. Luxemburg 2022 END mapping result - L_{den} (map: © wmts1.geoportail.lu/opendata)

5. CURRENT STATUS

In February 2025, SIG released a remote calculation service using LimA calculation cores. The user interface is a combination of freely available QGIS & a plugin interface, LimAQ, that links to LimA. LimAQ communicates with remote servers to undertake LimA noise calculations.
The model data refinement in cloud-processing as described in this paper follows a similar concept but makes use of other LimA modules.
In April 2025 a prototype of such an enhanced remote service has been tested. Support of cloud-processing on SIG's cluster for both services is therefore expected in Q3/Q4 2025.

CONCLUSIONS

- Initial model refinement is regarded as a potential bottle-neck in environmental noise calculations
- Remote noise calculation in external clusters or in the cloud (SaaS) make calculation time much less a concern
- To increase the capability of remote/cloud calculation, model refinement can be transferred into the cloud
- General or user-designed macros help to process the refinements and keep "expert" knowledge available
- The paper demonstrates the advantages in initial model refinement or result post-processing on the practical experience gathered during END work for the Grand Duchy of Luxemburg
- A concept for model data refinement in cloud-processing is introduced, as developed for the LimA software suite for environmental analysis

6. REFERENCES

[1] Environmental Noise Directive, *DIRECTIVE 2002/49/EC OF THE EUROPEAN PARLIAMENT AND OF THE COUNCIL of 25 June 2002*

[2] DEFRA's Noise Modelling System, *Department for Environment, Food and Rural Affairs: "Framework for the design and build of a Noise Modelling System (NMS)."*

DOI: 10.61782/fa.2025.0669



FORUM ACUSTICUM
EURONOISE 2025

OVERVIEW OF RESEARCH SUPPORTING DEVELOPMENT OF A NATIONAL NOISE MODELLING SYSTEM FOR ENGLAND

Simon Shilton[1*] **James Trow**[2] **Magdalena Wilczek**[3] **Katarzyna Fedyk**[3]
Hartmut Stapelfeldt[4] **Raymond Wong**[5] **Bert Peeters**[6] **Martin Toward**[7]
[1] Acustica Ltd, Cheadle Hulme, UK
[2] Noise Consultants Limited, Brighton, UK
[3] Mott McDonald, Bristol, UK
[4] Stapelfeldt Ingenieurgesellschaft mbH, Dortmund, Germany
[4] NGIS China Ltd, Hong Kong
[5] M+P Raadgevende Ingenieurs B.V., Aalsmeer, The Netherlands
[6] ISVR Consulting, University of Southampton, UK

ABSTRACT

The United Kingdom Department for Environment, Food and Rural Affairs (Defra) commissioned the design and build of an environmental noise modelling system (NMS). The NMS has been developed to support Defra in preparing its environmental noise evidence base by preparing national road and railway noise models. This paper provides an overview of the fourteen research projects undertaken to support the implementation of CNOSSOS-EU in England, and the development of the NMS. This includes sensitivity testing of the road and railway source emission models, developing localised input data for road traffic flows, road surfaces & road junctions; railway and light rail vehicles; ground cover, meteorology and calculation settings for propagation modelling. It highlights the NMS system design, and the open data standards developed to support both internal data process workflows, and interaction with third party systems.

Keywords: *environmental noise, noise mapping, big data, noise modelling, GIS*

[*]***Corresponding author***: *simon.shilton@acustica.co.uk*
Copyright: *©2025 Simon Shilton et al. This is an open-access article distributed under the terms of the Creative Commons Attribution 3.0 Unported License, which permits unrestricted use, distribution, and reproduction in any medium, provided the original author and source are credited.*

1. INTRODUCTION

The UK Department for Environment, Food and Rural Affairs (Defra) commissioned the design and build of an environmental noise modelling system (NMS). A functional requirement for the NMS is to support Defra in meeting its regulatory requirements to produce strategic noise models and maps for relevant road and railway sources in England, along with preparing analysis to fulfil the requirements of the Environmental Noise (England) Regulations 2006 (as amended) (the 'Regulations') [1], the Defra 25-year Environment Plan (25YEP) [2], and the Public Health Outcomes Framework (PHOF) [3]. These requirements are being delivered by producing a national environmental noise model with associated coverage, beyond the extents required by the Regulations. The noise models are being delivered in line with the requirements of the adapted assessment methods based on the Calculation of Road Traffic Noise (CRTN) [4] and Calculation of Railway Noise (CRN) [5], and CNOSSOS-EU [6].

While Defra had previously undertaken national coverage noise modelling in line with the Regulations during R1, R2 and R3 [7-10], the expansion of the coverage to include all roads and railways in England, and the first large scale implementation of the CNOSSOS-EU methodology in the UK, introduced a number of challenges and opportunities which Defra wished to investigate prior to the NMS system being implemented.

The aim of the research was to support the automated and reproducible modelling and calculations to be undertaken within by the NMS. The main objective developed out of

this aim was to support development of a national coverage noise calculation model, and in turn address queries including:

- What input data is required?
- Where does the model require high quality data?
- Who can supply the input data?
- How can the modelled reflect the UK situation?
- When could the calculations be completed?
- How could such a model be implemented?

2. RESEARCH PROJECTS

To address these queries and support the development of the NMS, and the implementation of CNOSSOS-EU in England, Defra commissioned 14 research studies projects investigating the following topics:

- CNOSSOS-EU Road Source:
  - Unknown traffic flows
  - Junction and roundabout flows
  - Junction and roundabout corrections
  - Road Surfaces
- CNOSSOS-EU Railway Source:
  - Heavy Rail Emissions
  - Light Rail Emissions
- CNOSSOS-EU Propagation:
  - Ground cover modelling
  - Meteo corrections
  - Calculation benchmark testing
- Noise Modelling System:
  - Input Data
  - Data Standards
  - System Design

The final reports for each of these projects are due to be published, and this paper provides a brief overview of the projects and highlights key findings.

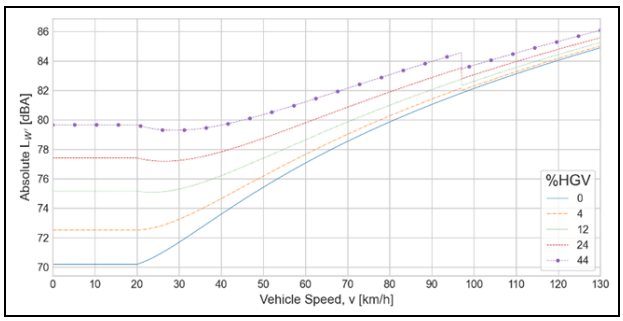


Figure 1. Vehicle speed sensitivity sweeps with composite flows: %HGV, showing discontinuity at 97 km/h.

3. ROAD SOURCE

The investigation of the CNOSSOS-EU road traffic source model aimed to gain an understanding of the effect of input data quality on the uncertainty of the resultant sound power emission levels.

Using an approach first used by the project team when investigating CRTN and NMPB'96 Interim Methods [11,12], a Python implementation of the CNOSSOS-EU road traffic source model was developed to enable parametric sensitivity analysis to be performed for each of the model input parameters. The output results were analysed to quantify accuracy implications & uncertainty, and identify parameters with the greatest influence on road SWL emissions.

The results indicated the input data sensitivity could be characterised as follows:

- **Vehicle speed:** Max uncertainty of ±11 km/h is recommended for traffic volumes typically dominated by cars
- **Surface type:** Deriving surface correction coefficients should be considered for each use case. Uncertainty is lowest where speeds are <30 km/h
- **Surface gradient:** Significant at low speeds for light vehicles (downhill), and at high speeds for medium/heavy emissions
- **Traffic flow:** Changing flow by a factor of 1.6 changes emissions by ±2 dBA. Sensitivity is greatest on lower trafficked roads
- **Flow composition:** Assumptions regarding the %HGVs is more important on lower speed roads
- **Air temperature:** Road traffic noise emissions are relatively insensitive to air temperature

More detail may be found in the 2022 paper [13], and the final report published by Defra.

4. ROAD SOURCE – UNKNOWN TRAFFIC FLOWS

The NMS includes all roads in England; however, traffic count and model data does not include all roads. The project aimed to develop a toolkit to convert 12-hour traffic flow data to annual average day, evening and night data required for strategic noise modelling with CNOSSOS-EU, and to identify approaches to fill gaps in road traffic flow data.

Scale factors were developed for three vehicle categories, and for three road classes, for situations where some road traffic count data was available, Figures 2. Where it was unavailable, and could not be derived based on adjacent

links in the network, a range of default traffic flows by road class were proposed, Figure 3.

	All Vehicle Types	Cars	LGVs	HGVs
Day (0700-1900)	0.806	0.808	0.820	0.740
Evening (1900-2300)	0.116	0.122	0.097	0.082
Night (2300-0700)	0.078	0.070	0.083	0.178

	A Road	B Road	Unclassified Road
Day (0700-1900)	0.834	0.835	0.903
Evening (1900-2300)	0.103	0.086	0.080
Night (2300-0700)	0.064	0.079	0.017

Figure 2. 12-hour Traffic Flow Expansion Factors derived from a sample of traffic counts, and proportion of 24-hour Traffic in other time periods based on a sample of traffic counts.

Category	24hr AADT flow	Source
B Road	3,000	DfT count database
C Road	1,000	DfT count database
Unclassified Road	400	DfT count database
Service Road	400	As Unclassified Road (DfT count database)
Dead end road	200	Breakpoint in DfT traffic estimates and approx. 3dB lower than 400 vehicles option for Service Road roads

Figure 3. Recommended Default values for different road types (24-hour AADT).

5. ROAD SOURCE – JUNCTION & ROUNDABOUT TRAFFIC FLOWS

The NMS includes all roads in England; however, traffic count and model data does not include slip roads and roundabout segments. The project aimed to develop a junction and roundabout traffic flow rulebook suitable for automation within the NMS input data transformation process. Based on a literature review, and analysis of National Highways Webtris data [14], 14 rulebook examples were developed, Figure 4.

6. ROAD SOURCE – JUNCTION & ROUNDABOUT CORRECTIONS

The CNOSSOS-EU road traffic source methodology includes corrections to account for accelerating and

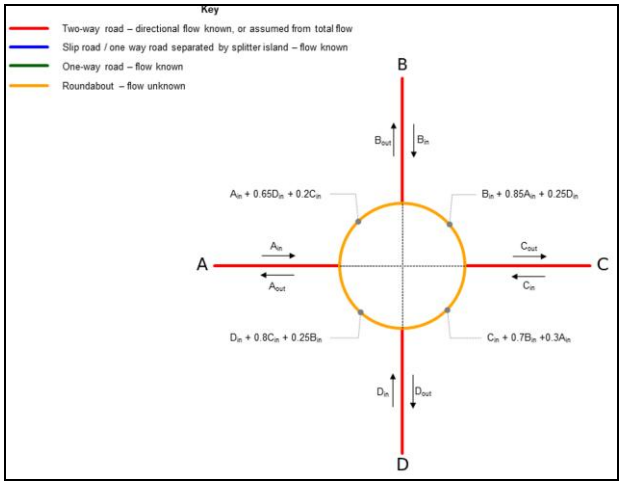


Figure 4. Example of a roundabout rulebook.

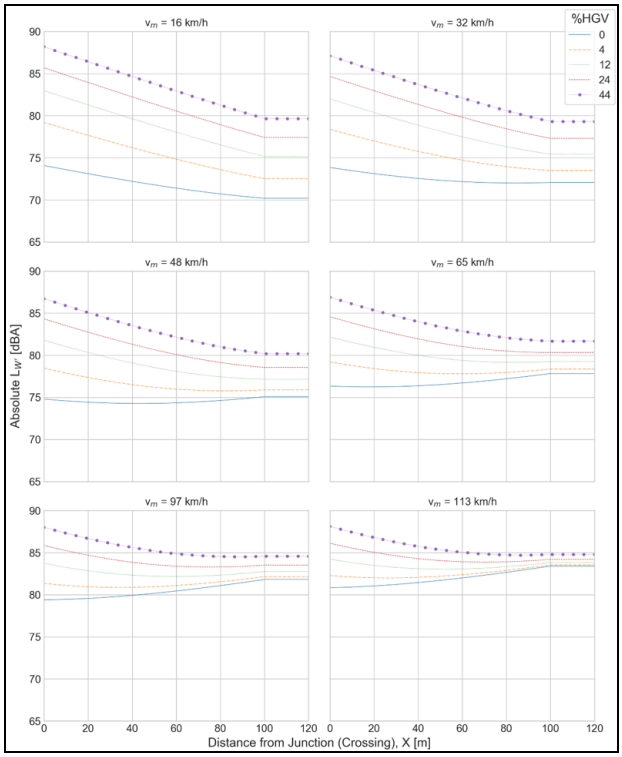


Figure 5. Distance to junction (crossing) with composite traffic flows and range of % HGV.

decelerating traffic within 100m of traffic light-controlled junctions and roundabouts. The project aimed

to quantity the change in calculated road traffic source emission near junctions and roundabouts, and identify how the model could be constructed to implement the corrections.
Parametric analysis was undertaken for each junction type, for each vehicle class, and for a range of composite traffic flows. It was identified that the corrections have larger effects near junctions, at low speeds, for high proportions of HGVs; up to about 7 dBA for composite traffic flows near junctions, and 5 dBA near roundabouts, Figure 5.
The report recommended to include the corrections, with road segments split into 25m lengths (or less) within 100m of the junctions.

7. ROAD SOURCE – ROAD SURFACES

The CNOSSOS-EU methodology includes a table of 17 road surface types in Appendix F Table F-1, these are based on pavement constructions typical within The Netherlands. The project aimed to develop road traffic source emission parameters, and road surface corrections, to represent the English road traffic fleet, and common UK road surfaces.
Based on literature review, existing CPX measurement data, and National Highways pavement management data (HAPMS) [15], source emissions parameters and road surface corrections were developed for UK values for CNOSSOS-EU database.

Category	Coefficient	63 Hz	125 Hz	250 Hz	500 Hz	1 kHz	2 kHz	4 kHz	8 kHz
1	A_R	80.22	86.32	84.82	90.22	97.22	93.82	83.92	73.32
	B_R	24.21	35.71	33.11	19.91	26.71	31.41	33.21	34.21
	A_P	95.19	89.79	87.99	84.49	81.99	85.29	81.69	74.39
	B_P	-4.12	4.38	4.88	5.18	5.18	5.18	5.18	5.18
2	A_R	88.23	92.73	95.23	100.43	101.23	94.63	87.33	83.13
	B_R	27.42	33.22	30.02	21.22	27.52	33.62	35.72	37.52
	A_P	105.10	99.80	100.10	98.30	100.60	97.40	90.80	84.60
	B_P	-3.19	3.41	5.11	5.21	5.21	5.21	5.21	5.21
3	A_R	91.23	95.73	97.73	104.43	104.63	98.03	90.63	85.13
	B_R	27.42	30.92	28.72	22.82	29.22	34.52	36.02	38.02
	A_P	108.40	103.80	103.10	102.50	102.20	98.10	93.40	87.10
	B_P	-1.29	1.71	3.31	3.71	3.71	3.71	3.71	3.71
4a	A_R	0.00	0.00	0.00	0.00	0.00	0.00	0.00	0.00
	B_R	0.00	0.00	0.00	0.00	0.00	0.00	0.00	0.00
	A_P	93.00	93.00	93.50	95.30	97.20	100.40	95.80	90.90
	B_P	4.20	7.40	9.80	11.60	15.70	18.90	20.30	20.60
4b	A_R	0.00	0.00	0.00	0.00	0.00	0.00	0.00	0.00
	B_R	0.00	0.00	0.00	0.00	0.00	0.00	0.00	0.00
	A_P	99.90	101.90	96.70	94.40	95.20	94.70	92.10	88.60
	B_P	3.20	5.90	11.90	11.60	11.50	12.60	11.10	12.00

Figure 6. CNOSSOS-UK proposed road noise emission parameters.

The project developed CNOSSOS-EU rolling & propulsion noise coefficients for UK fleet, Figure 6. Road surface corrections for six common pavement types in England were added to the CNOSSOS-EU database, Figure 7, and a lookup table was produced which aligned 162 road surface types from HAPMS to 23 surface types in the extended CNOSSOS-EU database.

ID	description	cat	α_m 63 Hz	α_m 125 Hz	α_m 250 Hz	α_m 500 Hz	α_m 1 kHz	α_m 2 kHz	α_m 4 kHz	α_m 8 kHz	β_m
CRTN01	Pervious macadam	1	6.2	-1.8	-1.8	-0.9	-5.5	-7.6	-5.4	-3.8	-1.8
		2	13.2	4.8	3.3	-1.0	-2.4	-2.7	-1.3	-0.8	0.5
		3	13.5	5.5	3.5	-1.0	-2.4	-2.7	-1.3	-0.8	0.3
CRTN02	Impervious macadam	1	0.0	0.0	0.0	0.0	0.0	0.0	0.0	0.0	0.0
		2	0.0	0.0	0.0	0.0	0.0	0.0	0.0	0.0	0.0
		3	0.0	0.0	0.0	0.0	0.0	0.0	0.0	0.0	0.0
CRTN03	Concrete	1	8.3	-0.4	5.1	2.5	1.5	2.9	1.8	-0.3	7.6
		2	0.5	8.9	7.4	3.5	3.9	3.4	1.0	0.4	3.2
		3	0.4	10.1	7.7	3.5	3.4	2.7	0.7	0.3	2.0
LA11101	LA111 Hot Rolled Asphalt	1	0.0	0.0	0.0	0.0	0.0	0.0	0.0	0.0	0.0
		2	0.0	0.0	0.0	0.0	0.0	0.0	0.0	0.0	0.0
		3	0.0	0.0	0.0	0.0	0.0	0.0	0.0	0.0	0.0
LA11102	LA111 Brushed Concrete	1	9.2	0.5	6.0	3.4	2.4	3.8	2.7	0.6	7.6
		2	1.4	9.8	8.3	4.4	4.8	4.3	1.9	1.3	3.2
		3	1.3	11.0	8.6	4.4	4.3	3.6	1.6	1.2	2.0
LA11103	LA111 Thin Surfacing	1	9.8	0.1	-1.2	-1.8	-3.6	-5.4	-4.0	-2.0	-2.9
		2	13.2	4.8	3.3	-1.0	-2.4	-2.7	-1.3	-0.8	0.5
		3	13.5	5.5	3.5	-1.0	-2.4	-2.7	-1.3	-0.8	0.3

Figure 7. CNOSSOS-UK road surface correction factors.

8. RAILWAY SOURCE

The investigation of the CNOSSOS-EU railway traffic source model aimed to gain an understanding of the effect of input data quality on the uncertainty of the resultant sound power emission levels.
Using an approach previously used by the project team when investigating CRN and RMR 1996 Interim Method [16,17], a Python implementation of the CNOSSOS-EU railway traffic source model was developed to enable parametric sensitivity analysis to be performed for each of the model input parameters. The output results were analysed to quantify accuracy implications & uncertainty, and identify parameters with the greatest influence on road SWL emissions.
More detail may be found in the 2022 paper [18], and the final report published by Defra.

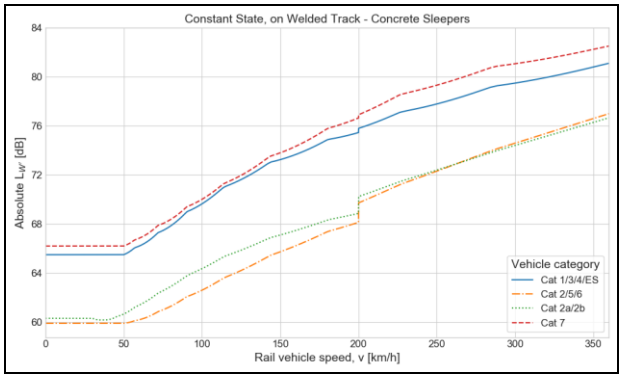


Figure 8. CNOSSOS-UK railway vehicle emission SWL with speed.

The results indicated the most important data collection considerations are to identify:

- Sections of track with impact sources such as joints, and joint density
- The mean speed per vehicle type
- Bridge types which incur a correction and where track is directly fastened to the bridge
- Braking systems
- Curved track, measures against squeal, and curved track known to not squeal, and calculate track curvature
- Rail flow per vehicle
- The number of axles per vehicle
- Wheel diameter for vehicles with cast iron tread brakes

9. RAILWAY SOURCE – HEAVY RAIL

The CNOSSOS-EU rail vehicle database, in Appendix G Table G-5, contains only five example vehicles. The project aimed to develop railway source terms to represent a range of English rail vehicles, on a range of English tracks, in order to improve the quality of the output from the railway source terms model.

Following a literature review, data from previous measurement campaigns and new trackside measurements, extended CNOSSOS-EU railway database tables were developed.

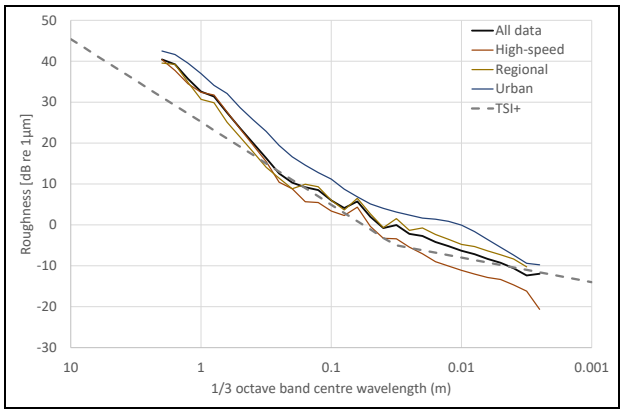


Figure 9. Average (mean) spectra for different track types. Compared to the average spectra across all track forms and the extrapolated TSI limit spectra.

The extended railway database covers:

- 47 CRN rail vehicles to aid model migration, and
- 16 additional CNOSSOS-EU rail vehicle types

The extended database tables also include:

- 4 additional wheel roughness spectra; cast iron tread, composite, disc, and metal sintered brakes
- 3 additional rail roughness spectra; high speed, regional, and urban lines, Figure 9

It was also identified that additional data on rail roughness, and rail fastener stiffness would help further improve the model.

10. RAILWAY SOURCE – LIGHT RAIL

The CNOSSOS-EU rail vehicle database does not contain any specific light rail or tram data. The project aimed to develop light rail source terms to represent a range of English light rail vehicles, on a range of light rail tracks, in order to improve the quality of the output from the railway source terms model.

Following extensive liaison with each of the light rail operators in England and Scotland, literature review and data from previous measurement campaigns, extended CNOSSOS-EU railway database tables were developed.

The extended database covers:

- 12 additional CNOSSOS-EU light rail vehicle types, one per light rail network

Extended database tables also include:

- 1 additional rail roughness spectra, for light rail network
- 1 additional track transfer function, for embedded track

It was also identified that additional data on rail roughness and rail fastener stiffness, and measurement of resilient wheels and traction noise of light rail vehicles, would help further improve the model.

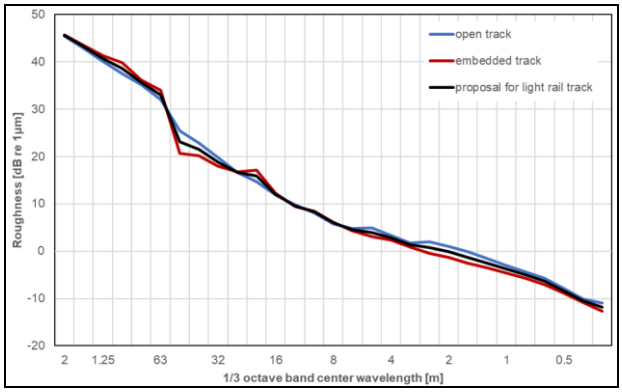


Figure 10. Proposed roughness spectrum for light rail track.

11.PROPAGATION – GROUND COVER MODELLING

The CNOSSOS-EU methodology includes Table 2.5a with G values and flow resistivity for eight different types of ground cover. The project aimed to investigate options available to describe the ground cover in England, and whether the resolution of the ground cover dataset affected the calculated time and the results generated.

Three options, offering broadly low (CLC) [19], medium (CEH LCM) [20], and high (OSMM Topo) [21] resolution description of ground cover areas were identified and tested.

The results of indicated that complexity could double the calculation time, but also appeared to improve the quality of the results. The recommendations were to use CEH LCM 2019 for national mapping, and that it may be preferable to use OSMM Topo data for smaller localised assessments.

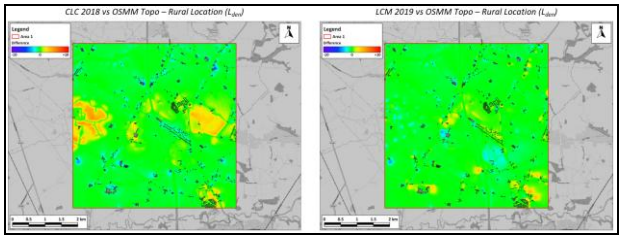


Figure 11. Calculated results difference grids for CLC (left) and LCM (right) compared to OSMM Topo.

12.PROPAGATION – METEO CORRECTIONS

The CNOSSOS-EU calculates propagation twice:

- Straight rays for homogeneous conditions; and
- Curved rays for conditions favourable to propagation from source to receiver

The long-term average sound level is derived using the percentage of favourable propagation (%FP), at the receiver point, based on the source location, for 20-degree increments, for day, evening and night periods, however it is not described how to prepare information of %FP based on long term weather data.

A literature review identified two methods used for NMPB2008 [22] and NORD2000 [23]. The NORD2000 method was fully documented, and all the required input data was available in the UK, namely: average wind speed; wind direction; cloud cover; and air temperature. The %FP was calculated across 131 meteo stations in England, and interpolated to 1 km raster for use within the NMS [24].

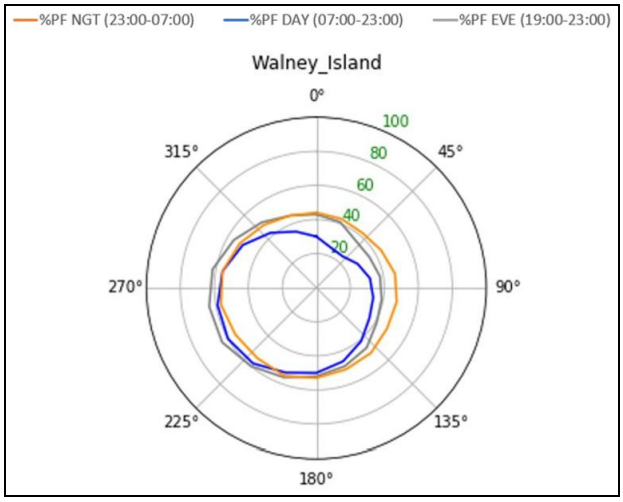


Figure 12. Example of %FP data prepared.

13.CALCULATION BENCHMARKING

The CNOSSOS-EU is a recent methodology, in 2021 when the project commenced there was very little experience in large area noise mapping using the new method.

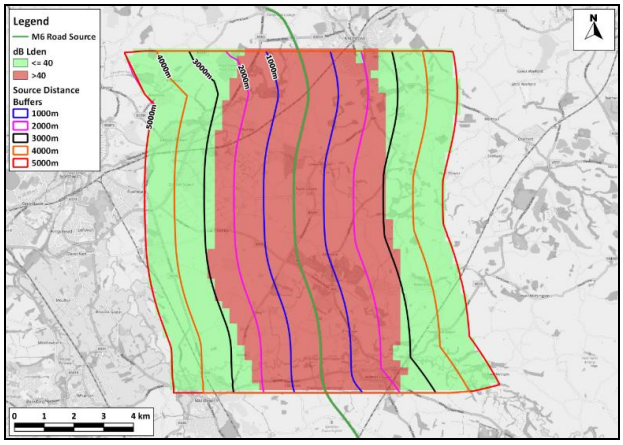


Figure 13. Propagation Distance Test – L_{den} Results.

This project aimed to support decision making on noise calculation parameters, and how this would affect calculation resources, and quality of noise mapping results:

- What source to receiver distance is required for calculated levels of 40 dB L_{den} and 35 dB L_{night} due to road and rail sources?
- What may be considered an optimum set of calculation settings, balancing calculation speed

with results uncertainty, having regard for the CNOSSOS-EU:2020 ±2.0 dB(A) quality criteria?

Using test models covering rural and urban areas, Figure 13, multiple calculation settings were tested one at a time, and in combination. Recommended calculation settings were proposed for delivery of national coverage noise mapping calculations.

14.NMS – INPUT DATA

Strategic noise mapping at national coverage requires a wide range of input datasets, many of which need to be spatially referenced, and come from a range of data suppliers and stakeholders. This project aimed to identify input data requirements, review options for required input data, and identify requirements for input data validation and pre-processing, including QA & QC processes.

Input parameters and results output requirements were identified for CNOSSOS-EU, CRTN, CRN, 25YEP, and PHOF, and reviewed against published literature. Almost 100 datasets were identified and screened, of which 39 underwent detailed review, and 37 were proposed as inputs for the NMS.

Recommended datasets were supplied by OS, EA, CEH, Met Office, NH, DfT, OpenStreetMap, OpenRailMap, RTT, Network Rail, ONS.

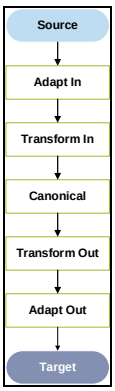


Figure 14. Seven-layer data architecture.

15.NMS – OPEN DATA STANDARDS

There are currently no open data standards for noise models which met all the requirements of the NMS. Open data standards help manage the flow of data through the NMS, and support interoperability with third party GIS and noise mapping software.

Existing spatial data, input data and output data standards, policy & regulatory requirements, government policy on open standards, Defra data principles, and published noise mapping data schemas, were reviewed including:

- INSPIRE, GEMINI, ISO 19100 series, ISO 196500 series, ISO 17534, ISO 15836, COVADIS and EEA Reportnet 3 noise reporting templates
- CadnaA, dBmap.net, eNoise City GML, DIN 45687, IMMI, LimA, MithraSIG, noise3D.net, NoiseMap, NoiseModelling, ODEN, Predictor/iNoise, SoundPlan

Conceptual and logical data models were developed for data flowing in and out of the NMS. The content and format of open data standards were proposed for a range of data layers supporting CNOSSOS-EU, CRTN and CRN, alongside proposals for metadata.

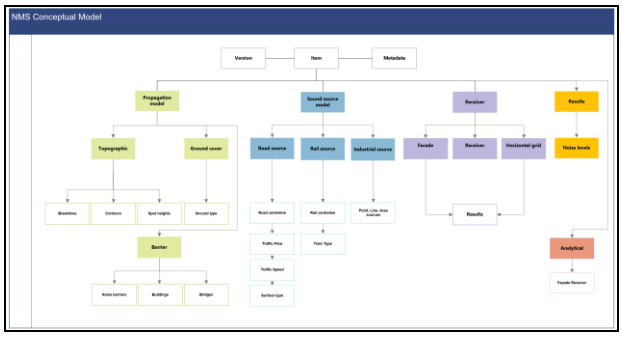


Figure 15. NMS conceptual model.

16.NMS – SYSTEM DESIGN

Off-the-shelf software components within the NMS conceptual design had not previously been combined. This project aimed to develop a mapping prototype of the NMS combining all key components within MS Azure cloud hosting:

- Web application firewall- security
- MS Azure Database for PostgreSQL – Hyperscale (Citus)
- Safe Software FME server – data integration and processing
- Oden – web-based environmental modelling tool
- Azure CycleCloud – HPC orchestrator
- LimA – propagation calculations

The prototype NMS was developed and included a test model area around Manchester [25], and subsequently scaled to full national coverage.

17.CONCLUSIONS

Fourteen research projects were undertaken to support the implementation of CNOSSOS-EU in England, and the development of the NMS. The findings and outputs for the projects were all used during delivery of the strategic noise mapping of roads and railways in England.

18.ACKNOWLEDGMENTS

We gratefully acknowledge Defra for commissioning the research studies in support of the NMS.

19. REFERENCES

[1] HM Government, *The Environmental Noise (England) (Amendment) Regulations 2018* (2018).

[2] HM Government, *A Green Future: Our 25 Year Plan to Improve the Environment* (2018).

[3] https://www.gov.uk/government/collections/public-health-outcomes-framework (accessed 28 March 2025)

[4] Department of Transport, Welsh Office. *Calculation of Road Traffic Noise* (CRTN). London, Her Majesty's Stationery Office (1988)

[5] Department of Transport, Welsh Office. *Calculation of Railway Noise* (CRN). London, Her Majesty's Stationery Office (1995)

[6] Annex II of Consolidated text: Directive 2002/49/EC of the European Parliament and of the Council of 25 June 2002 relating to the assessment and management of environmental noise, Document 02002L0049-20210729, July 2021.

[7] S. Shilton et al., *Managing Risk by Utilising an Integrated Approach to Quality Assurance During Strategic Noise Mapping*, Proc. Of Acoustics 08, Paris, 29 June to 4 July 2008.

[8] Department for Environment Food & Rural Affairs, *Strategic noise mapping - Explaining which noise sources were included in 2012 noise maps*, August 2015.

[9] S. Shilton et al., *Managing the production of the world's largest noise map*, Proc. Of InterNoise 2013, Innsbruck, October 2013.

[10] Department for Environment Food & Rural Affairs, *Strategic noise mapping - Explaining which noise sources were included in 2017 noise maps*, July 2019.

[11] Defra Research Project NANR 93, *WG-AEN Good Practice Guide and the implications for acoustic accuracy*, Hepworth Acoustics, 2004.

[12] S. Shilton et al., *Error Propagation Analysis of XPS 31-133 and CRTN to Help develop A Noise Mapping Data Standard*, Symp. on Uncertainties in Noise, Le Mans, June 2005.

[13] Phillips et al., *Sensitivity of Input Parameter on CNOSSOS-EU Road Emission Levels*, Proc. Of InterNoise 2022, Glasgow.

[14] National Highways Webtris service available at: https://webtris.highwaysengland.co.uk/

[15] National Highways HAPMS data available at: https://www.data.gov.uk/dataset/64df0f9e-cb98-4413-a88c-31dc55dd75f0/hapms

[16] Defra Research Project NANR 208, *Noise Modelling*, Hepworth Acoustics, 2007.

[17] S. Shilton et al., *Accuracy implications of using the WG-AEN "Good Practice Guide" toolkits for railways*, Proc. of InterNoise 2007, Istanbul, 28-31 August 2007.

[18] Phillips et al., *Sensitivity of Input Parameter on CNOSSOS-EU Rail Emission Levels*, Proc. Of InterNoise 2022, Glasgow.

[19] EU Copernicus CORINE Land Cover 2018 (CLC).

[20] UK Centre for Ecology & Hydrology Land Cover Map 2019 (CEH LCM).

[21] OS Mastermap Topography (OSMM Topo).

[22] *Road noise prediction - Noise propagation computation method including meteorological effects*, Sétra (NMPB 2008).

[23] Raimo Eurasto, *NORD2000 for road traffic noise prediction: Weather classes and statistics*, Vtt Technical Research Centre of Finland, 2006.

[24] D. Vinci & J. Nunn, *Approaches to determining and the effects of utilising Favourable Propagation on CNOSSOS-EU calculated levels*, Proc. Of InterNoise 2022, Glasgow.

[25] J. Trow et al., *Automation of a National Noise Model*, Proc. Of InterNoise 2022, Glasgow.

DOI: 10.61782/fa.2025.0685

FORUM ACUSTICUM EURONOISE 2025

A COMPARATIVE STUDY OF METHODS FOR THE DISTRIBUTION OF POPULATIONS IN RESIDENTIAL BUILDINGS FOR NOISE MAPPING PURPOSES

Álvarez Ruiz, Yesika Patricia[1] **Jiménez Pérez, Tamara**[2*] **Puyana Romero, Virginia**[1]
Sequera Soto, Martín[2] **Gey Flores, Ricardo**[3] **Cueto Ancela, José Luis**[1]

[1] Acoustic Engineering Laboratory. C.A.S.E.M. Building. Puerto Real. Spain
[2] Urci Consultores, S.L. Calle María de Guzmán, 54. Madrid. Spain
[3] Profcontrol Ingenieros S.L. Camino del granizo. Chiclana. Spain

ABSTRACT

This paper seeks to offer a thoughtful comparative analysis of different population distribution methods commonly used in the preparation of strategic noise maps, to assess their confidence levels. The examination encompasses three different approaches, including the one suggested by the Spanish Ministry of Transport, Mobility, and Urban Agenda. In the interest of studying which methods appear to be closest to reality, the paper proposes leveraging the "real" data provided by the city councils to serve as a reference ("benchmark") in the analysis. The statistical techniques employed in this study aim to identify statistical differences between the estimates derived from the various methods. Additionally, the study seeks to identify which methods provide estimates that are closest to the "benchmark." The findings from this study will hopefully allow for the formulation of recommendations that could contribute to more efficient territorial planning and better management of environmental noise in urban studies.

Keywords: *strategic noise maps,*

[*] ***Corresponding author***: *tamarajimenez@urciconsultores.com*
Copyright: *©2025 First author et al. This is an open-access article distributed under the terms of the Creative Commons Attribution 3.0 Unported License, which permits unrestricted use, distribution, and reproduction in any medium, provided the original author and source are credited.*

1. INTRODUCTION

From the perspective of the effective development of strategic noise maps, the geographic services providing spatial data in Spain have made a qualitative leap since the first round of strategic noise maps to the present. However, there are still data that must be estimated from proxy data and whose level of approximation to reality is questionable. Accurate population allocation on strategic noise maps is crucial for urban planning, as it enables an accurate assessment of environmental impacts and the development of effective mitigation strategies.

Regardless of the method used to assign noise exposure levels to the population residing in multi-occupied residential buildings, where the location of each dwelling within the building is unknown (tool 21.2 of GPG [1]), the population data for that building must be estimated accurately. In most cases, the municipality has the population by census tract, district, neighborhood, etc. (resolved by the tool 19.1: Number of residents of the mapping area or sub-area of GPG). The systematic use of GIS to obtain the residential area of each building within the district, and thus distribute the population by building seems quite reasonable. There are currently several estimation methods available, and the motivation for this study is to analyze the extent to which they deviate from reality. Therefore, this work aims to analyze the application of different population distribution methods in strategic noise mapping as this has an impact on the accuracy of estimates of the noise-exposed population.

2. METHODOLOGY

To this end, three different methods were implemented, since the fourth method corresponds to the actual figures provided by the Puerto Real City Council.

1. Method IMAGINE. The proposal was extracted from the IMAGINE project [2]. This method distributes the population based on the accommodation capacity of buildings. It starts with the number of dwellings per building and multiplies it by an average occupancy rate. The total population is then distributed proportionally across the study area according to accommodation capacity.
2. Method MTMUA. The proposal was extracted from the Ministry of Transport, Mobility, and Urban Agenda for the fourth round of strategic noise maps [3]. In this approach, the total number of dwellings per census tract is calculated, and then the population is assigned proportionally to each building according to its number of dwellings.
3. Method CADASTRE. Population Allocation Methods in Cadastral Parcels [4]. Residential Built-Up Area Method. This method assigns the population proportionally to the built-up area designated for residential use.
4. Benchmark. The Real-Data Method uses detailed census and administrative information to accurately assign the population to buildings and dwellings within a study area (the benchmark).

2.1 Case study and data collection before GIS estimation

Puerto Real (Figure 1) is a municipality in the province of Cádiz with approximately 42,000 inhabitants and an area of 197 km². Located on the Bay of Cádiz, it has important transportation infrastructure, such as the A-4 motorway and the AP-4 highway, which have a significant impact on environmental noise levels.



Figure 1. Aerial view of the municipality of Puerto Real showing the location of the two census tracts.

Census data from the Puerto Real municipality, cadastral records with information on buildings, and geospatial databases detailing urban characteristics and land use were collected. The collected information was integrated into a Geographic Information System (GIS) for subsequent analysis and application. Two census sections were chosen for the case study due to their different urban typologies.

- Census tracts 4-5 (Figure 2) present a high urban density, with mostly residential buildings of up to four stories, combined with small shops and public spaces.



Figure 2. Image of the typical type of configuration of residential building blocks (multi-story buildings) within census tracts 4-5.

- Census tract 3-10A, on the other hand, is characterized by a lower building density (Figure 3), with a predominance of single-family homes and some residential blocks of up to four stories. Its proximity to key road infrastructure exposes it to high noise levels, making it an area of interest for strategic noise mapping.



Figure 3. Image of the typical type of configuration of residential building blocks (semi-detached houses) within census tracts 3-10A.

For this study, 70 residential buildings containing 2,465 inhabitants were selected.

2.2 Statistical tests

To respond to the question that underlies this study, a proposal is hereby made for a comparison of the population data that has been generated by the four methods, on a building-by-building basis. This approach constitutes a relational (paired) analysis, as it involves the use of four quantitative estimates for the same units (buildings) which defines a data vector. Since we have the real data, the analysis consists of analyzing whether there are significant differences with respect to benchmarking using the three alternative estimation methods (named in this study IMAGINE, MTMUA, and CADASTRE). To this end, we will compute the Euclidean and Manhattan distances (also known as City Block) between the predictors with respect to the benchmark. Also, we estimate the Absolute Errors (AE) vector for each method with respect to the benchmark and the Mean Absolute Error (MAE). We will also measure the RMSE (Root Mean Square Errors) and corroborate the results using cluster analysis. Lower MAE & RMSE means a more accurate method, taking into account that RMSE penalizes large errors more than MAE. Take into account that Euclidean distance refers to a measurement metric between the two vectors in Euclidean space and, RMSE is the error function of the square root of the average square distance between the Benchmarking and predicted points of the two vectors. As MAE is the Manhattan distance divided by the sample size, only MAE is shown.

A nonparametric Friedman test is proposed for the absolute errors, wherein the medians are subjected to analysis. The null hypothesis is formulated as follows:

"Ho = there are no significant differences in the calculation and allocation of the population from building to building by the different methods with respect to the benchmark".

After the global omnibus test, in the event that the null hypothesis is rejected, a Bonferroni post-hoc test will be utilized to evaluate the specific differences on a case-by-case basis (for between-subject factors, i.e., method by method).

3. RESULTS AND DISCUSSION

First, the distance between two vectors is calculated to assess their data-to-data similarity (Table 1). Then the RMSE and MAE (Table 2) is used to measure the difference between the predicted and observed data (of the same two vectors).

Table 1. Euclidean distances of the results of the methods with respect to the benchmark.

Distance	IMAGINE	MTMUA	CADASTRE
Euclidean	69.6	93.8	147.7

Table 2. MAE and RMSE.

Error	IMAGINE	MTMUA	CADASTRE
MAE	5.7	7.4	12.9
RMSE	8.3	11.2	17.7

Table 1 and Table 2, indicate that the IMAGINE method is closer to the actual estimate of inhabitants per building.

The diagram for the Absolute Errors (AE) of the three methods in comparison to the benchmark (Figure 4) shows some outliers. IMAGINE method exhibits 3, MTMUA 5, while CADASTRE scores 7. MTMUA shows a Skewed Box Plot.

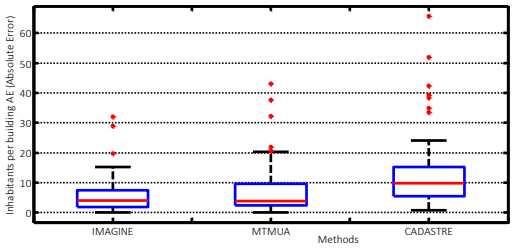


Figure 4. Boxplot of the distributions of population estimates building by building.

Meanwhile, the CADASTRE method points to the buildings with ID 1158548 and ID 600320. These last outliers are explained because the CADASTRE method makes estimates based on the built surface area per plot. If the area being analyzed is not occupied by buildings of a homogeneous type, this leads to large errors in population estimation sooner or later.



Figure 5. Picture of several single-family buildings that constitute a single cadastral reference with the largest area cataloged in the study.

There was an overall statistically significant difference between the mean ranks of the AE of the three methods with respect to the benchmark $\chi 2(2) = 28.9$ $p < 0.001$. As the Friedman test is an omnibus test, a post hoc analysis with Wilcoxon signed-rank tests was conducted with a Bonferroni correction applied, resulting in a significance level set at $p < 0.017$ (as we have 3 tests to perform). There were no significant differences between IMAGINE and MTMUA ($Z = -2.03$, $p = 0.042$). However, there were statistically significant differences with the method CADASTRE in the other two cases with $Z = -4.6$ and -3.7 respectively, and $p < 0.001$ in both cases).

When applying a hierarchical Cluster Method in SPSS using the between-groups of average linkage, with Euclidean distance, the dendrogram corroborates this fact, since both IMAGINE and MTMUA methods perform close results that form part of the same cluster (Figure 6).

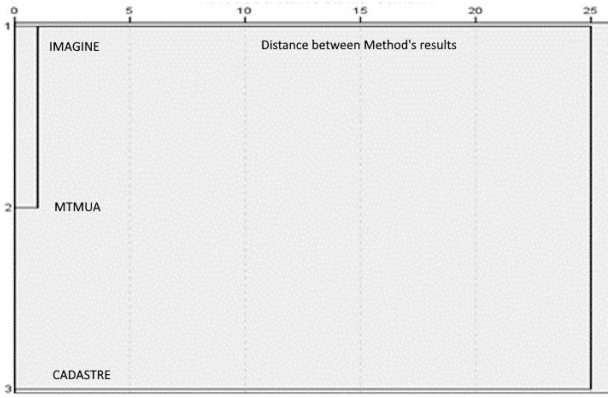


Figure 6. The dendrogram shows that Method 3 (CADASTRE) provides results very far from methods 1 and 2.

4. CONCLUSIONS

The results of this exploratory study indicate that the IMAGINE method is the most promising of the methods analyzed. Furthermore, the introduction of the complexity offered by the procedure proposed by Method 2 (Method MTMUA) appears to be unnecessary. Consequently, the number of dwellings per building does not guarantee a more accurate distribution of the population. A notable limitation of this study is its development in a case study context, indicating a need for further study that allows the generalization of the results. This study aims to advance toward a method that goes beyond those analyzed and that proposes the most interesting explanatory variables that complete the vision of estimating the number of people living in a building.

5. REFERENCES

[1] European Commission Working Group Assessment of Exposure to Noise (2006). Good Practice Guide for Strategic Noise Mapping and the Production of Associated Data on Noise Exposure Version 2. *https://sicaweb.cedex.es/docs/documentacion/Good-Practice-Guide-for-Strategic-Noise-Mapping.pdf*

[2] IMAGINE, (2007). Improved Methods for the Assessment of the Generic Impact of Noise in the Environment. *https://www.imagine-project.org/*

[3] INECO. (2023). Población y Vivienda en Mapas Estratégicos de Ruido. *https://www.m.gob.es /*

[4] Mora-García, R.T.; Marti-Ciriquian, P. "Desagregación poblacional a partir de datos catastrales". En: de la Riva, J., et al. (eds.). Análisis espacial y representación geográfica: innovación y aplicación. Zaragoza: Universidad de Zaragoza; AGE, 2015. ISBN 978-84-92522-95-8, pp. 305-314

DOI: 10.61782/fa.2025.0127



FORUM ACUSTICUM
EURONOISE 2025

AN OPEN-SOURCE TOOL FOR AIRCRAFT NOISE MODELING IN THE CONTEXT OF SPAIN'S GLOBAL NOISE ASSESSMENT (UNDER DEVELOPMENT)

Ignacio Soto-Molina[1,2*] **Rosa María Arce Ruiz**[2]

[1] Ministerio para la Transición Ecológica y el Reto Demográfico (SGPC-MITECO), Madrid, España
[2] Centro de Investigación del Transporte, TRANSyT, Universidad Politécnica de Madrid, España

ABSTRACT

As part of the global noise assessment initiative in Spain, through a National Noise Strategy, which aims to address the lack of a comprehensive understanding of noise pollution, we present progress in the development of an open-source Python tool for modeling and analyzing aircraft noise. Currently, strategic studies are limited to airports with more than 50,000 annual operations, which excludes a significant number of relevant aeronautical infrastructures. This limitation is insufficient to fully understand the global impact of aviation noise, especially in rural or less densely populated areas. Our tool implements the equations of ECAC Document 29, which will allow the calculation of key metrics, SEL and LAmax, on a large scale and on a periodic basis. Furthermore, it will facilitate the use of data from big data platforms such as OpenSky Network. Its modular and scalable design can allow for integration with other open-source software, expanding its functionality and adaptability to different scenarios, or for use on its own. With this initiative, we aim to address the current gaps in the strategic analysis of aircraft noise, promoting the development of more inclusive and accessible mitigation policies for the entire Spanish territory.

Keywords: *aircraft noise, open-source modeling, ECAC Doc 29, noise assessment, strategic noise mapping*

**Corresponding author*: isoto@miteco.es.

***Copyright**: ©2025 Soto-Molina et al. This is an open-access article distributed under the terms of the Creative Commons Attribution 3.0 Unported License, which permits unrestricted use, distribution, and reproduction in any medium, provided the original author and source are credited.*

1. INTRODUCTION

The challenges posed by aircraft noise have become a major public concern, recognized for their impact on both population health and environmental quality [1]. Long-term exposure to aircraft noise has been linked to various adverse effects, such as increased stress levels, and sleep disturbances [2, 3]. These impacts extend beyond simple annoyance, as demonstrated by systematic reviews emphasizing the correlation between noise exposure and psychological disorders such as anxiety or depression [2, 4].

Despite growing evidence of the negative implications of aircraft noise, current strategic assessments conducted in Spain, in accordance with the Environmental Noise Directive, appear to be insufficient. They focus primarily on large airports handling more than 50,000 operations per year, leaving a considerable number of smaller aviation infrastructures unaccounted for in the assessments [5]. Consequently, this omission limits comprehensive noise assessment efforts, resulting in a fragmented understanding of the broader implications of aircraft noise in different environments [3, 6]. A more comprehensive and inclusive assessment is needed to implement effective management and mitigation strategies, such as a National Noise Strategy, supported by reliable and accessible tools for environmental noise assessment.

The increasing availability of innovative technologies and open-source tools can significantly improve noise modeling initiatives [7]. An effective assessment tool not only provides accurate data on noise levels but also acts as a platform for public engagement, helping to bridge the gap between affected communities and regulators [2, 8].

2. OBJETIVES

The main objective of this study is to develop an open-source software tool for general-scale aircraft noise calculation, applicable at a national level, using flight trajectory data from various sources. To achieve this, two specific tools are being developed:

- **Flight Path Tool:** This tool extracts the required parameters from real flight data based on ECAC Doc 29 (ECAC29), Volume 2, Chapter 3: *Description of the Flight Path*.
- **Noise Calculation Tool:** This tool implements:
  - Chapter 4: *Noise Calculation for a Single Event*.
  - Chapter 5: *Calculation of Cumulative Levels*.
  - Chapter 6: *Calculation of Noise Contours*.

Once these modules are developed, the ultimate goal is to enable large-scale noise calculations by processing raw flight data, ensuring efficient and scalable analysis of aircraft noise impacts in a periodically updatable assessment.

3. MAIN REFERENCE WORKS

We highlight some of the works we consider most relevant related to the implementation of the ECAC29 [9] calculation model or other aeronautical noise calculation models in software, highlighting their contributions to understanding and mitigating aircraft noise. It is worth noting that the first [10] and second [11] works are related to a Matlab development of the ECAC calculation model. The first one code is available in the GitHub repository [1] .

The study by Casado, J., et al. (2023) [10] investigates missed approach maneuvers as a method to reduce noise and pollution associated with aircraft operations. By analyzing the implications of aircraft refueling strategies, the authors offer insights into practical approaches to minimizing the environmental impact of aviation activities, providing valuable data for regulatory measures and future modeling initiatives. The calculation tool is software developed by the authors.

The study by Zepeda Núñez, P.P.J. (2021) [11] focuses on the definition of a simplified aircraft noise model to study the impact of noise directivity patterns on a trajectory optimization tool called NOICE. This study underlines the importance of incorporating noise directivity into modeling to achieve more accurate assessments and effective noise mitigation strategies.

Meister, J., et al. (2021) [12] conducts a systematic comparison of different aircraft noise calculation software, providing critical assessments based on real-flight data. By highlighting discrepancies in noise predictions, it lays the groundwork for improving modeling accuracy and regulatory compliance.

Pretto, M. et al. (2020) [13] uses web data to predict noise emissions based on the ECAC Doc.29 model, demonstrating an innovative methodology that combines real-time data collection and predictive analytics to better inform noise management practices at airports.

Zellmann, A. et al. (2018) [14] presents an aircraft noise emission model that integrates detailed aircraft flight parameters into the noise calculation process. It serves to improve the predictive capability of noise emissions, representing a significant advancement in the modeling landscape.

Arntzen, K., et al. (2012) [15] explores the effects of varying weather conditions on noise contour predictions using the ECAC Doc. 29 model, highlighting important aspects of environmental influences on noise dispersion in urban environments.

These references, among many others, highlight the ongoing efforts to refine and expand noise modeling practices in the aviation sector, with particular attention to how various methodologies assess the environmental impact of aviation noise. They also emphasize the importance of applying crowdsourced data to modeling and its potential for studying aircraft noise.

4. METODOLOGY

The methodology applied in this work can be summarized in the selection of the programming language, the adaptation of the ECAC 29 prescriptions in the tools, and in the validation systems that are being applied.

4.1 Selected Programming Language

Although it is common for other projects to use MATLAB as the programming language for scientific tools [10], in this case, Python has been selected. Python is widely used in the scientific field due to its simplicity, readability, and extensive ecosystem of libraries that facilitate robust tool development [16]. Its clear syntax allows for easy code maintenance and debugging, which is crucial for scientific projects requiring verification and reproducibility [17]. Additionally, Python's large community provides

[1] https://github.com/GRCDEV/ANCM

access to numerous specialized libraries for data processing, mathematical computations, and geospatial analysis [18]. Its ability to seamlessly integrate various modules and file formats, such as CSV and JSON, makes it highly efficient for handling diverse datasets [19]. Moreover, its widespread adoption in research fosters collaboration and validation of methodologies [18].

Several key libraries, used in our code, enhance Python's capabilities in scientific applications. The **csv** library is used for tabular data processing, while the **os** library enables interaction with the operating system [20]. The **math** library provides essential mathematical functions, and **pandas** supports structured data analysis. For handling geospatial data, the **json** library is used for configuration files, and **shapely** enables geometric operations [21].

4.2 Flight Path Tool Implementation

Since the aim is to implement a segmentation tool that transforms massive flight data into segments compatible with the ECAC Doc. 29 model, no attempt has been made to emulate segmentation from the tables provided in ECAC29 Volume 3. Instead, work has been done on a tool that, by applying Chapter 3 of Volume 2 of ECAC Doc. 29, allows segmentation to be obtained from such massive data, for example, the OpenSky [2] Network [22].

Two modules have been depeloped at the moment. The first module prepares trajectory data from flight data sources, identifying distinct flight paths, ensuring chronological consistency, and computing distances between consecutive aircraft positions. Distance calculation between two geographical points (latitude and longitude) employs the Haversine Formula [23].

The second module segments the previously prepared trajectories strictly according to the guidance in ECAC Doc.29 (Section 3.6). It divides each flight trajectory into contiguous straight segments, performing linear interpolation of critical parameters such as height, velocity, and acoustic power, as explicitly indicated by the ECAC Equation 3.2a (Eqn. 1):

$$X(f) = X_{start} + f \cdot (X_{end} - X_{start}) \tag{1}$$

where $X(f)$ represents interpolated parameters (such as altitude, velocity, or power setting), and f is the fraction along the segment (0 at the beginning and 1 at the end).

Moreover, the segmentation procedure complies with ECAC guidelines for subdividing trajectory segments based on significant velocity changes. If the velocity difference between two consecutive points exceeds 10 m/s, the segment is subdivided according to the ECAC29 Equation 3.5 (Eqn. 2):

$$n_{seg} = \min\left(\left\lfloor 1 + \frac{\Delta V}{10} \right\rfloor, 5\right) \tag{2}$$

where ΔV is the absolute velocity difference between consecutive points (m/s), and n_{seg} is the resulting number of subsegments (up to a maximum of 5).

Additionally, vertical adjustments related to terrain elevation are applied in line with the ECAC methodology (section 3.3.4). The adjusted aircraft height relative to terrain or observer elevation is given by Equation 3:

$$z' = z - z_o \tag{3}$$

where z is the aircraft altitude, and z_o is the terrain (or observer) elevation.

Through this implementation, the Python code converts raw flight data into properly segmented flight paths in accordance with the ECAC Doc.29 Volume 2 (Section 3), ensuring accurate inputs for subsequent acoustic modeling procedures.

4.3 Noise Calculation Tool Implementation

The noise calculation tool implementation follows the methodology outlined in ECAC Doc 29 Volume 2 , Chapter 4, specifically focusing on the calculation of the segment-level noise metrics $L_{max,seg}$ and LE_{seg} (Sound Exposure Level).

The code structure is organized into distinct modules, each containing several scripts that, in summary, perform the following operations:

- **Input Data Module**: Responsible for loading aircraft performance and noise data from the ANP database, runway, and receptor information.
- **Geometric Calculations Module**: Calculates geometric parameters essential for determining distances, angles, and projection points.
- **Noise Calculation Module**: Computes the event noise levels per flight segment, implementing the equations described by ECAC.

The core of the noise calculation is based on the methodology described in ECAC Doc 29, particularly focusing on Equations (4-8a) and (4-8b):

[2] https://opensky-network.org/datasets/states/.

ECAC29 Equation (4-8a) defines the maximum level of noise for a single flight segment ($L_{max,seg}$) as:

$$L_{max,seg} = L_{max}(P,d) + \Delta I(\phi) - \Lambda(\beta,\ell) \quad (4)$$

Equation (4-8b) describes the sound exposure level for a segment ($L_{E,seg}$):

$$L_{E,seg} = L_E^{\infty}(P,d) + \Delta V + \Delta I(\phi) - \Lambda(\beta,\ell) + \Delta F \quad (5)$$

In the Python implementation, these equations are computed through several intermediate steps, structured as follows:

4.3.1 Baseline Noise Levels from NPD Data

First, the baseline event noise levels, $L_{max}(P,d)$ and $L_E^{\infty}(P,d)$, are interpolated from Noise-Power-Distance (NPD) tables, based on the corrected net thrust (power setting) and the slant distance (d) between the receptor and the flight segment midpoint.

4.3.2 Corrections

Duration Correction (ΔV): Implemented exclusively for sound exposure levels (SEL). This correction adjusts exposure based on the difference between actual segment duration and reference duration as provided by the NPD data:

$$\Delta V = 10 \log_{10}\left(\frac{V_{ref}}{V_{seg}}\right) \quad (6)$$

Engine Installation Correction:The engine installation correction ($\Delta I(\phi)$), which accounts for lateral directivity effects, is computed based on the depression angle (ϕ). This angle is calculated geometrically as the difference between elevation angle (β) and bank angle (ϵ).

Depending on the engine installation type defined for each aircraft (*'Fuselage'*, *'Wing'*, or *'Prop'*), specific empirical coefficients (as recommended by ECAC guidelines) are applied:

- For *'Fuselage'* installation:
  - $a = 0.1225$, $b = 0.329$, $c = 1$
- For *'Wing'* installation:
  - $a = 0.0039$, $b = 0.062$, $c = 0.8766$
- For *'Prop'* installation, no correction is applied:
  - $\Delta I(\phi) = 0$

Thus, the correction term $\Delta I(\phi)$ is calculated following the Equation 7 implemented in the Python code:

$$\Delta I(\phi) = 10 \cdot \log_{10}\left(\frac{\left(a \cdot \cos^2(\phi) + \sin^2(\phi)\right)^b}{c}\right) \quad (7)$$

Lateral Attenuation Calculation: The lateral attenuation, $\Lambda(\beta,\ell)$, is calculated following ECAC procedures, considering the elevation angle (β) and lateral distance (ℓ), applying empirical relationships provided in Section 4.5.4 and Equation 4-18 of ECAC and ECAC29 (Equation 8):

$$\Lambda(\beta,\ell) = \Gamma(\ell) \cdot \Lambda(\beta) \quad (8)$$

where $\Gamma(\ell)$ is a distance factor and $\Lambda(\beta)$ is long-range air-to-ground lateral attenuation calculated according to ECAC29 Equations 4-19 (a-d).

Finite Segment Correction (ΔF): The noise calculation for a single flight segment requires determining the fraction of sound energy contributed by each segment. In the implemented Python code, this fraction is computed for both SEL and L_{Amax} following ECAC Doc 29, using Appendix E equations, as well as the special cases defined by equations 4-20 and 4-21(a-b) for specific observer-segment positions.

In our the Python module, these calculations are performed sequentially. The structure of the Python code directly mirrors the ECAC methodology:

1. Calculate geometric parameters (β, ϕ, distances, etc.).
2. Extract NPD values and apply interpolations for baseline noise levels $L_{max}(P,d)$ and $L_E^{\infty}(P,d)$.
3. Apply corrections sequentially (engine installation, lateral attenuation, duration, and finite segment correction).

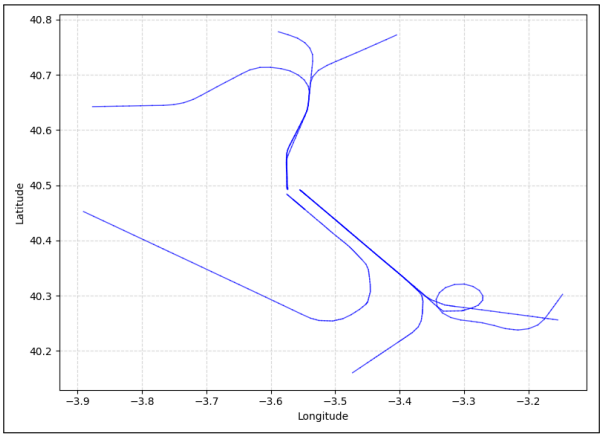
Thus, the Python implementation aims to closely adhere to the ECAC guidelines, to ensure that the calculations for $L_{max,seg}$ and $L_{E,seg}$ accurately reflect the intended methodology.

5. RESULT AND DISCUSSION

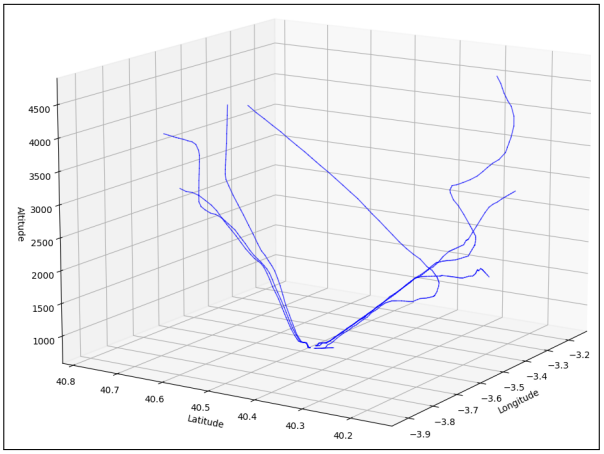
Below are the results obtained up to the time of writing this paper, highlighting that we are still in the process of developing and fine-tuning the tools described.

5.1 Flight Path Tool Implementation Status

The current development of this tool is considered satisfactory. It allows for the extraction of plausible flight paths from massive data, their representation, export to GIS, and height adjustment, if terrain is required (Figure 1).



(a) 2D trajectories.



(b) 3D trajectories.

Figure 1: 2D (a) and 3D (b) trajectories of Madrid-Barajas Airport, on June 27, 2022. Data source: OSN

However, the accuracy of noise calculations using ECAC Doc 29 is still unknown and requires further study. Since the ECAC Doc 29 developer volume does not include such comparison cases, it must be verified using available reference cases, such as the strategic noise maps prepared by the Kingdom of Spain for major airports [3] .

5.2 Noise Calculation Tool Implementation Status

This section presents, on one hand, the analysis of the global results (calculated vs. reference) of SEL in the receiver grid (Grid SEL) and, on the other hand, the detailed evaluation of various parameters influencing Segment SEL (dB) (individual trajectories, acoustic corrections, elevation angles and directivity, etc.). The ECAC Doc29 criterion is employed, which recommends monitoring δ_{RMS} (root mean square of the differences) to assess the agreement between the model and the reference data.

5.2.1 Grid SEL Analysis

Looking at Table 1, we see that globally, an RMS Difference (δ_{RMS}) of approximately 1.19 dB (Figure 2) is presented for the entire set of cases, with a correlation of 0.9738 and a mean difference of 0.16 dB. This indicates that, although the overall dispersion may exceed 1 dB, the spatial trend of SEL is reproduced quite consistently.

Table 1: Comparison of Grid SEL Analysis.

Case ID	r	Mean dB Diff.	δ_{RMS}
Global results	0.9738	0.1591	1.1897
JETFAC	0.9945	-0.1153	0.5211
JETFAS	0.9934	-0.1406	0.5774
JETFDC	0.9576	0.3253	1.6169
JETFDS	0.9579	0.3191	1.6150
JETWAC	0.9940	-0.0387	0.5292
JETWAS	0.9939	-0.0408	0.5305
JETWDC	0.9581	0.3975	1.6350
JETWDS	0.9583	0.3766	1.6332
PROPAC	0.9982	-0.0013	0.2805
PROPAS	0.9982	-0.0040	0.2805
PROPDC	0.9688	0.3343	1.4129
PROPDS	0.9686	0.2947	1.4131

Examining each specific case, a differentiated behavior is observed between straight (S) and curved (C) trajectories. In straight paths (AS, DS) or approaches/takeoffs without turns, δ_{RMS} usually remains very low (0.28–0.58

[3] https://www.transportes.gob.es/aviacion-civil/medioambiente/mapas-estrategicos-ruido

dB in some cases), with mean differences < 0.15 dB. However, when the trajectory includes a curved segment (AC, DC), the RMS increases significantly (1.4–1.6 dB). This suggests that, although the model satisfactorily handles straight operations, turning maneuvers require further adjustments, particularly regarding thrust, bank angle, and lateral directivity.

Cases with propeller aircraft (PROP) show very low RMS in straight operations ($\leq$0.28 dB), indicating a high level of refinement for that aircraft type and flight profile. However, in curved operations, RMS increases to around 1.4 dB, consistent with jet trends. Nevertheless, the global correlations in all cases typically exceed 0.95, supporting the robustness of the model in terms of spatial noise pattern.

In summary, the values in the Grid SEL (dB) confirm that the general approach is valid, with the largest differences concentrated in trajectories with pronounced curves, where δ_{RMS} exceeds 1 dB and reaches 1.6 dB.

5.2.2 *Segment Parameters and Acoustic Factors*

To understand the potential sources of discrepancy in the calculated noise levels, we performed a detailed analysis of the parameters that determine the Segment SEL(dB), as shown in Table 2 (Geometric Analysis), Table 3 (Acoustic Corrections) and Table 4 (Segment SEL Analysis).

Table 2: Geometric Analysis: Calculated vs. Reference Data

Variable	r	Mean Diff.
λ (ft)	1.000	0.000
d_{p} (ft)	1.000	0.063
d_1 (ft)	1.000	0.343
d_2 (ft)	1.000	0.349
q (ft)	1.000	-0.171
Lat_{displ} (ft)	1.000	0.058
d_{NPD} (ft)	1.000	0.065
$Thrust_{\text{P}}$ (lb/e)	0.993	-42.960
β (°)	0.573	-15.576
γ (°)	1.000	0.000
ϕ (°)	0.619	-12.705
θ_{bank} (°)	1.000	0.000

On one hand, the geometric distances (e.g., slant_distance, d_1, d_2, segment length λ, etc.) exhibit extremely high correlations (close to 1.0) and minimal mean differences.

Table 3: Acoustic Corrections: Calculated vs. Reference Data

Variable	r	Mean Diff.
SEL_{base} (dB)	0.997	0.245
$\Delta I(\phi)$ (dB)	0.739	-0.203
$\Lambda(\beta, \ell)$ (dB)	0.912	0.897
ΔV (dB)	0.976	0.740
ΔF (dB)	0.985	-0.979
ΔSOR (dB)	-	0.255
ΔImp (dB)	-	-0.070

This indicates that the positions of both the segment and the receiver are being represented with very high accuracy. However, the angles (i.e., β and ϕ) show lower correlations (about 0.57–0.62) along with average differences of around 10°–15° and standard deviations of 26°–29°. Because corrections such as lateral attenuation $\Lambda(\beta, \ell)$ and noise fraction ΔF depend strongly on these angles, even modest angular discrepancies tend to become amplified in the resulting acoustic calculations.

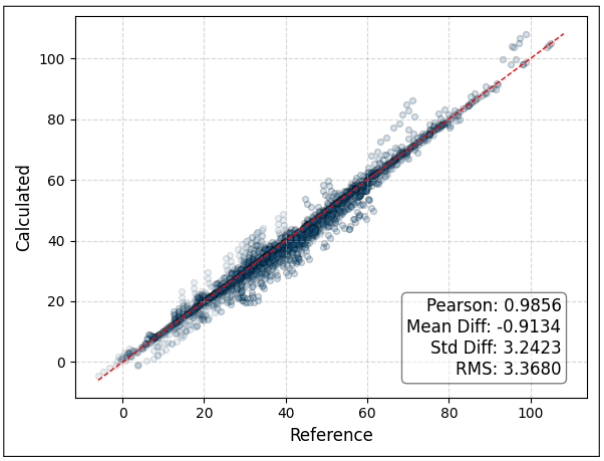
Table 4: Segment SEL Analysis: Calculated vs. Reference Data

Variable	r	Mean Diff.
δ_{RMS} (dB)	0.986	3.368
Mean Diff. (dB)	-	-0.913
Std Dev. (dB)	-	3.242

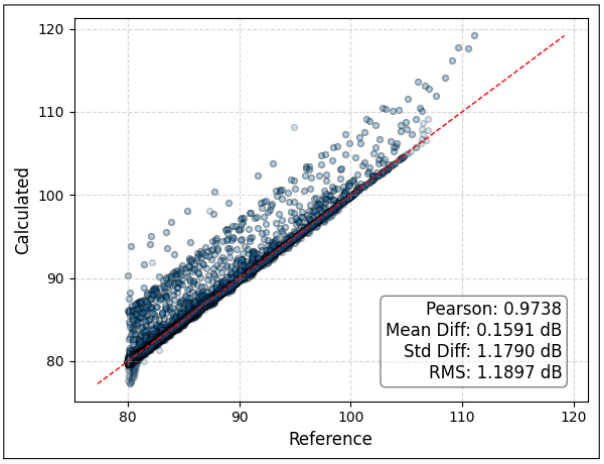
Regarding the acoustic corrections, the baseline SEL (the tabulated NPD reference) achieves excellent correlation ($\sim$0.997) but still exhibits a mean difference of about 0.24 dB, meaning that the overall NPD data are sound, but some residual inaccuracy remains when the final corrections are applied.

In addition, lateral attenuation and noise fraction show notably higher dispersion (with mean differences of $\sim$0.90 dB and $\sim$0.98 dB, respectively), consistent with the aforementioned angular issues. The engine installation correction $\Delta I(\phi)$ also introduces some scatter (correlation 0.739, mean difference ~ -0.20 dB) if the angles ϕ and β are not accurately captured. Finally, while the Segment SEL(dB) itself displays a very high correlation

(0.986), its δ_{RMS} of 3.37 dB indicates that some segments still deviate by a few decibels from their reference values (Figure 2a).



(a) Correlation Segment SEL(dB).



(b) Correlation Grid SEL(dB).

Figure 2: Correlation of Segment SEL(a) and Grid SEL(b) between reference and calculated results.

6. CONCLUSIONS

This work represents significant progress in the development of an open-source tool for large-scale aircraft noise assessment, in accordance with the guidelines of ECAC Doc. 29. The integration of two of its modules—the Flight Path Tool for data segmentation and the Noise Calculation Tool for calculating event noise levels—will allow for robust noise estimates.

This development currently presents reasonably good fits, especially for straight trajectories. In these cases, the model achieves very low RMS differences (often less than 0.6 dB) and high correlation coefficients, indicating the robustness of the basic methodology.

However, some challenges remain. On curved trajectories, δ_{RMS} differences tend to increase (reaching approximately 1.4−1.6 dB in grid analyses and even higher in segment-level assessments), primarily due to uncertainties in the estimation of angular parameters (elevation and directivity angles, β and ϕ). These angles are required for subsequent acoustic corrections (such as lateral attenuation and noise fraction), and even slight discrepancies in their values can be amplified, resulting in larger deviations in the final SEL calculations. Further refinement of the calculation of these angles is necessary to reduce these deviations and improve overall accuracy.

Looking ahead, tuning and calibration work is planned to improve the accuracy of the geometric and acoustic corrections, particularly in determining cases based on the relative position of the trajectory segment and the receiver, and corrections affected by angular parameters. Furthermore, the integration of noise segmentation and calculation modules into a unified framework is necessary to enable the agile use of big data.

Once finalized, the full code is intended to be made publicly available. This open-source tool is expected to not only advance the scientific assessment of aircraft noise at a general level, but also serve as a key resource to support the upcoming National Noise Strategy, thus contributing to more comprehensive and effective environmental noise management.

7. ACKNOWLEDGMENTS

The authors thank Miguel Ausejo Prieto (Eurocontrol SA) and Antonio Donoso López (SENASA) for their contributions and recommendations in this work.

8. REFERENCES

[1] W. H. Organization, "Environmental noise guidelines for the european region," *WHO Regional Office for Europe*, 2018.

[2] C. Clark and K. Paunović, "Who environmental noise guidelines for the european region: A systematic review on environmental noise and quality of life, well-being and mental health," *International Journal of*

Environmental Research and Public Health, vol. 15, no. 11, p. 2400, 2018.

[3] J. Feng *et al.*, "Review on metrics and prediction methods of civil aviation noise," *International Journal of Aeronautical and Space Sciences*, vol. 24, p. 67, 2023.

[4] P. Audrin *et al.*, "Aircraft noise and environmental equity in Montréal: A comparison of noise indicators and an analysis of the impacts of COVID-19," *Transportation Research Part D: Transport and Environment*, vol. 119, p. 103274, 2022.

[5] L. Budd *et al.*, "An assessment of the noise impacts of aviation in the UK," *Journal of Transport Geography*, vol. 25, pp. 1–8, 2012.

[6] D. Akdeniz *et al.*, "Assessment of aircraft noise emissions at International Eskisehir Hasan Polatkan Airport with multiple approach model," *Journal of Aerospace Technology and Management*, vol. 13, p. 1204, 2021.

[7] E. Bocher, G. Guillaume, J. Picaut, G. Petit, and N. Fortin, "Noisemodelling: An open source gis based tool to produce environmental noise maps," *ISPRS International Journal of Geo-Information*, vol. 8, no. 3, p. Article 130, 2019.

[8] Z. Peng *et al.*, "A rapid surrogate model for estimating aviation noise impact across various departure profiles and operating conditions," *Aerospace*, vol. 10, no. 7, p. 627, 2023.

[9] ECAC, "Doc. 29, report on standard method of computing noise contours around civil airports," tech. rep., European Civil Aviation Conference, Neuilly-sur-Seine, France, 2016. 4th Edition, December 2016.

[10] J. Casado *et al.*, "Pollution and noise reduction through missed approach maneuvers based on aircraft reinjection," *Transportation Research Part D: Transport and Environment*, 2023.

[11] P. P. J. Zepeda Núñez, "Aircraft sound modeling through simulation for route optimization," *Politecnico di Milano Thesis Repository*, vol. N/A, p. N/A, 2021.

[12] J. Meister *et al.*, "Comparison of the aircraft noise calculation programs sonAIR, FLULA2 and AEDT with noise measurements of single flights," *Aerospace*, vol. 8, no. 12, p. 388, 2021.

[13] M. Pretto *et al.*, "Forecasts of future scenarios for airport noise based on collection and processing of Web data," *European Transport Research Review*, vol. 12, p. 62, 2020.

[14] A. Zellmann *et al.*, "Aircraft noise emission model accounting for aircraft flight parameters," *Journal of Aircraft*, vol. 55, no. 6, pp. 2106–2116, 2018.

[15] K. Arntzen *et al.*, "A weather dependent noise contour prediction concept: Calculating multi-event noise contours with ray-tracing," in *Inter-Noise and Noise-Con Congress and Conference Proceedings*, (Chania, Greece), p. 5412, 2012.

[16] K. J. Millman and M. Aivazis, "Python for scientists and engineers," *Computing in Science & Engineering*, 2011.

[17] S. Gerhard, A. Daducci, A. Lemkaddem, R. Meuli, J.-P. Thiran, and P. Hagmann, "The connectome viewer toolkit: An open source framework to manage, analyze, and visualize connectomes," *Frontiers in Neuroinformatics*, 2011.

[18] A. Donath *et al.*, "Gammapy: A Python package for gamma-ray astronomy," *Astronomy and Astrophysics*, 2023.

[19] S. Hoyer and J. Hamman, "Xarray: N-D labeled arrays and datasets in Python," *Journal of Open Research Software*, 2017.

[20] J. G. Dunn and J. S. Weissman, "Plastid: Nucleotide-Resolution analysis of next-generation sequencing and genomics data," *BMC Genomics*, 2016.

[21] G. Boeing, "Street network models and measures for every U.S. city, county, urbanized area, census tract, and Zillow-Defined neighborhood," *Urban Science*, 2019.

[22] M. Schäfer, M. Strohmeier, V. Lenders, I. Martinovic, and M. Wilhelm, "Bringing up opensky: A large-scale ADS-B sensor network for research," pp. 83–94, April 2014.

[23] J. Z. Wells and M. Kumar, "Predicting sUAS conflicts in the national airspace with interacting multiple models and Haversine-based conflict detection system," *Frontiers in Aerospace Engineering*, 2023.

DOI: 10.61782/fa.2025.0186

FORUM ACUSTICUM EURONOISE 2025

CAN ROAD TRAFFIC NOISE ANNOYANCE MAPS DESCRIBE THE LACK OF MENTAL WELL-BEING IN AN URBAN AREA?

Alexandra L. Montenegro[1*] **Antonio Zumelzu**[2] **Gera Leal**[3] **Gaetano Licitra**[1,4]
[1] Department of Earth Sciences, University of Pisa, Italy
[2] Institute of Architecture and Urbanism, Austral University of Chile, Chile
[3] School of Sound and Musical Arts, Austral University of Chile, Chile
[4] Environmental Protection Agency of Tuscany Region (ARPAT), Pisa, Italy

ABSTRACT

The urban acoustic environment is often affected by road traffic noise, which has a negative impact on health and mental well-being by causing annoyance and discomfort to residents and visitors. Nevertheless, urban areas also have sounds that are pleasant to people. In this study, a mixed methodology was designed and applied in neighbourhoods in southern Chile. Urban road traffic noise and annoyance were quantified using noise maps estimated with open-source software and validated with measurements. In addition, walking interviews were conducted to assess self-reported mental well-being of residents. In parallel, the soundscape perceived by visitors was evaluated through guided soundwalks and surveys. Preliminary results suggest that in places where the population was highly annoyed, there was a lack of mental well-being. However, where the soundscape was dominated by natural sounds, mental well-being improved despite high estimated percentage of road traffic noise annoyance. Future studies aim to generalise our results and to investigate the observed positive influence of specific groups of sound sources on mental well-being in urban areas with high levels of road traffic noise.

Keywords: *road traffic noise, annoyance, well-being, soundscape, neighbourhoods*

[*] ***Corresponding author***: *alexandra.montenegro@dst.unipi.it.*
Copyright: *©2025 Montenegro et al. This is an open-access article distributed under the terms of the Creative Commons Attribution 3.0 Unported License, which permits unrestricted use, distribution, and reproduction in any medium, provided the original author and source are credited.*

1. INTRODUCTION

Road traffic noise damages physical and mental health [1]. Annoyance is one of the psychological adverse effects most studied, which has led to the definition of dose-effect relationships, allowing the estimation of the percentage of highly annoyed population (HA%) at specific levels of road traffic noise (Lden) [2]. Recently, it has been hypothesised that annoyance could be a mediator between noise and well-being. Relationships have been investigated linking noise exposure levels outside dwellings, neighbourhood urban characteristics and questionnaires associated with diagnoses of mental disorders such as anxiety and depression, both of which decrease well-being [3]. Nevertheless, clear connections are not yet established, especially considering that in public spaces many other elements of the built environment influence directly and indirectly mental well-being [4], which interact with the urban acoustic environment [5], affecting the short-term perceptions of visitors and residents. The aim of this study is to examine if annoyance (HA%) estimated based on a long-term health effects-related noise indicator (Lden) can be useful to describe and identify locations in public spaces of urban neighbourhoods where the acoustic environment affects mental well-being of residents and visitors.

2. METHODOLOGY

2.1 Study area: neighbourhoods

The study was carried out in two neighbourhoods in Valdivia, a city from southern Chile. Neighbourhood population differs according to their total area, as well as the availability of public space and green areas.

Figure 1 shows the difference between the scales of the studied neighbourhoods.

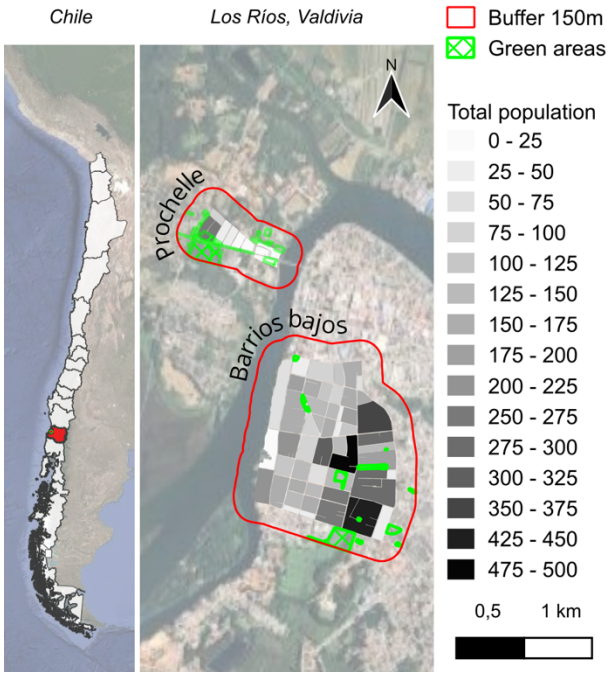


Figure 1. Barrios Bajos and Prochelle, Valdivia [6].

2.2 Noise measurements for noise mapping validation

Road traffic noise measurements were conducted on different streets in each neighbourhood to calibrate the noise maps. First, a street categorisation method was used to distinguish noise levels according to their functionality in an urban environment [7]. A simplified version was applied which requires data on transport infrastructure, road length, median width, sidewalk width, number of traffic lights at intersections and public transport bus routes [8]. Figure 2 identifies the three street groups and the measurement points. Category C1 groups the main streets of each neighbourhood, category C2 are the streets that connect C1 to residential streets C3.

All measurements lasted 15 min., under the supervision of an expert, and were carried out during the daytime, between 07.00–19.00 hrs on weekdays, avoiding periods of traffic congestion. A type 1 sound level meter was placed at 1.2 m from the roadside, following ISO 1996-2 standard for equipment location and favourable meteorological conditions, and checking the calibration of the instrument before and after each measurement campaign.

Additionally, speed and traffic flow were measured for the day, evening (19.00–23.00 hrs) and night (23.00–07.00 hrs), considering CNOSSOS categories [9], and segregating light and heavy public transport.

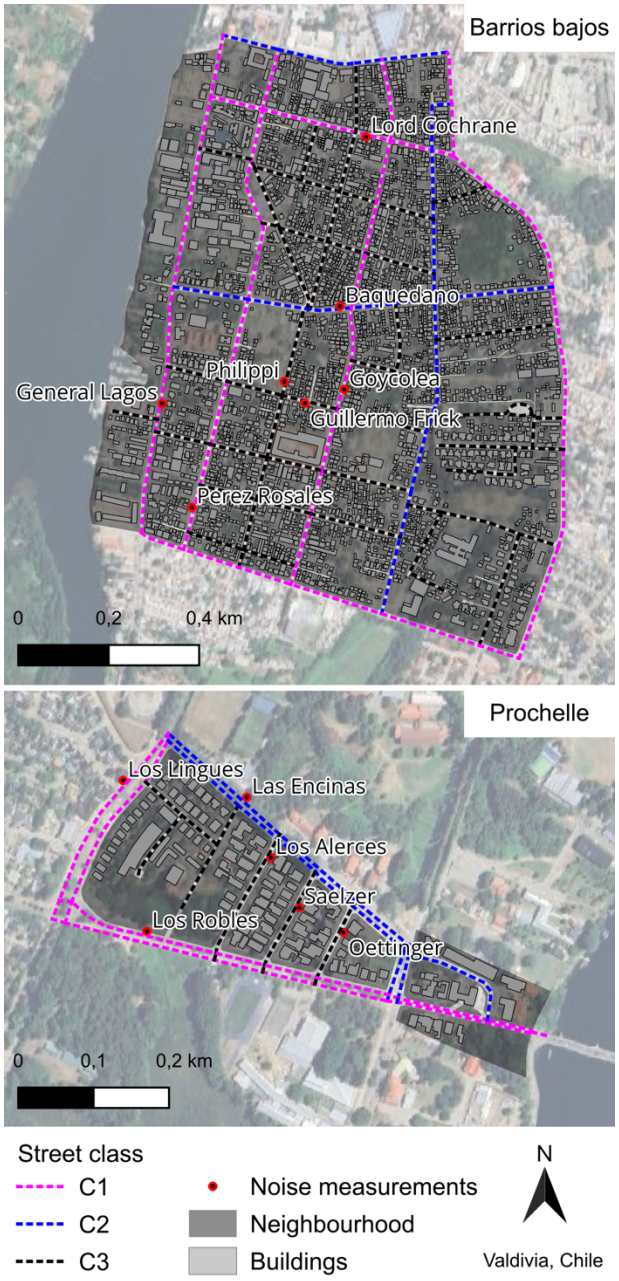


Figure 2. Street categorisation and noise measurement points in the studied neighbourhoods.

2.3 Road traffic noise annoyance maps

Noise maps and exposure were calculated using NoiseModelling [10]. Given the lack of reliable public databases in Chile, the buildings of each neighbourhood were mapped in-situ, their height was estimated through the number of floors of each site, assuming each floor height of 3 metres. The elevation of the terrain was generated from contour lines provided by the Municipality of Valdivia. The ground type and the acoustic absorption of the neighbourhood was obtained with the methodology described in other studies [11]. Weather conditions, traffic light intersections and street pavement type were determined in situ for each neighbourhood during the noise measurements.

Subsequently, the estimation of people highly annoyed by road traffic noise in public space was estimated using the equation described by *Guski et al. (2017)* [2], using isolines at a height of 1.5 metres from the ground. This represents the locations in the neighbourhood where a certain percentage of residents and visitors will potentially experience annoyance from road traffic noise.

2.4 Walking interviews to assess self-reported mental well-being of residents

For the assessment of mental well-being of neighbourhood residents, 76 volunteers from Barrios Bajos, and 56 from Prochelle participated. All of them recruited with the support of local associations.

A qualitative Walking Interview method was used with each resident, using the Natural Go–Along technique [12], to obtain recordings of residents' self-reported perceptions of their built environment. The interviews were conducted on weekdays between January 2023 and January 2024. The dialogue was 1:1 between the researcher and residents, capturing the usual hidden or unnoticed relationships with the places, highlighting environmental perception, spatial practices and social context, among other aspects. Each resident was asked to freely narrate their walking experience, and to stop at those places capable of evoking emotions or behaviours associated with greater affective impact.

General and then increasingly specific questions were asked to the residents, such as: *How do you feel while walking in this place?. What noises and sounds in this street provoke emotional reactions in you?*. The route of each interview was chosen voluntarily by the residents and recorded with the Strava app. Each conversation audio was recorded, coded and analysed by using Atlas.ti software. Photographs of aspects highlighted by the interviewers were also collected.

2.5 Guided soundwalks and surveys to assess soundscape perceived by visitors

The soundscape assessment involved 21 visitors in Barrios Bajos, and 16 in Prochelle. All volunteers had previously visited each neighbourhood, but no one was resident.

Their soundscape perception was assessed through Google form questionnaires using Method A of Part 2 of ISO/TS 12913 in Spanish [13, 14]. Complementarily, the taxonomy of sound sources was extended from traffic noise (e.g. cars, buses, trains, airplanes), other noise (e.g. sirens, construction, industry, loading of goods), sounds from human beings (e.g. conversation, laughter, children at play, footsteps), and natural sounds (e.g. birds call, flowing water, wind in vegetation), to a disaggregated version which includes sounds present in Latin American soundscapes (see Table 1). Also, at the start of each soundwalk, visitors were introduced to breathing and deep listening techniques, discussed in previous publications by the authors [15].

The soundwalks were organised in groups of no more than five volunteers, on different days of the week and at different times, between June 2023 and March 2024. Was required to not produce sounds that could interfere with the acoustic environment. Winter clothes like waterproof jackets and umbrellas sounds was not supposed to influence the responses of the participants. Eating and drinking were not allowed during the walks.

Every soundwalk route was designed by the researchers based on an ethnographic sound analysis of each neighbourhood, defining stop nodes that would represent each section of the route. The first questionnaire was applied at each node and was divided into three parts: identification of sound sources, soundscape quality and general evaluation. In this study, results are analysed with respect to the predominance of sound sources identified on each section between the stop nodes. Future publications by the authors will analyse all the findings.

Table 1. Sound taxonomy, adapted from [15].

Technophony
Transport
N1. Road traffic noise: car, bus, motorcycle, etc.
N2. Other transport noise: aircraft, vessels, etc.
N3. Non-motor traffic: bicycle, carriage, etc.
Urban noises
N4. Urban management: build-in, gardening, etc.
N5. Other noises: rumbles, gun shots, fans.
Music
AM. Amplified music: through loudspeakers.
NM. Non-amplified music: musical instruments.
Anthropophony
H. Human movement: footsteps, rubbing, etc.
S. Speech: conversations, whisper, voices, etc.
V. Vocal expressions: cry, laugh, cough, etc.
CT. Cultural or traditional: bell, siren, preach, etc.
Biophony
DA. Domestic animals: dog bark, cat meow.
FA. Farm animals: crow, bellow, neigh.
EA. Exotic animals: birds, amphibians, insects.
WA. Wild animals: hoot, roar, growl, howl, buzz.
Geophony
PN. Wind: Zum.
W. Water: rain, river, ocean waves, waterfall.

3. RESULTS

3.1 Noise mapping validation

Measurement points for noise, speed and traffic flow were included as receivers in each neighbourhood noise model to calculate differences between the measurements (see Table 2). Several iterations were performed by modifying the parameters of CNOSSOS model [9] to adapt them to the particularity of each neighbourhood in southern Chile.

Air temperature and relative humidity were set to 15°C and 70%. The most significant modification was the type of pavement in old streets. SMA surface with 8 mm stones (NL05) was assigned to consider the sound absorption due to the lack of maintenance of concrete pavements (NL06). An overall target accuracy of ±2 dB uncertainty in the emission level of the source is considered. For one point (see Table 2 (*)) the defined accuracy was not achieved, as the 15 min. measurement did not stabilise, because the flow was too low, and CNOSSOS overestimated in such situations. However, for most of the points the target was reached, therefore, every setting applied in the noise model was replicated in all other streets of the same road category for each neighbourhood.

Table 2. Differences between noise modelling and measurements at the neighbourhoods.

	Street		LAeq (dB)		
	Class	Name	Mea.	Mod.	Diff.
Barrios bajos	C1	P. Rosales	68,2	70,03	-1,8
		G. Lagos	70,2	71,41	-1,2
		Goycolea	66,1	67,97	-1,9
		L. Cochrane	68,0	69,07	-1,1
	C2	Baquedano	70,2	69,39	0,8
	C3	Phillippi	63,8	65,17	-1,4
		G. Frick	58,9	60,93	-2,0
Prochelle	C1	Los Lingues	68,6	69,2	-0,6
		Los Robles	71,9	72,6	-0,7
	C2	Los Encinos	61,6	64,1	-1,8
	C3	Los Alerces	49,8*	56,4	-6,6
		Saelzer	60,6	61,3	-0,7
		Oettinger	56,4	58,8	-1,6
*15 min measurements non-stabilized due to low traffic flow.					

3.2 Noise annoyance maps and source sources affecting mental well-being

Locations where people were annoyed by noise and places where sounds generated positive emotions are identified on maps. During the walking interviews, the acoustic environment was mentioned 65 times in Barrios Bajos, and 28 in Prochelle, playing an important role in the perception of well-being.

3.2.1 Barrios Bajos

Road traffic noise (N1) is predominant for visitors on the path between the start and nodes A and B. As well as between nodes E and F (see Figure 3). On the other hand, on the path between nodes B, C and D, visitors can distinguish an important presence of the sounds of domestic animals (DA) and exotic animals (EA). The proximity of the river at node E makes visitors perceive the sound of water. Along the whole route urban noises and music were present.

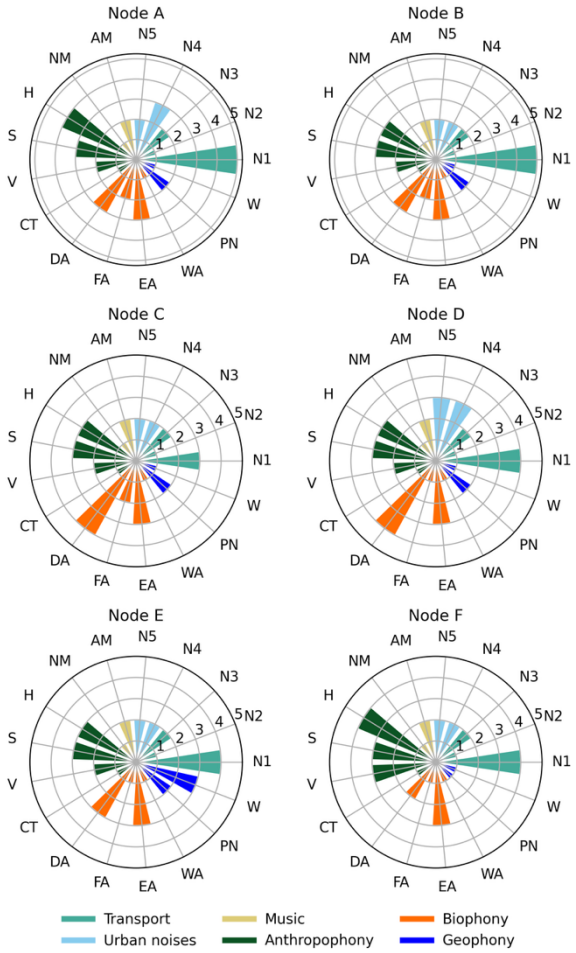


Figure 3. Sound source dominance at Barrios Bajos. 1) Not al all; 2) A little; 3) Moderately; 4) A lot; 5) Dominates completely.

Complementarily, Figure 4 shows the map of road traffic noise annoyance estimated for Barrios Bajos. Likewise, nodes A, B, C, D, E and F of the soundwalks were overlapped, together with the identification of public spaces where residents mentioned technophonic and anthropophonic noise sources that generated negative emotions, and biophonic and geophonic noise sources that generated positive feelings.

Two places were defined as quiet and positively valued. Quietness was a concept incorporated by the residents which was not defined in the taxonomy.

Among interviewed residents, high volume of traffic and vehicles parked on streets with multiple points of interest are associated with emotions of discomfort, insecurity, fear and stress. Likewise, heavy public transport operating at high speeds generates anger, rage, fear and insecurity. Moreover, streets with limited traffic led to emotions of insecurity and fear (women), especially when they walk late in the evening and at night.

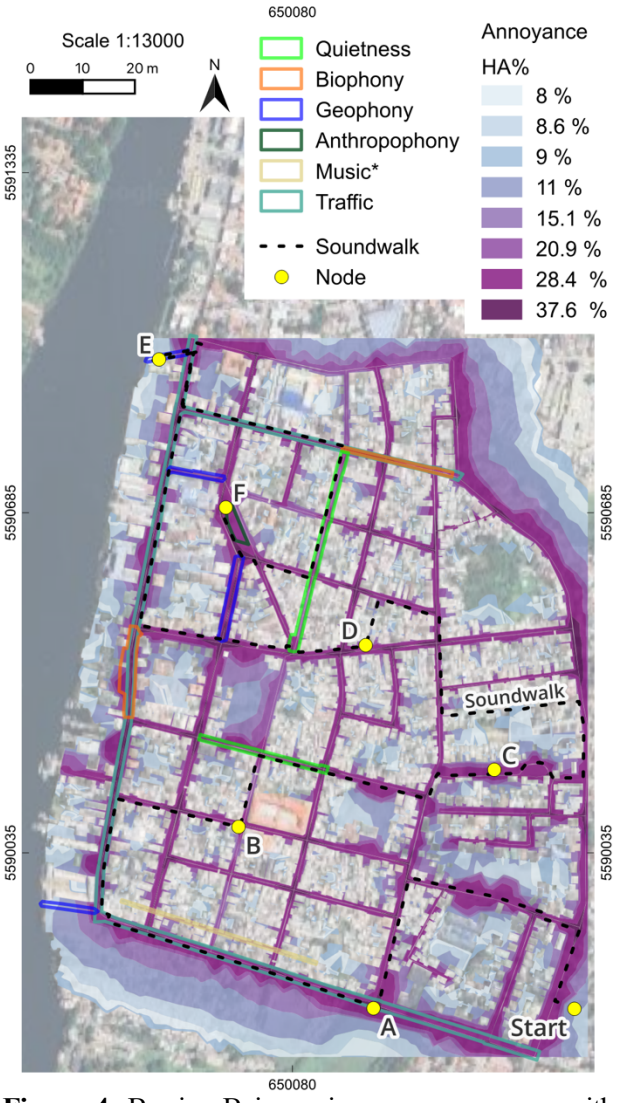


Figure 4. Barrios Bajos noise annoyance map with sound sources impacting mental well-being.

A negative externality of traffic is noise. Residents indicated that road traffic noise triggers annoyance and unpleasantness, especially the noise from heavy public transport in congested streets. Further sources of noise identified in the acoustic environment of the neighbourhood were the dogs' barking which created displeasure and

insecurity. As well as noise from neighbours and music in the street, which annoy residents and make them uncomfortable at night.

However, several sound sources generate positive emotions in residents. Children's voices in squares and playing in open spaces generate pleasure and joy. The sound of the wind produces tranquillity and calm in public spaces near or by the river. Similarly, when the wind interacts with trees, residents feel pleasure and joy. In addition, when birds are in the trees, the sound of their calls brings enjoyment and happiness, while in riverside locations it produces tranquillity, relaxation and joy. The absence of noise associated with urban life in wide and narrow streets are interpreted as quiet areas which give a sense of tranquillity among residents.

3.2.2 Prochelle

In this neighbourhood, road traffic noise (N1) and the sound of wind (PN) were predominant for visitors throughout the entire soundwalk. However, on the path between A and B, people perceived also exotic animals (EA) (see Figure 5).

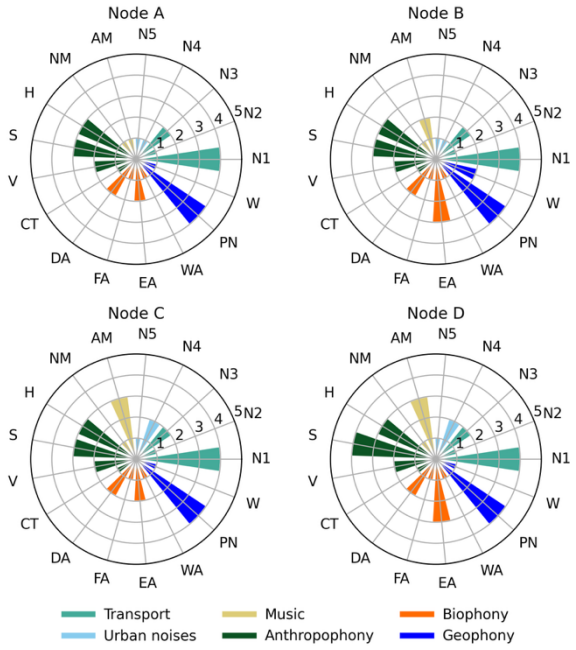


Figure 5. Sound source dominance at Prochelle.
1) Not al all; 2) A little; 3) Moderately; 4) A lot; 5) Dominates completely.

In addition, Figure 6 shows the road traffic noise annoyance map estimated for Prochelle, overlaying the soundwalk nodes, together with the identification of public spaces where residents recognised technophonic noise sources which generated negative emotions, and biophonic and geophonic sound sources which generated positive emotions.

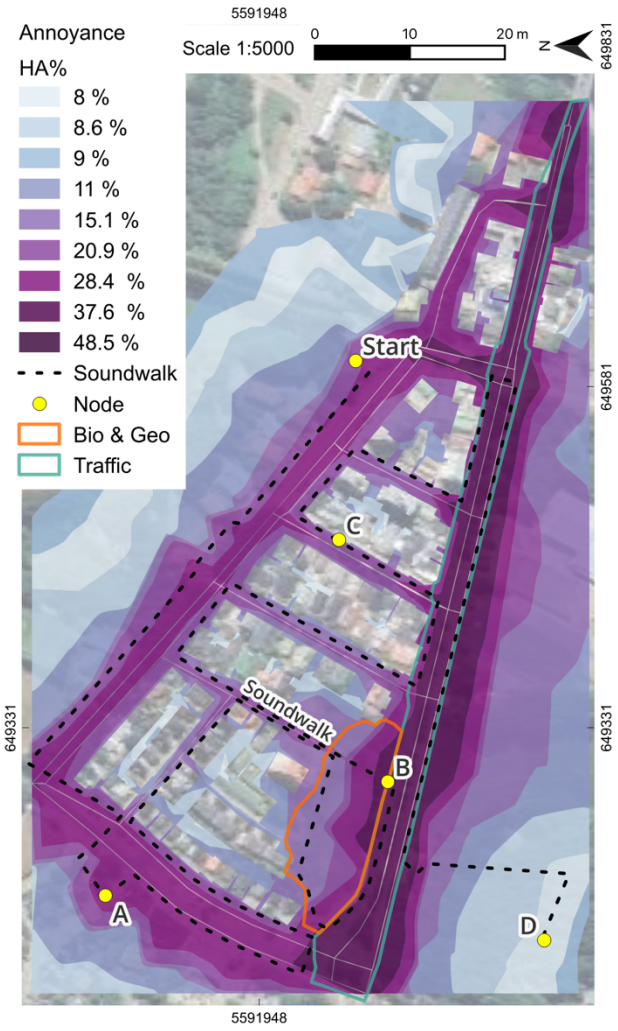


Figure 6. Prochelle noise annoyance map with sound sources impacting mental well-being.

Significant volumes of traffic flow at high speeds were associated with emotions of fear, stress, annoyance, discomfort, displeasure, and frustration among interviewees. Conversely, on narrow streets where vehicles drive at slow speeds, residents experienced peace, calm, security and tranquillity.

This result was directly related to places where sources of noise were explicitly identified (see Figure 6). Road traffic noise became associated with emotions of anger, anxiety, insecurity, unpleasantness and annoyance among respondents. In addition, at congested periods, the noise of horns generates mainly anxiety.

Meanwhile, the natural sounds of the acoustic environment were associated with emotions of pleasure, tranquillity, calm and enjoyment among residents. The sound of the wind interacting with the trees was associated with pleasure, enjoyment, calm, peace and satisfaction. Likewise, in some interviews it was mentioned that at a specific time of the year at Los Patos Lagoon (marked as Bio & Geo in Figure 6) the sound of frogs croaking was associated with feelings of calm, awe and satisfaction among residents. In the same area, several residents indicated that not hearing the typical noises associated with the city makes them feel quiet, calm, peaceful and safe.

4. DISCUSSION

Overall, when neither residents or visitors recognised a significant presence of sound sources different from traffic, annoyance maps were useful to locate places where road traffic noise negatively affects mental well-being. However, in Barrios Bajos, where HA% was between 20.9–28.4%, i.e. levels around 65–70 dBA, geophony (water flowering mostly produced by wind) enhanced well-being even though in the same area (path D–E) traffic noise was predominant. Likewise, in areas without heavy public transport routes but significant dominance of human movements sounds (path E–F), people perceived quietness. Furthermore, our findings suggest that even if there were high HA% levels (e.g. in the street parallel to the river) the sounds of exotic animals across the neighbourhood produce emotions associated with positive mental well-being. Similar patterns are observed in Prochelle, where despite HA% between 20.9–37.6% (levels around 65–75 dBA) with dominance of traffic noise (path A-B), in areas with wind sounds combined with trees and wild animals, people feel emotions that improve their mental well-being and make them perceive tranquillity regardless of the high noise levels. Consequently, noise annoyance maps can only describe a lack of mental well-being when there are no other biophonic and geophonic sound sources that potentially psychologically mask road traffic noise [5]. Such sounds are closely linked to other elements of the urban context which synergistically influence mental well-being [4].

5. CONCLUSIONS

- According to residents and visitors, road traffic noise was the most dominant source of noise in all the studied neighbourhoods, negatively affecting their mental well-being by generating emotions of annoyance and discomfort.
- In locations with elevated noise levels, annoyance due to road traffic noise, calculated through long-term indicators, identified areas that induce a lack of mental well-being.
- In places where geophonies and biophonies were present in combination with traffic, participants reported better mental well-being, as these sound sources induced positive emotional states such as quietness, calm, pleasantness, tranquillity, happiness, enjoyment and relaxation.
- It is not sufficient to generalise and use annoyance as an indicator of a lack of mental well-being, as in some urban environments there are also soundscapes that contribute to enhance the urban experience. These relationships need to be explored by considering all dimensions of the soundscape in future studies. As well as mapping other noise indicators which might be more related to short-term effects.
- Studying the acoustic environment from its noise and soundscape dimension is a good practice which helps to understand how people experience, listen and feel public spaces of the built environment.

6. ACKNOWLEDGMENTS

This research was funded by Chilean National Agency for Research and Development (ANID) through the project FONDECYT No. 1230027.

7. REFERENCES

[1] World Health Organization. Environmental Noise Guidelines for the European Region, 2018.

[2] R. Guski, D. Schreckenberg, R. Schuemer: "WHO Environmental Noise Guidelines for the European Region: A Systematic Review on Environmental Noise and Annoyance", *Int. J. Environ. Res. Public Health.* 14, 1539, 2017.

[3] J. Shi, J. Huang, M. Guo, L. Tian, J. Wang, T.W. Wong, Ch. Webster, G.M. Leung, M.Y. Ni: "Contributions of residential traffic noise to depression and mental wellbeing in Hong Kong: A prospective cohort study", *Environ. Pollut.* 338, 122641, 2023.

[4] A. Zumelzu, C. Heskia, M.G. Herrmann-Lunecke, G. Vergara, M. Estrada, C. Jara: "Street Design Elements That Influence Mental Well-Being: Evidence from Southern Chile", *Land*. 13, 1398, 2024.

[5] J. Kang. "Soundscape in city and built environment: current developments and design potentials", *City Built. Environ.* 1, 1, 2023.

[6] Instituto Nacional de Estadísticas de Chile. Geodatos abiertos, Microdatos Censo 2017 [database], 2018.

[7] G. Rey Gozalo, J.M. Barrigón Morillas, V. Gómez Escobar: "Urban streets functionality as a tool for urban pollution management", *Sci. Total Environ.* 461–462, 453–461, 2013.

[8] A.L. Montenegro, G. Rey Gozalo, J. Arenas, E. Suárez: "Streets classification models by urban features for road traffic noise estimation", *Sci. Total Environ.* 932, 173005, 2024.

[9] Directive 2015/996/EU of 19 May 2015 establishing common noise assessment methods according to Directive 2002/49/EC of the European Parliament and of the Council, 2015.

[10] E. Bocher, G. Guillaume, J. Picaut, G. Petit, N. Fortin: "NoiseModelling: An Open Source GIS Based Tool to Produce Environmental Noise Maps", *ISPRS Int. J. Geo-Inf.* 8, 130, 2019.

[11] A.L. Montenegro, A. Panci, M. Bolognese, D. Palazzuoli, M. Cerchiai, D. Melluso, G. Stasi, G. Licitra, "An open-source pipeline in noise modelling and noise exposure reduction in a port city", in *Proc. of the 30th International Congress on Sound and Vibration,* (Amsterdam), 2024.

[12] B. Piga, D. Siret, and J.P. Thibaud: *Experiential Walks for Urban Design: Revealing, Representing, and Activating the Sensory Environment*. Cham, Switzerland: Springer, 2021.

[13] J. Vida, J.A. Almagro, R. García–Quesada, F. Aletta, T. Oberman, A. Mitchell, J. Kang: "Soundscape attributes in Spanish: A comparison with the English version of the protocol proposed in Method A of the ISO/TS 12913–2", *Appl. Acoust.* 211, 109516, 2023.

[14] E. Suárez and M. Gueregat. Soundscape Evaluator [software]. Web, Android and iOS, 2021.

[15] G. Leal, A.L. Montenegro, A. Zumelzu, "Estimación del paisaje sonoro utilizando una escucha activa e integral en entornos urbanos del sur de Chile", in *Proc. of the XIII Congresso/Congreso Iberoamericano de Acústica FIA*, (Santiago), 2024.

DOI: 10.61782/fa.2025.0236

FORUM ACUSTICUM EURONOISE 2025

COMPARISON OF DIFFERENT URBAN TRAFFIC REPRESENTATIONS FOR ROAD TRAFFIC NOISE INDICATORS ESTIMATION

Yu Gao[1,2] **Sacha Baclet**[2,3] **Pierre Aumond**[1]
Romain Rumpler[2,3] **Arnaud Can**[1]*
[1] Univ Gustave Eiffel, CEREMA, UMRAE, F-44344 Bouguenais, France
[2] Department of Engineering Mechanics, KTH, Sweden
[3] ECO2 Vehicle Design, KTH, Sweden

ABSTRACT

This study designs a comparison of the estimation of road traffic noise from different urban traffic representations between their corresponding modelling chains. Based on a microscopic traffic dataset in Stockholm, three kinds of urban traffic representations (Microscopic traffic representations, Aggregated traffic representations, and Hybrid traffic representations) and their corresponding traffic noise estimation models are introduced from distinct perspectives. The distribution result of $L_{\mathrm{Aeq},1h}$ highlights that all models follow similar distribution patterns in noise exposure despite different traffic representations, while still slight differences in peak noise intervals remain. Two proposed hybrid traffic representation methods expand acoustic indicator sights from aggregated traffic representations by introducing dynamics and stochasticity, which can yield comparable noise estimates at high percentile indicators. The noise maps highlight that a general but uneven underestimation exists in all other modes compared to microscopic traffic representations. Desired improvements of hybrid traffic representation methods are discussed, aiming to bring acoustic evaluation enrichment in urban traffic environments.

Keywords: *Road traffic noise, Modelling chains, Traffic representations, Hybrid representations*

**Corresponding author*: *arnaud.can@univ-eiffel.fr* .
***Copyright**: ©2025 Yu Gao et al. This is an open-access article distributed under the terms of the Creative Commons Attribution 3.0 Unported License, which permits unrestricted use, distribution, and reproduction in any medium, provided the original author and source are credited.*

1. INTRODUCTION

Accurate noise estimation is critical for understanding the environmental impact of traffic systems. In recent years, various traffic output data from traffic simulation models have been widely utilized in estimating traffic noise. Stressed in different urban conditions and spatial scales, corresponding model chains provide unique analytical perspectives in traffic noise estimation [1–3]. Macroscopic traffic models provide aggregated link-based traffic speed and flow rate [4], while micro-simulation traffic models provide granular outputs (such as float point trajectories) as a basis for noise modelling. In addition, hybrid representations allow the gap between trajectories and aggregated representations to be bridged [5, 6]. This article aims to describe the state of the art of the various couplings and implementations currently available, and to propose a comparative analysis of their advantages and limitations, including implementation specificities, and resulting acoustic level accuracy.

These different traffic representation datasets are derived from the same micro-simulation scenario in an urban area in Stockholm. Noise levels are estimated for each dataset using established acoustic models in the latest version of CNOSSOS-EU [7, 8], and compared to the reference micro-simulation based estimation. This research provides insights into the influence of different traffic representation outputs from a microscopic traffic representation scenario on noise estimation, which could be referred to by practitioners in selecting traffic outputs for urban noise assessments.

2. METHODS

2.1 Traffic representations

The study is based on microscopic traffic data, typically representative of higher density traffic on the island of Södermalm in Stockholm, Sweden. In order to assess the impact of different traffic representations on noise estimations, three kinds of traffic representations are introduced from distinct perspectives in this part.

2.1.1 Microscopic traffic representations

SUMO Mode
The original traffic simulation is based on SUMO (Simulation of Urban Mobility) [9], which is an open-source, highly flexible microscopic traffic simulator widely used for modelling urban traffic dynamics. SUMO provides detailed vehicle-level movement data, including individual vehicle trajectories, acceleration, deceleration, lane-changing behavior, and interactions with traffic control mechanisms such as traffic lights and stop signs.

In this case study, the simulation is configured to simulate typically high traffic volumes and frequent stop-and-go movements.

2.1.2 Aggregated traffic representations

Computational efficiency and usability of microscopic traffic data in large-scale studies are usually limited. Aggregated traffic representations represent the classic approach commonly used in noise mapping [10], as it relies on available urban traffic counting loops or similar detection methods. Based on SUMO Mode, three distinct aggregated scenarios are analyzed: Flow Sensor Mode, Time Mean Speed Mode, and Space Mean Speed Mode. Each mode provides a unique perspective on link attributes including traffic flow rate and mean speed.

Flow Sensor Mode
In this mode, traffic speed is estimated using randomly placed flow sensors along each link. The methodology follows these steps:

- A single sensor point is randomly assigned to each road link.
- The sensor has a detection range of 10 meters, to avoid duplicate records, recording vehicle positions and passing time on the nearest link to the vehicles.
- As recorded vehicles pass through the sensor's detection area, their speeds are calculated.
- The link mean speed is then computed as the average speed of all vehicles detected by the sensor.

This approach mimics real-world traffic monitoring via stationary sensors but is limited by the fact that only a small portion of each road segment is observed, potentially leading to biases in speed estimation.

Time Mean Speed (TMS) Mode
The Time Mean Speed (TMS) [11] mode refines speed measurement from Flow Sensor Mode by considering all the appearances of vehicles on the same link. The process involves:

- Identifying vehicles that appear on the same nearest link at least twice within a given time window, capturing travel distance and time between vehicle positions.
- Calculating the speed of each detected vehicle along the nearest link.
- Computing the average speed of all identified vehicles on the link.

Space Mean Speed (SMS) Mode
The Space Mean Speed (SMS) [11] mode focuses on speed accuracy by incorporating the total travel time and travel distances regardless of the identification of single vehicles. This method follows a similar counting mechanism to the TMS mode but differs in speed computation:

- Vehicles are counted if they appear on the same nearest link at least twice.
- The total travel time and travel distance of all the vehicles along the link are recorded.
- The space mean speed is then computed as the ratio of the total travel distance to the total travel time for all vehicles on the link.

2.1.3 Hybrid traffic representations

In addition to the three traffic aggregation methods discussed earlier, this study explores two hybrid traffic representation methods. These methods aim to reconstruct individual vehicle movements along road links using link-aggregated traffic data, specifically traffic flow rates and average traffic speeds. By leveraging these hybrid techniques, we can generate a more detailed microscopic representation of traffic while preserving the macroscopic traffic characteristics derived from aggregated datasets, such as the traffic output from

macroscopic and agent-based simulation models.

Two proposed methods introduce stochastic variations to generate more dynamic vehicle trajectories: Density-Based Vehicle Movement Reconstruction [12] and Poisson-Based Vehicle Trajectory Reconstruction [13]. Each method uses different statistical modelling techniques to introduce variability in vehicle movements while maintaining consistency with the underlying link-aggregated data, giving an output similar to a microscopic traffic simulation with individual vehicle position and speed on 1-second time resolution. Time Mean Speed (TMS) Mode was selected as the base dataset. This choice ensures that vehicle movements are reconstructed based on a more refined speed estimation approach.

Density-Based Vehicle Movement Reconstruction Mode
This approach reconstructs individual vehicle movements at each predefined position based on the estimated road traffic density along each link. Traffic density is a key parameter in traffic flow theory, representing the number of vehicles per unit length of a roadway. The computed density determines the probability of vehicle occurrence at different positions along each road. Individual vehicle movements are then reconstructed through iterative probabilistic processes.

Poisson-Based Vehicle Trajectory Reconstruction Mode
The second method reconstructs vehicle trajectories using a Poisson process, which is commonly used to model the random arrival of vehicles in traffic flow theory. Unlike the density-based method, this approach does not rely on estimating the occurrence probabilities of all the possible positions along each road, but on distributing vehicles' trajectories under a Poisson random arrival model.

2.2 Modelling chains

All the noise simulation modelling chains in this article consist of two parts: the traffic model output representations and the noise calculation model. For aggregated scenarios, the noise levels emitted by road traffic are estimated based on the average flow rates and speeds of vehicle flows per road section. Alternatively, the noise source levels are estimated from the trajectory points along the roads for dynamic traffic scenarios including SUMO Mode, Density-Based Mode, and Poisson-Based Mode.

2.3 NoiseModelling

NoiseModelling [14] serves as the core computational framework for the noise calculation model, which is an open-source library capable of producing noise maps. This research employs the CNOSSOS-EU standard methodology to estimate noise emissions and propagation effects, utilizing its emission model, path-finding algorithm, and attenuation model to simulate noise transmission from traffic sources to receiver points. However, for the acceleration correction component, the IMAGINE method is applied over CNOSSOS-EU here. While CNOSSOS-EU includes a distance-based acceleration correction in relation to intersections, the choice made to use the IMAGINE method [15] offers a more precise approach to capture acceleration-induced noise variations by directly considering the actual accelerations.

2.4 Case Study and Parameters

This study is based on the traffic conditions in the Södermalm district, a central island in Stockholm, covering approximately 10 km² of urban traffic activity. Södermalm is a densely populated area with a well-developed road network, making it an ideal location for evaluating different traffic representation methods. (See Figure 1)

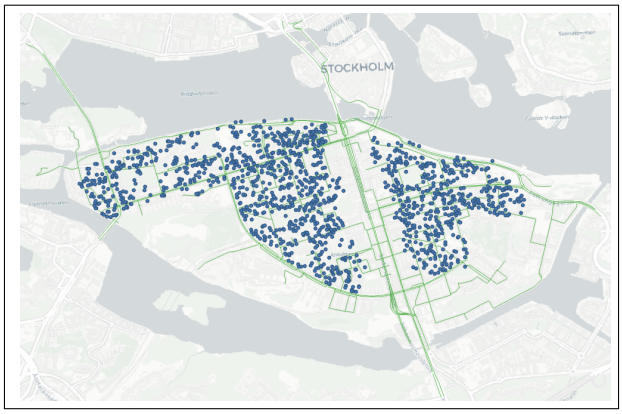


Figure 1. Network and position of noise receivers.

Most of the major roads within the study area are included in the simulation, with microscopic traffic data

suitable to capture a representative snapshot of urban mobility and one of the most significant noise sources throughout the day.

Since this research primarily investigates traffic representation methods, vehicle composition is intentionally simplified. To reduce complexity and maintain consistency in the analysis, only light vehicles are simulated, while heavy vehicles, buses, and motorized two-wheelers are excluded. These vehicle types introduce additional variability in both traffic dynamics and acoustic noise emissions, which may lead to increased uncertainty in hybrid traffic representation methods.

To assess the impact of traffic on noise levels, a total of 1,389 receiver points are strategically placed around buildings and along traffic corridors. The following noise level indicators are considered in the analysis: $L_{\text{Aeq},1h}$ (A-weighted equivalent continuous sound level per hour per point) is computed for all traffic scenarios. $L_{A10,1h}$, and $L_{A1,1h}$ are evaluated specifically for dynamic traffic representation scenarios (SUMO Mode, Density-Based Mode, and Poisson-Based Mode), where more detailed vehicle movement patterns are simulated.

Table 1 provides a summary of the key parameters used in the acoustic calculations for this study.

Table 1. Parameter values for sound propagation

Parameters	Configuration
Maximal order of reflection	1
Maximal order of diffraction	1
Maximal distance source-receiver	250m
Maximum source-reflection distance	50m
Receivers height	1.5m
Ground absorption coefficient	G=0
Spatial resolution	D=20m

3. RESULTS

3.1 Statistical results

Figure 2, 3, and 4 present the Kernel Density Estimation (KDE) curves of the road traffic noise indicators chosen $L_{\text{Aeq},1h}$, $L_{A10,1h}$, and $L_{A1,1h}$ across various modelling chains. These figures allow for a direct comparison of noise level distributions under the different traffic simulation approaches introduced in 2.1, including the initial SUMO microscopic mode, the density-based mode, and the Poisson-based mode.

As shown in Figure 2, the KDE curves of $L_{\text{Aeq},1h}$ illustrate the overall equivalent noise levels across different scenarios. Despite minor variations, all modes exhibit a similar bimodal distribution, indicating that the general noise exposure trends remain consistent regardless of the underlying traffic modelling approach. However, the SUMO mode (blue curve) shows slightly higher noise levels in the first and the second peaks, and gains more density in the highest noise interval (60 - 70 dB), which may be explained by a more detailed representation of vehicle flow dynamics.

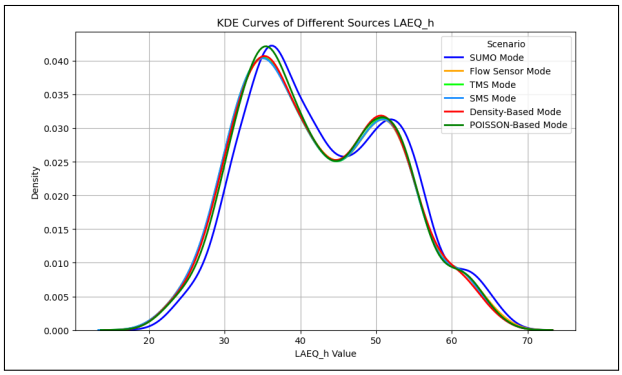


Figure 2. KDE Curves of Different $L_{\text{Aeq},1h}$.

Figure 3 presents the KDE curves for $L_{A10,1h}$. Unlike $L_{\text{Aeq},1h}$, which can be estimated from any aggregated traffic scenario, $L_{A10,1h}$ requires dynamic approaches to capture variations in noise over time. Therefore, only the SUMO microscopic mode, the Density-based mode, and the Poisson-based mode are represented in this figure. The Density-Based mode (red curve) and the Poisson-Based mode (green curve) align closely with the SUMO mode, particularly at lower noise levels. However, minor deviations appear in the tail of the distribution, indicating that high-intensity noise events may be influenced by traffic flow representation differences.

Figure 4 focuses on $L_{A1,1h}$, capturing the highest noise levels experienced during the simulation. Similarly to $L_{A10,1h}$, $L_{A1,1h}$ can only be derived from dynamic

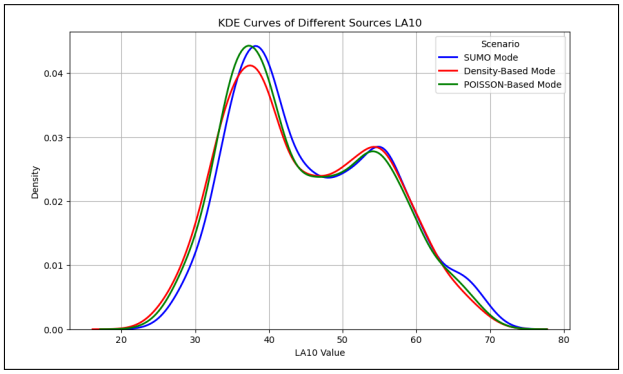


Figure 3. KDE Curves of Different $L_{A10,1h}$.

traffic models. The results indicate that the SUMO microscopic mode captures more pronounced peaks, reinforcing the idea that detailed vehicle-level modelling better represents transient events such as acceleration and braking. The Density-Based and Poisson-Based modes follow similar trends but exhibit smoother distributions, likely due to their simplified vehicle representation.

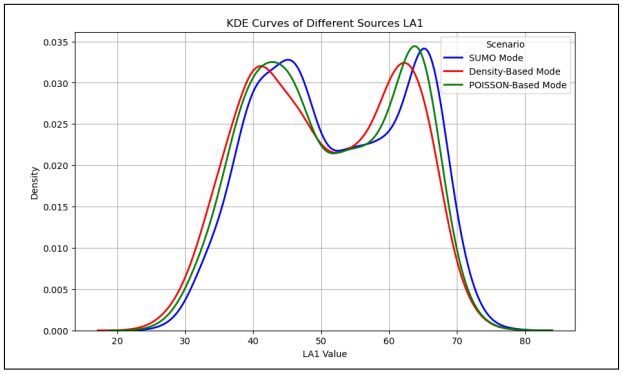


Figure 4. KDE Curves of Different $L_{A1,1h}$.

3.2 Noise mapping

Figures 5, 6, 7, 8, and 9 display the estimated $L_{\text{Aeq},1h}$ difference values of various scenarios compared with the reference SUMO mode. These figures contribute to explaining the deviations from the SUMO mode (blue curve), as most of the estimated $L_{\text{Aeq},1h}$ levels are underestimated while only a few of the receivers exhibit higher $L_{\text{Aeq},1h}$ levels in aggregated link-based scenarios.

Noteworthy is the fact that among these figures, the portion of receivers at which levels are greatly underestimated (deep blue color dots) is much reduced for Density-Based and Poisson-Based modes when compared to the other three aggregated traffic representation scenarios. This result suggests that hybrid traffic representations have the potential to alleviate the underestimation induced by the loss of details in the description of vehicle dynamics associated with aggregated traffic representations.

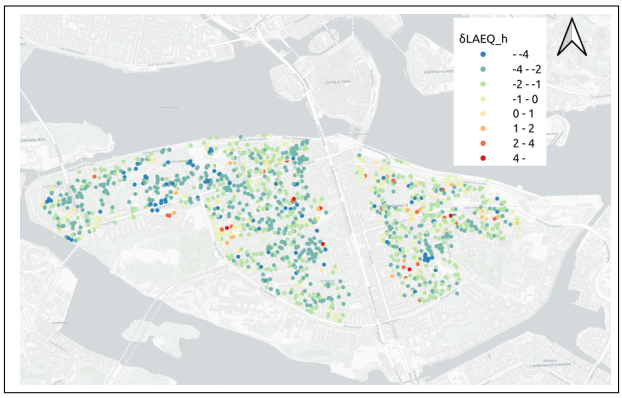


Figure 5. Sensor Mode acoustic indicators compared to SUMO Mode.

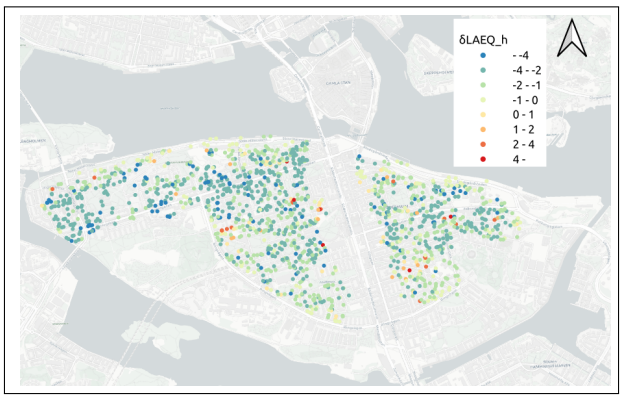


Figure 6. TMS Mode acoustic indicators compared to SUMO Mode.

4. CONCLUSIONS

This study offers a comparison of different modelling chains for estimating road traffic noise, focusing on

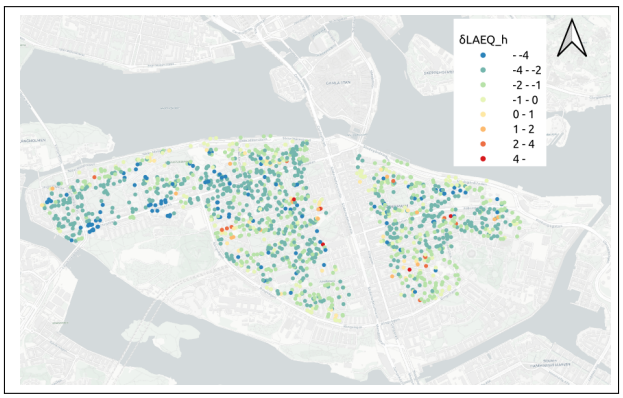


Figure 7. SMS Mode acoustic indicators compared to SUMO Mode.

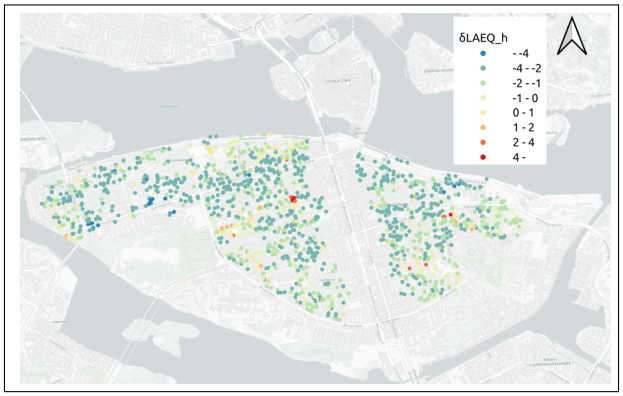


Figure 8. Density Mode acoustic indicators compared to SUMO Mode.

variations in noise distributions under distinct traffic representation approaches. By analyzing the Kernel Density Estimation curves of various noise indicators and noise indicator maps, several key observations are made.

First, despite differences in traffic representation, all models exhibit similar distribution patterns. This suggests that hybrid traffic modelling approaches, including Density-based and Poisson-based methods, can yield comparable noise estimates, especially at high percentile indicators. These indicators are limited in aggregated link-based scenarios, making hybrid methods a practical alternative when detailed microscopic data is unavailable.

However, the differences observed in the KDE curves and the distribution of noise maps indicate that while

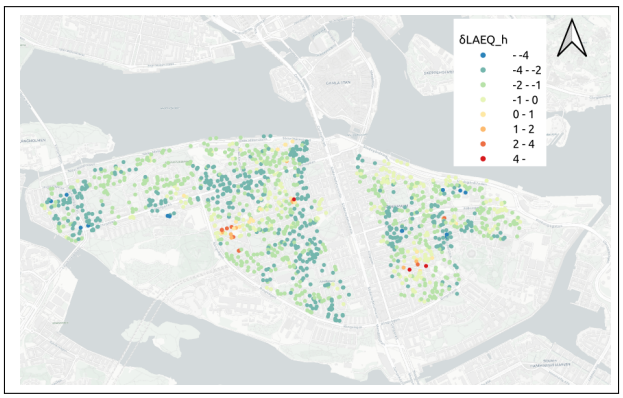


Figure 9. Poisson Mode acoustic indicators compared to SUMO Mode.

these methods effectively capture general trends, they may not fully account for noise from transient vehicle behaviors and uneven vehicle movement distributions. These factors can contribute to variations in high-noise conditions, generally leading to slightly lower noise level estimation when ignored.

Overall, this comparative analysis highlights the influence of different traffic representations on noise estimations with a range of noise indicators. While detailed microscopic simulations offer high-fidelity vehicle dynamics, Density-based and Poisson-based methods provide alternatives, particularly suited for scenarios with limited data availability. Compared to detailed microscopic simulations and static aggregated link-based scenarios, these approaches maintain a balance between broad accuracy insights and practicality. Future research could further refine these models by integrating detailed vehicle behaviors and improving their adaptability to complex urban traffic environments.

5. ACKNOWLEDGMENTS

This research was funded by the EU Horizon 2020 program under the Marie Skłodowska-Curie COFUND grant agreement No 101034248, City Lab Education and Research Doctoral Program.

6. REFERENCES

[1] V. Le Bescond, A. Can, P. Aumond, and P. Gastineau, "Open-source modeling chain for the dynamic assess-

ment of road traffic noise exposure," *Transportation Research Part D: Transport and Environment*, vol. 94, p. 102793, 2021.

[2] S. Baclet, K. Khoshkhah, M. Pourmoradnasseri, R. Rumpler, and A. Hadachi, "Near-real-time dynamic noise mapping and exposure assessment using calibrated microscopic traffic simulations," *Transportation Research Part D: Transport and Environment*, vol. 124, p. 103922, 2023.

[3] E. Chevallier, A. Can, M. Nadji, and L. Leclercq, "Improving noise assessment at intersections by modeling traffic dynamics," *Transportation Research Part D: Transport and Environment*, vol. 14, no. 2, pp. 100–110, 2009.

[4] C. F. Daganzo, "Urban gridlock: Macroscopic modeling and mitigation approaches," *Transportation Research Part B: Methodological*, vol. 41, no. 1, pp. 49–62, 2007.

[5] L. Leclercq and S. Moutari, "Hybridization of a class of "second order" models of traffic flow," *Simulation modelling practice and theory*, vol. 15, no. 8, pp. 918–934, 2007.

[6] Y. Imai, H. Fujii, K. Okano, M. Matsudaira, and T. Suzuki, "Development of dynamic micro-and macroscopic hybrid model for efficient highway traffic simulation: Model extension to merging sections and validation with probe data," *International Journal of Intelligent Transportation Systems Research*, vol. 22, no. 1, pp. 159–170, 2024.

[7] S. Kephalopoulos, M. Paviotti, F. Anfosso-Lédée, D. Van Maercke, S. Shilton, and N. Jones, "Advances in the development of common noise assessment methods in europe: The cnossos-eu framework for strategic environmental noise mapping," *Science of the Total Environment*, vol. 482, pp. 400–410, 2014.

[8] European Commission, "Commission Directive (EU) 2015/996 of 19 May 2015 establishing common noise assessment methods according to Directive 2002/49/EC of the European Parliament and of the Council (Text with EEA relevance)," *Official Journal of the European Union*, vol. OJ L, 2015.

[9] P. A. Lopez, M. Behrisch, L. Bieker-Walz, J. Erdmann, Y.-P. Flötteröd, R. Hilbrich, L. Lücken, J. Rummel, P. Wagner, and E. Wießner, "Microscopic traffic simulation using sumo," in *2018 21st international conference on intelligent transportation systems (ITSC)*, pp. 2575–2582, Ieee, 2018.

[10] A. Pascale, C. Guarnaccia, E. Macedo, P. Fernandes, A. I. Miranda, S. Sargento, and M. C. Coelho, "Road traffic noise monitoring in a smart city: Sensor and model-based approach," *Transportation Research Part D: Transport and Environment*, vol. 125, p. 103979, 2023.

[11] A. Mehar, S. Chandra, and S. Velmurugan, "Speed and acceleration characteristics of different types of vehicles on multi-lane highways," *European Transport*, vol. 55, no. 1, pp. 1–12, 2013.

[12] P. Aumond, L. Jacquesson, and A. Can, "Probabilistic modeling framework for multisource sound mapping," *Applied Acoustics*, vol. 139, pp. 34–43, 2018.

[13] S. R. de Donato and B. Morri, "A statistical model for predicting road traffic noise based on poisson type traffic flow," *Noise control engineering journal*, vol. 49, no. 3, pp. 137–143, 2001.

[14] E. Bocher, G. Guillaume, J. Picaut, G. Petit, and N. Fortin, "Noisemodelling: An open source gis based tool to produce environmental noise maps," *Isprs international journal of geo-information*, vol. 8, no. 3, p. 130, 2019.

[15] B. Peeters and G. Van Blokland, "The noise emission model for european road traffic," *IMAGINE deliverable*, vol. 11, no. 11, 2007.

DOI: 10.61782/fa.2025.0267

FORUM ACUSTICUM EURONOISE 2025

DELIVERING NATIONAL SCALE NOISE CALCULATIONS WITH CNOSSOS-EU THROUGH CLOUD COMPUTING AND SOFTWARE OPTIMISATION

Hartmut Stapelfeldt [1] **James Trow** [2] **Joe Madden**[3]

[1] Dipl.-Ing. Hartmut Stapelfeldt, Stapelfeldt Ingenieurgesellschaft mbH, D 44141 Dortmund, Germany
[2] Noise Consultants Limited, Warrington, UK
[3] Mott MacDonald, Glasgow, UK

ABSTRACT

The United Kingdom Department for Environment, Food and Rural Affairs (Defra) commissioned the design and build of an environmental noise modelling system (NMS). The NMS has been developed to support Defra in preparing its environmental noise evidence base by preparing national road and railway noise models. This paper discusses the challenges and solutions as part of Defra's NMS project to enable CNOSSOS-EU calculations to be delivered on 10 metres grids and at the facades of all residential buildings in England, Scotland and Wales.

Keywords: *noise mapping, cloud calculation, Defra noise modelling system (NMS)*

1. INTRODUCTION

The UK Department for Environment, Food and Rural Affairs (Defra) commissioned the design and build of an environmental noise modelling system (NMS) in 2021. The NMS has been developed to support Defra in preparing its environmental noise evidence base by preparing national road and railway noise models. Defra's model has been produced to fulfil the requirements of the Environmental Noise (England) Regulations 2006 (as amended) (the 'Regulations') [1], the Defra 25-year Environment Plan (25YEP) [2], and the Public Health Outcomes Framework (PHOF) [3]. This has required the model to incorporate all public road and railway noise sources and provide national coverage with respect to calculated noise maps and exposure statistics. The noise models have been delivered in line with the requirements of the adapted assessment methods based on the Calculation of Road Traffic Noise (CRTN) [4] and Calculation of Railway Noise (CRN) [5], and CNOSSOS-EU [6].

The NMS has been designed to connect a series of components secured behind a web application firewall. The design of the NMS has taken a 'decoupled' approach which utilizes existing commercial products with 'ground up' development in areas such as its database design and Extract Transform Load (ETL) tools [7].

At the heart of the NMS is a Postgres geospatial database served on Azure CosmosDB. The database has been designed to store noise model and noise exposure datasets alongside each other. In support of Defra's requirements, the NMS has been designed to deliver automated processes whereby selected input datasets are transformed into noise model datasets using Feature Manipulation Engine (FME) software.

The models are stored in a manner which conforms to its system's open data standards which have been developed in parallel to the NMS.

***Copyright**: ©2025 H. Stapelfeldt et al. This is an open-access article distributed under the terms of the Creative Commons Attribution 3.0 Unported License, which permits unrestricted use, distribution, and reproduction in any medium, provided the original author and source are credited.*

Noise calculations are delivered using a calculation engine which utilizes LimA [8] software modules including noise calculation cores. The calculation engine utilizes a range of components including Azure Cycle Cloud which provides flexibility by allowing calculations to scale up and down by deploying additional virtual machines to the calculation task.

The NMS and the calculation of Defra's model using CNOSSOS-EU has introduced unprecedented computation challenges with a need to balance scale with efficiency and accuracy demands. This paper discusses the key challenges and solutions to delivering CNOSSOS-EU calculations within the NMS at a national level.

2. KEY REQUIREMENTS

Defra set several requirements for its NMS and its noise model which have a direct impact on the approach and requirements for noise calculation. These are summarised as follows:

1) The NMS must be cloud based and scalable
2) Defra's noise model must be developed through automated processes, where practically possible, using authoritative datasets and stored centrally within geospatial database
3) The spatial quality of the noise model must be suitable for localised, detail applications as well as strategic use for national mapping exercises – this means that model simplification is not an option while setting up the geospatial database
4) The noise model must be stored in open standards independent of any noise modelling or calculation solution removing the ability to optimise the noise model itself for a particular calculation solution
5) The noise model must comprise of all public road and railway noise sources and not just those defined under the relevant Regulations
6) The NMS must be capable of delivering noise calculations down to 40 dB L_{den} and 35 dB L_{night} introducing the need for much larger calculation radius and introducing new efficiency techniques applicable to low noise level environments
7) Calculations must be capable of being run for England in 35 days
8) Any techniques adopted to increase computational efficiency should not result in a calculated uncertainty of more than ± 2dB for 90% of receiver point levels.

In combination, these requirements introduce an unprecedented calculation load with firm requirement with respect to the quality of the calculations.

3. RESPONDING TO REQUIREMENTS

During the development phase, focus on efficient, agile and scalable calculation was considered in three areas:

1) Calculation efficiency – Balancing accuracy and compliance with performance requirements at component level i.e. calculation at a single calculation core
2) Distributive Techniques – how to best distribute calculations within a single multi-core machine and across multiple machines
3) Calculation Management – bringing together calculation efficiency and distributive techniques in a managed way.

All three areas were subject to research and development, and associated testing as part of the NMS project.

4. CALCULATION STRATEGY

4.1 Technical challenges

The NMS project is ambitious with respect to extent of project area, detail of model and accuracy demands in calculation. Maximum calculation effort is required when applying CNOSSOS propagation logic.

4.1.1 CNOSSOS calculation method

Compared to CRTN which was previously adopted by Defra to deliver strategic noise maps, CNOSSOS requires working in octaves instead of main frequency and 8-fold propagation paths analysis for a single source-receiver constellation.

4.1.2 Highly detailed model data

NMS has been designed to provide noise modelling data ready for nationwide as well as localised assessment. The resolution of the model therefore needs to be high, as shown in Figure 1.

Noise emissions of sources are pre-calculated within Defra's model and stored in the central database. This avoids interpretations of emissions calculations by different

software tools which may introduce their own adaptation and same time allows for instant inqueries.
The central database delivers model data in a neutral, open format and enables its use by various software products.

The inclusion of all public road and rail sources results in a significant number of emission sources, beyond what would usually be considered in a conventional noise model. This is evidenced by the residential streets in Figure 1.

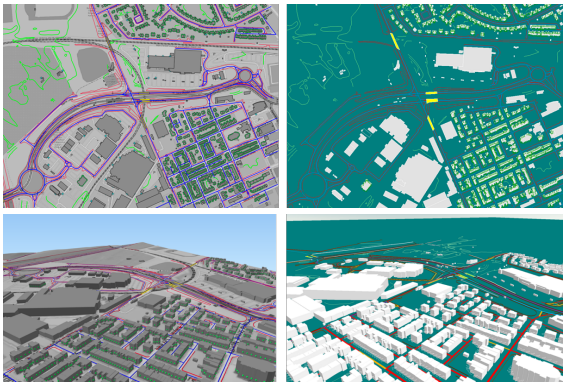


Figure 1. View of Defra's model in open standards (left) and in LimA (right)

4.1.3 Noise Apportionment

The NMS has been designed to support the estimate of noise exposure levels at calculated receiver positions in case of change in emission levels, based on noise apportionment data. For up to 30 most influential sources receptor level contribution per octave as well as the residual noise component need to be stored during the noise calculation. Data is delivered from the LimA calculation cores in a standardised CSV file format which is then ingested back into the central database. This increases calculation overhead by having to write additional information at the end of each calculations. It also requires extensions to LimA's handing of identifier strings to ensure are passed directly from the model into calculation and retained when reporting apportioned noise levels.

4.1.4 Low noise level requirement

To calculate noise at lower levels means that not only major and significant sources of emission are to be considered but rather all roads and rails need to be considered in the calculation. With respect to desired receiver levels in the range of 30 dB, the fetching radius for sources must be set to 3000 m in order to avoid discontinuities in noise grids due to distant high emission sources.

4.2 Calculation parameters and further settings

The immense calculation task does require a careful choice of calculation parameters and extra settings. Though long-standing experience in noise mapping e.g. already showed that small fetching radii for reflector search are reasonable, research was carried out for new parameters and to evidence selected choices in calculation parameters with respect to calculation efficiency (time) and introduce uncertainty (dB).

4.2.1 General calculation parameters

The values chosen for well-established calculation parameters were set to:

3000 m	Fetching radius for road sources
2000 m	Fetching radius for rail sources
25 m	Fetching radius for reflectors
30 dB	Min. relevant receptor levels at night
3 dB	Dynamic error margin (as extreme value)
No	Source segmentation due to ground cover

4.2.2 LimA's established efficiency tools

LimA offers a range of tuning settings to reduce calculation time and 2 key ones are mentioned here as examples. Both of them were introduced into the market by LimA more than 30 years ago.

Most renowned calculation speed tuning feature is the dynamic error margin, whereby a user limits the underestimation of calculated receiver levels, caused by neglection of less relevant sources. It represents a total effect. In many projects this has proven to be a very efficient way to speed up calculation and Figure 2 shows the effect on result and calculation time for a small example with 3 categories of road traffic emission intensity.

However, the need to report noise exposure for all and for major sources hampers the dynamic error concept, as even next to a highway the calculation core might still have to consider minor local roads at distance.

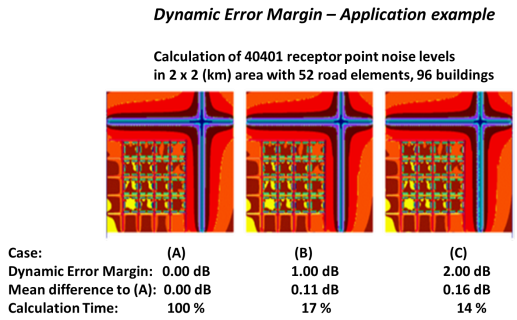


Figure 2. Dynamic Error Margin effects

Another tuning aspect deals with line source segmentation. LimA applies the 'method of projection' where sources are segmented with respect to segmentation of obstacles (e.g. each façade segment of a building) encountered between source and receiver in full 3D geometry analysis. This achieves best continuity for direct and reflected noise contributions.

The 'method of projection' was introduced into the market by LimA and by now is available in most noise mapping products and is described in ISO9613-2024 [8]. However, this only focusses on diffracting barriers.
In distinct model situations the propagation influence of ground cover may become important and an extra segmentation of line sources will be feasible. Therefor LimA does support an optional extra segmentation due to ground cover shapes. With respect to the highly detailed/scattered ground cover data and the fact that CNOSSOS does not deal with this issue, it was decided not to activate this feature.

But with source-receiver distances up to 3 km, and with buildings in urban areas, source segmentation needed further streamlining. Source line segmentation took full details of buildings at a maximum distance of the maximum of 8-fold maximum ground extent or at least 300 m from source or receiver. Source segmentation by further objects at larger distances were only considered with their individual total aperture angle. This technique was found to further rationalise the calculation load.

4.2.3 Efficiency tools developed alongside the project

To further enhance calculation performance it was accepted that under certain circumstances the dynamic error margin logic needed to be subject to 'pre-filtering' of certain sources. This was found to be the case where the calculations were subjected to significant densities of emitter with very similar noise emission levels due to the use of default values. Testing identified that
road and/or rail line sources with an emission level (SPL per m) below 75 dB could be filtered prior to the dynamic error margin when they are at a distance beyond 750 m whilst meeting calculation uncertainty requirement. This logic in effect introduced two calculation radii linked to the importance and influence of different types of sources i.e. high quantity low emission, and low quantity high emission.

Efforts in reflection calculation are reduced by limiting the number of reflecting surfaces next to receivers. Here a minimum aperture angle of 10 degree is used, with adjacent façade segments in same plain especially cared for.

4.2.4 Quality assessment

All strategies are subject to a specific study to ensure calculation accuracy remained within agreed tolerance. Recommended calculation settings result in calculation times of less than 0.4% of benchmark in urban areas, and less than 0.15% in rural areas, with mean difference of about 1.0 dB in urban areas, and 0.5 dB in rural areas, and 95% CI of 2.7 dB in urban areas, and 1.0 dB in rural areas.

4.3 Distribution Techniques

The model is stored in the central database in line with the Ordnance Survey tiling structure. This stores model data in 5 x 5 (km) project areas defined by their OS tile reference. A single CPU takes over a noise calculation task for a 1 x 1 (km) region. With 3 km buffer zone this already results in 49 km² model area to deal with per calculation run.

The NMS was designed to host a central controller node VM which manages a project processing queue and allocates individual projects by their OS tile reference to available VMs, known as the 'worker nodes'. Along with the project details it sends all model data required from central database. All this is organized by PowerShell scripts with the scaling of available worker node VMs managed by Azure Cycle Cloud. This logic is presented in Figure 3.

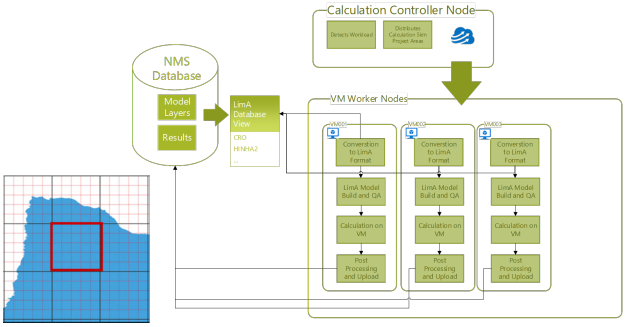


Figure 3. Calculation Distribution Logic

4.4 Calculation Management

Calculation management has to deal with model data transfer, initiating calculation jobs and collecting result files. The demand for apportionment results in massive size result data sets, which can run into several hundred MB per 1 x 1 (km) tile.

4.4.1 Calculation task description

Calculation requirements for project processing are written into Project Management File (*.PRM). This is the only initial user exercise and it is set up in a semi-automated process.

Table 1. Extract of PRM file defining calculation task

runID	nmsRailCNOSSOS_2021_Area8_SE47SE
userID	nmsAdmin
runDate	28.11.2023 16:20
calcDate	28.01.2023
runName	PRJ_320
runDescription	2021 Railway Noise Calculation - CNOSSOS-UK
runType	optimalNoiseMapping
processNodes	100
calcMethod	CNOSSOS-EU
calcSource	Rail
calcReceivers	Grid
gridSpacing	10
modelViews	CMTNMS CRA GBO GELCONT GELSPTH WGB HINHA3R HINHA3A LCMTOP HINHA7
calcRegion	nmsRailCNOSSOS_2021_Area8_PRJ_SE47SE_RLGD__calcRegion.lst
calcReflections	1
calcMargin	3
calcRadius	2000
calcTemplate	L_07M_CF_NMS.STD
calcOptions	BEW LDEN PEGMIN 30 GROUND 0.0001 L_DISLEV 750 75 RGEMI 1900 GEBNZ 4 SEG-TOP- DOPHIN
dbView	defra

4.4.2 Orchestrate the noise calculation

Once all data has been sent to a worker node, a LimA macro developed for the NMS takes over, defining jobs for LimA modules. The actions comprise:

1) Retrieving model data from the central database and converting the data into LimA format without simplification
2) Creating separate job files per 1 x 1 (km) calculation tile
   For each job the calculation input file is generated with respect to the information in the *.PRM file.
3) Job-files are stored in a central spool directory and are dispatched by LimA's DSERVER.EXE to any available out of 7 parallel processing queues. (One CPU is spared to support OS) with each worker node configured as an 8-core VM
4) When all jobs are finished data is zipped and handed over to separate processes for upload into the database.
5) Finaly the VM either takes over a next project or is powered down.

4.5 Hardware

Chosen hardware in the Azure cloud HPC environment is the result of efficiency tests, i.e. costs vs. calculation speed comparison. This testing demonstrated that the optimum configuration was an 8 core VMs with 32 GB RAM. Potential deployment of tasks on up to 150 VMs was ensured for the actual noise calculation as well as all other processes related to the project. Most of actual costs are linked to active processing and data communication across the network.

5. ACHIEVEMENTS

The NMS has been used to deliver noise calculations at national scale in England, Wales and Scotland. For grid calculations alone, the following number of calculation points have been generated:

- England, 1.329 billion
- Scotland, 803 million
- Wales, 212 million

The typical calculation times have been in the region of 0.2 seconds per calculation point. For England alone, national scale road traffic noise calculations on the NMS have a theoretical calculation time of around 2 days plus data transfer overheads across the NMS's 150 worker node VMs as opposed to 384 days on a single worker node VM. The Azure pricing logic means that the total calculation costs will be equal irrespective of the number of identical VMs involved.

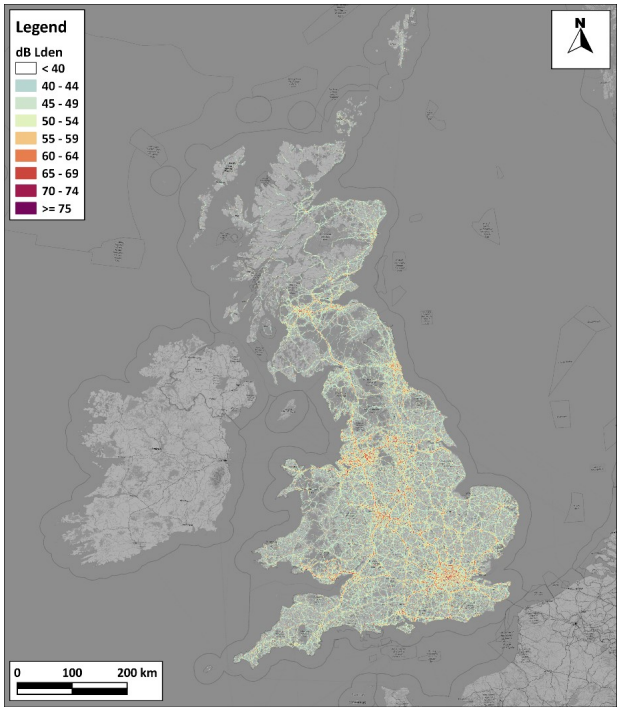


Figure 4. L_{den} road traffic noise map for England, Scotland and Wales

6. CONCLUSIONS

The NMS project demonstrates that detailed large area noise calculations delivered to much lower levels than previously considered are deliverable and achievable through a combination of traditional and optimised efficiency techniques and by utilising modern cloud solutions to create calculation environments.

7. REFERENCES

[1] HM Government, *The Environmental Noise (England) (Amendment) Regulations 2018* (2018).

[2] HM Government, *A Green Future: Our 25 Year Plan to Improve the Environment* (2018).

[3] https://www.gov.uk/government/collections/public-health-outcomes-framework (accessed 28 March 2025)

[4] Department of Transport, Welsh Office. *Calculation of Road Traffic Noise* (CRTN). London, Her Majesty's Stationery Office (1988)

[5] Department of Transport, Welsh Office. *Calculation of Railway Noise* (CRN). London, Her Majesty's Stationery Office (1995)

[6] Annex II of Consolidated text: Directive 2002/49/EC of the European Parliament and of the Council of 25 June 2002 relating to the assessment and management of environmental noise, Document 02002L0049-20210729, July 2021.

[7] J. Trow et al., *Automation of a National Noise Model*, Proc. Of InterNoise 2022, Glasgow.

[8] LimA Software Suite for environmental analysis, developed and distributed by Stapelfeldt Ingenieurgesellschaft mbH, D 44141 Dortmund

DOI: 10.61782/fa.2025.0238

FORUM ACUSTICUM EURONOISE 2025

COMPARISON OF INPUT DATA COLLECTION METHODS FOR ROAD TRAFFIC NOISE MODELS IN RESIDENTIAL AREA

Elena Ascari[1] **Luca Fredianelli**[1] **Mauro Cerchiai**[1]
Gaetano Licitra[1] **Cătălin Andrei Neagoe**[2,3] **Ana-Maria Mitu**[2] **Tudor Sireteanu**[2]
Daniel Cătălin Baldovin[2] **Domenico Profumo**[4] **Simon Kanka**[5*]
[1]Institute of Chemical and Physical Processes of National Research Council, Pisa, Italy
[2] Institute of Solid Mechanics of the Romanian Academy, Bucharest, Romania
[3] National University of Science and Technology POLITEHNICA Bucharest, Romania
[4] IPOOL s.r.l., Via Antonio Cocchi 3, 56121, Pisa, Italy
[5] Department of Physics of University of Pisa, Pisa, Italy

ABSTRACT

Whether it is NMPB96 or the newer CNOSSOS-EU model, all road traffic noise models require detailed inputs to provide the most reliable estimate of noise exposure.
The present work presents preliminary results of a bilateral project between the Italian National Council of Research (CNR) and Romanian Academy dedicated to the Comparison of different methods for road noise modeling in residential area.
The work presents a comparison of road traffic data acquired in both Italian and Romanian territory with 3 different traffic estimation methods: microwave radar traffic counter, Google API and cameras with recognition by machine learning.

Keywords: *transportation noise, noise mapping, traffic detection, crowd sourced data.*

1. INTRODUCTION

In 2002, the European Commission adopted the Environmental Noise Directive with the aim of preventing exposure, establishing a common methodology and exploring a way to reduce the excessive levels to which the population is exposed. The primary step in noise exposure assessment is acoustic mapping of the main sources (i.e. roads, railways, airports and industries), and this must be performed using a mathematical model. The CNOSSOS-EU method [1] was officially identified in 2015 as the new model to replace the previous NMPB interim method. This revised approach has been formally adopted by the two involved countries and will be mandatory from the 4th mapping round in 2022. The new model offered a great opportunity for European Country and at the same time new challenges in applying a different never tested large scale methodology [2].
Following extensive research, CNOSSOS-EU appears to exhibit certain discrepancies from its predecessor, predicting reduced levels of road traffic noise [3]. The difference can be attributed to several factors, including vehicle categorization and a novel formulation for absorption and diffraction effects. While an offset is expected to have no impact on the noise mitigation phase, it may be particularly relevant for health studies that require accurate noise estimation using validated maps.
In order to achieve this objective, it is imperative to acknowledge the assertion that, within a mathematical model, the quality of an output is contingent upon the quality of the inputs. Consequently, the focus should be directed towards the latter, with the establishment of clear definitions being of paramount importance.
This paper presents the findings from a collaborative study between IPCF, Institute of National Research Council of Italy, and IMSAR, Institute of Romanian Academy. The

[*]***Corresponding author***: *simon.kanka@phd.unipi.it*
Copyright: *©2025 Elena Ascari et al. This is an open-access article distributed under the terms of the Creative Commons Attribution 3.0 Unported License, which permits unrestricted use, distribution, and reproduction in any medium, provided the original author and source are credited.*

objective of the study was to evaluate the availability of the inputs required for the application of CNOSSOS-EU method in Romania, as well as to compare the results obtained from the NMPB and CNOSSOS-EU with respect to input data collection and results. The present paper offers the initial findings of the project, specifically the outcomes of data acquisition employing diverse methodologies, including microwave radar traffic counters, cameras with machine learning recognition, and Google API with Python script elaborations. Thereafter, a comparison will be drawn between the data sets, in order to ascertain potential discrepancies. Finally, these input data sets will be modelled in software to analyze the differences in terms of the derived noise compared to the actual measurements.

2. METHODS

2.1 Data acquisitions methods

A detailed description of the three methods identified for acquiring input data is presented hereafter. The acquisition of traffic data can be achieved through onsite measurements or remote analysis. Onsite measurements are performed with standard microwave radar traffic counters (TC) or with cameras that are optimized for vehicle recognition in the context of CNOSSOS-EU classification (CAM). The third method involves remote analysis, which exploits Google API traffic data (API). The installation of TC and CAM measurement systems is illustrated in Figure 1. The description will then proceed to detail how data are acquired and the flows derived, and the pros & cons of each methodology.

2.1.1 Microwave radar traffic counter (TC)

TC are situated at the roadside to monitor traffic on a maximum of two lanes. They can be installed in a low position (approximately 50 cm from the road surface) or in a high position (more than 2 m from the road surface) to monitor respectively roads with less or more traffic. As there may be occlusion from vehicles, the upper position should give a better view of the road if there are several lanes in the same direction. This system cannot differentiate between two lanes of traffic in the same direction, and passages are stored together. Traffic counting is based on the length of the vehicle as seen by the radar, so the same vehicle passing at different distances from the radar position will have different length values. Different lengths can be set for different vehicle categories in opposite directions, but not for two lanes in the same direction, so the thresholds between them should be set carefully. On the other hand, the system is very easy to install, it does not store any sensitive data and the analysis is done using spreadsheets.



Figure 1. Monitoring with TC and CAM – Bucharest testbed.

2.1.2 Camera with AI recognition (CAM)

AI-powered cameras are based on the YOLO (You Only Look Once) approach to object detection [4,5]. Vehicles are categorized according to a customized approach to CNOSSOS-EU categories identification. The employment of machine learning ensures the expeditious analysis of traffic flows, while a straightforward on-site measurement procedure enables speeds to be calculated. The system

utilized in this study is still required to undergo post-processing analysis in order to obtain flow and speed results, due to hardware constraints. In order to derive speeds, it is necessary to undertake local measurements of the distances between the camera and the road lanes. In order to perform this calibration phase, the road should be temporarily closed. Conversely, cameras have the capacity to detect up to four lanes and divide the flows, rendering them potentially very powerful, even in cases of high traffic volumes.

2.1.3 Google API & Python scripts (API)

Crowd-sourced data can be utilized to estimate traffic volumes. Google API provides travel times through specific calls for selected road stretch (origin-destination). The application of a basic transport equation [6] makes it possible to derive passenger car equivalent flows using Python scripts and then use standard percentages of vehicle categories to derive the flow of each. The API approach has been demonstrated to facilitate the derivation of a substantial database of flows in the absence of on-site measurements. However, it should be noted that API calls do incur a cost (0.01$ for each origin-destination and time). Additionally, transportation functions are incapable of deriving accurate flow in instances of both very high congestion and very low traffic. In both scenarios, the returned travel time, i.e. the speed, is independent of the actual flow, rather dependent upon driver behavior or the overall capacity of the network.

2.2 Testbeds

Two primary testbeds were identified in the project: a mitigated main regional road crossing a small village in Italy (SR 439) and two roads of a residential area in Bucharest (namely a residential road, Strada Secuilor, and the main boulevard, Constantin Brâncoveanu). Table 1 provides a synopsis of the characteristics, while Figure 2 illustrates the locations.

Table 1. Testbeds characteristics

Road, Country	Lanes	Speed limit (km/h)	Distance to houses (m)
Regional, IT	2	50	10-10
Residential, RO	2	30	15-20
Boulevard, RO	4	50	25-25

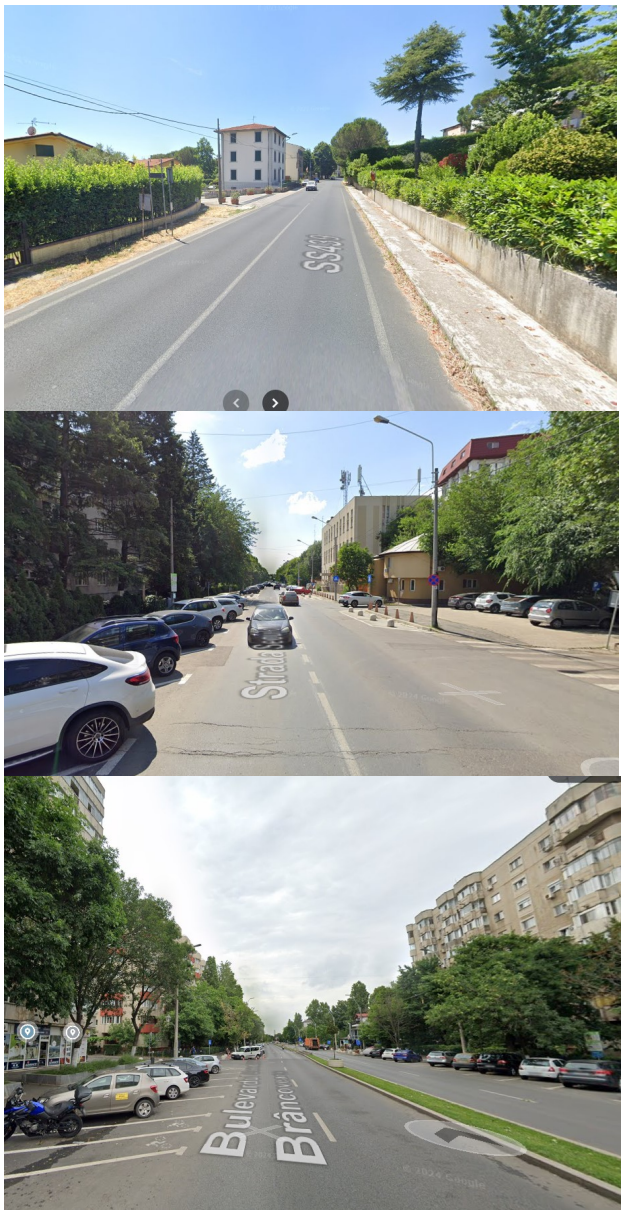


Figure 2. From top to down: SR 439 (IT), Strada Secuilor (RO) and Boulevard Constantin Brâncoveanu (RO).

2.3 Data comparison time base

In the course of the project, a comparison was made of input data gathering methods according to different time bases, depending on the purpose. For the purpose of END noise mapping, it is necessary to compare average day, evening and night-time slices. Furthermore, the 10-minute interval was analyzed in order to verify the suitability of the acquisition methods for advanced dynamic noise mapping, for example to manage congestion and other short-term effects. The focus of this paper is the presentation of results for END noise mapping estimates.

3. RESULTS

3.1 Measurements in testbeds

The first test was carried out in Italy: 24h measurements were taken in Massarosa on the SR439 during April 2024. Second test carried out in Romania: about 24h measurements were performed in Bucharest on the Boulevard Constantin Brâncoveanu and the street Strada Secuilor during September 2024.
All the acquisitions included:

- a roadside AI- camera monitoring all the lanes;
- the call to the API to acquire travel time data every 10 minutes for each direction of traffic;
- a noise level monitoring station.

Furthermore, the standard positioning of traffic counters was subject to variation across different roadways, with the objective of ensuring safety and optimizing traffic flow monitoring. The low position was utilized in Italy, while the high position was employed in Romania. Two traffic counters were installed to monitor the Boulevard; however, technical issues resulted in the failure to capture data from one of the four lanes. Consequently, the data from one of the lanes was doubled to account for the technical issues (modified data are marked with "*" in the following).

3.2 Comparison of average day evening night periods

In order to facilitate a comparison of the accuracy of the modelling process, the derived traffic data are compared in terms of flows and average speed in the three different time slices (day, evening and night) and on the three roads in each direction. The categorization of data is conducted in accordance with the CNOSSOS-EU classification system, which designates categories 1 as light vehicles, category 2 as medium trucks, category 3 as heavy vehicles (excluding urban areas in Romania, where heavy vehicles are not present), and category 4 as two-wheelers.

Acquisitions have demonstrated that the impact of categories other than light vehicles is negligible. Figure 3 illustrates the subdivision of traffic flows according to AI-camera data, for each designated time slice and testbed.

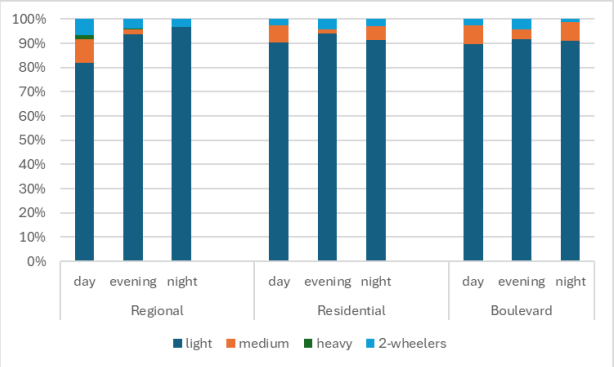


Figure 3. Vehicles categories subdivisions in flows for the three testbeds.

Therefore, the comparison of flows is reported only for light vehicles, as this is sufficient as a proxy for the expected noise differences. Tables 2, 3 and 4 present the estimated flows per hour for the three time slices and for all roads and directions according to the three input gathering approaches.
It is evident that the night-time slice of the Italian testbed reports significantly divergent values for the API method. This discrepancy can be attributed to the different method used to derive the flows: in Italy, the transport parameters were set to the same value in all time slices, whereas in Romania they were varied to reflect the different transport conditions in each time slice.

Table 2. Estimated light vehicles - day

Road, Country	TC	CAM	API
Regional, IT	332	310	350
	296	324	320
Residential, RO	114	166	169
	281	338	285
Boulevard, RO	459	614	603
	442*	704	704

Table 3. Estimated light vehicles - evening

Road, Country	TC	CAM	API
Regional, IT	207	236	369
	131	162	357
Residential, RO	86	107	201
	223	232	188
Boulevard, RO	449	542	558
	290*	506	601

Table 4. Estimated light vehicles - night

Road, Country	TC	CAM	API
Regional, IT	38	41	348
	37	52	323
Residential, RO	18	22	136
	38	39	121
Boulevard, RO	131	108	183
	177*	217	360

4. CONCLUSIONS

This work has presented the first results of a bilateral project between Italian National Research Council and Romanian Academy. While the whole project aims to analyze the effects of mapping road traffic noise with input gathered with different traffic flow measurements methodologies, the present work shows the results in terms of traffic counts from the testbeds situated in Italy and Romania. Three different methods were simultaneously used, and it results that when the traffic is low, the microwave traffic counter (TC) and camera with artificial intelligence recognition (CAM) methods are similar. CAM generally exhibits higher flows, which should be more realistic than the TC ones. The third approach, Google API approach, necessitates meticulous validation but could serve as a viable method for high traffic roads and average estimates. The transportation parameters that are conducive to deriving API data are the focus of ongoing research in related projects. Regarding noise mapping models, all methods are deemed suitable for deriving comparable noise levels during the day. For other time periods, the use of CAM is recommended, or, alternatively, TC, though only for low-traffic areas. Further analysis will allow for the establishment of variability in noise results due to the input data collection methods and the noise model applied (CNOSSOS-EU or interim NMPB method).

In order to achieve this objective, the remaining of the project will consist of a comparative analysis of the noise emissions of individual vehicles will be conducted. This will facilitate the verification of the similarity between the Italian and Romanian fleets. The measurement approach delineated in [7] will be utilized, and the potential establishment of NMPB or CNOSSOS-EU weighting coefficients for light vehicles will be considered.

5. ACKNOWLEDGMENTS

The study is funded by Bilateral project CNR – RA (Italy - Romania) “Comparison of CNOSSOS-EU and NMPB methods for road noise modelling in Italy and in Romania” 2023-2025 granted by CNR and RA

6. REFERENCES

[1] S. Kephalopoulos, M. Paviotti, F. Anfosso-Lédée, D. Van Maercke, S. Shiltonand N. Jones: “Advances in the development of common noise assessment methods in Europe: The CNOSSOS-EU framework for strategic environmental noise mapping” . *The Science of the total environment*, 482-483, 400–410. 2014.

[2] G. Licitra and E. Ascari, E. “Noise mapping in the EU: state of art and 2018 challenges” In proc. INTER-NOISE and NOISE-CON (Vol. 258, No. 7, pp. 714-718). Institute of Noise Control Engineering, December 2018.

[3] G. De Leon, F. Fidecaro, M. Cerchiai, M. Reggiani, E. Ascari, G. Licitra, Implementation of CNOSSOS-EU method for road noise in Italy. In: proc. 23rd International Congress on Acoustics. Aachen, September 2019.

[4] L. Fredianelli, S. Carpita, M. Bernardini, L.G. Del Pizzo, F. Brocchi, F., F. Bianco, and G. Licitra, G. “Traffic flow detection using camera images and machine learning methods in ITS for noise map and action plan optimization”. *Sensors,* 22(5), 1929. 2022.

[5] D. Profumo, G. de Leon, A. Monticelli, L. Fredianelli, ´and G. Licitra, “Quantized CNNs-based system for sustainable urban roads and noise management,” Submitted to Engineering Applications of Artificial Intelligence.

[6] E. Ascari, M. Cerchiai, P. Gorrasi, A. Longo, G. Mencagli, F. Miccoli, and M. Zappatore. “OUTFIT:

Crowdsourced Data Feeding Noise Maps in Digital Twins". In Proceedings of the 4th Workshop on Flexible Resource and Application Management on the Edge (pp. 39-46), June 2024.

[7] E. Ascari, M. Cerchiai, L. Fredianelli, and G. Licitra, "Statistical Pass-By for Unattended Road Traffic Noise Measurement in an Urban Environment." *Sensors,* 22(22), 8767. 2022

DOI: 10.61782/fa.2025.0324

FORUM ACUSTICUM EURONOISE 2025

EFFECT OF TRAFFIC FLOW ON URBAN NOISE MODELLING

Valentín Gómez Escobar[1*] **Sergio Paloqueme Váquez**[1] **Guillermo Rey-Gozalo**[1]
[1] Laboratorio de Acústica (Lambda), Departamento de Física Aplicada, Instituto Universitario de Investigación para el Desarrollo Territorial Sostenible (INTERRA), Escuela Politécnica, Universidad de Extremadura, Avda. de la Universidad, s/n, 10003 Cáceres, Spain

ABSTRACT

Noise mapping presents multiple challenges to ensure that the simulated values are as close as possible to the actual noise values.
For the optimization and testing of noise maps, it is necessary to measure control points (which must be characterized by a sound level and by a vehicle flow, in the case of road traffic noise maps).
A question arises: how to take into account the effect of traffic on streets near the control point?
This paper presents the preliminary study carried out in the city of Cáceres (Spain), on the effect on the simulated sound level of the variation of the flow of vehicles in the streets adjacent to the one in which a control point has been established. Different assumptions regarding the traffic on these streets have been considered.
The results show that, in streets without heavy traffic, the effect of traffic variation in adjacent streets can be significant.

Keywords: *Noise, noise mapping, traffic noise, uncertainty.*

1. INTRODUCTION

Noise is one of the main pollution factors that affect modern cities. Therefore, noise assessment is an important task in order to evaluate the quality of life of citizens.

Noise assessment can be carried out both from in situ measurement or by simulation software. In any case, both methodologies are complementary since, for instance, simulation results must necessarily be compared with in situ measurements to corroborate the quality of the developed noise model.

According the European Environmental Noise Directive (END), strategic noise maps are the main tool for noise assessment [1].

Noise simulation implies an adequate selection of the noise sources present in the environment. In this work only road traffic noise is considered, both in simulation and in the in situ measurements carried out. This noise source is one of the most important in modern developed cities and is related to different diseases [2,3]. For the strategic noise maps in which road traffic noise is considered, the European Commission established in 2019 a unique method for noise simulation (CNOSSOS-EU) [4].

When simulation an environment, it is necessary to collect different data such as meteorological conditions, road surface, absorption of buildings, vehicle categorization flows, vehicle speed, etc. Due to the large variability of this data, some assumptions are usually made, some of them included in official documents [5,6].

For the validation of noise models it is necessary de comparison of the noise levels obtained with the computational models with in situ measurements. The uncertainty obtained in this comparison can be influenced by different factors [7-8]

For the aforementioned validation, the characteristics of vehicles traffic at the point of evaluation are taken. However, in some streets, mainly in those with low vehicles

[*] ***Corresponding author***: valentin@unex.es. s
Copyright: *©2025 First author et al. This is an open-access article distributed under the terms of the Creative Commons Attribution 3.0 Unported License, which permits unrestricted use, distribution, and reproduction in any medium, provided the original author and source are credited.*

flow, the influence of noise coming from nearby streets could be important and data vehicles flow data from these streets are usually not available.

The purpose of this work is to make a first approximation to the possible effect of nearby streets on traffic noise assessment in noise modelling.

2. METHODOLOGY

2.1 Studied city

The simulation and measurements were carried in the city of Cáceres. The city of Cáceres is located in the southwest of the Iberian Peninsula. The population of the city is close to 95,000 inhabitants (although this number increase to more than 110,000 during most of the year due to the influx of more than 10,000 students at the University of Extremadura and, also, numerous tourists). Cáceres is a UNESCO World Heritage site.

2.2 Sampling methodology

For the present study, several sampling points were chosen in different streets of the city. To take into account la variability of traffic flow in the city, the sampling points were distribute among the different types of streets in Cáceres,

Thus, before the selection of sampling points, the streets were classified according to the previously proposed categorization method [9-10]. In Figure 1, a color-coded map of Cáceres is shown for the different categories of streets (only sampled streets are indicated).

Sampling points were randomly selected inside each category and prior to the measurement, each sampling point was analyzed in depth and possible adjacent streets that could influence noise were selected.

During sampling, some photographs of the sonometer location were taken.

At each sampling points, two measurements of 15 minutes of duration were carried out. All measurements were performed in diurnal period (from 7:00 to 19:00). The measurements were carried out on different working days, following the ISO 1996-2 standard [11].

All the measurement were carried out in years 2020 and 2021.

2.3 Noise modelling

The Predictor v.2024 software was used for noise mapping. The following configuration options was used for noise modelling:

- Computational model: CNOSSOS-EU
- Reflection number: 1
- Meteorological conditions: Default values of Toolkit 17 of the WG-AEN [5] were considered.
- Building height: Ground floor—4.5 m; each additional floor—3 m.
- Absorption of buildings and barriers: Reflective
- Vehicles speed: Maximum speed allowed for each street.

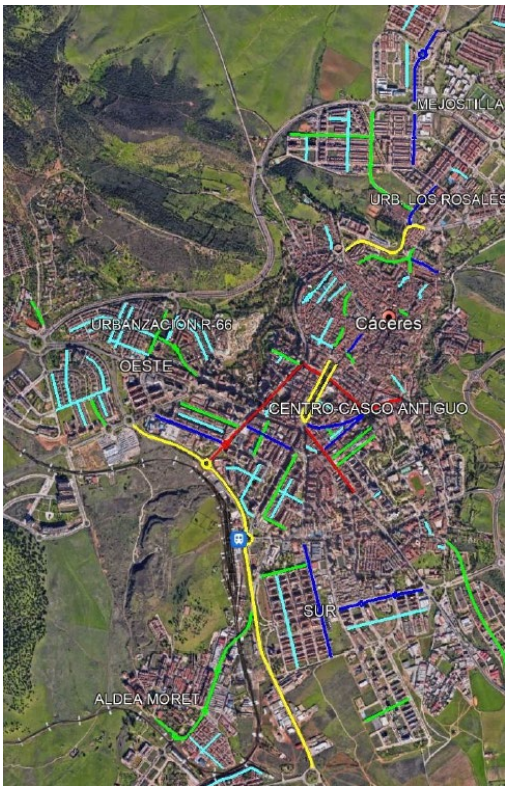


Figure 1. Sampled streets of Cáceres.

The receiver points were located in the noise model at the same position where in situ measurement were taken. In the case of photographs were the exact position of the sampling point could not be precisely determined, the sampling points was discarded.

A total of 100 sound measurements were estimated.

2.4 Street traffic flow

The traffic flow of the street on which the sampling point was placed was determined from the data obtained during sampling.
For the traffic flow of the adjacent streets, two cases were considered:

+ Case 1: No traffic flow
+ Case 2: Average traffic flow of the type of street.

For the present work, three types of street were considered [5]:

- Small main roads. In navy blue and red colors in Figure 1.
- Collecting roads (collecting traffic from service roads and leading it to & from main roads). In green color in Figure 1.
- Service roads: (mainly used by residents living there). In light blue color in Figure 1.

3. RESULTS AND DISCUSSION

As mentioned above, a total of 100 measurements/simulations were considered for the present study. These points were classified according to their location as shown in Table 1:

Table 1. Classification of sampling points considered.

Type	Description	Number
A	Small main roads	34
B	Collecting roads	33
C	Service roads	33

Noise values of the simulations for each sampling point for the two conditions considered (no traffic on adjacent streets and average traffic of the street type on adjacent streets) were compared with the measured level. The differences between the measured and the simulated levels are shown in Figure 2, for no traffic on adjacent streets, and in Figure 3, for average traffic flow.

As can be seen, in both cases, the simulated values are quite similar to the measured values, with very few points where the differences are greater than 3 dBA.

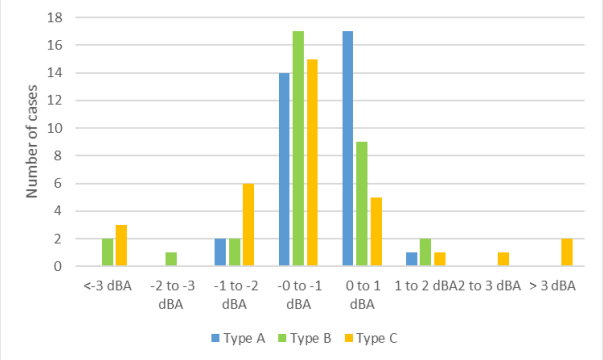


Figure 2. Differences intervals between measured and simulation noise values. Case 1.

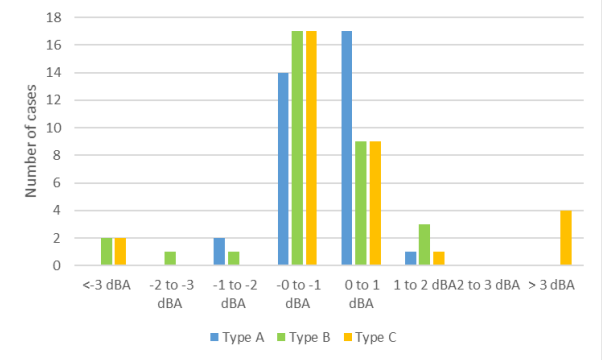


Figure 3. Differences intervals between measured and simulation noise values. Case 2.

In Table 2, comparison between the differences obtained for the two considered cases are shown

Table 2. Comparison between differences of the two considered cases.

	Type A	Type B	Type C
<-1 dBA	0	0	3
-0.5 to -1 dBA	0	0	5
-0 to -0.5 dBA	5	15	22
equal to 0	29	18	3

As can be seen, in the Type A sampling points, the differences between considering the traffic flow in the adjacent streets (case 1) and considering the average traffic flow (case 2) are very small and only in 5 points (15%) small variations (less than 0.5 dBA) are observed in the simulated values. In Type B sampling points, small variations (less than 0.5 dBA) are also observed, but in a larger number of points (45%). Finally, in the Type C streets, service roads, there are greater differences between the two cases considered. Thus, in eight of the considered points (24%) the differences are greater than 0.5 dBA (greater than 3 dBA in 3 points –9%-) and in 22 points the variations are small (less than 0.5 dBA) (67%).

4. CONCLUSIONS

The comparison between the measured and the simulated noise values at 100 measurement points in the city of Cáceres shows that the consideration of traffic on the adjacent streets to the street where measurements are taken can be important, mainly on service roads (those streets used mainly by the residents who live there).

Thus, in these streets, where the noise due to road traffic is not very important since the traffic flows are small, the influence of nearby streets with more traffic should be taken into consideration as, in some cases (about 35% in this study) the differences in the simulated values without consideration of traffic may lead to differences of more than 0.5 dB.

5. ACKNOWLEDGMENTS

This work was supported by the European Regional Development Fund (ERDF) and by Junta de Extremadura, Consejería de Educación, Ciencia y Formación Profesional (Grant GR24069).

6. REFERENCES

[1] END: *Directive 2002/49/EC of the European Parliament and of the Council of 25 June 2002 relating to the assessment and management of environmental noise (END)*. Brussels: The European Parliament and the Council of the European Union; 2002.

[2] A. Ndrepepa and D. Twardella: "Relationship between noise annoyance from road traffic noise and cardiovascular diseases: A meta-analysis", *Noise and Health*, 13, 5), 251-259, 2011.

[3] E. van Kempen and W. Babisch: "The quantitative relationship between road traffic noise and hypertension: A meta-analysis", *Journal of Hypertension*, 30, 6, 1075-1086, 2012.

[4] *Commission Directive (EU) 2015/996 of 19 May 2015 establishing common noise assessment methods according to Directive 2002/49/EC of the European Parliament and of the Council*. Brussels: The European Parliament and the Council of the European Union; 2015.

[5] WG-AEN: "Good Practice Guide for Strategic Noise Mapping and the Production of Associated Data on Noise Exposure". European Commission Working Group- Assessment of Exposure to Noise (WG-AEN); version 2, 13th August 2007.

[6] Spanish Government: "*Guía básica de recomendaciones para la aplicación de los métodos comunes de evaluación del ruido en Europa (CNOSSOS-EU)*", 2022

[7] G Rey Gozalo, V. Gómez Escobar, J.M. Barrigón Morillas, D. Montes González, and P. Atanasio Moraga:" Statistical attribution of errors in urban noise modeling," *Applied Acoustics*, 153, 20-29, 2019.

[8] G Rey Gozalo, and V. Gómez Escobar: "Uncertainty evaluation of road traffic noise models in two Ibero-American cities," *Applied Acoustics*, 180, 108134, 2021

[9] J.M. Barrigón Morillas, V. Gómez Escobar, J.A. Méndez Sierra, R. Vílchez-Gómez, J.M. Vaquero, and J. Trujillo Carmona: "A categorization method applied to the study of urban road traffic noise," *J. Acoust. Soc. Am.*, 117, 2844–2852, 2005.

[10] J.M. Barrigón Morillas, G. Rey Gozalo, D. Montes González, R. Vílchez-Gómez, and V. Gómez Escobar: "Variability of traffic noise pollution levels as a function of city size variables," *Environmental Research* 199 111303, 2021

[11] ISO 1996-2: 2017: *Acoustis- Description, measurement and assessment of environmental noise. Part 2: Determination of sound pressure levels*". International Organization for Standardization, Switzerland, 2017.

DOI:

Main theme: A05 Environmental Acoustics

Session A05.10/A14.09 Advanced air mobility noise

Chair(s): A. Torija Martinez, M. J. B. Lotinga

DOI: 10.61782/fa.2025.0610

FORUM ACUSTICUM EURONOISE 2025

Noise Impact Range Assessment Using UAM Noise Hemisphere

Seung-Min Lee[1] **Chan-Hoon Haan**[1*]
[1] Department of Architectural Engineering, Chungbuk National University, South Korea

ABSTRACT

The present study aims to investigate the noise impact range in urban areas around vertiport using a noise hemisphere model to simulate UAM noise propagation. In order to this three noise hemisphere methods were compared including Integrated, Interpolated, and Background noise compensation. SoundPLAN software was used for noise modeling in a specific area of a vertiport in Seoul. Both horizontal and vertical noise maps were drawn to evaluate the UAM noise effect on the buildings around vertiport. As a result, it was found that the noise impact range varied depending on the noise hemisphere model. In addition, the horizontal propagation range of noise was confirmed to be at least 200 m to 700 m. The vertical propagation range varied significantly depending on the building height, with higher noise levels observed around taller buildings. Based on the results, it is possible to predict the 3D noise impact range by combining horizontal and vertical noise maps when operating UAM in actual urban areas.

Keywords: *UAM(urban air mobility), noise impact range, noise assessment evaluation, noise hemisphere, noise map*

1. INTRODUCTION

UAM noise reduction research is being conducted in various fields, including motors and aircraft. Research on noise propagation, which is the focus of this study, is also being conducted in various directions. Several studies have analyzed UAM using the Federal Aviation Administration's (FAA) Aviation Environmental Design Tool (AEDT), which is efficiently used for aircraft noise analysis. One study conducted noise analysis for areas of value for UAM operation by setting fixed-point flight conditions.[1] In addition, a NASA time-marking simulation tool was used to generate noise exposure data for efficient operations to help differentiate differences associated with the integrated noise model implemented in AEDT. Possible changes to assess UAM community noise impact offered more consistently with simulation-based modeling.[2]

However, due to the lack of data, FAA's AEDT and other software do not yet support the operation and analysis of UAM aircraft performance models. Therefore, research on developing an appropriate tool for UAM analysis is also being conducted. For the real-time noise prediction of RPM-controlled multi-rotor configurations, a comprehensive multi-rotor noise assessment (CONA) framework based on a six-degrees-of-freedom flight simulation was developed.[3] Based on this, a study on noise evaluation during multi-rotor landing has been conducted. In addition, a psychoacoustical-based prediction was performed on the noise of the multi-rotor in gusty wind conditions.[4] In addition to references, there is a published study in terms of aircraft development that predicts that the noise characteristics generated by UAM-specific aircraft will be less noisy due to the low propeller load under experimental flight conditions.[5] As such, since UAM's noise analysis method is not standardized, research is continuing to determine the level of noise generated by UAM and the propagation of noise through each noise analysis method.

2. RESEARCH METHODS

Noise data were collected through the flight test of the Optionally Piloted Personal Air Vehicle (OPPAV), an eVTOL UAM aircraft being developed by the Korea Aerospace Research Institute (KARI). The flight test was conducted at the Goheung National Aviation Test Center (NATC) in Goheung, South Korea. Acoustic signals were measured hourly using 80 microphones on the ground runway. The test was conducted at an altitude of 60 m to construct a noise hemisphere. The noise data measured by the OPPAV aircraft using 80 microphones are shown in Fig.

*Corresponding author: Chhaan@chunbuk.ac.kr
Copyright: ©2025 First author et al. This is an open-access article distributed under the terms of the Creative Commons Attribution 3.0 Unported License, which permits unrestricted use, distribution, and reproduction in any medium, provided the original author and source are credited.

1. Averaging the noise measurements from the 80 microphones yielded an equivalent noise level of 64.0 dB and a maximum noise level of 70.9 dB. The measured noise data were used to generate a noise hemisphere using the SPHPERE-N noise hemisphere generation program.[6] The noise hemisphere with a null value was designated as the 'Integrated noise hemisphere,' and two additional noise hemispheres with corrected null values were added to compare a total of three types of noise hemispheres. Consequently, a 'Compensated noise hemisphere' was created by correcting the null values using background noise data, and an 'Interpolated noise hemisphere' was generated by applying the interpolation method to the null values. [7]

The simulation target areas are two areas in Phase 2-1, corresponding to the K-UAM Grand Challenge. [8] Based on the information presented in the Aeronautical Information Management (AIM), the location of the vertiport in the region and the UAM flight path were set. [9] The simulation was performed using two methods: a single noise source method and a multi-noise source method. The single noise source method aims to investigate the noise level affected by a single noise hemisphere in the region, and the multi-noise source method aims to determine the noise level propagating in the region according to the actual flight path. Both methods were calculated according to ISO 9613-2, and the radius of the noise source was set to 5 m. The color scale of the noise map was set to 5 dB.[10] Fig. 2 shows the location of flight lines and noise sources in the area.

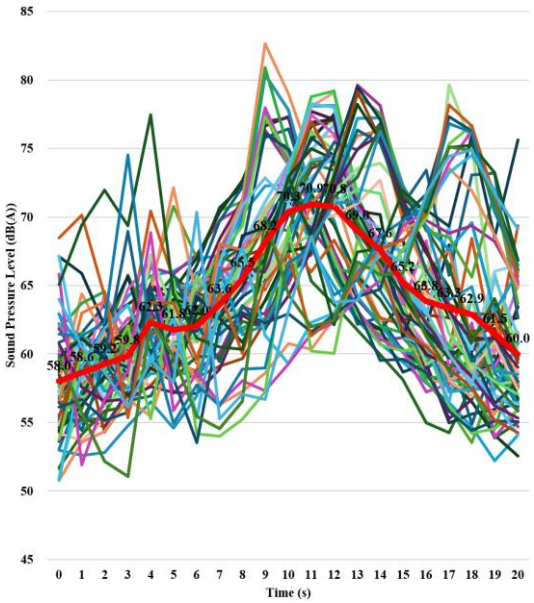


Figure 1. OPPAV noise measurement resluts.

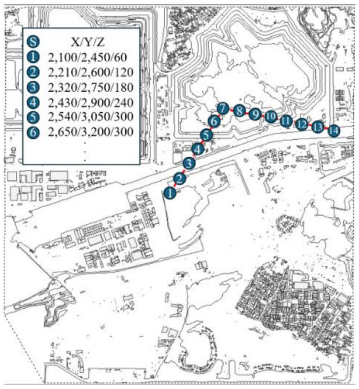
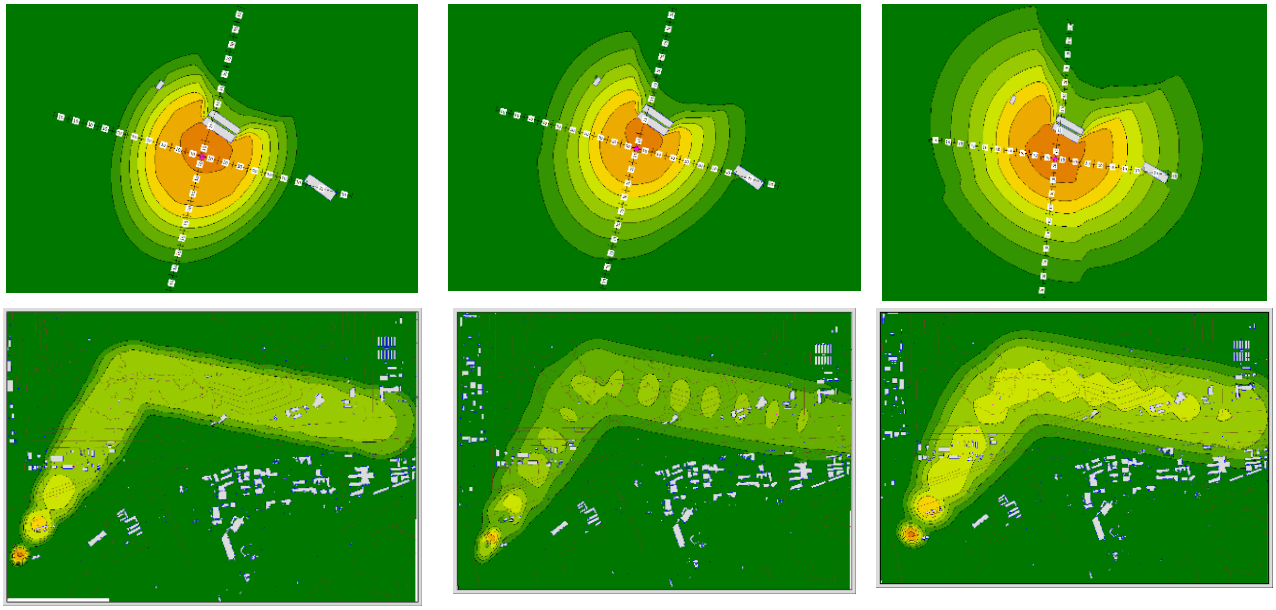


Figure 2. K-UAM Grand Challenge phase 2-1 vertiport and flight path.

3. RESULTS

The planar noise impact range of the Integrated Noise Hemisphere was investigated. The ranges to the left and right were 60 m, respectively, for a total influence of 120 m. In addition, the ranges to the front and rear were 50 m and 75 m, respectively, with the range of influence to the rear confirmed to be longer than that to the side. Investigating the planar noise impact range of the Compensated Noise Hemisphere revealed noise propagation up to 70 m from the left and right, respectively, for a total noise impact range of 140 m. In addition, the ranges to the front and rear were 80 m, respectively, for a total noise impact range of 160 m. Investigating the planar noise impact range of the Interpolated Noise Hemisphere revealed a total noise impact range of 200 m, at 100 m from the left and right. In addition, the total range of influence was 180 m, approximately 90 m from the front and rear. The results of the noise impact assessment using a single and multi-noise source can be seen in Figure 3.

In the Integrated Noise Hemisphere, S1 showed a shape, noise level, and range similar to that of a single noise source. The predicted noise level of S2 is 65 dB to 70 dB, a reduction of 10 dB within the same range, and the total impact range increases by 1.5 times to 200 m. The noise level predicted for S3 is 60 dB to 65 dB, a reduction of 5 dB, and the impact range is 300 m. From S4 onward, all noise sources were expected to be the same, with noise levels of 55 dB to 60 dB, and the impact range being 400 m.



(a) Integrated (b) Compensated (c) Interpolated

Figure 3. Noise impact assessment results

In the Compensated Noise Hemisphere, S1 was found to have a shape in which the noise level is concentrated in the front, unlike a single noise source. The noise impact range is approximately 160 m, and the noise level is predicted to be 70 dB to 75 dB. S2 is predicted to have a noise impact range of 200 m, and the noise level is predicted to be 60 dB to 65 dB, a reduction of 5 dB. S3 is predicted to have a noise impact range of 400 m, and the noise level is predicted to be 55 dB to 60 dB. Subsequently, it was confirmed that the noise sources were similar in noise level and influence range, and that the noise level partially exceeded 50 dB to 55 dB at certain points along the flight path.

In the Interpolated Noise Hemisphere, S1 showed noise levels and influence ranges similar to those of a single noise source. The noise level of S2 is 65 dB to 70 dB, and the noise impact range is predicted to be approximately 400 m. The noise level of S3 is 60 dB to 65 dB, and the noise impact range is predicted to be approximately 500 m. From S4 onward, the noise level was mainly predicted to be 55 dB to 60 dB, but it was also predicted to be 65 dB at some positions along the flight path. The noise impact range was predicted to be approximately 600 m.

4. CONCLUSIONS

Examining the three noise hemisphere influence ranges of UAM, noise propagation from a single noise source was expected to occur within a horizontal radius of approximately 60 m to 100 m, and within a vertical radius of approximately 10 m to 50 m. With multiple noise sources, the propagation range varied depending on the flight altitude. At the maximum altitude of 300 m, noise propagation was expected to occur within a horizontal radius of approximately 400 m to 600 m. Through this, the noise impact range can be predicted for an actual UAM flight path.

The noise measured by OPPAV was higher in the high-frequency band than in the low-frequency band. This is an electric signal generated by an electric motor and can have a strong effect at short distances. Therefore, due to the nature of UAM operations in urban areas, the subjective noise level perceived by occupants of nearby buildings may be higher than the expected noise level. Therefore, appropriate noise evaluation factors should be discussed for UAM noise evaluation.

5. REFERENCES

[1] Rizzi, S., and Rafaelof, M., “Community noise assessment of urban air mobility vehicle operations using the FAA Aviation Environmental Design Tool,”

in *INTER-NOISE and NOISE-CON Congress and Conference Proceedings*, (Washington DC, USA), pp. 450–461, 2021.

[2] Letica, S., and Rizzi, S., "On the modeling of urban air mobility vehicle takeoff and landing operations in the FAA Aviation Environmental Design Tool," in *INTER-NOISE and NOISE-CON Congress and Conference Proceedings*, (Washington DC, USA), pp. 270–282, 2024.

[3] Ko, J., Jeong, J., Cho, H., and Lee, S., "Real-time prediction framework for frequency-modulated multirotor noise," *Physics of Fluids*, vol. 34, no. 2, pp.027103 1-15, 2022.

[4] Thai, A., and Engineer, A. S., "Flyover Noise Computations of the Joby Aviation Aircraft," in *Vertical Flight Society 79th Annual Forum & Technology Display*, (Florida, USA), pp. 1–12, 2023.

[5] Wie, S.Y., Cho, T. H., Lee S. H., Jo Y. M., Lee, S. M., and C. H. Haan, "UAM Urban Noise Impact Analysis using Noise Measurement Data," in *The Korean Society for Aeronautical and Space Sciences (KSAS) 2024 Autumn Conference*, (Gangwon, South Korea), pp. 947–948, 2024.

[6] Jo, Y. M., Hwang, Y. H., and Lee, H. J., "A Study on UAM Noise Modeling and Environmental Noise Prediction based on Time- domain Noise Data." *The Acoustical Society of Korea (ASK) 2024 Autumn Conference*, (Busan, South Korea), 386. 2024.

[7] Lee, S. M., Wie, S. Y., and C. H. Haan, "Comparison of Measured Noise with the predicted value from UAM Noise Hemisphere Modeling," *The Acoustical Society of Korea (ASK) 2024 Autumn Conference*, (Busan, South Korea), 387-389. 2024.

[8] Korea Agency for Infrastructure Technology Advancement (KAIA), K-UAM technology ROADMAP, 2023.

[9] Ministry of Land, Infrastructure and Transport, Air Map for Urban Air Mobility (UAM), 2023.

[10] International Organization for Standardization (ISO), ISO 9613-2:2024. Acoustics − Attenuation of sound during propagation outdoors. Part 2: Engineering method for the prediction of sound pressure levels outdoors.

DOI: 10.61782/fa.2025.0656



FORUM ACUSTICUM
EURONOISE 2025

ON-FIELD MEASUREMENTS FOLLOWING THE EASA GUIDELINES ON NOISE MEASUREMENTS OF UNMANNED AIRCRAFT SYSTEMS LIGHTER THAT 600 KG

P. Miguel-Ayala[1*] **L. Estévez-Mauriz**[2] **C. Romero-Romero**[3]
A. J. Torija[3]

[1] Escuela de Ingenierías Industrial, Informática y Aeroespacial, Universidad de León, León, Spain
[2] Grupo de Investigación Ambiente Atmosférico (ATMOSENV), Área de Física Aplicada, Universidad de León, León, Spain
[3] Acoustics Research Centre, University of Salford, Salford, Greater Manchester, UK

ABSTRACT

Unmanned Aircraft Systems (UAS) have gained increasing attention, leading to the development of noise measurement protocols, such as the 2023 guidelines from the European Union Aviation Safety Agency (EASA). These guidelines focus on noise measurement procedures for UAS (lighter that 600 kg), outlining measurements and operational requirements. A key requirement is that the difference between the UAS sound pressure level and the background sound level must be at least 15 dBA. This study presents acoustic analysis results from three UAS (weighing under 600 kg) at three different heights, following EASA's guidelines. The study site was chosen with a background noise level of around 48 dBA. Results showed that only the largest UAS (7,3 kg) met the 15 dBA difference at all heights, while the smallest UAS (0,25 kg) did not meet this threshold at any height. Given that low background noise (below 45 dBA) is crucial to fulfilling the guidelines, the study concludes that it is challenging to apply these standards to small UAS. The study discusses whether the EASA guidelines require amendment for small size UAS.

*__Corresponding author__: pmigua01@estudiantes.unileon.es.
__Copyright__: ©2025 ; This is an open-access article distributed under the terms of the Creative Commons Attribution 3.0 Unported License, which permits unrestricted use, distribution, and reproduction in any medium, provided the original author and source are credited.

Keywords: *UAS, noise, guidelines*

1. INTRODUCTION

The use of Unmanned Aircraft Systems (UAS), has grown exponentially in recent years, expanding to a wide range uses such as mapping, surveillance, package delivery, and infrastructure inspection. However, this rapid expansion raises concerns regarding environmental impact and noise pollution, particularly in urban settings. It is worth noting that awareness of urban environmental quality is increasingly pronounced. A clear example of this is the European Green Deal [1] and the Sustainable Development Goals [2], which currently lead the vision for sustainability in the built environment. According to the European Green Deal [1], one of the main concerns is the negative impact of noise, primarily expressed through the annoyance caused by road traffic noise. Europe, along with other parts of the world, is facing a chronic issue in this regard, with estimates indicating that traffic-related noise (including road, rail, and air traffic) in Western Europe leads to the loss of at least one million healthy life years annually, with road traffic being the dominant source [1].

In order to regulate these aspects, the European Union Aviation Safety Agency (EASA) has established guidelines for drone noise measurement [3], including specific background sound level requirements for its

acoustic testing [3, p. 12]. However, these regulations impose constraints that can be difficult to meet for small UAS. Specifically, the requirement for low background noise levels (differences above 15 dBA) to obtain valid measurements, may hinder the feasibility of testing in real-world environments, where acoustic conditions are rarely ideal.

This paper, based on an experimental study of UAS sound levels, examines the methodology and the plausible limitations of current EASA criteria, raising awareness about the need to revise certain parameters to better align the regulations with the operational reality of certain UAS. By evaluating different models and measurement conditions, this study aims to provide a technical basis for optimizing regulatory procedures and ensuring a more realistic assessment of the acoustic impact of these aircraft.

2. EXPERIMENTAL STUDY'S DESCRIPTION

The main objective of the study is to carry out measurements on different UAS models according to EASA criteria and compare the sound pressure levels of the three UAS. This aimed to analyze noise differences based on UAS weight, proposing certain adjustments.

The experimental study consisted in the measurement of three different UAS, at three different heights. A location and date had to be selected that met specific requirements regarding pavement characteristics, wind speed, temperature, and humidity for the measurements to be carried out, according to regulations. Additionally, the recommendations specify the type of instrumentation to be used for the measurements, how they should be calibrated, and the setup. Finally, the guideline considers two study cases: level flight and overflight. Each of these must meet specific conditions regarding distances and areas of operation.

Specific information about how the experimental study was conducted are specified in sections 2.1, 2.2, 3 and 4

2.1 Flight

The first thing to select was the type of flight that was going to be measured. Due to its relevance and proximity with real situations, the chosen flight was a hover one.

For a hover flight the guidelines has some particular requirements [3, pp. 11-16]. In order to meet them, the three UAS were flown at three heights that were 12, 17 and 25 meters over the measurement point. Selecting these altitudes responds to the fact that 12 m is the minimum height allowed for measurements; 25 m is the reference height required by the regulations; and 17 m, was chosen as a relevant height to study scenarios where UAS fly at relatively low altitudes near people to assess their impact. The rest of the requirements such as the instrumentation and mounting, the operability limits and the measurements' number and duration were also followed precisely.

2.2 Place and date

To meet these requirements, the chosen location was a tennis court in the village of Ruiforco de Torío, in the province of León, Spain. This place was chosen for several reasons, including the fact that it was out of the airspace of Leon's airport. The surface of the tennis court was one of the one suggested in the guidelines [3, p. 10]. Finally, this space is located far from roads and urban areas, which minimizes background noise, however, sounds coming from nature were present (rustling leaves, stream). The days in which this study was conducted were the 29 May 2024 and 11 June 2024, both between 11:00 and 13:30. This dates fulfilled the guidelines recommendations of wind speed, temperature and humidity [3, pp. 8-9].

2.3 UAS

For this experimental study, the UAS used were provided by the Cartography Service from Universidad de León. The characteristics of each UAS is presented here, ordered from the smallest to the biggest:

- **DJI Mavic 4:**
  - Mass: 249 g.
  - Maximum autonomy: 34 minutes.
  - Diagonal size with propellers: ± 213 mm.
  - Maximum horizontal speed: 16 m/s
- **DJI Phantom 4 Pro Plus:**
  - Mass: 1375 g.
  - Maximum autonomy: 30 minutes.
  - Diagonal size with propellers: ± 490 mm.
  - Maximum horizontal speed: 20 m/s

- **DJI Matrice 300 RTK (sensor LIDAR Zenmuse L1):**
  - Mass: 7270 g.
  - Maximum autonomy: 55 minutes.
  - Diagonal size with propellers: ± 1150 mm.
  - Maximum horizontal speed: 23 m/s

3. INSTRUMENTATION AND SOFTWARE

The EASA guidelines also specifies the instrumentation needed to carry out the measurements properly [3, pp. 27-28]. The instruments used in the study were:

- *"Microphone CCLD Free-field 1/2 inch" type 4966-H-041"* by *"Brüel & Kjær"*. It was not necessary to calibrate it as it was brand new. The microphone fulfilled the guidelines. According to the EASA's guidelines, the microphone must be placed face down, over a plaque 7 mm above the ground, and it must be protected by a mesh [3, p. 28].
- Acoustic measurement system *"SQuadriga III"* by *"HEAD Acoustics"*. The only requirement from the EASA guidelines is to have a system that can store data.

For data extraction and analysis, the software *"ArtemiS SUITE"* version 15.7 by *"HEAD Acoustics"* was used. This software fulfills the regulatory requirements for data acquisition and analysis (such as slow analysis, the ability to extract "L_{Aeq}" and "L_{Amax}", A-weighted, etc.).

4. RECORDINGS

4.1 UAS noise recordings

As it is stated in subsection 2.1, the UAS had to fly within certain operability limits and during a certain time. Following the EASA's guidelines [3, p. 12], the UAS must remain within a 8° cone from the vertical above the noise measurement point during 30 seconds of noise recording. A minimum of six runs must be performed and the L_{Aeq} must result from the A-weighted sound level averaged over the 30 seconds.

In order to fulfill these recommendations the first step was to mark the ground with adhesive tape to indicate the action cone radius that the UAS should not exceed at each height. For the three chosen heights 12 m, 17 m, and 25 m, the corresponding action radius are 1.7 m, 2.4 m, and 3.5 m, respectively. The UAS were equipped with a camera system to trace the correct radio action. The dimensions of the action cone are shown in Fig. 1.

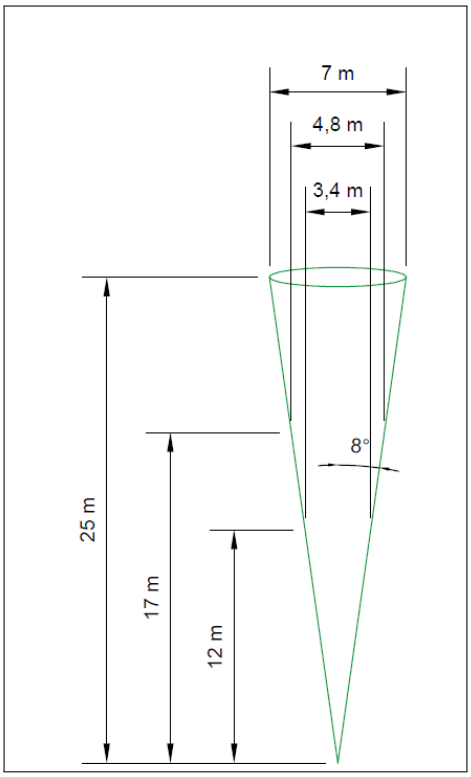


Figure 1. Operability limits for UAS' noise measurement. Adapted from [3, p. 15]

4.2 Background sound levels

To analyze the background noise, measurements were taken in complete silence, without any UAS operating, both before and after recording data for each UAS. The goal is to verify that the background noise remained stable throughout the measurements and, using these values, assess whether the 15 dBA difference between the equivalent background noise level (A-weighted) and the maximum noise level (A-weighetd) produced by the UAS.

The average sound level (L_{Aeq}), the 90th percentile ($L90$) and the maximum sound level (L_{Amax}) are chosen as representative of the background noise level. To compare the UAS' noise values with the background's sound pressure level, the L_{Aeq} of the background noise

must be taken by averaging the values before and after the measurement.

5. RESULTS

The measurements were processed using the *"ArtemiS SUITE"* software, version 15.7 by *"Head Acoustics"*, performing an analysis following the recommendations. According to the EASA's guidelines, for a hovering flight, the following data must be reported [3, p. 40]:

- The date on which the measurement was performed.
- The altitude at which the measurement was conducted.
- The equivalent sound pressure level, "L_{Aeq}".
- The maximum sound pressure level, "L_{Amax}".
- The background noise level, "L_{Aeq}".
- The 90th percentile, "L_{90}". That is, the sound pressure level above which the specified percentage of data is found, in this case, 90

The Tab. 1 contains the sound pressure level of the background noise for each UA test. The average values of L_{Aeq}, L_{Amax}, and L_{90} are shown for each test. The maximum sound pressure level recorded was 50.4 dBA whereas the three L_{Aeq} are around 48 dBA.

Table 1. Comparison of the background noise L_{Aeq}, L_{Amax}, and L_{90} for the three UAS.

	L_{Aeq}	L_{Amax}	L_{90}
DJI Mavic 4	48.2	49.6	47.7
DJI Phantom 4 Pro Plus	47.7	49.2	47.3
DJI Matrice 300 RTK	48.0	50.4	47.4

5.1 UAS' sound level

In the same way as for background noise, sound pressure level data was collected for each UAS at the three heights (12, 17, and 25 m). The following figures Fig. 2, Fig. 3 and Fig. 4 show the results for the three UA at 17 meters, as this height best illustrates which UAS seemed more likely to meet the 15 dBA difference requirement with the background noise. Nevertheless, all collected values are included in the Tab. 2.

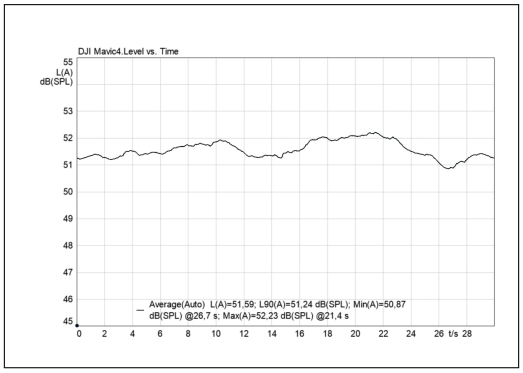


Figure 2. DJI Mavic 4 measurement at 17 m. Level Vs. time.

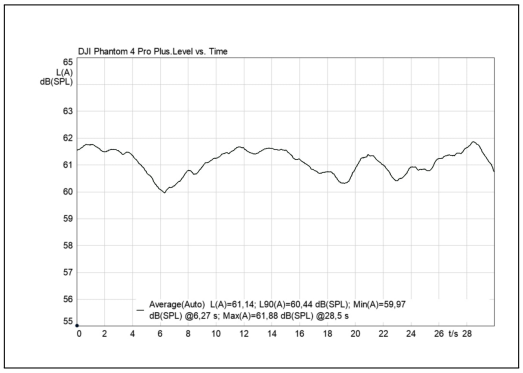


Figure 3. DJI Phantom 4 Pro Plus measurement at 17 m. Level Vs. time.

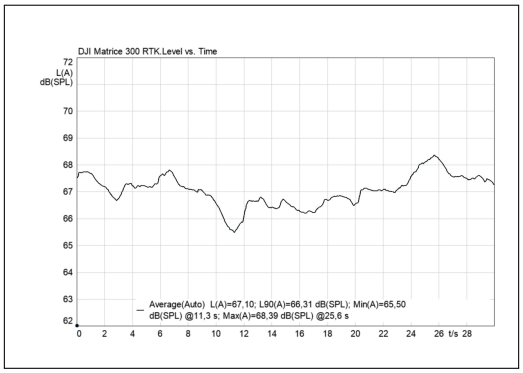


Figure 4. DJI Matrice 300 RTK measurement at 17 m. Level Vs. time.

In order to see the frequency content of the three UAS, the octave band spectrum (A-weighted) measured for the

hover procedure at 12 m (top), 17 m (middle) and 25 m (bottom) height is shown in Fig. 5.

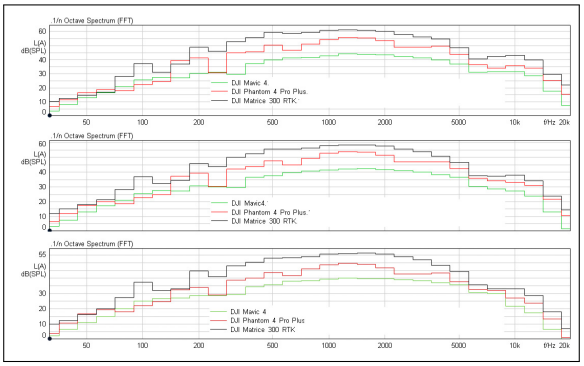


Figure 5. Octave band spectrum (A-weighted) for the three UAS at 12 m (top), 17 m (middle) and 25 m (bottom).

Since the regulations require the L_{Amax}, Tab. 2 shows the L_{Aeq}, L_{Amax} and L_{90} values for each UAS at each of the three different heights, having values between 50.6 and 71.0 dB (L_{Amax}).

Table 2. L_{Aeq}, L_{Amax} y L_{90} values for the three UAS

		12 m	17 m	25 m
DJI Mavic 4	L_{Aeq}	52.5	51.6	49.5
	L_{Amax}	53.7	52.2	50.6
	L_{90}	52.4	51.2	49.0
DJI Phantom 4 Pro Plus	L_{Aeq}	62.9	61.1	56.8
	L_{Amax}	63.8	61.9	57.8
	L_{90}	62.3	60.4	56.3
DJI Matrice 300 RTK	L_{Aeq}	69.9	67.1	64.8
	L_{Amax}	71.0	68.4	65.8
	L_{90}	69.1	66.3	64.1

Comparing Tab. 1 and Tab. 2, it can be observed that the 15 dBA difference with the background noise was not fulfilled in all cases (see Fig. 6). DJI Matrice 300 RTK, the largest of the three UAS, weighing 7270 g, is the only one that meets the 15 dBA difference requirement at all three heights (the differences for each height are: 23 dBA, 20.4 dBA, and 17.8 dBA, respectively). Therefore, this study complies with the recommendations. On the other hand, DJI Phantom 4 Pro Plus, the medium-sized UAS, weighting 1375 g, meets the 15 dBA difference at 12 m, though only marginally (16.1 dBA). At 17 m, it does not meet the requirement, despite being very close (14.2 dBA). However, at 25 m, it falls significantly short of the required difference (10.1 dBA). Finally, for the smallest UAS, the DJI Mavic 4, weighting only 249 g, the 15 dBA difference with the background noise is not met at any of the three heights (5.5 dBA, 4 dBA, and 2.4 dBA, respectively).

In Fig. 6, the difference between maximum noise level from the three UAS and the equivalent background noise for the three heights is shown.

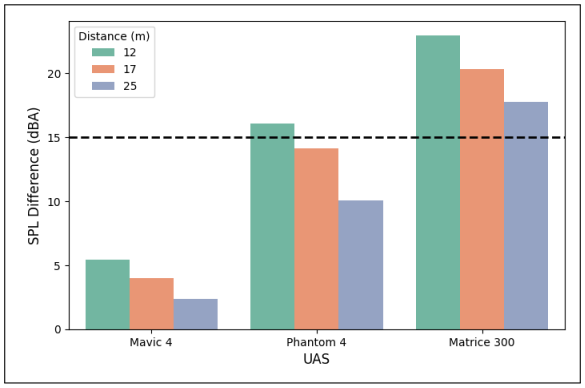


Figure 6. Difference between maximum noise level (L_{Amax}) from UAS and equivalent background noise level (L_{Aeq}). The level difference must be greater than 15 dBA to consider the run as a valid one.

6. DISCUSSION

As it is said in section 5.1 for UAS weighing less than 1.4 kg, it is very difficult to exceed the required 15 dBA difference from the background noise, even when measurements are conducted in a location outside urban areas.

For these reasons, based on this study, it is suggested EASA's recommendations to be revised. The proposed changes include adjusting the difference between maximum level from the UAS and background noise level, for UAS weighting and distance operation. It is suggested EASA's guidelines to study these limitations so it allows UAS below the black line on the Fig. 6 that have not exceed the 15 dBA difference with background noise reduce the threshold. To establish more precise limitations, additional tests should be conducted with UAS of different sizes and across a wider range of altitudes and situations. However, with the collected data,

a multiple linear regression can be established with the independent variables mass (X1) and height (X2), and the dependent variables considered as the difference between background noise level and UA maximum noise level (dBA):

$$y = 13,43747 + 0,001958X1 - 0,364728X2 \quad (1)$$

According to this, when mass increases, the difference in noise level is higher; and when height increases the difference in noise level is lower.

In order to fulfill the 15 dBA difference required, according to the regression with the collected data, a certain mass and height must me accomplished, shown in the Tab. 3:

Table 3. Mass and height requirements to fulfill the 15 dBA difference

Mass (g)	Height (m)
≤3100	12
3650	15
4000	17
5500	25

From this regression, mass below 3100 g requires less noise level difference at different heights. In Tab. 4 an example of plausible values with flights at 12 m height are presented. The same can be done for other height values, however, the intention in the present work is to highlight the variances and plausible adaptations.

Table 4. Minimum difference level for certain UA mass flying at 12 m height

Mass (g)	Difference level (dBA)
250	9
250 - 750	10
750 - 1250	11
1250 - 1750	12
1750 - 2300	13
2300 - 2800	14
2800 - 3100	14,5

Fig. 7 shows the limitations for the UAS Mavic 4 and Phantom 4 Pro Plus according to the values from Tab. 4. UAS Matrice 300 RTK is not included as it weights more than 3100 g.

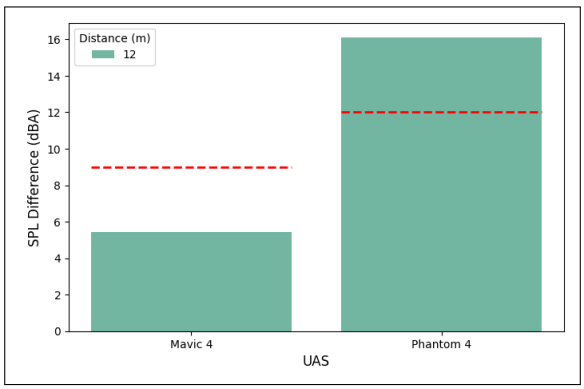


Figure 7. Difference between maximum noise level (L_{Amax}) from UAS and equivalent background noise level (L_{Aeq}) for UAS Mavic 4 and Phantom 4 Pro Plus at 12 m. The red line shows the limitations for each UAS according to Tab. 4

As it is highlighted, to establish more precise limitations, additional tests are needed, however, this work establishes a first relation between UA mass, test height, and required difference level between the background noise level (L_{Aeq}) and the UA maximum noise level (L_{Amax}).

7. ACKNOWLEDGEMENTS

We gratefully acknowledge the support of the Cartography Service from Universidad de León.
LEM and PMA would also like to thank the support from Universidad de León and the European Education and Culture Executive Agency, Project 101124439 — EURECA-PRO 2.0 — ERASMUS-EDU-2023-EUR-UNIV.
CRR and AJT would also like to acknowledge funding provided by EU Horizon Europe and UK Research and Innovation (UKRI) under the UK government's Horizon Europe funding guarantee (REFMAP project, grant number 10061935; and ImAFUSA project, grant number 101114776).

8. REFERENCES

[1] European Comission, *Communication from The Comission to the European Parliament, the Council, the European Economic and Social Committee and*

the Committee of the Regions. Pathway to a Healthy Planet for All EU Action Plan: 'Towards Zero Pollution for Air, Water and Soil' COM/2021/400 final, 2021.

[2] United Nations, *The Sustainable Developlment Goals Report 2024*, 2024.

[3] European Union Aviation Safety Agency, *Guidelines on Noise Measurement of Unmanned Aircraft Systems Lighter than 600 kg Operating in the Specific Category (Low and Medium Risk)*, 2023.

DOI: 10.61782/fa.2025.0762

FORUM ACUSTICUM EURONOISE 2025

ROTOR NOISE INTERFERENCE MECHANISMS FOR SIDE-BY-SIDE CO-ROTATING CONFIGURATIONS

T. Pagliaroli[1*] **P. Candeloro**[1] **F. Del Duchetto**[1]
J. Yin[2] **K.-S. Rossignol**[2]
[1] University Niccolò Cusano, Italy
[2] DLR German Aerospace Center, Germany

ABSTRACT

This study investigates the aeroacoustic effects of phase synchronization between co-rotating propellers in side-by-side configurations. Space-time Proper Orthogonal Decomposition (POD) is applied to pressure fluctuations to separate tonal and broadband components, enabling detailed analysis of the acoustic interference phenomena. Experimental results demonstrate that synchronization significantly influences the tonal component, highlighting distinct regimes of constructive and destructive interference at different rotor phase delays. Specifically, the analysis reveals a notable reduction in noise amplitude at certain phase shifts, particularly affecting the second harmonic. An explanation of this scientific outcome is provided and illustrated schematically. Additionally, probability density functions indicate clear changes in the statistical characteristics of pressure fluctuations due to rotor synchronization, reinforcing the effectiveness of the decomposition method. These findings confirm the potential of rotor synchronization as an efficient active noise-control technique capable of achieving substantial noise reduction.

Keywords: *aeroacoustics, rotor synchronization, noise reduction, proper orthogonal decomposition, acoustic interference.*

**Corresponding author*: *tiziano.pagliaroli@unicusano.it.*
***Copyright**: ©2025 T. Pagliaroli et al. This is an open-access article distributed under the terms of the Creative Commons Attribution 3.0 Unported License, which permits unrestricted use, distribution, and reproduction in any medium, provided the original author and source are credited.*

1. INTRODUCTION

U-space fosters drone integration in European airspace, yet noise pollution hinders public acceptance [1]. Studies on isolated rotor noise have intensified [2], but multirotor configurations require a broader aeroacoustic approach [1, 3, 4]. Passive noise control methods, such as serrated propeller edges, negatively affect aerodynamic performance [5], whereas active noise cancellation introduces additional weight and complexity [6]. Rotor phase synchronization emerges as a promising alternative, avoiding aerodynamic trade-offs [6]. This method manipulates rotor phase angles to induce destructive acoustic interference [7], achieving three main outcomes: noise amplitude reduction, modulation, and directivity alteration. Rotor synchronization can achieve significant noise reductions at blade passage frequency [5, 8–11], with co-rotating rotors benefiting more substantially than counter-rotating configurations [12]. Directivity modifications depend on phase differences, resulting in shifts between monopole and dipole radiation patterns [13–15]. Additionally, modulation effects introduce intermittent wave packets into pressure fluctuations [11, 14]. The present study employs space-time Proper Orthogonal Decomposition (POD) to separate the pressure fluctuation field, measured using a linear microphone array, into tonal and broadband components. This decomposition facilitates an in-depth analysis of the tonal component, typically the most annoying, offering detailed insights into the acoustic interference mechanisms between co-rotating rotors arranged in a side-by-side configuration. The paper is organized as follows. The experimental setup, instrumentation, and operating conditions are detailed in §2. Subsequently, the rotor acoustic interference phenomena are described and explained in §3. Finally, conclusions are presented in §4.

2. EXPERIMENTAL SETUP

The experiments were conducted in the Acoustic Wind Tunnel Braunschweig (AWB) optimised for noise measurements above 250 Hz. To simulate hovering conditions, the wind tunnel was deactivated during the tests. A total of 37 microphones were deployed in four non-equidistant linear arrays, with only arrays 1 and 4 used in this study. The acoustic signals were sampled at 102 kHz for 30 s per operating point. The microphone layout is illustrated in Figure 1. The setup comprised three-

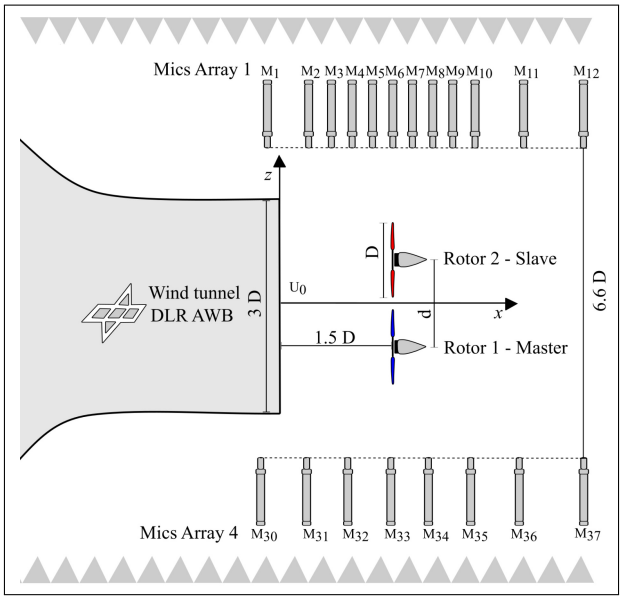


Figure 1. Microphone layout.

bladed KDE-CF155-TP propellers ($15.5'' \times 5.3$) mounted on vertical supports with adjustable spacing (d). The propellers had a diameter of 393.7 mm (D) and a mean aerodynamic chord of 28.5 mm. KDE4012XF-400 motors, controlled by KDEXF-UAS55 electronic speed controllers, powered the propellers. The two microphone arrays were positioned at $3.3D$ from the x-axis, ensuring pressure amplitudes were purely acoustic ($p' \propto 1/r$). A custom synchrophaser controlled the phase delay, $\psi(t)$, between the co-rotating rotors operating at a rotational speed $\omega(t)$. The system employed a Kübler 05.2400 incremental encoder (500 pulses per revolution) and National Instruments hardware, including an NI PXI-1031 chassis, an NI PXI-7350 motion controller, and an NI PXI-6259 multifunction DAQ. A PID controller regulated the phase shift, adjusting the slave rotor relative to the master rotor every 5 ms. The synchrophaser ensured stable rotational speeds and consistent phase differences. Experiments were conducted in hover conditions with phase differences varied in 15° increments. An inter-rotor distance was tested $d/D = 1.20$, with the rotational speed fixed at 5200 RPM. Several test cases were analysed, including an isolated rotor reference case. The blade tip Mach number was $M_{\text{tip}} = 0.31$, and the Reynolds number at 75% span was $Re_{c75} = 1.51 \times 10^5$.

3. RESULTS

The aerodynamic noise of propellers can be decomposed into two main components: tonal (narrow-band) and broadband noise. Tonal noise originates from the periodic blade motion, related directly to blade rotation speed, thickness, and aerodynamic loading. In contrast, broadband noise arises from turbulent structures and their interaction with blade edges, exhibiting random, incoherent characteristics in both space and time. The separation of these noise components is crucial for experimental analysis and validating simulations based on the Ffowcs Williams–Hawkings equation. Recent studies have introduced various separation techniques [16–19]. The space-time POD technique involves organizing collected microphone array data into limited-duration space-time fields structured into a matrix for POD analysis. The resulting modes, eigenvalues, and coefficients allow coherent and stochastic components to be separated through a truncated POD expansion. Key advantages of the space-time POD technique include ease of implementation, low sensitivity to the chosen truncation threshold and time window size, and effective performance even with relatively few microphones, aligning with common aeroacoustic experimental setups. By applying the space-time POD decomposition technique to the raw pressure data, the pressure fields were separated into tonal and broadband components. In Figure 2 the tonal component was notably smoother and perfectly in phase with the raw signal. Figure 3 illustrates the first six space-time modes, which appear pairwise. According to [20], such degeneracy, along with spatial-temporal translational symmetry, confirms the presence of travelling waves. Modes exhibit harmonic structure highlights the POD's effectiveness in isolating coherent periodic structures, aligning with harmonic orthogonal decomposition conditions discussed by [21]. Figure 4 presents the calculated Sound Pressure Spectral Level (SPSL), demonstrating that the coherent component spectrum aligns with the first three harmonics of the raw signal

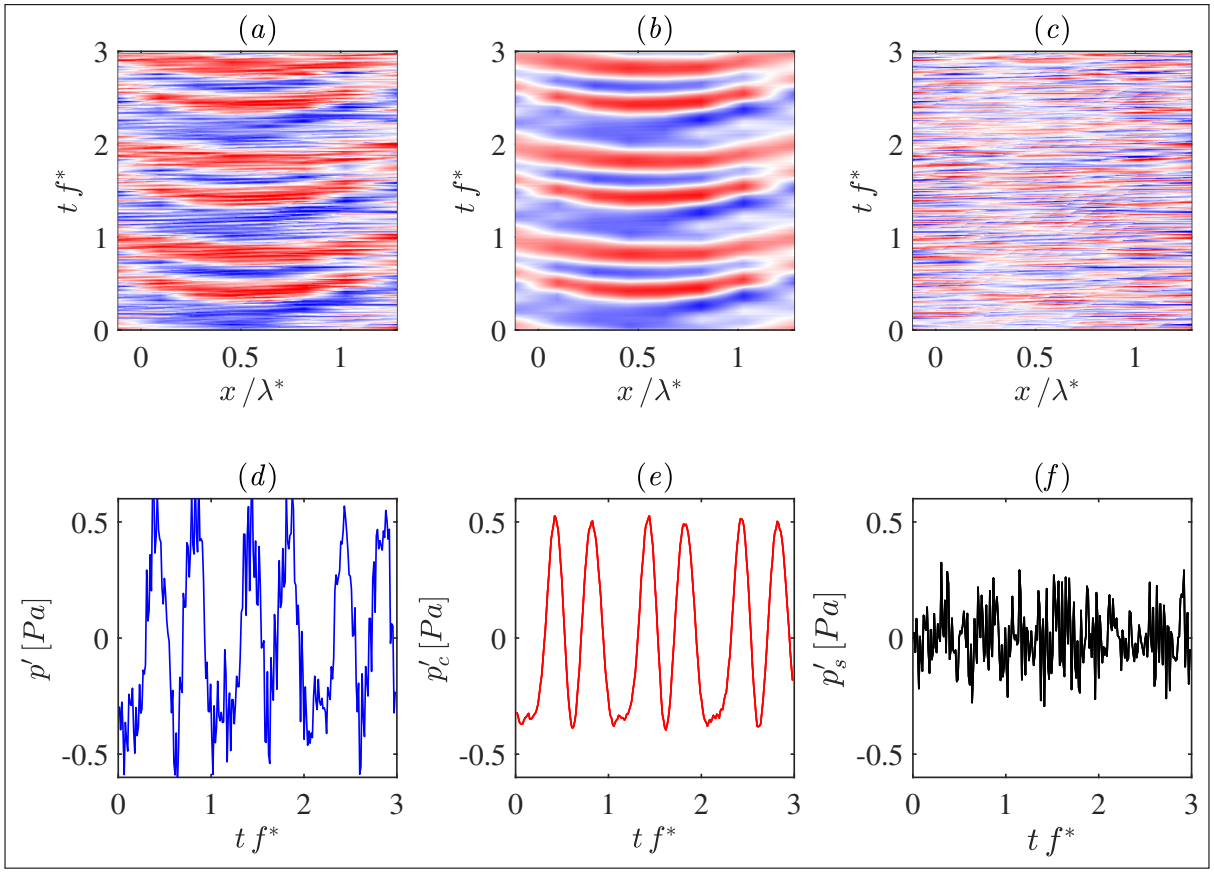


Figure 2. Input-output of the space-time POD decomposition applied to side-by-side rotor for constant phase delay $\psi = 0°$. The first column illustrates the raw data (a, d), the second column shows the tonal component (b, e), and the third column presents the broadband component (c, f). The top row represents space-time fields, while the bottom row shows a single time series at $x/\lambda^* = 0.45$, located in the rotor plane.

and remains nearly flat across the normalized frequency range $f/f^* \in [0.1, 1)$. Additionally, this decomposition technique effectively removes intermediate peaks between harmonics observed in the raw signal, distinguishing it from conventional band-pass filters. Figure 5 shows that the probability density function (PDF) of the incoherent signal closely follows a Gaussian distribution up to 3σ, confirming its stochastic nature. Conversely, the PDF of the coherent component is characterised by a bi-modal distribution, with peaks corresponding to blade passage events. These distinct PDF shapes validate the effectiveness of the decomposition technique in accurately separating tonal and broadband noise components. Figure 6 illustrates the effect of varying phase delay (ψ) between side-by-side rotors. At $\psi = 0°$ (Figure 6a), pairs of red-blue streaks appear for each blade passing period, with the delay between waves determined solely by rotor spacing. Increasing the phase delay to $\psi = 45°$ results in the alignment of compression waves from both rotors, producing constructive interference (Figure 6d). Conversely, at intermediate angles such as $\psi = 15°$ and $75°$, destructive interference occurs due to the overlap between expansion and compression waves, significantly reducing fluctuation amplitude. In Figure 7 is depicted pressure fluctuation time series showing the interference mechanism between side-by-side rotors for different phase delays (ψ). Figure 8 shows the Overall Sound Pressure Level (OASPL) for varying phase delays (ψ) between side-by-side rotors, comparing these results to the noise generated by a single rotor. This figure reveals promising findings, partic-

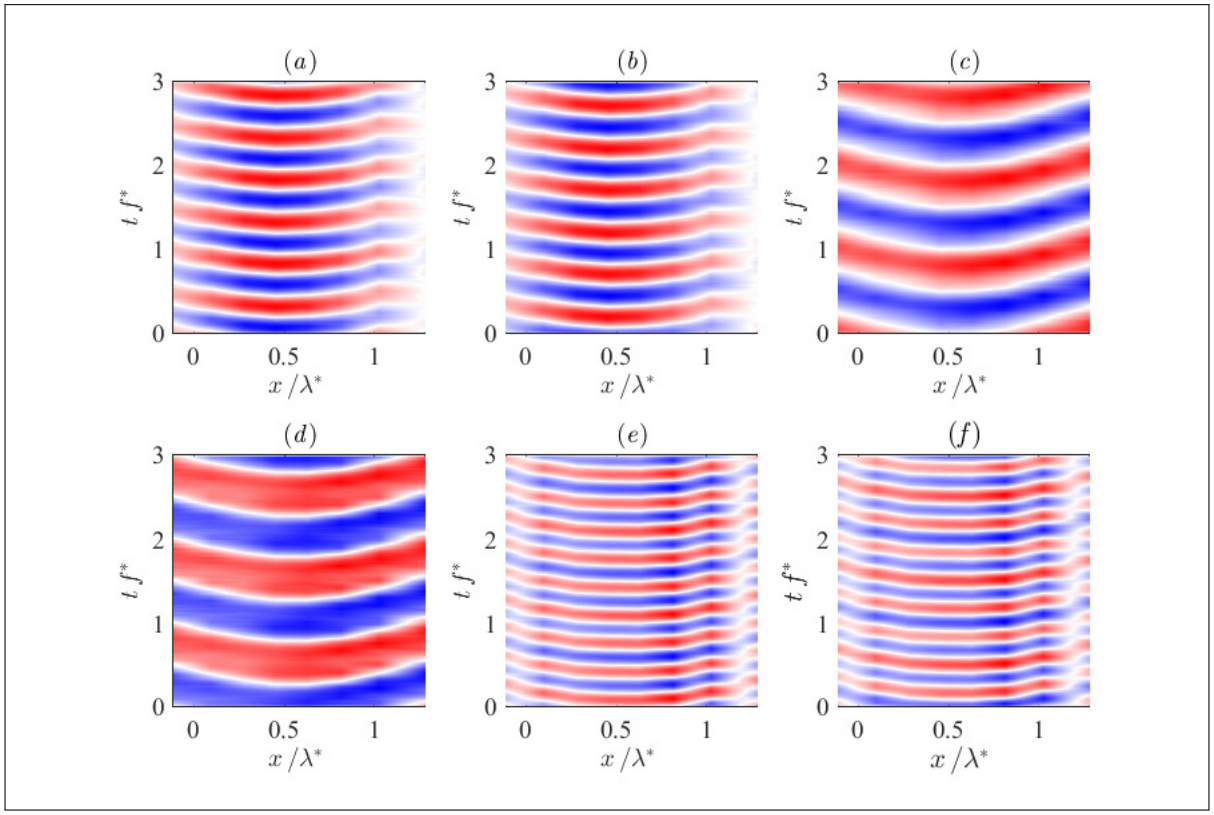


Figure 3. First six modes for side-by-side rotor for constant phase delay $\psi = 0°$ calculated using time history acquired by a linear array of microphones number 4.

ularly at angles associated with destructive interference ($\psi = 15°$ and $\psi = 75°$), where the noise produced by two synchronized rotors is notably lower than that of a single rotor. Conversely, constructive interference, observed at $\psi = 45°$, significantly increases the noise level. These findings confirm the potential of rotor synchronisation in effectively reducing aerodynamic noise through controlled interference. In Figure 9, the first harmonic is notably higher under constructive interference than in other cases. Consistent with [22], the second harmonic experiences the most significant mitigation due to destructive interference as reported in Table 1. Figure 7(f) clarifies why the second harmonic is mitigated: synchronisation of compression and expansion waves cancels fluctuations, resulting in a compression-expansion wave with reduced periodicity, as depicted by the grey-coloured fluctuation. The Probability Density Function (PDF) of pressure fluctuations provides valuable insights into how pressure signals change with varying phase delays. In Figure

Table 1. Sound Pressure spectral Level of the first and second harmonics by varying the rotor phase delay.

ψ, deg	$SPSL_1\,[dB]$	$SPSL_2\,[dB]$
0	75,3	74,4
45	82,2	82,4
75	79,6	62,4

10, at $\psi = 0°$, the PDF exhibits a distinct bi-modal distribution, clearly identifying two constant-intensity pressure fluctuations (expansion and compression). At $\psi = 45°$, these peaks shift outward, accompanied by the emergence of two lower-intensity internal peaks, ascribed to installation effects. At $\psi = 75°$, the PDF is dominated by

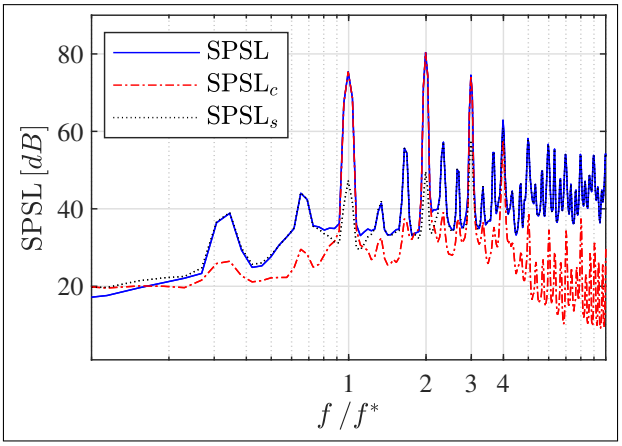


Figure 4. Sound pressure spectral levels calculated at $x/\lambda^* = 0.45$ for the raw data, tonal and broadband components.

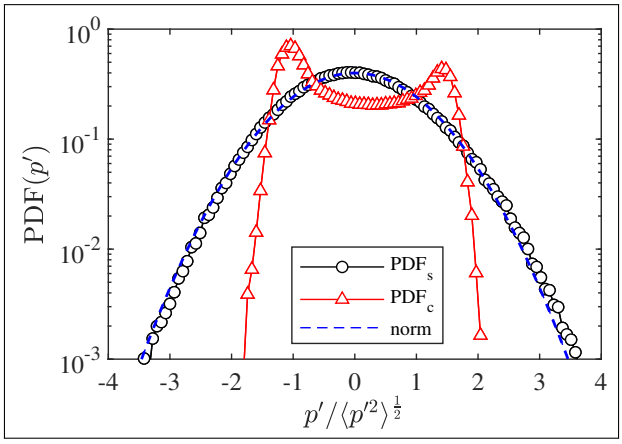


Figure 5. Probability density function of tonal and stochastic components of the pressure fluctuation.

a single expansion peak with an intensity very close to zero. This characteristic represents the acoustic footprint of noise cancellation due to destructive interference. Indeed, as illustrated in Figure 7f, the primary effect of destructive interference is the replacement of the positive-negative oscillation (see red and blue curves) with an extended sequence of values close to zero.

4. CONCLUSION

This investigation demonstrated the effectiveness of rotor phase synchronization as a passive noise reduction technique in co-rotating, side-by-side rotor configurations. Space-time Proper Orthogonal Decomposition (POD) successfully separated measured acoustic fields into tonal and broadband components, enabling precise analysis of acoustic interference mechanisms. Results revealed significant variations in noise levels due to constructive and destructive interference at specific phase angles, with notable reductions observed, particularly at second harmonic. Probability Density Function analyses confirmed clear distinctions in the statistical characteristics of pressure fluctuations, validating the decomposition technique's reliability. Overall, rotor synchronization emerged as a promising aeroacoustic control strategy, offering substantial noise mitigation potential.

5. ACKNOWLEDGMENTS

Research activities described in the manuscript are part of the work carried out by the GARTEUR AG-26 consortium, which has promoted the collaboration between DLR and Niccolò Cusano University. We sincerely thank Prof. Patanè for implementing the rotor synchronization software.

6. REFERENCES

[1] T. Dbouk and D. Drikakis, "Quadcopter drones swarm aeroacoustics," *Phys. Fluids*, vol. 33, no. 5, 2021.

[2] P. Candeloro, D. Ragni, and T. Pagliaroli, "Small-scale rotor aeroacoustics for drone propulsion: A review of noise sources and control strategies," *Fluids*, vol. 7, no. 8, p. 279, 2022.

[3] N. Intaratep, W. N. Alexander, W. J. Devenport, S. M. Grace, and A. Dropkin, "Experimental study of quadcopter acoustics and performance at static thrust conditions," in *22nd AIAA/CEAS Aeroacoustics Conference*, p. 2873, 2016.

[4] R. E. Nargi, P. Candeloro, F. De Gregorio, G. Ceglia, and T. Pagliaroli, "Fluid-dynamic and aeroacoustic characterization of side-by-side rotor interaction," *Aerospace*, vol. 10, no. 10, p. 851, 2023.

[5] B. Turhan, H. K. Jawahar, A. Gautam, S. Syed, G. Vakil, D. Rezgui, and M. Azarpeyvand, "Acoustic characteristics of phase-synchronized adjacent pro-

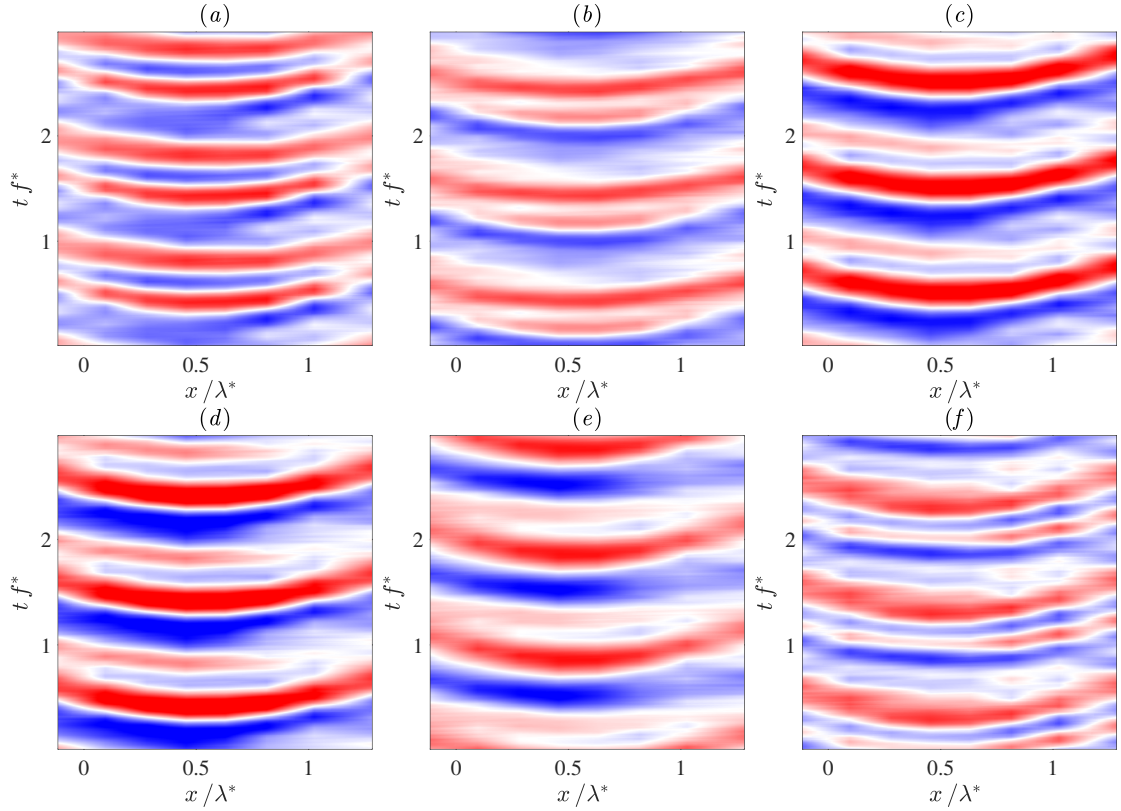


Figure 6. Pressure fluctuation space-time fields for side-by-side rotors with varying phase delays (ψ): (a) $\psi = 0°$, (b) $\psi = 15°$, (c) $\psi = 30°$, (d) $\psi = 45°$, (e) $\psi = 60°$, and (f) $\psi = 75°$.

pellers," *The Journal of the Acoustical Society of America*, vol. 155, no. 5, pp. 3242–3253, 2024.

[6] L. Chengyi, W. Yafeng, and C. Geng, "Active noise control experiment for unmanned aerial vehicle propeller," *Sci. Tech. and Eng.*, vol. 14, no. 9, pp. 1671–1815, 2014.

[7] Y. Cao, X. Huang, L. Sheng, and Z. Wang, "A flight experimental platform for synchrophasing control based on a small propeller uav," *Sci. China Technological Sciences*, vol. 61, pp. 1915–1924, 2018.

[8] A. Patterson, N. H. Schiller, K. A. Ackerman, A. Gahlawat, I. M. Gregory, and N. Hovakimyan, "Controller design for propeller phase synchronization with aeroacoustic performance metrics," in *AIAA Scitech 2020 Forum*, p. 1494, 2020.

[9] S. Guan, Y. Lu, T. Su, and X. Xu, "Noise attenuation of quadrotor using phase synchronization method," *Aerospace Sci. and Tech.*, vol. 118, p. 107018, 2021.

[10] O. Hertzman, S. Fligelman, and O. Stalnov, "Abatement of a multi-rotor tonal noise component with phase control technology," in *28th AIAA/CEAS Aeroacoustics 2022 Conference*, p. 2834, 2022.

[11] S. Zhong, P. Zhou, W. Chen, H. Jiang, H. Wu, and X. Zhang, "An investigation of rotor aeroacoustics with unsteady motions and uncertainty factors," *J. of Fluid Mech.*, vol. 956, p. A16, 2023.

[12] M. Shao, Y. Lu, X. Xu, S. Guan, and J. Lu, "Experimental study on noise reduction of multi-rotor by phase synchronization," *J. of Sound and Vib.*, vol. 539, p. 117199, 2022.

[13] K. Pascioni, S. Rizzi, and N. Schiller, "Noise reduction potential of phase control for distributed propul-

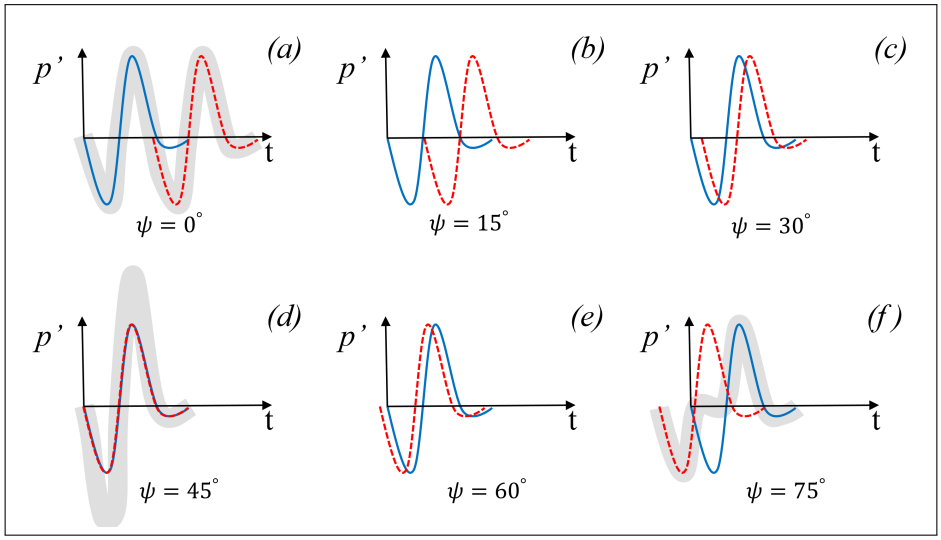


Figure 7. Schematic depiction of pressure fluctuation time series showing the interference effect between side-by-side rotors for different phase delays (ψ).

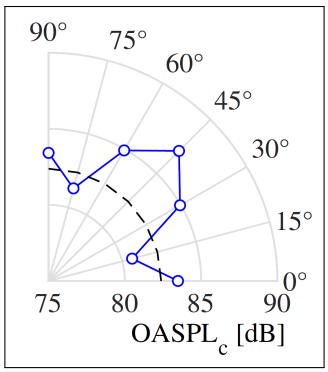


Figure 8. Overall Sound Pressure Level (OASPL) as a function of the phase delay (ψ). The dashed quarter circle represents the OASPL generated by an isolated rotor, providing a comparative reference for evaluating the effects of rotor interactions.

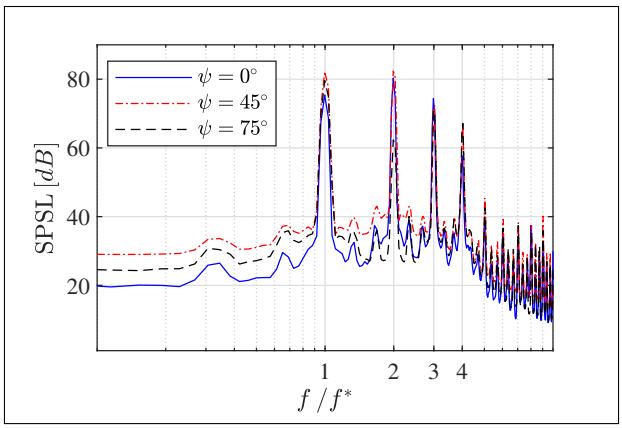


Figure 9. Sound pressure Spectra Level of the tonal component calculated for $\psi = 0°, 45°,$ and$75°$.

sion vehicles," in *AIAA Scitech 2019 Forum*, p. 1069, 2019.

[14] A. Celik, N. S. Jamaluddin, K. Baskaran, S. Meloni, D. Rezgui, and M. Azarpeyvand, "Experimental characterisation of rotor noise in tandem configuration," *Applied Acoustics*, vol. 222, p. 110053, 2024.

[15] N. Pandey, J. A. Valdez, W. Beaman, and C. E. Tinney, "Acoustics of side-by-side synchrophased rotors," in *30th AIAA/CEAS Aeroacoustics Conference (2024)*, p. 3218, 2024.

[16] L. A. Bonomo, J. A. Cordioli, A. K. Colaciti, J. V. N. Fonseca, and L. G. C. Simões, "A comparison of tonal-broadband decomposition algorithms for propeller noise," *Int. J. of Aeroacoustics*, vol. 23, no. 7-8, pp. 737–762, 2024.

[17] S. Meloni, E. de Paola, E. Grande, D. Ragni,

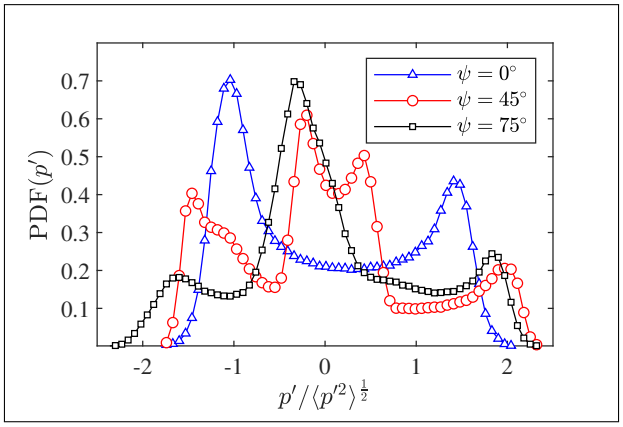


Figure 10. Probability Density Functions (PDFs) calculated ofr three condition: $\psi = 0°, 45°,$ and$75°$.

L. G. Stoica, A. Di Marco, and R. Camussi, "A wavelet-based separation method for tonal and broadband components of low reynolds-number propeller noise," *Measurement Science and Technology*, vol. 34, p. 044007, jan 2023.

[18] P. Candeloro, E. Martellini, R. Nederlof, T. Sinnige, and T. Pagliaroli, "An experimental study of the aeroacoustic properties of a propeller in energy harvesting configuration," *Fluids*, vol. 7, no. 7, p. 217, 2022.

[19] C. E. Tinney, Y. Zhao-Dubuc, and J. Valdez, "The space-time structure of sound produced by stacked rotors in hover using vold-kalman filters and proper orthogonal decomposition," *International Journal of Aeroacoustics*, vol. 22, no. 5-6, pp. 576–598, 2023.

[20] N. Hasan and S. Sanghi, "Proper orthogonal decomposition and low-dimensional modelling of thermally driven two-dimensional flow in a horizontal rotating cylinder," *J. of Fluid Mech.*, vol. 573, pp. 265–295, 2007.

[21] J. L. Lumley, "Coherent structures in turbulence," in *Transition and turbulence*, pp. 215–242, Elsevier, 1981.

[22] F. Del Duchetto, T. Pagliaroli, P. Candeloro, K.-S. Rossignol, and J. Yin, "Aeroacoustic study of synchronized rotors," *Aerospace*, vol. 12, no. 2, 2025.

DOI: 10.61782/fa.2025.0486

FORUM ACUSTICUM EURONOISE 2025

INTEGRATED U-SPACE SOCIETAL ACCEPTANCE ASSESSMENT: ENERGY-BASED AND PERCEPTION-BASED ACOUSTIC METRICS

Carlos Ramos-Romero[1*] **Michael J. B. Lotinga**[1] **Antonio J. Torija**[1]

[1] Acoustics Research Centre, University of Salford, UK

ABSTRACT

Innovative Air Mobility (IAM) systems are progressing within the European U-space framework to promote efficient and environmentally friendly air transport. The ImAFUSA project contributes by developing an integrated U-space assessment tool to evaluate environmental, societal, and safety impacts.

This paper focuses on acoustic metrics for assessing environmental noise and annoyance caused by unmanned aerial systems (UAS). It explores both energy-based and perception-based indicators to evaluate UAS noise. These metrics allow the U-space noise assessment accounting for the interaction between UAS and existing soundscapes and number of events.

The IAM noise assessment tool utilises acoustic pressure time-series at listener positions, which can be generated from measurements or auralised signals. In the latter case, the integration of aircraft noise synthesis, flight-control data, and sound propagation along the flight path is potentially feasible as input for the assessment tool. This flexibility highlights the usability of the proposed metrics across diverse input types, laying the groundwork for future extensions that incorporate a broader range of data, including varied operating conditions and advanced predictive models.

Therefore, the calculated metrics would provide insightful estimations for the societal and capacity impact of U-space, potentially contributing to the strategic noise management of the UAM operations.

*__Corresponding author__: c.a.ramosromero@salford.ac.uk.
__Copyright__: ©2025 Ramos-Romero, C. et al. This is an open-access article distributed under the terms of the Creative Commons Attribution 3.0 Unported License, which permits unrestricted use, distribution, and reproduction in any medium, provided the original author and source are credited.

Keywords: *U-space, environmental noise, urban air mobility, noise annoyance, psychoacoustics.*

1. INTRODUCTION

Innovative Air Mobility (IAM) solutions are anticipated to become a transformative element in the skies close to populated areas. In addition to the benefits IAM can offer to commerce, industry, and communication activities, their presence introduces a disruptive element to urban skies, potentially impacting various societal aspects, such as affordability and accessibility of the services and vertiports.

Such developments requires the use of multidisciplinary and innovative tools for precise U-space assessment. In this context, the **ImAFUSA** [1] project, funded by the Horizon Europe Programme, is developing an integrated assessment tool aimed at evaluating the impacts of Urban Air Mobility (UAM) within U-space. The project outputs comprise innovative tools to evaluate environmental, socio-economic, and safety aspects of IAM operations, as well as to analyse their effects on U-space capacity levels.

For the U-space environmental impact assessment, noise, visual and air pollution have been considered within the ImAFUSA framework. However, the focus on noise assessment in this paper reflects the specific scope of the current work, which is dedicated to the integration and application of noise metrics. While other societal and environmental factors are also relevant for IAM integration, noise was reported as a primary concern for EU citizens, as highlighted by the EASA report in 2021 [1]. This integrated Noise assessment tool will enable easy integration in decision-making processes and interdependency studies by taking into account the interaction between the source

[1] https://www.imafusa-sesar.eu

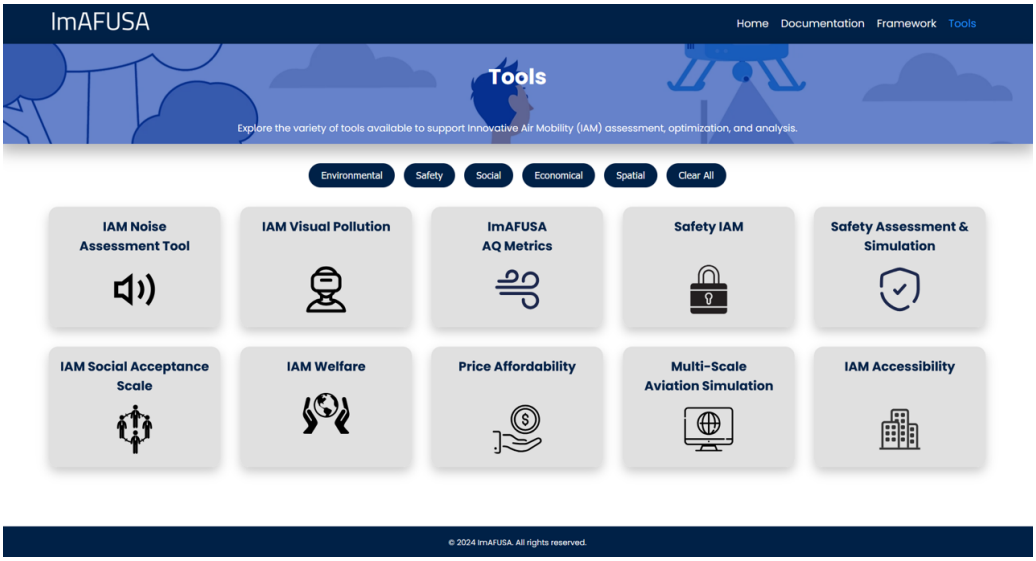


Figure 1. ImAFUSA integrated tools.

(unmanned aircraft), the environment (background noise — soundscape), and the listener (perception).

2. ASSESSMENT FRAMEWORK

ImAFUSA integrates state-of-the-art mathematical formulations and algorithms into an **Im**pact and capacity **A**ssesssment **F**ramework for **U**-space **S**ocietal **A**cceptance.

ImAFUSA focuses on assessing environmental factors such as noise, visual pollution, and air quality; safety considerations; and socioeconomic aspects including affordability, accessibility, economic development, public space utilisation, and connectivity (See. Fig. 1). By quantifying these elements through innovative performance indicators, the tool seeks to aid stakeholders in making informed and sustainable decisions, thereby promoting societal acceptance and positioning Europe as a leader in sustainable aviation.

In particular, the IAM noise assessment tool enables the evaluation of the acoustic impact of U-space use by incorporating both energy-based noise metrics and perception-based (psychoacoustic) metrics.

Expanding the analysis beyond traditional acoustic energy measures to include human perception is expected to enhance the environmental noise assessment of IAM operations. This approach allows for a more comprehensive understanding of community impact, capturing not only the additive effects of sound energy but also how noise is experienced by people in areas targeted for future IAM deployment [2].

These metrics have been extensively applied to single-aircraft and single-event operation scenarios. However, as periodicity or repetitiveness of UAM operations are expected for the potential definition of drone corridors or regular flight paths, a group of metrics should be further generated to quantify the effect of the number of flyover events and the number of people exposed along the flight paths [3]. In addition, high-order interactions between the target noise (aircraft), and masker noise (background noise), previously presented in the literature have also been integrated in the assessment framework [4].

3. NOISE ASSESSMENT METRICS

The set of metrics integrated into the IAM noise assessment tool, currently relies on acoustic pressure time-series data defined at a specific listener position. These signals can originate from various sources, including drone noise recording databases or auralised signals. From recordings, the tool can incorporate data for multiple UAS with varying sizes, take-off masses, numbers of rotors/blades, and operational variables such as altitude and speed (e.g., DroneNoise [5]). In cases where auralised signals are used, the integration of aircraft noise synthesis, operational flight control data, and sound propagation along the

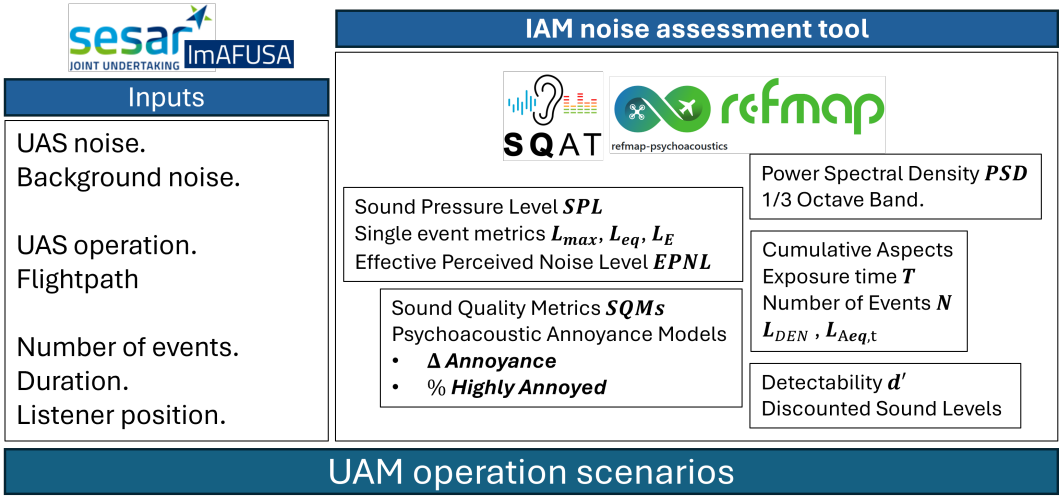


Figure 2. IAM noise assessment tool

flight path is feasible. This flexibility paves the way for future tool extensions that integrate even more comprehensive data sources, enhancing the versatility and applicability of the tool.

In addition to the aircraft noise signals, the tool also provides access to several examples of ambient sounds (e.g., EigenScape [6]). These capabilities enable a better assessment of IAM operation flight scenarios under different simulated operational conditions.

Firstly, energy-based metrics measure the acoustic intensity of the incident noise at a specific receiver point. This group of metrics has been used extensively for conventional aircraft noise assessment [7]. Secondly, the perception-based metrics evaluate the psychoacoustic effects of the sound signal on a human listener. This group of metrics considers the sound quality [8], which becomes important as the operation of IAM solutions is expected to be carried out at lower altitudes, closer to people than conventional aircraft systems [9].

The assessment tool also account for the masking effect of background environmental noise by using a discounting index. This index adjusts the acoustic metrics based on the detectability of the assessed noise source in relation to surrounding sounds. This approach includes in the analysis how much the annoyance response differs due to the non-constant prominence of the noise source in the presence of a masking sound, such as residual background noise along a flight path [4].

This ongoing project also aims to predict virtual scenarios in which more than one vehicle operates in the same urban area, and recurrent operations are expected to be carried out on an established drone path. In this regard, cumulative aspects such as exposure time and number of operations are required. Models incorporating the effects of multiple UAS events are being investigated as part of the ImAFUSA sister project, RefMap [2] [10].

To assess a UAM operation scenario, Fig. 2 illustrates the input parameters required by the IAM noise assessment tool. The inputs are the time-series data of acoustic pressure signals containing the operating source (target or UAS noise) and the soundscape where the source is expected to be operating (masker or background noise). Additional information on overflight operations will assist in the assessment of cumulative effects such as the number of operations and the number of aircraft in the flight corridor.

3.1 Energy-based metrics

3.1.1 Time-series

Sound Pressure Level SPL quantifies the wide variation in acoustic pressure from UAM operations and urban noise on a logarithmic scale in [dB]. SPL is calculated using the root-mean-square (RMS) of the pressure signal relative to a reference pressure (20 μPa). Since hu-

[2] https://www.refmap.eu The ImAFUSA and RefMap projects form the Aviation Twin Transition Cluster.

man hearing sensitivity differs from measurement devices, an A-weighting filter would be applied to better reflect perceived loudness, producing A-weighted SPL in [dBA]. As sound levels vary with source operation, time-window framing is used with exponential weighting to show SPL evolution (e.g., fast weighting: 0.125 s or slow weighting: 1 s).

Power Spectral Density PSD. represents the acoustic power distribution over frequency [11]. Spectral amplitudes are normalised by frequency resolution and expressed in [Pa^2/Hz]. Calculating power over successive time frames creates a 3D spectrogram (frequency vs. time vs. power), while averaging power over time yields a 2D plot spectrum (frequency vs. power), which also be expressed on a logarithmic scale as [dB/Hz]. PSD analysis across the full frequency range can be represented using frequency bands centred at standard frequencies f_c. Each band encompasses energy between a lower and upper cut-off frequency, with the ratio defined as $f_u = 2^n \times f_l$. An octave band corresponds to $n = 1$, where the upper-to-lower frequency ratio is 2. For greater detail, the analysis can use 1/3-octave bands, where $n = 1/3$ [12, 13].

3.1.2 Single-values

For aircraft noise emission, L_{max}, L_{eq}, and L_{E} are used to summarize the SPL evolution over time in a single value. When these metrics consider the sensitivity of the human ear, they are denoted with an A-weighting (e.g., L_{Amax}, L_{Aeq}, L_{AE}).

Maximum Sound Pressure Level L_{Amax} measures the maximum level of acoustic energy at the listener's position due to the operation of the UAM. For a flyover, it is expected to occur at the slant distance where the UAM is closest to the assessed point.

Continuous Equivalent Sound Pressure Level L_{Aeq} characterizes the time-varying acoustic event of duration T as a constant-amplitude sound, representing the averaged sound energy over the same time period.

The Sound Exposure Level L_{AE} allows for the comparison of different time-length signals by uniformly compressing their energy into a reference time T_{ref}. The total sound energy of a UAM operation is typically normalised to $T_{\text{ref}} = 1$ s. For aircraft flyovers, L_{AE} is accurately estimated by including only those sounds that lie within 10 dB of L_{Amax}. The L_{AE} increases by 3 dB if the duration is doubled while keeping the L_{Amax} value, because the energy is doubled [14].

These metrics have been extensively applied to conventional single-aircraft and single-event operation scenarios, and are still valid to evaluate IAM platforms. However, as periodicity or repetitiveness of IAM operations are expected for the potential definition of drone corridors or regular flight paths, a group of metrics should be further generated to quantify the effect of the number of flyover events and the number of people exposed along the flight paths [3].

If a series of non-consecutive overflights n_{eve}, each producing approximately the same SPL at the receiver location, occur over a given period, the cumulative sound pressure level can be estimated by accounting for the combined effect of these events. This scenario is plausible when periodic flights of the same aircraft follow the same path. The cumulative SPL_{eve} is expressed as:

$$\text{SPL}_{\text{eve}} = \text{SPL} + 10\log_{10}(n_{\text{eve}}) \tag{1}$$

This formulation captures the cumulative acoustic impact of repeated events at equal SPLs.

3.2 Perception-based metrics

Effective Perceived Noise Level EPNL was developed for assessing the annoyance characteristic of aircraft noise. It evaluates noise perception resulting from the combination of sounds from different source components, mechanisms, frequency emissions, intensity ranges, and time-series profiles. This metric is an improved version of Perceived Noise Level [14]. EPNL is calculated by measuring a sequence of 1/3-octave band spectra at 0.5-second intervals during the noise event. Each interval spectrum is examined for the presence of tones, and a tone-correction is computed to give the tone-corrected perceived noise level (PNLT). To determine EPNL, the complete set of 0.5-second PNLT values is integrated to calculate the level of the long-term steady sound.

Sound Quality Metrics SQMs are used to assess how sound is perceived by the human hearing system, considering features like tonal components, modulation effects, amplitude, and frequency [8]. These metrics evaluate subjective human sensations of sound, with a linear scale meaning that doubling a SQMs corresponds to doubling the perceived sensation. The following SQMs have been included as predictors of psychoacoustic annoyance models for UAM [15].

Loudness N is a measure of subjective sound strength, evaluated through models that account for non-linear amplitude response and critical bands. It is often considered the strongest indicator of annoyance and is measured in [sone].

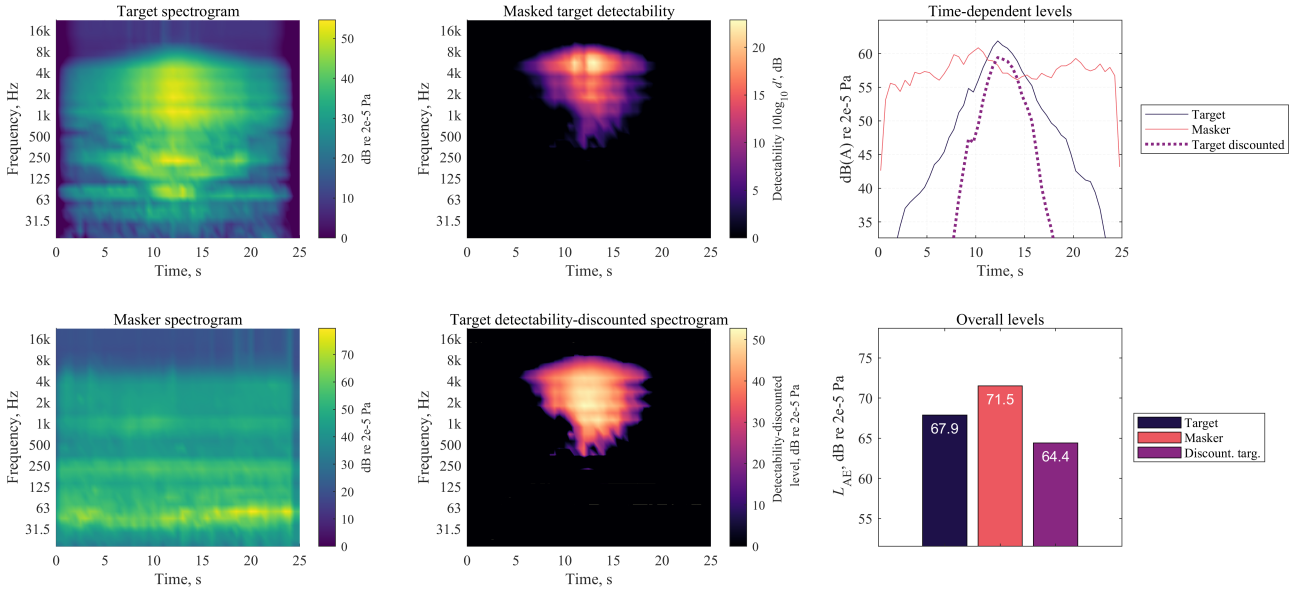


Figure 3. Example of detectability and discounting sound levels for UAS overflight (target) within urban street soundscape (masker).

Sharpness S quantifies the spectral character of a sound based on the balance between high- and low-frequency content. A sound with more high-frequency energy is perceived as sharper. It is measured in [acum].

Fluctuation Strength F assesses the perception of periodic variations in sound, comprising slow modulations (below 20 Hz, with a sensory peak ∼4 Hz) in amplitude or frequency, experienced as beating or pulsating. It is measured in [vacil].

Roughness R is similar to fluctuation strength, but it focuses on faster modulations (15-300 Hz with a sensory peak ∼ 70 Hz), causing the sound to be perceived as having a rough 'texture'. It is measured in [asper].

Tonality T evaluates the presence of pure tones or narrowband components in the sound. It tracks frequencies with salient amplitudes and is measured in tonality units [tu]. To evaluate these SQMs, computational tools have been implemented based on specific standards. The ImAFUSA toolkit integrates noise assessment algorithms developed in SQAT [16, 17] and RefMap [18].

Psychoacoustic Annoyance models use the aforementioned SQMs in non-linear models to assess annoyance. These models have shown good correlation with noise annoyance in jury tests. In one example [15], the 5% exceedance values (95th percentiles) are determined for each SQM. Other models have also been developed for UAS rotor sound [19]. These composite metrics have been found to be effective predictors for psychoacoustic annoyance assessment of UAM noise.

Detectability index d' incorporates ambient sound as a discounting factor for annoyance. Time series of 1/3-octave band power spectra are used to determine the time-dependent masking of the target source (the UAM vehicle) by the environment sound, affecting both audibility, and potentially, annoyance. To simplify the understanding of detectability, two scenarios can be considered. The first one occurs when the UAM signal is prominent over the ambient sound, i.e., it is clearly audible with no significant effect from the ambient sound on annoyance — for example, in a quiet environment. On the other hand, the second scenario involves a situation where the target sound is low compared to the ambient sound, rendering it partially masked, which may lead to a reduction in annoyance compared with the unmasked signal [4] — this scenario could occur environments with high levels of ambient sound.

The d' metric can be estimated from one-third octave band SPL data as a measure of the detectability of a signal. Then, discounted sound level metrics, which are determined from laboratory measurements of annoy-

ance responses, can be derived from the target signal detectability [20]. Fig. 3 presents an example of detectability and discounted sound levels for a UAS overflight which is masked by a urban soundscape: the first column depicts the spectrograms of the target signal (a UAS overflight, upper left panel) and the masker signal (urban street soundscape, bottom left panel); the second column shows the detectability index d' of the UAS (upper centre) in presence of the masking soundscape and the UAS discounted spectrogram (bottom centre); the third column presents the A-weighted SPL time series, with/without detectability-discounting (upper right) and overall A-weighted sound exposure levels, with/without detectability-discounting (bottom right). In the example, the UAS L_{AE} of 68 dB within the ambient sound of 72 dB L_{AE} (in this case, 58 dB L_{Aeq}) is discounted by 3.5 dB.

4. CONCLUSIONS

This document presents the structure and metrics of the IAM noise assessment tool, developed within the framework of the ImAFUSA project. While this work primarily focuses on acoustic impact evaluation, it is designed to be part of a broader set of U-space assessment indicators, including societal acceptance, safety, and environmental impacts. By combining both energy-based and perception-based acoustic metrics, the IAM noise assessment tool aims to support more accurate predictions of community noise impact and contribute to comprehensive capacity assessments for future Urban Air Mobility (UAM) operations within U-space.

5. ACKNOWLEDGMENTS

This work is supported by EU Horizon Europe and UK Research and Innovation (UKRI) under the UK government's Horizon Europe ImAFUSA project (101114776) and RefMap project (10061935).

6. REFERENCES

[1] E. U. A. S. Agency, "Urban air mobility survey evaluation report," tech. rep., European Union Aviation Safety Agency, 2021.

[2] M. J. Lotinga, C. Ramos-Romero, N. Green, and A. J. Torija, "Noise from unconventional aircraft: a review of current measurement techniques, psychoacoustics, metrics and regulation," *Current Pollution Reports*, vol. 9, no. 4, pp. 724–745, 2023.

[3] T. Krstić Simić, E. Ganić, B. Mirković, M. Baena, I. LeGriffon, and C. Barrado, "U-space social and environmental performance indicators," *Drones*, vol. 8, no. 10, p. 580, 2024.

[4] S. A. Rizzi, A. Christian, S. J. Letica, and S. V. Lympany, "Annoyance model assessments of urban air mobility vehicle operations," in *30th AIAA/CEAS Aeroacoustics Conference (2024)*, p. 3014, 2024.

[5] C. Ramos-Romero, N. Green, C. Asensio, and A. J. Torija, "Dronenoise databse," acoustics and pyschoacoustics metrics database from epsrc dronenoise project ep/v031848/1, Acoustics Research Centre - University of Salford, 2023.

[6] M. C. Green and D. Murphy, "EigenScape," oct 2017.

[7] G. J. Ruijgrok, *Elements of aviation acoustics*. TUDelft, 2004.

[8] E. Zwicker and H. Fastl, *Psychoacoustics: Facts and Models*. Berlin, Heidelberg: Springer, 3nd ed., 2007.

[9] M. Boucher, M. Rafaelof, D. Begault, A. Christian, S. Krishnamurthy, and S. Rizzi, "A psychoacoustic test for urban air mobility vehicle sound quality," in *INTER-NOISE and NOISE-CON Congress and Conference Proceedings*, vol. 266, pp. 794–807, Institute of Noise Control Engineering, 2023.

[10] M. J. B. Lotinga, M. C. Green, and A. J. Torija, "Human perception and response to sound from unmanned aircraft systems within ambient acoustic environments," *npj Acoustics*, vol. 1, no. 1, p. 2, 2025.

[11] P. D. Welch, "The use of fast fourier transform for the estimation of power spectra: A method based on time averaging over short, modified periodograms," *IEEE Transactions on Audio and Electroacoustics*, vol. 15, no. 2, pp. 70–73, 1967.

[12] "Electroacoustics – Octave-band and fractional-octave-band filters – Part 1: Specifications," 2014.

[13] R. D. Blevins, "Appendix c: Standard octaves and sound pressure," in *Formulas for Dynamics, Acoustics and Vibration*, pp. 343–350, John Wiley & Sons, Ltd, 2015.

[14] M. Jones and R. Cadoux, "Noise metrics for emerging aircraft technologies," in *15th AIAA/CEAS Aeroacoustics Conference*, AIAA, 2009.

[15] M. A. Boucher, A. W. Christian, S. Krishnamurthy, T. Tracy, D. R. Begault, K. Shepherd, and S. A. Rizzi, "Toward a psychoacoustic annoyance model for urban air mobility vehicle noise," Technical Memorandum NASA/TM-20240003202, National Aeronautics and Space Administration, June 2024.

[16] G. F. Greco, R. Merino-Martínez, A. Osses, and S. C. Langer, "SQAT: a MATLAB-based toolbox for quantitative sound quality analysis," in *Inter-Noise and Noise-Con Congress and Conference Proceedings*, vol. 268, pp. 7172–7183, Institute of Noise Control Engineering, 2023.

[17] G. Felix Greco, R. Merino-Martínez, A. Osses, and M. J. B. Lotinga, "SQAT: A sound quality analysis toolbox for MATLAB." Computer software version 1.3, 2025. https://doi.org/10.5281/zenodo.15148618.

[18] M. J. B. Lotinga, "refmap-psychoacoustics." Computer software version 2025, 2025. https://github.com/acoustics-code-salford/refmap-psychoacoustics.

[19] A. J. Torija, Z. G. Li, and P. Chaitanya, "Psychoacoustic modelling of rotor noise," *Journal of the Acoustical Society of America*, vol. 151, no. 3, pp. 1804–1815, 2022.

[20] A. Christian, "A construction for the prediction of noise-induced annoyance in the presence of auditory masking," tech. rep., NASA Langley Research Center, 2021.

DOI: 10.61782/fa.2025.0609

FORUM ACUSTICUM EURONOISE 2025

NOISE IMPACT OF DRONE PARCEL DELIVERY SCENARIO OVER MADRID

Ingrid LeGriffon[1*] **Elise Ruaud**[1] **Jovana Kuljanin**[2] **Emir Ganic**[3]
[1] DAAA, ONERA, Institut Polytechnique de Paris, 92322 Châtillon, France
[2] Computer Architecture Department, Technical University of Catalonia, Barcelona, Spain
[3] Faculty of Transport and Traffic Engineering, University of Belgrade, Belgrade, Serbia

ABSTRACT

To effectively integrate drones into densely populated urban infrastructures, it is crucial to assess their impact on the population's quality of life and mitigate any adverse effects. As noise pollution from drone overflights is a top concern, enhancing our numerical capabilities for predicting VTOL aircraft noise in urban environments is essential.
To achieve this goal, we have developed an integrated toolchain comprising three key components: Flight Mechanics, to accurately model aircraft behavior; Noise Emission at the Source: to quantify the noise generated by the drones and finally Urban Environment Noise Propagation using the open-source tool NoiseModelling.
This comprehensive toolchain enables the creation of detailed noise maps for specific drone scenario definitions.
This paper presents an application of our toolchain in a parcel delivery scenario, featuring DJI Matrice 600 drones operating over a 10 km² sector of Madrid in Spain within a day period, incorporating five distribution centers with varying hourly capacities. The results include a range of informative noise indicators, taking into account noise level, number of flyovers and background noise levels.

Keywords: *drone fleet noise, noise source modeling, urban propagation, parcel delivery, indicators*

[*]***Corresponding author***: *Ingrid.legriffon@onera.fr*
Copyright: *©2025 Ingrid LeGriffon et al. This is an open-access article distributed under the terms of the Creative Commons Attribution 3.0 Unported License, which permits unrestricted use, distribution, and reproduction in any medium, provided the original author and source are credited.*

1. INTRODUCTION

Urban Air Mobility (UAM) concepts, particularly those involving Vertical Take-Off and Landing (VTOL) aircraft, are increasingly being explored for applications such as passenger transport, medical logistics, and parcel delivery. As these operations move from theoretical frameworks to real-world implementation, ensuring that they integrate seamlessly into existing urban infrastructures has become a critical research and policy objective. Recent research has proposed a comprehensive U-Space Social and Environmental Performance Framework to assess the broad spectrum of Urban Air Mobility (UAM) impacts on citizens' quality of life, identifying key focus areas such as noise, visual pollution, privacy, equity, emissions, and public safety, and defining corresponding performance indicators for their evaluation [1].
Among the primary concerns associated with drone operations in urban environment and their potential impact on the quality of life of city residents, the focus of this research is on noise pollution. Consequently, the ability to model, predict, and manage noise generated by drones is essential for fostering public acceptance and informing regulation. To address these challenges, we have developed an integrated toolchain that combines three key components: (1) Flight Mechanics, which accurately models aircraft behavior; (2) Noise Emission at the Source, which quantifies noise generated by the drones; and (3) Urban Environment Noise Propagation, using the open-source tool NoiseModelling. This research presents an application of our toolchain in a parcel delivery scenario for the city of Madrid, in Spain, during a single day.
The paper is structured as follows: Chapter 2 describes the noise calculation tool. Chapter 3 defines the parcel delivery scenario. Chapter 4 presents the noise results, while Chapter 5 concludes the paper and outlines future work.

2. NOISE CALCULATION TOOL

The main structure of the noise calculation chain was presented in [2]. Once a drone fleet scenario is defined (by the consortium partner UPC), the ONERA in-house flight mechanics tool DynaPyVTOL [3] calculates all drone and propeller data that are necessary for the aircraft to comply with the target trajectories and velocities. These data (propeller thrust and RMP, vehicle orientation etc.) are used for the noise emission calculation tool CARMEN [4][5][6] that calculates at each time step along the mission trajectory the main noise sources; in this case propeller noise. Each resulting noise sphere is then combined in a traffic pattern by the UGE NoiseModelling urban propagation tool [7], and the main noise indicators are calculated (see [1]).

In the following, a DJI Matrice 600 type is used for calculation. The main noise source on this type of aircraft is propeller noise. For the purposes of this case study, the analysis focuses exclusively on tonal noise contributions. This deliberate scope limitation is driven by two key considerations: computational resource constraints and negligible omission error. Indeed, preliminary estimates indicate that omitting broadband noise components would introduce an error of negligible effect on the overall outcome, thus not significantly impacting the study's conclusions. This applies to our specific case study, but cannot, in any case, be generalized.

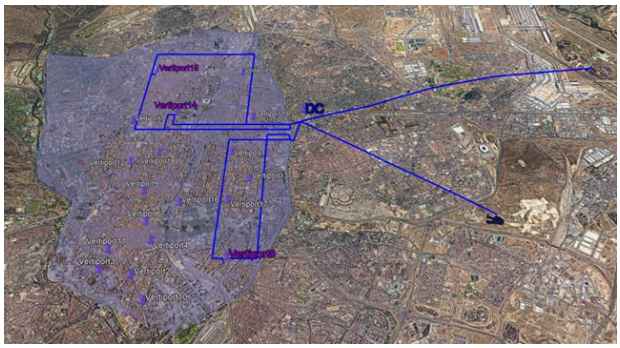
3. PARCEL DELIVERY SCENARIO

Mainly two types of drone usages were considered: parcel delivery and emergency delivery. Although emergency scenarios are very interesting for featuring access and equity indicators, they constitute only a minor fraction of future daily drone flights. For noise impact considerations the parcel delivery scenarios are much better suited, given that we are at liberty to set up as many distribution centers as we want, located all over the city and furthermore, deliveries are done to individuals all over the city and are not necessarily limited to fixed destinations such as hospitals.
After analyzing habits of already existing delivery hubs and taking into account results of the SESAR Metropolis 2 project [8], the consortium chose to set up five distribution centers, four located around the city center and one within. These distribution centers are configured to handle identical traffic volumes and rates, with two exceptions: one center is situated near a no-fly zone, and another is located in a sparsely populated area, each with adjusted traffic considerations.
A more detailed description of how these choices were made will be presented in further associated publications.

Two types of concepts of operations (ConOps) are considered: free route and constrained airspace. While the free route scenario links delivery hub and destination in the shortest possible way, the constrained airspace uses a free route when outside of the city center but follows a grid based network when inside the city limits (Fig. 1).



a)



b)

Figure 1. Two types of ConOps: a) free route, b) constrained airspace

One main difference between the two ConOps types has a noticeable impact on noise maps. While the free route drone altitude roughly follows the terrain, the constrained airspace presents four layers of flight altitudes. Those are calculated based on the highest point of the mission, leading to locally very important source – receiver distances (see Fig. 2 for one mission example).

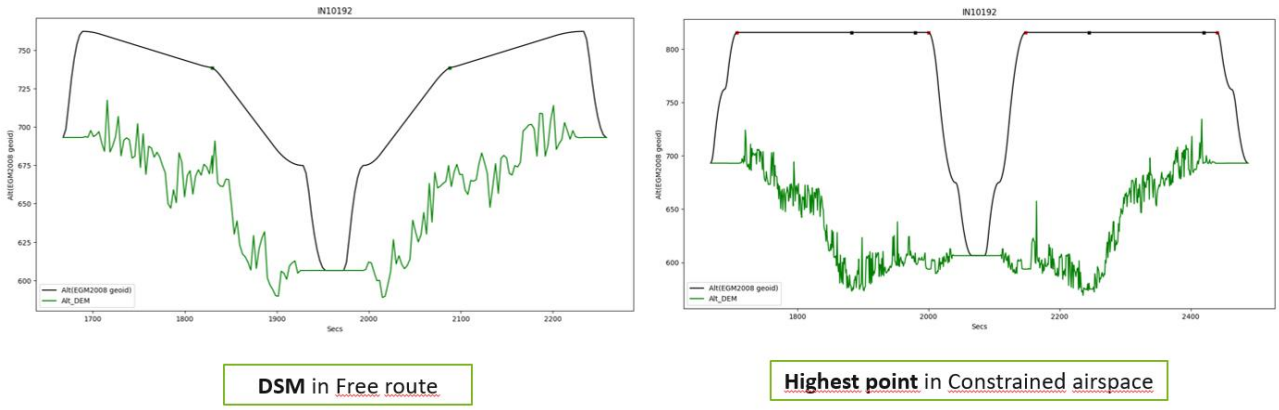


Figure 2. Reference for altitude in two ConOps

Mean height values are around 69 m for free route, and 125 m for constrained airspace, leading to enhanced propagation distances and variable ray paths in the urban environment.
All flight scenarios of the project were calculated by Polytechnic University of Catalonia (UPC) with their tool GEMMA [9].
In the cases presented in this paper, a mean flight frequency of 60 flights per hour (fph) is considered. This number is adapted to time of the day, i.e. one encounters more flights during late afternoon than in the morning for instance (see Fig. 3).

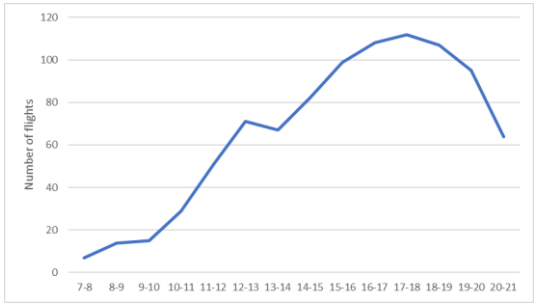


Figure 3. Operations per hour across the day in the area of interest

Lower flight frequencies have been evaluated as well, but are not presented here.
In order to assess the Performance Framework indicators (see [1]), we choose a specific of area of interest, covering a 5.9 km*1.7 km area in Madrid, that includes key elements such as residential areas, recreational zones, restricted locations (e.g., the Royal Palace in purple), and hospitals (see Fig. 4).

Several drone types are considered, which are most suitable for delivery and emergency operations. As explained in chapter 2, only one type is used in the parcel delivery scenarios that serve for noise indicator assessment: a DJI Matrice 600 that has a maximum take-off weight of 15.5 kg and 6 propellers equipped with 2 blades of approximately 0.5 m diameter.

4. NOISE RESULTS

Noise maps were calculated over the whole day for two ConOps (free route and constrained airspace) with varying flight numbers (60/40 fph). For visualization purposes only small time extracts are shown in this paper. Future analyses, scheduled for the upcoming months, will delve deeper into daily patterns and pinpoint locations yielding unforeseen results, providing a more comprehensive understanding.
In the following, two periods of day are considered: 9:00 – 9:15 am and 5:00 - 5:15 pm. These intervals are chosen for their variety in flight numbers (see Fig. 3 and Fig. 4). The only vertiport located inside the area of interest is in the upper part, centered.

Several noise metrics were calculated, including L_{Aeq}, L_{Amax}, ASEL, TA, NA and others.

Figure 5 shows L_{Aeq} noise maps integrated over a 15 minutes period for a morning and an afternoon period for a free route scenario, translating directly into a noise map the trajectory representation of Fig. 4. Noise levels depend on the number of drones, globally leading to a higher impact for the citizen on the afternoon. However, at a finer level of detail the precise flight altitude, urban architecture and the terrain have a non-negligible influence on the noise maps. A

quantification of each parameter's impact on noise levels on the ground needs to be done.

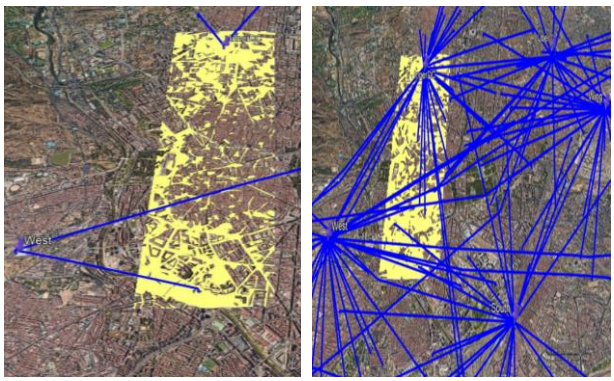


Figure 4. Drone traffic over 15 minutes: morning period (left), afternoon period (right)

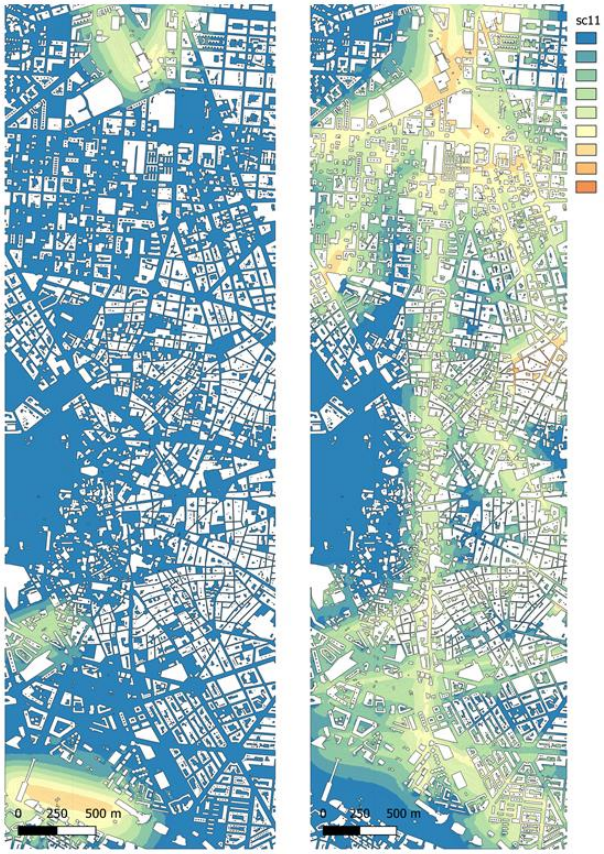


Figure 5. $L_{Aeq,15\ min}$ [dBA], free route : morning period (left), afternoon period (right)

Absolute noise levels are not shown for several reasons. Noise levels depend greatly on drone type and their flight configuration. In this test case the DJI Matrice 600 is equipped with propeller that have only 2 blades and rotate with relatively low rotation frequencies. This leads to extremely low frequency tonal noise content, to which the human ear is not well adapted and hence cannot hear very well. This is well translated by A-weighting filters. This configuration can be considered fortunate for the population since first psychoacoustic studies show that sharpness might be an important contributor to noise annoyance [10][11], and in general low frequencies are better masked by broadband urban background noise.

However for methodology demonstrations, levels are very limited. Other drone types with other propellers would have led to higher noise levels (either due to higher noise emission or higher, and hence less filtered, frequency content).

Another point is that, notably, the 15-minute integration period stands in contrast to commercial aviation norms (being relatively short) and drone flyover durations (being comparatively long), warranting further discussion on its applicability.

This "long" time integration also flattens out a lot L_{Aeq} values when only few drones overfly the receivers during the given time period.

Figure 6 shows a comparison of the two ConOps during the afternoon period. Changing the route type from free route to grid based necessarily implies that different sectors will be overflown. This will have consequences on the number of people exposed, when combining noise and population density. For noise considerations alone, the main impact will come from the difference in flight height as seen in the example of Fig. 2. Since mean flight heights are much higher for the grid based scenario, noise levels could be expected to be lower at receiver positions, since drone-receiver distances increase. However, the area of interest comprises densely built areas; the sound rays therefore encounter many buildings and are partially masked to the receivers. At higher altitudes rays propagate freely, without obstacles, towards the receivers. Contour maps for the grid based scenario are hence often more widespread than for the free route scenario where drones fly lower and are masked by the buildings (see Fig. 6).

In general, more detailed analyses are necessary for assessing what is the exact cause of increased or decreased noise levels: drone number, change in route, presence of buildings, flight height etc.

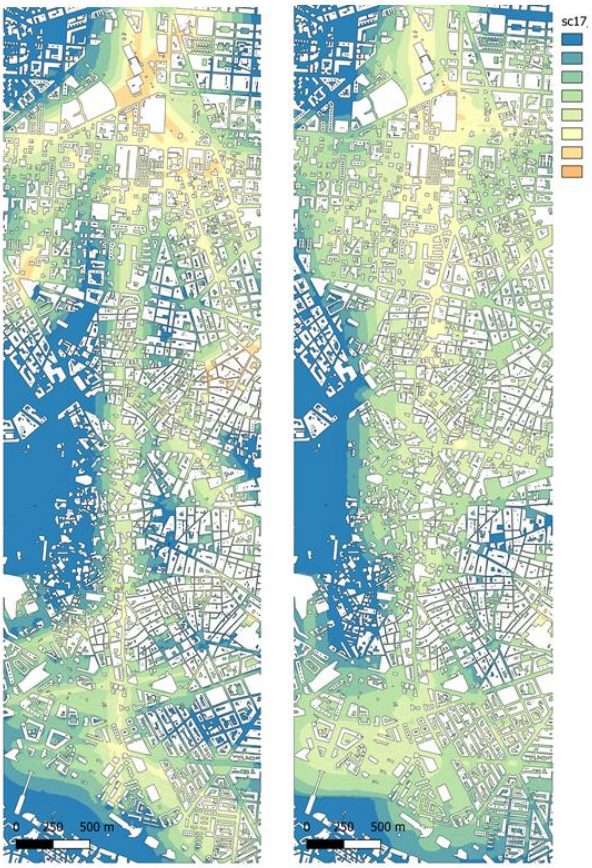


Figure 6. $L_{Aeq,15\ min}$ [dBA], afternoon : free route (left), grid based (right)

5. CONCLUSION

In the MUSE project, we enhanced a noise calculation toolchain to account for drone fleet scenarios, applying it to a parcel delivery case study in a Madrid area, Spain. Scenario types varied in route pattern, flight altitude, flight number etc. In this paper some results are shown for fleets composed of DJI Matrice 600 drones in different configurations, leading to interesting analyses with regard to flight height impact, importance of background noise and choice of drone type.

This work will be developed further in upcoming publications, with more detailed investigations of the impact of flight number per hour (20 / 40 fph) and impact of the considered hour of the day and hence varying number of flights and number of exposed people. Additionally, a more thorough discussion about the employed metrics and indicators will be led. These studies will refine our understanding of drone operations' noise effects, informing strategic decisions in aerospace.

6. ACKNOWLEDGMENTS

The authors acknowledge the MUSE consortium members who contributed to the creation of the scenarios and the discussion about noise indicators, i.e Miguel Baena, Marta Alonso and David Mocholi (NOMMON), Cristina Barrado (UPC), Emir Ganic and Tatjana Krstic (FTTE), Antoine Masse and An Vo Quang (IGN-FI).

This paper is part of a project that has received funding from the SESAR 3 Joint Undertaking (SESAR 3 JU) under grant agreement No 101114858. The JU receives support from the European Union's Horizon Europe research and innovation programme and the SESAR 3 JU members other than the Union. The results reflect only the author's view, and the SESAR 3 JU is not responsible for any use that may be made of the information it contains.

7. REFERENCES

[1] T. Krstić Simić, E. Ganić, B. Mirković, M. Baena, I. LeGriffon, and C. Barrado. "U-Space Social and Environmental Performance Indicators", *Drones* 8, no. 10: 580. https://doi.org/10.3390/drones8100580

[2] I. LeGriffon, E. Ruaud, "Drone fleet noise impact calculation – a methodology," in *Proc. of INTER-NOISE 2024*, (Nantes, France), 2024.

[3] R. Perret, F. Cuzieux, DynaPyVTOL: a flight mechanics code for VTOL evaluation and control, to be published in *Proceedings of 50th European Rotorcraft Forum*, Marseille, France, 10-12 Septembre 2024

[4] L. Bertsch, L. Sanders, R. Thomas, I. LeGriffon, J. June, I. Clark, M. Lorteau. "Comparative Assessment of Aircraft System Noise Simulation Tools", *Journal of Aircraft*, Vol. 58, No.4, July 2021, doi : https://doi.org/10.2514/1.C036124

[5] P. Beaumier, Y. Delrieux. "Description and validation of the ONERA computational method for the prediction of blade-vortex interaction noise". In *Proceedings of 29th European Rotorcraft Forum*, Friedrichshafen, Germany, 16-18 September, 2003

[6] G. Reboul, A. Taghizad. Semi-analytical modelling of helicopter main rotor noise. In *Proceedings of*

38th European Rotorcraft Forum, Amsterdam, Netherlands, 04-07 September, 2012

[7] G. Graziuso, A.B. Francavilla, S. Mancini, C. Guarnaccia. Open-source software tools for strategic noise mapping: a case study. *Journal of Physics: Conference Series*, Vol. 2162, 012014, 2022

[8] A. M. Veytia et al, "Metropolis II: Benefits of Centralised Separation Management in High-Denisty Urban Airspace", *in Proc. of 12th SESAR Innovation Days*, (Budapest, Hungary), 2022.

[9] C. Barrado, E. Salamí, A. Gallardo, L.X. Herranz, and E. Pastor, (2021). "Understanding the implications of the future unmanned air traffic growth". In IEEE/AIAA 40th Digital Avionics Systems Conference (DASC).

[10] D. Y. Gwak, D. Han, and S. Lee, (2020). "Sound quality factors influencing annoyance from hovering UAV," *Journal of Sound and Vibrations* 489, 115651

[11] C. Kawai, J. Jäggi, F. Georgiou, J. Meister, R. Pieren, and B. Schäffer. "Short-Term Noise Annoyance towards Drones and Other Transportation Noise Sources: A Laboratory Study*". The Journal of the Acoustical Society of America* 156, nº 4 (10/2024): 2578-95. https://doi.org/10.1121/10.0032386.

DOI: 10.61782/fa.2025.0863



FORUM ACUSTICUM
EURONOISE 2025

THE EFFECTS OF TIME-VARIANT CHARACTERISTICS OF UNMANNED AIRCRAFT SYSTEM NOISE ON REPORTED ANNOYANCE

Zuzanna Podwinska[1*] **Carlos Ramos-Romero**[1] **Marc Green**[1]
Antonio J Torija[1]
[1] Acoustics Research Centre, University of Salford, UK

ABSTRACT

Flight missions of Unmanned Aircraft Systems (UAS) are inherently unsteady due to the complex interactions between the environment (e.g., wind conditions) and the operative flight control system. These interactions result in the unsteadiness of the acoustic footprint, which affects psychoacoustic attributes even during apparently stable operations like hovering. This study investigated how time-varying characteristics of noise produced by hovering multi-rotor UAS affect human annoyance ratings. An in-house framework for synthesis and auralisation was applied to generate a corpus of UAS noise stimuli. The synthesis method allowed the modification of time-variant attributes of both the tonal and broadband components by altering frequency and amplitude modulation parameters. The stimuli were evaluated in a listening experiment in which participants were asked to rate their short-term annoyance in a relative magnitude estimation task. An analysis with mixed-effects linear models revealed that higher modulation depth and lower modulation frequency resulted in sounds rated as more annoying. Additionally, modulation parameters changing over time, particularly aperiodic modulation functions and signals with non-zero slope, produced less annoying sound than constant parameters. Overall, the results emphasise the importance of time-varying characteristics of sound for reported noise annoyance, with potential implications for flight control optimisation of UAS for lower noise annoyance.

Keywords: *environmental noise, drone noise, annoyance*

**Corresponding author*: z.m.podwinska@salford.ac.uk.
Copyright: *©2025 Zuzanna Podwinska et al. This is an open-access article distributed under the terms of the Creative Commons Attribution 3.0 Unported License, which permits unrestricted use, distribution, and reproduction in any medium, provided the original author and source are credited.*

1. INTRODUCTION

Since Unmanned Aircraft Systems (UAS) have started gaining interest as a novel resource for transportation systems, their potential contribution to changing the soundscape in populated environments has also emerged as a key topic in environmental acoustics and psychoacoustics. The UAS manoeuvring capabilities allow for rapid changes in flight profile, where integrated control systems (e.g., a proportional–integral–derivative controller) automatically regulate the rotational speeds of electric motors for safety requirements and adapt the operation to sudden changes in environmental conditions (e.g., wind gusts) [1]. These temporal variations in UAS operational conditions are also expected to affect the time-variant characteristics of the emitted noise, which subsequently can affect the response to the noise in affected populations.

This paper studies the potential effect of the time-variant characteristics of UAS noise that might contribute to annoyance ratings during hovering operations. UAS sound synthesis techniques were utilised to generate a corpus of stimuli. This approach allows for inducing time-variant characteristics regarding modulation in both amplitude and frequency over time in a controlled manner [2]. The perceived annoyance of the stimuli was tested in a laboratory listening experiment using relative magnitude estimation, and the relationship between the time-variant features and the reported levels of annoyance was studied.

2. METHODS

2.1 Stimuli

UAS sounds of hovering manoeuvres for two quadcopters were synthesised using additive methods [2]. The vehicles were a DJI Matrice 300 RTK [3] (referred to here as 'M3') which is a medium-size UAS, and a XAG P40 [4]

(referred to here as 'X1') which is a large-size UAS. The sounds consisted of a tonal component and a broadband noise component. The tonal component was expressed as a linear combination of tones tuned to the shaft frequencies, blade-passing frequencies (BPFs), and a corresponding set of harmonics of each rotor. In this study, the first 15 harmonics were considered a representative contribution of the tonal component. The broadband noise component was generated by filtering Gaussian white noise. The applied filter mimics the frequency response of the moving-media filter applied to the noise spectrum of a hovering recording [2]. To manipulate the time-variant characteristics of the generated sound in a controlled manner, modulation parameters for both amplitude and frequency are included in the model.

Amplitude modulation (AM) of the broadband component is controlled by the modulation depth m and an AM function which simulates interaction of two pair of propellers spinning at slightly different RPMs, defined as:

$$AM = (\sin(2\pi BPF_{max}t) + \sin(2\pi BPF_{min}t))/2 \quad (1)$$

where BPF_{max} and BPF_{min} were obtained by peak detection in the BPFs region of the recorded spectrum.

Frequency modulation (fm) of the tones is included in the model to simulate temporal fluctuations of each tone. In this regard, the frequency modulator considers two cases of how fast the tone fluctuates (i.e., high and low modulation frequency). This approach aims to simulate scenarios of instabilities on the motor controller systems as rapid (fm_{high}) or slow (fm_{low}) fluctuations in the RPMs, with resultant variations of tonal frequencies. In this study, the values for the modulator frequency are related with the detected BPFs and number of rotors n_{rotors} as:

$$fm_{low} = (BPF_{max} - BPF_{min})/n_{rotors} \quad (2)$$

$$fm_{high} = (BPF_{max} - BPF_{min}) \times n_{rotors} \quad (3)$$

The final parameter in the modulated tonal component is the frequency modulation index β, which is the ratio between the peak frequency deviation Δf and the frequency of the modulating signal fm. In this paper, the maximum frequency deviation of each tone was settled as constant $\Delta_f = 2.8$ to avoid over modulation.

Because of the differences in BPFs of the two simulated UAS, the high and low frequency modulation values were different for each vehicle. The low fm value was 4.8 Hz for M3 and 2 Hz for X1, while the high fm value was 77 Hz for M3 and 32 Hz for X1.

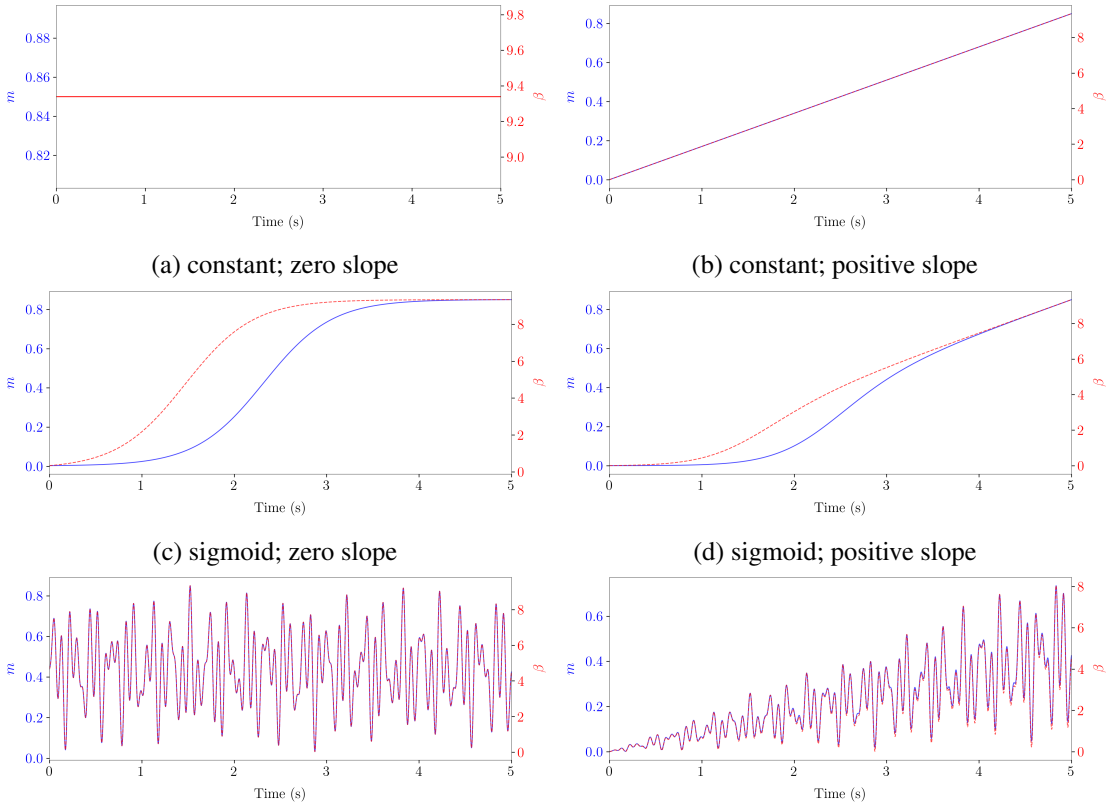
The modulation parameters described before (m and β) can remain unaltered throughout the signal duration, which is the case for an ideal stable flight hovering operation. However, to add time-variant features to the modulation parameters, two other variables have been included. The first one is the "slope", which indicates a potential increase (positive slope) of m and β over time. The second variable is the time varying profile (TVP) ("constant", "aperiodic", and "sigmoid"). The "constant" TVP means either no change over time (Fig. 1a) or a linear increment of the modulation variable over time (Fig. 1b). The "sigmoid" TVP (Fig. 1c and 1d) describes changes in modulation parameters that exhibit a sigmoid evolution over time, where minimal modulation occurs initially, followed by a rapid increase, culminating in the maximum modulation effect towards the end of the sound. The "aperiodic" TVP (Fig. 1e and 1f) induces changes in modulation variables driven by a function that introduces non-repeating variations in the constant modulation of amplitude and frequency factors Mf_{max} (m or β) (see. Eq. 4). The function comprises a sum of sinusoidal components with non-harmonic frequencies scaled by a modulation rate coefficient Q, which reflects environmental variability such as wind speed.

$$Mf(t; Mf_{max}, Q) = Mf_{max}\big[1 + \sin(2Qt) + \sin(2\pi Qt) + \sin(-2eQt)\big] \quad (4)$$

The resulting test matrix for stimuli generation is shown in Tab. 1, the rows of which correspond to the experimental variables used in the study. Note that for stimuli with a positive slope, their fm and m experimental variable values correspond to the maximum value of the slope.

Table 1: Time-variant characteristics

	M3	X1
FM frequency fm	low (4.8 Hz), high (77.03 Hz)	low (2 Hz), high (32 Hz)
AM depth m	0.4, 0.85	
Time varying profiles	constant, aperiodic, sigmoid	
Slope	none, positive	



(a) constant; zero slope

(b) constant; positive slope

(c) sigmoid; zero slope

(d) sigmoid; positive slope

(e) aperiodic; zero slope

(f) aperiodic; positive slope

Figure 1: Slope-shape variability for m and β.

2.2 Experimental procedure

The listening experiment was carried out in an acoustically-treated room. Participants were seated in the middle of the room and listened to the stimuli being played from a PC running a test interface created in MATLAB and connected to the loudspeaker via a RME MADIface XT USB interface.

A total of 50 5-second synthesised stimuli were used in the experiment. They were all A-weighted RMS normalised and the playback level was set to 65 dB(A). Participants were asked to listen to each stimulus and rate it on perceived annoyance using relative magnitude estimation. A reference sound was given which was a recording of the simulated UAS (either M3 or X1). The participants were asked to arbitrarily rate the test sound, assuming the reference sound was 100 on the annoyance scale. No lower or upper limits of the annoyance scale were given. The responses were provided by writing a number in an input field using a keyboard.

Each participant listened to and rated all of the stimuli, which included all combinations of the experimental variables: vehicle, amplitude modulation depth, modulation frequency, time varying profile and slope.

3. DATA ANALYSIS

Before any further analysis, participant ratings were normalised by subtracting 100 from the rating and then dividing by the difference between each participant's maximum and minimum rating. The limits of the rating scale were not given by experimenters, therefore participants were free to use their own estimate of range for rating the stimuli. The normalisation gives us a scale limited between -1 and 1 and allows us to interpret each rating with relation to each participant's individual scale. It also represents stimuli rated as more annoying than the reference as positive,

and less annoying than the reference as negative.

Then, the effects of the independent variables described in section 2.1 on the ratings were analysed using mixed-effects linear models. Participant ID was set as a random effect and the experimental variables as fixed effects. The interaction between vehicle and other variables was added to test if the choice of UAS model included in the experiment influenced the ratings. Additionally, the interaction between time varying profile and slope was included, as the combination of these two variables resulted in six distinct ways in which the modulation parameters could change (see Fig. 1). All statistical analysis was conducted in R, using packages lme4 [5] for fitting mixed linear models and emmeans [6] for calculating contrasts and marginal means.

To investigate the effect of the experimental variables on psychoacoustic metrics, the stimuli were recorded on a single measurement microphone in the middle of the room where the experiment was carried out, with a sampling rate of 48 kHz. A number of time-varying psychoacoustic metrics were then calculated from the recordings using Head Acoustics ArtemiS SUITE [7,8] and the SQAT Matlab toolbox [9]. Tab. 2 lists all the calculated metrics along with the corresponding window size. For statistical analysis, the first 1 s and last 1.5 s of all time-varying metrics except Fluctuation Strength were removed to avoid artefacts. For Fluctuation Strength, the first 4 seconds had to be removed and only the section of the file 1 second after that was stable enough to be included in the analysis. The 5th percentile values (the values exceeded 95% of the time) were calculated for each metric to represent each stimulus in the statistical analysis. These values were analysed with a Principal Component Analysis (PCA) using the FactoMineR package [10] in R. The data used in the PCA was scaled to unit variance.

Table 2: Psychoacoustic metrics used in the analysis

Metric	Source	Window size (ms)
Fluctuation Strength	ArtemiS	17.4
Impulsiveness	ArtemiS	0.9
Loudness DIN	ArtemiS	2.7
Loudness Hearing Model	ArtemiS	5.3
Loudness ISO 532-3	ArtemiS	1.0
Roughness	ArtemiS	20.0
Sharpness DIN	ArtemiS	2.7
Sharpness DIN/Aures	ArtemiS	2.7
Sharpness ISO 532-3/Aures	ArtemiS	1.0
Tonal Loudness	ArtemiS	5.3
Tonality Hearing Model	ArtemiS	5.3
Tonality Aures	SQAT	80

4. RESULTS

4.1 Annoyance ratings

41 participants took part in the experiment, recruited from University students and staff. The response range before normalisation varied significantly, with some participants using only values close to 100 (e.g. 98-112), and others a much wider range of values (e.g. 58-500). This confirms the need for normalising the data. All analysis results below are based on normalised ratings.

Tab. 3 shows the ANOVA table for the fitted mixed-effects linear model. UAS model as well as both modulation parameters (m and fm) were statistically significant variables. There was also a statistically significant interaction between the variables governing how modulation parameters changed over time: time-varying profile and slope. There was no significant interaction between the vehicle model and any of the other variables.

Table 3: ANOVA table for annoyance ratings

Variable	df	F value	p.value	
vehicle	1, 1996	4.00	0.046	*
m	1, 1996	90.24	<0.001	***
fm	1, 1996	319.25	<0.001	***
TVP	2, 1996	51.18	<0.001	***
slope	1, 1996	215.19	<0.001	***
vehicle × m	1, 1996	3.27	0.071	
vehicle × fm	1, 1996	0.43	0.510	
vehicle × TVP	2, 1996	1.37	0.254	
vehicle × slope	1, 1996	2.54	0.111	
TVP × slope	2, 1996	9.12	<0.001	***

Signif. codes: '***' <0.001, '*' <0.05

Tab. 4 shows a post-hoc contrast analysis for the significant variables and interactions. Annoyance ratings were significantly different between the two tested vehicles, with the X1 rated as slightly more annoying than the M3 ($MD = 0.02, p = 0.046$). Higher annoyance ratings were also found in response to high amplitude modulation depth m compared to low m ($MD = 0.09, p < 0.001$) and low fm versus high fm ($MD = 0.16, p < 0.001$). Overall, a positive slope of change was associated with less annoyance than zero slope (all $p < 0.001$) and this

difference was the largest for the constant time varying profile ($MD = 0.19$). The aperiodic profile was also consistently less annoying than the other profiles (all $p < 0.01$). Fig. 2 illustrates this interaction.

Table 4: Contrast analysis for annoyance ratings

Variable	Contrast	Estimate	p.value
vehicle	X1 − M3	0.02	0.046
m	0.85 − 0.4	0.09	<0.001
fm	low − high	0.16	<0.001
Slope			
TVP: constant	none − positive	0.19	<0.001
TVP: sigmoid	none − positive	0.10	<0.001
TVP: aperiodic	none − positive	0.11	<0.001
TVP			
slope: none	constant − sigmoid	0.10	<0.001
	constant − aperiodic	0.15	<0.001
	sigmoid − aperiodic	0.05	0.005
slope: positive	constant − sigmoid	0.02	0.618
	constant − aperiodic	0.07	<0.001
	sigmoid − aperiodic	0.06	0.001

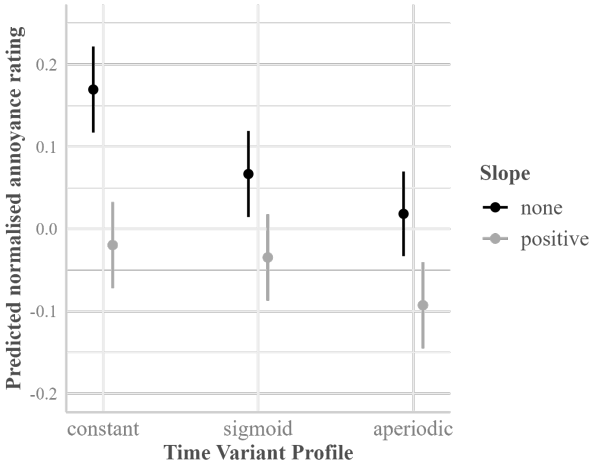


Figure 2: Marginal means calculated from the LMM model for different combinations of the slope × TVP interaction.

4.2 Psychoacoustic metrics

The psychoacoustic metrics were analysed with a PCA. The first 3 components were chosen for further analysis based on eigenvalues being larger than 1. The chosen number of components also corresponds to the most significant decreases in the scree plot gradient (just above the "elbow", see Fig. 3). Together they explain 91% of the variance in the data.

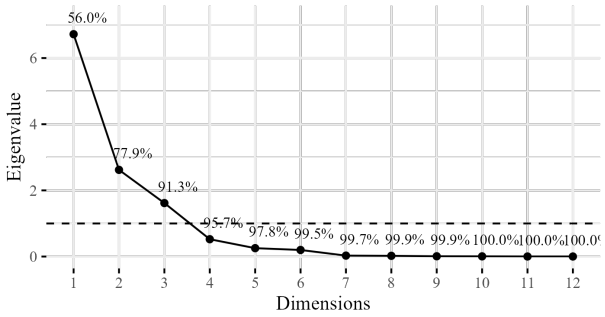


Figure 3: PCA scree plot. Labels show the cumulative variance explained for each additional principal component.

Tab. 5 shows the loadings of all variables on the three principal components. The first component is driven by a number of psychoacoustic metrics. It is positively correlated with Sharpness DIN, Fluctuation Strength and Tonality, and negatively correlated with Loudness ISO, Loudness DIN, and Sharpness ISO. The second component seems to be driven largely by the Loudness HM, but also by Aures Tonality, and to a smaller extent by Roughness, Impulsiveness, and Fluctuation strength. The third component is largely driven by Roughness and Impulsiveness, and to some extent by Aures Tonality. Fig. 4 shows the coordinates of the psychoacoustic metrics in the first two principal components.

Annoyance ratings were added to the PCA analysis as a quantitative supplementary variable. The square cosine metric was calculated between the annoyance ratings and principal components as a measure of their correlation. The correlation was high with PC2 ($cos^2 = 0.71$) and low with PC1 ($cos^2 = 0.006$) and PC3 ($cos^2 = 002$). Fig. 4 shows the projection of annoyance ratings on the 1st and 2nd PCA dimensions. To confirm that annoyance ratings were only related to PC2, a linear regression model was fitted with the annoyance ratings as the outcome variable and the first 3 principal components are predictors. Indeed, only the second component was a statistically significant predictor of annoyance ($\beta = -0.07, SE = 0.006, p < 0.001$).

Table 5: PCA loadings of the variables (psychoacoustic metrics)

Variable	PC1	PC2	PC3
Fluctuation Strength	0.26	−0.32	−0.07
Impulsiveness	−0.17	−0.34	0.55
Loudness DIN	−0.38	0.04	0.01
Loudness HM	−0.12	0.53	0.20
Loudness ISO	−0.38	0.10	−0.01
Roughnes	−0.04	−0.34	0.64
Sharpness DIN	0.37	−0.12	−0.01
Sharpness DIN/Aures	0.33	−0.16	−0.03
Sharpness ISO/Aures	−0.38	0.01	−0.05
Tonal loudness	0.33	0.29	0.13
Tonality HM	0.32	0.29	0.23
Tonality Aures	0.11	0.40	0.40

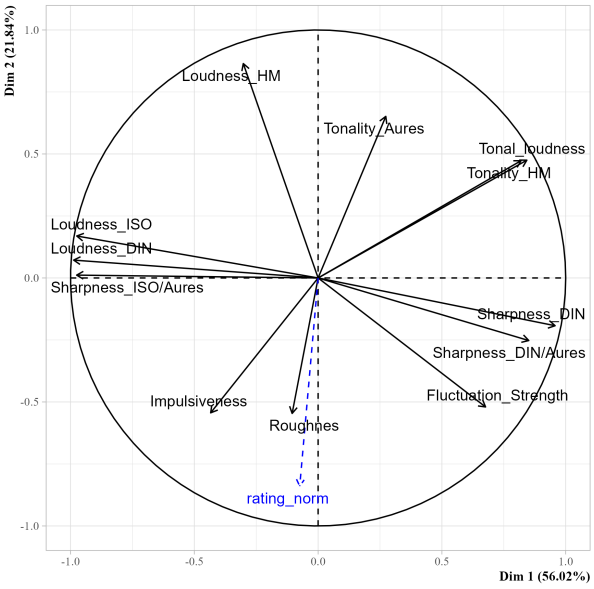


Figure 4: PCA variable plot. Each arrow represents the PC coordinates of one of the variables (psychoacoustic metrics). The dashed blue arrow shows normalised annoyance ratings plotted as a supplementary variable.

To explore the relationship between the psychoacoustic metrics and the experimental variables, the latter were added to the PCA results as qualitative supplementary variables. Tab. 6 illustrates the correlation between these variables and the principal components. The first component has a 99% correlation with vehicle type, indicating it is entirely driven by the difference between vehicles. The second component exhibits significant correlation with all variables except vehicle, while the third component shows significant correlations with fm, m and time varying profile.

Table 6: Square correlation coefficients between the supplementary variables and the principal components. Asterisks indicate statistically significant correlations ($p < 0.05$).

Variable	PC1	PC2	PC3
vehicle	0.982^*	0.000	0.000
fm	0.000	0.143^*	0.173^*
m	0.001	0.080^*	0.311^*
TVP	0.001	0.141^*	0.177^*
slope	0.000	0.273^*	0.006

Fig. 5 shows the individual stimuli divided by experimental variables on the 1st and 2nd principal components.

5. DISCUSSION

The results of the listening tests showed a number of variables that influenced annoyance ratings of simulated UAS noise. The X1 vehicle was rated as more annoying than the M3 vehicle, even with both being normalised to the same L_{Aeq}. The X1 is a larger UAS, with an overall lower pitch sound, which could have contributed to increased perceived annoyance. The difference however was small and the type of UAS did not affect responses to any of the other variables.

The amplitude modulation depth and value of modulation frequency were also significant predictors of annoyance. The higher modulation depth resulted in more pronounced modulation effects, which resulted in higher ratings of annoyance. Similarly, a low value of fm produced a "wobble" which made the modulation more noticeable than in the sound synthesised with high fm. Overall, sounds with more noticeable modulation effects were rated as more annoying.

How the modulation parameters changed over time also had an effect on annoyance. A positive slope in the function driving the change of parameters resulted in a less annoying sound. This could be the result of the modulation being introduced more gradually, making it less no-

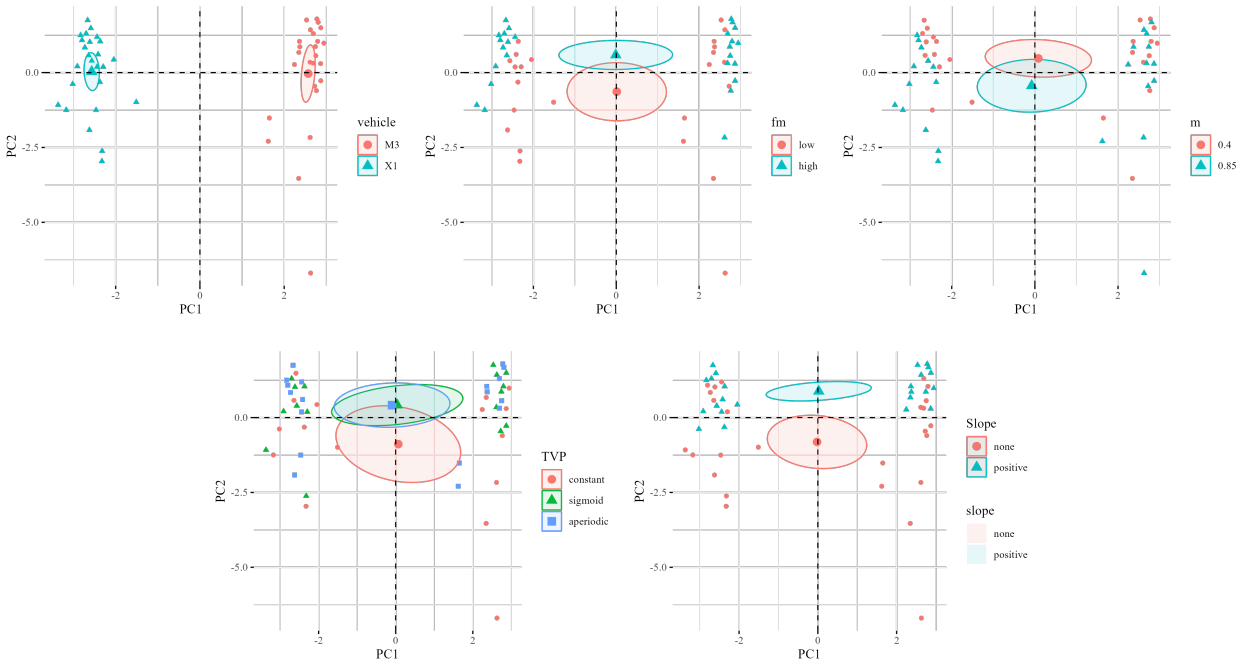


Figure 5: PCA plots of individuals (sound stimuli) with experimental variable means and confidence ellipses around the group means. Each plot shows a different experimental variable.

ticeable. However, the average amount of modulation in the sounds with positive slope was less than in the sounds with zero slope, and it could also be that it was this distinction that drove the ratings. In practical terms, a zero slope scenario would correspond to a static flyover within stable weather conditions, whereas a positive slope could be a result of aircraft movement or adverse evolution of environmental conditions such as an increase in wind speed. Sounds produced using aperiodically-changing modulation parameters were rated as less annoying than those with constant or sigmoidally increasing parameters. This likely is because the randomness of the modulation does not create a clear pattern in the sound and makes the modulation less perceivable. The aperiodic condition is in fact more realistic, whilst the constant condition is a hypothetical extreme.

A PCA analysis of psychoacoustic metrics revealed three principal components of interest. The first component was driven by a number of psychoacoustic metrics and is explained by the difference between the two vehicles. The smaller M3 vehicle was lower in Loudness, but higher in Sharpness, Fluctuation Strength, and Tonality, than the larger X1. The first component of the PCA was not correlated with annoyance ratings, despite the linear model analysis discussed above showing a small statistical difference in ratings between the two vehicles.

The second component of the PCA was strongly correlated with annoyance ratings. Roughness, Fluctuation Strength and Impulsiveness contributed to this component and were all positively correlated with annoyance. This is expected, as Roughness and Fluctuation Strength have been known to affect psychoacoustic annoyance [11], and likewise, the addition of Impulsiveness has been shown to improve predictions of annoyance in response to rotor noise [12]. The second component was also driven by Loudness HM and Aures Tonality, but somewhat surprisingly, these were negatively correlated with annoyance ratings. Loudness Hearing Model is a sophisticated metric which might be picking up a difference in the spectra of the stimuli which was not eliminated by L_{Aeq} normalisation. Regarding tonality, since only parameters related to amplitude and frequency modulation were included as variables in the experiment, and the amplitude of the tonal components remained unchanged, any variation in tonal-

ity values is likely due to an increase in the bandwidth or spread of energy around the tonal frequencies – that is, broader tonal components. This broader spectral content can make the tones less perceptually salient, especially if the energy spreads into adjacent critical bands.

One of the limitations of the current analysis is that the artefacts in calculated psychoacoustic metrics meant that a limited portion of the signals were used to calculate the statistics. This was particularly the case for Fluctuation Strength. In future analysis, metrics other than the 5th percentile might be used to test if we can better capture the changing nature of the modulation parameters. Additionally, a follow up study looks at longer fly-over sounds and methods of rating them in real-time.

6. CONCLUSIONS

This study highlights the significant impact of time-variant characteristics of UAS noise on perceived annoyance during hovering operations. In a laboratory experiment, modulation depth, modulation frequency and the temporal evolution of modulation parameters affected perceived annoyance of synthesised UAS sounds. Overall, low perceptibility of modulation, achieved with low modulation depth, high modulation frequency, as well as unpredictable patterns in the evolution of modulation parameters resulted in lower annoyance. Our analysis also confirmed the influence of Roughness, Fluctuation Strength and Impulsiveness on annoyance, for two different UAS types. Future research will focus on refining psychoacoustic metrics and exploring longer fly-over sounds to better understand the dynamic nature of UAS noise and its impact on human perception.

7. ACKNOWLEDGMENTS

The authors would like to acknowledge the funding provided by the UK Engineering and Physical Sciences Research Council for the DroneNoise project (EP/V031848/1). CRR and AJT would also like to acknowledge funding provided by EU Horizon Europe and UK Research and Innovation (UKRI) under the UK government's Horizon Europe funding guarantee (REFMAP project, grant number 10061935; and ImAFUSA project, grant number 101114776).

The authors also would like to thank Rory Stocks for his help in running the listening experiment.

8. REFERENCES

[1] M. L. Hoang, M. Carratù, V. Paciello, and A. Pietrosanto, "Noise attenuation on IMU measurement for drone balance by sensor fusion," in *2021 IEEE International Instrumentation and Measurement Technology Conference (I2MTC)*, pp. 1–6, IEEE, 2021.

[2] C. A. Ramos-Romero, M. Green, and A. J. Torija Martinez, "Synthesis and auralisations of quadcopter flyovers for psychoacoustic assessment.," in *30th AIAA/CEAS Aeroacoustics Conference (2024)*, p. 3272, 2024.

[3] C. Ramos-Romero, N. Green, C. Asensio, and A. J. Torija, "suas noise characterization during hovering operations," in *Forum Acousticum 2023*, pp. 661–666, 2023.

[4] M. Green and A. J. Torija Martinez, "Soundwalking in salford: A soundscape approach to drone noise assessment," in *QuietDrones Conference 2024*, University of Salford, 2024.

[5] D. Bates, M. Mächler, B. Bolker, and S. Walker, "Fitting linear mixed-effects models using lme4," *Journal of Statistical Software*, vol. 67, no. 1, pp. 1–48, 2015.

[6] R. V. Lenth, *emmeans: Estimated Marginal Means, aka Least-Squares Means*, 2025. R package version 1.11.0-001, https://rvlenth.github.io/emmeans/.

[7] Head Acoustics, "Loudness and sharpness calculation," Psychoacoustic Analyses I, HEAD acoustics, 2018.

[8] Head Acoustics, "Calculating psychoacoustic parameters in artemis SUITE," Psychoacoustic Analyses II, HEAD acoustics, 2018.

[9] G. Felix Greco, R. Merino-Martínez, and A. Osses, "SQAT: a sound quality analysis toolbox for MATLAB," Jan. 2025.

[10] S. Lê, J. Josse, and F. Husson, "FactoMineR: A package for multivariate analysis," *Journal of Statistical Software*, vol. 25, no. 1, pp. 1–18, 2008.

[11] H. Fastl and E. Zwicker, *Psychoacoustics: facts and models*, vol. 22. Springer Berlin / Heidelberg, 2006.

[12] A. J. Torija, Z. Li, and P. Chaitanya, "Psychoacoustic modelling of rotor noise," *The Journal of the Acoustical Society of America*, vol. 151, pp. 1804–1815, 03 2022.

DOI: 10.61782/fa.2025.0749



FORUM ACUSTICUM
EURONOISE 2025

REVIEW OF THE EFFECTS OF DRONE NOISE ON PEOPLE

Joel Li[1] **Brett R.C. Molesworth**[1] **Marion Burgess**[1*]
[1] School of Aviation, University of New South Wales, Sydney, Australia

ABSTRACT

The current use of drones includes, but is not limited to scientific, commercial, military, and surveillance applications. With the application of drones expanding, and to potentially include air mobility to transport people, they will become part of the transportation mix. The approvals from the government authorities for new uses will of course require evidence of safe operation but will also need to consider the noise impact on the communities. To establish clear guidelines there is a need to have knowledge of the effects of the noise on those in the communities. This paper will present findings from a systematic review on the effects of drone noise on people. The review follows the PRISMA-ScR (Preferred Reporting Items for Systematic reviews and Metanalysis extension for Scoping Reviews) methodology. It involved a search for publications that are available with full text in English from 2000 to 2024. The initial search protocol provided 10,613 unique publications. Of these, 32 studies were found to be relevant for further analysis. This has led to identification of the current gaps in knowledge relating to the effects of drone noise on people.

Keywords: *drone noise, effect of noise, uav noise.*

1. INTRODUCTION

Drones, otherwise known as remotely piloted aircraft (RPA), unmanned aerial vehicles (UAVs), or unmanned aircraft systems (UAS), or colloquially referred to as unmanned aircraft, are either fixed wing or rotating wing aircraft that are operated remotely. They can carry a range of tools including, sensors – thermal, infrared, cameras, data recording tools, transponders, winches and many more depending on the intended use of the aircraft. Future applications may even include the transportation of people.

The use of drones is growing. Drones currently have many uses such as for scientific, commercial, delivery, military, surveillance, and recreational purposes. More use cases for drones are being identified and implemented almost daily. With drones being projected to increase in usage by 20% annually [1], the concern about their noise impact on the community will grow alongside their increasing use.

The effects of noise, which is any unwanted sound, can be measured both subjectively and objectively. Subjective responses can include psychoacoustic effects, which is defined as the branch of psychology concerned with the perception of sound and its physiological effects [2]. Objective responses can include physiological responses to noise from drones.

Current regulations and guidelines used to regulate drone usage struggle to keep up to the rapid changes in development and application of drones. Drone usage and the associated noise impact are often regulated by different bodies. For example, in Australia, the regulations and guidelines from the Civil Aviation Safety Authority (CASA) focus on the safe operation of drones and CASA has stated that "*the issue of aircraft or RPA noise is not part of our role*" [3]. The Department of Infrastructure, Transport, Regional Development, Communications and the Arts in Australia is responsible for the management of drone noise. However the Aircraft Noise Regulations 2018 [4] exempt specific types and operations of drones. The rapid growth and development of drones has outpaced the regulatory framework and in regard to noise, research is needed to investigate the effects of the interaction of drones

[*] ***Corresponding author***: marion.burgess@unsw.edu.au.
Copyright: *©2025 First author et al. This is an open-access article distributed under the terms of the Creative Commons Attribution 3.0 Unported License, which permits unrestricted use, distribution, and reproduction in any medium, provided the original author and source are credited. Unported License, which permits unrestricted use, distribution, and reproduction in any medium, provided the original author and source are credited.*

and the people within the built environment so that the appropriate guidance and regulations can be created.

The aim of this systematic review is to synthesise and systematically map research that has investigated the effects that noise from drones have on people within the built environment. It is intended to provide the basis for directing future research on this topic by highlighting the gaps in knowledge that need to be addressed for the development appropriate regulations and guidelines on drone usage in Australia.

The following research question was developed to achieve the aims of this systematic review:

- What are the effects of drone noise on people?

2. METHODOLOGY

A systematic review approach was selected as the purpose aligned with the purpose of a systematic review as defined by Page et al[5]. Namely to identify the types of available evidence in a given field; to clarify key concepts/ definitions in the literature; to examine how research is conducted on a certain topic or field; to identify key characteristics or factors related to a concept; and to identify and analyse knowledge gaps. The PRISMA-ScR (Preferred Reporting Items for Systematic reviews and Metanalysis extension for Scoping Reviews)[5] methodology was selected.

Literature searches were limited to include full-text publications and government regulations that were available in English. The following selection criterion was used to determine whether the piece of literature was included in the review:

1. Studies involving healthy human adults with no hearing impediments. If the study included individuals from the excluded groups but reported the results for such participants separately, the study would then be included
2. Studies investigating the impact that drone noise has on humans; through:
    a. Subjective effects of drone noise on humans.
    b. Objective effects of drone noise on humans.
    c. Comparisons of subjective or objective effects of drone noise to other noise sources.
3. Studies including a source of noise that is perceived as a drone. This can include recording of drone noise, altering available drone noise, or altering any noise to replicate drone noise.

Three categories of search terms were created for this systematic review. The general search strategy is outlined below and was applied to SCOPUS, Dimensions, IEEE, Proquest, Environment Complete, Web of Science and Aerospace Research Central databases.

Table 1. Search terms used for the systematic review

Search Category	Search Terms Used
Drones	drone* OR rpa* OR "remotely piloted aircraft*" OR uav* OR "unmanned aerial*" OR "unmanned air*" OR "UAM*" OR "Urban air mobility*" OR "advanced air mobility" OR "AAM"
Noise	nois* OR acoustic* OR sound* OR psychoacoustic* OR auditory
Effect	impact* OR effect* OR perception* OR physio* OR objective* OR perform* OR task*

*Note * denotes a wildcard search term*

3. GENERAL FINDINGS

The search and selection process of the publications from the initial search strategy from the year 2000 to 2024 first resulted in the return of 16,024 publications. After removing duplications there were 10,613 publications. After a title search, 321 remained. All 321 abstracts, and if necessary full text, were then checked for relevance. After this final check, 31 papers were identified to be relevant of which 28 involved subjective assessments such as annoyance, loudness, threat, safety, pitch, tone, roughness, and other qualities of noise while 6 studies included objective measurements such as the ability to hear and/or identify sounds whilst drone noise is present. The initial findings highlight the diversity in the approach to the types of noise used to represent the noise from drones which is a reflection of the rapidly growing field. Similarly, there is a diversity in the approach to the methodology of assessing the noise from drones which makes selection of guidance on acceptable limits challenging. Thus, there are conflicting outcomes

indicating there is a need for more studies investigating the effects of noise from drones.

4. CONCLUSIONS

This paper summarises the work done up until the present day on this systematic review. By answering the research questions discussed above, this systematic review will be a significant contribution to the understanding the current research into the effects that the new technology of drones has on noise in the built environment. It will assist with development of regulations on the management of this new technology. Identifying the gaps in knowledge on the subjective and objective responses towards drone noise will assist to direct future research in this field.

5. ACKNOWLEDGMENTS

The authors would like to gratefully acknowledge the financial support from the research training program at the University of New South Wales (UNSW).

6. REFERENCES

[1] Scyne Advisory: “Sizing the future drone and advanced air mobility market in Australia”, Air Services Australia, 2024, available from https://www.airservicesaustralia.com/wp-content/uploads/2024/02/Sizing-the-Future-Drone-Industry-in-Australia_February.pdf

[2] Dictionary, O.E.: “psychoacoustics, n,” *Oxford English Dictionary*. Oxford University Press, 2023

[3] CASA: “Drone delivery services”, 2023, available from: https://www.casa.gov.au/drones/industry-initiatives/drone-delivery-services#Noisecomplaints

[4] Department of Infrastructure Transport Regional Development and Communications: “Emerging Aviation Technologies”, Department of Infrastructure Transport Regional Development and Communications, 2020, available from https://www.infrastructure.gov.au/infrastructure-transport-vehicles/aviation/emerging-aviation-technologies

[5] Page, M.J., et al.: “The PRISMA 2020 statement: an updated guideline for reporting systematic reviews.”, BMJ, **372**: p. n71., 2021.

DOI: 10.61782/fa.2025.0024



FORUM ACUSTICUM
EURONOISE 2025

A NOVEL PROCEDURE TO MINIMIZE THE ACOUSTIC AND ENVIRONMENTAL IMPACT OF EVTOL VEHICLES FOR INTRA-CITY MISSION PROFILES

Caterina Poggi[1*] **Giovanni Bernardini**[1] **Massimo Gennaretti**[1]

[1] Department of Civil, Computer Science and Aeronautical Technologies Engineering, University of Roma Tre, 00146, Rome, Italy

ABSTRACT

The paper applies a novel procedure to minimize the emitted noise or maximize vehicle performance for advanced air mobility applications. It considers a hexacopter configuration during the whole flight envelope for a typical intra-city mission profile. For a given flight trajectory conceived as a sequence of steady states segments, a trim solver, suitable for vehicle configurations with redundant controls, is applied in each segment to evaluate the optimal combination of control settings and vehicle attitude optimizing selected target functions like, for instance, noise and performance, while guaranteeing the desired flight condition. To this aim the trim solver is coupled with an aerodynamic solver based on the blade element momentum theory method and an acoustic solver based on the compact source version of the Farassat 1A formulation.

Keywords: *Advanced air mobility, noise reduction, eVTOL, trim procedure*

1. INTRODUCTION

Due to the exponential growth of city overcrowding and pollution, academia and industries are making a great effort to develop eco-friendly alternatives to standard urban mobility. Among them is urban air mobility (UAM), e scenario that is conceivable thanks to significant technological advances, including electric propulsion and batteries. Yet, to allow public acceptance and entry into the service of UAM, some critical issues should be addressed [1], such as environmental pollution and acoustic nuisance (mainly during take-off and landing operations).

In recent years, a great amount of research activities have been carried out to investigate viable strategies and technologies aimed at reducing the noise emitted by conventional vehicle designs, while maximizing aerodynamic performance to reduce fuel and electric energy consumption [2].

In typical eVTOL designs, as those commonly exploited for UAM applications, the propulsive system consists of more than one rotor, suitably tilted during the different flight envelope stages, eventually complemented by fixed wings to lift generation. In this perspective, to reduce the acoustic emissions of these concepts, several strategies can be exploited, from optimising each single rotor's geometrical characteristics [3] to defining optimal installation parameters to maximize the destructive interference of the signals radiated by each rotor [4] or the shielding effect of the vehicle airframe [5]. Even though great progress has been achieved so far, these strategies have the drawback of requiring the re-design of the whole configuration through costly optimization processes.

Recently, the authors proposed a novel procedure to minimize the emitted noise or maximize the aerodynamic performance of multi-rotor systems [6]. This approach overcomes the limitation of re-engineering the whole vehicle, by introducing strictly acoustic and aerodynamic

*__Corresponding author__: caterina.poggi@uniroma3.it.

__Copyright__: ©2025 First author et al. *This is an open-access article distributed under the terms of the Creative Commons Attribution 3.0 Unported License, which permits unrestricted use, distribution, and reproduction in any medium, provided the original author and source are credited.*

constraints since the earliest design phases, and is applicable as an easy retrofitting of already existing concepts. This strategy is based on the observation that typically eVTOL vehicles are conceived as multi-rotor systems, for which the number of available controls is generally greater than those required to trim the vehicle. In addition to the possible methods available in the literature for the control redundancy management [7, 8], recently the author proposed an alternative approach based on recasting the trim procedure into a constrained cost function minimization problem, which provides the optimal combination of control settings and vehicle attitude that guarantees the desired flight condition while achieving targeted design objectives [6]. It has already been successfully applied to minimize the acoustic emissions in terms of tonal and broadband components for specific flight condition cases [9, 10].

Here, the method is applied to minimize the noise emitted by a hexacopter configuration during the whole flight envelope for a standard intra-city mission profile. Starting from a given flight trajectory conceived as a sequence of steady-state segments, the trim solver is applied in each trajectory segment to evaluate the optimal combination of control settings and vehicle attitude to minimize the emitted noise while guaranteeing the desired flight condition. To this aim, the trim solver is coupled with an aerodynamic solver based on the blade element momentum theory method [11] and an acoustic solver based on the compact source version of the Farassat 1A formulation [12].

2. MINIMUM OBJECTIVE FUNCTION TRIM METHOD

For multi-rotor configurations with redundant controls the trim solution, in terms of attitude and control settings, can be achieved by the control identification method presented and validated through comparison with literature results in [6].

This method minimizes an objective function, $\mathcal{O}(\boldsymbol{z}, \boldsymbol{u})$, depending on the flight state parameters, $\boldsymbol{z}$, and the commands, $\boldsymbol{u}$, under the constraint to comply with the steady-state flight mechanics equations of trimmed flight. To this aim, the Lagrange multipliers, $\boldsymbol{\lambda}$, are introduced and the original minimization problem is recast into the following one

$$\mathcal{H}(\boldsymbol{z}, \boldsymbol{u}, \boldsymbol{\lambda}) = \mathcal{O}(\boldsymbol{z}, \boldsymbol{u}) + \boldsymbol{\lambda}^T \boldsymbol{f}(\boldsymbol{z}, \boldsymbol{u}) = min \quad (1)$$

where the $\boldsymbol{f}$ vector collects the equilibrium equations of trimmed flight. The solution of Eq. (1) requires the solution of the following system of equations:

$$\frac{\partial \mathcal{H}}{\partial \boldsymbol{z}} = 0 \; ; \qquad \frac{\partial \mathcal{H}}{\partial \boldsymbol{\lambda}} = 0 \; ; \qquad \frac{\partial \mathcal{H}}{\partial \boldsymbol{u}} = 0 \quad (2)$$

Thus, for a given steady-state flight condition, the system consists of 5 equations given by $\partial \mathcal{H}/\partial \boldsymbol{z} = 0$, N equations given by $\partial \mathcal{H}/\partial \boldsymbol{u} = 0$, and 9 equations provided by $\partial \mathcal{H}/\partial \boldsymbol{\lambda} = 0$, with $5 + N + 9$ unknowns, $(\boldsymbol{z}, \boldsymbol{u}, \boldsymbol{\lambda})$. Thus, Eqs. (2) yield a consistent nonlinear system that can be solved through the standard Newton-Raphson method. Although simple to implement, the drawback of this approach is the need to evaluate the Hessian matrix of $\mathcal{H}$. For this purpose, a standard finite difference algorithm can be exploited to evaluate the derivatives numerically, or, if available, the solution can be derived analytically. Alternatively, the computational burden of such an approach could be alleviated by using other solution approaches, such as the SLSQP (sequential quadratic programming) [13].

For a given set of kinematic variables and commands, the trim solver combines aerodynamic/propulsive loads, evaluated through a component build-up procedure, with the gravitational and inertial loads. The rotor blade is modeled as a hinged, rigid structure, with lead-lag and flap motion in addition to rotation about the feathering axis. The aerodynamic loads are determined by a quasi-steady Blade Element Momentum Theory, with section aerodynamic loads evaluated through a lookup table approach.

The trim problem is solved through two nested iterative loops, one for the solution of Eq. (1) and the other for the rotor dynamics equations solution through a harmonic balance approach. Specifically, starting from current states $(\mathbf{x}, \mathbf{u})$, the aerodynamic loads of each rotorcraft component are evaluated, including those from rotors given as output of the harmonic balance problem. Then, these are used to define a new value of the functions in Eq. (1) and hence of the unknowns to be applied in the next step of the trim loop. This procedure is iterated until convergence. Once the convergence is reached, the spanwise distribution of the blade section aerodynamic loads is determined.

As already stated, the designer can arbitrarily define the objective function in terms of suitable measures of targeted performance as long as they depend on any of the flight variables and the flight parameters involved in the problem. If the selected target function is an acoustic metric, the trim solver has to be suitably coupled with an aeroacoustic solver. In particular, the blade section aero-

dynamic loads, coming from the trim procedure, become the input of the aeroacoustic solver used to evaluate the vehicle radiated noise. The aeroacoustic solver is based on the compact-source version of the Farassat 1A boundary integral formulation [12]. Indeed, since the latter requires the knowledge only of section loads, it can be easily coupled with the blade element theory method implemented within the trim solver described above for the evaluation of aerodynamic loads. For rotors in a subsonic regime, this formulation yields the aeroacoustic pressure field as a superposition of a thickness noise term depending on the blade geometry and kinematics, and a loading noise term associated with the blade aerodynamic loads. Both can be suitably expressed as a combination of line integrals along the spanwise quarter-chord line of the rotor blades [14].

3. NUMERICAL RESULTS

The configuration considered herein consists of a hexacopter vehicle (schematically depicted in Fig. 1) with a maximum take-off weight of 3000 kg, six coplanar and identical three-bladed rotors, each with a radius, R = 3 m, in a vertex-first configuration. The blades have a linear twist of 12°, a mean chord c_w of 0.2711 m, and the airfoil shape is the VR7 profile. In the reference system depicted

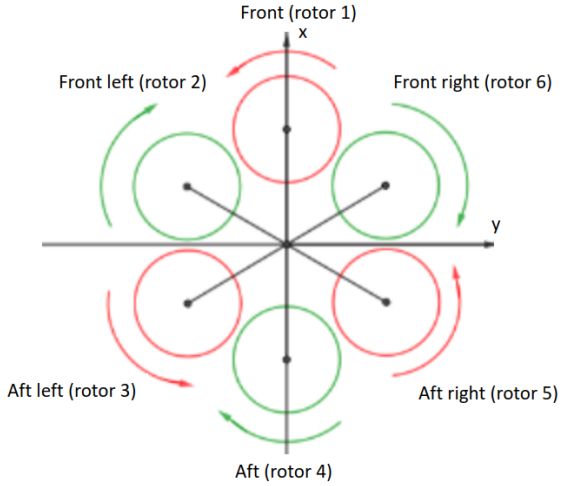


Figure 1. Schematic representation of the hexacopter configuration.

in Fig. 1, the rotors hubs coordinates are listed in Tab. 1.

The mission profile herein considered is schematically depicted in Fig. 2. The transient phases between the

	x [m]	y [m]	z [m]
Rotor 1	6.5	0.0	2.0
Rotor 2	3.25	-5.63	2.0
Rotor 3	-3.25	-5.63	2.0
Rotor 4	-6.5	0.0	2.0
Rotor 5	-3.25	5.63	2.0
Rotor 6	3.25	5.63	2.0

Table 1. Coordinates of the rotor hubs.

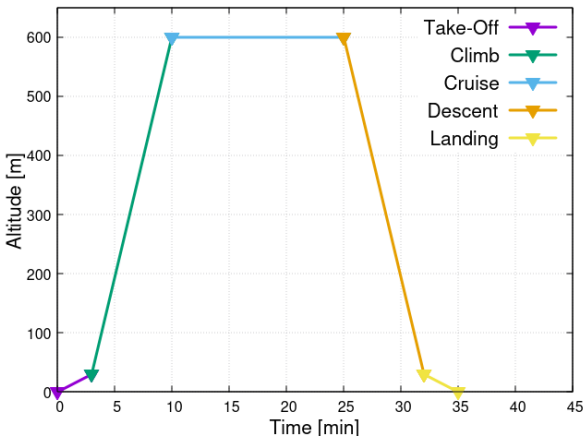


Figure 2. Mission profile.

different segments are ignored (they are assumed to be of short duration and, thus, scarcely affecting the overall nuisance generated).

The steady-state flight operative conditions in each segment of the mission profile are detailed in the following:

- Take-Off (TO): vertical flight from an altitude of 0 m to 30 m at 6 m/s;
- Climb (CL): from an altitude of 30 m to 600 m at 20 m/s, with a flight path angle equal to 12°;
- Cruise (CR): horizontal flight at an altitude of 600 m at 60 m/s;
- Descent (DS): from an altitude of 600 m to 30 m at 20 m/s, with a flight path angle equal to -12°;
- Landing (LN): vertical flight from an altitude of 30 m to 0 m at 6 m/s;

In each segment of the flight envelope, the trim procedure is applied considering two different objective functions to

be minimised:

- Strategy A, minimum torque condition: the objective function is the sum of all the dimensionless rotors' torque, defined as:

$$\mathcal{O}_t = \sum_{i=1}^{N_r} \hat{M}_{z_i}$$

where $\hat{M}_{z_i}$ denotes the dimensionless torque of the i-th rotor and N_r is the number of rotors;

- Strategy B, minimum noise condition: the objective function is the mean Overall Sound Pressure Level (OASPL) evaluated in a selected set of microphones, defined as:

$$\mathcal{O}_{ac} = \frac{1}{N_{mic}} \sum_{i=1}^{N_{mic}} OASPL_i$$

where N_{mic} is the number of microphones.

In particular, in the reference system shown in Fig. 1, the microphones lie over a circle in the xy plane, centred at the origin and having a radius equal to $40R$.

Note that for the evaluation of the radiated noise objective function (here accounting for the tonal contribution only), the frequency analysis required to evaluate the acoustic metric includes a windowing process of the signal recorded during a three-rotor-revolution period to deal with the presence of arbitrary rotor angular velocities. In particular, the Hann windowing is applied, and an energy correction factor is used to maintain the total energy content of the signal.

The blades are assumed to have a fixed pitch set equal to 11° (reference value). Thus, the only available controls are the six rotors' angular velocities. The control settings obtained through the application of strategies A and B are shown in Tab. 2 and Tab. 3, respectively.

The differences in control settings are negligible in all the mission phases except for the cruise. This means that, except for the cruise segment, the controls that minimize noise emissions and rotors' torque are the same. Instead, for the cruise condition, the control settings obtained by minimizing the torque or the noise are significantly different, even if both the minimization processes lead to a set of control settings where the angular velocity of rotor 1 is significantly lower than the others.

For the cruise segment the comparison of the noise and performance objective functions obtained through strategies A and B is reported in Tab. 4. A significant improvement of the value of the specific objective function minimized is obtained: when the torque is the objective function to be minimised, the dimensionless rotors' torque is reduced up to 45% with respect to that obtained through strategy B. On the contrary, when the target function is noise minimization, the average OASPL is reduced by 13 dB. This outcome is confirmed by Fig. 3 which shows the comparison of OASPLs evaluated at the selected set of microphones through the application of strategies A and B.

As already stated, the only active controls used up to this point are the rotor angular velocities, as typically assumed for multirotor control procedures. This means that the collective blade pitch angles are set a priori based on structural and aerodynamic considerations. An alter-

	TO	CL	CR	DS	LN
ω_1 [rad/s]	51.4	42.1	16.5	33.9	36.1
ω_2 [rad/s]	51.5	43.0	37.3	34.9	36.1
ω_3 [rad/s]	51.5	44.9	42.5	36.9	36.2
ω_4 [rad/s]	51.6	45.8	39.4	37.9	36.3
ω_5 [rad/s]	51.5	44.9	31.8	36.9	36.2
ω_6 [rad/s]	51.5	43.0	46.2	34.9	36.1

Table 2. Control settings during the whole mission profile as obtained by application of strategy A.

	TO	CL	CR	DS	LN
ω_1 [rad/s]	51.4	41.9	23.6	33.8	36.0
ω_2 [rad/s]	51.5	43.0	38.1	34.8	36.1
ω_3 [rad/s]	51.5	45.1	39.6	37.2	36.3
ω_4 [rad/s]	51.6	45.6	40.3	37.8	36.3
ω_5 [rad/s]	51.6	45.0	37.0	36.9	36.2
ω_6 [rad/s]	51.5	43.2	40.0	35.1	36.2

Table 3. Control settings during the whole mission profile as obtained by application of strategy B.

	$\mathcal{O}_t$	$\mathcal{O}_{ac}$
Strategy A	1.45	72.47
Strategy B	3.14	59.32

Table 4. Comparison of the objective function for the cruise condition as obtained by application of strategies A and B.

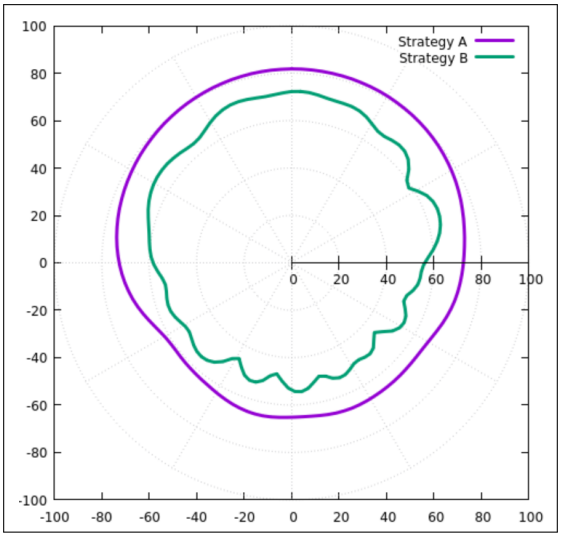


Figure 3. Comparison between the OASPL's directivities obtained for the minimum noise and minimum torque cases.

native approach might be considering the blade pitch angles as additional controls. But, being the use of variable blade pitch propellers unrealistic for standard configurations, the idea is to define an optimal pitch angle to be exploited for the whole flight envelope. To evaluate the optimal pitch, the trim procedure is applied considering 12 available commands for a selected flight condition. Once determined, the optimal pitch is kept fixed for the whole mission profile, and the trim procedure is applied with the angular velocities as the only available commands.

To this purpose, strategies A and B are applied in the takeoff condition, to evaluate the corresponding optimal collective angles, considering six angular velocities and six collective angles as available controls. The noise minimization leads to an increase of the collective pitch angle, with an optimal value of $12.7°$ (upper bound of the design space due to aerodynamic constraints), and equal for all the rotors. Instead, the minimization of the rotor torque results in a decrease of the pitch angle, with an optimal value of $9.3°$ (only slight differences are obtained among the rotors, less than 2%). The angular velocity control settings obtained through strategies A and B in combination with the optimal pitch angle setting are shown in Tab. 5 and Tab. 6, respectively.

The objective function obtained through the two strategies when applying the corresponding optimal pitch

	TO	CL	CR	DS	LN
ω_1 [rad/s]	60.0	48.7	36.7	38.5	40.7
ω_2 [rad/s]	60.0	49.5	38.8	39.3	40.7
ω_3 [rad/s]	60.0	51.4	43.2	41.3	40.7
ω_4 [rad/s]	60.0	52.2	45.6	42.2	40.7
ω_5 [rad/s]	60.0	51.2	43.2	41.3	40.7
ω_6 [rad/s]	60.0	49.5	38.8	39.3	40.7

Table 5. Control settings during the whole mission profile as obtained by application of strategy A with the optimal pitch setting.

	TO	CL	CR	DS	LN
ω_1 [rad/s]	47.5	37.7	31.4	31.4	33.1
ω_2 [rad/s]	47.4	40.4	32.0	32.3	33.2
ω_3 [rad/s]	47.5	42.6	35.1	35.3	35.5
ω_4 [rad/s]	47.5	41.3	42.2	35.6	33.2
ω_5 [rad/s]	47.4	42.8	35.4	34.4	33.3
ω_6 [rad/s]	47.5	40.3	31.4	33.3	35.3

Table 6. Control settings during the whole mission profile as obtained by application of strategy B with the optimal pitch setting.

angles are compared in Fig. 4 and Fig. 5 for the noise and torque objective functions, respectively. For the sake of completeness, the objective functions obtained by assuming the reference pitch angles are also depicted.

Concerning the rotor torque minimization, using an optimal pitch angle improves the target functions throughout the whole flight envelope. Instead, When the objective function is the emitted noise, the average OASPL is reduced in all the mission profile phases except for the cruise. In the latter case the average noise is 4 dB higher than that obtained by setting the reference pitch. In fact, since the optimal collective pitch angle is identified for a single flight condition, not necessarily it remains the optimal value for all the mission profile phases. Nevertheless, the average OASPL is still lower than the OASPLs resulting from a torque minimization strategy. These results confirm that even if an improved target function can be achieved by setting the same reference pitch angle for all the analyses, the application of a suitably determined optimal collective pitch can provide even better outcomes.

Finally, Fig. 6 shows comparisons between the OASPL directivities evaluated through the two strategies

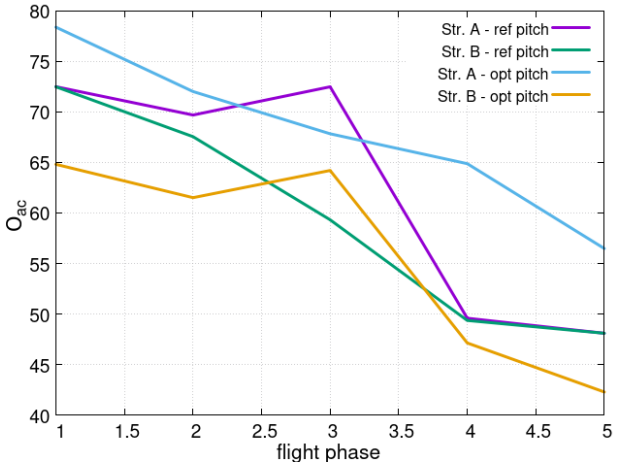


Figure 4. Comparison of the objective function $\mathcal{O}_{ac}$ obtained by application of strategies A and B with the reference and optimal pitch angle.

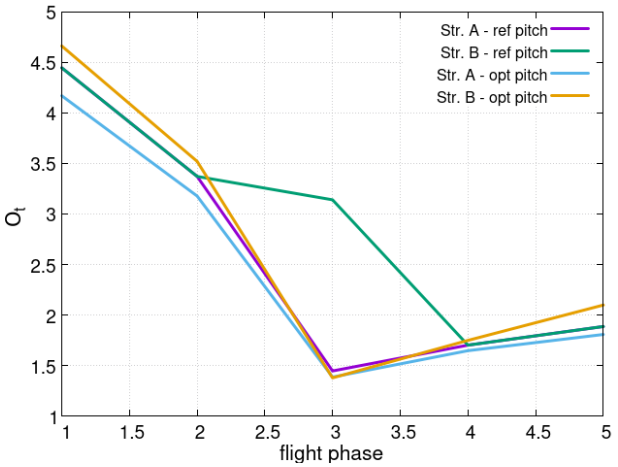
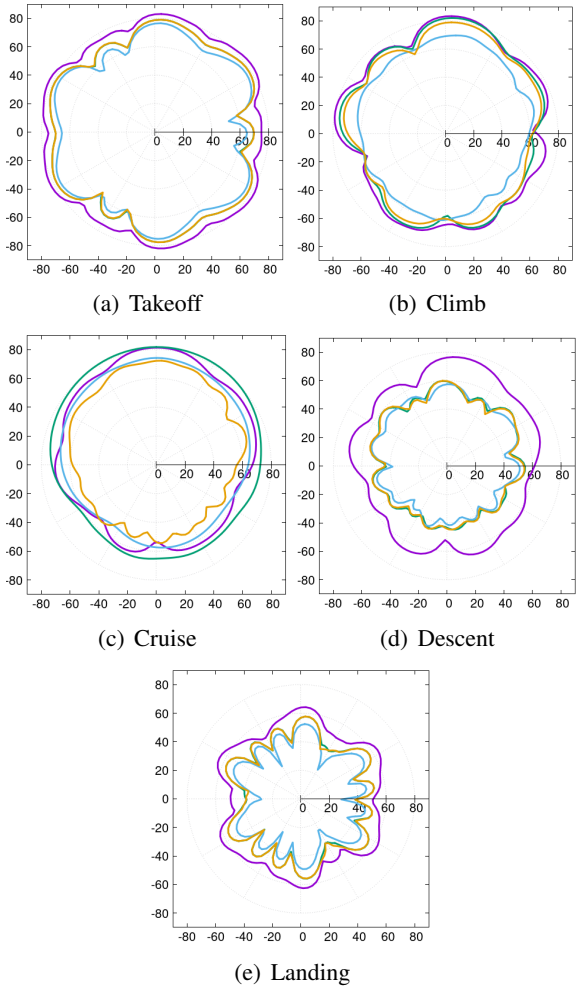


Figure 5. Comparison of the objective function $\mathcal{O}_t$ obtained by application of strategies A and B with the reference and optimal pitch angle.

by the two pitch settings for the whole mission profile.

The reduction in noise emission already observed in Fig. 5 is here confirmed. The decrease in the average OASPL is almost equally distributed among all the observers, with no microphones measuring an undesirable significant increase in noise. As already pointed out, the only exception is the cruise condition, where an increase of noise in all the microphones is observed with respect to



(a) Takeoff (b) Climb

(c) Cruise (d) Descent

(e) Landing

Figure 6. Comparison between the OASPL directivities obtained through the two strategies, with the optimal and the reference pitch angle. Purple line: strategy A - optimal pitch; Green line: strategy A - reference pitch; Light blue line: strategy B - optimal pitch; Orange line: strategy B - reference pitch;

that radiated in the case of noise minimization assuming the reference pitch angle.

4. CONCLUSIONS

This paper proposes a novel procedure to determine the trim condition of multi-rotor systems suitably exploiting the control redundancy to optimize selected target func-

tions, here related to noise emissions and aerodynamic performance. The configuration herein investigated is a hexacopter with a typical intra-city mission profile, which is conceived as a sequence of steady-state conditions. To demonstrate the capability of the proposed approach to achieve an effective improvement of the selected objective function, two different strategies are applied and compared which rely on the minimization of the acoustic emissions and the rotors' torque, respectively. The numerical investigations demonstrate that the minimization of both rotor torque objective function and acoustic metric objective function is successful when the rotor angular velocities are the set of controls to be identified. Furthermore, if the blade pitch angle is set a priori without involving any noise constraint, the improvements are limited. Instead, if the pitch angle is set through a preliminary trim analysis involving both the collective pitch angles and the angular velocities as active commands, the improvement strongly increases with a reduction of noise up to 8 dB, and a reduction of rotors' torque up to 5%.

5. ACKNOWLEDGMENTS

This work has been supported by the European Union HORIZON 2020 program under the project eVTOLUTION (EVTOL MULTI-FIDELITY HYBRID DESIGN AND OPTIMIZATION FOR LOW NOISE AND HIGH AERODYNAMIC PERFORMANCE), grant agreement No 101138209.

6. REFERENCES

[1] S. A. Rizzi, D. L. Huff, D. D. Boyd, P. Bent, B. S. Henderson, K. A. Pascioni, D. C. Sargent, D. L. Josephson, M. Marsan, H. B. He, *et al.*, "Urban air mobility noise: Current practice, gaps, and recommendations," tech. rep., 2020.

[2] I. A. T. Association *et al.*, "Aircraft technology roadmap to 2050," *IATA: Geneva, Switzerland*, 2019.

[3] C. Poggi, M. Rossetti, G. Bernardini, U. Iemma, C. Andolfi, C. Milano, and M. Gennaretti, "Surrogate models for predicting noise emission and aerodynamic performance of propellers," *Aerospace Science and Technology*, vol. 125, p. 107016, 2022.

[4] C. Poggi, M. Rossetti, J. Serafini, G. Bernardini, M. Gennaretti, and U. Iemma, "Neural network metamodeling for an efficient prediction of propeller array acoustic signature," *Aerospace Science and Technology*, vol. 130, p. 107910, 2022.

[5] J. Yin, K.-S. Rossignol, M. Barbarino, D. Bianco, C. Testa, H. Brouwer, S. R. Janssen, G. Reboul, L. Vigevano, G. Bernardini, *et al.*, "Garteur activities on acoustical methods and experiments for studying on acoustic scattering," *CEAS Aeronautical Journal*, vol. 10, pp. 531–551, 2019.

[6] C. Poggi, G. Bernardini, M. Gennaretti, and F. Porcacchia, "Optimal performance trim procedure for multirotor vertical takeoff and landing vehicles," *Journal of Aircraft*, vol. 61, no. 3, pp. 828–838, 2024.

[7] M. E. McKay, R. Niemiec, and F. Gandhi, "Analysis of classical and alternate hexacopter configurations with single rotor failure," *Journal of Aircraft*, vol. 55, no. 6, pp. 2372–2379, 2018.

[8] R. Niemiec and F. Gandhi, "Multi-rotor coordinate transforms for orthogonal primary and redundant control modes for regular hexacopters and octocopters," in *42nd Annual European Rotorcraft Forum*, Lille, France, 2016.

[9] C. Poggi, G. Bernardini, and M. Gennaretti, "A minimum objective function trim procedure for vtols noise reduction," *Aerospace Science and Technology*, vol. 147, p. 109004, 2024.

[10] G. Bernardini, C. Poggi, and M. Gennaretti, "A minimum objective function trim procedure for vtol boundary layer trailing edge broadband noise reduction," in *30th AIAA/CEAS Aeroacoustics Conference (2024)*, p. 3325, 2024.

[11] W. Johnson, *Rotorcraft aeromechanics*, vol. 36. Cambridge University Press, 2013.

[12] G. Bernardini, M. Gennaretti, and C. Testa, "Spectral-boundary-integral compact-source formulation for aero-hydroacoustics of rotors," *AIAA Journal*, vol. 54, no. 11, pp. 3349–3360, 2016.

[13] D. Kraft, *A Software Package for Sequential Quadratic Programming*. Deutsche Forschungs- und Versuchsanstalt für Luft- und Raumfahrt Köln: Forschungsbericht, Wiss. Berichtswesen d. DFVLR, 1988.

[14] K. Brentner and H. Jones, "Noise prediction for maneuvering rotorcraft," in *6th Aeroacoustics Conference and Exhibit*, p. 2031, 2000.

DOI: 10.61782/fa.2025.0299

FORUM ACUSTICUM EURONOISE 2025

DIFFERENCES IN SOUND EMISSION LEVEL OF MULTI-ROTOR UAS DURING HOVER AND CRUISE

Jonas Meister[1*] **Jonas Jäggi**[1]
Timothy Van Renterghem[2] **Reto Pieren**[1]

[1] Empa, Swiss Federal Laboratories for Materials Science and Technology, Switzerland
[2] Department of Information Technology, WAVES Research Group, Ghent University, Belgium

ABSTRACT

UAS noise is an increasing concern in today's society, necessitating effective control and monitoring. One approach to address this issue is the development of reliable UAS noise models. In some studies, the sound emission of multi-rotor UAS was characterized using hover measurements in an anechoic room; however, comparisons with forward-flight measurements revealed discrepancies for certain UAS. To investigate these differences, we conducted measurements during transitions from hover to cruise using an on-board measurement system mounted on the UAS. In addition to recording the emitted sound, the system acquires relevant flight data and the precise UAS position. In this paper, we present initial measurement results comparing the overall emitted sound pressure level (OSPL) at hover and across various flight speeds for two propeller types. For one propeller, the OSPL increases abruptly by 2 dB at low speeds, while a near-linear trend is observed for the other. The constant rotor speed during these changes suggests that aerodynamic factors are likely responsible. Although further analysis is needed, these findings emphasize the importance of assessing different flight conditions when modeling sound emission of UAS.

Keywords: *UAS noise, drone noise, noise measurements, sound emission, onboard measurement*

**Corresponding author*: *jonas.meister@empa.ch.*
***Copyright**: ©2025 Jonas Meister et al. This is an open-access article distributed under the terms of the Creative Commons Attribution 3.0 Unported License, which permits unrestricted use, distribution, and reproduction in any medium, provided the original author and source are credited.*

1. INTRODUCTION

Noise is an increasing concern in today's society and requires careful monitoring and control [1,2]. Depending on the field of investigation, different noise prediction models are necessary, ranging from those that generate overall sound pressure level (OSPL) at receiver positions to auralizations and annoyance models [3–6]. Most of today's existing unmanned aerial systems (UAS) noise models rely on lab measurements in hover mode or stationary ground microphone recordings during cruise.

Wunderli et al. [7] proposed a modeling approach to simulate third-octave band noise emission levels for various types of UAS, derived from lab recordings in hover. For each third octave band, a multi-regression model was developed using (1) rotor rotational speed and (2) emission angle as variables. During a validation study where these models were used to calculate noise levels in cruise flight sections, discrepancies of up to 10 dB were observed compared to models based on lab measurements, independent of rotor rotational speed or cruise speed. To account for this difference, a level correction term for cruise was applied to the OASPL, improving model performance with a maximum standard deviation of 1.8 dB between measurements and simulations. However, the physical cause of this level correction and the flight speed at which it should be applied remained unclear.

We hypothesize that noise emissions in hover and cruise phases may differ significantly, with strong dependence on the UAS and propeller type, and that a mea-

surable transition phase exists where this change occurs. Demonstrating this effect would have important implications for UAS noise measurements and modeling. To investigate this, we measured sound emissions during the transition between hover and cruise for a multi-rotor UAS equipped with two different propeller types. Using an onboard measurement system, we identified significant acoustic differences between these two flight states. In this paper, we present preliminary results from these measurements.

2. METHODS

Since the flight design consists of dynamic maneuvers, the use of stationary microphones would have been challenging. During cruise, the distance between the UAS and the microphone gets large quickly, leading to poor signal-to-noise ratio. Backpropagation of the signal to a fixed distance from the UAS is challenging due to the dynamic changes in geometry. In consequence, we used an onboard measuring system, keeping the distance between microphone and UAS short and constant. In this section, we describe the sound emission measurements with our developed onboard measurement system.

2.1 Experimental Setup

As UAS type, we selected the DJI Matrice 300 RTK [8], recently used in UAS noise studies (e.g. [4, 9]) and a common choice for inspection and mapping tasks. For each measurement, we equipped the UAS with two different commercially available propeller types: the standard R2110, referred to as "Propeller 1," and the R2195, referred to as "Propeller 2." The latter is designed for high-altitude operations, generating more lift per rotation than the standard model. These propellers have distinct shapes (especially the blade tips), as shown in Figure 1.

Table 1. Propeller types installed on the UAS during measurements.

Propeller 1	Propeller 2
	

To measure the emitted sound, the rotational speed of each rotor and the position/velocity of the UAS simultaneously, we used an onboard measurement system called "backpack", developed at the authors' institution (Empa). It has already been successfully used in a recent project, to record UAS sounds for auralization tasks [4] and is described in more detail in [10]. It consists of different parts, described in the following Table 2.

Table 2. Onboard measurement system ("backpack") and its components.

Component	Task
MEMS microphones (attached to arms)	Sound emission recording
Optical sensors	Tracking of rotor rotational speeds
GNSS antenna	Tracking of UAS position
Battery	Power supply
Microcontroller	Data acquisition
SD card	Data storage
Housing	Mounting structure for sensors and microcontroller

We used MEMS microphones (SPH0645LM4H, Knowles Electronics, Itasca, IL, USA) for sound recordings due to their lightweight design. Two microphones were mounted on carbon fiber tubes at a distance of 1.1 m from the nearest propeller tips, positioned symmetrically on either side at two different elevation angles relative to the rotor plane. One microphone was aligned with the rotor plane, while the other was angled 30° downward. To minimize wind-induced self-noise, we installed spherical foam windscreens, which also acted as vibration insulators (not measured). The MEMS microphones contain an AD converter and directly provide digital signals. Recordings were made with a sampling rate of 44.1 kHz and with 16 bit resolution. According to the manufacturers specification, the sensitivity of the MEMS microphones has a large range of 6 dB at 1 kHz. We therefore calibrated the MEMS microphones under free-field conditions. These calibration measurements were performed in an anechoic room with a loudspeaker and a free-field measurement microphone as a reference. The calibration measurements revealed an amplification of high frequencies due to pressure buildup at the added MEMS microphone circuit board. To equalize the frequency response of the microphones, we applied a second order high shelf filter.

To measure the rotational speed of each rotor, we

placed LEDs alongside photodiodes facing each motor. The LED continuously emitted infrared light, and its reflection was measured by the photodiode at a sampling frequency of 1 kHz. To reduce harmonics, we applied a grayscale strip with sinusoidal intensity around the rotating part of the motor.

For precise UAS position tracking, we used two GNSS receivers: one mounted on top of the backpack and one stationary on the ground. This setup enabled real-time kinematic (RTK) positioning in dual-band mode, achieving centimeter-level accuracy. With this configuration, we obtained position updates at a rate of 15 Hz. The complete setup, including the backpack and sensors, is shown in Figure 1.

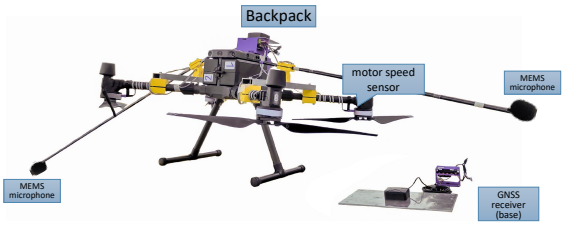


Figure 1. UAS equipped with the backpack and sensors. A second, stationary GNSS receiver (base) enables RTK positioning.

2.2 Flight Test Design

To ensure real-world flight conditions and avoid space limitations, we conducted the measurements outdoors in an open field. The UAS was manually operated, flying extended straight tracks at varying speeds. To minimize ground reflection influences, flights were conducted at an altitude of several 10 meters. The ambient temperature at the measurement site ranged between 5.9°C and 7.1°C, with relative humidity between 56% and 61%, and with low wind conditions (1.4 m/s at the nearest weather station, 10 m above ground).

Since the investigated UAS is designed to carry payloads of up to several kilograms, the attached backpack and sensors had minimal impact on flight performance. The UAS itself weighs 6.3 kg, while the backpack, including all sensors and sensor mounts, adds an additional 1.8 kg.

2.3 Data Processing and Analysis

From the in-flight recordings, time histories of the OSPL were computed, i.e. the unweighted short-term equivalent continuous OSPL with a time window of 1 s ($L_{\mathrm{eq},1s}$). In order to be comparable to the recordings of other UAS types, the obtained levels were scaled to a 1 m reference distance to the UAS's nearest propeller tips, by compensating for geometrical spreading. To obtain a corresponding OSPL assigned to every flight trajectory point, the $L_{\mathrm{eq},1s}$ was interpolated to the sampling rate of the GNSS receivers (15 Hz).

The rotational speed for each rotor was determined by applying Fast Fourier Transform (FFT) to the recorded signals. The rotational speed was then identified using a peak-finding method. For 2-bladed propellers, this corresponds to half the blade passing frequency.

3. RESULTS

This section presents initial measurement results for the UAS at different cruise speeds, equipped with two different propeller types. Figure 2 displays the $L_{\mathrm{eq},1s}$ for both propeller types, covering hover (very low cruise speed) up to cruise at speed of 9 m/s (max. possible speed $>$ 20 m/s). For each 1 m/s flight speed bin, we obtained an average of 75 seconds of flight data for Propeller 1 and 30 seconds for Propeller 2. We fitted the data points with a cubic smoothing spline using a smoothing parameter of 0.1.

Figure 2 shows that within the studied speed range, Propeller 2 exhibits 1 to 2 dB higher emissions compared to Propeller 1. For Propeller 1, a nearly linear increase in sound emission level with increasing cruise speed is observed. In contrast, Propeller 2 exhibits a sudden, sharp increase in emission level by 2 dB at a cruise speed of 3 to 4 m/s. Apart from this abrupt change, the emission levels remain largely unaffected by variations in cruise speed within the observed range. Additionally, the standard deviation of sound levels for Propeller 2 is noticeably higher at lower speeds, reaching almost 2 dB, but decreases at higher speeds. For Propeller 1, the standard deviation remains between 0.5 and 1 dB across all speeds.

Since the modeling approach in [7] uses rotor rotational speed as an input, we compare the emitted sound to the measured rotational speeds. Figure 3 presents the mean rotational speed across all four rotors as a function of cruise speed, with smoothing applied similarly to Figure 2. Within this speed range, the mean rotor rotational speed appears largely unaffected by increasing

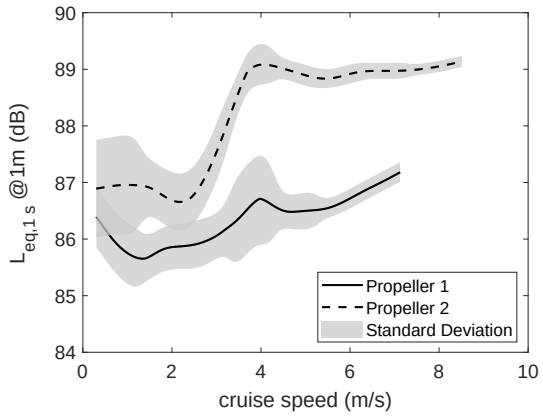


Figure 2. OSPL as a function of cruise speed for two propeller types under an elevation angle of -30° to the rotor plane at a 1 m reference distance to the nearest propeller tips.

cruise speed. As Propeller 2 is designed for higher altitudes, it generates more lift per rotation than Propeller 1, resulting in a noticeably lower rotor rotational speed.

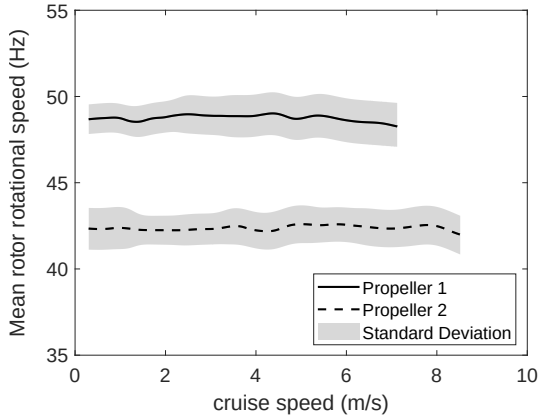


Figure 3. Mean rotational speeds and standard deviation of all four rotors for each measured propeller type as a function of cruise speed.

4. DISCUSSION

Both studied propeller types exhibit distinctly different behavior in terms of sound emission level at different cruise speeds, despite being used on the same UAS type. While the emitted OSPL of Propeller 1 changes only slightly with speed (showing a gradual increase), Propeller 2 displays a pronounced step-like behavior. However, measurements of rotor rotational speeds indicate that this sudden increase in sound level cannot be attributed to changes in rotational speed, as it remains relatively constant within this range. Consequently, we assume that the aerodynamics of the rotors must be influenced by changes in lateral inflow. This is, however, part of future investigations. Additionally the question arises, if a particular shape of the propellers favors this non-linear effect, such as for Propeller 2. Or if for any particular shape, generalizable statements regarding sound emission can be made.

For Propeller 2, applying the modeling approach of [7] would result in a cruise level correction of approximately 2 dB, whereas for the same UAS equipped with Propeller 1, no such correction would be necessary. Additionally, measurements taken within the rotor plane (not presented within this paper) revealed an even higher cruise level correction of 4 dB for Propeller 2. This dependence on the emission angle further indicates that the source directivity of the UAS also differs between hover and cruise.

5. CONCLUSION AND OUTLOOK

In this paper, we measured the emitted sound of a UAS equipped with two different propeller types at various flight speeds to investigate the transition between hover and cruise. Our results show that, depending on the UAS/propeller combination, the sound emission level can increase sharply at relatively low flight speeds, independent of rotor rotational speed. We assume that changes in the aerodynamics are responsible for this phenomena. When developing models for predicting or simulating UAS noise emissions for different flight states, it is therefore essential to measure the emitted sound for each propeller type separately and at both states, hover and cruise at various speeds.

Due to the assumption of aerodynamic changes in cruise flight, not only noise emission levels but also other characteristics of the emitted sound might be affected. Psychoacoustic aspects, as well as measurement data from a smaller UAS equipped with three different propeller types, are currently under investigation and will be presented in a future publication.

6. REFERENCES

[1] F. A. A. (FAA), "Faa aerospace forecast fiscal years 2024–2044," report, 2024.

[2] B. Aydin, "Public acceptance of drones: Knowledge, attitudes, and practice," *Technology in Society*, vol. 59, 2019.

[3] K. Heutschi, B. Ott, T. Nussbaumer, and P. Wellig, "Synthesis of real world drone signals based on lab recordings," *Acta Acust.*, vol. 4, no. 6, 2020.

[4] C. Kawai, J. Jäggi, F. Georgiou, J. Meister, R. Pieren, and B. Schäffer, "Short-term noise annoyance towards drones and other transportation noise sources: A laboratory study," *The Journal of the Acoustical Society of America*, vol. 156, no. 4, pp. 2578–2595, 2024.

[5] C. Ramos-Romero, M. C. Green, and A. J. Torija, "Synthesis and auralisation of quadcopter flyovers for psychoacoustic assessment," 2024.

[6] A. J. Torija and R. K. Nicholls, "Investigation of metrics for assessing human response to drone noise," 2022.

[7] J. M. Wunderli, J. Meister, O. Boolakee, and K. Heutschi, "A method to measure and model acoustic emissions of multicopters," 2023.

[8] DJI, "Dji official online store (https://store.dji.com/ch), visited 27.03.2025."

[9] C. Ramos-Romero, N. Green, A. J. Torija, and C. Asensio, "On-field noise measurements and acoustic characterisation of multi-rotor small unmanned aerial systems," *Aerospace Science and Technology*, vol. 141, p. 108537, 2023.

[10] J. Meister, J. Jäggi, T. van Renterghem, and R. Pieren, "Uav noise emission characterisation using a compact on-board measurement system," 2024.

DOI: 10.61782/fa.2025.0693

FORUM ACUSTICUM EURONOISE 2025

PREDICTION OF ENVIRONMENTAL NOISE FROM ROTORCRAFT USING A NOISE HEMISPHERE WITH TIME-DOMAIN DATA

Yeongmin Jo[1*] **Seong-Yong Wie**[2]
[1] Department of Unmanned Aircraft Systems, Hanseo University, Republic of Korea
[2] Korea Aerospace Research Institute, Daejeon, Republic of Korea

ABSTRACT

Recently, demand of UAM has been increasing because of the high versatility. However, there are several technical issues that makes the public acceptance about the UAM operation. One of the major issues is the environmental noise problem. The environmental noise should be quantified for the noise regulations issued by FAA or EASA.
Measurements of the noise in the urban areas would be the most reliable way for the quantification. However, it is impossible on the current step that any UAM vehicles have not got certification from FAA or EASA. Alternatively, numerical methods efficient for the environmental noise prediction could be used
In this study, we use an environmental noise prediction method based on noise hemisphere database (NHD). The NHD for a UAM vehicle is generated with using noise measurement data, which were obtained from flight tests conducted in K-UAM Grand Challenge. The noise propagation in an urban area is simulated to predict the noise data in the area. Then, the noise data is analyzed to estimate whether the noise satisfy the public acceptance in the urban area.

Keywords: *environmental noise, rotorcraft, noise hemisphere method, auralization*

1. INTRODUCTION

Environmental noise refers to sounds people hear in everyday environments, such as vehicle noise, mechanical noise, and conversational noise. Aircraft noise can also be classified as environmental noise, especially when sounds from aircraft operations like take-offs and landings impact daily life. Such environmental noise significantly affects public acceptance of aircraft. Indeed, the limited frequency of helicopter flights in urban areas can be attributed to their low public acceptance, resulting in frequent complaints.
This public acceptance issue is expected to become even more critical with the advent of Advanced Air Mobility (AAM). When dozens of small Unmanned Aerial Systems (sUAS) and Urban Air Mobility (UAM) vehicles fly within urban environments, citizens exposed to unfamiliar environmental noises may experience discomfort. This discomfort could ultimately undermine public trust in aviation systems, becoming a barrier to related industrial advancements.
Psychoacoustics quantitatively analyzes the psychological discomfort caused by audible noise. Although still relatively unfamiliar in the aviation field, psychoacoustics is essential for enhancing public acceptance of the upcoming AAM era. This analysis requires the subjective evaluation of listeners after auralizing the aircraft-generated noise. For accurate auralization, time-domain data is required instead of the frequency-domain data typically used in many aircraft noise studies.
Environmental noise can be analyzed through direct measurements from flight tests or predictive methods using

[*] ***Corresponding author***: yminjo@hanseo.ac.kr
Copyright: *©2025 First author et al. This is an open-access article distributed under the terms of the Creative Commons Attribution 3.0 Unported License, which permits unrestricted use, distribution, and reproduction in any medium, provided the original author and source are credited.*

analytical approaches. The noise hemisphere method is commonly used, storing aircraft noise data on a hemispherical surface to rapidly predict environmental noise by substituting the aircraft noise source with this hemisphere. However, existing noise hemisphere methods typically propagate sound in the frequency domain, complicating accurate auralization (1,2).
Considering these limitations, this study improved the existing environmental noise prediction code, enabling the creation of a noise hemisphere through noise back-propagation and facilitating noise predictions at specific locations in the time domain. The analysis primarily focused on noise back-propagation data.

2. NUMERICAL METHODS

2.1 Noise back-propagation and auralization

Microphones measure acoustic pressure in the time domain. Thus, noise back-propagation from microphone data to the hemisphere surface is performed for each time instance as described by Eqn. (1).

$$p'_{spr} = p'_{mic.} \times \frac{r_0}{r_s} \quad (1)$$

Here, the subscript denotes information on the hemisphere surface, represents information at the microphone, is the distance from the microphone to the hemisphere center, and is the radius of the hemisphere. This back-propagation is conducted for all measured time instances. The back-propagated noise data on the hemisphere surface does not initially account for physical phenomena such as atmospheric absorption and ground effects. To model these phenomena, previously proposed methods operate in the frequency domain. Therefore, back-propagated noise data is converted into narrow-band (NB) frequency-domain data using the Short Time Fourier Transform (STFT). Each modeling method then adjusts the amplitude of NB frequency-domain data for hemisphere construction.

2.2 Auralization through Grifin-Lim algorithm

Noise data converted to NB frequency-domain form via STFT can be returned to time-domain data using the Inverse STFT (ISTFT). However, the phase angle information of this reconstructed data often lacks accuracy. To resolve this, the Griffin-Lim Algorithm (GLA) is employed to reconstruct the phase angle using only the continuous amplitude of NB frequency-domain data. Figure 1 illustrates differences between original sounds restored with and without applying

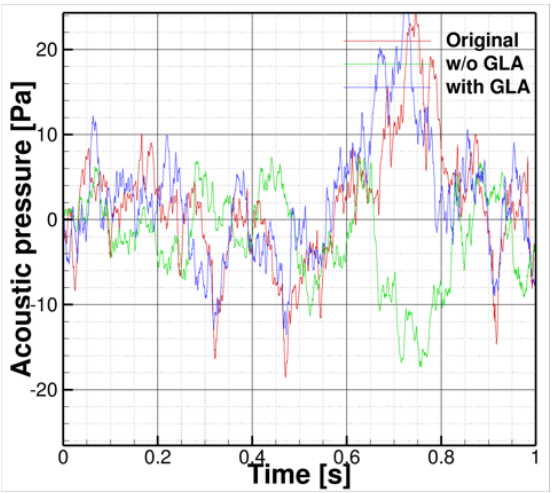


Figure 1. Comparison of restored time-domain data with and without GLA

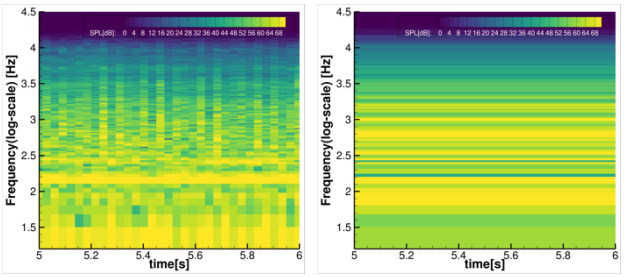
GLA. Although the reconstructed sound slightly differs from the original, GLA prevents critical errors like inverse phase reproduction. Sample points used for noise hemisphere construction are finalized through GLA.

2.3 Noise hemisphere generation using a surrogate model

Traditional noise hemisphere methods utilize grid-based data structures, storing noise data at grid centers or points. Interpolation with pre-generated noise samples often leads to unrealistic sound data due to insufficient grid resolution in time-domain noise prediction and auralization. To overcome this, the current study implements Kriging surrogate models for hemisphere generation, deriving noise information at various radiation angles required by the noise propagation algorithm. Figure 2 shows spectrograms comparing grid-based hemispheres and surrogate model-based hemispheres with the original sound. The surrogate model achieves more accurate restoration similar to the original, unlike the grid-based method, even at high grid resolutions

3. CONCLUSION

This study proposes a method to enable auralization in environmental noise prediction from rotorcraft by transitioning noise hemisphere techniques from frequency-domain to time-domain data. Implementing the Griffin-Lim Algorithm and surrogate models significantly improves the accuracy of sound reconstruction, closely matching original



(a) Original data

(b) Data using a noise hemisphere with 5° resolution

(c) Data using a noise hemisphere with 1° resolution

(d) Data using a surrogate model

Figure 2. Comparison of spectrogram for noise source data

sounds. Future research will utilize the developed time-domain noise hemispheres for noise propagation and auralization studies in both open and urban areas.

4. ACKNOWLEDGMENTS

This work is supported by the Korea Agency for Infrastructure Technology Advancement(KAIA) grant funded by the Ministry of Land, Infrastructure and Transport (Grant RS-2024-00444205).

5. REFERENCES

[1] Y. Jo, "Environmental Noise Prediction of Rotorcraft using Ray-Tracing Method and Noise Hemisphere," KSAS Spring Conference, Ramada Plaza Jeju, April 3-5, 2024.
[2] Y. Jo, H. Jo, W. Jeon, and T. Jo, "Aircraft Environmental Noise Analysis using Prediction Code," KSAS Fall Conference, Vivaldi Park, November 15-17, 2023.
[3] ISO, "ISO 9613-2:2024 - Acoustics - Attenuation of sound during propagation outdoors."
[4] G.A. Daigle, T.F.W. Embelton, and J.E. Piercy, "Some Comments on the Literature of Propagation Near Boundaries of Finite Acoustical Impedance," J. Acoust. Soc. Am., vol. 66, no. 3, pp. 918-919, 1979.
[5] N. Perraudin, P. Balazs, and P. L. Sondergaard, "A Fast Griffin-Lim Algorithm," 2013 IEEE Workshop on Application of Signal Processing to Audio and Acoustics, New Paltz, NY, USA, October 20-23, 2013.

DOI: 10.61782/fa.2025.0472



FORUM ACUSTICUM
EURONOISE 2025

INFLUENCE OF THE SURFACE ROUGHNESS ON THE AERODYNAMIC, AEROACOUSTIC AND PSYCHOACOUSTIC PERFORMANCES OF DRONE PROPELLERS

Giorgia Capobianchi[1*] **Alessandro Di Marco**[1] **Elisa de Paola**[1]
Luana G. Stoica[1]

[1] Roma Tre University, Department of Civil, Computer Science and Aeronautical Technologies Engineering, Via Vito Volterra, 62, 00146 Rome, Italy

ABSTRACT

The increasing air traffic of small multi-rotor UAVs for urban activities has led to a growing interest in the study of the flight noise emitted by these vehicles. Propeller noise has been recognized as a crucial issue, prompting efforts by the scientific community to search for mitigation strategies to reduce noise without compromising the propeller aerodynamic performance. The current research aims to analyze the effect of the propeller blades surface roughness on their aerodynamic, aeroacoustic and psychoacoustic performances. In order to carry out the study, an experimental campaign is conducted on a propeller, in isolated configuration at different rotational speeds. Tests involved the simultaneous measurements of the propeller thrust and noise, through a load cell and an array of microphones respectively. For each combination of parameters, a time-frequency analysis is performed, and a psychoacoustic annoyance model is used to evaluate five psychoacoustic metrics, loudness, sharpness, roughness, tonality and fluctuation strength.

Keywords: *propeller, roughness, psychoacoustics, noise, noise mitigation strategies.*

**Corresponding author*: *giorgia.capobianchi@uniroma3.it.*

***Copyright**: ©2025 G. Capobianchi et al. This is an open-access article distributed under the terms of the Creative Commons Attribution 3.0 Unported License, which permits unrestricted use, distribution, and reproduction in any medium, provided the original author and source are credited.*

1. INTRODUCTION

Unmanned aerial vehicles (UAVs) have experienced a significant increase in popularity over the last decade, due to the wide range of applications they can be used in. They are employed in military operations as well as civil applications such as traffic surveillance, packages delivery, wildfire monitoring, medical purposes, exploration of inaccessible areas etc. [1,2] Despite the advantages of using drones, noise is considered a crucial factor that limits their employability on a large-scale in urban environments. The main source of noise in multirotor vehicles is caused by the propulsion system, i.e. propellers. Since propellers are the components responsible for generating lift, in the effort to reduce propeller noise, particular attention must be paid to ensure that the aerodynamic performance of the propeller does not deteriorate. Noise reduction can be achieved by modifying the blade shape and structure, leading to a deep interdependence of noise and propeller efficiency.

Several studies have been conducted in order to achieve a better understanding of the noise generation mechanism of small rotating blades [3] and to explore the relationship between the aerodynamic performance and the acoustic signature of propellers [4]. These two aspects are naturally in competition. Therefore, to avoid that the reduction of noise is obtained to the disadvantage of the efficiency, multidisciplinary optimization algorithms are often employed in order to achieve a trade-off between the two aspects [5,6].

Recent researches have focused on the impact assessment on propeller aeroacoustics of the addition of roughness on the blade surface [7–9]. The application of a microfiber

coating on the propeller blades [7], or the use of propellers with high surface roughness values [8] have been found to lead to a noise reduction if compared with the baseline propeller. Hasegawa et al. [7], in particular, demonstrated that the application of a microfiber coating effectively reduces the broadband noise emitted by the propeller in the frequency range between 3 kHz and 10 kHz. The noise reduction becomes more pronounced as the position of the microfiber coating moves towards the blade tip. This, combined with the fact that the reduction occurs at high frequencies, suggests that the microfiber coating modifies the characteristics of the flow associated with the turbulent boundary layer trailing-edge noise (TBLTE) and the laminar boundary layer vortex-shedding noise (LBLVS).
Moreover, noise generated by UAVs is strongly related to a sense of annoyance in human listeners. The annoyance that people experience when exposed to UAVs noise is found to be greater than the one related to other vehicles, such as road vehicles [10]. Evidence highlights that environmental noise pollution significantly affects public health, well-being, and quality of life [11]. Recent focus on public health, encompassing both physical and mental dimensions, plays a crucial role in directing research and innovation in this area, aiming to ensure an improved quality of life and psychosocial well-being.
The indicators typically used to assess the acoustic behavior of a source, such as the overall sound pressure level (OASPL), calculated by integrating the power spectral density over the audible frequency range (between 20 Hz and 20 000 Hz), although very useful to determine the acoustic efficiency of a vehicle, can not be fully representative of the human perception. To evaluate the annoyance perceived under laboratory conditions, participants were exposed to specific noises and asked to numerically rate their level of annoyance. Statistical indicators were then derived from these ratings [10, 12–14]. Specifically, the mean annoyance indicator (MA) was calculated as the primary parameter, based on the average rating of all those involved in the study. However, the MA obtained from a specific laboratory trial can not be directly compared with the same parameter from another trial, unless additional tests are performed.
For this reason, psychoacoustic models have been developed to mathematically calculate and directly compare the relative annoyance degree of different sounds.
Since the perceived annoyance is found to be strongly dependent on the spectral characteristics of the sound, specific metrics are used to quantify these properties [15–17]. These metrics include loudness, sharpness, roughness, tonality and fluctuation strength. A weighted combination of these parameters enables the calculation of psychoacoustic annoyance (PA). According to Zwicker [18], PA can be described as a function of loudness, sharpness, fluctuation strength and roughness. This model, however, does not take tonality into account. To address this limitation, Di et al. [19] enhanced the model by including tonality as a dependency in the PA function, making it suitable for comparing tonal and atonal noises.
The present study intends to investigate the influence of the surface roughness on the aerodynamic, aeroacoustic and psychoacoustic behaviour of a propeller. The aim is to determine if an improvement can be achieved from the aeroacoustics and psychoacoustics point of view without compromising the propeller aerodynamic performance.
To this purpose, an experimental campaign has been carried out in the Fluid dynamics Laboratory of the University of Roma Tre. A load cell was used to measure thrust under static conditions while a linear microphone array was installed to collect acoustic data and, hence, to perform an analysis in terms of OASPL and psychoacoustic indicators.
The paper is organized as follows. Details about the experimental set-up and the measurement techniques are reported in Sec. 2. The results of the aerodynamic characterization and the acoustic and psychoacoustic measurements are presented in Sec. 3, with the conclusions drawn in Sec. 4.

2. METHODOLOGY

2.1 Experimental Setup

The experimental investigation was carried out in the Fluid dynamics Laboratory of the University of Roma Tre. The propellers used in this campaign are APC 8x6 E, with a diameter D of 20.48 cm and a pitch of 15.3 cm. Each propeller features a different surface roughness value. Apart from the commercial off-the-shelf propeller, the other roughness values were achieved by applying materials with varying grain sizes to the blades near the tip and in correspondence of the trailing edge in the suction side, as in Fig. 1, following the methodology in [7]. The grain sizes are equal to 27 µm, 50 µm, and a mixture of particles ranging from 70 to 110 µm. Tab. 1 provides a summary of the different values of the propeller's surface roughness along with the corresponding labels used in the graphs in Sec. 3.

The propellers were operated in static condition and

Table 1. Values of the propeller's surface roughness and the corresponding labels.

Roughness 1	R1	27 µm
Roughness 2	R2	70-100 µm
Roughness 3	R3	50 µm
Roughness 4	R4	baseline

in a pusher configuration at a maximum chord-based Reynolds number of about 7×10^4, based on the chord at 75% of the blade. The rotational speed of the propellers was set equal to six different values: 5500 RPM – 6000 RPM – 6500 RPM - 7000 RPM – 7500 RPM – 8000 RPM for the current experiment. The RPM control was managed through a LabVIEW program, which ensures that the RPM variation remains within 1.5% of the desired value.

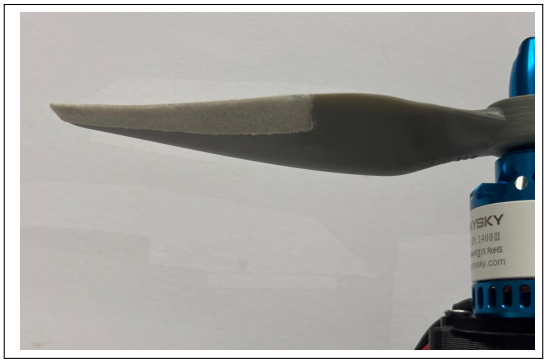


Figure 1. Propeller APC 8X6 E with a roughness value of 50 µm

2.2 Acoustic measurements

Four Microtech Gefell M360 electret microphones were used to perform the acoustic acquisitions. Each microphone has a diameter of 7 mm and has a flat frequency response in a range between 20 and 20 kHz with a maximum sound pressure level of 130 dB. The reference pressure is 20 µPa and the microphones have an integrated preamplifier. Microphone signals were recorded for a total of 10 s at 100 kHz. The microphones were mounted on a linear stand parallel to the propeller rotational axes and positioned at 0.7 m from it, that is equal to 3.5 D. The first microphone was aligned with the propeller plane, the others were positioned at 15°, 30° and 45° with respect to the propeller plane, in the outlet region. Fig. 2 shows in detail the setup used to perform the acoustic measurements. A fifth microphone was then placed in the nearfield of the propeller to perform the RPM control.

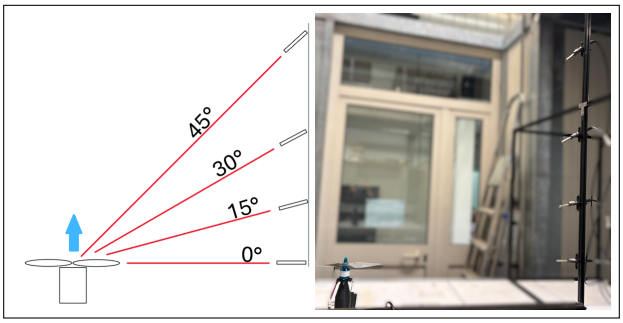


Figure 2. Schematic (left) and photo (right) of the experimental setup.

2.3 Thrust acquisitions

A RoHS low force compression load cell FS20 was used to perform thrust measurements. It can measure up to 1500 Grams-Force and the sensitivity was determined through the utilization of known weights. The signals were recorded for a total of 10 s at 100 kHz and the average values were calculated. The load cell was positioned into the propeller support specifically created to allow the transmission of the force in the x direction. Fig. 3 shows the load cell and the motor support.

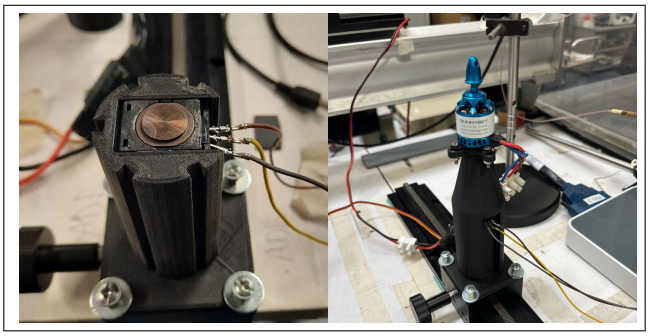


Figure 3. Load cell (left) and motor support (right).

2.4 Analysis

To perform the acoustic analysis, the sound pressure spectrum level (SPL) and the OASPL were calculated according to Eqn. (1) and Eqn. (2), respectively.

$$SPL(f) = 10\log_{10}\frac{PSD(f)}{p_{ref}^2} \tag{1}$$

$$OASPL = 20\log_{10}\frac{\sigma(p_m)}{p_{ref}} \tag{2}$$

where PSD is the power spectral density of the signal, calculated with a frequency resolution of $\Delta f = 3$ Hz, p_{ref} is the reference pressure and it is set equal to 20 µPa and $\sigma(p_m)$ is the standard deviation of the pressure signal from which the mean value has been subtracted.
Moving on to the psychoacoustic analysis, the open-source MATLAB toolboxSQAT (Sound Quality Analysis Toolbox) [20] was used. In particular, the model implemented here to calculate the perceived annoyance is the one proposed by Di et al. [18]. Psychoacoustic annoyance is defined as in Eqn. (3).

$$PA = N_5\left(1 + \sqrt{w_S^2 + w_{FR}^2 + w_T^2}\right) \tag{3}$$

where w_S, w_{FR} and w_T are defined as in Eqn. (4), Eqn. (5) and Eqn. (6).

$$w_S = \begin{cases} (S - 1.75)(0.25\log_{10}(N_5 + 10)), & S > 1.75 \\ 0, & S \leq 1.75 \end{cases} \tag{4}$$

$$w_{FR} = \frac{2.18}{N_5^{0.4}}(0.4F + 0.6R) \tag{5}$$

$$w_T = \frac{6.41}{N_5^{0.52}}T \tag{6}$$

where N_5 is the fifth percentile loudness and S, FS, R and T are the other psychoacoustic metrics: sharpness, fluctuation strength, roughness and tonality respectively.

3. RESULTS AND DISCUSSION

In this section the results are analyzed and commented. Starting from the analysis of thrust, Fig. 4 shows that the two propellers R1 and R2 exhibit better aerodynamic performance than the baseline propeller at all rotational speeds tested, with a maximum thrust gain of 0.3 N at 6000 RPM. The same cannot be said for the propeller R3, which instead shows lower performance than the baseline propeller at low RPM, but recovers from 7500 RPM onward, achieving the best overall performance at 8000 RPM.

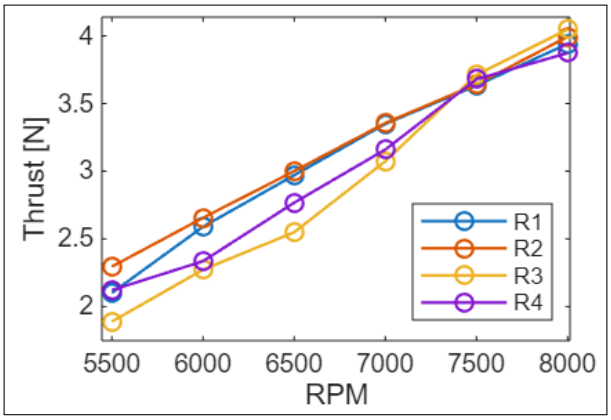


Figure 4. Thrust vs RPM

Fig. 5 shows the sound pressure spectrum level for a rotational speed of 7000 RPM and for all the propellers tested. The propellers with the add-on show a reduced broadband noise contribution than the baseline one, especially at the lower frequencies, up to 5 kHz. The same behavior is observed for all the rotational speeds tested and it is particularly pronounced for the propellers R1 and R2.
A zoom of the first 15 BPFs at 7000 RPM is provided in Fig. 6. In addition to the lower broadband noise, it can be observed that, in correspondence of the harmonics of the BPF, the propellers with the add-on reach higher values of SPL than the baseline (R4), i.e. the tonal noise contribution is higher, especially for R1 and R3.
In agreement with this observation, the values of tonality, the psychoacoustic indicator that evaluates the proportion of pure tones in a noise signal, are found to be higher for the propellers with the add-on compared to the baseline, which exhibits lower values across all RPM, as shown in Fig. 7. The greatest difference is observed at 7000 RPM, where the tonality value of the propeller R1 is 50% higher than the tonality of the baseline. Furthermore, it is worth emphasizing that the R2 propeller exhibits both a significantly reduced broadband noise and a relatively minor increase in tonal noise. This combination of contributions is expected to provide a good trade-off for achieving a better overall acoustic performance.

The OASPL values of the four propellers are com-

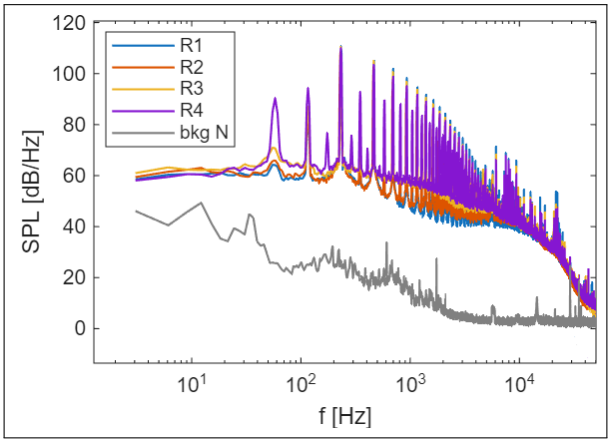


Figure 5. Spectra of the nearfield microphone at 7000 rpm

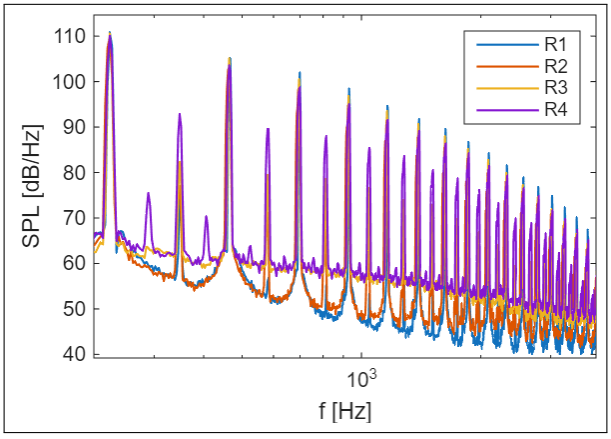


Figure 6. Zoom of the first 15 BPF at 7000 rpm

pared in Fig. 8 for all microphones and all the rotational speeds tested. As a general trend, we observe that the OASPL values tend to increase as the RPM increases, as expected. The baseline propeller has the worst aeroacoustic performance, exhibiting a higher acoustic energy content than the other propellers. Moreover, for most conditions, the R2 propeller appears to have the best acoustic performance, as previously suggested, with an average OASPL reduction of 0.9 dB compared to the baseline, versus an average reduction of 0.6 dB for the R1 propeller and 0.5 dB for the R3 propeller. However, at low speed, around 5500 RPM, and at high speed, around 8000 RPM, the lower value of OASPL is achieved by the R3 propeller. In the range between 6500 RPM and 7500 RPM, the R3

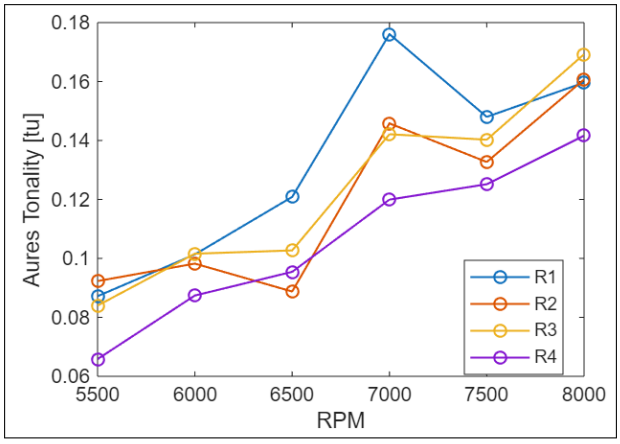


Figure 7. Tonality vs RPM for the microphone on the rotational plane of the propeller

OASPL values became similar to the ones of the baseline, deteriorating its overall acoustic performance. The maximum OASPL reduction, equal to 2.3 dB, with respect to the baseline, is achieved by the R2 propeller in correspondence of microphone 3 at 8000 RPM.

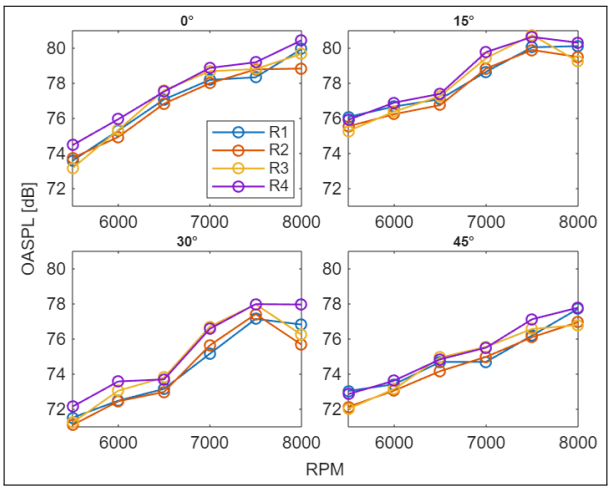


Figure 8. OASPL vs RPM for each microphone

From the psychoacoustic perspective, only the psychoacoustic annoyance (PA) is reported here, as it is calculated as a linear combination of all the other psychoacoustic parameters (see Eqn. 3). In Fig. 9, in particular, the annoyance versus the RPM is plotted for all the microphones. It can be observed that the trend of the PA curves is quite similar to the trend of the OASPL curves,

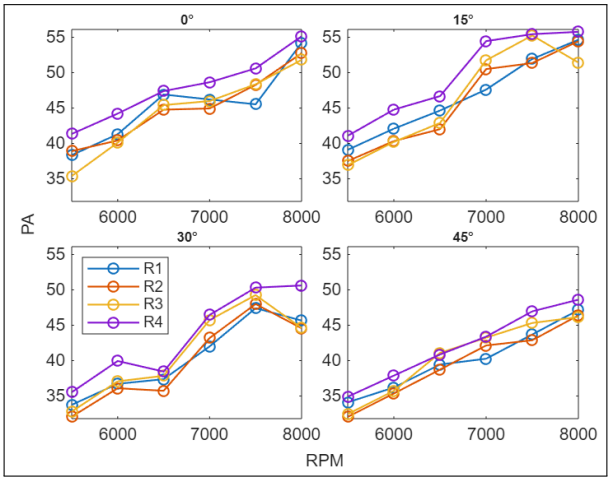


Figure 9. Psychoacoustic annoyance vs RPM for each microphone

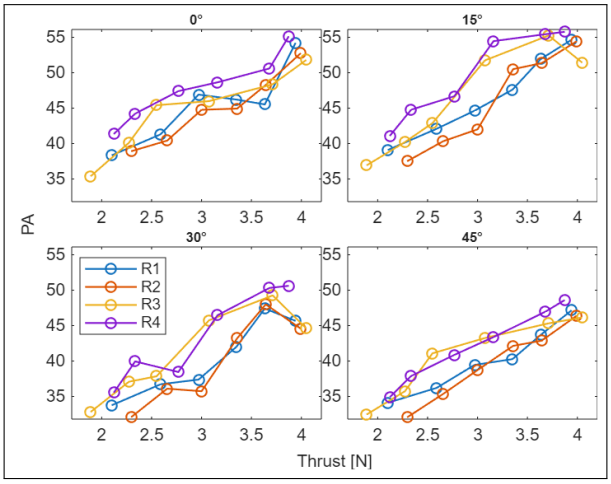


Figure 10. Psychoacoustic annoyance vs Thrust for each microphone

but the differences are more pronounced: the curves of the propellers are more spaced apart, revealing significant differences in terms of the annoyance caused. First, it is clearly visible that the baseline propeller is the most annoying along all the RPM and at all the locations. Regarding the lowest values, the situation is somewhat less clear. At low speed, between 5500 and 6000 RPM, the best psychoacoustic performance is reached by the roughness 3 and roughness 2 propellers. At 7000 and 7500 RPM the roughness 3 propeller became more annoying reaching, in some cases, values equal to the baseline. In this range of RPM, the best performance is prerogative of the R1 and, again, of the R2 propellers. At the maximum speed, 8000 RPM, once again the roughness 3 propeller achieves the best result. Anyway, the propeller with an overall greater average decrease in PA, compared to the baseline, is the R2 propeller, with a decrease of 3.2 units, whereas the other two propellers, R1 and R3, show a decrease of about 2.6 units.

As final comparison, Fig. 10 shows the psychoacoustic annoyance of the four propellers as function of the thrust produced. Here the situation is a bit different. For the same thrust, the most annoying propeller is, quite always, the baseline, but the values are often matched by the R3 propeller. For almost all the cases, the best psychoacoustic performance is achieved by the R2 propeller, followed by the R1. Only at the maximum thrust, the roughness 3 propeller achieves the best performance, since it combines the highest thrust at 8000 RPM (Fig. 4), if compared to the other propellers, and a relatively low psychoacoustic annoyance at 8000 RPM, as highlighted previously (Fig. 9).

4. CONCLUSIONS

An experimental investigation of the influence of the surface roughness on the aerodynamic, aeroacoustic and psychoacoustic behaviour of a propeller was carried out in the Fluid dynamics Laboratory of the University of Roma Tre. Four APC 8X6 propellers were tested: an off-the-shelf propeller and three propellers with an add-on of 27 µm, 50 µm, and a mixture of particles ranging from 70 to 110 µm, respectively. Thrust measurements were performed by means of a load cell, whereas 4 microphones were placed in the farfield, at a distance of 3.5 D from the hub of the propeller, for the acoustic characterization. Moreover, a fifth microphone was placed in the nearfield of the propeller. The psychoacoustic analysis was performed using the open-source MATLAB toolboxSQAT (Sound Quality Analysis Toolbox) that implemented the model proposed by Di to calculate the psychoacoustic annoyance. From the study of the spectra measured by the nearfield microphone, the propellers with an add-on show a reduced broadband noise contribution at the lower frequency, up to 5000 Hz. In the same frequency range, in correspondence of the BPF and its harmonics, the propellers with an add-on exhibit higher peaks than the baseline, showing an increased tonal noise contribution. In particular, the R2

propeller, with the add-on roughness ranging from 70 to 100 µm, displays both a significantly reduced broadband noise and a relatively minor increase in tonal noise, a combination that ensures a good performance overall from an aeroacoustic point of view, as demonstrated by the analysis of the OASPL. From the psychoacoustic perspective, the roughness 2 propeller shows an excellent performance relative to the psychoacoustic annoyance as function of the thrust produced. For the same RPM, R2 produces a greater thrust and a lower psychoacoustic annoyance than the other propellers tested, resulting in the best choice to improve the propeller performances.
Therefore, the addition of material which increases the surface roughness on the propeller's tip trailing edge surface is shown to improve the aerodynamic, aeroacoustic and psychoacoustic performances of the off-the-shelf propeller. In particular, among the particles sizes tested in this study, the best results were provided using the mixed particles ranging from 70 to 100 µm.

5. REFERENCES

[1] S. A. H. Mohsan, M. A. Khan, F. Noor, I. Ullah, and M. H. Alsharif, "Towards the unmanned aerial vehicles (UAVs): A comprehensive review," *Drones*, vol. 6, no. 6, p. 147, 2022.

[2] F. Ahmed, J. Mohanta, A. Keshari, and P. S. Yadav, "Recent advances in unmanned aerial vehicles: a review," *Arabian Journal for Science and Engineering*, vol. 47, no. 7, pp. 7963–7984, 2022.

[3] E. Pang, A. Cambray, D. Rezgui, M. Azarpeyvand, and S. A. Showkat Ali, "Investigation towards a better understanding of noise generation from UAV propellers," in *2018 AIAA/CEAS Aeroacoustics Conference*, p. 3450, 2018.

[4] W. A. Jordan, S. Narsipur, and R. Deters, "Aerodynamic and aeroacoustic performance of small uav propellers in static conditions," in *Aiaa Aviation 2020 Forum*, p. 2595, 2020.

[5] D. Xue, Q. Yan, Z. Li, and K. Wei, "Multidisciplinary optimization design of low-noise propellers," *Aerospace*, vol. 10, no. 3, p. 254, 2023.

[6] Y. Peixun, P. Jiahui, B. Junqiang, H. Xiao, and S. Xiang, "Aeroacoustic and aerodynamic optimization of propeller blades," *Chinese Journal of Aeronautics*, vol. 33, no. 3, pp. 826–839, 2020.

[7] M. Hasegawa and H. Sakaue, "Propeller-noise reduction by microfiber coating on a blade surface," *Sensors and Actuators A: Physical*, vol. 371, p. 115273, 2024.

[8] C. Chavez-Tolentino, X. Li, H. R. Siller, and H. Sadat, "Aerodynamic behavior and acoustic signature of propellers fabricated by additive manufacturing," *The International Journal of Advanced Manufacturing Technology*, vol. 129, no. 7, pp. 3403–3412, 2023.

[9] J. P. Cooke, M. F. Campbell, E. B. Steager, I. Bargatin, M. H. Yim, and G. I. Park, "Numerical and experimental study on the addition of surface roughness to micro-propellers," *Physics of Fluids*, vol. 35, no. 11, 2023.

[10] A. W. Christian and R. Cabell, "Initial investigation into the psychoacoustic properties of small unmanned aerial system noise," in *23rd AIAA/CEAS aeroacoustics conference*, p. 4051, 2017.

[11] W. R. O. for Europe, "Environmental noise guidelines for the European region," 2018.

[12] C. J. Hui, M. J. Kingan, Y. Hioka, G. Schmid, G. Dodd, K. N. Dirks, S. Edlin, S. Mascarenhas, and Y.-M. Shim, "Quantification of the psychoacoustic effect of noise from small unmanned aerial vehicles," *International Journal of Environmental Research and Public Health*, vol. 18, no. 17, p. 8893, 2021.

[13] D. Y. Gwak, D. Han, and S. Lee, "Sound quality factors influencing annoyance from hovering UAV," *Journal of sound and vibration*, vol. 489, p. 115651, 2020.

[14] R. Merino-Martínez, R. Pieren, and B. Schäffer, "Holistic approach to wind turbine noise: From blade trailing-edge modifications to annoyance estimation," *Renewable and Sustainable Energy Reviews*, vol. 148, p. 111285, 2021.

[15] M. J. Lotinga, C. Ramos-Romero, N. Green, and A. J. Torija, "Noise from unconventional aircraft: a review of current measurement techniques, psychoacoustics, metrics and regulation," *Current Pollution Reports*, vol. 9, no. 4, pp. 724–745, 2023.

[16] M. A. Boucher, A. W. Christian, S. Krishnamurthy, T. Tracy, D. R. Begault, K. Shepherd, and S. A. Rizzi, "Toward a psychoacoustic annoyance model for Urban Air Mobility vehicle noise," 2024.

[17] S. Schade, R. Merino-Martinez, P. Ratei, S. Bartels, R. Jaron, and A. Moreau, "Initial study on the impact of speed fluctuations on the psychoacoustic characteristics of a distributed propulsion system with ducted fans," in *30th aiaa/ceas aeroacoustics conference (2024)*, p. 3273, 2024.

[18] E. Zwicker and H. Fastl, *Psychoacoustics: Facts and models*, vol. 22. Springer Science & Business Media, 2013.

[19] G.-Q. Di, X.-W. Chen, K. Song, B. Zhou, and C.-M. Pei, "Improvement of Zwicker's psychoacoustic annoyance model aiming at tonal noises," *Applied Acoustics*, vol. 105, pp. 164–170, 2016.

[20] G. F. Greco, R. Merino-Martínez, A. Osses, and S. C. Langer, "SQAT: a MATLAB-based toolbox for quantitative sound quality analysis," in *Inter-Noise and Noise-Con Congress and Conference Proceedings*, vol. 268, pp. 7172–7183, Institute of Noise Control Engineering, 2023.

DOI: 10.61782/fa.2025.0567



FORUM ACUSTICUM
EURONOISE 2025

MID-FIDELITY FRAMEWORK FOR ROTOR NOISE PREDICTION AND PERCEPTION IN MANEUVERING FLIGHT

Marco Picillo[1*] **Mattia Barbarino**[2] **Francesco Avallone**[1]

[1] Department of Mechanical and Aerospace Engineering, Politecnico di Torino, Italy
[2] Centro Italiano Ricerche Aerospaziali, Capua, Italy

ABSTRACT

The goal of Urban Air Mobility (UAM) is to provide a safe, efficient, and sustainable transportation option to reduce traffic congestion and improve mobility in cities. However, the benefits, such as reduction of pollution and increase of public health, need to face important challenges related to safety, regulatory frameworks and public acceptance; the latter is highly driven by noise emissions. In this paper a mid/low-fidelity framework is used to investigate the effects of the acceleration between two steady conditions at different angular velocities for a small propeller. Far-field noise results are evaluated in terms of physical and psychoacoustic metrics. Differences in amplitude and directivity patterns suggest that in the presence of a fast transient, noise increases. Different angular velocity accelerations have also been investigated, highlighting their impact on noise perception.

Keywords: *Noise, UAM, Maneuver, Perception*

1. INTRODUCTION

Urban Air Mobility (UAM) refers to the use of advanced air transportation systems, including electric Vertical Takeoff and Landing (eVTOL) aircraft, to transport people and goods within urban and suburban areas. Beside this concept, Advanced Air Mobility (AAM) encompasses a range of new and emerging technologies in aviation, including UAM, but also includes larger and faster aircraft that are capable of longer-range flights. The development of these new concepts has been accelerated, in the recent years, thanks to the technological advance of VTOL, which are vehicles capable of take-off and landing in a small space [1] and are mainly driven by distributed propellers. Both AAM and UAM are expected to have significant impact on our future lives. However, the benefits, such as reduction of pollution, increase of public health and so on, need to face some important challenges related to safety, regulatory frameworks and public acceptance.

In the context of public acceptance, the analysis proposed by [2] shows that public acceptance is highly driven by noise. For this reason, it is crucial to correctly predict noise emissions from rotorcrafts in urban environments, which are characterized by non-uniform flows, gusts and turbulence [3], causing a non-uniform inflow condition at the rotor disk that determines a dramatic change in sound pressure levels and directivity [4]. Another important challenge in represented by the correct prediction of noise emissions in maneuvering flight and how noise is perceived by an observer. In order to predict noise emissions, different numerical methods are usually adopted, ranging from high-fidelity to low-fidelity. High-fidelity and low-fidelity approaches share the same philosophy, based on predicting blade loads and fluid displacement around the propeller, using an aerodynamic solver, which are then used to compute the acoustic pressure at a specific observer location. Classification is based on the accuracy of the aerodynamic and acoustic solvers that are used for the simulation. High-fidelity methods adopt high-fidelity Computational Fluid Dynamics (CFD) methods such as Reynolds Averaged Navier-Stokes (RANS) [5], Large Eddy Simulation (LES) [6] and Very Large Eddy

*__Corresponding author__: marco.picillo@polito.it.
__Copyright__: ©2025 Marco Picillo et al. This is an open-access article distributed under the terms of the Creative Commons Attribution 3.0 Unported License, which permits unrestricted use, distribution, and reproduction in any medium, provided the original author and source are credited.

Simulation (VLES) [4] to obtain near field description of noise sources, while the near to far field propagation is carried out by the Ffowcs Williams and Hawkings analogy (FW-H), which is a re-formulation of the linearized Euler equations using Lighthill's acoustic analogy [7]. On the other side, low-fidelity methods adopt low-fidelity CFD methods, such as Blade Element Momentum Theory (BEMT) [8], Lifting Line Theory (LLT) [9] and Potential Flow Methods [10] coupled with simplified versions of the FW-H equation such as Hanson's and Gutin's model in the frequency domain and Farassat 1 and 1A formulations in the time domain.

Although noise prediction for propellers in stationary and uniform-inflow conditions has been extensively studied, noise prediction from maneuvering rotorcraft remains a challenging problem. In practice, VTOLs and drones perform complex maneuvers. Rotorcraft flight, in general, can be described as a sequence of equilibrium states interspersed with transitional maneuvers. These maneuvers are marked by non-stationary and aperiodic effects, leading to noise generation mechanisms that significantly differs from the ones in stationary conditions [11]. This additional noise, which increases as the duration of the maneuver decreases, is not negligible as it is characterized by a time-dependent directivity [12].

The majority of studies in the literature employ a quasi-stationary approach, ignoring the transient that occurs when transitioning from one flight condition to another; only few works consider the effects of a short-time maneuver in terms of physical noise metrics. In [13] the noise of a helicopter transient maneuver is numerically simulated using the formulation 1A of Farassat, while [14] used a BEMT solver coupled with an acoustic solver, based on the formulation 1A of Farassat, to investigate the effects of a typical eVTOL mission on the noise of an observer fixed with the vehicle. However, most of the studies cited above focus primarily on physical noise metrics, such as Sound Pressure Level (SPL), while few address the effects of a short-time maneuver on noise perception. Ref. [15] highlights experimentally the effects of a drone transient flight in terms of sound quality metrics, such as loudness, sharpness and roughness with respect to the hovering case, while [16] focused on the effects of different type of propellers on the psychoacoustic annoyance, suggesting that perception-driven design can be performed by targeting the minimization of the perceived noise annoyance, rather that just reducing SPL. For this reason, with the aim of tackling the challenge of public acceptance, it is important to address the psychoacoustic effects of short-time maneuvers, in a fast and accurate way, due to the variety of eVTOL and drones architectures present in the market nowadays, and to include these metrics with the purpose of guiding future designs.

The purpose of this paper is to analyze the effects of angular velocity acceleration, for a small drone rotor, on physical and psychoacoustic metrics, using a low-fidelity framework. This paper is structured as follows: in Sec. 2 the simulation framework is introduced, in Sec. 3 a validation in uniform and non-uniform inflow conditions is presented, while in Sec. 4 the results of a short-time maneuver in terms of sound quality metrics and physical noise metrics will be discussed.

2. SIMULATION FRAMEWORK

In this section, the simulation framework is presented. The tool is composed of an aerodynamic solver, which is FLOWUnsteady [17], based on Vortex Particle Method and an in-house time-domain acoustic solver for the tonal component of the noise, based on the FW-H analogy [18]. The sketch, shown in figure Fig. 3, presents the workflow. First, the rotor geometry, defined with chord distribution, twist distribution, sweep distribution, rotor diameter, airfoils distribution and number of blades is passed to the aerodynamic solver, together with the operating conditions of the rotor. Then, the time history of the blade loading distribution along the radius of each blade is passed to the acoustic solver, together with the observer position, in order to compute a pressure signal at the observer position and finally the noise, in terms of physical noise metrics such as SPL and perception using the open-source python library MoSQUITo [19]. The acoustic solver is developed in Python, following the object-oriented paradigm, which make the software user-friendly and modular.

Vortex Methods are a class of meshless CFD solving the Navier-Stokes equations in their velocity-vorticity form. In particular, the method uses particles to discretize the Navier-Stokes equations. Each particle represents a Radial Basis Function that constructs a continuous vorticity field by carrying an integral quantity of vorticity that is convected by the velocity field. In FLOWUnsteady, blades are divided into blade elements that include 2D airfoil data, such as lift and drag, calculated by XFOIL. The forces on each blade are then reintroduced into the fluid domain by converting them into equivalent immersed vorticity. In this way, it is possible to compute the performance of one or multiple rotors under different operating conditions.

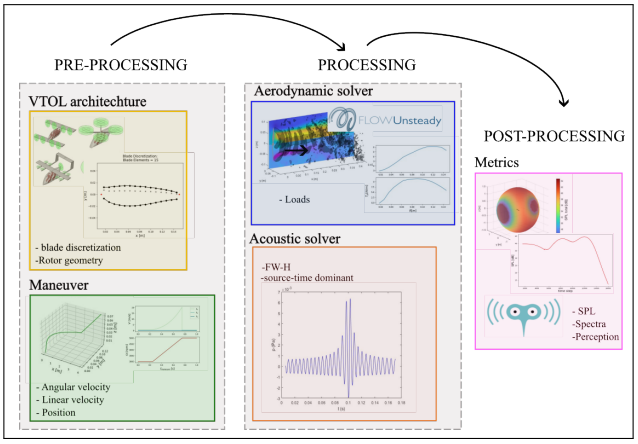


Figure 1. Simulation Framework.

For the acoustic solver we follow the procedure presented in [18]. Only the thickness and loading noise components are computed. More in detail, the FW-H equation, Eqn. (1), is simplified considering two hypotheses: observer placed in the far field and surface integrals calculated on the blade planform.

$$\begin{aligned}\rho'(\boldsymbol{x},t)c_\infty^2 = &\frac{\partial^2}{\partial x_i \partial x_j}\int_{V_0}\left[\frac{\boldsymbol{T}_{ij}}{4\pi r|1-M_r|}\right]_{\tau=\tau^*} dV(\boldsymbol{z}) \\ &- \frac{\partial}{\partial x_i}\int_{S_0}\left[\frac{p_{ij}\boldsymbol{n}_j}{4\pi r|1-M_r|}\right]_{\tau=\tau^*} dS(\boldsymbol{z}) \\ &+ \frac{\partial}{\partial t}\int_{S_0}\left[\frac{\rho_\infty V_j \boldsymbol{n}_j}{4\pi r|1-M_r|}\right]_{\tau=\tau^*} dS(\boldsymbol{z})\end{aligned} \tag{1}$$

Each integrand is then evaluated at the retarded time τ^* which is the time needed to the signal, emitted at time τ, to reach the observer position at time t. The retarded time equation, Eqn. (2), is solved implicitly.

$$t - \tau - \frac{|\boldsymbol{x} - \boldsymbol{y}(\tau)|}{c_\infty} = 0 \tag{2}$$

where $\boldsymbol{y}$ is the blade position in the fixed reference system, $\boldsymbol{x}$ the observer position and c_∞ the speed of sound.

3. VALIDATION

In this section, the noise generated by a rotor in a uniform and non-uniform inflow is compared against high-fidelity and experimental data, in order to partially validate the numerical tool. The geometrical characteristics of the propeller and reference values used for the simulations are summarized in Tab. 1, while geometric characteristics of the propeller can be seen in Fig. 2 and found in previous works from [20] and [4].

Table 1. Propeller parameters and reference values.

Propeller diameter (D)	0.3 m
Hub to tip ratio	0.13
Number of blades (N_b)	2
Blade aifoils	NACA 4412
Air density (ρ_∞)	1.18 kg/m^3
Speed of sound (c_∞)	343 m/s

For uniform inflow distribution we consider a condition in which the free-stream velocity vector, $\mathbf{V}_\infty$, is parallel to the blade rotational axis. On the other hand, a non-uniform inflow distribution consists of a free stream velocity vector which has an inclination, α, with respect to the propeller axis.

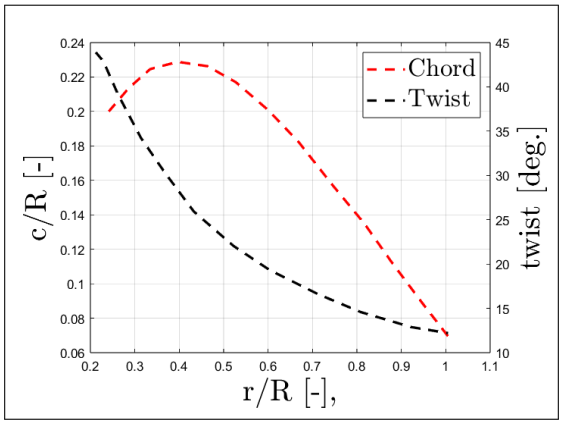


Figure 2. Blade geometry.

First, a comparison of the thrust coefficient C_T, the torque coefficient C_Q and the propulsive efficiency η, for different advance ratios J, calculated as in Eqn. (3), is shown in Fig. 3, Fig. 4 and Fig. 5. Here, the rotor is kept at a constant angular velocity of 4000 rpm, and the results are compared with respect to experimental data [20].

$$C_T = \frac{T}{\rho n^2 D^4} \qquad C_Q = \frac{Q}{\rho n^2 D^5} \qquad \eta = J\frac{C_T}{C_Q} \tag{3}$$

The numerical results match well with the experimental ones. The thrust coefficient is overpredicted for low

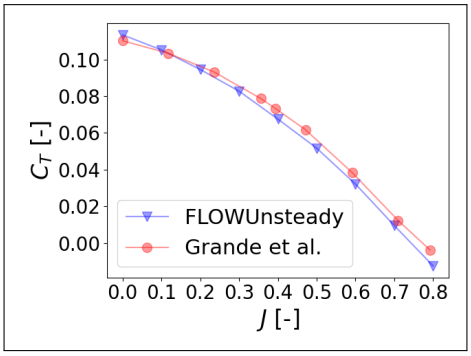


Figure 3. Thrust coefficient as a function of advance ratio.

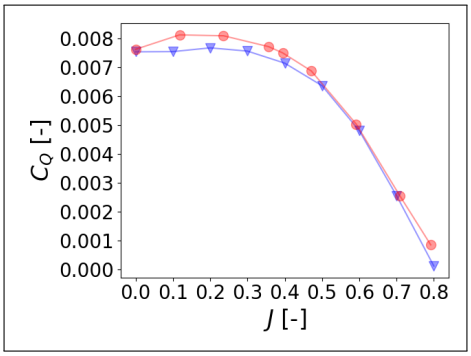


Figure 4. Torque coefficient as a function of advance ratio.

advance ratios, while it is underpredicted for higher ones; while the torque coefficient is underpredicted for low advance ratios in the order of 7%. This behavior reflects in the propulsive efficiency.

Acoustic results are compared with high-fidelity ones from [4] in terms of SPL directivity, for a uniform inflow condition, $\alpha = 0°$, and a non-uniform inflow condition, $\alpha = 15°$, both at $J = 0.4$. Fig. 6 shows the SPL directivity for the non uniform inflow distribution, and we can see that the low-fidelity results, computed with the present framework, match quite well with the high-fidelity data from [4].

4. RESULTS

In this section, the effects of a short-time maneuver are investigated, i.e. an angular velocity variation, between two steady conditions at constant angular velocity, for the rotor geometry described above. The maneuver is shown

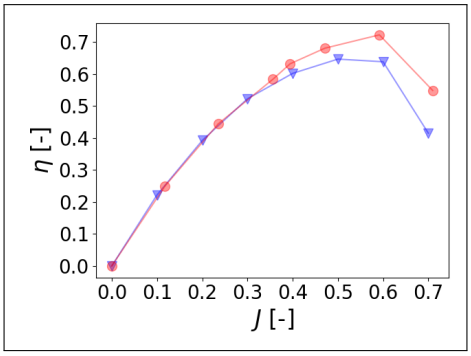


Figure 5. Propulsive efficiency as a function of advance ratio.

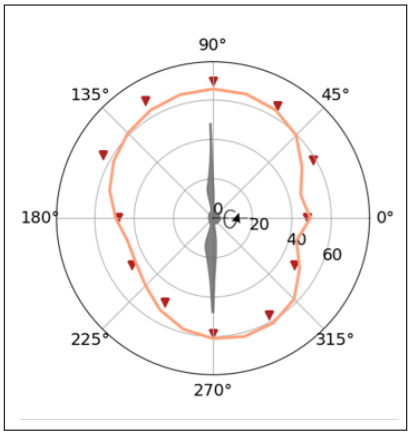


Figure 6. Thickness+Loading noise, $\alpha = 15°$. Solid line represents low-fidelity results. Results are in dB.

in Fig. 7.

Defined $t_{P_3} - t_{P_0}$ as the total time (t_{tot}) of the maneuver, and $t_{P_2} - t_{P_1}$ the transient time (Δt) between the two steady conditions, the transition between the two steady condition is obtained with different laws, a first order polynomial and a third order polynomial, and the transient time is varied in order to study the influence of both on physical noise metrics, such as SPL, and Sound Quality Metrics (SQM). In all the simulations the rotor position is fixed, with a uniform inflow ($V_x = V_\infty$) of 3 m/s, in order to speed up the convergence and eliminate the effects of a possible wake ingestion. The rotational speeds are set equal to $\Omega_{P_1} = 4000$ rpm $\Omega_{P_3} = 5000$ rpm. The selected transient times are $\Delta t = 0.1, 0.5$ s and the total time of the maneuver $t_{tot} = 1$ s. Tab. 2 summarizes the characteristic times, referring to Fig. 7, for each maneuver.

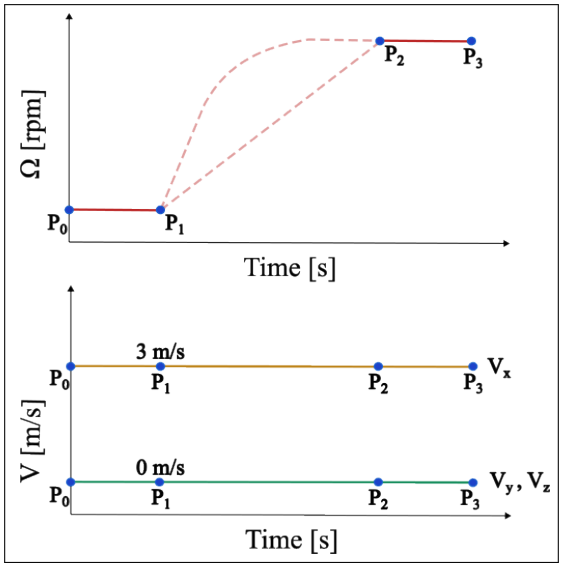


Figure 7. Reference maneuvers.

Table 2. Characteristic times of the maneuver.

Δt (s)	t_{P_1} (s)	t_{P_2} (s)
0.1	0.45	0.55
0.5	0.25	0.75

4.1 Physical Noise Metrics

In this section, the effect of the maneuver will be investigated in terms of SPL and its directivity. Fig. 8 and Fig. 9 show the directivity in time of the first order polynomial maneuver in terms of a difference in SPL, for the two transient times, defined as $\Delta SPL = SPL_{\Delta t=0.1} - SPL_{\Delta t=0.5}$, for the thickness and loading noise, respectively. Θ is the angle between the observer ad the propeller axis, see Fig. 6 for reference. Observing the figures, it can be stated that in the two stationary conditions, the two maneuvers have the same SPL values, but because of the different transient time, these stationary conditions are reached at different times. In fact, observing Fig. 8, the ΔSPL decreases from $0.25s$ to $0.45s$, approximately, becoming zero at $0.5s$, and then starts to increase until $0.55s$, where the maneuver with $\Delta t = 0.1s$ reaches the steady condition. This behavior appears to be independent of Θ, but dependent only on the angular speed value. Focusing on the loading noise, Fig. 9, we can observe an overshoot in SPL at the beginning and end of the transient of each maneuver. The overshoot seems to increase in magnitude and to affect a bigger range of Θ, decreasing the transient time. This behavior is related to the thrust derivative with respect to the retarded time in the FW-H equation, which becomes important approaching the propeller axis, and the effect becomes more evident as the transient time decreases.

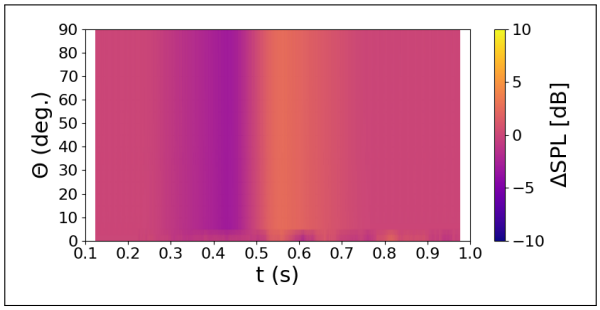


Figure 8. Thickness noise, first order polynomial.

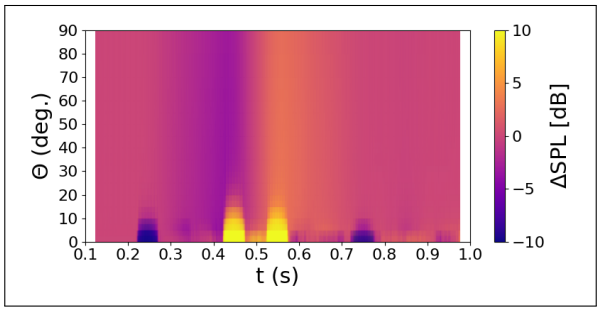


Figure 9. Loading noise, first order polynomial.

This effect can also be observed considering the spectrograms, Fig. 10 and Fig. 11, obtained for the first order polynomial transient with $\Delta t = 0.1s$. We can see that for $\Theta = 20°$, Fig. 11, SPL is higher in two low-frequency bands at the beginning and end of the transient and disappear for $\Theta = 90°$, Fig. 10.

The same behavior appears also for the third order polynomial at the beginning of the transient where the first order derivative of the thrust and angular velocity are greatest, Fig. 12.

Setting the transient time, it is possible to compare different transient laws, that are the third order polynomial and the first order polynomial, as presented in Fig. 7. Fig. 13 and Fig. 14 shows the thickness and loading noise, respectively, for $\Delta t = 0.5s$, in terms of $\Delta SPL =$

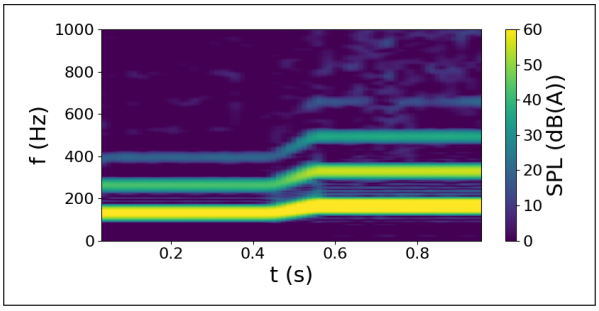


Figure 10. Spectrogram, poly1, $\Theta = 90°$, $\Delta t = 0.1$s.

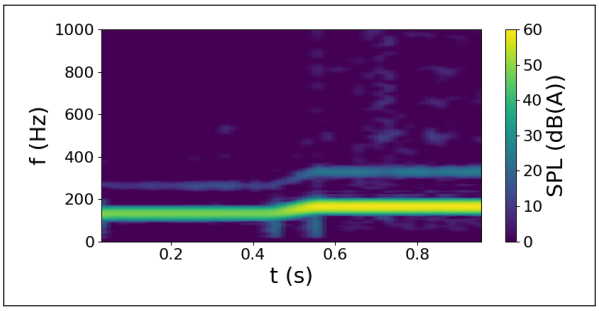


Figure 11. Spectrogram, poly1, $\Theta = 20°$, $\Delta t = 0.1$s.

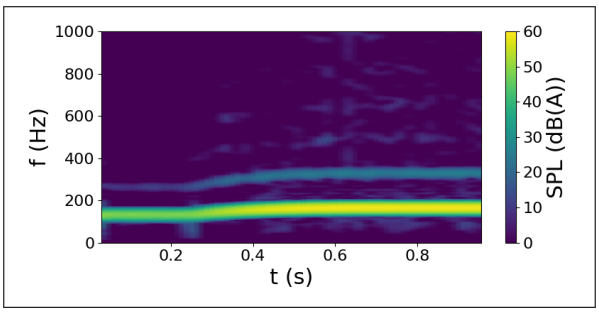


Figure 12. Spectrogram, poly3, $\Theta = 20°$, $\Delta t = 0.5$s.

$SPL_{poly3} - SPL_{poly1}$, which is the difference between the third order polynomial SPL and the first order polynomial SPL. As can be seen, from $t = 0.25s$ to $t = 0.75s$ the ΔSPL is positive, while it is zero during the two steady conditions. That is because the transient of the third order polynomial is characterized by higher angular velocities. The same behavior can be observed for the loading noise, with some differences from $\Theta = 0°$to $\Theta = 90°$. In fact, for $t = 0.25s$ the SPL of the third order polynomial is higher with respect to the first order polynomial; while the opposite behavior is observed for $t = 0.75s$. These results reflect the effect of the thrust derivative, which is higher, for the third order polynomial, at the beginning of the transient, and it is zero at the end of the transient.

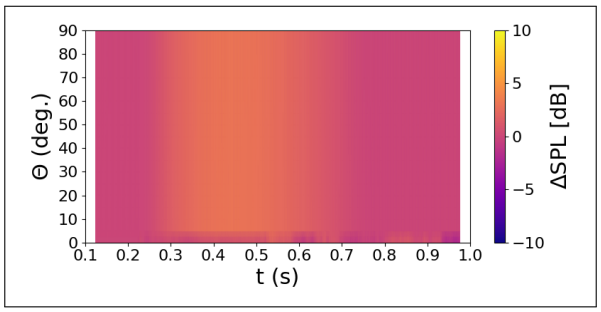


Figure 13. Thickness noise, $\Delta t = 0.5$s.

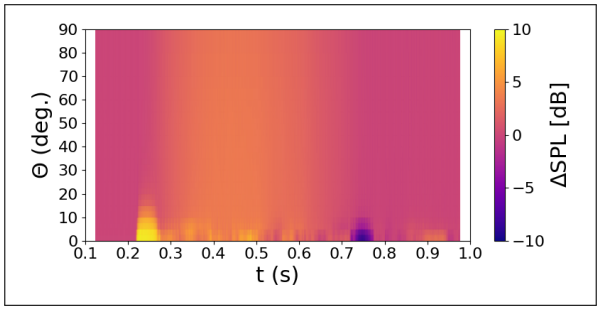


Figure 14. Loading noise, $\Delta t = 0.5$s.

4.2 Sound Quality Metrics

To understand if the effects described above affects the human perception, the SQM are analyzed. Fig. 15 and Fig. 16 show the loudness (ISO 532-1:2017) at $\Theta = 90°$and $\Theta = 20°$, respectively. As can be seen, the loudness increases as the observer approaches the rotor disk and it is dependent on the angular velocity variation law. In fact, the third order polynomial transient is characterized by higher loudness with respect to the first order polynomial, reflecting the angular velocity transient law, while during the two steady conditions the loudness remains constant, as expected.

Looking at the sharpness (DIN.45692:2009), Fig. 17 and Fig. 18, a peak in the transient region of the maneuver is observed. Moreover, the shape of the curve and the

magnitude of the peak seems to be dependent on the time variation of the angular velocity of the rotor. In fact, fixing the transient time, the third order polynomial transient law is characterized by a higher peak and this can be related to the effect of the higher derivative of the angular velocity at the beginning of the transient. The same observation can be made fixing the transient law and reducing the transient time.

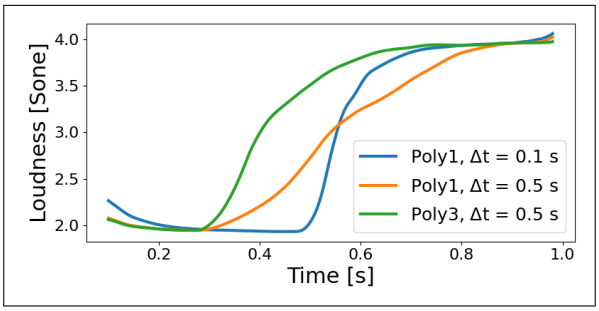


Figure 15. Loudness, $\Theta = 90°$.

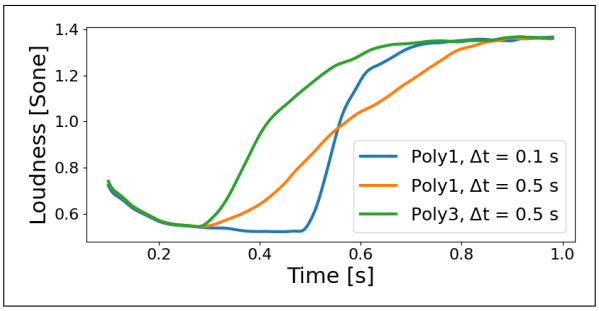


Figure 16. Loudness, $\Theta = 20°$.

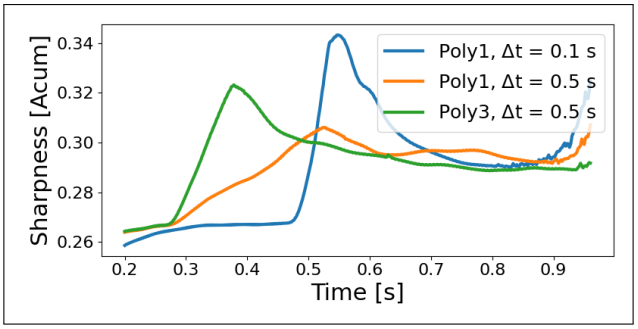


Figure 17. Sharpness, $\Theta = 90°$.

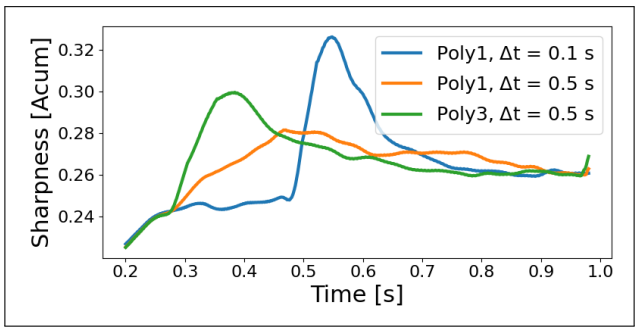


Figure 18. Sharpness, $\Theta = 20°$.

5. CONCLUSIONS

In this paper we presented a mid/low-fidelity tool for noise prediction of eVTOL vehicles. The framework is based on a Vortex Particle Method and a time-domain Ffowks Williams and Hawkings analogy. The framework is validated with high-fidelity and experimental data for a single propeller in uniform and non-uniform inflow conditions. The good agreement of low-fidelity data with respect to the high-fidelity ones gave confidence in employing the tool for the study of a maneuver. The maneuver consists of an angular velocity transient between two steady conditions, and the objective was to understand if the transient time and the angular velocity law affects physical and Sound Quality metrics, for a single two-bladed propeller. In particular, we observed the following features:

- time-dependent SPL directivity: from $\Theta = 0°$to approx. $\Theta = 30°$, we observed two overshoots in SPL at the beginning and end of the transient. These overshoots are carachterized by low-frequency noise, caused by the time variation of the thrust of the rotor, which becomes important as the observer approaches the propeller axis;
- transient time dependence: reducing the transient time, the overshoots increase in magnitude, both for the SPL and the sharpness;
- transient law dependence: how the two steady conditions are reached seems to influence the SPL and the sharpness. Highest time derivative of the angular velocity causes higher overshoots in SPL and sharpness;
- the loudness shape seems to be dependent only by the angular velocity.

In order to understand if these effects affect the noise perception, more in depth studies should be conducted, like sound perception tests on a sample of individuals and more specific maneuvers, representative of real eVTOL flight scenarios.

6. ACKNOWLEDGEMENTS

This publication is part of the project PNRR-NGEU which has received funding from the MUR-DM 117/2023 and is co-funded by C.I.R.A.

Finanziato dall'Unione europea NextGenerationEU | Ministero dell'Università e della Ricerca | Italiadomani

7. REFERENCES

[1] Y. Zhou, H. Zhao, and Y. Liu, "An evaluative review of the vtol technologies for unmanned and manned aerial vehicles," *Computer Communications*, vol. 149, 2019.

[2] S. Hasan, "Urban air mobility (uam) market study," 2018. NASA Urban Air Mobility Report.

[3] M. Al-Labbad, A. Wall, G. L. Larose, F. Khouli, and H. Barber, "Experimental investigations into the effect of urban airflow characteristics on urban air mobility applications," *Journal of Wind Engineering Industrial Aerodynamics*, vol. 229, 2022.

[4] G. Romani, E. Grande, F. Avallone, D. Ragni, and D. Casalino, "Computational study of flow incidence effects on the aeroacoustics of low blade-tip mach number propellers," *Aerospace Science and Technology*, vol. 120, 2022.

[5] P. W. Song, H. Z. Han, and D. Z. Qiao, "Prediction of hovering rotor noise based on reynolds-averaged navier-stokes simulation," *Journal Of Aircraft*, vol. 44, 2007.

[6] J. Yangzhou, J. Wu, Z. Ma, and X. Huang, "Aeroacoustic sources analysis of wake-ingesting propeller noise," *Journal of Fluid Mechanics*, vol. 962, 2023.

[7] M. J. Lighthill, "On sound generated aerodynamically i. general theory," in *Proc. of the Royal Society of London Series A, Mathematical and Physical Sciences*, 1952.

[8] J. B. H. M. Schulten, "Frequency-domain method for the computation of propeller acoustics," *AIAA Journal*, vol. 26, 1988.

[9] G. P. Succi, D. H. Munro, and J. A. Zimmer, "Experimental verification of propeller noise," *AIAA Journal*, vol. 20, 1982.

[10] D. Boots and D. Feszty, "Numerical investigation of the effect of wing position on the aeroacoustic field of a propeller," in *Proc. of AIAA/SAE/ASEE Joint Propulsion Conference*, (Salt Lake City, USA), 2016.

[11] G. A. Bres, S. K. Brentner, G. Perez, and H. E. Jones, "Maneuvering rotorcraft noise prediction," *Journal of Sound and Vibration*, vol. 275, 2004.

[12] H. Chen, S. K. Brentner, V. L. Lopes, and F. J. Horn, "An initial analysis of transient noise in rotorcraft maneuvering flight," *International Journal of Aeroacoustics*, vol. 5, 2006.

[13] S. K. Brentner and F. Farassat, "Modeling aerodynamically generated sound of helicopter rotors," *Progress in Aerospace Sciences*, vol. 39, 2003.

[14] O. Bergmann, F. Mohren, C. Braun, and F. Janser, "Propeller noise prediction for transient evtol mission," in *Proc. of AIAA SciTech Forum*, (Orlando, USA), 2024.

[15] E. Gallo, G. Beaulieu, and C. Schram, "Annoyance factors of a maneuvering multicopter drone," in *Proc. of AIAA/CEAS Aeroacoustics Conference*, (Southampton, UK), 2022.

[16] M. Snellen, R. Merino-Martinez, A. Altena, A. Amiri-Simkooei, C. Cappagli, A. Morin, L. Quaroni, F. Yunus, and R. Yupa-Villanueva, "Research on drone and urban air mobility noise: Measurement, modelling, and human perception," in *Proc. of Quietdrones Conference*, (Manchester, UK), 2024.

[17] E. J. Alvarez, *Reformulated Vortex Particle Method and Meshless Large Eddy Simulation of Multirotor Aircraft*. Ph.D. dissertation, Brigham Young University, Provo, UT, 2022.

[18] S. Glegg and W. Devenport, *Aeroacoustics of Low Mach Number Flows*. Academic Press, 2017.

[19] Green Forge Coop., "Mosqito."

[20] E. Grande, G. Romani, D. Ragni, F. Avallone, and D. Casalino, "Aeroacoustic investigation of a propeller operating at low reynolds numbers," *AIAA Journal*, vol. 60, 2022.

DOI: 10.61782/fa.2025.0711

FORUM ACUSTICUM EURONOISE 2025

PSYCHOACOUSTIC CHARACTERIZATION OF AN ISOLATED PROPELLER AT DIFFERENT INFLOW TURBULENCE CONDITIONS AND COLLECTIVE PITCH ANGLES

Roberto Merino-Martínez [1*] **Luca Nicola Quaroni**[1]

[1] Faculty of Aerospace Engineering, Delft University of Technology, the Netherlands

ABSTRACT

The far-field acoustic emissions of a six-bladed propeller were investigated in aeroacoustic experiments in an open-jet wind tunnel. The propeller was operating in different isotropic inflow turbulence conditions generated by turbulence grids placed upstream of the exit plane of the wind tunnel nozzle. In addition, the collective pitch angle of the propeller blades was also varied throughout the measurements. A preliminary directivity analysis of different acoustic and psychoacoustic metrics was performed to investigate the influence of the inflow turbulence intensity and collective pitch angle on the noise emissions and sound perception. In general, increasing the inflow turbulence levels did not modify the conventional metrics recorded, e.g. equivalent sound pressure level. Nevertheless, it considerably increased the broadband noise emissions of the propeller, the loudness, and the overall psychoacoustic annoyance metrics. However, notable reductions in tonality (due to partial tone masking because of the higher levels of broadband noise) and sharpness were reported for increasing turbulence intensities. Overall, this analysis is valuable for the perception-influenced design of devices equipped with propellers, such as drones or urban air mobility vehicles, to account for installation effects.

Keywords: *Propeller noise, psychoacoustics, sound quality metrics, tonality, turbulence ingestion.*

**Corresponding author*: r.merinomartinez@tudelft.nl.

Copyright: *©2025 Delft University of Technology This is an open-access article distributed under the terms of the Creative Commons Attribution 3.0 Unported License, which permits unrestricted use, distribution, and reproduction in any medium, provided the original author and source are credited.*

1. INTRODUCTION

An increasing number of devices employ propellers, such as drones [1] and urban air mobility vehicles [2,3], as well as aerospace technologies (e.g. distributed electric propulsion [4] and boundary layer ingestion systems [5]). Therefore, during the last years, considerable research has been devoted to investigating propeller noise emissions [6, 7] and, from a psychoacoustic point of view, the corresponding human perception [8, 9]. This has led to the use of perception-influence design of propellers to cause minimal noise annoyance during operation [10].

Most aeroacoustic experiments, for simplicity reasons, feature isolated propellers (typically conducted in anechoic chambers [10, 11] or wind tunnels [7]) and consider clean, low-turbulence inflow conditions. However, in practice, the usual installation of propellers close to the airframe (e.g. on aircraft or drones) typically causes turbulent inflow conditions [12]. Despite some studies on this topic [6,13,14], there is currently a lack of knowledge on how inflow turbulence influences propeller noise emissions, especially in terms of broadband noise and sound perception.

Therefore, the present paper provides a psychoacoustic characterization (using psychoacoustic sound quality metrics) based on a fundamental study conducted on an isolated propeller under different isotropic inflow turbulence conditions. In addition, the investigation is extended to different collective pitch angles of the propeller blades.

Section 2 describes the experimental setup employed for the aeroacoustic measurements and the acoustic equipment used. The conventional and psychoacoustic sound metrics used for the characterization are explained in section 3. Lastly, the main results are discussed in section 4, and the conclusions are drawn in section 5.

2. EXPERIMENTAL SETUP

The aeroacoustic measurements of the propeller were conducted at the anechoic, open-jet wind tunnel (A-Tunnel) at Delft University of Technology [15]. The wind tunnel circular outlet (exit diameter of 600 mm) placed on the floor of the facility has a contraction ratio of 15. An additional axisymmetric nozzle with an exit diameter D_{ext} of 420 mm was attached on top of the outlet, see Fig. 1, increasing the overall contraction ratio to approximately 30.

The experiments featured a six-bladed propeller made of steel with a diameter D_p equal to 203.2 mm (8") and a manually adjustable collective pitch angle β. In this study, β values of 25°, 27.5°, 30°, and 32.5° were investigated. This propeller (normally known as X-PROP-S) has been the subject of several publications; for its geometry, including spinner and nacelle dimensions, the reader is referred to [16]. The propeller was placed at a distance of 252 mm ($0.6\,D_{ext}$) from the exit plane of the nozzle. For additional information on the experimental setup the interested reader is referred to [6].

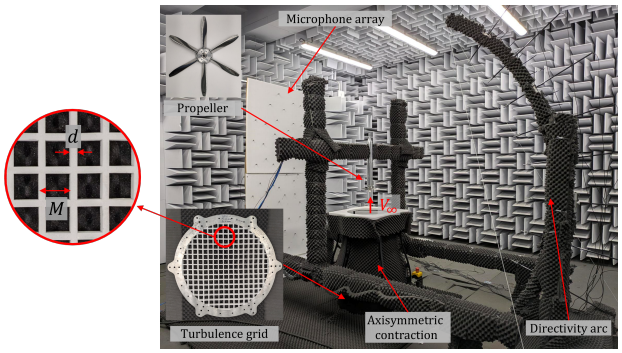


Figure 1: Experimental setup in the A-tunnel.

To investigate different inflow turbulence conditions, three different squared-mesh planar grids made of aluminum plates (thickness 5 mm) were placed at the junction between the axisymmetric nozzle and the wind tunnel outlet, see Fig. 1. The three grids (named A, B, and C) had the same open area ratio of 64% but different values for the bar width d and mesh length M, see Table 1 and Fig. 1. These differences in grid geometries enable various combinations of turbulence intensity TI (defined as the ratio between the root-mean-square velocity fluctuations u'_{rms} and the freestream velocity in the streamwise direction U_∞) levels and streamwise turbulence integral length scales Λ. Table 1 gathers these values for a freestream velocity U_∞ of 30 m/s and a streamwise distance of $x = 0.4\,D_{ext}$ downstream of the nozzle exit. The values for the reference grid-off case are also presented in the same table. All these values were obtained using hot-wire anemometry measurements [6].

Table 1: Bar width d, mesh length M, and turbulence intensity TI for each of the turbulence grids at a distance $x = 0.4\,D_{ext}$ downstream of nozzle exit for U_∞ of 30 m/s [6].

Grid	d, [mm]	M, [mm]	TI, [%]	Λ, [mm]
Off	N/A	N/A	<0.1	N/A
A	7	35	1.97	11.4
B	10	50	2.75	14.1
C	12	60	3.44	16.2

The acoustic measurements were performed using a phased array containing 63 free-field microphones and a directivity arc containing 8 microphones, see Fig. 1, spanning an emission angle range of 70° from $\theta = 70°$ to 140°, with the $\theta = 90°$ corresponding to the rotor disk plane and $\theta = 0°$ to the upstream direction. Both arrays of microphones were positioned at a distance of 1.3 m ($\approx 6.5 D_p$) from the propeller's axis, with the directivity arc centered at the propeller's rotation center. To account for the sound convection due to the flow, the acoustic data recorded was corrected in terms of amplitude and polar emission angle θ, following the guidelines explained in [17]. Therefore, the polar emission angles and amplitudes shown henceforth in directivity plots (Figs. 4-15) already present this correction. A sampling frequency of 51200 Hz and a recording time of 60 s were employed, which corresponds to approximately 10,000 propeller rotations acquired per operating condition.

In order to reduce acoustic reflections, acoustic absorbent materials (melamine and pyramidal polyurethane foam panels) were placed over all exposed surfaces within the anechoic plenum, see light and dark gray surfaces in Fig. 1, respectively. The turbulence grids were also equipped with 20-mm thick melamine foam panels, which were water-jet cut to the respective grid geometry and glued onto the downstream side to suppress both secondary reflections and the generation of tones by vortex-shedding mechanisms [18].

3. CONVENTIONAL AND SOUND QUALITY METRICS

Conventional sound metrics typically used in noise assessment pose challenges for quantifying noise annoyance [9]. Nevertheless, current noise regulations still employ these metrics for enforcing environmental noise laws. Therefore, the current study considers the equivalent sound pressure level $L_{\text{p,eq}}$, as well as the maximum tone-corrected perceived noise level (PNLT) to assess the noise emissions of both propellers. The latter is the base for the effective perceived noise level (EPNL) metric, which is typically employed during aircraft noise certification processes [19].

Unlike the sound pressure level L_{p} metric, which quantifies the purely physical magnitude of sound based on the pressure fluctuations, Sound Quality Metrics (SQMs) describe the subjective perception of sound by human hearing. Hence, SQMs are expected to better capture the auditory behavior of the human ear compared to conventional sound metrics typically employed in noise assessments. The five most commonly-used SQMs [20] are:

- Loudness (N): Perception of sound magnitude corresponding to the overall sound intensity.
- Tonality (K): Perceived strength of unmasked tonal energy within a complex sound.
- Sharpness (S): High-frequency sound content.
- Roughness (R): Hearing sensation caused by modulation frequencies between 15 Hz and 300 Hz.
- Fluctuation strength (FS): Assessment of slow fluctuations in loudness with modulation frequencies up to 20 Hz, with maximum sensitivity for modulation frequencies around 4 Hz.

These five SQMs were calculated for each recording and combined into a single global psychoacoustic annoyance (PA) metric following the model proposed by Di *et al.* [21]. Henceforth, the top 5% percentiles of these metrics (values exceeded 5% of the time) are reported (and hence the sub-index *5*). All the SQMs and the PA metric were computed using the open-source MATLAB toolbox SQAT (Sound Quality Analysis Toolbox) v1.2 [22]. The R and FS metrics evaluate the amplitude modulation and, since the result comparisons are made for the same propeller rotational speed, their variations were not as significant as for the other metrics and are, therefore, not presented in this paper for the sake of brevity.

4. RESULTS

From the different test conditions evaluated, the results presented in this paper correspond to a freestream velocity U_∞ of 30 m/s and a rotational frequency f_r of 166.76 Hz, resulting in a tip Mach number $M_{\text{tip}} = V_r/c_0$ of 0.325, where $V_r = \sqrt{(\pi f_r D_p)^2 + U_\infty^2}$ and $c_0 = 340$ m/s (speed of sound at 16°C).

4.1 Influence of the inflow turbulence intensity

Figure 2 depicts the comparison of the spectra for all grid cases for $\beta = 30°$ and a polar emission angle of $\theta = 140°$, i.e. downstream of the propeller plane. The frequency axis is normalized with respect to the blade passing frequency (BPF $= Bf_r \approx 1$ kHz, where $B = 6$ is the blade count). In general, it is observed that increasing TI causes a substantial raise in the broadband noise up to roughly the 7$^{\text{th}}$ BPF (≈ 7 kHz). On the other hand, a considerable reduction in high-frequency broadband noise is observed for all the grid cases after the 11$^{\text{th}}$ BPF (≈ 11 kHz).

For conciseness, the result comparison of varying turbulence grids in this section is limited here to the cases with $\beta = 30°$, although other collective blade pitch angles presented comparable findings.

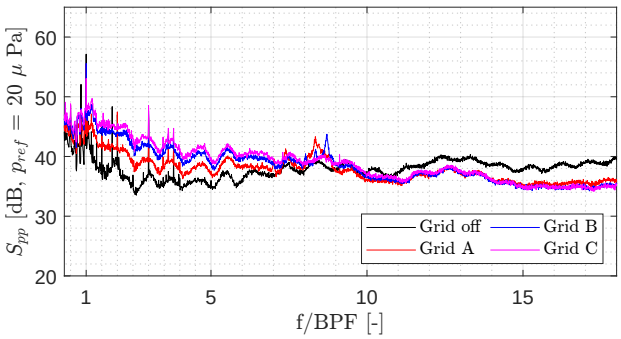


Figure 2: Power spectra S_{pp} of acoustic pressure for $\beta = 30°$ and all grids for $\theta = 140°$ ($\Delta f = 5$ Hz).

The influence of the inflow TI in the propeller far-field noise emissions was evaluated using directivity plots (Figs. 4-9) at the end of this paper for the different sound metrics considered (both conventional and psychoacoustic).

First of all, Fig. 4 depicts an almost omnidirectional (except for an outlier at $\theta \approx 150°$) emission pattern of the $L_{\text{p,eq}}$ metric that is essentially the same for all the four cases. This highlights the fact that this simple metric (lacking any frequency weighting) is not suitable for

making perceptual comparisons [23]. The PNLT_{max} metric (Fig. 5, on the other hand, starts showing larger differences between the four inflow TI cases, with (in general) larger emission values with increasing TI. Overall, larger values and variability are observed for larger polar emission angles θ. Nevertheless, the directivity patterns are not very uniform. Regarding loudness N_5, Fig. 6 presents a more dipole-like radiation pattern typical in propeller applications [6, 10, 11]. Since loudness is (to a certain extent) an energy-based metric, increasing the TI results in higher N_5 values for all emission angles, showing values up to 30% higher than the baseline grid-off case. This is explained by the higher broadband noise levels observed in the mid-frequency range in the spectra of Fig. 2. In terms of sharpness S_5 (see Fig. 7), the radiation patterns are again dipole-like, but in this case, the grid-off case (lowest inflow TI) presents the highest values. This is due to the fact that the sharpness metric employed represents the ratio of high-frequency loudness with respect to the total loudness. High-frequency noise is, in fact, affected by the presence of a turbulence inflow, but rather surprisingly, not by its turbulence intensity. Unexpectedly, its level is greater with a clean inflow and, therefore, the overall sharpness is roughly 10% lower for the cases with higher TI compared to the grid-off baseline. A similar trend (although with a considerably more irregular radiation pattern) is observed for the tonality K_5 (see Fig. 8). In this case, the additional broadband noise observed in the cases with higher TI (see Fig. 2) effectively masks the characteristic tones of the propeller noise signature (BPF and harmonics), providing K_5 values about half the baseline case without inflow turbulence. Finally, the global PA metric (see Fig. 9) combines the results of all SQMs and shows a similar radiation pattern as N_5 (since loudness heavily influences PA [20]). For the larger polar emission angles θ, the estimated psychoacoustic annoyance is up to about 25% higher than for the grid-off baseline case.

4.2 Influence of the collective blade pitch angle

In a similar way as Fig. 2, Fig. 3 compares the far-field noise emissions for all β cases considered when using Grid C and a polar emission angle of $\theta = 140°$. In contrast to the TI variation, increasing β seems to mostly affect the broadband noise emissions for frequencies higher than the 10^{th} BPF, with lower values reported for increasing β. The spectra below that threshold, on the other hand, roughly remained constant for varying β.

The effect of β on the directionality of the different

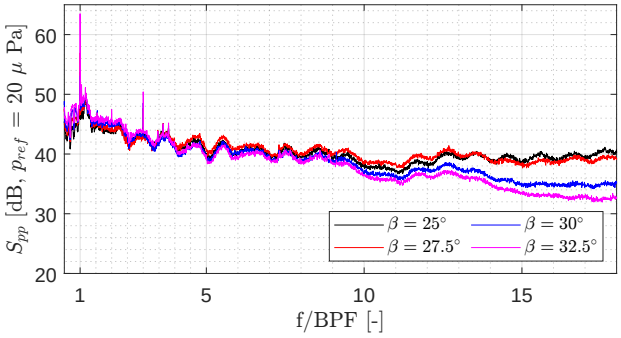


Figure 3: Power spectra S_{pp} of acoustic pressure for Grid C and all β for $\theta = 140°$ ($\Delta f = 5$ Hz).

sound and psychoacoustic metrics for the propeller was evaluated in Figs. 10-15 at the end of this paper. Only the results corresponding to Grid C (i.e. $TI = 3.44\%$) are presented for conciseness, but the conclusions can be extended to other cases.

The results for the $L_{\text{p,eq}}$ metric for this comparison are depicted in Fig. 10, which are essentially the same for all the cases evaluated, like in the TI comparison presented in Fig. 4. In contrast, the PNLT_{max} metric (Fig. 11 presents its largest variations (up to 4 PNTdB) closer to the propeller plane ($\theta \approx 90°$) with higher values for increasing β. This reflects the greater importance of loading noise mechanisms in the propeller's plane, as increasing β results in increased blade loading for a constant inflow velocity and rotational velocity. The loudness radiation patterns presented in Fig. 12 also show this feature, although with a more uniform dipole-like directivity pattern. Near the propeller plane emission angles, differences in N_5 up to 20% are reported, whereas for higher θ values, the results for all cases seem to collapse better. A more consistent variation with β is observed for the sharpness in Fig. 13, where the first two cases ($\beta = 25°$ and 27.5°) follow a very similar trend, but the two higher blade pitch angles present roughly 10% lower S_5 values. This is explained by the aforementioned reduction in high-frequency noise, as seen in Fig. 3. The tonality values for this comparison (with the highly-turbulent Grid C, see Fig 8) are all relatively low, but in the polar plot of Fig. 14, it is observed that the lower β cases present even lower K_5 values (below 0.05 t.u.). Once again, this is likely to be due to the lower masking because of the decrease in broadband noise that these cases present (see Fig. 3). Lastly, the global PA metric presents once again a dipole-like radiation pattern, but with a considerably smaller spread within

the different cases compared to the TI study. In fact, only significant reductions (about 10%) in PA are observed for the smaller β cases close to the propeller disk ($\theta \approx 90°$).

5. CONCLUSIONS

The current manuscript discussed the influence of the inflow turbulence intensity (TI) and the collective pitch angle on the noise emissions of an isolated propeller, evaluated with conventional and psychoacoustic metrics. The experimental data considered was measured using a directivity arc in an aeroacoustic wind tunnel campaign.

In general, it was found that increasing the inflow TI considerably raised the measured values of PNLT_{max} and loudness, whereas, on the other hand, sharpness and tonality decreased. The overall psychoacoustic annoyance metric (PA) roughly followed the same trend as loudness. Overall, larger PA values and variability were observed for higher polar emission angles (i.e. downstream of the propeller plane).

Increasing the collective propeller blade pitch angle β also caused a rise in PNLT_{max} and loudness, but also a moderate increase in tonality. This time, higher variations of these metrics were observed in the propeller plane direction ($\theta \approx 90°$). Conversely, sharpness seemed to decrease for increasing β angles. The combined effect of these changes caused a slight increase of PA with $beta$, but was considerably milder than for the TI comparison.

Future work will involve psychoacoustic listening experiments to confirm the findings in this paper and assess the somewhat contradicting trends between loudness and tonality and sharpness. In addition, applying acoustic imaging to the data recorded by the planar microphone array would also be of interest to localize, if possible, the noise sources responsible for these psychoacoustic features [24].

6. ACKNOWLEDGMENTS

This work is part of the HOPE (Hydrogen Optimized multi-fuel Propulsion system for clean and silEnt aircraft) project, and has received funding from the European Union's Horizon Europe research and innovation programme under grant agreement No. 101096275. Additionally, this publication is also a part of the *Listen to the future* project (project number 20247), a part of the Veni 2022 research programme (Domain Applied and Engineering Sciences). The latter project is granted to Roberto Merino-Martinez and is (partially) financed by the Dutch Research Council (NWO).

7. REFERENCES

[1] R. M. Yupa-Villanueva, R. Merino-Martinez, A. Altena, and M. Snellen, "Psychoacoustic Characterization of Multirotor Drones in Realistic Flyover Maneuvers," in 30th *AIAA/CEAS Aeroacoustics Conference, June 4 – 7 2024, Rome, Italy*, 2024. AIAA paper 2024–3015.

[2] S. A. Rizzi, D. L. Huff, D. D. J. Boyd, P. Bent, H. B., K. A. Pascioni, D. C. Sargent, D. L. Josephson, M. Marsan, B. He, and R. Snider, "Urban Air Mobility Noise: Current Practice, Gaps, and Recommendations," Tech. Rep. NASA Technical Memorandum 83199, NASA, 2020.

[3] S. Schade, R. Merino-Martinez, P. Ratei, S. Bartels, R. Jaron, and A. Moreau, "Initial Study on the Impact of Speed Fluctuations on the Psychoacoustic Characteristics of a Distributed Propulsion System with Ducted Fans," in 30th *AIAA/CEAS Aeroacoustics Conference, June 4 – 7 2024, Rome, Italy*, 2024. AIAA paper 2024–3273.

[4] F. Monteiro, R. Merino-Martinez, and L. T. Lima Pereira, "Psychoacoustic Evaluation of an Array of Distributed Propellers Under Synchrophasing Operation," in 30th *AIAA/CEAS Aeroacoustics Conference, June 4 – 7 2024, Rome, Italy*, 2024. AIAA paper 2024–3321.

[5] F. Ahmed, C. A. Ramos-Romero, A. J. Torija Martinez, and M. Azarpeyvand, "Boundary Layer Ingestion Ducted Fan: Aeroacoustic and Psychoacoustic Insights," in *30th AIAA/CEAS Aeroacoustics Conference (2024)*, (Rome, Italy), American Institute of Aeronautics and Astronautics, June 2024.

[6] L. N. Quaroni, R. Merino-Martinez, F. d. N. Monteiro, and S. S. Kumar, "Collective blade pitch angle effect on grid turbulence ingestion noise by an isolated propeller," in 30th *AIAA/CEAS Aeroacoustics Conference, June 4 – 7 2024, Rome, Italy*, 2024. AIAA paper 2024–3209.

[7] E. Grande, G. Romani, D. Ragni, F. Avallone, and D. Casalino, "Aeroacoustic Investigation of a Propeller Operating at Low Reynolds Numbers," *AIAA Journal*, vol. 60, pp. 860–871, Feb. 2022.

[8] A. J. Torija, C. Ramos-Romero, and N. Green, "Acoustic and Psychoacoustic Characterisation of Unmanned Aircraft Systems as a Function of Vehicle Mass and Flight Procedure," in 30th *AIAA/CEAS Aeroacoustics Conference, June 4 – 7 2024, Rome, Italy*, 2024. AIAA paper 2024–3235.

[9] R. Merino-Martinez, R. M. Yupa-Villanueva, B. von den Hoff, and J. S. Pockelé, "Human response to the flyover noise of different drones recorded in field measurements," in 3rd *Quiet Drones conference, September 8 – 11 2024, Manchester, United Kingdom*, 2024.

[10] R. Merino-Martinez, H. Ben-Gida, and M. Snellen, "Psychoacoustic Evaluation of an Optimized Low–Noise Drone Propeller Design," in 30th *International Congress on Sound and Vibration (ICSV), July 8 – 11 2024, Amsterdam, the Netherlands*, 2024.

[11] K. Heutschi, B. Ott, T. Nussbaumer, and P. Wellig, "Synthesis of real world drone signals based on lab recordings," *Acta Acoustica*, vol. 4, pp. 1–10, October 2020.

[12] T. Sinnige, B. Della Corte, R. de Vries, F. Avallone, R. Merino-Martinez, D. Ragni, G. Eitelberg, and L. L. M. Veldhuis, "Alleviation of Propeller–Slipstream–Induced Unsteady Pylon Loading by a Flow–Permeable Leading Edge," *Journal of Aircraft*, vol. 56, pp. 1214–1230, May–June 2019. DOI: 10.2514/1.C035250.

[13] F. Petricelli, P. Chaitanya, S. Palleja-Cabre, S. Meloni, P. F. Joseph, A. Karimian, S. Palani, and R. Camussi, "An experimental investigation on the effect of in-flow distortions of propeller noise," *Applied Acoustics*, vol. 214, p. 109682, Nov. 2023.

[14] N. S. Jamaluddin, A. Celik, K. Baskaran, D. Rezgui, and M. Azarpeyvand, "Experimental analysis of a propeller noise in turbulent flow," *Physics of Fluids*, vol. 35, p. 075106, July 2023.

[15] R. Merino-Martinez, A. Rubio Carpio, L. T. Lima Pereira, S. van Herk, F. Avallone, M. Kotsonis, and D. Ragni, "Aeroacoustic design and characterization of the 3D–printed, open–jet, anechoic wind tunnel of Delft University of Technology," *Applied Acoustics*, vol. 170, pp. 1–16, June 2020.

[16] N. Van Arnhem, R. De Vries, T. Sinnige, R. Vos, G. Eitelberg, and L. L. M. Veldhuis, "Engineering Method to Estimate the Blade Loading of Propellers in Nonuniform Flow," *AIAA Journal*, vol. 58, pp. 5332–5346, Dec. 2020.

[17] R. Amiet, "Correction of open jet wind tunnel measurements for shear layer refraction," in *2nd Aeroacoustics Conference*, (Hampton,VA,U.S.A.), American Institute of Aeronautics and Astronautics, Mar. 1975.

[18] L. Li, H. Zhu, R. Maryami, X. Zhang, and Y. Liu, "Flow and acoustic characterization of turbulence grids at wind tunnel nozzle exit," *Journal of Sound and Vibration*, vol. 590, p. 118535, Nov. 2024.

[19] R. Merino-Martinez, *Microphone arrays for imaging of aerospace noise sources*. PhD thesis, Delft University of Technology, 2018. ISBN: 978–94–028–1301–2.

[20] G. F. Greco, R. Merino-Martinez, A. Osses, and S. C. Langer, "SQAT: a MATLAB-based toolbox for quantitative sound quality analysis," in 52th *International Congress and Exposition on Noise Control Engineering, August 20 – 23 2023, Chiba, Greater Tokyo, Japan*, International Institute of Noise Control Engineering (I-INCE), 2023.

[21] G.-Q. Di, X.-W. Chen, K. Song, B. Zhou, and C.-M. Pei, "Improvement of Zwicker's psychoacoustic annoyance model aiming at tonal noises," *Applied Acoustics*, vol. 105, pp. 164–170, 2016.

[22] Greco, G. F. and Merino-Martinez, R. and Osses, A., "SQAT: a sound quality analysis toolbox for MATLAB (version v1.0)," May 2023. Accessed in May 2023.

[23] R. Merino-Martinez, R. Pieren, and B. Schäffer, "Holistic approach to wind turbine noise: From blade trailing–edge modifications to annoyance estimation," *Renewable and Sustainable Energy Reviews*, vol. 148, pp. 1–14, May 2021.

[24] R. Merino-Martinez, A. Vieira, M. Snellen, and D. G. Simons, "Sound quality metrics applied to aircraft components under operational conditions using a microphone array," in 25th *AIAA/CEAS Aeroacoustics Conference, May 20 – 24 2019, Delft, The Netherlands*, 2019. AIAA paper 2019–2513.

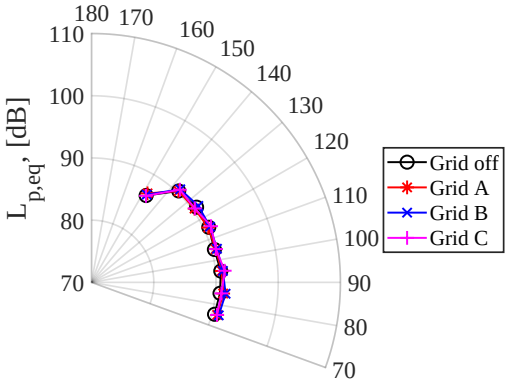


Figure 4: $L_{p,eq}$ directivity for $\beta = 30°$.

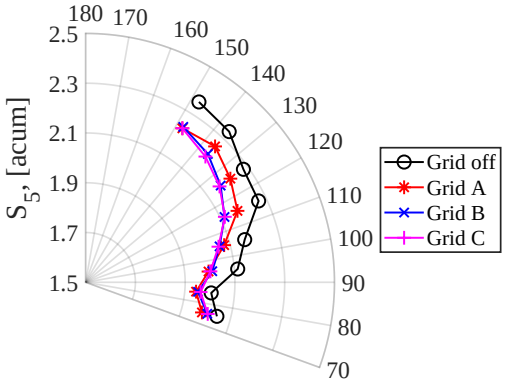


Figure 7: S_5 directivity for $\beta = 30°$.

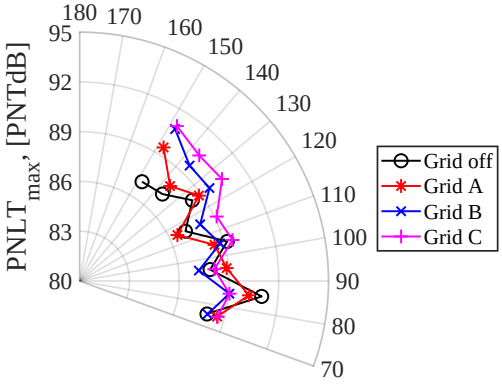


Figure 5: $PNLT_{max}$ directivity for $\beta = 30°$.

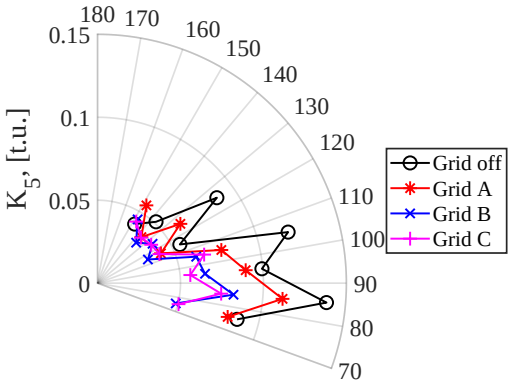


Figure 8: K_5 directivity for $\beta = 30°$.

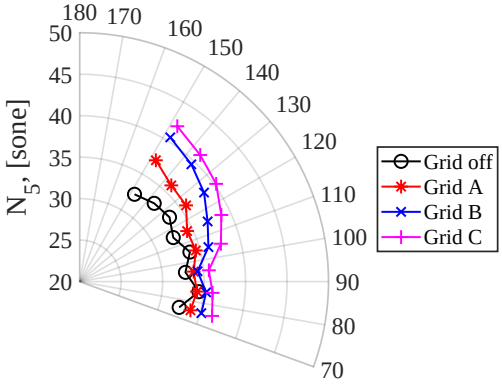


Figure 6: N_5 directivity for $\beta = 30°$.

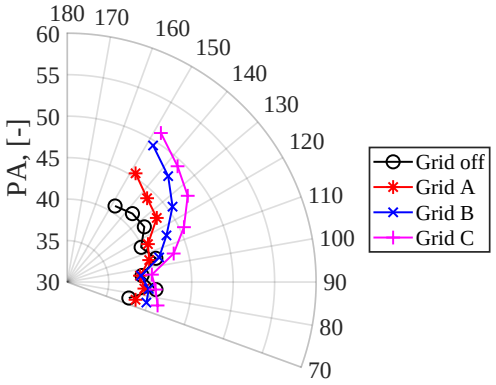


Figure 9: PA directivity for $\beta = 30°$.

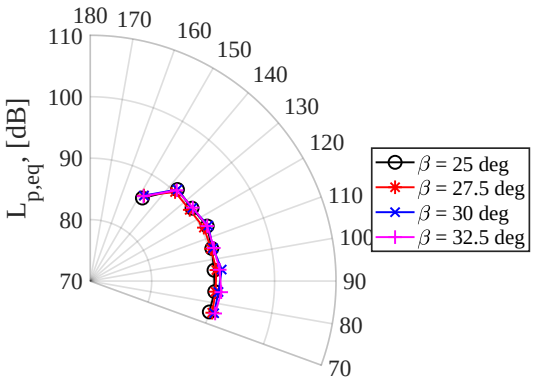


Figure 10: $L_{p,eq}$ directivity for Grid C.

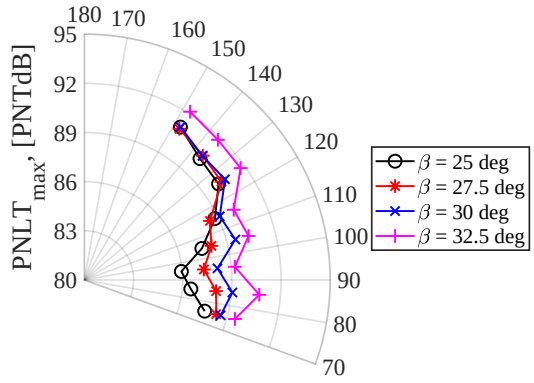


Figure 11: $PNLT_{max}$ directivity for Grid C.

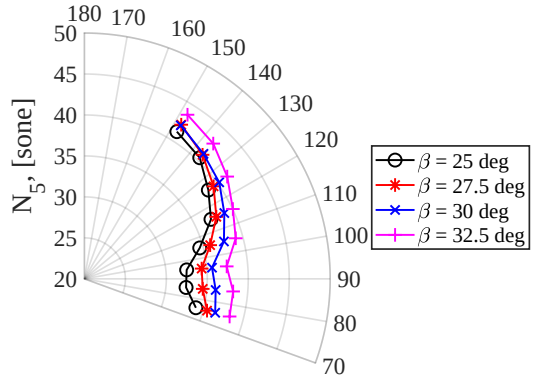


Figure 12: N_5 directivity for Grid C.

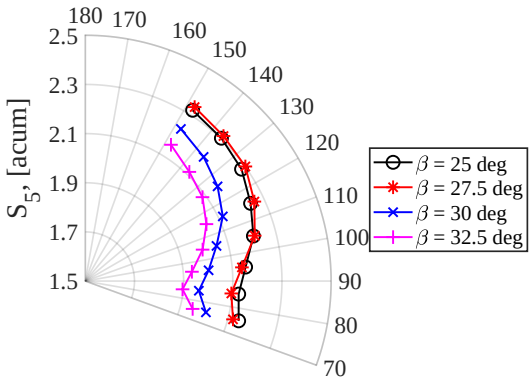


Figure 13: S_5 directivity for Grid C.

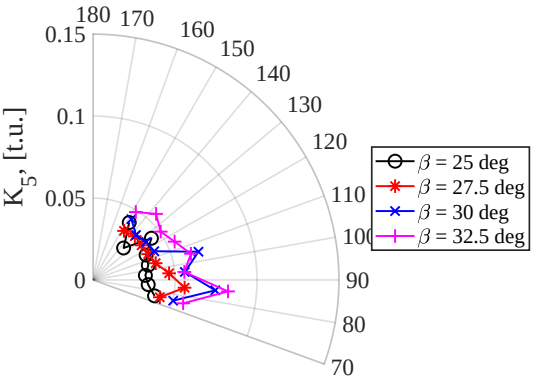


Figure 14: K_5 directivity for Grid C.

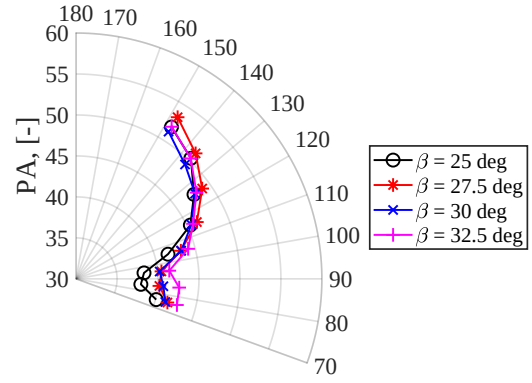


Figure 15: PA directivity for Grid C.

DOI: 10.61782/fa.2025.0541



FORUM ACUSTICUM
EURONOISE 2025

MACHINE LEARNING-BASED MODELLING OF UAV NOISE METRICS IN REAL CONDITIONS

Camilo I. Andino Cappagli[1*] **Alireza Amiri-Simkooei**[1] **Salil Luesutthiviboon**[1]
Tomáš Meiser[2] **Amy Morin**[1] **Michal Zajačík**[2]
Milan Rollo[2] **Mirjam Snellen**[1]
[1] Operations and Environment section, Faculty of Aerospace Engineering,
Delft University of Technology, Netherlands
[2] AgentFly Technologies, Prague, Czechia

ABSTRACT

Over the last decade, there has been a marked increase in the use of drones for various applications including emergency and natural disaster response, payload delivery, aerial imaging and surveillance. There are currently many private and public initiatives that aim to further increase the number of drones and diversify their tasks, offering many associated benefits such as reduction in emissions by replacing traditional and more polluting options with electric unmanned aerial vehicles (UAVs). However, several challenges have to be addressed before a broader implementation is accomplished. One of such challenges is the reported noise annoyance produced by UAVs. This study focuses on the development of data-driven models to predict the dynamics of noise metrics during real UAV operations. Extensive outdoor experimental campaigns were conducted, where array-based measurements were recorded during several manoeuvres performed by different types of drones. Beamforming techniques were applied to improve data quality and signal-to-noise ratio (SNR), and to synchronize telemetry and acoustics data streams. Using the improved experimental data, an initial machine learning model was developed to predict the back-propagated $OSPL$ as function of telemetry-derived operational parameters for ascent, hover, and descent. The model managed to accurately predict the experimental data, and it was found that the elevation angle was the most important predictor of $OSPL$ for the considered manoeuvres.

Keywords: Drones, noise metrics, noise prediction, machine learning models

*__Corresponding author__: c.i.andinocappagli@tudelft.nl.
__Copyright__: ©2025 Camilo I. Andino Cappagli et al. This is an open-access article distributed under the terms of the Creative Commons Attribution 3.0 Unported License, which permits unrestricted use, distribution, and reproduction in any medium, provided the original author and source are credited.

1. INTRODUCTION

Several factors have led to a sharp increase in the number of drones and tasks, some of which are due to the reduction of production costs, the development of more efficient and smaller technologies, critical for the manufacturing and control of these systems, and their versatility performing a large variety of tasks. Among these, photography and video recording capabilities have enabled drones to support, for example, infrastructure development and surveillance and security. Drones have also been employed to provide assistance in emergencies and natural disasters, in agricultural applications, and goods transportation [1]. Generally, they are considered to have great potential to serve as greener and more sustainable options to replace traditional, more contaminating methods. The number of tasks that UAVs can perform exceeds this list, but the critical natures of certain applications signify their importance.

However, one of the main barriers to the broader adoption and applications of UAVs is the reported acoustic annoyance caused by their operation [2–4]. To allow for the sector to sustainably grow, it is essential to address such reported acoustic annoyance. A predictive tool is needed to estimate representative psychacoustic metrics. Given the wide range in drone types and operational conditions, outdoor drone noise measurements are considered an important element in the efforts of working towards such a tool. These need to be developed based on studies of typical real UAV operations to understand the connections between operational parameters and the acoustics, as well as the influence of environmental factors.

The resulting tools will allow for adequate mission planning, manoeuvre optimization, and design improvements to mitigate acoustic annoyance. As the acoustics vary for different drone types and manoeuvres, these differences must be taken into account as well. At the same time, these tools need to remain computationally inexpensive for fast calculations and seamless

integration into optimization frameworks. Studying drone noise with the drone operating under realistic conditions is essential to ensure a realistic overview of the expected noise. Recent studies have explored UAV noise in such realistic and uncontrolled environments [5–7]. These works focused on measuring and characterising noise from specific drones under realistic conditions. In this study, we describe the development and initial results of a data-driven model that managed to predict experimentally measured acoustic features using telemetry-based variables, and identified important operational parameters as main predictors.

2. METHODS

2.1 Experimental campaigns

An experimental campaign was conducted in April 2024 at an airfield on the outskirts of Prague, Czechia. The site was chosen for its isolation from populations centers, and it was only close to a seldom-used road. Additionally, the airspace in the area was not crowded by air traffic, with only a few aircraft flying overhead throughout the campaign. These occurrences were noted in the experimental logs to account for their contributions, or remeasure if necessary. Taken all together, these conditions met the site goal which was to constitute a highly isolated environment in terms of additional noise sources, while still being an outdoor environment with its inherent variability, including occasional wind currents and gusts. The tested flight plan consisted of a series of manoeuvres including ascent, hover, descent, horizontal flights, and sudden changes in direction. All manoeuvres were performed by three different multirotor UAVs.

To start the model development, operations involving ascent, hover, and descent were analysed. Each operation was performed as follows: The drone took off and ascended vertically to 10 m above ground level (AGL), where it hovered for 15 seconds. It then ascended to 30 m where it hovered again for the same duration, and repeated the process at 50 m and 70 m. Once the hover at the last altitude was completed, the drone descended continuously until landing. The altitude profile, as a function of time, for this operation is shown in figure 1.

This operation was repeated for five different take off positions, where the ascent position, relative to the microphone array, was changed. The take off positions were located north, south, west, and east of the microphone array, at approximately 25 m distance, and an additional site at 50 m east of the array, resulting in five total take off positions. The combined altitude profile of these operations can be observed in figure 2. Differences in altitudes corresponding to different operations occurred due to pilot operations. The selected drone was a co-rotational (X8) quadcopter Gorgon, built, developed, and piloted by AgentFly Technologies, which can be observed in figure 3.

To measure the acoustic signal while the manoeuvre was performed, an array of 4 m of aperture, consisting of 64 microphones, with a sampling frequency of 62500 Hz was used. To attenuate ground reflections, a foam was placed under the entire array, and a secondary foam was placed in the central part of the array between the microphones and the array structure to avoid these reflections, had they appeared.

To record the operational parameters of the drone, the autopilot telemetry and ESCs were used. Among several others, these included the GPS-based information, position, velocity, and acceleration, the RPMs of individual rotors, and thrust, all recorded as a function of time.

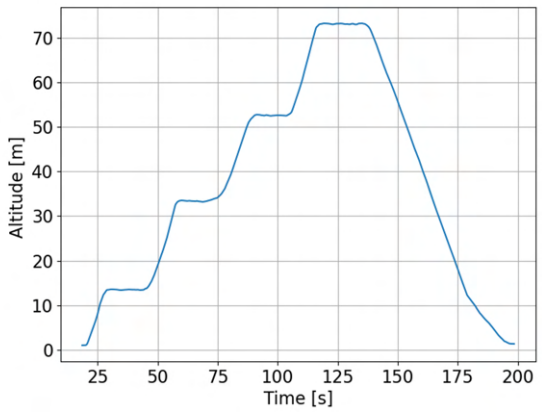


Figure 1. Altitude profile for a single ascent-hover-descent operation performed by the Gorgon X8.

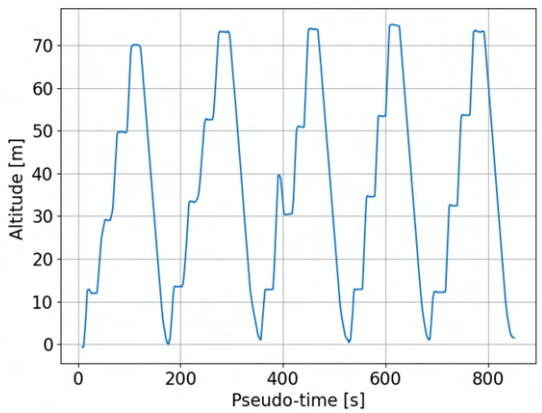


Figure 2. Altitude profile for five ascent-hover-descent operations performed by the Gorgon X8. The horizontal axis represents a sequential arrangement of time-series data rather than the actual time. Variability among signals is evident due to the manual piloting of these operations.



Figure 3. Photo of the selected drone, Gorgon X8, developed and operated by AgentFly Technologies. Credits: Dr. Milan Rollo, AgentFly Technologies.

2.2 Beamforming techniques

Given the goal of developing a data-driven model to describe the time dynamics of different acoustic metrics, it is necessary to first address two points. i) As explained in the previous section, different measures were taken to reduce the effect of ground reflections. However, it was impossible to eliminate them entirely during the data acquisition. ii) It is important to accurately synchronize all telemetry variables and acoustic data to increase the model validity. This involves both properly synchronizing the data and correcting the GPS readouts due to their uncertainties. To address the above issues, beamforming was used.

To do this, a beamformer for a fixed source position ξ_j is defined based on the following functional structure [8]:

$$B(r,\theta,\phi) = \frac{\mathbf{g}_j^* \langle \mathbf{p}\mathbf{p}^* \rangle \mathbf{g}_j}{|| \mathbf{g}_j ||^4} \tag{1}$$

where $\langle \mathbf{p}\mathbf{p}^* \rangle$ is the Cross-Spectral Matrix (CSM) of the measured pressures, which is generated by averaging the Fourier transforms of sample blocks of 0.1 s in our case, with no overlap considered, and $\mathbf{g}_j^*$ is the steering vector

$$g_{j,n} = \frac{\exp\left(-2\pi i f \Delta t_{j,n}\right)}{4\pi \, || \, \mathbf{x}_n - \xi_j \, ||} \tag{2}$$

with $\Delta t_{j,n}$ the delay between the emission at the position ξ_j and the receiver position $\mathbf{x}_n$. The beamformer (1) establishes a correlation between the actual location information of the source, contained within the CSM, and the source position considered, represented by the steering vector in Equation 2. By considering many potential source locations ξ_j, the location corresponding to the maximum of Equation 1 is used as the estimate of the source position from the array measurements.

This methodology was used to reconstruct the UAV trajectory, independent from the GPS information. Then, the acoustic localization-based and GPS-based trajectories were compared to estimate the corrections needed in the GPS telemetry data.

Once the corrections were implemented, the steering vector was no longer defined based on the estimated position, but rather in terms of the GPS-corrected trajectory. As the beamforming considers all microphones, while compensating for delays to effectively focus on the source, it generates a much cleaner spectrogram with improved SNR compared to single microphone measurements. Once the beamformed spectrogram was obtained, the signals were back-propagated for each beamformed frequency band according to:

$$SPL_{source}(f,t) = SPL_{ground}(f, t + \frac{r(t)}{c}) \tag{3}$$

$$+20 \log \frac{r(t)}{r_0} + \alpha(f) r(t) \tag{4}$$

where r is the distance between the array and the drone, $r_0 = 1$ m, c the sound speed, and $\alpha(f)$ is the coefficient of atmospheric absorption, which depends on the frequency, and also on relative humidity and temperature, both of which were recorded during the measurement campaign.

This procedure generated a cleaner, back-propagated to the source spectrogram, where ground reflections are attenuated. The single microphone and beamformed spectrograms for a single operation can be observed in figure 4

3. RESULTS

3.1 Correlation study

From the telemetry data, different observables were computed as inputs for the data-driven models. These were:

- Azimuthal angle $\phi(t)$: The angular position between the microphone array and the drone measured on the horizontal plane (on the ground).
- Elevation angle $\theta(t)$: The polar angle between the microphone array and the drone, with $\theta = 0$ when the drone is on the ground, and $\theta = \frac{\pi}{2}$ if the drone is overhead.
- Velocity vector absolute value $|\bar{v}(t)|$
- Acceleration vector absolute value $|\bar{a}(t)|$
- Thrust percentage T
- Each of the eight rotors rpm $\{n_{p,i}(t)\}_{i=1\ldots8}$

As the acoustic metrics were back-propagated to the source hemisphere, the range between the array and drone and altitude were not considered.

Since ascent, hover, and descent were the initially tested maneuvers, it is expected that under isolated, ideal conditions, all rpms should have the same absolute value at corresponding times. In the cases of ascent and descent, the absolute rpm of all rotors should be identical at each moment, whereas for hover,

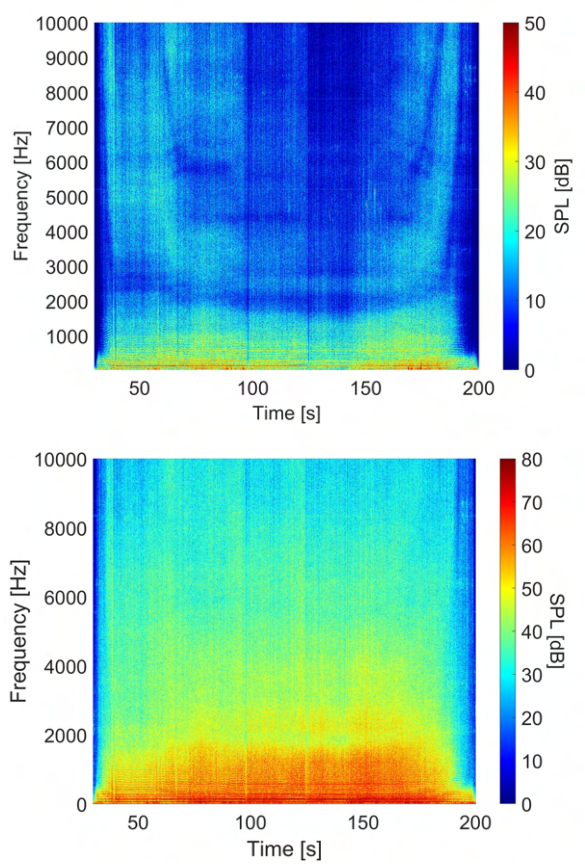


Figure 4. Top: Single microphone spectrogram from an ascent-hover-descent operation. Despite the measures taken during the experiments to attenuate reflections, some effects are still clear. These reflections however, do not appear to be due to ground effects but rather from the outermost parts of the array, which appear to act as spurious sources. Bottom: Beamformed spectrogram from a single ascent-hover-descent operation. Compared with the top, the reflections are greatly attenuated. The dB values increase as this spectrogram is back-propagated to the source. The tones are clearer than the top frame, and in particular, they are present up to 2 kHz. In this range, and for higher levels, the noise is dominated by its broadband component.

the rpm of all rotors would remain constant also during the duration of the manoeuvre. Therefore, the rpms time series were replaced, and the following observables were generated:

$$\langle n_p(t)\rangle = \frac{1}{N_r}\sum_{i=1}^{N_r} \mid n_p(t) \mid \tag{5}$$

$$\sigma_{n_p}(t) = \sqrt{\frac{1}{N_r}\sum_{i=1}^{N_r}(\mid n_p(t) \mid -\langle n_p(t)\rangle)^2} \tag{6}$$

where the average and standard deviations were calculated at equal times, thereby resulting in time series as well.

The $\langle n_p(t)\rangle$ measures the overall rpm, and $\sigma_{n_p}(t)$ is used to quantify how far from the ideal hover, ascent or descent the rpm activities are; a value of $\sigma_{n_p}(t_i) = 0$ indicates that at the time t_i, all the rotors had the same rpm. In other words, variations given by factors such as wind gusts and pilot-induced perturbations will cause this observable to vary from zero. The time over which each effect takes place depends on factors such as pilot reaction time, and wind gust intensity and duration.

The first step towards studying relations between both sets of variables (acoustic metrics and telemetry data) was to compute pair-wise correlations between each of the inputs and $OSPL$, considering a single ascent-hover-descent operation. The Spearman correlation was used as it can test for the existence of general monotonic correlations. The results are shown in figure 5.

As it can be observed from the correlation coefficients, the correlation between the $OSPL$ and the elevation angle θ is significantly increased. To validate the results, Pearson correlation was also used and displayed approximately the same coefficient between both of these variables (data not shown).

This study is a sufficient condition to establish that the elevation angle is a variable of importance to predict the $OSPL$, but it does not necessarily mean that the other variables are not relevant, as this is a pair-wise study and does not capture any coupling between input variables. Additionally, both metrics have limitations, with Spearman correlation allowing for non-linear but monotonic relations, and Pearson looking exclusively to linear relations; both could be excluding the discovery of more complex relations.

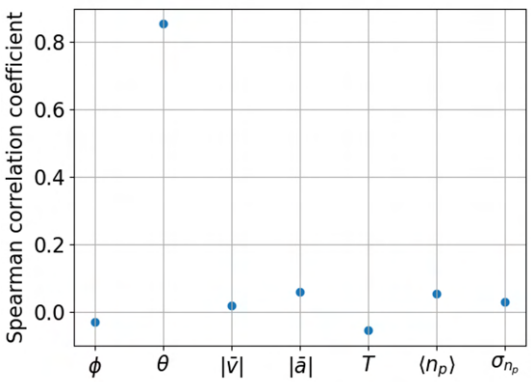


Figure 5. Spearman correlation of the $OSPL$ with each of the tested input parameters. A considerable increase is observed for the elevation angle. This implies the existence of a monotonic relation between both signals.

3.2 Model results

Because drone operations in uncontrolled environments tend to show a higher variability in terms of the drone flight dynamics and therefore in the generated acoustic signals, it is important to understand the model performance in representing this variability. To this end, all five ascent-hover-descent operations were integrated together into the dataset for the model. The altitude profile corresponds in this case with the one observed in figure 2 in the section 2.1.

As the correlation analysis showed that relations exist between at least one of the telemetry variables considered and the measured $OSPL$, the main goal was to find such relations and use them to predict this acoustic metric. To create a model capable of capturing complex relations between the operational parameters and the acoustic metrics, machine learning techniques were employed. In this work, we report the model results for the case of random forest regression (RFR). This method was chosen after comparing the prediction accuracy of different ML regression models, from which RFR proved to be the most accurate while remaining relatively simple. Additionally, Random Forest has also been used in other works related to assesment and prediction of aviation noise [9].

Initially, a series of studies were performed to optimize the number of decision trees. The optimization consisted of generating training, validation, and quality assessment of prediction procedures for each number of decision trees. Randomization and splitting were done before the optimization starts; dividing the randomized data into 80% training and 20% for validation. After the model for each number of trees is trained on the training set, the prediction is computed by applying it to the validation data and generating the model estimation. R^2, $RMSE$, and MAE were calculated based on the prediction and stored for each decision trees number. The optimal number of decision trees was set based on the highest value of R^2. It was also checked that the values of $RMSE$ and MAE have a local minimum at the chosen value. These results can be observed in the figures 6, 7, 8.

The optimization resulted in an optimal number of trees, which was then used to produce the optimal model predictions, which can be observed in figures 9 and 10, and the accuracy in figure 11. From figure 10, the dynamics of the $OSPL$ is accurately recovered by the model. There are sources of deviations arising from extreme values and stochastic experimental noise.

To assess the robustness of the model results, the optimization was repeated for different randomization of the dataset and the R^2, $RMSE$, and MAE were extracted again. No significant difference was observed for the optimized model, presenting similar values up to the 3 decimal place of R^2. The results obtained from the initial optimization are then robust relative to changes in the data randomization. Therefore, the model managed to generate accurately predictions of the experimentally obtained $OSPL$ when all operations are considered together.

To assess the relevance of each of the input variables to predict the $OSPL$, the feature importance of the model was studied, analyzing the mean decrease impurity (MDI). This metric measures how much each input variable reduces the variance of the target values after it is used to split the data. The results from

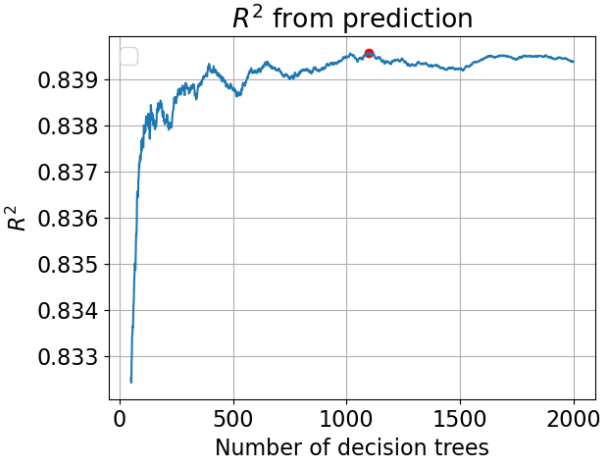


Figure 6. Optimization of the number of decision trees based on the highest R^2. In red, this maximum is shown. It can be observed that the variations on the R^2 are small, as it only changes a maximum of 0.007.

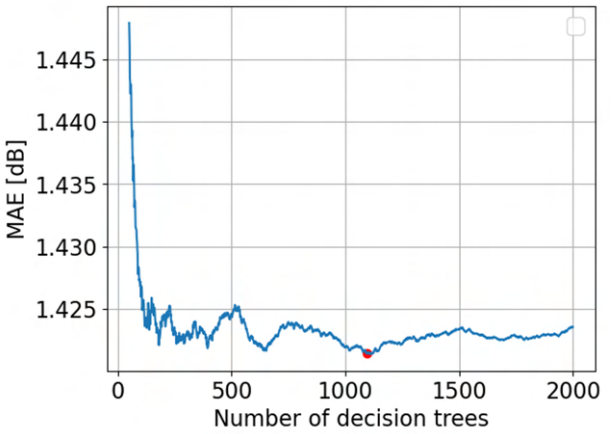


Figure 7. Values of the MAE calculated on the model prediction from each optimization run based on the highest R^2. In red, the number of decision trees for which the highest R^2 is obtained is displayed. It was observed that it corresponded to a local minima of the function. The variation on the MAE is small, with a maximum of 0.025 dB.

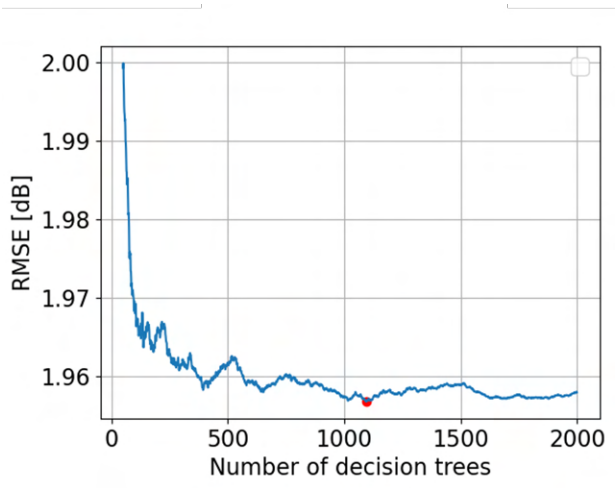


Figure 8. $RMSE$ of the prediction from each optimization run based on the highest R^2. In red, the number of decision trees for which the highest R^2 is obtained is displayed. The variation on the $RMSE$ is small, with a maximum of 0.05 dB across all tree values.

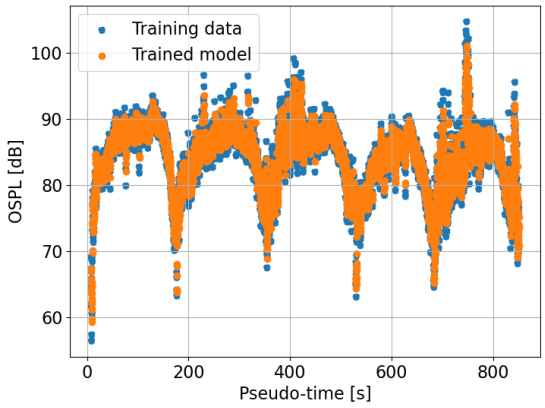


Figure 9. Trained RFR of the $OSPL$ data using the optimal number of decision trees.

this analysis can be observed in figure 12

As the MDI results show, the elevation angle results in the most important predictor of the $OSPL$, which implies that the information of both the $OSPL$ dynamics and intensity can be greatly explained by the elevation angle. Since all acoustic data was back-propagated to the 1 m hemisphere, the elevation angle is the angle between the horizontal plane of the drone and the field point.

This result implies that the $OSPL$ hemisphere behaviour

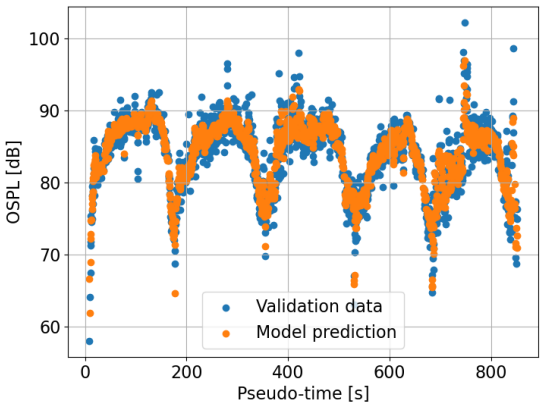


Figure 10. RFR prediction of the $OSPL$ using the optimal number of decision trees.

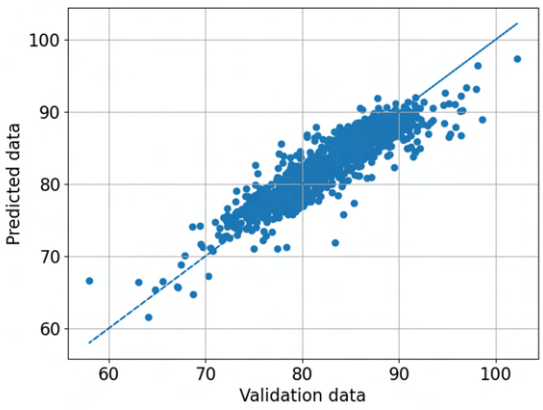


Figure 11. RFR prediction of the OSPL plotted as function of the validation data, for the case where all the operations were used. The model manage to capture most of the behaviour of the $OSPL$, with $R^2 = 0.84$

takes over other sound generating mechanisms when assessing predictor importance during realistic environmental conditions. The observed behaviour of the model in terms of R^2, deviation relative to the validation data, and feature importance, indicate that the prediction is accurate and robust to the high variability allowed. Furthermore, the ascent-hover-descent manoeuvres were performed manually, which adds a level of variability that is not usually present in systematic drone operations. Because of this, the model could show more accurate results when the automatic pilot commands the drone.

To visually verify the behaviour of the elevation angle, it

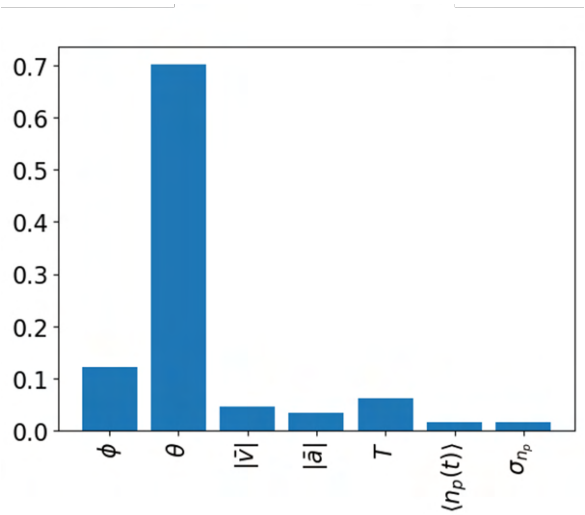


Figure 12. RFR parameter importance. The elevation angle scores the maximum MDI.

can be observed $OSPL$ for all the operations can be observed in figure 13.

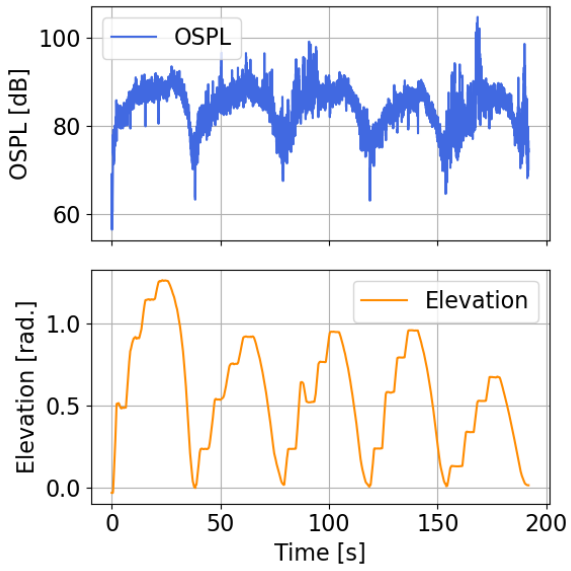


Figure 13. Comparison between the elevation angle (θ) and the $OSPL$ of all the ascent-hover-descent operations.

It is observed that the $OSPL$ increases as the elevation angle increases, which indicates that more frequency-integrated acoustic energy is measured when the field point is located closer to the bottom of the drone. As it can be observed in figure 13, this behaviour is not linear and the $OSPL$ increases more for smaller elevation angles, and it reaches an asymptotic behaviour for larger elevation angles.

4. CONCLUSIONS AND DISCUSSIONS

During the present work a machine learning model was developed and tested to predict the $OSPL$ caused by ascent, hover and descent operations of an X8 multirotor drone. The model managed to predict most of the variation observed in the acoustic metric calculated directly from experimental data, taken in realistic outdoor operational conditions. The elevation angle was found to be the most important predictor of the $OSPL$ in the tested manoeuvres, which indicates that the geometry of the hemisphere is more relevant than the other telemetry-based variables.

Consequently, the model is able to represent an effective geometry of the radiation lobe of the drone's $OSPL$. In particular, based on the observed non-linear behaviour, where the $OSPL$ increases more for smaller angles, and much less for larger angles, the model could indicate a sinusoidal/shifted-cosine dependency on the angle, which points at a dipolar behaviour of the sound propagation. This effect will be validated and further studied for other acoustic metrics in the future, as well as for the other manoeuvres and drones recorded during the experimental campaign.

This paper presents a method to generate predictions of total $OSPL$ prior to operations, involving ascent, hover, and descent. As these are critical manoeuvres for real UAV operations, they are highly relevant for assessing the impact of these operations on human populations nearby. During ascent and hover in real conditions, the drone has to accelerate or maintain an altitude, while adapting the rotors activities to compensate for any wind distortions, which in turn generate a fast variation of the acoustic dynamics. This first model managed to represent most of these variations based on telemetry-based features, accomplishing a good degree of accuracy and robustness, when analyzing all operations together.

Since the input features are directly derived from telemetry data, the model shows the potential to be also used as a way of interrogating the importance of physical drivers and guide the development of physics-based theories that can study from first principles, the dominant sound generating mechanisms in realistic, uncontrolled, conditions.

In a broader aspect, these results represent a first step into the development of a predictive tool to quantify the acoustic impact of drone operations. During the measurements campaign explained in section 2.1, several horizontal flight and changes in directions were measured, which are being used to extend the model to these different manoeuvres, hence more comprehensively studying a full flight envelope. To study how general the

predictors are, other multirotor systems that were used in the measurements campaign will be analysed.

Based on the measured manoeuvres, a series of uncertainty quantification studies are being developed with two objectives. Firstly, to quantify the accuracy of the model as well as its uncertainty for the different studied manoeuvres. Secondly, to study the role of wind gusts in the acoustic metrics and to quantify the effect on the model predictions.

5. ACKNOWLEDGMENTS

The authors are grateful to the EC for supporting the present work, performed within the REFMAP project, funded by the European Union's Horizon Europe research and innovation programme under grant agreement no. 101096698 (REFMAP). This publication solely reflects the authors' view and neither the European Union, nor the funding Agency can be held responsible for the information it contains.

6. REFERENCES

[1] C. Wankmüller, M. Kunovjanek, and S. J. Mayrgündter, "Drones in emergency response – evidence from cross-border, multi-disciplinary usability tests," *International Journal of Disaster Risk Reduction*, vol. 65, no. 102567, 2021.

[2] H. Eißfeldt and V. Vogelpohl, "Drone acceptance and noise concerns — some findings," in *20th International Symp. on Aviation Psychology*, (Dayton, Ohio, USA.), pp. 199–204, 2019.

[3] McKinsey and Company, *Study on the societal acceptance of urban air mobility in Europe*. EASA, 2021.

[4] D. Bajde, N. Woermann, M. H. Bruun, R. Gahrn-Andersen, J. K. Sommer, M. Nøjgaard, S. H. Christensen, H. Kirschner, R. H. Skaarup Jensen, and J. H. Bucher, *Public reactions to drone use in residential and public areas*. University of Southern Denmark / Aalborg University, 2021.

[5] C. Ramos-Romero, N. Green, A. J. Torija, and C. Asensio, "On-field noise measurements and acoustic characterisation of multi-rotor small unmanned aerial systems," *Aerosp. Sci. Technol*, vol. 141, no. 108537, 2023.

[6] N. Konzel and E. Greenwood, "Ground-based acoustic measurements of small multirotor aircraft," in *Vertical Flight Society's 78th Annual Forum & Technology Display*, (Fort Worth, Texas, USA.), 2022.

[7] T. Zhou, H. Jiang, and B. Huang, "Quad-copter noise measurements under realistic flight conditions," *Aerosp. Sci. Technol*, vol. 124, no. 107542, 2022.

[8] R. Merino-Martinez, P. Sijtsma, M.Snellen, T. Ahlefeldt, J. Antoni, C. J. Bahr, D. Blacodon, D. Ernst, A. Finez, S. Funke, T. F. Geyer, S. Haxter, G. Herold, X. Huang, W. M. Humphreys, Q. Leclère, A. Malgoezar, U. Michel, T. Padois, A. Pereira, C. Picard, E. Sarradj, H. Siller, D. G. Simons1, and C. Spehr, "A review of acoustic imaging methods using phased microphone arrays," *CEAS Aeronautical Journal*, vol. 10, pp. 197–230, 2019.

[9] J. Meister, "Power setting estimation of departing civil jet aircraft based on machine learning," *Journal of Aircraft*, vol. 61, no. 4, 2024.

DOI: 10.61782/fa.2025.0153

FORUM ACUSTICUM EURONOISE 2025

ASSESSMENT OF THE PSYCHOACOUSTIC PERFORMANCE OF THE VENUS PROJECT DISTRIBUTED ELECTRIC PROPELLERS CONFIGURATION

Alessandro Di Marco[1*] **Luana G. Stoica**[1]
Giorgia Capobianchi[1]
[1] DICITA, University of Roma Tre, Roma, Italy

ABSTRACT

The increasing use of aircraft concepts driven by distributed propulsion for urban and regional air mobility raises the issue of new sources of community noise and the prediction of the resultant annoyance. This paper addresses the assessment of the experimental measurements on a distributed electric propellers configuration in the framework of the EU project VENUS from a psychoacoustic point of view, framing the engineering design of these systems in a perception-driven perspective. The VENUS project was aimed to the aerodynamic and aeroacoustic design of a distributed electric propulsion aircraft. Acoustic, aerodynamic and wall pressure measurements were carried out on a wing model equipped with a flap and three propellers powered by electric motors in an open jet wind tunnel. The parameters changed during the tests included five blade pitch settings, an angle of attack sweep, take-off and landing flap configurations, a phase delay between the propellers, different relative distances between the propellers and with respect to the wing. An optimized liner was installed on the wing for acoustic mitigation, in selected configurations. The optimal geometric configuration was determined based on psychoacoustic metrics (i.e. loudness, fluctuation strength, roughness, sharpness and tonality) and psychoacoustic annoyance models.

*Corresponding author: alessandro.dimarco@uniroma3.it.

Copyright: ©2025 A. Di Marco et al. This is an open-access article distributed under the terms of the Creative Commons Attribution 3.0 Unported License, which permits unrestricted use, distribution, and reproduction in any medium, provided the original author and source are credited.

Keywords: *psychoacoustics, DEP, propellers, wind tunnel.*

1. INTRODUCTION

The main objective of the present study is to investigate to what extent a model based on sound quality metrics (SQMs) can predict the noise annoyance caused by a set of distributed electric propulsion layouts. The human perception of noise is influenced not only by personal qualities but also by their aesthetic and cognitive inclinations, along with their psychophysiological condition. While it's challenging to assess the latter factors, one can consider the unique aspects of how sounds are perceived acoustically, defining them through a model based on subjective qualities [1]. In psychoacoustic studies, different subjective qualities independent of each other have been identified: sharpness, fluctuation strength, roughness and tonality. By combining these qualities, a quantitative measure was established: the psychoacoustic annoyance (PA) can be calculated from a global point of view. The benefit of this approach is that it provides an overall estimate of the perceived annoyance level from a recorded sound without identifying the noise annoyance level among public residents through questionnaires. Additionally, the PA performance is compared to commonly used conventional noise metrics. The use of the PA approach in combination with the noise certification metric makes a perception-influenced acoustic design possible, in which the new vehicle design can simultaneously meet noise certification requirements while achieving low annoyance [2].

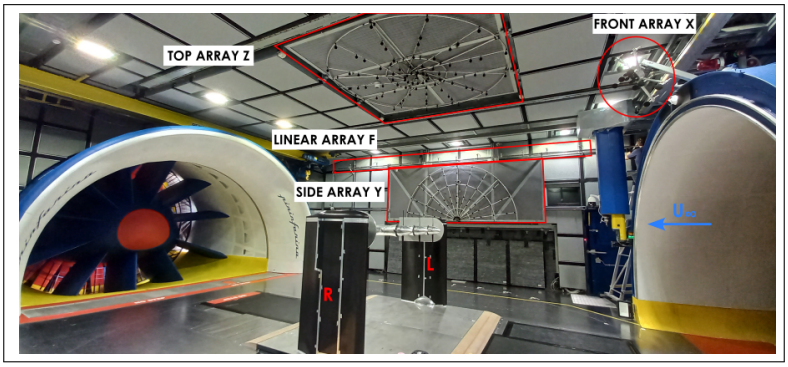


Figure 1. VENUS experimental setup.

2. METHODOLOGY

2.1 Wind Tunnel Aeroacoustic Measurements

Measurements in wind tunnels (WT) have been one of the main methods for aeroacoustic testing for the last decades, as they offer controllable conditions (flow velocity, angle of attack, etc.) repeatability of the results and, in most cases, accurate knowledge of the model position. One of the main challenges for wind-tunnel experiments is to replicate the exact conditions at full-scale. The smaller scale and usually less-detailed geometry of the wind-tunnel models, together with the typically lower flow velocities, can lead to a discrepancy in the Reynolds number. This effect was not taken into account. A model with three wing installed propellers (Fig. 1) was mounted on the floor of the Pininfarina WT test section with the central plane aligned with the WT balance.

Two aerodynamically shaped struts sustained the upside-down wing. The wing consisted in a non symmetric constant chord airfoil (NACA 63(2)415) with a deployable flap. The three propellers could be arranged in different geometrical configurations. The lateral propellers had two degrees of freedom on the wing whereas the central could be translated only in longitudinal direction. The propellers rpm were remotely controlled by an homemade software able to syncrophase the lateral propellers (followers) with respect to the central one (the leader). The model was instrumented with pressure taps, pressure transducers and load cells for thrust and torque measurements. During the test campaign, fluctuating pressure was acquired with four microphone arrays (Fig. 1) and the global aerodynamic coefficients were measured with the WT balance. Different DEP configurations were tested, those of interest are summarised in section 3 The reader is referred to [3] for more details on the experimental set-up.

Table 1. Parameters varied during VENUS wind tunnel tests.

Parameter	Value
AoA α	$-1° \rightarrow 11°$
Flap angle δ	0° (SL), 20° (TO), 35° (LA)
Phase shift $\Delta\varphi$	$0°, 35°$
DEP layout	XY1 $\rightarrow$ XY11
Low noise device	on, off

Tab. 1 provides a description about the tested conditions during the whole campaign. A reduced subset of the VENUS database is used here for to the psychoacoustic analysis. The data analysed herein correspond to an angle of attack (AoA) of $5°$, as it is the design angle in the landing phase. Regarding the nacelles layout, only the geometrical dispositions relevant to the study are selected as individuated in a preliminary numerical aeroacoustic study performed before the realization of the WT model. $XY*$ is a conventional name given to a specific combination of nacelle positions with respect to the baseline configuration, which is indicated with $XY1$.

The phase shift indicates the de-phasing of the lateral propellers with respect the central one. The wind tunnel air speed velocity was set at 20 $\mathrm{m/s}$ and the rotational speed of the three propellers was kept constant at 3300 rpm in all tests in order to guarantee the same advance ratio of $J = 0.65$.

2.2 Aeroacoustic and Psychoacoustic Sound Quality Metrics

Conventional acoustic/aeroacoustic metrics were used as a first ranking discriminant of the most/less annoying DEP configuration. To better assess the actual annoyance experienced by people, more sophisticated SQMs from the field of psychoacoustics were also implemented. In addition to SQMs, the relationship between annoyance of the sounds in this test and aircraft noise certification metrics was explored. Since the sounds were of short duration and constant, (those certification metrics involving summation and integration over time) metrics such as the effective perceived noise level were not analysed. Instead, the constituent metrics of these certification metrics were analysed. These constituent metrics are A-weighted sound pressure level ($L_{p,A}$), Z-weighted (or unweighted) sound pressure level ($L_{p,Z}$), perceived noise level (PNL) and tone-corrected perceived noise level (PNLT). In synthesis, without entering into the definitions, for each sound signal the following metrics were calculated:

- Loudness (N);
- Tonality (K);
- Sharpness (S);
- Roughness (R);
- Fluctuation strength (FS);

In this paper, a subset of these metrics is reported for the sake of conciseness. To reduce amplitude variation in some metrics, the 5 percent excess in the levels of the metrics are used to describe the metric levels for the duration of sound. If an SQM value is nearly constant over the sound duration the exceeded level will be approximately equal to the constant level [4].

From the SQMs, the PA metrics were calculated according to the models introduced by [5] and improved by [6]. The conventional sound metrics, SQMs and PA metrics were computed using the open-source MATLAB toolbox SQAT (Sound Quality Analysis Toolbox) [7].

3. TEST CASES

Three comparison scenarios are considered: (i) clean model versus model with installed propeller blades, (ii) five nacelle layouts for the take-off configuration with respect to the baseline layout, four nacelle layouts for the landing configuration with respect to the baseline layout and (iii) wing with/without noise reduction device for a selected nacelle layout. The clean configuration was obtained from the baseline layout removing the propellers blades and carrying out the tests with motors off. For this specific comparison a side-line (SL) configuration with the flap not deployed was also tested and presented in section 4. Take-off (TO) and landing (LA) configurations were obtained deploying the flap at 20° and 35° respectively. Fig. 2 shows the possible nacelle movements in $X-$ and $Y-$ direction. The central green lines indicate the positions of the baseline configuration. Note that the central nacelle can only translate in the streamwise direction.

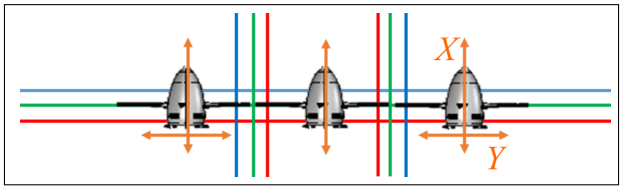


Figure 2. Sketch of the nacelles translation directions.

The nacelle layouts considered in this study are summarised in Tab. 2. ΔX and ΔY corresponds to the position variation with respect to the baseline configuration. Arrows indicate the longitudinal and transversal translation directions of the three nacelles (left L, central C and right R) for each layout. The values of the nacelle translations considered here were set at $\Delta X = 6$ cm for streamwise movements and $\Delta Y = 4$ cm for spanwise movements.

Table 2. Nacelle layout movements with respect to the baseline configuration.

Conf	ΔY_L	ΔX_L	ΔX_C	ΔX_R	ΔY_R
XY1	-	-	-	-	-
XY2	-	$\Downarrow$	$\Downarrow$	$\Downarrow$	-
XY3	-	$\Downarrow$	$\Uparrow$	$\Downarrow$	-
XY4	-	$\Uparrow$	$\Downarrow$	$\Uparrow$	-
XY6	-	-	$\Uparrow$	-	-
XY10	$\Rightarrow$	$\Downarrow$	$\Uparrow$	$\Downarrow$	$\Leftarrow$
XY11	$\Rightarrow$	$\Uparrow$	$\Downarrow$	$\Uparrow$	$\Leftarrow$

Table 3. Acoustic and Psychoacoustic metrics comparison of the baseline, clean and installed configurations.

	DEP Conf	$L_{p,A}$ [dBA]	PNLT [dB]	N [phon]	K [t.u.]	S [acum]	PA [-]
SL	Clean	63.3	76.9	19.6	0.07	1.10	21.2
	Installed	72.9	87.7	35.8	0.12	1.39	40.0
TO	Clean	64.6	78.3	21.5	0.07	1.11	23.4
	Installed	73.0	88.1	36.5	0.12	1.38	40.5
LA	Clean	65.8	79.5	23.3	0.08	1.11	25.5
	Installed	74.3	88.9	39.0	0.10	1.35	42.4

Table 4. Effect of the mitigation device on acoustic and psychoacoustic metrics.

	DEP Conf	$L_{p,A}$ [dBA]	PNLT [dB]	N [phon]	K [t.u.]	S [acum]	PA [-]
$\delta\varphi = 0°$	No Liner	75.2	89.4	40.5	0.1	1.33	44.1
	Liner	74.4	89.0	39.4	0.1	1.33	43.4
$\delta\varphi = 35°$	No Liner	74.8	89.2	40.1	0.11	1.33	44.0
	Liner	74.5	89.1	40	0.11	1.34	43.7

The noise reduction device consisted in a series of micro-perforated inserts mounted on the wing leading edge of the pressure side. The holes distribution and size and the cavities beneath the wing surface were specifically designed through an optimization procedure focused on the attenuation of the propeller tonal noise in a wide range of frequencies.

4. RESULTS

All the results presented in the following sections are obtained analysing the signal acquired by the central microphone from the array on the ceiling of the WT. In this way, the noise is perceived as an observer underneath the wing, similar to a fly-over manoeuvre. Sound propagation effects are not taken into account. All the signals are band-pass filtered in the range of interest of the installed propellers, discarding effects of the low frequency wind tunnel noise and high frequency disturbance due to the microphones and acquisition system. Furthermore, the signals are downsampled at 48 kHz in order to be compatible with psychoacoustic software requirements.

4.1 Clean vs Installed Configuration

Tab. 3 summarises the results of the comparison between the clean wing model and the wing with the propeller blades installed. The $L_{p,A}$ are found to be larger when the propellers are running, as expected, due to the noise contribution from the propeller rotation. The average level of this difference between the configurations amounts approximately to 8.8 dBA. For the clean model, the values increases with the flap deployment angle by 1 dBA when moving from SL to TO to LA. The effect of the flap with the propellers running only causes a rise of the $L_{p,A}$ in landing configuration, due to the greater deflection of the propeller wake. Similar trends are found for the PA. It is worth noting that installing the propellers doubles the estimated annoyance with respect to the clean model, for each manoeuvre setup.

4.2 Noise Mitigation Device Effect

The acoustic and psychoacoustic effects of the noise mitigation devices are summarised in Tab. 4. The results do not indicate a substantial modification of the perceived noise. The best performances are obtained for the in-phase

propellers ($\delta\phi = 0°$). The noise reduction device causes a slight reduction of the loudness, whereas the other metrics remain substantially unchanged.

4.3 Psychoacoustic Sound Quality Metrics of TO and LA setups

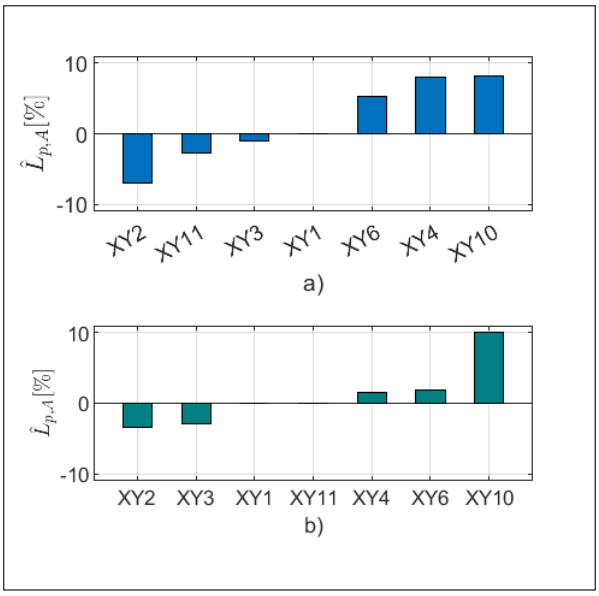


Figure 3. Normalized $L_{p,A}$ in TO for a) $\Delta\varphi = 0°$ and b) $\Delta\varphi = 35°$.

The results presented in this section for both setups are all referred to the baseline $XY1$ configuration. In order to adjust values measured on different scales to a comparable scale, the conventional metrics ($L_{p,A}$) and the psychoacoustic annoyance (PA) values are normalized as follows:

$$\hat{\sigma}_{p,A} = \frac{\sigma_{p,A,XY*} - \sigma_{p,A,XY1}}{\sigma_{p,A,XY1}} \tag{1}$$

and

$$\hat{PA}_{p,A} = \frac{PA_{XY*} - PA_{XY1}}{PA_{XY1}} \tag{2}$$

where XY^* indicates a generic nacelle layout, $XY1$ corresponds to the baseline layout and $\sigma_{p,A}$ is obtained from the A-weighted sound pressure level with the inverse formula assuming a reference pressure of 20 µPa.

The analysis of the conventional metrics and the PA model revealed some differences among the various layouts as illustrated in Fig. 3 and Fig. 4 for TO and in Fig. 5

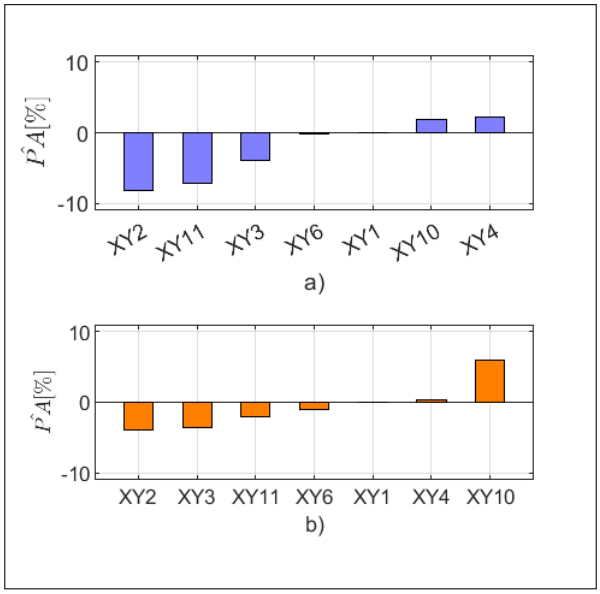


Figure 4. Normalized PA in TO for a) $\Delta\varphi = 0°$ and b) $\Delta\varphi = 35°$.

and Fig. 6 for the LA setup. In the figures, negative values express a reduction in the emitted noise compared to the baseline layout whereas positive values are an increment. On the abscissa, the layout ranks from the quietest to the noisiest; in each figure, results obtained at the two relative phase angles between the propellers are shown.

In TO, the quietest layout is the $XY2$ independently of the phase or the approach used. The layout consists of the three propellers discs aligned with each other at their closest position with respect to the wing. The noisiest configuration is the $XY10$ examining most metrics, although this result is questionable for the PA at $\Delta\varphi = 0°$ (Fig. 4). In this layout, the propeller discs are overlapping, with the two external propellers closest to the wing and the central at the farthest longitudinal position. Comparing the acoustic and psychoacoustic metrics at $\Delta\varphi = 0°$, the layout ranking remains almost unvaried, whereas changes occur when the propellers are not running in phase. A moderate noise reduction is obtained de-phasing the propellers in most cases.

For LA conditions, the worst case in terms of noise with respect to the baseline is represented by layout $XY4$. In this layout, the central nacelle is in the closest and the external nacelles in the farthest streamwise position. The estimated annoyance for this case is considerably lower than the conventional metric $L_{p,A}$. The quietest layout is

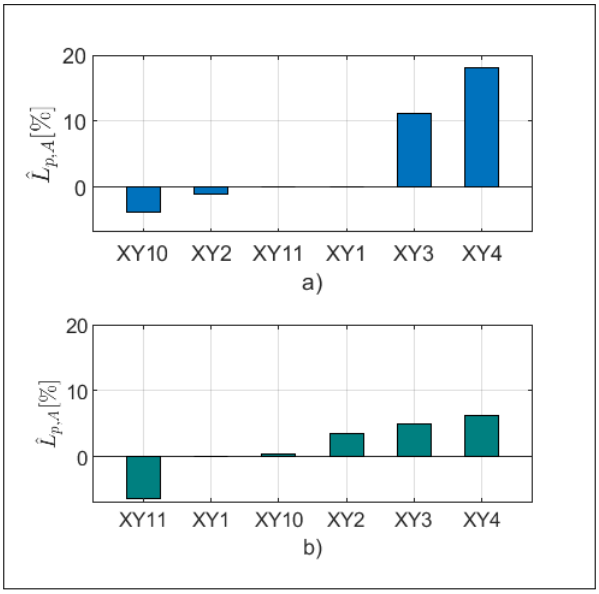


Figure 5. Normalized $L_{p,A}$ in LA for a) $\Delta\varphi = 0°$ and b) $\Delta\varphi = 35°$.

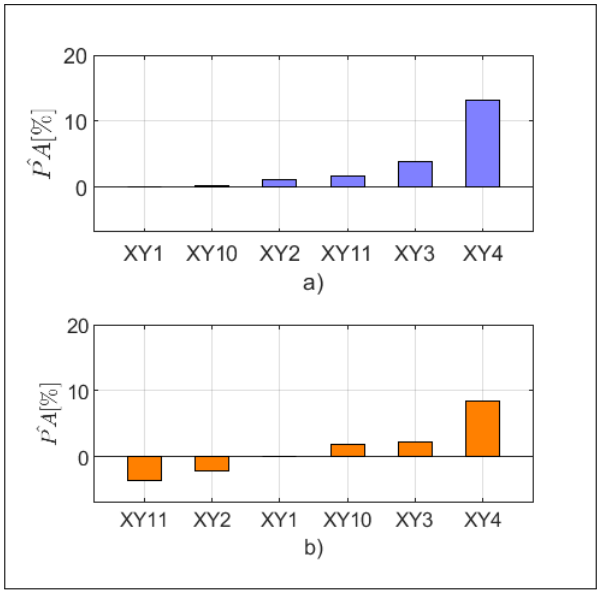


Figure 6. Normalized PA in LA for a) $\Delta\varphi = 0°$ and and b) $\Delta\varphi = 35°$.

not uniquely determined as it is the ranking.

Table 5. Overall ranking.

Tot points	Layout
15	XY2
20	XY11
27	XY1
30	XY3
37	XY10
48	XY4

In order to define the best and worst performing layout, a score was assigned based on the performances in both TO and LA configurations, for all the relative phase angles and for all the metrics used. The total points were counted summing each placement in the different rankings considered. The best overall configuration is thus found to be $XY2$ and $XY4$ as the worst. The overall ranking is reported in Tab. 5.

5. CONCLUSIONS

The aim of the paper is to gain insight into the wide variety of experimental tests performed within the VENUS project from a psychoacoustic perspective and compare it to classical aeroacoustic metrics. The model tested is a wing of a regional aircraft with an optimized distributed electric propulsion system composed of three tractor propellers powered by electric motors. The objective of the study was to compare different methods analysing the annoyance of noise perception. The classical method for annoyance estimation is to apply the A-weighting to the SPL, which roughly corresponds to the perceived loudness level. However, this method may only be suitable for certain types of noise.

Measurements of loudness are used to put policies in place that limit noise levels below reasonable bounds. But because of the informational value of noise and the notable decrease in noise levels that has already been attained, there are now additional techniques for measuring noise-induced irritation that supplement the conventional approaches. These include the rapid and effective computation of short-term psychoacoustic annoyance based on various subjective noise properties.

Results demonstrated that the noise emitted by the model with the installed propellers with respect to the

airframe only notably increases the human annoyance as confirmed by the conventional metrics. The effects of the noise mitigation device showed a moderate impact reduction on both conventional metrics and short-term annoyance. It was shown that the estimated human perception of the noise is different from the conventional approach, leading in some case to different results. A critical role is also held by the phase between the propellers. A deeper study on the phase effect and a hearing experiment would complete and validate this study.

6. ACKNOWLEDGMENTS

This work is part of the project VENUS (inVestigation of distributEd propulsion Noise and its mitigation through wind tUnnel experiments and numerical Simulations), which has received funding from the Clean Sky 2 Joint Undertaking under the European Union's Horizon 2020 research and innovation program under grant agreement 886019.

7. REFERENCES

[1] L. Rimskaya-Korsakova, P. Pyatakov, and S. Shulyapov, "Evaluations of the annoyance effects of noise," *Acoustical Physics*, vol. 68, no. 5, pp. 502–512, 2022.

[2] S. A. Rizzi, D. L. Palumbo, J. Rathsam, A. W. Christian, and M. Rafaelof, "Annoyance to noise produced by a distributed electric propulsion high-lift system," in *23rd AIAA/CEAS aeroacoustics conference*, p. 4050, 2017.

[3] E. De Paola, R. Camussi, G. Stoica, A. Di Marco, and G. Capobianchi, "Aerodynamic and aeroacoustic experimental investigation of a three propellers dep configuration," *Aerospace Science and Technology*, vol. 154, p. 109508, 2024.

[4] S. Krishnamurthy, M. A. Boucher, A. W. Christian, and S. A. Rizzi, "Rotorcraft sound quality metric test 1: Stimuli generation and supplemental analyses," *NASA/TM –20205008997*, 2021.

[5] E. Zwicker, H. Fastl, E. Zwicker, and H. Fastl, "Pitch and pitch strength," *Psychoacoustics: facts and models*, pp. 111–147, 1999.

[6] G.-Q. Di, X.-W. Chen, K. Song, B. Zhou, and C.-M. Pei, "Improvement of zwicker's psychoacoustic annoyance model aiming at tonal noises," *Applied Acoustics*, vol. 105, pp. 164–170, 2016.

[7] G. F. Greco, R. Merino-Martínez, A. Osses, and S. C. Langer, "Sqat: a matlab-based toolbox for quantitative sound quality analysis," in *Inter-Noise and Noise-Con Congress and Conference Proceedings*, vol. 268, pp. 7172–7183, Institute of Noise Control Engineering, 2023.

DOI: 10.61782/fa.2025.0225

FORUM ACUSTICUM EURONOISE 2025

COMPARATIVE DRONE NOISE FLIGHT TEST CAMPAIGN USING CONVENTIONAL PRECISION MICROPHONES AND AN ARTIFICIAL HEAD

Giovanni Fasulo[1*] **Francesco Petrosino**[1] **Mattia Barbarino**[1] **Luigi Federico**[1]

[1] Italian Aerospace Research Centre (CIRA), Capua (CE), 81043, Italy

ABSTRACT

This study investigates the acoustic signatures of a DJI Matrice 300 RTK during LiDAR and photogrammetric mapping missions at the Pianabella UrbanV vertiport in Rome. Utilizing a comprehensive setup that combines conventional precision condenser microphones with an artificial head, measurements were conducted throughout various drone flight phases. Analysis revealed that calculating advanced psychoacoustic metrics with the artificial head can introduce significant errors compared to conventional microphone measurements, for which these metrics were originally designed.

Keywords: *artificial head, psychoacoustic, drone noise, experimental test.*

1. INTRODUCTION

Small drones, known as Small Unmanned Aircraft Systems (sUAS), have become much more common in recent years, being used for commercial, security, and other purposes in areas that were previously unaffected [1]. As sUAS noise differs significantly from that of conventional aircraft [2], predicting resultant annoyance remains challenging. The numerous noise-generating components of sUAS experience constant variations in level, directionality, spectral content, and temporal characteristics during take-off, landing, and overflight maneuvers [3]. Moreover, the propagation of sUAS noise is highly sensitive to operating environment, weather, and wind conditions, complicating attempts to reliably forecast acoustic impacts. To address this, specialized flight tests are now crucial for better understanding sUAS noise and improving prediction models [4]. Within the European U-ELCOME project [5] framework, an extensive test campaign was carried out to investigate the acoustic signatures of different drone operations in real-world scenarios. Observations included different flight phases, such as take-off, overflight, and landing, to better characterize the role of operational aspects and external conditions on noise. A suite of precision microphones and an artificial head were deployed to capture a comprehensive dataset of both conventional and binaural acoustic measurements, which more accurately reproduce the subjective perception of human listeners. Traditional descriptors such as sound pressure level (SPL), along with psychoacoustic metrics including loudness, sharpness, fluctuation strength, roughness, and tonality, were computed for each audio sample. A comparative analysis between conventional microphone recordings and those acquired using an artificial head (both with and without the application of equalization curves) revealed significant discrepancies. These findings underscore the importance of a careful and informed application of psychoacoustic measurement equipment and metrics when assessing the potential disturbance caused by sUAS noise. Moreover, the results highlight the critical role of flight test data in developing robust acoustic impact evaluation methods, which are essential for guiding future regulatory frameworks and design considerations.

**Corresponding author*: G.Fasulo@cira.it.

Copyright: ©2025 First author et al. This is an open-access article distributed under the terms of the Creative Commons Attribution 3.0 Unported License, which permits unrestricted use, distribution, and reproduction in any medium, provided the original author and source are credited.

2. TEST GROUND AND EQUIPMENT

2.1 Test Ground

The acoustic test campaign was conducted on November 28th 2024 at the Pianabella UrbanV vertiport in Rome, Italy, with the primary objective of capturing and analyzing noise emissions during LiDAR and photogrammetric terrain mapping operations. The experimental setup involved the deployment of precision condenser microphones across the test field (Figure 1) to accurately record the acoustic signatures associated with various drone activities: takeoffs, landings, and flyovers. This approach enabled a comprehensive assessment of the drone's noise profile under realistic operational conditions.

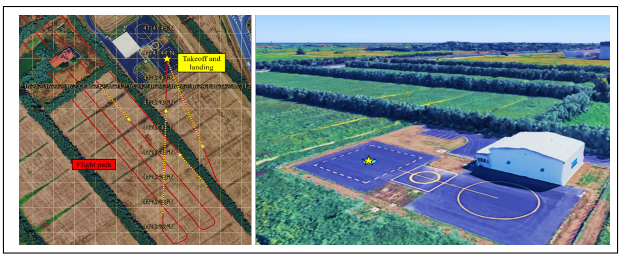


Figure 1. Test ground and planned drone flight path (Google Earth image).

2.2 Acoustic Equipment

Acoustic measurements were conducted using a comprehensive system that integrates data acquisition hardware, precision microphones, signal conditioning components, and calibration tools. The setup comprised a personal computer interfaced with an IMC C-SERIES PL3 analyzer, which provided eight channels at a sampling rate of 50 kHz per channel. Acoustic signal acquisition was achieved using a set of precision pre-polarized condenser microphones coupled with dedicated preamplifiers. Specifically, eight PCB model 377B11 microphones, which feature a pressure-field response were deployed. Each microphone has a nominal 1/2-inch diameter and a typical sensitivity of 50 mV/Pa, with the 377B11 units covering a frequency range of 3.15 to 10000 Hz (±2 dB) and a dynamic range of 146 dB re 20 µPa. Prior to measurements, each microphone was calibrated using a PCB model CAL250 acoustic calibrator that provides a 250 Hz output at 114 dB re 20 µPa (±0.2 dB) with distortion below 2%. Windscreens were employed on each microphone to mitigate wind-induced noise from high-speed airflow. To preserve signal integrity over long cable runs and extend the measurable frequency range, 8 microphone preamplifiers (PCB model 426A30) equipped with 7-pin LEMO connectors were used. These preamplifiers, which produce an output voltage of 28 Vpp, were supplied by 8 preamplifier power supplies (Larson Davis model 2221). These supplies offer selectable polarization settings (0 and 200 V) and weighting options (A, C, or Z), with a frequency response (Z-weighted) from 10 Hz to 100 kHz (±0.2 dB) and 1 Hz to 150 kHz at –3 dB. In addition, CIRA deployed a specialized acquisition system known as an artificial head, which replicates the acoustically significant features of the human ear, head, shoulders, and skin. This design filters incoming sound based on its direction, enabling the recorded signals to be perceived as if the listener were immersed in the original sound field. The artificial head HSU III.2 incorporates two precision pre polarized condenser microphones that have a nominal diameter of 1/2 inch and a typical sensitivity of 50 mV/Pa. These microphones operate over a frequency range of 3.5 to 20000 Hz, offer a dynamic range of 119 dB re 20 µPa, and can handle sound pressure levels up to 135 dB with less than 3% distortion at 1 kHz. Data acquisition and storage were managed using SQobold, a four channel recording and playback system for mobile sound and vibration measurements, providing two channels with a sampling rate of 48 kHz per channel.

Figure 2 is a sketch of the experimental apparatus schematic diagram:

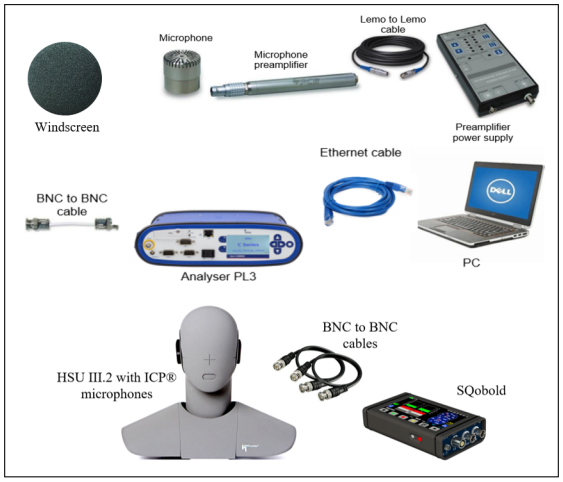


Figure 2. Experimental apparatus schematic diagram.

Microphone placements were determined based on the drone's designated flight paths (Figure 3). Three microphones were arranged in a quarter-circle with a 7-meter radius at a height of 1.5 meters, centered on the drone's takeoff point. A second array, consisting of three microphones, was configured in a quarter-circle with a 14-meter radius, also at 1.5 meters above ground level. In addition, two microphones were positioned along the drone's flight path within the terrain adjacent to the Pianabella vertiport, maintaining the same 1.5 meter elevation. Furthermore, the artificial head was mounted on a tripod and oriented such that its shoulders were perpendicular to the drone's flight trajectories, with the left ear directed toward the takeoff point, aligned with the position of microphone #8 (Ch8). The ear level was set at 1.5 meters from the ground.

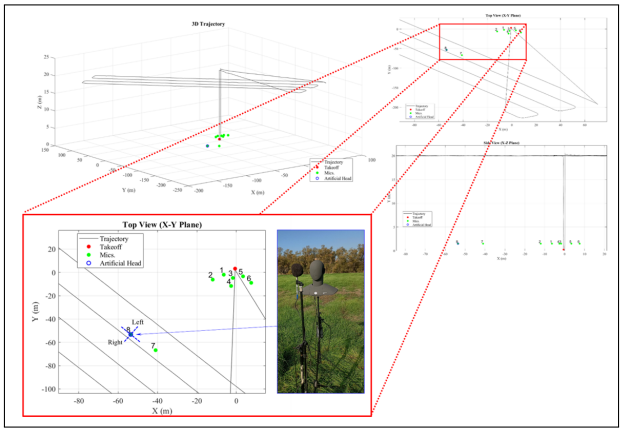


Figure 3. Drone trajectory and acoustic sensors locations.

2.3 Test Article

For the LiDAR and photogrammetric mapping operations, a DJI Matrice 300 RTK quad-rotor (Figure 4) was deployed. This versatile platform is engineered for a wide range of industrial applications and features a robust, foldable design that ensures both durability and ease of transport across various operational environments. Its support for multiple payload configurations allows for tailored setups to meet specific mission requirements, while advanced flight control algorithms and GPS positioning deliver precise navigation, stable hovering, and autonomous operation capabilities. The main technical specifications of the DJI Matrice 300 RTK are as follows: when unfolded (without propellers), its dimensions are 810 × 670 × 430 mm, and when folded (with propellers), 430 × 420 × 430 mm, with a diagonal wheelbase of 895 mm. The drone weighs approximately 3.6 kg without batteries and around 6.3 kg when equipped with batteries, with a maximum takeoff weight of 9 kg. It supports a maximum payload capacity of 2.7 kg and offers a flight time of up to 55 minutes with no payload.



Figure 4. DJI Matrice 300 RTK at UrbanV vertiport.

3. ACOUSTIC MEASUREMENTS AND POST-PROCESSING

This section presents the methodology employed for acoustic measurements at the UrbanV vertiport in Rome. Data acquired from both precision microphones and an artificial head were analyzed to assess the implications of the observed noise signatures.

3.1 Background Noise

Background noise plays a critical role in acoustic measurements as it represents the ambient sound environment in the absence of the primary noise source. In this study, the drone serves as the primary noise source, while the background noise is primarily attributable to operations at a nearby airport. This background noise includes sounds from aircraft takeoffs and landings, ground support equipment, vehicular traffic, and other related activities. Consequently, precise measurement of the background noise is imperative for establishing a reliable baseline that differentiates between ambient environmental noise and the noise generated specifically by the drone. To achieve this, acoustic signals were recorded and analyzed for approximately 150 seconds before to the beginning of the flight

test. The post-processing involved applying a Discrete Fourier Transform (DFT) with a Hanning window and a 50% overlap. Given the signal duration and segmentation, a sampling frequency of 0.01 Hz was achieved. Specifically, the signal was segmented into two overlapping frames, with each frame windowed by the Hanning function to minimize spectral leakage. The 50% overlap ensured that each consecutive frame shared half of its data points with the previous frame, thereby enhancing frequency resolution and yielding a smoother, more reliable frequency spectrum. The DFT was computed for each windowed segment, and the resulting spectra were averaged. To facilitate interpretation, the spectra were converted into 1/3 octave bands and adjusted using A-weighting (Figure 5) to account for the human ear's varying sensitivity across frequencies.

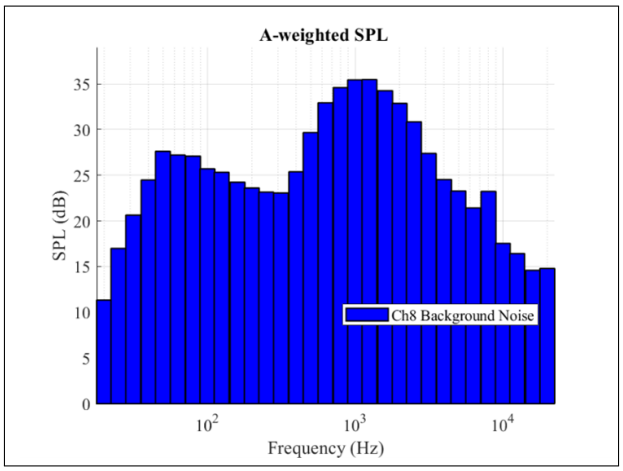


Figure 5. A-weighted 1/3 octave band spectra of background noise recorded by microphone #8.

Additionally, the mean A-weighted Overall Sound Pressure Level (A-OASPL) from all microphone measurements, which represents the mean total sound energy over the measurement duration, was computed. Specifically, two mean A-OASPL values were computed to reflect the distinct environmental conditions at different measurement locations. Microphones #1 to #6, positioned near the takeoff and landing area on rigid asphalt surfaces, exhibited a mean A-OASPL of 47.8 dBA, likely due to increased sound reflections. In contrast, microphones #7 and #8, deployed on grass and other absorptive surfaces, recorded a lower background noise level of 43.8 dBA, resulting from enhanced sound absorption.

3.2 Drone Noise

The acoustic signature of drones substantially differs from that of conventional aircraft. Drone noise is characterized by a complex frequency spectrum featuring multiple tones at harmonics of the blade passage frequency (BPF). Moreover, these acoustic emissions can vary considerably depending on factors such as drone type, size, propeller design, and operational conditions. Consequently, conventional noise metrics like $L_{A,eq}$ or L_{AE} are often inadequate to capture the annoyance of drone noise, thereby necessitating the use of psychoacoustic parameters that more accurately reflect human auditory perception.

Within the framework of the U-ELCOME project, a series of tests were conducted to characterize the noise generated by drones. The main test lasted 755 seconds, with signal acquisition for the eight microphones started and ended manually at the beginning and end of each test session. In contrast, the psychoacoustic head was activated manually prior to the initial test and deactivated after all tests, resulting in a continuous recording from which the relevant sections were later extracted. To analyze the temporal evolution of the drone's spectral content, a spectrogram was computed. This analysis utilized a Hanning window with a 50% overlap. The FFT was computed with a spectrum size of 65536 samples at a sampling rate of 50 kHz, resulting in time and frequency resolutions of 1.31 seconds and 0.76 Hz, respectively. Given the tonal nature of the recorded noise and the absence of impulsive characteristics, a larger FFT size was selected to achieve finer frequency resolution. Figure 6 presents the spectrograms for microphones #7 and #2.

These spectrograms reveal a predominance of continuous low-frequency noise attributable to background noise. In the recordings from microphone #2, peaks in the mid-to-high frequency range were observed at the beginning and end of the test, corresponding to the drone's noise during takeoff and landing. Conversely, recordings from microphone #7 exhibited peaks at regular intervals, characteristic of drone overflights. In the frequency domain, periodic spectral lines corresponding to the harmonics of BPF are clearly discernible. These harmonics are most marked when the drone is close to the microphones but become increasingly diluted by ambient noise as the drone moves farther away.

3.2.1 Artificial Head vs. Conventional Microphone

The artificial head employed in this study inherently incorporates multiple filtering phenomena, namely, pinna

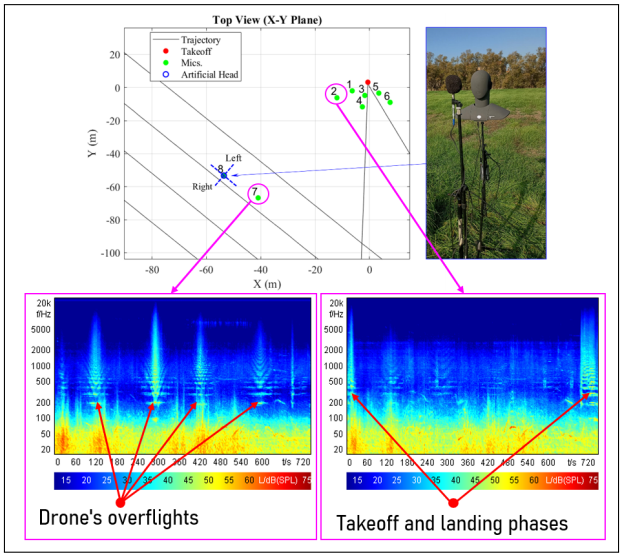


Figure 6. Drone path, placement of acoustic equipment, and corresponding spectrograms.

effects, ear canal resonance, diffraction and reflection due to the head's structure, acoustic shadowing, and skin absorption. These effects result in distortions that make the signals captured by the artificial head incompatible with those obtained from conventional measurement microphones [6]. Consequently, parameters such as the A-weighted sound pressure level and various other metrics cannot be reliably determined using a non-equalized artificial head measurement system. To address this limitation, HEAD Acoustics provides three distinct equalization options for the artificial head based on the direction of sound incidence:

- Free Field (FF): Sound arriving from the front in an anechoic environment, with the sound source located at least 3 meters from the artificial head;
- Diffuse Field (DF): Sound arriving uniformly from all directions;
- Independent of Direction (ID): Equalization tailored to the directional resonances of the cavum conchae and the ear canal entrance.

Since the sound field conditions during measurement rarely correspond exactly to any one of these idealized scenarios (FF, DF, or ID) this study examined the influence of various equalization curves on the evaluation of psychoacoustic metrics. For this purpose, microphone #8 was strategically positioned adjacent to the artificial head along the drone's flight path, specifically between the two ear microphones. A slight spatial displacement was compensated by temporally shifting the microphone pressure time histories by 0.45 seconds. Acoustic levels are presented in Figure 7 without the application of any weighting functions, ensuring an accurate representation of the total acoustic energy and to clarify the underlying noise generation mechanisms. Only a slow time weighting (1000 ms) was applied to smooth the output and enhance the readability of the plot.

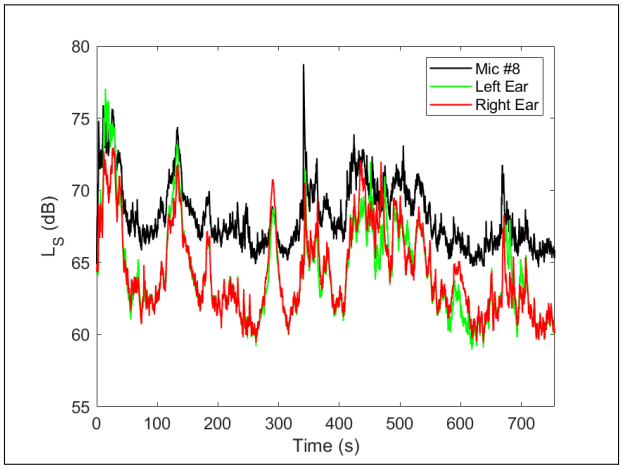


Figure 7. Acoustic levels with slow time weighting for conventional microphone #8 and the artificial head's ear microphones.

Microphone #8 generally records higher levels than the ear microphones, although there are time intervals where the levels converge or where the ear microphones briefly exceed those of microphone #8. Furthermore, the slight mismatch between left and right ear measurements arises from the head's asymmetry relative to the sound source. Refer to Figure 3 for an overview of the flight path and the artificial head's positioning.

The subsequent analysis focuses on a single forward flight segment, specifically, the time interval during which the drone is nearly overhead of the artificial head, as indicated between 200 and 370 seconds in the level graph (Figure 7). Figure 8 compares the spectral content of both recordings within the human auditory range (20 Hz–20 kHz). The spectra were computed using a Fast Fourier Transform (FFT) with a spectrum size of 16384 samples, a Hanning window, and 50% overlap. Given the 50 kHz

sampling frequency, the frequency resolution is approximately 3 Hz. These measurement do not incorporate any equalization curves, thereby representing the spectra of the original recorded sound.

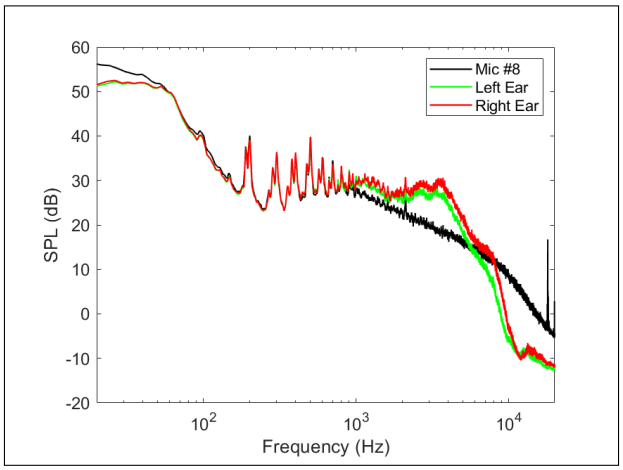


Figure 8. Comparison of the acoustic spectra obtained from conventional microphone #8 and the artificial head's ear microphones during the drone's forward flight.

The tonal components, specifically, the first eight harmonics of the blade passing frequency (BPF), are captured equally by both the conventional microphone and the artificial head. In the forward flight scenario, Figure 8 illustrates the separation of the BPFs between the forward and aft rotors, a result of the differing rotation rates during this flight condition. However, the artificial head also exhibits additional peaks at approximately 3 kHz, which indicate resonance associated with the ear canal's length [7], while a notch across the entire frequency band at 10 kHz can be attributed to the effect of the pinna [8]. The difference in the low-frequency region is likely due to the transition from free-field conditions to a duct configuration, which introduces a change in acoustic impedance that conventional microphones do not account for. This discontinuity may induce partial reflections of the acoustic wave at the entrance of the ear canal, thereby reducing the energy transmitted within the duct and consequently attenuating the signal detected by the artificial head microphones.

The following graphs present the FFT computed using equal input settings and time histories previously employed, incorporating the combined effect of the three equalization curves provided by HEAD Acoustics. In each instance, the resulting spectra are compared with those derived from conventional microphone recordings of the same noise event.

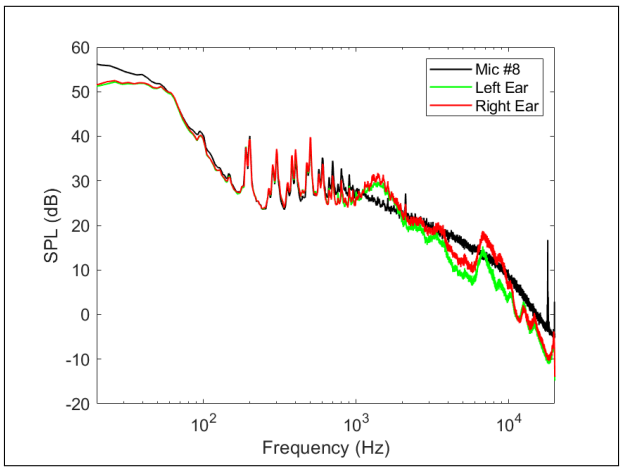


Figure 9. Conventional microphone #8 versus the artificial head's ear microphones (FF equalized).

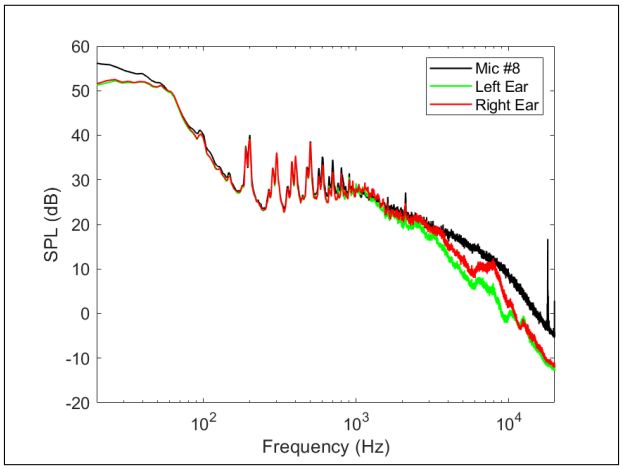


Figure 10. Conventional microphone #8 versus the artificial head's ear microphones (DF equalized).

Analysis reveals that the equalization curves do not reconstruct the spectral content of the conventional microphone signal from artificial head measurements with high fidelity. In this context, the diffuse field equalization appears to be a more suitable option. A quantitative evaluation of psychoacoustic metrics is provided in the subsequent part of this work. Specifically, Sound Quality (SQ)

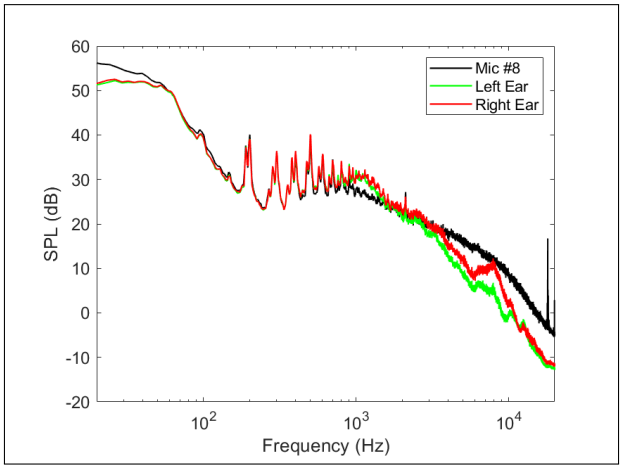


Figure 11. Conventional microphone #8 versus the artificial head's ear microphones (ID equalized).

metrics were computed for the conventional microphone recordings and for the artificial head measurements (both with and without equalization) across distinct phases of the drone mission. For this purpose, the levels shown in Figure 7 were segmented into six sub-signals with time ranges of 1–60, 60–200, 200–370, 370–530, 530–660, and 660–755 seconds. The analyses were conducted using the ArtemiS software from HEAD Acoustics, and the computed SQ metrics include Loudness (N), Roughness (R), Fluctuation Strength (F), Sharpness (S), and Tonality (T).

Loudness, Roughness, and Tonality were calculated according to ECMA-418-2 (2nd Edition), based on the Sottek Hearing Model [9]. In particular, for the computations of Loudness and Roughness, signals from both the right and left ears of the artificial head were combined. The calculation of Fluctuation Strength was derived from that of Roughness, with an adaptation ensuring that its maximum value occurs at a modulation frequency of 4 Hz. Finally, Sharpness was determined using the DIN 45692 standard. The maximum value, along with the 5th and 10th percentiles of each audio sample, was computed and analyzed. For metrics that lack an inherently defined combined left/right ear result (Fluctuation Strength, Sharpness, and Tonality) the arithmetic mean of the left and right ear values was employed as the representative single value metric for the artificial head. To ensure consistency, the mean absolute differences between the conventional and equalized curves, computed across all tests, were normalized by the mean metric value as estimated by the conventional microphone. Consequently, Figure 12 to Figures 15 illustrate the percentage deviation from the expected results for each single value metric and for each equalization curve adopted.

No eq. curve			
	Max	5%	10%
N	15.8	16.8	17.8
R	11.1	12.3	12.1
F	6.8	13.6	7.4
S	29.9	18.2	3.4
T	26.1	7.1	12.0

Figure 12. Percentage deviation from the expected results (Not Equalized).

FF			
	Max	5%	10%
N	2.8	3.6	3.4
R	13.9	16.3	17.9
F	3.7	7.6	4.3
S	31.9	22.2	2.9
T	8.2	9.6	9.6

Figure 13. Percentage deviation from the expected results (FF Equalized).

4. CONCLUSIONS

As part of the U-ELCOME project, an acoustic test campaign was conducted on November 28th 2024 at the Pianabella UrbanV vertiport in Rome, Italy. The study aimed to record and analyze the noise generated by a DJI Matrice 300 RTK during LiDAR and photogrammetric mapping operations. To achieve this, CIRA deployed eight 1/2-inch precision condenser microphones alongside an artificial head, strategically placing the sensors across the test field to capture noise during drone take-offs, landings, and overflights. A comparative analysis of psychoacoustic metrics derived from conventional microphone measurements and those obtained from the artificial head, both with and without equalization curve, revealed significant differences. Overall, the application of equalization curves substantially improves loudness estimation.

DF			
	Max	5%	10%
N	7.1	5.5	5.1
R	13.8	12.7	15.7
F	2.6	5.0	3.9
S	37.9	11.3	6.3
T	11.1	14.1	14.5

Figure 14. Percentage deviation from the expected results (DF Equalized).

ID			
	Max	5%	10%
N	3.3	4.2	3.9
R	16.0	19.5	24.5
F	3.2	8.5	4.3
S	39.1	7.5	9.1
T	11.1	14.6	17.8

Figure 15. Percentage deviation from the expected results (ID Equalized).

In particular, the "free-field" equalized curve yields the most accurate loudness estimates when compared with the reference measurement obtained from a conventional microphone. Other metrics did not exhibit a clear or consistent pattern. These results underscore that if the objective of using the head is to estimate psychoacoustic metrics in contexts that differ from the idealized conditions of a free-field or diffuse field, even when applying the "independent of direction" equalization curve as recommended by HEAD Acoustic for that cases, non-negligible errors may arise. Consequently, it may be valuable to develop specialized metrics for head measurements that eliminate the need for equalization by directly quantifying the external hearing effect during testing.

5. ACKNOWLEDGMENTS

The authors would like to thank all the partners of the U-ELCOME project, with special thanks to UrbanV for hosting the test campaign and to TopView for providing the drone.

6. REFERENCES

[1] B. Schäffer, R. Pieren, K. Heutschi, J. M. Wunderli, and S. Becker, "Drone noise emission characteristics and noise effects on humans—a systematic review," *International Journal of Environmental Research and Public Health*, vol. 18, no. 11, p. 5940, 2021.

[2] A. W. Christian and R. Cabell, "Initial investigation into the psychoacoustic properties of small unmanned aerial system noise," in *Proceedings of the 23rd AIAA/CEAS Aeroacoustics Conference*, p. 4051, 2017.

[3] A. J. Torija, Z. Li, and R. H. Self, "Effects of a hovering unmanned aerial vehicle on urban soundscapes perception," *Transportation Research Part D: Transport and Environment*, vol. 78, p. 102195, 2020.

[4] R. Cabell, F. Grosveld, and R. McSwain, "Measured noise from small unmanned aerial vehicles," in *Inter-Noise and Noise-Con Congress and Conference Proceedings*, vol. 252, pp. 345–354, Institute of Noise Control Engineering, June 2016.

[5] EUROCONTROL, "U-ELCOME." `https://www.eurocontrol.int/project/u-elcome`, January 25 2023. Accessed: [Insert access date here].

[6] H. acoustics GmbH, "Part 3: Equalization of binaural recording," in *Application Notes, SVP Series*, n.d. HEAD acoustics GmbH, 52134 Herzogenrath, Germany. Available at: `https://cdn.head-acoustics.com/fileadmin/data/global/Application-Notes/SVP/Part-3-Equalization_of_binaural_recording_e.pdf`.

[7] Sugiyama, Kiyoshi, Nishimoto, Mitsugu, and Satoh, Machiko, "Transmission characteristics of ear canal of artificial head," *Acoustical Science and Technology*, vol. 26, no. 1, pp. 67–70, 2005.

[8] Sugiyama, Kiyoshi, "Sound collection effect of a pinna of an artificial head," *Acoustical Science and Technology*, vol. 24, pp. 311–314, 2003.

[9] R. Sottek, "Application of the sottek hearing model for environmental noise assessment," in *Proceedings of the Institute of Acoustics, Vol. 46. Pt. 2*, 2024. HEAD acoustics GmbH, 52134 Herzogenrath, Germany.

DOI: 10.61782/fa.2025.0389

FORUM ACUSTICUM EURONOISE 2025

Exploring the Socio-spatial Pattern of Noise Impact of Advanced Air Mobility – A Case Study in West Yorkshire, England

Like Jiang[1*]
[1] Institute for Transport Studies, University of Leeds, UK

ABSTRACT

Using West Yorkshire in England as the case study area, this study assesses the potential noise impact of advanced air mobility (AAM) at reginal scale, and explores how the impact is distributed across different socio-economic groups. Using agglomerative hierarchical clustering (AHC), possible vertiport locations were identified based on commute travel demand. Then, two types of flying routes were tested: one prioritises distance reduction and one prioritises noise mitigation, each tested with 3 distances of noise footprints. Statistics of people exposed to the potential AAM noise were made with and without considering exposure to existing road and rail noise. The results show that AAM noise is likely to affect a large proportion of the population in West Yorkshire, and most of the affected population are not currently exposed to road and/or rail noise above 55dB $L_{Aeq,\ 16h}$. AAM noise is also likely to make the social inequality in transport noise exposure in West Yorkshire even worse. Using noise-priority routes seems to reduce the inequality, but there is a risk that the more deprived communities who are already exposed to high transport noise will bear disproportionally more burden of the new noise introduced by AAM.

Keywords: *advanced air mobility, vertiport, flying route, noise impact, social equity*

1. INTRODUCTION

Advanced air mobility (AAM), including passenger mobility such as air taxis, is becoming a reality. Real-world demonstrations have been taking place since at least 2017 with air taxi by Volocopter in Dubai, and commercially viable services are expected to be widely available by 2030 [1]. AAM will improve mobility and connectivity, stimulate economic growth, while at the same time reduce carbon emission [2]. However, it also comes with new problems. Despite lower noise emission from the emerging new flying vehicles such as electric vertical take-off and landing (eVTOL) aircrafts as compared to conventional aircrafts, lower flying paths, higher penetration into high density areas and higher frequency of operations mean AAM can potentially cause more noise impacts. According to a survey in Europe, noise is one of the public's most concerned issues regarding AAM [3].

There is a growing body of research addressing the noise issues of AAM. However, most of the focus has been on the modelling of noise emission from individual vehicles, along their flying paths or around vertiports where these vehicles take off and land [4-5], much less attention has been paid to assessing potential noise impact at city or reginal scale [6-8]. Studies at city and reginal scales can be useful in understanding spatial pattern and distribution of AAM noise impact. However, such studies are rare in Europe where land use and urban morphology are very different from those in US or in Asia. Moreover, none of these existing studies considered social distribution of the impact, while social equity could be an issue in public acceptance and AAM's uptake, given that AAM may only serve high value travelers, at least in the early stages. Therefore, this study explores the socio-spatial pattern of potential AAM noise impact using West Yorkshire in England as the case study area.

2. METHODS

To assess potential UAM noise impact, possible vertiport locations were first identified based on commute travel demand. Then, two types of flying routes were tested: one prioritises distance reduction and one prioritises noise

[*] ***Corresponding author***: l.jiang2@leeds.ac.uk
Copyright: *©2025 First author et al. This is an open-access article distributed under the terms of the Creative Commons Attribution 3.0 Unported License, which permits unrestricted use, distribution, and reproduction in any medium, provided the original author and source are credited.*

mitigation, each tested with 3 distances of noise footprints. Statistics of people exposed to the potential UAM noise were made with and without considering exposure to existing road and rail noise.

2.1 The case study area

West Yorkshire is a county in North England with a population of around 2.4 million in 2022 and governed by five metropolitan boroughs: City of Leeds, City of Bradford, City of Wakefield, Calderdale and Kirklees.

Analysis in this study was conducted at the spatial scale of Output Areas (OAs) which are the lowest level of geographical area for census statistics in England. Each OA has between 100 and 625 usual residents and there are 7345 OAs in West Yorkshire in the 2021 census. The 2019 English indices of deprivation (IMD) was used to divide the OAs into 10 deciles, with Decile 1 among the 10% most deprived OAs in England and Decile 10 among the 10% least deprived. As shown in Figure 1, there is a mixed levels of deprivation in West Yorkshire with OAs present in all the 10 deciles. However, the majority of the OAs are in the lower deciles and numbers of OAs generally decrease as deprivation decreases.

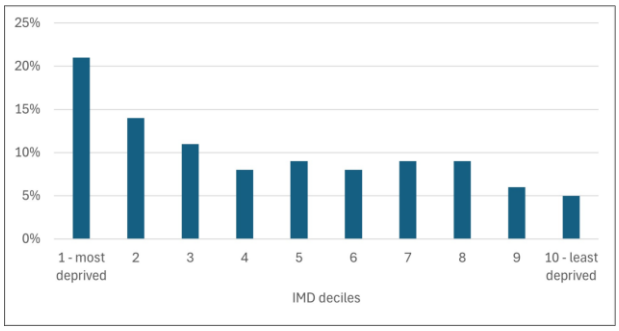


Figure 1. Distribution of West Yorkshire OAs in the English Indices of Multiple Deprivation (IMD) 2019 deciles.

2.2 Vertiport locations

Since one of the most promising use cases of AAM is envisaged to be for commute [6], possible vertiport locations in this study were identified based on travel to work demand. Number of residents as well as workplace population by distance travelled to work in each Middle Layer Super Output Area (MSOA) were obtained from census 2011. Census 2011 was used instead of census 2021 due to impact of Covid lockdowns on census 2021. MSOAs are higher level census geographical areas each containing between 5,000 and 15,000 residents. Given that AAM is unlikely to be appealing for very short distance travels, only residents and workplace population travelled longer than 10km were kept for analysis.

Clustering analysis is a popular approach to identify AAM vertiport locations [9] and agglomerative hierarchical clustering (AHC) was used in this study. To perform AHC, each MSOA centroid was broken down into demand point each representing 500 travellers (residents plus workplace population). Coordinates of the demand points were randomised by applying a random move of up to 500m so points belonging to the same MSOA do not overlap on each other. The resulted demand points are shown in Figure 2. The AHC was conducted in R using the *cluster* package [10] with the Ward.D2 linkage method. Figure 3 shows the resulted dendrogram. Based on the split pattern in the dendrogram and given that [6] used 100 vertiports for 21 million people while West Yorkshire has a population of around 2.4 million, number of vertiports was set to be 11 in this study. Locations of these vertiports was determined by calculating the arithmetic means of the coordinates of demand points within each cluster. Figure 2 shows the locations of the vertiports.

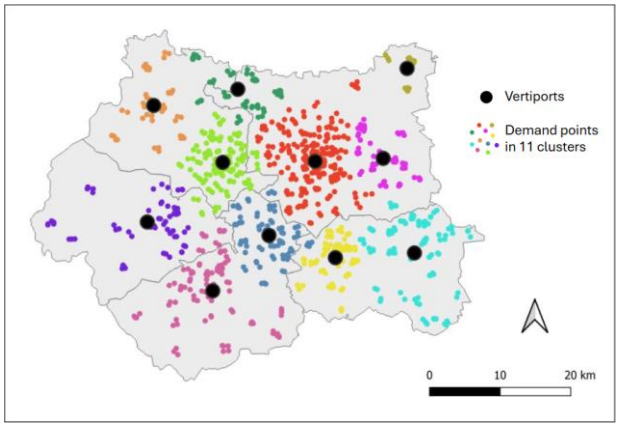


Figure 2. Vertiports and demand points in 11 clusters.

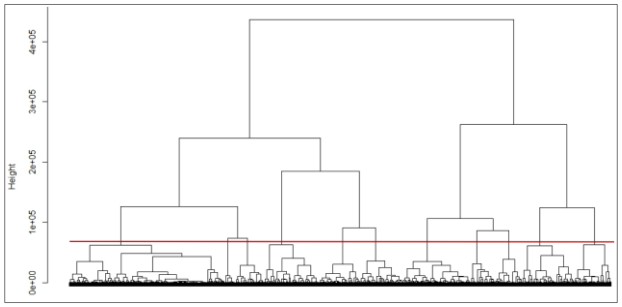


Figure 3. Dendrogram from the agglomerative hierarchical clustering (AHC) analysis with the cutoff line at 11 clusters.

2.3 Flying routes and noise footprints

Flying routes were assigned to provide good connections to the two largest settlements in West Yorkshire: Leeds and Bradfords. Two types of routes were tested: distance-priority routes which connect vertiports using straight lines; and noise-priority routes which follow major roads so the routes are above areas already exposed to high transport noise. The noise metric of $L_{Aeq,\ 16h}$ was used for road noise, as well as for all the noise levels mentioned in the rest of this paper, since AAM for commute is unlikely to operate over night so noise impact over the 16-hour period from 7am to 11pm would be most relevant. Figure 4 shows the two types of routes with road noise map from England Strategic Noise Mapping Round 4 (2022) in the background.

Noise footprints covering areas of within 500m, 1000m and 1500m distances along the flying routes were assumed and tested. AAM noise within these distances were assumed to be above 55dB $L_{Aeq,\ 16h}$. These distances were chosen based on noise maps produced in previous studies [6-8], and the fact that there is still uncertainty in AAM vehicle technologies and operation intensity which could affect noise footprint.

2.4 Noise impact assessment

Whether an OA is exposed to AAM noise is determined by whether the population-weighted centroid of the OA is within the noise footprint. Statistics were made for the 2 × 3 flying route and noise footprint scenarios, with and without considering existing road and rail noise.

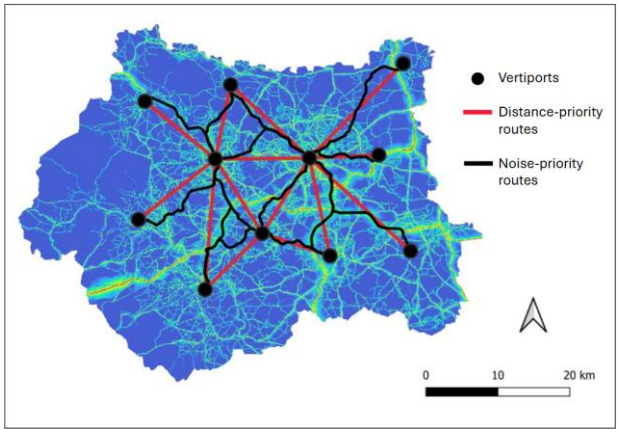


Figure 4. Distance-priority routes and noise-priority routes with road noise map in $L_{Aeq,\ 16h}$ from England Strategic Noise Mapping Round 4 (2022).

3. RESULTS

West Yorkshire is already facing serious transport noise issues, with 38% of the OAs exposed to road and/or rail noise above 55dB $L_{Aeq,\ 16h}$, while it was reported that "only" 27 % and 2.9 % of the adult population in England were exposed to road and rail noise above 53 and 54 dB L_{den} respectively [11]. Introduction of AAM will further increase noise exposure. As shown in Table 1, more than half of the OAs (53%) will be exposed to AAM noise above 55dB in our scenario if distance-priority routes are used and the wide 1500m noise footprint is assumed. Even with noise-priority routes and the narrow 500m noise footprint, the proportion of exposed OAs will still be high, around 1 in 5 (19%).

Table 1. Percentages of OAs in West Yorkshire exposed to AAM noise above 55dB.

	Noise footprint		
	500m	1000m	1500m
Distance-priority route	22%	39%	53%
Noise-priority route	19%	34%	48%

Among those exposed OAs, most are in quiet areas that are not currently exposed to road and/or rail noise above 55dB $L_{Aeq,\ 16h}$. As shown in Table 2, the percentage is highest

(60%) when distance-priority routes are used and the wide 1500m noise footprint is assumed, and lowest (53%) with noise-priority routes and the narrow 500m noise footprint. This indicates that AAM may pose new threat to areas that are otherwise not affected by transport noise, and the geographic coverage could be very wide and challenging.

Table 2. Percentages of OAs in West Yorkshire exposed to AAM noise in otherwise quiet areas (below 55dB $L_{Aeq,\ 16h}$ road and/or rail noise).

		Noise footprint		
		500m	1000m	1500m
% in all OAs	Distance-priority route	13%	23%	32%
	Noise-priority route	10%	19%	28%
% in exposed OAs	Distance-priority route	57%	59%	60%
	Noise-priority route	53%	56%	58%

Impacts of both the existing road and/or rail noise and the potential AAM noise are not evenly distributed across social groups. As shown in Figure 5, the more deprived OAs are more likely to be exposed to road and/or rail noise, with more than 40% of the OAs in Deciles 1, 2 & 3 exposed, while it is less 30% for OAs in Deciles 9 & 10.

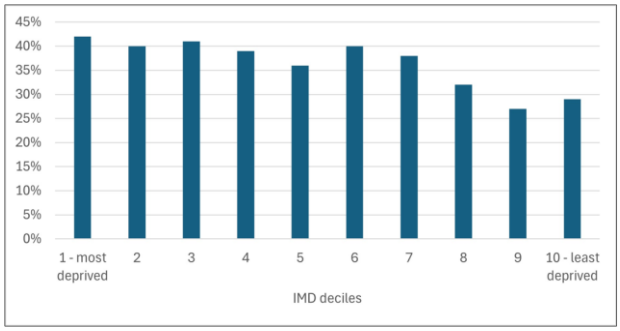


Figure 5. Percentage of OAs in West Yorkshire exposed to road and/or rail noise above 55dB $L_{Aeq,\ 16h}$ in each IMD decile.

The inequality could be even worse with AAM noise. As shown in Figure 6, when distance-priority routes are used, more than 30% of the OAs in Decile 1 will be exposed to AAM noise with 500m noise footprint. The percentages roughly go down as deprivation decreases, and are less than 10% for Deciles 8 & 9. Similar patterns are observed with 1000m and 1500m noise footprints, with OAs in lower deciles more than twice as likely to be exposed to AAM noise as compared to those in higher deciles.

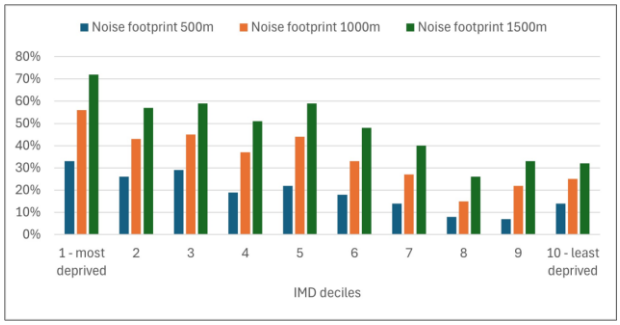


Figure 6. Percentages of OAs in West Yorkshire exposed to AAM noise above 55dB with distance-priority routes in each IMD decile.

Using noise-priority routes reduces the inequality. As shown in Figure 7, while lower deciles are still more likely to be exposed to AAM noise, the divides are not as large as when using distance-priority routes. With 500m noise footprint, around 25% and 10% of OAs are exposed in Decile 1 and in Deciles 8 & 9 respectively.

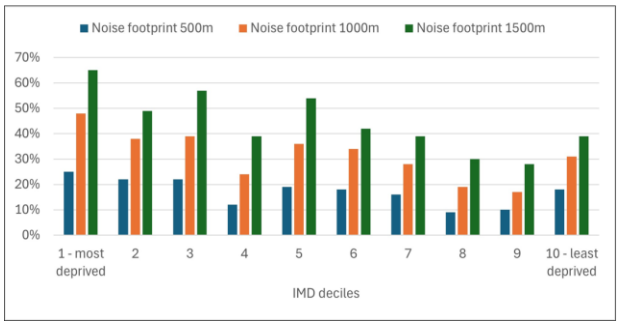


Figure 7. Percentages of OAs in West Yorkshire exposed to AAM noise above 55dB with noise-priority routes in each IMD decile.

When existing road and/or rail noise is considered, i.e., only counting OAs where road and/or rail noise does not exceed 55dB $L_{Aeq,\ 16h}$, the inequality becomes much less significant. With distance-priority routes, there are still higher proportions of OAs exposed to AAM noise in the lower

deciles, but generally less than twice as high as those in the higher deciles, especially when wider noise footprints are assumed (Figure 8). With noise-priority routes, the variation becomes even smaller and OAs in the lower deciles do not show remarkable disadvantages (Figure 9). However, this does not mean that AAM will not further contribute to social inequity in transport noise impact, or noise-priority routes are better at tackling the inequality. Rather, it indicates that the more deprived communities who are already suffering from more transport noise will bear disproportionally more burden of the new noise introduced by AAM.

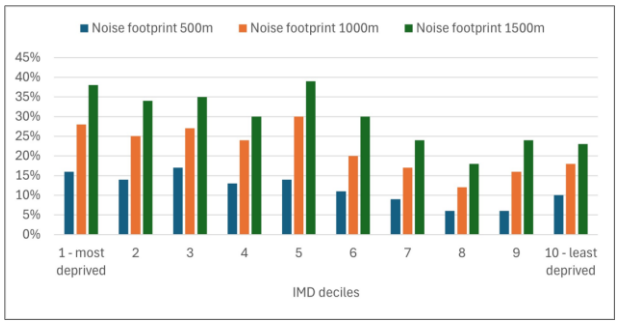


Figure 8. Percentages of OAs in West Yorkshire exposed to AAM noise above 55dB in otherwise quiet areas (below 55dB $L_{Aeq,\ 16h}$ road and/or rail noise) with distance-priority routes in each IMD decile.

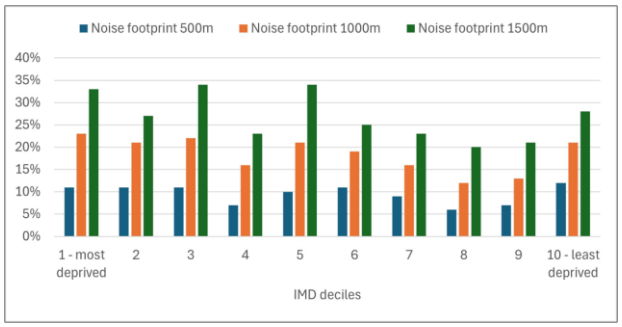


Figure 9. Percentages of OAs in West Yorkshire exposed to AAM noise above 55dB in otherwise quiet areas (below 55dB $L_{Aeq,\ 16h}$ road and/or rail noise) with noise-priority routes in each IMD decile.

4. CONCLUSIONS

This study shows that AAM noise is likely to affect a large proportion of the population in West Yorkshire even in the more conservative scenarios, and most of the affected population are not currently exposed to road and/or rail noise above 55dB $L_{Aeq,\ 16h}$. AAM noise is also likely to further impair social equity in transport noise impact in West Yorkshire, as the more deprived communities are more likely to be exposed to AAM noise. Using noise-priority routes seems to reduce the inequality, but there is a risk that the more deprived communities who are already exposed to high transport noise will bear disproportionally more burden of the new noise introduced by AAM.

This study however has some limitations. Vertiport locations and flying routes were decided only based on travel demand without considering other important factors such as land and airspace availability and land use sensitivity. Potential noise level and footprint of AAM was only roughly estimated. More accurate noise modelling could improve the rigorousness of this study.

5. REFERENCES

[1] Future Flight Challenge: *Future Flight Vision and Roadmap*. UK Research and Innovation, 2021.

[2] Swanson Aviation Consultancy & EAMaven: *UK Advanced Air Mobility (AAM) Market Assessment - An Analysis of 20 Potential Routes in the UK for AAM Aircraft Operations*. UK Research and Innovation, 2022.

[3] McKinsey & Company: *Study on the Societal Acceptance of Urban Air Mobility in Europe*. European Union Aviation Safety Agency, 2021.

[4] J. Hua and R.R. Mankbadi: "Prediction and Control of Broadband Noise Associated with Advanced Air Mobility—A Review," *Applied Sciences*, vol. 14, no. 18, pp. 8455, 2024.

[5] F. Yunus, D. Casalino, F. Avallone and D. Ragni: "Efficient prediction of urban air mobility noise in a vertiport environment," *Aerospace Science and Technology*, vol. 1, no. 139, pp. 108410, 2023.

[6] J. Jeong, M. So and H.Y. Hwang: "Selection of vertiports using k-means algorithm and noise analyses for urban air mobility (UAM) in the Seoul metropolitan area," *Applied Sciences*, vol. 11, no. 12, pp. 5729, 2021.

[7] J. Li, H.K. Ng, Y. Zheng and S. Gutierrez-Nolasco, "Noise exposure maps for urban air mobility," in *Proc. of AIAA Aviation 2021 Forum*, (virtual event), pp. 3203, 2021.

[8] S. Rizzi and M. Rafaelof, "Community noise assessment of urban air mobility vehicle operations using the FAA Aviation Environmental Design Tool," in Proc. of *INTER-NOISE and NOISE-CON Congress and Conference*, (Washington, D.C., USA), pp. 450-461, 2021.

[9] V. Volakakis and H.S. Mahmassani: "Vertiport infrastructure location optimization for equitable access to urban air mobility," *Infrastructures*, vol. 9, no. 12, pp. 239, 2024.

[10] M. Maechler, P. Rousseeuw, A. Struyf, M. Hubert and Hornik: "cluster: Cluster Analysis Basics and Extensions," R package: https://cran.r-project.org/web/packages/cluster/index.html

[11] C. Jephcote, S.N. Clark, A.L. Hansell, N. Jones, Y. Chen, C. Blackmore, ... and J. Gulliver: "Spatial assessment of the attributable burden of disease due to transportation noise in England," *Environment International*, vol. 178, pp. 107966, 2023.

DOI: 10.61782/fa.2025.0923

FORUM ACUSTICUM EURONOISE 2025

UAS-NOISECHECK - A SYSTEM IMPLEMENTING THE EASA GUIDELINES ON DRONE NOISE MEASUREMENT

Martin Blass* **Stefan Grebien** **Franz Graf**
JOANNEUM RESEARCH Forschungsgesellschaft mbH
DIGITAL – Institute for Digital Technologies

ABSTRACT

Unmanned aerial systems (UAS) are on the rise and are about to transform civil aviation. As their proliferation grows, the social and legal acceptance of drones is becoming increasingly important, particularly with regard to noise pollution. So far, the lack of standardized methods and systems to measure in-flight noise emissions of UAS has hindered the creation of legal frameworks. To close this gap, the EASA introduced guidelines for UAS noise measurement in October 2022, for which feedback is currently being collected on their practical implementation and measurement results. In this work, we present *UAS-NoiseCheck*, a prototype system designed to implement these guidelines. It integrates acoustic, visual, GNSS and meteorological components to enable comprehensive, multisensory data acquisition and thus represents a novelty in the multimodal metrological description of UAS. Since our system not only contains a single microphone as a sound level meter but also features a hemispherical 32-microphone array, it can also facilitate the certification and regulation of noise emissions when used in the context of drone detection and localization. In initial field experiments, we analyze noise emissions of different multicopter UAS recorded with a ground-based and an inverted microphone setup as well as the microphone array.

Keywords: *noise measurement, sound pressure level, sound emission, microphone array, uav, drone*

**Corresponding author*: martin.blass@joanneum.at.
Copyright: *©2025 Blass et al. This is an open-access article distributed under the terms of the Creative Commons Attribution 3.0 Unported License, which permits unrestricted use, distribution, and reproduction in any medium, provided the original author and source are credited.*

1. INTRODUCTION

Unlike conventional aircraft, UAS produce distinctive high-frequency and tonal noise signatures, which can lead to noise annoyance populated areas. Previous research studies have shown that UAS are likely to be perceived as more annoying than road vehicles, airplanes or helicopters at similar sound levels, in particular when combined with low-altitude flight maneuvers and hovering [1, 2].

In response to growing concerns [3], the European Union Aviation Safety Agency (EASA) introduced guidelines in 2022 [4] aimed at standardizing noise measurement for UAS operating in the *specific* category, which has not been addressed so far. These guidelines mark a significant step in bridging the gap between traditional noise assessment methods [5, 6] and the evolving acoustic profiles of modern UAS [7]. Previous studies have largely focused on controlled environments such as anechoic chambers, wind tunnels or complex and costly outdoor configurations [5, 8]. Nevertheless, field measurements are still essential to capture the complex interplay between UAS noise emissions and environmental factors such as ground effects and meteorological conditions.

In [9], sound pressure level (SPL) and noise variability under different flight conditions was analyzed in an extensive flight test campaign for small UAS, focusing on the comparison between ground-plane and elevated microphones. [10] presents a robust framework for field measurements to accurately characterize UAS noise emissions during flyovers, using multiple measurement positions and backpropagation techniques to calculate directivity noise hemispheres. In this comprehensive work the inverted microphone setup over a ground plate proposed in [4, 6] is used. Similar measurements were performed in [11] with results providing insights into sound pressure, sound power, spectral content and directional patterns.

At the same time, numerous papers have been published on the human perception of drone sounds, with the aim of finding a link between objective noise metrics and psychoacoustic sound quality metrics. [1] used the sound exposure levels (SEL), effective perceived noise level (EPNL), and loudness exceeded 5% of the time (L5) together with subjective listening tests, to compare human annoyance responses to noise from UAS flyovers and road vehicle drive-bys. [2] recommends a combination of qualitative and quantitative methods, including laboratory studies and real-world testing to understand human responses to UAS and to develop the most meaningful noise metrics. In particular, loudness, sharpness, tonality and roughness should be considered, as A-weighted SPL, SEL or EPNL are considered insufficient.

There exist only few works on the noise measurement including SPL estimation with microphone arrays. In [12] the use of microphone arrays is recommended due to their localization capabilities and improved signal-to-noise ratio (SNR) given by possibility of focusing in a desired direction via beamforming (BF). In a previous paper [13], we presented a hemispherical 32-microphone array specifically designed to capture typical UAS noise and investigated its performance in fixed and mobile setups.

In this paper, we present *UAS-NoiseCheck*, a research project and equally named system, designed to implement the EASA noise measurement guidelines [4]. By integrating ground-plate microphones, a sound level meter (SLM) and a microphone array from [13], with visual, GNSS and meteorological components, our system enables a comprehensive, multimodal characterization of drone noise. Based on the results of initial field tests, we show that the system has the potential to combine noise measurement with acoustic drone tracking to enable directional SPL estimation in future regulatory tasks.

2. METHODOLOGY

The guidelines of [4] describe two different approaches for the objective measurement of UAS noise: a level-flight to estimate the A-weighted sound exposure level (L_{AE}) and a hover procedure to compute the A-weighted equivalent continuous SPL (L_{Aeq}) recorded using the inverted setup (INV) with a 1/2" microphone spaced 7 mm above a ground plate [6] and an SLM, both complying with IEC 61672-1 (Class 1). This setup is recommended for its simplicity instead of a ground-based microphone (GND) mounted flush with the plate. In *UAS-NoiseCheck*, we implement both setups to analyze potential SPL differences.

Similar to our previous work [13], we use an acoustic localization algorithm providing DOA estimation (DOAE) of multiple sound sources in order to track potential UAS targets. The algorithm relies on the BF steered response power and adopts a Gaussian Mixture Model (GMM) based approach for the use in 3D with custom frequency and sampling grid settings to enable probabilistic modeling and tracking of an unknown number of sources and signal extraction using masked delay-and-sum beamforming (DSB) [14]. It provides good localization accuracy even with coarse spatial scanning grids with a computational load that enables real-time application.

3. SENSOR SYSTEM

The sensor system consists of the following components that provide data streams a central unit (CORE):

- SPL: *GRAS 67AX* (INV, GND) + *NTi Audio XL2* SLM → 2x audio via USB, 1x JSON message via LAN,
- ARR: *JR-IcoDome32* microphone array + *MOTU AVB* → 32x audio via USB,
- CAM: 2x *FLIR Blackfly GigE* + *NVIDIA Jetson Orin* → 1x JSON message via LAN,
- GNSS: *Holybro H-RTK F9P GNSS* + *Pixhawk 6X* → 1x GNSS message via USB from *RFD868x-EU*,
- METEO: *DAVIS Vantage Pro 2* + *Weatherlink LIVE* → 1x JSON message via LAN.



Figure 1: Measurement setup: SPL with GNSS for positioning (top left), ARR with windscreens (top right), CAM in case (bottom left), and a *ViewCopter V6H* with payload for MTOM (bottom right).

Figure 1 shows the measurement setup during the initial field test in 2024. All components are synchronized in time by an NTP server on an LTE router. For SPL, we use a *GRAS 47AX* (GND) and a *Z-TECH 333-507* (INV) microphone. The audio signal of INV is split with an XLR Y-adapter and used as SLM input. ARR has 32 ICP electret array microphones, 26 of which are arranged on a geodesic dome and 5 as a pentagon, with one in the center of a solid plate. Signal conditioning, A/D conversion and time synchronization is done with *MOTU AVB* USB audio interfaces. CAM only sends position estimates to CORE and stores video data locally. GNSS is used to record sensor positions and is mounted on the UAS during flights.

For our initial field test, we used four UAS [1] [2]:

UAS	**DIM** (cm)	$\mathbf{V_{Gref}}$ (m/s)	**MTOM** (kg)
ViewCopter V6H	150x150x45	10	32
twinFOLD KAT	173x187x30	10	12
twinFOLD GEO	125x115x26	10	5
twinFOLD SCI	52x52x17	15	2

Table 1: UAS with dimensions, reference ground speed V_{Gref} and maximum take-off mass (MTOM).

According to [4], UAS must be operated at V_{Gref}, i.e. at the fastest speed at which the level-flight can be maintained under the atmospheric reference conditions, with their maximum take-off mass (MTOM) at an altitude between 17 m and 150 m and ensuring a lateral deviation of $\pm 10°$ from the vertical above the noise measurement point (SPL). For the hover procedure, the UAS must maintain a stabilized position for 30 s at an altitude between 12 m and 50 m within a cone of 8° from the vertical above the noise measurement point. For both level and hover scenarios at least 6 valid runs must be performed.

4. RESULTS

The first field tests were carried out at *UMFC Stocking* airfield in November 2024. All microphones and the SLM were calibrated with a 1 kHz sine signal at 94 dB. Audio data was recorded at a sampling rate of 48 kHz at 24 bits together with the SLM metrics L_{AF} and L_{AS} logged at 5 Hz for fast and slow time weightings, respectively. For FFT processing in DOAE, we set the size of the time window (square-root Hann) and the FFT to 4096, with a frame overlap of 50% to ensure perfect reconstruction of the DSB signals extracted from the estimated source tracks. Considering the predominant characteristics of drone sound, i.e. rotor noise, the frequency range for DOAE was set to [300 2300] Hz and for DSB signal extraction to the whole range [0 24] kHz. As scanning grid we choose a hemisphere of 200 quasi-uniformly distributed points. The number of initial and maximum sound sources was set to 3 and 16, respectively [13].

In Figures 2 and 3 we show exemplary runs for a level and a hover flight of the *ViewCopter V6H*, respectively. The top two subplots represent the DOAE tracking results of three sound source hypotheses (SRC1-3) compared to the GNSS based position ground truth (TRUE) in terms of azimuth and elevation angles. The respective absolute angle error for each source is shown in the third diagram. The fourth subplot shows the distance and velocity profile of the UAS flight with respect to SPL as origin. The bottom two plots display the SPL recordings of INV as reference (which is also used as input to SLM), GND, ARR as the central microphone on the array base, and DSB as the extracted beamformer output of the SRC closest to TRUE.

The measurement results for the entire dataset are presented as follows: Table 2 provides the calculated noise metrics defined in [4] for each UAS: the arithmetic average sound level L_{AEref_av} and L_{Aeqref_av} for level and hover flight, with the corresponding standard deviation (SD).

UAS	$\mathbf{L_{AEref_av}}$ (dBA)	$\mathbf{L_{Aeqref_av}}$ (dBA)
ViewCopter V6H	77.6 ± 0.81	77.6 ± 0.76
twinFOLD KAT	74.4 ± 0.67	66.4 ± 1.09
twinFOLD GEO	77.3 ± 0.48	57.6 ± 1.73
twinFOLD SCI	66.3 ± 0.39	50.8 ± 1.32

Table 2: UAS noise metrics L_{AEref_av} and L_{Aeqref_av} averaged over runs for level-flight and hover, resp.

Scenario	**GND** (dB)	**ARR** (dB)	**DSB** (dB)
level	0.23 ± 0.06	-0.03 ± 1.84	-2.69 ± 2.63
hover	0.06 ± 0.83	0.50 ± 4.82	-3.86 ± 4.88
level & hover	0.17 ± 0.71	0.16 ± 3.24	-3.11 ± 3.64

Table 3: SPL differences of GND, ARR and DSB w.r.t. INV: mean $\pm$ SD for level-flight and hover.

[1] https://www.vcopter.net/drohnenbau.html
[2] https://www.twins.co.at/multirotorsysteme

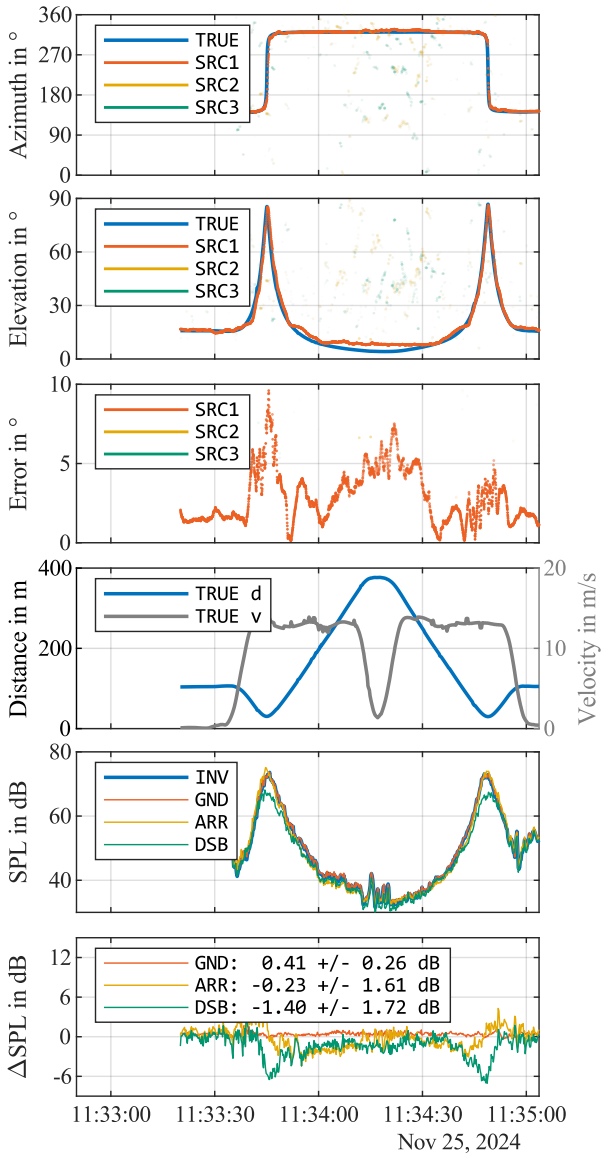


Figure 2: Level-flight example of *ViewCopter V6H*: The UAS is tracked during the entire run up to a distance of 400 m with a DOAE error below 10°. The average SPL differences w.r.t. INV are within 1.5 dB for all signal types. The deviations in ARR and DSB are mainly due to time differences during overflights. The relatively large SPL differences in DSB of -6 dB indicate that the tracker is not able to follow the UAS fast enough, leading to steering errors and unwanted attenuation of the target signal in the BF process.

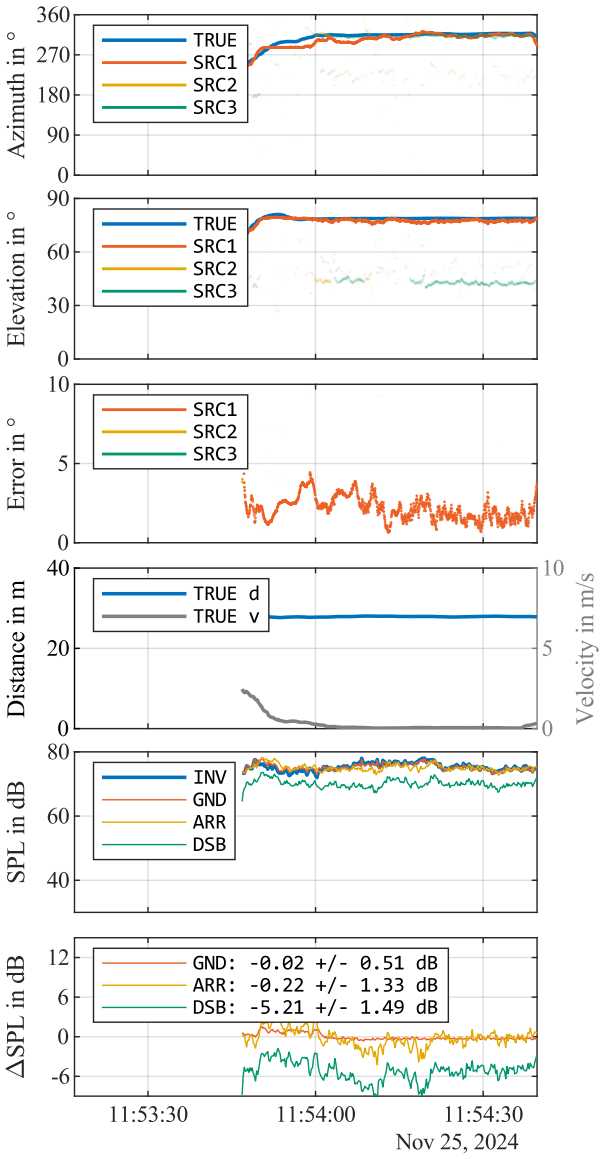


Figure 3: Hover-flight example of *ViewCopter V6H*: The UAS is stabilized at a height of 31 m above the ground plate (SPL) and tracked with a DOAE error below 5°. The average SPL differences w.r.t. INV are within 1 dB for GND and ARR. The deviations at DSB of -6 dB are due to spatial filtering effects, such as suppressed ground reflections, turbulent incoherent noise etc., and possibly also due to the fact that the array mainlobe is too narrow to focus on the UAS as a whole and therefore does not capture its entire frequency content.

Table 3 examines the SPL differences in terms of L_{AF} of GND, ARR and DSB compared to the inverted setup microphone signal (INV) averaged over all runs. To get a more detailed insight, we divide the analysis into the contributions of level, hover, and both scenarios.

Table 4 shows a statistical evaluation of the DOAE in terms of mean absolute error (MAE) including SD and median absolute deviation with the respective interquartile ranges, which represents a more outlier prone error metric. Again, we split the evaluation into level, hover, and both.

Scenario	**MAE** $\pm$ **SD** (°)	**MAD** (°)	**IQR** (°)
level	5.94 $\pm$ 8.27	3.63	[2.08, 7.25]
hover	6.08 $\pm$ 5.36	3.69	[2.34, 8.83]
level & hover	5.99 $\pm$ 7.37	3.65	[2.16, 7.88]

Table 4: DOAE performance: mean $\pm$ SD, median and IQR of absolute error for level-flight and hover.

5. CONCLUSION

We have presented *UAS-NoiseCheck*, a multimodal system for UAS noise measurement. We draw the following conclusions from our results obtained in a first field test:

- Both the inverted and the ground microphone setup are suitable for accurately measuring UAS noise metrics.
- The DOAE performance highlights the effectiveness of microphone arrays to automatically localize UAS.
- To accurately measure SPL based on BF, special care must be taken to ensure robust sound source tracks and to compensate for the spatial array response.

Future work lies in extensive field testing to verify the results on larger datasets and improve DOAE tracking.

6. ACKNOWLEDGMENTS

The project *UAS-NoiseCheck* has received funding from the research, technology and innovation funding program Take Off of the Republic of Austria, Ministry for Climate Action. The Austrian Research Promotion Agency (FFG) has been authorized for the program management.

7. REFERENCES

[1] A. W. Christian and R. Cabell, "Initial investigation into the psychoacoustic properties of small unmanned aerial system noise," in *23rd AIAA/CEAS aeroacoustics conference*, p. 4051, 2017.

[2] A. J. Torija and C. Clark, "A psychoacoustic approach to building knowledge about human response to noise of unmanned aerial vehicles," *Int. Journal of Environmental Research and Public Health*, vol. 18, 2021.

[3] EASA, "Study on the societal acceptance of urban air mobility in Europe," 2021.

[4] EASA, "Guidelines on Noise Measurement of Unmanned Aircraft Systems Lighter than 600 kg Operating in the Specific Category," 2022.

[5] ISO, *3744:2010 – Acoustics – Determination of sound power levels of noise sources using sound pressure – Engineering method in an essentially free field over a reflecting plane*, 3 ed., 2010.

[6] ICAO, *Annex 16 – Environmental Protection, Volume I: Aircraft Noise*, 8 ed., 2017.

[7] G. Malaval, "Approach to Noise Regulation of Unmanned Aviation in the European Union," in *Quiet Drones*, 2024.

[8] ISO, *5305:2024 Noise measurements for UAS (unmanned aircraft systems)*, 1 ed., 2024.

[9] E. Greenwood and N. B. Konzel, "Measurement and characterization of multirotor unmanned aerial system noise," in *INTER-NOISE and NOISE-CON Proceedings*, vol. 264, pp. 662–672, 2022.

[10] C. Ramos-Romero, N. Green, A. J. Torija, and C. Asensio, "On-field noise measurements and acoustic characterisation of multi-rotor small unmanned aerial systems," *Aerospace Science and Technology*, vol. 141, 2023.

[11] A. Nash and J. Kennedy, "In Flight Evaluation of UAV Noise Emission," in *Quiet Drones*, 2024.

[12] M. Snellen, R. Merino-Martinez, A. Altena, A. Amiri-Simkooei, C. Cappagli, A. Morin, L. Quaroni, F. Yunus, and R. Yupa-Villanueva, "Research on drone and urban air mobility noise: Measurement, modelling, and human perception," in *Quiet Drones*, 2024.

[13] M. Blass, S. Grebien, and F. Graf, "Experimental Evaluation of Acoustic Drone Tracking using Mobile Microphone Arrays," in *Quiet Drones*, 2024.

[14] N. Madhu and R. Martin, "A versatile framework for speaker separation using a model-based speaker localization approach," *IEEE Transactions on Audio, Speech and Language Processing*, vol. 19, no. 7, pp. 1900–1912, 2011.

DOI: 10.61782/fa.2025.0615

FORUM ACUSTICUM EURONOISE 2025

NOISE MODELING OF UAM AROUND VERTIPORTS BY SOUND BARRIER

Seung-Min Lee[1] **Chan-Hoon Haan**[1*]
[1] Department of Architectural Engineering, Chungbuk National University, South Korea

ABSTRACT

The present study aims to propose practical solutions to control the noise issue, which is a key challenge for the commercialization of Urban Air Mobility (UAM). Noise levels around vertiports during UAM urban operations were predicted using the SoundPLAN program, and the noise reduction effects were assessed through simulation modeling when various heights of noise barriers were applied at different distances and receiver heights. The comparison factors to confirm the noise reduction effect were set to L_{den}, L_{eq}, and L_{max}. The height of the sound barrier was investigated up to 27 m at 3 m intervals. In the present study, for noise prediction, two major vertiports on the K-UAM Grand Challenge phase 2-1 Ara Waterway demonstration route were targeted. As a result, it was found that significant noise reduction was observed at receiver points lower than the sound barrier. However, the noise reduction effect was minimal or absent at receiver points of similar or greater height than the sound barrier. This indicated that as the distance from the vertiport decreased, the noise reduction effect increased with the height of the sound barrier. Thus, it can be expected that the findings of this study could contribute to noise mitigation of UAM.

Keywords: *UAM(urban air mobility), sound barrier, vertiport, noise modeling, noise map*

1. INTRODUCTION

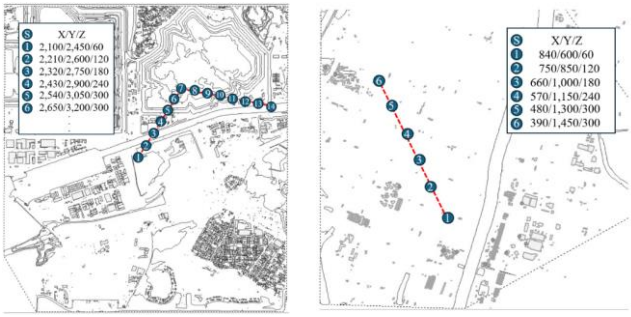
A significant challenge in the commercialization of Urban Air Mobility (UAM) is noise.[1] Aircraft like helicopters have caused disturbance to those living near airports due to elevated noise levels, frequently sparking community opposition. Because UAM utilizes electric vertical take-off and landing (eVTOL) technology, it is anticipated to produce less noise compared to traditional aircraft.[2] However, given that UAM operations primarily occur over urban centers, even with reduced noise compared to conventional aircraft, they will operate much closer to where people live and work. Consequently, UAM operation could introduce a new source of noise in existing urban areas, potentially increasing how intensely noise is perceived and raise concerns about sensitive reactions from city dwellers.[3] Therefore, to successfully commercialize UAM, the development and application of UAM-specific noise analysis and mitigation techniques are essential.

Sound barriers are recognized as important elements in decreasing environmental noise. In the transportation sector, they are installed alongside highways and railways to effectively lessen noise impacting nearby residential and commercial zones. [4] Sound barriers function by creating a physical obstruction that prevents sound from traveling directly to the listener. Beyond just traffic noise, these sound barriers are also employed to control noise from industrial activities, aiding in adherence to local noise ordinances and minimizing noise pollution in adjacent areas. This study proposes a method for reducing noise generated by UAM operations through the use of an established technology: sound barriers. To achieve this, SounPLAN software is employed to predict and analyze noise levels by strategically placing sound barriers around vertiports, which are the take-off and landing locations for UAM within the city. The aim is to identify ways to lessen the noise impact of UAM operations on urban environments and to significantly contribute to the protection of the living environment for city residents

[*]***Corresponding author***: Chhaan@chunbuk.ac.kr
Copyright: *©2025 First author et al. This is an open-access article distributed under the terms of the Creative Commons Attribution 3.0 Unported License, which permits unrestricted use, distribution, and reproduction in any medium, provided the original author and source are credited.*

Table 1. UAM noise level by frequency

	63	125	250	500	1,000	2,000	4,000	8,000
Departure	83.7	69.5	64.7	62.9	62.7	62.2	63.3	32.6
Approach	77.1	74.8	78.1	75.5	84.8	79.9	72.3	38.5



(a) V1) (b) V2

Figure 1. Noise reduction rate according to the height of sound barrier.

2. RESEARCH METHOD

Noise maps were generated, and noise levels were predicted using the SoundPLAN program. Sound barriers were positioned along the road adjacent to the vertiport, and the material of the sound barriers was set to be reflective. The area simulated was the vertiport location of the K-UAM Grand Challenge. Table 1 shows the noise level of the UAM input into SoundPLAN. The height of the sound barriers was compared from 12 m to 27 m at 3 m intervals.

3. RESULTS

L_{eq} and L_{max} were predicted at two different points. L_{eq} prediction results showed that the noise level continuously decreased as the height of the sound barrier increased in 3 m increments. Furthermore, when the increase/decrease rate was compared, the noise level reduction was greater as the height of the sound barrier increased. This trend was consistent at both sound-receiving points. L_{max} did not show a decreasing trend up to 18 m. However, when the height of the sound barrier exceeded 20 m, the noise level was reduced by nearly 2% compared to the previous measurement. At R2, the noise level was nearly double that at R1.

4. CONCLUSION

In this study, the noise level according to the height of the sound barrier was predicted and analyzed using the SoundPLAN program. As a result of analyzing the noise reduction effect, there was a difference in the noise reduction rate depending on the height of the sound barrier and the distance from the sound source. Therefore, when determining the height of sound barriers to prevent noise impact on buildings around the vertiport, the appropriate height should be calculated considering the distance between the vertiport and the sound-receiving location. In addition, there was a difference in the noise reduction rate depending on the noise evaluation factors. In the case of UAM, L_{max} is a noise evaluation factor that requires more careful examination than L_{eq}. Therefore, selecting the height of the sound barrier that is most effective for L_{max} reduction will be effective in reducing overall noise.

5. REFERENCES

[1] Jang, H. W., Choi S. I., Kim, H. Y., "A Study on the Design Criteria of Lateral Direction for Urban Air Mobility (UAM) Flight Path Construction", *Journal of the Korean Society for Aeronautical & Space Sciences*, vol. 52, issue 7, pp. 559-566, 2024.

[2] Lee, S. M., Wie S. Y., Haan, C. H., "Noise Evaluation of K-UAM by Current Noise Crieteria", *Journal of the Korean Society for Aeronautical & Space Sciences*, vol. 52, issue 12, pp. 1063-1071, 2024.

[3] Kim, J. S. "A study on subjective noise evaluation of residential area on aircraft noise near airport: case study on Teagu airport", *Kor Soc Noi Vibr Eng*, 10, pp. 41-48, 2000.

[4] Im, H. S., "A study on the characteristics of road traffic noise and the performance of noise barriers", *Fire Protection Technology*, pp. 33-37, 2001.

DOI:

Main theme: A05 Environmental Acoustics

Session A05.11 Heat pump sounds in residential settings: challenges and solutions

Chair(s): J. Harvie-Clark, C. Reichl, G. Fusaro

DOI:

Main theme: A06 Electro-Acoustics

Session A06.02 Microphones (theory, measurement, applications, MEMS technology, etc.)

Chair(s): P. Honzík, S. Durand

DOI: 10.61782/fa.2025.0624



FORUM ACUSTICUM
EURONOISE 2025

NONLINEAR BEHAVIOR OF CONDENSER MICROPHONES: ANALYTICAL MODELING AND EXPERIMENTAL VALIDATION

Jan Plaček[1] **Petr Honzík**[1*]
[1] Department of Radioelectronics, Faculty of Electrical Engineering,
Czech Technical University in Prague, Technická 2, 166 27 Praha, Czech Republic

ABSTRACT

This study investigates the nonlinear behavior of condenser microphones, with a focus on nonlinear capacitance as the primary source of nonlinearity. An experimental transducer was developed, consisting of a circular membrane and a fixed electrode with a central hole leading to a backing cavity. A linear analytical model for membrane displacement was derived using a multimodal approach, while a nonlinear model from the literature was used to relate the membrane displacement to the output voltage of the microphone. Experimental measurements of the nonlinear output of the transducer were conducted. A harmonic correction method from the literature was used to linearize the acoustic pressure incident on the transducer's membrane. These measurements were compared with theoretical predictions. The dependence of the first, second, and third harmonics of the output voltage on the input acoustic pressure level was analyzed. The results show good agreement between theoretical predictions and experimental data, particularly for the first and second harmonics, demonstrating the effectiveness of the proposed model in capturing the nonlinear characteristics of condenser microphones.

Keywords: *nonlinear behavior, condenser microphones, analytical modeling, harmonic correction, experimental validation*

**Corresponding author*: honzikp@fel.cvut.cz.
***Copyright**: ©2025 Jan Plaček et al. This is an open-access article distributed under the terms of the Creative Commons Attribution 3.0 Unported License, which permits unrestricted use, distribution, and reproduction in any medium, provided the original author and source are credited.*

1. INTRODUCTION

Condenser microphones offer several advantages, including a flat frequency response, low inherent noise, and relatively high sensitivity. Like many electroacoustic transducers, they exhibit a certain level of nonlinear distortion [1]. Among the various sources of nonlinearity, the nonlinear variation of capacitance is widely recognized as the dominant contributor [2]. This nonlinear distortion can be both measured [3, 4] and, to some extent, reduced [5, 6].

In this paper, we first present an analytical model of an experimental condenser microphone composed of a circular membrane and a fixed electrode with a central hole leading to a backing cavity. A linear formulation is used to determine the membrane displacement, which is then applied to compute the nonlinear output voltage of the microphone. The experimental device is subsequently described, along with a measurement setup based on recent techniques for nonlinear characterization and signal correction [4, 7]. Finally, the measured results are presented and compared with theoretical predictions to assess the accuracy and limitations of the model.

2. ANALYTICAL MODEL

This section presents an analytical model of the electrostatic (condenser) microphone, which consists of a circular membrane of radius R, separated by an air gap of thickness h_g from a fixed electrode of thickness l_h. The electrode contains a central hole of radius R_h, which opens into a backing cavity with volume V_c, as illustrated in Figure 1.

2.1 Nonlinear ouput voltage

First, the model of the microphone output voltage incorporating nonlinearities due to the nonlinear variation of

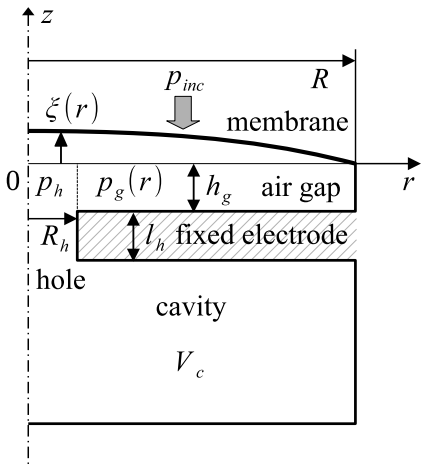


Figure 1. Axisymmetric schematic cross-sectional view of the transducer.

capacitance is summarized from [4]. Since the polarization voltage U_0 is applied to the fixed electrode through a high-value polarization resistor (on the order of GΩ), the charge variation is negligible, and the output voltage can be expressed as

$$u = -U_0 \frac{\mathrm{d}C}{C}. \tag{1}$$

Assuming that the time-dependent capacitance is given by

$$C(t) = C_p + \frac{\varepsilon_0 S}{h_g + \tilde{\xi}(t)} = C_p + C_0 \frac{1}{1 + \frac{\tilde{\xi}(t)}{h_g}}, \tag{2}$$

where $\tilde{\xi}(t)$ denotes the spatial average of the membrane displacement over the active area of the fixed electrode, the capacitance can be expressed as the sum of the parasitic capacitance C_p, transducer's static capacitance C_0 and a time-varying component $\mathrm{d}C(t)$. Applying a Taylor series expansion, the output voltage (1) can be written as

$$u(t) = U_0 \frac{C_0}{C_p + C_0} \left(\frac{\tilde{\xi}(t)}{h_g} - \left(\frac{\tilde{\xi}(t)}{h_g} \right)^2 + \right. \\ \left. + \left(\frac{\tilde{\xi}(t)}{h_g} \right)^3 - \dots \right) \tag{3}$$

The nonlinearities in the output voltage are thus clearly apparent.

2.2 Equations governing the displacement of the membrane

The membrane displacement ξ, required for evaluating the output voltage in (3), is governed by the following wave equation [8–10]

$$T(\Delta_r + K^2)\xi(r) = p_{inc} - p(r), \tag{4}$$

where T denotes the membrane tension, K is the membrane wavenumber, p_{inc} is the incident acoustic pressure, and $p(r)$ represents the $r-$dependent acoustic pressure behind the membrane. The solution to equation (4) is searched for in the form of an eigenfunction expansion

$$\xi(r) = \sum_n \xi_n \Psi_n(r), \tag{5}$$

where the eigenfunctions $\Psi_n(r)$ are given by

$$\Psi_n(r) = \frac{1}{\sqrt{\pi} R J_1(K_n R)} J_0(K_n r), \tag{6}$$

with K_n determined by the membrane boundary conditions $\xi(R) = 0$. The modal coefficients ξ_n are expressed as

$$\xi_n = \frac{1}{T(K^2 - K_n^2)} \iint_S (p_{inc} - p(r)) \Psi_n \mathrm{d}S, \tag{7}$$

where $S = \pi R^2$ denotes the membrane surface area.

2.3 Acoustic pressure inside the transducer

The acoustic pressure behind the membrane comprises two parts

$$p(r) = \begin{cases} p_h = \text{const.} & \text{for } r \in (0, R_h), \\ p_g(r) & \text{for } r \in (R_h, R), \end{cases} \tag{8}$$

where p_h is assumed to be constant over the cross-sectional area of the central hole $S_h = \pi R_h^2$. Following the approach in [9], the acoustic pressure in the air gap is governed by the wave equation

$$\Delta_r p_g(r) + \chi^2 p_g(r) = \zeta\, \xi(r), \tag{9}$$

where ζ is an auxiliary source term and χ is a complex wavenumber that accounts for thermoviscous losses, as described in [9]. The solution to equation (9) is sought in the form

$$p_g(r) = A J_0(\chi r) + B Y_0(\chi r) + \sum_n p_n \Psi_n(r), \tag{10}$$

where A and B are integration constants determined by the following boundary conditions: (i) zero acoustic velocity at $r = R$, (ii) continuity of the acoustic pressure at $r = R_h$, and (iii) continuity of the volume velocity at $r = R_h$.

2.4 Coupling between membrane displacement and acoustic pressure

Substituting the expression for the acoustic pressure $p(r)$ into equation (7), the modal coefficients are obtained as follows

$$\frac{T(K^2 - K_n^2)}{2\pi}\xi_n = b_n + \sum_{mn} \xi_m C_{mn}, \tag{11}$$

which can be rewritten in matrix form as

$$\{[\mathbb{U}] - [\mathbb{C}]\}(\Xi) = (B), \tag{12}$$

where $[\mathbb{C}]$ is the matrix composed of elements C_{mn}, and $[\mathbb{U}]$ is a diagonal matrix with elements $T(K^2 - K_n^2)/2\pi$. The vectors (Ξ) and (B) represent the modal coefficients ξ_n and the excitation terms $b_n = p_{inc}\int_0^R \Psi_n(r) r \mathrm{d}r$, respectively.

2.5 Mean displacement and pressure sensitivity

The mean value of the membrane displacement over the active area of the fixed electrode S_e is given by

$$\begin{aligned}\tilde{\xi} =& \frac{1}{S_e}\iint_{S_e} \xi(r)\mathrm{d}S_e = \\ =& \frac{2\pi}{S - S_h}\sum_n \xi_n \frac{RJ_1(K_nR) - R_hJ_1(K_nR_h)}{K_n\sqrt{\pi}RJ_1(K_nR)},\end{aligned} \tag{13}$$

where $S_e = S - S_h$.

Finally, the acoustic pressure sensitivity of the microphone is expressed as

$$\sigma = \frac{U_0}{p_{inc}}\frac{\tilde{\xi}}{h_g}. \tag{14}$$

2.6 Theoretical results

The results of the linear microphone model are presented in this section. The physical properties of air and the geometrical and material parameters of the microphone used in the theoretical calculations are summarized in Tables 1 and 2, respectively.

Table 1. Properties of the air

Parameter	Value	Unit
Adiabatic sound speed c_0	343.2	m/s
Air density ρ_0	1.2	kg/m^3
Shear dyn. viscosity μ	$1.8{\cdot}10^{-5}$	Pa·s
Thermal conductivity λ_h	$24{\cdot}10^{-3}$	W/(m·K)
Specific heat at constant press. per unit of mass C_p	1005	J/(kg·K)
Ratio of specific heats γ	1.4	-

Table 2. Dimensions of the system and material properties of the moving component

Parameter	Value	Unit
Membrane radius R	$18{\cdot}10^{-3}$	m
Membrane thickness h_m	$25{\cdot}10^{-6}$	m
Air-gap thickness h_g	$230\cdot10^{-6}$	m
Radius of the hole R_h	$0.8{\cdot}10^{-6}$	m
Length of the hole R_h	$1.6{\cdot}10^{-6}$	m
Back cavity volume V_c	$7.74{\cdot}10^{-6}$	m^3
Membrane density ρ_m	1944	kg/m^3
Membrane tension T	116.27	N/m^1
Polarization voltage U_0	165	V

The absolute value of the acoustic pressure sensitivity, expressed in decibels and computed using the linear analytical model described above, is shown in Figure 2 (blue curve). This analytical result is compared with a reference numerical model based on the finite element method (FEM), formulated according to [11] and implemented in the Comsol Multiphysics software (red dots). The comparison demonstrates good agreement between the two models when the first 10 modes are included in the analytical solution.

Using the calculated mean displacement (13), the nonlinear output voltage of the microphone (3) was computed, and the levels of the first three harmonic components were determined at each frequency. These frequency-dependent output levels, calculated for an incident acoustic pressure of $p_{inc} = 1$ Pa, are presented in Figure 3. A relatively large level difference between the harmonic components can be observed at this input pressure.

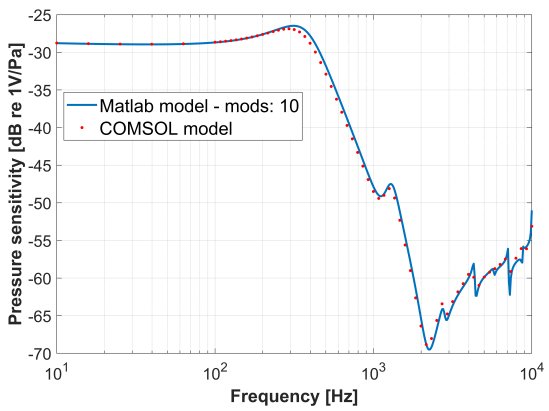


Figure 2. Comparison of the bsolute value of the acoustic pressure sensitivity in dB, calculated analytically (blue curve) and numerically using COMSOL Multiphysics (red dots).

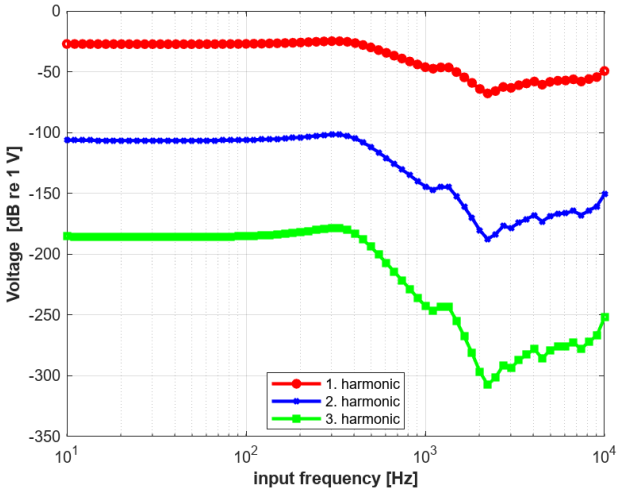


Figure 3. Absolute values of the harmonic components of the microphone output voltage in dB for $p_{inc} = 1$ Pa: 1st (fundamental) harmonic (red curve), 2nd harmonic (blue curve), and 3rd harmonic (green curve).

3. EXPERIMENTAL DEVICE AND MEASUREMENT SETUP

The experimental transducer (see Figure 4) consists of a circular membrane made of aluminum-metallized plastic foil, clamped at its periphery within a rigid 3D-printed frame. The fixed electrode, separated from the membrane by spacers forming the air gap, is fabricated from a printed circuit board (PCB) metallized with copper and coated with a thin gold layer on the side facing the membrane. The opposite side of the PCB hosts electronic components for signal amplification and power supply. A 3D-printed component forms the backing cavity and includes a threaded mechanism, which, when tightened, presses the PCB and spacers against the membrane, thus adjusting its tension. The dimensions of the system correspond to those listed in Table 2.

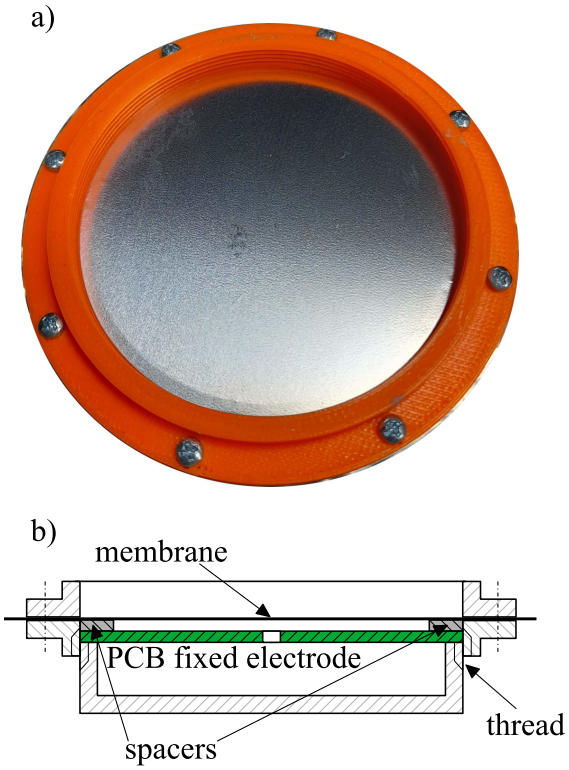


Figure 4. The experimental transducer: (a) top-view photograph; (b) schematic view of the assembly.

The measurement setup is shown in Figure 5. The experimental transducer, together with a reference microphone (B&K 4944-B, 3% THD at 170 dB SPL), is placed inside a measurement chamber between two loudspeakers (Visaton FR 12) arranged in a push-push configuration to generate high sound pressure levels with low distortion. The loudspeakers and both microphones are connected, via amplifiers, to a sound card (RME Fireface

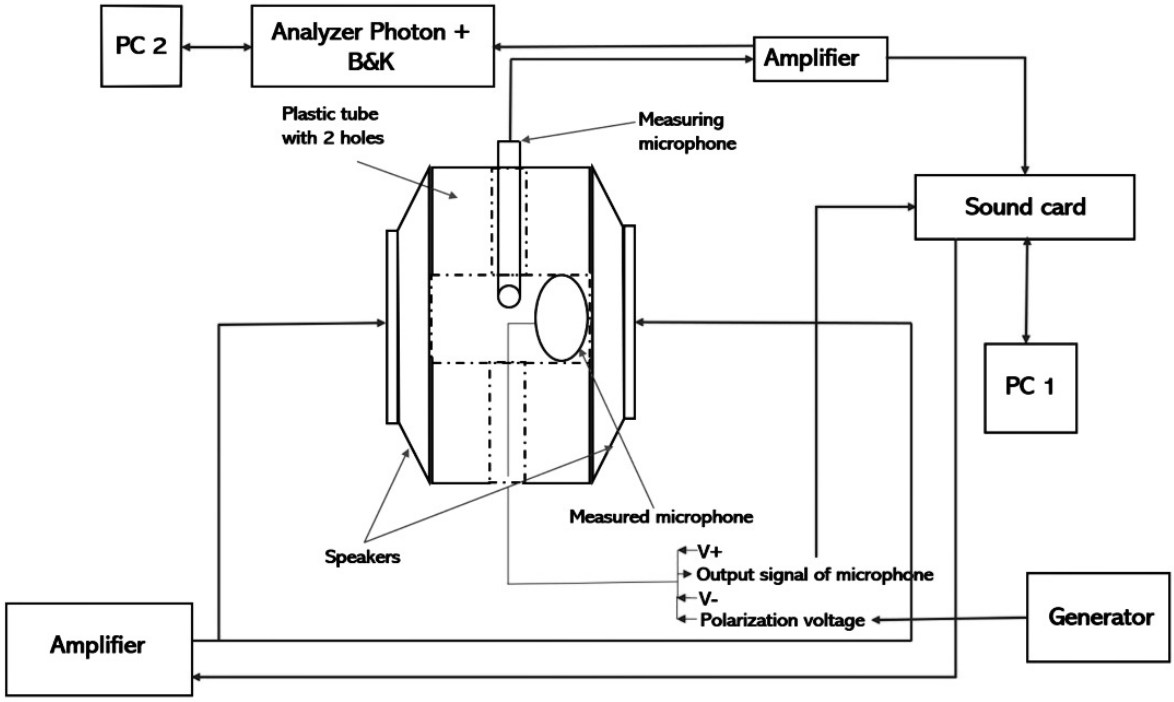


Figure 5. Schematic view of the measurement setup.

UCX), which is interfaced with computer PC1. Additionally, the output of the reference microphone is connected through an amplifier to a B&K Photon+ analyzer, which is linked to computer PC2 to monitor the exact sound pressure level inside the measurement chamber. To ensure purely harmonic excitation, a nonlinear harmonic correction technique was applied [7], effectively suppressing all undesired higher-order harmonics to the noise level. As a result, any nonlinearities observed in the output signal of the tested microphone originate solely from the microphone itself.

4. RESULTS

The measurement procedure described in the previous section was repeated for various levels of incident acoustic pressure and at different frequencies. For each measurement, the levels of the first three harmonics were extracted from the recorded output voltage of the tested microphone using a Fast Fourier Transform (FFT).

Figure 6 presents the results obtained at 110 Hz, which lies below the first resonance frequency of the transducer, for incident acoustic pressure levels ranging from 100 to 140 dB SPL. The points indicate the measured values for the first (blue points), second (orange points), and third (green points) harmonic components. The continuous lines represent the theoretical predictions based on the model described in the preceding sections. Similarly, Figure 7 shows results measured at 1 kHz, which is above the first resonance frequency of the transducer, for pressure levels between 90 and 130 dB SPL.

In both figures, the first and second harmonics are accurately predicted by the model. However, the third harmonic is observed to be between several decibels and approximately 40 dB higher than the levels predicted by the model. This discrepancy indicates that the third harmonic is influenced by additional sources of nonlinearity not accounted for in the analytical model, such as varying damping in the air gap with changing thickness or acoustic nonlinearities at high sound pressure levels within the gap.

5. CONCLUSION

An analytical model of an electroacoustic transducer with a circular membrane and a fixed electrode was developed, incorporating the coupling between membrane displace-

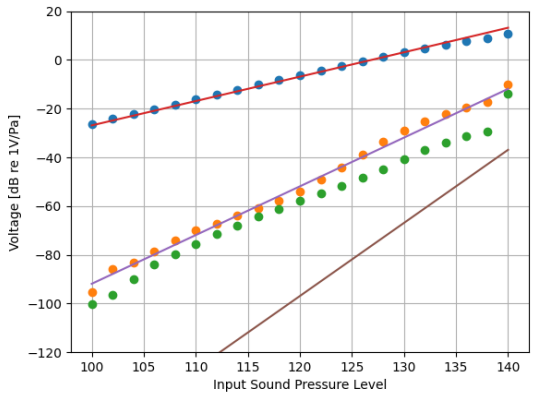


Figure 6. First three harmonic components of the microphone output voltage for different input sound pressure levels at 110 Hz.

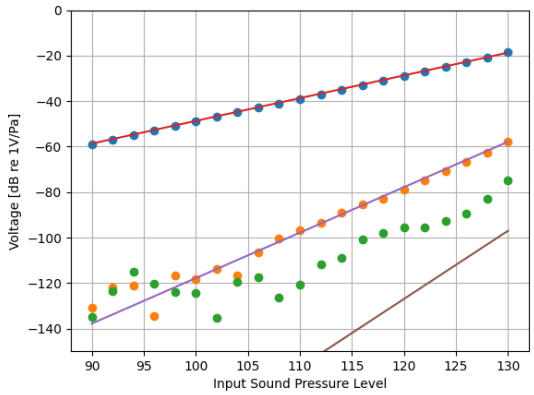


Figure 7. First three harmonic components of the microphone output voltage for different input sound pressure levels at 1 kHz.

ment and acoustic pressure in the air gap, as well as nonlinearities due to time-varying capacitance. The membrane response was expressed via eigenfunction expansion, leading to a formulation of the nonlinear output voltage. The model's predictions of acoustic pressure sensitivity were validated against numerical FEM results from COMSOL Multiphysics, showing good agreement when using the first ten modes.

An experimental transducer was built and measurements were carried out using harmonic excitation with nonlinear correction to isolate the transducer's intrinsic nonlinearities. The results confirmed that the model accurately predicts the first and second harmonic components. However, the third harmonic was significantly underestimated, indicating the presence of additional nonlinear effects, such as pressure-dependent damping or nonlinear acoustics in the air gap, not captured by the current model.

6. ACKNOWLEDGMENTS

This work was supported by grant No. SGS23/185/OHK3/3T/13 of the Czech Technical University in Prague.

7. REFERENCES

[1] A. Dessein, *Modelling distortion in condenser microphones*. PhD thesis, Technical University of Denmark, DTU, DK-2800 Kgs. Lyngby, Denmark, 2009.

[2] H. Pastillé, "Electrically manifested distortions of condenser microphones in audio frequency circuits," *J. Audio Eng. Soc.*, vol. 48, no. 6, pp. 559–563, 2000.

[3] E. Frederiksen, "System for measurement of microphone distortion and linearity at very high sound levels," *The Journal of the Acoustical Society of America*, vol. 110, pp. 2670–2670, 11 2001.

[4] A. Novak and P. Honzík, "Measurement of nonlinear distortion of mems microphones," *Applied Acoustics*, vol. 175, p. 107802, 2021.

[5] E. Frederiksen, "Reduction of non-linear distortion in condenser microphones by using negative load capacitance," in *Proceedings of InterNoise 96*, (Liverpool, UK), pp. 2679–2684, Institute of Noise Control Engineering, June 30–August 2 1996.

[6] P. Honzík and A. Novak, "Reduction of nonlinear distortion in condenser microphones using a simple post-processing technique," *The Journal of the Acoustical Society of America*, vol. 157, pp. 699–705, February 2025.

[7] A. Novak, P. Lotton, and L. Simon, "A simple predistortion technique for suppression of nonlinear effects in periodic signals generated by nonlinear transducers," *Journal of Sound and Vibration*, vol. 420, pp. 104–113, 2018.

[8] M. Bruneau, A.-M. Bruneau, Z. Škvor, and P. Lotton, "An equivalent network modelling the strong coupling between a vibrating membrane and a fluid film," *Acta Acustica*, vol. 1994, pp. 223–232, 06 1994.

[9] P. Honzík, A. Podkovskiy, S. Durand, N. Joly, and M. Bruneau, "Analytical and numerical modeling of an axisymmetrical electrostatic transducer with interior geometrical discontinuity," *The Journal of the Acoustical Society of America*, vol. 134, pp. 3573–3579, 11 2013.

[10] M. Bruneau and T. Scelo, *Fundamentals of Acoustics*. London: ISTE, 2006.

[11] N. Joly, "Finite element modeling of thermoviscous acoustics on adapted anisotropic meshes: Implementation of the particle velocity and temperature variation formulation," *Acta Acustica united with Acustica*, vol. 96, no. 1, pp. 102–114, 2010.

DOI: 10.61782/fa.2025.0195



FORUM ACUSTICUM
EURONOISE 2025

CHARACTERIZATION OF PLANAR CIRCULAR AND SQUARE MEMS MICROPHONE ARRAYS FOR LOW-POWER ACOUSTIC APPLICATIONS

Ricardo Moreno[1*] **Jorge Ortigoso-Narro**[2] **Marco Raiola**[1]
Luis A. Azpicueta-Ruiz[2] **Daniel de la Prida**[3]

[1] Department of Aerospace Engineering, Universidad Carlos III de Madrid, Spain
[2] Department of Signal Theory, Universidad Carlos III de Madrid, Spain
[3] Grupo de Investigación en Acústica Arquitectónica, Universidad Politécnica de Madrid, Madrid, Spain

ABSTRACT

Advancements in microphone arrays are transforming acoustic sensing and innovating applications such as speech enhancement, beamforming, source localization, and environmental noise monitoring. On the way to developing low-cost phased arrays with numerous sensors, MEMS microphones have become a preferred solution whose distribution and positioning can boost their acoustic capabilities. The performance of both circular concentric and square grid geometries is characterized. A square grid array prioritizes low-cost scalability for high-efficiency data acquisition, while the circular concentric design optimizes directivity. Both compared arrays use the same MEMS microphone model and electronic configuration, but differ in the number of elements and aperture size. The microphone model used for both arrays allows using Time-Division Multiplexing for streamlined data collection through a single data line with an I^2S interface and integrated PCB design. The frequency response, directivity, and data transfer efficiency are analyzed by conducting experiments with a sound source at various positions within an anechoic chamber. The results demonstrate trade-offs between geometric configurations, providing valuable insight into the design of low-power, flexible, and scalable acoustic sensing systems.

*__Corresponding author__: jonmoren@ing.uc3m.es.

__Copyright__: ©2025 R. Moreno et al. This is an open-access article distributed under the terms of the Creative Commons Attribution 3.0 Unported License, which permits unrestricted use, distribution, and reproduction in any medium, provided the original author and source are credited.

Keywords: *MEMS, Phased Microphone Arrays, Time-Division Multiplexing, Inter-IC Sound*

1. INTRODUCTION

The growing demand for low-cost and scalable acoustic sensing systems has fueled advancements in microphone array technology. These arrays are essential tools for applications such as noise source identification, beamforming, and environmental noise monitoring [1, 2]. Among the available technology solutions, MEMS (Micro-Electro-Mechanical Systems) microphones have gained prominence due to their reduced and compact size, low-power consumption, affordability, and integration versatility with development boards. The ease of deployment in various geometric configurations significantly influences the array's spatial resolution, directivity, and overall performance.

A critical challenge in developing massive acoustic cameras is optimizing the microphone distribution while ensuring efficient data capturing [3]. To diagnose noise generation, expensive FPGA-based acquisition systems commonly use the Inter-IC Sound (I^2S) protocol. However, standard I^2S interfaces can only support up to two microphone channels per data line, requiring multiple physical connections for larger arrays [4]. To address this limitation, the Time-Division Multiplexing (TDM) interface extends I^2S capabilities by allowing up to 16 microphone channels to be transmitted on a single data line. Thus, the number of connections can be significantly reduced, streamlining system integration and enabling a cost-effective and scalable architecture. By using

a multiplexed acquisition system, we can systematically assess the performance of different microphone distributions while ensuring consistency in sensor characteristics.

To evaluate the impact of these configurations, we compare two distinct microphone array geometries: a circular concentric array CCA and a square grid array SGA. Both arrays utilize the same MEMS microphone model and electronic setup, differing only in their spatial arrangement, number of elements, and aperture. These configurations are designed as a complete acquisition system intended for use with a low-cost microprocessor development board. The acquired signals must undergo post-processing after acquisition, meaning that all analyses are conducted offline. As it can be seen in Fig. 1, the CCA features a completely solid design, whereas the SGA distributes its microphones along a grid structure, and therfore is expected to behave more transparently concerning wave incidence.

Experiments in this study focus on analyzing the frequency response of each microphone within both array configurations to determine potential variations across the array, and also considering different orientations with respect to the noise source, i.e., the array directivity. Additionally, we assessed whether the multiplexing process impacts measurement accuracy. To demonstrate the synchronization of the multiplexed system, we evaluate its functionality with the worst-case scenario (SGA), where signals are stressed at the maximum trace length recommended by the manufacturer and the one that multiplexes the maximum number of channels supported. These results will provide insights into the reliability of TDM acquisition for scalable, low-power microphone arrays and contribute to optimizing array design for acoustic sensing applications.

The breakout of this document is as follows: Section 2 describes the design of both microphone arrays, explaining the criteria behind their geometries and detailing the composition of the acquisition system. Section 3 outlines the methodology used to evaluate their performance, focusing on three key aspects: frequency response, directivity, and TDM synchronization. In Section 4, the results of these evaluations are presented, supported by graphs and performance parameters. Finally, Section 5 provides a discussion of the findings and summarizes the main conclusions of this work.

2. MICROPHONE ARRAY DESIGNS

2.1 Hardware Development

The modular SGA design has been explained in detail in [5]. Such array follows a scalable architecture consisting of four identical modules, each containing 16 daisy-chain microphones model ICS-52000 [6]. For this study, we assessed the performance of one 16-microphone submodule. Microphones of this array design are evenly spaced and arranged in a 4×4 square grid, with $62.5\,\mathrm{mm}$ between adjacent microphones. To minimize propagation delay mismatches, all electrical connections adhere strictly to the manufacturer's recommendations, with trace lengths set to the maximum allowable limits and matched impedance at clock frequency.

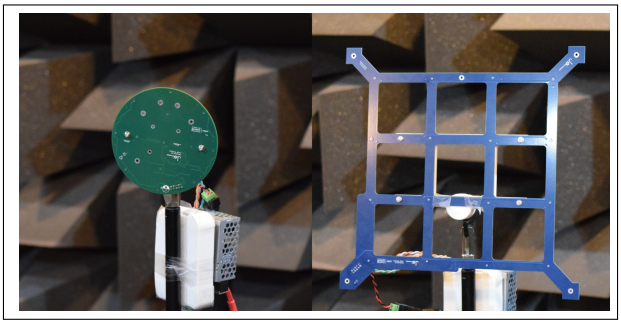


Figure 1. On the left-hand side, the CCA composed of 13 MEMS microphones. The blue printed circuit board corresponds to the SGA with 16 microphones distributed in a Cartesian grid.

Beyond electrical considerations, the SGA's mechanical design was developed to be minimally intrusive to the test environment, reducing the risk of potential airborne disturbances. The printed circuit board occupies a considerable surface area, which could reflect sound energy and introduce pressure variations that degrade acoustic measurements. To counteract this, sections of the structure between microphones have been removed, allowing air to pass freely through the array. This design choice minimizes reflections and potential aerodynamic artifacts. By balancing electrical, spatial, and mechanical constraints, this microphone array optimizes acoustic performance and modular scalability. Moreover, if this microphone array design were used for beamforming applications, its aperture size and microphone separation would impose limitations, e.g., reduced spatial resolution and grating lobes generation, for frequencies under

$f_L \approx 1\,\mathrm{kHz}$ and above $f_H \approx 2.7\,\mathrm{kHz}$, respectively.

A different approach is observed in the CCA, which consists of 13 microphones: one at the center, four distributed along a $2.5\,\mathrm{cm}$ radius, and eight along a $4.5\,\mathrm{cm}$ radius. Compared to SGA from a theoretical point of view, the microphone distribution of this CCA would offer improved directionality and isotropic coverage, making it more suitable for applications requiring omnidirectional sound capture and robust source localization [7], although it is expected that its solid design will affect the directivity in the high frequency range. Furthermore, due to its short and non-uniform spacing, the array may introduce more spatial aliasing effects depending on the frequency range of interest. Additionally, its smaller aperture limits its ability to resolve lower frequency sources as effectively as the larger square array. For this setup, the approximate lower and upper frequency bounds are $f_L \approx 3.8\,\mathrm{kHz}$ and $f_H \approx 8.5\,\mathrm{kHz}$, respectively.

2.2 Data Transmission to BeagleBone Black Board

To handle the signal acquisition, a BeagleBone Black board (BBB) was chosen as the main processing unit. The primary reason for this selection was its Multichannel Audio Serial Port (McASP), which enables seamless interfacing with TDM digital audio streams. Since the MEMS microphones used in both designs output data via this protocol, the acquisition system must be capable of demultiplexing the interleaved audio channels correctly. The BBB, running a Linux-based system, provided this capability while allowing efficient real-time data acquisition.

This transmission format implies that the board manages precisely a bit clock (BCK) and frame synchronization (FS) signals. The data transfer rate is defined by BCK, while FS triggers the start of the first microphone. This means that the following microphone has to wait until the first microphone finishes writing a 32-bit word and commands the word select output (WSO), as shown in Fig. 2.

For a fair comparison between both microphone arrays, the acquisition system was configured to record 16 channels at a sample frequency of $8\,\mathrm{kHz}$. In the case of the 13-microphone CCA, the last three channels were ignored during processing.

3. MEASUREMENT PROCEDURES

Measurements were carried out in an anechoic chamber to ensure a controlled acoustic environment, free from unwanted reflections and external noise. This facility is located at the Signal Theory and Communications Department of the University Carlos III de Madrid. The chamber's interior dimensions of $6.5\,\mathrm{m} \times 4.5\,\mathrm{m} \times 3.85\,\mathrm{m}$, combined with $60\,\mathrm{cm}$-long absorbing wedges, effectively attenuate reflections across a wide frequency range.

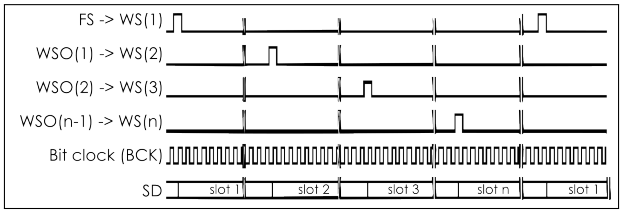


Figure 2. In the microphone datasheet, the terminology describes the Word Select (WS) and Word Select Output (WSO) as the propagation of the Frame Sync (FS) throughout the daisy-chain system. This pulse triggers the bit writing of each microphone to the Serial Data line (SD) at the Bit Clock rate (BCK), sequentially.

3.1 Frequency Response

The frequency response of both microphone arrays was evaluated following two distinct procedures, both using a domestic speaker as a sound source, specifically an Alexa Echo Pop, and generating a white noise signal.

In the first procedure, each microphone was assessed individually at a distance of $1\,\mathrm{m}$ from the sound source. The objective of this measure was to compare the magnitude of the frequency response of each microphone when positioned at the same location relative to the source. To achieve precise positioning, a cross-line laser was used to mark the exact spot on each microphone, always keeping the 1-meter distance throughout the procedure, as shown in Fig. 3. Measurements were conducted sequentially, displacing the arrays in a parallel plane to the source position, and ensuring that only the channel that corresponds to the microphone positioned at the spot is analyzed at a time.

We calculate the deviation in the frequency response of the i-th microphone using $\Delta H_i(f)$ as figure of merit, denoted as

$$\Delta H_i(f) = H_i(f)\ (\mathrm{dB}) - H_{\mathrm{av}}(f)\ (\mathrm{dB}), \qquad (1)$$

where $H_i(f)$ represents the magnitude of the i-th microphone in decibels, and $H_{\mathrm{av}}(f)$ is the reference value to compare, obtained as the average of all the frequency re-

sponses magnitudes across the array, also expressed in decibels.

To ensure the stability of the sound source throughout the measurements, a Brüel & Kjær Type 2250 Light Hand-Held Sound Frequency Analyzer was placed at a fixed reference point within the anechoic chamber (see Fig. 4). This device monitored continuously the level of the sound source to allow a source stability correction in the event of a slight change in the loudspeaker's power efficiency.

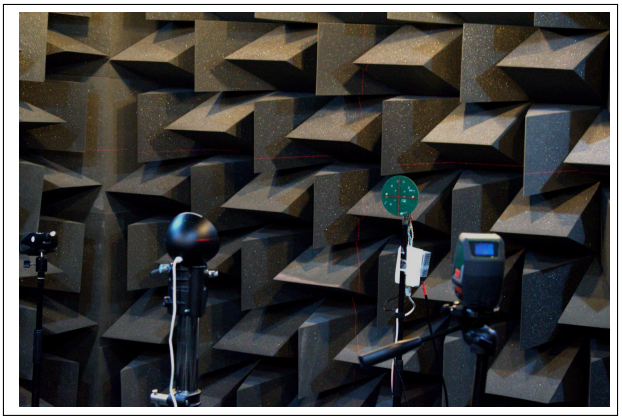


Figure 3. Cross-line laser positioning to maintain the measurement spot at 1 m from the sound source. In the picture, the laser aims at the central microphone of the concentric array.

In the second procedure, the microphone array was positioned at a greater distance of 2.5 m from the sound source. The purpose of this measurement was to assess the collective response of the array, assuming that at this distance, the sound waves would approximate a plane wavefront, meaning that all microphones would receive the signal with minimal differences in amplitude and frequency content due to source directivity. This measurement approach allowed for the characterization of the array's response under conditions where spatial variations in the sound field were minimized, avoiding an iterative relocation of the array. All the recorded signals from the microphones were compared to determine variations in frequency response across the array and to evaluate the consistency of microphone performance.



Figure 4. SGA positioned at one meter from the sound source. A sound frequency analyzer was placed at a fixed position to control the sound source's stability.

3.2 Directivity

The directivity of both microphone arrays was measured by rotating the array in 30-degree increments relative to the sound source in the horizontal plane. The sound-receiver distance was marked at 2.5 m. The frequency response at each angle was normalized by the response measured at 0 degrees (frontal incidence), representing the direction of maximum sensitivity [8]. Specifically, we define the directivity function $D(\phi, f)$, quantified in decibels, as

$$D(\phi, f) = H_{\text{av}}(\phi, f)\ (\text{dB}) - H_{\text{av}}(0^\circ, f)\ (\text{dB}), \qquad (2)$$

where $H_{\text{av}}(\phi, f)$ is the average of the frequency response magnitudes across all microphones at a specific rotational angle ϕ and frequency f, expressed in decibels. The term, $H_{\text{av}}(0^\circ, f)$, represents the reference response measured when the microphone cavities and PCB orifices directly face the sound source ($\phi = 0^\circ$), also in decibels.

3.3 Time-Division Multiplexing Synchronization

An additional experiment was conducted to validate the integrity of the TDM acquisition process and the phase response of the microphones, which consisted of placing the microphone array at a distance of 2.5 m from the sound source, emitting a low-frequency tone through the speaker. Thus, potential time delays between channels can be visualized by comparing the recorded signals across

the microphones. Since the TDM protocol transmits microphone signals sequentially, a key concern was whether the multiplexing process introduced any artifacts or synchronization errors by analyzing the phase alignment of the recorded signals.

4. RESULTS

4.1 Microphone Frequency Response

All presented spectral results were processed using one-third octave band filtering for a clearer comparison and interpretation.

As detailed in 3.1, the individual microphone response was captured at a time and compared to the average, as Equation (1) indicates. Figure 5 displays the range of values in which all the frequency responses are found, observed across the entire set of microphones, as well as selected examples from individual microphones of the CCA. For the SGA, the same experiment was performed for each of its 16 microphones, whose results are displayed in Figure 6.

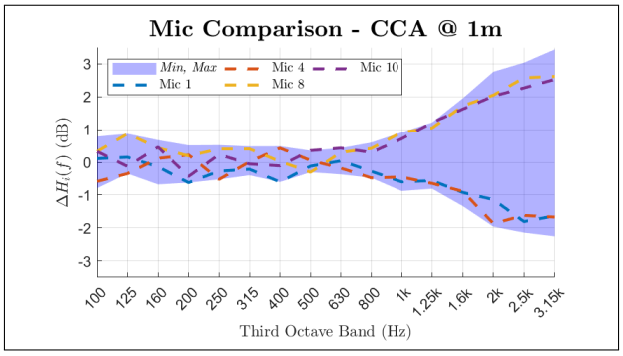


Figure 5. Comparison of the Frequency Response of microphones 1, 4, 8, and 10 of the CCA placed at 1 m from the source. The purple region corresponds to the minimum and maximum frequency response values.

Fig. 7 shows the frequency response evaluated following our second procedure. In this case, with the array positioned at 2.5 m from the source, all microphones were assessed simultaneously, under conditions approximating a plane wavefront. It is important to note that this second procedure was carried out as an alternative to the first one, aiming to reduce its associated uncertainty due to its iterative process which involves the array repositioning for each microphone, and that could be affected by small

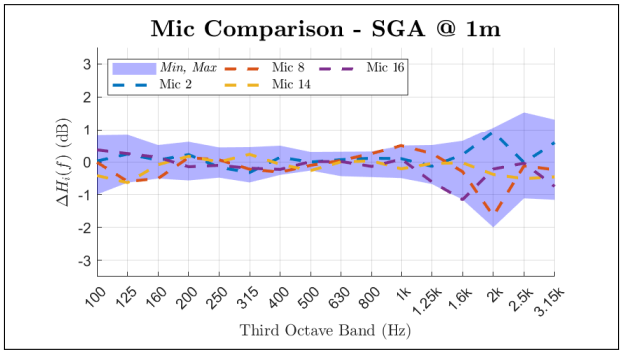


Figure 6. Comparison of the individual frequency response of microphones 2, 8, 14, and 16 of the SGA placed at 1 m from the source. The purple region corresponds to the minimum and maximum frequency response values.

changes in the source stability. For this reason, we only present here the results for the SGA.

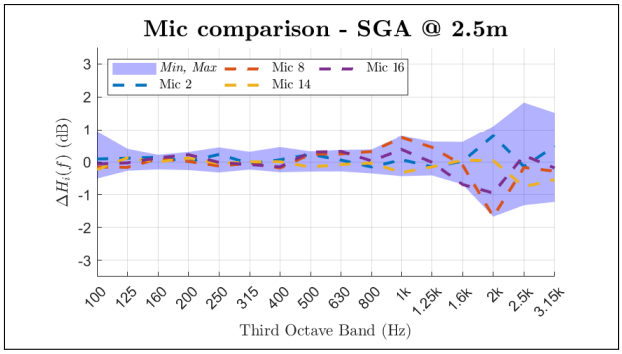


Figure 7. Comparison of the simultaneous frequency response of microphones 2, 8, 14, and 16 of the SGA placed at 2.5 m from the source. The purple region corresponds to the minimum and maximum frequency response values.

4.2 Directivity

The directivity measurement was carried out rotating both arrays in 30° increments over the horizontal axis, keeping a fixed 2.5 m distance to the sound source. The 0° orientation was used as the reference since it aligns with the main axis of sensitivity, as stated in (2). Figures 8 and 9 show the difference between the average response relative

to the reference direction and the rotation angle of ϕ for the CCA and SGA, respectively. Four selected frequency bands are also displayed to ease the visualization.

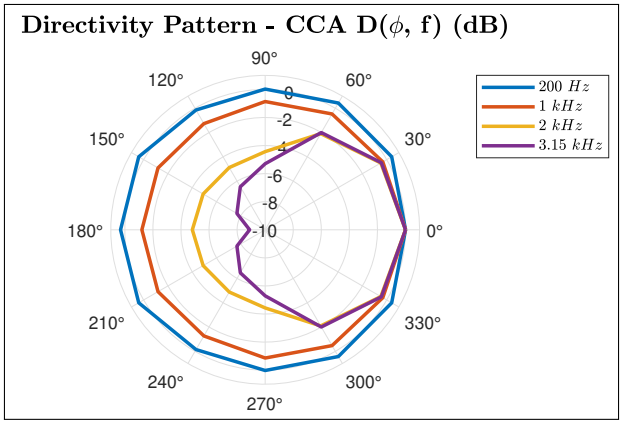


Figure 8. Directivity pattern of the frequency response of the CCA, measured at 2.5 m for the 1/3 octave bands of 200 Hz, 1 kHz, 2 kHz, and 3.15 kHz.

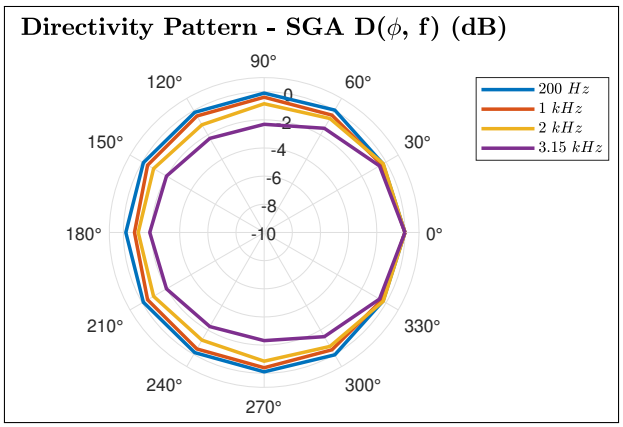


Figure 9. Directivity pattern of the frequency response of the SGA, measured at 2.5 m for the 1/3 octave bands of 200 Hz, 1 kHz, 2 kHz, and 3.15 kHz.

4.3 TDM Synchronization

The integrity of the TDM data acquisition system was examined using a low-frequency signal, which has to be at least higher than the anechoic chamber cut-off frequency, i.e., above 143 Hz. Two sinusoidal signals were tested at 200 Hz and 500 Hz, chosen for its relatively long period (5 ms and 2 ms respectively) compared to the sampling interval (125 µs at the 8 kHz sampling rate). Given that the SGA poses the worst-case scenario, with 16 audio channels and the longest data line traces, it was chosen for this test. The array was positioned at 2.5 m, minimizing the paths differences with respect to the wavelength. To quantify synchronization offsets $\Delta(\tau)$, the signal from each microphone channel was compared against the signal from microphone 1, which served as a stable reference for being the first channel in the TDM data stream. This comparison was performed using a cross-correlation calculated over sliding windows of 600 samples. The analysis was systematically swept along the entire signal length for all microphones. Fig. 10 presents the results of this analysis at 200 Hz, only plotting the calculated time delay evolution of the reference microphone and any detected to be off-sync. For the test using 500 Hz signal, no off-sync was detected.

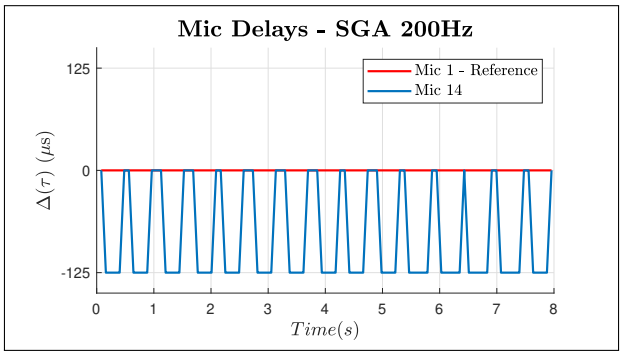


Figure 10. Delay pattern over time using a 200 Hz signal with SGA. Delays are shown in steps of 125 µs due to the sample frequency employed in this acquisition.

As can be seen, only channel 14 shows a fluctuation in synchronization, appearing to drift in and out of phase alignment with the reference channel. Fig. 11 provides a snapshot in the time domain, illustrating a moment when microphone 14's signal is visibly delayed compared to microphone 1, confirming the detected synchronization drift.

5. DISCUSSION AND CONCLUSIONS

This study presents an experimental evaluation of two microphone array prototypes (CCA and SGA), developed using identical MEMS sensor models and the same data transmission protocol to the same BeagleBone Black

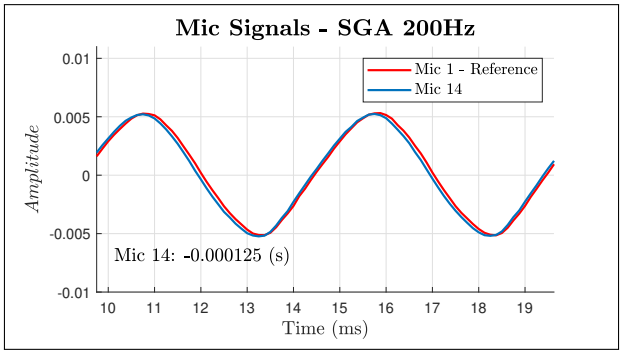


Figure 11. Snapshot in the time domain of waveforms from microphones 1 and 14 when desynchronized. Note that both are overlaid at the moment where the difference becomes most evident.

board, in order to ensure a fair and consistent comparison. The characterization experiments demonstrated the overall functional performance of both the CCA and SGA. Individual microphone frequency responses showed good consistency across both arrays, particularly within the stable 100 Hz to 1 kHz range. Minor deviations observed at higher frequencies are likely due to small positioning variations and inherent microphone differences, while the CCA's response above 1 kHz suggested additional scattering effects, possibly influenced by its solid central mounting board. This structural component may introduce diffraction or reflection that becomes more relevant as frequency increases.

Comparing the former procedure with measurements taken at 2.5 m with SGA, results show a similar behavior, with an even more uniform frequency response, especially when compared to sequential measurements taken at 1 m. Rather than thinking in different frequency responses depending on the distance, we consider that this difference could be caused by a reduced uncertainty in the procedure because of simultaneous measurements that avoids the reallocation of the array and prevent small fluctuations in the emitted sound power of the source. Nevertheless, small differences remained at higher frequencies, indicating that individual microphone characteristics still play a role even under more ideal conditions.

Directivity analysis allows concluding that SGA exhibits a sensitivity with lower dependency on the angle. This behavior seems related to the construction of the arrays (solid design for CCA vs grid structure for SGA). In fact, for the CCA, rotation in 30º increments revealed significant attenuation of high-frequency content when the array was turned around 180º from the source. These results underline the impact of array geometry, construction, and orientation, particularly in aeroacoustic environments where source directionality is a key factor.

The TDM synchronization test for SGA using a 200 Hz signal revealed detectable, periodic time delays for at least one channel relative to the reference. While these delays are bounded by the system's sampling step of 125 µs, their presence suggests that in applications requiring very precise phase alignment, such as beamforming or source localization, potential channel-specific compensation must be applied. That said, the overall results showed that the multiplexing process did not introduce significant artifacts, and most microphones remained well-aligned over time, especially those that are at the end of the stream (microphones 15 and 16), which could have been the most delayed. As a conclusion, a deeper study about the delay evaluation should be performed in order to conclude if this behavior is only related to the phase response of the microphone.

In summary, the experiments provide a solid baseline for understanding the operational characteristics of both arrays. While their overall behavior supports their use in typical aeroacoustic applications, special attention should be given to high-frequency variability, directional response, and synchronization fidelity when designing experiments that rely on fine spatial or temporal resolution.

6. ACKNOWLEDGMENTS

This work has been supported by Grant TED2021-130909A-I00, funded by MCIN/AEI/10.13039/501100011033 and by the European Union NextGenerationEU/PRTR.

7. REFERENCES

[1] J. Yan, C. Chen, Z. Wu, X. Ding, and L. Lou, "An acoustic localization sensor based on mems microphone array for partial discharge," *Sensors*, vol. 23, no. 3, 2023.

[2] J. Picaut, A. Can, N. Fortin, J. Ardouin, and M. Lagrange, "Low-cost sensors for urban noise monitoring networks—a literature review," *Sensors*, vol. 20, no. 8, 2020.

[3] I. Hafizovic, C.-I. C. Nilsen, M. Kjølerbakken, and V. Jahr, "Design and implementation of a mems mi-

crophone array system for real-time speech acquisition," *Applied Acoustics*, vol. 73, no. 2, pp. 132–143, 2012.

[4] M. Turqueti, J. Saniie, and E. Oruklu, "Mems acoustic array embedded in an fpga based data acquisition and signal processing system," in *2010 53rd IEEE International Midwest Symposium on Circuits and Systems*, pp. 1161–1164, 2010.

[5] J. O. Narro and R. Moreno, "64-microhpone module for a massive acoustic camera," in *Proc. of the Tecniacustica*, 2024.

[6] Invensense, "ICS-52000 Datasheet."

[7] Z. Prime and C. J. Doolan, "A comparison of popular beamforming arrays," in *Proc. of ACOUSTICS*, 2013.

[8] L. L. Beranek and T. Mellow, *Acoustics: sound fields and transducers*. Academic Press, 2012.

DOI: 10.61782/fa.2025.0701



FORUM ACUSTICUM
EURONOISE 2025

PRESSURE-COMPARISON CALIBRATION OF MEMS MICROPHONES IN THE REVERBERATION CHAMBER

Fabio Saba[1*] **María Campo-Valera**[2*] **Mario Corallo**[1]
Giovanni Durando[1]
[1] Istituto Nazionale di Ricerca Metrologica (INRiM), Torino, 10135, Italy
[2] Telecommunication Research Institute (TELMA), Universidad de Málaga, 29010 Málaga, Spain

ABSTRACT

The demand of metrological traceability to the International System of units (SI) for Micro-Electro-Mechanical Systems (MEMS) microphones poses new challenges for the development of reliable, fast, and cost-effective calibration methods. This work proposes novel solutions to meet these requirements, improving the capabilities of secondary calibration methods by pressure-comparison. Specifically, it addresses the effects of acoustic field irregularities and different frequency response of microphones under comparison in the determination of MEMS microphone sensitivity in the reverberation chamber. We present numerical techniques for predicting the sound pressure distribution within the narrow gap between reference and test microphones, along with the experimental evaluation of the deviation of calibration results when microphones of different frequency response characteristics are compared. The validity of the measurements in the reverberation chamber, is demonstrated comparing the calibration results obtained by different implementations of the pressure-comparison method, like in closed pressure-couplers and in the anechoic chamber.

Keywords: *MEMS microphone, sound field corrections, pressure-comparison calibration, reverberant chamber, diffuse field.*

**Corresponding author*: *f.saba@inrim.it, maria.campo@ic.uma.es.*

***Copyright**: ©2025 Fabio Saba et al. This is an open-access article distributed under the terms of the Creative Commons Attribution 3.0 Unported License, which permits unrestricted use, distribution, and reproduction in any medium, provided the original author and source are credited.*

1. INTRODUCTION

MEMS microphones are critical components in various acoustic applications, prized for their compact size, low power consumption, and cost-effective production [1, 2]. They are commonly used in consumer electronics and wireless sensor networks, playing a vital role in urban and natural soundscape analysis [3, 4]. Additionally, their small size makes them ideal for sound source localization in applications like seismic detection, traffic monitoring, and security systems.

Traditional calibration methods, like the pressure-comparison method, struggle to fully account for geometric differences between MEMS and reference microphones, leading to systematic errors, especially at high frequencies. These methods also fail to consider the complex acoustic interactions within pressure-couplers, affecting accuracy and repeatability. To overcome these issues, proper correction methods are essential to handle geometric discrepancies [5, 6].

This study integrates Finite Element Method (FEM) simulations with experimental implementations of the pressure-comparison technique for the calibration of MEMS microphones within a reverberation chamber. It addresses the challenges associated with the compensation of acoustic field irregularities between reference and test microphones using FEM, as well as the comparison of microphones exhibiting significantly divergent sensitivity responses across the frequency interval. The results obtained in the reverberation chamber demonstrate good consistency with those from other applications of the pressure-comparison method, including closed pressure-coupler and anechoic chamber set-ups.

2. PRESSURE-COMPARISON CALIBRATION OF MEMS MICROPHONES

The comparison method is crucial for calibrating non-conventional microphones, including miniaturized MEMS microphones, ensuring traceability to primary standards. It uses a reference microphone with known sensitivity, often determined by the reciprocity technique. For smaller microphones, especially MEMS, calibration under pressure-field conditions has the advantage to replicate real operating environments. Studies highlight the importance of using small-size Laboratory Standard (LS) microphones that can ensure the traceability of measurements.

2.1 Numerical simulation of sound field non-uniformities

FEM is widely used to solve complex acoustics problems, especially in cases where analytical solutions are impractical. It is particularly useful for modeling sound fields between microphones in scenarios involving intricate geometries, such as the small sensing areas of MEMS microphones. The acoustic pressure distribution p is governed by the Helmholtz equation:

$$\Delta p + k^2 p = 0 \tag{1}$$

where $k = \omega/c$ represents the wave number, ω is the angular frequency, and c is the speed of sound in air. FEM effectively handles boundary conditions, including rigid, vibrating with finite acoustic impedance, and sound source boundaries with known particle velocity distributions, which are crucial for simulating real-world microphone configurations.

Recent studies demonstrate the effectiveness of applying FEM with a lumped-parameter approach to model acoustic impedance boundaries [5, 6], simplifying a 3D problem to a 2D axisymmetric one. This approach aids in simulating MEMS microphones during pressure-comparison calibration, ensuring reproducible results. Numerical models have been proposed to correct sensitivity differences caused by acoustic pressure non-uniformity between reference and test microphones, which become more significant at high frequencies and as size dissimilarity of transducers gets more pronounced.

FEM results show the radial distribution of acoustic pressure, influenced by the impedance characteristics of microphones and boundaries, and are validated with experimental data. Fig. 1 illustrates the sound pressure distribution between a reference LS microphone and a MEMS test microphone under pressure-comparison at 6.3 kHz sine-type acoustic excitation, as obtained by FEM. The simulation mesh has a maximum element size of $\lambda/30$, being λ the sound wavelength, with 7214 elements covering an area of $12.12\,\mathrm{mm}^2$. The highest simulation frequency is $f_{max} = 30\,\mathrm{kHz}$.

2.2 Differences in microphones frequency response

The choice of the type of acoustic excitation and signals analysis for microphones calibration by the pressure-comparison method depends on the time efficiency of the measurement procedure, the type of acoustic environment, and the discrepancy of frequency responses of reference and test microphones' sensitivities. Broadband noise sources and third-octave bands analyses are advisable for fast calibrations, but if there are significant differences in microphones frequency responses, the use of sine-type signals and FFT analysis is recommended, especially for MEMS microphones calibration against LS reference microphones. In reverberation chambers, care should be taken in narrowing the bandwidth of the analysis with broadband noise sources, particularly as far as the degradation of the signal-to-noise ratio is concerned. Furthermore, long time-averaging of microphones signals and multi-position measurements should be performed to increase calibration accuracy.

3. REVERBERATION CHAMBER SET-UP

The pressure-comparison method for the calibration of MEMS microphones has been implemented inside the INRiM reverberation chamber of 294 m^3 volume, able to maintain the conditions of an acoustic diffuse field in the frequency range from 250 Hz to 12.5 kHz. The acoustic excitation is provided by two omnidirectional sound sources, placed at specific positions inside the chamber. The reference microphone was an LS2 type (LS microphone of 13.2 mm outer diameter, and 9.3 mm diaphragm diameter) HBK 4180, calibrated by the pressure reciprocity method at the centre frequencies of third-octave bands. The test microphone was an analog MEMS microphone on the evaluation board STMicroelectronics STEVAL-MKI139V5 fit into a custom cartridge that mimics the typical shape of LS2 microphones with a front recessed cavity. Reference and test microphones were coaxially aligned, facing each other with a very small separation gap lower than 2

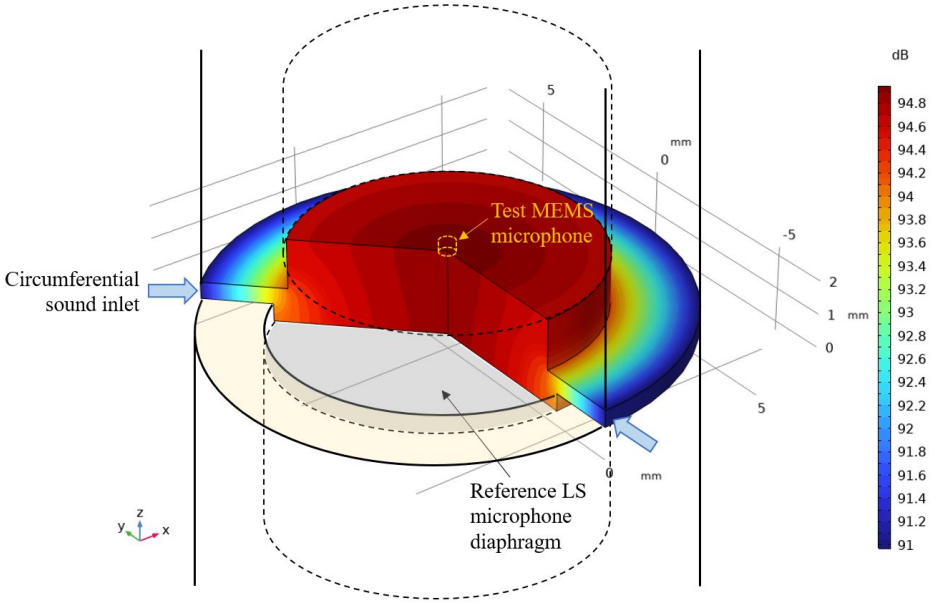


Figure 1. FEM simulation of the acoustic field for pressure-comparison calibration of a test MEMS microphone against an LS2 type reference microphone (LS microphone of 13.2 mm outer diameter, and 9.3 mm diaphragm diameter) with sine-type excitation at a frequency of 6.3 kHz.

mm. The coaxial alignment of the two microphones was realized along a direction non-parallel to any of the walls of the room as show in Fig. 2.

Signal acquisition and analysis were carried out using the ONO SOKKI DS-3200 data station, acting as a spectrum analyzer in third-octave bands. A 15-minute time-averaging was applied, with measurements repeated at various positions within the chamber to account for the diffuseness of the environment. A custom signal conditioner for the MEMS microphone, along with an HBK 2673 preamplifier for the reference microphone connected to the power and polarization module through a custom switch box, allowed applying the insert voltage technique to compensate for gain differences.

4. RESULTS

A broadband noise signal in the frequency range from 100 Hz to 16 kHz, properly amplified and equalized, was supplied to the sound sources to get a uniform sound pressure level (SPL) of about 80 dB over the third-octave bands from 250 Hz to 12.5 kHz. Because of the electro-acoustic characteristic of the sound sources, the SPL at the third-octave band of 16 kHz resulted of around 70 dB, still high enough with respect to the background noise, which was lower than 30 dB in the whole spectrum.

The frequency response of the sensitivity of the MEMS test microphone differs significantly from that of the LS2 reference microphone, as observed in previous calibrations by pressure-coupler and free field implementations of the pressure-comparison method. The dependence of calibration results on the bandwidth of the analysis was investigated by comparing the results obtained in the reverberation chamber with broadband noise stimuli analyzed in third-octave bands, with calibrations in pressure-coupler (active coupler) and free field (anechoic chamber) implementations using sine-type signals at the centre frequencies of third-octave bands. Fig. 3 shows the deviation of the calibration results due to the band-averaging in the reverberation chamber, calculated with respect to the average sensitivity curve of the MEMS microphone normalized to 1 kHz. Results are shown from 500 Hz to 16 kHz.

A marked deviation has been observed at frequency higher than 10 kHz, with a frequency response of about



Figure 2. Reference LS2 HBK 4180 microphone (right) faced to the test STEVAL-MKI139V5 MEMS microphone fit into the custom cartridge (left) for pressure-comparison calibration inside the reverberation chamber.

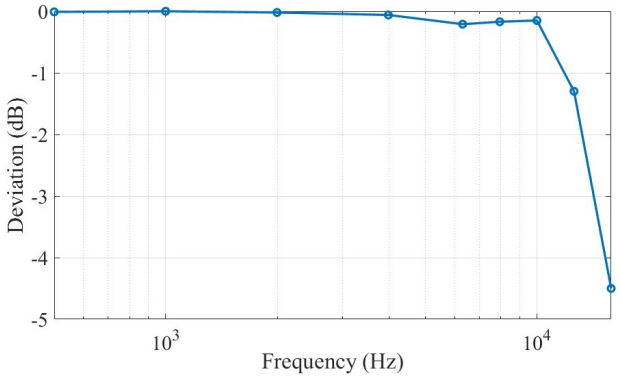


Figure 3. Deviation of pressure-comparison calibration results in the reverberation chamber with respect to the results obtained in pressure-coupler and free field implementations, due to third-octave band-averaging error.

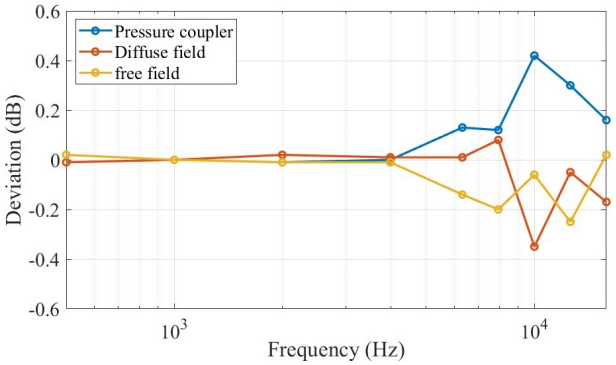


Figure 4. Deviation of pressure-comparison calibration results using sine-type signals in pressure-coupler, free field, and diffuse field implementations.

5 dB lower than those obtained with sine-type excitation. To evaluate the influence of the bandwidth of the analysis on the calibration results, sine-type signals have been used instead of broadband noise, along with the FFT analysis of microphones signals. Despite the possible onset of standing waves would be enhanced by such a tone excitation, the signal-to-noise ratio was higher compared to the case of a broadband noise source with bandwidth analysis narrower than third-octave. Fig. 4 shows the deviations from the mean sensitivity curve of the MEMS microphone normalized to 1 kHz, as obtained from pressure-comparison calibrations with sine-type signals in all acoustic environments: closed pressure-coupler (active coupler), free field (anechoic chamber), and diffuse field (reverberation chamber).

With sine-type signals excitation all calibration results were observed consistent within 0.5 dB. The increasing deviations above 4 kHz are likely due to the worse repeatability of measurements in the reverberation chamber, and to the uncertainty associated to the evaluation of the sound field corrections for the compensation of acoustic field non-uniformities between reference and test microphones.

5. CONCLUSION

This study presents a detailed analysis of pressure-comparison calibration of MEMS microphones

in a reverberation chamber. Although this approach can be time efficient, it is critical to account for significant differences in frequency response between reference and test microphones, which is common for MEMS microphones. In such cases, a trade-off between accuracy and time must be considered, as sine-type excitation provides more accurate results but requires longer measurements. However, sine-type signals can be affected by standing waves in the acoustic field. The results obtained in the reverberation chamber show good agreement with previous pressure-comparison calibrations performed in pressure-coupler and free field implementations. Improvements can be achieved by optimizing the numerical evaluation of sound field corrections and by implementing automatic positioning systems to improve the repeatability of the measurements.

6. ACKNOWLEDGMENTS

Fabio Saba acknowledges the support from the Italian Ministry of University and Research (MUR) in the framework of the continuing-nature project "NEXT-GENERATION METROLOGY", under the allocation of the Ordinary Fund for research institutions (FOE) 2023 (Ministry Decree n. 789/2023).

María Campo-Valera acknowledges the support from the ThinkInAzul and AgroAlNext programmes, funded by Ministerio de Ciencia, Innovación y Universidades (MICIU) with funding from European Union NextGenerationEU/PRTR-C17.I1 and by Fundación Séneca with funding from Comunidad Autónoma Región de Murcia (CARM).

7. REFERENCES

[1] M. A. Shah, I. A. Shah, D.-G. Lee, S. Hur, *et al.*, "Design approaches of MEMS microphones for enhanced performance," *J. Sens.*, vol. 2019(1), p. 9294528, 2019.

[2] Y. He, A. Yu, X. Liu, and Y. Wang, *Micro-Electro-Mechanical Systems (MEMS). In Handbook of Integrated Circuit Industry*, pp. 895–911. Wang, Y., Chi, M.H., Lou, J.J.C., Chen, C.Z., Eds.; Springer: Singapore, 2024.

[3] J. Picaut, A. Can, N. Fortin, J. Ardouin, and M. Lagrange, "Low-cost sensors for urban noise monitoring networks—a literature review," *Sensors*, vol. 20, no. 8, p. 2256, 2020.

[4] A. Izquierdo, L. Del Val, J. J. Villacorta, W. Zhen, S. Scherer, and Z. Fang, "Feasibility of discriminating UAV propellers noise from distress signals to locate people in enclosed environments using MEMS microphone arrays," *Sensors*, vol. 20, no. 3, p. 597, 2020.

[5] F. Saba, G. Durando, D. Paesante, M. Corallo, A. Schiavi, and A. Prato, "An experimental setup for the metrological characterization of MEMS microphones," in *24th International Congress on Acoustics (ICA 2022) - A05: Electro-acoustics*, 24–28 October 2022.

[6] F. Saba, M. Campo-Valera, D. Paesante, G. Durando, M. Corallo, and D. Pugliese, "Effectiveness of sound field corrections for high-frequency pressure comparison calibration of MEMS microphones," *Sensors*, vol. 25, no. 5, p. 1312, 2025.

DOI: 10.61782/fa.2025.0620

FORUM ACUSTICUM EURONOISE 2025

NOISE SOURCE DIRECTION ESTIMATION USING FLOW-SENSING MEMS MICROPHONES

Thomas Röck[1*] **Martin Hagmüller**[2] **Franz Zotter**[1]
[1]Institute of Eletronic Music and Acoustics, University of Music and Performing Arts Graz, 8010 Graz, Austria
[2]Signal Processing and Speech Communication Laboratory, Graz University of Technology, 8010 Graz, Austria

ABSTRACT

Unattended noise monitoring systems can be used to track the sound level over an extensive amount of time and record whenever the level exceeds a threshold. Direction-of-Arrival (DoA) measured with a microphone array can add relevant information about the noise captured.
This paper investigates a prototype application employing novel directional flow-sensing Micro-Electro-Mechanical Systems (MEMS) microphones integrated into a highly compact array for DoA-detecting noise monitoring. Such sensors are supposed to exhibit a consistent directivity over the audible frequency range and to hereby enable frequency-independent DoA estimation for broadband noise sources. An array prototype is designed on an energy efficient micro controller unit (MCU) that runs three different DoA-estimation methods under test.
The resulting prototype uses one omnidirectional and three directional, flow-sensing MEMS microphones. Measurements confirm that a high spatial aliasing limit could be reached without sacrificing low-frequency directivity. Our field study validates applicability to DoA-detecting noise monitoring at cheap computational costs.

Keywords: *Acoustic DoA estimation, MEMS velocity microphone array, ARM microcontroller*

1. INTRODUCTION

Compliance with noise regulations typically requires monitoring acoustic emissions from specific sources and the comparison to legal limits [1]. In unattended noise monitoring systems, the sound level is tracked over a long period of time. When the level surpasses a threshold, the system activates an alarm, requiring a human operator to restore order manually. This is time-consuming, especially if the object to monitor is near roads, railways and airports. Using Artificial Intelligence (AI) for unattended noise monitoring systems allows for the automatic classification of triggering events and potential exclusion from the overall measurement [2, 3]. Deep learning methods are remarkably successful in Sound-Event-Detection (SED). However, the current leading models still encounter errors, especially when having to distinguish between different types of vehicles [4] or distinct soundscapes [5]. However, there is more information than what can be contained in single-channel sound. For instance, Direction-of-Arrival (DoA) offers useful additional information. In particular, DoA allows to limit the solid angle/field of view, within which noise shall be monitored. Current methods in DoA estimation for noise monitoring applications investigate arrays incorporating mainly omnidirectional MEMS microphones. The “Noise Compass” [6] is an array that includes eight omnidirectional MEMS microphones and computes the DoA of the dominant noise source using a Time-Difference-of-Arrival method. Another work proposes the design of a 3D sound intensity probe using eight MEMS pressure microphones on the vertices of a 2cm × 2cm cube [7].
This work investigates the performance of novel directional, flow-sensing MEMS microphones [8, 9] that sense acoustic particle velocity. An orthogonal arrangement of velocity microphones combined with an omnidirectional pressure microphone enables the computation of the three-dimensional pseudo-intensity vector, which indicates the direction of sound propagation and, accordingly, the direction of the sound source emitting the sound field. We derive and compare three DoA-estimation methods applicable to the proposed array geometry, which are implemented on a low-power ARM microcontroller. Additionally, the results of directivity measurements used

*Corresponding author: roeck@iem.at.
Copyright: ©2025 Thomas Röck et. al. This is an open-access article distributed under the terms of the Creative Commons Attribution 3.0 Unported License, which permits unrestricted use, distribution, and reproduction in any medium, provided the original author and source are credited.

to verify the figure-of-eight polar pattern of the velocity microphones are discussed. Finally, we present two case studies to demonstrate the array's performance in the field. The proposed array prototype is suitable for noise DoA-estimation applications and produces good results with minimal signal processing. Drawbacks such as the influence of wind on the velocity microphones should be discussed and addressed.

2. SIGNAL MODEL

We assume an acoustic signal $s(t)$ emitted by a sound source that lies at some distance along the unit DoA vector

$$\boldsymbol{u} = \begin{pmatrix} \cos(\varphi)\cos(\vartheta) \\ \sin(\varphi)\cos(\vartheta) \\ \sin(\vartheta) \end{pmatrix}, \tag{1}$$

where $\varphi \in [0, 2\pi[$ is the azimuth angle and $\vartheta \in [-\frac{\pi}{2}, \frac{\pi}{2}]$ is the elevation angle of the source. For our array with 4 microphones located at the center of a coordinate system, let there be K sources at the directions $\boldsymbol{u}_k$ with the signals $s_k(t)$, and an $\mathbb{R}^{4\times 1}$ signal vector recorded by the array

$$\boldsymbol{x}(t) = \sum_{k=1}^{K} s_k(t)\, \boldsymbol{y}(\boldsymbol{u}_k) + \boldsymbol{v}(t). \tag{2}$$

Here, $\boldsymbol{y}(\boldsymbol{u}) \in \mathbb{R}^{4\times 1}$ is the array manifold vector for a continuous direction $\boldsymbol{u}$, and $\boldsymbol{v}(n) \in \mathbb{R}^{4\times 1}$ is a vector that contains the additive zero-mean self noise of each microphone.
Similar to [10], we assume the following conditions:

A) Incident waves are local plane waves at the array, implying (i) far-field conditions characterized by array-to-source distances much greater than a wavelength, and (ii) array dimensions much smaller than a wavelength to avoid both diffraction and time differences of arrival.
B) Band limitation: The signal is bandlimited accordingly, $\omega_{\min} < \omega < \omega_{\max}$, such that both conditions are fulfilled.

The microphone array in this work follows a WXYZ (B-format) layout with three orthogonal velocity microphones and one omnidirectional pressure microphone. The resulting array manifold vector $\boldsymbol{y}(\boldsymbol{u}) \in \mathbb{R}^{4\times 1}$ is defined as

$$\boldsymbol{y}(\boldsymbol{u}) = \begin{pmatrix} 1 \\ \boldsymbol{u}\sqrt{3} \end{pmatrix}. \tag{3}$$

We further assume consistent microphone directivity within the frequency range of interest, which is why $\boldsymbol{y}(\boldsymbol{u})$ is assumed to be frequency-independent.

3. FLOW-SENSING MEMS MICROPHONE

The Soundskrit directional MEMS microphone is the result of a collaboration between researcher Ronald N. Miles, who has extensively studied sound velocity sensing [11–13], and Stephane Leahy from Soundskrit, who designed a new transducer based on capacitive sensing [8]. The sensing element consists of multiple porous plates, fixed beams, and cantilevers, creating a highly flexible membrane designed to enhance the influence of air viscosity on its movement due to its material properties. Two port holes on the front and back of the microphone allow sound to flow through the sensing element. In our array prototype as seen in Fig. 1, we incorporate three of Soundskrit's SKR0410 first-generation digital MEMS microphones in an orthogonal alignment. An omnidirectional microphone by Infineon is brought into the center of the array using a Flex PCB. The coupon board PCBs of the velocity microphones are attached to a hollow 3D-printed housing. The distance between the orthogonal microphone and the three velocity microphones is $d = 6.5$ mm, resulting in a maximum microphone distance of $d_{\max} = \sqrt{2}\, d = 9.2$ mm and consequently a minimum aliasing frequency at $\frac{c}{2d_{\max}} = 18657$ Hz where $c = 343$ m/s is the speed of sound.

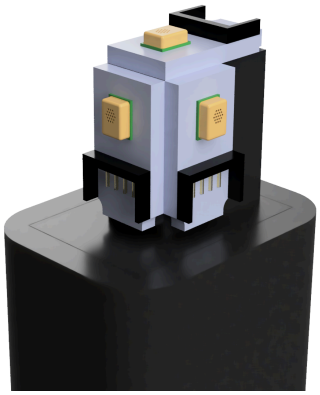


Figure 1: The array prototype. The MEMS velocity microphones are mounted on the white PCB coupon boards. The omnidirectional MEMS microphone is located in the center of the array. The largest distance between any two microphones is 9 mm.

3.1. Directivity measurements of the microphones

The polar pattern of the MEMS velocity microphones is specified as a figure-of-eight (Fo8) and has been verified through directivity measurements. These measurements utilize an array of loudspeakers mounted on a circular frame with radius $r = 1.5\text{m}$ facing the circle's center point where the microphone array specimen is located, as seen in Fig. 2. The array is mounted on a stand on a turntable that rotates the array along the vertical axis in 10° azimuthal steps, resulting in an angular resolution of $\Delta\varphi = 10°$. The elevation resolution is given by the spacing of the loudspeakers, which is $\Delta\vartheta = 11.25°$.

Overlapping exponential sweeps were employed as the measurement signal [14]. The loudspeaker's individual frequency response is equalized by measurements recorded with an *Earthworks* measurement microphone. Spherical surface plots are generated with a MATLAB tool[1] that interpolates the 10° × 11.25° sample grid using 14th-order spherical harmonics and performs far-field extrapolation in the spherical harmonics domain.

We observed a consistent phase difference of approximately 60° between the omnidirectional MEMS and the Fo8 microphones. This difference must be accounted for to prevent a sign flip of the pseudo-intensity vector. Therefore, the Fo8 microphones are equalized to the frequency response of the omnidirectional microphone.

Furthermore, the orthogonal MEMS microphones exhibit an orientation misalignment, especially the X- and Z microphones (as depicted in Fig. 3). Fortunately, this misalignment can be easily corrected through a change of basis transformation

$$\hat{\boldsymbol{u}}' = \boldsymbol{D}\left(\tilde{\boldsymbol{D}}^{\mathrm{T}}\right)^{-1}\hat{\boldsymbol{u}}. \tag{4}$$

This transformation projects the estimated DoA vector onto the inverse of a matrix containing the actual alignment of the microphones, transforming the vector to lie within the orthonormal Cartesian basis. Here, $\boldsymbol{D} = \boldsymbol{I}$ denotes the Cartesian basis which is an identity matrix and $\tilde{\boldsymbol{D}}$ contains the actual alignment of the Fo8 microphones determined by the measurement.

The measured polar pattern of a cardioid beam steered to $\varphi = 90°$ is shown in Fig. 4 a). In this depiction, the magnitude is normalized for each frequency bin as the MEMS microphones are less sensitive at lower frequencies but that sensitive was also not considered in the simulation. However, the directionality and consequently the beampattern is maintained even for lower frequencies. We do observe inconsistencies in the beampattern with frequencies starting at 4000 Hz which could be attributed to temporal measurement errors or acoustic turbulences within the case. The simulated energy response of a cardioid beamformer steered to $\varphi_s = 90°$ and $\vartheta_s = 0°$ is depicted in Fig. 4 b). Initial interference patterns can be observed at $\frac{c}{4d} = 13192$ Hz. Below that frequency, the beamformer consistently favours the steering direction without spatial aliasing.

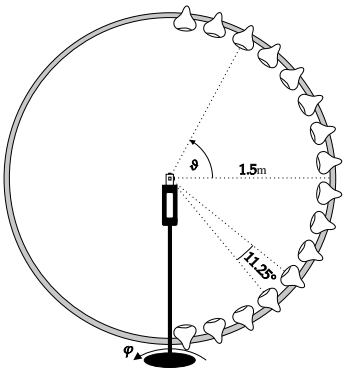
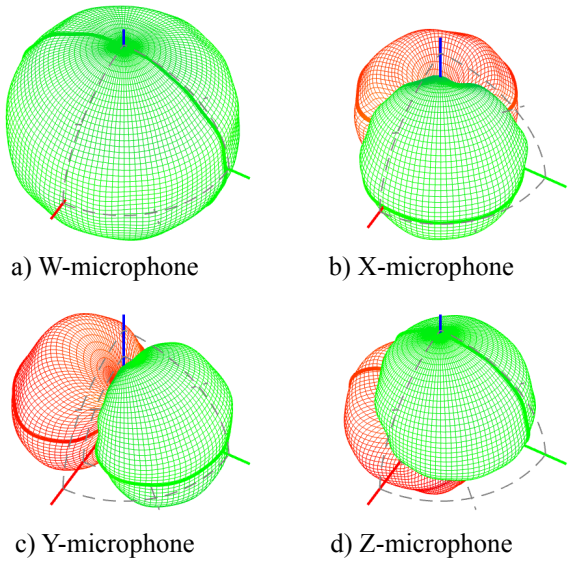


Figure 2: The measurement setup. 16 loudspeakers with a spacing of 11.25°, mounted on a circular frame with radius $r = 1.5\text{m}$, face the microphone array.

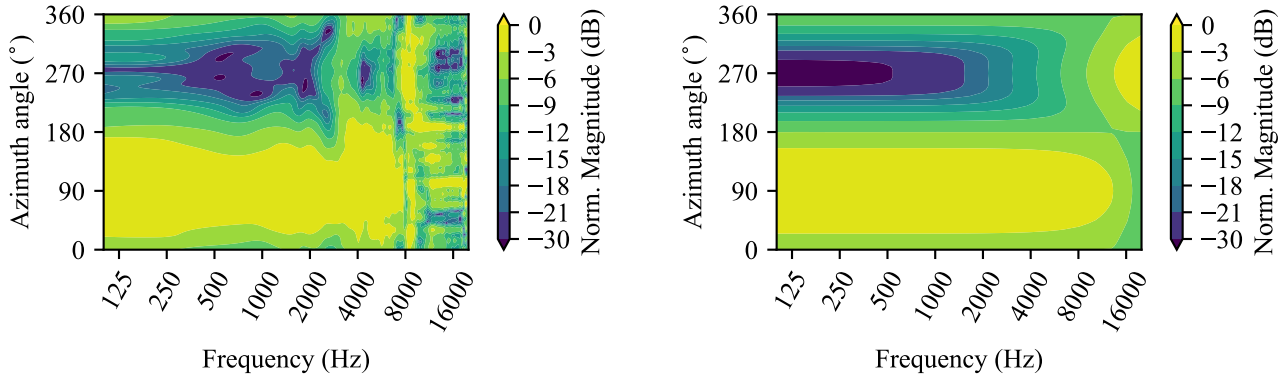
[1] https://git.iem.at/p2774/balloon_holo



a) W-microphone b) X-microphone

c) Y-microphone d) Z-microphone

Figure 3: Directivity for the W, X, Y, and Z microphone measured at a frequency of 500 Hz. The colors indicate the phase response of the micorphones.



a) Measured polar pattern.

b) Simulated array response.

Figure 4: A cardioid beam (linear combination of the omni- and Fo8 microphones) is steered to a direction of $\varphi = 90°$ and $\vartheta = 0°$. In the measurement in a), the magnitude is normalized per frequency. In reality, the MEMS microphones are less sensitive in the lower frequency range but that sensitivity was also not considered in the simulation depicted in b) which is performed by placing sound sources around the array and evaluating Green's function for planar waves that depends on the distance between the source and receiver.

4. DOA ESTIMATION METHODS

In this section we present three DoA-estimation methods. We extend a simple beamforming approach with a seasoned, well-established subspace algorithm applicable for any kind of array-geometry, followed by a pseudo-intensity method that makes use of the sampling of the sound pressure and velocity vector.

4.1. Steered Response Power (SRP)

The Steered Response Power (SRP) method is fundamentally based on beamforming, utilizing the array response vector $\boldsymbol{y}(\boldsymbol{u})$ as defined in Eqn. (3) and an estimation of the covariance matrix

$$\boldsymbol{C}_{\mathrm{xx}} = \boldsymbol{X}^{\mathrm{T}}\boldsymbol{X} \tag{5}$$

of a N-sample signal block $\boldsymbol{X} \in \mathbb{R}^{N\times M}$. For a set of $\mathcal{G}$ discrete points on the surface of a unit-sphere, sampled using a Fibonacci lattice, we compute

$$P(\boldsymbol{u}) = \boldsymbol{y}^{\mathrm{T}}(\boldsymbol{u})\,\boldsymbol{C}_{\mathrm{xx}}\,\boldsymbol{y}(\boldsymbol{u}). \tag{6}$$

The point that maximizes this power is the estimated direction of arrival

$$\hat{\boldsymbol{u}} = \underset{\boldsymbol{u}\in\mathcal{G}}{\operatorname{argmax}}\, P(\boldsymbol{u}). \tag{7}$$

4.2. Multiple Signal Classification (MUSIC)

Introduced in 1986 [15], MUSIC is a renowned subspace method and extends the aforementioned beamforming technique. It relies on the eigen-decomposition of the covariance matrix $\boldsymbol{C}_{\mathrm{xx}}$ and successive separation of the eigenvectors into a signal- and noise subspace. The signal model claims that the wavefronts received at the M microphones are a linear combination of D incident wavefronts and noise. After the eigendecomposition of the covariance matrix of the signal vector $\boldsymbol{x}$, the D largest eigenvalues and their corresponding eigenvectors span the signal subspace, whereas the eigenvectors corresponding to the $M - D$ smallest, clustered eigenvalues span the noise subspace $\boldsymbol{E}_{\mathrm{n}}$. A pseudo spectrum $\hat{P}_{\mathrm{MU}}(\boldsymbol{u})$ is introduced, which computes to the squared norm of the projection of $\boldsymbol{y}(\boldsymbol{u})$ onto the noise subspace. The direction that maximizes the pseudo spectrum

$$\hat{P}_{\mathrm{MU}}(\boldsymbol{u}) = \frac{1}{\left\|\boldsymbol{E}_{\mathrm{n}}^{\mathrm{T}}\,\boldsymbol{y}(\boldsymbol{u})\right\|^2} \tag{8}$$

is the predicted direction of arrival $\hat{\boldsymbol{u}}$

$$\hat{\boldsymbol{u}} = \underset{\boldsymbol{u}\in\mathcal{G}}{\operatorname{argmax}}\, \hat{P}_{\mathrm{MU}}(\boldsymbol{u}). \tag{9}$$

4.3. Active Intensity Measurement (AIM)

Euler's equation relates the acoustic pressure p to the sound velocity vector $\boldsymbol{v}$

$$-\nabla p = \rho_0 \frac{\partial \boldsymbol{v}}{\partial t} \tag{10}$$

where $\rho_0 \approx 1.2 \frac{\text{kg}}{\text{m}^3}$ is the atmospheric density. For sufficiently far away sources, i.e. plane-wave conditions, the ∇-operator is equal to $\partial(\boldsymbol{u}_\text{s}/c)/\partial t$ and Eqn. (10) becomes

$$\boldsymbol{v} = -\frac{\boldsymbol{u}\, p}{\rho_0 c}. \tag{11}$$

As the B-format signals of a first-order ambisonics microphone are $W = p$ and $[X, Y, Z]^\text{T} = -\rho_o c \sqrt{2}\, \boldsymbol{v}$, the predicted direction by AIM is

$$\begin{aligned} \hat{\boldsymbol{u}} &= -\frac{\rho_0 c\, \boldsymbol{I}}{|p|^2} = -\frac{\rho_0 c\, p \boldsymbol{v}}{|p|^2} = \frac{\rho_0 c\ |p|^2\ \boldsymbol{u}}{\rho_0 c\ |p|^2} = \boldsymbol{u} \\ &= \frac{W\,[X, Y, Z]^\text{T}}{\sqrt{2}\ |W|^2} \end{aligned} \tag{12}$$

and the estimator averaging over one block of samples is

$$\hat{\boldsymbol{u}} = \frac{\mathbb{E}(W[X, Y, Z]^T)}{\sqrt{2}\mathbb{E}(W^2)}. \tag{13}$$

5. HARDWARE IMPLEMENTATION

The microphone array is powered by a *STM32U5A9NJ* ARM microcontroller which also runs the DoA-estimation algorithms and performs 1/1 octave band filtering for eight octave bands with center frequencies from 31.5 Hz - 4000 Hz. The built-in interleaved sampling mode of the Multi-Function-Digital-Filter (MDF) of the ST guarantees precise sampling of the four microphone channels. After acquiring a block of $N = 2048$ samples, that block is filtered eight times by 4$^\text{th}$ order IIR butterworth bandpass filters following the ANSI S1.11-2004 specifications [16], effectively whitening the signal in its respective band. A separate recording mode allows for the transmission of the recordings to a host computer for postprocessing and the results shown in Sec. 6 were obtained by offline analysis of the recordings.

5.1. Computational effort of the algorithms on the chip

The *STM32U5A9NJ* MCU contains a single-core *Cortex-M33* ARM processor operating at a system clock frequency of up to 160 MHz. We benchmarked the algorithms by executing a Monte Carlo simulation comprising 1000 trials and selecting the median number of clock cycles required for the algorithm to finish. We set an external timer to the same system clock rate $f_\text{CLK} = 160$ MHz. Computational improvements could be made using the CMSIS DSP library[2] tailored towards the specific CPU architecture of the *Cortex-M33*.

[2]https://arm-software.github.io/CMSIS_5/DSP/html/index.html

Table 1: Computational effort of the three algorithms for different sample sizes N. The numbers below the algorithm's names denote the number of clock cycles required for the algorithm to finish.

N	SRP	MUSIC	AIM
512	739 384	1 948 476	35 779
1024	808 535	2 039 794	71 133
2048	946 834	2 192 544	141 815

For an efficient processing of the MUSIC algorithm, the property of the covariance matrix $\boldsymbol{C}_\text{xx}$ as real-valued and positive semi-definite was exploited to efficiently use a real-valued Schur decomposition for eigendecomposition $\boldsymbol{C}_\text{xx} = \boldsymbol{E}\,\text{diag}(\boldsymbol{s})\,\boldsymbol{E}^\text{T}$, where $\boldsymbol{E}$ contains all eigenvectors and $\text{diag}(\boldsymbol{s})$ the eigenvalues. The noise subspace $\boldsymbol{E}_\text{n}$ corresponds to the 3 smallest eigenvalues with the signal subspace set to $D = 1$. The number of points for SRP and MUSIC is set to $\mathcal{G} = 1650$ to achieve an angular resolution of approximately $\Delta\boldsymbol{u} = \sqrt{\frac{4\pi}{1650}} \frac{180}{\pi} = 5°$.
Tab. 1 shows the measured clock cycles for different block lengths N. AIM is faster than both MUSIC and SRP, mainly because of their expensive grid search over $\mathcal{G}$ directions. Complexity roughly scales with $\mathcal{O}(N)$ for AIM, in contrast to $\mathcal{O}(N) + \mathcal{O}(\mathcal{G})$ for SRP and MUSIC. The computation of the SRP power spectrum is cheaper than Schur decomposition.

6. CASE STUDIES

Case studies on the array performance in real-world scenarios were carried out, of which two are presented in the following sections. The first scenario demonstrates the array performance on a low-frequency sound source. The second study investigates the influence of wind, which is particularly evident in recordings of the flow-sensing microphones. Direction estimates are performed individually for eight 1/1 octave bands with center frequencies ranging from 31.5 Hz to 4 kHz and additionally for the A-weighted recording. The system's sampling rate is set to 16 kHz. The number of discrete unit vectors $\mathcal{G}$ for SRP and MUSIC is 1650, resulting in an angular resolution of approximately 5°. The number of signals in MUSIC is assumed to be $D = 1$. The individual 5-minute recordings are buffered into blocks of $N = 2048$ samples, each block yielding a direction estimate for segments where a noise source is present with certainty. Given that the true direction of the sound source is unknown, we can only analyse the scattering of direction estimates. For this purpose, we

analyse boxplots containing samples of the angle between an estimate $\hat{\boldsymbol{u}}$ and the mean direction $\boldsymbol{\mu}_{\mathrm{A}}$ of the A-weighted filter bank, i.e. $\arccos(\boldsymbol{u}^{\mathrm{T}}\boldsymbol{\mu}_{\mathrm{A}})$. The boxes in the boxplots shown extend from the first to the third quartile with a line at the median. The whiskers extend from the box to the farthest data point, lying within 1.5 times the interquartile range. Fliers are shown as grey circles. Additionally, histograms counting direction samples estimated by AIM are presented.

6.1. Low-frequency screed silo pump

The first study was conducted next to a construction site during the operation of a silo pump. Free-field conditions could not be fulfilled as the recording area was surrounded by residential houses, as can be seen in Fig. 5. Nevertheless, this example should demonstrate the direction estimation capabilities of the miniature array for low-frequency sources. As can be seen in the spectrogram segment shown in Fig. 6, the silo pump emits a particularly dominant tone at 50 Hz and additional harmonic overtones. For conventional, small-aperture microphone arrays, the accurate detection of a noise source in this frequency range should pose a great challenge. However, as evident in the boxplots presented in Fig. 7, the direction estimates exhibit minimal deviation from the mean direction $\boldsymbol{\mu}_{\mathrm{A}}$ in the 31.5- and 63 Hz frequency bands. Notably, in the 31.5 Hz band, a remarkably precise direction estimate of AIM's histogram for a single frame is discernible in Fig. 8. Comparing the algorithm's performance in this scenario, we can note that SRP, AIM, and MUSIC yield similar estimation outcomes. However, AIM does show greater scattering of its direction estimates in the frequency bands from 250 Hz to 4000 Hz.



Figure 5: In the first scenario, a silo pump next to a construction site in a residential area was recorded.

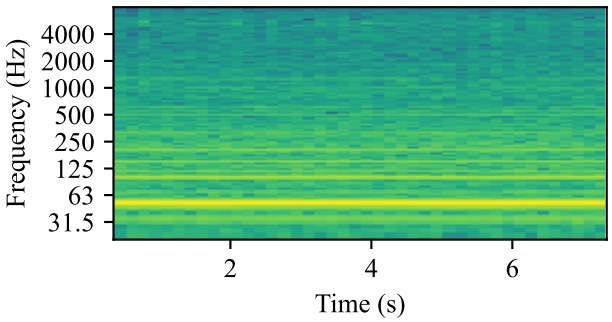


Figure 6: Spectrogram of the pump recording in a segment where an especially dominant low-frequency tone at 50 Hz is present.

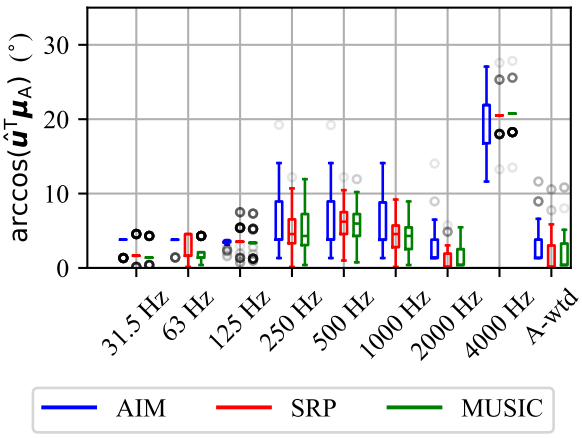


Figure 7: Angle between the direction estimates $\hat{\boldsymbol{u}}$ and the mean direction of the A-weighted filter $\boldsymbol{\mu}_A$ for the silo pump recording.

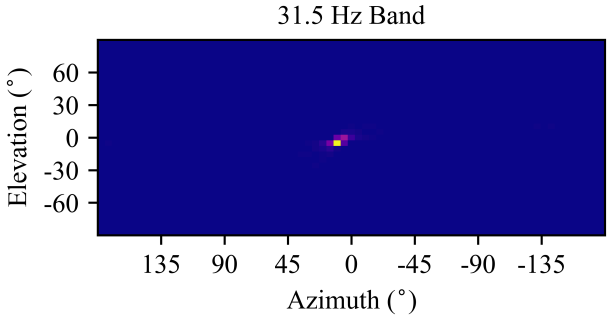


Figure 8: A histogram counting direction estimates for a single block of the silo recording. Computed by AIM, evaluated for the 31.5 Hz octave band.

Such behaviour could be attributed to the reflective recording scenario and, consequently, additive wavefronts from mirror sources, causing more deviations in the per-sample estimates of the pseudo intensity vector. Notably, in the 4000 Hz band, an angular discrepancy of 20° is evident. Further examination of this band revealed that the elevation of the estimation is 20° higher than for $\boldsymbol{\mu}_{\mathrm{A}}$ but with similar azimuth. It is possible that a more prominent noise source, perhaps originating from another point on the silo itself, is present at higher elevations.

6.2. Parked airplane in the presence of wind gusts

For the second study, the array was mounted on a terrace of an airport facing the runway, as shown in Fig. 9. We want to demonstrate the array's performance in non-ideal weather conditions, such as in the presence of wind gusts that interfere with the recording. Occasional wind gusts can be seen in Fig. 10 where they occupy the frequency range of 20 Hz to 100 Hz. We observed that recordings captured by the Fo8, flow-sensing microphones were significantly more influenced by wind compared to recordings captured by the omnidirectional pressure microphone. Evidently, as wind gusts distort the recording, they will deteriorate the performance of the direction estimation. A greater scattering of direction estimates can be seen in Fig. 11, vastly influencing the performance of all algorithms in the 31.5 Hz and 63 Hz band. Turbulent - but optically quite artistic estimations of the direction of the pseudo intensity vector can be appreciated in Fig. 12. This picture further emphasizes the impact of wind at lower frequencies. However, with increasing center frequency, the performance improves for all algorithms. In comparison to the scenario in Sec. 6.1, their prediction performance seems to be even more similar.

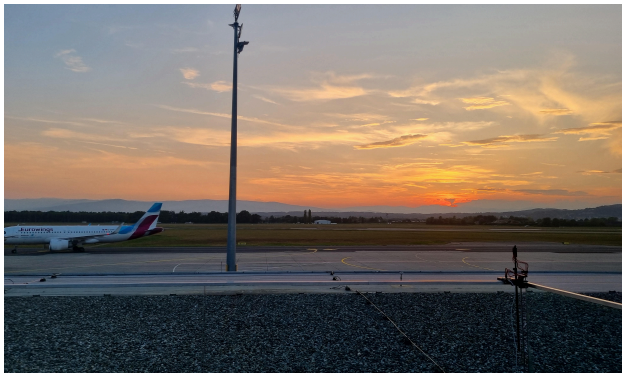


Figure 9: The second recording scenario was conducted at an airport and the sound source was the parked airplane seen on the left.

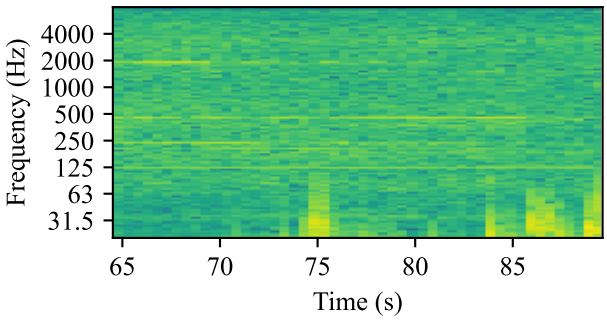


Figure 10: Spectrogram of the airplane source. Occasional wind gusts can be seen occupying the frequency range from 20 Hz to 100 Hz.

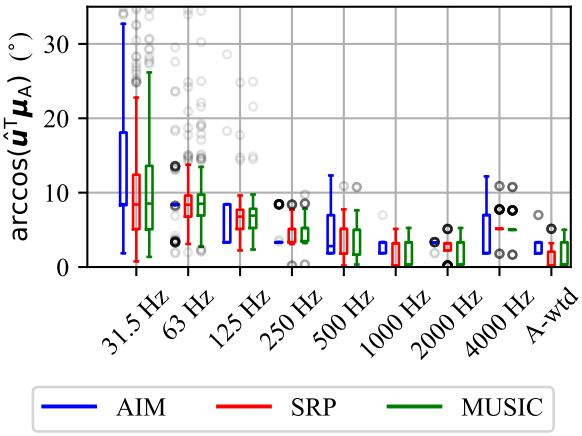


Figure 11: Angle between the direction estimates $\hat{\boldsymbol{u}}$ and the mean direction of the A-weighted filter $\boldsymbol{\mu}_A$ for the airport recording.

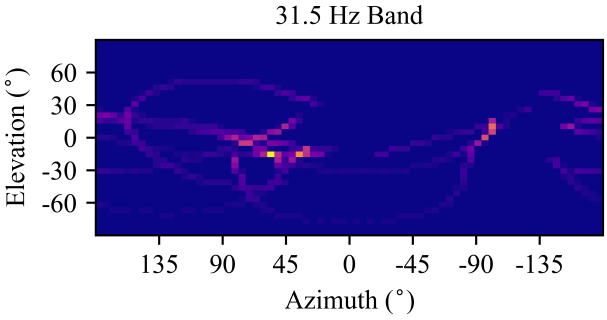


Figure 12: A histogram counting direction estimates computed by the AIM algorithm. Evaluated for the 31.5 Hz octave band for the airplane source.

7. CONCLUSION

We presented a miniature microphone array comprising directional, velocity-sensing MEMS microphones suitable for broadband noise source direction estimation. We verified the individual microphone and array directivities over a broad frequency range, and showed that the small sensor spacing provides a high spatial aliasing frequency limit. For the array prototype, three direction-of-arrival detection algorithms were implemented on an energy-efficient MCU. It was shown that the computational load varied depending on the complexity of the underlying algorithm. Field studies further verified the applicability of the microphone array in real-world scenarios, demonstrating comparable estimation performance for the different algorithms, but also highlighting the influence of wind, primarily on the velocity microphones. Consequently, users should consider their windscreen solution when incorporating flow-sensing microphones. Compared to conventional microphone arrays using non-coincident, omnidirectional sensors, the microphones in this configuration can be brought together as closely as possible without sacrificing low-frequency directivity performance. This not only reduces spatial aliasing but also enables the design of a very small microphone array module, that could potentially be installed directly in a class-1 measurement microphone e.g. with a 1/2″ capsule form factor.

8. REFERENCES

[1] D. Manvell and K. Andersen, "Developments in specific noise determination in continuous unattended monitoring systems," *Proc. of Euronoise 2018*, 2018.

[2] K. Zaman, M. Sah, C. Direkoglu, and M. Unoki, "A Survey of Audio Classification Using Deep Learning," *IEEE Access*, vol. 11, pp. 106620–106649, 2023, doi: 10.1109/access.2023.3318015.

[3] Z. Mnasri, S. Rovetta, and F. Masulli, "Anomalous sound event detection: A survey of machine learning based methods and applications," *Multimedia Tools and Applications*, vol. 81, no. 4, pp. 5537–5586, 2022.

[4] E. Betton-Ployon, A. Kacem, J. Mars, and N. Martin, "Enhanced railway sound event detection using YAMNet and classification criteria," *INTER-NOISE and NOISE-CON Congress and Conference Proc.*, vol. 270, no. 3, pp. 8834–8843, Oct. 2024, doi: 10.3397/in_2024_4148.

[5] K. H. Ejdfors, N. SATO, and L. A. SæLE, "A comparative study of noise event identification using AI in unattended monitoring," in *INTER-NOISE and NOISE-CON Congress and Conference Proc.*, 2024, pp. 7670–7678.

[6] D. T. Helboe and E. Fasting, "Automatic detection of source direction and exclusion of irrelevant sounds in unattended noise monitoring systems," *INTER-NOISE and NOISE-CON Congress and Conference Proc.*, vol. 268, no. 7, pp. 1131–1142, Nov. 2023, doi: 10.3397/in_2023_0172.

[7] E. Aflalo and T. Hupp, "Unattended noise measurements: use of new technologies to automatically qualify noise events for greater efficiency, precision and time savings," *Internoise 2024*, 2024.

[8] R. N. Miles, M. Farahikia, S. Leahy, and A. A. Aziz, "A flow-sensing velocity microphone," in *2019 IEEE SENSORS*, IEEE, Oct. 2019. doi: 10.1109/sensors43011.2019.8956947.

[9] Soundskrit Inc., "SKR0410 - PDM Directional Microphone Datasheet," 2023.

[10] A. Nehorai and E. Paldi, "Acoustic vector-sensor array processing," *IEEE Transactions on Signal Processing*, vol. 42, no. 9, pp. 2481–2491, 1994, doi: 10.1109/78.317869.

[11] J. Zhou and R. N. Miles, "Sensing fluctuating airflow with spider silk," *Proc. of the National Academy of Sciences*, vol. 114, no. 46, pp. 12120–12125, Oct. 2017, doi: 10.1073/pnas.1710559114.

[12] J. Zhou and R. N. Miles, "Directional Sound Detection by Sensing Acoustic Flow," *IEEE Sensors Letters*, vol. 2, no. 2, pp. 1–4, Jun. 2018, doi: 10.1109/lsens.2018.2843376.

[13] R. Miles, "Most animals hear acoustic flow instead of pressure; we should too," *The Journal of the Acoustical Society of America*, vol. 145, no. 3_Supplement, p. 1698, Mar. 2019, doi: 10.1121/1.5101224.

[14] P. Majdak, P. Balazs, and B. Laback, "Multiple exponential sweep method for fast measurement of head-related transfer functions," *Journal of the Audio Engineering Society*, vol. 55, no. 7/8, pp. 623–637, 2007.

[15] R. Schmidt, "Multiple emitter location and signal parameter estimation," *IEEE Transactions on Antennas and Propagation*, vol. 34, no. 3, pp. 276–280, doi: 10.1109/TAP.1986.1143830.

[16] "ANSI S1.11-2004: Specification for Octave-Band and Fractional-Octave-Band Analog and Digital Filters." New York, NY, 2004.

DOI: 10.61782/fa.2025.0117

FORUM ACUSTICUM EURONOISE 2025

AMPLITUDE MODULATION DISCRIMINATION IN COCHLEAR IMPLANT LISTENERS: EFFECTS OF CARRIER FREQUENCY AND 'INTERFERING' MODULATED SIGNALS

Nicholas R. Haywood [1*], Brian C. J. Moore[1], Ben Williges[2], Patrick Boyle[3], Marina Salorio-Corbetto[1], Josef Schlittenlacher[1,4], Charlotte Harbottle[5], Deborah A. Vickers[1]

[1] Cambridge Hearing Group, University of Cambridge, Cambridge, United Kingdom

[2] University of Essen, Essen, Germany

[3] Advanced Bionics GMBH, Hannover, Germany

[4] Speech, Hearing and Phonetics Sciences, University College London, London

[5] University of Nottingham, Nottingham, UK

ABSTRACT

For cochlear implant (CI) listeners, speech comprehension relies on sensitivity to amplitude modulation (AM) cues across different electrode channels. For a given channel, envelope sensitivity may be impaired for many reasons, not least due to the spread of electrical current and/or neural degeneration.

We used a psychoacoustic task to explore AM discrimination in adult CI listeners (n=12). Listeners discriminated a 40 Hz sinusoidally amplitude-modulated (SAM) pure tone from a 13 Hz SAM tone in a three-interval task, where the modulation depth was varied adaptively. Testing was conducted in the presence or absence of speech envelope modulated interferer tones targeting neighboring electrode channels (± adjacent+1). Stimuli were delivered through headphones, all front-end noise reduction features were de-activated on the speech processor, and the level of each interval was roved (3 dB). By varying carrier frequencies, we measured AM thresholds across a range of targeted electrodes.

AM discrimination was poorer in the presence of interferers, and poorer at higher carrier frequencies. CI performance is also compared to normal hearing cohort (n=12): Although performance was more variable across CI listeners, both groups achieved comparable mean thresholds. Individual thresholds will be correlated with panoramic ECAPs and measures of speech in noise performance.

Keywords: *cochlear implants, amplitude modulation, psychophysics*

[*] ***Corresponding author***: nh572@cam.ac.uk

Copyright: *©2025 First author et al. This is an open-access article distributed under the terms of the Creative Commons Attribution 3.0 Unported License, which permits unrestricted use, distribution, and reproduction in any medium, provided the original author and source are credited.*

1. INTRODUCTION

Cochlear implants (CIs) most commonly function by filtering the acoustic signal into a limited number of frequency channels. The amplitude modulation (AM) envelope within each channel is extracted, and used to modulate a fixed-rate electrical pulse train delivered by a corresponding intra-cochlear electrode. For the perceived sound to correspond meaningfully with the external source, the listener must detect, track, and discriminate temporal envelope cues, both within and across channels. Many factors may limit the transmission of AM cues to a CI listener, but those most pertinent to this research concern the spread of electrical current within the cochlear, and the extent of neuronal survival of the auditory nerve at the corresponding frequency region. Any measure which could estimate these factors on an individual basis would likely prove helpful in guiding implant fitting [e.g., 1, 2, 3].

To this end, we are currently testing and comparing a range of measures to characterize information transmission and selectivity at different electrode sites within the cochlear. These measures include evoked responses to changes in AM rate [4], panoramic ECAP recordings [3], behavioral measures of stream segregation, and behavioral measures of AM discrimination [5]. A overview of the latter measure is presented here, alongside data from two experimental conditions.

2. METHOD

2.1 Listeners

Twelve CI listeners who used Cochlear® devices took part. During the experiment, listeners used their everyday map, but with any noise reduction and automatic scene classification (SCAN) features disabled via clinical software. Twelve normal hearing (NH) listeners also took part and were presented with the default stimuli described below.

2.2 Stimuli

The test signal typically comprised an acoustic tone, of a frequency corresponding to the centre frequency (CF) of electrode 16. This was 1000 Hz for those with maps comprising default electrode-frequency allocations. Listeners discriminated a 'target' test signal from two 'reference' signals. The target rate of sinusoidal AM (SAM) was 40 Hz, and the reference rate of SAM was 13 Hz.

When present, two interferers were presented with frequencies corresponding to the CFs of electrodes 17 and 15 (875 Hz and 1125 Hz by default). Each interferer was modulated with an envelope extracted from an independent sample of speech [6], lowpass filtered at 50 Hz.

Stimuli were presented via an RME Fireface UCX soundcard (Haimhausen, Germany) and Sennheiser HD-600 headphones (Hannover, Germany). Each stimulus component was presented at a random level between 62-65 dB SPL, as calibrated using a Tektronix MDO3024 oscilloscope (Beaverton, OR, USA).

2.3 Method

In a 3I-3AFC adaptive procedure; listeners discriminated a target test signal from two reference signals. There was a 500 ms silence between intervals, and visual feedback was provided.

The experiment used a two-down, one-up adaptive procedure to estimate the 71% correct point on the psychometric function [7]. The depth of SAM applied to the test signal was varied, starting at 80% (i.e., where 100% corresponds to full modulation). The step size was a factor of 1.7 for the first two reversals, reduced to 1.4 for another two reversals, and finally held at 1.15 for four reversals. The geometric mean of the final four reversals is taken as the threshold estimate.

Interferer modulation depth began at 10%, but *increased* when test signal modulation *decreased*, and vice versa. At each step change, interferer modulation depth was scaled by the same factor as that for the test signal.

Listeners completed two runs of each of experimental conditions, and their final threshold estimate was taken as the geometric mean of the estimates derived both each run.

3. RESULTS AND DISCUSSION

Mean thresholds for both CI and NH groups are plotted in Figure 1. Performance was broadly similar across the two groups – both were able to discriminate modulation rates at relatively shallow modulation depths in the absence of interferers, but the presence of interferers markedly impaired performance. A mixed-design ANOVA confirmed a significant effect of interferers [$F(1,22)=161.55$, $p<0.001$, $\eta_p^2=0.88$], but not of group [CI vs. NH, $F(1,22)=2.21$, $p=0.15$, $\eta_p^{2=}0.09$]. The interaction was not significant [$F(1,22)=1.17$, $p=0.29$, $\eta_p^2 0.05$]

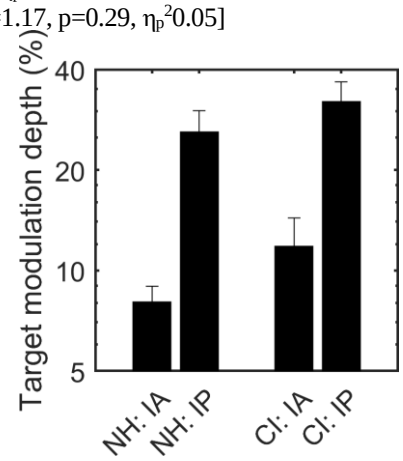


Figure 1. AM discrimination thresholds normal hearing (NH) and cochlear implant (CI) listeners. The task was performed in the absence (IA) or presence (IP) of interferers. Error bars indicate +1 standard error.

Overall, these results show that the task is generally suitable for CI listeners – all performed below ceiling and above floor. The comparable performance between CI and NH groups is consistent with other research showing that CI listeners are broadly as sensitive to SAM as those with NH [8,9]. Further data will be presented which explores 1) changes in performance over carrier frequencies/electrode locations, and the extent to which greater individual variability across frequencies in the CI group may be indicative of poorly functioning electrode regions, 2) correlations between behavioral measures of SAM discrimination and objective measures (ECAPs and EEG-observed cortical evoked responses), and 3) correlations between AM discrimination thresholds and a measure of speech in noise performance [10].

4. ACKNOWLEDGMENTS

This research was supported by an MRC Senior Fellowship in Hearing Research (MR/S002537/1). We thank our CI volunteers for their valuable time and help with this study.

5. REFERENCES

[1] C. J. Long, T. A. Holden, G. H. McClelland, W. S. Parkinson, C. Shelton, D. C. Kelsall, and Z. M. Smith: "Examining the electro-neural interface of cochlear implant users using psychophysics, CT scans, and speech understanding," *Journal of the Association for Research in Otolaryngology*, vol 15, pp. 293–304, 2014.

[2] B. E. Pfingst, N. Zhou, D. J. Colesa, M. M. Watts, S. B. Strahl, S. N. Garadat, and T. A. Zwolan; "Importance of cochlear implant health for implant function," *Hearing Research*, vol. 322, pp. 77–88, 2015.

[3] C. Garcia, T. Goehring, S. Cosentino, R. E. Turner, J. M. Deeks, T. Brochier, T. Rughooputh, M. Bance, and R. P. Carlyon: "The Panoramic ECAP Method: Estimating Patient-Specific Patterns of Current Spread and Neural Health in Cochlear Implant Users," *Journal of the Association for Research in Otolaryngology*, vol. 22, no. 5, pp. 567-589, 2021.

[4] J. A. Undurraga, L. V. Yper, M. Bance, M., D. McAlpine, and D. Vickers: "Neural Encoding of Spectro-Temporal Cues at Slow and Near Speech-Rate in Cochlear Implant Users," *Hearing Research*, vol. 403, article 108160, 2020.

[5] D. A. Vickers, B. C. J. Moore, B. Williges, P. Boyle, M. Salorio-Corbetto, J. Schlittenlacher, and N. R. Haywood: "Using Measures of Amplitude Modulation Processing to Understand Function of Electrically Stimulated Auditory Pathways," *Proceedings of Forum Acusticum*. European Acoustics Association. 2023.

[6] I. Holube, S. Fredelake, M. Vlaming, and B. Kollmeier: "Development and analysis of an International Speech Test Signal (ISTS)," *International journal of audiology*, vol. 49, no. 12, pp. 891–903, 2010.H. C. C.

[7] H. Levitt: "Transformed up-down methods in psychoacoustics," *The Journal of the Acoustical society of America*, vol. 49, no. 2B, pp. 467-477, 1971.

[8] M. Chatterjee, and C. Oberzut: "Detection and rate discrimination of amplitude modulation in electrical hearing," *The Journal of the Acoustical Society of America*, vol. 130, 2pp. 1567-1580, 2011.

[9] M. Fraser, and C. M. McKay: "Temporal modulation transfer functions in cochlear implantees using a method that limits overall loudness cues," *Hearing Research*, vol. 283, no. 1-2, pp. 59-69, 2012.

[10] D. S. Brungart: "Evaluation of speech intelligibility with the coordinate response measure," *The Journal of the Acoustical Society of America*, vol. 109, no. 5, 2pp. 276-2279, 2001.

DOI:

Main theme: A06 Electro-Acoustics

Session A06.03 Loudspeakers and headphones (theory, measurement, applications, MEMS technology, etc.)

Chair(s): L. Rufer, F. Stoppel

DOI: 10.61782/fa.2025.0078

FORUM ACUSTICUM EURONOISE 2025

ACOUSTIC METAMATERIALS FOR ATTENUATING UNWANTED WAVE PHENOMENA IN LOUDSPEAKER ENCLOSURES

Bartłomiej Chojnacki[1*] **Aleksandra Chojak**[1] **Wojciech Binek**[1]
Jan Pawlik[1] **Julia Idczak**[1]
[1] Department of Mechanics And Vibroacoustics, AGH University of Krakow, Mickiewicza Av. 30, 30-059 Cracow, Poland

ABSTRACT

The rapid development of sound-absorbing acoustic metamaterials has opened new ideas for their application. Innovations shared in metamaterial designs — such as reduced material thickness compared to traditional solutions and precise control over absorption bandwidth — show promise in the design of loudspeaker enclosures. This presentation will detail recent advancements at AGH University of Krakow, demonstrating the use of acoustic metamaterials to attenuate standing waves within loudspeaker enclosures and to mitigate back-propagation effects from the driver diaphragm. We will discuss the methodologies for designing metamaterial structures using Transfer Matrix Method simulations, optimization techniques, and neural networks to establish a reliable design and manufacturing process. Results from anechoic chamber experiments conducted for test enclosures equipped with metamaterials will be presented. These cavity-based materials, in both broadband and multi-resonance configurations, offer solutions to problematic wave phenomena within enclosures and present advantages over traditional porous materials, such as improved speaker sensitivity by 1 dB and the elimination of VAS increase due to the use of rigid materials instead of porous ones.

Keywords: electroacoustics, standing waves, loudspeaker sensitivity, resonances, 3D printed metamaterials, acoustic measurement

[*]***Corresponding author***: *bchojnacki@agh.edu.pl*
Copyright: *©2025 First author et al. This is an open-access article distributed under the terms of the Creative Commons Attribution 3.0 Unported License, which permits unrestricted use, distribution, and reproduction in any medium, provided the original author and source are credited.*

1. INTRODUCTION

The utilization of acoustic metamaterials is rapidly expanding across various fields of acoustics. They are particularly noted for their effectiveness in low-frequency absorption when compared to porous or fibrous materials of the same size [1]. This characteristic enables the use of metamaterial absorbers in applications where a low material thickness is essential. One such application is in loudspeaker enclosures, which is the focus of this paper. Previously, acoustic metamaterials in electroacoustics were primarily employed as broadband sound-absorbing structures to mitigate diaphragm back propagation [2], [3]. However, they had not been previously utilized to address the issue of standing waves. This paper presents preliminary research on the application of metamaterial absorbers for standing wave attenuation within loudspeaker enclosures. By employing cavity-based acoustic metamaterials that are tuned to the multiple resonant frequencies of the test enclosure, we demonstrate that metamaterials can effectively reduce standing wave interference. Despite a smooth frequency response in the resonant frequency region, the use of rigid metamaterial structures mitigates the adverse effects of fibrous materials, which usually reduce loudspeaker sensitivity.

2. MULTI-RESONANCE CAVITY-BASED ACOUSTIC METAMATERIALS

Acoustic metamaterials are often designed as cavity-based structures, which may include a combination of quarter-wavelength absorbers [4], [5] or Helmholtz-type absorbers [6], [7]. In this study, we used a set of Helmholtz resonators with a common inlet canal. The desired sound absorption was optimized for the frequency ranges of 215 Hz and 320 Hz, which were previously identified as the first two standing wave frequencies in the measured enclosure. The

sample design process utilized Particle Swarm Optimization (PSO) algorithms alongside the Transfer Matrix Method (TMM), following methodologies established in prior research [8], [9], [10]. The finalized model was encased in a cylinder with a diameter of 100 mm and a depth of 100 mm, ensuring both metamaterial sample and fibrous material used in this investigation had the same depth. Figure 1 illustrates the shape of the canals used in the tested sample and the printed model.

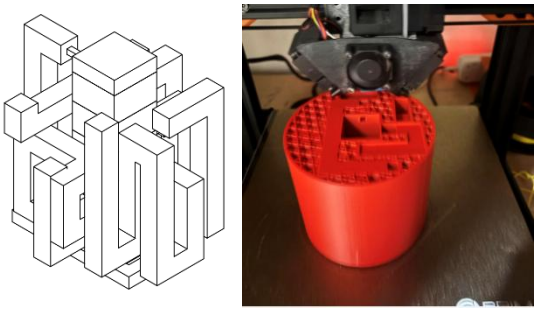


Figure 1. The scheme of the used metamaterial sample (left) and the printed model (right)

To confirm that the manufactured sample met the absorption criteria, its sound absorption coefficient was measured in an impedance tube using the transfer function method. The final sample shape was adjusted to fit into a standard impedance tube with a diameter of 100 mm.

3. MEASUREMENTS OF LOUDSPEAKER ENCLOSURE IN ANECHOIC CHAMBER

To evaluate the influence of the metamaterial samples placed within the loudspeaker enclosure, we conducted acoustic measurements. The enclosure was prepared in three variants: 1) empty, with no absorbing materials inside; 2) with polyester fibers, using a fibrous material of 100 mm depth; and 3) with metamaterials, incorporating six samples of cavity-based metamaterials tuned to the frequency ranges matching the first two modes of air inside the enclosure. Figures 2 and 3 show images of the enclosure's interior with fibrous materials and metamaterials, respectively. Figure 4 depicts the measurement setup.

Acoustic measurements were carried out with a free-field microphone (GRAS46AE) positioned 1 m from the enclosure, aligned with the loudspeaker, similar to loudspeaker sensitivity measurements. A sine sweep signal was utilized to acquire the frequency response of the loudspeaker in the enclosure.



Figure 2. Test enclosure – polyester fibers variant



Figure 3. Test enclosure – metamaterial variant

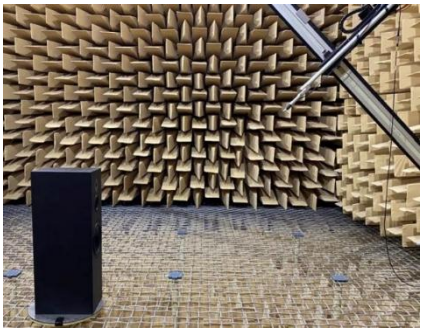


Figure 4. Test enclosure during the acoustic measurements in an anechoic chamber

The frequency response of the loudspeaker was assessed to evaluate the effectiveness of the metamaterial absorbers. The results are presented in Figure 5, which displays the Sound Pressure Level (SPL) measurements alongside the sound absorption coefficients of the metamaterial sample obtained in the impedance tube, which is a common method for this type of material research [11], [12].

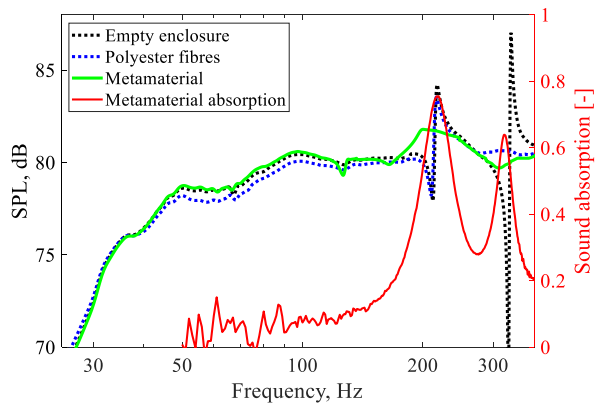


Figure 5. Frequency response of the measured loudspeaker enclosure in three variants

This study aimed to reduce the first two modal frequencies of the air mass confined within the enclosure. It is evident that the metamaterial samples absorbed the resonant frequencies at 215 Hz and 320 Hz, which were observed in the measurements of the empty enclosure, resulting in a smoother frequency response. As shown in Figure 5, the first resonant frequency at 215 Hz was only absorbed with the use of metamaterial samples, while the polyester fibers did not effectively address this low-frequency issue. Moreover, the use of fibrous materials resulted in a significant drop in loudspeaker sensitivity, whereas the incorporation of rigid metamaterial samples allowed for a recovery of the loudspeaker sensitivity.

During the research, it was observed that the absorption bandwidth may be a critical factor for the effective attenuation of standing waves within the enclosure. Designing a single, perfectly tuned resonator would be inefficient as a wider absorption range is typically necessary. This need is evident in the absorption curve, particularly around the 215 Hz point of the tested metamaterial sample. Consequently, an optimized metamaterial design is essential to achieve the desired sound absorption curve.

4. SUMMARY

The preliminary research data presented in this paper demonstrates that cavity-based metamaterial absorbers can effectively reduce the standing wave phenomenon in loudspeaker enclosures. This solution has two main advantages:

- Metamaterials enable absorption of lower frequencies without requiring an increase in the thickness of the absorbing materials.
- The rigid metamaterials used in this research eliminate the sensitivity drop often associated with fibrous materials, resulting in a 1 dB gain in sensitivity.

Metamaterial absorbers hold significant potential for further research in electroacoustics. However, it is crucial to address potential issues that may arise from their application. During the project, it was observed that full-cylinder samples placed inside the enclosure reduced the overall volume, which could negatively impact the loudspeaker's low-frequency response.
Therefore, sound absorption measurements for the samples used are necessary, and it is important to maintain the impedance tube size. It would be beneficial to design samples that do not substantially alter the enclosure volume and could be constructed without an external cylinder. Additionally, further development and testing on various enclosures are required to ensure that the design and manufacturing processes are consistent and that the technology can be successfully transitioned to the development stage.

5. ACKNOWLEDGMENTS

Development of the metamaterial absorbers for loudspeaker enclosures was funded and supported by the Polish Government, National Centre of Research and Development, agreement no. LIDER/11/0065/L-12/20/NCBR/2021.

6. REFERENCES

[1] M. Yang and P. Sheng, “Sound Absorption Structures: From Porous Media to Acoustic Metamaterials,” *Annu Rev Mater Res*, vol. 47, pp. 83–114, 2017, doi: 10.1146/annurev-matsci-070616-124032.

[2] S. Degraeve and J. Oclee-Brown, “Metamaterial Absorber for Loudspeaker Enclosures,” in *Audio Engineering Society Convention 148*, 2020. [Online]. Available: http://www.aes.org/e-lib/browse.cfm?elib=20758

[3] L. Chisari, M. Di Cola, and P. Martignon, “Acoustic metamaterials in loudspeaker systems design,” *147th Audio Engineering Society International Convention 2019*, 2019.

[4] G. Memoli, M. Caleap, M. Asakawa, D. R. Sahoo, B. W. Drinkwater, and S. Subramanian, "Metamaterial bricks and quantization of meta-surfaces," *Nat Commun*, vol. 8, pp. 1–8, 2017, doi: 10.1038/ncomms14608.

[5] Y. Tang *et al.*, "Hybrid acoustic metamaterial as super absorber for broadband low-frequency sound," *Sci Rep*, vol. 7, no. 1, p. 43340, 2017, doi: 10.1038/srep43340.

[6] N. Jiménez, V. Romero-García, V. Pagneux, and J. P. Groby, "Rainbow-trapping absorbers: Broadband, perfect and asymmetric sound absorption by subwavelength panels for transmission problems," *Sci Rep*, vol. 7, no. 1, pp. 1–13, 2017, doi: 10.1038/s41598-017-13706-4.

[7] Y. Li and B. M. Assouar, "Acoustic metasurface-based perfect absorber with deep subwavelength thickness," *Appl Phys Lett*, vol. 108, no. 6, p. 063502, Feb. 2016, doi: 10.1063/1.4941338.

[8] B. Chojnacki, A. Chojak, W. Binek, J. Idczak, and J. Pawlik, "Numerical modeling of the elementary metamaterial cells for the sound-absorbing structure preparation," *Vibrations in Physical Systems*, vol. 35, no. 1, 2024, doi: https://doi.org/10.21008/j.0860-6897.2024.1.14.

[9] A. Chojak, W. Binek, B. Chojnacki, J. Pawlik, and J. Idczak, "The effect of sound-absorbing walls on the acoustic properties of the modelled unit cell of a sound-absorbing metamaterial," *Vibrations in Physical Systems*, vol. 34, no. 2, 2023.

[10] B. Chojnacki, A. Chojak, J. Pawlik, W. Binek, and J. Idczak, "Acoustic metamaterial samples preparation for impedance tube measurements—The influence of different 3D printing techniques and mechanical post-processing on the simulation compliance," *J Acoust Soc Am*, vol. 155, no. 3_Supplement, pp. A59--A59, 2024.

[11] K. Kosała, "Comparative Analysis of the Acoustic Properties of Granular Materials Determined with the Use of Impedance Tube," *Vibrations in Physical Systems*, vol. 33(3), 2022, doi: 10.21008/j.0860-6897.2022.3.21.

[12] A. Flach, "Research on the Influence of Airflow Resistance of Layered Porous Structures on the Sound Absorption Coefficient," *Vibrations in Physical Systems*, vol. 33(3), 2022, doi: 10.21008/j.0860-6897.2022.3.11.

DOI: 10.61782/fa.2025.0405



FORUM ACUSTICUM
EURONOISE 2025

FLAT AND CURVED PARAMETRIC ACOUSTIC LOUDSPEAKERS MEASURED WITH EXPONENTIAL SINE SWEEPS

Augusto Fantinelli[1] **Marc Arnela**[1*]

[1] Human-Environment Research (HER) group, La Salle, Universitat Ramon Llull, Barcelona, Catalonia, Spain

ABSTRACT

Parametric Acoustic Loudspeakers (PALs) utilise ultrasounds to generate an audible field thanks to a non-linear effect in air. This phenomenon is difficult to simulate, so an alternative is to rely on prototyping devices and test them experimentally. Several options exist to manufacture a PAL, the flat surface being the most common. However, transducers can also be set on curved surfaces to attain specific effects. In this paper, a set of four prototypes with different transducer dispositions on flat and convex surfaces are constructed and tested in free-field conditions at several distances. A methodology based on the Exponential Sine Sweep is used for this aim, which allows us to obtain their ultrasonic and audible frequency responses simultaneously. The results were compared with those of a single transducer, revealing significant differences between flat and curved PALs attributed to constructive and destructive interference patterns that vary with transducer arrangement.

Keywords: *parametric acoustic loudspeakers, frequency response, ultrasonic and audible sound fields, exponential sine sweeps, spatial sound-field sampling*

1. INTRODUCTION

Parametric acoustic loudspeakers (PAL) are devices that generate audible sound using ultrasonic transducers [1, 2]. They rely on the Parametric Acoustic Array (PAA) effect, in which the propagation of two ultrasonic frequencies in a medium generates a secondary field that oscillates with the difference between the frequencies. This difference can be tuned to be audible, allowing these devices to reproduce audio focused through the ultrasonic beam, making them useful for a vast gamma of applications [3].

The PAA effect results from the non-linear behaviour of the propagation media at elevated frequencies, and the equations that describe this phenomenon tend to have elevated mathematical and computational complexity [2, 4–7]. This makes the numerical modelling of this type of device difficult. To circumvent the need for simulations, prototypes of PALs can be constructed at relatively low costs since the ultrasonic transducers are inexpensive and 3D printing is currently an accessible process. Notwithstanding, the differences in the sound fields generated by different prototype models still need to be assessed.

This paper presents a comparison between 4 different prototypes of PAL that differ in shape (flat or curved), size, and amount of transducers. Two of them are flat, with one laying 96 transducers in concentric rings up to a diameter of 195 mm [8], while the other has 19 of them in a compact hexagonal distribution with diameter 82 mm. The other two are curved, with one of them being an omnidirectional source with 750 transducers placed on a sphere of 250 mm of diameter [9], and the other being a spherical cap of 91 mm and 19 transducers with the same curvature than the omnidirectional source. Exponential Sine Sweeps (ESS) were adapted and employed to be used in these loudspeakers, allowing the simultaneous measurement of the frequency response in the audible and ultrasonic ranges [10, 11]. A robotic system was used to

*__Corresponding author__: marc.arnela@salle.url.edu.

__Copyright__: ©2025 Augusto Fantinelli and Marc Arnela. This is an open-access article distributed under the terms of the Creative Commons Attribution 3.0 Unported License, which permits unrestricted use, distribution, and reproduction in any medium, provided the original author and source are credited.

place the transducer at increasing distances from 10 mm up to 2.13 m, and the frequency responses were taken at each point.

This paper is structured as follows. Section 2 presents the prototypes and the method used to measure the sound field they generate. Section 3 shows the results obtained for each prototype and presents considerations regarding their differences. Section 4 closes the paper with the conclusions.

2. METHODOLOGY

2.1 Exponential Sine Sweep methodology applied to PAL

An Exponential Sine Sweep (ESS) can be defined as [10]

$$s(t) = K \sin\left[K\ (\exp(t/L) - 1)\right], \tag{1a}$$

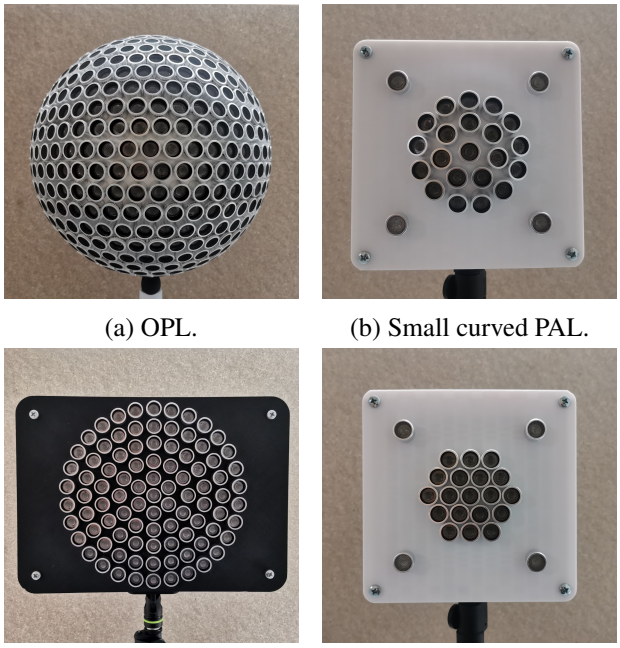
in which

$$K = \frac{2\pi f_1 T}{\ln(f_2/f_1)}, \tag{1b}$$

$$L = \frac{T}{\ln(f_2/f_1)}, \tag{1c}$$

and f_1 and f_2 are the lower and upper frequencies of the sweep, respectively. This represents a sine function of amplitude K in which the argument exponentially increases in time. This sweep is played through a loudspeaker inside an enclosure and recorded by a microphone. The deconvolution of the recorded signal through an inverse filter corresponding to the sweep results in an impulse response that contains information about the speaker, room and microphone. This technique has been vastly used in acoustics due to its robustness to noise and distortion [12–14].

The utilisation of ESSs in PALs [10, 11] requires the sweep to be modulated into a frequency range appropriate to the ultrasonic transducers that form the PAL. The signals, therefore, go through an upper side-band amplitude modulation (USBAM) with a transmitted carrier component. This, in practice, means that the transducers are constantly emitting the transmitted carrier with frequency f_c and whatever the frequency of the sweep signal at that moment. The simultaneous emission of both frequencies triggers the PAA effect. This allows for the frequency responses in the audible and ultrasonic ranges to be measured simultaneously [10, 11].



(a) OPL. (b) Small curved PAL.

(c) Flat PAL. (d) Small flat PAL.

Figure 1: PALs analysed in this work.

2.2 Prototypes

Four prototypes of PAL are considered. They all employ the same transducer model (Multicomp Pro MCUST16A40S12RO), varying in quantity and/or disposition. These transducers are ultrasonic piezoelectric transducers (PZTs) and are connected in parallel in all models. Figure 1 displays the four parametric loudspeakers analysed in this work. The Omnidirectional Parametric Loudspeaker (OPL) was designed and constructed in [9], characterised in [10, 11] and applied in [15] for measuring the random-incidence sound absorption. It has 750 transducers arranged in a sphere with 250 mm of diameter following an equal-area distribution [9]. The OPL directly inspires the next prototype. It is based on its top spherical cap, with 91 mm of diameter and 21 transducers. Next is the flat PAL described in [8], with 96 transducers laid out in six circular rings up to 195 mm of diameter. The last prototype has its transducers set in a hexagonal manner, with three layers and 19 transducers, and has 82 mm of diameter. In addition to the PALs, the same transducer that composed all prototypes was also analysed.

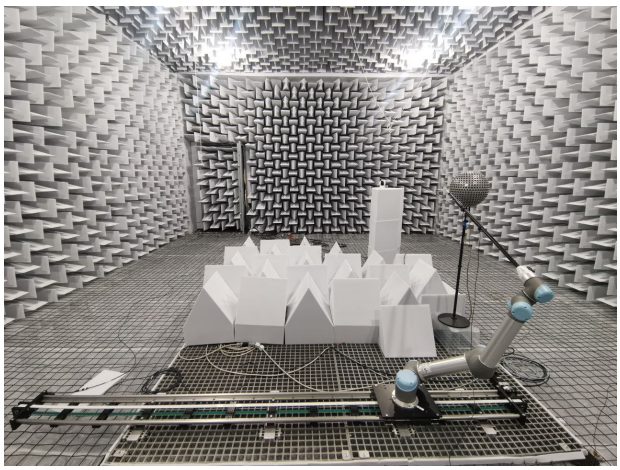


Figure 2: Experimental setup in the anechoic chamber of La Salle - Universitat Ramon Llull, with the robot, the track and the OPL installed.

2.3 Experimental setup

A UR5 (Universal Robots) robotic arm was used to position the microphone aligned with the centre of the irradiation. The robot is mounted over a $2.45\,\mathrm{m}$ linear track (IGUS) so it can be moved around parallel to the x axis of the speaker. The sound field emitted by the prototypes was measured along the centre of the propagation axis for all loudspeakers (aligned with the movement axis of the track) with an interval of $0.04\,\mathrm{m}$, from $0.01\,\mathrm{m}$ to $2.13\,\mathrm{m}$ of distance from the closest transducer. A GRAS 46BF-1 1/4" microphone was attached to the robot by a $1\,\mathrm{m}$ microphone holder, long enough so the robot causes minimal effects in the measured sound field. The generation of the sine sweep and the recordings were made using a Type 3160-A-042 Brüel & Kjaer LANXI module with a UA-3102-041 front end. The signal was amplified using an Ecler XPA3000 amplifier with its gain set in such a way that it provides a peak voltage of $17\,\mathrm{V}$ to avoid damaging the transducers. Fig. 2 displays the experimental setup with the UR5 cobot and the Igus track used to scan the sound field generated by the OPL [9], assembled in the anechoic chamber at La Salle - Universitat Ramon Llull.

The ESSs emitted by the PALs were $1\,\mathrm{s}$ long, from $20\,\mathrm{Hz}$ to $14\,\mathrm{kHz}$, with $2\,\mathrm{s}$ and $3\,\mathrm{s}$ of silence before and after the sweep, respectively. Linear ramps from $20\,\mathrm{Hz}$ to $80\,\mathrm{Hz}$ and $12\,\mathrm{kHz}$to $14\,\mathrm{kHz}$ were added to the sweeps to avoid pre-ringing artefacts, as proposed in [10]. Due to the changes in impedance from one prototype to another and the response of the amplifier, an equalization of the sweep was done to compensate for the change in waveform and maintain the excitation voltage constant [15]. This is specifically important when employing the OPL due to its very capacitive load [15]. In addition, a $1\,\mathrm{kHz}$ modulated pure tone was measured to calibrate the measurement chain. This pure tone was measured at the central position of the array $10\,\mathrm{mm}$ from the loudspeaker. The ESSs were modulated using USBAM with carrier frequency $f_c = 41.4\,\mathrm{kHz}$, selected based on [10]. The same carrier frequency was used for all devices.

3. RESULTS AND DISCUSSIONS

Fig. 3 shows the frequency responses in front of the four PALs and the single PZT transducer for four different distances in the audible and ultrasonic frequency ranges. The first thing of note is that the audible frequency responses have shapes that follow the ultrasonic ones. This is especially noticeable when comparing the frequency responses between the two ranges close to the source, where the highest sound pressure levels (SPLs) occur. It can also be seen that very close to the source, the curved designs produce higher levels than the flat prototypes, except at about $54\,\mathrm{kHz}$, which is the second resonance of this transducer [16]. Note also that they produce the highest levels at low frequencies. This is likely related to the constructive and destructive interaction of the sound waves generated by the arrays, which is modified depending on whether the prototype is flat or curved. With increasing distance, the only PALs that generate over $60\,\mathrm{dB}$ are the flat PAL and the OPL, which have more transducers than the rest. The small flat PAL does not reach large distances compared to other prototypes. This indicates that the constructive and destructive interactions between the individual transducers influence the behaviour of the PAL, and the final resulting emission cannot be estimated with only the amount and the shape of the distribution. As expected, the single transducer also does not generate high level audible sound fields due to insufficient ultrasonic power in the far-field to trigger the PAA.

Fig. 4 displays the generated audible and ultrasonic SPLs along a straight line following the propagation axis in front of the PALs, for $500\,\mathrm{Hz}$, $1000\,\mathrm{Hz}$, $5000\,\mathrm{Hz}$, and $10\,000\,\mathrm{Hz}$. The sound field cast by a PAL can be divided into three zones regarding the distance: a near-field in which there are successive local minima and maxima of

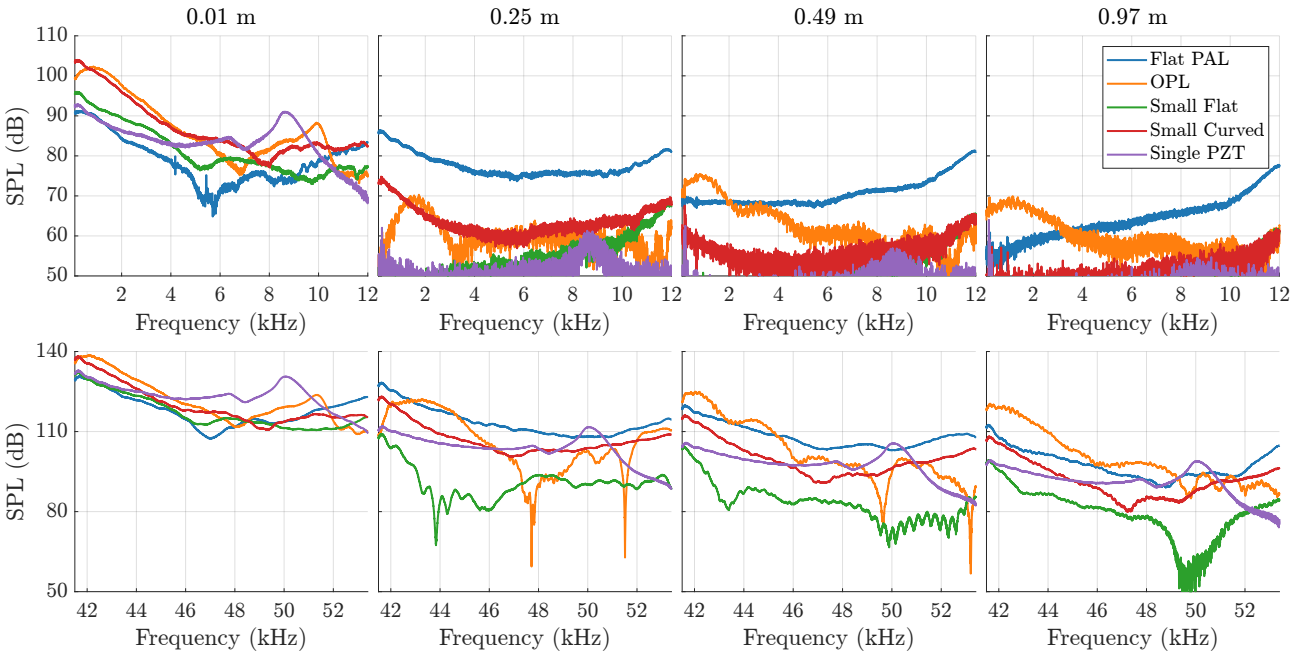


Figure 3: Frequency responses for the four PALs and the single transducer.

sound pressure; the Westervelt far-field, in which the PAL behaves like an infinitely large virtual volume source; and the inverse-law field, in which the inverse-square-law is valid [2]. The inverse-law field typically exists very far from the source, exceeding the dimensions of the anechoic chamber. Therefore, it was not assessed. The transition between near-field and Westervelt far-field can be identified following the criterion introduced by Zhong *et al.* [2]. This transition can be determined by finding the last local maxima of the SPL in the distance. The Westervelt far-field transition distances for the flat circular PAL (F. C. PAL), the flat hexagonal PAL (F. H. PAL), the OPL, and the spherical cap PAL (S. C. PAL) are displayed in Tab. 1. The small flat PAL and the single transducer do not produce high audible SPLs beyond the near-field, likely due to destructive interferences in the former and lack of power in the latter. Another thing of notice is that the flat PAL has a pronounced peak around the transition distance at 500 Hz, 1 kHz, and 5 kHz. Relating with Zhong *et al.*'s analysis [17], this indicates that this corresponds to a region where the sound energy is focused. At 10 kHz, the peak is not as pronounced, and the levels are higher in the Westervelt far-field, indicating the formation of a sound beam despite an initial concentration of energy.

Table 1: Westervelt far-field transition distance (m) at 500 Hz, 1 kHz, 5 kHz and 10 kHz for the flat PAL, the small flat PAL, the OPL, and the small curved PAL prototypes.

	500 Hz	1 kHz	5 kHz	10 kHz
Flat PAL	0.25 m	0.25 m	0.25 m	0.29 m
Small Flat	0.17 m	0.13 m	0.17 m	0.13 m
OPL	0.41 m	0.45 m	0.33 m	0.37 m
Small Curved	0.09 m	0.09 m	0.09 m	0.13 m

Regarding the ultrasonic field generated along the propagation axis (see Fig. 4), observe that the local maxima in the ultrasonic range coincide with the local maxima at the audible range. This indicates that the ultrasonic fields could also be used to determine the transition between near-field and Westerwelt far-field. Another remark is that the ultrasonic levels for the small flat PAL are very low, even lower than the single transducer. This means that, despite this PAL having 19 transducers, their ultrasonic signals suffer destructive interferences, and the generated levels are even lower than for the single transducer. Transducer placement and phase mismatch might be the causes of this phenomenon.

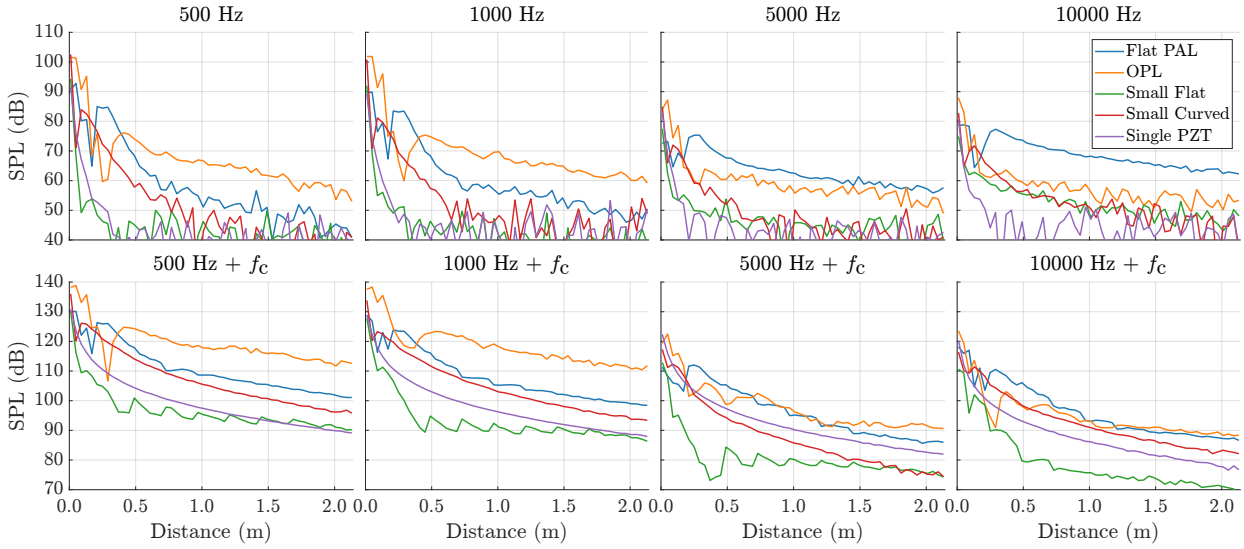


Figure 4: Audible (top) and ultrasonic (bottom) sound pressure levels (SPLs) for each device as a function of the distance from the speaker. $f_c = 41.4$ kHz.

4. CONCLUSIONS

This work has explored the performance of four prototypes of PAL with distinct characteristics: a flat circular PAL (flat PAL), a flat hexagonal PAL (small flat), an omnidirectional PAL (OPL), and a spherical cap PAL (small curved), aiming to assess differences between flat and curved layouts. Their audible and ultrasonic frequency responses were simultaneously measured in free-field conditions using exponential sine sweeps, as well as that of the transducer used to build the arrays. Their behaviour was examined at several distances aligned to their centres employing a robotic system that moved and positioned a microphone.

Results show that the audible and the ultrasonic frequency responses match each other in shape, indicating proportionality between the primary (ultrasonic) and secondary (audible) fields. The curved designs produced higher levels in the near field and reached longer distances compared to the flat prototypes for low and mid frequencies (< 2 kHz), while the flat prototypes have the opposite behaviour and generate the highest values at high frequencies. The flat PAL has a focusing behaviour in lower frequencies, in which the sound energy is concentrated in the transition region of the PAL. The prototypes with curved designs did not present this behaviour and, instead, tended to carry part of the sound energy throughout the distance, although with a pronounced decay at higher frequencies, while retaining part of the energy in the near-field. The small flat PAL generated very low ultrasonic levels in the far-field, which were not enough to trigger the PAA effect. All in all, the above behaviours could be justified by the constructive and destructive interaction of the ultrasonic sound fields generated by each of the transducers that form the array. It seems clear that modifying the number of transducers and their arrangement in the array, whether curved or flat, greatly affects the behaviour of the PAL.

Future work will involve applying near-field acoustical holography (NAH) to these and other prototypes and transducers to investigate the mechanisms of ultrasonic and audible sound generation, as well as the interactions among individual transducers. Their sound fields will also be analysed using pressure maps obtained with the assistance of a robotic measurement system.

5. ACKNOWLEDGMENTS

This work has been funded by MCIN/AEI/10.13039/501100011033 and the European Union - NextGenerationEU through project Sonora (TED2021-132376A-I00). The authors thank the support of the Catalan Government (Departament de Recerca i Universitats) for the grant 2021 SGR 01396 given to the HER group.

6. REFERENCES

[1] F. J. J. Pompei, *Sound from ultrasound*. PhD thesis, Massachusetts Institute of Technology, 2002.

[2] J. Zhong, R. Kirby, and X. Qiu, "The near field, westervelt far field, and inverse-law far field of the audio sound generated by parametric array loudspeakers," *J. Acoust. Soc. Am.*, vol. 149, no. 3, pp. 1524–1535, 2021.

[3] Holosonics, "Audio spotlight directional speakers." `https://www.holosonics.com/applications`. Last accessed 2025-04-07.

[4] O. Guasch and P. Sánchez-Martín, "Far-field directivity of parametric loudspeaker arrays set on curved surfaces," *Appl. Math. Model.*, vol. 60, pp. 721–738, 2018.

[5] J. Zhong, S. Wang, R. Kirby, and X. Qiu, "Insertion loss of a thin partition for audio sounds generated by a parametric array loudspeaker," *J. Acoust. Soc. Am.*, vol. 148, no. 1, pp. 226–235, 2020.

[6] J. Zhong, S. Wang, R. Kirby, and X. Qiu, "Reflection of audio sounds generated by a parametric array loudspeaker," *J. Acoust. Soc. Am.*, vol. 148, no. 4, pp. 2327–2336, 2020.

[7] J. Zhong, R. Kirby, M. Karimi, H. Zou, and X. Qiu, "Scattering by a rigid sphere of audio sound generated by a parametric array loudspeaker," *The Journal of the Acoustical Society of America*, vol. 151, pp. 1615–1626, 03 2022.

[8] M. Avelar, M. Arnela, C. Martínez-Suquía, L. Sant'Ana, and E. Brandão, "Medicão de coeficiente de espalhamento sonoro (scattering) em câmara anecoica, com auxílio de fontes sonoras paramétricas," in *XIII Iberoamerican Congress of Acoustics*, (Santiago, Chile), Iberoamerican Acoustics Federation, 2024.

[9] M. Arnela, O. Guasch, P. Sánchez-Martín, J. Camps, R. M. Alsina-Pagès, and C. Martínez-Suquía, "Construction of an omnidirectional parametric loudspeaker consisting in a spherical distribution of ultrasound transducers," *Sensors*, vol. 18, no. 12, p. 4317, 2018.

[10] M. Arnela, C. Martínez-Suquía, and O. Guasch, "Characterization of an omnidirectional parametric loudspeaker with exponential sine sweeps," *Appl. Acoust.*, vol. 182, p. 108268, 2021.

[11] M. Arnela, C. Martínez-Suquía, and O. Guasch, "Carrier frequency influence on the audible and ultrasonic fields generated by an omnidirectional parametric loudspeaker excited with exponential sine sweeps," *Appl. Acoust.*, vol. 200, p. 109073, 2022.

[12] A. Farina, "Simultaneous measurement of impulse response and distortion with a swept-sine technique," in *Audio Engineering Society Convention 108*, (Paris, France), pp. 1–24, Audio Engineering Society, 2000.

[13] S. Müller and P. Massarani, "Transfer-function measurement with sweeps," *Journal of the Audio Engineering Society*, vol. 49, pp. 443–471, 2001.

[14] A. Farina, "Advancements in impulse response measurements by sine sweeps," in *Audio Engineering Society Convention 122*, (Vienna, Austria), pp. 1–21, Audio Engineering Society, 2007.

[15] M. Arnela, R. Burbano-Escolà, R. Scoczynski Ribeiro, and O. Guasch, "Reverberation time and random-incidence sound absorption measured in the audible and ultrasonic ranges with an omnidirectional parametric loudspeaker," *Applied Acoustics*, vol. 229, p. 110414, 2025.

[16] A. Fantinelli, M. Arnela, R. Burbano-Escolà, and J. Vaquerizo-Serrano, "A study of the ultrasonic and audible frequency response of commercial loudspeakers for use as parametric acoustic arrays," in *Inter-noise 2024*, (Nantes, France), International Institute of Noise Control Engineering, 2024.

[17] J. Zhong, T. Zhuang, R. Kirby, M. Karimi, X. Qiu, H. Zou, and J. Lu, "Low frequency audio sound field generated by a focusing parametric array loudspeaker," *IEEE/ACM Transactions on Audio, Speech, and Language Processing*, vol. 30, pp. 3098–3108, 2022.

DOI: 10.61782/fa.2025.0468

FORUM ACUSTICUM EURONOISE 2025

INFLUENCE OF COIL WINDING MATERIAL ON THE PERFORMANCE OF ELECTRODYNAMIC LOUDSPEAKERS

Martínez-Iranzo, José [1*] **Martínez-Piá, Carla** [2] **Carbajo-San Martin, Jesús** [1]
Poveda-Martínez, Pedro [1] **Ramis-Soriano, Jaime** [1] **Segovia-Eulogio, Enrique G.** [3]
[1] Department of Physics, Systems Engineering, and Signal Theory, University of Alicante, Spain
[2] Department of Technology, Montmeló High School, Montmeló, Spain
[3] Civil Engineering Department, University of Alicante, Spain

ABSTRACT

This work presents an analytical method to determine which material -copper or aluminum- is more suitable for coil winding, based on the initial specifications of the transducer. The proposed approach compares the coil mass to the total moving mass and establishes a threshold value that defines the suitability of each material for achieving maximum efficiency.
Initial method relies on minimal variables, primarily derived from the original loudspeaker model. These variables include the total moving mass (M_{MS}), encompassing all moving parts, such as the air load on both sides of the diaphragm, and the material used for the coil conductor.
The role of the voice coil, however, differs from some perspectives presented in the literature, particularly those equating the coil mass to the total moving mass, a simplification that is not realistic for a transducer characterized by inherently low efficiency.
Additionally, the analysis accounts for variations in the Bl force factor caused by the physical differences between copper and aluminum for the same electrical resistance, due to the alterations in the air gap volume.

Keywords: *Electrodynamic loudspeaker, voice coil, moving mass, transducer efficiency.*

1. INTRODUCTION

This article proposes a novel approach in the development of the electrodynamic loudspeaker, focusing on the optimization of the voice coil. The objective is to achieve results comparable to those obtained through conventional methods but with lower time and costs, as well as a significant reduction in the carbon footprint during the manufacturing process.
To this end, a comprehensive study of the voice coil is presented, analyzing various improvement criteria and refining its performance to achieve an optimal balance between performance and cost. The importance of optimizing the coil mass in relation to the moving masses is discussed, and a solution based on the limit value theory is proposed. This approach allows for performance maximization through changes in the material of the winding wire as well as in the geometry of its cross-section.
As mentioned, equating the coil mass to the remaining moving masses would require a significant increase in the size of the magnetic circuit, which is economically unfeasible [1]. On the other hand, some authors propose reducing the coil size to match the total moving mass [1, 2], but this would introduce technical challenges that are difficult to resolve. Therefore, the approach should focus on maximizing efficiency while retaining the original components, with some modifications in the properties of the voice coil conductor.
For certain types of loudspeakers, copper is traditionally preferred for voice coil construction due to its excellent conductivity and mechanical strength. Consequently, it is the most widely used material in low and mid-frequency direct-radiation models. Conversely, aluminum is recommended in high-frequency loudspeakers and compression drivers, mainly due to its low density [3].
Although this criterion may involve some subjectivity, it is the most applied approach in loudspeaker manufacturing. This study challenges this practice and proposes a method to determine the suitability of one material over another to

[*] ***Corresponding author***: jmi21@alu.ua.es
Copyright: *©2025 First author et al. This is an open-access article distributed under the terms of the Creative Commons Attribution 3.0 Unported License, which permits unrestricted use, distribution, and reproduction in any medium, provided the original author and source are credited.*

achieve maximum loudspeaker performance if that is the objective or to optimize the magnetic circuit for a given performance level.

2. APPROACH

In loudspeaker design, it is not usual to conduct a preliminary study to determine the optimal coil mass to maximize system performance. Typically, the dimensions and construction characteristics of the voice coil -such as diameter, conductor material, winding width, among others- are dictated by parameters such as electrical resistance, power capacity, maximum linear displacement, or peak displacement, etc. However, this study aims to justify the need to refine the coil based on additional criteria that enable maximum performance. This includes improving the *Bl* product with an optimized moving mass and dissipation while also achieving the desired power and efficiency characteristics through magnetic circuit optimization. The latter is a critical component in terms of weight and cost, highlighting its relevance in the overall design and efficiency of the system.

2.1 Voice coil mass versus efficiency

The efficiency of the loudspeaker in the mid-frequency range can be expressed using the following equation:

$$\eta = K\frac{{S_D}^2 B^2 l^2}{R_E M_{MS}^2} \quad (1)$$

Where the terms affected by the change in the coil are the wire length l of the coil and the moving mass M_{MS}.

This expression can be expanded by substituting the electrical resistance R_E in terms of the resistivity of the material ρ, as well as the length l and cross-sectional area s of the conductor. Additionally, M_{MS} can be replaced by the sum of the individual masses that comprise it.

$$\eta = K\frac{{S_D}^2 B^2 l^2}{\rho\frac{l}{S}\cdot(2M_A+M_{MD}+M_{MVC})^2} = K\frac{{S_D}^2 B^2 lS}{\rho(2M_A+M_{MD}+M_{MVC})^2} \quad (2)$$

With M_A being the mass of the air load on the membrane, M_{MD} the mass of the membrane, spider, and dust cap, and M_{MVC} the mass of the coil.

In the numerator, the product of l and S appears, representing the volume of the winding. By mathematical adjustment, the coil mass M_{MVC} is obtained.

$$\eta = K'\frac{{S_D}^2 B^2 M_{MVC}}{(2M_A+M_{MD}+M_{MVC})^2} \quad (3)$$

By taking the derivative of Equation (3) with respect to M_{MVC} and equating it to zero, the condition for maximizing efficiency is found.

$$M_{MVC} = 2M_A + M_{MD} \quad (4)$$

This condition suggests that the coil mass M_{MVC} must equal the mass of the remaining moving components (Fig. 1, solid line).
However, this solution is unrealistic. Compelling the coil mass to match the total moving mass would require an extremely powerful magnetic circuit to maintain a constant *Bl* product, resulting in prohibitively high costs. Nevertheless, even with a variable *Bl* product, there is an optimal value for the coil mass relative to the total moving mass that maximizes efficiency (Fig. 1, dashed line).

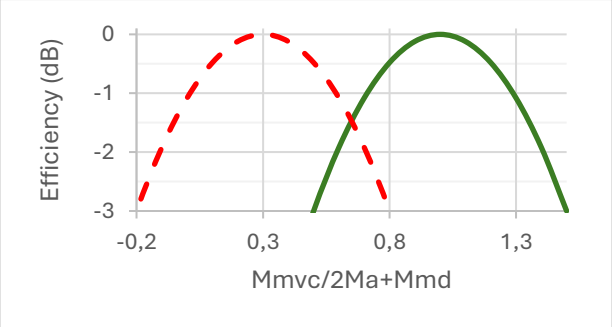


Figure 1. Efficiency versus voice coil mass

2.2 Influence of the conductor material on efficiency

This study aims to determine which of the two analyzed materials (copper or aluminum) is more suitable for voice coil construction to optimize loudspeaker efficiency. To achieve this, the expression for efficiency in Equation (1) is considered, depending on the *Bl* product and the moving mass.
Since efficiency is directly proportional to the first term and inversely proportional to the second- both terms squared- it can be stated that this relationship serves as the determining criterion, as the other terms in the equation remain constant regardless of the material used for the winding.

2.3 Determination of variables affecting efficiency

From the expression for the electrical resistance of the loudspeaker coil:

$$R_E = \rho \frac{l}{S} \quad (5)$$

The ratio of the aluminum wire diameter, w_{DAl}, to the copper wire diameter, w_{DCu}, is obtained:

$$w_{DAl} = 1{,}17 w_{DCu} \quad (6)$$

Using these values and taking μ as the material density, the coil mass M_{MVC} can be calculated as:

$$M_{MVC} = \mu l S \quad (7)$$

From this, it follows that the mass of the aluminum coil M_{MVCAl} relative to the copper coil mass M_{MVCCu} is:

$$M_{MVCAl} = 0{,}355 M_{VCCu} \quad (8)$$

This indicates that, for a coil with the same electrical resistance R_E, voice coil diameter V_{CD}, and winding width w_L, the aluminum wire diameter must be 17% larger than that of copper. Furthermore, based on this relationship, the aluminum coil mass is approximately one-third that of the copper coil.

2.4 Variation of the *Bl* product due to the change in the voice coil material

For magnetic systems such as the one illustrated in Fig. 2, empirical studies have shown that the magnetic flux Φg in the air gap can be calculated using the following expression [4]:

$$\Phi_g = \frac{L_m B_R / 1.07\mu_0}{(L_g/\mu_0 A_g)(27.5\mu_0 L_m R_m + 1.55) + L_m/1.07\mu_0 A_m} \quad (9)$$

Where

B_R Residual induction
R_m Magnet reluctance
A_m Magnet cross section area

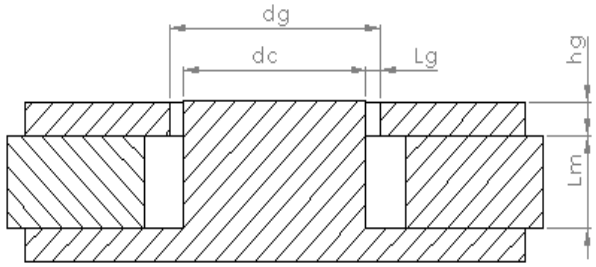


Figure 2. Section of the loudspeaker magnet system

By applying these results, it is possible to determine the variation in the air gap size and, using Eq. (10) and (11), calculate the difference in magnetic induction B between the two coils:

$$B = \frac{\Phi_g}{A_g} \quad (10)$$

Where the air gap area Ag is given by:

$$A_g = \pi(d_c + L_g)h_g \quad (11)$$

Initial calculations performed with the air gap dimensions for the copper coil, and subsequently adjusted for the aluminum coil, reveal a 3.5% reduction in magnetic induction B when switching from copper to aluminum. On the other hand, the reduction in the second term, l, is due to the increase in the wire diameter when using aluminum, which leads to a decrease in the number of turns and, consequently, in the total wire length, according to the following relationship:

$$l_{Al} = 0.854 l_{Cu} \quad (12)$$

Based on these variations, the ratio of the Bl product for the aluminum coil to that of the copper coil can be expressed as:

$$Bl_{Al} = 0.824 Bl_{Cu} \quad (13)$$

3. CONCEPT OF THE LIMIT VALUE BASED ON THE COIL MATERIAL

As discussed earlier, this study aims to select the voice coil wire material based on criteria for either maximizing efficiency or optimizing the magnetic motor. Without requiring prior analysis of the magnetic circuit, the choice between copper and aluminum can be deduced using the criteria outlined below.

3.1 Initial considerations

In the early loudspeaker design, constraints related to the moving mass (e.g., membrane, suspensions, and other moving parts) are established. Similarly, the geometric dimensions of the coil are defined based on power handling, electrical resistance, linear displacement, etc. With these values and Equation (1), the efficiency equivalence for both materials can be expressed as:

$$K \frac{(Bl)^2_{Cu}}{R_{ECu}(M_{MS})^2_{Cu}} = K \frac{(Bl)^2_{Al}}{R_{EAl}(M_{MS})^2_{Al}} \quad (14)$$

Since the electrical resistance is the same (R_{ECu}= R_{EAl}), it cancels out along with other constants. On the other hand:

$$2M_A + M_{MD} = M_X \quad (15)$$

Substituting M_{MS} according to Equations (1) and (15), and simplifying, yields:

$$\frac{Bl_{Cu}}{M_{MX}+M_{MVC_{Cu}}} = \frac{Bl_{Al}}{M_{MX}+M_{MVC_{Al}}} \quad (16)$$

Reordering terms:

$$\frac{Bl_{Cu}}{Bl_{Al}} = \frac{M_{MX}+M_{MVCCu}}{M_{MX}+M_{MVCAl}} \quad (17)$$

Substituting and solving using Equations (8) and (13),

$$\frac{M_{MX}}{M_{MVC_{Cu}}} = 2.66 \quad (18)$$

This implies that when the ratio of M_{MX} to the copper coil mass equals 2.66, both materials yield equivalent performance. For ratios below 2.66, aluminum is better, whereas ratios above 2.66 favor copper (Fig. 3).
It is easy to deduce that, when the ratio in Equation (18) exceeds the indicated value, the weight of the moving parts other than the voice coil becomes predominant. As a result, the coil mass is not as critical, and a higher *Bl* product is preferable.

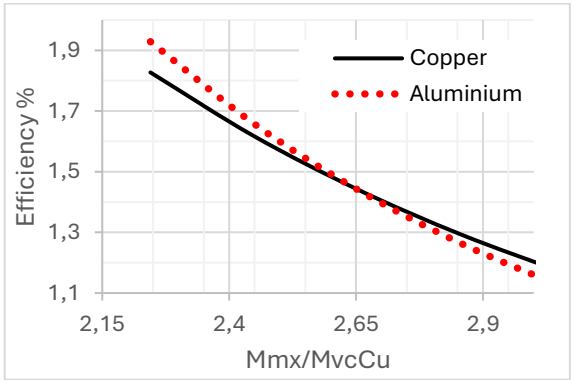


Figure 3. Variation of the efficiency

According to Equation (13), this is achieved with a copper coil. On the other hand, if the value is below 2.66, the coil mass becomes dominant. In this case, the lightest possible coil is desirable, which is achieved with aluminum, despite having a lower *Bl* product.

3.2 Example

A loudspeaker is selected from a well-known manufacturer that provides the following data: Loudspeaker size: 18" (46 cm), with 100 mm voice coil diameter, made of 0.50 mm diameter copper wire. The M_{MX}/M_{MV} value is 1,32, so less than 2.66. According to this, the efficiency will be higher with an aluminum coil. A 30% increase in efficiency has been confirmed by changing the coil wire material, according to the procedure seen above (Tab. 1).

Table 1

Coil Material	M_{MVC} Kg	M_{MS} Kg	M_{MX} Kg	Bl N/A	η %
Copper	0,099	0,23	0,131	29	2,7
Aluminun	0,035	0,166	0,131	23,9	3,5

4. PERFORMANCE VARIATION DUE TO WIRE CROSS-SECTION GEOMETRY

The conventional geometry for the voice coil conductor is circular, from which the packing factor can be obtained. This factor represents the ratio between the actual volume of the wire and the total volume of the winding (Fig. 4a). In this case, the packing factor is 78.5%. It is also possible to use rectangular cross-section wire, which achieves a 100% packing factor (Fig. 4b).

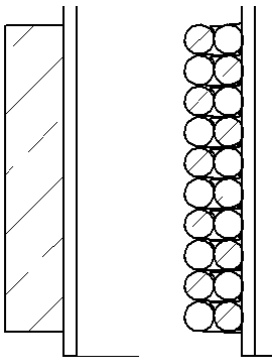


Figure 4a. Difference between voice coil volume (left) and wire volume (right)

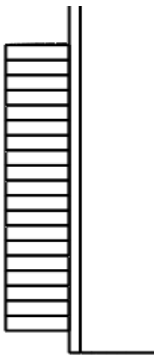


Figure 4b. Voice coil with edge wound rectangular wire

This allows the wire length and cross-sectional area to be increased while maintaining the electrical resistance. Obviously, this configuration enhances the Bl product.

4.1 Calculation of rectangular cross-section voice coil parameters

When switching from one geometry to the other, certain dimensions are preserved, such as the winding length (w_L) and the inner and outer diameters of the winding, which avoids modifications to the air gap dimensions.
Additionally, while the round-wire coil uses two layers in the winding, the rectangular-wire coil only uses one. Consequently, the height of the rectangular-section wire (h) will be equal to $2w_D$.

$$l = \frac{2w_L V c_D \pi}{w_D} \tag{20}$$

By substituting (considering the number of layers n is equal to 1, and the wire thickness denoted as t.

$$l = \frac{w_L V c_D \pi}{t} \tag{21}$$

4.2 Rectangular vs. Circular Cross-Section Conductor

Due to its higher packing factor, the rectangular cross-section coil will have a greater number of turns, thereby increasing the Bl product.
Expressing the electrical resistance based on the rectangular wire cross-section geometry:

$$R_{E\,FLAT} = \rho \frac{w_L V c_D \pi}{h t^2} \tag{22}$$

4.2.1 Calculation of wire thickness

As previously defined, $h = 2w_D$. The thickness can be obtained from the following expression:

$$R_E = \rho \frac{2w_L V c_D \pi}{\frac{w_D{}^2 \pi}{4}} = \rho \frac{w_L V c_D \pi}{h t^2} \tag{23}$$

Solving for t:

$$t = 0{,}44 w_D \tag{24}$$

4.2.2 Determination of rectangular wire coil mass

The mass is expressed as:

$$M_{MVC\,Round} = lS\mu = \frac{2w_L V c_D \pi^2 w_D^2}{4w_D}\mu \tag{25}$$

$$M_{MVC\,FLAT} = lS\mu = \frac{w_L V c_D \pi}{t} h t \mu \tag{26}$$

Resulting in:

$$M_{MVC\,FLAT} = 1{,}273 M_{MVC\,Round} \tag{27}$$

Since the air gap volume remains unchanged, the new value of l is derived using equations (25) and (26):

$$l_{Rect} = 1{,}136 l_{Round} \tag{28}$$

Thus

$$Bl_{FLAT} = 1{,}136 Bl_{ROUND} \tag{29}$$

4.3 Critical value between round and rectangular wire coils

Following the methodology in Section 4.1, equation (16) is adapted by substituting materials with the cross-sections:

$$\frac{Bl_{ROUND}}{M_{MX} + M_{MVC\,ROUND}} = \frac{Bl_{FLAT}}{M_{MX} + M_{MVC\,FLAT}} \tag{30}$$

From this, it results:

$$\frac{M_{MX}}{M_{MVC\,ROUND}} \approx 1 \tag{31}$$

This solution demonstrates that no critical value exists to equalize the performance of voice coils with circular versus rectangular cross-section geometries. In practice, since the rectangular wire coil mass M_{MVC} is significantly smaller than other moving masses, the improvement in Bl product will enhance overall performance. This improvement depends on the ratio M_{MX}/M_{MVC}, with greater benefits as this ratio increases.

5. CONCLUSION

It has been possible to establish the advantages of analyzing the loudspeaker coil to achieve a balance between the mass of moving parts, excluding the voice coil and the voice coil mass itself.
While the optimal solution -equating both masses- is economically unviable or practically unattainable, it has been demonstrated that selecting the appropriate conductor material, copper or aluminum, allows for

either maximizing efficiency or optimizing the magnetic circuit. This approach offers both economic and technical advantages.

Additionally, the feasibility of using alternative wire cross-section geometries to increase the packing factor and consequently, the Bl product, has been outlined. This improvement is universally beneficial, particularly in bigger diameter models. In such cases, the higher manufacturing cost of flat wire voice coil (compared to more economical round wire voice coil) is compensated by the potential to reduce the magnetic circuit volume.

6. ACKNOWLEDGMENTS

This publication is part of the project PID2021-127426OB-C22, funded by MCIN/AEI/10.13039/501100011033 and by the European Union "NextGenerationEU"/PRTR," with the reference indicated in the grant resolution. MCIN stands for the Ministry of Science and Innovation; AEI stands for the State Research Agency; 10.13039/501100011033 is the Digital Object Identifier (DOI) of the Agency; and PRTR stands for the Recovery, Transformation, and Resilience Plan.

8. REFERENCES

[1] F. Brouchier: *Haut-parleurs et Enceintes Acoustiques, Théorie et Pratique.* Accessed March 4, 2025. https://orba.cpd.ua.es/?_task=mail&_frame=1&_mbox=INBOX&_uid=393&_part=2&_action=get&_extwin=1 ,

[2] L. L. Beranek and T. J. Mellow: *Acoustics: Sound Fields and Transducers,* UK: Academic Press, 2012

[3] J. King: "Loudspeakers Voice Coils," in *Journal of the Audio Engineering Society*, Volume 18, Issue 1, pp 34–43

[4] Philips. (1984). *Permanent magnet materials*: *Data handbook.*

[5] L. L. Beranek: *Acoustics,* USA: McGraw-Hill, 1954

[6] M. R. Gander: "Moving Coil Loudspeaker Topology as an Indicator of Linear Excursion Capability", in *Journal of the Audio Engineering Society*, vol. 29, no. 1, 1981, pp. 36–43

[7] J. Borwick: *Loudspeaker And Headphone Handbook,* London: Butterworths and Co, 1988

DOI: 10.61782/fa.2025.0662

FORUM ACUSTICUM EURONOISE 2025

OPTIMIZATION OF CAVITIES AND SUSPENSIONS IN UNDERWATER ACOUSTIC PROJECTORS: ANALYTICAL AND EXPERIMENTAL STUDY

Martínez-Iranzo, José [1*] **Carbajo-San Martín, Jesús**[1] **Poveda-Martínez, Pedro**[1]
Ramis-Soriano, Jaime[1] **Segovia-Eulogio, Enrique G.**[3] **Martínez-Piá, Carla**[2]
[1] Department of Physics, Systems Engineering and Signal Theory, University of Alicante, Spain
[2] Department of Technology, Montmeló High School, Montmeló, Spain
[3] Civil Engineering Department, University of Alicante, Spain

ABSTRACT

This paper focuses on the design and analysis of an underwater acoustic projector based on a conventional loudspeaker, with particular emphasis on the role of the intermediate cavity between the loudspeaker and the radiating diaphragm, as well as the suspension properties of both components. The design, which eliminates direct contact between the loudspeaker and the diaphragm, presents unique challenges in efficiently transmitting mechanical energy from the former to the latter while minimizing losses.
The study explores how the cavities volume and suspension characteristics (linearity, stiffness, and damping) influence the low-frequency response by analyzing the first modes of the diaphragm. Using analytical approaches and experimental models, comparative studies are presented to optimize the system configuration.
This arrangement offers a significant advantage by eliminating the need for compensating the fluid pressure exerted on the diaphragm in shallow waters, without affecting the coil rest position within the magnetic gap.

Keywords: *Underwater projector, loudspeaker, radiating diaphragm, cavity volume.*

[*] ***Corresponding author***: *jmi21@alu.ua.es*
Copyright: *©2025 First author et al. This is an open-access article distributed under the terms of the Creative Commons Attribution 3.0 Unported License, which permits unrestricted use, distribution, and reproduction in any medium, provided the original author and source are credited.*

1. INTRODUCTION

The purpose of this work is to analyze the behavior of the cavities that form the projector, particularly their influence on the response and passband. Additionally, it aims to define the type of suspension and dimensions based on the piston size to optimize the low cutoff frequency and performance in water, for submersions up to 3 meters deep, while avoiding nonlinearities caused by the static displacement of the resting point of the coil.
In this type of design, numerous references exist for audio applications [1, 2, 3], highlighting the possibility of varying the passband or efficiency [2, 3], as well as limiting low frequency displacement due to the membrane being loaded on both sides. A vent is typically used because of the ease of tuning the enclosure to the desired frequency. The use of a passive diaphragm has been described on some occasions [3, 4], but no practical or commercial applications are known in this field.

2. PROJECTOR DESCRIPTION

To protect the inside loudspeaker from the effects of hydrostatic pressure when submerged in water, a system has been conceived based on the symmetrical loading system used in some speaker enclosures. This system consists of placing the loudspeaker inside an enclosure formed by two cavities (Fig. 1, 2). The rear cavity (V1) is airtight, while the other (V2) contains a passive diaphragm that allows sound to propagate outward.

2.1 Design of the prototype

This design, reminiscent of one previously presented in an earlier communication [5], differs primarily in the absence

of the element that connected the loudspeaker coil to the external diaphragm. This significantly reduces the displacement of the coil from its resting point due to the hydrostatic pressure exerted on the diaphragm. This aspect is crucial since, as will be discussed later, the aim is to use a loudspeaker with a very short voice coil.

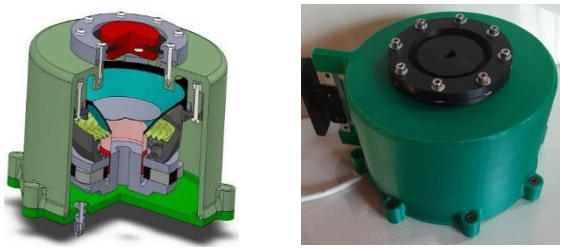


Figure 1. Section of the projector (left), and prototype photo (right)

This type of assembly is derived from the sealed back chamber bandpass enclosure, used in audio systems for very low-frequency applications. It is characterized by a frequency response like a bandpass filter, with a bandwidth of slightly more than two octaves. Since the loudspeaker is loaded on both sides, it exhibits minimal displacement. This allows for the use of a voice coil with a very short winding width. As a result, with all the turns remaining within the magnetic gap, both efficiency and power handling capacity are improved.

2.2 Construction

Obviously, models that radiate into the air require a large loudspeaker size and a significant volume to achieve a low cutoff frequency with high sensitivity. In the case of the described model, due to the difference in radiation impedance between air and water, a small diaphragm with a relatively high mass is used (Fig. 2).

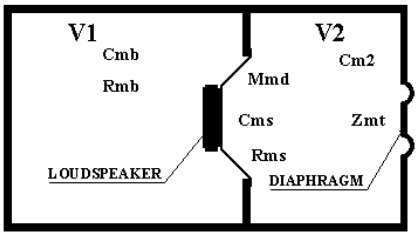


Figure 2. Band pass cabinet

3. ELECTRO-MECHANICAL CIRCUIT

Fig. 3 shows the mechanical circuit, with all the elements involved in it.

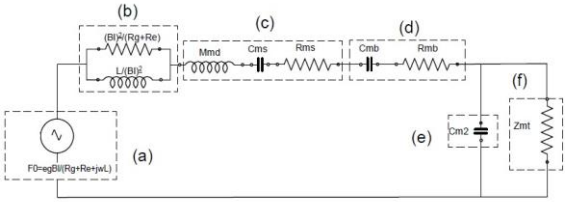


Figure 3. Mechanical circuit of the direct-radiator loaded on both sides: (a) force, (b) electrical components referred to the mechanical side, (c) mechanical elements of the loudspeaker, (d) rear side box, (e.) front side box, (f) mechanical impedance of the passive diaphragm

4. RESULTS AND DISCUSSION

Based on previous model experience, a free air resonance frequency is established around 100 Hz, as the increase in moving mass—due to the added mass of water—will shift the main mode below this value, which is the requested low cutoff frequency for this model.

4.1 Passive diaphragm characteristics

To minimize the efforts induced by hydrostatic pressure, the area is reduced to one-fourth of the total area of the membrane. A suspension with the required stiffness is employed to match the properly required free air resonance, as described above. To confirm this value, a known mass is applied, and the resulting displacement is measured using a laser sensor (Fig. 4).



Figure 4. Measurement of the resting point (left), and the displacement with a known mass (right)

This experiment is conducted using the same piston diameter, but with different suspension areas.
The first suspension, (model C), has a smaller area than model D. This difference has a strong impact on stiffness K and in the free air resonant frequency, (Tab. 1). The diaphragm mass is defined by the material and production conditions, in this case printing 3D techniques.

Table 1

Diaphragm Model	Suspension Area cm^2	K N/m	Diaphragm Mass Kg	Fs Hz
C	4,5	30430	0,038	142
D	9,5	9360	0,038	79

4.2 Parametric study

Different measurements are conducted on both the active and the passive model, while also analyzing the influence of the cavities. Because the nature of the components, an impedance measurement of the 5" loudspeaker (active model), will be done. On the other hand, the passive diaphragm has no way to achieve a direct electrical measure, so a sensor (accelerometer) will be affixed to the piston, to see how it performs.

4.2.1 Influence of the passive diaphragm

The accelerometer is placed on the back side of the piston and is excited by the loudspeaker in all the audible range of frequencies (Fig. 5).

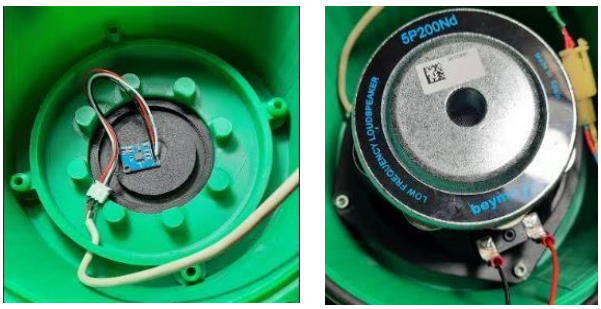


Figure 5. Accelerometer fixed on the back side of the piston (left) with the 5" unit mounted inside the cabinet (right)

Figure 6 shows the shift in the first peak of impedance when replacing the diaphragm. In the case of model C, this peak is located around 200 Hz (solid line), whereas in model D, a downward shift is observed, placing it around 105 Hz (dashed line).

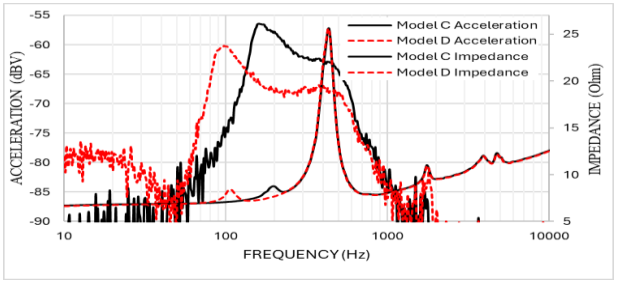


Figure 6. Impedance and Acceleration, with models C and D diaphragms

The first mode has a very low amplitude due to the air load enclosed in both cavities, on both sides of the loudspeaker. The second mode remains unchanged in both frequency and amplitude. The tuning frequency, which is the minimum value between both peaks, is also clearly modified. The acceleration measurements show a broader frequency response for diaphragm D (dashed line), while for model C, the response is substantially reduced at lower frequencies (solid line). As the passband widens, efficiency decreases.

4.2.2 Influence of the front cavity

This cavity, located between the loudspeaker and the diaphragm, behaves as a low-pass filter. Therefore, it should affect the response at the upper cutoff frequency. Figure 7 exhibits the behavior, with the first peak located around 150 Hz, and the second one, at 445 Hz.

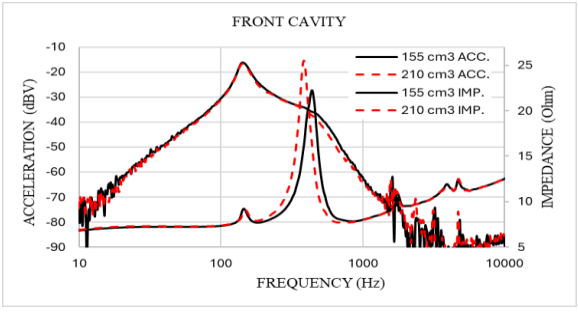


Figure 7. Impedance and acceleration for different volumes

After modifying the volume, increasing up to 210 cm^3, the first peak remains at the same value, meanwhile the second is placed at 390 Hz. The amplitude of the peak rises due to the increase of the air chamber compliance.

4.2.3 Influence of the rear cavity

The rear cavity is completely sealed, loading the loudspeaker from the rear side. The air enclosed inside represents an added rigidity to the loudspeaker suspension. The volume of his cavity increased from 800 cm³ (Fig. 8) to 1300 cm³, while the original front volume of 155 cm³ remains unchanged.
It can be observed a shift in the first two peaks toward the lower frequency region.

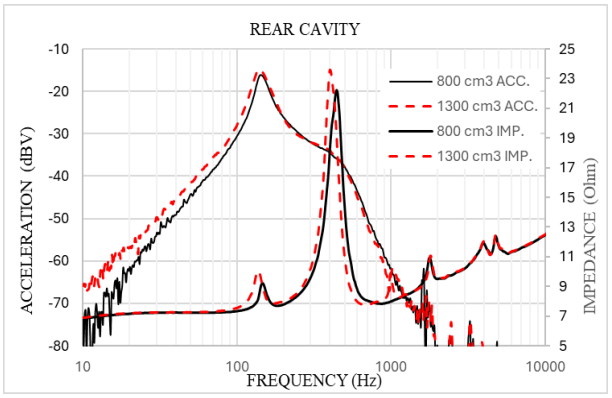


Figure 8. Impedance and acceleration when modifying the rear volume

Additionally, a peak appears at 1 kHz, likely caused by a resonance due to the larger cavity size and the absence of damping material.
The increase in the rear volume V1 affects the low frequency cutoff, and very lightly the higher cutoff frequency.
Meanwhile, the variation in the front volume, that behaves as a low pass filter, has some incidence in the higher cutoff frequency, but none in the low frequency.

4.3 Analytical results

A parametric study, leveraging a MATLAB-based implementation of the mechanical model (Fig. 3), revealed strong agreement between theoretical predictions and experimental outcomes (Fig. 9)

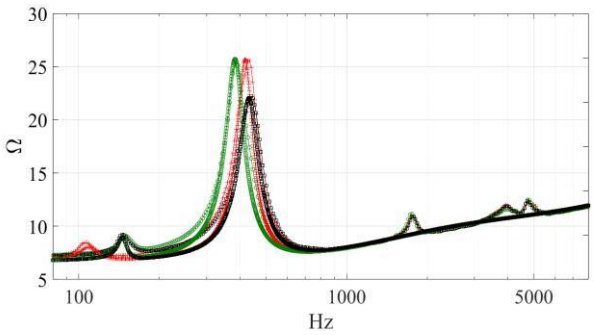


Figure 9. Validation of the analytical model: Diaphragm model D, (lines); 210 cm^3 front volume cavity: (squares); 1300 cm^3 rear volume cavity:
(circles)

4.4 Pressure frequency response

Although this model is intended for underwater applications [6, 7], SPL measurements in free air are carried out to confirm the previously described results (Fig. 10).

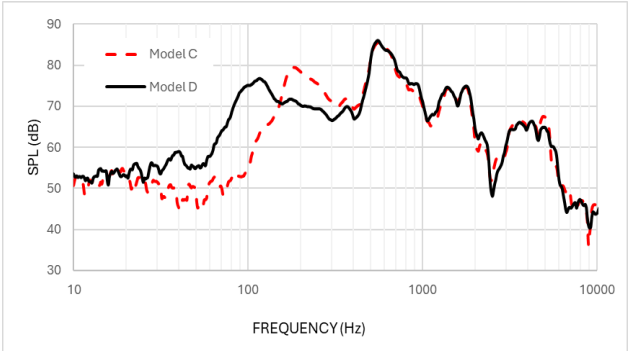


Figure 10. Frequency response at free air

It is possible to verify that the SPL aligns well with the measurements performed with the accelerometer, and verifies the wider response of model D but also the higher efficiency of model C.

5. CONCLUSION

This study has investigated an innovative underwater projector design, inspired by electrodynamic loudspeaker principles, which introduces a novel decoupling mechanism to mitigate hydrostatic pressure effects on the

voice coil at rest. By eliminating direct mechanical coupling between the external diaphragm and the loudspeaker assembly, the proposed configuration demonstrates a marked reduction in static load-induced deformations.

The analysis further reveals that careful optimization of the diaphragm suspension system yields substantial improvements in both frequency response linearity and acoustic sensitivity, while the dimensions of the front and rear cavities exhibit measurable influence on bandwidth behavior, their impact plays a secondary role compared to suspension tuning.

Notably, the striking concordance between experimental measurements and analytical predictions validates the theoretical framework as a robust predictive tool.

The validated model provides a foundation for optimizing similar pressure-resilient projectors, particularly in applications requiring precise acoustic performance in shallow-water environments. Future work should explore the long-term stability of the decoupled assembly under cyclic loading and investigate advanced materials to further enhance sensitivity without compromising structural robustness.

5 ACKNOWLEDGMENTS

This publication is part of the project PID2021-127426OB C22, funded by MCIN/AEI/10.13039/501100011033 and by the European Union "NextGenerationEU"/PRTR," with the reference indicated in the grant resolution. MCIN stands for the Ministry of Science and Innovation; AEI stands for the State Research Agency; 10.13039/501100011033 is the Digital Object Identifier (DOI) of the Agency; and PRTR stands for the Recovery, Transformation, and Resilience Plan.

6 REFERENCES

[1] M. Rossi: *Audio,* Lausanne : Presses Polytechniques et Universitaires Romandes, 2007

[2] V. Dickasen: *Enceintes acoustiques & Haut-Parleurs*, Paris : Publitronic/Eleknor,1996

[3] P. Augris et D. Santens: *L'Audiophile*, Paris : Editions Fréquences, 1982

[4] V. Dickasen: *The Loudspeaker Design Cookbook,* Peterborough: Audio Amateur Press, 1991

[5] J. Martinez, J. Carbajo, P. Poveda and J. Ramis: "Proyectores acústicos submarinos basados en el altavoz electrodinámico", in *Acústica 2024*, Faro, Portugal, pp. 469-473, 2024

[6] H.F. Olson: *Acoustical Engineering,* Philadelphia: Professional Audio Journals, 1991

[7] F. Fahy: *Engineering Acoustics,* London: Academic Press, 2001

[8] J. L. Butler and C. H. Sherman: *Transducers and Arrays for Underwater Sound,* Springer International Publishing Switzerland 2007, 2016

[9] B. S. Willard: "A Towable, Moving-Coil Acoustic Target for Low Frequency Array Calibration" - *Naval Underwater Systems Center,* Newport, Rhode Island, New London, Connecticut, 1981

DOI: 10.61782/fa.2025.0496



FORUM ACUSTICUM
EURONOISE 2025

INVESTIGATING SPATIAL ALIASING AND FRESNEL ZONES OF LINE AND PLANAR SOURCES FOR SOUND REINFORCEMENT

Lukas Gölles[1,2*] **Franz Zotter**[1,2]
[1] Institute of Electronic Music and Acoustics, Graz, Austria
[2] University of Music and Performing Arts, Graz, Austria

ABSTRACT

Modern large-scale sound reinforcement systems predominantly utilize line-source arrays and, more recently, planar matrix arrays due to their flexibility in shaping direct sound pressure coverage across the listening area. In these arrays, the received sound pressure level is influenced, not only by the listener's distance, but also by the size of the first Fresnel Zone on the array, particularly around the origin of the earliest wavefront. The size of this zone varies with both frequency and source dimensions, and it can be adjusted through curvature and time delays. However, comb filtering effects inevitably arise, especially at higher frequencies, due to contributions from later Fresnel Zones and the finite size of the array. Additionally, the discrete spacing of drivers in both line and planar sources introduces spatial aliasing. This contribution presents simulations that analyze the impact of Fresnel Zones, driver spacing, and driver arrangements on frequency response and direct sound coverage within the listening area.

Keywords: *line array, planar arrays, spatial aliasing, Fresnel Zones, sound reinforcement*

1. INTRODUCTION

The field of sound reinforcement is fundamentally concerned with the precise reproduction, control, and propagation of sound waves to ensure optimal audio quality and spatial fidelity. Line-source arrays have long been the standard for large-scale sound reinforcement systems, but more recently, planar arrays have also gained prominence. In this context, spatial aliasing and Fresnel Zones play an essential role in shaping the performance of sound systems. These phenomena are central to the design and operation of modern sound reinforcement systems and present significant challenges that must be addressed to guarantee high-fidelity audio reproduction across diverse environments, ranging from concert halls to outdoor venues.
Fresnel Zones, derived from wave interference theory, define regions of constructive and destructive interference that arise as sound waves propagate from a linear or planar source to a receiver. These zones are particularly relevant in large-scale sound reinforcement, where the interaction of wavefronts over extended distances can result in variations in sound pressure levels and phase coherence. The concept of Fresnel Zones, initially developed in optical theory to describe the diffraction of light waves [1], has proven to be an invaluable tool in acoustics for understanding how sound waves interact with physical obstacles and how these interactions influence perceived sound quality. Notably, Kuttruff's work [2] underscores the importance of Fresnel Zones in room acoustics, emphasizing their role in shaping the spatial distribution of sound energy and the clarity of audio signals. In sound reinforcement systems, effective consideration of Fresnel Zones is critical for minimizing interference effects and ensuring uniform coverage, especially in line and planar array configurations.
Spatial aliasing, in contrast, occurs when the spatial sampling of sound sources is inadequate to excite the wave field with sufficient continuity. This issue is particularly prominent in line and planar sound sources, where the discrete arrangement of transducers can introduce artifacts and distortions in the reproduced sound. Berkhout et al. [3] provide a foundational understanding of spatial aliasing in array-based sound systems, demonstrating how

*Corresponding author: goelles@iem.at.
Copyright: ©2025 L. Gölles et al. This is an open-access article distributed under the terms of the Creative Commons Attribution 3.0 Unported License, which permits unrestricted use, distribution, and reproduction in any medium, provided the original author and source are credited.

transducer spacing and the frequency content of sound signals contribute to aliasing phenomena. Line arrays, composed of multiple closely spaced transducers arranged in a vertical configuration, are widely used in sound reinforcement for their ability to provide controlled directivity and extended range. However, the discrete nature of line arrays makes them vulnerable to spatial aliasing, particularly at higher frequencies. Heil et al. and Urban et al. offer valuable insights into the properties of arrays composed by multiple sources and outline five essential criteria that line arrays must satisfy [4, 5]. Planar arrays, which extend line arrays into two dimensions, encounter similar challenges, albeit with greater complexity due to the increased number of transducers and the multidimensional nature of wave propagation.

This paper explores the effects of Fresnel Zones and spatial aliasing in the context of linear and planar sound sources, focusing on their implications for sound reinforcement systems. The goal is to offer a comprehensive understanding of the challenges they present and the strategies available to mitigate their impact on the listening area. Through a combination of theoretical analysis and numerical simulations, we will demonstrate how optimizing transducer spacing, array geometry, and signal processing algorithms can enhance sound quality and spatial fidelity in practical applications.

2. PHASED LINE SOURCE

2.1 Line Source Phasing

Recently, a theory for line array curving and phasing has been introduced [6], presenting a nonlinear differential equation for the total inclination $\vartheta_\mathrm{T} = a\,\vartheta + (1-a)\,\vartheta_\mathrm{w}$ which is linearly decomposed into a curving component ϑ and a phasing/beamforming component ϑ_w,

$$\dot{\vartheta}_\mathrm{T} = -\frac{r^{2\,\beta}}{g^2}\,\frac{1}{r^2\,\cos\vartheta_\mathrm{w}} + \frac{\cos\vartheta_\mathrm{w}}{r}\,, \qquad \text{with } r = \frac{z}{\sin\vartheta_\mathrm{T}}\,. \tag{1}$$

Here, r represents the distance between the source and receiver, and z is the current z-coordinate of the source when solving the differential equation stepwise. The parameter g determines the radius of curvature at the highest point, while β is a design parameter controlling the direct sound level roll-off, resulting in a decay of $-6\cdot\beta$ dB per distance doubling (dod) across the listening area. Using the Frenet-Serret formulas, which describe arbitrary spatial trajectories, the tangent at any point on the curved line source is given by $\boldsymbol{t} = \begin{bmatrix}\sin\vartheta & 0 & \cos\vartheta\end{bmatrix}^\mathsf{T}$. The geometry of the source is then computed by integrating along the natural source length parameter,

$$\boldsymbol{x}(s) = \int_0^S \boldsymbol{t}\,\mathrm{d}s + \boldsymbol{x}_0 \qquad \boldsymbol{x}_0 = \begin{bmatrix}0 & 0 & z_0\end{bmatrix}^\mathsf{T}\,, \tag{2}$$

where z_0 defines the mounting height of the line source. The delay introduced along the curve acts as a progressive delay and summing beamformer, with the delay length determined by integrating over the sine,

$$w = -\int_0^S \sin\vartheta_\mathrm{w}\,\mathrm{d}s\,. \tag{3}$$

It has been shown, that this formalism is directly applicable to line-array curvature design after discretization [7]. Furthermore, for optimal frequency homogeneity across distance and a balanced trade-off between preserving the mixing balance and enhancing envelopment in immersive sound reinforcement at off-center listening positions, it is recommended to use line sources with a direct sound level decay of -1.5 dB/dod [8]. Accordingly, the simulations in this study are conducted for sources exhibiting this specific decay characteristic.

2.2 Simulation Procedure

We consider a mid-scale sound reinforcement scenario. To align with the results presented in [6], we employ a linear arrangement of the line array prototype [9] consisting of 12 elements.

The continuous line source contour, along with the phasing profile,cf. Eq. (1), (2), and (3), is computed through numerical simulation, following Algorithm 1 in [6]. The simulation parameters are set as follows: $x_{r,0} = 10\,\mathrm{m}$, $z_0 = 2\,\mathrm{m}$, $g = 0.4093$, and $\beta = 0.25$. The phasing profile is discretized based on the element height of the line array prototype, which measures $8.2\,\mathrm{cm}$ [9].

To simulate a piston-shaped driver, we employ a circular arrangement of ideal point sources positioned at $1\,\mathrm{mm}$ intervals. Each source is described using Green's function, with a total diameter of $6.35\,\mathrm{cm}$ (2.5 inches). A Gaussian filter is applied as an amplitude kernel to each element, under the assumption that the driver's edge contributes less to radiation than its center,

$$K[m,n] = \left[e^{-\frac{m^2+n^2}{2\,\sigma^2}}\right]^5\,. \tag{4}$$

Here, σ^2 represents the standard deviation, defining the width of the Gaussian kernel, and is set to $\sigma = 0.83$.

The exponent of five is chosen based on simulation results from [6, 10], as there the results of the measurement match well to the simulation using the prototype array of [9].
For equalization, a filter is applied whose magnitude increases by 3 dB per octave up to the spatial aliasing frequency, compensating for the pink frequency response characteristic of a line source composed of ideal point sources, as described in [6].
At each observation point, the sound pressure is evaluated over a frequency range from 20 Hz to 24 kHz with a linear resolution of 512 points. To visualize the coverage as a broadband result, the frequency responses are third-octave smoothed, followed by A-weighting before summation.

2.3 Spatial Aliasing

Fig. 1 presents the simulated frequency responses of discrete line sources composed of 12 elements. Due to the driver spacing of 8.2 cm, spatial aliasing is expected to occur at approximately $f_{\mathrm{spat.al}} \approx 4.2\,\mathrm{kHz}$ which is clearly reflected in the graphs.
The impact of spatial aliasing can potentially be mitigated through the use of waveguides, f.e. DOSC (Diffuseur d'onde sonor cylindrique [11]), HRW (Hyperbolic Reflective Waveguide [12]), or multi-driver systems. A key advantage of a multiway system incorporating smaller drivers for high frequencies is, that the required curvature of the outlet for near-field sound reinforcement can be more effectively achieved due to the closer spacing of the drivers.
Fig. 2 illustrates the simulated on-axis frequency responses at various distances for a two-way system. In this setup, 2.5-inch drivers spaced at 8.2 cm intervals are used for the lower frequencies, while 1-inch drivers positioned at 2.9 cm intervals handle the higher frequencies. The crossover frequency is set at 2 kHz, and each filter (high-pass and low-pass) is a 4th-order Butterworth filter with a cutoff frequency at 2 kHz. Notably, the two-way system increases the spatial aliasing frequency to approximately 14 kHz due to the reduced driver spacing.

2.4 Fresnel Zones

Figures 3 and 4 illustrate the sizes of the various Fresnel Zones for a discrete line source with 12 elements at the observation points $\boldsymbol{x}_\mathrm{r} = \begin{bmatrix}1 & 0 & 0\end{bmatrix}^\mathsf{T}$ and $\boldsymbol{x}_\mathrm{r} = \begin{bmatrix}2 & 0 & 0\end{bmatrix}^\mathsf{T}$. The regions marked in black represent the first Fresnel Zone, which is the most significant. As the zone number increases, the regions become progressively brighter. For clarity, only the first five Fresnel Zones are depicted.

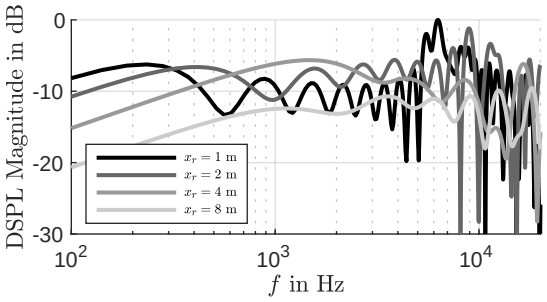


Figure 1. On-axis frequency responses of a 12-element discrete line array at different distances to the source.

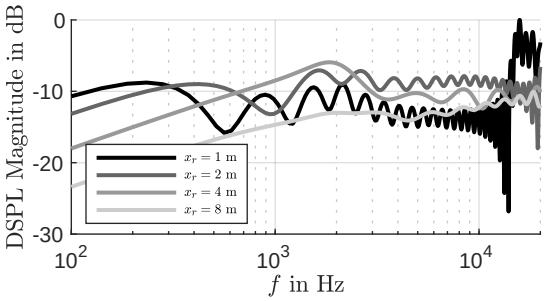


Figure 2. On-axis frequency responses of a 12-element discrete line array (two way system) at different distances to the source.

At both observation points, the Fresnel Zones exhibit asymmetry. At $x_\mathrm{r} = 1\,\mathrm{m}$, the second Fresnel Zone becomes evident at 500 Hz, contributing to the first notch in the frequency response, as shown in Fig. 1. As the frequency increases, the Fresnel Zone diminishes in size, resulting in comb filtering effects in the frequency response. At $x_\mathrm{r} = 2\,\mathrm{m}$, the entire source lies within the first Fresnel Zone. The size of the first Fresnel Zone at 1 kHz at $x_\mathrm{r} = 2\,\mathrm{m}$ is comparable to that at 500 Hz for $x_\mathrm{r} = 1\,\mathrm{m}$. This causes a shift in the first notch to approximately 1 kHz, resulting in an additional comb filter pattern.
Tapering, a well known technique from phased antenna theory [13] and also known as shading in the theory of constant-beamwidth transducer in acoustics [14], can be applied to the array to mitigate the effects of comb filtering. Fig. 5 presents the on-axis frequency responses at different distances of the dual-driver array, consisting of 12 low-frequency drivers and 33 high-frequency drivers, with amplitude tapering applied. For amplitude tapering,

we used a Hann window

$$a[n] = \frac{1}{2}\left(1 - \cos\frac{2\,\pi\,n}{M-1}\right)\,, \tag{5}$$

where the window length M is chosen such that the outermost element is attenuated by 10 dB. This condition is expressed as $a\left[\frac{(M+1)}{2} - \frac{N}{2}\right] = 10^{\frac{-10}{20}}$, where N denotes the number of array elements. By rearranging Eq. (5), the required parameter M is determined

$$M = \mathrm{rd}\left\{\frac{\pi\,(N+1) - \arccos\left(1 - 2\cdot 10^{\frac{-10}{20}}\right)}{\pi - \arccos\left(1 - 2\cdot 10^{\frac{-10}{20}}\right)}\right\}\,. \tag{6}$$

Subsequently, only the symmetric section centered around the peak of the window function is utilized, ensuring it aligns with the number of array elements N. While this tapering results in a noticeable reduction of the notches in the frequency response, it also limits the coverage area, leading to excessively small levels at close observation points, as seen in Fig. 7.
To increase coverage (with $g = 0.38$) while maintaining tapering such that the closest desired observation point is closer to the source, i.e., $x_r = -0.14\,\mathrm{m}$, frequency responses similar to those in Fig. 5 are achieved, c.f. Fig. 6. Additionally, the A-weighted sum of the direct sound level over the distance is comparable to the setup without tapering, as shown in Fig. 7.

3. PHASED PLANAR SOURCES

3.1 Planar Source Phasing

The formalism introduced in [6] has been extended to planar arrays in [10] by introducing a horizontal spread parameter a and a lateral distance range parameter b as design parameters in addition to g and β. Since implementing a two-dimensional curved source is challenging, the proposed method relies on flat planar sources, where delays are used to achieve the desired $-6\cdot\beta$ dB/dod in the listening area. The formalism employs a set of three differential equations to calculate the delay length $w = c\cdot\tau$, where c represents the speed of sound and τ denotes the equivalent delay:

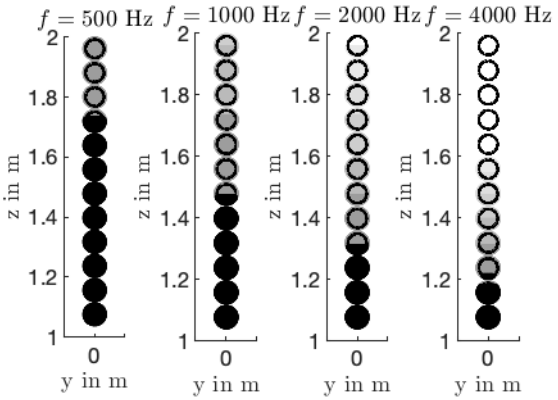


Figure 3. Fresnel Zones (1st=black) on the source at observation point at $x_\mathrm{r} = 1\,\mathrm{m}$ for different frequencies.

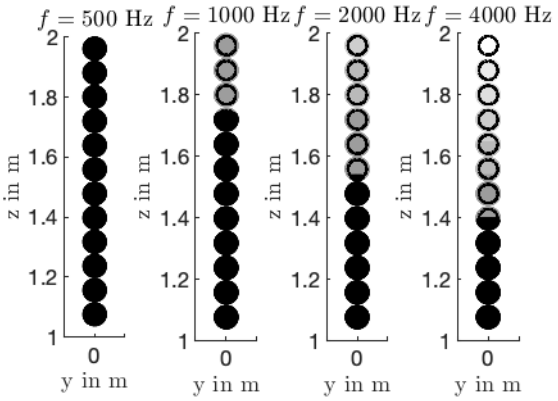


Figure 4. Fresnel Zones on the source at observation point at $x_\mathrm{r} = 2\,\mathrm{m}$ for different frequencies.

$$\frac{\partial^2 w}{\partial h^2} = a + \frac{1}{r}\left(\frac{\partial w}{\partial h}\right)^2 \tag{7}$$

$$\frac{\partial^2 w}{\partial h\,\partial v} = b + \frac{1}{r}\frac{\partial w}{\partial h}\frac{\partial w}{\partial v} \tag{8}$$

$$\frac{\partial^2 w}{\partial v^2} = \frac{1}{r}\left[\frac{g^{-2}\,r^{2\beta} + r^2\,b^2}{1 + r\,a} + \left(\frac{\partial w}{\partial v}\right)^2 - 1\right] \tag{9}$$

$$\text{with } r = \frac{v\,\cos\eta + z_0}{-\frac{\partial w}{\partial v}\,\cos\eta + \sin\eta\,\sqrt{1 - \left(\frac{\partial w}{\partial h}\right)^2 - \left(\frac{\partial w}{\partial v}\right)^2}}\,.$$

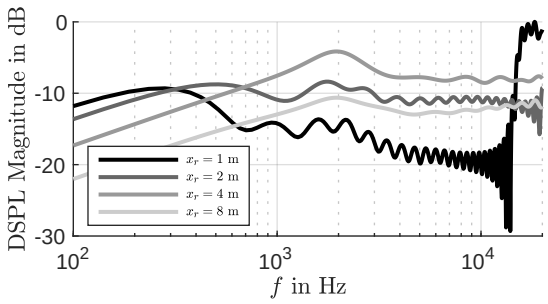


Figure 5. On-axis frequency responses of a 12-element discrete line array (two way system) at different distances to the source with applied tapering.

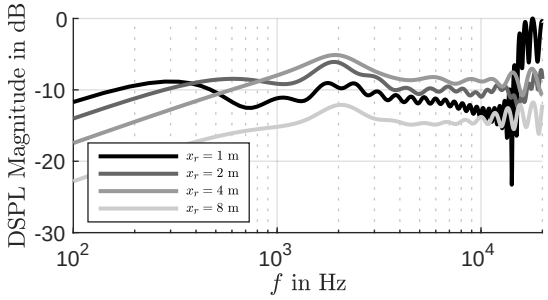


Figure 6. On-axis frequency responses of a 12-element discrete line array (two way system) at different distances to the source with applied tapering and modified coverage.

Here, η denotes the inclination of the planar source, v defines the source length in the vertical direction (i.e., $v \in [0, -V]$), and h represents the width in the horizontal direction ($h \in \left[-\frac{H}{2}, \frac{H}{2}\right]$). z_0 is the mounting height of the planar source, which corresponds to the distance between the highest point of the source and the listening area (assumed to be on the x-y plane). The geometry of the planar source is described using the unit vectors $\boldsymbol{e}_\mathrm{h} = \begin{bmatrix}0 & 1 & 0\end{bmatrix}^\mathsf{T}$ and $\boldsymbol{e}_\mathrm{v} = \begin{bmatrix}\sin\eta & 0 & \cos\eta\end{bmatrix}^\mathsf{T}$,

$$\boldsymbol{x}_\mathrm{s} = \boldsymbol{x}_0 + h\,\boldsymbol{e}_\mathrm{h} + v\,\boldsymbol{e}_\mathrm{v} \qquad \text{with } \boldsymbol{x}_0 = \begin{bmatrix}0 & 0 & z_0\end{bmatrix}^\mathsf{T}. \tag{10}$$

3.2 Simulation Procedure

To make the results from both sources comparable, a planar source with 9×10 elements of size $8.2\,\mathrm{cm} \times 8.2\,\mathrm{cm}$ is chosen. The differential equations (7), (8), and (9) are solved numerically, following Algorithm 3 from [10], using the parameters $x_{\mathrm{z},0} = 10\,\mathrm{m}$, $z_0 = 2\,\mathrm{m}$, $\eta = 11.3°$, $\beta = 0.25$, $g = 0.2492$, $a = 1.9684$, and $b = 0.3902$. The parameters a and b control the coverage width, while η defines the total inclination of the source. In this case, an outermost observation point at $\boldsymbol{x}_\mathrm{r} = \begin{bmatrix}5 & 5 & 0\end{bmatrix}^\mathsf{T}$ is targeted. The values of a and b are derived from a fixed-point iteration as described in Algorithm 1 of [10]. Subsequently, the phasing profile is discretized as proposed in [10].
The individual elements are simulated in the same manner as the linear sources described earlier.

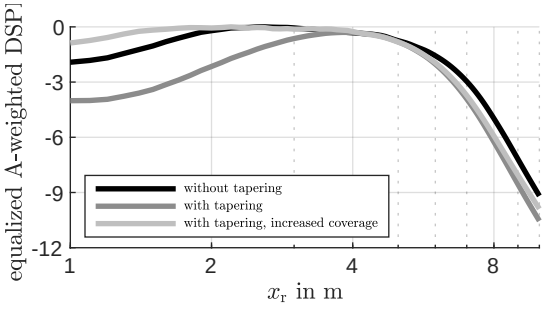


Figure 7. Equalized A-weighted direct sound level in ox-axis direction.

3.3 Spatial Aliasing

Spatial aliasing presents challenges similar to those encountered with linear sources. The top panel of Fig. 8 displays the frequency responses at various observation points. However, for practical reasons, employing an array with smaller, more densely spaced drivers is not a viable solution, as smaller drivers are generally less effective at reproducing lower frequencies. Additionally, a two-way system with an auxiliary array of smaller, denser drivers positioned in front of the main array is not feasible, as it would adversely affect the radiation of lower frequencies. A possible approach to mitigate spatial aliasing effects, at least along the depth dimension, involves placing a vertical array of smaller, densely packed drivers in front of each vertical loudspeaker line. Fig. 8 compares the frequency responses of an array using 2.5 inch drivers across the entire frequency range to an alternative array that employs 2.5 inch drivers for lower frequencies and 1 inch drivers for higher frequencies. The crossover frequency is set at 2 kHz, with each filter (high-pass and low-

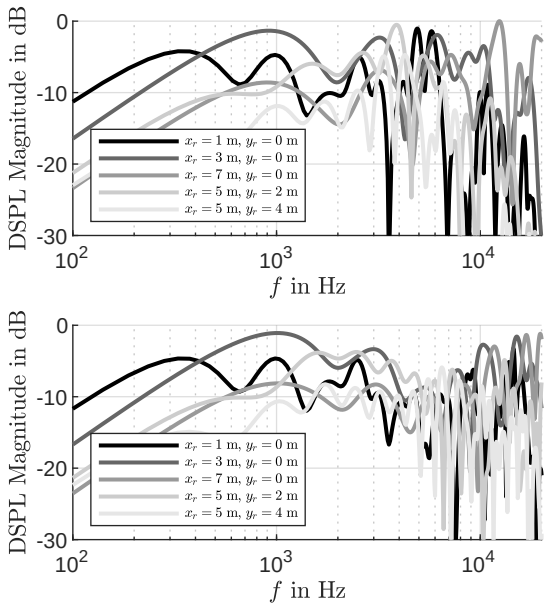


Figure 8. Comparing the frequency responses of a planar array as one-way system (top) and a two-way system (bottom) at different observation points that lie within the desired coverage region.

pass) implemented as a 4th-order Butterworth filter with a cutoff frequency of 2 kHz. Notable improvements in the frequency response are observed in the range of 3 kHz to 6 kHz. However, spatial aliasing at high frequencies remains unavoidable.

3.4 Fresnel Zones

Figures 9 and 10 depict the Fresnel Zones on the planar source at various frequencies for two different observation points. As with the line sources, it is observed that nearly the entire source lies within the first Fresnel Zone at 1 kHz for both observation points. For other frequencies, the size and shape of the Fresnel Zones vary with distance. The observed discontinuities in the zones arise from the fact that the phase profile of an element has been discretized, and the Fresnel Zone is calculated for multiple points on the driver. Consequently, only part of the driver falls within one Fresnel Zone, while the remainder belongs to the next higher Fresnel Zone.
As previously conducted for line sources, tapering is applied to mitigate the effects of comb filtering. The top panel of Fig. 11 illustrates the frequency responses at various observation points for the phased planar source without tapering. The center panel presents the corresponding results after tapering is applied. The same window function as for line sources was selected for tapering, but the outermost elements were attenuated only by 6 dB in both

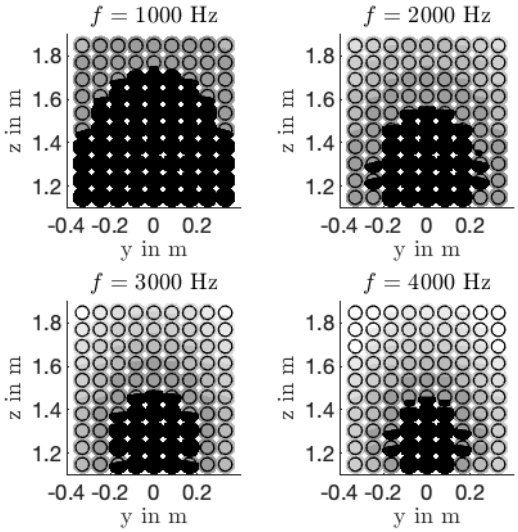


Figure 9. Fresnel Zones on the source at observation point at $\boldsymbol{x}_\mathrm{r} = \begin{bmatrix} 2 & 0 & 0 \end{bmatrix}^\mathsf{T}$ for different frequencies.

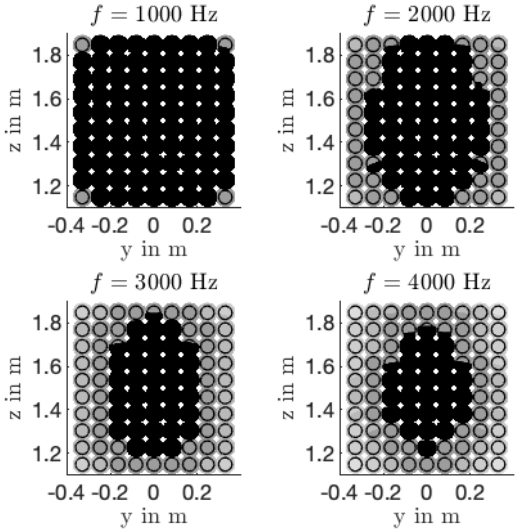


Figure 10. Fresnel Zones on the source at observation point at $\boldsymbol{x}_\mathrm{r} = \begin{bmatrix} 4 & 0 & 0 \end{bmatrix}^\mathsf{T}$ for different frequencies.

the horizontal and vertical directions.
Similar to line sources, the implementation of tapering enhances the frequency response below the aliasing frequency but simultaneously reduces the coverage area, comparing the top and center panels of Fig. 12. To address this limitation, the coverage can be strategically designed for a broader region by adjusting the parameters defining the horizontal coverage to $a = 2.295$ and $b = 0.2919$, thereby targeting an outermost observation point at $\boldsymbol{x}_\mathrm{r} = \begin{bmatrix}5 & 8 & 0\end{bmatrix}^\mathsf{T}$. Additionally, the nearest observation point is repositioned to $x_\mathrm{r} = 0.22\,\mathrm{m}$. A comparison of the results indicates that the coverage achieved with these modifications is comparable to that of the untapered source, cf. Fig. 12. The frequency response characteristics of the tapered source exhibit noticeable improvements, cf. Fig. 11.

4. CONCLUSION

This contribution investigated the effects of spatial aliasing and Fresnel Zones for both line and planar sources in sound reinforcement systems. To improve the frequency responses, tapering can be applied; however, this comes with the trade-off of restricting the coverage area. It was demonstrated that designing for an extended area yields similar results in terms of the covered region when compared to the source without tapering, but with the added improvements in the frequency response achieved through the application of tapering.
Further research should focus on measuring the prototype array and comparing the simulation results with practical applications. Additionally, the impact of individual filtering of the array enclosure should be explored to determine whether further improvements in coverage and frequency homogeneity over distance can be achieved.

5. ACKNOWLEDGMENTS

Our research was funded by the Austrian Science Fund (FWF): P 35254-N (Envelopment in Immersive Sound Reinforcement, EnImSo).

6. REFERENCES

[1] A. Fresnel, “Mémoire sur la diffraction de la lumière,” in *Annales de Chimie et de Physique*, 1816.

[2] H. Kuttruff, *Room Acoustics, Fourth Edition*. E-Libro, Taylor & Francis, 2000.

[3] A. J. C. Berkhout, D. de Vries, and P. Vogel, “Acoustic control by wave field synthesis,” *Journal of the Acoustical Society of America*, vol. 93, pp. 2764–2778, 1993.

[4] C. Heil and M. Urban, “Sound fields radiated by multiple sound sources arrays,” in *Audio Engineering Society Convention 92*, Mar 1992.

[5] M. Urban, C. Heil, and P. Bauman, “Wavefront sculpture technology,” *J. Audio Eng. Soc*, vol. 51, no. 10, pp. 912–932, 2003.

[6] L. Gölles and F. Zotter, “Theory of continuously curved and phased line sources for sound reinforcement,” *Acta Acust.*, vol. 7, p. 52, 2023.

[7] L. Gölles and F. Zotter, “Dual-target design for large-scale sound reinforcement: Simulation and evaluation,” in *Audio Engineering Society Conference: AES 2024 International Conference on Acoustics & Sound Reinforcement*, Jan 2024.

[8] L. Gölles, M. Frank, and F. Zotter, “Evaluating a dual-target line-array design for medium-scale surround sound reinforcement,” in *Audio Engineering Society Convention 156*, (Madrid), 06 2024.

[9] L. Gölles, F. Zotter, and L. Merkel, “Miniature line array for immersive sound reinforcement,” in *Proceedings of AES SIA Conf.*, (Huddersfield), 08 2023.

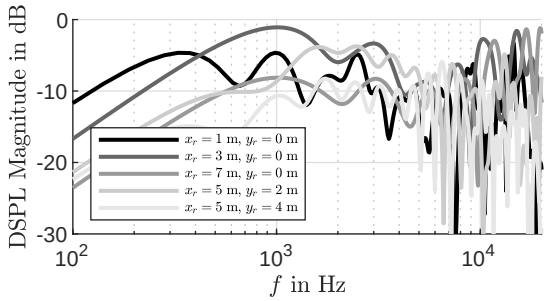
[10] L. Gölles and F. Zotter, “Theory of continuously phased planar sources for sound reinforcement,” *Acta Acust.*, vol. 8, p. 77, 2024.

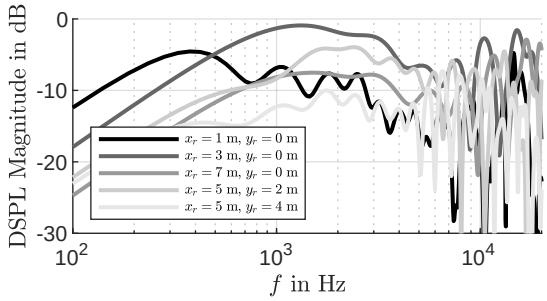
[11] C. Heil, “Sound wave guide,” U.S. Patent 5163167A, Oct. 1992.

[12] E. Vincenot and F. Deffarges, “Sound-Producing Device With Acoustic Waveguide,” U.S. Patent 6585077B2, Jul. 2003.

[13] R. Mailloux, *Phased Array Antenna Handbook*. Antennas and Propagation Library, Artech House, 2005.

[14] taylor richard, manke kurtis, and keele d.b. (don), “circular-arc line arrays with amplitude shading for constant directivity,” *journal of the audio engineering society*, vol. 67, pp. 400–413, june 2019.





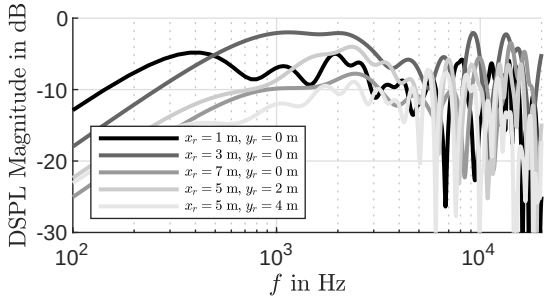
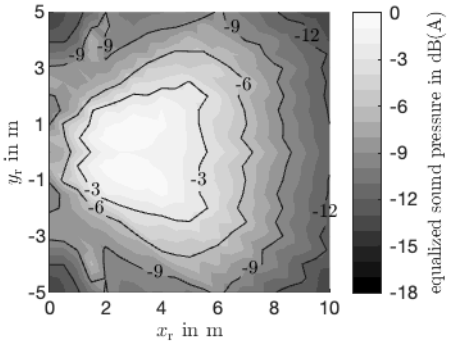
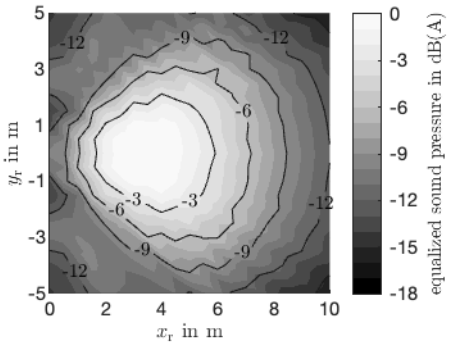


Figure 11. Frequency responses of a planar array at different observation points that lie within the desired coverage region.





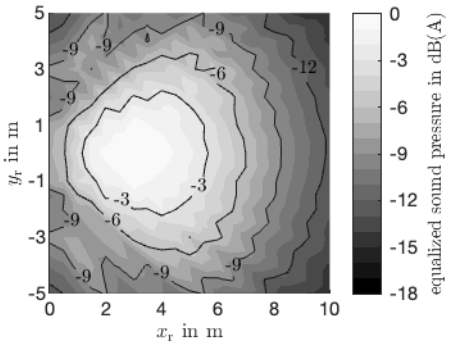


Figure 12. Equalized A-weighted direct sound level in ox-axis direction with applied tapering.

DOI: 10.61782/fa.2025.0034

FORUM ACUSTICUM EURONOISE 2025

A SIMULATION FRAMEWORK FOR PIEZOELECTRIC MEMS SPEAKERS: MODELING, INTEGRATION, AND VALIDATION

Fabian Bachl[1*] **Samu Horváth**[1]
[1] USound GmbH, Gutheil-Schoder-Gasse 8-12, Vienna, Austria

ABSTRACT

We present a simulation framework for piezoelectric, cantilever based Micro-Electro-Mechanical-Systems (MEMS) Speakers. Contrary to electrodynamic speakers, those speakers present a capacitive electrical load, necessitating a modified modeling approach.

Using measurements from a Laser-Doppler-Vibrometer (LDV) we determine a set of parameters derived from the well known Thiele-Small-Parameters (TSP) using the Known Mass Method.

The acoustic load on the back of the membrane is strongly influenced by the cavity structure within the speaker. We use Finite-Element-Analysis (FEA) to calculate the acoustic impedance acting on the membrane back side. A lumped element representation of this impedance is included in the full model.

We present the integration of a MEMS speaker into an earphone design using a simulation driven approach based on the previously described model.

The acoustic effects of the enclosure, as well as the artificial ear are simulated using the finite element method. The results are validated against acoustic measurements of a 3D printed version of the earphone. We show that the models can accurately predict the frequency response of the MEMS speakers, also under complex acoustic load conditions.

Keywords: *MEMS Speakers, Transducer Simulation, Microspeakers*

**Corresponding author*: *fabian.bachl@usound.com.*
***Copyright**: ©2025 Fabian Bachl et al. This is an open-access article distributed under the terms of the Creative Commons Attribution 3.0 Unported License, which permits unrestricted use, distribution, and reproduction in any medium, provided the original author and source are credited.*

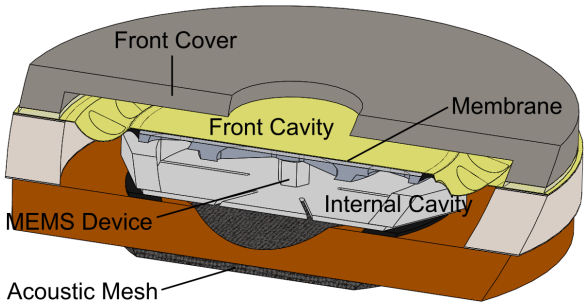


Figure 1. A drawing of the MEMS speaker's internal structure. (Diagonal Cross Cut). The overall diameter of the speaker is 5 mm

1. INTRODUCTION

1.1 Piezoelectric MEMS Speakers

Cantilever based piezoelectric Micro-Electro-Mechanical-Systems (MEMS) Speakers are transducer elements utilizing the force provided by the inverse piezoelectric effect to actuate a moving surface, leading to the radiation of sound. There are two distinct approaches. While some designs use the surface of the piezoelectric MEMS device itself [1], our work concerns itself with designs that utilize an additional membrane component that is connected mechanically to the piezoelectric cantilever element.

Figure 1 shows a cross cut through such a MEMS speaker. The acoustically active area (membrane) is shown in yellow. The MEMS device is shown in light gray. The two elements are mechanically connected to each other.

The MEMS device is the active motor unit of the

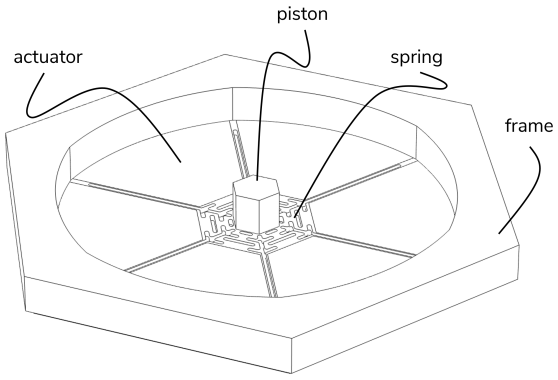


Figure 2. Architecture of the MEMS device

speaker. It consists of four main structural building blocks. (Figure 2)

The frame supports the MEMS device and provides mechanical and electrical connection towards the base of the speaker assembly.

The actuators are piezoelectric cantilevers that provide the driving force. The composite layer stack of the actuators consists of the electrodes, the active piezoelectric layer and the passive structural layer. Due to the inverse piezoelectric effect, applying a voltage at the electrodes across the active layer leads to a deformation, this results in a bending motion of the cantilever. Moving the central region of the device upward and downward where the piston and springs couple the movement to the membrane element of the speaker.

The active piezoelectric layer is made from Lead zirconate titanate (PZT), specifically, epitaxial PZT with highly ordered crystal structure, providing self-poling and high linearity. [2] The passive structural layer is a polymeric film. It provides a large elastic reserve for the structure, which is especially crucial for the device to withstand not only normal operation but also extreme events such as drops while handling.

Generally, there are many similarities between this type of piezoelectric MEMS speakers and "traditional" electrodynamic (micro-)speakers. While the motor principle is fundamentally different, both rely on a moving membrane, the movement of which can be described by a single degree-of-freedom oscillator. This is why a slightly modified version of the Thiele-Small Model [3,4] can also be used for piezoelectric MEMS speakers.

The difference is in the transformation between the electrical domain and the mechanical domain. While the force output of an electromagnetic motor is proportional to the current flow through the voice coil, the force output from a piezoelectric element is proportional to voltage. [5]

1.2 TSP Measurement

Traditional parameter measurement involves adding a known mass or enclosing the speaker in a small, known, volume, both altering the resonance frequency. The change in resonance frequency is then used to conclude the values of the TSP [6]. Since resonance appears as a clearly visible peak in electrical impedance, commercial systems typically use impedance measurements for both methods.

However, the usage of this approach is limited for piezoelectric MEMS speakers due to two factors. First, their impedance is predominantly capacitive. Figure 3 shows the difference to the impedance of an electrodynamic (ED) speaker. Common algorithms are designed for ED speaker impedance profiles. Making them incompatible with the capacitive impedance of piezoelectric MEMS devices.

Secondly, the very small internal dimensions of piezoelectric MEMS speakers (as shown in Figure 1) have a significant influence on the acoustic speaker performance. These internal cavities act as acoustic impedance, influencing all moving surfaces within the speaker, and therefore the speaker's movement.

1.3 Ear Simulators

Ear simulators, or couplers, play a crucial role in the accurate and standardized assessment of auditory devices by mimicking the acoustic impedance of the human ear. The IEC 60318 series defines various coupler types, among which the occluded ear simulator specified in IEC 60318-4 is the most widely used in earphone design. However, its specification is limited to the 100 Hz to 10 kHz frequency range.

The RA0403 (GRAS Sound Vibration A/S, Holte, Denmark) is compatible with the IEC 60318-4 standard but includes design modifications that extend its operational frequency range up to 50 kHz. [7]

2. METHODS

2.1 Model Structure

The piezoelectric MEMS speaker is modeled as a damped mass spring resonator with one degree of freedom. This corresponds to the membrane moving as a piston. All

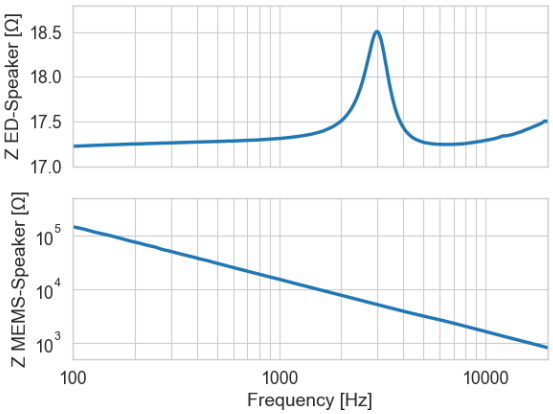


Figure 3. Comparison between the typical impedance curve of a electrodynamic (ED) speaker (RB-E06016F-007R) and a piezoelectric MEMS speaker (USound UA-C0503-3T)

higher order modes, like membrane deformation, are not considered.

The response of a dampened mass-spring resonator is given by the equation of motion. (1)

$$F_p = M_{ms}\frac{d^2x}{dt^2} + R_{ms}\frac{dx}{dt} + K_{ms}x \tag{1}$$

Expressing the frequency response

$$\begin{aligned} x = A\frac{1-T^2}{(1-T^2)^2+(2\zeta T)^2} \\ +jA\frac{2\zeta T}{(1-T^2)^2+(2\zeta T)^2} \end{aligned} \tag{2}$$

where A is the deflection per voltage, T is the tuning and ζ is the damping ratio.

$$T = \frac{2f\pi}{\omega_0} \tag{3}$$

$$\omega_0 = \sqrt{\frac{K_{ms}}{M_{ms}}} \tag{4}$$

$$\zeta = \frac{R_{ms}}{2\sqrt{K_{ms}M_{ms}}} \tag{5}$$

$$a = x \cdot (2j\pi f)^2 \tag{6}$$

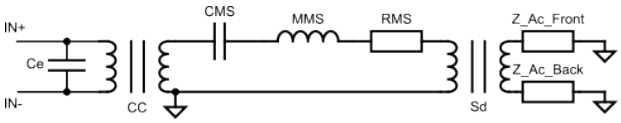


Figure 4. The basic equivalent circuit used to describe the MEMS speaker. $C_{MS} = {}^1/_{K_{MS}}$

The model is represented using and lumped parameters with the equivalent circuit shown in Figure 4. We use the Force-Voltage (FU) analogy for the mechanical domain. As the force provided by the MEMS device is directly proportional to the voltage applied, the effort variable voltage in the electrical domain is directly transformed into the effort variable force in the mechanical domain.

To model this relation a parameter referred to as the Coupling Constant (CC) is introduced. It replaces the Force Factor (B_L) typically used in loudspeaker models. The Coupling Constant is given in ᴺ/ᵥ.

$$A = \frac{CC}{K_{ms}} \tag{7}$$

Allowing the use of a ideal transformer to interface the two domains in the equivalent circuit. The mechanical spring stiffness K_{ms} is represented by its inverse, the compliance C_{ms}

The full model and any Finite-Element-Analysis (FEA) is set up and solved in COMSOL Multiphysics 6.3 (COMSOL Inc. Stockholm, Sweden). We use the lumped electrical circuit physics interface to model the mechanical and electrical domains of the lumped representation. Acoustical simulations are done using FEA.

As with the majority of other transducer principles, the piezoelectric MEMS speaker in question (USound UA-C0504-3T) features an active area (membrane) that is moved to create acoustic pressure. The membrane separates the acoustic front from the acoustic back. An acoustic impedance acts on both sides. The impedance on the front (Z_Ac_Front) is dominated by the ear simulator and the earphone. But, the acoustic impedance on the back (Z_Ac_Back) mainly arises in the small air cavities within the speaker. (Assuming a reasonably open ventilation towards the back)

We calculate Z_Ac_Back using FEA. A 3D representation of the cavity within the speaker is created based on technical drawings. ⅙ of the speaker is used for the sim-

ulation as it is rotationally symmetric and this makes the model computationally less expensive. Due to the small structure sizes found inside the speaker, the calculations are done in the "Thermoviscous Acoustics, Frequency Domain Interface" of the COMSOL Acoustics Module. This interface calculates the viscous and thermal losses occurring in close vicinity to the boundaries. [8]

The external back volume of the speaker is assumed to be infinitely big. In this model, the membrane is moved with a constant velocity for each frequency point. This allows the calculation of the acoustical impedance by evaluating the acoustic pressure on the membrane surface.

$$Z = \frac{p}{q} \tag{8}$$

Where p is the average acoustic pressure at the active area ("membrane") and q is the volume flow rate. This is equal to the integral of the mechanical velocity over the active area. The calculated impedance is a complex valued function of frequency. Discrete frequency points are exported.

The frequency points are then included for "Z_Ac_Back" as seen in Figure 4. As described before, this circuit is implemented in the COMSOL model. "Z_Ac_Back" is integrated as a "User Defined" impedance in the Lumped Speaker Boundary Condition. "Z_Ac_Front" however is dependent on the acoustical load from the ear(-simulator) and the coupler adapter/earphone.

2.2 Added Mass Method

The TSP are typically measured in free air, where results are affected by acoustic impedance. To eliminate these external acoustic influences and accurately determine the intrinsic mechanical parameters of the speaker assembly, measurements were carried out in a vacuum using a Laser-Doppler-Vibrometer (LDV) (PSV 500, Polytec GmbH, Waldbronn, Germany). The vacuum environment effectively isolates the system from acoustic loading, allowing for the characterization of its purely mechanical behavior.

Equation 1 to 6 describe the frequency response function of a dampened mass spring resonator. The least_squares function of Scipy v1.15.2 is used to determine a set of parameters that satisfactorily describe the loaded and unloaded cases.

2.2.1 *Known Mass*

We cut circular pieces of adhesive copper tape. The pieces used had a mass of 2.5 mg each. The front cover was removed from the speakers to reveal the whole membrane. The speakers were then measured under vacuum ($< 8.7 \cdot 10^{-2} hPa$), so as to remove effectively all influences from the air load (unloaded case). The copper pieces were attached, as shown in Figure 6, and the measurements were repeated within the same conditions (loaded case).

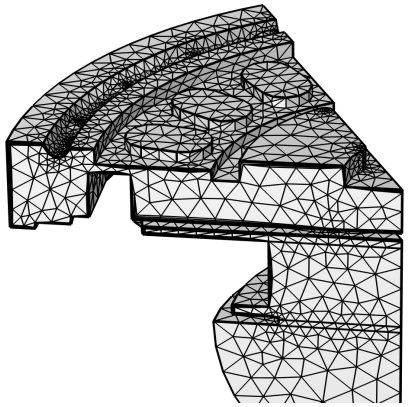


Figure 5. Mesh used to calculate the acoustic impedance of the volume within the speaker packaging

2.3 Acoustic Validation

The predictive quality of the model is validated acoustically by comparing the output to measurements of two scenarios. We use a 1.8 mm long coupler adapter with a diameter of 3 mm to connect the speakers acoustic output to the coupler input. The coupler is used without the conical earmould adapter.

Also, the speaker model is compared to the speaker performance within an earphone prototype. The earphone in question is shown in Figure 7. The piezoelectric MEMS speaker is used as a tweeter. Hence, the design features space for the integration of a ring-shaped electrodynamic woofer, which is outside the scope of this paper. A detailed description of the earphone is provided in [9].

We use a RA0403 (GRAS Sound & Vibration A/S, Holte, Denmark) "High-Resolution" ear simulator to do all reference measurements. The ear simulator is represented in the model by a slightly modified version of the "generic_711_coupler" available in the COMSOL appli-



Figure 6. A circular piece of copper tape is attached to the speaker membrane. Increasing the moving mass by 2.5 mg

cation library. An acoustic impedance of $9000^{Pas}/_{m^2}$ is added to the central, tube shaped, volume of the coupler. Figure 8 shows the alignment of this model and the calibration data provided by the manufacturer.

3. RESULTS

3.1 TSP Measurement

The TSP are calculated with a least squares fit of Equation 2, to both the loaded and unloaded cases. Figure 9 shows the alignment of the fit to the acceleration measured using LDV.

From fitting Equation 6 to the measurement data we can extract the modified TSP, resulting in the values shown in Table 1.

Table 1. The calculated modified TSP

Parameter	Value
M_{ms}	$1.57mg$
K_{ms}	$1.86 \cdot 10^{3N}/_{m}$
R_{ms}	$4.2 \cdot 10^{-3Ns}/_{m}$
CC	$818 \cdot 10^{-6N}/_{V}$

3.2 Acoustic Measurements

The simulation model is compared with the acoustical test results gathered in a G.R.A.S RA0403/04 ”Hi-Res” Ear Simulator. The comparative plot is shown in Figure 10. The deviation up to 20 kHz is below $\pm 1\,dB$.

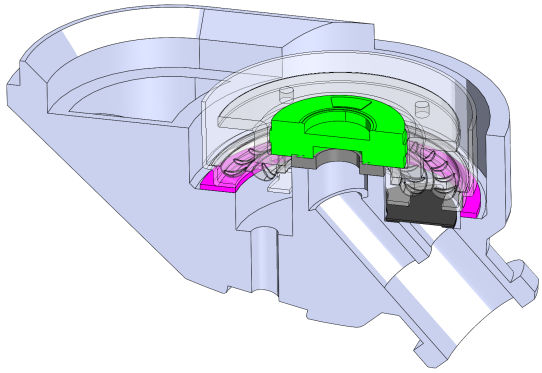


Figure 7. Cross cut of the earphone Design used for model validation. The piezoelectric MEMS speaker is shown in green. The woofer is shown in transparent gray. The silicone rubber eartip is not shown.

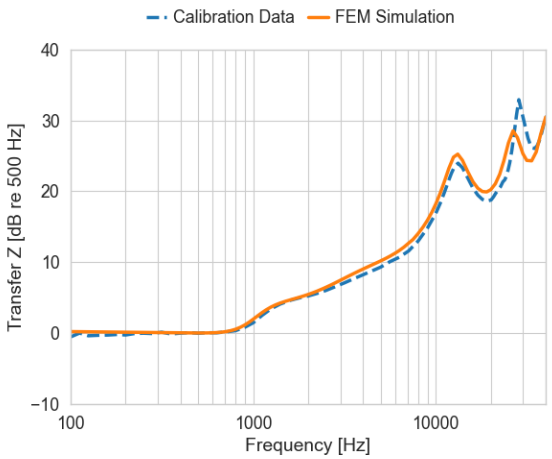


Figure 8. Relative transfer impedance of the used FEM Model of the G.R.A.S RA0403 ”Hi-Res” Ear Simulator and the corresponding calibration data provided by the manufacturer

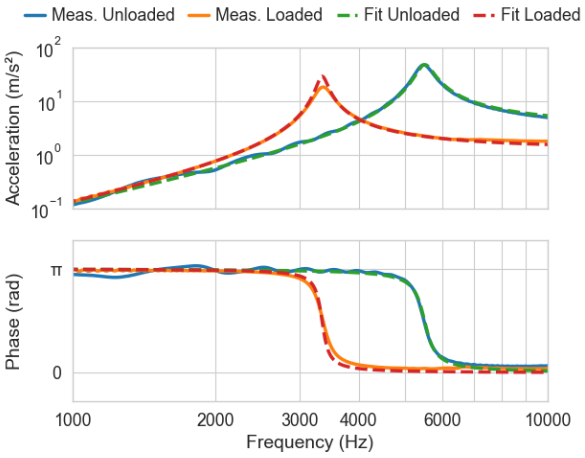


Figure 9. Result of the least squares fit in comparison with the LDV measurement results. The loaded case has a lower resonance frequency.

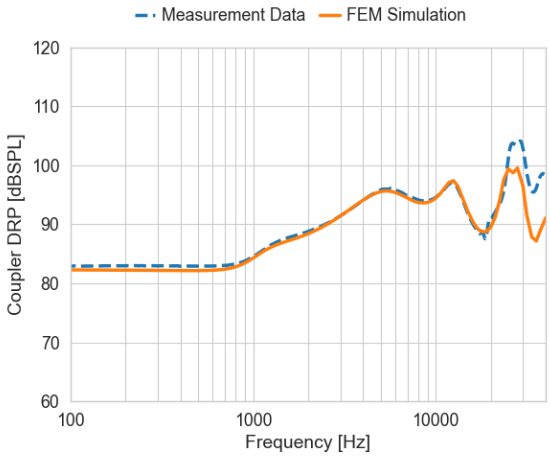


Figure 10. Comparison between the simulation result and the measured performance of the piezoelectric MEMS speaker in the G.R.A.S RA0403/04 "Hi-Res" Ear Simulator. With two different adapter systems

Above the audible range, the deviation increases continuously. Showing the limit of the single degree-of-freedom approach.

In addition, speakers are evaluated in an application-focused way using a previously developed earphone design. The predictive performance of the model is shown in Figure 11. Within the audible range, the deviation is below $\pm 1.5\,dB$. The position of the resonances is accurate to $\pm 300\,Hz$

4. DISCUSSION

The simulation framework presented addresses the unique characteristics of piezoelectric Micro-Electro-Mechanical-Systems (MEMS) speakers, particularly their capacitive electrical load, which requires a modified modeling approach compared to traditional electrodynamic speakers. We show the adaption of the Thiele-Small-Parameters (TSP) for these speakers and present a way to measure them using Laser-Doppler-Vibrometer (LDV) measurements under vacuum with the Known Mass Method, effectively eliminating the influence of acoustic impedance. The calculated TSP values appropriately describe the speakers mechanical behavior in the audible frequency range.

The integration of the MEMS speaker model into an earphone design was achieved using a simulation-driven

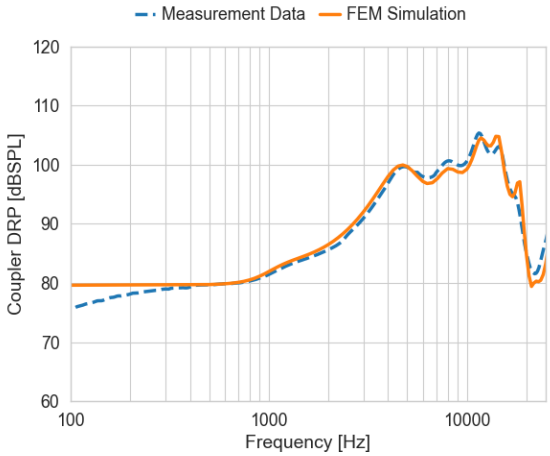


Figure 11. Comparison between the simulation result and the measured performance of the MEMS speaker in the earphone design.

approach incorporating Finite-Element-Analysis (FEA) to model enclosure and artificial ear acoustics. The significant influence of internal acoustic impedance, calculated via FEA of the speaker's cavities, was included in the model.

Acoustic validation demonstrated good agreement between simulation and measurements using a GRAS RA0403/04 "Hi-Res" Ear Simulator and an earphone prototype. Deviations were generally below ±1 dB up to 20 kHz for the ear simulator and below ±1.5 dB within the audible range for the earphone, with accurate resonance prediction. The increased deviation at frequencies above the audible range shows a limitation of the single degree-of-freedom model.

In conclusion, this simulation framework provides a valuable tool for the design and optimization of piezoelectric MEMS speakers and their integration into audio devices by accurately predicting frequency response under various acoustic loads while considering their unique electrical and acoustic characteristics.

Future work could focus on more complex mechanical models. A promising approach would be to go towards lumped representation of a multi degree of freedom model. We would expect this to improve the high-frequency accuracy.

5. ACKNOWLEDGMENTS

We would like to thank our colleagues at USound GmbH for all their previous contributions that went into this paper. Although they are too many to mention individually, we would like to especially thank Paul Heyes for his help with the Laser-Doppler-Vibrometer measurements and Jascha Blinzer for providing the cross sectional view from Figure 1.

6. REFERENCES

[1] C. Gazzola, V. Zega, F. Cerini, S. Adorno, and A. Corigliano, "On the design and modeling of a full-range piezoelectric mems loudspeaker for in-ear applications," *Journal of Microelectromechanical Systems*, vol. 32, no. 6, pp. 626–637, 2023.

[2] M. Teuschel, P. Heyes, S. Horvath, C. Novotny, and A. Rusconi Clerici, "Temperature stable piezoelectric imprint of epitaxial grown pzt for zero-bias driving mems actuator operation," *Micromachines*, vol. 13, no. 10, 2022.

[3] R. Small, "Direct-radiator loudspeaker system analysis," *IEEE Transactions on Audio and Electroacoustics*, vol. 19, pp. 269–281, Dec. 1971.

[4] A. Thiele, "Loudspeakers in vented boxes," *Journal of the Audio Engineering Society*, vol. 19, pp. 382–392, May 1971.

[5] A. Rusconi Clerici, "Mems speaker modeling," in *MikroSystemTechnik Congress 2021*, (Berlin), VDE Verlag, 2021. "Organisatoren: VDE/VDI-GMM-Gesellschaft für Mikroelektronik, Mikrosystem- und Feinwerktechnik (GMM); VDI/VDE Innovation + Technik GmbH (VDI/VDE-IT)" - Kongress-Homepage ('Programm').

[6] R. Gomez-Meda, "Measurement of the thiele-small parameters for a given loudspeaker, without using a box," in *Audio Engineering Society Convention 91*, Audio Engineering Society, 1991.

[7] GRAS Sound Vibration A/S, *GRAS RA0403 Externally Polarized Hi-Res Ear Simulator*, 2025.

[8] COMSOL, *COMSOL 6.3 Acoustics Module User's Guide*, 2024.

[9] USound GmbH, *Greip 1.0 UAM-C1001 Acoustic design*, 2024. Available upon request (sales@usound.com).

DOI: 10.61782/fa.2025.0557

FORUM ACUSTICUM EURONOISE 2025

MECHANICALLY-OPEN AND ACOUSTICALLY-CLOSED MEMS LOUDSPEAKERS FOR IN-EAR APPLICATIONS

Chiara Gazzola[1*] **Filippo Perli**[1] **Fabrizio Cerini**[2] **Silvia Adorno**[2]
Pierrick Lotton[3] **Manuel Melon**[3] **Alberto Corigliano**[1]
[1] Department of Civil and Environmental Engineering, Politecnico di Milano, Italy
[2] STMicroelectronics, 20007 Cornaredo, Italy
[3] Laboratoire d'Acoustique de l'Université du Mans (LAUM), UMR 6613,
Institut d'Acoustique - Graduate School (IA-GS), CNRS, Le Mans Université, France

ABSTRACT

MEMS loudspeakers for in-ear applications have been attracting a growing interest in recent years, promising to overcome the limits in terms of form factor, power efficiency and cost of non-MEMS loudspeakers. The piezoelectric actuation principle is one of the most investigated, thanks to the introduction of high precision piezoelectric thin films with high electro-mechanical coupling coefficients in the microfabrication processes. This work presents a new set of high-performance piezoelectric MEMS speakers, consisting of PZT-driven thin plates properly shaped through a set of narrow slits. The latter serve the twofold purpose of enhancing the mechanical compliance of the speaker diaphragm and limiting the acoustic short-circuit between the speaker front and rear side. The diaphragm geometry, evolution of a design previously proposed by the Authors, is properly modified to improve the acoustic output and power efficiency. The proposed devices feature a Sound Pressure Level (SPL) at 30 V_{pp} greater than 108 dB SPL in the whole audible range, a Total Harmonic Distortion (THD) at 1 kHz at 94 dB SPL lower than 1% and a compact footprint of 4.5x4.5 mm^2. Experimental results are compared with a FEM-assisted lumped element model demonstrating a good match between them.

*__Corresponding author__: chiara.gazzola@polimi.it.
__Copyright__: ©2025 Gazzola et al. This is an open-access article distributed under the terms of the Creative Commons Attribution 3.0 Unported License, which permits unrestricted use, distribution, and reproduction in any medium, provided the original author and source are credited.

Keywords: Piezoelectric thin films, MEMS, Microspeaker, Lumped Element Method, IEC 60318-4 coupler

1. INTRODUCTION

The integration of loudspeakers into devices such as smartphones, laptops, earphones, and hearing aids underscores their critical role in modern audio technology. The miniaturization of these systems into MEMS loudspeakers offers several advantages, including a compact form factor, low power consumption, and cost-efficient manufacturing, facilitating their widespread adoption in true wireless systems and in-ear applications, where power and space constraints are increasingly stringent.

To date, diaphragm actuation in MEMS loudspeakers can be achieved through electrodynamic (see *e.g.* [1, 2]), electrostatic (see *e.g.* [3, 4]), thermoacoustic (see *e.g.* [5, 6]), or piezoelectric (see *e.g.* [7–10]) forces. Among these, piezoelectric actuation has emerged as the most viable approach due to its ability to generate high driving forces at relatively low voltages. That is due to key technological advancements, including the development of piezoelectric materials with high electromechanical coupling, refined sputtering techniques enabling precise deposition in complex patterns, and the introduction of the mechanically-open and acoustically-closed (MOAC) design concept [8, 11]. This design strategy involves integrating a series of openings into the diaphragm to reduce its mechanical stiffness, thereby allowing for greater displacements. Simultaneously, these openings are designed so that the viscosity of the air within them limits the acoustic short-circuit between the front and rear side of

the MEMS loudspeaker. Piezoelectric MEMS loudspeakers have achieved Sound Pressure Levels (SPL) exceeding 100 dB SPL in all the audible range, starting to close the performance gap with widely adopted non-MEMS loudspeakers. However, their sound pressure output per unit area has not yet reached its full potential.

This work presents a new set of high-performance piezoelectric MEMS speakers, whose diaphragms consists of PZT-driven thin plates separated by narrow slits. The devices were designed with the support of a FEM-assisted lumped element model [12], whose predictions are compared with in-ear acoustic measurements carried out on prototypes fabricated by STMicroelectronics (Cornaredo, Italy).

2. DESIGN CONCEPT

For a single-degree-of-freedom loudspeaker radiating in a cavity, the output pressure can be computed as [8]:

$$\Delta p = \gamma P_0 \frac{\Delta \mathcal{V}}{V_0} = \gamma P_0 \frac{d_{\max} S_{\text{eff}}}{V_0}, \tag{1}$$

where $\Delta\mathcal{V}$ is its volume displacement, given by the product of the speaker maximum displacement $d_{\max}$ and the speaker effective area S_{eff}, while γ is the adiabatic index (equal to 1.4 for dry air at 20 ° C), P_0 the ambient pressure and V_0 the volume of the cavity. The effective area of the speaker is computed as:

$$S_{eff} = \int_{\partial\Omega_f} \mathbf{\Phi} \cdot \boldsymbol{n} \, dS, \tag{2}$$

where $\mathbf{\Phi}$ is the modal shape function, $\partial\Omega_f$ is the surface area of the front side of the speaker and $\boldsymbol{n}$ its outward normal. Consequently, the parameters to address to maximize the speaker's acoustic performance are its maximum displacement and effective area, which are related respectively to the diaphragm mechanic stiffness and its movement type. The first can be reduced by implementing the MOAC design principle while the second can be maximized by encouraging the central part of the membrane to move like a piston. Following these design guidelines led to the diaphragms presented in Fig. 1, where a schematic cross-section of their structure is also given (Fig. 1c). The first design (Fig. 1a) consists of eight trapezoidal plates fabricated from a 13 µm-thick Epi-Poly silicon layer, partially coated with a 2 µm-thick Lead Zirconate Titanate (PZT) layer. These plates are connected to the central region of the MEMS loudspeaker through a

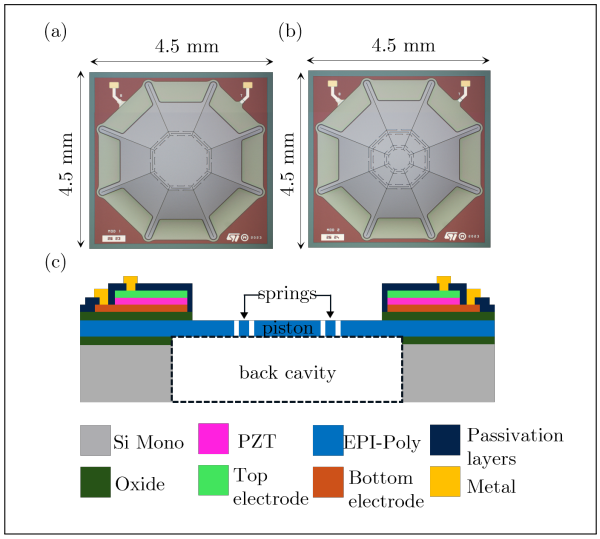


Figure 1. (a) Microscope optical images and (b) cross-sectional view of the proposed MEMS loudspeakers.

network of elastic springs and are anchored to an external fixed frame. The eight plates are designed to be actuated synchronously, moving the diaphragm central part that they keep suspended like a piston. The mechanical gaps between adjacent trapezoidal plates extend from the fixed frame to the central region, effectively segmenting the PZT patches, which remain interconnected at the fixed frame. This distinct separation between plates, combined with the low stiffness of the elastic springs at their extremities, allows to mitigate the hardening effect that a clamped-clamped configuration would otherwise experience. The second device (Fig. 1b) features a reduced central region, leaving space for an additional set of elastic springs positioned along the extended trapezoidal plates. This modification aims to further enhance the maximum displacement of the diaphragm, albeit at the cost of deviating from an ideal piston-like motion. The two devices features a footprint of $4.5 \times 4.5\,\text{mm}^2$.

The proposed diaphragm geometries are an evolution of the design previously proposed by the Authors in [8]. Compared to the previous generation, the diaphragm structure is properly modified to improve the acoustic output with a halved piezoelectric capacitance, which is directly related to the power consumption. In particular, the air-gaps are reduced from 10 µm to 5 µm, to improve the sound pressure at low frequency by limiting the acous-

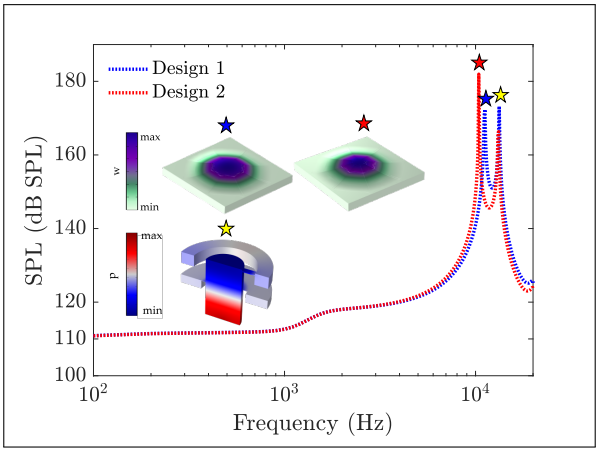


Figure 2. Equivalent circuit SPL predictions for design 1 and 2 at a bias voltage of 15 V_{DC} plus an alternating voltage of 30 V_{pp}. The insets report the loudspeakers deformed shape at their resonance frequency and the acoustic pressure distribution at the half wavelength resonance of the ear simulator.

tic short-circuit. The piezoelectric capacitance is reduced from 70 nF to 35 nF.

3. NUMERICAL RESULTS

The acoustical performances of the proposed loudspeakers are simulated through the FEM-assisted lumped element model reported in [12]. In particular, a FEM prestressed eigenfrequency analysis is exploited for the derivation of the electro-mechanical parameters whereas acoustical parameters are computed through analytical formulas.

The acoustic performance for a bias voltage of 15 V_{DC} plus an alternating voltage of 30 V_{pp} are reported in Fig. 2. The actuated loudspeaker mode, occuring at 11.6 kHz for design 1 and at 10.7 kHz for design 2, determines the first peak of the SPL curves. The second peak is instead due to the half wavelength resonance of the ear simulator. The simulations predict a SPL greater than 110 dB SPL from 100 Hz onwards and a relatively flat response at low frequency, due to the reduced slit width.

4. EXPERIMENTAL RESULTS

The numerical SPL predictions are compared with experimental measurements carried out on nine prototypes of

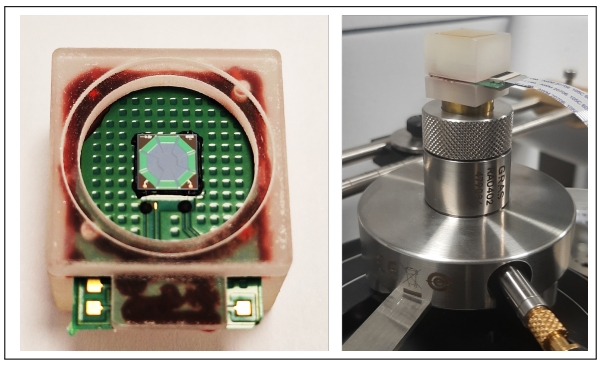


Figure 3. Fabricated microspeaker mounted on a custom PCB and coupled with the package for in-ear acoustic tests (left). Device Under Test (DUT) mounted on the ear simulator G.R.A.S. RA0402 (right).

the proposed microspeakers, fabricated by STMicroelectronics. For experimental tests, the device is mounted on a custom printed circuit board (PCB) and coupled with an acrylonitrile butadiene styrene (ABS) thermoplastic package composed of a back chamber of 1 cm^3 and a front adapter of 1 mm height to connect the speaker with the ear simulator (Fig. 3).

The experimental SPL curves for a bias voltage of 15 V_{DC} plus an alternating voltage of 30 V_{pp} is reported in Fig. 4, for design 1 and 2. The acquisition is stopped at 10 kHz to avoid the break-up of the prototypes. Overall, the numerical vs experimental matching is good (overestimation at 100 Hz of 2.3 dB SPL for design 1 and 2.7 dB SPL for design 2). As reference, the experimental SPL curve for the design of the previous generation [12] is reported in the same figure with black solid line. It can be confirmed that the reduction of the slit width from 10 µm to 5 µm leads to a significant SPL improvement at low frequency (+5 dB SPL at 100 Hz). Moreover, despite the halved piezoelectric surface area, the output pressure is overall higher for the new devices.

The THD has also been evaluated at 1 kHz at 94 dB SPL, obtaining 0.68% for design 1 and 0.72% for design 2 (previous design 1.5%).

5. CONCLUSIONS

Two full-range piezoelectric MEMS loudspeakers for in-ear applications are designed, simulated, fabricated and experimentally characterized. The good match between

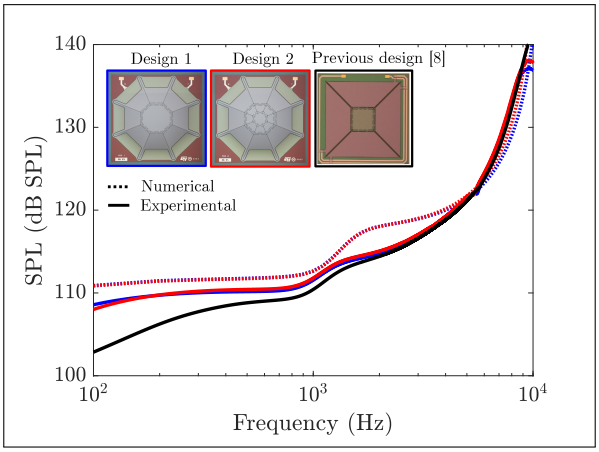


Figure 4. (a) Comparison between numerical (dotted lines) and experimental (solid lines) SPL frequency spectra for a bias voltage of 15 V_{DC} plus 30 V_{pp}, for design 1, design 2 and the design reported in [8].The acquisition is stopped at 10 kHz to avoid the break-up of the prototypes.

simulations and experiments demonstrates that, with respect to the previous generation, the proposed designs gain up to 5 dB SPL at low frequency and more than halve the previous THD, while keeping the same device footprint and a halved piezoelectric surface area.

6. REFERENCES

[1] I. Shahosseini, E. Lefeuvre, J. Moulin, E. Martincic, M. Woytasik, and G. Lemarquand, "Optimization and microfabrication of high performance silicon-based mems microspeaker," *IEEE Sensors Journal*, vol. 13, no. 1, pp. 273–284, 2013.

[2] I. Shahosseini, E. L. M. Woytasik, J. Moulin, X. Leroux, S. Edmond, E. Dufour-Gergam, A. Bosseboeuf, G. Lemarquand, and V. Lemarquand, "Towards high fidelity high efficiency mems microspeakers," *IEEE SENSORS*, 2010.

[3] M. V. Garud and R. Pratap, "A novel mems speaker with peripheral electrostatic actuation," *Journal of Microelectromechanical Systems*, vol. 29, no. 4, pp. 592–599, 2020.

[4] C. Sano, M. Ataka, G. Hashiguchi, and H. Toshiyoshi, "An electret-augmented low-voltage mems electrostatic out-of-plane actuator for acoustic transducer applications," *Micromachines*, vol. 11, no. 3, p. 267, 2020.

[5] H. Tian, T. Ren, D. Xie, Y. Wang, C. Zhou, T. Feng, D. Fu, Y. Yang, P. Peng, L. Wang, and L. Liu, "Graphene-on-paper sound source devices," *IEEE 34th International Conference on Micro Electro Mechanical Systems (MEMS)*, vol. 6, no. 5, pp. 4878–4885, 2011.

[6] W. Fei, J. Zhou, and W. Guo, "Low-voltage driven graphene foam thermoacoustic speaker," *Small*, no. 19, p. 2252–2256, 2014.

[7] H.-H. Cheng, S.-C. Lo, Z.-R. Huang, Y.-J. Wang, M. Wu, and W. Fang, "On the design of piezoelectric mems microspeaker for the sound pressure level enhancement," *Sensors and Actuators A: Physical*, vol. 306, p. 111960, 2020.

[8] C. Gazzola, V. Zega., F. Cerini, S. Adorno, and A. Corigliano, "On the design and modeling of a full-range piezoelectric mems loudspeaker for in-ear applications," *Journal of Microelectromechanical Systems*, vol. 99, pp. 1–12, 2023.

[9] R. Liechti, S. Durand, T. Hilt, F. Casset, C. Dieppedale, and M. Colin, "High performance piezoelectric mems loudspeaker based on an innovative wafer bonding process," *Sensors and Actuators A: Physical*, vol. 358, p. 114413, 2023.

[10] F. Stoppel, J. Fankhänel, T. Giese, C. Eisermann, I. Pieper, and F. Lofink, "Highly miniaturized 115 db full-range mems loudspeaker for in-ear applications," *Sensors and Actuators A: Physical*, p. 116373, 2025.

[11] F. Stoppel, A. Männchen, F. Niekiel, D. Beer, T. Giese, and B. Wagner, "New integrated full-range mems speaker for in-ear applications," *IEEE Micro Electro Mechanical Systems (MEMS)*, 2018.

[12] C. Gazzola, V. Zega, A. Corigliano, P. Lotton, and M. Melon, "A reduced-order-model-based equivalent circuit for piezoelectric micro-electro-mechanical-system loudspeakers modeling," *The Journal of the Acoustical Society of America*, vol. 155, no. 2, pp. 1503–1514, 2024.

DOI: 10.61782/fa.2025.0447



FORUM ACUSTICUM
EURONOISE 2025

IMPACT OF IMPEDANCE MISMATCH ON CROSSTALK CANCELLATION WITH MICRO-SPEAKER ARRAYS

Francesco Veronesi[1*] **Filippo M. Fazi**[1] **Jacob Hollebon**[2]

[1]Institute of Sound and Vibration Research, University of Southampton, United Kingdom
[2]Audioscenic Limited, Enterprise Road Southampton, United Kingdom

ABSTRACT

Crosstalk Cancellation (CTC) is an audio technology designed to deliver binaural sound from loudspeaker arrays. Recently, its application has been extended to portable devices with miniature loudspeakers, hereafter referred to as micro-speakers. This paper investigates the effect of manufacturing inconsistencies causing variations in micro-speaker characteristics on CTC performance using numerical simulations. A lumped element model, based on measured electrical impedance of several identical micro-speakers, is used as the transfer functions between the array input signals and the loudspeaker diaphragm velocity. This, together with a rigid sphere acoustic head model or measured Head-Related Transfer Functions (HRTFs), is used to simulate the pressure signals at the listener's ears. Key findings reveal the sensitivity of CTC to specific parameter variations.

Keywords: crosstalk cancellation, micro-speakers, binaural audio, electroacoustic modeling, head-related transfer function

1. INTRODUCTION

The widespread use of mobile devices, including smartphones, laptops and tablets, has led to a significant increase in the integration of miniature speakers, or micro-speakers, to deliver high-quality audio in portable electronics. Advances in digital signal processing have led to the testing of sound and noise control technologies in portable devices with embedded micro-speakers [1], including binaural 3D audio reproduction over loudspeakers – a technique known as Crosstalk Cancellation (CTC) [2–4].

A potential challenge in using micro-speakers for such applications is the variability introduced by manufacturing inconsistencies, which can lead to discrepancies between expected and actual performance [5, 6]. This paper investigates the effect of micro-speakers manufacturing variations on CTC performance by analysing a set of micro-speakers of the same model, produced by the same manufacturer. These variations are assessed by measuring the electrical impedance of the micro-speaker voice coils, and a lumped element model is used to estimate key parameters such as voice coil resistance, inductance, suspension damping, compliance and the electrodynamic transduction coefficient (force factor). The effect of parameter variations on the transfer function relating input voice coil voltage to diaphragm velocity is analysed and the resulting impact on CTC performance is assessed. This is done by combining the transfer function with both rigid sphere and measured Head-Related Transfer Functions (HRTFs) to investigate how variations in micro-speaker parameters affect the reproduced pressure at the listener's ears.

2. THEORETICAL FRAMEWORK

2.1 Micro-speaker lumped element model

The electrical impedance of the blocked voice coil, Z_{EB}, at a given frequency ω is modelled as

$$Z_{EB} = R_E + j\omega L_E, \tag{1}$$

where R_E is the DC voice coil resistance, and L_E is its ideal inductance without considering the losses generated

*Corresponding author: F.Veronesi@soton.ac.uk.
Copyright: ©2025 Francesco Veronesi et al. This is an open-access article distributed under the terms of the Creative Commons Attribution 3.0 Unported License, which permits unrestricted use, distribution, and reproduction in any medium, provided the original author and source are credited.

by eddy currents at higher frequencies [7]. The mechanical impedance describing the diaphragm and voice coil dynamic is computed as:

$$Z_{MD} = R_{MS} + j\omega M_{MD} + \frac{1}{j\omega C_{MS}}. \quad (2)$$

In Equation (2), the parameter M_{MD} models the mechanical mass of the diaphragm and voice coil assembly, C_{MS} defines the mechanical compliance of the diaphragm suspension, and R_{MS} models the mechanical losses in the suspension [8]. The micro-speaker is mounted in a closed-box enclosure. Therefore, the total mechanical impedance, Z_M, can be modelled by introducing the rear-acoustic loading radiation impedance as follows [9],

$$Z_M = Z_{MD} + j\omega M_A + S_D^2 \frac{\rho_0 c^2}{j\omega V_c}. \quad (3)$$

where ρ_0 is the air density, c is the speed of sound, S_D is the effective radiating area of the micro-speaker diaphragm, V_c is the cabinet's volume, and M_A represents the effective mass of acoustic loading on the speaker diaphragm. By combining Equations (1) and (3), the electrical voice coil impedance is given by [8, 9]:

$$Z_E = Z_{EB} + \frac{(Bl)^2}{Z_M}, \quad (4)$$

where the force factor, Bl, is the electro-mechanical transduction coefficient representing the force exerted on the diaphragm by the magnetic motor [8]. It can be further shown [9] that the ratio between the velocity of the diaphragm and voice coil assembly, u_D, and coil input voltage, v_E, is given by:

$$\psi \triangleq \frac{u_D}{v_E} = \frac{Bl}{Z_{EB}Z_M + (Bl)^2}. \quad (5)$$

Assuming that the loudspeaker radiates sound omnidirectionally, Equation (5) can be used to express the ratio of acoustic pressure, p, to input voltage [9]:

$$\frac{p}{v_E} = j\omega\rho_0 S_D \psi \cdot G(\boldsymbol{r}, \boldsymbol{r}_s) \triangleq \Gamma \cdot G(\boldsymbol{r}, \boldsymbol{r}_s), \quad (6)$$

where $G(\boldsymbol{r}, \boldsymbol{r}_s)$ is the Green's function modelling the acoustic field produced by the speaker located at $\boldsymbol{r}_s$ at point $\boldsymbol{r}$. In this work, Equation (6) and the transfer element Γ are used to model the micro-speaker transfer function and investigate the effect of parameters variations on Crosstalk Cancellation.

2.2 Crosstalk Cancellation

Crosstalk Cancellation (CTC) is a method for reproducing binaural audio over loudspeakers, achieved by sound field control via inverse filtering [4, 10]. A single listener, L-channel CTC system ensures accurate binaural reproduction by controlling the sound pressure at two control points (the listener's ears) using L loudspeakers. The system may be described in the frequency domain as [4]

$$\boldsymbol{p} = \boldsymbol{C}\boldsymbol{H}\boldsymbol{d}, \quad (7)$$

where $\boldsymbol{p}$ is the pressure reproduced at the listener's ears, $\boldsymbol{C}$ is the $2 \times L$ plant matrix describing the system's complex frequency responses between the L loudspeakers and the left and right ear, $\boldsymbol{H}$ is the $L \times 2$ matrix of the CTC filters, and $\boldsymbol{d}$ is the target pressure to be reproduced. The CTC filters $\boldsymbol{H}$ are typically obtained by minimising the squared error norm $\|\boldsymbol{p} - \boldsymbol{d}\|^2$. To ensure causality, a modelling delay is usually introduced during filter design [3]; for simplicity, this delay term is omitted here. Solving this minimisation problem involves inverting the plant matrix $\boldsymbol{C}$. Since $\boldsymbol{C}$ is generally non-square, the filters are computed using the Moore-Penrose pseudoinverse [10].

The computation of the CTC filters, $\boldsymbol{H}$, with an accurate plant matrix, $\boldsymbol{C}$, is often impractical as it requires a thorough calibration and measurement process. Therefore, system models are commonly used, making assumptions about the listener's Head-Related Transfer Function (HRTF) and loudspeaker radiation. For instance, loudspeakers could be modelled as monopole sources [2, 11]. However, errors in the reproduced signals and a degraded binaural effect can result from inaccurate plant models [4]. Moreover, at certain frequencies, the plant matrix undergoing inversion may be ill-conditioned. Thus, to control the loudspeaker gains and the sensitivity of the pseudoinverse solution to errors in the plant matrix, Tikhonov regularisation is used to compute the CTC filters as [11]

$$\boldsymbol{H} = \boldsymbol{C}^H[\boldsymbol{C}\boldsymbol{C}^H + \beta\boldsymbol{I}]^{-1}, \quad (8)$$

where β is the regularisation parameter, $\boldsymbol{I}$ is the 2×2 identity matrix and $[\cdot]^H$ denotes the Hermitian transpose. In Equation (8), β determines the relative weight assigned to the electrical power required to drive the loudspeakers – referred to as control effort and defined as $\|\boldsymbol{H}\boldsymbol{d}\|^2$. As β changes from zero to infinity, the solution changes from minimising only the performance error to minimising the control effort [3].

In this paper, Equation (8) is used to calculate the CTC filters employed to drive L micro-speakers arranged

in a linear configuration, adopting a rigid sphere head model for the plant matrix, $\boldsymbol{C}$, as outlined in [12]. To include the micro-speaker characteristics, Equation (7) is modified as follows,

$$\boldsymbol{p} = \boldsymbol{G}\boldsymbol{\Gamma}\boldsymbol{H}\boldsymbol{d}, \tag{9}$$

where $\boldsymbol{\Gamma}$ is a $L \times L$ diagonal matrix populated with transfer elements Γ as defined in Equation (6), $\boldsymbol{G}$ is the matrix of Green's functions modelling the acoustic field between the array speakers and the listener's ears, and $\boldsymbol{d} = [1, 0]^T$ is the target binaural signal [4]. In this work, $\boldsymbol{G}$ contains the transfer responses associated with a rigid sphere head model or Neumann KU 100 HRTFs [13], and is hereafter referred to as *forward* plant matrix.

2.3 Crosstalk Cancellation system description

The CTC system under consideration consists of $L = 5$ sources and two control points corresponding to the ears of a dummy head. The sources considered, all of the same model and from the same manufacturer, are rectangular microspeakers with diaphragm dimensions of 9.2 mm $\times$ 32.2 mm, giving an area of $S_D = 2.9$ cm^2. Each transducer is mounted in a cabinet with a volume of approximately $V_C = 13.0$ cm^3. Figure 1 illustrates the listener and loudspeakers configuration.

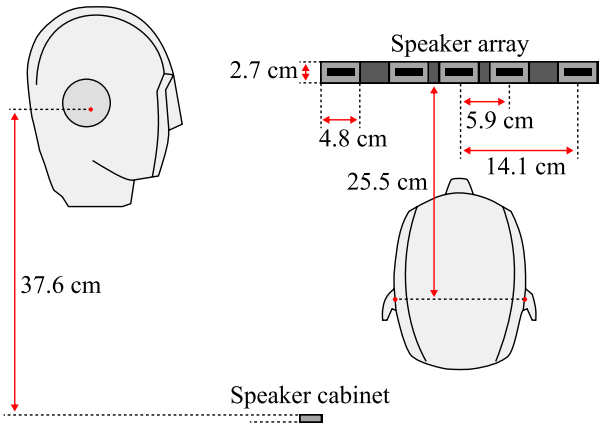


Figure 1: Graphical representation of the CTC system (side and top view).

3. SENSITIVITY ANALYSIS OF PARAMETERS

This section illustrates how the parameters of the model introduced in Equation (4) are estimated from measured voice coil electrical impedances and how they affect the transfer function ψ defined in Equation (5).

3.1 Parameter estimation

The voice coil impedance of 12 micro-speakers was measured between 100 Hz and 20 kHz using the method described in [14]. The resulting data were then analysed using the function introduced in Equation (4) for the least-squares estimation of the Thiele-Small (T-S) parameters of the micro-speakers. Table 1 presents the mean value of the fitted parameters, along with their corresponding percent Relative Standard Deviation (RSD), and maximum mismatch ($m_{\%}$), equivalent to three deviation standards. The total mass $M_{MT} = M_{MD} + M_A$ represents the mechanical mass of loudspeaker diaphragm assembly including air load and voice coil, and f_0 the resonance frequency of the micro-speakers.

Table 1: Estimated mean, percent Relative Standard Deviation (RSD), and maximum mismatch ($m_{\%}$) of model parameters.

Parameter	Mean value	RSD (%)	$m_{\%}$
R_E	3.7 Ω	3.3%	9.9%
L_E	0.025 mH	0.8%	2.4%
Bl	3.5 N/A	2.5%	7.5%
R_{MS}	4.8 Kg/s	6.4%	14.4%
C_{MS}	0.015 mm/N	5.9%	17.3%
M_{MT}	3.7 g	4.8%	14.4%
f_0	678.8 Hz	2.3%	6.9%

The table shows that the estimated parameters with the largest variation are the suspension resistance and compliance, followed by the mechanical mass and electrical resistance. This result is consistent with the level of manufacturing imperfection reported in other studies [6, 9, 15, 16], where it is observed that C_{MS}, R_{MS}, and R_E are typically the micro-speaker parameters that are the most subject and sensitive to variations in the production line. It is further noted that the estimated voice coil DC resistance, resonance frequency, and mechanical mass align with the specification provided in the micro-speaker data sheet.

Figure 2 shows the measured voice coil impedance and the reference impedance curve calculated using the mean values from Table 1. The figure clearly illustrates the manufacturing inconsistencies in micro-speakers across the entire frequency range. It should also

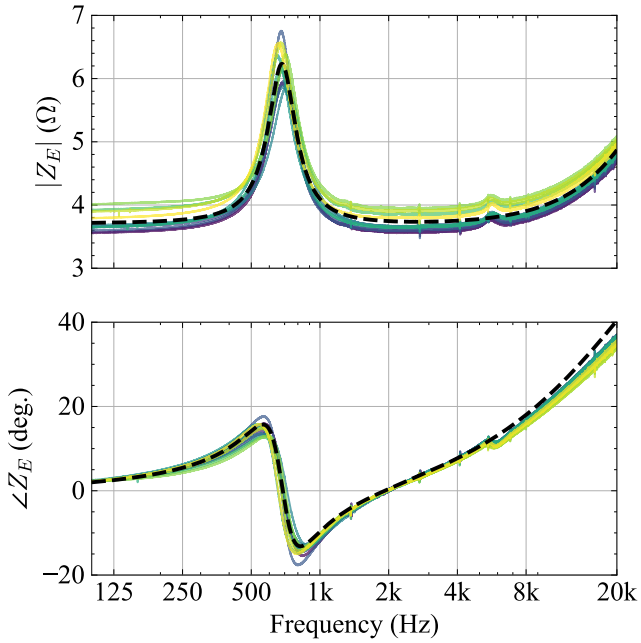


Figure 2: Measured (coloured, solid) and average (black, dashed) voice coil electrical impedance. The average curve is computed using the mean parameters of Table 1.

be noted that the lumped element model considered replicates the impedance curve well, but is unable to reproduce the resonance peak at 5.5 kHz, which might be a higher-order mechanical vibration mode of the micro-speaker [7].

3.2 Effect of parameter variations on ψ

Each parameter of the micro-speaker model has a different effect on the transfer function ψ (Equation (5)) and thus on the radiated acoustic pressure (Equation (6)). Figure 3 illustrates the effects caused by variations of individual parameters on the magnitude and phase of ψ. The black solid and dashed lines respectively represent the magnitude and phase of ψ calculated using the mean parameter values from Table 1, with $\rho_0 = 1.204$ kg/m^3 and $c = 343$ m/s. Deviations from the mean are indicated by the shaded areas, transitioning to blue for negative variations and red for positive variations.

The variation of the voice coil resistance R_E is inversely proportional to the variation of the magnitude of ψ. Without altering the system's resonance frequency, increasing R_E reduces both the magnitude of ψ and the radiated acoustic pressure. Significant phase variations primarily occur at high frequencies. The electrical inductance L_E affects ψ only at high frequencies, with a smaller effect compared to R_E. Conversely, the variation of the magnitude of ψ is directly proportional to the variation of the force factor Bl, with limited phase variations. The suspension resistance R_{MS} modifies the sharpness of the resonance peak without changing its frequency, where higher mechanical losses due to the suspension reduce the radiated sound. The phase response is only slightly affected by large variations in R_{MS}. Differently to the previous cases, the resonance frequency of the system is significantly influenced by changes in C_{MS} or M_{MT}, as expected. An increase in these parameters will lower the resonance frequency and alter the phase response of ψ. These observations align with the results discussed in [17].

4. EFFECT OF PARAMETER VARIATIONS ON CROSSTALK CANCELLATION

This final section examines how mismatches in loudspeaker impedance – resulting from variations in selected T-S parameters between different micro-speakers – affect the CTC level achieved by the system, based on the model introduced in Equation (5). The tuning of the regularisation parameter, the modelling of the inverse filters, and the evaluation of CTC performance are discussed, followed by simulation results based on two forward plant matrices, $\boldsymbol{G}$.

4.1 CTC filters and CTC level

The CTC filters are computed as shown in Equation (8), using a rigid sphere head model to design the plant matrix. This choice is motivated by the variability introduced by micro-speaker manufacturing variations, as observed in Figure 2. Such inconsistencies can lead to inaccurate plant models when using speakers different from those used during the calibration process. In these cases, regularisation would improve the robustness of the system to loudspeaker variations, but also reduces the CTC performance in the ideal case. Additionally, previous research has shown that CTC levels obtained with measured HRTFs and those derived from rigid sphere head models are comparable [4]. Therefore, for simplicity, in this work the plant matrix elements used for the CTC filter design utilise a rigid sphere head model. The mathematical formulation for the responses follows [12], with the head radius set to 87.5 mm.

To determine the appropriate level of regularisation, the control effort was analysed. Specifically, a frequency-independent regularisation parameter of $\beta = 0.00023$ was

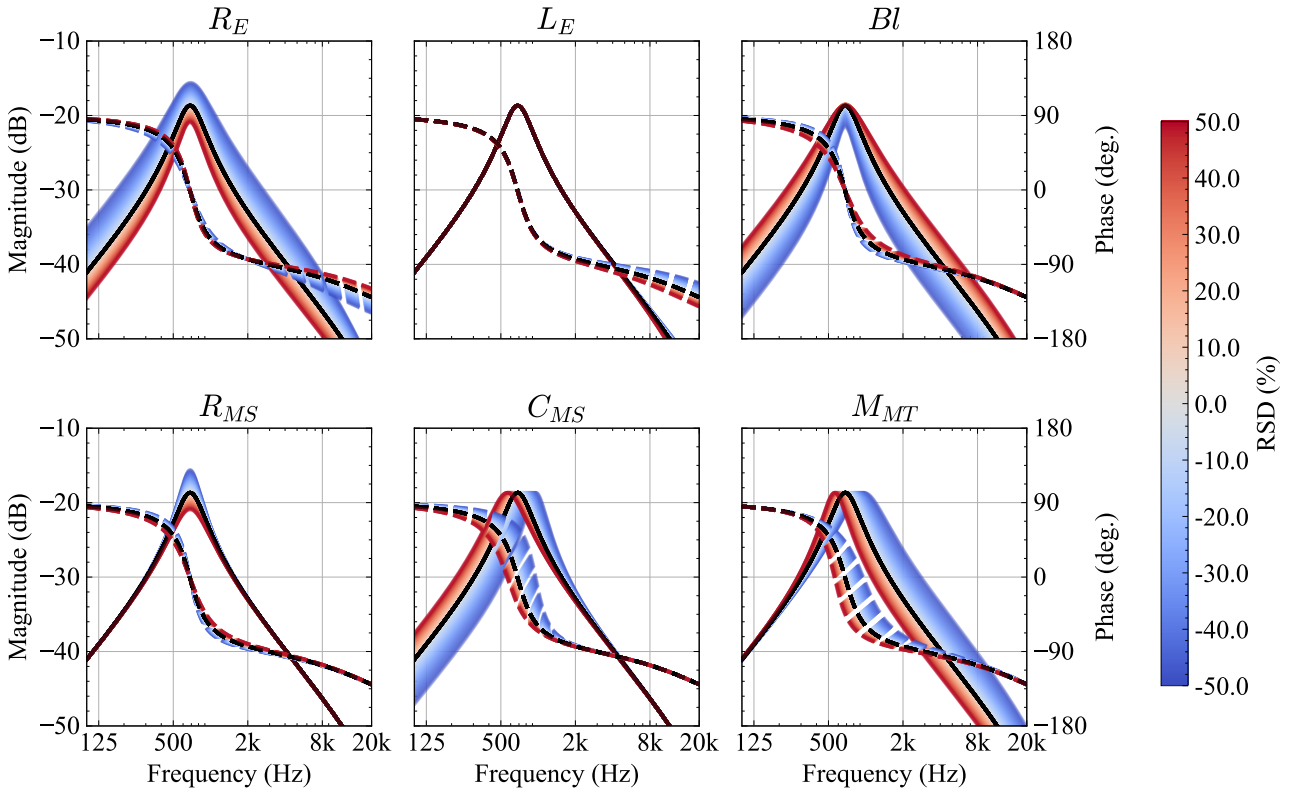


Figure 3: Effect of parameter variations on the magnitude and phase of the transfer function ψ. The black line represents ψ computed using mean parameter values (solid for magnitude, dashed for phase). Shading transitions toward blue for negative variations, measured in terms of the percent Relative Standard Deviation (RSD), and red for positive variations.

chosen to ensure that the control effort variation remained within 18 dB over the 100 Hz to 20 kHz range.

The performance of the system is evaluated using the CTC level, defined as the ratio of the squared reproduced pressures at the listener's ears for a target binaural signal $\boldsymbol{d} = [1, 0]^T$ [4]:

$$\text{CTCL} = 10 \log_{10} \left(\frac{|p_1|^2}{|p_2|^2} \right). \tag{10}$$

The CTC level quantifies the amount of CTC achieved between the listener's ears. In general, a minimum CTC level of 20 dB is required to achieve the desired binaural effect [4].

4.2 Simulation outline

The behaviour of the system under parameter variation was simulated for different levels of percentage mismatch. Previous studies [9,15,16] indicate that the parameters most subject to manufacturing variations in microspeakers are C_{MS}, R_{MS} and R_E. Specifically, these studies suggest that the suspension compliance has an imperfection tolerance of about $\pm 30\%$, while the mechanical and electrical resistances typically vary within $\pm 10\%$. For these reasons, and given the levels of variation reported in Table 1, the T-S parameters R_E, R_{MS}, C_{MS} and M_{MT} are selected for analysis.

The simulation follows this procedure: a single T-S parameter is selected, and a set of $L = 5$ random values is generated for a given percentage mismatch level. The manufacturing imperfections are assumed to follow a normal distribution with a mean μ – the nominal values from Table 1 – and a standard deviation σ given by

$$\sigma = \frac{m_{\%}}{3 \cdot 100} \mu. \tag{11}$$

In Equation (11), $m_{\%}$ represents the maximum deviation from the mean that the random value of the T-S param-

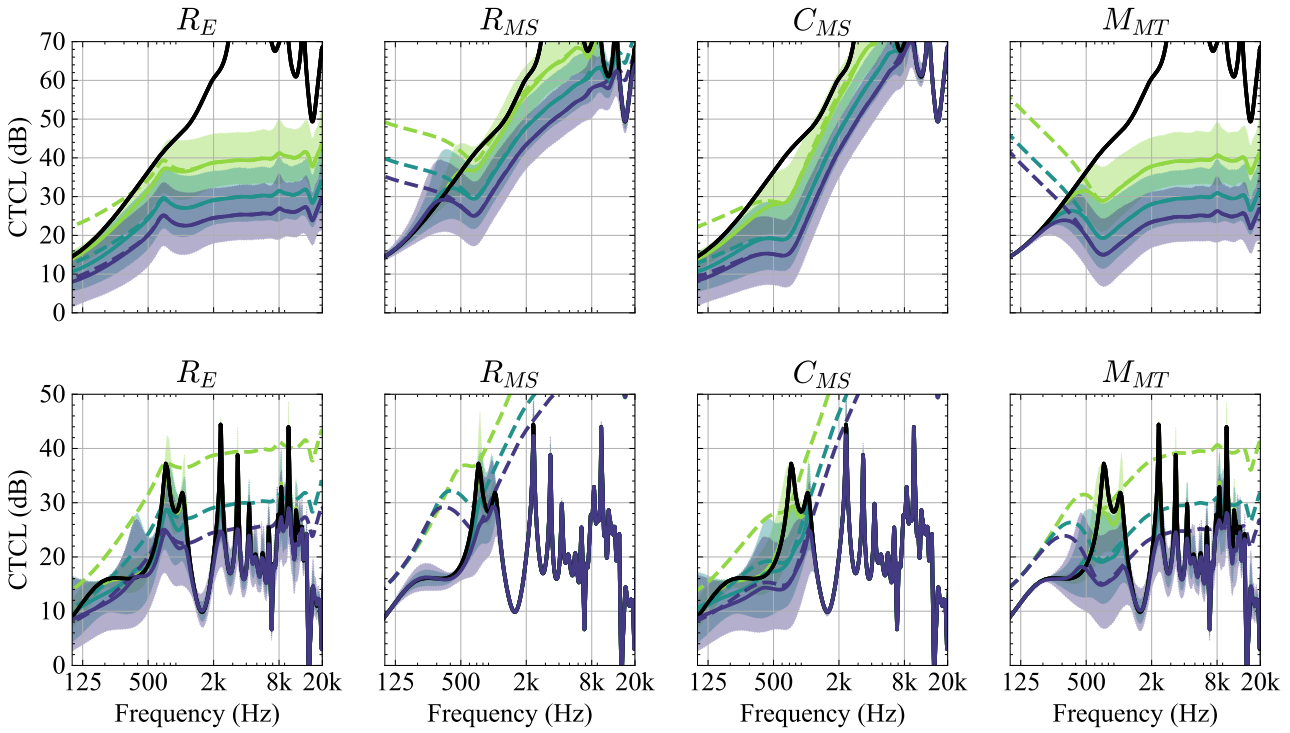


Figure 4: Average CTC level for different parameter mismatch values and forward plant matrix choices. Top: forward plant modeling with rigid sphere HRTFs; bottom: forward plant modeling with KU 100 HRTFs. Mismatch values: 0% (—), 10% (—), 30% (—), 50% (—). Dashed lines show CTC levels with reduced regularisation ($\beta = 10^{-9}$) in the first row and with rigid sphere forward plant matrix in the second. Shaded regions indicate the 10th to 90th percentiles.

eter can assume. Therefore, 'thirding' $m_{\%}$ ensures that nearly all randomly generated values are within three standard deviations. The selected values for maximum mismatch are $m_{\%} = 10\%$, 30% and 50%. This latter value is considered because, in addition to discussed manufacturing imperfections, further variations can occur during sound reproduction due to the non-linear and time-variant behaviour of micro-speakers, which significantly affects their response [5, 7, 18]. While keeping all other parameters fixed at their nominal mean values, the generated random parameters are used to compute five distinct transfer functions, ψ and Γ. These modified transfer functions populate the diagonal transfer function matrix $\mathbf{\Gamma}$. In this way, the effect of parameter variations on the CTC level can be examined by computing and analysing the reproduced pressure, as described in Equations (9) and (10). This procedure is repeated 10^4 times for the four selected parameters and across all percentage mismatch values to ensure statistical reliability of the results. Finally, the retrieved CTC levels are averaged.

4.3 Performance Analysis

The results of the simulation are illustrates in Figure 4, which shows the average CTC level obtained for the three different parameter mismatch values and four model parameters, for the two distinct forward plant matrix choices. The top row of the figure displays the results corresponding to the choice of a rigid sphere forward plant matrix, while the bottom row corresponds to the KU 100 HRTF plant matrix. Dashed lines are introduced in the plots. In the first row they represent the CTC levels obtained by reducing the regularisation parameter to $\beta = 10^{-9}$. In the second row, they show the CTC level obtained using the rigid sphere forward plant matrix (with $\beta = 0.00023$). The averaged CTC level is compared with the performance level obtained without introducing any parameter variation (black line). Moreover, the statistical dispersion of the CTC level obtained for each simulation

is illustrated with shaded regions, whose boundaries define respectively the 10th and 90th percentiles.

4.3.1 *Forward plant modeling with rigid sphere HRTFs*

Figure 4 shows that when the same rigid sphere head model used to compute the CTC filters is also used to design the forward plant matrix, the CTC level achieved by the system, when no mismatch is considered, is well above the 20 dB threshold over most of the frequency range considered. At low frequencies, especially below 200 Hz, the plant matrix is highly ill-conditioned, resulting in poor CTC levels regardless of parameter mismatch. In this range, β regulates the stability of the solution and prevents energy loss, but at the cost of reduced control performance. When parameter variations are introduced, a reduction in the CTC level is observed. The reductions are consistent with the variations in the transfer function ψ observed in Figure 3. In particular, changes in R_E and M_{MT} affect the CTC level over the entire frequency range, especially above the resonance frequency, where losses of more than 20dB occur above 2kHz. Variations in mechanical resistance mainly affect and reduce the CTC level about and below the resonance frequency, while variations in C_{MS} lead to reductions at frequencies below resonance. The results obtained with reduced regularisation (dashed lines) highlight an important property of the system: at low frequencies, the performance degradation is driven by regularisation rather than impedance mismatch. This proves that regularisation imposes a performance limit on the system, regardless of parameter variations.

4.3.2 *Forward plant modeling with KU 100 HRTFs*

When the reproduced pressure is derived by modeling the forward plant matrix with KU 100 HRTFs, the CTC level significantly reduces compared to the case in which the rigid sphere head model is employed. The forward plant matrix is not accurate and the system results in a lower CTC performance, in line with what is observed in [4]. Nonetheless, similar trends to those observed in the previous case occur. T-S parameter variations reduce the CTC level in proportion to the parameter mismatch, matching the variations in the transfer function ψ. It is further noted that at certain frequencies the CTC level matches that of the rigid sphere (dashed lines), indicating that the reduction is driven by the largest mismatch – whether from regularisation, head model differences, or variations in micro-speaker parameters. For the chosen level of regularisation, errors from mismatched head models dominate over most of the frequency spectrum, while CTC degradation due to parameter mismatch is mainly confined to mid-low frequencies, especially below 1 kHz and about resonance. At these frequencies, the performance loss due to parameter mismatch is less severe than in the previous case, even for large variations. This suggests that in practice, even with extremely poor manufacturing tolerances, parameter mismatches have a negligible effect on CTC performance, provided that the CTC filters and the forward plant matrix are designed with different models.

5. CONCLUSIONS

The increasing integration of miniature loudspeakers in mobile devices has enabled the use of advanced audio technologies, such as Crosstalk Cancellation (CTC), to improve the audio experience on these devices. However, manufacturing inconsistencies in micro-speakers can introduce variability that affects performance. This paper has investigated the effect of these variations on CTC using a lumped element model to design two transfer functions: one for diaphragm velocity to voice coil input voltage, ψ, and the other for acoustic pressure to input voltage. Manufacturing variations in 12 micro-speakers were measured, revealing a maximum variation of up to 20% in the Thiele-Small parameters. The effect of parameter mismatch on CTC was investigated by analysing different model parameters considering typical manufacturing variations.

The CTC filters have been designed using Tikhonov regularisation with a rigid sphere head model. The reproduced pressure was computed using a forward plant matrix whose entries are populated either with the same rigid sphere responses used for the CTC filters, or with measured HRTFs. The results have shown that when a rigid sphere head model is used, the CTC level variations due to parameter mismatch are more pronounced, as the ideal CTC level is very high and there are no errors in the sound path transfer responses. The variations are consistent with those observed in the transfer function ψ. At low frequencies, the degradation in performance is driven by regularisation rather than impedance mismatch, highlighting that regularisation sets a performance limit independent of parameter variations. When KU 100 HRTFs are used, the CTC level is significantly reduced due to the differences in the head models. At some frequencies, the CTC level is equal to that of the rigid sphere, indicating that the reduction is dominated by the largest mismatch – whether from regularisation, head model differences or micro-speaker

parameter variations.

The results presented in this paper suggest that CTC performance may be further compromised when multiple mismatches are combined. Future research could also explore the effects of extending the micro-speaker model to account for non-linear behaviour, as well as analysing the effects of varying the number of loudspeakers in the array, or testing the system's robustness across different listener positions.

6. ACKNOWLEDGMENTS

This work was supported by Audioscenic Limited as part of the project "Understanding, Modelling and Improving Various Aspects of Crosstalk Cancellation Systems" (Contract No 9747105).

7. REFERENCES

[1] M. Homaei, M. Fathalilou, R. Shabani, and G. Rezazadeh, "Application of the electrostatic micro-speakers for producing audible directional sound," *International Journal of Applied Mechanics*, vol. 12, no. 04, 2020.

[2] O. Kirkeby, P. A. Nelson, and H. Hamada, "Local sound field reproduction using two closely spaced loudspeakers," *The Journal of the Acoustical Society of America*, vol. 104, no. 4, pp. 1973–1981, 1998.

[3] O. Kirkeby, P. Nelson, H. Hamada, and F. Orduna-Bustamante, "Fast deconvolution of multichannel systems using regularization," *IEEE Transactions on Speech and Audio Processing*, vol. 6, no. 2, pp. 189–194, 1998.

[4] J. Hollebon, E. Hamdan, and F. Fazi, "A comparison of the performance of hrtf models in inverse filter design for crosstalk cancellation," in *Proceedings of the Institute of Acoustics*, vol. 41, Curran Associates, Inc., 2020.

[5] M. Colloms and P. Darlington, *Loudspeaker Assessment*, ch. 10, pp. 513–634. John Wiley & Sons, Ltd, 2018.

[6] B. Chojnacki, "Dispersion influence of electroacoustic transducer parameters in the design process of miniature loudspeaker arrays and omnidirectional sound sources," *Sensors*, vol. 24, no. 15, 2024.

[7] K. Wolfgang, "Micro-speakers – hybrids between headphones and loudspeakers," *Journal of the Audio Engineering Society*, no. K-1, 2016.

[8] J. W. Marshall Leach, *Introduction to Electroacoustics and Audio Amplifier Design*. Kendall Hunt Publishing Company, 4 ed., 2009.

[9] A. Bright, F. Jacobsen, J.-D. Polack, and K. Rasmussen, *Active control of loudspeakers: An investigation of practical applications*. PhD thesis, 2002.

[10] J. Bauck and D. H. Cooper, "Generalized transaural stereo and applications," *journal of the Audio Engineering Society*, vol. 44, pp. 683–705, 1996.

[11] T. Takeuchi and P. A. Nelson, "Optimal source distribution for binaural synthesis over loudspeakers," *The Journal of the Acoustical Society of America*, vol. 112, no. 6, pp. 2786–2797, 2002.

[12] R. O. Duda and W. L. Martens, "Range dependence of the response of a spherical head model," *The Journal of the Acoustical Society of America*, vol. 104, no. 5, pp. 3048–3058, 1998.

[13] B. Bernschütz, "A spherical far field hrir/hrtf compilation of the neumann ku 100," in *AIA-DAGA 2013 Merano*, vol. 41, 2013.

[14] T. Steve and S. Tony, "Advances in impedance measurement of loudspeakers and headphones," *Journal of the Audio Engineering Society*, no. 8991, 2013.

[15] J. R. Chang and C. N. Wang, "Acoustical analysis of enclosure design parameters for microspeaker system," *Journal of Mechanics*, vol. 35, no. 1, pp. 1–12, 2017.

[16] J. R. Chang and C. N. Wang, "Bass extension of microspeaker system on mobile device," *Journal of Mechanics*, vol. 35, no. 4, pp. 487–498, 2018.

[17] S. J. Pawar, H. C. Her, and J. H. Huang, "Parametric simulation study of miniature loudspeaker for performance evaluation and improvement," in *ICA2010: 20th International Congress on Acoustics*, vol. 20, 2010.

[18] M. Zilletti, A. Marker, S. J. Elliott, and K. Holland, "Identifying the nonlinear mechanical behaviour of micro-speakers from their quasi-linear electrical response," *Mechanical Systems and Signal Processing*, vol. 88, pp. 212–223, 2017.

DOI: 10.61782/fa.2025.0291

FORUM ACUSTICUM EURONOISE 2025

DEVELOPMENT OF AN OMNIDIRECTIONAL CYLINDRICAL SOUND SOURCE WITH A CORONA DISCHARGE TRANSDUCER

Hervé Lissek[1*] **Tirui Wang**[1] **Rahim Vesal**[1]

[1] Laboratory of Wave Engineering, Ecole Polytechnique Fédérale de Lausanne, Switzerland

ABSTRACT

The Corona Discharge Transducer (CDT) relies on the electroacoustic actuation of a ionized layer of air through an oscillatory electric field. This device allows sound generation without an intermediate mechanical radiator such as a membrane, making it an almost perfect particle velocity source, with ideal impulse response. Thanks to its membrane-less and construction and its continuous arrangement of uniform linear acoustic antennas, it also permits the development of ideal monopolar sources. This paper presents a cylindrical CDT concept, its design and optimization through numerical models (COMSOL), in a view to the realization of a future experimental prototype. The discussion on the acoustic performance obtained on the models will lead to concluding remarks on its applicability to acoustic metrology.

Keywords: *Plasma physics, corona discharge, directional loudspeakers*

1. INTRODUCTION

In their vast majority, loudspeakers rely on the acoustic radiation of a mechanical component (circular or rectangular diaphragm) or through an acoustical radiator (horn), actuated by an electromechanical driver, most often electrodynamic (although electrostatic, piezoelectric, or pneumatic transducers also exist) [1]. Therefore, the whole electro-acoustic transduction cannot happen without an intermediate, likely to degrade the response to transients (due to the inertia of the membrane), thus yielding audible phase distortions [2].

Besides their limitations in the time domain, loudspeakers relying on mechanical membrane do not allow the effective construction of actual omnidirectional sources, unless through the faceting of polyhedrons, such as dodecahedrons used in room acoustic measurements [3]. These sound sources present directivity pattern close to ideal pulsating spheres at low frequencies (as long as the wavelength remain much larger than the polyhedron dimensions [4]), but become nonetheless directive at higher frequencies.

The development of electroacoustic transducers relying on the Corona Discharge mechanism has been reported back to the 1970's, but the 2000's have seen a surge of interest with the work of Béquin et al with mathematical models [5, 6] allowing their design in different configurations ("point-to-grid", "wire-to-grid", etc.). More recently, a planar loudspeaker relying on a "wire-to-grid" Corona Discharge configuration has been developed by Sergeev et al [7, 8] for applications to active noise control, but also as an "ideal" source of sound (transparent, massless, resonant-free, ideal flow velocity source...).

One interesting property of this device is the combination of two colocated sound sources. A first monopolar source results from the heat release around the ultra-thin electrode (designated "corona electrode") responsible for the ionization of the surrounding medium. The second dipolar source is linked to the electrostatic force responsible of the bulk acceleration/decelaration of positive ions and their consecutive non-elastic collisions with the surrounding (neutral) fluid medium in the "drift region" between the corona electrode and a grounded coarsely perforated metallic electrode (designate "collector electrode").

**Corresponding author*: *herve.lissek@epfl.ch.*

Copyright: *©2025 Hervé Lissek et al. This is an open-access article distributed under the terms of the Creative Commons Attribution 3.0 Unported License, which permits unrestricted use, distribution, and reproduction in any medium, provided the original author and source are credited.*

In short, the two processes are responsible of the simultaneous generation of two flow velocities, one symmetric and the other anti-symmetric with respect to the median plane of the transducer. It has also been shown that the ratio between the two flow velocity sources was of the order 1:5 (the dipole source being about 5 times stronger than the monopole source), depending on the transducer geometry.

While constructing an ideal spherical source with a corona discharge transducer represents an obvious challenge with the "wire-to-grid" configuration, the cylindrical geometry is much more straightforward to design, and should allow validating the concept of an ideally omnidirectionnal sound source. This paper aims at presenting the development of a cylindrical loudspeaker based on the corona discharge principle with a wire-to-grid configuration, allowing achieving an omnidirectionnal source in the plane perpendicular to its axis of symmetry. In a first section, the principle of the corona discharge and its application to electroacoustic transducers will be shortly reminded, followed by the description of a very simple numerical model on COMSOL Multiphysics, allowing its further design. Finally, preliminary simulation results will be presented, justifying the timeliness of the proposed design, and paving the way to future experimental validations.

2. THE CORONA-DISCHARGE ELECTROACOUSTIC TRANSDUCER

2.1 Reminder of the principle in a "wire-to-grid" configuration

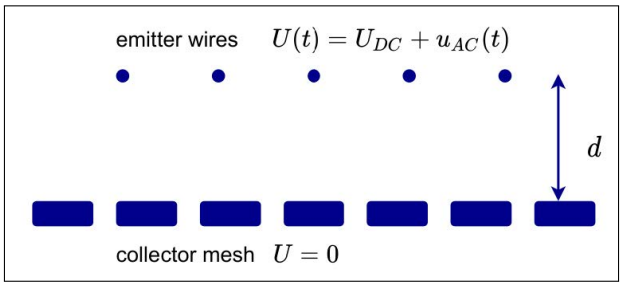


Figure 1. Sketch representing a cut view of the electrode pair: corona electrode (emitter wires)/collector electrode (grounded perforated grid)

Corona discharge loudspeakers allow for sound generation due to the ionization of molecules in the surrounding fluid, moved by an intense oscillating electric field. In the "wire-to-grid" configuration, the transducer is constituted by a pair of electrodes (forming two parallel planes, as illustrated in the sketch of Fig. 1): the first one is a perforated metallic grid connected to the ground, and is designated the "collector electrode"; the second one, designated "corona electrode", is made of an ultra thin wire (diameter of the order of 100 μm), arranged in a pattern of parallel lines along a same plane parallel and distant of d to the collector plane, put at a sufficiently high voltage so as to trigger the extraction of electrons from surrounding molecules. The breakdown voltage, above which ionization is possible, is designated U_0 and is of the order of a few kV.

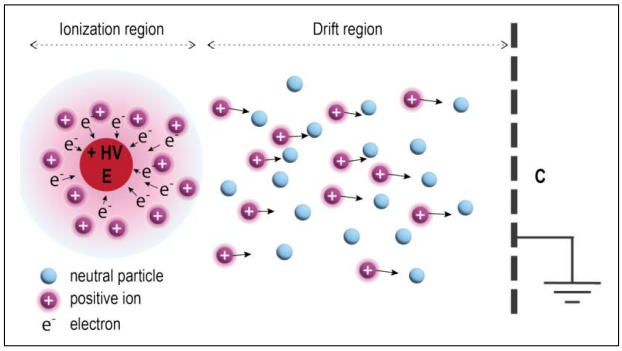


Figure 2. Corona discharge principle

When applying an offset voltage U_{DC} higher than U_0, positive ions are accelerated inside the ionization region towards the collector electrode. They then collide with the neutral particles present in the drift region, which are then moved, giving rise to an "ionic wind" (constant flow).

If an alternating voltage $u_{ac}(t)$, of the order of 1 kV, is superimposed to U_{DC} (while total voltage $U_{DC} + u_{ac}$ still remains higher than the breakdown voltage, as well as not exceeding a value above which arcing may occur), the transducer generates acceleration/deceleration of the surrounding fluid layers, responsible for sound generation.

The preceding studies show that this corona discharge transducer configuration could be modelled as the combination of two volumic sound sources, one monopolar "heat" source H (due to the heat release at the corona electrodes), and another dipolar "force" source F (relative to the electrostatic force moving the surrounding fluid back and forth).

An extremely simple electroacoustic model can be deduced from the coupling equations between the plasma

generation and actuation, and the generated sound field. Indeed, it has been shown that the offset voltage U_{DC} can be linked to the current I flowing through the corona wire according to the Townsend formula:

$$I = CU_{DC}(U_{DC} - U_0) \tag{1}$$

where C is a constant that depends on the transducer geometry, and that can be experimentally determined. It is then possible to express the two sources H and F as a function of the voltage feeding the transducer [7, 8]:

$$\begin{aligned} H &= C(3U_{DC}^2 - U_{DC}U_0)u_{ac} \text{ [W]} \\ F &= \frac{C.d}{\mu_i}(2U_{DC} - U_0)u_{ac} \text{ [N]} \end{aligned} \tag{2}$$

where μ_i designates ions mobility, and d is the distance between the two electrodes (or the plasma thickness).

Equation (1) can then be used to express the "Heat Source" power density (in W/m^3), and the "Dipolar Domain Source" force density (in N/m^3), by dividing these two expressions by the plasma volume ($S.d$, where S is the transducer effective area) in the COMSOL model.

2.2 Case of a cylindrical "wire-to-grid" configuration

In this study, we investigate a alternative geometry of the corona discharge electroacoustic transducer, where the collector electrode is composed of a cylindrical perforated metallic grid (alternatively, composed of cylindrical rods arranged to form a cylinder shape around the symmetry axis), of height h, bounded by two rigid plates on both sides, over which an ultrathin wire can be arranged to form a network of parallel wires distant of e from each others, and distant of d from the collector. Fig. 3 illustrates the proposed configuration.

It seems quite obvious that, in this configuration, the dipolar force source is cancelled by the axisymmetry of the transducer, giving rise to the only monopolar heat source. It should then behave as an ideal omnidirectional sound source in the horizontal plane, or in azimuth (according to the convention of Fig. 3, the symmetry axis being along the vertical). Note that the transducer directivity in elevation (with respect to the z axis) should correspond to the one of a finite radiating cylinder, according to Williams et al [9].

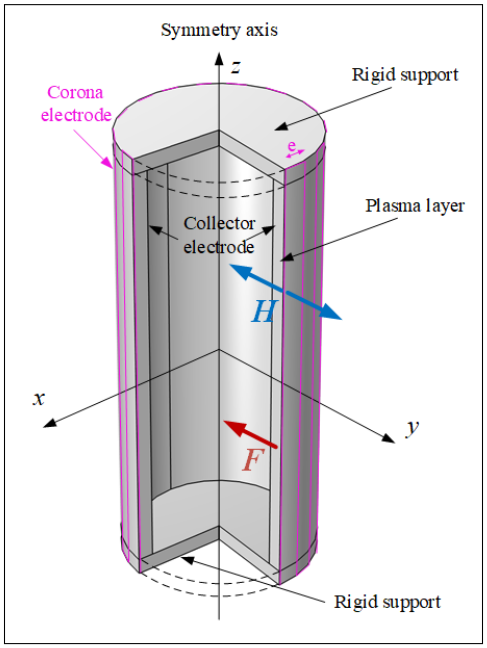


Figure 3. Cylindrical plasma loudspeaker geometry

3. NUMERICAL MODEL

3.1 Description of the COMSOL model

A COMSOL Multiphysics model has been developped to verify the acoustic properties of the transducer elaborated before. The model uses the only *Pressure Acoustics, Frequency Domain* (acpr). We have chosen to develop a full 3D model of the transducer in a view to assess further configurations in the future, not only the axisymmetric one (for which the only 2D Axisymmetric Space Dimension would have been sufficient). Especially, we will be interested in investigating a dipolar transducer configuration in the future (not presented here). However, in order to save computational time, we assumed the horizontal plane xOy and the vertical plane xOz are planes of symmetry, thus limiting the 3D model to a quadrant of a sphere.

We start by modeling the geometry in the xOz plane, and generate the 3D model by semi-revolution along axis z. In this plane, we draw the propagating domain as a quadrant of a circle of radius $D = 1$m, surrounded by a Perfectly Matched Layer of depth $D/5 = 0.2$ m. The cylindrical loudspeaker is represented by a rectangular layer of height $h/2$ and width d, shifted by distance R from the axis of symmetry z. This plasma layer is capped by a rigid frame of width $R + d$ and height t, which is

substracted from the propagation domain, the remaining boundaries being set as "Sound Hard Boundary".

Here, we will consider the plasma layer model presented by Sergeev et al [7, 8], namely considering the plasma layer of volume $V = \pi(d^2 + 2d.R).h$ as an homogenous air medium embedding one "Heat Source" domain (power density $Q_{heat} = H/V$, to which we should precise the isobar heat capacity C_p and adiabatic coefficient γ), and a "Dipolar Domain Source" (power density $q_d = -F/V$ along the xOy plane, the - sign indicating that the corona electrode is located on the exterior side of the cylinder, although this component should have no effect in this geometry). Fig. 4 illustrates the chosen model geometry in 2D.

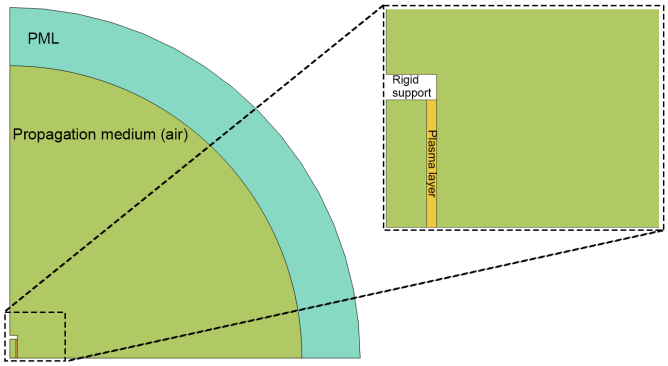


Figure 4. Intermediate 2D COMSOL model

The parameters used to design the COMSOL model are given in Tab. 1. Note that the dimensions have been chosen to meet the ones of a planar version of the corona discharge loudspeaker, assuming the electroacoustic properties (especially coefficient C) is only dependant on the transducer dimensions (inter-electrode distance d, corona wire diameter, and overall corona wire length, linked to the effective area of the transducer S). With these assumptions, there is no need to build a prototype to evaluate the electroacoustic model parameters, which simplifies the modeling and design phase. The following parameters mostly refer to a former design reported in [10].

Table 1. Model parameters

Parameter	Symbol	Value	Unit
Medium (air) properties			
Density	ρ_0	1.23	kg.m^{-3}
Speed of sound	c	343	m.s^{-1}
Isobar heat capacity	C_P	1015	J.kg^{-1}K^{-1}
Adiabatic coefficient	γ	1.4	-
Ions mobility	μ_i	1.1.10^{-4}	m^{2}V^{-1}s^{-1}
Transducer dimensions			
Plasma thickness	d	5	mm
Wires spacing	e	10	mm
Height	h	13	cm
Internal radius	R	2.5	cm
Support thickness	t	13	mm
Electrical characteristics			
DC voltage	U_{DC}	8	kV
Breakdown voltage	U_0	6.16	kV
Current/voltage constant	C	1.8 10^{-11}	A V^{-2}

Last, the 2D model drawn in the xOz *Work Plane* is extruded in semi-revolution to obtain the 3D model of Fig. 5.

The simulations are performed in the frequency domain, for ISO frequencies split in 1/24th octave spanning the [125 Hz - 2000 Hz] range. The tetrahedral meshing was limited to one sixth of a wavelength at 2000 Hz. Presented results will limit to octave bands central frequencies.

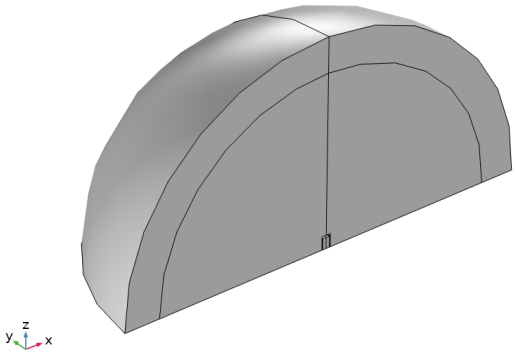


Figure 5. Full 3D COMSOL model

3.2 Simulations results

We present the directivities of the cylindrical plasma loudspeaker in azimuth (Fig. 6) and elevation (Fig. 7). Regarding the directivity in azimuth, it is obvious that the transducer is perfectly omnidirectionnal in the xOy plane, which justifies the chosen geometry. Moreover, the achieved directivities in elevation confirm that the sound radiation conforms to the one of a finite pulsating cylinder, as described by Williams et al. [9].

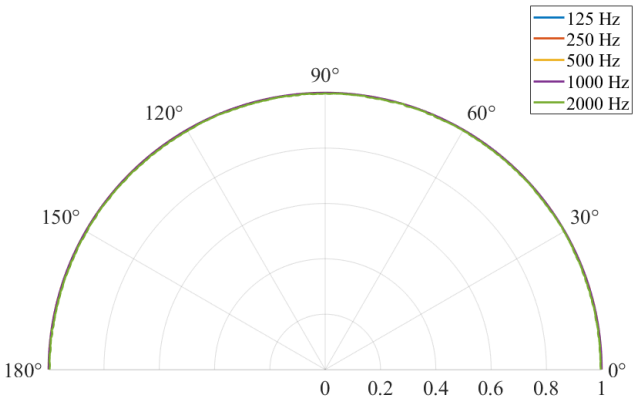


Figure 6. Directivity in azimuth

Moreover, the acoustic pressure along the Ox axis, illustrated on Fig. 8 corresponds to the sound radion model of a finite cylinder reported in [9].

Last, the radiation impedance of the cylindrical plasma transducer is obtained by first integrating the sound pressure and the normal velocity over the plasma outter boundary to derive the net pressure force and flow velocity, and then expressing their ratio normalized by $Z_c = \rho_0.c_0$. The normalized radiation impedance is illustrated on Figure 9.

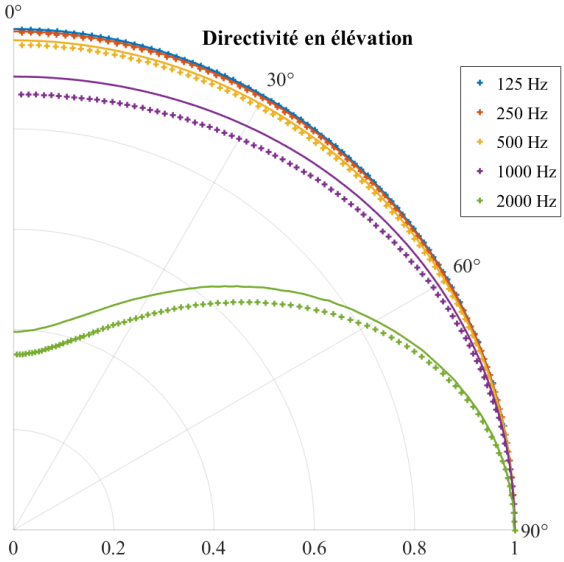


Figure 7. Directivity in elevation (lines: COMSOL simulations; + markers: theoretical results after Williams et al [9])

4. CONCLUSIONS AND PERSPECTIVES

We have been able to verify, with the COMSOL model, the hypothesis after which a corona discharge loudspeaker following a cylindrical geometry behaves as a monopolar sound source in a first approximation (ie. considering the cylindrical plasma layer generates the same amount of monopolar / dipolar sound sources than a plane geometry of same dimensions), the dipolar force source being cancelled by symmetries. The main drawback is the lower sound pressure amplitude radiated by the monopolar source compared to the dipolar (about 5 times less), explaining the low acoustic efficiency of the transducer. Another drawback (also visible on other geometries) is its high-pass filter behaviour, linked to its ideal flow velocity source characteristics, associated to the radiation impedance of a pulsating cylinder. Last, the finite dimension of the transducer yields a directivity in elevation similar to the one of a finite pulsating cylinder of radius R and

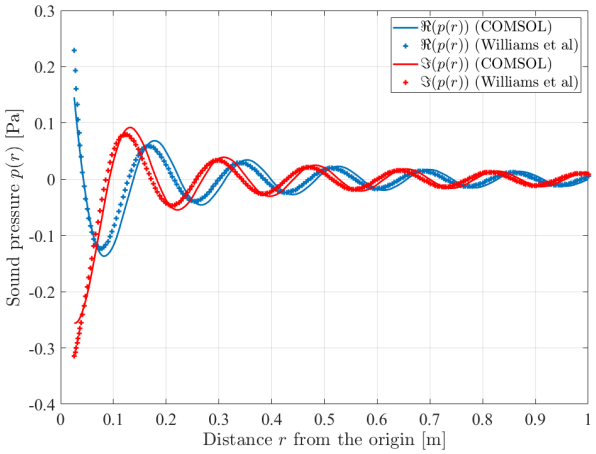


Figure 8. Acoustic pressure along Ox, at 2000 Hz: lines: COMSOL simulation results (blue: real part, red: imaginary part); markers: theoretical results after Williams et al [9] (blue: real part, red: imaginary part)

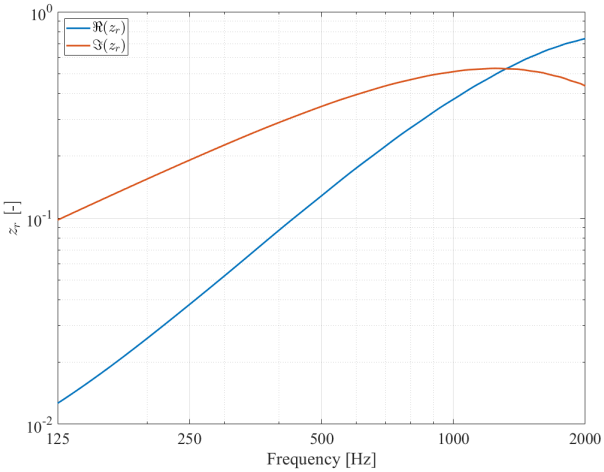


Figure 9. Normalized radiation impedance derived with the COMSOL model (blue: radiation resistance; red: radiation reactance)

height h [9].

The next step will consist in constructing a prototype based on the proposed geometry, and the assessment of its acoustic radiation in an anechoic facility. Moreover, we anticipate to test some alternative transducer configurations, for example in a "dipolar-only" version, where the transducer would be made of two half-cylinders, each fed with its own voltage amplifier, one with voltage $u_{ac,1}$ and the other with out of phase voltage $u_{ac,2} = -u_{ac,1}$. These planned experiments should confirm the results of this preliminary simulation study and open the way to new controllable directionnal sound sources, allowing changing the directivity from omnidirectionnal to bidirectionnal (two-sided), and beyond, multipolar by further partitions of the cylinder.

The applications of such an omnidirectionnal source are manifold: it first allows verifying sound radiation models used for the design of ideal sound sources, such as pulsating spheres and cylinders, which are accessible to experiments only through the simplification of their geometry as polyhedrons. Besides this theoretical interest, having effective omnidirectionnal sound sources could be an important asset for acoustic metrology, more specifically for room acoustics measurements, as a substitute to state-of-the-art dodecahedrons.

5. ACKNOWLEDGMENTS

The authors would like to honor the memory of Tirui Wang, a student in Micro-Engineering at EPFL, having collaborated to the development of the cylindrical plasma loudspeaker, who tragically passed away in China, his home country, on February 14, 2025.

6. REFERENCES

[1] F. V. Hunt. *Electroacoustics: the Analysis of Transduction, and its Historical Background*. New York: American Institute of Physics for the Acoustical Society of America (1982).

[2] S. P. Lipshitz, M. Pocock, J. Vanderkoy, On the Audibility of Midrange Phase Distortion in Audio Systems, *Journal of the Audio Engineering Society*, **30**(9), 580-595 (1982).

[3] C. C. J. M. Hak, Remy H.C. Wenmaekers, Jan P.M. Hak, Renz C.J. van Luxemburg, The Source Directivity of a Dodecahedron Sound Source determined by Stepwise Rotation, Proc. of Forum Acusticum 2011, Aalborg, Denmark, 1875-1879 (2011).

[4] ISO 3382-1 International Standard ISO/DIS 3382-1: Acoustics Measurement of room acoustic parameters – Part 1: Performance rooms. International Organization for Standardization, 2009.

[5] P. Béquin, P. Herzog, Model of acoustic sources related to negative point-to-plane discharges in ambiant air, *Acta Acustica*, **83**, 359–366 (1997).

[6] P. Béquin, K. Castor, P. Herzog, V. Montembault, Modeling plasma loudspeakers, *Journal of the Acoustical Society of America*, **121**(4), 1960–1970 (2007).

[7] S. Sergeev, H. Lissek, A. Howling, I. Furno, G. Plyushchev, and P. Leyland, Development of a plasma electroacoustic actuator for active noise control applications *Journal of Physics D: Applied Physics* **53**, 495202 (2020)

[8] S. Sergeev, Plasma-based Electroacoustic Actuator for Broadband Sound Absorption, EPFL PhD Thesis N. 9784 (2022).

[9] W. Williams, N.G. Parke, D.A. Moran, C. H. Sherman, Acoustic radiation from a finite cylinder, *Journal of the Acoustical Society of America*, **36**(12), pp. 2316-2322 (1964).

[10] S. Sergeev, M. Donaldson, H. Lissek, Ultrabroadband sound control of 3D spaces using plasmacoustic metalayers, Proc. of Inter-noise 2024, Nantes, France, August 25-29, 2024.

DOI:

Main theme: A06 Electro-Acoustics

Session A06.06 Acoustic-based sensors, actuators and microsystems for diverse applications

Chair(s): V. Ferrari, A. Carlosena

DOI: 10.61782/fa.2025.0642



FORUM ACUSTICUM
EURONOISE 2025

ON BIOTELEMETRY'S BIDIRECTIONAL ACOUSTIC TAG

Gerard Batet[1*] **David Sarria**[1] **Spartacus Gomariz**[1]
Ivan Masmitja[2] **Joaquin del Rio**[1]
[1] SARTI Research group, Universitat Politècnica de Catalunya, Spain
[2] Institut de Ciències del Mar, Consejo Superior de Investigaciones Científicas

ABSTRACT

Acoustic tagging is one of the primary resources for tracking marine species and understanding their behaviors within these protected zones. However, traditional acoustic tags have several limitations, resulting in data loss or inaccuracies, complicating ecological studies. In this work, we describe the deployment of BTAGs in high-density and elongated array configurations, alongside USBL-based direction and range measurements, providing a versatile toolset for ecological studies, improving the ability to monitor marine species, assess Marine Protected Areas (MPAs), and contribute to the sustainable management of marine ecosystems.

Keywords: *acoustic biotelemetry, bidirectional acoustic tag, usbl*

1. INTRODUCTION

Marine and oceanic ecosystems face significant threats from climate change and overfishing, necessitating continuous monitoring to assess and mitigate their impact [1]. Marine Protected Areas (MPAs) have been introduced to counteract these challenges, but their effectiveness depends on robust data collection methods [2]. Acoustic tagging is one of the primary resources for tracking marine species and understanding their behaviors within these protected zones [3].

The use of acoustic tagging in marine research dates back to the mid-20th century. Early acoustic tags were relatively simple, relying on ultrasonic pulses that could be detected by hydrophones placed in strategic locations. [4]. By the 1970s and 1980s, advancements in electronics and miniaturization enabled the tagging of smaller fish, broadening the scope of research beyond large commercial species. Acoustic telemetry soon became a widely used tool for studying fish behavior, habitat use, and population dynamics, contributing to the development of Marine Protected Areas (MPAs) as a key conservation strategy [5].

Despite its success, traditional acoustic tagging technology has had several limitations. The most significant drawback is the unidirectional nature of data transmission, where tags send signals to receivers but cannot receive information or be reprogrammed remotely [6]. This constraint limits real-time data retrieval, which can be time-consuming and resource-intensive to process.

To solve those unidirectional constraints, a bidirectional acoustic tag has been developed, enabling the acoustic transceivers to send commands to the tags, compute the time of flight (ToF) and receive real-time feedback, thereby improving data accuracy and monitoring efficiency [7].

In this work, the bidirectional acoustic tag (BTAG) system and its deployment options are presented alongside its main specifications.

2. SYSTEM IMPLEMENTATION

The BTAG system is a miniaturisation of a common modem system with tailored solutions to system specifications; these specifications are i. full encapsulation to withstand depths of 500 m, ii. miniaturised design to be able to be carried by a *Nephrops Norvigecus* (i.e., Norway Lobster) following the 2% tag mass to body mass rule [8] and iii. an ultra-low power design to maintain the operativity for a minimum of 3 months up to a 1-year life.

*Corresponding author: gerard.batet@upc.edu.
Copyright: ©2025 Gerard Batet et al. This is an open-access article distributed under the terms of the Creative Commons Attribution 3.0 Unported License, which permits unrestricted use, distribution, and reproduction in any medium, provided the original author and source are credited.

The system has been designed to comply with these requirements, as seen in Fig.1, with three main blocks in mind, i. the power electronics, which comprises a high energy density lithium thionyl-chloride, a hall effect sensor working with a power switch, enabling the tag's activation and deactivation via an external magnet, ii. the microcontroller from ST Microelectronics, which has the ability to access an ultra-low power sleep mode and a low-power dynamic run mode and iii. the transmission and reception circuitry composed by the input and output amplifier and the piezoelectric transducer.

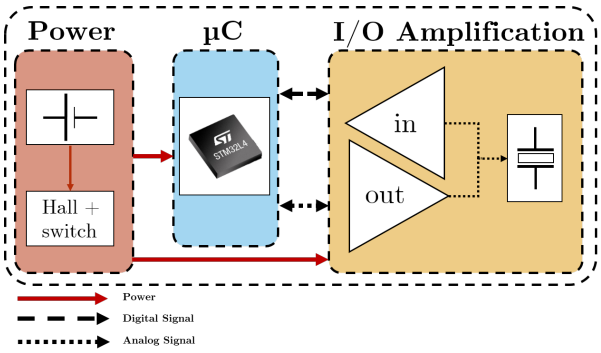


Figure 1. Basic electronic building blocks graphical representation being i. power with the battery and a magnet activated hall sensor with the power switch, ii. ST Microelectronics's ultra-low power microcontroller, and iii. electronic instrumentation with output and input amplification to the piezoelectric element

The output amplifier is a common type D audio amplifier to reduce the power consumption, the input amplifier has been tailored to bandpass 69 kHz which is the most used in the acoustic tagging, being the carrier of the pulse position modulation (PPM) used to transmit the ID of the tag, the polling message from the transceiver station and the response of the BTAG.

The BTAG is encapsulated in a hard resin to ensure the mechanical and water ingress protection (See Fig. 2), and for this size, the battery life in days can be estimated using battery tests resulting in the Table 1.

3. DEPLOYMENT TOPOLOGY

Receivers are typically deployed using two primary configurations: i. a high-density array designed to precisely monitor a specific area and ii. an elongated array or straight-line arrangement used for tracking movements along coastlines, migration routes, or changes in marine habitats. The BTAG system is compatible with these deployment strategies, complementing traditional methods while incorporating transceivers to obtain range measurements.

Table 1. Battery life in days depending on the cycle time and the reception window on the cycle

Cycle time	60 s	120 s	180 s
No Rx	3650	3650	3650
Rx 7.45 s	121	230	326
Rx 12.45 s	75	145	210

Additionally, recent tests utilizing Ultra-Short Baseline (USBL) technology from Evologics have demonstrated the capability to determine both the direction of arrival (bearing) and the range through time-of-flight measurements, enhancing the accuracy and efficiency of tracking efforts.

To ensure full compatibility with the other systems, the BTAG employs the Open protocol developed by the European tracking network (ETN) (https://europeantrackingnetwork.org/en) [9] [10].



Figure 2. Bidirectional acoustic tag transparent test encapsulation showing i. the piezoelectric element (white cylinder), ii. the electronics (blue board), and iii. the battery (purple cylinder)

4. CONCLUSIONS

The introduction of the BTAG technology represents a significant advancement in marine species monitoring. The BTAG system addresses key limitations of traditional acoustic tags by enabling real-time data retrieval and range measurements, thus enhancing tracking accuracy and efficiency.

The miniaturized design, coupled with ultra-low power consumption, ensures extended operational life, up to 10 years when unidirectional mode and 1 year when bidirectional.

Additionally, the integration of an open communication protocol allows for seamless compatibility with existing tracking networks, facilitating broader adoption in marine research.

The deployment of BTAGs in high-density and elongated array configurations, alongside USBL-based direction and range measurements, provides a versatile toolset for ecological studies. These innovations improve the ability to monitor marine species, assess MPA effectiveness, and contribute to the sustainable management of marine ecosystems.

Future developments may focus on further miniaturization, enhanced battery performance, and the incorporation of additional environmental sensors to expand the system's capabilities.

5. ACKNOWLEDGMENTS

This work received financial support from the Spanish Ministerio de Economía y Competitividad BITER project (PID2020-114732RB-C32), MINKE TNA USBL4TAGS project and Generalitat de Catalunya's "SARTI-MAR" 2021 SGR 259. GB received the support of Secretaria d'Universitats i Recerca del Departament d'Empresa i Coneixement de la Generalitat de Catalunya, ref. BDNS 612831. IM is funded by the Spanish National Program Ramón y Cajal RYC2022-038056-I. This work acknowledges the 'Severo Ochoa Centre of Excellence' accreditation (CEX2019-000928-S) and the Research Unit Tecnoterra (ICM-CSIC/UPC)

6. REFERENCES

[1] E. Goyet, "Thermodynamic forecasts of the mediterranean sea acidification," *Mediterranean Marine Science*, vol. 17, no. 2, p. 508–518, 2016.

[2] P. Afonso, J. Fontes, K. N. Holland, and R. S. Santos, "Small marine reserves can offer long-term protection to an endangered fish," *Biological Conservation*, vol. 144, no. 11, pp. 2739–2744, 2011.

[3] G. C. Hays, H. Bailey, and S. J. e. a. Bograd, "Translating marine animal tracking data into conservation policy and management," *Trends in Ecology and Evolution*, vol. 34, no. 5, p. 459–473, 2019.

[4] P. S. Trefethen, "Acoustic equipment for tracking individual fish," *U.S. Fish and Wildlife Service Special Scientific Report – Fisheries*, vol. 179, pp. 1–11, 1956.

[5] M. R. Heupel, J. M. Semmens, and A. J. Hobday, "Automated acoustic tracking of aquatic animals: scales, design, and deployment of listening station arrays," *Marine and Freshwater Research*, vol. 57, no. 1, pp. 1–13, 2006.

[6] G. Batet, I. Masmitja, D. Sarria, S. Gomariz, and J. del Rio, "Engineering a testbed for bidirectional acoustic tag development," *IEEE Access*, 2024.

[7] I. e. a. Masmitja, "Miniaturized bidirectional acoustic tag to enhance marine animal tracking studies," in *IEEE International Instrumentation and Measurement Technology Conference (I2MTC)*, 2021.

[8] M. Newton, J. Barry, J. A. Dodd, M. Lucas, P. Boylan, and C. E. Adams, "Does size matter? a test of size-specific mortality in atlantic salmon salmo salar smolts tagged with acoustic transmitters," *Journal of Fish Biology*, vol. 89, no. 3, pp. 1641–1650, 2016.

[9] J. Reubens, K. Aarestrup, C. Meyer, A. Moore, F. Okland, and P. Afonso, "Compatibility in acoustic telemetry," *Animal Biotelemetry*, vol. 9, no. 1, p. 33, 2021.

[10] E. Aspillaga, S. Bruneel, J. Alós, P. Verhelst, D. Abecasis, K. Aarestrup, K. Birnie-Gauvin, P. Afonso, M. Palmer, and J. Reubens, "Open protocols, the new standard for acoustic tracking: results from interoperability and performance tests in european waters," *Animal Biotelemetry*, vol. 12, no. 1, p. 40, 2024.

DOI: 10.61782/fa.2025.0532



FORUM ACUSTICUM
EURONOISE 2025

LOW ORDER LATERAL MODES OF PLATE TRANSDUCERS AS BASIS FOR EFFECTIVE AND REPRODUCIBLE ACOUSTOFLUIDIC DEVICES

Andreas Fuchsluger[1*] **Annalisa De Pastina**[2] **Bernhard Jakoby**[1]
[1] Institute for Microelectronics and Microsensors, Johannes Kepler University Linz, Austria
[2] Microsystems, Silicon Austria Labs, Villach, Austria

ABSTRACT

Acoustofluidics is a contactless and thus gentle method for handling objects from the sub-micrometer to the millimeter length scale. Making use of the radiation force, small objects can be aligned at the pressure nodes or antinodes of a stationary acoustic field generated inside microfluidic structures. Besides the intensity and frequency of the acoustic field, the acoustic force on an object purely relies on its mechanical properties, and therefore, no special requirements or treatments are necessary. We designed and built numerically optimized acoustofluidic devices consisting of microfluidic silicon-glass chips actuated by attached piezoelectric plate transducers. The specialty in our design is the utilization of a low order lateral width mode of the plate transducer, which stands in contrast to the usually used thickness mode. A glycerol layer between the transducer and the chip ensures weak coupling of the lateral mode, meaning that the resonance frequency of the transducer is barely altered when attached to the chip. Together with low patch-to-patch variation of the used components, this altogether leads to very reliable and reproducible operating devices. We will demonstrate the performance of our concept by manipulating objects in millimeter-sized structures and in the milliseconds-timeframe, reaching acoustic energy densities close to $3000\,\mathrm{J/m^3}$.

Keywords: *Acoustofluidics, Acoustopheresis, Ultrasound, Lateral Modes, Particle Focusing*

**Corresponding author*: *andreas.fuchsluger@jku.at.*
Copyright: *©2025 Andreas Fuchsluger et al. This is an open-access article distributed under the terms of the Creative Commons Attribution 3.0 Unported License, which permits unrestricted use, distribution, and reproduction in any medium, provided the original author and source are credited.*

1. INTRODUCTION

Small particles suspended in a fluid and exposed to a standing acoustic plane wave experience a force that, depending on the mechanical properties of the involved materials, will either drive them toward the pressure nodes or antinodes of the acoustic field, where the particles accumulate. This force is known as the acoustic radiation force [1]

$$F_{\mathrm{rad}} = 3V\,\Phi\,E_{\mathrm{ac}}\,k\sin(2kx), \tag{1}$$

which depends on the particle volume V, the acoustic contrast factor Φ, and on the acoustic energy density E_{ac} and the wave-number k of the standing pressure-wave $p_0\cos(kx)$ oriented along the x-direction with the pressure amplitude p_0. The acoustic contrast factor Φ characterizes the influence of the mechanical properties of both the fluid and the particle. Its sign determines the direction of the force. The particles used in our experiment have a density similar to that of the surrounding fluid but lower compressibility, resulting in a positive Φ. Consequently, F_{rad} directs the particles toward the pressure nodes of the wave.

2. THE DEVICE

The core elements of our device are formed by the microfluidic silicon-glass chip and the piezoelectric plate transducer for ultrasonic actuation shown in Fig. 1. The chip is mounted into our custom-made chip holder [2], where the transducer is clamped towards the bottom of the chip using a thin layer of glycerol in between as an acoustic coupling medium.

The chip geometry is numerically optimized for particle focusing in the center of the channel relying on the second-order lateral extensional width mode of the plate

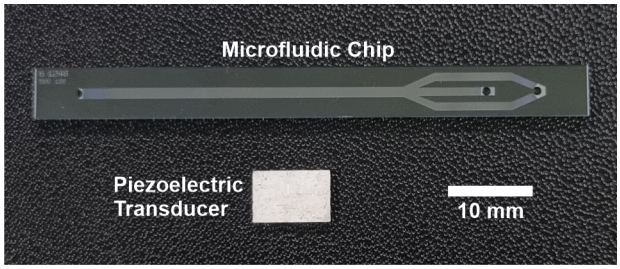


Figure 1. The core elements of the device are formed by a microfluidic chip made out of silicon and glass, and a piezoelectric plate transducer that is attached to the bottom of the chip for ultrasonic actuation.

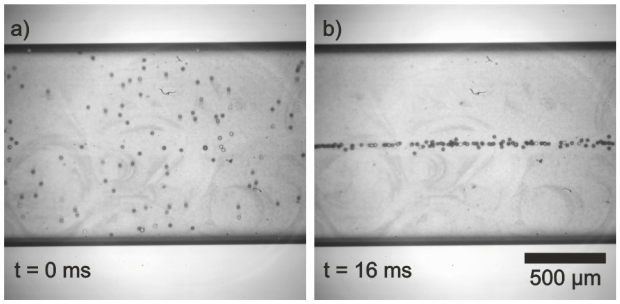


Figure 2. Particle focusing in a 1240-μm wide channel within 16 milliseconds, corresponding to an acoustic energy density of $E_{\mathrm{ac}} = 2770\,\mathrm{J/m^3}$. The actuation frequency and the actuation voltage are $547\,\mathrm{kHz}$ and approximately $70\,\mathrm{V_{pp}}$, respectively.

transducer. Minimizing the focusing time and improving the setup is ongoing work [3,4]. As a final goal, using the trifurcation at the end of the channel, the system should operate as an effective flow-through separator using the lateral mode of the transducer instead of the usually employed thickness modes, e.g., as implemented in [5].

The lateral mode of the transducer, which is fundamental to our actuation, exhibits only a weak coupling with the microfluidic chip. Consequently, the lateral resonance of the transducer remains nearly unchanged when the transducer is attached to the microfluidic chip. Conversely, the thickness mode demonstrates strong coupling, resulting in significant alteration of the behavior at resonance [4].

3. RESULTS

With an actuation voltage of approximately $70\,\mathrm{V_{pp}}$, we cleared the outer region of a 1240-μm wide channel of 20-μm polystyrene (PS) particles, focusing them at its center within $16\,\mathrm{ms}$. By measuring the focusing time and using the method from [6], which is based on equating the acoustic radiation force to the drag force experienced by a particle when moving through the fluid, we obtained an acoustic energy density of $E_{\mathrm{ac}} = 2770\,\mathrm{J/m^3}$.

4. REFERENCES

[1] H. Bruus, "Acoustofluidics 7: The acoustic radiation force on small particles," *Lab Chip*, vol. 12, pp. 1014–1021, 2012.

[2] A. Fuchsluger, A. De Pastina, R. Ecker, T. Mitteramskogler, T. Voglhuber-Brunnmaier, N. Andrianov, N. Cselyuszka, and B. Jakoby, "Acoustofluidic particle trapping in a structured microchannel using lateral transducer modes," *IEEE Sensors Journal*, vol. 24, no. 24, pp. 40274–40285, 2024.

[3] A. Fuchsluger, A. De Pastina, N. Cselyuszka, N. Andrianov, A. Roshanghias, T. Mitteramskogler, R. Ecker, T. Voglhuber-Brunnmaier, M. Moridi, and B. Jakoby, "Utilizing lateral plate transducer modes for high quality acoustofluidics in silicon-based chips," in *2022 IEEE Sensors*, pp. 1–4, 2022.

[4] A. Fuchsluger, A. De Pastina, T. Mitteramskogler, R. Ecker, T. Voglhuber-Brunnmaier, N. Andrianov, A. Shatalov, N. Cselyuszka, M. Moridi, and B. Jakoby, "Ultra-fast acoustofluidic particle focusing using lateral modes of a plate transducer," in *2023 22nd International Conference on Solid-State Sensors, Actuators and Microsystems (Transducers)*, pp. 1333–1336, 2023.

[5] F. Petersson, A. Nilsson, C. Holm, H. Jönsson, and T. Laurell, "Separation of lipids from blood utilizing ultrasonic standing waves in microfluidic channels," *Analyst*, vol. 129, pp. 938–943, 2004.

[6] R. Barnkob, P. Augustsson, T. Laurell, and H. Bruus, "Measuring the local pressure amplitude in microchannel acoustophoresis," *Lab Chip*, vol. 10, pp. 563–570, 2010.

DOI: 10.61782/fa.2025.0076

FORUM ACUSTICUM EURONOISE 2025

ACOUSTIC LEVITATION IN AIR: NOVEL TECHNIQUES AND APPLICATIONS

Asier Marzo[1*]
[1] Department of Computer Science, Universidad Publica de Navarra, Spain

ABSTRACT

Acoustic levitation can hold different material in mid-air. Typically, an emitter and an opposed reflector form a standing wave. Millimetric particles significantly smaller than the wavelength can be trapped in the nodes of the standing wave. Despite the limitations on particle size, the diversity of supported materials enables multiple applications. Metals, liquids, gases, plastics or small living beings can be trapped with acoustic levitation. Some applications are contactless spectroscopy or the study of crystallization of levitated samples. In this presentation, novel techniques beyond standing waves will be presented such as acoustic vortices or bottle beams that provide positional and orientation control on the levitated particles. We will highlight emerging applications in additive manufacturing, particle agglomeration, aerosol control, patterning, or pick and place of fragile samples. Finally, we will present some opportunities to get started in mid-air acoustic levitation using devices that can be built at the lab or even at home with off-the-shelf components.

Keywords: acoustic levitation, radiation force, acoustic traps, beamforming

1. INTRODUCTION

Sound can held in mid-air small particles made of different materials [1]. Acoustic levitation in air typically uses an ultrasonic emitter and an opposed reflector [2] to create a standing wave, with particles levitating at its nodes. Other setups use two opposed emitters [3], an array of emitters and reflectors to enable transportation, and recently, phased-arrays [4] are used to levitate multiple particles independently [5]. Trapping on a standing-wave node limits the particle size to half-wavelength, and emitters should be around the particle. Recent research showed that single-beams can trap particles [6, 7] and that particles larger than the wavelength can be trapped in vortices [8] and special acoustic bottles [9].

More advances can be found in acoustic levitation reviews: general [10, 11], liquids [12], biomaterials [13], airborne chemistry [14] or soft matter [15].

2. HOMEMADE LEVITATORS

Lab equipment can be expensive and hard to access, thus limiting exploration and accessibility to acoustic levitators. In the past decade, various levitators that can be built with off-the-shelf components have been shown and successfully used for research activities. Homemade devices are not as accurate or powerful as lab equipment, but they are available to a wider range of researchers, including hobbyists and schools.

TinyLev [16] is a single-axis standing-wave levitator, it has two opposed bowls made of 36 emitters each. The emitters are off-the-shelf $40\,\mathrm{kHz}$ transducers that are arranged around a sphere of 13 cm diameter. This gives the setup a natural focus, and can levitate liquids and samples of densities up to $2.4\,\mathrm{g/cm^3}$ and $3\,\mathrm{mm}$ diameter. The electronics are simplified and use an Arduino Nano and a motor driver (L298N). The levitator and some levitated samples are shown in Figure 1. Modifications of TinyLev make it more compact (Mk3 [17]) or able to levitate denser particles (MightyLev [18]).

SonicSurface [19] is an integrated $40\,\mathrm{kHz}$ phased-array of 16×16 emitters, with individual control of phases

*Corresponding author: asier.marzo@unavarra.es.
Copyright: ©2025 Marzo et al. This is an open-access article distributed under the terms of the Creative Commons Attribution 3.0 Unported License, which permits unrestricted use, distribution, and reproduction in any medium, provided the original author and source are credited.

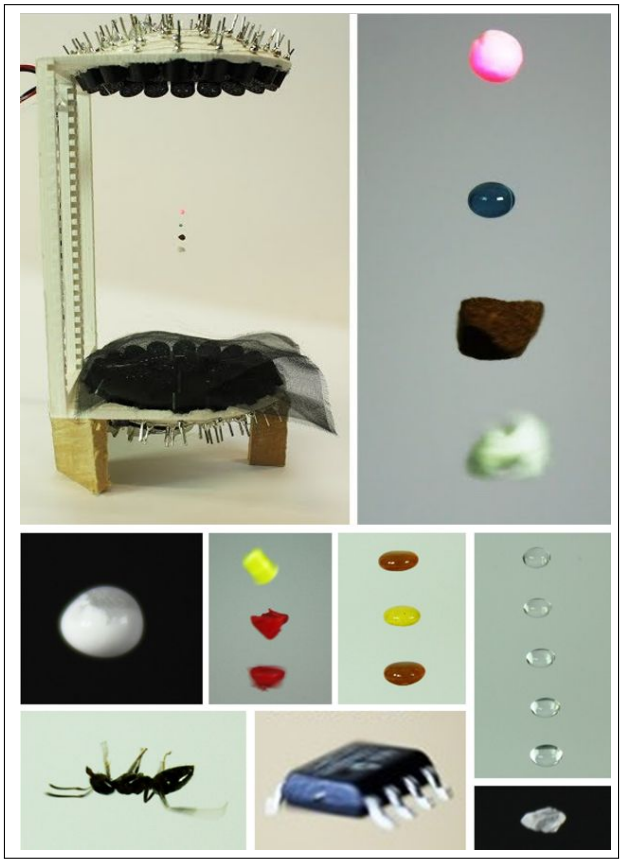


Figure 1. TinyLev is made of two opposed bowls with 36 ultrasonic emitters each, the bowls have a separation of 10 cm. Bottom) some levitated samples, left to right: titanium dioxide in water, plastics, ketchup and mustard, water, ant, integrated circuit and salt.

(see Figure 2). It has been used in various research projects [5, 20–22]. Other open phased-arrays have been published [23–25].

3. EMERGING APPLICATIONS

Apart from the applications referenced in the introduction, we describe some recent explorations that go beyond containerless and contactless processing.

Aerosols falling into a substrate get patterned along the high-amplitude areas where an acoustic field is applied [26]. The variety of aerosols enables application in bio-fabrication but also for printed electronics when conductive powder is mixed with the liquid medium.

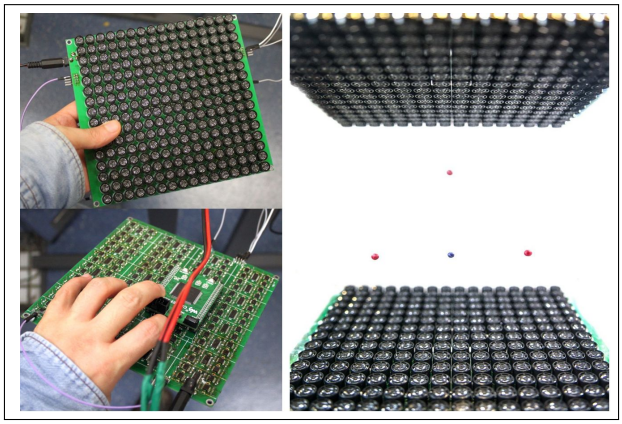


Figure 2. SonicSurface is an integrated phased-array with 256 emitters of 1 cm-diameter. It can levitate multiple particles and control them individually.

LeviPrint [20] explores the levitation of droplets of glue, solid particles and elongated thin objects to build structures in a contactless way. Traditional standing waves can hold droplets and spherical particles whereas other fields are optimized to held in position and orientation elongated sticks. The assembly can be done without touching the pieces to avoid cross-contamination, and the structure can be built inside a container as long as there is a small aperture for the parts to enter. Figure 3 shows a structure built with levitated sticks.

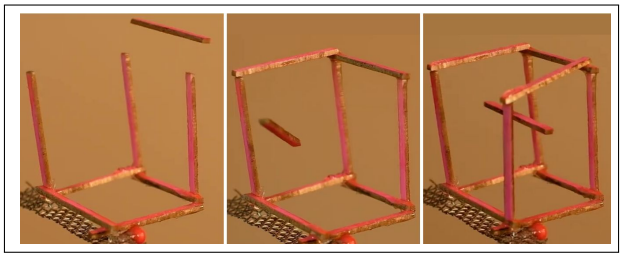


Figure 3. A cube built with sticks connected with UV-curable glue. The cube has 5 cm side, the sticks and the glue were levitated in a contactless way.

Electric sparks can be guided with ultrasound [27]. Electric sparks heat up the air, it expands and becomes less dense. This lower-density air gets shaped by the ultrasonic field due to the acoustic contrast in comparison with the surrounding ambient air. Also, less dense air

has lower breakdown voltage and is a preferred discharge path. The process repeats and the ultrasonic field can guide the sparks along the high-amplitude areas. Being able to guide electric sparks enables new applications in high-voltage switching and selective welding. A guided electric spark is shown in Figure 4.

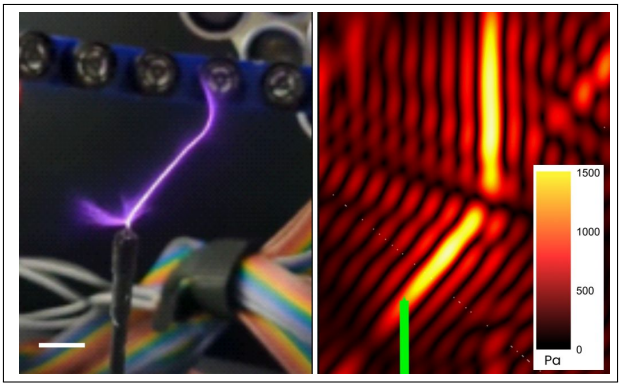


Figure 4. An electric spark is guided along the high-amplitude region of a 40 kHz ultrasonic field. left) guided spark. right) amplitude field. scale bar is 1 cm.

4. CONCLUSION

Acoustic levitation keeps evolving both in techniques and applications. Its low cost and larger scale of manipulation when compared with optical trapping makes acoustic levitation an active research topic.

5. ACKNOWLEDGMENTS

This research was funded by the European Research Consortium under grant agreement No 101042702 Intevol-ERC2021-STG.

6. REFERENCES

[1] E. Brandt, "Suspended by sound," *Nature*, vol. 413, no. 6855, pp. 474–475, 2001.

[2] R. Whymark, "Acoustic field positioning for containerless processing," *Ultrasonics*, vol. 13, no. 6, pp. 251–261, 1975.

[3] J. Weber, C. Rey, J. Neuefeind, and C. Benmore, "Acoustic levitator for structure measurements on low temperature liquid droplets," *Review of scientific instruments*, vol. 80, no. 8, 2009.

[4] D. Foresti, M. Nabavi, M. Klingauf, A. Ferrari, and D. Poulikakos, "Acoustophoretic contactless transport and handling of matter in air," *Proceedings of the National Academy of Sciences*, vol. 110, no. 31, pp. 12549–12554, 2013.

[5] A. Marzo and B. W. Drinkwater, "Holographic acoustic tweezers," *Proceedings of the National Academy of Sciences*, vol. 116, no. 1, pp. 84–89, 2019.

[6] D. Baresch, J.-L. Thomas, and R. Marchiano, "Observation of a single-beam gradient force acoustical trap for elastic particles: acoustical tweezers," *Physical review letters*, vol. 116, no. 2, p. 024301, 2016.

[7] A. Marzo, S. A. Seah, B. W. Drinkwater, D. R. Sahoo, B. Long, and S. Subramanian, "Holographic acoustic elements for manipulation of levitated objects," *Nature communications*, vol. 6, no. 1, p. 8661, 2015.

[8] A. Marzo, M. Caleap, and B. W. Drinkwater, "Acoustic virtual vortices with tunable orbital angular momentum for trapping of mie particles," *Physical review letters*, vol. 120, no. 4, p. 044301, 2018.

[9] S. Inoue, S. Mogami, T. Ichiyama, A. Noda, Y. Makino, and H. Shinoda, "Acoustical boundary hologram for macroscopic rigid-body levitation," *The Journal of the Acoustical Society of America*, vol. 145, no. 1, pp. 328–337, 2019.

[10] M. A. Andrade, N. Pérez, and J. C. Adamowski, "Review of progress in acoustic levitation," *Brazilian Journal of Physics*, vol. 48, pp. 190–213, 2018.

[11] M. A. Andrade, A. Marzo, and J. C. Adamowski, "Acoustic levitation in mid-air: Recent advances, challenges, and future perspectives," *Applied Physics Letters*, vol. 116, no. 25, 2020.

[12] A. Amoochi, M. Sheykholeslami Borghani, R. Mohammadi, and S. Mazdak, "Systematic review of the theories and applications of acoustic levitation of liquids," *Mechanic of Advanced and Smart Materials*, vol. 3, no. 3, pp. 310–324, 2023.

[13] R. J. Weber, C. J. Benmore, S. K. Tumber, A. N. Tailor, C. A. Rey, L. S. Taylor, and S. R. Byrn, "Acoustic levitation: recent developments and emerging opportunities in biomaterials research," *European Biophysics Journal*, vol. 41, pp. 397–403, 2012.

[14] S. Santesson and S. Nilsson, "Airborne chemistry: acoustic levitation in chemical analysis," *Analytical and bioanalytical chemistry*, vol. 378, pp. 1704–1709, 2004.

[15] H. Chen, Z. Hong, and D. Zang, "New insights into suspended drops: When soft matter meets acoustic levitation," *Droplet*, vol. 3, no. 1, p. e95, 2024.

[16] A. Marzo, A. Barnes, and B. W. Drinkwater, "Tinylev: A multi-emitter single-axis acoustic levitator," *Review of Scientific Instruments*, vol. 88, no. 8, 2017.

[17] S.-M. Argyri, C. Andersson, N. Paillet, L. Evenäs, J. Ahrens, A. Marzo, V. Contreras, and R. Bordes, "Customized and high-performing acoustic levitators for contact-free experiments," *Journal of Science: Advanced Materials and Devices*, vol. 9, no. 3, p. 100720, 2024.

[18] J. W. Drewitt, B. Emmens, Z.-H. Kong, B. W. Drinkwater, and A. C. Barnes, "Mightylev: An acoustic levitator for high-temperature containerless processing of medium-to high-density materials," *Review of Scientific Instruments*, vol. 95, no. 10, 2024.

[19] R. Morales, I. Ezcurdia, J. Irisarri, M. A. Andrade, and A. Marzo, "Generating airborne ultrasonic amplitude patterns using an open hardware phased array," *Applied Sciences*, vol. 11, no. 7, p. 2981, 2021.

[20] I. Ezcurdia, R. Morales, M. A. Andrade, and A. Marzo, "Leviprint: Contactless fabrication using full acoustic trapping of elongated parts.," in *ACM SIGGRAPH 2022 Conference Proceedings*, pp. 1–9, 2022.

[21] M. A. Andrade, T. S. Camargo, and A. Marzo, "Automatic contactless injection, transportation, merging, and ejection of droplets with a multifocal point acoustic levitator," *Review of Scientific Instruments*, vol. 89, no. 12, 2018.

[22] Y. Koroyasu, T.-V. Nguyen, S. Sasaguri, A. Marzo, I. Ezcurdia, Y. Nagata, T. Yamamoto, N. Nomura, T. Hoshi, Y. Ochiai, *et al.*, "Microfluidic platform using focused ultrasound passing through hydrophobic meshes with jump availability," *PNAS nexus*, vol. 2, no. 7, p. pgad207, 2023.

[23] A. Marzo, T. Corkett, and B. W. Drinkwater, "Ultraino: An open phased-array system for narrowband airborne ultrasound transmission," *IEEE transactions on ultrasonics, ferroelectrics, and frequency control*, vol. 65, no. 1, pp. 102–111, 2017.

[24] R. Montano-Murillo, R. Hirayama, and D. Martinez Plasencia, "Openmpd: A low-level presentation engine for multimodal particle-based displays," *ACM Transactions on Graphics*, vol. 42, no. 2, pp. 1–13, 2023.

[25] S. Zehnter and C. Ament, "A modular fpga-based phased array system for ultrasonic levitation with matlab," in *2019 IEEE International Ultrasonics Symposium (IUS)*, pp. 654–658, IEEE, 2019.

[26] J. M. Shapiro, B. W. Drinkwater, A. W. Perriman, and M. Fraser, "Sonolithography: In-air ultrasonic particulate and droplet manipulation for multiscale surface patterning," *Advanced Materials Technologies*, vol. 6, no. 3, p. 2000689, 2021.

[27] J. Irisarri, I. Ezcurdia, N. Iriarte, M. Sirkka, D. Nikolaev, J. Mäkinen, A. Martinez-Marchese, D. Iablonskyi, A. Salmi, and A. Marzo, "Electric plasma guided with ultrasonic fields," *Science Advances*, vol. 11, no. 6, p. eadp0686, 2025.

DOI: 10.61782/fa.2025.0681

FORUM ACUSTICUM EURONOISE 2025

Piezoelectric MEMS Temperature Sensor based on Acoustic Flexural Plate Waves

Stefano Bertelli[1*] **Alessandro Nastro**[1] **Marco Baù**[1] **Marco Ferrari**[1]
Libor Rufer[2] **Skandar Basrour**[3] **Vittorio Ferrari**[1]
[1] Department of Information Engineering, University of Brescia, 25123, Brescia, Italy
[2] ADT MEMS, France
[3] Univ. Grenoble Alpes, CNRS, Grenoble INP*, TIMA, 38000 Grenoble, France

ABSTRACT

Piezoelectric sensors based on acoustic waves propagating into micro electro-mechanical systems (MEMS) are a lively research area, with devices based on flexural plate waves (FPW) finding applications across various fields, including industrial and biological sectors. In this paper, a temperature sensor based on a piezoelectric MEMS that exploits the first antisymmetric mode, denoted as the A_0 or FPW mode, of Lamb waves generated in a diaphragm is presented. The micromachined diaphragm is composed of a stack of doped silicon and an aluminum nitride (AlN) piezoelectric layer with aluminum interdigital transducers (IDTs) employed for wave generation and detection. The proposed MEMS sensor exploits the variation of the FPW propagation velocity in the diaphragm due to temperature. The sensor expected working temperature range is at least 20 to 80 °C and in this preliminary phase has been tested from 25 to 45 °C by means of a tailored PID controlled temperature chamber including a Peltier cell and a Pt100 sensor while measuring the electrical admittance of a single IDT. The working principle has been validated within the frequency range from 11.185 to 12.88 MHz. Measurements have confirmed the sensor working principle, demonstrating a sensitivity of -426.5 Hz/°C and highlighting its potential for extending the operating temperature range.

Keywords: *Lamb waves, MEMS, piezoelectric, temperature sensor.*

[*] ***Corresponding author***: *stefano.bertelli@unibs.it.*
Copyright: *©2025 S. Bertelli et al. This is an open-access article distributed under the terms of the Creative Commons Attribution 3.0 Unported License, which permits unrestricted use, distribution, and reproduction in any medium, provided the original author and source are credited.*

1. INTRODUCTION

MEMS-based sensors are extensively employed in several research fields [1], including environmental monitoring [2], biomedical diagnostics [3], and industrial automation [4]. MEMS temperature sensors play a critical role in various applications where precise temperature monitoring is essential, such as tracking the internal temperature of smartphones [5], measuring human body temperature [6], or regulating indoor environments in heating, ventilation, and air conditioning (HVAC) systems [7]. Given the widespread adoption of MEMS temperature sensors, significant efforts have been made to develop and optimize different transduction principles, including resistive [8], optical [9], and piezoelectric [10], the latter being particularly notable for its high responsivity to temperature variations and suitability for harsh environments [10]. Specifically, among piezoelectric sensors, acoustic wave-based sensors have gained attention due to their high sensitivity and reliability [11]. Typically, acoustic wave MEMS temperature sensors are based on surface acoustic wave (SAW) [12], bulk acoustic wave (BAW) [13], and flexural plate wave (FPW) [14]. Among acoustic wave sensors, FPW MEMS exploit the propagation of Lamb waves in thin diaphragms and exhibit several advantages, including the operating frequency range typically in the tens of MHz and the ability to operate in contact with liquids with low losses [15,16]. In this context, this work presents a novel piezoelectric MEMS temperature sensor based on flexural plate waves, specifically exploiting the first antisymmetric mode (A_0) of Lamb waves. The sensor exploits the variation in the propagation velocity of FPWs in a micromachined piezoelectric diaphragm as a function of temperature, enabling thermal measurements.

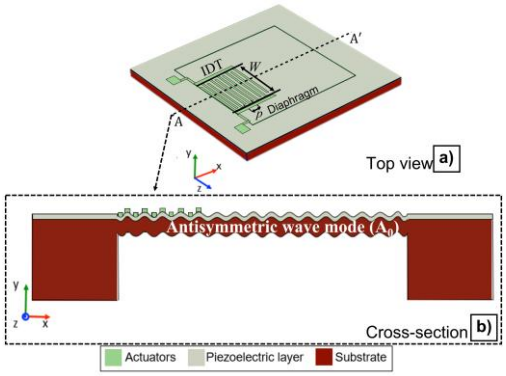


Figure 1. Top (a) and cross-section (b) schematic views of the proposed piezoelectric temperature sensor.

2. DESCRIPTION AND WORKING PRINCIPLE OF THE PROPOSED MEMS TEMPERATURE SENSOR

Fig. 1a shows a schematic representation of the top view of the proposed MEMS. The device is composed of a square diaphragm with an interdigital transducer (IDT), positioned close to the edge of the diaphragm, which comprises two interleaved comb-shaped electrodes. Each electrode consists of equally spaced fingers with a pitch p and aperture W, located on top of a piezoelectric layer. By applying a sinusoidal voltage across the IDT fingers, a perturbation in the thickness of the AlN layer, and consequently in the diaphragm, is induced, as schematically shown in the cross-section view A-A' of Fig. 1b. At specific frequencies, this perturbation induces mechanical vibrations in the diaphragm in the form of Lamb waves. Specifically, the first antisymmetric mode (A_0) has been excited at the synchronous frequency $f_{A0}=v_{A0}/p$ where v_{A0} represents the propagation velocity of the A_0 mode. The proposed MEMS has been manufactured by means of the PiezoMUMPs process [17]. The device features overall dimensions of 9 mm × 9 mm and incorporates a 6 mm × 6 mm squared composite diaphragm. The top and bottom views of the manufactured device are shown in Fig. 2a and 2b, respectively. The diaphragm consists of a material stack composed of a 10 µm thick silicon (Si) layer and a 0.5 µm thick piezoelectric aluminum nitride layer. The AlN layer on the composite diaphragm can be actuated by eight IDTs, positioned on the inner and outer edges of the diaphragm and arranged symmetrically with respect to its center.

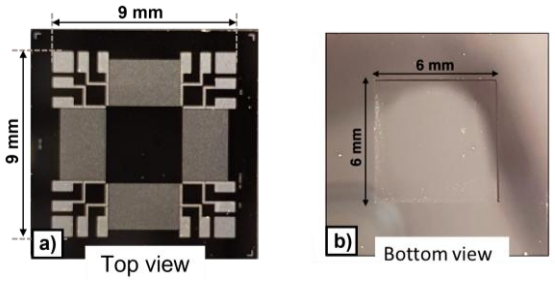


Figure 2. Top (a) and bottom (b) views of the fabricated piezoelectric MEMS sensor.

Each IDT comprises two interleaved comb-shaped electrodes. Each electrode consists of $N = 10$ equally spaced fingers, with a pitch $p = 112$ µm and an aperture $W = 3.5$ mm. By considering the tolerances of the fabrication process the frequency f_{A0} is expected to be between 11 and 15 MHz [15]. The proposed MEMS sensor exploits the variation of the FPW propagation velocity v_{A0} in the diaphragm due to thermal expansion and changes in the Young's modulus of the materials as a function of temperature [18,19]. The device was configured as a one-port transducer and the electrical admittance $G(f)$ of a single IDT has been analyzed as a function of temperature. This is expected to produce a frequency shift in the IDT admittance pattern centered at f_{A0} of the A_0 mode [14, 20], with a downshift in frequency as the temperature increases. The expected working temperature range is at least 20 to 80 °C as observed in similar AlN-based MEMS devices, [21] while in this preliminary phase it has been tested within 25 and 45 °C.

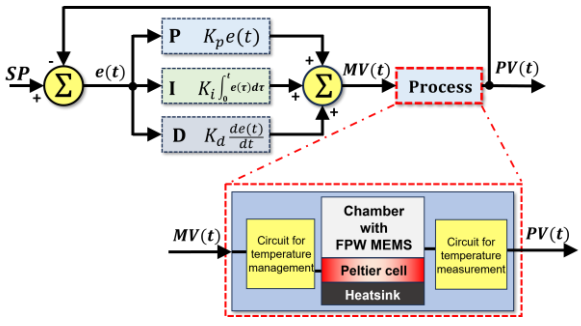


Figure 3. Schematic representation of the implemented PID controller. The enlarged view shows a detail of the controlled process, embedding the FPW MEMS temperature sensor, the actuator (Peltier cell), and auxiliary circuits.

3. EXPERIMENTAL SETUP

The operating principle was experimentally investigated using an HP4194A impedance analyzer and a custom experimental setup, including a thermal chamber regulated by a proportional-integral-derivative (PID) controller. Fig. 3 shows the block diagram of the implemented PID controller. The time-dependent process variable *PV(t)* corresponds to the chamber temperature *T*, which is measured using a dedicated temperature sensing circuit and compared with the setpoint variable *SP*, representing the desired operating temperature. The error $e(t) = SP - PV(t)$ is processed by the PID control algorithm, which incorporates proportional, integral, and derivative control actions with gains K_p, K_i, and K_d, respectively. The resulting manipulated variable *MV(t)* feeds a thermal management circuit to control the chamber temperature *T*. The system is specifically designed to establish and maintain predefined temperature profiles, enabling a precise characterization of the proposed MEMS temperature sensor. Fig. 4a illustrates the developed thermal chamber, which has been built using insulating foam layers. A Marlow TG12-6 Peltier cell has been employed as the heating element and is positioned at the bottom of the chamber, with a heat sink attached to its outer surface as shown in Fig. 4b. The Peltier cell is driven by a Pulse-Width Modulation (PWM) controller, which facilitates power regulation.

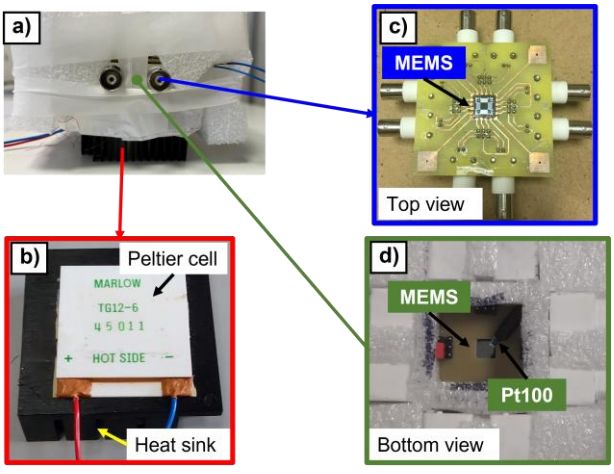


Figure 4. Experimental setup. Thermal chamber made of insulating foam (a). Peltier cell and the heat sink used to control the chamber temperature (b). Top view of the PCB adapter for the proposed MEMS sensor (c). Bottom view of the PCB adapter and Pt100 reference sensor positioned inside the chamber (d).

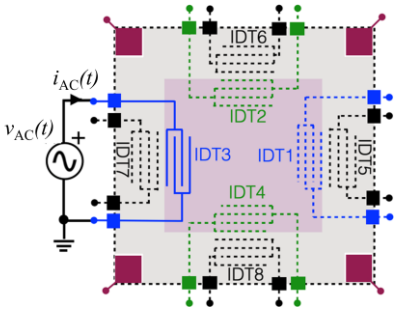


Figure 5. Simplified schematic representation of the proposed MEMS sensor configured for electrical admittance measurements.

The PWM driver is controlled via the PID algorithm, implemented through a LabVIEW interface. The chamber temperature *T* is measured using an HP34401A multimeter connected to a Pt100 resistive temperature detector (RTD) temperature sensor located inside the chamber, with a sampling time of 1 s. The FPW MEMS temperature sensor was fixed on a printed circuit board, as shown in Fig. 4c and Fig. 4d.

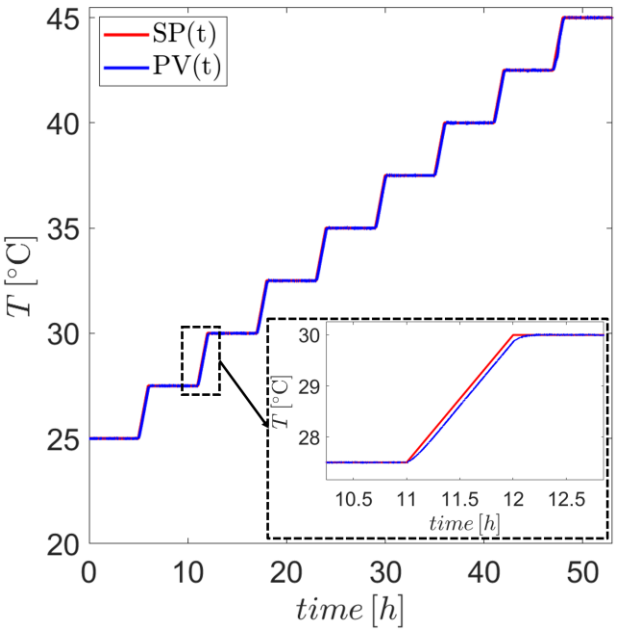


Figure 6. Setpoint (*SP*) and measured chamber temperature (*PV*) as a function of time. The inset shows the transient response to a heating step of 2.5 °C.

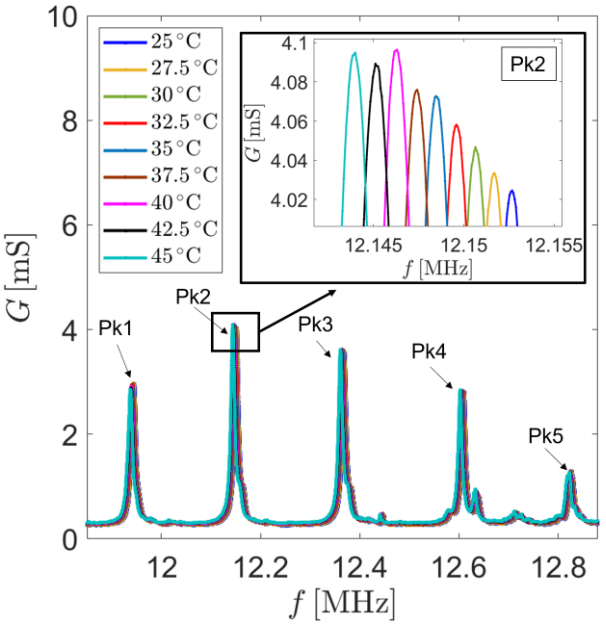


Figure 7. Measured conductance *G(f)* of a single IDT as a function of the excitation frequency *f* at different temperature *T*. The inset shows an enlarged view of the second peak Pk2 of *G(f)* at different temperatures.

4. EXPERIMENTAL RESULTS

To validate the proposed MEMS temperature sensor, the electrical conductance *G(f)* of a single IDT, namely IDT3, was measured according to the schematic diagram shown in Fig. 5, while the remaining IDTs were left floating, i.e., electrically unconnected. A sinusoidal excitation with a rms amplitude V_{AC} of 1 V was applied, while the frequency *f* was swept between 11.185 and 12.88 MHz with a step size of 70 Hz at different temperatures. The proposed sensor has been tested within the temperature range of 25°C to 45°C, while varying the setpoint *SP* with a 2.5°C step as shown in Fig. 6. The time required to achieve steady state after each 2.5°C step was set as 1 hour, as illustrated in the inset of Fig. 6. An additional delay of 30 minutes after the beginning of the steady state was introduced before conducting admittance measurements. Thanks to the continuous real-time temperature control implemented via the PID, the *PV* accurately followed the *SP* ensuring precise thermal regulation, as shown in the inset of Fig. 6. Measurements were performed while maintaining a stable temperature over time, with a variation of approximately ±0.02 °C. Fig. 7 shows the measured *G(f)* of IDT3 as a function of the excitation frequency *f*. The obtained conductance patterns show five distinctive main peaks within the considered bandwidth caused by the IDT3 location on the diaphragm and by the diaphragm dimensions [15, 22]. A conductance peak is obtained when the wavelength is an integer submultiple of the propagation path, defined as twice the distance between the center of the IDT and the outermost constraint of the diaphragm [22]. The obtained series of peaks (Pk1-5) exhibits a rigid downshift in frequency as the temperature *T* increases, as visible in the inset of Fig. 7, where the second peak of *G(f)* is shown. Fig. 8 illustrates the frequency shifts Δf as a function of ΔT, where $\Delta T = T - T_0$ with T_0 = 25 °C. The frequency shift is defined as $\Delta f = f_m - f_{m0}$, where f_m represents the frequency at which the conductance *G(f)* reaches its maximum for the five measured conductance peaks, and f_{m0} the corresponding values at the reference temperature T_0. The dashed line represents the linear fitting of the average frequency shifts obtained by averaging the individual shifts of the conductance peaks as a function of ΔT. For ΔT = 25 °C, a frequency variation of -8.628 kHz has been measured. The proposed MEMS sensor exhibits a sensitivity of -426.5 Hz/°C, with a maximum nonlinearity error, referred to the full scale, of 1.18%.

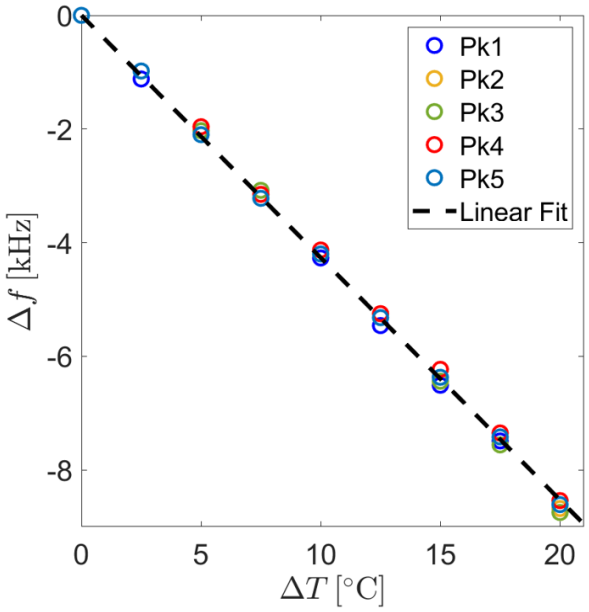


Figure 8. Frequency shifts Δf as a function of ΔT for the five conductance peaks. The dashed line represents the linear fit of the average frequency shifts obtained for the five peaks.

5. CONCLUSIONS

In this work, a piezoelectric FPW MEMS temperature sensor was presented. The proposed sensor exploits the first antisymmetric (A_0) vibration mode of Lamb waves to measure the surrounding temperature. The operating principle was experimentally validated using a custom PID-controlled temperature chamber, ensuring precise measurement conditions, accurate characterization, and minimal external interferences. The sensor was validated over the temperature range of 25 °C to 45 °C within the 11.185 to 12.88 MHz frequency range. For ΔT = 25 °C, a frequency shift of -8.628 kHz was measured. The proposed MEMS sensor exhibits a sensitivity of -426.5 Hz/°C with a maximum nonlinearity error of 1.18% referred to the full scale. The results obtained demonstrate the feasibility of using FPW-based piezoelectric MEMS for temperature sensing applications, confirming the expected downshift in frequency of the conductance pattern as the temperature increases and highlighting its potential to operate over an extended temperature range.

6. ACKNOWLEDGMENTS

The work has been carried out within the research project funded by the European Union NextGenerationEU.

7. REFERENCES

[1] J. Bryzek, S. Roundy, B. Bircumshaw, C. Chung, K. Castellino, J. Stetter and M. Vestel, "Marvelous MEMs," *IEEE Circuits and Devices Magazine*, vol. 22, no. 2, pp. 8–28, Mar. 2006, doi: 10.1109/MCD.2006.1615241.

[2] S. E. Moon, N. J. Choi, H. K. Lee, J. Lee, and W. S. Yang, "Semiconductor-type MEMS gas sensor for real-time environmental monitoring applications," ETRI Journal, vol. 35, no. 4, pp. 617–624, Aug. 2013, doi: 10.4218/etrij.13.1912.0008.

[3] K. Menon, R. A. Joy, N. Sood, and R. K. Mittal, "The Applications of BioMEMS in Diagnosis, Cell Biology, and Therapy: A Review," Bionanoscience, vol. 3, no. 4, pp. 356–366, Dec. 2013, doi: 10.1007/s12668-013-0112-7.

[4] A. A. M. Faudzi, Y. Sabzehmeidani, and K. Suzumori, "Application of Micro-Electro-Mechanical Systems (MEMS) as Sensors: A Review," Journal of Robotics and Mechatronics, vol. 32, no. 2, pp. 281–288, Apr. 2020, doi: 10.20965/jrm.2020.p0281.

[5] R. Bogue, "Recent developments in MEMS sensors: a review of applications, markets and technologies," Sensor Review, vol. 33, no. 4, pp. 300–304, Sep. 2013, doi: 10.1108/SR-05-2013-678.

[6] B. Padha, I. Yadav, S. Dutta, and S. Arya, "Recent Developments in Wearable NEMS/MEMS-Based Smart Infrared Sensors for Healthcare Applications," Oct. 24, 2023, American Chemical Society. doi: 10.1021/acsaelm.3c00860.

[7] Izhar, X. Zhao, H. Tavakkoli, W. Xu, and Y. K. Lee, "Performance Improvement of Integrated MEMS Temperature, Humidity, and Air Velocity Sensors for Application in Smart Buildings," IEEE Trans Electron Devices, vol. 71, no. 3, pp. 2064–2071, Mar. 2024, doi: 10.1109/TED.2024.3353147.

[8] Z. Stanimirovic and I. Stanimirovic, "Pt Resistive Film Sensors," in 2019 IEEE 31st International Conference on Microelectronics (MIEL), IEEE, Sep. 2019, pp. 145–148. doi: 10.1109/MIEL.2019.8889625.

[9] W. Tomboza, R. Cotillard, N. Roussel, M. C. P. Huy, G. Bouwmans, and G. Laffont, "Characterization of femtosecond laser micromachined fiber in-line pressure sensor for simultaneous measurement of high temperature and pressure," in Optica Advanced Photonics Congress 2022, Washington, D.C.: Optica Publishing Group, 2022, p. BTh2A.3. doi: 10.1364/BGPPM.2022.BTh2A.3.

[10] W. Sui, T. Kaisar, H. Wang, Y. Wu, J. Lee, H. Xie, and P. Feng, "Micromachined Thin Film Ceramic PZT Multimode Resonant Temperature Sensor," *IEEE Sens J*, vol. 24, no. 6, pp. 7273–7283, Mar. 2024, doi: 10.1109/JSEN.2023.3294125.

[11] H. Qian et al., "A High Sensitivity Temperature Sensor Using High-Q NS-SAW Resonator," in 2022 Joint Conference of the European Frequency and Time Forum and IEEE International Frequency Control Symposium (EFTF/IFCS), IEEE, Apr. 2022, pp. 1–4. doi: 10.1109/EFTF/IFCS54560.2022.9850684.

[12] X. Q. Bao, W. Burkhard, V. V. Varadan, and V. K. Varadan, "SAW Temperature Sensor and Remote Reading System," in IEEE 1987 Ultrasonics Symposium, IEEE, 1987, pp. 583–586. doi: 10.1109/ULTSYM.1987.199024.

[13] K.-H. Chiu, H.-R. Chen, and S. R.-S. Huang, "High-Performance Film Bulk Acoustic Wave Pressure and Temperature Sensors," *Jpn J Appl Phys*, vol. 46, no. 4R, p. 1392, Apr. 2007, doi: 10.1143/JJAP.46.1392.

[14] S. W. Wenzel and R. M. White, "A multisensor employing an ultrasonic Lamb-wave oscillator," IEEE Trans Electron Devices, vol. 35, no. 6, pp. 735–743, Jun. 1988, doi: 10.1109/16.2525.

[15] A. Nastro, M. Baù, M. Ferrari, L. Rufer, S. Basrour, and V. Ferrari, "Cell Alignment in Aqueous Solution Employing a Flexural Plate Wave Piezoelectric MEMS Transducer," IEEE Access, vol. 11, pp. 130755–130762, 2023, doi: 10.1109/ACCESS.2023.3333694.

[16] M. Reusch, K. Holc, A. Zukauskaite, V. Lebedev, N. Kurz, and O. Ambacher, "Flexural plate wave sensors with buried IDT for sensing in liquids," in 2017 IEEE SENSORS, IEEE, Oct. 2017, pp. 1–3. doi: 10.1109/ICSENS.2017.8234418.

[17] A. Nastro, L. Rufer, M. Ferrari, S. Basrour, and V. Ferrari, "Piezoelectric Micromachined Acoustic Transducer with Electrically-Tunable Resonant Frequency," in 2019 20th International Conference on Solid-State Sensors, Actuators and Microsystems & Eurosensors XXXIII (TRANSDUCERS & EUROSENSORS XXXIII), IEEE, Jun. 2019, pp. 1905–1908. doi: 10.1109/TRANSDUCERS.2019.8808488.

[18] Z. Yu, Y. Yue, Z. Liang, X. Zhao, F. Li, W. Peng, Q. Zhu and Y. He, "Physical Sensors Based on Lamb Wave Resonators", Micromachines (2024), 15, 1243. https://doi.org/10.3390/mi15101243.

[19] P. Kropelnicki et al., "CMOS-compatible ruggedized high-temperature Lamb wave pressure sensor," Journal of Micromechanics and Microengineering, vol. 23, no. 8, Aug. 2013, doi: 10.1088/0960-1317/23/8/085018.

[20] H. Jia, R. Duhamel, J.-F. Manceau, M. de Labachelerie, and F. Bastien, "Improvement of Lamb waves sensors," Sens Actuators A Phys, vol. 121, no. 2, pp. 321–326, Jun. 2005, doi: 10.1016/j.sna.2005.02.014.

[21] B. Cunningham, M. Weinberg, J. Pepper, C. Clapp, R. Bousquet, B. Hugh, R. Kant, C. Daly, E. Hauser, "Design, fabrication and vapor characterization of a microfabricated flexural plate resonator sensor and application to integrated sensor arrays," Sens Actuators B Chem, vol. 73, no. 2–3, pp. 112–123, Mar. 2001, doi: 10.1016/S0925-4005(00)00664-X.

[22] S. Bertelli, A. Nastro, M. Ferrari, M. Baù, and V. Ferrari, "Simulation and Experimental Validation of a Flexural Plate Wave Piezoelectric MEMS Transducer," in 2024 IEEE Sensors Applications Symposium (SAS), IEEE, Jul. 2024, pp. 1–6. doi: 10.1109/SAS60918.2024.10636618.

DOI: 10.61782/fa.2025.0704



FORUM ACUSTICUM
EURONOISE 2025

PRODUCTIZATION CHALLENGES OF ACOUSTIC MEMS SENSORS AND ACTUATORS

Anton Lagosh[1] **Adrien Piot**[1] **Sanjay Nayak**[1] **Rodrigo T. Rocha**[1] **Humberto Campanella**[1*]
[1] Silicon Austria Labs GmbH, High Tech Campus Villach - Europastraße 12, 9524 Villach, Austria

ABSTRACT[*]

Silicon-based MEMS technologies for acoustic transducers are mature, widely available and have enabled a strong industry for consumer and niche markets while fulfilling the More-than-Moore promise. Nevertheless, mass production faces continuous innovation, manufacturability and testing challenges that prevent a higher market implantation of proof-of-concept acoustic MEMS devices. In response to these challenges, this paper discusses new integration trends involving the hybrid integration of polymeric materials into the flow of MEMS manufacturing. New test and modeling methodologies to address corresponding performance and data handling challenges are also discussed in this paper.

Keywords: *polymer acoustic MEMS, wafer temporary bonding, thin wafer handling, non-ideal MEMS modeling, manufacturing of acoustic MEMS devices.*

1. INTRODUCTION

Nowadays, majority of micro electromechanical system (MEMS) devices in industrial production have leveraged on pure silicon-based processes. More recently, thin-film piezoelectric materials have enabled a whole new range of miniaturized acoustic MEMS devices, from microphones to speakers, from audio to ultrasound bands, and to serve a wide variety of consumer and industrial applications. While conventional sets of materials and silicon-based processes used in these devices demonstrate proof-of-concept feasibility and functionality, performance for industrialization and mass production is not yet there. To address performance practical implementation issues, recent trends in acoustic MEMS device development have seen increasing efforts in polymeric materials integration (moving on from pure-silicon processes to heterogeneous polymer-MEMS materials) [1-5]. Nevertheless, and while polymers bring in a whole new range of convenient mechanical properties that enable new and competitive applications, it also poses new challenges to micromachining and wafer handing for mass production environments. In the following sections, we compare techniques for polymer film transfer as well as properties crucial for manufacturability and device reliability, which involve crucial temporary bonding and debonding processes, to enable safe and reliable processing of thin wafers. We highlight advantages and disadvantages of state-of-the-art techniques like thermal slide-off, UV and IR laser debonding.

Stress control and tunability is another key challenge faced by MEMS devices, which greatly impact manufacturability and device performance. In Section 4 we discuss the impact of stress performance and methods to carry out stress control to accomplish specific performance goals. Finally, Section 5 proposes a brief discussion on testing challenges associated with non-linear and non-ideal behavior of MEMS devices, and handling, analysis and postprocessing of large amount of test data required in production.

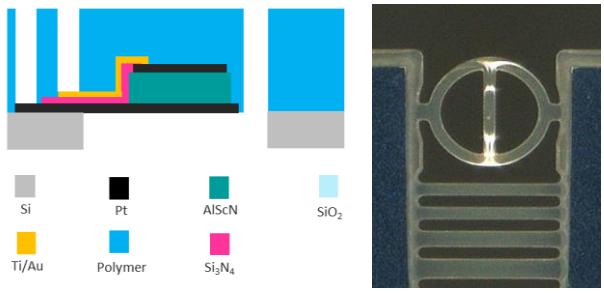
2. POLYMER INTEGRATION TO MEMS PROCESS FLOW

2.1 Polymer film and challenges

Figure 1 shows an example process of an acoustic MEMS device integrating a polymer layer and more *conventional* stacked structure and micromachining techniques. Polymer

[*]***Corresponding author***:
humberto.campanella@silicon-austria.com

Copyright: *©2025 Humberto Campanella et al. This is an open-access article distributed under the terms of the Creative Commons Attribution 3.0 Unported License, which permits unrestricted use, distribution, and reproduction in any medium, provided the original author and source are credited.*



a. b.

Figure 1. Example process of an acoustic MEMS device integrating polymer: (a) Schematic of a cross section; (b) realization o of a polymer-based piezo cantilever and Guckel ring stress test structures

integration in the flow of acoustic MEMS devices is challenging as polymers are usually sensitive to temperature. Requirements involve thick layers that are usually in the range of a 10-100 µm, and that require coating of the polymer on a micromachined surface with high aspect ratio features and finally patterning of the thick polymer layer should be achieved while keeping reachable critical dimensions (CD) as low as possible and side walls as vertical as possible. In the following sections, we discuss the best coating techniques and polymer materials candidate for MEMS integration.

2.2 Polymer selection and coating technique

Specifications and constraints were given for the polymer. This polymer needed to be patterned with a required CD of 10 µm, a minimum reachable aspect ratio of 1, a Young's Modulus higher than 3 GPa, a glass transition temperature (Tg) >150°C, a total thickness of 45 µm. Coating should be conformal on a substrate with surface features consisting in steps of 1 to 4 µm and aspect ratio below 1. And lastly all processes need to be compatible with mass production.

2.3 Polymer dry film

Different coating techniques can be used to realize the dry film, including spin coating, dip coating, spray coating, lamination and vacuum bonding. Among all the different coating techniques, thick layers are mostly coated using dip coating, lamination or vacuum bonding. In general, only lamination and vacuum bonding are mostly used with batch processes. In the end, we selected vacuum bonding to perform conformal coating and potentially reduce the number of trapped air bubbles between the substrate and the polymer. Vacuum bonding is performed with polymer dry films. For this process we selected a 45 µm SU8-based dry-film from Nippon with an expected Young's Modulus of 3.5 GPa and Tg of 280°C. This polymer dry film is a negative photoresist.

2.4 Dry film adhesion and patterning

After substrate plasma O_2 treatment and dry-film vacuum bonding with the EVG 520IS bonder we processed the dry-film using post bonding bake, then UV-exposure, post exposure baking and development using PGMEA. Hard bake was finally performed in an oven at 170°C for at least 80 min. First trials demonstrated vertical sidewalls -see **Figure 2.**

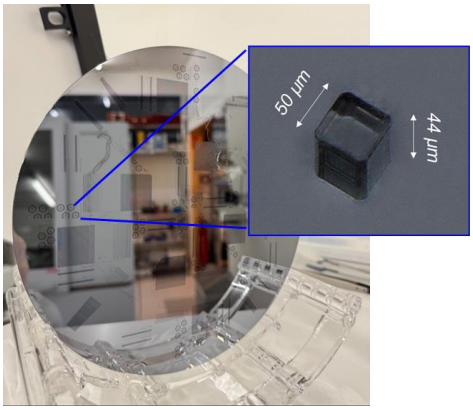
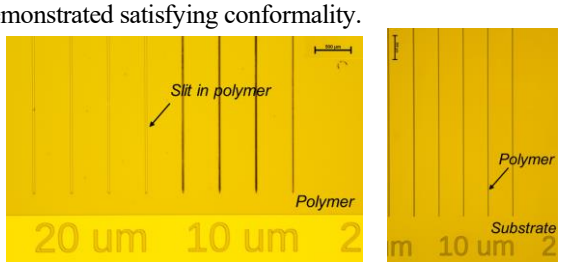


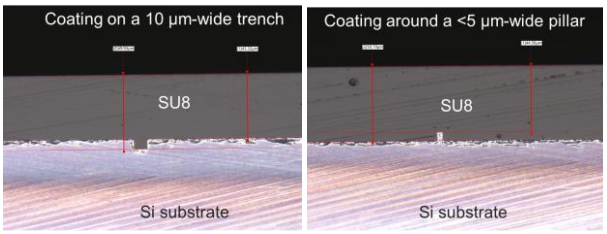
Figure 2. Bird's eye view of a patterned polymer square on 200mm wafer for sidewall characterization.

Error! Reference source not found.3 shows a successful i mplementation example, which reaches a maximum aspect ratio of 2.25 in polymer (**Error! Reference source not f ound.**3a), and a minimum CD of 10 µm see **Error! Reference source not found.**b. On the other hand, **Figure 4** shows test structures with conformal coating on steps with a width of 10 µm and depth of 5 µm were also validated as well as conformal coating of pillars down to a width and height of 5 µm. No trapped air bubbles were noticeable near the patterned features in the silicon substrate. The coating demonstrated satisfying conformality.



a. b.

Figure 3. Optical microscope images of: (a) patterned slits in polymer (AR 2.25); (b) Polymer lines with CD 10um.



a. b.

Figure 4. Cross section images of a. polymer coating and the silicon substrate with a trench, b. polymer coating and the silicon substrate with a pillar.

2.4.1 Adhesion test and Mechanical Properties

To be noted that the substate was coated with a 100 nm-thick SiO_xN_y layer, as for the final device, thus we performed a pull-off adhesion test using a Zwick/Roell Z2.5 apparatus to validate adhesion of the polymer film on the substrate, see **Figure 5**.

Adhesion loss, delamination occurred at ~ 0.31 MPa between the dolly and the double-sided tape used to fix the sample. The 3M LSE-160WF double-sided tape has a theoretical pull-off adhesion limit at 0.47 MPa. We failed to de-bond the polymer layer from its substrate and concluded to a satisfying adhesion of the polymer to the SiO_xN_y layer. The reduced Young's Modulus of the SU-8-based dry-film was measured using the FT-104 Femto-Indenter from Femtotools. We obtain a reduced modulus equal to 5.3 GPa, meaning a Young's Modulus of 4.8 GPa assuming for dry film a poisson coefficient, ν, close to 0.32 [6].

We measured the Young's Modulus, *E*, 137 % higher than

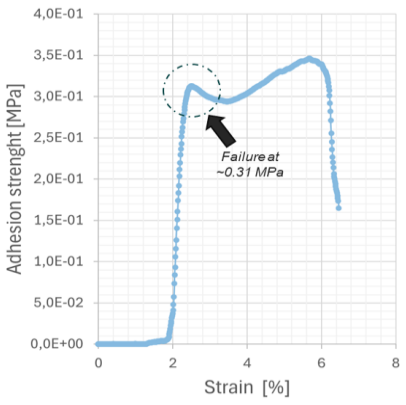


Figure 5. Pull-off test showing dry film adhesion strength vs strain.

what was expected from the datasheets. The discrepancy still needs to be investigated and could be attributed to different characterization techniques and scale between this work and the dry-film manufacturer. However, a higher Young's Modulus than expected is beneficial for the final MEMS device as E > 3 GPa leading to a stiffer structure.

Using our FT-104 Femto-Indenter, we performed continuous stiffness measurement (CSM) nanoindentation from ambient temperature up to 200°C and observed a drop of around 35% of the storage Young's Modulus at 170°C, thus we could assume a Tg close to 170°C which is higher than 150°C, but lower than expected from datasheet. Finally, we measured relatively low residual tensile stress in the blanked polymer layer close to 27 MPa. Ultimately, we selected the dry film polymer from datasheets provided by the manufacturer, development of the processing recipes was performed, and we confirmed its mechanical properties and productization. The next step will be grinding and polishing the silicon substrate to obtain small form factor and thin devices. More details are given in the next section.

3. THIN WAFER HANDLING AND PROCESSING

3.1 Why is temporary bonding needed?

Current mainstream in industrial applications requires miniaturized and cost-effective solutions. Thus, the demand for thin and ultrathin wafers is growing. Temporary bonding is a crucial process that enables safe and reliable processing of thin or to-be-thinned wafers [7, 8]. Thin wafers are very fragile, and as a result chips and cracks can easily occur. Thus, the final yield is at a high risk since these wafers should pass through processing steps like lithography, etching, deposition and others. The industry seeks reliable batch solutions in temporary bonding and debonding that ensures repeatability and high productivity at reasonable cost [9].

3.2 Temporary bonding technologies

A first technique involves direct bonding of MEMS device wafers and a carrier wafer using a special Temporary Bonding Material (TBM) [10] as shown in Figure 5(I). This material is an organic thermoplastic or thermoset adhesive spin coated on a carrier or device MEMS wafer. This process is suitable for simple chemical release debonding. A more complex process combines TBM with a thin Layer Release Material (LRM) [11, 12], intended for UV or IR debonding process -see Figure 5(II).

Typically, the bonding step occurs via thermocompression in vacuum or, in some cases, using UV radiation. The TBM is selected tailored to the intended application considering ease of coating, shorten processing time and simplified cleaning. Ideally, it is applied using single coat step ensuring uniform, void free and low stress interface between carrier and device MEMS wafer. The thickness should be enough to cover all topography on device MEMS wafer. The adhesive should be compatible with the intended thermal budget for subsequent process steps. The choice of carrier wafer is based on the target debonding process and CTE match with the device MEMS wafer to minimize induced thermomechanical stress. For example, silicon carrier is a perfect match for silicon device MEMS wafer. However, the technique such as UV laser debonding is not an option in this case since it requires transparent carriers such as glass.

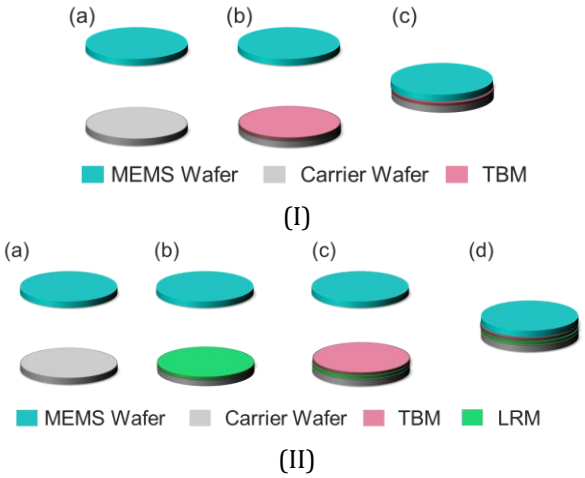


Figure 5. Temporary bonding process designed for: (I) chemical release debonding or thermal slide off; (II) UV or IR laser debonding.

3.3 Chemical release debonding

The chemical release debonding is established and reliable technique for temporary bonded wafers. The temporarily bonded stack is placed in a solvent bath to separate carrier and device MEMS wafer, and then a second bath is used to clean off any remaining adhesive. One can expect an approximate throughput of 25 wafers per debonding cycle that can be up to 4 hours. The main advantage of this technique is low induced stress. However, this technique is comparably slow and, in the end, expensive for high volume production. This pushes industry to develop new temporary bonding materials and corresponding processes.

3.4 Thermal slide-off debonding

In case of thermal slide off debonding, the wafer stack is heated up and separated by sliding wafers apart as Figure 6 illustrates. There is a trade-off between temperature, mechanical force and sliding rate. The maximum throughput is higher, up to 15 wafers per hour. Unfortunately, the stress induced by this debonding technique can be critical for fragile MEMS devices, limiting total yield.

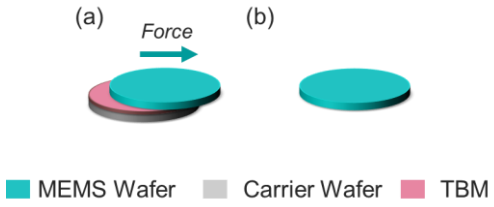


Figure 6. Thermal slide-off debonding process.

3.5 Laser debonding

Laser debonding technique offers high throughput up to 50 wafers per hour and low induced stress that is required to maximize yield in case of sensitive MEMS devices. This technique requires a special inorganic LRM layer [11, 12] that has high absorbance at specific wavelengths in UV (254 nm, 308 nm, 355 nm) or IR (1064 nm) band. This material is decomposed due to photochemical or photothermal effects leaving almost no residues. These residues can be later cleaned using oxygen plasma or an oxidizing solvent. After laser exposure happens, the temporary bonded stack can be separated with almost no force that is a great advantage for fragile structures. Figure 7 illustrates a simple laser debonding process involving (a) laser rastering and heating of the LRM layer; (b) wafers separation; (c) TBM removal.

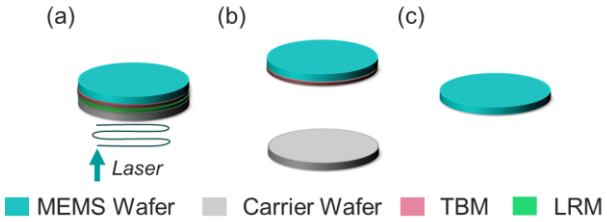


Figure 7. UV or IR laser debonding process.

4. STRESS TUNING FOR ACOUSTIC PERFORMANCE AND MANUFACTURABILITY

4.1 Why is stress control needed?

Stress becomes an important factor for acoustic performance, as it impacts both the geometry, the small and large signal performance and functionality, and the long-term reliability of the device. Geometric parameters include residual deflection of a cantilevered structure, or mismatch of deflections in arrays, buckling, and offsetting of key layout features. Functionality is also affected as losses, electrical, dielectric and piezoelectric performance rely on stress. This has direct consequences on key figures of merit of the device like sensitivity, SNR, resonance frequencies, and electromechanical coupling coefficients, among others. On the other hand, it is worth clarifying that stress is, rather than a problem, a physical situation intrinsic to stacked-layer devices. Also, that stress engineering problems become visible when MEMS manufacturing leave the early R&D proof-of-concept phase, typically done on small wafers, and move to large 200mm wafer format. Therefore, there is a need to tune stress to the performance goals of the MEMS device. This is discussed in the next paragraphs.

4.2 Stress tunability in c-axis textured piezoelectric AlScN thin films

The stress in polycrystalline and textured thin films can be controlled by adjusting various factors. These factors include both extrinsic and intrinsic components. Extrinsic stress is primarily influenced by the processing temperature, known as thermal stress. Intrinsic stress is more complex and arises from the kinetics of film growth, grain boundary densification, and the generation of point defects in the bulk. Chason *et al.* [13] have proposed a kinetic model for stress, which describes *total stress* as the sum of three components, namely growth-related stress, grain boundary energetics-related stress, and bulk energetics-related stress. This model suggests that by controlling the RF bias power of the tools carrying out physical deposition or growth of the acoustic MEMS layers and that affects the kinetic energy of incoming ions, one can manipulate all three components of stress.

As an example, we deposit scandium-doped aluminum nitride (AlScN), a piezoelectric thin-film that we use as active transducer layer of the acoustic MEMS device. Deposition is carried out by physical vapor deposition (PVD) using an industrial cluster tool Cluster 200E from Evatec. In our work, we tune the residual stress of c-axis textured AlScN films by applying an RF bias power to the chuck during deposition. The RF bias power varies from 50 W to 250 W, which leads to a linear increase in compressive stress with increasing power. The residual stress was measured using a Toho Stress measurement system, which employs Stoney's equation to relate the wafer curvature to the film stress [14]. The standard Stoney's equation used is:

$$\sigma = \frac{E \times t_s^2}{(1-\nu) \times t_f}\left[\frac{1}{R_f} - \frac{1}{R_s}\right] \qquad (1)$$

Where E and ν are the Young's modulus and Poisson's ratio of the substrate, t_s and t_f are the thicknesses of the substrate and film, and R_f and R_s are the radii of curvature after and before film deposition, respectively. Our experimental results show that for 500 nm thick Al0.64Sc0.36N films on Pt/AlN/Si100 electrodes, the average biaxial compressive residual stress is linearly dependent on the applied RF bias power. After laser exposure happened, temporary bonded stacks can be separated with almost no force that is a great advantage for fragile structures.

The plot in Figure 5 shows how stress control is a function of RF bias power. Selected bias point is defined by the target value defined by the application and stack of layers in the acoustic MEMS device.

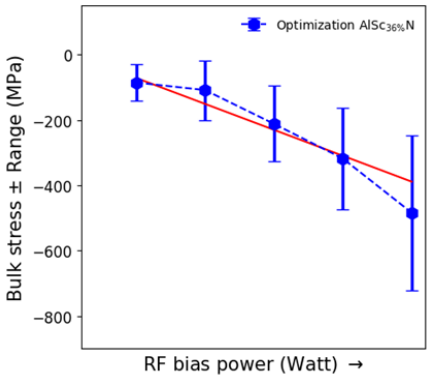


Figure 5. Dependence of RF power chuck bias to the residual stress of the AlScN thin film deposited on a 200 mm silicon wafer.

5. FEW WORDS ABOUT TESTING CHALLENGES

Testing of MEMS devices in the production environment poses several challenges. First of all, foundry setup is typically prepared for pure electrical testing, while MEMS devices generally require multi-physical domain environment. Adapting fab resources away from conventional *e-test* (electrical testing) is far from trivial.

This issue has direct impact in the cost of final application, as MEMS yield has to be characterized, modeled and improved at reasonable cost. Later stages of production will involve singulation of MEMS devices and testing them either integrated with electronic components in a module, or as stand-alone chips. Then, events such as crosstalk due to acoustic waves interfering in the data acquisition, robustness of die bonding using flexible glues, or even clamping losses will affect performance. A fully manufacturable flow will need test methodologies that integrate seamlessly in the manufacturing setup of standard foundries.

6. CONCLUSION

This paper has reported on relevant technologies needed for industrialization and successful inception of MEMS technologies in markets, namely polymeric dry film integration, handling of thin wafers as part of flow, MEMS stack stress management and tuning, and testing methodologies. Dry film integration enables new applications and performance of acoustic devices. MEMS wafer temporary bonding to carrier wafers in turn enables polymer processing, while debonding enables final MEMS device release for acoustic performance. Batch testing finally enables new wafer sorting methodologies.

7. REFERENCES

[1] Z.S. Hu, C.H. Lin, S.C. Lo and W. Fang, “Design of Piezoelectric MEMS Microspeaker with Parylene Spring for Performance Improvement,” In *2025 IEEE 38th International Conference on Micro Electro Mechanical Systems (MEMS)* (pp. 775-778), 2025, January IEEE.

[2] Q. Wang, Z. Yi, T. Ruan, Q. Xu, B. Yang and J. Liu, “Obtaining high SPL piezoelectric MEMS speaker via a rigid-flexible vibration coupling mechanism,” *Journal of Microelectromechanical Systems*, *30*(5), 2021, pp.725-732.

[3] A. Rosa, W. Mühleisen, A. De Pastina and J. Abbaszadeh, "Bandwidth and Thermal Stability Enhancement of Polymer-Integrated Piezoelectric Micromachined Ultrasonic Transducer Array for Air-Coupled Applications," 2025 IEEE 38th International Conference on Micro Electro Mechanical Systems (MEMS), Kaohsiung, Taiwan, 2025, pp. 655-658

[4] P. -H. Huang et al., "3D Printed Mems," 2025 IEEE 38th International Conference on Micro Electro Mechanical Systems (MEMS), Kaohsiung, Taiwan, 2025, pp. 62-67

[5] L. Wang *et al.*, "Ultra-Sensitive Wireless Pressure Sensor for Real-Time Cardiovascular Restenosis Monitoring in Smart Stents," *2025 IEEE 38th International Conference on Micro Electro Mechanical Systems (MEMS)*, Kaohsiung, Taiwan, 2025, pp. 12-15.

[6] S. Chung, and S. Park, “Effects of temperature on mechanical properties of SU-8 photoresist material,” *Journal of Mechanical Science and Technology*, *27*, 2013, pp.2701-2707.

[7] D. Wuensch et al., "Temporary wafer bonding - key technology for MEMS devices," 2017 Pan Pacific Microelectronics Symposium (Pan Pacific), Kauai, HI, USA, 2017, pp. 1-7

[8] Q. Ren, W. L. Loh, S. K. Neo and K. -J. Chui, "Temporary Bonding and De-bonding Process for 2.5D/3D Applications," 2020 IEEE 22nd Electronics Packaging Technology Conference (EPTC), Singapore, Singapore, 2020, pp. 27-31

[9] Mo, Z.; Wang, F.; Li, J.; Liu, Q.; Zhang, G.; Li, W.; Yang, C.; Sun, R. Temporary Bonding and Debonding in Advanced Packaging: Recent Progress and Applications. Electronics 2023, 12, 1666.

[10] W. L. Tsai *et al.*, "How to select adhesive materials for temporary bonding and de-bonding of 200mm and 300mm thin-wafer handling for 3D IC integration?," *2011 IEEE 61st Electronic Components and Technology Conference (ECTC)*, Lake Buena Vista, FL, USA, 2011, pp. 989-998

[11] Y. -s. Yang, K. -s. Hwang and R. Gorrell, "Laser Releasable Temporary Bonding Film with High Thermal Stability," 2019 IEEE 69th Electronic Components and Technology Conference (ECTC), Las Vegas, NV, USA, 2019, pp. 330-333

[12] S. C. Roy and S. Merugu, "Polymer Materials for Temporary Bonding and Laser Debonding for MEMS Based Applications: An Evaluation," 2024 IEEE 26th Electronics Packaging Technology Conference (EPTC), Singapore, 2024, pp. 768-773

[13] E. Chason, M. Karlson, J. J. Colin, D. Magnfalt, K. Sarakinos, and G. Abadias. A kinetic model for stress generation in thin films grown from energetic vapor fluxes. J. Appl. Phys. 119, 145307 (2016)

[14] Stoney G G. The tension of metallic films deposited by electrolysis *Proceedings of the Royal Society of London. Series A, Containing Papers of a Mathematical and Physical Character* **82** 172–5 (1909).

DOI: 10.61782/fa.2025.0226

FORUM ACUSTICUM EURONOISE 2025

COMPARATIVE STUDY OF THE FREQUENCY RESPONSE OF SMARTWATCH SENSORS FOR HUMAN MOVEMENT ASSESSMENT

María Centeno-Cerrato[1*] **Carlos Polvorinos-Fernández**[1] **Guillermo de Arcas**[1]
Luis Sigcha[2] **Ignacio Pavón**[1]
[1] Department of Mechanical Engineering, Instrumentation and Applied Acoustics Research Group, ETS Ingenieros Industriales, Universidad Politécnica de Madrid, Madrid, Spain
[2] Department of Physical Education and Sports Science, Health Research Institute, & Data-Driven Computer Engineering (D2iCE) Group, University of Limerick, Limerick, Ireland

ABSTRACT

Smartwatches are wearable devices designed for continuous and precise data collection, ensuring minimal disruption or discomfort for the user. Their ability to monitor movement makes them particularly effective for applications such as health monitoring or workplace risk evaluation. However, the inertial sensors embedded in these devices may exhibit inaccuracies in data acquisition, which could compromise the quality of the results. Therefore, thorough characterization is essential to understand their response under specific excitation conditions.

This study evaluates the performance of accelerometers in four commercially available smartwatches, by assessing their frequency responses using two different calibration methods. Method 1, considered the reference method and involving individual sensor calibration, produced minimal deviations, validating the reliability of the devices within the tested ranges. In contrast, Method 2, intended for quicker calibration of multiple devices, showed greater deviations due to limitations in the calibration process.

The results revealed discrepancies in performance based on the calibration method used, highlighting the importance of selecting an appropriate technique to ensure more reliable and accurate measurements, especially for critical human movement monitoring applications.

Keywords: *calibration, accelerometer, wearables, human movement monitoring.*

[*] ***Corresponding author***: *maria.centeno.cerrato@upm.es*
Copyright: *©2025 María Centeno-Cerrato et al. This is an open-access article distributed under the terms of the Creative Commons Attribution 3.0 Unported License, which permits unrestricted use, distribution, and reproduction in any medium, provided the original author and source are credited.*

1. INTRODUCTION

Wearable technology has experienced significant growth in recent years, driven by the integration of advanced sensors into portable devices such as smartwatches, smart glasses, or biometric rings. These systems are widely adopted due to their ease of use, portability, and real-time data collection capabilities. Their main applications include occupational risk assessment, human movement and physical activity analysis [1], with increasing potential in healthcare [2]. Nevertheless, despite their advanced capabilities, multiple studies [3-5] have identified critical technical limitations in the embedded sensors of these devices, particularly regarding the accuracy and reliability of data acquisition.

Smartwatches are among the most common and widely adopted wearable devices [1] due to user familiarity and their integration into daily life. These devices are equipped with inertial sensors, including triaxial accelerometers and gyroscopes. The combined use of these sensors enables a detailed analysis of the user's dynamic behavior.

Periodic calibration or verification of sensors is essential, as factors such as environmental variations, temporal drift or device configuration changes can affect measurement reliability. To address this challenge, a thorough analysis of the sensor's dynamic behavior is required, focusing on its frequency and amplitude response under controlled vibratory excitation conditions [5]. This evaluation allows for the identification of the ranges where the sensor performs with maximum accuracy, while also revealing potential limitations in its measurement capabilities.

This study focuses on the characterization of accelerometers integrated into four commercial smartwatches of the same specific model. In healthcare and other movement monitoring studies, it is common to work with multiple identical devices. Therefore, ensuring that all devices

exhibit a similar and consistent response is essential for making reliable comparisons between the recorded data.

It is essential to determine the relevant amplitude and frequency ranges associated with human movement dynamics (hand-arm), with the aim of aligning the procedure with the specific operating conditions of the sensor. In this context, the frequency ranges extend up to 10 Hz, corresponding to physiological tremors [6], while typical amplitudes reach 4 m/s², as observed during human gait [7]. These parameters enable the assessment of smartwatch accelerometers in real-world applications.

This study employs two approaches for characterizing accelerometers to compare and analyze sensor performance variations under different calibration procedures.

The first method uses a uniaxial vibration bench, which allows for individual sensor characterization by applying precise vibratory excitation at different frequencies and amplitudes. While effective in terms of accuracy, this method can be time-consuming when calibrating multiple devices sequentially, making it less efficient for large-scale applications. This method was validated in [5], and is therefore considered the reference approach for comparison.

The second method utilizes a vibration platform, which generates vibrations on a surface. Unlike the previous approach, it allows for the simultaneous evaluation of multiple sensors, significantly reducing calibration time.

The study focuses on the comparative evaluation of the two calibration methodologies mentioned, employed to characterize accelerometers in smartwatches [8]. Through this analysis, the aim is to identify the advantages and limitations of each method in assessing sensor performance within the frequency and amplitude ranges associated with human movement. The ultimate goal is to optimize the calibration procedure, enhancing the reliability of measurements in biomechanical applications.

2. CALIBRATION METHODOLOGY

In studies related to human movement monitoring, particularly in healthcare or in safety fields such as risk assessments, multiple devices of the same type and model are typically used. Therefore, it is crucial that the data recorded by these sensors are comparable, meaning that all sensors must exhibit a precise and consistent response when subjected to the same mechanical vibration signal.

Consequently, this study focuses on characterizing the integrated accelerometers of four commercially available smartwatches of the same model by analyzing their frequency and amplitude response and verifying the consistency of their behavior. The sensors were configured with a sampling rate of 50 Hz and a maximum amplitude range of ±2 g, values considered appropriate for recording typical human movement dynamics in real-world scenarios.

Considering that the main objective of this study is not to fully characterize the accelerometer but to compare two calibration methodologies and evaluate their effectiveness, the analysis was intentionally limited to examining the frequency response of the Z-axis of the sensor. The axes orientation in the employed devices is shown in Figure 1.



Figure 1. Axes orientation in the employed sensor.

A vibratory excitation source is a device specifically designed to generate controlled vibrations, adjustable in terms of both frequency and amplitude, with the aim of subjecting sensors to defined testing conditions. The input signal applied is a sinusoidal waveform, as shown in Figure 2, whose characteristics are defined according to the sampling plan specifically designed for each study.

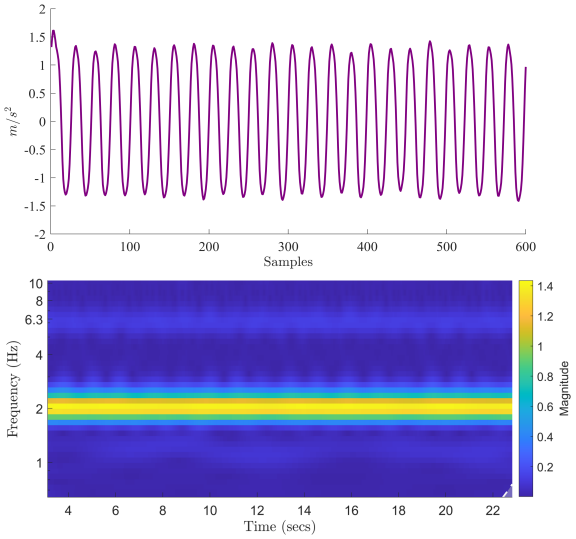


Figure 2. Signal captured by the accelerometer in a 2 Hz and 1 m/s² test. Top: time signal; Bottom: scalogram.

The quality of the calibration process is highly dependent on the performance of the excitation source. This study

employs two methodologies, each involving a different excitation source: Method 1, based on a uniaxial vibration bench, which enables the individual calibration of accelerometers through the application of precise and controlled vibrations; and Method 2, which utilizes a vibration platform capable of subjecting multiple sensors to uniform oscillations simultaneously, with the vibrations applied at a 45º angle relative to the horizontal plane.

The characterization of accelerometers is performed following the ISO 16063-21:2003 [9], which establishes a comparison methodology based on the use of a reference transducer. This method consists of rigidly coupling a calibrated reference accelerometer, which is presumed to function with a high level of accuracy, to the structure of the smartwatch, ensuring that both sensors are simultaneously exposed to the same controlled mechanical vibration.

2.1 Sampling plan

It is essential to establish a sampling protocol that clearly defines the specific frequencies and amplitudes to be used during the calibration process. It should guarantee that the characterization of the sensors is performed under controlled conditions that accurately replicate typical real-world hand-arm vibration scenarios.

Regarding the frequencies to be used for calibration, ISO 16063-21:2003 [9] recommends performing sensor characterization using vibratory excitations at standardized one-third octave frequencies, defined by ISO 266:1997 [10]. In the context of accelerometers designed for human movement analysis, it is crucial to adapt the excitation parameters to the typical frequency range characteristic of human activities in a variety of real-world contexts, which remains below 10 Hz [6, 11]. Accordingly, this study selected the frequencies of 1 Hz, 2 Hz, 4 Hz, 6.3 Hz, 8 Hz, and 10 Hz to evaluate the sensors' frequency response.

Concerning amplitude, the calibration was performed within an acceleration range of 1 m/s² to 4 m/s², reflecting the magnitudes encountered during common activities such as walking, running, or manual operations [7].

However, to develop a sampling plan suited to each calibration method, it is essential to carefully determine the operating range of the vibration sources used. In this context, multiple tests were conducted, establishing the operational interval for each method, as shown in Figure 3.

The common range shared by both calibration methods reaches up to 4 m/s² within the frequency band of 4 Hz to 6.3 Hz and decreases to 1 m/s² at 2 Hz. Method 1 offers the advantage of enabling excitations at higher frequencies (above 6.3 Hz), whereas Method 2 is particularly suitable for excitations at lower frequency ranges (below 4 Hz).

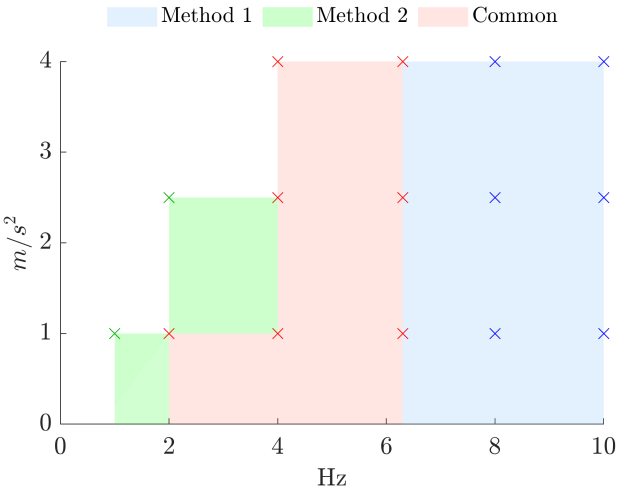


Figure 3. Specific operating range of the excitation sources in Method 1 and Method 2, including the common interval.

2.2 Setup

The calibration test setup is characterized by notable variations between both methods. In Method 1, the excitation source generates vibrations in a uniaxial configuration and, due to its geometric and dimensional constraints, it allows for the placement of only one device at a time, as shown in Figure 4 (left). Consequently, the smartwatch is positioned to ensure that the induced vibrations are applied exclusively along the Z-axis of its accelerometer. Additionally, the device is placed on a rigid and properly fixed holder, preventing the introduction of any undesired vibrations, guaranteeing the reliability and repeatability required for the calibration process.

In Method 2, the vibration excitation source consists of an actuator that induces vibrations on a platform at an angle of 45° relative to the horizontal plane, as illustrated in Figure 4 (right). Due to the dimensions of the surface where the vibration is generated, it is possible to place multiple devices simultaneously for calibration, thus facilitating a more efficient calibration process compared to Method 1.

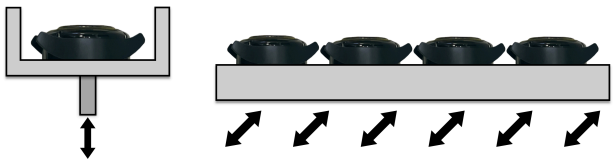


Figure 4. Movement induced by the excitation sources and placement of the smartwatches. Left: Method 1; right: Method 2.

Considering the characteristics of the excitation source in Method 2, there are two possible mounting configurations for placing the devices on the vibrating surface. The first option involves positioning the devices directly on the horizontal plane of the vibratory platform, as illustrated in Figure 5 (left). However, under this particular configuration, the excitation generated would simultaneously affect both the Z-axis and Y-axis of the device's accelerometer, resulting in a biaxial excitation. Although the mechanical implementation of this configuration is simple, it is not suitable for reproducing the Z-axis specific excitation carried out in Method 1.

Furthermore, to achieve the acceleration levels previously defined in the sampling plan, a, positioning the devices on the horizontal plane would necessitate that the platform generates an excitation with an amplitude equal to $\sqrt{2}a$, exceeding the acceleration levels intended for analysis during the calibration procedure. This requirement could lead to nonlinear behavior of the excitation source, particularly at low frequencies where higher amplitudes are required. Such nonlinearities may compromise the accuracy of the calibration and even pose a risk of structural damage to the platform due to excessive excitation levels.

In light of these considerations, the horizontal mounting option was deemed unsuitable for the intended calibration process. Instead, it was proposed to design and manufacture a custom support that holds the devices at a 45° inclination, aligned with the direction of excitation imposed by the actuator, as shown in Figure 5 (right). This approach ensures that the smartwatch experiences a uniaxial excitation along its Z-axis, replicating the conditions of Method 1 and thus enabling a direct comparison between both calibration methods.

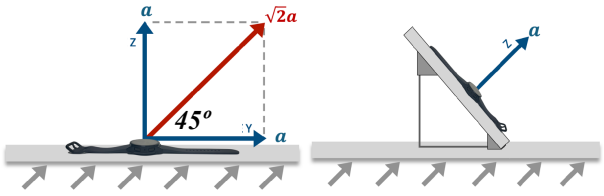


Figure 5. Smartwatch setup in Method 2. Left: horizontal plane, solution excluded from consideration; right: 45º, adopted solution.

The design of a custom fixture to support the devices must be carefully addressed, as several factors may influence the validity of the results. Among these, special attention must be given to the rigid attachment of the fixture to the vibrating platform and to the mounting of the devices on the fixture itself. Any looseness, misalignment, or insufficient clamping force could generate unwanted movements, resulting in distortion of the transmitted accelerations and, consequently, in erroneous calibration data.

Moreover, it is essential to consider that all mechanical structures subjected to dynamic excitations inevitably experience some degree of elastic deformation. If the fixture's natural frequencies fall within or close to the study's frequency range, undesired resonances may occur, potentially amplifying the input vibrations and introducing unwanted acceleration components into the measured signals. This phenomenon could significantly compromise the calibration process, leading to incorrect and unreliable estimations of the acceleration levels in the sensors.

Therefore, to mitigate this risk, it is necessary to ensure that the fixture behaves as a rigid body within the working frequency range, without exhibiting local modes or flexural deformations. To address these concerns, a modal analysis of the fixture was performed. The results revealed that the first resonance frequency is located at 56 Hz (Figure 6), which is above the operational frequency range of interest, since the calibration tests do not exceed 10 Hz. Based on these findings, it can be concluded that no significant resonances that could compromise the accuracy of the calibration results are present within the working interval.

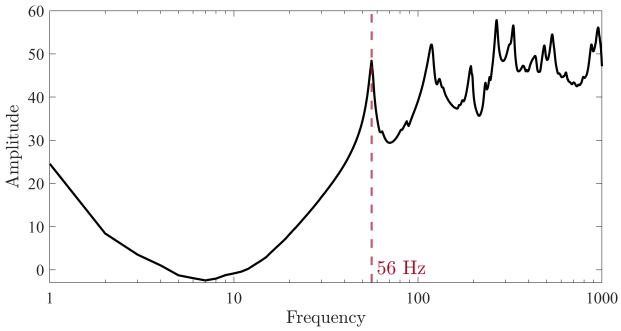


Figure 6. Fixture's global frequency response.

Regardless of the calibration method employed, since the comparative methodology is followed, a reference accelerometer was mounted onto the structure where the devices under evaluation were placed. This setup ensures that both the smartwatches and the reference sensor are exposed to the identical mechanical vibration signal.

2.3 Calibration procedure

In accordance with ISO 8041:2007 [12], for the calibration of hand-arm vibration measuring systems, each test had a duration of 30 seconds. This period was extended as needed to ensure that the excitation source reached a steady-state condition. To guarantee the validity and reproducibility of

the results, three measurements were performed for every combination of frequency and amplitude assessed. Following the sampling plans, Method 1 involved a total of 13 tests, while Method 2 consisted of only 9 tests.

The input signal was adjusted according to the specific test being conducted, with the frequency and amplitude modified as needed to align accurately with the defined sampling plan. This adjustment ensured that the reference accelerometer recorded root mean square (RMS) values of 1 m/s², 2.5 m/s², and 4 m/s², with the signals filtered through a second-order Butterworth bandpass filter.

2.4 Data processing

After completing the tests, the data recorded by the sensors were processed using an identical procedure for both calibration methods, thereby ensuring the comparability of the results. This step involved filtering the raw data from the Z-axis, which is critical to isolate the frequency range of interest and eliminate any unwanted noise that could distort the vibration signal. The filtering was performed using the same filter settings as applied to the reference accelerometer during the tests; specifically, a second-order Butterworth bandpass filter with a one-third octave bandwidth, centered on the relevant frequency band for each specific test.

In addition to removing noise from the source and the measurement environment, filtering also eliminates the effect of gravity. The accelerometer measures the sum of all forces acting on the sensor, which includes both the acceleration due to movement and due to gravity (a low-frequency signal, below 0.5 Hz, that is nearly constant). To focus specifically on the motion-induced data, it is necessary to filter out this low-frequency component.

Figure 7 presents an example of the signal recorded by the accelerometer of a smartwatch during a 1 Hz and 1 m/s² test, both before and following the filtering process.

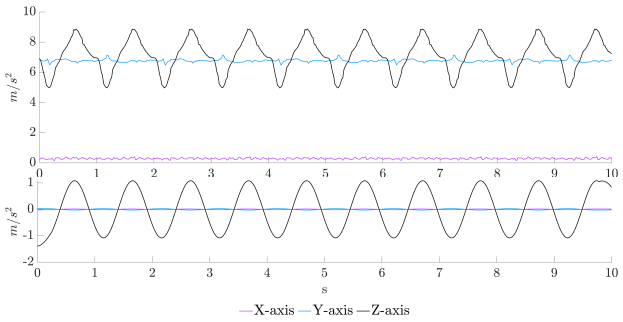


Figure 7. Signal captured by the smartwatch in a 1 Hz and 1 m/s² test. Top: before filtering; Bottom: after filtering.

Following the filtering process, the RMS value, which reflects the total energy of the input signal over a defined period, was calculated. The primary parameter under evaluation during the data processing phase is the error, which quantifies the deviation between the measurements from the test devices and the reference accelerometer.

3. RESULTS

A comparative analysis was performed to evaluate the results obtained with both calibration methods. This comparison considered the RMS values recorded by the smartwatches and their deviations relative to the reference accelerometer, which, during the tests conducted, recorded RMS-filtered accelerations of 1 m/s², 2.5 m/s², and 4 m/s².

Figure 8 presents the frequency and amplitude response of the smartwatches using calibration Method 1. The results indicate that, for all tests conducted, the values recorded by the accelerometers of the four smartwatches are almost identical. This consistency demonstrates that the devices are responding similarly to the applied vibrations. Furthermore, the measurements obtained from the smartwatches align with the recorded values from the reference accelerometer, demonstrating a high level of accuracy.

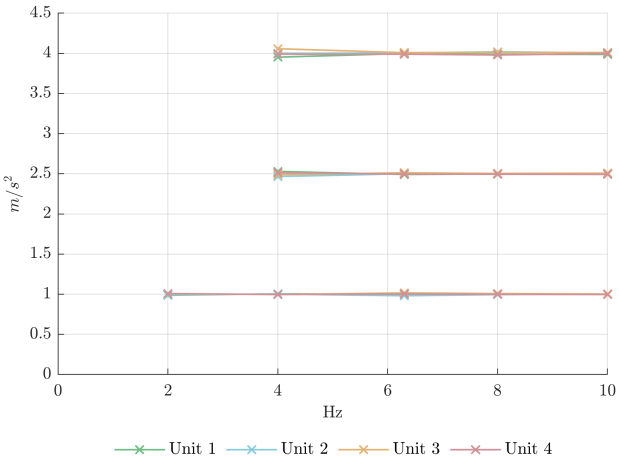


Figure 8. RMS values recorded by the smartwatches in Method 1.

Figure 9 presents the frequency and amplitude response obtained in Method 2. In contrast to Method 1, these results show some differences between the devices tested. The most significant discrepancies between smartwatches in Method 2 are observed when the input signal amplitude is 2.5 m/s², with deviations reaching up to 0.14 m/s². In comparison, the maximum deviation recorded across all tests in Method 1 was notably lower, 0.06 m/s². This

demonstrates that, despite using the same devices, their accelerometers respond differently depending on the applied calibration methodology. These differences suggest that the reliability of the measurements depends not only on the smartwatch hardware but also on the calibration method employed, which may contribute to additional variability and impact the overall validity of the collected data.

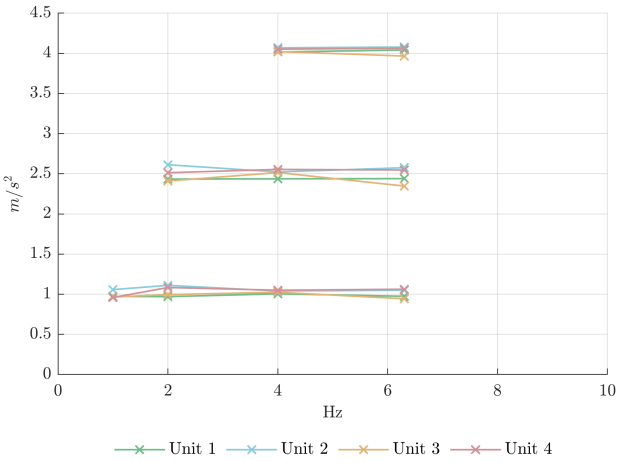


Figure 9. RMS values recorded by the smartwatches in Method 2.

According to ISO 8041:2007 [12], a smartwatch can be used for monitoring human movement and measuring hand-arm vibrations only if its frequency and amplitude response deviation remains within defined limits. These thresholds are defined as percentage-based limits, meaning that higher input amplitudes allow for a greater margin of error. They are set at 0.06 m/s² for an input of 1 m/s²; 0.15 m/s² for 2.5 m/s²; and 0.24 m/s² for an excitation of 4 m/s². Tables 1 through 4 present the absolute deviations of smartwatches relative to the reference sensor. Tests exceeding the limits defined by the standard are highlighted in red for clarity.

In Method 1, all smartwatches fully complied with the required specifications, showing deviations significantly below the established limits. The most notable discrepancies occurred with an input excitation of 4 m/s² at 4 Hz, with deviations of 0.05 m/s² in unit 1 and 0.06 m/s² in unit 3. However, these values fall well within the 0.24 m/s² limit and do not present any significant issue.

In most conducted, the deviations between the smartwatches and the reference sensor remained below 0.01 m/s², which corresponds to an error of less than 1% for all three input amplitudes. These results clearly demonstrate the high level of consistency and accuracy achieved by calibration Method 1 for hand-arm vibration measurements.

Focusing on Method 2, the deviations relative to the reference sensor remained within the permissible error margin in almost all cases, with only two exceptions. For the excitation of 1 m/s² at 2 Hz, units 2 and 4 showed errors of 0.09 m/s² and 0.08 m/s², respectively, slightly exceeding the 0.06 m/s² limit. However, considering that, using this method, a total of 36 tests were conducted across 4 smartwatches, and only 2 tests exceeded the established limit (representing less than 6% of the total tests), these discrepancies can be regarded as isolated incidents. Therefore, they do not compromise the overall reliability or effectiveness of the proposed method.

A comparison of the deviations between methods shows that, in most cases, the error is slightly greater in Method 2. This suggests that, while Method 2 provides reliable results, there is still potential to refine the methodology and achieve the level of accuracy demonstrated by Method 1.

Table 1. Absolute deviations of unit 1 relative to the reference sensor.

	1 m/s²		2,5 m/s²		4 m/s²	
	Method 1	Method 2	Method 1	Method 2	Method 1	Method 2
1 Hz		0,03				
2 Hz	0,01	0,03		0,07		
4 Hz	0,01	0,00	0,03	0,06	0,05	0,02
6,3 Hz	0,00	0,03	0,01	0,06	0,00	0,04
8 Hz	0,00		0,00		0,01	
10 Hz	0,00		0,00		0,01	

Table 2. Absolute deviations of unit 2 relative to the reference sensor.

	1 m/s²		2,5 m/s²		4 m/s²	
	Method 1	Method 2	Method 1	Method 2	Method 1	Method 2
1 Hz		0,06				
2 Hz	0,00	0,09		0,11		
4 Hz	0,00	0,04	0,03	0,02	0,00	0,07
6,3 Hz	0,02	0,05	0,00	0,08	0,00	0,08
8 Hz	0,00		0,00		0,02	
10 Hz	0,00		0,00		0,01	

Table 3. Absolute deviations of unit 3 relative to the reference sensor.

	1 m/s²		2,5 m/s²		4 m/s²	
	Method 1	Method 2	Method 1	Method 2	Method 1	Method 2
1 Hz		0,03				
2 Hz	0,01	0,00		0,09		
4 Hz	0,00	0,02	0,01	0,02	0,06	0,02
6,3 Hz	0,02	0,05	0,01	0,14	0,01	0,03
8 Hz	0,01		0,00		0,01	
10 Hz	0,00		0,01		0,01	

Table 4. Absolute deviations of unit 4 relative to the reference sensor.

	1 m/s²		2,5 m/s²		4 m/s²	
	Method 1	Method 2	Method 1	Method 2	Method 1	Method 2
1 Hz		0,04				
2 Hz	0,01	0,08		0,01		
4 Hz	0,00	0,05	0,01	0,05	0,01	0,05
6,3 Hz	0,00	0,06	0,00	0,05	0,01	0,06
8 Hz	0,00		0,01		0,02	
10 Hz	0,00		0,01		0,00	

4. DISCUSSION

This study assesses the performance of smartwatch accelerometers subjected to two distinct calibration procedures. The following analysis reviews the main results and identifies factors that may have contributed to any variations observed between the two methods.

The response obtained from the four smartwatches using Method 1 indicates that the deviations are minimal and can be considered negligible. This suggests that the behavior of the devices is highly precise and reliable within the tested frequency and amplitude range. Consequently, the devices do not introduce significant errors in their measurements relative to the excitations they are exposed to.

It is important to emphasize that Method 1 was validated in [5], thereby establishing it as the reference method for this study. Consequently, the outcomes derived from this approach are considered both reliable and accurate.

When analyzing Method 2, the deviations obtained by the tested devices are noticeably larger compared to those in Method 1. As concluded in the validated reference method, the performance of the smartwatches closely mirrors that of the reference accelerometer. Therefore, the errors observed in Method 2 are not attributable to the smartwatches' behavior itself. Instead, these discrepancies are more likely the result of errors inherent in the calibration process of this method. This suggests that improvements in the calibration procedure are necessary for Method 2 to achieve accuracy comparable to Method 1.

The differences observed in Method 2 can largely be attributed to the mounting procedure. Despite efforts to secure the devices as firmly as possible, the fixation method used was relatively rudimentary. This approach may have resulted in imperfect attachment of some smartwatches, causing slight displacements during the measurement process. These movements could have occurred not only along the Z-axis but also along the other two axes that were not considered in the analysis. These uncontrolled shifts in position may explain the variations in error observed among the different smartwatches, with some exhibiting more significant deviations related to the reference sensor.

The limitations associated with the manual fixation method suggest that a more precise, automated mounting system would be beneficial in future experiments to minimize these sources of error and improve the reliability of the results.

In addition to the calibration methodologies and mounting procedures, environmental factors could have also contributed to the observed variations between the two methods. Fluctuations in temperature and relative humidity, as well as vibrations in the surrounding environment may have influenced the measurements, particularly in Method 2, where the manual fixation may have been more susceptible to external disturbances. Future studies could address this by conducting tests in more controlled environments, where these factors are continuously monitored and regulated.

5. CONCLUSIONS

Smartwatches are increasingly utilized in applications such as healthcare or occupational risk assessment, where precision and reliability of data are critical. Consequently, a deeper understanding of the behavior of their inertial sensors is essential to accurately interpret the data they generate. For this purpose, this study presents a comparative analysis of two calibration methods used to characterize the frequency and amplitude response of the accelerometers embedded in four smartwatches of the same model.

Method 1 used a uniaxial vibration bench, which allows for individual sensor characterization, while Method 2 used a vibration platform that generates vibrations on a surface, allowing the simultaneous evaluation of multiple sensors. Method 1, previously validated, was established as the reference for evaluating sensor performance. As the goal is to calibrate multiple devices in the shortest time, this study, along with future research, focuses on refining Method 2 based on the comparison with Method 1.

In this research, only the Z-axis was analyzed. However, once the calibration method is optimized, the procedure should be extended to evaluate all three axes of the triaxial sensor, in order to fully characterize the smartwatch for acceleration measurement applications.

Since these smartwatches are used for collecting data related to human movement, it is essential to characterize their accelerometers within the amplitude and frequency ranges typical for these activities. These ranges include amplitudes up to 4 m/s² and frequencies up to 10 Hz. However, each calibration method has its own limitations in terms of excitation sources. Method 1 enables high-amplitude excitation at higher frequencies but is more restricted at lower frequencies. In contrast, Method 2 can generate larger excitation amplitudes at lower frequencies, but it is less effective at reaching higher frequencies.

The results from Method 1 showed that the smartwatches exhibited minimal deviations relative to the reference sensor, demonstrating their precise behavior under vibratory excitations. This suggests that the smartwatches' accelerometers can provide reliable measurements within the tested frequency and amplitude ranges, supporting their potential for high-precision human motion analysis.

Method 2 revealed larger deviations from the reference method, primarily due to limitations in the calibration

process. These discrepancies are not attributed to inherent issues with the smartwatches' sensors but are likely caused by the mounting procedure. The manual fixation of the devices may have caused uncontrolled movements during measurements, which contributed to the observed errors.

While these unwanted displacements did not significantly impact the overall accuracy and reliability of the method, they highlight the need for a more robust and automated mounting system to enhance the consistency of results. In future studies employing this calibration method, a more controlled mounting procedure will be adopted to minimize uncertainties and guarantee more repeatable measurements.

Additionally, environmental factors, such as temperature and vibrations, may also influence sensor performance and should be carefully considered in future evaluations.

In summary, the precise calibration of smartwatch accelerometers is crucial for their reliable application in human movement analysis and related fields. This study highlights the need to select a calibration method that optimizes both accuracy and efficiency. Future work will focus on refining the accelerometer characterization procedure to minimize uncertainties and, thereby, improve the reliability of inertial sensor measurements.

6. ACKNOWLEDGMENTS

Thanks to the Sociedad Española de Acústica (SEA) for funding this paper in recognition of achieving the highest academic record in the Master's Degree in Acoustic Engineering at the Universidad Politécnica de Madrid during the 2023/2024 academic year.

The authors also acknowledge to the *Earthquake Engineering: dynamics of soils and structures* research group of the Universidad Politécnica de Madrid for allowing us to conduct the experiments in their laboratories.

This study is part of the BIOCLITE research project PID2021-123708OB-I00, funded by MCIN/AEI/ 10.13039/501100011033/FEDER, EU.

7. REFERENCES

[1] Y. Bello and E. Figetakis, *IoT-based Wearables: A comprehensive Survey*. 2023.

[2] C. Polvorinos-Fernández *et al.*, "Evaluating Motor Symptoms in Parkinson's Disease Through Wearable Sensors: A Systematic Review of Digital Biomarkers," *Applied Sciences*, vol. 14, no. 22, doi: 10.3390/app142210189.

[3] D. Bravo and C. Rengifo, "Calibración de la Unidad de Medida Inercial de un Dispositivo Móvil," *Revista Mexicana de Física E,* vol. 21, pp. 1-6, 07/01 2024, doi: 10.31349/RevMexFisE.21.020215.

[4] Y. Li, J. Georgy, X. Niu, Q. Li, and N. El-Sheimy, "Autonomous Calibration of MEMS Gyros in Consumer Portable Devices," *IEEE Sensors Journal,* vol. 15, pp. 1-1, 07/01 2015, doi: 10.1109/JSEN.2015.2410756.

[5] L. F. Sigcha, I. Pavón, P. Arezes, N. Costa, G. Arcas, and J. M. Lopez Navarro, "Occupational Risk Prevention through Smartwatches: Precision and Uncertainty Effects of the Built-In Accelerometer," *Sensors,* vol. 18, 11/06 2018, doi: 10.3390/s18113805.

[6] J. A. B. Hernández, H. Alonso-Navarro, M. R. L. Piudo, and F. J. J. Jiménez, "Protocolo diagnóstico y terapéutico del temblor," *Medicine - Programa de Formación Médica Continuada Acreditado,* vol. 11, no. 74, pp. 4483-4486, 2015/03/01/ 2015, doi: https://doi.org/10.1016/j.med.2015.02.016.

[7] S. R. Hamner and S. L. Delp, "Muscle contributions to fore-aft and vertical body mass center accelerations over a range of running speeds," *Journal of Biomechanics,* vol. 46, no. 4, pp. 780-787, 2013/02/22/ 2013, doi: https://doi.org/10.1016/j.jbiomech.2012.11.024.

[8] M. Centeno-Cerrato, "Metodología para caracterizar sensores inerciales orientado al análisis de movimiento humano utilizando diferentes bancos de ensayo," Master's Degree in Acoustic Engineering *(Master's Thesis)*, Escuela Técnica Superior de Ingenieros Industriales & Escuela Técnica Superior de Ingenieros de Telecomunicación, Universidad Politécnica de Madrid, 2024.

[9] *ISO 16063-21:2003. Methods for the Calibration of Vibration and Shock Transducers-Part 21: Vibration Calibration by Comparison to a Reference Transducer*, ISO: Geneva, Switzerland, 2003.

[10] *ISO 266:1997. Acoustics-Preferred Frequencies*, ISO:Geneva, Switzerland, 1997.

[11] D. Rincón *et al.*, "Wristbands Containing Accelerometers for Objective Arm Swing Analysis in Patients with Parkinson's Disease," *Sensors,* vol. 20, p. 4339, 08/04 2020, doi: 10.3390/s20154339.

[12] *ISO 8041:2007. Human Response to Vibration-Measuring Instrumentation*, ISO:Geneva, Switzerland, 2007.

DOI:

Main theme: A06 Electro-Acoustics

Session A06.07 Active metamaterials

Chair(s): T. Bravo, H. Lissek, C. De Marqui Jr

DOI:

Main theme: A07 Flow Acoustics

Session A07.01 Flow acoustics - General

Chair(s): S. Becker, D. Ragni, R. Camussi

DOI: 10.61782/fa.2025.0242



FORUM ACUSTICUM
EURONOISE 2025

COMPARISON OF WAVEPACKET MODELS FOR SUPERSONIC TWIN JETS AGAINST NEAR-FIELD PRESSURE MEASUREMENTS

Iván Padilla-Montero[1*] **Daniel Rodríguez**[1] **Vincent Jaunet**[2]
Peter Jordan[2]
[1] ETSIAE - Universidad Politécnica de Madrid, 28040 Madrid, Spain
[2] Institut Pprime, CNRS - Université de Poitiers - ISAE - ENSMA, 86036 Poitiers, France

ABSTRACT

Plane-marching PSE wavepackets for a supersonic twin-jet operating at perfectly-expanded conditions are compared against near-field pressure measurements with the purpose of validating the modelling strategy. Two streamwise phased-microphone arrays distributed close to the external mixing-layer boundary of each jet are employed to obtain pressure measurements in the linear hydrodynamic fluctuation region. PM-PSE calculations are performed for the symmetric toroidal mode (mode SS0) based on a tailored twin-jet mean flow constructed via an analytical profile fitted from PIV measurements. Comparisons of the amplitude evolution in the streamwise direction for different frequencies reveal a very remarkable agreement between the SS0 PSE prediction and the symmetry-decomposed pressure signals, particularly when SPOD-filtered experimental measurements are considered. These results constitute a new validation of PM-PSE for modelling twin-jet wavepackets related to mixing noise.

Keywords: *jet noise, wavepackets, twin jets, supersonic*

1. INTRODUCTION

Twin-jet-powered aircraft and launch vehicles generate noise footprints with significant impact on both civil and military applications. The control of such systems at an aeroacoustic level requires a fundamental understanding of the noise-generation mechanisms in the turbulent flow. Under the knowledge gathered from the study of planar mixing layers and single round jets in the past decades [1], it is well established that the machinery of noise generation in turbulent shear flows is mainly powered by the large-scale coherent structures present in the flow [2–6], and that such structures can, in most cases, be predicted by linear stability theory in the form of what is commonly known as wavepackets [7]. On the modelling side, linear parabolized stability equations (PSE) have been found to deliver excellent wavepacket predictions for both subsonic and supersonic jets [8–10].

The existence wavepackets (and their significant role) in twin jets is expected by extension of the insights accumulated for single jets. In fact, late modelling efforts based on plane-marching PSE calculations [11, 12] have produced wavepacket models for twin jets that exhibit similar characteristics to those for single jets, but which no longer feature axisymmetric structures. However, experimental works aimed at their validation and characterization in twin-jet systems are recent and still very sparse, and mainly focused on the screech resonance phenomenon [13]. Following the need for experimental characterization of mixing-noise wavepackets in twin jets, in a recent work [14] we employ high-speed schlieren visualizations to educe coherent structures present in twin jets at perfectly-expanded conditions, and compare them against PM-PSE modes for validation purposes. While good agreement is found in terms of fluctuation structure, the comparison of PSE models with the schlieren images has inherent limitations due to the implicit line-of-sight integration: one of the symmetry planes of the system is inaccessible and the identification of the different oscillation modes (toroidal, flapping) is non-trivial. For this reason, the use of discrete-point experimental techniques

*Corresponding author: ivan.padilla@upm.es.
Copyright: ©2025 Iván Padilla Montero et al. This is an open-access article distributed under the terms of the Creative Commons Attribution 3.0 Unported License, which permits unrestricted use, distribution, and reproduction in any medium, provided the original author and source are credited.

such as microphone pressure measurements has also been recently considered as a complementary source of empirical data [15].

Using phased microphone arrays positioned just outside of the turbulent mixing layer, combined with cross-correlation techniques such as spectral proper orthogonal decomposition (SPOD), has proven effective to analyze coherent fluctuations in natural subsonic single jets [8, 9, 16–18]. By placing the microphones near the mixing-layer boundary, the measured pressure fluctuations mainly reflect linear irrotational components, with nonlinear perturbations linked to small-scale turbulent structures being, in turn, negligible. Applying SPOD to the phased measurements from multiple microphones enables the successful extraction of the wavepackets, which agree well with PSE predictions [9, 18]. In the case of supersonic jets, the use of the same idea to study mixing noise is virtually non-existent (mainly due to the ubiquity of screech), let alone its application to twin-jet configurations. Recently, we performed an experimental investigation [15] of near-field twin-jet pressure fluctuations employing an azimuthal array of microphones distributed following the mixing layer contours from RANS simulations. Although good agreement was obtained between the experimentally-determined amplitudes and the predicted wavepackets in a significant number of cases, the limitation of measuring one streamwise position at a time prevented the application of SPOD to filter the streamwise wavepacket structure.

The aim of this work is to provide a new quantitative validation of PM-PSE wavepacket models for supersonic twin jets against near-field pressure measurements obtained using a linear microphone array distributed in the streamwise direction, thus enabling the application of SPOD to educe the coherent information contained in the pressure signals. These comparisons complement the aforementioned quantitative analyses based on schlieren visualizations and on an azimuthal microphone array. The manuscript is organized as follows. Section 2 describes the twin-jet experimental apparatus and the adopted processing strategy, section 3 summarizes the numerical methodology employed for the calculation of PM-PSE wavepacket models, section 4 presents the results for the measured pressure signals and the comparison against the computed PM-PSE modes, and section 5 provides concluding remarks.

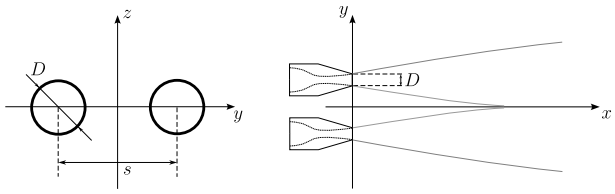


Figure 1. Sketch of the studied twin-jet configuration.



Figure 2. T200 experimental setup: (left) twin-jet system with linear microphone arrays installed; (right) twin-jet system with the 3D-printed part used for microphone positioning.

2. EXPERIMENTAL SETUP

The studied twin-jet configuration consists of two round convergent-divergent nozzles separated by a distance $s = 1.76D$ operating at perfectly-expanded conditions ($M_j = 1.54$), see Fig. 1. The jets are not isothermal and are subject to a total temperature equal to the ambient temperature ($T_0 = T_\infty = 300$ K).

The employed experimental setup is illustrated in Fig. 2, which is built on the T200 wind tunnel facility at Institut Pprime (Poitiers, France). Near-field pressure measurements are carried out using two symmetric streamwise arrays of microphones distributed near the outer mixing-layer boundaries of the twin-jet system. The microphones are located at the symmetry plane containing both jets (xy plane at $z = 0$), with 8 microphones mounted on each array. The left pic-

ture on Fig. 2 shows the microphone arrays mounted on the experimental model. The respective streamwise positions of the microphones on each array are $x/D = [0.5, 1, 1.5, 2, 3, 4, 5, 6]$. Their relative position with respect to the twin-jet mixing layers can be observed in Fig. 3.

A 3D-printed part designed using streamwise velocity contours of RANS calculations is employed for adjusting the position of each microphone (see the right picture in Fig. 2). The geometry of this part approximately follows the evolution of the mixing-layer boundary of the twin jet for the conditions under study, such that microphones located right at its surface would be placed in the desired near-field region. More details on the strategy employed for microphone positioning can be found in [15].

2.1 Processing of microphone signals

The symmetries of the twin-jet geometry can be exploited to decompose the microphone signals into symmetric and antisymmetric fluctuations. For the current experimental setup, the symmetry of the configuration across the xz plane allows the calculation of the following symmetry-decomposed pressure signals:

$$p_{0\mathrm{S}} = \frac{p_t + p_b}{2}, \quad p_{0\mathrm{A}} = \frac{p_t - p_b}{2}, \tag{1}$$

where p_t refers to those pressure signals measured by microphones located near the top mixing layer ($y > 0$) and p_b to those measured near the bottom mixing layer ($y < 0$).

The power spectral density (PSD) of each signal is calculated following Welch's method. First, the pressure fluctuation is obtained by removing the mean from the measured signal:

$$p'(t) = p(t) - \frac{1}{N}\sum_{i=1}^{N} p_i. \tag{2}$$

Then, the power spectral density is computed as:

$$P_{xx}(f) = \frac{1}{\Delta f N_b G_w}\sum_{j=1}^{N_b} |\hat{p}_j(f)|^2, \tag{3}$$

where $\hat{p}_j(f)$ denotes the windowed Fourier-transform of the pressure fluctuation signal for block j, expressed in terms of the fast Fourier transform (FFT) as:

$$\hat{p}_j(f) = \frac{1}{N_{\mathrm{FFT}}}\mathrm{FFT}[w(t)p'_j(t)], \tag{4}$$

where $w(t)$ is a window function and N_{FFT} denotes the block size. The quantity Δf is the frequency bin size, N_b denotes the total number of blocks, and G_w is the energy correction associated to the applied window function (a Hamming window in this case), defined by

$$G_w = \frac{1}{N_{\mathrm{FFT}}}\sum_{i=1}^{N_{\mathrm{FFT}}} w_i^2. \tag{5}$$

The pressure fluctuation signals are split into 487 blocks of 8192 samples each featuring a 50% overlap. The PSD results are converted to dB using the auditory threshold pressure ($p_{\mathrm{ref}} = 20$ µPa) as a reference, i.e. $P_{xx}\,[\mathrm{dB\ SPL}] = 10\log(P_{xx}/p_{\mathrm{ref}}^2)$.

Since all microphone signals are recorded at the same time and the twin-jet dynamics are assumed to be statistically stationary, the spatio-temporal coherence present in the data can be extracted via spectral proper orthogonal decomposition (SPOD). In this case, the SPOD eigenvalue problem takes the form [19]:

$$\mathbf{S}_k\mathbf{\Psi}_k = \mathbf{\Psi}_k\mathbf{\Lambda}_k, \tag{6}$$

where $\mathbf{S}_k$ is the 8×8 cross-spectral density tensor for the kth frequency, defined as:

$$\mathbf{S}_k = \frac{1}{\Delta f N_b G_w}\hat{\mathbf{Q}}_k\hat{\mathbf{Q}}_k^H, \tag{7}$$

with $\hat{\mathbf{Q}}_k$ being the matrix of frequency-domain realizations. $\mathbf{\Psi}_k$ is the matrix containing the eigenvectors for the kth frequency and $\mathbf{\Lambda}_k$ denotes the diagonal matrix containing the associated eigenvalues λ_i, which represent the PSD associated with the ith SPOD mode. The superscript H denotes the complex-conjugate transpose.

The same block size, overlap and window function used for the calculation of the PSD are employed for the SPOD. Since for the current analysis the number of blocks is much larger than the number of spatial points, the formulation of the SPOD problem given by equation (6) requires much less computational effort than the more typical snapshot method formulation [20].

3. NUMERICAL METHODOLOGY

3.1 Mean flow

In this work, the twin-jet mean flow is constructed from the linear superposition of two single-jet mean flows, usually known in previous investigations [11, 12] as a tailored

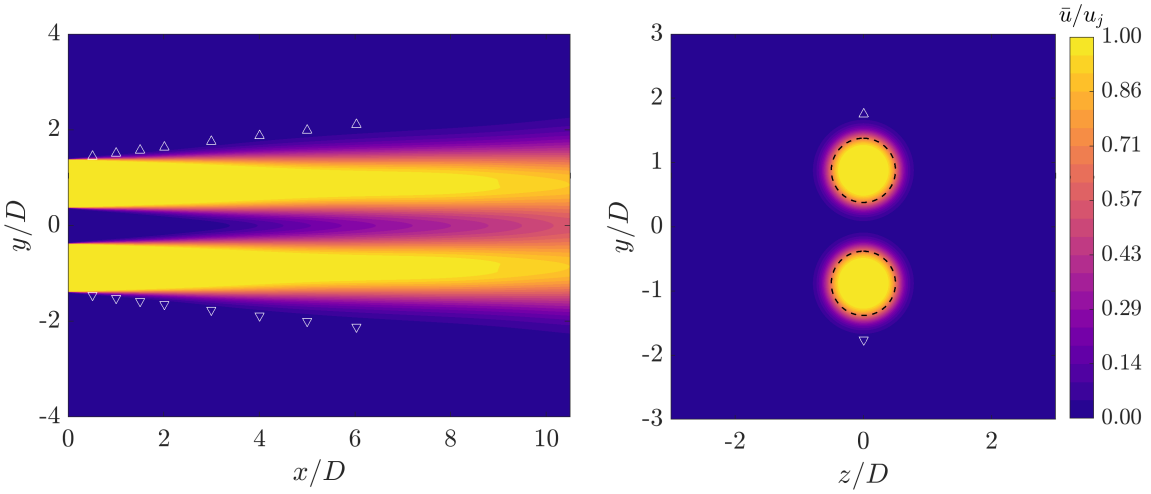


Figure 3. Contours of the tailored twin-jet mean flow employed for the PM-PSE calculations: (left) symmetry plane at $z = 0$; (right) cross-stream plane at $x/D = 3$. The white symbols illustrate the measurement position of the microphones with respect to the mean flow solution.

twin-jet model. The tailored twin-jet mean streamwise velocity component $\bar{u}$ is obtained as the sum (linear combination) of the streamwise velocity fields of two single jets with centers respectively located at $y = \pm s/2$. Here, the velocity components in the y and z directions are neglected. The mean temperature field of the twin jet is estimated from the constructed streamwise velocity field through the following Crocco-Busemann relation:

$$\frac{\bar{T}}{T_j} = \left[1 + \frac{\gamma - 1}{2} M_j^2 \left(1 - \frac{\bar{u}}{u_j}\right)\right] \frac{\bar{u}}{u_j} + \left(1 - \frac{\bar{u}}{u_j}\right) \frac{T_\infty}{T_j}, \tag{8}$$

where T_j and u_j refer to the isentropic jet-exit conditions fixed by M_j and T_0, while the mean density field is obtained from the perfect gas equation of state under the assumption of a constant static pressure field $\bar{p} = p_\infty = 10^5$ Pa.

To obtain the single-jet mean flow, an analytical profile based on the Gaussian function introduced by [21,22] is fitted to PIV measurements of the xy twin-jet symmetry plane. This profile has been used in recent studies of single jets [9] and twin jets [11, 12] with satisfactory results. It is defined as follows:

$$\bar{u}(x,r) = \begin{cases} \bar{u}_c(x), & r < R(x), \\ \bar{u}_c(x) \exp\left[-\dfrac{(r - R(x))^2}{\delta(x)^2}\right], & r \geq R(x), \end{cases} \tag{9}$$

where r denotes the radial coordinate. The parameters $\bar{u}_c$, R and δ respectively represent the mean streamwise velocity of the jet along the nozzle axis, the radial extent of the potential core and the thickness of the mixing layer, which are functions of the streamwise coordinate. These parameters are fitted from the PIV data using a cubic spline, similarly to [9, 12]. More details on the employed PIV measurements can be found in [23]. Although the PIV data corresponds to a twin-jet mean flow and therefore contains both the outer and inner shear layers of each jet, only the external mixing layer of one of the two jets is used for the estimation of $\delta(x)$.

Fig. 3 depicts contours of the tailored twin-jet mean flow obtained following the aforementioned procedure. The triangular symbols represent the position of the different microphones involved in the experimental pressure measurements, showing that they are placed right outside of the external mixing layer of each jet.

3.2 Wavepacket modelling via plane-marching PSE

Twin-jet wavepackets under perfectly-expanded conditions are modelled by means of linear plane-marching parabolized stability equations (PM-PSE). This extension of the classical PSE formulation accounts for mean flows featuring a strong inhomogeneity in two spatial directions, namely, the cross-stream planes in this case. Details on the employed PM-PSE formulation can be found in [11]. In brief, a perturbation ansatz of the following form is considered:

$$\hat{\mathbf{q}}_\omega(x,y,z) = A_\omega \tilde{\mathbf{q}}_\omega(x,y,z) \exp\left(\mathrm{i}\int_{x_0}^{x} \alpha_\omega(\xi)\mathrm{d}\xi\right), \tag{10}$$

where $\hat{\mathbf{q}}_\omega$ denotes the fluctuation at the angular frequency $\omega = 2\pi f$, which is split into a three-dimensional shape function with a slow evolution in the streamwise direction, given by $\tilde{\mathbf{q}}_\omega$, and a wave function featuring a rapid variation along x, given by the exponential term. A_ω represents the initial amplitude and $\alpha_\omega = \alpha_r + \mathrm{i}\alpha_i$ corresponds to the streamwise wavenumber, for which a slow variation with x is also assumed.

The substitution of (10) into the linearized Navier-Stokes equations, together with an order of magnitude analysis that neglects terms of order $1/Re^2$, yields a parabolized initial value problem that can be solved by marching in the streamwise direction.

4. RESULTS

4.1 Measured pressure spectra

The obtained PSD of the symmetry-decomposed pressure signals is displayed in Fig. 4, which shows maps of P_{xx} as a function of x and St for $p_{0\mathrm{S}}$ and $p_{0\mathrm{A}}$. These maps illustrate the range of frequencies at which mixing noise is dominant in the studied twin jet, namely $St \approx [0.1, 1]$. This is the range of interest for comparison against the wavepackets predicted by PM-PSE. As expected in the near-field region where hydrodynamic fluctuations remain important, the streamwise range of linear amplitude growth becomes shorter as the frequency is increased.

Both the symmetric and antisymmetric pressure signals reveal similar spectral signatures, indicating that both kinds of fluctuations are present and are equally important in the twin-jet system.

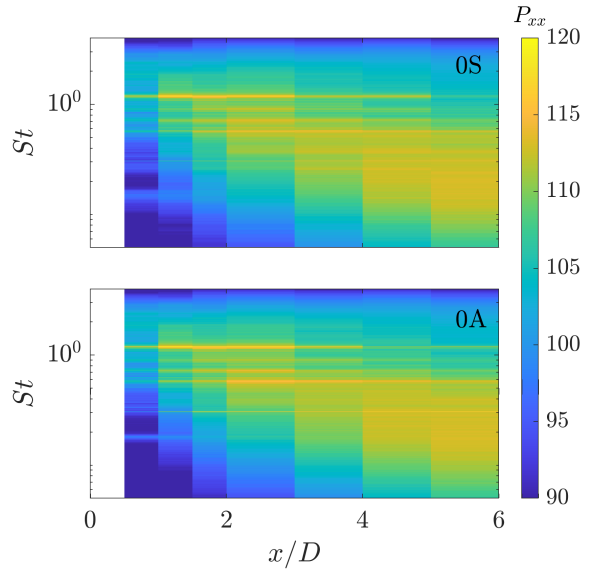


Figure 4. PSD (in [dB SPL/Hz]) of the symmetry-decomposed pressure signals ($p_{0\mathrm{S}}$ and $p_{0\mathrm{A}}$) as a function of x and St.

4.2 Comparison of modelled wavepackets against measured signals

The results presented herein focus on the comparison between the symmetric pressure signal $p_{0\mathrm{S}}$ and the PM-PSE mode SS0, which corresponds to a wavepacket that is symmetric with respect to both twin-jet symmetry planes and represents toroidal Kelvin-Helmholtz instabilities which are analogous to those of $m = 0$ modes in axisymmetric single jets. To illustrate its three-dimensional structure, Fig. 5 displays contours of the PM-PSE mode SS0 for $St = 0.7$ in two different cutplanes: the twin-jet symmetry plane at $z = 0$ and the cross-stream plane at $x/D = 3$. The ring-like structures are clearly visible in the cross-stream plane, which are not axisymmetric owing to the close spacing between the two jets. The fluctuation contours in the symmetry plane highlight the Mach-wave radiation associated with the wavepacket that is typical of mixing noise in supersonic jets. The relative position of the microphone probes with respect to the predicted wavepacket structure are indicated by the triangular symbols.

The initial amplitude of wavepackets calculated via linear stability theory is defined up to an arbitrary constant. For the purpose of comparison against experimen-

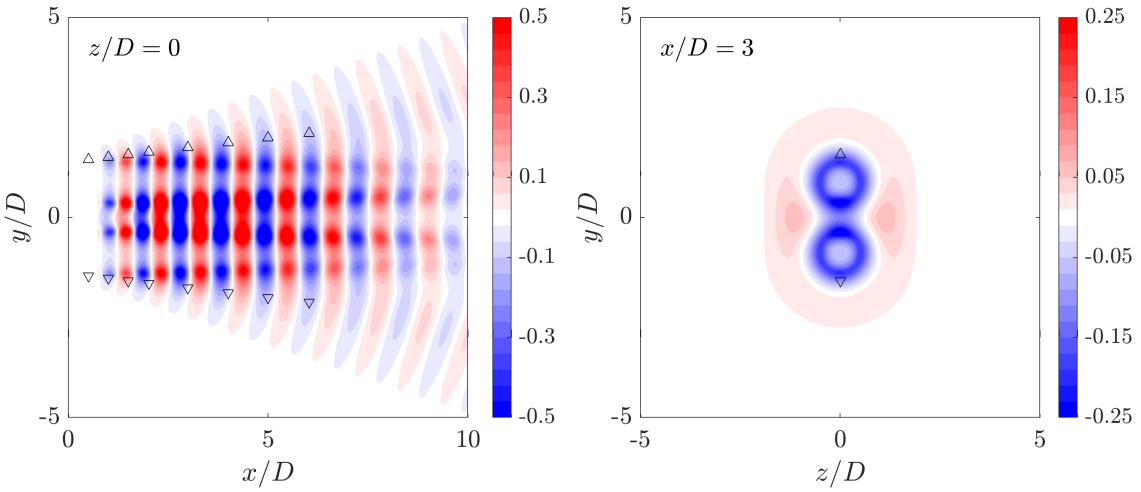


Figure 5. Contours of the real part of the pressure fluctuation for PM-PSE mode SS0 at $St = 0.7$: (left) symmetry plane at $z/D = 0$; (right) cross-stream plane at $x/D = 3$. The contours are normalized with respect to the maximum value of the real part of $\hat{p}$. The black symbols denote the measurement positions of the microphones.

tal measurements, the value of A_ω for a given PM-PSE mode at a given frequency is calibrated by means of a least squares fit to the amplitude of the measured pressure signals, resulting in the following estimation:

$$A_{\omega,p} = \frac{\sum_{j=1}^{N_{\text{mic}}} |\hat{p}_\omega(x_j, y_j, z_j)| \sqrt{P^j_{xx,\omega}}}{\sum_{j=1}^{N_{\text{mic}}} |\hat{p}_\omega(x_j, y_j, z_j)|^2}, \qquad (11)$$

where $\hat{p}_\omega(x_j, y_j, z_j)$ denotes the PM-PSE pressure fluctuation for frequency ω evaluated at the measurement position of microphone j, while $P^j_{xx,\omega}$ represents the PSD of the pressure signal measured by microphone j for frequency ω. This is also the approach followed by previous works on single jets (see e.g. [9]).

The comparison between the measured symmetric pressure signal and PM-PSE mode SS0 is presented in Fig. 6, which shows the evolution of the amplitude as a function of the streamwise coordinate for different frequencies spanning the previously identified range of interest. Two different sets of experimental data are included for each case, namely, the original symmetric pressure signal, marked with star symbols, and the first SPOD mode obtained from the SPOD-filtered symmetric pressure signal, marked with square symbols. Correspondingly, two different curves are represented for mode SS0: that with the initial amplitude calibrated with the original measurements (solid lines, labelled A_p), and that with the amplitude calibrated using the first SPOD mode extracted from the measurements (dashed line, labelled A_Ψ). Overall, a very good agreement is obtained between the PM-PSE wavepacket predictions and the experimental measurements for most of the studied frequencies. Except for the lowest frequency ($St = 0.1$), the match between the PM-PSE model and the measured amplitudes is significantly improved when the SPOD-filtered measurements are considered, especially near and downstream of the saturation point for higher frequencies.

These results suggest that, even though no azimuthal mode decomposition is applicable in the twin-jet case, and therefore the measured signals are expected to contain contributions from multiple modes, the SS0 wavepacket is one of the most dominant contributions to the dynamics of the system, since by itself it can represent the measured amplitude evolution with remarkable accuracy for most frequencies. This comparison constitutes a new quantitative validation of the ability of PM-PSE to model mixing-noise wavepackets in twin jets, which complements our previous quantitative comparisons based on the coherent structures educed from high-speed experimental measurements [14].

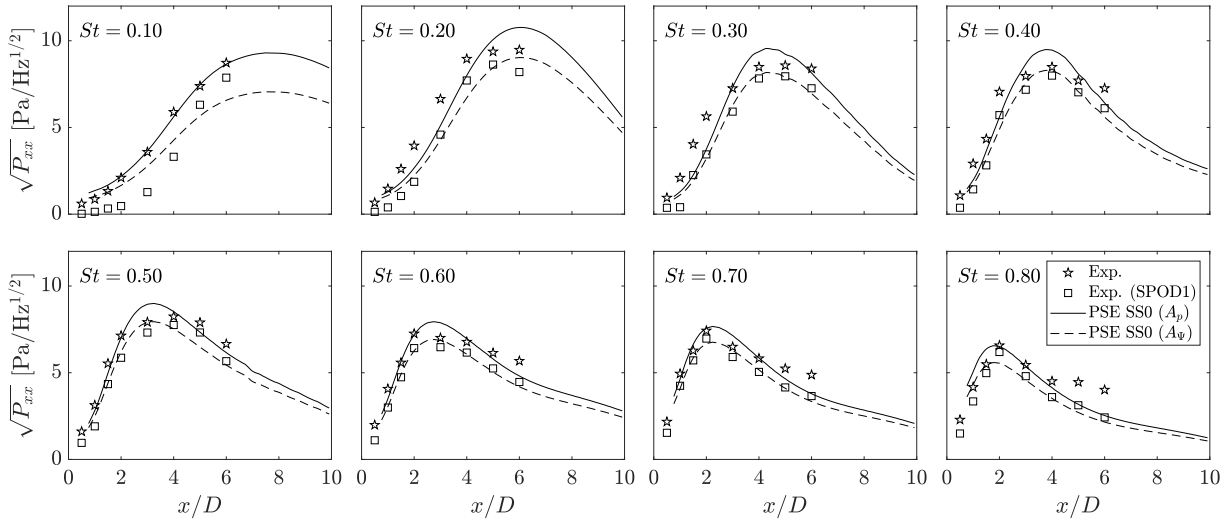


Figure 6. Amplitude comparison between the measured symmetric pressure signal (p_{0S}) and the PM-PSE wavepacket for mode SS0 as a function of the streamwise coordinate for different frequencies. The star symbols denote the experimental measurements; the squared symbols represent the first SPOD mode extracted from the experimental signals; the solid lines indicate the PM-PSE amplitude evolution calibrated directly with the experimental measurements (A_p); the dashed lines correspond to the PM-PSE amplitude evolution calibrated with the first SPOD mode of the experimental results (A_Ψ).

5. CONCLUSIONS

Wavepacket models for mixing noise in twin jets are still premature and require comparison against experimental measurements to assess their validity and accuracy. In this work, wavepackets predicted by plane-marching PSE for a supersonic twin jet operating at perfectly-expanded conditions have been compared against experimental pressure measurements in the near field.

Two streamwise arrays with 8 microphones each are employed to obtain phased measurements in the symmetry plane containing the two jets, with the microphones positioned right outside of the external mixing layer of each jet to target the linear region of the hydrodynamic fluctuation field. The spectral characteristics of the obtained measurements exhibit the desired features expected in the linear hydrodynamic regime and reveal the range of frequencies at which mixing noise is dominant ($St \approx [0.1, 1]$), which in turn guide the wavepacket modelling.

PM-PSE calculations are performed based on a tailored twin-jet mean flow obtained by fitting an analytical axisymmetric jet profile to PIV measurements of the twin jet system. The analysis focuses on the symmetric toroidal mode SS0, for which the predicted wavepackets feature three-dimensional Kelvin-Helmholtz instabilities which deviate from the familiar axisymmetric structures known from single jets.

The comparison between the amplitude of the symmetry-decomposed pressure measurements and the PM-PSE mode SS0 yields a very good agreement for most frequencies in the studied range, particularly when the SPOD-filtered pressure measurements are considered. The obtained results provide a new quantitative assessment of the capability of plane-marching PSE to model twin-jet wavepackets associated with mixing noise. Future work should involve the linear combination of multiple PM-PSE modes in the comparison, as well as the validation of antisymmetric fluctuations.

6. ACKNOWLEDGMENTS

This work has received funding from the EU's Horizon Europe programme under the Marie Skłodowska-Curie grant agreement no. 101063992 and from the Government of the Community of Madrid (V-PRICIT line 3).

7. REFERENCES

[1] P. Jordan and T. Colonius, "Wave Packets and Turbulent Jet Noise," *Annu. Rev. Fluid Mech.*, vol. 45, no. 1, pp. 173–195, 2013.

[2] S. Crow and F. Champagne, "Orderly structure in jet turbulence," *J. Fluid Mech.*, vol. 48, no. 3, pp. 547–591, 1971.

[3] D. Juvé, M. Sunyach, and G. Compte-Bellot, "Intermittency in the noise emission in subsonic cold jets," *J. Sound Vib.*, vol. 71, pp. 319–332, 1980.

[4] C. Tam, "Supersonic jet noise," *Annu. Rev. Fluid Mech.*, vol. 27, no. 1, pp. 17–43, 1995.

[5] A. V. G. Cavalieri, G. Daviller, P. Comte, P. Jordan, G. Tadmor, and Y. Gervais, "Using large eddy simulation to explore sound-source mechanisms in jets.," *J. Sound Vib.*, no. 330, pp. 4098–4113, 2011.

[6] A. Cavalieri, P. Jordan, T. Colonius, and Y. Gervais, "Axisymmetric superdirectivity in subsonic jets," *J. Fluid Mech.*, vol. 704, pp. 388–420, 2012.

[7] D. G. Crighton and M. Gaster, "Stability of slowly diverging jet flow," *J. Fluid Mech.*, vol. 77 (2), pp. 397–413, 1976.

[8] T. Suzuki and T. Colonius, "Instability waves in a subsonic round jet detected using a near-field phased microphone array," *J. Fluid Mech.*, vol. 565, pp. 197–226, 2006.

[9] K. Gudmundsson and T. Colonius, "Instability wave models for the near-field fluctuations of turbulent jets," *J. Fluid Mech.*, vol. 689, pp. 97–128, 2011.

[10] A. Sinha, D. Rodríguez, G. Brès, and T. Colonius, "Wavepacket models for supersonic jet noise," *J. Fluid Mech.*, vol. 742, pp. 71–95, 2014.

[11] D. Rodríguez, M. R. Jotkar, and E. M. Gennaro, "Wavepacket models for subsonic twin jets using 3D parabolized stability equations," *Comptes Rendus Mécanique*, vol. 346, pp. 890–902, oct 2018.

[12] D. Rodríguez, "Wavepacket models for supersonic twin-jets," in *AIAA AVIATION 2021 FORUM*, (Reston, Virginia), pp. 1–16, American Institute of Aeronautics and Astronautics, aug 2021.

[13] T. Y. Wong, M. N. Stavropoulos, J. R. Beekman, A. Towne, P. A. Nogueira, J. Weightman, and D. Edgington-Mitchell, "Steady and unsteady coupling in twin weakly underexpanded round jets," *J. Fluid Mech.*, vol. 964, pp. 1–43, 2023.

[14] I. Padilla-Montero, D. Rodriguez, V. Jaunet, and P. Jordan, "Experimental validation of pse wavepacket models for supersonic twin jets using schlieren imaging and potential-momentum-theory-based spod," *30th AIAA/CEAS Aeroacoustics Conference (2024)*, AIAA 2024-3146.

[15] I. Padilla-Montero, D. Rodriguez, V. Jaunet, S. Girard, D. Eysseric, and P. Jordan, "Pressure measurements at the mixing-layer boundary of supersonic twin jets," *30th AIAA/CEAS Aeroacoustics Conference (2024)*, AIAA 2024-3147.

[16] R. E. A. Arndt, D. F. Long, and M. N. Glauser, "The proper orthogonal decomposition of pressure fluctuations surrounding a turbulent jet," *J. Fluid Mech.*, vol. 340, pp. 1–33, 1997.

[17] C. E. Tinney and P. Jordan, "The near pressure field of co-axial subsonic jets," *J. Fluid Mech.*, vol. 611, pp. 175–204, 2008.

[18] D. E. S. Breakey, P. Jordan, A. V. G. Cavalieri, P. A. Nogueira, O. Léon, T. Colonius, and D. Rodríguez, "Experimental study of turbulent-jet wave packets and their acoustic efficiency," *Phys. Rev. Fluids.*, vol. 2, p. 124601, 2017.

[19] A. Towne, O. T. Schmidt, and T. Colonius, "Spectral proper orthogonal decomposition and its relationship to dynamic mode decomposition and resolvent analysis," *J. Fluid Mech.*, vol. 847, pp. 821–867, jul 2018.

[20] L. Sirovich, "Chaotic dynamics of coherent structures. parts i-iii," *Quarterly of Applied Math.*, vol. XLV, no. 3, pp. 561–582, 1987.

[21] T. R. Troutt and D. K. McLaughlin, "Experiments on the flow and acoustic properties of a moderate Reynolds number supersonic jet," *J. Fluid Mech.*, vol. 116, pp. 123–156, 1982.

[22] C. Tam and D. Burton, "Sound generated by instability waves of supersonic flows. Part 2. Axisymmetric jets.," *J. Fluid Mech.*, vol. 138, pp. 273–295, 1984.

[23] I. Padilla-Montero, D. Rodríguez, V. Jaunet, S. Girard, D. Eysseric, and P. Jordan, "Mean flow and linear stability analysis of twin supersonic jets," *AIAA Aviation Forum 2023, June 12-16, 2023, San Diego, CA, AIAA Paper 2023-3350*, 2023.

DOI: 10.61782/fa.2025.0545



FORUM ACUSTICUM
EURONOISE 2025

MATCHING PURSUIT DECOMPOSITION OF JET NEAR-FIELD PRESSURE DATA

Roberto Camussi[1*] **Matteo Mancinelli**[1] **Elisa de Paola**[1]

[1] Department of Civil, Computer Science and Aeronautical Technology Engineering, University Roma Tre, Via della Vasca Navale 79, 00146 Roma, Italy

ABSTRACT

The Matching Pursuit (MP) decomposition is applied to an extensive set of pressure data obtained in experiments carried out in two distinct laboratories, at the University Roma Tre and at the École Centrale de Lyon. Both data sets contain pressure signals measured simultaneously in the near and in the far-field of free stream compressible circular jets of different diameters and different subsonic Mach numbers. The MP method provides a decomposition of the pressure time series into a linear combination of waveforms selected from a dictionary composed of Gabor atoms. A subset of these waveforms is chosen to provide a Reduced Order Model of the original pressure signals that matches at best the energy content at the frequencies of interest. It is demonstrated that the reconstructed signals preserve significant features related to the near-field hydrodynamic pressure field and the far-field noise generation mechanisms. Additionally, it is shown that relevant statistical properties are universal and can serve as a valuable foundation for future modeling.

Keywords: *Reduced Order Modeling, Jet Noise, Matching Pursuit*

[*] ***Corresponding author***: *roberto.camussi@uniroma3.it*
Copyright: *©2025 First author et al. This is an open-access article distributed under the terms of the Creative Commons Attribution 3.0 Unported License, which permits unrestricted use, distribution, and reproduction in any medium, provided the original author and source are credited.*

1. INTRODUCTION

The far-field noise in compressible jets arises from the high-speed flow exiting the jet, which is inherently unsteady and spatially random. In fact, acoustic analogies that model pressure wave radiation in subsonic jets identify the turbulent flow—represented by the Reynolds stress tensor—as the primary source of noise [1]. According to this view, experiments targeted to characterize the jet noise sources, necessities the measurement and processing of non-deterministic signals characterized by time-localized events and time-varying frequency content. To this extent, the application of Time-Frequency decomposition techniques is crucial to overcome the limitations of standard Fourier analysis that is not well-suited for extracting time-localized features.

In the present approach, to the purpose of analyzing efficiently complex signals with time varying characteristics, we propose the use of the Matching Pursuit (MP) method, a technique that has not been used extensively in aeracoustics so far, except for a few applications for beamforming analyses [2] and [3]. The MP procedure provides the decomposition of a given signal (time series) into a linear combination of waveforms taken from a predefined set of functions called Dictionary. The algorithm selects the best basis, not necessarily orthogonal, that efficiently approximates the signal of interest overcoming the limitations of other more traditional approaches, such as the Short Time Fourier Transform, or the Wavelet Transform.

The objective of this work is to demonstrate the method's capability to provide a reliable reduced order modeling of jet noise data while preserving relevant physical properties related to both the evolution of near-field

pressure and its correlation with the far field. Additionally, potential advancements in jet noise modeling are outlined, along with examples of statistical outcomes that highlight universal features.

2. THE PROCESSING METHOD AND THE EXPERIMENTAL DATABASE

The main features of the MP technique are briefly worked out in the following, while details can be found in the literature. This method has been introduced by Mallat & Zhang [4] and has been successively applied for the analysis of temporal signals or images in several fields out of aeroacoustics or aerodynamics (e.g. [5-7]). The MP decomposition provides an optimal non-linear approximation of a signal by adaptively choosing the proper basis depending on the signal nature. The basic idea is to construct an optimal basis, not necessarily orthogonal, that approximates efficiently the signal of interest. The MP algorithm iteratively constructs an approximation by selecting a set of elementary waveforms, called *atoms*, chosen from an over-complete set of functions, called Dictionary, such that they represent at the best the inherent signal features. To the purpose of the present application, the dictionary is composed of Gabor atoms that provide optimal joint time–frequency localization. The Gabor dictionary indeed contains functions obtained by the combination of a Gaussian envelope of variable time location and extension, with a cosine function of variable frequency. The extraction of the atoms is based on an iterative process that maximizes the correlation between the signal reconstructed through the combination of the atoms and the original signal. We remind to the literature for the details on the procedure and the implementation of the algorithm.

In the present analysis, the MP processing procedure has been applied to two distinct data sets obtained in experiments carried out in two different facilities, hereinafter denoted as ECL and UR3.

The experimental database ECL consists of near and far-field pressure signals synchronously measured in the anechoic wind tunnel of the Laboratoire de Mecanique des Fluides et d'Acoustique (LMFA) of the Ecole Centrale de Lyon. The setup provided near field pressure measurements using a linear array of microphones and far-field pressure measurements through a microphone array displaced on a circular arc. Details about the experimental setup can be found in [8].

The experiment denoted as UR3, has been carried out in the semi-anechoic chamber available at the Laboratory of Fluid Dynamic "G. Guj" of the University Roma Tre of Rome. Also in this case near field measurements have been carried out through a linear array of microphones whereas only one microphone was located in the far field. Details about this second setup are given in [9].

We underline that in both experiments the Mach numbers were subsonic and varied between M=0.6 and M=0.9. On the other hand, the jet diameters in the two experiments were significantly different therefore corresponding to different Reynolds numbers.

3. RESULTS

As pointed out above, the Dictionary used in the present analyses is composed of Gabor atoms obtained by a combination of a trigonometric function with a Gaussian envelope. Figure 1 reports examples of those atoms corresponding to different scales. It is pointed out that the minimum and maximum time-scales are selected in order to be compatible with the frequency range of interest for the present applications.

An example of a signal reconstructed through the combinations of atoms selected from the Dictionary is given in Figure 2. It is shown that the reconstructed signal consists of a few selected atoms randomly distributed in time (thus with a random phase), having different frequencies and amplitudes. Indeed, to the purpose of providing a reduced order modeling of the measured pressure signals, in the present analysis the reconstruction is accomplished using only a few thousand atoms. It is also important to point out that the frequency, amplitude, and timing of the selected atoms are not predetermined, but rather derived as outputs of the MP algorithm. In this sense the MP method is considered an *adaptive* approach.

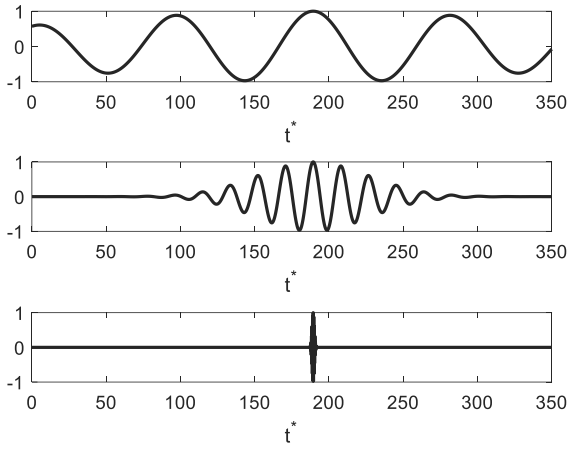


Figure 1. Examples of Gabor functions composing the Dictionary. Amplitudes are normalized in order to vary between -1 and 1.

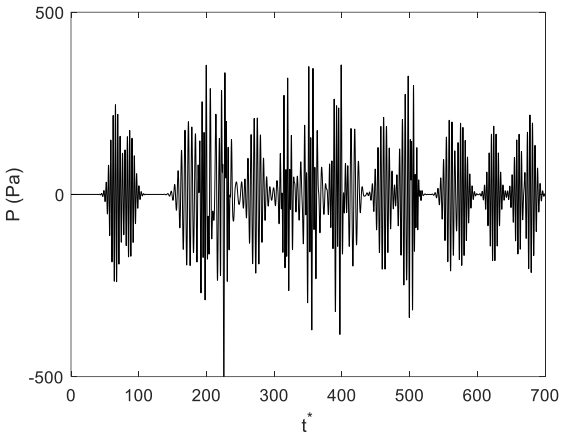


Figure 2. Examples of signal reconstruction. The case reported refers to the UR3 experiment at M=0.7 and x/D=2.

The adaptive nature of the algorithm is demonstrated by the spectral content of the reconstructed signals. An example is given in Figure 3 along with the spectrum of the original signal. The two spectra look very similar in the region where an energy bump related to the Kelvin-Helmholtz (K-H) instability mechanisms, is present. According to the nature of the algorithm, a greater number of atoms results in a more accurate reconstruction of the original signal. However, this analysis demonstrates that a limited number of atoms can still yield a satisfactory reproduction of the signal, particularly within the frequency range that is of primary interest from a physical perspective.

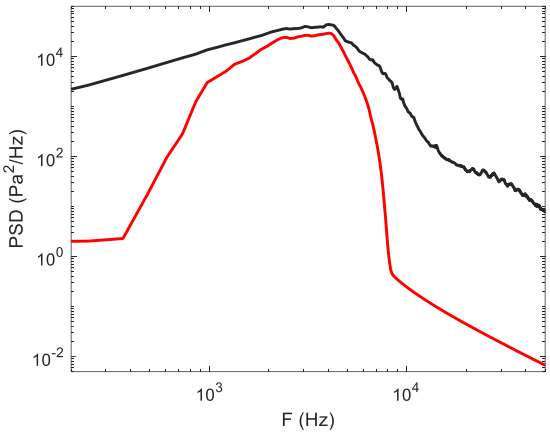


Figure 3. Examples of PSD of the original (black) and reconstructed signal (red). Same case as Figure 2.

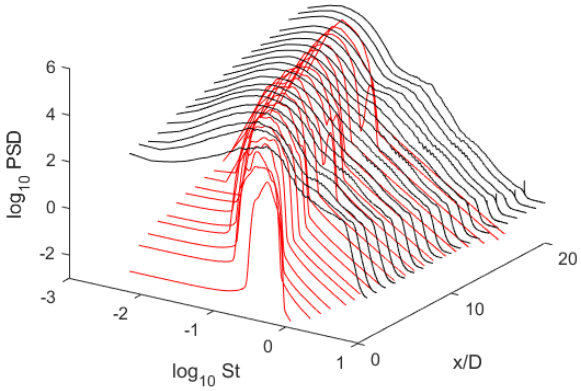


Figure 4. Fourier auto-spectra of the original (black curves) and reconstructed (red curves) signals. Data refers to the UR3 database at M=0.9.

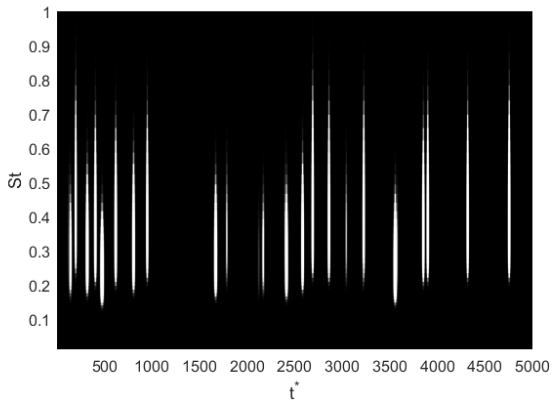


Figure 5. Modulus of the Wavelet Cross-Spectrum between near-field reconstructed signals at x/D=1 and x/D=3. Data refers to the ECL database at M=0.9.

The capability of the method to preserve the physical properties of the original pressure field is examined by analyzing the evolution of atoms in the near field and their correlation with the far field.

The evolution of the auto-spectra in the streamwise direction is examined and examples are reported in Figure 4. It is shown that even though more narrow-banded, the spectra of the reconstructed signals reproduce correctly the energy content of the original signals in the region corresponding to the K-H instability frequency. The reconstruction is satisfactory not only in terms of amplitude but also in terms of its evolutionary behavior along x/D. Similar results are obtained in all the other cases and not reported here for brevity.

Another way to assess the physical significance of the extracted atoms is to verify their *convective* nature, that is to verify whether their trace is presented over different distances from the jet exit. Indeed, atoms that are artifacts generated by the algorithm should not exhibit any coherence in the streamwise direction. Due to the local nature of the atoms in the time frequency domain, the only way to extract a localized coherence is to compute the Wavelet Cross Spectrum (WCS) and an example is reported in Figure 5. The WCS is obtained using a consolidated algorithm [10] and the example reported refers to near-field microphones separated by a distance of 2D. The trace of the atoms is clearly visible (white stripes) showing that most of them are physically correct and are not artifacts generated by the algorithm. It has been checked that the percentage of atoms showing zero correlation length, and thus originated by spurious effects of the algorithm, is less than 10%.

In order to maximize the reliability of the results, all the reconstructed signals are distilled from the spurious atoms and only those showing a non-zero coherence over a distance of at least two diameters are preserved.

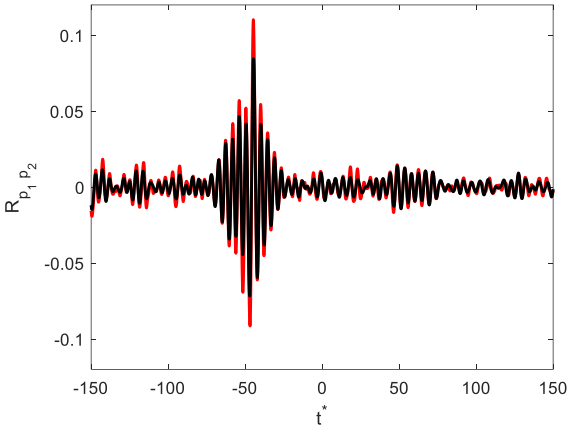


Figure 6. Examples of near- far-field cross-correlations of the original (red) and reconstructed signal (black). Same case as Figure 4.

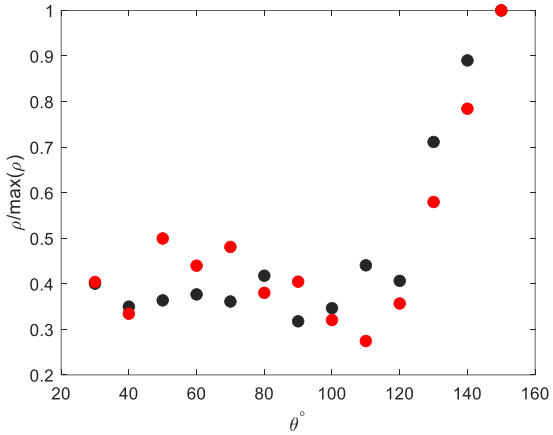


Figure 7. Normalized cross-correlation maxima computed between a near-field microphone located at x/D=1 and all the microphones in the far-field. Black dots refer to the original signals, red dots to the reconstructed ones. The analysis refers to the ECL database at M=0.9.

The set of reconstructed near field pressure time series are correlated with the far field signals in order to verify their

connection with the radiated noise. An example of correlations obtained from the UR3 database is given in Figure 6. The original and reconstructed signals exhibit a very similar behavior both in terms of amplitude and in terms of the time location of the correlation maxima. This time delay, when converted to space using the speed of sound, reproduce exactly the distance between the near field and the far field microphone.

The ECL database allowed us to better clarify the correlation between near and far field microphones thanks to the availability of a polar arc in the far field. In order to characterize the directivity patterns, correlations between near field microphones and all the far field sensors have been computed. To this purpose, the normalized amplitudes of the correlation maxima have been extracted. Results obtained at M=0.9 are reported in Figure 7 and 8 considering a reference near-field microphone located within the jet potential core and in the turbulent region, respectively. A normalization has been employed in both cases to emphasize the dependency upon the polar angles rather than the differences in amplitudes, which are inevitably significant due to the limited number of atoms used to reconstruct the signals.

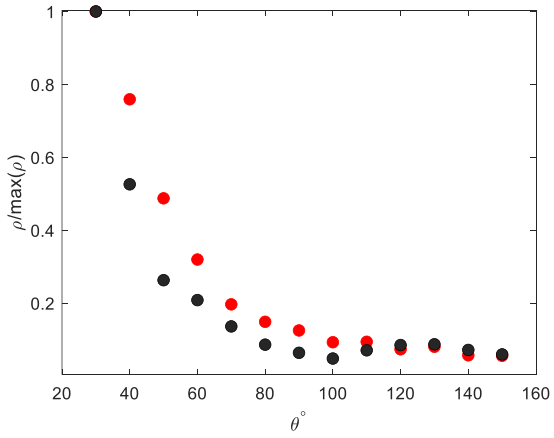


Figure 8. Same as Figure 5 but considering a near-field microphone at x/D=8.

The amplitudes are normalized with respect to the one exhibiting the maximum correlations. As expected, for the microphone located close to the jet exit (Figure 7) the maximum directivity is achieved at around 150° and the trend is very similar for the original and reconstructed cases. When the far field is correlated with a near-field microphone located far from the jet exit, the trend completely changes and the maximum correlation corresponds to very small angles. This is shown in Figure 8 where, again, reconstructed and original cases exhibit very simal behaviors.

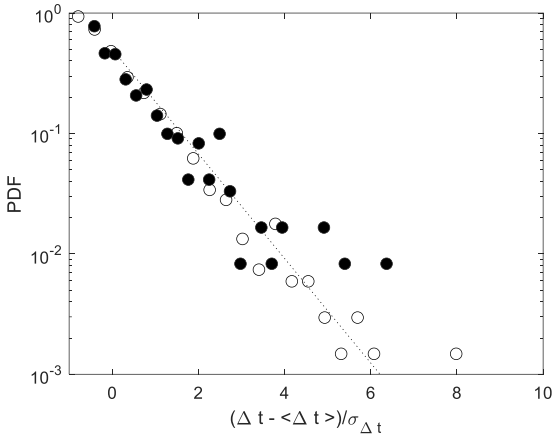


Figure 9. PDFs of the waiting time computed from the UR3 (empty symbols) and the ECL (full symbols) datasets. Both cases are referred to M=0.9 and x/D=3.

The results presented thus far highlight the physical significance of the reconstructed signals, as they accurately reproduce the near-field pressure properties and exhibit proper correlation with the far-field pressure, thereby maintaining the connection with the radiated noise.

The temporal behavior of the extracted waveforms is further explored by extracting the statistics of the time delay between successive atoms. This quantity is often denoted as the waiting time and its statistics is connected with intermittency, an intrinsic property of the turbulent flow. The analysis provides the Probability Distribution Functions (PDF) reported in the so-called reduced form, i.e. by subtracting the mean value from the analyzed random variable and dividing by the standard deviation. Examples are given in Figures 10 where explanatory results obtained in the two experiments are reported. According to the larger number of acquired samples, a better statistical convergence is achieved from the UR3 database but a very good agreement among the normalized PDFs is observed in all cases. For the cases reported, the PDFs exhibit a pure exponential decay, and the exponential fit reported in the figures is very simple, its analytical expression being $F(x) = 0.5\, e^{-x}$.

The same result has been obtained from all the other cases confirming that the time of appearance of the atoms follows a universal statistics.

This universal form of the PDF, together with other statistical properties of the waveforms, can be used to set up a model for reproducing the jet dynamics responsible for the noise emission. This task remains an objective for future studies currently being conducted by the authors, and preliminary results will be presented at the conference.

4. CONCLUSIONS

The MP procedure has been applied to a comprehensive database comprising pressure signals from two distinct laboratory experiments. Both experiments provide pressure signals in the near and far field of circular compressible jets operating at subsonic Mach numbers. The main outcomes obtained can be summarized as follows:

- The MP procedure offers a reduced-order representation of the original signals by reconstructing them through the superposition of a limited number of Gabor atoms extracted from a specified dictionary.
- The overall properties of the near-field pressure are correctly preserved by the reconstructed field. The modelled signals reproduce correctly different features: the energy contained by the pressure spectra around the Kelvin-Helmholtz frequency; the spectra evolution along the streamwise direction; the convective nature of the selected atoms.
- The correlation between near and far field signals is preserved. According to the expected behavior, the reconstructed signals close to the jet exit exhibit good correlations with far field microphones at aft angles. Also, the measured time delay is in line with the distance between the near and far microphones.
- The statistics of the waiting time between successive atoms are universal, supporting the notion of using the reduced-order representation of the signals as potential components for developing predictive models of jet noise.

We emphasize that the similarity of the results obtained across various configurations demonstrates their independence from flow conditions and, more importantly, from the experimental facility. This outcome represents the basis for setting up a reliable model of the atoms' properties that can be used for jet noise predictions. Further studies on this aspect are currently underway by the authors and, hopefully, will be available by the time of the conference.

5. ACKNOWLEDGMENTS

T. Castelain of the Ecole Central de Lyon, is sincerely acknowledged for providing access to the experimental database named ECL.

6. REFERENCES

[1] Lighthill, M. J., & Newman, M. H. A. (1952). On sound generated aerodynamically I. General theory. *Proceedings of the Royal Society of London. Series A. Mathematical and Physical Sciences*, *211*(1107), 564–587.

[2] Bergh, T. F. (2019). Deconvolution approach to the mapping of acoustic sources with matching pursuit and matrix factorization. *Journal of Sound and Vibration*, *459*, 114842.

[3] Padois, T., & Berry, A. (2015). Orthogonal matching pursuit applied to the deconvolution approach for the mapping of acoustic sources inverse problem. *J. Acoust. Soc. Am.*, *138*(6), 3678–3685.

[4] Mallat, S. G., & Zhang, Z. (1993). Matching Pursuits With Time-Frequency Dictionaries. *IEEE Transactions on Signal Processing*, *41*, 3397–3415.

[5] Ray, S., Crone, N. E., Niebur, E., Franaszczuk, P. J., & Hsiao, S. S. (2008). Neural Correlates of High-Gamma Oscillations (60–200 Hz) in Macaque Local Field Potentials and Their Potential Implications in Electrocorticography. *The Journal of Neuroscience*, *28*, 11526–11536.

[6] Kuś, R., Różański, T., & Durka, P. J. (2013). Multivariate matching pursuit in optimal Gabor dictionaries: theory and software with interface for EEG/MEG via Svarog. *Biomedical Engineering Online*, *12*(1), 94.

[7] Jabbari, S., & Ghassemian, H. (2011). Modeling of heart systolic murmurs based on multivariate matching pursuit for diagnosis of valvular disorders. *Computers in Biology and Medicine*, *41*, 802–811.

[8] Mancinelli, M., Pagliaroli, T., Di Marco, A., Camussi, R., & Castelain, T. (2017). Wavelet decomposition of hydrodynamic and acoustic

pressures in the near field of the jet. *Journal of Fluid Mechanics, 813*, 716–749.

[9] Camussi R., Mancinelli M. and Di Marco A., Intermittency and stochastic modeling of hydrodynamic pressure fluctuations in the near field of compressible jets International Journal of Heat and Fluid Flow 68, 180–188 (2017)

[10] Torrence, C. and Compo, G. P. 1998 A practical guide to wavelet analysis. Bull Am. Met. Soc. 79, 61–78.

DOI: 10.61782/fa.2025.0457

FORUM ACUSTICUM EURONOISE 2025

IMPACT OF THE NOZZLE EXHAUST TEMPERATURE ON THE NEAR-FIELD NOISE EMITTED BY SUBSONIC JETS

Stefano Meloni[1*] **Giorgio Palma**[2]
Roberto Camussi[3] **Christophe Bogey**[4]
[1] University of Tuscia, 01100 Viterbo, VT, Italy
[2] CNR-INM, National Research Council-Institute of Marine Engineering, 00128 Roma, Italy
[3] Roma Tre University, 00146 Roma, RM, Italy
[3] Laboratoire de Mécanique des Fluides et d'Acoustique, LMFA, UMR 5509, 69130 Ecully, France

ABSTRACT

This study provides an analysis of the impact of temperature on the near pressure field of three subsonic jets, using data from well-resolved compressible Large-Eddy Simulations. The jets have nozzle-exit temperatures equal to 1, 1.5, and 2.25 times the ambient temperature, an acoustic Mach number of $M_a = 0.9$ and a Reynolds number of $Re_D = 10^5$. Pressure time series were extracted from several virtual probes distributed in the near field of the jets, covering a region extending up to 20 jet diameters in the streamwise direction and 3 jet diameters radially, repeating this planar distribution across different azimuthal angles. The data were analyzed in both the Fourier and Wavelet domains, facilitating simultaneous representation in the time-frequency domain. The analysis focused on evaluating the influence of nozzle exhaust temperature on pressure fluctuations in the near field of the single-stream jets. In addition, a wavelet-based acoustic decomposition technique was applied to assess the effects of nozzle exit temperature on both the acoustic and hydrodynamic pressure fields. The parameters of a wave-packet model for subsonic jet noise were finally analyzed and systematically optimized.

*__Corresponding author__: *stefano.meloni@unitus.it.*
__Copyright__: *©2025 Stefano Meloni et al. This is an open-access article distributed under the terms of the Creative Commons Attribution 3.0 Unported License, which permits unrestricted use, distribution, and reproduction in any medium, provided the original author and source are credited.*

1. INTRODUCTION

The noise generated by high-speed turbulent jets remains a critical challenge in the design of modern civil aircraft, particularly during take-off when engine thrust is maximized. Since Lighthill's pioneering formulation of aeroacoustic theory [1], extensive research has sought to unravel the physical mechanisms through which turbulent jet flows produce sound. Seminal contributions by [2, 3], and [4], among others, have established that coherent turbulent structures within the jet shear layer act as primary noise sources. Recent advances in modeling, particularly through wavepacket-based approaches and linear stability analysis, have significantly improved the predictions of jet noise radiation. Studies such as those by [5,6], and [7,8] demonstrate the efficiency of these frameworks in linking hydrodynamic instabilities to far-field acoustics.

Despite these advancements, the existing models often rely on simplifications, such as assuming steady base flows, neglecting temperature variations, or linearizing sound propagation that limit their applicability to idealized configurations. While analytical studies such as those of Kam et al. [9] and the experimental analysis by Vishwanathan [10] have explored heated jets, most numerical and experimental efforts focus on jets at ambient temperatures, leaving

a gap in understanding how elevated exhaust temperatures, typical of aeronautical engines, influence noise generation and propagation.

This work addresses these limitations by investigating the generation of acoustic waves in high-speed turbulent jets with temperature ratios ranging from 1 to 2.25 relative to ambient conditions. The jets have an acoustic Mach number of 0.9 and are highly disturbed at the nozzle exit. They have been computed using compressible Large-Eddy Simulations (LES). The LES datasets allow for a comprehensive analysis of both acoustic and hydrodynamic fields through a combination of Fourier and wavelet-based techniques. A wavelet-based acoustic decomposition method [11, 12] is applied to the jet near pressure field to highlight the effects of temperature on jet noise radiation.

Furthermore, this study systematically optimizes the parameters of a wavepacket noise prediction model, based on the methodology of [7,8]. Although earlier work demonstrated strong agreement with experimental data for cold subsonic jets, the extension to heated flows presented here aims to increase the fidelity of the model.

Details on the numerical setup and the wavelet-based processing procedure are given in Sections II and III, respectively. The main results are reported in Section IV while concluding remarks are given in Section V.

2. NUMERICAL SETUP

The LES simulations were performed by solving the three-dimensional compressible Navier-Stokes equations in cylindrical coordinates, using low-dissipation and low-dispersion explicit schemes [13]. The computational grid extends up to $x/D = 20$ in the axial direction and up to $r/D = 7.5$ in the radial direction, where D if the jet nozzle diameter.

For this analysis, we considered three jets with nozzle exhaust temperatures $T = T_a$, $T = 1.5T_a$, and $T = 2.25T_a$, where T_a is the ambient temperature. The jet acoustic Mach number are fixed at $M_a = 0.9$, resulting in jet Mach numbers decreasing with the nozzle-exhaust temperature. The jet Reynolds number is equal to 10^5 in all cases. Finally, the turbulence levels at the nozzle exit has been fixed to $TI = 9\%$ by tripping the boundary layers inside the nozzle.

More information on the LES and properties of the jet flow and acoustic fields can be found in previous papers [13, 14]

3. POST-PROCESSING PROCEDURE

3.1 Wavelet-based analysis

The data processing relies on separating the acoustic component of the pressure signals from the hydrodynamic counterpart. This goal is achieved by applying the procedure proposed by [15] and [11, 12, 16] that is briefly worked out in what follows.

The method is based on the wavelet transform of pressure signals and an appropriate filtering of the resulting wavelet coefficients. It is known that the wavelet transform performs well in identifying and isolating intermittent or time-dependent features. For a pressure time series $p(t)$, the wavelet transform can be formally represented by the following expression [17–21]:

$$w(s,t) = C_\psi^{-\frac{1}{2}} s^{-\frac{1}{2}} \int_{-\infty}^{\infty} p(\tau)\psi^*\left(\frac{t-\tau}{s}\right)d\tau, \quad (1)$$

where s is the wavelet scale, τ is a time shift, $C_\psi^{-\frac{1}{2}}$ is a constant that takes into account the mean value of $\psi(t)$ and $\psi^*\left(\frac{t-\tau}{s}\right)$ is the complex conjugate of the dilated and translated mother wavelet $\psi(t)$.

To perform the acoustic/hydrodynamic separation, the wavelet coefficients can be separated by assuming that the hydrodynamic contribution, being related to localized eddy structures, compresses well onto the wavelet basis so that it originates, in the transformed domain, few but with large amplitude wavelet coefficients [11,12]. Thus, the so-called pseudo-sound (i.e., the hydrodynamic component of pressure fluctuations) can be extracted by selecting

the wavelet coefficients exceeding a proper threshold. In the present approach, the threshold is identified through the so-called WT3 technique. The procedure is based on an iterative process originally developed for signal denoising [22] and then applied to the analysis of coherent structures in turbulence [23]. Details about the procedure have been reported in [11]

Specifically, the chosen method is based on single-point statistics. Thus it does not require any additional signals taken from other virtual probes. Furthermore it has been applied successfully also to configurations out of jet noise (e.g. [24–26]). In the present approach, the application of the decomposition procedure provides the reconstruction in the physical domain both of the hydrodynamic and acoustic pressure in the near field of the jet.

The two time series are then processed separately and the statistical properties are eventually computed.

3.2 Wave-packet modeling

The wavepacket approach considered in this work follows the method described in [7, 8]. Specifically, the wave-packet noise source introduces some parameters whose value can be adjusted to match the pressure fluctuations from the reference jet using LES. A wave-packet describing the pressure fluctuations for a free jet is obtained by optimizing its parameters with near-field data on co-axial lines at two radial distances from the jet axis, namely $r/D = 2$ and 2.5. The radial distance of the near field probes has been chosen considering that the wavepacket model is valid for lines that are outside of the jet stream, and at the same time sufficiently close to the jet to sense and provide information about the hydrodynamic component of the pressure fluctuation. In the following, the data at the mentioned lines are referred to as *training* set, meaning that the model is informed by these data, while a *test* set is composed of the pressure field at other monitoring points.

4. RESULTS

A frequency-domain analysis of the wavelet-decomposed near-pressure field is first presented. The frequency dependence of the near-field acoustic component is evaluated through the spectra of both hydrodynamic and acoustic pressure, expressed in terms of the Sound Pressure Level (SPL) using the following equation:

$$SPL = 10\log_{10}\left(\frac{\mathrm{PSD}\Delta f_{\mathrm{ref}}}{p_{\mathrm{ref}}^2}\right), \qquad (2)$$

where PSD denotes the power spectral density evaluated using Welch's method setting Nyquist frequency at St = 12.8, with 256 samples per bin, and applying a Hanning window.

The SPL of the acoustic pressure field obtained at a radial distance of $r/D = 2$ in the jet near pressure field are shown in Figure 1 . It reveals a reduction in the acoustic component across all frequencies with increasing temperature, with the attenuation being more pronounced at higher axial distances.

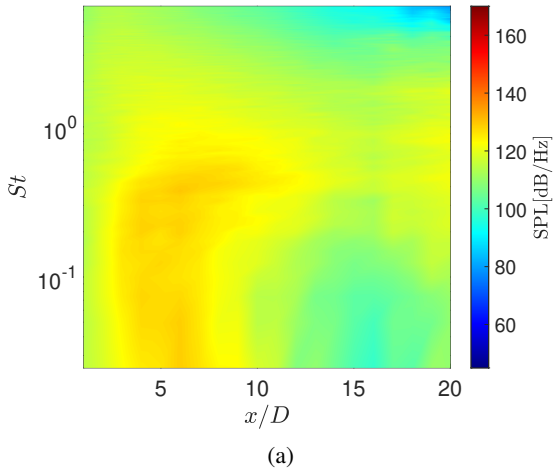
The SPL frequency peak is also significantly reduced with the increase in nozzle exhaust temperature. This can be attributed to the more rapid development of the Kelvin-Helmholtz shear-layer wave instabilities in the hot jets.

Conversely, in Figure 2, the SPL of the hydrodynamic pressure field appear to weakly depend on the jet temperature. Notably, a significant difference between Figures 2(a) and (c) is only observed at low x/D.

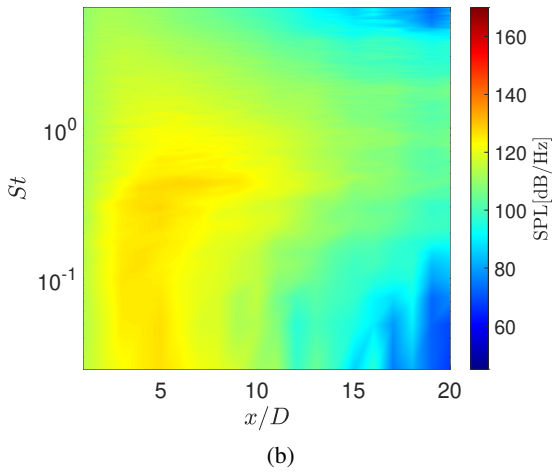
The variation in acoustic pressure field intensity indicates a change in directivity. To illustrate this, the OASPL maps obtained for the acoustic field, evaluated using the following equation:

$$\mathrm{OASPL} = 20\log_{10}\left(\frac{\sigma}{p_{\mathrm{ref}}}\right), \qquad (3)$$

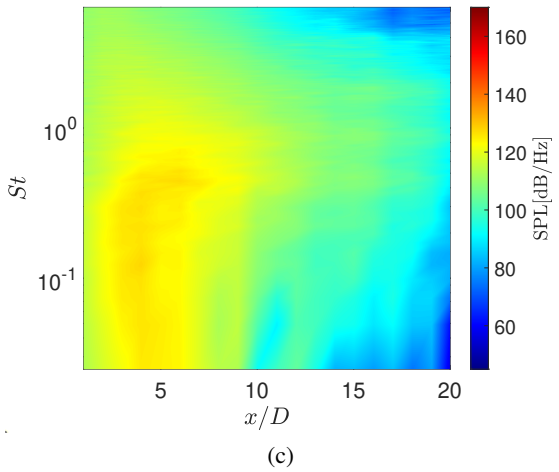
are presented in figure 3, where σ is the standard deviation of the pressure signal and p_{ref} is a reference pressure whose value is $20\mu Pa$.



(a)

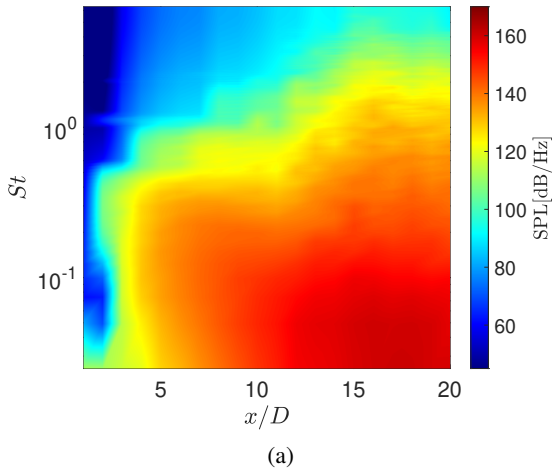


(b)

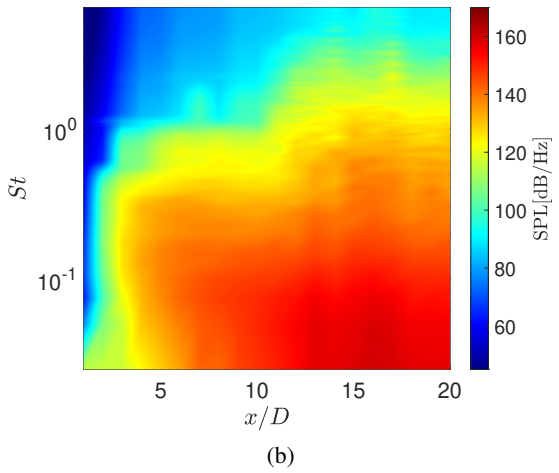


(c)

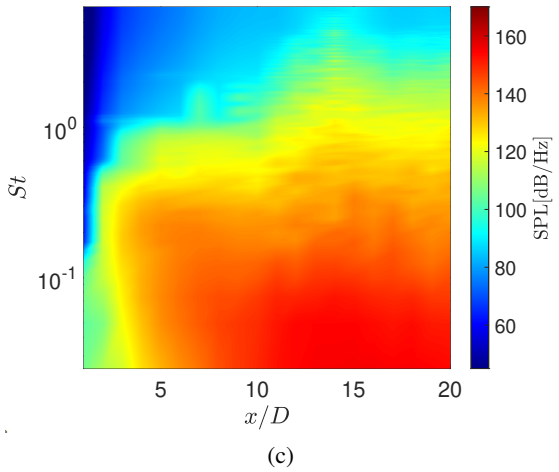
Figure 1: SPL of the acoustic pressure field at $r/D = 2$: : (a) $T = T_a$; (b) $T = 1.5T_a$; (c) $T = 2.25T_a$.



(a)



(b)



(c)

Figure 2: SPL of the hydrodynamic pressure field $r/D = 2$: (a) $T = T_a$; (b) $T = 1.5T_a$; (c) $T = 2.25T_a$.

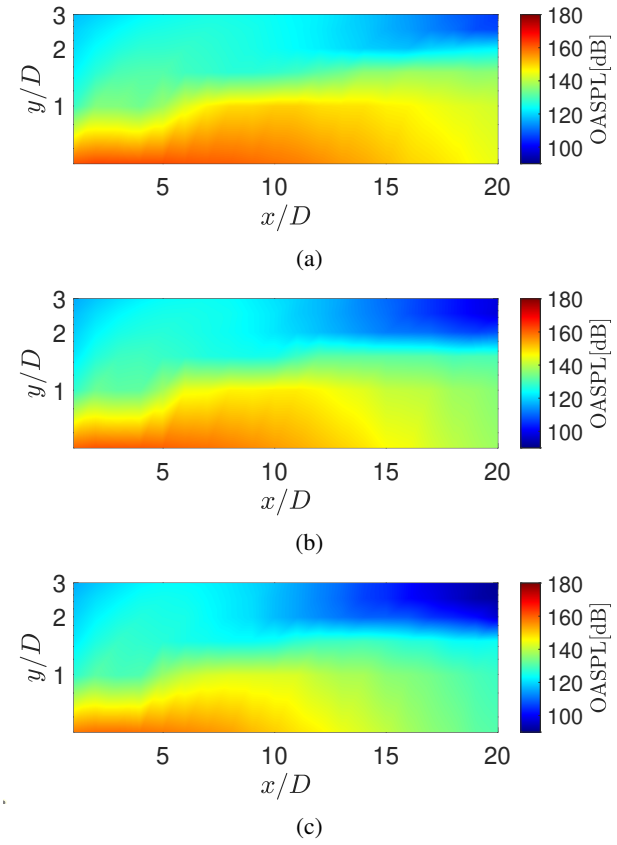


Figure 3: OASPL of the acoustic pressure field: (a) $T = T_a$; (b) $T = 1.5T_a$; (c) $T = 2.25T_a$.

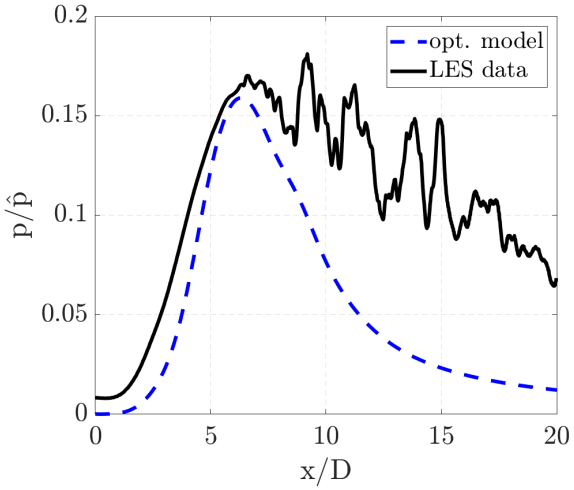
It clearly appears that the amplitude and the directivity of the acoustic pressure field are both significantly affected by the jet temperature, especially further downstream of the jet. Specifically, a reduction in OASPL is observed at high x/D values. Additionally, the OASPL distribution indicates a progressive sideline spread of the noise field as the temperature increases. This can be ascribed to the faster breakdown of large-scale structures as they develop more rapidly.

It is interesting to note that the high-intensity region near the jet axis (represented by the dark red areas in Figure 3) extends from the nozzle exit to a distance between 10 and 15 diameters, depending on the temperature. More specifically, as the nozzle exhaust temperature increases, the axial extent of this high-intensity region contracts, reaching approximately $x/D = 10$ for the highest temperature. This is due to the faster breakdown of large-scale structures.

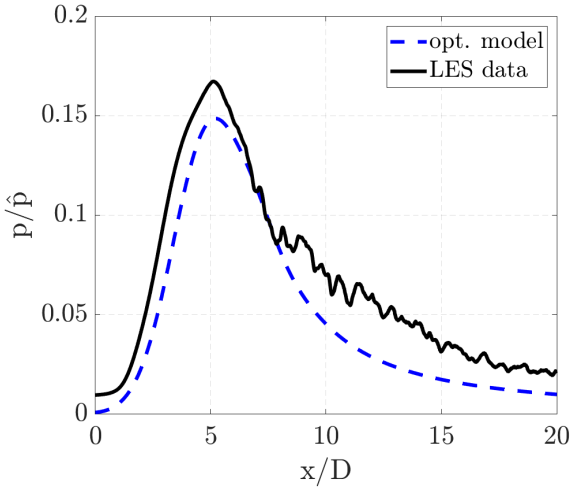
Comparisons of the LES pressure field and that predicted by the optimal wave-packets (see [8] for the approach used) for $T = T_a$ and (b) $T = 2.25T_a$, at a Strouhal number of $St = 0.25$, are finally provided in Figure fig:enter-label. The predictions closely match the shape of the reference data along the near-field lines, but only up to the axial position where the lines begin to interact with the jet flow for the considered Strouhal number. The modification in jet structure due to the higher temperature enhances the effectiveness of wavepacket optimization.

5. CONCLUSIONS

This paper presented an analysis of the effect of nozzle-exit temperature on the near-field acoustic pressure of compressible subsonic jets. The study is based on a high-fidelity, well-resolved large-eddy simulation (LES) database, conducted at fixed acoustic Mach and Reynolds numbers, and turbulence intensity. The acoustic and hydrodynamic pressure components were separated using an established wavelet-based procedure, enabling the reconstruction of both pressure time series with high accuracy. The OASPL maps show a shortening of the high-intensity region observed which suggests a faster breakdown of large-scale coherent structures, shifting the dominant noise sources upstream. A key finding is the shift in noise directivity with increasing temperature. While lower-temperature jets predominantly radiate noise in the aft direction, higher-temperature jets exhibit a more pronounced sideline directivity. The SPL frequency peak is also significantly reduced with increasing nozzle exhaust temperature, likely due to the more rapid development of the Kelvin-Helmholtz instabilities. Finally, the optimized wavepacket approach better predicts the jet pressure field for higher temperature.



(a)



(b)

Figure 4: Comparison between reference and optimized wave-packet normalized pressure at $r/D = 1.5$: (a) $T = T_a$ and (b) $T = 2.25T_a$.

6. REFERENCES

[1] M. J. Lighthill, "On sound generated aerodynamically," *General theory. Proc. R. Soc. Lond.*, pp. 564–587, 1952.

[2] M. E. Goldstein, "Aeroacoustics of turbulent shear flows," *Annu. Rev. Fluid Mech.*, vol. 16, no. 1, pp. 263–285, 1984.

[3] G. Lilley, "On the noise from air jets.," *AGARD CP 131*, pp. 13.1–13.2, 1974.

[4] A. V. G. Cavalieri, P. Jordan, A. Agarwal, and Y. Gervais, "Jittering wave-packet models for subsonic jet noise," *J. Sound Vib.*, vol. 330, no. 18-19, pp. 4474–4492, 2011.

[5] P. Jordan and T. Colonius, "Wave packets and turbulent jet noise," *Annu. Rev. Fluid Mech.*, vol. 45, no. 1, pp. 173–195, 2013.

[6] A. V. G. Cavalieri, P. Jordan, and L. Lesshafft, "Wave-packet models for jet dynamics and sound radiation," *Appl. Mech. Rev.*, vol. 71, no. 2, 2019.

[7] G. Palma, S. Meloni, R. Camussi, U. Iemma, and C. Bogey, "Data-driven multiobjective optimization of wave-packets for near-field subsonic jet noise," *AIAA Journal*, vol. 61, no. 5, pp. 2179–2188, 2023.

[8] G. Palma, S. Meloni, R. Camussi, U. Iemma, and C. Bogey, "Subsonic jet noise prediction in near and far field with optimized wave-packet approach," *AIAA Journal*, vol. 62, no. 11, pp. 4144–4152, 2024.

[9] E. W. S. Kam, R. M. C. So, S. C. Fu, and R. C. K. Leung, "Finite difference Lattice Boltzmann method applied to acoustic-scattering problems," *AIAA Journal*, vol. 48, no. 2, pp. 354–371, 2010.

[10] K. Viswanathan, "Aeroacoustics of hot jets," *Journal of Fluid Mechanics*, vol. 516, p. 39–82, 2004.

[11] R. Camussi and S. Meloni, "On the application of wavelet transform in jet aeroacoustics," *Fluids*, vol. 6, no. 8, p. 299, 2021.

[12] S. Meloni, R. Camussi, and C. Bogey, "An analysis of the effect of the jet initial conditions on the wavelet separated near-field acoustic pressure," *Theoretical and Computational Fluid Dynamics*, vol. 39, no. 1, p. 5, 2025.

[13] C. Bogey, "Acoustic tones in the near-nozzle region of jets: characteristics and variations between Mach numbers 0.5 and 2," *Journal of Fluid Mechanics*, vol. 921, 2021.

[14] C. Bogey, "Properties of the tones emerging in the near-field pressure spectra of hot high-speed jets," in *30th AIAA/CEAS Aeroacoustics Conference*, p. 3031, 2024.

[15] S. Grizzi and R. Camussi, "Wavelet analysis of near-field pressure fluctuations generated by a subsonic jet," *Journal of Fluid Mechanics*, vol. 698, pp. 93–124, 2012.

[16] Camussi, Roberto, Meloni, Stefano, and Bogey, Christophe, "On the influence of the nozzle exhaust initial conditions on the near field acoustic pressure," *Acta Acustica*, vol. 6, p. 57, 2022.

[17] M. Farge, "Wavelet transform and their applications to turbulence," *Annual Review of Fluid Mechanics*, vol. 24, no. 1, pp. 395–458, 1992.

[18] R. Camussi, G. Robert, and M. C. Jacob, "Cross-wavelet analysis of wall pressure fluctuations beneath incompressible turbulent boundary layers," *Journal of Fluid Mechanics*, vol. 617, p. 11–30, 2008.

[19] S. Meloni and H. Kamliya Jawahar, "A wavelet-based time-frequency analysis on the supersonic jet noise features with chevrons," *Fluids*, vol. 7, no. 3, 2022.

[20] G. L. Micci, R. Camussi, S. Meloni, and C. Bogey, "Intermittency and stochastic modeling of low- and high-Reynolds-number compressible jets," *AIAA Journal*, vol. 60, no. 3, pp. 1983–1990, 2022.

[21] R. Camussi and C. Bogey, "Intermittent statistics of the 0-mode pressure fluctuations in the near field of Mach 0.9 circular jets at low and high Reynolds numbers," *Theoretical and Computational Fluid Dynamics*, vol. 35, no. 2, pp. 229–247, 2021.

[22] D. L. Donoho and J. M. Johnstone, "Ideal spatial adaptation by wavelet shrinkage," *Biometrika*, vol. 81, no. 3, pp. 425–455, 1994.

[23] J. Ruppert-Felsot, M. Farge, and P. Petitjeans, "Wavelet tools to study intermittency: application to vortex bursting," *J. Fluid Mech.*, vol. 636, pp. 427–453, 2009.

[24] S. Li, D. E. Rival, and X. Wu, "Sound source and pseudo-sound in the near field of a circular cylinder in subsonic conditions," *Journal of Fluid Mechanics*, vol. 919, p. A43, 2021.

[25] A. Hajczak, L. Sanders, F. Vuillot, and P. Druault, "Wavelet-based separation methods assessment on the near pressure field of a landing gear subcomponent," in *25th AIAA/CEAS Aeroacoustics Conference*, p. 2482, 05 2019.

[26] C. Pérez Arroyo, G. Daviller, G. Puigt, C. Airiau, and S. Moreau, "Identification of temporal and spatial signatures of broadband shock-associated noise," *Shock Waves*, vol. 29, no. 1, pp. 117–134, 2019.

DOI: 10.61782/fa.2025.0751



FORUM ACUSTICUM
EURONOISE 2025

REVISITING THE EFFECTS OF MEAN VELOCITY PROFILES SHAPE ON SOUND PROPAGATION THROUGH TWO-DIMENSIONAL DUCTS

Lucas A. Bonomo[1*] **Julio A. Cordioli**[1] **Edward J. Brambley**[2]
[1] Federal University of Santa Catarina, Florianópolis, Brazil
[2] University of Warwick, Coventry, United Kingdom

ABSTRACT

Previous publications suggest that the acoustic attenuation rate in lined two-dimensional ducts with grazing flow depends on the shape of the boundary layer's mean velocity profile. Nayfeh et al. (1974) showed that for downstream-propagating waves, similar attenuation rates can be achieved for different profile shapes if the boundary layer displacement thickness remains constant. However, for upstream propagation, the attenuation rate also varies with the boundary layer shape factor. This study revisits Nayfeh et al.'s work, focusing on small ducts, particularly within the typical Helmholtz number range used in acoustic liner impedance eduction test rigs. Three profile shapes are considered: the sinusoidal flow profile, the hyperbolic tangent profile, and the universal law of the wall, which represents a more realistic turbulent boundary layer. The exact wavenumbers from the Pridmore–Brown equation for these flow profiles are compared with the approximation obtained using a uniform flow and the Ingard–Myers boundary condition applied to the lined wall with slipping grazing velocity.

Keywords: *duct acoustics, acoustic liners, sheared flow profile, impedance eduction.*

1. INTRODUCTION

Acoustic liners are essential noise-reducing treatments applied to the nacelles of turbofan engines. They typically consist of a perforated facesheet, a honeycomb core, and a hard backplate. These liners are characterised by their acoustic impedance, $\tilde{Z}(\omega) = \theta + \mathrm{i}\chi$, where θ is the resistance and χ is the reactance. The impedance, which depends on both liner geometry and operational conditions such as grazing flow velocity and incident Sound Pressure Level (SPL), serves as a boundary condition in noise propagation models, enabling accurate noise predictions while circumventing the computational cost of explicitly modelling the liner.

Liner impedance is typically characterised using experimental methods under conditions as close as possible as those in turbofan engines, with impedance eduction being the most widely used approach [1]. These techniques often assume uniform mean flow and apply the Ingard–Myers boundary condition to describe liner interaction with acoustic and flow fields. However, recent findings challenge these assumptions.

One key issue is the dependence of educed impedance on the wave propagation direction relative to the mean flow, which contradicts the locally reacting hypothesis. This discrepancy has been consistently observed across different experimental facilities, suggesting a fundamental limitation in the standard modelling approach. Initial studies [2] attributed this behaviour to a failure of the Ingard–Myers boundary condition, prompting alternative formulations that introduce additional degrees of freedom, such as viscosity [3], shear stress [4,5], or boundary layer effects [6]. These modifications aim to remove the directional dependence of the educed impedance. However, experimental validation remains inconclusive, as adjustments to the model fit experimental data regardless of the specific physical mechanism introduced.

An alternative line of research replaces the uniform flow assumption with a sheared velocity profile. While several studies have employed one-dimensional shear flow models [5,7,8], results indicate that incorporating sheared

*Corresponding author: lucas.bonomo@lva.ufsc.br.
Copyright: ©2025 Lucas Bonomo et al. This is an open-access article distributed under the terms of the Creative Commons Attribution 3.0 Unported License, which permits unrestricted use, distribution, and reproduction in any medium, provided the original author and source are credited.

flow alone does not fully resolve the impedance mismatch [9]. A recent parametric study [8] found that shear effects become more significant at higher frequencies and larger Helmholtz numbers but remain a reasonable approximation for small ducts at low frequencies.

Beyond one-dimensional shear models, some studies have explored the impact of fully three-dimensional flow. Numerical experiments comparing solutions from the Convected Helmholtz Equation (CHE) with those from the Linearised Euler Equations (LEE) [10] indicate that assuming uniform flow introduces a bias error. This bias appears to be a significant contributor to the upstream-downstream impedance mismatch observed experimentally. Furthermore, when impedance eduction is performed using wavenumbers derived from a more physically accurate flow representation, the mismatch is significantly reduced, especially at higher frequencies [11].

A common assumption in the literature is that the specific formulation of the boundary layer profile does not significantly influence acoustic propagation, provided that the displacement thickness remains unchanged. However, early investigations [12] suggest that while this holds for downstream propagation, upstream propagation is sensitive to the boundary layer shape. Despite this, the influence of boundary layer shape on impedance eduction remains largely unexplored.

In this work, we propose a numerical experiment to evaluate how different boundary layer formulations affect impedance eduction. We use the Pridmore–Brown equation [13] to obtain axial wavenumbers for a sheared mean flow and apply these wavenumbers in a traditional impedance eduction routine [14] assuming uniform flow. By comparing realistic turbulent boundary layer profiles with simplified formulations commonly used in the literature, we assess the extent to which small variations in wavenumbers influence the educed impedance. Our findings aim to provide further insight into the limitations of current eduction methods and their sensitivity to flow representation.

2. GOVERNING EQUATIONS

For this study, we consider the infinite 2D duct depicted in Figure 1. The duct has width W and an axial flow $\mathbf{u}_0 = U_0(x)\hat{\mathbf{e}}_z$, assumed invariant in the axial direction. The wall at $x = -W/2$ has a locally reacting impedance $Z(\omega)$, while the other wall is rigid.

Acoustic propagation of a wave with $\exp(\mathrm{i}\omega t)$ time-dependence follows the Pridmore–Brown Equation (PBE)

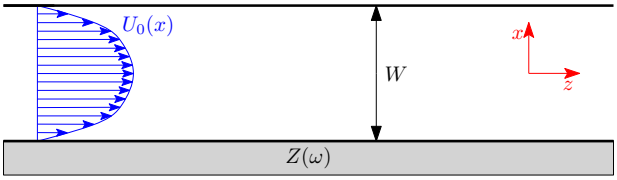


Figure 1. Schematic duct and coordinate system.

[13], given by

$$(\mathrm{i}\omega + \mathbf{u}_0 \cdot \nabla)\left(\frac{1}{c_0^2}(\mathrm{i}\omega + \mathbf{u}_0 \cdot \nabla)^2\tilde{p}' - \nabla^2\tilde{p}'\right) + 2\frac{\partial}{\partial z}\left(\nabla\tilde{p}' \cdot \nabla U_0\right) = 0. \quad (1)$$

Assuming an axial modal solution of the form $\tilde{p}'(x,z) = \tilde{p}'(x)\exp(-\mathrm{i}k_z z)$, with k_z the axial wavenumber, we obtain

$$0 = \left(\nabla_\perp^2 + \frac{\omega^2}{c_0^2} - k_z^2\right)\tilde{p}' - k_z\left(\frac{U_0}{\omega}\nabla_\perp^2 - \frac{2}{\omega}\nabla_\perp U_0 \cdot \nabla_\perp + \frac{3\omega U_0}{c_0^2}\right)\tilde{p}'. \quad (2)$$

For boundary conditions, at the rigid wall $x = W/2$, the normal acoustic velocity vanishes, while at $x = -W/2$, the impedance boundary condition is

$$\frac{\mathrm{d}\tilde{p}'}{\mathrm{d}x} = -\frac{\mathrm{i}\omega}{Z}\tilde{p}'. \quad (3)$$

For a uniform flow, the PBE simplifies to the Convected Helmholtz Equation (CHE), and the impedance boundary condition reduces to the Ingard–Myers condition [15]. The problem is discretised using Chebyshev polynomials [16] and solved as a generalised eigenvalue problem.

3. VELOCITIES PROFILE SHAPE FUNCTIONS

The simplest formulation considered in this work is the sinusoidal flow profile, as presented by Ref. [17]. In this case,

$$\frac{U_0(x)}{c_0} = \begin{cases} M_s \sin\left(\dfrac{\pi\xi}{2\delta_s}\right), & 0 \le \xi \le \delta_s \\ M_s, & \xi > \delta_s, \end{cases} \quad (4)$$

where M_s is the free-stream Mach number, and δ_s is the boundary layer thickness.

A commonly employed formulation nowadays is the hyperbolic tangent profile introduced by Ref. [18], given by

$$\frac{U_0(r)}{c_0} = M_c \Bigg[\tanh\left(\frac{1-r}{\delta_t}\right) + (1 - \tanh(1/\delta_t)) \times \left(\frac{1+\tanh(1/\delta_t)}{\delta_t} r + (1+r)\right)(1-r) \Bigg], \quad (5)$$

where M_c is the centreline Mach number, r is the radial position, and δ_t is a shape factor. In this work, we use the coordinate transformation $r = 2|x|/W$ to obtain the flow profiles in the x coordinate system.

For a realistic boundary layer velocity profile, we employ the universal wall law [19]

$$U^+ = \Pi + \int_0^{y^+} \frac{2}{1 + \sqrt{1 + 4\kappa^2 {y^+}^2 (1 - \exp(-y^+/A^+))^2}} \mathrm{d}y^+, \quad (6)$$

where Π is given by

$$\int_0^{y^+_{\max}} \frac{2}{1 + \sqrt{1 + 4\kappa^2 {y^+}^2 (1 - \exp(-y^+/A^+))^2}} \mathrm{d}y^+ \times (y^+_{\max} - y^+) \left(\frac{y^+}{y^+ \max}\right)^2 = \Pi. \quad (7)$$

where $y^+_{\max,x} = W u_\tau / \nu / 2$. This formulation ensures continuity in the velocity profile derivative at the duct centreline.

4. MATERIAL AND METHODS

In this work, we consider a small rectangular duct representative of traditional liner impedance eduction facilities. The initial dimensions follow the Liner Impedance Test Rig from UFSC (LITR/UFSC), with a width of $W = 40\,\mathrm{mm}$, and a parametric study on the effect of duct width is planned.

For the lined wall impedance, we adopt an SDOF-like impedance given by

$$Z_{\mathrm{SDOF}}(\omega) = 2 - \mathrm{i}\left(\cot(k_0 h) - (0.03 k_0)^2\right), \quad (8)$$

with $h = 35\,\mathrm{mm}$, $k_0 = \omega/c_0$ is the free-field wavenumber, with ω the frequency in $\mathrm{rad\,s^{-1}}$ and c_0 the speed of sound in $\mathrm{m\,s^{-1}}$, which is representative of a typical liner in the considered frequency range and Mach number. The frequency range considered is 500–3000 Hz. The reference impedance is shown in Figure 2.

Velocity profiles are examined using three formulations presented: the turbulent universal wall law, Eqn. (6), a hyperbolic tangent profile, Eqn. (5), and a sinusoidal profile, Eqn. (4). The wall law parameters are fitted to experimental data from LITR/UFSC, yielding an average Mach number of $M = 0.279$, boundary layer thickness $\delta_{99\,\%} = 15.72\,\mathrm{mm}$, and displacement thickness $\delta^* = 1.70\,\mathrm{mm}$.

To assess the impact of velocity profiles on impedance eduction, we fit the hyperbolic tangent and sinusoidal profiles to match either the same bulk Mach number and boundary layer thickness or the same bulk Mach number and displacement thickness. The considered flow profiles are depicted in Figure 3

The number of points in the computational domain used for the pseudospectral solver was determined based on the critical case, which, for this study, corresponds to the universal wall law due to its high gradient near the walls.

For the numerical experiment eduction, we consider the traditional straightforward wavenumber based impedance eduction first proposed by Ref. [14]. Applying the Ingard–Myers boundary condition on the lined wall the CHE solution, it leads to the eigenvalue problem

$$k_x \tan(k_x W) - \frac{1}{\mathrm{i}k_0 Z}(\mathrm{i}k_0 - \mathrm{i}M k_z)^2 = 0, \quad (9)$$

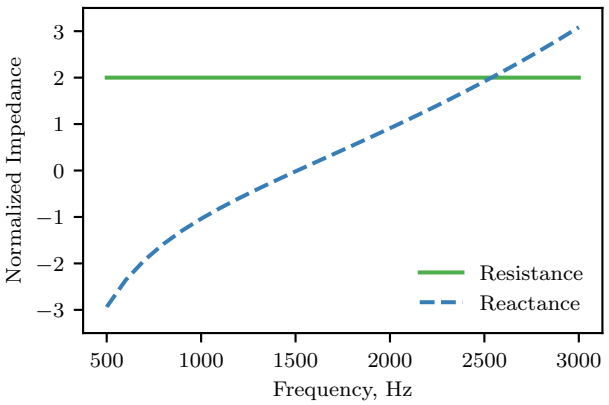


Figure 2. Reference impedance for the numerical experiments.

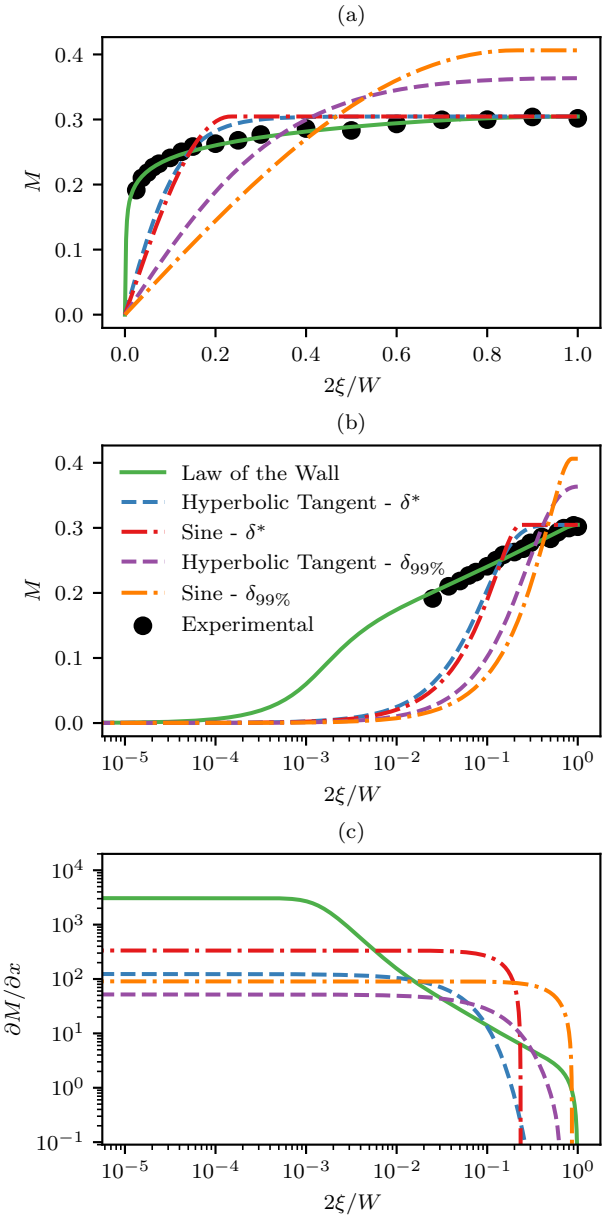


Figure 3. Flow velocities profiles in linear (a) and logarithmic (b) and velocities gradient (c) considered in the first step of this work.

where k_x is the transverse wavenumber, and the dispersion relation given by

$$k_x^2 = (k_0 - Mk_z)^2 - k_z^2. \tag{10}$$

Once the axial wavenumber is known, it is straightforward to calculate the liner impedance from Eqn. (9) and Eqn. (10).

5. RESULTS AND DISCUSSION

First, we examine the wavenumbers obtained from the Pridmore–Brown equation for different velocity profile shapes, all with the same boundary layer thickness, $\delta_{99\,\%}$, and average Mach number M. These results are compared with the wavenumbers derived from the Convected Helmholtz equation with the Ingard–Myers boundary condition, which models the refraction at the boundary layer considering the average Mach number. The wavenumbers for the least attenuated mode, for both upstream (k_z^-) and downstream (k_z^+) propagation (corresponding to upstream and downstream sources, respectively), are presented in Figure 4.

Results suggest good agreement between all considered velocity profiles and the predictions from the CHE-IMBC for the real component of the wavenumber in both propagation directions. However, for the imaginary component of the wavenumber, which corresponds to the attenuation rate, significant differences are observed between the wavenumbers obtained for the hyperbolic tangent and sinusoidal flow profiles, compared to those obtained for the more realistic distribution given by the universal wall law, particularly for upstream propagation. Good agreement is observed between the CHE-IMBC solution and both the wall law and PBE solutions. This suggests that the IMBC may provide a good approximation for the typical range of impedance eduction. A possible explanation is that, due to the high gradient near the wall, even though the velocity distribution extends nearly across the entire duct half-width, the region where refractive effects are significant is confined to a much thinner region, making the infinitely thin hypothesis of the IMBC reasonable

Next, we consider the case where the different velocity distributions are adjusted to match the average Mach number and the boundary layer displacement thickness, δ^*, rather than the boundary layer thickness, $\delta_{99\,\%}$. This approach is expected to improve the agreement between the acoustic attenuation predicted by the different flow profiles, particularly for downstream propagation [12]. The wavenumbers for the least attenuated mode in both upstream and downstream propagation are shown in Figure 5.

As expected, a better agreement is observed for the

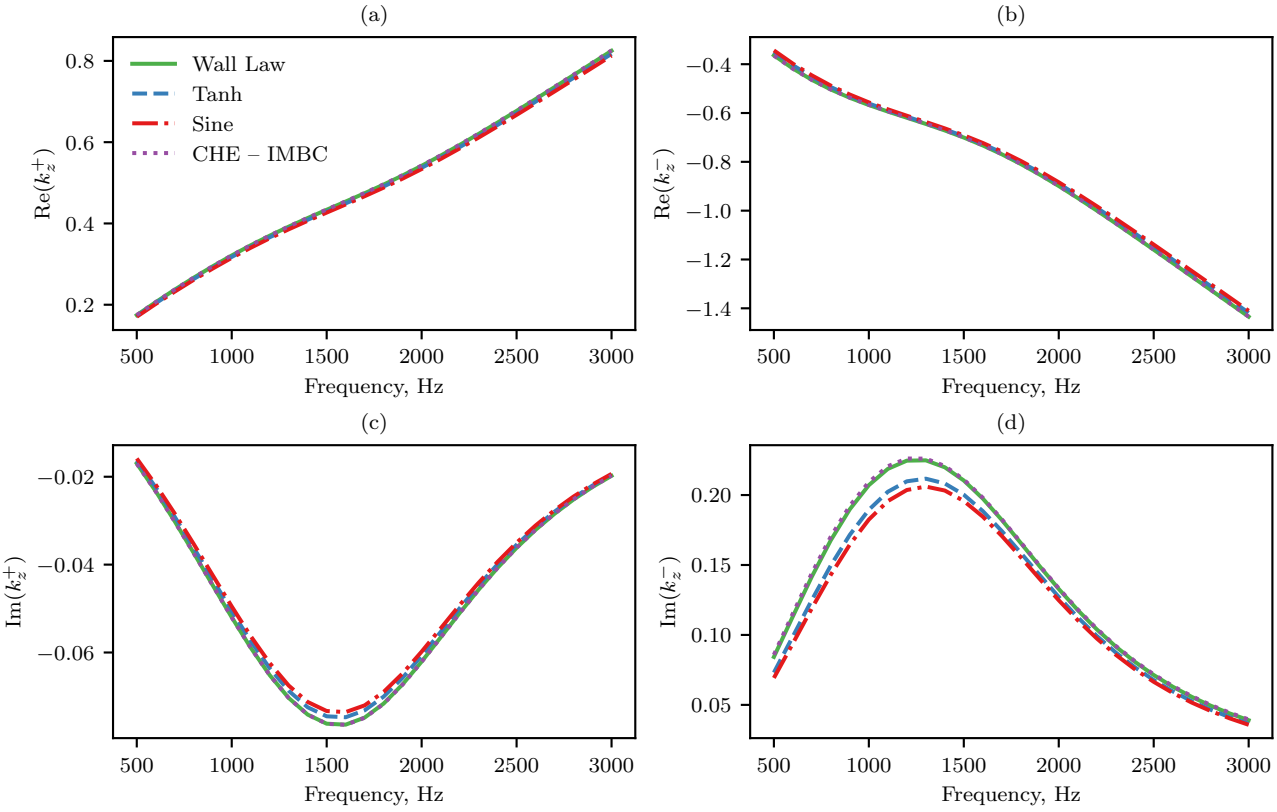


Figure 4. Wavenumbers obtained with different velocities distributions for the same M and $\delta_{99.9\,\%}$.

wavenumbers obtained for the different velocity distributions, especially for downstream propagation. However, for upstream propagation, the wavenumbers for the hyperbolic tangent and sinusoidal flow profiles agree well with each other, but diverge from the solution for the wall law and the prediction for the CHE-IMBC. These initial results suggest that assuming a uniform flow and compensating for the refraction within the boundary layer using the Ingard–Myers boundary conditions provides better estimates of the acoustic field in impedance eduction facilities under typical test conditions, compared to solving for an explicit velocity distribution that is not representative of realistic conditions.

The next step, which is the main goal of this study, is to evaluate the impact of considering different flow velocity distribution shapes on the evaluation of the acoustic field in impedance eduction. We use the wavenumbers obtained for the least attenuated mode, considering the different velocity profile formulations, in the classical straightforward impedance eduction routine. This routine assumes uniform flow and the Ingard–Myers boundary condition to model the slip velocity at the wall. The impedances educed with the proposed numerical experiment, along with the wavenumbers obtained for the different velocity profiles in the PBE, are shown in Figure 6.

The impedances educed using the wavenumbers obtained from the exact solution of the hyperbolic tangent and sinusoidal flow profiles exhibit a similar trend regarding the mismatch observed experimentally between upstream and downstream acoustic sources (downstream and upstream propagation, respectively). At the lower frequency end, the upstream source case results in a lower resistance, with the opposite trend observed at higher frequencies. This behaviour is similar to what has been observed by Ref. [10]; however, in our case, the reference impedance is not the midpoint between the two curves. For the most realistic flow profile, the wall law, the conclusions differ significantly. At the lower frequency end,

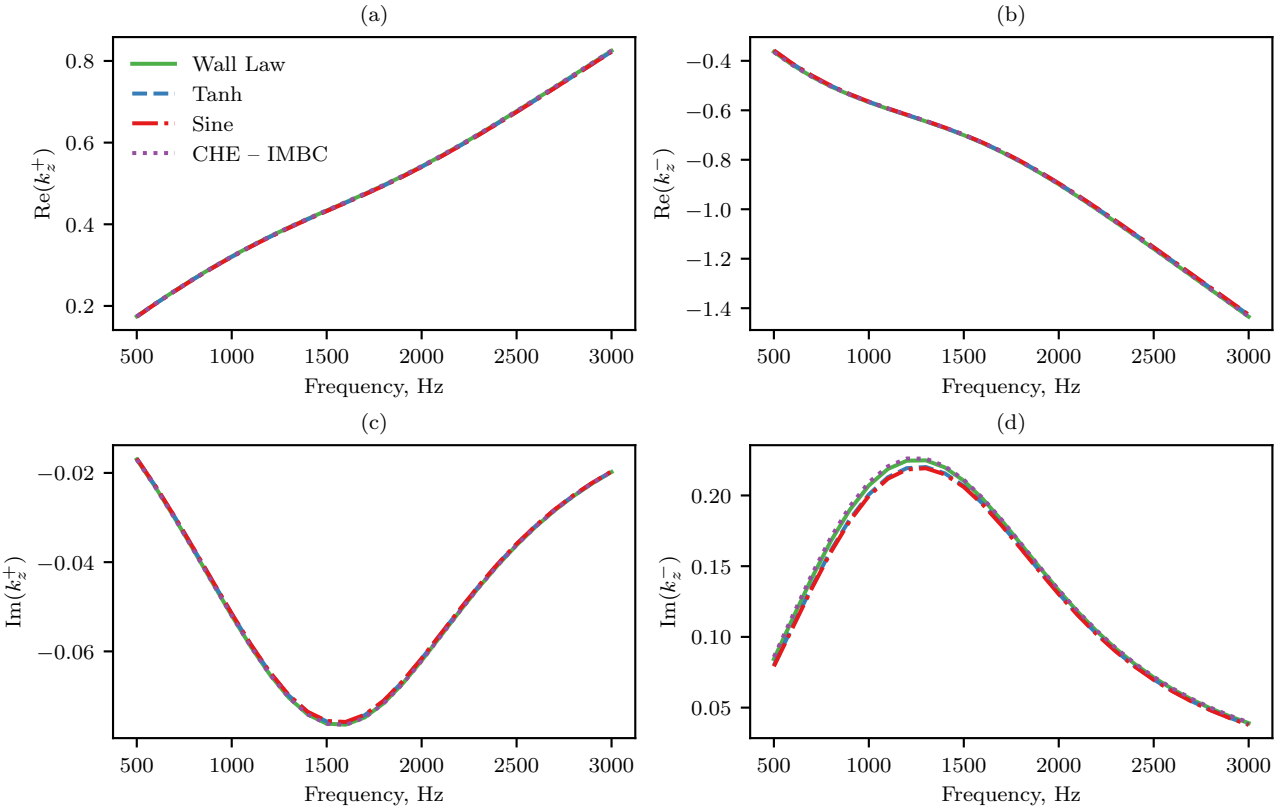


Figure 5. Wavenumbers obtained with different velocities distributions for the same M and δ^*.

the assumption of uniform flow with the IMBC introduces a small bias for both acoustic source positions, with good agreement observed between them. At higher frequencies, the curves diverge, with the upstream source (downstream propagation) surprisingly showing a greater deviation from the reference impedance.

6. CONCLUDING REMARKS

This work revisited the influence of sheared flow profiles on acoustic propagation in a 2D duct, extending Ref. [12] to impedance eduction. Comparing wavenumbers from the Pridmore–Brown equation with those from the Convected Helmholtz equation using the Ingard–Myers boundary condition (IMBC) showed that the IMBC performs well when the velocity profile is realistic, with improved agreement when matching the boundary layer displacement thickness.

A numerical experiment confirmed that IMBC-based eduction may introduce errors for non-realistic profiles but remains accurate for realistic flows. Iterative eduction with experimental data supported the findings of Ref. [5], showing reasonable agreement with the IMBC solution.

Overall, the IMBC is a reasonable simplification for low Mach number, small-duct impedance eduction in 2D ducts. Future work should extend this approach to realistic 3D ducts, as in Ref. [10], while preserving accurate flow profile representation.

7. ACKNOWLEDGMENTS

On behalf of L.A. Bonomo and J.A. Cordioli, this research was partially funded by CNPq (National Council for Scientific and Technological Development). L.A. Bonomo acknowledges that this study was financed in part by the Coordenação de Aperfeiçoamento de Pessoal de Nível Superior – Brasil (CAPES), Finance Code 001. E.J. Brambley gratefully acknowledges the support of the UK Engineering and Physical Sciences Research Council (EPSRC grant EP/V002929/1).

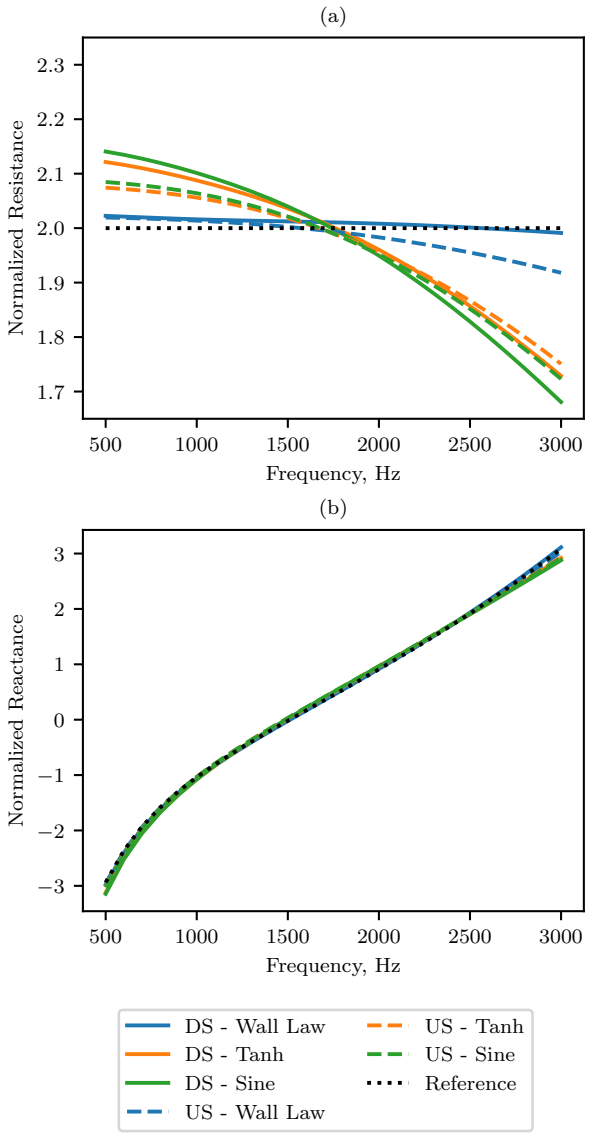


Figure 6. Educed impedances obtained for the wavenumbers evaluated for the PBE considering different velocities profile shapes with the same δ^*. US - Upstream Source (downstream propagation), and; DS - Downstream Source (upstream propagation).

8. REFERENCES

[1] L. A. Bonomo, N. T. Quintino, A. M. N. Spillere, P. B. Murray, and J. A. Cordioli, "A comparison of in situ and impedance eduction experimental techniques for acoustic liners with grazing flow and high sound pressure level," *International Journal of Aeroacoustics*, p. Article in Advance, Jan. 2024.

[2] Y. Renou and Y. Aurégan, "Failure of the Ingard–Myers boundary condition for a lined duct: An experimental investigation," *The Journal of the Acoustical Society of America*, vol. 130, p. 52, July 2011.

[3] D. Khamis and E. J. Brambley, "Acoustics in a two-deck viscothermal boundary layer over an impedance surface," *AIAA Journal*, vol. 55, pp. 3328–3345, Oct. 2017.

[4] Y. Aurégan, "On the use of a stress–impedance model to describe sound propagation in a lined duct with grazing flow," *The Journal of the Acoustical Society of America*, vol. 143, pp. 2975–2979, May 2018.

[5] C. Weng, A. Schulz, D. Ronneberger, L. Enghardt, and F. Bake, "Flow and Viscous Effects on Impedance Eduction," *AIAA Journal*, vol. 56, pp. 1118–1132, Mar. 2018.

[6] E. J. Brambley, "Well-posed boundary condition for acoustic liners in straight ducts with flow," *AIAA Journal*, vol. 49, no. 6, pp. 1272–1282, 2011.

[7] X. Jing, S. Peng, L. Wang, and X. Sun, "Investigation of straightforward impedance eduction in the presence of shear flow," *Journal of Sound and Vibration*, vol. 335, pp. 89–104, Jan. 2015.

[8] J. Yang, T. Humbert, J. Golliard, and G. Gabard, "Shear flow effects in a 2D duct: Influence on wave propagation and direct impedance eduction," *Journal of Sound and Vibration*, vol. 576, p. 118296, Apr. 2024.

[9] A. M. N. Spillere, L. A. Bonomo, J. A. Cordioli, and E. J. Brambley, "Experimentally testing impedance boundary conditions for acoustic liners with flow: Beyond upstream and downstream," *Journal of Sound and Vibration*, vol. 489, p. 115676, Dec. 2020.

[10] R. Roncen, E. Piot, F. Méry, F. Simon, M. G. Jones, and D. M. Nark, "Wavenumber-Based Impedance Eduction with a Shear Grazing Flow," *AIAA Journal*, vol. 58, no. 7, pp. 3040–3050, 2020.

[11] D. M. Nark, M. G. Jones, and E. Piot, "Assessment of axial wave number and mean flow uncertainty on acoustic liner impedance eduction," in *2018*

AIAA/CEAS Aeroacoustics Conference, (Reston, Virginia), pp. AIAA Paper 2018–3444, American Institute of Aeronautics and Astronautics, June 2018.

[12] A. H. Nayfeh, J. E. Kaiser, and B. S. Shaker, "Effect of mean-velocity profile shapes on sound transmission through two-dimensional ducts," *Journal of Sound and Vibration*, vol. 34, pp. 413–423, June 1974.

[13] D. C. Pridmore-Brown, "Sound propagation in a fluid flowing through an attenuating duct," *Journal of Fluid Mechanics*, vol. 4, pp. 393–406, Aug. 1958.

[14] X. Jing, S. Peng, and X. Sun, "A straightforward method for wall impedance eduction in a flow duct," *The Journal of the Acoustical Society of America*, vol. 124, no. 1, pp. 227–234, 2008.

[15] M. K. Myers, "On the acoustic boundary condition in the presence of flow," *Journal of Sound and Vibration*, vol. 71, pp. 429–434, 1980.

[16] J. Boyd, *Chebyshev and Fourier Spectral Methods*. Dover Books on Mathematics, Dover Publications, 2 ed., 2001.

[17] G. Gabard and R. Astley, "A computational mode-matching approach for sound propagation in three-dimensional ducts with flow," *Journal of Sound and Vibration*, vol. 315, no. 4, pp. 1103–1124, 2008.

[18] S. Rienstra and G. Vilenski, "Spatial instability of boundary layer along impedance wall," in *14th AIAA/CEAS Aeroacoustics Conference (29th AIAA Aeroacoustics Conference)*, p. 2932, 2008.

[19] E. R. Van Driest, "On turbulent flow near a wall," *Journal of the aeronautical sciences*, vol. 23, no. 11, pp. 1007–1011, 1956.

DOI: 10.61782/fa.2025.0424

FORUM ACUSTICUM EURONOISE 2025

GPU-BASED AEROACOUSTIC SIMULATION OF LOW-SPEED AXIAL FANS ACROSS THEIR CHARACTERISTIC FAN CURVES

Alessandra Verza[1*] **Peter Altmann**[2] **Lars Erbig**[2]
[1] Siemens Digital Industries Software, Spain
[2] Siemens Digital Industries Software, Germany

ABSTRACT

Over the past years, several papers dealt with numerical simulations of EAA's axial fan benchmark at its design point. Since all these publications used different simulation techniques and mesh types, but still delivered meaningful results, we assess how different levels of mesh resolution on the fan surfaces and motion modeling approaches impact the accuracy of the simulations when looking at more extreme operating conditions close to stall or free flow. Our simulations are based on constant-density Large Eddy Simulation coupled to a Perturbed Convective Wave equation and are run on 8 Nvidia A100 GPUs, which allows us to return results significantly more quickly than on CPUs. We find that accurately predicting aerodynamic quantities on all considered operating points requires a fine normal, and surface resolution on the fan blades as well as accurate motion modeling. In contrast, the acoustic far field predictions on all operating points except the free-flow condition are significantly less dependent on meshing and motion modeling decisions.

Keywords: *fan noise, large eddy simulation, les, pcwe, gpu.*

1. INTRODUCTION

Fast and reliable aeroacoustics simulation methods are key to enabling manufacturers to develop fan designs for a broad set of applications, such as automotive, wearable technology and appliances. Lowering the noise from components is one of the main concerns for fan manufacturers.

The most common approach in literature to this kind of problem mainly focuses on finding the best set up to accurately resolve the design operating point. This can be observed in numerous papers, for example by Ghodake et al. [1] and Antoniou et al. [2] show results on different meshes both at 1.4 m^3/s, and Erbig et al. [3] solved for the same mass flow rate on very coarse and fine grids. All these papers present good correlation with the experimental results, but so far there have been significantly less research efforts on the robustness of a simulation across a range of operating conditions.

The purpose of this study was to understand the variation in accuracy of the results when key aspects of the simulation and operating conditions were changed. In particular, changes in mesh resolution and motion modeling methods were studied to understand their effects on both aerodynamic and acoustic fields.

The experimental benchmark data that this study refers to, was based on a test series run by Krömer at the Friedrich-Alexander Universität Erlangen-Nürnberg on low-pressure axial fans [4].

Both aerodynamics and acoustic results are compared to the test data across the different mass flow rates to provide better insight into the requirements needed for the set up according to which quantities are of interest for the user.

2. THEORY

In this section, the theoretical background of the simulations is introduced, distinguishing between flow and acoustics modeling, and modeling of the fan motion itself. Finally, the evaluated quantities of interest are introduced.

[*] ***Corresponding author***: *alessandra.verza@siemens.com.*
Copyright: *©2025 Alessandra Verza et al. This is an open-access article distributed under the terms of the Creative Commons Attribution 3.0 Unported License, which permits unrestricted use, distribution, and reproduction in any medium, provided the original author and source are credited.*

2.1 Flow and Acoustic Modeling

The simulations follow a hybrid finite-volume approach that splits the aeroacoustic problem into a constant-density Large Eddy Simulation (LES) that is one-way coupled to a Perturbed Convective Wave Equation (PCWE) that uses instantaneous flow fields to model convective effects, as originally introduced by Piepiorka and von Estorff [5]. Both flow and acoustics use a 2nd order discretization in space and an implicit 2nd order temporal discretization. For flow, the temporal discretization is based on backward differencing, and the PCWE is discretized using a Newmark Alpha scheme [3]. It is worth noting that a constant density flow simulation allows fixing the volumetric flow rate at the inlet and is therefore particularly well suited to simulate a range of operating points across an unknown characteristic fan curve.

2.2 Motion Modeling

There are different approaches to model motion or to be more precise fan rotation in numerical simulations. The so-called moving reference (MRF) method was originally developed for axial flows and utilizes momentum equation source terms to approximate rotation [6]. Since no real rotation takes place, it is a numerically cost efficient, pragmatic approach, but with limitations in terms of accuracy. A high-fidelity simulation requires the real motion of the fan. This aspect is enabled with the so-called rigid body motion (RBM) model. The simulation domain gets divided into two parts/regions: the stationary region is the test chamber fluid volume, and the rotating region is the fluid volume surrounding the fan. The latter gets the fan rotation rate assigned and is normally modelled as a cylinder and contains the fan and in case of an axisymmetric shroud the entire shroud fluid volume. Consequently, the interface between the two regions must be re-calculated at every time-step. Past publications [3, 7] used intersection algorithms that lead to topologically valid cells, this paper is based on a more lightweight, "metrics-based", intersection algorithm that does not generate new polygonal faces [6]. While this approach is potentially less accurate, it also minimizes the memory footprint of the intersection and is better suited for running on GPUs.

2.3 Quantities of Interest

The aerodynamic performance of the fan is characterized by its total-to-static efficiency η_{ts} and its total-to-static pressure coefficient ψ_{ts}. Let Q denote the volume flow rate through the fan, and Δp_{ts} its total-to-static pressure difference. Then, the total-to-static pressure coefficient is defined by

$$\psi_{ts} = \frac{2\Delta p_{ts}}{\rho(\pi n d_{\text{fan}})^2} \quad , \tag{1}$$

where ρ is the fluid density, n is the number of blades, and d_{fan} the fan diameter. The total-to-static efficiency is given by

$$\eta_{ts} = \frac{Q\Delta p_{ts}}{M_s 2\pi n} \quad , \tag{2}$$

where M_s is the shaft torque. The acoustic performance of the fan is presented at far field microphones by evaluating its Sound Power Level (SWL) from the A-weighted time signals at the 7 microphones following the standard procedure outlined in DIN EN ISO 3746:2011-03.

3. TEST CASE

3.1 Experimental Setup

The original case was published by the European Acoustics Association [4] including both acoustics and aerodynamics experimental data. The fan was tested in a standardized inlet test chamber with a flow straightener upstream, and the exact volume flow rates were achieved by using an auxiliary fan in the inlet section. The acoustic experimental data was collected across 7 microphones located in an arc 1 m away from the inlet nozzle of the fan, as can be seen in Figure 1.

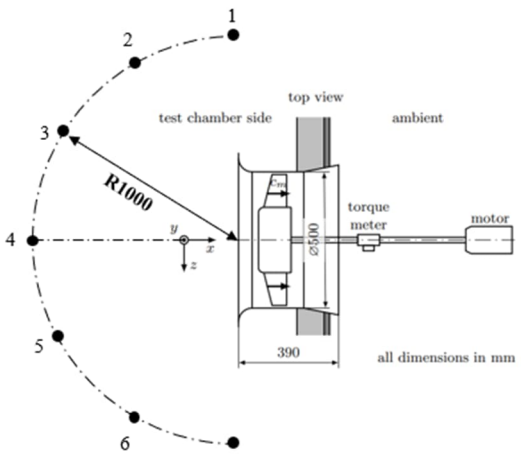


Figure 1. Detail of experimental setup with microphone arc [4].

The geometry here considered consists of an axial fan with a diameter of $d_{\text{fan}} = 0.495\,\text{m}$ and with $n = 9$ blades (referred to as "S1U" by Krömer [8]), mounted inside a duct 0.5 m in diameter, showed in Figure 2. The fan was tested across its complete operating curves, from stall to free flow, which means the inflow rate varied between 0.2 m^3/s to 2.1 m^3/s. Additional equipment was used to provide more

data on the flow behavior, such as time signals from differential pressure transducers to measure wall pressure fluctuations in the duct, and Laser Doppler Anemometer measurements on both sides of the fan.

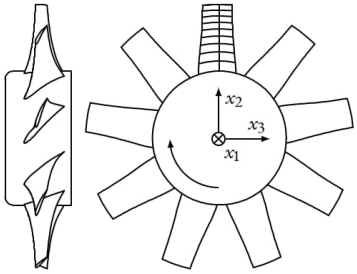


Figure 2. Tested axial fan with unskewed blades [4].

3.2 Numerical Setup

The computational setup replicates the experimental test facility and consists of two large rectangular chambers that are separated by a partition and the duct which hosts the axial fan. The top, bottom and side surfaces and the partition are modeled as non-reflecting, rigid walls. Inlet and outlet boundaries are parallel to the partition and prescribe a mass flow rate at the suction side and enforce a pressure on the pressure side of the fan (as shown in Figure 3). A hex dominated, so-called trimmed mesh in combination with prism layers at the surfaces was used to discretize the simulation domain. In total four different volume meshes were generated to analyze the impact of spatial discretization on runtimes and accuracy. The global mesh size (base size) for all meshes was 13.6 mm. Table 1 provides an overview of the relevant mesh parameters, relative to the base size if applicable, to create the different volume meshes. The total cell count varies between 55 M for the finest and 29 M for the coarsest mesh.

Table 1. Investigated volume meshes.

	Fan prism layers	Prism layer thickness (mm)	Fan target surface size (mm)	Fan minimum surface size (mm)	Volume cells (× 1E6)
Mesh 1	8	0.50	0.43	0.11	55
Mesh 2	2	0.75	0.43	0.11	40
Mesh 3	2	0.75	0.85	0.21	30
Mesh 4	2	0.75	1.70	0.43	26

A hemisphere was used to refine the mesh from the fan up to the far-field microphone locations. To capture the propagating sound waves, a uniform mesh size of 6.8 mm was used. This spatial resolution ensures 12 cells per wavelength up to 4 kHz.
The following image of Mesh 1, the finest volume mesh with around 55 M cells, visualizes the simulation domain, the overall mesh topology and refinement level around the fan and the fan tip gap.

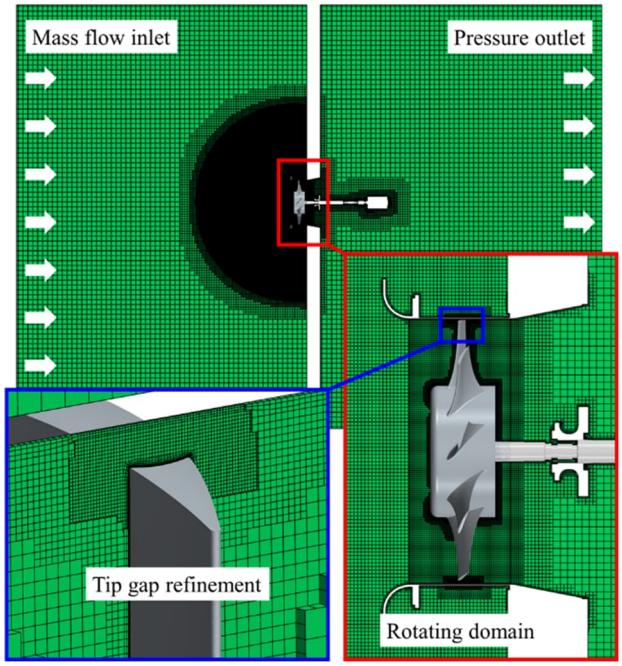


Figure 3. Finest volume mesh, topology and details.

All simulations were performed with Simcenter STAR-CCM+ version 2502. The unsteady, scale-resolving runs were initialized with a steady state Reynolds-averaged Navier-Stokes solution and utilize a segregated solver based on the SIMPLEC algorithm to solve the transient flow equations in an uncoupled manner. Fan motion was modelled with MRF for the steady, initial step and RBM for the unsteady part. The latter uses a wall-modelled Large Eddy Simulation (WMLES) approach based on the Wall-Adapting Local Eddy-Viscosity (WALE) subgrid-scale model [9] for turbulence modelling.
Each run featured eight fan revolutions with 2,000 time-steps per rotation, which equals 12.5 time-steps per period at 4 kHz. The convective wave equation is activated after the first rotation and the Newmark Alpha scheme uses $\alpha = -1/3$. Acoustics data sampling took place over the last six rotations.

4. RESULTS

In this section, we will analyze simulation results obtained on several operating points distributed over the entire characteristic fan curve. We will particularly investigate the dependency of these results on the spatial discretization on the fan blades, as well as the impact of the different motion modeling approaches. The key enabler for performing these numerous simulations were 8 NVIDIA A100 GPUs, each with 40 GB GPU memory. On this hardware, elapsed simulation times varied between 16.8 hours on Mesh 1 with RBM, and 6.8 hours on Mesh 3 with MRF, where MRF motion modeling accelerated the simulations by about 35% compared to RBM.

4.1 Analysis of different operating points

Typically, the degree of resolution of LES simulations of wall-bounded flows are judged upon the sizes of the dimensionless wall distance y^+, and the dimensionless cell sizes in the streamwise direction Δx^+, and the spanwise direction Δz^+ of the flow. These quantities are governed by

$$y^+ = \frac{u_\tau y}{\nu}, \Delta x^+ = \frac{u_\tau \Delta x}{\nu}, \text{and } \Delta z^+ = \frac{u_\tau \Delta z}{\nu}, \quad (3)$$

where u_τ is the friction velocity and ν the kinematic viscosity of the fluid, y is the wall distance of the cell center of the first cell next to the wall, and Δx and Δz denote the local edge lengths in the respective flow directions. Usual criteria [10] consider an LES simulation to be properly wall-resolved if

$$y^+ \sim 1, \Delta x^+ < 100, \text{and } \Delta z^+ < 30, \quad (4)$$

and wall-modeled if

$$y^+ > 30, \Delta x^+ \approx \Delta z^+ < 500. \quad (5)$$

In day-to-day engineering applications, the flow is usually not following a single, well-defined direction, and meshes are often isotropic on the wall. Hence, it is particularly difficult to judge the validity of the dimensionless cell sizes. In this paper, we approximate these quantities by evaluating

$$\Delta^+ := \frac{u_\tau \sqrt{A}}{\nu} \approx \Delta x^+ = \Delta z^+, \quad (6)$$

where A denotes the local face area at the walls.

The obtained upper limits for these values on the leading edges of the blades, and the blades themselves are presented in Table 2. It is evident that Mesh 1 can be considered a classical representative of a wall-resolved LES, whereas Mesh 4 is a clear representative of a wall-modeled LES, while Meshes 2 and 3 are hybrid states that independently vary y^+ or Δ^+.

Table 2. Realized wall discretization on the four considered volume meshes.

	Mesh 1	Mesh 2	Mesh 3	Mesh 4
Max. y^+ Leading Edge	1.2	4	6	14
Max. Δ^+ Leading Edge	22	14	26	50
Max. y^+ Blade	2.5	27	32	32
Max. Δ^+ Blade	98	85	166	320

In an initial attempt, the volumetric flow rate at the inlet was varied from 0.6 m³/s to 2.0 m³/s on the same grid and the mean total-to-static efficiency and total-to-static pressure coefficient were evaluated over the last sampled revolution of the fan. Figure 4 shows that especially the total-to-static pressure coefficient on Mesh 1 aligns very well with the test data.

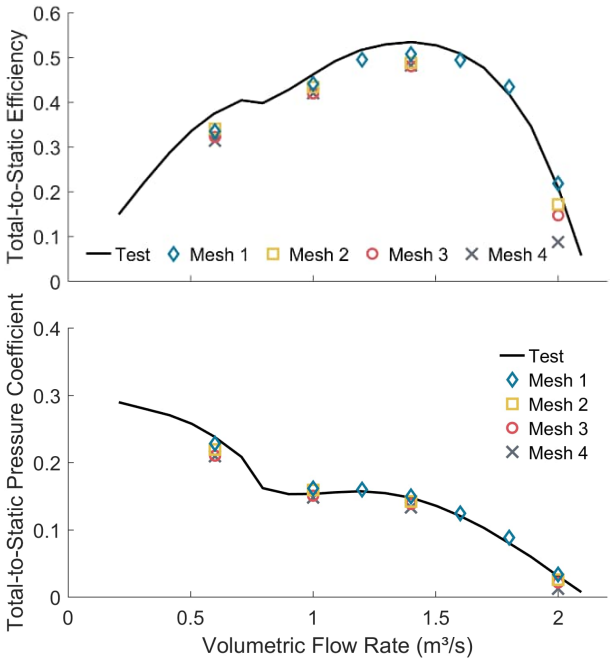


Figure 4. Mesh dependency of the total-to-static efficiency and pressure coefficient.

The efficiency shows slightly larger deviations, with a slightly flatter area around the design point and an underprediction at 0.6 m³/s. Based on these results, we decided to focus the further analysis on the limits of the expected fan operating range, 1.0 m³/s, and 2.0 m³/s, the design point 1.4 m³/s and the case at 0.6 m³/s. It is clearly visible that each individual mesh coarsening, including the independent increase of only y^+, leads to an increased under-prediction of the aerodynamic predictions. And even though this effect is most pronounced for the highest mass flow rate, the data points still follow the measured curves.

By inspecting the wall shear stress on Mesh 1 in Figure 5, one can identify the difference between the various volumetric flow rates: particularly at the lowest considered volumetric flow rate of 0.6 m³/s the flow is highly turbulent on the entire fan blade, and the vortical structures extend upstream throughout the whole shroud, typical for the stall regime. As the volumetric flow rate increases, the upstream vorticity drops, and the flow at the design point of 1.4 m³/s is dominated by the tip gap dynamics and becomes less turbulent on the blade.

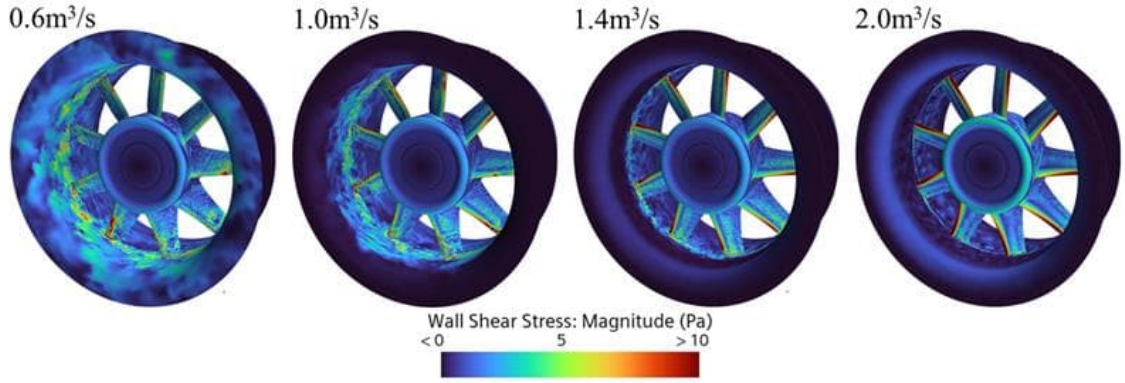


Figure 5. Instantaneous wall shear stress from Mesh 1 on fan and shroud.

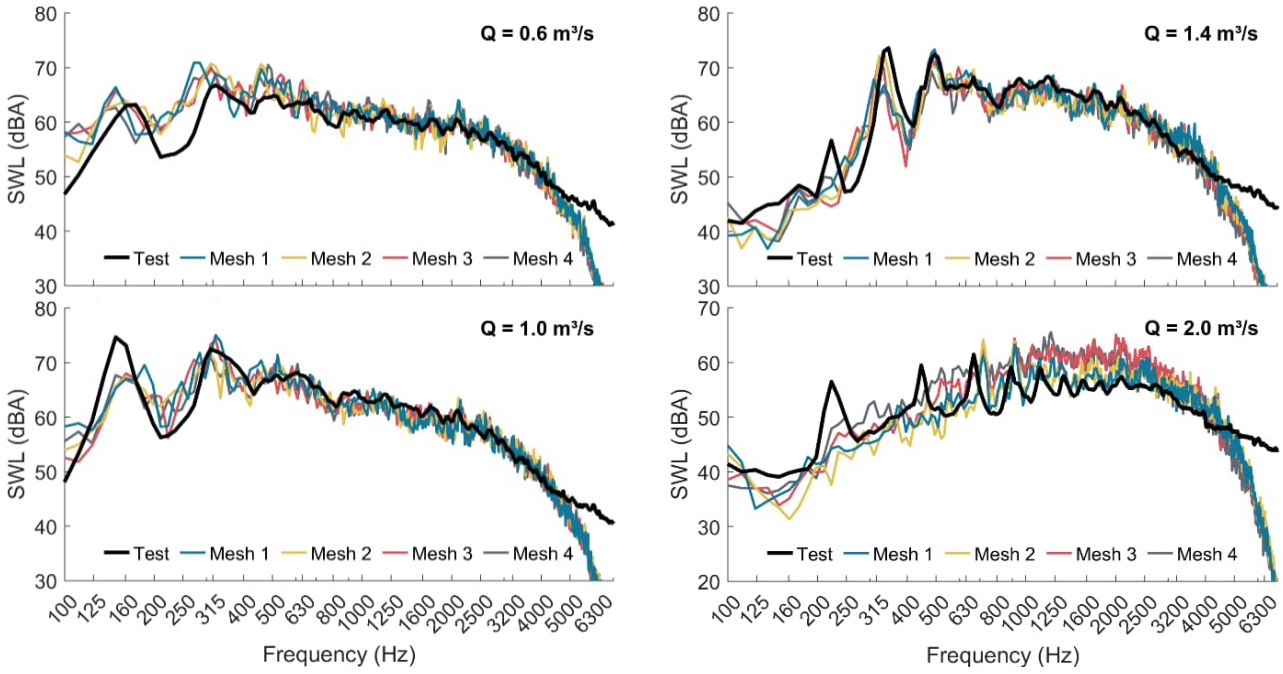


Figure 6. Mesh dependency of the Sound Power Level obtained from the 7 far field microphones.

Finally, at 2.0 m³/s, the trace of the tip gap vortex becomes much more localized and the flow around the blades transitions significantly later, a typical characterization of free flow conditions.

In this context, we can attempt to analyze the Sound Power measured at the 7 far field microphones which are shown in Figure 6. The test data from Krömer's experiments [8] shows a clear dependency on the considered operating point. The spectrum at the design point has already been analyzed in much detail [1, 8], and it is characterized by low low-frequency levels, which are followed by a relatively subtle peak at the blade passing frequency and two strong subharmonic peaks due to the tip gap dynamics. The highest frequencies above 2 kHz are then dominated by trailing edge noise of the blades. In comparison, the spectra at lower volumetric inflow rates show subharmonic peaks that are shifted to lower frequencies, and similar high frequency characteristics. In contrast, the spectrum at the highest volumetric inflow rate appears highly different: The subharmonic peaks vanish entirely, but the blade passing frequency with several harmonics is strongly excited. Furthermore, the overall level of the broadband high frequency content decreases by more than 5 dBA and finally remains more stable towards the highest frequencies.

The simulation results at the design point and the mass flow rate of 1.0 m³/s are highly consistent across all considered meshes and agree well with those reported in the literature, i.e. they show sensitivities at the subharmonic peaks, and they don't capture the blade passing tones. The results at the lowest volumetric inflow rate are also highly consistent and match excellently above 300 Hz, but they overpredict the noise due to the vortex dynamics at the lowest frequencies.

Overall, these results indicate that the acoustics predictions at these volumetric flow rates are much less sensitive to any meshing considerations than the aerodynamic quantities – which are presumably dominated by the strong tip gap vortex dynamics. In agreement with the aerodynamic results, the spectra at the highest volumetric inflow rate show the greatest dependency on the meshes: While the results from the finest mesh (Mesh 1) match the test results quite well, apart from the missing blade passing tones, the results on the coarsest grid leads to a strong offset of more than 5 dBA in almost the entire frequency range. However, it should be noted that the independent modification of y^+ does not affect the acoustic results, it is only the increase of Δ^+ that leads to deteriorated results. Hence, the aerodynamics seem to depend much more on the wall normal resolution in the vicinity of the wall, than the acoustics, which rely much more on the surface resolution. To understand the reasons for these differences, we can analyze the instantaneous wall shear stress and the surface trace of the acoustic source term of the PCWE in Figure 7. In these images, it is clearly visible that the flow structure around the blades changes immediately with increasing y^+, whereas the increase of Δ^+ in Mesh 3 and Mesh 4 only coarsens the flow pattern found on Mesh 2.

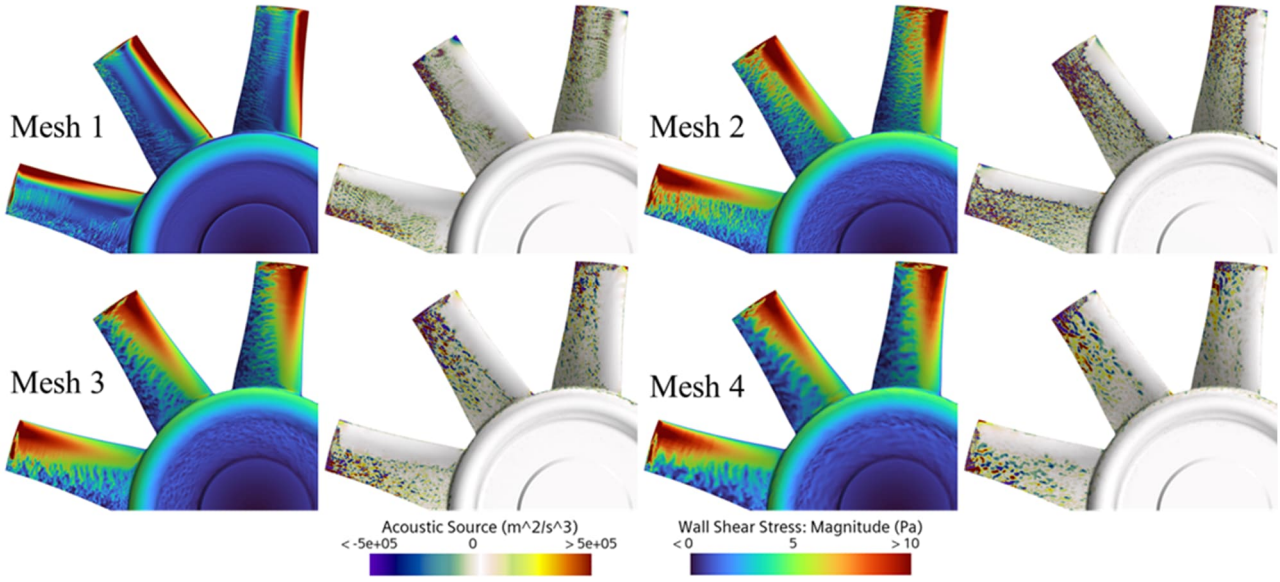


Figure 7. Wall shear stress and trace of the volumetric acoustic source term of the PCWE of the fan.

In contrast, it can also be seen that the acoustic source term changes going from Mesh 1 to Mesh 2, but we still see sources everywhere on the downstream parts of the blades. But with increasing Δ^+ on Mesh 3 and Mesh 4, the sources on the blade itself become weaker and the source term accumulates around the tip gap, which likely indicates a shift of the dominant noise generation mechanism.

4.2 Influence of Motion Modeling

Separately from coarsening the mesh or the time-step it is also possible to consider switching the motion modeling from RBM modeling with a rotating and a stationary domain, to MRF modeling that keeps a stationary mesh but introduces a moving reference frame. While this clearly reduces the computational costs per time-step, the individual impact on aerodynamics and acoustics predictions in a scale-resolving simulation is relatively unclear. To address this question, Meshes 1 and 3 were additionally simulated with MRF. In Figure 8, one can see the aerodynamics results on the different meshes and it can be clearly seen that the MRF motion modeling has a significant impact on both meshes, leading to bigger deviations from the test results. Again, particularly the volumetric inflow rate of 2.0 m³/s is most sensitive to these changes. Very much in contrast to this, especially the broadband acoustic results at the fan's design point shown in Figure 9 are consistent across the entire frequency range. Again, a big deviation is visible on Mesh 3 for the first subharmonic peak, which correlates well with strong sensitivity of the aerodynamic results on the motion modelling approach. The results on the other volumetric inflow rates were highly consistent with those from the design point.

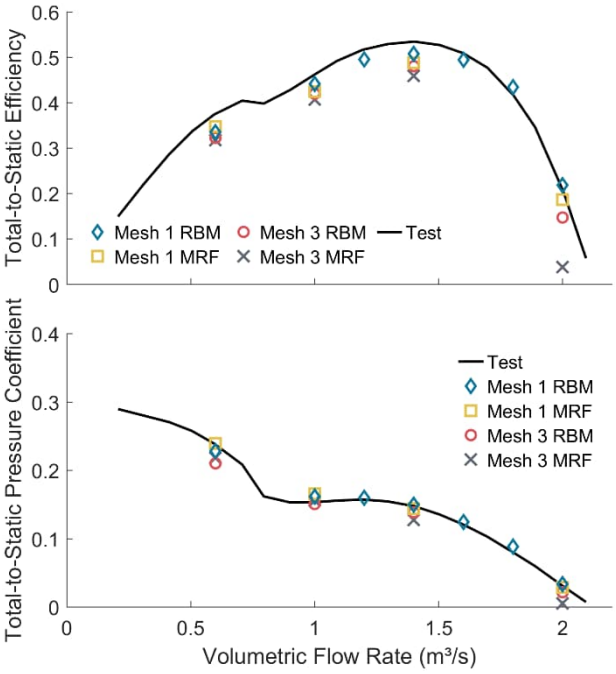


Figure 8. Dependency of the total-to-static efficiency and pressure coefficient on motion modeling.

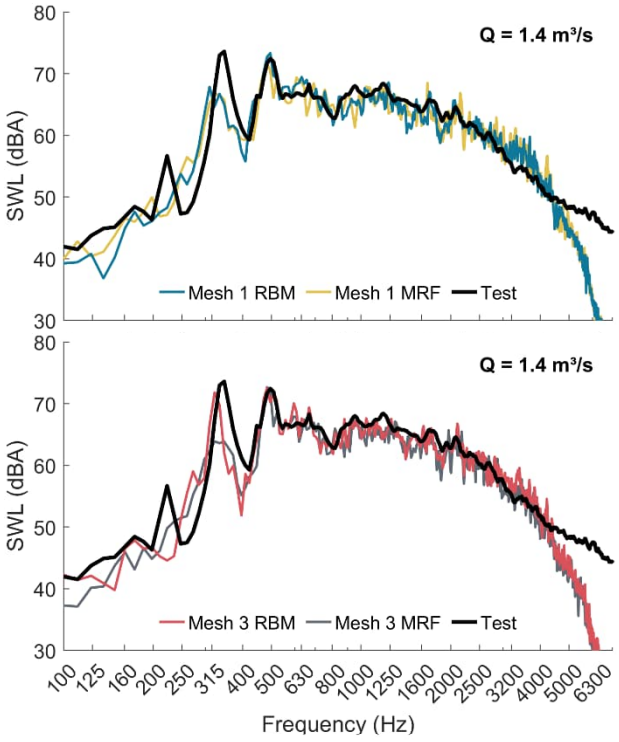


Figure 9. Dependency of the Sound Power Level obtained from the 7 far field microphones on motion modeling.

5. SUMMARY & CONCLUSION

In this paper, scale-resolving hybrid aeroacoustic simulations of the EAA benchmark fan across almost its entire operating range were performed on 8 NVIDIA A100 GPUs. The GPUs helped to reduce the computational costs of each simulation to significantly less than a day. In the simulations, we particularly studied the sensitivity of the aerodynamic and acoustic results on y^+ and Δ^+, as well as on different motion modelling approaches. The operating points were varied by modifying only the volumetric inflow rate. Overall, good results were achieved for all operating points without changing the mesh. It was found that the aerodynamic

predictions rely much more on highly resolved y^+ values and RBM than the acoustic results in the far field. Only the tones due to the subharmonic tip gap vortices as well as the free-flow operating point showed sensitivities to the Δ^+ mesh resolution and the motion modelling approach. Overall, this demonstrates that acoustics and aerodynamics converge at different rates towards their mesh-converged values.

Hence, one can potentially conduct comparably pragmatic acoustic simulations that do not attempt to answer aerodynamics and acoustics at the same time. Such an approach could be considered feasible in most of the fan's operating range. Such a split would be another step towards efficient utilization of the different length and timescales of aerodynamics and aeroacoustics.

To further investigate such splitting the authors intend to better understand the reasons for the mesh dependency at the free flow condition and look deeper into the vortex shedding mechanism at the blade tip. Furthermore, we intend to test these procedures on additional fan designs, such as those simulated by Ghodake [1] and further investigate the validity of MRF motion modelling in cases with more significant rotor stator interactions.

6. ACKNOWLEDGMENTS

The authors would like to thank Felix Czwielong and Stefan Becker from the Institute of Fluid Mechanics of Friedrich-Alexander Universität Erlangen-Nürnberg for providing the additional test data and for consenting to this publication.

7. REFERENCES

[1] Ghodake, D., et al.: "Effect of Sweep on Axial Fan Noise Sources Using the Lattice Boltzmann Method," in *Int. J. of Turbomachinery, Propulsion and Power*, vol. 7, no. 4, 2022.

[2] Antoniou, E., et al.: "Numerical flow noise simulation of an axial fan with a Lattice-Boltzmann solver," in *Acta Acustica*, 7, 65, pp. 1–14, 2023.

[3] L. Erbig, and S. Lardeau: "Hybrid Aeroacoustic Simulation of EAA's Axial Fan Benchmark," in *Fortschritte der Akustik – DAGA 2022*, (Stuttgart, Germany), pp. 360–363, 2022.

[4] EAA benchmark database, URL: https://eaa-bench.mec.tuwien.ac.at/

[5] Piepiorka, J. and Estorff, O.: "Numerical investigation of hydrodynamic/acoustic splitting methods in finite volumes including rotating domains," in *Proc. of the 23rd Int. Congress on Acoustics*, (Aachen, Germany), 2019.

[6] Siemens Industry Software, Simcenter STAR-CCM+ User Guide, Version 2502, 2025

[7] S. Schoder, C. Junger, and M. Kaltenbacher: "Computational aeroacoustics of the EAA benchmark case of an axial fan," in *Acta Acustica*, 4, 22, pp. 1–17, 2020.

[8] Krömer, F: "Sound emission of low-pressure axial fans under distorted inflow conditions," Erlangen: FAU University Press, 2018.

[9] Nicoud, F. and Ducros, F.: "Subgrid-Scale Stress Modelling Based on the Square of the Velocity Gradient Tensor," in *Flow, Turbulence, and Combustion*, vol. 62, no. 3, pp. 183–200, 1999

[10] J. Fröhlich: *Large Eddy Simulation turbulenter Strömungen*. Wiesbaden: Vieweg+Teubner Verlag, 2007.

DOI: 10.61782/fa.2025.0498

FORUM ACUSTICUM EURONOISE 2025

INVESTIGATING THE ACOUSTIC RADIATION OF COHERENT STRUCTURES IN A SUBSONIC JET

Yihong Fang[1*] **Zhengxuan Song**[1] **Xufeng Yang**[1] **Jingrui Liu**[1]
[1] Department of Mechanics, School of Mechanical Engineering, Tianjin University
Tianjin 300072, China

ABSTRACT

In the present paper, a non-Lighthill approach based on first principles is developed. The physical sound sources were clearly defined, and two acoustic radiation mechanisms were investigated. The sound field spectrum obtained by calculation was found to be in relatively good agreement with previous study.

Keywords: *jet noise; hybrid methods; equivalent sound source; acoustic radiation mechanism.*

1. INTRODUCTION

Turbulent jets at high subsonic Mach numbers account for a significant proportion of commercial aircraft noise. Despite considerable advances in the characterisation and reduction of jet noise, this subject persists as a salient issue, primarily due to a lack of understanding of the physical mechanisms underlying sound generation.

A turbulent jet is composed of two distinct structures: large orderly coherent structures (CS) and fine-scale random fluctuations [1]. A substantial corpus of research has indicated that the generation of noise is predominantly associated with the evolution and interaction of coherent structures [2-4].

Computational aeroacoustics, defined as solving the full compressible Navier-Stokes equations numerically within a sufficiently large domain encompassing both the near and far fields, is an extremely challenging task, even for the most powerful computers at present.

Theoretical approaches based on reduced equations are indispensable, and two theoretical methods have been developed by taking different perspectives to generation of noise by unsteady flows. The primary approach to aeroacoustics is acoustic analogy, a concept initially proposed by Lighthill [5].

A methodology that differs from the acoustic analogy is the asymptotic approach, which examines the sound waves radiated to the far field as the asymptotic behaviour of the near-field hydrodynamic fluctuations. The mechanism of acoustic radiation was initially investigated using matched asymptotic expansion by Tam & Burton [6]. Building upon this, Zhang and Wu [7-10] have extended the analysis to study the nonlinear evolution and acoustic radiation of coherent structures in subsonic turbulent jets. The physical sound source can be derived directly.

The objective of the present study is to formulate a hybrid method based on first principles. The near/hydrodynamic field is simulated numerically, while the far acoustic field integrates with asymptotic theoretical analysis. The physical sound sources were calculated, and two acoustic radiation mechanisms were identified.

2. HYBRID METHOD

The two-dimensional compressible Navier-Stokes equations in cylindrical coordinates are solved by a finite-difference DNS code. The axial and radial derivatives are computed with sixth-order center difference scheme, while the second-order total-variation-diminishing (TVD) Runge-Kutta scheme is used for time integration.

According to latest research, we know that the nonlinear evolution of large-scale coherent structure produces the

[*] ***Corresponding author***: yhfang@tju.edu.cn.
Copyright: *©2025 Yihong Fang et al. This is an open-access article distributed under the terms of the Creative Commons Attribution 3.0 Unported License, which permits unrestricted use, distribution, and reproduction in any medium, provided the original author and source are credited.*

equivalent sound source $\widehat{a_M^+}$ consist of three parts, namely $\mathcal{U}$, $\mathcal{S}$ and $\mathcal{Y}$. The formula is as follows, and only the upper half of the solution of the free shear flow is considered:

$$\widehat{a_M^+}(\omega,k)=\frac{\hat{\mathcal{E}}_-(\omega,k)}{\hat{\mathcal{E}}_+ +\hat{\mathcal{E}}_-}\left[\frac{ik\hat{\mathcal{U}}(\omega,k)}{c(k-\omega)^2}+\int_{-\infty}^{\infty}\frac{\hat{\mathcal{S}}(\omega,k,y)}{(\bar{U}k/c-\omega)^2}dy\right]-\frac{\hat{\mathcal{Y}}(\omega,k)}{\hat{\mathcal{E}}_+ +\hat{\mathcal{E}}_-} \quad (1)$$

where $\mathcal{U}$ is contributed by the interactions in the critical layer, corresponding to the streamwise velocity jump across the critical layer, $\mathcal{S}$ is reflected in the effect of the small-scale structure on the coherent structure, $\mathcal{Y}$ represents the back action from the sound field acted on the source, corresponding to the pressure jump, k is the axial wavenumber, c is the phase speed, y represents the transverse direction, $\mathcal{E}_+$ and $\mathcal{E}_-$ are functions related to the boundary conditions, $\hat{\blacksquare}$ means the Fourier transform of the corresponding quantity. More details can be found in [9].

Then the acoustic pressure $\tilde{P}^+$ can be obtained by integrating the sound source. Here, we directly give the final far-field pressure at any equivalent distance $\bar{R}$ and angle θ to jet axis as follows,

$$\tilde{P}^+\sim\frac{1}{2\pi^2\bar{R}}\int_{-\infty}^{\infty}e^{sgn[\phi''(\omega,k_s,\theta)]i\pi/4-i\pi/4}D_P(\omega,k_s)\widehat{a_{Ml}^+}(\omega,k_s)e^{i\phi(\omega,k_s,\theta)\bar{R}-i\omega\tau}d\omega \quad (2)$$

3. NUMERICAL RESULTS

In present study, the parameters of disturbance waves were listed in table 1, and ω_1, ω_2 are the two inflow primary waves. It should be noted that this simplified "double-wave" model was proposed by Sandham [11-12], and they pointed out there would be a strong nonlinear interaction creating the difference mode wave. Therefore, we calculated these classic cases to verify the feasibility of our hybrid method on the one hand, and on the other hand to analysis the mechanisms of sound radiation of this simplified model in detail.

The dimensionless parameters, Mach number and Reynolds number, are chosen the same as the experimental parameters of Stromberg *et al*. [13], which are *M=0.9* and *Re=3600* respectively.

Table 1. Parameters of inflow.

ω_1	ω_2
2.2	3.4

Figure 1 shows the instantaneous dilation rate field calculated by the present method. The sound radiation is highly directional, and noise is emitted from the vortex roll-up position, implying that the sound sources are just hidden here. The wavelength of the emitted sound corresponds to the difference mode frequency $\Delta\omega=1.2$, which means that the difference mode generated by the nonlinear interaction between two inflow disturbances dominates the acoustic radiation.

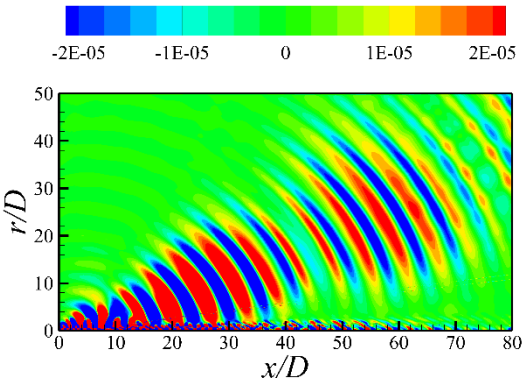


Figure 1. The instantaneous dilation rate field.

By integrating the equivalent sound source, the far-field pressure can be easily obtained. For an intuitive description, the sound pressure level was calculated and compared with the results of DNS, see in Figure 2. And the results of DNS are calculated by the empirical formula

$$SPL=20log_{10}\left(\frac{p'_{DNS}p_s}{p_c p_{ref}}\right), \quad (3)$$

where p'_{DNS} is the calculated pressure of DNS, the relative pressure $p_{ref}=2\times10^{-5}N/m^2$, p_s is the standard atmospheric pressure and $p_c=0.0072p_s$.

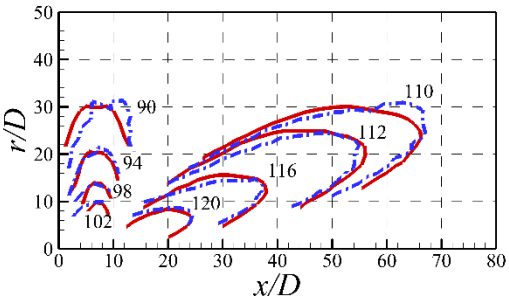


Figure 2. The sound pressure level contours. (red line for present result; blue dashed line for DNS)

It is evident that the results of the present method are exactly congruent with those of direct simulation. For the low angle region, the sound radiation exhibits super-directive characteristics at an angle of nearly *30* °relative to the jet axis. This radiation mechanism can be considered as an extension of the Mach-wave radiation.
In addition, there is another direction of radiation at an angle approximately *90* °to the jet axis. This finding is an indication of the presence of an additional high angle radiation mechanism. The nonlinear interaction of the instability waves gives rise to a mean-flow distortion. This distortion is slowly modulated in both time and space and acts as an emitter, radiating low-frequency sound waves on the scale of the wavepacket envelope at a high angle. This phenomenon is so called envelope radiation.

4. CONCLUSION

This paper presents a novel non-Lighthill hybrid method for the study of the acoustic radiation of axisymmetric modes in subsonic jets. The results, of our hierarchical hybrid methodology, exhibit a remarkable agreement with experimental observations and those obtained from DNS. It is therefore concluded that the non-Lighthill hybrid method is a feasible approach for predicting acoustic noise in subsonic jets.
The findings also indicate the presence of two distinct sound sources and two sound radiation mechanisms: general Mach-wave radiation and envelope radiation.

5. ACKNOWLEDGMENTS

This work is being supported by National Natural Science Foundation of China (Grant 91852110) and State Key Laboratory of Hydraulic Engineering Simulation and Safety (HESS-1812).

6. REFERENCES

[1] Crow, S. C., and Champagne, F. H.: "Orderly structure in jet turbulence," *Journal of Fluid Mechanics*, Vol. 48, pp. 547–591, 1971.
[2] Armstrong, R. R., Michalke, A., V. Fuchs, H: "Coherent structures in jet turbulence and noise," *AIAA Journal*, 15 (7), 1011-1017, 1977.
[3] Tam, C. K. W., Viswanathan, K., Ahuja, K. K., Panda, J.: "The sources of jet noise: experimental evidence," *Journal of Fluid Mechanics*, Vol. 615, 2008, pp. 253-292.
[4] Mitchell, B. E., Lele, S. K., Moin, P.: "Direct computation of the sound generated by vortex pairing in an axisymmetric jet," *Journal of Fluid Mechanics*, Vol. 383, 1999, pp. 113-142.
[5] Lighthill M. J.: "On sound generated aerodynamically. I. General theory," *Proc. R. Soc. Lond. A*, 211: 564–587, 1952.
[6] Tam C. K. W., Burton D. E.: "Sound generated by instability waves of supersonic flow. Part 2. Axisymmetric jets," *J. Fluid Mech.*, 138: 273–295, 1984.
[7] Wu, X. S.: "Mach wave radiation of nonlinearly evolving supersonic instability modes in shear layers," *Journal of Fluid Mechanics*, Vol. 523, 2005, pp. 121-159.
[8] Wu, X. S., Huerre, P.: "Low-frequency sound radiation by a nonlinearly modulated wavepacket of helical modes on a subsonic circular jet," *Journal of Fluid Mechanics*, Vol. 637, 2009, pp. 173-211.
[9] Z. Zhang and X. Wu: "Nonlinear evolution and low-frequency acoustic radiation of ring-mode coherent structures on subsonic turbulent circular jets," *J. Fluid Mech.* 940(A39), 1-56, 2022.
[10] Z. Zhang andhere X. Wu: "A unified theory for the envelope radiation of ring-mode coherent structures in the very-near nozzle and developed regions of circular jet." *Phys. Fluids.* 35(10), 014113, 2023.
[11] N. D. Sandham and A. M. Salgado: "Nonlinear interaction model of subsonic jet noise," *Phil. Trans. R. Soc. London*, Ser. A. 366, 2745-2760, 2008.
[12] Sandham, N. D., and Salgado, A. M.: "Nonlinear interaction model of subsonic jet noise," *Philosophical Transactions of the Royal Society A: Mathematical, Physical and Engineering Sciences*, Vol. 366, 2008, pp. 2745-2760.
[13] Stromberg, J. L., Mclaughlin, D. K., and Troutt, T. R.: "Flow field and acoustic properties of a Mach number 0.9 jet at a low Reynolds number," *Journal of Sound and Vibration*, Vol. 72, 1980, pp. 159-176.

DOI:

Main theme: A07 Flow Acoustics

Session A07.02 Aeroacoustics of aircraft and urban air vehicles

Chair(s): R. Camussi, D. Ragni, D. Casalino

DOI: 10.61782/fa.2025.0110



FORUM ACUSTICUM
EURONOISE 2025

AEROACOUSTICS OF UAV PROPELLERS WITH UNEQUALLY SPACED BLADES

Dima Usov[1*] **Antonio Filippone**[1]
Caterina Poggi[2] **Giovanni Bernardini**[2]
[1] The University of Manchester, United Kingdom
[2] Roma Tre University, Italy

ABSTRACT

The study delves into the characterisation of the aeroacoustic response of low-Reynolds number propellers subjected to blade spacing angle modification. A numerical investigation was carried out on two-bladed propellers featuring blade spacing angles from 30 to 150 degrees, in 30-degree increments, as well as a conventional propeller with 180-degree blade spacing. The non-uniform blade spacing can mitigate tonal contributions at the blade passing frequency and its harmonics while introducing non-zero contributions at odd multiples of the shaft frequency. The objective of this work is to determine the effect of the blade spacing angle on the distribution of the acoustic energy spectrum and the aerodynamic quality of the propeller. The numerical analyses were performed by a potential aerodynamic solver based on a boundary integral method and an aeroacoustic solver based on the Farassat 1A formulation. The predictions were validated against experimental measurements for conventional and 90-degree blade spacing propellers. The time-averaged propeller thrust and tonal overall sound pressure level were accurately predicted. Propellers with uneven obtuse blade spacing angles displayed the largest addition of the acoustic energy towards the lower frequency domain while preserving the aerodynamic performance of the reference propeller.

Keywords: *aeroacoustics, aerodynamics, propellers.*

*__Corresponding author__: *dmitrij.usov@manchester.ac.uk..*
__Copyright__: *©2025 Dima Usov et al. This is an open-access article distributed under the terms of the Creative Commons Attribution 3.0 Unported License, which permits unrestricted use, distribution, and reproduction in any medium, provided the original author and source are credited.*

1. INTRODUCTION

The prevalence of unmanned aerial vehicles (UAVs) utilising low-Reynolds number propellers is increasing, leading to the establishment of new economic sectors. The perception of noise pollution by humans and the subsequent public acceptance of UAVs represent one of the major barriers to the widespread adoption of these aircraft [1]. The optimisation of propeller designs aimed at mitigating the adverse effects of noise pollution presents significant advantages to emerging aerial robotics services. For this reason, academia and industry are making considerable efforts to investigate and design innovative solutions aimed at reducing the acoustic nuisance of these vehicles [2–4]. To this aim, it is evident that a profound understanding of the mechanism governing noise generation is essential to characterise the acoustic footprint of low-Reynolds number propellers, a topic that has become the focus of extensive literature [5–9].

This study investigates an approach to mitigate acoustic emissions, by manipulating the blade spacing angle that eliminates radial symmetry. Under the assumption of identical and evenly spaced blades, the tonal components of the emitted noise emerge at frequencies that are multiples of the blade passing frequency (BPF) [10]. Contrarily, with blades that are not equally spaced, the tonal noise components manifest at harmonics of the revolution frequency. Therefore, the premise is to utilise this redistribution of the energy content resulting from the uneven blade spacing to diminish the noise emitted at the multiples of the BPF, while recognising that the drawback is the onset of tonal contributions at the revolution frequency and its odd harmonics. It is critical to emphasise that the blade spacing, in principle, influences the aerodynamic perfor-

mance. Hence, a balance between acoustic benefits and performance deterioration should be found.

In this context, a characterisation of the aeroacoustic response of uneven-blade spaced propellers was conducted. Six distinct propeller configurations were examined, featuring blade spacings of 30, 60, 90, 120, 150, and 180 degrees. Due to the apparent radial asymmetry due to uneven blade spacing, these propellers can be referred to as "asymmetric" propellers. The numerical analysis was performed through the application of an aerodynamic solver based on a boundary integral formulation for potential flows and an aeroacoustic solver based on the Farassat 1A formulation for tonal noise prediction. Numerical simulations were supplemented by the experimental measurements of a conventional propeller configuration described by blade spacing of 180 degrees, referred to as VP-R, and a non-conventional design with blade spacing of 90 degrees, denoted by VP-9.

2. NUMERICAL METHOD

The aerodynamic analysis was performed through a Boundary Element Method (BEM) solver based on the boundary integral formulation introduced in [11], able to take into account the effects of significant body-wake interactions. Under the assumption of potential and incompressible flows, the potential field was defined as the superposition of an incident field, generated by doublets over the wake portion not in contact with the trailing edge (far wake), and a scattered field, generated by sources and doublets over the body and doublets over the wake portion very close to the trailing edge (near wake). This procedure allows the removal of the numerical instabilities arising when a doublet wake comes too close to or impinges on the body. Recalling the equivalence between the surface distribution of doublets and vortices, the contribution of the far wake was expressed as a net of thick vortices (i.e., Rankine vortices). In this approach, the wake shape can be either assigned (prescribed-wake analysis) or obtained as a part of the solution (free-wake analysis) by a time-marching integration scheme in which the wake points move according to the local velocity field.

Once the potential field was obtained, the Bernoulli theorem yielded the pressure distribution on the body that, in turn, was used both to determine the aerodynamic loads and to predict the radiated noise, being the input of the aeroacoustic solver. The aeroacoustic analysis was performed by a prediction tool based on the linear Farassat 1A boundary integral formulation [12]. Specifically, the acoustic pressure field was given as the superposition of only the thickness noise depending on body geometry and kinematics and the loading noise related to the pressure distribution over body surfaces (being the quadrupole term negligible in the analysed flight condition).

3. VALIDATION

The numerical aerodynamic and aeroacoustic solvers used in this study have undergone extensive validation against empirical data [13–15]. However, due to the unconventional propeller geometries examined herein, an additional validation set involving a propeller with unequal blade spacing angles has been presented.

All the numerical results presented in the paper were obtained by discretising each propeller blade in $6,000$ panels, whereas $43,200$ panels are used over the corresponding wake surface, which was assumed to be eight revolutions long, with 60 panels distributed along the radial direction. A schematic representation of the discretised geometry is shown in Figure 1 for the baseline propeller configuration. A free-wake algorithm was used for the aerodynamic solution. A non-dimensional time-step of 3 degrees was used for the aerodynamic analysis, whereas a step of $1/2$ degrees was used for the aeroacoustic one. It was verified that these computational mesh characteristics and time discretisation guaranteed converged numerical results.

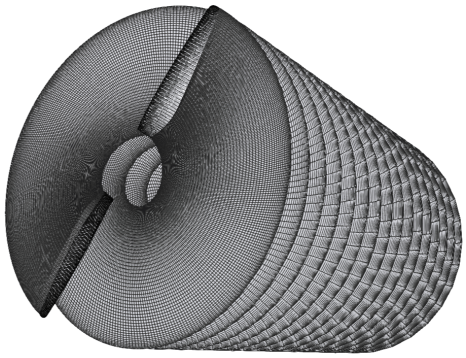


Figure 1. Discretisation of the reference propeller, VP-R.

3.1 Propellers

For validation of the numerical solver, two fixed-pitch, 16×5.5 inches lifting propellers were examined: the con-

ventional, reference off-the-shelf propeller (VP-R) and a custom propeller with 90-degree blade spacing (VP-9), as illustrated in Figure 2. The designation "VP" refers to V-Propeller, named for its characteristic shape. Both propellers had equivalent blade geometry, solidity and tip radius, and were fabricated by a company specialising in the low-Reynolds number propellers manufacturing. To address the inertial imbalance in the plane of rotation for the VP-9 configuration, a finely tuned counterbalance pellet was fitted into the elongated hub of the propeller.

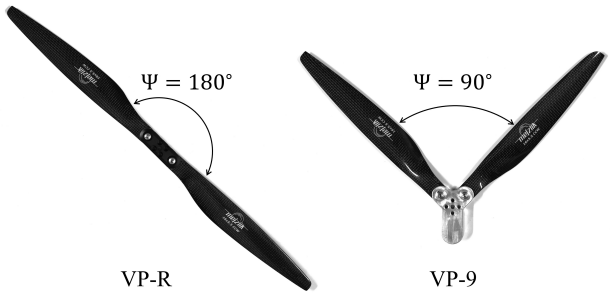


Figure 2. Propeller set. Reference propeller, VP-R, and propeller with 90-degree blade spacing angle, VP-9.

3.2 Test procedure

The aeroacoustic response measurements were carried out in an anechoic chamber with a cut-off frequency of 50 Hz at the University of Salford, instrumented to measure far-field aeroacoustic response for different observation angles. In particular, nineteen 1/2-inch far-field pressure microphones – nine Brüel and Kjær 4963 and nine GRAS 46AO – were installed on a two-and-half meter arc centred in the propeller hub and lying in the plane orthogonal to the propeller plane of rotation. The microphones were uniformly spaced across observation angles, θ, ranging from 0 to 180 degrees, in 10-degree increments, with the microphone at a 180-degree observation angle located within the propeller wake. The microphone signals were recorded at a sampling rate of 50 kHz.

3.3 Aerodynamic response

The comparison of the time-averaged static thrust predictions with the experimental data is presented in Figure 3 for the VP-R and VP-9 propeller. The agreement between simulated results and test data was deemed satisfactory, particularly in the $3,500$ to $5,000$ rpm domain. At rotational speeds below $3,500$ rpm the Reynolds number at 75% tip radius falls below $50,000$, leading to augmented effects of viscosity terms. At speeds exceeding $5,000$ rpm, the influence of compressibility becomes substantial. These effects are not captured by the governing equations of the aerodynamic solver, resulting in a slight decline in the level of agreement within these speed domains. Nonetheless, the observed discrepancies remained marginal. At a speed of interest, $5,000$ rpm, the percentage error between predicted and mean measured thrust for VP-R and VP-9 propellers were 2.9% and 1.6%, respectively. Regarding the effect of the blade spacing, it only

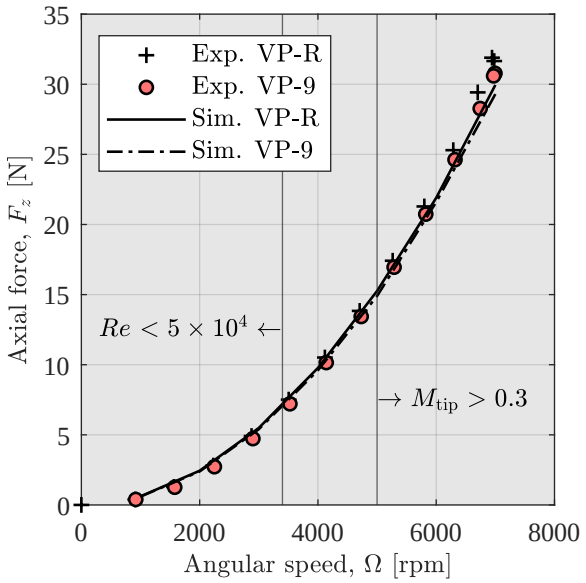


Figure 3. Validation of the predicted time-averaged static propeller thrust.

slightly affects the aerodynamic performance, and mainly for angular velocities higher than $6,000$ rpm. In particular, a thrust decrease as the propeller blade spacing decreases is observed, as captured both numerically and experimentally.

3.4 Aeroacoustic response

For the spectral analysis of the experimental data, a Hanning window was used, characterised by a constant partition size of 2^{17} and 75% overlap, giving a frequency resolution of 0.38 Hz. The power spectral density was

obtained using Welch's method. The reference acoustic pressure level was assumed at 20 µPa.

The noise directivity in terms of zero-weighted overall sound pressure level (OASPL) is shown in Figure 4. The simulated OASPL had a tonal nature and solely incorporated the first ten harmonics of the rotational frequency. Consequently, only the tonal contributions of the measured sound pressure level spectrum were extracted and truncated at a fifth BPF harmonic, $0 < f^+ \leq 5$, to ensure that the experimental results remained directly comparable to the simulation output. The acoustic response was not reported for emission angles between 170 and 180 degrees due to the contamination of the recorded sound pressure signal by the propeller wake. In the case of a conventional propeller, VP-R, the mean discrepancy between the measured data and the simulation for all reported emission angles was found to be 3.9 dB. The most considerable discrepancies were observed at the emission angles corresponding to the suction side of the propeller, ranging from 0 to 20 degrees. In contrast, the OASPL predictions for the propeller with 90-degree blade spacing, VP-9, displayed a strong agreement with the experimental data, yielding a mean difference of 2.3 dB, with discrepancies consolidated in the domain from 60 to 110 degrees.

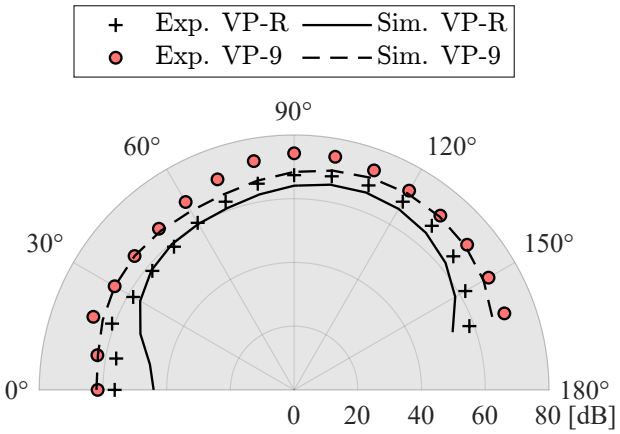


Figure 4. Tonal **OASPL** polar.

4. RESULTS

Upon validating the numerical solver against the experimental data corresponding to both the VP-R and VP-9 configurations, the solver was subsequently employed to asses the influence of the blade spacing angle on the aerodynamic and aeroacoustic responses of the propeller. Figure 5 shows the effect of the blade spacing angle on the time-averaged propeller thrust coefficient – computed at 5,000 rpm in static flight conditions. In agreement with the experimental observation for the VP-R and VP-9 propellers, as well as findings reported in prior publications [16, 17], a decrease in blade spacing angle corresponded with a reduction in time-averaged propeller thrust. Especially, at a blade spacing angle of 30 degrees, a thrust reduction of approximately 9% was observed, a trend that displayed lesser impact for obtuse angles, with thrust reduction diminishing to less than 1% for blade spacing angles greater than 120 degrees.

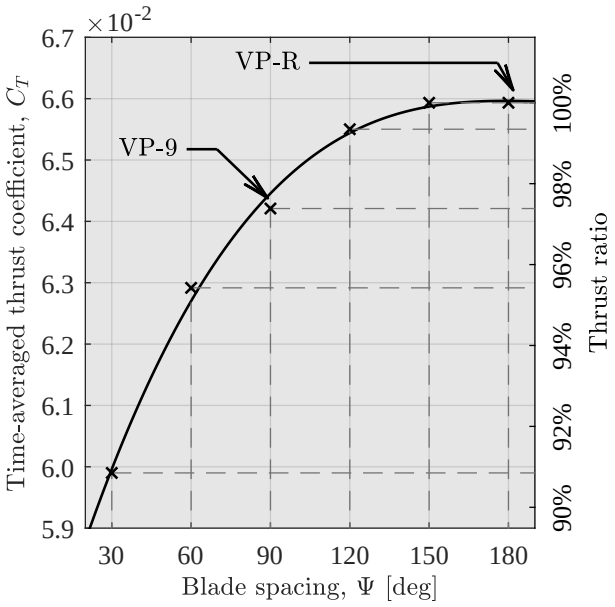


Figure 5. Variation of time-averaged propeller thrust coefficient as a function of the blade spacing angle.

The predicted tonal components of the sound pressure level are illustrated in Figure 6. As anticipated, propellers featuring uneven blade spacing demonstrated the emergence of tones at odd multiples of the shaft frequency. This observation suggests that the uneven blade spacing angle has indeed facilitated a redistribution of acoustic energy within the frequency spectrum. Furthermore, as the blade spacing was reduced a greater amount of acoustic energy was added to the spectra within the analysed frequency interval, $0 < f \leq 833$ Hz. However, it would be a misinterpretation to assert that reduced blade spac-

ing negatively affects acoustic performance, as only the first five BPF harmonics were identified. The observed increase in peak amplitudes may be correlated with a shift in tonal energy toward the lower frequency domain, which must occur at the expense of the higher frequency energy content, thereby the total radiated acoustic energy must be preserved – subject to further investigation.

5. CONCLUDING REMARKS

A numerical and experimental study was conducted to analyse the aerodynamic and aeroacoustic characteristics of a two-bladed low-Reynolds number propeller with uneven blade spacing under static flight conditions. The correlation found between the measured experimental data and the numerical results enhances the fundamental understanding of the key factors affecting both the aerodynamic efficiency and the sound signatures linked to these configurations, while also confirming the effectiveness of the numerical solver for unconventional propeller designs.

A parametric analysis was performed to investigate how different blade spacing angles affect aerodynamic and aeroacoustic behaviours in propellers. The blade spacing angles considered were 30, 60, 120, and 150 degrees.The purpose of this study was to explore the possibility of optimising the blade spacing angle to shift acoustic energy content toward the lower frequency domain while also minimising negative effects on aerodynamic performance.

The implementation of uneven blade spacing facilitates a redistribution of the acoustic energy content towards the lower frequency domain. The uneven blade spacing added more energy into the spectrum in the frequency interval up to the fifth BPF harmonic. Understanding whether this increase in acoustic energy at the lower end of the frequency spectrum occurs at the expense of the higher frequency content remains a topic for further investigation.

6. ACKNOWLEDGMENTS

This research is funded by the U.K. Engineering and Physical Sciences Research Council (EPSRC) Grant EP/W010119/1 Greener Aviation with Advanced Propulsion Systems (GAAPS). The authors would like to thank Antonio J. Torija and acknowledge the funding provided by the U.K. Engineering and Physical Sciences Research Council for the DroneNoise project (EP/V031848/1) and by Innovate U.K. for the InCEPTion (Integrated Flight Control, Energy Storage and Propulsion Technologies for Electric Aircraft) project (ref. 73692).

7. REFERENCES

[1] A. J. Torija, Z. Li, and P. Chaitanya, "Psychoacoustic modelling of rotor noise," *The Journal of the Acoustical Society of America*, vol. 151, no. 3, pp. 1804–1815, 2022.

[2] D. Ingraham, J. S. Gray, and L. V. Lopes, "Gradient-based propeller optimization with acoustic constraints," in *Aiaa scitech 2019 forum*, p. 1219, 2019.

[3] C. Poggi, M. Rossetti, G. Bernardini, U. Iemma, C. Andolfi, C. Milano, and M. Gennaretti, "Surrogate models for predicting noise emission and aerodynamic performance of propellers," *Aerospace Science and Technology*, vol. 125, p. 107016, 2022.

[4] L. Abergo, A. Guardone, and G. Gori, "Towards a two-stage multi-fidelity shape optimization approach to noise reduction in urban air mobility applications," in *AIAA Scitech 2025 Forum*, p. 0245, 2025.

[5] D. Casalino, E. Grande, G. Romani, D. Ragni, and F. Avallone, "Definition of a benchmark for low reynolds number propeller aeroacoustics," *Aerospace Science and Technology*, vol. 113, p. 106707, 2021.

[6] G. Romani, E. Grande, F. Avallone, D. Ragni, and D. Casalino, "Performance and noise prediction of low-reynolds number propellers using the lattice-boltzmann method," *Aerospace Science and Technology*, vol. 125, p. 107086, 2022.

[7] E. Grande, D. Ragni, F. Avallone, and D. Casalino, "Laminar separation bubble noise on a propeller operating at low reynolds numbers," *AIAA Journal*, vol. 60, no. 9, pp. 5324–5335, 2022.

[8] L. T. Lima Pereira, D. Ragni, G. Romani, and D. Casalino, "Accuracy of tonal noise prediction of propellers via numerical simulations and experimental campaigns," in *30th AIAA/CEAS Aeroacoustics Conference (2024)*, p. 3267, 2024.

[9] A. D. Thai, E. De Paola, A. Di Marco, L. G. Stoica, R. Camussi, R. Tron, and S. M. Grace, "Experimental and computational aeroacoustic investigation of small rotor interactions in hover," *Applied Sciences*, vol. 11, no. 21, p. 10016, 2021.

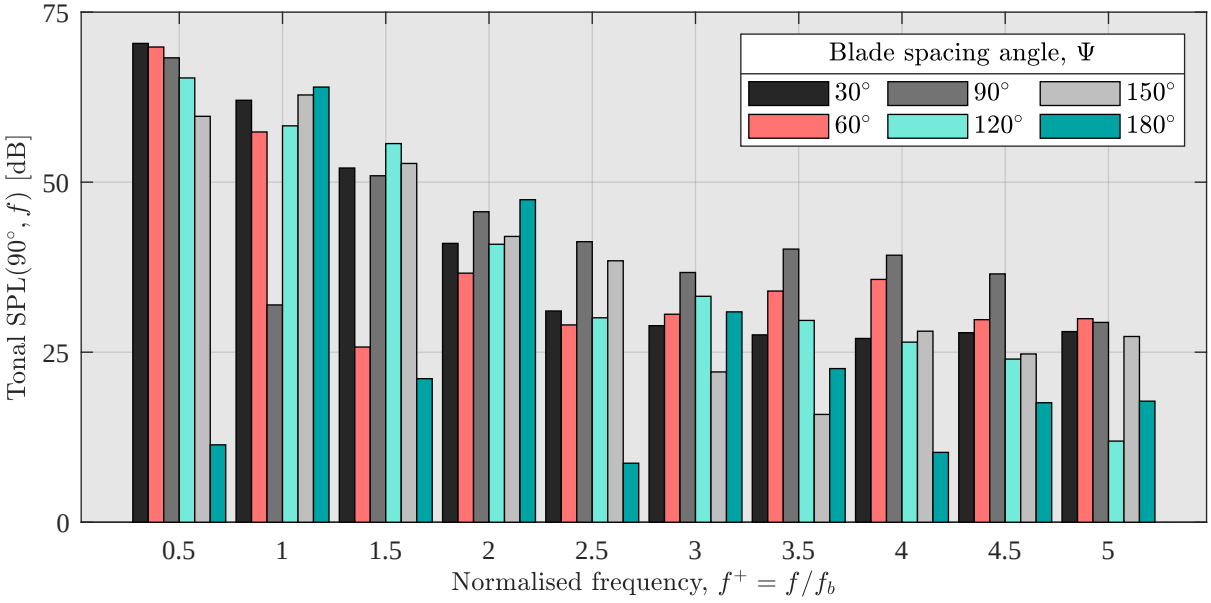


Figure 6. Frequency response of tonal sound pressure level as a function of the blade spacing angle in decibels at 5,000 rpm for an observer in the plane of rotation.

[10] W. Johnson, *Rotorcraft Aeromechanics*, vol. 36. Cambridge university press, 2013.

[11] M. Gennaretti and G. Bernardini, "Novel boundary integral formulation for blade-vortex interaction aerodynamics of helicopter rotors," *AIAA journal*, vol. 45, no. 6, pp. 1169–1176, 2007.

[12] F. Farassat, "Derivation of formulations 1 and 1A of Farassat," Tech. Rep. TM-2007-214853, NASA Langley Research Center, Hampton, VA, Mar 2007.

[13] M. Gennaretti, G. Bernardini, J. Serafini, and G. Romani, "Rotorcraft comprehensive code assessment for blade–vortex interaction conditions," *Aerospace Science and Technology*, vol. 80, pp. 232–246, 2018.

[14] C. Poggi, E. de Paola, L. G. Stoica, and A. Di Marco, "Numerical and experimental characterization of an isolated low-reynolds rotor in pusher configuration," in *FORUM ACUSTICUM 2023*, 2023.

[15] J. Yin, F. Gregorio, K.-S. Rossignol, L. Rottmann, G. Ceglia, G. Reboul, G. Barakos, G. Qiao, M. Muth, M. Kessler, *et al.*, "Acoustic and aerodynamic evaluation of dlr small-scale rotor configurations within garteur ag26," *CEAS Aeronautical Journal*, 2024.

[16] D. Usov, T. Chronis, A. Filippone, and N. Bojdo, "Performance of asymmetric propellers under varying blade spacing," in *49th European Rotorcraft Forum*, (Buckebürg, Germany), 2023.

[17] D. Usov, D. Koning, T. Chronis, A. Filippone, D. Akiwate, and A. J. T. Martinez, "Aerodynamics and acoustics of asymmetric propellers with uneven blade spacing," in *30th AIAA/CEAS Aeroacoustics Conference*, 6 2024.

DOI: 10.61782/fa.2025.0406

FORUM ACUSTICUM
EURONOISE 2025

FLOW CHARACTERISATION USING PIV TO OPTIMISE MICROPHONE WINDSCREENS FOR ON-BOARD SELF-NOISE MEASUREMENTS OF A MULTICOPTER (UAV) UNDER DIFFERENT FLIGHT CONDITIONS

Julian Benz[1*] **Christoph Heigl**[1] **Felix Czwielong**[1]
Andreas Gründer[2] **Jörg Franke**[2] **Stefan Becker**[1]
[1] Institute of Fluid Mechanics,
Friedrich-Alexander-University Erlangen-Nuremberg, 91058 Erlangen, Germany
[2] Institute for Factory Automation and Production Systems,
Friedrich-Alexander-University Erlangen-Nuremberg, 91058 Erlangen, Germany

ABSTRACT

Accurately measuring the self-noise of unmanned aerial vehicles (UAVs) is crucial for acoustic characterisation, noise reduction optimisation, and gaining public acceptance and certification of these aircraft. An on-board measurement setup allows direct and flexible detection of acoustic phenomena in different flight conditions, without the need for external sensor installations with the problem of continuously changing measurement distance and a complex measurement setup. For reliable measurements, especially at higher flight or wind speeds, an effective microphone windscreen is essential. This windscreen should ideally shield the microphone from ambient and propeller airflow while introducing minimal additional turbulence noise, which could otherwise mask the UAV's self-noise and reduce measurement accuracy. In this study, the airflow around the microphone of a quadrocopter UAV was experimentally analysed for different flight conditions using stereo PIV measurements and a wind tunnel. Based on the results, optimisation possibilities for the microphone windscreen solution were investigated in an aeroacoustic wind tunnel. Starting from commercially available windscreens, different designs were investigated and refined to effectively suppress hydrodynamic pressure fluctuations that overlap with the UAV self-noise. The results illustrate how airflow patterns change in different flight situations and highlight practical optimisation strategies to improve the accuracy of UAV self-noise measurements.

Keywords: *multicopter, PIV, noise, microphone, windscreen*

**Corresponding author: julian.benz@fau.de.*
***Copyright**: ©2025 Julian Benz This is an open-access article distributed under the terms of the Creative Commons Attribution 3.0 Unported License, which permits unrestricted use, distribution, and reproduction in any medium, provided the original author and source are credited.*

1. INTRODUCTION

Multirotors, commonly known as drones or Unmanned Aerial Vehicles (UAVs), have evolved rapidly from futuristic concepts to practical tools used in diverse commercial and public service applications. Examples of their widespread adoption include autonomous package deliveries already operational in regions such as Australia [1] and upcoming implementations planned in the United Kingdom and elsewhere [2]. Additionally, their inherent flexibility has enabled them to perform various specialized tasks, ranging from media production, such as aerial photography and videography, to medical logistics like the rapid transport of blood samples [3], and critical roles in rescue and reconnaissance missions [4–6] or in the agriculture [7]. The increased use of UAVs introduces significant challenges, most notably the issue of noise emissions [8]. Drone-related noise pollution has become a contentious issue, often leading to public concern and regulatory scrutiny. Engineers and developers thus face the dual challenge of effectively reducing noise emissions while si-

multaneously adhering to regulatory acoustic limits, similar to those established for other technical equipment like heat pumps [9]. Moreover, enhancing energy efficiency remains crucial, as it directly affects the operational range and flight duration of multirotor systems. Prior research at the Chair of Fluid Mechanics (LSTM) has investigated correlations between propeller-generated thrust and noise emissions under controlled hover conditions, confirming a strong link between aerodynamic performance and acoustic output [10]. However, to thoroughly characterize and understand UAV acoustics, it is essential to expand analyses beyond hover conditions. Realistic flight operations, including horizontal, climbing, and descending maneuvers, involve complex aerodynamic interactions that significantly influence the acoustic footprint of the aircraft. The reason for this is that each of these flight maneuvers exhibits specific aerodynamic characteristics [11] and phenomena also known from helicopters. These include the vortex ring state in vertical flight, blade-vortex interactions, flow separations, or Mach number effects [12]. In order to capture the noise emissions of multirotors, there are essentially two approaches: external measurements using microphone(s) on the ground or direct onboard measurements with microphone(s) on the drone itself. However, external measurements are associated with drawbacks, as they usually require a multitude of specifically arranged microphones [13], entail complex evaluations, and the variability of the drone's position during flight as well as atmospheric sound propagation effects [14] limit the measurement accuracy. An on-board measurement using one or more microphones offers a flexible and practical alternative, allowing acoustic data to be recorded directly and continuously during flight. Nevertheless, other challenges arise, particularly due to hydrodynamic pressure fluctuations caused by the propeller flow as well as the self-motion of the multirotor and ambient wind. Previous studies have shown that, especially at higher flight speeds, significant masking effects due to hydrodynamics impair the measurement of the actual self-noise [10]. Furthermore, it has been demonstrated that the positioning of the microphone has a significant impact on the measured sound spectrum. While other publications have positioned microphones on lateral arms [15], future placement is intended to be centrally above the drone, near the horizontal center of mass and without altering the moments of inertia about the horizontal axes. This positioning reduces unwanted influences on flight stability and agility, enables better comparability of the measurements. Furthermore, as demonstrated in the volumetric PIV investigation by Wolf [16], is that in the suction area, where significantly less turbulence occurs compared to a placement beneath the drone. This study clearly illustrated not only the reduction in turbulence but also the behavior of the flow—including blade vortices and other flow phenomena during various flight maneuvers—in different regions around the drone. For our purposes, it is particularly important to analyze how the flow behaves in the suction area, especially in terms of flow direction and turbulence levels, where the effects of the drone's body flow are most pronounced. Therefore, the subsequent analysis will focus on characterizing the flow in this critical region.

2. FLOW CHARACTERIZATION

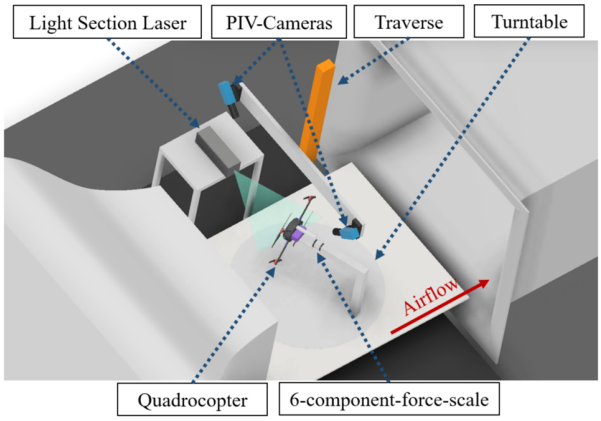


Figure 1. The measurement setup.

To enable future investigations of wind protection variants under realistic conditions, a detailed flow analysis using Stereo-PIV is conducted. The measurements were carried out in the wind tunnel of the Chair of Fluid Mechanics (LSTM). This wind tunnel has a cross-sectional area of $B = 1.87\,\mathrm{m} \times H = 1.40\,\mathrm{m}$ and a test section length of $L = 2.4\,\mathrm{m}$, featuring a central test table and an integrated turntable. A schematic picture of the measurement setup is shown in Fig. 1.

The quadrocopter used for the measurements was equipped with $D = 15$-inch propellers (T-Motor NS15x5) and has a flight weight without payload of $m_{\mathrm{Quadrocopter}} = 3.1\,\mathrm{kg}$. This UAV represents a typical 5-kg class system with a payload capacity of 2 kg, providing an excellent research platform. As shown in Fig. 2, the quadrocopter has canopy with an oval planform and proper extrusion to facilitate a better characterization of its surrounding airflow. Most of the onboard electronics, are housed within

the canopy and the battery hangs under it, so there is a minimal influence to the flow above, with only the electronic speed controlers slightly outside the canopy.

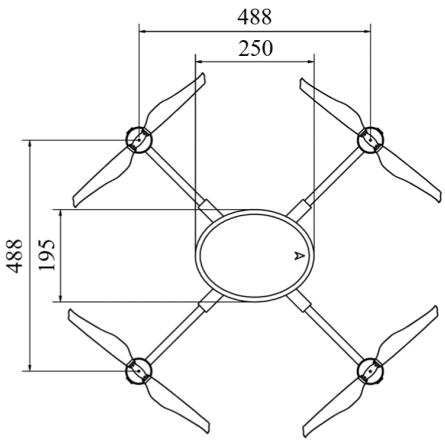


Figure 2. Dimensions of the investigated quadrocopter.

For the Stereo-PIV measurements, two *PCO.2000* cameras with *Sigma* lenses (f = 18–35 mm F1.8) and Scheimpflug adapters were employed. The system was calibrated and aligned using a specialized calibration device and an optical calibration plate. Scheimpflug optics ensured that both cameras shared the same focal plane, allowing reliable three-dimensional (XYZ) measurements. Particular care was taken to ensure that the seeding particles (propylene glycol) were accurately assigned throughout the measurement volume. The flow was illuminated by a pulsed Nd:YAG laser (*Quantel Twins BSL 200*), and data evaluation was performed using the software *PIVView3C*. The measured plane was located centrally between the rotors of the multirotor, as illustrated in Fig. 3. This plane is particularly relevant for understanding the flow, as the measurement microphone will be positioned here in the future.

The current and rotational speed were individually set and monitored for each motor. The multirotor was mounted on a 6-component force balance for the simultaneous measurement of aerodynamic forces on the turntable. The propeller thrust for each flight condition was validated using the 6-component force balance. The relative deviation between the experimentally measured thrust F_{meas} and the theoretically required thrust for weight compensation at a tilt angle θ was calculated as:

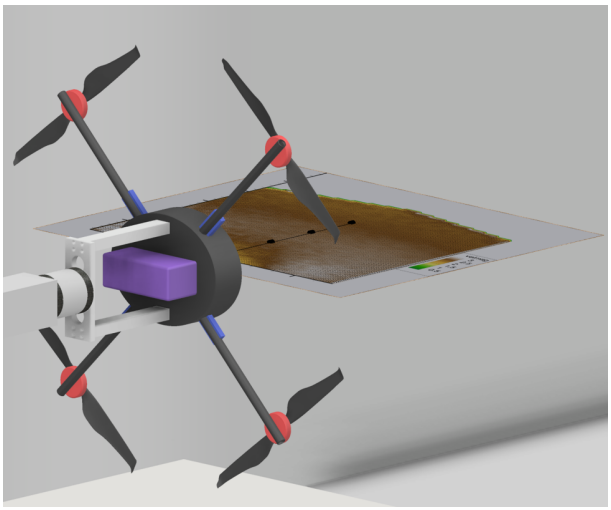


Figure 3. Illustration of the investigated measurement plane.

$$\Delta F_{\%} = \left(\frac{F_{\text{meas}} \cos(\theta)}{m\, g} - 1 \right) \times 100\,\%. \qquad (1)$$

The rotor speeds were determined experimentally during several test flights, with each relevant flight maneuver being performed multiple times and the recorded rotational speeds and currents averaged. These averaged rotor speeds were then precisely reproduced for each motor seperately in the wind tunnel.

2.1 Hover Case

In a hover case no external airflow is applied, which poses a challenge for PIV measurements since, without additional flow, the seeding particles are not sufficiently transported to characterize the velocity field. To overcome this, the airflow generated by the propellers was utilized. The thrust produced by the rotating propellers induces a passive airflow in our closed-loop wind tunnel (Göttinger design), that transports the particles. However, this passive flow leads to a circulation that establishes a relative airflow of approximately $v_{passive} = 1.86\,\text{m/s}$. This passive flow reduces the inflow angle on the propeller blades and consequently diminishes the generated thrust, so that the expected $T = 30.5$ N for hover is not fully reached, as seen in Fig. 4. To compensate, the propeller speed was increased by 200 rpm, which in turn raised the passive airflow to about $v_{passive} = 1.94\,\text{m/s}$. As a result, instead of a pure hover, the condition is more akin to a slow climb

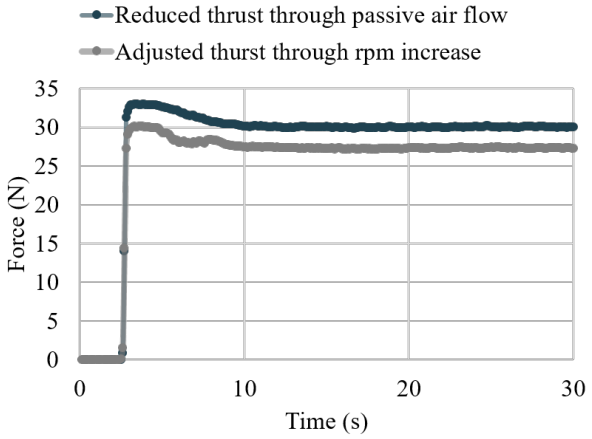


Figure 4. Thrust curve in hover case through passive air flow after turning on the motors at 2 s.

at $v_{vertical} = 1.94\,\mathrm{m/s}$. Analysis of the flow field in Fig. 5 shows that at a distance of the Z-coordinate in the body-fixed frame, $Z_{UAV} = 100\,\mathrm{mm}$ from the drone a stagnation zone with low velocities between $1\,\mathrm{m/s} \leq u \leq 1{,}5\,\mathrm{m/s}$ exists; at $Z_{UAV} = 200\,\mathrm{mm}$ and $Z_{UAV} = 300\,\mathrm{mm}$ the velocity increases to $v \approx 2.5\,\mathrm{m/s}$, and then decreases again to about $v = 2\,\mathrm{m/s}$ at $Z_{UAV} = 400\,\mathrm{mm}$. Furthermore, the flow direction remains largely consistent with only minor deflections very close to the drone at $Z_{UAV} \approx 50\,\mathrm{mm}$, where slight redirection components are observed.

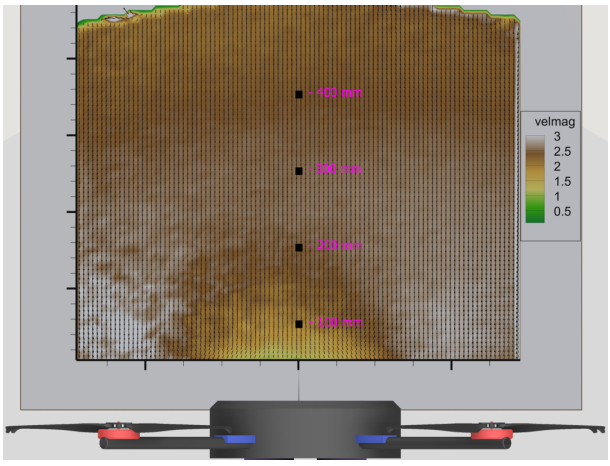


Figure 5. Averaged flow field at $v_{horizontal} = 5\,\mathrm{m/s}$ with the Z-coordinate indicated in the body-fixed frame.

2.2 Horizontal Flight with a Speed of 5 m/s

The conditions for the case of $v_{\text{horizontal}} = 5\,\mathrm{m/s}$ are summarized in Table 1.

Parameter	$v_{\text{horizontal}} = 5\,m/s$
Tilt Angle, θ [°]	4.1
Thrust Deviation, $\Delta F\%$	1.08%

Table 1. Flight conditions at $v_{\text{horizontal}} = 5\,m/s$.

Figure 6 illustrates the averaged flow field obtained under these conditions. The analysis reveals a pronounced stagnation zone in the immediate vicinity of the multirotor body, where the local flow velocity drops to approximately $v = 3.5\,\mathrm{m/s}$. At a distance of around $Z_{UAV} = 100\,\mathrm{mm}$ from the vehicle, distinct velocity peaks emerge, reaching up to $v = 8\,\mathrm{m/s}$. As the distance from the multirotor increases further, the flow velocity gradually diminishes, converging to the nominal flight speed of $v_{\text{horizontal}} = 5\,\mathrm{m/s}$. Moreover, while the flow direction near the body exhibits significant deviations, it increasingly aligns with the flight trajectory at larger distances.

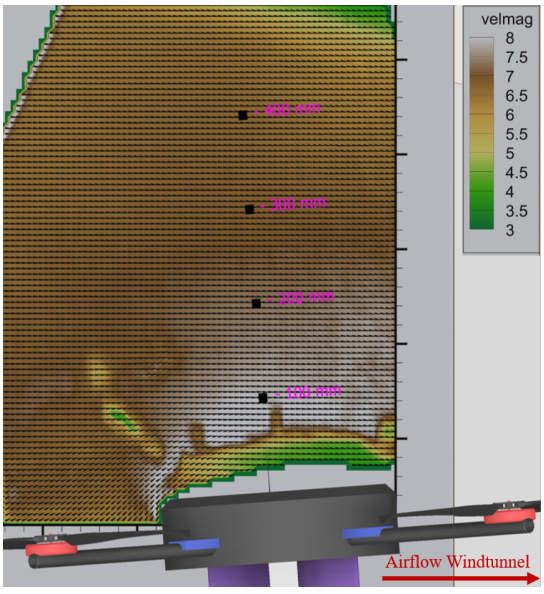


Figure 6. Averaged flow field at $v_{\text{horizontal}} = 5\,\mathrm{m/s}$ with the Z-coordinate indicated in the body-fixed frame.

2.3 Horizontal flight with a speed of 10 m/s

The conditions for the case of $v_{\text{horizontal}} = 10\,\text{m/s}$ are summarized in Table 2.

Parameter	$v_{\text{horizontal}} = 10\,m/s$
Tilt Angle, θ [°]	10.0
Thrust Deviation, $\Delta F\%$	2.98%

Table 2. Conditions at $v_{\text{horizontal}} = 10\,m/s$.

A similar flow pattern is observed at a higher horizontal flight speed of $v_{horizontal} = 10\,\text{m/s}$, as shown in Fig. 7. Here is also a strong stagnation zone was observed immediately at the multirotor body, which, at a distance of $Z_{UAV} = 100$ mm, exhibits strong flow velocity peaks of up to $v = 12\,\text{m/s}$. This increased velocity then continuously decreases with further distance and approaches the actual flight speed. Again, it is evident that near the multirotor body there are significant deviations in the flow direction from the actual flight direction, while at greater distances the flow direction corresponds to the flight trajectory.

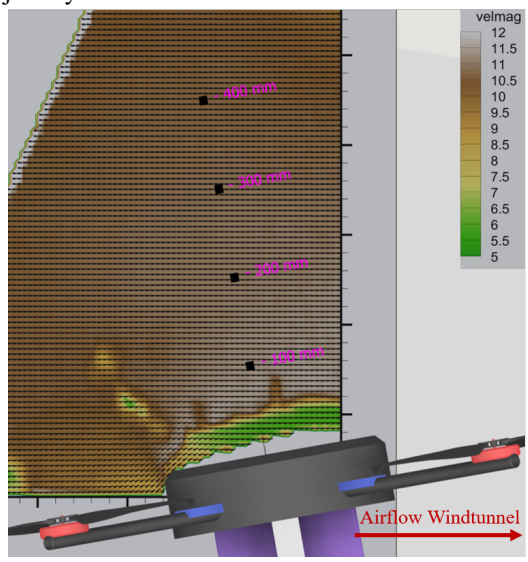


Figure 7. Averaged flow field at $v_{horizontal} = 10\,\text{m/s}$ with the Z-coordinate indicated in the body-fixed frame.

2.4 Horizontal Flight with a Speed of 15 m/s

For the case of $v_{\text{horizontal}} = 15\,\text{m/s}$ the conditions are shown in Table 3.

Parameter	$v_{\text{horizontal}} = 15\,m/s$
Tilt Angle, θ [°]	16.6
Thrust Deviation, $\Delta F\%$	-2.98%

Table 3. Flight conditions for $v_{\text{horizontal}} = 15\,m/s$.

In the $v_{horizontal}$ = 15 m/s case (see Fig. 8), a similar behavior is observed as in the previously investigated horizontal flow fields at different speeds. Very close to the drone, within less than $Z_{UAV} = 100$ mm, a stagnation zone with considerably reduced flow velocities $v \approx 8$ m/s is present, accompanied by strong flow deflections near the drone body. At a distance of around $Z_{UAV} = 100$ mm, a pronounced velocity peak is observed, reaching $v \approx 15$ m/s. With increasing distance from the drone, the flow velocity gradually decreases and eventually converges to the nominal flight speed of $v_{horizontal}$ = 15 m/s at about $Z_{UAV} = 400$ mm. Moreover, the flow direction progressively aligns with the flight trajectory of the drone.

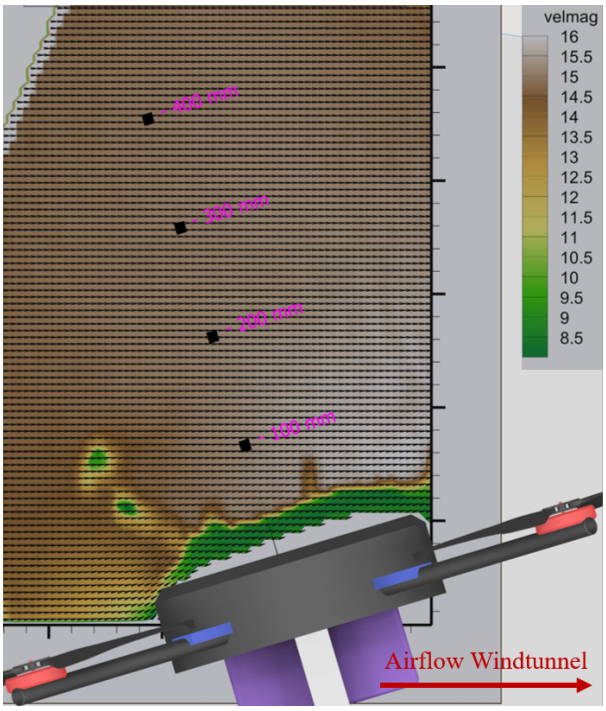


Figure 8. Averaged flow field at $v_{horizontal} = 15\,\text{m/s}$ with the Z-coordinate indicated in the body-fixed frame.

2.5 Summary of Flow Conditions

The present measurements reveal that in all investigated flight maneuvers, a pronounced stagnation zone develops in close proximity to the drone body. At approximately $Z_{UAV} = 80\,\text{mm}$ from the drone, the flow field exhibits significantly increased velocities, with local speeds exceeding the nominal flight speed of up to 60%. As the distance from the drone increases, the flow gradually aligns with the flight trajectory and approaches the vehicle's actual speed. At $Z_{UAV} = 200\,\text{mm}$, the velocities remain slightly elevated compared to the flight speed, while from around $Z_{UAV} = 300\,\text{mm}$ onward, the measured flow velocity essentially matches the nominal flight speed. Although a larger separation, such as $Z_{UAV} = 400\,\text{mm}$, would provide even more favorable flow conditions, it would necessitate a considerably larger mounting structure for the microphone.

These findings are critical for the future design of the wind protection system. The windscreen should be strategically positioned to avoid the stagnation zone, where elevated flow velocities are very close to and the directions the flow are changing. It is also expected that there is higher turbulence intensity within the stagnation region. So it is advisable to place the microphone in an area where the flow has already aligned with the flight trajectory and speed. Future investigations will focus on a detailed analysis of the turbulence distribution and its impact on the measurements, ultimately guiding the optimal positioning of the wind protection.

3. INVESTIGATION OF VARIOUS WIND PROTECTION VARIANTS

In future investigations, the characterized flow conditions will serve as the basis for evaluating various wind protection variants under realistic conditions. To illustrate the potential of these designs, preliminary results from experiments conducted in an aeroacoustic wind tunnel are presented in Fig. 9. These measurements were performed at an approach velocity of $v = 10\,\text{m/s}$ with a 90° incidence angle (i.e., perpendicular to the microphone). The following wind protection variants were tested:

- *MTG* Standard Foam Wind Protection 50 mm (referred to in the spectrum as *Foam*)
- *Rycote Baseball* (referred to in the spectrum as *Baseball*)
- *Rycote Cage with foam + Deadcat* (referred to in the spectrum as *Deadcat*)
- *Rycote Classic Softie* (referred to in the spectrum as *RCS*)
- *Rycote Super Softie* (referred to in the spectrum as *RSS*)

Figure 9 provides a comparison of the different wind protection variants at $v = 10\,\text{m/s}$. Additionally, two microphones were placed outside the primary flow region, and their averaged measurements (denoted as 'outside' in the spectrum) were used as reference values to account for the baseline hydrodynamic influence. The external measurements consistently showed low flow-induced noise, whereas significant differences became apparent when evaluating the wind protection variants.

Notably, the standard foam wind protection (*Foam*) exhibited average sound pressure levels of approximately $L_{p,\text{Mittel}} \approx 48\,\text{dB}$, similar to those observed for the *RSS* and *Baseball* variants. In contrast, the *Deadcat* demonstrated a considerable advantage over the foam by reducing overall sound pressure levels by roughly $\Delta L_{p,\text{Mittel}} \approx 4\,\text{dB}$. This improvement is particularly pronounced in the low-frequency range ($f < 500\,\text{Hz}$), where hydrodynamic pressure fluctuations are most influential. The *Deadcat* achieves a sound level reduction of about $\Delta L_p \approx 11\,\text{dB}$ compared to the foam there. Moreover, the frequency responses of the variants differ significantly in certain ranges. For instance, a switching behavior is observed where the *Foam* variant outperforms *RSS* in specific frequency bands, and vice versa. In some cases, characteristic spectral peaks, presumably due to flowinduced effects or structural noise from the wind protectors, were also detected and warrant further investigation.

At a higher approach velocity of $v = 20\,\text{m/s}$, even more pronounced differences emerge (see Fig. 10). Under these conditions, the classic foam variant performs the poorest. Although its performance up to about $f > 100$ Hz remains comparable to that of the other variants, from around $f < 200$ Hz onward its sound pressure levels increase dramatically by at least 10 dB compared to all other wind protection types a trend that continues well into the high kHz range. Of course it is not made for such flow velocities, it is more like a reference in this case. In contrast, the *RCS* variant performs best in the low-frequency range $f < 300$ Hz but exhibits a significant level increase at higher frequencies. Overall, when the entire frequency spectrum is considered, the *Deadcat* consistently shows

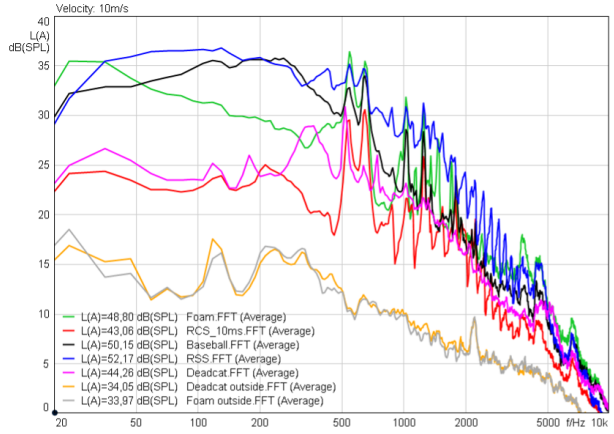


Figure 9. Comparison of the different wind protection variants at a flow velocity of $v = 10\,\mathrm{m/s}$.

the best performance, achieving an overall improvement of $\Delta L_p \approx 17\,\mathrm{dB}$ compared to the classic foam. The presence of characteristic peaks in some of the spectra suggests specific flow-induced components or inherent structural noise from the wind protectors, aspects that will be examined in more detail in future studies.

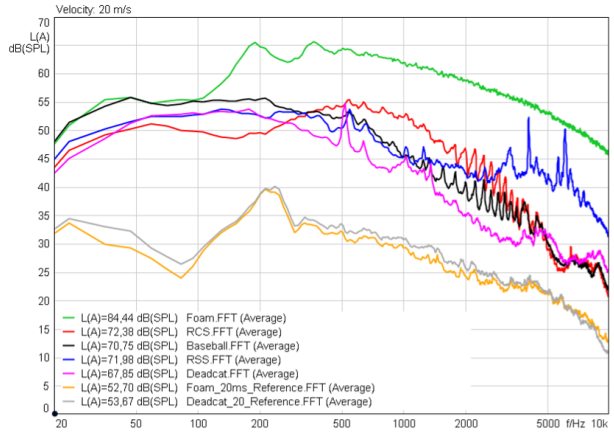


Figure 10. Comparison of the different wind protection variants at a flow velocity of $v = 20\,\mathrm{m/s}$.

Lastly, it is important to note the varying sizes of the wind protection variants. In drone applications, where size and weight are critical parameters, finding an optimal balance between effective wind protection and minimal impact on the vehicle is essential. Future work will focus on refining this balance under realistic flow conditions.

4. CONCLUSION AND OUTLOOK

By employing Stereo-PIV measurements in a wind tunnel, we characterized the complex airflow around a quadrocopter under various flight conditions. Our analysis revealed that, regardless of the maneuver, a pronounced stagnation zone develops in close proximity to the drone body, with local velocities exceeding the nominal flight speed of up to 60%. As the distance increases, the flow gradually aligns with the flight trajectory and converges to the actual movement speed, highlighting the importance of sensor placement for accurate noise measurements. Furthermore, we evaluated several wind protection variants in the aeroacoustic wind tunnel. Preliminary results indicate that commercially available windscreens, particularly the *Deadcat* variant, can significantly reduce the impact of hydrodynamic pressure fluctuations on the measured sound pressure levels. Notable differences in the frequency response among the tested variants emphasize the need for an optimized design that minimizes additional turbulence and noise while maintaining a compact form factor. Looking ahead, future work will focus on a more comprehensive analysis of the turbulence distribution within the stagnation zone and its impact on acoustic measurements. This will enable further refinement of the wind protection design, ensuring optimal microphone placement. The goal is to develop a universally applicable windscreen that reliably isolates the UAV's self-noise, thereby improving measurement accuracy and facilitating broader acceptance of UAV operations in both commercial and regulatory contexts.

5. REFERENCES

[1] E. Visontay, E. V. Transport, and u. a. reporter, "'We don't stop for red lights': drone deliveries take off as Australian regulators prepare for air traffic boom," *The Guardian*, Aug. 2024.

[2] BBC, "Amazon picks Darlington for drone deliveries trial," *BBC News*, Jan. 2025.

[3] S. W. R. Aktuell, "Klingt nach Science Fiction, ist aber wahr: Hier werden Blutproben bald per Drohne verschickt," *SWR Aktuell*, Mar. 2025.

[4] Z. Fang and A. V. Savkin, "Strategies for Optimized UAV Surveillance in Various Tasks and Scenarios: A Review," *Drones*, vol. 8, p. 193, May 2024.

[5] M. Erdelj, E. Natalizio, K. R. Chowdhury, and I. F. Akyildiz, "Help from the Sky: Leveraging UAVs for

Disaster Management," *IEEE Pervasive Computing*, vol. 16, pp. 24–32, Jan. 2017.

[6] W. Schmidbauer, C. Jänig, E. Vits, T. Gruebl, S. Sauer, N. Weller, K. Kehe, F. Holzapfel, T. Lüth, K. G. Kanz, E. Rittinghaus, and P. Biberthaler, "Ein neues Rettungskonzept für Schwerstverletzte in militärischen und zivilen Großschadenslagen: DRONEVAC," *Notfall + Rettungsmedizin*, Aug. 2023.

[7] R. Guebsi, S. Mami, and K. Chokmani, "Drones in Precision Agriculture: A Comprehensive Review of Applications, Technologies, and Challenges," *Drones*, vol. 8, p. 686, Nov. 2024.

[8] E. Thalheimer, "Community Acceptance of Drone Noise," *INTER-NOISE and NOISE-CON Congress and Conference Proceedings*, vol. 263, pp. 913–924, Aug. 2021.

[9] BMDV, "BMDV - Lärmvorsorge und Lärmsanierung an Bundesfernstraßen," Dec. 2018.

[10] J. Benz, A. Gründer, F. Czwielong, and S. Becker, "Acoustic Self-Noise Measurement of a Quadcopter (UAV) in Flight with Focus on Data Acquisition, Microphone Position, and Microphone Wind Protection," 2024. Artwork Size: 1336090 Bytes Pages: 1336090 Bytes.

[11] Y. Yang, Y. Liu, Y. Li, E. Arcondoulis, and Y. Wang, "Aerodynamic and Aeroacoustic Performance of an Isolated Multicopter Rotor During Forward Flight," *AIAA Journal*, vol. 58, pp. 1171–1181, Mar. 2020.

[12] B. G. Wall, *Grundlagen der Hubschrauber-Aerodynamik*. Berlin, Heidelberg: Springer Berlin Heidelberg, 2015.

[13] A. Nash and J. Kennedy, "In Flight Evaluation of UAV Noise Emission,"

[14] A. Ziemann and K. Balogh, "Gekoppelter Atmosphäre-Boden-Einfluss auf die Schallausbrei- tung einer höher gelegenen Schallquelle," 2006.

[15] J. Meister and R. Pieren, "UAV noise emission characterisation using a compact on-board measurement system,"

[16] C. C. Wolf, D. Schanz, C. Schwarz, A. Heintz, J. Bosbach, T. Strübing, and A. Schröder, "Volumetric wake investigation of a free-flying quadcopter using Shake-The-Box Lagrangian particle tracking," *Experiments in Fluids*, vol. 65, p. 152, Oct. 2024.

DOI: 10.61782/fa.2025.0137



FORUM ACUSTICUM
EURONOISE 2025

ANECHOIC NOISE CHARACTERIZATION OF SUB-7KG MULTI-ROTOR DRONES: CONFIGURATION EFFECTS AND SPL SCALING MODELS

Runzhen Cao[1] **Zhicheng Zhang**[1] **Zhenjun Peng** [1]
Zhida Ma[1] **Wangqiao Chen**[1] **Peng Zhou** [1] **Xin Zhang**[1*]
[1] Department of Mechanical and Aerospace Engineering,
The Hong Kong University of Science and Technology,
Clearwater Bay, Kowloon, Hong Kong SAR, China

ABSTRACT

The rapid development of multi-rotor drones has accelerated the growth of the low-altitude economy (LAE), yet expanding applications demand rigorous noise evaluation and regulation due to varying acoustic characteristics across different sizes and configurations. This study investigates the acoustic emissions of sub-7 kg multi-rotor drones during hovering, using both curved and planar phased microphone arrays in an anechoic chamber. Five drone models (0.25 kg to 6.5 kg) were tested to analyze directional noise radiation and spectral behavior. Results show a shift from tonal to broadband-dominant noise as drone size increases, along with lower blade-passing frequencies and smoother directivity patterns in larger platforms. Notably, the heaviest model exhibited lower overall noise than a lighter one, highlighting the impact of aerodynamic design. A logarithmic-linear model incorporating disk area ratio (DAR) was proposed to predict A-weighted sound pressure levels, with strong accuracy ($R^2 > 0.95$) for broadband and overall sound pressure level (SPL). These findings contribute to drone acoustic databases and offer a practical framework for noise prediction, aiding standardization, low-noise design, and regulatory development in urban air mobility. Future work will expand to dynamic flight conditions and other configurations to further enhance model robustness.

*__Corresponding author__: *aexzhang@ust.hk.*

__Copyright__: *©2025 Prof. Xin Zhang This is an open-access article distributed under the terms of the Creative Commons Attribution 3.0 Unported License, which permits unrestricted use, distribution, and reproduction in any medium, provided the original author and source are credited.*

Keywords: *drone noise, multi-rotor acoustics, anechoic measurement, low-altitude economy*

1. INTRODUCTION

With the rapid development of the low-altitude economy (LAE), small multi-rotor drones are increasingly used in logistics, surveillance, and urban mobility [1] . As their deployment expands in urban environments, aerodynamic noise emerges as a key barrier, affecting both human well-being and public acceptance [2] . Accordingly, both the component level and full-vehicle level should be considered, as noise characteristics differ significantly between them. In addition, a standardized noise database and evaluation framework are essential to support drone development, manufacturing, and operational management.

Numerous studies have investigated the aerodynamic noise of drones, particularly from rotor systems. Some have focused on modeling and experimental validation of tonal and broadband noise generated by individual or paired rotors [3, 4] . Others have examined multi-rotor configurations—including coaxial [5, 6] and side-by-side layouts [7–9] —to understand how geometric parameters such as rotor spacing and relative phase affect acoustic performance. In addition, full-vehicle level interactions, including rotor-airframe and rotor-flow coupling effects, have been shown to play a significant role in shaping the overall acoustic behavior of small drones [10–12].

To better reflect realistic flight conditions and capture system-level acoustic effects, recent studies have conducted full-vehicle noise measurements of drones using microphone arrays in both anechoic and outdoor environments. These works typically evaluate key metrics such as

overall sound pressure level (OASPL), blade-passing frequency (BPF) harmonics, broadband noise components, and radiation directivity. Controlled indoor experiments have examined how factors such as observer position, payload, and rotor geometry affect acoustic signatures, while also addressing far-field criteria to ensure the validity of measurements [13, 14] . In contrast, outdoor studies focus on capturing noise during realistic flyover conditions and often employ 3D acoustic field reconstruction techniques [15] . Some investigations further incorporate Geographic Information Systems (GIS)to assess the large-scale environmental impact of drone operations [16] . Together, these efforts underscore the importance of spatially resolved, system-level acoustic measurements and highlight the need for standardized evaluation frameworks to support drone noise regulation and sustainable low-altitude integration.

Although existing studies have improved the understanding of drone noise and informed regulatory efforts, most measurements remain limited to one or two models with narrow variations in size or configuration. To better reflect real-world operations, testing should include larger and more capable drones, as maximum takeoff mass (MTOM) is closely linked to rotor size, configuration layout, and rotational speed—all of which directly influence acoustic performance. For instance, many FAA-approved platforms for advanced operations exceed $5\,\mathrm{kg}$, highlighting the need to study noise behavior in this practically relevant range [17] . While classification systems by EASA, FAA, and CAAC use MTOM thresholds, the category intervals are often too broad to capture meaningful acoustic trends. For example, EU Class C1 includes drones up to $0.9\,\mathrm{kg}$, while C2 extends to $4\,\mathrm{kg}$ [18, 19] . The relationship between drone mass and noise output within these ranges remains poorly understood, motivating higher-resolution measurements across MTOM levels. For untested platforms, anechoic chamber measurements provide a controlled baseline for early-stage acoustic assessment, minimizing environmental interference and supporting consistent noise modeling, design decisions, and policy development [20].

This paper presents a series of acoustic measurements conducted in the anechoic chamber of the Aerodynamics and Acoustics Facility (AAF) at the Hong Kong University of Science and Technology, focusing on typical multi-rotor drones with varying maximum takeoff mass (MTOM) and configurations. The tests were performed under hovering conditions using a curved microphone array to capture noise radiation. Drones under the $7\,\mathrm{kg}$ threshold were selected to span finer MTOM intervals, representing the majority of platforms used in industrial and logistics applications. This work aims to support the sustainable development of the low-altitude economy (LAE), which encompasses drone-based services in logistics, inspection, and urban mobility. To enable cross-platform comparison, dimensionless acoustic parameters were employed to describe noise characteristics within a unified framework. In addition, a logarithmic-linear scaling model incorporating MTOM and disk area ratio (DAR) was developed to predict A-weighted sound pressure levels with high accuracy. The resulting database enhances the understanding of drone acoustics and provides a foundation for future research, regulatory development, and environmentally responsible design.

2. METHODOLOGY

This section outlines the experimental setup for measuring the acoustic emissions of multi-rotor drones under controlled conditions. Five platforms, including both commercial and custom-built models, were selected to represent a range of takeoff weights and configurations relevant to low-altitude operations. Experiments were conducted by using a curved microphone array to capture noise during steady hovering. Measurement feasibility and reliability considerations are also discussed.

2.1 Drone platforms and configurations

Five multi-rotor drones with takeoff masses ranging from approximately $0.25\,\mathrm{kg}$ to $6.5\,\mathrm{kg}$ were selected to represent typical configurations under the $7\,\mathrm{kg}$ threshold. The set includes both commercial and custom-built quadcopters commonly used in consumer, industrial, and commercial applications. All feature a standard X-type layout with two-blade propellers, ensuring structural consistency while varying in frame size, rotor geometry, and propulsion systems. Key physical parameters—such as takeoff mass, propeller diameter, motor spacing, and vertical clearance—are summarized in Tab. 1 . Since most tested platforms are commercial products, only the two custom-built models, X 450 and ZD 680, are shown in Fig. 1.

The selection aligns with regulatory classification systems from EASA, FAA, and CAAC, which define drone categories based on weight. For example, EU categories range from $250\,\mathrm{g}$ (C0) to $4\,\mathrm{kg}$ (C2) [18, 19], FAA defines small UAS under $25\,\mathrm{kg}$ [21], and CAAC classifies drones under $7\,\mathrm{kg}$ as light [22] . This selection increases sam-

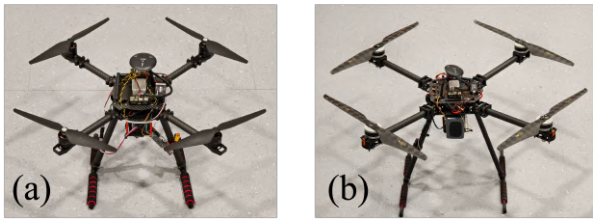


Figure 1. Photographs of the two custom-built platforms: (a) X 450 and (b) ZD 680.

pling density across MTOM levels and configurations, enabling more detailed analysis of acoustic characteristics.

Table 1. Physical parameters of the five tested multirotor drones. "Diag." denotes the diagonal motor-to-motor spacing, "Prop." indicates the propeller diameter, and "Area" refers to the area bounded by the motor layout.

Model	Mass [g]	Diag. [mm]	Prop. [mm]	Clear. [mm]	Area [mm²]
Mini 3	249	247	152	24	39950
Mavic 3	895	380	239	50	74400
X 450	1395	450	254	272	101250
ZD 680	3784	680	432	380	231200
Matrice 350	6470	895	538	239	542700

To better characterize the aerodynamic and geometric properties of the tested drones, the disk area ratio (DAR) was calculated as a dimensionless parameter reflecting the spatial efficiency of the propulsion system. It is defined as the ratio of total rotor swept area to the area enclosed by the motors:

$$\mathrm{DAR} = \frac{n \cdot \frac{\pi D_{\mathrm{prop}}^2}{4}}{A_{\mathrm{enclosed}}} \tag{1}$$

where n is the number of rotors (four in this study), D_{prop} is the propeller diameter, and A_{enclosed} is the area bounded by the motor layout just shown in Tab. 1. Related parameters, including disk loading and layout ratio—which are based on the same core variables such as takeoff mass, propeller diameter, and frame geometry—are also listed in Tab. 2 but are not further analyzed in this study. DAR was later used to develop a scaling model for A-weighted sound pressure levels.

Table 2. Derived parameters of the five tested multirotor drones.

Model	Disk area ratio (DAR)	Disk load	Layout ratio
Mini 3	1.82	10.78	0.62
Mavic 3	2.41	15.67	0.63
X 450	2.00	21.62	0.56
ZD 680	2.54	20.28	0.64
Matrice 350	1.68	22.35	0.60

2.2 Test environment and acoustic measurement setup

All experiments were conducted in the anechoic chamber room. The chamber, measuring $8.1\,\mathrm{m} \times 6.0\,\mathrm{m} \times 5.1\,\mathrm{m}$, is fully wedge-lined and provides free-field conditions above $100\,\mathrm{Hz}$. A nylon safety cage was installed to define an internal working volume of $6.8\,\mathrm{m} \times 4.8\,\mathrm{m} \times 4.0\,\mathrm{m}$, ensuring a minimum $600\,\mathrm{mm}$ clearance from all walls. A net was also placed at the bottom for failsafe protection. High-contrast ground markers were used to support visual-based positioning, especially for lightweight drones operating in GPS-denied indoor environments.

To capture radiated noise under steady hovering, a semi-circular microphone array was deployed at a $2.5\,\mathrm{m}$ radius from the chamber center. The array spanned a $120°$ vertical arc and consisted of thirteen GRAS 46BE 1/4-inch microphones, spaced at $10°$ intervals. The vertical angle of each microphone is denoted by θ, measured from the downward vertical direction ($\theta = 0°$) upward toward the drone's front axis. This angular configuration allows for directional analysis of noise radiation.The array was tilted $60°$ from the chamber's short axis, with the central microphone aligned to the drone's nominal hovering position. Each microphone was fitted with a windscreen to reduce flow-induced noise. A schematic and chamber photo are shown in Fig. 3 and Fig. 2 , including microphone locations, coordinate systems, and marker placement. Drone position and yaw were tracked by a VICON

system with eight Vero V2.2 cameras operating at 50 Hz , using reflective markers beneath each rotor and on the airframe. The system was synchronized with acoustic measurements acquired via NI cDAQ-9189 and NI-9231 modules at 50 kHz . To minimize acoustic interference, metal components of the safety cage were acoustically treated with foam.

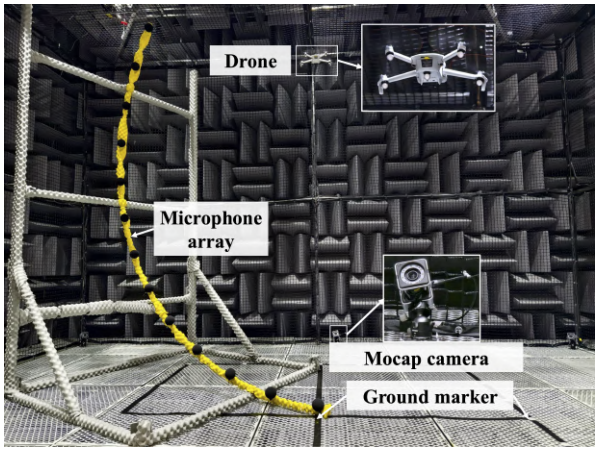


Figure 2. Experimental setup in the AAF anechoic chamber room.

2.3 Test procedure and evaluation of measurement validity and repeatability

Each drone was tested under consistent procedures to characterize its directional acoustic behavior. The drone hovered at the geometric center of the chamber, 2.5 m above the floor (Fig. 3), and was rotated about its vertical body axis (z_b) from 0° to 180° in 15° increments. At each orientation, a 20 s recording was made using synchronized systems: acoustic signals were captured at 50 kHz by the 13-microphone array, while position and yaw were tracked at 50 Hz via the VICON system. Each drone completed three full test cycles to evaluate repeatability.

Measurement validity was ensured through chamber background noise checks and array configuration validation. Ambient noise levels were maintained below 20 dB across the frequency range of interest to achieve sufficient signal-to-noise ratio. The microphone array design was evaluated against ISO 3745:2012 [23] far -field criteria. For the largest drone, Matrice 350 RTK ($L = 1.433$ m), the array radius fell slightly short of the $2L$ condition but exceeded other requirements [14], with a 13 % deviation

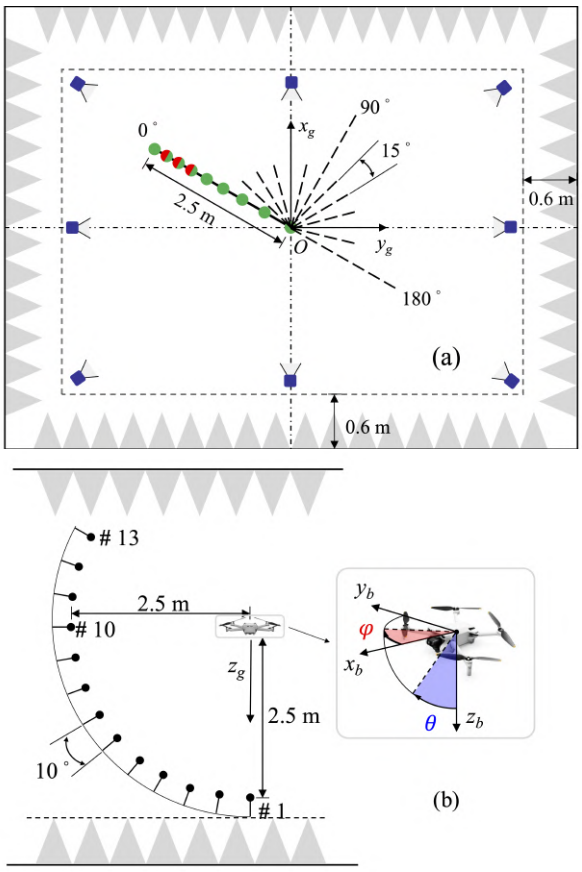


Figure 3. Schematic diagrams of the acoustic measurement setup: (a) top view showing the microphone array orientation; (b) side view including the drone body coordinate system.

deemed acceptable. All smaller drones fully met the criteria. Additionally, the influence of rotor downwash and recirculating flow was considered. Previous studies [24] indicate that such effects cause minor spectral shifts and entropy changes, but their impact on A-weighted broadband SPL remains within 2 dB , and thus does not compromise measurement reliability.

3. RESULTS AND DISCUSSIONS

This section presents the acoustic analysis of all tested multi-rotor drones during steady hovering. Each platform was incrementally rotated in yaw, and sound pressure levels were recorded at 13 microphone positions along a 120°

vertical arc. The signals were post-processed to extract A-weighted overall sound pressure levels (OASPL), narrowband SPL spectra, and directional features, including 2D directivity plots and interpolated 3D fields. The analysis focuses on identifying shared acoustic characteristics across platforms, yaw-dependent frequency behaviors, and trial-to-trial consistency. In addition, scaling relationships between A-weighted OASPL and maximum takeoff mass (MTOM) are evaluated to investigate how noise radiation evolves with platform size.

3.1 Hovering stability evaluation via motion capture

To assess the hovering stability of the tested multi-rotor drones, we analyzed the standard deviation of body center positions and yaw angles during a steady 20-second hover at $0°$ yaw, as summarized in Tab. 3. All five platforms maintained sub- $6\,\mathrm{mm}$ deviations across all spatial axes. The Matrice 350 exhibited the most stable performance, with variations under $3\,\mathrm{mm}$ and minimal yaw fluctuation ($0.77°$). In contrast, the ZD 680 showed the largest vertical ($3.42\,\mathrm{mm}$) and yaw ($1.16°$) deviations, which may be attributed to increased inertia or less refined control tuning. The Mini 3 displayed slightly larger vertical fluctuation ($5.16\,\mathrm{mm}$), likely due to its lower mass and greater susceptibility to recirculating flow , although further testing would be required to confirm this. Overall, all platforms demonstrated sufficient stability to support repeatable and reliable indoor acoustic measurements.

Table 3. Standard deviation of motion capture measurements under hovering at $0°$ yaw for each drone model (unit: mm / °).

Model	X std [mm]	Y std [mm]	Z std [mm]	Yaw std [°]
Mini 3	3.47	2.56	5.16	0.92
Mavic 3	3.13	2.61	2.69	1.06
X 450	3.65	2.96	3.71	0.93
ZD 680	5.06	3.31	3.42	1.16
Matrice 350	2.66	1.99	2.12	0.77

3.2 Acoustic characteristics analysis

Acoustic analysis was based on signals recorded at a microphone positioned at $\theta = 30°$, oriented perpendicular to the drone's forward axis. This angle was selected because the bottom-mounted microphone, affected by rotor downwash, failed to clearly capture tonal components such as the first blade-passing frequency (BPF) . The $30°$ position provided a more representative signal across platforms. Given the presence of multiple tonal peaks around BPFs due to rotor asymmetry and aerodynamic interactions, each BPF in this study is defined as a frequency band rather than a single frequency. The reported SPL values represent the A-weighted energy integrated over each corresponding band.

The A-weighted narrowband SPL spectra of the five drones under hover are shown in Fig. 4 . The Mini 3 exhibits the lowest SPL, with acoustic energy concentrated in the low-frequency region, while the Mavic 3 and X 450 display stronger tonal peaks in the mid-frequency range. The heavier ZD 680 and Matrice 350 generate higher SPL across a broader spectral range (1–6 kHz), consistent with their greater thrust demand and more complex aerodynamic interactions. As maximum takeoff mass (MTOM) increases, the spectra become increasingly broadband, with relatively diminished tonal peaks, broader spectral ridges, and lower blade-passing frequencies. These trends suggest more distributed and diffuse acoustic signatures in larger drones. Design asymmetries such as staggered rotor heights or center-of-mass offsets may further suppress tonal coherence and reduce directional radiation. All spectra remain well above the background noise floor, confirming measurement fidelity.

Fig. 5 illustrates the relationship between maximum takeoff mass (MTOM) and A-weighted SPL across multiple frequency bands, including 1BPF, 2BPF, 3BPF, broadband, and overall. In general, SPL increases with MTOM across all bands, with the most pronounced growth observed at 1BPF and 2BPF, reflecting stronger tonal components in heavier platforms. Broadband and higher-order components exhibit a more gradual increase, suggesting a more distributed energy spectrum. An exception to this trend is the Matrice 350, which, despite its higher MTOM compared to the ZD 680, exhibits slightly lower A-weighted SPL across all metrics—likely due to noise reduction measures such as optimized propeller geometry and a more aerodynamically refined fuselage.

The observed trends in A-weighted SPL are further visualized in Fig. 6 , which presents 3D directivity maps

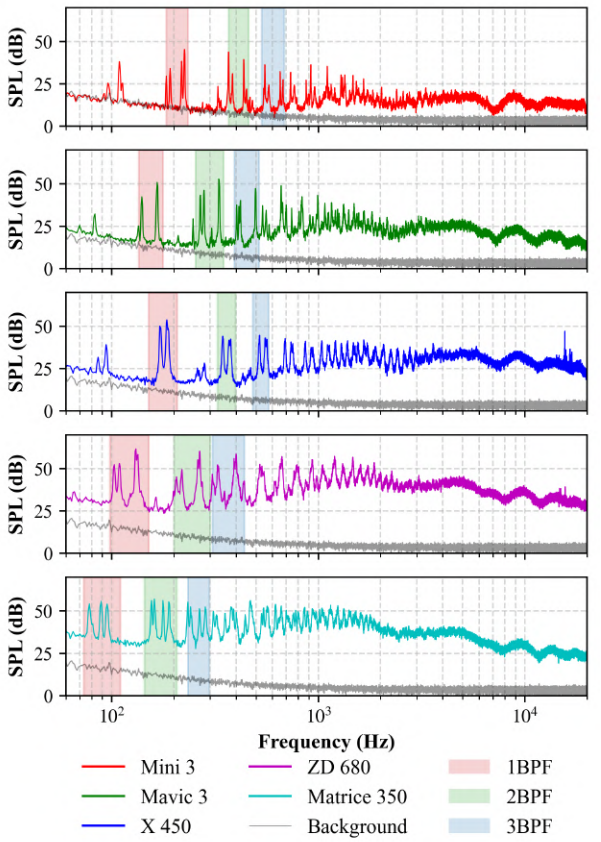


Figure 4. Comparison of SPL spectra measured at the $\theta = 30°$ microphone for all drones under hover condition. The shaded regions represent the respective BPF bands.

of A-weighted OASPL for all five platforms. The X 450 exhibits a fragmented and irregular radiation pattern, likely resulting from structural resonance and less coherent rotor interaction. In contrast, the ZD 680 shows a well-defined downward lobe with elevated levels, reflecting high rotor loading and more focused downward radiation. The Matrice 350, despite its larger size, displays a smooth and symmetric pattern with noticeably lower peak levels, consistent with its overall reduced SPL observed in Fig. 5 . These results suggest that aerodynamic refinements—such as smoother fuselage contours and optimized propeller design—can effectively mitigate directional noise radiation even in larger multirotor systems.

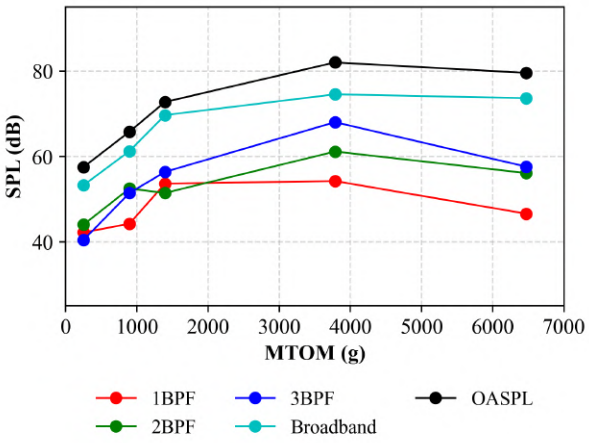


Figure 5. Variation of A-weighted Sound Pressure Level (SPL) with Maximum Takeoff Mass (MTOM) across different frequency bands: 1BPF, 2BPF, 3BPF, Broadband, and OASPL.

3.3 Model fitting and data analysis

To characterize how A-weighted SPL varies with platform mass and configuration, we adopted a logarithmic-linear model incorporating disk area ratio (DAR). This model provides a more accurate representation of the noise emissions across different frequencies using the following equation(2):

$$\mathrm{SPL} = a \cdot \ln(\mathrm{MTOM}) + b \cdot \mathrm{MTOM} + c \cdot \mathrm{DAR} + d \quad (2)$$

Due to the higher variability and less consistent results at blade-passing frequencies (1BPF–3BPF), and given that OASPL is easier to manage and unify in regulatory contexts, we focused our analysis on Broadband SPL and OASPL. The fitted parameters for all frequency bands are summarized in Tab. 4.

4. CONCLUSION

This study examined the acoustic characteristics of multirotor drones with varying maximum takeoff masses and configurations under controlled hovering conditions. Results show that A-weighted sound pressure levels (SPL) scale with drone mass. To quantify the influence of mass and geometry, a logarithmic-linear model incorporating disk area ratio (DAR) was developed to predict A-weighted SPL across frequency bands, achieving strong

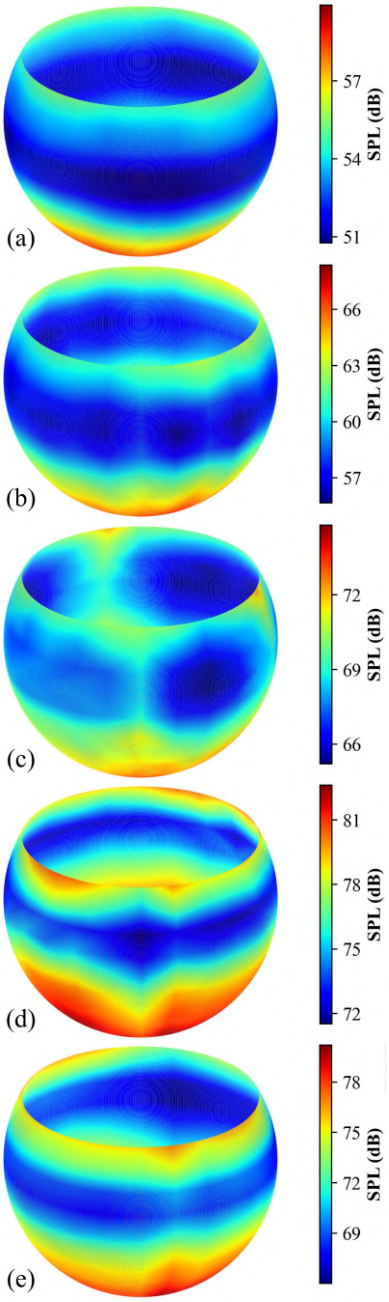


Figure 6. A-weighted OASPL directivity maps from a 45° view: (a) Mini 3, (b) Mavic 3, (c) X 450, (d) ZD 680, (e) Matrice 350.

accuracy for broadband and overall levels. These findings contribute a standardized acoustic dataset and modeling approach that support low-noise drone design, regulatory development, and integration into urban air mobility. Future work will extend to dynamic flight conditions, transitional states, and a broader range of configurations to improve the generalizability of the predictive model and facilitate sustainable development of the low-altitude economy.

Table 4. Fitted coefficients for the A-weighted SPL log-linear model defined in (2), incorporating maximum takeoff mass (MTOM) and disk area ratio (DAR). "B'band." refers to broadband SPL.

P.	1BPF	2BPF	3BPF	B'band.	OASPL
a	9.521	2.897	9.555	11.66	9.273
b	-3.83 $\times 10^{-3}$	7.10 $\times 10^{-4}$	-1.63 $\times 10^{-3}$	-2.60 $\times 10^{-3}$	-9.10 $\times 10^{-4}$
c	-2.589	8.991	8.461	-2.890	2.060
d	-6.260	11.227	-28.65	-6.118	1.737
R^2	0.6858	0.9942	0.9348	0.9628	0.9574

5. ACKNOWLEDGMENTS

This work was supported by the Hong Kong Research Grant Council (RGC 16201923 and 16202519).

6. REFERENCES

[1] X. Huang, "The small-drone revolution is coming — scientists need to ensure it will be safe," *Nature*, vol. 637, pp. 29–30, Jan. 2025.

[2] B. Schäffer, R. Pieren, K. Heutschi, J. M. Wunderli, and S. Becker, "Drone Noise Emission Characteristics and Noise Effects on Humans—A Systematic Review," *International Journal of Environmental Research and Public Health*, vol. 18, p. 5940, June 2021.

[3] H. Wu, P. Zhou, P. Wang, G. Zhou, B. Chen, S. Zhong, and X. Zhang, "Broadband noise of a hovering rotor: Measurement, prediction, and reduction," *AIAA Journal*, vol. 0, no. 0, pp. 1–13, 0.

[4] X. Li, H. Wu, Y. Li, P. Zhou, S. Zhong, X. Zhang, and Z. Ma, "Experimental study of the effect of boundary-layer transition on rotor aeroacoustics," *AIAA Journal*, vol. 62, no. 5, pp. 1974–1981, 2024.

[5] R. S. McKay, M. J. Kingan, S. T. Go, and R. Jung, "Experimental and analytical investigation of contra-rotating multi-rotor uav propeller noise," *Applied Acoustics*, vol. 177, p. 107850, 2021.

[6] W. Chen, Z. Ma, Étienne Spieser, J. Guo, P. Zhou, S. Zhong, X. Zhang, and X. Huang, "Acoustic imaging of the broadband noise arising in contra-rotating co-axial propellers," *Aerospace Science and Technology*, vol. 141, p. 108531, 2023.

[7] X. Xu, Y. Lu, C. Lan, M. Shao, and J. Lu, "Mechanism analysis of the influence of rotor-to-rotor interactions on global rotor noise," *Journal of Sound and Vibration*, vol. 585, p. 118473, 2024.

[8] H. Bu, H. Wu, C. Bertin, Y. Fang, and S. Zhong, "Aerodynamic and acoustic measurements of dual small-scale propellers," *Journal of Sound and Vibration*, vol. 511, p. 116330, 2021.

[9] K. A. Pascioni, S. A. Rizzi, and N. Schiller, "Noise Reduction Potential of Phase Control for Distributed Propulsion Vehicles," in *AIAA Scitech 2019 Forum*, (San Diego, California), American Institute of Aeronautics and Astronautics, Jan. 2019.

[10] S. Cantos, P. Zhou, Z. MA, and Y. Li, *A Numerical Study on the Reduction of Rotor Blade-Airframe Interaction Noise Through Airframe Permeability*.

[11] J. Whelchel and W. N. Alexander, *sUAS Rotor-Airframe Interaction*.

[12] J. Wu, O. Stalnov, W. Chen, Z. Yang, and X. Huang, "Transient analysis of blade-vortex interaction noise," *Aerospace Science and Technology*, vol. 120, p. 107294, 2022.

[13] M. Alkmim, J. Cardenuto, E. Tengan, T. Dietzen, T. Van Waterschoot, J. Cuenca, L. De Ryck, and W. Desmet, "Drone noise directivity and psychoacoustic evaluation using a hemispherical microphone array," *The Journal of the Acoustical Society of America*, vol. 152, pp. 2735–2745, 11 2022.

[14] Z. Ma, H. Wu, J. Mao, G. Liu, P. Zhou, and S. Zhong, "Noise measurement of a quadrotor drone in an anechoic chamber," *INTER-NOISE and NOISE-CON Congress and Conference Proceedings*, vol. 268, pp. 4659–4670, Nov. 2023.

[15] C. Ramos-Romero, N. Green, A. J. Torija, and C. Asensio, "On-field noise measurements and acoustic characterisation of multi-rotor small unmanned aerial systems," *Aerospace Science and Technology*, vol. 141, p. 108537, 2023.

[16] F. Škultéty, E. Bujna, M. Janovec, and B. Kandera, "Noise impact assessment of uas operation in urbanised areas: Field measurements and a simulation," *Drones*, vol. 7, no. 5, 2023.

[17] F. A. Administration, "Nepa and drones: Guidance for environmental review of uas operations," 2023.

[18] E. Commission, "Commission delegated regulation (eu) 2019/945 of 12 march 2019 on unmanned aircraft systems and on third-country operators of unmanned aircraft systems," 2019.

[19] E. Commission, "Commission delegated regulation (eu) 2020/1058 of 27 april 2020 amending delegated regulation (eu) 2019/945 as regards the introduction of two new unmanned aircraft systems classes," 2020.

[20] T. Zhou, H. Jiang, and B. Huang, "Quad-copter noise measurements under realistic flight conditions," *Aerospace Science and Technology*, vol. 124, p. 107542, 2022.

[21] "14 cfr part 107: Small unmanned aircraft systems." `https://www.ecfr.gov/current/title-14/chapter-I/subchapter-F/part-107`, 2024. Accessed: 2025-04-03.

[22] "Interim regulations on unmanned aircraft flight management." `https://www.caac.gov.cn/XXGK/XXGK/FLFG/202401/t20240115_222642.html`, 2023. In Chinese; Accessed: 2025-04-03.

[23] International Organization for Standardization, "Acoustics – determination of sound power levels and sound energy levels of noise sources using sound pressure – precision methods for anechoic rooms and hemi-anechoic rooms," Standard ISO 3745:2012, International Organization for Standardization, Geneva, CH, 2012.

[24] Z. Ma, P. Zhou, X. Zhang, and S. Zhong, "Experimental assessment of the flow recirculation effect on the noise measurement of a free-flying multi-rotor uas in a closed anechoic chamber," *Acoustics Australia*, pp. 1–10, 2024.

DOI: 10.61782/fa.2025.0632

FORUM ACUSTICUM EURONOISE 2025

NUMERICAL INVESTIGATION ON TONAL NOISE DIRECTIVITY IN DISTRIBUTED PROPULSION SYSTEMS

Alessandro Zarri[12*] **Frits de Prenter**[2]

[1] Aeronautics and Aerospace Department, von Karman Institute for Fluid Dynamics, Belgium
[2] Department of Flow Physics and Technology, Delft University of Technology, The Netherlands

ABSTRACT

The potential of distributed electric propulsion to mitigate noise environmental impact has been increasingly explored for UAV and UAM applications. However, when rotors are placed in close proximity, strong aerodynamic interactions and complex acoustic phenomena are induced. Phase synchronization has been proposed as a tonal noise mitigation strategy. Significant reductions in tonal levels have been reported under various configurations, though the extent and nature of such reductions remain debated. Previous assessments have relied on sparse sound pressure measurements, potentially misrepresenting global noise attenuation due to altered directivity. To address this experimental limitation, high-fidelity simulations are carried out for a multi-propeller configuration, focusing on the effects of phase synchronization. The influence of a 30°-phase offset between three co-rotating six-blade rotors is evaluated against an in-phase configuration. A spherical microphone array was used to determine the spatial directivity and total radiated sound power. Results show that phase-angle differences substantially redistribute the acoustic energy toward different spatial locations. Nevertheless, it also impacts the global noise emission, mitigating the sound power level of the opposite-phase configuration by 7.47 dB in acoustic power for the first BPF harmonic and 4.79 dB for the second.

Keywords: DEP, propeller noise, aeroacoustics, directivity, phase synchronization

**Corresponding author*: alessandro.zarri@vki.ac.be.
***Copyright**: ©2025 Zarri et al. This is an open-access article distributed under the terms of the Creative Commons Attribution 3.0 Unported License, which permits unrestricted use, distribution, and reproduction in any medium, provided the original author and source are credited.*

1. INTRODUCTION

The emergence of urban air mobility (UAM) and small-scale unmanned aerial vehicles (UAVs) has spurred interest in novel propulsion systems that reduce environmental impact while improving efficiency. Distributed electric propulsion (DEP) systems, comprising arrays of electrically driven propellers, are promising for enhancing aerodynamic performance and lowering pollutant emissions [1]. When propellers are positioned nearby, as is common in DEP systems, their interactions give rise to complex aerodynamic and acoustic phenomena [2]. These interactions not only affect the aerodynamic loads, leading to increased tonal and broadband noise [3], but also alter the spatial directivity of the blade passing frequency (BPF) harmonics. One proposed method for mitigating such noise is the synchronization of adjacent rotors, typically by imposing a constant phase angle between them. Recently, several studies have investigated the potential of phase synchronization to reduce tonal noise, particularly in hover:

- Pascioni et al. [4] found a 6 dB reduction at the BPF for a 3-bladed, 16-inch propeller at 5100 rpm.
- Shao et al. [5] reported 1–11 dB reductions using 2-bladed, 12-inch propellers at 4000 rpm.
- Guan et al. [6] observed 11–30 dB reductions under hover and low-speed flight (advance ratio 0–0.1) using 2-bladed, 12.5-inch rotors at 6000 rpm.

In forward-flight conditions:

- Turhan et al. [7] measured a 24 dB reduction at the first BPF harmonic with a 90° phase offset between

2-bladed propellers.

- De Paola et al. [8] reported a 5 dB reduction using 4-bladed rotors.

These studies suggest that phase synchronization can suppress tonal emissions without compromising thrust, and they often attribute this effect to acoustic interference between the propellers. In contrast to aerodynamic installation effects, which depend on unsteady flow phenomena, acoustic interference stems from phase-coherent sound fields overlapping and interfering destructively or constructively in the far field [9]. However, reported noise reductions vary widely, from 1 dB up to 30 dB for a single-observation microphone. A key limitation of many studies is that only a few microphones are deployed to capture sound pressure levels (SPL) at discrete positions due to limitations in space, time, and cost. Since phase synchronization drastically alters the directivity of tonal components, local SPL measurements may misleadingly suggest strong attenuation, even though sound is merely redirected elsewhere in space. Without capturing the full spatial radiation pattern, it's unclear whether noise is truly reduced or just redistributed. To address this ambiguity, the present study uses high-fidelity numerical simulations to compute the full 3D directivity patterns of DEP systems and to determine the sound power level (SWL), which integrates radiation over all directions. Unlike isolated SPL measurements, SWL offers a global, physically meaningful quantification of noise reduction. This work, therefore, aims to re-evaluate the noise mitigation claims found in the literature by examining the extent to which phase synchronization alters both the directionality and total radiated acoustic power.

2. MATERIALS AND METHODS

2.1 Computational Setup

The simulations replicate the TUD-XPROP-S propeller setup from de Vries et al. [10], involving three six-blade rotors (diameter $D = 0.2032$ m) spaced along the Y-axis, as depicted in Figure 1a. The present work focuses exclusively on two specific phase-synchronized distributed-propulsion configurations, namely with a relative phase angle $\Delta\phi = 0°$ and $\Delta\phi = 30°$, corresponding to the in-phase and opposite-phase rotation, respectively. The simulations analyzed here are the same as those originally introduced in [11] and further extended in [12], to which the reader is referred for additional details on the numerical setup and methodology. The propeller geometry involves a pitch angle of 30° at 70% span and root chord of 16.3 mm, and it was provided by TU Delft. The system rotates anticlockwise with an inflow velocity of $V_\infty = 30$ m/s, and advance ratio $J = 0.8$. The flow around propellers is simulated using SIMULIA PowerFLOW® (version 6-2021-R2), a commercial CFD that employs the Lattice-Boltzmann (LB) method. It solves the LB equation for the particle distribution function $f(\boldsymbol{x}, \boldsymbol{v}, t)$, describing the probability density of particles with velocity $\boldsymbol{v}$ at location $\boldsymbol{x}$ and time t. The simulation uses a D3Q19

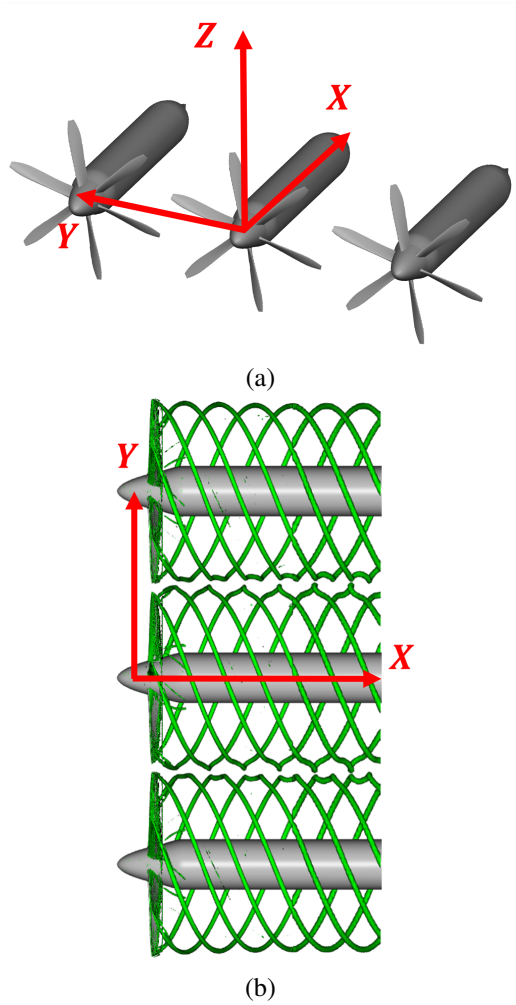


Figure 1: (a) View of the simulated setup with three distributed propellers and the GRS. (b) Visualization of vortex structures with $\lambda 2$ method for the in-phase configuration (b).

stencil for 19 discrete velocity directions and a regularized Bhatnagar-Gross-Krook collision operator. The LB equations are solved on a Cartesian grid with cubic volumetric elements (voxels) and solid objects discretized with planar surface elements (surfels). The solver incorporates a very large eddy simulation (VLES) approach, utilizing a k-ϵ turbulence model. A pressure-gradient extended wall model approximates the no-slip boundary condition. The grid contains approximately 225.5 million voxels, ensuring $y^+ \approx 15$ over the blade surfaces. CPU costs reach roughly 112,000 hours per case. The flow solution can be visualized *via* λ_2 method in Figure 1b.

2.2 Far-Field Noise Computation

The far-field noise formulation used in this work is described and validated in [12]. It exploits the axial and tangential forces computed on the propeller disks as dipole sources radiating sound to the far-field. These forces include the aerodynamic interactions caused by the propellers' proximity. The SPL of the BPF harmonic tones is determined from the measured amplitudes ($p_{\mathrm{BPF_n}}$) using the following equation:

$$L_p(f) = 10\log_{10}\frac{0.5p^2_{\mathrm{BPF_n}}}{p^2_{ref}}, \tag{1}$$

which results in the output in acoustic decibels. In this equation, $p_{ref} = 20\,\mu\mathrm{Pa}$ is the reference pressure, while the subscript n indicated the chosen BPF harmonic. For the calculation of the SWL, a spherical microphone array consisting of 2500 microphones is arranged around the propeller at a distance of $100D$ from the global reference system (GRS) origin, ensuring a comprehensive capture of the sound field in all directions. It was confirmed that increasing the number of microphones and the distance from the origin did not affect the SWL. The root mean square (RMS) pressure was computed at all microphone locations. The RMS pressure squared, p^2_{rms}, is the average of the square of the pressure levels at the selected BPF harmonic over all microphone positions. The emitted sound power is then calculated as:

$$\mathrm{W} = p^2_{\mathrm{rms}} A_m / \rho_\infty\, c_\infty, \tag{2}$$

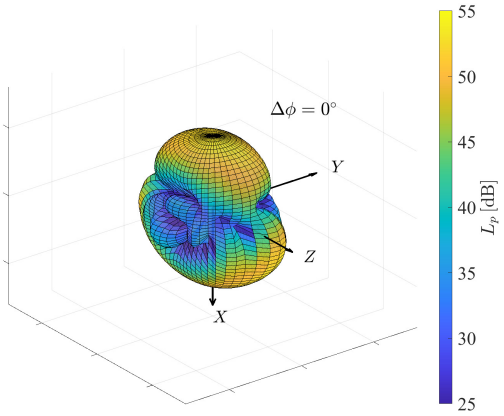
where ρ_∞ is the air density, c_∞ is the speed of sound in air, and the area $A_m = 4\pi R^2_m$ represents the surface area of the sphere formed by the microphone array, with $R_m = 100D$ being the distance from the source to each microphone. Finally, the SWL is computed as:

$$L_w = 10\log_{10}\left(\frac{\mathrm{W}}{\mathrm{W_{ref}}}\right), \tag{3}$$

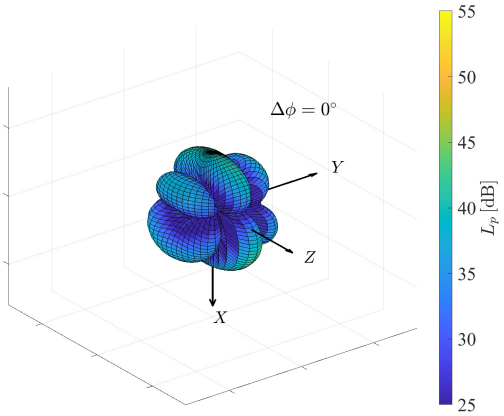
where $\mathrm{W_{ref}} = 1\times10^{-12}\,\mathrm{W}$ is the reference sound power. This formula yields the SWL in decibels, which quantifies the total acoustic power radiated by the source in all directions.

3. RESULTS

The spatial distribution of sound emissions from a system of three rotors is examined. This distribution is determined by the aerodynamic interaction resulting from the proximity of adjacent propellers, as well as by the interference among the acoustic fields generated by each of the three propellers. In Figure 2a, the $\Delta\phi = 0°$ configuration at the first BPF harmonic is analyzed, and the spatial distribution of the SPL around the propellers' GRS is presented. The SPL mostly contributes around the XY plane and reaches its maximum along the X-axis, with values around $52.7\,\mathrm{dB}$. Along the Y-axis, a lobed pattern is observed, with reduced amplitudes not exceeding $19\,\mathrm{dB}$. In contrast, as shown in Figure 3a for the $\Delta\phi = 30°$ configuration, the directivity pattern of the first BPF harmonic is significantly altered, particularly along the X and Z directions. For instance, if the SPL is measured by a microphone placed along the X-axis, at a distance of $100D$ from the GRS, a substantial reduction of approximately $43\,\mathrm{dB}$ is observed. While this reduction can be attributed to the effect of phase synchronization, an inspection of the directivity in Figure 3a reveals that certain regions still exhibit emissions reaching about $48\,\mathrm{dB}$; however, these regions are located differently compared to those observed in the $\Delta\phi = 0°$ case. For this reason, a less ambiguous method for evaluating the effect of noise reduction caused by the phase angle is employed by computing the SWL, as explained in Section 2.2, and by interpreting results in terms of acoustic power levels expressed in decibels. For the first BPF harmonic, values of $L_w = 85.71\,\mathrm{dB}$ and $L_w = 78.24\,\mathrm{dB}$ are obtained for the in-phase and opposite-phase cases, respectively. This corresponds to a reduction of $\Delta L_w = 7.47\,\mathrm{dB}$ in acoustic power due to the phase angle effect. Turning to the second BPF harmonics, these are shown in Figure 2b for $\Delta\phi = 0°$ and in Figure 3b for $\Delta\phi = 30°$. Unlike the first harmonic, the tonal directivity is found to be very similar and is characterized by a lobed spatial distribution that peaks along the X-axis in both cases. When the SWL is computed, values

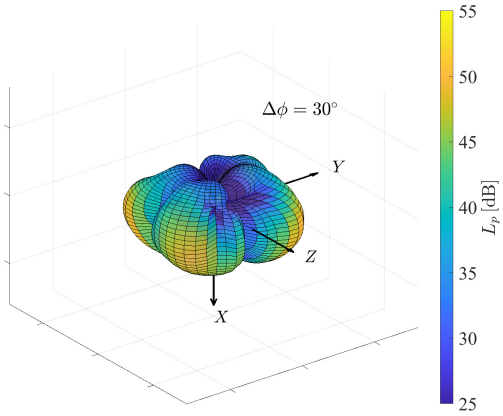


(a) 1st BPF harmonic.

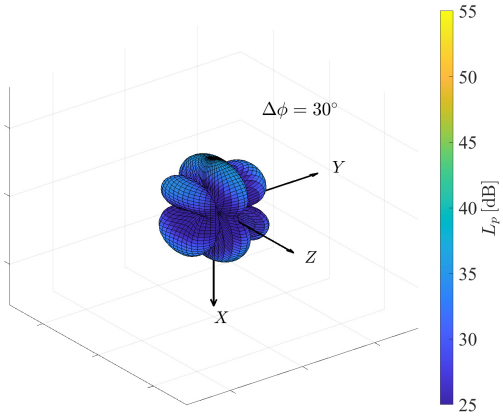


(b) 2nd BPF harmonic.

Figure 2: Three-dimensional L_p directivity of the BPF harmonic tones for the $\Delta\phi = 0°$ configuation.



(a) 1st BPF harmonic.



(b) 2nd BPF harmonic.

Figure 3: Three-dimensional L_p directivity of the BPF harmonic tones for the $\Delta\phi = 30°$ configuration.

of $L_w = 73.76\,\mathrm{dB}$ and $L_w = 68.97\,\mathrm{dB}$ are obtained for the two configurations, respectively. This indicates a reduction of $\Delta L_w = 4.79\,\mathrm{dB}$ in acoustic power due to the phase angle for the second BPF harmonic.

4. CONCLUSIONS

In recent years, significant tonal noise attenuation has been reported in several experimental studies on phase synchronization in DEP systems. However, these conclusions have often been based on discrete SPL measurements taken at isolated locations, which may not fully capture the three-dimensional nature of acoustic radiation. As a result, the spatial redirection of tonal components may have been misinterpreted as global attenuation, raising questions about the generalizability of the findings. To address this limitation, a methodology has been employed in the present study, relying on high-fidelity numerical simulations already available in the literature [12], combined with a dipole-based far-field noise formulation and a

dense spherical microphone array. Through this approach, the spatially integrated SWL can be computed, providing a global and physically meaningful metric for quantifying tonal acoustic emissions. A three-propeller DEP configuration has been considered in the analysis, with a comparison made between in-phase ($\Delta\phi = 0°$) and opposite-phase ($\Delta\phi = 30°$) operation under forward-flight conditions. It has been shown that in-phase rotation produces highly directional radiation patterns at the first BPF harmonic, particularly along the X and Z axes, whereas the opposite-phase configuration yields a markedly different spatial distribution, with peak emissions occurring elsewhere. This suggests that tonal energy is drastically redistributed by phase synchronization, resulting in either mitigation or amplification depending on the spatial location considered. Nevertheless, notable reductions in SWL have been observed in the $\Delta\phi = 30°$ case, with decreases of $\Delta L_w = 7.47\,\mathrm{dB}$ in acoustic power for the first BPF harmonic and $\Delta L_w = 4.79\,\mathrm{dB}$ for the second. In future studies, a broader range of phase angles, rotor counts, and operating conditions should be explored, and hybrid strategies that combine synchronization with aerodynamic optimization should be considered for more effective and scalable noise control.

5. ACKNOWLEDGMENTS

This research was carried out within the framework of the H2020 Research and Innovation Actions ENODISE (ENabling Optimized DISruptivE airframe-propulsion integration concepts) and eVTOLUTION (eVTOL Multi-fidelity Hybrid Design and Optimization for Low Noise and High Aerodynamic Performance), both funded by the European Commission under Grant Agreement numbers 860103 and 101138209, respectively. Furthermore, the authors would like to acknowledge Prof. Daniele Ragni and Prof. Damiano Casalino from TU Delft (The Netherlands) and Prof. Francesco Avallone (Politecnico di Torino, Italy) for the inspiring discussions about aeroacoustics and computational fluid mechanics.

6. REFERENCES

[1] NASA, "Strategic implementation plan: 2017 update." `https://www.nasa.gov/sites/default/files/atoms/files/sip-2017-03-23-17-high.pdf`, 2017.

[2] A. Zarri, E. Dell'Erba, W. Munters, and C. Schram, "Aeroacoustic installation effects in multi-rotorcraft: Numerical investigations of a small-size drone model," *Aerospace Science and Technology*, vol. 128, p. 107762, 2022.

[3] H. Lee and D.-J. Lee, "Rotor interactional effects on aerodynamic and noise characteristics of a small multirotor unmanned aerial vehicle," *Physics of Fluids*, vol. 32, no. 4, 2020.

[4] K. A. Pascioni, S. A. Rizzi, and N. Schiller, "Noise reduction potential of phase control for distributed propulsion vehicles," American Institute of Aeronautics and Astronautics, 2019.

[5] M. Shao, Y. Lu, X. Xu, S. Guan, and J. Lu, "Experimental study on noise reduction of multi-rotor by phase synchronization," *Journal of Sound and Vibration*, vol. 539, p. 117199, Oct. 2022.

[6] S. Guan, Y. Lu, T. Su, and X. Xu, "Noise attenuation of quadrotor using phase synchronization method," *Aerospace Science and Technology*, vol. 118, p. 107018, 2021.

[7] B. Turhan, H. K. Jawahar, A. Gautam, S. Syed, G. Vakil, D. Rezgui, and M. Azarpeyvand, "Acoustic characteristics of phase-synchronized adjacent propellers," *The Journal of the Acoustical Society of America*, vol. 155, pp. 3242–3253, May 2024.

[8] E. De Paola, R. Camussi, G. Stoica, A. Di Marco, and G. Capobianchi, "Aerodynamic and aeroacoustic experimental investigation of a three propellers DEP configuration," *Aerospace Science and Technology*, p. 109508, 2024.

[9] M. Roger, D. Acevedo-Giraldo, and M. C. Jacob, "Acoustic versus aerodynamic installation effects on a generic propeller-driven flying architecture," *International Journal of Aeroacoustics*, vol. 21, no. 5-7, pp. 585–609, 2022.

[10] R. de Vries, N. van Arnhem, T. Sinnige, R. Vos, and L. L. Veldhuis, "Aerodynamic interaction between propellers of a distributed-propulsion system in forward flight," *Aerospace Science and Technology*, vol. 118, p. 107009, Nov. 2021.

[11] A. Zarri, A. Koutsoukos, F. Avallone, F. de Prenter, D. Ragni, and D. Casalino, "Aerodynamic and acoustic interaction effects of adjacent propellers in forward flight," *AIAA AVIATION 2023 Forum*, 2023.

[12] F. D. Prenter, A. Zarri, and D. Casalino, "Low-cost computational modeling of aeroacoustic interactions between adjacent propellers," *30th AIAA/CEAS Aeroacoustics Conference (2024)*, 2024.

DOI: 10.61782/fa.2025.0328

FORUM ACUSTICUM EURONOISE 2025

EFFECTS OF BOUNDARY LAYER INGESTION ON DUCTED PROPELLER NOISE

M. Daroukh[1*] **F. Ahmed**[2] **T. Le Garrec**[1]
M. Azarpeyvand[2] **E. Manoha**[1]
[1] DAAA, ONERA, Institut Polytechnique de Paris, 92320 Châtillon, France
[2] Department of Aerospace Engineering, University of Bristol, Bristol, BS8 1TR, United Kingdom

ABSTRACT

In this paper, the effects of boundary layer ingestion on the noise emitted from an academic ducted propeller are evaluated using lattice Boltzmann simulations and wind tunnel experiments. The boundary layer is generated by an aggressive S-plate placed upstream of the propeller and its impact is assessed by comparison with an isolated ducted propeller configuration. Three operating conditions are studied, which correspond to a free-stream velocity of 32 m/s and rotational speeds of 6000, 8000, and 11,000 rpm. Aerodynamic results are compared between simulations and experiments and show a good agreement. They highlight the increase in flow asymmetry and turbulence ingested by the ducted propeller in the presence of the S-plate. Direct acoustic results are extracted from the simulations at the position of the two experimental microphone arrays and compared against experiments in terms of tonal and broadband contributions. Similar trends are observed despite some quantitative discrepancies. In the presence of the S-plate, the stronger flow distortion is responsible for an increase of tonal noise at the blade passing frequencies, while the higher turbulence intensity generates increased broadband noise levels.

Keywords: *ducted propeller noise, boundary layer ingestion, lattice Boltzmann method, wind tunnel experiments*

**Corresponding author*: *majd.daroukh@onera.fr.*
***Copyright**: ©2025 M. Daroukh et al. This is an open-access article distributed under the terms of the Creative Commons Attribution 3.0 Unported License, which permits unrestricted use, distribution, and reproduction in any medium, provided the original author and source are credited.*

1. INTRODUCTION

In order to reduce aircraft fuel consumption, alternative propulsion systems are investigated, such as open fan [1], distributed electric propulsion [2], or boundary layer ingestion (BLI) [3] architectures. The present paper focuses on the latter configuration, which has been the subject of several concepts of aircraft in recent years [3–5].

The principle of BLI is to minimize the net drag force of the airframe-propulsion arrangement by ingesting and re-energizing the airframe wake through the propulsion system [3]. Some concepts have already shown promising results in terms of fuel savings [5], but they also highlight challenges in terms of noise emissions. In particular, the engines ingest an incoming flow with high turbulence intensity and strong azimuthal mean flow distortion. These characteristics are expected to affect both the tonal and broadband components of the noise emitted by the engines [6, 7].

The present study aims to understand the main mechanisms of noise emission in a BLI configuration by focusing on an academic setup composed of a ducted propeller and a S-plate, as investigated in the European Union's Horizon 2020 ENODISE project (`https://cordis.europa.eu/project/id/860103`). Numerical simulations based on the lattice Boltzmann method (LBM) and wind tunnel experiments are conducted at different operating conditions on this so-called "A2-ducted" configuration. A large database has been generated and is available on Zenodo (`https://doi.org/10.5281/zenodo.14041712`). In this paper, we focus only on a few illustrative results.

The configuration and experimental setup are first described in Sec. 2, before detailing the numerical methodology in Sec. 3. Some aerodynamic results are then pre-

sented in Sec. 4, followed by some acoustic results in Sec. 5. Finally, conclusions are drawn in Sec. 6.

2. CONFIGURATION AND EXPERIMENTAL SETUP

The configuration studied in this paper is composed of a ducted propeller which can be placed above an S-plate to investigate the effects of boundary layer ingestion. The setup, tested in the aeroacoustic wind tunnel facility at the University of Bristol [8], is briefly described below (see the paper of Ahmed *et al.* [9] for a complete description).

The propeller is composed of three blades based on X22A NACA23012 profiles and has a diameter D of 0.254 m. It is placed inside a 0.175 m long duct with inner and outer diameters of 0.255 m and 0.279 m respectively, leaving a tip clearance of 0.5 mm. The position of the propeller inside the duct is such that the distance x_{LE} from the tip leading edge to the duct inlet plane equals $0.0627D$. Three struts are positioned downstream of the propeller to maintain the assembly. Other tip clearance and propeller position values have been tested in the experiments but they are not detailed in this paper. In installed configurations, an S-plate with a total length of 1.69 m and a total width of 1 m is added. It is characterized by an height variation of 0.2 m over a length of 1 m, with a maximum local curvature of 75%. The S-plate is placed in direct continuation of the bottom part of the wind tunnel nozzle. The ducted propeller is located 0.8 m downstream of the nozzle exit plane and touches the plate. As a result, the propeller axis is shifted downwards from the nozzle axis by 0.3 m. The setup in the presence of the S-plate is illustrated in Fig. 1.

In this paper, only one wind tunnel velocity U_∞ of 32 m/s and three rotation speeds N of 6000, 8000 and 11,000 rpm are investigated, but other conditions have been tested experimentally. The three studied regimes are characterized by a tip Mach number M_{tip} of 0.22, 0.33 and 0.44, an advance ratio J of 1.26, 0.94 and 0.69, and a blade passing frequency f_{BPF} of 300, 400 and 550 Hz respectively. These conditions are summarized in Tab. 1.

Many measurements are included in the setup. Pressure taps and microphones are incorporated in the S-plate and hotwire measurements at different axial positions allow an assessment of the flow field development. Regarding acoustics, two farfield microphone arcs are used. One is placed along the plane of the plate (top arc) while the other is in the transverse direction (side arc), as shown in Fig. 1. One microphone is put every 5 degrees but the

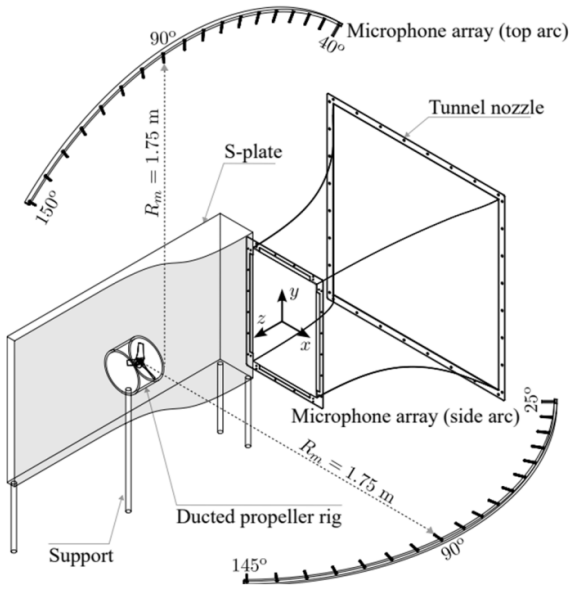


Figure 1. Experimental setup in the presence of the S-plate.

Table 1. Operating conditions investigated in this paper.

U_∞ (m/s)	N (rpm)	M_{tip}	J	f_{BPF} (Hz)
32	6000	0.22	1.26	300
32	8000	0.33	0.94	400
32	11,000	0.44	0.69	550

polar range of the two arcs differ because of installation reasons. The top arc goes from 40 to 150 degrees while the side arc covers the 25-145 degrees range.

3. NUMERICAL METHODOLOGY

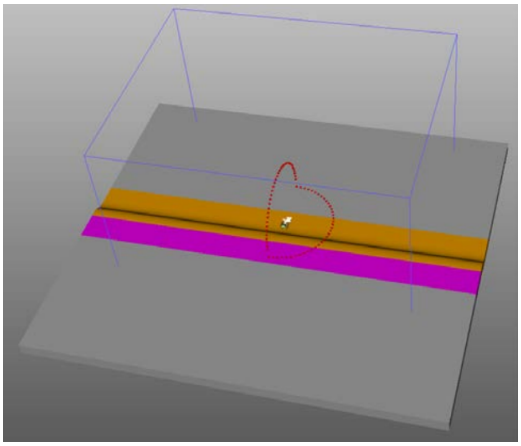
In addition to the experiments, numerical simulations based on the lattice Boltzmann method are performed with the *ProLB* solver (`http://www.prolb-cfd.com/`) which is developed by a French consortium composed of universities, research institutes, and industries. The hybrid recursive regularized Bhatnagar-Gross-Krook (HRR-BGK) collision model [10] is used and the lattice is composed of 19 velocities (D3Q19 lattice). The shear-improved Smagorinsky model of Lévêque *et al.* [11] is chosen for turbulence modeling, while the transfer of in-

formation from rotating to fixed parts is managed by an arbitrary Lagrangian-Eulerian approach.

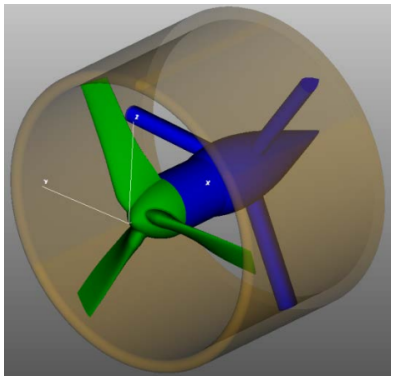
Only part of the setup is included in the simulations for limitation of the computational cost. The isolated cases are thus only composed of the ducted propeller and do not include the wind tunnel nozzle nor the propeller support. The propeller is placed at the center of a cubic fluid domain of size 10 m x 10 m x 10 m. Outlet pressure conditions (with $p_\infty = 101325$ Pa) are prescribed at all external fluid boundaries, except on the one that face the duct inlet where an inlet velocity condition (with $U_\infty = 32$ m/s) is imposed. In order to avoid reflections, absorbing regions are also added close to these external boundaries. Finally, wall boundary conditions (with the use of a wall function) are applied on all solid surfaces. The setup of installed cases slightly differs because it additionally accounts for the S-plate which is assumed to be infinite along its width. The domain is therefore no longer cubic with the replacement of one lateral fluid boundary by the plate. The position of the upstream fluid boundary face is also adjusted to account for the plate length. Note that in order to get a correct boundary layer development over the plate, an artificial plate with a 2 m length is added upstream of the real plate. The first part (1 m) is considered as a frictionless wall while the second part (1 m) is considered as a real wall. A view of the setup defined in installed configurations is given in Fig. 2.

The meshes are done such that the region with the smallest cell size of $\Delta x = 0.1$ mm encompasses the propeller blades, which leaves the place for 5 cells in the radial direction in the tip gap area. The maximum cell size up to the farfield microphones is set to 6.4 mm in order to have least 10 points per wavelength associated to $10 f_{\mathrm{BPF}}$ in the most restrictive case (highest rotation speed), thus allowing for direct noise evaluation. In the installed setup, the plate is added with a prescribed cell size of 0.2 mm in its vicinity. As a result, the isolated setup comprises 500 million nodes and 125 million fine-equivalent nodes (*i.e.* the number of nodes effectively updated at each time step) while the installed setup totalizes 884 million nodes and 330 million fine-equivalent nodes.

The smallest time step is of 168.35 ms, making one full rotation to be described by 59,400, 44,550 and 32,400 iterations at 6000 rpm, 8000 rpm and 11,000 rpm respectively. In all cases, 20 propeller rotations are computed to get converged statistics. The isolated simulations are launched on 1056 processors and last between 60 and 100 h depending on the case, while the installed ones use 2112 processors and last between 100 and 120 h and 100 h. The 11,000 rpm case in installed setup failed to converged, probably because of the appearance of too high local velocities, hardly reachable with such an athermal version of the LBM.



(a) Overview



(b) Zoom into the ducted propeller

Figure 2. Numerical setup for installed cases: limits of the fluid domain in blue lines, far field microphones as red dots, real S-plate in orange, artificial upstream plate in purple, blades and spinner in green, hub and struts in blue, duct in transparent orange.

4. AERODYNAMIC RESULTS

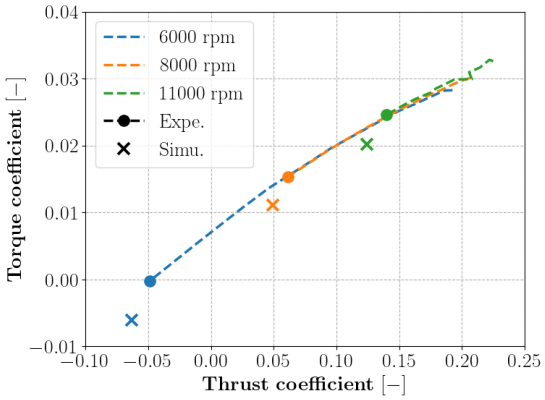
Some aerodynamic results are given in this section. The performance map is given for all engine rotation speeds but the flow profiles are only illustrated on the intermediate case ($N = 8000$ rpm) for conciseness, noting that

similar behavior is obtained at other regimes.

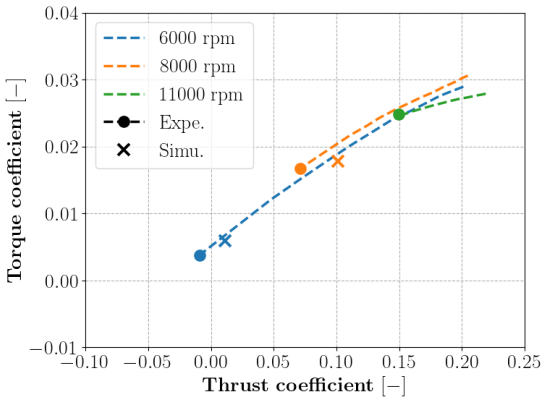
We first focus on aerodynamic performance by plotting in Fig. 3 the thrust and drag coefficients obtained in the experiments and in the simulations (averaged value on the last ten rotations). Lines are drawn for experimental results where the wind tunnel speed is varied from 8 m/s to 32 m/s. The points highlight the 32 m/s condition which is the same as the one used in the simulations. For isolated ducted propeller, we observe slightly different operating conditions between experiments and simulations, with an underestimation of both thrust and drag coefficients at all rotation speeds. The tendency is reversed for the installed ducted propeller at 6000 rpm and 8000 rpm where these coefficients are overestimated in the numerical results (recalling that there is no simulation result for the 11,000 rpm case). As a consequence, the effect of BLI on aerodynamic performance (thrust and torque increase) is more marked in the simulations than in the experiments. These observations should be kept in mind when comparing absolute levels between experiments and simulations in the following.

To get an overview of the flow field topology, simulation contour maps of the axial velocity averaged over the last rotation are given in Fig. 4 for both setup at 8000 rpm. In the isolated configuration, the flow is symmetric and we can notice the potential effect of the duct in the vicinity of the inlet plane, as well as the wakes that develop past the hub and duct ends. In the installed case, we clearly see the development of the boundary layer over the plate and its impact with the propeller around $x = 0$ m. The velocity field inside the duct is no longer symmetric as are the duct end wakes. It is interesting to note that the averaged flow velocity ingested by the propeller is slightly lower in the BLI configuration.

In order to provide more insights into the flow field ingested by the propeller, mean and root mean squared (RMS) velocity profiles are extracted at $x = -0.02$ m (just upstream of the inlet plane) and are compared against experiments in Figs. 5 and 6 respectively. We observe a good agreement in both setups in terms of mean flow velocity. In particular, the lobes due to the hub and shroud potential effect are recovered in the isolated case, and the boundary layer development is correctly reproduced in the installed configuration. This result highlights the asymmetry of the mean flow in the presence of the plate. Regarding the RMS profiles, the agreement between simulations and experiments is less good in terms of absolute values, probably because of a small background residual turbulent level in the experiments, but the trends are correctly reproduced. We indeed observe a strong increase of the turbulent levels ingested by the ducted propeller in the installed configurations, especially in the bottom part of the duct.



(a) Isolated ducted propeller

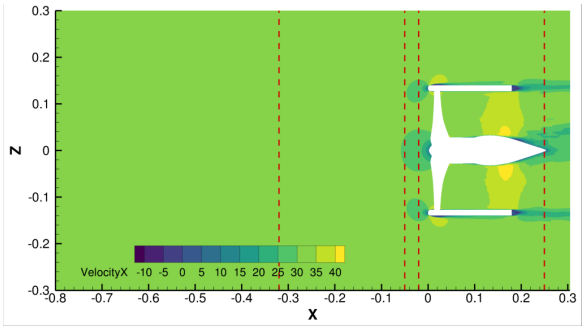


(b) Installed ducted propeller

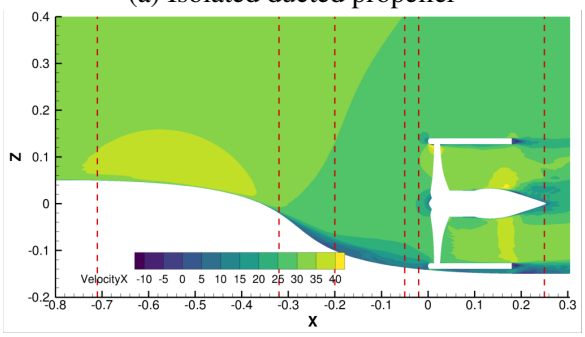
Figure 3. Thrust and drag coefficients from experiments and simulations. Experimental lines show the evolution for different wind tunnel velocities ($U_\infty = 8 - 32$ m/s), with the dots corresponding to the $U_\infty = 32$ m/s condition.

5. ACOUSTIC RESULTS

The main acoustic results are now provided in this section, by first focusing on the broadband noise and then considering the tonal noise.

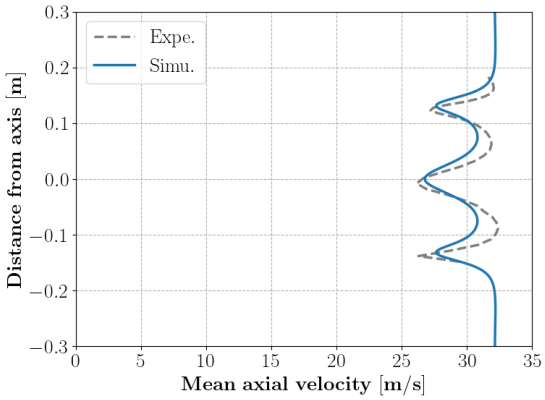


(a) Isolated ducted propeller

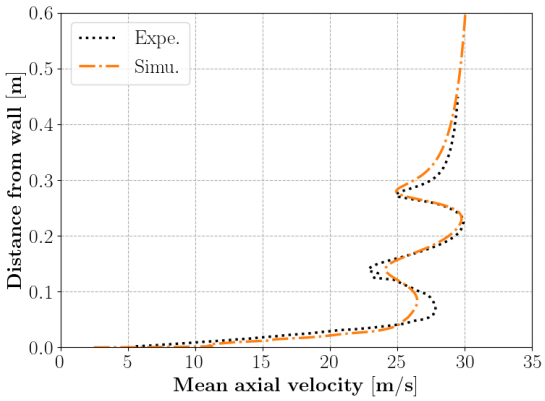


(b) Installed ducted propeller

Figure 4. Contour maps of mean axial velocity obtained from simulations at $y = 0$ m (case $N = 8000$ rpm).



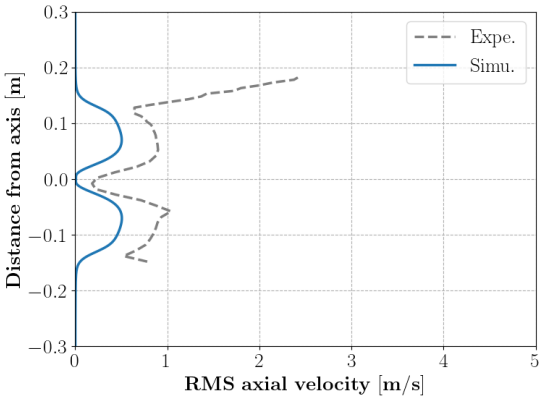
(a) Isolated ducted propeller



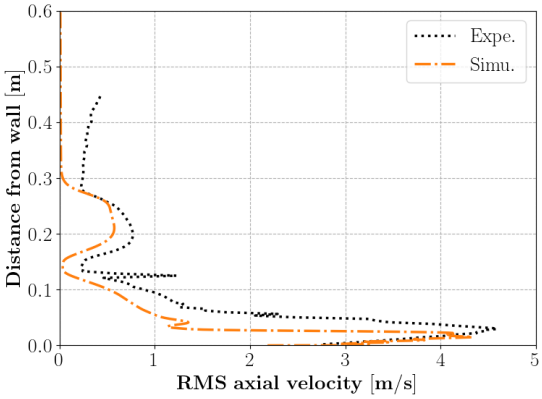
(b) Installed ducted propeller

Figure 5. Mean axial velocity profiles extracted at $x = -0.02$ m from experiments and simulations (case $N = 8000$ rpm).

In order to assess broadband noise, power spectral densities (PSDs) are computed from experimental and numerical time series recorded at the microphones/probes. The time series are first filtered by removing the blade passing phase average in order to remove the tonal component. In the simulations, the PSDs are computed from the last ten rotation signals using the Welch's method with 10 blocks and 50% overlapping. In the experiments, around 30 s of signal (equivalent to $\sim$ 3000 to $\sim$ 6000 rotations depending on the speed) is recorded, thus giving a very small frequency step compared to the numerical one. However, no top tour was included in the setup, which makes the phase average removing quite inefficient. In order to compare broadband noise with a minimal pollution by tonal peaks, only the last ten rotations from experimental measurements are also kept for experimental PSD computations, using again the Welch's method with 10 blocks and 50% overlapping. The tonal component is indeed incorrectly captured in these 10 last rotations because of the engine speed fluctuations, making the tonal contribution much more attenuated. The results for one representative microphone, the one at 90 deg of the side arc (along the propeller plane, see Fig. 1), are given for both setups and for the three rotation speeds in Fig. 7. The low frequencies (lower than $0.5 f_{\mathrm{BPF}}$) are not reliable as there are strong discrepancies between numerical and experimental results, probably because of installation effects in the experiments and/or short statistics in the simulations. In the mid-frequency range (between $0.5 f_{\mathrm{BPF}}$ and 1.5 kHz), the agreement between simulations and experiments is correct, which allows driving some conclu-



(a) Isolated ducted propeller



(b) Installed ducted propeller

Figure 6. RMS axial velocity profiles extracted at $x = -0.02$ m from experiments and simulations (case $N = 8000$ rpm).

sions on the effects of BLI. The levels in the installed configurations are indeed much stronger than in the isolated setup, with 10 to 15 dB increase in average. This increase is probably due to the interaction of incoming turbulence with the rotating blades (rotor leading edge noise), which is to be added to the two other main expected broadband noise sources *i.e.* rotor self noise (trailing edge noise) and wakes/struts interaction noise. Above 1.5 kHz, there is a strong mismatch between numerical and experimental levels for the isolated configurations only. Parametric studies performed experimentally (not shown in this paper for conciseness) have shown that this increase is caused by the tip gap noise, a mechanism that is badly captured in the simulations with only 5 points along the radial extent of the tip gap. This noise mechanism seems to be predominant at high frequencies in the isolated setup only. Indeed, in the installed setup, the agreement between experiments and simulations is correct in this frequency range, thus indicating the predominance of the other acoustic sources mentioned above.

The focus is now put on the tonal noise results. The tonal noise is extracted from time signals recorded at the microphones/probes by doing the blade passing phase average over the whole available signals (*i.e.* the last ten rotations in the simulations, and the whole 30 s in the experiments). The directivities of the overall sound pressure level (OASPL) obtained by integrating the contribution from f_{BPF} to $6f_{\mathrm{BPF}}$ are given in Fig. 8. We can observe significant differences in terms of absolute levels between experiments and simulations, with no clear trend. The OASPL is indeed globally overestimated in the simulations at 6000 rpm and 11,000 rpm, while it is underestimated at 8000 rpm. Still, the relative effect of BLI is coherent between measurements and computations, with an average increase of the OASPL by about 10 dB at 6000 rpm and 8000 rpm. There is no simulation for the installed case at 11,000 rpm, but the penalty induced by BLI found experimentally seems to be slightly lower at this condition. This tonal noise increase is to be mainly caused by the propeller unsteady loadings due to the asymmetric flow in the installed configuration (distortion/rotor interaction noise). The other contributors to tonal noise *i.e.* the propeller steady loading and thickness noise and the wakes/struts interaction noise might also be altered by the boundary layer ingestion.

6. CONCLUSION

The effects of boundary layer ingestion are investigated in this paper on an academic setup composed of a ducted propeller that can be placed over an aggressive S-plate. Experiments have been made in the wind tunnel of the University of Bristol and numerical simulations have been performed using the *ProLB* solver based on the lattice Boltzmann method. Many operating points have been measured in the experiments, but we focused in this paper on the three ones that have been considered in the simulations (wind tunnel speed of 32 m/s and propeller rotation speeds of 6000, 8000 and 11,000 rpm). A large database has been generated and is available on Zenodo. Only a few illustrative results have been presented in this paper.

We have shown in particular that the flow ingested by the ducted propeller is largely asymmetric in the presence of the S-plate, which creates an important flow distortion that interacts with the rotating propeller blades. This creates unsteady loading on the blades, an additional source of tonal noise radiation at the blade passing frequencies. The two other main mechanisms, *i.e.* propeller steady loading and thickness noise and propeller-strut interaction noise, might also be altered by the boundary layer ingestion. As a result, the tonal noise levels are significantly increased at all engine rotation speeds, with a 5 to 10 dB penalty.

In addition, the flow ingested by the propeller is also shown to be significantly more turbulent in the bottom part of the duct. The interaction of this turbulence with the rotating blades adds a contribution to broadband noise, which is caused by the rotor trailing edge and tip gap noise and the propeller-strut interaction noise in the isolated setup. The broadband noise levels in the farfield are therefore strongly increased in the presence of the S-plate, with about 10-15 dB in the mid-frequency range. After 1.5 kHz however, the penalty is no more visible in the measurements, probably because of the predominance of tip gap noise. This mechanism is poorly captured in the simulations which explains the discrepancies in this frequency range.

Those results highlight the strong effect of boundary layer ingestion on both tonal and broadband noise. They also show that the tip gap noise is an important contributor to broadband noise in such a setup, which was not necessarily anticipated in the preparation of numerical simulations. Further analyses should be made to better understand the impact of boundary layer ingestion on the different acoustic sources.

7. ACKNOWLEDGMENTS

This work is supported by the European Union's Horizon 2020 research and innovation program through the project ENODISE (ENabling Optimized DISruptivE airframe-propulsion integration concepts) under grant agreement no. 860103.

8. REFERENCES

[1] D. Lewis, C. Perrin, and F. Falissard, "Tonal Noise Predictions of a Generic Open-Fan Based on a Hybrid URANS Approach," in *30th AIAA/CEAS Aeroacoustics Conference*, 2024.

[2] P. Schmollgruber, O. Atinault, I. Cafarelli, C. Döll, C. François, J. Hermetz, R. Liaboeuf, B. Paluch, and M. Ridel, "Multidisciplinary Exploration of DRAGON: an ONERA Hybrid Electric Distributed Propulsion Concept," in *AIAA Scitech 2019 Forum*, 2019.

[3] L. Wiart and C. Negulescu, "Exploration of the Airbus 'Nautilius' engine integration concept," in *31st Congress of the International Council of the Aeronautical Sciences*, 2018.

[4] S. A. Pandya, A. Uranga, A. Espitia, and A. Huang, "Computational Assessment of the Boundary Layer Ingesting Nacelle Design of the D8 Aircraft," in *52nd Aerospace Sciences Meeting*, 2014.

[5] L. Menegozzo and E. Benini, "Boundary Layer Ingestion Propulsion: A Review on Numerical Modeling," *Journal of Engineering for Gas Turbines and Power*, vol. 142, no. 12, 2020.

[6] G. Romani, Q. Ye, F. Avallone, D. Ragni, and D. Casalino, "Numerical analysis of fan noise for the NOVA boundary-layer ingestion configuration," *Aerospace Science and Technology*, vol. 96, p. 105532, 2020.

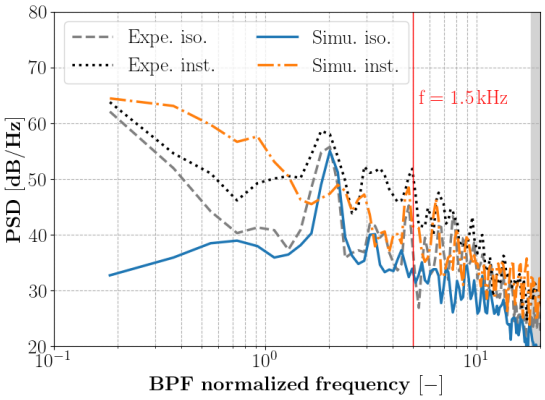
[7] M. Daroukh, C. Polacsek, and M. Carini, "Acoustic Assessment of BLI Effects on Airbus Nautilius Engine Integration Concept - Part I: Noise Generation," in *28th AIAA/CEAS Aeroacoustics Conference*, 2022.

[8] Y. D. Mayer, H. Kamliya Jawahar, M. Szőke, S. A. Showkat Ali, and M. Azarpeyvand, "Design and performance of an aeroacoustic wind tunnel facility at the University of Bristol," *Applied Acoustics*, vol. 155, pp. 358–370, 2019.

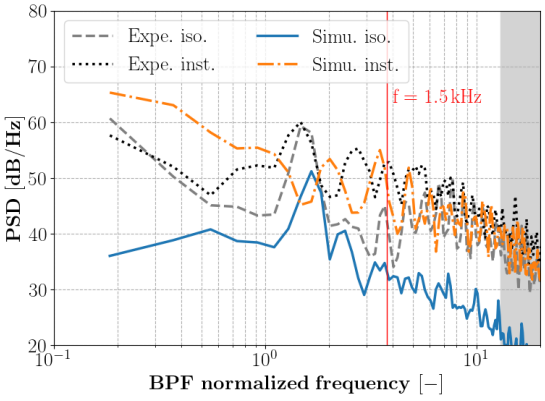
[9] F. Ahmed, I. Zaman, D. Rezgui, and M. Azarpeyvand, "Aeroacoustics of a ducted fan ingesting an adverse pressure gradient boundary layer," *Journal of Fluid Mechanics*, vol. 985, p. R1, 2024.

[10] J. Jacob, O. Malaspinas, and P. Sagaut, "A new hybrid recursive regularised Bhatnagar–Gross–Krook collision model for Lattice Boltzmann method-based large eddy simulation," *Journal of Turbulence*, vol. 19, no. 11-12, pp. 1051–1076, 2018.

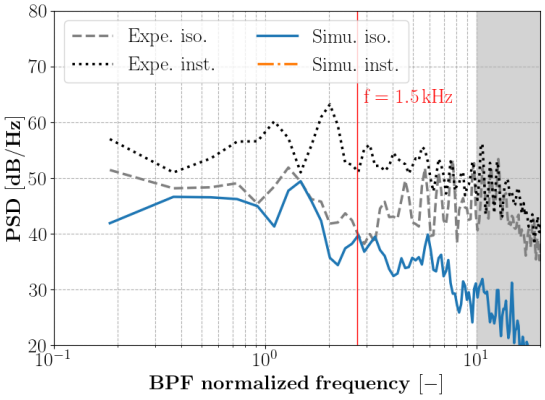
[11] E. Lévêque, F. Toschi, L. Shao, and J. P. Bertoglio, "Shear-improved Smagorinsky model for large-eddy simulation of wall-bounded turbulent flows," *Journal of Fluid Mechanics*, vol. 570, pp. 491–502, 2007.



(a) $N = 6000$ rpm

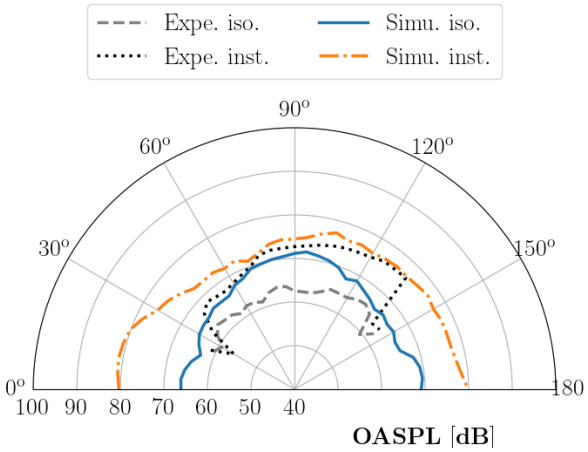


(b) $N = 8000$ rpm

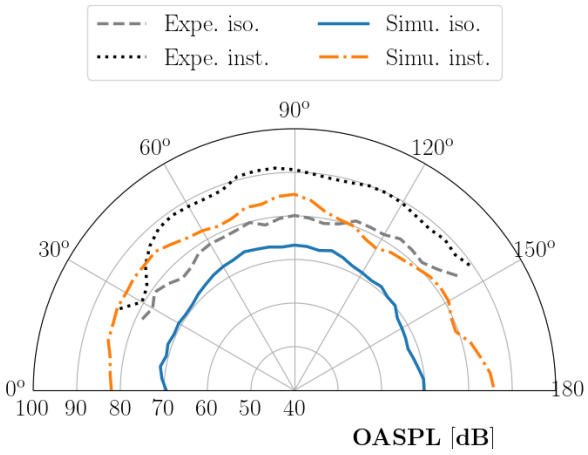


(c) $N = 11,000$ rpm

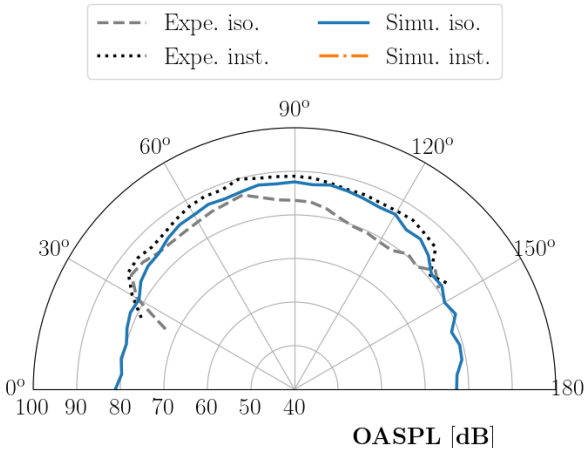
Figure 7. PSDs computed from experiments and simulations on the 90 deg microphone of the side arc. The grey areas show the mesh cut-off region. The vertical red line highlights the frequency above which the tip gap noise is predominant in isolated setups.



(a) $N = 6000$ rpm



(b) $N = 8000$ rpm



(c) $N = 11,000$ rpm

Figure 8. OASPL directivity over the side arc computed from experiments and simulations by integrating the contribution from f_{BPF} to $6f_{\mathrm{BPF}}$.

DOI: 10.61782/fa.2025.0966

FORUM ACUSTICUM EURONOISE 2025

WALL PRESSURE FLUCTUATIONS AND IMPACT ON THE NOISE FROM DISTRIBUTED ELECTRIC PROPELLERS

Luana G. Stoica[1*] **Elisa de Paola**[1] **Giorgia Capobianchi**[1]
Alessandro Di Marco[1] **Roberto Camussi**[1]
[1] DICITA, University of Roma Tre, Roma, Italy

ABSTRACT

In the pursue of new urban air mobility solutions, the VENUS project served as a test bench for a real-world application of distributed electric propulsion aircraft. Experimental investigations were carried out on a wing model, equipped with three tractor propellers, derived from a realistic regional aircraft configuration inside an open jet acoustically treated wind tunnel. Wall pressure fluctuations induced by the multiple propeller configuration on the wing were investigated, in particular on the leading edge of the wing, on the flap, and inside the gap between the flap and the wing. Measurements of the acoustic footprint and of the polar directivity were carried out using three far-field microphone arrays. The parameters varied during the measurements included propeller blade pitch angle, flap deflection angle and wing angle of attack, as well as the distances between the propellers and with respect to the wing. The importance of the different generation mechanisms on the far-field noise and their dependency on the position along the wing and test parameters was assessed applying two-point statistics.

Keywords: *wall pressure fluctuations, DEP, propellers, wind tunnel.*

1. INTRODUCTION

In recent years we witnessed the increased popularity of the distributed electric propulsion (DEP) with a variety of new technologies and aircraft concepts being developed. DEP aircraft concepts feature multiple electric propulsors around an airframe and one or more independent electric generators or energy storage devices [1].

Experimental investigations using high resolution PIV, force and aeroacoustic measurements were carried out in [2] finding that the noise distribution for twin-rotor configurations is a function of azimuthal angle and separation distance. Systematic testing on different dual propeller configurations were conducted both numerically and experimentally in [3] in order to gain insight in the mutual interaction effect on thrust and noise levels. In these two latter papers, two-bladed propellers for UAV applications were considered. A benchmark experiment on wake-ingesting propellers is discussed in [4], including fluctuating pressure and aeroacoustic analysis.

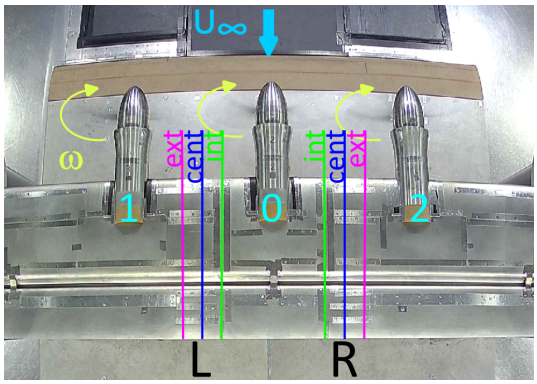
Realistic wing models with multiple bladed propellers were investigated in three different EU funded projects. In [5] we find the results of the study of a wing model equipped with three propellers with three blades each, both in tractor and pusher configuration in the framework of the ARTEM project. The project ERaCLE was focused on the aeroacoustics of a wing model propelled by two five-bladed pusher propellers [6]. In the current paper, the experimental database of the VENUS project was investigated with a focus on the wall pressure fluctuation analysis, and its correlation to the emitted far-field noise.

2. EXPERIMENTAL SET-UP

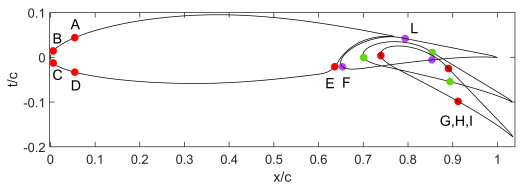
The VENUS model is inspired by a short range regional aircraft, with each wing powered by three distributed propellers to be used mainly in take-off and landing. Each propeller is composed of four blades. The blade geometry and the propellers positions along the wing were op-

*__Corresponding author__: luana.stoica@uniroma3.it.
__Copyright__: ©2025 L.G. Stoica et al. This is an open-access article distributed under the terms of the Creative Commons Attribution 3.0 Unported License, which permits unrestricted use, distribution, and reproduction in any medium, provided the original author and source are credited.

timized with aerodynamic and aeroacoustic constraints. The experimental set-up is described in detail in [7].



(a) Upper view model - pressure side wing



(b) Cross-section view

Figure 1: Fluctuating pressure sensors positions. The wing is seen from the pressure side.

A picture of the wing with the baseline DEP relative position and the position of the sensors is shown in Fig. 1 a, as seen from the pressure side of the wing, as the wing model was installed upside-down inside the wind tunnel. The unsteady pressure sensors (Knowles FG-23629-P16 capsule electret microphones) were installed on both sides of the central propeller, named left (L) and right (R) as seen when facing the flow, on three lines (internal, central and external with respect to the centre of the wing) with the aim of covering the interaction area between the propellers. Along the airfoil, the positions are marked with different letters and are mainly gathered around the leading edge, on the flap and in the gap between wing and flap. All the propellers spin counter-clockwise as seen from the flow, with a blade pitch angle of 17°. In the baseline position, the propeller blades are aligned on the same plane, at a distance from the wing of $0.52D$ and a hub to hub distance of $1.05D$. The wing chord is equal to $1.14D$. All the tested propellers positions can be found in Tab. 1. The wing is also equipped with a high lift device: the flap deflection angles are $\delta = 20°$ in take-off and $\delta = 35°$ in landing position. The wing pitch angle is set to 5° in both cases.

Table 1: Propellers' position in the DEP configurations tested.

	$\Delta Y/D$ 0-1, 0-2	$\Delta X/D$ 1, 2	$\Delta X/D$ 0
XY1	1.05	0.52	0.52
XY2	1.05	0.41	0.41
XY3	1.05	0.41	0.63
XY4	1.05	0.63	0.41
XY5	1.05	0.52	0.63
XY6	0.984	0.41	0.63
XY7	0.984	0.63	0.41

3. RESULTS AND DISCUSSION

The fluctuating pressure signals from the wall microphones on the wing are analysed in this section. The tests analysed herein are performed in take-off wing configuration (AoA=5°, flap deflection 20°) with all three propellers running in-phase at an advance ratio of $J = 0.654$. The Reynolds number of the incoming flow is $Re_\infty = 0.81 \cdot 10^6$, whereas for the propeller, $Re_{0.75} = 1.3 \cdot 10^5$, based on the propeller chord at the 75% propeller-blade station. The fluctuating pressure coefficient is defined as $c_{p,rms} = \frac{\sigma_p}{q}$, where σ_p is the standard deviation of the fluctuating pressure and q is the dynamic pressure measured in the wind tunnel test section.

An interesting feature is that sensors on the central lines show a notable difference in the spectra on both sides of the wing as we can see from the spectra measured in the baseline configuration in Fig. 2. We notice that the sensors on the external and internal lines of microphones exhibit tonal components up to around the 12th shaft frequency, whereas the central line of microphones exhibits an additional set of tonal spikes at higher frequency, in some cases up to the 36th BPF in some cases. This effect may be ascribable to the interaction between the vortices from the two adjacent propellers, and it is registered on both right and left side of the wing (see convention in Fig. 1). As the AoA is increased, this effect remains evident only on the pressure side of the wing, as probably

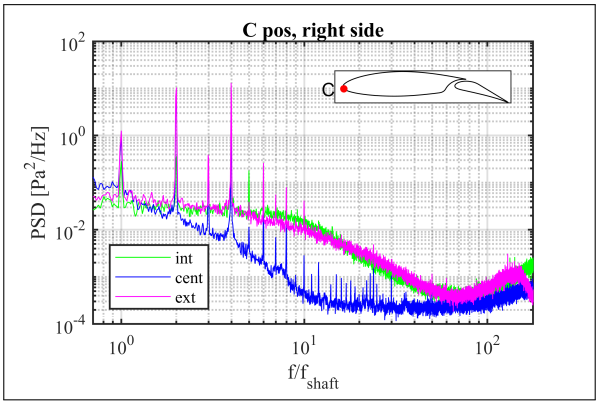


Figure 2: PSD of the fluctuating pressure from sensors in position C, right side of the wing - baseline.

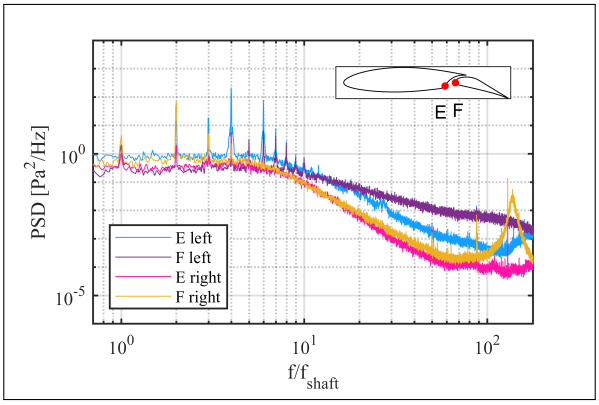


Figure 3: PSD of the fluctuating pressure from sensors in the gap between flap and wing - baseline.

the sensors on the upper side are screened by the airflow separating at the leading edge.

In Fig. 3, the spectra of the wall pressure in the gap between wing and flap are shown for the baseline configuration. These sensors are only installed on the line denoted as internal (green line in Fig. 1). On the right side of the wing, where we expect the disturbed wake of the central propeller to be impinging on the pressure side, the high frequency decay of the spectra has the same rate in E and F, around $f^{(-7/2)}$. On the left side of the wing, where the tip vortices from the central propeller are not impinging on these sensors, we have different features in the E and F positions. For the sensor E, we notice that the tone at the shaft frequency is not present, whereas the successive harmonics have a higher amplitude than in the F position.

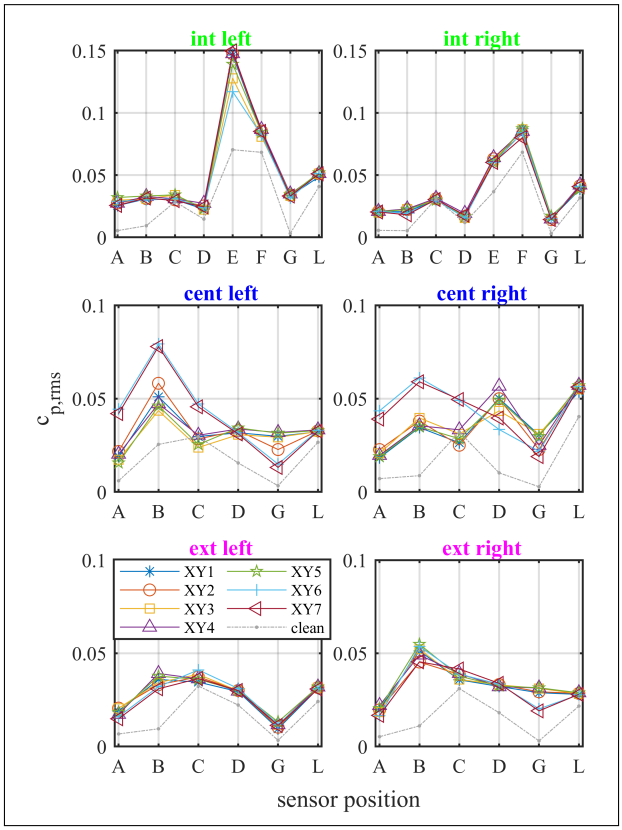


Figure 4: Trends of $c_{p,rms}$ along the wing model in different DEP configurations.

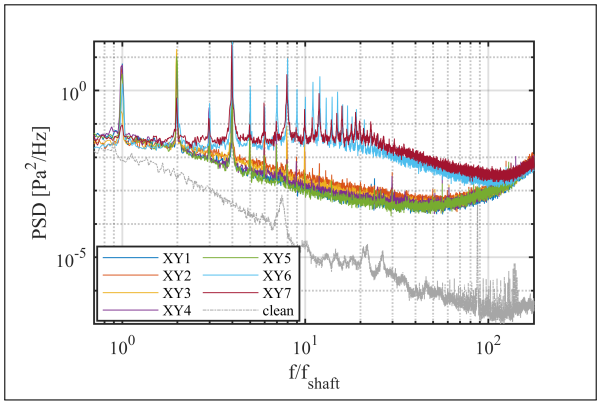


Figure 5: PSD of the fluctuating pressure from sensor B, central line, right side - DEP configuration effect.

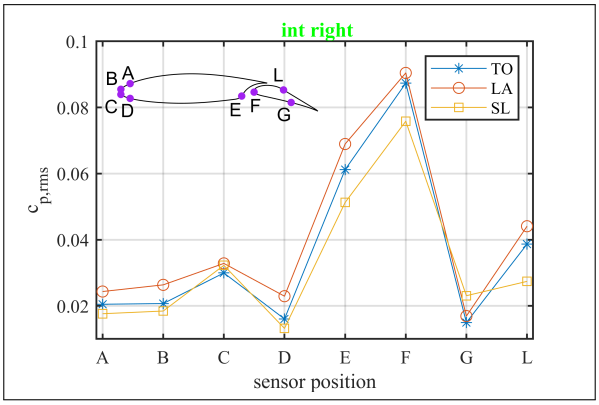


Figure 6: Trends of $c_{p,rms}$ along the wing model with different flap deflection angles.

Also the high frequency decay has a lower rate in F with respect to E, and in both cases is lower than the right side.

The effect of the different DEP configurations on the fluctuating pressure is investigated in Fig. 4, where also the results on the clean wing (i.e. without propeller blades) are included. Notable differences may be observed on the central lines of microphones, where the interaction between adjacent propellers is captured. In particular, configurations $XY6$ and $XY7$ exhibit the highest maximum value in position B and the lowest minimum in position G. This effect may be ascribed to the propellers planes overlapping or to the increased distance between the propellers axes. An intermediate value is found for position $XY2$, which has the three aligned propellers in their closest position with respect to the wing. The trends of the $c_{p,rms}$ on the external and internal lines are quite similar, with a local maximum on the leading edge, in position B or C depending on the line, and with another local maximum in position L on the upper side of the flap. The pressure fluctuations in the gap between the flap and the wing exhibit the highest values, with differences with respect to the other sensors up to 0.05 on the right side and up to 0.1 on the left side. This latter value may be be affected by the impinging wake from the propellers. Similar results are obtained in take-off and landing configurations.

In order to further investigate the origin of the maximum value of the fluctuating pressure, in Fig. 5, the spectra in position B from the central (blue) line on the right side of the wing are shown, for all the DEP configurations tested. The difference between the overlapping discs configurations and the others becomes obvious looking at the mid-high frequency part of the spectra, where a substantially higher level of energy is observed. The high frequency decay of the spectra from configurations XY6 and XY7 is approximately $f^{(-7/3)}$, typical value for the turbulent boundary layer acoustic-transition [8]. For the configurations with no overlap, the slope of the spectra decreases rapidly after the second shaft frequency.

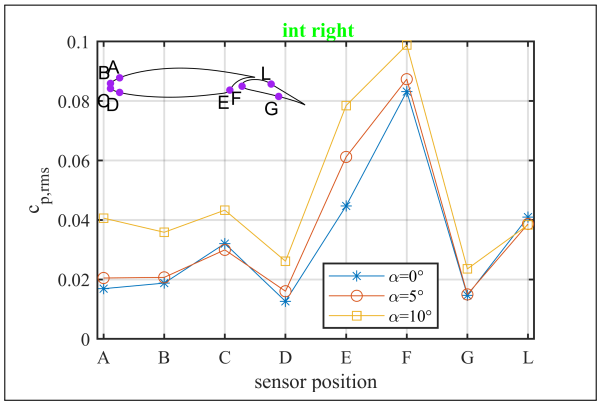


Figure 7: Trends of $c_{p,rms}$ along the wing model with different wing pitch angles.

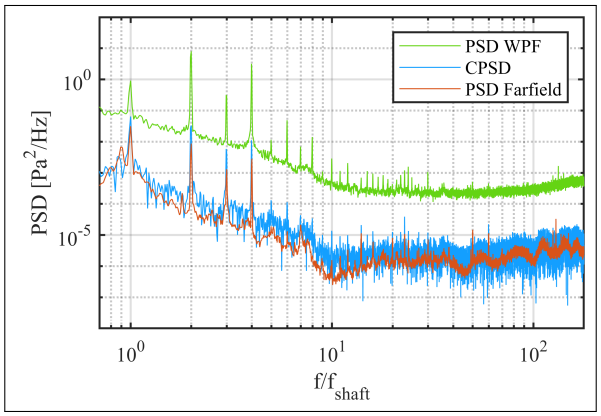


Figure 8: Comparison between PSD of the fluctuating pressure, farfield noise and cross-spectrum.

The effect of the flap deflection on the fluctuating pressure is shown in Fig. 6 for the baseline configuration in take-off, with the results from the sensors located along the internal line on the right side as an example. The landing configuration ($\delta = 35°$) exhibits the higher fluctuation, followed by the take-off and the side-line, with differences in the order of 0.005. This is especially true

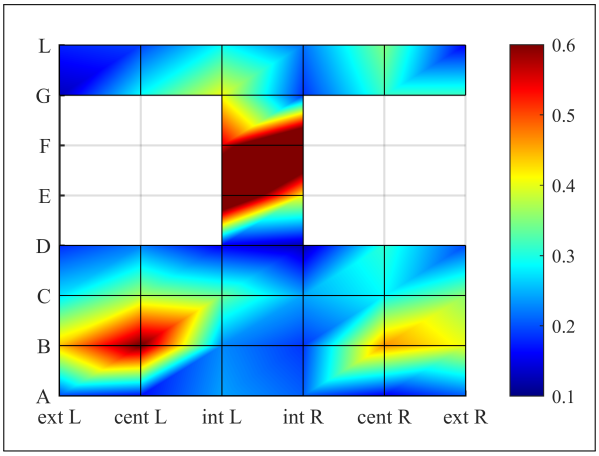


Figure 9: Covariance between the fluctuating pressure sensors and farfield noise.

for the sensors in the gap between the wing and the flap.

In Fig. 7, the results from the same sensors are plotted at different wing pitch angles. At $10°$, there is a $c_{p,rms}$ up to 0.02 higher, due to separation effects. For angles between $0°$ and $5°$ the values are similar, whereas for exceeding angles the fluctuations increase with the AoA, indicating a flow separation occurring. For the sensors in the gap between wing and flap the situation is different, with the fluctuations increasing with the AoA at all angles.

The cross-spectra were computed between the pressure sensors on the wing and one farfield sensor located at the centre of the acoustic footprint of the wing, near the propeller plane. An example is shown in Fig. 8, for the sensor in position C on the central line on the right side of the wing. The baseline configuration in take-off is considered. We can see a strong correlation on the first four shaft frequencies. The cross-spectrum also unveils the higher frequency tonal components which are more evident in the wall pressure spectra. The broadband component maintains the same shape as the far-field noise.

The covariance between the signals was then obtained integrating the cross-spectra, in order to understand which positions affect mostly the emitted noise (Fig. 9). The maximum correlation between the signals is found in the gap between the flap and the wing, although there are other areas concurring in a notable manner to the noise emission. In particular, we find a second maximum at the sensors in position B on the central lines, where the vortices from the adjacent propellers are interacting and impinging on the wing. In this position, flow separation may occur at the examined AoA of $5°$. A lower local maxima is also found at sensors in position C on the internal lines, which are closest to the central propeller. When comparing different flap positions, we find a higher correlation on sensors positions D and L when the flap is deflected with respect to the sideline configuration. As the the angle of attack is increased, the maximum correlation moves towards positions C and D on the left side of the wing, i.e. where the outflow from the propeller is impinging on the wing. Also the correlations measured on the flap in G and L increase with the AoA.

4. CONCLUSION

Wall pressure fluctuations on a DEP configuration were analysed in order to find the underlying mechanisms leading to noise generation. Signals are acquired from 44 fluctuating pressure sensors installed at different stations along the wing, surveying different areas on the airfoil, such as the leading edge of the wing, the gap between wing and flap and the flap.

The interaction between the adjacent propellers has a visible effect on the wall pressure fluctuations and is highly correlated with the acoustic footprint. Regarding the propellers relative position, the configurations with overlapping propellers discs and the greatest distance between their axes are responsible for the highest wall pressure fluctuations impinging on the wing. An influence of the flap deflection angle is also visible, with pressure fluctuations increasing with increasing deflection. The wing angle of attack is in its turn responsible for increasing the fluctuations, especially above $5°$, due to separation effects.

The cross-correlation between the wall pressure fluctuations on the wing and the farfield emitted noise was then examined. The highest correlation with the farfield noise is found in the gap between the wing and the flap, which is also responsible for the highest contribution to the pressure fluctuations on the wing. In addition, the points where the interacting tip vortices from the adjacent propellers are impinging on the wing are the second highest correlated with the acoustic footprint.

5. ACKNOWLEDGMENTS

This work is part of the project VENUS (inVestigation of distributEd propulsion Noise and its mitigation through wind tUnnel experiments and numerical Simulations), which has received funding from the Clean Sky 2 Joint

Undertaking under the European Union's Horizon 2020 research and innovation program under grant agreement 886019.

6. REFERENCES

[1] H. D. Kim, A. T. Perry, and P. J. Ansell, "A review of distributed electric propulsion concepts for air vehicle technology," in *AIAA/IEEE Electric Aircraft Technologies Symp. (EATS)*, pp. 1–21, IEEE, 2018.

[2] T. Zhou and R. Fattah, "Tonal noise acoustic interaction characteristics of multi-rotor vehicles," in *23rd AIAA/CEAS Aeroacoustics Conference*, p. 4054, 2017.

[3] H. Bu, H. Wu, C. Bertin, Y. Fang, and S. Zhong, "Aerodynamic and acoustic measurements of dual small-scale propellers," *Journal of Sound and Vibration*, vol. 511, p. 116330, 2021.

[4] K. Brown, J. Fleming, M. Langford, W. Walton, W. Ng, K. Schwartz, D. Wisda, and R. Burdisso, "Reduced-order prediction of unsteady propeller loading and noise from pylon wake ingestion," *AIAA Journal*, vol. 59, no. 9, pp. 3304–3316, 2021.

[5] J. Drofelnik, M. Andrejasic, B. Mocan, T. Kosel, *et al.*, "Measurement and modelling of aero-acoustic installation effects in tractor and pusher propeller architectures," in *AIAA AVIATION FORUM*, p. 2301, 2021.

[6] L. G. Stoica, S. Mancini, A. Di Marco, E. de Paola, R. Camussi, C. Aquilini, A. Kolb, and N. Paletta, "Experimental investigation and numerical modeling of noise generated by installed pusher propellers," *Journal of Aircraft*, vol. 0, no. 0, pp. 1–13, 0.

[7] E. De Paola, R. Camussi, G. Stoica, A. Di Marco, and G. Capobianchi, "Aerodynamic and aeroacoustic experimental investigation of a three propellers DEP configuration," *Aerospace Science and Technology*, vol. 154, p. 109508, 2024.

[8] M. K. Bull, "Wall-pressure fluctuations beneath turbulent boundary layers: some reflections on forty years of research," *Journal of Sound and Vibration*, vol. 190, no. 3, pp. 299–315, 1996.

DOI: 10.61782/fa.2025.0136

FORUM ACUSTICUM EURONOISE 2025

ANALYTICAL INVESTIGATION OF ROTOR-STRUT POTENTIAL INTERACTION NOISE

Riccardo Zamponi[1,2*] **Alessandro Zarri**[1] **Julien Christophe**[1]
[1] von Karman Institute for Fluid Dynamics, Sint-Genesius-Rode, Belgium
[2] Technische Universiteit Delft, Delft, The Netherlands

ABSTRACT

This paper presents a methodology to predict the tonal noise radiated by a propeller-strut configuration by modeling the potential inflow distortion induced by the strut. The approach combines a theoretical description of the potential flow around a circular cylinder with the force distribution and induced velocity computed using an unsteady panel method. The analytical results show satisfactory agreement with measurements from previous studies, demonstrating the suitability of the proposed methodology as a fast and effective prediction tool.

Keywords: *Propeller noise, potential interaction noise, noise prediction, urban air mobility.*

1. INTRODUCTION

A significant part of the aerodynamic noise radiating from an unmanned aerial vehicle (UAV) arises from the interaction between the turbulent wake and the acoustic field produced by the rotors and the supporting strut located downstream. The intensity of such interaction depends on the proximity between these components and encompasses several noise generation mechanisms, including the sound emitted by the rotor operating in the potential distortion of the strut. Clarifying these mechanisms can offer guidelines for the future design of quieter UAVs and foster the development of analytical noise prediction tools to exploit in the early design stage, where the detailed geometry of the propulsion systems is still unknown.

Several studies in the literature have focused on the analytical modeling of propeller-strut potential interaction noise [1–6]. However, most of these relied on measurement data or high-fidelity numerical simulations to provide input to the prediction models, particularly for the propeller-induced velocity. Low-fidelity methods, such as blade element momentum theory (BEMT), have been regarded as subject to significant uncertainties [4]. In this study, we propose an alternative approach, making use of a fast mid-fidelity simulation framework coupled for the estimation of the aerodynamic data required by the model.

2. METHODOLOGY

2.1 Experimental setup

The analytical results presented in this study are intended to reproduce the measurements performed by Gallo *et al.* [3] in the JAFAAR anechoic room of the von Karman Institute for Fluid Dynamics. Acoustic measurements were performed using a 7-microphone directivity arc (with radiation angles ranging from $0°$ to $90°$ relative to the propeller axis) to investigate the noise emitted by a propeller operating upstream of a cylindrical rod (see Figure 1). A two-bladed Mejzlik 13”x4.2 propeller, driven by a T-motor AT 2814 KV1050 and controlled by a Scorpion Tribunus II 12-80 A, was tested for different rod diameters and propeller-strut distances. For comparison with noise prediction results, the case with the propeller operating at $6000\,\mathrm{RPM}$ and with a strut radius of $a_c = 0.02\,\mathrm{m}$ located at $d = 0.01\,\mathrm{m}$ from the rotor plane is selected.

2.2 Analytical model

The analytical flow-distortion model used in this paper is based on the classical incompressible solution for the flow past a circle. The two-dimensional nature of the model of-

*Corresponding author: riccardo.zamponi@vki.ac.be.
Copyright: ©2025 Riccardo Zamponi. This is an open-access article distributed under the terms of the Creative Commons Attribution 3.0 Unported License, which permits unrestricted use, distribution, and reproduction in any medium, provided the original author and source are credited.

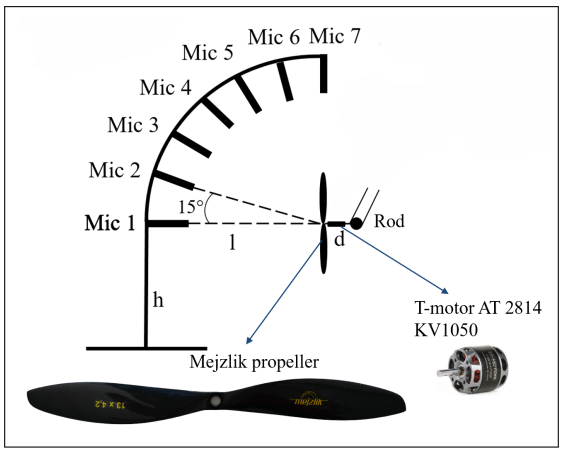


Figure 1. Propeller-strut experimental setup [3].

fers an advantage when dealing with struts of non-uniform cross-section, as it allows the structure to be divided into segments in accordance with a strip-theory approach for rotor noise prediction. Following Roger *et al.* [7], the expression for the upwash velocity w in the direction normal to the blade chord in the polar coordinates (r, ϕ) along the mean circle of the considered blade strip reads

$$\frac{w(r,\phi)}{U_z(r)\,a_c^2} = \sin\alpha\sin\alpha_0\,C_d(r,\phi) - \sin\alpha\cos\alpha_0\,D_d(r,\phi) + \cos\alpha\cos\alpha_0\,A_d(r,\phi) + \cos\alpha\sin\alpha_0\,B_d(r,\phi), \quad (1)$$

where

$$A_d(r,\phi) = \frac{(d^2 - r^2\sin^2\phi)}{(d^2 + r^2\sin^2\phi)^2};\; B_d(r,\phi) = \frac{2d\,r\sin\phi}{(d^2 + r^2\sin^2\phi)^2}$$
$$C_d(r,\phi) = \frac{\cos\phi(d^2 - r^2\sin^2\phi)}{(d^2 + r^2\sin^2\phi)^2};\; D_d(r,\phi) = \frac{d\,r\sin 2\phi}{(d^2 + r^2\sin^2\phi)^2}.$$

Here, α, and α_0 are the blade pitch angle and the flow swirl angle with respect to the rotor axis, respectively, while U_z is the propeller induced velocity. Since the strut only extends on half of the rotor disk plane, w is set equal to zero for $\phi \in [3\pi/2; \pi/2]$ [6]. Although w is stationary, the blade experiences periodic distortion in its reference frame, whose k-th harmonic can be computed through a Fourier series:

$$w_k(r) = \frac{1}{2\pi}\int_0^{2\pi} w(r,\phi)e^{ik\phi}d\phi, \quad k \geq 1. \quad (2)$$

The harmonics of lift per unit span can be subsequently derived from the coefficients w_k by means of Sears' theory [8], according to

$$L_k(r) = \pi\rho_0 c U_r w_k(r) \times \left[C(\sigma)(J_0(\mu) - iJ_1(\mu)) + \frac{i\sigma}{\mu}J_1(\mu)\right]^*, \quad (3)$$

with

$$\sigma = \frac{k\Omega c}{2U_r}; \quad \mu = \frac{ikc}{2r}e^{-i\gamma},$$

where U_r is the velocity at the blade section, C is the Theodorsen function, Ω is the rotational speed, c is the chord of the blade section, γ is the blade stagger angle, and * denotes the complex conjugate. L_k can now be decomposed into an axial and tangential force distribution and used in Hanson's model [9] to calculate the tonal far-field noise radiated at the m-th harmonic of the blade passing frequency (BPF). It is important to specify that the formulation of Hanson's model implemented in this paper is valid for acoustically compact cases, which limits the investigation presented here up to the 5th BPF harmonic.

2.3 Unsteady panel method

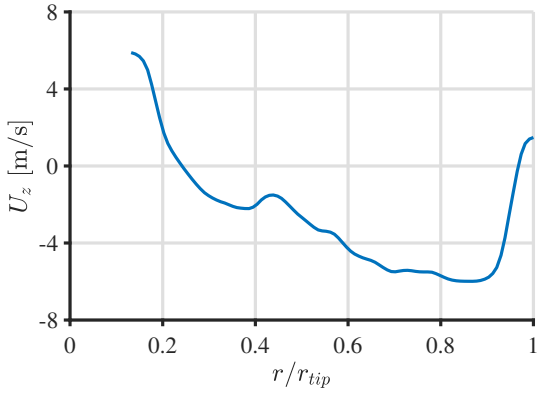


Figure 2. Induced velocity of the isolated propeller extracted 0.01 m from the rotor disk.

The model presented in Section 2.2 relies on the distributions of force per unit span along the propeller blade and the rotor-induced velocity, as well as the flow swirl angle. In the present study, these

quantities are computed using the commercial unsteady panel method software FlightStream, which employs a surface vorticity approach augmented with a Prandtl–Glauert correction to account for compressibility effects and a viscous correction that couples the potential flow solution with a numerical boundary layer. The simulation comprises 2568 surface elements, with a mesh resolution of 2.1 mm at the blade tip and along the leading and trailing edges, and 4.2 mm elsewhere. The numerical calculation is performed for the isolated propeller spinning at 6000 RPM, and the data are averaged over 8 propeller revolutions. An example of an induced velocity profile extracted downstream of the propeller is shown in Fig. 2, whereas an overview of the inflow distortion induced by the strut and experienced by the blades is illustrated in Fig. 3.

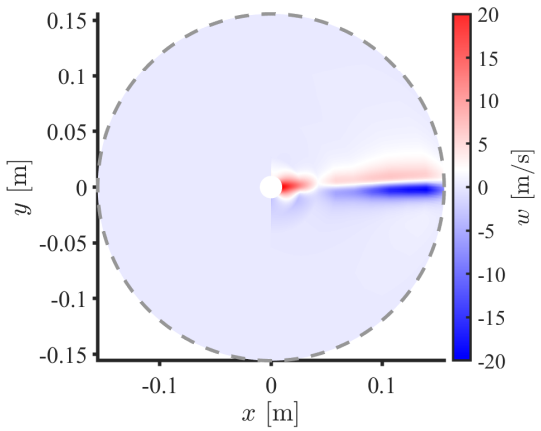


Figure 3. Upwash velocity distortion induced by the strut on the rotor disk.

3. RESULTS AND DISCUSSION

The analytical prediction of the potential interaction noise radiated by the propeller up to a frequency of 5 × BPF is compared to the experimental results of Gallo *et al.* [3] in Fig. 4. The data refer to a radiation angle of 0° (see Fig. 1).

In general, the prediction results agree satisfactorily with the measurements for the considered tonal

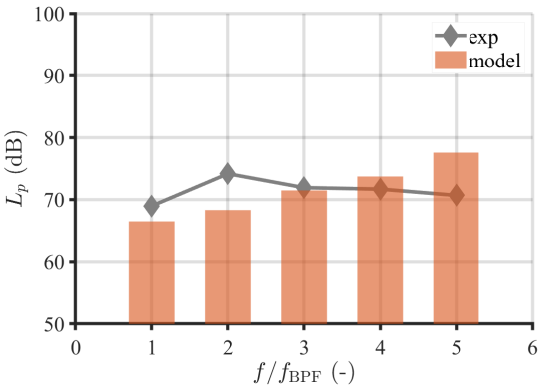


Figure 4. Analytical and experimental sound pressure levels computed with a reference pressure of 20 µPa and referred to the main BPF and its harmonics.

peaks. The model successfully captures the increase in unsteady loading noise due to the inflow distortion, although the first harmonic is under-predicted. This effect may be due to the diffraction of rotor noise by the strut, which is not taken into account in the analytical model and has been shown to play a significant role at low frequencies [4, 5].

These results confirm that a reasonable potential interaction noise prediction can be achieved without relying on experiments or high-fidelity simulations. In particular, the use of an unsteady panel method, such as FlightStream, provides the input data required for the analytical model with sufficient accuracy and little computational effort, making it an attractive tool for the early-design and optimization stages of UAVs. Further developments of this research will involve the inclusion of sound diffraction effects in the noise prediction model, as well as the potential interaction noise that arises from the unsteady loading of the strut due to the passage of the blade [2].

4. ACKNOWLEDGMENTS

The research presented in this paper has been funded by the European Union's Horizon Europe Re-

search and Innovation program under grant agreement No. 101138209 (eVTOLUTION). Views and opinions expressed are, however, those of the authors only and do not necessarily reflect those of the European Union or the European Climate, Infrastructure and Environment Executive Agency (CINEA). Neither the European Union nor the granting authority can be held responsible for them. The authors would also like to thank E. Passelac Estrada and A. Beni for their support in this research.

5. REFERENCES

[1] M. Roger and S. Moreau, "Tonal-noise assessment of quadrotor-type uav using source-mode expansions," vol. 2, no. 3, pp. 674–690, 2020.

[2] Y. Wu, M. J. Kingan, and S. T. Go, "Propeller–strut interaction tone noise," *Physics of Fluids*, vol. 34, p. 055116, 05 2022.

[3] E. Gallo, A. Zarri, G. Bampanis, M. C. Fasinella, and C. Schram, "Simplified Models for Propeller Potential Interaction Noise," in *28th AIAA/CEAS Aeroacoustics 2022 Conference*.

[4] M. Roger, E. Vella, J. Rendon, and S. Moreau, *Aerodynamic and Sound-Scattering Effects in Rotor-Strut Interaction Noise of Small-Size Drones*.

[5] J. Rendon, A. A. Ramo, S. Moreau, and M. Roger, *A Numerical and Analytical Approach of the Sound-Scattering Effects in Rotor-Strut Interaction Noise of Small-Size Drones*.

[6] E. Vella, R. Gojon, H. Parisot-Dupuis, N. Doué, T. Jardin, and M. Roger, *Mutual Interaction Noise in Rotor-Beam Configuration*.

[7] M. Roger, S. Moreau, and A. Guédel, "Vortex-Shedding Noise and Potential-Interaction Noise Modeling by a Reversed Sears' Problem," in *12th AIAA/CEAS Aeroacoustics Conference (27th AIAA Aeroacoustics Conference)*.

[8] W. R. Sears, "Some Aspects of Non-Stationary Airfoil Theory and Its Practical Application," *Journal of the Aeronautical Sciences*, vol. 8, no. 3, pp. 104–108, 1941.

[9] D. B. Hanson and D. J. Parzych, "Theory for noise of propellers in angular inflow with parametric studies and experimental verification," tech. rep., National Aeronautics and Space Administration, Scientific and Technical Information Program, Washington, DC, 1993.

DOI: 10.61782/fa.2025.0430



FORUM ACUSTICUM
EURONOISE 2025

HOVERING SMALL-SCALE LOW REYNOLDS NUMBER ROTOR-BEAM SOURCE LOCALIZATION USING BOTH NEARFIELD AND FARFIELD MEASUREMENTS

H. Parisot-Dupuis[1*] **B. Mellot**[1] **N. Gariglio** [1] **F. Méry**[2]

[1] ISAE-SUPAERO, University of Toulouse, Toulouse, France
[2] ONERA, University of Toulouse, Toulouse, France

ABSTRACT

The sound radiation of small-scale low Reynolds number rotor in interaction with a beam is measured in anechoic room in hovering condition. The experimental setup is composed by a farfield acoustic instrumentation, a directivity antenna and an array of 45 microphones, and nearfield acoustic intrumentation, a microphone and an array of 16 microphones located near the rotor and flush-mounted on the beam. Both nearfield and farfield microphones are used to characterize the different rotor-beam noise source components, tonal noise associated to the blade passing frequency (BPF) and its harmonics which increases in the presence of the beam, and high frequency broadband noise. The coherent output power (COP) spectral analysis is also used to obtain sound source maps coherent or anti-coherent with nearfield signals. This methodology is first assessed on loudspeakers in anechoic room before to be applied to the rotor-beam test case. Nearfield and farfield acoustic signatures show similar radiation patterns. Tonal noise components are very coherent with nearfield signals and their evolution along the beam differs between low frequency and high frequency BPF harmonics. The high frequency broadband noise is contrarly anti-coherent with nearfield signals and its evolution along the beam shows a maximum level near the blade tip.

***Corresponding author**: *helene.parisot-dupuis@isae-supaero.fr.*

Copyright: *©2025 Parisot-Dupuis et al. This is an open-access article distributed under the terms of the Creative Commons Attribution 3.0 Unported License, which permits unrestricted use, distribution, and reproduction in any medium, provided the original author and source are credited.*

Keywords: *aeroacoustics, source localization, coherent output power, rotor, UAV*

1. INTRODUCTION

The sound generated by bodies in interaction with an airflow is a concern for many applications, especially for noise pollution due to transportation in cities [1]. Transportation noise present often multiple aeroacoustic sources and/or complex interaction phenomenon with possible correlation between sources. This is the case of new unmanned aircraft systems for which the developement leds to many aeroacoustic studies last years [2–8].

In order to reduce the noise coming from these equipments, it is necessary to understand the physical mechanisms responsible for their generation. An interesting way of improving aeroacoustics noise sources understanding is the use of microphone array measurements associated with source localization methods. Indeed, such approach allows to discriminate the different sources while providing a ranking of each of them for the frequencies of interest. The most famous source localization algorithm is the conventional beamforming (CBF) method developed by Billinglsey et al. [9], which is based on the assumption that the sound field radiated by the sources under study follows a certain source model (uncorrelated monopoles). The principle is to localize the sound sources from farfield microphone array measurements by interpreting the propagation delays measured between each microphone of the array and knowing the source-array distance. Parallely, coherent output power (COP) spectral analysis has been developped and was recently applied to microphone array measurements for denoising or source separation purposes [10–12].

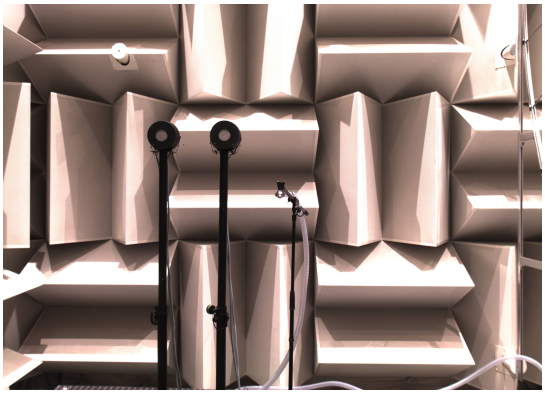


Figure 1. Loudspeakers configuration: S1 (center) and S2 sources (upper left).

This paper proposes to use the degree of coherence of farfield microphone signals with nearfield microphone ones to improve the characterization of complex aeroacoustic noise sources. First, the experimental campaign and associated post processing methodology is presented. Then, the results of preliminary tests on loudspeakers with different degree of coherence are discussed. Finally, the methodology is applied to an aeroacoustic test case: a hovering small-scale low Reynolds number UAV rotor in interaction with a beam.

2. EXPERIMENTAL CAMPAIGN

2.1 Sources configurations

Measurements are performed in ISAE-SUPAERO anechoic room, which is acoustically treated in the frequency range $80 - 16000\ Hz$, and has wedge-tip to wedge-tip dimensions of $5.02 * 5.24 * 5.34\ m^3$ $(L * W * H)$.

A first set of measurements was performed on loudspeakers: a monopolar source Siemens Q-MHF, called $S1$, and two compression drivers BMS 4592, called $S2$. A white noise signal on the frequency range $100-20000\ Hz$ is sended to this three sources. The generation setup allowed to send uncoherent signal, in-phase signal and signals in phase opposition to the two sources $S2$. The positionning of the three sources is shown Figure 1.

A second set of measurements was performed on a hovering small-scale low Reynolds number UAV rotor in interaction with a beam. The rotor has two blades with a NACA0012 blade cross section profile extruded in the radial direction, a constant chord of 0.025 , a constant pitch of $10°$ and a radius $R = 0.1\ m$. The beam is a cylinder

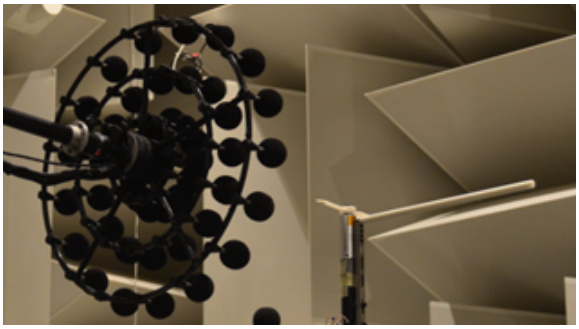


Figure 2. UAV rotor-beam configuration with the 45-channels microphone array.

of diameter $0.02\ m$ and length $0.4\ m$ whose axis is located $0.02\ cm$ below the rotor disk plane. The rotor-beam setup is visible Figure 2 and is described in more details in [6]. Measurements were performed at a rotational speed of $8000\ RPM$.

2.2 Acoustic measurements

The farfield noise radiated by sources is measured by a 2D array of 45 microphones and diameter $0.5\ m$ developed by MicrodB. This array is composed by GRAS 40PH microphones located on 3 concentric circles with irregular spacing (see Figure 2). The array plane was located at a distance of $1\ m$ from the loudspeakers plane and $0.56\ m$ from the rotor-beam setup. For the rotor-beam test case, a directivity antenna of 13 microphones, covering elevation angles $[-60 : 10 : 60]°$, $0°$ being the rotor disk plane, located $1.62\ m$ from the rotor center and perpendicular to the beam was also used. More details about the farfield acoustic instrumentation can be found in [8].

For this study, nearfield measurements were also performed in both cases. The volume acceleration sensor integrated at the exit nozzle of the S1 source is used for the loudspeakers configuration. A microphone GRAS 48LX-1 located on the top of the beam at a distance of $0.8R$ from the rotor axis was used for the rotor-beam configuration. Additionally, a small array of 16 MEMs microphones ICS-40619 was developed to study specifically to study nearfield noise. MEMs were located any $0.005\ m$ between $0.35R$ and $1.1R$ and positionned at the top of the beam instead of the nearfield microphone for some measurements.

Both data acquisition and post-processing were perfomed using Siemens Simcenter Testlab software. Mea-

surements were performed at a sampling frequency of 51.2 kHz during 16.16 s. The fast Fourier transform (FFT) on those signals was computed with a Hanning window applied on 100 segments and a sample overlap of 50%, leading to a frequency resolution of 3.125 Hz. Source maps have been computed with a sample overlap of 50% for FFT in order to have a frequency resolution of 10 Hz with a source grid cells of size 0.01 m.

3. METHODOLOGY

3.1 Conventional beamforming

The conventional beamforming source localization algorithm is based on the propagation delays measured between each microphones that are related to the source-microphone distance. It uses the cross-spectral matrix C, which contains microphones auto-spectra on its diagonal and cross-spectra outside its diagonal, and the free space Green's function g to estimate the sources' position and amplitude q in Pa^2 from the farfield sound pressure measurements p':

$$q = \frac{g^H C g}{||g||^4} \quad \text{with} \quad g = \frac{e^{jkr}}{r} \quad \& \quad C = p' p'^H \tag{1}$$

where ^{H} the complex conjugate transpose, j the imaginary unit, k the wavenumber and r the distance between microphones and focal points.

The cross-spectral matrix diagonal removal technique is used for maps averaging computation to obtain a single acoustic map from a time selection including multiple FFT time segments, while removing the noise contained associated to microphones auto-spectra. This allows to obtain source maps for each frequency or frequency range of interest.

3.2 Coherence with nearfield data

When reference data are available near sources they can be used to separate the different sources' contributions at other microphone's locations. This can be done by calculating the coherent or anti-coherent output power (COP or ACOP) spectra [10]:

$$COP_{rm} = \gamma_{rm}^2 * S_{mm} \tag{2}$$

$$ACOP_{rm} = (1 - \gamma_{rm}^2) * S_{mm} \tag{3}$$

with

$$\gamma_{rm}^2 = \frac{|S_{rm}|^2}{S_{rr} * S_{mm}} \tag{4}$$

where γ_{rm} and S_{rm} are respectively the coherence and the cross-power between a microphone, denoted m, and the nearfield reference signal, denoted r, and S_{mm} and S_{rr} arer respectively the auto-spectra of the microphone and the reference signal. This methodology was used recently to denoise microphone array signals or to separate different noise source contributions [11, 12].

Reference nearfield data can also be used to distinguish different sources' contributions on beamforming source maps. This is obtained using the COP and ACOP principles by weighting microphone averaged auto-spectra S_{mm} and by adding a phase relationship related to this reference:

$$S'_{mm} = COP_{rm} * \frac{{S_{rm}}^2}{|S_{rm}|^2} \quad \text{or} \quad ACOP_{rm} * \frac{{S_{rm}}^2}{|S_{rm}|^2} \tag{5}$$

The beamforming processing is then applied to those new microphone averaged autospectra S'_{mm}, to obtain source maps coherent or anti-coherent with the reference signal.

3.3 Assessment on loudspeaker test case

Measurements were performed with the three loudspeakers in three cases: sources S2 uncoherent, coherent in phase and coherent in phase opposition. Coherent and anti-coherent beamforming maps are then obtained by using S1 volume acceleration sensor as reference.

As expected, the coherent beamforming map obtained for the case of three uncoherent sources highlights the source S1, whereas the anti-coherent beamforming maps highlights S2 sources. This allows to identify the contribution of the source S1 even if its amplitude is lower. Figure 3 shows as example source maps obtained at 2000 Hz. Symbols indicate sources locations, S1 source being at the center. Others cases are not presented here but confirmed the ability of the methodology to separate coherent and anti-coherent sources contributions.

4. ROTOR-BEAM NOISE CHARACTERIZATION

4.1 Farfield spectra

Previous papesr shows that the rotor noise is characterized by tonal noise at the blade passing frequency (BPF) and its harmonics as well as a high frequency broadband noise (BBD), and that the presence of the beam increases the magnitude of BPF harmonics leading to a hump with a maximum level around $5 * BPF$ [4, 6].

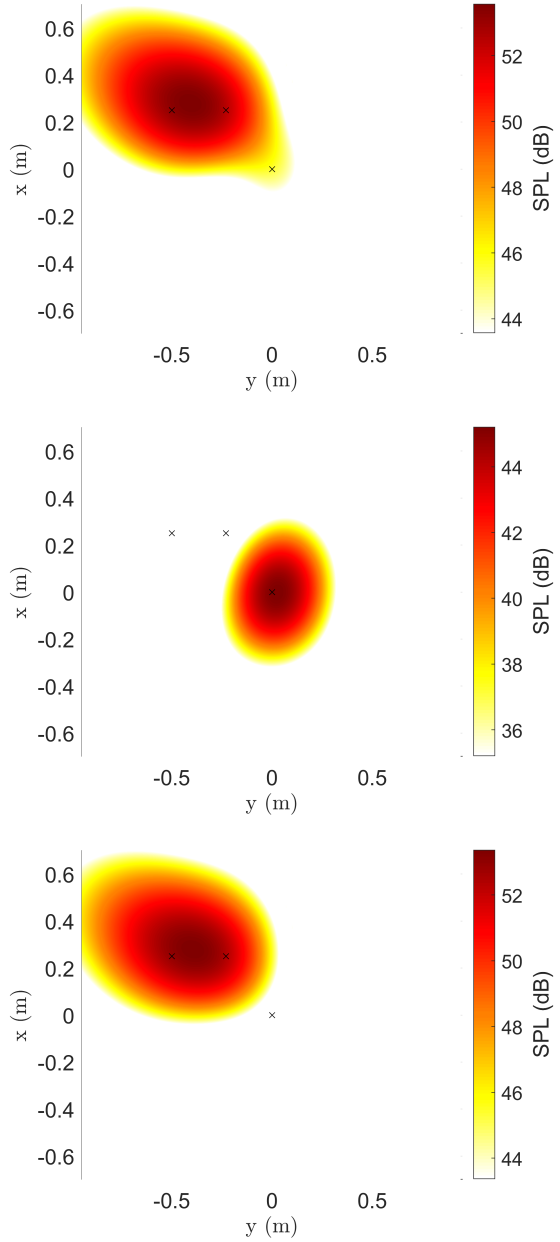


Figure 3. Maps obtained for 3 uncoherent sources at 2000 Hz: CBF (top), coherent CBF (center) & anti-coherent CBF (bottom).

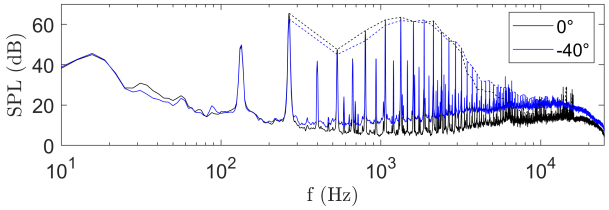


Figure 4. Spectra obtained for rotor-beam in the rotor disk plane $0°$ & toward the ground $-40°$.

A numerical study [8] showed that the BPF harmonics increase seems to be mainly due to the beam radiation, suggesting a noise generation mechanism related to unsteady loading when the blade passes above the beam. Figure 4 highlights those noise components, with the hump of BPF harmonics and the impact of the elevation angle on the high BPF harmonics and broadband noise levels.

4.2 Source maps

Source maps were here obtained using conventional beamforming based on fixed sources to focus on the intetaction noise with the array plane parallel to the beam as described in [8]. Coherent and anti-coherent source maps targeting the different noise components have been computed taking nearfield microphone on the beam as reference sensor. Locations of the rotor, the beam and the test stand are indicated by black lines on the source maps. To complete the source maps, farfield directivity diagrams with and without coherent or anti-coherent with the reference beam microphone are plotted for tonal components $5 * BPF$, $22 * BPF$ and the high frequency broadband noise (BBD) Figure 5.

For the highest BPF harmonic of the hump, $5 * BPF$, the CBF source map is identical to the CBF source map coherent with the beam nearfield microphone, whereas the anti-coherent source map is several orders of magnitudes below. This confirms the relationship between this BPF harmonic level and the periodic blade passing above the beam, and source maps indicate an omnidirectional radiation which corresponds to the farfield directivity perpendicular to the beam (see Figure 5).

Then, it was chosen to study the BPF harmonic $22 * BPF$ which corresponds to a frequency for which the tonal level is decreasing but the broadband level is increasing. In this case, source maps highlight that the main source remains here the one coherent with the beam

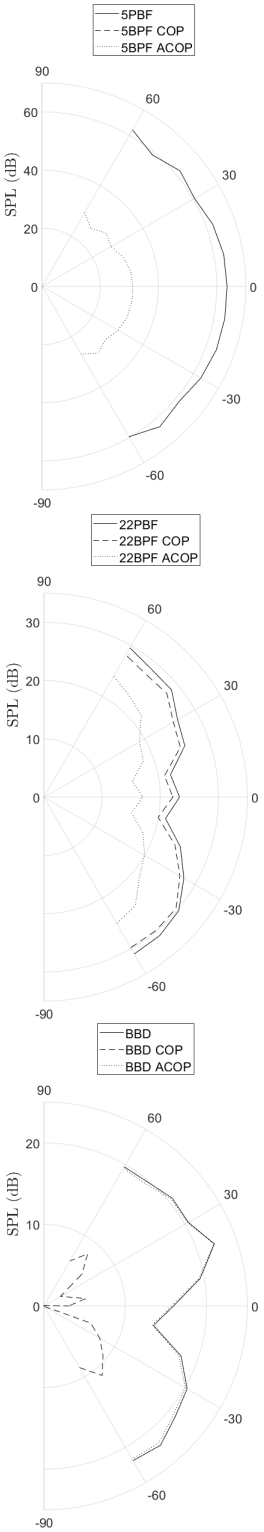


Figure 5. Farfield directivity obtained for rotor-beam at $5*BPF$, $22*BPF$ & BBD with and without coherent or anti-coherent weighting with nearfield data.

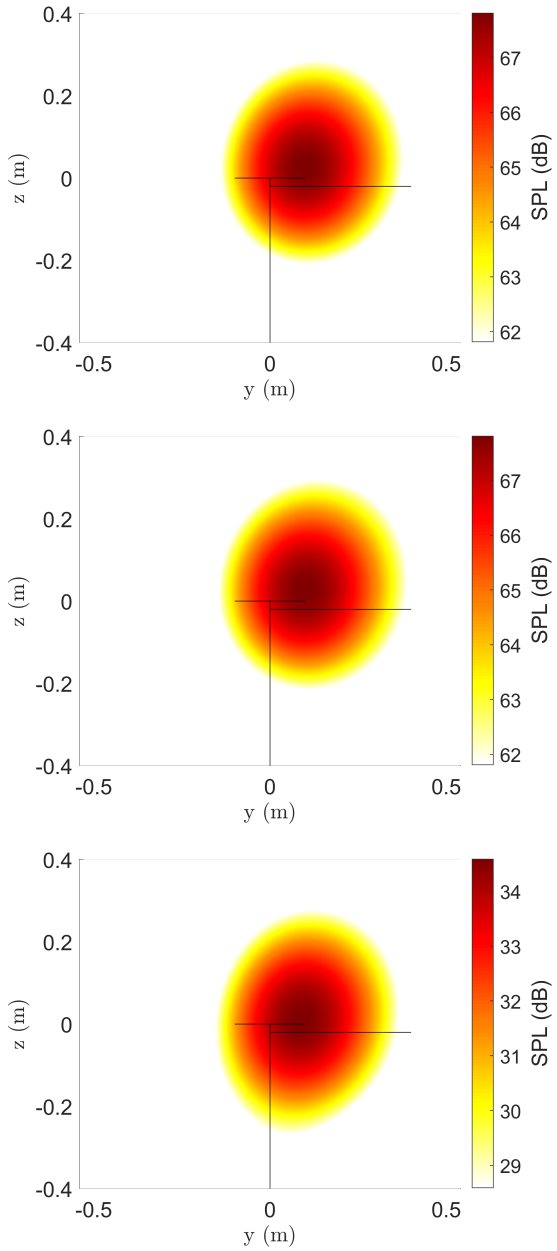


Figure 6. Source maps obtained for rotor-beam at 5*BPF: CBF (top), coherent CBF (center) & anti-coherent CBF (bottom).

nearfield microphone, but the anti-coherent source map allows to identify another source component slightly lower in terms of level and with a different radiation pattern. Looking at the corresponding farfield directivity (Figure 5) we can see that both noise components seem to dipole-like patterns.

Finally, the high frequency broadband noise in the frequency region without tones is studied (frequency of 13000 Hz was chosen). For this noise component we can observe that source map is entirelly determined by the anti-coherent source map, confirming that the sources anti-coherent with the reference beam microphone are associated to the broadband part of the spectrum. The shape of the corresponding source maps indicates a dipolar radiation, as well as the directivity diagrams Figure 5, which is consistent with the trailing edge broadband noise directivity previously identified [6].

4.3 Noise components evolution along the beam

Additionnally, the MEMs linear array was used to plot sound pressure levels (SPL) evolution of each noise component along the beam. COP and ACOP SPL evolutions respect to the MEMs located at $0.8R$ to be consistent with the beam nearfield microphone location.

For the main BPF harmonic an increase along the beam is observed with a maximum at $0.9R$ which is consistent with previous numerical simulation results, and the coherence of this phenomenon with the reference MEMs is confirmed. A previous numerical study showed that the beam was the main contributor to the farfield noise radiation at this BPF harmonic and that the main beam radiating area was around $80 - 90\%$ of the blade radius [7], which is similar to the maximum level location. The $22 * BPF$ harmonic present a diffrent behaviour with a first increase until $0.6R$, then a minimum, and after a second increase with a maximum at $0.95R$, with again the part coherent with the reference MEMs being the main one.

In the case of the high frequency broadband noise the evolution is quite flat between $0.4R$ and $0.9R$ and a peak is observed at $1.05R$. The level of this noise component along the beam is mainly anti-coherent with the reference MEMs but the trend along the beam is the same for both coherent and anti-coherent parts. Anti-coherent parts of tonal noise components present very similar behaviour with a peak at $1R$. The location of those peaks seems to suggest that this noise component might be due to blade tip wake impingement on the beam.

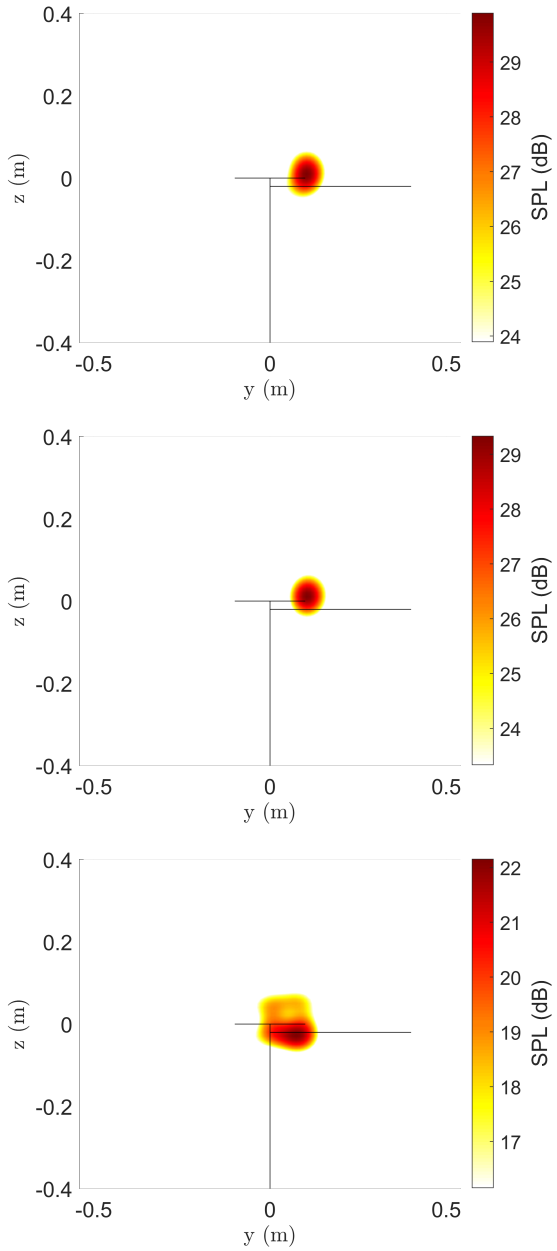


Figure 7. Source maps obtained for rotor-beam at 22*BPF: CBF (top), coherent CBF (center) & anti-coherent CBF (bottom).

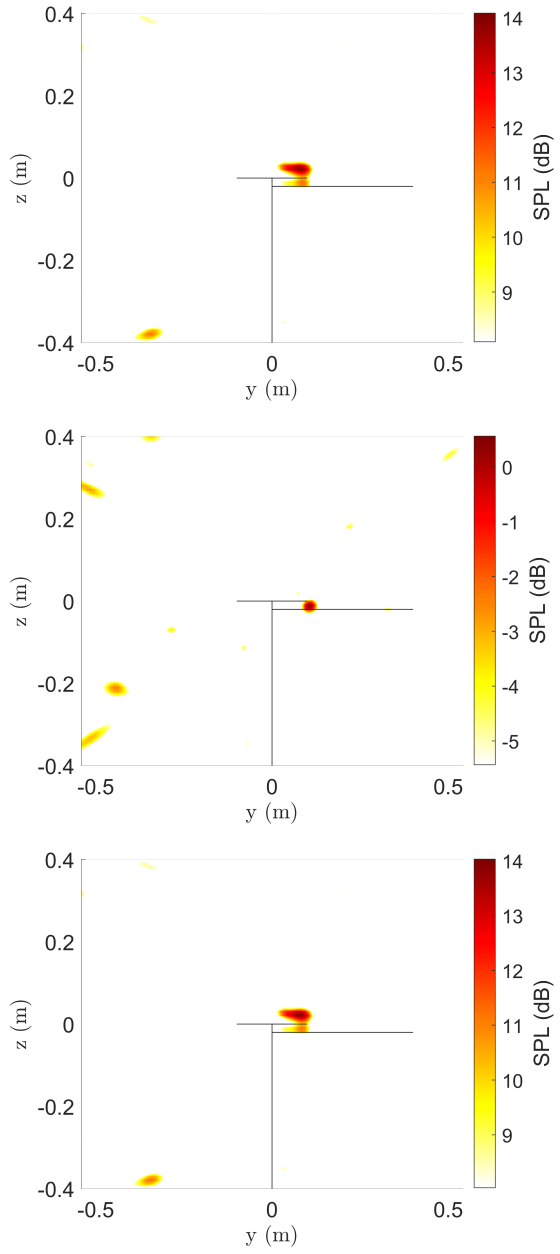


Figure 8. Source maps obtained for rotor-beam at BBD: CBF (top), coherent CBF (center) & anti-coherent CBF (bottom).

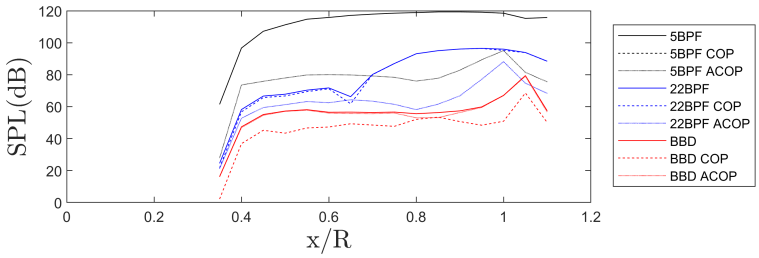


Figure 9. SPL along the beam for $5 * BPF$, $22 * BPF$ & BBD: total, coherent & anti-coherent with the MEMs located at $0.8R$.

5. CONCLUSIONS

Microphone array measurements were performed in anechoic room synchroneously with other acoustic nearfield and farfield measurements in order to help the identification of the different noise components associated to complex aeroacoustic sources. The proposed methodology is to compute beamforming source maps coherent or anti-coherent with nearfield reference signals using the coherent output power (COP) spectral analysis.

Preliminary tests on loudspeakers with different degree of coherence were first performed. The ability of the proposed methodology to distinguish source contributions coherent or anti-coherent with a nearfield reference signal was demonstrated, even when there is a significative difference of levels between the two contributions.

The methodoloy was then applied to an areoacoustic test case: a hovering small-scale low Reynolds number UAV two-bladed rotorof diameter $0.2\ m$ and NACA0012 blade profile in interaction with a cylindrical beam of diameter $0.02\ m$. Previous studies showed tonal noise at the blade passing frequency (BPF) and its harmonics, increased by the presence of the beam with a maximum around $5 * BPF$, and high frequency broadband noise.

Conventional beamforming was used to obtain source maps coherent and anti-coherent with a nearfield microphone located on the beam at 80% of the blade radius. The strongest BPF harmonic appeared to be coherent with the beam nearfield microphone, confirming the relationship between this BPF harmonic level and the periodic blade passing above the beam. High frequency BPF harmonics in the frequency region where the broadband increases appeared to be coherent with the beam nearfield microphone too, but another anti-coherent source with a dipolar radiation pattern and lower level was also identified. The high frequency broadband noise is contrarly

perfectly anti-coherent with the beam nearfield microphone with a dipolar radiation pattern associated to trailing edge noise. Farfield directivity diagrams coherent or anti-coherent with the beam nearfield microphone allowed to confirm the radiation patterns visibles on source maps.

Additionally, a linear MEMs array located on the beam was used to determine the sound pressure levels (SPL) evolution of each noise component along the beam, coherent and anti-coherent respect to the MEMs located at 80% of the blade radius. The evolution of the low frequency BPF harmonic level along the beam leads to one hump coherent with the reference MEMs, whereas the one of the high frequency BPF harmonic leads to two humps also coherent with the reference MEMs. For the high frequency broadband noise a flat evolution, mainly anti-coherent with the reference MEMs, with a maximum level near the blade tip is found.

Complementary post processing are planned and this methodology will be also used to study the different noise source components evolution with the rotational speed, the beam diameter, and the rotor-beam distance. It is also envisaged to apply it to more realistic configurations: different airflow conditions, rotor-airframe and/or multiple rotors interactions for instance.

6. ACKNOWLEDGMENTS

The authors gratefully acknowledge financial support from the French Defense Procurement Agency (DGA). They are grateful to ISAE-SUPAERO technical staff for their contribution to the experimental campaign.

7. REFERENCES

[1] C. Marquis-Favre, E. Premat, and D. Aubrée, "Noise and its effects - a review on qualitative aspects of sound. part ii: Noise and annoyance.," *Acta Acust united Ac*, vol. 91, no. 17, pp. 626–642, 2005.

[2] N. Zawodny, D. Boyd, and C. Burley, "Acoustic characterization and prediction of representative, small-scale rotary-wing unmanned aircraft system components," in *In Proc. of the American Helicopter Society (AHS) 72nd Annual Forum*, pp. 16–19, 2016.

[3] N. Zawodny and D. Boyd, "Investigation of rotorairframe interaction noise associated with small-scale rotary-wing unmanned aircraft systems," in *In Proc. of the American Helicopter Society (AHS) 73rd Annual Forum*, 2017.

[4] R. Gojon, T. Jardin, and H. Parisot-Dupuis, "Experimental investigation of low reynolds number rotor noise," *The Journal of the Acoustical Society of America*, vol. 149, no. 6, pp. 3813–3829, 2021.

[5] Y. Wu, M. Kingan, and S. Go, "Propeller-strut interaction tone noise," *Physics of Fluids*, vol. 34, pp. 3813–3829, 2022.

[6] R. Gojon, H. Parisot-Dupuis, B. Mellot, and T. Jardin, "Aeroacoustic radiation of low reynolds number rotors in interaction with beams," *The Journal of the Acoustical Society of America*, vol. 154, no. 2, p. 1248–1260, 2023.

[7] N. Doué, R. Gojon, and T. Jardin, "Numerical investigation of the acoustics radiation of a two-bladed rotor in interaction with a beam," in *In Proc. of Numerical investigation of the acoustics radiation of a two-bladed rotor in interaction with a beam*, 2023.

[8] H. Parisot-Dupuis, R. Gojon, and N. Doué, "Feasibility of hovering small-scale low reynolds number rotor-beam source localization by microphone array measurements," in *In Proc. of 30th AIAA/CEAS Aeroacoustics Conference*, p. 3063, 2024.

[9] J. Billinsgley and R. Kinns, "The acoustic telescope," *J. Sound Vib.*, vol. 48, no. 4, pp. 485–510, 1976.

[10] W. G. Halvorsen and J. S. Bendat, "Noise source identification using coherent output power spectra," *Journal of Sound and Vibration*, vol. 9, no. 8, pp. 15–24, 1975.

[11] P. Sijtsma, M. Dreux, B. Delescluse, R. Leneveu, and J. Mardjono, "Coherent output power with groups of microphones," in *30th AIAA/CEAS Aeroacoustics Conference (2024)*, (Rome, Italy), p. 3330, 2024.

[12] N. Auquier, J. Cuenca, and L. D. Ryck, "Coherence-based nearfield acoustic holography for damage detection in plates," in *In Proc. of ISMA*, pp. 2899–2907, 2020.

DOI: 10.61782/fa.2025.0647



FORUM ACUSTICUM
EURONOISE 2025

ON THE IMPACT OF TURBULENT INFLOW ON THE NOISE GENERATED BY A PROPELLER OPERATING AT LOW REYNOLDS NUMBER

Mario Alì[1*] **Andrea Piccolo**[2] **Riccardo Zamponi**[2,3]
Daniele Ragni[2] **Francesco Avallone**[1]
[1] Dipartimento di Ingegneria Meccanica e Aerospaziale, Politecnico di Torino, Torino, Italy
[2] Department of Flow Physics and Technology, Delft University of Technology, Delft, The Nederlands
[3] von Kàrmàn Institute for Fluid Dynamics, Rhode-Saint-Genèse, Belgium

ABSTRACT

Ingested turbulence affects propeller noise at frequencies higher than the 2nd blade passing frequency. The extension of Amiet's model to rotating blades represents a useful tool for predicting this phenomenon. However, it relies on assumptions that are not fully valid in reality, e.g., it neglects the distortion of turbulence. This paper investigates how the propeller-induced flow field alters incoming turbulence paving the way, in future studies, to extend Amiet's model with these features. Lattice Boltzmann Very Large Eddy Simulations of a reference propeller, for which experimental data exist, operating at low-Reynolds number and subject to turbulent inflow are performed. The spatial and temporal evolution of isotropic grid-generated turbulence approaching the propeller plane is characterized. It is found that the propeller leading edge interacts with anisotropic turbulence. This is due to the rotational flow induced by the propeller, stream tube contraction, and leading-edge distortion. In addition, the impact of the inflow turbulence on the laminar separation bubble on the propeller suction side, whose dynamic affects the acoustics at high frequencies, is analyzed. Finally, the aerodynamics flow features are linked to the far-field acoustic spectra, obtained through the Ffowcs-Williams and Hawkings analogy applied to the propeller surface.

*__Corresponding author__: *mario.ali@polito.it.*
__Copyright__: *©2025 Mario Alì et al. This is an open-access article distributed under the terms of the Creative Commons Attribution 3.0 Unported License, which permits unrestricted use, distribution, and reproduction in any medium, provided the original author and source are credited.*

Keywords: *turbulence ingestion noise, turbulence distortion, laminar separation bubble*

1. INTRODUCTION

The growing interest in small Unmanned Aerial Vehicles (UAVs), driven by a wide range of potential applications, poses the need to integrate this technology into an urban environment. Given their impact on public acceptance [1], it is crucial to account for the aerodynamic noise generated by these devices when operating in an urban environment, which is characterized by different scales of turbulence.

From an aerodynamic point of view, small UAVs' propellers typically operate at low Reynolds numbers, resulting in a transitional regime extremely susceptible to inflow disturbances and characterized by complex phenomena such as the presence of laminar separation bubble (LSB) [2]. Furthermore, incoming turbulence interacting with the propeller produces an unsteady pressure field over the surface, that is radiated as broadband and/or quasi-tonal noise in the far field [3, 4]. LSB, whose presence on a small propeller was assessed for the first time by Grande et al. [5] under clean inflow, plays an important role in the far-field noise in the high-frequency [6]. It causes laminar boundary layer vortex shedding noise with frequency varying along the propeller radius, thus resulting in a high-frequency hump. Casalino et al. [2, 3] showed that, under clean inflow conditions, the mean behavior of the LSB is mostly determined by the propeller advance ratio; furthermore, in hovering, the mean LSB is

unaffected by the recirculating flow in the testing environment.

Most of the work on rotors in turbulent inflow focuses on helicopter and engine rotors, typically operating at higher Reynolds numbers, and they do not consider the effect of turbulence on LSB. Sevik [7] proposed a prediction method of turbulence ingestion noise based on the two-dimensional aerodynamic response function and dipolar radiation pattern of the unsteady loading. This retrieved the broadband component of the acoustic spectrum but missed the quasi-tonal content. Blake [8] recovered the latter by introducing blade-to-blade correlation. Hanson [9] attributed the quasi-tonal noise to the streamwise elongation of the eddies that, chopped several times by the rotor, produce blade-to-blade coherence in the unsteady loading. This is reflected in the narrow-band content around the BPF harmonics in the acoustic spectrum.

Amiet extended the prediction model for airfoils in turbulent inflow [10] to the case of rotating blades [11] approximating the circular motion to a rectilinear motion in the limit of acoustic frequencies much higher than the rotational one. The model obtains the acoustic spectrum from the characteristics of incoming turbulence through an acoustic transfer function, neglecting the effects of turbulence distortion. Capobianchi et al. [12] employed two analytical models based on Amiet's theory for noise prediction: the first one considers turbulence characteristics at a specific representative radial location while the second accounts for blade geometry and turbulence parameters along the blade and exploits the inverse strip theory [13], providing better results. Raposo et al. [14] proposed a prediction model that includes the effects of rotation and spanwise coherence. They proved that Amiet's model recovers the haystacking tones when revised with a correct calculation of the time between two consecutive chops of the same eddy. They highlighted that haystacking is underpredicted when the integral length scale of the flow is large compared to the blade, likely because of the lack of spanwise correlation in the direct strip approach adopted. In these studies, the effect of including turbulence distortion in Amiet 's model is not considered.

The purpose of this study is two-fold. First, the analysis of turbulence near the leading edge reveals the effect of the propeller-induced flow field on the turbulent inflow, inspecting the validity of the assumptions of Amiet 's model. The effect of including turbulence distortion in Amiet 's model prediction will be presented in future work. Additionally, the solid formulation of the FWH analogy, applied to the propeller surface, allows to characterize the effects of ingested turbulence on the aerodynamic sources across different frequency ranges. To address these points, three different setups (only turbulence, propeller in turbulent inflow, and propeller in clean inflow) have been simulated in PowerFLOW 6-2022-R1 3DS.

The paper is structured as follows: the numerical setup is described in sec.2.2 and validated in sec.2.3. In sec.3 the main results are discussed, and sec.4 summarizes the conclusions of this work.

2. METHODOLOGY

2.1 Computational method

The study is based on data obtained with PowerFLOW 6-2022-R1, based on a Lattice-Boltzmann Method (LBM). Here, the only unknown quantity is the particle-probability distribution function $f(\mathbf{x}, t, \mathbf{v})$, representing the probability for a particle at location $\mathbf{x}$ and instant t to have velocity $\mathbf{v}$. The macroscopic quantities are retrieved from the statistical moments of f. The evolution of $f(\mathbf{x}, t, \mathbf{v})$ is described by the Boltzmann equation, which relies on gas-kinetic theory. The discrete Boltzmann equation is then solved on a Cartesian mesh, whose base elements are called voxels, whose size halves from a resolution region to the next finer one. Since reaching a y^+ lower than 1 in a Cartesian mesh is computationally prohibitive, a fully turbulent wall function model, extended to include the effects of pressure gradient, is adopted in this work.

2.2 Numerical setup

The computational domain is a cube with a side length of 100 D_{prop}. The region of interest with the turbulence grid and the propeller is located at the center of the computational domain, which is discretized into 17 Variable Resolution (VR) regions, numbered from 0 to 16, gradually increasing the resolution from the outer region to the area of interest. VR11 resolves the turbulence from the grid to $2D_{prop}$ downstream of the propeller plane, to enclose the nacelle. The voxel size in this region is 0.88 mm. 5 inner levels, defined as offsets of the blades, are introduced to achieve a $y^+_{MAX} \approx 9$ at the wall to capture the separation bubble [2, 3]. The total number of voxels in the computational domain is approximately 1.2×10^7, with the smallest voxel size equal to 0.03 mm. The numerical setup (fig.1) reproduces the experimental one [12]. The flow exits from a cylindrical pipe with a diameter $D = 0.6m$, whose wall is treated as frictionless. The turbulence grid

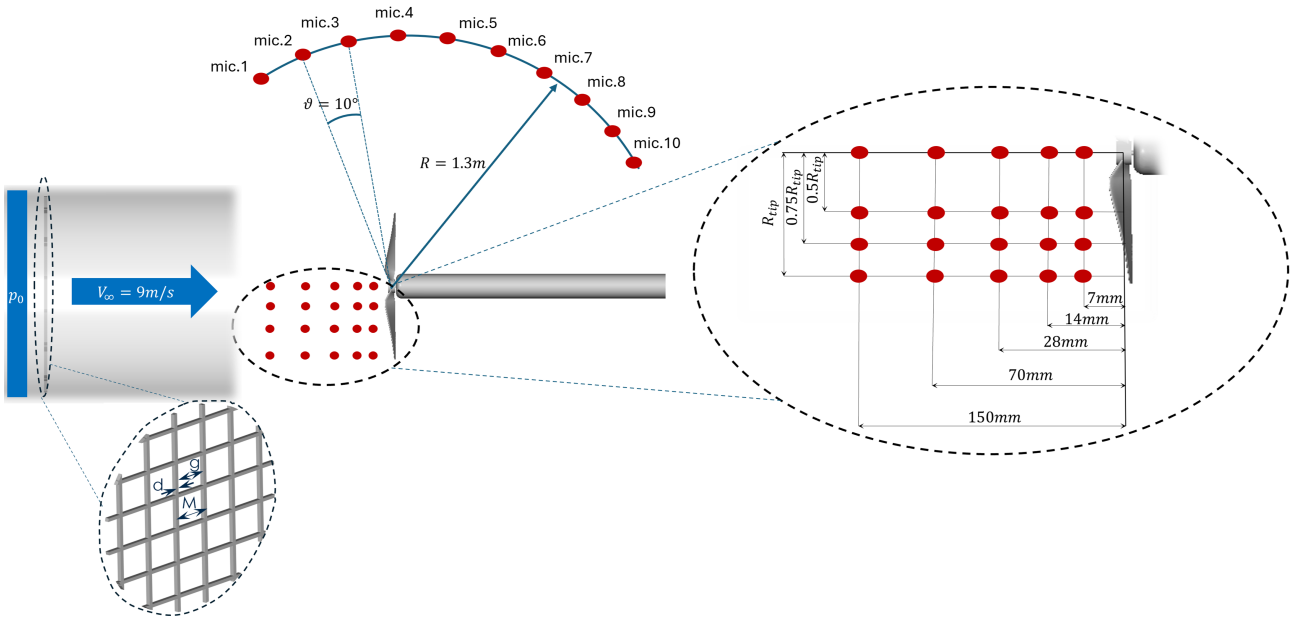


Figure 1: Numerical setup and turbulence grid - $g = 9cm$, $d = 1cm$, $M = 10cm$

is enclosed into the pipe $0.6m$ upstream from the exit and at $1m$ from the propeller plane. The propeller is the same as previous works [2, 5, 15]; the diameter is $0.3m$ and the airfoil profile is the NACA-4412. The rotational speed is $\Omega = 6000RPM$.

The total pressure p_0 is prescribed as a boundary condition upstream of the grid to match the reference mean velocity value $V_\infty = 9m/s$. It is computed accounting for the local pressure losses introduced by the grid, Δp^0 as [16]:

$$\frac{\Delta p^0}{q} = A\left(\frac{1}{\beta^2} - 1\right)^B, \tag{1}$$

where q is the upstream dynamic pressure, β is the grid porosity, and A and B are functions of Reynolds number, Mach number, and grid geometry. For a square-mesh grid, porosity is given by:

$$\beta = \left(1 - \frac{d}{M}\right)^2 \tag{2}$$

Free-stream and ambient static pressure are imposed as boundary conditions at the borders of the computational domain to prevent flow recirculation.

20 probes are distributed upstream of the propeller plane to characterize the inflow (fig.1). After 3 initial settling revolutions, data are sampled for 10 revolutions with sampling frequency $f_s = 20kHz$. The signal is then divided into 4 Welch blocks with 50% overlap, resulting in a resolution frequency $\Delta f = 20Hz$. Surface pressure is sampled at $f_s = 367kHz$ with a spatial averaging of $0.4mm$ over the propeller and nacelle surfaces to feed the FWH analogy and obtain acoustic spectra.

The setup for the clean case is obtained by removing the turbulence grid and resetting the total pressure. In addition, VR 11, previously used to resolve incoming turbulence, is reduced to an offset of the propeller to keep the same resolution at the propeller while reducing the computational cost.

2.3 Validation

Grid convergence is assessed for all tested cases and the results are validated against data from the reference experiment [12]. Two meshes (coarse and medium) are analyzed. The results of the fine resolution will be presented in the future. The characteristic length M (fig.1) is discretized with 80 and 120 voxels for the coarse and medium grid, respectively.

Since the load cell was not used in the experiment, the numerical thrust and torque coefficients, C_T and C_Q, are compared in tab.1 with the ones available in the literature [2], obtained through a BEMT approach. A good match

is observed for all the meshes, with the C_T from the LBM being slightly lower than BEMT prediction.

Table 1: Convergence of C_T and C_Q

	Coarse	Medium	BEMT ([2])
C_T	0.087	0.088	0.09
C_Q	0.008	0.0081	0.008

Table 2 compares the mean velocity V_m, the turbulence intensity TI, and the turbulence integral time scale T_{uu} obtained from the numerical simulations and the experiments at $x/R_{tip} = 1$, $r/R_{tip} = 0.5$ without and with the propeller. The integral time scale T_{uu} is used in the table because the mean velocity gradients introduced by the propeller invalidate Taylor's hypothesis for the computation of the integral length scale $\Lambda_{uu,x}$.

Table 2: Flow quantities at $x/R_{tip} = 1$, $\frac{r}{R_{tip}} = 0.5$

	$V_m[m/s]$		$TI[\%]$		$T_{uu}[s]$	
	Num.	Exp.	Num.	Exp.	Num.	Exp.
wo prop.	9.55	9	6.98	7.13	0.17	0.25
with prop.	10.3	9.68	6.3	6.4	0.16	0.2

Mean velocity and velocity fluctuations are computed considering the velocity measured by the hot wire as described by Zamponi et al. [17].

The integral time scale T_{uu} is obtained as the integral of the autocorrelation function in the interval from its maximum to the point where it decreases to $1/e^2$ [17]. For the case with turbulent inflow, the phase-locked average is subtracted from the instantaneous signal to remove the periodicity introduced by the blade passage. Numerical and experimental results show good agreement, with the numerical V_m being up to $0.6m/s$ higher than the experimental one.

Similarly, the comparison of the turbulence spectra (fig. 2) shows a good agreement on the frequency range considered. The drop in the spectra at the 5^{th} and 8^{th} harmonics of the Blade Passing Frequency (BPF) in the coarse and medium/fine cases, respectively, is due to the filtering effect of the mesh. The numerical scheme requires at least 10 voxels per wavelength to resolve the wave. An increase in the overall resolution will solve the turbulence up to the 10^{th} BPF harmonic, but the computational cost will be prohibitive. However, as proved later, the far-field noise is well captured making the increase of computational cost not needed for the scope of this paper.

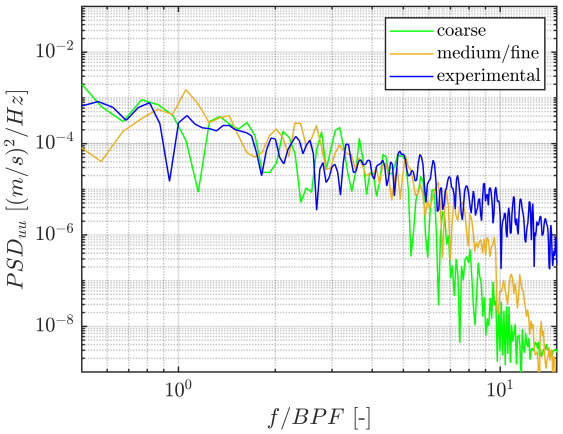
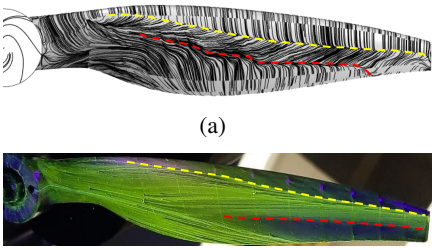


Figure 2: Turbulence spectrum at $x = 1R$, $r/R = 0.5$ without propeller



(a)

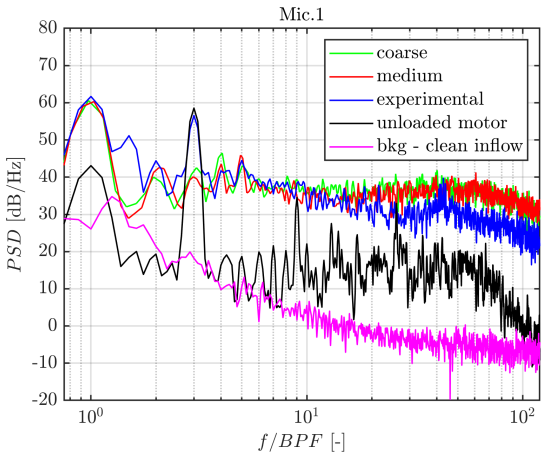
(b)

Figure 3: Time-averaged surface streamlines 3(a) and oil flow visualization 3(b)

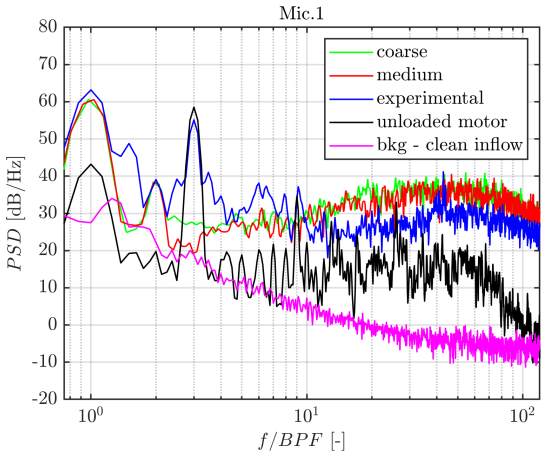
To further support the validation of the numerical database, the time-averaged surface streamlines are compared with oil flow visualization in fig. 3 only for the turbulent case, for conciseness. Separation and reattachment lines, indicated by yellow and red dotted lines, respectively, are slightly delayed with respect to the experimental result. This can be due to the still high y^+, the adopted wall model, and the slightly higher mean velocity in the numerical simulations. Improvement in fine resolution is expected. The effect of different wall models on the LSB prediction will be the objective of future studies.

Acoustic spectrum at mic.1 (fig. 1) is shown for both the turbulent (fig.4(a)) and clean (fig.4(b)) inflows. The slight underprediction (less than $2dB$) at the 1^{st} harmonic, mostly influenced by steady loading and thickness noise, is likely due to the higher numerical mean velocity, which

reduces the steady loading, consequently under-predicting C_T. The experimental result at the third harmonic is dominated by motor noise, while the tones at half of the BPF harmonic originate from the motor shaft frequency. For the clean inflow case, the difference between numerical and experimental results from the 3^{th} to the 8^{th} BPF harmonic is likely due to the loaded motor noise, not present in the simulations. The over-prediction at frequencies higher than the 20^{th} harmonic is ascribed to inaccuracies in reattachment point prediction. The mesh refinement from coarse to medium does not affect the acoustics.



(a)



(b)

Figure 4: (a) Acoustic spectra for turbulent (b) and clean inflow

3. RESULTS AND DISCUSSION

3.1 Characterization of turbulence

3.1.1 Absolute frame of reference

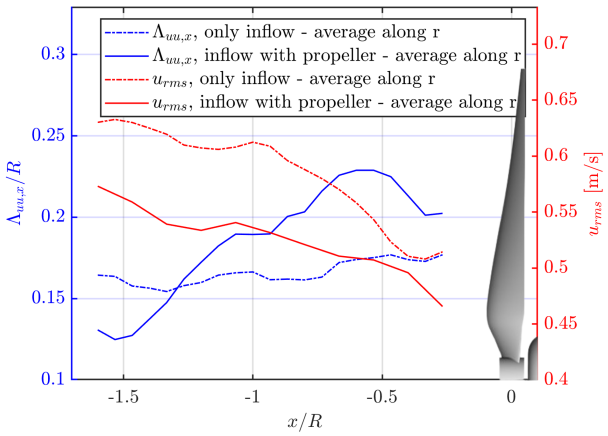


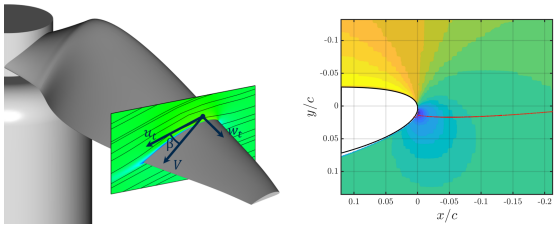
Figure 5: $\Lambda_{uu,x}(x)$ and $u_{rms}(x)$, radially averaged, with and without the propeller

Figure 5 shows the evolution of the integral length scale $\Lambda_{uu,x}(x)$ and root mean square $u_{rms}(x)$, with and without the propeller. The quantities have been radially averaged to highlight the general trend, although inhomogeneity remains present along the span. It can be observed that, without the propeller, $\Lambda_{uu,x}$ is almost constant, with $\Lambda_{uu,x} \approx 2.4cm$. In the presence of the propeller, the integral length scale grows faster approaching the propeller plane, as a result of the stream tube contraction. $u_{rms}(x)$ presents lower values and a faster decay in the presence of the propeller because of the stream tube contraction that, while elongating the eddies in the streamwise direction, reduces the fluctuation of the axial component.

3.1.2 Relative frame of reference

The analysis presented in this section refers to a plane at $r/R_{tip} = 60\%$ in the rotating frame of reference, normal to the spanwise direction (fig. 6(a)). The in-plane components, u, and v are projected along the mean local direction to obtain u_t and v_t, the tangential and normal components, respectively, relative to the mean streamline (fig. 6(b)), while w_t is the out-of-plane component.

Figure 7 presents the root mean square of the three velocity components along the mean stagnation line. Approaching the propeller plane, u_t decelerates and $u_{t,rms}$ decreases, while $v_{t,rms}$ increases, and w_t shows a weaker



(a) (b)

Figure 6: (a) Visualization of the rotating frame of reference and (b) mean stagnation line s at $r/R = 60\%$

increase. This observation suggests a momentum transfer from u_t to v_t, aligning with the physical description of the Rapid Distortion Theory (RDT) [18] showed with the dashed line in the figures.

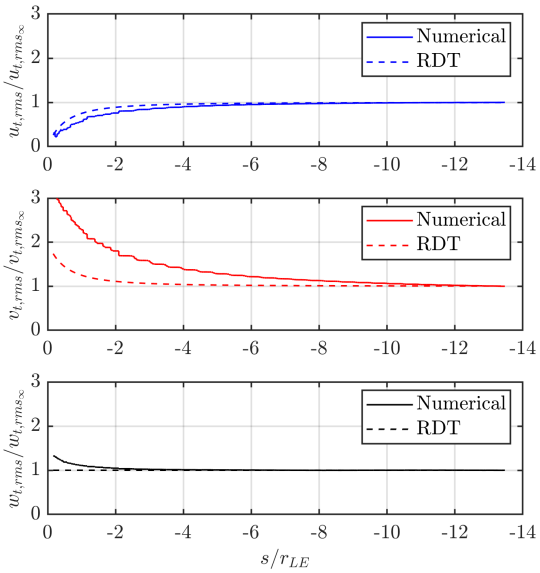


Figure 7: $u'_{t,rms}$, $v'_{t,rms}$ and $w'_{t,rms}$ along the mean stagnation line

More specifically, $u_{t,rms}$ obtained from the numerical simulations follows the RDT prediction well up to $-4r_{LE}$, then approaching the stagnation point it decreases a bit faster than predicted; $v_{t,rms}$ diverges from the RDT prediction already at $s = -10r_{LE}$, reaching values up to 3 times the undisturbed level. The early increase in $v_{t,rms}$, occurring before the decrease in $u_{t,rms}$, suggests the existence of an additional mechanism - beyond the momentum transfer from the streamwise component - that enhances $v_{t,rms}$. In this case, a possible explanation can lie in the curvature of the mean streamline, which is not accounted for in RDT: streamwise velocity fluctuations induce oscillations in the centrifugal force acting on fluid particles, leading to fluctuations in the radial pressure gradient. These fluctuations influence the normal velocity component. To validate this hypothesis, a comparison with a 2D simulation of a wing section will be conducted in future studies.

Figure 8 shows the spatial distribution of the integral length scales $\Lambda_{u_t u_t,s}(s)$ and $\Lambda_{v_t v_t,span}(s)$ along the mean stagnation line. These quantities are normalized with respect to their value at $s/r_{LE} = -6$. Approaching the leading edge, $\Lambda_{u_t u_t,s}(s)$ decreases, while $\Lambda_{v_t v_t,span}(s)$ increases. This indicates that vortices are compressed against the leading edge and elongated in the spanwise direction, enhancing the spanwise coherence of normal velocity fluctuations.

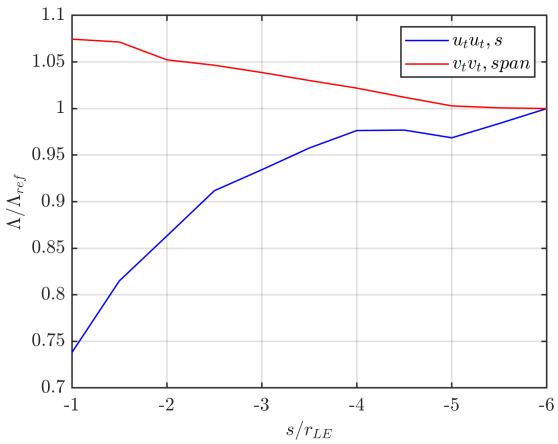


Figure 8: Spatial distribution of the integral length scales $\Lambda_{u_t u_t,s}(s)$ and $\Lambda_{v_t v_t,span}(s)$ along the mean stagnation line

3.2 Laminar separation bubble

The time-averaged surface streamlines, superimposed to the standard deviation of the surface pressure fluctuations coefficient c_{p_σ}, are shown in fig. 9 for both turbulent and clean inflows. No significant difference is observed in the mean flow features of the LSB, visualized through

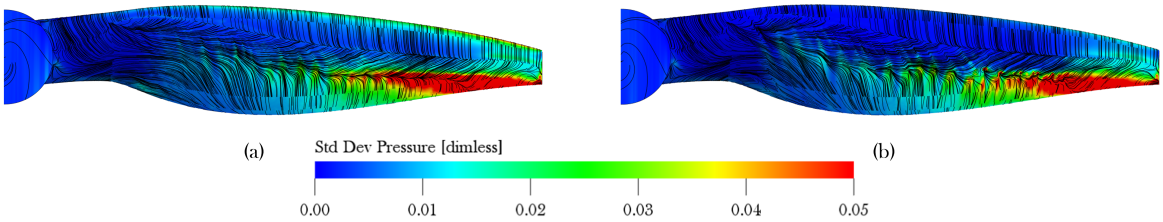


Figure 9: Time-averaged surface streamlines, superimposed to the standard deviation of the surface pressure fluctuations coefficient c_{p_σ} over the blade surface for turbulent (a) and clean (b) inflow

the surface streamlines. The impact of turbulence on noise sources becomes evident by looking at c_{p_σ}. Incoming turbulence increases the amplitude of the surface pressure fluctuations at the leading edge, along the separation line, and inside the bubble itself. This suggests that incoming turbulence enhances the unsteadiness of the LSB.

3.3 Far-field noise

Figure 10 shows the far-field noise spectrum at mic.1 for the turbulent and clean inflows, while the noise sources are described in fig. 11.

Ingested turbulence increases broadband noise up to the 30^{th} harmonic and introduces tones at the harmonics higher than the 2^{nd}. The first harmonic is dominated by the steady loading and therefore is not affected by the presence of free-stream turbulence. At $f > 30BPF$, where trailing-edge noise is the dominant source, all the spectra collapse meaning that the surface pressure fluctuations at the trailing edge are weakly affected by the inflow turbulence .

Figure 11 shows the constructive (CP) and destructive (DP) contribution maps, expressed in dB, to the far-field noise at mic.1 in the frequency $1.3kHz < f < 1.5kHz$, where the difference between the turbulent and clean acoustic spectra is $5dB$. CP and DP are computed from the coherence between the acoustic pressure radiated from the surface element and the total acoustic pressure at the same location ([3]). The CP map shows noise sources, that constructively interfere, due to inflow turbulence at the leading edge and on the suction side up to the laminar separation bubble. The DP map shows that the leading edge, in clean inflow, generates destructive contribution in this frequency range, which is canceled in the turbulent case. After reattachment, the sources are influenced by the mean LSB characteristics and therefore they are not affected by the ingested turbulence.

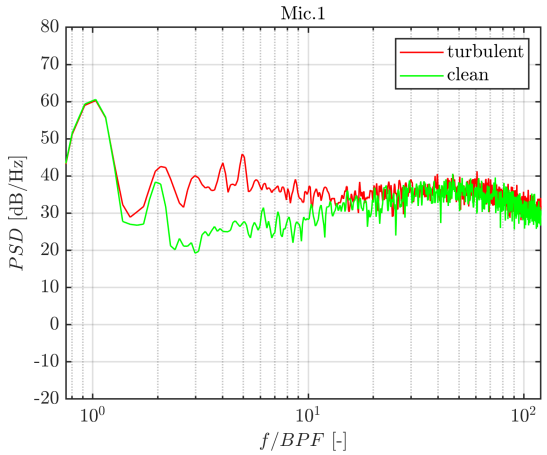


Figure 10: Acoustic spectrum for turbulent and clean inflow at mic.1

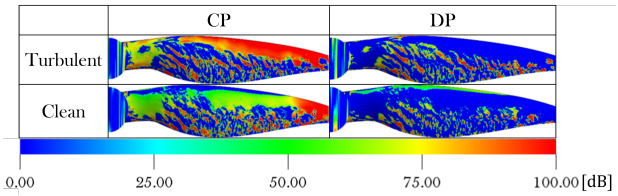


Figure 11: constructive (CP) and destructive (DP) contribution maps for turbulent and clean inflow

4. CONCLUSIONS

This paper investigated the interaction of a low Reynolds propeller with incoming turbulence, both in terms of turbulence distortion and the impact of turbulence on the generated far-field noise. Streamtube contraction induces elongation of the largest eddies in the streamwise direction, reducing the intensity of u_{rms}, while the leading

edge distortion increases the intensity and spanwise coherence of normal fluctuations. These results will be exploited in a future work to evaluate the performances of Amiet's model when turbulence distortion is taken into account. In addition, incoming turbulence was shown to have an impact on the unsteady behavior of the laminar separation bubble, increasing the unsteady loading on the blade. In this configuration, trailing edge noise is not affected by ingested turbulence.

5. ACKNOWLEDGMENTS

The authors acknowledge Compagnia di San Paolo for funding and supporting the present project and ISCRA for the providing computational resources.

6. REFERENCES

[1] M. M. Connors, "Factors that influence community's acceptance of noise: An introduction for urban air mobility," tech. rep., 2019.

[2] D. Casalino, G. Romani, R. Zhang, and H. Chen, "Lattice-boltzmann calculations of rotor aeroacoustics in transitional boundary layer regime," *Aerospace Science and Technology*, vol. 130, p. 107953, 2022.

[3] D. Casalino, G. Romani, L. M. Pii, and R. Colombo, "Flow confinement effects on suas rotor noise," *Aerospace Science and Technology*, vol. 143, p. 108756, 2023.

[4] C. S. Thurman, N. S. Zawodny, and N. A. Pettingill, "The effect of boundary layer character on stochastic rotor blade vortex shedding noise," in *The Vertical Flight Society's 78th Annual Forum and Technology Display*, 2022.

[5] E. Grande, G. Romani, D. Ragni, F. Avallone, and D. Casalino, "Aeroacoustic investigation of a propeller operating at low reynolds numbers," *AIAA Journal*, vol. 60, no. 2, pp. 860–871, 2022.

[6] E. Grande, D. Ragni, F. Avallone, and D. Casalino, "Laminar separation bubble noise on a propeller operating at low reynolds numbers," *AIAA Journal*, vol. 60, no. 9, pp. 5324–5335, 2022.

[7] M. Sevik, "Sound radiation from a subsonic rotor subjected to turbulence," *Fluid Mech., Acoustics, and Design of Turbomachinery, Pt. 2*, 1974.

[8] W. K. Blake, "Mechanics of flow-induced sound and vibration. volume 1 general concepts and elementary source. volume 2-complex flow-structure interactions," *Aplikace Matematiky, Applied Mathematics*, vol. 1, 1986.

[9] D. B. Hanson, "Spectrum of rotor noise caused by atmospheric turbulence," *The Journal of the Acoustical Society of America*, vol. 56, no. 1, pp. 110–126, 1974.

[10] R. K. Amiet, "Acoustic radiation from an airfoil in a turbulent stream," *Journal of Sound and vibration*, vol. 41, no. 4, pp. 407–420, 1975.

[11] R. Amiet, "Noise produced by turbulent flow into a propeller or helicopter rotor," *AIAA Journal*, vol. 15, no. 3, pp. 307–308, 1977.

[12] G. Capobianchi, S. Montagner, A. Piccolo, A. Di Marco, F. Avallone, G. Cafiero, D. Ragni, E. de Paola, and L. G. Stoica, "Impact of turbulent inflow on the far-field noise generated by a propeller operating at low reynolds number," in *30th AIAA/CEAS Aeroacoustics Conference (2024)*, p. 3154, 2024.

[13] J. Christophe, J. Anthoine, and S. Moreau, "Amiet's theory in spanwise-varying flow conditions," *AIAA journal*, vol. 47, no. 3, pp. 788–790, 2009.

[14] H. Raposo and M. Azarpeyvand, "Turbulence ingestion noise generation in rotating blades," *Journal of Fluid Mechanics*, vol. 980, p. A53, 2024.

[15] L. van Beek, "The distortion of turbulence by a low reynolds number uav propeller and the effect on aeroacoustics: An analytical and experimental study," 2021.

[16] P. Roach, "The generation of nearly isotropic turbulence by means of grids," *International Journal of Heat and Fluid Flow*, vol. 8, no. 2, pp. 82–92, 1987.

[17] R. Zamponi, S. Satcunanathan, S. Moreau, D. Ragni, M. Meinke, W. Schröder, and C. Schram, "On the role of turbulence distortion on leading-edge noise reduction by means of porosity," *Journal of Sound and Vibration*, vol. 485, p. 115561, 2020.

[18] J. Hunt, "A theory of turbulent flow round two-dimensional bluff bodies," *Journal of Fluid Mechanics*, vol. 61, no. 4, pp. 625–706, 1973.

DOI: 10.61782/fa.2025.0039



FORUM ACUSTICUM
EURONOISE 2025

A STUDY OF URBAN AIR MOBILITY ROTOR NOISE AT MODERATE REYNOLDS NUMBERS WITH COLLECTIVE PITCH CONTROL.

Charles E. Tinney[1†] **John Valdez**[1] **Yingjun Zhao-Dubuc**[1]
[1] Applied Research Laboratories, The University of Texas at Austin, Austin, Texas, USA
https://www.arlut.utexas.edu/gdl

ABSTRACT

Measurements of hover performance and acoustics of a Mach-tip scaled notional rotor for urban air mobility is presented. The blade shape is a 35% geometrically scaled replica of an earlier generation Joby rotor blade first studied by Tinney and Valdez [1] and is evaluated for changes to blade tip Mach number (between 0.28 and 0.40), rotor collective pitch angle, as well as rotor solidity (number of blades). The findings demonstrate that, in general, sound levels decay with increasing collective pitch angle, while they increase with increasing blade count. A delay in the collective pitch angle, where decreasing noise transitions to increasing noise with increasing collective, is also observed. When using thrust coefficient as the performance metric for comparing different rotor operating conditions, the transition point from decreasing noise to increasing noise is delayed to higher collective pitch angles as blade count increases. This tends to occur for the same range of rotor figures of merit between 0.65 and 0.70; peak hover efficiency is found for a figure of merit of 0.75. The findings provide a first principals understanding of the tradespace between hover performance and acoustics using a UAM relevant blade shape at Reynolds numbers of practical importance.

Keywords: *eVTOL, UAM, AAM, Rotor Noise.*

**Corresponding author*: ✉ *charles.tinney@arlut.utexas.edu.*
***Copyright**: ©2025 The authors. This is an open-access article distributed under the terms of the Creative Commons Attribution 3.0 Unported License, which permits unrestricted use, distribution, and reproduction in any medium, provided the original author and source are credited.*

1. BACKGROUND

A low noise rotor capable of efficient take-off, landing and hovering operations is a prerequisite to the successful integration of urban air mobility (UAM) vehicles into the transportation network. This is an ambitious undertaking as the features of the blade that enhance propulsive efficiency in either hover or forward flight are different from the ones that are needed for low noise operations. To develop a blade shape that can satisfy all of these targets requires a contemporaneous understanding (either measured or simulated) of both rotor performance and its sound field, and at scales that are large enough to overcome Reynolds number effects. The last of these is problematic for most indoor test facilities and has averted the refinement of some rotor noise prediction methods, especially lower-fidelity approaches that lean on experimental validation for confidence. A second issue is concerned with identifying a metric that can capture community annoyance. One of the most commonly adopted metrics for static rotor noise tests is overall sound pressure level (OASPL). Corrections for human perception effects using well established weighting functions are easily incorporated into the OASPL metric and can improve insight into the effect of rotor operating conditions on community annoyance. Though these traditional metrics may not be the best indicators of annoyance, and one might consider other metrics that are designed to be sensitive to impulsive and distorted features in the acoustic waveform [2].

In this study, we present measurements from a test campaign performed in 2022 at The University of Texas at Austin to characterize the hover performance and acoustics of a notional UAM (or eVTOL) rotor blade. A description of this database was first presented by Tinney and Valdez [1] and focused mostly on reporting experi-

mental uncertainties and characterizing facility enclosure effects. Unlike a number of the laboratory-scale rotor tests being reported in the open literature using fixed pitch drone scale rotors, the rotor geometry studied here is a Mach tip scale rotor with collective pitch control, and with chord and twist distributions that are representative of the ones found on nearly all UAM platforms. An analysis of the trade-space between hover performance and perceived noise using this notional UAM rotor blade is presented for different blade number combinations and collective pitch settings of the rotor. The results are part of a larger effort by this group to characterize the performance and acoustic trade space of these unique UAM rotors and are complementary to the experimental and numerical studies reported by Brentner et al. [3], Baskaran et al. [4], and Pascioni et al. [5].

2. HARDWARE AND SETUP

Hover performance and acoustic measurements of a 35% scale UAM rotor were acquired in the Gas Dynamics Laboratory (GDL) of the Applied Research Laboratories, The University of Texas at Austin (ARL-UT). The GDL is a fully enclosed and acoustically treated laboratory encompassing $\dot{V} = 30,100$ ft^3 of climate controlled open air space over 1,500 ft^2 of floor space with an average ceiling height of 21 ft. ARL-UT is located in Austin, Texas near sea-level conditions ($p_\infty = 14.7$ psia (103,325 Pa), $T_\infty = 529$ R (294 K), $\gamma = 1.4$, $\rho = 2.33 \times 10^{-3}$ slug/ft^3) with a sound speed of air being estimated at $a_\infty = 1128$ ft/s. The blade is fabricated from 6061 aluminum using CNC machining and is a geometrically scaled replica of the blade shape flown on an earlier generation Joby Aviation prototype vehicle in 2017 and described recently by Stoll and Bevirt [6]. The 35% scale blade has a diameter of $D = 39.96$ in. (0.665 m) and has non-uniform chord and twist distributions, as shown in Fig. 1a where $cmax = 3.2976$ in. while the blade twist at the root is $\beta_0 = 26.15$ deg. Changes to rotor solidity were evaluated by changing the blade count from $N_b = 2$ to 5, thereby resulting in changes to the blade area from $A_b = 110$ in^2 to 276 in^2, respectively. Additional details concerning the GDL at ARL:UT, as well as the rotor and test stand are provided by Tinney and Valdez [1].

During testing, a magnetic rotary encoder tracks and records the angular speed and phase to within 0.0879 deg over the full duration of testing while a triad of hi-torque servos control collective pitch angles over the range $0 \leq \alpha \leq 18$ in $\delta\alpha = 3$ deg. increments. Blade pitch angles are routinely measured using a 0.1 deg accurate inclinometer while rotor collectives are referenced to a blade pitch angle of zero at $r = 0.75R$. An image of the 5-bladed rotor during testing is shown in Fig. 2. A test matrix of available databases that have been generated for this rotor is provided in Table 1. Symbols identified by (●) pertain to databases encompassing hover performance measurements only, whereas (▶) identify measurements comprising both performance and acoustics. Only a subset of this database will be used in the current discussion. The peak Reynolds numbers ($\mathrm{Re}_c = u(r)c(r)/\nu$) for these three rotor speeds occur at $r/R = 0.82$ and are valued at $Re_c = [3.7, 4.3, 4.9] \times 10^5$ with blade tip Mach numbers $M_t = \Omega R/a_\infty$ valued at 0.28, and 0.32, and 0.37, respectively.

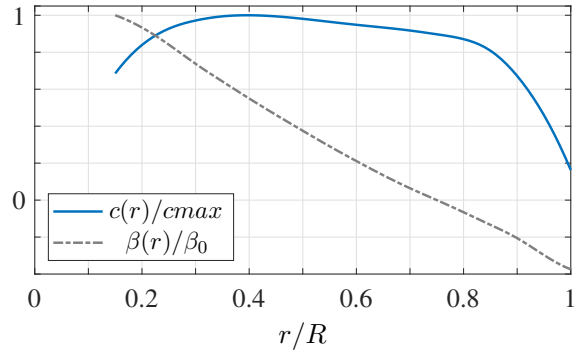


Figure 1. Chord and twist distribution of this notional UAM blade.

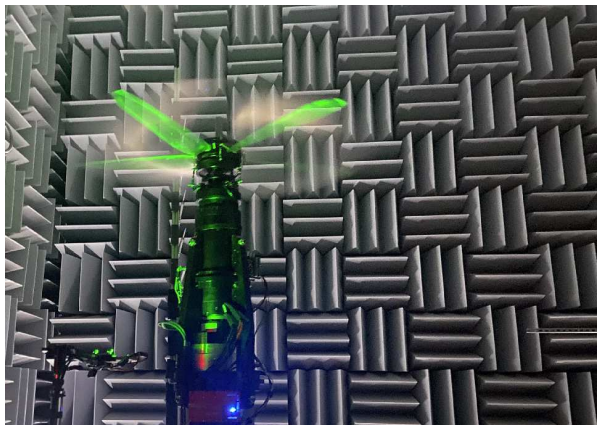


Figure 2. Testing of the notional UAM rotor with five blades.

N_b	σ	30 [rps]	35 [rps]	40 [rps]
2	0.088	▶	●	●
3	0.132	▶	▶	▶
4	0.176	▶	●	
5	0.220	▶	●	
	M_t:	0.28	0.32	0.37

Table 1. Test matrix of hover performance and acoustics of the 35% UAM rotor for all pitch angles ($\alpha = 0,\ 3,\ 6,\ 9,\ 12,\ 15$ deg).

3. HOVER SLIPSTREAM

Visualizations of the rotor slipstream were realized using a laser with sheet forming optics and a high-speed digital camera synchronized to the 1/rev magnetic encoded. The flow is seeded using a combination of atomized olive oil and glyceron fog with particle sizes ranging between 1-10μm; this is the same kind of setup used for Particle Image Velocimetry [7, 8]. The laser sheet is 2-3mm thick and is aligned with the quarter-chord of the blade to capture the tip-vortices, slipstream and blade wake generated by the different rotor configurations in hover. This is shown for the 3-bladed rotor in Fig. 3 at $\alpha = 12$ deg pitch and $M_t = 0.28$ (grid lines have increments of $0.1R$). The image is a pseudo-instantaneous snapshot made up of several images that are combine using Adobe Photoshop v.24. The process involves substitution (not addition or averaging) and works well for this kind of flow. Vortex centers are identified by hand (no vortex centering technique) and are labeled in degrees according to their wake age, ψ_v. The image is rich with information that is expected of this kind of flow. That is, the large radial displacement of the tip vortex up until the first blade pass is observed, followed by an abrupt change in its trajectory towards large axial displacements and increased vortex wander. Between the first and second blade passes, the blade wake passes from the roll-up of the first tip vortex, down to the second. The downwash reveals strong radial dependence at this rotor collective setting with the largest values residing at approximately 30% of the rotor radius. At higher rotor collectives (not shown) the downwash is relatively uniform across the slipstream. A broad range of turbulence scales are observed in the blade wake, while streamlines corresponding to the slipstream between subsequent blade wakes are smooth. This suggest that the rotor inflow is relatively free of turbulence.

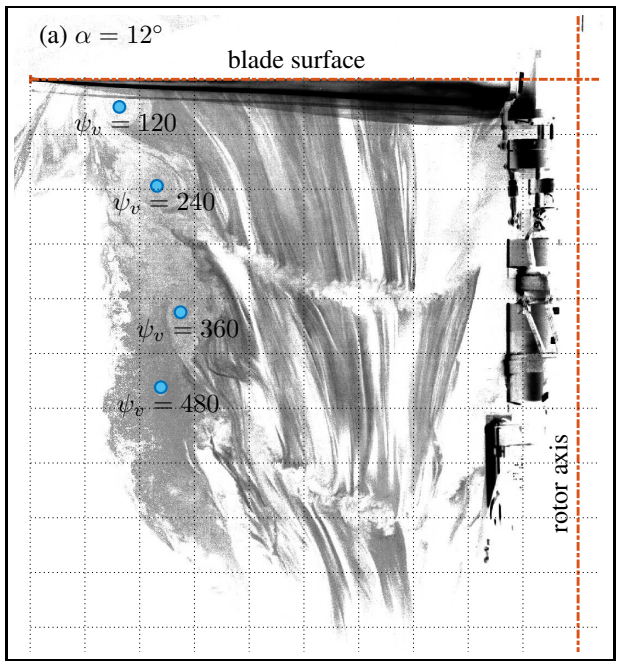


Figure 3. Visualization of the rotor wake generated by the 3-blade rotor at $\alpha = 12$ deg pitch and $M_t = 0.28$.

4. HOVER PERFORMANCE

Rotor torque and thrust were measured using an Interface Model 1216 bi-axial load cell with a 1000-lbf axial force T range (± 0.4 lbf) and a 500 lbf-in. torque Q range (± 0.35 lbf-in.). For each rotor condition, a minimum of three tests were conducted with each test encompassing 32.77 s of interrupted recordings. Measurements were recorded after the wake had stabilized and with the rotor disk elevated three rotor diameters above the facility floor [9]. Thrust coefficient $C_T = F_z/(\rho A(\Omega R)^2)$, power coefficient $C_P = \tau\Omega/(\rho A(\Omega R)^3)$ and rotor figure of merit $FM = C_T^{3/2}/(\sqrt{2}C_P)$ were calculated where $A = \pi D^2/4$ is the disk area, $\Omega = 2\pi\omega$ is the motor rotation speed in rad/s, and $P = Q\Omega$. Large changes in the facility time-scale ($t_v = \dot{V}/Av_i$ where $v_i = \lambda_i \Omega R$ is the rotor inflow and $\lambda_i = \sqrt{C_T/2}$), were observe and found to range from 351 s (for low collective settings of the 2-bladed rotor) to 96 s for the 5-bladed rotor at $\alpha = 15$ deg. collective. Blade loading coefficients (C_P/σ and C_T/σ) are shown in Fig. 4a for different blade number combinations and increasing collective pitch control. Hover efficiency is then reported in Fig. 4b for the same conditions

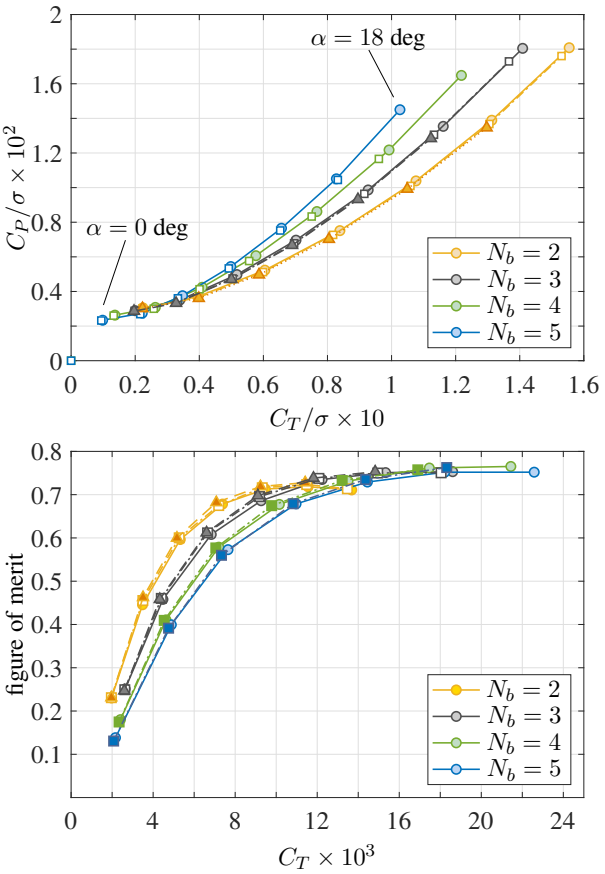


Figure 4. a) Blade loading coefficient and b) figure of merit for $M_t = 0.28$.

where colors are used to distinguish between blade numbers while symbols identify different rotor speeds. Low thrust coefficient and low figure of merit corresponds to low collective, while high thrust coefficient identifies the largest collective setting of the rotors. Peak figure of merit is valued at 0.75 and is achieved by the 4-bladed and 5-bladed rotors. The thrust coefficient where peak hover efficiency is achieved increases with blade count. For a given blade number count, increases to rotor speed have negligible effect on hover performance, thereby demonstrating that the performance of this scale rotor appears to be independent of Reynolds number effects.

5. HOVER ACOUSTICS

The sound field generated by this rotor was captured using a line array of 12 G.R.A.S. IEPE-type free-field microphones (combination of quarter-inch and half-inch capsules). Data was recorded uninterrupted for 20.48 s at 50 kHz sample rate using two NI-PXI-4472 boards (24-bit A/D converters with Butterworth filters). The microphone array was positioned so that the forth sensor was located at the rotor disk plane with remaining sensors being biased towards observers located below the rotor. The array was then traversed radially to create a 2D grid of measurements between $1.0 \leq r/D \leq 3.5$ in increments of $\delta r/D = 0.5$. Ensemble averaged sound pressure spectrum levels (SPSL, re: 20μPa) are computed using a hanning window with 75% overlap and a spectral resolution of $f_s/N = \delta f = 2.0345$ Hz. Microphone corrections (diffraction effects) are implemented following manufacturer guidelines [10]. In Fig. 5, a comparison between facility noise, motor noise and noise from the rotor are shown for an observer located below the rotor disk plane. Motor noise penetrates the rotor noise spectra at the fifth bpf harmonic, but is otherwise too low to contaminate the rotor noise measurement.

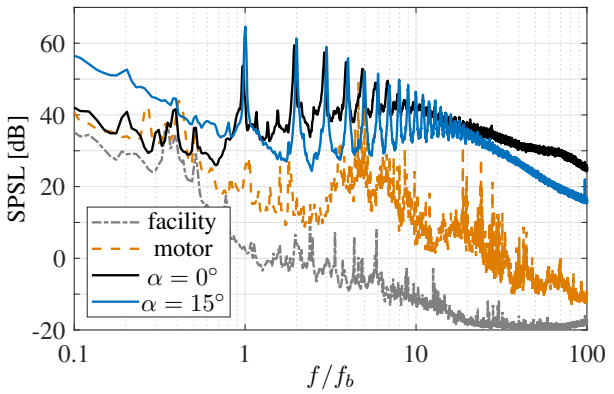


Figure 5. Sound pressure spectrum level [dB, re: 20μPa] of the facility background noise, motor noise and rotor noise at $M_t = 0.28$ for two pitch angles of the 5-bladed rotor as seen by a ground observer.

For the same observer and rotor operating conditions, the effect of blade pitch on the SPSL is shown in Fig. 6 with subsequent spectra being shifted by 20 dB to reduce clutter. An increase in rotor collective from $\alpha = 0$ deg to 6 deg is shown to shift rotor broadband noise to higher frequencies and is attributed to a reduction in blade vortex interaction noise. For $\alpha \geq 6$ deg, and higher, the characteristic frequency of the broadband noise hump is unaffected by changes in rotor collective, or the changes are too small to quantify.

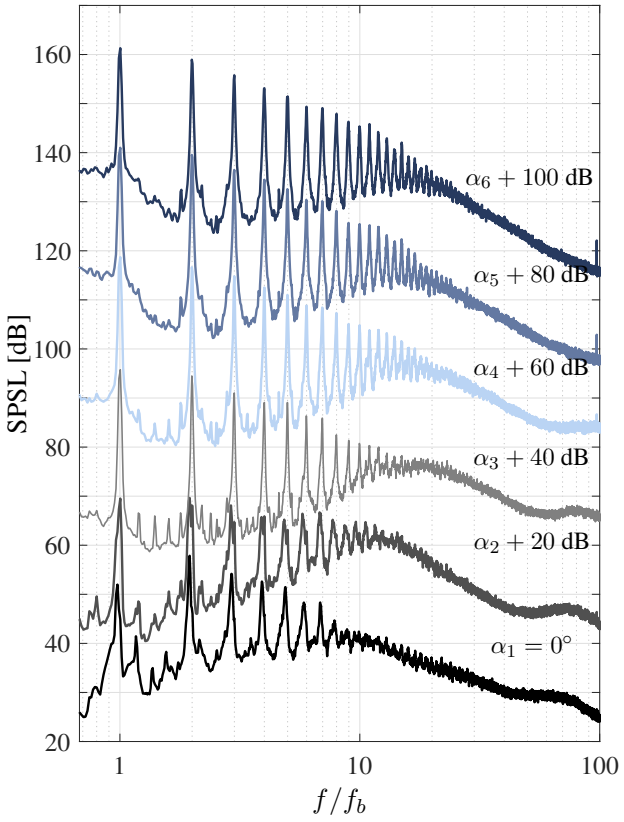


Figure 6. Effect of blade pitch angle on SPSL [dB] for an observer located at $r/D = 2.5$ at the a) rotor disk plane, and b) below ($\theta = -38$ deg). This is for the 5-bladed rotor at $M_t = 0.28$.

6. SCALING AND PERCEPTION

Rotor noise measurements are scaled to full scale conditions and then weighted using the A-weighting noise standard. Scaling is achieved by matching the product of Strouhol number with Mach number which produces Helmholtz number $H_m = fD/(\Omega R) \cdot M_{tip}$. Since blade tip Mach numbers are matched, the scaling reduces to changes in the source frequency using $f^* = \xi f$, where ξ is the geometrical scale factor between the laboratory and full-scale blades and is valued at 0.35. A demonstration of this is shown in Fig. 7 where both unweighted (dB) and weighted (dBA) SPSL are shown for an observer located below the rotor disk plane for the 5-bladed rotor at 30 rps and 15 deg blade pitch. As expected, the effect of A-weighting is a significant reduction in rotor harmonic noise, while rotor broadband noise remains unaffected and is now the dominant noise source. The high frequency peaks are electrical noise and are not related to the rotor or test stand.

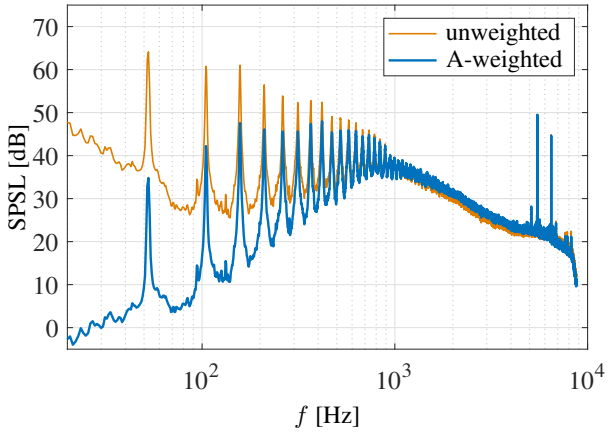


Figure 7. Scaled SPSL [dB] for the microphone observer located at $r/D = 3.05$ and $\theta = -35$ deg for the 5-bladed rotor operating at $M_t = 0.28$ and $\alpha = 15$ deg blade pitch.

The broader impacts of scaling and weighting the SPSL is demonstrated using contours of overall sound pressure level (OASPL) in Fig. 8 for the full 2D grid array. This is first demonstrated using the 3-bladed and 5-bladed configuration at $M_t = 0.28$ and $\alpha = 15$ deg pitch angle. Alongside these unweighted contours are contours of the scaled and weighted values. Comparing the two reveals the significant reductions in noise over all observer locations when human perception effects are included. As most of the low-frequencies associated with thickness and loading noise have been removed, self-noise from boundary layer turbulence on the pressure and suctions sides of the blade are shown to generate a sound field that is directive above and below the rotor. While these patterns signify dipole behavior, it is known that self-noise source mechanisms are quadrupoles and that their directivity is governed by the turbulence in the boundary layer whose spatial wavenumbers convect at speeds that allow them to become acoustically matched with the surrounding gas. The dipole shape is due to individual contributions of self-noise from the suction and high-pressure sides of the rotor. Fig. 8 shows this to be the case for both the 3-bladed and 5-bladed rotors.

Scaled and weighted SPSL are then evaluated in

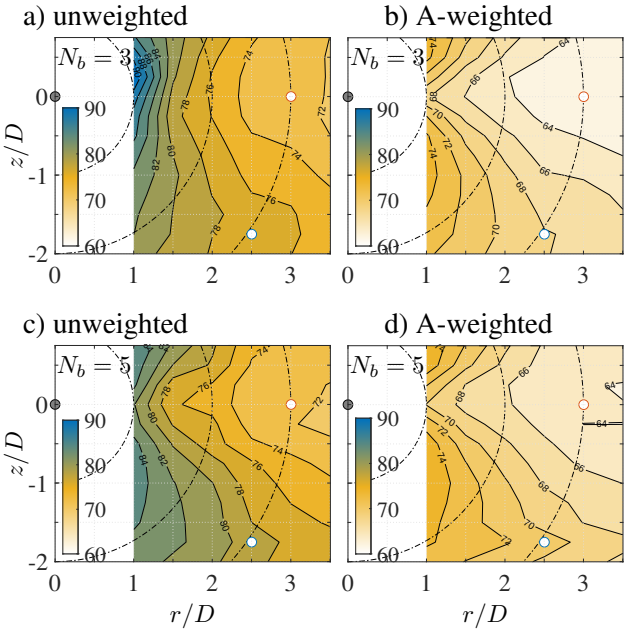


Figure 8. a,c) Unweighted and b,d) weighted OASPL at $M_t = 0.28$ and $\alpha = 15$ deg blade pitch for the a,b) 3-bladed and c,d) 5-bladed rotor.

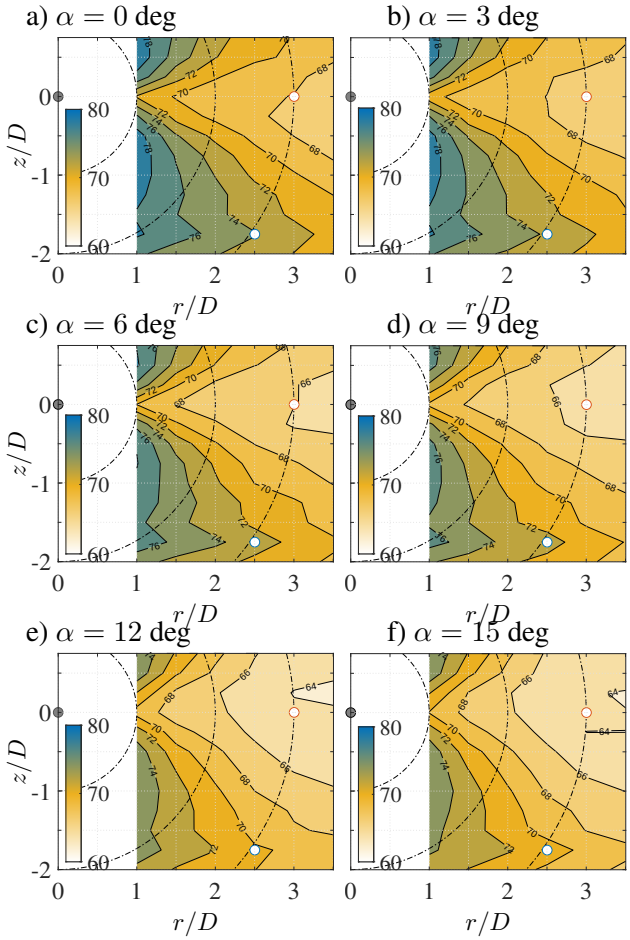


Figure 9. A-weighted OASPL at $M_t = 0.28$ for the 5-bladed rotor and all blade collective pitch angles.

Fig. 9 for all blade collectives to see the effect of rotor inflow on the self-noise. This is demonstrated using the 5-bladed rotor at $M_t = 0.28$. The contour decrements have been enhanced to accommodate the new A-weighted range of sound levels with each illustration comprising the same color scale so that direct comparisons can be made. The findings demonstrate negligible changes in contour shapes and sound directivity pattern on account of changes to rotor collective. Furthermore, OASPL levels are mostly unaffected by increasing rotor collective. In fact, at the highest collective pitch setting of $\alpha = 15$ deg, rotor noise amplitudes are shown to decrease over the entire observer space.

Scaled and weighted OASPL are now used to evaluate the trade-space between perceived noise and hover performance for all blade numbers and collective pitch settings. A presentation of findings from this can be overwhelming so the analysis is isolated to a single ground observer identified by blue circles in Figs 8 and 9; this is the same ground observer used to generate the SPSL in Fig. 7. The results are first reported in Figs. 10a and 10b without and with the effect of A-weighting, respectively, and with thrust coefficient as the performance metric. Starting with the 2-bladed and 3-bladed rotors, minimum perceived noise is achieved at moderate rotor collectives. As blade count advances to the 4-bladed and 5-bladed rotors, minimum perceived noise levels migrate towards higher rotor collectives thereby demonstrating that higher blade count rotors have increased inflow and subsequently generate more downwash which reduces the ingestion of turbulence from the wakes generated by preceding blades. For the 5-bladed configuration, the A-weighted noise decreases with increasing thrust, and complements the observations made concerning the contours in Fig. 9.

The same rotor conditions are then evaluated in Fig. 11 to reveal the trade-space between figure of merit and weighted/unweighted OASPL. For all blade number counts and at low hover efficiency conditions, as rotor collective increase, and consequently hover efficiency in-

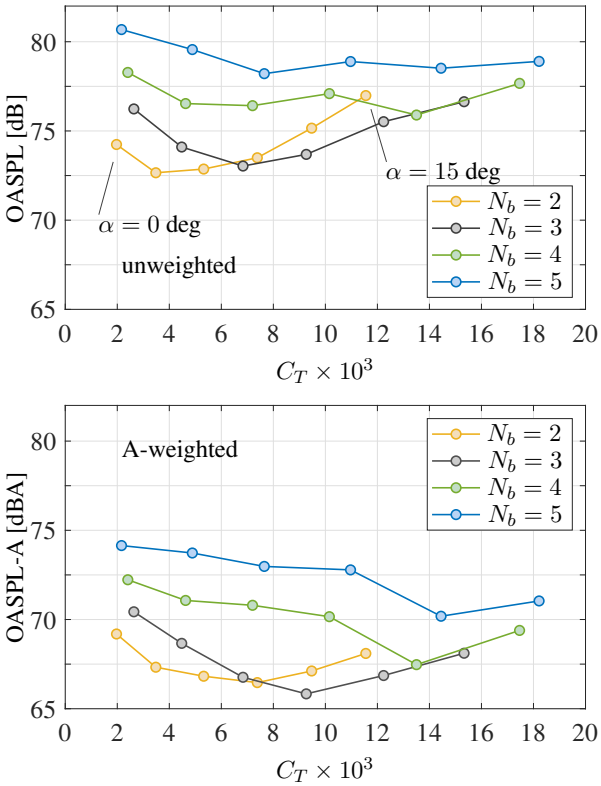


Figure 10. a) unweighted and b) weighted OASPL [dB] for the microphone observer located at $r/D = 3.05$ and $\theta = -35$ deg at $M_t = 0.28$.

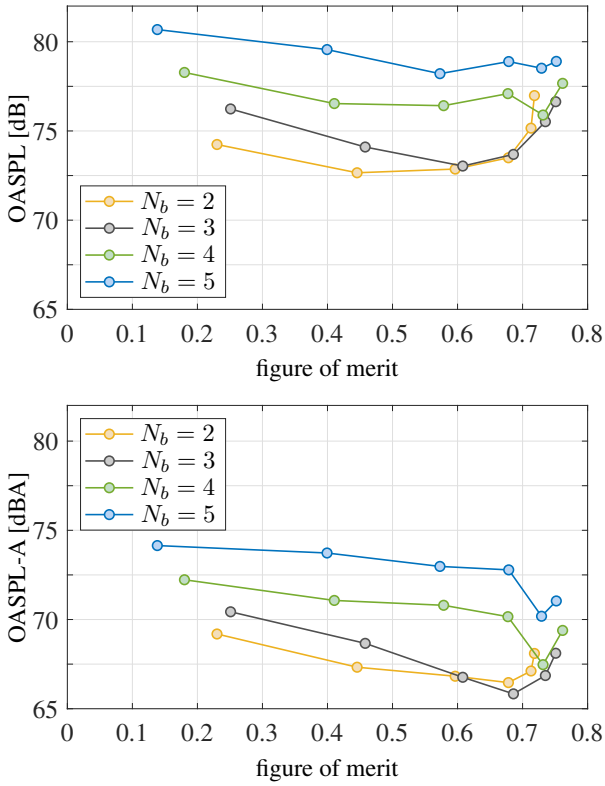


Figure 11. a) unweighted and b) weighted OASPL [dB] for the microphone observer located at $r/D = 3.05$ and $\theta = -35$ deg at 30 rps.

creases, perceived noise decreases. Eventually as the rate of change in hover efficiency begins to roll off, overall perceived noise levels begin to rise. This change is nearly consistent for all blade number combinations and occurs around a figure of merit between 0.65 and 0.7. The change is attributed to thickening of the boundary layers on the suction sides of the blades which promotes turbulence production. Regions of the blade close to the hub may be incipiently separated or stalled. Flow measurements / visualizations (like the one shown in Fig. 3) with the interrogation region being perpendicular to the rotor radius (complementary to the smoke visualizations of Yarusevych et al. [11]) are needed to address this question, and are currently underway. As hover efficiency approaches peak values of 0.75 for the different blade number counts, noise levels generated by all blade number combinations are within 3 dB for both the unweighted and A-weighted values.

7. SUMMARY

An analysis of hover performance and acoustics of a 35% scale UAM blade shape was presented using the experimental database described by Tinney and Valdez [1]. Performance measurements were acquired using a bi-axial load cell so that traditional metrics like thrust coefficient, power coefficient and rotor figure of merit were evaluated. The acoustic field was captured along a two-dimensional grid covering observer locations both above and below the rotor and between 1.0 and 3.5 rotor diameters from the hub; pressure measurements in this region are shown to transition from hydrodynamic to acoustic waveforms. Both hover performance and acoustics are evaluated for changes to the rotor collective pitch angle and for different blade number counts as well as increasing rotor speed (tip Mach numbers ranging between 0.28 and 0.37). At this scale, rotor performance was shown to be independent of Reynolds numbers while the thrust coefficient where peak

hover efficiency resided increased with increasing blade count. Contour maps of unweighted and A-weighted overall sound pressure levels were then evaluated for different collective pitch settings of the 3-bladed and 5-bladed rotor and by scaling the rotors to match full-scale conditions. As expected, a significant increase in loading noise and self-noise (rotor broadband noise) was observed while thickness noise, which is predominantly monopole-like, was suppressed. When the blade count advanced from a 4-bladed rotor to a 5-bladed rotor, minimum perceived noise levels were shown to migrate towards higher rotor collectives thereby demonstrating that higher blade count rotors have increased inflow and subsequently generate more downwash. The additional downwash reduces the ingestion of turbulence from the wakes generated by preceding blades.

8. ACKNOWLEDGMENTS

Support for this effort was graciously provided through an internal research and development award with the Signal and Information Sciences Laboratory of the Applied Research Laboratories, The University of Texas at Austin.

9. REFERENCES

[1] C. E. Tinney and J. Valdez, "Hover performance and acoustics of a 35% scale notional evtol rotor," *AIAA Paper 2024-3219*, pp. 1–14, 2024.

[2] C. E. Tinney and J. Valdez, "Higher-order statistical metrics for characterizing multirotor acoustics," *AIAA Journal*, vol. 62, no. 11, pp. 4431–4441, 2024.

[3] K. S. Brentner, B.-E. Zolbayar, and T. F. Jaworski, "An investigation of noise from electric, low-tip-speed aircraft propellers," *in: AHS International Technical Meeting on Aeromechanics Design for Transformative Vertical Flight*, pp. 1–10, 2018.

[4] K. Baskaran, N. S. Jamaluddin, A. Celik, and D. Rezgui, "Effects of number of blades on propeller noise," *Journal of Sound and Vibration*, vol. 572, no. 118176, pp. 1–17, 2024.

[5] K. A. Pascioni, A. C. Thai, and J. J. Bain, "Propeller source noise separation from flight test measurements of the joby aviation aircraft.," *AIAA Paper 2024-3231*, pp. 1–14, 2024.

[6] A. Stoll and J. B. Bevirt, "Development of evtol aircraft for urban air mobility at joby aviation," *Vertical Flight Society Forum 78, Paper 2022-17528*, 2022.

[7] S. Mula, J. Stephenson, C. E. Tinney, and J. Sirohi, "Dynamical characteristics of the tip vortex from a four-bladed rotor in hover," *Experiments in Fluid*, vol. 54, no. 1600, 2013.

[8] S. Mula and C. E. Tinney, "A study of the turbulence within a spiralling vortex filament using proper orthogonal decomposition," *Journal of Fluid Mechanics*, vol. 769, pp. 570–589, 2015.

[9] E. A. Fradenburgh, "The helicopter and the ground effect machine," *Journal of the American Helicopter Society*, vol. 5, pp. 24–33, 1960.

[10] S. Rayes, "How to match a measurement microphone to a sound field," *G.R.A.S. Sound and Vibration Handbook*, p. 12, 2021.

[11] S. Yarusevych, P. E. Sullivan, and J. G. Kawall, "On vortex shedding from an airfoil in low-reynolds-number flows," *Journal of Fluid Mechanics*, vol. 632, pp. 245–271, 2009.

DOI:

Main theme: A07 Flow Acoustics

Session A07.03 Active and passive noise reduction technologies

Chair(s): M. Raiola, A. Schulz

DOI: 10.61782/fa.2025.0650

FORUM ACUSTICUM EURONOISE 2025

ON THE INTERACTION OF GRAZING ACOUSTIC WAVES AND TURBULENT BOUNDARY LAYER OVER ACOUSTIC LINERS

Angelo Paduano[1*] **Francesco Scarano**[1] **Damiano Casalino**[2]
Julio Cordioli[3] **Francesco Avallone**[1]
[1]Department of Mechanical and Aerospace Engineering, Politecnico di Torino, Torino, Italy
[2] Flow Physics and Technology, Delft University of Technology, Delft, Netherlands
[3]Department of Mechanical Engineering, Federal University of Santa Catarina, Florianópolis, Brazil

ABSTRACT

Acoustic liners, passive devices to mitigate engine noise, operate under high-speed grazing flow and grazing acoustic waves. To investigate the complex physics governing this interaction, high-fidelity numerical simulations of a spatially evolving turbulent boundary layer grazing a multi-orifice acoustic liner at a bulk Mach number of 0.32 are performed. The simulations replicate conditions from a reference experiment. Grazing tonal plane acoustic waves with amplitudes of 130 dB and 145 dB and propagating in the same direction and the direction opposite to the mean flow are analyzed. The results show that the boundary layer displacement thickness doubles in the presence of the liner and its growth rate is affected by the amplitude and propagation direction of the acoustic wave. The acoustic liner also promotes the formation of an outer hump in both the logarithmic region of the streamwise and wall-normal velocity variance, with these effects becoming more pronounced under acoustic forcing. Furthermore, impedance estimation, using Dean's method, reveals that near-wall flow modifications, quantified through the displacement thickness, influence the local value of the computed impedance.

Keywords: *aeroacustics, acoustic liners, impedance, semi-empirical model.*

**Corresponding author*: *angelo.paduano@polito.it.*
***Copyright**: ©2025 Angelo Paduano et al. This is an open-access article distributed under the terms of the Creative Commons Attribution 3.0 Unported License, which permits unrestricted use, distribution, and reproduction in any medium, provided the original author and source are credited.*

1. INTRODUCTION

Acoustic liners are essential components to reduce noise in aircraft engines. They are typically installed in the intake and core jet sections of aircraft engines. The advent of ultra-high bypass ratio engines, characterized by larger fan diameters, has significantly increased the contribution of fan noise, comprising a tonal component at the Blade-Passing Frequency (BPF) and broadband noise due to rotor-stator turbulence interaction [1–3].

Acoustic liners vary in complexity and absorption properties. Conventional Single Degree-Of-Freedom (SDOF) liners consist of a perforated face sheet, a backing cavity, and a rigid backplate, operating as Helmholtz resonators tuned to the fan's BPF or harmonics [4]. A widely used approach to characterize the acoustic liner is to measure its acoustic impedance, a quantity defined in the frequency domain as:

$$\hat{Z}(\omega) = \frac{\hat{p}}{\hat{v} \cdot \mathbf{n}} = \theta + i\chi, \tag{1}$$

where p is the acoustic pressure, u_n the acoustic particle velocity normal to the face sheet, θ the resistance, and χ the reactance. Although impedance is an intrinsic property of the liner surface, studies have shown that it is highly sensitive to the eduction technique used for its calculation [5]. Furthermore, impedance is strongly influenced by the presence of grazing flow, with research highlighting its dependence on boundary layer parameters, particularly the displacement thickness δ^* [6].

The presence of a grazing flow adds complexity to impedance eduction, requiring an appropriate boundary condition. The most widely adopted boundary condition is the Ingard-Myers one [7], which assumes an in-

finitely thin vortex sheet along the liner surface. To improve accuracy, several studies have incorporated boundary layer profiles with finite thickness in impedance modeling [8–10]. To characterize the flow near the wall, fully three-dimensional numerical simulations of sound interacting with laminar and turbulent boundary layers were performed by Zhang and Bodony [11]. Although this computational study provided valuable information on flow-acoustic interactions within a single orifice, it remained limited to single-resonator configurations and did not account for boundary layer modifications induced by multiple cavities.

A step forward was taken by Shahzad et al. [12], who performed pore-resolved compressible direct numerical simulations of a turbulent flow that grazes a multi-cavity acoustic liner. Their findings show that the turbulent flow over an acoustic liner behaves similarly to flow over a porous surface. However, their study did not consider the presence of acoustic waves.

A comprehensive analysis of the acoustic and aerodynamic fields over multi-cavity liners, particularly the boundary layer evolution and its effect on impedance, remains lacking. This study employs high-fidelity numerical simulations using the Lattice-Boltzmann Very-Large-Eddy-Simulation (LB/VLES) approach to model a turbulent boundary layer grazing an acoustic liner in the presence of grazing acoustic waves. The simulated geometry corresponds to the one experimentally investigated by Bonomo et al. [6].

The paper is structured as follows: section 2 details the methodology and the computational setup. Section 3 presents and discusses the numerical results. Section 4 summarizes the main findings.

2. METHODOLOGY

2.1 Solver

The commercial software 3DS Simulia PowerFLOW version 6 is adopted. It is based on an extended LB method. A VLES approach is used, which resolves only the large turbulent scales. It accounts for sub-grid effects using a turbulence model based on two-equation renormalization group theory k-ϵ. This approach differs from the computation of an equivalent eddy viscosity. It dynamically adjusts the Boltzmann model to match the characteristic time scales of turbulent flow. Reynolds stresses are not explicitly added to the governing equations; they arise implicitly from the chaotic exchange of momentum in turbulent flow, where characteristic times are shorter than the slowly varying turbulent flow.

To reduce the computational approach, a wall-model based on the extended law-of-the-wall is adopted [13]. This solver has been widely used to study fluid dynamic and aeroacoustic fields over acoustic liners [14–16].

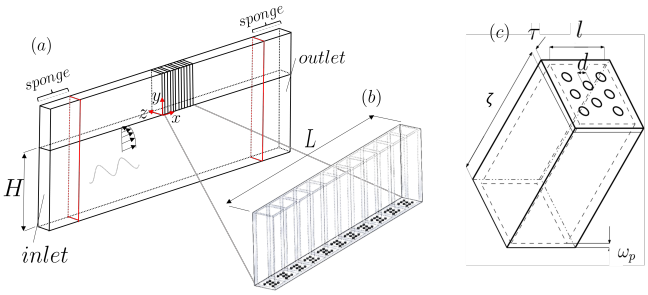


Figure 1: Overview of the computational domain: (a) schematic of the simulation setup, (b) detailed view of the acoustic liner, and (c) magnified depiction of a single cavity.

2.2 Numerical set-up

The computational domain, shown in Fig. 1, replicates the UFSC grazing flow test facility [17]. The liner is positioned on the top wall of a channel with rectangular cross section. The channel height is $H = 2h = 40$ mm. Each cavity, with a square cross-section $l = 8.46d$ and depth $\zeta = 32.56d$ ($d = 1.17$ mm is the orifice diameter), has eight orifices, partition walls with thickness $w_p = 2.17d$, and a face sheet $\tau = 0.46d$ thick. This configuration results in a cavity porosity of 5.63%. The simulated liner consisted of a row of eleven cavities, yielding a total streamwise length of $L = 116.23d$. A zig-zag trip with a height of $0.21d$ and length of $1.71d$ is placed upstream at $x = -1367d$ to match the experimental velocity profile [17].

The simulation is initialized with the flow at rest. A inflow velocity boundary condition is applied at the inlet, allowing the flow to develop spatially within the channel until statistical convergence is reached. For the acoustic simulations, an instantaneous flow field is saved and modified by superimposing a plane acoustic wave with a specified frequency and amplitude using the *OptydB* toolkit. This modified flow field serves as the initial condition for the simulations that include the acoustic excitation.

A total of five cases are tested, as summarized in Table 1. The first case is the smooth wall one; it serves as the baseline reference. The second case has a lined wall subjected to the same turbulent boundary layer. In the remaining cases, acoustic excitation is added at a fixed frequency of 1400 Hz, with SPLs equal to 130 dB and 145 dB. For both SPLs, cases with upstream and downstream acoustic wave propagation are tested. However, since the 130 dB cases exhibited trends similar to those at 145 dB, only the latter are presented for brevity.

2.3 In-situ technique

In this work, impedance is computed using the in-situ technique proposed by Dean [18]. It involves measuring unsteady pressure at the face sheet and the bottom of the cavity. This method provides a local measurement of impedance. It is based on the following key assumptions: the wavelength of the incident acoustic wave is significantly larger than the cavity width; the walls of the cavity are considered to be sufficiently thick, resulting in the liner being locally reactive; any wave entering the cavity is assumed to be completely reflected at the backplate. Consequently, the acoustic pressure of the standing wave within the cavity is the sum of the incident and reflected waves. Using the linearized momentum equation, it is possible to calculate the acoustic-induced velocity and, subsequently, the impedance as:

$$Z_f = \frac{Z}{Z_0} = -i\tilde{H}_{fb}\frac{1}{\sin(k\lambda)}; \qquad (2)$$

where Z_0 is the characteristic impedance of air, $\tilde{H}_{fb}$ is the transfer function defined as the ratio between the pressure measured at the face sheet $\tilde{p}_f$ and at the backplate $\tilde{p}_b$, and $k = \omega/c_0$ is the free-field wavenumber, with ω being the acoustic wave angular frequency. This technique has been widely used for calculating the impedance of acoustic liners in the presence of grazing flow [11, 19]. Unlike impedance eduction techniques [17], a model of the acoustic field is not required for the in-situ technique, so boundary conditions to model the presence effects of the boundary layer are unnecessary. However, studies have underlined the sensitivity of this technique on the sampling position [20, 21].

Mach	Case	SPL (dB)	Freq. kHz	ac. pos.
0.32	Smooth	-	-	-
0.32	Lined	-	-	-
0.32	Lined	130	1.4	up
0.32	Lined	145	1.4	up
0.32	Lined	145	1.4	down.

Table 1: List of simulations carried out.

3. RESULTS

3.1 Mean flow velocity profiles

Figure 2 presents streamwise velocity profiles sampled at three locations along the liner: $x/L = 0$, $x/L = 0.5$ and $x/L = 1$. The velocity profiles are expressed in outer coordinates, where U_∞ denotes the centerline streamwise velocity, and h is the half height of the channel.

Figure 2a compares the mean velocity profiles with and without the liner and in the absence of grazing acoustic wave. It can be observed that introducing a liner causes a velocity shift. Figure 2b compares the velocity profiles at $x/L = 0$ and $x/L = 0.5$ in the absence of acoustic excitation. The presence of cavities affects the near-wall flow, with a further velocity shift of $\Delta U = -14\%$ in the range $0.01 < y/h < 0.04$ at $x/L = 0.5$ compared to $x/L = 0$. Conversely, comparing the velocity profiles at $x/L = 1$ with the one at $x/L = 0.5$ (Figure 2c) it can be observed that the velocity shift is reduced to $\Delta U = -3\%$.

The effect of the presence of the acoustic wave is visible already upstream of the lined section. As a matter of fact, a slight downward shift in velocity compared to the no-acoustic case, $\Delta U = -4\%$, is found in the region $0.01 < y/h < 0.04$ for the upstream propagating wave with SPL equal to 145dB. At $x/L = 0.5$, the influence of acoustic waves is more pronounced than in the upstream region. As shown in Figure 2e, a higher SPL increases the velocity deficit. As a matter of fact, for the cases with SPL = 130 dB the differences with respect to the no-acoustic cases are smaller ($\Delta U = -4\%$) than for the cases with higher SPL ($\Delta U = -8\%$). At the end of the liner ($x/L = 1$, Figure 2f) the differences between acoustically excited cases and the no-acoustic case are within 3%.

The comparison of the velocity profiles between upstream and downstream propagating wave shows that the largest difference appears at $x/L = 0.5$ (Figure 2h); the downstream case exhibits a velocity profile closer to the no-acoustic case, with deviations remaining below -4%. Furthermore, downstream of the liner, the combined effect of the cavities and grazing acoustic waves diminishes.

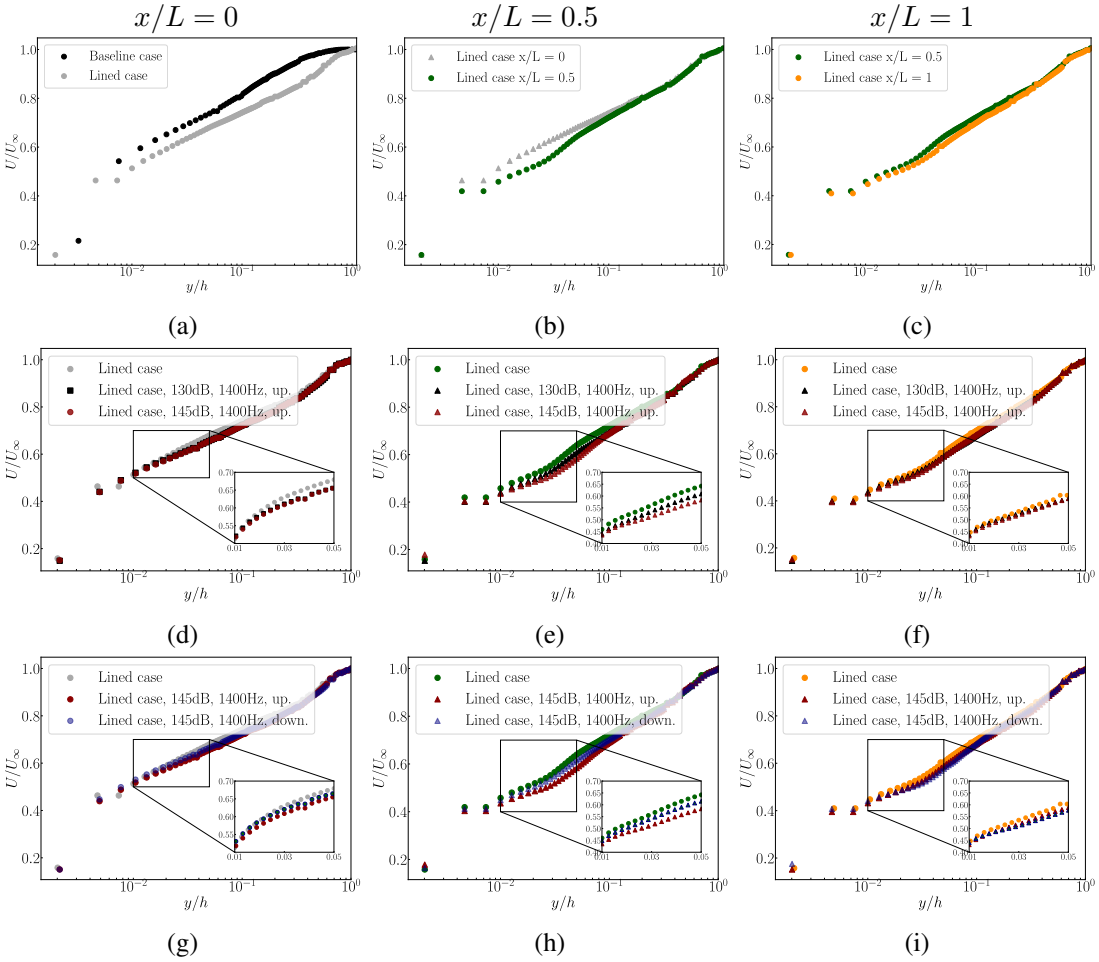


Figure 2: Streamwise velocity profiles in outer coordinates at three different locations along the liner: (left column) $x/L = 0$, (center column) $x/L = 0.5$, and (right column) $x/L = 1$. Velocity profiles are normalized by the centerline velocity U_∞ and channel half-height.

3.2 Integral boundary layer parameter streamwise evolution

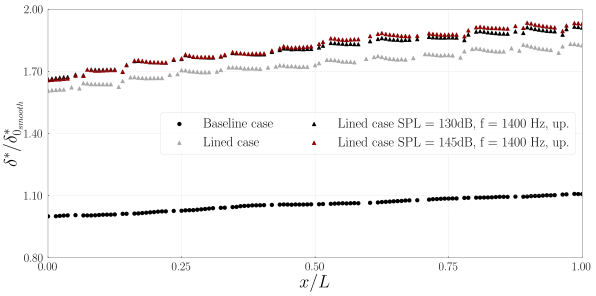
Although these parameters are not commonly used for turbulent channel flows, some, such as δ^*, are present in the semi-empirical model for predicting impedance .

In this context, the boundary layer displacement thickness δ^* is defined as:

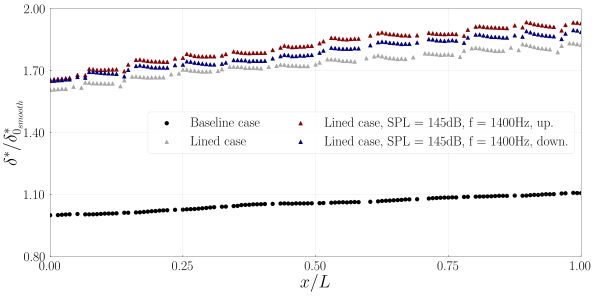
$$\delta^* = \int_0^h \left(1 - \frac{U(y)}{U_\infty}\right) dy \tag{3}$$

Figure 3 shows that, in the presence of the liner, δ^* increases by approximately 50% with respect to the smooth wall case. δ^* shows localized humps after each orifice, followed by a slight decrease until the next pair of orifices is encountered. This periodic variation results in an overall displacement thickness increase of 13% at the end of the liner.

The streamwise development of δ^* is also dependent on the presence of the acoustic wave, its amplitude and direction of propagation. As shown in Figure 3a, the presence of the acoustic wave increases the δ^*; starting from $x/L = 0.5$ the impact of the SPL also is visible even if it is not very strong. On the other hand, differences become more relevant when assessing the impact of the direction of propagation of the acoustic wave: the case



(a)



(b)

Figure 3: Streamwise evolution of δ^* over the liner: (a) effect of different sound pressure levels at a fixed frequency of 1400 Hz, (b) effect of acoustic wave propagation direction at SPL = 145 dB.

with a downstream-propagating wave exhibits a slightly lower increase in δ^* compared to the upstream propagating case. Nonetheless, differences in boundary layer displacement thickness remain below 5% relative to the no-acoustic case, whereas the most significant effect is the 50% increase in δ^* caused by the presence of the liner and the oscillatory variations over the cavities. These findings highlight that the presence of the lined surface is the most important factor that affects the boundary layer development.

3.3 Variance of the velocity fluctuations

The variance of streamwise and wall-normal velocity fluctuations normalized by the centerline velocity are reported in Figure 4. The variance profiles are sampled at three different streamwise locations: $x/L = 0$, $x/L = 0.5$ and $x/L = 1$.

Upstream of the liner, profiles of both the streamwise and wall-normal velocity variance collapse, closely resembling the one obtained for the smooth wall. At $x/L = 0.5$, an outer hump emerges in the variance of the streamwise velocity component for the no-acoustic case. This indicates that the lined surface alters the distribution and amplitude of the velocity fluctuations within the boundary layer. A clear secondary peak in streamwise velocity turbulent fluctuations appears at $y/h \approx 0.1$. At the same location, also the fluctuations of the wall-normal velocity component show an increase. These findings align with previous results on porous material [22, 23] and are likely related to a development of secondary flow structures, due to the injection of momentum near the wall [24]. The intensity of both peaks increases at downstream locations (i.e., $x/L = 1$), with the vertical velocity component showing a larger increase than the wall-parallel one.

It is interesting to note that the introduction of acoustic excitation modifies the turbulence statistics. The outer hump is more pronounced as the SPL increases. This is demonstrated by comparing Figure 4 (b) and (c). At the most downstream location $x/L = 1$, the amplitude of the acoustic source is higher for the downstream acoustic source because the acoustic amplitude is higher. Furthermore, it is also possible to notice that the development of the flow has also an impact on the wall-normal profile of the variance of the streamwise velocity fluctuations. At the most downstream location, a higher amplitude of the acoustic wave shows a more uniform high-intensity fluctuations region with a less evident difference between the inner and outer peaks. Conversely, the wall-normal velocity fluctuations show less dependence on the intensity of the acoustic source with the peak at $x/L = 1$ being very similar.

3.4 Impedance streamwise analysis

Using the in-situ technique on a numerical database, it is possible to analyze the distribution of impedance on the entire liner surface, thus providing insights into how individual orifices affect locally the impedance value.

Figures 5 show the distribution of resistance and reactance values computed on all the streamwise points at $z/l = 0.5$. A periodic pattern emerges in the distribution of resistance for all cases, with values doubling along each cavity peaking after the orifices and tending to decrease near the end of the cavity. This pattern follows the one discussed for δ^* (Figure 3). This is observed regardless of SPL value and the acoustic wave propagation direction; however, the downstream case shows higher variation of resistance compared to the upstream one. Considering the

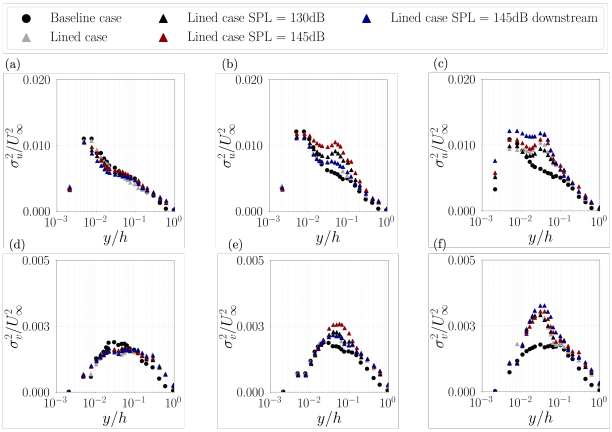


Figure 4: Streamwise (top row) and wall-normal (bottom row) velocity variance at three streamwise locations: $x/L = 0$ (a-d), $x/L = 0.5$ (b-e), and $x/L = 1$ (c-f).

variation of resistance along each cavity, this is enhanced for the downstream propagating case.

Considering the mean resistance value, small differences are found between the cases analyzed. The upstream acoustic source case yields $\theta = 0.78$ for SPL = 130 dB and $\theta = 0.80$ for SPL = 145 dB, while for the downstream case at SPL = 145 dB $\theta = 0.82$.

Reactance exhibits spatial variations across each cavity, following a trend that depends on the propagation direction of the acoustic wave. This is consistent with the established relationship between reactance and the phase of the acoustic wave. In the downstream acoustic source case, reactance variation is reduced compared to the upstream case. However, as for the resistance, the differences in the mean values are not large. Specifically, for SPL = 130 dB the mean reactance is $\chi = -0.52$, while, for SPL = 145 dB, the upstream acoustic source case yields $\chi = -0.46$ and the downstream case $\chi = -0.47$. Previous studies employing in-situ measurement techniques [16] have reported similar spatial dependencies in resistance and reactance within a single cavity.

These findings indicate that the wake generated by each orifice has a relevant impact on the impedance computed with the Dean's method.

To evaluate the impact of the local boundary layer profiles, Figure 5 compares the computed components of impedance with the one predicted by a semi-empirical model [25]. This model requires as input the value of δ^*. In this case, the prediction obtained using the δ^* from the smooth-wall simulation upstream of the liner, as it is typically done, and the prediction obtained using the δ^* obtained at each streamwise location in the presence of the liner. Results obtained with the latter agree better with the simulation results, regardless of the acoustic wave propagation direction. When the smooth-wall displacement thickness is used in the semi-empirical model, the discrepancy in impedance estimation is 17%, whereas incorporating the local boundary layer displacement thickness it reduces to 3%. Similar results are found for the reactance.

4. CONCLUSION

This study investigates the interaction between grazing acoustic waves and a turbulent boundary layer over an acoustic liner using high-fidelity numerical simulations. The study revealed that the presence of the liner leads to a 50% increase in displacement thickness (δ^*) compared to a smooth wall, with an additional 13% streamwise growth. The downstream-propagating wave results in a slightly lower δ^* growth compared to the upstream case. Overall, the impact of acoustic waves remains secondary to that of the cavities. This confirms that the liner geometry plays a dominant role in modifying the boundary layer, with the impact of acoustic forcing diminishing towards the liner's downstream end. The lined surface alters second-order flow statistics, promoting the formation of an outer hump in the streamwise and wall-normal velocity variance. This effect is amplified by acoustic forcing, particularly at higher SPLs, causing an increased inner-outer interaction within the boundary layer. The modifications in the grazing flow streamwise evolution have been linked to impedance through in-situ eduction technique. The impedance eduction analysis reveals significant spatial variations in resistance and reactance. The periodic pattern in resistance, peaking just after each orifice and decreasing within the cavity, closely follows the displacement thickness evolution. The study highlights that assuming a uniform boundary layer profile different from the local one leads to inaccuracies in impedance predictions, particularly when using semi-empirical models. The direction of acoustic wave propagation affects both flow statistics and impedance characteristics. However, differences in mean resistance and reactance values remain minimal, reinforcing the idea that local variations play a more significant role than acoustic propagation direction.

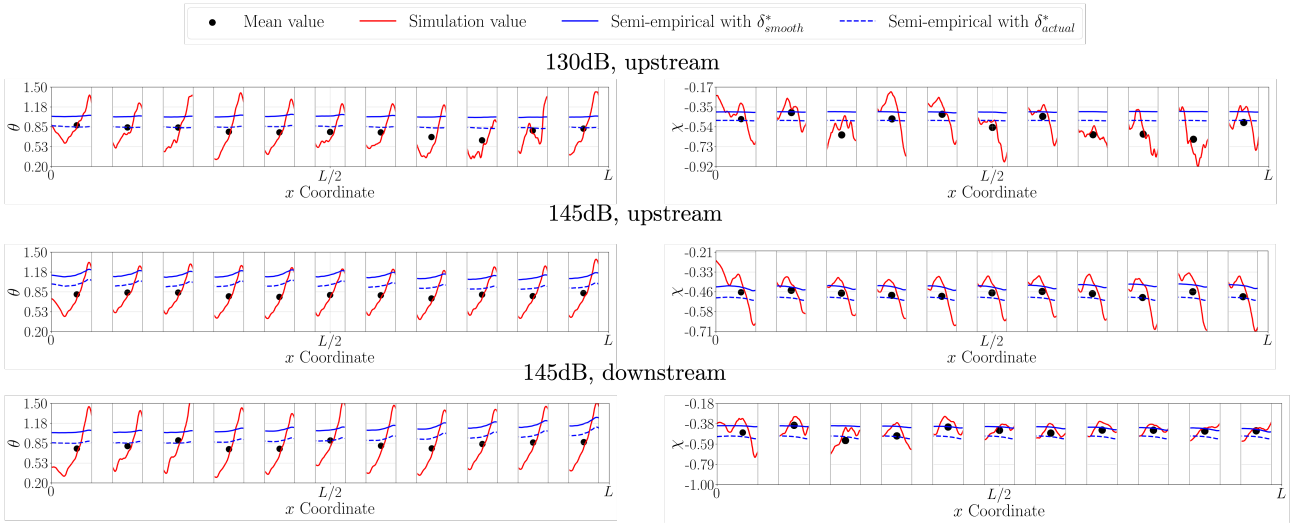


Figure 5: Streamwise distribution of (left) resistance, and (right) reactance along the liner surface for different acoustic wave's SPLs and direction of propagation at fixed $f = 1400$ Hz.

5. ACKNOWLEDGMENTS

The work of A. Paduano and F. Avallone is co-funded by the European Union (ERC, LINING, 101075903). Views and opinions expressed are however those of the author(s) only and do not necessarily reflect those of the European Union or the European Research Council. Neither the European Union nor the granting authority can be held responsible for them. This work was partially supported by the AeroAcoustics Research Consortium (AARC). The AARC is a government-industry partnership supporting pre-competitive research for aircraft noise reduction. J.A. Cordioli gratefully acknowledge funding from Conselho Nacional de Desenvolvimento Científico e Tecnológico (CNPq), project number 407583/2022-0.

6. REFERENCES

[1] S. Mallat, "A theory for multiresolution signal decomposition: the wavelet representation," *IEEE Transactions on Pattern Analysis and Machine Intelligence*, vol. 11, no. 7, pp. 674–693, 1989.

[2] C. Hughes, "The Promise and Challenges of Ultra High Bypass Ratio Engine Technology and Integration," *AIAA Aero Sciences Meeting*, pp. 0–11, 2011.

[3] D. Casalino, A. Hazir, and A. Mann, "Turbofan broadband noise prediction using the lattice boltzmann method," *AIAA Journal*, vol. 56, no. 2, 2018.

[4] R. E. Motsinger and R. E. Kraft, "4 Design and Performance of Duct Acoustic Treatment," in *NASA. Langley Research Center, Aeroacoustics of Flight Vehicles: Theory and Practice. Volume 2: Noise Control*, 1991.

[5] F. Avallone, A. Paduano, L. M. Pereira, L. A. Bonomo, J. A. Cordioli, D. Casalino, and D. Cerizza, "On the comparison of different methods for impedance eduction applied to a numerical database," in *30th AIAA/CEAS Aeroacoustics Conference (2024)*, 2024.

[6] L. A. Bonomo, N. Quintino, J. A. Cordioli, F. Avallone, M. G. Jones, B. M. Howerton, and D. M. Nark, "A Comparison of Impedance Eduction Test Rigs with Different Flow Profiles," in *AIAA AVIATION 2023 Forum*, 2023.

[7] U. Ingård and S. Labate, "Acoustic circulation effects and the nonlinear impedance of orifices," *The Journal of the Acoustical Society of America*, vol. 22, pp. 211–218, 03 1950.

[8] E. J. Brambley, "Well-posed boundary condition for acoustic liners in straight ducts with flow," *AIAA Journal*, vol. 49, no. 6, pp. 1272–1282, 2011.

[9] S. W. Rienstra and M. Darau, "Boundary-layer thickness effects of the hydrodynamic instability along an impedance wall," *Journal of Fluid Mechanics*, vol. 671, p. 559–573, 2011.

[10] Y. Aurégan, R. Starobinski, and V. Pagneux, "Influence of grazing flow and dissipation effects on the acoustic boundary conditions at a lined wall," *The Journal of the Acoustical Society of America*, vol. 109, no. 1, 2001.

[11] Q. Zhang and D. J. Bodony, "Numerical investigation of a honeycomb liner grazed by laminar and turbulent boundary layers," *Journal of Fluid Mechanics*, vol. 792, pp. 936–980, 3 2016.

[12] H. Shahzad, S. Hickel, and D. Modesti, "Turbulence and added drag over acoustic liners," *Journal of Fluid Mechanics*, vol. 965, 6 2023.

[13] B. E. Launder and D. B. Spalding, "The numerical computation of turbulent flows," *Computer Methods in Applied Mechanics and Engineering*, vol. 3, no. 2, 1974.

[14] A. Hazir and D. Casalino, "Effect of temperature variations on the acoustic properties of engine liners," in *23rd AIAA/CEAS Aeroacoustics Conference, 2017*, 2017.

[15] A. Mann, F. Pérot, M. S. Kim, and D. Casalino, "Characterization of acoustic liners absorption using a lattice-Boltzmann method," in *19th AIAA/CEAS Aeroacoustics Conference*, 2013.

[16] F. Avallone, P. Manjunath, D. Ragni, and D. Casalino, "Lattice-boltzmann very large eddy simulation of a multi-orifice acoustic liner with turbulent grazing flow," in *25th AIAA/CEAS Aeroacoustics Conference, 2019*, 2019.

[17] L. A. Bonomo, N. T. Quintino, A. M. Spillere, J. A. Cordioli, and P. B. Murray, "A Comparison of In-Situ and Impedance Eduction Experimental Techniques for Acoustic Liners with Grazing Flow and High SPL," in *28th AIAA/CEAS Aeroacoustics Conference, 2022*, 2022.

[18] P. Dean, "An in situ method of wall acoustic impedance measurement in flow ducts," *Journal of Sound and Vibration*, vol. 34, no. 1, pp. 97–IN6, 1974.

[19] B. Schuster, "A comparison of ensemble averaging methods using Dean's method for in-situ impedance measurements," in *18th AIAA/CEAS Aeroacoustics Conference (33rd AIAA Aeroacoustics Conference)*, 2012.

[20] L. M. Pereira, L. A. Bonomo, N. T. Quintino, A. R. da Silva, J. A. Cordioli, and F. Avallone, "Validation of high-fidelity numerical simulations of acoustic liners under grazing flow," in *AIAA AVIATION 2023 Forum*, 2021.

[21] F. Avallone and D. Casalino, "Acoustic-induced velocity in a multi-orifice acoustic liner grazed by a turbulent boundary layer," in *AIAA Aviation and Aeronautics Forum and Exposition, AIAA AVIATION Forum 2021*, American Institute of Aeronautics and Astronautics Inc, AIAA, 2021.

[22] P. Jaiswal and B. Ganapathisubramani, "Effects of porous substrates on the structure of turbulent boundary layers," *Journal of Fluid Mechanics*, vol. 980, p. A39, 2024.

[23] F. Scarano, M. C. Jacob, and E. R. Gowree, "Drag reduction by means of an array of staggered circular cavities at moderate reynolds numbers," *International Journal of Heat and Fluid Flow*, vol. 102, p. 109142, 2023.

[24] M. Kadivar, D. Tormey, and G. McGranaghan, "A review on turbulent flow over rough surfaces: Fundamentals and theories," *International Journal of Thermofluids*, vol. 10, p. 100077, 2021.

[25] J. Yu, M. Ruiz, and H. W. Kwan, "Validation of Goodrich perforate liner impedance model using NASA langley test data," in *14th AIAA/CEAS Aeroacoustics Conference (29th AIAA Aeroacoustics Conference)*, 2008.

DOI: 10.61782/fa.2025.0742



FORUM ACUSTICUM
EURONOISE 2025

RELEVANCE OF RADIATOR INSTALLATION ON THE EFFICACY OF NOISE REDUCTION STRATEGIES IN AN INDUSTRIAL ENGINE COOLING FAN

Francesco Bellelli* **Renzo Arina** **Francesco Avallone**
Department of Mechanical and Aerospace Engineering, Politecnico di Torino, Torino, Italy

ABSTRACT

Engine cooling fans must be efficient and quieter, as their acoustic contribution is today more noticeable considering the reduced noise from electric motors. Therefore, more effective noise reduction technologies must be designed. This paper investigates how noise reduction technologies, designed for an isolated fan, are impacted by the presence of a radiator pulling upstream. Two modifications to the baseline fan geometry are studied: (i) one with a ring shape that mitigates the backflow-rotor interaction and (ii) one with stator vane azimuthal spacing optimized to reduce rotor-stator interaction tonal noise. They are assessed with high-fidelity simulations performed both on an isolated fan and a full cooling module including the radiator, which is simulated using an equivalent porous medium. Results reveal that the modified ring shape effectively prevents backflow-rotor interaction on the isolated fan, reducing broadband noise by radially redirecting the backflow. However, its performance is less effective when a radiator is present due to the presence of the casing. Conversely, stator vane optimized spacing shows robust noise reduction in both configurations, because the effect of distributing tonal energy across several modes is not altered by the presence of the radiator.

Keywords: *Radiator, installation, fan, noise sources, noise reduction*

**Corresponding author*: *francesco.bellelli@polito.it.*
***Copyright**: ©2025 Francesco Bellelli et al. This is an open-access article distributed under the terms of the Creative Commons Attribution 3.0 Unported License, which permits unrestricted use, distribution, and reproduction in any medium, provided the original author and source are credited.*

1. INTRODUCTION

With the transition to electric motors, reducing car component noise emissions has become a critical focus. This shift has led the scientific community to investigate several conventional [1] and bio-inspired [2] noise reduction strategies.

One of the main noise contribution for low-speed fans is tip-clearance noise, generated by coherent vortex structures present in the tip-gap region [3]. Tip-clearance noise is usually mitigated by introducing a rotating ring [4] to prevent the formation and growth of coherent structures responsible for sub-harmonic humps. However, a rotating ring may generate unwanted flow patterns if the fan is subjected to a pressure rise, causing backflow end increasing unsteady loading noise. It has been demonstrated that rotor-backflow interaction is a major source of unsteady loading noise even at design conditions [5, 6]. Strategies such as tailored short ducts [7], porous leading edges [8], or serrated bio-inspired designs [9] have been conceived to mitigate this noise source, albeit they increase high-frequency broadband noise.

Rotor-stator interaction is another significant noise source [10] for fans. If the rotor-stator axial clearance is short, aerodynamic potential effect dominates over wake impingement [11]. Geometrical azimuthal inhomogeneities might increase noise [12] and give rise to additional azimuthal pressure modes. Unevenly spacing the vanes with specific modulations, as done by Duncan [13] and Mellin-Sovran [14], is a typical solution. However, these approaches act only in a discrete fashion on the vanes spacing, eventually discarding optimal solutions, as repoted in Ref. [15].

A comprehensive understanding of how these strategies influence backflow-rotor interactions still deserves

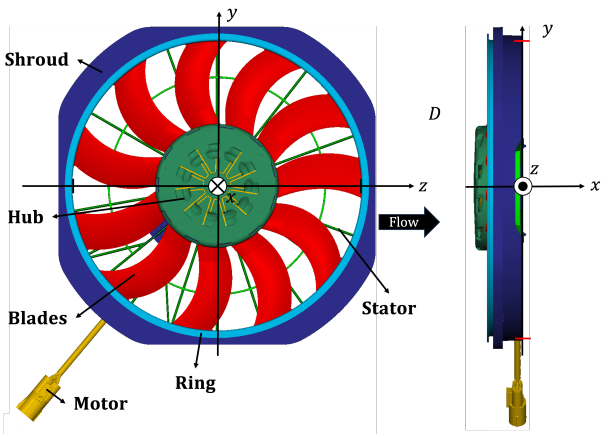


Figure 1: Tested automotive engine fan. The main parts in which the fan consists are shown with different colors.

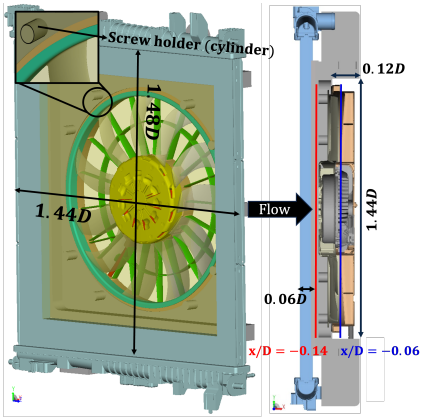


Figure 2: Tested radiator. The heat exchanger is shown in light blue (solid part) and yellow (coolant tubes part), while the square casing is shown in grey.

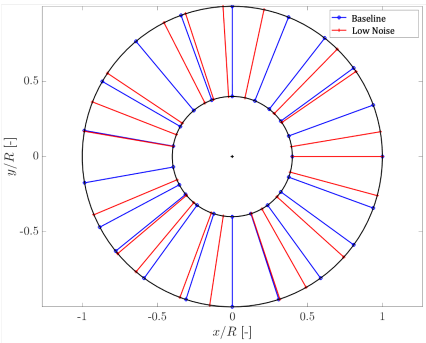


Figure 3: Baseline and low-noise stator-vane azimuthal distributions.

further studies. Deterministic unsteady loading contributions such as non-viscous rotor-stator interaction are rarely addressed, and optimization procedures to mitigate these effects are almost absent. Finally, most noise reduction techniques are evaluated on isolated fans rather than on the real installed configuration. This must be considered when the same casing, for the fan and the radiator, is used to test different configurations [16]. This aspect is expected to impact the efficacy of noise reduction techniques when applied to a baseline fan.

This paper examines numerically the influence of shape modifications of the rotating ring to mitigate the backflow-rotor interaction noise and explores the effects of stator-vane uneven spacing to minimize rotor-stator interaction tonal noise. Furthermore, the paper considers how the radiator installation impacts the performance of noise reduction strategies in typical operations.

2. FAN AND RADIATOR GEOMETRY

The fan consists of a 465 mm diameter (D) rotor with $B = 11$ unevenly spaced blades connected to a ring, a hub, a driving electrical motor, $N_v = 20$ unevenly spaced stator-vane, and a shroud, as shown in Fig. 1. The fan tip-clearance is equal to $0.009D$. The radiator consists of a heat exchanger of $1.44D \times 1.48D$ placed $0.02D$ upstream of the fan hub and of a square casing that joins it to the fan, as shown in Fig. 2.

A first modification to the ring geometry was performed with the scope of preventing the backflow to interact with the blades. The ring shape was modified to further redirect the backflow from the blades. The axial spacing between the ring and stator-vane was reduced by 30% to mitigate adverse flow in the tip-clearance. The shroud was shifted forward in the x direction of the top structure to keep constant the axial spacing with respect to the ring.

A second modification concerned the stator vane azimuthal distribution. The spacing was designed following the random spacing approach as described in Ref. [15]. This allows to redistribute more efficiently the acoustic energy of the rotor-stator interaction tones. In Fig. 3 the baseline and low-noise stator-vane azimuthal distributions are represented.

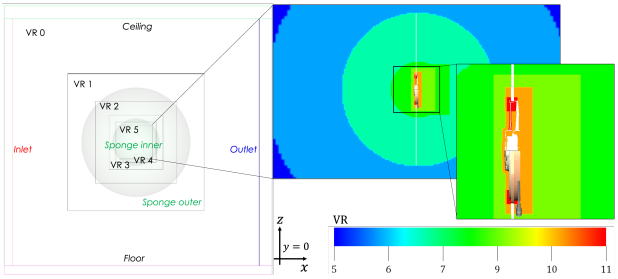


Figure 4: Sketch of the computational domain in the plane at $y/D = 0$.

3. NUMERICAL SETUP

Simulations have been performed with the commercial software 3DS PowerFLOW version 6, based on the lattice-Boltzmann method (LBM) [17].

The computational domain used to simulate all the configurations is shown in Fig. 4. A large fluid domain of $135D \times 135D \times 135D$ was built to simulate a free-field environment that encloses the fan. The ceiling and the floor of the simulation domain were modelled as a solid reflecting wall, while both inlet and outlet had a static ambient pressure boundary condition. A discretization strategy based on 11 Variable Resolution (VR) regions was adopted. The regions with maximum resolutions were set around the rotating blades and near the tip gap region, where there are 11 voxels in the tip-clearance. The resolution in the tip gap region was similar to the one adopted by Avallone et al. [18]. The voxel size between one VR region and the adjacent one was doubled. In the VR3 region, a sponge region was defined by an artificial change of viscosity of a factor of 100, with an exponential function between the inner and outer region, as outlined in Fig. 4. Both the increase in voxel size and the sponge region were used to mitigate reflections of acoustics waves at the domain boundaries.

In the isolated fan configuration, an anechoic wall separating the two environments was introduced so that a pressure rise Δp across the fan could be imposed [6]. The fan maximum efficiency point was simulated, corresponding to a load coefficient of $\psi = \frac{\Delta p}{\frac{1}{2}\rho v_{tip}^2} = 0.14$, where ρ is the ambient density and v_{tip} is the tip velocity, and a flow coefficient of $\varphi = \frac{\dot{V}}{\pi(R_{tip}^2 - R_{hub}^2)v_{tip}} = 0.10$, where $\dot{V}$ is the volume flow rate through the fan. R_{tip} and R_{hub} are respectively the tip and hub radii. In the full cooling module configuration, the heat exchanger was modelled as an equivalent porous medium [19]. No pressure difference was imposed in this configuration, as the equivalent porous medium provided the fan with a pressure loss which corresponded roughly to the maximum efficiency point of the complete cooling module system.

A physical time of 20 revolutions was simulated at a resolution of 1200 voxel per diameter (vox/D) in the finest VR region. A grid resolution study was performed on this setup in a previous work [6]. Data was saved only during the last 10 revolutions. Two planes parallel to the fan were sampled at $x/D = -0.14$ and $x/D = -0.06$ to compute averaged flow fields. The locations correspond respectively to the rotating ring upstream boundary and the rotor-stator interstage. Pressure on all the solid surfaces of the cooling module was sampled at a frequency of $48,000\,Hz$ and the volume flow rate was sampled, at the same frequency, on a plane at $x = 0/D$. Finally, a fully circular array of 12 equally spaced far-field probes, located in the plane $z/D = 0$ at a radius $r/D = 2.15$ far from the fan centre, was used to sample directly the acoustic field from the simulations. The spectral content of the signals was computed through the Welch averaging algorithm [20] with 8 Hamming windows and 50% of overlap, resulting in a frequency resolution of $11.8\,Hz$.

4. RESULTS

4.1 Isolated fan

ΔT [%]	$\Delta \dot{V}$ [%]	ΔQ [%]	$\Delta \eta$ [%]
+2.0	+6.4	+10.9	-6.0

Table 1: Aerodynamic performance variation between the baseline and low-noise geometries in the isolated fan configurations.

First, the effects of the proposed noise reduction strategies on the aerodynamic performance is discussed. In Tab. 1 the variations of axial thrust force (T), volume flow rate through the fan ($\dot{V}$), aerodynamic torque (Q), and aerodynamic efficienc of the low-noise geometry with respect to the baseline geometry are reported. The efficiency is calculated as

$$\eta = \frac{\frac{T}{\pi(R_{tip}^2 - R_{hub}^2)}\dot{V}}{Q\Omega}, \tag{1}$$

where Ω is the fan rotational speed in rad/s. The low-noise configuration displays an increase of both thrust and

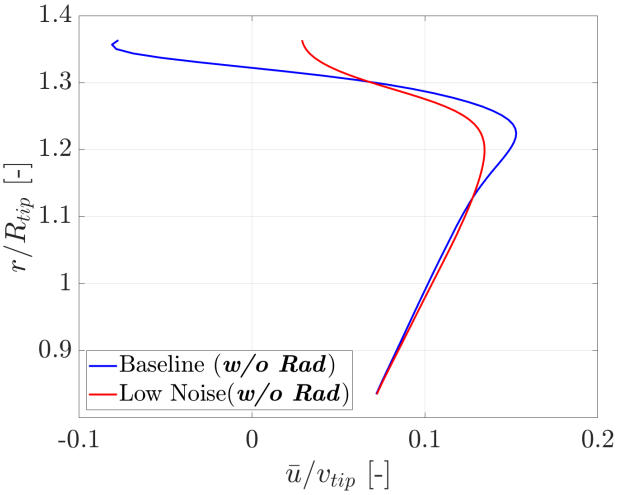


Figure 5: Mean axial velocity in the near-tip region ($0.8 \leq r/R_{tip} \leq 1.1$), at $x/D = -0.14$, azimuthally averaged.

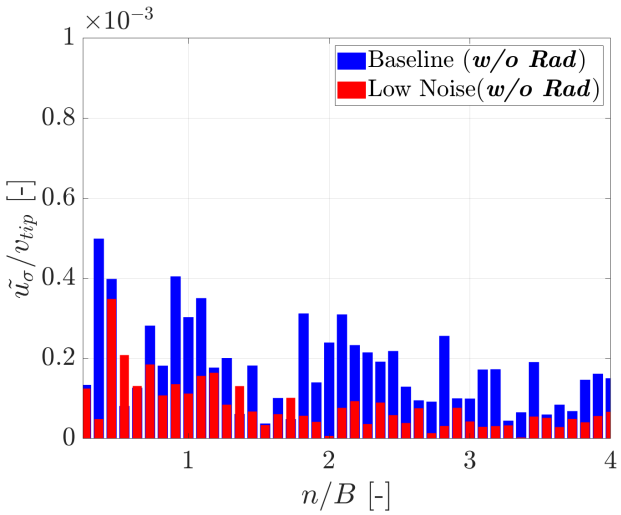


Figure 6: Azimuthal mode decomposition of the axial velocity root mean square (rms) sampled on a fully circular line at $r/R_{tip} = 0.9$ in a plane located at $x/D = -0.14$. n is the mode order and B is the number of rotor blades.

torque due to the increase of aerodynamic surface, as well as an increase of volume flow rate through the fan that can be explained with a decrease in backflow. However, both the increase in thrust and flow rate cannot compensate the increase in torque, leading to an aerodynamic efficiency reduction.

The impact of the ring shape on the upstream flow is analyzed. In Fig. 5 the time and azimuthally averaged axial velocity sampled on a plane at $x/D = -0.14$ is shown. The velocity is made dimensionless with the tip velocity. It is observed that the low-noise configuration reduces the velocity gradient in the region $1.1 \leq r/R_{tip} \leq 1.4$; $\bar{u}/v_{tip}$ does not attain negative values on the low-noise configuration, proving absence of the backflow.

The azimuthal mode decomposition of the axial velocity root mean square is shown in Fig. 6. The quantity is sampled on a plane at $x/D = -0.14$ and along a circular line at $r/R_{tip} = 0.9$. Results confirm previous observations, as the low-noise configuration is characterized by a considerable decrease in the axial velocity modal content among all the frequencies of interest. This is associated with the redirection of the backflow achieved by the modified ring geometry, reducing blade-backflow interaction.

The relevance of stator-vane azimuthal distribution is now discussed by looking at the azimuthal mode decomposition of the mean axial velocity in Fig. 7. The velocity is sampled on a plane at $x/D = -0.06$, which cor-

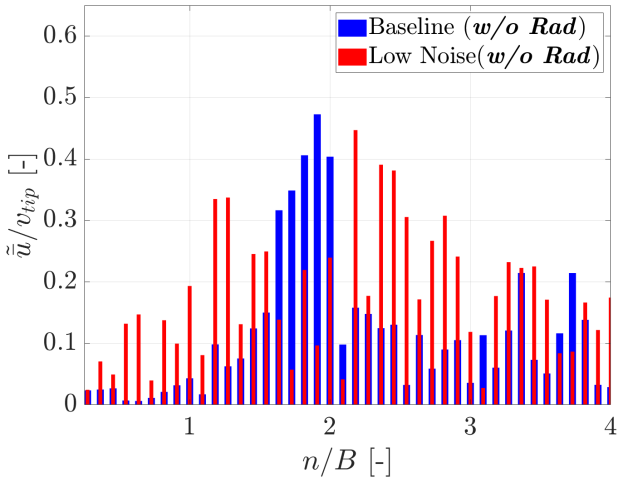


Figure 7: Azimuthal mode decomposition of the mean axial velocity sampled on a fully circular line at $r/R_{tip} = 0.7$ in a plane located at $x/D = -0.06$.

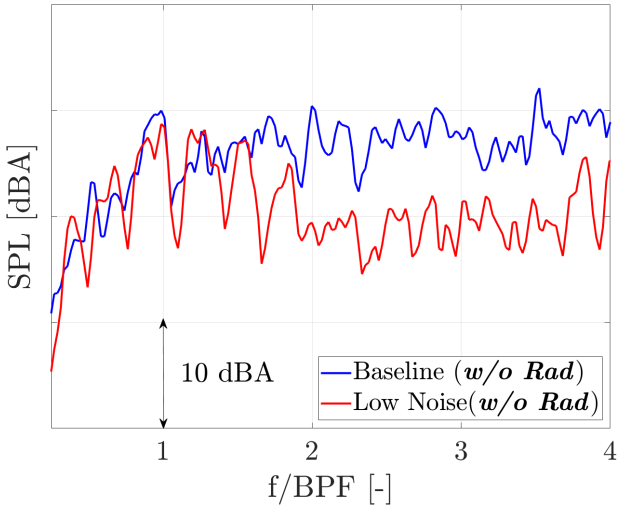


Figure 8: Pressure fluctuations at $x/D = -2.15$, $y/D = 0$, and $z/D = 0$.

responds to the rotor-stator interstage, and on a circular line located at $r/R_{tip} = 0.7$. The low-noise configuration positively contributes to the redistribution of energy among several other modes n. In particular, the low-noise configuration can substantially reduce the modal content in the range $1.5 \leq n/B \leq 2$, which has been previously shown by the authors [6] to be critically dominated by aerodynamic potential rotor-stator interaction on this fan configuration.

Finally, the efficacy of the proposed noise reduction strategies is discussed in Fig. 8, where the spectra of sound pressure fluctuations sampled at $x/D = -2.15$, $y/D = 0$, and $z/D = 0$ are shown in terms of Sound Pressure Level (SPL). The probe lies on the fan rotational axis, at a distance of $2.15D$ upstream of the fan. The frequency axis is made dimensionless with the blade passing frequency ($BPF = \omega B$, where ω is the fan rotational frequency in Hz). The spectrum clearly shows that the low-noise configuration is characterized by a considerable decrease in broadband content for $f/BPF \geq 1.5$. This improvement is attributed to the absence of backflow-rotor interaction in the low-noise configuration, achieved through the modified ring shape that redirects the backflow far from the blades. Moreover, it should be noted that also the tonal content of the low-noise configuration is reduced, especially in the range $1.5 \leq f/BPF \leq 2$, as a result of the optimized vane distribution. Both noise reduction strategies led to a decrease in Overall Sound Pressure Level (OASPL) of about $4.9\,dBA$.

ΔT [%]	$\Delta \dot{V}$ [%]	ΔQ [%]	$\Delta \eta$ [%]
-0.4	-2.6	+2.9	-5.7

Table 2: Aerodynamic performance variation between the baseline and low-noise geometries in the full cooling module configurations.

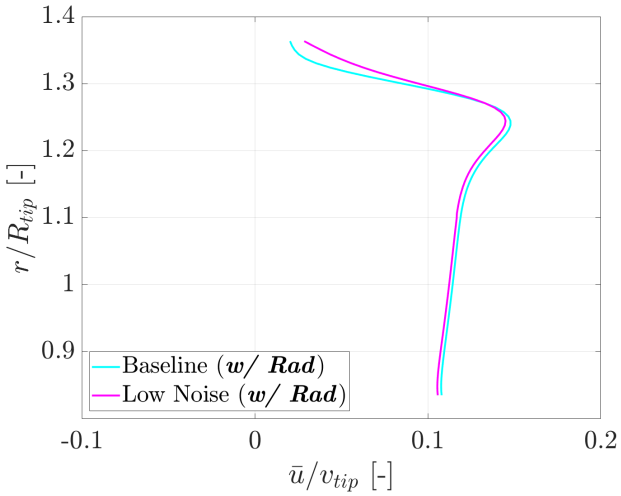


Figure 9: Mean axial velocity in the near-tip region ($0.8 \leq r/R_{tip} \leq 1.1$), at $x/D = -0.14$, azimuthally averaged.

4.2 Full cooling module

The variations in aerodynamic performance for the full cooling module baseline and low-noise configurations is assessed in Tab. 2. Overall, the low-noise geometry results in smaller variations of almost every investigated quantity. The thrust is mainly unaltered and the torque is only slightly increased. However, the volume flow rate through the fan is decreased, unlike the isolated fan configurations. This is due to a different flow physics associated with the backflow when considering the radiator installation. These differences in aerodynamic quantities lead to an aerodynamic efficiency decrease less important than the one for the isolated fan configurations (Tab. 1).

In Fig. 9 the time and azimuthally averaged axial velocity sampled on a plane at $x/D = -0.14$ is shown for the full cooling module configurations. The baseline and low-noise configurations have an almost identical spanwise trend of mean axial velocity near the tip, with a sub-

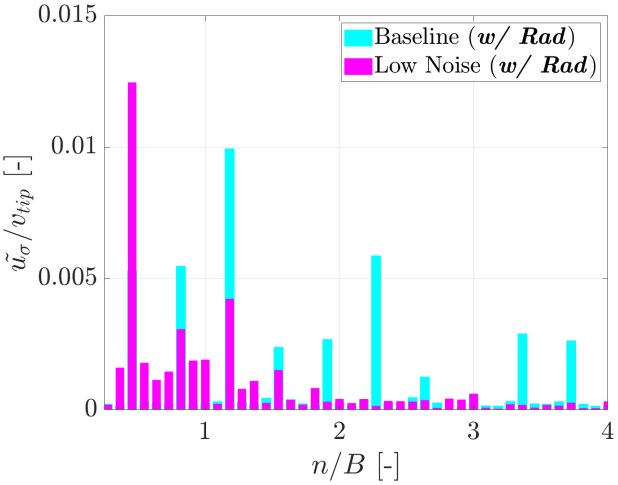


Figure 10: Azimuthal mode decomposition of the axial velocity root mean square (rms) sampled on a fully circular line at $r/R_{tip} = 0.9$ in a plane located at $x/D = -0.14$.

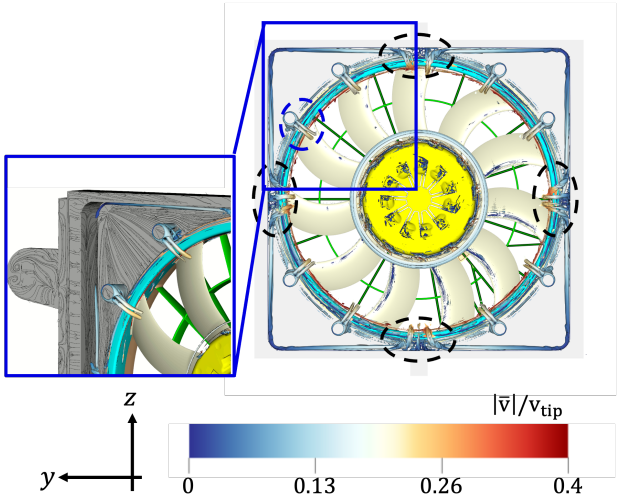


Figure 11: Mean $\Lambda_2 = -2.5 \cdot 10^5 1/s$ iso-surfaces coloured with velocity magnitude in the upstream casing for the baseline configurations.

stantial reduction of the mean axial velocity gradient with respect to the isolated fan, as seen in Fig. 5. This is associated with the presence of the equivalent porous medium, that has been previously shown by the authors [21] to locate the pressure losses on the fan disk up to $r/R_{tip} \leq 0.9$.

The azimuthal mode decomposition of the axial velocity root mean square at $x/D = -0.14$ and $r/R_{tip} = 0.9$ is shown in Fig. 10. It is observed an increase in the low frequency modal content up to $n/B \leq 2$ which is associated with the highly limited space in the radial extent due to the presence of the casing. This prevents the backflow to be radially redirected. Conversely, a stronger recirculation takes place in the casing upstream of the fan and is expected to negatively influence the acoustic performance of the system. The highly tonal content observed in both the baseline and low-noise configurations is instead associated with periodic recirculation spot in the casing that are due to the flow distortion induced by the square-to-round shape transition from the casing to the fan and by the presence of several cylindrical screw holders that are present in the casing. These features in the flow field are outlined for the baseline configuration only in Fig. 11, where $\Lambda_2 = -2.5 \cdot 10^5 1/s$ iso-surfaces are shown, colored by velocity magnitude.

In Fig. 12 the azimuthal mode decomposition of the mean axial velocity at $x/D = -0.06$ and r/R_{tip} shows that the stator-vane distribution is consistently able

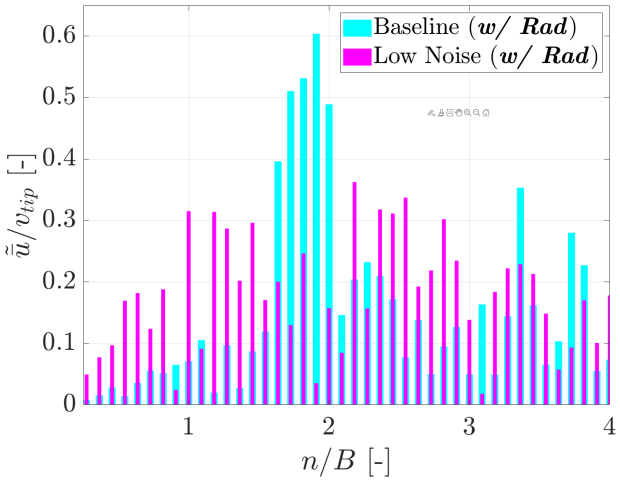


Figure 12: Azimuthal mode decomposition of the mean axial velocity sampled on a fully circular line at $r/R_{tip} = 0.7$ in a plane located at $x/D = -0.06$.

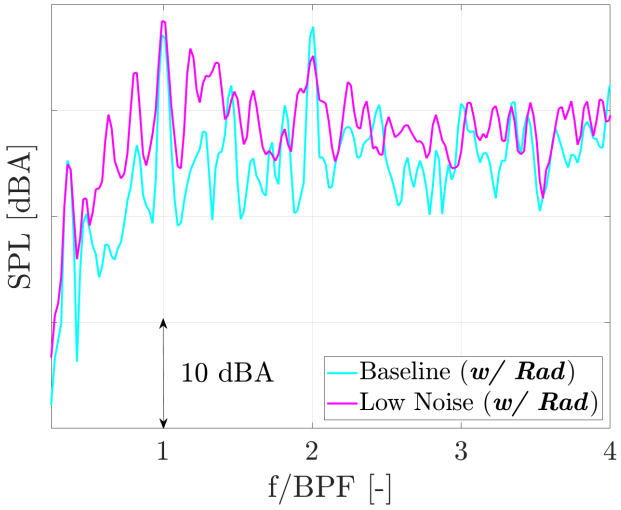


Figure 13: Pressure fluctuations at $x/D = -2.15$, $y/D = 0$, and $z/D = 0$.

to reduce the prominence of single modes n by heterogeneously distribute the energy, as seen also in Fig. 7 for the isolated fan configurations. As a matter of fact, the radiator installation does not influence the flow physics in the interstage between rotor and stator, leading to considerably similar results between the isolated fan and the full cooling module configurations.

In Fig. 13 the spectra of sound pressure fluctuations sampled at $x/D = -2.15$, $y/D = 0$, and $z/D = 0$ are shown. The probe location is upstream of both the fan and the radiator. The low frequency ($0.5 \leq f/BPF \leq 2$) broadband content of the low-noise configuration is higher than the baseline configuration, meaning that the modification on the ring shape is not consistently able to reduce the backflow-rotor interaction noise contribution. This results in a higher noise contribution in the low frequency range. From $f/BPF \geq 2$ the broadband content is similar to the baseline configuration. Nevertheless, the tonal content of the low-noise configuration is consistently lower than the baseline configuration, as a result of the stator-vane redistribution. It has been shown in Fig. 12 that the vanes are not influenced by the presence of the upstream radiator. The OASPL is increased by $2.5\,dBA$ because of the broadband content increase.

5. CONCLUSIONS

Two modifications to the baseline geometry of an engine cooling fan are studied: one with a ring shape that mitigates the backflow-rotor interaction and one with stator vane's spacing optimized to reduce rotor-stator interaction tonal noise. They are investigated on an isolated fan and a full module where the radiator is simulated as an equivalent porous medium. Results revealed that the proposed noise reduction strategies slightly reduced the aerodynamic performance, mainly because of the increased aerodynamic surface of the modified ring shape that led to a drastic increase in torque. The low-noise ring prevented backflow-rotor interaction on the isolated fan, but showed poor performance when the radiator is present because of its casing. On the other hand, stator vane spacing showed robust noise reduction in both configurations since the effect of distributing tonal energy across several modes is not altered by the presence of the radiator upstream. Results shown in this paper highlight the importance of considering the radiator installation when designing possible noise reduction strategies, especially when the flow physics exploited to reduce noise can be substantially altered by the presence of the radiator.

6. REFERENCES

[1] M. Piwowarski and D. Jakowski, "Areas of Fan Research—A Review of the Literature in Terms of Improving Operating Efficiency and Reducing Noise Emissions," *Energies*, vol. 16, p. 1042, Jan. 2023.

[2] W. Zhou, P. Zhou, C. Xiang, Y. Wang, J. Mou, and J. Cui, "A Review of Bionic Structures in Control of Aerodynamic Noise of Centrifugal Fans," *Energies*, vol. 16, p. 4331, May 2023.

[3] T. Zhu, D. Lallier-Daniels, M. Sanjosé, S. Moreau, and T. Carolus, "Rotating coherent flow structures as a source for narrowband tip clearance noise from axial fans," *Journal of Sound and Vibration*, vol. 417, pp. 198–215, Mar. 2018.

[4] F. Han, X. Chen, Y. Yang, and C. Wang, "Numerical and Experimental Study on the Effect of Rotor–Stator Distance on Rotor–Stator Interaction Strength within Mixed-Flow Centrifugal Pumps," *Journal of Marine Science and Engineering*, vol. 10, p. 1114, Aug. 2022.

[5] S. Magne, S. Moreau, and A. Berry, "Subharmonic tonal noise from backflow vortices radiated by a low-speed ring fan in uniform inlet flow," *The Journal of*

the Acoustical Society of America, vol. 137, pp. 228–237, Jan. 2015.

[6] F. Bellelli, R. Arina, and F. Avallone, "On the impact of operating condition and testing environment on the noise sources in an industrial engine cooling fan," *Applied Acoustics*, vol. 227, p. 110252, Jan. 2025.

[7] Z. Sun, J. Tian, T. Zhang, Z. Du, and H. Ouyang, "Cooling fan aerodynamic noise reduction with short inlet duct and its applicability," *International Journal of Refrigeration*, vol. 148, pp. 117–130, Apr. 2023.

[8] C. Teruna, L. Rego, D. Casalino, D. Ragni, and F. Avallone, "A Numerical Study on Aircraft Noise Mitigation Using Porous Stator Concepts," *Aerospace*, vol. 9, p. 70, Jan. 2022.

[9] Z. Liang, J. Wang, W. Wang, B. Jiang, Y. Ding, and W. Qin, "Numerical and Experimental Investigations of Axial Flow Fan with Bionic Forked Trailing Edge," *Machines*, vol. 11, p. 155, Jan. 2023.

[10] J. M. Tyler and T. G. Sofrin, "Axial Flow Compressor Noise Studies," in *Pre-1964 SAE Technical Papers*, vol. Pre-1964 SAE Technical Papers, p. 620532, Jan. 1962.

[11] E. Canepa, A. Cattanei, and F. Mazzocut Zecchin, "Effect of the rotor–stator gap variation on the tonal noise generated by axial-flow fans," *Applied Acoustics*, vol. 94, pp. 29–38, July 2015.

[12] M. Pestana, M. Sanjosé, S. Moreau, M. Roger, and M. Gruber, "Investigation on the noise of an axial low mach-number fan stage with a heterogeneous stator," *FAN 2018*, 2018.

[13] P. Duncan and B. Dawson, "Reduction of interaction tones from axial flow fans by suitable design of rotor configuration," *Journal of Sound and Vibration*, vol. 33, pp. 143–154, Mar. 1974.

[14] R. C. Mellin and G. Sovran, "Controlling the Tonal Characteristics of the Aerodynamic Noise Generated by Fan Rotors," *Journal of Basic Engineering*, vol. 92, pp. 143–154, Mar. 1970.

[15] A. Cattanei, F. Mazzocut Zecchin, A. Di Pasquali, and A. Lazari, "Effect of the uneven blade spacing on the noise annoyance of axial-flow fans and side channel blowers," *Applied Acoustics*, vol. 177, p. 107924, June 2021.

[16] M. Sortor, "On-System Engine Cooling Fan Measurement as a Tool for Optimizing Cooling System Airflow Performance and Noise," *SAE International Journal of Materials and Manufacturing*, vol. 4, pp. 1221–1230, Apr. 2011.

[17] X. He and L.-S. Luo, "Theory of the lattice Boltzmann method: From the Boltzmann equation to the lattice Boltzmann equation," *Physical Review E*, vol. 56, pp. 6811–6817, Dec. 1997.

[18] F. Avallone, D. Ragni, and D. Casalino, "On the effect of the tip-clearance ratio on the aeroacoustics of a diffuser-augmented wind turbine," *Renewable Energy*, vol. 152, pp. 1317–1327, June 2020.

[19] M. Piellard, B. B. Coutty, V. Le Goff, V. Vidal, and F. Perot, "Direct aeroacoustics simulation of automotive engine cooling fan system: effect of upstream geometry on broadband noise," in *20th AIAA/CEAS Aeroacoustics Conference*, (Atlanta, GA), American Institute of Aeronautics and Astronautics, June 2014.

[20] P. Welch, "The use of fast Fourier transform for the estimation of power spectra: A method based on time averaging over short, modified periodograms," *IEEE Transactions on Audio and Electroacoustics*, vol. 15, pp. 70–73, June 1967.

[21] F. Bellelli, R. Arina, S. Moreau, and F. Avallone, "Aeroacoustics analysis of radiator installation effects in a pulling engine cooling module," in *FAN2025 Conference*, FAN2025 Conference, Apr. 2025.

DOI: 10.61782/fa.2025.0761



FORUM ACUSTICUM
EURONOISE 2025

ROTOR NOISE CONTROL USING COAXIAL CO-ROTATING ROTORS.

Charles E. Tinney[1†] **Yingjun Zhao-Dubuc**[1] **John Valdez**[1]
[1] Applied Research Laboratories, University of Texas at Austin, Austin, Texas, USA
https://www.arlut.utexas.edu/gdl

ABSTRACT

The development of a low-noise rotor blade has received considerable attention in recent years due to emerging interests in electric vertical take-off and landing (eVTOL) vehicles. One of the most impact-full methods for reducing the acoustic footprint from multirotor platforms is by augmenting the angular phase between neighboring rotors so that sound waves interfere either constructively or destructively for an observer in the far-field. For stacked, co-rotating rotors operating in hover, this form of noise control has been shown to augment rotor performance, thereby providing a trade-space between changes in noise, versus changes in performance. Here we evaluate the same trade-space using a combination of low-order analysis methods capable of filtering out the most energetic waveforms that make up the sound field of this rotor. This combines the conventional form of the proper orthogonal decomposition (POD) with vold-kalman filters (VKF) to filter structures in both space and time, respectively. The findings show that for an observer located below the rotor disk plane, sound pressure levels corresponding to the first few blade pass frequency harmonics can be reduced by as much as 4 dB with only moderate losses in hover efficiency.

Keywords: *Drone noise, eVTOL, UAM, AAM, co-rotating rotors, rotor noise control, proper orthogonal decomposition, Vold-Kalman filters.*

**Corresponding author*: ✉ *charles.tinney@arlut.utexas.edu.*
***Copyright**: ©2025 The authors. This is an open-access article distributed under the terms of the Creative Commons Attribution 3.0 Unported License, which permits unrestricted use, distribution, and reproduction in any medium, provided the original author and source are credited.*

1. BACKGROUND

Most studies concerned with the acoustics of multirotor platforms focus on side-by-side configurations with or without synchrophase control. The coaxial (stacked), co-rotating rotor is another multirotor configuration that, unlike the traditional side-by-side setup, ha an acute sensitivity to both performance and acoustics on account of changes to rotor operating conditions. As such, the co-rotating offers a much more promising approach for controlling rotor noise through the constructive and destructive interference (CDI) of sound waves generated by neighboring rotors. These sources of noise are the result of thickness noise and blade loading noise, which are impulsive (unlike rotor broadband noise), and are the key drivers of community annoyance. In 2018, a number of initiates began at the Applied Research Laboratories, The University of Texas at Austin (ARL:UT) to study this trade-space with key findings being published in a number of conference papers [1, 2] and journal articles [2–4]. This paper serves to review the highlights of these findings, while providing new results for the interested reader. Other efforts to characterize the hover performance and acoustics of stacked rotors can be found in the literature [5, 6].

2. HARDWARE AND SETUP

Measurements were performed in the Gas Dynamics Laboratory (GDL) at ARL:UT near standard sea level conditions ($p_\infty = 14.7$ psia (103,325 Pa), $T_\infty = 526$ R (292 K), $\rho = 2.34 \times 10^{-}3$ slug/ft^3 and $a_\infty = 1.126 \times 10^3$ ft/s). A description of the GDL can be found here: `https://www.arlut.utexas.edu/gdl/` and is a 24 ft tall acoustically treated facility enclosing $\dot{V} = 30,100$ ft^3 of open air space over 1,500 ft^2 of floor space. The performance and acoustics of various rotor platforms covering

Table 1. Definitions for rotor index angle ϕ [deg] and rotor lead/lag φ [deg].

j	1	2	3	4	5	6
ϕ_j [deg]	12	30	48	66	84	102
φ_j [deg]	12	30	48	66	84	-78
k	7	8	9	10	11	
ϕ_j [deg]	120	138	156	174	192	
φ_j [deg]	-60	-42	-24	-6	12	

a range of scales have been tested over the years at the GDL, [7,8]. For now, we will concentrate on a stacked co-rotating configuration using model 18×5.5 MR-P blades ($D = 18$ in.) manufactured by APC Propellers. These blade shapes are highly twisted and are inverted with the rotor disk plane elevated 105 inches from the laboratory floor so that the thrust vector points down. This equates to a distance of sixteen rotor diameters between the rotor disk plane and the virtual floor (ceiling) to reduce ground effects.

The upper blade assembly was designed so that changes to both rotor index angle (angle between upper and lower rotors ranging between $\phi_1 = 12$ deg and $\phi_{11} = 192$ deg with $\delta\phi = 18$ deg increments) and stacking distances between rotors could be tightly controlled. Table 1 lists the notation used to identify the differences between index angle (ϕ_j) and lead/lag angle (φ_j) where φ is positive when the upper rotor is leading the lower rotor in the direction of rotation. The third variable of interest is rotor rotation speed, which varied from $\omega = 50$ rotations per second (RPS) to 90 rps, in 10 rps increments. Only the $\omega = 90$ rps and $\delta z/D = 0.061$ condition will be evaluated here and corresponds to a blade chord Reynolds number at $r = 0.75R$ of $\mathrm{Re}_{c75} = 1.9 \times 10^5$ and a blade tip Mach number valued at 0.38. An illustration of the upper assembly with rotor blades is shown in Fig. 1a.

3. ROTOR PERFORMANCE

Several instruments were used to understand the mechanisms governing the trade-space between hover performance and acoustics, and the effect of synchrophasing on rotor noise control. The first of these was a Futek model MBA500 bi-axial load cell for measuring axial thrust and torque with reported errors of 0.125 lbf and 0.125 in-lbf, respectively. Thrust coefficient $C_T = F_z/(\rho A \Omega^2 R^2)$, torque coefficient $C_\tau = \tau/\rho A_d (\Omega R)^2 R$, and rotor figure

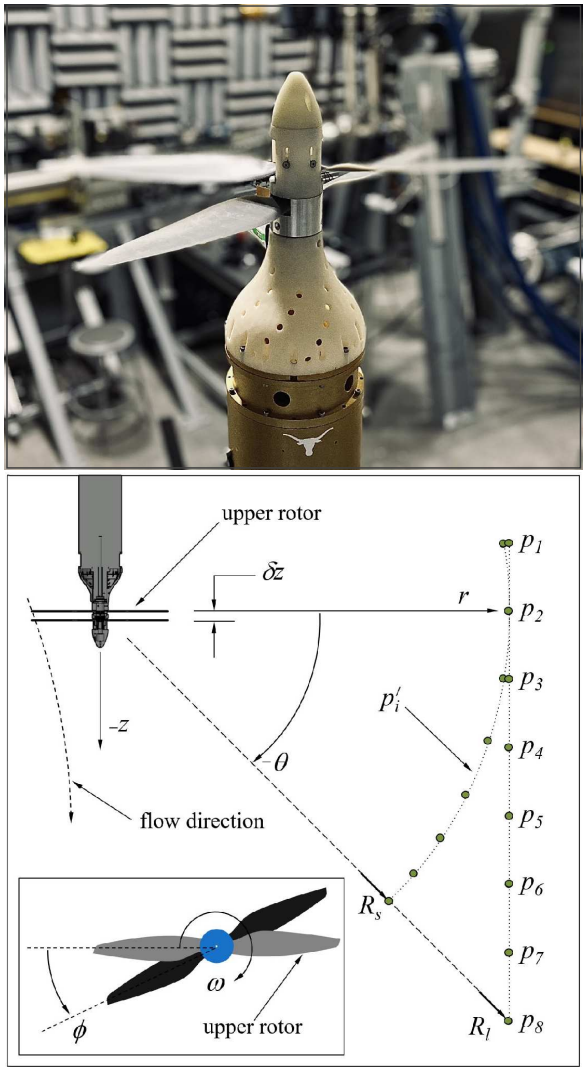


Figure 1. a) The coaxial, co-rotating rotor used by Tinney and Valdez [1] with APC propeller models 18×5.5 MR(P) b) Orientation of rotor test stand with coordinate system.

of merit $FM = C_T^{3/2}/\sqrt{2}/C_\tau$, were calculated for each test case where $R = D/2$ is rotor radius, $A = \pi D^2/4$ is rotor disk area and Ω is motor rotation speed in rad/s ($\Omega = 2\pi\omega$). In Fig. 2a, thrust coefficient and torque coefficient are reported for the 90 rps rotor speed and with systematic changes to rotor index angle. Rotor efficiency is reported in Fig.2b and is typical of rotors of this scale [7]. The findings demonstrate the key features of the stacked, co-rotating rotor. The first is that changes in rotor index

angle have a profound impact on hover performance and that the optimum hover performance is achieved when the upper rotor lags the lower rotor. This occurs for this rotor configuration around $\varphi = -30$ deg.

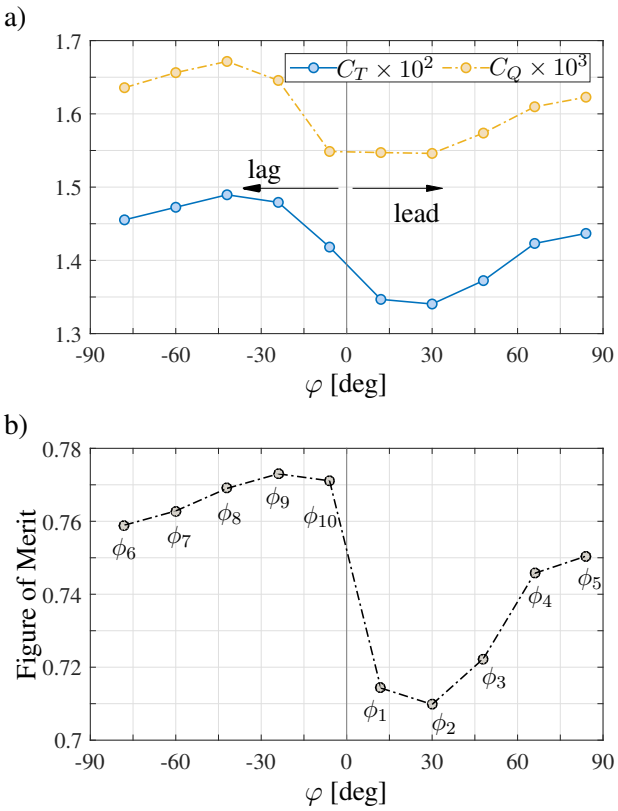


Figure 2. a) Thrust coefficient, torque coefficient, and b) rotor figure of merit at 90 rps rotor speed.

4. ROTOR WAKE AND SLIPSTREAM

A single camera PIV system mounted to a two-stage linear traverse was then used to measure the wake and slipstream boundaries generated by the stacked rotor [3]. The measurement window was oriented to capture vortices from both the upper and lower blades including provisions for wander. The principal components of the PIV system comprised a Nd-YAG laser, a single 2M pixel CCD camera operating at sample rate of 7 Hz (double frame mode), as well as a PIVTEC 14 Laskin nozzle seeder for generating 0.1 to 1.0μm size olive oil particles. A total of 250 statistically independent image pairs were captured for each of the 37 wake ages ($0° \leq \psi \leq 360°$ deg in increments of $\Delta\psi = 10$ deg) and all eleven index angles thereby resulting in a total of 101,750 image pairs that were converted to vector maps using DaVis v.10.1. The location of the slipstream boundary was identified using the Γ_1-method to correct for vortex jitter. Numerous reviews on both integral-based and divergence-based schemes for characterizing vortex jitter are provided by Mula et al. [9] and the references therein.

A sample result from the PIV system is shown in Fig. 3 for the stacked rotor operating at 90 rps with $\delta z/D = 0.061$ and $\phi_1 = 12$ deg. At each wake age, small grey symbols identify the instantaneous locations of jittering vortices from all snapshots, followed by the average value (large color symbols). Lines are drawn connecting the trajectory of vortices generated by the upper and lower rotors with increasing wake age. The full PIV database is then compiled to identify the flow mechanisms responsible for effecting changes to hover performance. This is accomplished by evaluating the miss distance between the upper rotor vortices with the lower rotor blade, which is plotted in Fig. 4. Here, the solid symbols are from direct measurements while open symbols are extrapolated from trajectories of the vortex using the last known measurements from that index angle. The findings demonstrate that for a given rotor speed, index angle and stacking distance of the co-rotating rotor, thrust is maximum when the tip vortex generated by the upper rotor grazes the low pressure side of the lower rotor.

5. ROTOR ACOUSTICS

The last of the instruments used for this study was a line array of eight 1/2-inch free-field microphones (G.R.A.S. model 46AE with matching preamplifiers) positioned three rotor diameters from the hub with equal spacings of $z_i/D = 0.5$, and with the second microphone aligned with the rotor disk plane as shown in Fig. 1b. Remaining sensors were then biased towards locations below the rotor resulting in an acoustic corridor between $\theta_1 = 9.5°$ (above the rotor) and $\theta_8 = -45°$ (below the rotor). Microphone signals were sampled uninterrupted for 20.48 seconds at a rate of $f_s = 40$ kHz using 24 bit accurate A/D converters. Acoustic waveforms were then propagated using $p \propto 1/r$ decay to a virtual arc array located three rotor diameters from the hub and identified by p' in Fig. 1b. Ensemble averaged sound pressure spectrum levels (SPSL, Re: 20μPa) are computed using a Hanning window with 75% overlap and a spectral resolution of $f_s/N = \delta f = 2.0345$ Hz. No corrections for atmospheric absorption or human ear effects are employed. Albeit, precautions should be taken when conducting acous-

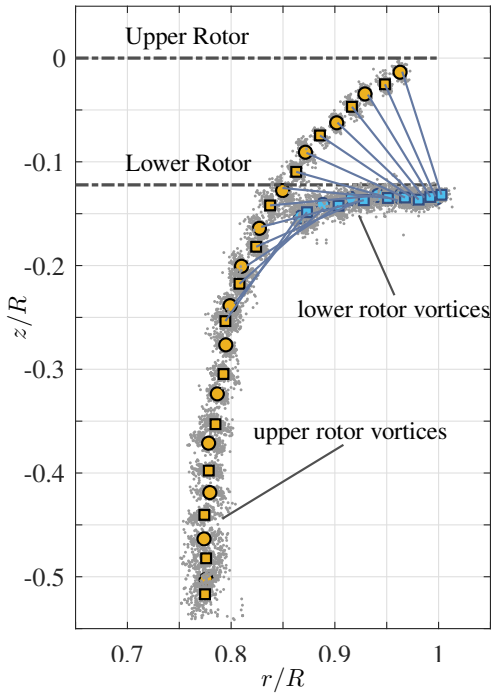


Figure 3. Average vortex locations from the upper and lower rotors of the stacked rotor operating at 90 rps with $\delta z/D = 0.061$ and $\phi_1 = 12$ deg.

tic and performance measurements in enclosed facilities which warrant some discussion.

5.1 Gauging Facility Enclosure Effects

Determining whether facility effects are corrupting one's measurements continues to be a contentious topic of discussion at conferences and workshops. While there is no unified framework for gauging these effects, some simple exercises can be performed during testing and are listed as follows:

i ***Facility time-scale:*** The first of these seeks to estimate the time required for the rotor to fully digest the volume of air enclosed by the facility. This was proposed by [8] and was motivated by concerns over recirculation effects [10]. This facility time-scale is determined by $t_v = \dot{V}/(Av_i)$ and uses rotor inflow $v_i = \lambda\Omega R$ and inflow ratio $\lambda_i = \sqrt{C_T/2}$ as inputs. For the highest thrust generating condition of this stacked rotor, the facility time scale is valued at $t_v = 465$ [s] and is sufficiently large for enclosure effects to be considered negligible.

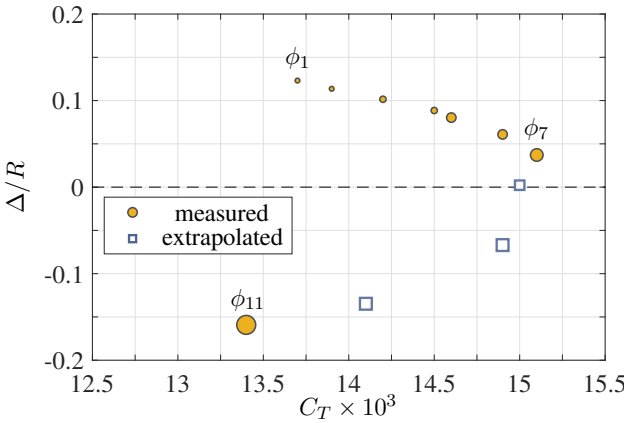


Figure 4. Miss-distance (Δ) between the upper rotor tip vortex and the lower rotor centerline versus thrust coefficient for ω_5 and δz_1. Symbol size increases with increasing index angle ϕ_k.

ii ***Spherical decay:*** If measurements are in the acoustic field and the source is compact, then pressure amplitudes should follow the $p \propto 1/r$ decay law. A simple check for this was performed using the isolated rotor spinning at $\omega = 90$ rps and by traversing a single microphone radially along the rotor disk plane between $1.0 \leq r/D \leq 8.0$. The findings are shown in Fig. 5 where the onset of spherical decay appears around $r/D \sim 2.5$ from the hub. Errors, relative to the spherical decay law, are 1.17 dB for $r/D \geq 2.5$, that then reduce to 1.03 dB for $r/D \geq 3.0$.

iii ***Isolating motor noise:*** Most drone scale rotor measurements are powered using outrunner type brushless DC motors, which are notoriously loud. The source of motor noise is well known and is caused by the first few structural modes of the motor casing [11]. Most motor noise falls into the same frequency bands where rotor broadband noise is prevalent. As such, SPSL provides an easy metric for gauging whether facility or motor noise tones are leaking into the rotor noise measurements. This is evaluated using the isolated rotor operating at 90 rps and is shown in Fig. 6 where $f_b = N_b \cdot \omega$ is the blade-pass frequency. Noise from the motor appears in some of the higher frequency tones (above $10 f_b$). The shapes and amplitudes are what one might expect for rotors of this scale.

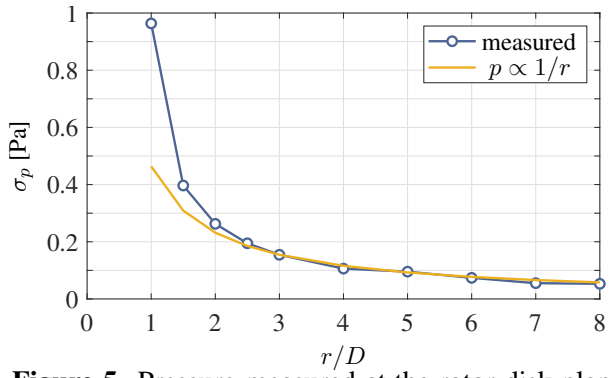


Figure 5. Pressure measured at the rotor disk plane compared with the $1/r$ decay for the isolated rotor at 90 rps.

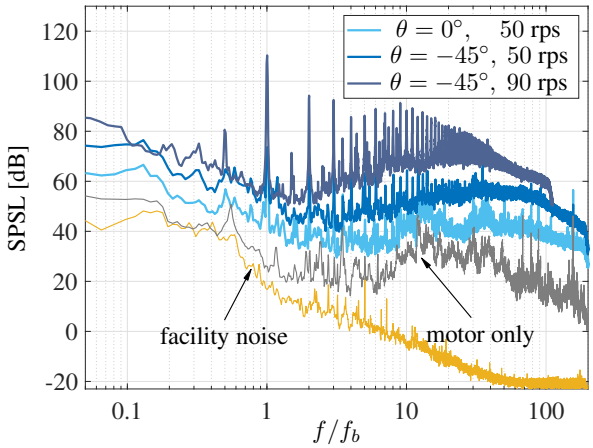


Figure 6. Background noise relative to the isolated two-blade rotor. Subsequent spectra are shifted upwards by 10 dB.

5.2 Constructive and Destructive Interference

A known feature of synchrophased rotors is the constructive and destructive interference of sound waves generated by neighboring blades and their effect on the far-field noise. This is not limited to co-rotating stacked rotors and is a common discussion point for studies involving multi-rotor platforms operating numerous motors independently without phase-synchronized control. That is, tones appear intermittently, due to nonlinear coupling between neighboring rotors and was shown early on using wavelet spectra of Tinney and Sirohi [12]. A simple demonstration of this is shown in Fig. 7 using two acoustic pressure time series from an isolated rotor (some filtering of the data has been performed to improve clarity). The pressure waveforms are identical and are used to generate a new waveform $\hat{p}(\tau) = p(t) + p(t+\tau)$ by retarding the same measured waveform using $\tau = \phi_k/\omega \cdot 360$ as the retarded time. Calculating this effect over all rotor index angles ϕ_k demonstrates the change from constructive interference to destructive interference.

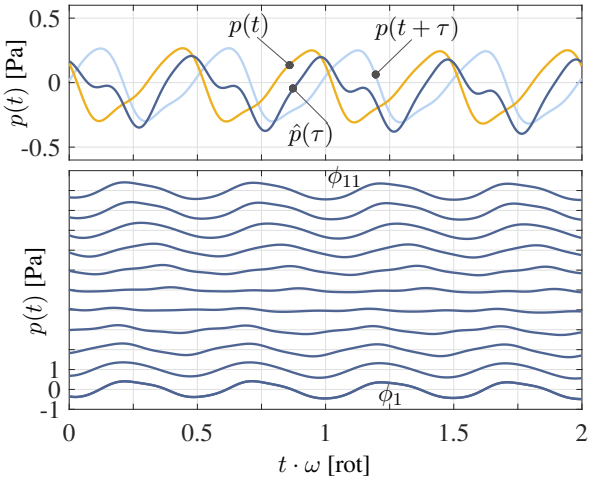


Figure 7. Top: Linear superposition of an acoustic pressure time series with its retarded time. Bottom: Comparison between estimates and measurements of acoustic pressure time series for ω_5 and δz_1. Adapted from Tinney and Valdez [1].

5.3 Analysis methods.

Data reduction techniques play a pivotal role in separating out features responsible for governing the bulk physics of a system. To this end, a number of techniques have been proposed that combine various forms of the POD (conventional, spectral, gappy) with Vold Kalman filters, to distill structure from unsteady stationary signals. In what follows, the outline of one such approach is described and is leveraged to flush out the mechanisms responsible for generating the abundance of noise generated by synchrophased stacked rotors. The process first decomposes spatially evolving acoustic waveforms using the conventional form of the POD, followed by filtering of the first few rotor harmonics using Vold Kalman filters.

5.3.1 *Conventional POD*

The simplest form of Lumley's POD is one where the kernel comprises a covariance matrix that forms from the inner product of one of two variables that make up the vector

space. In this case, the two variables stretch over space (θ) and time (t), so that

$$R(\theta,\theta') = \sum_t p(\theta,t)p^*(\theta',t) \tag{1}$$

which is self-adjoint: $\det([R_{\theta\theta'}]^{-1}) = 0$. An eigenvalue problem then forms: $R(\theta,\theta')\Phi(\theta',n) = \Lambda(n)\Phi(\theta,n)$ whose solution generates a discrete set of eigenvalues $\Lambda(n)$ with corresponding eigenvectors $\Phi(\theta,n)$ where n is an integer corresponding to the mode number ($n \in m$). Since eigenvectors are properties of the kernel, they can be used to reconstruct the variable space in two simple steps

$$a(t,n) = \sum_\theta p(\theta,t)\Phi(\theta,n) \tag{2}$$

$$\hat{p}^{(m)}(\theta,t) = \sum_n^m a(t,n)\Phi(\theta,n) \tag{3}$$

The reconstruction process is what allows certain signals to be retained while others are discarded (or filtered out). If ever a bias is introduced by the user, it occurs in the reconstruction process. If $m = \text{rank}(R_{\theta\theta'})$, then $\hat{p}^{(m)}(\theta,t) = p(\theta,t)$, and no filtering has been performed.

While POD can be used to decompose both variables, we will resort to Vold-Kalman filters (VKF) to decompose the other variables as this has the option of being performed in real time. In this case, a second generation Vold-Kalman multi-order tracking method is proposed.

5.3.2 *Vold-Kalman Multi-Order Tracking Filter*

Like POD, the VKF separates structure $P(\theta,t)$ from noise $\eta(\theta,t)$ using a two step reconstruction process as follows

$$s_k^\theta(t) = [H_{ttk}]^{-1}\Theta_k(t)^* p(\theta,t) \tag{4}$$

$$P(\theta,t) = \sum_k s_k^\theta(t)\Theta_k(t) \tag{5}$$

where $p(\theta,t) = P(\theta,t) + \eta(\theta,t)$ is the full signal, $s_k^\theta(t)$ is a low-frequency complex envelop, $\Theta_k(t)^*$ is a complex phasor, and the order of the filter k is denumerable. In practice, k defines the number of waveforms to be extracted. Similar to the role of the eigenvectors in the POD, the phasor serves to extract waveforms that make up the structured components of $p(\theta,t)$. The extraction is achieved by minimizing the error between the phasor and the raw signal and is performed using backward finite differencing. The crux of the problem is the formation of a multi-order difference matrix

$$[H_{ttk}]^{-1} = \begin{cases} r^2[A]^T[A] + [I], & \text{for} \quad k = l \\ \Theta_k(t)^*\Theta_l(t), & \text{for} \quad k \neq l \end{cases} \tag{6}$$

where r is a weighting parameter that depends on the number of poles in the filter, $[A]$ is a triangular array of coefficients and $[I]$ is an identity matrix. For a 2-pole filter, the weighting function is approximated numerically while the coefficients are based on Pascal's triangle and is written as

$$\begin{aligned} \nabla^2 s_k(t_i) &= s_k(t_{i+2}) - 2s_k(t_{i+1}) + s_k(t_i) \\ &= \epsilon(t_i) \end{aligned} \tag{7}$$

For a multi-order approach of order k, Eq. (7) resorts to an inverse problem of the form $[A][s_k^\theta(t)] = [\varepsilon_k(t)]$.

5.3.3 *Combining Methods*

There are several ways in which the POD and VKF techniques can be combined to dissect the different variables that make up the signal, thus making them complementary techniques. For the conventional POD, two options are proposed. The first uses VKF to filter the time variable by substituting $p(\theta,t)$ with its structured component $P(\theta,t)$ followed by a calculation of the POD coefficients. That is, Eqs. (4) and (5) are repeated for all of θ followed by the substitution of $P(\theta,t)$ into Eqs. (2) and (3) so that,

$$a_k(t,n) = \sum_\theta P(\theta,t)\Phi(\theta,n) \tag{8}$$

$$\hat{p}^{(mk)}(\theta,t) = \sum_n^m a_k(t,n)\Phi(\theta,n) \tag{9}$$

A potentially less costly alternative is to use the VKF to filter the POD coefficients $a(t,n)$ in place of the physical variable $p(\theta,t)$ since the opposing variable θ is suppressed during the summation process. In this case, the VKF is applied to individual POD expansion coefficients.

5.3.4 *Results*

In Fig. 8, normalized eigenvalues are shown for changes in rotor index angle where the denominator comprises the total resolved signal: $E = \sum_\theta \sum_t p(\theta,t)^2 = \sum_n \Lambda(n)$. The decay in convergence is less rapid as rotor index angle increases and advances from being dominated by two blade passes per rotation, to four blade-passes per rotation. As such, the sound field should be less structured and is an indicator of CDI rotor noise control.

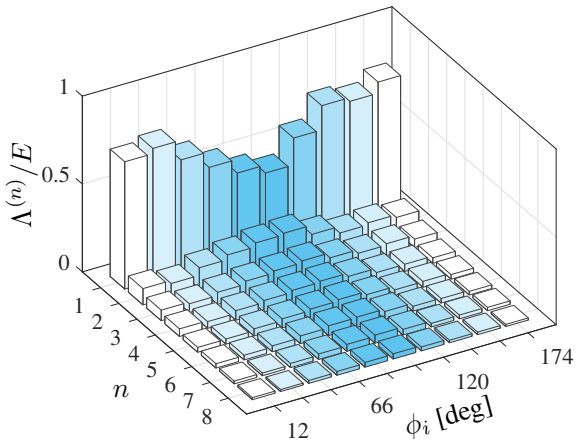


Figure 8. a) Normalized eigenvalue convergence and b) cumulative sum.

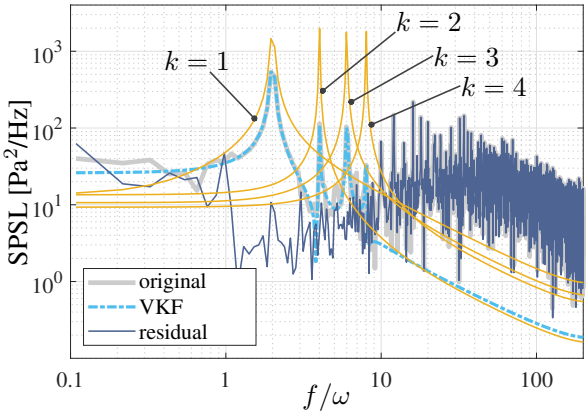


Figure 9. a) Sample acoustic time series with and without filtering, and b) its corresponding spectra superimposed the first four VKF phasors, the structural and residual components of the signal.

As for the VKF method, the instantaneous spectra of the raw acoustic pressure time series are shown in Fig. 9 superposed the structured component and its residual. Filtering is performed using $k = 4$ phasors corresponding to the first four blade pass frequency harmonics. Several reconstructions of the filtered sound field are then shown in Fig. 10 for changes to the rotor index angle and using the same combination of POD modes and VKF orders. When the upper and lower rotors are aligned and the sound field is a manifestation of constructive interference, sound waves are shown to extend over all observer positions. Eventually destructive interference takes over as the rotor index angle advances to a four blade configuration as seen in Figs. 10c and 10d.

5.4 Performance trade-space

An evaluation of the trade-space between rotor noise and hover performance is evaluated using Sound Pressure Levels (SPL) of the filtered waveforms at two observer locations in the far-field. The first is located at the rotor disk plane ($\theta = 0$ deg) while the second is where a ground observer would reside ($-\theta = 45$ deg). Symbol sizes increase with increasing index angle (ϕ). As seen in Fig. 11, rotor hover efficiency ranges from a maximum of 0.77 at $\varphi = -6$ deg, and then drops to 0.72 at $\varphi = 30$ deg. This change generates a 8% increase in hover performance with only a 0.40 dB and 0.03 dB increase in SPL for the rotor disk plane and ground observers, respectively. When implementing noise control measures through changes in rotor index angle, SPL levels drop by as much as 6 dB and 4 dB for the rotor disk plane and ground observers, respectively, while the rotor advances from $\varphi = -78$ deg to $\varphi = -6$ deg. This equates to a moderate loss in hover efficiency by -2%.

6. ACKNOWLEDGMENTS

Support for this effort was graciously provided through an internal research and development award with the Signal and Information Sciences Laboratory of the Applied Research Laboratories, The University of Texas at Austin.

7. REFERENCES

[1] C. E. Tinney and J. Valdez, "Thrust and acoustic performance of small-scale, coaxial, co-rotating rotors in hover," *AIAA Journal*, vol. 58, no. 4, pp. 1657–1667, 2020.

[2] C. E. Tinney, Y. Zhao-Dubuc, and J. Valdez, "The space-time structure of sound produced by stacked rotors in hover using vold-kalman filters and proper orthogonal decomposition," *Int. J. Aeroacoustics*, vol. 22, no. 5-6, pp. 576–598, 2023.

[3] J. Valdez and C. E. Tinney, "Wake of a coaxial, corotating rotor in hover," *AIAA Journal*, vol. 60, no. 8, pp. 4829–4839, 2022.

[4] C. E. Tinney and J. Valdez, "Higher-order statistical metrics for characterizing multirotor acoustics," *AIAA Journal*, vol. 62, no. 11, pp. 4431–4441, 2024.

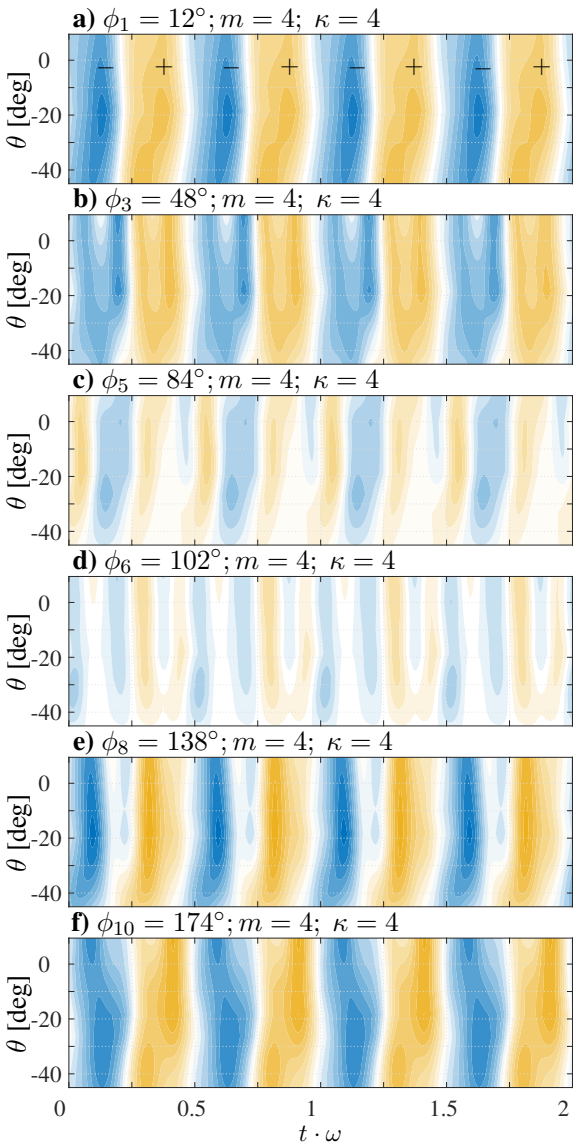


Figure 10. The sound field generated by the coaxial, corotating rotor for various index angles and filtered using $m = 4$ POD modes and $k = 4$ VKF phasors assigned to the first four blade pass frequency harmonics.

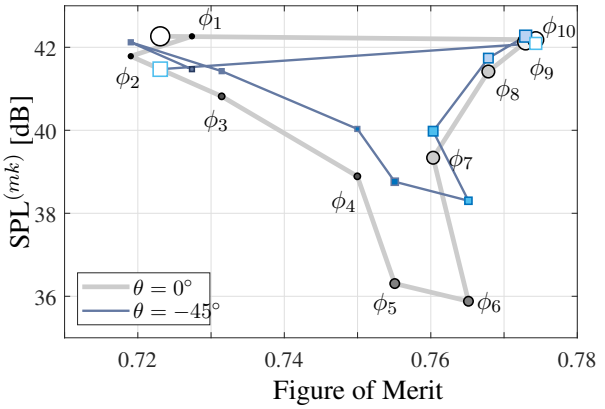


Figure 11. Trade space between filtered SPL and a) thrust coefficient, b) power coefficient, and c) rotor figure of merit.

[5] C. G. Cameron, A. Karpatne, and J. Sirohi, "Performance of a mach-scale coaxial counter-rotating rotor in hover," *Journal of Aircraft*, vol. 53, no. 3, pp. 746–755, 2016.

[6] E. Grande, S. Shubham, F. Avallone, and D. Ragni, "Computational aeroacoustic study of co-rotating rotors in hover," *Aerospace Science and Technology*, vol. 153, no. 109381, pp. 1–12, 2024.

[7] C. E. Tinney and J. Valdez, "Acoustic scaling for small rotors in hover," *Vertical Flight Society Forum 75, Paper 2019-14457*, 2019.

[8] C. E. Tinney and J. Valdez, "Hover performance and acoustics of a 35% scale notional evtol rotor," *AIAA Paper 2024-3219*, pp. 1–14, 2024.

[9] S. Mula, J. Stephenson, C. E. Tinney, and J. Sirohi, "Dynamical characteristics of the tip vortex from a four-bladed rotor in hover," *Experiments in Fluid*, vol. 54, no. 1600, 2013.

[10] D. Weitsman, J. H. Stephenson, and N. S. Zawodny, "Effects of flow recirculation on acoustic and dynamic measurements of rotary-wing systems operating in closed anechoic chambers," *Journal of the Acoustical Society of America*, vol. 148, no. 3, pp. 1325–1336, 2020.

[11] B. Henderson, D. Huff, J. Cluts, and C. Ruggeri, "Electric motor noise from small quadcopters: Part ii - source characteristics," *AIAA Paper 2018-2953*, pp. 1–23, 2018.

[12] C. E. Tinney and J. Sirohi, "Multirotor drone noise at static thrust," *AIAA Journal*, vol. 56, no. 7, pp. 2816–2826, 2018.

DOI: 10.61782/fa.2025.0419

FORUM ACUSTICUM EURONOISE 2025

FURTHER INVESTIGATION OF THE SIMPLIFIED SEPTA ACOUSTIC LINER CONCEPT

Brian M. Howerton[1*] **Jordan R. Kreitzman**[1]
[1] Applied Acoustics Branch, NASA Langley Research Center, USA

ABSTRACT

Additional refinements of an acoustic liner design incorporating single-hole perforate septa were evaluated by the NASA Langley Liner Physics Team. The design, termed the 'Simplified Septa' concept, incorporates embedded septa as found in traditional, multidegree-of-freedom liners. Typically, such septa are either multihole perforates or porous mesh, whereas the Simplified Septa uses only one hole per cell. An optimization scheme was employed to determine the liner geometry based on a target absorption cost function. These optimized designs incorporating one and two septa were tested in the NASA Langley Normal Incidence Tube (NIT) to determine impedance and absorption spectra for swept tonal excitation at 120 and 140 dB. Experimental results were compared to predictions from a liner model based on the Zwikker-Kosten Transmission Line (ZKTL) code and showed good agreement for no-flow conditions. Absorption performance was found to be good over a wide portion of the frequency range tested. The single-septum design geometry was applied to a larger sample suitable for evaluation in the NASA Langley Grazing Flow Impedance Tube (GFIT). The sample was subjected to grazing flow speeds up to Mach 0.5 and swept tonal excitation at 120 and 140 dB to determine its impedance under these conditions. The results gave confidence that the concept could be used successfully in a grazing flow environment.

Keywords: *acoustic liner, impedance, septa, normal incidence, optimization*

1. INTRODUCTION

Certification requirements limit the noise levels commercial aircraft can produce during operations. Aircraft engines are typically the primary contributor to the overall noise spectrum with the engine fan being a significant contributor [1]. The application of acoustic liners to the walls of the inlet and aft bypass ducts of turbofan engines has been highly effective in reducing total engine noise [2–4]. Engine design trends have led to reduced tonal levels relative to the broadband components of the total noise spectrum [5]. Thus, liner concepts with wider absorption bandwidth are of interest for future applications.

Examples of liners typically used in aircraft engines are shown in Figure 1. Single-degree-of-freedom (SDOF) liners provide excellent absorption for a narrow range of frequencies (approximately one octave) controlled through the choice of cavity depth and facesheet geometry. Widening this frequency range can be achieved by embedding a porous septum within the liner core to create a two-degree-of-freedom (2DOF) liner. The additional resonant frequencies extend the effective absorption range to two octaves. Using additional septa can widen this further but with additional complexity and cost.

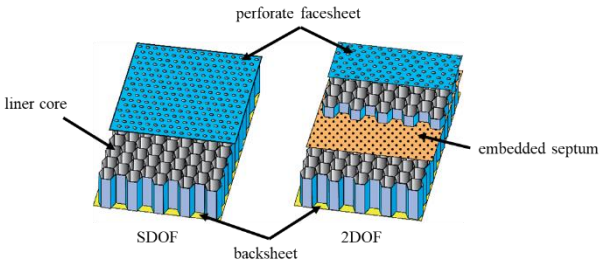


Figure 1. Conventional liner construction.

[*] ***Corresponding author***: *brian.m.howerton@nasa.gov*
Copyright: *©2025 United States Government as represented by the Administrator of the National Aeronautics and Space Administration. No copyright is claimed in the United States under Title 17, U.S. Code. All Other Rights Reserved.*

A previous paper detailed the development of the Simplified Septa (SS) liner concept whereby embedded septa employing a single perforation were used. Results showed good broadband performance for optimized 2- and 3-septa configurations [6]. The current work continues the development of the concept through testing a new set of 1- and 2-septa designs optimized for absorption from 600-3000 Hz at 140 dB tonal excitation. Samples were manufactured using stereolithography and evaluated in the NASA Langley Normal Incidence Tube (NIT) at source sound pressure levels (SPLs) of 120 and 140 dB to determine their acoustic performance. One configuration was also evaluated using the NASA Langley Grazing Flow Impedance Tube (GFIT) for the same frequencies and SPLs at Mach numbers up to 0.5 to determine if the concept performs adequately when exposed to flow.

2. BACKGROUND

2.1 Simplified Septa Concept

The SS concept is an alternative embodiment of the typical 2DOF liner that may be attractive for certain applications. The use of a single-hole septum perforate can simplify manufacturing of the liner core. The required perforations could be punched, drilled or lasered (depending on diameter) either before or after septum placement. Additive manufacturing (AM) could be readily applied as the perforations are large enough to be within the limits of such methods. The use of a single hole generates dissipation through the creation of vortical structures separating from the hole edges, especially at high SPLs. The resultant liner is, therefore, nonlinear with increasing acoustic levels.

2.2 Septa Optimization

Determination of the liner facesheet properties along with septa placement, hole diameter and liner depth were done via an optimization process. The liner was modeled using a version of the NASA Zwikker and Kosten Transmission Line (ZKTL) impedance prediction code [7–10]. The impedance modeling approach was implemented in a set of Python scripts and coupled with a nonlinear optimization routine, NLopt [11]. Specifically, the BOBYQA [12] algorithm was implemented, which is a derivative free bound constrained local minimum solver.

Constraints were imposed upon the various geometric parameters of the liner as shown in Table 1. The bounds were chosen to ensure resulting designs could be manufactured with available methods but provides latitude for parameter values outside of those found in production liners. Note that septa placement was done as a percentage of the available height and bounded to prevent placement either too close to the facesheet, backplate or other septa. Figure 2 provides a diagram of a liner unit cell with pertinent dimension labels. Note that the number of septa used was a fixed parameter, not a variable in the optimization.

Table 1. Simplified Septa liner optimization constraints.

	Description	Lower Bound	Upper Bound
Facesheet	hole dia. (d_n)	0.51 mm	1.52 mm
	thickness (t_n)	0.51 mm	2.54 mm
	POA	4 %	16 %
Septa	hole dia. (d_n)	0.51 mm	3.81 mm
	thickness (t_n)	0.51 mm	1.52 mm
Cavities	total length (L)	7.62 mm	43.18 mm
	L_n (% of available height)	10	90

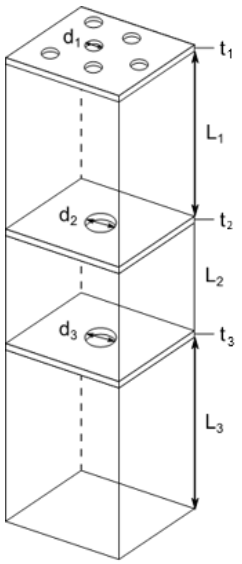


Figure 2. AM liner core unit cell diagram.

An objective function based on maximizing the computed absorption coefficient over a desired frequency range was used. If X is a vector of the liner design variables, then the

average absorption coefficient over a given frequency range can be expressed as:

$$\bar{\alpha} = \frac{1}{f_2 - f_1}\int_{f_1}^{f_2} \alpha(X)df \quad (1)$$

where f_1 and f_2 are the lowest and highest frequencies of interest. For the current study, these frequencies were set to 600 and 3000 Hz to reflect the majority of the testing range. A source SPL of 140dB was chosen for the optimization to more closely match the expected SPLs of a practical engine application.

3. EXPERIMENT

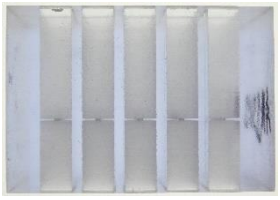
Liner samples were constructed using AM and consist of the liner core and a separable facesheet fabricated via a stereolithography process whereby liquid plastic resin is photopolymerized to build the part. The experimental investigation involves two phases of testing. The first evaluated two configurations in the NASA Langley NIT to determine their impedance and absorption spectra. These results were used to downselect a configuration for Phase 2 testing in the grazing flow environment of the GFIT test rig.

3.1 Liner Core Construction

The AM liners for the NIT testing employed a 5x5 grid of 7.62 mm square unit cells separated by 2.54 mm partitions forming a total sample area of 2581 mm^2. This sample area matches the cross-section area of the NIT waveguide. Table 2 lists dimensions for the two Phase 1 core samples, the first with one embedded septum per cell (AM1S) and the second with two embedded septa per cell (AM2S). Images of the core samples are provided in Fig. 3 showing the embedded septa in each cell.

Table 2. Liner core unit cell dimensions.

Dimension (mm)	1 Septa (AM1S)	2 Septa (AM2S)
t_1	1.32	1.35
d_1	0.56	0.99
L_1	26.49	24.08
t_2	0.30	0.30
d_2	1.19	1.42
L_2	16.76	12.19
t_3	N/A	0.30
d_3	N/A	0.79
L_3	N/A	7.7
Total Length	29.85	



a) AM1S



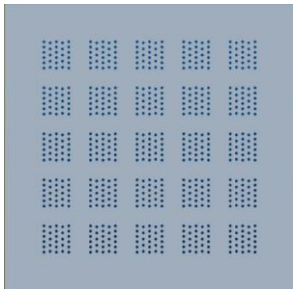
b) AM2S

Figure 3. Side view of AM liner core samples.

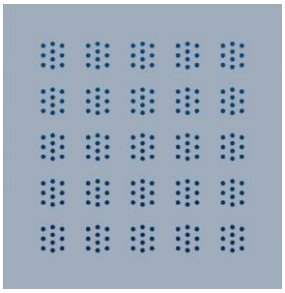
An additional core sample, based on the AM1S unit cell geometry, was constructed for Phase 2 testing in the GFIT. The sample was an extended replication of the NIT liner geometry, creating a 5x40 cell grid with dimensions of 50.8 x 254 mm (width x length).

3.2 Liner Facesheet Construction

Each core was paired with a printed facesheet with unique porosity, hole geometry, spacing and thickness. The AM1S sheet (Fig. 4a) is 1.32 mm thick and has a percent open area (POA) of 13.3 using 28 0.56 mm diameter circular holes per cell distributed in a staggered pattern. The facesheet for AM2S (Fig. 4b) is 1.35 mm thick with a POA of 11.8 and ten 0.99 mm diameter holes per cell (again in a uniform, staggered pattern). The facesheet for the GFIT sample is based on the AM1S geometry from Table 2, but rather than being a separate part, was integrally constructed with the core.



a) AM1S



b) AM2S

Figure 4. Top view of AM liner facesheets.

3.3 Experimental Test Rigs

3.3.1 Normal Incidence Tube (Phase 1)

The NIT consists of a group of six electromagnetic acoustic drivers coupled radially into a cylindrical tube that transitions to the 50.8 mm x 50.8 mm square cross-section waveguide. Samples are placed at the exit of the tube to be exposed to the generated sound field. Individual digital-to-

analog converters for each speaker allow for the creation of arbitrary waveforms to energize each driver. Typically, tonal or broadband signals are employed for impedance eduction. Impedance spectra for each sample are obtained in the NIT via the switching Two-Microphone Method (TMM) [13] and the Multipoint Method of Jones and Stiede [14]. Figure 5 is a diagram of the acquisition system while Figure 6 is a rendering of the NIT showing the pertinent features. Further details on the experimental setup can be found in Ref. 6.

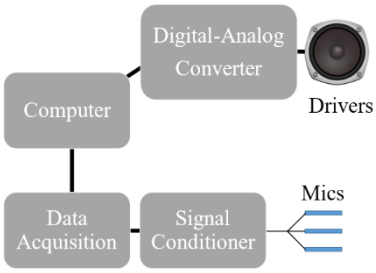


Figure 5. Normal Incidence Tube acquisition system diagram.

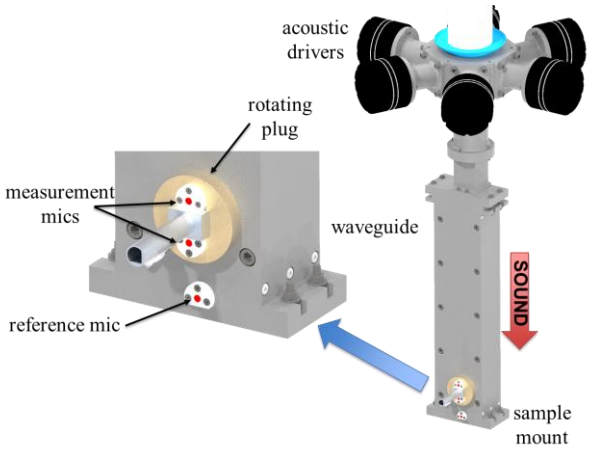


Figure 6. NASA Langley Normal Incidence Tube (NIT) general arrangement.

3.3.2 Grazing Flow Impedance Tube (Phase 2)

Grazing flow tests are performed on the liner samples using the GFIT. A schematic diagram of the setup is shown in Fig. 7. The GFIT is an acoustic wind tunnel with a 50.8 mm x 63.5 mm cross-section at the test section capable of centerline flow Mach numbers up to 0.6. Either of the two speaker arrays can be energized to achieve SPLs up to 150 dB depending on the desired orientation. For this investigation, the upstream array was employed to simulate conditions in the aft duct of a turbofan engine. An array of 95 pressure-field condenser microphones positioned along the length of the duct were used to measure the acoustic pressure profile. SPL and phase readings from each microphone were used to educe the liner acoustic impedance using the Straightforward Method of Watson and Jones [15].

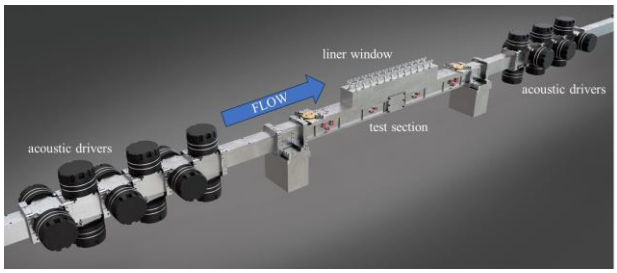


Figure 7. NASA Langley Grazing Flow Impedance Tube (GFIT) general arrangement.

3.3.3 Measurement Process

For both phases of testing, the Swept-Sine Method (SSM) [16] was used to obtain the complex acoustic cross spectra between the measurement microphones and the source signal supplied to the acoustic drivers. The acoustic source signal increases linearly in frequency from 400 to 3000 Hz during the measurement process and was amplitude modulated such that the total SPL at the sample surface was constant. A Vold-Kalman order tracking filter was employed to extract complex acoustic pressures at each microphone for the frequencies of interest. These pressures provided input for the various impedance eduction methods employed.
In the GFIT, grazing flow speed was set to duct centerline Mach numbers of 0.0, 0.3, and 0.5. At each Mach number, the acoustic source generates sine sweeps at SPLs of 120 dB and 140 dB for the same frequency range as used in the Phase 1 NIT testing.

4. RESULTS

4.1 Phase 1 - NIT

The impedance spectra for sample AM1S are shown in Figs. 8–9 at the two SPLs along with matching predictions. For both sound pressure levels, the model predicts the impedance behavior well with some deviation around antiresonance (~1800 Hz). Such deviations can be expected between model and experiment at 140 dB because the

model does not account for nonlinearities that create a reactance loss associated with perforates at high SPLs. There is work planned to incorporate a correction. Note that the frequency variation in both resistance and reactance decreases for the higher SPL which is a desired characteristic in a broadband absorber.

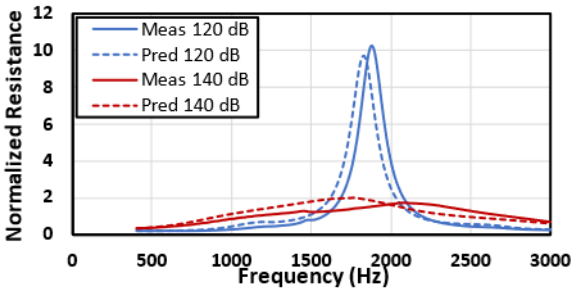


Figure 8. Comparison of measured AM1S acoustic resistance spectra to model predictions.

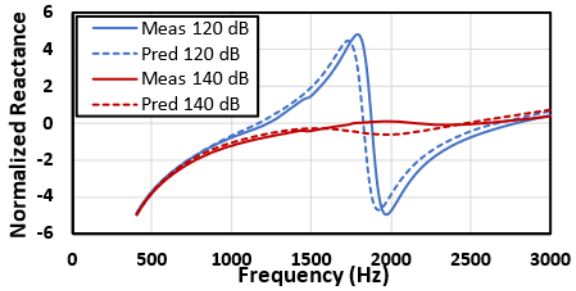


Figure 9. Comparison of measured AM1S acoustic reactance spectra to model predictions.

Figure 10 shows the computed and predicted absorption coefficient spectra for this configuration. As with impedance, the predictions are well matched to experimental results. Liners with normal incidence absorption coefficients above 0.4 have, historically, provided significant attenuation when evaluated in a grazing incidence environment such as the GFIT. Thus, one could expect reasonable broadband performance for this configuration above approximately 800 Hz and especially for higher sound pressure levels.

The addition of a second septum to the AM2S sample altered the characteristics of the impedance spectra as evident in Figs. 11–12. One can see in the 120 dB resistance spectra the appearance of a second antiresonance peak in the upper frequency range. The magnitudes of the peaks, however, are lessened compared to AM1S. Similar behavior is noted in the reactance, where the antiresonant spikes are not as sharp as AM1S.

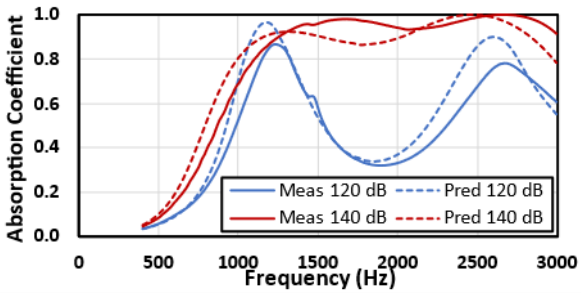


Figure 10. Comparison of measured AM1S absorption spectra to model predictions.

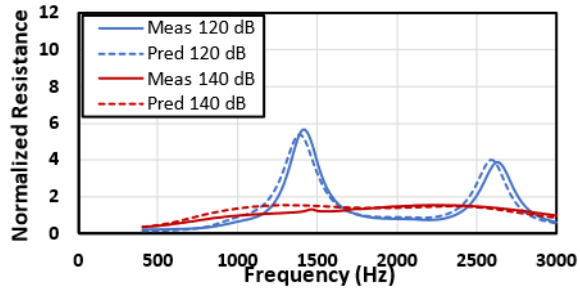


Figure 11. Comparison of measured AM2S acoustic resistance spectra to model predictions.

At 140 dB, there is little difference between the impedance spectra for both configurations. Interestingly, the agreement between experiment and modeling improved slightly for this configuration especially at the antiresonance frequencies. Enhanced absorption characteristics in the midfrequency range are observed for the 120 dB SPL case (Fig. 13), but performance at the design point of 140 dB was relatively unchanged compared to the simpler AM1S design.

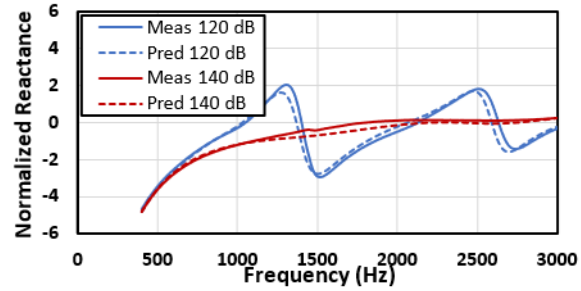


Figure 12. Comparison of measured AM2S acoustic reactance spectra to model predictions.

Based on these results, a decision was made to downselect the AM1S configuration for Phase 2 testing in the grazing flow environment of the GFIT. The addition of the second septum for AM2S does not appear to offer a significant acoustic benefit to justify the complexity and cost of production for flightworthy engine applications.

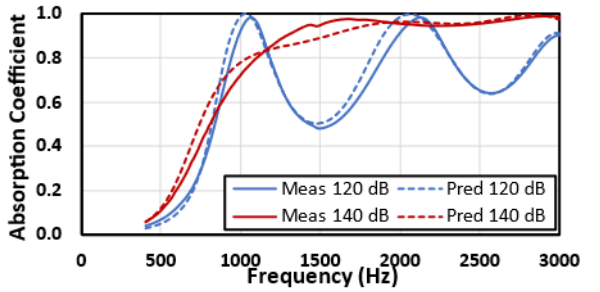


Figure 13. Comparison of measured AM2S absorption spectra to model predictions.

4.2 Phase 2 - GFIT

The intent of this investigation phase is to determine if the broadband absorption performance of the Simplified Septa concept observed in Phase 1 would carry over to a grazing flow environment. Ideally, one would see similar impedance characteristics for the design between the two test rigs, but it should be noted that the liner geometry was not optimized for the GFIT and grazing flow.

For the AM1S liner geometry, educed resistance and reactance spectra for an SPL of 120 dB are provided in Fig. 14 and 15, respectively, at the three test Mach numbers. At M=0.0, resistance and reactance are very similar to that seen in Phase 1 (Figs. 8–9) testing. Increasing flow speed shifts antiresonance to slightly higher frequencies with reduced peak values for both impedance quantities.

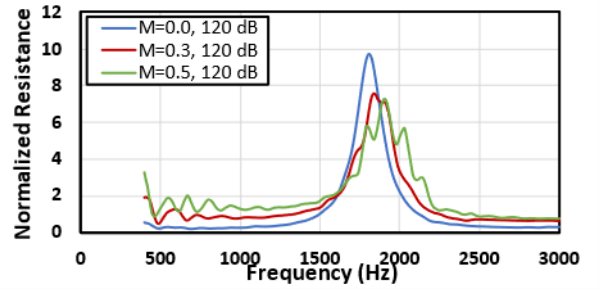


Figure 14. Educed AM1S acoustic resistance spectra for various flow Mach numbers, 120 dB SPL.

Resistance away from the peak increases as expected while reactance seems to flatten slightly for frequencies below antiresonance.

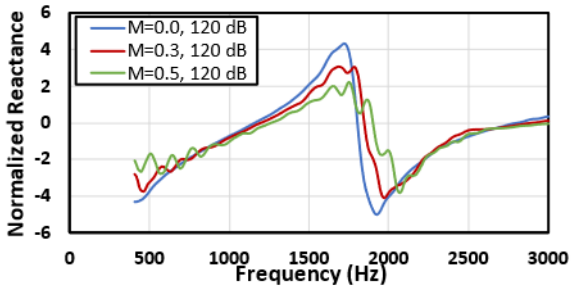


Figure 15. Educed AM1S acoustic reactance spectra for various flow Mach numbers, 120 dB SPL.

Increasing the acoustic excitation levels to 140 dB reduces the frequency variation in the impedance spectra for all Mach numbers, but variation is greater than observed in Phase 1 (Fig. 16–17). Resistance follows similar trends as the 120 dB data while reactance is only marginally affected by increasing the flow Mach number. The relative

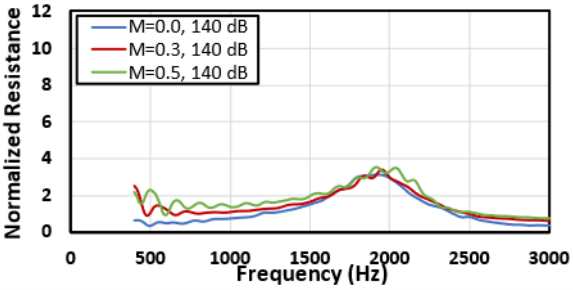


Figure 16. Educed AM1S acoustic resistance spectra for various flow Mach numbers, 140 dB SPL.

insensitivity to Mach number is somewhat expected given the POA of the facesheet as it is on the higher end of values used in engine liners. Such behavior could be desired in achieving predictable acoustic performance in practical applications.

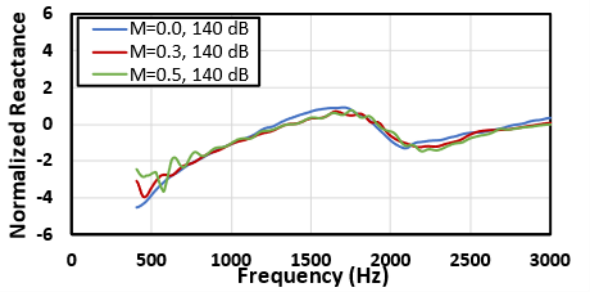


Figure 17. Educed AM1S acoustic reactance spectra for various flow Mach numbers, 140 dB SPL.

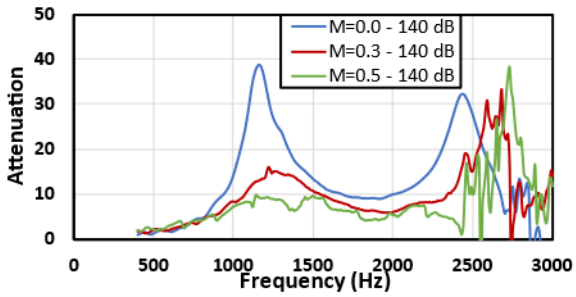


Figure 18. Calculated AM1S attenuation spectra for various flow Mach numbers, 140 dB SPL.

For both source SPLs, the educed impedance spectra exhibit an interesting characteristic with grazing flow. Some 'waviness' is observed in the impedance spectra, especially at lower frequencies and around antiresonance and becomes more pronounced at the higher Mach numbers. As the effect appears at both source levels, it is likely not acoustically induced but driven by some flow phenomenon. An initial hypothesis centers around possible compliance of the septum as its thickness (0.3 mm) is less than half of a typical facesheet. Further study is warranted to determine the cause, but the effect does not change the overall character of the spectra or the conclusions from this investigation.

Combining microphone SPL, relative phase and location data, one can compute the incident and reflected levels upstream and downstream of the liner sample. By subtracting pressure levels of the waves travelling with the flow, a simple measurement of liner attenuation can be computed. Data for both SPLs showed similar trends as the flow Mach number increased. As the higher source SPL is more relevant to most applications of this concept, only those results are presented. Figure 18 provides frequency spectra of this attenuation calculation for the AM1S sample at the three flow conditions for an SPL of 140 dB.

In keeping with the results from Phase 1 where the calculated absorption coefficient was above 0.4 for frequencies above 800 Hz, attenuation levels are generally greater than 5 dB up to the point the first higher-order mode is cut on (~2700 Hz @ M=0.0, ~2400 Hz @ M=0.5). Such levels have been shown previously to be sufficient for accurate impedance eduction [17]. The peaks in attenuation seen for the no-flow case are significantly reduced as Mach number increases. This is expected as the propagating wave has less time to interact with the liner due to flow convection.

Improved performance could be realized by altering the optimization objective function to target an impedance spectrum that produces greater attenuation in the GFIT. In developing SS liners for practical applications, this would be the likely approach.

5. CONCLUSIONS

Liner samples based on the Simplified Septa concept were constructed via AM and tested to determine their acoustic performance. Data from NIT were used to calculate impedance and absorption coefficient spectra for optimized single- and two-septa liners at two SPLs for frequencies between 400 and 3000 Hz. Comparisons of experimental results to predictions from a liner model based on ZKTL showed very good agreement. Both designs provided good absorption over a wide frequency range. The single-septa configuration was employed to create a larger liner for use in the GFIT to explore the effect of grazing flow. Acoustic data over the same frequency range, at 120 and 140 dB SPL and for Mach numbers up to 0.5 was used to educe impedance spectra and calculate the resulting attenuation levels. This phase of testing confirmed the introduction of grazing flow did not markedly alter the impedance characteristics of the liner. Thus, there is confidence the concept can be successfully employed in such noise control applications.

6. ACKNOWLEDGMENTS

The authors would like to thank Robert Andrews of the NASA Langley Additive Manufacturing Center for his efforts to construct the test samples. Appreciation also goes to NASA Langley Liner Physics Team members Christopher Shoemaker for processing the GFIT test data and Alonzo 'Max' Reid for acquiring the NIT data.

7. REFERENCES

[1] Van Zante, D, Nark, D. M., Fernandez, H., "Propulsion Noise Reduction Research in the NASA Advanced Air Transport Technology Project," *International Society for Air Breathing Engines 2017*, Manchester, UK, Sept 2017.

[2] "The NASA Acoustically Treated Nacelle Program," *Proc. of the Aircraft Noise Symp.* (Acoustical Duct Treatments for Aircraft), Invited Tutorial Papers presented at the *77th Meeting of the Acoustical Society of America*, Philadelphia, PA, Apr. 1969.

[3] "Study and Development of Turbofan Nacelle Modifications to Minimize Fan-Compressor Noise Radiation," Vol. IV – Flight-worthy Nacelle Development, Prepared by The Boeing Company, NASA CR-1714, Jan. 1971.

[4] Nark, D. M. and Jones, M. G., "Design of an Advanced Inlet Liner for the Quiet Technology Demonstrator 3," AIAA 2019-2764, *25th AIAA/CEAS Aeroacoustics Conference*, Delft, The Netherlands, May 2019.

[5] Bielak, G. W., Premo, J. W., and Hersh, A. S., "Advanced Turbofan Duct Liner Concepts," NASA CR-1999-209002, February 1999.

[6] Howerton, B. M., Kreitzman, J., and Solano, C., "Extending Acoustic Liner Bandwidth with Simple Embedded Septa," AIAA 2024-3302, *30th AIAA/CEAS Aeroacoustics Conference*, Rome, Italy, June 2024.

[7] Zwikker, C., and Kosten, C., *Sound Absorbing Materials*, Elsevier, Amsterdam, 1949.

[8] Tijdeman, H., "On the propagation of sound waves in cylindrical tubes," *Journal of Sound and Vibration*, Vol. 39, No. 1, pp. 1–33, March 1975.

[9] Parrott, T., and Jones, M., "Parallel-element liner impedances for improved absorption of broadband sound in ducts," *Noise Control Engineering Journal*, Vol. 43, No. 6, pp. 183–195, 1995.

[10] Kreitzman, J., and Jones, M., "Toward Fully 3D-Printed Two Degree of Freedom Acoustic Liners," AIAA Paper 2024-2801, *AIAA SCITECH 2024*, Orlando, FL, Jan 2024.

[11] Johnson, S., "The NLopt nonlinear-optimization package," 2021. http://github.com/stevengj/nlopt.

[12] Powell, M., "The BOBYQA algorithm for bound constrained optimization without derivatives," *Department of Applied Mathematics and Theoretical Physics, Cambridge England, technical report NA2009/06*, 2009.

[13] J. Chung and D. Blaser, "Transfer function method of measuring in-duct acoustic properties: I. theory," *Journal of the Acoustical Society of America*, vol. 68, pp. 907–921, 1980.

[14] Jones, M. G., and Stiede, P. E., "Comparison of Methods for Determining Specific Acoustic Impedance," *Journal of the Acoustical Socicy of America*, Vol. 101, No. 5, Pt. 1, pp. 2694-2704, May 1997.

[15] Watson, W. R., and Jones, M. G., "A comparative study of four impedance eduction methodologies using several test liners," AIAA 2013-2274, *19th AIAA/CEAS Aeroacoustics Conference*, Berlin, DE, May 2013.

[16] Howerton, B. M., Vold, H, and Jones, M. G., "Application of Swept-Sine Excitation for Acoustic Impedance Eduction," AIAA 2019-2487, *25th AIAA/CEAS Aeroacoustics Conference*, Delft, NE, May 2019.

[17] Jones, M. G., Nark, D. M., and Howerton B. M., "Impedance eduction for uniform and multizone acoustic liners". *International Journal of Aeroacoustics*, Vol. 20, Nos. 5-7, pp. 458-477, Sept. 2021.

DOI: 10.61782/fa.2025.0921

FORUM ACUSTICUM EURONOISE 2025

TURBULENCE EFFECT ON THE ACOUSTIC BOUNDARY LAYER OF PERFORATED ACOUSTIC LINERS

Anita Schulz[1*] **Dirk Ronneberger**[2]
[1] University of Applied Sciences (HTW) Berlin, 12459 Berlin, Germany
[2] retired, formerly Drittes Physikalisches Institut, 37077 Göttingen, Germany

ABSTRACT

In this work the shear stress effect on the acoustic boundary condition of liners with grazing turbulent mean flow is investigated. The lined wall is supposed to be rigid and homogeneously permeable. We have derived two semi-analytical models supplemented by DNS data which provide insight in the qualitative dependencies and the governing parameters of the turbulence effect. We found a critical frequency $\omega_c^+ = 10^{-2}$, which separates two regimes: For high frequencies the sound-synchronous shear stress does not reach beyond the viscous sublayer and the turbulence has no impact on the acoustic boundary condition. However, for low frequencies the shear wave penetrates into the turbulent flow layer and deforms the turbulent vorticity field. This causes an increased magnitude of sound-coherent wall shear stress as well as a significant change of the wall shear stress impedance and of the effective acoustic boundary condition. It was found that the latter depends particularly strongly on the dynamic processes which take place in the near-wall region of the turbulent wall boundary layer. In order to get more insight into the course of these processes impulse response functions of the sound-coherent shear stress have been calculated from existing DNS data. The results confirm a previous hypothesis that a shear wave propagates from the wall into the viscous sublayer, triggers a reaction of the turbulent shear stress in the turbulent region of the boundary layer, which in turn generates a viscous shear stress field that extends to the wall. This latter reaction manifests itself in a distinct 'turbulent portion' of the sound-coherent wall shear stress. It was found also that this dynamic process takes a characteristic time of $t^+ \approx 160$.

Keywords: *liner, acoustic boundary condition, turbulent flow*

*__Corresponding author__: anita.schulz@htw-berlin.de.
__Copyright__: ©2025 Anita Schulz This is an open-access article distributed under the terms of the Creative Commons Attribution 3.0 Unported License, which permits unrestricted use, distribution, and reproduction in any medium, provided the original author and source are credited.

1. INTRODUCTION

Passive acoustic linings are widely used to reduce noise emission for instance in the inlet or bypass duct of aircraft engines or in the duct walls of gas turbines. In most of these applications, the liner is naturally exposed to a highly turbulent grazing flow. It is well known from experiments that the acoustic properties of liners, especially the impedance and the sound absorption, can change significantly due to the grazing mean flow. The mean grazing flow is to be expected to interact with the acoustic particle velocity through the perforations of the rigid face-sheet of the liner. This induces a sound-coherent ('acoustic') shear stress at the wall which can exceed the well-known shear stress of the no-flow case by orders of magnitude. This shear stress plays an essential role in the acoustic boundary condition and its correct consideration is crucial for the design of liners if precise predictions of the sound attenuation of the liner should be achieved. The propagation of shear stress in the so-called acoustic boundary layer is strongly affected by the Reynolds stresses of the turbulence, which in turn depends on the sound-induced temporal change of the acoustic boundary condition. However, little is known about the involved physical effects and its governing parameters and in most models, the acoustic shear stress and the turbulence effect are ignored completely.

This report presents the current status of an ongoing study on the turbulent shear stress effect. The long-term goal from an engineering point of view is to derive an 'effective' acoustic boundary condition which includes the

distribution of shear stress caused by turbulence together with the effect of the wall impedance. However, for this purpose we must first investigate how sound-coherent shear stress is generated and propagates in the turbulent boundary layer, how the Reynolds stress and other turbulence characteristics react spatially and dynamically to the acoustic perturbation of the mean flow, and what the governing parameters of these processes are.
It has to be noted that in the course of the study and as a first step we have limited ourselves to a particular and somewhat artificial type of liner wall: the rigid homogeneously permeable wall with infinitesimally small pores. For this wall, the acoustic effects due to the macroscopic openings of realistic liners (e.g. propagation and scattering of sound waves and hydrodynamic waves, local production of shear stress, shear layer instabilities) can be neglected and the no-slip condition applies. [1, 2] This is beneficial since it allows a simplified theoretical description and precisely defines the generation of a shear wave and the wall-normal gradient of acoustic shear stress at the wall. Moreover, we assume that the solutions for the homogeneously permeable wall will be at least part of the solution of the full problem (when the effects of the macroscopic openings are included).

2. INFLUENCE OF THE TURBULENCE ON THE EFFECTIVE BOUNDARY CONDITION

In our previous work [2, 3], the influence of turbulence on the effect of the acoustic boundary condition of a rigid, but homogeneously permeable liner has already been qualitatively investigated and some of the governing factors have been determined. These findings are summarized here briefly in order to build on this with further conclusions and analysis on the generation of sound-coherent shear stress:

1. The distribution of sound-coherent shear stress in the acoustic boundary layer is modified by two individual effects or properties of the turbulence:

   - Shear deformation of the turbulent vorticity field: The turbulence in the acoustic boundary layer is sheared and deformed by the shear wave which is exited at the wall. This results in a modulated or sound-synchronous part of the Reynolds shear stress which must be modeled somehow. In the few available models [4–8] the classic Boussinesq hypothesis associated with a fictive 'eddy viscosity' was used, which is a well-established concept for mean flow turbulence. However, the transfer of this concept to the acoustic case is questionable and the results of a direct numerical simulation (DNS) [9] have supported this concern.

   - Relaxation due to wall-normal displacement of the turbulent vorticity field: In a flow in equilibrium, also the statistical characteristics of the turbulent tangle of vortex filaments is in a state of equilibrium depending on the distance from the wall. If the vortex filaments are displaced due to the acoustical flow through the wall, turbulent relaxation processes will set in which seek to restore the previous state of equilibrium. This turbulent relaxation has never been investigated before in case of turbulent flow with an acoustical displacement at the boundary.

2. We have developed two semi-analytical models to include the above mentioned turbulence effects. Both models are based on extremely different physical assumptions:

   - The first model ('Model 1') follows the traditional concept of an eddy viscosity, i.e. it assumes a strictly local relationship between turbulent shear stress and strain rate. The parameter of the eddy viscosity was estimated by DNS data of Hartmann [9].

   - The second model ('Model 2') is based on the rather speculative hypothesis, suggested by the results of the DNS, that the sound-synchronous Reynolds stress, at least near the wall, is controlled solely by the acoustic wall shear stress and is independent of any local properties of the flow field. The wall shear stress parameter in this model was also estimated by DNS data.

It has to be emphasized that both models present two very hypothetical and simplified physical concepts and, in fact, we have no idea which approach is closer to reality. Moreover, the models represent two extreme cases for the interaction between the turbulent shear stress and the flow field: Model 1 assumes a strictly local interaction, whereas Model 2 is based on an extreme remote effect. The models can be used to show how strong the influence of the previously neglected effects can be in general and what the qualitative dependencies and the governing parameters of the turbulence effect are.

3. A representative result for the two models is

shown in Fig. 1 for the wall shear stress impedance

$$z_\tau^+ = \frac{1}{\rho_0 u_\tau} \frac{\widetilde{\tau}_w}{\widetilde{u}_0}. \tag{1}$$

We consider z_τ^+ [9, 10] as an appropriate quantity to discuss the turbulence effect since, in first instance, it can be regarded as measure for the acoustic wall shear stress $\widetilde{\tau}_w$ reacting to the streamwise acoustic velocity $\widetilde{u}_0$ at the wall. Also, it has been found that z_τ^+ determines directly the effective admittance of the liner if the Doppler-shift of the frequency is disregarded (not shown here). Note that we use the common normalization by turbulent boundary layer quantities, i.e. the kinematic viscosity $\nu = \mu/\rho$ and the friction velocity u_τ in Eq. 1. Figure 1 depicts the magnitude and phase of the wall shear stress impedance as a function of the normalized frequency $\omega^+ = \omega\nu/u_\tau^2$. The colors of the curves mark the solutions for the two extreme cases of turbulent relaxation: non-relaxed flow (red) or fully-relaxed flow (black). By 'non-relaxed flow' we refer to the initial state of flow before relaxation processes set in after a sudden wall-normal displacement $\widetilde{\xi}$ of the fluid at the boundary. In this case, the displacement would lead to an immediate shift of the flow profile, the turbulent vortex filaments, and their inherent velocity correlations as a whole to a new distance from the wall. This is because the time scales of the acoustic displacement are small compared to the time scales of the turbulent boundary layer. The subsequent start of turbulent relaxation rebalances the flow, i.e. eventually adapt the flow profile and the velocity correlations to the new wall distance. We refer to this second state of flow as the 'fully-relaxed' flow. Note that the solution for a real relaxing flow, which relaxes with a finite relaxation time, is supposed to be somewhere between the solutions of the two relaxation limits. Previous models [4–8, 11, 12] have only considered implicitly the limit of a fully-relaxed flow which implies that the turbulence always adjusts without the slightest delay to the wall-normal displacement.

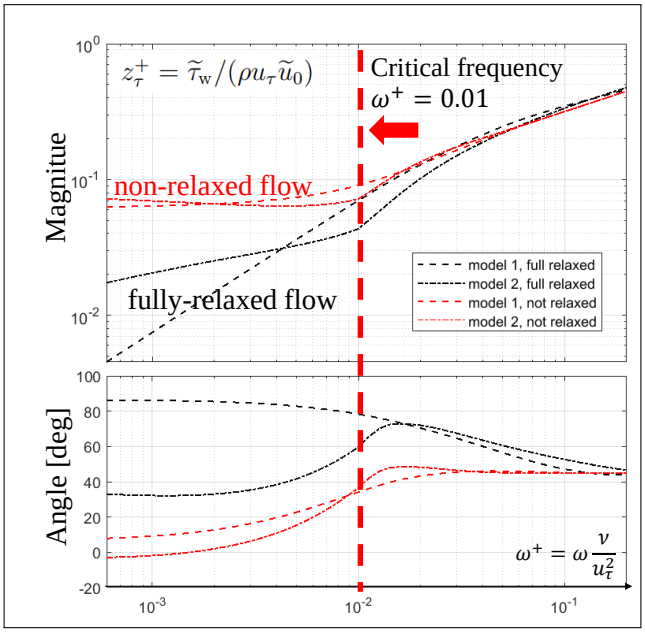


Figure 1. Results for the wall shear stress impedance $z_\tau^+ = \frac{1}{\rho_0 u_\tau} \frac{\widetilde{\tau}_w}{\widetilde{u}_0}$ normalized with wall parameters as a function of the normalized angular frequency.

The results, which are shown in Fig. 1 among others, can be interpreted as follows.

- We found a **'critical frequency'** $\omega_c^+ \approx 10^{-2}$, which separates two regimes of impact of turbulent shear stress on the acoustic boundary condition. This frequency is highlighted in Fig. 1. For 'high' frequencies $\omega > \omega_c$ the results become more and more independent of the applied turbulence model and of the state of relaxation effect. This is because at high frequencies the sound-synchronous shear stress decays close to the wall due to the short wavelength of the according diffusion wave and does not reach beyond the viscous sublayer. Thus, in this regime the turbulence has no impact on the effective boundary condition and can be ignored in practical situations.

- However, for 'low' frequencies $\omega < \omega_c$ the acoustic shear stress wave penetrates into the turbulent flow (at least into the buffer layer) which causes a great change in the spatial distribution of sound-coherent shear stress. This is more pronounced and covers a larger distance from the wall the lower the frequency is. On the one hand, this results in a strongly increased magnitude of acoustic wall shear stress and accordingly on a change of the wall shear stress impedance z_τ^+. On the other hand, it leads to a major change of the effective impedance relative to the liner impedance (not shown here, see [3]) which can reach orders of magnitude depending on the Mach number and the streamwise wavenumber of the sound wave. Also, completely different trends have been found for wave propagation in or against the flow direction. Even nega-

tive real parts of the effective impedance have been found for cases of wave propagation against the flow and it is still unclear if this indicates production of sound or just an energy transport in the opposite direction.

- Unfortunately, in the low-frequency regime not only the deviation between the solutions for the two limiting flow states, non-relaxed and fully-relaxed flow, are increasing, but also the discrepancies between the solutions of the two models. Fig. 1 gives us a rough estimate of the range of possible solutions, but the uncertainty between the models is considerably increased at low frequencies.
- It is noteworthy, that the low frequency regime is actually achieved in practical liner applications, so the effect cannot simply be neglected. To give a practical example: For a Mach number of 0.17 the critical frequency would be at $f = 1$ kHz. For $M = 0.4$, however, the affected frequency range would be already stretched up to 5 kHz. Moreover, the effect is supposed to be even more pronounced at realistic liner surfaces where the wall is usually not hydraulically smooth but somewhat rough. At a rough wall the viscous sublayer is thinner compared to a smooth wall. Hence, a shear wave that has decayed in the viscous sublayer for a smooth wall would interact with the turbulence (i.e. the turbulent buffer layer) at a rough wall. Thus, the critical frequency is shifted towards higher frequencies and the turbulence effect applies at a wider frequency range.

3. DYNAMIC REACTION OF THE TURBULENT FLOW TO THE ACOUSTIC DISTURBANCE AT THE WALL

3.1 Frequency response and impulse response function of z_τ^+

To overcome the great uncertainty in choosing the right turbulence model ('model 1/2'? or something else?) at low frequencies $\omega < \omega_c$, it is crucial to obtain more insight in the mechanisms of generation and propagation of sound-coherent shear stress in the boundary layer. This includes the question of how the system of the turbulent flow (with its inherent Reynolds shear stresses) reacts dynamically to the sound-induced temporal variation of the boundary condition and how this ultimately results in a certain distribution of the total sound-coherent shear stress in the acoustic boundary layer. To this end an understanding of the temporal sequence of the (local or global) physical mechanisms involved would be beneficial.

A useful base for this could be provided by the impulse response function (IRF) of the sound-coherent shear stress. We have started this investigation by evaluating the impulse response function of the shear stress impedance z_τ^+ (Eq. 1). This corresponds to the temporal response of the wall shear stress to a dirac pulse of the streamwise velocity at the wall (which would be observed at the wall without the no-slip condition). Note that the latter velocity can be also regarded as the difference between the streamwise velocities of the bulk flow and the fluid which sticks to the wall. The impulse response function is obtained by an inverse Fourier transformation (ifft) of the frequency response of z_τ^+. The latter was evaluated from the DNS data of Hartmann [9] and from corresponding measurements [10]. Note that the original frequency response was multiplied with a Gaussian function first since the ifft cannot be applied to a monotonically increasing function (as $z_\tau^+ \propto \sqrt{i\omega^+}$). The real and imaginary part of the frequency response for the DNS data (multiplied with the

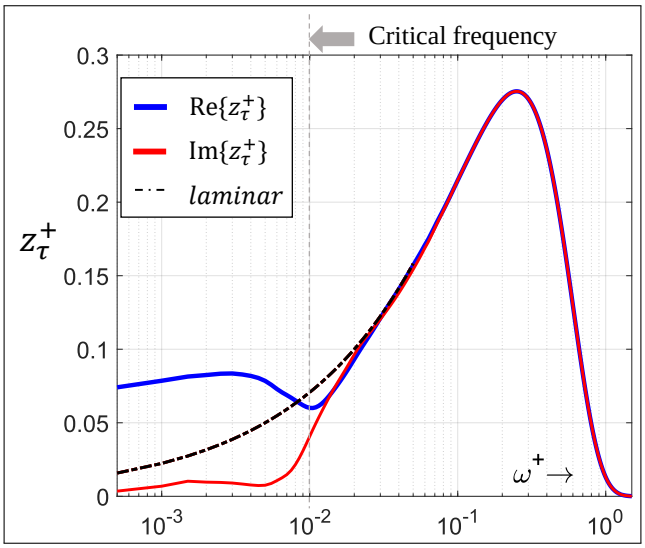


Figure 2. Real and imaginary part of the frequency response (multiplied with a Gaussian function) of the wall shear stress impedance z_τ^+ which was evaluated from the DNS data [9]. The normalization is the same as in Fig. 1. The black dash-dotted curve shows both the real part and the imaginary part of z_τ^+ in a laminar flow.

Gaussian function) is shown in Fig. 2 together with the solution for a laminar flow (black dash-dotted line), i.e. the shear stress is governed only by the molecular viscosity and the shear rate.
Note that the calculation of the impulse response was prone to considerable uncertainties since the frequency response is given only for a certain number of frequencies in both data sets. Thus, some effort has been put in an appropriate data processing which conditions the shear stress impedance by a cost function first (details not shown here).

3.2 Results

Fig. 3 shows the results for the evaluated impulse response function as a black, solid line. Note that the impulse response is causal (there are no contributions at negative times except of a small portion due to the convolution with the Gauss function) which confirms that the streamwise change in the position of the wall relative to the bulk flow can indeed been considered to be the cause of the shear stress. Fig. 3 a) shows that mainly a high, somewhat deformed peak is obtained at $t^+ = 0$, which - physically speaking - reflects the infinitely high wall shear stress at the infinitely high wall velocity during the delta pulse. The deformation of the peak is caused by the dynamics of the radiated viscous shear wave. The corresponding impulse response, which accounts for the purely laminar flow case, is shown as a red dashed line. Since it can hardly be distinguished from the actual impulse response in Fig. 3 b) the same information is shown with an enlarged scaling of the ordinate and a broader time scale. The difference between the total and the laminar impulse response is caused by the reaction of the turbulent shear stress on the wall shear stress. This difference (total solution minus laminar solution) is specifically shown in Fig. 3 c) and compared between the DNS data and the experimental data.

4. CONCLUSIONS AND OUTLOOK

The turbulent portion of the impulse response in Fig. 3 c) clearly reveals a distinct peak after a time $t^+ \approx 160$ (note that t is made dimensionless by ν/u_τ^2). This fits into our previously expected view of the physical processes: Since the wall is smooth, it is directly exposed to the viscous sublayer of the turbulent boundary layer which means that the sound-coherent shear stress at the wall has to be generated exclusively by viscous forces (viscosity times shear rate). Thus, the information of the turbulent shear stress (which originates from e.g. the buffer layer of the turbulent boundary) cannot pass directly to the wall, but is instead (indirectly) transmitted by shear waves. These shear waves propagate from the wall through the viscous sublayer, then trigger a reaction of the turbulent shear stress in the turbulent region of the boundary layer, which in turn generates a viscous shear stress field that extends back to the wall. The result of this latter portion manifests itself in a distinct sound-coherent wall shear stress in Fig. 3 c). This idea is further confirmed by the position of the maximum of the impulse response at a characteristic time $t^+ \approx 160$, which interestingly corresponds to the reciprocal of the characteristic frequency $\omega_c^+ \approx 10^{-2}$. It is assumed that this time span contains the sum of the shear wave transit times and the time required by the turbulence to respond to the shear rate.
Recent results indicate that the impulse responses of the turbulent shear stress and the shear rate as a function of wall distance provide further insight into these processes. In fact, the acoustic boundary condition of the homogeneously-permeable wall with grazing turbulent mean flow depends particularly strongly on the processes that take place in the near-wall region of the turbulent wall boundary layer. The estimation of the impulse responses thus proves to be a meaningful addition to the frequency responses that have been considered almost exclusively up to now. However, due to the difficulty of data preparation in obtaining the impulse response from the frequency response, it would be beneficial in the future to obtain the data directly from a numerical or real experiment, which provides the impulse response of the shear stress to a pulse of the streamwise velocity.

5. ACKNOWLEDGMENTS

The authors gratefully acknowledge the financial support of the German Research Foundation (project *SCHU 3376/2-1*).

6. REFERENCES

[1] A. Schulz, C. Weng, F. Bake, L. Enghardt, and D. Ronneberger, “Modeling of liner impedance with grazing shear flow using a new momentum transfer boundary condition,” in *23rd AIAA/CEAS Aeroacoustics Conference, 5 - 9 June 2017, Denver, CO*, no. AIAA 2017-3377, 2017.

[2] A. Schulz and D. Ronneberger, “Effect of momentum transfer on the acoustic boundary condition of perfo-

rated liner walls with grazing flow," in *Forum Acusticum 2020, Lyon*, pp. 793–800, 2020.

[3] D. Ronneberger and A. Schulz, "The effect of the turbulent shear stress on the acoustic boundary condition of liners with grazing mean flow," in *30th AIAA/CEAS Aeroacoustics Conference (2024)*, no. AIAA-2024-3252, 2024.

[4] R. Starobinski, "Sound propagation in lining duct with essentially non-uniform distribution of velocity and temperature," in *Noise of jet engines, Issue 2, CIAM*, 752, pp. 155–181, 1978.

[5] M. S. Howe, "Damping of sound and vibration by flow nonlinearity in the apertures of a perforated elastic screen," *Journal of Applied Mathematics*, vol. 55, pp. 221–242, 1995.

[6] Y. Aurégan, R. Starobinski, and V. Pagneux, "Influence of grazing flow and dissipation effects on the acoustic boundary conditions at a lined wall," *Journal of the Acoustical Society of America*, vol. 109, no. 1, pp. 59–64, 2001.

[7] C. Weng, S. Boij, and A. Hanifi, "The attenuation of sound by turbulence in internal flows," *Journal of the Acoustical Society of America*, vol. 133, pp. 3764–3776, 2013.

[8] C. Weng, S. Boij, and A. Hanifi, "Numerical and theoretical investigation of pulsatile turbulent channel flows," *Journal of Fluid Mechanics*, vol. 792, pp. 98–133, 4 2016.

[9] M. Hartmann, *Zeitlich modulierte Statistik der periodisch gestörten turbulenten Kanalströmung*. Phd thesis, Georg-August-Universität, Göttingen, 2002.

[10] D. Ronneberger and C. D. Ahrens, "Wall shear stress caused by small amplitude perturbations of turbulent boundary-layer flow: An experimental investigation," *Journal of Fluid Mechanics*, vol. 83, no. 3, pp. 433–464, 1977.

[11] J. Rebel and D. Ronneberger, "The effect of shear stress on the propagation and scattering of sound in flow ducts," *Journal of Sound and Vibration*, vol. 158, pp. 469–496, 1992.

[12] C. Weng, A. Schulz, D. Ronneberger, L. Enghardt, and F. Bake, "Flow and viscous effects on impedance eduction," *AIAA Journal*, vol. 56, pp. 1118–1132, December 2018.

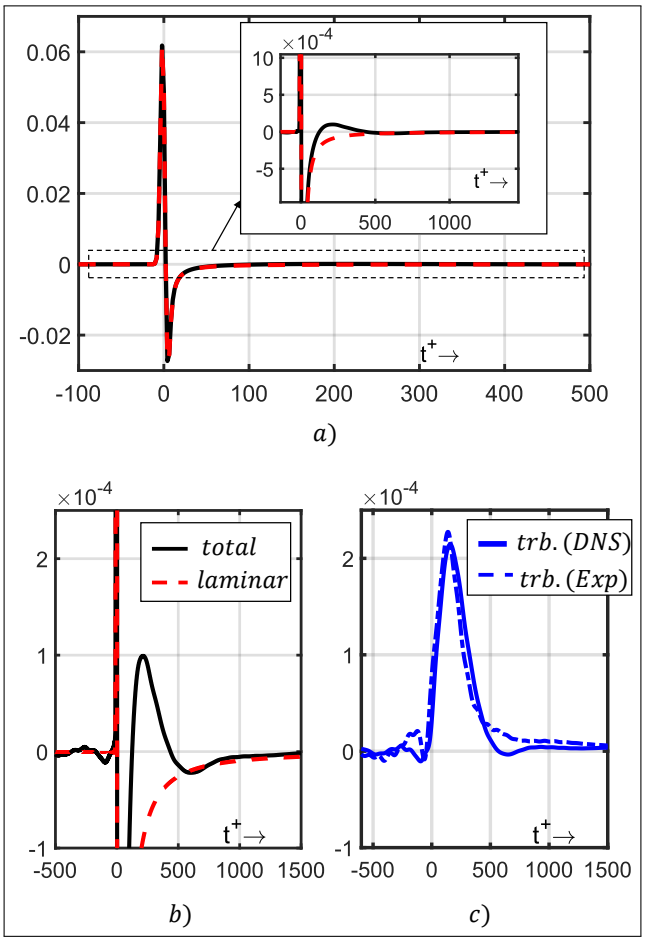


Figure 3. Impulse response of z_τ^+ (which was multiplied with a Gaussian function): a) Black curves represent the actual impulse response, red dashed curves represent the laminar case (no turbulence). b) Enlargement for small values. c) Purely turbulent portion (subtraction of the laminar solution from the total solution), solid line for the results from the DNS data [9], dash-dotted line for results from the experimental data [10].

DOI: 10.61782/fa.2025.0646



FORUM ACUSTICUM
EURONOISE 2025

ON THE IMPACT OF THE ORIFICE GEOMETRICAL FEATURES ON THE PERFORMANCE OF AN ACOUSTIC LINER

Francesco Avallone[1*] **Amr Khedr**[1] **Angelo Paduano**[1]
Francesco Scarano[1] **Lucas Meirelles**[2] **Julio Cordioli**[2]
[1] Department of Mechanical and Aerospace Engineering, Politecnico di Torino, Italy
[2] Department of Mechanical Engineering, Federal University of Santa Catarina, Brazil

ABSTRACT

This computational study investigates the impact of manufacturing inaccuracies of face sheet orifice geometries on acoustic liners' impedance and flow dynamics. Normal Impedance Tube (NIT) lattice-Boltzmann very-large eddy simulations at 130 and 145 dB and 800, 1400, and 2000 Hz reveal that sharp-edged geometries present increased acoustic resistance and absorption than geometries with smoother edges. Rounded and double-chamfered edge shapes, mimicking real-world imperfections, reduce the resistance component of impedance by up to 28%, thus reducing the absorption coefficient. The inspection of the velocity field shows the flow features that cause these differences. Results demonstrate that minor edge imperfections, potentially due to manufacturing, may alter liner performance. This underscores the need to account for geometric imperfections in industrial design and quality control.

Keywords: *acoustic liners, orifice geometry, impedance, computational fluid dynamics, manufacturing imperfections*

1. INTRODUCTION

Reducing fan noise in turbofan engines is a critical area of research; acoustic liners are one of the most effective noise mitigation strategies [1]. Acoustic liners generally consist of a perforated face sheet, a honeycomb core, and a rigid backing, forming a structure that enhances sound attenuation [2]. The perforated face sheet facilitates acoustic dissipation through viscous and thermal losses at the orifice walls, whereas the backing structure enables reactive interference, effectively reducing noise levels. This configuration is particularly efficient in attenuating noise within a narrow frequency range, typically centered around the fundamental blade passing frequency (BPF) during take-off and landing conditions [3].

The shape of the perforations of the face sheet represents a key geometrical parameter in the design and optimization of acoustic liners. Recent advancements in liner performance have focused on modifying the geometry of these perforations or orifices to enhance their effectiveness [4]. Modifications to traditional Helmholtz resonator (HR) liners, particularly through additive manufacturing techniques, have led to the development of novel liner configurations. Examples include HRs with extended necks [5], inserted necks [6], spiral necks [7], and tapered necks [8]. These modifications allow for a reduction in the overall absorber thickness without compromising sound absorption performance, highlighting the critical role of perforation shape in acoustic liner efficiency. However, given the small size of these perforations and their significant influence on liner performance, achieving precise manufacturing tolerances remains a major challenge.

In an ongoing experimental study conducted by the present research group on the effect of grazing flow on acoustic liner performance, it was observed that the manufacturing finish of perforation edges plays a crucial role [9]. Specifically, when liners are 3D-printed, the edges tend to be filleted, whereas in metal-machined liners, the perforation edges are chamfered. With more advanced machining techniques, sharper edges can be maintained. These variations in edge geometry have been found to

*__Corresponding author__: francesco.avallone@polito.it.
__Copyright__: ©2025 Avallone et al. This is an open-access article distributed under the terms of the Creative Commons Attribution 3.0 Unported License, which permits unrestricted use, distribution, and reproduction in any medium, provided the original author and source are credited.

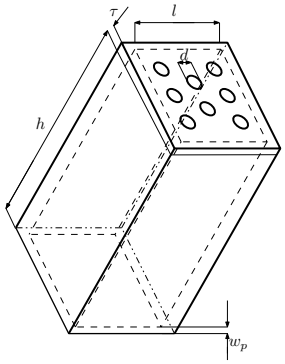


Figure 1. Schematic of the liner cavity.

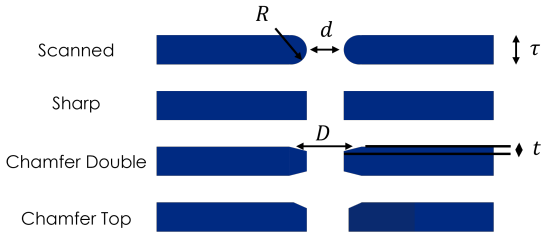


Figure 2. Liner geometries, with different edges' finish, analyzed with the normal impedance tube setup.

Table 1. Geometrical parameters of the liners tested with the normal impedance tube setup.

τ	d	D	R	t
0.55 mm	1.17 mm	1.29 mm	0.066 mm	0.1 mm

have a pronounced impact on liner performance.

Motivated by these observations, the present study aims to numerically investigate and quantify the effect of small modifications of perforation edge shape on acoustic liner performance. The analysis is conducted using computational fluid dynamics (CFD) simulations under normal sound plane wave excitation, without a grazing flow, to isolate the effect of perforation edge shape. Simulations are performed at different sound pressure levels (130 dB and 145 dB) and frequencies (800 Hz, 1400 Hz, and 2000 Hz) to evaluate the impact of the orifices edge geometry on the liner performance.

2. COMPUTATIONAL SETUP AND TEST CASES

The liner geometry investigated in this study consists of 33 cells, each featuring a face sheet with eight orifices positioned over a rectangular cavity, as illustrated in Figure 1. The parametric analysis was carried out on four different face sheet orifice geometries, as shown in Figure 2. These geometries were derived by modifying a reference experimental geometry, named scanned. This was obtained through the 3D scanning of the geometry experimentally available. In addition to the scanned geometry, three alternative configurations were considered: sharp, chamfer double, and chamfer top. The corresponding geometrical parameters are provided in Table 1. The height of the cavity h is 38.1 mm and the side of the square cavity l is 9.89 mm

The four liner geometries were tested numerically using the commercial software PowerFLOW. A Normal Impedance Tube (NIT) setup was automatically constructed using $OptydB - Kundt$. The NIT setup consists of a tube, positioned above the simulated acoustic liner, whose length varies based on the minimum frequency of interest. For the present case, the duct has a length of 2.28 m and a diameter of 0.08 m.

Tonal acoustic plane waves with amplitudes of 130 dB and 145 dB and frequencies of 800, 1400, and 2000 Hz were tested. An example of the spectral content of the input acoustic waves for the two investigated amplitudes at a tonal frequency of 1400 Hz is shown in Figure 3. The theoretical resonance frequency of the current acoustic liner geometry is 1170 Hz [10], making 1400 Hz the closest tested frequency to resonance. Therefore, this frequency is selected as the representative case, particularly at the high sound pressure level of 145 dB, for which flow details will be further analyzed and discussed in the results section.

The computational domain was discretized using nine variable-resolution regions, with a minimum voxel size of 20 vx/τ (0.0274 mm). The grid resolution was highest near the face-sheet orifice and decreased further away. It was ensured that the resolution remained above 15 vx per wavelength for the shortest wavelength of interest. In the present setup, the minimum and maximum frequencies of interest were set to 50 Hz and 2500 Hz, respectively, leading to a total simulation time of 0.02 s.

Data were sampled at a frequency of 50 kHz at both the backplate and face sheet to compute the surface impedance distribution using Dean's method [11]. Additionally, ten virtual probes were placed along the cen-

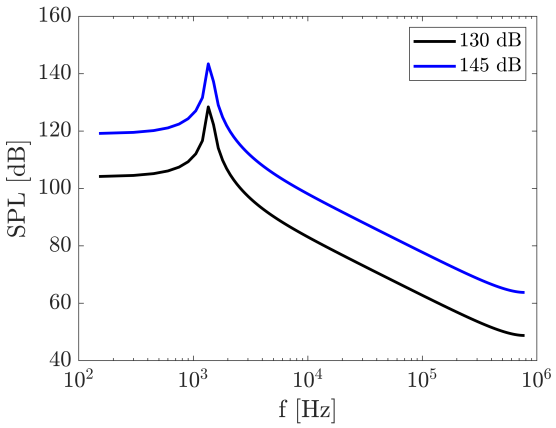


Figure 3. Sound pressure level spectra given as input to the normal impedance tube simulations.

terline of the duct, evenly spaced between 0.228 m and 1.144 m above the liner. These probes were used to compute impedance, following the same methodology as in the experiments. In the subsequent analysis, data from the ten probes were averaged, and error bars indicate the minimum and maximum values of the computed impedance and absorption coefficients.

Before conducting simulations for all geometries of interest and plane acoustic waves, a grid resolution study was performed using three different resolutions: 10 vx/τ, 20 vx/τ, and 40 vx/τ. The face sheet thickness τ was chosen as the reference length scale since it is smaller than the orifice diameter [12]. The geometry selected for this study was the scanned configuration, owing to the availability of experimental results obtained using the normal impedance tube at the Federal University of Santa Catarina (UFSC), Brazil. The grid resolution study was conducted for a single condition: a tonal acoustic plane wave with an amplitude of 145 dB and a frequency of 1400 Hz due to significant nonlinear effects.

Results from the grid resolution study are presented in Figures 4 and 5, alongside experimental data for comparison. Two experimental datasets are reported: the black curve corresponds to results obtained using broadband noise excitation with an overall sound pressure level of 145 dB; the blue curve represents results from tonal acoustic wave excitation at 145 dB. The error bars indicate the minimum and maximum values obtained by performing experiments on four parts of the liner sample. As observed, the experimental NIT results with tonal acoustic excitation exhibit large fluctuations and trends that do not fully align with theoretical expectations. Consequently, the broadband source excitation case is considered as the reference.

The comparison between experimental and numerical results indicates that the simulations slightly overpredict the experimental resistance θ, while reactance χ values are in closer agreement. This discrepancy may arise from minor differences between the orifice geometries in the numerical simulations and those in the experiments, and differences in the acoustic excitation. The computational results demonstrate a converging trend with increasing grid resolution. A resolution of 20 vx/τ was selected as a suitable compromise between computational accuracy and cost.

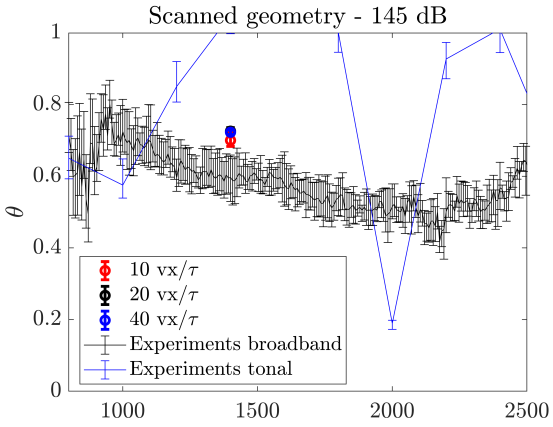


Figure 4. Resistance comparison between experiments and simulations carried out with three gird resolutions.

3. RESULTS

Acoustic results are presented in Figures 6, 7, and 8, where resistance and reactance components of impedance and the absorption coefficient are shown. The error bars indicate the maximum and minimum values computed using different virtual probes.

The analysis highlights the influence of the face sheet orifice geometry on the computed impedance and absorption coefficients. It is observed that resistance and reactance, as well as the absorption coefficient, vary with the orifice geometry. Specifically, the scanned and double chamfer geometries exhibit the lowest resistance, re-

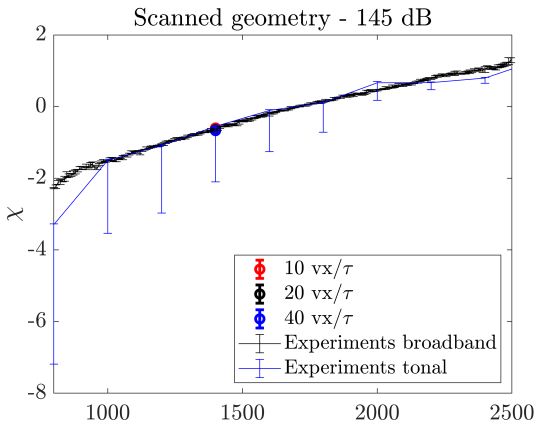


Figure 5. Reactance comparison between experiments and simulations carried out with three gird resolutions.

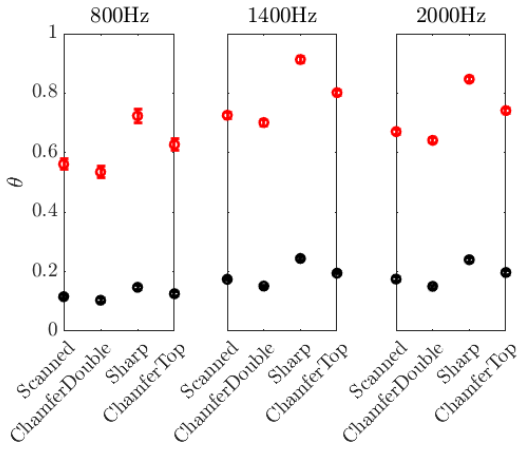


Figure 6. Resistance component comparison between geometries. Simulations were performed with acoustic plane waves with different frequencies and amplitudes equal to 130 dB (black) and 145 dB (red).

actance, and absorption, with minimal difference. When one edge is sharpened, as in the chamfer top geometry, resistance, reactance, and absorption increase, and they reach their highest values when both sides are sharpened in the sharp geometry for all the frequencies and SPLs.

The maximum mass flow rate across the orifices, obtained during the inflow and outflow phases, are presented in Figure 9 for all the test cases. It is observed that the trend of the in- and out-mass flow rate is the opposite of that seen in the acoustic impedance and absorption results. Specifically, the scanned and double chamfer geometries exhibit the highest mass flow rates, with minimal differences. When one edge is sharpened, as in the chamfer top geometry, the mass flow rate decreases, reaching its lowest values for the sharp geometry across all frequencies and SPLs.

Figure 10 presents the quality factor Q, computed by optimizing the fit between the theoretical and simulated vertical velocity across the analyzed frequencies (800, 1400, and 2000 Hz). The results indicate that, for most cases, Q follows a similar trend to the impedance, increasing as the orifice edges become sharper. This behavior is consistent with the theoretical relationship between Q and acoustic resistance, where a higher resistance leads to lower damping and thus a higher Q factor [13]. The scanned and double chamfer geometries exhibit the lowest Q values suggesting greater energy dissipation. Conversely, the chamfer top and sharp geometries yield the highest Q, indicating reduced dissipation. This trend is influenced by the vena-contracta effect, which alters the effective orifice area and modifies the in-orifice velocity dynamics [13], which will be discussed in the following.

The vertical velocity profiles, perpendicular to the face sheet, nondimensionalized by the speed of sound in air (a_∞), within the orifice at the midplane of the face sheet during the inflow and outflow phases are shown in Figure 11 for all SPL and frequency values. Each subfigure presents the velocity profiles for the four geometries, extracted in the middle of the face sheet thickness. The spanwise location corresponds to the plane crossing two orifices in the streamwise direction (refer to Figure 1). Notably, at 1400 Hz, the vertical velocities during both inflow and outflow phases exhibit the highest values. For SPL=130 dB, the peak velocity is significantly lower, approximately five times smaller than that at SPL=145 dB.

Comparing the different geometries, the sharp-edged orifice consistently exhibits the highest inflow velocities across nearly all SPL and frequency combinations. Conversely, the scanned and double chamfer geometries display similar velocity profiles, both during the inflow and outflow phases due to their comparable edge designs. The chamfer top geometry typically shows intermediate inflow velocities; however, during the outflow phase, it occasionally surpasses the sharp geometry in velocity magnitude. This velocity profile trend aligns with impedance and mass flow results (Figures 6–9). Sharp geometries, with the highest acoustic resistance and absorption, gener-

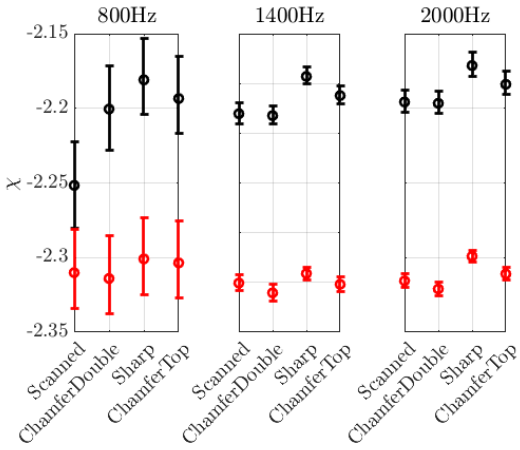


Figure 7. Reactance component comparison between geometries. Simulations were performed with acoustic plane waves with different frequencies and amplitudes equal to 130 dB (black) and 145 dB (red).

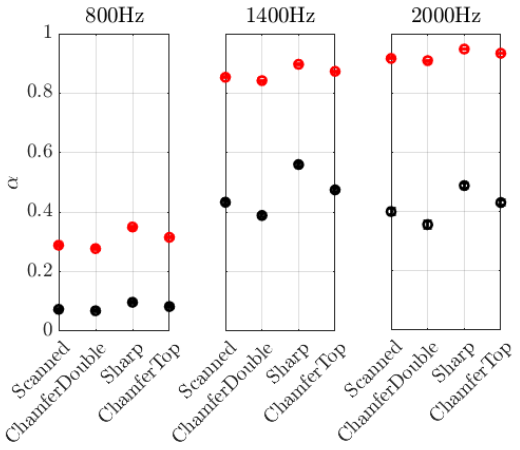


Figure 8. Absorption comparison between geometries. Simulations were performed with acoustic plane waves with different frequencies and amplitudes equal to 130 dB (black) and 145 dB (red).

ate intense localized inflow velocities, due to the vena contracta effect, also visible in the vertical velocity contours in Figure 12 (1st and 2nd rows). These contours highlight the pronounced flow contraction at the sharp inflow edge, which restricts the effective cross-sectional flow area, resulting in the lowest net mass flow. Scanned and double-chamfered geometries reduce flow contraction through symmetric edge treatments, lowering resistance and enabling higher mass flow despite diminished peak velocities. The chamfer top geometry balances these effects: its chamfered inflow edge mitigates separation, reducing resistance compared to the sharp case, while the sharp outflow edge increases expulsion resistance. This asymmetry explains why the chamfer top geometry achieves intermediate absorption (Figure 8) and occasionally exceeds the sharp geometry in outflow velocity acceleration. However, its overall mass flow remains lower than the scanned and double-chamfered cases due to residual outflow losses. These mechanisms scale consistently with SPL, reflecting acoustic forcing intensity.

It is interesting to notice, that the velocity profiles, for all the cases, are not symmetric within the orifice, thus suggesting that there is a fluid dynamic interaction between the orifices, even at the lowest SPL analyzed.

The horizontal velocity contours (Figure 12, 3rd & 4th rows) further clarify these dynamics. During the inflow (3rd row), sharp geometries exhibit larger recirculation zones that restrict mass flow. During the outflow (4th row), the sharp geometry's horizontal velocity field reveals a narrow, high-speed jet, whereas the scanned and double-chamfered geometries produce broader, slower jets. Chamfer top's outflow (4th row) combines features of both: its sharp bottom edge generates a jet, while the chamfered top edge from the inflow phase minimally perturbs the expelled flow, explaining its intermediate mass flow and occasional velocity exceedance.

Figure 13 illustrates the root-mean-square (RMS) contours of vertical velocity fluctuations during the inflow and outflow phases at 145 dB and 1400 Hz. During the inflow (1st row), the sharp-edged orifice exhibits the highest RMS values near the orifice walls, consistent with intense turbulent shear layers generated by abrupt flow contraction and vena contracta effects. The chamfer top geometry shows moderately high RMS levels at the orifice walls but the highest fluctuations inside the cavity, likely due to asymmetric vorticity generation from its chamfered inflow edge interacting with the sharp outflow edge. In contrast, scanned and double-chamfered geometries display minimal RMS amplitude at the walls and low fluctuations within the cavity, reflecting their smoother inflow patterns and reduced flow separation. During the outflow (2nd row), the sharp geometry produces the strongest RMS fluctuations outside the orifice, indicative of turbulent jet expulsion, while the chamfer top shows elevated wall-adjacent fluctuations. Scanned and double-chamfered cases maintain low RMS values at both loca-

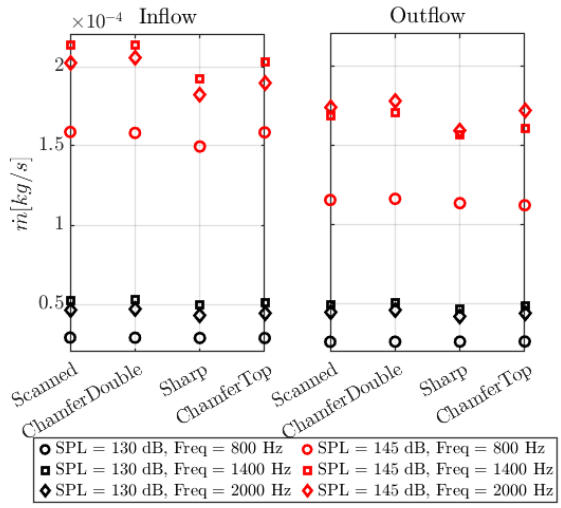


Figure 9. Mass flow comparison between geometries.

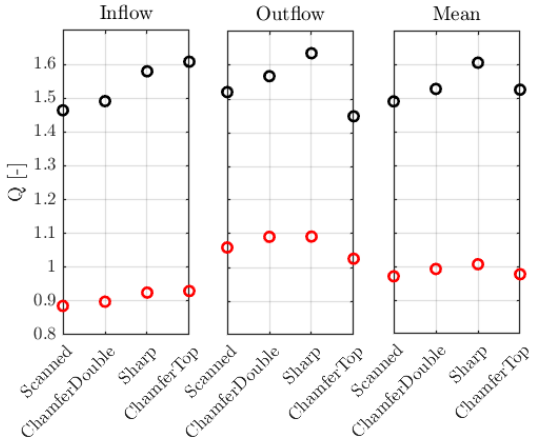


Figure 10. Quality factor comparison between geometries. (130 dB (black) and 145 dB (red))

tions. Asymmetry in the RMS contours across all geometries emphasizes the three-dimensional nature of vortex shedding and turbulence.

4. CONCLUSIONS

This work systematically evaluates the influence of orifice edge geometry on the performance of acoustic liners through high-fidelity CFD simulations. By analyzing four configurations under varying SPLs and frequencies, key insights into the interplay between edge geometry, acoustic impedance, and flow dynamics are established. The sharp-edged orifice maximizes acoustic resistance and absorption. In contrast, unsharpened edges (scanned and double-chamfered geometries) reduce acoustic absorption and facilitate higher mass flow rates within the orifices.

RMS velocity fluctuations highlight the role of edge geometry in vortex generation, with the sharp edges producing intense shear layers. These findings emphasize that manufacturing imperfections—often dismissed in idealized models—critically influence liner performance. For industries relying on perforated liners, this study underscores the importance of stringent quality control to minimize geometric deviations and calibrate predictive tools to account for real-world imperfections.

5. ACKNOWLEDGMENTS

The is co-funded by the European Union (ERC, LINING, 101075903). Views and opinions expressed are however those of the author(s) only and do not necessarily reflect those of the European Union or the European Research Council. Neither the European Union nor the granting authority can be held responsible for them. The work is partially supported by the AeroAcoustics Research Consortium (AARC), a government-industry partnership supporting pre-competitive research for aircraft noise reduction. L. Meirelles acknowledges scholarship funding from CNPq (168115/2023-9). The authors acknowledge Fundação CERTI (Brazil) for their contributions to the metrological aspects of this research.

6. REFERENCES

[1] D. Casalino, F. Diozzi, R. Sannino, and A. Paonessa, "Aircraft noise reduction technologies: A bibliographic review," *Aerospace Science and Technology*, vol. 12, no. 1, pp. 1–17, 2008.

[2] M. J. Smith, *Aircraft Noise*, vol. 3. Cambridge, UK: Cambridge University Press, 2004.

[3] E. Envia, "Fan noise reduction: an overview," *International Journal of Aeroacoustics*, vol. 1, no. 1, pp. 43–64, 2002.

[4] K. Mahesh, S. K. Ranjith, and R. Mini, "Recent advancements in helmholtz resonator based low-frequency acoustic absorbers: a critical review,"

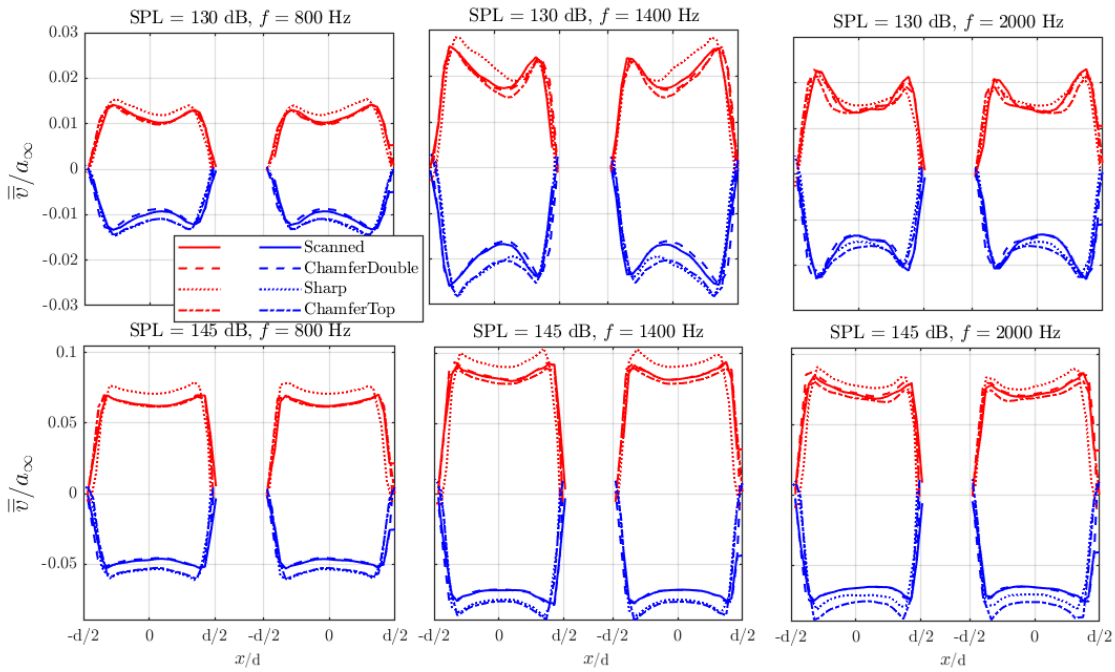


Figure 11. Phase-averaged velocity profiles at the center of the circular apertures for all investigated cases during the inflow (red) and outflow (blue) phases.

Archives of Computational Methods in Engineering, vol. 31, no. 4, pp. 2079–2107, 2024.

[5] A. Selamet and I. Lee, "Helmholtz resonator with extended neck," *The Journal of the Acoustical Society of America*, vol. 113, no. 4, pp. 1975–1985, 2003.

[6] S. Huang, X. Fang, X. Wang, B. Assouar, Q. Cheng, and Y. Li, "Acoustic perfect absorbers via helmholtz resonators with embedded apertures," *The Journal of the Acoustical Society of America*, vol. 145, no. 1, pp. 254–262, 2019.

[7] J. Guo, X. Zhang, Y. Fang, and Z. Jiang, "A compact low-frequency sound-absorbing metasurface constructed by resonator with embedded spiral neck," *Applied Physics Letters*, vol. 117, no. 22, 2020.

[8] C. Song, S. Huang, Z. Zhou, J. Zhang, B. Jia, C. Zhou, Y. Li, and Y. Pan, "Perfect acoustic absorption of helmholtz resonators via tapered necks," *Applied Physics Express*, vol. 15, no. 8, p. 084006, 2022.

[9] L. A. Bonomo, N. T. Quintino, J. A. Cordioli, F. Avallone, M. G. Jones, B. M. Howerton, and D. M. Nark, "A Comparison of Impedance Eduction Test Rigs with Different Flow Profiles," in *AIAA AVIATION 2023 Forum*, (San Diego, CA, USA), American Institute of Aeronautics and Astronautics, 2023.

[10] P. Morse and U. Ingard, *Theoretical Acoustics*. Princeton, New Jersey, USA: Princeton University Press, 1 ed., 1986.

[11] P. Dean, "An in situ method of wall acoustic impedance measurement in flow ducts," *Journal of Sound and Vibration*, vol. 34, pp. 97–IN6, May 1974.

[12] F. Avallone and C. Damiano, "Acoustic-induced velocity in a multi-orifice acoustic liner grazed by a turbulent boundary layer," in *AIAA AVIATION 2021 FORUM*, AIAA AVIATION Forum, American Institute of Aeronautics and Astronautics, July 2021.

[13] O. Léon, F. Méry, E. Piot, and C. Conte, "Near-wall aerodynamic response of an acoustic liner to harmonic excitation with grazing flow," *Experiments in fluids*, vol. 60, pp. 1–18, 2019.

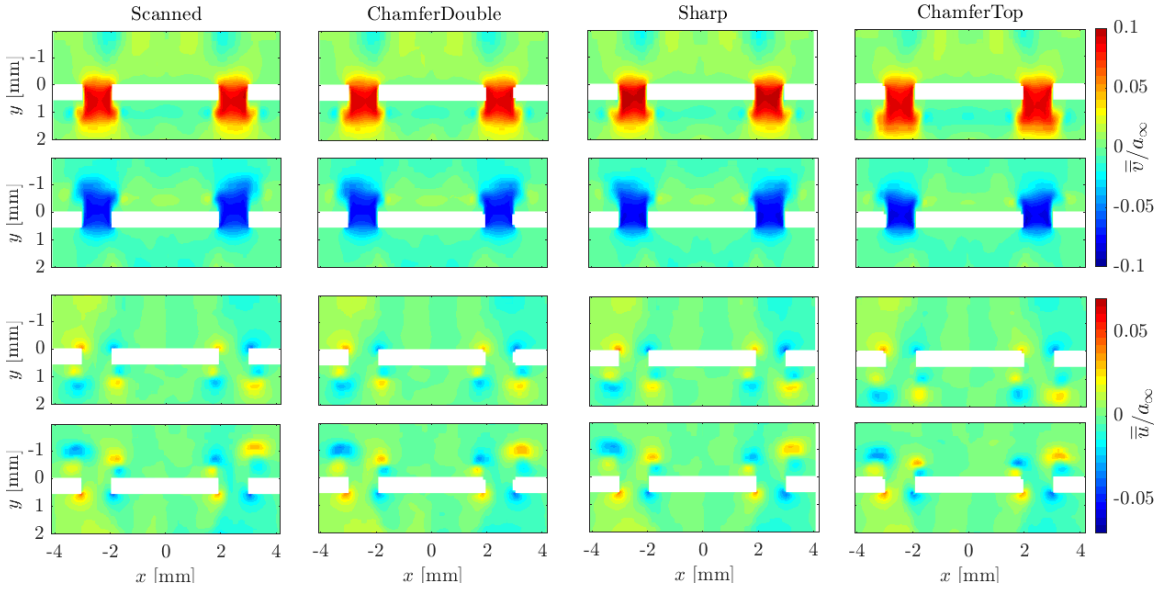


Figure 12. Comparison between geometries of the phase-averaged contours of the vertical velocity (1st & 2nd rows) and the horizontal velocity (3rd & 4th rows), at inflow (1st & 3rd rows), and outflow (2nd & 4th rows) at 145 dB and 1400 Hz.

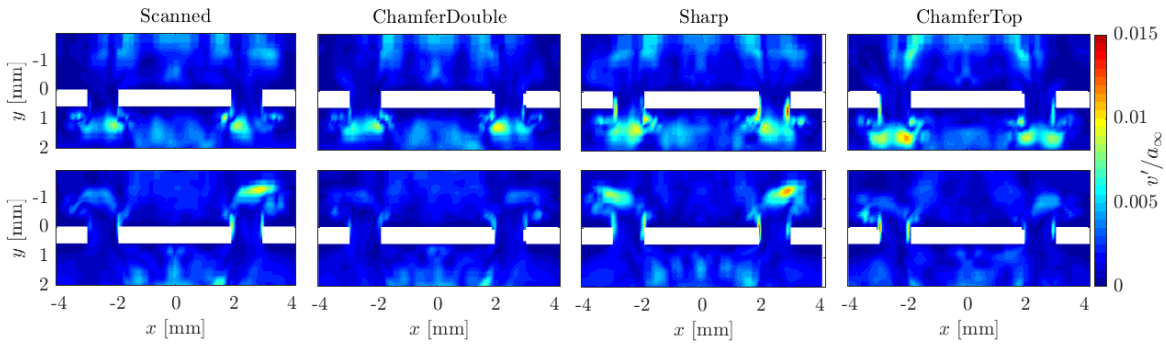


Figure 13. Comparison between geometries of the RMS contours of the vertical velocity at inflow (1st row), and outflow (2nd row) at 145 dB and 1400 Hz.

DOI: 10.61782/fa.2025.0376



FORUM ACUSTICUM
EURONOISE 2025

EXPERIMENTAL INVESTIGATION INTO THE SUPPRESSION OF PROPELLER NOISE USING OVER-TIP-ROTOR LINERS

Sergi Palleja-Cabre[1*] **Jona Ballgjati**[2] **Chaitanya Paruchuri**[1]
Phillip Joseph[1] **Francesco Avallone**[2]
[1] Institute of Sound and Vibration Research, University of Southampton, Southampton, UK
[2] Department of Mechanical and Aerospace Engineering, Politecnico di Torino, Torino, Italy

ABSTRACT

This paper presents an experimental study on suppressing propeller noise in a short duct configuration by installing Over-Tip-Rotor (OTR) liners on the wall casing. Far-field noise measurements are reported alongside in-duct pressure measurements at the wall obtained using an axial and azimuthal microphone array installed upstream of the propeller plane. In-duct measurements reveal that the OTR liner is effective in reducing broadband noise, achieving up to 4 dB of noise reduction over 1-5 BPFs. The axial decay of tonal components was compared with an analytical solution based on the Green's function of an axial dipole source, requiring a large number of cut-off modes to match the experimental observations. The findings emphasise the importance of evanescent modes in compact duct acoustics, with direct implications for source modification, scattering effects, and far-field radiation.

Keywords: *OTR liners, propeller noise, noise suppression, ducted rotors*

1. INTRODUCTION

Compact ducted propellers, also known as shrouded propellers, have regained attention in the development of Unmanned Aerial Vehicles (UAVs) and Urban Air Mobility (UAM) solutions due to their potential advantages in thrust augmentation, noise reduction, and operational safety. Several studies have shown that incorporating a duct can lead to a significant increase in thrust compared to an open propeller configuration [1, 2]. The integration of a duct enhances safety by providing a protective barrier or blade containment. This feature is particularly advantageous in densely populated areas where UAVs and UAM vehicles are expected to operate.

Recent studies have investigated the effect of a short duct on propeller noise. Overall noise reductions can be achieved in some conditions, but the effect of the duct on noise radiation can vary significantly between hover and in-flight conditions. Malgoezar et al. [3] conducted experiments on both isolated and shrouded propellers in hover and in-flight conditions. In hover, the use of the duct reduced the Blade Passing Frequency (BPF) tone while increased broadband noise by up to 20 dB. In contrast, the increase in broadband noise was significantly lower in-flight conditions. Cuppoletti and Riley [4] also found an increase in tonal noise at all BPFs and in broadband noise when including a shroud in their experimental investigation of ducted and unducted propellers at hover and at constant RPM. More recently, Go et al. [5] studied a 12-inch propeller experimentally and numerically with and without a shroud, finding that the shroud reduced propeller loading by generating additional thrust. This led to lower tonal noise from the blades in comparison to an isolated propeller. However, while the shroud decreased tonal noise downstream, it increased it upstream compared to an isolated propeller.

Ducted propellers can accommodate the installation of acoustic treatments to further mitigate propeller noise. Acoustic liners are widely used in aero engines, and maximising the treatment area is desirable for noise reduction. The treatment of the area directly above the fan

*__Corresponding author__: s.palleja-cabre@soton.ac.uk.
__Copyright__: ©2025 Sergi Palleja-Cabre et al. This is an open-access article distributed under the terms of the Creative Commons Attribution 3.0 Unported License, which permits unrestricted use, distribution, and reproduction in any medium, provided the original author and source are credited.

casing, i.e., Over-Tip-Rotor/Over-The-Rotor (OTR) liners, has been investigated experimentally by NASA over the last two decades [6] and has shown the potential of this technology to increase the treated area and enhance the suppression of fan noise.

The mechanisms of noise reduction of OTR liners have been investigated analytically [7–9], numerically [10, 11] and experimentally [6, 12] in recent years. The noise reductions are mainly attributed to a combination of: (1) conventional noise attenuation by the liner, which can be enhanced by a larger fluid particle oscillation through the acoustically treated wall due to the close proximity to the fan [8], and (2) source modification effects, which include both acoustic back-reaction effects changing the power output of the source [7, 11], and hydrodynamic changes affecting the unsteady blade loading [8, 10, 12].

Despite OTR liners were originally developed for aero-engine applications, recent work has been carried out to investigate their application for smaller, more compact, ducted propellers for UAV and UAM vehicles. The technology is particularly suitable for such applications due to the much lower area available for acoustic treatments. Some of these works include an experimental investigation by Zhong et al. [13] with OTR side-branch tubes to reduce tonal noise and the numerical work of Zhao et al. [10] showing the influence of the liner on the tip leakage flow.

The current paper is an extension of a previous study by the authors investigating the reduction of shrouded propeller noise with OTR liners [14]. Far-field noise results were presented in [14] for two types of liners - a Single Degree of Freedom (SDOF) liner and a grooved metal foam liner - placed in an OTR position, upstream and downstream of the propeller. The modular shroud used in the experiment featured either a bellmouth intake or an unflanged intake. The geometry of the intake was found to have a major influence on the flow characteristics upstream of the propeller plane and the sources of propeller noise. The study found that OTR liners can reduce overall sound pressure levels by up to 5 dB near the propeller axis, with peak noise reductions in the PWL spectra reaching 6 dB in both tonal and broadband noise. The current study extends this previous investigation by instrumenting the propeller duct with an axial and azimuthal array to gain understanding of the source near-field and how it is impacted by the OTR liner.

2. EXPERIMENTAL SET-UP

2.1 Shrouded propeller rig

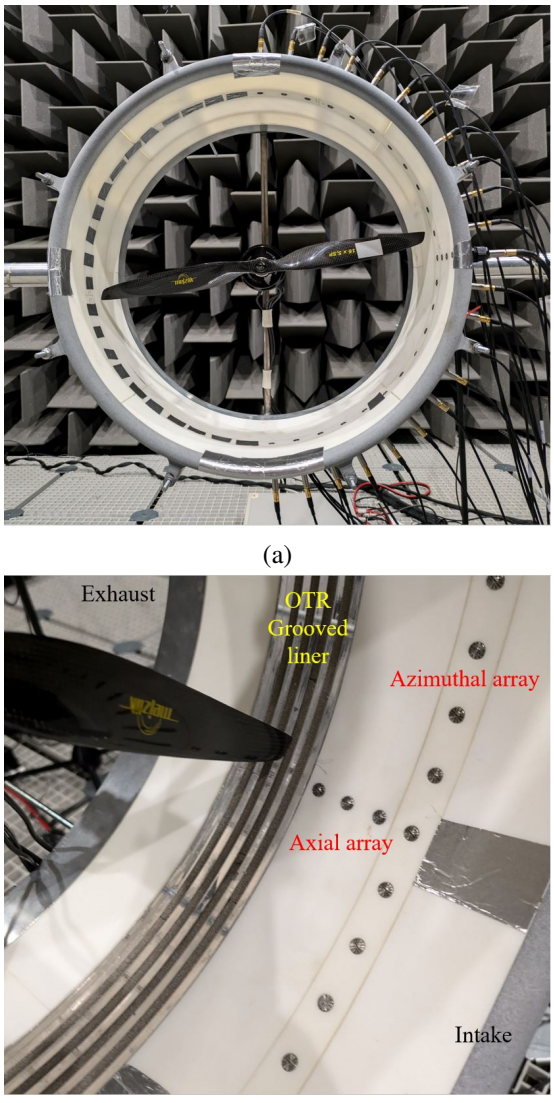
The experiments were carried out on a modular ducted rotor rig with a single propeller, described in [14]. The propeller, motor, and loadcell are held on the shroud axis by a pair of vertical rods. The duct consists of a series of modular sections that allow for varying the length of the shroud, instrumenting the duct with in-duct microphones, installing acoustic treatments in the casing, and modifying the intake geometry. The current investigation was performed with a simple rounded intake and for two configurations: (a) hard wall baseline, and (b) an acoustic liner installed over the propeller tip. The picture of the rig for each configuration is shown in Fig. 1. In both cases, the length of the duct is $L = 260$ mm and the diameter is $D = 410$ mm, resulting in a compact ducted propeller configuration with $L/D \approx 0.6$. The propeller is at an axial distance $z_{prop} = 105$ mm from the duct exhaust.

The rotor was powered by a U7-V2.0 KV420 Brushless T-motor mounted on a MINI45 ATI 6-axis loadcell. The electronic speed controller used in conjunction with the motor was a Master Mezon 135 opto unit. An ICP Laser Tachometer sensor was used to measure the propeller rotational speed (Rotations Per Minute, RPM). A 2-bladed MEJZLIK propeller with a diameter of 16 inches was used in this investigation. All the results in this article were acquired with a constant thrust of the propeller of $T = 10$ N with a corresponding RPM of approximately $N = 4600$. The thrust provided by the shroud has not been considered in this investigation.

2.2 Microphone instrumentation

The experiments were carried out at the Institute of Sound and Vibration Research's anechoic chamber of dimensions 6.7 m $\times$ 6.7 m $\times$ 4.9 m. The walls are acoustically treated with open-cell polyurethane wedges whose cut-off frequency is 70 Hz. Far-field noise measurements were obtained by using 3 1/4" GRAS 40PL-10 CCP microphones located in the forward arc (upstream of the propeller). The microphones were located at a distance of 2.5 m centred on the propeller rig and at polar angles of $\phi = 0°$, 45°, and 90°, where 0° is on the propeller axis. In-duct pressure measurements were performed by using an axial and azimuthal array in a cross-configuration, as shown in Fig. 1b. A total of 25 quarter-inch GRAS 40PL-10 CCP microphones were flush mounted on the intake casing, 3 (+1) on the axial array ($z_{axial} = 32 - 85$ mm

upstream of the propeller plane), and 22 in the azimuthal array ($z_{azm} = 85$ mm upstream of the propeller plane), equally spaced between $\theta = 0°$ and 180°. The data were acquired for a duration of 10 s at a sampling frequency of 40 kHz.



(a)

(b)

Figure 1: Ducted propeller rig; photograph of the rig with for the (a) hard wall baseline (front view), and (b) OTR liner configuration (detailed view of instrumentation).

2.3 Acoustic liner properties

The acoustic liner considered in this investigation is a grooved liner in which the annular grooves are filled with a nickel chromium alloy metal foam flush with the inner wall of the duct. This is a semi-locally reacting liner that is locally reacting in the axial direction and non-locally reacting in the azimuthal direction, as described in [15, 16]. The liner has a Percentage Open Area POA$= 44\%$ [1], a cavity depth $d = 17.5$ mm and a porosity of the metal foam $\sigma = 90\%$. The total length of the liner module on the tip of the propeller is $l = 50$ mm long, as for the hard-wall baseline configuration.

3. FAR-FIELD NOISE REDUCTION

The aim of this section is to present the far-field noise spectra for the hard wall baseline and the acoustically treated configuration. Results are only presented for the microphone on-axis ($\theta = 0°$) for brevity. The far-field PWL noise spectra integrated in the forward arc and the directivity of these two configurations were presented in the preceding investigation [14].

The Sound Pressure Level (SPL) spectra for the hard wall baseline and lined configurations are shown in Fig. 2a. Measurements of the flow characteristics upstream of the propeller for the 'lip' intake, used in the current investigation, identified a region of flow separation at the lip centred around 90% of the radius [14]. This was related to significantly higher levels of tonal and broadband noise than with a streamlined bellmouth intake that prevents such separation from occurring. The current configuration with the 'lip' intake, therefore, presents stronger tones than the bellmouth, likely caused by the periodic chopping of eddies in the incoming separated flow (tonal) and turbulence leading edge interaction noise (broadband). This discussion is recalled here to explain the strong broadband component of the SPL spectra in Fig. 2a, which becomes dominant over tonal noise from about $10 \times$ BPF.

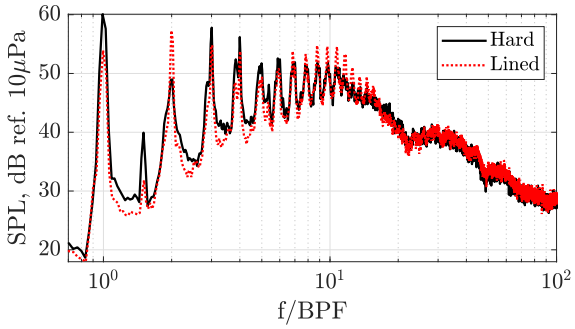
The noise sources outlined above are arguably independent of whether a hard or lined configuration is considered, other than possible hydrodynamic modifications on the source caused by the OTR liner, which shall be discussed in further detail later in the paper. The results in Fig. 2a show that the OTR liner yields modest reductions

[1] This POA only accounts for the grooved area relative to the total liner area and not the open area of the metal foam within the grooves.

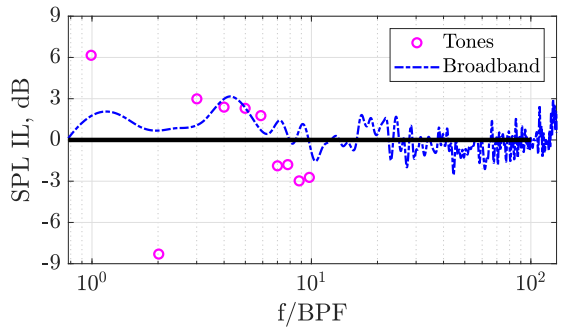
in broadband noise of 1-3 dB at frequencies between BPF and 10 × BPF. The first BPF tone is reduced by 6 dB, but the reductions are smaller at other harmonics, and the higher harmonics in the liner configuration can even be larger than for the hard wall baseline. The same results are shown in Fig. 2b in the form of SPL Insertion Loss (IL), that is,

$$\mathrm{IL} = \mathrm{SPL_H} - \mathrm{SPL_L} \quad , \quad \mathrm{dB}, \tag{1}$$

where $\mathrm{SPL_H}$ and $\mathrm{SPL_L}$ are the SPLs for the hard and lined configurations, respectively. The SPL IL in Fig. 2b is separated into the tonal and broadband contributions. Tonal SPL IL is only plotted up to 10 × BPF since broadband noise becomes dominant at higher frequencies. The observations from Fig. 2a are now clearer, and it also becomes evident that a strong noise increase is caused by the liner at the 2 × BPF tone, with some increase of tonal noise also at 6-10 × BPF. The broadband noise at frequencies above 10 × BPF is not significantly affected by the liner at this measurement location on the propeller axis.



(a) Sound Pressure Level (SPL)



(b) Insertion Loss (IL)

Figure 2: Far-field SPL and IL spectra at $\theta = 0°$.

4. IN-DUCT PRESSURE MEASUREMENTS

This section aims to present the pressure characteristics on the duct wall to understand the effect of the OTR liner on the near-field of the source and the propagation in the duct. To highlight the compactness of the problem, key length scales of the problem are compared to the wavelength at BFP ($\lambda \approx 2.2$ m) and harmonics in Table 1, namely duct diameter D, duct length L, and liner length l.

Table 1: Compactness of the problem at BPF and harmonics.

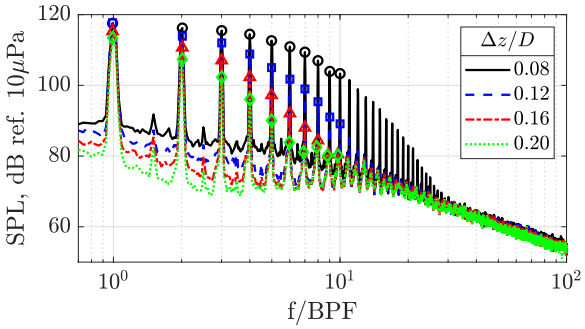
Frequency	D/λ	L/λ	l/λ
BPF	0.18	0.12	0.02
2 × BPF	0.37	0.23	0.05
3 × BPF	0.55	0.35	0.07
5 × BPF	0.92	0.59	0.11
10 × BPF	1.85	1.17	0.23

The compactness of the problem highlighted in Table 1 suggests that the role of evanescent or cut-off duct modes excited by the propeller and the struts can have a significant impact on the problem:

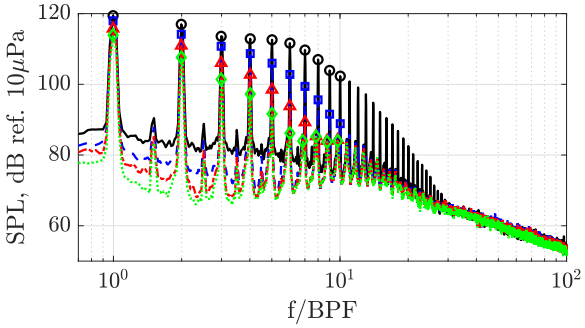
- Contributions to the far-field noise from evanescent modes scattered at the intake/exhaust [17].
- 'Trapped' modes in the short duct caused by evanescent modes reflected at the intake/exhaust.
- In the liner case, the effects of the acoustic back-reaction on the source can be significant at these low frequencies (low D/λ), which have been reported to be stronger for $e/\lambda < 0.5$ [7], were e is the distance between the source and the duct wall.
- Also in the case with the liner, scattering of evanescent modes acoustically close to the impedance discontinuity (low l/λ) can have a significant effect on the noise reduction performance [11].

The SPL spectra, measured along the axial array, are shown in Fig. 3a and Fig. 3b for the hard wall and lined configurations. Also shown are the tonal amplitudes of the first 10 BPFs. The distances Δz shown in the legend are relative to the propeller plane. The general trends in both configurations show a rapid decay of the tonal components when increasing the axial separation distance to

the source plane Δz. Furthermore, significant decay in broadband noise of up to 10 dB can also be observed in both cases for frequencies below 10 × BPF.



(a) Hard wall



(b) Lined

Figure 3: Axial variation of the wall SPL spectra for the hard wall and lined configurations.

The decay in tonal SPL at the harmonics of the BPF is found to be close to exponential. The SPL decay for the first 3 BPFs is shown in Fig. 4a for both the hard wall and lined configurations. Also shown is a linear fit of the tonal levels along the array. The decay rates in dB/m are summarised in Table 2. It can be observed that the decay is similar in both configurations, which is expected since these measurements are obtained at the hard wall section upstream of the propeller.

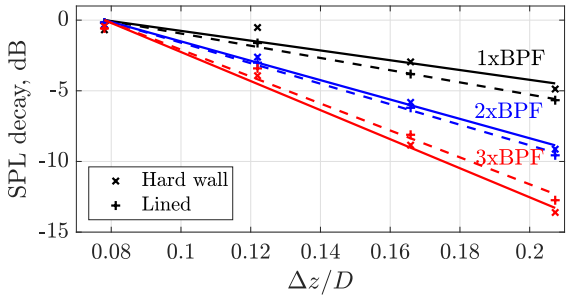
The measured decay of the BPF tone is compared with analytical predictions [7] in Fig. 4b. The predictions are obtained by evaluating the wall pressures at the wall of an infinite hard wall duct containing a point axial dipole located at 95% of the radius. The Green's function formulation used in this instance [7] is obtained from the monopole Green's function in Rienstra and Tester [18]. The number of modes included in the solution is controlled by the Cut-Off Ratio (COR). The definition used here for the COR for a mode with radial wavenumber α, at frequency ω and mean flow Mach number M is

Table 2: Tonal decay rates in dB/m for the lined and hard wall configurations.

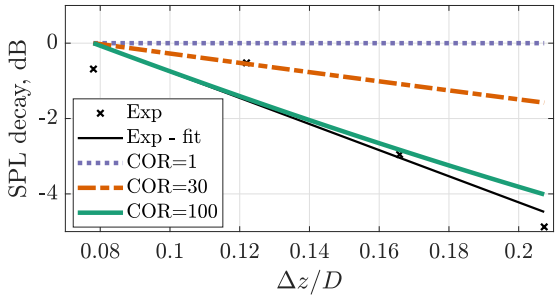
BPF	Hard wall	Lined
1	-84.5	-105.4
2	-167.2	-177.1
3	-250.8	-223.3

$$\text{COR} = \frac{\alpha\sqrt{1-M^2}}{\omega} \quad . \tag{2}$$

For a given COR, all the modes with α smaller than $\omega\text{COR}/\sqrt{1-M^2}$ are therefore included in the solution.



(a) Measured decay of the BPF, 2xBPF and 3xBPF tones.



(b) Measured and predicted decay of the BPF tone.

Figure 4: Decay of tonal SPL along the axial array.

The analytical solutions shown in Fig. 4b are obtained with a COR of 1, 30 and 100. For the case with COR=1, only cut-on modes are included in the solution.

At the BPF frequency, only the plane wave is cut-on. The other two cases, COR=30 and COR=100, include a certain number of evanescent modes. At the BPF frequency, COR=30 corresponds to a total of 20 evanescent modes included in the solution and COR=100 corresponds to a total of 425. The comparison in Fig. 4b shows that a large number of evanescent modes are required in the analytical solution to obtain the rapid decay observed in the experiment. This result highlights the importance of the cut-off modes in the current problem and the need for further investigation to clarify its impact on the noise reduction characteristics of OTR liners and the noise radiation to the far-field.

The Insertion Loss spectra are presented in Fig. 5 to appreciate more clearly the effect of the OTR liner in the in-duct pressure field. It is observed that the liner only has a modest effect of ± 2 dB in the tonal noise, and that the variation across different axial locations is within 2 dB. In contrast, 4 dB of broadband noise reduction can be observed at most microphone locations for frequencies below 10 $\times$ BPF, with some variation across the array. In particular, weaker reductions are observed in the microphone closest to the propeller plane ($\Delta z = 0.08$).

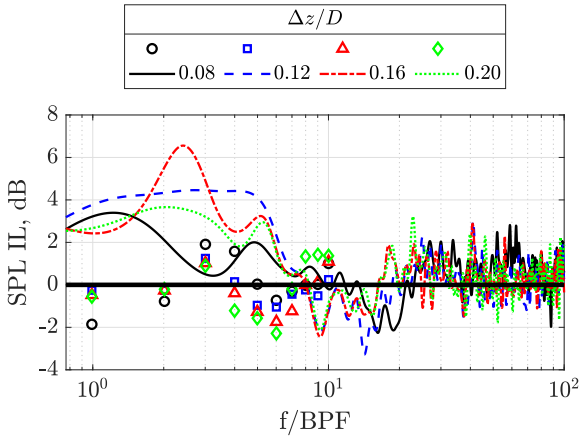
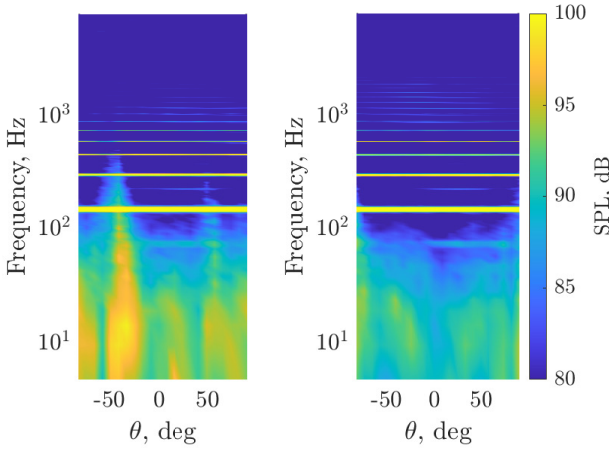


Figure 5: Axial variation of the Insertion Loss measured at the duct wall.

Very little variation in SPL IL would be expected between microphones in the axial array since they are all located in the hard wall section upstream of the liner. The differences observed in Fig. 5 may therefore be attributed to a different distribution of the modal amplitudes between the hard wall and lined case between the two configurations caused by (1) changes on the source caused by the OTR liner (source modification effects), and/or (2) modal scattering at the impedance discontinuity between the OTR liner and the hard wall section.

The azimuthal microphone array is now used to show the SPL spectra variation along the circumference over the 180° aperture of the array. This is presented in the form of contour plots in Fig. 6a and Fig. 6b for the hard wall and lined configurations, respectively. The wall pressure fluctuations around the duct present significant non-uniformity, especially at low frequencies below the first BPF, with up to 10 dB variations along the circumference. These results suggest significant non-uniformities in the flow field, potentially caused by the separation at the inlet lip, the development of the boundary layers, or non-uniformities in the impinging flow itself. Further investigation is needed to characterise the flow in the duct and provide insights into this discrepancy. However, the frequencies at which the liner has been found to be most effective in reducing noise in the far-field and in the in-duct axial array results are not affected by this contamination (the axial array is located at $\theta = 0°$).



(a) Hard wall (b) Lined

Figure 6: Azimuthal variation of the wall SPL spectra for the hard wall and lined configurations.

5. CONCLUSIONS

This paper has presented an experimental investigation on the reduction of propeller noise with Over-Tip-Rotor liners on a modular compact ducted propeller rig. In-duct wall pressure measurements indicate that OTR liners are effective in reducing broadband noise, yielding some 4 dB of noise reduction at frequencies between BPF and 5xBPF. This is in contrast to a modest effect of the liner of only ± 2 dB in tonal noise. Conversely, the far-field results (on axis) show up to 6 dB of noise reduction at the BPF tone and almost 9 dB of noise increase at the 2xBPF tone. The axial decay in the amplitude of the tones was compared to an analytical solution based on the Green's function of an axial dipole source. A large number of cut-off modes were required in the analytical solution to match the decay observed in the experiments. The main observation of this investigation is the importance of the evanescent modes in such compact ducts. This has direct implications for the source modification and scattering effects associated with OTR liners and in the radiation of these evanescent modes to the far-field. Future work is planned to understand the flow non-uniformities in the duct and the sources, as well as to investigate further the role of evanescent modes in hard and lined compact ducts.

6. ACKNOWLEDGMENTS

This project was supported by the Department for Science, Innovation and Technology and the Royal Academy of Engineering under the Research Fellowships scheme (RF-201819-18-194 and RF-2324-23-289). The work of F.A. is co-funded by the European Union (ERC, LINING, 101075903). Views and opinions expressed are however those of the author(s) only and do not necessarily reflect those of the European Union or the European Research Council. Neither the European Union nor the granting authority can be held responsible for them.

7. REFERENCES

[1] S. Yilmaz, D. Erdem, and M. S. Kavsaoglu, "Performance of a ducted propeller designed for UAV applications at zero angle of attack flight: An experimental study," *Aerospace Science and Technology*, vol. 45, pp. 376–386, 2015.

[2] T. Zhang and G. N. Barakos, "High-fidelity numerical analysis and optimisation of ducted propeller aerodynamics and acoustics," *Aerospace Science and Technology*, vol. 113, p. 106708, 2021.

[3] A. M. Malgoezar, A. Vieira, M. Snellen, D. G. Simons, and L. L. Veldhuis, "Experimental characterization of noise radiation from a ducted propeller of an unmanned aerial vehicle," *International Journal of Aeroacoustics*, vol. 18, no. 4-5, pp. 372–391, 2019.

[4] D. R. Cuppoletti and T. Riley, "Time-Resolved Flow Field and Acoustic Measurements of a Ducted and Unducted Rotor," in *28th AIAA/CEAS Aeroacoustics Conference, 2022*, 2022.

[5] S. T. Go, M. J. Kingan, Y. Wu, and R. N. Sharma, "Experimental and numerical investigation of the sound field produced by a shrouded UAV propeller," *Applied Acoustics*, vol. 211, p. 109523, 2023.

[6] D. L. Sutliff, R. F. Bozak, M. G. Jones, and D. M. Nark, "Investigations of three over-the-rotor liner concepts at various technology readiness levels," *International Journal of Aeroacoustics*, vol. 20, no. 5-7, pp. 826–866, 2021.

[7] S. Palleja-Cabre, B. J. Tester, and R. J. Astley, "Modelling of ducted noise sources in the proximity of acoustic liners," *Journal of Sound and Vibration*, vol. 517, no. October 2021, p. 116548, 2022.

[8] Y. Sun, X. Wang, L. Du, and X. Sun, "On the flow-acoustic coupling of fan blades with over-the-rotor liner," *Journal of Fluid Mechanics*, vol. 941, pp. 1–35, 2022.

[9] S. Palleja-Cabre, B. J. Tester, and R. J. Astley, "Modeling of Over-Tip-Rotor Liners for the Suppression of Fan Noise," *AIAA Journal*, vol. 60, no. 11, pp. 6361–6373, 2022.

[10] P. Zhao, Z. Zhao, and C. Yang, "Investigation of the orifice flow of over-the-rotor liner and its interaction with the rotor flow field," *Physics of Fluids*, vol. 35, no. 10, 2023.

[11] R. R. Subramanyam, S. Palani, P. Chaitanya, and S. Palleja-Cabre, "On the noise reduction mechanisms of over-tip liners," vol. 43, pp. 29–43, 2024.

[12] S. Palleja-Cabre, I. Saraceno, and P. Chaitanya, "On the modification of tip leakage noise sources by over-tip liners," *Physics of Fluids*, vol. 36, no. 2, 2024.

[13] T. Zhong, C. Yang, and M. Åbom, "Tonal noise reduction of an electric ducted fan using over-the-rotor acoustic treatment," *Applied Acoustics*, vol. 205, p. 109298, 2023.

[14] S. Palleja-Cabre, E. Macey, P. Chaitanya, and P. Joseph, "Reduction of shrouded propeller noise with Over-Tip-Rotor liners," in *30th AIAA/CEAS Aeroacoustics Conference, 2024*, vol. AIAA 2024-, pp. 1–14, 2024.

[15] S. Rienstra, "Contributions to the theory of sound propagation in ducts with bulk-reacting lining," *Journal of Acoustical Society of America*, vol. 77, no. 5, pp. 1681–1685, 1985.

[16] S. Palleja-Cabre, B. J. Tester, R. J. Astley, and H. Beriot, "Impedance modelling of acoustically treated circumferential grooves for over-tip-rotor fan noise suppression," *International Journal of Aeroacoustics*, vol. 0, no. 0, pp. 1–17, 2020.

[17] B. Baddour, P. Joseph, A. McAlpine, and R. Leung, "Acoustic radiation characteristics of cutoff modes from ducts," *Journal of Sound and Vibration*, vol. 541, no. June, p. 117306, 2022.

[18] S. W. Rienstra and B. J. Tester, "An analytic Green's function for a lined circular duct containing uniform mean flow," *J. Sound Vib.*, vol. 317, no. 3-5, pp. 994–1016, 2008.

DOI: 10.61782/fa.2025.0438



FORUM ACUSTICUM
EURONOISE 2025

IDENTIFICATION OF AN ACTUATION MANIFOLD FOR OPEN-LOOP CONTROL OF SUBSONIC JET NOISE WITH ACOUSTIC-BASED EXCITATION

Luca Franceschelli* **Marco Raiola** **Andrea Ianiro** **Stefano Discetti**

Department of Aerospace Engineering, Universidad Carlos III de Madrid,
Avda. Universidad 30, Leganés, 28911, Madrid, Spain

ABSTRACT

Subsonic jet noise remains a key contributor to aircraft noise, particularly during takeoff. While reducing jet velocity has helped, further mitigation requires controlling turbulent structures in the shear layer, which are primary sound sources. Active jet control offers a promising solution with minimal efficiency loss. This study investigates acoustic-based actuation in a turbulent subsonic jet. Experiments are conducted in the jet facility of the anechoic chamber at Universidad Carlos III de Madrid. Acoustic excitation is provided by counter-facing loudspeakers in the stagnation chamber, following an open-loop control strategy. The goal of this work is to explore the actuation manifold produced by the acoustic excitation using data-driven dimensionality-reduction techniques. Isometric Mapping (ISOMAP) and Proper Orthogonal Decomposition (POD) are applied to phase-averaged velocity fields measured via Particle Image Velocimetry, phase-locked with the actuation. The impact of actuation is further assessed using hydrodynamic pressure measurements in the shear layer and acoustic pressure in the far field. Results confirm the existence of an actuation manifold in the phase-averaged velocity fields. The influence of actuation on the jet is further supported by both shear-layer and far-field pressure measurements.

Keywords: Jet noise, Reduced Order Modelling, ISOMAP, flow control

**Corresponding author*: lfrances@ing.uc3m.es.

Copyright: *©2025 Franceschelli et al. This is an open-access article distributed under the terms of the Creative Commons Attribution 3.0 Unported License, which permits unrestricted use, distribution, and reproduction in any medium, provided the original author and source are credited.*

1. INTRODUCTION

Jet noise is a major contributor to aircraft noise pollution, particularly during takeoff and landing. Although advances in engine design and reductions in jet exhaust velocity have led to significant improvements, further noise reduction requires direct control of the turbulent structures in the jet shear layer, which are the primary sources of subsonic jet noise. Among emerging strategies, active flow control using acoustic excitation has shown promise in modifying the jet dynamics with minimal aerodynamic penalties [1].

Reduced-Order Modeling (ROM) has become central in the analysis and control of such complex flows. Classical techniques like Proper Orthogonal Decomposition (POD) offer a linear, energy-optimal decomposition of flow fields, providing compact representations useful for modeling and control [2, 3]. However, the inherently nonlinear behavior of turbulent and transitional jets often limits the effectiveness of such linear approaches in capturing the full extent of flow dynamics.

To overcome these limitations, nonlinear manifold learning methods aim to identify low-dimensional embeddings that reflect the true geometry of high-dimensional flow data. Isometric mapping (ISOMAP) [4], which preserves geodesic distances between flow snapshots, has recently shown promise in uncovering coherent structures in complex shear flows [5]. Compared to POD, ISOMAP has demonstrated better separation of flow regimes in experimental settings [6]. Furthemore, Marra et al. [7] have demonstrated that ISOMAP can be used to unveil "actuation manifolds", i.e., manifolds of flows under different types of actuations, with interpretable coordinates.

In this work, we apply ISOMAP to experimental data

from an acoustically-excited subsonic jet in a transitional regime, at $Re = 10,000$ (with the Reynolds number Re being based on the bulk jet velocity U_j and the nozzle diameter D). Open-loop actuation is applied via counter-facing loudspeakers mounted in the stagnation chamber, operating in phase. Measurements of the velocity field are acquired using Particle Image Velocimetry (PIV). Additionally, synchronized acoustic measurements using two sets of microphones are performed: four placed along the jet axis in the near field to track the evolution of pressure fluctuations, and two in the far field positioned at 30° and 90° relative to the jet axis. Synchronization with the actuation signal enables the computation of phase-averaged flow fields, capturing several phases of each periodic control actuation. The ability of ISOMAP to identify a low-dimensional actuation manifold in both turbulent and transitional regimes is assessed on phase-averaged flow fields. Results are compared with those obtained using POD, highlighting the advantages of nonlinear manifold learning in revealing coherent flow structures under periodic forcing. A similar analysis performed on the near- and far-field microphone temporal signals, however, failed in identifying a low-dimensional manifold, not providing a conclusive answer to whether a control manifold exists for the instantaneous noise measurements.

2. METHODOLOGY

The actuation manifold is identified using the ISOMAP algorithm, a nonlinear dimensionality-reduction technique that seeks to uncover a low-dimensional embedding that preserves geodesic distances between flow snapshots in a high-dimensional feature space. This section outlines the core steps of the methodology, which are further detailed in [7].

Let us consider a collection of M snapshots, each represented as a high-dimensional vector $\mathbf{u}_i \in \mathbb{R}^d$. The first pairwise distances between snapshots using the standard Euclidean norm are equal to:

$$\|\mathbf{u}_i - \mathbf{u}_j\| = \left(\sum_{m=1}^{d} \left| u_i^{(m)} - u_j^{(m)} \right|^2 \right)^{1/2}. \quad (1)$$

A neighborhood graph is constructed by connecting each snapshot to its k-nearest neighbors according to the Euclidean distance. The geodesic distances between all pairs of snapshots are then estimated as the shortest paths on this graph. The resulting geodesic distance matrix $\boldsymbol{D}_{\mathrm{G}} \in \mathbb{R}^{M \times M}$ approximates the manifold distances and serves as the basis for the embedding.

Classical multidimensional scaling (MDS) is then applied to compute the low-dimensional embedding $\Gamma = (\tilde{\gamma}_{ij})_{1 \le i \le M,\, 1 \le j \le n} \in \mathbb{R}^{M \times n}$. The optimal set of coordinates is obtained from the eigenvectors corresponding to the largest n eigenvalues of the double-centered squared distance matrix. Each snapshot $\mathbf{u}_i$ is mapped to $\boldsymbol{\gamma}_i \in \mathbb{R}^n$, preserving its geodesic relationships with other samples.

The quality of the embedding is evaluated using the *residual variance*, R_v, which measures how faithfully the embedding represents the geometry of the original dataset.

In this work, the ISOMAP algorithm is applied to a velocity field ensemble including 20 phase-averaged fields for each actuation at a distinct frequency, yielding a closed trajectory in the reduced-order manifold that captures the system's coherent response to forcing. ISOMAP has also been tested on portions of the time signal provided by the 2 sets of microphones. In this latter case no coherent trajectory has been identified in the reduced-order manifold, leaving open the question if a control manifold can be identified for the non-phase-averaged data.

3. EXPERIMENTAL SET-UP

The experiments are conducted in the jet facility located inside the anechoic chamber of Universidad Carlos III de Madrid [8]. The setup consists of an air jet issuing from a round nozzle with exit diameter $D = 10\,\mathrm{mm}$. The jet flow condition investigated correspond to a transitional jet at Reynolds number $Re = 10{,}000$, with natural transition inside the nozzle.

Open-loop acoustic forcing is applied in both cases using two counter-facing loudspeakers mounted in the stagnation chamber. A purely sinusoidal excitation is imposed through the loudspeakers at a set of discrete actuation frequencies f, selected to span a typical range of Strouhal numbers, defined as $St = fD/U_j$. The explored range covers $St \in [0.05, 1.2]$, with increments of 0.05. This corresponds to 24 actuation frequencies between 75 Hz and 1800 Hz. The acoustic signal is generated using two ND654 2 $\frac{1}{2}$" aluminum cone full-range drivers (4 Ω impedance), mounted in a counter-facing configuration. The input waveform is amplified using a Fosi Audio V1.0B stereo audio amplifier, and the output power supplied to the loudspeakers is fixed at 25 W. This configuration provides repeatable and robust acoustic excitation across the entire frequency range explored.

Two-component velocity fields are measured using

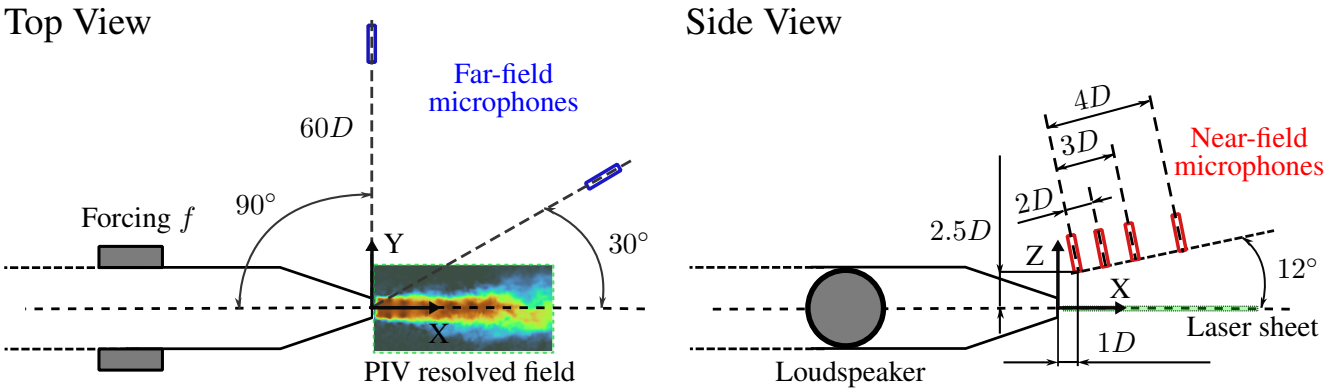


Figure 1: Sketch of the experimental setup. The top view (left) illustrates the positioning of the far-field microphones, while the side view (right) shows the placement of the near-field microphones.

PIV in the symmetry plane of the jet that intersects the axis of the two loudspeakers. The acquisition system consists of a 5.5 Mpx Andor Zyla sCMOS camera and a dual-cavity Nd:YAG laser operating up to 15 Hz with a pulse energy of 200 mJ. The flow is seeded with DEHS particles with a mean diameter of approximately 1 μm. The spatial resolution of the PIV setup is equal to 22.7 px/mm.

Image processing is performed using the PaIRS software developed at the University of Naples [9], with a final interrogation window of 32×32 px and 75% overlap. Optical reflections caused by the presence of four near-field microphones partially degrade the image quality. To mitigate this, a pre-processing step is applied to remove the background contribution. This is achieved using a POD-based technique, following the method described in [10], which enables efficient separation of the flow-induced particle signal from persistent light artifacts.

For each actuation frequency, phase-averaged velocity fields are obtained by synchronizing the non-temporally-resolved acquisition with the sinusoidal excitation signal. For each phase bin, 100 instantaneous velocity fields are recorded to ensure statistical convergence of the phase average. In total, 24 actuation frequencies are tested per flow condition, resulting in $M = 20 \times 24 = 480$ phase-averaged velocity fields for each case, which serve as the input for ISOMAP.

A rake of four Adafruit 1016 Electret Microphone Amplifier Boards (MAX4466) was installed in the near field, along with two GRAS 46AE microphones positioned in the far field. Microphone signals were acquired synchronously with both the actuation signal and the PIV system, at a sampling frequency of 200 kHz. A schematic of the experimental arrangement is shown in figure 1. The near-field microphones were arranged linearly along the jet development direction, inclined at 12° with respect to the jet axis. They were positioned at streamwise distances of 1, 3, 6, and 10 nozzle diameters D from the jet exit and mounted in a plane perpendicular to the PIV measurement plane. The far-field microphones were placed at a distance of $60D$ from the nozzle exit: one at an angle of 90° and the other at 30° relative to the jet axis.

4. RESULTS

To ensure consistent scaling across the dataset and enable meaningful comparison across different forcing conditions, the fluctuating phase-averaged velocity components u and v are normalized independently by their respective root-mean-square (rms) values, computed for each actuation case:

$$\bar{u} = \frac{u_{\text{PIV}}}{\text{rms}(u)}, \qquad \bar{v} = \frac{v_{\text{PIV}}}{\text{rms}(v)} \tag{2}$$

The ISOMAP and POD algorithms are then applied to the resulting normalized velocity field $\bar{\boldsymbol{u}} = [\bar{u}, \bar{v}]$, allowing for consistent low-dimensional analysis across the full range of forcing frequencies. This normalization prevents the dimensionality reduction methods from being biased toward actuation cases with inherently larger fluctuation amplitudes, ensuring that all cases contribute comparably to the extracted flow structures.

Before analyzing the embedding results in detail, we first assess the dimensionality reduction behavior of the two methods. Figure 2 compares the ISOMAP resid-

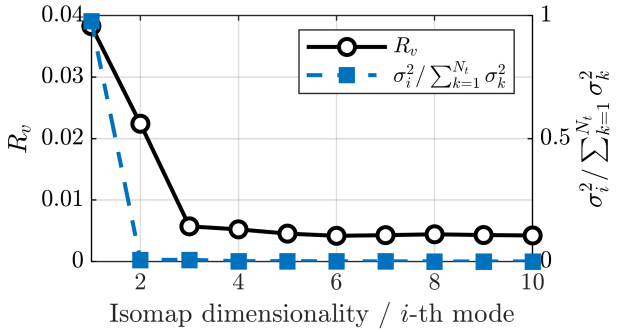


Figure 2: Comparison of dimensionality reduction: ISOMAP residual variance R_v (black) versus normalized POD eigenvalues $\sigma_i^2 / \sum \sigma_k^2$ (blue).

ual variance R_v and the normalized POD eigenvalues $\sigma_i^2 / \sum_k \sigma_k^2$ as functions of the mode index.

To further compare the effectiveness of the two methods, Figure 3 shows the pairwise projections of the first four low-dimensional coordinates obtained from ISOMAP (a) and POD (b), applied to the normalized fluctuating velocity fields. Each point corresponds to a phase-averaged snapshot and is color-coded by the Strouhal number St of the forcing. A neighborhood size of $k = 10$ is used for ISOMAP.

While POD succeeds in compressing the dataset energy into a few dominant modes, the resulting embedding fails to organize the snapshots coherently across the Strouhal number range. As shown in Figure 3b, the projections exhibit partial circular arrangements in the ψ_2-ψ_3 plane, which are reminiscent of phase-resolved dynamics for certain intermediate actuation frequencies. However, this structure fades significantly at low St, leading to a disordered and overlapping distribution of snapshots, where phase information is lost and actuation cases become indistinguishable.

In contrast, ISOMAP yields a more structured and physically interpretable embedding, as shown in Figure 3a. The pairwise projections of the first four coordinates reveal organized manifolds with clear geometric patterns—such as rings, spirals, and bifurcated surfaces—that consistently vary with the forcing frequency. Unlike POD, ISOMAP preserves the continuity of the phase trajectories even at low St, highlighting its ability to retain the intrinsic geometry of the flow dynamics and to represent both temporal evolution and actuation mechanisms in a unified low-dimensional space.

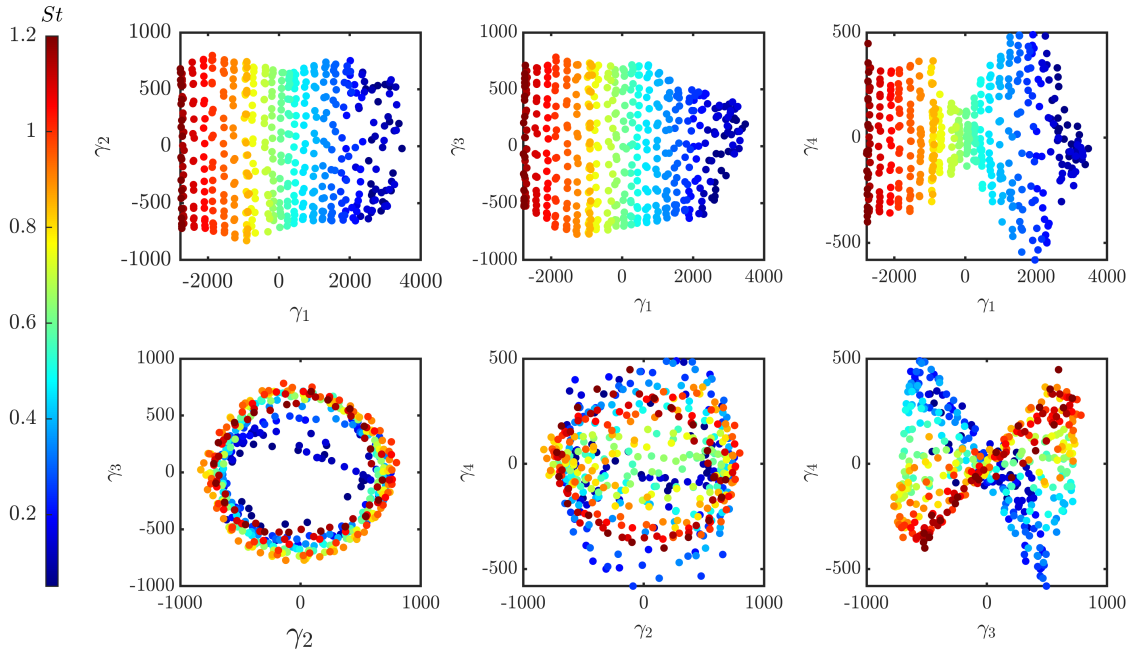
The contrast between actuation regimes is further explored by examining the flow structures associated with representative Strouhal numbers. Figure 4 shows the first spatial POD mode ϕ of the streamwise velocity fluctuations for three selected cases: $St = 0.15$, $St = 0.45$, and $St = 1$. The modes are normalized by $\sqrt{N_p}$, where N_p is the number of grid points. In the low-St case (top), the spatial mode reveals large-scale, nearly steady structures that extend over several jet diameters, reflecting a strong mean-flow pumping effect. At higher St, the modes become increasingly compact and periodic, with the $St = 1$ case (bottom) dominated by wave-like features consistent with Kelvin–Helmholtz vortices synchronized with the actuation.

To further investigate the flow response at different forcing frequencies, the phase-averaged voltage signals recorded from four near-field microphones are presented in Figure 5, for actuation cases $St = 0.15$, 0.45, and 1. The microphones are aligned along the jet centerline at axial distances of $1D$, $3D$, $6D$, and $10D$ from the nozzle exit (top to bottom).

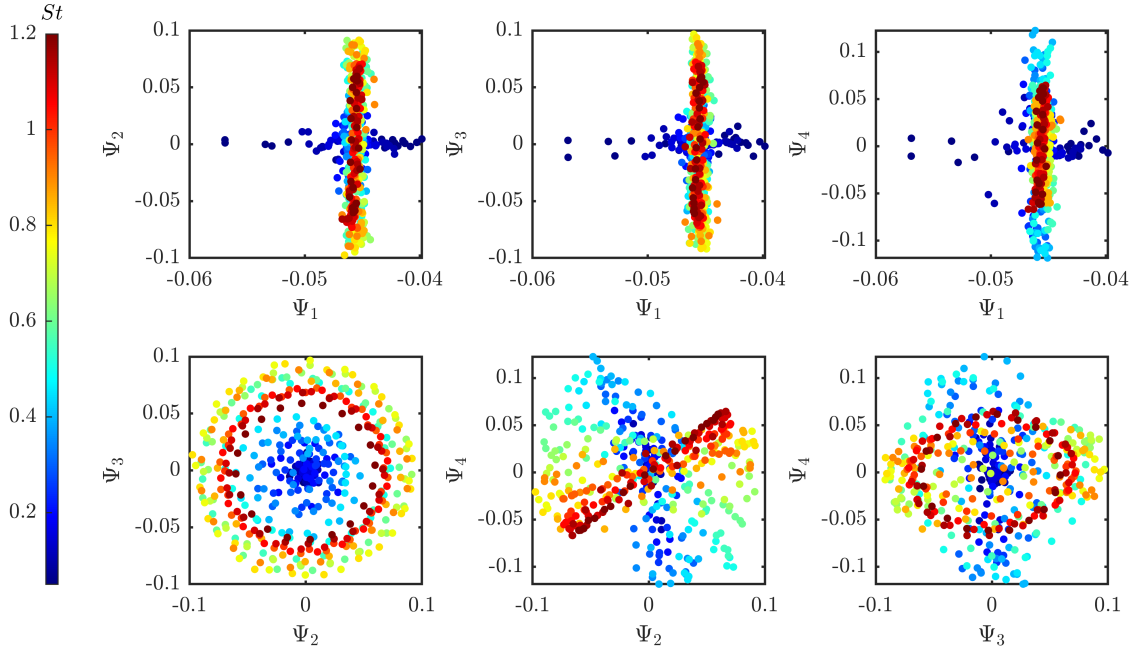
At $St = 0.15$, the signals exhibit high-amplitude oscillations with a smooth and coherent phase shift across the microphones. The temporal behavior of the signals show a strong modulation, differing from the expected sinusoidal behavior typical of travelling waves. This pattern maintains its structure and shifts without significant deformation — likely driven by acoustic resonance within the facility. For $St = 0.45$ and $St = 1$, the voltage signals are significantly weaker but still exhibit low-amplitude oscillations. Interestingly, the waveform remains nearly unchanged across the four microphones, indicating limited spatial evolution and suggesting the presence of weak convective fluctuations rather than amplified coherent structures. In contrast, the $St = 0.15$ case shows strong spatial modulation of the waveform, with amplitude decreasing notably by $10D$, consistent with a resonance-driven wave confined to the near-nozzle region.

These findings reinforce the interpretation that the low-St regime excites a distinct, facility-driven mechanism with a strong near-field signature. This behavior differs fundamentally from the convective responses at higher frequencies, and explains why POD struggles to represent both within a common basis. ISOMAP, on the other hand, successfully embeds this physical variation into its low-dimensional manifold.

Finally, Figure 6 presents the power spectral density (PSD) of the far-field pressure signals acquired by the GRAS microphones placed at 30° (Mic1) and 90° (Mic2)



(a) ISOMAP



(b) POD

Figure 3: Pairwise projections of the first four low-dimensional coordinates obtained with ISOMAP **(a)** and POD **(b)**, applied to the normalized streamwise velocity fluctuations. Each point corresponds to a phase-averaged snapshot and is color-coded by the Strouhal number St. While POD compresses energy in a few modes, ISOMAP reveals a more structured and physically interpretable manifold.

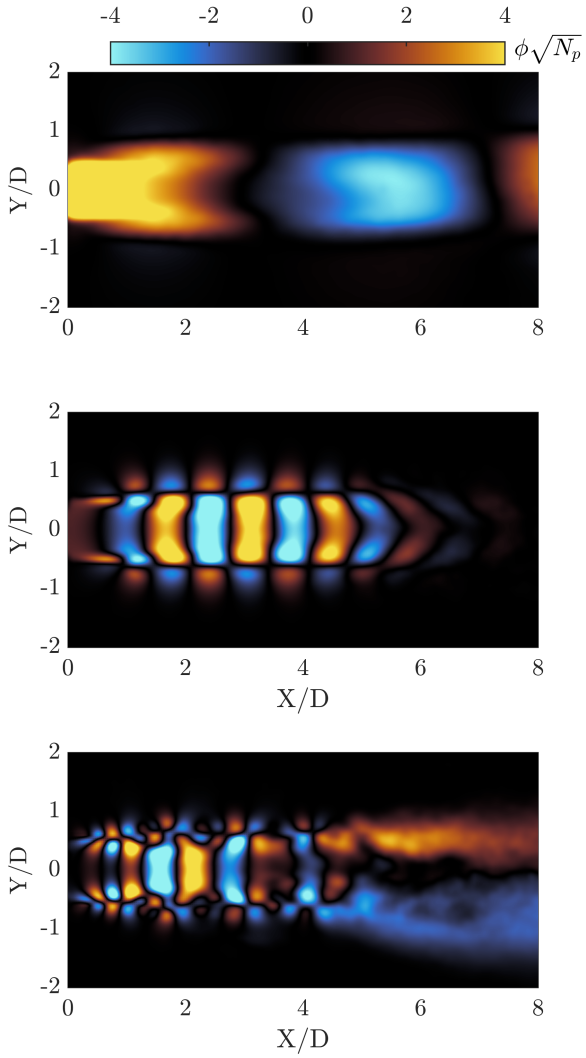


Figure 4: First spatial POD mode ϕ of the streamwise velocity fluctuations for the cases $St = 0.15$ (top), $St = 0.45$ (middle), and $St = 1$ (bottom). The modes are normalized by $\sqrt{N_p}$, where N_p is the number of grid points.

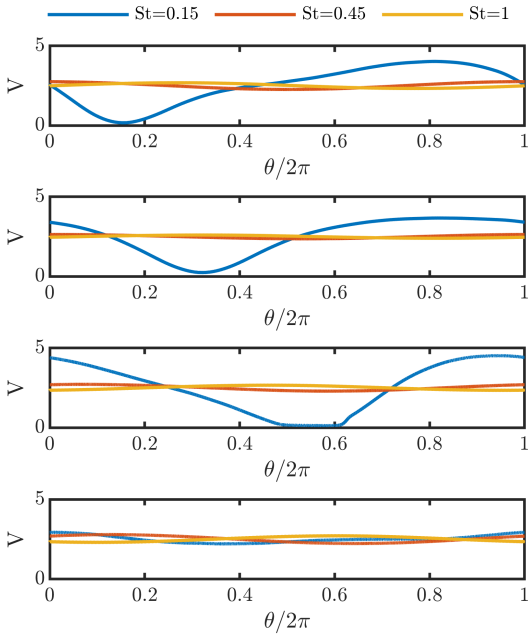


Figure 5: Phase-averaged voltage signals from four near-field microphones placed along the jet centerline at axial distances of $1D$, $3D$, $6D$, and $10D$ (top to bottom), for actuation cases $St = [0.15, 0.45, 1]$.

from the jet axis, comparing the uncontrolled and actuated cases at $St = 0.50$ and $St = 1.00$. The power spectra are plotted as Sound Pressure Levels (SPL), using a reference pressure of 20 μPa. The dominant peak observed in each actuated spectrum corresponds to the acoustic wave produced by the loudspeaker at the forcing frequency. However, the most informative effects of the actuation lie in the surrounding broadband spectral content. At 90° (Mic2), a substantial elevation of the high-frequency floor is observed in the actuated cases. This increase indicates enhanced radiation from small-scale turbulent structures, which typically dominate the side-radiated acoustic field [11]. In contrast, the spectra at 30° (Mic1) show more selective changes and are generally associated with sound generated by large-scale coherent structures aligned with the jet axis. These directional differences confirm that actuation not only injects tonal energy but also reorganizes the turbulence dynamics and their acoustic signatures in a frequency- and angle-dependent manner.

Overall, the results reveal that the acoustic impact of

actuation is far from trivial: while the forcing introduces energy at a specific tone, it also modifies the structure and distribution of broadband noise in ways that reflect deeper changes in the flow field. This complex interplay warrants further investigation to understand the link between actuation, turbulent structures, and jet noise generation mechanisms.

5. CONCLUSIONS AND FUTURE WORKS

The present work explores the existence of an actuation manifold for open-loop control of a subsonic transitional jet. The control action has been performed using acoustic excitation inside the stagnation chamber. Data-driven dimensionality reduction techniques have been applied to the phase-averaged velocity field measurements to identify the actuation manifold. Results shown the existence of a low-dimensional manifold for such data. The ISOMAP techniques, in particular, revealed to provide a more clear manifold than POD, being capable of coherently embedding different behaviors of the flow, i.e. "jet-pumping" mechanisms at low Strouhal numbers and Kelvin-Helmholtz vortices excitation at higher Strouhal numbers. The existence of a clear actuation manifold confirms the capability of the selected control action to affect the flow. This is further reinforced by the difference in behavior measured by both near-field microphones and the far-field microphones. Further work will focus in identifying a control manifold for non phase-averaged quantities.

6. ACKNOWLEDGMENTS

This work has been supported by the project EXCALIBUR, grant PID2022-138314NB-I00, funded by MCIN/AEI/10.13039/501100011033 and by "ERDF A way of making Europe".

7. REFERENCES

[1] A. Ginevsky, Y. V. Vlasov, E. V. Vlasov, and R. Karavosov, *Acoustic control of turbulent jets*. Springer Science & Business Media, 2004.

[2] G. Berkooz, P. Holmes, and J. L. Lumley, "The proper orthogonal decomposition in the analysis of turbulent flows," *Annual review of fluid mechanics*, vol. 25, no. 1, pp. 539–575, 1993.

[3] B. R. Noack, K. Afanasiev, M. Morzyński, G. Tadmor, and F. Thiele, "A hierarchy of low-dimensional models for the transient and post-transient cylinder wake," *Journal of Fluid Mechanics*, vol. 497, pp. 335–363, 2003.

[4] J. B. Tenenbaum, V. d. Silva, and J. C. Langford, "A global geometric framework for nonlinear dimensionality reduction," *science*, vol. 290, no. 5500, pp. 2319–2323, 2000.

[5] E. Farzamnik, A. Ianiro, S. Discetti, N. Deng, K. Oberleithner, B. R. Noack, and V. Guerrero, "From snapshots to manifolds–a tale of shear flows," *Journal of Fluid Mechanics*, vol. 955, p. A34, 2023.

[6] S. E. Otto and C. W. Rowley, "Inadequacy of linear methods for minimal sensor placement and feature selection in nonlinear systems: a new approach using secants," *Journal of Nonlinear Science*, vol. 32, no. 5, p. 69, 2022.

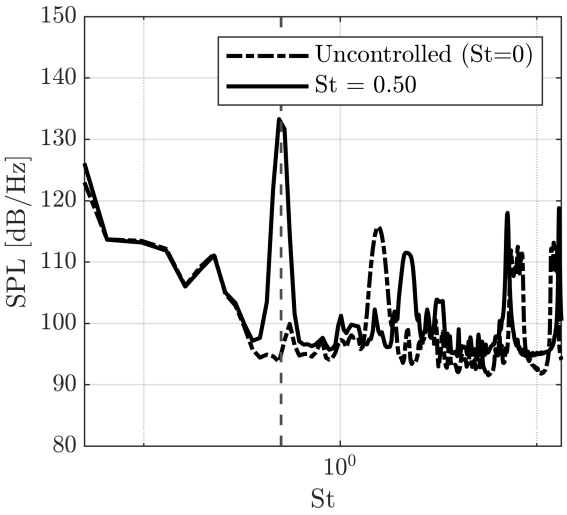
[7] L. Marra, G. Y. C. Maceda, A. Meilán-Vila, V. Guerrero, S. Rashwan, B. R. Noack, S. Discetti, and A. Ianiro, "Actuation manifold from snapshot data," *Journal of Fluid Mechanics*, vol. 996, p. A26, 2024.

[8] J. R. Moreno, L. Franceschelli, D. De la Prida, L. A. Azpicueta-Ruiz, and M. Raiola, "Implementation of a jet collector and dissipation cavity into a closed anechoic chamber for jet noise studies," in *30th AIAA/CEAS Aeroacoustics Conference (2024)*, p. 3066, 2024.

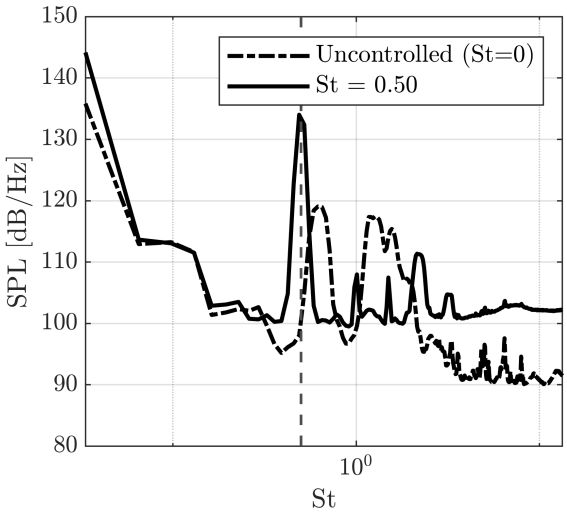
[9] G. Paolillo and T. Astarita, "Pairs-unina: A robust and accurate free tool for digital particle image velocimetry and optical camera calibration," in *Proceedings of 21st International Symposium on Applications of Laser and Imaging Techniques to Fluid Mechanics*, (Lisbon, Portugal), July 08–11 2024.

[10] M. A. Mendez, M. Raiola, A. Masullo, S. Discetti, A. Ianiro, R. Theunissen, and J.-M. Buchlin, "Pod-based background removal for particle image velocimetry," *Experimental Thermal and Fluid Science*, vol. 80, pp. 181–192, 2017.

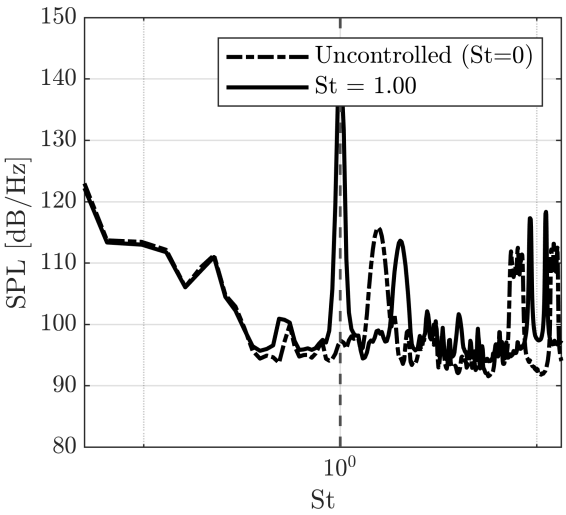
[11] C. Tam, M. Golebiowski, and J. Seiner, "On the two components of turbulent mixing noise from supersonic jets," in *Aeroacoustics conference*, p. 1716, 1996.



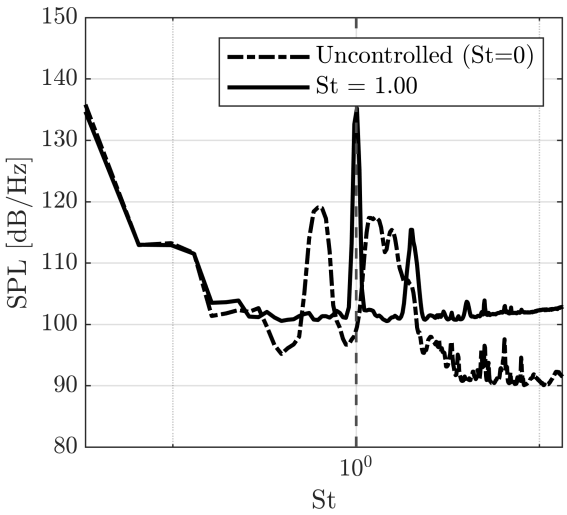
(a) Mic1 at 30°, $St = 0.50$.



(b) Mic2 at 90°, $St = 0.50$.



(c) Mic1 at 30°, $St = 1.00$.



(d) Mic2 at 90°, $St = 1.00$.

Figure 6: Power spectral density (PSD) of far-field pressure signals measured by GRAS microphones at 30° (Mic1) and 90° (Mic2), comparing the uncontrolled case (dashed) with actuation at $St = 0.50$ and $St = 1.00$. Actuation introduces sharp tonal peaks and modifies the surrounding spectral distribution, highlighting complex, angle-dependent flow–acoustic interactions.

DOI: 10.61782/fa.2025.0631



FORUM ACUSTICUM
EURONOISE 2025

NUMERICAL INVESTIGATION ON NOISE REDUCTION OF DISTRIBUTED PROPELLERS BY PHASE SYNCHRONIZATION

Zhe Yang[1*] **Matthias Meinke**[1] **Dominik Krug**[1] **Wolfgang Schröder**[1]
[1] Institute of Aerodynamics, RWTH Aachen University, Wüllnerstr. 5a, 52062 Aachen, Germany

ABSTRACT

Distributed propulsion systems represent a promising solution for future Urban Air Mobility (UAM) aircraft, offering benefits such as noise reduction, improved efficiency, and enhanced maneuverability. Recent studies highlight propeller phase synchronization as an effective active control strategy for mitigating noise in distributed propellers with compact installation clearance.

To further explore the mechanisms underlying noise reduction through phase synchronization, large-eddy simulations with adaptive mesh refinement are conducted to investigate co- and counter-rotating propeller pairs with relative phase angles of 0° and 90°. The far-field noise signals are predicted from the LES flow field by a time-domain formulation of the Ffowcs-Williams and Hawkings analogy. The results exhibit good agreement with wind tunnel measurements in terms of noise spectra and directivity patterns.

The findings indicate that synchronized propellers with a 90° relative phase angle achieve noise reductions greater than 20 dB at the blade passing frequency across all directions. Additionally, the acoustic signals of two isolated propellers are superimposed and compared with dual-propeller configurations. The observed tonal noise reduction is attributed to two key mechanisms: (a) reduced aerodynamic interaction at the propeller tips, which mitigates unsteady loading noise that propagates in the streamwise direction; and (b) destructive acoustic interference between counter-phase neighboring propellers.

*__Corresponding author__: z.yang@aia.rwth-aachen.de.
__Copyright__: ©2025 Zhe Yang et al. This is an open-access article distributed under the terms of the Creative Commons Attribution 3.0 Unported License, which permits unrestricted use, distribution, and reproduction in any medium, provided the original author and source are credited.

Keywords: distributed propulsion, propeller noise, phase synchronization, large eddy simulations.

1. INTRODUCTION

As a key driver of the emerging low-altitude economy, Urban Air Mobility (UAM) [1] has attracted significant attention as an innovative transportation solution. By leveraging advanced flight control and electric propulsion technologies, UAM aims to meet the increasing demand for efficient point-to-point travel in congested metropolitan areas or regions with limited road infrastructure. Despite its potential, the widespread adoption of UAM faces significant challenges, with aircraft generated noise being a major regulatory societal concern.

Among the various technologies explored for UAM applications, distributed electric propulsion (DEP) has emerged as a leading solution [2]. Characterized by multiple electrically driven propellers distributed along the airframe, DEP enhances aerodynamic performance, increases safety redundancy, provides acoustic shielding, and reduces propeller loading, thereby lowering overall noise emissions. Nonetheless, the compact installation of propellers introduces engineering challenges related to inter-propeller interactions and propeller–airframe coupling [3]. These complexities underscore the need for in-depth investigations into the noise and performance characteristics of DEP systems.

The aerodynamic and acoustic interactions between closely installed propellers have been the focus of extensive research. When the tip-to-tip separation is below 0.5 times the propeller diameter, significant thrust fluctuations have been observed [4–6], leading to a measurable reduction in propulsive efficiency, typically in the range of 1% to 2% [4, 7]. The interaction of tip vortices between adjacent propellers results in the distortion of he-

lical vortical structures [5, 8, 9], elevating turbulence intensity in the wake [4]. From an acoustic perspective, studies have reported increased noise levels at the blade passing frequency (BPF) and overall sound pressure level (OASPL) [4, 5]. Variations in sound pressure levels of up to ±10 dB at specific observation points have been documented [7], highlighting the significance of inter-propeller interactions in shaping the acoustic footprint of DEP systems. Additionally, noise source localization studies have identified the primary noise source within the gap region between adjacent propeller disks, where noise intensity is approximately 5 dB higher than that of blade tip noise [10]. This phenomenon is attributed to intensified blade-turbulence interactions and unsteady blade loading effects.

To mitigate noise emissions in DEP configurations, active noise control strategies, such as propeller phase synchronization, have been proposed. By precisely controlling the relative phase angles between adjacent propellers, this technique has demonstrated the potential to achieve noise reductions by 15 to 46 dB at the BPF and up to 6 dB in OASPL [11, 12]. The primary mechanism responsible for this noise reduction is destructive acoustic interference between phase-locked propellers [4]. However, recent findings indicate that reduced aerodynamic interactions between adjacent propellers also contribute significantly to noise mitigation [7, 9]. A comparative analysis of noise spectra from two-propeller configurations and superimposed isolated propeller signals further supports the coexistence of these two mechanisms [13]. Notably, in configurations with minimal tip clearance, nonlinear aerodynamic interactions become increasingly dominant, influencing overall noise emissions.

Building upon prior research, this study aims to further elaborate on the underlying mechanisms of noise reduction through propeller phase synchronization in distributed propulsion systems using high-fidelity numerical simulations. The paper is structured as follows: Section 2 provides an overview of the flow solver and numerical methodologies. Section 3 details the computational setup, including the test geometry and simulation parameters. Section 4 presents the results and discusses the key findings of the study. Finally, Section 5 summarizes the conclusions and outlines potential directions for future research.

2. NUMERICAL METHODS

Large-eddy simulations (LES) are performed based on the flow solver multiphysics-Aerodynamics Institute Aachen (m-AIA) [14]. The simulation workflow is illustrated in Fig. 1. First, an unstructured hierarchical Cartesian mesh is automatically generated by a parallel grid generator according to predefined mesh parameters for the target geometry. To track the rotating geometry of the propeller blades, a level-set solver based on the kinematic motion level-set approach [15] is employed, providing information about the surface location for solution adaptive mesh refinement (AMR) during the simulation run. The Navier-Stokes equations are solved by a finite-volume (FV) solver [16] at second-order accuracy in time and space to perform wall-resolved LES of the turbulent flow field. A postprocessing module is integrated into the simulation workflow to conduct time averaging or time-series data sampling on the dynamically changing mesh. For the far-field noise, Farassat's time-domain formulation 1A [17] of the Ffowcs-Williams and Hawkings (FW-H) method is used to predict the pressure signals at far-field observer positions. Dynamic load balancing (DLB) [18] is used to alleviate workload imbalances among the parallel processes generated by AMR to improve the computational efficiency on high-performance computing systems.

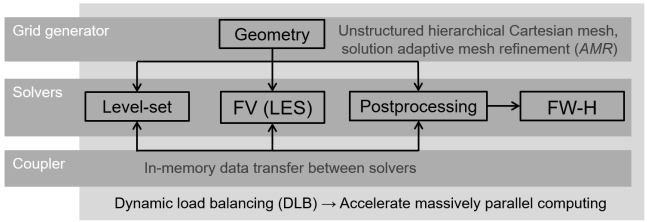


Figure 1. Overview of the m-AIA framework [14]

3. COMPUTATIONAL SETUP

3.1 Test geometry

Turhan et al. [12] have developed an experimental setup, shown in Fig. 2, to investigate the interaction noise of the closely arranged distributed propellers and evaluate the effectiveness of phase-synchronization for propeller noise reduction. The experiments were performed with two 2-bladed propellers manufactured by Mejzlik with a diameter of $D = 228.6\ mm$ (9 inch) and a pitch-to-

diameter ratio of $P/D = 1$. The center-to-center separation distance between adjacent propellers is $S/D = 1.05$. The two propellers were mounted 150 mm upstream of a supportive NACA0018 airfoil, with a chord length of $c_{wing} = 300$ mm, and a span of 940 mm.

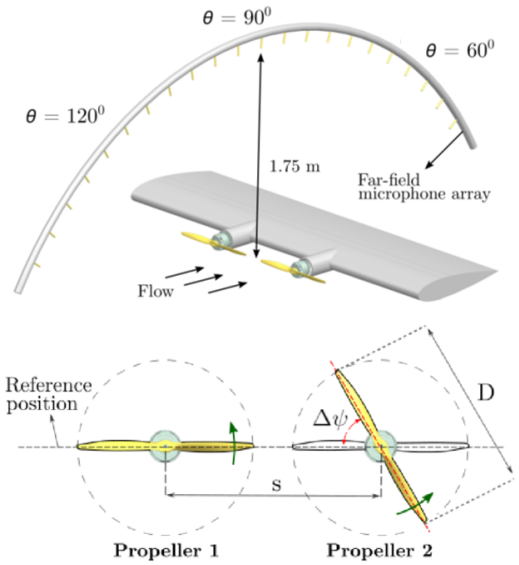


Figure 2. Experimental setup for propeller-propeller interaction noise [12].

The incoming freestream velocity is $U_\infty = 10$ m/s with a wing angle of attack $AoA = 0°$. The chord Reynolds number is approximately $Re_{wing} = 2 \cdot 10^5$. The two propellers rotate in the same direction at the speed of $n = 5000$ rpm, giving a blade tip tangential Mach number of about $M_{tip} = 0.17$, a blade passing frequency of $BPF = 166.7$ Hz and a propeller advance ratio of $J = U_\infty/(nD) = 0.53$. Two propeller blade relative phase angles, $\Delta\psi = 0°$ and $90°$ are tested.

3.2 Flow simulation setups

Based on the previous experimental/numerical observations by [19, 20] that the propeller-propeller interaction is a major noise source of the distributed propulsion system and has a much higher contribution to the far-field noise than the propeller-airfoil interaction, the flow field of only the two propellers are simulated and the supportive nacelle and airfoil are omitted to reduce the computational cost. The lengths $L_x = 1400$ mm, $L_y = 1200$ mm, and $L_z = 1000$ mm define the size of the computational domain. The no-slip boundary condition is imposed on all surfaces which are assumed to be adiabatic. Subsonic inlet and outlet conditions with an acoustic sponge layer are used for the far-field boundaries to absorb any spurious reflected pressure waves.

The computational mesh is shown in Fig. 3. To resolve the turbulent boundary layer near the solid surfaces, the minimum spatial step near solid surfaces is $4.3 \cdot 10^{-5}$ m. Approximately 300 cells are distributed along the propeller chord. Adaptive mesh refinement is applied to the fluid-solid interface with the minimum spatial resolution and coarsening towards the far field until a maximum spatial step of $1.4 \cdot 10^{-3}$ m is reached. Patch refinement boxes are implemented in the near field to better resolve the propeller slipstream. Overall, this leads to approximately $500 \cdot 10^6$ cells. The rotating propeller and the high-frequency turbulent scales are resolved by a time step of $1 \cdot 10^{-7}$ s, which is determined by the stability limit of the numerical method.

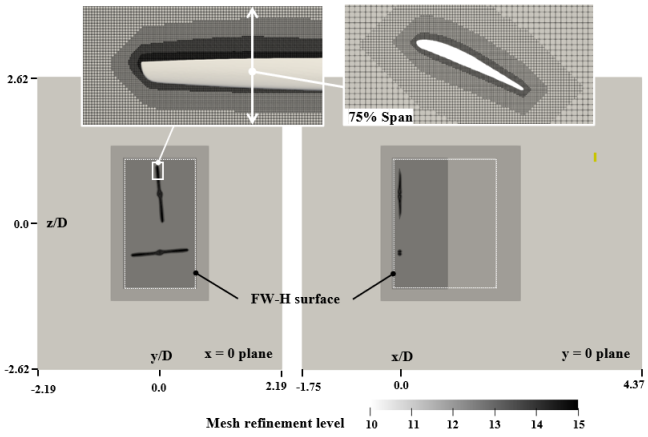


Figure 3. Illustration of the computational domain and mesh

3.3 Far-field noise prediction setups

A permeable FW-H surface around the vortex core of the propeller pairs is employed to record the near-field perturbations. The surface is a rectangular box, as defined by the white dashed lines in Fig. 3. The leeward side of the FW-H surface is left open to avoid spurious noise generated by hydrodynamic perturbations traveling over the sampling surface. The spatial resolution of the sampling surface is $2 \cdot 10^{-3}$ m. The sampling frequency is 65 kHz and data for 10 propeller revolutions are recorded.

4. RESULTS

4.1 Flow field

The generation and propagation of the instantaneous vortex structures of the co-rotating propeller pairs with relative phase angle $\Delta\psi = 0°$ are shown in Fig. 4.

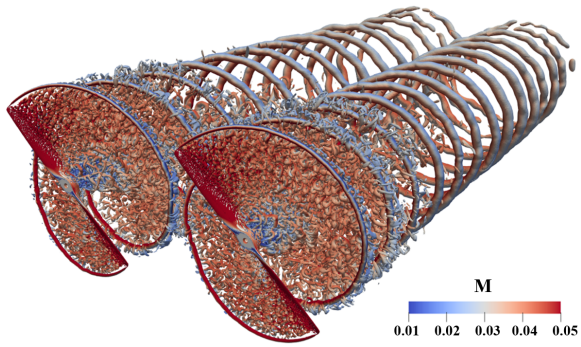


Figure 4. Vortex structures denoted by the Q-criterion [21] with an iso-surface value of $\tilde{Q} = 2$.

The time-averaged statistics of the thrust coefficient $C_T = F_T/(\rho_0 n^2 D^4)$ is provided in Tab. 1. The time histories of the thrust coefficient for propeller 1 at relative phase angles of $\Delta\psi = 0°$ and $90°$ are illustrated in Fig. 5, co-rotating propellers in Fig. 5 (a) and counter-rotating propellers in Fig. 5 (b). Both cases are compared against the isolated propeller.

The results indicate that closely installed propeller pairs exhibit an approximately 0.5% higher time-averaged thrust coefficient compared to an isolated propeller. Furthermore, the time-averaged thrust coefficient at a relative phase angle of $\Delta\psi = 0°$ is slightly higher than that at $\Delta\psi = 90°$.

The instantaneous thrust coefficients of installed propeller pairs show clear periodic fluctuations dominated by the blade passing frequency (BPF). The root-mean-square fluctuation of the thrust coefficient at a relative phase angle of $\Delta\psi = 0°$ is roughly 45% higher than that of an isolated propeller. For the $\Delta\psi = 90°$ phase angle, this increase reduces to about 24%. This demonstrates that adopting a relative phase angle of $\Delta\psi = 90°$ helps mitigate aerodynamic interference between adjacent propellers, and reduce periodic unsteady loading on the blades.

To further investigate the aerodynamic interactions between adjacent propellers, Fig. 6 presents the total pressure perturbation at the propeller tip gap located at

Table 1. Time-averaged thrust coefficient of propeller 1.

	C_T	C_{Trms}
Isolated propeller	0.083 25	0.000 62
co-r, $\Delta\psi = 0°$	0.083 68	0.000 92
co-r, $\Delta\psi = 90°$	0.083 63	0.000 78
counter-r, $\Delta\psi = 0°$	0.083 74	0.000 89
counter-r, $\Delta\psi = 90°$	0.083 62	0.000 76

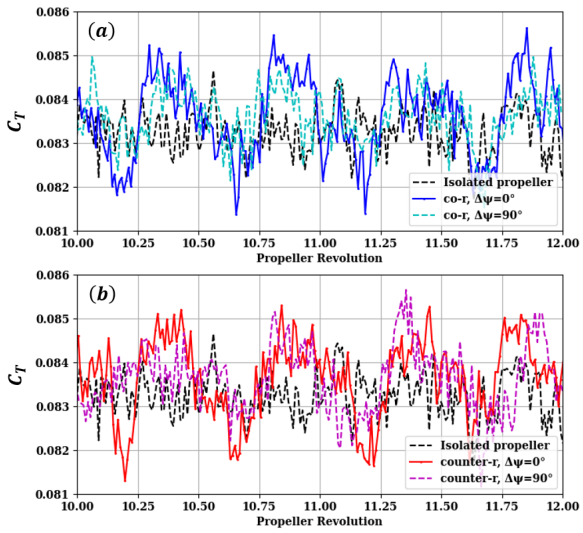


Figure 5. Time history of the propeller thrust coefficient of propeller 1; (a) co-rotating propellers, (b) counter-rotating propellers.

$(x, y, z) = (0, 0, 0)$. The nondimensional perturbed total pressure is defined as $\tilde{p_T'} = (p_T - \bar{p}_T)/(0.5\rho_\infty U_\infty^2)$. For an isolated propeller, the total pressure fluctuation at the blade tip exhibits periodicity corresponding to the blade passing frequency, with a clear pressure drop when each blade passes.

Considering the installed propeller pairs with a relative phase angle of $\Delta\psi = 0°$, the amplitude of the total pressure fluctuation approximately doubles due to simultaneous blade passages from both propellers through the tip gap. However, at a phase angle of $\Delta\psi = 90°$, the total pressure fluctuations are periodic at twice the rotor frequency, as blades from each propeller pass through the tip gap alternately. The fluctuation amplitude in this scenario is comparable to that of an isolated propeller. Moreover,

the rotation direction of the propellers has negligible influence on the total pressure fluctuations at the blade tip.

A comparison between Fig. 5 and Fig. 6 reveals that variations in total pressure fluctuations in the tip gap align closely with changes in propeller thrust. This correlation suggests that aerodynamic interference between adjacent propellers significantly contributes to unsteady aerodynamic loading on the rotor, which potentially increase noise generation.

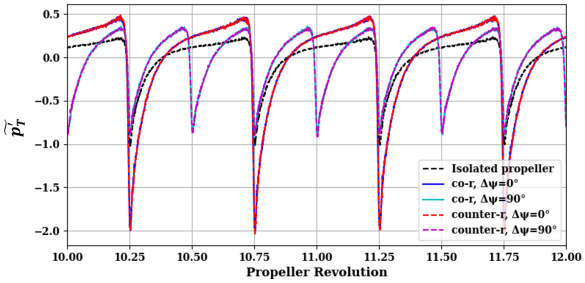


Figure 6. Total pressure perturbation in the tip gap.

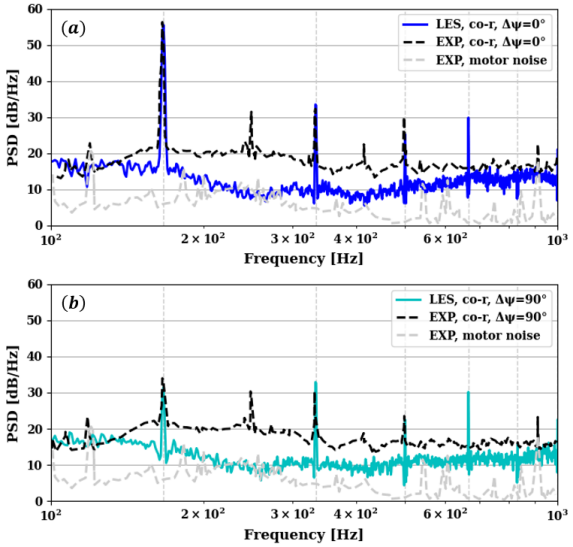


Figure 7. Predicted power spectral density of the co-rotating propeller pairs with relative phase angle (a) $\Delta\psi = 0°$, and (b) $\Delta\psi = 90°$.

4.2 Acoustic Field

The far-field noise of the synchronized propellers is determined by the permeable FW-H approach and compared with the wind tunnel measurements from [12]. The microphone is located 1.75 m off the propeller in the vertical plane with an angular position of $\theta = 90°$. The power spectral density (PSD) of the acoustic signal is calculated using Welch's method, 50% overlap, filtered by a Hanning window, with a frequency resolution of $\Delta f = 1.0\ Hz$, and the reference pressure is $2 \cdot 10^{-5}\ Pa$. The grey dashed lines in the plots represent the propeller blade passing frequency (BPF) and its harmonics.

Fig. 7 compares the predicted far-field noise spectra with the experimental reference data in the frequency range from 100 Hz to 1000 Hz. It can be seen that the propeller tonal noise at the first and second BPF frequencies is accurately predicted by the numerical method. The reference data showed a higher amplitude of broadband noise, which was mainly caused by the background motor noise in the wind tunnel experiment.

Next, the predicted noise spectra at the angular position of $\theta = 90°$ for cases with different rotation directions and relative phase angles are shown in Fig. 8. No significant difference in broadband noise was observed among the cases; variations mainly occurred in propeller tonal noise. A close look at the first two blade passing frequencies (BPF) reveals that the relative phase angle primarily affects the first BPF. At a relative phase angle of $\Delta\psi = 0°$, cases with different rotation directions exhibited similar far-field noise levels of approximately 55 dB at the first BPF. In contrast, at $\Delta\psi = 90°$, the first BPF noise level for the co-rotating case decreased by about 24 dB. Remarkably, in the counter-rotating case at $\Delta\psi = 90°$, the first BPF tonal noise was nearly eliminated, achieving a noise reduction exceeding 50 dB. This finding is consistent with experimental results reported by Shao et al. [11]. As a trade-off for the reduction in the first BPF, the second BPF tonal noise increases by approximately 1 dB for the cases with a $\Delta\psi = 90°$ relative phase angle. The above findings evidence that propeller phase synchronization effectively reduces the first BPF tonal noise, especially for counter-rotating propellers.

The directivity of the propeller far-field noise compared with experimental measurements is presented in Fig. 9. Fig. 9 (a) shows the sound pressure level (SPL) at the first BPF and Fig. 9 (b) illustrates the overall sound pressure level (OASPL) within the frequency range of 100 to 1000 Hz. As shown in Fig. 9 (a), the numerical predictions agree well with the experimental data upstream of the propeller but underestimate the SPL downstream. This

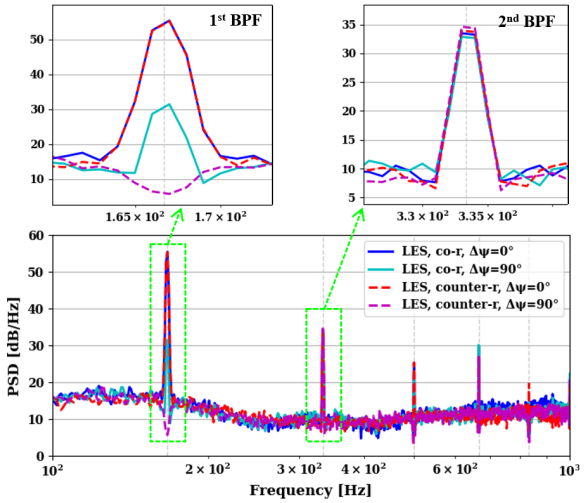


Figure 8. Comparison of predicted noise spectra for several test cases.

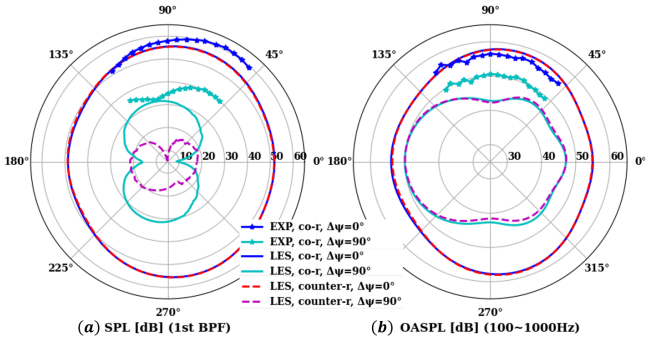


Figure 9. Directivity of the propeller noise.

discrepancy may arise from the scattering effect of the airfoil located downstream in the experiment, which alters the directivity of the sound field. A similar discrepancy was observed by Turhan et al. [22] in their mid-fidelity Vortex Lattice Method (VLM) simulations with the same test geometry. Consistent with Fig. 8, noise directivities for cases with a relative phase angle of $\Delta\psi = 0°$ are nearly identical. A relative phase angle of $\Delta\psi = 90°$ reduces far-field noise by over 20 dB at the first BPF in all directions. Compared to co-rotating propellers, counter-rotating propellers achieve an additional 10 dB noise reduction at $\theta = 90°$ and 270°, i.e. perpendicular above and below the propeller.

For the OASPL shown in Fig. 9 (b), numerical predictions at $\Delta\psi = 0°$ match very well with the experimental data, whereas at $\Delta\psi = 90°$, the numerical results exceed the experimental values on the top and bottom sides. The reduction of the OASPL ranges from 5 to 15 dB for different directions. The findings reveal that a staggered relative phase angle $\Delta\psi = 90°$ significantly reduces the overall noise levels in all directions, while the influence of different rotation directions on the OASPL is negligible.

4.3 Superposition of the isolated propeller noise

The principle of superposition [13] is employed to further understand noise-reduction mechanisms due to propeller phase synchronization. The far-field noise signal of a simulated isolated propeller is spatially and temporally shifted to construct a two-propeller system identical to the experimental setup but without aerodynamic interactions. The noise signals from these two isolated propellers are linearly superimposed to represent the dual-propeller noise, accounting only for acoustic interference. A comparison of the superimposed results with direct dual-propeller simulations in Fig. 10 shows the contributions from aerodynamic interactions and purely acoustic interference between adjacent propellers to far-field noise can be distinguished.

Figs. 10 (a) and (c) show the far-field noise for co-rotating and counter-rotating propeller pairs at a relative phase angle $\Delta\psi = 0°$. The isolated superimposed propellers exhibit a dipole-like directivity for the first BPF noise, with acoustic energy mainly concentrated on the top and bottom sides of the propellers, and relatively low noise levels upstream and downstream. In contrast, the dual-propeller simulation results show significantly increased noise upstream and downstream of the propellers. Specifically, tonal noise levels at $\theta = 0°$ and 180° increase by approximately 30 dB. This indicates that aerodynamic interactions between adjacent propellers generate strong additional noise sources, primarily propagating upstream and downstream.

Fig. 10 (b) presents the far-field noise of co-rotating propeller pairs at a relative phase angle of $\Delta\psi = 90°$. Due to the reduced aerodynamic interactions at the blade tips, the dual-propeller simulation results exhibit dipole patterns consistent with those predicted by linear superposition. Destructive wave interactions occur at the far-field microphone locations due to the phase difference between the two propellers, leading to a significant reduction in noise levels. The pure acoustic noise cancellation is most pronounced in the case of counter-rotating propellers with

$\Delta\psi = 90°$. As shown in Fig. 10 (d), the first BPF noise is nearly completely eliminated, such that the noise level is reduced to that of the background broadband noise.

In addition, we observed that in certain cases, such as at $\theta = 0°$ in Figs. 10 (a), (b), and (c), the noise level of the dual-propeller simulations are lower than the predicted value based on linear superposition. This indicates the presence of nonlinear effects in the dual-propeller case, which influence the directivity of propeller far-field noise.

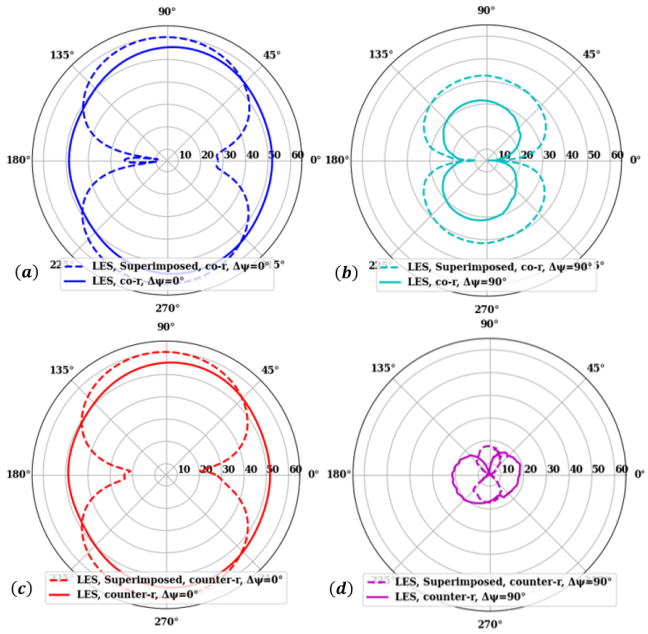


Figure 10. Comparison of first BPF noise directivity of the superimposed propellers and simulated propeller pairs.

5. CONCLUSIONS

The noise reduction mechanisms of distributed propeller systems through phase synchronization are investigated by a hybrid LES/FW-H approach. The numerical method accurately captures aerodynamic interactions and acoustic interference between adjacent propellers and is validated against wind tunnel measurements.

Results show that the relative phase angle of $\Delta\psi = 90°$ effectively reduces the tonal noise at the first blade passing frequency. Specifically, the co-rotating configuration achieves a noise reduction of approximately 24 dB, while the counter-rotating configuration yields an even greater reduction, with the first BPF tonal noise reduced by over 50 dB. Additionally, phase synchronization leads to an overall sound pressure level reduction of 5 to 15 dB, depending on the direction.

The observed noise reduction is primarily attributed to two mechanisms: (1) a reduction in aerodynamic interactions at the propeller tips, which mainly propagate upstream and downstream, and (2) destructive acoustic interference between counter-phase neighboring propellers which effectively cancels the first BPF noise component, particularly in counter-rotating configurations.

The present work offers practical insights into integrating phase synchronization in urban air mobility propulsion systems, emphasizing dual control of aerodynamic and acoustic sources. Future research could investigate additional propeller parameters, including tip clearance variations, transitional inflow conditions, elastic propeller blades, and multi-propeller configurations, to further refine noise mitigation strategies.

6. ACKNOWLEDGMENTS

The present work has received funding from the European Union's Horizon 2020 research and innovation program under the project ENODISE (Enabling optimized disruptive airframe-propulsion integration concepts) (`www.vki.ac.be/index.php/about-enodise`) grant agreement No. 860103. The authors would like to thank B. Turhan and M. Azarpeyvand from the University of Bristol (United Kingdom) for providing the test geometry and experimental data. The authors also gratefully acknowledge the Gauss Centre for Supercomputing e.V. (`www.gauss-centre.eu`) for funding this project by providing computing time on the GCS Supercomputer HAWK at Höchstleistungs-Rechenzentrum Stuttgart (`www.hlrs.de`).

7. REFERENCES

[1] A. Straubinger, R. Rothfeld, M. Shamiyeh, K.-D. Büchter, J. Kaiser, and K. O. Plötner, "An overview of current research and developments in urban air mobility–setting the scene for uam introduction," *Journal of Air Transport Management*, vol. 87, p. 101852, 2020.

[2] A. S. Gohardani, G. Doulgeris, and R. Singh, "Challenges of future aircraft propulsion: A review of distributed propulsion technology and its potential application for the all electric commercial aircraft,"

Progress in Aerospace Sciences, vol. 47, no. 5, pp. 369–391, 2011.

[3] E. Greenwood, K. S. Brentner, R. F. Rau, and Z. F. Ted Gan, "Challenges and opportunities for low noise electric aircraft," *International Journal of Aeroacoustics*, vol. 21, no. 5-7, pp. 315–381, 2022.

[4] W. Zhou, Z. Ning, H. Li, and H. Hu, "An experimental investigation on rotor-to-rotor interactions of small uav propellers," in *35th AIAA Applied Aerodynamics Conference*, p. 3744, 2017.

[5] H. Lee and D.-J. Lee, "Rotor interactional effects on aerodynamic and noise characteristics of a small multirotor unmanned aerial vehicle," *Physics of Fluids*, vol. 32, no. 4, 2020.

[6] A. D. Thai, E. De Paola, A. Di Marco, L. G. Stoica, R. Camussi, R. Tron, and S. M. Grace, "Experimental and computational aeroacoustic investigation of small rotor interactions in hover," *Applied Sciences*, vol. 11, no. 21, p. 10016, 2021.

[7] R. de Vries, N. van Arnhem, T. Sinnige, R. Vos, and L. L. Veldhuis, "Aerodynamic interaction between propellers of a distributed-propulsion system in forward flight," *Aerospace Science and Technology*, vol. 118, p. 107009, 2021.

[8] D. Shukla and N. Komerath, "Multirotor drone aerodynamic interaction investigation," *Drones*, vol. 2, no. 4, p. 43, 2018.

[9] A. Zarri, A. Koutsoukos, and F. Avallone, "Aerodynamic and acoustic interaction effects of adjacent propellers in forward flight," in *AIAA Aviation 2023 Forum*, p. 4489, 2023.

[10] T. Zhou, H. Jiang, and X. Sun, "Noise source imaging measurements for small-scale multi-propeller systems," *Applied Acoustics*, vol. 194, p. 108801, 2022.

[11] M. Shao, Y. Lu, X. Xu, S. Guan, and J. Lu, "Experimental study on noise reduction of multi-rotor by phase synchronization," *Journal of Sound and Vibration*, vol. 539, p. 117199, 2022.

[12] B. Turhan, H. K. Jawahar, A. Gautam, S. Syed, G. Vakil, D. Rezgui, and M. Azarpeyvand, "Acoustic characteristics of phase-synchronized adjacent propellers," *The Journal of the Acoustical Society of America*, vol. 155, no. 5, pp. 3242–3253, 2024.

[13] M. Bhardwaj, T. P. Chong, C. Paruchuri, and P. Joseph, "Noise decomposition of dual synchronized propellers in hover," in *30th AIAA/CEAS Aeroacoustics Conference (2024)*, p. 3045, 2024.

[14] Institute of Aerodynamics, RWTH Aachen University, "m-AIA multiphysics flow solver." `https://doi.org/10.5281/zenodo.13350586`, 2024.

[15] A. Pogorelov, L. Schneiders, M. Meinke, and W. Schröder, "An adaptive cartesian mesh based method to simulate turbulent flows of multiple rotating surfaces," *Flow, Turbulence and Combustion*, vol. 100, pp. 19–38, 2018.

[16] M. Meinke, W. Schröder, E. Krause, and T. Rister, "A comparison of second-and sixth-order methods for large-eddy simulations," *Computers & Fluids*, vol. 31, no. 4-7, pp. 695–718, 2002.

[17] K. S. Brentner and F. Farassat, "Analytical comparison of the acoustic analogy and kirchhoff formulation for moving surfaces," *AIAA Journal*, vol. 36, no. 8, pp. 1379–1386, 1998.

[18] A. Niemöller, M. Schlottke-Lakemper, M. Meinke, and W. Schröder, "Dynamic load balancing for direct-coupled multiphysics simulations," *Computers & Fluids*, vol. 199, p. 104437, 2020.

[19] T. Sinnige, B. D. Corte, R. De Vries, F. Avallone, R. Merino-Martínez, D. Ragni, G. Eitelberg, and L. L. Veldhuis, "Alleviation of propeller-slipstream-induced unsteady pylon loading by a flow-permeable leading edge," *Journal of Aircraft*, vol. 56, no. 3, pp. 1214–1230, 2019.

[20] Y. Zhe, M. Meinke, and W. Schröder, "Numerical analysis of propeller-airfoil interaction in a distributed propulsion system using a hybrid LES and FW-H approach," in *30th AIAA/CEAS Aeroacoustics Conference (2024)*, p. 3211, 2024.

[21] J. Jeong and F. Hussain, "On the identification of a vortex," *Journal of Fluid Mechanics*, vol. 285, pp. 69–94, 1995.

[22] B. B. Turhan, L. F. Lopes de Moraes Filho, S. Pullin, B. Y. Zhou, H. K. Jawahar, A. Gautam, D. Rezgui, and M. Azarpeyvand, "Numerical and experimental analysis of synchronized propellers for noise mitigation," in *30th AIAA/CEAS Aeroacoustics Conference (2024)*, p. 3237, 2024.

DOI: 10.61782/fa.2025.0571

FORUM ACUSTICUM EURONOISE 2025

MITIGATION STRATEGIES FOR ACOUSTIC REFLECTIONS GENERATED BY AN AXISYMMETRIC WIND TUNNEL NOZZLE

Luca Nicola Quaroni [1*] **Roberto Merino-Martínez** [1]

[1] Faculty of Aerospace Engineering, Delft University of Technology, the Netherlands

ABSTRACT

The issue of acoustic reflections caused by an axisymmetric nozzle is addressed both numerically and experimentally. The contraction (with an exit diameter of 420 mm and a contraction ratio of 2) is representative of typical open-jet wind tunnel exits. Such a category of wind tunnels are extensively used in aeroacoustic studies due to the possibility of acoustic treatment of the test chamber (plenum) walls and the placement of acoustic sensors outside of the flow. The distance between the wind tunnel's nozzle exit and the model being tested is usually limited to around one hydraulic diameter in order for the model to be fully contained within the exit jet's core. Partly for this reason, the wind tunnel nozzle normally protrudes inside the anechoic plenum to distance the tested model from the (acoustically-treated) walls. This effectively creates a cavity, which is in communication with the test section. Acoustic simulations through a commercial finite-element code (COMSOL Multiphysics) show that the presence of the nozzle leads to interference patterns within the test section and a substantial modification of a source's measured directivity pattern. Experimental measurements in a fully anechoic chamber confirm these results. Melamine foam inserts on both the exit flange and part of the inner walls of the contraction are shown to mitigate the issue partly.

Keywords: ***Acoustic reflections, Aeroacoustic wind tunnel, Melamine foam inserts.***

Corresponding author: *l.n.quaroni@tudelft.nl.*

***Copyright**: ©2025 This is an open-access article distributed under the terms of the Creative Commons Attribution 3.0 Unported License, which permits unrestricted use, distribution, and reproduction in any medium, provided the original author and source are credited.*

1. INTRODUCTION

Awareness of the adverse health effects of noise exposure from the aviation sector has been steadily increasing over the past few decades as the volume of flights has increased globally [1]. Furthermore, in an effort to increase propulsive efficiency, novel architectures (i.e. distributed propellers, boundary layer ingestion, etc.) have been introduced, potentially contributing to and altering the noise generation [2]. Improvements in control technologies and the lowering of production costs have then led to the widespread use of small Unmanned Aerial Vehicles (UAVs) for both professional and entertainment purposes, further exacerbating the issue [3]. Research for mitigation strategies has therefore followed suit, with experimental testing usually involving anechoic chambers and/or open-jet wind tunnels. While offering anechoic conditions (i.e. free-field sound propagation) over a large frequency range, anechoic chambers lack the possibility of adding any inflow, restricting their use to hovering UAVs [4]. Open-jet wind tunnels, on the other hand, allow for the presence of low-turbulence subsonic inflows in an anechoic environment, making them the perfect candidates for aeroacoustic studies. Common designs present a turbulence-reducing contracting nozzle protruding into an anechoic plenum, matched by a collector on the opposite side for the creation of a semi-closed air circuit [5]. Recent contributions involving anechoic open-jet wind tunnels focused on isolated propellers [6, 7], propeller installation effects [8], and turbulence-airfoil interaction [9,10].

Because of the widespread use of open-jet anechoic wind tunnels in aeroacoustic investigations, a clear understanding of the effects related to their specific testing environment is essential for a correct interpretation of

the results obtained. The present paper focuses on the issue of acoustic reflections caused by an axisymmetric contracting nozzle designed for an open-jet wind tunnel facility. It summarizes the results of a numerical and experimental investigation of the acoustic interference patterns generated by a simple point sound source located outside of the nozzle's exit, representative of the typical location of test models. The effectiveness of acoustically absorbing panels at mitigating the issue is also discussed.

2. PROBLEM OVERVIEW

2.1 Contraction geometry

An axisymmetric contraction was designed as part of a broader investigation [7] of turbulence-ingestion noise generation by an isolated propeller at the anechoic wind tunnel facility (A-Tunnel) of Delft University of Technology [11]. The nozzle is intended to both improve the isotropy of grid-generated turbulence and reduce the grids' self-noise, following suggestions by Bowen et al. [12]. The contraction follows the fifth-order polynomial wall profile indicated by Bell & Mehta [13]:

$$\mathrm{D(z)} = \mathrm{D_{wt}} + (\mathrm{D_{wt}} - \mathrm{D_{ext}}) \left[-10 \left(\frac{z}{\mathrm{L_c}} \right)^3 + \right.$$
$$\left. + 15 \left(\frac{z}{\mathrm{L_c}} \right)^4 - 6 \left(\frac{z}{\mathrm{L_c}} \right)^5 \right], \quad (1)$$

where all the geometrical parameters and their values are shown in Fig. 1. The additional cylindrical section after the contracting profile, of length $\mathrm{L_a} = \mathrm{R_{wt}}/2 = 150$ mm, was inserted to improve the flow's homogeneity at the nozzle's exit. Two flanges with a thickness of 15 mm and six aluminum struts (see top view in Fig. 2) were included for both structural and practical reasons and for compatibility with existing nozzles designed for the same wind tunnel, e.g. [11, 14]. A hot-wire anemometry campaign showed that the contraction produces streamwise turbulence intensity levels u'/U_∞ lower than 0.1% with good flow homogeneity within the first diameter $\mathrm{D_{ext}}$ from the nozzle exit [7].

2.2 Example: interference patterns in turbulence-interaction noise investigation

Fig. 3 shows the experimental setup used for the aforementioned investigation of turbulence-interaction noise by

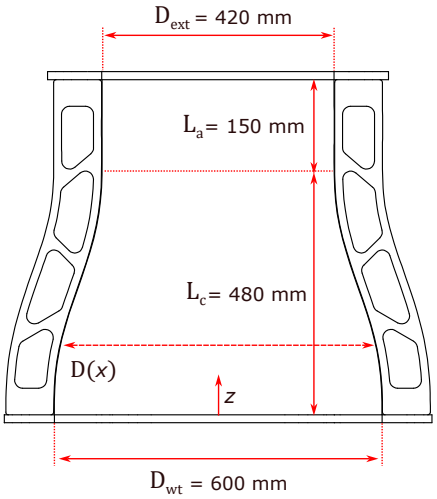


Figure 1. Sectional view of the axisymmetric contraction. The flow is in the positive z direction.

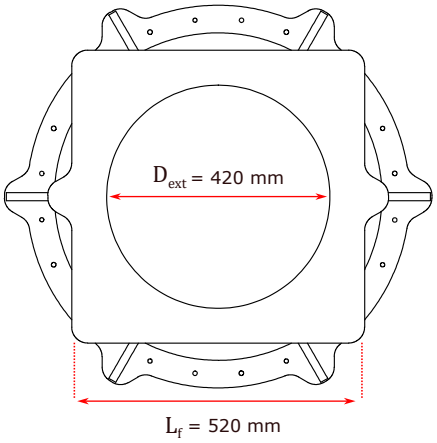


Figure 2. Top view of the axisymmetric contraction.

an isolated propeller. A turbulence-generating grid was inserted between the main wind tunnel's exit on the floor and the inlet of the additional contraction, allowing for the generation of turbulence intensity levels in the streamwise direction z of approximately 3% at the location of the propeller's disk ($z = 0.4\,\mathrm{D_{ext}}$, with $z = 0$ m at the nozzle exit plane). For further details, the reader is referred to Quaroni et al. [7]. The self-noise produced by the supporting structure and the propeller's nacelle was obtained by substituting the propeller with a dummy spinner and installing or removing the turbulence-producing grid at the base of the additional contraction. The self-noise of the system

composed of the nozzle and grid only was also tested by removing the propeller's setup altogether.

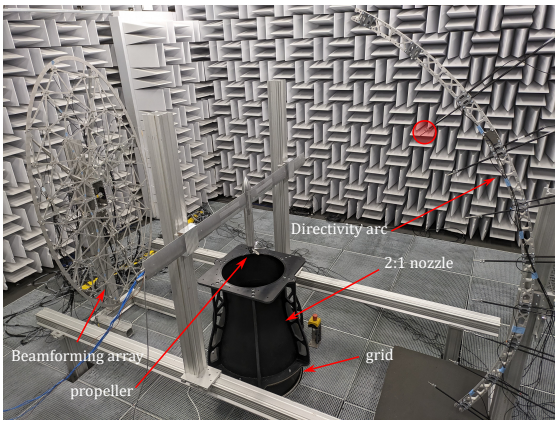


Figure 3. Overview of the setup for the study of turbulence-interaction noise by an isolated propeller, from [7]. Microphone at $\vartheta = 50°$ highlighted.

Fig. 4 reports the power spectral density (PSD) of the acoustic pressures measured at a distance $r = 1.3$ m from the center of the propeller's disk and at emission angle $\theta = 50°$ downstream of the propeller's disk for the self-noise cases and the condition with an operational propeller spinning at 180.57 Hz; a common inflow velocity of $V_\infty = 30$ m/s was set. Characteristic undulations in the broadband spectra are clearly visible in all cases. Oscillation 'amplitudes' increase while their 'wavelengths' remain constant when going from the case of clean inflow to the support structure to the case of turbulent inflow and installed propeller. This observation seems to indicate that the behavior might be related to the acoustic response of the overall wind tunnel system rather than to a particular sound generation mechanism (e.g. turbulence-ingestion noise). For the cases of 'grid on' and 'propeller setup on-off', the spectral oscillations almost perfectly overlap for frequencies higher than $\approx$ 2000 Hz, indicating that the acoustic scattering due to the support structure has a limited effect. Finally, a previous characterization of the wind tunnel facility showed that the anechoic plenum has a cut-off frequency of 200 Hz [11]. This leads to the conclusion that the newly designed axisymmetric nozzle might be responsible for the introduction of spurious acoustic reflections, leading to complex interference patterns within the anechoic plenum of the wind tunnel. The following sections explore this possibility through a numerical and experimental investigation of the acoustic properties of the contraction.

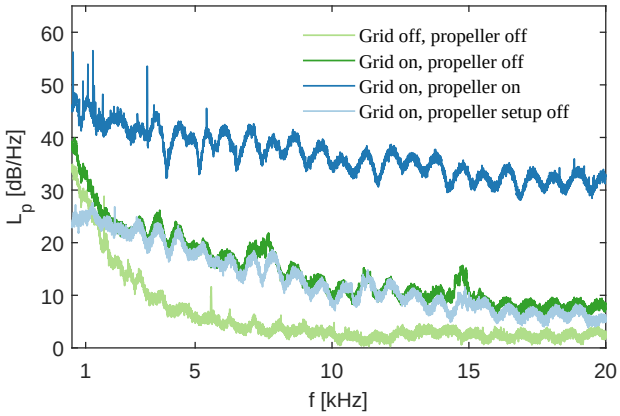


Figure 4. Power spectral density (L_p, $\Delta f = 1$ Hz) of acoustic pressure at $r = 1.3$ m and $\theta = 50°$ downstream of propeller's disk for the case of: no grid and dummy spinner, grid and dummy spinner, grid and propeller, grid on and propeller setup off ($V_\infty = 30$ m/s).

3. NUMERICAL INVESTIGATION

The commercial software COMSOL Multiphysics 6.2 was used to gain insight into the acoustic scattering effects caused by the introduction of the axisymmetric nozzle to the wind tunnel's anechoic plenum.

3.1 Numerical model

A simplified geometry of the nozzle was considered in order to reduce the problem to a 2D axisymmetric one. Both the bottom flange and the side struts were removed, while the shape of the top flange was converted from a square with rounded edges to an infinitely thin circular plate. This allowed for a considerable reduction in computational costs while maintaining the main parameters of interest to the problem. Fig 5 reports a sketch of the numerical domain. An acoustic point source of strength Q_s was placed at $z_s = \mathrm{L}_c + \mathrm{h}_s$, with $\mathrm{h}_s = 0.4\,\mathrm{D}_{\mathrm{ext}} = 164$ mm being the distance of the source from the nozzle exit (same as the distance to the propeller disk in the example before). The value of Q_s was computed from the formula for monopole sources [15]:

$$p_{rms}^2 = \frac{Q_s^2 k^2 (\rho_0 c^2)}{16\pi^2 r^2 (1 + k^2 a^2)} \tag{2}$$

where $k = 2\pi f_s/c = \omega_s/c$ is the wave number and a is the source radius. Letting $a \to 0$ and imposing p_{rms} such that the sound pressure level $L_p = 45$ dB/Hz at a distance $r = 1.3$ m, a value of for Q_s could be computed for each simulated source frequency f_s. Such distance was set equal to the inner radius of the directivity arc shown in Fig. 4 (and used in the experimental analysis discussed in Section 4).

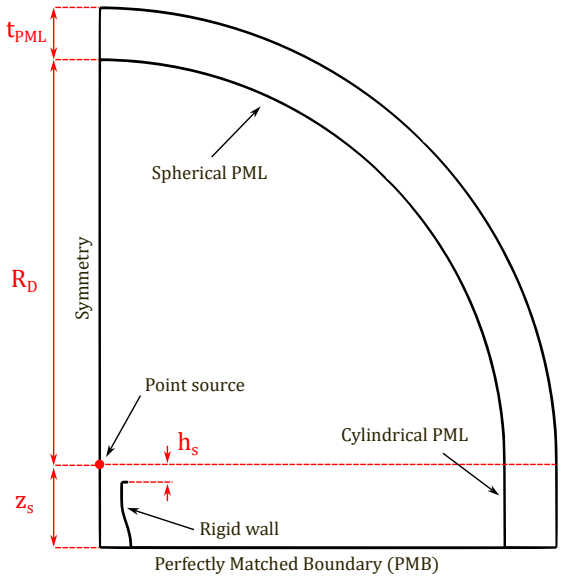


Figure 5. Sketch of the numerical domain including source position and boundary conditions.

To reproduce acoustic free-field propagation conditions, Perfectly Matched Layers (PML) and a Perfectly Matched Boundary (PMB) were added to the numerical domain's boundaries. A spherical and a cylindrical PML enclosed the top and right boundaries while a PMB represents the floor of the anechoic chamber. At least 5 cells per acoustic wavelength λ are recommended for a correct discretization of an acoustic field [16]. In the present case, the maximum cell size in the domain was set to $h_{max} = \lambda/8$. Preliminary simulations without the inclusion of the rigid-walled contraction showed that free-field conditions were obtained when imposing a radius of the numerical domain $\mathrm{R}_D = 4$ m $\approx 20\mathrm{D}_{ext}$ and a PML thickness $t_{PML} = 0.5$ m. This last value is related to the ability of the PML to absorb incoming waves and should be in the order of the largest wavelength to absorb. The application of acoustically absorbing panels to mitigate the interference caused by the nozzle was also numerically explored. Melamine foam was selected over other materials (e.g. glass wool, polyurethane foam) due to its better acoustic performance when grazing flows are involved [17]. Foam inserts were applied on both the upper flange and on the internal walls of the end (cylindrical) section of the nozzle (Fig. 6). This was done to minimize the possible influence of the foam layers on the flow quality (homogeneity and turbulence intensity) of the nozzle. The Johnson-Champoux-Allard (JCA) model was used to model the acoustic absorption by the melamine foam inserts, with the required physical properties listed in Table 1.

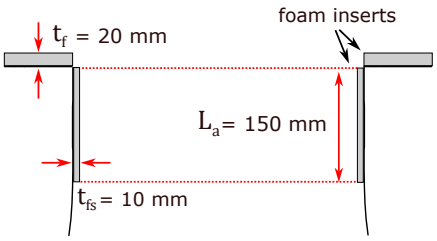


Figure 6. Diagram of melamine foam inserts on the upper end of the simplified contraction geometry.

Table 1. Melamine foam properties, from [18].

Quantity	Symbol	Value
Porosity	ε_p	0.95
Flow resistivity	R_f	10500 Pa · s/m^2
Drained density	ρ_d	11 kg/m^3
Viscous length (coeff.)	s	0.49
Thermal length	L_{th}	470 μm

3.2 Results

The sound pressure level distribution over the numerical domain for the untreated contraction and a source frequency $f_s = 4000$ Hz is reported in Fig. 7. Such frequency corresponds to a Helmholtz number $He = 2\pi L/\lambda \approx 31$, where $L = D_{ext}$, which is within the typical frequency range of interest for aeroacoustic testing. A complex pattern of alternating lobes is present due to constructive and destructive interference. This clearly shows the deviation in terms of directivity with respect to the

spherical propagation expected for a point sound source and typically assumed in acoustic beamforming [11].

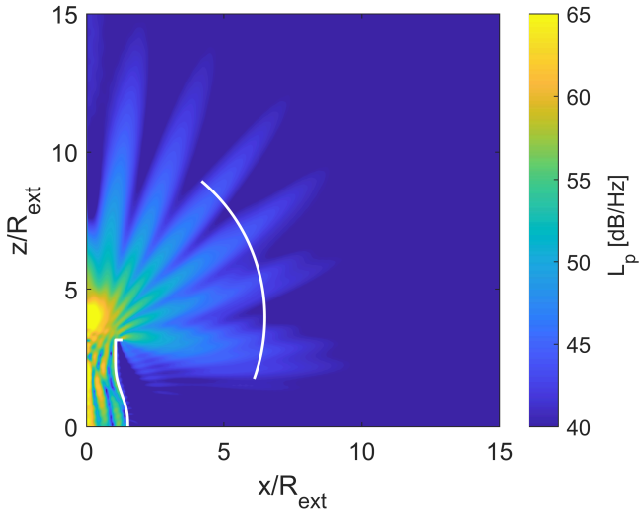


Figure 7. Simulated sound pressure level (L_p) distribution for the case of the untreated (simplified) nozzle geometry and an acoustic point source with frequency $f_s = 4000$ Hz at a distance $h_s = 0.4\mathrm{D}_{ext}$ from the nozzle exit. The directivity arc and nozzle outline are highlighted in white.

Figs. 8-10 depict the directivity patterns of L_p at $r = 1.3$ m and polar angles $\vartheta = [-20°, 50°]$ (with $\vartheta = 0°$ corresponding to the nozzle exit plane and ϑ positive anti-clockwise) for three different source frequencies $f_s = 1000$ Hz, 4000 Hz and 6300 Hz. Both cases of untreated and acoustically treated nozzle are reported. The range for ϑ is chosen to be consistent with the angle covered by the directivity arc shown in Fig. 3 and used in the experimental investigation (Sec. 4). The source frequencies f_s correspond to a selection of typical 1/12-octave band center frequencies of interest during aeroacoustic investigations. Large differences in L_p along the arc length are visible at all source frequencies, with the number of lobes increasing with increasing f_s. The addition of melamine foam helps to some extent in reducing the amplitude of the lobes and its effectiveness increases with increasing f_s. This last consideration had to be expected since the foam inserts' small thickness limits the dampening of longer wavelengths (i.e. lower frequencies).

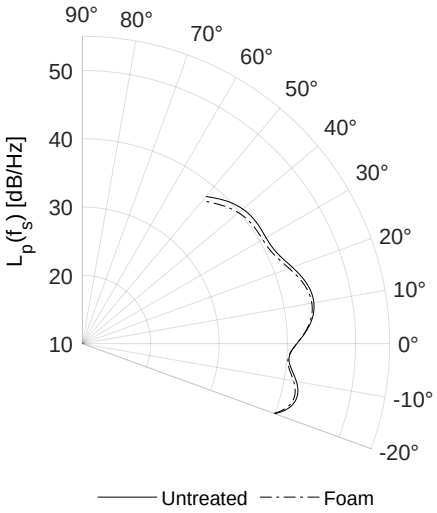


Figure 8. Simulated sound pressure level L_p directivity at $r = 1.3$ m ($r/R_{ext} \approx 6$) for a single source frequency of $f_s = 1000$ Hz.

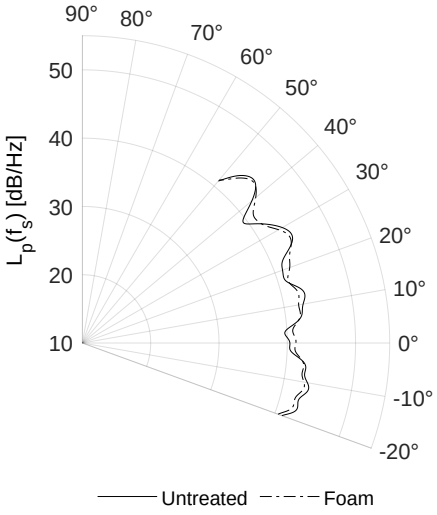


Figure 9. Simulated sound pressure level L_p directivity at $r = 1.3$ m ($r/R_{ext} \approx 6$) for a single source frequency of $f_s = 4000$ Hz.

4. EXPERIMENTAL INVESTIGATION

An experimental campaign was conducted to confirm the effectiveness of the melamine foam treatment in mitigating the issue of acoustic reflections by the presence of the nozzle.

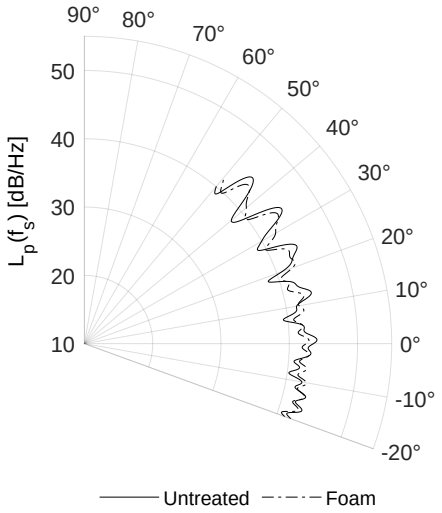


Figure 10. Simulated sound pressure level L_p directivity at $r = 1.3$ m ($r/R_{ext} \approx 6$) for a single source frequency of $f_s = 6300$ Hz.

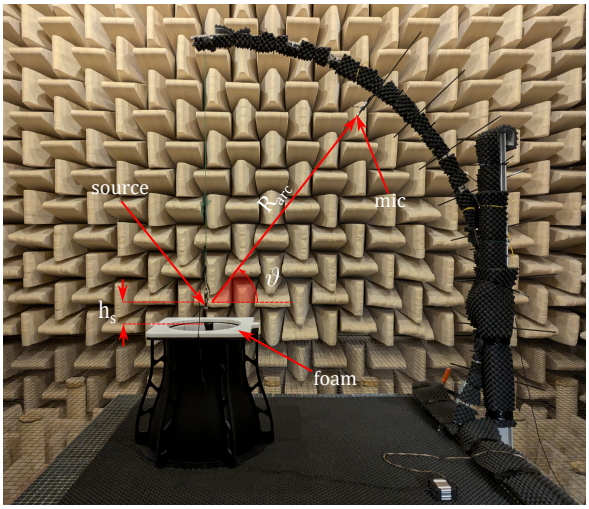


Figure 11. Experimental setup at the anechoic chamber of Delft University of Technology.

4.1 Experimental setup

The experiment was conducted at the 8 m × 8 m × 8 m anechoic chamber of the Applied Sciences faculty of Delft University of Technology (Fig. 11). A miniature sound source (Qsources, type QindW) was positioned at a distance $h_s = 0.4\mathrm{D_{ext}}$ above the center of the contraction's exit ($r = 0$). The source presents good omnidirectionality properties over the frequency range from 500 Hz to 7000 Hz and an accompanying amplifier allows for the production of white noise in this range [19]. The same directivity arc shown in Fig. 3 was employed to sample the acoustic pressure field at a distance $r = R_{arc} = 1.3$ m over the polar angle range $\vartheta = [-20°, +50°]$ with a step $\Delta\vartheta = 10°$. A prepolarized 1/2-inch free-field microphone (Brüel & Kjær, Type 4189) was sequentially moved along the directivity arc and its signal was acquired for 45 s and sampled at 40 kHz through a hand-held analyzer (Brüel & Kjær, Type 2250).

4.2 Results

Figure 12 presents the power spectral density at $\vartheta = 50°$ for the untreated and the acoustically treated nozzle. Oscillations in the spectra are visible in both cases. However, the addition of the melamine foam layer effectively reduces their amplitude over the considered frequency range. Figs. 13-15 report the 1/12-octave band sound pressure level $L_{p_{1/12}}$ directivity plots for the center frequencies of $f_c = 1000$ Hz, 4000 Hz, and 6300 Hz. The $L_{p_{1/12}}$ is computed as:

$$L_{p_{1/12}}(f_c) = 10\log_{10}\left(\sum_{n=1}^{N}\frac{S_{pp}(f_i)\Delta f}{p_{ref}^2}\right), \qquad (3)$$

where $f_1 = f_L$ and $f_N = f_U$ are the lower and upper bounds of the 1/12-octave band with center frequency f_c, S_{pp} is the acoustic power spectral density, Δf is its frequency interval, and $p_{ref} = 20$ μPa is the reference acoustic pressure. At the lowest frequency, the pattern is highly non-omnidirectional but foam addition seems to nonetheless mitigate the issue by reducing the $L_{p_{1/12}}$ difference between points along the arc. For the larger center frequencies, the increase in frequency bandwidth considered in the computation of the $L_{p_{1/12}}$ makes the overall directivity closer to the omnidirectional one. However, it is also evident that adding foam has the effect of improving the source omni-directionality, especially at larger polar angles ϑ.

5. CONCLUSIONS

The present paper has dealt with the issue of acoustic interference by an axisymmetric contraction in an open-jet wind tunnel exit. It was shown through both numerical

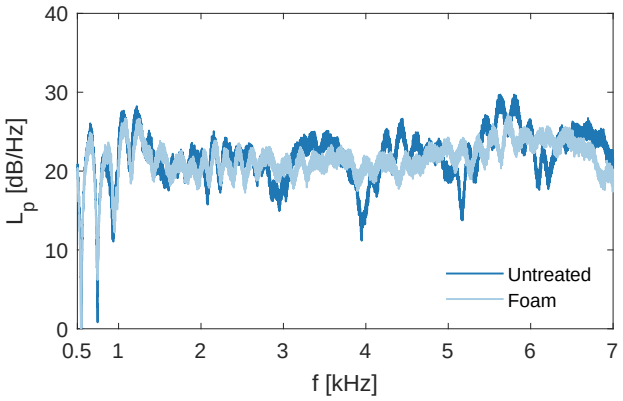


Figure 12. Power spectral density of microphone signal at $\vartheta = 50°$ for both acoustically treated and untreated nozzle ($\Delta f = 1$ Hz).

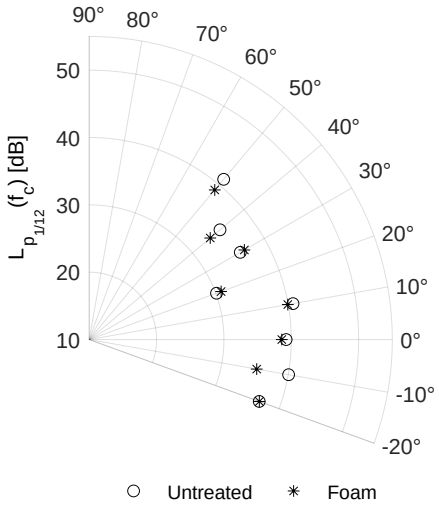


Figure 13. Directivity of 1/12-octave band sound pressure level $L_{p_{1/12}}$ at center frequency $f_c = 1000$ Hz and $r = 1.3$ m ($r/R_{ext} \approx 6$) for both acoustically treated and untreated nozzle.

and experimental analyses that the introduction of the nozzle to an anechoic environment caused substantial modifications in the directivity pattern of a simple point source placed at a typical position of aeroacoustic sources in wind tunnel testing. Adding melamine foam inserts on the upper flange and along the end section of the internal wall of the contraction helped mitigate the issue to some extent.

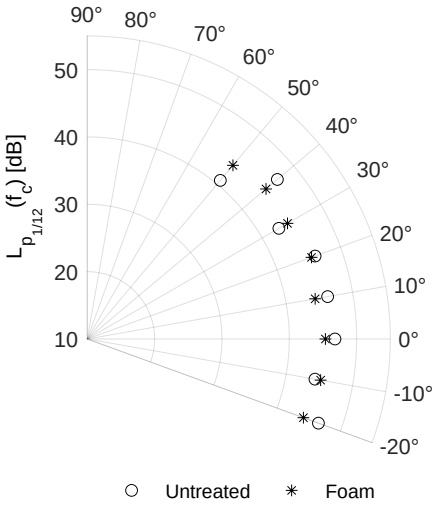


Figure 14. Directivity of 1/12-octave band sound pressure level $L_{p_{1/12}}$ at center frequency $f_c = 4000$ Hz and $r = 1.3$ m ($r/R_{ext} \approx 6$) for both acoustically treated and untreated nozzle.

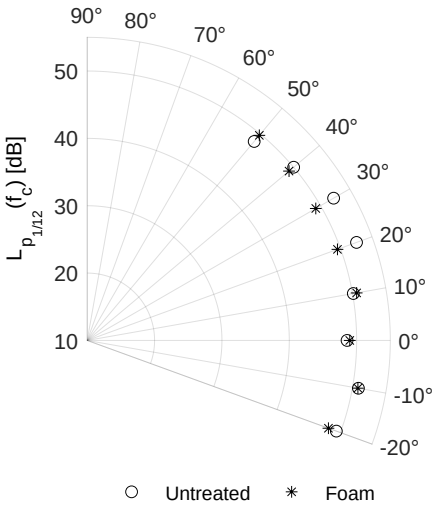


Figure 15. Directivity of 1/12-octave band sound pressure level $L_{p_{1/12}}$ at center frequency $f_c = 6300$ Hz and $r = 1.3$ m ($r/R_{ext} \approx 6$) for both acoustically treated and untreated nozzle.

6. ACKNOWLEDGMENTS

This work is part of the HOPE (Hydrogen Optimized multi-fuel Propulsion system for clean and silEnt air-

craft) project and has received funding from the European Union's Horizon Europe research and innovation programme under grant agreement No. 101096275. The authors would also like to acknowledge the help of Bieke von den Hoff during the experimental campaign in the anechoic chamber, as well as the support from Henry den Bok from the faculty of Applied Sciences.

7. REFERENCES

[1] L. Leylekian, A. Covrig, and A. Maximova, eds., *Aviation Noise Impact Management: Technologies, Regulations, and Societal Well-being in Europe*. Cham: Springer International Publishing, 2022.

[2] N. van Arnhem, *Unconventional PropellerAirframe Integration for Transport Aircraft Configurations*. PhD thesis, Delft University of Technology, 2022.

[3] N. Green, A. J. Torija, and C. Ramos-Romero, "Perception of noise from unmanned aircraft systems: Efficacy of metrics for indoor and outdoor listener positions," *The Journal of the Acoustical Society of America*, vol. 155, pp. 915–929, Feb. 2024.

[4] C. E. Tinney and J. Sirohi, "Multirotor Drone Noise at Static Thrust," *AIAA Journal*, vol. 56, pp. 2816–2826, July 2018.

[5] C. S. Allen, W. K. Blake, R. P. Dougherty, D. Lynch, P. T. Soderman, and J. R. Underbrink, *Aeroacoustic Measurements*. Berlin, Heidelberg: Springer Berlin Heidelberg, 2002.

[6] K. Baskaran, N. S. Jamaluddin, A. Celik, D. Rezgui, and M. Azarpeyvand, "Effects of number of blades on propeller noise," *Journal of Sound and Vibration*, vol. 572, p. 118176, Mar. 2024.

[7] L. N. Quaroni, R. Merino-Martinez, F. D. Monteiro, and S. S. Kumar, "Collective blade pitch angle effect on grid turbulence ingestion noise by an isolated propeller," in *30th AIAA/CEAS Aeroacoustics Conference (2024)*, (Rome, Italy), American Institute of Aeronautics and Astronautics, June 2024.

[8] F. Petricelli, P. Chaitanya, S. Palleja-Cabre, S. Meloni, P. F. Joseph, A. Karimian, S. Palani, and R. Camussi, "An experimental investigation on the effect of in-flow distortions of propeller noise," *Applied Acoustics*, vol. 214, p. 109682, Nov. 2023.

[9] T. Geyer, S. Wasala, and E. Sarradj, "Experimental Study of Airfoil Leading Edge Combs for Turbulence Interaction Noise Reduction," *Acoustics*, vol. 2, pp. 207–223, Apr. 2020.

[10] L. Bowen, A. Celik, and M. Azarpeyvand, "A thorough experimental investigation on airfoil turbulence interaction noise," *Physics of Fluids*, vol. 35, p. 035123, Mar. 2023.

[11] R. Merino-Martínez, A. Rubio Carpio, L. T. Lima Pereira, S. Van Herk, F. Avallone, D. Ragni, and M. Kotsonis, "Aeroacoustic design and characterization of the 3D-printed, open-jet, anechoic wind tunnel of Delft University of Technology," *Applied Acoustics*, vol. 170, p. 107504, Dec. 2020.

[12] L. Bowen, A. Celik, M. Azarpeyvand, and C. R. I. Da Silva, "Grid Generated Turbulence for Aeroacoustic Facility," *AIAA Journal*, vol. 60, pp. 1833–1847, Mar. 2022.

[13] J. Bell and R. Mehta, "Contraction Design for Small Low-Speed Wind Tunnels," Contractor report 177488, NASA, 1988.

[14] E. Grande, G. Romani, D. Ragni, F. Avallone, and D. Casalino, "Aeroacoustic Investigation of a Propeller Operating at Low Reynolds Numbers," *AIAA Journal*, vol. 60, pp. 860–871, Feb. 2022.

[15] M. Norton and D. Karczub, "2 Sound waves: a review of some fundamentals," in *Fundamentals of Noise and Vibration Analysis for Engineers*, Cambridge University Press, 2nd ed., 2003.

[16] COMSOL, "Acoustics Module: User's Guide," 2018.

[17] H. F. Bento, D. Ragni, F. Avallone, D. Simons, and M. Snellen, "Acoustic wall treatments for wind tunnel aeroacoustic measurements," *Applied Acoustics*, vol. 199, p. 108989, Oct. 2022.

[18] N. Kino and T. Ueno, "Comparisons between characteristic lengths and fibre equivalent diameters in glass fibre and melamine foam materials of similar flow resistivity," *Applied Acoustics*, vol. 69, pp. 325–331, Apr. 2008.

[19] H. F. Mourão Bento, C. P. VanDercreek, F. Avallone, D. Ragni, P. Sijtsma, and M. Snellen, "Wave propagation modelling approach for improved assessment of the acoustic field in closed test section wind tunnels," *Journal of Sound and Vibration*, vol. 600, p. 118858, Mar. 2025.

DOI:

Main theme: A07 Flow Acoustics

Session A07.04 Fluid structures acoustic coupling

Chair(s): S. Becker, E. Ferrer

DOI: 10.61782/fa.2025.0841

FORUM ACUSTICUM EURONOISE 2025

SUPPRESSION OF AN AEROACOUSTIC FEEDBACK MECHANISM IN A COMPLEX PIPELINE

Erika Quaranta[1*] **Malcolm Smith**[1]
[1]ISVR Consulting, University of Southampton, UK

ABSTRACT

This paper describes a study aimed at understanding and controlling an unsteady flow induced resonance in the metering system of a gas production platform, which had constrained the platform's operating conditions for many years. The resulting high-level vibrations posed a risk of fatigue failures in the attached pipework.
Various numerical flow and aeroacoustic modelling techniques were used to simulate the flow through the different parts of the system to identify the main physical excitation mechanism. This was found to be analogous to a so-called Rossiter tone, commonly occurring in grazing flows over cavities. In this case, vortex shedding at bifurcations in different parts of the pipeline were identified as sources of flow instability, associated with an aeroacoustic feedback mechanism from features further downstream. The numerical analysis also enabled an understanding of the persistence and varying strength of this mechanism along the entire pipeline, also depending on the flow regime at which the pipeline was operated.
The in-depth understanding provided by this analysis enabled recommendations for an efficient redesign of the entire system to control the problem at source.

Keywords: ***Aeroacoustics, resonance, numerical modelling, computational fluid dynamics.***

1. INTRODUCTION

A comprehensive review on resonance due to flow-induced pulsation in pipelines with various configurations of closed branches was presented in 2011 [1]. The review primarily focused on the aeroacoustic feedback mechanism, where boundary layer-excited vorticity couples with acoustic modes in the cavity. Many studies have investigated the aeroacoustics of cavities in pipelines, using both experimental and numerical approaches, with some of the most recent being [2-4]. Additionally, other aeroacoustic sources in a pipeline are T junctions, where vortex shedding from the junction can couple with an acoustic resonant mode of a nearby portion of the piping system [5-6].
The present study addresses a real-world problem, where for decades gas production on a platform has been disrupted by flow-induced vibrations in the gas metering ductwork, depending on flow regimes and velocity. At higher flow velocities, instabilities within the 30-35 Hz range triggered structural response in a mode of vibration at 34 Hz, causing significant issues.
The pipeline design includes an inlet duct where flow bifurcates into a header, then redirects into the metering system, and finally into the outlet duct (Fig. 1). Previous studies suggested various possible causes of instability, but our 2023 study [7] combined CFD and acoustic FEM analysis to confirm that vortex shedding and flow instability in the inlet header create an aeroacoustic feedback mechanism coupling with the pipeline's acoustic modes.
A follow-on study [8] extended the analysis to the outlet manifold, indicating a strong possibility of resonance in the outlet header, analogous to that previously identified in the inlet.
Based on our findings, the platform management company proposed a complete redesign of the entire pipeline aim to eliminate these issues at source.
After summarizing the aeroacoustic results and our proposed interpretation of the feedback mechanisms at the two different flow regimes in the current pipeline, this paper aims to present the equivalent results obtained for the redesigned pipeline and so demonstrate the improvements achieved by implementing the proposed modifications.

[*]***Corresponding author***: e.quaranta@soton.ac.uk.
Copyright: *©2025 Erika Quaranta et al. This is an open-access article distributed under the terms of the Creative Commons Attribution 3.0 Unported License, which permits unrestricted use, distribution, and reproduction in any medium, provided the original author and source are credited.*

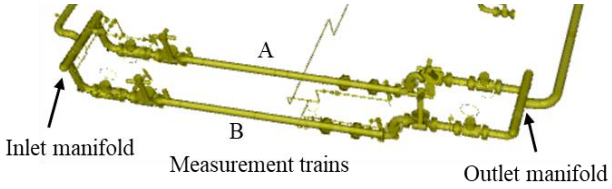


Figure 1: The current gas production pipeline.

2. AEROACOUSTIC MODELLING

In this study we utilised compressible Unsteady Reynolds-Averaged Navier-Stokes (URANS) simulations with the k-ω SST turbulence model to analyse turbulent and acoustic pressure fluctuations in the pipeline. Despite the average Mach number being characteristic of incompressible flow, compressible analysis was necessary to capture the relevant aeroacoustic phenomena.

We used the open-source software OpenFOAM [9], because it was the most efficient and cost-effective solution, in conjunction with High-Performance Computing (HPC).

Key Aeroacoustic Insights:

- The focus was on low-frequency interactions between vortex shedding and acoustic waves, which are crucial for understanding flow physics and providing design modification recommendations.
- Standard CFD tools face challenges such as dissipative numerical schemes that damp acoustic wave propagation and boundary conditions that reflect acoustic waves. Accurate modelling required careful treatment of these factors.
- Fully structured meshes were used to minimise numerical dissipation, allowing sound wave propagation without compromising stability. Non-reflective boundary conditions and progressively increasing aspect ratio meshes were employed to reduce wave reflection at inlets and outlets.

The pipeline system operates in single and dual stream regimes, with the inlet manifold feeding two metering trains. This study's findings aimed to mitigate flow-induced vibrations by addressing aeroacoustic feedback mechanisms in both regimes.

From test data measured on the platform, it was identified that the critical inlet velocity of 20 m/s triggered high vibration levels. In the dual stream case, this results in 10 m/s flow at each metering duct inlet, while in the single stream case, it remains 20 m/s at the single inlet. In the headers, due to expansion into a wider duct, the flow decelerates to 6 m/s in the dual stream case and 12 m/s in the single stream case.

The pipeline carries a mixture of natural gases, with a static outlet pressure of 11.3 MPa, and constant temperature and density of 330 K and 80 kg/m³, respectively. The speed of sound in the duct was 430 m/s.

3. ANALYSIS OF THE CURRENT PIPELINE

As reported in the previous studies [7] and [8], CFD analysis has been performed to identify the aeroacoustic feedback mechanism responsible for the resonance in the two different flow regimes.

We have employed wavenumber analysis to examine the spatial-frequency distribution of unsteady pressure perturbations. This powerful tool is used to plot the power spectral density of a wave over frequency f and wavenumber k, enabling the identification of standing and traveling waves and their propagation velocities. This method helps determine whether perturbations are turbulence, propagating at the speed of the flow, or acoustic waves, propagating at the speed of sound. More details on the application of this methodology were explained in our previous paper [7].

Using this method, we analysed both the inlet and outlet separately and surprisingly found both similarly problematic, despite the differences in flow patterns.

This is a summary of our findings and interpretations.

3.1 Dual Stream Case

The CFD model of the pipeline in this flow regime is shown in Fig. 2. The flow bifurcates at the inlet manifold, which feeds two metering ducts, and then rejoin in the outlet manifold.

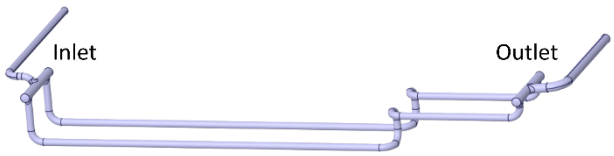


Figure 2: The current pipeline model in the dual stream flow regime.

Wavenumber analysis on the headers and metering ducts are shown in Figs. 3, 4, 5 and 6. In the headers dominant tones result from a combination of turbulence and acoustics. However, in the metering ducts the same tones are propagating as purely acoustic waves. Even if mechanisms differ significantly between the inlet and outlet manifold.

These are indications of vortex instability in the header triggering acoustic waves travelling in the metering duct.
In the case of flow over a cavity, discrete acoustic frequencies arise from the interaction between vortices formed over the cavity and the cavity's acoustic modes. This phenomenon is known as Rossiter tone feedback mechanism [10]. It is generally associated with shear layer vorticity generating acoustic waves when impinging on the downstream edge of the cavity, then travelling upstream through the cavity. The pressure disturbances are converted back into vorticity waves in the shear layer, completing the feedback loop, which is strongly dependent on the flow velocity. This mechanism is particularly critical when the pressure disturbances couple with the acoustic modes of the cavity.
The Rossiter formula calculates the Strouhal number (non-dimensional frequency) at which resonance occurs, as

$$St = \frac{fD}{U} = \frac{n-\alpha}{1/k + M}, n = 1,2,3 \ldots \quad (1)$$

where:

- D is the cavity opening,
- U is the mean flow velocity,
- M is the Mach number,
- α is the phase delay (approximately 0),
- k is the ratio between the convection speed and the mean speed (experimentally 0.6).

In the current case, the flow is within the cavity rather than over it, but the vorticity generated by the flow instability can trigger the same aeroacoustic feedback mechanism.
Using Eq. 1, we can evaluate the critical frequencies. Given that both the headers have similar geometry, using D = 1.1 m (distance between the T-junction and the bifurcation), U = 6 m/s (mean speed in the header), and M = 0.014, the Rossiter frequencies are approximately multiple of 3.2 Hz. The wavenumber analysis of the inlet header (Fig. 3) shows dominant tones at 18 and 36 Hz, while the outlet header (Fig. 5) shows dominant tones at 12, 32, and 48 Hz. There appears to be an approximate 6 Hz factor, which can lock in with the header cavity modes. Specifically, 36 Hz corresponds to a quarter wavelength of the entire header, and the distance between the T-junctions of 2.3 m is a quarter wavelength at 48 Hz.

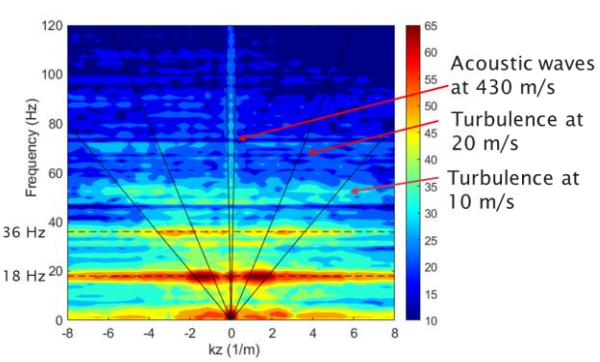


Figure 3: Wavenumber analysis in the inlet header.

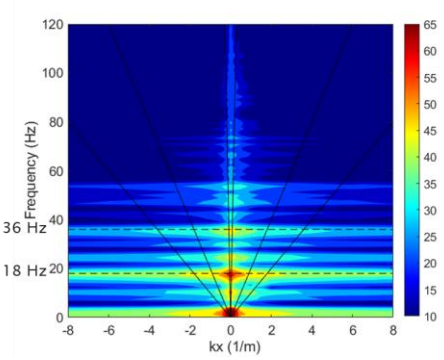


Figure 4: Wavenumber analysis in the metering duct, when only the inlet header is modelled.

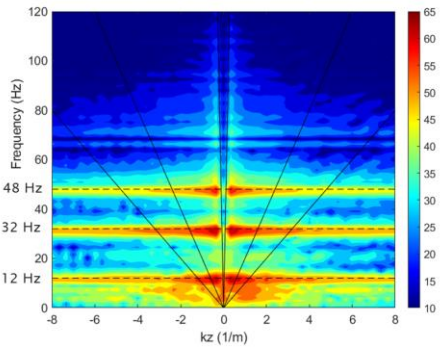


Figure 5: Wavenumber analysis in the outlet header.

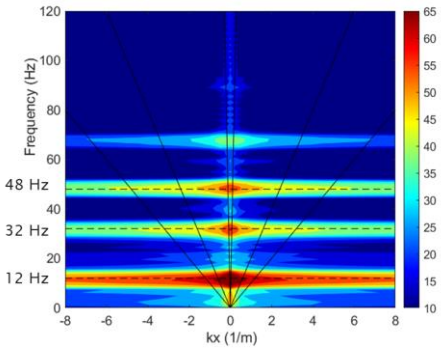


Figure 6: Wavenumber analysis in the metering duct, when only the outlet header is modelled.

3.2 Single Stream Case

The CFD model of the pipeline in this flow regime is shown in Fig. 7. With only one metering duct open, branches are present on the closed line.
For brevity, only the wavenumber analysis on the headers are shown in Figs. 8 and 9. The instability is even more pronounced in both the inlet and outlet headers, as the mean velocity is effectively doubled in this case. There is also evidence of the same Rossiter feedback mechanism, with a similar 6 Hz factor, which is further amplified by the presence of the closed branches. In fact, the two dominant tones 12 and 20 Hz are the same in both headers, as the two branches have similar lengths, approximately a quarter wavelength at 20 Hz.



Figure 7: The current pipeline model in the single stream flow regime.

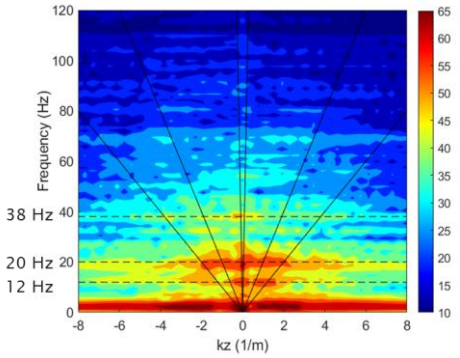


Figure 8: Wavenumber analysis in the inlet header.

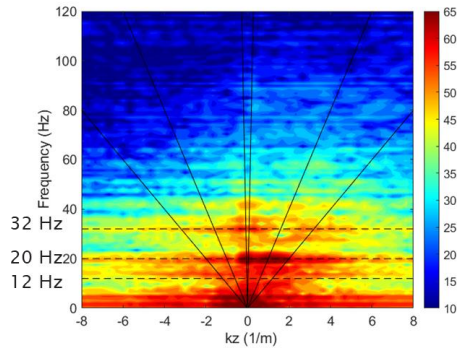


Figure 9: Wavenumber analysis in the outlet header.

4. REDESIGN OF THE PIPELINE

Our study has identified that the main cause of flow instability leading to aeroacoustic resonance is the flow bifurcation and convergence occurring in the header, coupled with the expansion of the flow from a narrower to a wider duct.
Therefore, we have recommended eliminating the headers and finding alternative, smooth solutions to redesign the pipeline avoiding sharp edges, which are strong sources of turbulence. Figures 10 and 11 illustrate the proposed design for the new inlet and outlet, which primarily utilise T-junctions only, as T-junctions itself have not shown potential to be a source of vortex shedding, when using smooth rounded joints.
Further analysis of the proposed design has demonstrated significant improvements in both the flow stability and acoustics of the pipeline.

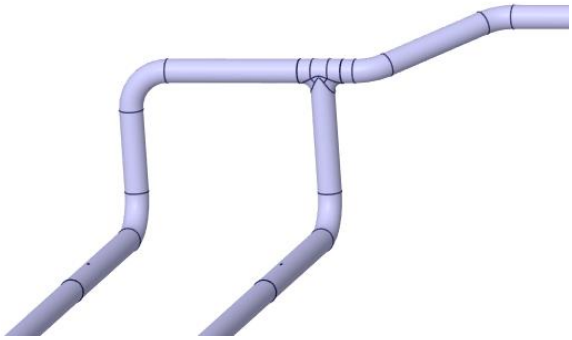


Figure 10: New design of the inlet header.

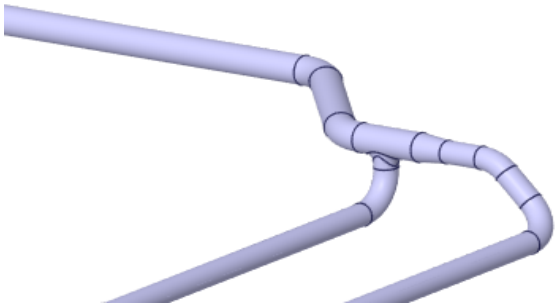


Figure 11: New design of the outlet header.

4.1 Dual Stream Case

The wavenumber analysis shown in Figs. 12 and 13 reveal a complete absence of strong tonal components. There is no evidence of a potential aeroacoustic problem.

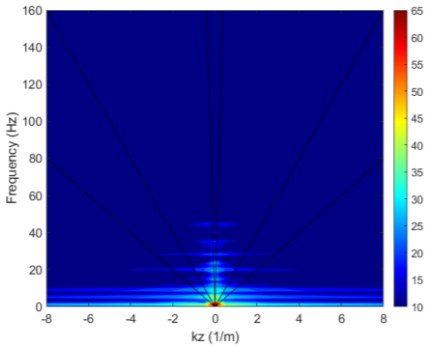


Figure 12: Wavenumber analysis in the inlet header.

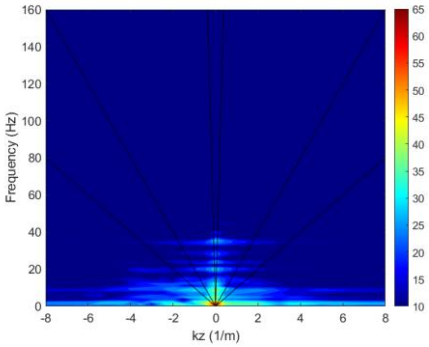


Figure 13: Wavenumber analysis in the outlet header.

4.2 Single Stream Case

Despite showing an overall improvement on the tonal content, the wavenumber analysis (Figs. 14 and 15) in this case still reveals some evident tonal components.
Flow analysis (Fig. 16) indicates that flow instability arises from the expansion occurring upstream of the T junction. This expansion is necessary as the outlet duct is wider than the metering ducts, but we have argued that moving the expansion downstream of the T junction would be beneficial to stabilise the flow.

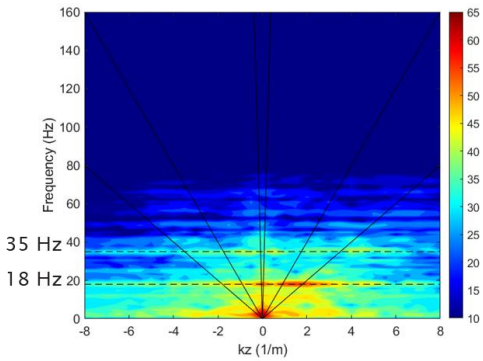


Figure 14: Wavenumber analysis in the outlet header.

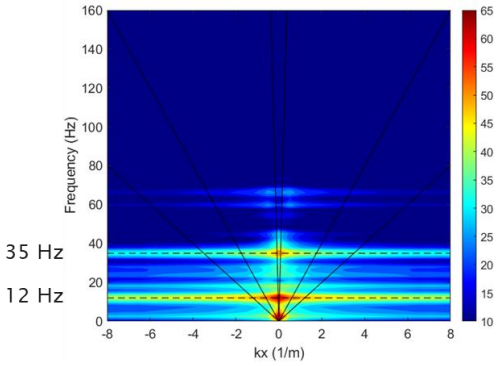


Figure 15: Wavenumber analysis in the outlet header.

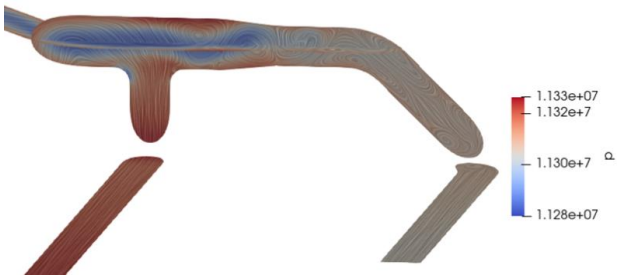


Figure 16: Pressure instability arising at the flow expansion.

5. REDESIGN OF THE OUTLET EXPANSION

To prove our hypothesis with the minimum effort, instead of redoing the full CFD analysis on a redesigned outlet, which would have required issuing an updated CAD and remeshing it, we modified the inlet model by adding an expansion duct to transition from the metering duct to the outlet duct size.

This model is shown in Fig. 17 and was used as an outlet with flow only inlet into the metering duct connected by the T junction to demonstrate the beneficial effect of the smooth transition downstream of the T junction.

Wavenumber analysis in the header of this fictitious outlet (Fig. 18) confirms our assumption, by showing a lack of tonal component.

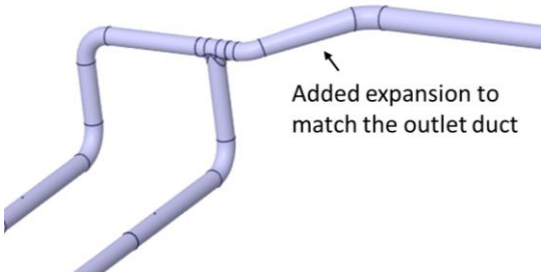


Figure 17: Using the inlet header to prove the effect of moving the expansion downstream the T junction.

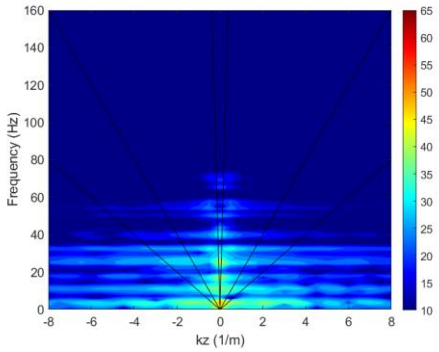


Figure 18: Wavenumber analysis in the header.

6. CONCLUSIONS

The CFD analysis successfully identified the aeroacoustic feedback mechanisms responsible for resonance in two distinct flow regimes. By employing wavenumber analysis, we examined the spatial frequency distribution of unsteady perturbations and revealed that both the inlet and outlet headers exhibited similar problematic behaviour despite differences in flow patterns.

The wavenumber analysis indicated dominant tones resulting from a combination of turbulence and acoustics, with evidence of vortex instability triggering acoustic waves. The single stream case showed even more pronounced instability, amplified by the acoustic modes of closed branches.

To address these issues, we recommended eliminating the headers and redesigning the pipeline using only T-junctions, which have not shown potential to be a source of instability. Further analysis of the proposed design demonstrated significant improvements in both flow stability and acoustics.

However, in the single stream case, despite overall improvement, some evident tonal components remained. Further analysis confirmed that moving the expansion downstream of the T-junction removed the strong tonal components.
This numerical modelling approach provided powerful insights to identify the physical mechanisms involved in this complex engineering problem and has the potential to be applied to a wide range of other aeroacoustic problems.

7. ACKNOWLEDGMENTS

We want to acknowledge the use of the HPC facility Iridis 5 and 6 at the University of Southampton for running all the CFD cases.
We also want to thank the offshore engineering and petrochemical industry participants in this project for their permission to publish this paper.

8. REFERENCES

[1] D. Tonon, A. Hirschberg, J. Golliard and S. Ziada, "Aeroacoustics of pipe systems with closed branches", *International Journal of Aeroacoustics*, vol. 10, no. 2&3, pp. 201–276, 2011.

[2] S. K. Tanga and Y. Tang, "On the length scale and Strouhal numbers for sound transmission across coupled duct cavities at low Mach number", *JASA*, vol. 150, no. 6, pp 4232–4243, 2021.

[3] M. Hanna, A. Mohany, "Aeroacoustics and shear layer characteristics of confined cavities subject to low Mach number flow", *Journal of Fluids and Structures*, vol. 121, art. no. 103949, 2023.

[4] P. Wang, S. Jia, Z. He, C. He, H. J. Sung and Y. Liu, "Flow–acoustic resonance mechanism in tandem deep cavities coupled with acoustic eigenmodes in turbulent shear layers", *Journal of Fluid Mechanics*, vol. 984: A19, 2024.

[5] P. Wang, X. Qiang, H. Jin Sung, Y. Liu, "Data assimilation for turbulence-merged channel branches with the simultaneous enhancement of hydrodynamics and aeroacoustics", *Journal of Fluids and Structures*, vol. 134, art. no. 104283, 2025.

[6] H. Zhang, P. Wang, H. Liu, B. Wang, Y. Liu, "Unsteady flow behaviours and flow-induced noise characteristics in a closed branch T-junction", *Physics of Fluids*, vol. 36, no. 6, 2024.

[7] E. Quaranta, M. Smith and S. Taggart: "Aeroacoustic analysis of flow induced resonance in a gas pipeline" in 53rd International Congress & Exposition on Noise Control Engineering (Internoise), Nantes, France, 2024.

[8] E. Quaranta and M. Smith: "Computational aeroacoustic analysis of a complex pipeline" in the 20th NAFEMS World Congress, Saltzburg, Austria, 2025.

[9] OpenFOAM v10. https://doc.cfd.direct/openfoam/user-guide-v10.

[10] J. E. Rossiter: "Wind-tunnel experiments on the flow over rectangular cavities at subsonic and transonic speeds", Aeronautical Research Council Reports and Memoranda, No. 3438, 1964.

DOI: 10.61782/fa.2025.0452

FORUM ACUSTICUM EURONOISE 2025

IMPACT OF RESONANCE LOADING ON THE SOUND GENERATION FROM IN-DUCT POINT SOURCES

Maximilian Behn* **Ulf Tapken**
German Aerospace Center, Institute of Propulsion Technology, Engine Acoustics Department
Berlin, Germany

ABSTRACT

Analytical models of the sound generation from ducted turbomachinery stages often apply spatially distributed point sources such as monopoles and dipoles, which can be derived from the in-duct Green's function. Another important application of point source models is the localisation of sound source distributions, which is done inside ducts so far mainly for fan stages. One difficulty with current point source models is the unconstrained excitation of resonant modes at their cut-on frequencies leading to unrealistically high sound power levels. Simultaneously, the resonant modes manifest an immense loading on the point sources according to Newton's third law. To achieve more realistic predictions, an extension of the point source models is developed that accounts for the impact of resonance loading by including an internal source impedance. The resulting sound power distribution over the range of cut-on modes is derived for relevant source configurations and compared with reference models and experimental data from a fan test rig.

Keywords: acoustic point source model, mode excitation, sound power, flow ducts

1. INTRODUCTION

The design and further improvement of turbomachinery stages with low noise excitation relies on accurate prediction tools to support the design process during the pre-design phase. These tools are often semi-analytical, and model the sound generation from the rotor and stator by application of equivalent, spatially distributed point sources [1, 2]. Depending on the sound generating mechanism, the point sources can have monopole, dipole and quadrupole characteristics. Another important application of in-duct point source models is the localisation of source distributions from microphone array measurements [3, 4]. In both fields of application, the reliability of existing tools and methods is impeded at the mode cut-on frequencies, where single modes are resonant, and an infinite mode amplitude and sound power is predicted, which overestimates the resonant mode excitation in comparison with experimental observations. Different approaches have been proposed in the past, ranging from sound power correction terms for the sound power radiated into the far field, as proposed by Moreau [2], to a complete disregard of the resonant mode behaviour, as proposed by Dougherty [5] for the localisation of in-duct noise sources.

In order to provide a physics-based source model that achieves more realistic predictions of the resonant mode excitation, the in-duct point source model of Goldstein [1] is extended by including an internal source impedance. Doak stated that acoustic sources in turbomachinery stages are constrained by an internal source impedance, but did not provide an explicit expression of the form of the source model [6]. So far, the concept of internal source impedance has been applied in ducted systems only for frequencies below the cut-on frequency of the first higher-order modes (e.g. [7–9]). This article describes an extended in-duct point source model for the prediction of the excitation of higher-order, acoustic modes in resonant and off-resonant conditions. The impact of the model extension is evaluated by example of monopole and dipole source distributions and by comparison with experimental results from a fan test rig.

**Corresponding author*: maximilian.behn@dlr.de.
Copyright: ©2025 Maximilian Behn & Ulf Tapken. This is an open-access article distributed under the terms of the Creative Commons Attribution 3.0 Unported License, which permits unrestricted use, distribution, and reproduction in any medium, provided the original author and source are credited.

2. POINT SOURCES IN FLOW DUCTS

The sound radiation from a monopole source at position $(\check{x}, \check{r}, \check{\phi})$ in a cylindrical flow duct of radius R is described as a superposition of acoustic modes and can be derived from the in-duct Green's function (see e.g. [1]):

$$p^{\pm}_{\text{monopole}}\left(x, r, \phi|\check{x}, \check{r}, \check{\phi}\right) = q\frac{\rho c}{4\pi R^2}\cdot \sum_{m=-\infty}^{\infty}\sum_{n=0}^{\infty}\frac{f_{mn}(r)f_{mn}(\check{r})}{\alpha_{mn}}e^{im(\phi-\check{\phi})}e^{ik^{\pm}_{mn}(x-\check{x})} \tag{1}$$

with volume flow q as source strength, density ρ and speed of sound c. Each mode is described in terms of the azimuthal order m, radial order n, axial wave number $k^{\pm}_{mn}$ and radial mode shape factor $f_{mn}(r)$, which in combination yield the mode transfer function $f_{mn}(r)e^{i\left(m\phi+k^{\pm}_{mn}x\right)}$ [10]. The generated mode amplitude $A^{\pm}_{mn}$ is proportional to $q\frac{\rho_0 c}{4\pi R^2}\frac{1}{\alpha_{mn}}$, where α_{mn} denotes the mode propagation factor, which ranges between 0 and 1 above the mode cut-on frequency and is imaginary for cut-off modes. As a consequence, the mode amplitude reaches infinite sound pressure at the mode cut-on frequency. In terms of sound power, which is given for cut-on modes by the following expression

$$P^{\pm}_{mn} = \frac{\pi R^2}{\rho c}\frac{\alpha_{mn}(1-M_x^2)^2}{(1\mp\alpha_{mn}M_x)^2}|A^{\pm}_{mn}|^2, \tag{2}$$

The $1/\alpha_{mn}$-term in the expression of the mode amplitude cancels the α_{mn}-term in Eq. (1) resulting in an infinite sound power of resonant modes with $\alpha_{mn} = 0$ excited by a monopole source. Therefore, similarly to the mode amplitude, the mode sound power $P^{\pm}_{mn}$ is proportional to $\frac{1}{\alpha_{mn}}$.

At subsonic operating conditions, the dominant acoustic sources in turbomachinery stages have dipole characteristics [1]. The generated sound pressure from a dipole source is obtained from the directional derivative of the monopole Green's function in Eq. (1) with respect to the dipole axis given by vector $\mathbf{n} = [\cos\alpha_{\text{dipole}};\ 0;\ \sin\alpha_{\text{dipole}}]^T$ [11] [1]:

$$\begin{aligned} p^{\pm}_{\text{dipole}}\left(x, r, \phi|\check{x}, \check{r}, \check{\phi}\right) &= \partial_{\mathbf{n}} p^{\pm}_{\text{monopole}}\left(x, r, \phi|\check{x}, \check{r}, \check{\phi}\right) \\ &= \nabla p^{\pm}_{\text{monopole}}\cdot\mathbf{n} \\ &= q_d\frac{\rho c}{4\pi R^2}\cdot \end{aligned} \tag{3}$$

$$\sum_{m=-\infty}^{\infty}\sum_{n=0}^{\infty} -i\left(k^{\pm}_{mn}\cos\alpha_{\text{dipole}} + \frac{m}{\check{r}}\sin\alpha_{\text{dipole}}\right)\cdot \frac{f_{mn}(r)f_{mn}(\check{r})}{\alpha_{mn}}e^{im(\phi-\check{\phi})}e^{ik^{\pm}_{mn}(x-\check{x})} \tag{4}$$

with dipole moment q_d. Note, that the gradient ∇ is evaluated with respect to the source position $(\check{x}, \check{r}, \check{\phi})$. Equation (4) shows that the mode amplitude and, hence, the mode sound power have generally the same proportionality with $\frac{1}{\alpha_{mn}}$ as for the monopole source. Only for $M_x = 0$, the $\frac{1}{\alpha_{mn}}$-term is lifted for modes with azimuthal mode order $m = 0$.

3. MODEL EXTENSION BY SOURCE IMPEDANCE

The infinite sound power output from in-duct point sources at the mode cut-on frequencies stands in contradiction to two experimental observations of the excited sound field from turbomachinery stages. Firstly, an increased sound pressure is indeed measured at the mode cut-on frequencies, typically at low frequencies, but it does not reach infinite amplitudes. Therefore, according to Eq. (4) with $\alpha_{mn} = 0$ the resulting, measured mode sound power is zero in contrast to the analytical model, which predicts an infinite sound power. Secondly, towards higher frequencies the density of mode cut-on frequencies increases exponentially, which leads to a high number of resonance peaks in the analytically modelled spectra, but measured sound pressure spectra do not show any resonance effects in this frequency range.

In comparison, the sound power output from a point source in free field conditions increases monotonously with [12]

$$P = \frac{k^2\rho c}{8\pi}q^2 \tag{5}$$

for a monopole source, respectively

$$P = \frac{k^4\rho c}{12\pi}q_d^2 \tag{6}$$

[1] The assumption that the dipole axis lies in the x-ϕ-plane is valid for blades with sufficiently small lean.

for a dipole source. It appears plausible that a point source in a duct at high characteristic frequencies kR should generate a sound power output at a similar level to that in free field conditions. Albeit, the point source model in Eq. (1) predicts much higher sound power levels, in particular for modes near their cut-on frequencies. In the following, the in-duct point source model of a monopole source is extended in order to achieve a more realistic characteristics of the sound power output. The transfer to dipole sources is easily made using Eq. (3).

The mode impedance $Z^{\pm}_{mn} = A^{\pm}_{mn}/q$ is chosen as the starting point for the model extension. More precisely, it is given by the following expression:

$$Z^{\pm}_{mn}\left(\check{x},\check{r},\check{\phi}\right) = \frac{\rho c}{4\pi R^2}\frac{f_{mn}(\check{r})}{\alpha_{mn}} e^{-im\check{\phi}} e^{-ik^{\pm}_{mn}\check{x}}. \quad (7)$$

The mode impedance describes the ratio of the excited mode amplitude to the source volume flow. However, it can also be interpreted as the pressure on the source as a back reaction of the mode relative to the source strength [6]. At the mode cut-on frequencies the pressure of the resonant modes becomes infinite. In the idealised point source models in Eq. (1) and (4) the back reaction of the modes on the source is not considered, so that the source effectively acts as a constant volume flow source. Morfey [13] investigated the behaviour of this source type as well as constant pressure sources and showed that in the latter case no resonance phenomena occur. A more realistic source model, whose behaviour lies somewhere between these two extremes, is obtained by including an internal source impedance for each cut-on mode. An illustration of the extended model is given in Fig. 1.

The model is based on an electroacoustic analogy, which considers the volume flow q as current and pressure resp. mode amplitude as voltage. It is assumed that the loading due to each mode does not depend on the source position. Therefore, the factors of the mode impedance in Eq. (7) that are independent from the source position are separated from the position-dependent terms, i.e. $\hat{Z}^{\pm}_{mn} = \frac{\rho c}{4\pi R^2}\frac{1}{\alpha_{mn}}$. The model's network structure allows a straightforward analysis employing Kirchhoff's loop and node laws. For each mode, the mode impedance is connected in parallel with the internal source impedance resulting in the effective mode impedance of the internal source impedance (ISI-)model given by:

$$\hat{Z}^{\pm}_{mn,\mathrm{ISI}} = \frac{Z_S \cdot \hat{Z}^{\pm}_{mn}}{Z_S + \hat{Z}^{\pm}_{mn}}. \quad (8)$$

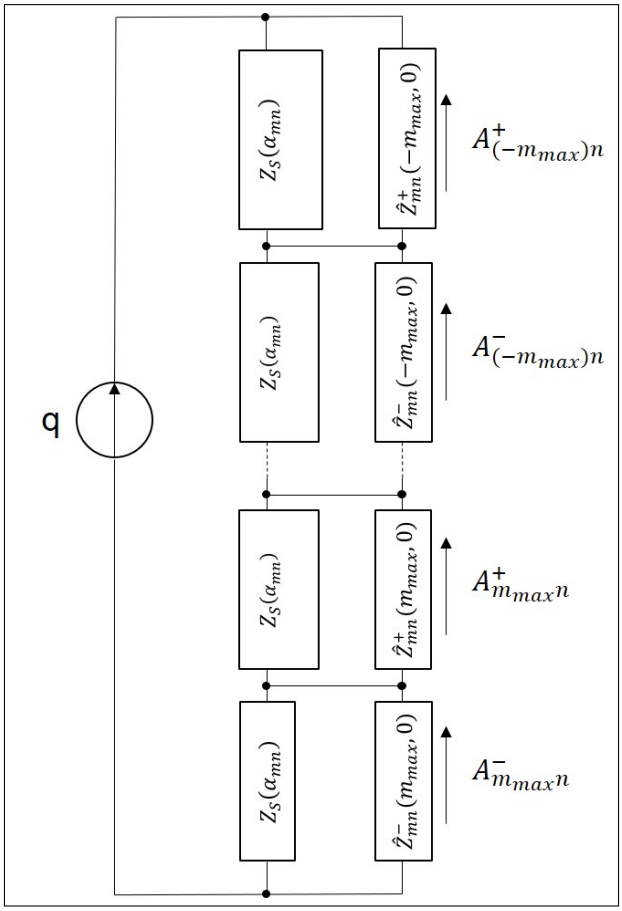


Figure 1. Illustration of the extended source model with internal source impedance Z_S and radiation impedances $Z^{\pm}_{mn}$.

In combination with the source position-dependent terms, the excited mode amplitude according to the ISI-model is expressed as:

$$Z^{\pm}_{mn,\mathrm{ISI}} = \frac{A^{\pm}_{mn}}{q} = \hat{Z}^{\pm}_{mn,\mathrm{ISI}} f_{mn}(\check{r}) e^{-im\check{\phi}} e^{-ik^{\pm}_{mn}\check{x}}. \quad (9)$$

At the mode cut-on frequencies, the loading due to $Z^{\pm}_{mn}$ is very high, so that the effective mode impedance of the ISI-model yields:

$$Z^{\pm}_{mn,\mathrm{ISI}}\left(\alpha_{mn}=0\right) \approx Z_S. \quad (10)$$

Thus, modes are not excited with infinite pressure at their cut-on frequencies, but instead the mode amplitude yields $A^{\pm}_{mn}\Big|_{\alpha_{mn}=0} = Z_S q$.

Additional fundamental assumptions are:

1. each mode is an additional load for the source,
2. the source impedance relates the in-duct source output to the free field case, and
3. the influence of the source impedance is maximal for resonant modes and diminishes for $\alpha_{mn} \to 1$.

A natural choice for the internal source impedance of an in-duct monopole source is the radiation impedance of a monopole source in free field conditions, which is given by [12]:

$$Z_{FF} = \frac{p_{FF}}{q} = \frac{\rho c}{4\pi R^2} (kR)^2 . \tag{11}$$

However, Z_{FF} shows a low sound pressure excitation at low frequencies. In order to achieve a realistic resonance behaviour at low frequencies, an additional term $\chi(kR)$ is included that increases the mode excitation at low frequencies. Finally, the first and last assumptions lead to the following expression of the internal source impedance:

$$\begin{aligned} Z_S(\alpha_{mn}) =& \frac{Z_{FF} + \chi(kR)}{N_M \cdot (1 - \alpha_{mn})} \\ =& \frac{\rho c}{4\pi R^2} \frac{(kR)^2 + \frac{25}{kR}}{N_M \cdot (1 - \alpha_{mn})}. \end{aligned} \tag{12}$$

with the number of cut-on modes N_M. The expression of the additional term $\chi(kR)$ is hypothetical and primarily included to demonstrate the behaviour of the proposed model extension. The low-frequency characteristics of the internal source impedance requires further investigation.

The internal source impedance in Eq. (12) distributes the sound generation potential according to the free field radiation impedance over all cut-on modes by division by the number of cut-on modes N_M. The additional term $1/(1 - \alpha_{mn})$ corresponds to the third fundamental assumption. This choice increases the impact of resonance loading on the excitation of modes, which are close to their cut-on frequencies, while modes with a high propagation factor, i.e. $\alpha_{mn} \to 1$, are not affected by resonance loading. As a result, the internal source impedance Z_S approaches infinity for modes with a high propagation factor, which means that for these modes the ISI point source model acts a constant volume flow source.

The effective mode impedance in Eq. (9) yields after some rearrangement:

$$Z^{\pm}_{mn,\mathrm{ISI}} = \frac{Z^{\pm}_{mn}\left(\check{x}, \check{r}, \check{\phi}\right)}{1 + \frac{N_M}{(kR)^2 + \frac{25}{kR}} \frac{1 - \alpha_{mn}}{\alpha_{mn}}}. \tag{13}$$

4. EVALUATION OF SOURCE DISTRIBUTIONS USING THE EXTENDED SOURCE MODEL

The extended source model is evaluated for dense distributions of two different source types:

- incoherent monopoles and
- incoherent dipoles with $\alpha_{\mathrm{dipole}} = -\frac{\pi}{4}$,

which are distributed equally over the duct cross-section.

As an example, the duct geometry and flow conditions of DLR's fan test rig CRAFT (Co-/Counter-Rotating Acoustic Fan Test Rig) are considered. The duct diameter is 453.6 mm. The flow Mach number in the inlet is $M_x = 0.11$ at the fan design point. Further information is provided in [14].

Figure 2 shows the development of the internal source impedance as a function of the non-dimensional frequency kR for $\alpha_{mn} = 0$. The internal source impedance approaches an asymptotic limit of approximately 2 already at relatively low frequencies. Between $kR = 5$ and 25, the normalised internal source impedance is almost constant and predominantly determined by Z_{FF}/N_M. The results show that the additional term $\chi(kR)$ has an impact only at low frequencies $kR < 5$.

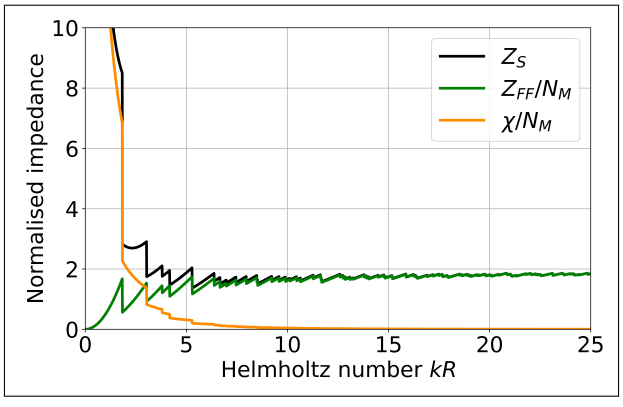


Figure 2. Internal source impedance Z_S and its components as a function of non-dimensional frequency. Values are normalised by $\frac{\rho c}{4\pi R^2}$.

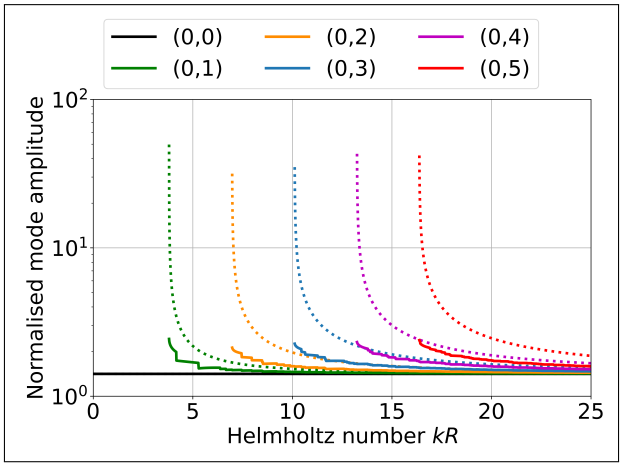


Figure 3. Mode amplitudes for azimuthal mode order $m = 0$ excited by a dense distribution of incoherent monopole sources. Values are normalised by $\frac{\rho c}{4\pi R^2}$. Solid lines show results for the ISI-model and dashed lines for the Goldstein point source model.

The mode amplitudes with azimuthal mode order $m = 0$ that are excited by the distribution of monopole sources, are displayed in Fig. 3. The plane wave mode $(0, 0)$ has a propagation factor $\alpha_{00} = 1$ and therefore, is not affected by resonance loading. All higher radial mode orders exhibit significantly lower amplitudes close to the cut-on frequencies in comparison to the reference point source model by Goldstein (cp. Eq. (1)). The mode amplitude of mode $(0, 1)$ is characterised by two larger discontinuities, which occur due to a discrete increase of N_M at neighbouring mode cut-on frequencies. With increasing frequency, the cut-on of additional mode orders has a small impact on the mode amplitude curves, because the number of cut-on modes N_M is growing exponentially. Furthermore, both point source models converge asymptotically towards high frequencies. However, whereas for mode $(0, 1)$ the predicted mode amplitudes are almost equal within $\Delta kR = 5$ to 6 from the mode cut-on frequency, the convergence of the predicted mode amplitudes extends over a much larger frequency range for higher radial mode orders. For example, for mode $(0, 4)$ convergence is observed for approximately $\Delta kR = 10$. Thus, the impact of resonance loading is stronger towards high frequencies.

The most important characteristics of the newly proposed ISI-model is observed from the development

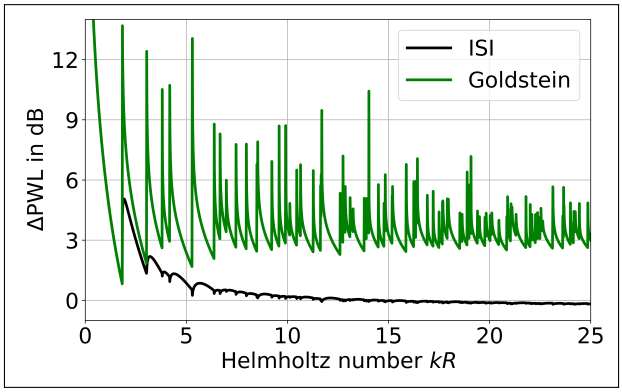


Figure 4. Total sound power generated by a dense distribution of incoherent monopole sources relative to the sound power output of a monopole source in free field conditions (cp. Eq. (5)).

of the total sound power, which is depicted in Fig. 4. At low frequencies, both source models show significantly increasing sound power levels at the mode cut-on frequencies, but the levels of the ISI-model are limited with e.g. an increase of 4 dB at the cut-on frequency of the modes $(\pm 1, 0)$ compared to more than 11 dB for the Goldstein point source model. Towards high frequencies, the ISI-model approaches the sound power level of the free field source asymptotically, while the results of the Goldstein model exhibit strongly fluctuating sound power levels and an average offset of approximately 2.5 dB.

The second source distribution consists of dipole sources, whose dipole axes are oriented at -45 degrees with respect to the duct axis. The excited mode amplitudes of azimuthal mode order $m = 0$ are presented in Fig. 5 and the total sound power in Fig. 6.

The trend of the mode amplitude curves for the distribution of dipole sources is almost inverted to those for the monopole distribution. The results for the reference model indicate a very narrow notch of the mode amplitude curves near to the cut-on frequencies and an asymptotic increase towards high frequencies. The impact of the ISI-model is twofold. Firstly, the maximum mode amplitude at the cut-on frequency is strongly reduced. And secondly, the rate of increase is reduced, which is particularly pronounced with increasing radial mode order. Both characteristics of the ISI-model can also be identified in Fig. 6. Due to the limitation of the

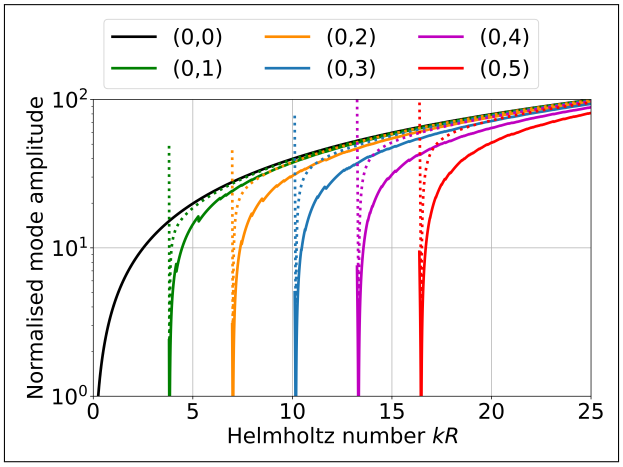


Figure 5. Mode amplitudes for azimuthal mode order $m = 0$ excited by a dense distribution of incoherent dipole sources. Values are normalised by $\frac{\rho c}{4\pi R^2}$. Solid lines show results for the ISI-model and dashed lines for the Goldstein point source model.

maximum mode amplitude at the cut-on frequencies, the total sound power exhibits a smooth development with respect to frequency above $kR = 5$ in contrast to the results of the Goldstein point source model. Furthermore, the general rate of increase of the sound power predicted by each model is similar to that of the free field dipole source. An offset of approximately 2.5 dB for both source models is reached at $kR = 25$, which is similar to the monopole case. Note, however, that the difference between the ISI-model and the free field dipole does not indicate a less accurate prediction, because, unlike in the free field, the sound power output of the ducted dipole sources is influenced by the dipole angle with respect to the duct axis.

5. COMPARISON WITH EXPERIMENTAL RESULTS

In this section, the sound power distributions obtained with the Goldstein and the ISI point source models are compared with experimentally determined mode sound powers using radial mode analysis. The details of the measurements on the CRAFT test rig and the analysis of the measurement data are given in [15].

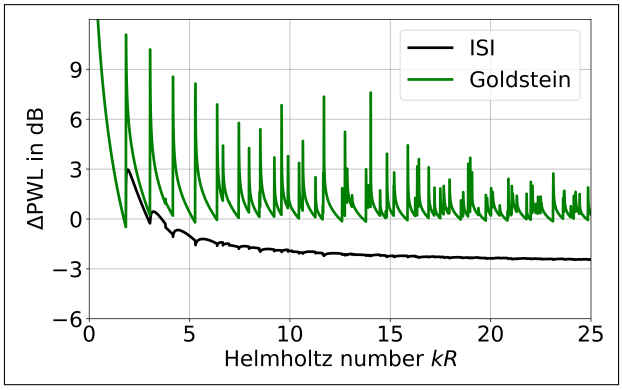


Figure 6. Total sound power generated by a dense distribution of incoherent dipole sources relative to the sound power output of a dipole source in free field conditions (cp. Eq. (6)).

Figures 7 and 8 show the mode sound power distribution of the rotor-incoherent, broadband sound field component at $kR \approx 20$, which were measured in the inlet and outlet of the CRAFT at the aerodynamic design point of the fan stage. In the inlet, only upstream propagating and rotor co-rotating modes are considered for the comparison, because the rotor shielding effect has an additional effect on the sound power distribution that is not included in the modelling discussed here. In contrast, in the outlet only downstream propagating, rotor counter-rotating modes considered. Additionally, modelled mode sound power distributions according to distributions of dipole sources with $\alpha_{\text{dipole}} = -\frac{\pi}{4}$ using the Goldstein and the ISI point source models as well as two mode energy distribution models: "'equal mode energy"' (EME) and "'equal mode energy density"' (EDEM), which are matched to the total measured sound power.

The modelling results show two different trends. On the one hand, the "'equal mode energy"' distribution corresponds to a constant sound power level independent of the mode propagation factor. Interestingly, the results of the Goldstein point source model show a trend that is similar to the EME distribution. On the other hand, the "'equal mode energy density"' predicts an increasing sound power level for high values of the mode propagation factor. A very similar trend is observed for the ISI point source model.

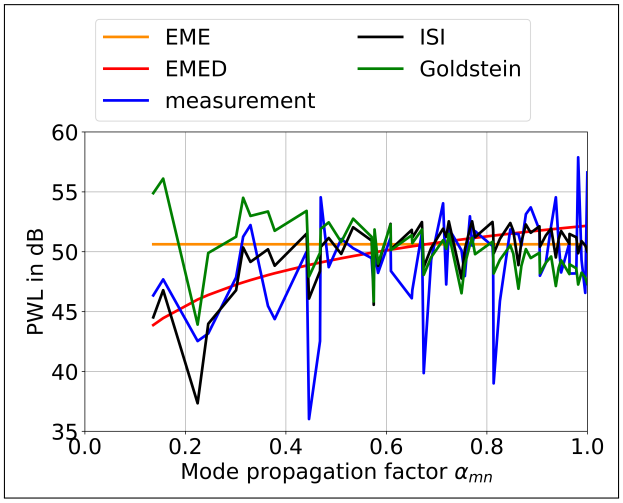


Figure 7. Comparison of measured mode sound power in the inlet of the CRAFT test rig and matched distributions from different source and mode energy distribution models at $kR \approx 20$.

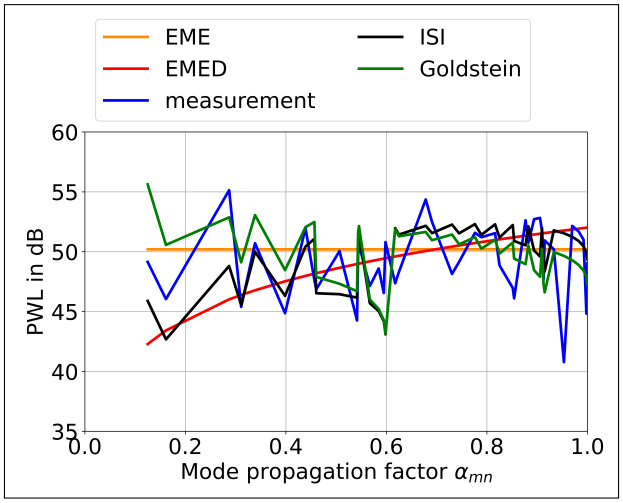


Figure 8. Comparison of measured mode sound power in the outlet of the CRAFT test rig and matched distributions from different source and mode energy distribution models at $kR \approx 20$.

In comparison with the measured sound power distribution, the EMED distribution and the prediction using the ISI-model achieve a very good agreement in the inlet regarding the overall trend. In case of the ISI-model, the distribution of dipole sources at a single axial plane is insufficient in order to predict dips in the mode sound power distribution like the ones at $\alpha \approx 0.45$, 0.67 and 0.81, which correspond to the modes $(-1, 3)$, $(-1, 4)$ and $(-1, 5)$.

In the outlet, the results of the ISI-model are in good agreement with the measured sound power levels above $\alpha = 0.3$. For modes that are closer to their cut-on frequencies, the measured sound power levels are elevated, which is caused by resonant excitation of the modes, but also by stronger reflections at the rotor of the corresponding modes $(18, 0)$, $(13, 1)$ and $(9, 2)$.

6. CONCLUSION

The widely used point source models by Goldstein are extended by incorporation of an internal source impedance (ISI) with the aim to achieve a more realistic excitation of acoustic modes in resonant conditions. For the internal source impedance, the radiation impedance of a monopole point source in free field conditions is taken in combination with an additional term, that boosts the mode excitation at low frequencies. The evaluation of monopole and dipole distributions demonstrates the effective reduction of overestimated mode sound powers at the cut-on frequencies leading to a continuous total sound power spectrum above $kR = 10$. A good agreement of the predicted sound power distribution using the ISI-model is found in comparison with experimental data from DLR's CRAFT fan test rig. Furthermore, the trend of the sound power distribution from the ISI-model resembles the "'equal mode energy density"' (EMED) distribution in contrast to the original Goldstein model, which shows a stronger resemblance to the "'equal mode energy"' model (EME). The demonstrated characteristics of the ISI-point source model are particularly beneficial for the robustness of noise prediction tools and source localisation techniques for turbomachinery stages, especially, at high frequencies, where the modal density increases exponentially.

7. ACKNOWLEDGMENTS

The authors are grateful for the support of Lukas Klähn and Wolfram Köhler in providing the experimental data from the CRAFT test rig.

This research has been performed in the frame of the project COMPANION (COMmon Platform and

Advanced iNstrumentration readIness for ultra efficient propulsiON), which is funded by the European Union Clean Aviation Joint Undertaking program, under grant agreement No. 101140627.

CLEAN AVIATION Co-funded by the European Union

8. REFERENCES

[1] M. E. Goldstein, *Aeroacoustics*. New York: McGraw-Hill International, 1976.

[2] A. Moreau, *A unified analytical approach for the acoustic conceptual design of fans of modern aero-engines*. Dissertation, Technical University Berlin, Berlin, Germany, 2017.

[3] C. R. Lowis, *In-duct measurement techniques for the characterisation of broadband aeroengine noise*. Dissertation, University of Southampton, Southampton, UK, 2008.

[4] H. Brouwer and P. Sijtsma, "Phased array beamforming to identify broadband noise sources in the interstage section of a turbofan engine," in *25th AIAA/CEAS Aeroacoustics Conference*, (Delft, Netherlands), May 2019.

[5] R. P. Dougherty and J. M. Mendoza, "Nacelle in-duct beamforming using modal steering vectors," in *14th AIAA/CEAS Aeroacoustics Conference*, (Vancouver, Canada), May 2008. 10.2514/6.2008-2812.

[6] P. E. Doak, "Excitation, transmission and radiation of sound from source distributions in hard-walled ducts of finite length (i): The effects of duct cross-section geometry and source distribution space-time pattern," *Journal of Sound and Vibration*, vol. 31, pp. 1–72, 1973.

[7] P. K. Baade, "Effects of acoustic loading on axial flow fan noise generation," *Noise Control Engineering Journal*, vol. 8, pp. 5–15, 1977.

[8] M. G. Prasad, "A four load method for evaluation of acoustical source impedance in a duct," *Journal of Sound and Vibration*, vol. 114, pp. 347–356, 1987.

[9] H. Bodén, "The multiple load method for measuring the source characteristics of time-variant sources," *Journal of Sound and Vibration*, vol. 148, pp. 437–453, 1991.

[10] U. Tapken, *Analyse und Synthese akustischer Interaktionsmoden von Turbomaschinen*. Dissertation, Technical University Berlin, Berlin, Germany, 2016.

[11] E. Williams, *Fourier Acoustics*. London: Academic Press, 1999.

[12] K. U. Ingard, *Fundamentals of waves and oscillations*. Cambridge: Cambridge University Press, 1988.

[13] C. L. Morfey, "Rotating pressure patterns in ducts: Their generation and transmission," *Journal of Sound and Vibration*, vol. 1, pp. 60–87, 1964.

[14] U. Tapken, L. Caldas, R. Meyer, M. Behn, L. Klähn, R. Jaron, and A. Rudolphi, "Fan test rig for detailed investigation of noise generation mechanisms due to inflow disturbances," in *AIAA AVIATION 2021 FORUM*, (virtual), August 2021.

[15] L. Klähn, R. Meyer, and U. Tapken, "Inflow distortion noise and turbulence measurements in a low speed fan test rig," in *30th AIAA/CEAS Aeroacoustics Conference*, (Rome, Italy), June 2024.

DOI: 10.61782/fa.2025.0670

FORUM ACUSTICUM EURONOISE 2025

PARAMETRIC STUDY OF TURBULENCE INGESTION NOISE FOR MARINE PROPELLERS

Romain Lavanant[1,2*] **Benjamin Cotté**[2] **Gilles Serre**[1]
Jean-François Mercier[3]
[1] Naval Group, CEMIS, Ollioules, France
[2] IMSIA, ENSTA, CNRS, CEA, EDF, Institut Polytechnique de Paris, France
[3] POEMS, CNRS, INRIA, ENSTA, Institut Polytechnique de Paris, France

ABSTRACT

Hydrodynamic noise is an important component of the overall noise radiated by a ship, particularly at low frequencies where propeller noise could be dominant especially at high speed. This study proposes a simplified analytical solution of the phenomenon of spectral humps of propeller noise due to the interaction between a rotating propeller and an incident turbulent flow. The acoustic radiation is described by the Ffowcs-Williams and Hawkings analogy in the compact approximation. The inflow turbulence field is assumed to be homogeneous and isotropic and is modeled using a von Kármán spectrum. Experimental validation and comparison with more costly analytical solutions demonstrate the ability of the developed model to correctly capture the characteristics of the humps related to turbulence ingestion. From the results obtained, a parametric analysis enables us to define a criterion for the emergence and shape of turbulence ingestion humps according to the propeller advance ratio, improving the criterion proposed by Ffowcs-Williams and Hawkings in 1969.

Keywords: *turbulence ingestion, marine propellers, noise prediction, spectral humps, parametric analysis*

**Corresponding author*: *romain.lavanant@ensta.fr.*
***Copyright**: ©2025 Romain Lavanant et al. This is an open-access article distributed under the terms of the Creative Commons Attribution 3.0 Unported License, which permits unrestricted use, distribution, and reproduction in any medium, provided the original author and source are credited.*

1. INTRODUCTION

In the context of propeller hydroacoustics, turbulence ingestion noise is due to the interaction between the rotating blades and the turbulent wake of a submarine or a surface vessel. The development of predictive models to better understand the physical origins of turbulence ingestion noise and estimating its levels is critical to enhance ship discretion. Understanding fundamental noise generation mechanisms allows architects to propose solutions like optimized blade and hull geometries or operational adjustments. Integrated early in design, it can reduce detectability by passive sonar in defense contexts and mitigate environmental impacts on marine life (Fig. 1).

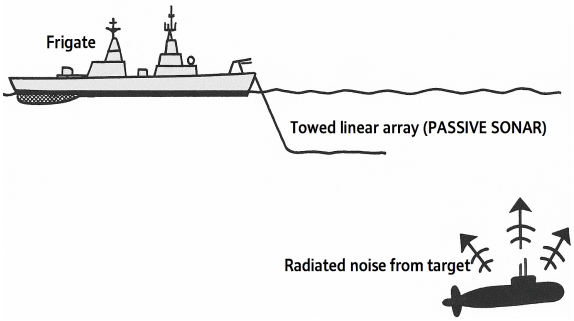


Figure 1. Detection of a submarine by passive SONAR in anti-submarine warfare.

This study targets low-frequency noise, specifically turbulence ingestion humps. When a turbulent flow is ingested by a rotating propeller, the incoming eddies are periodically chopped by the propeller. This interaction can potentially lead to a correlation (depending on the config-

uration) between the broadband turbulence spectrum and the periodic passage of the blades. This correlation creates a series of humps centered at blade passage frequency (BPF) harmonics on the resulting spectrum. The objective is to study the influence of propeller's parameters on the spectral humps and to define a criterion for the appearance of these humps, building on prior research to fully resolve turbulence-blade interactions while keeping computational costs industrially feasible.

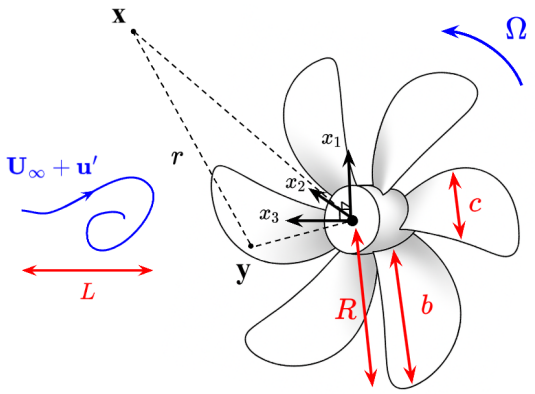


Figure 2. Fixed reference frame, with origin at the center of the propeller. $\boldsymbol{x}$ corresponds to the receiver's coordinate, and $\boldsymbol{y}$ to the coordinate within the volume containing the sources near the propeller (Ffowcs-Williams and Hawkings analogy).

2. NOISE RADIATION MODELING

To predict turbulence ingestion noise, this study employs a simplified version of the Ffowcs-Williams formulation for moving surfaces under the compact source approximation : $K_0 c < 1$, $K_0 R < 1$, where $K_0 = \omega/c_\infty$ is the acoustic wavenumber, c is the blade chord and R the propeller radius (see Fig. 2). For a propeller with N blades rotating at angular velocity Ω, the far-field ($|\boldsymbol{x}| \gg R$) acoustic pressure spectrum is thus expressed as in [1] section 6.6.2:

$$\widehat{p}(\boldsymbol{x},\omega) \simeq \frac{iK_j}{8\pi^2|\boldsymbol{x}|} e^{i\boldsymbol{K}\cdot\boldsymbol{x}} \widehat{F_j}(\omega), \tag{1}$$

with the acoustic wave vector in a convected medium:

$$\boldsymbol{K} = \frac{\omega}{c_\infty}\left(\frac{\boldsymbol{x}}{|\boldsymbol{x}|} - \boldsymbol{M}_\infty\right), \quad \boldsymbol{M}_\infty = (0,0,M_\infty), \tag{2}$$

$\widehat{F_j}(\omega)$ represents the force fluctuation spectrum and is expressed as [2],

$$\widehat{F_j}(\omega) = \sum_{n=0}^{N-1} \int_{-\infty}^{+\infty} \int_{S(\tau)} f_j(\boldsymbol{y}^{(n)},\tau) dS(\boldsymbol{y}^{(n)}) e^{i\omega\tau} d\tau, \tag{3}$$

with f_j is the surface force fluctuation, N the number of blades and S the surface of each blade. The radiated pressure spectral density in the far-field, is then derived as:

$$S_{pp}(\boldsymbol{x},\omega) \simeq \frac{K_i K_j}{64\pi^4|\boldsymbol{x}|^2} S_{F_iF_j}(\omega), \tag{4}$$

where the force spectral density $S_{F_iF_j}(\omega)$ is computed using a rotating reference frame and Taylor's frozen turbulence hypothesis. For propellers with low twist angle, $S_{F_iF_j}(\omega)$ can be approximated only by it's axial contribution $S_{F_3F_3}(\omega)$, that can be expressed as an integral over the blade radius r and the chordwise wavenumber k_2 (see [1] section 6.6.2) for waves propagating from the leading edge to the trailing edge ($k_2 \geq 0$):

$$S_{F_3F_3}(\omega) = \int_{R-b}^{R} \int_0^\infty A(r)|H(k_2)|^2 \cdot B(k_2,r)\psi_{33}(\omega,k_2,r)\, dk_2\, dr. \tag{5}$$

Here, A accounts for the axial force amplitude,

$$A(r) = \frac{1}{U_\infty}(2\pi^2\rho_\infty c(r)U(r))^2, \tag{6}$$

where $U(r)$ is the total effective speed perceived by the blades:

$$U(r) = \sqrt{U_\infty^2 + (r\Omega)^2}. \tag{7}$$

B captures inter-blade correlations,

$$B(k_2,r) = \frac{\sin^2(\pi k_2 r)}{\sin^2(\pi k_2 r/N)}. \tag{8}$$

H is the blade response function, given in the low frequency regime by the Sears function [3] of modulus approximated by [4] equations 6.4.3 and 6.4.4:

$$|H(k_2)|^2 \simeq \frac{1}{1+\pi c(r)k_2}, \quad k_2 \geq 0. \tag{9}$$

Finally, ψ_{33} is the turbulence spectrum in the rotating frame in the axial direction and will be given in the next section. This framework provides the foundation for the parametric analysis detailed later.

3. TURBULENCE MODELING

The incident turbulence is modeled as homogeneous and isotropic using the von Kármán spectrum [5] section 9.1:

$$\phi_{ij}(\boldsymbol{k}) = \frac{E(\boldsymbol{k})}{4\pi|\boldsymbol{k}|^2}\left(\delta_{ij} - \frac{k_i k_j}{|\boldsymbol{k}|^2}\right), \tag{10}$$

$$E(\boldsymbol{k}) = A_\phi \frac{|\boldsymbol{k}|^4/k_e^4}{(1+|\boldsymbol{k}|^2/k_e^2)^{17/6}}, \tag{11}$$

where $\boldsymbol{k} = (k_1, k_2, k_3)$ and the constants are defined by:

$$A_\phi = \frac{55}{9\sqrt{\pi}}\frac{\Gamma(5/6)}{\Gamma(1/3)}\frac{\overline{u^2}}{k_e}, \tag{12}$$

$$k_e = \frac{\Gamma(5/6)}{\Gamma(1/3)}\frac{\sqrt{\pi}}{L}, \quad \overline{u^2} = I_t U_\infty.$$

where I_t is the turbulent intensity. In the rotating frame, the turbulence spectrum is given by

$$\psi_{33}(\omega, k_2, r) = \phi_{33}\left(0, k_2, \frac{\omega - k_2 r\Omega}{U_\infty}\right), \tag{13}$$

providing the turbulence inputs for the the equations (5) and (4) of the noise model.

4. MODEL VALIDATION

The model is validated against Blake's analytical results [1] associated with Wojno experimental data [6] reproducing a similar configuration of the famous Sevik's study [7] with a ten-blades rotor. The parameters used for this configuration are listed in Tab. 1. The comparison, shown in Fig. 3, demonstrates good agreement, despite differences arise because Blake uses the frozen turbulence hypothesis on the chordwise wavenumber $k_2 = \omega/U(r)$ while we use the frozen turbulence hypothesis on the upstream axial wavenumber $k_3 = \omega/U_\infty$. Moreover, an offset of $10\log_{10}(U_\infty)$ has been removed from Blake's data due to the absence of normalization by U_∞ in Blake's model. This normalization is necessary when making the frozen turbulence hypothesis.

The compact source approximation leads to good predictions when the observer is located near the rotor rotational axis, where the sound level is maximum. It is underpredicted when the observer is positioned far from the axis of rotation. This underestimation is illustrated in Fig. 4, where the compact model is compared to the non-compact

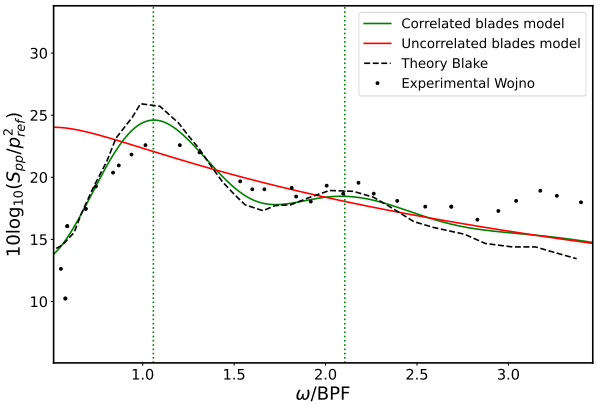


Figure 3. Comparison of radiated pressure spectrum with Blake's model and Wojno's measurements. The green solid line corresponds to the model (4) used with data from Tab. 1 and the red solid line corresponds to the same but with $B = 1$ in (5) (uncorrelated blades noise).

Table 1. Parameter values from Blake's study [1].

Parameter	Value	Unit
p_{ref}	20	μPa
ρ_∞	1.2	kg/m^3
c_∞	340	m/s
M_∞	0.037	-
I_t	0.06	-
L	1.9	cm
J_Ω	1.14	-
c	2.54	cm
R	10	cm
b	7.6	cm
N	10	-
(x_1, x_2, x_3)	(64, 0, 64)	cm

model of Raposo and Azarpeyvand [8] for an observer located at 90 degrees from the axis of rotation. Used parameters values correspond to the wind turbine case from Table 1 in [8].

Despite this, it is observed in Fig. 3 and Fig. 4, that the

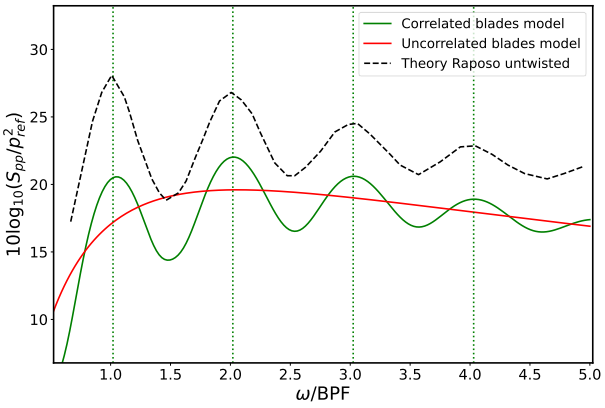


Figure 4. Comparison of radiated pressure spectrum with Raposo and Azarpeyvand's untwisted model. The green solid line corresponds to the model (4) used with data from Table 1 in [8] data and the red solid line corresponds to the same but with $B = 1$ in (5) (uncorrelated blades noise).

shape of the turbulence ingestion humps is correctly reproduced. Moreover, it is precisely this criterion (humps shape) that will be important later in the analytical definition of the emergence of these humps.

5. PARAMETRIC ANALYSIS

This section leverages the noise radiation model, specifically equation (5), to conduct a detailed parametric study of the spectral humps generated by turbulence ingestion. The analysis focuses on hump positions, their bandwidths, and the critical conditions under which these humps emerge or disappear, providing insights into noise characteristics and design implications.

5.1 Positions of the spectral humps

The positions of the spectral humps are determined by analyzing the peaks in the radiated pressure spectrum. The peak frequencies of the force spectrum (5) are derived by finding the maximum of the turbulence spectrum $\psi_{33}(\omega, k_2, r)$ with respect to ω. Setting the partial derivative $\partial\psi_{33}/\partial\omega = 0$, the resulting frequencies are:

$$\omega_{T,n} = r\Omega k_2 = nN\Omega. \tag{14}$$

These frequencies correspond to the blade-passing frequency ($BPF = N\Omega$) harmonics of harmonic number n reflecting the periodic chopping of turbulent eddies by the blades. In (14), the condition $k_2 = nN/r$ has been used indicating that the inter-blade interference term B reaches its maximum, as illustrated in the force spectrum construction process (Fig. 5).

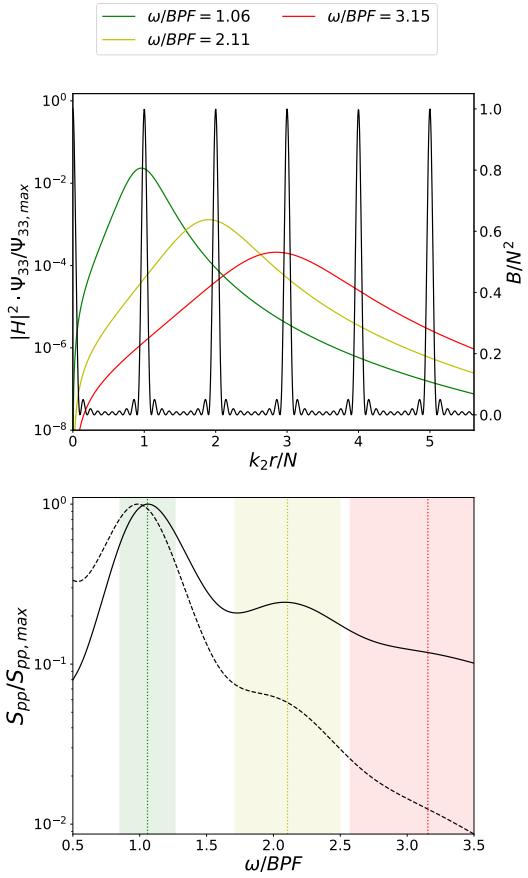


Figure 5. Normalized construction of the pressure spectrum S_{pp} (solid line lower figure) and force spectrum $S_{F_3F_3}$ (dotted line) from the integration over the chordwise wavenumber of the diffracted turbulence $|H|^2\psi_{33}$ (wide curves upper figure) times the inter-blade interference function B (narrow curve).

5.2 Bandwidths of the spectral humps

The bandwidths of the spectral humps, defined as the frequency range at half-height of their peaks, quantify their

spread and influence their distinguishability in the spectrum. For turbulence humps, the bandwidth at half-height is calculated by solving $\psi_{33}(k_2,\omega) = \frac{1}{2}\psi_{33}(k_2,\omega_T)$, yielding:

$$\Delta\omega_{T,n} \simeq U_\infty \sqrt{\frac{n^2N^2}{R^2} + k_e^2}. \tag{15}$$

This expression shows that the bandwidth increases with the inflow velocity U_∞, the harmonic number n, and the number of blades N, while being moderated by the radial position r and the turbulence integral scale $L \propto 1/k_e$. In Fig. 5, shaded zones correspond to the bandwidth predicted by (15). The relative bandwidth, normalized by the peak frequency, is:

$$\frac{\Delta\omega_{T,n}}{\omega_{T,n}} = \sqrt{\frac{J_\Omega^2}{\pi^2} + \frac{9}{16n^2N_h^2}}, \tag{16}$$

where $J_\Omega = \pi U_\infty / R\Omega$ is the propeller tip advance ratio and $N_h = N\Omega L/U_\infty$ is the chopping number introduced by Ffowcs-Williams and Hawkings in their humps prediction criterion [9] eq. 8, predicting $\Delta\omega_{T,n}/\omega_{T,n} \propto 1/N_h$ implying narrow humps when $N_h \gg 1$. This criterion is used in several studies such as Homicz and George [10], Martinez [11], Glegg et al. [12], Glegg and Devenport [4], Raposo and Azarpeyvand [8]. Unlike Ffowcs-Williams and Hawkings prediction, the present criterion (16) indicates a stronger dependence on the advance ratio J_Ω, meaning that a large N_h does not necessarily imply narrow humps. Note that this new formulation is equivalent to that of Ffowcs-Williams and Hawkings when $J_\Omega \to 0$.

5.3 Hump emergence criteria

The emergence of spectral humps is a pivotal concept in this study, as it directly informs strategies for noise control in propeller design. Turbulence humps are distinguishable in the spectrum when their bandwidths do not exceed the frequency spacing between consecutive humps, given by $N\Omega$. If the bandwidth $\Delta\omega_{T,n}$ surpasses this threshold, the humps overlap and the spectrum flattens into a broadband signature. Mathematically, this condition is expressed as:

$$\frac{\Delta\omega_{T,n}}{N\Omega} > 1. \tag{17}$$

Substituting the bandwidth from Equation (15), this inequality becomes:

$$J_\Omega > \frac{\pi}{\sqrt{n^2 + \frac{r^2k_e^2}{N^2}}}, \tag{18}$$

meaning that the n-th turbulence hump vanishes if J_Ω is superior to a critical advance ratio, as their bandwidth exceeds the BPF spacing. This critical advance ratio is defined by:

$$J_{\Omega,c}(n) = \frac{\pi}{\sqrt{n^2 + \frac{r^2k_e^2}{N^2}}}. \tag{19}$$

The most restrictive case occurs at the first harmonic ($n = 1$), where overlap eliminates all subsequent humps if exceeded. Fig. 6 illustrates this effect, showing how increasing J_Ω beyond the critical value leads to a loss of distinct humps. A trend consistent with experimental observations where humps disappear at higher inflow velocities relative to rotation speed even with the number N_h being fixed (see [8] section 4.2). Given the expression (19), we can reformulate the relative bandwidth (15) only in terms of the advance ratio :

$$\frac{\Delta\omega_{T,n}}{\omega_{T,n}} = \frac{J_\Omega}{nJ_{\Omega,c}(n)}. \tag{20}$$

Physically, a high J_Ω implies a faster axial inflow U_∞ compared to the rotational speed $R\Omega$, increasing the frequency at which eddies are chopped and thus broadening the spectral humps to the shape of the turbulence spectrum. For the Blake's parameters in Tab. 1, $J_{\Omega,c}(1) \simeq 2.92$, $J_{\Omega,c}(2) \simeq 1.54$ and $J_{\Omega,c}(3) \simeq 1.04$. Thus the experimental $J_\Omega = 1.14$ suggests overlap after the second humps, which is what we observe in Fig. 3. This criteria for hump emergence offer actionable insights for propeller design. Optimizing parameters like blade count N, turbulence integral scale L, and rotor's radius R can suppress humps, by diminishing the critical advance ratio $J_{\Omega,c}$ an thus reducing ship's detectability.

5.4 Spectral humps perceived by the observer

The spectrum perceived by the observer is that radiated by the pressure fluctuations (4) resulting from the propagation and deformation of the force spectrum from the blades such that $S_{pp} \propto \omega^2 S_{F_3F_3}$. The frequency of the perceived humps $\omega_{p,n}$ (peaks of S_{pp}) is therefore different from that of the turbulent humps (peaks of $S_{F_3F_3}$). The link between the perceived humps and turbulence's humps is established by expressing the peaks of S_{pp} in function of the peaks of $S_{F_3F_3}$ using (4) and (2):

$$\omega_{p,n} \simeq \frac{\omega_{T,n}}{2} + \frac{1}{2}\sqrt{\omega_{T,n}^2 + \frac{\Delta\omega_{T,n}^2}{\ln(2)}}. \tag{21}$$

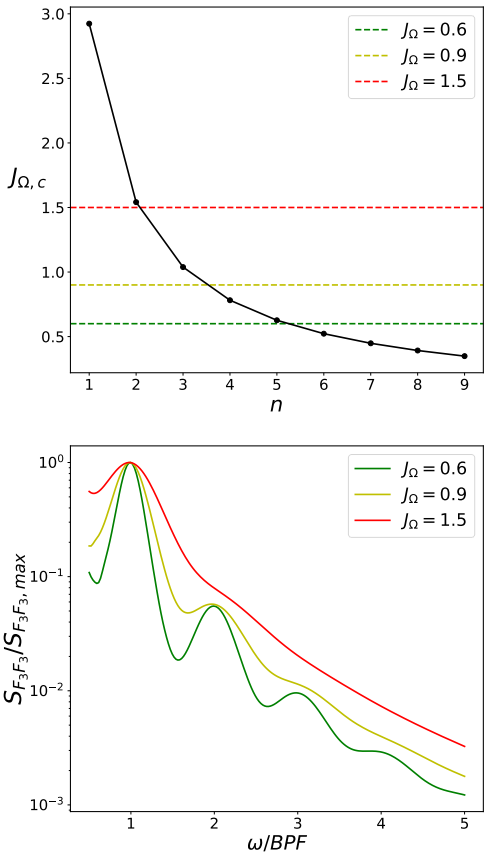


Figure 6. Impact of critical advance ratio on turbulence hump visibility, showing $J_{\Omega,c}$ versus harmonic number (upper figure) and normalized force spectrum flattening (lower figure). Parameters values are from Tab. 1.

It is therefore noted that the position of the humps perceived by the observer is slightly shifted to the right (higher frequencies) as the humps bandwidths increases, consequence of the propagation from the propeller to the observer. This phenomenon is illustrated in Fig. 5. Recently, this 'blue shifting' phenomenon has been qualitatively described by Huang [13] and numerically studied by Qin et al. [14]. Moreover, Martinez [15] made a theory for large N, predicting the first hump's 'blue shifting' of the force spectrum $S_{F_3F_3}$ (i.e. on the shift of $\omega_{T,n} > nN\Omega$ which is not seen here) but not for the pressure spectrum S_{pp} (i.e. not for $\omega_{p,n}$). By injecting the expression (15) obtained for the bandwidths into (21), we derive the explicit expression of $\omega_{p,n}$ as a function of the problem's parameters:

$$\omega_{p,n} = \frac{\omega_{T,n}}{2}\left(1 + \sqrt{1 + \frac{1}{n^2 \ln(2)}\frac{J_\Omega^2}{J_{\Omega,c}^2}}\right). \qquad (22)$$

with $\omega_{T,n} = nN\Omega$. It is interesting to note that there exists a maximum shift, dependent only on n, when $J_\Omega = J_{\Omega,c}$, since the n-th peak overlaps for higher advance ratio (when $J_\Omega > J_{\Omega,c}$). The first peak satisfies $\max(\omega_{p,1}) \simeq 1.28\omega_{T,1}$, corresponding to a maximum shift of 28%. The maximum shift then rapidly decreases with n, such that $\max(\omega_{p,2}) \simeq 1.08\omega_{T,2}$ and $\max(\omega_{p,3}) \simeq 1.04\omega_{T,3}$, corresponding to 8% and 4%, respectively. For the parameters of Tab. 1, we obtain a shift of $\omega_{p,1} \simeq 1.06\omega_{T,1} = 1.06BPF$, which is a better prediction of the experimental shift observed in Fig. 3 (dotted vertical lines).

6. SPECIFIC CASES

In this last section, an analysis of special cases of the previous model is presented to demonstrate its equivalence with theories in the literature dealing with limit cases.

6.1 Static propeller

When the propeller is static ($\Omega = 0$) and has only one blade ($N = 1$), the model reduces to leading edge diffraction noise as in section 14.3 of [4]:

$$S_{F_2F_2}(\omega) = 4\pi^4 \rho_\infty^2 c^2 U_\infty b \left|H\left(\frac{\omega}{U_\infty}\right)\right|^2 \Phi_{22}\left(0, \frac{\omega}{U_\infty}\right),$$

$$S_{pp}(\boldsymbol{x}, \omega) = \left(\frac{\omega x_2}{8\pi^2 c_\infty |\boldsymbol{x}|^2}\right)^2 S_{F_2F_2}(\omega). \qquad (23)$$

with $\Phi_{22}(k_1, k_3) = \int_{-\infty}^{+\infty} \phi_{22}(k_1, k_2, k_3) dk_2$ the two-dimensional turbulence spectrum in the blade plane. This model thus reproduces the result of Glegg and Devenport [4], for a fixed wing in turbulent flow, modulo a factor 2π, given that the normalization of the Fourier transform used is not the same as here (see appendix).

6.2 Uncorrelated blades

The cross-correlation function between the blades B is responsible for the periodic reproduction of the turbulence spectrum (and thus the production of the humps) in (5).

Setting $B = 1$ amounts to neglecting the interaction between the incident turbulent field and the periodicity of the blade passage, which thus eliminates the humps while still preserving the average trend of the spectrum (red mean line without humps in Fig. 3 and 4) given by the diffraction of the turbulence corresponding to $|H|^2 \cdot \psi_{33}$ in (5). This uncorrelated approach has already been theorized by Sevik during his experiment in 1971 [7].

7. CONCLUSION

This study has successfully developed a simplified analytical model to predict turbulence ingestion noise for marine propellers, focusing on the characterization of spectral humps. The key steps undertaken include: (1) the adaptation of the Ffowcs-Williams and Hawkings formulation to model acoustic radiation from moving surfaces, incorporating a homogeneous and isotropic von Kármán turbulence spectrum; (2) validation of the model against Blake's and Raposo's analytical and experimental results, confirming its ability to reproduce hump shapes despite some underpredictions in non-compact scenarios; (3) a detailed parametric analysis to determine hump positions, bandwidths, and emergence criteria, introducing a refined critical advance ratio $J_{\Omega,c}(n)$ that improves upon the original Ffowcs-Williams and Hawkings criterion; and (4) an exploration of special cases, such as static propellers and uncorrelated blades, demonstrating equivalence with established theories. Future works will focus on implementing realistic propeller geometry (with twist, sweep and skew angles, etc.) into the models and relaxing compacity hypothesis to study the potential influence on humps positions, and bandwidths.

8. APPENDIX

8.1 Fourier transform conventions

For the Fourier transforms in time and space, the following conventions and notations are used:

$$\widehat{f}(\omega) = \frac{1}{2\pi} \int_{-\infty}^{+\infty} f(t) e^{i\omega t} dt,$$

$$f(t) = \int_{-\infty}^{+\infty} \widehat{f}(\omega) e^{-i\omega t} d\omega$$

9. REFERENCES

[1] W. K. Blake, "Chapter 6 - noise from rotating machinery," in *Mechanics of Flow-Induced Sound and Vibration, Volume 2 (Second Edition)* (W. K. Blake, ed.), pp. 505–658, Academic Press, second edition ed., 2017.

[2] M. Goldstein, "Unified approach to aerodynamic sound generation in the presence of solid boundaries," *The Journal of the Acoustical Society of America*, vol. 56, pp. 497–509, 08 1974.

[3] W. R. Sears, "Some aspects of non-stationary airfoil theory and its practical application," *Journal of the Aeronautical Sciences*, vol. 8, no. 3, pp. 104–108, 1941.

[4] S. Glegg and W. Devenport, "Aeroacoustics of low mach number flows," Academic Press, 2017.

[5] S. A. Glegg, W. Devenport, and N. Alexander, "Broadband rotor noise predictions using a time domain approach," *Journal of Sound and Vibration*, vol. 335, pp. 115–124, 2015.

[6] J. P. Wojno, T. J. Mueller, and W. K. Blake, "Turbulence ingestion noise, part 2: Rotor aeroacoustic response to grid-generated turbulence," *AIAA Journal*, vol. 40, no. 1, pp. 26–32, 2002.

[7] M. Sevik, "Sound radiation from a subsonic rotor subjected to turbulence," Fluid Mechanics, Acoustics and Design of Turbomachinery NASA SP-304, 1974.

[8] H. Raposo and M. Azarpeyvand, "Turbulence ingestion noise generation in rotating blades," *Journal of Fluid Mechanics*, vol. 980, 02 2024.

[9] W. J. E. Ffowcs and D. L. Hawkings, "Theory relating to the noise of rotating machinery," *J. Sound Vib*, pp. 10–21, 1969.

[10] G. Homicz and A. George, "Broadband and discrete frequency radiation from subsonic rotors," *Journal of Sound and Vibration*, vol. 36, no. 2, pp. 151–177, 1974.

[11] R. Martinez, "Asymptotic theory of broadband rotor thrust, part i: Manipulations of flow probabilities for a high number of blades," *Journal of Applied Mechanics*, vol. 63, pp. 136–142, 03 1996.

[12] S. Glegg, M. Morton, and W. Devenport, "Rotor inflow noise caused by a boundary layer: Theory and examples," in *18th AIAA/CEAS Aeroacoustics Conference*, (Colorado Springs, CO), American Institute of Aeronautics and Astronautics, June 2012.

[13] X. Huang, "Convolution for haystacking in turbulence-ingesting rotor noise," *AIAA Journal*, vol. 61, 11 2023.

[14] D. Qin, O. Stalnov, and X. Huang, "Numerical investigation of parameters influencing the turbulence-ingesting noise of a ten-bladed propeller," *Ocean Engineering*, vol. 300, p. 117237, 2024.

[15] R. Martinez, "Asymptotic theory of broadband rotor thrust, part ii: Analysis of the right frequency shift of the maximum response," *Journal of Applied Mechanics*, vol. 63, pp. 143–148, 03 1996.

DOI: 10.61782/fa.2025.0330



FORUM ACUSTICUM
EURONOISE 2025

EFFECTS OF INFLOW CONDITIONS ON TURBULENCE-INGESTION NOISE PREDICTION

Andrea Piccolo[1*] **Riccardo Zamponi**[1,2]
[1] Technische Universiteit Delft, Delft, The Netherlands
[2] von Karman Institute for Fluid Dynamics, Sint-Genesius-Rode, Belgium

ABSTRACT

In this paper, we present a modification of Amiet's model for rotating systems aimed at enhancing the assessment of inflow-conditions effects on turbulence-interaction noise generation and prediction. This involves replacing the original three-dimensional turbulence input, which is particularly challenging to measure both experimentally and numerically, with a one-dimensional term, enabling probe measurements to be directly used as input. The proposed modification also allows for the extension to rotating systems of turbulence-distortion models developed for rectilinear motion to account for realistic geometry effects in sound prediction. The approach is validated against experimental acoustic data obtained for a low-Reynolds two-bladed propeller interacting with grid-generated turbulence.

Keywords: *Rotating Systems, Turbulence Modeling, Turbulence-Ingestion Noise, Low-Fidelity Noise Prediction.*

1. INTRODUCTION

Aeroacoustic optimization of urban aerial vehicles is essential for the successful implementation of urban air mobility. Such a necessity arises from strict urban regulations and the complex, heterogeneous flow conditions that characterize urban environments. This highlights the importance of analyzing turbulence-ingestion noise (TIN), which results from the interaction between the incoming turbulence structures and the rotor. The complexity is further increased by the growing diversity of rotor geometries and configurations, making flow-structure interactions even more challenging to predict and control.

The interaction of turbulence with a rotating system can be divided into three distinct phases. In the first phase, the streamtube contraction induced by the rotating system elongates the turbulence structures in the streamwise direction [1]. Consequently, even if the incoming turbulence is homogeneous and isotropic far upstream, the rotor encounters anisotropic flow conditions [1, 2]. In the second phase, these elongated structures are chopped by the rotor blades, generating coherent unsteady surface pressure across different blades. This blade-to-blade correlation introduces narrow-band quasi-tonal peaks to the mainly broadband features of the TIN spectra. Finally, in the third phase, the elongated and chopped structures undergo distortion as they interact with the blade leading edge, accelerating along its surface. Although the impact of this mechanism on noise generation has been extensively studied in the context of rectilinear motion [3, 4], its potential effects on rotating systems remain largely unexplored.

Since the identification of this flow-induced noise source by Sharland in the 1960s [5], several low-fidelity models — mainly used for the optimization phase — have been developed, with Amiet's model [6] standing out for its robustness and simplicity. Despite its numerous simplifying assumptions, this model has proven capable of providing accurate predictions across a wide range of conditions [7]. It also accounts for blade-to-blade correlation and partially incorporates rotor geometry by discretizing the blade into narrow strips using a strip-theory approach [8]. However, its implementation depends on precise modeling or extensive characterization of inflow conditions, which poses a significant limitation for many

*Corresponding author: a.piccolo@tudelft.nl.
Copyright: ©2025 Andrea Piccolo and Riccardo Zamponi This is an open-access article distributed under the terms of the Creative Commons Attribution 3.0 Unported License, which permits unrestricted use, distribution, and reproduction in any medium, provided the original author and source are credited.

cutting-edge configurations currently under development.

The purpose of this study is hence to propose a modification to Amiet's model that enables the use of direct, simple flow measurements as input. This modification is especially useful for complex configurations where low-fidelity noise prediction is needed but a detailed description or reliable model of the inflow is unavailable, allowing the use of hot-wire anemometry measurements to assess the acoustic performances. The modified model has been validated against experimental measurements from a simple turbulence-rotor configuration.

The outline of the paper is the following. The experimental setup is presented in Sec. 2, while the modification and the results are reported in Sec. 3. The conclusions are then drawn in Sec. 4.

2. METHODOLOGY

The experimental campaign has been carried out in the anechoic open-jet wind tunnel (A-Tunnel) at the Low-Speed Laboratory of TU Delft, shown in Fig. 1a and extensively described by Merino-Martinez *et al.* [9]. A turbulence-generating grid (with rectangular rods $0.01\,\mathrm{m}$ wide separated by $0.10\,\mathrm{m}$) has been placed at the exit of the tunnel, followed by a $0.60\,\mathrm{m}$ long circular nozzle with a diameter of $0.60\,\mathrm{m}$. This configuration was chosen to prevent microphone measurements from being contaminated with grid noise.

The propeller is an APC 9×6 rescaled to have a diameter of $0.30\,\mathrm{m}$ and modified to feature a NACA 4412 as blade section. Positioned $0.40\,\mathrm{m}$ from the nozzle exit, the propeller is powered by a Lehner Motors LMT 2280/34 brushless inrunner. Further information about the propeller manufacturing and the support nacelle is provided by Grande *et al.* [10]. A single rotational speed of $6000\,\mathrm{RPM}$ has been considered, resulting in an advance ratio $J = W_\infty/nD$, with n being the rotational speed in Hz, of 0.30.

Figure 1b shows a schematic of the experimental setup. The reference frame is centered on the rotor hub, with the z axis aligned along the axial (streamwise) direction, pointing upstream. The x and y axes lie within the rotor plane, forming a right-handed coordinate system. The corresponding velocity components are denoted as w, u, and v.

The sketch also illustrates the placement of ten G.R.A.S. 40PH microphones along the directivity arc at a radius of $R_{\text{mic}} = 1.3\,\mathrm{m}$, positioned between $\theta_{\text{mic}} = 60°$ and $\theta_{\text{mic}} = 150°$ in increments of $10°$, with θ_{mic} measured relative to the z axis. The microphones have a frequency range of 10 to $20\,\mathrm{kHz}$ and a maximum sound pressure level of $135\,\mathrm{dB}$.

Aerodynamic measurements were conducted using hot-wire anemometry (HWA). Axial velocity fluctuations were recorded at the grid points shown in Fig. 1b. The probe used is a platinum-plated tungsten Dantec Dynamics P11, with a width of $5\,\mu\mathrm{m}$ and a length of $1.25\,\mathrm{mm}$. HWA data were used to characterize the flow at the nozzle exit, where the free-stream velocity is $W_\infty = 9.5\,\mathrm{m\,s^{-1}}$, the turbulence intensity $\sqrt{\overline{w'^2}}$ is $6\,\%$, and the integral length scale L^z_{ww} is $0.018\,\mathrm{m}$.

Acoustic and aerodynamic data were collected for $60\,\mathrm{sec}$ at a sampling rate of $51.2\,\mathrm{kHz}$. The power spectral densities (PSDs) were computed using Welch's method with a Hanning window and a $50\,\%$ overlap, achieving a frequency resolution of $1\,\mathrm{Hz}$.

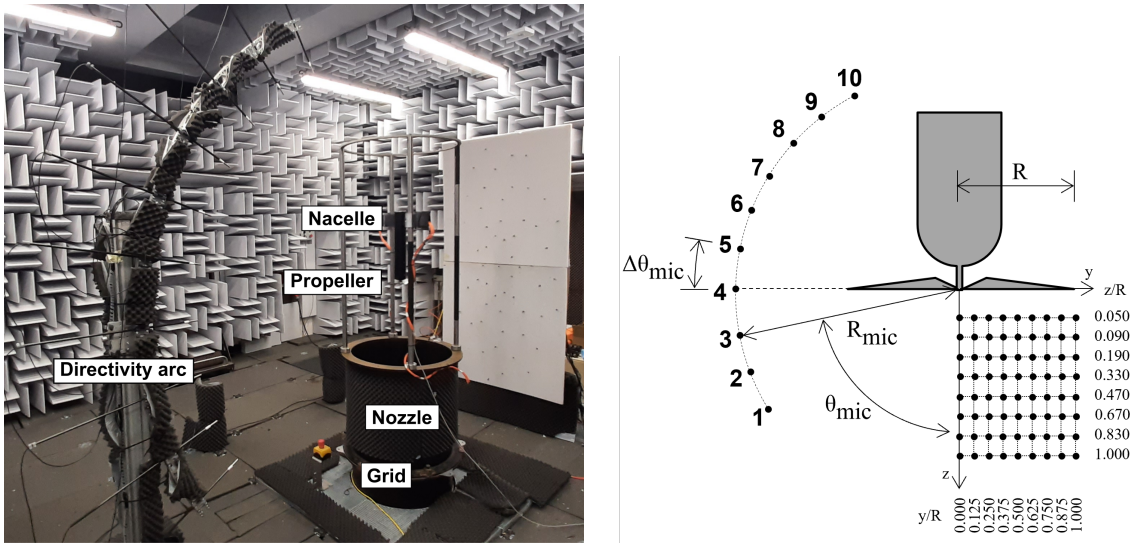
3. RESULTS

Amiet's model for turbulence-ingestion noise prediction [6] is based on the analytical approach developed in the two-dimensional regime [11]. This is used to calculate the instantaneous sound emission of the blade at each azimuthal position γ, which is hence modeled as if the blade were moving in rectilinear motion. This assumption holds as long as the considered noise frequencies are much higher than the rotational frequency of the propeller.

From a modeling perspective, the implementation of the rectilinear motion model requires three key considerations. First, an average must be taken over the azimuth. Second, the relative motion of the source with respect to the listener's position must be taken into account, which means that the listener's position $\mathbf{x}_\mathrm{B} = (x_\mathrm{B}, y_\mathrm{B}, z_\mathrm{B})$ should be calculated in the reference frame moving with the blade (from which the subscript $_\mathrm{B}$). Third, the Doppler effect must be incorporated into the calculation. The following equation is then finally retrieved for the far-field acoustic pressure $S_{pp}\left(\mathbf{x}_\mathrm{B}, \omega_0\right)$

$$S_{pp}\left(\mathbf{x}_\mathrm{B}, \omega_0\right) = \frac{1}{2\pi}\int_0^{2\pi}\left(\frac{\omega_\mathrm{B}}{\omega_0}\right)^2 S_{pp}\left(\mathbf{x}_\mathrm{B}, \omega_\mathrm{B}, \gamma\right)\mathrm{d}\gamma, \tag{1}$$

with $\omega_\mathrm{B}/\omega_0$ indicating the Doppler's effect as the ratio between ω_B, i.e., the "de-Dopplerized" frequency in the rotating reference frame, and ω_0, i.e., the "Dopplerized" sound frequency as heard by the observer in the fixed reference frame.



(a) (b)

Figure 1: (a) Picture and (b) sketch of the experimental setup at the TU Delft A-tunnel facility.

In the formulation incorporating blade-to-blade correlation, the instantaneous noise emission generated by the blade in the rotating reference system $S_{pp}\left(\mathbf{x}_\mathrm{B}, \omega_\mathrm{B}, \gamma\right)$ is expressed as

$$S_{pp}\left(\mathbf{x}_\mathrm{B}, \omega_\mathrm{B}, \gamma\right) = \left(\frac{\omega_\mathrm{B} z_\mathrm{B} \rho_0 c}{2 c_0 \sigma^2}\right)^2 \pi U_\mathrm{x} \left(\frac{L}{2}\right) \times \overline{w'^2} \left(\frac{c}{2}\right)^2 \left|\mathcal{L}\left(K_x, K_y, M_x\right)\right|^2 \times \sum_{n=-\infty}^{\infty} \Phi_{ww}\left(K_x, K_y, K_z^{(n)}\right) \frac{2\pi}{\left(\frac{c}{2}\right)^2 \overline{w'^2} Z}, \quad (2)$$

with ρ_0 being the flow density, c_0 is the speed of sound, c the chord and L the span, while $\sigma_0 = \sqrt{x_\mathrm{B}^2 + \beta_x^2 \left(y_\mathrm{B}^2 + z_\mathrm{B}^2\right)}$, with $\beta_x = \sqrt{1 - M_x^2}$, considers convection effects. U_x, with the respective Mach number M_x, indicates the flow velocity along the blade chord that accounts for the local pitch angle, as in the approach of Sinayoko *et al.* [12]. $\mathcal{L}\left(K_x, K_y, M_x\right)$ is the aeroacoustic transfer function, for which the original formulation of Amiet [13] has been implemented, and $\Phi_{ww}\left(K_x, K_y, K_z^{(n)}\right)$ is the three-dimensional turbulence spectrum. The wavenumbers are obtained as $K_x = \frac{\omega_\mathrm{B}}{U_\mathrm{x}}$, $K_y = \frac{\omega_\mathrm{B} y_\mathrm{B}}{c_0 \sigma}$, and $K_z^{(n)} = \frac{2\pi n + \omega_0 T_2}{Z}$. The expression for $K_z^{(n)}$ is obtained in the framework of the blade-to-blade correlation: T_2 is the time between the eddie chops as heard by the listener, Z can be defined as the distance between the blade paths in fluid, and n is an index representing the correlation between the 0-th and the n-th blade. As a detailed overview of the model falls outside the scope of the present manuscript, the reader is referred to Amiet [6, 13] for the derivation and expressions of all the parameters.

The present implementation considers the inverse strip theory approach proposed by Christope *et al.* [8] to calculate the blade noise emission. With this methodology, the blade is divided into M narrow-span strips of width L/M, whose emitted sound is calculated as the difference between a wing of span L_1 and a wing of span $L_2 = L_1 - L/M$, with $L_1, L_2 >> 1$. Referring to Eq. 2, this hence leads for $S_{pp}\left(\mathbf{x}_\mathrm{B}, \omega_\mathrm{B}, \gamma\right)$ for the m-th strip to

$$S_{pp}\left(\mathbf{x}_\mathrm{B}, \omega_0, \gamma\right)\Big|_m = \Big(S_{pp}\left(\mathbf{x}_\mathrm{B}, \omega_0, \gamma\right)\Big|_{L_1} + - S_{pp}\left(\mathbf{x}_\mathrm{B}, \omega_0, \gamma\right)\Big|_{L_2}\Big)\Big|_m. \quad (3)$$

Finally, Eq. 1 must be applied for all the M strips and the B blades, yielding

$$S_{pp}\left(\mathbf{x}_\mathrm{B}, \omega_0\right) = B \sum_{m=1}^{M} S_{pp}\left(\mathbf{x}_\mathrm{B}, \omega_0\right)\Big|_m. \quad (4)$$

The present study proposes the substitu-

tion of the three-dimensional turbulence spectrum $\Phi_{ww}\left(K_x, K_y, K_z^{(n)}\right)$ in Eq. 2 with a one-dimensional one $\Theta_{ww}\left(K_x\right)$ to allow the use of direct probe measurements. This is carried out using the analytical results of Wilson [14] on the multi-dimensional correlation and wavenumber spectra of homogeneous isotropic turbulence. The findings indeed show that it is possible to write

$$\Phi_{ww}\left(K_x, K_y, K_z^{(n)}\right) = \Psi_{ww}\left(K_x, K_y\right) \times \tilde{A}\left(K_x, K_y, K_z^{(n)}\right), \quad (5)$$

with $\tilde{A}\left(K_x, K_y, K_z^{(n)}\right)$ indicating an auxiliary function and $\Psi_{ww}\left(K_x, K_y\right)$ being the two-dimensional wavenumber spectrum. $\tilde{A}\left(K_x, K_y, K_z^{(n)}\right)$ can be calculated by performing the ratio of the von Kármán analytical expression of $\Phi_{ww}\left(K_x, K_y, K_z^{(n)}\right)$ and $\Psi_{ww}\left(K_x, K_y\right)$ [15], obtaining

$$\tilde{A}\left(K_x, K_y, K_z^{(n)}\right) = \left(\frac{55}{16}\frac{L_{ww}^z}{\pi}\right) \times \frac{\left(1+\left(\frac{K_x}{k_e}\right)^2+\left(\frac{K_y}{k_e}\right)^2\right)^{\frac{7}{3}}}{\left(1+\left(\frac{K_x}{k_e}\right)^2+\left(\frac{K_y}{k_e}\right)^2+\left(\frac{K_z^{(n)}}{k_e}\right)^2\right)^{\frac{17}{6}}}, \quad (6)$$

with $k_e = \pi/L_{ww}^z \Gamma\left(5/6\right)/\Gamma\left(1/3\right)$.

The two-dimensional wavenumber spectrum is then converted into a one-dimensional spectrum following the formulation of Amiet [11]

$$\Psi_{ww}\left(K_x, K_y\right) = \frac{1}{\pi}\Theta_{ww}\left(K_x\right) l_y\left(K_x\right), \quad (7)$$

with l_y being the spanwise coherence length of the upwash velocity component, for which the following expression is derived:

$$l_y\left(K_x\right) = \frac{8L_{ww}^z}{3}\left[\frac{\Gamma\left(1/3\right)}{\Gamma\left(5/6\right)}\right]^2 \times \frac{\left(\frac{K_x}{k_e}\right)^2}{\left(3+8\left(\frac{K_x}{k_e}\right)^2\right)\sqrt{1+\left(\frac{K_x}{k_e}\right)^2}}. \quad (8)$$

The introduction of the two auxiliary functions $\tilde{A}\left(K_x, K_y, K_z^{(n)}\right)$ and $l_y\left(K_x\right)$ thus allows the turbulence term in Eq. 2 to be expressed in terms of the one-dimensional spectrum, finally leading to

$$S_{pp}\left(\mathbf{x}_\mathrm{B}, \omega_\mathrm{B}, \gamma\right) = \left(\frac{\omega_\mathrm{B} z_\mathrm{B} \rho_0 c}{2c_0\sigma^2}\right)^2 \pi U_\mathrm{x}\left(\frac{L}{2}\right) \times \overline{w'^2}\left(\frac{c}{2}\right)^2 \left|\mathcal{L}\left(K_x, K_y, M\right)\right|^2 \left(\frac{1}{\pi}\Theta_{ww}\left(K_x\right) l_y\left(K_x\right)\right) \times \sum_{n=-\infty}^{\infty} \tilde{A}\left(K_x, K_y, K_z^{(n)}\right) \frac{2\pi}{\left(\frac{c}{2}\right)^2 \overline{w'^2} Z}. \quad (9)$$

The inclusion of a one-dimensional turbulence term enables the application of the altered spectra provided by turbulence-distortion models [3, 16]. Originally developed for bidimensional regime, these approaches effectively characterize the impact of thick airfoil geometries on noise generation.

Alternatively, the one-dimensional spectrum can be obtained using a direct probe measurement in the frequency domain as input, such as the frequency spectra of axial velocity - corresponding to the upwash component with respect to the propeller - obtained by means of HWA in the rotor inflow. These are shown in Fig. 2, which compares the measurements taken far upstream at $z/\mathrm{R} = 1.000$, at an intermediate distance $z/\mathrm{R} = 0.470$, and in the vicinity of the propeller at $z/\mathrm{R} = 0.050$ for 4 radial positions ($y/\mathrm{R} = 0.125$, $y/\mathrm{R} = 0.375$, $y/\mathrm{R} = 0.625$, and $y/\mathrm{R} = 0.875$). A decrease in velocity fluctuations in the low-frequency range, up to $f/\mathrm{BPF} \simeq 0.7$, can be observed as the frequency spectrum of the axial velocity is sampled closer to the rotor plane, especially for the mid-radial positions. This results from the alteration of turbulent structures as they are elongated in the streamtube contraction induced by the propeller, as in the case of the converging section of a wind tunnel [17, 18].

Such a mechanism also impacts sound production, as can be inferred by applying Amiet's model with the HWA spectra as input using Eq. 9. A filtering operation was applied to the velocity spectra sampled at intermediate distances and very close to the rotor plane to remove the tones caused by the blade passage. The resulting noise prediction is shown in Fig. 3, which shows the sound pressure level (SPL) at microphone positions 1 and 8. A clear variation in noise levels is observed in the low-frequency range when the sampling position of the velocity spectrum

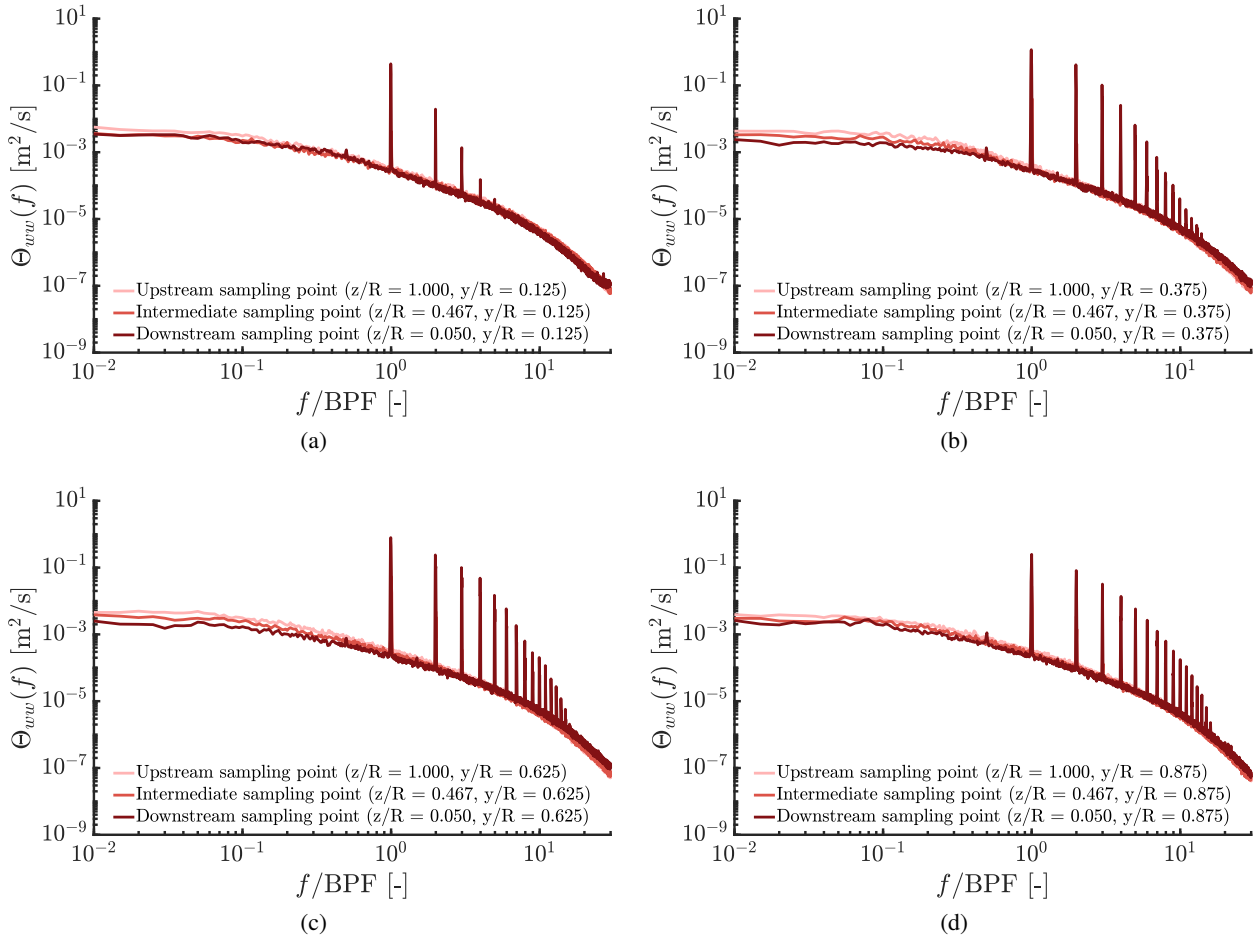


Figure 2: Frequency spectra of the axial velocity at radial positions (a) $y/\mathrm{R} = 0.125$, (b) $y/\mathrm{R} = 0.375$, (c) $y/\mathrm{R} = 0.625$, and (d) $y/\mathrm{R} = 0.875$. The spectra sampled far upstream at $z/\mathrm{R} = 1.000$, at intermediate distance $z/\mathrm{R} = 0.470$, and in the vicinity of the propeller at $z/\mathrm{R} = 0.050$ are compared.

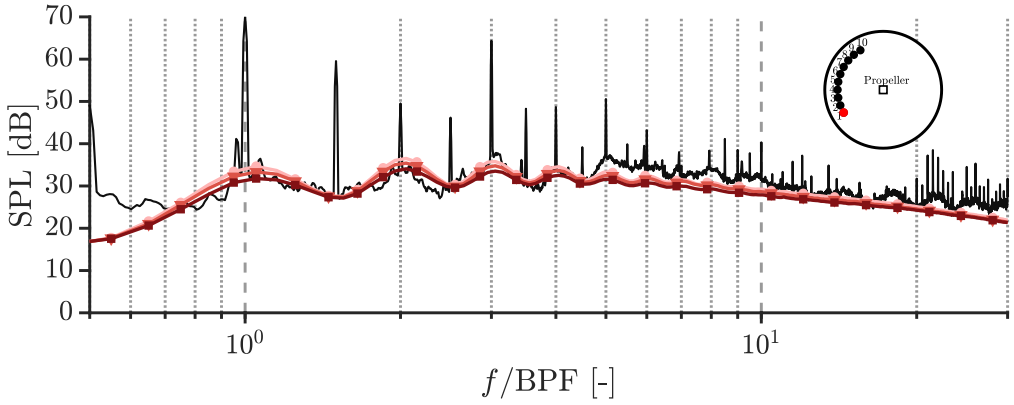
is changed, with higher accuracy achieved by sampling closer to the rotor plane.

4. CONCLUSIONS

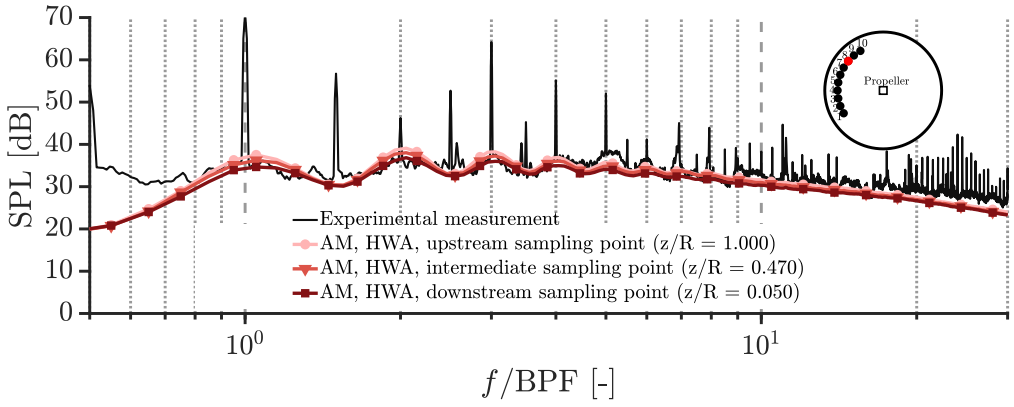
An implementation of Amiet's model for turbulence-ingestion noise in rotating systems has been proposed to allow direct flow measurements obtained through hot-wire anemometry to be used as input. This modification was validated using experimental data from a two-bladed propeller interacting with grid-generated turbulence. It was found that the variation in the inflow characteristics as the rotor plane is approached significantly affects the noise generation and prediction. This effect was evaluated by changing the position at which the HWA velocity spectrum, used as input for the model, is sampled. The results confirm that this modification of Amiet's model can effectively assess the impact of inflow conditions and play a crucial role in providing low-fidelity predictions of acoustic performance for configurations with limited availability of flow measurements and modeling.

5. REFERENCES

[1] D. B. Hanson, "Spectrum of rotor noise caused by atmospheric turbulence," *The Journal of the Acoustical Society of America*, vol. 55, pp. S3–S4, Apr. 1974.



(a)



(b)

Figure 3: Sound pressure level calculated with Amiet's model (AM) applied using HWA spectra sampled far upstream ($z/\mathrm{R} = 1.000$), at an intermediate distance ($z/\mathrm{R} = 0.470$), and in the vicinity of the propeller ($z/\mathrm{R} = 0.050$) compared to experimental measurements for (a) Microphone 1 and (b) Microphone 8. The reference pressure used to calculate the SPL is 2×10^{-5} Pa.

[2] S. J. Majumdar and N. Peake, "Noise generation by the interaction between ingested turbulence and a rotating fan," *J. Fluid Mech.*, vol. 359, pp. 181–216, Mar. 1998.

[3] F. L. dos Santos, L. Botero-Bolívar, C. Venner, and L. De Santana, "Modeling the Turbulence Spectrum Dissipation Range for Leading-Edge Noise Prediction," *AIAA Journal*, pp. 1–12, Mar. 2022.

[4] A. Piccolo, R. Zamponi, F. Avallone, and D. Ragni, "Turbulence distortion and leading-edge noise," *Physics of Fluids*, 2024.

[5] I. J. Sharland, "Sources of noise in axial flow fans," *Journal of Sound and Vibration*, vol. 1, pp. 302–322, July 1964.

[6] R. Amiet, "Noise produced by turbulent flow into a propeller or helicopter rotor," in *3rd Aeroacoustics Conference*, Aeroacoustics Conferences, American Institute of Aeronautics and Astronautics, July 1976.

[7] H. Raposo and M. Azarpeyvand, "Turbulence ingestion noise generation in rotating blades," *Journal of Fluid Mechanics*, vol. 980, p. A53, Feb. 2024.

[8] J. Christophe, J. Anthoine, and S. Moreau, "Amiet's

Theory in Spanwise-Varying Flow Conditions," *AIAA Journal*, vol. 47, pp. 788–790, Mar. 2009.

[9] R. Merino-Martínez, A. Rubio Carpio, L. T. Lima Pereira, S. Van Herk, F. Avallone, D. Ragni, and M. Kotsonis, "Aeroacoustic design and characterization of the 3D-printed, open-jet, anechoic wind tunnel of Delft University of Technology," *Applied Acoustics*, vol. 170, p. 107504, Dec. 2020.

[10] E. Grande, G. Romani, D. Ragni, F. Avallone, and D. Casalino, "Aeroacoustic Investigation of a Propeller Operating at Low Reynolds Numbers," *AIAA Journal*, vol. 60, pp. 860–871, Feb. 2022.

[11] R. K. Amiet, "Acoustic radiation from an airfoil in a turbulent stream," *Journal of Sound and Vibration*, vol. 41, pp. 407–420, Aug. 1975.

[12] S. Sinayoko, M. Kingan, and A. Agarwal, "Trailing-edge noise theory for rotating blades in uniform flow," 2013.

[13] R. K. Amiet, "Noise Produced by Turbulent Flow into a Rotor: Theory Manual for Noise Calculation," NASA Report, 1989.

[14] D. K. Wilson, "Three-Dimensional Correlation and Spectral Functions for Turbulent Velocities in Homogeneous and Surface-Blocked Boundary Layers.:," tech. rep., Defense Technical Information Center, Fort Belvoir, VA, July 1997.

[15] S. Glegg and W. Devenport, "Chapter 9 - Turbulent flows," in *Aeroacoustics of Low Mach Number Flows* (S. Glegg and W. Devenport, eds.), pp. 185–220, Academic Press, Jan. 2017.

[16] D. De Santana, J. Christophe, C. Schram, and W. Desmet, "A Rapid Distortion Theory modified turbulence spectra for semi-analytical airfoil noise prediction," *Journal of Sound and Vibration*, vol. 383, pp. 349–363, Nov. 2016.

[17] R. K. Amiet, J. C. Simonich, and R. H. Schlinker, "Rotor noise due to atmospheric turbulence ingestion. II - Aeroacoustic results," *Journal of Aircraft*, vol. 27, pp. 15–22, Jan. 1990.

[18] G. K. Batchelor and I. Proudman, "The Effect of Rapid Distortion of a Fluid in Turbulent Motion," *The Quarterly Journal of Mechanics and Applied Mathematics*, vol. 7, pp. 83–103, Jan. 1954.

DOI: 10.61782/fa.2025.0048

FORUM ACUSTICUM EURONOISE 2025

VIBRO-ACOUSTIC CALIBRATION FOR THE FEM SIMULATION OF A THIN-WALLED DUCT SYSTEM AND FAN HOUSING

Patrick Heidegger[1*] **Felix Czwielong**[2] **Stefan Schoder**[1]
Stefan Becker[2] **Manfred Kaltenbacher**[1]
[1] Institute of Fundamentals and Theory in Electrical Engineering, Graz University of Technology, Austria
[2] Institute of Fluid Mechanics, Friedrich-Alexander-University Erlangen-Nuremberg, Germany

ABSTRACT

Evaluating the acoustic behavior of a ducted ventilation system poses multiple challenges, e.g., possibly changing cross-sections, a lack of symmetry due to a non-straight layout, or a thin-walled structure acting as a bypass for sound waves traveling to the exterior. These aspects can be tackled via numerical simulation methods, like the finite element method, but uncertainties remain. Examples are the necessity to omit geometrical details for obtaining a computable model, the unknown and often non-ideal behavior of parts like the suspension or connecting joints, and unknown material properties. This proceeding discusses the calibration process for the vibroacoustic simulation of a thin-walled aluminum duct and a centrifugal-fan housing belonging to a high-precision aeroacoustic test rig.

Keywords: *centrifugal fan, finite element method, duct acoustics, model calibration*

1. INTRODUCTION

Centrifugal fans transport air and gases for industrial and civilian applications, e.g., in building ventilation systems. In ducted ventilation systems, the noise produced by the operating fan may propagate over wide distances within the ducts. The noise approaches the exterior field either via duct openings or by transmission through the duct walls (acoustic breakout) [1] and may constitute a source disturbance for potential listeners.

Acoustic breakout may contribute significantly to the total sound emission of the ducted ventilation system, depending on various parameters such as the construction material, the wall thickness, and the duct cross-section [2]. Understanding the vibroacoustic behavior of the duct can thus be essential for classifying the sound emission of a ducted ventilation system.

Numerical simulation methods are widely employed to gain such insights, but obtaining a valid computational model that reflects the actual real-world system poses multiple challenges. Examples are non-symmetric duct layouts, the necessity to omit geometrical details in the meshing process, the unknown and usually non-ideal behavior of mountings or connecting joints, and unknown material properties. For investigating the complex fluid-structure-acoustic interactions occurring in ducted centrifugal fans, a benchmark case for an academic centrifugal fan is being established in a research project. The benchmark case is an extension to the test rig proposed in [3] and covers simulations of the fluid mechanical, structural mechanical, and acoustic fields, accompanied by extensive measurements of all three physical domains.

This work in progress describes the vibroacoustic finite-element (FE) model of the fan housing, the duct walls, and the surrounding air of the benchmark case. Further, two approaches for tuning the simulation models to reference measurements are discussed. One refers to laser-vibrometry scans on parts of the mechanical structure excited by an impact hammer (method 1). The other refers to exterior microphone signals, excited via a voice-coil loudspeaker attached to the duct end (method 2).

*__Corresponding author__: patrick.heidegger@tugraz.at.
__Copyright__: ©2025 Patrick Heidegger et al. This is an open-access article distributed under the terms of the Creative Commons Attribution 3.0 Unported License, which permits unrestricted use, distribution, and reproduction in any medium, provided the original author and source are credited.

2. EXPERIMENTAL SETUP

The housing of the test fan consists of an 8 mm aluminum sheet connected by flanges. The duct system is mainly made of a 2 mm aluminum sheet, connected by flanges or welded joints. It consists of a narrowing transition piece (close duct) mounted on the downstream side of the fan housing and an extension part with a constant cross-section (extended duct). The two duct parts are connected by a flexible connector (canvas sleeve) made of truck tarpaulin, which has the purpose of mitigating the coupling of mechanical vibrations between the parts. The test rig is located in an acoustically treated chamber to reduce the room-acoustic impact on the sound radiation of the structure. A photograph of the setup is depicted in Fig. 1.

A system identification was performed using two types of measurements. Method 1: an impact hammer was used to excite the structure on the front flange of the fan housing in the surface-normal direction. The vibration response was scanned on the front, upper, and lower surfaces of the fan housing and the closed duct by 3D laser-vibrometry. The back-side surfaces could not be scanned due to the limited space. Method 2: An enclosed voice-coil loudspeaker was installed on the end of the extended duct to excite the system, and the sound radiation was recorded in twelve different positions.

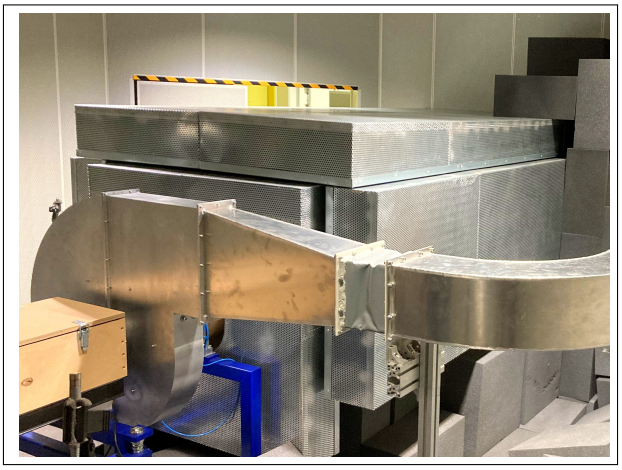


Figure 1. Photograph of the centrifugal test fan and duct system.

3. SIMULATION MODELS

The measured data should be reproduced by numerical simulations. For this purpose, FE models for the interior acoustic field and the mechanical field, as well as the exterior sound field, were set up. Two types of models are required. One high-fidelity model is backed by grid-refinement studies, and one low-fidelity model is used in the procedure of tuning the model parameters to satisfy the reference data. The solutions are computed for the time-harmonic case. The frequency band of interest is 20 Hz - 3000 Hz.

3.1 Method 1

Here, only the mechanical FE system should be calibrated, where the acoustic domain and the extended duct part are omitted. A unit normal force is applied to the same position as the hammer impact of the measurement. The time-harmonic structural vibration can be described by the Fourier-transformed linearized Navier's equation. Finite-element discretization and including a damping model leads to a system of equations of the form

$$\left(\underline{\boldsymbol{K}} - \mathrm{j}\omega\underline{\boldsymbol{C}} + \omega^2\underline{\boldsymbol{M}}\right)\underline{\boldsymbol{u}} = \underline{\boldsymbol{f}}, \tag{1}$$

where $\underline{\boldsymbol{K}}$, $\underline{\boldsymbol{C}}$, and $\underline{\boldsymbol{M}}$ are the stiffness, damping, and mass matrices, respectively. Furthermore, $\underline{\boldsymbol{u}}$ is the solution vector holding the mechanical displacements, $\underline{\boldsymbol{f}}$ the right-hand-side excitation vector, ω the angular frequency, and j the imaginary unit. The boundary conditions for Eqn. (1) are defined on the one hand by the natural (traction) boundary conditions arising due to the finite-element procedure. On the other hand, zero-displacement boundary conditions are set on all mounting positions of the construction and on the connecting surfaces to the omitted duct parts, respecting the direction of the opposing force.

In addition to the boundary conditions, the solution of Eqn. (1) depends on several material properties. Coefficients in the mass matrix are proportional to the material density ρ, while the stiffness-matrix coefficients are related to the elasticity modulus E_m and the Poisson ratio ν_P [4]. For the coefficients of the damping matrix, the most common approach is to exploit a linear combination of the stiffness and mass matrices (Rayleigh damping),

$$\underline{\boldsymbol{C}} = \alpha_R\underline{\boldsymbol{M}} + \beta_R\underline{\boldsymbol{K}}, \tag{2}$$

with the mass- and stiffness-proportional coefficients α_R and β_R, respectively. This leads to five parameters needed

to be specified for an entirely unknown isotropic material: ρ, E_m, ν_P, α_R, and β_R.

The material properties are given to a sufficient extent in the datasheet of the main construction material, aluminum "AlMgSi1-3.2315". However, the exact material properties of the canvas sleeve and the plastic flanges of the sleeve connector are not known. Additionally, all flanges contain screws and are sealed by a thin rubber tape in between, features that are not included in the finite-element mesh. Also, the welding seams connecting the edges of the aluminum plates and the suspension behavior of the mountings might influence the solution.

The model validity at a single frequency can be indicated by considering the normalized root-mean-squared error (RMSE) of the transfer functions over all positions i on the measured surfaces,

$$\mathrm{RMSE}_\omega = \sqrt{\frac{\sum_i (H_{ref,i} - H_{sim,i})^2}{\sum_i H_{ref,i}^2}}, \tag{3}$$

where the transfer function is calculated from the surface-normal velocities divided by the normal excitation force,

$$H_i(\omega) = \frac{\boldsymbol{n}_i \cdot \boldsymbol{v}_i(\omega)}{f_{n,i}(\omega)}. \tag{4}$$

For calculating Eqn. (3) the transfer functions need to be determined on the same positions. Hence, the measured and simulated data needs to be interpolated to the cell centroids of the finite-element grid's outer surfaces and projected into the surface-normal direction beforehand. A k-nearest-neighbor interpolation with inverse-distance weighting was employed for this purpose, using the Python package pyCFS-data [5].

An initial simulation run of the high-fidelity model, where the canvas sleeve material was roughly estimated based on online available data sheets and the rest of the structure set to the properties of aluminum "AlMgSi1-3.2315" revealed an unsatisfactorily high RMSE over the investigated frequency range.

3.2 Method 2

The second validation method is complementary to method 1. Here, the mechanical FE model should produce sufficiently valid results already. The aim of method 2 is to include the left-out duct parts and the air domain to the calibration procedure. Here, the whole vibroacoustic FE model is solved, which leads to significantly higher computational cost. The loudspeaker is modeled as an acoustic normal-velocity boundary condition on the corresponding surface.

The direct-coupled vibroacoustic finite element simulation solves for Eqn. (1) and the system for the acoustic wave equation simultaneously. The system for the homogeneous acoustic wave equation in the time-harmonic case is of the form

$$\left(\underline{\boldsymbol{K}}_a + \omega^2 \underline{\boldsymbol{M}}_a\right) \boldsymbol{p} = \boldsymbol{0}, \tag{5}$$

where $\boldsymbol{p}$ holds the acoustic pressures. The systems are coupled by applying the correct interface conditions to the corresponding domain boundaries in the weak form [4]. Here, for a homogeneous fluid, the terms of the mass matrix are inversely proportional to the squared speed of sound, which can be specified via the mean fluid density ρ_0 and the compression modulus K, so that

$$c_0^2 = \frac{K}{\rho_0}. \tag{6}$$

Similarly to method 1, the model validity can be evaluated via the RMSE between measured and simulated results, Eqn. (3). Here, however, the excitation signal cannot be recorded from the loudspeaker. Hence, the frequency response of the loudspeaker mounted in a large baffle was determined in a separate laser-vibrometry measurement. As there is an expected deviation between the baffled and the duct-mounted frequency response, this topic is part of ongoing investigations.

4. OPTIMIZATION WORKFLOW

The model calibration should be done in three steps. First, evaluate the most relevant material parameters and boundary/interface conditions to vary in the mechanical model. Second, an optimized mechanical model can be determined via method 1. Third, calibration method 2 is used to optimize what is left: the acoustic material parameters and the extended duct.

For determining the most significant regions and material parameters to vary in the mechanical model, their effect should be tested with respect to the RMSE in method 1. For this purpose, the model is separated into multiple regions of different (effective) materials, which are sampled using Latin hypercube sampling and scaled to subjectively estimated bounds, considering available material catalogs and data sheets. For the boundary conditions modeling the suspension behavior of the mountings, spring elements can be applied and varied instead of using fixed boundary conditions.

Due to the initial high dimension of the parameter space and the high computation time required to solve for the mechanical FE model, the method for the significance ranking should be chosen carefully. The Spearman rank coefficient has been employed to evaluate correlations when the feature space is sparse. It is a non-parametric measure that assesses the strength and direction between two ranked variables [6]. Additionally, a Least Absolute Shrinkage and Selection Operator (LASSO) regression could be employed. This method is a form of regression that allows coefficients to shrink to zero. Thus, it is especially useful for variable selection and sparsely sampled data [7]. As a third method, the feature-importance values of a trained random forest (RF) regression model can be used to rank the feature significance. RF regressors are robust to overfitting and inherently handle nonlinear relationships and interactions between variables [8]. Combining these three methods is expected to provide a robust significance estimation, even when applied to sparsely sampled data.

After reducing the feature space to sufficiently few features, optimization can be performed by using the trained RF regressor as a surrogate model and determining the optimized parameter set for a minimum RMSE. The optimization can be done, e.g., by exploiting a stochastic optimization algorithm.

5. CHALLENGES FOR THE METHOD

The major challenge of the optimization is the exceedingly high computational cost of evaluating the FE simulations. Hence, it is not feasible to evaluate the eigenfrequencies of the system via an eigenvalue analysis or to compute the full frequency band of interest in a sufficient resolution. Additionally, the low-fidelity model, which is required to save computation time, deviates significantly from the high-fidelity model for higher frequencies. Further, the measured transfer functions yield insufficiently high noise rates at frequencies below 60 Hz. For the calibration method 2, the unknown excitation of the loudspeaker might impact the result. Finally, the high initial RMSE of the mechanical simulation complicates the determination of significant variables and optimized solutions.

A first attempt to optimize the mechanical FE model was already conducted. Here, only seven frequencies in non-integer ratios ranging between 70 Hz and 780 Hz were simulated. Only material parameters, but no boundary conditions, varied. The procedure was conducted in three rounds of 650 simulation evaluations. The first two rounds were used to reduce the feature space from initially 65 to 13 features. The third round was then used to determine optimized parameters. This first attempt did not lead to satisfactory results.

6. CONCLUSIONS AND OUTLOOK

This proceeding discusses the workflow to calibrate the vibroacoustic system for a thin-walled duct system and the housing of a centrifugal fan. It documents the current state of a work in progress and outlines methods and difficulties for achieving the goal of a calibrated simulation model.

7. ACKNOWLEDGMENTS

This research was funded in whole, or in part, by the Austrian Science Fund (FWF) [I 5515-N] and by the German Research Foundation (DFG) [468338100]. The computational results presented have been achieved, in part, using the software openCFS.

8. REFERENCES

[1] C. Burgess and R. Thomspon, "Practical consideration of noise from fans," in *INTER-NOISE and NOISE-CON Congress and Conference Proceedings*, 2014.

[2] A. Cummings, "SOUND TRANSMISSION THROUGH DUCT WALLS," *Journal of Sound and Vibration*, vol. 239, pp. 731–765, Jan. 2001.

[3] T. Uffinger, F. Czwielong, A. Renz, P. Heidegger, S. Schoder, M. Kaltenbacher, and S. Becker, "Development of a test rig for the investigation of flow-induced mechanisms of sound generation at radial fans," *Applied Acoustics*, vol. 211, p. 109553, 2023.

[4] M. Kaltenbacher, *Numerical Simulation of Mechatronic Sensors and Actuators: Finite Elements for Computational Multiphysics*. Berlin, Heidelberg: Springer Berlin Heidelberg, 2015.

[5] "pyCFS." `https://pypi.org/project/pyCFS/`, 2025. Accessed: 2025-04-01.

[6] J. H. Zar, "Spearman rank correlation," *Encyclopedia of Biostatistics*, 2005.

[7] C. S. Signorino and A. Kirchner, "Using lasso to model interactions and nonlinearities in survey data," *Survey Practice*, vol. 11, pp. 1–10, 2018.

[8] G. Biau and E. Scornet, "A random forest guided tour," *Test*, vol. 25, pp. 197–227, 2016.

DOI: 10.61782/fa.2025.0768



FORUM ACUSTICUM
EURONOISE 2025

SHAPE OPTIMISATION FOR THE AEROACOUSTICS, AERODYNAMICS AND HEAT TRANSFER OF ROUND HOLES

Yifei Wang[1*] **Juan Guzmán-Iñigo**[2] **Aimee S. Morgans**[1]

[1] Department of Mechanical, Imperial College London, London, UK.
[2] Department of Engineering, City University of London, London, UK.

ABSTRACT

Acoustic liners are comprised of small holes in the walls of gas turbine combustors. The flow through them both cools the combustion chamber and absorbs acoustic energy, such that their aeroacoustic, aerodynamic, and heat transfer performance are all important. Their circular holes typically have straight edges, whose length (compared to the radius) plays a significant role in their acoustic behaviour. In the case of "short" holes, where the flow through the hole separates without reattaching within it, there can be an amplification of acoustic energy at certain frequencies, leading to a phenomenon known as "whistling". Previous analyses suggests that heat transfer can either exacerbate or mitigate this undesirable occurrence. Furthermore, altering the inlet or outlet geometry of the holes can eliminate the whistling effect, shifting the acoustic behaviour toward damping. Such geometry changes will also affect the holes' aerodynamic and heat transfer performance. This research numerically investigates optimisation of the hole geometry, considering aeroacoustic, aerodynamic performance and heat transfer performance. Simulations integrate the energy equation into a linearised Navier-Stokes solver and employ Bayesian optimisation to refine the orifice shape based on a cost function that combines acoustic absorption, aerodynamic and heat transfer measures. The results indicate that heat transfer through the orifice surface significantly impacts acoustic performance. To enhance the acoustic absorption, a large downstream chamfer is optimal, while for aerodynamics, a moderate upstream chamfer is best. For optimal heat transfer, or to achieve a combined multi-objective target, a large upstream chamfer is identified as the most effective geometry.

Keywords: *Acoustic damping, Optimisation, Holes, Orifices, Acoustic liners, Heat transfer*

1. INTRODUCTION

Thermoacoustic instability occurs when acoustic waves interact with unsteady heat release during combustion. This phenomenon can lead to significant pressure fluctuations within combustors, negatively impacting operational performance and potentially damaging components [1]. The challenge of thermoacoustic instability is especially pertinent when using decarbonised fuels such as hydrogen, with hydrogen flames being especially sensitive to acoustic disturbances due to their high flame speed. Acoustic dampers, like liners and Helmholtz resonators, are often installed in engines to mitigate these issues. These devices absorb acoustic perturbations and help suppress thermoacoustic instability in various industrial applications, including gas turbines and rocket engines.

Acoustic liners consist of multiple circular holes through which a bias flow passes. When the flow travels through these holes, it can significantly enhance the acoustic absorption and effective bandwidth of a perforated liner. Additionally, its tunable properties can be adjusted by varying the mean flow velocity [2]. The mechanism underpinning the acoustic damping is recognised as the conversion of acoustic energy into vortical energy,

*__Corresponding author__: yifei.wang20@imperial.ac.uk.
__Copyright__: ©2025 Yifei Wang et al. This is an open-access article distributed under the terms of the Creative Commons Attribution 3.0 Unported License, which permits unrestricted use, distribution, and reproduction in any medium, provided the original author and source are credited.

which is then dissipated as heat [3, 4]. Furthermore, the bias flow from the orifice also provides an impingement jet for cooling the combustor surface [5]. Thus, the effect of heat transfer within the hole must be taken into account.

Howe's model [6] has been widely used to predict the acoustic absorption of holes. It assumes that the hole is infinitely thin and that there is a straight vortex-shedding path from the hole downstream. It predicts that an orifice can absorb sound energy, but cannot generate it. Subsequent research [7] indicates that the dimensions of the orifice significantly impact its acoustic behaviour, and the thickness of the orifice must also be taken into account.

A "short" hole, defined as having a length-to-diameter ratio of less than one but not close to infinitesimal, exhibits flow characteristics that can amplify acoustic energy at certain frequencies, a phenomenon referred to as "whistling" [8–10]. This occurs due to the two-way interaction between acoustic waves and vortical disturbances. It presents challenges in engineering design, as it can decrease the acoustic absorption capability and may even amplify acoustic perturbations, potentially leading to structural failures. The above works considered isothermal hole flows: recent research on heat transferring flows suggests that a temperature gradient can alter the acoustic behaviour of a flow, either increasing or decreasing its acoustic absorption ability [11].

For isothermal hole flows, recent theoretical and numerical studies have shown that the acoustic characteristics of short holes are highly sensitive to their geometry [12,13]. Even minor changes in shape can significantly alter the acoustic response, causing a hole's behaviour to shift from amplification to damping [13, 14]. The present study numerically investigates the optimal performance of short holes, considering aeroacoustic, aerodynamic and heat transfer performance.

2. PROBLEM FORMULATION

2.1 Simulation configuration

To evaluate the aeroacoustic performance, a two-step simulation method is employed [15, 16]. In the first step, the mean flow field is obtained using a Reynolds-Averaged Navier-Stokes (RANS) k-ω-SST turbulence model. Next, acoustic perturbations are added to the mean flow field, which is then solved using a linearised Navier-Stokes Equation (LNSE) solver in the frequency domain. This method has been validated against experimental data and direct simulation techniques, demonstrating greater computational efficiency compared to more intensive methods like Large Eddy Simulation (LES) [13]. Additionally, Bayesian optimisation is utilised as a powerful approach for black-box problems with costly evaluations [17, 18]. The high resource cost associated with each evaluation during the optimisation process limits the number of sampling operations.

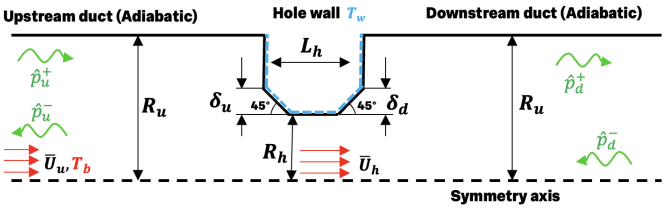


Figure 1. Schematic of the hole configuration, with heat transfer through the wall of the hole.

The configuration studied is a single axisymmetric hole, whose wall is subject to heat transfer. A turbulent mean flow passes through the hole, as illustrated in Figure 1. The radii of the upstream and downstream ducts are R_u, while the radius of the concentric circular hole is R_h. The ratio of the duct radius to the hole radius is $R_u/R_h = 2$. The length of the hole is set to $L_h = 0.66R_h$, which is typical for a short hole. To account for a heat transfer effect, the mean flow is considered to have a temperature of $T_b = 500$ K, while the orifice wall is considered to be at a cooler fixed temperature of $T_w = 300$ K, with the upstream and downstream duct walls considered adiabatic.

A subsonic mean flow with an inlet velocity $\bar{U}_u$ is defined at the inlet boundary as a fully developed turbulent profile. The mean flow is characterised by two dimensionless parameters: the Reynolds number and the Mach number. At the orifice, the Reynolds number is defined as:

$$Re = \frac{R_h \bar{U}_h}{\nu} = 20,000 \tag{1}$$

where $\bar{U}_h$ represents the average flow velocity at the orifice, and ν denotes the kinematic viscosity of the average flow. The Mach number is defined as:

$$M = \frac{\bar{U}_h}{\bar{c}_u} = 0.104 \tag{2}$$

where $\bar{c}_u$ represents the mean speed of sound in the flow. Previous simulations and experimental results [8, 10] suggest a potential for whistling under these flow conditions with a straight hole geometry in adiabatic conditions.

To optimize the geometry, two chamfers are added to the hole edges at both the upstream and downstream sides of the hole. Each edge features a fixed chamfer angle of 45 degrees with variable length, denoted as δ_u for the upstream edge and δ_d for the downstream edge.

The Strouhal number, denoted St, is a dimensionless quantity used to describe normalised frequencies of sound waves. It is defined as:

$$St = fL_h/\bar{U}_h = \frac{\omega}{2\pi} L_h/\bar{U}_h \tag{3}$$

where f is the frequency of the acoustic wave, ω is the angular velocity of the wave and $\bar{U}_h$ represents the mean flow velocity passing through the orifice. In this research, our focus is on Strouhal numbers ranging from 0 to 0.5, as this range is linked to the first whistling mode of the geometry under investigation.

The absorption coefficient, represented as Δ [14, 19, 20], is used as a measure of the aeroacoustic performance of the hole. It is defined as:

$$\Delta = 1 - \frac{|W_u^-| + |W_d^+|}{|W_u^+| + |W_d^-|} \tag{4}$$

where $W_j^{\pm}$ $(j = u, d)$ represents the averaged acoustic energy flux of a plane wave propagating in the positive (+) or negative (-) directions, at the upstream (u) or downstream (d) locations, respectively. It represents the ratio of acoustic energy moving away from the orifice to that entering it. A value of $\Delta = 1$ indicates full absorption, meaning that all incoming energy is absorbed and no acoustic energy escapes the hole. Conversely, $\Delta = 0$ signifies that the acoustic energy remains unchanged by interaction with the hole. If $\Delta < 0$, the acoustic energy is amplified by the presence of the hole, a phenomenon commonly referred to as "whistling".

The aerodynamic characteristics of the orifice are represented by the discharge coefficient, C_d. This is defined as the ratio of the actual discharge to the theoretical discharge from an orifice, expressed as:

$$C_d = \frac{Q_{\text{real}}}{Q_{\text{ideal}}} = \frac{\dot{m}}{A\sqrt{2\rho\Delta P}} \tag{5}$$

where, $\dot{m}$ is the mass flow rate through the hole, A is the cross-sectional area of the hole, ρ is the fluid density, and ΔP is the pressure difference across the hole. Knowing the value of C_d is essential for designing the air distribution system within gas turbine engines [21].

To characterise the heat transfer performance of the hole, we define a normalised power coefficient, denoted P^*, given by:

$$P^* = \frac{P_{wall}}{\rho \bar{U}_h^3 L_{wet}^2} \tag{6}$$

where, P_{wall} represents the power transferred from the orifice wall to the flow. The sign of P_{wall} indicates the direction of heat transfer: a positive value means that the wall loses heat to the flow, while a negative value indicates that the wall absorbs heat from the flow. The denominator, $\rho \bar{U}_h^3 L_{wet}^2$, represents the kinetic power of the flow and has units of Watts. ρ is the mean flow density, $\bar{U}_h$ is the mean flow velocity, and L_{wet} refers to the total length of the orifice wall, which includes the hole length, chamfer length, and radial length in cross-section. The coefficient P^* quantifies the ratio between the energy transferred into the flow and the flow kinetic energy through the hole.

2.2 Numerical Implementation

To evaluate all of the aerodynamic, heat transfer and aeroacoustic performance, a two-step simulation method was employed [15, 16] which decomposed the fluid variables into mean and perturbation terms. The first step involved obtaining the mean turbulent flow field using a compressible Reynolds-Averaged Navier-Stokes (RANS) simulation with the open-source solver OpenFoam (version 11). A steady-state simulation solution was achieved using the SIMPLE algorithm along with the K-Omega SST turbulence model. A fully developed turbulent flow profile was imposed at the inlet boundary, where the inlet pressure was defined as a zero gradient, and the outlet pressure was set to zero gauge pressure. The temperature of the flow inlet is assigned $T = 500$ K. The upstream and downstream walls are set to adiabatic and the hole wall is set to a fixed temperature T_{wall} = 300 K. The upstream, downstream, and wall surfaces were assigned a no-slip condition.

The second step then involved solving for the linearised flow perturbations using a compressible linearised Navier-Stokes Equation (LNSE) solver. This was performed in the frequency domain using a finite element method within the open-source computing framework FEniCS [22], with more detail provided in [23]. Non-reflecting boundary conditions were implemented at both the inlet and outlet boundaries, and acoustic waves of different frequencies were forced from the inlet boundary into the downstream flow. The acoustic response was evaluated using the two-microphone method at the inlet and outlet boundaries to distinguish between the acoustic waves. For the acoustic perturbations, the walls of the hole

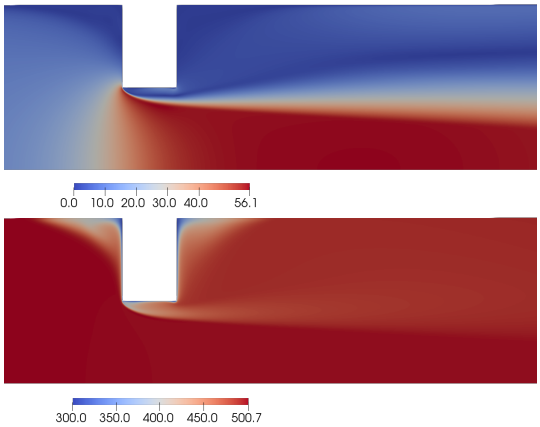


Figure 2. Magnitude of the mean flow velocity field (upper) and temperature field (lower) for the original, unmodified hole geometry with a wall temperature $T_{wall} = 300K$.

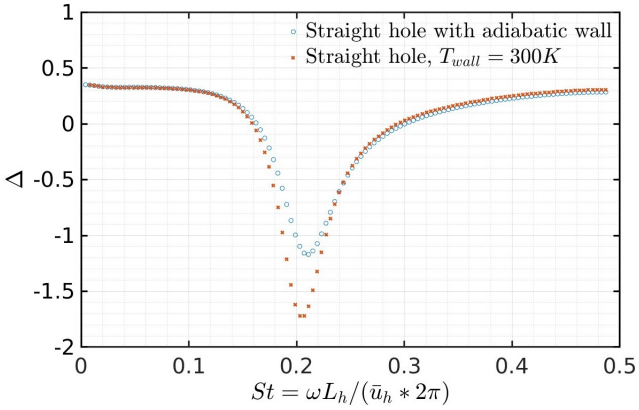


Figure 3. Absorption coefficient Δ of original geometry with an adiabatic wall and with a cooler wall. Negative Δ indicates the acoustic amplifying phenomenon known as "whistling".

were defined as non-slip boundaries with $\hat{\mathbf{u}} = 0$. The upstream and downstream walls were assigned slip boundary conditions $\hat{\mathbf{u}} \cdot \mathbf{n} = 0$ to reduce the computational costs that would be associated with acoustic boundary layers along the upstream and downstream duct walls.

For isothermal flows, the two-step method was validated for straight holes against experimental data and direct simulation techniques, demonstrating accuracy and computational efficiency [13]. For the present work, validation was for the isothermal straight hole geometry, with the $u_d, u_u = 0$, condition validated by comparison to experimental data and numerical simulations [23]. The mean velocity and temperature fields of the straight hole (δ_u, δ_d = 0) with $T_{wall} = 300K$ are shown in Figure 2. This mean flow field is subsequently used in the perturbation solver to determine the acoustic response to an input acoustic wave. The absorption coefficient Δ as a function of frequency St is shown in Figure 3.

2.3 Optimisation configuration

The geometry of a straight hole serves as the baseline for optimizing the aeroacoustic, aerodynamic, and heat transfer performance. With the acoustic performance known to be sensitive to geometry [13], two 45-degree chamfers of variable length were added to the upstream (inlet) and downstream (outlet) edges of the hole to modify the energy amplification. The optimisation algorithm controls the depths of the two chamfers, δ_u,δ_d, while keeping the total length of the hole constant ($\delta_u + \delta_d < L_h$).

For the optimisation procedure, Bayesian optimisation was chosen, this being a powerful approach for black-box problems with costly evaluations [17, 18]. For the present numerical problem, computing the mean flow solution and perturbations at a single frequency takes approximately 500 CPU hours, primarily due to the mean flow simulation. Bayesian optimisation is performed using a modified version of the scikit-optimize library that includes a constraint function [24] [25]. The acquisition function is set to the probability of improvement (EI), and the acquisition optimizer function is configured as "lbfgs." The optimisation problem is formulated as follows:

$$\arg\max_{\delta_u, \delta_d} f(\delta_u, \delta_d) \tag{7}$$

subject to $\delta_u \in [0, L_h]$, $\delta_d \in [0, L_h]$ and $\delta_u + \delta_d \leq L_h$ to maintain the geometry's topology. 45 initial sampling points, selected using the grid method, were computed in advance to initiate the optimisation. The optimisation was performed for 5 steps to provide a fast indication of the potential optimal geometry.

The acoustic absorption coefficient, Δ, of a straight hole with and without heat transfer is shown in Figure 3. Δ shows acoustic energy amplification in the frequency range $0.16 < St < 0.30$, with the most pronounced whistling effect occurring at $St = 0.20$, for which Δ reaches its minimum value of -1.72. The presence of a hot bias flow and heat transfer increased the maximum nega-

tive value of Δ; this is consistent with recent research [11] suggesting that heat transfer out of a flow can increase Δ and vice versa.

In this study, the acoustic absorption coefficient at frequency $St = 0.20$, denoted $\Delta_{st=0.20}$, is identified as the aeroacoustic parameter that needs optimisation. The aerodynamic performance is represented by the discharge coefficient, C_d, and the heat transfer performance by the normalised heat transfer power, $P*$, both of which depend only on the mean flow solution. The values of these three performance parameters for the straight (unmodified) hole are summarised in Table 1.

Table 1. Aeroacoustic, aerodynamic and heat transfer performance of unmodified straight hole geometry.

Geometry	$\Delta_{st=0.20}$	C_d	$\lvert P^* \rvert$
$\delta_u, \delta_d = 0$	-1.72	0.66	0.77

In order to perform an optimisation which accounts for aeroacoustic, aerodynamic and heat transfer performance, an objective function f is defined which combines all three using weighting factors α, β and γ:

$$f = \alpha\,\Delta_{st=0.20} + \beta\,C_d + \gamma|P^*| \tag{8}$$

By altering these weight factors such that they sum to unity, optimal geometries can be obtained which differently prioritise the three performances.

3. RESULTS

3.1 Optimisation of only the acoustic absorption coefficient $\Delta_{st=0.20}$

When optimisation is performed for solely the aeroacoustic performance (i.e. $\alpha = 1$, $\beta = 0$, $\gamma = 0$), the results in Figure 4 show that an orifice with a large downstream chamfer would provide the best aeroacoustic absorption performance. The mechanism of the improved performance is likely to be associated with the downstream edge being moved further from the vortex shedding path, weakening the generation of acoustic waves at the hole opening.

3.2 Optimisation of only the aerodynamic performance, C_d

When optimisation is performed for solely the aerodynamic performance (i.e. $\alpha = 0$, $\beta = 1$, $\gamma = 0$),

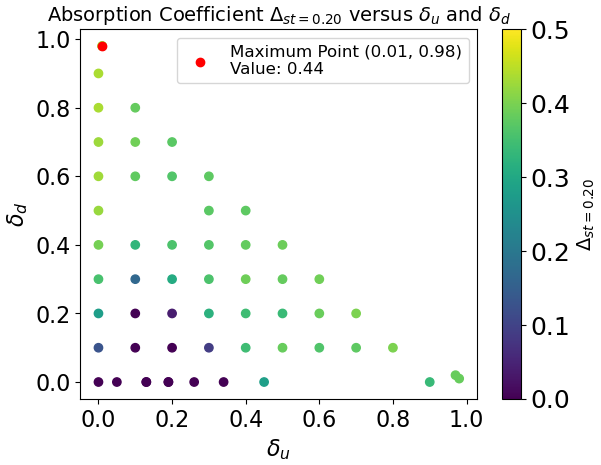


Figure 4. Acoustic absorption coefficient $\Delta_{st=0.20}$ versus δ_u and δ_d. An optimised value of $\Delta_{st=0.20} = 0.44$ was found for which $\delta_u = 0.01L_h$ and $\delta_d = 0.98L_h$.

the optimisation results in Figure 5 show that a moderate upstream chamfer of size $\delta_u = 0.19L_h$ and no downstream chamfer($\delta_d = 0$) is best. The presence of an upstream chamfer reduces flow separation at the upstream edge, which ultimately helps to alleviate the pressure drop across the hole.

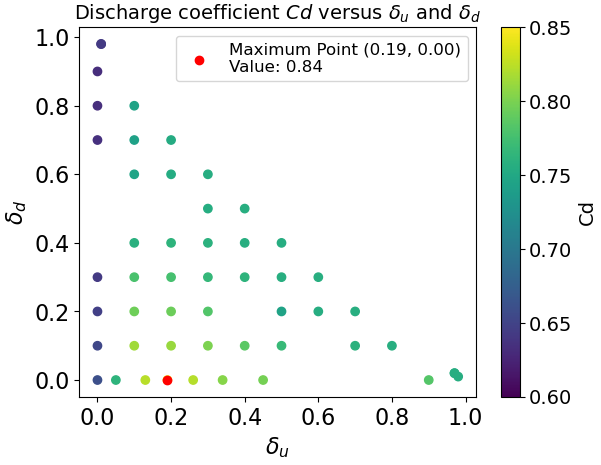


Figure 5. Discharge coefficient C_d versus δ_u and δ_d. An optimised value of $C_d = 0.84$, was found for which $\delta_u = 0.19L_h$ and $\delta_d = 0.0$.

3.3 Optimisation of only the heat transfer performance, $|P*|$

When optimisation is performed for solely the heat transfer performance (i.e. $\alpha = 0$, $\beta = 0$, $\gamma = 1$), the optimisation results in Figure 6 show that a large upstream chamfer provides the highest heat transfer. This outcome can be attributed to the larger contact area created with the flow upstream, which enhances heat transfer.

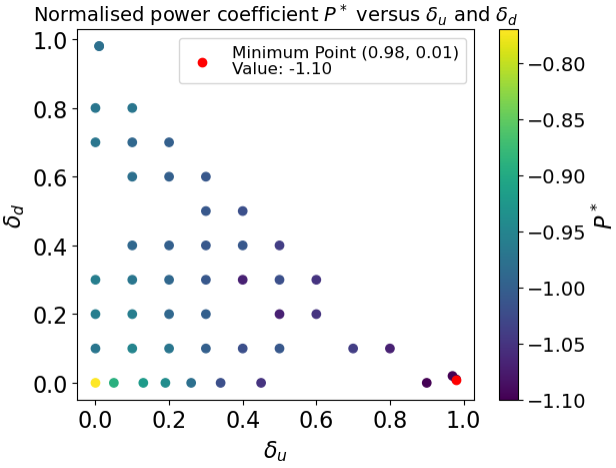


Figure 6. Normalised power coefficient P^* versus δ_u and δ_d, with the highest heat transfer performance obtained for $\delta_u = 0.98L_h, \delta_d = 0.01L_h$

3.4 Optimisation for combined objective function

For the multi-objective optimisation, the combined objective function in Equation 8, is applied using weight factors of $\alpha = 0.33$, $\beta = 0.33$, and $\gamma = 0.33$. With this combination of weight factors, the optimisation process returns an optimal geometry characterised by a large upstream chamfer, consistent with the results of P^*. This results in a high heat transfer power transfer coefficient while causing only minor reductions (compared to the best achievable) in $\Delta_{st=0.20}$ and C_d. A summary of these geometries is presented in Table 2. The aeroacoustic performance of the optimized geometry is illustrated in Figure 3, while the mean flow fields are depicted in Figure 2.

4. CONCLUSION

The present work has presented a two-step simulation method for simultaneously characterising the aeroacous-

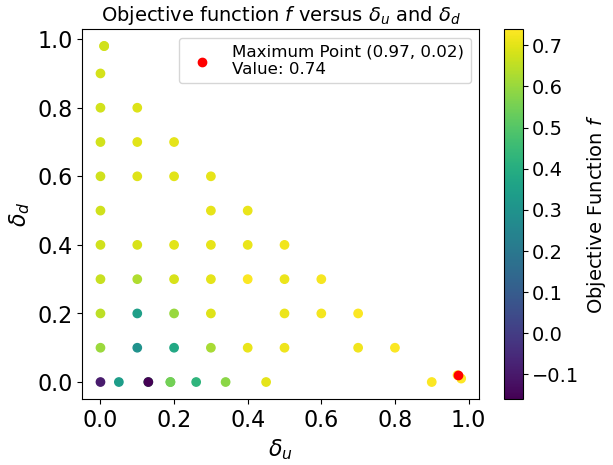


Figure 7. The combined cost function f, which accounts for aeroacoustic, aerodynamic, and heat transfer performance, δ_u and δ_d.

Table 2. Summary of the performance of the original and optimised geometries.

Geometry(δ_u, δ_d)	$\Delta_{st=0.20}$	C_d	$\lvert P^* \rvert$	f
Straight(0,0)	-1.72	0.66	0.77	-0.09
$(0.01L_h, 0.98L_h)$	0.43	0.64	0.98	0.68
$(0.19L_h, 0)$	-0.17	0.86	0.97	0.55
$(0.98L_h, 0.01L_h)$	0.38	0 .76	1.10	0.74

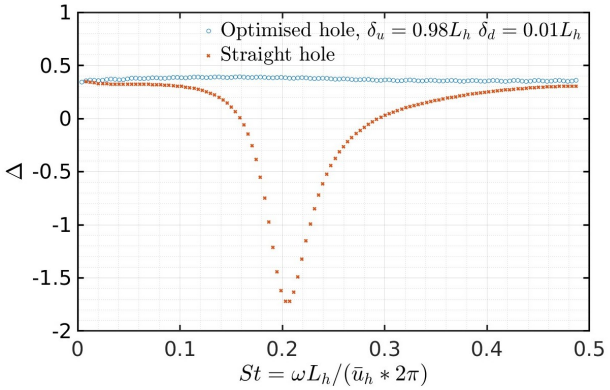


Figure 8. Absorption coefficient Δ of original straight geometry and optimised geometry under objective function f.

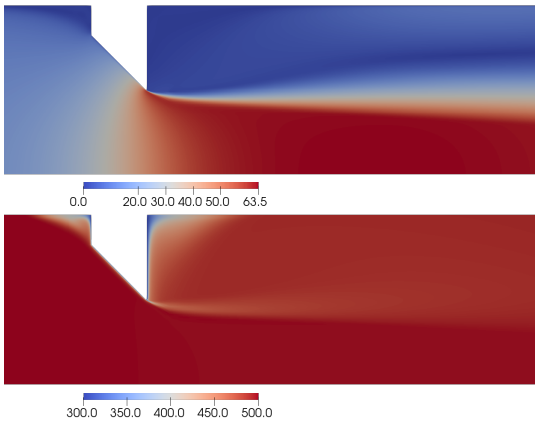


Figure 9. Magnitude of the mean flow velocity field (upper) and temperature field (lower) for the optimised hole.

tic, aerodynamic and heat transfer performance of a hole flow with heat transfer. Heat transfer through the wall of the hole is seen to accentuate the acoustic whistling effect in the absence of hole geometry changes. A Bayesian optimisation technique for optimising the chamfer lengths of 45 degree chamfers at both the hole inlet and hole outlet was then employed.

The optimisation can target the individual aeroacoustic, aerodynamic, and heat transfer performances resulting in three distinct optimal geometries. It was also shown that it is possible to apply a combined objective function which incorporates different combinations of the above three performance measures. The optimal geometry then obtained involves a large upstream chamfer which ensures good heat transfer, aerodynamic and aeroacoustic performance.

This work thus represents a step in being able to design the shapes of orifices according to acoustic, aerodynamic and heat transfer priorities, with finer geometry control being possible through additive manufacturing.

5. REFERENCES

[1] A. S. Morgans and D. Yang, "Thermoacoustic instability in combustors," *Annual Review of Fluid Mechanics*, vol. 57, pp. 9–33, 2025.

[2] X. Jing and X. Sun, "Experimental investigations of perforated liners with bias flow," *The Journal of the Acoustical Society of America*, vol. 106, p. 2436–2441, 1999.

[3] J. D. Eldredge and A. P. Dowling, "The absorption of axial acoustic waves by a perforated liner with bias flow," *Journal of Fluid Mechanics*, vol. 485, pp. 307–335, 2003.

[4] I. J. Hughes and A. P. Dowling, "The absorption of sound by perforated linings," *Journal of Fluid Mechanics*, vol. 218, pp. 299–335, 1990.

[5] J. G. von Saldern, M. E. Eck, J. P. Beuth, B. Ćosić, and K. Oberleithner, "Acoustic characteristics of impingement cooling sheets; effect of bias-grazing flow interaction on the liner impedance in a thin annulus," *Journal of Sound and Vibration*, vol. 527, p. 116818, 2022. Available online 18 February 2022, © 2022 Elsevier Ltd. All rights reserved.

[6] M. Howe, "On the theory of unsteady high reynolds number flow through a circular aperture," *Proc. R. Soc. A*, vol. 366, no. 1725, pp. 205–23, 1979.

[7] X. Jing and X. Sun, "Effect of plate thickness on impedance of perforated plates with bias flow," *AIAA Journal*, vol. 38, no. 9, 2000.

[8] P. Testud, Y. Aurégan, P. Moussou, and A. Hirschberg, "The whistling potentiality of an orifice in a confined flow using an energetic criterion," *Journal of Sound and Vibration*, vol. 325, pp. 769–780, Sept. 2009.

[9] J. Su, J. Rupp, A. Garmory, and J. F. Carrotte, "Measurements and computational fluid dynamics predictions of the acoustic impedance of orifices," *Journal of Sound and Vibration*, vol. 352, p. 174–191, 2015.

[10] R. Lacombe, S. Föll, G. Jasor, W. Polifke, Y. Aurégan, and P. Moussou, "Identification of aero-acoustic scattering matrices from large eddy simulation: application to whistling orifices in duct," *Journal of Sound and Vibration*, vol. 332, pp. 5059–5067, 2013.

[11] S. R. Yeddula, R. Gaudron, and A. S. Morgans, "Acoustic absorption and generation in ducts of smoothly varying area sustaining a mean flow and a mean temperature gradient," *Journal of Sound and Vibration*, vol. 515, p. 116437, sep 2021. Available online 16 September 2021.

[12] D. Yang and A. S. Morgans, "Asemi-analytical model for the acoustic impedance of finite length circular holes with mean flow," *Journal of Sound and Vibration*, vol. 384, p. 294–311, 2016.

[13] J. Guzmán-Iñigo, D. Yang, H. G. Johnson, and A. S. Morgans, "Sensitivity of the acoustics of short circular holes with bias flow to inlet edge geometries," *AIAA Journal*, vol. 57, no. 11, pp. 4835–4844, 2019.

[14] J. Guzmán-Iñigo and A. S. Morgans, "Designing the edges of holes(with bias flow) to maximise acoustic damping," *Journal of Sound and Vibration*, vol. 575, no. 11, p. 118224, 2024.

[15] A. Kierkegaard, S. Boij, and G. Efraimsson, "A frequency domain linearized navier–stokes equations approach to acoustic propagation in flow ducts with sharp edges," *The Journal of the Acoustical Society of America*, vol. 127, pp. 710–719, 2010.

[16] J. Guzmán-Iñigo and A. S. Morgans, "Influence of the shape of a short circular hole with bias flow on its acoustic response," in *28th AIAA/CEAS Aeroacoustics Conference*, (Southampton, UK), June 2022.

[17] B. Shahriari, K. Swersky, Z. Wang, R. P. Adams, and N. de Freitas, "Taking the human out of the loop: A review of bayesian optimization.," *Proceedings of the IEEE*, vol. 104, no. 1, p. 148–175, 2016.

[18] M. T. Morar, *Bayesian Optimisation over Mixed Parameter Spaces*. PhD thesis, University of Manchester, Manchester, United Kingdom, 2021. Doctoral Dissertation. Engineering and Physical Sciences. https://pure.manchester.ac.uk/ws/portalfiles/portal/194689010/FULL_TEXT.PDF.

[19] R. Gaudron, J. Guzmán Iñigo, and A. S. Morgans, "Variation of acoustic energy across sudden area expansions sustaining a subsonic flow," *AIAA Journal*, vol. 6, no. 1, 2023.

[20] I. D. J. Dupere and A. P. Dowling, "The use of helmholtz resonators in a practical combustor," *Journal of engineering for gas turbines and power*, vol. 127, no. 2, p. 268–275, 2005.

[21] N. Hay and A. Spencer, "Discharge coefficients of cooling holes with radiused and chamfered inlets," *Journal of Turbomachinery*, vol. 114, no. 4, p. 701–706, 1992.

[22] M. S. Alnæs, J. Blechta, J. Hake, A. Johansson, B. Kehlet, A. Logg, C. Richardson, J. Ring, M. E. Rognes, and G. N. Wells, "The FEniCS project version 1.5," *Archive of Numerical Software*, vol. 3, no. 100, pp. 9–23, 2015. Received: May 28, 2015; Final revision: December 1, 2015; Published: December 7, 2015.

[23] J. Guzmán-Iñigo, D. Yang, R. Gaudron, and A. S. Morgans, "On the scattering of entropy waves at sudden area expansions," *Journal of Sound and Vibration*, vol. 540, p. 117261, 2022.

[24] scikit-optimize developers, "scikit-optimize: Sequential model-based optimization in python," 2021.

[25] S. Torbati, A. Daneshmehr, H. Pouraliakbar, M. Asgharian, S. H. Ahmadi Tafti, D. Shum-Tim, *et al.*, "Personalized evaluation of the passive myocardium in ischemic cardiomyopathy via computational modeling using Bayesian optimization," *Biomech. Model. Mechanobiol.*, 2024. Available online 2024.

DOI: 10.61782/fa.2025.0407

FORUM ACUSTICUM EURONOISE 2025

FLOW-ACOUSTIC COUPLING IN VORTEX WHISTLE

Muriel Amielh[1*] **Daniel Mazzoni**[1] **Yann Pley**[1]
Jean-Jacques Lasserre[2]
[1] Aix Marseille Univ, CNRS, Centrale Méditerranée, IRPHE UMR 7342, 13384, Marseille, France
[2] Dantec Dynamics AS, DK-2740 Skovlunde, Denmark

ABSTRACT

The acoustic source we study is a vortex whistle composed of three parts of geometry and dimension similar to that of a bottle. The device consists of a cylindrical cavity with a circular base, a single fluid inlet tangential to the base of the cylinder and a cylindrical fluid outlet downstream which is a cylinder with a radius smaller than that of the cavity. The fluid (here air) entering the cavity generates a circular motion in the cavity and in the downstream cylinder. This device produces a sound with a dominant frequency. The frequency of the sound is controlled by the fluid flow rate. The characterization of the fluid vortex is performed in air by stereo-PIV (Particle Image Velocimetry), a laser optical diagnostics, resolved temporally and spatially, combined with acoustic measurements by microphone. In the exit section of the whistle, the center of the vortex circulates with a precession motion. From a decomposition into eigenmodes of the velocity field, the contributions to this motion are specified. The directivity diagram is established by calculating the Rayleigh integral based on the measured velocity fluctuations. The coupling between the acoustic field and the flow dynamics is thus highlighted and analyzed.

Keywords: *aero-acoustics, dipole source, time resolved stereo-PIV, proper orthogonal decomposition.*

**Corresponding author*: *muriel.amielh@univ-amu.fr.*
***Copyright**: ©2025 First author et al. This is an open-access article distributed under the terms of the Creative Commons Attribution 3.0 Unported License, which permits unrestricted use, distribution, and reproduction in any medium, provided the original author and source are credited.*

1. INTRODUCTION

The Vortex Whistle (Vonnegut, 1954 [1]) is a device generating sound by rotating a vortex within a cylindrical section with a tangential inlet. Vonnegut was the first to explain that the sound frequency generated at the outlet of the device is proportional to the fluid flow rate. At the outlet of the device, the fluid movement becomes unstable and generates a vortex agitated by a precessional movement. This instability is the cause of the sound emitted and an empirical formula in which the sound frequency varies according to the inlet-outlet pressure gradient and the dimensions of the device was proposed. His experiments showed that the Vortex Whistle works equally well in air and water. In 1963, Chanaud [2] sought to demonstrate the relationship between the vortex generated by instability and the sound frequency. His experimental work allowed him to explain that the sound frequency is the same as the frequency of the vortex's precessional motion at the device's outlet. Both Vonnegut and Chanaud mentioned the importance of considering friction losses in order to establish a right relation between frequency and flow rate, this being taken into account through a fitting empirical parameter in the law proposed by Vonnegut.
In the 2000s, applications for the Vortex Whistle emerged. For example, in 2013, Di et al. [3] suggested using it as a flow meter, given that frequency varies linearly with flow rate. In 2016, the device began to be used as a spirometer for medical applications [4].
In 2020, Kristiansen et al. [5] proposed a model based on the conservation of angular momentum, including friction losses. This model predicts the frequency as a function of the flow rate and device dimensions. The agreement was obtained with experiments in air and water for two different Vortex Whistles, respectively. The vortex precession at the outlet section of the Whistle was quantified by velocity

measurements by PIV ($2D-2C$) associated to acoustics measurements by microphone in air. A technique of phase averaging was performed in order to reconstruct the temporal dynamic of the vortex since the PIV was performed at 10 Hz whereas the characteristic flow frequency is in the range $200-1500Hz$. Their experiments allow them to characterize the acoustic radiation of the source, which they find similar to that of a dipole, confirming the previous result of Chanaud [2].
The objective of the present study is to identify the main contribution of the flow dynamics to sound generation. The detailed characterization of the vortex at the Vortex Whistle outlet is performed in air by fast stereo-PIV (Particle Image Velocimetry, $2D-3C$), a laser optical diagnostic, resolved temporally and spatially, combined with acoustic measurements by microphone. The experimental setup is described in Section 2. The velocity and acoustics results are analyzed in Section 3. By considering the helicoidal movement in the two cylinders constituting the Vortex Whistle, some improvements of the model initially developed in [5] are proposed. A Proper Orthogonal Decomposition is performed on the velocity field in order to highlight the cyclic movement associated to the dominant frequency for a given flow rate (Section 4).

2. EXPERIMENTAL SETUP

The geometry of the Vortex Whistle is presented in (Fig. 1). The main core of the Vortex Whistle with air tangential inlet is in aluminum, it is quite long compared to those studied by [2] and [5] with a length-to-diameter ratio of $L_c/D_c = 3.5$ (Tab. 1). For the nozzle, designed in plexiglass, this ratio is $L_o/D_o = 3.0$. The sudden reduction between these two parts is characterized by a diameter ratio $D_c/D_o = 2.5$. The surface of the internal wall is considered smooth.

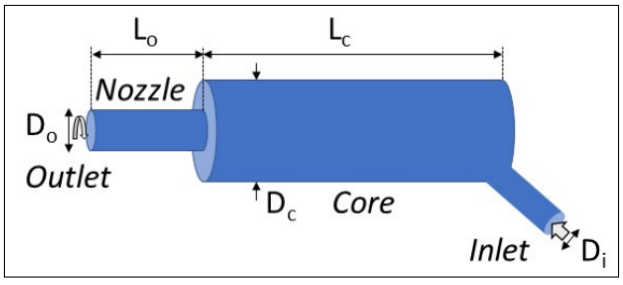


Figure 1. Geometry of the Vortex Whistle.

Table 1. Dimensions of the Vortex Whistle.

Geometry	Dimension
Inlet diameter, $D_i = 2R_i$	$14mm$
Outlet diameter, $D_o = 2R_o$	$20mm$
Oulet pipe length , L_o	$60mm$
Core diameter, $D_c = 2R_c$	$50mm$
Core length, L_c	$175mm$

Stereo-PIV images are acquired by a Dantec Dynamics system (RapiDO) that includes two T4040 SpeedSense Phantom high-speed cameras (2560×1664 $pixels$, 12 bits), and a double pulsed laser (Fig. 2). The pulsed laser is a Photonics laser (527nm, $2 \times 30mJ$ at a nominal 1kHz repetition rate). The DynamicStudio software controls synchronization of image acquisition. A laser sheet generator constituted of several suited lenses is installed at the end of the optical arm so that a flow field of $75.5 \times 49mm^2$ is illuminated. Stereo-PIV needs a depth calibration in order to correctly measure the U_z velocity component. This is performed with five calibration images of a motorized target positioned at $Z = 200\mu m$, $100\mu m$ and $0\mu m$, the laser sheet center. PIV images are acquired at a $4kHz$ rate and the time delay between two associated pulses is $5\mu s$. The flow is seeded by olive oil droplets of $2-3\mu m$ diameter introduced in the air circuit upstream the inlet of the Vortex Whistle.

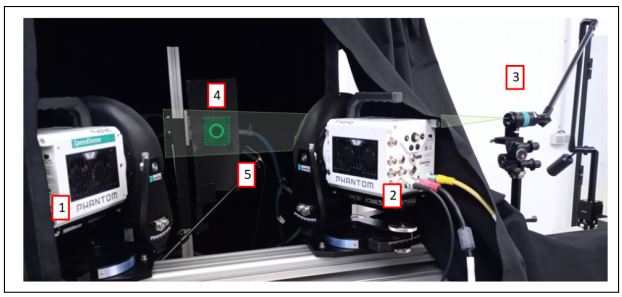


Figure 2. Set up of the nozzle outlet (4) flow investigation by high-speed stereo-PIV including two cameras (1 and 2), a laser sheet generator (3) and a microphone (5).

The spatial resolution is $\delta_x = \delta_y = 472\mu m$. The (O, X, Y, Z) coordinate system is centered on the exit cross-section on the nozzle where the investigation is fo-

cused. The three instantaneous components ($3C$) of velocity (U_x, U_y, U_z) are measured on the plane ($2D$) $Z = 0$ specified in (Fig. 2) by a green dotted line square. The velocity components in polar coordinates are (U_r, U_θ, U_z). 4000 instantaneous velocity fields are acquired for each flow conditions during $1s$. In the same time of PIV measurements, the acoustic pressure is measured by a microphone (1/4", GRAS) located at $(83mm, -63mm, 60mm)$ during $10s$ at a $25.6kHz$ sample frequency. Statistics and other post-processing on velocity fields and acoustic signals are performed by homemade codes developed in Matlab.

3. FLOW CHARACTERIZATION

The whistling is clearly detected by spectral analysis of acoustic pressure measured by microphone in the range $135 - 1200Hz$. Five flow conditions with velocity-pressure measurements are performed for the whistling frequencies $F_w = 135$, 410, 520, 620, 720 Hz. The flow rates q associated to these frequencies F_w are deduced from integration of the U_z velocity component over the exit cross-section of the nozzle. A summary of the flow conditions is given in Tab. 2.

Table 2. Flow conditions. $\tilde{U} = q/(\pi R_o^2)$, $\omega_o = 2\pi F_w$, $\overline{U}_z^* = \overline{U}_{z,max}/\tilde{U}$, $\overline{U}_\theta^* = \overline{U}_{\theta,max}/(\omega_o R_o)$, $S_w = \overline{U}_{\theta,max}/\overline{U}_{z,max}$.

F_w	$\tilde{U}$	$\omega_o R_o$	$\overline{U}_z^*$	$\overline{U}_\theta^*$	S_w
(Hz)	(m/s)	(m/s)			
135	2.15	3.92	1.48	0.474	0.583
410	12.5	25.8	1.58	0.523	0.682
520	15.3	32.8	1.59	0.500	0.674
620	18.0	39.0	1.57	0.500	0.689
720	19.8	45.2	1.58	0.473	0.684

Fig. 3 presents the mean velocity field at the section $Z = 0$. The rotating movement is in agreement with a tangential inlet located in the quarter ($X > 0, Y < 0$). In the outer region, for radius $R > 10mm$, the velocity vectors orientations highlight the external flow entrainment. This external part of the flow is not considered for the flow rate calculation.

The $\overline{U}_\theta$ (shown in Fig.4) and $\overline{U}_z$ mean velocity components are not maximum in the same regions of the flow,

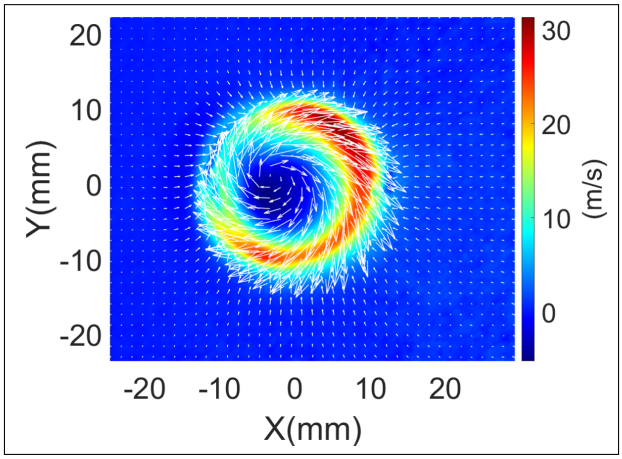


Figure 3. Mean velocity for $F_w = 720Hz$: ($\overline{U}_r$, $\overline{U}_{theta}$) vectors and $\overline{U}_z$ contours (see colorbar).

their maximum occur on rings centered on a radius of $8.3mm$ and $9.5mm$, respectively and independently of the flow conditions investigated here by PIV. In the quarter ($X < 0$, $Y > 0$) where $\overline{U}_z$ presents a minimum on its ring, it corresponds to a local maximum $\overline{U}_{\theta,max}$ of $\overline{U}_\theta$. The local maximum of $\overline{U}_z$ is named $\overline{U}_{z,max}$. Thus, the averaged velocity field is not axisymmetric. The similar non-dimensionalized values of $\overline{U}_\theta^*$ and $\overline{U}_z^*$ and of the swirl number S_w gathered in Tab. 2 for different F_w suggest a regime in similarity in the range $410 - 720Hz$.

Negative values of $\overline{U}_z$ in the center of this ring are significative of a flow reverse inside the nozzle due to the high level of swirl. The mean vortex center observed in Fig. 3 is in the region of negative $\overline{U}_z$. However, this mean position must be considered carefully, since actually, the instantaneous vortex follows a precession movement so that it is never at this position as shown in Fig. 5. The mean trajectory of the vortex center is shifted from the nozzle cross-section center and is located in the quarter ($X < 0, Y > 0$).

Thanks to the high speed PIV system, the instantaneous three velocity components are acquired at a sufficient high frequency in order to allow a right spectral analysis. Fig. 6 highlights the presence of the same predominant frequency in the velocity component signals extracted at the position ($X = 5mm$, $Y = 5mm$, $Z = 0mm$) than in the acoustic pressure signal measured by microphone according to the frequency resolution of 3.91 Hz for velocity and 1.56 Hz for acoustics. This

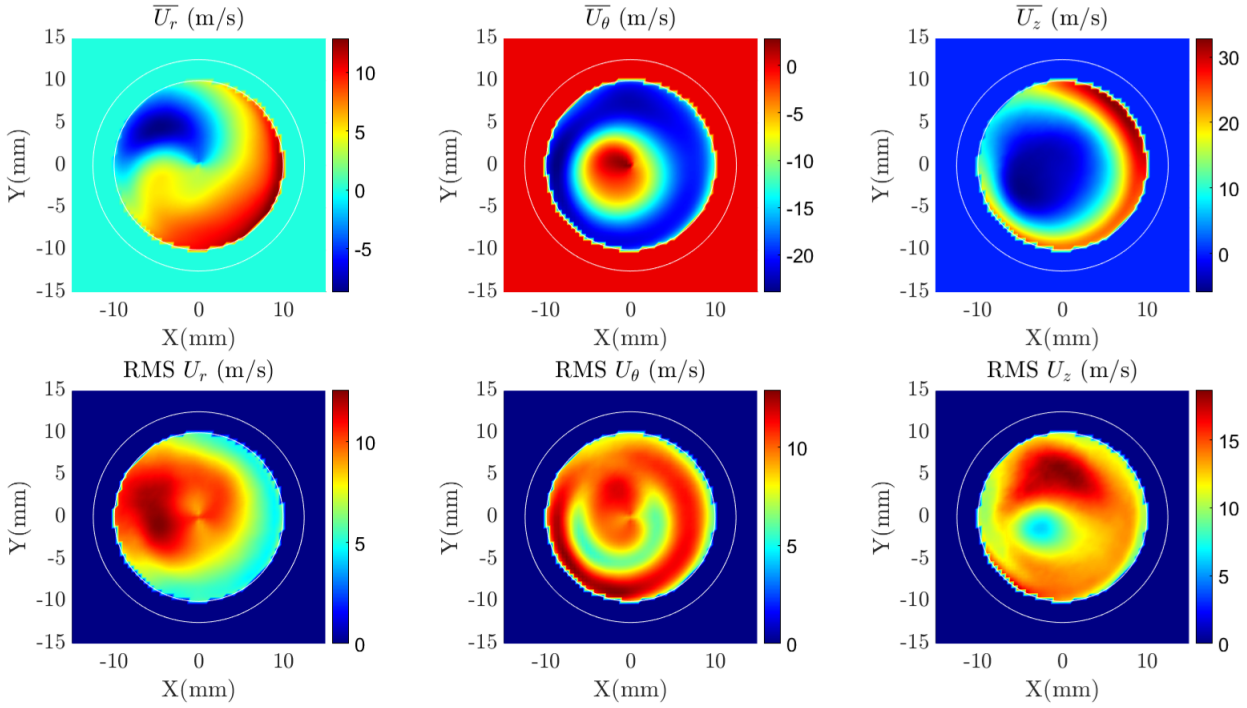


Figure 4. Velocity statistics in the exit cross-section of the nozzle from stereo-PIV measurements. Mean velocity components $\overline{(.)}$ (up) and velocity root mean square (RMS, down) for $F_w = 720Hz$.

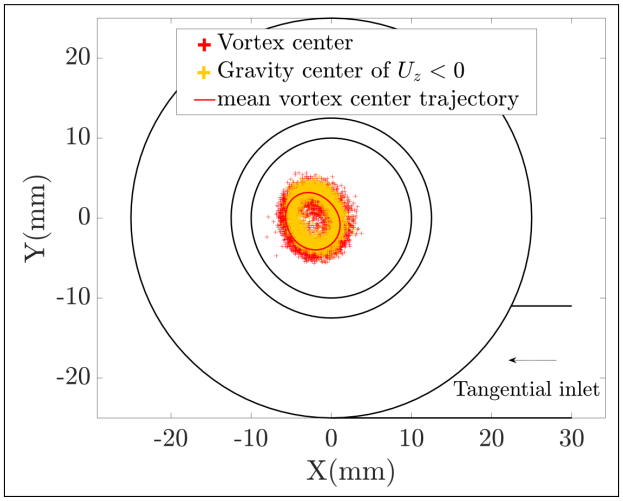


Figure 5. Instantaneous vortex and negative U_z region center positions detected from the 4000 PIV fields for $F_w = 720Hz$.

concordance is true in the whole velocity field and for all investigated flow rates.

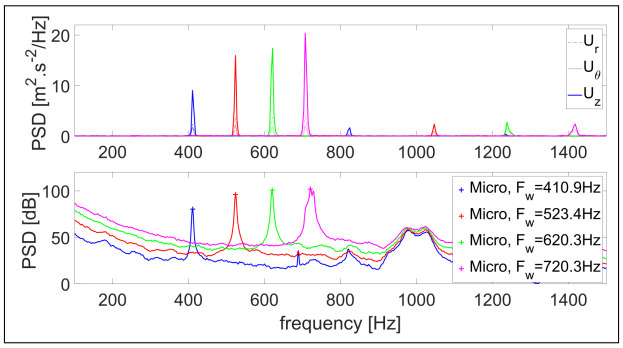


Figure 6. Spectral analyses of velocity components extracted at ($X_e = 5mm$, $Y_e = 5mm$, $Z_e = 0mm$) and pressure for different flow rates.

The linear dependency between flow rate q and whistling frequency F_w is confirmed as usually observed

for Vortex Whistle ([1, 2, 5]) as shown in Fig. 7. The model proposed by Kristiansen et al. [5] is compared with the present experimental results. Their relation between the whistling frequency F_w and the volume flow rate q was deduced from the balance of the kinetic momentum. The expression obtained without wall friction was :

$$F_w = \frac{q}{(\pi R_i R_o)^2}\,(R_c - R_i) \tag{1}$$

When considering the wall friction along the L_c and L_o lengths of the core and the nozzle respectively, the expression becomes:

$$F_w = q\frac{\sqrt{1 + 16\dfrac{(C_{F_c}L_c + C_{F_o}L_o)\,(R_c - R_i)}{R_i^2}} - 1}{8\pi^2\,(C_{F_c}L_c + C_{F_o}L_o)\,R_o^2} \tag{2}$$

where C_{F_c} and C_{F_o} are the friction coefficients in the core and the nozzle.

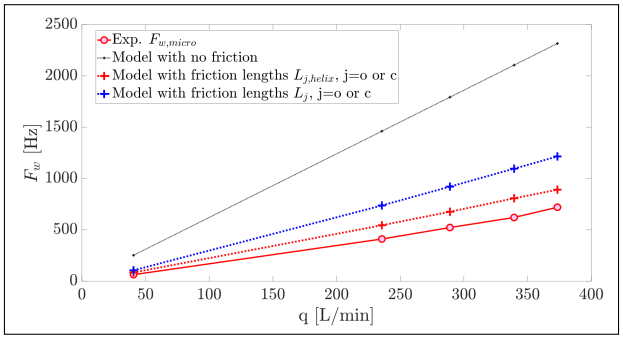


Figure 7. Whistling frequency vs flow rate. Adjustment of the model [5] by considering an elongation of friction length due to the helical movement inside the core and the nozzle.

While the model was in a good agreement with the results obtained by Kristiansen et al. [5] for Vortex Whistle with $L_c/D_c = 1.76$ and 1.94, the agreement is not so good with the present experimental results because the present frequencies are lower than those expected by the original model. The decrease of whistling frequencies for similar flow rate but with larger ratio length/diameter was also observed by Chanaud when varying L_o/D_o while keeping the same L_c/D_c. In the present experiment, the ratio $L_o/D_o = 3$ is smaller than those of the vortex whistles of Kristiansen et al. [5] where $L_o/D_o = 3.42$ and 3.85 while the D_i/D_c ratio are quite similar: respectively 0.28 here, and 0.30 and 0.26 for [5]. Thus, the lower experimental frequencies is not due to the variation of the parameter L_o/D_o, but probably to the larger ratio L_c/D_c = 3.5 for the present experiment. It means that friction is probably not sufficiently taken into account in the model. A proposed improvment of the model is to consider that a fluid particle will follow a helical trajectory both in the core and the nozzle, so that the friction length L_j ($j = o$ or c) to be considered in the model will become the length of the helix in each part of the Vortex Whistle by considering the translation velocity $q/\pi R_j^2$ and the rotation velocity $\omega_j R_j$:

$$L_{j,helix} = \frac{\pi R_j^2 L_j \sqrt{(\frac{q}{\pi R_j^2})^2 + \omega_j^2 R_j^2}}{q} \tag{3}$$

Results presented in Fig. 7 show a better agreement with this proposed model, but some differences remain, that can not be fully solved with this simple model.

4. FLOW FOOTPRINT ON ACOUSTICS

4.1 POD of the velocity field

In order to typify the effect of flow fluctuations on acoustics, the coherent structures that contribute to the dynamics are sought. The POD (Proper Orthogonal Decomposition) [6] is a right tool for the analysis of the fluctuating part of the velocity field. The POD principle is based on the decomposition on a basis of eigen modes sorted by their energetic contribution to the quantity of interest, here the velocity components. The decomposition is performed on 4000 uncorrelated snapshots of the three velocity components (U_r, U_θ, U_z), which determines a number of modes equal to the number of realizations. The interest is here focused on the ten first energetic modes.

Fig. 8 illustrates the cumulative energy for modes 1 to n when non-dimensionalized by the cumulative energy for mode 1 up to mode 10. When considering the cumulative energy of the two first modes (condition named POD [1 2] in Fig. 9 for e.g.), almost 50% of the cumulative energy of the 10 first modes (POD [1 ... 10]) is reached.

A spectral analysis made on the U_z signal extracted at the position ($X_e = 5mm$, $Y_e = 5mm$, $Z_e = 0mm$) from the PIV field measured for $F_w = 720Hz$ is presented in Fig. 9. The power spectral density (PSD) is compared with different POD reconstructed signals

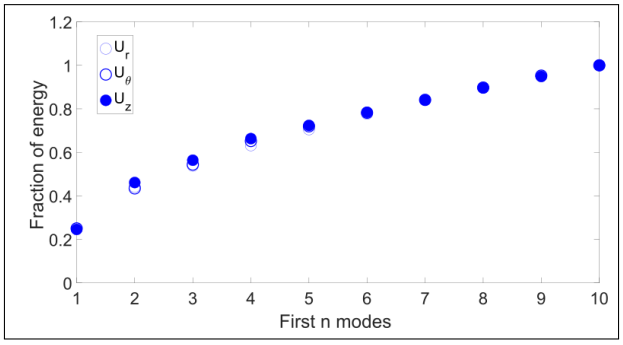


Figure 8. Fraction of energy captured by POD according to the ($n \leq 10$) considered modes for $F_w = 720Hz$.

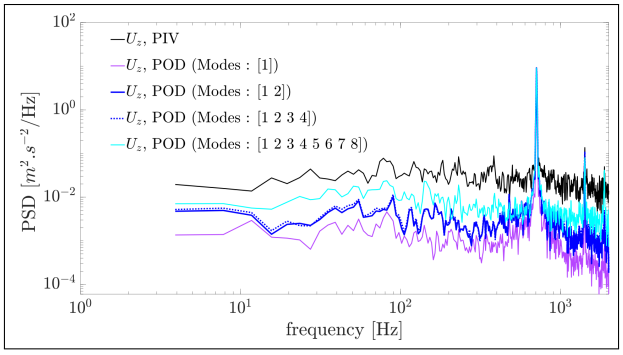


Figure 9. Spectral analysis of PIV and POD velocity signals at the position ($X_e = 5mm$, $Y_e = 5mm$, $Z_e = 0mm$) for $F_w = 720Hz$.

of U_z including only the first mode (POD [1]) up to eight modes ([POD [1...8]). For all the reconstructed POD signals, the predominant frequency F_w is preserved while the noise energy level is reduced. The energy related to the predominant peak is also respected since $PSD = 9.29m^2/s^2/Hz$ for the PIV and 9.16 and $9.11m^2/s^2/Hz$ for POD [1 2] and POD [1 2 3 4], respectively. Note that for POD [1] the PSD is only $3.88m^2/s^2/Hz$. Since no great difference in energy level is observed between the POD reconstructed PSD for POD [1 2] and POD [1 2 3 4], the rest of the following POD analyses will be based on the two first modes.

An example of velocity time series reconstitution by POD [1 2] at the position (X_e, Y_e, Z_e) is given in Fig. 10 (right) for the three velocity components (U_r, U_θ, U_z). The harmonic behaviour of the velocity signals is highlighted by POD while the phase is respected. In the left part of the figure is presented an instantaneous velocity field for (U_r, U_θ) where only one vector out of three is plotted for the sake of readability. The vector field obtained from POD is obviously smoothed and the instantaneous position of the vortex center is clearly detected.

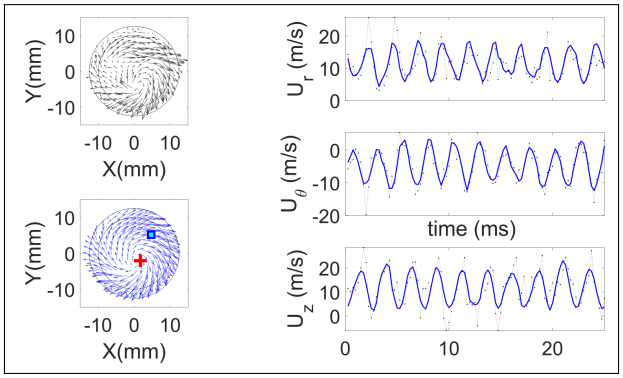


Figure 10. Comparison between PIV (black) measurements and POD analysis (blue) with the two first modes [1 2] for $F_w = 410Hz$. Instantaneous velocity vector (U_r,U_θ) at the exit cross-section of the nozzle (left). Extracted velocity signals (U_r, U_θ, U_z) at the position ($X_e = 5mm$, $Y_e = 5mm$, $Z_e = 0mm$) located by a blue square on the left figure (right). The red cross indicates the vortex center.

4.2 Directivity diagram

Since the signal $U_z(X, Y, Z, t = time)$ is available in the whole exit cross-section of the nozzle, the next step is to check if it is possible to estimate the acoustic pressure level and the directivity diagram from the POD [1 2] reconstruction. This estimation is performed by Rayleigh integral applied in the time domain, that can be written:

$$P(M,t) = \rho \iint_{\Sigma} \frac{1}{2\pi r_{MS}} \frac{dv_n(S, t - \frac{r_{MS}}{c})}{dt} dS \qquad (4)$$

where c is the sound speed, Σ is the source area and $v_n = U_z$ is the fluctuating velocity component normal to the exit cross-section of the nozzle. M is an observation point situated at a radius R_M from the center O of the nozzle exit section and at the angle ϕ where the contribution to the directivity diagram will be calculated. Fig. 11 illustrates the geometry for this pressure model. The red

radius is the location of the observation points M. dS (white square) is a surface element centered on the source point S located on the exit cross-section of the nozzle colored in blue in Fig. 11. The Rayleigh integral is calculated for $R_M = 0.5m$ using POD [1 2] reconstruction of U_z for $F_w = 410Hz$ and $720Hz$.

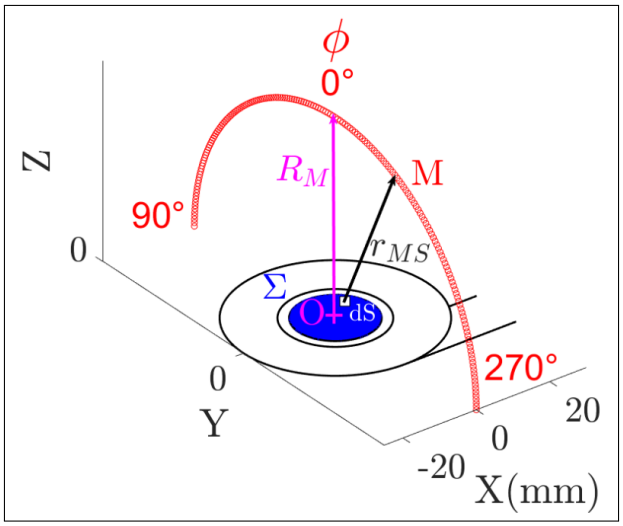


Figure 11. Angular positions of microphone (in red) for diagram directivity measurements.

The results are compared to measurements made at the same distance R_M with the microphone previously described (See Section 2) for three whistling frequencies $F_w = 606, 700$ and $725Hz$. For this experiment, the Vortex Whistle exit cross-section was installed flush with a rigid panel of large dimensions $1.5m \times 2.5m$. The results are presented as a directivity diagram in Fig. 12. The values of sound pressure level are overestimated by Rayleigh integral calculated with POD modes comparatively to experiments and no minimum is obtained at ϕ=0°. Contrariwise, such minimum of radiation at 0° angle, the main outlet flow direction, and larger values towards 90° and 270° are observed with experimental data, it could be associated to a dipole radiation as previously suggested by [2] and [5]. However the radiation is not symmetric against angles, a larger radiation is detected for the three experimental frequencies F_w in the angle range $300 - 330$, this is probably to be associated to the asymmetry of the real flow. Another proposed approach is to modeled the $U_z(R, \theta, z, t)$ by a sinus whose amplitude $A(R)$ is the radial profile of the experimental U_z root mean square deduced from PIV statistics post-process (See Fig.4), multiplied by $\sqrt{2}$. The proposed formulation is :

$$U_z(R, \theta, z, t) = A(R)\ sin(\omega_o\, t + \theta) \qquad (5)$$

The Rayleigh integral is calculated with this sinus model for $F_w = 720Hz$. A comparison between dU_z/dt calculated from POD modes or this sinus model is presented in Fig. 12 Due the symmetry of the sinus model, the typical radiation of a dipole is obviously obtained, but it is interesting to note that the maximum sound pressure levels are in good agreement with the experimental results as seen in the angle range 30-180°.

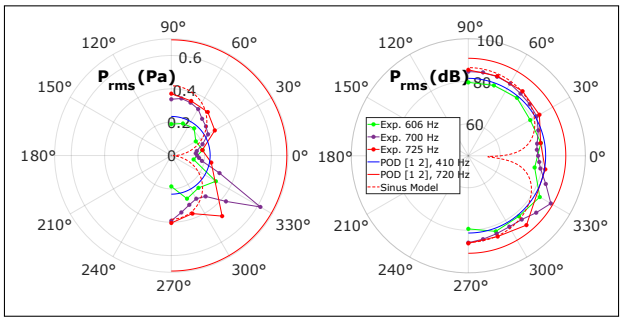


Figure 12. Directivity diagram in Pa (left) and in dB (right). The angle ϕ=0° corresponds to measurements on the axis on the outflow side.

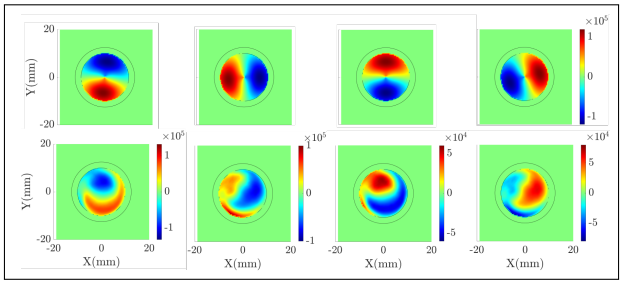


Figure 13. dU_z/dt with U_z estimated by sinus model (up) and POD (modes [1 2]) (down) for $F_w = 720Hz$ at four typical instants.

In order to check if acoustic radiation of the present experimental source embraces other characteristics of a dipole, one analyses the SPL level according to the whistling frequency. By considering that the sound power level Lw at distance R_S from the sound source, located in free field positioned over a rigid plane, can approximately

related to sound pressure level (SPL) by the relation:

$$Lw = SPL + 10log10(\frac{2\pi R_M^2}{S_0}) \quad (6)$$

where $S_0 = 1m^2$ and R_M is the radius of a large hemisphere enclosing the source, a study of the SPL will give some information on Lw. Fig. 14 illustrates the increase of SPL with the whistling frequency F_w for the acoustic pressure measured by microphone at the angle ϕ=30°. Comparisons are made with SPL calculated for the microphone signal filtered with a narrow pass-band filter around F_w and also with the SPL deduced from the Rayleigh integral on POD [1 2]. The typical slope 6 of a sound power level for a dipole is rather in a good agreement with the present results.

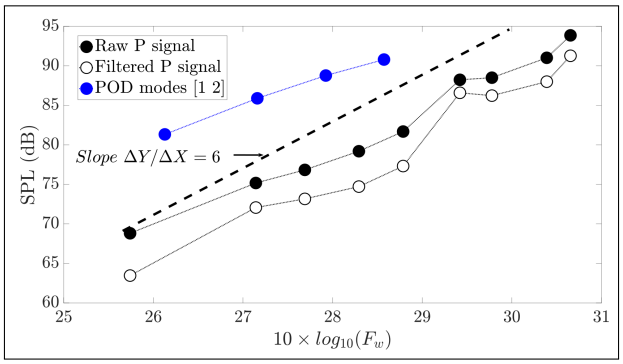


Figure 14. Sound pressure level *vs.* whistling frequency.

5. CONCLUSION

The flow dynamics in the exit section of a Vortex whistle was characterized by high-speed stereo-PIV velocity measurements combined with acoustic pressure measurements by microphone. Using POD, the spatio-temporal organization of the flow was highlighted. The main characteristics of Vortex Whistles previously studied in the literature were found, the dynamics of the velocity field and the acoustic pressure being interdependent. However, it seems that the length of the main cylinder influences the characteristics of the acoustic source that the Vortex Whistle simulates. If the acoustic levels and their radial distribution remain close to that typical of an acoustic dipole, the decentering of the precession movement seems to induce an additional complexity that a simple radiation model does not fully describe.

6. ACKNOWLEDGMENTS

The IRPHE technical staff is acknowledged for the design of the Vortex Whistle.
The high-speed stereo PIV system RapiDO is a funded project of A*Midex (Aix Marseille University).

7. REFERENCES

[1] B. Vonnegut, "A vortex whistle," *The Journal of the Acoustical Society of America*, vol. 26, no. 1, pp. 18–20, 1954.

[2] R. C. Chanaud, "Experiments concerning the vortex whistle," *The Journal of the Acoustical Society of America*, vol. 35, pp. 953–960, 1963.

[3] Y. Di, C. Gerhardy, and W. K. Schomburg, "Vortex whistles employed as remote micro flow sensors," *Flow Measurement and Instrumentation*, vol. 34, pp. 11–18, 2013.

[4] S. Kaiser, A. Parks, P. Leopard, J. C. Charlie Albright, M. Goel, D. Nassehi, and E. C. Larson, "Design and learnability of vortex whistles for managing chronic lung function via smartphones," in . *UbiComp '16*, (Heidelberg Germany), 2016.

[5] U. Kristiansen, M. Amielh, and D. Mazzoni, "On the sound production in vortex whistle," in *e-Forum Acusticum, 9th Edition*, (Lyon, France), 2020.

[6] G. Berkooz, P. Holmes, and J. Lumley, "The proper orthogonal decomposition in the analysis of turbulent flows," *Annual Review of Fluid Mechanics*, vol. 25, p. 539–575, 1993.

DOI:

Main theme: A07 Flow Acoustics

Session A07.05 Methods for advanced computational aeroacoustics

Chair(s): S. Schoder, G. Bernardini, F. Avallone

DOI:

Main theme: A07 Flow Acoustics

Session A07.06 Modern experimental techniques in aeroacoustics

Chair(s): S. Jacob, M. Jacob

DOI: 10.61782/fa.2025.0377

FORUM ACUSTICUM EURONOISE 2025

EXPERIMENTAL INVESTIGATION OF ROTOR SHIELDING EFFECTS ON AXIAL FLOW FAN USING AN INTERSTAGE ARRAY

Manju ADHIKARY[1,2*] **Antonio PEREIRA**[1]
Marc JACOB[1] **Ricardo BLAZQUEZ-NAVARRO**[2]
Johan THISSE[2]
[1] Ecole Centrale de Lyon, CNRS, Universite Claude Bernard Lyon 1, INSA Lyon, LMFA, UMR5509, 69130, Ecully, France
[2] AIRBUS OPERATIONS SAS, 316 Route de Bayonne, 31060 Toulouse, France

ABSTRACT

An experimental investigation is performed on a small-scale axial flow fan in a ducted configuration to observe rotor shielding effects. The study focuses on spinning azimuthal modes incident on a rotor-stator layout in the presence of flow. The sources considered are a ring of loudspeakers generating a particular spinning mode. Along with the reflection and modified transmission, several phenomena like mode scattering and mode trapping are expected. An array of 64 microphones is employed in the interstage, i.e. between the rotor and stator rows. The microphones are arranged in two rings and two spirals on the duct surface using a remote probe configuration and its axial extent is 40mm. The interstage array helps in providing a detailed understanding of the noise propagation between the rotor-stator rows. The modal decomposition is based on a Bayesian inversion method. Both the frequency dependence and the spin direction are examined at various engine operating points.

Keywords: rotor shielding, interstage array, experimental studies, axial fan

**Corresponding author*: manju.adhikary@ec-lyon.fr.
Copyright: *©2025 Manju ADHIKARY et al. This is an open-access article distributed under the terms of the Creative Commons Attribution 3.0 Unported License, which permits unrestricted use, distribution, and reproduction in any medium, provided the original author and source are credited.*

1. INTRODUCTION

Despite considerable advancement in the recent years to reduce noise emission by aircraft, fan noise remains to be one of the major contributors of noise generated by aircraft engines during all phases of operation. Several studies have been conducted to model the sound generation mechanisms in an engine and the free-field propagation [1, 2]. However, the study of noise transmission inside turbofan engines poses some specific challenges owing to the presence of complex geometries and heterogenous flow, and in turn, multiple noise generation and propagation mechanisms. One of the main noise source mechanisms is the rotor-wake and stator interaction noise, that generates Tyler and Sofrin modes [3]. The noise radiates in both upstream and downstream directions. A deeper understanding of the noise transmission through the rotor blades is therefore crucial for enabling more accurate assessments of noise.

One of the first analytical models to study noise transmission through static rotor blades was proposed by Kaji and Okazaki [4, 5] known as 'Cascade theory'. The blades are modelled as a cascade of finite chord length and infinitesimal blade thickness. The angle of incidence of the propagating waves has been shown to influence the reflection and transmission coefficients across the blades. The theory was further developed by using mode-matching technique to model sound generation and propagation in outlet guide vanes [6, 7]. A comparative study of different 2D and 3D analytical approaches has been performed to estimate sound transmission across stator blades [8]. Three phenomena are described based on the direction of prop-

agation of incident waves: Venetian blind, Modal condition and Blocking condition. Experimental studies have also been performed to estimate modal amplitudes generated at the inlet of a ducted fan by inverting the modal directivity matrices [9] and also using compressed sensing based mode analysis [10]. The flow between the rotor and stator blades are characterised by swirl effects, which can alter modal behaviour. A qualitative analytical model to explain transmission of BPF tones in the swirl region and through the rotor blades have been proposed [11].
In the present study, spinning azimuthal modes are generated using a ring of loudspeakers. The propagation of these modes across rotor and stator blades are observed using microphone arrays and an iterative Bayesian Inverse Approach. The experimental setup and analysis methodology are presented in the following sections. The results and comparison of transmission loss across fan stages for different modes are presented in Sec. 3, followed by a brief conclusion.

2. METHODOLOGY AND EXPERIMENTAL SETUP

Assuming linear acoustics behavior and a stationary sound field, the complex acoustic pressure inside a hard-wall cylindrical duct with a circular or annular cross-section and in the presence of a flow, can be expressed as a weighted sum of modes as shown in Eqn. 1 [12]:

$$p(r,\theta,z,t) = \sum_{m=-\infty}^{\infty}\sum_{n=0}^{\infty}[A^{+}_{mn}e^{ik^{+}_{z,mn}z} + A^{-}_{mn}e^{ik^{-}_{z,mn}z}]f_{mn}(r)e^{im\theta}e^{i\omega t} \quad (1)$$

where A^{+}_{mn} and A^{-}_{mn} are complex-valued mode amplitudes propagating downstream and upstream respectively. The subscripts m and n are the azimuthal and radial mode orders. $f_{mn}(r)$ is a normalised modal shape factor depending on the duct's cross section (circular or annular) and hard-wall boundary conditions. The axial wavenumbers $k^{\pm}_{z,mn}$ of a particular mode (m,n) in both downstream $(^{+})$ and upstream $(^{-})$ directions in the presence of a flow of Mach number M are given by

$$k^{\pm}_{z,mn} = \frac{\mp Mk_0 + \sqrt{k_0^2 - (1-M^2)k^2_{r,mn}}}{1-M^2} \quad (2)$$

where, $k_{r,mn}$ is the radial wave number of mode (m,n) obtained from the solutions of Bessel functions constituting modal shape factor $f_{mn}(r)$. The purpose of the study is to generate particular modes inside a duct and observe the behavior across different blade rows of a fan.

2.1 Experimental setup

The experimental setup consists of a circular duct with a radius of 0.085 m. A low-speed electrical HVAC (Heating, ventilation and air-conditioning) fan, henceforth known as LP3, manufactured by Safran Ventilation Systems is installed inside the duct. Modular rings are present between the rotor and the stator blades in order to increase or decrease the gap among them. A Turbulent Control Screen (TCS) upstream of the fan at the inlet minimizes inflow distortions. A vane at the end of the duct can be opened or closed as required to control the mass flow inside the duct. Pressure probes and thermo-couples are fitted before and after LP3 and venturi to measure the physical parameters in the duct during operation. The parameters of LP3 are listed below:

Rotor blades number	B	17
Stator vanes number	V	23
Diameter	ϕ	17 cm
Hub to tip ratio	R_H/R_T	0.55
Tip Mach number	M_{tip}	0.3
Maximum rotational speed	Ω_{max}	$\sim$ 10000 rpm
Maximum mass flow rate	Qm	$\sim 1\ kg\ s^{-1}$
Maximum mean axial flow velocity	U_0	$\sim 40\ m\ s^{-1}$

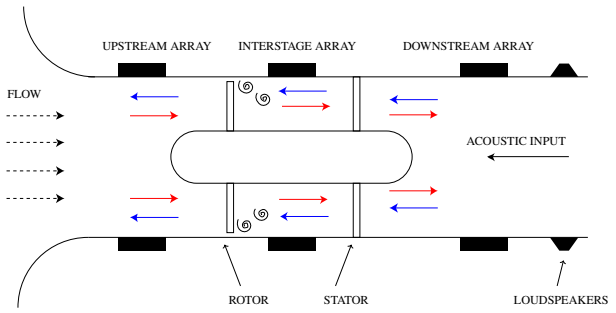


Figure 1: Schematic diagram of the experimental setup showing the positions of microphone antenna and direction of acoustic wave propagation, blue arrows depict the incident direction of modes *i.e.* the same direction as that of acoustic input and the red arrows depict the reflected direction of mode propagation

A ring of 13 loudspeakers downstream of LP3 generate a particular azimuthal mode inside the duct based on relative phase difference as explained in the methodology. The acquisition system consists of 25 nos. 1/4" microphones upstream and 25 nos. 1/4" microphones downstream with respect to the fan mounted in pin-hole configuration, and 64 nos. 1/4" microphones in the interstage mounted remotely. Fig. 1 gives a pictorial representation of the experimental setup. The fan is operated at three rotational speed and mass flow rate combinations. The performance map of the fan at these operating points are shown in Fig. 2. One of these points (9800 rpm and 30 mm vane opening) is chosen as the baseline configuration (marked with an 'o' symbol) and the corresponding results are present in the following section. The number of loudspeakers used for mode generation limits the maximum mode number that can be excited without aliasing, which is determined as half of the number of loudspeakers. Thus, for the experimental campaign modes -6 to +6 are chosen. The generation are pure tones excited individually at 30 frequencies between 500 Hz and 10000 Hz for each azimuthal mode.

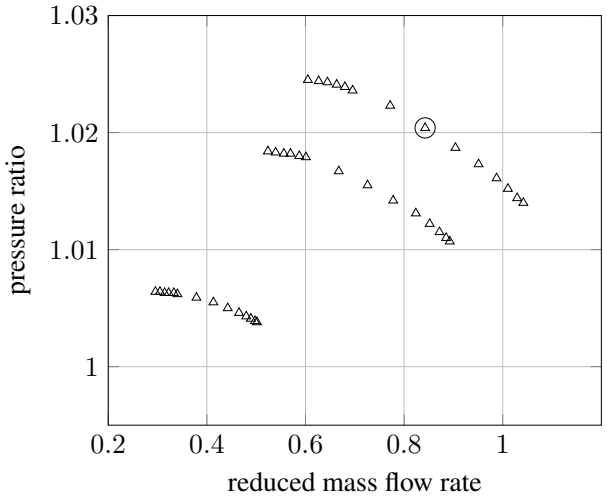


Figure 2: Performance map of the LP3 fan used in the experimentation with considered operating point marked in 'o'

2.2 Calibration of microphone arrays

The installation of the microphones on the duct is an important aspect of the experimental setup. A common method is to mount them flushed to the duct inner surface, with or without the protection grid. However, such a configuration is prone to measurement of pressure fluctuations due to turbulent boundary layer at the duct surface, along with the acoustic pressure. Furthermore, the distance between the rotor-stator rows in the long configuration is 40mm, not sufficient for flush-mounting the necessary number of microphones required for the study. Using a remote sensor installation, known as pin-hole system provides flexibility in designing a more efficient microphone array [13]. The pin-hole system creates a small cavity in front of the microphone, which acts as a Helmholtz resonator and modifies the frequency response of the microphone. Two methods of calibration are employed- individual and global calibration [14]. For individual calibration of microphones, a calibrating device consisting of a flush-mounted reference microphone and an already calibrated microphone are used. The transfer function between the target microphone and the reference microphone is measured. This is followed by the measurement of the transfer function between the reference microphone and the already calibrated microphone placed on a controlled surface. The ratio of the two transfer functions provide the calibration factor of the target microphone. The method is time-consuming and very sensitive to the position of the reference microphone in front of the pin-hole, thus difficult to reproduce. Moreover, once the setup is installed, the downstream and interstage microphones arrays are inaccessible. Therefore, individual calibration is performed for all the arrays, once before mounting the setup. Then global calibration is performed regularly during the experimental campaign. Fig. 3 gives an example of the calibration curves of microphone arrays obtained upon performing the abovementioned procedure. The curves are then used during post-processing to account for the frequency amplification and signal attenuation due to remote installation.

2.3 Mode generation

A particular spinning mode can be generated inside a duct using a combination of phased loudspeakers ([15,16]). To generate a spinning wave of azimuthal mode 'm' using 'K' monopole sources, the phase of the 'j^{th}' source is given by:

$$\phi_j = \frac{2\pi m}{K}(j-1) \tag{3}$$

The 13 loudspeakers are connected to the duct using waveguides of diameter 14 mm, resulting in a cut-off fre-

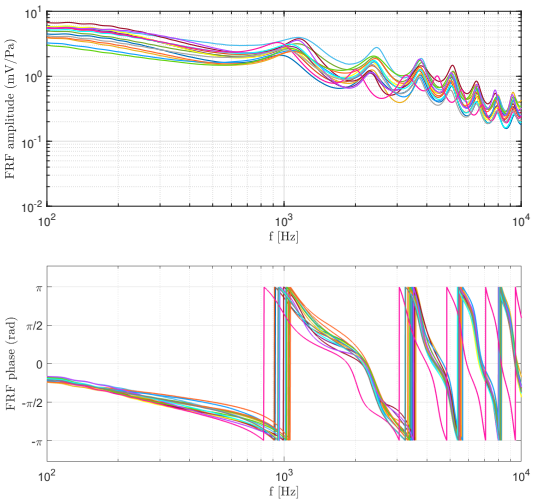


Figure 3: Sensitivity curves (amplitude and phase) for a group of microphones in the interstage array

quency of 14240.4 Hz. This ensures that the loudspeakers can be modelled as monopole sources for the range of frequencies considered in the study. The generation of radial modes cannot be controlled owing to the fact that the loudspeakers are positioned along a unique axial and radial position. The generation is performed considering a cylindrical duct, which is applicable at the position of the loudspeakers. However, at the location of the fan, notably at the Interstage array, the geometry transitions to an annular duct. It has to be noted that certain modes might become propagative, *i.e.* cut-on, as the sound propagates due to the aforementioned transition.

2.4 Analysis methodology

The iterative Bayesian Inverse Approach (iBIA) has been implemented to perform the modal analysis [17]. Eqn. 1 can be represented in a matrix notation.

$$\mathbf{p} = \mathbf{\Phi c} + \mathbf{n} \tag{4}$$

where, $\mathbf{p} \in \mathbb{C}^K$ is a vector of complex pressure coefficients (result of a Fourier transform) from measurements at a given frequency ω, $\mathbf{n} \in \mathbb{C}^K$ accounts for additive noise, $\mathbf{c} \in \mathbb{C}^L$ is a vector containing the unknown complex coefficients ($A^{\pm}_{mn}$) and $\mathbf{\Phi} \in \mathbb{C}^{K\times L}$ depends on the problem being solved ($\mathbf{\Phi} = e^{ik^{\pm}_{z,mn}z} f_{m,n}(r) e^{im\phi}$ in this case). The unknowns $\mathbf{c}$ and observations $\mathbf{p}$ are considered as random variables which are modelled through probability density functions and an algorithm based on the majorisation–minimisation (MM) principle is employed to solve the problem. Since, recorded sound pressure includes effects of the fan itself, notably when the excitation frequency is close to the blade passing frequency (BPF) or its harmonics, it is important to filter out the recorded data from these effects. To achieve that, a frequency band of 200 Hz is chosen around the excitation frequency and analysis is performed only within this range.

3. RESULTS

Upon post-processing the recorded microphone signals using the methodology explained above, the amplitudes of all cut-on modes present inside the duct are obtained. The mode amplitudes correspond to respective array locations and frequencies put to the test during the experiment. The results are presented in terms of acoustic power of the excited modes. Experiments have been conducted at specific test points. Continuous lines joining these points in the figures are for better visualisation.

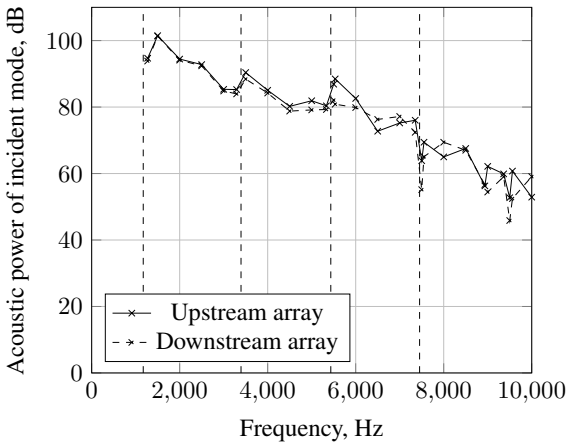
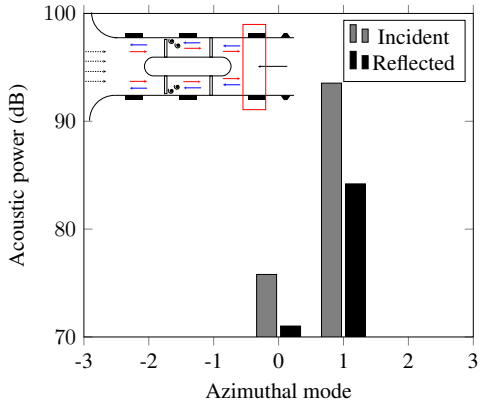


Figure 4: Acoustic power of azimuthal mode -1 (summed for all cut-on radial modes) along incident direction for upstream and downstream arrays in the case of an empty circular duct (dashed vertical lines represent the cut-off frequencies of subsequent radial modes)

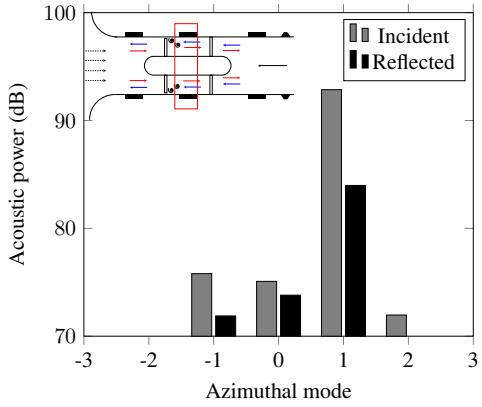
For the first part of the analysis, simpler configurations have been investigated: an empty circular duct

and the duct with LP3 but without rotation of blades or flow. These analyses demonstrate the performance of the methodology in conditions where the behaviour is theoretically predictable. Further, such an analysis enables the separation of the shielding due to the setup geometry from that generated due to the blades rotation and the effect of the flow. Fig. 4 presents the acoustic power of azimuthal mode -1 along the incident direction recorded by microphones of the upstream and downstream arrays. As theoretically expected, the acoustic power is conserved across the microphone arrays, specially at low frequencies where very few radial modes are cut-on. At higher frequencies, the acoustic power decrease in general and their values at upstream and downstream arrays diverge from each other. This is due to the presence of several radial modes and also spurious azimuthal modes which are excited by the loudspeakers. The method struggles to differentiate the modes, when several modes are present with comparable energy. Jumps in the power values are also observed near the cut-off frequencies of radial modes. Near the cut-off frequencies, evanescent modes with longer axial wavelength are present and recorded by the microphones. These modes have not been taken into account during the analysis. The analysis has been limited to low frequencies and test points near cut-off frequencies have been removed to ensure that observations are made within the limits of the method. Similar observations have been made for the other azimuthal modes. The results are comparable and reinforce the confidence on the generation and post-processing methodology.

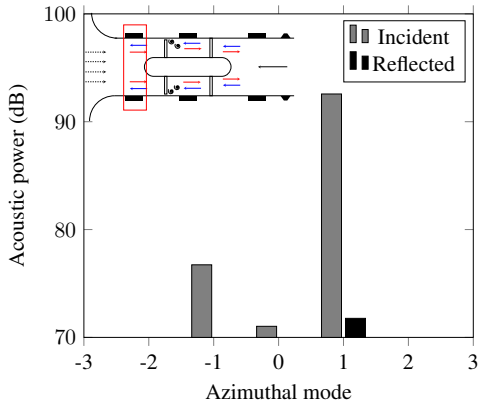
The next step is to analyse the effect of the rotor rotation on the noise transmission. Fig. 5 presents an example of the results obtained when mode 1 is excited at 2000 Hz with LP3 at 9800 rpm and vane opening of 30 mm. It is the operating point marked with 'o' in Fig. 2. 'Incident' and 'reflected' represent the direction of mode propagation with respect to the acoustic input. It can be seen that the difference in amplitude of incident $m = 1$ across different antenna is negligible ($\sim$ 0.6 dB). However, the amplitude of reflected mode is considerably high at the interstage array compared to upstream array, indicating that the rotor blades are the major contributors towards reflecting $m = 1$. It can also be observed that other cut-on modes like $m = 0, -1$ are excited, however their amplitudes are negligible compared to those of $m = 1$. The overall decrease in transmission can be obtained by taking the difference of incident mode power at upstream array from that at downstream array. Fig. 6 shows the transmission loss of mode -1 with frequency for different con-



(a) Downstream array



(b) Interstage array



(c) Upstream array

Figure 5: Acoustic power of cut-on modes (along incident and reflected direction of propagation with respect to acoustic input) present at different microphone array locations upon excitation of azimuthal mode 1 at 2000 Hz with LP3 rotating at 9800 rpm and vane opening of 30 mm (operating point marked with 'o' in Fig. 2)

figurations. Higher difference in mode power (y-values) means lower transmission across blades. The presence of LP3 slightly decreases the transmission of mode -1. However, higher transmission loss is detected when LP3 rotates at 9800 rpm with 30 mm vane opening. The rotation of rotor blades and presence of flow are possible causes for this transmission loss. Transmission loss across each blade rows of the fan can be obtained by using the microphone measurements of interstage array. The difference in incident power of excited azimuthal mode across the downstream and interstage arrays (depicting transmission loss across stator blades) and that across the interstage and upstream arrays (depicting transmission loss across stator blades) are calculated and shown in Fig. 7 for modes $m = -1$ and $m = 1$. For the present study, $m = 1$ represents a co-rotating mode and $m = -1$ a counter-rotating mode with respect to the rotor rotation. For $m = 1$, the transmission loss across stator blades are slightly higher at low frequencies compared to rotors but above 2000 Hz, transmission loss across rotors dominate. The trend is consistent for $m = -1$, in which case, the transmission loss across rotor blades dominate throughout. The stators are slightly more efficient in blocking $m = 1$ compared to $m = -1$ but the differences are quite small and maybe accounted from the uncertainties of measurement or post-processing. However, the rotor blades are more efficient in blocking $m = -1$ upto 3 dB at 2500 Hz.

Fig. 8 shows the transmission loss across LP3 at 9800 rpm and vane opening of 30 mm for various modes. The values are obtained by taking the difference in acoustic power along incident direction of upstream array from downstream array. The lower order modes follow the trend as explained above at frequencies below 4000 Hz. With increase in frequency, transmission loss across the fan increases. However, at higher frequencies and for higher order modes, no conclusion can be drawn. It is to be noted that, along with the mode required to be excited, aliased modes are also being generated. These aliased modes are related to the number of loudspeakers present in the generation system and are given by Eq. 5.

$$m_{\text{aliased}} = m_{\text{desired}} \pm \text{Nos. of loudspeakers} \qquad (5)$$

These modes are cut-on for higher order modes and thus are generated by the loudspeakers. One example of this phenomenon can be observed in Fig. 9 where mode -7 is excited along with the intended mode 6 at downstream array inside a circular duct even without LP3. The acoustic power of both these modes are comparable with a difference of ~ 1 dB. Since, both the desired and aliased modes

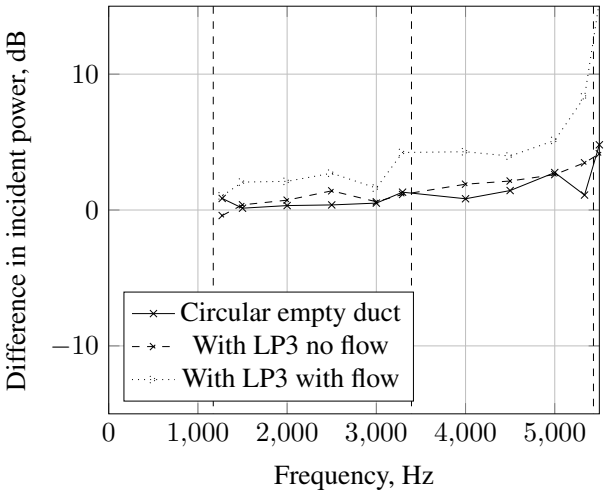


Figure 6: Difference in acoustic power along incident direction of upstream array from downstream array of azimuthal mode -1 (summed for all cut-on radial modes) for three different configurations (dashed vertical lines represent the cut-off frequencies of subsequent radial modes)

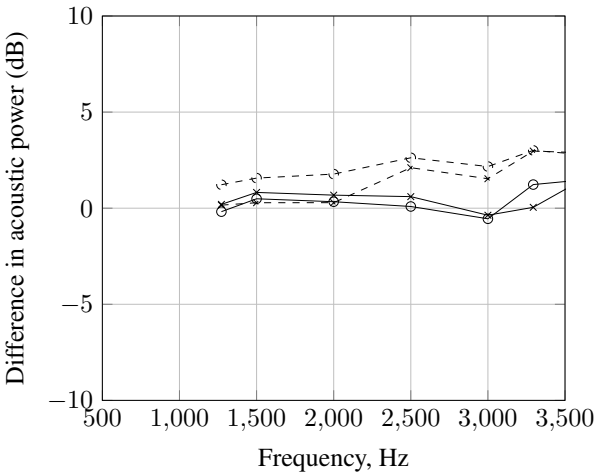


Figure 7: Difference in acoustic power of incident azimuthal mode $m = 1$ (x) and $m = -1$ (o) across stator (solid) and rotor (dashed) blades with LP3 rotating at 9800 rpm and vane opening of 30 mm

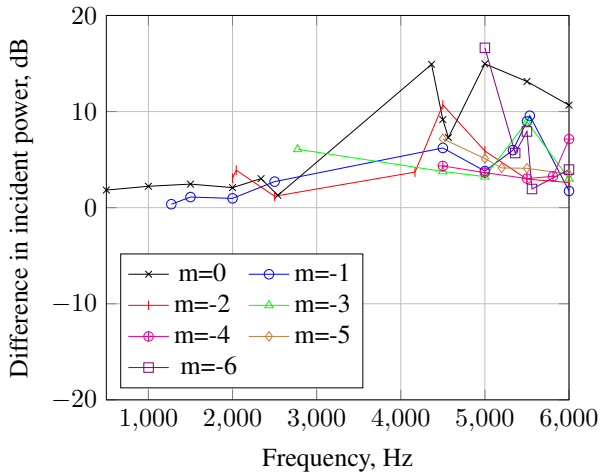


Figure 8: Difference in acoustic power along incident direction of upstream array from downstream array for different azimuthal modes (summed for all cut-on radial modes) with LP3 rotating at 9800 rpm and vane opening of 30 mm

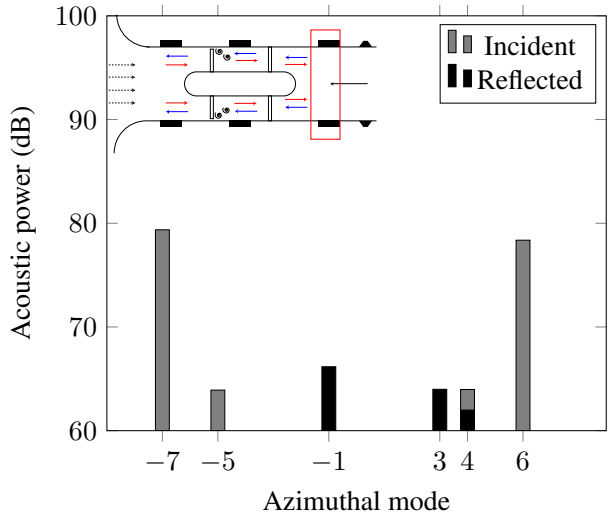


Figure 9: Acoustic power of cut-on modes (along incident and reflected direction of propagation with respect to acoustic input) present at downstream array location upon excitation of azimuthal mode 6 at 6500 Hz inside a circular duct without LP3

are generated by the same sources, they are correlated and create interference patterns inside the duct. It is possible that the energy of the aliased modes are transferred to the desired modes and vice-versa during the application of the inverse method.

4. CONCLUSION AND DISCUSSIONS

Rotor shielding across an axial fan comprising of rotor and stator blades has been studied experimentally. The analysis of lower order modes provides some information regarding rotor-shielding effects. The rotation of blades and the presence of flow increase rotor shielding effects across a fan. Stator blades are relatively transparent to the modes owing to their low stagger angles. The counter-rotating modes are shielded more efficiently by the rotor blades than the co-rotating modes. However, the analysis of higher order modes and high frequency excitation pose several challenges. It has been observed that other cut-on modes are also excited along with the desired azimuthal modes. In most cases, the mode amplitudes are considerably lower to those of the excited mode but can be comparable at certain frequencies. Due to the use of a single ring of loudspeakers, the generation of radial modes cannot be controlled. Thus, at higher frequencies and higher modes, the analysis becomes more complex and uncertain. Near the cut-off frequencies, evanescent modes are present and recorded by the microphones. Mainly at the interstage array, these modes and also the evanescent modes generated at rotor and stator edges are recorded. The evanescent modes have been ignored in the analytical formulation and thus in the modal basis of analysis. Further, the flow between the rotor and stator features swirl. For the present study, the swirl has been approximated to an equivalent axial velocity. Including the swirl effects and adding evanescent modes in the modal basis will lead to better estimation of the mode amplitudes at the interstage array. Moreover, several phenomena occur inside the experimental setup like transition from circular to annular duct, multiple reflections between rotor and stator rows and coupled effect of transmission and reflection at both the blade rows. These effects cannot be decoupled by merely investigating the mode amplitudes at microphone arrays. A numerical study is presently being conducted to simulate the experimental setup and estimate the propagation of modes across the fan. The numerical study would enable understanding of each individual phenomenon. The information will then be used to deepen the experimental analysis.

5. ACKNOWLEDGMENTS

This work was granted access to the HPC resources of PMCS2I (Pôle de Modélisation et de Calcul en Sciences de l'Ingénieur de l'Information) of École Centrale de Lyon, Écully, France. The authors acknowledge Safran Ventilation Systems and in particular, Patrice CAULE, for providing the LP3 fan-OGV module. The authors would like to thank Jean-Charles VINGIANO for the fabrication of the interstage array and mounting of the test bench. This works was performed in the framework of the Labex CeLyA (grant number ANR-10-LABX-0060) of the University of Lyon, within the program "Investissements d'Avenir" (grant number ANR-16-IDEX-0005) operated by the French National Research Agency.

6. REFERENCES

[1] W. Eversman and I. D. Roy, "Ducted Fan Acoustic Radiation Including the Effects of Nonuniform Mean Flow and Acoustic Treatments," tech. rep., NASA Lewis Research Center, 1993.

[2] M. Roger, S. Moreau, and A. Guédel, "Vortex-Shedding Noise and Potential-Interaction Noise Modeling by a Reversed Sears' Problem," in *12th AIAA/CEAS Aeroacoustics Conference, Cambridge, MA*, 2006.

[3] J. M. Tyler and T. G. Sofrin, "Axial flow compressor noise studies," *SAE Tech Papers*, 1962.

[4] S. Kaji and T. Okazaki, "Propagation of sound waves through a blade row: I. analysis based on the semi-actuator disk theory," *J. Sound Vib.*, vol. 11 (3), 1970.

[5] S. Kaji and T. Okazaki, "Propagation of sound waves through a blade row: Ii. analysis based on the acceleration potential method," *J. Sound Vib.*, vol. 11 (2), 1970.

[6] S. Bouley, B. François, M. Roger, and S. Moreau, " On a mode-matching technique for sound generation and transmission in a linear cascade of outlet guide vanes," in *21st AIAA/CEAS Aeroacoustics Conference, AIAA AVIATION Forum, Dallas, Texas*, 2015.

[7] S. Bouley, B. François, M. Roger, H. Posson, and S. Moreau, "On a two-dimensional mode-matching technique for sound generation and transmission in axial-flow outlet guide vanes," *J. Sound Vib.*, vol. 403, 2017.

[8] M. Behn, U. Tapken, P. Puttkammer, R. Hagmeijer, and N. Thouault, "Comparative study of different analytical approaches for modelling the transmission of sound waves through turbomachinery stators," in *22nd AIAA/CEAS Aeroacoustics Conference, Lyon, France*, 2016.

[9] F. O. Castres and P. F. Joseph, "Mode detection in turbofan inlets from near field sensor arrays," *J. Acoust. Soc. Am.*, vol. 121 (2), 2007.

[10] M. Behn and U. Tapken, "Investigation of Sound Generation and Transmission Effects Through the ACAT1 Fan Stage using Compressed Sensing-based Mode Analysis," in *25th AIAA/CEAS Aeroacoustics Conference, Delft, The Netherlands*, 2019.

[11] D. A. Topol, S. C. Holhubner, and D. C. Mathews, "A reflection mechanism for aft fan tone noise from turbofan engines," in *11th AIAA Aeroacoustics Conference, Palo Alto, California*, 1987.

[12] M. L. Munjal, *Acoustics of ducts and mufflers: with application to exhaust and ventilation system design*. Wiley-Interscience, 1 ed., 1987.

[13] E. Salze, C. Bailly, O. Marsden, E. Jondeau, and D. Juvè, "An experimental characterisation of wall pressure wavevector-frequency spectra in the presence of pressure gradients," in *20th AIAA/CEAS Aeroacoustics Conference, no. 2909*, (Atlanta, GA), 2014.

[14] Q. Leclère, A. Pereira, A. Finez, and P. Souchotte., "Indirect calibration of a large microphone array for in-duct acoustic measurements," *J. Sound Vib.*, vol. 376, 2016.

[15] J. M. Seiner and G. Reethof, "Design and Development of the Spinning Mode Synthesizer," tech. rep., National Aeronautics and Space Administration, 1973.

[16] S. Huang, X. Pan, L. Yu, and W. Jiang, "Achieving cylindrical duct modes generation in spinning mode synthesizer via a least-square identification of the global calibration factor," *Appl Acoust*, vol. 186, 2022.

[17] A. Pereira and M. Jacob, "Modal analysis of in-duct fan broadband noise via an iterative bayesian inverse approach," *J. Sound Vib.*, vol. 520, no. 116633, 2022.

DOI: 10.61782/fa.2025.0829



FORUM ACUSTICUM
EURONOISE 2025

STOCHASTIC APPROACH FOR ESTIMATING THE SOUND POWER OF TONAL MODE COMPONENTS IN FLOW DUCTS BASED ON AZIMUTHAL MODE ANALYSIS

Maximilian Behn* **Ulf Tapken**
German Aerospace Center, Institute of Propulsion Technology, Engine Acoustics Department
Berlin, Germany

ABSTRACT

The accurate experimental determination of the sound power in the ducts of aircraft engines, engine demonstrators and turbomachinery test rigs is challenging due to limited installation space for sensor arrays. Particularly in the inlet, a high number of propagating modes requires sensor arrays with multiple axial positions in order to decompose the measured sound field into its radial mode constituents. As an alternative, a sensor ring array requires a minimum of axial installation space and provides insight into the mode distribution using an azimuthal mode analysis (AMA). In this case, it is necessary to use radial mode distribution models, such as "equal mode energy" in order to estimate the sound power. However, the difficulty with tonal components, e.g. those generated by rotor-stator interaction, is that the radial modes are mutually coherent. This leads to a complex relation between the azimuthal mode amplitudes and the underlying mode distribution, which varies with the individual case, e.g. operating parameters of the rotor-stator configuration. To account for this variability, a stochastic approach is proposed in which, in particular, the phase relationships of the modes are varied and a distribution of sound power is determined. Its validity is evaluated by comparison with the results of a radial mode analysis obtained at a fan test rig.

Keywords: tonal sound power, azimuthal mode analysis, flow ducts

**Corresponding author*: maximilian.behn@dlr.de.
Copyright: *©2025 Maximilian Behn & Ulf Tapken. This is an open-access article distributed under the terms of the Creative Commons Attribution 3.0 Unported License, which permits unrestricted use, distribution, and reproduction in any medium, provided the original author and source are credited.*

1. INTRODUCTION

The next generation of UHBR aircraft engines will be equipped with shorter nacelles in order to reduce the overall engine weight. This development has an impact on the fan inflow and the resulting fan noise excitation, which needs to be assessed experimentally under realistic conditions. Engine demonstrators, just like the real aircraft engines, provide a very limited installation space for microphone arrays, particularly in the inlet. Therefore, microphone ring arrays are applied in many cases enabling the decomposition of the measured sound field into azimuthal modes. In contrast to radial modes, which are determined by radial mode analysis, azimuthal modes do not allow a direct computation of the propagating sound power. Based on the original work of Joseph et al. [1], a sound power estimation technique had been developed on the basis of azimuthal mode spectra and radial mode distribution models and applied to experimental data from small and large-scale test rigs [2–4]. One of the fundamental assumptions of this estimation technique is mutual incoherence of all radial mode constituents, which is an appropriate assumption for broadband sound field components. Regarding tonal mode components, this approach neglects the fact, that all radial modes are fully coherent resulting in interference of the modes and strongly fluctuating sound pressure levels depending on the axial position of the microphone ring array. Despite the inappropriateness of the assumption of mutual mode incoherence, the approach for the broadband case was applied to the analysis of tonal mode components on a LPT rig [2] and on a radial compressor rig [5].

This article explores a stochastic approach that allows to take coherent modes into account and to evaluate the

impact of varying phase relations between the modes. Just like in the broadband case, the magnitudes of the radial mode amplitudes are prescribed according to radial mode distribution models. Additionally, the individual radial modes are assigned with randomly selected phases so that the resulting interference can be evaluated stochastically in a Monte Carlo study. The result of this approach is a distribution of sound power, of which the spread and the usefulness of the median value as a possible sound power estimation value are evaluated using measured data from a fan test rig and compared with reference results from radial mode analysis.

2. SOUND POWER ESTIMATION BASED ON AZIMUTHAL MODE ANALYSIS

Sound fields in cylindrical and annular flow ducts with a uniform background flow with Mach number M_x can be decomposed into radial modes of the form

$$p\left(x,r,\phi\right) = \sum_{m=-\infty}^{\infty}\sum_{n=0}^{\infty}\left(A_{mn}^{+}e^{ik_{mn}^{+}x} + A_{mn}^{-}e^{ik_{mn}^{-}x}\right)\cdot e^{im\phi}f_{mn}(r) \tag{1}$$

with azimuthal mode order m, radial mode order n, mode amplitudes $A_{mn}^{\pm}$, axial wave number $k_{mn}^{\pm}$, and radial mode shape function $f_{mn}(r)$ [6]. On the basis of the mode amplitude, the mode sound power is calculated as:

$$P_{mn}^{\pm} = \frac{\pi R^2}{\rho c}\frac{\alpha_{mn}(1-M_x^2)^2}{\left(1\mp\alpha_{mn}M_x\right)^2}|A_{mn}^{\pm}|^2, \tag{2}$$

with the outer duct radius R, static density ρ and speed of sound c. The term α_{mn} is called the mode propagation factor and plays a particular role in the estimation of the mode sound power. It is defined as:

$$\alpha_{mn} = \sqrt{1-\left(1-M_x^2\right)\frac{\sigma_{mn}^2}{\left(kR\right)^2}}, \tag{3}$$

where σ_{mn} is the radial-transversal eigenvalue. For propagating modes, α_{mn} ranges between 0 at the mode cut-on frequency and 1. It is imaginary for cut-off modes and determines the rate of decay in axial direction through its relation to the axial wave number $k_{mn}^{\pm} = \frac{k}{1-M_x^2}\left(-M_x \pm \alpha_{mn}\right)$.

The determination of the radial mode amplitudes in Eq. (1) via Radial Mode Analysis (RMA) requires a considerable effort in equipment (microphones, traversing devices) and measurement duration. The microphone arrays, that are typically installed at the duct walls, extend over an axial installation space, which increases depending on the highest frequency of interest and is usually limited due to spatial constraints of the test environment [6]. An alternative analysis technique is the azimuthal mode analysis (AMA) (see e.g. [7]), which requires a ring array of wall-flush mounted microphones and can be realised in spatially limited test environments such as the inlets of aero engines or engine demonstrators. Mathematically, AMA corresponds to the discrete form of the spatial Fourier transform of the in-duct sound field in circumferential direction conducted e.g. with microphones installed flush at the outer duct wall:

$$A_m(x) = \frac{1}{N_{\text{mic}}}\sum_{j=1}^{N_{\text{mic}}} p(x, r=R, \phi_j)\cdot e^{-im\phi_j}. \tag{4}$$

The relation of the azimuthal mode amplitude A_m and the amplitudes of the underlying radial modes is obtained from eq. (4):

$$A_m(x) = \sum_{n=0}^{n_{\max}}\left(A_{mn}^{+}e^{ik_{mn}^{+}x} + A_{mn}^{-}e^{ik_{mn}^{-}x}\right)\cdot f_{mn}(R) \tag{5}$$

as a summation over all cut-on radial mode orders. In contrast to the radial mode amplitudes, the azimuthal mode amplitude can vary strongly depending on the axial position of the ring array. In order to estimate the mode sound power from azimuthal mode amplitudes, Eqs. (2) and (5) need to be combined. Since the axial wave numbers are determined from the known duct geometry, frequency and flow conditions, the main difficulty in estimating the mode sound power from azimuthal mode amplitudes lies in the estimation of the unknown amplitudes and phases of the radial modes. In previous studies, the mode sound power in broadband sound fields was estimated using mode distribution models such as "'equal mode energy"' or "'equal mode energy density"' to relate the magnitude of the radial mode amplitudes to single parameters of the corresponding mode distribution model [1,3,4] with the assumption of mutual incoherence of the radial modes, which makes it possible to neglect the mode phases and the axial propagation terms $e^{ik_{mn}^{-}x}$. In combination with

the assumption that only modes propagating in a single direction, e.g. upstream, are present, the square of Eq. (5) yields for the broadband case:

$$|A_m|^2 = \sum_n |A_{mn}^-|^2 f_{mn}^2(R). \tag{6}$$

Equation (6) can be solved for the radial mode amplitudes $|A_{mn}^-|^2$ using a mode distribution model.

Tonal sound field components comprise coherent modes whose phase relations have to be considered. Because the mode phases are unknown and can not be retrieved via AMA, a stochastic approach is sought. The initial equation, which relates A_m to A_{mn}^-, then yields:

$$A_m = \sum_n |A_{mn}^-| f_{mn}(R) e^{i2\pi\mathcal{U}(1,0)}. \tag{7}$$

In Equation (7), the mode phases are randomly selected from a uniform distribution with unit standard deviation and zero mean. As a consequence, the radial mode amplitudes and the resulting mode sound powers are random variables. An efficient evaluation of these random variables can be realised by Monte Carlo simulations.

3. MODE SOUND POWER DISTRIBUTION MODELS

Currently, generalised mode distribution models are lacking for the tonal mode components from turbomachinery stages. Therefore, two mode distribution models (see [1]), "'equal mode energy"' (EME) and "'equal mode energy density"' (EMED), that are widely applied for the analysis of fan broadband noise, and the sound power distribution according to point source models are introduced in the following to demonstrate the stochastic approach for mode sound power estimation. However, the expressions can easily be adapted to other mode distribution models in the future.

3.1 "'Equal mode energy"' model

The EME model assumes that all propagating modes with the same azimuthal mode order have the same sound energy and as a result, the same mode sound power, i.e. $P'_m := P^-_{mn}$. Now P'_m is inserted in Eq. (2), which is then solved for $|A_{mn}^-|^2$. From Eq. (7) the following expression for the azimuthal mode amplitude is obtained:

$$|A_m|^2 = \frac{\rho c}{\pi R^2} \frac{1}{\left(1 - M_x^2\right)^2} P'_m \cdot \left| \sum_n \frac{1 + \alpha_{mn} M_x}{\sqrt{\alpha_{mn}}} f_{mn}(R) e^{i2\pi\mathcal{U}(1,0)} \right|^2. \tag{8}$$

Then, the summed sound power $P_m^{\text{EME,-}} = N_n \cdot P'_m$ yields:

$$P_m^{\text{EME,-}} = N_n \frac{\pi R^2}{\rho c} \left(1 - M_x^2\right)^2 |A_m|^2 \cdot \left| \sum_n \frac{1 + \alpha_{mn} M_x}{\sqrt{\alpha_{mn}}} f_{mn}(R) e^{i2\pi\mathcal{U}(1,0)} \right|^{-2}. \tag{9}$$

The EME model is sensitive to modes that are close to their cut-on frequencies and whose propagation factor α_{mn} is close to 0. In this case, the summation over all radial mode orders is dominated by the contribution of the highest cut-on radial mode order, which effectively is closest to its cut-on frequency. Because the $1/\sqrt{\alpha_{mn}}$-term is unbounded at the cut-on frequency, the estimated sound power is zero directly at this frequency. Hence, the EME model is prone to underestimate the sound power.

3.2 "'Equal mode energy density"' model

For the EMED model, the sound power is expressed in terms of the energy density $\Pi_{mn}^{\pm}$ [1]:

$$P_{mn}^{\pm} = \Pi_{mn}^{\pm} S c_{\text{g,mn}} = \Pi_{mn}^{\pm} S c \frac{\alpha_{mn}\left(1 - M_x^2\right)}{1 \mp \alpha_{mn} M_x}, \tag{10}$$

with the duct cross-section S and the mode group velocity $c_{\text{g,mn}}$. It is assumed that all upstream propagating modes with the same azimuthal mode order have the same energy density, i.e. $\Pi'_m := \Pi^-_{mn}$. Modes propagating downstream are neglected at this point. Setting Eq. (10) equal to Eq. (2) and solving for $|A_{mn}^-|^2$ yields:

$$|A_{mn}^-|^2 = S \frac{\rho c^2}{\pi R^2} \frac{1 + \alpha_{mn} M_x}{1 - M_x^2} \Pi'_m. \tag{11}$$

From Eq. (7) the relation between azimuthal mode amplitude and mode energy density reads:

$$|A_m|^2 = S \frac{\rho c^2}{\pi R^2} \frac{1}{1 - M_x^2} \Pi'_m \cdot \left| \sum_n \sqrt{1 + \alpha_{mn} M_x} f_{mn}(R) e^{i2\pi\mathcal{U}(1,0)} \right|^2. \tag{12}$$

The summed sound power is computed as follows:

$$P_m^{\text{EMED,-}} = Sc\left(1-M_x^2\right)\Pi_m' \sum_n \frac{\alpha_{mn}}{1+\alpha_{mn}M_x}. \quad (13)$$

Combining Eqs. (12) and (13) provides the estimation equation for the EMED model:

$$P_m^{\text{EMED,-}} = \frac{\pi R^2}{\rho c}\left(1-M_x^2\right)^2 |A_m|^2 \cdot \frac{\sum_n \frac{\alpha_{mn}}{1+\alpha_{mn}M_x}}{\left|\sum_n \sqrt{1+\alpha_{mn}M_x} f_{mn}(R) e^{i2\pi\mathcal{U}(1,0)}\right|^2}. \quad (14)$$

In comparison to the EME model, the EMED model is less sensitive to low values of the mode propagation factor α_{mn}.

3.3 ISI point source model

Point source models such as monopoles and dipoles are suitable to model the sound generation from different interaction mechanisms in turbomachinery stages [8]. For high accuracy of the determined sound power, the blade geometries and aerodynamic properties need to be modelled in detail to calculate the source strengths. Instead, a dense distribution of point sources is assumed across the duct cross-section as a substitute model, which ensures that each mode order can be excited effectively. A distribution of a high number of densely positioned point sources is equivalent to a continuous source distribution as described in [1]. The integration of the contribution of each point source over the duct cross-section yields the total radiated mode field, which depends on mode-specific parameters like the mode propagation factor α_{mn}, but is independent of the radial and azimuthal mode shape. Furthermore, the stochastic sound power estimation approach based on the azimuthal mode analysis is chosen, in which only the distribution of mode amplitudes is predicted by the point source models and the mode phases is selected randomly from a random distribution.

The absolute values of the radial mode amplitudes are predicted on the basis of the mode impedance $\hat{Z}_{mn}^{\pm}$ and the source strength q, which are described for different source types in more detail e.g. in [9]. In this reference, the ISI point source model is introduced, which is characterised by a more realistic excitation of modes close to their cut-on frequencies by virtue of an internal source impedance and applied in the following investigation:

$$|A_{mn}^{\pm}| = |\hat{Z}_{\text{mn,ISI}}^{\pm} q|. \quad (15)$$

The mode impedance of the source distribution with an assumed dipole characteristic is approximated as:

$$\hat{Z}_{\text{mn,ISI}}^{\pm} = -i\frac{\rho c}{4\pi R^2}\frac{1/\alpha_{mn}}{1+\frac{N_M}{(kR)^2+\frac{25}{kR}}\cdot\frac{1-\alpha_{mn}}{\alpha_{mn}}} \cdot \left(k_{mn}^{\pm}\cos\alpha_{\text{dipole}} + \frac{\sigma_{mn}}{R}\sin\alpha_{\text{dipole}}\right) \quad (16)$$

with the total number of cut-on modes N_M and the dipole angle α_{dipole}.

From Eq. (7) the azimuthal mode amplitude can be expressed as:

$$A_m = |q|\sum_n |\hat{Z}_{\text{mn,ISI}}^{-}| f_{mn}(R) e^{i2\pi\mathcal{U}(1,0)}. \quad (17)$$

Likewise, the summed mode sound power is directly computed by inserting Eq. (15) in Eq. (2):

$$P_m^{\text{ISI,-}} = \sum_n \frac{\pi R^2}{\rho c}\frac{\alpha_{mn}(1-M_x^2)^2}{(1+\alpha_{mn}M_x)^2}|\hat{Z}_{\text{mn,ISI}}^{-} q|^2 \quad (18)$$

$$= \frac{\pi R^2}{\rho c}|A_m|^2 \sum_n \frac{\alpha_{mn}(1-M_x^2)^2}{(1+\alpha_{mn}M_x)^2} \cdot \frac{|\hat{Z}_{\text{mn,ISI}}^{-}|^2}{|\sum_{\tilde{n}=0}^{n_{\max}}|\hat{Z}_{\text{m}\tilde{n},\text{ISI}}^{-}| f_{m\tilde{n}}(R) e^{i2\pi\mathcal{U}(1,0)}|^2}. \quad (19)$$

4. APPLICATION TO FAN TEST RIG DATA

The stochastic approach for sound power estimation based on azimuthal mode amplitudes is demonstrated on both, synthesized and experimental data from DLR's fan test rig CRAFT (Co-/Counter-Rotating Acoustic Fan Test Rig). It is equipped with a fan stage whose rotor has 18 blades and stator has 21 vanes. The duct diameter at the inlet test section is 453.6 mm. At the fan design point, the flow Mach number in the inlet is $M_x = 0.11$. Typically, the upstream radiated sound power of the tonal mode components is determined by radial mode analysis on the basis of traverse measurements with an axial microphone array, which is depicted in Fig. 1. The RMA results serve as reference data for the comparison with the estimated sound powers using the measured data from the ring array in combination with the stochastic estimation approaches.

For further information on the CRAFT test rig itself as well as on the measurements and data analysis of the data used here, the interested reader is referred to Ref. [10] and Ref. [11].

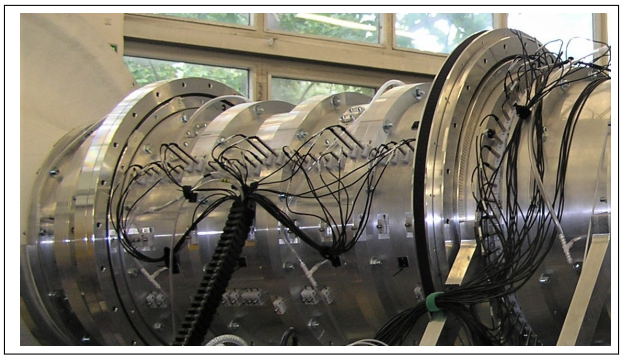


Figure 1. Microphone arrays in the inlet of the CRAFT fan test rig [11]: a traversable, axial line array (left) and ring array (right).

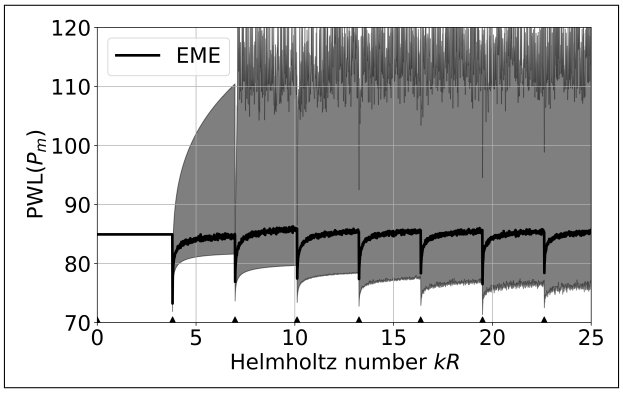


Figure 2. Sound power estimation results for constant azimuthal mode amplitude $A_0 = 1$ assuming "'equal mode energy"'.

First, the stochastic sound power estimation procedure is demonstrated for a synthetic case with constant azimuthal mode amplitude $A_0 = 1$. The results in Figs. 2, 3, and 4 show the estimation results for $m = 0$ using the mode distribution models EME and EMED and the ISI point source model. For the Monte Carlo study, a total of 1000 iterations were performed. The shaded areas indicate the complete dynamic range from the minimum to the maximum of the distribution of

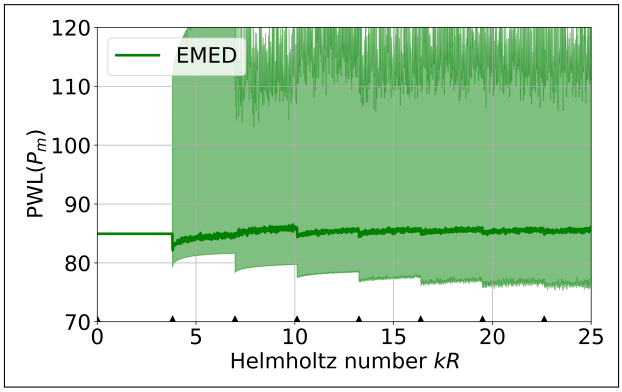


Figure 3. Sound power estimation results for constant azimuthal mode amplitude $A_0 = 1$ assuming "'equal mode energy density"'.

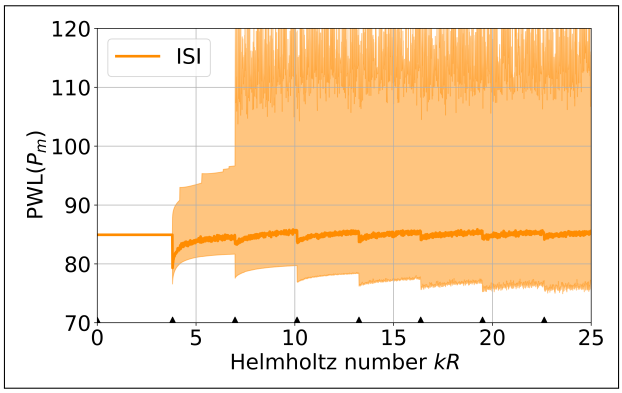


Figure 4. Sound power estimation results for constant azimuthal mode amplitude $A_0 = 1$ using the ISI point source model.

estimated sound powers. The median value of the sound power distribution is shown by the darker lines. Below $kR \approx 4.5$, only the radial mode order $n = 0$ is cut-on, which leads to the same sound power estimation for all models. Furthermore, in this case the sound power distribution is concentrated at a constant value, despite the variation of the mode phase terms. Hence, the stochastic variation, which is introduced in Eq. (7), only has an impact if several radial mode orders are cut-on for the same azimuthal mode order. Also, although no particular sound power distribution is assigned in the comparison of the different models, that is supposed to be reconstructed, it seems plausible that if the azimuthal mode amplitude is constant, the sound power lies in a rather narrow dynamic

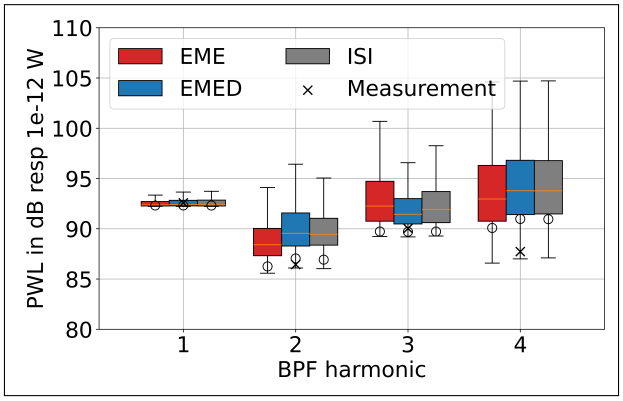


Figure 5. Total estimated sound power for the tonal mode components at 1BPF to 4BPF in comparison to reference measurement data (indicated by crosses) and estimation results assuming mutual mode incoherence (cp. (6), indicated by circles).

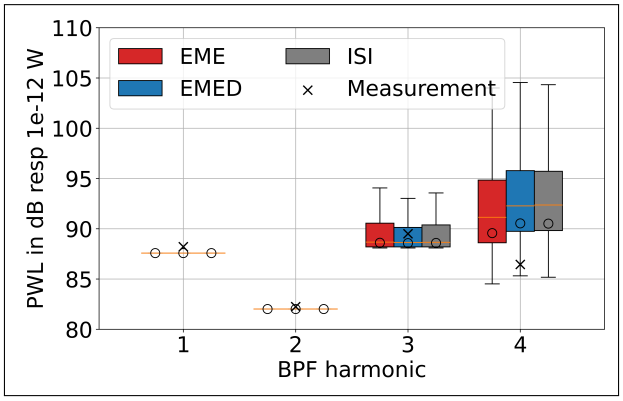


Figure 6. Estimated sound power of the rotor-stator interaction modes at 1BPF to 4BPF in comparison to reference measurement data (indicated by crosses) and estimation results assuming mutual mode incoherence (indicated by circles).

range.

Above the cut-on frequency of $n = 1$, which is indicated by a small triangle at $kR \approx 4.5$ at the bottom of the figure, the dynamic range of the sound power distribution increases rapidly and asymmetrically. The results for the EMED model exhibit the steepest increase reaching a maximum dynamic range of more than 40 dB just below the cut-on frequency of the next higher radial mode order $n = 2$. For the EME model, the estimated sound power drops directly at the mode cut-on frequencies and then increases monotonically up to a dynamic range of about 30 dB, at least up to the cut-on frequency of $n = 2$. The sound power distribution for the ISI model extends over a smaller dynamic range of about 15 dB below the cut-on frequency of $n = 2$. However, above approximately $kR = 7.5$ the dynamic range of the sound power distributions fluctuates between 30 and 45 dB independent of the underlying model.

The median proves to be a robust descriptor for the estimated sound power. For the EME model, the median sound power drops at each mode cut-on frequency and then increases approaching a sound power level of approximately 85 dB. In contrast, the median sound power for the EMED model is almost constant, except for small drop at the cut-on frequency of the mode order $n = 1$. The ISI model leads to results that combine the characteristics of the EME and the EMED model. At relatively low frequencies, the median curve is similar to the one of the EME model, particularly at the cut-on frequency of mode order $n = 1$. With increasing frequency, the median curve of the ISI model becomes more similar to the median curve of the EMED model with very small fluctuations close to the mode cut-on frequencies.

In the following, the stochastic approach is applied to measured data from the inlet of the CRAFT fan test rig in order to estimate the sound power of the tonal components radiated upstream at the blade passing frequency (BPF) and its harmonics. Figure 5 shows the distributions of the estimated total sound power for the three different models in comparison with the reference results, which were obtained by RMA. Additionally, the estimation results under the assumption of mutual mode incoherence, which is a common assumption for the analysis of broadband sound fields, are indicated with circles. Except for 1BPF, the median of the estimated distributions overestimates the radiated sound power in comparison with the RMA results by 2 to 3 dB at the second and third harmonic, and approximately 9 to 10 dB at 4BPF. The results show that none of the three applied models leads to a significantly better agreement with the experimental data than the others.

In Fig. 6, the sound power levels are shown only for

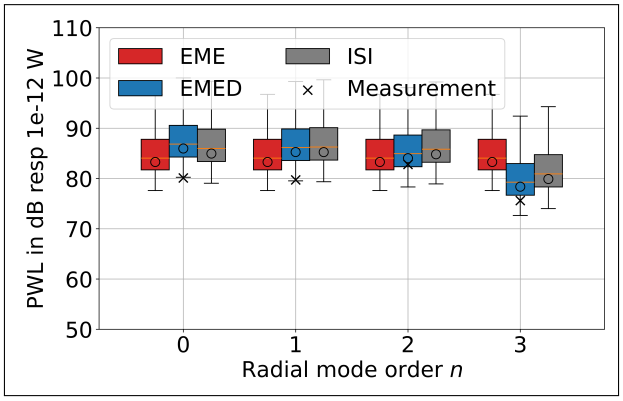


Figure 7. Estimated sound power of the rotor-stator interaction mode with mode order $m = -9$ at 4BPF in comparison to reference measurement data (indicated by crosses) and estimation results assuming mutual mode incoherence (indicated by circles).

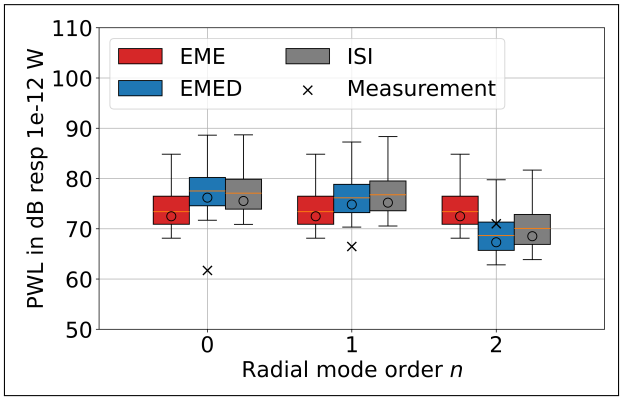


Figure 8. Estimated sound power of the rotor-stator interaction mode with mode order $m = 12$ at 4BPF in comparison to reference measurement data (indicated by crosses) and estimation results assuming mutual mode incoherence (indicated by circles).

the rotor-stator interaction modes, which are obtained from the Tyler-Sofrin rule [12]. For 1BPF and 2BPF, only radial mode order $n = 0$ is cut-on for the respective azimuthal mode orders, so that all models yield the same result for the tonal and broadband analysis. The corresponding sound power estimation results are in very good agreement with the reference results. At 3BPF, the median values of the three estimated distributions are nearly equal and lie within 1 dB of the measurement result. Similar to the results of the total sound power, for 4BPF the median values of all three distributions overestimate the radiated sound power by 9 to 10 dB in comparison with the reference results, which is further investigated next.

The first rotor-stator interaction mode at 4BPF has the azimuthal mode order $m = -9$. Figure 7 shows the sound power levels and distributions for each propagating radial mode order. It is evident, that the relative distribution of sound power over the radial mode orders matches relatively well with the EMED and ISI model. However, for the low radial mode orders both models overestimate the sound power stronger than the EME model.

The mismatch between the actual sound power levels of the propagating radial mode orders and the mode distribution models is even more pronounced for the second rotor-stator interaction mode at 4BPF with the azimuthal mode order $m = 12$. As shown in Fig. 8, the sound power levels of the reference results increase from low to higher radial mode order, which is in contrast to the mode distribution models. This mismatch leads to a strong overestimation of 10 to 12 dB for mode order $n = 0$ and 4 to 6 dB for mode order $n = 1$. This example illustrates an important deficiency of the available mode distribution models: their inability to represent the complex source distribution of turbomachine blade tones, which vary significantly with the rotor-stator stage geometry and the operating-point-dependent rotor wake characteristics (see e.g. [8]). These complex relations are not considered in any of the available mode distribution models.

5. CONCLUSION

A stochastic approach for sound power estimation based on azimuthal mode analysis is proposed, which takes into account the mutual coherence of tonal mode components radiated from turbomachinery stages. The approach combines prescribed magnitudes of the radial modes according to mode distribution models and randomly selected mode phases. Evaluating the sound power estimation in a Monte Carlo study yields a sound power distribution. It is shown that the spread of the distribution depends strongly on the number of propagating radial mode orders, whereas the median value of the distribution is a robust indicator of the estimated sound power. Besides two commonly used mode distribution models, "'equal mode

energy"' and "'equal mode energy density"', a third distribution model is developed based on a dense distribution of point sources, which is equivalent to constant source distribution over the duct cross-section. Here, the internal source impedance model for dipole sources from [9] is applied. However, the results for the estimated sound power from the three distribution models do not show a clear superiority of any distribution model. In the investigated test case from a fan test rig, the estimated sound power is in good agreement with the reference results obtained by radial mode analysis for the first three BPF harmonics. At 4BPF, the sound power is overestimated by 9 to 10 dB, which is likely to be linked to an insufficient match between the mode distribution models and the actual mode sound power distribution with respect to the radial mode order. Due to complex relations between the geometric and aerodynamic design of the rotor-stator configuration and the generated distribution of the radiated mode sound power, it is difficult to determine a generally valid mode distribution model for tonal fan noise. Therefore, the sound power estimation for tonal components based on azimuthal mode analysis is challenging, but it can be useful to determine trends of the radiated sound power in test environments with limited installation space.

6. ACKNOWLEDGMENTS

The authors are grateful for the support of Lukas Klähn and Wolfram Köhler in providing the experimental data from the CRAFT test rig.

This research has been performed in the frame of the project COMPANION (COMmon Platform and Advanced iNstrumentration readIness for ultra efficient propulsiON), which is funded by the European Union Clean Aviation Joint Undertaking program, under grant agreement No. 101140627.

CLEAN AVIATION Co-funded by the European Union

7. REFERENCES

[1] P. Joseph, C. L. Morfey, and C. R. Lowis, "Multimode sound transmission in ducts with flow," *Journal of Sound and Vibration*, vol. 264, pp. 523–544, 2003.

[2] A. Serrano and R. Vazquez, "Feasibility of using single mode rings for characterization of turbine tone noise," in *17th AIAA/CEAS Aeroacoustics Conference*, (Portland, Oregon (USA)), June 2011.

[3] U. Tapken, B. Pardowitz, and M. Behn, "Radial mode analysis of fan broadband noise," in *23rd AIAA/CEAS Aeroacoustics Conference*, (Denver, Colorado (USA)), June 2017.

[4] U. Tapken, M. Behn, M. Spitalny, and B. Pardowitz, "Radial mode breakdown of the acat1 fan broadband noise generation in the bypass duct using a sparse sensor array," in *25th AIAA/CEAS Aeroacoustics Conference*, (Delft, Netherlands), May 2019.

[5] J. D. Hurst, *Efficient in-duct tonal sound power estimation methods for radial compressors*. Dissertation, Technical University Berlin, Berlin, Germany, 2024.

[6] U. Tapken, *Analyse und Synthese akustischer Interaktionsmoden von Turbomaschinen*. Dissertation, Technical University Berlin, Berlin, Germany, 2016.

[7] M. Behn, R. Kisler, and U. Tapken, "Efficient azimuthal mode analysis using compressed sensing," in *22nd AIAA/CEAS Aeroacoustics Conference*, (Lyon, France), June 2016.

[8] A. Moreau, *A unified analytical approach for the acoustic conceptual design of fans of modern aeroengines*. Dissertation, Technical University Berlin, Berlin, Germany, 2017.

[9] M. Behn and U. Tapken, "Impact of resonance loading on the sound generation from in-duct point sources," in *Forum Acusticum Euronoise 2025*, (Málaga, Spain), June 2025.

[10] U. Tapken, L. Caldas, R. Meyer, M. Behn, L. Klähn, R. Jaron, and A. Rudolphi, "Fan test rig for detailed investigation of noise generation mechanisms due to inflow disturbances," in *AIAA AVIATION 2021 FORUM*, (virtual), August 2021.

[11] L. Klähn, R. Meyer, and U. Tapken, "Inflow distortion noise and turbulence measurements in a low speed fan test rig," in *30th AIAA/CEAS Aeroacoustics Conference*, (Rome, Italy), June 2024.

[12] J. M. Tyler and T. G. Sofrin, "Axial flow compressor noise studies," *SAE Transactions*, vol. 70, pp. 309–332, 1962.

DOI: 10.61782/fa.2025.0485



FORUM ACUSTICUM
EURONOISE 2025

INSTRUMENTATION AND MEASUREMENT VALIDATION APPROACH FOR AN AERO-ACOUSTIC CIRCULAR TESTRIG BASED ON TEMPORAL, FREQUENCY, AND MODAL CRITERIA

Jérémie Derré[1*] **Nicolas Aujogue**[2] **Paúl Rodríguez García**[1]
[1] Acoustic testing team, Flight test and integration center
[2] Acoustic design office, Propulsion center
Airbus Operations SAS, 316 route de Bayonne, 31060 Toulouse Cedex 03, France

ABSTRACT

This paper presents the study of a multi-criteria approach for the instrumentation and measurement validation of an experimental testrig. The study case is an aircraft engine liner characterization bench (named CANNELLE) which is a 3m-long circular duct, based on higher-order modal generation and detection principles. This approach has been initiated for rigs with a large number of sensors, being in this case two arrays of a hundred flush mounted microphones, distributed in an optimized pseudo-random arrangement. Heavy experimental campaigns with associated large test matrices lead to huge datasets, which need to be rapidly validated after the recording, and before moving forward to the next testpoint. Therefore, the proposed validation is based on a multiple criteria approach, and aims at comparing them with target values and associated confidence intervals. Thus, the final objective is to identify potential anomalies in each measurement run among the three following categories: a priori validated data, with nominal criteria; the "should be ok" data, with barely nominal criteria, and little investigation to perform; and the data with severe defaults, which require further analysis. The proposed paper presents the outcomes of this study, exploring criteria on the temporal, frequency, and modal domains when applied to a fully rigid bench without aerodynamic excitation flow.

*__Corresponding author__: jeremie.derre@airbus.com.
__Copyright__: ©2025 Derré et al. This is an open-access article distributed under the terms of the Creative Commons Attribution 3.0 Unported License, which permits unrestricted use, distribution, and reproduction in any medium, provided the original author and source are credited.

Keywords: Experimental testbench / Aeroacoustics / Higher-order modes / Data validation

1. INTRODUCTION

In the civil aircraft industry, the turbofan engines are the standard today for most of the mid- to long-range commercial flights. As the overall traffic is increasing and will continue to grow, the aircraft and engine manufacturers are more and more preparing their next products with a sustainable approach. Meanwhile, the latest international regulations, the ICAO chapter 14 [1] and the FAA stage 5 [2], are reinforcing the emission targets. For instance, they are imposing for the external noise a cumulative reduction of 7 EPNdB versus the previous version chapter 4 / stage 4, and further restrictions are expected for the next generation of aircraft. Therefore, it is of paramount importance to design and validate model of acoustic liner with efficiency and reliability. For that, testing is a key feature, especially when disruptive design are proposed, for which precise modeling and simulations are not mature or fast enough.

Research on liners is very abundant and diversified [3–12], as being at the crossroad of several disciplines, including for instance pure acoustics, aerodynamics, thermic coupling, or icing. Higher-order (also called transverse) acoustic modal content is a specific research field. Indeed, it is not that easy to set-up and measure, requiring several sources and microphones which quantities can be quite large, especially for turbofan engine experiments, whose number of blades is high, so that is the modal order. At the origin of the present paper, there are two

testrigs developed at the acoustic testing laboratory of Airbus Commercial Aircraft (Toulouse, France), which are heavily instrumented, with more than 150 sensors: a rectangular cross-section bench and a circular one. The testcampaigns performed with these benches are often parametric, to have a deep understanding of the physics, which leads to large temporal datasets. During the testcampaign, it is mandatory to validate the running testpoint before moving to the next one, in order to ensure the quality of the data, as the testmatrix sequences are optimized depending on priorities and added value.

To do so, data validation must be specific to guide the experimenter towards the potential issues and facilitate their root cause analysis. The proposed strategy is to work both on the microphone temporal data, their frequency transforms, and finally the modal calculations, by computing criteria on these three datasets. To be more specific, each criterion is compared to a target value, and several thresholds are defined, allowing to classify the criterion into three categories: a priori validated data; the "should be ok" data; and the data with severe defaults. The criteria have been chosen to explore three domains: the instrumentation, the measurement and the experiment quality. This approach has been developed for the above-mentioned rectangular cross-section bench called ModSquare [13, 14] at the Airbus acoustic lab, and its extension to the circular one named CANNELLE is proposed in this study.

The paper as proposed by the authors is organized in two main parts. The first one introduces some of the key features of the CANNELLE bench, including an overview of the test rig, its instrumentation, and post-processing. A focus is made on the bench specificities, based on modal generation and detection principles, with multiple sources arranged azimuthally, generating higher-order transverse modes in the duct. The second part presents the validation methodology of the generation, acquisition and test quality, based on experimental results, using temporal, frequency and modal data. Then, the chosen criteria are explained in detail. The proposed analysis is based on the canonical case of a purely rigid duct, without any aerodynamic excitation. Indeed, this configuration is used as a reference, and has been characterized several times during each campaign, for validation, repeatability and reproducibility purposes since the bench entry into service. Finally, the criteria results are discussed, as well as the thresholds and global outcomes of this analysis.

2. TESTRIG PRESENTATION

The following section presents the bench chosen for this paper, named CANNELLE. The main features of the testrig are presented, as well as its experimental set-up and operations.

2.1 Bench overview

The testrig chosen for this study is called CANNELLE, which stands in French for *Caractérisation des traitements Acoutiques Nacelle en eNvironnement et EcouLement réaListEsEs*. It has been developed in between the late 2000s and early to mid 2010s at the Airbus acoustic testing laboratory in Toulouse, with the motivation to validate modeling and numerical simulations with experimental data for impedance eduction, mainly applied to the liners of the engine's nacelles. It is a straight duct of about 3m-length, with a circular cross section of 350 mm diameter, whose walls are made of thick aluminum. The bench is based on higher-order modal generation and detection principles. The in-duct acoustic modal theory is not reminded in this paper, as already well documented in many publications and books [15, 16]. Fig. 1 proposes a picture of the CANNELLE bench when installed in "pure acoustic" configuration, meaning that there is no aerodynamic flow in the duct. The rig can be decomposed into several

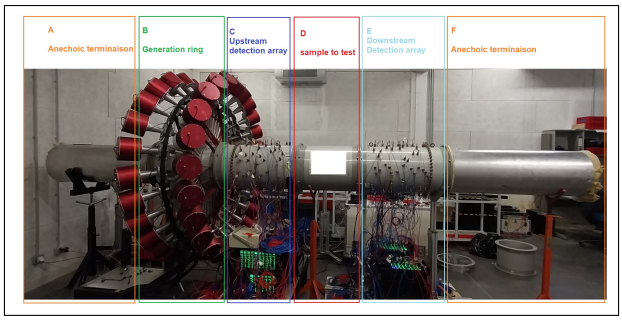


Figure 1. Picture of the CANNELLE bench in the Airbus acoustic laboratory, Toulouse (France).

sub-parts such as follow:

- the part [A], a first ending of about 1m, filled with glasswool;
- the part [B], the generation ring composed of 50 loudspeakers, used for modal excitation;
- the part [C], a first modal detection ring, consisting of an azimuthal array of 50 microphones equally

spaced, and an optimized pseudo-random array of 100 microphones;
- the part [D], the location for the sample to test;
- the part [E], the second modal detection ring, with the same arrangement than the part [C], except that sensor positions are symmetrical regarding the sample;
- the part [F], the second ending, as part [A].

The parts [A] and [F] are considered anechoic at the frequency and levels of interest, based on preliminary studies performed during the bench development phase. All parts are aligned with pins, ensuring a fair flushness into the bench. This aspect is very important because the bench can also be used in wind tunnels, in order to combine the aerodynamic flow to the acoustic excitation. In such a case, the parts [A] and [F] are removed, and the wind tunnel is connected on one side (let's say instead of part[A]), whereas a sonic throat of the Mach number of interest is plugged at the other end (instead of part [F]). There are three sonic throats built to this day, designed for Mach numbers 0.3, 0.45 and 0.6. The specificity of the CANNELLE bench is that the acoustic excitation could be-mounted both for parallel or counter flows. Indeed, by moving the generation ring (part B) after the downstream detection array (part [E]), the acoustic excitation is traveling against the aerodynamic flow. If acoustic liners of an engine nacelle are tested in the bench, and the generation ring (part [B]) is simulating a fan, counter flow is representing the inlet configuration, whereas parallel flow aims for bypass or exhaust.

2.2 Instrumentation and operations

During the bench design and development phases, a compromise has been made between the maximal modal order, the maximal frequency and the generation (the number of loudspeakers) and instrumentation size (the number of microphones), leading to approximately 40 cut-on modes at 5000 Hz, linked to the duct diameter. The generation signal is a sinusoidal pure tone, sent to all loudspeakers with the appropriate phase delays, in order to directly generate the desired azimuthal mode shape. As loudspeakers only control the pressure on the duct wall, selecting a specific radial mode is not possible. Thus, all cut-on radial modes are excited simultaneously. The gain is adjusted to reach the expected level based on the acoustic pressure level, once averaged over all the microphones of the upstream acoustic array (part [B] in Fig. 1). The MaxMSP software is used to master the generation. A digital signal is sent encoded into MADI (Multichannel Audio Digital Interface) format towards two chained digital-to-analog RME M-32 DA converters, which output are the 50 analog lines sent to the 25 double channel QSC Audio RMX 2450 amplifiers. Finally, the amplified signals are sent to the 50 BMS 4599 compression drivers.

When used in the Airbus acoustic lab, the bench is in a "pure acoustic" configuration, meaning there is no aerodynamic flow. A temperature sensor (PT100) is installed flush mounted at the end of the bench, and recorded simultaneously with the microphones. The atmospheric pressure is manually entered in the testcampaign log, allowing to compute the sound wave celerity combined with the temperature. Only the 100 optimized pseudo-random microphones of each detection array (parts [C] and [E]) are used. These 200 sensors are 1/4 inch pressure field microphones with front-vented cartridges, mounted flush without their protection grids. To record, Brüel and Kjær 6-channel Lan-xi acquisition systems are used, powered and mounted on rack frames. The clock synchronization is managed by a B&K layer using PTP (Precision Time Protocol), with a classical master-slave architecture. A local network is connecting all the rack frames, the generation and acquisition computers using a network switch.

A record for one given frequency and modal configuration lasts 5 seconds, using a 7 seconds generation that includes a fade-in and a fade-out. A trigger signal sent from the MaxMSP patch is used to synchronize the acquisition. There is no feedback control loop or enslavement: indeed, the gain adjustment is done separately, at the beginning of the campaign. As already mentioned, the target is to reach a level on the average of the upstream detection array, when the bench is fully rigid, meaning that there is no liner installed. The usual target is around 120 or 130 dB for linear regime, and between 140 and 150 dB to reach non linearity. Parallel to the record, a "perfo" file is created, logging data such as the absolute and unique number of the run, the generation frequency, the targeted mode, and the atmospheric pressure for instance. All the frequency data (auto and inter-spectra, transfer function and coherence) are computed from the temporal raw data file, using B&K Connect version v26.0.0.241. Finally, the modal amplitudes and intensities are computed from the frequency data using an in-house code called MoDe, which has been validated on canonical cases with Actran FEM simulations in 2013 [17]. The transmission loss can be calculated by computing the modal difference between the two detection arrays, providing a direct evaluation of the acoustic sample efficiency.

3. CRITERIA METHODOLOGY AND APPLICATION

This chapter presents the validation methodology developed from the experimental results, and based on temporal, frequency and modal data. The chosen criteria are detailed, with their expected targeted values based on experience from the past campaigns, and on engineering judgment. They are applied to the purely rigid duct measurements in the CANNELLE bench without aerodynamic flow, which is considered as a reference measurement. To ease the presentation, a given testpoint, called α chosen randomly, is used in this chapter. A testpoint is the triplet combination of a target frequency, its associated level, and the azimuthal order of the mode to generate.

3.1 Validation based on criterion in the time domain

It is firstly proposed to simply compute the overall sound pressure level (OASPL) as a function of time, and to verify that it is somehow constant / stable during the acquisition. To save some computation time, it has been chosen to compute it on one microphone only. Indeed, the purpose here is to verify that the generation is stable, not the microphones during a record, so that it is assumed here that the acquisition chain is behaving as expected (this aspect is detailed later in this paper). The first microphone of the upstream detection array (part [C] in Fig. 1) has been chosen, as also being used for the cross-spectral computation as the reference for this detection barrel. The criterion C1 is the OASPL computed with a time integration step of 0.25s, and compared the the target level during the 5 second of record. The chosen thresholds are summarized in Table 1, and the data are considered such as validated if the OASPL lies within a range of +/- 1dB around the target level.

Table 1. Criterion C1: OASPL VS time.

C1 $\in$ target +/- 1dB	Validated data
C1 $\ni$ target +/- 1dB	Defaults

This criterion is not intended to evaluate in detail the issues that could appear at different steps, such as:

- problems in the generation chain itself (from the generation computer, the digital to analog conversion, or from the amplification);
- issues due to the loudspeakers distortion;
- unknown effects during the propagation of the acoustic waves inside the duct;
- noise pollution linked to the acoustic background noise of the lab;
- issues in the acquisition chain (electrical noise, grounding issues, etc.).

Several of these points are addressed in the next section.

3.2 Validation based on criteria in the frequency domain

As described in section 2.1, there are two microphone arrays in the bench, one upstream and one downstream of the sample, with 100 pseudo-randomly distributed microphones each. It is proposed to compute the "mean auto-spectrum" for each array, which corresponds to the mean of all the microphone auto-spectra over the 5-second record. This quantity gives an overview of the sensors and signals behaviors in each array. The next six criteria are all based on this mean auto-spectrum for the upstream microphone array, the one between the source and the sample, as the example of Fig. 2.

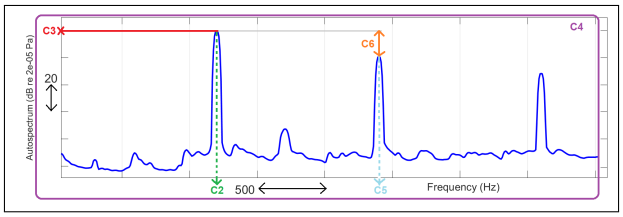


Figure 2. Mean auto-spectrum and schematic criteria representation for the testpoint α.

First, in order to ensure that the generated frequency is indeed the targeted one, the maximum peak frequency is detected in the mean auto-spectrum, and the difference with targeted frequency is computed, sketched as the criterion C2 in Fig 2. Any deviation would discard the testpoint, and a root cause analysis must follow.

Table 2. Criterion C2: max frequency identification.

C2 $= 0$	Validated data
C2 $\neq 0$	Severe defaults

The chosen thresholds are summarized in Table 2, and the data are considered as validated if there is no difference between the maximal frequency of the mean auto-spectrum, and the target frequency. This of course assumes that the generation frequency is piloted in accordance with the frequency step of the delta f used in the spectrum computations.

Directly after, the level of this maximum peak, identified as criterion C3, is compared to the generation target, ensuring proper correspondence. As above mentioned, all the generation gains are adjusted in the campaign preparation phase, and there is no enslavement or feedback control loop during a record. Any discrepancy in the productive tests has to be identified and investigated. A threshold value of 2dB is proposed, as presented in Table 3.

Table 3. Criterion C3: max level identification.

C3 $\in$ target +/- 2dB	Validated data
C3 $\ni$ target +/- 2dB	Defaults

It has to be noted that the gains are derived for the fully rigid sample, and applied then for all samples to be tested. Due to their impedance, or the quality of the mechanical flushness of the tested sample, the reflected energy will change, and can affect then the levels on the upstream array.

In a third step, the next criterion compares the target level at the targeted frequency with the global OASPL, in order to detect any significant perturbations. Indeed, most of the energy should be carried by the targeted frequency in a laboratory environment such as the CANNELLE one. The C4 criterion is the absolute value of the difference between the max SPL at the targeted frequency with the OASPL averaged of the 100 microphones of the mean auto-spectrum, both on the upstream array. Based on the past experiences, and expectations of such a set-up, it has been decided to build two thresholds values, leading to the three categories mentioned in Table 4.

Considering the high levels injected in the bench, the harmonics of targeted frequency are often generated by the compression drivers. If harmonic distortion occurs, the second highest level of the mean auto-spectrum might probably be a peak, and the first harmonic of the targeted frequency. For that, the second highest level is detected, and the ratio between the first and second max level frequencies is computed, to validate if it is indeed a harmonic. For the search of the second maximum, it is proposed to explore all the rest of the spectrum. However, a certain distance to the first peak has been set. Working with a delta f of 4 Hz, several values have been tested, and the selected distance is further than 20Hz (so 5 spectral lines) on each side of the first maximum. As summarized in Table 5, this is an all-or-nothing criterion. When it is different of two, so not an harmonic, it could have several root causes, like the generation chain (digital to analog conversion, the amplification), the loudspeakers distortion, the lab acoustic background noise, or the acquisition chain (electrical noise, grounding issues, etc.).

Table 4. Criterion C4: max level and OASPL difference

C4 ≤ 0.1	Validated data
$0.1 >$ C4 ≤ 0.5	Should be ok data
C4 > 0.5	Severe defaults

Table 5. Criterion C5: 2^{nd} and 1^{st} max level frequencies ratio.

C5 $= 2$	Validated data
C5 $\neq 2$	Defaults

Immediately after, if the second peak is indeed the first harmonic, it is proposed to compare it to the first maximum. The difference of the two is computed, leading to criterion C6. This is mainly providing information on the compression drivers health. The threshold of this criterion are difficult to set, mainly because it is directly linked to the targeted level. Indeed, if for instance, 130 dB is expected, the distortion is reasonable, and the C6 can be up to 20 dB when there is no default on the generation. However, if the target is 140 or 150 dB, then C6 criterion can easily be 5 dB or less, even when the compression drivers are working properly. Table 6 summarizes the threshold values for the C6 criterion.

The last criterion in the frequency domain is based on

Table 6. Criterion C6: difference between 1^{st} and 2^{nd} max levels.

C6 $>$ 20dB	Validated data
C6 $\in$ [10 ; 20] dB	Should be ok data
C6 $<$ 10dB	Defaults

coherence. It is quite straightforward in order to detect any issue linked to one or several microphones. Fo that, the coherence is computed for all microphones of both upstream and downstream arrays, with the reference sensor being the first microphone of each array. The criterion C7 is computed by extracting the coherence values at the generated frequency, as shown in Fig 3.

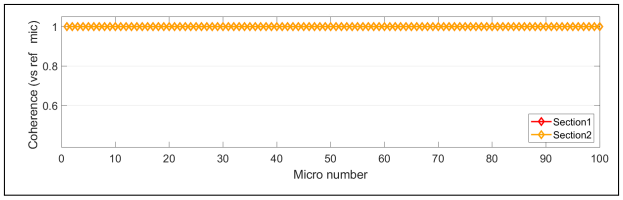


Figure 3. Coherences at the excitation frequency of all microphones of the two detection arrays for the testpoint α.

Table 7 summarizes the thresholds values for this criterion.

Table 7. Criterion C7: coherence values at the target frequency.

C7 $>$ 0.99	Validated data
C7 $\in$ [0.9 ; 0.99] dB	Should be ok data
C7 $<$ 0.9	Defaults

As the CANNELLE set-up is in a lab environment, the coherence is expected to be very close to 1, considering that there is no flow, and that all the microphones are in the same waveguide. A lower coherence might indicate a defect on the SPL at targeted frequency, a mic issue, or the presence of parasitic noise, either acoustic background or electrical noise. A value lower than 0.99 illustrates a significant difference. Furthermore, a value lower than 0.9 directly shows a severe default on the concerned microphone.

3.3 Validation based on criteria in the modal domains

As the purpose of the bench is the modal generation, it is important to verify that the test has reached its objectives.

First, only the upstream detection array is considered. Figure 4 represents the intensities of the incident and reflected propagative modes of the testpoint α. The maximum modal intensity is identified, and its associated azimuthal order is compared to the target, and the criterion C8 is their difference. Any deviation would discard the testpoint, and a root cause analysis follows, as summarized in Table 8.

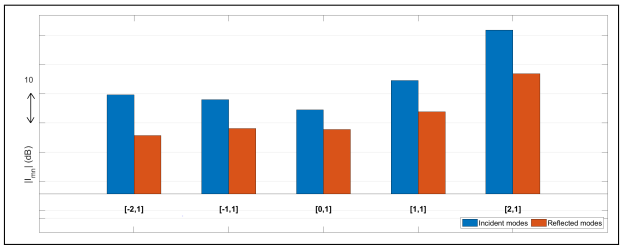


Figure 4. Intensities of the incident (blue) and reflected (orange) propagative modes in the upstream detection array for the testpoint α.

Table 8. Criterion C8: dominant mode identification.

C8 $= 0$	Validated data
C8 $\neq 0$	Severe defaults

Then, the second maximum modal intensity is identified and analyzed. First, its modal intensity is compared to the maximum one, leading to Table 9 threshold values for this C9 criterion.

The way this criterion is computed has to be adapted when at least one second-order radial mode is cut-on. Indeed, the modal energy of the same azimuthal order will be spread over all radial cut-on modes.

Moreover, it is interesting to analyze which mode is the one with the second largest modal intensity. It could be the same mode but its reflected part, meaning the acoustic waves traveling backwards. It could also be another

Table 9. Criterion C9: difference between 1^{st} and 2^{nd} max modal intensities.

C9 $>$ 20dB	Validated data
C9 $\in$ [10 ; 20] dB	Should be ok data
C9 $<$ 10dB	Defaults

mode: the closest one in terms of azimuthal content, or the mode with the cut-on frequency being the nearest to the generation frequency for instance. There is no criterion on this aspect because it has to be analyzed case by case. Then, this C9 criterion can be computed for the downstream detection array as well, and the results have to be put into perspective regarding what has been found on the upstream detection array.

Finally, the last criterion is the transmission loss (TL) on the generated mode. With the bench in a "pure acoustic" configuration, it is assumed that it is equal to 0 when the rigid section is installed (if the viscous dissipation on the duct wall is not taken into account). Even if the approach followed in this study does not aim at assessing the experiment uncertainty, this final criterion provides a fair idea of the full method reliability and robustness, because it includes the impact of the bench mounting, the generation, the acquisition and the full data post-processing chain. A confidence interval of +/-1dB is proposed, as presented in Table 10.

Table 10. Criterion C10: transmission loss.

C10 $\in$ [-1 ; 1] dB	Validated data
C10 $\ni$ [-1 ; 1] dB	Defaults

4. DISCUSSION AND CONCLUSION

This study presents a methodology for the validation of experimental data, applied to a circular testrig that works on the principle of higher-order modal generation and detection. The approach is based on the computation of criteria in the temporal, frequency and modal domains, and to compare them with the target values and their associated thresholds.

The bench considered is CANNELLE, a circular waveguide built on modal generation and detection principles, generally used for acoustic liner characterization in pure acoustic or in aero-acoustic configurations, mounted in this study with a rigid part considered as a reference set-up. Several criteria are computed from the microphone temporal raw data: 1 in the temporal domain, 6 in the frequency domain, and 3 in the modal domain. One or several thresholds are proposed, in order to establish if the criterion is considered: as nominal and lies within the expected target, so that the data are a priori validated; as barely nominal , with little investigation to perform, so that data "should be ok"; or as a default (more or less severe), which are requiring further analysis.

Several conclusions are drawn from this study. First, the criteria provide information for different validation aspects: at the instrumentation level, the measurement and the experiment itself. For the instrumentation, it can reflect if the acquisition has properly worked (no electrical perturbations or large faulty contact, microphones capturing the signal, etc.). About the measurement, it helps to identify if the generation is working as expected, or if the generated signal is emerging from the background noise, or if there are any other perturbations in the record, electrical or acoustical. Concerning the experiment, it helps to understand if the experiment has worked, meaning that the targeted mode is the dominant one, and that other cut-on modes, either created by error in the generation or by some modal re-distribution during propagation for instance are not perturbing the test. One of the key features of the criteria analysis is that these indicators clearly prepare the testpoint validation, and allows to put the focus towards particular results that might need further investigations to understand the abnormal behavior.

However, it clearly appears that the target values and their associated thresholds need to be refined. Although the values proposed in this study are based on the past experiences and testcampaign observations, with engineering judgment, a previous study on another testbench [14] has shown that a statistical analysis of a representative dataset could help to fine tune the values. Moreover, it is obvious that some thresholds should be adapted to the target level. Indeed, the compression drivers do not have the same behavior when excited to reach 130dB or 150dB. For instance, the harmonic distortion is strongly dependent on the voltage of the excitation. A consequence could be directly observed on the C6 criterion, the difference between the first and the second maximum levels of the mean-spectrum. Following the same reasoning, the thresholds should also be adapted to the frequency: the responses of

the compression drivers differ a lot between 300 Hz and 5000 Hz. This might be considered in the next improvement phase of the methodology, to have frequency and level dependent thresholds for some specific criteria.

In order to continue the development of such a methodology, it will be interesting to apply this approach to other reference samples, which are measured several times during each testcampaign, mainly for reproducibility purposes.

Then, the step after could be to evaluate the limit of the criteria and associated target values, with for instance their application to *a priori* unknown liner sample. In addition, this method is planned to be extended to the bench when used in wind tunnel testing for aero-acoustic liner tests. The target values and the thresholds might be adapted, as well as some criteria (e.g. C5). Indeed, it sometimes happens that wind tunnel aerodynamic flow carries some tonal component, linked to the fan of the facility. In addition, the frequency computations might also be modified to use synchronous averaging as in [12].

5. REFERENCES

[1] ICAO, *Annex 16 to the Convention on International Civil Aviation : Environment Protection*, vol. I — Aircraft Noise. City: International Standards and Recommended Practices, 8 ed., July 2017.

[2] D. o. T. FAA, *Title 14, Chap. I, Subchap. C, Part 36 - Noise standards: aircraft type and airworthiness certification, Stage 5*. Code of Federal Regulations, 2017.

[3] C. H. Gerhold, R. H. Cabell, and M. C. Brown, "Development of an experimental rig for investigation of higher order modes in ducts," *AIAA Paper 2006-2637*, pp. 1–19, May 2006.

[4] Y. Aurégan and Y. Renou, "Failure of the ingard-myers boundary condition for a lined duct: An experimental investigation," *J. Acoust. Soc. Am.*, vol. 130, no. 1, pp. 52–60, 2001.

[5] S. Busse-Gerstengarbe, F. Bake, L. Enghardt, and M. G. Jones, "Comparative study of impedance eduction methods, part 1: Dlr tests and methodology," *AIAA Paper 2013-2124*, pp. 1–13, May 2013.

[6] J. Primus, E. Piot, F. Simon, and M. G. Jones, "Onera-nasa cooperative effort on liner impedance eduction," *AIAA Paper 2013-2273*, pp. 1–15, May 2013.

[7] L. Zhou, H. Boden, C. Lahiri, F. Bake, L. Enghardt, S. Busse-Gerstengarbe, and T. Elnady, "Comparison of impedance eduction results using different methods and test rigs," *AIAA Paper 2014-2955*, June 2014.

[8] M. G. Jones, W. R. Watson, D. M. Nark, B. M. Howerton, and M. C. Brown, "A review of acoustic liner experimental characterization at nasa langley," *NASA report*, vol. TP–2020–220583, pp. 1–52, April 2020.

[9] Q. Leclère, A. Pereira, A. Finez, and P. Souchotte, "Indirect calibration of a large microphone array for in-duct acoustic measurements," *J. Sound Vib.*, vol. 376, pp. 48–59, August 2016.

[10] J. Golliard, E. Portier, J.-C. L. Roux, and T. Humbert, "Maine flow facility for measurement of liner properties in multimodal acoustic field with grazing flow: Qualification and first liner characterization," *AIAA Aviation Forum*, August 2021.

[11] D. L. Sutliff and T. Marotta, "Measurements of interaction and scattered modes in a mixed bypass/core duct due to multiple rotating source," *22nd AIAA/CEAS Aeroacoustics Conference*, May 2016.

[12] A. Pereira and M. C. Jacob, "Modal analysis of in-duct fan broadband noise via an iterative bayesian inverse approach," *Journal of Sound and Vibration*, vol. 520, p. 116633, 2022.

[13] J. Derré, F. Mercat, O. Deille, and E. Julliard, "Multi-criteria approach for instrumentation and measurement validation," in *Proc. of the CFA22*, (Marseille, France), pp. 1–8, 2022.

[14] J. Derré, F. Mercat, O. Deille, and E. Julliard, "Validation of the instrumentation and measurement of an acoustic liner test rig by a combined frequency and modal approach," in *Proc. of the 28th AIAA/CEAS Aeroacoustics Conference*, (Southampton, UK), pp. 1–15, 2022.

[15] M. Bruneau, *Manuel d'acoustique fondamentale*. Etudes en mécanique des matériaux et des structures, Hermes, 1998.

[16] S. W. Rienstra, *Fundamentals of duct acoustics*. Von Karman Institute, Lecture Series 2, 2016.

[17] M. Lavieille, "Cannelle : Large scale bench numerical modeling," *Airbus internal - Tech. Report*, no. RP1349302, 2013.

DOI: 10.61782/fa.2025.0628



FORUM ACUSTICUM
EURONOISE 2025

NUMERICAL ASSESSMENT OF A MODE DETECTION ARRAY FOR AZIMUTHAL DECOMPOSITION

Hugo Vincent* **Antonio Pereira** **Marc C. Jacob**

Ecole Centrale de Lyon, CNRS, Universite Claude Bernard Lyon 1, INSA Lyon, LMFA, UMR5509, 69130, Ecully, France

ABSTRACT

The efficiency of a mode detection array for azimuthal mode decomposition in turbofan nacelle experiments is numerically investigated by analyzing acoustic solutions computed using the commercial finite-element code ACTRANTM. First, irrotational inviscid mean flow fields are computed for sideline conditions, with and without an external flow at a Mach number of 0.2. Then, the upstream propagation of duct modes representing fan noise components is performed for three frequencies by solving the Möhring equation in the frequency domain using ACTRANTM. The acoustic solutions are interpolated to the microphone locations of the mode detection array. In all cases, the azimuthal structure of the interpolated data is obtained using Fourier transforms. It is compared to a reference one, determined by a duct mode decomposition of the full acoustic solution. The results provide guidelines for the analysis of ongoing experiments. They indicate that the detection antenna will be able to efficiently capture the azimuthal mode distributions, but not the radial structure. The procedure can be applied to design improved microphone arrays by defining judicious axial and radial positions for azimuthal and radial mode decompositions. Moreover, the approach can determine the optimum discretization for azimuthal mode decomposition.

Keywords: *aeroacoustics, duct mode, modal analysis*

**Corresponding author*: *hugo.vincent@ec-lyon.fr.*

***Copyright**: ©2025 H. Vincent et al. This is an open-access article distributed under the terms of the Creative Commons Attribution 3.0 Unported License, which permits unrestricted use, distribution, and reproduction in any medium, provided the original author and source are credited.*

1. INTRODUCTION

Aircraft produce noise that affects the health of people living near airports. Acoustic radiation originates mainly from the engine and, in particular, from the jet and the fan stage. With the development of Ultra-High Bypass Ratio (UHBR) engines, the noise produced in the fan stage has become the main noise contributor, as described in the recent review by Moreau [1]. The noise generated in the fan stage is characterized by tonal and broadband components. The tonal noise is produced at the Blade Passing Frequency (BPF) and its harmonics [2]. It is reduced by the use of acoustic liners [3], the optimization of which requires an in-depth knowledge of the acoustic field properties.

During their propagation in a turbofan intake, the acoustic waves reflect on the nacelle walls, leading to constructive and destructive interference at specific radial and azimuthal locations. As a result, the acoustic field can be decomposed into azimuthal and radial duct modes [4, 5]. The duct modes satisfy specific dispersion relations whose properties are used to determine key features of the acoustic field from in-duct experimental measurements [6–8].

The measurements are generally performed with wall-flush mounted microphones. The azimuthal structure of the acoustic field can easily be estimated from pressure measurements obtained on a microphone ring using Fourier transforms in the azimuthal direction. Computing the radial-mode amplitudes is more challenging since it is not possible to put microphones in the radial direction in a turbofan without significantly disturbing the flow. To the best of the authors' knowledge, Moore [6] was the first to describe a method for performing radial decomposition.

This method consists in projecting the acoustic field onto Bessel functions. Using this method, Moore [6] was able to decompose a synthetic field into azimuthal and radial modes. He also successfully applied the method to circumferential and radial measurements for a ventilation fan. Considering only measurements obtained in the azimuthal and axial directions, with rings and lines of microphones, and using the properties of the solutions of the convective wave equation, Enghardt *et al.* [7] were able to carry out an azimuthal and radial mode decomposition of the pressure fields measured in an axial-flow fan, using a method similar to the one introduced by Moore [6].

From measurements in the radial, azimuthal, and axial directions, it is possible to separate the upstream and downstream waves and to determine the amplitudes of the duct modes by applying procedures described by Rienstra [9]. However, in practice, such a full-mode decomposition cannot usually be performed because it requires microphones in the radial direction.

In the framework of the COMPANION (COMmon Platform and Advanced iNstrumentration readIness for ultra efficient propulsiON) project, pressure measurements obtained on a mode detection antenna will be analyzed to characterize the propagation of fan noise in a new-generation nacelle intake. The antenna is represented in figure 1. It is made of two rings and 4 axial lines linked to the azimuthal angles $\theta = 0, \pi/2, \pi$ and $3\pi/2$. All microphones are uniformly spaced and flush-mounted in the wall. A part of the nacelle intake is also depicted in figure 1. The geometry is non-axisymmetric and has a plane of symmetry.

The objective of the present work is to assess the capacity of the detection antenna to perform an azimuthal and radial decomposition. The study is conducted by analyzing pressure fields associated with fan noise propagating upstream through the nacelle intake. These pressure fields are simulated using the commercial finite element code ACTRANTM. Two flow configurations for sideline conditions and three frequencies are considered.

The remainder of this paper is organized as follows. Mean flow computations are documented in section 2. The numerical methods used for acoustic propagation calculations, as well as the pressure fields obtained, are described in section 3. A full mode breakdown is described in section 4. The capability of the antenna to perform azimuthal and radial decompositions is assessed in section 5. Concluding remarks are provided in section 6.

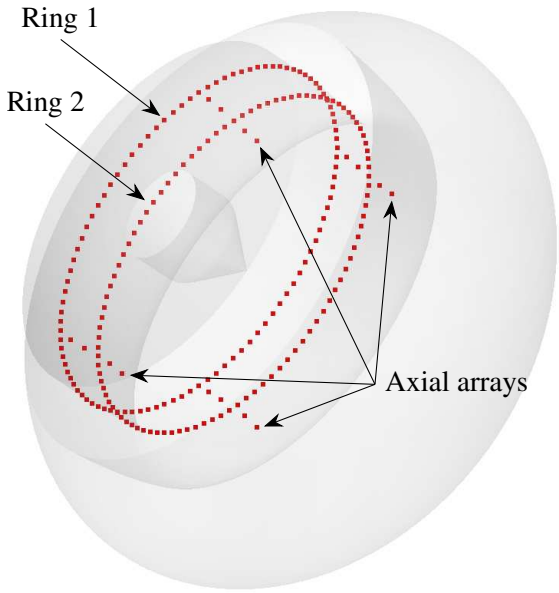


Figure 1. Representation of the inlet acoustic antenna composed of 2 rings and 4 axial lines; A part of the nacelle intake is displayed with transparency.

2. MEAN FLOW COMPUTATIONS

Two flow configurations associated with sideline conditions with and without an external flow at a Mach number of 0.2 are considered. Compressible irrotational inviscid mean flow fields are calculated using a potential flow solver implemented in ACTRAN. For that, an almost cylindrical computational domain is defined using the open-source software GMSH [10]. It is closed by an outlet surface normal to the flow direction located slightly downstream of the intersection between the rotor blades and the spinner. The rotor blades are not considered.

Mean pressure, density, and velocity fields are obtained by solving a generalised Laplace equation for the scalar potential using the finite element method. This equation is solved for an unstructured mesh composed of 9.4 million first-order triangles and tetrahedra generated using GMSH [10]. The element sizes were determined by a mesh sensitivity study, not described in this paper for the sake of brevity. The calculations required 28 GB of memory and less than one CPU hour. The mean flow fields were stored in all the mesh elements. They were used by ACTRANTM to solve the convected wave equation.

Cross-sections of the mean velocity fields obtained for $\mathrm{M_{ext}} = 0$ and $\mathrm{M_{ext}} = 0.2$ are represented in figures 2(a,b). For both cases, outside the nacelle, the levels are close to the exterior velocity associated with $\mathrm{M_{ext}} = 0$, as expected. Inside the geometry, they are higher and the mean velocity fields are nearly uniform, with velocity values around $165\,\mathrm{m/s}$. The strongest levels are found inside the geometry near the inlet lips. They are around $250\,\mathrm{m/s}$ for $\mathrm{M_{ext}} = 0$ and $200\,\mathrm{m/s}$ for $\mathrm{M_{ext}} = 0.2$. The flow near the inlet lips is thus more accelerated for $\mathrm{M_{ext}} = 0$ than for $\mathrm{M_{ext}} = 0.2$. These results are consistent with those reported by Doherty & Namgoong [11] and Xiong *et al.* [12].

3. ACOUSTIC PROPAGATION COMPUTATIONS

The acoustic propagation computations are carried out using ACTRANTM by solving a frequency domain formulation of the Möhring's equation [13], i.e. the convected wave equation for a non-uniform irrotational flow. Acoustic modes are injected slightly downstream of the intersection between the rotor blades and the spinner. Three arbitrarily chosen frequencies $f = 1000\,\mathrm{Hz}$, $3000\,\mathrm{Hz}$ and $5000\,\mathrm{Hz}$ are considered. They are associated with the Helmholtz numbers $\mathrm{He} = 2\pi f R/c_0 = 6, 18, 30$, where R is the outer duct radius and c_0 is the speed of sound in ambient medium. For each frequency, the propagation of all acoustic modes with a cut-off frequency below $3000\,\mathrm{Hz}$ is computed. The amplitude of the modes is set to $1\,\mathrm{Pa}$ at the injection plane. Thus, 16 modes are considered for $f = 1000\,\mathrm{Hz}$, whereas 126 modes are taken into account for $3000\,\mathrm{Hz}$ and $5000\,\mathrm{Hz}$.

The numerical methods used for the simulations are very similar to those recommended by Van Antwerpen *et al.* [14]. The computational domains are semi-elliptical and their size varies with frequency. Exploiting the planar symmetry of the nacelle intake, half-domain computations are performed using a fully automated strategy for decomposing the acoustic solutions into symmetric and anti-symmetric parts implemented in ACTRANTM. Acoustic meshes are generated using GMSH [10]. They are made of quadratic triangles and tetrahedra, and are refined so that each acoustic wavelength is discretized by at least four elements. The Perfectly matched layers (PMLs) described by Hu [15] are used at the boundaries considering non-uniform mean flow fields. Their thickness varies with frequency and is equal to $\lambda = c_0/f$. Six different meshes are thus considered. They contain between 710 000 and 7 200 000 nodes.

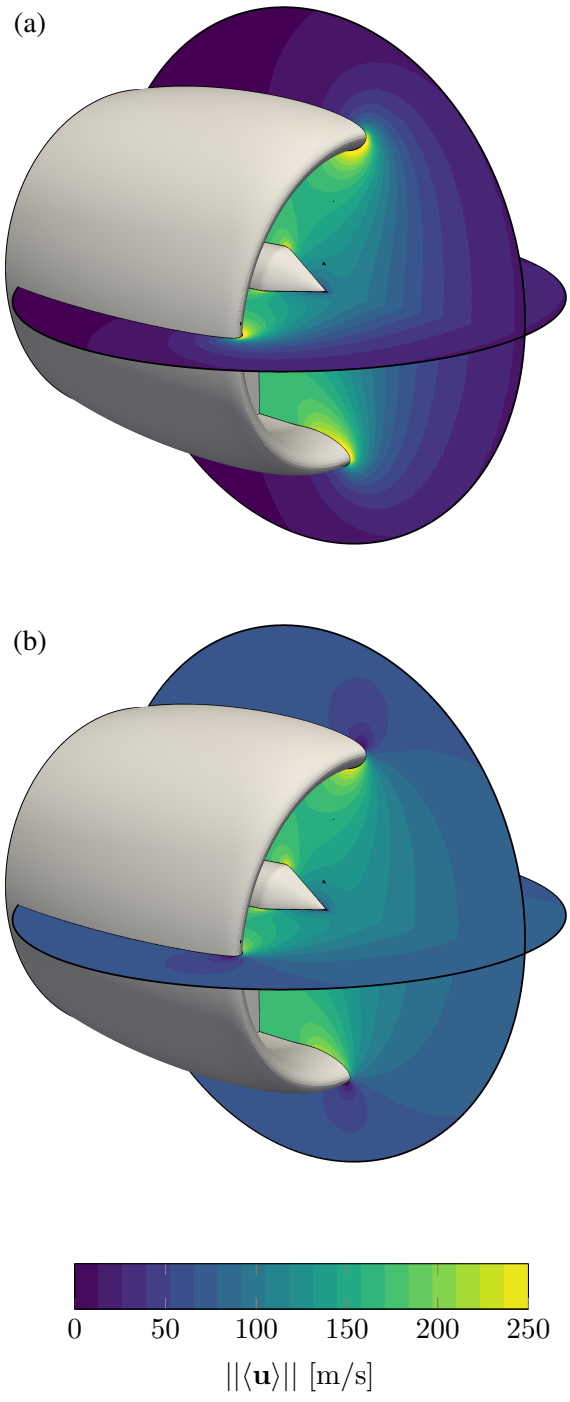


Figure 2. Magnitude of mean velocity vector on two longitudinal slices for sideline conditions and an external flow at (a) $\mathrm{M_{ext}} = 0$ and (b) $\mathrm{M_{ext}} = 0.2$.

For $f = 1000\,\text{Hz}$, the computations require around 8 GB of memory and less than one hour of CPU time. For $f = 5000\,\text{Hz}$, the simulations need approximately 200 GB of memory and 10 CPU hours. For each frequency and mode, the solutions have been stored on a full 3D mesh associated with the computational domain without the PML, on the microphone locations of the detection antenna, and on a cylindrical structured grid. The solutions for more than 500 modes were thus stored, constituting a database of approximately 700 GB.

The pressure fields obtained for the three frequencies 1000 Hz, 3000 Hz and 5000 Hz, for the two flow conditions with $\text{M}_{\text{ext}} = 0$ and $\text{M}_{\text{ext}} = 0.2$, for the plane mode, are represented in figures 3(a-f). In all cases, the propagation of acoustic waves through the inlet geometry and in the near field can be seen. The wavelengths are shorter for higher frequencies, and near the high velocity regions, as expected. For $f \geq 3000\,\text{Hz}$ in figures 3(b,c) and 3(e,f), the footprints of modes with radial orders $n \geq 0$ can be observed on the upstream boundaries of the domains.

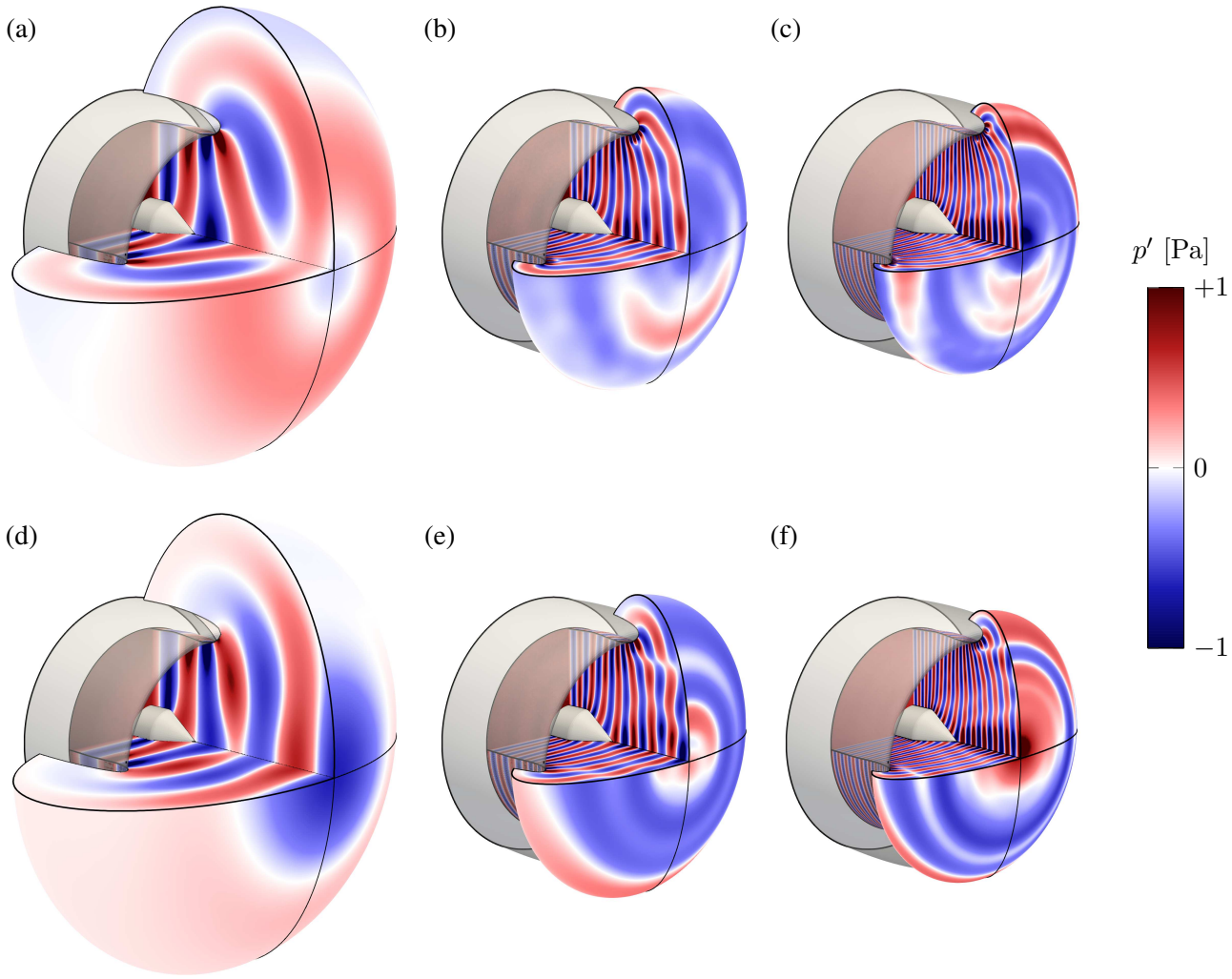


Figure 3. Representations of the real part of the pressure fields obtained for (a-c) $\text{M}_{\text{ext}} = 0$ and (d-f) $\text{M}_{\text{ext}} = 0.2$, and (a,d) $f = 1000\,\text{Hz}$, (b,e) $f = 3000\,\text{Hz}$ and (c,f) $f = 5000\,\text{Hz}$; three quarters of the computational domains without the PMLs are shown, and the geometry is displayed in gray with transparency.

4. DUCT-MODE DECOMPOSITION

The acoustic solutions are decomposed into upstream and downstream propagating azimuthal and radial modes by applying a procedure described by Rienstra [9]. The pressure fields satisfy equation (1), where $A_{m,n}$ and $B_{m,n}$ are respectively the amplitudes of the upstream and downstream propagating modes associated with the eigenfunctions for annular and circular duct sections $f_{m,n}$, and $k^+_{z_{m,n}}$ and $k^-_{z_{m,n}}$ are the associated axial wavenumbers, m and n are the azimuthal and radial orders, and i is the imaginary unit. The decomposition is performed for the duct-modes with azimuthal and radial orders between $m = 0$ and 4 and $n = 0$ and 4, using the complex pressure and axial velocity obtained on the structured grid previously mentioned. This grid is uniform and contains $N_r = 50$, $N_\theta = 64$, and $N_z = 60$ points in the radial, azimuthal, and axial directions. It extends radially from $r = 0$ up to the outer radius, and axially from $z = 0$ up to the end of the duct at $z \simeq 0.92R$. For each axial position, the amplitudes of the upstream and downstream propagating azimuthal and radial duct modes are estimated.

The contributions of the first five azimuthal modes to the sound pressure levels (SPL) of the upstream propagating fluctuations, obtained from the decomposition for the plane mode for $f = 3000\,\text{Hz}$, for $\text{M}_{\text{ext}} = 0$ and $\text{M}_{\text{ext}} = 0.2$ are represented as functions of the axial distance in figures 4(a,c). The axial positions of the two rings of the detection antenna are also depicted. In both cases, the dominant mode is axisymmetric, as expected for the plane mode. Upstream of the first ring for $z \gtrsim 0.25R$, strong levels are found for higher azimuthal orders $m = 1{-}4$, indicating that a proportion of the plane mode energy is redistributed on higher azimuthal modes during the propagation through the inlet. This was also the case in other studies [11, 12], and is certainly due to the non-axisymmetric geometry of the intake. The SPL of the axisymmetric mode for the first five radial modes in the flow conditions with $\text{M}_{\text{ext}} = 0$ and $\text{M}_{\text{ext}} = 0.2$, are displayed in figures 4(b,d). The plane mode is initially the mode with the highest energy content. This is not the case at the end of the duct, for $z \gtrsim 0.7r_0$, where the contributions of the radial modes with $n = 1 - 4$ are predominant, in agreement with the pressure fields in figures 3(b,e).

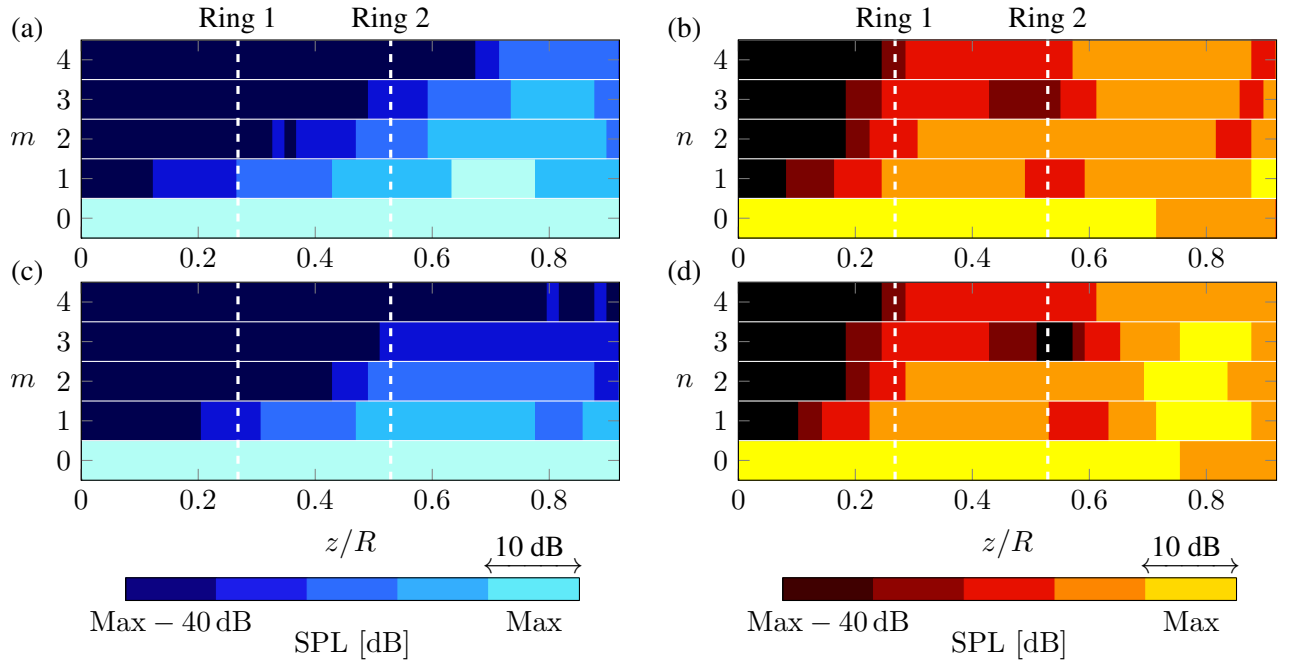


Figure 4. Sound pressure levels for the plane mode for $f = 3000\,\text{Hz}$ for (a,b) $\text{M}_{\text{ext}} = 0$ and (c,d) $\text{M}_{\text{ext}} = 0.2$, for upstream propagating (a,c) azimuthal modes and (b,d) axisymmetric radial modes ($m = 0$).

$$p\left(r,\theta,z\right)=\sum_{m=-\infty}^{\infty}\sum_{n=0}^{\infty}\left(A_{m,n}e^{ik_{z_{m,n}}^{+}z}+B_{m,n}e^{ik_{z_{m,n}}^{-}z}\right)f_{m,n}\left(r\right)e^{im\theta} \tag{1}$$

5. ASSESSMENT OF THE ANTENNA

To assess the capability of the antenna, only the complex pressure values obtained at the microphones of the detection antenna are analyzed in what follows. First, an azimuthal decomposition is performed by applying Fourier transforms to the pressure determined at the microphones of the two rings. The SPL obtained for the plane mode are represented as a function of the azimuthal order for the three frequencies for $\mathrm{M_{ext}} = 0$ in figures 5(a-c). They are displayed in red for Ring 1 and in blue for Ring 2. For both rings, the levels for the helical modes are stronger for higher frequencies, indicating that the redistribution of the plane mode energy on higher azimuthal modes is more important for these frequencies. Moreover, for $f = 5000\,\mathrm{Hz}$ in figure 5(c), the SPL associated with the first helical mode is approximately $15\,\mathrm{dB}$ higher than for the axisymmetric mode.

For all frequencies, the contributions of azimuthal modes with $m \geq 1$ are higher for Ring 2 than for Ring 1. They are therefore consistent with those determined along the duct axis, shown in figure 4(a). This indicates that the mode detection antenna can be useful for performing an azimuthal decomposition. Similar results, omitted here for clarity, are obtained for the other flow configuration with $\mathrm{M_{ext}} = 0.2$.

To investigate the ability of the mode detection antenna to perform a radial decomposition, the complex pressures obtained on the two rings and on the four axial lines are first arranged in a matrix $\mathbf{\Phi} \in \mathbb{C}^{K\times L}$, where L is the number of modes computed at a given frequency and K the total number of microphones in the antenna. Then, the modal coherence matrix [8, 16]

$$\mathbf{\Gamma} = \max_{1\leq i<j\leq L} \frac{|\langle \mathbf{\Phi}_i, \mathbf{\Phi}_j\rangle|}{\|\mathbf{\Phi}_i\|_2 \|\mathbf{\Phi}_j\|_2}, \tag{2}$$

where $\mathbf{\Phi}_i$ is the ith column of $\mathbf{\Phi}$, is computed for all cases. It quantifies the linear interdependence between two modes [17] and is therefore linked to the ability of the detection antenna to dissociate two modes.

The modal coherence values obtained for the first six cut-on axisymmetric modes for $f = 3000\,\mathrm{Hz}$ and $5000\,\mathrm{Hz}$ for $\mathrm{M_{ext}} = 0$ are presented in figures 6(a,b). In both cases, the values are equal to 1 along the diagonal since they are associated with the coherence of a mode with itself. They are also equal to 1 for the radial modes with $n \leq 3$, indicating that the footprints of these modes on the detection antenna are similar. This suggests that the antenna will not be able to separate these different radial modes. Overall, the coherence levels for $f = 5000\,\mathrm{Hz}$ in figure 6(a) are higher than those for $f = 3000\,\mathrm{Hz}$ in figure 6(b). This indicates that the capability of the

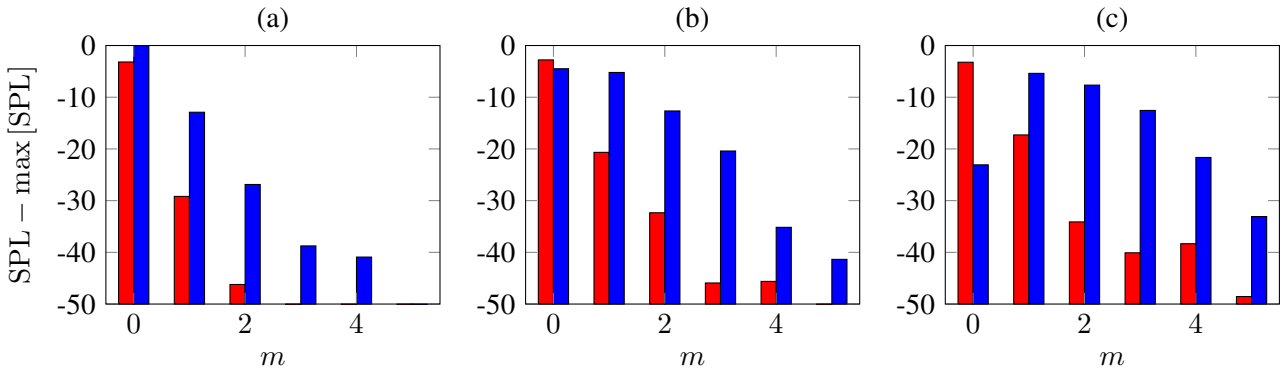


Figure 5. SPL for the plane mode as a function of the azimuthal order for (a) $f = 1000\,\mathrm{Hz}$, (b) $f = 3000\,\mathrm{Hz}$, (c) $f = 5000\,\mathrm{Hz}$ for $\mathrm{M_{ext}} = 0$, for the pressure obtained at the microphones of Ring 1 and Ring 2. The common SPL reference for the three plots is arbitrary.

antenna to distinguish two modes with the same azimuthal structure is reduced for a higher frequency.

The modal coherence levels obtained for 5000 Hz for $M_{ext} = 0.2$ are represented in figure 6(c). They are similar to those for $M_{ext} = 0$ in figure 6(a), suggesting that the ability of the antenna to separate two modes does not depend on the external flow Mach number.

A Tyler & Sofrin [2] mode linked to rotor-stator interaction is now considered. Its azimuthal order is $m = -4$. The coherence values obtained for the first five cut-on modes with $m = -4$ are displayed in figures 6(d-f). They exceed 0.5, suggesting that the detection antenna is not suitable for separating the radial modes of the Tyler & Sofrin mode under consideration. Moreover, the coherence levels for $m = -4$ are slightly lower than those for the plane mode in figures 6(a-c). The antenna therefore seems slightly better suited to separate modes with relatively high azimuthal modes.

6. CONCLUSIONS

The ability of a mode detection array for duct-mode decomposition in turbofan nacelle experiments is numerically investigated by analyzing acoustic solutions computed using the commercial code ACTRANTM. A full-mode breakdown is performed to obtain reference amplitudes for the upstream and downstream propagating azimuthal and radial modes. The detection antenna effectively captures azimuthal mode distributions. However, its capability to distinguish between modes with the same azimuthal structure remains limited. This provides guidelines for the analysis of future experimental measurements. In future work, it will be interesting to compare the results with solutions obtained using analytical models [18] or a Green's function discretization technique [19]. It could also be interesting to apply an inverse method [20] to determine the modal amplitudes.

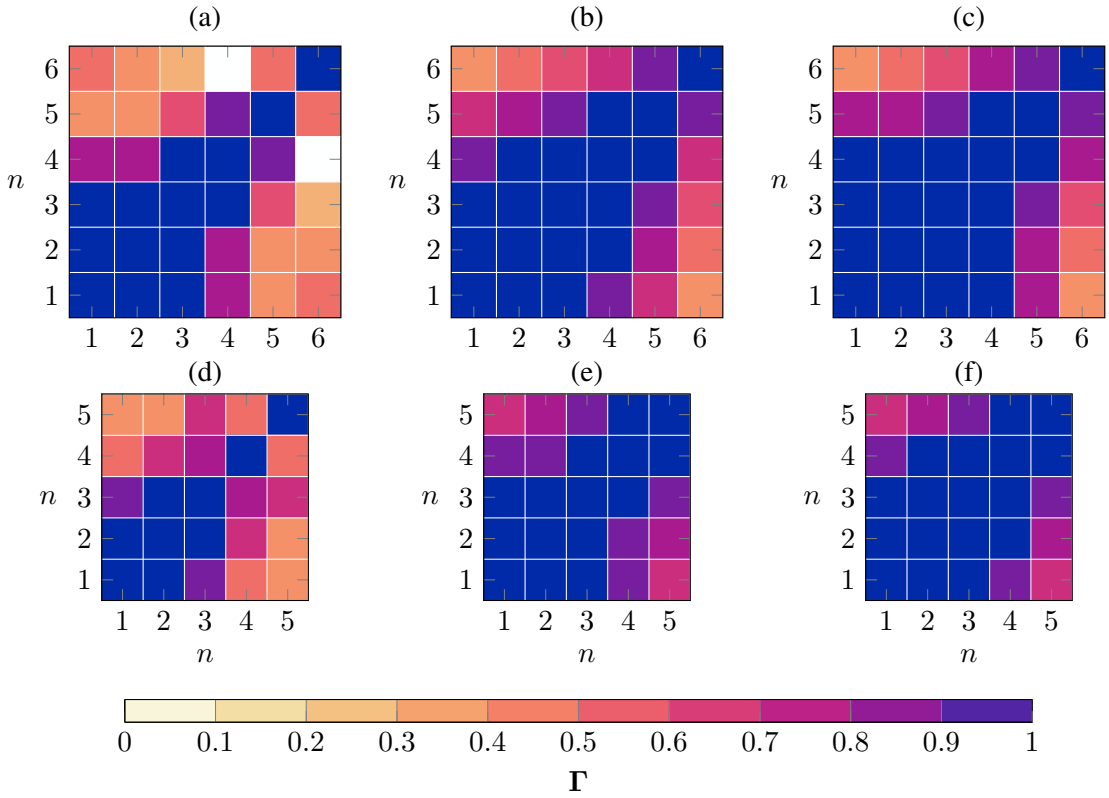


Figure 6. Modal coherence for (a,d) $f = 3000$ Hz and (b,e) $f = 5000$ Hz for $M_{ext} = 0$, and (c,f) $f = 5000$ Hz for $M_{ext} = 0.2$, for (a-c) the first six axisymmetric modes ($m = 0$) and (d-f) the first five modes with $m = -4$, which is the azimuthal order of a Tyler & Sofrin mode.

7. ACKNOWLEDGMENTS

This research has been performed in the frame of the project COMPANION (COMmon Platform and Advanced iNstrumentration readIness for ultra efficient propulsiON), which is funded by the European Union Clean Aviation Joint Undertaking program, under grant agreement No. 101140627. The authors gratefully acknowledge Emmanuel Julliard (Airbus) for useful discussions. This work was granted access to the HPC resources of PMCS2I (Pôle de Modélisation et de Calcul en Sciences de l'Ingénieur de l'Information) of Ecole Centrale de Lyon. It was performed within the framework of the LABEX CeLyA (ANR-10-LABX-0060) of Université de Lyon, within the program *Investissements d'Avenir* (ANR-16-IDEX-0005) operated by the French National Research Agency (ANR).

8. REFERENCES

[1] S. Moreau, "Turbomachinery noise predictions: present and future," *Acoustics*, vol. 1, no. 1, 2019.

[2] J. M. Tyler and T. G. Sofrin, "Axial flow compressor noise studies," *SAE Technical Paper 620532*, 1962.

[3] M. G. Jones, W. R. Watson, D. M. Nark, B. M. Howerton, and M. C. Brown, "A review of acoustic liner experimental characterization at NASA Langley," *NASA Technical Report 2020-220583*, 2020.

[4] C. Morfey, "Rotating pressure patterns in ducts: Their generation and transmission," *Journal of Sound and Vibration*, vol. 1, no. 1, 1964.

[5] S. W. Rienstra and A. Hirschberg, *An introduction to acoustics*. Eindhoven University of Technology, 2004.

[6] C. Moore, "Measurement of radial and circumferential modes in annular and circular fan ducts," *Journal of Sound and Vibration*, vol. 62, no. 2, 1979.

[7] L. Enghardt, Y. Zhang, and W. Neise, "Experimental verification of a radial mode analysis technique using wall-flush mounted sensors," *Meeting of the Acoustical Society of America*, 1999.

[8] A. Pereira, A. Finez, Q. Leclere, E. Salze, and P. Souchotte, "Modal identification of a small-scale ducted fan," *AIAA Paper 2016-3063*, 2016.

[9] S. W. Rienstra, "Fundamentals of duct acoustics," *Von Karman Institute Lecture Notes*, vol. 589, 2015.

[10] C. Geuzaine and J.-F. Remacle, "Gmsh: A 3-D finite element mesh generator with built-in pre- and post-processing facilities," *International Journal for Numerical Methods in Engineering*, vol. 79, no. 11, 2009.

[11] M. Doherty and H. Namgoong, "Impact of turbofan intake distortion on fan noise propagation and generation," *AIAA Paper*, 2016.

[12] L. Xiong, R. Sugimoto, and E. Quaranta, "Effects of turbofan engine intake droop and length on fan tone noise," *AIAA Paper 2019-2581*, 2019.

[13] W. Mohring, "A well posed acoustic analogy based on a moving acoustic medium," *Aeroacoustic Workshop SWING*, 1999.

[14] B. V. Antwerpen, Y. Detandt, D. Copiello, E. Rosseel, and E. Gaudry, "Performance improvements and new solution strategies of Actran/TM for nacelle simulations," *AIAA Paper 2014-2315*, 2014.

[15] F. Q. Hu, "A perfectly matched layer absorbing boundary condition for linearized euler equations with a non-uniform mean flow," *Journal of Computational Physics*, vol. 208, no. 2, 2005.

[16] M. Behn, R. Kisler, and U. Tapken, "Efficient azimuthal mode analysis using compressed sensing," *AIAA Paper 2016–3038*, 2016.

[17] F. O. Castres and P. F. Joseph, "Experimental investigation of an inversion technique for the determination of broadband duct mode amplitudes by the use of near-field sensor arrays," *The Journal of the Acoustical Society of America*, vol. 122, no. 2, 2007.

[18] D. Lewis, J. de Laborderie, M. Sanjosé, S. Moreau, M. C. Jacob, and V. Masson, "Parametric study on state-of-the-art analytical models for fan broadband interaction noise predictions," *Journal of Sound and Vibration*, vol. 514, 2021.

[19] D. Casalino, M. Roger, and M. C. Jacob, "Prediction of sound propagation in ducted potential flows using Green's function discretization," *AIAA Journal*, vol. 42, no. 4, 2004.

[20] A. Pereira and M. C. Jacob, "Modal analysis of in-duct fan broadband noise via an iterative bayesian inverse approach," *Journal of Sound and Vibration*, vol. 520, 2022.

DOI: 10.61782/fa.2025.0141

FORUM ACUSTICUM EURONOISE 2025

APPLICATION OF ATMOSPHERIC WIND FILTER ARRAYS FOR ACOUSTIC MONITORING UAVS

Ramesh Raja Subramanyam[1*] **Criostoir Gerasch**[1] **Stefan Jacob**[1]
[1] National Metrology Institute (PTB), Braunschweig, Germany - 38116

ABSTRACT

The application of Uncrewed Aerial Vehicles (UAVs) in low frequency acoustic measurements is, among other factors, limited by the disturbances induced by atmospheric wind noise. The infrasound sensor networks used in the seismic activity monitoring consists of a wind filter array that filter the acoustic disturbances caused by the atmospheric turbulence. These arrays function as spatial filters, eliminating the incoherent noises generated by the wind. In this study we design and test wind filter arrays for their application in a UAV based measurement platform. Different configurations of the wind filters such as the Rosette filter, porous circular pipes and several other derived configurations were studied. The frequency response function of the filters indicated a significant distortion from the acoustic resonance in the filter tube for some designs. Acoustic plane wave theory is used to tune these wind filter arrays for shifting these resonances beyond the frequency range of the measurement. In addition, an investigation is made by coupling arrays of varying dimensions to increase the effective frequency range of the filter.

Keywords: *infrasound measurement, wind noise filter, atmospheric turbulence, sensor array, uav measurement*

1. INTRODUCTION

The increasing growth of renewable energy converters, e.g. Wind turbines, has raised a low frequency noise concern in the nearby residential areas [1], [2]. The blade passing frequency of wind turbines and rotor blade interaction with wind generates an infrasound noise that are measured several kilometres in the downwind direction [3]. Sound power characterisation of wind turbines involves ground based measurements based on the standard guidelines in IEC 61400 – 11 [4]. Microphones equipped with spherical windscreens are used to measure the Sound Pressure Level (SPL) in a linear array of points to estimate the sound power of the wind turbines. Application of this technique for infrasound frequencies is infeasible because longer wavelengths require measurements with network arrays. Moreover, the acoustic signal in the low frequencies is masked by atmospheric wind noise making it difficult to measure infrasound noise.

Infrasound Monitoring Stations (IMS) developed as a part of the Comprehensive Nuclear Test Ban Treaty Organisation (CTBTO) employ wind filter arrays to reduce the disturbance caused by atmospheric wind [5], [6]. These filter arrays are constructed with a series of pipes and their working principle is that the atmospheric wind induced turbulence is incoherent with a shorter wavelength in comparison to the infrasound signal which is filtered with a sensor array larger than the turbulent scale. The most common design is the rosette filter, consisting of multiple pressure sensing inlets distributed in a geometric pattern in a larger perimeter. As stated in the reference text, for filtering the wind noise in the frequencies below 5 Hz, a filter diameter of at least 18 m is required. The rosette filter design is limited by the acoustical resonance effect which is addressed with another form of wind filter design using porous pipe in a circular loop [7], [8]. It differs from the rosette filter design in that a single tube with porous inlets is used rather than a series of tubes. The circular filter, however, undergoes degradation due to defects arising over time. Furthermore, the remote location of IMS permits the

[*] ***Corresponding author***: rameshraja14@hotmail.com.
Copyright: *©2025 First author et al. This is an open-access article distributed under the terms of the Creative Commons Attribution 3.0 Unported License, which permits unrestricted use, distribution, and reproduction in any medium, provided the original author and source are credited.*

construction of these large infrasound filter arrays which are otherwise difficult to build near a residential area. For the measurement of infrasound noise in areas with limited spaces, spherical porous domes or large windscreens are used to shield the microphone from turbulence effects producing a maximum of 7 dB noise reduction [9], [10].

In recent times, the application of UAVs for remote sensing and environmental condition monitoring has gained traction for its improved accessibility to remote terrains [11]. The limiting factor in the use of UAVs for acoustic monitoring is the inherent noise they generate, which has been studied extensively [12], [13]. In our previous experimental study [14], we measured the low frequency noise signature of UAVs and concluded that in the low frequencies, the self-noise of the drone is minimal. Hydrodynamic fluctuations caused by the rotor thrust masked the acoustic signal in low frequencies, but it was limited to the downstream direction of the rotors. Having figured out the sweet spot for sensor location, in this study, we construct a wind filter array for measuring the infrasound noise using UAVs. We equip the UAV with the rosette filter, porous hose filter, and circular filter configuration and measure the filter response in the vicinity of the reference infrasound source of known sound power output [15].

While the porous wind filter domes are effective in infrasound range [10], their application in UAV measurements is prevented by the payload limitations of the drone. Except for the dimensional differences, both windscreens and wind domes average out the turbulence effects in the wind by integrating the sound pressure over a larger surface area. In addition, the porosity of the windscreen creates viscous and inertial losses which further reduces the atmospheric turbulence effects [16]. Measurements performed with various windscreens in a wind tunnel showed a significant noise reduction performance in low frequencies [17]. So, we constructed a circular microphone array using the microphones equipped with windscreens. Further, to filter the incoherent turbulences in the atmosphere, the spatial filter technique from the rosette pipe design was adopted. The construction of the array and the filters are explained in section. Results for each of the filter configurations tested are summarised in section 3. Finally, discussions and conclusions from the present study are provided in section 4 along with the future research plan.

2. METHODOLOGY

2.1 Measurement setup

2.1.1 UAV assembly

Measurements in this study are performed with PM X6 Pro Hexacopter drone with a payload capacity of 5 kg. We equipped the drone with 3D - printed attachments to carry the measurement hardware. Measurement data is acquired remotely using National Instruments NI 9181 DAQ. The sound pressure signal was recorded with a half - inch infrasound condenser microphone GRAS 47 AC powered by GRAS 12 AL CCP power module. The measured data is then relayed to a PC through a Wi-Fi router. For extending the Wi-Fi range while flying, a Wi-Fi bridge is mounted on the drone along with the power backup. The assembly of the measurement system on the drone is shown in Fig 1 (a).

2.1.2 Rosette filter design

Flexible PET pressure hose of 4 mm inner diameter and 1 mm wall thickness were used in constructing the filter. Filter was designed using the parametric relations given in the electroacoustic model developed by B. Alcoverro [6]. The inlet pipes of the filter are supported by the carbon tubes attached to the arms of the drone. Pneumatic connectors were used in connecting the inlet pipes to the secondary pipes. The secondary pipe is interfaced to the infrasound microphone through a 3D printed manifold of 30 mm × 30 mm × 5 mm volume. The constructed filter has a diameter span of 2.32 m and consists of six pressure inlets. The assembly of the rosette filter is shown in Fig 1 (b).

2.1.3 Porous hose design

For the porous filter design, holes of 2 mm diameter were drilled in the inlet pipes of the rosette filter. Holes were made for 300 mm length from the open end with an interval of 50 mm resulting in 36 pressure inlets in total. Porosity length was limited to avoid hydrodynamic fluctuations of the rotor. The rest of the assembly of the filter is similar to the rosette filter design described above.

2.1.4 Circular filter design

For the circular filter, 7.5 m pressure hose is made porous with 1 mm diameter hole with 100 mm interval. There were a total of 69 pressure inlets and the filter was looped around the ends of the carbon tubes at 2.32 m diameter. While one end of the filter was closed the other end was connected to the manifold. The filter construction is shown in Fig 1 (c).

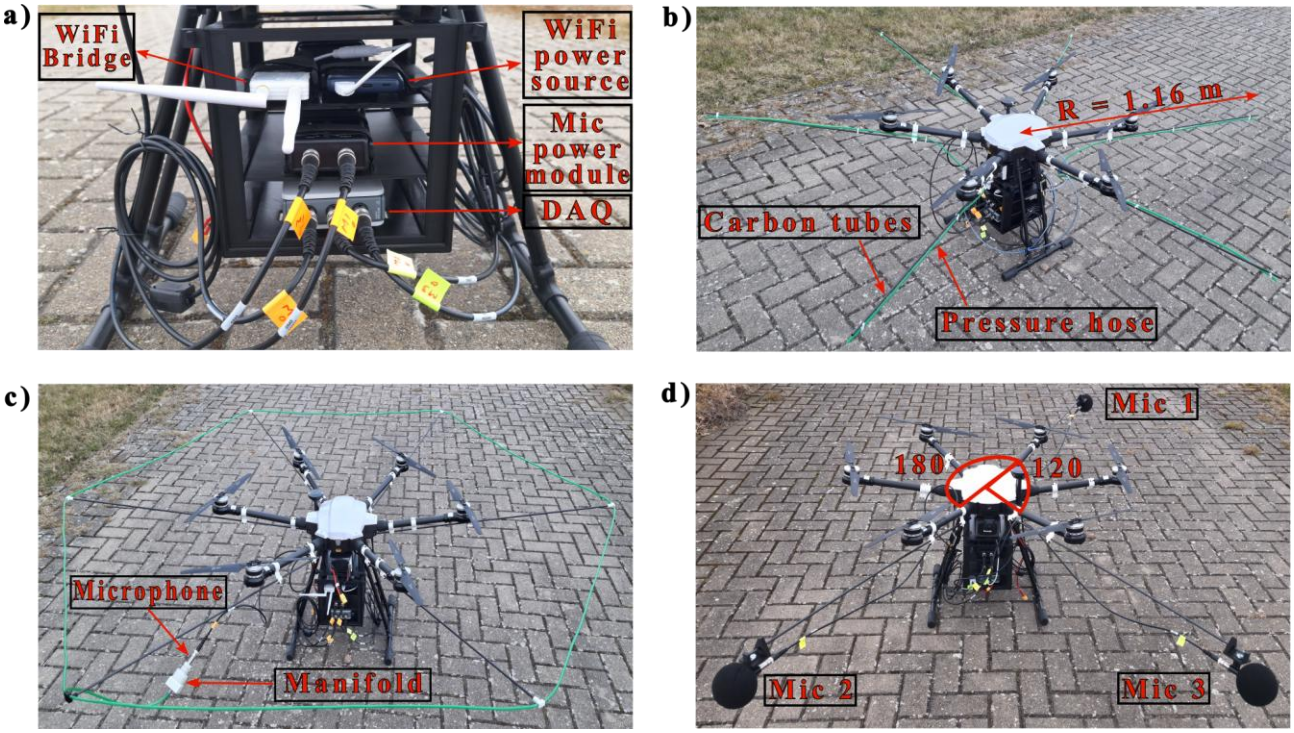


Figure 1. Picture showing the measurement setup in the UAV. a) DAQ hardware assembly, b) Rosette filter assembly, c) Circular filter assembly, d) Three microphone array assembly.

2.1.5 Three microphone array

A circular microphone array was built with three infrasound microphones (GRAS 47 AC). At the end of the carbon tubes, the microphones were mounted with a 3D printed support and GRAS 90 mm windscreens were attached to the microphones. The microphone filter array has a diameter span of 2.37 m. Two microphones were mounted 180 degrees apart and the third microphone was mounted at 120 degrees from the first mic to have a different separation distance as shown in Fig 1 (d).

2.2 Data acquisition

Measurements were performed at PTB's open field on a slightly windy day with an average wind speed of 10 kmph (forecasted value). The reference infrasound source [15] was used to radiate a 10 Hz tonal noise. Sound pressure was measured at ground level at 10 m from the source with the drone turned off and at an altitude of 10 m above the reference source with the drone in hover mode. The time signal was acquired for 300 seconds. Using Welch's algorithm [18] in Python, the measured time signal is converted to the frequency domain with 1 Hz resolution and 300 averages. Further, the background wind noise is measured without the infrasound source for comparative study. In addition, sound pressure is measured using a reference microphone stationed at the geometric centre of the filters tested.

3. RESULTS

The measurement results are plotted in terms of SPL spectra for a frequency bandwidth of 1 – 100 Hz. While the Power Spectral Density (PSD) is used for calculating the filter array SPL, Cross Spectral Density (CSD) is used for three microphone array results. The window correction factor, bandwidth correction factor, and microphone sensitivity are applied in estimating the exact SPL values in each case.

Fig 2 shows the comparison of SPL spectra measured with the three filter configurations (Rosette filter, Porous hose filter, and Circular filter) along with SPL spectra measured with the reference microphone. The

background noise measured at the ground level in Fig 2 a) indicates that the designed filter is less effective in reducing the wind induced noise compared to the single microphone with windscreen attached. Comparing the spectra of the three filter configurations, the rosette filter provides a better noise reduction for most of the bandwidth. Particularly in the infrasound range, the rosette filter response was 10 dB lower than the other two filter configurations. From the electroacoustic model [19], the high frequency cut off for the rosette filter with the given dimensions and 10 kmph wind speed was calculated to be 70 Hz (approx.) which agrees with the measurement result. As pointed out in the literature, the rosette filter response was affected by the internal resonances of the pipes around 40 Hz frequency.

The porous hose filter response resembles the rosette filter response except for the higher amplitude level. The increase in the SPL can be an effect of an increased number of pressure inlets. Likewise, for the circular filter, the SPL level is identical to that of the porous hose filter, but the resonance effects were shifted towards higher frequencies. Despite the absence of resonance in the frequency range of interest, the circular filter was least effective in filtering the wind noise.

However, the comparison of background noise at 10 m altitude in Fig 2 b) indicates a better performance with the circular filter. This is mainly due to the resonance effects in the rosette and porous hose filter amplifying the background noise. Also, the porous hose filter provides a better noise reduction in frequencies below 8 Hz, unlike the background noise measured at ground level. At higher altitudes, tonal noise corresponding to the shaft frequency of the drone rotors is generated around 70 Hz which is measured in all filters. Because of the variation in the rotational frequency of the rotor in each arm of the drone, the peak appears broader. However, the overall noise level measured with the filter has increased further by 10 to 15 dB at higher altitudes in comparison to the spectra measured at the ground.

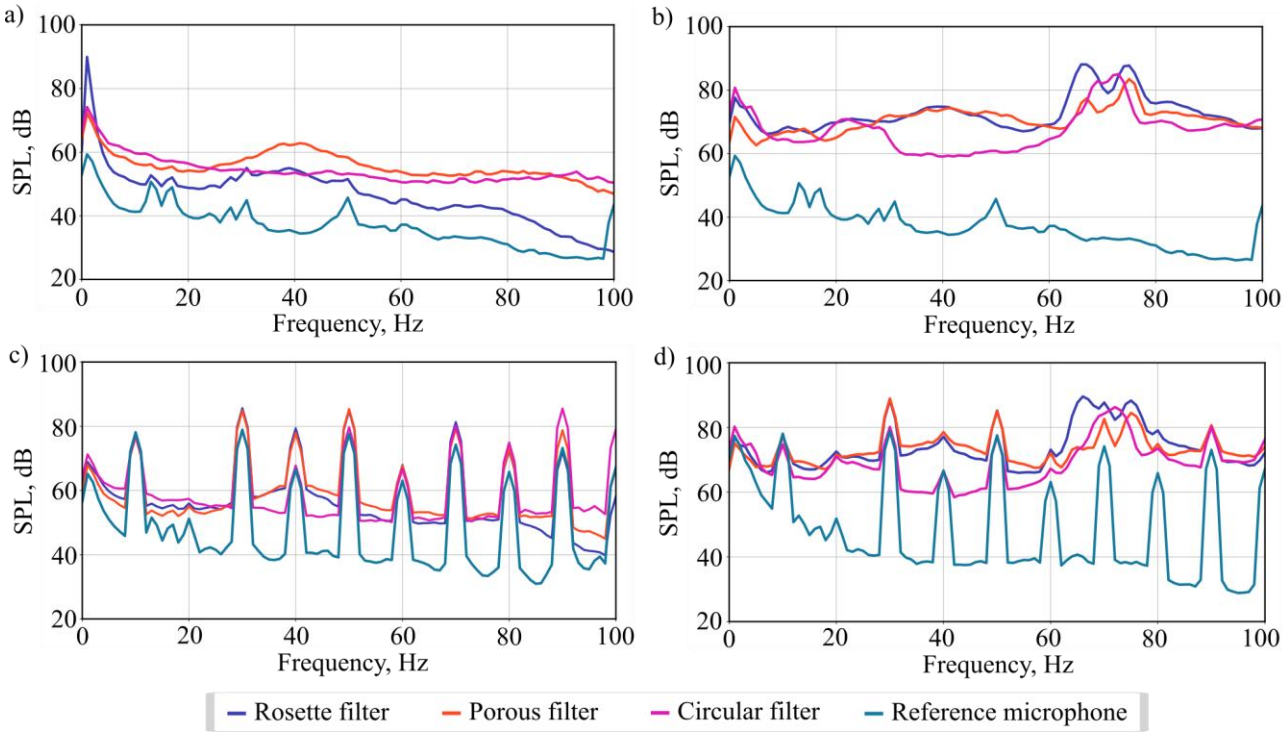


Figure 2. Comparison of SPL spectra measured with the filters and the reference microphone. a) Background noise at ground, b) Background noise at 10 m height, c) Infrasound source noise measured at ground, d) Infrasound noise measured at 10 m height.

To quantify the filter effects on the measured amplitude levels, an investigation using the infrasound noise source is performed. The source noise measured at the ground level is plotted in Fig 2 c). All filter configurations measured the same amplitude level of the 10 Hz tone as the reference microphone. The amplitude levels of the overtones between 30 Hz to 50 Hz were higher with rosette and porous hose filter due to the internal resonances. Beyond 70 Hz, the porous hose filter and circular filter gives a higher amplitude level, which could be the result of amplification caused by the increased number of inlets.

The source noise measured at 10 m altitude plotted in Fig 2 d) shows little difference in the frequency response of the filters. The 10 Hz amplitude peak remained identical among the filter spectra while the overtone peaks were amplified due to resonance and shaft noise of the rotor. Nevertheless, it is evident from Figure 2 that the spatial filter configurations tested had a minimal effect on the wind noise reduction in comparison to the spherical windscreens. Therefore, the three-microphone array was investigated as an alternative solution.

The advantage of using two or more microphones over a single microphone for filtering the atmospheric wind noise is showcased through the comparison of the CSD of the microphones with the auto spectra of a single microphone in Figure 3. Note, in the figure only the CSD spectra of Mic 1 and Mic 2 is plotted. The background noise comparison at ground level is shown in Fig 3 a). As seen from the plot, the frequency response with the microphone array overlaps the single microphone response in higher frequencies. But, in infrasound frequencies below 15 Hz, noise reduction of at least 10 dB is achieved. Similarly, the background noise measured at 10 m height is plotted in Fig 3 b) and it shows that the microphone array gives a noise reduction of at least 7 dB across the bandwidth. Furthermore, the source noise measured with the microphone array at 10 m height is shown in Fig 3 c) and it indicates negligible difference in the amplitude levels.

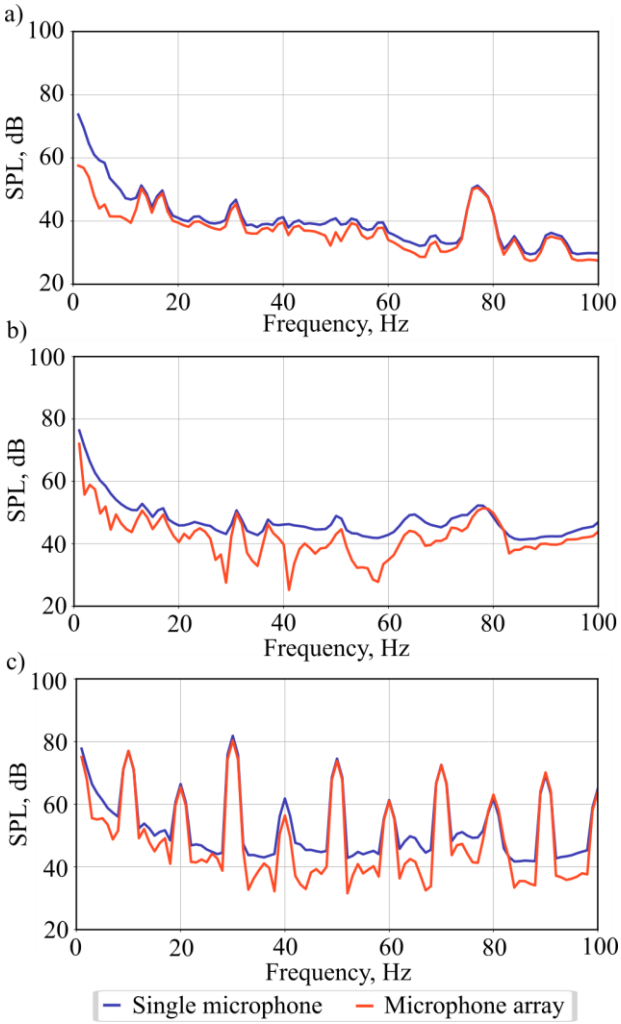


Figure 3. SPL spectra of microphone array compared to a single microphone spectra a) Background noise at ground level, b) Background noise at 10 m altitude, c) Infrasound source noise at 10 m altitude.

4. DISCUSSIONS AND CONCLUSION

The lack of effectiveness of the wind filter arrays in comparison to a microphone with windscreens is a result of the design complications involved in the filter construction. Only the rosette filter with solid pipes gave a better noise reduction efficiency in the comparative study with various filter configurations. However, one of the primary limitations in the rosette filter design is the resonance effects that reduce the effective bandwidth of the measurement. By combining arrays of different sizes, the measurement range can be extended like in the study performed by Hedlin [5] and Alcoverro [6], where 18 m and 70 m rosette filters were used to measure two different frequency ranges. Nevertheless, implementing those designs on UAV based measurement platform is difficult as we end up in the downwash region of the rotor that masks the actual acoustic signal. Further, the resonance effects arising due to the impedance mismatch in the filter design were found to introduce phase delays in the measured signal [20]. Capillary plugs matching the characteristic impedance of the tube were used to break the internal resonances in the

tube. However, the design complications of the capillary plugs further result in a complex filter design. Also, the efficiency of the rosette filter was found to be dependent on the grazing angle of the waves at the inlet [6], [21]. This might introduce some decay in the frequency response and geometric symmetry of the filter must be ensured to eliminate these effects [21]. Since the filter is subjected to vibration during the flight, geometrical symmetry becomes questionable at higher altitudes with UAVs.

The porous hose filter was tested with the assumption that multiple inlets of varying distances increase the bandwidth of the measurement. Rather these inlets only increased the averaging effect which was confirmed in a previous empirical study as well [22]. While the filter was partially effective in frequencies below 10 Hz, they were found to amplify the signals in higher frequencies making their application obsolete. The circular filter configuration, which is an extension of a porous filter, suffered from a similar issue, though the resonance issues in the low frequency were eliminated.

Considering the aforementioned reasons, the application of a microphone with a windscreen for low frequency measurement in UAVs seems beneficial. A comparative measurement was performed on a windy day (15 kmph forecasted value) between the microphone with and without windscreen attached and noise reduction of at least 10 dB was achieved in the infrasound range. Also, previous experimental studies revealed that larger windscreens (> 60 mm diameter) effectiveness in low frequencies [17] which explains the better performance achieved in our case with 90 mm windscreens.

However, the efficiency of windscreens in high turbulence conditions is reduced [23]. The analytical model [24] and numerical simulation model [25] can be used in estimating the turbulence induced noise in the measurement. But these methods are complicated in that the turbulence parameters such as stability and roughness, and the stagnation pressure are to be estimated. Also, the application of the models is limited by the estimation accuracy of these parameters. In comparison, by using the CSD of two or more microphones that are spatially separated, the incoherent atmospheric turbulence effects are straightaway averaged out resulting in a simpler measurement protocol. Hence, the noise reduction mechanism of a windscreen is combined with the mechanism of a spatial filter array improving the noise reduction further. But the wind noise reduction achieved with the microphones separated by 60 degree angle (Mic 2 and Mic 3) was less than the noise reduction attained with 180 degree separation (Mic 1 and Mic 2). This implies that a longer separation distance between the sound pressure inlets provides a better averaging of the turbulence effects.

For further validation of this experimentation method, a comparison study with the analytical and numerical models discussed before would be beneficial. Also, measurement campaigns on varying wind profile conditions are required to quantify the efficiency and applicability of the microphone array for low frequency noise measurements with UAVs. Moreover, studies targeting design variations of the array and improving the data processing techniques are necessary for increasing the number of sensors thereby, to have better averaging of atmospheric turbulence.

5. ACKNOWLEDGMENTS

This research was funded by the Deutsche Forschungsgemeinschaft (DFG, German Research Foundation) – JA 3325/4-1. We also acknowledge the support provided by Mohammad Mkanna (PhD researcher in our working group) during the measurement campaign.

6. REFERENCES

[1] E. Blumendeller, M. Hofsäß, A. Goerlitz, and P. W. Cheng, 'Impact of wind turbine operation conditions on infrasonic and low frequency sound induced by on-shore wind turbines', *J. Phys. Conf. Ser.*, vol. 2265, no. 3, p. 032048, May 2022, doi: 10.1088/1742-6596/2265/3/032048.

[2] J. Jakobsen, 'Infrasound Emission from Wind Turbines', *J. Low Freq. Noise Vib. Act. Control*, vol. 24, no. 3, pp. 145–155, Sep. 2005, doi: 10.1260/026309205775374451.

[3] O. Marcillo, S. Arrowsmith, P. Blom, and K. Jones, 'On infrasound generated by wind farms and its propagation in low-altitude tropospheric waveguides', *J. Geophys. Res. Atmospheres*, vol. 120, no. 19, pp. 9855–9868, 2015, doi: https://doi.org/10.1002/2014JD022821.

[4] S. E. Keith *et al.*, 'Wind turbine sound power measurements', *J. Acoust. Soc. Am.*, vol. 139, no. 3, pp. 1431–1435, Mar. 2016, doi: 10.1121/1.4942405.

[5] M. A. H. Hedlin, B. Alcoverro, and G. D'Spain, 'Evaluation of rosette infrasonic noise-reducing spatial filters', *J. Acoust. Soc. Am.*, vol. 114, no. 4, pp. 1807–1820, Oct. 2003, doi: 10.1121/1.1603763.

[6] B. Alcoverro and A. Le Pichon, 'Design and optimization of a noise reduction system for infrasonic measurements using elements with low

acoustic impedance', *J. Acoust. Soc. Am.*, vol. 117, no. 4, pp. 1717–1727, Apr. 2005, doi: 10.1121/1.1804966.

[7] R. Burridge, 'The Acoustics of Pipe Arrays', *Geophys. J. Int.*, vol. 26, no. 1–4, pp. 53–69, Dec. 1971, doi: 10.1111/j.1365-246X.1971.tb03382.x.

[8] F. H. Grover, 'Experimental Noise Reducers for an Active Microbarograph Array', *Geophys. J. Int.*, vol. 26, no. 1–4, pp. 41–52, Dec. 1971, doi: 10.1111/j.1365-246X.1971.tb03381.x.

[9] B. Zajamšek, K. L. Hansen, C. J. Doolan, and C. H. Hansen, 'Characterisation of wind farm infrasound and low-frequency noise', *J. Sound Vib.*, vol. 370, pp. 176–190, May 2016, doi: 10.1016/j.jsv.2016.02.001.

[10] J. Noble, W. Alberts, R. Raspet, S. Collier, and M. Coleman, 'Infrasound wind noise reduction via porous fabric domes', *J. Acoust. Soc. Am.*, vol. 135, p. 2409, Apr. 2014, doi: 10.1121/1.4877982.

[11] M. Ghamari, P. Rangel, M. Mehrubeoglu, G. S. Tewolde, and R. S. Sherratt, 'Unmanned Aerial Vehicle Communications for Civil Applications: A Review', *IEEE Access*, vol. 10, pp. 102492–102531, 2022, doi: 10.1109/ACCESS.2022.3208571.

[12] B. Schäffer, R. Pieren, K. Heutschi, J. M. Wunderli, and S. Becker, 'Drone Noise Emission Characteristics and Noise Effects on Humans—A Systematic Review', *Int. J. Environ. Res. Public. Health*, vol. 18, no. 11, p. 5940, Jun. 2021, doi: 10.3390/ijerph18115940.

[13] N. Intaratep, W. N. Alexander, W. J. Devenport, S. M. Grace, and A. Dropkin, 'Experimental Study of Quadcopter Acoustics and Performance at Static Thrust Conditions', in *22nd AIAA/CEAS Aeroacoustics Conference*, Lyon, France: American Institute of Aeronautics and Astronautics, May 2016. doi: 10.2514/6.2016-2873.

[14] R. R. Subramanyam, R. Castro Mota, K. Picker, V. Wittstock, and S. Jacob, 'Experimental Low-Frequency Noise Characterization of an Octocopter Drone', in *30th AIAA/CEAS Aeroacoustics Conference (2024)*, in Aeroacoustics Conferences. , American Institute of Aeronautics and Astronautics, 2024. doi: 10.2514/6.2024-3343.

[15] R. R. Subramanyam, R. Castro Mota, and S. Jacob, *A quarter wave infrasonic noise generator*. INTER-NOISE Congress and Conference Proceedings, 2024.

[16] S. Zhao, M. Dabin, E. Cheng, X. Qiu, I. Burnett, and J. C. Liu, 'On the wind noise reduction mechanism of porous microphone windscreens', *J. Acoust. Soc. Am.*, vol. 142, no. 4, pp. 2454–2463, Oct. 2017, doi: 10.1121/1.5008860.

[17] G. F. Hessler, D. M. Hessler, P. Brandsta¨tt, and K. Bay, 'Experimental study to determine wind-induced noise and windscreen attenuation effects on microphone response for environmental wind turbine and other applications', *Noise Control Eng. J.*, vol. 56, no. 4, pp. 300–309, Jul. 2008, doi: 10.3397/1.2949926.

[18] P. Welch, 'The use of fast Fourier transform for the estimation of power spectra: A method based on time averaging over short, modified periodograms', *IEEE Trans. Audio Electroacoustics*, vol. 15, no. 2, pp. 70–73, Jun. 1967, doi: 10.1109/TAU.1967.1161901.

[19] B. Alcoverro and A. Le Pichon, 'Design and optimization of a noise reduction system for infrasonic measurements using elements with low acoustic impedance', *J. Acoust. Soc. Am.*, vol. 117, no. 4, pp. 1717–1727, Apr. 2005, doi: 10.1121/1.1804966.

[20] M. A. H. Hedlin and B. Alcoverro, 'The use of impedance matching capillaries for reducing resonance in rosette infrasonic spatial filters', *J. Acoust. Soc. Am.*, vol. 117, no. 4, pp. 1880–1888, Apr. 2005, doi: 10.1121/1.1760778.

[21] D. J. Brown, C. A. L. Szuberla, D. McCormack, and P. Mialle, 'The Influence of Spatial Filters on Infrasound Array Responses', *Pure Appl. Geophys.*, vol. 171, no. 3, pp. 575–585, Mar. 2014, doi: 10.1007/s00024-012-0586-1.

[22] K. T. Walker and M. A. H. Hedlin, 'A Review of Wind-Noise Reduction Methodologies', in *Infrasound Monitoring for Atmospheric Studies*, A. Le Pichon, E. Blanc, and A. Hauchecorne, Eds., Dordrecht: Springer Netherlands, 2009, pp. 141–182. doi: 10.1007/978-1-4020-9508-5_5.

[23] P. Rasmussen, 'Windscreens – Practical Guidelines for Acoustic Measurements in Situations with Wind Flow', 2016.

[24] G. P. Van Den Berg, 'Wind-induced noise in a screened microphone', *J. Acoust. Soc. Am.*, vol. 119, no. 2, pp. 824–833, Feb. 2006, doi: 10.1121/1.2146085.

[25] R. Raspet, J. Webster, and K. Dillion, 'Framework for wind noise studies', *J. Acoust. Soc. Am.*, vol. 119, no. 2, pp. 834–843, Feb. 2006, doi: 10.1121/1.2146113.

DOI:

Main theme: A08 Industrial, Machinery, Equipment Noise and Vibration

Session A08.03 Advances in machinery noise and vibration control

Chair(s): E. A. Piana, J. Ramis-Soriano, S. Anda

DOI: 10.61782/fa.2025.0042

FORUM ACUSTICUM EURONOISE 2025

A STUDY ON THE TRANSFER CHARACTERISTICS OF IN-WHEEL MOTOR SYSTEM BASED ON EV PLATFORM

Park, Sangwon[1*] **Lee, Jongwha**[1] **Lee, Minsung**[1] **Woo, Jongmun**[1]
Jung, Jinnyon[2] **Lee, Sangil**[2] **Sohn, Byunggil**[2]
[1] HYUNDAI MOBIS, South Korea
[2] JINN, South Korea

ABSTRACT

The In-Wheel motor system is mounted directly on the inside of the tire where the road load comes in and increases the unsprung mass, which has a critical effect on the NVH performance of the vehicle. Although the evaluation of the In-Wheel motor at the component and vehicle level is performed respectively, performance at the system level is difficult to predict due to the absence of a test system. In this study, two types of test system are developed to verify the integrated platform performance at the level of the drive unit + suspension system in order to predict the characteristics of vehicles assembled with the in-wheel motor system. So, the dynamic performance difference is analyzed by the load transfer ratio between the suspension system in which the EV motor and the in-wheel motor are assembled.

Hyundai Mobis Restricted

Keywords: *In-Wheel Motor System, Suspension system, Dynamic Performance, Load Transfer Ratio.*

1. INTRODUCTION

Recently, according to the global interest in eco-friendliness, electrification is being carried out at a rapid pace in the automobile industry. Representatively, the strengthening of CO_2 regulations and tax benefits for eco-friendly cars require automobile manufacturers to develop low-emission and high-energy-efficient vehicles.[1] Following this trend, various types of motors are being developed for the purpose of driving automobiles. This study deals with the contents of the direct drive type In-Wheel system. In the direct drive type In-Wheel system, the motor and brake system are mounted directly inside the wheel of the vehicle and directly drive the wheel without a drive shaft. Compared to existing vehicles, it has the advantage of a simple path and structure for transmitting power.[2] Since the motor support structure is designed in a small space inside the wheel and the motor is directly coupled to the suspension system, there is a disadvantage in that the excitation force of the motor is directly transmitted to the vehicle body.[3][4]. And the road load also comes in directly and increases the unsprung mass, which has a critical effect on the NVH performance of the vehicle. In order to predict this problem in advance, it is necessary to study not only the component and vehicle level, but also the system level as the intermediate stage. [5] In this study, an integrated platform evaluation system for drive unit + suspension system + tire level was developed to analyze the NVH characteristics in order to analyze the NVH characteristics of the suspension system applied to the in-wheel system.

2. TEST SYSTEM I : ROLLER BENCH

In order to simulate the driving conditions of an actual vehicle, a roller bench test device was built as an integrated platform consisting of a drive unit + suspension system + tire, and the system was configured as shown in Fig. 1. The load transfer characteristics of the suspension system level were verified by utilizing the input load from the roller-tire patch surface, which implements the same surface friction coefficient as the asphalt road, and the output load of the vehicle body mountings. In addition, the roller base height was adjusted to generate a pre-load of the actual vehicle. The input force can be measured from the wheel force transducer (WFT) mounted on the tire and the output force

[*] ***Corresponding author***: *summul100@mobis.com*
Copyright: *©2025 First author et al. This is an open-access article distributed under the terms of the Creative Commons Attribution 3.0 Unported License, which permits unrestricted use, distribution, and reproduction in any medium, provided the original author and source are credited.*

can be measured from the force sensor mounted on the vehicle body jig mount to obtain the load transfer ratio at the ratio of the two loads. This load transfer ratio can be defined as a characteristic of the system.

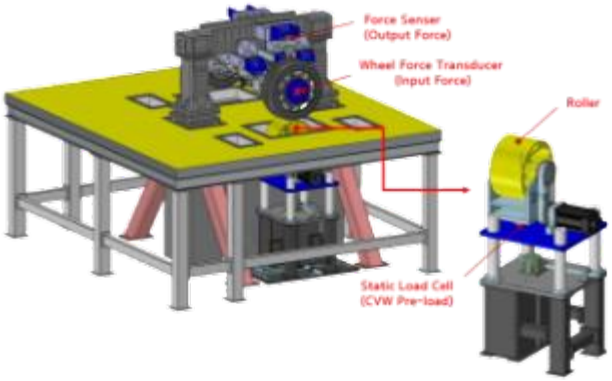


Figure . Roller Bench Test System.

2.1 Input Force

In this study, the roll bench system was operated by a test mode that simulated run-up 0 to 100 kph based on the actual vehicle drive mode. Analyzing the characteristics of the input load shown in Fig. 2, the 1st and harmonics are generated under system conditions, which does not occur in In-Wheel single-component dynamo evaluation, due to unbalance of tire deformation caused by pre-load. In addition, the tire resonance mode moves from 190 Hz to 200 Hz according to the sweep speed, and In-Wheel motor (64 pole 60 slots) mounted directly inside the tire generates 32nd/60th/64th order and sideband components by electromagnetic force of motor.

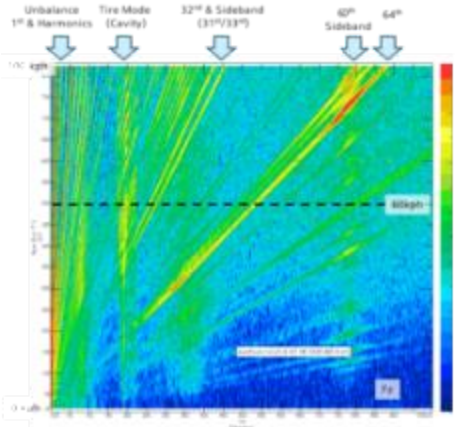


Figure 2. Input Force of Tire Wheel Center in In-Wheel Motor System

2.2 Output Force

In order to obtain the output force of the suspension system, the dynamic force sensor was directly mounted on four body mounts (Shock Absorber, Spring, Member FR/RR Mount). Finally, the Z-direction load, which is the most dominant force according to the mounting direction, was selected as the representative value.

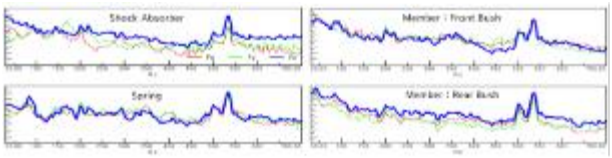


Figure 3. Output Force of Tire Wheel Center in In-Wheel Motor System

2.3 Load Transfer Ratio

It is possible to define the load transfer ratio of the system by the measured input/output force. Using this quantitative value, the contribution of transfer path of the suspension system the vehicle body transfer path can be analyzed on target frequency band.

Hyundai Mobis Restricted

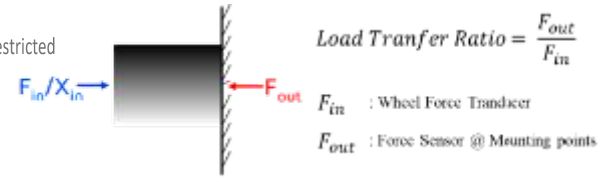


Figure 4. Definition for the Load Transfer Ratio

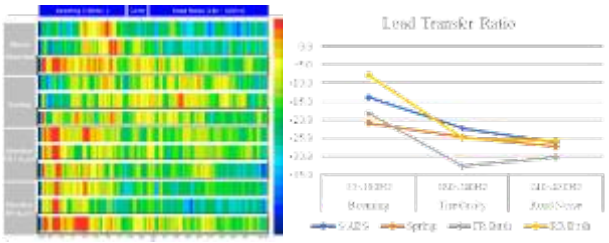


Figure 5. Load Transfer Ratio on Mounting Points at Roller Bench Test.

To define the load transfer characteristics of the frequency band, it is classified and analyzed into three bands according to the noise pattern: booming noise below 180 Hz, tire cavity between 180 and 240 Hz, and road noise band up to 500 Hz based on frequency range.

First, in the booming noise band (180 Hz ↓), the transmission is large in the order of rear bush > shock absorber > front bush > spring.
Second, the contribution can be found in the order of shock absorber > rear bush ≒ spring > front bush in the tire cavity band (180 Hz ~ 240 Hz).
Lastly, in the road noise band (240 Hz to 500 Hz), it can be seen that a large amount of load is transmitted in the order of rear bush ≒ shock absorber ≒ spring > front bush.
Comprehensively looking at contributions across all frequency bands, the suspension system can determine that the transfer paths to the member rear bush and shock absorber are dominant.

2.4 Analysis of Dynamic Characteristics for Suspension System

In addition to the load, the vibration transfer phenomenon of each system component was verified. As shown in Fig. 6, the vibration is amplified in the suspension arms compared to the input part equipped with the in-wheel motor. In addition, when the vibration is transmitted to the member after the suspension bushes, the vibration is reduced again.
A mode map of dynamic characteristics of the suspension system was constructed to analyze the contribution of load transfer by components in more detail. As shown in Fig. 7, it can be seen that the resonance mode of each component element occurs at frequencies where the load transfer ratio peaks. Particularly, the global mode of the suspension system is the main cause in a band of 100 Hz or less, and that the load transfer ratio is deteriorated by the individual modes of the members/arms and the mode coupling between parts more than 100 Hz. This mode map is meaningful in that it has established a process of selecting an improvement target by checking the cause parts of the problem frequency in the future.

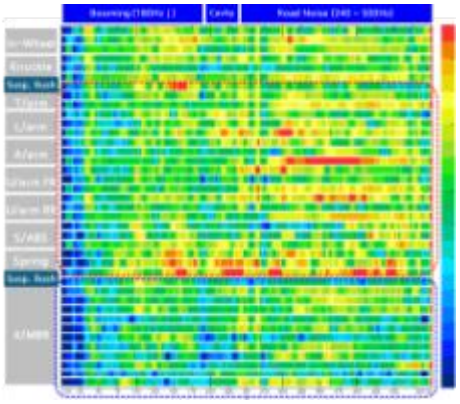


Figure 6. Vibration Transfer characteristics of components

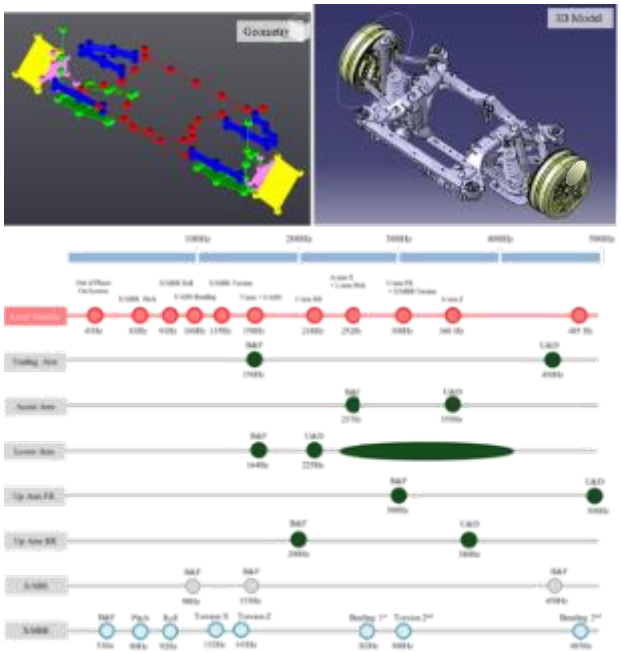


Figure 7. Geometry and Mode Map for the In-Wheel System

Hyundai Mobis Restricted

2.5 Comparison between In-Wheel and EDU System

The test results were analyzed to compare In-Wheel type and the EDU system, which are currently mass-produced electric vehicles. In-wheel shows different characteristics in input load and load transfer ratio because there is a structural difference in which the motor is rigidly fastened directly to the inside of the tire and the EDU type is fastened to the member by mount bushes. Due to these structural differences, it was verified that tire components (180 to 220 Hz) and unbalanced components due to pre-load are equally generated at the input load, but motor/gear order components are not generated in the EDU type at 500 Hz or less, as shown in Fig. 7.
As shown in Fig. 8, by quantitatively comparing the load transfer ratio of the two systems, it can be seen that the In-Wheel motor system has a superior load transfer ratio compared to the EDU system in all frequency range and transfer paths. In other words, it can be predicted through system level evaluation that In-wheel system's road noise is better than EDU system in real vehicles.

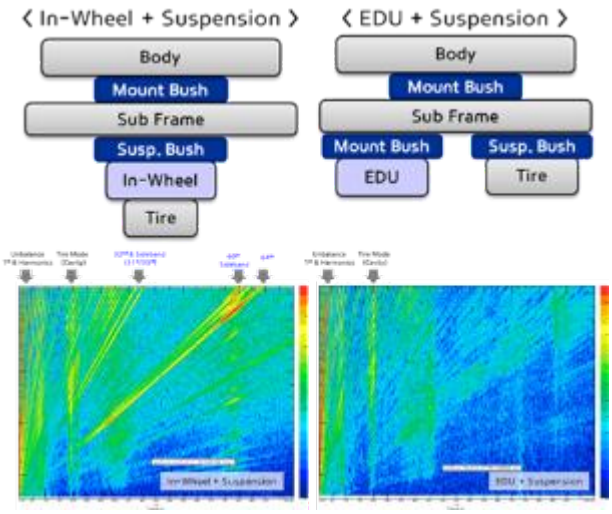


Figure 8. Comparison between In-Wheel and EDU System

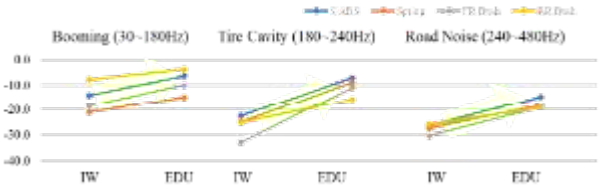


Figure 9. Result of Load Transfer Ratio between In-Wheel and EDU System at Roller Bench Tester

3. TEST SYSTEM II : LINEAR ACTUATOR

The second evaluation system developed is a linear actuator type as shown in Fig. 10. In this test system, a large-capacity excitation motor of 1 ton was newly developed and applied to control the static pre-load and the dynamic force at the same time. Compared to the roller bench type, it is evaluated as a system that combines only the drive unit + suspension system excluding the tire, so the difference is that it reflects the original characteristics of the suspension.
In the linear excitation test, sweep the LH/RH vertical axis to the 30 to 300 Hz in both the in-phase and out-of-phase to obtain the load transfer ratio. Based on this linear actuator system, the load transfer ratio can be compared for two drivetrain types, In-Wheel and EDU, and the results are shown in Fig. 11.

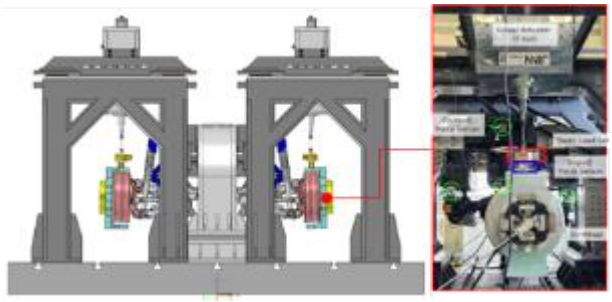


Figure 10. Linear Actuator Test System

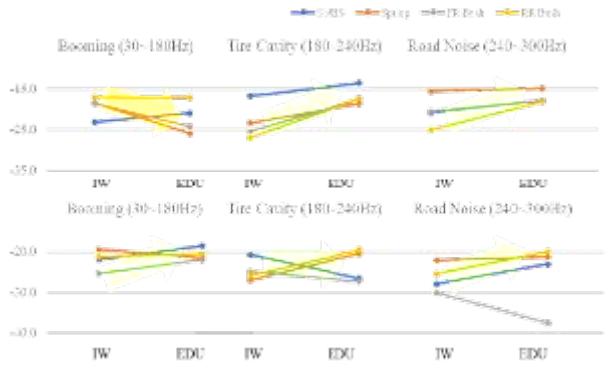


Figure 11. Result of Load Transfer Ratio between In-Wheel and EDU System at Linear Actuator Tester

Hyundai Mobis Restricted

Overall, the In-Wheel system has a superior load transfer ratio than the EDU system, just like the previous roller bench test. However, when the linear actuator tester is in-phase excited, the result is opposite to the roller bench test in which the In-Wheel type is inferior only in the booming noise band (30 ~ 180 Hz). When the test results are compared in detail in the frequency domain, the load transfer ratio in the 140 ~ 180 Hz band is amplified in the In-Wheel type, which can be judged as the effect of the boundary conditions of the two excitation systems. Although there are differences in boundary conditions such as whether tires are mounted or not, or excitation conditions such as roller/linear exciters, it can be seen that each test has independent characteristics at the same time.

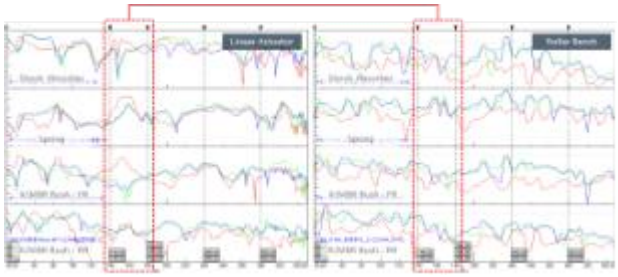


Figure 12. Comparison between Linear Actuator and Roller Bench Test System

4. CONCLUSION

So far, we have introduced the development of an evaluation system for verifying system-level NVH performance for the In-Wheel motor. In addition, the NVH performance of the system level due to the difference in the drive unit (In-Wheel vs EDU) was extracted and compared with a quantitative value called the load transfer ratio. And a mode map was constructed to analyze the causative component for selecting the target component when improving performance. Using this study, we laid the foundation for verifying the performance of the integrated platform level including the drive unit and suspension system.

Hyundai Mobis Restricted

5. REFERENCES

[1] Wellmann, T., Govindswamy, K., and Tomazic, D., “Impact of the Future Fuel Economy Targets on Drive unit, Driveline and Vehicle NVH Development”, *SAE Int. J. Veh. Dyn., Stab., and NVH* 1(2), pp. 428–438, 2017

[2] Itoh, Y., Sakai, K. and Makino, Y., “In-Wheel Motor System”, *NTN Technical Review*, no. 79, pp. 22–28, 2011

[3] Bohyeong Kim, Jungi Hong, Seen Yun, Gyoungho Shin, Gyeongwhi Min and Jintai Chung, “Noise Reduction of an In-Wheel Motor System for an Electric Vehicle”, *Transactions of the Korean Society for Noise and Vibration Engineering*, vol. 29, no. 3, pp. 422–428, 2019

[4] Yeonghwi Min, Gyoungho Shin, Jinmoo Jeon, Sohee Park, Donghyun Kim, “A Study on vibration reduction with In-Wheel planetary gear bearing support structure change”, KSAE 2020 Annual Autumn Conference & Exhibition, pp. 1151–1154, 2018

[5] Sangyoung Park, Injeong Choi, and Jinnyeon Jung. "Development and Application of Test and Simulation Technology." *Proceedings of the Spring Conference of the Korean Society of Automotive Engineers*, pp. 261-266, 2023

DOI: 10.61782/fa.2025.0739



FORUM ACUSTICUM
EURONOISE 2025

RELATIONSHIP AMONG NOISE, CAVITATION STRUCTURE AND EROSION RISK IN INDUSTRIAL CENTRIFUGAL PUMPS WITH A FAN-TYPE INDUCER

Shimpei Narimatsu[1*] **Haruto Utsumi**[1] **Shinichiro Ejiri**[2] **Masahiro Miyabe**[1]
[1]Osaka Institute of Technology, Osaka, Japan
[2]Nikkiso Co., Ltd. , Tokyo, Japan

ABSTRACT

There is a strong demand for pump manufacturers to prevent problems such as noise, vibration and erosion due to cavitation before delivering products to the site. This study aims to establish a practical technique for predicting the occurrence, structure, and erosion risk of cavitation by noise measurements. A centrifugal pump with a fan-type inducer was operated to measure noise both outside and inside of pipes at various suction conditions and flow rates. Visualization experiments around the inducer were also conducted to identify the cavitation structure. In addition, the paint erosion test was conducted to estimate the cavitation erosion risk at the blades of the inducer. From these experiment results, the relationship between noise, cavitation structure and erosion risk were discussed. The overall sound pressure level measured by air-borne noise measurements was found to be characterized as the increase with the enlarged peeling area obtained from the paint erosion test. Furthermore, the overall sound pressure level measured by the liquid-borne noise measurements was also confirmed to be related with the vibration due to cavitation instability phenomena.

Keywords: *Turbopump, Cavitation, Inducer, Noise*

[*]***Corresponding author***: *m1m24426@st.oit.ac.jp*
Copyright: *©2025 First author et al. This is an open-access article distributed under the terms of the Creative Commons Attribution 3.0 Unported License, which permits unrestricted use, distribution, and reproduction in any medium, provided the original author and source are credited.*

1. INTRODUCTION

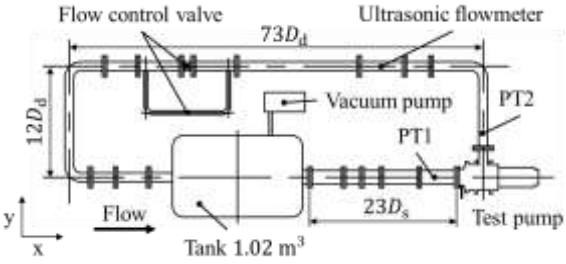
Cavitation in turbopumps is a serious problem due to the vibration, noise, and damage it causes in comparison to the stability of the pump[1]. Therefore, pump manufacturers are required to identify problems caused by cavitation before delivering products to the site. Predictions have been made by experimental methods and numerical fluid analysis, but users and designers may determine the existence of cavitation from noise. Dong[2] et al. attempted to visualize the occurrence of cavitation in centrifugal pumps and to measure liquid-borne noise with the hydrophone. The results indicate the feasibility of detecting the presence of cavitation from the over-all value of the liquid-borne noise. In terms of Air-borne noise, Chudina[3] measured audible external noise for a centrifugal pump impeller. As a result, there is a large change in the 1/2BPF (Blade Passing Frequency) before and after the occurrence of cavitation, and it is thought that the change in this frequency band may be used to detect cavitation. Černetič[4] et al. made the similar measurement and confirmed that besides discrete frequencies, there are also large changes in a wide frequency range of 20 Hz to 20 kHz, indicating that it can be used for detection. In addition, Iga[5] et al. used a centrifugal pump with the visualization system to measure the unsteady flow and external noise using the microphone during cavitation instability phenomena. As a result, it was confirmed that the external noise had a predominant swirling frequency component during the occurrence of the rotating cavitation, and the possibility of inferring the occurrence of the cavitation was reported. As described above, liquid-borne and air-borne noise measurements have shown positive results in detecting the occurrence of cavitation. However, since noise measurement is greatly affected by component materials, pump geometry, and measurement environment, various research results are

needed for further practical application. Furthermore, the prediction of cavitation erosion has been studied by numerical fluid dynamics analysis[6-7], but experimental prediction is also important due to its sophistication, as it must consider the collapse and growth of individual bubbles. In this study, a fan-type inducer, with cavitation instability phenomenon[8] confirmed at low flow rates, will be experimentally investigated and analyzed to establish a practical method for noise by investigating the occurrence and development of cavitation, its morphology, and the risk of erosion. The effects of varying the blade leading edge geometry on the cavitation collapse area and the noise are investigated.

2. EXPERIMENTAL FACILITY

2.1 Test Facility

Figure 1 indicates the experimental apparatus mainly consists of suction pipes D_s (JIS (Japan Industrial Standards) 125A), discharge pipes D_d (JIS 80A), a control valve, an ultrasonic flow meter, a vacuum pump, and a tank. A pump is placed in the test section and motor is electronically controlled to maintain the rotational speed constant at any set value. The working fluid is fresh water. The pump performance is evaluated from shaft rotational speed, torque, flow rate, and the difference of static pressure between section A and B. The flow rate is adjusted to any set value with a control valve and is measured by an ultrasonic flowmeter. The pressure of the liquid level in the tank is adjusted by a vacuum pump to change the pressure of the entire piping system. The centrifugal pump used in the present study is a vertical pump that is mainly used for transporting Liquified Natural Gas. The discharge port was modified by turning sideways to apply to Osaka Institute of

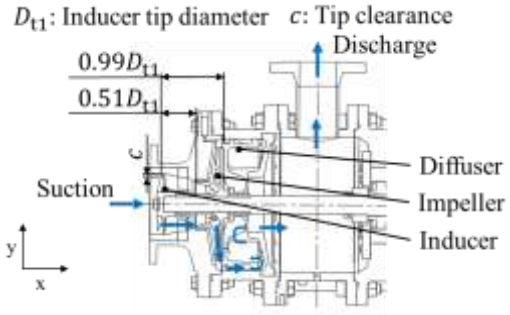


Technology test facility.

Figure 1. Test Facility

2.2 Test Pump

Figure 2 shows the cross sectional view of the test pump. The test pump has a 4-blade fan-type inducer, a 9-blade closed impeller, and an 8-vane axial diffuser with vane slit[9].



D_{t1} represents the inducer diameter. The impeller inlet is $0.51D_{t1}$ axially away from the trailing edge of the inducer and the diffuser inlet is $0.99D_{t1}$. The type number of this pump is 156 (specific speed :138 m^3/min,m,min^{-1}).

Figure 2. Cross-sectional view of the test pump

2.3 The fan-type Inducer

Figure 3 shows the external view of the fan-type inducer (Base type). Table 1 shows the primary geometrical properties of the fan-type inducer[10]. It summarizes the parameters that relate to the cavitation performance. The design parameter that represents the most significant feature of this inducer is solidity which is defined as equation (1). This type of inducer is suitable for high flow rate and low head specifications and is used in industrial applications, but few studies have been conducted. Inlet flow rate / inlet tip blade tip angle ratio, m_1 satisfies recommended value, m_1>0.4 defined as equation (2). In comparison with the design guideline of the turbopump for a rocket[11]. It indicates that flow instabilities due to backflow such as cavitation surge are unlikely to occur at the design flow rate for this inducer. In addition, inlet tip blade angle, β_{t1} meets within recommended value which should be less than 20 deg. However, the outlet tip bade angle is larger and the backflow is likely to occur at low flow rate. On the other hand, the hub / tip ratio, ν_1 is larger than the recommended value 0.25 to 0.35[11] and it suppresses to occur backflow at low flow rate because average flow velocity is relativity large at the inducer inlet. The diameter of the inducer hub is determined by that of the shaft and pump performance is well balanced by those two parameters, β_{t1} and ν_1. However, cavitation is relativity easy to occur. Furthermore, the tip

clearance ratio, c is smaller than recommended value 0.009 to 0.011 to achieve high efficiency.

Table 1. Design parameters of fan-type inducer

Number of blades [-] : n_1	4
Tip diameter [mm] : D_{t1}	125.3
Hub diameter [mm] : D_{h1}	51.0
Hub height [mm] : h_1	40.0
Solidity at tip [-] : S_t	0.77
Solidity at hub [-] : S_h	0.83
Inlet flow rate/Inlet blade tip angle ratio [-] : m_1	0.47
Inlet blade tip angle [deg.] : β_{t1}	10.5
Hub/Tip ratio [-] : ν_1	0.41
Tip clearance [mm] : c	0.65

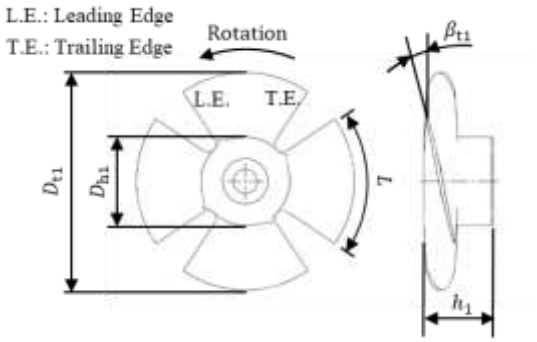


Figure 3. External view of a fan-type inducer (Base)

3. EXPERIMENTAL METHODS

3.1 NPSH test

NPSH test is conducted to measure pump cavitation performance. The pressure of the inlet is decreased by the vacuum pump, the pump total head at each cavitation number is recorded. Experiment is conducted until the condition where pump head drop is confirmed by 3 % (NPSH3). The rotational speed is 3000 min^{-1}.

3.2 Noise measurement test

Air-borne and liquid-borne noise were measured to clarify the effectiveness of noise measurements in detecting cavitation and the characteristics of the collapse sound. The locations of the air-borne and liquid-borne noise measurements are shown in Fig. 4. For the air-borne noise measurements, a microphone (BOYA, PVM1000) was placed 5 mm away from the outside wall of the casing. These measurements were based on previous studies by Saito[12]. The measured sound pressure was passed through an amplifier and frequency analyzed using an FFT (Fast Fourier Transform) analyzer(ONOSOKKI, CF-5210). The frequency range was recorded from 25 Hz to 20 kHz, which is the audible range, and from 25 Hz to 5 kHz to observe the BPF in detail. The frequency-weighted A-weighted characteristics were evaluated in consideration of human hearing. For the liquid-borne noise measurements, a hydrophone (Brüel & Kjær, Type 8103) was installed inside the pipe upstream of the inducer. The tip of the hydrophone was placed at the same position as the inner wall of the pipe. Liquid-borne sound pressure data acquired by a data logger (KEYENCE, NR-X100, CA04) was subjected to FFT analysis using a data evaluation code written in Python 3.13.2. The frequency range is 25 Hz to 5 kHz.
In this study, an anechoic chamber was not used, assuming a factory environment where industrial pumps are operated.

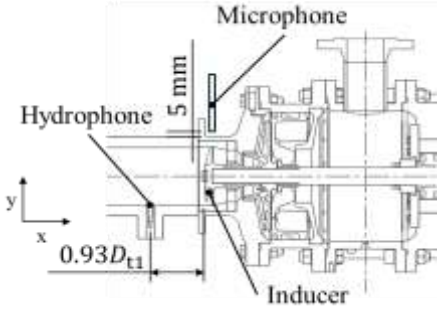


Figure 4. Positions of a microphone and a hydrophone

3.3 Visualization test

Visualization experiments were conducted to observe and identify cavitation foam. Figure 5 shows a schematic view. The inducer casing is made of acrylic, and a high-speed camera (Photron, FASTCAM Mini AX100) was used to capture images at a speed of 6,000 fps. The brightness of the images was adjusted by using a 500 W halogen light source (EARTH MAN, WLT-260).

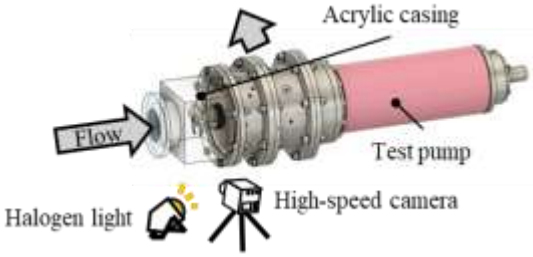


Figure 5. Schematic view of visualization test rig

3.4 Paint erosion test

Paint erosion test is conducted to observe paint removal area due to cavitation on the blade surface of a fan type inducer. Blue varnish (JIP 101) is painted on the inducer blade surface with reference to Fukaya[6]. After 30 minutes of operation with constant flow rate and cavitation number, the inducer is removed from the test stand and the condition of the blade surface is observed.

4. EXPERIMENTAL RESULTS AND DISCUSSION

4.1 Results of NPSH tests and visualization tests

Figure 6 shows the suction performance curve of the test pump and the development and form of cavitation under each operating condition. For ϕ/ϕ_d =0.50, 0.70, 1.00, and 1.20, ψ dropped sharply after maintaining a constant value with the decrease in σ. The visualization experiments revealed that cavitation occurred at the inducer (○ in the figure) and then developed into the shaft and impeller (△ and ◇ in the figure), which may be due to the blockage of the flow channel by the cavities. Focusing on ϕ/ϕ_d =0.30, vortex cavitation in reverse flow occurred in the range of σ =0.057 to 0.541 (□ in the figure). Furthermore, below σ = 0.051, a cavitation surge was observed, with intermittent cavitation expansion and contraction. Under conditions where cavitation surges occurred, the pump system vibration increased, so measurements could not be taken until the head dropped (x in the figure).

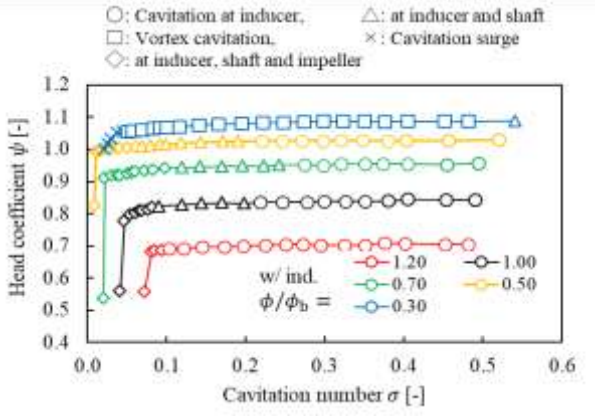
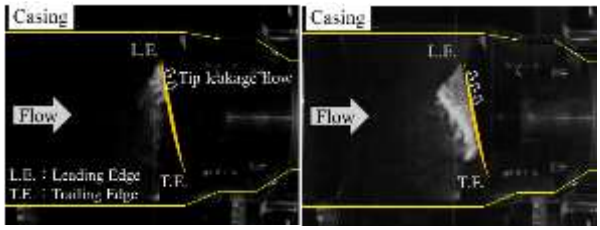
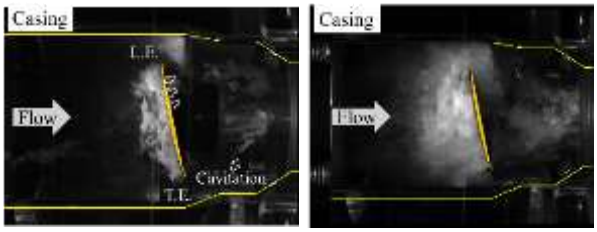


Figure 6. Suction performance curve of test pump and cavitation patterns

Next, we show the development form of cavitation based on the results of the visualization experiment. Figure 7(a) shows the cavitation morphology at the rated flow rate of the pump. σ = 0.453, cavitation occurred with the same shape on the negative pressure surface of all inducer blades. Cavitation originated at the leading edge of the blade and fluctuated at the trailing edge due to the gap leakage from the casing, confirming the release of a group of bubbles. These cavitation patterns are a mixture of sheet cavitation, crevice cavitation, and bubble cavitation[13]. Figure 7(b) shows a visualization image of the same flow rate with lower pump suction pressure. As σ decreases, the cavities expand to the trailing edges of the blades, and the leakage cavitation expands at the same time. Cavitation was also observed around the shaft and continued to the impeller inlet with a swirling element. Cavitation was also observed at the impeller inlet in Fig. 7(c), the point of 3% drop in pump head. Since the flow path between the inducer blades is not completely blocked by cavitation, the drop in pump head is considered due to channel blockage caused by cavitation in the impeller. The same cavitation development process was also observed for ϕ/ϕ_d =0.50, 0.70, and 1.20. Figure 7(d) shows the vortex cavitation in reverse flow with ϕ/ϕ_d =0.30 and σ =0.324, exhibiting a cluster of fine bubbles around the inducer blade. The cavitation form was not changed with a decline in suction pressure, and intermittent expansion and contraction of a cluster of fine bubbles were observed during the cavitation surge. Visualization experiments confirmed the cavitation occurred at the leading edge of the blades and developed in the direction of the trailing edge.



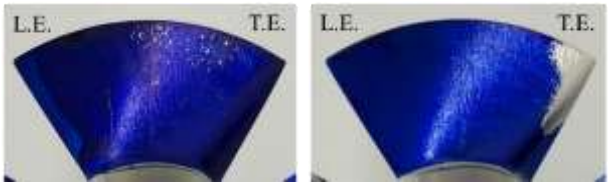
(a) ϕ/ϕ_d =1.00, σ =0.453, (b) ϕ/ϕ_d =1.00, σ =0.170



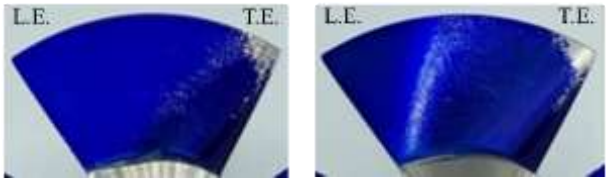
(a) ϕ/ϕ_d =1.00, σ = 0.453, (b) ϕ/ϕ_d =1.00, σ =0.170

Figure 7. Cavitation development around inducer

The following sections compare the paint removal on the suction side of the inducer blade in the paint erosion test. As shown in Fig. 8(a), a small detachment was observed from the center of the blade edge to the trailing edge at ϕ/ϕ_d =1.00 and σ =0.197. Decreasing the pump suction pressure, σ =0.052 in Fig. 8(b), shows the change to a plane delamination extending to the trailing edge of the airfoil. Figure 8(c) and (d) with ϕ/ϕ_d =1.20 also resulted in a plane delamination. For other ϕ/ϕ_d conditions, sparse and areal detachment was not observed at the point of head reduction. Cavitation collapse was stronger on the trailing edge of the inducer blade, suggesting a high risk of erosion near the trailing edge for ϕ/ϕ_d =1.00 and 1.20.



(a) ϕ/ϕ_d =1.00, σ =0.197 (b) ϕ/ϕ_d =1.00, σ =0.052



(c) ϕ/ϕ_d =1.20, σ =0.094 (b) ϕ/ϕ_d =1.20, σ =0.058

Figure 8. Paint peeling area at suction surface

4.2 Relationship between cavitation erosion area and noise characteristics

This section compares the relationship between paint erosion test results and noise measurement results. Figure 9 shows the relationship between the overall noise level and each of the operational conditions, and as in Fig. 6, markers are used to classify the development and form of cavitation in the visualization experiment. The markers are filled in the conditions with surface delamination confirmed by the paint erosion test. The air-borne noise in Fig. 9(a) shows a similar trend with decreasing σ for ϕ/ϕ_d =0.50, 0.70, 1.00, and 1.20, and different trend for σ <0.250. At ϕ/ϕ_d =1.00 and 1.20, there is an increase in noise at higher σ than the operating conditions in both cases with areal exfoliation observed. This range is the transition from sparse exfoliation to areal exfoliation and is considered to capture the collapse of cavitation. Paint erosion tests help to predict in advance the conditions under high risk of erosion. Also, at ϕ/ϕ_d =0.50 and 0.70, the overall value increased rapidly at the 3% drop point of the pump head. The trend was consistent with the results of Dong et al[3], considering the fluid force due to cavitation blockage was converted to acoustic energy. Comparing the suction condition of vortex cavitation in reverse flow at ϕ/ϕ_d =0.30 with other ϕ/ϕ_d conditions, the overall value was decreased. Since the visualization test showed fine bubble clusters and the paint erosion test showed no areal detachment, it is assumed the bubble clusters always weakened the sound propagation without collapsing it. Therefore, predicting cavitation instability phenomena from external noise is difficult with current measurement methods. In addition, the characteristic noise change during the cavitation surge was not observed. The liquid-borne noise in Fig. 10 exhibited similar trends for all ϕ/ϕ_d conditions. Characteristic changes in the noise measurements were not observed for the operating conditions with a high risk of erosion. A previous study[3] showed a positive relationship between the development of cavitation and an increase in noise. The difference in the liquid-borne noise trend indicates the position of the hydrophone. In this study, the hydrophone was installed upstream of the inducer, resulting in the inability to measure localized changes in sound pressure due to cavity collapse. On the other hand, cavitation surge with ϕ/ϕ_d =0.30 indicates significant increase in noise and good response to reverse flow and fluctuations in the internal flow.

FFT analysis was performed on the air-borne noise measurements for each ϕ/ϕ_d condition to confirm the validity for the prediction of erosion risk. Figure 11 shows the results for each ϕ/ϕ_d condition at σ =0.143. The horizontal axis indicates the dimensionless frequency divided by the revolution frequency, and the vertical axis is the sound pressure value [dB] measured at the pressure [Pa] and converted by the equation (4). The BPF of the inducer and impeller and its higher-order components appear in the low frequency range of 25 to 800 Hz. Therefore, discrete specific frequencies due to geometry and flow are affected in the low-frequency range. At high risk of erosion ϕ/ϕ_d =1.00,1.20, the increase was observed in a wide band of high frequencies above 1 kHz. In particular, the increase was significantly larger at 3kHz to 4kHz, and the peak was found to increase around 3.5kHz. These results are similar to the experimental results of Matsumoto et al[14] in their liquid injection method, concluding this phenomenon is the frequency of intermittent release of bubbles from the tail of the cavity. Figure 12 shows the liquid-borne noise at the onset of the cavitation surge; σ =0.051 has a prominent peak below 20 Hz, which is consistent with the frequency

response measured in a previous study[8]. Therefore, it is considered that the air-borne noise was strongly affected by the flow control valve and BPF and could not be captured under the occurrence of cavitation surges.

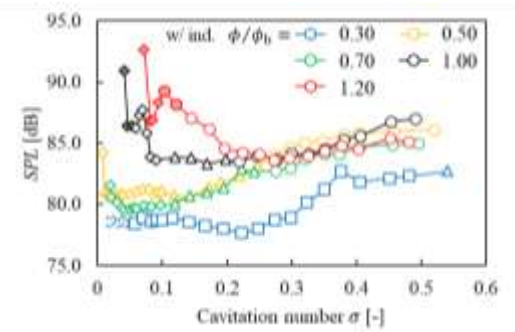


Figure 9. Relationship between cavitation number and air-borne noise

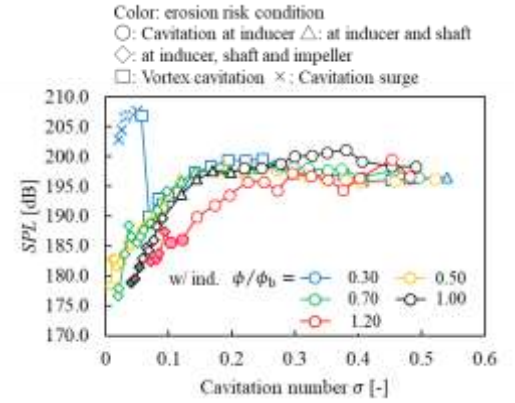


Figure 10. Relationship between cavitation number and liquid-borne noise

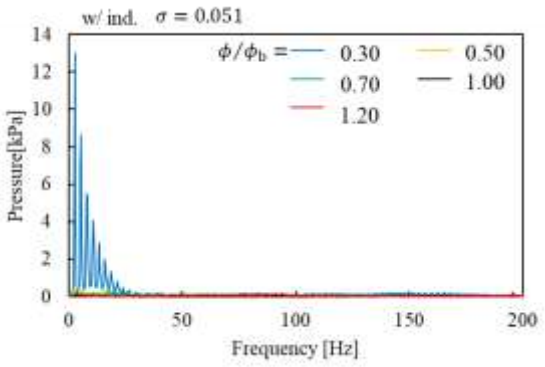


Figure 11. Comparison of air-borne noise spectrum with different flow rate

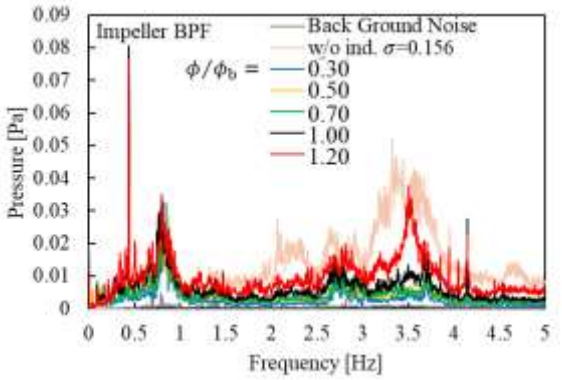


Figure 12. Overall value of high-pass filtered air-borne noise (evaluated range is from 25Hz to 20kHz)

Based on the above results, the measurement in the high-frequency band above 3.0 kHz is considered to be effective for noise evaluation of the risk of erosion. Figure 11 shows the results of applying a high-pass filter above 3.0 kHz in the human audible range of 25 Hz to 20 kHz. It is possible to determine the risk of erosion based on differences in air-borne noise tendency and improve the prediction reliability of erosion risk by using a high-frequency bandwidth.

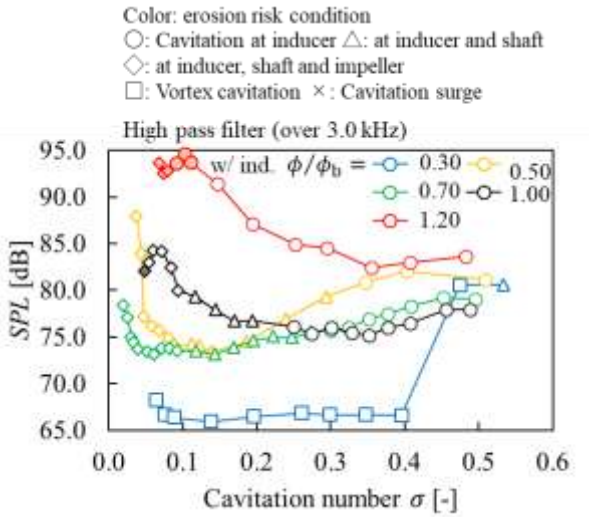


Figure 12. Overall value with 3.0 kHz high pass filter of air-borne noise; 25 Hz to 20 kHz

4.3 Suppression of cavitation erosion by modifying the blades' geometry

Paint erosion experiments showed the area of high erosion risk to be the trailing edge of the inducer blades. Therefore, the geometry of the leading edge of the blade tip was modified to lower the risk of erosion. The effects of applying a borehole or a sweep angle were also investigated. The inducer with the forward sweep angle that had the most significant effect on cavitation instability and noise reduction is shown below. Figure 13 shows the view of the inducer with forward sweep; the leading and trailing edges of the blade tip are swept upstream. In this study, the inlet and outlet angles are the same as the base geometry without the sweep angle. The comparison of the overall values of air-borne noise with and without sweep angle is shown in Fig. 14. Applying the leading edge sweep angle, the noise reduction was confirmed even under the σ condition at ϕ/ϕ_d =1.00, with a high risk of erosion.

The visualization test in Fig. 15 shows the forward sweep is effective in suppressing the development of cavitation generated at the leading edge to the blade tip direction. Furthermore, the paint erosion experiment in Fig. 15 shows the lower risk of erosion, since no areal detachment was observed. These results suggest the cavitation collapse at the inducer blade tip leads to higher risk of erosion with more noise increase. The addition of a forward sweep angle is expected to lower the noise level and decrease the risk of erosion. On the other hand, the sound pressure level did not increase significantly at ϕ/ϕ_d =1.20, although it remained consistently higher than for the other ϕ/ϕ_d conditions. Therefore, employing the forward sweep enables to lower both the noise and the risk of erosion, but further investigation of the blade geometry is required to determine the cause of the noise gain in the high flow region.

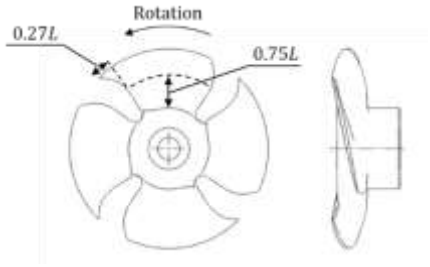


Figure 13. Fan-type inducer with forward sweep

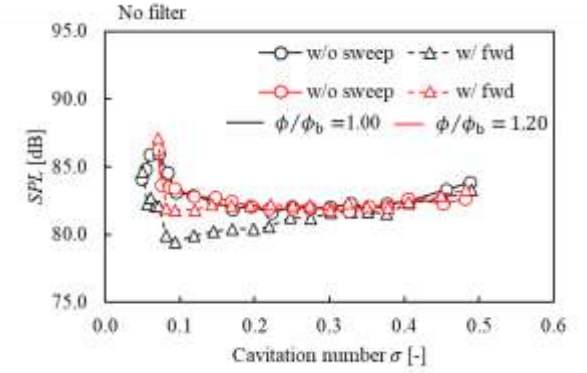
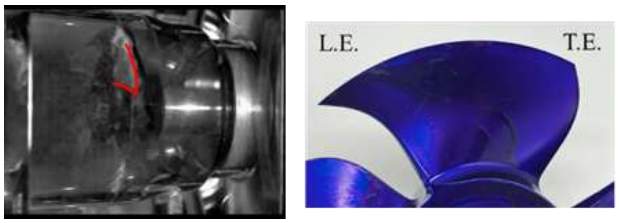


Figure 14. Comparison of air-borne noise with two different inducers



(a) Visualization; σ =0.291 (b) paint erosion; σ= 0.052

Figure 15. Inducer with forward sweep at ϕ/ϕ_d=1.00

5. CONCLUSIONS

- It is possible to predict erosion risk by the tendency of air-borne noise.
- It is also possible to make the prediction accuracy higher using high pass filter over 3.0kHz.
- The cavitation surge can be detected by liquid-borne noise.
- The erosion risk and noise are reduced by adopting the forward sweep geometry.
- The cavitation development near the inducer tip is suppressed by the forward sweep geometry.

6. EQUATIONS

The equations used in this study are shown below.

$$s_t = l_t / t_t \quad (1)$$

$$m_1 = \varphi_{1t} / \tan\beta_{1t} \quad (2)$$

$$\psi = \frac{p_{out} - p_{in}}{\rho u^2} \quad (2)$$

$$\varphi = \frac{Q}{Au^2} \quad (3)$$

$$\sigma = \frac{p_{in} - p_v}{\frac{1}{2}\rho u 2} \quad (4)$$

$$SPL = 10\log_{10}\frac{p^2}{p_0^2} = 20\log_{10}\frac{p}{p_0} \quad (5)$$

$$OA = 10\log_{10}\left(\sum_{i=1}^{n} 10^{\frac{SPL}{10}}\right) \quad (6)$$

7. ACKNOWLEDGMENTS

The authors would like to thank NIKKISO Co., Ltd. For permission to present this paper.

8. REFERENCES

[1] Brennen, C. E., “Hydrodynamics of Pumps”, Cambridge University Press, 1994.

[2] Dong, L., Zhao, Y. and Dai, C., “Detection of Inception Cavitation in Centrifugal Pump by Fluid-Borne Noise Diagnostic”, Hindawi Shock and Vibration, Vol. 2019.

[3] Chudina, M., “Noise as an Indicator of Cavitation in a Centrifugal Pump”, Acoustic Physics, Vol. 49, No. 4, pp. 463-474, 2003.

[4] Černetič, J. and Čudina, M., “Estimating uncertainty of measurements for cavitation detection in a centrifugal pump”, Measurement, Vo. 44, No. 7, pp. 1293-1299, 2011.

[5] Iga, Y., Yokoi, T., Moriya, S., Okajima, R., Nomi, M., ”Noise Measurement of Rotating Cavitation Arising in a Centrifugal Pump (in Japanese)”, Turbomachinery, Vol. 52, No. 6, pp.334-343, 2024.

[6] Fukaya, M., Tamura, Y. and Matsumoto, Y., “Prediction of Cavitation Intensity and Erosion Area in Centrifugal Pump by Using Cavitation Flow Simulation with Bubble Flow Model”, Journal of Fluid Science and Technology, Vol. 5, No. 2, pp. 305-316, 2010.

[7] Miyabe, M. and Maeda, H., “Numerical Prediction of Pump Performance Drop and Erosion Area due to Cavitation in a Double-Suction Centrifugal Feedpump”, Proc. of ASME-JSME-KSME 2011 Joint Fluids Engineering Conference, AJK2011-06023, pp. 121-128, 2011.

[8] Narimatsu, S., Nakayama, S., Konno, S., Ejiri, S. and Miyabe, M., “Analysis of Instability Phenomena Occurring in a Centrifugal Pump with a Low-solidity Fan-type Inducer”, Proc. of the ASME 2024 Fluids Engineering Division Summer Meeting, FEDSM2024-130433, 2024.

[9] Takao, S., Konno, S., Ejiri, S., Miyabe, M., ”Experimental Investigation on the Suppression of Diffuser Rotating Stall in a Centrifugal Pump Using Diffuser Vane Slits (in Japanese)” , Turbomachinery, Vol. 50, No. 2, pp. 101-109, 2020.

[10] Ejiri, S., “Fan Type Inducer for a Centrifugal Pump by Wire Arc Additive Manufacturing and Machining”, International Journal of Fluid Machinery and Systems, Vol. 16, No. 2, pp. 184-191, 2023.

[11] Furukawa, A., Ishizaka, K., “Inducer design and instability phenomena (in Japanese)”, JSME, RC 178, 2002.

[12] Saito, S., “Generation Mechanism and Transition Process of Cavitation Noise”, JSME international journal, Ser. 2, Vol. 32, No. 2, pp. 189-198, 1989.

[13] Turbomachinery Society of Japan, ”Guideline for Prediction and Evaluation of Cavitation Erosion in Pumps (in Japanese)”, TSJ G 011: 2011, 2016

[14] Matsumoto, M., Inoue, Y., Kobashi, Y., Matsumura, E., Senda, J., ”Effect of Cavitation inside Injection Nozzle on Spray Characteristics for Direct Injection”, Transactions of the Japan Society of Mechanical Engineers, Part B, Vol. 79, No. 806, 2013.

DOI: 10.61782/fa.2025.0867

FORUM ACUSTICUM EURONOISE 2025

THE INFLUENCE OF HELIX ANGLE AND GEAR WIDTH ON THE NOISE RADIATED BY A GEARBOX

Francesco Mori[1*] **Andrea Santoni**[1] **Nicolò Zuccherini Martello**[2]
Roberto Grimaldi[2] **Simone Chiari**[2] **Patrizio Fausti**[1]
[1] Department of Engineering, University of Ferrara, Italy
[2] Baker Hughes – Nuovo Pignone Tecnologie srl, Via Felice Matteucci 2, Firenze, Italy

ABSTRACT

The noise spectrum generated by a gearbox depends on multiple factors, such as gear design parameters, casing geometry, rotational speed of the shafts and the presence of imperfections. This numerical study analyses the influence of the helix angle and gear width on the noise radiated by a gearbox through parametric studies. The numerical investigation combines a time-domain analysis on a multibody model of the gearbox with a frequency-domain analysis on a boundary element model of the air to evaluate noise radiation in an open space in free-field conditions. The simulations assume a constant workload and a constant rotational speed of the shafts. The results indicate that increasing the helix angle and gear width leads to a smoother noise spectrum and modifies its shape. Compared to spur gears, helical gears generate lower sound power levels due to a reduced variation in the meshing stiffness.

Keywords: *gearbox, noise radiation, helical gears, numerical prediction.*

1. INTRODUCTION

Gearboxes, essential components of mechanical transmission systems, typically consist of one or more pairs of gears enclosed in a casing. They are widely employed in applications such as compressors, pumps and fans to regulate motion and torque. Acoustically, gearboxes are often part of complex noise generation systems, in which multiple noise sources interact, making it difficult to isolate and identify individual contributions. As a result, experimentally evaluating the noise generated by gears meshing and radiated in the surrounding fluid by the casing in real operating conditions is typically challenging.

The noise spectrum radiated by a gearbox depends on various factors, including gear geometry, rotational speed, axis misalignment, and surface imperfections [1,2]. In a previous study, the effect of the workload was assessed for a pair of spur gears [3]. These gears exhibit a distinct harmonic component at the meshing frequency, which is associated with significant variations in the meshing stiffness throughout the meshing cycle. This study employed a coupled numerical approach to evaluate the radiated noise: a time-domain multibody analysis on a finite element (FE) model of the gearbox to determine the dynamic response of the casing and a frequency-domain acoustic analysis on a boundary element (BE) model of the semi-infinite fluid domain to determine noise radiation in free-field conditions [4].

This paper investigates the influence of the helix angle and gear width on the noise radiated by a gearbox employing the same numerical method. Section 2 describes the numerical model used for the study and outlines the parametric analysis conducted to assess the effects of helix angle and gear width. Section 3 presents the results of this parametric analysis. First, the influence of these two parameters on the meshing stiffness function is analyzed. Then, their effects on the sound power spectrum and overall sound power level are examined. Finally, Section 4 discusses the key findings of this study and the potential follow-up for future research.

[*] ***Corresponding author***: *francesco.mori@unife.it*
Copyright: *©2025 Francesco Mori et al. This is an open-access article distributed under the terms of the Creative Commons Attribution 3.0 Unported License, which permits unrestricted use, distribution, and reproduction in any medium, provided the original author and source are credited.*

2. METHODOLOGY

The parametric analysis to assess the influence of the helix angle and gear width is structured into three main stages. The first stage evaluates the meshing stiffness of helical gears. For this purpose, a helical gear of width L is assumed to be composed of a series of spur gears with an infinitesimal width dz, each rotated by a small angle determined by the helix angle β. Specifically, the meshing stiffness $K_{G,H}$ of the helical gears as a function of the rotational angle θ is determined as:

$$K_{G,H}(\theta) = \int_0^L K_{G,S}\left(\theta + \frac{z}{R}\tan\beta\right)\frac{dz}{L_0}, \quad (1)$$

where R represents the pinion pitch radius and $K_{G,S}(\theta)$ is the meshing stiffness of the spur gears with the same cross-section as the helical gears. This function is computed from a multibody simulation in which the spur gears of width L_0 are treated as elastic bodies in contact: the pinion rotates of a certain angle θ, while the wheel rotates of the same angle plus an additional twist $\theta + \mathrm{d}\theta$.

Once the meshing stiffness $K_{G,H}(\theta)$ is determined, the second stage consists of a time-domain analysis on the multibody model shown in Fig. 1. This model consists of two helical gear pairs, treated as rigid bodies with geometrical characteristics detailed in Tab. 1. The helix angle β and the gear width L are varied as part of the parametric study. The elasticity of these elements is incorporated into the meshing stiffness function $K_{G,H}(\theta)$ previously determined. The steel casing measures 250 mm x 150 mm x 120 mm, with a thickness of 3 mm and is modelled through isotropic linear elastic 3D elements, with an elastic modulus $E = 200$ GPa, Poisson's ratio $\nu = 0.3$, damping factor $\eta = 5\%$ and density $\rho = 7850\ \mathrm{kg/m^3}$. The casing is assumed to be fixed to the ground at four localized points, while the two shafts are supported by the walls perpendicular to the y-axis through two pairs of hinges, which allow rotation around their respective axes. The analysis considers a pinion rotational frequency of $f_p = 100$ Hz and a resisting torque of $T = 100$ Nm applied to the wheel. The duration and the time step imposed in the time-domain simulations are set to 0.021 s and $3.5 \cdot 10^{-5}$ s respectively.

In the final stage, the normal acceleration computed on the casing, which is responsible for the noise radiation in the free field, is transformed into the frequency domain using a Fourier transform. The resulting acceleration field is mapped onto a BE model representing the infinite acoustic domain, which, in this study, is bounded by the source boundaries, corresponding to the external surface of the casing. The acoustic model is discretized with a maximum element size equal to one-fifth of the shortest wavelength, which, in this study, is associated with the highest analyzed frequency of 5000 Hz. The radiated sound power is determined by integrating the sound intensity field over the upper hemisphere of a sphere with a radius of 2 m, enclosing the noise source.

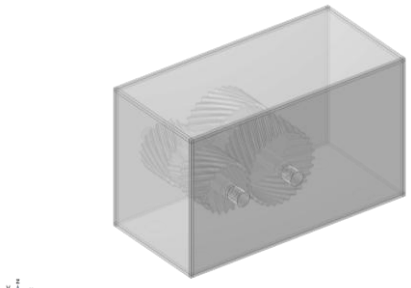


Figure 1. Geometry of the gearbox employed in numerical simulations.

Table 1. Geometric characteristics of the gears.

	Pinion	Wheel
Teeth Number	20	30
Pitch Diameter	50 mm	75 mm
Pressure Angle	25°	25°
Shaft Diameter	15 mm	15 mm
Teeth Height	4.5 mm	4.5 mm

3. RESULTS

3.1 Meshing stiffness analysis

In the first stage, the meshing stiffness was evaluated for helix angles ranging from 0° (spur gears) to 40° and for gear widths varying between 10 mm and 50 mm. Fig. 2 shows the meshing stiffness function over the meshing cycle for different helix angles. The increase of the helix angle reduces the oscillation of this function. Similar conclusions can be deduced for the increase of the gear width. Fig. 3 illustrates the normalized amplitude difference Δ_n for different helix angles and gear widths, defined as:

$$\Delta_n = \frac{K_{G,H,max} - K_{G,H,min}}{K_{G,H,avg}} \cdot 100, \quad (2)$$

where the $K_{G,H,max}$, $K_{G,H,min}$ and $K_{G,H,avg}$ represent the maximum, minimum and average value of the meshing

stiffness over the meshing cycle, respectively. For spur gears, the gear width acts as an identical scaling factor for all three values (maximum, minimum and average). Thus, the normalized amplitude difference Δ_n does not depend on the gear width. In contrast, for helical gears, the effect of helix angle and gear width are combined. As both parameters increase, the normalized amplitude difference Δ_n progressively decreases. This trend can be attributed to the fact that, compared to spur gears, helical gears have more teeth simultaneously engaged in meshing at any given instant, leading to a smoother and more continuous load distribution.

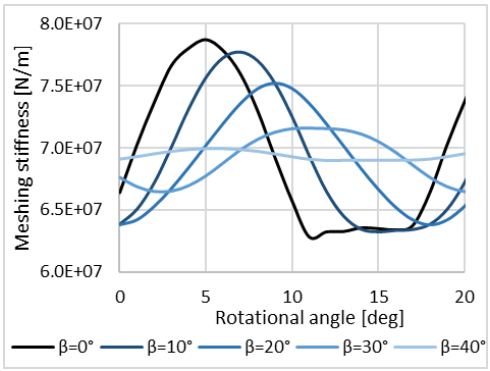


Figure 2. Meshing stiffness for different helix angles.

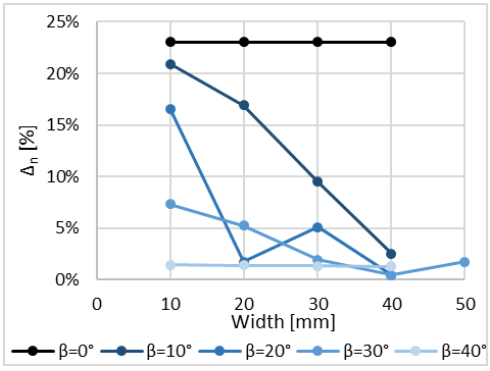


Figure 3. Normalized amplitude difference of meshing stiffness.

3.2 Effect of the parameters on the spectrum

Fig. 4 presents the sound power spectra for various helix angles, keeping the gear width constant at 30 mm. As the helix angle increases, the amplitude of the meshing frequency component decreases. This trend suggests that a larger helix angle results in smoother meshing between the gear teeth, reducing the impact of this tonal component. As a result, a significant reduction of the global level is observed, since the component associated with the meshing frequency represents the main contribution to the overall sound power level. On the other hand, there is a relevant increase in noise levels at lower frequencies, indicating a redistribution of energy across the spectrum. This shift may be due to changes in the dynamics of the gear meshing as the helix angle varies, affecting how vibrations are transmitted to the casing.

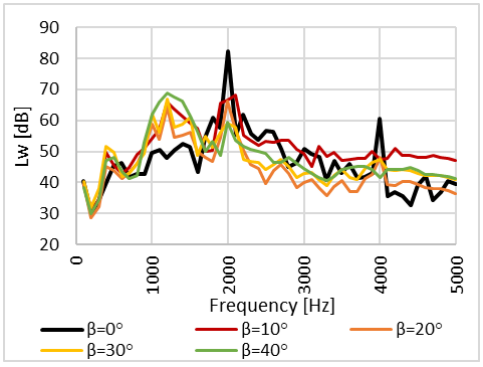


Figure 4. Sound power spectrum for different helix angles (width L = 30 mm).

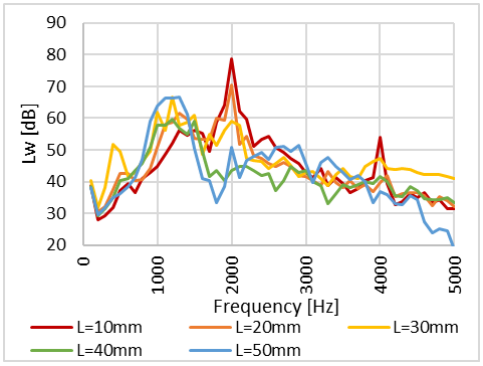


Figure 5. Sound power spectrum for different gear widths (helix angle $\beta = 30°$).

Fig. 5 shows the sound power spectra for different gear widths, while maintaining constant the helix angle value, $\beta = 30°$. Similar to the previous case, the increase in gear width provides a reduction in the amplitude of the meshing frequency component. This reduction can be attributed to a smaller amplitude difference in the meshing stiffness, leading to less pronounced fluctuations in the force

transmitted between the gear teeth. Additionally, there is a noticeable increase in noise levels below the meshing frequency, suggesting that as the gear width increases, more energy is distributed into lower frequencies, possibly due to changes in the contact mechanics and in the overall stiffness of the system.

3.3 Effect of the parameters on the overall level

The overall noise level as a function of the normalized amplitude difference Δ_n is shown in Fig. 6. This parameter accounts for the combined effects of both helix angle and gear width, providing a comprehensive measure to assess their influence on noise levels radiated by the gearbox. As shown in this figure, an increase in the normalized amplitude difference results in a higher sound power level radiated by the gearbox. Thus, larger variations in the meshing stiffness lead to an amplification of the generated noise. A non-uniform gear meshing, for which the helix angle and the gear width play an important role, will thus lead to higher vibration amplitude or more significant impacts during the meshing cycle.

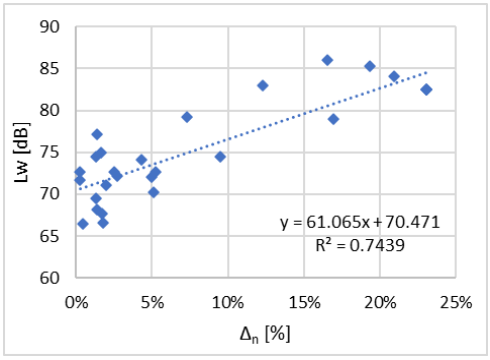


Figure 6. Correlation between the sound power level and the normalized amplitude difference of the meshing stiffness.

4. CONCLUSIONS

In this article, a numerical analysis is presented to investigate the influence of helix angle and gear width on noise radiated by a gearbox. In particular, the study focuses on how these two parameters influence the shape of the meshing stiffness function, which plays a crucial role in the acoustic behavior of the system. This function can be used as a control variable to assess and optimize the influence of helix angle and gear width on the overall noise level. A direct relationship between the sound power level and the normalized amplitude difference of the meshing stiffness was identified. This relationship shows that a larger variation in the amplitude of the meshing stiffness corresponds to a proportional increase in the overall sound power level. Since the meshing stiffness variation is significantly influenced by gear geometrical characteristics such as helix angle and gear width, an optimal design of these parameters can provide a reduction of noise radiated by the gearbox. Additionally, this study revealed that increasing either the gear width or the helix angle leads to a reduction in the amplitude of the meshing frequency component. However, this reduction also increases radiated noise at lower frequencies, suggesting a redistribution of the vibrational energy across the spectrum.
Through this analysis, a clear correlation between the key design parameters of the gears and the sound power level is established. Future research should aim at conducting experimental measurements to validate the trends observed in the numerical analysis. Furthermore, the effects of other geometrical factors and working parameters should be explored.

5. ACKNOWLEDGMENTS

This work was supported and financed by the collaboration with Nuovo Pignone Tecnologie (Baker Hughes).

6. REFERENCES

[1] F.B. Oswald, D.P. Townsend, M.J. Valco, R.H. Spences, R.J. Drago, and J.W. Lenski: "Influence of gears design parameters on gearbox radiated noise," *NASA Technical Memorandum,* 106511, Army Research Laboratory Memorandum ARL-TR-381, 1994.

[2] J.W. Lenski, R.H. Spences, R.J. Drago, M.J. Valco, and F.B. Oswald: "Gear sound levels with various tooth contact ratios and forms," *NASA Technical Memorandum,* 106432, Army Research Laboratory Memorandum ARL-MR-122, 1993.

[3] F. Mori, A. Santoni, and P. Fausti: "A preliminary numerical analysis of the noise radiated by a gearbox," in *Proc. of Forum Acusticum 2023,* (Turin, Italy), pp. 539–542, 2023.

[4] F. Mori, A. Santoni, and P. Fausti: "Valutazione numerica della potenza sonora emessa da un gearbox con metodi FEM e BEM," in *Proc. of 49th National Congress on the Italian Acustic Association 2023,* (Ferrara, Italy), 2023.

DOI: 10.61782/fa.2025.0538

FORUM ACUSTICUM EURONOISE 2025

LPSCAN – A PROJECT TO STANDARDIZE SOUND POWER DETERMINATION FROM SOUND PRESSURE SCANS

Fabian Heisterkamp[1*] **Volker Wittstock**[2] **Deborah Brosig**[2]
[1] Federal Institute for Occupational Safety and Health (BAuA), 44149 Dortmund, Germany
[2] Physikalisch-Technische Bundesanstalt, 38118 Braunschweig, Germany

ABSTRACT

Noise emissions from machinery are the main source of noise exposure for workers. To combat this risk at source, the European Machinery Directive requires the declaration of the main noise emission parameter, the sound power level. This quantity is determined according to 10 different EN ISO standards, requiring special laboratory environments or complex measurement techniques (reference sound sources, intensity probes, etc.). This high level of effort is considered to be a major reason why, despite legal requirements, noise data in instructions for 80% of machinery is unreliable or unavailable (NOMAD study). This project aims to reduce the measurement effort for machinery manufacturers, test houses and occupational health and safety personnel. To this end, existing methods, e.g., EN ISO 3744, that determine sound power from sound pressure measurements at discrete positions on the enveloping measurement surface around the machine shall be complemented by a new method based on manual sound pressure scans on the measurement surface. Ideally, these can be performed with a single microphone connected to a sound level meter. We present the results of first measurements on a model machine.

Keywords: *sound power, sound pressure scanning, basic sound power standards*

[*] ***Corresponding author***: *heisterkamp.fabian@baua.bund.de*
Copyright: *©2025 F. Heisterkamp et al. This is an open-access article distributed under the terms of the Creative Commons Attribution 3.0 Unported License, which permits unrestricted use, distribution, and reproduction in any medium, provided the original author and source are credited.*

1. INTRODUCTION

Noise-induced hearing loss remains an important occupational safety issue. A significant contribution to reduce the noise hazard for workers can be made by purchasing "quiet machines", which, in addition to suitable characteristics, are also characterized by the lowest possible noise emissions, in line with the "Sell and Buy Quiet" concept [1]. In order for companies to be able to choose quieter machines ("Buy Quiet"), manufacturers must provide comparable and reliable noise emission data ("Sell Quiet").

However, a European market surveillance exercise, the so-called NOMAD (Noise Machinery Directive) survey revealed significant problems with the noise emission data provided in the instructions of machinery to be sold on the EU Single market [2]: 80 % of the noise emission declarations in more than 1500 investigated instructions did not meet the requirements of the EU Machinery Directive 2006/42/EC [3].

This rather poor compliance with legal requirements might – in part – be caused by the complicated basic noise emission standards that manufacturers have to apply to determine the noise emissions of their machines. Sec. 2 explains the application and as well the limitations of the existing standards in more detail, while Sec. 3 describes previous projects aimed at improving and simplifying the existing basic noise emission standards. Sec. 4 outlines the project LpScan, which aims to develop a new sound power standard, based on sound pressure scans instead of sound pressure level measurements at specified, fixed positions. Sec. 5 explains the methodology of this project, Sec. 6 presents the results of sound power measurements according to the existing ISO 3744 on a model machine and Sec. 7 concludes the paper with a summary and an outlook.

2. LIMITS OF EXISTING SOUND POWER STANDARDS

In accordance with the New Approach, many European Directives, such as the Machinery Directive [3], only define essential health and safety requirements, but not how they are to be achieved in detail/for each specific product. The EU-wide harmonization of product safety requirements is then achieved by means of harmonized standards, which are listed in the Official Journal of the European Union under the respective directive and the application of which is associated with a presumption of conformity (with regard to the requirements of the directive covered by the standard).

With regard to the noise emissions of machines, but also in general for other requirements of the Machinery Directive, a distinction is made between machine-specific standards, so-called C-standards, basic standards for specific hazards, etc. (B-standards) and basic standards (A-standards), defining principles, etc. (e.g. ISO 12100).

To determine the noise emission of a specific machine type, type-C standards define the applicable measurement methods by references to one or more B-standards, further measurement requirements, and the operating and mounting conditions.

There are many basic noise emission standards (B-standards) for determining the key noise emission quantity sound power level L_W. ISO 3740 [4] provides an overview of and information on when to use which B-standard/measurement method. The most important methods are the enveloping surface method (ISO 3744, ISO 3745 & ISO 3746), the reverberation room method (ISO 3741, ISO 3743-1, -2), the reference source method (ISO 3747) and the sound intensity method (ISO 9614, parts 1 to 3). The enveloping surface method, in particular the ISO 3744 and ISO 3746, makes relatively few demands on the measurement equipment, which is why the ISO 3744 method is the most widely used method. Most regulations, C-standards and product specifications refer to this accuracy grade 2 method.

However, ISO 3744 requires the determination of the environmental correction K_2 when used indoors outside of a hemi-anechoic test room and relies on fixed measurements positions. Both aspects may represent a challenge for machinery manufacturers, especially small- and medium-sized enterprises (SMEs), when determining the sound power level of their products on their own premises.

Measurements on larger machines and in particular on machines with a directed noise emission, e.g., from openings, vents, etc. require measurements on 21 or even more measurements positions (see Figure 7 showing the setup for model machine 1.)

This can increase the costs for the measurement equipment or when performed with a single sound level meter the measurement effort. Although sound intensity measurements according to ISO 9614-2 and ISO 9614-3 can be performed by intensity scans on the enveloping surface, using this method is no practical solution for SMEs. The measurement equipment is much more expensive than a sound level meter and the measurements require more expertise. Especially, since the current standards require the determination of partly unnecessary field indicators, which are not correlated to the accuracy of the determined L_W (see also Sec. 3) [5].

Thus, there is a need to develop an alternative method based on sound pressure level measurements that combines the low equipment costs of sound pressure level measurements and the reduction in measurement effort by scanning on the enveloping surface/measurement surface instead of measuring sound pressure on many fixed positions (see Sec. 4).

3. PREVIOUS PROJECTS AIMED AT IMPROVING BASIC NOISE EMISSION STANDARDS

In the course of its focus project “Practice-oriented simplification of noise emission measurement methods”, the Federal Institute for Occupational Safety and Health (BAuA) conducted several research projects aimed at a simplification of noise emission measurement of machines.

Project F 2438 “Simple approximate determination of the environmental correction” explored the feasibility of replacing expensive reference sound sources (RSS) with other small machines with sufficiently stable noise emission. The goal was to enable machinery manufacturers, in particular SMEs, to determine the environmental correction K_2 for the in-situ determination of the sound power level L_W themselves [6].

The local environmental correction K_3 for the in-situ determination of the emission pressure sound level requires even more effort. Project F 2495 “Determining the local environmental correction for the emission sound pressure level” investigated possibilities to simplify its determination and the effects of an amendment to ISO 11202:2010 [7].

Project F 2450 “Improving the practicability of the sound intensity method” was setup by BAuA and conducted by PTB in Braunschweig. It investigated potential simplifications to ISO 9614, parts 1 to 3 [5]. The project report contains drafts of a simplified ISO 9614, but these proposals have yet to be adopted in a revised version of the standard. Although the revision process has been started

already, it will still take a while until the revision will be completed.

4. CURRENT PROJECT: LPSCAN – DETERMINATION OF SOUND POWER LEVEL BY SOUND PRESSURE SCANNING (F 2571)

The project F 2571 “Determination of sound power level by sound pressure scanning (LpScan)” is a joint research project of BAuA and PTB, the national metrology institute of Germany, setup in the framework of the BAuA focus project “Practice-oriented simplification of noise emission measurement methods”. The aim of project “LpScan” is to develop a measurement method that determines the sound power level by scanning the sound pressure level around the machine [9]. Such a method has the advantage that the measurement can be carried out quickly using a single sound level meter. Compared to the sound intensity method (ISO 9614-2 and ISO 9614-3), which already works by scanning intensity on the enveloping surface, scanning with a single microphone connected to a sound level meter would offer great cost advantages (cost of measurement equipment). By moving the scans in the acoustic near-field of the machine, it might even be possible to perform the measurements without determining the background noise correction K_1 and the environmental correction K_2, making the method ideal for in-situ measurements on the premises of SMEs.
The project is planned for three years and the final result will be a draft for a standard to determine the sound power level of machines and other products from sound pressure scans on the enveloping surface, in openings of the encapsulation and in a few centimeters from the machine surface.

5. METHODOLOGY OF PROJECT LPSCAN

5.1 General

The research question is: Can the sound power of a machine be determined with sufficient accuracy and reproducibility by scanning the sound pressure level on an imaginary surface (called the measurement surface or enveloping surface) around the machine with a microphone, and is this a useful addition to existing standardized measurement methods?
Based on theoretically describable model radiators (e.g. monopole, dipole, etc.), the sound pressure scanning method is first analyzed at a typical measurement distance of 1 m. The deviations of the results obtained with this method from the known sound power of the model radiators are determined by varying the parameters such as enveloping surface shape, scanning speed, density of the scanning paths, shape of the paths, required stationarity of the sound field, level and distribution of the background noise level, orientation of the microphone or hand-held sound level meter. In addition to the results for sound pressure scanning, the results for discrete measurement point arrays are also used for comparison. The result of this work package is a basic understanding of the sound pressure scanning method at typical measurement distances and the most important parameters to be considered. At the same time, appropriate measurements will be performed to determine the sound power of model machines (see 5.3) using sound pressure scanning to verify the theoretical results.
Another application of sound pressure level scanning, which will be investigated in the project and developed into a measurement method, is the relocation of the scans in the near-field of the source. At distances of only a few centimeters to the surface of the machine, it may be possible to dispense with both the background noise correction K_1 and the correction for noise reflected in the measurement environment (environmental correction K_2).

5.2 Near-field scanning

In the case of near-field scanning, two methods can be distinguished:
In near-field full-surface scanning, the microphone is scanned over the entire surface of the machine to be tested at a distance of a few centimeters. It is also suitable for determining the sound power of individual components of linked systems.
Near-field partial surface scanning is based on the assumption that the sound power of the source is essentially radiated from certain spatially limited partial surfaces, so that the sound power can be determined only by scanning these areas. This method is also highly relevant in practice, since it can be used whenever machines are encapsulated for noise reduction, but openings in the encapsulation must be present for the machine to operate (e.g. in beverage filling machines).
In the context of near-field partial surface scanning, analytical calculations are conducted using synthetically generated sound pressure distributions that are strongly inhomogeneous on enveloping surfaces. These distributions are designed to model, for instance, openings in source enclosures. The study investigates the conditions under which it is feasible to determine the total sound power that passes through the enveloping surface by measuring solely at the most radiating partial surfaces. The validity of these

calculations is substantiated by measurements conducted on model machines.

5.3 Model machines

For this project, three model machines with variable "configurations" will be used to simulate measurements on real life machines under reproducible conditions. The machines are built from aluminum profiles and dampened aluminum sheets (see Figure 1 [7]).



Figure 1. Model machine 1 with a circular opening (Configuration I).

Three to four Brüel & Kjaer (Type 4204) aerodynamic reference sound sources (RSS) are placed in the model machines to ensure a sufficient, stable, reproducible and broadband noise emission. Each RSS has a sound power level $L_{WA} \approx 93$ dB. The configurations of openings in the model machines can be varied to allow the testing of different, but yet "challenging" configurations that have a directed, non-uniform noise emission in common.

5.3.1 Model machine 1

Model machine 1 has the following dimensions:
1,74 m×1,12 m×1,67 m (length × width × height).
The dimensions shall represent the dimensions of realistic machines, but yet have to be handled under laboratory conditions.

Figure 2 shows a sketch of the model machine 1 in the configuration with a circular opening that represents a small area dominating the noise emission on that side (configuration I).

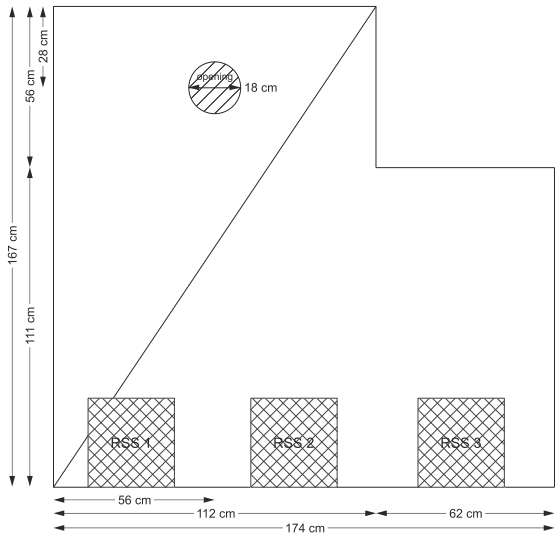


Figure 2. Sketch of model machine 1 with a circular opening (configuration I) [7].

The panel with the opening can be replaced with an open frame (configuration II (see Figure 3)) or a completely closed panel (configuration III).

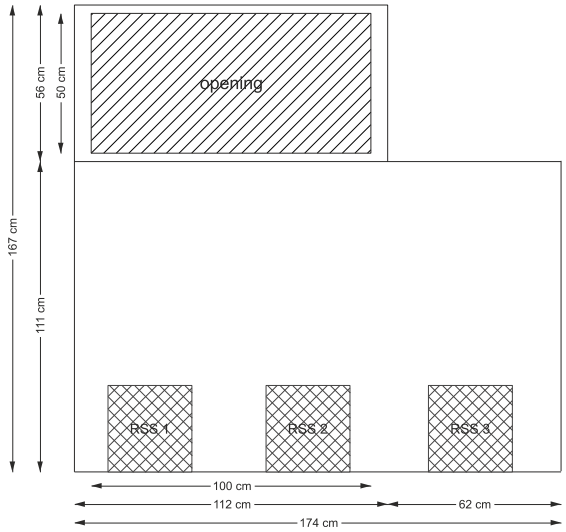


Figure 3. Sketch of model machine 1 with an open frame (configuration II) [7].

5.3.2 Model machine 2

Figure 4 shows a sketch of model machine 2 seen from the side. It has the following dimensions:
3,24 m×1,12 m×1,65 m (length × width × height).

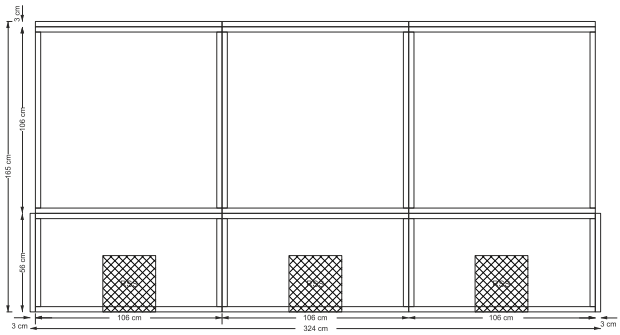


Figure 4. Sketch of model machine 2 (side view).

With openings at the ends, model machine II is designed to investigate partial-surface near-field scanning, where the goal is to determine the sound power level by scanning in these openings only.

5.3.3 Model machine 3

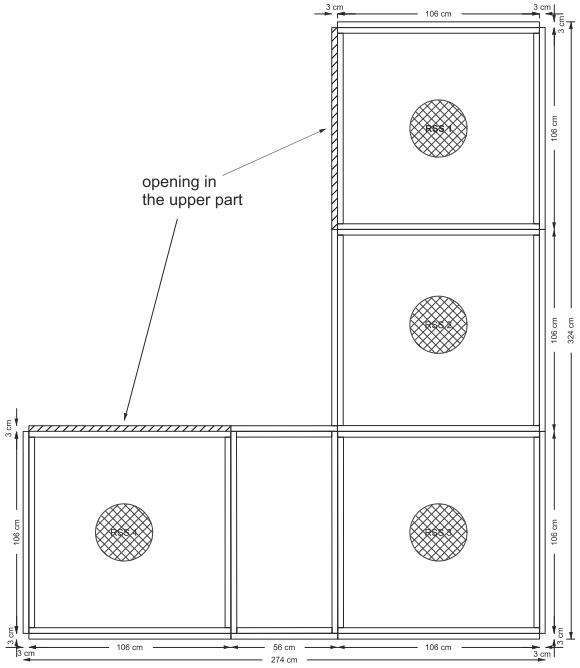


Figure 5. Sketch of model machine 3 (top view).

Figure 5 shows a sketch of the L-shaped model machine 3 seen from the top. Here, four RSS ensure a sufficiently high level of noise emission. The L-shape will be particularly demanding for full-surface near-field scanning, as noise emissions from the other opening might disturb the measurement, and maybe even when scanning at typical distances from the surface (d = 1 m).

5.4 Analysis of the results and comparative measurements

The findings from the calculations as well as the measurements on the model machines are then used to define a measurement method, which is subsequently tested through comparative measurements involving at least BAuA and PTB as participants. If feasible, additional cooperation partners should be sought to participate in these measurements, with the aim of determining the standard deviation of reproducibility of the measurement method.

5.5 Finalizing the report including a draft standard

The project will be concluded with a comprising report in English. As the key part of the report, the measurement method developed will be formalized as a draft standard. It is to be standardized as an EN ISO standard and will constitute a basic noise emission standard (B-standard) equivalent to ISO 3744. This basic standard for determining the sound power level by means of enveloping surface sound pressure scanning will also include criteria for the circumstances under which full-surface near-field scanning or partial-surface near-field scanning can be used while ensuring sufficient accuracy and reproducibility.

6. FIRST MEASUREMENTS ON MODEL MACHINE 1

We determine the sound power level of model machine 1 according to ISO 3744:2010 [10] using measurements at discrete positions on an enveloping surface/measurement surface. Due to the size and shape of model machine 1 a parallelepiped measurement surface with a distance d = 1 m from the reference box was chosen. According to ISO 3744, this meant that already 21 measurement positions were necessary (see Figure 6) – not taking account of possible non-uniform noise emission yet.
Figure 6 shows the setup for the sound power determination in the hemi-anechoic chamber. This test room is qualified from 63 Hz to 12,5 kHz according to ISO 3745.

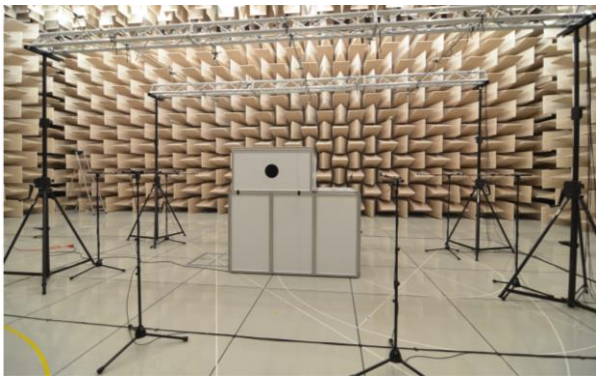


Figure 6. Model machine 1 and the setup according to ISO 3744 in the hemi-anechoic chamber at BAuA.

The measurements are conducted with 21 Brüel & Kjaer Type 4190 1/2-inch free-field microphones (IEC 61672 class 1) connected to a Brüel & Kjaer PULSE LAN-XI measurement system with 28 channels. This system is calibrated by an accredited external laboratory every two years. A system unavailable to most machinery manufacturers, especially SMEs.
However, even this high number of measurement positions is not sufficient to fully meet the requirements of ISO 3744 for configurations I and II of model machine 1, where sound pressure levels at the microphones near the circular opening and open frame, respectively, are higher. Here, 18 additional measurement positions are placed near the opening to ensure a proper sound power determination despite the directed emission of the source (see Figure 7).



Figure 7. Model machine 1 and 18 additional measurement positions according to ISO 3744 in the hemi-anechoic chamber at BAuA.

The sound power level L_W was calculated from the sound pressure level measurements at these 21 plus 18 measurement positions using the method described in Ref. [11]. Table 1 shows the sound power level for all three configurations of model machine 1. Note that the L_W of configuration III (closed) was determined from 21 measurement positions only.

Table 1. Sound power level of model machine 1 in different configurations, determined according to ISO 3744 [10].

	Conf. I Circ. open.	Conf. II Open. fr.	Conf. III Closed
L_W (dB)	88,8	93,0	87,4
L_{WA} (dB)	83,9	91,7	81,3

As expected, the sound power level of the configuration with the largest opening (configuration II, open frame) is the highest.

7. SUMMARY & OUTLOOK

We describe the details of Project LpScan. This project aims at developing a sound power standard based on (manual) sound pressure scanning. First results characterize the sound power level of model machine 1 using the existing enveloping surface method and demonstrate how much effort the established method according to ISO 3744 requires for such a machine (especially configurations I and II with a non-uniform noise emission).
As the main goal, the project will result in a new sound power standard (EN ISO) to be harmonized under the European Machinery Directive 2006/42/EC. This standard will support machinery manufacturers, in particular SMEs, to properly determine the sound power level of their products on their own premises with reduced effort. In turn, reliable noise emission data for machinery will improve market transparency regarding low noise machines. This enables employers to better protect their workers from noise by “Buying Quiet” when purchasing or hiring new machinery.

8. ACKNOWLEDGMENTS

We thank Anke Berger for carrying out the measurements on model machine 1 in the “Products and Work Systems Laboratory” at BAuA.

9. REFERENCES

[1] F. Heisterkamp, J. Bengtsson Ryberg, J. Jacques und A. Verdaasdonk, Sell and Buy Quiet - the extended concept to reduce noise (at work and at home). *Inter-Noise 2021*, **263(4)**, 2011-2019, 2021. DOI: 10.3397/IN-2021-2027

[2] J. Châtillon und M. Szyszko, Technical Note. The "NOMAD" Project – A Survey of Instructions Supplied with Machinery with Respect to Noise. *Archives of Acoustics* **38(2)**, 271-275, 2013. DOI: 10.2478/aoa-2013-0033

[3] Directive 2006/42/EC of the European Parliament and of the Council of 17 May 2006 on machinery, and amending Directive 95/16/EC (recast). *OJEU* L 157/24, 9 June 2006.

[4] ISO 3740:2019, Acoustics – Determination of sound power levels of noise sources - Guidelines for the use of basic standards. International Organization for Standardization: Geneva, Switzerland, 2019.

[5] V. Wittstock, S. Brezas, F. Heisterkamp; Sound power determination by intensity – Are field indicators and criteria in ISO 9614 meaningful? *J. Acoust. Soc. Am.*, **155 (1)**, 588–599, 2024. DOI: 10.1121/10.0024361

[6] F. Heisterkamp, I. Arendt, Simplified determination of the environmental correction for noise emission measurements. *INTER-NOISE and NOISE-CON Congress and Conference Proc.*, Chicago, IL, pages 994 - 1998, pp. 1286-1295(10), 2018. DOI

[7] F. Heisterkamp, Machine Noise—Experimental Study of the Local Environmental Correction for the Emission Sound Pressure Level. *Acoustics*, **6(1)**, 177-203, 2024. DOI: 10.3390/acoustics6010010

[8] S. Brezas, F. Heisterkamp, V. Wittstock, Practice-oriented simplification of noise emission measurement methods, subproject 2: Practical adaptation of the sound intensity measurement method. BAuA, Dortmund, 2021. DOI: 10.21934/baua:report20210914

[9] Project homepage (accessed: 2025-03-18): https://www.baua.de/EN/Research/Research-projects/f2571

[10] ISO 3744:2010, Acoustics – Determination of Sound Power Levels and Sound Energy Levels of Noise Sources Using Sound Pressure – Engineering Methods for an Essentially Free Field over a Reflecting Plane. International Organization for Standardization: Geneva, Switzerland, 2010.

[11] V. Wittstock, Unequal segment areas and corner positions with the enveloping surface method for sound power determination, Internoise, 25.-29. August 2024, Nantes, France, 2024.

DOI: 10.61782/fa.2025.0135

FORUM ACUSTICUM EURONOISE 2025

ANALYTICAL AND EXPERIMENTAL INVESTIGATION OF STATOR ASSEMBLY VIBRATIONS IN ELECTRIC MOTORS

Panagiotis Andreou[1] **Amal Z. Hajjaj**[1] **Mahdi Mohammadpour**[1]
Stephanos Theodossiades[1*]
[1] Loughborough University, School of Mechanical, Electrical and Manufacturing Engineering, Loughborough University, UK

ABSTRACT

This work presents a novel analytical model for the stator of an electric motor, modelled as a thick segmented cylindrical shell, to accurately capture its vibrational behaviour. The methodology employs the First-order Shear Deformation Stress Theory (FSDST) with considerations of mechanical property anisotropies and dimensional variations to represent the system's complex dynamics. An Experimental Modal Analysis (EMA) was performed using an impulse hammer, to identify the stator's modal characteristics. The analytical model demonstrated exceptional accuracy in capturing these features. The experimental results were used to enhance the Rayleigh damping approximation implemented in the model. The enhanced model was applied to predict the forced response of the system under impulse excitation. Comparisons between analytical predictions and experimental measurements revealed excellent agreement, validating the model's reliability in capturing the stator's dynamic response. This approach not only provides a comprehensive understanding of both the free and forced vibrational behaviour of electric motor stators but also establishes a dependable framework offering valuable insights for mitigating vibrations and improving the overall electric motor performance.

Keywords: *experimental modal analysis, e-motor stator assembly, analytical structural dynamics, forced response.*

1. INTRODUCTION

Electric motor noise, vibration, and harshness (NVH) are critical concerns in modern powertrain development, with stator vibrations being a dominant source of acoustic emissions [1]. Predicting accurately the natural frequencies and mode shapes of a stator assembly is essential for understanding its dynamic response under electromagnetic excitation and avoiding resonances that can lead to excessive noise and structural fatigue. While numerical methods provide detailed modal and dynamic predictions, their computational expense remains a major limitation, especially for high-frequency analyses requiring fine meshes and small time steps [2], [3]. Prior reduced-order and analytical approaches [4]-[6] have been proposed, however, they typically rely on simplifying assumptions, such as reducing the problem to two dimensions or neglecting critical structural and geometric complexities of the stator assembly, thereby limiting their applicability.

This paper proposes an analytical modelling framework for the modal and dynamic analysis of electric motor stator assemblies based on the First-order Shear Deformation Stress Theory (FSDST). The proposed methodology offers a highly accurate, computationally efficient alternative to numerical approaches. By axially segmenting the assembly and introducing continuous functions to characterise the material properties across its thickness, the model effectively captures the effects of anisotropic parameters as well as dimensional variations. The displacement field is formulated using orthogonal Jacobi polynomial functions and the natural frequencies and mode shapes are computed via the Lagrangian energy method. The Newmark-β integration technique is then employed for the evaluation of the forced response of the system under an impulse excitation. The methodology is outlined in Section 2, and results of the analytical model are presented and assessed against experimental data in Section 3.

[*] ***Corresponding author***: *s.theodossiades@lboro.ac.uk*
Copyright: *©2025 First author et al. This is an open-access article distributed under the terms of the Creative Commons Attribution 3.0 Unported License, which permits unrestricted use, distribution, and reproduction in any medium, provided the original author and source are credited.*

2. METHODOLOGY

2.1 Mechanical Model and Material Characterisation

The stator assembly is modelled as a thick cylindrical shell of length L and radius R, divided into P segments, each with a thickness h_P and length L_P. This segmentation allows for the incorporation of dimensional variations within the cylindrical shell. To accurately represent the complex material properties of the assembly – including the stator windings, teeth, stator yoke, and cooling jacket or housing – carefully formulated continuous functions are introduced. These functions characterise the orthotropic nature of the stator lamination and the variation of material properties across the shell's thickness. More specifically, they comprehensively characterise the modulus of elasticity, shear modulus, Poisson's ratio, and density.

2.2 Displacement and Energy Equations

Through the assumptions that the shell displacements are small relatively to their thickness and that normal shear stresses are negligible, the displacement field can be expressed in accordance with first-order shear deformation shell theory (FSDST) as [7]:

$$\boldsymbol{u^p(x,\varphi,z,t) = u_0^p(x,\varphi,t) + z\beta_x^p(x,\varphi,t)} \quad (1)$$

$$\boldsymbol{v^p(x,\varphi,z,t) = v_0^p(x,\varphi,t) + z\beta_\varphi^p(x,\varphi,t)} \quad (2)$$

$$\boldsymbol{w^p(x,\varphi,z,t) = w_0^p(x,\varphi,t)} \quad (3)$$

where u, v, and w are the mid-surface displacements in the axial, circumferential and normal directions, and β_x and β_φ are the mid-surface rotations in the axial and circumferential directions, respectively. Once these functions are established, the FSDST is employed to express the kinetic energy T^P, potential energy U^P , and external work W^P associated with each segment, as follows:

$$U^p = \frac{R}{2}\int_0^{L_p}\int_{-h_p/2}^{h_p/2}\int_0^{2\pi}\left(\sigma_{xx}^p\varepsilon_x^p + \sigma_{\varphi\varphi}^p\varepsilon_\varphi^p + \tau_{x\varphi}^p\gamma_{x\varphi}^p + \tau_{xz}^p\gamma_{xz}^p + \tau_{\varphi z}^p\gamma_{\varphi z}^p\right)\left(1+\frac{z}{R}\right)d\varphi\,dz\,dx \quad (4)$$

$$T^p = \frac{R}{2}\int_0^{L_p}\int_{-h_p/2}^{h_p/2}\int_0^{2\pi}\rho_p\left(\dot{u}_p^2 + \dot{v}_p^2 + \dot{w}_p^2\right)\left(1+\frac{z}{R}\right)d\varphi\,dz\,dx \quad (5)$$

$$W^p = \frac{R}{2}\int_0^{L_p}\int_{-h_p/2}^{h_p/2}\int_0^{2\pi}\left(f_u^p u_0^p + f_v^p v_0^p + f_w^p w_0^p + f_{\beta_x}^p\beta_x^p + f_{\beta_\varphi}^p\beta_\varphi^p\right)\left(1+\frac{z}{R}\right)d\varphi\,dz\,dx \quad (6)$$

where σ, ε, τ and γ represent the normal stress, normal strain, shear stress and shear strain in each direction for the p-th segment, ρ is the density and f denotes the external force.

2.3 Boundary and Continuity Enforcement

To satisfy continuity between adjacent segments and ensure that transverse and shear displacements at the end of one segment match the start of the next segment, artificial massless springs are introduced. Similarly, artificial springs are incorporated at each end of the cylindrical shell, allowing for any possible boundary condition to be imposed, by varying the appropriate spring stiffnesses. The energy stored in the artificial continuity and boundary springs is calculated according to the penalty method [8], denoted as U_c and U_b, respectively.

2.4 Eigenvalue Analysis

Having established the energy formulations, the Lagrangian energy function $\mathcal{L}$, may be expressed as:

$$\mathcal{L} = \sum_{p=1}^{P}(T^p - U^p + W^p) - \sum_{p=1}^{P-1}U_c^{p,p+1} - U_b \quad (7)$$

Minimising the Lagrangian energy function with respect to each of the generalised coordinate variable yields:

$$\boldsymbol{M\ddot{q} + Kq = F} \quad (8)$$

where $\boldsymbol{q}$ is the global generalised coordinate vector, $\boldsymbol{M}$ and $\boldsymbol{K}$ are respectively the mass and stiffness matrices and $\boldsymbol{F}$ is the external load vector. For the eigenvalue analysis, external work is neglected, and the system is assumed to undergo free harmonic motion, i.e. $\boldsymbol{F = 0}$ and $\boldsymbol{q(t) = \bar{q}e^{i\omega t}}$. Substituting these into Equation 8 yields:

$$\boldsymbol{[-\omega_{nat}^2 M + K]\bar{q} = 0} \quad (9)$$

The solution of the above expression returns the natural frequencies of the system, ω_{nat} and their corresponding eigenvectors, $\bar{\boldsymbol{q}}$.

2.5 Forced Response

For the evaluation of the dynamic response of the system under impulse load, the Newmark-β integration method was utilised, due to its numerical stability, computational efficiency and versatility [9]. Having obtained the modal damping ratios from the Experimental Modal Analysis (EMA) performed on the actual system, the damping matrix was constructed following the Rayleigh damping method. The applied force in the analytical model, at location (x_0, θ_0, z_0), is expressed as:

$$f_w(x,\theta,t) = A(t)\delta(x-x_0)\delta(\theta-\theta_0)\delta(z-z_0) \quad (10)$$

where $A(t)$ denotes the time-dependent force amplitude obtained experimentally, and δ is the Dirac delta function, which allows for spatial localisation of the applied force.

3. RESULTS AND DISCUSSION

Having applied the methodology outlined above to a real stator assembly from an electric vehicle powertrain, this section presents and discusses some of the results obtained, with comparisons against experimental data. **Table 1** presents the results of the EMA compared against the analytical natural frequency predictions for the first five vibration modes of the system. The average error across the presented modes is -1.03% (maximum error 7.54%), thus within an acceptable range, confirming that the analytical method effectively captures the modal characteristics of the complex stator assembly, and that the assumptions utilised within the model are successful. The accuracy of the model is also shown in **Figure 1**, with the analytically derived cylindrical mode shapes being in very close conformity with the ones obtained from the EMA.

Table 1. Comparison of EMA results with analytical natural frequency predictions

Mode *(n,m)*	Exp. (Hz)	Damp. (%)	Ana. (Hz)	Error (%)
(2,0)	604	1.11	609	0.85
(3,0)	1692	0.99	1589	-6.07
(2,1)	2088	1.03	2172	4.00
(3,1)	2598	1.05	2692	3.61
(4,0)	2976	1.56	2751	-7.54

Finally, the experimental and analytical acceleration signals following the impulse excitation described in Section 2 are presented in the time-domain in **Figure 2**. It can be observed that both systems exhibit a sharp initial acceleration peak due to the applied impulse, followed by rapidly decaying oscillatory motion, as the stator assembly is allowed to come to rest. The peak acceleration values in both signals are similar, indicating that the application of the excitation in the analytical model is consistent with the experiment. There is however a slight discrepancy in the amplitude decay rate, which could be justified by the simplified damping representation implemented in the analytical model, as well as additional energy dissipation in the real system. This energy dissipation could be a result of friction at the interfaces between the assembly's layers or between the system and the elastic supports used to approximate free boundary conditions.

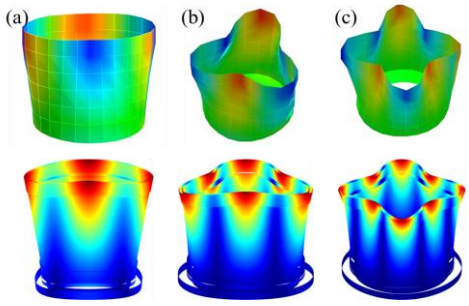


Figure 1. Comparison of experimentally obtained mode shapes (top) with analytically derived ones (bottom) for mode (a) (2,0), (b) (3,0) and (c) (4,0).

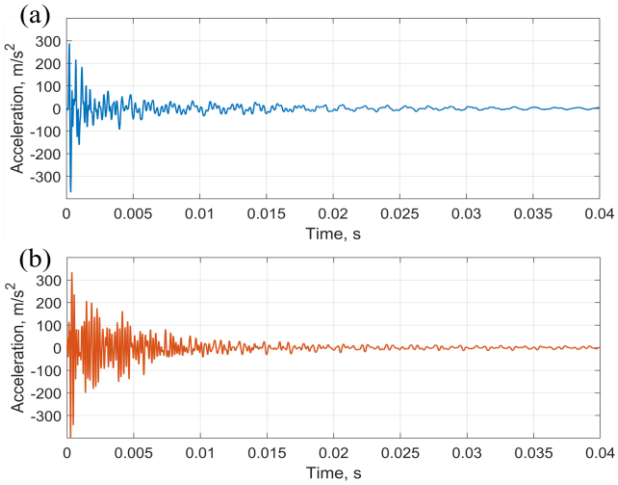


Figure 2. Experimentally obtained (a) and analytically predicted (b) acceleration response at a random location mode on the stator assembly following impulse excitation.

The Frequency Response Function (FRF) of the acceleration signals, shown in **Figure 3**, provides further insight into the accuracy of the analytical model in capturing the dynamic behaviour of the stator assembly. The dominant resonant peaks predicted analytically align well with those observed experimentally, confirming that the developed methodology accurately identifies the primary vibration modes of the structure. The discrepancies in the locations of the peaks are mostly explained by the errors in the calculation of the natural frequencies. Additionally, in the experimental signal there appear to be contributions in the range of 800-1350 Hz, as well as 1750-2000 Hz, which are caused by the degenerate mode pairs of vibration modes (2,0) and (3,0), but due to geometric asymmetries in the real system they have different frequencies. These asymmetries cannot be captured by the cylindrical analytical model hence there is no contribution

at those frequencies. Furthermore, minor discrepancies at higher frequencies may again be attributed to the assumptions introduced by the Rayleigh damping method and may be minimised through further damping refinement.

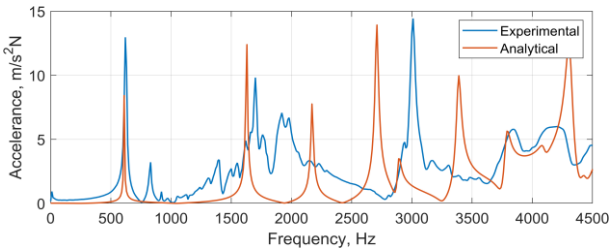


Figure 3. Acceleration Frequency Response Function (FRF) of the structure following impulse excitation.

4. CONCLUSIONS

This work introduces an accurate, yet highly computationally efficient framework for identification of the modal characteristics and the dynamic response analysis of electric motor stator assemblies. The overall agreement between analytical and experimental results demonstrates the effectiveness of the proposed methodology in predicting the dynamic behaviour of complex stator assemblies. The natural frequency and mode shape predictions of the analytical model are in excellent agreement with EMA results, with a maximum error of 7.54%. The dynamic response of the system to an impulse excitation is captured with great qualitative agreement, considering the differences in peak amplitudes can be attributed to damping simplifications, while the frequency deviations are a direct result of the deviations in natural frequency predictions. However, further refinement of damping parameter estimation could enhance the model's predictive capability. Incorporating additional experimental data to fine-tune damping coefficients or employing a more detailed dissipation model could further improve the accuracy of time-domain responses.

Despite these minor discrepancies, the developed analytical approach provides a computationally efficient and reliable tool for modal analysis of stator assemblies. Its ability to closely match experimental results highlights its potential for early-stage NVH assessment and optimization in electric powertrains.

5. ACKNOWLEDGMENTS

The authors would like to thank Arrival Ltd for their technical support, as well as the EPSRC [EP/T518098/1 – DTP 2020-2021 & EP/V053353/1 – Automotive electric powertrain whistling and whining: fundamental root cause analysis to novel solutions], the UKRI [2585407 – Electric motor and transmission coupled vibro-acoustics of electric powertrains] and the Loughborough University Doctoral College for supporting this work.

6. REFERENCES

[1] N. Morris *et al*, "4 - tribodynamic analysis of electric vehicle powertrains," in *Electric Vehicle Tribology*, L. I. Farfan-Cabrera and A. Erdemir, Eds. 2024. DOI: 10.1016/B978-0-443-14074-7.00004-2.

[2] X. Liang *et al*, "Comparative Study of Classical and Mutually Coupled Switched Reluctance Motors Using Multiphysics Finite-Element Modeling," *IEEE Transactions on Industrial Electronics,* vol. 61, *(9),* pp. 5066–5074, 2014. DOI: 10.1109/TIE.2013.2282907.

[3] Y. S. Wang *et al*, "Electromagnetic noise analysis and optimization for permanent magnet synchronous motor used on electric vehicles," *EC,* vol. 38, *(2),* pp. 699, 2020. DOI: 10.1108/ec-02-2020-0070.

[4] P. Andreou *et al*, "Analytical Multiphysics Methodology to Predict Vibroacoustics in PMSMs Combining Tangential Electromagnetic Excitation and Tooth Modulation Effects," *IEEE Transactions on Transportation Electrification,* vol. 10, *(3),* pp. 5997–6009, 2024. DOI: 10.1109/TTE.2023.3325350.

[5] R. Sun *et al*, "A novel forward computational modal analysis method of the motor stator assembly considering core lamination and winding stacking," *Mechanical Systems and Signal Processing,* vol. 208, pp. 110920, 2024. DOI: 10.1016/j.ymssp.2023.110920.

[6] P. Andreou *et al*, "Reduced Order Model for Modal Analysis of Electric Motors Considering Material and Dimensional Variations," SAE Technical Paper 2024-01-2945, 2024, https://doi.org/10.4271/2024-01-2945.

[7] M. S. Qatu, "Accurate equations for laminated composite deep thick shells," *Int. J. Solids Structures,* vol. 36, *(19),* pp. 2917–2941, 1999. DOI: 10.1016/S0020-7683(98)00134-6.

[8] L. Lu *et al*, "Dynamic analysis of stepped functionally graded conical shells with general boundary restraints using Jacobi polynomials-Ritz method," *Thin-Walled Structures,* vol. 204, pp. 112304, 2024. DOI: 10.1016/j.tws.2024.112304.

[9] C. Gao *et al*, "Free and forced vibration analysis of uniform and stepped combined conical-cylindrical-spherical shells: A unified formulation," *Ocean Eng.,* vol. 260, pp. 111842, 2022. DOI: 10.1016/j.oceaneng.2022.111842.

DOI: 10.61782/fa.2025.0713

FORUM ACUSTICUM EURONOISE 2025

PSYCHOACOUSTIC INVESTIGATION OF THE SOUND RADIATION OF ROTARY DRILLING RIGS

Jörg Riedel[1*] **Gabriel Beer**[1] **Franz Froschmeir**[2]
Thomas Uhlemann[2] **Stefan Becker**[1]
[1] Institute of Fluid Mechanics (LSTM), FAU Erlangen-Nürnberg, Germany
[2] BAUER Maschinen GmbH, BAUER-Straße 1, 86529 Schrobenhausen, Germany

ABSTRACT

The acoustic emission of rotary drilling rigs consists of the partial sound sources of the diesel engine, the fans of the cooling system and the rotary drive. Usually, the machines are acoustically characterised according to the outdoor noise directive 2000/14/EC with a value for the averaged sound power. However, the subjective noise exposure for construction site employees can differ from the measured sound power level depending on their location on the construction site. In our test setup, we examine the acoustic emission of the device from the perspective of the construction site workers, once from the machine operator in the operator's cab and once from the site assistant giving instructions outside. Using artificial head measurements, we analyse the psychoacoustic parameters of loudness, sharpness, roughness and tonality at different operating points of the drilling rig. It turns out that, despite similar values for the sound power, the psychoacoustic parameters can characterise the sound radiation of the drilling rig in a more differentiated way at specific operating points.

Keywords: *psychoacoustics, construction site noise, rotary drilling rigs*

1. INTRODUCTION

According to a report by the German Federal Ministry of Labour and Social Affairs, noise-induced hearing loss is the second most common recognised work-related disease in Germany. In 2023, 18,076 new cases of occupational noise-induced hearing loss were reported to the relevant accident insurance companies. Of these, 7,889 new cases have already been confirmed and in 283 cases, noise-induced hearing loss was the reason for early retirement [1]. A significant proportion of these cases affect employees in the construction industry, with around 1,500 new cases of noise-induced hearing loss being recognised in this sector each year [2].

Particularly on major construction and civil engineering sites, construction workers and residents are exposed to high noise emissions due to the heavy construction machinery used. One machine type frequently employed in this context are rotary drilling rigs, which are used to drill piles, carry out soil mixing procedures or prepare the ground for following process steps [3]. An example of such a machine is shown in Fig 1.



Figure 1. Example for a rotary drilling rig.

[*] ***Corresponding author***: joerg.riedel@fau.de
Copyright: *©2025 Jörg Riedel et al. This is an open-access article distributed under the terms of the Creative Commons Attribution 3.0 Unported License, which permits unrestricted use, distribution, and reproduction in any medium, provided the original author and source are credited.*

2. PSYCHOACOUSTIC PARAMETERS

The application of psychoacoustic methods for product optimisation is nowadays well established in the mobility sector. Some examples in this context are the characterisation of automotive HVAC noise [4], sound design of warning signals for electric cars [5], or the characterisation of motors in pedelecs [6]. We apply the software ArtemiS SUITE 16.0 from HEAD acoustics to calculate the psychoacoustic parameters mentioned below.

2.1 A-weighted sound pressure/power level

For practical applications, the A-weighted sound power level is a commonly used metric to quantify the acoustic emission of a machine. The A-weighting takes into account the fact that the human ear is less sensitive to particularly low and high frequencies. However, strictly speaking, the A-weighting filter only corresponds to the curve of equally loud perceived tones at a volume between approximately 20 and 40 phon. Nevertheless, A-weighting is a very good approximation for the evaluation of tones, narrow-band noise and simple A-B comparisons, where A and B have the same sound characteristics. For broadband noise and when comparing noises that differ greatly in their underlying characteristics (e.g. additional tonal components), pure A-weighting however underestimates the volume compared to subjective volume perceptions from listening tests [7].

2.2 Loudness

When assessing the volume of a noise signal, loudness takes into account the physiological characteristics of human hearing. This includes, among other things, taking into account frequency-dependent masking effects and incorporating different rating curves depending on the maximum sound pressure level being present [7]. A 1 kHz sinusoidal tone with a sound pressure level of 40 dB is assigned the unit 1 *sone*. In our investigations, we use the calculation of loudness according to DIN 45631/A1, which is based on the frequency group method according to ZWICKER.

2.3 Sharpness

Speaking figuratively, sharpness describes the location of the centroid of the loudness-corrected spectrum of a sound. Noises with a focus in the high-frequency sound range are perceived as sharper [7]. A narrowband noise around the centre frequency of 1 kHz with the width of one critical band and a sound pressure level of 60 dB corresponds to 1 *acum*. In the present case, we use the calculation model according to AURES with an underlying loudness calculation according to DIN 45631/A1.

2.4 Roughness

The roughness indicates a parameter for characterising frequency- and amplitude-modulated sounds. A 1 kHz sine tone at 60 dB, which is amplitude-modulated with a frequency of 70 Hz and a modulation degree of 1, corresponds to a roughness of 1 *asper* [8]. We use the procedure according to DIN 38455 to calculate roughness.

2.5 Tonality

The tonality parameter is used to rate noise in terms of the annoyance of specific tonal components it contains. We use the tonality according to the SOTTEK hearing model, as shown in ECMA 418-2, in our analyses. A 1 kHz tone with a level of 40 dB receives the unit 1 tu_{HMS} (tonality units according to the hearing model of Sottek). Compared to other methods of calculating tonality, such as the tone-to-noise ratio or DIN 45681, the metric used here has the advantage that it uses psychoacoustic loudness as the basis for its calculations [9].

3. MEASUREMENT SET-UP

Construction equipment and machinery used outdoors are sound-characterised in Europe in accordance with the outdoor directive 2000/14/EG. This directive refers to EN ISO 3744 for determining the sound power of rotary drilling rigs. Accordingly, the sound power of rotary drilling rigs is determined using an enveloping surface method for a free sound field above one reflecting surface Fig. 2 shows the measurement set-up in this case. 12 microphone positions are defined around the device in a hemisphere with a radius of 16 m, in line with the standard. The microphones used for the sound power measurement are ½”- free-field microphones of the type MK 255 from MTG.

We use the KEMAR Head & Torso 45BB-10 with anthropometric ears as the artificial head. The artificial head is placed at a distance of 4 m from the outer contour of the machine, which is a typical working position for the drilling assistant (see Fig. 1). Data acquisition is carried out with an SQuadriga II from HEAD acoustics. During the measurements, the machine operator inside the device wears the Mobile Headset BHS II together with the mobile recorder SQobold from HEAD acoustics.

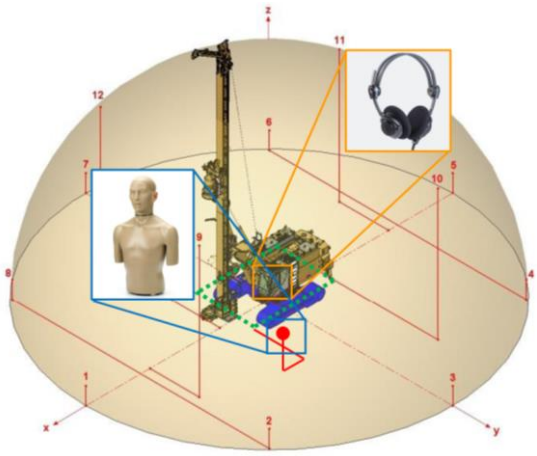


Figure 2. Set-up for determining the sound power of a rotary drilling rig according to EN ISO 3744. Also highlighted is the measurement equipment for the binaural recordings at the related positions

In our tests, we analyse a medium-powered rotary drilling rig with a 6-cylinder 4-stroke diesel engine. As already mentioned, the main sources of noise on such a machine are the diesel engine itself, the fans for cooling the engine, hydraulic circuit and charge air, and the operation of the power rotary head. In our measurement programme, we analyse the device in four different operating modes, which are summarised in Tab. 1. We examine time periods of 15 s for each operating point.

Table 1. Test plan of the considered operating points of the rotary drilling rig with corresponding sound power levels according to EN ISO 3744.

#	engine speed	fan speed	rotary drive	sound power level
M000	85 %	70 %	off	$L_{w,min}$
M100	100 %	70 %	off	$L_{w,min}$ +0,7dB(A)
M010	85 %	100 %	off	$L_{w,min}$ +7,5dB(A)
M011	85 %	100 %	on	$L_{w,min}$ +8,3dB(A)

In the first operating condition, M000, the engine is running at 85% of its nominal speed. All the fans are manually controlled at 70% of their maximum speed and the rotary drive is not in operation. In this setting, the lowest of all sound power levels, $L_{w,min}$, is measured and used as a reference for the other operating conditions. In the second operating state, M100, the speed of the diesel engine is then increased to nominal speed (100%). This results in a sound power increased by 0.7 dB(A) compared to the initial variant. In the third operating state, M010, the engine speed is reduced again to 85% of the nominal engine speed and the speed of the fans is increased to 100% instead; the rotary drive remains switched off. Compared to the initial variant M000, a sound power level increased by 7.5 dB(A) is now measured. In the last set-up, M011, the rotary drive is switched on, the motor engine speed remains at 85 % of its maximum and the speed of the fans are operated at 100 %. This results in an 8.3 dB(A) increase in sound power compared to the initial variant.

4. RESULTS

In Fig. 3, the results of the psychoacoustic analysis at the four different operating points are shown with the help of bar charts. Each row of the subplot represents a separate metric. Starting with level in dB(A) and moving on to loudness, sharpness, roughness and tonality. The results for the operator's position are shown in orange bars, and the results for the assistant are shown in blue.

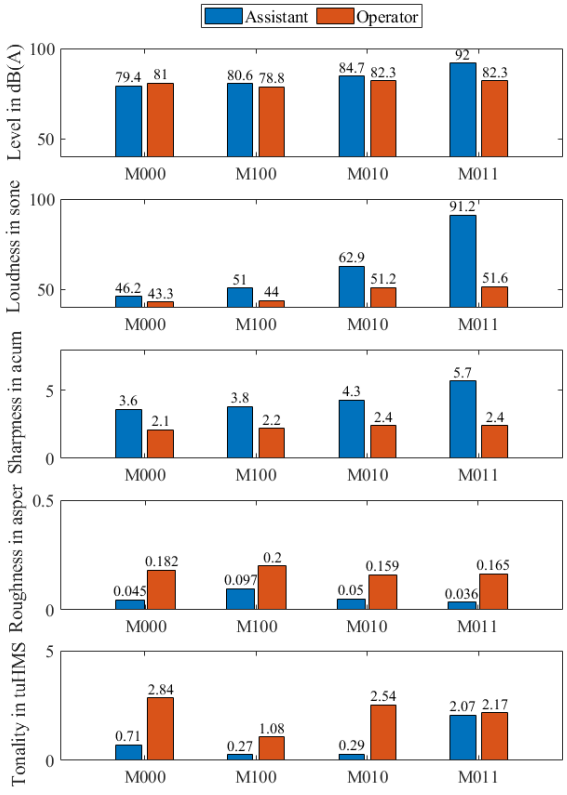


Figure 3. Single value results for the five different metrics of the psychoacoustic analysis.

4.1 Increased diesel engine speed

First, we investigate how an increase in engine speed (M000->M100) affects the sound perception for the operator and the assistant. According to Tab.1, this change results in a minimal increase in sound power of 0.7 dB(A). At the assistant's position, a slight increase in loudness of 4.8 sone is measured. While the pure A-weighted sound pressure level at the operator's position decreases by 2.2 dB(A) for this setting, the loudness increases by 0.7 sone. When listening to the sound recordings of the two operating points at the two positions, it becomes clear that the increase in engine speed is most clearly described by the parameters roughness and tonality. For both the operator and the assistant, the increase in engine speed results in a significant increase in the parameter roughness. At the same time, the parameter tonality decreases strongly at both observer positions.

4.2 Increased fan speed

Subsequently, we analyse how an increase in the fan speed (M000->M010) affects the sound perception of the construction site workers. With this particular modification, an increase of 7.5 dB(A) was observed for the sound power in Tab.1. In this case, an increase in loudness of 7.9 sone can be measured for the operator, and for the worker in front of the drilling rig, the increase is 16.7 sone. In addition to the volume, the sensation of sharpness changes when the fan speed is increased. The tonal components of the secondary aggregates are suppressed by the noise of the fan, which is expressed in the tonality parameter.

4.3 Switching on the rotary drive

Finally, we consider how an additional switch-on of the rotary drive (M010->M011) affects the noise perception of the construction site workers. The sound power level changes by only 0.8dB(A) at this setting. From the operator's position, it is almost impossible to detect the switching on of the rotary drive acoustically. However, the most significant differences for the assistant in the whole measurement campaign arise with this variation. The loudness increases in this case by 28.3 sone. The measured sharpness changes from 4.3 to 5.7 acum. And the tonality for the assistant increases by 1.78 tu_{HMS}.

5. CONCLUSION

In the present study, we examined how a change in characteristic machine parameters of a rotary drilling rig affects the subjective sound perception of construction site employees. Due to the fact that the machine emits a broadband noise spectrum with many different partial sound sources, the measured sound power level does not always adequately reflect the perceived noise exposure at the positions of the construction workers. Our research showed that the assistant perceives the various operating states of the machine in a much more differentiated way than the machine operator. This indicates that the machine's cab provides sound insulation and shields the operator. The work carried out shows that the psychoacoustic parameters are suitable for assessing the subjective noise exposure of construction workers.

6. ACKNOWLEDGMENTS

The authors would like to thank the German Federal Ministry for Economic Affairs and Climate Protection, which is funding the underlying work through the Projektträger Jülich (PTJ) with grant number 03EN5034D.

7. REFERENCES

[1] Bundesanstalt für Arbeitsschutz und Arbeitsmedizin: “Sicherheit und Gesundheit bei der Arbeit – Berichtsjahr 2023“, Dortmund, 2025.

[2] BG BAU: “Lärm in der Bauwirtschaft-Handlungshilfe zur Umsetzung der Lärm- und Vibrations- Arbeitsschutzverordnung,” 2019.

[3] BAUER Maschinen GmbH: https://equipment.bauer.de/de/drehbohrgeraete

[4] S. Hohls et al.: “Psychoacoustic analysis of HVAC noise with equal loudness”, in *INTER-NOISE and NOISE-CON congress and conference*, 2014.

[5] D. Menzel et al.: “Psychoacoustic experiments on feasible sound levels of possible warning signals for quiet vehicles”, in *Tagungsband Fortschritte der Akustik-DAGA 2011*, Düsseldorf, 2011.

[6] S. Becker et al.: “Akustik von E-Bikes”, *DEGA Akustik Journal*, no. 02/20, pp. 41-49, 2020.

[7] Gh. R. Sinambari and S. Sentpali: *Ingenieurakustik Physikalische Grundlagen und Anwendungsbeispiele*. Wiesbaden: Springer-Vieweg, 2014.

[8] H. Fastl and E. Zwicker: *Psychoacoustics Facts and Models*. Berlin Heidelberg: Springer, 2006.

[9] HEAD acoustics GmbH: *Tonality (Hearing Model)*. Application Note, 2018.

DOI: 10.61782/fa.2025.0077

FORUM ACUSTICUM EURONOISE 2025

ACOUSTIC MEASUREMENTS AND EMPLOYEE FEEDBACK: ADDRESSING NOISE IN INDUSTRIAL WORK ENVIRONMENTS – A CASE STUDY.

Pascal van Dort*
Rockfon (ROCKWOOL B.V.)
Industrieweg 15, 6045JG Roermond
Netherlands

ABSTRACT

(introduction) This study aims to evaluate the impact of high noise levels in an industrial hall on workers' health, wellbeing and productivity, with a focus on room acoustic measurements and employee feedback. (method) Various room acoustic measurements were conducted within the production hall to assess reverberation time and sound levels. Additionally, a survey was distributed to 83 workers to collect qualitative data on their experiences with noise exposure and its effects on their work environment. (results) The measurements indicated reverberant noise levels (L_{eq}) reaching up to 92 dB(A), and performed dosimeter readings among employees showed noise levels (L_{ex}) between 85 and 89 dB(A), highlighting a challenging indoor acoustic environment. Survey results revealed that a significant number of workers found their workplace to be excessively noisy, negatively affecting their stress levels, wellbeing, productivity, concentration and communication. (conclusions) The findings suggest that implementing sound-absorbing materials, such as suspended acoustic ceilings, could reduce noise levels by 5 to 6 dB(A), thereby improving working conditions. This study underscores the importance of addressing noise in industrial settings to enhance worker wellbeing and productivity, indicating that effective acoustic treatments can lead to a healthier and more happier workplace.

*Corresponding author: pascal.van.dort@rockfon.com
Copyright: ©2025 First author et al. This is an open-access article distributed under the terms of the Creative Commons Attribution 3.0 Unported License, which permits unrestricted use, distribution, and reproduction in any medium, provided the original author and source are credited.

Keywords: *industry hall, noise exposure, health impact, wellbeing, employee feedback*

1. INTRODUCTION

Noise pollution in industrial work environments is a significant concern that can have far-reaching effects on employee health, wellbeing and productivity. In industrial settings, where machinery and equipment are primary noise sources, sound levels can easily exceed the World Health Organization's recommended level of sound exposure of 80 dB(A) for a maximum of 40 hours per week [1].

1.1 Noise exposure and its' impact on health and wellbeing

Short-term and long-term health effects have been associated with prolonged exposure to high levels of noise. Transient auditory fatigue and noise annoyance are short-term health effects of high noise levels (88 – 92 dB(A)) in factories, leading to substantial discomfort among workers [2]. Moreover, >85 dB(A) sound exposure during a working day dramatically raises the levels of the stress marker cortisol, and consequently fatigue and irritability [3]. Chronic noise exposure is associated with psychological symptoms such as anxiety and sleep disturbances. Workers in automotive industries reported increased stress and fatigue due to prolonged noise exposure [4-5]. Long-term health effects due to prolonged exposure to high-intensity noise is a leading cause of occupational hearing loss. According the WHO there is an increase in prevalence of all grades of hearing loss in Europe. In 2019 it was 197 million people and estimated that it will be 236 million in 2050 [1]. Studies

in various industries, including automotive and textile manufacturing, have documented a high prevalence of Noise-Induced Hearing Loss (NIHL), often progressing to permanent sensorineural hearing loss if left unaddressed [6-7].

1.2 Impact on productivity and job satisfaction

Noise levels in production facilities has negative effect on human productivity which leads to decrease in organization productivity and decrease in quality and quantity of services and products [8]. Another study on press machine operators found that reducing reflected and direct sound levels improved both health outcomes and production quality [9]. Poor acoustic conditions can reduce job satisfaction and overall engagement. A study comparing two industries found that reducing noise levels led to greater environmental satisfaction and improved company attachment [5].

2. GENERAL INFORMATION ABOUT THE INDUSTRY HALL

The investigated industry hall is located near Antwerp in Belgium. The hall has different production lines used for the production of metal profiles, key activities include cutting metal sheets or coils into specific shapes, roll forming to shape the profiles, cutting to different sizes and punching to create holes or slots. The total production area covers 8000m^2 with an average ceiling height of 8,20m[1]. The hall has a concrete floor, brick and steel walls and the ceiling has an unperforated steel deck, see Fig. 1.



Figure 1. Production lines in the industry hall

3. ACOUSTIC PARAMETERS; METHODS, MEASUREMENTS RESULTS AND CALCULATIONS

Room acoustic measurements were conducted within the production hall to assess reverberation time (RT) and sound levels. Equivalent sound pressure levels (L_{Aeq}) were measured to determine the overall noise exposure. These measurements provide quantitative data on the noise environment to which workers are exposed. Dosimeter readings were also taken for some employees to assess personal noise exposure levels (L_{ex}), giving a more detailed understanding of individual noise exposure variations throughout the workday.

3.1 Acoustic measurements methods

Acoustic measurements are performed on Sept. 16th 2021 using a Class 1 calibrated sound level meter Norsonic type Nor140. The noise levels were measured in more than 150 points in the entire production hall. In all points, measurement durations of ca. 1 minute were appropriate since the noise field was sufficiently stable.



Figure 2. Employee with dosimeter

In total 6 workers were equipped with a noise dosimeter. This dosimeter measured the noise pressure level at about 10 cm distance from the ear, see Fig.2. The results of the measurement render a realistic representation of the daily noise exposure of each participant. According to the European and Belgian labour legislation this “daily dose” of noise exposure is the most important indicator for

determining the risk of noise induced hearing damage [10]. Raw measurement results were elaborated such that a correct interpretation of the legislation is possible. For the calculations of the $L_{EX,8h,}$ the working conditions during the measurement period were evaluated as representative for the activities during the whole day.

3.2 Measurements results

The data obtained from acoustic measurements are analysed to determine compliance with regulatory limits and assess the potential risk to worker health, see Table 1.

Table 1. Legal limits according the 2003/10/EU directive.

Legal limits	Doses	
	$L_{EX,8H}$ dB(A)	L_{peak} dB(C)
No legal health risk	< 80	< 135
Exceedance of the lower action value	≥ 80	≥ 135
Exceedance of the upper action value	≥ 85	≥ 137
Exceedance of the limit value when not wearing hearing protection	≥ 87	≥ 140

Equivalent sound pressure levels (L_{Aeq}) were measured to determine the overall noise exposure, see Fig. 3. The active production lines are highlighted in white, and the most important operator positions are indicated by grey rectangles. Numerous areas exhibit noise exposure levels exceeding 85 dB(A), with operators frequently working in close proximity to the noisiest zones. The decay of sound levels is rather limited, indicating that noise from one production line can easily affect adjacent lines. Acoustic measurements conducted on June 22nd 2020, revealed L_{Aeq} levels reaching even up to 92 dB(A).

All operators equipped with a dosimeter exceed the upper legal limit values according the 2003/10/EU directive, see Table 2. There is a substantial risk of noise induced hearing loss when not wearing hearing protectors. Five out of six operators even exceeded the limit value of 87 dB(A) when not wearing hearing protectors. The Lpeak-values values are less critical in determining health risk and remain within the legal limits. For a more detailed description of the noise sources that are responsible for the measured $L_{EX,8H}$-values, of one of the participants see Fig.4. The graphs shows the measurement dB(A) levels per minute.

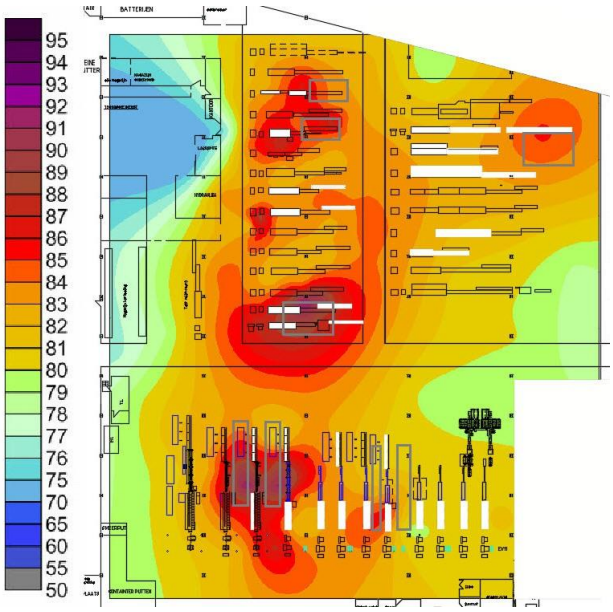


Figure 3. Noise map (L_{Aeq}) in dB(A)

Table 2. Measured dosimeter levels

Participant	Measurement duration (hr)	$L_{EX,8H}$ dB(A)	L_{peak} dB(C)
Operator 1.	5:25	87	131
Operator 2.	5:20	85	133
Operator 3.	5:25	88	127
Operator 4.	5:25	87	132
Operator 5.	5:19	89	132
Operator 6.	5:39	87	131

3.3 Acoustic modeling and calculations

To improve the indoor acoustic environment, it was recommended to add sound-absorbing materials. Given that the ceiling is the largest available surface, the impact of installing a highly sound-absorbing suspended ceiling was calculated. To predict the effect of the added sound-absorbing material on the ceiling, the production hall was modeled using Catt Acoustic / TUCT software. The reverberation time was measured at five locations and used to calibrate the model. During measurements, the signal-to-

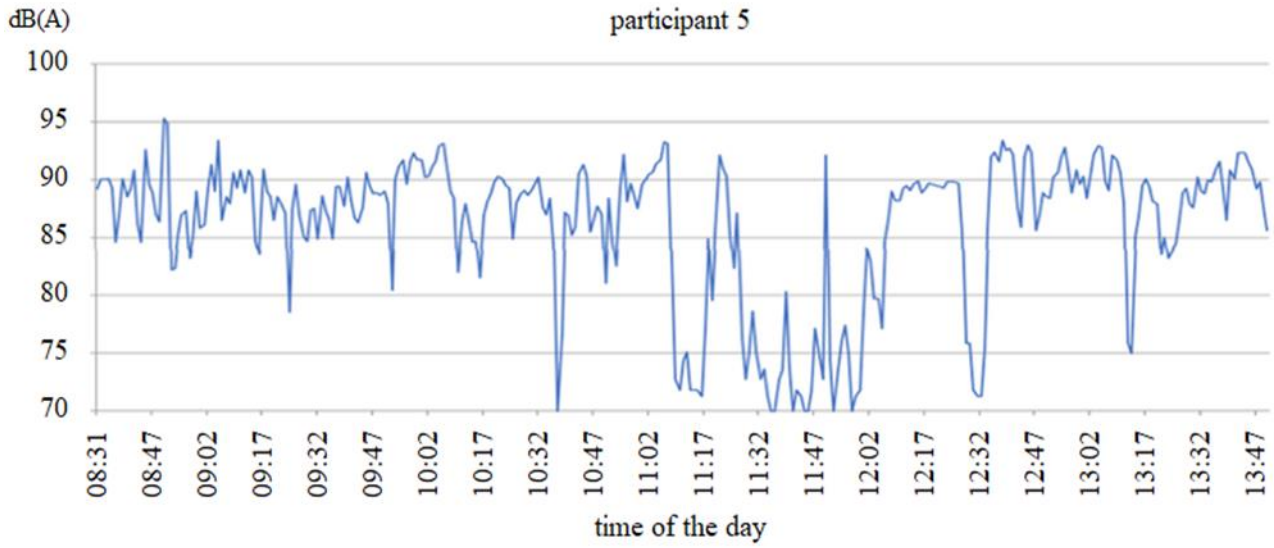


Figure 4. Dosimeter measurements per minute

noise ratio was often too weak in the 125 Hz octave band. The results of the reverberation time measurements are presented in Table 3. Room acoustic modelling shows that a Class A sound absorbing suspended ceiling will reduce the reverberant sound level by 5 to 6 dB(A).

Table 3. Measured reverberation times

Frequency	250 Hz	500 Hz	1 kHz	2 kHz	4 kHz
Reverb. time (sec.)	2,7	2,3	2,6	2,4	1,9

4. QUESTIONNAIRE; METHODS AND RESULTS

A survey was distributed among the employees to collect qualitative data on their experiences with noise exposure and its effects on their work environment. The survey aimed to capture the subjective impact of noise on various aspects of their work, including stress levels, wellbeing, productivity, concentration and communication. This feedback provides valuable insights into how workers perceive and are affected by the noise environment.

4.1 Questionaire methods

Surveys were administered from March 8 to March 14, 2022, to collect subjective feedback from employees (n=83). Participants used tablets and were provided with information about the study, along with a link to the questionnaire facilitated by the online tool 'SurveyMonkey'. Table 4 presents the age distribution of the participants, while Table 5 details their tenure with the company.

Table 4. Age range of the participants

Age	Number of employees	
(years)	(n)	(%)
18 - 24	9	11
25 - 40	21	25
41 - 56	31	38
57 - 67	22	26
Total	83	100

Table 5. Tenure with the company of the participants

Years working	Number of employees	
(years)	(n)	(%)
< 1	17	21
1 - 5	11	13
6 - 10	7	8
11 - 20	4	5
> 20	44	53
Total	83	100

Table 6. Sound environment

	totally don't agree	don't agree	neutral	agree	totally agree
My workplace is too noisy	2%	6%	16%	56%	20%
I have to raise my voice to be able to talk to my colleagues	1%	2%	16%	51%	30%
I need a quiet work environment to perform my tasks well.	5%	15%	42%	30%	8%

Table 7. Health and wellbeing

	never	seldom	sometimes	often	always
I have headache after a working day	22%	19%	40%	11%	8%
I hear a 'beeb' in my ears	40%	11%	31%	5%	13%
I lose my voice because of shouting to my colleagues	45%	29%	17%	4%	5%
I get home exhausted after a working day	16%	16%	45%	13%	10%
I get stressed at work	19%	23%	40%	10%	8%

4.1 Questionaire results

From the participants of the survey 76% indicate (agree and totally agree) that their workplace it too noisy. Because of that, 81% indicates (agree and totally agree) that they have to raise their voices to be able to talk to their colleagues. See Table 6. Health and wellbeing related questions are shown in Table 7. One of the results that stands out is the questions about *"I hear a 'beeb' in my ear"*, which is related to tinnitus. Tinnitus is characterized by the perception of sound without an external source, often described as ringing or beeping in the ears, and can be constant or intermittent [11]. In the survey, participants reported their experiences with hearing a beeping sound in their ears as shown in Table 7. Seldom beeping might not necessarily indicate tinnitus, as transient auditory perceptions can result from temporary factors such as exposure to loud noise, earwax buildup, or certain medications [12]. However, persistent or frequent beeping is more indicative of tinnitus, a condition that significantly impacts quality of life [13]. The prevalence of tinnitus varies, but it is commonly reported that at least 10% of the global population experiences tinnitus at some point in their lives [13-14]. With 18% of participants indicating to have a beebing sound (often and always), we can conclude a very high average of workers in the industry hall suffer from tinnitus.

Survey results revealed that a significant number of workers found their workplace to be excessively noisy, negatively affecting their stress levels, wellbeing, productivity and concentration. Fig. 5 shows the percentage answers 'often' and 'always'.

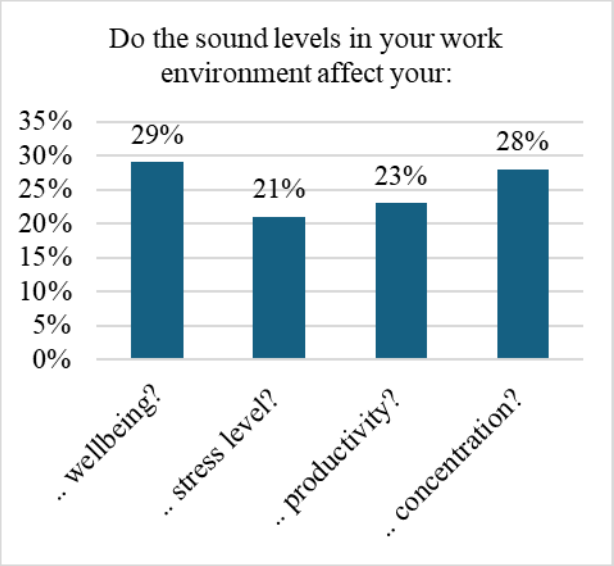


Figure 5. Subjective experience of sound levels

According to Directive 2003/10/EC [10], hearing protection must be worn when exposed to noise levels above 85 dB(A). When asking *'how often do you wear personal hearing protection'* only 20% replied with *'always'*, see Fig. 6. The stated reason is that some employees find hearing protection devices uncomfortable to wear for extended periods and some say they find it challenging to communicate with colleagues while wearing hearing protection, especially in areas where verbal communication is essential.

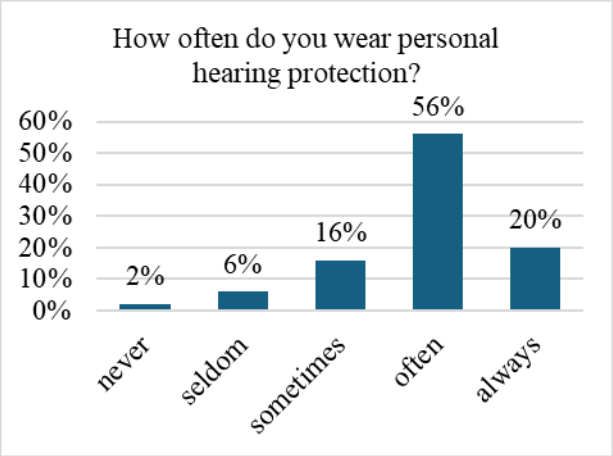


Figure 6. Personal hearing protection

5. CONCLUSION

This study evaluated the impact of high noise levels in an industrial hall, focusing on room acoustic measurements and employee feedback on their health, wellbeing and productivity. The measurements indicated noise levels (L_{eq}) reaching up to 92 dB(A), and dosimeter readings among employees showed noise levels (L_{ex}) between 85 and 89 dB(A), underscoring a challenging indoor acoustic environment. Survey results revealed that a significant number of workers found their workplace excessively noisy, negatively affecting their stress levels, wellbeing, productivity, concentration and communication. The findings suggest that implementing sound-absorbing materials, such as Class A sound absorbing suspended ceiling and wall panels, could reduce noise levels by 5 to 6 dB(A), thereby improving working conditions. This study emphasizes the importance of addressing noise in industrial settings to enhance worker wellbeing and productivity, indicating that effective acoustic treatments can lead to a healthier and more satisfying workplace. Future research should focus on long-term monitoring and the effectiveness of various acoustic interventions, specifically evaluating how the indoor acoustic environment is improved after installing the acoustic ceiling and wall panels, to ensure sustained improvements in industrial work environments.

6. ACKNOWLEDGMENTS

We would like to express our gratitude to acoustic consultant Tom Segers from Bureau De Fonseca in Belgium for his invaluable contribution to this study. Tom conducted the measurements and calculations, providing critical insights into the acoustic environment of the industrial hall.

7. REFERENCES

[1] World Health Organization. 2021. World report on hearing. Geneva, Switzerland: *World Health Organization. 2021*; Retrieved from: https://www.who.int/publications/i/item/world-report-on-hearing

[2] Yaman, M. "Analysis of textile industry noise through noise exposure, noise sensitivity and noise annoyance of workers." Pamukkale University *Journal of Social Sciences Institute*, 2024 https://doi.org/10.30794/pausbed.1542527

[3] Melamed, S., & Bruhis, S., "The effects of chronic industrial noise exposure on urinary cortisol, fatigue and irritability: a controlled field experiment." *Journal of Occupational and Environmental Medicine*, 38(3), 252–256., 1996 https://doi.org/10.1097/00043764-199603000-00009

[4] Mucci, N., Traversini, V., Lulli, L. G., Vimercati, L., Rapisarda, V., Galea, R., De Sio, S., & Arcangeli, G., "Neurobehavioral Alterations in Occupational Noise Exposure: A Systematic Review." *Sustainability*, 13(21), 12224., 2021 https://doi.org/10.3390/SU132112224

[5] Raffaello, M., & Maass, A., "Chronic Exposure to Noise in Industry: The Effects on Satisfaction, Stress Symptoms, and Company Attachment." *Environment and Behavior*, 34(5), 651–671., 2002 https://doi.org/10.1177/0013916502034005005

[6] Marijanti, L. T., "Noise Exposure and Hearing Health in the Workplace." *Jurnal Biomedika Dan Kesehatan*, 5(3), 132–135., 2022 https://doi.org/10.18051/jbiomedkes.2022.v5.132-135

[7] Michael, K. L., & Byrne, D. C., "Industrial Noise and Conservation of Hearing." In R.L. Harris (Ed.), *Industrial hygiene* (5th ed., pp. 15-16)., 2001 https://doi.org/10.1002/0471435139.HYG019

[8] Akbari, J., Dehghan, H., Azmoon, Hiva, and Forouharmajd, F., "Relationship between Lighting and Noise Levels and Productivity of the Occupants in Automotive Assembly Industry". Journal of Environmental and Public Health.., 2013 https://doi.org/10.1155/2013/527078

[9] Veljović, F., Burak, S., Begic, E., & Masic, I., "Redesign of Work Space in Order to Reduce Noise" *Health Effects*. 31(2), 135–140., 2019 http://doi.org/10.5455/msm.2019.31.135-140

[10] *Directive 2003/10/EC* of the European Parliament and of the Council of February 6, 2003 on the Minimum Health and Safety Requirements Regarding the Exposure of Workers to the Risks Arising from Physical Agents (Noise). https://eur-lex.europa.eu/eli/dir/2003/10/

[11] Baguley, D., McFerran, D., & Hall, D. "Tinnitus." *The Lancet*, 382(9904), 1600-1607., 2013 http://dx.doi.org/10.1016/S0140-6736(13)60142-7

[12] Henry, J. A., Dennis, K. C., & Schechter, M. A. "General review of tinnitus: prevalence, mechanisms, and management." *Journal of Speech, Language, and Hearing Research*, 48(5), 1204-1235., 2005 https://doi.org/10.1044/1092-4388(2005/084)

[13] Jastreboff, P. J. "Phantom auditory perception (tinnitus): mechanisms of generation and perception." *Neuroscience Research*, 8(4), 221-254., 1990 https://doi.org/10.1016/0168-0102(90)90031-9

[14] McCormack, A., Edmondson-Jones, M., Fortnum, H., & Dawes, P. "The Prevalence of Tinnitus and the Relationship With Neuroticism in a Middle-Aged UK Population." *Journal of Psychosomatic Research*, Volume 76, Issue 1, January 2014, Pages 56-60., 2014 https://doi.org/10.1016/j.jpsychores.2013.08.018

[15] James A. Henry, et al. "Tinnitus: An Epidemiologic Perspective." *Otolaryngologic Clinics of North America*, Volume 53, Issue 4, 2020, Pages 481-499., 2020 https://doi.org/10.1016/j.otc.2020.03.002.

DOI: 10.61782/fa.2025.0234

FORUM ACUSTICUM EURONOISE 2025

COMPARISON OF CONTROL LOGIC DRIVING INVERTER COMPRESSORS IN REFRIGERATORS AND POTENTIAL IMPACT ON CUSTOMER SOUND QUALITY ASSESSMENT

Piotr Kosowski[1*] **Serkan Atamer**[2] **Ercan Altinsoy**[2]

[1] Beko Europe, Bora-Komorowskiego 6, 51-210 Wrocław, Poland
[2]Chair of Acoustics and Haptics, TU Dresden, Helmholtzstr. 18, 01069, Dresden, Germany

ABSTRACT

Acoustics and vibrations improvement developments in household appliances is usually based on basic Source, path and receiver problem solving model. The engineering sector has moved across the years from simple additions of acoustic or vibration damping materials (focused on path improvement) towards optimization of sound sources (like motors, for source improvement) where greater gains were possible. Notably, the latest and modern appliances take advantage of variable speed inverter motors, running at minimal speeds most of the time, producing little noise and vibration, resulting in very low sound power level claims on energy labels. Authors of this text found out however that the applied algorithms to control speed of inverter compressors on refrigerators can vary significantly. This study aims to compare various approaches from appliance manufacturers to control the speed of inverter compressors, targeting greater customer satisfaction once the product is running at end user premises. It engages also into a debate which algorithms are more favorable from developmental engineering perspective as well from final customer.

Keywords: *inverter compressors, household appliances, noise control, psychoacoustics, sound quality*

1. INTRODUCTION

The research area of noise reduction in household appliances business, as well as adjacent businesses, is frequently modelled as “Source, Path and Receiver” [1]. In that model a source of noise is being considered a compressor or fan motor (in typical, simpler type of refrigerators [2]) as well as valves, gears, flow in tubes, etc. (in more efficient refrigerators). Since the primary goal of acoustic or noise reduction treatment is to not detriment the core function of a product (i.e. cooling in case of refrigerator), the majority of engineering interventions were focused on optimizing the path that leads from a source to receiver (i.e. microphone or final user). Typical ways of achieving this in refrigerators are additional rubber or viscoelastic components (or equivalently, bitumen or foam components in dishwashers). Since addition of these components has strong implications on cost of the product (serious concern for manufacturers), the producers of sources started to put more emphasis on the design of components, consequently moving the attention from path to source of the aforementioned model. The area of improvement is related to internal design of components, for example, compressors, such as internal tubing’s and suspension [3].

This paper analyzes another aspect of noise reduction engineering, related to the way the new type of inverter compressors are controlled in refrigerators. This is especially important, as according to information from suppliers [4], there are expected rather large differences in acoustic performance of inverter compressors when running at different speeds.

[*]***Corresponding author***: *pio.kosowski@gmail.com.*
Copyright: *©2025 First author et al. This is an open-access article distributed under the terms of the Creative Commons Attribution 3.0 Unported License, which permits unrestricted use, distribution, and reproduction in any medium, provided the original author and source are credited.*

2. MOTIVATION

Authors of this text were motivated by the outcome of earlier studies [5], where survey participants were commenting how they perceive the noise of modern refrigerators at home. Especially the reflections on the responses to the questions "Can you particularly notice when the compressor works at high speed" and "How often do you notice that your refrigerator is working in high speed mode?" were worthy of further studies. Based on that survey, 43.4% of respondents indicated awareness of changes in the compressor operating condition in response to the question "Do you notice when the working condition of your compressor changes". It is a known phenomenon that human hearing is sensitive to small changes in sound [6], and since modern refrigerators are mostly equipped with inverter compressors (which changes speeds based on electronic system inputs), the motivation existed to measure how often that situation occurs in normal usage, what is the rate of change, how many different conditions are present, etc.

Authors suspected that this could be an area of differentiation between manufacturing brands, in an attempt to please its customers with a sound of product and avoid unnecessary annoyance and disturbances to achieve proper sound quality level. The experimental space of testing included various refrigerators' models from the European market, produced by locally available manufacturers. All of these were using inverter compressors.

3. MEASUREMENTS & ANALYSIS

3.1 Testing conditions

A key aspect was trying to obtain various working conditions of tested refrigerators. To achieve this goal the tested objects were put into two conditions:

- normal working mode, representing running explained in IEC 60704-2-14 standard [7] as "steady-state", where product is supposed to maintain the internal temperature with highly reproducible compressor running cycle
- first working mode, representing a situation as if a user would plug in the product for the very first time, where the product (initially warm) is supposed to start cooling down towards the desired nominal temperatures.

The idea behind the latter working mode is that authors expected the object would go through various modes along with the reduction of internal temperature. Indeed, later testing results proved the assumption, as it is revealed in the next sections.

3.2 Sensors position & software for analysis

Sound Power level (IEC) procedure microphone layout was used to record the sound from one of its microphones (the frontal one, which sits more or less 1m from the refrigerator front door and 1,5m above the floor). To have a better understanding of compressor speeds during the cycles, the additional accelerometer was used, mounted on the compressor. Registration of all signals was done in a hemi-anechoic chamber using HBK Pulse Labshop software, while the psychoacoustic analysis was done using Head Acoustics Artemis.

3.3 FFT spectrograms analysis

The FFT spectrograms below represent the vibrations obtained from the accelerometers mounted on compressors of three selected refrigerator models, each displaying a different method of controlling inverter compressor speed. Main emphasis in analysis is on tracing the vertical lines in frequency axis (x-axis), representing the changing fundamental frequency of compressor vibration, thus compressor speed. The next three spectrograms (Figures 1 - 3) represent first working mode cycles (as explained in 3.1) and the time span (Y-axis) covers the entire compressor running cycle, from the moment it was powered on until the natural stop (related to achievement of nominal temperatures) for three different brands. From the first look at the graphs, it is clear that the strategy of signal control is very different for each brand.

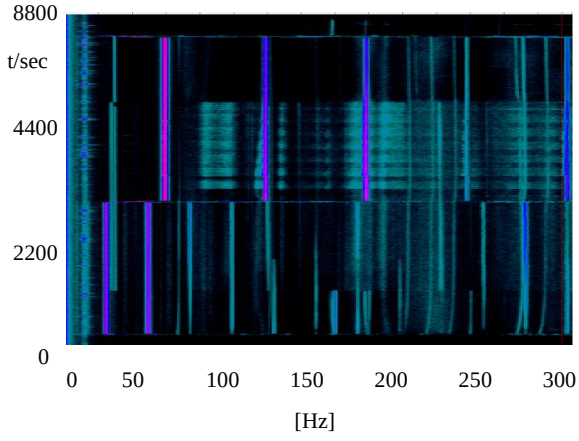


Figure 1. Vibration spectrogram of the first working mode, refrigerator brand 1.

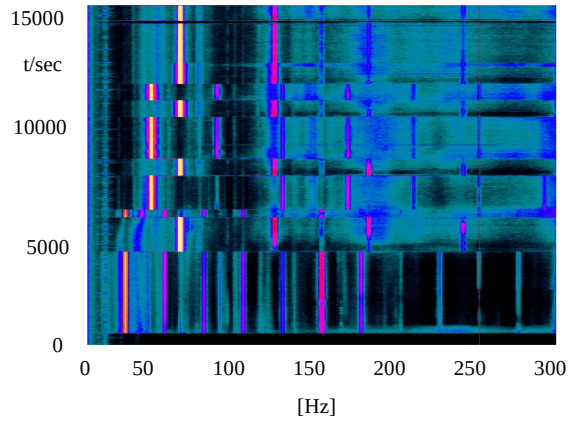


Figure 2. Vibration spectrogram of the first working mode, refrigerator brand 2.

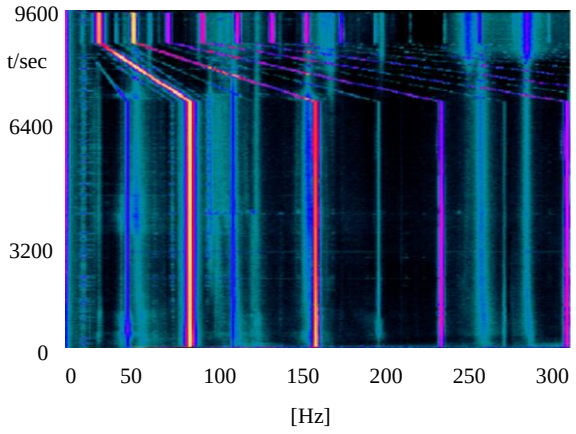


Figure 3. Vibration spectrogram of the first working mode, refrigerator brand 3.

Each brand has a different strategy engaging inverter compressors to cool down the product. Brand 1 is using just two discrete speed steps (lower fundamental frequency around 20 Hz corresponding to 1200 rpm, and higher frequency 60Hz, corresponding to 3600 rpm). Between these two, there is just one change in the middle of the running cycle (Figure 1).

On brand 2's refrigerator, the compressor is changing speed 8 times in the cycle. Time at each speed is unequal and three distinctive speed steps are distinguished (around 20, 40 and 60Hz, corresponding to, respectively, 1200, 2400 and 3600 rpm) (Figure 2).

The graph representing measures of brand 3 is again different. Again only 2 main speeds are detected (around 75Hz and 20 Hz, corresponding to 4500 and 1200rpm), but the majority of the time it works at first running speed, followed by a lengthy period of transition from initial speed to final speed (Figure 3). Figure 4 shows, zoomed in, the area of transition from one speed to the next with a highlighted time for brand 1.

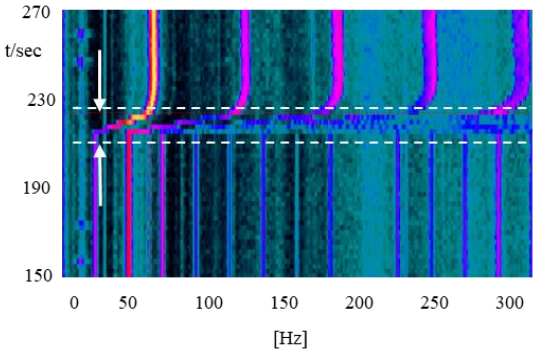


Figure 4. Vibration spectrogram of the area of transition from one speed to the next with the highlighted time for brand 1.

For each brand the respective time to transition between desired speeds was 60 seconds, 10 seconds and 18 minutes (respectively for brands 1, 2 and 3).Such varying transition times can have a significant impact on perceived sound quality, depending on the presence of structural resonances in the range of speeds selected. The next three spectrograms represent a different approach to speed control of the compressor during normal working mode (as in 3.1).

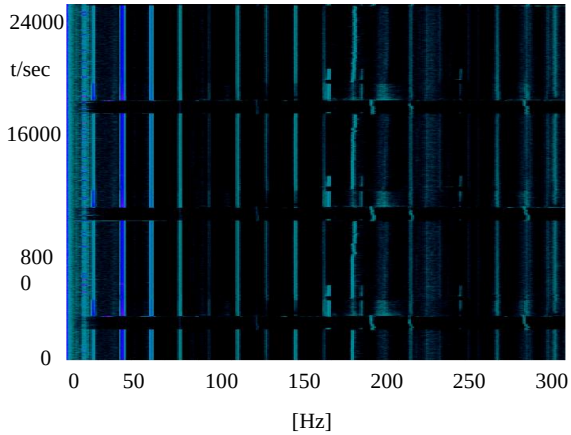


Figure 5. Vibration spectrogram of the normal working mode, refrigerator brand 4.

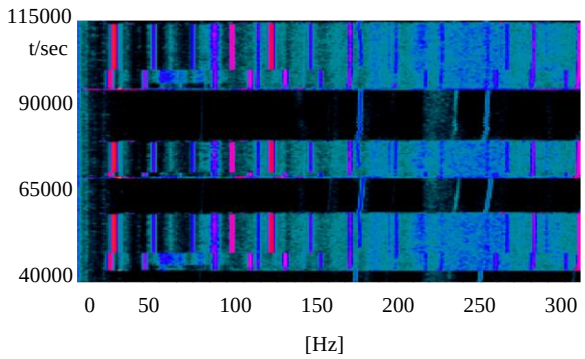


Figure 6. Vibration spectrogram of the normal working mode, refrigerator brand 5.

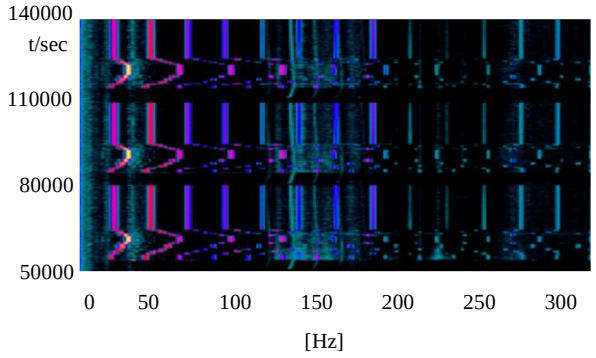


Figure 7. Vibration spectrogram of the normal working mode, refrigerator brand 6.

Compared to the first working mode, the normal working mode tends to engage only one compressor speed around 20Hz (corresponding to 1200rpm) for each of three brands, however still some noticeable differences between brands are present like either keeping one speed flat, changing sharply between two speeds or slowly modulating the speed close to the nominal.

3.4 Psychoacoustic analysis

The variation in compressor driving speed is primarily determined by the required cooling demand. Based on this demand, a specific RPM value is set. Accordingly, the compressor either accelerates from zero to reach this target speed (first working mode) or maintains a stable temperature by adjusting its speed accordingly (normal working mode). The decisions made at this stage—such as how quickly the compressor should reach the target RPM or which intermediate steps it should follow—significantly impact noise emissions and, to a large extent, psychoacoustic parameters. Different numbers of steps, varying frequencies (hence different RPMs), and different transition lengths all influence the compressor's operation. RPM changes can create BSR problems (buzz, squeak and rattle), lead to resonance issues, which not only elevate overall noise levels but also enhance tonal components, affecting the perceived sound quality.

To evaluate the various vibroacoustic issues that may arise from RPM changes and their corresponding psychoacoustic effects, a sample recording was analyzed. Figure 8 presents the spectrograms of this recording. The upper panel, plotted only up to 300 Hz with higher FFT resolution, focuses on better visualizing the compressor's operating conditions. In contrast, the lower panel displays all audible sound events. In this example, the compressor initially runs at approximately 60 Hz before gradually reducing its speed over an extended period. As expected, strong resonances can be observed during this deceleration phase, particularly in the lower panel as indicated by the yellow areas. Figure 9 presents a magnified view of the lower panel from Figure 8, providing a more detailed representation of time- and frequency-dependent sound events for better analysis.

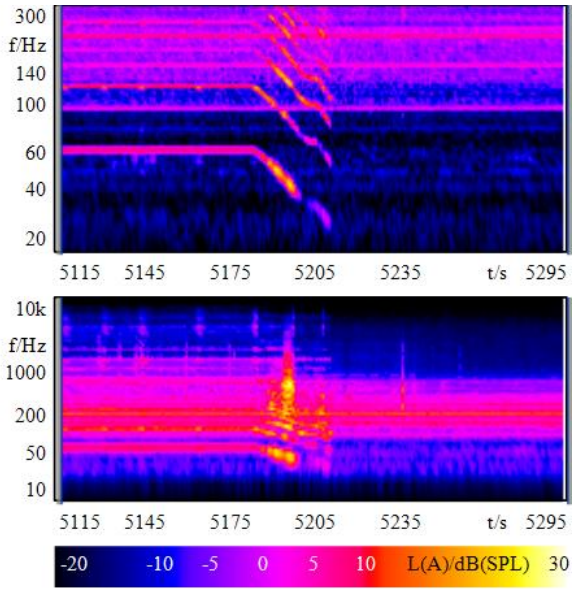


Figure 8. Spectrograms of an example compressor deceleration. (Upper panel spectrum size: 16384, lower panel spectrum size: 4096, A-weighted).

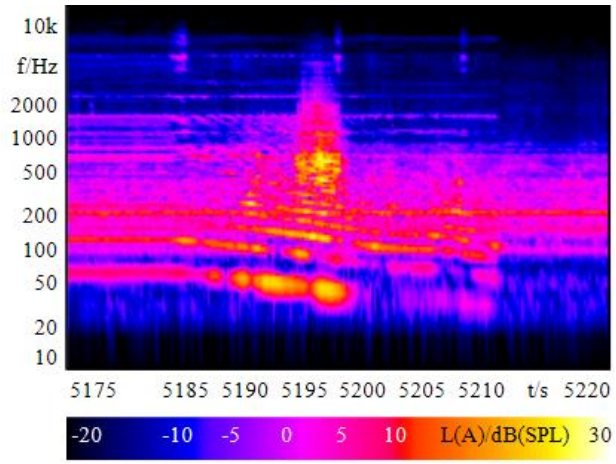


Figure 9. Spectrogram of an example compressor deceleration (detailed view of lower panel from Figure 8, spectrum size: 4096, A-weighted).

As expected, resonance issues arise during this transition, significantly degrading sound quality. Figure 10 illustrates the A-weighted sound level and the loudness level according to ISO 532 during this phase. Considering that these recordings were made in an anechoic environment—and that these values could be higher in a real room—it would not be incorrect to state that the refrigerator transitions from being "inaudible" to "noticeably disturbing" during this period [5]. Similarly, the hearing model tonality values during this resonance phase are presented in Figure 11. Even under anechoic conditions, the tonality values rise from very low levels to exceed the threshold value of 0.40 [8].

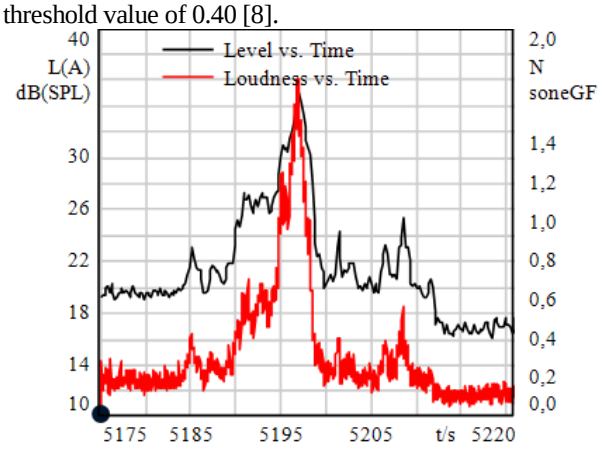


Figure 10. A-weighted levels and loudness levels (ISO 532) over time for the example case in Figure 9.

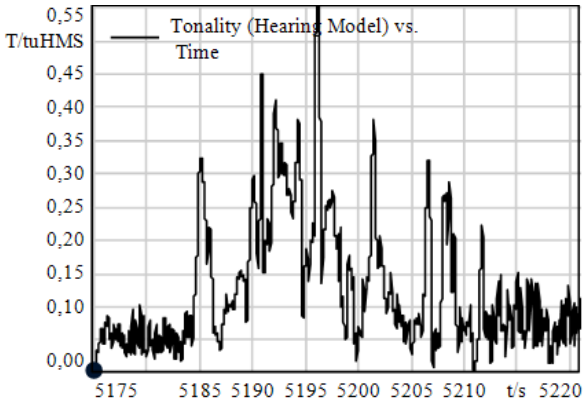


Figure 11. Hearing model tonality over time for the example case in Figure 9.

From this perspective, continuous and slow RPM changes can be considered detrimental to sound quality. The literature already suggests that compressors should operate in a stepwise manner rather than with continuous adjustments [9]. However, determining which RPM values should be used as steps becomes a challenging design problem, especially when considering the complex vibration transfer paths of the devices. Moreover, based on these specific insights on possible transfer paths, RPM steps and their durations should be selected and optimized for the particular characteristics of the device, ensuring better acoustic performance and reduced user annoyance. This approach demonstrates that significant improvements in sound quality can be achieved solely by modifying the compressor's operating algorithm, without the need for additional materials or components. As a result, manufacturers can enhance acoustic performance without incurring extra costs, making this an efficient and cost-effective solution.

As a general rule, higher RPM corresponds to higher noise levels [2, 9]. In particular, high RPM can push a modern refrigerator from being inaudible to clearly perceptible noise levels [5]. Due to both noise concerns and energy consumption, lower operating speeds are typically preferred. However, in specific cases—such as newly stored groceries—algorithms often opt for much higher speeds. High RPM directly translates to higher sound levels, increased loudness, and potentially elevated tonality, all of which contribute to increased annoyance and reduced sound quality. As a trade-off, rather than using the highest RPM values, a moderate speed can be employed, as long as it does not significantly reduce cooling performance and speed. This selected RPM should not coincide with any

resonance. In this way, a significant improvement in sound quality can be achieved with just an algorithm change.

Another important aspect is the speed at which transitions between defined RPM steps should occur. From a psychoacoustic perspective, two key points can be highlighted. While rapid changes are generally perceived as more disturbing and attention-grabbing, psychoacoustic evaluations focusing on product sound quality must also consider the operational context and user interaction. Although very short-duration changes may be noticeable, their low frequency of occurrence throughout the day reduces possible user exposure, ultimately contributing to a higher overall perception of sound quality. This hypothesis is based on initial observations and should be further investigated in future studies in controlled listening experiments.

From a control algorithm perspective, another factor that may not cause operational issues but can be highly detrimental to sound quality is the defined minimum RPM step size. Figure 12 provides an example illustrating this issue. This example presents the noise characteristics of a refrigerator, specifically detailing the 50–80 Hz range with high FFT resolution. As shown in this detailed view, the compressor undergoes very small speed variations, sometimes as little as 2–3 Hz. At this already high operating speed, the device's perceived noise level is elevated. One can argue that, even the elevated levels can be accustomed after some time as long as the stationarity can be achieved. However, this type of very small fluctuations can attract constant attention of the user, deteriorating the sound quality of the device. Ultimately, it can be argued that annoyance is, to some extent, linked to attention.

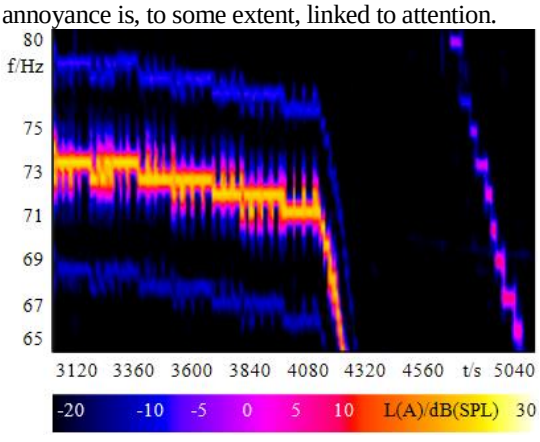


Figure 12. Spectrogram of an example refrigerator in the 50–80 Hz, illustrating small speed variations (2–3 Hz) of the compressor at high operating speeds (spectrum size: 65536, A-weighted).

4. CONCLUSION

The modern refrigerators, at the example of popular models from the European market, are built with inverter compressors [4]. These compressors usually have a significant range of speeds available and are an interesting challenge from acoustic and vibration-engineering standpoint. Authors have shown that although the majority of these products converged their claims (like on Energy Label, based on standardized conditions [7]) towards similar values, yet in practice, while running in a way similar to what end-users would experience, have substantial differences in control algorithms. These differences are related to how many different speed steps are used, how often they are engaged and how quickly the algorithm transitions from one to another speed.

The results show that speed changes have a significant impact on both sound levels and user perception (based on loudness and tonality examples). Therefore, optimizing the compressor's speed transitions, rather than just focusing on low RPMs (for the sake of Energy Label claim), is crucial for balancing effective performance with user satisfaction and preventing a poor overall product image.

In summary, as it was presented, the control algorithm adaptation becomes another interesting aspect of acoustic and vibrations optimization and a battlefield between the manufacturers trying to achieve customer greater satisfaction with the product. Consequently, manufacturers can improve acoustic performance without additional expenses, making it a practical and cost-efficient solution.

5. REFERENCES

[1] S. Fatima, A. Mohanty, S. Paradhe, and S. T. Tamizharasan, "Vibro-acoustic source path characterization of a domestic refrigerator," 20th International Congress on Sound and Vibration 2013, ICSV 2013, vol. 2, pp. 1265–1272, Jan. 2013.

[2] R. Zárate-Espinosa, J. Poblet-Puig, M. Ortega, and M. Parra, "Case study: Experimental characterization of noise and vibration sources in a refrigerator," Noise Control Engineering Journal, vol. 69, pp. 477–489, Nov. 2021, doi: 10.3397/1/376945.

[3] S. Wu, J. Luo, and Y. Li, "Study on Vibrations of Inverter Refrigerator Compressor," presented at the 23nd International Compressor Engineering Conference, Purdue, 2016

[4] "Embraco - Variable Speed Solutions." Accessed: Feb.24, 2025. [Online]. Available:

https://materials.refrigerationclub.com/embracovariblespeed

[5] Atamer, Serkan, Piotr Kosowski, and Ercan Altinsoy. "A study on the perception of refrigerator noise in everyday life." INTER-NOISE and NOISE-CON Congress and Conference Proceedings. Vol. 270. No. 4. Institute of Noise Control Engineering, Nantes, 2024

[6] You, Jin, and Jin Yong Jeon. "Just noticeable differences in sound quality metrics for refrigerator noise." Noise Control Engineering Journal 56., 414-424, 2008

[7] IEC 60704-2-14:2013. "Household and Similar Electrical Appliances - Test Code for the Determination of Airborne Acoustical Noise - Part 2-14: Particular Requirements for Refrigerators, Frozen-Food Storage Cabinets and Food Freezers." International Electrotechnical Commission, 2013

[8] "ECMA-418-2 :Psychoacoustic Metrics for ITT equipment - Part 2, Methods for Describing Human Perception Based on the Sottek Hearing Model, 3rd edition" 2024.

[9] Schwarz, M. "Variable Capacity Compressors, a new dimension for refrigeration engineers to explore." Embraco 111 (2001)

DOI: 10.61782/fa.2025.0312

FORUM ACUSTICUM EURONOISE 2025

DOUBLE AND SINGLE ELASTIC SUPPORT FOR LARGE GENERATOR SETS

Sergio Anda[1*]
[1] Technical & Sales Manager, Viblens, Spain

ABSTRACT

Currently, when a high-level vibration and shock attenuation is required, a two-level series isolation (2 degree of freedom system) to get the highest filtration (very characteristic of naval environment). The present document shows a study case from the beginning selecting the best antivibration strategy to reach the targets.

Keywords: *bench, double, vibration, shock, 2DOF*.

1. INTRODUCTION

Large diesel generator sets generate considerable dynamic forces due to combustion, rotating mass imbalance, and torque pulsations. To prevent the transmission of vibrations and shocks to the surrounding structure, elastic support systems are employed. These systems, often using elastomeric or spring-type isolators, aim to reduce the transmissibility of both steady-state vibrations and transient shocks. In marine and industrial installations, proper mounting design is critical not only for operational efficiency but also for structural integrity, acoustic comfort, and to reduce noise radiated into the water.

This paper presents a comparative analysis between single and double elastic support configurations, focusing on a case study with a 10,000 kg generator set. The study first evaluates three different masses for the base frame in a single elastic support system. Then, a second stage of elastic isolation is introduced by adding an intermediate mass, forming a double elastic support configuration. The results illustrate the influence of support design on vibration isolation performance.

2. THEORETICAL BACKGROUND

2.1 Single Elastic Support

In a single elastic support configuration, the generator and its base frame are mounted on a set of vibration isolators directly coupled to the final foundation (either a ship structure or building). This forms a single-degree-of-freedom (SDOF) system. The vibration isolation depends on the ratio between the excitation frequency and the natural frequency of the mounted system, with better performance achieved when the natural frequency is much lower than the excitation frequency.

The natural frequency is calculated by Eqn. (1):

$$f_n = \frac{1}{2\pi}\sqrt{\frac{k}{m}} \tag{1}$$

Where k is the stiffness of the isolators and m is the total suspended mass.

The transmissibility T of the system, which expresses the ratio of transmitted force to input force, is given by Eqn. (2):

$$T = \frac{\sqrt{1+(2\zeta r)^2}}{\sqrt{(1-r^2)^2+(2\zeta r)^2}} \tag{2}$$

Where:

$$r = \frac{f}{f_n} \tag{3}$$

- Υ is the frequency ratio
- ζ is the damping ratio
- f is the excitation frequency
- f_n is the natural frequency

*Corresponding author: sergio.anda@viblens.com
Copyright: ©2025 First author et al. This is an open-access article distributed under the terms of the Creative Commons Attribution 3.0 Unported License, which permits unrestricted use, distribution, and reproduction in any medium, provided the original author and source are credited.

As the excitation frequency increases beyond the natural frequency (especially for $r > \sqrt{2}$), the transmissibility drops below 1, indicating effective vibration isolation.

2.2 Double Elastic Support

A double elastic support introduces an intermediate base frame between two sets of isolators, effectively creating a two-degree-of-freedom (2DOF) system. This configuration allows for two distinct natural frequencies, offering improved isolation over a wider frequency range. However, it also introduces a second resonance that must be carefully managed through system tuning and damping.

Double elastic systems are especially effective in environments with strict vibration or shock limits, such as naval vessels or high-precision industrial setups.

3. CASE STUDY: 10,000 KG GENERATOR SET

3.1 Introduction

The isolators used in this study are Willbrandt SES 5010 series, selected based on the expected load per support and mounting layer:

3.1.1 First layer (primary supports)
Willbrandt SES 5010 55 ShA – designed for lower load per mount and optimized for vibration isolation.

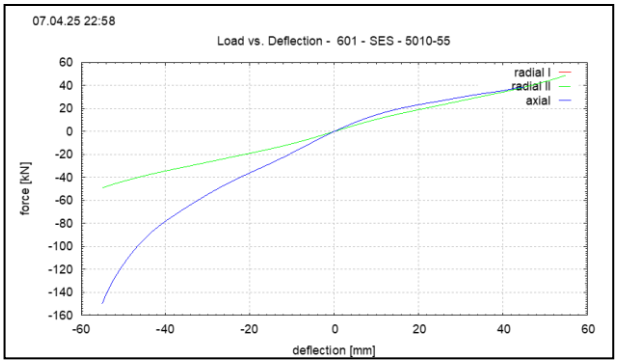


Figure 1. Load vs Deflection SES 5010 55Sh

3.1.2 Second layer (secondary supports):
Willbrandt SES 5010 65 ShA – suited for higher loads and structural damping.

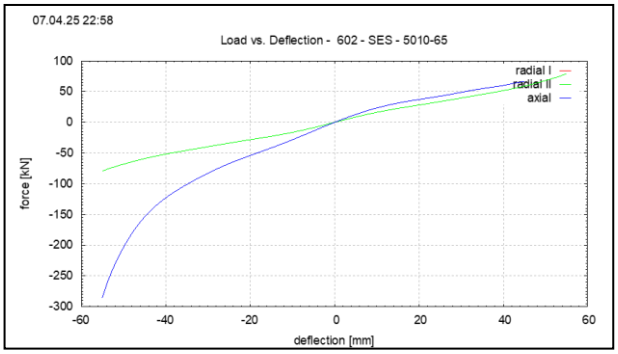


Figure 2. Load vs Deflection SES 5010 65Sh

3.2 Configuration Overview

A generator set with a total mass of 10,000 kg (engine + alternator) is considered. The analysis proceeds in two phases:

3.2.1 Phase 1: Single Elastic Support

The generator is mounted on three different base frames to study the effect of base mass on isolation. The entire set (generator + base) is mounted on a single layer of vibration isolators.

Table 1. Single Elastic Support Configurations

Case	Generator Mass (kg)	Base Frame Mass (kg)	Total Suspended Mass (kg)	Base Mass Ratio
1	10,000	1,000	11,000	10%
2	10,000	2,000	12,000	20%
3	10,000	4,000	14,000	40%

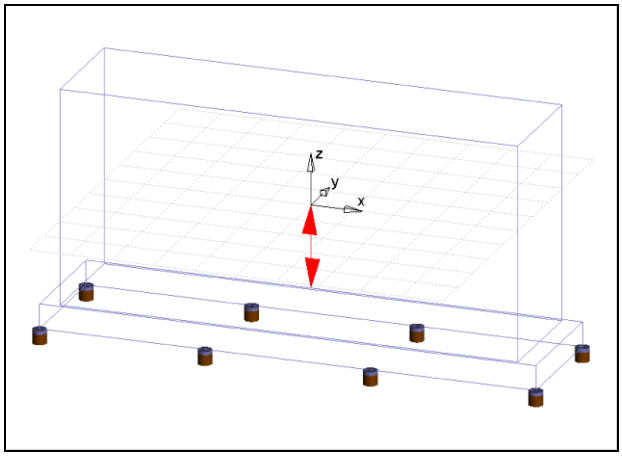


Figure 3. Full assembly view (single elastic configuration)

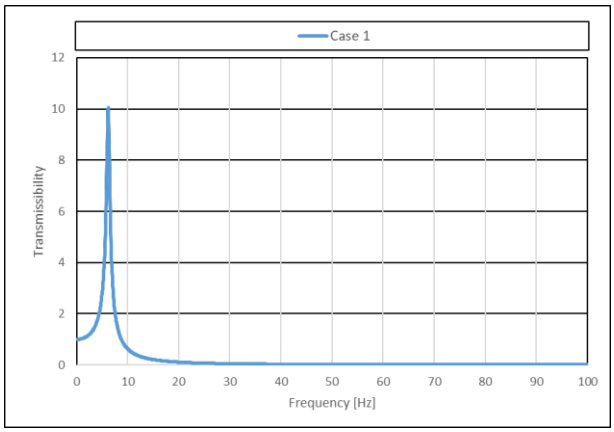


Figure 4. Case 1 transmissibility (vertical axis)

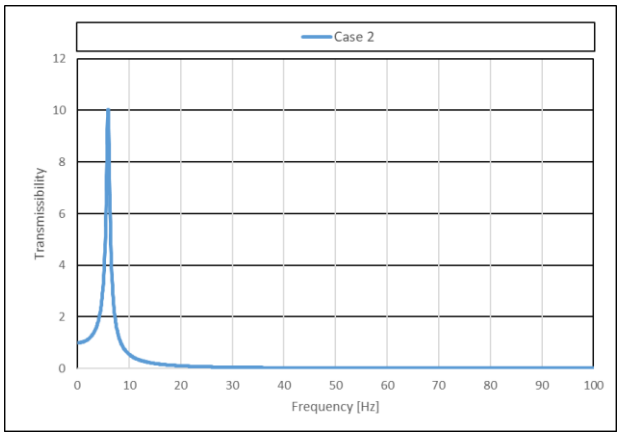


Figure 5. Case 2 transmissibility (vertical axis)

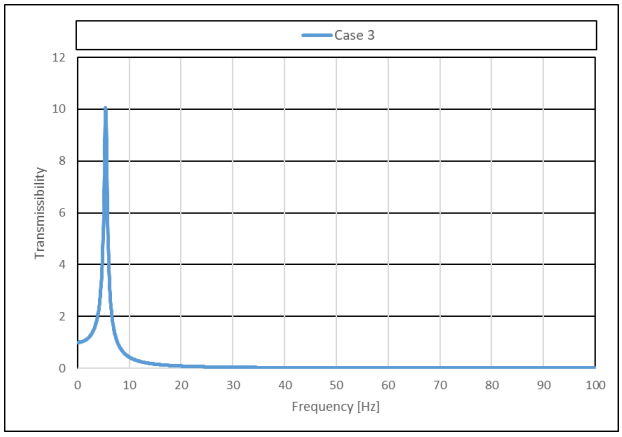


Figure 6. Case 3 transmissibility (vertical axis)

3.2.2 Phase 2: Double Elastic Support

For each configuration from Phase 1, a second base frame weighing 1,000 kg is added below a new layer of isolators. This forms a two-stage isolation system.

Table 2. Double Elastic Support Configurations

Case	Generator Mass (kg)	Base Frame Mass (kg)	Total Suspended Mass (kg)
1+BF2	11,000	1,000	12,000
2+BF2	12,000	1,000	13,000
3+BF2	14,000	1,000	15,000

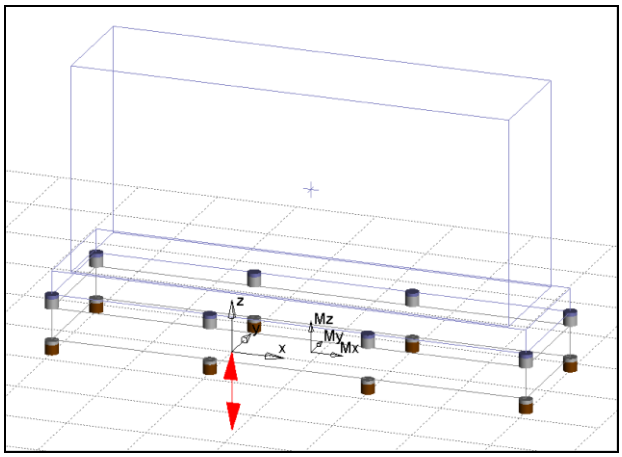


Figure 7. Full assembly view (double elastic configuration)

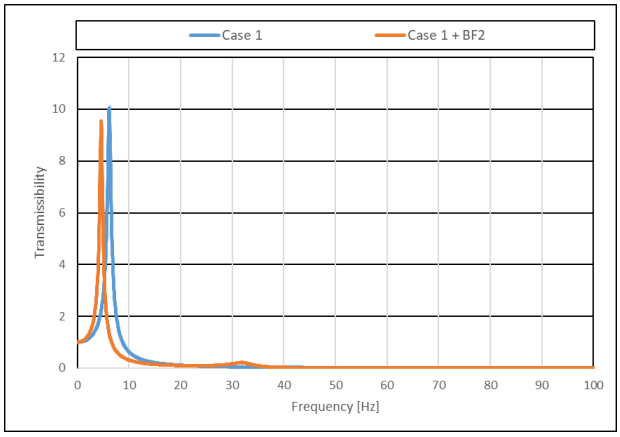


Figure 8. Case 1 and Case 1 + BF2 transmissibility (vertical axis)

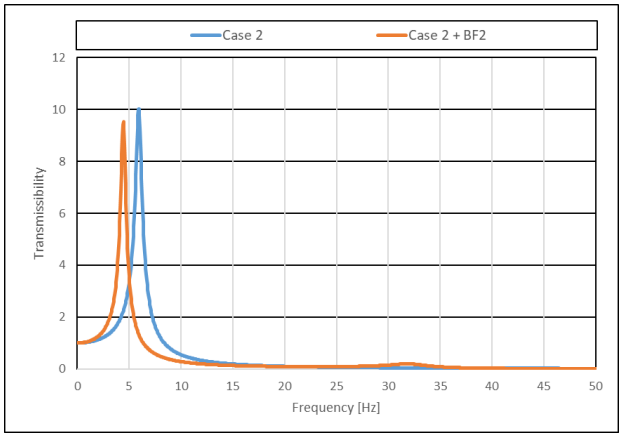


Figure 11. Case 2 and Case 2 + BF2 transmissibility (vertical axis)

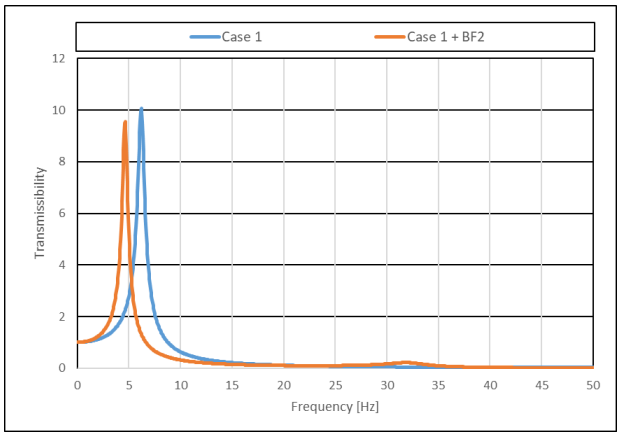


Figure 9. Case 1 and Case 1 + BF2 transmissibility (vertical axis)

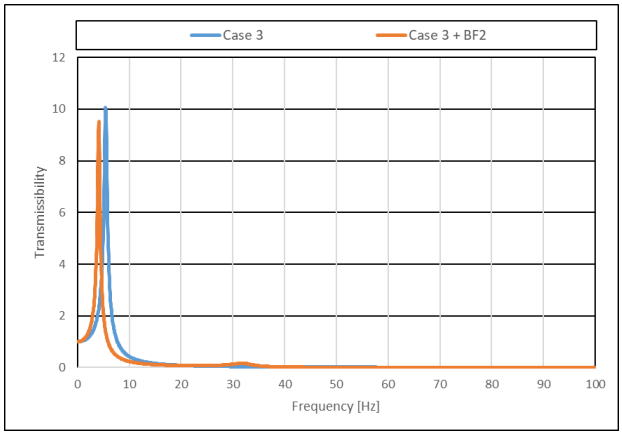


Figure 12. Case 3 and Case 3 + BF2 transmissibility (vertical axis)

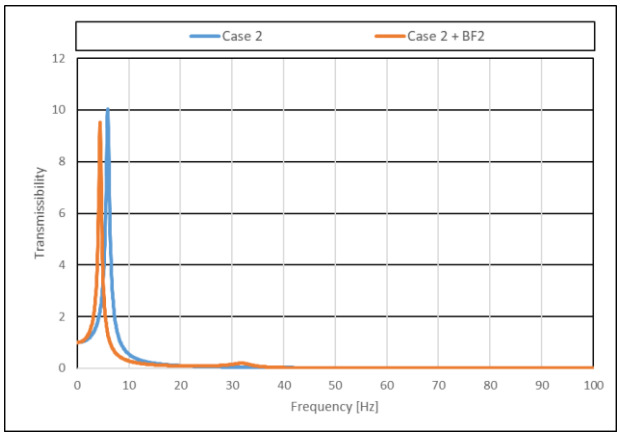


Figure 10. Case 2 and Case 2 + BF2 transmissibility (vertical axis)

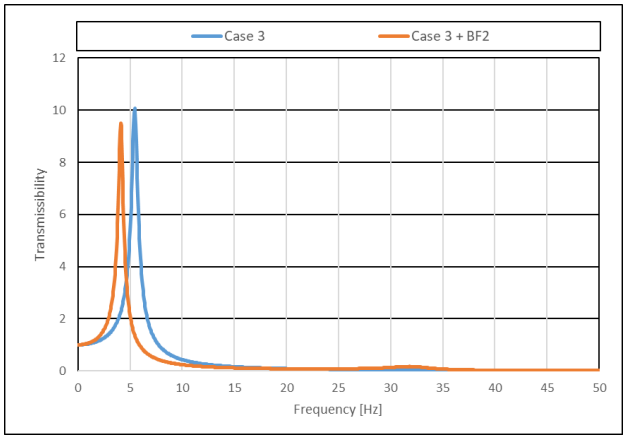


Figure 13. Case 3 and Case 3 + BF2 transmissibility (vertical axis)

4. COMPARATIVE DISCUSSION

The results show that increasing the base frame mass in a single support system effectively lowers the system's natural frequency, improving vibration isolation. However, this comes at the cost of added weight and structural demands. Introducing a second elastic support stage significantly improves isolation, particularly from approximately twice the natural frequency, due to the cascading effect of two mass-spring stages.

The double support reduces transmissibility by increasing system compliance and energy absorption capacity. This makes it ideal for marine environments where shock events are common.

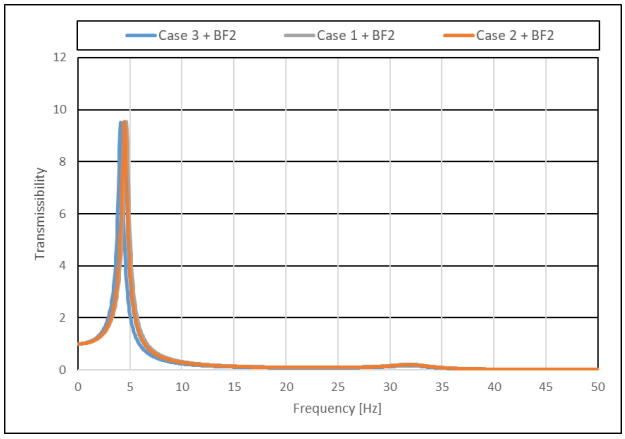


Figure 14. Cases 1, 2 and 3 + BF2 transmissibility (vertical axis)

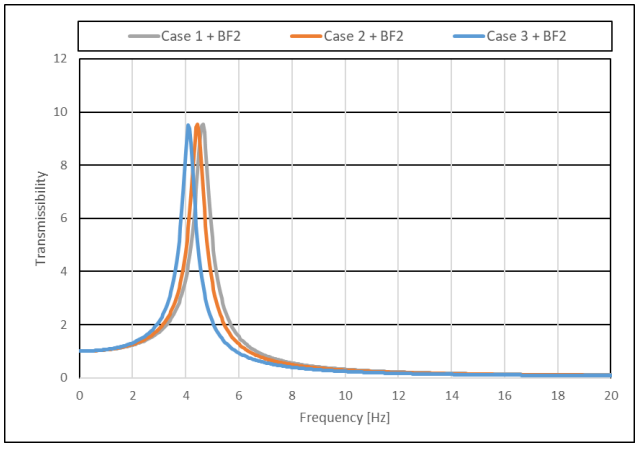


Figure 15. Cases 1, 2 and 3 + BF2 transmissibility (vertical axis)

5. CONCLUSIONS

Elastic mounting systems are essential for protecting structures and machinery from harmful vibrations and shocks. This study demonstrates how base frame mass impacts isolation in single elastic support systems and highlights the superior performance of double elastic support configurations.

For the 10,000 kg generator analyzed, using a base frame of 1,000–4,000 kg already yields substantial improvement, and adding a 1,000 kg intermediate frame further enhances isolation. These results support the adoption of double elastic support in high-demand installations, especially where acoustic, vibratory, or shock criteria are stringent.

6. REFERENCES

[1] ISO 20154:2017 – Mechanical vibration – Measurement and evaluation of vibration isolation systems.

[2] MTU Friedrichshafen GmbH – Installation Guidelines for Marine Generator Sets.

[3] Caterpillar Inc. – Generator Set Mounting and Vibration Control Guidelines.

[4] Engineering Dynamics Inc. – Practical Solutions for Machinery Isolation and Shock Protection.2.

[5] WILLBRANDT Shock absorbers (German/English) - S10201 – Technical brochure

DOI: 10.61782/fa.2025.0210

FORUM ACUSTICUM EURONOISE 2025

COMBINED THERMAL AND ACOUSTIC DESIGN OF ENCLOSURES FOR OUTDOOR APPLICATIONS

Edoardo A. Piana[1*] **Jorge Joaquin Garcia**[1]
Diego Tonetti[1] **Roberto Spezie**[2]

[1] Applied Acoustic Laboratory, University of Brescia, Italy
[2] TERNA Rete Italia S.p.A., Rome, Italy

ABSTRACT

One of the most effective methods to control the noise spreading of sound sources is to put them inside sound-absorbing/insulating enclosures. When such sources also generate a certain amount of heat, the panels separating the source and the receiver must be provided with ventilation openings that can greatly reduce the effectiveness of the enclosure from an acoustic point of view. The issue gets significantly more difficult if the system must be installed outdoors and only natural convection is to be used, as this requires taking into account the effects of wind, air temperature, and solar radiation. All these factors usually require increasing the dimensions of the openings and then a lower sound attenuation. The framework used to conduct a combined thermodynamic and acoustic investigation on a high-voltage device that produces impulsive sound and is intended for placement in residential areas is described in this paper.

Keywords: *high voltage switchgear, dynamic thermal analysis, sound insulation, noise spreading.*

1. INTRODUCTION

The availability of electricity and the possibility of dispatching it in a safe and sensible way, depending on the customers' needs, is becoming fundamental. In the past years, TERNA Rete Italia S.p.A. developed a number of solutions to improve the lines capacity [1] and to maintain the network with real-time operations [2].
In this framework, the new Compact Pole System (CPS) project was recently presented. The idea is to be able to install the switchgear needed for the operations also in urban areas, close to the receivers. Being the switches high-voltage elements that need to be protected from undesired access and based on mechanical parts producing impulsive noise, it is important to place these elements inside an enclosure. On the other hand, the heat generated by the high-voltage elements needs to be dissipated outside the volume of the enclosure. A further difficulty is that the CPS could be placed in any type of environment. This means that it must withstand not only low temperatures, but mainly the components must be able to survive the typical summer temperatures and the heat caused by the radiation of the sun. In this framework, it is necessary to perform a thermal study that considers not only the environmental variables but also the thermal characteristics of the materials used to assemble the building. Moreover, some openings are necessary to guarantee the heat exchange, and such openings must be small enough to avoid noise spreading from the switchgear to the surrounding area.
The paper is organized as follows: Section 2 describes the building where the CPS is located, and the thermal/sound sources placed inside. Section 3 shows the thermal model implemented in Energy+. Section 4 illustrates the acoustic model for the noise spreading. Section 5 discusses the thermal and acoustic results. Finally, Section 5 concludes the work.

[*] ***Corresponding author***: edoardo.piana@unibs.it.
Copyright: *©2025 Edoardo A. Piana et al. This is an open-access article distributed under the terms of the Creative Commons Attribution 3.0 Unported License, which permits unrestricted use, distribution, and reproduction in any medium, provided the original author and source are credited.*

2. DESCRIPTION OF THE CSP BUILDING AND OF THE THERMAL/ACOUSTIC SOURCES

The system is made of:
- a main volume, containing the switchgear and the accessories, called the GIS room;
- some panels with aesthetic functions, placed at 40 cm from the GIS room walls;
- a steel framework;
- a shelter containing the accessory devices.

Figure 1 shows an outline of the system.

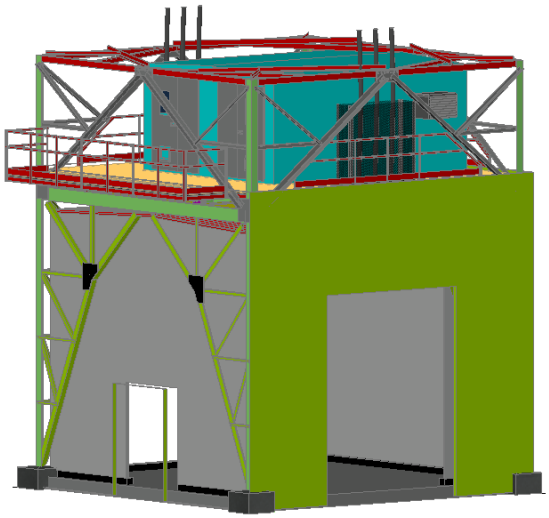


Figure 1. 3D outline of the system.

The green panels of Figure 1 are placed in the lower part of the trellis and have an aesthetic purpose. They are attached to the trellis beams and conceal a second set of inner panels, forming the vertical walls of the GIS room. The big hatch is normally closed and is used for the maintenance of the switchgear placed inside, while the small door is used for the access of the personnel. Above the GIS room is placed a small shelter, hosting the control and service devices.

The foot plant of the GIS room is 8 x 8 m^2, with a height of 6.5 m. To guarantee a sufficient number of air changes per hour due to natural convection, and thus the cooling of the high voltage devices, some openings are placed on two opposite sides of the room. These openings, represented in Figure 2, are:

- two inlets, placed in the lower part of the front side (dimensions 3.125 x 0.5 m^2);
- an outlet, in the higher part of the panel opposite the one where the inlets are located (dimensions 0.675 x 7.0 m^2).

The inlets are symmetrical to the vertical centreline of the panel. The openings will be protected by grilles, introducing a pressure drop of about 20 Pa. The position and dimensions of the openings have been decided after some fluid dynamic simulations carried out with COMSOL Multiphisics® in order to obtain a fair distribution of the air flows inside the GIS room.

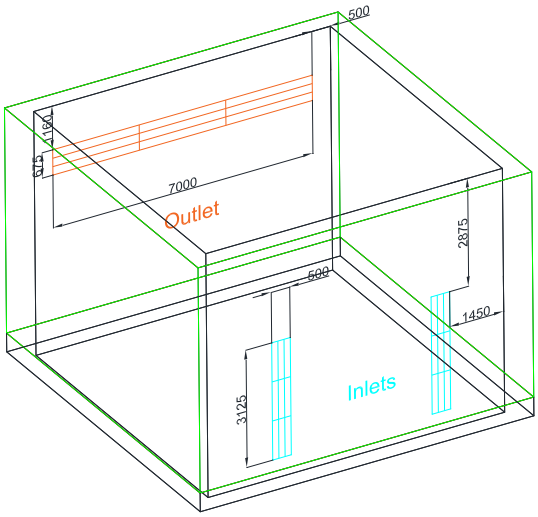


Figure 2. Positions of the inlets and the outlets.

3. THERMAL MODEL

The CPS will be subject to interactions with the environment: temperature changes, radiation of the sun, and wind. All these elements change with time and are a function of the location selected for the system. Using a finite element model such as COMSOL to predict the thermal behavior of the system is particularly challenging if the effect of non-stationary weather conditions must be captured. For this reason, after performing a validation of the COMSOL model [3], it was decided to switch to EnergyPlus. This software allows an estimation of the temperature inside the GIS room in non-stationary conditions. For this reason, EnergyPlus takes into account both the thermal conductivity and the thermal capacity of the walls. The assumptions adopted for the simulations are the following:

- Location: Catania. The weather data have been retrieved from those available from the local airport.
- To consider the increase of the temperature due to global warming, the weather data have been morphed to

simulate the conditions in 2050 (https://energy.soton.ac.uk/ccworldweathergen/)
- Time span for the calculation: solar year (01 January – 31 December)
- Time step: hour + day
- Aesthetic panels: trapezoidal steel sheet 1 mm; rockwool, density 70 kg/m^3, thickness 78 mm; perforated sheet steel, thickness 1 mm – overall thickness 80 mm.
- GIS room panels: trapezoidal steel sheet 1 mm; rockwool, density 70 kg/m^3, thickness 48 mm; perforated sheet steel, thickness 1 mm – overall thickness 50 mm.
- Distance between the aesthetic walls and the walls of the GIS room: 400 mm
- Height of the aesthetic panels from the floor: 500 mm
- Model used for the airflow in EnergyPlus: Airflow Network
- WindPressureCoefficientArray computed using fluid dynamic simulations (Figure 3) carried out on the system for 5 different angles of incidence of the wind on the structures (Table 1).

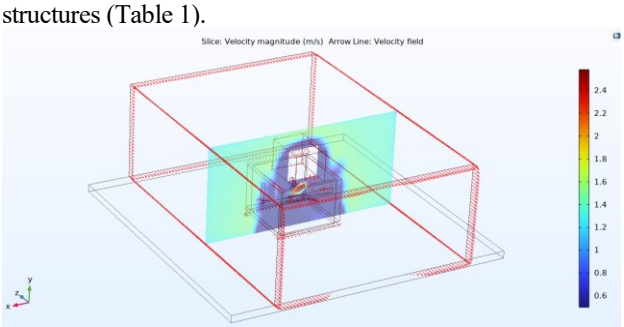


Figure 3. Example of fluid dynamic simulation for the computation of the wind pressure coefficients.

Table 1. Wind pressure coefficients.

	Wind pressure coefficients	
Angle of incidence	Inlet	Outlet
0	-1.99636	-1.09497
23	-1.08254	-0.14105
45	-5.79697	.1026984
68	0.38094	0.610374
90	0.14567	0.824607

- Thermal power to be dissipated in the GIS room: 5300 W
- The assumptions made allow us to consider also the effect of the wind
- The temperature computed by EnergyPlus must be intended as the average temperature inside the GIS room

4. ACOUSTIC MODEL

After defining the thermal characteristics of the CPS, it is possible to move on to the acoustic simulations. First, it is necessary to feed the simulation program with the acoustic emission characteristics of the source. For this purpose, the measurements conducted in the field for the switchgear of a specific supplier were used. On that occasion, the sound energy during the opening (O) and closing (C) events of the actuators was estimated. These characteristics were then composed to obtain the sound energy of an OCO+2CO event. Based on the hypotheses made with TERNA regarding the standard operations, this sequence occurs every 15 minutes.
As regards the sound power level to be associated with the sources was:

- Event power level OCO+2CO in 15 minutes = 93.2 dB(A)
- Event power level OCO+2CO diluted in 8 hours (night period) = 84.2 dB(A)

The spectrum associated with the events is reported in Figure 4, representing the average sound pressure level measured on the envelope surface during the tests.

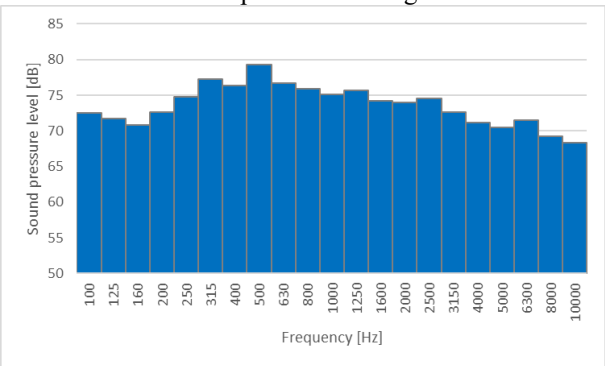


Figure 4. Spectrum used for the power levels.

The characteristics of the panels were derived, based on what was established for the thermal part, from the Metecno catalog for the "Wall Panel" type of products with the thicknesses indicated in the previous section. Figure 5 and Figure 6 show the graphs of the sound absorption and sound insulation offered by the Metecno panels respectively. These values were inserted into Ramsete to carry out simulations of the sound pressure level propagating outside the GIS room. The software can consider the diffraction effect and the transmission effect at the same time.

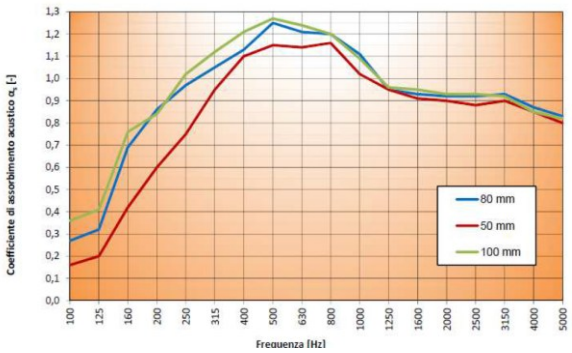


Figure 4. Sound absorption of the panels.

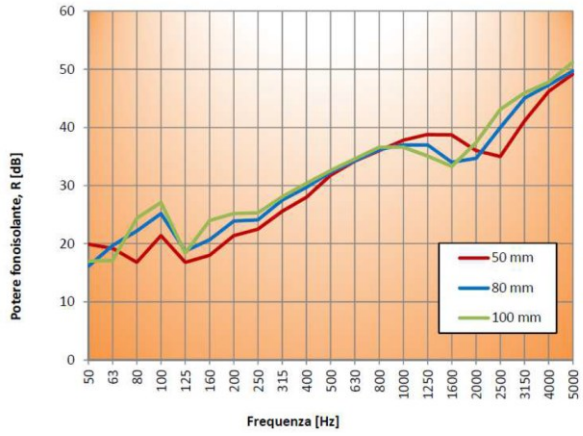


Figure 5. Sound insulation of the panels.

In Ramsete, the following assumptions were adopted:
- Insulation of the GIS room panels equal to that of the 50 mm Metecno panels
- Insulation of the openings equal to 0 dB
- Absorption of the GIS room panels and aesthetic panels equal to the absorption declared for the 50 and 80 mm panels
- Calculations at the receivers made at distances of 15 and 30 m and at heights of 2 m, 5 m, 8 m and 11 m.
- Distribution of sound pressure levels symmetrical to the axis that joins the two faces with the vents (only the series of receivers placed on the right side will be considered)

5. THERMAL AND ACOUSTIC RESULTS

Figure 6 shows the average temperature inside the GIS room on a 1-hour basis during the year. The limit temperature given by the company making the switchgear is 40 °C. It can be observed that this temperature is exceeded only in limited times:

o at 14.00 - 06 July (T_in=40.0 °C) with an outdoor temperature T_out=37.1 °C
o at 11.00 - 9 August (T_in=40.5 °C) with an outdoor temperature T_out=37.7 °C
o at 11.00 - 18 August (T_in=40.3 °C) with an outdoor temperature T_out=37.4 °C

Moreover:
- The thermal inertia of the panels leads to a phase shift in the thermal load due to solar radiation
- The maximum air speed in the inlet openings corresponds to 0.3 m/s for a volumetric flow rate of approximately 0.5 m^3/s

Since suppliers also ask not to exceed 35 °C of average temperature during the 24 hours, in Figure 7 the annual trend of the average daily temperatures is reported. The limit value of 35 °C is never exceeded.

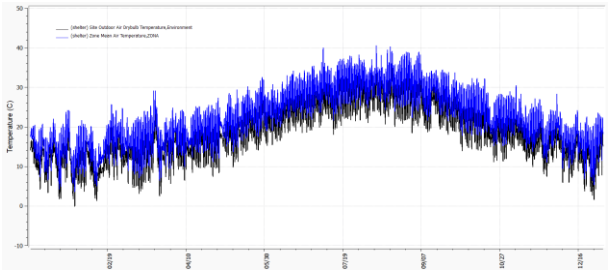


Figure 6. Indoor (blue line) and outdoor (black line) profiles with 1 hour time step.

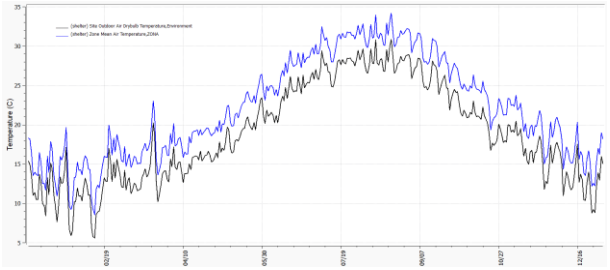


Figure 7. Indoor (blue line) and outdoor (black line) profiles with 1 day time step.

As concerns the acoustic results, Figure 8 shows the result of the simulation made with Ramsete. According to Italian legislation, the results of the simulations were compared to the emission, immission, and differential limits.
- Emission: is to be intended as the sound pressure level emitted only by the specific sound source to be investigated
- Immission: is the energetic sum of the sound pressure level emitted by the specific sound source that is intended to be investigated with the background sound pressure level

- Differential: difference between the immission levels and the background noise level (algebraic difference)

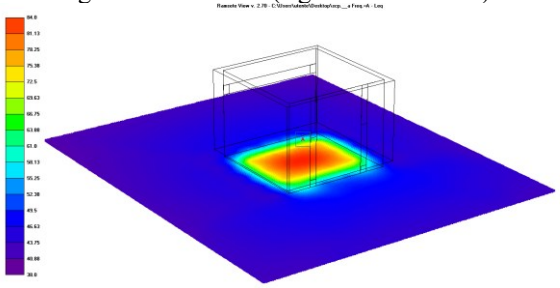


Figure 8. Sound pressure level computed by Ramsete.

The emission and immission limits are a function of the acoustic class being investigated and must be evaluated by diluting the source's contribution over the 16 hours for the daytime period (6-22) and 8 hours for the night-time period (22-6). The tables below provide the limit values and the predicted ones. The limits are based on the acoustic classes established by the Municipality where the installation will take place.

The differential must instead be evaluated in correspondence with the living environments and must not exceed 5 dB during the day and 3 dB during the night.

Table 2 shows, for the various measurement points considered, the values of the sound pressure levels estimated by the calculation code for the dilution of an event in 8 hours and for 15 minutes.

Table 2. Emission values and comparison with the legislation limits. A green cell indicates the limits are fulfilled.

Punto di stima	SPL(dB(A)) per 8 ore	SPL(dB(A))-15'	Classe I	Classe II	Classe III	Classe IV	Classe V	Classe VI
I15_2	19.9	29.3	35	40	45	50	55	65
I15_5	20.3	30.7	35	40	45	50	55	65
I15_8	21.4	32.8	35	40	45	50	55	65
I15_11	22.1	34	35	40	45	50	55	65
I30_2	14.6	24.6	35	40	45	50	55	65
I30_5	14.9	25.6	35	40	45	50	55	65
I30_8	16	26.4	35	40	45	50	55	65
I30_11	16.4	28.2	35	40	45	50	55	65
L15_2	18.7	28.8	35	40	45	50	55	65
L15_5	19.2	30.2	35	40	45	50	55	65
L15_8	21.2	32.4	35	40	45	50	55	65
L15_11	23.4	33.7	35	40	45	50	55	65
L30_2	13.7	24.6	35	40	45	50	55	65
L30_5	14	25.5	35	40	45	50	55	65
L30_8	15.8	26.3	35	40	45	50	55	65
L30_11	16.3	28.1	35	40	45	50	55	65
O15_2	20.2	32.6	35	40	45	50	55	65
O15_5	21	33.1	35	40	45	50	55	65
O15_8	22.2	34	35	40	45	50	55	65
O15_11	22.9	34.8	35	40	45	50	55	65
O30_2	15	27.1	35	40	45	50	55	65
O30_5	15.4	27.6	35	40	45	50	55	65
O30_8	16.5	28	35	40	45	50	55	65
O30_11	17	29.2	35	40	45	50	55	65

The estimation points are indicated with a code of the type XDIST_h where:

- X can assume the values: I (inlet face), L (lateral face), or O (outlet face)
- DIST indicates the distance from the side of the GIS room at which the estimate was performed (15 m or 30 m)
- h indicates the height from the ground at which the estimate was performed (2 m, 5 m, 8 m or 11 m).

It can be observed that the emission limits are always respected.

As regards the immission values, given by the energetic sum of emissions and background noise, some assumptions must be made on the value of the residual noise level, which depends on the position of the area considered, the quality of the acoustic classification, and the presence of sources in neighbouring areas. Since the most critical period is the night-time period, the assessment was made only in that period. In the calculations, the assumption was made that the residual noise is 5 dB lower than the night-time emission limit for the area considered.

Table 3 shows the immission values calculated for the various points and the class limits. In this case, the limit values are respected for all points. The values shown in grey are lower than the limit of applicability of the differential with open windows for the night-time period.

Table 3. Immission values and comparison with the legislation limits. A green cell indicates the limits are fulfilled.

Punto di stima	Classe I	Classe II	Classe III	Classe IV	Classe V	Classe VI	Classe I	Classe II	Classe III	Classe IV	Classe V	Classe VI
I15_2	32.7	36.0	40.4	45.1	50.0	60.0	40	45	50	55	60	70
I15_5	33.4	36.4	40.5	45.2	50.1	60.0	40	45	50	55	60	70
I15_8	34.6	37.0	40.8	45.3	50.1	60.0	40	45	50	55	60	70
I15_11	35.5	37.5	41.0	45.3	50.1	60.0	40	45	50	55	60	70
I30_2	31.1	35.4	40.1	45.0	50.0	60.0	40	45	50	55	60	70
I30_5	31.3	35.5	40.2	45.0	50.0	60.0	40	45	50	55	60	70
I30_8	31.6	35.6	40.2	45.1	50.0	60.0	40	45	50	55	60	70
I30_11	32.2	35.8	40.3	45.1	50.0	60.0	40	45	50	55	60	70
L15_2	32.5	35.9	40.3	45.1	50.0	60.0	40	45	50	55	60	70
L15_5	33.1	36.2	40.4	45.1	50.0	60.0	40	45	50	55	60	70
L15_8	34.4	36.9	40.7	45.2	50.1	60.0	40	45	50	55	60	70
L15_11	35.2	37.4	40.9	45.3	50.1	60.0	40	45	50	55	60	70
L30_2	31.1	35.4	40.1	45.0	50.0	60.0	40	45	50	55	60	70
L30_5	31.3	35.5	40.2	45.0	50.0	60.0	40	45	50	55	60	70
L30_8	31.5	35.5	40.2	45.1	50.0	60.0	40	45	50	55	60	70
L30_11	32.2	35.8	40.3	45.1	50.0	60.0	40	45	50	55	60	70
O15_2	34.5	37.0	40.7	45.2	50.1	60.0	40	45	50	55	60	70
O15_5	34.8	37.2	40.8	45.3	50.1	60.0	40	45	50	55	60	70
O15_8	35.5	37.5	41.0	45.3	50.1	60.0	40	45	50	55	60	70
O15_11	36.0	37.9	41.1	45.4	50.1	60.0	40	45	50	55	60	70
O30_2	31.8	35.7	40.2	45.1	50.0	60.0	40	45	50	55	60	70
O30_5	32.0	35.7	40.2	45.1	50.0	60.0	40	45	50	55	60	70
O30_8	32.1	35.8	40.3	45.1	50.0	60.0	40	45	50	55	60	70
O30_11	32.6	36.0	40.3	45.1	50.0	60.0	40	45	50	55	60	70

As regards the comparison with the differential limit, the same assumptions made for the calculation of the emissions regarding the residual noise level apply. Since the most critical period is the night-time, the evaluation was made only considering a maximum differential of 3 dB. Table 4 shows the result of this calculation. The cells for which the value is higher than the legal limit for Class I (3 dB) have been highlighted in red, while the numerical values shown in grey refer to those points where the differential cannot be

applied because the emissions are lower than 40 dB(A) with the windows open.
The result is that, only for Class I there are exceedances below 15 m of distance. For the higher classes (II - V) the differential is always respected.

Table 2. Differential and comparison with the legislation limits.

	Differenziale Classe I	Differenziale Classe II	Differenziale Classe III	Differenziale Classe IV	Differenziale Classe V
I15_2	2.7	1.0	0.4	0.1	0.0
I15_5	3.4	1.4	0.5	0.2	0.1
I15_8	4.6	2.0	0.8	0.3	0.1
I15_11	5.5	2.5	1.0	0.3	0.1
I30_2	1.1	0.4	0.1	0.0	0.0
I30_5	1.3	0.5	0.2	0.0	0.0
I30_8	1.6	0.6	0.2	0.1	0.0
I30_11	2.2	0.8	0.3	0.1	0.0
L15_2	2.5	0.9	0.3	0.1	0.0
L15_5	3.1	1.2	0.4	0.1	0.0
L15_8	4.4	1.9	0.7	0.2	0.1
L15_11	5.2	2.4	0.9	0.3	0.1
L30_2	1.1	0.4	0.1	0.0	0.0
L30_5	1.3	0.5	0.2	0.0	0.0
L30_8	1.5	0.5	0.2	0.1	0.0
L30_11	2.2	0.8	0.3	0.1	0.0
O15_2	4.5	2.0	0.7	0.2	0.1
O15_5	4.8	2.2	0.8	0.3	0.1
O15_8	5.5	2.5	1.0	0.3	0.1
O15_11	6.0	2.9	1.1	0.4	0.1
O30_2	1.8	0.7	0.2	0.1	0.0
O30_5	2.0	0.7	0.2	0.1	0.0
O30_8	2.1	0.8	0.3	0.1	0.0
O30_11	2.6	1.0	0.3	0.1	0.0

6. CONCLUSIONS

The non-stationary thermal simulations have provided comforting results, with occasional exceedances of the maximum temperature of 40 °C in the hypothesis of placing the SCP in Catania and projection of meteorological data to 2050. As regards the acoustic part, having maintained the size and position of the ventilation openings as studied with the thermal analyses, there would be exceedances of the legal limits only for the receptors positioned below 15 m. and belonging to Class I.

7. REFERENCES

[1] M.R. Guarniere, F. Palone, R. Spezie, L. Buono, L. Papi, G. Tresso, S. Lauria, M. Maccioni, Loadability curves for the new Terna's "5F" high capacity overhead lines, in: 2023 IEEE Int. Conf. Environ. Electr. Eng. 2023 IEEE Ind. Commer. Power Syst. Eur. EEEIC ICPS Eur., IEEE, Madrid, Spain, 2023: pp. 1–6. https://doi.org/10.1109/EEEIC/ICPSEurope57605.2023.10194723.

[2] E.A. Piana, F. Bignucolo, A. Donini, R. Spezie, Maintenance of a high-voltage overhead transmission line: Sustainability and noise impact assessment, Sustain. Switz. 10 (2018). https://doi.org/10.3390/su10020491.

[3] S. Basu, E. Piana, Thermal and Acoustic Design of a Shelter for High-Voltage Electrical Equipment, Appl. Sci. 15 (2025) 957. https://doi.org/10.3390/app15020957.

DOI: 10.61782/fa.2025.0099



FORUM ACUSTICUM
EURONOISE 2025

ACTIVE STRUCTURAL ACOUSTIC CONTROL WITH REMOTE MICROPHONE TECHNIQUE FOR NOISE RADIATED BY A THIN PLATE

Francesco Mori[1*] **Andrea Santoni**[1] **Cristina Marescotti**[1]
Patrizio Fausti[1] **Francesco Pompoli**[1] **Pietro Nataletti**[2] **Paolo Bonfiglio**[3]
[1] Department of Engineering, University of Ferrara, Italy
[2] INAIL, National Institute for Insurance against Accidents at Work, Rome, Italy
[3] Materiacustica srl, Via C. Ravera 15/A, Ferrara, Italy

ABSTRACT

Noise pollution in industrial environments can significantly impact workers' health and productivity, necessitating effective control measures. This preliminary study investigates the feasibility of an active structural acoustic control (ASAC) system to mitigate noise radiated by an industrial cabin wall. A cabin mock-up was created for this purpose, designed with passive acoustic treatments to improve noise insulation on three walls, the floor and the roof. Conversely, one of the cabin walls was realized with a thin steel plate without passive acoustic treatments. The ASAC system, applied to this plate, uses a single inertial actuator to suppress noise induced by an acoustic source inside the cabin and radiated to the external environment. The system employs the remote microphone technique (RMT) to attenuate the noise at a specific distance from the cabin. The experimental validation was conducted for different types of disturbing noise signals. The results highlight the potentiality of this method to control radiated noise. This work lays the foundation for scalable ASAC solutions in industrial environments, offering a promising path toward quieter workplaces.

Keywords: *industrial cabin, active structural acoustic control, FXLMS algorithm, remote microphone technique*

[*] ***Corresponding author***: *francesco.mori@unife.it.*
Copyright: *©2025 Francesco Mori et al. This is an open-access article distributed under the terms of the Creative Commons Attribution 3.0 Unported License, which permits unrestricted use, distribution, and reproduction in any medium, provided the original author and source are credited.*

1. INTRODUCTION

In industrial environments, enclosures are commonly used to reduce airborne noise propagation and workers' exposure. These structures typically consist of a mass-spring-mass system, with an outer continuous plate, an inner perforated plate inside and a fibrous material in between, acting as both a spring of the system and noise absorber. However, these enclosures can often have untreated parts, such as panels and windows, reducing the overall effectiveness. In such cases, an active structural acoustic control (ASAC) system can help mitigate low-frequency noise radiation toward the external environment. An ASAC system employs one or more actuators on a vibrating surface to generate an anti-vibration signal that counteracts noise radiation. This signal is computed in real-time through an adaptive algorithm after the acquisition of some signals from error and reference sensors, similarly to an active noise control (ANC) system. Literature discourages the use of accelerometers as error sensors due to the need of multiple sensors and actuators [1]. Several studies explored the optimization of number and placement of actuators on radiating surfaces [2]. However, practical industrial applications [3] remain limited compared to numerical studies and laboratory experiments.

This study, part of the BRIC Inail 2022 ID-11 project, investigates the feasibility of applying an ASAC system to an industrial cabin mock-up. The system was applied on a thin steel plate representing one cabin wall, radiating noise generated by a simulated source enclosed in the cabin and emitting different types of signals. The system operates in a feedforward configuration with one reference microphone inside the cabin, one inertial actuator on the radiating plate and one error microphone near the outer plate. Additionally, a remote microphone technique (RMT) was employed for

far-field noise attenuation [4] and feedback compensation was used to prevent reference signal corruption [5]. The implemented adaptive algorithm was the filtered-X least mean squares (FXLMS) [6], chosen for its simple scalability for further developments. Section 2 provides an overview of the case study, detailing the ASAC system design and the implemented algorithm. Section 3 presents the study findings, including the preliminary characterization of the impulse responses and the attenuation obtained for different noise signals. Finally, Section 4 outlines the conclusions and potential future developments to enhance the system performance.

2. EXPERIMENTAL SETUP AND ASAC SYSTEM

The tests were conducted on the reproduction of an industrial enclosure, as shown in Fig. 1. The structure measures 1.5 × 1.5 × 2.0 m and features a 1 mm-thick steel plate on one side. The remaining walls and the roof are made of similar steel plates, internally treated with sound-absorbing fibrous material and a metallic mesh. Conversely, the floor features a 5 mm-thick steel plate instead of the metallic mesh. Inside the enclosure, an acoustic dodecahedron reproduces synthetized signals and recordings of industrial machineries as a simulated noise source.

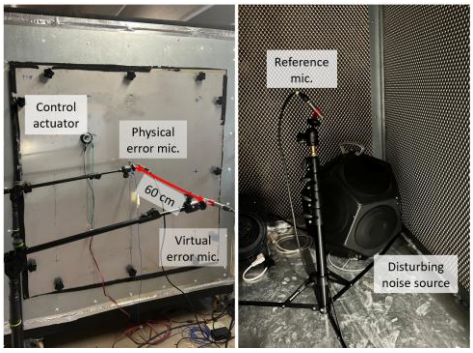


Figure 1. Experimental setup outside and inside the enclosure.

The ASAC system was implemented on the steel plate in a feedforward configuration. The reference microphone was placed inside the cabin, near the noise source. The inertial actuator, generating the control signal, was selected based on the frequency response comparison of several actuators and placed on the plate away from the edges, where distortions were observed in some preliminary tests probably related to the boundary rigidity. The system adopts the remote microphone technique (RMT), which virtualizes the error microphone position to prevent a physical obstacle during the real application [4]. In this setup, the physical error microphone was placed outside, near the steel plate, while the virtual error microphone was positioned 60 cm from the surface. The entire ASAC system is driven by a NI cRIO 9063 real-time target, acquiring and generating signals at a 3200 Hz sampling rate. Due to this rate and device placement, the system does not meet the causality constraint, making it ineffective for unpredictable signals. The algorithm employed to compute the adaptive filter was the feedforward filtered-X least mean squares with acoustic feedback compensation (FF_FBFXLMS) [5], chosen to prevent reference signal corruption caused by plate excitation.

The whole procedure executed by the ASAC system is hereinafter described. In a preliminary stage, the virtual and physical secondary paths (s_v and s_p respectively) and the feedback path (f) are estimated generating a white noise with the control source and computing the filter with a least mean square (LMS) approach [6]. Similarly, the virtual and physical primary paths (p_v and p_p) are estimated emitting white noise with the disturbing source. The impulse response h_{pv} between the physical and the virtual positions can be derived from the ratio of the two primary paths in the frequency domain. After this stage, the virtual error microphone is no longer involved in the ASAC operations and assumes a simple monitoring function. During the online operations, the ASAC system works iteratively as follows:

- the reference signal $u(n)$ is acquired and the contribution from the control actuator is subtracted:

$$x(n) = u(n) - f * y(n), \tag{1}$$

  where $y(n)$ is the output of the control source and $*$ is the convolutional operator.
- The disturbing signal in the physical position is computed from the physical error signal $e_p(n)$ as:

$$d_p(n) = e_p(n) - s_p * y(n). \tag{2}$$

- The virtual error signal $e_v(n)$ is evaluated as:

$$e_v(n) = h_{pv} * d_p(n) + s_v * y(n). \tag{3}$$

- The FXLMS computes the adaptive filter and drives the inertial actuator with the classical

procedure, using the virtual error signal $e_v(n)$ and the cleaned reference signal $x(n)$ as inputs.

3. RESULTS

3.1 Estimation of the impulse responses

The secondary and primary paths, used for the identification of the system impulse responses, are illustrated in Fig. 2 and Fig. 3, respectively, for both the physical and the virtual positions. These functions are shown in terms of transfer function magnitude in the frequency domain for easier interpretation. As can be observed, the secondary paths exhibit higher amplitude than the primary paths across the entire spectrum. This means that for equal power of the sources, actuator saturation can be avoided. The amplitude at the virtual position is lower than at the physical position due to the larger distance from the radiating surface. Fig. 4 shows the feedback path. The contribution of the control actuator on the reference microphone is particularly relevant at low frequency (< 50 Hz). However, its importance depends on the noise level produced by the disturbing source. A filter length of 2000 elements was assumed for primary, secondary and feedback paths.

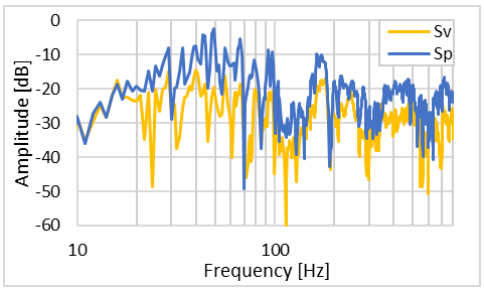


Figure 2. Physical and virtual secondary paths.

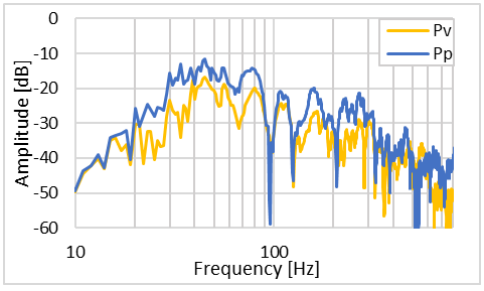


Figure 3. Physical and virtual primary paths.

The transfer function H_{pv} (with a capital letter to indicate the frequency domain) used to model the disturbance signal at the virtual position, is reported in Fig. 5. This function was obtained as the ratio between the spectra of the virtual and the physical primary paths. A positive value means that the sound pressure level at the virtual position assumes a larger value with respect to the physical position for that frequency. It should be noted that this function models the acoustic field at the virtual position starting from the sensing of the acoustic field in one point near the radiating plate. However, the noise at the virtual position can be radiated from different points of the plate. Thus, this function considers only a part of the disturbing noise. A filter length of 500 elements was considered for the physical-virtual impulse response.

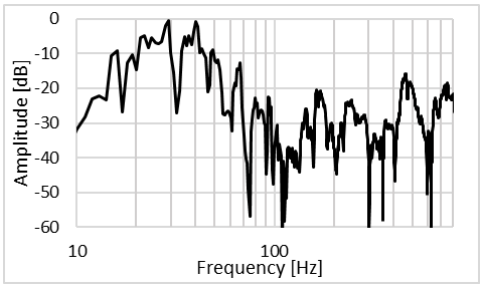


Figure 4. Feedback path.

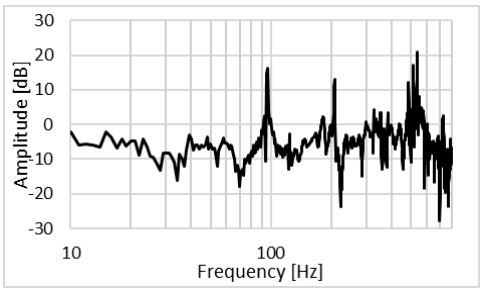


Figure 5. Physical-virtual transfer functions.

3.2 Attenuation of noises

The results obtained with different pure tones are shown in Tab. 1. These frequencies were selected as the central frequencies of the third octave bands within the range of interest, independently of the plate modal frequencies.
The ASAC system successfully attenuates noise at the virtual position for all the tones, except for the 125 Hz frequency, where a slight amplification occurs. This particular tone is characterized by a low level on the primary paths. Thus, the estimation of H_{pv} at that frequency can be not accurate. The 160 Hz tone coincides with a

radiating mode, as indicated by the peaks in the primary and secondary path spectra.
Secondly, a pseudo-random noise signal was used for the performance evaluation. This signal contains a broad frequency range but maintains a periodic pattern, repeating every 0.2 s. The results for this signal are shown in Fig. 6. In this case, the ASAC system faces more difficulties in providing a good performance, although noise attenuation is observed across all the bands of interest. This results in an overall noise attenuation of 1.6 dB – 1.9 dB(A).
Finally, Fig. 7 shows the effect of the ASAC system on the noise generated by an industrial compressor. The system reduces noise across the bands from 80 Hz to 500 Hz, especially on the main components at 80 Hz and 200 Hz, achieving an overall attenuation of 3.5 dB – 2.9 dB(A).

Table 1. Attenuation for different pure tones.

Frequency [Hz]	125	160	200	250	315	400
Attenuation [dB]	-2.3	4.8	3.9	7.0	13.6	2.4

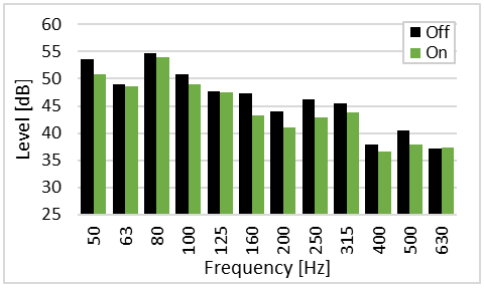


Figure 6. Results for a pseudo-random noise signal.

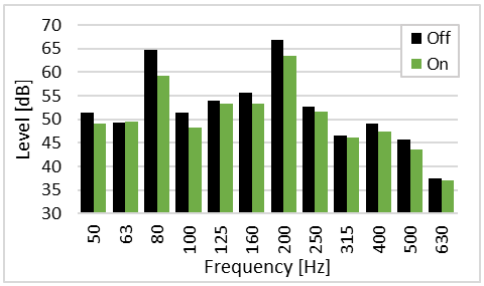


Figure 7. Results for an industrial compressor recording.

4. CONCLUSIONS

In this paper, an experimental study on the potentiality of a feedforward ASAC system with RMT and feedback compensation was analyzed. The results show that the ASAC system can act on all the components in the frequency range of interest, when the physical-virtual impulse response in effectively modelled. No tests with pure broadband signals were carried out, since the causality constraint was not respected. However, the ASAC system was effective in the cases of a pseudo-random noise signal and industrial compressor recording. The possible future steps of this study could regard the optimization of number and placement of error microphones and actuators, for extending the zone of quiet at the virtual position. Furthermore, tests with actuators applied to the treated panels could be explored.

5. ACKNOWLEDGMENTS

This work was supported by the BRiC 2022 ID-11 project from INAIL (National Institute for Insurance against Accidents at Work).

6. REFERENCES

[1] V.L. Metcalf, C.R. Fuller, R.J. Silcox, and D.E. Brown: "Active control of sound transmission/radiation from elastic plates by vibration inputs, II: Experiments", *J. Sound Vib.*, Vol. 153, no. 3, pp. 387-402, 1992.

[2] S. Wrona, and M. Pawelczyk: "Experimental investigation on inertial actuators arrangement optimization for active control applications", in *Proc. of Forum Acusticum 2023,* (Turin, Italy), 2023.

[3] S. Wrona: "Performance analysis of active structural acoustic control applied to a washing machine", *Sensors*, Vol. 22, no. 7357, 2022.

[4] J. Cheer, and S. Daley: "Active structural acoustic control using the remote sensor method", *J. Phys.: Conf. Ser.*, Vol. 744, no. 012184, 2016.

[5] F. Mori, A. Santoni, P. Fausti, F. Pompoli, P. Bonfiglio, and P. Nataletti: "The effectiveness of least mean squared-based adaptive algorithms for active noise control system in a small confined space", *App. Sci.*, Vol. 13, no. 11173, 2023.

[6] S.M. Kuo, I. Panahi, K.M. Chung, T. Horner, M. Nadeski, and J. Chyan: *Design of active noise control systems with the TMS320 family*, Texas Instruments, 1996.

DOI: 10.61782/fa.2025.0276

FORUM ACUSTICUM EURONOISE 2025

DESIGN OF A TRIPOD VIBRATION ACTUATOR FOR ACTIVE REDUCTION METHODS

Stanislaw Wrona[1*] **Federico Caroppo**[2] **Rocco Scarano**[2]
Marek Pawelczyk[1]

[1] Silesian University of Technology, Department of Measurements and Control Systems, Gliwice, Poland
[2] Politecnico di Milano, Department of Mechanical Engineering, Milan, Italy

ABSTRACT

Every active noise and vibration reduction system needs actuators capable of controlling the considered vibroacoustic system. Structural actuators are commonly utilized for this purpose. Inertial actuators are particularly convenient to use due to their simple audio-type amplifiers and relatively low cost. However, due to the fact that they are relying on inertia in order to generate force, they are rather inefficient for lowest frequencies. In this paper a novel concept is investigated, which adds a tripod structure to the seismic mass, allowing controlled structure displacement even for a constant voltage. Advantages and drawbacks of such a design are investigated numerically and experimentally.

Keywords: *mathematical modelling, actuation, experimental measurements*

1. INTRODUCTION

Vibration and noise control are vital aspects of many engineering applications, ranging from industrial machinery in manufacturing facilities to everyday household appliances. Effectively managing vibrations, and the noise they generate, has long been a focus of research aimed at enhancing both performance and acoustic comfort.

The most practical strategy for noise reduction is to address it directly at the source. While passive vibration and sound-absorbing materials are commonly used for this purpose, they come with significant limitations—particularly at low frequencies, where their effectiveness drops considerably. Achieving sufficient attenuation at these frequencies often requires barriers that are impractically thick or heavy. These constraints have driven growing interest in active control systems, which can effectively target low-frequency noise and serve as a valuable complement to passive solutions in areas where they fall short [1]. In recent years, various solutions have been developed [2], in which actuators are used to control the vibrations of thin barriers, thereby reducing both noise transmission and acoustic radiation. Numerous applications use thin panels and shells as sound barriers to reduce the spread of acoustic noise [3, 4]. Such an approach can be applied to many different types of structures, including aircraft fuselage [5, 6]. To improve the effectiveness of these barriers, active control systems with inertial actuators can are used. When applied to individual panels or entire device casings, active structural acoustic control (ASAC) systems exhibit superior performance [7]. However, to ensure efficient operation of an active system, the actuators must be efficiently controlling vibrations.

This paper introduces the design and preliminary analysis of a novel tripod-supported electromagnetic actuator intended to improve the effectiveness of vibration control, especially in the case of thin metal plates. Conventional electromagnetic inertial actuators often face challenges due to their single-point actuation, which can result in poor force transmission when placed on vibrational nodal lines. The proposed tripod structure overcomes this limitation by distributing the actuation force across multiple contact points, increasing the system's adaptability to various vibrational modes and enabling the use of a single actuator where traditionally multiple actuators might be required for successful vibration control.

*__Corresponding author__: stanislaw.wrona@polsl.pl.
__Copyright__: ©2025 Stanislaw Wrona et al. This is an open-access article distributed under the terms of the Creative Commons Attribution 3.0 Unported License, which permits unrestricted use, distribution, and reproduction in any medium, provided the original author and source are credited.

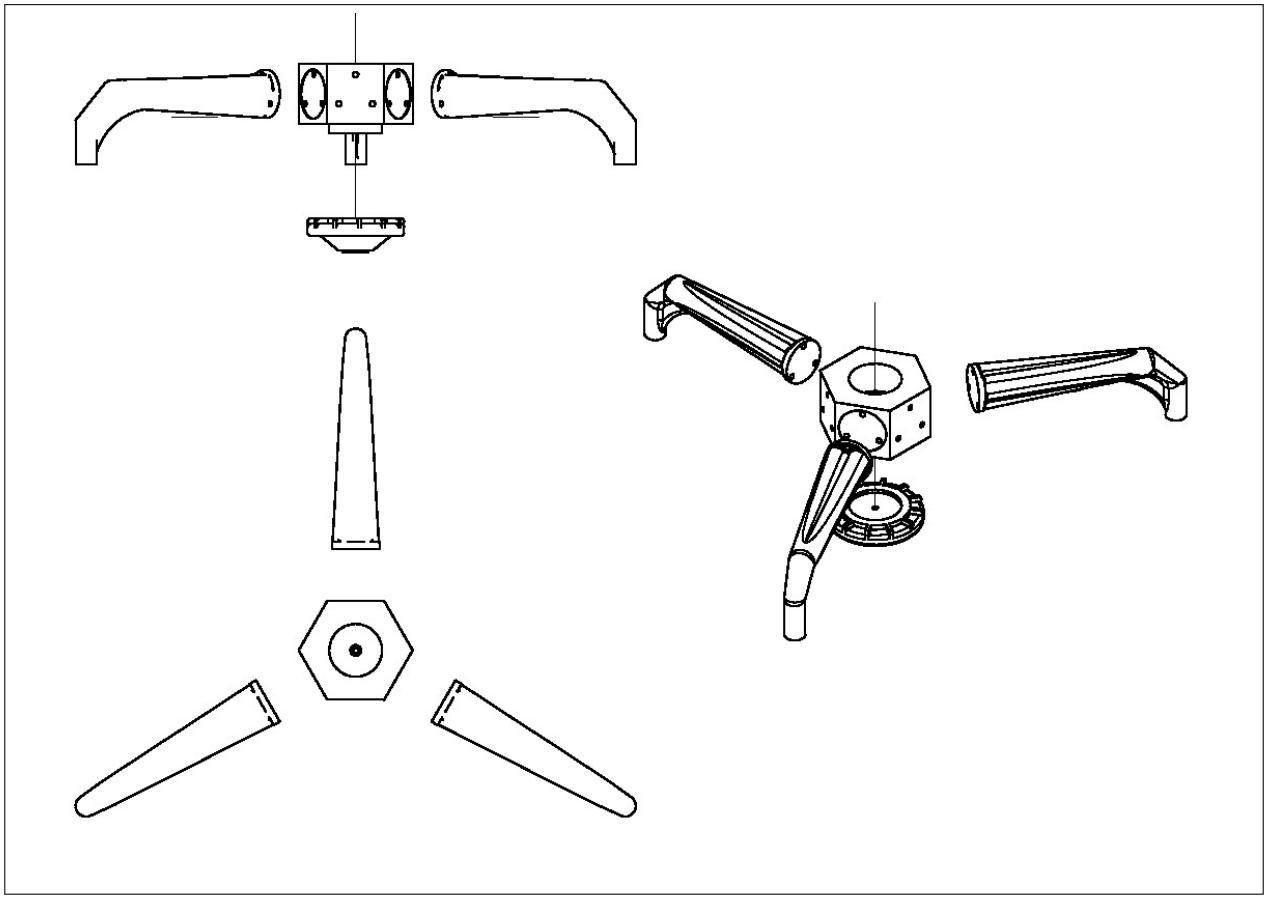


Figure 1. Schematic of a tripod structure attached to the inertial actuator. [8]

2. TRIPOD-SUPPORTED ELECTROMAGNETIC ACTUATOR

This study focuses on a novel electromagnetic actuator design that does not require a grounded frame for installation, nor relies on inertia. Instead, it can be directly mounted onto the target structure using a magnetic attachment system (employing neodymium magnets attracted to steel structures). The actuator features a unique tripod geometry, making contact with the vibrating structure at four distinct points: three legs provide mechanical support and anchorage, while a central piston, also magnetically coupled to the target structure, is actively driven by a control signal. As the piston applies force, a reactive force is simultaneously generated through the legs, resulting in a distributed stress and strain pattern across the contact area. This interaction enables the actuator, which becomes an integral part of the structure, to bend the target itself using it as the supporting frame. Conceptual schematic of the actuator is shown in Figure 1. The design is intended to deliver substantial actuation force and displacement, promoting consistent control over a distributed surface area. This minimizes the risk of ineffective operation due to the piston coinciding with a vibrational nodal line.

The prototype of the actuator, presented in Figs. 2-3, consists of 3D-printed body (the hexagonal central part), to which three 3D-printed legs are attached. To the bottom of the body, a formerly inertial actuator Dayton Audio DAEX32EP-4 if firmly attached, acting now as a voice coil actuator driving the piston.

Utilization of a ready-made inertial actuator not only solves difficulties in manufacturing our own dedicated voice coil actuator. It also allows a fair comparison of the exactly same actuator operating based on inertia principle and employing the tripod support.



Figure 2. Prototype of the actuator attached to the steel metal plate in the test rig.

3. EXPERIMENTAL MEASUREMENTS

In order to experimentally evaluate the performance of the actuator, it was attached to a thin steel plate of dimensions 420 mm × 420 mm × 1 mm. The plate was rigidly clamped to a heavy frame, as depicted in Fig. 3. The actuator has been evaluated in three configurations. The first consisted in using the actuator in its original form, basing of the inertia principle. In the second configuration, the 3D-printed hexagonal body was attached to the actuator. The actuator still operated basing of the inertia principle, but this test was done of investigate the impact of adding an extra mass to the actuator. Finally, in the third configuration, the legs have been attached, altering the actuator's operating principle. The actuator, in this paper, was always mounted centrally on the plate.

Two main measurement series were done for each aforementioned configurations. In the first series, the actuator excited the plate with a frequency sweep, generating single tone at a time, in the range between 20 Hz and 500 Hz, with an increment of 2 Hz. The vibrations of the excited plate were measurement with a laser vibrometer PDV-100 centrally, at the location of the actuator's piston. Based on this series, both excitation efficiency and non-

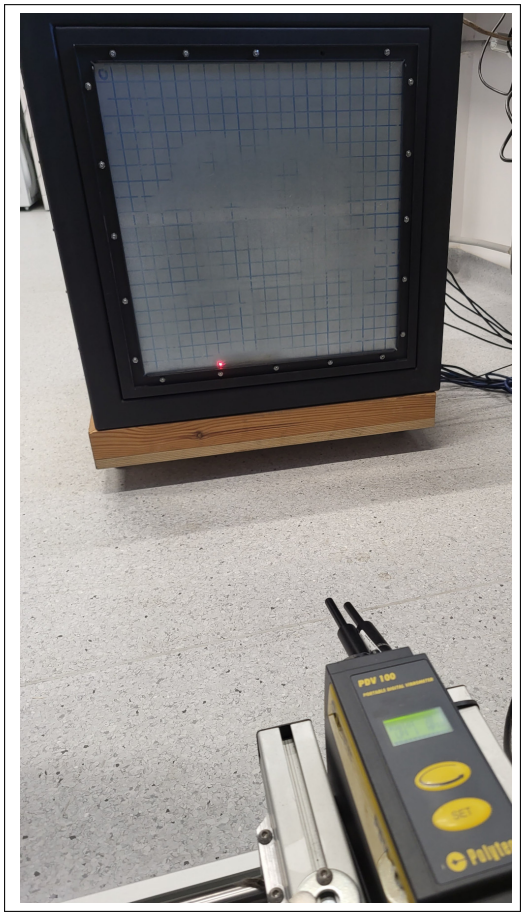


Figure 3. Other side of the steel metal plate, which vibrations are measured with a laser vibrometer PDV-100.

linearity was studied. The obtained plots are presented in Figs. 4-6. The Total Harmonic Distortion (THD) measure was calculated based on the following equation:

$$\mathrm{THD} = \frac{\sqrt{V_2^2 + V_3^2 + V_4^2 + \cdots}}{V_1}, \tag{1}$$

where V_n is the RMS value of the n^{th} harmonic voltage, and V_1 is the RMS value of the fundamental tone.

The second series was measured for a plate exposed to a broadband signal, exciting all frequencies in the considered frequency range at once. Then, the laser vibrometer measured vibrations at a grid of 22 × 22 points, uniformly distributed over the plate with an interval of 20 mm. The surface-averaged vibration frequency response of the plate

is presented in Fig. 7. This series allowed to capture all excited modes, showing a certain advantage of the tripod support—the third configuration of the actuator allowed to control more modes in the same frequency range than former two configurations. This leads to a conclusion that the multiple points of contact prevents the lack of controllability for certain modes with a nodal line going through the actuator's piston. The actual modes of the plates with and without the tripod support cannot be directly compared, because the presence itself of the additional structure at the plate surface alters its mode shapes, but there were no uncontrollable modes observed for the tripod configuration, which were present in the case of the former two actuator configurations.

4. CONCLUSIONS

This paper presented the design and preliminary analysis of a novel tripod-supported electromagnetic actuator. A series of tests were carried out to evaluate its performance. While the tripod configuration successfully excited multiple target modes at very low frequencies, the improvement over conventional inertial actuators was somewhat less than initially anticipated. However, the tripod configuration allowed to control more modes in the considered frequency range than the former two configurations, most probably due to multiple points of contact with the plate.

Another key outcome of the study was the measurement of Total Harmonic Distortion (THD), where the tripod actuator demonstrated significantly lower nonlinearity within the same frequency range compared to the inertial type. This results in notable benefits for signal fidelity, system efficiency, and operational stability. An actuator with low THD maintains signal clarity, allowing for accurate transfer of vibrational energy with minimal spectral distortion. This improves control precision, reduces unwanted harmonic components, and enhances the predictability of system behavior.

Although in this paper the actuator has been centrally mounted on the plate, it is noteworthy that the further study should involve the optimization of the tripod position and orientation, taking into account the overall mathematical model of the plate and attached actuator [9].

5. ACKNOWLEDGMENTS

The work was supported by the project IN-NOVA: Active reduction of noise transmitted into and from enclosures through encapsulated structures, which has received funding from the European Union's Horizon Europe programme under the Marie Sklodowska-Curie grant agreement no. 101073037.

6. REFERENCES

[1] K. Mazur, S. Wrona, and M. Pawelczyk, "Performance evaluation of active noise control for a real device casing," *Applied Sciences*, vol. 10, no. 1, p. 337, 2020.

[2] Q. Mao, "Improvement on sound transmission loss through a double-plate structure by using electromagnetic shunt damper," *Applied Acoustics*, vol. 158, p. 107075, 2020.

[3] B. Lam, W.-S. Gan, D. Shi, M. Nishimura, and S. Elliott, "Ten questions concerning active noise control in the built environment," *Building and Environment*, vol. 200, p. 107928, 2021.

[4] C. W. Isaac, M. Pawelczyk, and S. Wrona, "Comparative study of sound transmission losses of sandwich composite double panel walls," *Applied Sciences*, vol. 10, no. 4, p. 1543, 2020.

[5] X.-X. Xie, Z.-X. Yuan, and W.-B. Shangguan, "Sound transmission loss of a metal panel with rib reinforcements and pasted damping," *International Journal of Acoustics and Vibration*, vol. 25, no. 4, pp. 513–525, 2020.

[6] M. Misol, "Full-scale experiments on the reduction of propeller-induced aircraft interior noise with active trim panels," *Applied Acoustics*, vol. 159, p. 107086, 2020.

[7] S. Wrona, M. Pawelczyk, and L. Cheng, "Sound transmission through a panel with a hybrid active and semi-active control system," *Journal of Sound and Vibration*, p. 117172, 2022.

[8] R. Scarano, *A novel tripod electromagnetic actuator designed to control vibrations of a thin metal plate*. Politecnico di Milano, Milan, Italy: Master's thesis, 2025.

[9] F. Caroppo, *Modeling of a Novel Voice Coil Actuator for Noise and Vibration Control of Thin Plates*. Politecnico di Milano, Milan, Italy: Master's thesis, 2025.

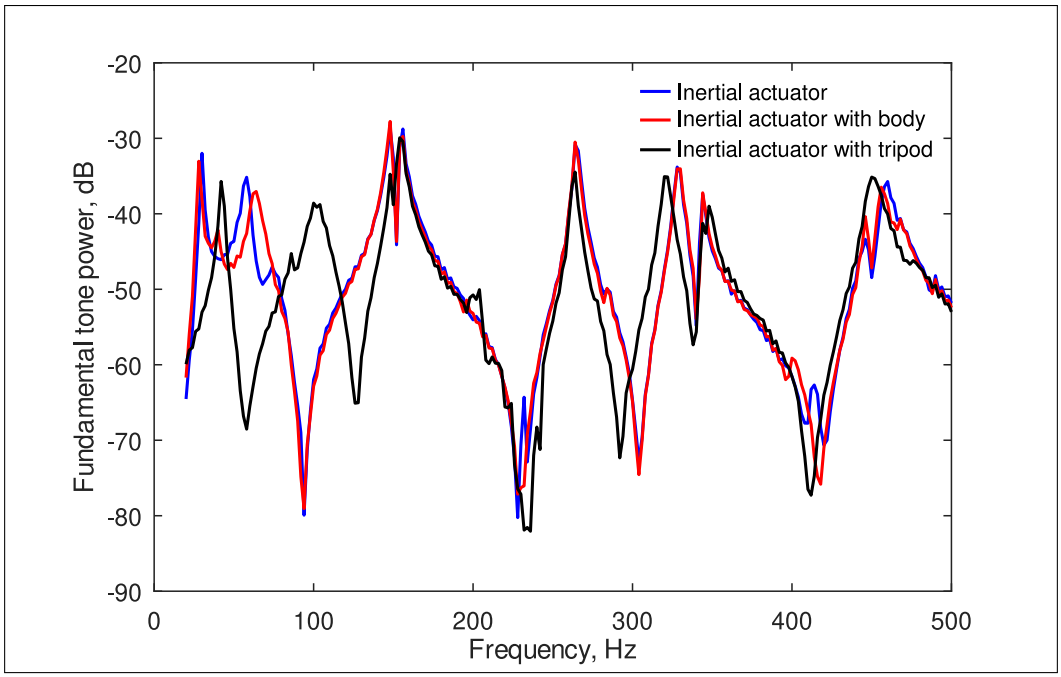


Figure 4. Fundamental frequency power of the three configurations of the actuator. The resulted were obtained using the frequency-sweep excitation by the actuator.

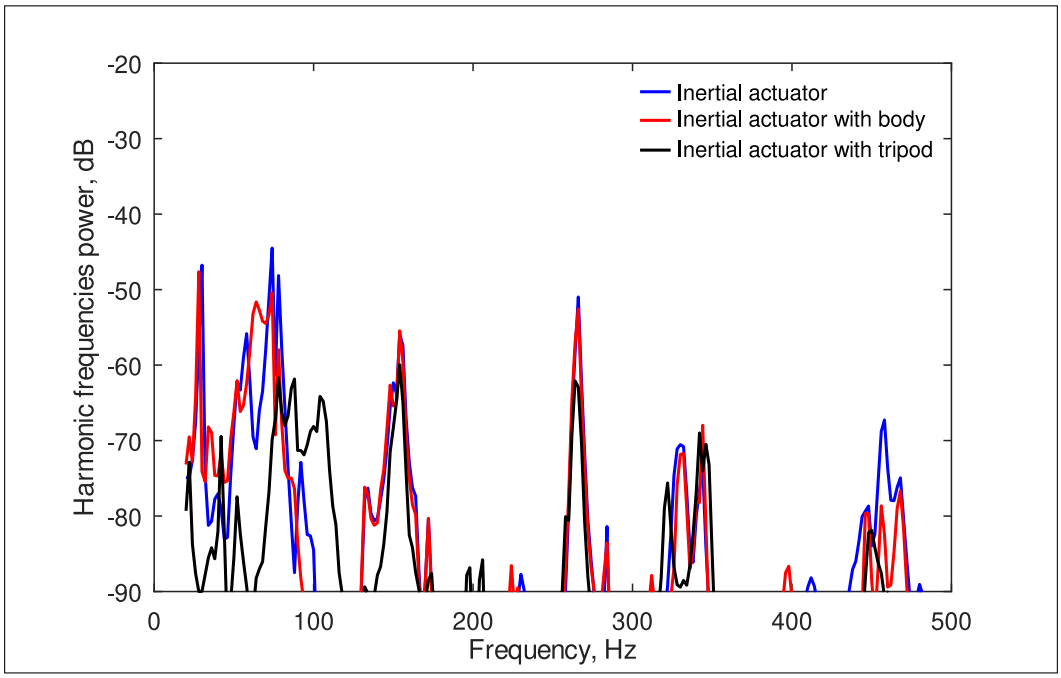


Figure 5. Power of the harmonic frequencies of the three configurations of the actuator. The resulted were obtained using the frequency-sweep excitation by the actuator.

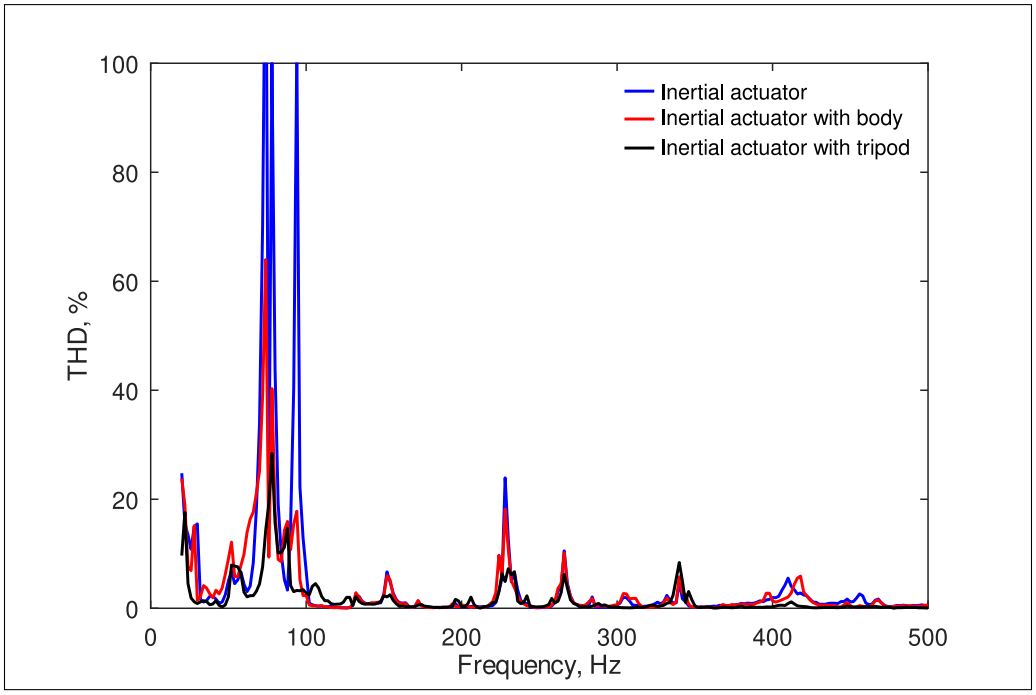


Figure 6. Total Harmonic Distortion (THD) of the three configurations of the actuator. The resulted were obtained using the frequency-sweep excitation by the actuator.

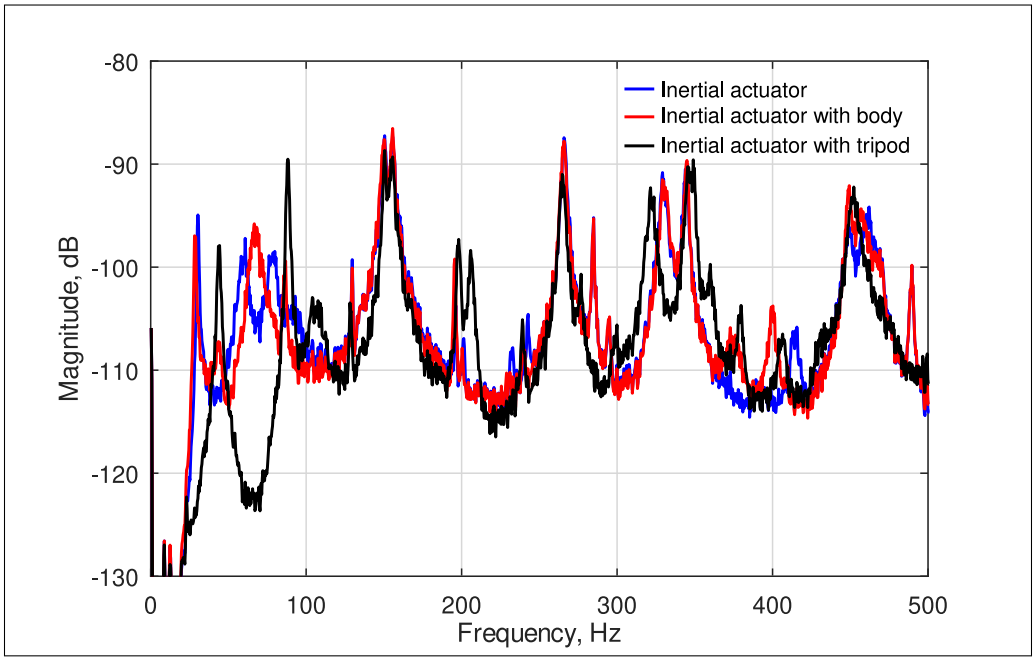


Figure 7. Surface-averaged vibration frequency response of the plate due to broadband excitation by the actuator.

DOI: 10.61782/fa.2025.0613



FORUM ACUSTICUM
EURONOISE 2025

NOISE MEASUREMENTS PERFORMANCE GUARANTEE ON A FLOATING LIQUIFIED NATURAL GAS PLANT

Bruno Crivelli[1*] **Dominique Vincent**[1]
[1] Technip Energies France, 2126 Boulevard de la Défense - CS10266 – 92000 Nanterre, France

ABSTRACT

In the energy industry, noise impact is commonly evaluated during the engineering phase as part of the work process for new plant development. However, even if noise regulations shall be applied, a noise performance guarantee is generally not required, demonstrated or is limited to individual equipment. This situation is currently changing, and plant noise performance guarantee tends to become widespread in contracts. Its goal is to ensure compliance with local regulations, environmental and social impact assessment and/or clients' standards.
As a major energy industry engineering contractor, Technip Energies faces this challenge with the projects it executes. To deal with this emerging contractual requirement and due to the lack of acoustic measurements standards for offshore, Technip Energies has developed its own validation methodology for noise performance guarantee on a Floating Liquified Natural Gas (FLNG) facility.
This paper presents the methodology developed by Technip Energies to validate the noise performance guarantee on a FLNG, the feedback on the noise measurements and a summary of the measurements results recorded on an operational facility.

Keywords: *measurements, performance guarantee, offshore, industry.*

1. INTRODUCTION

Airborne noise control in the energy industry is of major importance to ensure safe work conditions. Information on the design methodology, including main noise sources and mitigation measures are provided in different papers such as "Controlling Vibration and Noise Hazards to Insure Safe Work Conditions in Oil and Gas Plants"[1] and "Acoustic Design of Alarming System in the Energy Industry"[2]. However, these scientific articles do not provide any information regarding noise performance guarantee that can be dealt with by the contracts.
In this paper, the methodology developed by Technip Energies to validate the noise performance guarantee on a FLNG is presented.
This methodology starts from the conformity criterion definition to the noise measurements results. Consequently, it completes the work performed for several years during the design phase.
The following sections will be developed in the context of a FLNG:

- Definition of conformity criterion,
- Definition of acoustic measurement procedure and measurement material,
- Encountered difficulties during measurements,
- Summary of measurement results and compliance.

2. MEASUREMENTS PREPARATION

2.1 Definition of acceptance criterion

As a FLNG is located offshore and most of the time there is no specific noise limit for airborne noise in the environment, it is necessary to define a specific acceptance criterion.
During the engineering phase, the noise generated by the FLNG has been modelled and noise maps have been issued for each module and each deck.
The acceptance criterion is based on these noise maps. Considering the loudest predicted noise level on the noise map (not less than 1m from a noise source) a different acceptance criterion is set for each deck. Due to the

[*] ***Corresponding author***: bruno.crivelli@ten.com.
Copyright: *©2025 Bruno Crivelli et al. This is an open-access article distributed under the terms of the Creative Commons Attribution 3.0 Unported License, which permits unrestricted use, distribution, and reproduction in any medium, provided the original author and source are credited.*

measurement material, a positive tolerance of 1.5 dB is added to the maximum predictive noise level.
An extract of a noise map is presented below (see Fig. 1) with a major noise source hatched in the center and the highest noise level achieved identified by an arrow and surrounded with a rectangular shape.

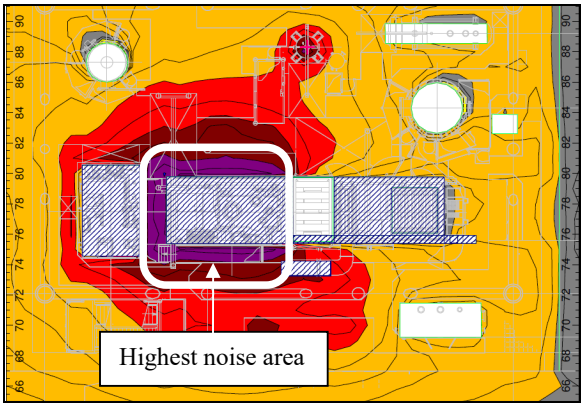


Figure 1. Extract of a noise map with a noise source and some equipment modelled as obstacles.

This criterion has been discussed and approved by all the parties involved in the project.

2.2 Measurement procedure and material

There is no recognized international standard specifically dedicated to noise measurements for offshore applications. The procedure presented in the following sections is influenced by ISO 11201 [3] and ISO 1996-2 [4] respectively related to noise measurements at a work station and related to description, measurement and assessment of environmental noise.

2.2.1 Measurements' locations and heights

For each deck or area, a minimum of 4 to 10 measurement points is defined depending on the deck or area size. Each measurement location is identified with a number on a plan, for example: see Fig. 2.
Noise measurements shall be performed 1.5 m above the floor.

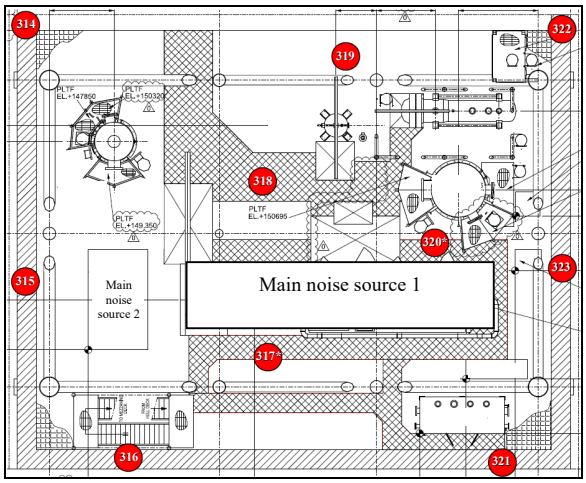


Figure 2. Example of measurement point identifications and locations.

2.2.2 Operating conditions

Noise measurements shall be performed during normal operation of the FLNG provided that:

- The rotating equipment and packages have proven stable reliable operation,
- All instruments related to the rotating equipment and packages are commissioned and have been operational for a sufficient period to prove their reliability.

During noise measurements, only necessary workers for the operation and the measurements shall be present in the area.

2.2.3 Measurement material

The following equipment used for the measurements shall be class 1 as per IEC 60942 [5], IEC 61260 [6] and IEC 61672-1 [7]:

- Calibrator,
- Sound level meter.

These devices shall be periodically verified by a national standard laboratory or a competent accredited laboratory.

2.2.4 Measurement time intervals and data to be recorded

For steady noise emissions the measurement time interval shall be at least 30 s.
If a noise level variation of more than 5 dB is identified during the 30 s measurement, the point shall be considered as non-steady, and the measurement shall cover one or more complete cycles to determine a representative average level. The source of the intermittence shall be investigated.

The operation time and time interval shall be noted and reported in the test results.
The equivalent sound pressure level shall be recorded in decibels using A-weighting filter (LAeq,1s). Additionally, during each measurement, octave band analysis between 31.5 Hz and 8000 Hz shall be recorded as well as the peak sound pressure level using C-weighting filter (LCpeak).

2.2.5 Calibration check

A calibration shall be performed before and after each series of measurements. If a gap higher than 0.5 dB is identified between the results of a calibration before and after the measurements, the results of this series shall be discarded, and the measurements shall be repeated.

3. MEASUREMENTS FEEDBACK AND RESULTS

3.1 Difficulties encountered during measurements

Conducting noise measurements on an FLNG is a challenging task due to the complexity of its environment. The combination of industrial activity, marine, weather conditions and spatial constraints creates a unique set of difficulties that must be carefully managed to ensure reliable results. This section outlines the challenges that could be encountered during the noise measurements.
To perform noise measurements on a FLNG, training and administrative work are necessary. This includes the Basic Offshore Safety Induction and Emergency Training (BOSIET) to access the FLNG. The specific regulations of the country and temporary admission for the measurement equipment shall also be considered, which means the need to gather all necessary documentation for foreign customs.
Additionally, one of the main challenges is that the noise measurement material may not be ATEX-certified. In these conditions, to conduct in-plant noise measurements, a hot work permit shall be requested daily. The purpose of the hot work permit is to ensure that the work is performed in safe conditions. Thus, it evaluates the different risks linked to the activity and details all necessary safety measures including the need for personal protection. As an example, a personal gas monitor to detect and prevent the presence of hazardous gas leaks could be permanently worn for field operations.
To validate the permit, the purpose of the noise measurements shall be explained to the different working areas safety representatives and their approval signatures shall be collected. This adds complexity and requires meticulous planning to ensure compliance and safety during noise measurements.

As the noise performance test occurs after the first start-up of the plant, unforeseen events could happen. This includes:

- Malfunctioning or under-maintenance equipment,
- FLNG shutdowns due to defective operation.

This would result in modification or cessation of ongoing measurements and therefore delays in the on-site measurements schedule.
Finally, unplanned measurements stoppages due to the noise generated by chopper traffic, bad or extreme weather conditions could further complicate the work progress.

3.2 Summary of measurements results and compliance

Despite the difficulties presented above, Technip Energies has implemented its procedure on an operational FLNG and the measurements have been performed. Main results are provided in Tab. 1.

Table 1. Measurements noise results.

Area	Number of measurements	Number of uncompliant measurements
Portside	265	13
Starboard	246	16
Hull Deck	173	25
Turret	15	0

The overall results of the noise measurements campaign show that 54 noise measurements exceed the acceptance criterion, over the 699 measurement points.
These exceedances are primarily located on the hull deck, resulting from:

- The main deck's configuration, which includes expansion holes not accounted for in the modeling phase,
- Reciprocating pumps generating high noise levels due to vibrations transmitted to the deck.

Exceeding measurement points on the topsides (portside and starboard) are mainly attributed to insufficient acoustic insulation on powerful compressors and pumps.

4. CONCLUSION

As previously mentioned, there are no specific international standards dedicated to noise performance tests for offshore applications. Consequently, it is incumbent upon acousticians to develop an appropriate methodology. The first step is the definition of the acceptance criterion.

This should be discussed with the different parties involved throughout the project.
Then, the noise measurement procedure shall be established to define the location of measurements points but also the measurement material, the interval duration of noise measurement points and the data to be recorded.
During the offshore noise measurements on a FLNG, safety shall not be compromised, and thus administrative work (permit to work) is of major importance.
In addition, measurement schedule can be impacted by unplanned events related to operation troubles, chopper traffic and/or extreme weather conditions.
Based on experience, it is advised to work with ATEX-certified sound level meters to reduce the risk associated with an explosion. Another point is to allocate extra time in case of unforeseen events that could disrupt the schedule.
Experience has demonstrated that the presented noise measurements procedure is appropriate for this type of work and environment.
Noise measurement results, with only 7% of the points exceeding the acceptance criterion, have been considered acceptable by all the parties. Thus, noise guarantee has been satisfied and FLNG is currently operating.

5. REFERENCES

[1] N. Souil, J. Jacq, B. Crivelli, C; Deslot-Marongiu, P. Vouagner, S. Lacolle and P. Pischedda, "Controlling Vibration and Noise Hazards to Insure Safe Work Conditions in Oil and Gas Plants," in *Proc. of the International Petroleum Technology Conference,* (Bangkok, Thailand), IPTC-18923-MS, 2016.

[2] B. Crivelli, and N. Gorilliot, "Acoustic Design of Alarming System in the Energy Industry," in *Proc. of the Forum Acusticum,* (Lyon, France), pp.2739-2742, 2020.

[3] ISO 11201 (2010): *Acoustics — Noise emitted by machinery and equipment — Determination of emission sound pressure levels at a work station and at other specified positions in an essentially free field over a reflecting plane with negligible environmental corrections.*

[4] ISO 1996 (2017): *Acoustics — Description, measurement and assessment of environmental noise Part 2: Determination of sound pressure levels.*

[5] IEC 60942 (2017): *Electroacoustics - Sound calibrators.*

[6] IEC 61260-1 (2014): *Electroacoustics - Octave-band and fractional-octave-band filters - Part 1: Specifications.*

[7] IEC 61672-1 (2013): *Electroacoustics - Sound level meters - Part 1: Specifications.*

DOI:

Main theme: A08 Industrial, Machinery, Equipment Noise and Vibration

Session A08.04/A10.04 Materials and systems for noise and vibration reduction

Chair(s): F. Pompoli, J. Carbajo San Martín, J. Arenas

DOI: 10.61782/fa.2025.0370

FORUM ACUSTICUM EURONOISE 2025

EXPERIMENTAL APPROACHES FOR THE CHARACTERIZATION OF THE VIBROACOUSTIC BEHAVIOUR OF A DOMESTIC COFFEE APPARATUS

Federico Castellini*[1] **Arianna Cavallo**[1] **Marco Rossoni**[1] **Francesco Ripamonti**[1]
Giorgio Colombo[1] **Roberto Corradi**[1] **Gennaro Cimmino**[2]
[1] Department of Mechanical Engineering, Politecnico di Milano, Via Giuseppe La Masa 1, 20156 Milan
[2] De'Longhi Appliances S.r.l., Via L. Seitz 47, 31100 Treviso, Italia

ABSTRACT

The growing demand for more comfortable and quieter household appliances reflects the increasing customer expectations for enhanced user experiences. In a competitive market, manufacturers are continuously seeking innovations that balance performance with noise reduction. To address this demand, experimental methodologies that characterize the vibroacoustic behaviour of devices can provide valuable support during the design phase. In this context, this paper focuses on a domestic coffee apparatus for coffee preparation as a case study to analyse its vibroacoustic behaviour, evaluating the acoustic emissions during operation and demonstrating the effectiveness of vibroacoustic testing for enhanced design insights. Noise and vibration measurements are conducted in a semi-anechoic chamber using accelerometers, microphones, a sound camera and a 3D sound intensity probe. The results of the proposed methodology highlight its potential for improving the acoustic performance of similar devices.

Keywords: *sound power, beamforming, sound intensity measurements, noise localization, vibroacoustic analysis*

*__Corresponding author__: federico.castellini@polimi.it
__Copyright__: ©2025 Castellini et al. This is an open-access article distributed under the terms of the Creative Commons Attribution 3.0 Unported License, which permits unrestricted use, distribution, and reproduction in any medium, provided the original author and source are credited.

1. INTRODUCTION

In recent years, domestic comfort has become a relevant aspect for customers, who require household appliances that are not only efficient but also quiet. In a competitive market, the attention to technical solutions that reduce acoustic impact without compromising performance is in constant growth. To this end, the adoption of experimental and numerical methods to study the vibroacoustic behaviour of such devices is one of the key elements in the process of product development and optimization.
The article presents a methodology to characterize in detail the vibroacoustic performance of a generic household appliance. The methodology is applied to a domestic apparatus for coffee preparation as a case study. The outcomes of a set of experimental approaches are compared, highlighting the potential benefits and the main limitations of adopting different measurement techniques and data processing methods. The procedure is designed to establish a setup that identifies the primary noise and vibration transmission paths, providing guidelines for acoustically driven design improvements or optimizing the acoustic performance of the product under analysis. The overview of the methodology is provided in Section 2. The preliminary acoustic analysis of the coffee machine is carried out in Section 3 through sound pressure and sound power measurements [1]. The detailed acoustic characterization of the product is described in Section 4. The identification of the main noise sources is conducted through beamforming algorithm [2] and sound intensity measurements [3]. The spatial reconstruction of the noise generated by the machine is suitable for the definition of a hybrid setup including accelerometers and microphones for the identification of the main acoustic and vibration transmission paths, which in turn allows for the definition

of possible mitigation actions and the evaluation of their effectiveness.

2. METHODOLOGY AND TEST CASE OVERVIEW

The most commonly performed acoustic tests for characterizing a product's acoustics rely on sound pressure measurements and sound power calculations (Figure 1a). These approaches only provide the possibility to have a general description of the product and do not allow for the identification of the location of the critical noise sources. In parallel with these measurements, noise source localization analysis is performed using a beamforming algorithm applied to a microphone array or by employing sound intensity measurements (Figure 1b). The combination of these two sets of tests enables a detailed characterization of the machine's acoustic behaviour, offering guidelines for developing a refined vibro-acoustic setup aimed at achieving a comprehensive vibroacoustic analysis (Figure 1c).

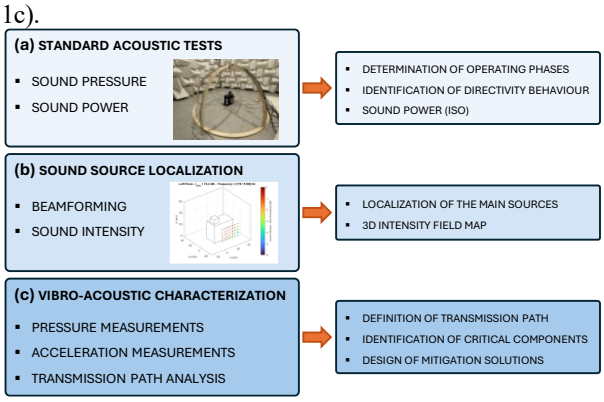


Figure 1. Overview of the methodology: (a) standard pressure and power measurements, (b) sound source localization techniques and (c) comprehensive vibro-acoustic characterization.

The machine under examination features an internal supporting frame that houses the components (motors, coffee grinder, handling and brewing systems) along with the external panels. Excluding components that are not involved in the grinding phase (the only operational phase analysed in this paper), the machine can be schematized as a combination of the following components. The "source group", consisting of the motor and grinding system, is positioned inside the machine and supported by the frame via supports. It is also connected to the coffee bean container through a channel passing through the upper panel. The external panels are, in turn, connected to the frame. Ventilation grids are installed on each panel, necessary for cooling the electrical circuits and for dissipating condensation (see Figure 2).

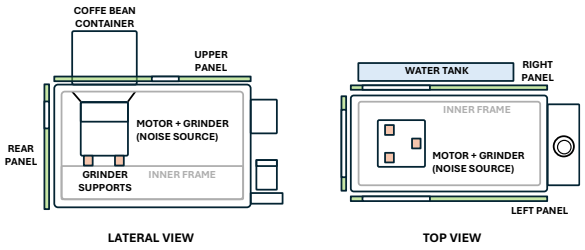


Figure 2. Schematic overview of the coffee machine. The ventilation grids on the external panels are indicated with a, b, c and d.

3. IDENTIFICATION OF THE ACOUSTIC BEHAVIOUR

The acoustic behaviour of the coffee machine is determined through a preliminary assessment of pressure measurements and sound power calculation. The analysis is carried out using a hemisphere (1m radius) designed for sound power measurements (ISO 3744 [1]). Measurements are conducted with 10 microphones located in different positions of the sphere, measuring the sound pressure in the position highlighted in Figure 3.

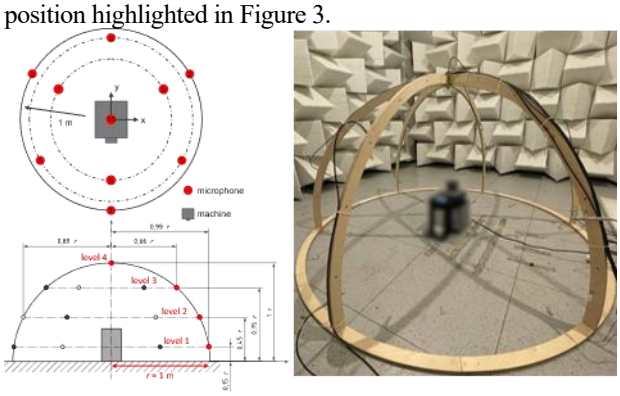


Figure 3. Setup of the sound power measurements [1].

Data from these microphones can be first used to highlight the different operating phases of the machine and to highlight possible non-stationary behaviour during each phase. This is performed by computing sound pressure levels using the fast-weighting data processing (see [4]), which allows for estimating the total sound level over time. The results of this procedure are collected in Figure 4a.

Microphone 10 is considered (see the scheme of Figure 3). The operating phases of the coffee machine (grinding, brewing and internal movement operations) are clearly evident when observing the overall Sound Pressure Level (SPL) over time ($p_{ref} = 2 \cdot 10^{-5}$ Pa). The grinding phase is the most critical and the loudest operational phase, as shown in Figure 4a. A time-frequency domain analysis is also conducted to highlight any critical frequencies associated with the noise phenomena. The spectrogram of the noise levels recorded by microphone 10 is shown in Figure 4b.

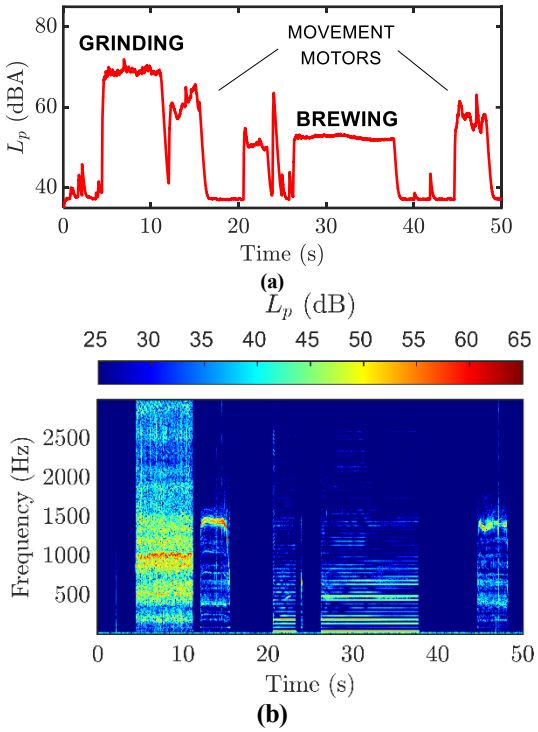


Figure 4. Identification of the machine operational phases (microphone 10): (a) fast weighted SPL (dBA) and (b) spectrogram (dB).

The noise generated during the grinding phase is mostly concentrated in the one-third octave band at 1 kHz and is related to the interaction between the grinder and the coffee beans. During the motor movement phase, it is possible to highlight that most of the noise is concentrated around 1500 Hz, which corresponds to the frequencies associated with the rotation of the motor that moves the coffee container to prepare the brewing phase. A peculiar frequency pattern is highlighted during the brewing phase, where it is possible to recognize the contribution of the motor pump, which is directly powered by household electricity (generating noise at the main electric frequency and at the higher order harmonics). In this research, the focus is given to the analysis of the grinding phase, which is, as explained above, the most annoying one considering the noise levels and the high-frequency content. All the following analyses are related to this phase only. One of the most important outcomes of the sound pressure measurements using a hemisphere in a hemi-anechoic chamber is the sound power of the machine, which can be computed following the procedure reported in ISO3744 [1]. Sound power provides an overall description of the noise generated by the machine and allows for comparison between similar products, as reported in Figure 5, where the sound power levels of the described reference Coffee Machine (CM1) are compared with those computed from sound pressure measurements of three other similar devices (CM2, CM3, CM4).

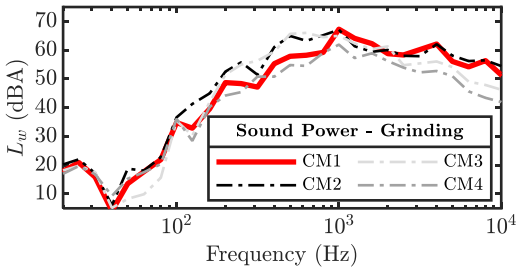


Figure 5. Third-octave band sound power levels of the grinding phase for different Coffee Machines (CM).

It must be noted that sound power can be considered a good index for initial assessment or for comparison between similar devices, but also to evaluate the overall impact of possible mitigation solutions. However, sound power is the result of the integration of the sound intensity normal to the hemisphere, so it represents the sum of the contributions of all the noise sources, which can also be localized in specific areas of the machine. Thus, to achieve a comprehensive acoustic characterization, further analysis is required, focusing on sound source localization and identification.
The techniques required to achieve these objectives are described in Section 4.

4. DETAILED ACOUSTIC CHARACTERIZATION

This section presents the techniques used for a detailed acoustic characterization by identifying the main noise sources. Preliminary sound source localization is conducted using a beamforming algorithm applied to measurements taken with a microphone array. Further investigation is carried out through sound intensity measurements.

4.1 Preliminary sound source localization through acoustic camera

The delay and sum algorithm, which serves as the foundation of beamforming [2], is one of the most common techniques adopted to locate the main sound sources on complex systems. Beamforming is typically employed to process the signals measured by one or more microphone arrays, enabling the generation of the beampattern, which is an acoustic map that highlights the loudest sound sources over a reference plane. In this research, preliminary sound source localization is carried out through the acoustic camera type 9712-W-FEN by Bruel & Kjer [5], which allows for obtaining real-time visualization of the acoustic field around the object analysed. In this context, the camera is used to scan each panel of the coffee machine by moving the microphone array. The acoustic maps of the left, right, rear, and top/upper panels are reported in Figure 6a, 6b, 6c, and 6d, respectively.

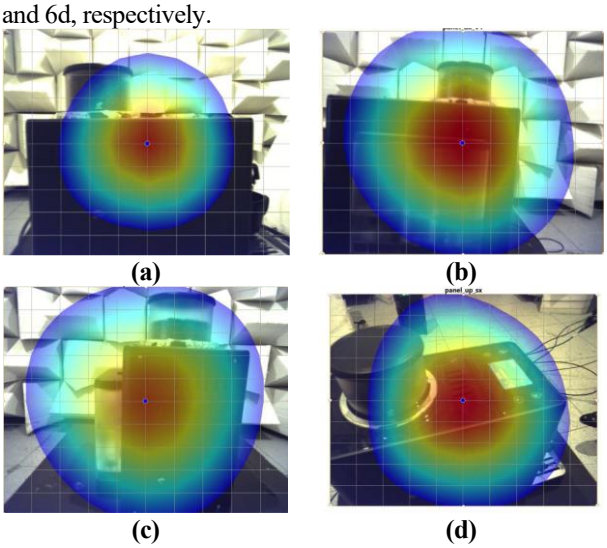


Figure 6. Results of the beamforming analysis through the acoustic camera: (a) left panel, (b) right panel, (c) rear panel and (d) upper panel.

The main noise emission is found to be located close to the ventilation grids, suggesting that this area may be the most significant transmission path for the noise produced in the internal part of the machine as a result of the vibrations generated during coffee bean grinding. However, the acoustic map produced by the camera may not always provide accurate noise level results due to several limitations. The operator's movement during the acoustic scanning process causes variations in the relative position between the microphone array and the source, introducing errors. Additionally, the beamforming technique has limited spatial resolution at low frequencies, making it less effective in accurately locating low-frequency noise sources. It is also sensitive to environmental reflections and background noise, which can distort the identification of sound sources. Moreover, when multiple noise sources are close to each other and operate at similar frequencies, beamforming may struggle to separate them clearly. In conclusion, it is able to provide only a qualitative representation of noise distribution rather than absolute sound intensity values. For this reason, in the next section, the noise generated by the machine will be accurately mapped using sound intensity measurements.

4.2 Detailed sound source identification: 3D sound intensity map

Sound intensity measurements can be used to refine the results obtained through the acoustic camera by reconstructing the sound intensity field surrounding the machine. To this end, a G.R.A.S. 3D sound intensity probe head type 60LK is used to estimate the sound intensity vector in different positions close to the left, right, rear, and top panels (see Figure 7).

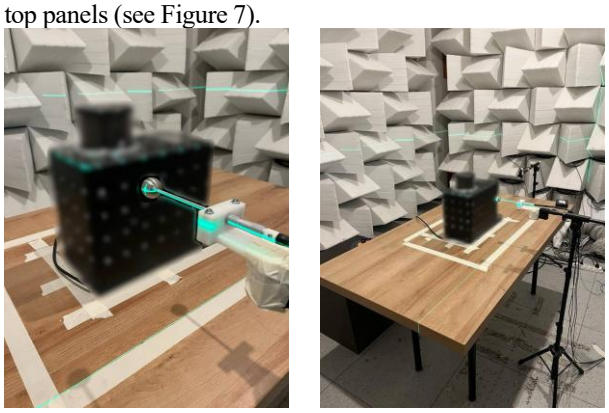


Figure 7. Measurement setup of the sound intensity measurements.

The measurements are carried out thanks to four ¼" microphones embedded in a rigid spherical shell with a diameter of 30 mm, which are organised in a regular tetrahedron configuration. A dedicated MATLAB software was developed to process and visualize the data acquired by the 3D sound intensity probe. In this process, a correction was applied to account for the acoustic scattering caused by the sensor's rigid spherical surface in the acoustic field, following the formulation proposed in [6,7]. The output of the algorithm is the estimation of the sound intensity vector at the centre of

the sphere, which allows tracking the magnitude and the direction of the sound intensity field in different positions surrounding the coffee machine. During the tests, the sound probe is positioned 15 cm from each of the panels. A total number of 118 measurement points is created, adopting a spatial distance between points of 5 cm. Unlike beamforming, sound intensity measurement offers higher accuracy in quantifying noise levels, is less affected by background noise, and allows for direct identification of sound transmission paths. Additionally, it enables analysis in low-frequency ranges and provides vectorial information about the direction of the sound energy flow, offering a more detailed characterization of noise sources. Another key advantage is its ability to analyse both near-field and far-field noise propagation, making it particularly useful for distinguishing between localized sources and the overall noise radiation of the machine. The results of the sound intensity measurements are reported in Figure 8. The sound intensity vectors are normalised with respect to the maximum value obtained in each panel. The analysed frequency range includes all one-third octave bands from 200 Hz to 10 kHz. A colormap of 6 dB is employed for the sound intensity field representation. The maximum value of sound intensity (78.1 dB) is obtained on the upper panel, just in front of the top grid. Slightly lower sound intensity magnitude is obtained on the rear panel (77.7 dB) and on the left and right panels (74.2 dB and 73.5 dB). The differences between the left and the right panels are due to the presence of the water tank on the right side, which creates an additional shield for sound transmission.

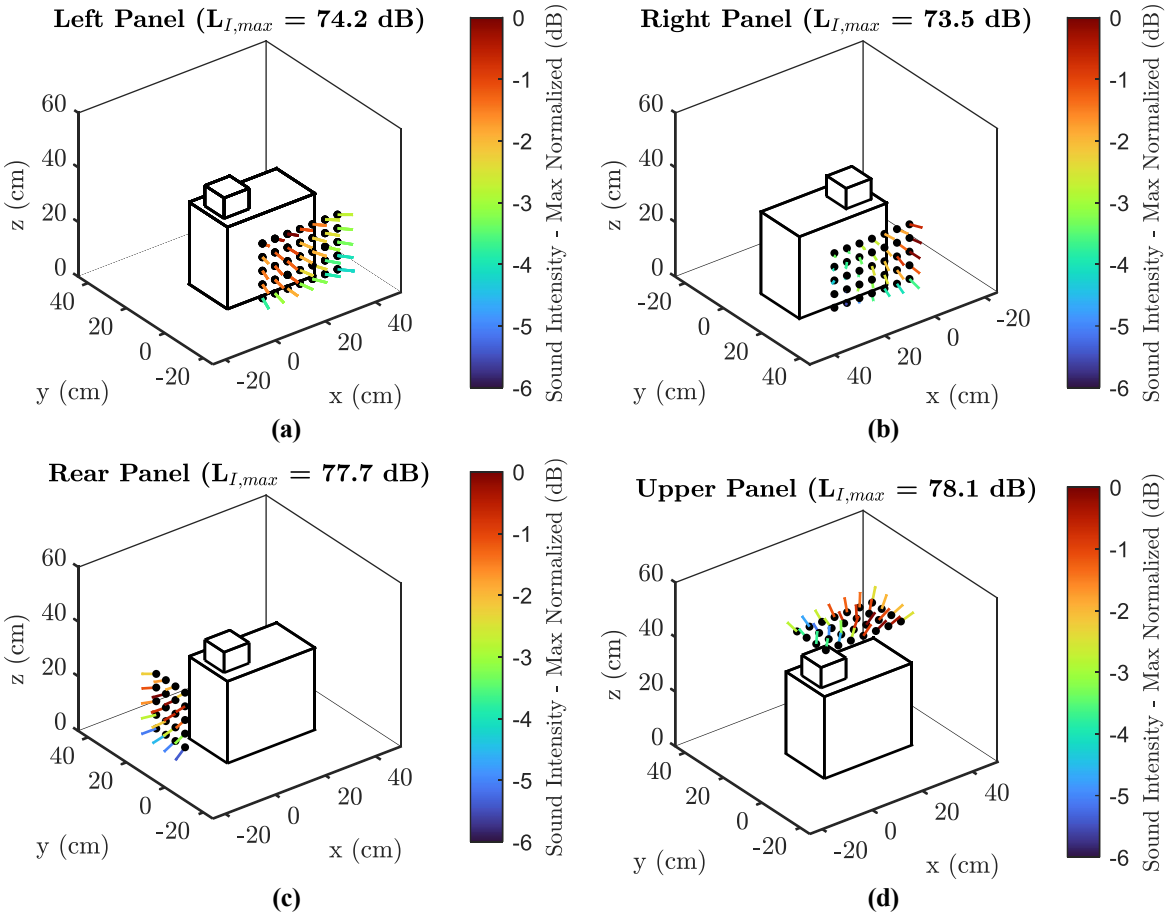


Figure 8. 3D sound intensity maps: (a) left panel, (b) right panel, (c) rear panel and (d) upper panel.

5. VIBROACOUSTIC ANALYSIS

The identification of the sound sources through beamforming and sound intensity measurements reveals some localized potential critical areas associated with noise emission during the grinding phase. Thus, a measurement setup dedicated to further refinement of these findings has been developed. The main scope of this third experimental session is to understand if the noise is mostly generated by acoustic leakages, such as the ventilation grids, or if there are other phenomena associated with structural contributions only. Determining noise and vibration transmission paths is fundamental to identifying potential mitigation solutions. This analysis requires not only pressure measurements but a combination of noise and vibration tests. A hybrid setup is therefore designed, including accelerometers and microphones mounted in different positions. The description of the measurement setup is provided in Section 5.1, while the results of the tests are analysed in Section 5.2.

5.1 Measurement setup

The final tests are carried out by organising sensors in three layers: source sensors (layer 1, accelerometers), "near field" sensors (layer 2, accelerometers and microphones at 5 cm relative to the ventilation grids) and "far field" sensors (layer 3, two microphones located 1m away from the front and the rear of the coffee machine). Please note that layer 3 has been designed to be representative of a generic customer position. These sensors are useful for estimating the average noise level to which the user is exposed during the coffee preparation and to investigate the possible impact of different design solutions on user annoyance. This is not the aim of the present paper, so the analysis of layer 3 is not reported here. The overview of the entire setup is illustrated in Figure 9.

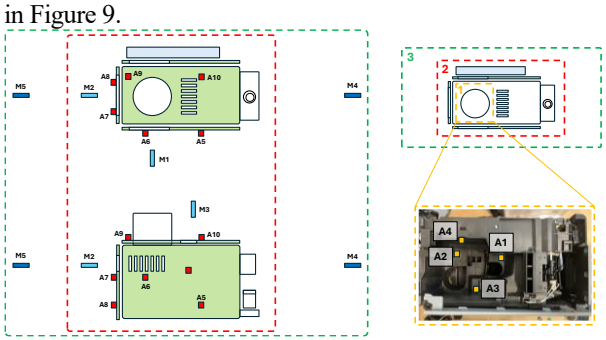


Figure 9. Refined setup for vibro-acoustic characterisation.

5.2 Transmission path analysis

Three of the four accelerometers of layer 1 are mounted close to the supports of the grinder, and they collect the vibration transmitted by the source to the main frame of the machine. As highlighted in Figure 10, these supports are not the only possible structural transmission path for vibration induced by the grinding process. In fact, the grinder is connected to the upper panel also through the canal for the passage of coffee beans from the coffee container. The main challenge is to determine the impact of the possible transmission path. This is carried out by comparing the vibration measured by the accelerometers mounted on layer 1 and the sensors mounted on layer 2.

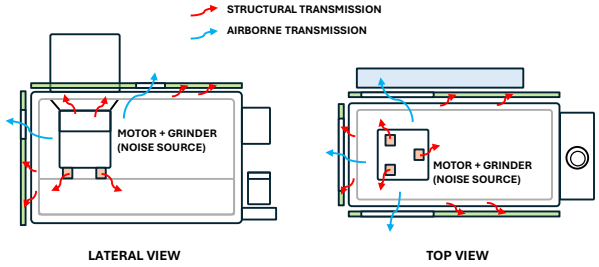


Figure 10. Identification of potential structural and acoustic transmission paths.

First, the comparison between the acceleration measured on the inner frame (layer 1) and that of the panels is performed. The spectrogram of the acceleration levels ($a_{ref}=1\cdot10^{-6}$ m/s) is employed. The most important results of the analysis are now presented. The accelerometer 1 (A1) is chosen as the reference channel for layer 1, while A5, A8, and A9 are the reference channels for the left, rear, and top panels, respectively. The results are reported in Figure 11. Similar vibration contributions are observed comparing the acceleration measured by A1 and the ones measured by A5 and A8 (left and rear panels). A low-frequency dynamic amplification is detected on the panel's accelerometers only (below 500 Hz) and it is therefore attributed to the panel dynamics. However, as it will be visible in the microphone data, the low-frequency vibration does not contribute significantly to the noise emission. The vibration peaks observed in A1 around 1 kHz are also partially visible on the left and rear panels, although they are significantly attenuated compared to the layer 1 measurements. A different vibration pattern is observed in the spectrograms of the levels of channel A9. The contribution at 1 kHz is much more evident here and is correlated with the measurements from the layer 1 accelerometers. Strong transient peaks in the vibration levels are observed at t=5s,

t=6s and t=7.5s. These vibration peaks are related to the random hits generated during the grinding of coffee beans and seem to be much more evident in the top panel vibration compared to the other panels or to the layer 1 accelerometers (see A1 spectrogram). This confirms that there is a direct structural transmission of vibration from the grinder to the upper panel, in addition to the transmission of the vibration from the grinder support to the inner frame (as highlighted by looking at the correlation in the spectrograms of A1, A5, and A8).

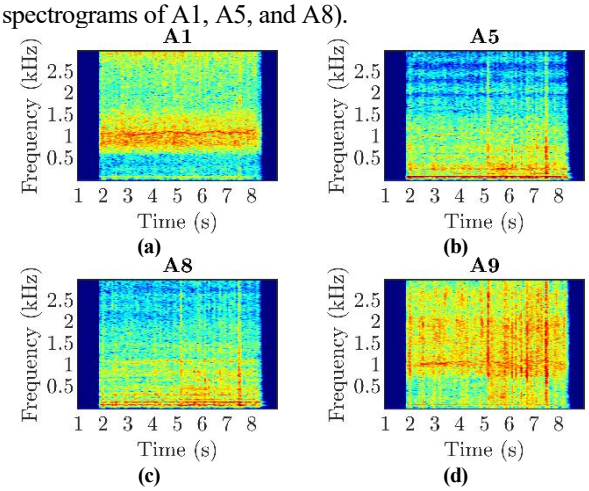


Figure 11. Spectrograms of the vibration levels (dB): (a) A1, (b) A5, (c) A8 and (d) A9.

The impact of the structural transmission on vibration can be evaluated by analysing the signal measured by the microphones located surrounding the coffee machine. The analysis of the grinding phase is repeated by closing the ventilation grids to discover if the noise emitted is mainly due to the structural transmission of the vibration from the grinder to the panel (which results in noise radiation) or if it is due to the acoustic transmission through ventilation grids. The results on the rear and the upper panels are shown in Figure 12 and Figure 13, respectively. As mentioned above, the low-frequency vibration of the panels is not found to generate a significant contribution to the noise emission (see Figure 12b). The rear panel vibration spectrogram (A8) is very similar to the one of the rear microphone (M2) at frequencies above 300-400 Hz. However, in the test with the ventilation grid closed, a significant reduction in the noise levels measured by M2 is observed (see Figure 12d). This confirms that a significant part of the noise radiated by the machine seems to be transmitted through the ventilation grids. Similar results are obtained by analysing the left panel.

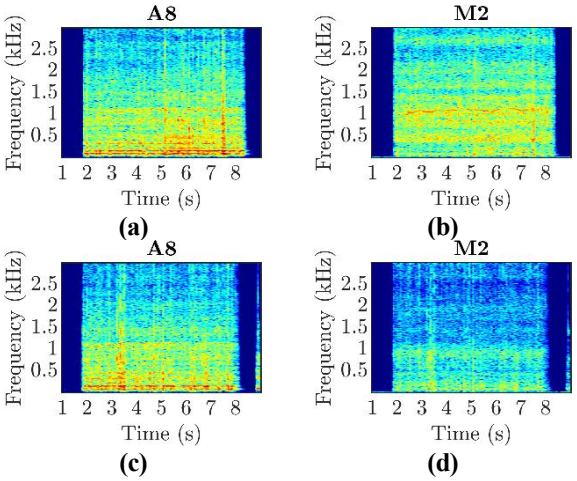


Figure 12. Spectrograms of noise and vibration levels (dB) on the rear panel: (a,b) with ventilation grids open, (c,d) with ventilation grids closed.

The analysis of the upper panel comparing the tests with the ventilation grids open and closed (see Figure 13) confirms the previous considerations regarding a possible structural transmission of vibration between the grinder and the upper panel.

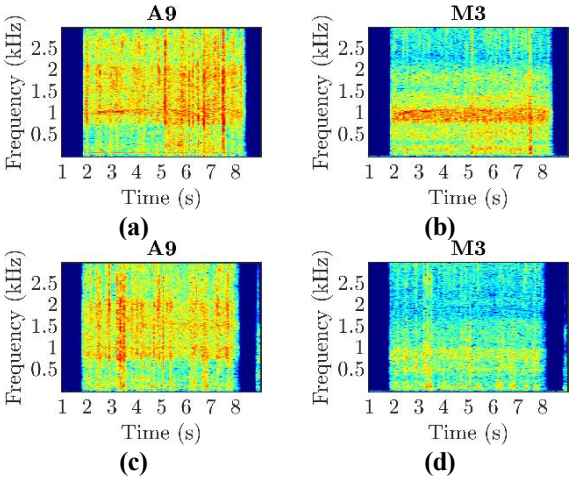


Figure 13. Spectrograms of noise and vibration levels (dB) on the upper panel: (a,b) with ventilation grids open, (c,d) with ventilation grids closed.

Noise emission is mainly related to the transmission through the ventilation grids, but the contribution from the hits of the coffee beans during grinding, along with some of the broadband vibrations around 1 kHz, is also transmitted to the upper panel through structural pathways (see Figure 13).

6. CONCLUSIONS

In this research, a methodology for vibroacoustic characterisation of household appliances is described. The use of standard sound pressure and sound level measurements, supported by noise source localisation techniques such as beamforming and sound intensity measurements, is shown to provide a comprehensive characterisation of the tested product. These experimental techniques also allow for the design of a dedicated setup in which, thanks to sound pressure and acceleration measurements, it is possible to identify the main noise and vibration transmission paths. The methodology is applied to a test case with the aim of characterising the vibroacoustic behaviour of a household coffee machine. The analysis shows that acoustic leakages, due to the presence of ventilation grids, may result in a significant impact on the overall noise emission. However, through combined noise and vibration analyses, a critical structural transmission path has also been identified. The results of these experiments highlight several key aspects of the product that can be optimized to reduce overall noise emission. The experimental techniques presented in this article can be adopted for the identification of potential mitigation measures for the noise generated by any kind of household appliance, or can be used for the definition of guidelines for an acoustically oriented design of new products.

7. ACKNOWLEDGMENTS

The authors would like to thank De'Longhi Appliances S.r.l for providing the tested product and for their technical assistance during the experimental phase. Their support has been a significant added value to our research.

8. REFERENCES

[1] ISO 3744:2010 Acoustics - Determination of sound power levels and sound energy levels of noise sources using sound pressure - Engineering methods for an essentially free field over a reflecting plane.

[2] Cigada A, Ripamonti F, Vanali M. The delay & sum algorithm applied to microphone array measurements: Numerical analysis and experimental validation. Mech Syst Signal Process. 2007;21(6):2645–2664.

[3] F. J. Fay, “Sound Intensity,” Elsevier Applied Science, Amsterdam, 1989.

[4] BS EN 61672-1:Electroacoustics. Sound level meters - Specifications. 2013.

[5] BK Connect Acoustic Camera | Brüel & Kjær.

[6] Sondergaard T, Wille M. Optimized vector sound intensity measurements with a tetrahedral arrangement of microphones in a spherical shell. J Acoust Soc Am. 2015;138(5):2820–2828.

[7] Rapino L, Cavallo A, La Paglia I, et al. Combined acoustic testing of home appliances: a case study. Internoise 2022 - 51st International Congress and Exposition on Noise Control Engineering. :Glasgow.

DOI: 10.61782/fa.2025.0296

FORUM ACUSTICUM EURONOISE 2025

DEVELOPMENT OF SUSTAINABLE SOUND ABSORBING PANELS MADE OF JUTE FIBERS

Francesco Pompoli[1*] **Peter Dagø**[2] **Cristina Marescotti**[1]
Andrea Santoni[1] **Patrizio Fausti**[1]
[1] Department of Engineering – University of Ferrara, Ferrara, Italy
[2] Hubbub ApS, Copenhagen, Denmark

ABSTRACT

This paper presents an optimization study of sustainable sound-absorbing panels made of jute fiber, developed for two different applications: the first, with a thickness of 40 mm, is optimized for wall mounting, while the second consists of a 20 mm thick panel designed for suspended ceiling installations with an air cavity. The design process began with an experimental study of the acoustic performance of loose jute fibers, with the objective of achieving Class A performance ($\alpha_w \geq 0.90$) according to ISO 11654. This study was conducted in collaboration with the Danish company Hubbub ApS.

Keywords: *acoustic optimization, sound absorption, jute fibers, natural fibers, sustainable material.*

1. INTRODUCTION

In recent years, the development of sustainable sound-absorbing materials has gained significant interest due to global CO_2 emission reduction targets. Natural and recycled fibers, which find applications both in building construction and industrial noise control engineering, may represent a more sustainable solution for thermal and sound insulation compared to traditional synthetic fibrous materials. While a knowledge gap still exists between traditional synthetic fibers, which have been studied for over fifty years, and natural fibers, an extensive body of literature is now available on fibrous materials of plant origin, such as hemp, wood fibers, and coconut fibers [1][2].

However, unlike traditional fibrous materials, whose acoustic performance can be optimized through the manufacturing process, the physical characteristics of natural fibers cannot be precisely engineered and generally exhibit significant variability in diameter, distribution, and orientation; factors that strongly affect their acoustic performance. Therefore, the acoustic optimization of sound-absorbing products made from plant-based fibers must consider and fine-tune other parameters that play a fundamental role in the acoustic behavior of the fibrous material and strongly affect its overall performance.
The present project was promoted by the company Hubbub ApS to develop fully natural indoor sound-absorbing panels, including both the fibers, the binder that provides structural cohesion, and the aesthetic covering.

2. MATERIALS AND METHODS

The aim of this study was to develop two jute fiber-based sound-absorbing panels for indoor environments: a thicker panel (40 mm) for wall applications and a thinner panel (20 mm) for suspended ceilings with an air cavity. The panels were manufactured in India using jute fibers and natural latex as a binder. The jute fibers were obtained without the use of chemicals from plants of the *Corchorus Capsularis species*, belonging to the *Malvaceae family*, which are abundant in the monsoon regions of the East. The production process, which employs natural latex as a binder, results in a panel that is 100% biodegradable.
The Johnson-Champoux-Allard (JCA) [3][4] equivalent dissipative fluid model was employed for the acoustic design

[*] ***Corresponding author***: *francesco.pompoli@unife.it.*
Copyright: *©2025 First author et al. This is an open-access article distributed under the terms of the Creative Commons Attribution 3.0 Unported License, which permits unrestricted use, distribution, and reproduction in any medium, provided the original author and source are credited.*

and optimization process of the two panels. The transport parameters, required as input data for implementing the JCA model, were determined through an inverse characterization approach, based on the experimental measurement of the normal incidence sound absorption coefficient on a small quantity of loose fibers (**Figure 1**), progressively compressed to test different densities. A variation of the sample density ρ implies a change in the material's open-cell porosity ϕ, which can be evaluated from the density of the solid skeleton ρ_s as:

$$\phi = 1 - \frac{\rho}{\rho_s} \tag{1}$$

The airflow resistivity σ can be related to the material porosity ϕ and to the effective radius r_e of the equivalent monodisperse fibrous medium:

$$\sigma = \frac{\eta}{(2r_e)^2} \times \frac{\sqrt{1-(1-\phi)}}{0.21\left(\frac{0.71}{1-\phi} - 3\sqrt{\frac{0.71}{1-\phi}} + 3 - \sqrt{\frac{1-\phi}{0.71}}\right)} \tag{2}$$

Analytical equations were used to express the remaining three transport parameters – tortuosity α_∞, viscous and thermal characteristics lengths Λ, and Λ' – either as a function of the porosity ϕ or the effective radius r_e:

$$\alpha_\infty = \left(\frac{1}{\phi}\right)^{0.9574} \tag{3}$$

$$\Lambda = A_1 r_e (1-\phi)^{-A_2} \tag{4}$$

$$\Lambda' = A_3 r_e (1-\phi)^{-A_4} \tag{5}$$

The effective radius r_e and the unknown coefficients A_i were determined through a minimization procedure, described in detail in reference [5], based on the experimental results of the normal incidence sound absorption coefficient, measured at different combinations of thickness and density according to the ISO 10543-2 standard. This approach allowed us to correlate variations in transport parameters with changes in material density. Considering these density-functions for the transport parameters used as input in a JCA model, along with the diffuse field assumption and the finite-size correction method proposed by Rhazi et al. [6], the panels' thickness and density were optimized. The optimization process involved evaluating different combinations of thickness, density, and air cavity, based on predictions of the random incidence sound absorption coefficient, which represents the acoustic performance measurable in a reverberation chamber according to the ISO 354 standard. The optimization target, requested by Hubbub ApS, was to develop two panels capable of achieving Class A performance ($\alpha_w \geq 0.90$) according to ISO 11654. The entire process was experimentally validated at the end of the design phase on 10.8 m^2 of panels, specifically produced in accordance with the optimization results, tested in a reverberation chamber.



Figure 1. Loose jute fibers and their installation in the plane wave impedance tube.

3. EXPERIMENTAL RESULTS

The experimental normal incidence absorption coefficients measured on loose fibers at different combinations of thickness and density are shown **Figure 2**.

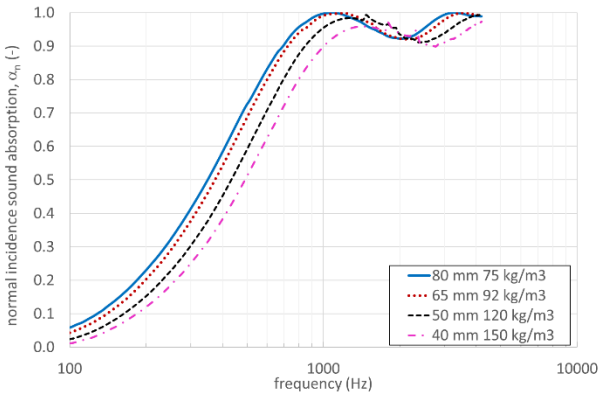


Figure 2. Normal incidence sound absorption: experimental measurements on loose fibers for different combinations of thickness and density.

The loose fibers were compressed from 80 mm to 40 mm, enabling the experimental measurement of densities within the range of 75 – 150 kg/m^3. The five transport parameters – including porosity, airflow resistivity, tortuosity, and the characteristic viscous and thermal lengths – were determined as a function of material density, as described in the previous paragraph. **Table 1** presents the values of these parameters for densities ranging from 120 to 240 kg/m^3.

A comparison between the experimentally investigated densities and the values for which the transport parameters were estimated suggests that the applicability of the optimization approach extends across the experimental interval. However, for values outside the investigated range, a higher degree of uncertainty should be expected. Since the target performance was expressed in terms of average sound absorption α_w, the random incidence sound absorption coefficients were computed from the density-dependent transport parameters and considering a finite-size correction for a 10.8 m² surface. The results are shown in **Figure 4**.

Table 1. Physical parameter values derived from measurements on loose fibers as a function of density.

ρ [kg/m^3]	ϕ [-]	σ [kNs/m^4]	α_∞ [-]	Λ [μm]	Λ' [μm]
120	0.91	15.9	1.10	65	133
140	0.89	21.1	1.12	50	123
160	0.88	27.3	1.13	39	115
180	0.86	34.8	1.15	32	108
200	0.85	43.7	1.17	27	102
220	0.83	54.3	1.19	23	97
240	0.82	66.8	1.22	19	93

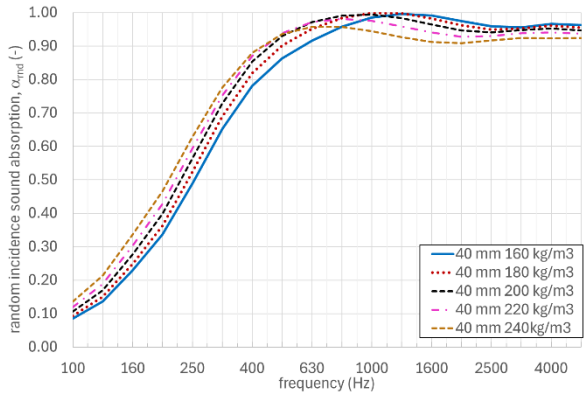


Figure 3. Random incidence sound absorption coefficient: JCA prediction at different densities.

From these results, the average sound absorption coefficient α_w was computed according to ISO 11654 for each density. For instance, **Figure 4** presents the calculated diffuse incidence sound absorption values in octave bands and illustrates the α_w computation procedure for the 40 mm panel at different densities.

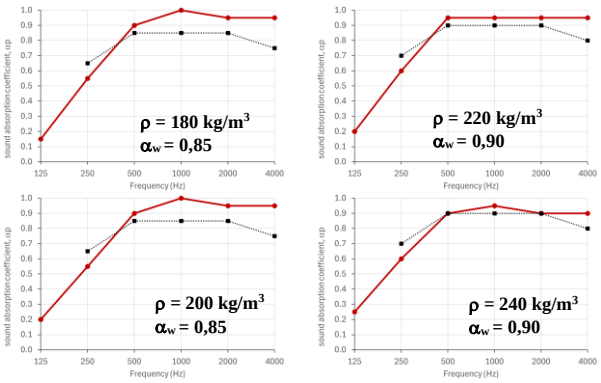


Figure 4. Diffuse incidence sound absorption values in octave bands, computed for the 40 mm panel at different densities, and the α_w reference curve as provided by the ISO 11654.

Table 2 summarizes the results of the optimization approach, presenting the average sound absorption coefficient α_w, which was evaluated from the random incidence sound absorption. This was computed using the transfer matrix method (TMM) at different densities, for two panel configurations: *i)* 40 mm wall-flush mounted, and *ii)* 20 mm ceiling mounted with a 200 mm airgap.

Table 2. Calculated α_w values as a function of panel density for wall-mounted and suspended ceiling configurations.

Density [kg/m^3]	***160***	***180***	***200***	***220***	***240***
α_w *wall- mounted*	0.80	0.85	0.85	0.90	0.90
Density [kg/m^3]	***120***	***140***	***160***	***180***	***200***
α_w *ceiling-mounted*	0.80	0.85	0.90	0.90	0.90

The performance target for Class A sound absorption is met for $\alpha_w \geq 0.90$. Therefore, results indicate that for the 40 mm wall-mounted panel, a minimum density of 220 kg/m^3 is required to achieve Class A performance,

while for the 20 mm ceiling panel with a 200 mm air cavity, a minimum density of 160 kg/m^3 is necessary. At the end of the analytical optimization phase, for each configuration nine prototype panels measuring 1 m x 1.6 m were produced for experimental testing in a reverberation chamber, according to ISO 354. The experimental results, representing diffuse incidence sound absorption (third-octave bands), are compared with the analytical predictions in **Figure 5**.

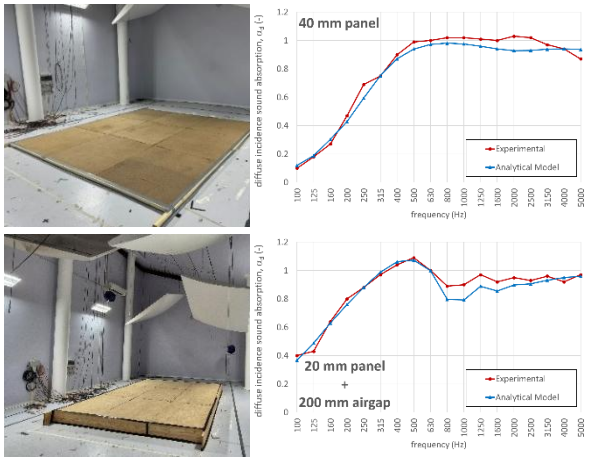


Figure 5. Comparison between experimental results and analytical predictions for 40 mm panels (wall-mounted, density 220 kg/m^3) and 20 mm panels (suspended ceiling with 200 mm air cavity, density 160 kg/m^3).

Reaching an average sound absorption coefficient $\alpha_w = 0.95$, both the configurations were certified with a Class A acoustic performance, thus confirming the predicted results. The analytical model proved to be reliable, accurately approximating the diffuse incidence sound absorption across the entire frequency range. However, it slightly underestimated the acoustic performance for $\alpha_{rnd} > 1.00$, which is physically meaningless and highly dependent on laboratory characteristics.

4. CONCLUSIONS

In this project, two sound-absorbing panels made of jute fiber were developed, both fully biodegradable, thanks to the natural origin of the fibers and the use of a natural latex binder. The adopted acoustic optimization process allowed the development of two Class A panels ($\alpha_w = 0.95$) for both the 40 mm wall-mounted and the 20 mm suspended ceiling solutions.

The proposed methodology demonstrated high reliability while minimizing experimental efforts, as measurements were conducted on a small quantity of fibers using a widely available plane wave impedance tube. These measurements were complemented by a fast analytical processing step, implemented in MATLAB, which enabled the calculation of the physical and acoustic properties of the fibrous material as a function of density.

The adoption of this procedure significantly reduces panel prototyping efforts, cutting costs and development time.

Additional technical information regarding natural-based fibrous panels can be find [7].

5. REFERENCES

[1] Asdrubali, F., Schiavoni, S., and Horoshenkov, K. V. (2012). A review of sustainable materials for acoustic applications. *Building Acoustics*, *19*(4), 283-311.

[2] Santoni, A., Bonfiglio, P., Fausti, P., Marescotti, C., Mazzanti, V., Mollica, F., and Pompoli, F. (2019). Improving the sound absorption performance of sustainable thermal insulation materials: Natural hemp fibres. *Applied Acoustics*, *150*, 279-289.

[3] Johnson, D. L., Koplik, J., and Dashen, R. Theory of dynamic permeability and tortuosity in fluid-saturated porous media, Journal of fluid mechanics, 176, 1987, pp. 379-402.

[4] Champoux, Y., and Allard, J. F. Dynamic tortuosity and bulk modulus in air - saturated porous media. Journal of applied physics, 70(4), 1991, pp. 1975-1979.

[5] Santoni, A., Pompoli, F., Marescotti, C., Fausti, P. Characterization of fibrous media transport parameters from multi-compression ratio measurements of normal incidence sound absorption, J. Acoust. Soc. Am. 157 (2), 2025, pp. 1185–1201, https://doi.org/10.1121/10.0035847.

[6] Rhazi, D., and Atalla, N., A. Simple Method to Account for Size Effects in the Transfer Matrix Method, J. Acoust. Soc. Am., 127(2), 2010, pp. EL30–EL36.

[7] https://hubbub.space/Home

DOI: 10.61782/fa.2025.0534

FORUM ACUSTICUM EURONOISE 2025

LOW-FREQUENCY ACOUSTIC AND VIBROACOUSTIC TREATMENTS TO REDUCE SOUND TRANSMISSION WITH DUCTS

Clément Lagarrigue* **Damien Lecoq**[1] **Julie Perchaud**[1]
Marianne Fruchart[1]
[3] Metacoustic, 57 Boulevard Demorieux, 72000 Le Mans, France

ABSTRACT

This study addresses the attenuation of low-frequency noise in ducts without modifying the cross-sectional geometry or introducing pressure losses. Conventional solutions, such as porous materials or reactive silencers, typically show limited effectiveness below 500 Hz and suffer from degradation under airflow. We propose two compact and robust alternatives: a mechanical elastic approach and an acoustic resonator-based approach. The elastic solution uses a soft viscoelastic material to create a mass–spring system that efficiently attenuates low frequencies through mechanical resonance. The acoustic solution is based on an array of quarter-wavelength resonators with a spatial gradient, designed to target a broader low-frequency band while minimizing flow-induced noise regeneration. Both silencers were manufactured and experimentally tested in laboratory conditions, including under airflow, to evaluate their acoustic performance and robustness. The results show significant transmission loss in the sub-500 Hz range without additional noise generation, confirming the relevance of resonance-based mechanisms for compact low-frequency silencers.

Keywords: *Metamaterial, duct, Experimental measurement, Silencer, flow*

**Corresponding author*: clement.lagarrigue@metacoustic.com
***Copyright**: ©2025 Lagarrigue et al. This is an open-access article distributed under the terms of the Creative Commons Attribution 3.0 Unported License, which permits unrestricted use, distribution, and reproduction in any medium, provided the original author and source are credited.*

1. INTRODUCTION

Ventilation systems represent a significant source of noise pollution in both industrial and residential environments, necessitating the implementation of effective acoustic attenuation devices. Ventilation duct silencers have been extensively studied, but they still present major limitations, particularly concerning their size, low-frequency attenuation, and impact on airflow.

The most commonly used solution in the industry today is the parallel baffle. These consist of parallel sound-absorbing panels, typically made of mineral wool or fiberglass, covered with fabric or a perforated sheet. These devices provide effective attenuation at mid and high frequencies [1]. However, their limited performance in the low-frequency range (<500 Hz) is well known [2] and particularly problematic in many industrial applications, as they can induce significant aerodynamic pressure losses, which in turn increase the operating energy costs of ventilation systems [3-4]. Dissipative cylindrical silencers, used in circular ducts, are also widely employed in the industry and exhibit similar low-frequency limitations as parallel baffles [5]. To mitigate these issues, a larger-diameter casing can be used, with dissipative material applied to its inner walls. This design preserves the original duct cross-section, minimizing pressure losses. In any case, absorbing materials (such as mineral wool, foam, or fiberglass) are vulnerable to humidity and particulate contamination, reducing their durability, which can lead to delamination and potential health concerns when exposed to strong airflow. To address these issues and the low-frequency shortcomings of dissipative silencers, reactive silencers have been investigated as an alternative solution. By utilizing resonance phenomena, these silencers aim to

improve attenuation in targeted frequency ranges. Resonator silencers, such as Helmholtz or quarter-wave types, provide targeted attenuation of specific frequencies [6-7]. Furthermore, flow-induced noise regeneration remains a key limitation for many existing solutions, requiring careful design to prevent unwanted acoustic emissions.

This study focuses on developing new proposals for dissipative-like silencers that are effective at low frequencies, particularly below 500 Hz, while maintaining performance even in the presence of airflow without generating additional noise. By leveraging resonance-based mechanisms, these treatments aim to enhance sound attenuation while maintaining compactness and robustness in demanding environments. Two different strategies are investigated: an elastic approach utilizing soft and flexible materials, and an acoustic approach based on resonance gradients, offering a practical solution to mitigate flow-induced noise regeneration.

2. USE CASE CONFIGURATION

All results presented in this paper will be experimental transmission losses shown for "dissipative-like silencer" configurations (i.e. where the internal guide cross section remains unchanged). Two examples are displayed and each example has been tested with a different setup for practical reasons (Fig.1): A square duct with a cross-section of 10 cm × 10 cm for the elastic solution (a) and a circular duct with a 16 cm diameter for the acoustic solution (b).

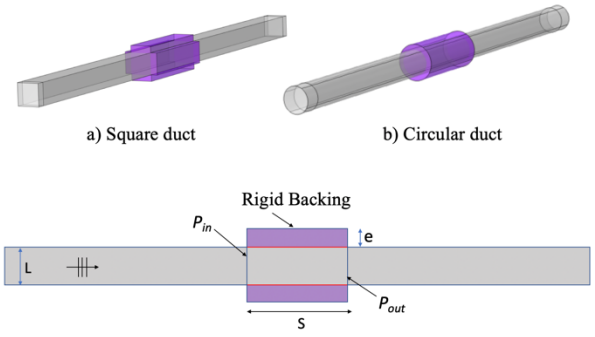


Figure 1. Experimental setups

A silencer is placed at the center of the duct, with the treatment thickness fixed at e = 3 cm in all cases to ensure compactness while addressing the target frequency ranges for attenuation. The transmission loss (TL) is determined by measuring the acoustic pressure upstream and downstream of the silencer using the microphone doublet method. In this configuration, the squared duct cutoff frequency is 1600 Hz, while the cutoff frequency of the circular duct is 1256 Hz. All configurations are first modeled and dimensioned numerically using the Finite Element Method (FEM) implemented in COMSOL Multiphysics. Once the numerical models are established, prototypes are fabricated and tested experimentally to validate the numerical predictions. In this paper, we will only present the experimental results.

3. MITIGATION STRATEGIES

3.1 Elastic Approach

In this approach, we aim to excite elastic phenomena to create, for example, a mass-spring system using a lightweight and flexible material, allowing us to control its resonance behavior. The objective is to fine-tune the system by either adjusting the mass (by adding elements to the flexible material) or modifying the stiffness (by softening the material). For practical reasons, we found no better compromise between mass and Young's modulus than using a porous material. Therefore, we utilize Melamine foam, but instead of exploiting its acoustic properties, we apply an impervious film to excite only its mechanical properties.

3.1.1 Simple case: soft elastic material

The film prevents acoustic propagation within the foam pores but allows mechanical deformation of the porous skeleton, effectively turning the foam + film system into a mass-spring resonator with a resonance frequency dependent on the Young's modulus of the foam and the mass of the system. With a Young's modulus of 100 kPa for Melamine foam, we estimate the resonance frequency to be 1200 Hz. However, this frequency is too high compared to our target of 500 Hz. To address this, we propose making the structure more flexible by introducing a periodic network of cylindrical holes filled with air, which allows local deformations of the foam and reduces the equivalent Young's modulus (Fig. 2). The experimental device

consists of cylindrical air inclusions with a diameter of 12 mm and a periodicity of 3 cm.

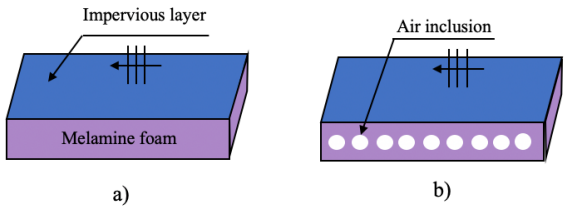


Figure 2. Liners constituting the dissipative-like silencer composed in both cases of 420x100x30mm melamine foam and 50 µm Mylar impervious layer.

Experimental results comparing these two configurations are shown in Fig. 3, where the mass-spring resonance of the homogeneous foam is clearly visible at 1150 Hz, achieving a dip with a maximum transmission loss of 30 dB. On the other hand, the TL of the sample with air inclusions shows multiple dips, achieving a significant TL enhancement over a large frequency range, particularly between 600 Hz and 1200 Hz.

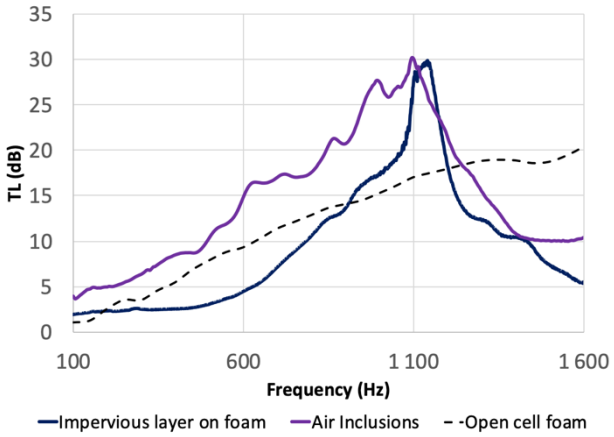


Figure 3. Experimental transmission loss comparison between the homogeneous liner and the air inclusion liner. Experimental TL of 3cm open cell foam is also plotted for information

Even though the TL is clearly enhanced, we did not achieve a sufficient improvement below 500 Hz with this solution, as we have already reached the manufacturing limit: Drilling larger holes can result in the destruction of the foam during the process. For this reason, we decided to change our approach by modifying the phenomenon involved and using local resonance instead of global deformation.

3.1.2 Elastic plate with locally resonant effects

By considering the foam with its impervious film as a soft elastic material it is relatively simple to create locally resonant phenomena by adding new elements within the plate thickness. This concept can be implemented using various types of inclusions, such as solid inclusions that act as local masses, with the matrix functioning as the spring, or flexural plates that bend and oscillate with the deformation of the soft material. By carefully tuning these inclusions, the system can be optimized to provide significant transmission loss at targeted low frequencies. In this study, we present results only for cylindrical aluminum inclusions with a diameter of 12 mm, embedded in the same foam as before, with a periodicity of 3 cm (Fig. 4). The thickness of the inclusions is 1 mm.

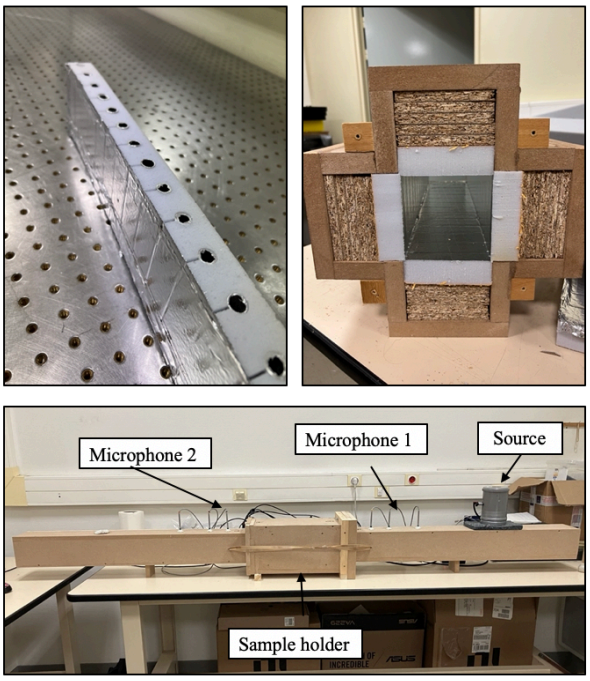


Figure 4. Pictures of the experimental setup for the elastic use case

Fig. 5 shows the experimental TL obtained with the homogeneous liner and with the sample containing aluminum inclusions. The effect of the inclusions is clearly visible between 200 and 500 Hz, with a TL of around 10 dB. As a result, beyond this frequency band, the system is no longer effective. It is therefore not suitable as a standalone solution, but it can serve as the low-frequency component of a hybrid silencer, incorporating an additional section to address mid- and

high-frequency noise, while maintaining a compact form factor and avoiding pressure drop or flow-induced noise regeneration. In parallel, we also investigated another way to reach the same target, but using an acoustic approach.

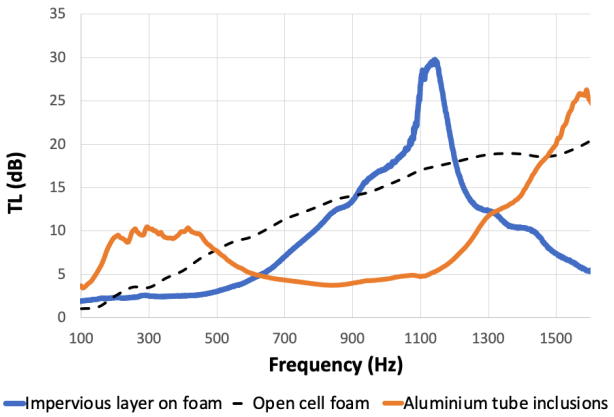


Figure 5. Experimental transmission loss comparison between the homogenous impervious foam liner and the rigid inclusion liner. Experimental TL of 3cm open cell foam liner is also plotted for information (dashed line).

3.2 Acoustic Approach

In many industrial applications, traditional porous materials cannot be used due to high temperatures, harsh environments (e.g., humidity, gas exposure, abrasion, or dust), or the need for high-pressure cleaning. Therefore, alternative transmission loss mechanisms based on reactive devices with resonator gradients are worth to investigate. In this study, we explore the potential of quarter-wavelength resonators. Unlike Helmholtz resonators, which require precise dimensional tuning due to the critical coupling of losses and sensitivity to aspect ratio, quarter-wavelength resonators are primarily controlled by the length of the duct. Although achieving low-frequency attenuation requires relatively long ducts, these can be coiled to fit within the available space. For this use case, we designed a 3 cm thick, 25 cm long silencer aimed at achieving a 10 dB transmission loss in the [250–450] Hz range (Fig. 6). The main challenge with this approach is maintaining performance in the presence of airflow. The addition of cavities directly connected to the duct walls increases local surface roughness and pressure losses, potentially inducing turbulence and noise regeneration at resonance frequencies. To address this issue, we covered the entire silencer surface with a micro-perforated mesh (25% perforation rate).

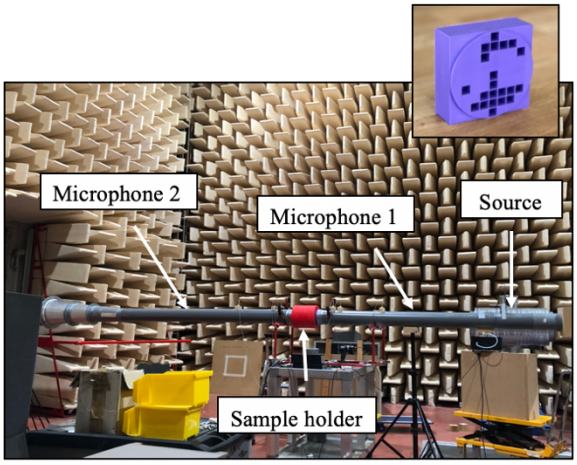


Figure 6. Experimental setup for the graded 1/4 wavelength resonator silencer with flow. Top picture depicts the unit cell sample used and wrapped to obtain the final circular silencer

The resulting transmission loss curve shows that at Mach 0.1, the device maintains 10 dB attenuation over the targeted frequency range (Fig. 7).

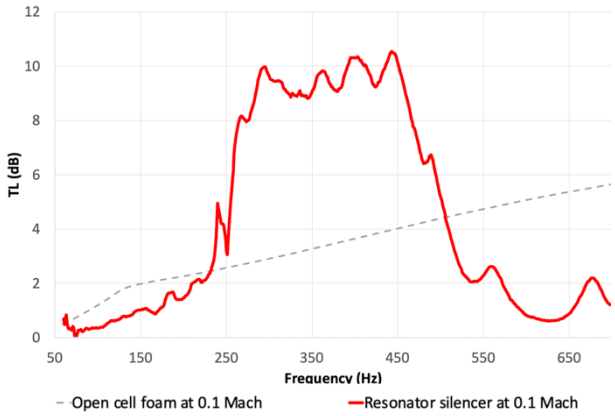


Figure 7. Experimental TL obtained for graded resonator device covered with 25% micro-perforated plate and measured with 0.1 Mach flow. Open cell foam TL for 0 and 0.1 Mach are also plotted for information.

Furthermore, we performed noise regeneration measurements and confirmed that with the micro-perforated mesh, the regenerated noise level is as low as that observed when the experimental setup is tested without a silencer. As previously mentioned, resonator-

based silencers are not effective beyond their frequency range of interest and must be combined with a mid- to high-frequency system to achieve broadband transmission loss. However, they can be highly valuable in meeting industrial constraints particularly in terms of compactness.

4. CONCLUSION

In this study, we have explored two alternative silencing strategies tailored for low-frequency noise attenuation while maintaining a constant duct cross-section. The elastic approach, based on a flexible material forming a mass-spring system, demonstrated its effectiveness in leveraging mechanical properties for improved low-frequency attenuation. The acoustic approach, using quarter-wavelength resonators, provided an alternative solution suitable for harsh industrial environments where porous materials are not viable. Both silencers were designed and tested in controlled laboratory conditions, ensuring a realistic evaluation by incorporating airflow considerations. The results confirm that these solutions achieve significant transmission loss in the targeted low-frequency range without introducing additional noise due to flow effects.

Looking forward, future work will aim to enhance the robustness and efficiency of these silencers under real operating conditions. This includes manufacturing, material choice, long-term performance assessments in the presence of humidity, dust, and temperature variations, as well as their integration into complex duct systems. Optimization strategies could be employed to fine-tune the geometric and material parameters for targeted industrial use cases. Additionally, hybrid designs combining both elastic and acoustic mechanisms may open new avenues for compact, broadband, and flow-resistant silencers, meeting the increasingly stringent acoustic and environmental requirements in ventilation and process industries.

Finaly, this paper has focused on the experimental validation of these concepts, providing key insights into their feasibility and limitations. Further details, including advanced numerical optimizations and potential industrial applications, will be discussed in our oral presentation.

5. REFERENCES

[1] Fuchs, H. V. (2013). *Applied Acoustics: Concepts, Absorbers, and Silencers for Acoustical Comfort and Noise Control*. Springer Science & Business Media, Berlin.

[2] Cummings, A., & Chang, I. J. (1988). Internal mean flow effects on the characteristics of bulk-reacting liners in circular ducts. *Acta Acustica united with Acustica*, 64(3), 169-178.

[3] Munjal, M. L. (2014). *Acoustics of Ducts and Mufflers with Application to Exhaust and Ventilation System Design*. 2nd. John Wiley & Sons, Chichester.

[4] Åbom, M. (2016). Acoustic modelling of silencers, in: *Handbook of Manufacturing Engineering and Technology*. Springer, London, 3341–3377.

[5] Kirby, R., & Cummings, A. (1998). The impedance of perforated plates subjected to grazing gas flow and backed by porous media. *Journal of Sound and Vibration*, 217(4), 619-636.

[6] Tang, S. K. (2012). A review on natural ventilation-enabling façade noise control devices for congested high-rise cities. *Applied Acoustics*, 73(8), 746-758.

[7] Seo, S. H., & Kim, Y. H. (2005). Silencer design by using array resonators for low-frequency band noise reduction. *Journal of the Acoustical Society of America*, 118(4), 2332-2338.

DOI: 10.61782/fa.2025.0902

FORUM ACUSTICUM EURONOISE 2025

TOWARDS A UNIFIED APPROACH TO CHARACTERIZE VENTILATED ACOUSTIC METAMATERIALS

Francesco Martellotta[1*] **Chiara Rubino**[1] **Stefania Liuzzi**[1]
Francesco Bianco[2] **Chiara Scrosati**[2]
[1] Politecnico di Bari, DARCOD, via Orabona, 4, Bari, 70125, Italy
[2] CNR-ITC, via Lombardia, 49, San Giuliano Milanese, 20098, Italy

ABSTRACT

Ventilated acoustic metamaterials have become increasingly popular among researchers given their ability to combine contrasting needs like sound insulation and air change, contributing to improved indoor environment quality. However, being a topic where contributions come from different disciplines, a literature review pointed out significant discrepancies in measuring (or more often simulating) approaches, used to both characterize acoustic and ventilation performances. Thus, published results are often difficult to compare. Starting from a preliminary subdivision of the metamaterial-based solutions into micro and macro-scale approaches and taking into account existing standardized procedures in use in acoustics and (more broadly) in building regulations, the present work investigates which might be the most reliable and appropriate techniques. This might represent a first important step towards defining consensus procedures and metrics to be used in acoustic metamaterial research, allowing for fully comparable results.

Keywords: ventilation, acoustic metamaterials, windows

1. INTRODUCTION

In recent years, ventilated acoustic metamaterials have emerged as promising candidates for novel window structures that attenuate transmitted sound waves while ensuring ventilation [1]. In urban areas, integrating metamaterials into window frames or glass can absorb or redirect traffic noise, enhancing indoor environmental quality by reducing sound transmission.

However, the design of acoustic metamaterials can be fine-tuned to balance noise control and airflow, ensuring proper air circulation. To this purpose, their ventilation performance should be carefully evaluated. A literature review [2] highlighted a critical lack of consistent metrics for assessing the ventilation properties of acoustic metamaterials. Additionally, the limited number of researchers studying ventilation performance resulted in further complicating comparisons among published results.

The real difficulty is to quantitatively determine the ventilation performance of the metamaterial unit. Most studies simply report open area or airflow resistance, without a consistent framework that defines how and where to measure the pressure difference, its magnitude, or how to evaluate the airflow rate.

A common method for evaluating the ventilation performance of metamaterials is to analyze the pressure drop across the material when an airflow occurs. The general idea is that, according to Bernoulli's equation, a change in velocity implies a change in pressure. In this way it is possible to evaluate the air flow resistance of the material. Higher-pressure drop indicates higher resistance offered by the material, reducing the efficiency of the ventilation system. Kumar et al. [3] showed the pressure drop versus flow rate characteristics for different opening percentages, registering an increase in the required pressure drop with increasing in airflow rate. A similar approach is followed by Fusaro et al. [4] and Kumar et al. [5] who analyzed the required pressure drop across the opening by varying the inlet airflow velocity. However, all authors studied the pressure drop resulting from modifying the opening percentage verifying that smaller openings offer high air flow resistance, establishing a high air pressure

[*] ***Corresponding author***: *francesco.martellotta @poliba.it.*
Copyright: *©2025 Martellotta et al. This is an open-access article distributed under the terms of the Creative Commons Attribution 3.0 Unported License, which permits unrestricted use, distribution, and reproduction in any medium, provided the original author and source are credited.*

drop across the window by wind and buoyancy forces. Dong et al [6] and Xiang et al [7] generated the air flow by an electric fan installed at the inlet of a tube containing the metamaterial in the middle section. The sample, obstructing the movement of air, reduces its velocity which is measured by an anemometer placed at the outlet of the tube.
To overcome the limitations related to the lack of a defined approach, this research aims to propose a methodology for testing the ventilation properties of metamaterials at the laboratory scale.

2. EXISTING STANDARDIZED METHODS

A survey of existing standards identifies three key metrics for characterizing and comparing ventilated metamaterials: airflow resistance *Rs*, discharge coefficient *Cd*, and air change rate *ACR*. *Rs* value evaluates pressure drop across a porous material, *Cd* value assesses efficiency through openings under varying pressures, and *ACR* value expresses basically the same concept but with reference to the room volume and under well defined pressure drop. Despite their different purposes, each test relies on measured pressure differences and air flow rate to calculate the figures of merit.
Specific airflow resistance is a key parameter in determining the acoustic properties of a material, as it measures how easily air can pass through it. According to ISO 9053-1 [8], *Rs* is defined as the ratio between the pressure drop Δp and the linear flow velocity w of air inside the testing rig:

$$Rs = \frac{\Delta p}{w} \quad (1)$$

A steady air source generates unidirectional laminar airflow through a cylindrical sample at velocities as low as 0.5 mm/s. A differential manometer, measuring down to 0.1 Pa, records the pressure drop to determine specific airflow resistance.
Standard EN 13141-1 [9] proposes a method to calculate the air flow rate value by gradually increasing the pressure difference across the device. The method involves the application of various static pressure differences (1–100 Pa) to an air transfer device, while measuring the corresponding volume flow rates and defining the flow rate vs pressure characteristic curve. Depending on the device type, 8 to 12 pressure measurement points are taken. The *Cd* can be obtained by regressing the measured values according to a generalized flow equation:

$$q = C \cdot \Delta p^n \quad (2)$$

where q is the volume airflow rate, Δp is the pressure difference, n is the flow exponent (n = 1 for laminar flow, n = 0.5 for turbulent flow) and C is the airflow coefficient.
The discharge coefficient is a dimensionless coefficient commonly used to characterize openings by quantifying the reduced flow resulting from the formation of the so called "vena contracta". It reflects the deviation of the actual flow rate from the ideal flow rate, accounting for factors like the geometry of the window opening, surface roughness, and turbulence. By analyzing the pressure difference across the opening and measuring the airflow, it is possible to calculate the coefficient *Cd*, which gives insight into how effectively air passes through the opening under specific conditions.
Mathematically, it is expressed as:

$$Cd = \frac{q_{actual}}{A} \cdot \sqrt{\frac{\rho}{2\Delta P}} \quad (3)$$

ISO 9972 [10] evaluates building infiltration rates through the measurement of the *ACR* value. The test is based on pressurizing or depressurizing the building using a fan to force airflow through the envelope. Airflow is measured at pressure from 50 Pa to 100 Pa. *ACR* is calculated by dividing the air leakage rate at 50 Pa *q50* by building volume V:

$$ACR = \frac{q_{50}}{V} \quad (4)$$

3. TOWARDS A UNIFIED APPROACH

Standardized methods previously analysed measures the same quantities (pressure differences and volume flow rate or average air velocity across the opening section), but they derive different parameters. In order to characterize the air permeability of ventilated metamaterial units (i.e. devices individually tested in a small equipment like standing wave tubes but intended for use in planar or spatial arrays), none of the test procedures fits perfectly In fact, flow resistance tests are suitable for porous materials with low-velocity laminar flow (≤15 mm/s), but may fail to detect pressure variations in open structures. Conversely, EN 13141 [9] method can induce turbulence in small metamaterial openings. Considering that it is known from the theory [11] that the pressure variation can be expressed as a function of the volume airflow (q) (and consequently of the mean velocity w across the section) as the sum of a linear and a quadratic term respectively representing the laminar and the turbulent component:

$$\Delta p = a \cdot w + b \cdot w^2 \quad (5)$$

Some authors also express the above relationship taking into account that the linear term related to laminar flow

($Re < 1000$) is strongly influenced by viscous losses, equivalent to the airflow resistance and quantified using the Hagen-Poiseuille equation [12] that assumes, for a circular orifice having radius *r* and length *L* and resulting in an open fraction $\phi = A_{open}/A_{tube}$:

$$a = R_s = \frac{8\eta L}{r^2 \phi} \quad (6)$$

where η is the fluid viscosity.

On the other hand, the second term applies to turbulent flow ($Re > 2000$) and can be expressed as a function of the inertial losses depending on the opening geometry, flow separation, etc., whose combined effect is given by the loss factor ($\xi = 1/Cd^2$) applied to the pressure variation resulting from the Bernoulli equation:

$$\Delta p = \frac{\zeta \rho w^2}{2} \rightarrow b = \frac{\xi \rho}{2} \quad (7)$$

Thus, the equation can be rewritten as a function of *Rs* and *Cd* as follows:

$$\Delta p = R_s \cdot w + \frac{\rho}{2C_d^2} \cdot w^2 \quad (8)$$

The two terms could be consequently determined from a proper regression analysis performed over a sufficiently large interval of *w* values, capable of keeping into account different flow rates, and, consequently, different Reynolds numbers (Re). However, as turbulence needs space to fully develop, in short openings it is not obvious that this condition takes place even at higher *Re*. Conversely, presence of sharp edges may promote flow separation and turbulence even at lower *Re*.

It is worth noticing that the standard procedure to determine air flow resistance is based on plotting *Δp* as a function of *w* and then fitting the values with a quadratic equation. Subsequent calculation of *Rs* as $\Delta p/w$ and plotting as a function of *w* should consequently return a linear distribution where the constant term coincides with the *Rs* term in Eqn. 8 which, consequently, corresponds to flow resistance when flow tends to zero.

In a similar way, collected data about pressure drops and flow rate might be directly used to calculate *Cd* for each combination. It is known from the theory that *Cd* is generally dependent on *Re* (or *w*) and becomes independent when high *Re* values are reached, while at low values viscous and laminar effects tend to reduce the value. As a consequence the EN 13141 [9] suggests to plot the values and use a power law for interpolation, assuming that, in the most general case, under fully developed turbulent flow the previous equation may not apply. However, if Eqn. 5 is assumed to be valid, it is possible to replace *Δp* in the *Cd* equation, which yields, after some steps:

$$C_d = w \cdot \sqrt{\frac{\rho}{2\Delta p}} \rightarrow C_d^2 = \frac{1}{a + \frac{2b}{\rho w}} \quad (9)$$

From which it appears that the *Cd* value appearing in Eqn. 8, and obtainable from the regression analysis, is actually corresponding to the limiting value towards which *Cd* tends when *w* grows.

In other words, plotting data and calculating regression parameters is consequently the best way to understand whether the data can fit the model represented by Eqn. 8 or more complex turbulent flows appear.

4. NUMERICAL VALIDATION

In order to test whether the proposed approach could be conveniently applied in practice, a "virtual experiment" was carried out using Comsol 6.3 and, considering that most experiments on ventilated metamaterials are carried out on simple "units" that are tested in impedance tubes, a comparable setup was explored. A simple metamaterial employing a labyrinthine structure built around a square opening [13] was modelled. A 3D printed sample of the same design was tested according to the ISO 9053-1 method [8] without success due to the very low pressure drops that appeared. So the device was modelled in Comsol and, for the sake of simplicity, only the open square was modelled. Square dimensions were 14 mm by 14 mm and 8 mm height. Inlet and outlet tubes were modelled as 60 mm cylinders long enough to let the streamline as regular as possible (Fig. 1).

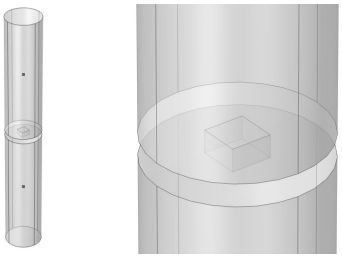


Figure 1. Schematic of the simulation set-up.

A pressure drop ranging from 0.1 Pa to 20 Pa was modelled obtaining the flow velocity distribution given in Fig. 2. Extraction of the parameters from the coefficients of the regression curve returns a Cd = 0.055 which is well aligned with analytical results given by Idelchick [16], while *Rs* shows bigger fluctuations compared to the theoretical value returned by Eqn. 4 and equal to 0.3 Pa.s/m. Extraction of values based only on the lowest *Δp* values and an increased number of

simulation points in that range, significantly improved the accuracy.

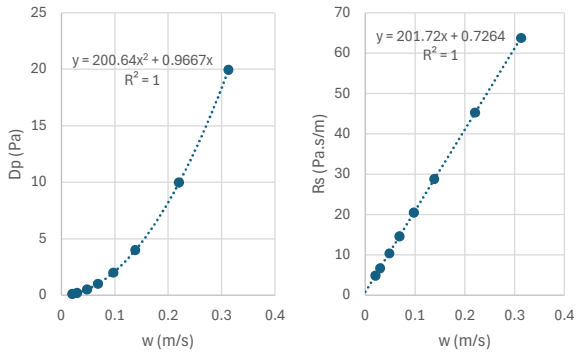


Figure 2. Velocity *w* versus Pressure drop *Δp* and air flow resistance *Rs*.

5. CONCLUSIONS

The method proposed by ISO 9053-1 can be considered, with the proposed amendments, a valid alternative for evaluating the ventilation performance of a metamaterial unit. In fact, the necessary adjustments to the velocity and pressure difference ranges make it suitable for applications with open structures and collected data can be interpreted obtaining representative parameters (Rs and Cd) that could ease comparisons among different devices.

6. ACKNOWLEDGMENTS

Project funded under the National Recovery and Resilience Plan (NRRP), Mission 4, Component 2, Investment 1.1 by the Italian Ministry of University and Research (MUR), funded by the European Union – NextGenerationEU– Project Title METAWAVE (New METAmaterial Window for simultaneous Acoustic, Ventilation and Energy performance) – Grant 2022RA785R-PE8-PRIN2022.

7. .REFERENCES

[1] S.H. Kim, S.H. Lee: "*Air transparent soundproof window*", AIP Advances 4, 117123, 2014.

[2] C. Rubino, S. Liuzzi, G. Fusaro, F. Martellotta, C. Scrosati, M. Garai: "Balancing ventilation and sound insulation in windows by means of metamaterials: A review of the state of the art", *Building and Environment* 275, 112780, 2025.

[3] S. Kumar, T.B. Xiang, H.P. Lee: "Ventilated acoustic metamaterial window panels for simultaneous noise shielding and air circulation", *Applied Acoustics* 159 107088, 2020.

[4] G. Fusaro, X. Yu, Z. Lu, F. Cui, J. Kang: "A metawindow with optimized acoustic and ventilation performance," *Applied Science* 11, 3168, 2021.

[5] S. Kumar, T. B. Xiang, H. P. Lee: "Ventilated acoustics metamaterial window panels for simultaneous noise shielding and air circulation", *Applied Acoustics* 159, 107088, 2020.

[6] R. Dong, D. Mao, X. Wang, Y. Li: "Ultra-broadband acoustic ventilation barriers via hybrid-functional metasurfaces", *Phys. Review Appl.* 15, 024044, 2021.

[7] X. Xiang, X. Wu, X. Li, P. Wu, H. He, Q. Mu, S. Wang, Y. Huang, W. Wen, "Ultra-open ventilated metamaterial absorbers for sound-silencing applications in environment with free air flows", *Extreme Mechanics Letters* 39, 100786, 2020.

[8] ISO 9053-1:2018, Acoustics - Determination of Airflow Resistance, Part 1: Static Airflow Method, ISO, Geneva, 2018.

[9] UNI EN 13141-1:2019, Ventilation for buildings - Performance testing of components/products for residential ventilation - Part 1: Externally and internally mounted air transfer devices.

[10] ISO 9972:2015, Thermal Performance of Buildings - Determination of Air Permeability of Buildings - Fan Pressurization Method, ISO, Geneva, 2015.

[11] D. Etheridge: Natural ventilation of buildings: Theory, measurements and design. United Kingdom: John Wiley & Sons, Ltd, 2012.

[12] J.F. Allard and N. Atalla: Propagation of sound in porous media: Modelling sound absorbing materials. United Kingdom: John Wiley & Sons, Ltd, 2009.

[13] J. Yang, J.S. Lee, H.R. Lee, Y.J. Kang, Y.Y. Kim: "Slow-wave metamaterial open panels for efficient reduction of low-frequency sound transmission", *Applied Physics Letters*, 112, 091901, 2018.

[14] I.E. Idelchik: Handbook of hydraulic resistance. 4th Revised And. Augmented Edition New York: English Edition Editor, 2007.

DOI: 10.61782/fa.2025.0268



FORUM ACUSTICUM
EURONOISE 2025

DEMONSTRATING THE EFFECTIVENESS OF A MULTI-LAYER THIN MINERAL SOUND ABSORBER FOR COURTYARD NOISE REDUCTION

Bart Van Damme[1*] **Jean-Marc Wunderli**[1] **Liviu Zambila**[1]
Théo Cavalieri[1,2]

[1] Laboratory for Acoustics/Noise Control, Empa, Ueberlandstrasse 129, 8600 Dübendorf, Switzerland
[2] L-Acoustics, 13 rue Levacher Cintrat, 91460 Marcoussis, France

ABSTRACT

Reducing traffic noise in urban environments has a proven positive effect on the wellbeing. It is known that sound absorbing façades can improve the noise level in streets and courtyards, but practical large-scale surface treatments are scarce. Porous absorbers are typically bulky, and resonant absorbers too expensive for this kind of application. We have shown previously that perforated mineral foams (PMFs) yield high sound absorption levels over a relatively wide frequency range, while requiring only a fraction of the thickness of open-pore absorbers. In this work, a multi-layer PMF absorber is demonstrated. In a first step, the optimal configuration of four PMF layers with a total thickness of 55 mm is shown to yield high diffuse-field sound absorption in the 500-1000 Hz range. Based on this result, a 12 m^2 surface is manufactured and its absorption coefficient measured in a reverberation room. Finally, the demonstrator is tested in realistic conditions, and shows a significant reduction of broadband noise transmission through a courtyard entrance. The controlled measurements are supported by finite element simulations to improve their effectiveness by optimal placement considerations.

Keywords: *sound absorption, demonstrator, acoustic optimization*

**Corresponding author*: *bart.vandamme@empa.ch.*
***Copyright**: ©2025 Bart Van Damme et al. This is an open-access article distributed under the terms of the Creative Commons Attribution 3.0 Unported License, which permits unrestricted use, distribution, and reproduction in any medium, provided the original author and source are credited.*

1. INTRODUCTION

Acoustic absorbers are crucial in creating a pleasant environment. By reducing reflections and reverberation time, the overall noise level can be lowered, the intellegibility improved, or the musical quality enhanced [1]. Acoustic absorbers also play a crucial role in reducing engine, turbine, and ventilation noise. This paper presents a method to achieve high diffuse acoustic absorption in a chosen broad frequency range. Using an optimized layering of perforated mineral foams, the absorber can be devised considerably thinner than when conventional porous media are used. The effectiveness is illustrated with a large-scale demonstrator, designed to reduce street noise transmission through a courtyard entrance.

2. ACOUSTIC ABSORPTION BY PERFORATED FOAMS

2.1 Homogenization of the acoustic properties

The use of perforated rigid foams for low-frequency sound absorption was shown in previous studies [2, 3]. By combining foam properties (pore size and wall thickness) with an appropriate perforation pattern (diameter and spacing), the absorption spectrum can be tuned to a desired frequency range. The modelling is done in two steps. First, a numerical simulation of a representative volume element of the perforated foams allows us to calculate homogenized fluid properties, i.e. complex valued bulk modulus and mass density, based on the Johnson-Champoux-Allard description of viscous and thermal losses [4]. In a second step, a combination of the four foam parameters is chosen to achieve the desired absorption spectrum.

In our previous work, we showed that the tortuosity of such structures is considerably higher than for open-pore

foams [3, 5]. However, high tortuosity typically comes at the cost of higher flow resistivity. Therefore, a compromise between absorption amplitude and the frequency of maximum absorption has to be found. It is practically possible to achieve absorption levels higher than 0.8 for a layer thickness equal to or smaller than 1/15 of the wavelength in air. This is similar to several advanced absorber designs based on coiled or resonant structures.

2.2 Optimization of layered sound absorbers

The homogenization step allows to generate a library of acoustic materials with various sound propagation properties. In collaboration with a foam manufacturing company, de Cavis AG, gypsum foams with pore sizes varying between 1 and 3 mm, and a constant wall thickness between 0.1 and 0.3 mm, can be reliably produced in batches of 1 m^3. Due to advanced stabilizers, a total porosity higher than 90% can be achieved, yielding a mass density below 150 kg/m^3 for the lightest materials. The foams are cut to the desired thickness, and can be perforated by needle punching or water jet cutting.

It is known that layered sound absorbers can outperform homogeneous porous media in terms of thickness and band width [6,7]. For our application, we aim for high sound absorption in the range between 400 and 1000 Hz. To achieve this, we can use three foam types, combined with several perforation patterns. The perforations can be either 0.5 or 1 mm in diameter, and 5 or 10 mm apart in a rectangular pattern. In total, ten combinations have desirable acoustic properties and are considered useful for the absorber design.

The optimization process aims to achieve a minimal absorption level within prescribed frequency bounds, by finding a suitable stack of materials with optimized thickness and order. Limitations such as total thickness, minimal layer thickness, and maximum amount of layers can be easily introduced. The absorption of the rigidly backed stack is calculated by a transfer matrix approach, and the optimization is done by a particle swarm optimization. To further improve the design space, air is allowed as one of the layers.

3. LARGE ABSORBER DEMONSTRATOR

3.1 Optimized absorber layout and construction

For a practical implementation, we aim for absorption levels higher than 0.8 starting at 400 Hz and up to 1000 Hz. The absorber stack should not be thicker than 55 mm, which is thinner than 1/15 of a wave length in air and thus considerably thinner than traditional porous absorbers. In order to reduce fragility, the layers should not be thinner than 10 mm and the amount of layers cannot be higher than 4.



Figure 1. Top: layered setup of the opimized absorber panel. Bottom: Placement of the absorber panels in the courtyard entrance.

Several combination of layers yield a suitable absorption spectrum, and further practical considerations can be taken into account for the final choice. In this case, it turns out that only one foam type is necessary: a lightweight gypsum foam with 3 mm pore size and 0.1 mm wall thickness. Combining one type of perforated and one non-perforated layer, in which case only the inherent microporosity is considered, the prescribed absorption can be achieved. The layers are cut to size and placed in wooden frames for easy transportation and placement. In total, 72 panels of 40×40 cm^2 are made, yielding a 12 m^2 surface. Each panel weighs less than 1.5 kg and has a total thickness of 57 mm, making it ideal for treating walls without increasing the demands on bearing capacity, or taking too much space. the structure of the panels is shown in Fig. 1.

3.2 Reverberation room measurement

In order to validate the optimization and the models, the diffuse sound absorption is measured according to EN ISO 354. The entire sample is placed on the floor of a reverberation room, including the beams that will be used for installation in situ (see Fig. 2). This slightly increases the total surface, and therefore reduces the diffuse absorption coefficient. Despite this small difference, it can be seen in Fig. 2 that the absorption reaches a peak value of 1.1 at 400 Hz. At frequencies higher than 1200 Hz the absorption is reduced, since the stack was not optimized in this range. This is however not necessarily negative. In many real situation, the higher frequency range is sufficiently absorbed by other effects, and additional absorption might reduce intellegibility and could make the room sound too dry.

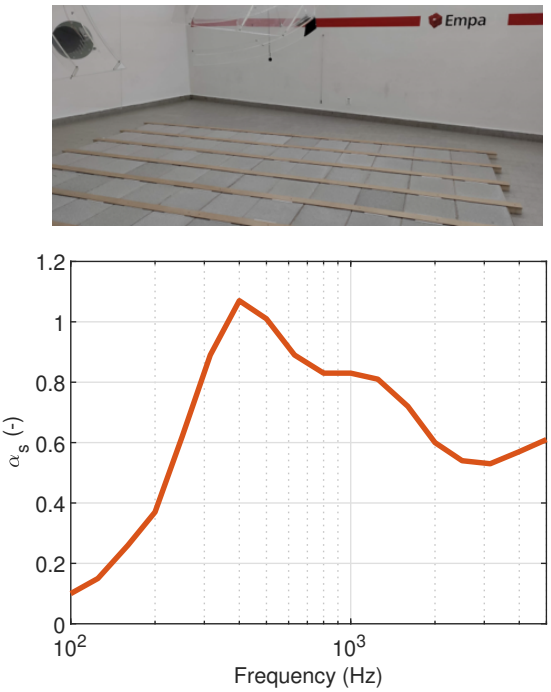


Figure 2. Diffuse absorption coefficient measurement according to EN ISO 354. Top: experimental setup in the Empa reverberation room. Bottom: measured absorption curve.

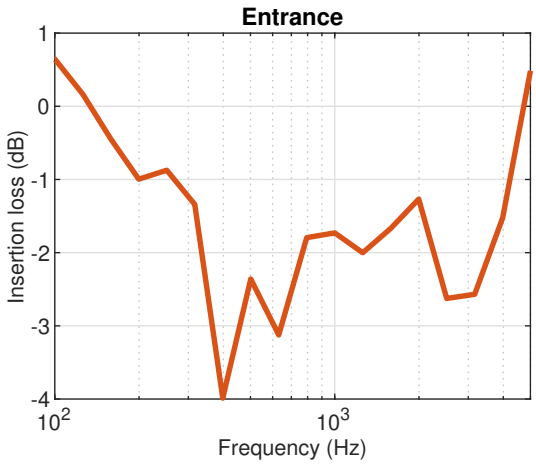


Figure 3. Measured insertion loss comparing the sound transmission through the entrance with and without absorber panels.

3.3 Noise transmission reduction in a courtyard entrance

The efficiency of the absorber panels to reduce street noise transmission is tested in a passage to a courtyard with dimensions 3 × 3 × 12 m^3. The panels are placed on both side walls in a symmetric way, close to the street side entrance, in a 3 × 12 panel arrangement. This way, 1.2 × 4.8 m^2 of each wall is covered, which is around 1/6 of the walls' surface. The final setup is shown in the bottom image of Fig. 1.

Pink noise is generated by an omnidirectional loudspeaker, placed 3 m away from the entrance, and measured by microphones placed at the entrance and exit of the passage. To mimic a car pass-by, the loudspeaker is moved parallel to the street, starting in the middle of the passage and spanning 6 positions with 0.5 m steps. The sound transmission loss is calculated as the transfer function between the entrance and exit in third octave bands for each loudspeaker position, for the situation with and without absorbing panels. Finally, the insertion loss is calculated as the difference between the situations with and without absorbers of the mean SPL.

The correlation between the insertion loss and the diffuse sound absorption spectrum is clearly seen in Fig. 3. At the frequency of maximum absorption, an insertion loss of 4 dB can be measured. At very low (¡200 Hz) and at very high (¿4000 Hz) frequencies, the insertion loss is minimal.

4. CONCLUSION

Layered sound absorbers consisting of perforated mineral foams can be optimized to achieve broadband high absorption, while only needing a fraction of the thickness of conventional porous absorbers. Since the base material is a mineral foam, their application is similar to standard absorbing materials, and they can be fabricated in bulk. Moreover, mineral foams offer unique properties, e.g. external use (in case of cement foams), or high-temperature environments (in case of ceramic foams). A large demonstrator of 12 m^2 allowed us to confirm the validity of the optimization by standardized absorption testing. Moreover, it was possible to measure a 4 dB sound transmission reduction in realistic conditions, showing that effective acoustic treatments can be realized with thin structures.

5. ACKNOWLEDGMENTS

This work was funded by Innosuisse project IP-EE 56633.1 and by the City of Zurich, Environmental and Health Protection Department. We gratefully acknowledge the support of de Cavis AG.

6. REFERENCES

[1] T. Cox and P. d'Antonio, *Acoustic absorbers and diffusers: theory, design and application*. CRC press, 2016.

[2] F. Chevillotte, C. Perrot, and R. Panneton, "Microstructure based model for sound absorption predictions of perforated closed-cell metallic foams," *The Journal of the Acoustical Society of America*, vol. 128, no. 4, pp. 1766–1776, 2010.

[3] B. Van Damme, T. Cavalieri, C.-T. Nguyen, and C. Perrot, "Enhancement of the sound absorption of closed-cell mineral foams by perforations: Manufacturing process and model-supported adaptation," *Materials & Design*, vol. 249, p. 113540, 2025.

[4] C. Perrot, R. Panneton, and X. Olny, "Linking microstructure and acoustic properties of open-cell foams," *The Journal of the Acoustical Society of America*, vol. 120, no. 5_Supplement, pp. 3145–3145, 2006.

[5] T. Cavalieri and B. Van Damme, "Sound pressure-dependent acoustic absorption by perforated rigid-frame porous materials," *Acta Acustica*, vol. 8, p. 79, 2024.

[6] M. D. Guild, V. M. García-Chocano, W. Kan, and J. Sánchez-Dehesa, "Acoustic metamaterial absorbers based on multilayered sonic crystals," *Journal of Applied Physics*, vol. 117, no. 11, 2015.

[7] J. Boulvert, T. Cavalieri, J. Costa-Baptista, L. Schwan, V. Romero-García, G. Gabard, E. R. Fotsing, A. Ross, J. Mardjono, and J.-P. Groby, "Optimally graded porous material for broadband perfect absorption of sound," *Journal of Applied Physics*, vol. 126, no. 17, 2019.

DOI: 10.61782/fa.2025.0041

FORUM ACUSTICUM EURONOISE 2025

A Study on the Prediction Method of Bush Dynamic Characteristics in Used and High Frequency Domain

Young Eun Ahn[1]

[1] Hyundai Motor Company, Korea

ABSTRACT

As electric vehicles become more prevalent, NVH (Noise, Vibration, and Harshness) performance requirements extend into higher frequency bands (1 kHz and above) due to motor excitation characteristics. Performance verification is often conducted at the concept stage using virtual models. In the medium and high frequency ranges, where mode density is high, NVH problems are typically addressed by reducing the response magnitude rather than designing for mode avoidance. This highlights the critical role of the bush system. However, obtaining bush characteristics that accurately capture the high frequency response remains challenging. This study performs a dynamic stiffness analysis of bushes using a three-dimensional finite element (3D FE) model to validate the approach and explores a method for extending the analysis to the medium and high frequency domains for direct application in vehicle development.

Keywords: NVH Performance, Bush and Mount System, Dynamic Stiffness, Rubber, System Analysis, Prediction Methodology

1. INTRODUCTION

Recently, in the automotive industry, performance evaluations extending to high frequency bands of 1 kHz or more have become necessary for NVH performance, due to motor excitation characteristics and the shift to electric vehicles. Unlike low frequency bands—which check mode frequencies to avoid resonance—medium and high frequency bands have high mode density. Therefore, NVH issues are generally addressed by reducing the magnitude of the response rather than by designing to avoid specific modes. This necessitates the efficient design of vibration-proof and sound-absorbing materials within a bush system or a final response system that reduces vibration transmission through insulation during electric vehicle development.

Performance verification is carried out at the conceptual stage using virtual models to secure target vehicle performance early. In particular, bush characteristics represent a critical factor that often conflicts with both NVH and ride & handling (R&H) performance. Thus, it is important to promptly evaluate NVH performance in a design review that meets both criteria.

In a typical bush virtual model for predicting NVH performance, the dynamic characteristics for six degrees of freedom are represented as constants using a spring element. These dynamic properties are usually derived by applying a lump sum multiplier—typically 1.5 or 2 times—to the static characteristic design targets. Additionally, when the developed bush is applied to a new vehicle, dynamic properties measured at a specific frequency (usually 100 Hz) from test reports are used. Although this method offers a simple approach for constructing a performance prediction model during the design stage, it is somewhat insufficient for addressing vibration noise problems that require precise frequency response characterization. Moreover, while test reports typically provide dynamic characteristics in the translational direction (owing to test equipment limitations), evaluating dynamic characteristics in the rotational direction remains challenging.

Furthermore, although recent dynamic characteristic test equipment can evaluate up to approximately 1 kHz, obtaining bush dynamic data at this frequency is not

*Corresponding author: ahnyoungeun@hyundai.com

Copyright: ©2025 First author et al. This is an open-access article distributed under the terms of the Creative Commons Attribution 3.0 Unported License, which permits unrestricted use, distribution, and reproduction in any medium, provided the original author and source are credited.

straightforward. More importantly, to address NVH issues arising from electric vehicle motor excitation forces, bush characteristics at even higher frequency ranges (e.g., 1.5 to 2 kHz) are required.

To overcome this limitation, a bush dynamic analysis method using an FE model was investigated to achieve a high correlation between test and analysis results. However, securing accurate rubber material properties—which critically influence the analysis—proved difficult, rendering the method unsuitable for immediate application in vehicle development.

In this study, a bush dynamic analysis using a 3D FE model was conducted to verify its accuracy, and a method applicable to actual vehicle development—with extension to the medium and high frequency domains—was explored.

2. MAIN TEXT

2.1 Rubber properties for analysis

In order to determine the characteristics of the bush through analysis, the following analytical properties, obtained from rubber specimen tests, are required:

1. Static Properties: Strain-energy function and material constants for expressing hyper-elastic behavior.
2. Dynamic Properties: Storage modulus and loss factor for viscoelastic characterization.
3. Poisson's Ratio.

Conventional elastic materials, such as metals, exhibit linear elastic behavior, meaning that they maintain a proportional relationship between load and deformation and return to their original state once the load is removed. In contrast, rubber materials exhibit elastic behavior even under large deformations where the relationship between load and deformation becomes nonlinear; this behavior is known as hyper-elasticity. When the strain-energy function is modeled as a polynomial that accurately represents this behavior, and the corresponding material constants are determined through tensile and compression tests on the rubber specimen, these properties can be used for analysis. In this study, the hyper-elastic behavior is modeled using the Yeoh function, as illustrated in Figure 1.

$$U = \sum_{i=1}^{N} C_{i0}\left(\bar{I}_1 - 3\right)^i + \sum_{i=1}^{N} \frac{1}{D}\left(J^{el} - 1\right)^{2i}$$

Yeoh (N=3)	Ci0	D
i=1	security	
i=2		
i=3		

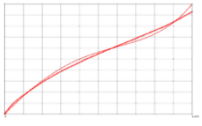


Figure 1 Hyper-elastic Material Constants of Rubber

Viscoelasticity refers to the coexistence of viscosity and elasticity in a material. Unlike metals, rubber materials dissipate energy through internal friction. This behavior is characterized by a complex modulus comprising two components: the storage modulus and the loss factor. These parameters are obtained by subjecting rubber specimens to dynamic strain testing. In this study, the storage modulus and loss factor measured up to 300 Hz, as shown in Figure 2, were used.

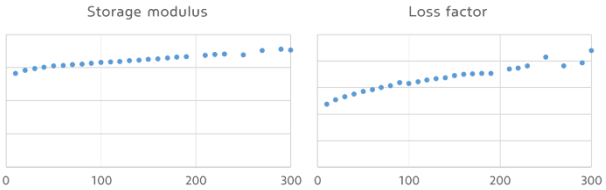


Figure 2 Complex Elastic Modulus of Rubber

Since rubber materials are generally considered to be nearly incompressible, a Poisson's ratio appropriate for this is used.

2.2 3D Bush Dynamic Characteristics Analysis Accuracy Verification

The accuracy of the 3D FE analysis was verified using a G BUSH component from a midsize sedan, which allowed for accurate rubber material characterization. Based on the physical property evaluation of the rubber specimen, the rubber properties used in this analysis included the viscoelastic (hyperelastic, Yeoh model) modulus and the viscoelastic modulus and loss factor measured up to 300 Hz. The static properties of the G BUSH were determined by averaging the stiffness between displacements of 0.5 mm and 2 mm, and the error defined as the difference between the test report and the analysis results is at the level of 7%.

For the dynamic characteristic analysis, although the viscoelastic properties of the rubber specimen were evaluated up to 300 Hz, the analysis was performed at 100 Hz for accuracy verification. The corresponding analysis results were compared with the test report values. As illustrated in Figure 4, the static characteristics in the translational direction were predicted with a maximum error of 7%. Regarding the dynamic characteristics, although the Q direction could not be compared due to the absence of test data, the errors in the P1 and P2 directions were 2% and 14%, respectively, indicating that the dynamic characteristics were predicted with an error within 15%. In the rotational direction, the error in the static characteristics was relatively larger—up to 24% compared to the translational direction—

but this is considered acceptable given that dynamic evaluation in the rotational direction is not feasible, and the analysis method provides values under conditions similar to those used in the static evaluation with high accuracy.

DIR	단위	Static			Dynamic		
		TEST	CAE	Error	TEST	CAE	Error
P1	N/mm	security		7%	security		2%
P2				0%			14%
Q				3%			-
S1	N*mm/rad			24%			-
S2				-			
R				22%			

Figure 4 Comparison of Test/CAE results and errors in all directions

2.3 2.3 Problems and Hypothesis Establishment and Verification

For conventional elastic materials such as metals and glass, "standard physical properties" are typically used to predict performance under uniform conditions, regardless of variations in vehicle type or the personnel responsible for the virtual model. In contrast, due to significant variations in rubber material properties—dependent on material type, mixing ratio, and manufacturing process—it is challenging to adopt a single set of standard physical properties for rubber. When accurate rubber properties corresponding to the manufactured parts (such as those of the G BUSH in a medium-sized sedan) are available, bush characteristics can be predicted within the test error range. In particular, using viscoelastic properties that incorporate frequency characteristics enables the development of bush models that accurately reflect NVH performance.

However, it is impractical to secure all the appropriate rubber material properties for every bush, given the wide range of bush types, manufacturers, hardness levels, and other factors present in actual vehicles. To address this limitation, the hypothesis was proposed that if the ratios of the characteristics in all six degrees of freedom are proportional to the shape of the rubber part, the primary characteristics could be determined using the available properties. Consequently, it was hypothesized that the static and dynamic characteristics in all directions could be obtained through post-processing of the test results available in some directions. The conceptual diagram illustrating this approach is shown in Figure 5.

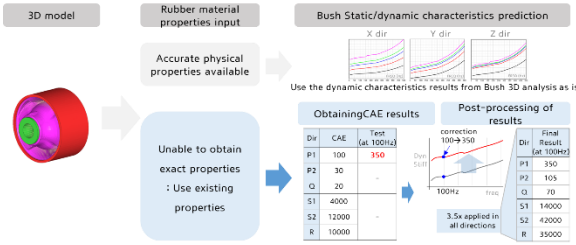


Figure 5 Conceptual diagram for predicting characteristics of Busch 3D analysis

For verification, the previously validated G BUSH model of a medium-sized sedan was employed. The analysis was performed using rubber material properties obtained from other manufacturers that did not match the properties used for the G BUSH model. As shown in the left table of Figure 6, the positive characteristics in the translational and rotational directions exhibited errors of 38% and up to 58%, respectively, compared to the test report.

To adjust for these discrepancies and align the analysis results more closely with the test report, a correlation coefficient of 0.79 was derived by dividing the test report value (237) in the P2 direction by the analysis result (300). This coefficient was then applied uniformly to the basic analysis results in all six directions, as illustrated in Figure 7. The adjusted results yielded a final error of up to 9% in the translational direction and up to 28% in the rotational direction, which is comparable to the results obtained using the accurate rubber properties for the actual G BUSH (with errors of up to 7% and 24% in the translational and rotational directions, respectively).

DIR	Unit	Static of G bush		
		Test	CAE	Error
P1	N/mm	Security		7%
P2				-
Q				3%
S1	N*mm/rad			24%
S2				-
R				22%

Fig. 6 G BUSH Static Characteristics Results



Figure 7 Prediction Results of Using and Aftertreatment of Physical Properties

To extend the validated hypothesis to various types of bushes, the static characteristics of all bushes in a small SUV were evaluated using the same methodology previously applied to the G BUSH of a medium-sized sedan. First, the primary direction—typically the VOID direction (P2) or the axial direction for a shock absorber bush—was identified. The ratio of the test report value to the analysis result in this primary direction was then used as a correlation coefficient, which was uniformly applied across all directions.

Figure 8 presents the static and dynamic characteristics calculated using the proposed method. For static characteristics, the final adjusted results closely matched those from the test report. For dynamic characteristics, values for the remaining five directions—where test data were unavailable—were successfully obtained. Notably, both the static correlation coefficient (c = a/b) and the dynamic correlation coefficient (C = A/B) were determined to be 1.3, an observation that merits further attention.

	dir	Static				Dynamic			
		Test (a)	CAE (b)	Correlation Coefficient1 (c=a/b)	Static (d=b*c)	Test (A)	CAE (B)	Correlation Coefficient2 (C=A/B)	Dynamic (D=B*C)
G BUSH	P1								
	P2	390	300		390	1040	800		1040
	O			1.3		-		1.3	
	S1			※ P2				※ P2	
	S2					-			
	R								

Figure 8. Prediction Results of G BUSH Static and Dynamic Characteristics of Small SUV

Since the dynamic characteristic correlation coefficient cannot be determined without results from the dynamic test report (as illustrated by the strut insulator in Figure 9), the final static characteristic value (d) was first calculated using the static characteristic correlation coefficient (c = a/b), as described above. The final dynamic characteristic value (F) was then obtained by multiplying this static value (d) by the dynamic ratio (E = B/b) between the static and dynamic characteristics.

	Dir	Static				Dynamic		
		Test (a)	CAE (b)	Correlation Coefficient1 (c=a/b)	Static (d=b*c)	CAE (B)	Ratio (Dynamic/Static) (E=B/b)	Dynamic (F=d*E)
FR STRUT INSULATOR	X							
	Y							
	Z	1200	1500	0.8	1200	3450	2.3	2760
	RX			※ 대입항				
	RY							
	RZ							

Fig. 9 Prediction method of FR STRUT INSULATOR static and dynamic characteristics of a small SUV (1)

However, given that the static and dynamic characteristic correlation coefficients derived from the G BUSH results for the small SUV (as shown in Figure 8) are identical, the final dynamic characteristic can be calculated as illustrated in Figure 10. This result is consistent with the final dynamic characteristic obtained in Figure 9.

	dir	Static				Dynamic			
		Test (a)	CAE (b)	Correlation Coefficient1 (c=a/b)	Static (d=b*c)	Test (A)	CAE (B)	Correlation Coefficient2 (C=A/B)	Dynamic (D=B*C)
FR STRUT INSULATOR	P1								
	P2								
	O	1200	1500	0.8	1200	-	3450	0.8	2760
	S1			※ O				※ O	
	S2								
	R								

Figure 10. FR STRUT INSULATOR Static and Dynamic Characteristics Prediction Method (2)

Based on two prediction methods—one utilizing the dynamic test report and one without—it was possible to predict both static and dynamic characteristics for a total of 10 bushes in small SUV vehicles, and compare them with the test report. Although verifying the accuracy of dynamic characteristics is challenging—since most bushes provide test data for only one major direction—the excellent prediction accuracy for static characteristics, using the same model and analysis method, suggests that the derived dynamic characteristic values are reliable for use in the NVH performance review model.

2.4 Dynamic Properties Prediction Frequency Extension and Application Method

Finally, an approach was reviewed to expand the frequency range over which dynamic characteristics can be predicted. Since the viscoelastic properties of the rubber specimen are measured only up to 300 Hz, the bushing characteristics for a single component are likewise limited to this range. Due to equipment limitations, evaluating material properties at higher frequencies is challenging. Therefore, a linear extrapolation method was employed to extend the available physical property data into the higher frequency domain.

As illustrated in Figure 12, the linear trend of the storage modulus as a function of frequency is first extracted from the measured data (up to 300 Hz). This trend is then extended into the desired higher frequency range, with the measured data used directly up to 300 Hz and the extrapolated data applied beyond that, as shown in Figure 13. The loss factor was similarly extended to 1000 Hz using the same method.

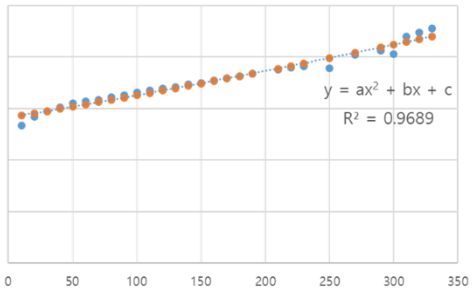


Figure 12 Extracting the Storage Modulus linear trend line of viscoelastic elasticity

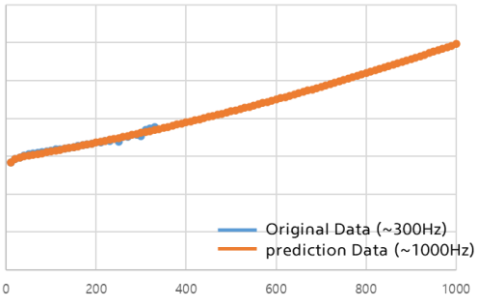


Fig. 13 0~1000 Hz Storage Modulus Prediction Data

The predicted dynamic characteristics of the G BUSH for a small SUV—obtained by extending the rubber properties to a frequency domain of 1000 Hz—are presented in Figures 14.

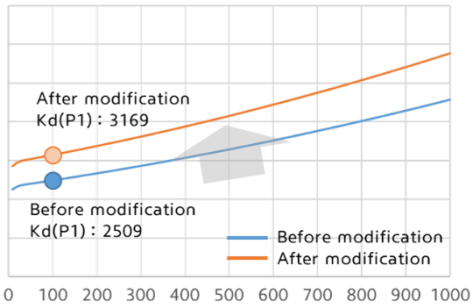


Figure 14 Prediction Results of G BUSH P1 Dynamic Characteristics of Small SUV (~1000 Hz)

3. CONCLUSION

3.1 Conclusion

In this study, we addressed the challenge of obtaining bush dynamic characteristics—required for predicting NVH performance in the middle and high frequency domains—that are difficult to measure in all six degrees of freedom due to limitations of test equipment. To overcome this issue, a 3D shape-based bush dynamic characteristics prediction method was developed, and the following conclusions were reached:

1. Comprehensive Data Acquisition: To improve the accuracy of NVH performance predictions, it is essential to obtain dynamic characteristic values in all six degrees of freedom over the frequency region of interest and incorporate these values into the analysis model. By inputting accurate material properties specific to the bush and utilizing its 3D shape, it is possible to predict properties that fall within the test error range across all directions.
2. Use of Correlation Coefficients: When accurate material properties are unavailable for all directions, a correlation coefficient can be derived using dynamic test results from a specific primary direction (obtained via the initial 3D shape-based analysis and previously secured physical properties). This coefficient can then be applied uniformly to estimate accurate dynamic characteristics in all directions.
3. Frequency Range Extension via Extrapolation: Even when viscoelastic material properties of the rubber specimen are evaluated, securing data up to the desired high frequency range remains challenging. In such cases, extending the measured material property data to the required frequency range via linear extrapolation enables the calculation of bush dynamic characteristics over the higher frequency domain.

Overall, the study demonstrates that predicting bush dynamic characteristics in the middle and high frequency domains using a 3D shape-based approach is a promising method. This approach effectively overcomes equipment limitations and reduces time and cost constraints, ensuring that sufficient dynamic characteristics can be secured for accurate NVH performance evaluation.

.

4. REFERENCES

[1] Lee Shin -bok,“Development of Rubber Dynamic Characteristics Analysis Technology”, 2012/10, Internal Report.

[2] Jeong Heon-seop,“ Construction of Suspension Bush Material Material Materials DB Phase 2 ”, 2018/04 , Internal Report.

[3] Hyundai NGV,“ Engineering Technology_Understanding the Characteristics of Rubber Materials for Automobiles ”, 2019/05, Internal Report.

DOI: 10.61782/fa.2025.0553

FORUM ACUSTICUM EURONOISE 2025

MEASUREMENTS OF THE ACOUSTIC PROPERTIES OF MYCELIUM-BASED MATERIALS USING AN IMPEDANCE TUBE

György Wersényi[1*] **Zsófia Németh**[1] **Attila Schweighardt**[2]
[1] Department of Telecommunications, Széchenyi István University, Hungary
[2] Department of Whole Vehicle Engineering, Széchenyi István University, Hungary

ABSTRACT

Mycelium-based materials were tested for acoustic purposes. Different fungi were grown on substrates and formed to fit into the available impedance tube for transmission loss (TL) and absorption rate (AR) measurements. Results supported previous findings about mycelia being acoustically appropriate for sound insulation, especially in the spectral region of speech. Absorption rates between 0.1 and 0.6 were measured. Furthermore, thickness appears to be the most important factor. However, large-scale production, design, and lifespan are critical issues, and further experiments are needed to develop industry-level products.

Keywords: *transmission, impedance tube, speech intelligibility, mycelium, sustainability*

1. INTRODUCTION

Acoustic paneling for room acoustic or automotive solutions incorporate various materials. These are generally foams, porous structures with high absorption coefficients allowing for acoustic damping and isolation in many application areas. On the other hand, the use of natural materials can contribute to sustainability. Especially, biodegradability plays a significant role in environment friendly production and recycling. It is the capability of a material to be broken down by living organisms, such as bacteria, fungi, or water molds, and reabsorbed by the natural environment.

1.1 Mycelium as material

The mycelium is a root-like structure of a fungus consisting of a mass of branching, a network of fungal threads or hyphae. Mycelia often grow underground, but can also thrive in other substrates. The fruiting bodies of fungi, such as mushrooms, can sprout from a mycelium.
To create the optimum substrate for culturing and breeding, a temperature of 18-25 Celsius, HEPA-filtered air, and a sequentially operated mixer are needed. An additional cold vaporizer with hydrogen peroxide would be an innovative solution in optimization. In the substrate, the mycelium will grow and penetrate 1-4 weeks in case of constant temperature. For the substrate, different materials can be used - i.e., hemp, sawdust, wood waste, coffee-ground - anything with high cellulose content. The substrate must be pasteurized, free from fungicide materials and other fungus (this happens in heat stress for several hours around 80°C), and dried on air or in a heated oven. In contrast to usual materials, mycelium is different in production, storage and design. Only a few companies offer industry grade and high quality solutions, e.g., by providing pre-mixed substrate and mycelium [1, 2].
Mycelium has an uneven growth, it is inhomogeneous, especially by contrasting surface and internal part. The substrate (which is generally responsible for the mass) produces larger cavities and gaps that are filled by the mycelium. Some strains of fungus have good water solubility, and thus, the liquid can be sprayed over the substrate. For example, the *Ganoderma* fungi can be breed in big tanks under sterile circumstances (Fig.1.).
At the end, high temperature (overheating) is used to stop the growing process. Forming, cutting and designing can be performed before and/or after the heat stress. For example, if the material is to replace wood or plastic, the overheating

[*] ***Corresponding author***: *wersenyi@sze.hu*
Copyright: *©2025 First author et al. This is an open-access article distributed under the terms of the Creative Commons Attribution 3.0 Unported License, which permits unrestricted use, distribution, and reproduction in any medium, provided the original author and source are credited.*

and forming take place in a pneumatic heat press. If the application area is acoustics, a foam-like state without pressing is recommended. Fire, moisture resistance, tension and compression tests are also important for usability [3].



Figure 1. Example of mycelium-based materials of different forms and sizes.

More research is needed to optimize the manufacturing process, especially in larger "industrial" scale in a time- and cost-effective way. Currently, industry-grade production offers a wide range of applications on large scale, especially on the field of packaging [4]. Acoustic paneling is very similar in size and form. Furthermore, on a smaller scale, local production contributes to sustainability (by avoiding long-distance shipping and enabling local recycling), to local employment and individual production.

1.2 Acoustic measurements

The most important material properties to describe acoustic behavior of porous absorbers are tortuosity, porosity, flow resistivity, and surface openness [5, 6]. They can be measured directly with dedicated equipment or indirectly.

There are two main methods to measure acoustic properties (indirect methods). One of them is using a Kundt's tube also known as an impedance tube [7, 8]. The material is located at the one end of a tube, while the other end is closed with a loudspeaker producing a standing wave. Microphones are fixed along the tube, and the acoustic properties can be calculated by the transfer function method. This compares the sound pressure levels as function of frequency. Small sample sizes can be used, but it is assumed to have perpendicular sound incidence, which is usually an invalid assumption in real life environments. The other method is having a reverberant or anechoic room. This is more realistic, but deals with very large sample (and room) sizes.

This paper presents the method of breeding, followed by the acoustic measurement setup to determine the basic acoustic properties. Based on the results, current state and future perspectives will be discussed from the engineering point of view, focusing on the spectral range of speech.

2. MEASUREMENT SETUP

To create the samples, different types of fungal germ were used on different substrates. After 5-6 weeks, six samples were selected for the measurement. Beech wood chip substrate was used for two *Ganoderma* and two *Pleurotus* samples (see Fig.2.). The diameter of the samples shrank from 45 mm to 42 mm after drying, thickness was 36 mm. Two additional *Ganoderma* samples were grown on a mixture of fine beech wood sawdust and hemp junk (thickness only 12 mm). These were then compressed in a heat press, followed by CNC cutting.



Figure 2. Examples of homemade breeding on beech wood chips substrates using *Ganoderma lucidum* and *Pleurotus* in small size for acoustic testing.

In the experiment, the measurement system of the Mecanum company was used. A detailed description of the equipment with a video of the procedure can be found on the homepage [9]. Although the two- and four-microphone methods are the most common, we opted for a three-mic solution (Fig. 3.) [10]. Both absorption and transmission loss could be measured simultaneously. During repeated sessions, all six samples were measured with both sides (flipped) facing the sound source, thus,

12 curves were plotted on AR and TL diagrams, respectively.



Figure 3. The measurement setup with the impedance tube and data acquisition device.

The frequency range was from 115 Hz to 4300 Hz, sufficient for most of transportation noise and speech experiments.

3. RESULTS

Absorption coefficient is measured directly, whilst transmission lost is calculated. In a normal Sound Transmission Loss (TL) test, a sample is placed between two test chambers in the tube. Based on the sound level reduction the material provides and various acoustical characteristics of the test chambers, the TL can be determined. Generally, heavier walls and acoustic barriers have a higher transmission loss than lighter materials.

Figures 4-5 show measurement results of the sound absorption coefficient and transmission loss for all samples on a linear frequency scale. GBSH denotes the thin, GBC denotes the thick *Ganoderma* samples, PBC denotes the *Pleurotus* samples. The numbers and the letter indicates sample number and side.

4. DISCUSSION

There exist only a few products commercially available for acoustic purposes, i.e., the Sinewave panel (diffusor), or the Mogu, based on textile waste substrate with only a thin layer of mycelium on top [1, 2]. As a result, only a few papers are available about acoustic testing, focusing on the role of the substrate mix and density during absorption [5, 11-13]. It was demonstrated that the mycelium performs well in contrasted to conventional materials (plywood, foam, etc.). The measurements were generally between 300 Hz and 4 kHz using road noise for vehicle industry applications. However, this range is also important for building acoustics and speech technology (intelligibility measurements). The main finding is that lower density gives a higher absorption and lower through transmission protection. Denser material results in better through transmission shielding and lower absorption.

In a master thesis, results were presented using two tubes with 100 mm and 29 mm diameter [3]. The upper working frequency for the smaller tube was 6860 Hz, and only 1990 Hz for the larger tube. The measurement was evaluated from 50 to 6400 Hz and 1600 Hz respectively. Results showed good acoustic absorption. Most of the hemp/straw samples performed equally with low effects of thickness and density. Denser and samples with a closed surface showed a shift to the lower spectrum. Increasing density generally improved the absorption until a certain point, and it can contribute to lower fragility as well. Reverberation room results supported the main findings, absorption values were all above 0.8 in the one-third-octave-band 315 Hz and up [3, 14]. Impedance tube tests were not too optimistic; absorption can be even better in reality.

In our measurement, absorption greater than 0.1 can be observed above about 500 Hz, reaching a maximum of about 0.6. There are large differences among the samples and also between the two sides of a sample indicating an inhomogeneous inner structure. Absorption results are noisy below 400 Hz, because the setup was originally optimized for measurements focusing on the 800-3500 Hz frequency range. The results could be improved at lower frequencies by increasing the tube diameter (and with different microphone spacing).

The pressed GBSH samples are more effective at lower frequencies, below 2500 Hz, while the PBC is more linear over the entire range. On the other hand, one PBC sample showed a continuous rise as function of frequency. Large differences are present in the absorption using the same sample reversed, which makes a conclusive evaluation difficult.

TL is a quantification of how much sound energy is prevented from traveling through an acoustic treatment, it is the ratio of the sound energy transmitted through a sample versus the amount of sound energy on the incident side of the material. TL values were calculated from measurement data and show very low level of noise. The thin samples (brown curves) are the least effective, while the thicker samples provide better results. Although there are variations among the samples based on the placement (which side faces the source), thickness seems to be the most important parameter, as expected.

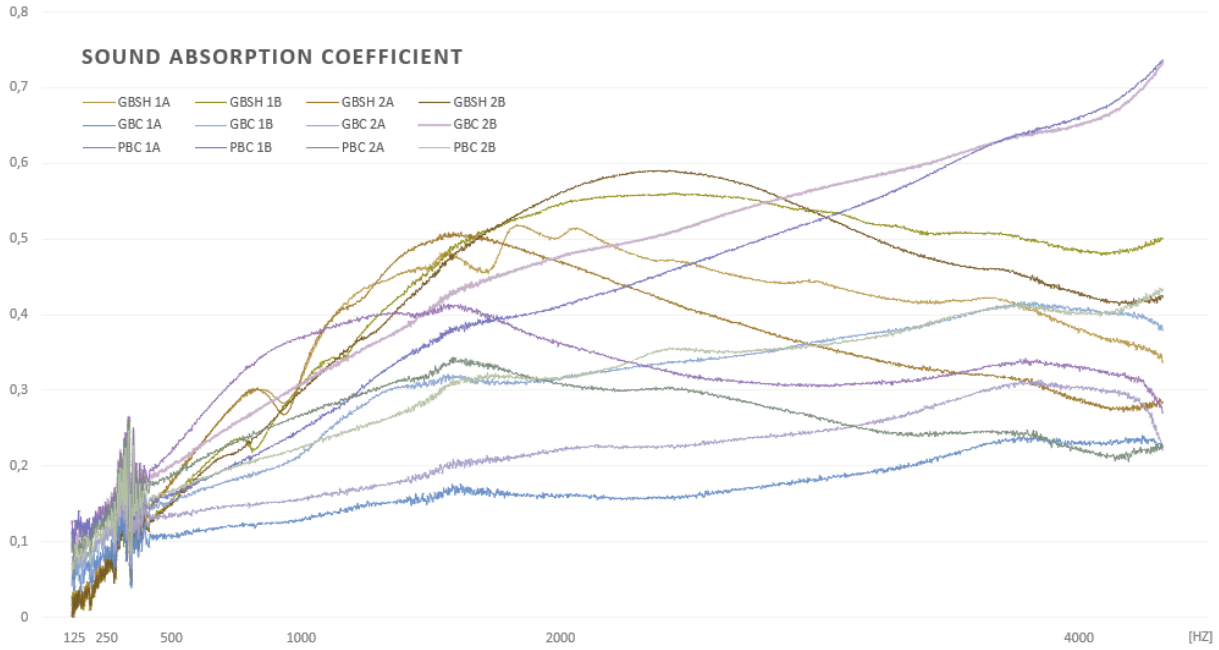


Figure 4. Results of six samples, each with both sides facing the sound source (denoted side A and side B).

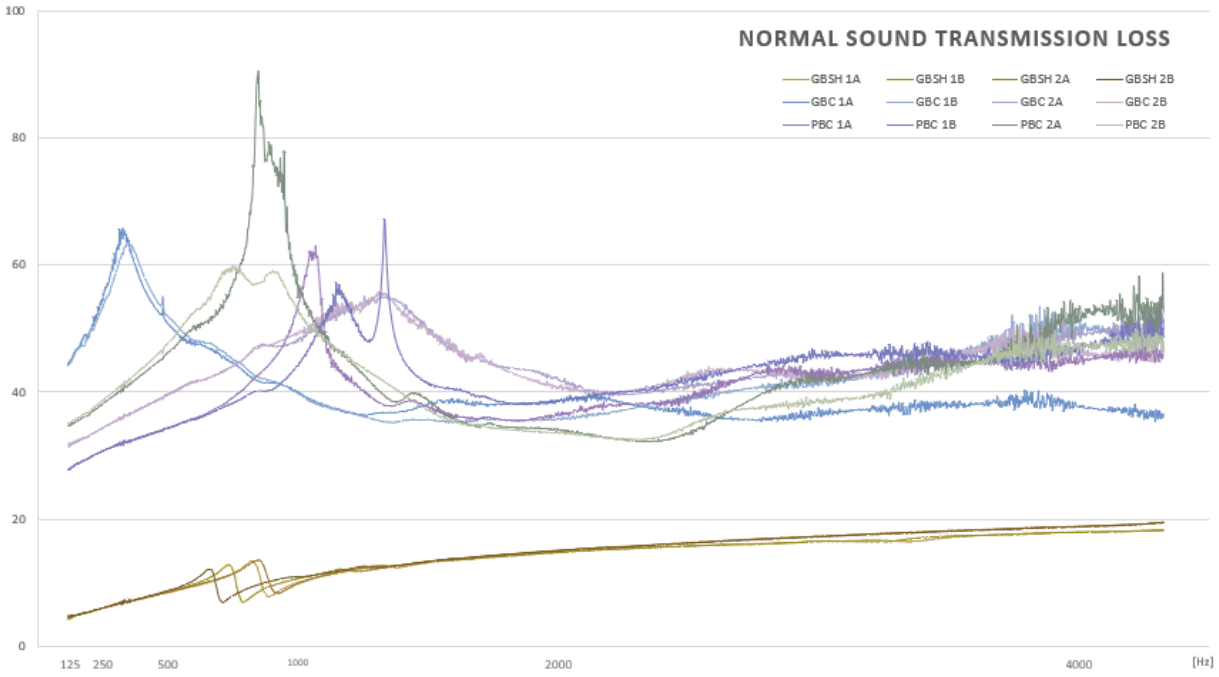


Figure 5. Results of six samples, each with both sides facing the sound source (denoted side A and side B).

4.1 Planting and harvesting

Creating larger size samples and panels takes more time than conventional materials used in sound proofing. Particle size can matter during compression. Using beech saw dust it was shown that reducing the particle size and increasing the compression pressure and/or temperature, results in increasing density that is significant from the point of view of friction [15].
A literature study on material properties shows that acoustic absorption and thermal insulation are suitable functions for this material [16-19]. A designed panel was compared with existing mycelium, other bio-based and more conventional products in terms of acoustics, safety, health, durability, sustainability and price [3]. Balancing acoustic absorption with mechanical properties and connecting the panels to the wall are important issues.

4.2 Future perspectives in sound engineering

Mycelium is a biodegradable material with light weight, good thermal and acoustic properties. On the other hand, samples could be fragile that makes production, design and application (screwing on the wall) difficult [20-23]. Furthermore, the effect of aging is unknown. More research is needed on mechanical properties and optimization, but both building acoustics (speech intelligibility) and automotive industry (traffic noise) could benefit, as the lower frequency range up to 4 kHz can be damped effectively.

5. CONCLUSION

This paper presented impedance tube measurements of acoustic properties of mycelium based materials. Two strains and two different substrates were used for sample sizes with different thickness. Impedance tube measurements were performed for determining the absorption and transmission loss in the 115-4300 Hz range using a 3-microphone method. Differences between the samples showed large variability. Due to the unsymmetrical structure of the samples, measurements were sensitive to the placement of the samples (which side is facing the sound source). Mycelium-based materials can be a good alternative for sound absorbing. Durability (fragility) and lifespan (unknown aging) are the most important problems. Although production is more difficult, sustainability could be a key issue in future developments.

5. REFERENCES

[1] https://www.ecovative.com/pages/mycocomposite

[2] https://mogu.bio/mycelium-acoustic-panels/

[3] J. Vos, “Mycelium Acoustic Panel: Growing, testing and designing with a novel bio-composite material,” Master thesis, TU Delft, http://resolver.tudelft.nl/uuid:a90154e6-c705-482e-a5d2-f03bfe236e34, 2020.

[4] R. Abhijith, A. Ashok, and C.R. Rejeesh, “Sustainable packaging applications from mycelium to substitute polystyrene: a review,” *Materials today: proceedings*, vol. 5, no. 1, pp. 2139-2145, 2018.

[5] N. Walter, and B. Gürsoy, “A Study on the Sound Absorption Properties of Mycelium-Based Composites Cultivated on Waste Paper-Based Substrates,” *Biomimetics*, vol. 7, no. 3, p. 100, 2022.

[6] T. Cox, P. D’Antonio, and M. Schroeder, *Acoustic Absorbers and Diffusers: Theory, Design and Application*, vol. 117, 2015.

[7] E. Labašová, and R. Ďuriš, “Measurement of the Acoustic Absorption Coefficient by Impedance Tube,” *Research Papers Faculty of Materials Science and Technology Slovak University of Technology*, vol. 27, no. 45, pp. 94-101, 2019.

[8] M. Vercammen, “Improving the accuracy of sound absorption measurement according to ISO 354,” in *Proceedings of the International Symposium on Room Acoustics*, Australia, Melbourne, pp. 1-4, 2010.

[9] https://mecanum.com/measuring-instruments/impedance-transmission-tubes/conventional-tubes/

[10] A. Schweighardt, B. Vehovszky, M. Szendrő, Z. Gazdagh, and B Kuti, “Development of 1D and 3D Acoustic Simulation Methods for Transmission Loss based on Transfer Matrix Measurement Results,” *in Proc. of the 27th International Congress on Sound and Vibration (ICSV27)*, online, pp. 11-16, 2021.

[11] M.G. Pelletier, “Acoustic evaluation of mycological biopolymer, an all-natural closed cell foam

alternative," *Industrial Crops and Products*, vol. 139, 111533, 2019.
[12] M.G. Pelleter, "An evaluation study of mycelium based acoustic absorbers grown on agricultural by-product substrates," *Industrial Crops and Products*, vol. 51, pp. 480-485, 2013.
[13] M.G. Pelletier, G.A. Holt, J.D. Wanjura, A.J. Lara, A. Tapia-Carillo, G. McIntyre, and E. Bayer, "An evaluation study of pressure-compressed acoustic absorbers grown on agricultural by-products," *Industrial Crops and Products*, vol. 95, pp. 342-347, 2017.
[14] J. Pfretzschner, and R. Rodriguez, "Acoustic properties of rubber crumbs," *Polymer Testing*, vol. 18, no. 2, pp. 81-92, 1999.
[15] P. Križan, M. Matúš, L. Šooš, and J. Beniak, "Behavior of beech sawdust during densification into a solid biofuel," *Energies*, vol. 8, no. 7, pp. 6382-6398, 2015.
[16] E. Moretti, E. Belloni, and F. Agosti, "Innovative mineral fiber insulation panels for buildings: Thermal and acoustic characterization," *Applied Energy*, vol. 169, pp. 421-432, 2016.
[17] S. Manan, "Synthesis and applications of fungal mycelium-based advanced functional materials," *Journal of Bioresources and Bioproducts*, vol. 6, no. 1, pp. 1-10, 2021.
[18] O. Robertson, "Fungal Future: A review of mycelium biocomposites as an ecological alternative insulation material," *DS 101: Proceedings of NordDesign*, Lyngby, Denmark, pp. 1-13, 2020.
[19] A. Javadian, "Application of mycelium-bound composite materials in construction industry: A short review," *SOJ Materials Science and Engineering*, vol. 7, pp. 1-9, 2020.
[20] M. Jones, "Mycelium composites: a review of engineering characteristics and growth kinetics," *Journal of Bionanoscience*, vol. 11, no. 4, pp. 241-257, 2017.
[21] M. Jones, "Engineered mycelium composite construction materials from fungal biorefineries: A critical review," *Materials & Design*, vol. 187, 108397, 2020.
[22] L. Yang, D. Park, and Z. Qin, "Material function of mycelium-based bio-composite: A review," *Frontiers in Materials*, vol. 8, 737377, 2021.
[23] C. Girometta, "Physico-mechanical and thermodynamic properties of mycelium-based biocomposites: A review," *Sustainability*, vol. 11, no. 1, p. 281, 2019.

DOI: 10.61782/fa.2025.0733

FORUM ACUSTICUM EURONOISE 2025

RECYCLED MATERIALS AS ABSORBENT LAYER IN ACOUSTIC CEILINGS: NON-WOVEN POLYPROPYLENE

M. Galindo[1*] **E. Alberdi**[1] **M. A. Sánchez-Burgos**[1]
F. J. Nieves[1] **I. Flores-Colen**[2]
[1] Instituto Universitario de Arquitectura y Ciencias de la Construcción (IUACC), Escuela Técnica Superior de Arquitectura, Universidad de Sevilla. Av. Reina Mercedes 2, 41012, Sevilla, Spain
[2] CERIS-DECivil, Instituto Superior Técnico, University of Lisbon, Lisbon, Portugal

ABSTRACT

Polypropylene is widely used nowadays, generating an important volume of waste that, in general, has a very low recycling rate. This study proposes the use of non-woven polypropylene, discarded in hospital - sanitary uses and not reused for other uses, as an absorbent layer for acoustic ceilings. For this purpose, and in comparison with absorbent layers of mineral wool from international manufacturers commonly used in the construction sector, the combination of thickness and treatment of the waste is sought, which offers the most suitable acoustic absorption coefficient depending on the density for the usual thicknesses used by commercial houses. The results obtained are comparable to or better than those of mineral wool. The study is complemented by a comparative life cycle analysis of both materials, considering the optimal combination of density and treatment of polypropylene waste. This analysis shows an improvement for non-woven polypropylene over mineral wool in all impact categories.

Keywords: *Sustainable materials, Sound absorption, Acoustic ceilings, Life cycle assessment, Polypropylene nonwoven waste.*

1. INTRODUCTION

The challenge of sustainability in the building materials sector leads to the prioritization of the use of environmentally friendly materials to reduce environmental impact. At the same time, comfort standards in buildings constructed today establish acoustic insulation as a fundamental aspect [1-2]. In this line of research Pedroso *et al.* [3] analyse different materials available in the market, concluding that there are alternative materials that, from the point of view of their acoustic behaviour, embodied energy and costs, are a viable alternative to replace those commonly used in the sector.

The use of natural fibres as thermal and acoustic insulation material has been analysed by different researchers [4-6]. However, researchers point out limitations regarding the behaviour of these materials against humidity, parasites and fungi that may make it necessary to spray the fibres with silicones and apply specific treatments, thus reducing sustainability. Another aspect to be considered is the limitation of the fire performance of natural fibres, which must conform to the requirements of the inherent limitations of building materials.

Islam and Bhat [7], jointly analyse different investigations, observing that recycled polyester, wool, cotton and jute fibres have good acoustic absorption properties at medium and high frequencies. With respect to polypropylene, they analyse studies using composite materials (polypropylene (PP) with bamboo, banana, cotton, wool, jute), with the absorption coefficients being more favourable when incorporating PP.

[*] ***Corresponding author***: mgalindo@us.es.
Copyright: *©2025 First author et al. This is an open-access article distributed under the terms of the Creative Commons Attribution 3.0 Unported License, which permits unrestricted use, distribution, and reproduction in any medium, provided the original author and source are credited.*

The significant increase in demand for nonwoven fabric products, including PP, was a consequence of the COVID 19 pandemic, although in later years, such as in 2023, with the critical stage of the pandemic over, a growth trend in the volume of this waste generated continued to be observed [8]. As indicated by Karimi *et al*. [9], the good chemical behaviour, low moisture absorption and density, as well as its good thermal and acoustic properties, make PP fabrics a material with potential use in the field of construction. Therefore, the increase in the volume of waste produced, its good acoustic behaviour and the opportunity to give a second life to waste products, focus the interest on the study of PP nonwovens for applications in the field of construction.

In this field, the works carried out by Ali *et al*. [10], Maderuelo *et al*. [11], Fabiani *et al*. [12] and Dehdashti *et al*. [13] should be highlighted. The joint analysis of the four referenced investigations allows us to establish the significant aspects when analysing the possibility of using nonwoven fabric from recycled face masks as an acoustic absorber. The main ones are the following:

- Disinfection treatment: To eliminate biological contaminants only Ali and Maderuelo introduce in their methodology disinfection processes applying temperature on the samples, Ali at 120ºC for 1 h and Maderuelo 70ºC for 30 minutes. In the case of Ali's research, the result of heating at 120ºC is to melt the material generating a rigid sample.

- Sample treatment: Maderuelo crushed short fibres, Fabiani 1x1 cm^2 squares and the samples analysed by Dehdashti are prepared using a fibrous mass to which he adds bio-base binder. Finally, Ali keeps the masks stacked one on top of the other.

- Thickness: The investigations analyse varying thicknesses. Ali 1.2 cm, Maderuelo 3, 6 and 9 cm, Fabiani 0.5, 1, 2 and 3 cm and Dehdashti between 1 and 3 cm with steps every 0.5 cm.

- Density: Expressing densities in g/cm^3, Ali 0.11, Maderuelo, variable for the different thicknesses between 0.05 and 0.15, Fabiani 0.127 and Dehdashti between 100 and 300.

- Test method: In all cases the impedance tube is used.

- Life cycle study: Only Fabiani and Dehdashti analyse the life cycle for the tested material, although they do not compare with life cycles of materials commonly used as acoustic absorbers in construction processes.

As for the results Ali and Fabiani obtain the absorption coefficient α, although in the case of Ali for 580 Hz and Fabiani for 2 kHz. The Sound Absorption Average (SAA) values vary between 0.58 and 0.83 for Maderuelo's tests and between 0.28 and 0.53 for Dehdashti and, finally, only Maderuelo obtains the Noise Reduction Coefficient (NCR=0.60, 0.75, 0.75 values, (density=0.10, 0.07, 0.005 g/cm^3). The values obtained are hardly comparable since the treatments used for the samples are disparate, as well as the thicknesses and densities.
The research work presented here has been developed within the RAECE research project, which analyses the treatment of these materials, with special emphasis on the analysis of the sustainability of the proposal based on the life cycle study in comparison with mineral wool insulation. The full results can be found in the publication by Galindo et al. [14].

2. ACOUSTIC TESTING

For the acoustic analysis, several factors were studied on which the sound absorbing layer depends: disinfection of the waste, its treatment, density and thickness.

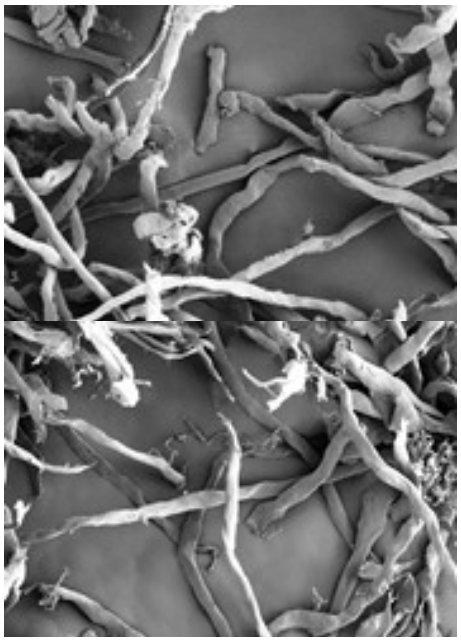


Figure 1. Microscopy. Detail of nonwoven fabric fibre from face masks. Up. Unwashed fabric. Down. Washed fabric.

For disinfection, a treatment with a bleach wash cycle at concentrations between 500 mg/L and 1000 mg/L was chosen [15-17]. In addition, the possibility that the mechanical properties of the material are affected by the washing cycle has been investigated [18]. Fig. 1 shows an electron microscopic scan of fibres of the material used before and after the washing process. It can be seen that the fibres do not undergo a structural change after the washing cycle.

The treatment of the material summarises the two possibilities most commonly used by other researchers, a finish after shredding the sample or its execution in strips (see Fig. 2). For this, a treatment has been carried out that can be faithfully reproduced. In the case of shredding, the RESTCH SM 2000 cutter was used, which produces pieces of material with a fineness of 2 mm. For the strips, an A3 PROFESSIONAL GUILLOTINE from MTEXTIL was used.

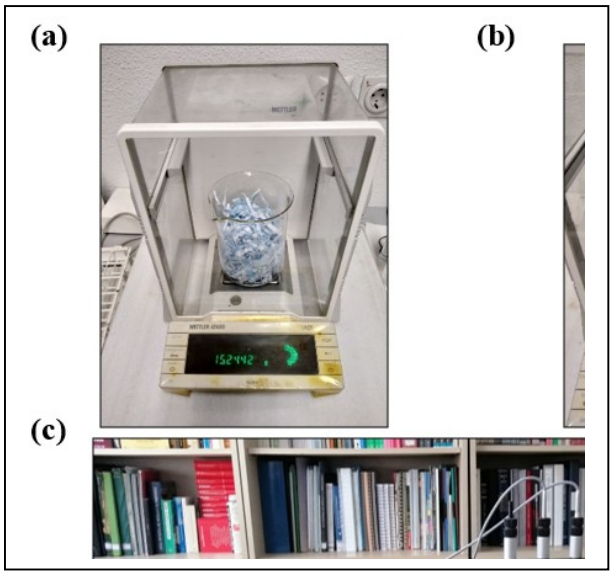


Figure 2. Tested samples. a) Strips of PP, b) Shredded PP, c) Impedance tube and power amplifier.

The density of each treatment is closely linked to the measuring equipment used to determine the sound absorption. An Impedance Tube Kit Type 4206 from B&K has been used (Fig. 2), which combines the material in a fixed diameter portion of the tube, so the densities are limited by this diameter. The layer of material tested must be uniform, without the material collapsing due to low densities or becoming reflective due to excess density. The described equipment complies with ISO 10534-2:2023 [19] and ASTM E1050 [20], which allows the determination of the sound absorption coefficient, the complex reflection coefficient and the acoustic impedance of the material, under conditions of normal sound wave incidence. In addition, the dimensions of the impedance tube also force a certain frequency range corresponding to the interval from 50 Hz to 6.4 kHz. Two different tubes are used to cover this range. The large 100 mm tube covers the range from 50 Hz to 1.6 kHz, while the small 29 mm tube covers the range from 500 Hz to 6.4 kHz.

Under these conditions, the shredded PP layer has been tested for three densities (0.15, 0.20 and 0.25 g/cm^3), while seven different densities (0.050, 0.075, 0.080, 0.085, 0.090, 0.095 and 0.100 g/cm^3) have been tested for the strip-finished layer.

In order to compare the results obtained, a sample of mineral wool (MW) from an international manufacturer was tested and used as a reference. This fact has conditioned the thickness of the tested solutions, as the usual thicknesses used by this manufacturer have been used, which are approximately the same as those used worldwide by the rest of the manufacturers (20, 48 and 65 mm).

All these factors resulted in tests of 33 layers of absorbent (PP and MW).

The Impedance Tube Kit Type 4206 from B&K allows the transfer function of the sample to be obtained by measuring the sound pressure at two fixed positions on the tube. For this purpose, two B&K Type 4187 ¼' condenser microphones and a stationary acoustic signal generated by a sound source located at the opposite end of the tube to the sample location are used. This signal is adjusted with a 2735 B&K power amplifier. During the measurement, the atmospheric conditions of air pressure, temperature and relative humidity are adjusted. In addition, the impedance tube rested on an elastic anti-vibration material.

3. RESULTS

The results correspond to the averaging of 3 different samples for each diameter analysed. For the 33 samples and in order to compare and qualify them on a commercial and

technical level, different single number or letter indices have been calculated. These correspond to the Noise Reduction Coefficient (NRC), ASTM C423-22 [21], Sound Absorption Average (SAA), ASTM C423-22, Practical Sound Absorption Coefficient (α_p), ISO 11654 [22], Weighted Sound Absorption Coefficient (α_w), ISO 11654 and Absorption Class (A_E), ISO 11654.

Table 2 shows all samples tested, labeled as S1 to S33. These correspond to the reference MW and the two different PP finishes, for each density and thickness, together with the single letter or number indices. The results of these indices appear in bold when they are better for the PP than for the MW, remaining unemphasized when the results are equal, or underlined when they are lower.

Table 2. Tested materials, densities, thicknesses and rating indexes

Material	Density (g/cm^3)	Samples	Thickness (cm)	NRC	SAA	α_w	Absorption Class
MW	0.023	S1	2.0	0.30	0.32	0.20 (H)	E
		S2	4.8	0.70	0.68	0.50 (MH)	D
		S3	6.5	0.75	0.78	0.65 (MH)	C
Shredded PP	0.150	S4	2.0	**0.40**	**0.42**	**0.25(MH)**	E
		S5	4.8	*0.65*	*0.67*	**0.65**	**C**
		S6	6.5	0.75	*0.73*	**0.75**	C
	0.200	S7	2.0	**0.45**	**0.45**	**0.30 (MH)**	**D**
		S8	4.8	*0.60*	*0.58*	**0.60**	**C**
		S9	6.5	*0.60*	*0.58*	*0.55 (H)*	*D*
	0.250	S10	2.0	**0.50**	**0.49**	**0.40 (MH)**	**D**
		S11	4.8	*0.55*	*0.49*	0.50 (H)	D
		S12	6.5	*0.45*	*0.43*	*0.45*	*D*
Strips PP	0.050	S13	2.0	0.30	*0.28*	*0.15 (H)*	E
		S14	4.8	*0.55*	*0.57*	*0.40 (MH)*	D
		S15	6.5	*0.65*	*0.65*	*0.45 (MH)*	*D*
	0.075	S16	2.0	**0.45**	**0.45**	0.20 (MH)	E
		S17	4.8	0.70	0.68	0.50 (MH)	D
		S18	6.5	0.75	*0.76*	**0.70**	C
	0.080	S19	2.0	**0.50**	**0.47**	**0.25(MH)**	E
		S20	4.8	0.70	**0.69**	**0.55(MH)**	D
		S21	6.5	0.75	*0.77*	**0.75**	C
	0.085	S22	2.0	**0.50**	**0.50**	**0.25(MH)**	E
		S23	4.8	0.70	**0.70**	**0.60(M)**	**C**
		S24	6.5	0.75	*0.76*	**0.75**	C
	0.090	S25	2.0	**0.50**	**0.49**	**0.25(MH)**	E
		S26	4.8	0.70	**0.70**	**0.65**	**C**
		S27	6.5	0.75	*0.75*	**0.80**	**B**
	0.095	S28	2.0	**0.50**	**0.50**	**0.30(MH)**	**D**
		S29	4.8	0.70	**0.72**	**0.70**	**C**
		S30	6.5	0.75	*0.75*	**0.80**	**B**
	0.100	S31	2.0	**0.50**	**0.52**	**0.30 (MH)**	**D**
		S32	4.8	0.70	**0.70**	**0.70**	**C**
		S33	6.5	0.75	*0.73*	**0.75**	C

The results of the table show equal or better index values for PP than for MW for PP densities higher than MW.

The values for shredded PP only exceed or equal all single number or letter indices for the densities of 0.200 and 0.250 g/cm^3 and a thickness of 2 cm, so no better results are found for the usual thicknesses of acoustic ceilings. Only the value of α_w is exceeded by PP versus MW for all thicknesses when the density is 0.150 g/cm^3. This rules out the results of crushed PP samples versus strips for use in an acoustic ceiling.

For PP strips, similar or better results than for MW are achieved at densities of 0.075 g/cm^3 and above. In addition, all single letter or number indices improve for the 2 cm and 4.8 cm thicknesses. For the 6.4 cm thickness, the only exception is for the SAA index with values slightly lower than those of the MW. Taking into account these variables, the most appropriate density is 0.095 g/cm^3, which manages to improve, compared to MW, the single letter index for each thickness. This seems to worsen at higher densities.

Fig. 3 presents the values of the sound absorption coefficient versus frequency in thirds of octave for the operating range of the impedance tube. For each thickness, the values for MW, shredded PP and strips are presented. For each of the finishes, three densities are shown. These correspond to the 3 densities used in the crushed material and, for reasons of visual clarity, to only 3 of the 7 tested in the strips, one of them being the one with the best acoustic performance.

Figure 4 shows the absorption coefficient against frequency, measured in third-octave bands, for four densities of PP across all thicknesses tested. MW is included as reference. Figure 4(a), with the lowest density, relates to shredded PP, while the other three depict PP strips. Looking at the ratings, only this shredded PP option is considered commercially viable. Furthermore, Figure 4(d) is deemed the optimal choice within the studied density range (0.080 to 0.100 g/cm³). Figures 4(b) and (c), which represent the lower density values, are included to demonstrate how the absorption behaviour changes as density increases.

Across all samples, the absorption characteristics of PP closely resemble those of MW. The shredded layer, within the impedance tube's limitations, effectively eliminates any air gap between the sample and the tube's rigid wall. This leads to an increase in absorption with increasing frequency. The three PP strip densities exhibit behaviour like MW, thus validating PP's correctness as a porous sound-absorbing material.

4. LIFE CYCCLE ASSESMENT

A Life Cycle Analysis has been carried out, comparing the absorbing material layer selected for the PP with the commercial MW one. MW is the most common insulating and acoustic material in the Spanish construction market.

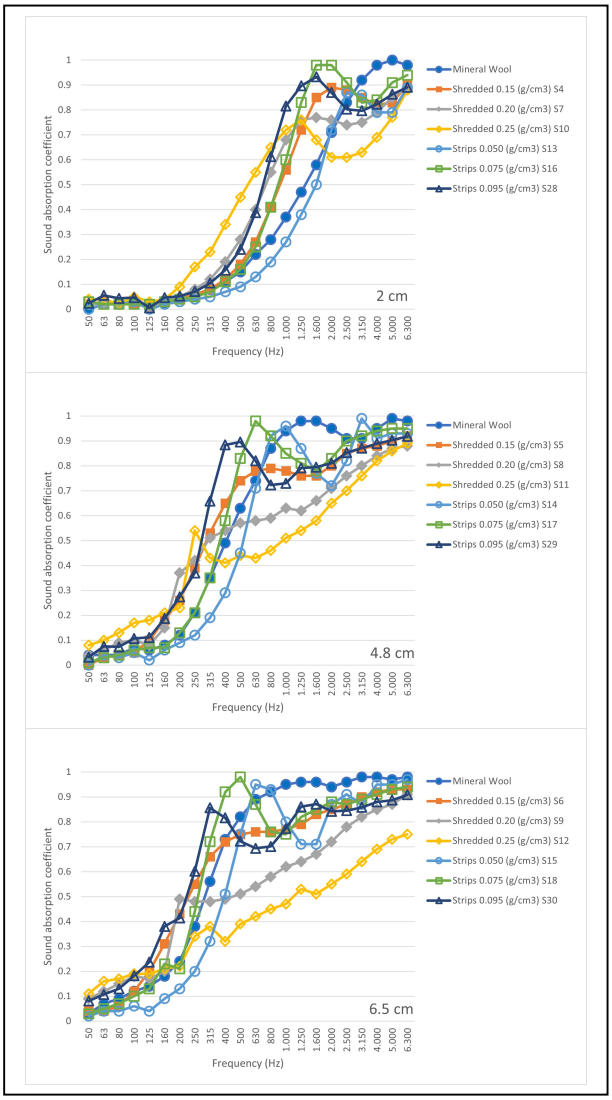


Figure 3. Sound absorption coefficient versus frequency in third octave bands for the different materials and thicknesses.

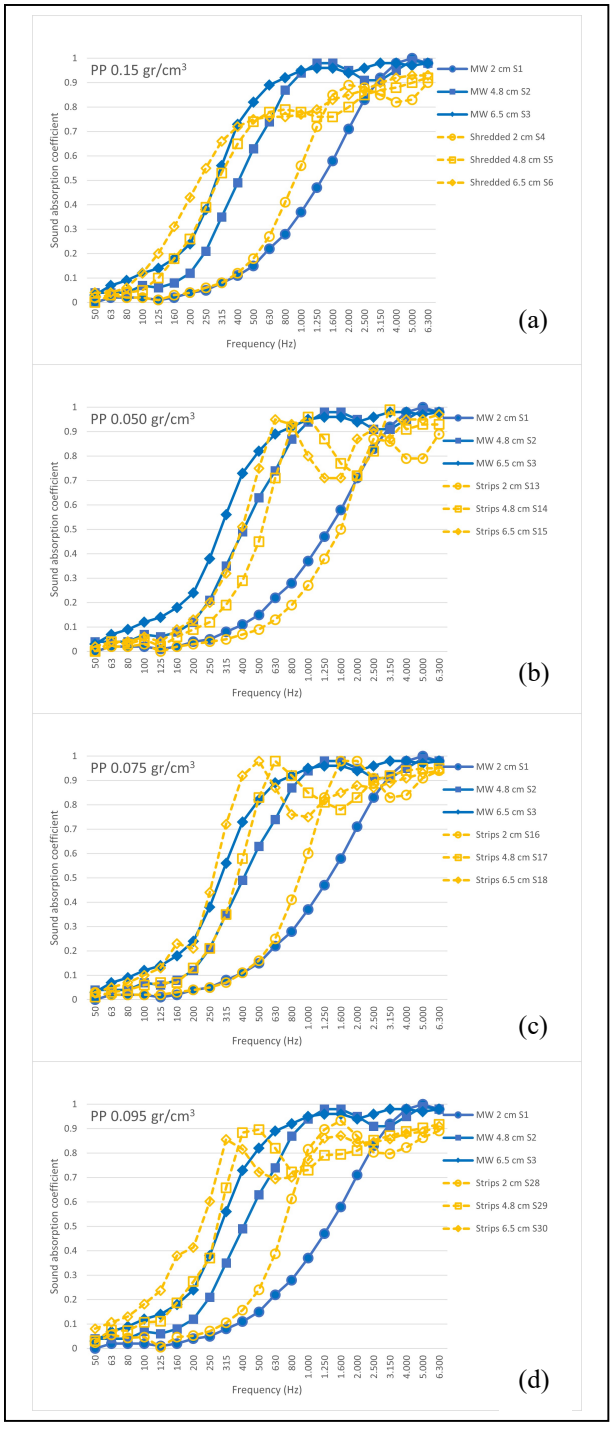


Figure 4. Absorption coefficient versus frequency in thirds of octave for the different materials and sample thicknesses.

A "cradle to gate" analysis (Stages A1 to A3, EN 15804 [23]) was performed. The data obtained to evaluate the consumption and emissions of the samples tested for the PP have been obtained from the prototype production process. The environmental data used for the MW were obtained from the corresponding Environmental Product Declaration of the commercial product.

This LCA study follows the attributional approach, which represents current market conditions in Spain. The impact score calculations have been calculated according to the Ecoinvent and ELCD databases [24], which represent the current technology in Europe. The Simapro tool from Pré Consultants was used to calculate the impact scores.

The result of the calculation shows significantly lower scores for PP in all impact categories evaluated.

In addition, the sensitivity analysis performed shows that the reduction of electricity use in PP production results in a further reduction of the impact scores obtained in all categories. It should be emphasized that this scenario can be achieved following current trends in the green electricity market.

5. CONCLUSIONS

The present work studies discarded materials from healthcare protective equipment made of non-woven polypropylene, for use as an absorbent layer in acoustic ceilings.

Two forms of waste treatment have been analysed, strips of 4×100 mm^2 and shredded PP with a fineness of 2 mm. The study contemplates samples for different thicknesses, typical of commercial solutions common in the international market for mineral wool layers, and different densities, making it possible to obtain the most suitable density of PP for use as an absorbent layer in acoustic ceilings.

For this purpose, we have compared the achievable values obtained for PP, of acoustic indices to number or single letter, with those declared for the reference mineral wool. These indexes have been obtained from the results of the acoustic absorption coefficient for each sample obtained in impedance tubes under normal incidence conditions.

According to the results, the environmental performance of the PP layer outperforms that of conventionally produced acoustic MW and benefits environmental sustainability.

Future research will analyse the acoustic performance and life cycle of the complete acoustic ceiling solution, including the thickness of the air gap and the plasterboard sheet.

6. ACKNOWLEDGMENTS

The project PID2021-123192OB-I00 was financed by the Spanish Ministry of Science and Innovation, the State Research Agency and the EU ERDF. (Ministerio de Ciencia e Innovación, la Agencia Estatal de Investigación y por el Fondo Europeo de Desarrollo Regional de la Unión Europea).

The authors would like to thank the FCT (Fundação para a Ciência e Tecnologia) and the support of the CERIS Research Centre (UIDB/04625/2020). The cutting process for the shredded PP was performed in the LAPIST lab at CERENA (Centro de Recursos Naturais e Ambience).

7. REFERENCES

[1] J. Ahmad, A. Majdi, A. Babeker Elhag, A.F. Deifalla, M. Soomro, H.F. Isleem and S. Qaidi., "A Step towards Sustainable Concrete with Substitution of Plastic Waste in Concrete: Overview on Mechanical, Durability and Microstructure Analysis," *Crystals*, vol. 12, no. 7, pp. 944, 2022.

[2] G. K. Oral, A. K. Yener, and N. T. Bayazit, "Building envelope design with the objective to ensureing thermal, visual and acoustic comfort conditions," *Building and Environment*, vol. 39, no. 3, pp. 281–287, 2004.

[3] M. Pedroso, J. de Brito, and J. D. Silvestre, "Characterization of eco-efficient acoustic insulation materials (traditional and innovative)," *Construction and Building Materials*, vol. 140, pp. 221–228, 2017.

[4] A. Patnaik, M. Mvubu, S. Muniyasamy, A. Botha, and R. D. Anandjiwala, "Thermal and sound insulation materials from waste wool and recycled polyester fibers and their biodegradation studies," *Energy and Building*, vol. 92, pp. 161–169, 2015.

[5] U. Berardi and G. Iannace, "Acoustic characterization of natural fibers for sound absorption applications," *Building Environment*, vol. 94, pp. 840–852, 2015.

[6] U. Berardi and G. Iannace, "Predicting the sound absorption of natural materials: Best-fit inverse laws for the acoustic impedance and the propagation constant," *Applied Acoustics*, vol. 115, pp. 131-138, 2017.

[7] S. Islam and G. Bhat, "Environmentally-friendly thermal and acoustic insulation materials from recycled textiles," *Journal of Environmental Management*, vol. 251, pp. 109536, 2019.

[8] Edana, "Nonwovens," *Nonwovens Industry*. [Online]. Available: https://www.nonwovens-industry.com/contents/view_breaking-news/2023-04-05/edana-releases-overview-of-nonwovens-production-figures; Accessed 2024-02-15

[9] F. Karimi, P. Soltani, M. Zarrebini, and A. Hassanpour, "Acoustic and thermal performance of polypropylene nonwoven fabrics for insulation in buildings," *Journal of Building Engineering*, vol. 50, pp. 104125, 2022.

[10] M. Ali, R. Almuzaiqer, K. Al-Salem, A. Alabdulkarem, and A. Nuhait, "New novel thermal insulation and sound-absorbing materials from discarded facemasks of COVID-19 pandemic," *Scientific Reports*, vol. 11, no. 1, pp. 1–15, 2021.

[11] R. Maderuelo-Sanz, P. Acedo-Fuentes, F. J. García-Cobos, F. J. Sánchez-Delgado, M. I. Mota-López and J. M. Meneses-Rodríguez, "The recycling of surgical face masks as sound porous absorbers: Preliminary evaluation," *Science of The Total Environment*, vol. 786, pp. 147461, 2021.

[12] C. Fabiani, S. Cavagnoli, C. Chiatti, and A. L. Pisello, "Management of disposable surgical masks for tackling pandemic-generated pollution: Thermo-acoustic investigations and life cycle assessment of novel recycled building panels," *Resources Conservation Recycling*, vol. 186, pp. 106509, 2022.

[13] Z. Dehdashti, P. Soltani, and E. Taban, "Utilizing discarded face masks to fabricate sustainable high-performance panels for enhanced building thermal and acoustic comfort," *Journal of Cleaner Production*, vol. 446, pp. 141304, 2024.

[14] M. Galindo, E. Alberdi, M. A. Sánchez-Burgos, F. J. Nieves, and I. Flores-Colen, "Polypropylene as an absorbent layer for acoustic ceilings: Sound

absorption and life cycle assessment," *Journal of Building Engineering*, vol. 96, pp. 110655.

[15] J. Wang, J. Shen, D. Ye, X. Yan, Y. Zhang, W. Yang, X. Li, J. Wang, L. Zhang, L. Zhang and L. Pan, "Disinfection technology of hospital wastes and wastewater: Suggestions for disinfection strategy during coronavirus Disease 2019 (COVID-19) pandemic in China," *Environmental Pollution*, vol. 262, pp. 114665, 2020.

[16] W. A. Rutala and D. J. Weber, "Uses of inorganic hypochlorite (bleach) in health-care facilities," *Clinical Microbiology Reviews*, vol. 10, no. 4, pp. 597–610, 1997.

[17] S. Fukuzaki, "Mechanisms of actions of sodium hypochlorite in cleaning and disinfection processes," *Biocontrol Science*, vol. 11, no. 4, pp. 147–157, 2006.

[18] P. Heikkilä, M. Määttänen, P. Jetsu, T. Kamppuri, and S. Paunonen, "Nonwovens from Mechanically Recycled Fibres for Medical Applications," *VTT Technical Research Centre of Finland.*, vol. VTT-R-0092, 2020, [Online]. Available: https://cris.vtt.fi/en/publications/nonwovens-from-mechanically-recycled-fibres-for-medical-applicati Accessed 2024-02-15

[19] "ISO 10534-2:2023 Acoustics — Determination of acoustic properties in impedance tubes — Part 2: Two-microphone technique for normal sound absorption coefficient and normal surface impedance," 2023.

[20] "ASTM E1050 Standar Test Method for Impedance and Absorption of Acoustical Materials Using a Tube, Two Microphones and a Digital Frequency Analysis System," 2023.

[21] "ASTM C423-22 Standard Test Method for Sound Absorption and Sound Absorption Coefficients by the Reverberation Room Method," 2022.

[22] "ISO 11654. Acoustics Sound absorbers for use in buildings Rating of sound absorption," 1997.

[23] EN 15804, "Standards Publication Sustainability of construction works — Environmental product declarations — Core rules for the product category of construction products," *Comité Européen de Normalisation (CEN),* 2019.

[24] Ecoinvent, "Ecoinvent Database.". [Online]. Available: https://ecoinvent.org/database/. Accessed: Jun. 25, 2025

DOI:

Main theme: A08 Industrial, Machinery, Equipment Noise and Vibration

Session A08.05 NVH damage detection, condition monitoring, diagnostics of machinery

Chair(s): E. Mucchi, P. Poveda Martinez, M. Battarra

DOI: 10.61782/fa.2025.0047

FORUM ACUSTICUM EURONOISE 2025

A VIBRATION BASED HEALTH MONITORING SYSTEM FOR AN AUTOMATIC PACKAGING MACHINE

Ilaria Rizioli[1] **Giulia Cristofori**[1]
Mattia Battarra[1] **Emiliano Mucchi**[1]
[1] Department of Engineering, University of Ferrara, Ferrara FE-44121, Italy

ABSTRACT

This study focuses on the design and development of a condition monitoring system for automatic packaging machines using accelerometer-based measurements. The purpose is to detect defects on the rotating components to enhance machine reliability and operational efficiency. A critical aspect of the study involved determining the optimal placement of accelerometers to maximize sensitivity to wheel defects. The investigation involved extensive testing under controlled conditions with several combinations of working conditions, various artificially induced defects and sensor locations. Data collected from the accelerometers were processed and analyzed using multiple statistical indicators, including bearing-related techniques and cyclostationary approaches. These analyses enabled the identification of key patterns and thresholds indicative of wheel defects. Preliminary results demonstrate the feasibility of detecting early-stage anomalies through accelerometer data and highlight the relevance of sensor positioning in capturing meaningful signals. The ongoing phase of the project focuses on refining the system's accuracy and robustness through additional testing and refining of the data processing procedure. Future developments aim to integrate the system into machine control units for automated defect detection and alerts.

Keywords: *Condition monitoring, NVH, industrial machinery, wheel fault.*

**Corresponding author*: *mattia.battarra@unife.it.*
***Copyright**: ©2025 Ilaria Rizioli et al. This is an open-access article distributed under the terms of the Creative Commons Attribution 3.0 Unported License, which permits unrestricted use, distribution, and reproduction in any medium, provided the original author and source are credited.*

1. INTRODUCTION

In modern industrial environments, ensuring the reliability and efficiency of machinery is critical for maintaining productivity and reducing operational costs. Predictive maintenance, driven by advanced diagnostic techniques, plays a key role in detecting potential failures before they lead to costly downtime. Among various approaches, as also shown by Jardine A. et al. in [1], vibration-based health monitoring has proven to be effective in assessing rotating and mechanical components.

The effectiveness of accelerometers in condition monitoring is well-documented in several books, including the work by Wu et al. [2] that discusses the application of vibration-based condition monitoring in hydraulic machinery. The authors emphasize the role of accelerometers in measuring the absolute vibration of machine components. In this context, it is crucial to underline that acceleration measurements are used to assess the health conditions of the most critical components of automatic machines, e.g. rolling element bearings [3,4] and gears [5,6]. In this context, it is mandatory to underline that acceleration measurements have become the reference approach, also thanks to a vast community of research groups that have continuously developed a variety of signal processing techniques with the purpose to maximize the extraction of information. Their use is currently so widespread that acceleration signals represent a reference source of information also in physics-based diagnostic and prognostic protocols, since they are used for tuning and validation of digital twins of faulty mechanical components [7–9].

As a matter of fact, signal processing techniques play a pivotal role in vibration-based condition monitoring. Feature extraction methods, such as time-frequency analysis, enhance the detection of faults in machinery com-

ponents such as rolling bearings. A study by Zhang et al. [10] provides a review of these techniques, emphasizing their application in estimating degradation trends in low-speed slew bearings. This context is particularly proficient in the case of mechanical rotating machines, which have been largely proven to behave as cyclo-stationary systems [11]. Based on this observation, several techniques have been developed with the purpose to define diagnostic indicators from acceleration signals by taking advantage of the cyclo-stationary behavior of the system. In this framework, works such as the one reported in [12] propose approaches to detect the appearance of pitting phenomena in gears, while others such as the one in [13] are devoted to define specific techniques for rolling element bearings.

The described scenario clarifies as the specialized literature may currently provide a relevant variety of case studies, open-source datasets with experimental results and innovative research project outcomes regarding the diagnostics of rotating mechanical components, however their application on actual machines and production lines is certainly less common. Within this context, the present work has the purpose to provide insights regarding the use of well-established indicators, commonly adopted for the diagnostics of single mechanical components, in real machines adopted in an industrial environment. In particular, the study focuses the attention on automatic packaging machines, which are widely used in packaging industries and are commonly subject to wear and mechanical degradation over time. Implementing a vibration-based monitoring system can enhance their operational efficiency by identifying early signs of malfunction, enabling timely maintenance interventions.

The following section is devoted to the description of the mechanical system under study and the experimental tests carried out to characterize the vibration behavior of the machine. Section 3 reports the results of the analysis applied to the experimental results. Eventually, the last section is devoted to concluding remarks.

2. MECHANICAL SYSTEM DESCRIPTION

The study focuses on a automated packaging machine with rotative mechanical subsystems, which are supported by groups of wheels located in circle. Each group is constituted by three polymer wheels, two of them with axes of rotation disposed along the ring radial direction and the remaining one with axis of rotation disposed along the ring axial direction.

The experimental study has been carried out with the purpose to fully characterize the behavior of a complete wheel group through the entire available working conditions of the machine. In this context, three triaxial accelerometers have been placed on top of the bearings of the three wheels constituting a wheel group, while other three triaxial accelerometers have been placed on the ring frame. An optical tachometer is used to assess the wheel position and the instantaneous rotational speed of the machine. Tests have been conducted at four different workin conditions, with speed varied from 25% to 100% of the maximum available value, with each acquisition lasting for 60 s and the sampling frequency set to 25600 Hz. The test campaign involved the baseline condition, i.e. the machine in nominal condition, and eight different artificial faults.

3. RESULTS AND DISCUSSION

The present section reports the results of the different signal processing techniques applied on the data obtained from the experimental study described in section 2. Figure 1 reports Root Mean Square (RMS) and Kurtosis values referring to the data acquired from the two accelerometers placed on the radial axes wheels of a wheel group. Data are expressed as the difference with respect to the analogous value computed from the baseline condition. As it may be observed, both statistical indicators are capable to recognize the presence of defects located on the wheels of the same wheel group where the accelerometers are mounted, while their sensitivity to faults located on other wheel groups is almost negligible. Moreover, both RMS and Kurtosis appears to be highly sensitive to faults involving faceted wheels, while other modifications do not seems to produce significant modifications in the values of the indicators.

The analysis is then repeated for the data acquired with the accelerometers located on the ring frame, as reported in Fig. 2. As it may be observed, the presence or absence of the film does not alter the results significantly, with the x direction, which coincides with the radial one, being the most sensitive. Again, artificial faults involving the faceted wheel appear to have a more significant effect on both indicators, while other modifications, such as displacing the gear along the ring center, lead to RMS and Kurtosis values almost superimposed to the baseline condition.

In order to deepen the analysis and define a wider set of indicators with significant sensitivity to all the simu-

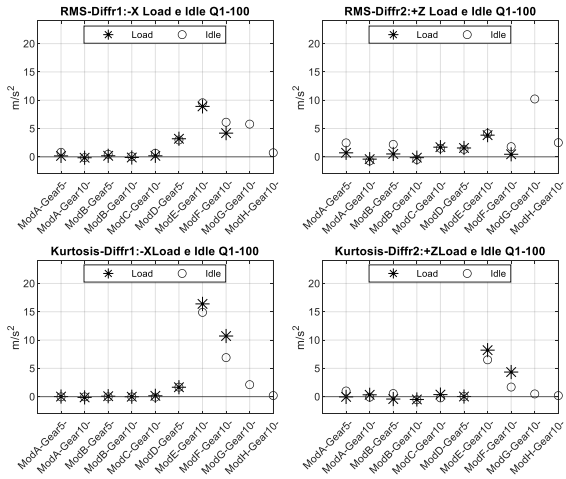


Figure 1. RMS and Kurtosis values for the two accelerometers placed on the radial axis wheels of a wheel group, expressed as difference with respect to the values computed from baseline conditions.

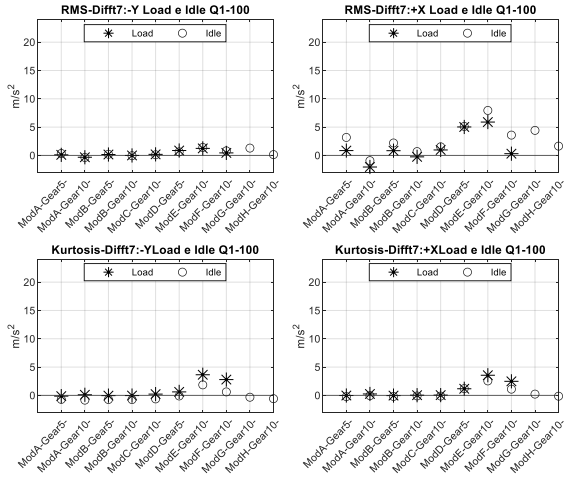


Figure 2. RMS and Kurtosis values for one of the accelerometers placed on the ring frame, expressed as difference with respect to the values computed from baseline conditions.

lated faults, the acquired data have been further processed by using five additional indicators: skewness, Teager-Kaiser Energetic Operator (TKEO), Power Spectral Entropy (PSE), Peak-to-Peak value and the Hillbert indicator. Figure 3 reports the results of this analysis applied to the same accelerometer observed in Fig. 1. The results show that most of the indicators demonstrate a relevant sensitivity to the proposed modifications, with the Hillbert indicator that certainly achieve the highest sensitivity while PSE seems almost not-influenced by the considered faults. Moreover, it is worth underlining that similar results have been obtained from the signals collected by all the involved accelerometers, both located on the wheel group and the ring frame.

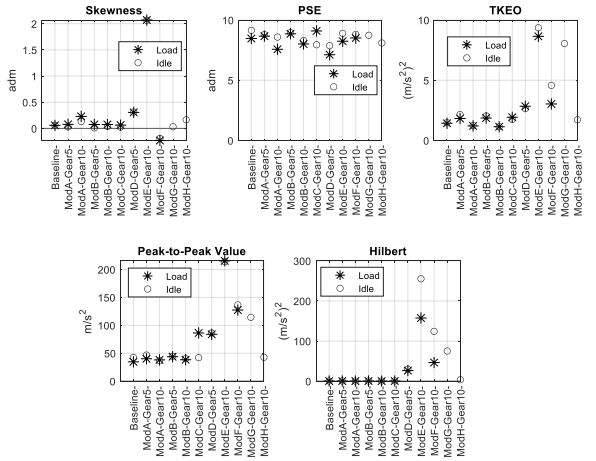


Figure 3. Computation of additional indicators on the data obtained from the same accelerometer adopted in Fig. 1.

4. CONCLUDING REMARKS

This study focused on the design and development of a condition monitoring system for automatic packaging machines using accelerometer-based measurements. The purpose was to detect defects on the wheels to enhance machine reliability and operational efficiency. The study is based on an extensive experimental analysis, involving six triaxial accelerometers, 16 different working conditions and 8 artificial faults, from wheel displacement to wheel faceting.

The acquired signals have been post-processed with different techniques: the first analysis is focused on statistical indicators, such as RMS and Kurtosis, showing that faults involving faceted wheels have significant effects on them. On the other hand, artificial faults involving wheel

displacements are less observable. The analysis has been further deepened by including additional indicators such as skewness, Teager-Kaiser Energetic Operator (TKEO), Power Spectral Entropy (PSE), Peak-to-Peak value and the Hillbert indicator. The outcomes of this second round of post-processing demonstrated that faceted wheel faults produce significant effects on several indicators, on all the applied accelerometers. Conversely, wheel displacement faults probably do not alter the energy content of the phenomenon and therefore are less prone to be observed with these indicators. In addition, as a whole consideration, the analysis has demonstrated that the diagnostic protocol could be applied during both load and idle conditions. Further works will be focused on defining an artificial intelligence approach capable to take into account all the defined indicators in order to classify faults according to their nature.

5. REFERENCES

[1] A. K. Jardine, D. Lin, and D. Banjevic, "A review on machinery diagnostics and prognostics implementing condition-based maintenance," *Mechanical Systems and Signal Processing*, vol. 20, no. 7, p. 1483 – 1510, 2006.

[2] Y. Wu, S. Li, S. Liu, H.-S. Dou, and Z. Qian, *Vibration-Based Condition Monitoring*, pp. 431–477. Dordrecht: Springer Netherlands, 2013.

[3] E. Soave, G. D'Elia, M. Cocconcelli, and M. Battarra, "Blind deconvolution criterion based on fourier–bessel series expansion for rolling element bearing diagnostics," *Mechanical Systems and Signal Processing*, vol. 169, 2022.

[4] A. Gabrielli, M. Battarra, E. Mucchi, and G. Dalpiaz, "A procedure for the assessment of unknown parameters in modeling defective bearings through multi-objective optimization," *Mechanical Systems and Signal Processing*, vol. 185, 2023.

[5] F. Pizzolante, M. Battarra, G. D'Elia, and E. Mucchi, "A rattle index formulation for single and multiple branch geartrains," *Mechanism and Machine Theory*, vol. 158, 2021.

[6] N. Sawalhi and R. B. Randall, "Gear parameter identification in wind turbines using diagnostic analysis of gearbox vibration signals," *Lecture Notes in Mechanical Engineering*, vol. 5, p. 273 – 285, 2014.

[7] A. Gabrielli, M. Battarra, E. Mucchi, and G. Dalpiaz, "Physics-based prognostics of rolling-element bearings: The equivalent damaged volume algorithm," *Mechanical Systems and Signal Processing*, vol. 215, 2024.

[8] P. McFadden and J. Smith, "The vibration produced by multiple point defects in a rolling element bearing," *Journal of Sound and Vibration*, vol. 98, no. 2, p. 263 – 273, 1985.

[9] Z. Li, R. Zhu, T. Verwimp, H. Wen, and K. Gryllias, "Estimation of remaining useful life of rolling element bearings based on the adaptive kernel kalman filter," *Mechanical Systems and Signal Processing*, vol. 229, 2025.

[10] C. Zhang, A. A. Mousavi, S. F. Masri, G. Gholipour, K. Yan, and X. Li, "Vibration feature extraction using signal processing techniques for structural health monitoring: A review," *Mechanical Systems and Signal Processing*, vol. 177, p. 109175, 2022.

[11] J. Antoni, "Cyclostationarity by examples," *Mechanical Systems and Signal Processing*, vol. 23, no. 4, p. 987 – 1036, 2009.

[12] F. Berlato, G. D'Elia, M. Battarra, and G. Dalpiaz, "Condition monitoring indicators for pitting detection in planetary gear units," *Diagnostyka*, vol. 21, no. 1, p. 3 – 10, 2020.

[13] H. Qiu, J. Lee, J. Lin, and G. Yu, "Wavelet filter-based weak signature detection method and its application on rolling element bearing prognostics," *Journal of Sound and Vibration*, vol. 289, no. 4-5, p. 1066 – 1090, 2006.

DOI: 10.61782/fa.2025.0014



FORUM ACUSTICUM
EURONOISE 2025

A MATHEMATICAL MODEL BASED DIGITAL TWIN FOR GEARBOXES OPERATING AT VARIABLE SPEEDS

Shahis Hashim **Sitesh Kumar Mishra** **Piyush Shakya***

Engineering Asset Management Group, Indian Institute of Technology Madras, Chennai, India

ABSTRACT

The gearboxes are vital components of most drive trains. The operation of gearboxes in applications such as wind turbines and manufacturing tools is characterised by sudden changes in loads, which may lead to variations in operational speed. Hence, visualising system dynamics in varied conditions becomes vital to operation planning. The role of the digital twins in industrial applications has led to streamlined virtual learning of the system dynamics. Further, the mathematical model-based digital twin is faster in computation than its counterpart, the finite element model, thus meeting the demand for real-time system simulations. The study presents a digital twin based on a mathematical model for simulating the vibration response of a fixed-axis single-stage spur gearbox operating at variable speed. A detailed study of the simulated vibration response and a detailed discussion of its time, frequency, and time-frequency domains are also presented.

Keywords: *Dynamic model, vibration analysis, gearbox, digital twin*

1. INTRODUCTION

Lack of proper maintenance is the most prominent reason for gearbox failures [1]. Further, the failure of gearboxes may lead to extensive hazards ranging from operational downtime to loss of personal life [2]. Historically, gearbox failure has been the primary cause of aviation hazards. Notably, gearbox failures of the Boeing-made V-22 Osprey and the Airbus-made super-puma family helicopters have resulted in multiple fatal accidents over the years, with loss of life amounting to dozens [3]. Hence, visualising the gearbox's operation and the associated system dynamics is paramount for operation planning [4, 5]. The analyst may simulate varying operational conditions of the gearbox in a virtual system to understand the safe operational parameters. Such virtual visualisations are aided by a Digital twin (DT) capable of simulating the operational characteristics of the gearbox in a display unit.

A vast range of research addresses the DT analysis by Finite element modelling (FEM). However, the FEM is computationally intensive, requiring dedicated workstations and associated equipment. The FEM-based DTs are thus limited to industrial units that may afford such costly tools for operational optimisation. Most industrial units and primary employment providers in the developing and under-developed nations are categorised as micro, small, and medium enterprises (MSMEs). The non-availability of advanced algorithms for optimised operations significantly hinders developing nations' inclusive progress. As such, the dynamic model-based DTs that provide low-cost computation may be more suited to the context of MSMEs [6].

Researchers have tried to generate a dynamic model-based DT for gearboxes at various degrees of freedom [7]. Patel and Shakya demonstrated a model capable of addressing the variable speed but limited the study to signal processing of the simulated vibration response [8]. The present study explores the characteristics of the simulated vibration response during the presence of the fault, as well as during variations in speed, a vital aspect of the digital twin's onboard application.

*Corresponding author: pshakya@iitm.ac.in.

Copyright: ©2025 Dr. Piyush Shakya This is an open-access article distributed under the terms of the Creative Commons Attribution 3.0 Unported License, which permits unrestricted use, distribution, and reproduction in any medium, provided the original author and source are credited.

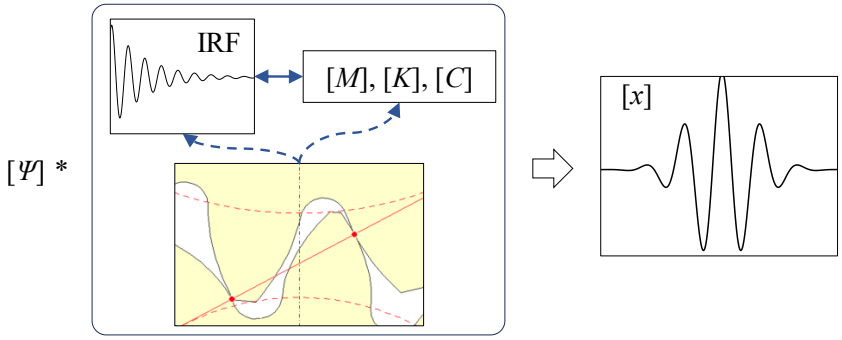


Figure 1: Schematic representation of vibration response during gear tooth meshing

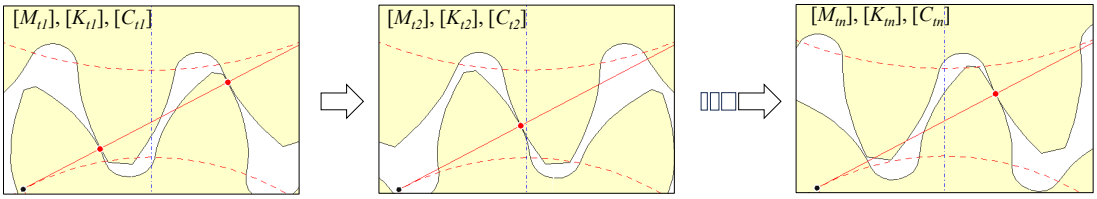


Figure 2: Gear mesh at different instants

2. VIBRATION RESPONSE SIMULATION

The vibration response-based analysis has emerged as the norm in contemporary gearbox monitoring practices. The wide acceptance of vibration analysis is due to its ability to reflect highly correlated fault information swiftly. The vibration response of a structural element is governed by its Impulse response function (IRF), which is dependent on the system's dynamic properties. The Figure 1 illustrates the instantaneous vibration response ($[x]$) generation during the gear tooth meshing under the influence of external and internal forces ($[\Psi]$). At any instant, the meshed gear tooth may be assumed as a structure with a set of dynamic properties dependent on the combined meshed geometry of the interacting gear tooth. The dynamic properties such as the mass ($[M]$), stiffness-coefficient ($[K]$), and damping-coefficient ($[C]$) influence the IRF of the said structure. However, the meshing of the gearbox generates complex meshed structures and dynamic forces at every instant, generating a complex vibration response over time (Figure 2). Nonetheless, understanding the vibration response is fundamental to the study. The following sections of the current study analyse the gearbox vibration response using the proposed dynamic model. The vibration response's time, frequency, and time-frequency domain characteristics are studied.

3. THE DYNAMIC MODEL

The dynamic property most influential in the vibration response generation is the instantaneous stiffness during the gear tooth meshing, termed the time-varying mesh stiffness (TVMS). The dynamic model consists of two integral parts: the TVMS calculation and the lumped-mass dynamic model. The root-crack growth under different speed variations is analysed in the present discussion to understand the complex nature of gearbox vibration response under fault growth and operational variations.

3.1 TVMS calculation

The dynamics of a single tooth during the gear mesh is assumed to be that of a cantilever beam under a moving load (Ψ). The Ψ results in a set of deformation modes of the gear tooth governed by the associated stiffness. Specifically, the gear tooth undergoes axial deformation, bending and shearing, fillet foundation deflection, and contact deformation. The present analysis adopts the Mohammed et. al. [9] model for the axial, bending, and shear stiffness (K_a, K_b, and K_s); Sainsot model [10] for fillet foundation stiffness (K_f); and Yang model [11] for the Hertzian contact stiffness (K_h).

The strain energies (U_a, U_b, and U_s) stored in the gear tooth due to the axial, bending, and shear deformation are

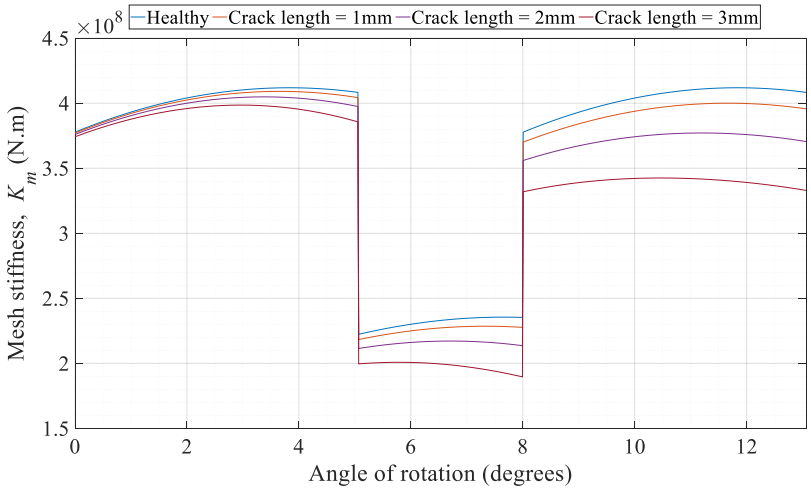


Figure 3: Calculated mesh stiffness for contact ratio of 1.5

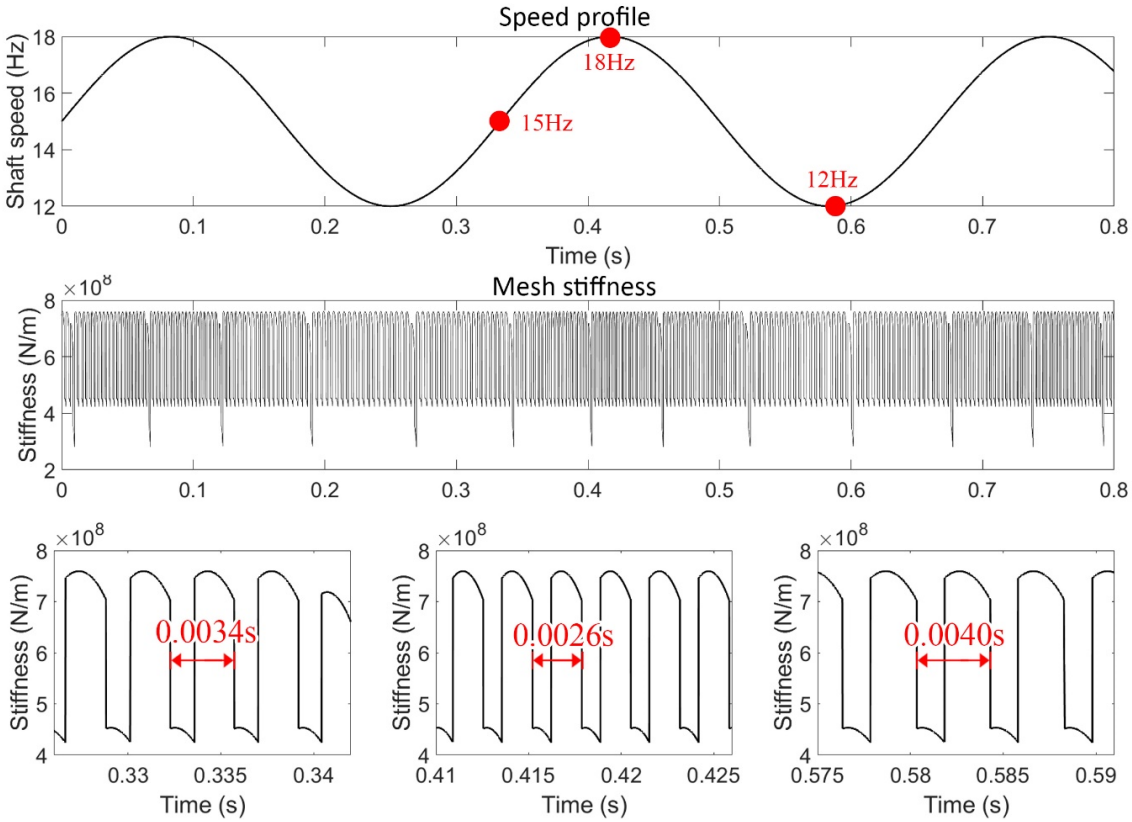


Figure 4: Instantaneous shaft speed and corresponding mesh stiffness of the gear operating at 15% speed fluctuation.

as follows:

$$U_a = \frac{\Psi^2}{2K_a} = \int_0^d \frac{\Psi_a^2}{2EA_X} dX \ , \Psi_a = \Psi \cos(\theta_1) \quad (1)$$

$$U_s = \frac{\Psi^2}{2K_s} = \int_0^d \frac{\Psi_b^2}{2EA_X} dX \ , \Psi_b = \Psi \sin(\theta_1) \quad (2)$$

$$U_b = \frac{\Psi^2}{2K_b} = \int_0^d \frac{J^2}{2EI_X} dX \ , \quad J = [\Psi_b.(d-X)] - [\Psi_a.h] \quad (3)$$

Here, the variables h, d, and X are associated with the gear tooth geometry and the point of contact. The E and G are the elastic and shear modulus. The I_X and A_X are the moments of inertia and cross-sectional area of the tooth section at a distance of X. The I_X and A_X are calculated as follows:

$$I_X = \begin{cases} \frac{1}{12}(h_X + h_X)^3 db; & h_x \leq H_o \\ \frac{1}{12}(h_X + H_o)^3 db; & h_x > H_o \end{cases} \quad (4)$$

$$A_X = \begin{cases} (h_X + h_X) db; & h_x \leq H_o \\ (h_X + H_o) db; & h_x > H_o \end{cases} \quad (5)$$

Here, H_o is the geometric parameter associated with the crack.

Further, the fillet foundation stiffness (K_f) and the Hertzian contact stiffness due to the Ψ is calculated by the following equation:

$$\frac{1}{K_f} = \frac{\cos^2(\alpha_1)}{bE} \left\{ L^* \left(\frac{d}{S_f}\right)^2 + M^* \left(\frac{d}{S_f}\right) + P^* \left(1 + Q^* \tan^2(\theta_1)\right) \right. \quad (6)$$

$$\frac{1}{K_h} = \frac{4(1-\nu^2)}{\pi E b} \quad (7)$$

Here b is the tooth width, and S_f is the tooth thickness at the fillet foundation. The $L*$, $M*$, $P*$, and $Q*$ are coefficients calculated empirically.

The total mesh stiffness (K_m) for the gear pair [1] at any instant is given by the following equation [2]:

$$\frac{1}{K_m} = \left(\frac{1}{K_{ag}} + \frac{1}{K_{bg}} + \frac{1}{K_{sg}} + \frac{1}{K_{fg}} + \frac{1}{K_{hg}}\right) + \left(\frac{1}{K_{ap}} + \frac{1}{K_{bp}} + \frac{1}{K_{sp}} + \frac{1}{K_{fp}} + \frac{1}{K_{hp}}\right) \quad (8)$$

[1] Note that the calculation shown here is for a single gear pair. Twice the value may be taken when multiple gear pairs are in mesh, i.e. when the contact ratio is more than one.

[2] The annotations p represents the pinion and g represents the gear.

The mesh stiffness for healthy and cracked gear tooth pair is simulated using the gear parameters given in [8] (Figure 3). It may be noted that the stiffness reduces with the increase in crack length. Also, at angular positions of multiple gear meshes, the K_m is higher due to the combined geometry. The period of engagement and disengagement of the gear tooth pair varies according to the instantaneous speed. The meshing is faster at higher speeds, while the meshing is slower at lower speeds. Hence, the mesh stiffness follows a scaling pattern driven by the speed of the instantaneous shaft. Figure 4 shows the speed profile, corresponding mesh stiffness and enhanced portions of the mesh stiffness time snippets. The scaling effect of the mesh stiffness across the time domain may be visualised by the period of engagement and disengagement at different speeds (15Hz, 18Hz and 12Hz).

3.2 Lumped mass model

A six-degree-of-freedom lumped mass model is used for the analysis [8]. Figure 5 shows a schematic representation of the model. A set of ordinary differential equations governs the dynamics of the said system. The equations of motion of the model are as follows:

$$I_g\ddot{\theta_g} = T_{fg} + r_g W_0 + T_g \quad (9)$$

$$I_p\ddot{\theta_p} = T_{fp} - r_p W_0 + T_p \quad (10)$$

$$m_g\ddot{v_g} + c_{gv}\dot{v_g} + k_{gv}v_g = -W_0 \quad (11)$$

$$m_p\ddot{v_p} + c_{pv}\dot{v_p} + k_{pv}v_p = W_0 \quad (12)$$

$$m_g\ddot{u_g} + c_{gu}\dot{u_g} + k_{gu}u_g = -\Psi \quad (13)$$

$$m_p\ddot{u_p} + c_{pu}\dot{u_p} + k_{pu}u_p = \Psi \quad (14)$$

$$W_0 = C_m(r_p\dot{\theta_p} - r_g\dot{\theta_g} + \dot{v_p} - \dot{v_g}) + K_m(r_p\theta_p - r_g\theta_g + v_p - v_g) \quad (15)$$

In the above-given equations, u, v, and θ represent the horizontal, vertical, and angular displacements; m is the mass, and r is the base radius; c and k represent the damping coefficient and stiffness of the gearbox bearings; T represents the input/output torque; T_f represents the frictional torque; K_m and C_m represent the mesh stiffness and the mesh damping coefficient respectively. The following paragraphs analyse the vibration response generated by the above-described dynamic model. Analyses based on time, frequency, and time-frequency domains are presented. Two cases of analyses are presented: Case 1, crack growth model and Case 2, speed variation model.

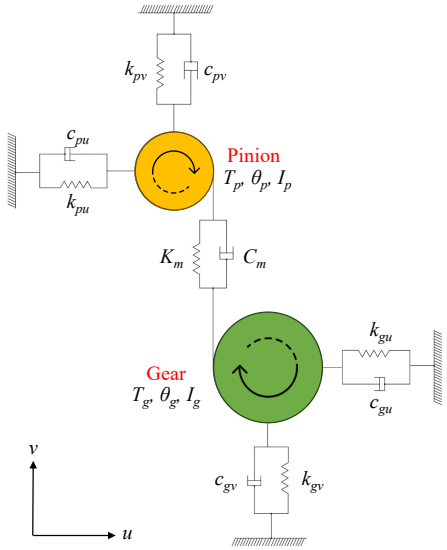


Figure 5: Six degree-of-freedom lumped mass model of a single-stage fixed-axis gearbox

The Case 1 is analysed using responses generated for K_m values given in the Figure 3. A sinusoidal variation with fluctuations 0%, 1%, 2.5%, and 5% are considered for Case 2.

4. RESULTS AND DISCUSSION

Analyses based on time, frequency, and time-frequency domains are presented in the following paragraphs. Two cases of analyses are presented: Case 1, crack growth model and Case 2, speed variation model. Case 1 is analysed using responses generated for K_m values in Figure 3. A sinusoidal variation (Figure 6) with fluctuations (F_l) 0%, 1%, 2.5%, and 5% are considered for Case 2.

4.1 Time domain analysis

The time domain representations of the vibration response generated for both cases are shown in Figures 7 and 8. The crack growth model shows the transient response in faulty gear mesh instances. Further, the transients correspond to the diminished stiffness of the meshed tooth pair, as shown in Figure 3. It may be noted that the damping of transient response after the impact of the faulty gear pair meshing has shown visible Amplitude Modulation (AM) (as shown in Figure 7). However, the direct visualisation of fault information from the time domain is impossible

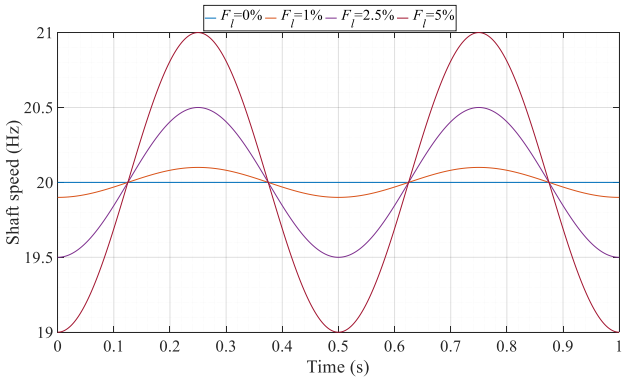


Figure 6: Speed variation for the simulation model

for very early faults. The said conundrum is multi-fold for real-life systems where external noise, sub-component vibrations, and transfer path effect mask the sensor-acquired vibration response. The variation in tooth contact force during the speed variation has resulted in a corresponding variation in the vibration response for Case 2 [3]. AM corresponding to the speed profile is apparent only in the vibration response corresponding to higher speed fluctuations. Intuitively, since the angular displacement is non-constant during the rotation of the gear pair, Frequency modulation (FM) is also expected in the response.

4.2 Frequency domain analysis

The frequency domain representation is a global illustration of the energy distributed among the constituent frequencies of the vibration response. The basis of the frequency domain representation is the Fourier transform. The Fourier transform facilitates any function to be represented as a combined set of scaled sinusoidal functions at different frequencies and phases. The Fourier transform of the vibration response ($x(t)$) is as follows:

$$\hat{x}(\omega) = \int_{-\infty}^{\infty} x(t) \mathrm{e}^{-i\omega t} dt \tag{16}$$

Theoretically, the gear pair meshes at constant operational speeds at a constant frequency, termed the Gear Mesh Frequency (GMF) [4]. Hence, the vibration responses will have a higher energy concentration at the GMF harmonics. Further, the gear tooth bends at every gear mesh. Hence, a

[3] The variation in shaft speed corresponds to variation in power transmission. Correspondingly, the torque load changes with respect to the speed variation.

[4] GMF is the fault frequency (f_0) for gearboxes.

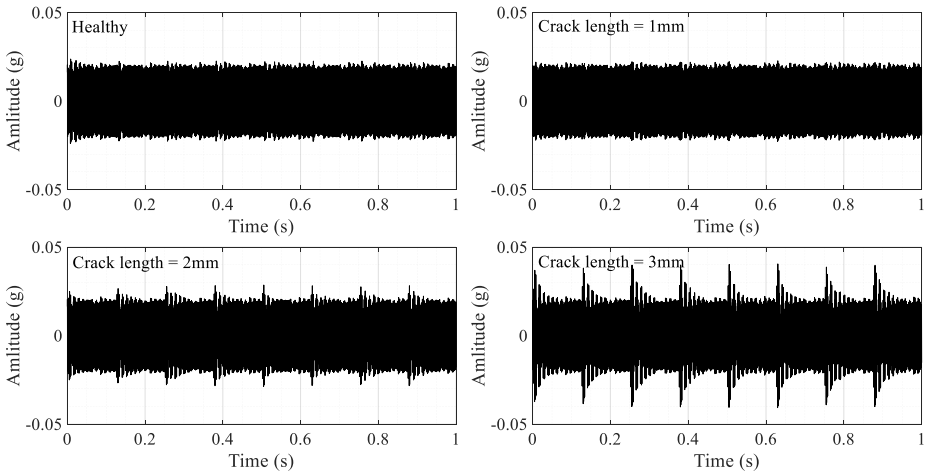


Figure 7: Time domain representation of the dynamic model simulated vibration response for different crack size

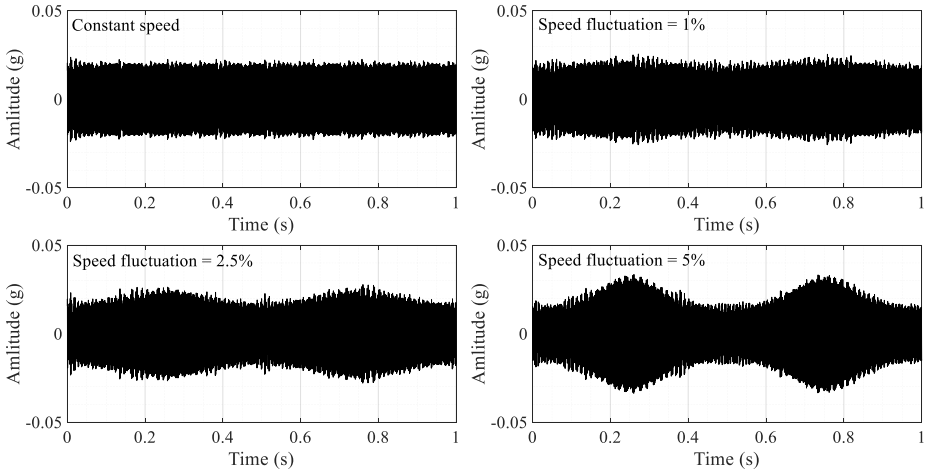
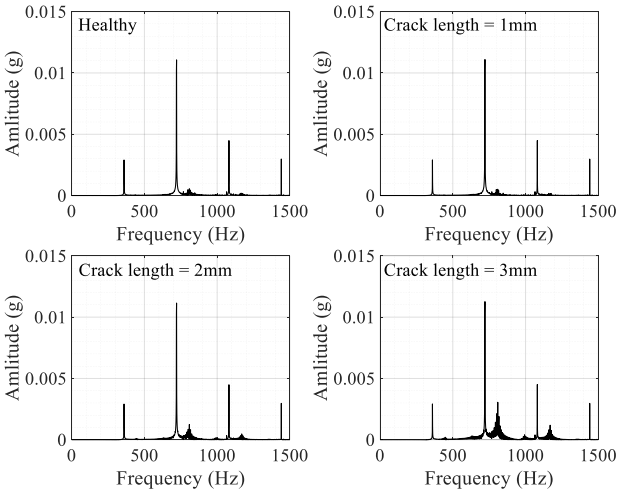


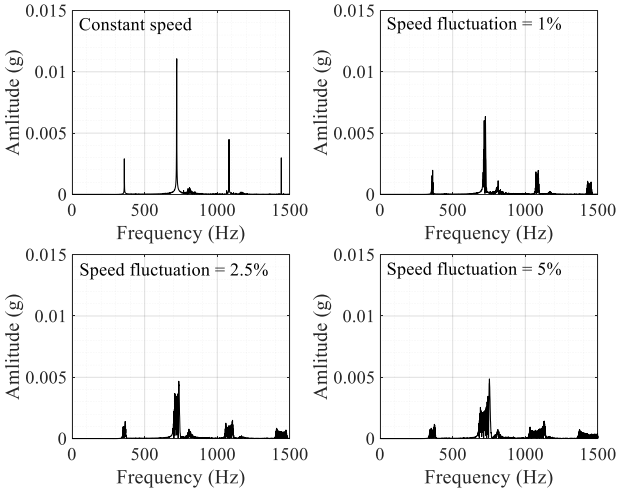
Figure 8: Time domain representation of the dynamic model simulated vibration response for different speed fluctuation

slight variation in transmission ratio at the tooth meshes leads to FM, which, along with the AM due to gear mesh impacts, leads to sidebands around the GMF. Further, the AM-FM at the faulty gear pair mesh is higher than the rest due to the relatively lower K_m. Hence, the presence of the fault leads to disturbance in the sideband energy, which is apparent in the frequency domain representation of the crack growth model's vibration response (Figure 9a). The basic assumption of frequency domain representation is the constant operational speed. As such, the frequency domain representation of the vibration response of gearboxes operating at variable speeds results in a smeared spectrum (Figure 9b). Specifically, the global GMF variation across the gearbox's operation varies; hence, the vibration response energy gets smeared across those frequencies. Further, a decrease in the spectral amplitude is also apparent, possibly due to the smearing of energy across the earlier frequencies concentrated at singular frequency values [5] .

[5] Note that the total vibration energy stays conserved.

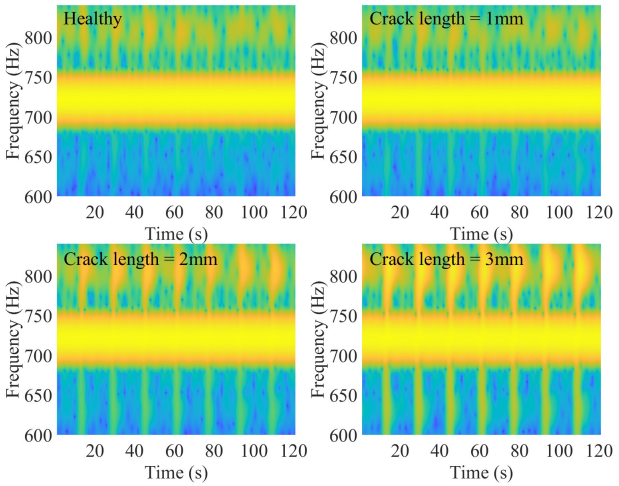


(a) Frequency domain representation of the dynamic model simulated vibration response for different crack sizes.

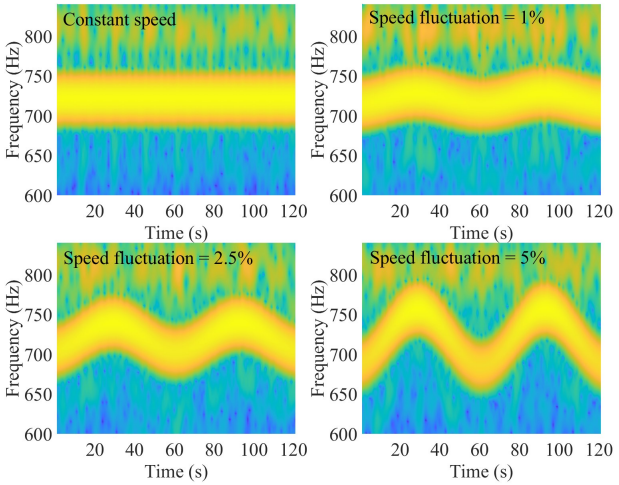


(b) Frequency domain representation of the dynamic model simulated vibration response for different speed fluctuations.

Figure 9: Frequency domain representations of simulated vibration responses for different conditions.



(a) Time-frequency domain representation of the dynamic model simulated vibration response for different crack sizes.



(b) Time-frequency domain representation of the dynamic model simulated vibration response for different speed fluctuations.

Figure 10: Time-frequency domain representations of simulated vibration responses for different conditions.

4.3 Time-frequency domain analysis

In contrast to the frequency domain representation, a global representation of vibration response energy across the frequencies, the time-frequency domain representation illustrates a temporal localised frequency distribution. The time-frequency domain is the frequency domain amalgamation of time-windowed signal sections of the vibration response.

$$\hat{x}(\tau,\omega) = \int_{-\infty}^{\infty} x(t)w(t-\tau)\mathrm{e}^{-i\omega t}dt \qquad (17)$$

Here, $w(.)$ represents the windowing function. The time-frequency domain representation provides insights into the localised variation in frequencies. Specifically, the

frequency variations, which are difficult to capture by the frequency domain analysis due to spectral smearing, are easily comprehensible in the time-frequency domain representation.

Figures 10a and 10b show the time-frequency domain representations of vibration responses generated for the crack growth and speed variation models. The variations in instantaneous frequency are apparent in both cases [6]. Specifically, the crack growth model was simulated at a constant speed; hence, the GMF stays constant over time. However, in the speed variation model, the time-frequency representation aptly illustrates the variations in GMF due to shaft frequency fluctuation. In the crack growth model, frequency variations may be observed at the fault transients due to their FM nature. The time-frequency representation provides clear insight into the frequency variation of the vibration response across time. However, the spectral coherence of the representation is limited by the time and frequency resolution balance across the respective axes [7]. Hence, spectral energy quantification for fault severity estimations is not easily possible in the time-frequency domain. When combined with appropriate fault enhancement algorithms, the frequency domain analysis has shown better quantification of fault severity. Nonetheless, the time-frequency representation is ideal for reverse estimation of instantaneous frequency in the unavailability of tacho-pulse signals.

5. CONCLUSION

The study presents a digital twin based on a dynamic model for simulating gearbox vibration response in the presence of a fault and variable operational speed. The six-degree-of-freedom model successfully simulates the vibration response characteristic of a gearbox with root cracks and operates at variable speed. Further, a detailed study of the vibration response in its time-domain, frequency-domain, and time-frequency domain is presented. The presented model can simulate the vibration response's spectral distortions and amplitude-frequency modulations indicative of fault information and speed variations.

[6] The second GMF harmonic is shown in the figures due to its higher spectral energy concentration, as apparent in the frequency domain representations.

[7] Heisenberg's uncertainty principle.

6. REFERENCES

[1] J. R. Davis, *Gear materials, properties, and manufacture*. ASM international, 2005.

[2] S. Hashim and P. Shakya, "Tacho-less spur gear condition monitoring at variable speed operation using the adaptive application of variational mode extraction," *Structural Health Monitoring*, 2024.

[3] L. Zhou, F. Duan, M. Corsar, F. Elasha, and D. Mba, "A study on helicopter main gearbox planetary bearing fault diagnosis," *Applied Acoustics*, vol. 147, pp. 4–14, 2019.

[4] S. Hashim and P. Shakya, "Variational mode decomposition based vibro-acoustic analysis for spur gear fault detection," in *Internoise and Noisecon Congress and Conference Proceedings*, pp. 1995–2994, Institute of Noise Control Engineering, 2023.

[5] S. Hashim, S. K. Mishra, and P. Shakya, "An approach for adaptive filtering with reinforcement learning for multi-sensor fusion in condition monitoring of gearboxes," *Computers in Industry*, vol. 164, p. 104214, 2025.

[6] G. Sariyer, S. Mangla, Y. Kazancoglu, C. O. Tasar, and S. Luthra, "Data analytics for quality management in industry 4.0 from a msme perspective," *Annals of Operations Research*, 2021.

[7] X. Liang, M. Zuo, and Z. Feng, "Dynamic modeling of gearbox faults: A review," *Mechanical Systems and Signal Processing*, vol. 98, pp. 852–876, 2018.

[8] A. Patel and P. Shakya, "Spur gear crack modelling and analysis under variable speed conditions using variational mode decomposition," *Mechanism and Machine Theory*, vol. 164, 2021.

[9] O. Mohammed and M. Rantatalo, "Gear fault models and dynamics-based modelling for gear fault detection – a review," *Engineering Failure Analysis*, vol. 117, 2020.

[10] P. Sainsot, P. Velex, and O. Duverger, "Contribution of gear body to tooth deflections—a new bidimensional analytical formula," *J. Mech. Des.*, vol. 126, no. 4, pp. 748–752, 2004.

[11] D. Yang and Z. Sun, "A rotary iodel for spur gear dynamics," *Journal of Mechanical Design, Transactions of the ASME*, vol. 107, no. 4, p. 529 – 535, 1985.

DOI: 10.61782/fa.2025.0022



FORUM ACUSTICUM
EURONOISE 2025

A NEW FEATURE EXTRACTION FRAMEWORK FOR SOURCE-FREE DOMAIN ADAPTATION IN BEARING FAULT DIAGNOSIS

Sakthisandron Arunagiri **Sitesh Kumar Mishra** **Piyush Shakya***
Engineering Asset Management Group, Department of Mechanical Engineering,
Indian Institute of Technology Madras, Chennai-36, India

ABSTRACT

Condition monitoring of machine elements is critical in industrial applications, drawing significant attention to cross-domain bearing fault diagnosis. However, data privacy concerns and storage limitations pose significant challenges. To address these issues, source-free domain adaptation networks, consisting of a feature extractor and a fault classifier, have been developed. In these frameworks, the parameters of both components are trained using only source-domain data. During testing on target-domain data, the extractor's parameters are initialized with the learned source-domain parameters and allowed to adapt, while the classifier's parameters remain fixed. Although the proposed approach effectively tackles privacy and storage concerns, it falls short in providing a unique feature representation for each domain, limiting its generalization capability. The present work seeks to overcome the mentioned limitation by employing auto-regressive models to generate unique feature representations for individual domains. Additionally, self-organizing maps are utilised to explore similarities across domains and various fault types. The robustness of the proposed approach is validated through extensive experiments, demonstrating its effectiveness in improving cross-domain fault diagnosis performance.

Keywords: *bearing diagnosis, source free domain adaptation, auto-regressive model, self-organizing map.*

**Corresponding author*: *pshakya@iitm.ac.in.*

***Copyright**: ©2025 Shakya et al. This is an open-access article distributed under the terms of the Creative Commons Attribution 3.0 Unported License, which permits unrestricted use, distribution, and reproduction in any medium, provided the original author and source are credited.*

1. INTRODUCTION

In modern industrial systems, predictive maintenance plays a crucial role in ensuring safety and minimizing downtime. Significant research efforts have been dedicated to developing data-driven methods for early fault detection [1, 2], which can assist in effective decision-making. However, real-world implementation faces several challenges, including large data storage requirements, data privacy concerns, and the increased difficulty of domain adaptation when applying models across different operating conditions. Recent studies [3,4] have attempted to address these issues by developing source-free domain adaptation frameworks. This work aims to tackle these challenges by introducing a novel feature extraction approach that provides a unique representation of the dataset, ensuring more distinctive and domain-specific feature learning.

A source-free domain adaptation approach for bearing fault diagnosis begins with feature extraction from the source-domain bearing data followed by training a classifier using the corresponding fault labels. Notably, training is performed exclusively on the source data, without access to target labels. Once trained, the same feature extraction procedure is applied to the target-domain bearing data, and the classifier is expected to accurately classify faults in the target domain despite distributional differences.

Mathematically, the labelled source-bearing dataset is represented as $D_S = \{x_i^S, y_i^S\}_{i=1}^{N_S}$, where x_i^S and y_i^S denote the vibration signal and the corresponding fault label for the i^{th} sample, respectively. The unlabelled target-bearing dataset is given by $D_T = \{x_i^T\}_{i=1}^{N_T}$, where N_S and N_T represent the number of samples in the source and target datasets, respectively. Since the source and target data distributions may differ, the key challenge is to

learn a mapping function: $f : x_i \rightarrow y_i$ using only the source data, such that it can effectively classify faults in the target domain despite the absence of target labels.

2. PROPOSED METHOD

2.1 Overview

The proposed method consists of three main stages: feature extraction, feature representation, and classification. In the feature extraction stage, the vibration signal is modelled as the output of an Auto-Regressive (AR) process [5]. The AR model parameters and the residual variance are extracted as features to ensure a unique representation for each sample. In the feature representation stage, the extracted features are structured using Self-Organizing Maps (SOMs) [6]. The transformation organizes the samples based on similarity, improving feature discrimination and clustering. In the classification stage, a deep neural network (DNN) is trained on the SOM-structured feature representations of the source domain. Once trained, the parameters of both the SOM and the classifier are frozen. The same feature extraction and representation process is then applied to the target domain data. The structured representations of the source and target samples are clustered independently. To facilitate unsupervised domain adaptation, the target clusters are mapped to the closest corresponding source clusters. Finally, the mapped target samples are classified using the trained DNN. An overview of the proposed method is illustrated in Fig. 1.

2.2 Mathematical Framework of the Proposed Method

2.2.1 Feature Extraction Using AR Model

All vibration signals in the dataset are modelled as the output of an AR process of order five as

$$x(k) = \sum_{j=1}^{5} \alpha_j x(k-j) + \epsilon(k) \tag{1}$$

where $\epsilon(k)$ is white noise with variance σ^2, and α_j represents the j^{th} coefficient. These coefficients, along with the residual noise, constitute the feature vector for each vibration signal, expressed as $\mathbf{f} = [\alpha_1, \alpha_2, \alpha_3, \alpha_4, \alpha_5, \sigma^2]$. Consequently, the transformed dataset is given by $\bar{D}_S = \{\mathbf{f}_i^S, y_i^S\}_{i=1}^{N_S}$ and $\bar{D}_T = \{\mathbf{f}_i^T\}_{i=1}^{N_T}$.

2.2.2 Structured Representation via SOM

The extracted features are mapped to a structured 2D latent space using a SOM consisting of a 20×20 neuron lattice, with $\mathbf{w_{ij}}$ representing its weights. The iterative process for updating these weights is as follows:

- Find the Best Matching Unit (BMU):

$$(i^*, j^*) = \arg\min_{(i,j)} \|\mathbf{f}_i - \mathbf{w}_{ij}\|$$

- Update neuron weights:

$$\mathbf{w}_{ij} \leftarrow \mathbf{w}_{ij} + \eta.h(i,j)(\mathbf{f}_i - \mathbf{w}_{ij})$$

  where η is the learning rate, and $h(i,j) = e^{\frac{(i-i^*)^2+(j-j^*)^2}{2\beta^2}}$ is the Gaussian neighborhood function with β as the neighborhood radius.
- Repeat until the weights converge.
  After convergence, the structured representations from SOM_S and SOM_T are denoted as $\mathbf{w}_{ij}^S$ and $\mathbf{w}_{ij}^T$, respectively.

2.2.3 Training DNN-Based Classifier

The updated weights $\mathbf{w}_{ij}^S$ from SOM_S are stacked to form $\mathbf{z}^S$, which serves as input to the DNN for training its weights and biases. The DNN architecture is mathematically expressed as:

$$\hat{y}_S = \sigma_3(\mathbf{W}_3(\sigma_2(\mathbf{W}_2(\sigma_1(\mathbf{W}_1\mathbf{z}^S + \mathbf{b}_1)) + \mathbf{b}_2) + \mathbf{b}_3)) \tag{2}$$

where $\mathbf{W}_*, \mathbf{b}_*$, and σ_* denote the weights, biases, and ReLU activation functions, respectively. Training is performed for 2000 epochs to minimize the cross-entropy loss between $\hat{y}_S$ and the true source labels using the Adam optimizer.

2.2.4 Unsupervised Domain Adaptation and Classification

After training, the weights $\mathbf{w}_{ij}^S$ of SOM_S and the parameters of the DNN are frozen while adapting to the target dataset. The procedure for aligning $\mathbf{w}_{ij}^T$ to $\mathbf{w}_{ij}^S$ is as follows:

- Apply K-means clustering to the neurons of SOM_S and SOM_T:

$$C^S = \{c_{ij}^S\}_{(i,j)\in \text{SOM}_S}, \quad C^T = \{c_{ij}^T\}_{(i,j)\in \text{SOM}_T}$$

  where c_{ij}^S and c_{ij}^T represent the cluster assignments for each neuron.

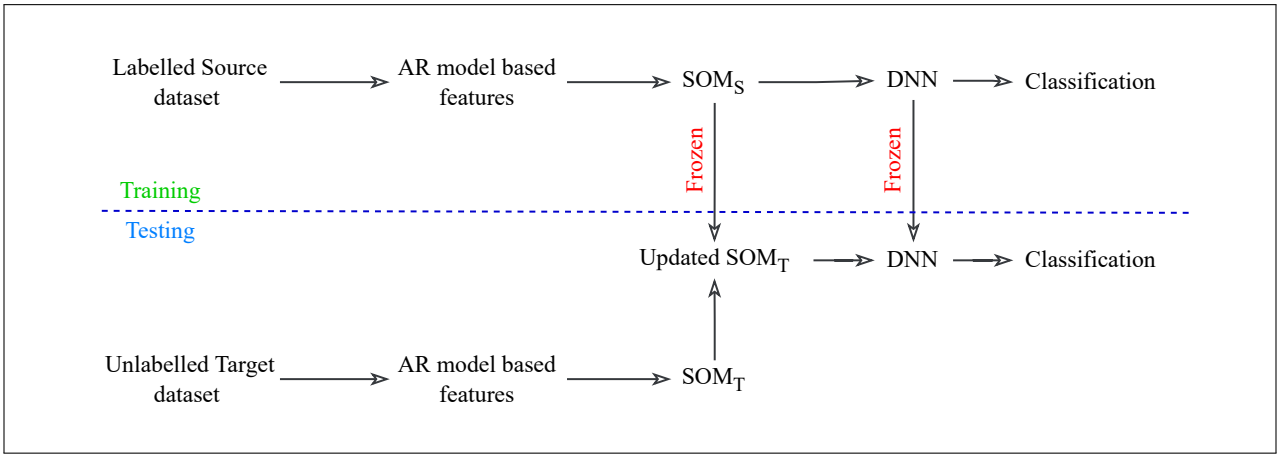


Figure 1. Overview of the proposed method.

- Compute the centroid of source clusters:

$$\mu_k^S = \frac{1}{|C_k^S|} \sum_{(i,j)\in C_k^S} \mathbf{w}_{ij}^S$$

where C_k^S is the set of neurons assigned to cluster k.

- Update target weights iteratively:

$$\mathbf{w}_{ij}^T \leftarrow \lambda \mathbf{w}_{ij}^T + (1-\lambda)\mu_k^S$$

Finally, the updated $\mathbf{w}_{ij}^T$ is fed into the DNN for fault classification:

$$\hat{y}_T = DNN(\mathbf{w}_{ij}^T) \tag{3}$$

3. DISCUSSION

3.1 Dataset and Tasks

The proposed method is validated on both same-domain and cross-domain tasks using bearing vibration data from the CWRU dataset [7] and the IMS dataset [8]. For the CWRU dataset, vibration data collected from both the drive end (CWRU$_d$) and fan end (CWRU$_f$) are used. The fault types considered are Rolling Element (RE), Outer Race (OR), Inner Race (IR), and the Healthy condition. To ensure uniformity, vibration signals from both datasets are resampled to 12 kHz and 20 samples are used for each fault type. The tasks defined for evaluation are summarized in Tab. 1.

Table 1. Description of diagnostic tasks for same-domain and cross-domain fault classification.

Task	Type	Source	Target
T1	Same-domain	CWRU$_d$	CWRU$_f$
T2	Same-domain	CWRU$_f$	CWRU$_d$
T3	Cross-domain	CWRU$_d$	IMS
T4	Cross-domain	CWRU$_f$	IMS
T5	Cross-domain	IMS	CWRU$_d$
T6	Cross-domain	IMS	CWRU$_f$

3.2 Comparison

The classification accuracy of the proposed method is compared with three existing methods: Source HypOthesis Transfer (SHOT) [9], Contrastive Test-Time Adaptation (AdaContrast) [10] and Tent [11]. The accuracy results for each task are presented in Tab. 2.

3.3 Observations

The observation of the confusion matrices reveals that SHOT, AdaContrast, and the proposed method successfully cluster the fault types, whereas Tent struggles significantly. However, the relatively low accuracy scores across all methods highlight the inherent challenge of unsupervised domain adaptation in a source-free setting. The slight improvement in accuracy observed with the proposed method can be attributed to the adaptive weight

Table 2. Classification accuracy (%) of different methods for same-domain and cross-domain diagnostic tasks.

Task	SHOT	AdaContrast	Tent	Proposed
T1	50	50	22.45	50
T2	50	46.06	27.98	50
T3	50	25	23.94	50
T4	0	25	27.02	47.34
T5	75	25	28.94	50
T6	25	25	22.13	25
Avg	41.67	32.67	25.41	45.39

update strategy, wherein the SOM_T cluster centroids are adjusted towards the nearest cluster centroid in SOM_S. This adjustment enhances feature alignment between the source and target domains, leading to better classification performance. For instance, in Task 4 (cross-domain adaptation), the SHOT approach successfully identified three distinct fault types in the target dataset. However, it failed to assign the correct labels, leading to significant misclassification. The corresponding confusion matrix for Task 4 using SHOT is shown in Fig. 2. The proposed method consistently achieved around 50% accuracy in all tasks except Task 6 and was outperformed only in Task 5 by the SHOT approach.

4. CONCLUSION

The current study presents a source-free domain adaptation approach for bearing fault diagnosis, leveraging AR modelling, SOM, and a DNN. While AR modelling captures a unique representation of vibration data, the structured feature representation via SOM enhances clustering, leading to improved classification accuracy. Experimental results demonstrate that the proposed method outperforms existing approaches in both same-domain and cross-domain tasks. By addressing the challenge of domain shift in a source-free framework, the proposed method improves the feasibility of deploying machine learning models in real-world fault diagnosis applications. While the results are promising, further research is needed to refine pseudo-labelling strategies for better accuracy and to enhance robustness in noisy environments.

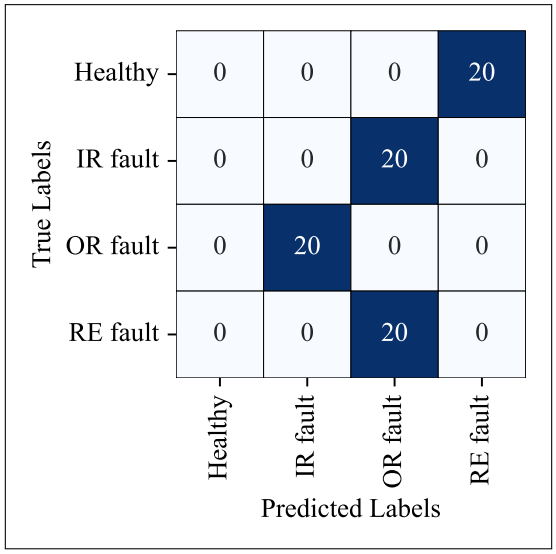


Figure 2. Confusion matrix for Task 4 using the SHOT approach.

5. ACKNOWLEDGMENTS

The authors genuinely thank Shahis Hashim for his constructive feedback and unwavering support throughout the presented research.

6. REFERENCES

[1] L. Cui, Z. Jiang, D. Liu, and D. Zhen, "A novel weighted sparse classification framework with extended discriminative dictionary for data-driven bearing fault diagnosis," *Mechanical Systems and Signal Processing*, vol. 222, p. 111777, 2025.

[2] S. Hashim, S. K. Mishra, and P. Shakya, "An approach for adaptive filtering with reinforcement learning for multi-sensor fusion in condition monitoring of gearboxes," *Computers in Industry*, vol. 164, p. 104214, 2025.

[3] Y. Wang, F. Jia, J. Shen, and L. Hao, "Source-free domain adaptation network for rolling bearing fault diagnosis," in *2023 IEEE International Conference on Mechatronics and Automation (ICMA)*, pp. 1691–1696, IEEE, 2023.

[4] H.-W. Yeh, B. Yang, P. C. Yuen, and T. Harada, "Sofa: Source-data-free feature alignment for unsupervised domain adaptation," in *Proceedings of the IEEE/CVF*

Winter Conference on Applications of Computer Vision, pp. 474–483, 2021.

[5] A. K. Tangirala, *Principles of system identification: theory and practice*. CRC press, 2018.

[6] T. Kohonen, "Self-organized formation of topologically correct feature maps," *Biological cybernetics*, vol. 43, no. 1, pp. 59–69, 1982.

[7] C. W. R. U. B. D. Center, "Case western reserve university bearing data center website," 2009.

[8] H. Qiu, J. Lee, J. Lin, and G. Yu, "Wavelet filter-based weak signature detection method and its application on rolling element bearing prognostics," *Journal of sound and vibration*, vol. 289, no. 4-5, pp. 1066–1090, 2006.

[9] J. Liang, D. Hu, and J. Feng, "Do we really need to access the source data? source hypothesis transfer for unsupervised domain adaptation," in *International conference on machine learning*, pp. 6028–6039, PMLR, 2020.

[10] D. Chen, D. Wang, T. Darrell, and S. Ebrahimi, "Contrastive test-time adaptation," in *Proceedings of the IEEE/CVF Conference on Computer Vision and Pattern Recognition*, pp. 295–305, 2022.

[11] D. Wang, E. Shelhamer, S. Liu, B. Olshausen, and T. Darrell, "Tent: Fully test-time adaptation by entropy minimization," *arXiv preprint arXiv:2006.10726*, 2020.

DOI: 10.61782/fa.2025.0131

FORUM ACUSTICUM EURONOISE 2025

ANALYSIS OF DEFECTS IN ROLLING BEARINGS USING VIBROACOUSTIC AND ULTRASONIC TECHNIQUES

Emanuele Voltolini [1] **Mirko Monaco**[1] **Enrico Armelloni**[1]
Marco Cocconcelli[3] **Andrea Toscani**[2] **Fabio Immovilli**[3] **Elisabetta Manconi**[*1]
[1] Department of Engineering for Industrial Systems and Technologies, University of Parma, Italy
[2] Department of Engineering and Architecture, University of Parma, Italy
[3] Department of Engineering Science and Methods, University of Modena and Reggio Emilia, Italy

ABSTRACT

This study explores the comparative effectiveness of microphones (standard and ultrasonic) and accelerometers in detecting defects in bearings. Defects in rolling bearings generate acoustic waves with a rich content in high frequencies. Both accelerometer and microphone data allow for Envelope Analysis or Amplitude Demodulation (low frequency), while only ultrasonic microphone data enable high-frequency analysis. The study investigates the advantages of using non-contact microphones to capture this high-frequency content easily. The non-contact nature of microphones also eliminates the risk of altering the machine's operational conditions, ensuring easy and secure data collection. Various bearings with different defects were investigated by conducting controlled experiments on a test bench. The analysis was carried out by exploiting statistical indicators, e.g., Kurtosis, Crest Factor, Impulse Factor, etc., and energy-based analysis techniques to compare low- and high-frequency results. Results of the different analyses were presented and discussed, showing the potential use of mixed accelerometric, acoustic, and ultrasonic measurements for practical predictive maintenance of rotating machines.

Keywords: *bearings, predictive maintenance, ultrasound microphone, microphone, accelerometer.*

1. INTRODUCTION

In recent years, predictive maintenance has become increasingly important in industry due to its ability to predict failures and reduce downtime [1-3]. Vibration analysis, primarily based on the use of accelerometers, is one of the most established techniques for monitoring the condition of rotating machinery [4]. In fact, it can provide accurate and repeatable data for condition monitoring of industrial machines, and it is a well-developed and thoroughly studied technique. However, accelerometers need to be installed on the machine in close proximity to the component being analyzed [5-7]. This can pose a challenge since there are practical situations where the sensors cannot be mounted properly or may interfere with the machine's structure. In more severe cases, they might not be installable close to the area that needs monitoring, or, even more critically, they cannot be utilized at all, such as for safety concerns. Compared to acceleration analysis, acoustic analysis using microphones offers several advantages, including the ability to detect signals at higher frequencies than traditional accelerometers and the capability to monitor machines without direct contact. In this context, this paper investigates the use of microphones, particularly ultrasonic microphones, in addition to accelerometers for monitoring the condition of mechanical components, particularly rolling bearings [8]. In addition, the combined use of vibration and acoustic signals could improve the accuracy of early fault detection, allowing more timely and efficient maintenance intervention. The paper focuses on the analysis of the energy content in the acoustic signal and the use of statistical indicators, without going into details of advanced spectral processing or machine learning techniques. The aim is to assess the effectiveness of an approach based on simple, yet meaningful, metrics that complement traditional

[*] ***Corresponding author***: elisabetta.manconi@unipr.it
Copyright: *©2025 Elisabetta Manconi et al. This is an open-access article distributed under the terms of the Creative Commons Attribution 3.0 Unported License, which permits unrestricted use, distribution, and reproduction in any medium, provided the original author and source are credited.*

predictive maintenance methods, enhance early failure detection, and to evaluate the effectiveness of the hybrid accelerometric-microphonic approach applied to these techniques.

2. ANALYSIS PARAMETERS

This study uses low-complexity signal analysis parameters to assess their applicability in industrial predictive maintenance [9-10].
Kurtosis is here applied as a key indicator. It measures the deviation from the mean and reflects the presence of sharp peaks or heavy tails in a signal. Statistically, it is defined as the fourth standardized moment:

$$Kurtosis = E\left[\left(\frac{X-\mu}{\sigma}\right)^4\right] = \frac{\mu_4}{\sigma^4}$$
$$\frac{\mu_4}{\sigma^4} = \frac{\frac{1}{N}\sum_{i=1}^{N}(x(i)-\mu)^4}{\left(\frac{1}{N}\sum_{i=1}^{N}(x(i)-\mu)^2\right)^2} \quad (1)$$

A normal distribution of data presents a kurtosis equal to 3, and distributions with a kurtosis greater than that value are defined as leptokurtic. Leptokurtic distributions present thicker tails, i.e. have more data far from the mean value; typically, vibrations produced by defects in rolling bearings show Leptokurtic behavior.
The second indicator used is the RMS (Root Mean Square), defined as:

$$RMS = \sqrt{\frac{1}{N}\sum_{i=0}^{N}\left(x^2(i)\right)} \quad (2)$$

The RMS value of vibrations produced by a damaged bearing is sensibly greater than a healthy bearing one.
Some impulsive metrics indicators, such as the crest factor and the impulse factor were used to evaluate the peak component of the signal. Crest factor is defined as the peak value divided by the RMS value:

$$Crest\ Factor = \frac{|x_{peak}|}{\sqrt{\frac{1}{N}\sum_{i=0}^{N}\left(x^2(i)\right)}} \quad (3)$$

The impulse factor is defined as the ratio of the peak value to the arithmetic mean of the absolute values of the signal:

$$Impulse\ Factor = \frac{|x_{peak}|}{\frac{1}{N}\sum_{i=0}^{N}|x(i)|} \quad (4)$$

Impulsive metrics are important in bearings fault analysis because the formation and growth of defects cause impulsive forces to be generated during bearing operation.

To conclude, spectral energy was used to represent the energy contained in the various third octave frequency bands. Spectral energy is defined as the sum of the squared absolute value of the Fourier-transformed signal:

$$E(f) = \sum |X(f)|^2 \quad (6)$$

According to Percival's theorem, the spectral energy calculated over the whole spectrum is equal to the overall signal energy. In this study, particular attention was paid to the relationship between the spectral energies calculated from the signals of damaged bearings to those from healthy bearings for each data acquisition batch.

3. METHODOLOGY

3.1 Data Acquisition

Several data acquisitions were conducted by varying both fault type and bearing operating condition. This section details the equipment and sensors used, including their technical specifications. In addition, a brief overview of the test environments and experimental settings are provided. All the measurements were carried out at the laboratories of the University of Modena and Reggio Emilia.

3.1.1 Sensors and data acquisition devices

The same data acquisition systems were used in the tests to ensure consistency and comparability of results. The whole system is composed of a data acquisition system, one measurement microphone, one ultrasound microphone and one accelerometer. The ZoTech[1] Data Acquisition System (DAQ) was used to record the microphone and accelerometer signals, composed of a Sensor Network Interface (DIN0264) and a Sensor Acquisition Node (AIN0824). This architecture makes use of a digital bus implemented on an Unshielded Twisted Pair to connect one or more AIN0824 boards to a data storage system (e.g., a laptop or an industrial PC) using a DIN0264 board. The implementation of a digital communication guarantees perfect synchronization between the acquired signals, both in term of jitter and latency [9-10] making it a perfect system for acquiring many transducers with time synchronization, mandatory for the computation of the most advanced diagnostic metrics [11-12]. The system operates at a sampling rate of 48 kHz with a resolution of 24 bits, ensuring accurate signal representation. A full-scale range of ±5V was configured for both sensors to optimize

[1] www.zotech.it/en

dynamic range and measurement fidelity. Further specifications are given in Tab. 1.

Table 1. ZoTech data acquisition system

Specification	Value
Number of inputs	64
Sampling Rate	48 kHz
Resolution	24 bits
Connection	USB 2.0

The Ultramic 384K WIND ultrasonic microphone (Tab. 2) has a built-in recording system with a sampling rate of 384 kHz and a resolution of 16 bits. This configuration allows accurate acquisition of ultrasonic signals up to 192 kHz, effectively covering the entire operating range of the microphone, which is critical for detecting high-frequency fault signatures.

Table 2. Ultrasound Microphone Ultramic 384K WIND (Dodotronic), technical data.

Specification	Value
Frequency Range	1 to 100 kHz
Sampling Rate	384 kHz
Resolution	16 bits
Connection	USB 2.0

For vibration measurements, the Piezotronics 603M170 PCB sensor was used (Table 3), which offers a frequency range up to 14 kHz and a sensitivity of 100 mV/g over one axis (mono-axial). This ensures the detection of mechanical vibrations in the typical range of failure frequencies.

Table 3. Accelerometer PCB Piezotronics 603M170, technical data.

Specification	Value
Sensitivity (±10%)	100 mV/g
Measurement Range	±80g
Frequency Range	0.4 Hz to 14 kHz

The Brüel & Kjær 4189 omnidirectional microphone was used as the acoustic transducer (Table 4), which offers a flat frequency response from 6 Hz to 20 kHz with a sensitivity of 50 mV/Pa. Its wide and stable response range enables accurate capture of low-frequency and high-frequency acoustic emissions, facilitating a comprehensive analysis of how potential damage affects the entire acoustic spectrum.

Table 4. Microphone and Preamplifier Bruel&Kjaer 4189-1706, technical data.

Specification	Value
Diameter	½inch
Sensitivity	50 mV/Pa
Frequency Range	6.3 Hz to 20 kHz

3.1.2 First test condition

In Fig. 1(a), a schematic diagram illustrates the configuration of the first test condition. The system consists of a three-phase motor with a bearing mounted directly on the shaft. An accelerometer is placed over the bearing seat to capture vibrations in the radial direction.
The Ultramic 384K WIND is placed 20 cm in front of the bearing, directly aligned with it. The microphone is connected via USB 2.0 to a PC running Audacity software, which records the signal at 384 kHz.
The measurement microphone (Brüel & Kjær 4189) is placed 45 cm from the bearing to capture the machine's overall acoustic emissions. This microphone and accelerometer are connected to the ZoTech data acquisition system. Data from these sensors are recorded on a separate PC, as different interfaces are needed for different sampling rates.
The motor speed was set to 1000 rpm, and all test bearings were evaluated under this nominal operating condition. Measurements were conducted on a series of three SKF 6205 bearings, each subjected to different laboratory-induced wear conditions. The first bearing was new and served as a reference. The second bearing had damage to the outer ring induced by acid exposure, and the third was damaged by compression with a force greater than its rated load capacity. SKF 6205 bearing specifications are given in Tab. 5.

Table 5. SKF 6205 bearing specifications.

Specification	Value
Number of balls	9
Diameter of balls	7.94 mm
Pitch diameter	39.04 mm
Contact angle	0°

3.1.3 Second test condition

The second set of measurements, shown in Fig. 1.b, was conducted on a test bench specially designed for bearing analysis, the AV TEST BENCH, manufactured by AMC Vibro. This test bench consists of two three-phase asynchronous motors, one operating as a main motor and the other as a braking system, together with a gearbox

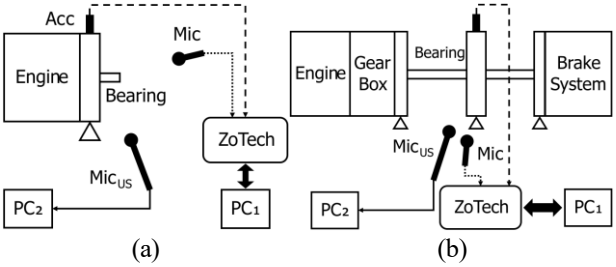


Figure 1. (a) First test condition, (b) second test condition

(transmission rate 2,91:1) and a shaft supported by three rolling bearings. The test stand was used with a three-stage speed profile consisting of three constant-speed strokes at 1000-1500-2000 RPM measured on the motor side. The corresponding shaft speeds at which the bearing was tested were 343.64 RPM, 515.46 RPM and 687.29 RPM, due to the speed reduction of the gearbox. For these measurements, the accelerometer was mounted on the center bearing, and the two microphones were placed 15 cm in front of the bearing. The parameters of the data acquisition system remained unchanged from the previous test to ensure consistent measurement conditions. Measurements were conducted using two SKF YAR 204-2F bearings: the first bearing was healthy, with a minimum number of operating hours, while the second had a lab welding-induced damage on the outer ring. SKF YAR 204- bearing technical specifications are given in Tab. 6.

Table 6. SKF YAR 204 2F bearing specifications.

Specification	Value
Number of balls	8
Diameter of balls	7.938 mm
Pitch diameter	33.5 mm
Contact angle	0°

3.2 Data Processing

To ensure consistent and reliable statistical parameters for the detection of potential failures, the acquired signals were subjected to pre-processing, which included data slicing and filtering. Next, theoretical failure frequencies of the tested bearings were calculated based on their geometric parameters and rotational speed. Finally, envelope analysis and spectrogram visualization were performed to characterize the damage signatures of the defective bearings with respect to the healthy reference. The following subsections detail each step of the data processing workflow.

3.2.1 Pre-processing

In all test conditions, at least 1 minute of audio was recorded to ensure that the system reached a steady state condition. From each recording, 15 seconds of steady-state data are selected. In Fig. 2, an example of the raw, trimmed signal data from the three sensors is presented in both "healthy" and "damaged" conditions of the bearing. The data are then filtered with a Butterworth-type bandpass filter of order 5, matched to the characteristic frequency range of each sensor: for the accelerometer, the used filter range is 2 Hz to 14 kHz; for the microphone, the range is 6 Hz to 20 kHz and for the ultrasonic microphone goes from 1 to 100 kHz.

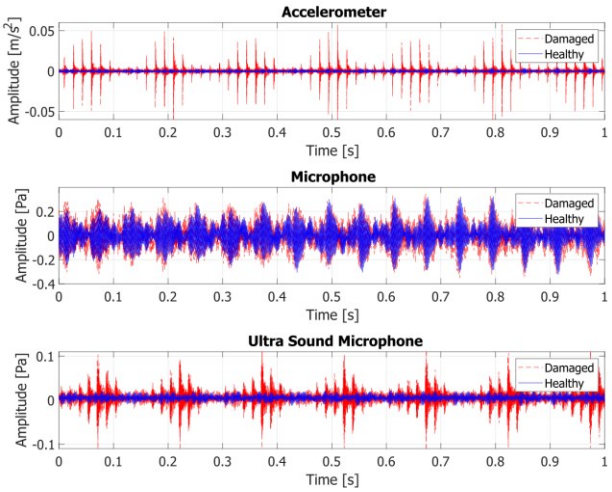


Figure 2. Time plot of 1 s for each sensor.

3.2.2 Calculus of bearings fault frequencies

To confirm and characterize the presence of defects manually induced on the bearings, characteristic failure frequencies were calculated based on bearing's geometric parameters and rotational speed, following the methodology described in [13]. These failure frequencies aid in identifying specific types of defects. The equations used are as follows:

$$f_{BPFO} = \frac{n}{2} f_r \left(1 - \frac{BD}{PD}\cos\beta\right) \quad (7)$$

$$f_{BPFI} = \frac{n}{2} f_r \left(1 + \frac{BD}{PD}\cos\beta\right) \quad (8)$$

$$f_{BFF} = \frac{PD}{BD} f_r \left[1 - \left(\frac{BD}{PD}\cos\beta\right)^2\right] \quad (9)$$

$$f_{FTF} = \frac{1}{2} f_r \left(1 - \frac{BD}{PD}\cos\beta\right) \quad (10)$$

where f_r is the shaft rotational frequency (in Hz), BD is the ball diameter and PD is the pitch diameter (distance

between opposite rolling elements). The n parameter indicates the number of rolling elements and β is the contact angle of the rolling elements. The frequencies f_{BPFO}, f_{BPFI}, f_{BFF} , f_{FTF} are respectively: the Ball Pass Frequency Outer Race (characteristic of an outer ring fault), the Ball Pass Frequency Inner Race (for inner ring faults), the Ball Spin Frequency (related to rolling element defects), the Fundamental Train Frequency (associated with cage or retainer faults). The results are collected in Table 7.

Table 7. Bearings' fault frequencies with shaft speed respectively of 1000 and 343.64 rpm.

Parameters [Hz]	SKF 6205	SKF YAR204
Rotation Freq.	16.67	5.73
BPFO	59.75	20.53
BPFI	90.25	31.01
BFF	78.56	27.00
FTF	6.64	2.28

To confirm the presence of these defects in the recorded signals, Hilbert envelope analysis was applied to the accelerometer signal [13] to enhance the impulsive components caused by the bearing defects, making the defect-related frequencies more visible in the frequency domain. The Hilbert envelope spectrum, shown in Fig. 3, reveals the dominant spectral components associated with different types of damage. In the healthy bearing (black solid line), the spectrum is predominantly characterized by the shaft rotation frequency of 16.67 Hz and its harmonics, indicating normal operation. In contrast, for the first type of damage (dashed blue line), the spectrum has a distinct peak at the ball passage frequency on the outer raceway (BPFO) of 59.75 Hz, confirming the damage on the outer raceway. In addition, the presence of a peak at the train fundamental frequency (FTF) suggests a cage defect, while the side bands around the BPFO, spaced twice the FTF, indicating modulation effects due to the interaction between these fault components. For the second type of damage (dashed red line), the dominant peak at 78.6 Hz corresponds to the ball rotation frequency (BFF), while distinct peaks at the ball passage frequency within the stroke (BPFI), BPFO and FTF further confirm the presence of the multiple damages, induced by compression of the bearing.

3.2.3 Calculus of parameters in ⅓-octave band approach

To calculate statistical parameters for bearing defect detection, a preliminary analysis was performed on the entire spectrum of the pre-filtered signal.

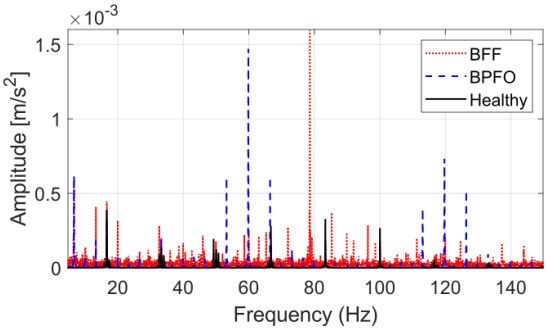


Figure 3. Spectrum of the Hilbert envelope of the accelerometer signal (SKF6205).

Subsequently, a ⅓-octave band approach was adopted to obtain a more in-depth view. This method was chosen because it offers an optimal compromise between frequency resolution and data manageability. Starting from the pre-processed signal (section 3.2.1), the data were segmented into one-third octave bands spanning the frequency range defined by the minimum and maximum central frequencies reported in Tab. 8. For each band, a 4th-order bandpass Butterworth filter was applied. The cutoff frequencies were calculated as:

$$f_{low} = \frac{f_c}{2^{1/6}} \;\; ; \;\; f_{high} = f_c \times 2^{1/6} \qquad (11)$$

where f_c is the central frequency of each band. Once the signal was filtered into its component ⅓ octave bands, the statistical parameters described in section **Errore. L'origine riferimento non è stata trovata.** were calculated for each band. These parameters provide insights into the signal's energy distribution and impulsiveness, which are critical in identifying the occurrence of bearing failures.

Table 8. 1/3 octave maximum and minimum central frequencies for all the sensors.

[kHz]	Acc	Mic	UltraMic
f_{c_min}	1	1	20
f_{c_max}	12.5	16	100

4. RESULTS AND DISCUSSION

This chapter presents the overall results of the two test conditions described in Sections 3.1.2 and 3.1.3, analyzed in terms of statistical parameters and spectral energy factor. Section 4.1 focuses on the first test condition, illustrating the results obtained for different types of damage at constant velocity. Section 4.2, on the other hand, examines the effects of a single type of damage at varying speeds.

4.1 Results at constant speed

The first testbed demonstrated promising results, showing clear distinctions in both statistical parameters and spectral energy analysis.

4.1.1 Statistical Parameter

Before calculating the parameters within one-third-octave bands, as shown in section 3, they were calculated over the entire spectrum. In Tab. 9, only the results for the ultrasonic microphone are presented because previous research has already validated the use of these statistical parameters with accelerometers. As is evident from the data, both types of bearing damage result in significant deviations from the "healthy" case, making these parameters an effective means of distinguishing between undamaged and damaged bearings. Fig. 4 shows the results obtained for the kurtosis for the three sensors, applying it to the one-third-octave bands as described in section 3.2.3. As expected, the accelerometer provided excellent results, particularly in the mid-to-high frequency ranges (3.5-5 kHz and 6-12 kHz), where the damage effects were most pronounced. The results obtained from the two microphones are also interesting, showing a significant increase in kurtosis at higher frequencies, particularly between 8 and 16 kHz. Although the difference between the "healthy" and the "damaged" cases is relatively small compared to the accelerometer results, it is noteworthy that despite being placed at a considerable distance from the bearing, the microphone still managed to detect the changes between the two conditions. The ultrasonic microphone, on the other hand, provided even sharper and more reliable results. It differentiated effectively between the two bearings, with damage to the outer ring (red bars) mainly affecting bands between 20 and 31.5 kHz. In the case of compression damage (ochre bars), the affected frequency range was from 20 to 63 kHz, with a peak at 40 kHz.

Table 9. Mean Statistical Parameters of different condition of the bearing, computed using ultrasonic microphone recordings.

	Healthy	BPFO Damaged	BFF Damaged
Kurtosis	2.4849	15.1926	11.1764
Impulse Factor	4.8443	19.7021	22.8560
Crest Factor	4.0316	12.0241	15.3572
RMS	0.0016	0.0105	0.0181

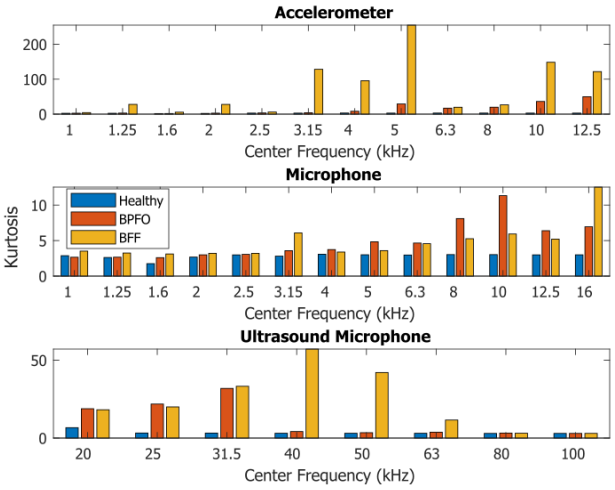


Figure 4. Kurtosis parameter in 1/3 octave bands representation, calculated for each sensor.

4.1.2 Spectral Energy Confrontation

Although spectral energy is not typically used as an absolute indicator of defects, the energy comparison between healthy and damaged bearings demonstrated significant results in this sense. As we did for the previous parameters, the spectral energy ratio was calculated in one-third octave bands to highlight the differences between damaged and healthy bearings. As shown in Fig. 5, the accelerometer reveals that the most significant energy differences between healthy and damaged bearings are concentrated in the mid- to high-frequency range, between 4 and 12.5 kHz, with a clear increase in spectral energy in the damaged cases. An interesting observation emerges from the analysis of the microphone measurement. In the case of compression damage, the increase in spectral energy is mainly in the low-mid frequencies, with a prominent peak at 1 kHz. In contrast, for outer ring damage, the frequencies affected are mainly in the upper-mid range, between 4 and 16 kHz, similar to what was observed with the accelerometer. For the ultrasonic microphone, the spectral energy increases significantly in the 20–40 kHz range, particularly in the compression-damaged bearing. The peak distribution differs with damage type: outer ring damage shows a dominant increase in the 20 kHz band, while compression damage peaks in the 35 kHz band.

4.2 Results at varying speed

This section presents the results referred to the second testbench, described in section 3.1.3. In Fig.6, we can observe the most statistically significant parameters (section

2) calculated over the entire signal spectrum at all three speeds tested.

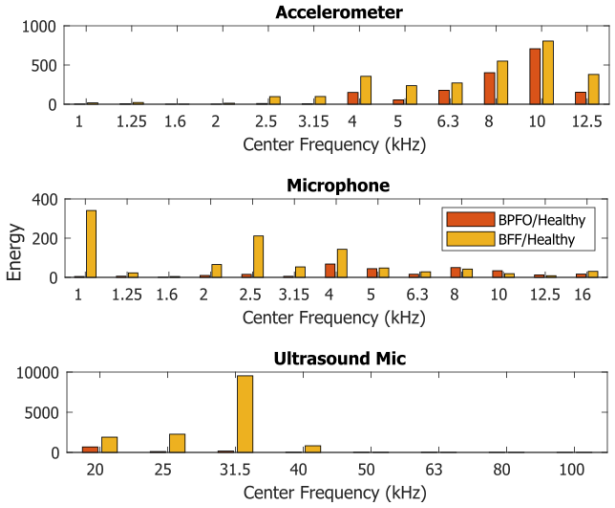


Figure 5. Spectral energy ratio between the damaged and healthy bearing signal, calculated for each sensor.

The first notable observation is that both the accelerometer and the ultrasonic microphone clearly distinguish between healthy and damaged bearings across all calculated parameters. Among these, impulse factor and kurtosis stand out as the most effective indicators. This demonstrates that full-band statistical analysis alone can reliably detect potential damage, regardless of shaft speed. In contrast, the standard microphone shows minimal variation across different speeds and conditions, indicating limited effectiveness over the entire frequency range. However, as shown in Fig. 7, when the analysis is narrowed to third-octave bands, this sensor also reveals useful information about fault presence. The plots illustrate only the kurtosis parameter for simplicity and clarity. A particularly noteworthy result is shown in Fig. 8, which illustrates the spectral energy ratio between damaged and healthy signals for both sensors, calculated on the 1/3-octave spectrum. The results clearly indicate a gradual increase in the energy ratio with increasing shaft speed for both microphones. In particular, the measurement microphone shows an increase in spectral energy in the range from 6.3 to 16 kHz, peaking at 8 kHz. On the other hand, the ultrasonic microphone reveals two distinct regions of energy increase: one between 20 and 25 kHz and the other between 31.5 and 63 kHz. Interestingly, both microphones' effectiveness is significantly influenced by shaft speed, revealing weaker energy ratios at lower speeds. This tendency is more pronounced in the ultrasonic microphone but is also slightly evident in the measurement microphone. The accelerometer does not exhibit this velocity-dependent behavior, showing the highest energy ratio in the upper bands, particularly from 8 to 12.5 kHz. As might have been expected, in terms of amplitude of the spectral energy ratio, the accelerometer provides the most pronounced and reliable results.

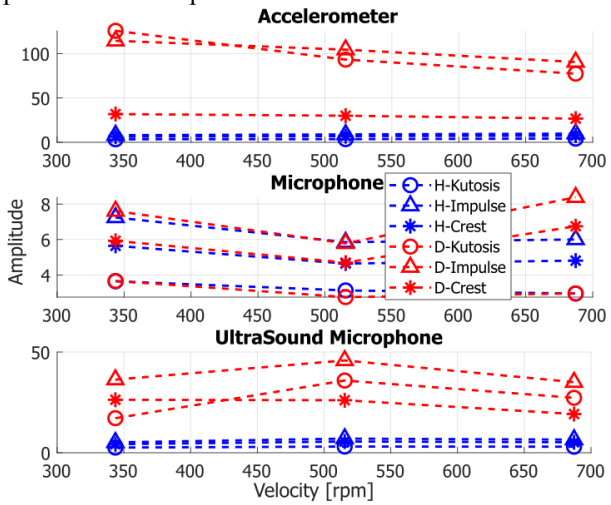


Figure 6. Statistical indicators at varying speeds.

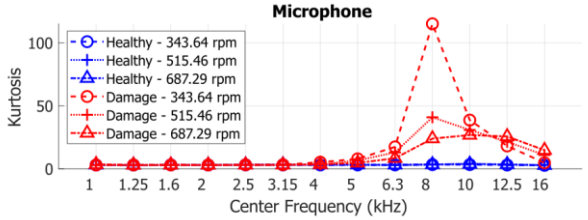


Figure 7. Microphone signal kurtosis in 1/3-octave bands.

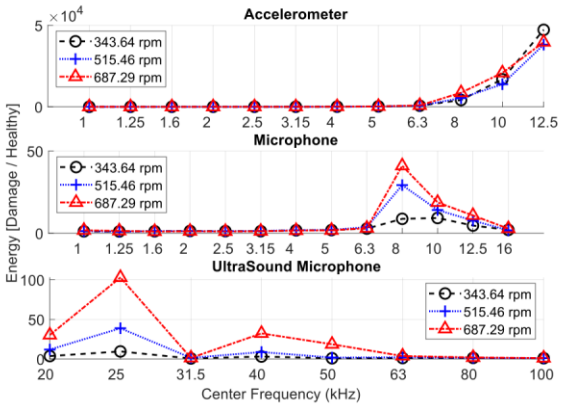


Figure 8. Energy Ratio between damaged and healthy bearings at varying speeds.

5. CONCLUSION

Microphones have proven to be a viable solution for detecting faults in rolling bearings under controlled conditions, offering a useful alternative in scenarios where accelerometers cannot be used. This study explored two basic data analysis techniques, both of which yielded promising results. In particular, the energy ratio method demonstrated strong potential for predictive maintenance applications, with performance comparable to that of traditional statistical indicators. While kurtosis can be an absolute indicator of failure, this is not necessarily true for the other statistical parameters or energy-based approaches. These methods were selected for their low computational cost and practical applicability in real-world predictive maintenance systems. The findings suggested that integrating ultrasonic microphones into vibroacoustic analysis frameworks can enhance the monitoring and maintenance of industrial systems. This approach was shown to be promising for improving the sensitivity of defect detection and providing, at the same time, practical benefits regarding ease of installation and maintenance.

6. FUTURE WORKS

This preliminary study applied classical statistical parameters and energy-based analysis techniques to signals acquired from accelerometric, acoustic, and ultrasonic measurements. Future work will explore advanced diagnostic signal processing methods and compare sensor performance under varying operating conditions, including changes in position and rotational speed. In particular, the influence of microphone distance will be investigated to simulate scenarios in which contact sensors, such as accelerometers, are not a feasible solution.

7. REFERENCES

[1] P. Nunes, J. Santos, and E. Rocha, “Challenges in predictive maintenance – A review,” *CIRP J Manuf Sci Technol*, vol. 40, pp. 53–67, 2023.

[2] T. Zonta, C. A. da Costa, R. da Rosa Righi, M. J. de Lima, E. S. da Trindade, and G. P. Li, “Predictive maintenance in the Industry 4.0: A systematic literature review,” Comput Ind Eng, vol. 150, p. 106889, 2020.

[3] M. Pech, J. Vrchota, and J. Bednář, “Predictive Maintenance and Intelligent Sensors in Smart Factory: Review,” *Sensors*, vol. 21, no. 4, 2021.

[4] S. A. McInerny and Y. Dai, “Basic vibration signal processing for bearing fault detection,” IEEE Transactions on Education, vol. 46, no. 1, pp. 149–156, 2003.

[5] J. Coady, D. Toal, T. Newe, and G. Dooly, “Remote acoustic analysis for tool condition monitoring,” Procedia Manuf, vol. 38, pp. 840–847, 2019.

[6] A. Morhain and D. Mba, “Bearing defect diagnosis and acoustic emission,” Proceedings of the Institution of Mechanical Engineers, Part J, vol. 217, no. 4, pp. 257–272, 2003.

[7] E. Y. Kim, A. C. C. Tan, J. Mathew, and B. S. Yang, “Condition monitoring of low speed bearings: A comparative study of the ultrasound technique versus vibration measurements,” Australian Journal of Mechanical Engineering, vol. 5, no. 2, pp. 177–189, 2008.

[8] A. Rai and S. H. Upadhyay, “A review on signal processing techniques utilized in the fault diagnosis of rolling element bearings,” Tribol Int, vol. 96, pp. 289–306, 2016.

[9] N. Rocchi, A. Toscani, G. Chiorboli, D. Pinardi, M. Binelli, and A. Farina, “Transducer Arrays over A^2B Networks in Industrial and Automotive Applications: Clock Propagation Measurements,” *IEEE Access*, vol. 9, pp. 118232–118241, May 2021.

[10] A. Toscani, F. Immovilli, D. Pinardi, and L. Cattani, “A Novel Scalable Digital Data Acquisition System for Industrial Condition Monitoring,” IEEE Transactions on Industrial Electronics, vol. 71, no. 7, pp. 7975–7985, Jul. 2024.

[11] N. Rocchi et al., “A Modular, Low Latency, A 2 B-based Architecture for Distributed Multichannel Full-Digital Audio Systems,” in 2021 Immersive and 3D Audio: from Architecture to Automotive (I3DA), IEEE, Sep. 2021.

[12] D. Pinardi, L. Arpa, A. Toscani, E. Manconi, M. Binelli, and E. Mucchi, “A Novel Hybrid Acquisition System for Industrial Condition Monitoring and Predictive Maintenance,” IEEE Access, vol. 12, pp. 98121–98129, 2024.

[13] R. B. Randall, Vibration-based condition monitoring: industrial, automotive and aerospace applications. John Wiley & Sons, 2021.

DOI: 10.61782/fa.2025.0898



FORUM ACUSTICUM
EURONOISE 2025

TOOL WEAR PREDICTION IN CNC TURNING OPERATIONS USING ULTRASONIC MICROPHONE ARRAYS AND CNNS

Jan Steckel[1,2,*] **Arne Aerts**[3] **Erik Verreycken**[1,2]
Dennis Laurijssen[1,2] **Walter Daems**[1,2]
[1] Cosys-Lab, Faculty of Applied Engineering, University of Antwerp, Antwerp, Belgium
[2] Flanders Make Strategic Research Centre, Lommel, Belgium
[3] Service Group Materials, Mechanical Engineering, University of Antwerp, Antwerp, Belgium

ABSTRACT

This paper introduces a novel method for predicting tool wear in CNC turning operations, combining ultrasonic microphone arrays and convolutional neural networks (CNNs). High-frequency acoustic emissions between 0 kHz and 60 kHz are enhanced using beamforming techniques to improve the signal-to-noise ratio. The processed acoustic data is then analyzed by a CNN, which predicts the Remaining Useful Life (RUL) of cutting tools. Trained on data from 350 workpieces machined with a single carbide insert, the model can accurately predict the RUL of the carbide insert. Our results demonstrate the potential gained by integrating advanced ultrasonic sensors with deep learning for accurate predictive maintenance tasks in CNC machining.

Keywords: *condition monitoring, predictive maintenance, ultrasound signal processing, deep learning, beamforming*

1. INTRODUCTION

Predictive maintenance is the process of using sensor data to infer the state of a machine, and detect flaws or failures before they happen from that sensor data [1, 2]. Predictive maintenance is a rising trend in virtually all industry branches, ranging from bearing fault detection [3], gear wear detection [4] or piston wear in reciprocating machines [5] amongst many other examples. A plethora of sensors is being applied for predictive maintenance, ranging from acoustics, vibration signals, thermal sensors, current sensors, and virtually any other sensing modality that can be imagined [1, 3]. In previous work, we demonstrated bearing fault detection using ultrasound signals in the band of 0 kHz to 60 kHz, measured with a microphone array and subsequent beamforming techniques [6].

When machining complex parts with axis-symmetry, CNC lathes are the de-facto standard manufacturing technique. In a CNC lathe, the work piece is mounted to a spindle which is then being rotated, and cutting is performed by means of a stationary cutting tool. There is a wide variety of cutting tool geometry and materials, with carbides being the dominantly used material for fabricating these cutting tools. While the variety in geometry and material type is vast, one recurring and important feature of these tools is the sharpness. Indeed, the sharpness of the cutting tool often directly correlates to the finished quality of the workpiece [7, 8]. A tool that is too dull will not cut adequately, leaving a poor surface finish, while a tool that is overly sharp is brittle and wears quickly. Manufacturers of CNC tools often specify a tool life parameter, expressed in hours, which indicates how long a tool can be utilized. However, these estimates are sometimes too conservative [7, 9], and therefore lead to premature replacement of still useful tools. Furthermore, some tools might fail prematurely, causing problems in automated manufacturing applications, which results in scrapped parts and lost revenue.

To combat the problem with tool wear inherent to CNC machining, various techniques for automated tool wear estimation have been devised [9, 10]. Similar as to

*Corresponding author: jan.steckel@uantwerpen.be.
Copyright: ©2025 Jan Steckel et al. This is an open-access article distributed under the terms of the Creative Commons Attribution 3.0 Unported License, which permits unrestricted use, distribution, and reproduction in any medium, provided the original author and source are credited.

the general field of predictive maintenance, a wide range of sensing modalities is being used, such as consumed spindle power/current [11], vibration measurements [12], Doppler radar [13] and acoustics [14–16]. In many previous publications, combinations of these aforementioned sensor modalities are used to perform the tool wear or tool life prediction.

In this paper, we will focus on the use of ultrasonic acoustic signals in the range of 0 kHz to 60 kHz using an array sensor, similar to our previous work on bearing fault detection [6]. The sensor is based around our eRTIS ultrasonic sensor [17] which allows the implementation of broadband spatial filters through beamforming. Using beamforming in high-noise scenarios such as CNC operations should improve the SNR of the signal, by filtering out unwanted noise sources. We will use our eRTIS sensor to measure the ultrasonic spectrogram acoustic signals generated by the cutting operation, and use beamforming to remove unwanted interference. Then, we will employ a convolutional neural network to perform Remaining Useful Life (RUL) prediction [18] of the cutting tool, using data obtained from 350 work pieces turned using a single carbide insert.

2. HARDWARE SETUP

In this section we will provide some details on the experimental setup. We used an industrial CNC lathe (Mazak QT10N), which is shown in figure 1 panel b). On this lathe, we turned a batch of tensile test specimen used in the mechanical engineering curriculum of our university until tooling insert failure (350 pieces). The model of this tensile test specimen can be seen in figure 1, panel e). We used two materials for making these test pieces, more specifically 1.1191 (C45) and 1.7225 (Chromoly), distributed as randomly as possible during the production run. We used a depth of cut of 0.3 mm, a feed rate of 0.5 mm per revolution and a surface speed of 120 m min^{-1}. As tooling insert we used an Iscar GRIP 3015Y in grade IC808.

As ultrasonic sensors we used two eRTIS sensors [17], which are ultrasonic microphone-array sensors with 32 microphones, sampled at 450 kHz. The individual sensors are synchronized using our pseudo-random 1-bit synchronization method described in [19]. One eRTIS sensor was placed inside of the lathe, another outside right where the operator would stand. In addition, we recorded the spindle current using a Fluke i1000s current clamp, connected to a National Instruments NI-USB6363 DAQ, which sampled both the current signal as well as the synchronization signal at 500 kHz. The eRTIS sensors measured chunks of acoustic data of 40 ms at a rate of 10 Hz (i.e., the signal is sampled intermittently).

3. SIGNAL PROCESSING AND EXPERIMENTAL RESULTS

In this paper, we treat each eRTIS sensor independently - i.e. there is no sensor fusion using multiple sensors. Each sensor measures 32 microphone signals $s_m(t)$. These microphone signals are passed through a beamformer B_ψ pointing in direction ψ, which is the vector pointing from the sensor to the tool position. The beamformed signals are also filtered using a bandpass filter $h_{bp}(t)$, which is set to be a Butterworth filter of order 6 between 0 kHz and 60 kHz. The overall output of each datasample of 40 ms can then be calculated as:

$$s_o(t) = h_{bp}(t) * \sum_{i=1}^{32} B_\psi \Big(s_m(t) \Big) \tag{1}$$

This output signal is then transformed to a magnitude spectrum $S_n(\omega)$ using a Welch Power Spectral Density estimator, using a window length of 1024 samples and Hamming weighting. In this spectrum $S_n(\omega)$, the index n represents the frame number of that data section (sampled at 10 Hz, and 40 ms). These spectra are all concatenated into a large matrix S, which then represents a spectrogram-like representation:

$$S(\omega, n) = \Big[S_1(\omega) \quad S_2(\omega) \quad \dots \quad S_N(\omega) \Big] \tag{2}$$

Examples of these spectrogram-like representations can be seen in figure 2. Panel a) shows the spectrogram of a run recorded using an eRTIS outside of the lathe, and panel b) shows the spectrum recorded inside the machine. The main difference between the data recorded by these two sensors can be found in i) the low-frequency motion sounds, which are more clearly visible in the spectrum measured outside of the machine, and ii) the cutting noise, which is high in frequency and more prominent in the data in panel b). Both representations are shown on a logarithmic dB scale, normalized between 0dB and 90dB. One of these spectrograms is recorded for each of the 350 pieces that is being manufactured.

Finally, we implemented a convolutional neural network which solves the following regression task: estimating the work-piece number based on a acoustic spectrogram data (ie, a number between 1 and 350). The CNN



Figure 1. Overview of the hardware setup used in this paper. Panel a) shows the eRTIS sensor, an ultrasonic array sensor with 32 microphones arranged in a pseudorandom pattern. The sensor is waterproofed using a membrane material from the Acoustic Protective Material line manufactured by W. L. Gore and Associates. Panel b) shows the CNC lathe being used, a Mazak Quickturn 10N, using Iscar GRIP 3015Y grade IC808 inserts. Panel c) shows the inside eRTIS sensor mounted in the lathe. Panel d) shows the turned materials, and e) shows the model of the piece that has been turned during this experiment.

is a standard feed-forward CNN with four convolutional layers, leaky ReLu function, max pooling, layer normalization and dropout (10 percent). After the four convolutional layers the output gets flattened into a vector, and passed through two fully connected (FC) layers, where the first FC layer has an output dimension of 10 and a ReLu nonlinearity, and the last FC layer has a single output. We trained the neural network using the Adam optimizer, with a learning rate of 0.01 for a maximum of 100 epochs, and used the best validation loss checkpoint as the final network. We used data augmentation (shifting in the time dimension and additive noise), and split the augmented dataset randomly into a training set (75%), validation (10%) and test (15%) sets. In the ideal case, we would perform this split before augmentation (or even use a complete second run), which would required a more extensive dataset, and that was not available at the time of writing. Training of the CNN on a single NVidia RTX4090 took around one hour, including data pre processing.

After training we used our test data to evaluate the model's performance, for which the results can be seen in figure 4. In that figure, panel a) shows the run number prediction based on a single acoustic spectrogram, and panel b) shows the prediction when combining the predictions of five spectrograms centered around the desired run number. Panels c) and d) show the mean run number prediction error including the variance bands on the prediction (grey shadows), in percentage of the total tool life. The maximum error of this prediction is plus or minus 6 percent of the total tool life when using the averaged result. This estimator allows tracking the health of the cutting tool, and allows interventions or continued operation based on the real-world state of tool sharpness. Including a window around the current run number decreases the variance on the estimation and estimation error, as is to be expected.

4. DISCUSSION AND CONCLUSION

In this paper, we showed a multi-modal sensor setup for estimating tool wear in CNC turning operations. We discussed the data-acquisition process, and explained what pre-processing steps were taken in data preparation. Subsequently, we detailed the architecture of a convolutional neural network which was applied to the prediction of remaining useful life of the CNC cutting insert. Using an extensive dataset, consisting of 350 tensile test pieces in two materials, we showed the performance of the regression capabilities of these CNNs. We showed that these CNNs are able to estimate the tool life with a maximum error of 6 percent within the total tool life, illustrating the rich data that ultrasonic sensing provides to extract the relevant metrics for predictive maintenance. In future work, we will benchmark our approach to existing approaches in the literature, and evaluate in detail which aspects of the system are relevant: what advantages does a microphone array bring, what benefit has a CNN, and how important is the CNN architecture.

Furthermore, we will evaluate the problem of generalizing this method to different machines/parts. The system

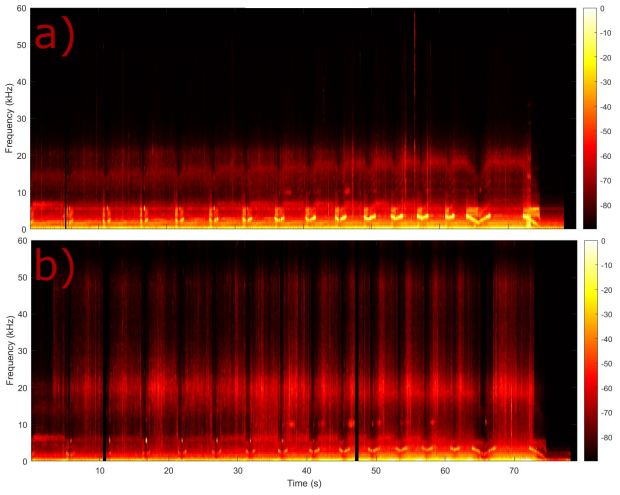


Figure 2. Spectrogram representation of the acoustic data recorded by the eRTIS sensors during a turning run. Panel a) shows the data of measured by the eRTIS sensor ouside of the machine, and panel b) shows the data recorded from inside the machine. In the low frequency parts, the signal is dominated by the motion sounds of the machine, and the high frequency parts of the spectrogram are generated by the cutting operations.

as it is currently proposed, requires a training run for each machine/part/tool combination. In industrial practice, this is not a major hindrance, because each part is often run over multiple weeks, and performing a single training run on an insert is not a large hindrance. However, it would be interesting to implement models which are capable of generalization. For this, larger datasets need to be captured on different machines, making different parts, which is why we classify this as future work.

5. REFERENCES

[1] T. Zonta, C. A. Da Costa, R. da Rosa Righi, M. J. de Lima, E. S. da Trindade, and G. P. Li, "Predictive maintenance in the Industry 4.0: A systematic literature review," *Computers & Industrial Engineering*, vol. 150, p. 106889, 2020.

[2] W. Zhang, D. Yang, and H. Wang, "Data-driven methods for predictive maintenance of industrial equipment: A survey," *IEEE systems journal*, vol. 13, no. 3, pp. 2213–2227, 2019.

[3] S. Schwendemann, Z. Amjad, and A. Sikora, "A survey of machine-learning techniques for condition monitoring and predictive maintenance of bearings in grinding machines," *Computers in Industry*, vol. 125, p. 103380, 2021.

[4] S. Raadnui, "Spur gear wear analysis as applied for tribological based predictive maintenance diagnostics," *Wear*, vol. 426, pp. 1748–1760, 2019.

[5] V. V. Shanbhag, T. J. Meyer, L. W. Caspers, and R. Schlanbusch, "Failure monitoring and predictive maintenance of hydraulic cylinder—State-of-the-art review," *IEEE/ASME Transactions on Mechatronics*, vol. 26, no. 6, pp. 3087–3103, 2021.

[6] T. Verellen, F. Verbelen, K. Stockman, and J. Steckel, "Beamforming applied to ultrasound analysis in detection of bearing defects," *Sensors*, vol. 21, no. 20, p. 13 p., 2021.

[7] H. Gökkaya and M. Nalbant, "The effects of cutting tool geometry and processing parameters on the surface roughness of AISI 1030 steel," *Materials & design*, vol. 28, no. 2, pp. 717–721, 2007.

[8] P. Sivaiah and U. Bodicherla, "Effect of surface texture tools and minimum quantity lubrication (MQL) on tool wear and surface roughness in CNC turning of

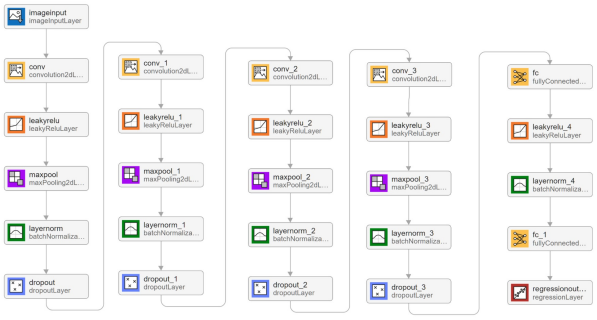


Figure 3. Overview of the CNN architecture, consisting of 4 convolutional layers, followed by a leaky ReLu activation, average pooling, batch normalization and dropout. After the convolutional layers, fully connected layers are used to form the regression outputs.

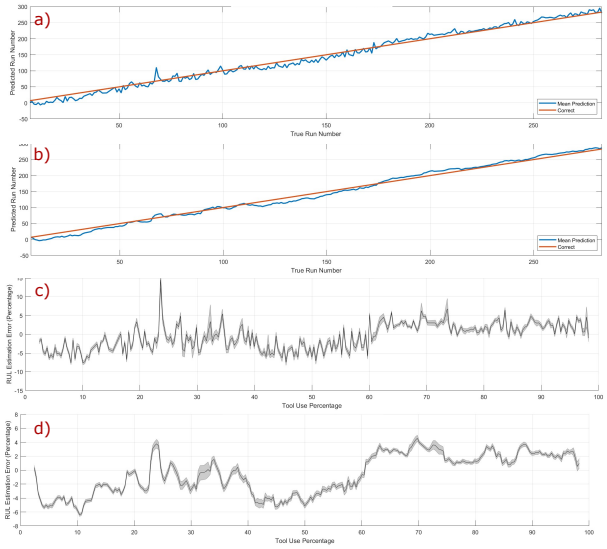


Figure 4. Results of the tool life prediction performed using the CNN networks based on the spectrogram inputs. Panel a) shows the run-number prediction based on a single spectrogram, and panel b) shows the prediction when using the predictions of five spectrograms centered around the desired run number. Panels c) and d) show the mean run number prediction error including the variance bands on the prediction (grey shadows).

AISI 52100 steel," *Journal of The Institution of Engineers (India): Series C*, vol. 101, no. 1, pp. 85–95, 2020.

[9] C. K. Chan, M. Wong, and Z. Siang, "CNC Cutting ToolsLife Prediction Using Data Mining Approach," *Journal of Innovation and Technology*, vol. 2022, no. 11, pp. 1–7, 2022.

[10] T. Szecsi, "Automatic cutting-tool condition monitoring on CNC lathes," *Journal of Materials Processing Technology*, vol. 77, no. 1-3, pp. 64–69, 1998.

[11] B. Neef, J. Bartels, and S. Thiede, "Tool wear and surface quality monitoring using high frequency CNC machine tool current signature," in *2018 IEEE 16th International Conference on Industrial Informatics (INDIN)*, pp. 1045–1050, IEEE, 2018.

[12] H. Arslan, ALİ. ER, S. Orhan, and E. Aslan, "Tool condition monitoring in turning using statistical parameters of vibration signal," *International Journal of Acoustics and Vibrations*, vol. 21, no. 4, 2016.

[13] G. C. Smith and S. S. Lee, "A method for detecting tool wear on a CNC lathe using a doppler radar detector," *The International Journal of Advanced Manufacturing Technology*, vol. 25, pp. 270–280, 2005.

[14] M.-K. Liu, Y.-H. Tseng, and M.-Q. Tran, "Tool wear monitoring and prediction based on sound signal," *The International Journal of Advanced Manufacturing Technology*, vol. 103, pp. 3361–3373, 2019.

[15] D. R. Salgado and F. J. Alonso, "An approach based on current and sound signals for in-process tool wear monitoring," *International Journal of Machine Tools and Manufacture*, vol. 47, no. 14, pp. 2140–2152, 2007.

[16] N. Seemuang, T. McLeay, and T. Slatter, "Using spindle noise to monitor tool wear in a turning process," *The International Journal of Advanced Manufacturing Technology*, vol. 86, pp. 2781–2790, 2016.

[17] R. Kerstens, D. Laurijssen, and J. Steckel, "eRTIS: A fully embedded real time 3D imaging sonar sensor for robotic applications," in *IEEE International Conference on Robotics and Automation*, pp. 1438–1443, Ieee, 2019.

[18] Y. Wang, Y. Zhao, and S. Addepalli, "Remaining useful life prediction using deep learning approaches: A review," *Procedia manufacturing*, vol. 49, pp. 81–88, 2020.

[19] D. Laurijssen, E. Verreycken, I. Geipel, W. Daems, H. Peremans, and J. Steckel, "Low-cost synchronization of high-speed audio and video recordings in bio-acoustic experiments," *The journal of experimental biology*, vol. 221, no. 4, pp. 1–6, 2018.

DOI:

Main theme: A08 Industrial, Machinery, Equipment Noise and Vibration

Session A08.06 Innovative noise barriers to enhance acoustic comfort

Chair(s): M. Pawelczyk, J. Kang, A. González, S. Wrona, M. Ferrer

DOI:

Main theme: A08 Industrial, Machinery, Equipment Noise and Vibration

Session A08.07 Artificial intelligence for industrial applications

Chair(s): R. M. Alsina-Pagès, G. Licitra

DOI:

Main theme: A09 Machine learning and Artificial Intelligence in Acoustics

Session A09.01 Machine learning and artificial intelligence in acoustics - General

Chair(s): D. Botteldooren, M. Sobreira, R. M. Alsina-Pagès, M. Plumbley, W. Want

DOI: 10.61782/fa.2025.0602



FORUM ACUSTICUM
EURONOISE 2025

NEURAL NETWORK-BASED SOLUTIONS FOR THE LINEARIZED EULER EQUATIONS IN OUTDOOR SOUND PROPAGATION

Hessel Juliust[1,2] **Katharina Baumann**[1] **Arthur Schady**[1]
Sirine Gharbi[1] **Felix Dietrich**[2]
[1] Institute of Atmospheric Physics, German Aerospace Center
[2] School of Computation, Information and Technology, Technische Universität München

ABSTRACT

The Linearized Euler Equations (LEE) are a system of partial differential equations that provide a framework for modeling outdoor acoustic wave propagation, capturing atmospheric and topographic effects. Solving LEE using traditional numerical methods demands fine spatial and temporal resolutions, leading to high computational costs over large domains. This study uses established neural network approaches to solve LEE and evaluates their performance and scalability for outdoor acoustic wave propagation. Included approaches are Physics-Informed Neural Networks (PINNs) and the sampled network-based Extreme Learning Machine Ordinary Differential Equations (ELM-ODE). We use a SIREN-based architecture in our PINNs for wave-like solutions. In the 1D case, PINNs achieved higher accuracy but required significantly more training time due to the complexity of training over a spatiotemporal domain. Meanwhile, ELM-ODE provided competitive accuracy with much lower computational cost. In the 2D case, ELM-ODE again showed computational advantages over SIREN-PINNs while delivering great accuracy. However, its scalability is constrained by the coupled velocity–pressure matrix, which increases costs in cases like outdoor noise mapping, where velocity data eventually are unused. Addressing boundary conditions, such as frequency-dependent impedance, remains a challenge.

*__Corresponding author__: *hessel.juliust@dlr.de.*
__Copyright__: *©2025 Juliust et al. This is an open-access article distributed under the terms of the Creative Commons Attribution 3.0 Unported License, which permits unrestricted use, distribution, and reproduction in any medium, provided the original author and source are credited.*

Keywords: *linearized euler equations, outdoor acoustics, PINNs, ELM-ODE, sampled networks*

1. INTRODUCTION

Modeling outdoor acoustic wave propagation is important with a lot of applications, including noise mapping for urban planning [1], environmental monitoring [2], and aviation acoustics [3]. The propagation of sound in the atmosphere is affected by atmospheric factors such as wind, temperature gradients, and topographic features [2]. These factors introduce complexities into predicting acoustic wave behavior accurately, especially when considering high-frequency waves or large spatial domains.

The Linearized Euler Equations (LEE) provide a mathematical framework for modeling outdoor acoustics by capturing the interactions among acoustic velocity, pressure fluctuations, and the background atmospheric flow [4, 5]. Unlike simpler acoustic models, the LEE take account for the convective effects and the compressible nature of sound waves, making them particularly well-suited for simulating realistic outdoor conditions. However, traditional numerical methods for solving the LEE, such as finite-difference time-domain (FDTD) schemes [6, 7], often require substantial computational resources. This is especially true for scenarios involving high frequencies or extended spatial domains [8].

Recent advances in machine learning offer a new way to solve LEE. In particular, *physics-informed neural networks* (PINNs) have been proposed as an effective means to solve partial differential equations (PDEs) by embedding the governing equations directly into the loss function during training [9]. This approach ensures that the neural network follows the underlying physics. How-

ever, PINNs can be computationally demanding and may encounter convergence issues when dealing with high-frequency oscillations and multi-scale features [10], especially for solving time dependent PDEs like LEE which need to be trained for the whole time domain.

An alternative strategy, the *sampled neural network method* to solve PDE has been introduced to overcome some of these challenges. In the work of Datar *et al.* [11], the authors propose the *Extreme Learning Machine Ordinary Differential Equations* (ELM-ODE) framework, which applies a shallow neural network with fixed, randomly sampled weights to represent spatial basis functions. The time evolution of the solution is then captured by solving a system of ordinary differential equations for the time-dependent coefficients. This decoupling of the spatial and temporal components leads to a dramatic reduction in training time while still achieving high accuracy in modeling the wave dynamics inherent in the LEE.

In this paper, we present a comparative study of the PINNs and ELM-ODE approaches for solving the Linearized Euler Equations in the context of outdoor acoustic propagation. We present how to implement each framework to solve LEE and assess the methods' performance in terms of accuracy and computational efficiency. Our goal is to explore the strengths and limitations of these techniques for simulation of outdoor acoustics.

2. METHODS

2.1 Linearized Euler Equations

The linearized Euler equations have become a widely accepted model for simulating outdoor sound propagation. Their time-domain formulation offers several key advantages. First, a single simulation can generate comprehensive frequency responses. Second, they accommodate nonlinear effects while accounting for moving, realistic sources. When dealing with a moving medium, it is essential to use numerical methods that accurately capture both the medium's velocity and the acoustic pressure [12]. For instance, models described in [7] employ finite-difference time-domain (FDTD) methods to simulate sound wave motion in a moving medium. Atmospheric conditions significantly influence outdoor sound propagation, further highlighting the need to consider the medium's dynamics. The LEE consists of coupled equations for the velocity and pressure components, defined as follows:

The velocity component of LEE is given by:

$$\begin{aligned}\frac{\partial \mathbf{v}_{\text{acc}}}{\partial t} + (\mathbf{v}_{\text{met}} \cdot \nabla)\mathbf{v}_{\text{acc}} + (\mathbf{v}_{\text{acc}} \cdot \nabla)\mathbf{v}_{\text{met}} \\ = -\alpha_{\text{met}} \nabla p_{\text{acc}} - \alpha_{\text{acc}} \nabla p_{\text{met}} + \nu \nabla^2 \mathbf{v}_{\text{acc}}.\end{aligned} \tag{1}$$

Similarly, the pressure component is given by:

$$\begin{aligned}\frac{\partial p_{\text{acc}}}{\partial t} + \mathbf{v}_{\text{met}} \cdot \nabla p_{\text{acc}} + \mathbf{v}_{\text{acc}} \cdot \nabla p_{\text{met}} \\ = -\kappa p_{\text{met}} \nabla \cdot \mathbf{v}_{\text{acc}} - \kappa p_{\text{acc}} \nabla \cdot \mathbf{v}_{\text{met}}.\end{aligned} \tag{2}$$

The coefficients are defined as:

$$\alpha_{\text{met}} = \frac{1}{\rho_{\text{met}}}, \alpha_{\text{acc}} \quad = -\frac{1}{\kappa} \frac{p_{\text{acc}}}{p_{\text{met}}} \frac{1}{\rho_{\text{met}}}, \kappa = \frac{c_p}{c_v}.$$

The numerical solver will then solve for $\mathbf{v}_{\text{acc}}$ (the velocity of the particle) and p_{acc} (the pressure of the acoustic wave), with other variables such as p_{met} (the pressure of the flow field), $\mathbf{v}_{\text{met}}$ (the velocity of the flow field), ρ_{met} (the air density), and κ (the ratio of specific heats at constant pressure (c_p) and constant volume (c_v)) given. Note that κ can also be obtained from the speed of sound (c), p_{met}, and ρ_{met}.

2.2 Physics-Informed Neural Networks (PINNs)

Physics-Informed Neural Networks (PINNs) are neural networks trained to satisfy partial differential equations (PDEs), initial conditions (IC), and boundary conditions (BC) simultaneously [13]. The network receives spatiotemporal coordinates as input and outputs the physical fields to be learned. These outputs are differentiated with respect to the inputs using automatic differentiation [14], and then substituted into the PDE to obtain the residual. The residual quantifies how much the predicted fields violate the governing equations and is evaluated at a set of collocation points in the domain. The total loss is defined as:

$$\mathcal{L} = \mathcal{L}_{\text{phys}} + \mathcal{L}_{\text{IC}} + \mathcal{L}_{\text{BC}}, \tag{3}$$

where each term is a mean-squared error loss for the PDE residual $\mathcal{L}_{\text{phys}}$, the initial condition loss $\mathcal{L}_{\text{IC}}$, and the boundary condition loss $\mathcal{L}_{\text{BC}}$. Note that it can also include additional loss term if data are available such as from old simulation or measurements.

When applied to the Linearized Euler Equations (LEE), the neural network takes spatial-temporal input coordinates (x, t) or (x, y, t) and outputs pressure and velocity components as continuous functions. The network utilizes sinusoidal activation functions based on the SIREN

architecture [15], where each layer applies

$$\sigma(z) = \sin(\omega_0 z)$$

with a fixed frequency scaling constant ω_0 in order to approximate the wavy behaviour better.

2.3 Sampled Neural Network Approach

The Sampled Neural Network approach used in this study follows the Extreme Learning Machine-based ODE (ELM-ODE) method introduced in [11]. This method approximates the solution of a time-dependent PDE by separating spatial and temporal components. The spatial part is represented using a shallow neural network with fixed, randomly sampled weights, while the temporal part is evolved by solving an ordinary differential equation (ODE) system.

Let $\phi_k(x) = \sigma(w_k^\top x + b_k)$ denote the k-th basis function, where σ is a nonlinear activation function also w_k and b_k are weights and biases sampled from prescribed distributions (e.g., $w_k \sim \mathcal{N}(\eta_1, \eta_2)$ and $b_k \sim \mathcal{U}[-\eta_3, \eta_3]$), as originally proposed in the Extreme Learning Machine framework [16]. The solution is expressed as:

$$\hat{u}(x,t) = \sum_{k=1}^{K} c_k(t) \cdot \phi_k(x), \tag{4}$$

where $c_k(t)$ are time-dependent coefficients.

This ansatz is substituted into the governing PDE, and the residual is evaluated at a set of collocation points. The resulting system is projected onto the fixed spatial basis, resulting an ODE system for the temporal coefficients $c(t) = [c_1(t), \ldots, c_K(t)]^\top$, which is then integrated forward in time using standard solvers. For linear PDEs such as the simplified Linearized Euler Equations (LEE), the resulting ODE system remains linear.

Boundary conditions can be incorporated in two main ways, either by constructing basis functions that satisfy the boundary constraints, or by introducing additional terms to the ODE system that enforce the conditions weakly.

3. FORMULATING SOLUTIONS TO LEE WITH NEURAL NETWORKS

We started from the full Linearized Euler Equations given in Equations (1) and (2), however, in order to focus on the dominant convective and acoustic effects, we neglect the nonlinear advection due to acoustic perturbations, the weak coupling with background pressure gradients, viscous dissipation, and the divergence of the background flow.

Therefore, omitting these effects, the governing system simplifies to:

$$\frac{\partial \mathbf{v}_{\text{acc}}}{\partial t} = -\left(\mathbf{v}_{\text{met}} \cdot \nabla\right) \mathbf{v}_{\text{acc}} - \frac{1}{\rho_{\text{met}}} \nabla p_{\text{acc}}, \tag{5}$$

$$\frac{\partial p_{\text{acc}}}{\partial t} = -\left(\mathbf{v}_{\text{met}} \cdot \nabla\right) p_{\text{acc}} - \kappa\, P_{\text{met}}\, \nabla \cdot \mathbf{v}_{\text{acc}}. \tag{6}$$

3.1 Formulation of LEE in the PINNs Framework

We first nondimensionalize the governing equations. Let L_{ref} denote a characteristic length scale, and define the reference time scale as $T_{\text{ref}} = L_{\text{ref}}/c$, where c is the speed of sound. Pressure is scaled by a reference value p_c, and velocity by $v_c = p_c/(\rho_{\text{ref}} c)$, where ρ_{ref} is the reference density. This yields a nondimensional domain $(x, y, t) \in [-1, 1]^2 \times [0, 1]$, with all physical constants absorbed into the transformed variables. The nondimensional background wind velocities are defined as $M_x = v_{\text{met},x}/c$ and $M_y = v_{\text{met},y}/c$. Note that this can vary along the spaces or be constant values.

We apply this nondimensionalizing to Equations (5) and (6), resulting in the following system:

$$\frac{\partial v_{acc,x}}{\partial t} = -M_x \frac{\partial v_{acc,x}}{\partial x} - M_y \frac{\partial v_{acc,x}}{\partial y} - \frac{\partial p}{\partial x}, \tag{7}$$

$$\frac{\partial v_{acc,y}}{\partial t} = -M_x \frac{\partial v_{acc,y}}{\partial x} - M_y \frac{\partial v_{acc,y}}{\partial y} - \frac{\partial p}{\partial y}, \tag{8}$$

$$\frac{\partial p}{\partial t} = -M_x \frac{\partial p}{\partial x} - M_y \frac{\partial p}{\partial y} - \frac{\partial v_{acc,x}}{\partial x} - \frac{\partial v_{acc,y}}{\partial y}. \tag{9}$$

Then, we define a neural network that takes spatiotemporal coordinates (x, y, t) as input and outputs the predicted fields $\tilde{v}_{acc,x}$, $\tilde{v}_{acc,y}$, and $\tilde{p}$. The residuals are defined as:

$$\mathcal{R}_{v_{\text{acc},x}} = \frac{\partial \tilde{v}_{\text{acc},x}}{\partial t} + M_x \frac{\partial \tilde{v}_{\text{acc},x}}{\partial x} + M_y \frac{\partial \tilde{v}_{\text{acc},x}}{\partial y} + \frac{\partial \tilde{p}}{\partial x}, \tag{10}$$

$$\mathcal{R}_{v_{\text{acc},y}} = \frac{\partial \tilde{v}_{\text{acc},y}}{\partial t} + M_x \frac{\partial \tilde{v}_{\text{acc},y}}{\partial x} + M_y \frac{\partial \tilde{v}_{\text{acc},y}}{\partial y} + \frac{\partial \tilde{p}}{\partial y}, \tag{11}$$

$$\mathcal{R}_p = \frac{\partial \tilde{p}}{\partial t} + M_x \frac{\partial \tilde{p}}{\partial x} + M_y \frac{\partial \tilde{p}}{\partial y} + \frac{\partial \tilde{v}_{\text{acc},x}}{\partial x} + \frac{\partial \tilde{v}_{\text{acc},y}}{\partial y}. \tag{12}$$

These residuals are evaluated at collocation points and minimized during training. In the one-dimensional variant, all y-dependent terms are removed.

The neural network takes as input the spatiotemporal coordinates (x, y, t) and outputs the nondimensional fields p, v_x, and v_y. We employ a fully connected deep neural network using sinusoidal activation functions (SIREN) [15]. Derivatives of the output fields with respect to the inputs are computed via automatic differentiation [14].

The total loss minimized during training is composed of three terms such as in Equations (3), where the physics-based residual loss is defined as

$$\mathcal{L}_{\text{PDE}} = \text{MSE}(\mathcal{R}_{v_x}) + \text{MSE}(\mathcal{R}_{v_y}) + \text{MSE}(\mathcal{R}_p). \quad (13)$$

The initial condition loss $\mathcal{L}_{\text{IC}}$ is computed from a Gaussian pressure pulse centered in the domain with zero initial velocity. Boundary conditions are incorporated through $\mathcal{L}_{\text{BC}}$, enforced by included as supervised data points.

Training points are sampled uniformly across the nondimensional domain. The network is optimized using the AdamW optimizer, combined with a cosine annealing learning rate schedule [17]. Optionally, dynamic loss weighting based on Neural Tangent Kernel (NTK) sensitivity are applied in 2D case to balance contributions from different residuals during training [18, 19].

3.2 LEE Solution via ELM-ODE

Following the sampled neural network approach described above, we approximate the acoustic fields using a shallow NN with fixed, randomly sampled weights and biases. In this formulation, the only unknowns are the time-dependent coefficients. In particular, we write the Galerkin ansatz for the fields as

$$v_{acc,x}(t,x,y) = c_0(t) + \sum_{k=1}^{K} c_k(t)\,\phi(w_k^1\,x + w_k^2\,y + b_k), \quad (14)$$

$$v_{acc,y}(t,x,y) = d_0(t) + \sum_{k=1}^{K} d_k(t)\,\phi(w_k^1\,x + w_k^2\,y + b_k), \quad (15)$$

$$p_{acc}(t,x,y) = e_0(t) + \sum_{k=1}^{K} e_k(t)\,\phi(w_k^1\,x + w_k^2\,y + b_k), \quad (16)$$

where ϕ is the chosen activation function, and $\{w_k^1, w_k^2, b_k\}$ are fixed through random sampling. In this way, we seek only the time-dependent coefficients $c(t)$, $d(t)$, and $e(t)$ rather than training the full set of network parameters.

3.2.1 *Galerkin Projection of the Derivatives*

The time derivatives of the fields are obtained by differentiating the coefficients:

$$\frac{\partial v_{acc,x}}{\partial t} = c_{0,t}(t) + \sum_{k=1}^{K} c_{k,t}(t)\,\phi(w_k^1\,x + w_k^2\,y + b_k), \quad (17)$$

$$\frac{\partial v_{acc,y}}{\partial t} = d_{0,t}(t) + \sum_{k=1}^{K} d_{k,t}(t)\,\phi(w_k^1\,x + w_k^2\,y + b_k), \quad (18)$$

$$\frac{\partial p_{acc}}{\partial t} = e_{0,t}(t) + \sum_{k=1}^{K} e_{k,t}(t)\,\phi(w_k^1\,x + w_k^2\,y + b_k). \quad (19)$$

Spatial derivatives are computed by differentiating the NN ansatz. For instance, the x-derivative of p_{acc} is given by

$$\frac{\partial p_{acc}}{\partial x} = e_0(t) + \sum_{k=1}^{K} e_k(t)\,\phi'(w_k^1\,x + w_k^2\,y + b_k)\,|w_k^1|, \quad (20)$$

with analogous expressions for the spatial derivatives of $v_{acc,x}$ and $v_{acc,y}$.

These evaluations at the collocation points are collected into matrices: let $\mathbf{A}^{(i)}$ denote the matrix of basis function evaluations for the i-th field and $\mathbf{B}_x^{(i)}$ and $\mathbf{B}_y^{(i)}$ denote the corresponding spatial derivative matrices (with $i = 1$ for $v_{acc,x}$, $i = 2$ for $v_{acc,y}$, and $i = 3$ for p_{acc}). We then form the block matrices

$$\mathbf{A} = \begin{bmatrix} \mathbf{A}^{(1)} & 0 & 0 \\ 0 & \mathbf{A}^{(2)} & 0 \\ 0 & 0 & \mathbf{A}^{(3)} \end{bmatrix}, \quad (21)$$

$$\mathbf{B}^{(x)} = \begin{bmatrix} \mathbf{B}_x^{(1)} & 0 & 0 \\ 0 & \mathbf{B}_x^{(2)} & 0 \\ 0 & 0 & \mathbf{B}_x^{(3)} \end{bmatrix}, \quad (22)$$

$$\mathbf{B}^{(y)} = \begin{bmatrix} \mathbf{B}_y^{(1)} & 0 & 0 \\ 0 & \mathbf{B}_y^{(2)} & 0 \\ 0 & 0 & \mathbf{B}_y^{(3)} \end{bmatrix}. \quad (23)$$

3.2.2 Assembly of the ODE System

The coupling terms from the Linearized Euler Equations, such as the pressure gradient and the divergence of velocity, are incorporated into the coupling matrix

$$\mathbf{K} = \begin{bmatrix} 0 & 0 & \alpha_{met}\,\mathbf{B}_x^{(3)} \\ 0 & 0 & \alpha_{met}\,\mathbf{B}_y^{(3)} \\ \kappa p_{met}\,\mathbf{B}_x^{(1)} & \kappa p_{met}\,\mathbf{B}_y^{(2)} & 0 \end{bmatrix}. \quad (24)$$

Defining the combined coefficient vector

$$\mathbf{Y}(t) = \begin{bmatrix} c(t) \\ d(t) \\ e(t) \end{bmatrix}, \quad (25)$$

the Galerkin projection leads to:

$$\mathbf{A}\frac{\partial \mathbf{Y}}{\partial t} = -\Big[V_{met,x}\,\mathbf{B}^{(x)} + V_{met,y}\,\mathbf{B}^{(y)} + \mathbf{K}\Big]\mathbf{Y}.$$

Because the NN weights and biases are already obtained by sampling, we solve only for the coefficients. Inverting $\mathbf{A}$ (or solving the associated least-squares problem) yields

$$\begin{aligned} \frac{\partial \mathbf{Y}}{\partial t} &= -\mathbf{A}^{-1}\Big[V_{met,x}\,\mathbf{B}^{(x)} + V_{met,y}\,\mathbf{B}^{(y)} + \mathbf{K}\Big]\mathbf{Y} \\ &\equiv \mathbf{B}_{combined}\,\mathbf{Y}. \end{aligned} \quad (26)$$

This linear ODE system for $\mathbf{Y}(t)$ is then integrated in time using standard solvers, after which the full solution is reconstructed by evaluating the NN basis functions weighted by the computed coefficients.

4. PARAMETER DETAILS

4.1 One Dimensional Case

The one-dimensional case serves as a preliminary test to compare the accuracy, convergence, and computational performance of both PINNs and ELM-ODE methods under simplified conditions. The physical parameters used in this setup are listed in Tab. 1, while the configuration details for the PINNs and ELM-ODE implementations are given in Tab. 2 and 3, respectively. Both methods are tested on the same domain and initial conditions, allowing for a fair comparison. This setup provides insights into the strengths and limitations of each approach before scaling up to higher-dimensional problems.

Table 1. Physical parameters for 1D simulation

Parameter	Value
Space Domain	$x \in [-100, 100]$ m
Time Domain	$t \in [0, 1]$ s
Medium flow velocity	5 m/s
Speed of sound	340 m/s
Initial pressure	Gaussian at $x = 0$, $\sigma = 5$ m
Boundary condition	Total reflection

Table 2. PINNs configuration for 1D simulation

Component	Value
Architecture	3 hidden layers, 30 neurons each (SIREN)
Activation	Sinusoidal, $\omega_0 = 3.0$
Input/Output	(x, t) input; $(v_{acc},\ p_{acc})$ output
Collocation points	8,000 (PDE), 200 (BC), full grid (IC)
Optimizer	Adam (lr=10^{-3}, exponential decay)
Epochs	500,000
Computing Device	Nvidia P100

Table 3. ELM-ODE configuration for 1D simulation

Component	Value
Neuron Basis	600 per field (velocity and pressure)
Activation	$\tanh$
Sampling	Randomized with scaling
Boundary	Total Reflection
Basis Fitting	Least-squares projection with regularization (10^{-6})
Spatial Resolution	400 points over the domain
Time Integration	RK45
Computing Device	Intel Xeon Gold 5218R (1 core)

4.2 Two Dimensional Case

The two-dimensional case extends the previous 1D setup to a more realistic scenario of outdoor sound propagation

with a horizontal background wind. It evaluates the methods' performance in capturing wavefront changes, directional propagation, and boundary interactions.

Table 4. Physical parameters for 2D simulation

Parameter	Value
Space Domain	$x, y \in [-100, 100]$ m
Time Domain	$t \in [0, 1]$ s
Medium Flow velocity	$V_x = 40$ m/s, $V_y = 0$ m/s
Initial pressure	Gaussian, $\sigma = 20$ m
Boundary condition	Total reflection

Table 5. PINNs configuration for 2D simulation

Component	Value
Architecture	6 hidden layers, 80 neurons each with SIREN activation ($\omega_0 = 1$)
Input/Output	(x, y, t) input; (p, v_x, v_y) output
Collocation points	50,000 (PDE), 3,000 (BC), 5,000 (IC)
Optimizer	AdamW (lr=10^{-3}, cosine annealing)
Epochs	400,000
NTK	EMA with $\beta = 0.99$
Computing Device	Nvidia A100

Table 6. ELM-ODE configuration for 2D simulation

Component	Value
Neuron Basis	1500 per field (velocity v_x, velocity v_y, pressure)
Activation	$\tanh$
Sampling	Randomized with scaling
Boundary	Total Reflection
Basis Fitting	Least-squares projection with regularization (10^{-8})
Spatial Resolution	500 points per dimension
Time Integration	RK45
Computing Device	Intel Xeon Gold 5218R (1 core)

5. RESULTS AND DISCUSSION

5.1 1D Cases

Fig. 1 compares the solutions of the 1D Linearized Euler Equation obtained using finite-difference (FD), ELM-ODE, and PINNs approaches. The FD solution acts as the ground truth for evaluating the performance of neural network-based methods.

Both ELM-ODE and PINNs solutions accurately reproduce the overall wave dynamics, including reflections at domain boundaries and the propagation of the pressure pulse across the simulation domain. However, noticeable differences exist in their error distributions. The absolute error for the ELM-ODE solution (bottom-left panel of Fig. 1) primarily concentrates along the primary wavefront paths, indicating that ELM-ODE slightly underpredicts rapid changes. In contrast, the error distribution for the PINNs solution (bottom-right panel) shows more evenly dispersed, finer-scale errors across the domain. This behavior suggests that while PINNs captures the overall wave patterns very well, it exhibits smaller-scale oscillations or numerical artifacts.

Quantitatively, as shown in Tab. 7, PINNs achieve a lower mean absolute error (0.001851 Pa) than the ELM-ODE method (0.007404 Pa), confirming that PINNs offer better accuracy overall in the tested scenario. However, this comes at the cost of significantly higher computational demands, PINNs require approximately one hour of training, while ELM-ODE produces results within seconds.

Table 7. Accuracy and cost for 1D simulation

Metric	PINNs	ELM-ODE
MAE	1.851×10^{-3}	7.404×10^{-3}
Training Time	1 h 2 min	2.98 s

5.2 2D Cases

Extending the methods from Section 5.1 to two dimensions allows for more realistic outdoor acoustic propagation scenarios, such as a planar Gaussian pressure pulse advected by a horizontal background wind. Fig. 2 compares the solutions at two different time instants, $t = 0.2$ s and $t = 0.6$ s. Both PINNs and ELM-ODE solutions closely match the finite-difference (FD) reference, capturing wavefront propagation and boundary reflections effectively. At early times ($t = 0.2$ s) (as it is written in Tab. 8),

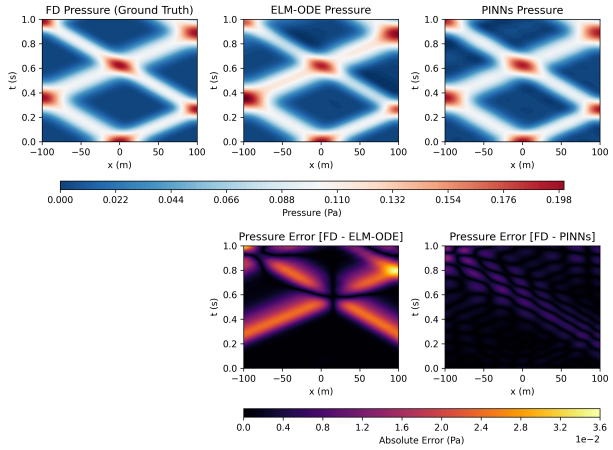


Figure 1. Comparison of pressure fields (top row) and absolute error (bottom row) for the 1D Linearized Euler Equation simulation. The FD solution serves as ground truth.

both methods yield mean absolute errors (MAE) in the order of 10^{-3}. At later times ($t = 0.6\,\mathrm{s}$), the error increases to the order of 10^{-2}, consistent with expected dispersion and diffusion. Spatially, PINNs errors are more uniformly distributed across the domain, while ELM-ODE shows errors along high-gradient regions.

Despite these similar accuracies, the two methods differ significantly in runtime. The PINNs approach required roughly 7.6 hours of training, whereas ELM-ODE finished in about 23 minutes. Important is, most of the ELM-ODE cost does not come from integrating the ordinary differential equation system, rather, it is spent assembling and factorizing the large block matrices (as discussed around Equations (21), (22), (23), (24), and (26)). Once those matrices are formed and factorized, the subsequent time-integration step involves repeated matrix-vector multiplications, which are relatively cheap.

An additional observation is that both methods must solve for all three fields (v_x, v_y, p). Even if we are mainly interested in the acoustic pressure p, the Linearized Euler Equations intrinsically couple pressure and velocity via gradients and divergences, making it physically incorrect to omit the velocity unknowns. Consequently, the coefficient vector in ELM-ODE must span three fields, substantially inflating the block matrices and their factorization cost. In three dimensions, the velocity field gains a third component, further increasing memory usage and computational effort. Nevertheless, for moderate 2D problems at practical accuracy, ELM-ODE can be significantly faster than a PINN-based solution while maintaining physically consistent results.

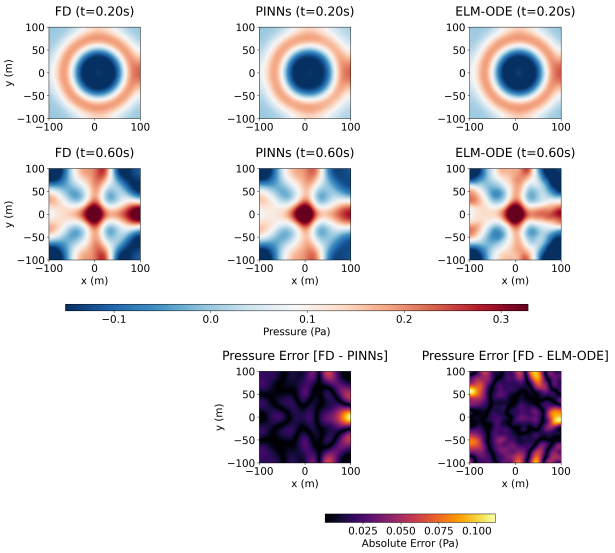


Figure 2. Comparison of FD, PINNs, and ELM-ODE solutions at $t = 0.2\,\mathrm{s}$ and $t = 0.6\,\mathrm{s}$ for the 2D domain. The bottom row shows the absolute errors for PINNs and ELM-ODE compared to the FD reference.

Table 8. Accuracy and cost for 2D simulation

Metric	PINNs	ELM-ODE
MAE $(t = 0.2)$ s	6.2221×10^{-3}	2.8990×10^{-3}
MAE $(t = 0.6)$ s	1.6631×10^{-2}	2.5553×10^{-2}
Training Time	7h 36m 52s	1362.424 s

6. CONCLUSION AND FUTURE WORK

We applied PINNs and ELM-ODE to solve the Linearized Euler Equations for outdoor acoustics in both 1D and 2D. ELM-ODE decoupled the spatial approximation from time integration and delivered faster solutions, despite with slightly larger errors in the same order. By contrast, PINNs attained slightly higher accuracy but demanded extensive training due to the full spatiotemporal residual.

Future work requires applying complex boundary conditions with frequency-dependent impedance and realistic ground surfaces to better match real-world acoustics. Scaling these methods to 3D remains challenging due to increased computational costs from the additional velocity component. Moreover, exploring alternative PDEs such as the convective Helmholtz equation or combining neural PDE solvers with measurement data or precomputed simulations appears promising.

7. REFERENCES

[1] M. Hornikx, "Ten questions concerning computational urban acoustics," *Building and Environment*, vol. 106, p. 409, 2016.

[2] J. E. Piercy, T. F. W. Embleton, and L. C. Sutherland, "Review of noise propagation in the atmosphere," *Journal of the Acoustical Society of America*, vol. 61, no. 6, pp. 1403–1418, 1977.

[3] R. Kapoor, N. Kloet, A. Gardi, A. Mohamed, and R. Sabatini, "Sound propagation modelling for manned and unmanned aircraft noise assessment and mitigation: A review," *Atmosphere*, vol. 12, no. 11, p. 1424, 2021.

[4] C. Tam, "Computational aeroacoustics: Issues and methods," *AIAA Journal*, vol. 33, no. 10, pp. 1788–1796, 1995.

[5] C. Bailly and D. Juve, "Numerical solution of acoustic propagation problems using linearized euler equations," *AIAA Journal*, vol. 38, no. 1, pp. 22–29, 2000.

[6] D. Botteldooren, "Finite-difference time-domain simulation of low-frequency room acoustic problems," *Journal of the Acoustical Society of America*, vol. 98, no. 6, pp. 3302–3308, 1995.

[7] R. Blumrich and D. Heimann, "A linearized eulerian sound propagation model for studies of complex meteorological effects," *The Journal of the Acoustical Society of America*, vol. 112, no. 2, pp. 446–455, 2002.

[8] N. Morales, V. Chavda, R. Mehra, and D. Manocha, "MPARD: A high-frequency wave-based acoustic solver for very large compute clusters," *Applied Acoustics*, vol. 121, pp. 82–94, 2017.

[9] M. Raissi, P. Perdikaris, and G. E. Karniadakis, "Physics-informed neural networks: A deep learning framework for solving forward and inverse problems involving nonlinear partial differential equations," *Journal of Computational Physics*, vol. 378, pp. 686–707, 2019.

[10] A. Krishnapriyan, A. Gholami, S. Zhe, R. Kirby, and M. W. Mahoney, "Characterizing possible failure modes in physics-informed neural networks," in *Advances in Neural Information Processing Systems*, vol. 34, 2021.

[11] C. Datar, T. Kapoor, A. Chandra, Q. Sun, I. Burak, E. L. Bolager, A. Veselovska, M. Fornasier, and F. Dietrich, "Solving partial differential equations with sampled neural networks," *arXiv preprint arXiv:2405.20836*, 2024.

[12] T. Van Renterghem, "Efficient outdoor sound propagation modeling with the finite-difference time-domain (fdtd) method: a review," *International Journal of Aeroacoustics*, vol. 13, no. 5-6, pp. 385–404, 2014.

[13] G. E. Karniadakis, I. G. Kevrekidis, L. Lu, P. Perdikaris, S. Wang, and L. Yang, "Physics-informed machine learning," *Nature Reviews Physics*, vol. 3, no. 6, pp. 422–440, 2021.

[14] A. G. Baydin, B. A. Pearlmutter, A. A. Radul, and J. M. Siskind, "Automatic differentiation in machine learning: A survey," *Journal of Machine Learning Research*, vol. 18, no. 153, pp. 1–43, 2018.

[15] V. Sitzmann, J. Martel, A. Bergman, D. Lindell, and G. Wetzstein, "Implicit neural representations with periodic activation functions," *Advances in neural information processing systems*, vol. 33, pp. 7462–7473, 2020.

[16] G.-B. Huang, Q.-Y. Zhu, and C.-K. Siew, "Extreme learning machine: theory and applications," *Neurocomputing*, vol. 70, no. 1-3, pp. 489–501, 2006.

[17] I. Loshchilov and F. Hutter, "Decoupled weight decay regularization," in *International Conference on Learning Representations (ICLR)*, 2019. arXiv:1711.05101.

[18] A. Jacot, F. Gabriel, and C. Hongler, "Neural tangent kernel: Convergence and generalization in neural networks," in *Advances in Neural Information Processing Systems (NeurIPS)*, vol. 31, pp. 8571–8580, 2018.

[19] S. Wang, X. Yu, and P. Perdikaris, "When and why PINNs fail to train: A neural tangent kernel perspective," *Journal of Computational Physics*, vol. 449, p. 110768, 2021.

DOI: 10.61782/fa.2025.0947

FORUM ACUSTICUM EURONOISE 2025

UTILIZING LARGE LANGUAGE MODELS FOR OPTIMIZING SOUND SELECTION IN DEMENTIA CARE ENVIRONMENTS

Arezoo Talebzadeh[1*]

[1] Department of Information Technology - Ghent University.
Technologiepark 126, 9052, Ghent, Belgium

ABSTRACT

The effect of soundscape on people with dementia has been studied, with established links between acoustic environments and Behavioral and Psychological Symptoms of Dementia. Previous research has demonstrated promising results in using soundscape augmentation for dementia care interventions. However, selecting appropriate sound segments remains challenging due to the heterogeneous nature of dementia and varying individual needs. This study explores the innovative application of Large Language Models (LLMs) in selecting appropriate sound segments for soundscape augmentation. By analyzing responses from Claude 3.5 and GPT-4 to systematically designed prompts, the potential to recommend suitable sound segments based on the specific auditory deficits associated with different types of dementia was investigated. The LLMs were provided with semantic complexity ratings and affective information of pre-labelled sound segments and then tasked with matching appropriate sounds to various dementia types. Results demonstrate LLMs' capability to consider multiple factors, including semantic complexity, emotional impact, and specific auditory processing challenges when making recommendations. Key findings indicate that LLMs can effectively differentiate between suitable sound segments for various dementia types. This research suggests potential benefits in using AI-assisted sound selection to enhance personalized soundscape design in dementia care while acknowledging the importance of human oversight and individual patient preferences.

Keywords: *Large Language Models, Soundscape, Dementia, Prompt Engineering.*

1. INTRODUCTION

The effect of soundscape on people with dementia has been studied [1-3], with established links between acoustic environments and Behavioral and Psychological Symptoms of Dementia [4]. Previous research has demonstrated promising results in using soundscape augmentation for dementia care interventions [5]. However, selecting appropriate sound segments remains challenging due to the heterogeneous nature of dementia and varying individual needs (Talebzadeh, Botteldooren et al., 2023). Recently, there has been an interest in using large language models (LLMs) in soundscape studies. Hou et al. used LLM for soundscape captioning, identifying sound sources, and predicting annoyance [7-8].

Selecting suitable sound segments for soundscape augmentation is challenging as human bias and prejudice may unknowingly play a role. LLMs and Generative Pre-Trained transformers (GPT) have shown promising results in minimizing bias when prompted correctly and monitored.

This study aims to use LLMs to select suitable sounds for soundscape augmentation in dementia care settings based on specific subtypes of dementia, the auditory symptoms and deficits related to each type and the appropriate sound segment based on theoretical frameworks. To examine the

[*] ***Corresponding author***: arezoo.talebzadeh@ugent.be
Copyright: *©2025 Talebzadeh et al. This is an open-access article distributed under the terms of the Creative Commons Attribution 3.0 Unported License, which permits unrestricted use, distribution, and reproduction in any medium, provided the original author and source are credited.*

possibility of LLMs as a tool to help select suitable sound, Claude 3.5 and Chat GPT 4o were prompted, and results were analyzed for homogeneity and reliability.

2. METHODOLOGY

2.1 Experimental Design

This study employed a methodological approach to evaluate the potential of LLMs in selecting appropriate sound segments for people with dementia. Claude 3.5 and GPT-4o were utilized to analyze and recommend suitable sound segments based on different types of dementia and their associated auditory deficit. The study followed a three-phase process:

1. Initial general prompting to access LLM understanding of sound selection for dementia
2. Specific prompts addressing specific dementia types and their auditory deficit
3. Complex scenario-based prompts with detailed sound segment information to design a soundscape

2.2 Prompt Engineering

To evaluate the LLM's capabilities, a series of specific prompts were developed from general to specific, using four elements: instruction, context, input data, and output indicator [9].

1. **General question**: "How can LLM be used to enhance sound segment selection for people with dementia when designing soundscapes?"
2. **Specific segment selection**: "I need your help locating the most suitable sound segments to enhance the auditory environment for individuals with dementia."
3. **Auditory deficit inquiry**: "What are the auditory deficits of each type of dementia?"
4. **Scenario**-based prompts: Two specific scenarios were presented:
    a. **Scenario A:** Sound selection for frontotemporal dementia in long-term care home
    b. **Scenario B:** Comparison of sound selection for Alzheimer's disease (AD) vs. frontotemporal dementia (FTD)

2.3 Sound Segment Analysis

The sound segment labelling was conducted online through online Audio Captioning: https://huggingface.co/spaces/wsntxxn/efficient_audio_captioning

The program labelled a comprehensive set of sound segments from previous research [6]. Each segment was then characterized by:

1. Identification number (e.g., W0004, W00026)
2. Audio caption (e.g., "rain falling on a surface", " a crowd of people are talking")
3. Semantic complexity rating (low, moderate and high)

Recognizing the inability of LLMs to directly process audio files (at the time of experience), the pre-labelled sound segments were utilized for the study. LLMs were provided with this information to make recommendations.

2.4 Evaluation Framework

LLM responses were evaluated based on:

1. Understanding of dementia-specific auditory deficits
2. Appropriate matching of sound segments to dementia type
3. Consistency of recommendation across models

3. RESULTS

3.1 LLM Understanding of Sound Selection for Dementia

Both LLMs demonstrated a sophisticated understanding of using sound segments for dementia interventions. In response to general prompts, both models provided structured approaches:

GPT-4o outlined a six-stage process:

1. Personalized Sound Recommendations
2. Tailoring to Specific Auditory Deficits
3. Adapting to Cognitive and Emotional States
4. Contextual Sound Placement
5. Data-Driven Sound Optimization
6. Combining with Assistive Technologies

Claude 3.5 proposed an eight-step framework:

1. Content analysis
2. Personalization
3. Emotional response prediction
4. Narrative generation
5. Temporal sequencing
6. Interaction analysis
7. Metadata enhancement
8. Contextual adaptation

3.2 Dementia-Specific Auditory Deficits

Both LLMs were able to identify and describe the distinctive auditory deficits associated with the most known types of dementia:
For Alzheimer's Disease (AD):

- Auditory agnosia
- Impaired sound localization
- Reduced auditory memory
- Speech comprehension difficulties

For Lewy Body Dementia (LBD):

- Auditory hallucinations
- Impaired speech understanding
- Auditory distortion

For Frontotemporal Dementia (FTD):

- Auditory neglect
- Difficulty with voice recognition
- Impaired auditory attention

For Vascular Dementia (VD):

- Auditory processing deficits
- Reduced speech discrimination
- Slower auditory processing

3.3 Sound Segment Recommendations for Specific Scenarios

For **Scenario A** (FTD), both LLMs recommended similar sound segments with GPT-4o using a time-sequenced approach.

GPT-4o suggestion:

1. Soft Outdoor Ambience (7:00-7:15 am): birds chirping, distant wind through trees, soft morning rain
1. Subtle Household Sounds (7:15-7:30 am): muffled kitchen activity, footsteps, water running
2. Neutral, Natural Soundscapes (7:30-7:45 am): ocean waves, rustling grasses, distant farm animals
3. Morning Outdoor Ambience (7:45-8:00 am): urban morning sounds, faint church bells, light wind chimes

Claude 3.5 recommendation:

1. Gentle nature sounds: birds chirping, rain, rustling leaves
2. Household sounds: kitchen noises, clock ticking, footsteps
3. Animal sounds: purring cat, quiet dog barking, cow mooing
4. Weather sounds: light wind, distant thunder, waves
5. Human voices: soft speech, quiet laughter, humming
6. Ambient outdoor sounds: park sounds, street sounds, market sounds
7. Calming white noise: fan or air conditioning hum, soft static

For scenario B (comparing AD to FTD), both LLMs highlighted specific distinctions:

For AD:

- Familiar, memory-evoking sounds
- Simple and repetitive patterns
- Emotionally positive or natural sounds

For FTD, both emphasized on:

- Non-social, neutral sounds
- Simple, non-triggering sounds
- Avoiding complex social cues

3.4 3.4 Comprehensive Sound Segment Matching

When provided with detailed information about sound segments (including ID, labelling, semantic complexity, and affective information), both LLMs demonstrated matching capabilities with some similarities:

GPT-4o recommended:

- For AD: W0026 (rain falling), W0211 (birds chirping), W0088 (stream flowing), W0013 (music)
- For LBD: W0026, W0088, W0211, W0107 (crickets chirping)
- For FTD: W0088, W0016 (birds chirping), W0006 (frogs croaking), W0026
- For Posterior Cortical Atrophy: W0026, W0088, W0010 (ocean waves), W0211

Claude 3.5 recommended:

- For AD: W0016, W0026, W0088
- For VD: W0212, W0072, W0013
- For FTD: W0162, W0144, W0015
- For LBD: W0060, W0152, W0213

4. DISCUSSION

4.1 Comparative Analysis of LLM Performance

Both LLMs demonstrated some capabilities in understanding the complex relationship between dementia types, auditory deficits, and appropriate sound selection. However, notable differences emerged in their approaches:
GPT-4o tended to provide more structured, sequential recommendations with detailed explanations of why particular sounds would benefit specific dementia types. Its recommendations align with established therapeutic approaches, emphasizing familiarity for Alzheimer's and neutral, non-triggering sounds for frontotemporal dementia.
Claude 3.5 offered more diverse sound segment suggestions with greater attention to the affective dimensions and semantic complexity. It demonstrated some potential in distinguishing subtle differences between dementia types and providing tailored recommendations based on specific auditory deficits.

4.2 Semantic Complexity Considerations

The LLMs effectively utilized semantic complexity ratings in their recommendations, showing appropriate general selection patterns:

- Low complexity sounds (e.g., rain falling, stream flowing) were consistently recommended for Alzheimer's disease and other conditions with significant auditory processing deficits
- Moderate complexity sounds were selectively recommended for conditions where some auditory processing remained intact
- High-complexity sounds were generally avoided for most dementia types, with exceptions made for specific therapeutic purposes

4.3 Integration of Affective Information

Both LLMs demonstrated sophisticated use of affective information in their recommendations. They consistently preferred segments described as "pleasant," "calming," or "soothing" for conditions with anxiety features, while moderately stimulating sounds described as "vibrant" or "engaging" were recommended when appropriate for maintaining cognitive engagement.

4.4 Discrepancy between LLMs

Although both LLMs demonstrated the ability to select suitable segments based on specific dementias, their choices were inconsistent on specific segments.

4.5 Limitations and Ethical Considerations

Several limitations must be acknowledged:

1. Lack of direct audio processing: Current LLMs cannot directly analyze audio files, necessitating pre-labeled segments
2. Absence of personalization: Recommendations were based on dementia types rather than individual preferences and histories
3. Limited validation: The recommendations have not been extensively validated in clinical settings
4. Ethical considerations: The use of AI in dementia care raises important questions about agency, consent, and technological dependency

5. CONCLUSION

This study demonstrates the potential of LLMs to assist in selecting appropriate sound segments for soundscape augmentation in dementia care. By leveraging their ability to process complex information about dementia types, auditory deficits, semantic complexity, and affective dimensions, LLMs can provide nuanced recommendations that may enhance therapeutic interventions.
The findings suggest that LLMs could serve as valuable co-creators in designing personalized soundscapes, particularly in addressing the heterogeneity within dementia and tailoring interventions to specific auditory needs. However, LLMs should complement rather than replace human expertise at this time, with the final selection incorporating patient preferences, caregiver insights, and clinical judgment.
Future research should focus on:

1. Developing LLMs capable of directly processing audio files
2. Creating more personalized approaches that incorporate individual histories and preferences
3. Conducting clinical validation studies to assess the effectiveness of LLM-recommended sound segments
4. Establishing ethical frameworks for AI integration in dementia care
5. Exploring longitudinal applications to accommodate the progressive nature of dementia

This initial exploration suggests that integrating LLMs in soundscape design for dementia care represents a promising direction for enhancing the quality of life and reducing behavioural and psychological symptoms through personalized auditory environments.

6. REFERENCES

[1] P. Devos *et al.*, "Soundscape design for management of behavioral disorders: a pilot study among nursing home residents with dementia," 2018.

[2] T. De Pessemier *et al.*, "Personalising augmented soundscapes for supporting persons with dementia," *Multimed Tools Appl*, 2022, doi: 10.1007/s11042-022-13839-3.

[3] F. Aletta *et al.*, "Awareness of 'sound' in nursing homes: A large-scale soundscape survey in Flanders (Belgium)," *Building Acoustics*, vol. 25, no. 1, pp. 43–59, Mar. 2018, doi: 10.1177/1351010X17748113.

[4] A. Talebzadeh *et al.*, "The Influence of Everyday Acoustic Environments on the Challenging Behavior in Dementia: A Participatory Observation Study in Nursing Homes," *Int. J. Environ. Res. Public Health*, vol. 20, p. 4191, 2023, doi: 10.3390/ijerph20054191.

[5] A. Talebzadeh *et al.*, "Effect of soundscape augmentation on behavioural symptoms in people with dementia: A pilot randomized controlled trial," *Innov Aging*, p. igae069, Aug. 2024, doi: 10.1093/geroni/igae069.

[6] A. Talebzadeh *et al.*, "Sound augmentation for people with dementia: Soundscape evaluation based on sound labelling," *Applied Acoustics*, vol. 215, p. 109717, Dec. 2023, doi: 10.1016/j.apacoust.2023.109717.

[7] Y. Hou *et al.*, "AI-based soundscape analysis: Jointly identifying sound sources and predicting annoyance," *J Acoust Soc Am*, vol. 154, no. 5, pp. 3145–3157, Nov. 2023, doi: 10.1121/10.0022408.

[8] Y. Hou *et al.*, "Soundscape Captioning using Sound Affective Quality Network and Large Language Model," Jun. 2024, [Online]. Available: http://arxiv.org/abs/2406.05914

[9] L. Giray, "Prompt Engineering with ChatGPT: A Guide for Academic Writers," Dec. 01, 2023, *Springer*. doi: 10.1007/s10439-023-03272-4.

DOI: 10.61782/fa.2025.0224

FORUM ACUSTICUM EURONOISE 2025

COMPARATIVE ANALYSIS ON THE USE OF LINEAR AND NON-LINEAR METHODS FOR AUDITORY ATTENTION DECODING (AAD)

Iñigo García-Ugarte[1*] **Rubén Eguinoa**[1] **Carmen Vidaurre**[2]
Daniel Paternain[2] **Ricardo San Martín**[1]
[1] Acoustics Laboratory, Public University of Navarre, Spain
[2] Department of Computer Science, Public University of Navarre, Spain
[3] Basque Center on Cognition, Brain and Language, San Sebastian, Spain

ABSTRACT

In a cocktail party scenario, the human auditory system can focus on a single stimulus while suppressing others identified as noise [1]. In the context of neuro-steered hearing devices, auditory attention decoding (AAD) aims to replicate this process using different algorithms that decode electroencephalography (EEG) signals to identify the attended stimulus. Traditional approaches often rely on linear models to establish relationships between neural activity and auditory inputs. However, linear algorithms face significant limitations when decoding a complex non-linear system like the brain. The emergence of deep learning has enabled the development of novel non-linear algorithms, which have shown promising results. In this study, different linear and non-linear algorithms are implemented and evaluated using publicly available data. Furthermore, different methods for training deep learning models are considered to enhance the final model accuracy. The results are analyzed to assess the advantages and limitations of linear versus non-linear approaches in real-world scenarios. This work provides a detailed comparison between different AAD methodologies, offering valuable insights for applications in smart hearing aids, auditory prostheses, and hearing-related medical diagnoses.

*__Corresponding author__: inigo.garciaugarte@unavarra.es.
__Copyright__: ©2025 Iñigo García-Ugarte et al. This is an open-access article distributed under the terms of the Creative Commons Attribution 3.0 Unported License, which permits unrestricted use, distribution, and reproduction in any medium, provided the original author and source are credited.

Keywords: *Auditory attention decoding (AAD), electroencephalography (EEG), speech envelope, deep learning.*

1. INTRODUCTION

In scenarios where multiple speakers, background noise, or music are present, our auditory system can distinguish the attended speaker from other sources by suppressing or ignoring them [1]. This auditory ability diminishes with age, and individuals with congenital hearing impairment are similarly affected. Current hearing devices and cochlear implants often perform poorly in complex listening environments—such as at a cocktail party, in eavesdropping situations, or while driving—because they typically identify the attended source based on loudness or location. Decoding the desired auditory source directly from the user's brain activity could provide crucial information for neuro-steered hearing devices, thereby enhancing the performance of traditional devices in challenging scenarios.

The electroencephalogram (EEG) is the preferred method for measuring brain activity for auditory attention decoding (AAD) because it is non-invasive, cost-effective, and scalable; features that facilitate its use in everyday settings. In [2,3], the authors established a direct relationship between the EEG signal and the low-frequency envelope of the attended stimulus. When linking the attended stimulus with the brain activity, researchers distinguish between forward and backward models based on whether the stimulus or the EEG signal is predicted. Backward

models have demonstrated superior performance by predicting the attended speech envelope from the EEG signal [4]. Consequently, this study primarily considers the backward paradigm (see Fig. 1 a)).

Several real-time [5] and real-life [6] AAD implementations have been conducted, and new portable, comfortable EEG devices continue to emerge [6]. These experiments only considered classical approaches—specifically linear methods—which have been regarded as state-of-the-art in terms of efficiency and performance. However, in recent years the advent of deep learning techniques significantly impacted data processing tasks. In the field of AAD, recent studies introducing new non-linear methods [7–9] and more extensive datasets [10] have enabled the development of complex non-linear models that outperform classical methods.

Unlike previous works, our study incorporates innovative deep learning models using the same dataset, allowing for a rigorous analysis of their advantages and limitations compared to traditional methods. This provides a comprehensive evaluation of the current state of auditory attention decoding.

2. AAD ALGORITHMS REVIEW

2.1 Linear models

2.1.1 Linear regression

Linear supervised AAD models facilitate the estimation of the attended stimulus by reconstructing the speech envelope ($\hat{\mathbf{s}}_\mathbf{a}$) applying a decoder matrix on the EEG lagged signal [3]. This reconstruction is achieved by linearly combining time-lagged sequences from the EEG channels, as expressed by:

$$\hat{s}_a(t) = \sum_{c=1}^{C} \sum_{l=0}^{L-1} d_c(l) x_c(t+l) \tag{1}$$

where $x_c(t)$ denotes the value of the c-th EEG channel at time t, $d_c(l)$ represents the decoder coefficient corresponding to the l-th time lag corresponding to the c-th channel, and L and C indicate the total number of time lags and EEG channels, respectively.

Assuming T samples, the decoding coefficients are obtained by minimizing the mean squared error (MSE) between the predicted speech envelope $\hat{\mathbf{s}}_\mathbf{a} = \mathbf{Xd}$ and the actual envelope $\mathbf{s_a}$:

$$\mathbf{argmin}||\mathbf{s_a} - \mathbf{Xd}||_\mathbf{2}^\mathbf{2} \tag{2}$$

with $\mathbf{X} = [x(0)...x(T-1)] \in \mathbb{R}^{T \times LC}$ and $\mathbf{s(a)} = [s(0)...s(T-1)] \in \mathbb{R}^{T \times LC}$. This leads to the solution $\hat{\mathbf{d}} = (\mathbf{X^T X})^{-1} \mathbf{X^T s_a}$ [4], where $\mathbf{R_{xx}} = (\mathbf{X^T X})^{-1}$ corresponds to the autocorrelation matrix and $\mathbf{R_{xs_a}} = \mathbf{X^T s_a}$ represents cross-correlation matrix. Thus, the decoder matrix is estimated as: $\hat{\mathbf{d}} \in \mathbb{R}^{LC \times 1}$.

Although these linear models offer simplicity with considerable performance, overfitting remains a common issue in AAD due to the typically limited size of available datasets. To mitigate this, Ridge regression is frequently employed, incorporating to Equation 1 an L2-norm regularization term when computing the decoder matrix: $\lambda \mathbf{z} ||\mathbf{d}||^\mathbf{2}$ with $\mathbf{z} = \mathbf{trace(XX^T)}/LC$ [11] Here, λ denotes the regularization hyperparameter that penalizes large decoder weights, and it is determined by selecting an optimal value from a predefined range using a validation procedure.

In this model the reconstructed envelope is correlated with both the attended (ρ_1) and the ignored (ρ_2) real envelopes. The higher correlation coefficient, ρ, is associated with the attended stimulus, providing a measure of the model's accuracy in decoding auditory attention in a multi-speaker scenario (Fig. 1 a)).

2.1.2 Canonical correlation analysis CCA

In section 1, backward models are presented as the top-performing models in Auditory Attention Decoding (AAD). However, Canonical Correlation Analysis (CCA) offers a hybrid approach (see Fig. 1 b)), integrating both forward and backward modeling techniques to enhance decoding performance. This model proposed in [12] to solve the AAD problem, identifies optimal linear transformations for both EEG signals and speech envelopes, thereby minimizing irrelevant variance and maximizing mutual correlation between the transformed domains.

Mathematically, CCA seeks to determine a set of backward spatiotemporal filters, denoted as $\mathbf{w_x} \in \mathbb{R}^{LC \times 1}$, and forward temporal filters, $\mathbf{w_{s_a}} \in \mathbb{R}^{L_a \times 1}$, applied to the EEG and stimulus domains, respectively. These filters maximize the correlation:

$$\max_{\mathbf{w_x}, \mathbf{w_{s_a}}} \frac{\mathbf{w_x^T R_{xs_a} w_{s_a}}}{\sqrt{\mathbf{w_x^T R_{xx} w_x}} \sqrt{\mathbf{w_{s_a}^T R_{s_a s_a} w_{s_a}}}} \tag{3}$$

This optimization is typically solved via generalized eigenvalue decomposition, where the optimal filters correspond to the eigenvectors with the largest eigenvalues. By selecting the top J eigenvectors, we obtain filter matrices $\mathbf{W_x} \in \mathbb{R}^{LC \times J}$ and $\mathbf{W_{s_a}} \in \mathbb{R}^{L_a \times J}$. As depicted

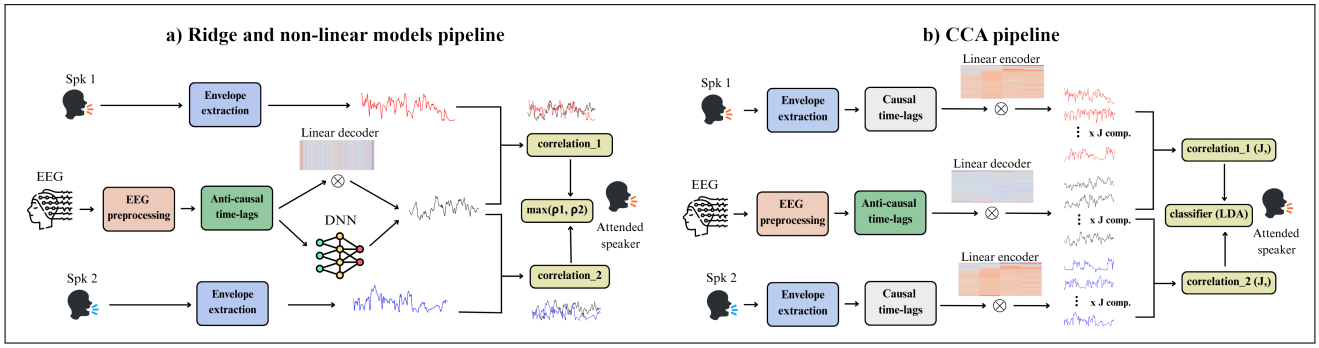


Figure 1. Different analytical pipelines followed for Auditory Attention Detection (AAD). (a) Implements only a backward decoder for Ridge regression and non-linear models. (b) Incorporates both a backward decoder and a forward encoder for Canonical Correlation Analysis (CCA), extracting multiple components.

in Fig. 1 b) for the classification task, these J correlation coefficients, both the ignored and the attended, serve as features for linear discriminant analysis (LDA) classifiers. Further details regarding specific model parameters and implementation can be found in Section 4.

2.2 Non linear models

2.2.1 CNN

In [8], two deep-learning-based backward models (map EEG signal to stimulus) are proposed. These algorithms predict the ongoing sample of the input sequence, operating in an anti-causal fashion. Among the two models presented in the study, we selected the Convolutional Neural Network (CNN) model, based on the original network EEGNet [13], as it proved to be a more efficient network when compared with the alternative Fully-Connected Neural Network (FCNN) solution. This model applies convolution operations along both temporal and channel dimensions to extract features from the EEG. After that, a depth-wise separable convolution is employed to capture global features, which are fed into a linear classifier to predict the initial sample of attended stimulus.

2.2.2 EEG Conformer

Recognizing that the CNN model is relatively simple, we explored more complex architectures in this study. The network proposed in [9], known as EEG Conformer, is considered state-of-the-art for EEG classification, having achieved superior results on motor-imagery (MI) and emotion detection datasets. This network integrates some Convolutional modules from EEGNet with a transformer self-attention block, thereby combining local feature extraction with global context modeling. For adaptation to the auditory attention decoding (AAD) paradigm, the network was modified to predict the ongoing segment of the envelope, as for the CNN approach, and an extensive hyperparameter search was conducted.

2.2.3 VLAAI

The study in [7] describes a convolutional network architecture, VLAAI, which was evaluated on the SparrKULee dataset [10] and outperformed both CNN (see section 2.2.1) and linear models. The architecture comprises N distinct blocks, each containing a CNN module with M consecutively stacked convolutional layers. The model also includes an output context module that applies a left zero padding to the convolutional operation. Unlike the previous non-linear models, which predict only the ongoing segment of the sequence, VLAAI predicts the entire window at each forward pass. Moreover, since the dataset used differed from that used in the original study, we performed an independent parameter search.

3. DATA: DTU DATASET

This work relies on a well-established dataset, known as the DTU dataset [14], to train and evaluate the models described in previous sections. The dataset comprises recordings from 18 subjects who listened to one of two competing audio streams, each featuring a male and a female narrator reading a book in Dutch. All subjects were young, normal-hearing individuals, and the recordings were obtained under various simulated reverberation

scenarios. A 64-channel BioSemi ActiveTwo system sampled at a frequency of 512 Hz is employed to obtain the EEG signals.

The extraction of the speech envelope was conducted using the `COCOHA MATLAB toolbox` [15]. The function `co_auditoryfilterbank.m` is used to implement a Gamma-tone filter bank on the unprocessed audio signal, sampled at $f_s = 44100Hz$. The signal is decomposed into 31 frequency bands, with center frequencies equally spaced on the Equivalent Rectangular Bandwidth (ERB) scale, ranging from 80 Hz to 8000 Hz. The envelope of each sub-band is then computed by taking the absolute value of the filtered signal and applying a nonlinear compression by raising it to the power of 0.3. Subsequently, the audio is down-sampled to align with the EEG sampling rate ($f_s = 64Hz$), and all frequency components are aggregated to compute the average and establish the final envelope.

The `COCOHA MATLAB toolbox` was also utilized to preprocess the EEG signal for the Auditory Attention Decoding (AAD) task. The signal is down-sampled to $f_s = 64Hz$ and subjected to a second-order Butterworth filter operating within the frequency range of $f_l = 0.5Hz$ to $f_h = 32Hz$. For further details on EEG preprocessing and artifact removal, refer to the preprocessing pipeline implemented in `preproc_data.m`, as described in [14].

4. METHODS

4.1 Validation procedure

AAD datasets contain subject-specific information recorded across different trials. Including data from the same trial in both training and validation could lead to misleading results, as models might learn trial-specific patterns, causing overfitting [16]. To prevent this, we implement a cross-trial validation procedure, distinguishing between three different approaches: subject-specific (SS), subject-independent (SI) and population procedures.

For subject-specific decoders (SS), models are trained and evaluated using data from the same individual, resulting in one model per subject. Given the limited availability of subject-specific data, we applied a 5-fold cross-validation strategy. The total number of trials was divided into five equal sets (e.g.: 12 trials per set in the DTU dataset). One set was used for validation, another for testing, and the remaining three for training.

For subject-independent decoders (SI), we used a leave-one-subject-out (LOSO) validation approach. The test set consisted of a single subject, while the remaining subjects were included in the training and validation sets. Five randomly selected subjects were assigned to the validation set and the rest of them formed the training set. A single model per subject is obtained when using this validation paradigm.

In addition to these validation strategies, we implemented a population-level baseline model, trained on data from all subjects. In this case, we applied the same 5-fold cross-validation strategy as in the subject-specific approach to enhance robustness. This resulted in a single model per dataset per fold. The population model served as a baseline for the subject finetuning (SF) training strategy (see Section 4.3).

4.2 Evaluation metrics

4.2.1 Decoding accuracy

The accuracy obtained by the model is calculated by comparing the Pearson r coefficients of the attended and unattended stimuli. This Pearson correlation coefficient r quantifies the similarity between two temporal sequences ranging from -1 to 1, where 1 indicates maximum correlation and 0 denotes no correlation. The envelope corresponding to the higher coefficient is identified as the attended one. Classification accuracy is determined as the ratio of correctly predicted windows to the total number of windows. Accuracy depends on window size, as larger windows incorporate more samples, increasing the likelihood of correct classification. Six window sizes were evaluated, ranging from 1s to 50s, the last one corresponding to the trial length of the DTU dataset.

4.2.2 MESD

Decoding accuracy, as previously mentioned, is a length-dependent metric that yields varying results based on the evaluation window. In [17], a unique metric is introduced to assess overall model performance. This metric offers insight into the model's potential performance in a real hearing-aid device by quantifying the minimal-expected switch duration (MESD) using a Markov chain approach. It is measured in seconds, and a lower value is preferable for the model, as it indicates the minimum expected duration required for an attention shift. Its computation relies on an adaptive gain system that depends on a hypothetical number of gain levels. All calculations were performed using the `MESD-toolbox` implemented in Python [18], which processes classification window results and returns

an estimate for the duration of a hypothetical attention switch.

4.3 Training process

In linear decoders, time-lag matrices were computed by fixing the time-lag value to $L = 26$ in LSR, which left-shifts the EEG signal by up to 400 ms. For CCA, we set $L_a = 80$ for the encoder and $L = 16$ for the decoder, corresponding to a right-shift of the stimulus by up to 1.25 s and a left-shift of the EEG by up to 250 ms. These time-lag values were chosen based on previous studies [3,4]. To determine the optimal number of components J for CCA, we first trained a CCA model with $\min(L_a, L)$ components and then optimized an LDA classifier via grid-search over J (ranging from 1 to $\min(L_a, L)$); the J yielding the best validation performance was selected. Similarly, for Ridge regression, a grid-search was performed for the regularization parameter λ over the range 10^{-7} to 10^{7}. Both linear models were implemented using the scikit_learn library, specifically `cross_decomposition.CCA` and `linear_model.Ridge` functions.

For non-linear models, the optimization objective was to minimize the negative correlation coefficient. The Adam optimizer was employed and models were trained for up to 200 epochs with early stopping after 5 epochs without improvement in validation loss. A hyperparameter search was conducted for the VLAAI and Conformer models, as they were originally designed for different tasks and datasets. All deep learning models were implemented in PyTorch using an NVIDIA A600 GPU.

Two training strategies were adopted to obtain the best subject-specific model. For non-linear models, we compared performance when training the model from scratch (see SS in 4.1) versus fine-tuning a pre-trained baseline model (see population in 4.1), where the final classification layers were adapted to subject-specific data while the rest of the model remained with the same parameters. A parametric paired test with Bonferroni correction was used for the statistical analysis.

5. RESULTS

5.1 Hyper-parameter search

To ensure a fair comparison among the reviewed models, we performed a hyperparameter search for all models except the CNN, which was already optimized in [8] for the dataset used.

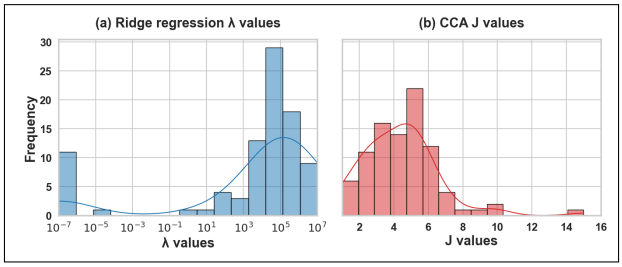


Figure 2. Linear models parameter distribution: a) Ridge regression λ values b) CCA J values

Fig. 2 a) illustrates the λ values for the Ridge regression model during subject-specific validation, selected based on validation loss. Most models yielded high regularization values that penalize large weights.

Fig. 2 b) displays the optimal J values for the CCA models under subject-specific validation. Typically, the best J values involve seven or fewer components, indicating that additional components are unnecessary.

For the non-linear models originally trained on different datasets, we conducted a hyperparameter search on the VLAAI and Conformer models. Tab. 1 summarizes the differences in model sizes and validation performance, with results averaged across folds. Note that the window sizes differ: the VLAAI model was trained on 5-second windows, while the Conformer and CNN models predicted 2-second windows on the training stage.

Table 1. Model sizes and validation results for non-linear models

Model	Size	Loss (ρ)	Accuracy (%)
CNN [8]	**9.65K**	**0.150**	**61.32**
VLAAI [7]	1.71M	0.058	56.40
VLAAI (enhanced)	**1.71M**	**0.069**	**57.08**
Conformer [9] (adapted)	241K	0.139	60.34
Conformer (enhanced)	**508K**	**0.144**	**60.62**

5.2 Subject-finetuning (SF)

Each population model was fine-tuned with subject-specific data to compare two training methodologies: subject-specific versus subject-fine-tuned (see Section 4.3). As shown in Fig. 3, except for VLAAI, fine-tuning did not improve validation accuracy, with Con-

former and CNN models showing no significant differences between the two strategies. Therefore, we will use subject-specific validation for these models. In contrast, the VLAAI model exhibited a significant improvement with fine-tuning ($p < 0.01$), consistent with [7]. Hence, this strategy will be applied to VLAAI in the subsequent evaluation.

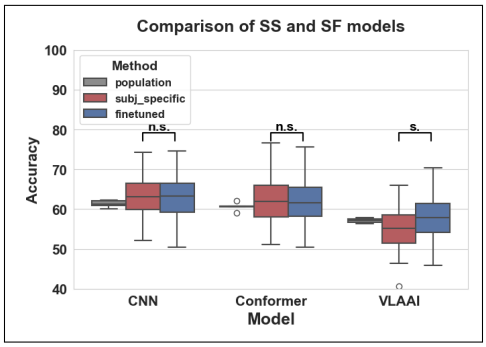


Figure 3. Subject specific and subject finetuned comparison based on the validation accuracy. Statistical analysis: **n.s.** : $p > 0.01$; **s.** : $p < 0.01$

5.3 Subject-specific (SS) and Subject-independent (SI)

Fig. 4 a) presents the subject-specific evaluation results, comparing accuracies across different window lengths and corresponding inter-model MESD values. The CNN and Conformer models achieve the best median MESD values, at 16.7 and 17.4 respectively. Although the CCA model appears to perform better for long windows, for short decision windows (1–2 seconds) the CNN and Conformer models outperform the others, thereby significantly influencing the overall MESD. Conversely, for long windows the CCA model performs better, reaching 92.2% at 50s, also producing fewer MESD outliers. The Ridge regression model performed substantially worse in both MESD and accuracy, while the VLAAI model performed close to the singnificance level, indicating its unsuitability for this dataset.

The results for subject-independent methodology, which renders the system ready for use (see Section 4.1), are illustrated in Fig. 4 b). As expected, subject-independent models performed significantly worse than subject-specific ones; the VLAAI model was excluded since it did not exceed the significance level. Nevertheless, the remaining models achieved above-chance, and even acceptable accuracies with long decision windows. The CCA model attained the best performance for long windows, reaching an accuracy of 83.6% on a 50-second window, whereas the CNN model—excelling in short decision windows—delivered the best MESD at 33.3 seconds. These findings indicate that the models can generalize across subjects when subject-specific data is unavailable.

6. DISCUSSION

6.1 Linear vs. non-linear models

Results in Section 5.3 show that the best linear model (CCA) and the CNN performed similarly in terms of MESD. However, these models differ in accuracy across different window lengths, highlighting the MESD metrics sensitivity to short-time windows. We attribute the superior performance of these models to two factors. First, CCA leverages both stimulus and EEG information to capture relevant variance from each domain [12]. Second, the performance of the CNN and Conformer nonlinear models can be attributed to their ability to adapt to a relatively small dataset, such as the DTU dataset.

In many machine learning applications, the trend is to develop larger, more complex models trained on extensive datasets. Following this approach, a non-linear model that integrates both stimulus and EEG signals could potentially yield even better performance. Nonetheless, when selecting an algorithm for AAD, linear models offer clear advantages: they provide lightweight solutions and simpler, more interpretable pipelines. In many cases, these characteristics may be prioritized over marginal gains in final performance.

6.2 Non-linear models prediction

In Section 5.2, the only model that benefited from subject fine-tuning was VLAAI. However, this model exhibited the poorest overall performance, in contrast to [7]. We attribute this discrepancy primarily to the window prediction paradigm, as other linear models predicting the ongoing sample performed much better. Furthermore, the DTU dataset [14] differed substantially in both experimental design and size from that in [7], which further explains the under-performance of VLAAI in Section 5.3. In contrast, the CNN and Conformer nonlinear models adequately fit the dataset, achieving the best results in terms of MESD and accuracy for small window sizes. When comparing these two models, despite expectations regarding model

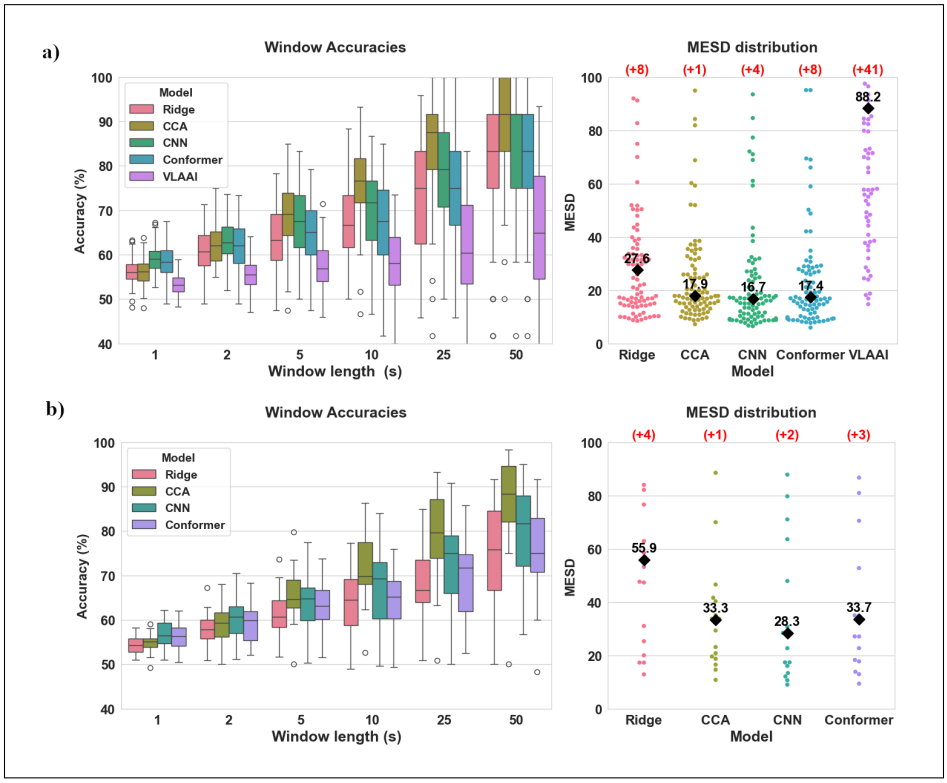


Figure 4. a) Subject-specific (SS) model comparison, b) Subject-independent (SI) model comparison.

size and complexity, empirical results indicate that the CNN outperformed the Conformer model. This results suggest that a depth-wise block is sufficient to learn from EEG signals, rather than relying on a self-attention layer.

6.3 AAD feasibility and actual constraints

The reviewed models demonstrated robust performance for the AAD paradigm. However, when implementing an AAD system in real-life scenarios, several constraints must be considered. First, all algorithms rely on access to clean envelopes, which requires an effective speech separation algorithm. Second, the data in this study were recorded using a wet 64-electrode EEG system in a controlled environment, a setting that does not reflect real-world conditions. Another critical factor is the computational cost and real-time feasibility, both aspects not addressed by the pipelines developed in this work.

Ultimately, accurately measuring attention remains challenging. In experimental settings, attention is typically inferred from participant's responses to a series of questions after completing the trials. However, in real-world situations, attention fluctuates dynamically and cannot be directly measured, making it fundamentally different from controlled experimental assessments. Thus, future studies must search for an adequate trade-off between window length and accuracy and incorporate an adaptive gain system that allows users to switch attention.

Although significant progress has been made to overcome these issues [5, 6], further research is essential to transform neuro-steered hearing aids into a practical solution.

7. CONCLUSION

In this study, different linear and non-linear auditory-attention decoding (AAD) models were presented and evaluated using the same dataset. All models were adjusted to the dataset through a hyperparameter search to obtain the optimal configuration. For non-linear models, a subject fine-tuning training strategy was considered. The CNN model of [8], performed the best on short de-

cision windows achieving the lowest MESD on both SS and SI models by predicting the ongoing sample of the introduced context. Nevertheless, the CCA linear model achieved higher accuracies on long decision windows and similar MESD results, offering a simpler and more interpretable alternative to non-linear models. In conclusion, this work provides a fair comparison between different AAD algorithms using the same dataset and may serve as a basis for future studies evaluating alternative AAD approaches. It also contributes to further research by linking brain activity with auditory stimuli, thereby providing useful insights for neuro-steered hearing aids and hearing-related medical diagnoses.

8. REFERENCES

[1] E. C. Cherry, "Some Experiments on the Recognition of Speech, with One and with Two Ears," *The Journal of the Acoustical Society of America*, vol. 25, pp. 975–979, June 2005.

[2] S. J. Aiken and T. W. Picton, "Human Cortical Responses to the Speech Envelope," *Ear & Hearing*, vol. 29, pp. 139–157, Apr. 2008.

[3] J. A. O'Sullivan, A. J. Power, and Mesgarani, "Attentional Selection in a Cocktail Party Environment Can Be Decoded from Single-Trial EEG," *Cerebral Cortex*, vol. 25, pp. 1697–1706, July 2015.

[4] S. Geirnaert and Vandecappelle, "Electroencephalography-Based Auditory Attention Decoding: Toward Neurosteered Hearing Devices," *IEEE Signal Processing Magazine*, vol. 38, pp. 89–102, July 2021. Conference Name: IEEE Signal Processing Magazine.

[5] J. Hjortkjær and Wong, "Real-time control of a hearing instrument with EEG-based attention decoding," *Journal of Neural Engineering*, vol. 22, p. 016027, Feb. 2025. Publisher: IOP Publishing.

[6] L. Straetmans, K. Adiloglu, and S. Debener, "Neural speech tracking and auditory attention decoding in everyday life," *Frontiers in Human Neuroscience*, vol. 18, Nov. 2024. Publisher: Frontiers.

[7] B. Accou and Vanthornhout, "Decoding of the speech envelope from EEG using the VLAAI deep neural network," *Scientific Reports*, vol. 13, p. 812, Jan. 2023. Publisher: Nature Publishing Group.

[8] M. Thornton and Mandic, "Robust decoding of the speech envelope from EEG recordings through deep neural networks," *Journal of Neural Engineering*, vol. 19, p. 046007, Aug. 2022.

[9] Y. Song, Q. Zheng, B. Liu, and X. Gao, "Eeg conformer: Convolutional transformer for eeg decoding and visualization," *IEEE Transactions on Neural Systems and Rehabilitation Engineering*, vol. 31, pp. 710–719, 2022.

[10] L. Bollens, B. Accou, H. Van hamme, and T. Francart, "SparrKULee: A Speech-evoked Auditory Response Repository of the KU Leuven, containing EEG of 85 participants," 2023.

[11] D. D. E. Wong and Fuglsang, "A Comparison of Regularization Methods in Forward and Backward Models for Auditory Attention Decoding," *Frontiers in Neuroscience*, vol. 12, p. 531, Aug. 2018.

[12] A. de Cheveigné and Wong, "Decoding the auditory brain with canonical component analysis," *NeuroImage*, vol. 172, pp. 206–216, May 2018.

[13] V. J. Lawhern and Solon, "Eegnet: a compact convolutional neural network for eeg-based brain–computer interfaces," *Journal of neural engineering*, vol. 15, no. 5, p. 056013, 2018.

[14] S. A. Fuglsang and Wong, "EEG and audio dataset for auditory attention decoding," Mar. 2018.

[15] D. D. Wong and Hjortkjær, "COCOHA Matlab Toolbox," Mar. 2018.

[16] I. Rotaru and Geirnaert, "What are wereallydecoding? Unveiling biases in EEG-based decoding of the spatial focus of auditory attention," *Journal of Neural Engineering*, vol. 21, Feb. 2024.

[17] S. Geirnaert and Francart, "An Interpretable Performance Metric for Auditory Attention Decoding Algorithms in a Context of Neuro-Steered Gain Control," *IEEE Transactions on Neural Systems and Rehabilitation Engineering*, vol. 28, pp. 307–317, Jan. 2020. Conference Name: IEEE Transactions on Neural Systems and Rehabilitation Engineering.

[18] EXPORL, "Mesd-toolbox: A toolbox for model-based evaluation of speech detectors." `https://github.com/exporl/mesd-toolbox`, 2024. GitHub repository.

DOI: 10.61782/fa.2025.0235



FORUM ACUSTICUM
EURONOISE 2025

Comparison of Deep Learning and Psychoacoustic Models to Predict UAV Noise Impact in Soundscapes

Max W. Ellis[1*] **Marc C. Green**[1] **Michael J. B. Lotinga**[1]
Antonio J. Torija Martínez[1]

[1] Acoustics Research Centre, University of Salford, England (UK)

ABSTRACT

The increasing prevalence of Unmanned Aircraft Systems in urban environments necessitates a deeper understanding of their impact on the experience of urban soundscapes. This study presents Machine Learning models aimed at predicting perceived annoyance of UAS noise. Deep learning models were generated using convolutional recurrent neural networks, trained on a dataset incorporating data from multiple listening experiment. The model predictions are compared with various existing nonlinear models for Psychoacoustic Annoyance. Our expanded dataset includes recent field studies across England and Greece, enhancing the robustness and generalisability of our models. The broader aim of this research is development of a comprehensive soundscape model for UAS noise, which could be incorporated into future 'next generation' smart sound level meters and be used to inform urban planning decisions.

Keywords: *Artificial Intelligence, Machine Listening, Psychoacoustic Annoyance, Soundscape, UAS*

1. INTRODUCTION

Noise signatures from emergent technologies in both civil and commercial domains have prompted growing concern regarding their acoustic impact on the perception of urban soundscapes. As frameworks develop for UAS, commonly referred to as *drones,* to integrate into transport infrastructure, small drones are already employed in agriculture for crop sowing, health monitoring, and logistics for both NHS and Royal Mail deliveries. These drones elicit complex perceptual responses by introducing novel, often highly tonal noise signatures that deviate from broadband noise typical of road or rail transport. Conventional noise assessment methods – historically reliant on A-weighted scales – are insufficient in capturing these effects.

Recent years have seen increased emphasis on applying the soundscape approach [1], acknowledging human perception of environmental sound is shaped not only by acoustic levels but also by context and emotional affect. This shift has encouraged the development of methods that predict perceived affect directly from audio features, whether through psychoacoustic modelling or data-driven approaches such as deep learning. However, while psychoacoustic metrics have been widely used in industrial noise prediction, their application to UAS noise, particularly in complex or multi-source sound environments, remains under investigation.

Our previous work using convolutional neural networks (CNNs) to predict perceived annoyance ratings from mel-spectrograms indicated that deep learning may offer enhanced predictive capabilities for UAS noise perceived annoyance [2]. This study introduces a new convolutional recurrent neural network (CRNN) architecture and three new soundwalk datasets (on top of the previous CNN model and 5 datasets). The objective is to determine which model architectures best predict subjective UAS noise annoyance ratings.

2. BACKGROUND

2.1 Soundscapes and Contextual Perception

The concept of soundscapes, introduced by R. M. Schafer [3], describes how sound interacts with environments and shapes human perception. ISO-12913 [1] formalised this

[*] ***Corresponding author***: *M.Ellis6@edu.salford.ac.uk*
Copyright: *©2025 First author et al. This is an open-access article distributed under the terms of the Creative Commons Attribution 3.0 Unported License, which permits unrestricted use, distribution, and reproduction in any medium, provided the original author and source are credited.*

framework, defining soundscapes as "the acoustic environment as perceived or experienced and/or understood by a person or people, in context". A significant advancement in soundscape research is the Circumplex Model [4], which organises soundscapes along dimensions of pleasantness and eventfulness, varying combinations of which can yield soundscapes described as calm, exciting, monotonous, and chaotic. Despite these advances, the influence of *auditory salience* – the prominence of a sound object – remains understudied [5], particularly in relation to electric vehicles (EV's) and UAVs. As next-generation technologies introduce novel noise sources, often containing high-frequency tonal components, their interaction with existing soundscapes can vary dramatically depending on listener expectations, use case, emotional factors and context [6].

2.2 Psychoacoustic Modelling and Annoyance Frameworks

Psychoacoustic annoyance refers to a modelled estimate derived from quantifiable sound quality metrics such as loudness, sharpness, fluctuation strength, and tonality. In contrast, perceived annoyance (PA) is a subjective judgement made by listeners, typically gathered through listening tests, and reflects the complex interplay of acoustic, contextual, and individual factors not fully captured by existing models. Widmann's annoyance model, originally developed for traditional noise sources [7], has required significant adaptations for UAS noise profiles. Di *et al.* [8] enhanced the model by integrating tonality penalties that account for an additional 0.5 – 1.5 units of annoyance depending on tonal strength and frequency, and an adjusted sharpness rating that is approximately 20% higher than ISO and DIN standards [9]. This adaptation improved prediction accuracy with a reduction in Root Mean Squared Error (RMSE) from 1.27 to 0.89, though limitations remain when analysing complex environments with non-tonal noise characteristics. Ramos-Romero *et al.* (2024) [10] developed a comprehensive taxonomy for assessing UAS noise, examining relationships between design parameters, operational conditions, and psychoacoustic metrics. Their measurements revealed that multirotor UAS produced noise with higher sharpness and tonal components compared to fixed-wing designs. UAS noise typically ranges between 500 Hz – 5 kHz, with tonal peaks in the 1 kHz – 2 kHz range contributing significantly to perceived annoyance. Contextual variations were notable, with sharpness levels measuring 1.9 acums in urban settings versus 1.5 acums in rural areas. Lotinga *et al.* (2023) [11] investigated psychoacoustic metrics for potential integration into UAS noise regulations. Smaller UAVs (e.g. DJI Matrice 300) exhibited higher levels of sharpness and roughness, while larger aircraft produced greater tonal fluctuation strength. Tonal components between 200 Hz – 800 Hz were found to significantly increase annoyance, with sharpness levels exceeding 1.5 acum, correlating with a 25% increase in reported annoyance even when overall sound levels remained constant. Subsequent research from Lotinga [12] found that the adapted Torija et al. [13] PA model demonstrated superior performance to Widmann, More [14] and Di et al. The Sottek Hearing Model [15] offers an advanced framework that simulates human auditory perception by modeling the basilar membrane's response to sound. This physiological approach accounts for nonlinear auditory filtering and is particularly effective for analysing drone noise in varying flight conditions, due to its increased precision in quantifying slow amplitude modulation. While psychoacoustic annoyance models offer interpretable predictions based on engineered features, they are limited by their reliance on fixed-weight formulations and assumptions derived from traditional noise sources. These models often fail to account for contextual variation, spectral complexity, and perceptual non-linearity present in UAV noise. A deep learning approach could learn context-sensitive acoustic representations directly from data, across varying environments and sound source types, perhaps resulting in more accurate predictions.

2.3 Deep Learning Models for Noise Analysis and Prediction

Green and Torija [2] demonstrated that CNNs, an architecture ideal for processing gridlike data such as audio spectrograms, achieves 85% accuracy in predicting perceived annoyance from UAV noise using mel-spectrograms, substantially outperforming traditional regression models that reach only 70% accuracy. The optimal time-frequency resolution parameters were found to be a Fast Fourier-Transform (FFT) length of 256 and hop length of 64 samples, yielding a Mean Absolute Error (MAE) of 0.58 and an R^2 value of 0.72. This performance exceeded traditional PA metrics that predominantly emphasise loudness, suggesting CNNs can identify additional perceptually relevant features such as fluctuation strength and roughness. However, challenges remain in generalising these models across varied environments and UAS types due to differences in noise profiles based on altitude, speed, and environmental conditions. For sequential audio analysis, Recurrent Neural Networks (RNNs) have proven effective in capturing temporal patterns. Grekow's

research on music emotion recognition demonstrated RNNs achieving 83% accuracy in predicting emotional responses along arousal and valence dimensions [16], analogous to the affective eventfulness and pleasantness dimensions specified in ISO 12913. The model showed stronger performance in predicting arousal (correlation coefficient of 0.72) than valence (correlation coefficient of 0.55), using features including tempo, loudness, pitch, and timbre across a dataset of 5,000 music tracks. Addressing the complexity of polyphonic soundscapes, Çakır *et al.* [17] proposed a CRNN utilising convolutional layers to extract spectral features while recurrent layers model temporal dependencies. This resulted in a 10 – 15% improvement in F1 scores compared to standard CNN and RNN models when applied to overlapping urban sounds. This architecture is particularly suitable for UAV noise detection within complex soundscapes, though computational demands may challenge realtime deployment. Casabianca and Zhang [18] introduced a late fusion ensemble approach for acoustic UAV detection, combining multiple deep neural networks through both hard and weighted soft voting strategies. Their ensemble, comprising CNNs trained on mel-spectrograms, achieved up to 94.7% accuracy on unseen augmented datasets, significantly outperforming individual models. The study also highlighted the role of data augmentation in improving scalability across drone types and recording conditions.

3. METHODS

3.1 Datasets

This study retains the five datasets introduced in Green and Torija [2], comprising a total of 587 audio clips with associated annoyance ratings. These were recorded across various controlled listening studies involving both conventional and UAV aircraft, with annotations collected using continuous ratings (KTH dataset) rescaled to match. To extend the data and explore the applicability of existing models, in this work, three new datasets are introduced, collected in: (i) Crescent Meadow, Salford, UK (23 clips) (Green and Torija, 2024) [19]; (ii) Athens, Greece (56 clips) (Green *et al.*, 2025) [20]; (iii) the Isles of Scilly, UK (27 clips) (Green and Torija, 2025) [21], amounting to an increased total of 693 clips. These datasets are distinct from those included in the previous study in that they were collected in field-based soundwalk studies, rather than in a lab-based setting. Participants were exposed to take-off, flyover, and landing UAS maneuvers, conducted at a range of altitudes, and responses were gathered along soundscape dimensions specified in ISO 12913-2, as well as annoyance based on ISO 15666 [22]. The latter were used as target ratings in the present study. Baseline annoyance ratings were gathered from soundwalk locations prior to the commencement of drone operations, and the average annoyance of all respondents at each stop/location were assigned to audio clip names from all eight datasets. Audio recordings were made at each stop using the Zoom H3VR portable Ambisonic recorder[1], with the omnidirectional channel used to derive monaural stimuli for the present study. These soundwalks were conducted as part of a series with the specific aim of investigating the perception of UAS noise introduced within a variety of existing environmental contexts, including a busy city street, quieter park and meadow, and a remote rural island. The extracted clips include both ambience and UAS noise. In line with the original methodology, all audio clips were resampled and trimmed to the loudest six-second segment based on total spectrogram amplitude. Mel-spectrograms were then generated for each clip up to a frequency of 8 kHz, represented by 96 mel-spaced bins with a total dynamic range of 60 dB.

Table 1. Summary of included datasets

Dataset	Participants	Clips	Response Type
MJL	42	80	Single
NG23	41	71	Single
NG22	30	51	Single
RN	50	120	Single
AJ	25	9	Continuous
Meadow	16	24	Single
Scilly	22	27	Single
Athens	110	56	Single

[1] https://www.zoom-europe.com/en/handy-recorders/zoom-h3-vr

3.2 Psychoacoustic Annoyance Models

Sound quality metrics required for Widmann's psychoacoustic annoyance model were derived from the raw audio files using the SQAT library in MATLAB [19]. Pearsons *R* was used to quantify correlations between the Mean Perceived Annoyance's (MPA) and the sound quality metrics. Scatter plots showing correlations between perceived and psychoacoustic annoyance, as well as those with individual SQMs, are shown in Figure 1.

3.3 Deep Learning Models

Two deep neural network architectures were developed to predict perceived annoyance directly from audio spectrograms: a CNN and a CRNN. Similarly to the previous study [2], input spectrograms were generated using the *torchaudio* library [20], with particular attention to time-frequency resolution parameters which were previously found to significantly impact model performance. The CNN architecture consists of two convolutional layers with 3×3 kernels outputting 96 and 32 channels respectively, each followed by 2×8 max pooling and batch normalisation. These feed into three fully-connected layers of 1000, 100, and 1 output units with ReLU activation functions and dropout regularisation (p=0.2) between all layers except the final output. The CRNN extends this architecture by incorporating recurrent processing after the convolutional feature extraction. It utilises the same initial convolutional layers but then reshapes the output for sequential processing through two bidirectional LSTM layers with 128 and 64 hidden units respectively. An attention mechanism focuses on the most relevant temporal features before passing through fully-connected layers of 512 and 128 units, then finally one single unit. The CRNN employs higher dropout (p=0.3) and gradient clipping at a maximum norm of 5.0 to stabilise training. Through systematic grid search of FFT lengths {512, 256, 128, 64} and hop lengths {256, 128, 64, 32}.

3.4 Training & Testing

The models were implemented using PyTorch [21] and trained with MSE loss and Adam optimiser (learning rate 1×10^{-3} for CNN, 5×10^{-4} for CRNN). Early stopping with 40 epochs patience prevented overfitting across a maximum of 200 epochs with batch size 16. The dataset was randomly split into training (75%, n=520), validation (13%, n=91), and test (12%, n=83) sets, with shuffling to ensure even distribution across data sources. Performance was evaluated using MAE and coefficient of determination (R^2).

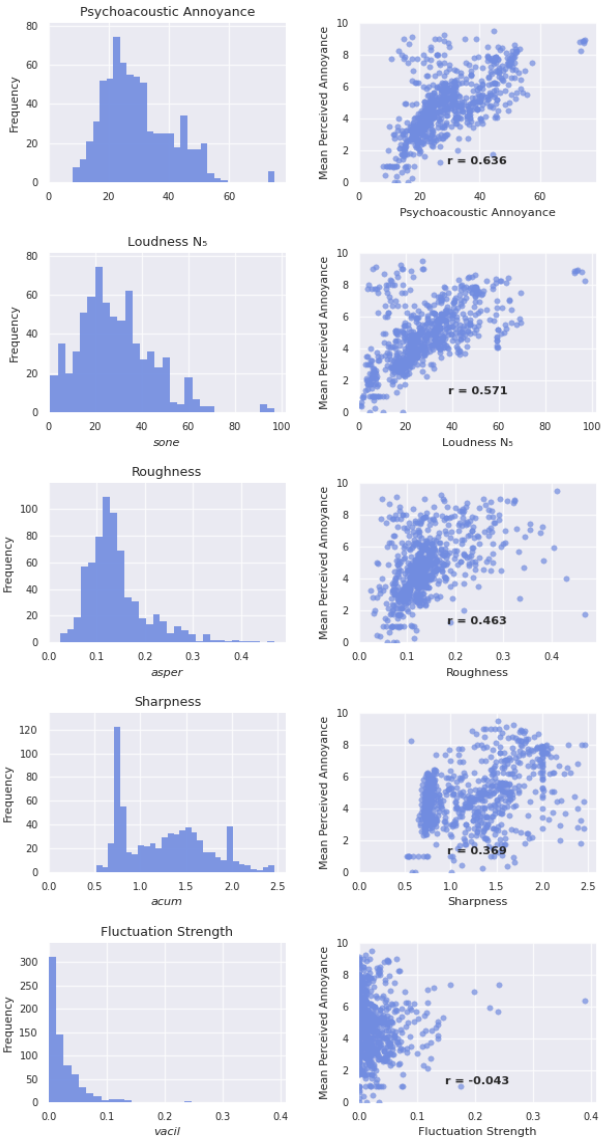


Figure 1. Histograms of psychoacoustic features and correlations of these to perceived annoyance.

Regularisation techniques included weight decay (1×10^{-5}) and gradient clipping at a maximum norm of 5.0 to prevent overfitting and stabilise training. Computation time per epoch ranged from 70 to 120 seconds, with training conducted on a Mac Mini M2 to utilise Metal Performance Shaders (MPS) backend for GPU training acceleration [22]. For comparison, two Support Vector Regression (SVR) baseline models were implemented: one with sigmoid kernel fitted directly to Widmann psychoacoustic annoyance values, and another with polynomial kernel (degree 3)

trained on the raw sound quality metrics.

4. RESULTS AND DISCUSSION

The SVR model trained on PA values using a sigmoid kernel achieved an MAE of 0.87 and an R^2 of 0.49, while the polynomial SVR trained on raw psychoacoustic features yielded a marginally better performance, with an MAE of 0.77 and R^2 of 0.56. As seen in the previous study, this suggests that a model trained directly on the constituent features of PA can outperform the composite metric itself. The sigmoid curve fit, shown in Figure 2, follows a similar logistic shape to that reported in earlier work, with perceived annoyance values beginning to plateau at higher PA levels. A notable concentration of moderate-to-high annoyance ratings (7-10 range) was identified, predominantly originating from the Athens dataset. This clustering suggests potential contextual influences beyond the immediate acoustic stimuli. Qualitative observations during the soundwalk revealed localised environmental factors that may have significantly influenced participant responses. Specifically, the Athens dataset exhibited a marked tendency toward elevated annoyance ratings, potentially attributable to pre-existing environmental disturbances independent of the specific acoustic stimulus. Despite these potential outliers, the SVR model maintained robust predictive performance, demonstrating remarkable resilience to dataset heterogeneity.

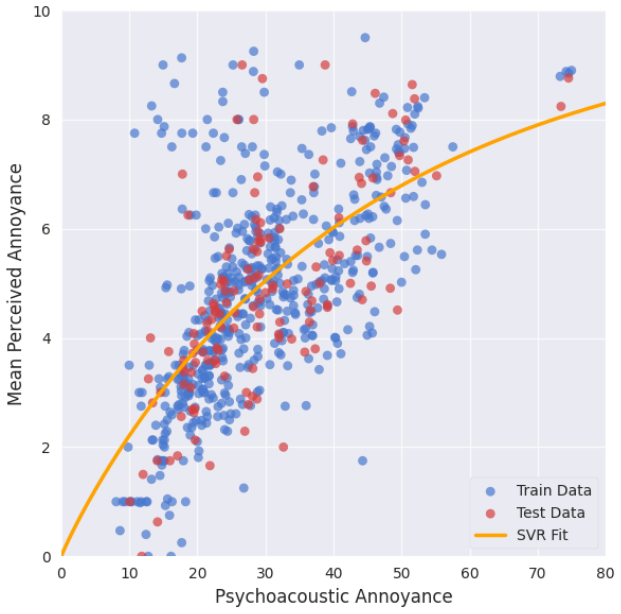


Figure 2. Fit of perceived annoyance to Widmann psychacoustic annoyance values by SVR model.

Table 2. Results for each network architecture and frame/hop length combination.

Frame / Hop	CNN		CRNN	
	MAE	R^2	MAE	R^2
512 / 256	0.77	0.55	0.65	0.66
512 / 128	0.84	0.29	0.62	0.7
512 / 64	**0.56**	**0.75**	0.55	0.76
512 / 32	0.85	0.54	0.7	0.78
256 / 128	0.76	0.62	0.56	0.81
256 / 64	0.64	0.71	**0.49**	**0.86**
256 / 32	0.87	0.39	0.83	0.46
128 / 64	0.72	0.56	0.58	0.79
128 / 32	0.81	0.46	0.71	0.63
64 / 32	0.77	0.5	0.94	0.44

Table 2 shows that CNN models exhibited varied performance across different time-frequency resolutions. The optimal configuration was identified as an FFT length of 512 samples and hop length of 64 samples, achieving MAE 0.56 / R^2 0.75. This configuration demonstrated a robust balance between spectral and temporal feature extraction. Configurations with shorter hop lengths (32 samples) consistently underperformed, with MAE values ranging from 0.85 to 0.87 and lower R^2 values. The 256 / 64 configuration also showed strong performance, with MAE 0.64 / R^2 0.71.

The CRNN models demonstrated superior performance compared to the CNN models. The 256 / 64 configuration in particular emerged as the standout, with an impressive MAE 0.49 / R^2 0.86, indicating a significant improvement in predictive accuracy over the CNN. The recurrent architecture showed more consistent performance across different FFT and hop length configurations. The 512 / 64 configuration also performed well, with MAE 0.55 / R^2 0.76. Configurations with 32-sample hop lengths showed decreased performance, with the 512 / 32 configuration achieving an R^2 of 0.78 but other configurations showing less consistent results.

The lower MAE and higher R^2 values of the CRNN results suggest that the bidirectional LSTM layers and attention mechanism provide additional context for predicting perceived annoyance. All models achieved their best ratings with hop 64 and FFT 256 or 512, aligning with the previous hypothesis about capturing perceptually relevant acoustic fluctuations. This configuration provides a 4ms time resolution, potentially capturing psychoacoustic features analogous to roughness and temporal modulation.

5. CONCLUSIONS AND FUTURE WORK

Several promising avenues for future research emerge from this study. First, investigating transfer learning techniques could potentially enhance model generalisability. The incorporation of additional datasets from various acoustic environments might improve model robustness and predictive capabilities. Expanding the research to other sound sources beyond UAS could establish a more comprehensive framework for sound affect prediction. As tonal, high-frequency and synthetic novel noises from e-mobility proliferate into urban environments, it would be invaluable to expand on the current models to classify sounds in noise clips and apply weightings based on source type, detectability and intermittency to better measure more eventful soundscapes. Finally, exploring objective ratings of annoyance from psychoacoustic models from Di, More, Torija *et al*. and NASA, along with their relative metrics, could help better calculate both subjective target annoyances and objective annoyance-model based ratings. This could, in theory, lead to a framework for open-source sound libraries to become extremely useful and adaptable to noise annoyance prediction, classification, training and learning.

6. ACKNOWLEDGMENTS

The authors would like to sincerely thank Abertay University, Dundee, for the support and supervision of work carried out during Max W. Ellis' postgraduate study, where the research framework, spectrograms, and data processing of this study were developed.

7. REFERENCES

[1] ISO, 2014. *ISO 12913-1:2014. Acoustics – Soundscape – Part 1: Definition and conceptual framework.* Geneva: ISO.ISO, 2014. ISO 12913-1:2014. Acoustics – Soundscape – Part 1: Definition and conceptual framework. Geneva: ISO.

[2] Green, M. C. and Torija, A. J., 2024. *Soundwalking in Salford: A Soundscape Approach to Drone Noise Assessment.* Quiet Drones, Manchester.

[3] Schafer, R. M., 1993. *The Soundscape: Our Sonic Environment and the Tuning of the World.* Rochester, VT: Destiny Books.

[4] Axelsson, Ö., Nilsson, M.E. & Berglund, B. (2010) 'A principal components model of soundscape perception', The Journal of the Acoustical Society of America, 128(5), 2836–2846.

[5] Podwinska, Z., Fazenda, B.M. & Davies, W.J. (2019). Testing spatial aspects of auditory salience. Proc. of the 25th International Conf. on Auditory Display (ICAD).

[6] Fang, X., Aletta, F., Mitchell, A., Oberman, T., and Kang, J., 2024. *Determining factors for the appropriateness of soundscapes: A cross-sectional large-sample study in London (UK). J. Acoust. Soc. Am.*, 156(5), pp.3588–3607.

[7] Zwicker, E. and Fastl, H., 2013. Psychoacoustics: Facts and Models. 3rd ed. Berlin: Springer.

[8] Di, Z., Shi, L., Chen, Y., Li, X. and Zhang, M., 2022. Annoyance prediction of substation noise based on the modified psychoacoustic annoyance model. Appl. Acoust., 188, p.108594.

[9] DIN, 2010. *DIN 45631/A1: Calculation of loudness level and loudness from the sound spectrum – Zwicker method – Amendment 1: Calculation procedure for loudness above 10 kHz.* Berlin: Beuth Verlag.

[10] Ramos-Romero, M. F., Green, N., and Torija, A. J., 2024. *How do flight operations and ambient acoustic environments influence the noticeability and noise annoyance associated with UAS?* Proc. INTER-NOISE 2024.

[11] Lotinga, M. J. B., Torija, A. J., and Green, M. C., 2023. *Dose–response function of community annoyance to urban air mobility (UAM) noise. Appl. Acoust.*, 210, p.109369.

[12] Lotinga, M. J. B., 2024. *Psychoacoustic modelling of UAS noise in diverse acoustic environments.* Proc. INTER-NOISE 2024.

[13] Torija Martínez, A. J., Self, R. H., and Li, Z., 2020. *Effects of a hovering unmanned aerial vehicle on urban soundscapes perception. Transp. Res. Part D: Transp. Environ.*, 78.

[14] More, S., 2010. *Aircraft noise characteristics and metrics.* PhD Thesis. Purdue University.

[15] Sottek, R. and Genuit, K., 2005. *Models of signal processing in human hearing. Int. J. Electron. Commun. (AEÜ)*, 59(3), pp.157–165.

[16] Grekow, J., 2021. *Music emotion recognition using recurrent neural networks with attention. Neural Comput. Appl.*, 33, pp.13227–13236.

[17] Çakır, E., Parascandolo, G., Heittola, T., Huttunen, H. and Virtanen, T., 2017. *Convolutional recurrent neural networks for polyphonic sound event detection. IEEE/ACM Trans. Audio Speech Lang. Process.*, 25(6), pp.1291–1303.

[18] Casabianca, T. and Zhang, Y., 2021. *Late Fusion CNN Ensemble for UAV Sound Detection in Complex Environments. Drones*, 5(3), p.54.

[19] Green, M. C. and Torija, A. J. (2024). Soundwalking in Salford: A Soundscape Approach to Drone Noise Assessment. Quiet Drones, Manchester.

[20] Green, M.C., Lotinga, M. J., and Torija, A. J. (2025). Shaping future soundscapes: Affective impact of unmanned aircraft systems noise in urban environments. Submitted for publication, 2025.

[21] Green, M.C., & Torija, A.J. (2025). Soundwalking in Scilly: UAS Noise Impact on Remote Soundscapes. DAS / DAGA, Copenhagen, Denmark, March 2025.

[22] ISO, 2021. *ISO/TS 15666:2021. Acoustics – Assessment of noise annoyance by means of social and socio-acoustic surveys.* Geneva: ISO.

[23] Greco, G. F., Merino-Martínez, R., Osses, A., and Langer, S. C., 2023. *SQAT: A MATLAB-based toolbox for quantitative sound quality analysis.* In: *Proc. INTER-NOISE 2023.*

[24] Yang, Y., et al., 2021. *Torchaudio: Building audio and speech ML tools for PyTorch.* In: *Proc. IEEE Int. Conf. Acoust., Speech Signal Process. (ICASSP)*, pp.675–679.

[25] Paszke, A., Gross, S., Massa, F., et al., 2019. *PyTorch: An imperative style, high-performance deep learning library. Adv. Neural Inf. Process. Syst.*, 32, pp.8024–8035.

DOI: 10.61782/fa.2025.0659



FORUM ACUSTICUM
EURONOISE 2025

OPEN-SOURCE SYSTEM FOR MULTILINGUAL TRANSLATION AND CLONED SPEECH SYNTHESIS

Mateo Cámara[1,2*] **Juan Gutiérrez**[1] **María Pilar Daza**[1] **José Luis Blanco**[1,2]

[1]ETSI de Telecomunicación, Universidad Politécnica de Madrid, Spain
[2]Information Processing and Telecommunications Center, Universidad Politécnica de Madrid, Spain

ABSTRACT

We present an open-source system designed for multilingual translation and speech regeneration, addressing challenges in communication and accessibility across diverse linguistic contexts. The system integrates Whisper for speech recognition with Voice Activity Detection (VAD) to identify speaking intervals, followed by a pipeline of Large Language Models (LLMs). For multilingual applications, the first LLM segments speech into coherent, complete sentences, which a second LLM then translates. For speech regeneration, the system uses a text-to-speech (TTS) module with voice cloning capabilities to replicate the original speaker's voice, maintaining naturalness and speaker identity.

The system's open-source components can operate locally or via APIs, offering cost-effective deployment across various use cases. These include real-time multilingual translation in Zoom sessions, speech regeneration for public broadcasts, and Bluetooth-enabled multilingual playback through personal devices. By preserving the speaker's voice, the system ensures a seamless and immersive experience, whether translating or regenerating speech.

This open-source project is shared with the community to foster innovation and accessibility. We provide a detailed system performance analysis, including latency and word accuracy, demonstrating its potential to enable inclusive, adaptable communication solutions in real-world multilingual scenarios.

*__Corresponding author__: mateo.camara@upm.es.

__Copyright__: ©2025 Mateo Cámara et al. This is an open-access article distributed under the terms of the Creative Commons Attribution 3.0 Unported License, which permits unrestricted use, distribution, and reproduction in any medium, provided the original author and source are credited.

Keywords: *simultaneous spoken language translation, voice cloning, machine translation, speech-to-speech*

1. INTRODUCTION

In an era where global collaboration and mobility are redefining human interaction, the ability to communicate across languages in real time has transitioned from a futuristic vision to a technological imperative. Traditional translation pipelines, reliant on sequential human intervention or disjointed automated tools, are ill-suited for dynamic environments—from international conferences to emergency response scenarios—where managing latency and coping with naturalness is critical [26]. Artificial intelligence (AI)-powered speech translation systems promise to address this gap. Yet, their practical use remains constrained by competing priorities: the need for accuracy, computational efficiency, and the preservation of speaker identity [12, 5]. While recent breakthroughs in neural architectures have accelerated progress, the field remains divided between two competing paradigms—end-to-end and cascade systems—each with distinct trade-offs in performance, adaptability, and scalability [1].

End-to-end speech translation systems, which directly map source-language speech to target-language text or audio, have gained prominence for their potential to minimize error propagation through joint optimization of transcription and translation tasks. Pioneering works [7, 13, 15, 16] demonstrated the feasibility of unified frameworks implemented on neural networks, while recent breakthroughs like Meta's SeamlessM4T [5] have elevated the paradigm by supporting multilingual translation across 100+ languages. SeamlessM4T exemplifies the allure of end-to-end architectures: it eliminates modular bottle-

necks by training on massive multimodal corpora, achieving state-of-the-art BLEU scores [19] while preserving prosody. However, as Bahar et al. [3] note, such systems remain constrained in streaming applications due to their reliance on full input sequences. The same ability to cope with extended semantic contexts, from which they excel in performance, makes them prone to latency spikes in real-time scenarios. Moreover, end-to-end models struggle with interpretability and robustness, mainly when dealing with noisy input or domain shifts. Anyhow, SeamlessM4T is not yet publicly available, and its real-world applicability beyond controlled demonstrations remains to be thoroughly evaluated.

By contrast, cascade systems modularize translation into discrete stages—ASR, text refinement, Machine Translation (MT), and TTS—leveraging specialized models optimized for each subtask. This decoupled architecture, as explored by Iranzo-Sánchez et al. [12] and Arivazhagan et al. [2], benefits from abundant monolingual ASR and MT datasets, enabling robust performance in high-resource settings. However, cascade pipelines inherit vulnerabilities from the accumulation of errors between stages and segmentation challenges in continuous speech streams [9, 17]. Despite these challenges, recent evaluations confirm that cascade systems retain a performance edge over end-to-end models in standardized benchmarks, particularly for high-resource language pairs [1]. Like those by Bahar et al. [4], hybrid solutions integrate streaming ASR with simultaneous MT models to mitigate latency. Their reliance on proprietary components limits reproducibility, a critical barrier for academic and low-budget implementations.

This work presents a fully open-source, modular cascade system designed for conferences to harmonize the strengths of pre-trained models while mitigating their weaknesses and delivering a complete end-to-end experience. Figure 1 shows the schematic of our solution. Implements a four-stage pipeline. Unlike end-to-end frameworks, our system emphasizes transparency and adaptability by integrating best-performant, independently validated, state-of-the-art open-source modules. We selected the following for our implementation: 1) Whisper [20] for low-latency ASR; 2) a Llama 3 model [10] serves as a contextual buffer, correcting or substituting misrecognized phonemes and deciding whether the sentence is ready for translation, by leveraging contextual and syntactic cues; 3) a second Llama 3 LLM conditioned to perform translation; and 4) MeloTTS [27], offline fine-tuned for voice cloning to mimic the speaker.

We have developed and publicly released this solution for general use, [1] including detailed descriptions of the system and demo's software and hardware implementations. Specifically, we created a low-power analog radio transmitter setup to take advantage of the limits of commercial FM band frequencies, allowing easy reception through standard consumer radio devices. The design simplifies accessibility, accommodating users less comfortable with advanced technology. Additionally, we provide clear instructions for integrating the system with video conferencing sessions and Bluetooth-enabled devices, enhancing its versatility and user-friendliness.

We have validated this solution objectively by measuring latency (between both ends), Word Error Rate (WER) for ASR, and BLEU [19] and COMET [21] scores for translation quality. Regarding the speech synthesis module, we conducted a subjective evaluation of the voice cloning component using a speaker and a small group of evaluators. While this subjective evaluation is informal and not exhaustive in terms of languages or vocabulary, we deem it sufficient for our demonstration.

The remainder of this document is as follows. Section 2 describes the software development aspects, including system architecture and implementation details. Section 3 covers the hardware development, particularly the analog radio setup designed for ease of use. Section 4 discusses the tests conducted and the validation metrics obtained to ensure the system's reliability and effectiveness. Finally, Section 5 concludes the document.

2. SOFTWARE IMPLEMENTATION

2.1 Automatic Speech Recognition (ASR)

The ASR module forms the foundational layer of our cascade system, delivering timely transcriptions from the input speech. For this module, we use Whisper [20], an open-source, multilingual model pre-trained on five million hours of diverse labeled audio data. We selected it for its proven robustness to accents, background noise, and streaming compatibility. Unlike proprietary alternatives (e.g., Google Speech-to-Text, Amazon Transcribe), Whisper's architecture and weights are publicly accessible. Specifically, we utilize whisper.large-v3.turbo [2] (1,550M parameters), which achieves a WER of 9.5% on average for the 15 most common languages, just 1% higher than

[1] https://github.com/MateoCamara/speech-translator-with-voice-cloning

[2] openai/whisper-large-v3-turbo

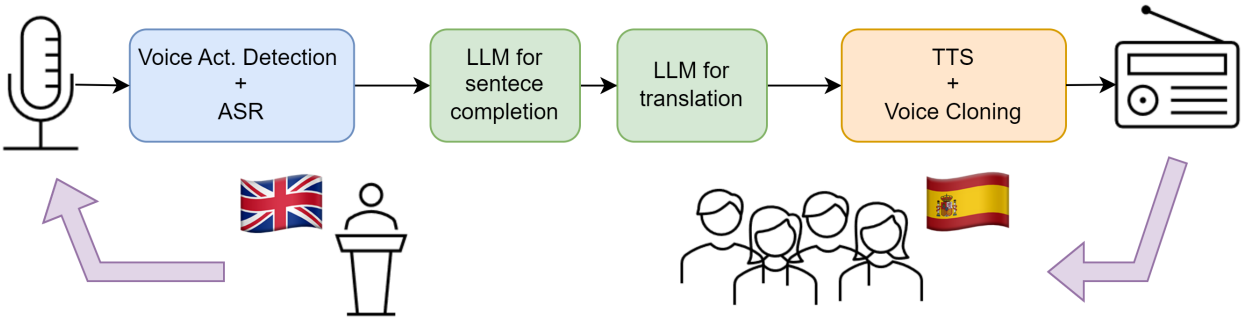


Figure 1: Schema of the solution for multilingual speech recognition (left), translation, and synthesis (right).

the non-distilled version of the model, being 5.4 faster on inference.

A critical limitation of conventional ASR systems in real-time applications is in managing non-speech intervals (e.g., silence, background noise), wasting computational resources, and introducing additional latency with spurious outputs. To minimize computational overhead and false activations, we integrated Silero VAD [24], a lightweight, open-source voice activity detector optimized for real-time applications. Silero VAD processes audio 30 times faster than real-time on CPU, achieving an accuracy score of 91% on their validation dataset. We use it to activate Whisper only when speech probability exceeds a threshold of 0.5, reducing idle inference cycles.

2.2 LLMs for Context Refinement and Translation

To address the inherent challenges of real-time speech processing—such as disfluencies, fragmented phrases, and contextual ambiguity—we deploy two specialized LLMs in cascade. This modular design ensures robustness while balancing latency and semantic coherence.

2.2.1 Context-Aware Phrase Refinement

The first LLM acts as a linguistic validator tasked with resolving ambiguities, correcting ASR errors, and determining phrase completeness. Built on LLama-3 architecture [25], the module leverages a five-sentence context stored in a buffer for semantic continuity. We found this effectively complements Whisper's 30-second speech context. Specifically, we use the LLaMA 3.3-70B-Instruct [3] model, which offers an optimal balance between quality and inference speed, achieving 51.14 tokens per second.

[3] `meta-llama/Llama-3.3-70B-Instruct`

As a new chunk of transcription arrives from Whisper, this LLM is prepared to account for:

- Completeness: Whether the chunk forms a grammatically and semantically self-contained unit (e.g., ending with punctuation or a natural pause).
- Anomaly Detection: Identifies and removes extraneous elements (e.g., filler words, misrecognized phonemes) using syntactic and contextual cues.

The module retains incomplete phrases in a rolling buffer with a capacity of five chunks. If the buffer reaches its maximum capacity, the chunks are forcibly flushed to the translation module, prioritizing low latency over prosodic perfection.

2.2.2 Translation

The second LLM handles translation, converting validated phrases into the target language. Built on LLaMA 3.3-70B, it offers native high multilingual performance, supporting eight languages, including English, Spanish, French, and German. Each complete phrase from the previous LLM is translated, preserving semantic integrity.

Alternative implementations may merge these two LLM instances. For the sake of simplicity and at the cost of increased latency, we did not address such considerations, leaving them for future work.

2.3 Text-to-Speech with voice cloning

To bridge the gap between translated text and natural-sounding speech, our system integrates a hybrid TTS pipeline that combines high-quality synthesis and voice cloning for a specific speaker. This dual-stage approach ensures linguistic clarity and preserves the original speaker's vocal identity.

2.3.1 *MeloTTS for Speech Synthesis*

For the text-to-speech process, we employ MeloTTS [27], an open-source, non-autoregressive TTS framework optimized for low-latency streaming. It supports real-time inference (i.e., speech synthesis) on both CPU and GPU, delivering 44.1 kHz audio with high fidelity. Despite its quality, the model remains efficient, operating smoothly even on mid-range hardware. MeloTTS leverages non-autoregressive architectures, allowing for single-step audio generation. It supports multiple languages and accents, including English, Spanish, French, Chinese, Japanese, and Korean. Additionally, it enables speech rate adjustment, offering flexibility for various applications.

2.3.2 *Voice Cloning Via Full Retraining*

Unlike methods that adapt pre-trained models through style transfer (e.g., "voice color" tuning with 30 seconds of audio), we adopt a full retraining strategy to clone speaker identities with high fidelity. This approach addresses the limitations of zero-shot cloning systems, which often struggle to preserve personal vocal traits (e.g., breathiness, pitch contours) in low-resource scenarios. The implementation workflow is as follows:

- Base Model Selection: We initialize MeloTTS with weights pre-trained on a target-language corpus (in the case of Spanish, 25 hours of clean and consistent audio), prioritizing phonetic coverage of the target deployment language.
- Speaker-Specific Retraining: We used 30 minutes of clean audio from the target speaker (industry-standard duration) to fine-tune the model parameters. For the MeloTTS, these included the audio generator, the duration predictor, and the audio discriminator models. Based on our tests, the latter could be frozen, accelerating the process.

We trained our base model for a male Spanish speaker on the LibriVox datasets [14]. The retraining of the speaker-specific model was covered on a NVIDIA A100@40GB GPU for 56 hours. The process stopped after 235k epochs as the losses stabilized.

3. HARDWARE IMPLEMENTATION

To ensure inclusivity across diverse user demographics—particularly those with limited technological literacy, such as elderly populations—our system prioritizes analog FM radio transmission while retaining compatibility with modern digital interfaces. The FM-based design guarantees universal accessibility through low-cost, widely available receivers (e.g., portable transistor radios). Bluetooth multicast and virtual audio routing remain as supplementary options for tech-literate users.



Figure 2: Radio Transmitter and laptop.

3.1 Analog FM Radio for Universal Deployment

The core hardware deployment lies in a compact, low-power FM transmitter designed to operate at the edges of commercial frequency bands (87.5-108 MHz). It allows reception on conventional devices while avoiding interference with licensed broadcasts. The system comprises three key components:

- Transmitter Module: We included a DSP PLL FM transmitter module operating at carrier frequency 105.1 MHz with a default output power of 0.5 W.
- Amplification Stage: A Class-A amplifier (gain ×100, 12 V input) boosts the signal to 2.0 W, enabling coverage of large indoor spaces (e.g., auditoriums).
- Antenna System: A vertically polarized mini patch panel antenna with +3 dB gain, 50 Ω impedance ensures robust coverage while minimizing signal leakage beyond 100 m.

It supports 12 V DC input from batteries or wall adapters. Thermal fuses and current limiters prevent overheating. Figure 2 shows a picture of the hardware display used in our tests, housed in a PBS enclosure. The system offers versatile audio input via a 3.5 mm jack, micro-USB, or built-in microphone. It features an LCD screen that displays transmission information with volume, play/pause, and frequency selector buttons.

3.2 Complementary Digital Interfaces

For users with smartphones or computers, the system optionally routes translated audio to Bluetooth headphones (via multicast pairing) or virtual microphone outputs for video conferencing tools. However, these interfaces are secondary to the FM radio, which remains the primary channel for its simplicity, cost-effectiveness, and compatibility with legacy devices. The associated GitHub page provides an explanation of how to set these up.

4. EXPERIMENTS AND EVALUATION

We evaluated our solution using the Europarl dataset [11], which contains recordings from the European Parliament. Speeches are delivered and translated into multiple languages. We selected the test subset for validation and assessed the system's performance in translating from English to Spanish on up to three hours of speech and the corresponding transcripted sentences.

The analysis included hereafter covers several key aspects: system latency, errors in speech recognition and translation, voice cloning quality (for a single user), and the performance of the hardware radio setup.

4.1 Latency Tests

This experiment quantifies the latency from the moment a speaker begins a sentence until playback starts. Figure 3 presents an example of a 10-minute speech, illustrating latency variations over time. This fragment is the first eight audio files of the Europarl test set, consisting of political speeches delivered by different speakers. These speeches offer a variety of vocal characteristics, accents, and speaking styles. The total latency averages around 2.5 seconds, with peaks reaching 5 seconds, highlighting the system's behavior with diverse input signals. Most components remain within a stable range. The literature considers 2.5 seconds a valid threshold for real-time translation [1].

Whisper and MeloTTS ran in parallel on an RTX 5090 GPU, while LLM tasks relied on cloud-hosted A100 units accessed via API. The primary latency contributors are the LLM-related tasks, which are challenging to control due to shared cloud resources. Dedicated inference services could help reduce variability. The peak latencies are infrequent and not representative of typical system performance. Latency would likely increase significantly on less powerful hardware. Therefore, deploying cloud-based resources similar to those used in our experiments is recommended.

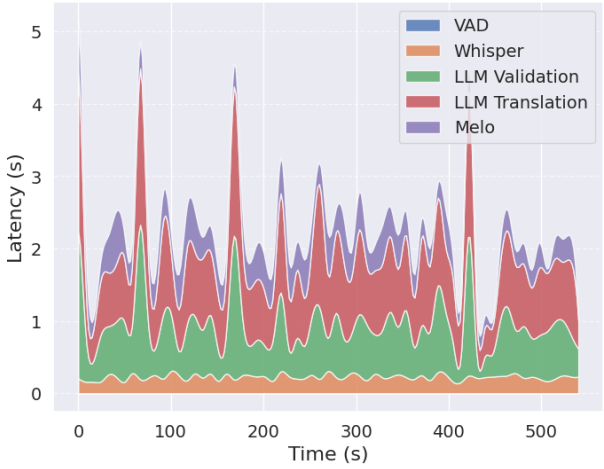


Figure 3: Results on the latency test with 10 minutes speech including all pipeline modules.

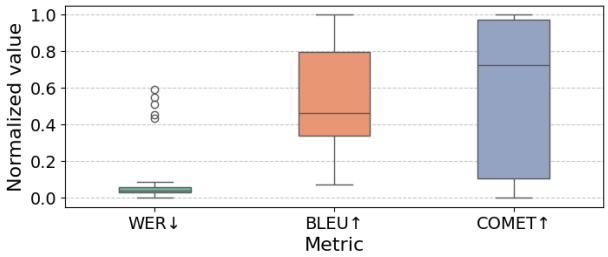


Figure 4: WER for Whisper evaluation and BLEU and COMET for LLM-translation evaluation.

4.2 Intelligibility tests

Figure 4 presents the intelligibility results, with WER evaluated for Whisper, and BLEU and COMET scores for the translation LLM. The reported WER agrees with the values found in the literature. The reference WER for this Whisper model is approximately 9.5%, while our dataset evaluation yielded a median value of 4.5%. This slightly improved performance may be attributed to the dataset-specific characteristics, as no modifications were made to the model.

Regarding translation quality, the BLEU score shows a median of around 0.5, indicating that the translations are not highly reliable and contain significant errors. Meanwhile, the higher COMET score suggests that translations are generally acceptable despite existing errors, with some sentences being mistranslated. The translation direction is

from English to Spanish. While Llama 3.3 does not explicitly report BLEU or COMET scores for Spanish-to-English, it scored 91.1 in the Multilingual MGSM (zero-shot) test [23], demonstrating strong overall performance.

The discrepancy between our results and those reported in the literature may be primarily due to how our pipeline processes the data. Our evaluation does not merely compare two languages but assesses real-world speech records. To minimize latency, some segments may be truncated, and pauses made by the speaker may be misinterpreted as sentence boundaries. Although an additional validation LLM is used to mitigate these issues, the results remain below the state of the art. This bottleneck in translation quality has been identified as a critical area for improvement, and future iterations of the system should focus on enhancing this aspect.

However, research has indicated that automatic translation metrics may be unreliable for evaluating translation quality [28], as human evaluation remains a superior approach. Our observations confirm this: in many cases, translations are perfectly understandable, yet the metrics assign poor scores due to word order changes or structural variations introduced by the LLM. We report the standard metrics used in the recent literature without highlighting their absolute values, as we concur that their relevance is limited.

4.3 Voice cloning subjective evaluation

We conducted subjective evaluations to assess the quality of the generated speech based on user perception, following [22]. Participants were required to use wired headphones, have no hearing impairment, and complete the test in a quiet environment. We also collected information about their native language and proficiency in Spanish: speaking, writing, and listening.

The evaluation followed a standardized MOS rating system implemented using the GoListen platform [6]. The online test consisted of 28 questions across two parts: (1) synthesized audio without reference to the original human recordings, [8], and (2) comparisons between synthesized and original recordings, [18]. Each question was rated on a scale of 1 (poor) to 5 (excellent). The audio samples included phonetically balanced sentences.

The analysis was structured into two parts. First, we evaluated items across all subjects per sentence. Second, we analyzed the dispersion for each sentence on all evaluated items. Thirty evaluators completed the test. Sentences 1 and 3 received the highest ratings overall, as shown in Fig.5a. Sentence 3 particularly excelled in listening effort, comprehension, and speaking rate, with most ratings at 5 (Fig.5b). However, pleasantness scored slightly lower. Sentence 4 showed good overall quality but required more listening effort and had articulation issues. Sentence 2 performed well in comprehension but struggled with pronunciation and speaking rate.

In summary, evaluators rated the synthetic audio highly, especially compared to original human recordings. These promising results highlight the potential of our solution while identifying areas for improvement, such as voice pleasantness and articulation. For further details, refer to the test [4] and to the published repository. [5]

4.4 Hardware Tests

To validate the performance of our FM transmitter, we assessed operational reliability and signal confinement within the designated area. We collected our measurements in the ETSIT-UPM auditorium, where irregular wall absorption, physical obstructions, and ambient noise affected propagation. The room can accommodate up to

[4] https://golisten.ucd.ie/task/mushra-test/67d296bf75e8b306f88e3908

[5] https://mateocamara.github.io/s2s

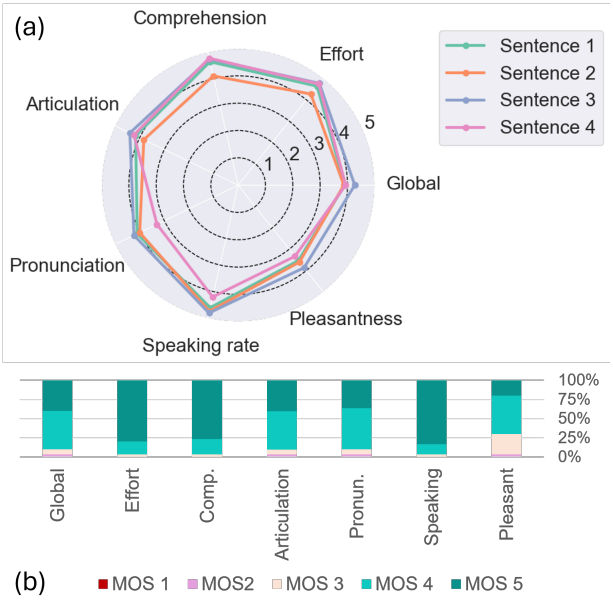


Figure 5: Results of the subjective tests: (a) chart on all sentences, (b) stacked ratings on Sentence 3.

Table 1: Measured performance parameters of the FM transmitter at various auditory locations

Location	Peak Power (dBm)	Signal Power (dBm)	SNR (dB)
Antenna	-53.8	-56.0	59.1
First Row Middle (Best Case)	-75.4	-77.6	47.3
Interior (Avg ± S.D.)*	-82.0±7.3	-83.1±7.0	38.2±5.7
Far Corner (Worst Case)	-93.2	-95.1	33.7
Adjacent Room	-106.0	-108.3	20.5

* Average room values were computed by excluding the antenna and adjacent room locations.

195 people. The floor plan is 12.50 m × 14.60 m. The transmitter antenna was centered in the stage 2 m high, oriented toward the audience to optimize coverage.

In this controlled environment, we used a calibrated handheld spectrum analyzer N9342C with a test antenna from the ETS Lindgren Model 7405 kit. We used a set of reference signals, a constant 440Hz (A note), white noise, and a 20-second-long speech record. Measurements were collected in strategic locations within the auditorium to capture spatial variations in signal performance and assess leakage in adjacent rooms.

Average measures on signal-to-noise ratio (SNR), frequency band leakage, and signal strength are listed in Table 1. In the auditory area, the SNR was consistently above 30 dB, which indicates good reception quality. In contrast, measurements outside the auditorium produced SNR values around 20 dB, suggesting minimal signal quality; however, the observed leakage remains below acceptable interference thresholds. We also observed frequency shifts of 33.31 ± 10.2 kHz, which falls within reasonable limits. A subjective test with three volunteers provided uniformly positive feedback on audio clarity.

5. CONCLUSION

We successfully designed, implemented, and tested a system for multilingual translation and cloned speech synthesis, adapting state-of-the-art open-source components. Users can listen to our broadcast using standard radio or Bluetooth devices.

In our tests on English-to-Spanish translation, the system introduced a 5-second delay in the communication, with an average of 4.5% WER in the transcription, 0.5 BLEU, and 0.75 COMET scores, respectively.

From our subjective tests, we conclude that the results achieved an average rating of 4.20 on the MOS scale. In addition, our hardware tests verified reliable signal confinement and robust performance in the real environment under varying conditions, with an average SNR of 38.2 dB inside the auditorium.

The proposed system is subject to several improvements. The MeloTTS essentially conditions the latency. Optimizations to the model, particularly in how the models are handled internally, could reduce this number. The two LLM models, used for sentence completion and translation, may be integrated to accelerate execution without compromising performance.

6. ACKNOWLEDGMENTS

M. Cámara, J. Gutiérrez, M.P. Daza, and J.L. Blanco, are with the Signal Processing Applications group (GAPS-UPM). These activities were partially funded by the Horizon 2020 Research and Innovation EU Programme under grant agreement No. 101003750; and by the Ministry of Economy and Competitiveness of Spain under grant No. PID2021-128469OB-I00.

7. REFERENCES

[1] Milind Agarwal et al. “Findings of the IWSLT 2023 Evaluation Campaign”. In: *Proc. of the 20th Int. Conf. on Spoken Language Translation (IWSLT)*. Association for Computational Linguistics, July 2023, pp. 1–61.

[2] Naveen Arivazhagan et al. *Monotonic Infinite Lookback Attention for Simultaneous Machine Translation*. June 2019.

[3] Parnia Bahar, Tobias Bieschke, and Hermann Ney. *A Comparative Study on End-to-end Speech to Text Translation*. Nov. 2019.

[4] Parnia Bahar et al. “Start-Before-End and End-to-End: Neural Speech Translation by AppTek and RWTH Aachen University”. In: *Proc. of the 17th Int. Conf. on Spoken Language Translation*. July 2020, pp. 44–54.

[5] Loïc Barrault et al. “Joint speech and text machine translation for up to 100 languages”. In: *Nature* 637.8046 (Jan. 2025), pp. 587–593.

[6] D. Barry et al. “Go Listen: An End-to-End Online Listening Test Platform”. In: *Journal of Open Research Software* 9 (July 2021).

[7] Alexandre Bérard et al. “End-to-End Automatic Speech Translation of Audiobooks”. In: *Proc. - ICASSP IEEE Int. Conf. Acoust. Speech Signal Process*. Apr. 2018, pp. 6224–6228.

[8] Marc Bruyninckx et al. “Language-induced voice quality variability in bilinguals”. In: *Journal of Phonetics* 22.1 (1994), pp. 19–31.

[9] Christian Fügen, Alex Waibel, and Muntsin Kolss. “Simultaneous translation of lectures and speeches”. In: *Machine Translation* 21.4 (Dec. 2007), pp. 209–252.

[10] Aaron Grattafiori et al. *The Llama 3 Herd of Models*. Nov. 2024.

[11] Javier Iranzo-Sánchez et al. “Europarl-ST: A Multilingual Corpus for Speech Translation of Parliamentary Debates”. In: *Proc. - ICASSP IEEE Int. Conf. Acoust. Speech Signal Process*. 2020, pp. 8229–8233.

[12] Javier Iranzo-Sánchez et al. “Streaming cascade-based speech translation leveraged by a direct segmentation model”. In: *Neural Networks* 142 (Oct. 2021), pp. 303–315.

[13] Ye Jia et al. “Direct Speech-to-Speech Translation with a Sequence-to-Sequence Model”. In: *Proc. Annu. Conf. Int. Speech Commun. Assoc.* 2019, pp. 1123–1127.

[14] Jodi Kearns. “LibriVox: Free Public Domain Audiobooks”. In: *Reference Reviews* 28.1 (Jan. 2014), pp. 7–8.

[15] A. Lavie et al. “Janus-III: speech-to-speech translation in multiple languages”. In: *Proc. - ICASSP IEEE Int. Conf. Acoust. Speech Signal Process*. Vol. 1. Apr. 1997, 99–102 vol.1.

[16] Ann Lee et al. *Direct speech-to-speech translation with discrete units*. Mar. 2022.

[17] Yusuke Oda et al. “Optimizing segmentation strategies for simultaneous speech translation”. In: *Proc. of the 52nd Annu. Meeting of the Assoc. for Computational Linguistics*. 2014, pp. 551–556.

[18] J. Ortega, J. González Rodríguez, and V. Marrero. “AHUMADA: A large speech corpus in Spanish for speaker characterization and identification”. In: *Speech Comm.* 31.2–3 (2000), pp. 255–264.

[19] Kishore Papineni et al. “BLEU: a method for automatic evaluation of machine translation”. In: *Proc. of the 40th Annu. Meeting on Assoc. for Computational Linguistics*. July 2002, pp. 311–318.

[20] Alec Radford et al. “Robust Speech Recognition via Large-Scale Weak Supervision”. In: *Proc. of the 40th Int. Conf. on Machine Learning*. July 2023, pp. 28492–28518.

[21] Ricardo Rei et al. “COMET: A Neural Framework for MT Evaluation”. In: *Proc. of the Conf. on Empirical Methods in Natural Language Processing (EMNLP)*. Nov. 2020, pp. 2685–2702.

[22] P. L. Salza et al. “MOS and pair comparison combined methods for quality evaluation of text-to-speech systems”. In: *Acta Acustica united with Acustica* 82.4 (1996), pp. 650–656.

[23] Freda Shi et al. *Language Models are Multilingual Chain-of-Thought Reasoners*. Oct. 2022.

[24] Silero Team. *Silero VAD: pre-trained enterprise-grade Voice Activity Detector (VAD), Number Detector and Lang Classifier*. `https://github.com/snakers4/silero-vad`. 2024.

[25] Hugo Touvron et al. *LLaMA: Open and Efficient Foundation Language Models*. Feb. 2023.

[26] Brian Yan et al. “CMU‘s IWSLT 2023 Simultaneous Speech Translation System”. In: *Proc. of the 20th Int. Conf. on Spoken Language Translation (IWSLT)*. July 2023, pp. 235–240.

[27] Wenliang Zhao, Xumin Yu, and Zengyi Qin. *MeloTTS: High-quality Multi-lingual Multi-accent Text-to-Speech*. 2023.

[28] Vilém Zouhar et al. “Pitfalls and Outlooks in Using COMET”. In: *Proc. of the 9th Conference on Machine Translation*. Nov. 2024, pp. 1272–1288.

DOI: 10.61782/fa.2025.0019



FORUM ACUSTICUM
EURONOISE 2025

A MODEL FOR IMPROVING THE PERFORMANCE OF LARGE LANGUAGE MODELS ON SOUNDSCAPE DESCRIPTION TASKS

Zhongju Yuan[1] **Dick Botteldooren**[1*]

[1] Department of Information Technology, Ghent University, Belgium

ABSTRACT

Generative AI is increasingly used in acoustic scene analysis and environmental soundscape description. Audio Language Models (ALMs) are key in this field but have two main drawbacks: they don't provide human-like survey responses and require significant computational resources, making real-time monitoring impractical. These issues stem from differences in how ALMs and humans assess and store sensory experiences. We propose a computationally efficient model with a three-layer architecture. The top layer features an advanced ALM for recognizing, grouping, and remembering audio events. The intermediate layer includes a local salient change detector based on sound feature embedding, which identifies meaningful changes in the auditory environment. When a change is detected, the ALM interprets and remembers the sound. The bottom layer has a memory cell mimicking echoic memory, retaining and reconstructing recent audio inputs. This reconstructed memory is passed to the ALM for recognition when triggered by the salient detector. Tested on the Urban Soundscapes of the World dataset, our model balances computational efficiency with real-time recognition accuracy, paving the way for scalable, intelligent acoustic monitoring solutions.

Keywords: *soundscape, saliency, large language models*

1. INTRODUCTION

Soundscape, the sonic environment as perceived and understood by persons of society within context, is increasingly used to assess and design the (urban) sound environment. With this definition in mind, measuring the soundscape remains a challenge. The ISO/TS 12913-2 standard series suggests surveys, sound walks, and focused listening to assess the soundscape. Artificial intelligence (AI) today allows us to recognize sounds and relate them to emotional attributes, e.g. annoyance [1]. However, such models are not very biologically plausible. Generative AI has recently seen tremendous expansion. Audio Language Models (ALMs), a special branch of large language models, offer the advantage that they can take into account context and common expectations, aspects that were shown to be extremely important in soundscape evaluation [2], [3], [4].

However, a direct use of ALMs on continual sound streams detected in urban public places does not account for the critical role of human attention in urban sound perception, which has often been overlooked in soundscape research. In fact, in daily life, the urban sound environment is seldom the focus of attention of the space user. Therefore in previous work, we have introduced an additional dimension orthogonal to the two-dimensional pleasure - arousal plane, backgrounding, measuring the degree of influence on overall perception of the space [5].

Allowing the sound to be backgrounded, that is gated out from further cognitive processing, also alows to reduce the amount of effort the ALM needs to put in analyses of the sound. Inference of answers from generative AI is a highly energy consuming process [6]. When connected to edge devices for monitoring soundscape, the combined process becomes extremely energy unfriendly and expensive. Nature has solved this problem also encountered by biological brains by allowing to gate out any repeated, continuous or otherwise uninformative sound. To assure that the function of hearing as an alerting and situation monitoring system is kept intact, gating out or in-

**Corresponding author*: dick.botteldooren@ugent.be.

Copyright: *©2025 Dick Botteldooren, Zhongju Yuan. This is an open-access article distributed under the terms of the Creative Commons Attribution 3.0 Unported License, which permits unrestricted use, distribution, and reproduction in any medium, provided the original author and source are credited.*

hibition must be accompanied by a saliency detection that triggers attention bottom up [7]. Auditory saliency has been widely studied [8] and has been related to changes in acoustical features [9], extending the classical Kayser-model [10].

In this paper, we propose a hierarchical framework to model the auditory processing system. The bottom layer functions as the echoic memory, responsible for memorizing and retrieving short audio segments. These sliding short segments are passed to the upper short-term memory layer for pattern change detection. When a change in the pattern is detected compared to the previous segment, the higher cognitive layer—referred to as ALM in our context—takes over the processing. At this stage, a longer auditory memory span is analyzed, and responses to several predefined questions are generated.

The proposed framework demonstrates that the model can significantly reduce the workload of the ALM by decreasing query frequency, while maintaining overall performance. By offloading routine pattern recognition and memory operations to the lower layers, the ALM is only engaged when higher-level cognitive processing is required. This hierarchical design not only improves computational efficiency but also better reflects the biological plausibility of human auditory processing. Furthermore, the reduction in unnecessary queries enables the ALM to allocate more resources to complex tasks, thereby enhancing the system's scalability and responsiveness in dynamic auditory environments.

2. MODEL

The proposed model is subdivided in large blocks that roughly correspond to functions in the biological system. The cochlear and brain-stem model conducts the primary spectral filtering. For the purpose of this paper, a simple gammatone filter bank is used for calculation speed, but this block can easily be replaced by a more precise model such as CONNear [11].

The block labeled "echoic memory" stores time traces of the (filtered) sensory input. In line with observations in humans, it allows to go back in time for about 4 seconds. This is essential to allow analysing a salient event that might be detected slightly after it has actually happened. Biologically plausible implementations of sensory, echoic memory might reveal special effects in real-time applications, but for the current paper the stored audio file is simply recalled when needed.

A central element is the predictive model used for detecting changes and saliency. In contrast to earlier work, no attempt is made to extract features that might influence the detection of sensory salient signals. Instead, it is assumed that a convolutional neural network (CNN) trained to detect sounds that are of relevance for humans will identify those features that define a sound object. Thus unpredictable changes of the embedding resulting from encoding a short epoch of sound can be seen as changes in the sound environment that might warrant re-evaluation of the soundscape. If such detections occur, the gate connecting the sensory memory to the large language model is opened for a predefined amount of time. The latter could still be a point of discussion. If the sound is of low interest for the person visiting the environment, top down attention will fade quickly and further processing will stop. However, conversations or longer bird songs may keep attention focussed. In earlier work on notice events we estimated that the decay time of top down attention for uninteresting sounds could be up to 10 seconds [12]. In this paper a fixed time interval of 15 seconds is used.

Any pretrained large generative model can be used as a cognitive model in this framework. We associate these models with human cognition because for soundscape assessment they fulfill roles that are usually associated with cognitive processes: (1) recognizing sounds and associating meaning where meaning is seen as the complex set of associations that are triggered by the sound; (2) putting the sound in a context, e.g. by specifying that a recording is made in an outdoor public place; (3) associating affect (e.g. calming, stimulating). The appropriateness of using the ALM for the latter could be debated as it probably only covers the common sense evaluation. For example, such models may easily link voices of people and traffic to lively environments and birds and water to calming environments, but they do not adequately account for the complexity of sound mixtures [13], where complexity is understood as the effort needed to analyze the auditory scene [14].

Prompt engineering, the craft of prompting a generative model properly, requires some attention. Here, we employ *Qwen-audio* [15] to generate the final responses. After several preliminary experiments, the following prompt was selected for use in the experimental setting:

> **Prompt:** Assume that you are a human in a public place, answer the following questions:
>
> 1. Can you describe what sounds you

hear?

2. What type of public place do you think you are in?
3. In general, how would you categorize the environment you just experienced?
(Options: calming / tranquil, lively / active, or neither)

Provide a structured response for all these questions.

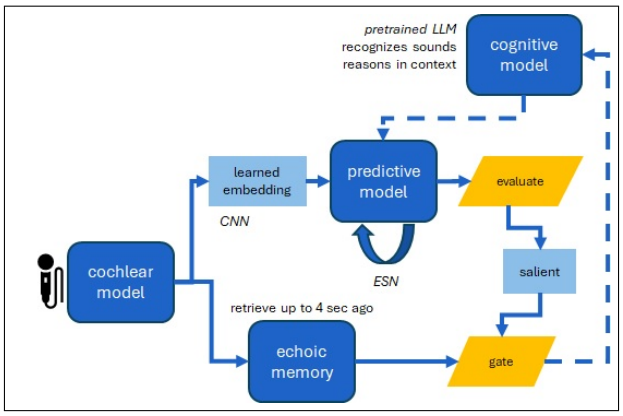


Figure 1. Connection between main components in the proposed model: the predictive model uses a learned embedding of the sound to detect any unpredictable changes in the sound; if such a change occurs it opens the gate to feed the cognitive model with new sound input; the echoic memory allows to retrieve the sound up to 4 seconds before the detection of a change, a salient event.

3. URBAN SOUNDSCAPES OF THE WORLD

As a test case for the approach, we used the Urban Soundscape of the World dataset. This database has been recorded at carefully selected locations in multiple cities across the globe [16]. The database contains high quality 4-channel ambisonics and binaural recordings and is supported by 360 degree video. The original recordings are around 10 minutes long, but 1-minute excerpts have been used in this work [17].

The Urban Soundscapes of the World database has been used in several lab studies. Here, the evaluation of each audiovisual recoding by 20 persons in a carefully constructed virtual reality experiment will be used [5]. In this work, participants are questioned in a much more subtle way than ISO/TS 12913-2. In brief: participants are first ask to rate the environment as a whole on a calming/tranquil to lively/active scale; then they are triggered to reflect on the activities that they could do in this environment in order to set a context for further evaluation; they are then asked whether the sound has drawn their attention during the AV experience (this leads to a rating on the *backgrounded* axis); they are then queried about the possible interruption of the activities they had in mind by the sound (this leads to a rating on the *disruptive* axis); depending on their answer to the first question, they are then asked to rate to what extend the sound environment contributed to that experience (this leads to a rating on the *calm/tranquil* and *lively/active* rating dimensions).

4. RESULTS

4.1 Overall accuracy

The model proposed in this paper is purely auditory, hence it has no visual context or any other stimulus. Thus, it is not possible for the model to rate whether the sound environment would be *backgrounded*. For the same reason *disruption* of potential activities is hard to rate as these potential activities depend largely on the overall knowledge about the place that human participants in an experiment would largely get from visual input. Therefore, this evaluation is restricted to the *calm/tranquil* and *lively/active* dimensions. 2 shows the distribution of average rating by the 20 participants from [5] for two classes predicted by the model: tranquil and lively. In the left figure, all sound fragments are used, in the right figure only those where the people rated that the sound environment had at least a moderate influence on the overall perception. By restricting the evaluation to sound environments that were rated by people, on average, to have an influence on the perception, the two distributions become more disjoint. Yet the model still classifies several sound environments as tranquil while persons would give them a more lively rating.

4.2 Ablation study

The proposed framework improves the ALM's ability to handle real-time scenarios. In this subsection, we demonstrate the performance of the framework. We evaluate its efficiency based on two metrics: the final tranquility level output by Qwen, and the total audio duration processed

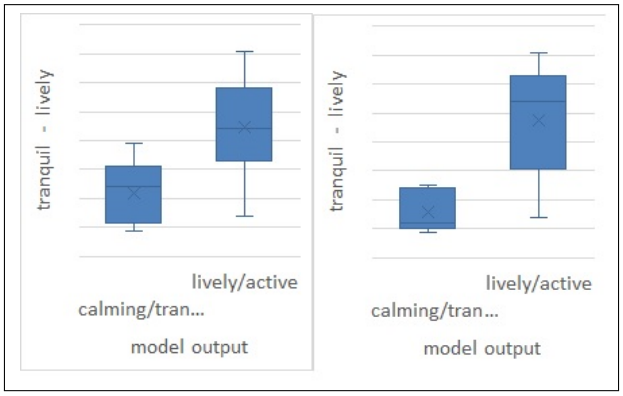


Figure 2. Box plot of the rating by participants of the environments on a *calm/tranquil* and *lively/active* dimension for the group of soundscapes rated as tranquil or lively by the model; left: all recordings, right: only environments where the sound is rated as influential by people.

per sample—since it's not feasible to send audio to the ALM every second for description generation.

First, we compare the tranquil/lively classification produced by Qwen using the complete sound fragment and the excerpt selected by the proposed model (cosine similarity threshold 0.9). We remind the reader that our model only sends a 15-second segment for evaluation when a pattern change is detected. The description from the most recent segment is used to determine tranquil/lively.

A confusion matrix has been calculated comparing the classifications based on analysing the full minute and a classification based on the proposed model. This showed that 54 recordings are classified as *lively/active* by both approaches and 10 recordings are classified as *calm/tranquil* by both approaches. However, 9 recordings that were classified as classified as *lively/active* on the basis of the full minute get classified as *calm/tranquil* by the proposed model and 4 recordings that were classified as *calm/tranquil* on the basis of of the full minute get classified as *lively/active* by the proposed model.

Figure 3 shows the same results as Figure 2 but now using the classification based on an evaluation of the full minute recording by Qwen. Both results are very similar and small differences tend to show that the proposed model slightly better predicts the evaluation by people. The latter observation should be interpreted with caution as no statistical significance of this difference is shown.

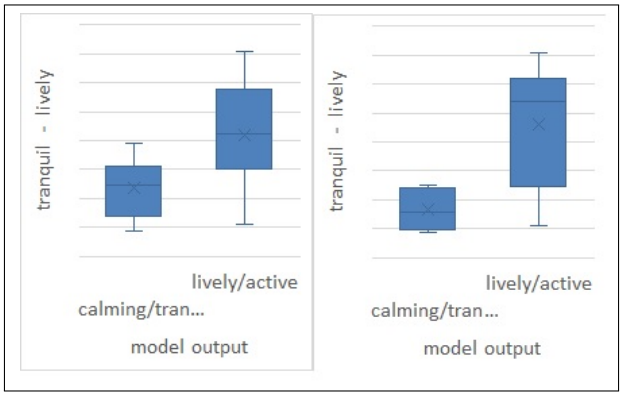


Figure 3. Box plot of the rating by participants of the environments on a *calm/tranquil* and *lively/active* dimension for the group of soundscapes rated as tranquil or lively based on the full one minute recording; left: all recordings, right: only environments where the sound is rated as influential by people.

To clarify that the time length processed by Qwen is significantly shorter, we provide statistical analysis of the processed durations across all audio samples. The results are presented in Fig. 4.

This violin plot shows the distribution of audio segment lengths sent to the Qwen model at a 0.9 threshold, combining density, individual data points, and a box plot. The distribution is bimodal with peaks at 15 and 30 seconds. The mean (22.51s) exceeds the median (15.00s), indicating right skew due to longer segments. Most data range from 15 to 60 seconds, with clusters in the lower range and a few high-value outliers. From Fig. 4, it is evident that approximately half of the audio fragments in the dataset do not exhibit significant pattern shifts. As a result, the framework sends only the initial 15 seconds to Qwen. This shortened processing time does not affect the resulting tranquility level.

5. DISCUSSION

Acoustic Language Models, a special subbranch of Large Language Models that combine sound recognition with the *common sense* knowledge embedded in these pretrained models are becoming notoriously powerful for describing acoustic scenes. However, directly applying such models to continuous sound streams recorded in urban

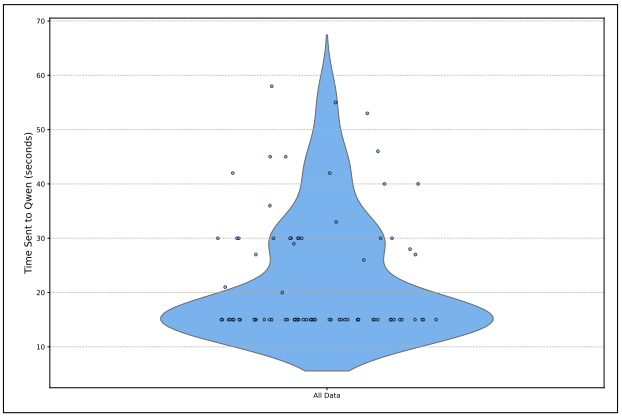


Figure 4. Distribution of Time Length Sent to Qwen at Threshold 0.9. This violin plot illustrates the distribution of audio time lengths processed and sent to the Qwen model at a threshold of 0.9.

sound monitoring for example, is extremely energy consuming and expensive. Inspired by human auditory scene analysis, we propose a model that decides which sound can safely be gated out without losing any essential information.

Environmental sounds often fade into the background for individuals enjoying public spaces. After an initial assessment of the sonic environment, the human mind tends to wander, only reassessing the surroundings when a notable sound event occurs. Numerous models have been proposed to identify these salient sounds, typically grounded in psychoacoustic principles. The proposed model, however, takes a different path. It posits that Artificial Learning Models (ALMs) trained to recognize sounds relevant to humans will develop embeddings that emphasize the features the human auditory system is attuned to. Consequently, a change in these embeddings would signal a shift in sounds significant to human perception, thereby suggesting triggering a release of gating.

This model is used here to assess sound environments available in the urban soundscape of the world database, with soundscape in mind. In particular, the labeling of the sound environment as *lively/active* or *calm/tranquil* is considered. For this, results obtained by human participants evaluation an audiovisual environment in virtual reality [5] can be used as a reference. It is shown that the proposed model predicts human evaluation at least as good as an evaluation based on the whole fragment. At the same time, very often, processing as little as 15 seconds using the ALM is sufficient. Only very seldom more than 30 seconds of sound is needed to reach the decision.

6. ACKNOWLEDGMENTS

This work was supported in part by the Research Foundation - Flanders, Belgium under grant number G0A0220N (FWO WithMe project), and the Flemish Government, Belgium under the "Onderzoeksprogramma Artificiele Intelligentie (AI) Vlaanderen"

7. REFERENCES

[1] Y. Hou, Q. Ren, H. Zhang, A. Mitchell, F. Aletta, J. Kang, and D. Botteldooren, "Ai-based soundscape analysis: Jointly identifying sound sources and predicting annoyance," *The Journal of the Acoustical Society of America*, vol. 154, no. 5, pp. 3145–3157, 2023.

[2] K. Filipan, M. Boes, B. De Coensel, C. Lavandier, P. Delaitre, H. Domitrović, and D. Botteldooren, "The personal viewpoint on the meaning of tranquility affects the appraisal of the urban park soundscape," *Applied Sciences*, vol. 7, no. 1, p. 91, 2017.

[3] Z. Kankhuni and C. Ngwira, "Overland tourists' natural soundscape perceptions: influences on experience, satisfaction, and electronic word-of-mouth," *Tourism Recreation Research*, vol. 47, no. 5-6, pp. 591–607, 2022.

[4] H. I. Jo and J. Y. Jeon, "Urban soundscape categorization based on individual recognition, perception, and assessment of sound environments," *Landscape and urban planning*, vol. 216, p. 104241, 2021.

[5] K. Sun, B. De Coensel, K. Filipan, F. Aletta, T. Van Renterghem, T. De Pessemier, W. Joseph, and D. Botteldooren, "Classification of soundscapes of urban public open spaces," *Landscape and urban planning*, vol. 189, pp. 139–155, 2019.

[6] A. A. Chien, L. Lin, H. Nguyen, V. Rao, T. Sharma, and R. Wijayawardana, "Reducing the carbon impact of generative ai inference (today and in 2035)," in *Proceedings of the 2nd workshop on sustainable computer systems*, pp. 1–7, 2023.

[7] C. N. Price and D. Moncrieff, "Defining the role of attention in hierarchical auditory processing," *Audiology Research*, vol. 11, no. 1, pp. 112–128, 2021.

[8] N. Huang and M. Elhilali, "Auditory salience using natural soundscapes," *The Journal of the Acoustical Society of America*, vol. 141, no. 3, pp. 2163–2176, 2017.

[9] S. R. Kothinti, N. Huang, and M. Elhilali, "Auditory salience using natural scenes: An online study," *The Journal of the Acoustical Society of America*, vol. 150, no. 4, pp. 2952–2966, 2021.

[10] C. Kayser, C. I. Petkov, M. Lippert, and N. K. Logothetis, "Mechanisms for allocating auditory attention: an auditory saliency map," *Current biology*, vol. 15, no. 21, pp. 1943–1947, 2005.

[11] D. Baby, A. Van Den Broucke, and S. Verhulst, "A convolutional neural-network model of human cochlear mechanics and filter tuning for real-time applications," *Nature machine intelligence*, vol. 3, no. 2, pp. 134–143, 2021.

[12] B. De Coensel, D. Botteldooren, T. De Muer, B. Berglund, M. E. Nilsson, and P. Lercher, "A model for the perception of environmental sound based on notice-events," *The Journal of the Acoustical Society of America*, vol. 126, no. 2, pp. 656–665, 2009.

[13] D. Botteldooren, "Urban sound design for all," in *INTER-NOISE and NOISE-CON Congress and Conference Proceedings*, vol. 261, pp. 2012–2017, Institute of Noise Control Engineering, 2020.

[14] A. S. Bregman, *Auditory scene analysis: The perceptual organization of sound*. MIT press, 1994.

[15] Y. Chu, J. Xu, X. Zhou, Q. Yang, S. Zhang, Z. Yan, C. Zhou, and J. Zhou, "Qwen-audio: Advancing universal audio understanding via unified large-scale audio-language models," *arXiv preprint arXiv:2311.07919*, 2023.

[16] B. De Coensel, K. Sun, and D. Botteldooren, "Urban soundscapes of the world: Selection and reproduction of urban acoustic environments with soundscape in mind," in *INTER-NOISE and NOISE-CON Congress and Conference Proceedings*, vol. 255, pp. 5407–5413, Institute of Noise Control Engineering, 2017.

[17] B. De Coensel, D. Botteldooren, S. Kang, and T. Van Renterghem, *Urban soundscapes of the world*. zenodo: https://zenodo.org/records/10106181.

DOI: 10.61782/fa.2025.0785

FORUM ACUSTICUM EURONOISE 2025

SOUND ENVIRONMENTS CLASSIFICATION OF A UNIVERSITY CAMPUS USING UNSUPERVISED MACHINE LEARNING TECHNIQUES

Jose Montoya Belmonte[1*] **Antonio Pita Lozano**[1] **Juan Miguel Navarro Ruiz**[1]
[1] Research Group in Advanced Telecommunications (GRITA),
UCAM Universidad Católica de Murcia, 30107 Guadalupe, Spain

ABSTRACT

A university campus, often comparable to a small city, faces similar challenges in monitoring and managing noise pollution within their environments. This study presents a methodology to classify the diverse soundscapes of a university campus using long-term acoustic measurements collected through a network of acoustic sensors. The research was conducted at the Catholic University of San Antonio in Murcia, where sound data was captured and analyzed based on sound pressure levels. In addition to using overall sound pressure levels data, the study explores the advantages and limitations of incorporating more detailed information, such as sound pressure levels segmented by frequency bands, for identifying acoustic patterns. Unsupervised machine learning techniques, specifically the k-means clustering algorithm, were applied to process the extensive dataset generated by continuous monitoring. This methodology facilitated the identification of distinct acoustic patterns across the campus. The results demonstrate the potential of combining acoustic sensor networks with machine learning algorithms to efficiently monitor and categorize urban-like environments such as university campuses. This approach provides a scalable and cost-effective solution for soundscape management, while highlighting the potential benefits of integrating more granular acoustic data for enhanced pattern recognition.

Keywords: *soundscape, university campus, sound pressure level, IoT, monitoring*

**Corresponding author*: jmontoya3@ucam.edu.

***Copyright**: ©2025 J Montoya et al. This is an open-access article distributed under the terms of the Creative Commons Attribution 3.0 Unported License, which permits unrestricted use, distribution, and reproduction in any medium, provided the original author and source are credited.*

1. INTRODUCTION

The contemporary university campus presents a complex acoustic environment where diverse sound sources, ranging from human activities to transportation noise, affect both outdoor and indoor soundscapes [1], [2]. The soundscape of university environment plays a pivotal role in influencing students' well-being, cognitive performance, and academic satisfaction [3]. Furthermore, in recent years, the concept of soundscape has gained increasing relevance in the design and management of campus environments [4].

The implementation of Wireless Acoustic Sensor Networks (WASN) has revolutionized acoustic monitoring methodologies by providing systems for real-time data collection and transmission in a distributed and scalable manner [2]. These networks enable a more precise and dynamic characterization of soundscapes, facilitating the detection of relevant acoustic events and the spatial and temporal analysis of noise. The measurement of sound pressure level (SPL) serves as a fundamental indicator to characterize acoustic environment and evaluate exposure to noise and its potential health impacts [5]. Despite its widespread use, conventional approaches to noise assessment typically emphasize the average SPL values, which can overlook the intricate temporal and spatial fluctuations present in complex soundscapes.

To address these shortcomings, unsupervised machine learning methods, such as k-means clustering, have gained traction as effective strategies for analyzing large acoustic datasets. These techniques allow for the automatic grouping of sound pressure data into clusters that exhibit similar properties, thereby facilitating the discov-

ery of distinct noise patterns and acoustic zones that traditional methods might miss.

This paper is focused on evaluating the suitability of applying a WASN-based system for long-term temporal monitoring of acustics parameters in order to assess the acoustic environment in a High Education institutions for this purpose. This work explores the integration of unsupervised machine learning techniques, specifically k-means clustering, for analyzing SPL data in complex environments, with the aim of enhancing noise management strategies and improving acoustic comfort.

2. MATERIALS AND METHODOLOGY

This smart campus initiative involves the design and implementation of WASN strategically placed at various indoor and outdoor locations. For this work, four sensor nodes are deployed, one of then are located outdoor. The outdoor area is a highly frequented space utilized by staff and students during break periods and for hosting special events such as forums and exhibitions. Consequently, it serves as an open venue for the entire university community, with the primary source of noise being predominantly anthropogenic. While the rest of nodes are indoors, in particular, an office, a classroom and an entrance hall.

Each WASN is capable of continuously acquiring valuable acoustic data over extended periods. Each node is equipped with sensors for capturing sound signals, and calculating acoustic metric such as the sound pressure level (SPL) in dB, along with the SPL values in several octave frequency bands (dB), specifically 125 Hz band, 250 Hz band, 1 kHz band, 2 kHz band, 4 kHz band. Moreover, As well as embedded software for processing audio inputs and computing key acoustic parameters.

Monitoring is performed for four months, twenty four hours per day, with data capture every minute in different scenarios.

For the input data, no preprocessing or aggregation is applied; thus, the model's input consists solely of the metrics corresponding to the octave frequency bands.

Subsequently, the collected data are analyzed, preprocessed, and cleaned to ensure quality and reliability. Once the data is properly prepared, it is utilized in an unsupervised learning approach using the k-means clustering algorithm, For a given value of k, k-means algorithm groups the nodes in k-clusters. This technique enables the identification of homogeneous groups within the dataset, thereby facilitating the classification of different acoustic environmental sound patterns. Where the parameter K denotes the predetermined number of clusters specified prior to the execution of the algorithm, guiding the iterative assignment of data points to the nearest cluster centroid based on a defined distance metric.

The algorithm iterates in two steps until the centroids have stabilized. In the first stage of the process, known as the assignment step, each node is associated with the closest centroid according to the computed distance. The second step, known as the update phase, involves recalculating the centroid positions by determining the element-wise arithmetic mean of all data points associated with each cluster [6].

Software and Technology

Data preparation, transformation, analysis, and modeling were carried out using the open-source programming language R [7], version 4.3.2. The computational environment included an AMD Ryzen 7 5800X 8-core processor running at 3.80 GHz, 32 GB of RAM, and an Nvidia GTX 3050 GPU with 8 GB GDDR6 memory. The analysis utilized several R libraries: dplyr (version 1.1.4), lubridate (version 1.9.3), tidyr (version 1.3.0), cluster (version 2.1.4), clValid (version 0.7), mclust (version 6.1.1), Kohonen (version 3.0.12) and ggplot2 (version 3.4.4). To ensure the reproducibility of results, a fixed seed was set using the `set.seed()` function for all tasks involving random processes. Furthermore, given the changes in random number generation introduced in R version 4.0.0, additional steps were taken to standardize the methodology and guarantee consistent outcomes across different R versions.

3. RESULTS AND DISCUSSION

In this section, results obtained from applying the clustering technique, K-means, to the collected data are analyzed and discussed.

To determinate the appropriate amount of clusters, k-means algorithm has been trained for k = 1, . . . , 12, being this one with 5 clusters the best of them for Silhouette metric [8]. Therefore, the model has been trained with k=5, as it maximizes the Silhouette. This indicates that clusters of sounds are formed based on their similar behavior with respect to the five selected variables, namely, the SPL in several octave frequency bands, i.e. from 125 Hz to 4,000 Hz. Centroids, in dB, are calculated according to [9].

Tab. 1 shows the clusters' centroids created by clustering.

The data obtained allow for the identification of multiple sound sources impacting the acoustic environment of

Table 1. Centroid of clusters using data collected during monitoring the university.

Group	125 Hz band	250 Hz band	1 kHz band	2 kHz band	4 kHz band	Colour
1	32.94	30.20	23.97	21.11	18.45	black
2	36.72	18.29	18.28	48.81	24.57	pink
3	39.53	38.55	33.43	26.68	22.84	cyan
4	51.32	43.08	40.77	31.81	30.02	brown
5	56.32	47.38	48.13	54.76	33.72	blue

the university.

Group 1 shows a constant decreasing trend from 125 Hz band to 4 kHz band.This reduction suggests a predominance of low-frequency sound sources, potentially associated with structure-borne noise. Additionally, the presence of furniture in the area may contribute to acoustic absorption, while the attenuation of high frequencies indicates that they are being absorbed or dispersed within the environment.

Group 2 has a sharp drop at 250 Hz band, staying at low values until 1 kHz band.Then, at 2 kHz band, it experiences a sharp peak before dropping again at 4 kHz band.This suggests that this group is very sensitive to certain frequencies, especially in the 2 kHz region, where the dB level is the highest.

Group 3 also presents a progressive reduction in dB, although less pronounced than group 1.

Group 4 exhibits a higher value in the 125 Hz frequency band, suggesting the influence of ventilation systems and structure-borne noise.

Group 5 highlights two frequency bands: 2 kHz frequency band and 125 Hz frequency band. This cluster represents an outdoor node where students gather on benches during breaks. The 2 kHz frequency band is associated with human speech, indicating that conversations significantly contribute to the acoustic environment in this area. Meanwhile, the 125 Hz frequency band component is influenced by its proximity to the transportation zone, where external noise sources, such as vehicle traffic, play a role.

The values obtained from the Tab. 1 are represented in Figure 1, which illustrates the variation in dBA levels across different frequency bands for distinct groups.

Group 3 and 5 have peaks in 2 kHz band, suggesting that this band has a greater impact in certain scenarios.

Group 1 and 2 show a downward trend, which may be related to energy loss at high frequencies.

In order to show the relevance and the relation between these indicators 125 Hz Band, 250 Hz band, 1 kHz band, 2 kHz band and 4 kHz band. A smoothed color density scatterplot representing all monitoring can be seen in

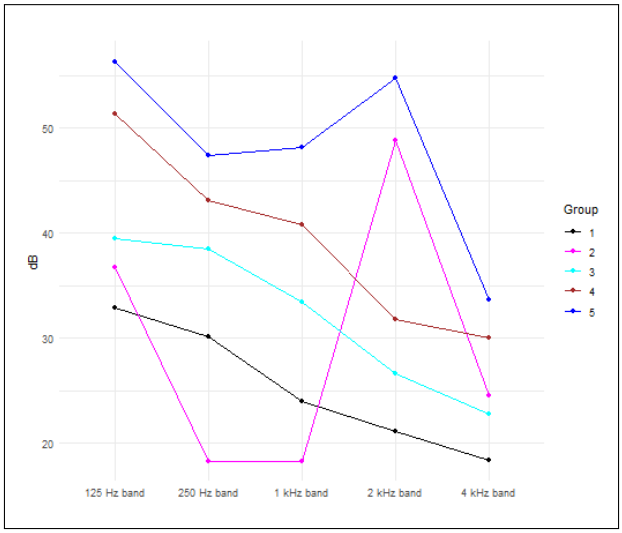


Figure 1. Centroids according to cluster and their respective frequency bands.

Figure 2. The smoothed color density helps to identify dense zones that groups nodes with similar behavior.

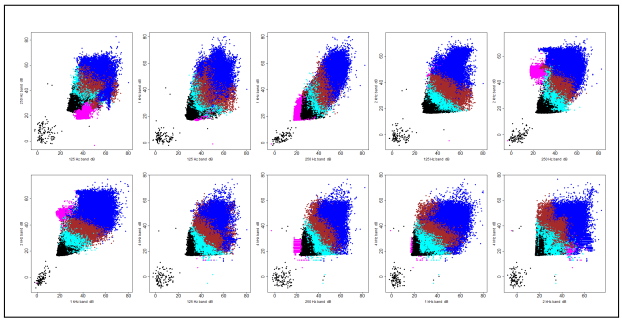


Figure 2. Scatter plot of the 125 Hz band, 250 Hz band, 1 kHz band, 2 kHz band and 4 kHz band metrics representing all time frames.

4. CONCLUSIONS

The acoustic environment within a university setting should be continuously monitored, as various sound sources can significantly impact the well-being and academic performance of the university community. WASN represents an effective tool for environmental acoustic monitoring, enabling the collection of large volumes of data. However, due to the magnitude of the captured in-

formation, conventional data processing methods may be insufficient. To address this challenge, the implementation of machine learning algorithms allows for data analysis, pattern recognition, predictive modeling, and the extraction of meaningful insights, enhancing decision-making in acoustic management.

This study presents a preliminary analysis of an urban acoustic environment within a university setting, employing unsupervised machine learning techniques, specifically the k-means clustering algorithm to determine whether the analysis of the values obtained from sound pressure level bands allows for the identification of specific acoustic characteristics. This technique is a good tool for analyzing large amounts of data obtained from the monitoring of sound environments. According to the data obtained, higher SPL values are observed in the low frequency values, 125 Hz band, which present higher SPL than at higher frequencies, Based on the obtained data, it is valid for identifying different sound sources that impact the university environment. In future projects, subjective values such as loudness and sharpness will be added in order to know the correlation that may exist with the band values and to be able to know how these sources are affected.

5. REFERENCES

[1] J. Segura-Garcia, J. M. Navarro-Ruiz, J. J. Perez-Solano, J. Montoya-Belmonte, S. Felici-Castell, M. Cobos, and A. M. Torres-Aranda, "Spatio-temporal analysis of urban acoustic environments with binaural psycho-acoustical considerations for iot-based applications," *Sensors*, vol. 18, no. 3, p. 690, 2018.

[2] J. Montoya-Belmonte and J. M. Navarro, "Long-term temporal analysis of psychoacoustic parameters of the acoustic environment in a university campus using a wireless acoustic sensor network," *Sustainability*, vol. 12, no. 18, p. 7406, 2020.

[3] Q. Liand, S. Lin, F. Yang, and Y. Yang, "The impact of campus soundscape on enhancing student emotional well-being: A case study of fuzhou university," *Buildings*, vol. 15, no. 1, p. 79, 2025.

[4] P. Croce, F. Leccese, G. Salvadori, C. Bartalucci, F. Borchi, and P. Pulella, "Soundscape assessment of the school of engineering external area at the university of pisa," in *Proc. 10th Convention of the European Acoustics Association*, (Turin, Italy), 2023.

[5] R. Guski, D. Schreckenberg, and R. Schuemer, "Who environmental noise guidelines for the european region: A systematic review on environmental noise and annoyance," *International Journal of Environmental Research and Public Health*, vol. 14, no. 12, p. 1539, 2017.

[6] J. MacQueen, "Some methods for classification and analysis of multivariate observations," in *Phe Fifth Berkeley Symposium on Mathematical Statistics and Probability, Volume 1: Statistics*, (University of California press.), pp. 281–298, January 1967.

[7] "R, free software environment for statistical computing and graphics.," *Accessed on Apr, 29, 2024 [Online]. Available: https://www.r-project.org/,*.

[8] A. Dudek, "Silhouette index as clustering evaluation tool. in classification and data analysis: Theory and applications," *Springer International Publishing*, vol. 28, pp. 19–33, 2020.

[9] A. Pita, F. J. Rodriguez, and J. M. Navarro, "Cluster analysis of urban acoustic environments on barcelona sensor network data," *Int. J. Environ. Res. Public Health*, vol. 18, no. 16, p. 8271, 2021.

DOI:

Main theme: A09 Machine learning and Artificial Intelligence in Acoustics

Session A09.03/A02.07 AI and machine learning in bioacoustics

Chair(s): Y. Jadoul, V. Lostanlen

DOI: 10.61782/fa.2025.0165

FORUM ACUSTICUM EURONOISE 2025

AUTOMATED ECOACOUSTIC MONITORING: EVALUATING CLASSIFIER PERFORMANCE FOR COMMON CUCKOO (*CUCULUS CANORUS*) DETECTION

Helen C Whitehead[1*] **William J Davies**[1] **Sergey Gashchak**[2] **Michael D Wood**[1]

[1] School of Science, Engineering & Environment, University of Salford, Manchester, United Kingdom

[2] Chornobyl Center for Nuclear Safety, Radioactive Waste & Radioecology, Slavutych, Ukraine.

ABSTRACT

This study evaluates the effectiveness of automated bioacoustic classifiers in detecting the vocal activity of the common cuckoo (*Cuculus canorus*) within the Chornobyl Exclusion Zone (CEZ). Data were collected from 12 recording locations using Wildlife Acoustics Songmeter 3 (SM3) units during May 2015. Acoustic data were analysed using Kaleidoscope Pro, focusing on the left channel to avoid duplicate detections. The classifier scanned recordings for target sounds based on specified signal parameters and employed cluster analysis to categorise events. The classifier demonstrated high precision (95.1%) and a low false negative rate (0.5%), with most misclassifications due to other bird species with similar frequencies. The recall rate averaged 61%, varying from 40% to 100% across different recorders. Variations in recall rate were influenced by habitat structure, environmental noise, and distance between the target species and the recorder. This study highlights the potential of automated classifiers in ecoacoustic monitoring.

Keywords: *ecoacoustics, biodiversity, monitoring,*

1. INTRODUCTION

Ecoacoustics, the study of environmental sounds and their relationship with the ecosystem, plays a crucial role in monitoring biodiversity. Automated classification, a method that uses machine learning algorithms to identify species from acoustic data, enhances the efficiency and accuracy of such studies. By leveraging these technologies, researchers can effectively monitor species.

The common cuckoo (*Cuculus canorus*) is a migratory brood parasite that relies on other species to raise its young. Females remove host species' eggs and nestlings before laying their eggs in the nest [1]. Common cuckoo breed extensively in Europe and parts of North Africa, and winter in Africa and southern Asia. In Europe, they are summer visitors from April to September, with peak breeding in May and June [2,3]. They inhabit diverse habitats, including woodlands, forests, scrub, heathland, meadows, reedbeds, lowlands, and moorlands. Their diet mainly consists of insects, particularly caterpillars, crickets, and dragonflies [2].

Common cuckoos are solitary outside the breeding season but communicate vocally during breeding [2]. Detection through traditional methods like point counts and line transects is challenging due to their isolated behaviour. The species is characterised by distinct vocalisations, with males emitting loud "cu-coo" calls audible over 2-3 km. These vocalisations make acoustic monitoring highly effective for detecting common cuckoos [4].

[*] ***Corresponding author***: H.C.Whitehead1@salford.ac.uk.

Copyright: *©2025 Whitehead et al. This is an open-access article distributed under the terms of the Creative Commons Attribution 3.0 Unported License, which permits unrestricted use, distribution, and reproduction in any medium, provided the original author and source are credited.*

Here, the vocal activity of the common cuckoo was monitored throughout May 2016, one of the most active months for this species [5], to investigate the common cuckoo across the CEZ. The objective of the study was to evaluate the effectiveness of automated detection for this species.

2. METHODS

2.1 Data Collection

Wildlife Acoustics Songmeter 3 (SM3) units were deployed in the CEZ. In total, 12 locations were used. Data were collected continuously between 10th May 2016 and 3rd June 2016.

2.2 Acoustic Data Analysis

The data collected during the specified period was analysed using Kaleidoscope Pro (ver 5.3.6) (Wildlife Acoustics, https://www.wildlifeacoustics.com). To avoid duplicate detections, only the left channel of the recordings was used (channel 0), a method validated by previous studies [6,7,8]. Kaleidoscope Pro scanned recordings for target sounds based on specified signal parameters, including minimum and maximum frequency (Hz), minimum and maximum length of detection (s), and maximum inter-syllable gap (ms). These parameters were determined using 40 manually located cuckoo calls from the study area with Raven Pro 1.5 (Bioacoustics Research Program 2014). Kaleidoscope Pro's cluster analysis function was used, extracting the Discrete Cosine Transform coefficient (DCT) of the spectrum of candidate sounds. A Hidden Markov Model (HMM) was constructed using the vector of the DCT of each signal frame, and vectors were grouped based on K-Means clustering. Clusters were labelled as "cuckoo" or "other sounds" based on the first 50 events of each cluster. Each sound was visually/acoustically checked to determine classifier performance, including precision and recall rate.

Table 1. Signal parameters derived from Raven Pro were input into Kaleidoscope to detect common cuckoo calls.

Species	Min Freq (Hz)	Max Freq (Hz)	Min Length (s)	Max Length (s)	Intersyllable Gap (s)
Common Cuckoo	250	900	0.3	1	0.6

The recall rate was estimated by dividing the total number of calls detected by Kaleidoscope Pro by the total number of actual cuckoo vocalizations (determined by manual analysis). A total of 108, 15-minute recordings were randomly selected to determine the recall rate.

3. RESULTS

The common cuckoo was detected through the cluster analysis function within Kaleidoscope Pro at every recording location across the CEZ. The number of calls detected ranged from 2163 to 16,062. Kaleidoscope Pro reported a total of 128,527 events matching the signal parameters. These were divided into "other sounds" (29,437 events, 22.9%) and "cuckoo" (99,090 events, 77.1%).

The precision of the classifier was 95.1%, with a false positive rate of 3.3%. Most false positives were vocalisations from birds with similar frequencies, including the common woodpigeon (*Columba palumbus*), Eurasian hoopoe (*Upopa epops*), Eurasian collared dove (*Streptopelia decaocto*), and tawny owl (*Strix aluco*). The mean recall rate for the entire dataset was 61% (5058 calls detected out of 8363 calls annotated in the 108 recordings of the validation dataset), ranging from 40% to 100% for each recorder.

Table 2. Recall rate for each acoustic recorder used in this study. The number of manual annotations represents the number of calls detected through manually inspecting the validation dataset, whereas the number of calls detected through automated classification represents how many calls the classifier in Kaleidoscope Pro detected. The recall rate column expresses the percentage of calls correctly detected by the automated classifier in relation to the calls detected through manual annotations.

Recorder	No. of calls manual annotations	No. of calls automated classifier	Recall Rate
303715	1158	773	67%
303712	2087	1145	55%
303160	1074	434	40%
303727	403	205	51%
303719	302	265	88%
303724	331	178	54%
303137	563	298	53%
303138	25	25	100%

303736	794	614	77%
303183	548	271	50%
303146	425	379	90%
303139	653	471	72%

4. DISCUSSION

The classifier showed high precision (95.1%) and a low false negative rate (0.5%), indicating few misclassifications, mainly due to other bird species with similar frequencies. It performed well in detecting common cuckoo calls within the CEZ, achieving a recall rate of 61%, though this varied from 40% to 100% across different recorders.

Variations in recall rate were likely influenced by factors such as habitat structure, environmental noise, and the distance between the target species and the recorder. Habitat characteristics can affect sound transmission, leading to signal attenuation and impacting detectability. Environmental noise, especially during adverse weather conditions and high biophonic noise during the dawn chorus, can also challenge accurate detection. The distance between the target species and the recorder further affects the classifier's ability to detect vocalisations.

5. REFERENCES

[1] V. Jelínek, P. Procházka, M. Požgayová, and M. Honza: "Common Cuckoos Cuculus canorus change their nest-searching strategy according to the number of available host nests," Ibis, vol. 156, no. 1, pp. 189–197, 2014.

[2] R. B. Payne: The Cuckoos. New York: Oxford University Press, 2005.

[3] M. Honza, B. Taborsky, M. Taborsky, Y. Teuschl, W. Vogl, A. Moksnes, and E. Røskaft: "Behaviour of female common cuckoos, Cuculus canorus, in the vicinity of host nests before and during egg laying: A radiotelemetry study," Animal Behaviour, vol. 64, no. 6, pp. 861–868, 2002.

[4] J. Shonfield and E. M. Bayne: "Autonomous recording units in avian ecological research: current use and future applications," Avian Conservation and Ecology, vol. 12, no. 1, 2017

[5] J. Mei, S. M. Puswal, M. Wang, and F. Liu: "Diurnal and Seasonal Patterns of Calling Activity of Seven Cuculidae Species in a Forest of Eastern China," Diversity, vol. 14, no. 4, pp. 1–18, 2022.

[6] E. C. Knight, K. C. Hannah, G. J. Foley, C. D. Scott, R. M. Brigham, and E. Bayne: "Recommendations for acoustic recognizer performance assessment with application to five common automated signal recognition programs," Avian Conservation and Ecology, vol. 12, no. 2, 2017.

[7] C. Pérez-Granados and K. L. Schuchmann: "Monitoring the annual vocal activity of two enigmatic nocturnal Neotropical birds: the Common Potoo (Nyctibius griseus) and the Great Potoo (Nyctibius grandis)," Journal of Ornithology, vol. 161, no. 4, pp. 1129–1141, 2020.

[8] C. Pérez-Granados and K. L. Schuchmann: "Seasonal climate impacts on vocal activity in two neotropical nonpasserines," Diversity, vol. 13, no. 7, pp. 1–13, 2021.

DOI: 10.61782/fa.2025.0231

FORUM ACUSTICUM EURONOISE 2025

CLUSTERING AND NOVEL CLASS RECOGNITION: EVALUATING BIOACOUSTIC DEEP LEARNING FEATURE EXTRACTORS

Vincent S. Kather[1,2*] **Burooj Ghani**[2] **Dan Stowell**[1,2]
[1] Department of Cognitive Science and Artificial Intelligence, Tilburg University, Netherlands
[2] Naturalis Biodiversity Center, Leiden, Netherlands

ABSTRACT

In computational bioacoustics, deep learning models are composed of feature extractors and classifiers. The feature extractors generate vector representations of the input sound segments, called embeddings, which can be input to a classifier. While benchmarking of classification scores provides insights into specific performance statistics, it is limited to species that are included in the models' training data. Furthermore, it makes it impossible to compare models trained on very different taxonomic groups. This paper aims to address this gap by analyzing the embeddings generated by the feature extractors of 15 bioacoustic models spanning a wide range of setups (model architectures, training data, training paradigms). We evaluated and compared different ways in which models structure embedding spaces through clustering and kNN classification, which allows us to focus our comparison on feature extractors independent of their classifiers. We believe that this approach lets us evaluate the adaptability and generalization potential of models going beyond the classes they were trained on.

Keywords: *deep learning, bioacoustics, embeddings*

1. INTRODUCTION

Human-driven climate change and deforestation have caused a rapid decline in global biodiversity [1]. Using sensor arrays for biodiversity monitoring, ecologists can gather information on environments and investigate how human pressures affect biodiversity and how we can halt its decline [2]. Passive acoustic monitoring (PAM) is one method that provides a low-cost and non-invasive way to monitor biodiversity [3]. The vast amount of data generated by PAM sensors has led to the rapid development of bioacoustic deep learning models to help researchers reduce the annotation effort [4]. The use of these state-of-the-art models has proven valuable in ecological studies, for example, in general species assessments [5] or detection of endangered species [6].

While bioacoustic deep learning models are a useful asset in ecology, it is crucial to understand the models' limitations based on their training setup. The two main training strategies to develop bioacoustic deep learning models are supervised learning and self-supervised learning. Supervised learning models require large amounts of annotated data to be trained [7]. The models classify sounds based on a fixed number of predefined classes representing annotated sounds in the dataset. While supervised learning can have the benefit of instructing models to differentiate between species vocalizations, it requires annotated datasets. This limits supervised learning models to known and annotated classes and makes them sensitive to class imbalance and label quality. Alternatively, self-supervised learning can be trained without annotated data, enabling models to learn meaningful representations directly from the data. For example, in a paradigm called masked prediction, the model is trained to predict a masked portion of the audio, thus modeling bioacoustic characteristics without supervision [8]. With growing annotated databases, supervised learning models like BirdNET [9] improve in performance, yet recent developments in self-supervised learning on models like An-

*Corresponding author: vincent.kather@naturalis.nl.
Copyright: ©2025 Vincent S. Kather et al. This is an open-access article distributed under the terms of the Creative Commons Attribution 3.0 Unported License, which permits unrestricted use, distribution, and reproduction in any medium, provided the original author and source are credited.

imal2vec [10] indicate a promising new direction for the field requiring less manual annotation. Not requiring annotations, self-supervised learning models can be trained on far larger datasets, however there is no control of what is being learned. The model might, for instance, learn to differentiate between sounds based on characteristics very different from the species that produces them.

To evaluate bioacoustic deep learning models, a comparison of just the classifier performance obscures the fine-grained differences between models and the way they analyze input sounds. Bioacoustic deep learning models consist of artificial neural networks that can be subdivided into feature extractors and classifiers. The feature extractor creates an embedding (vector representation) of an input sound and the classifier (which corresponds to the final dense layer of the model) maps the embedding onto classes. Commonly, in bioacoustics, a suite of established benchmarks is used to compare the classifier performance of state-of-the-art models [11]. This requires the models to have been trained on the classes present in the benchmarking datasets. However, there is an alternative: using the embeddings created by the feature extractors, the embedding spaces can be analyzed with regard to their structural characteristics, irrespective of what the classifiers were trained on.

Due to their size, datasets that are used to train bioacoustic models for bird detection are often based on citizen science data (e.g., xeno-canto [12]). The majority of these recordings are focal recordings of individuals which are weakly labeled with little polyphony. When models are applied to large PAM datasets, especially outside of North America (where the majority of the training data originates), the difference in recording conditions causes performance drops [13]. To accurately evaluate the models in this study, we use a PAM bird vocalization dataset from Colombia and Costa Rica [14], as well as a dataset of frog vocalizations from Brazil [15]. Both datasets are comprised of PAM recordings in noisy environments and can therefore be considered as challenging datasets. With this, we hope to on the one hand emphasize the performance differences between the models and on the other hand produce results that will reflect in real world applications.

This study aims to showcase the potential for evaluating and especially comparing bioacoustic deep learning models with regard to their training paradigm and training data. The evaluation focuses on the structuring capabilities of each feature extractor, as measured by clustering and classification performance. Classification in this case refers to recognition of novel classes, as none of the models have been pretrained on the classes selected here. This way, classification heads are attached to each feature extractor, all of which are trained on the same evaluation sets (bird and frog vocalizations), i.e. same classes and same data, allowing us to compare their performance. Classification is done using a k-nearest neighbor (kNN) approach. This method of analysis opens up the possibilities for a fair comparison of deep learning feature extractors guiding the field to a better understanding of how training configurations affect downstream performance.

2. METHODS

To incorporate a variety of training setups, covering popular models as well as models targeted to various species groups, we compare a total of 15 pretrained bioacoustic feature extractors (Table 1). This includes both self-supervised and supervised learning feature extractors. Furthermore, large variations in input length, embedding dimension and training data provide a diverse landscape of feature extractors, allowing us to analyze performance of differently structured embedding spaces.

2.1 Dataset

The evaluation datasets that were used for this study are a bird vocalization dataset (bird dataset) recorded in coffee farms in Colombia and Costa Rica [14] and a frog vocalization dataset (frog dataset) recorded in Brazil [15]. The recordings in these datasets feature challenging soundscape recordings with overlapping vocalizers and noisy environments. Both datasets have been reduced from their original size to only include sound events corresponding to classes with more than 150 annotations. Due to the high amount of polyphony, the frog dataset has furthermore been reduced to only contain sound events with non-overlapping annotations, i.e. turning it into a single-label dataset. It is worth mentioning, that by excluding overlapping annotations, only polyphony of frog species is removed, the complex background of overlapping sounds created by insects and birds in the recordings remain.

For the bird dataset this results in 11 classes, while for the frog dataset 18 classes are included in the final dataset. We intentionally selected soundscape recordings with gradual changes of background noise and overlapping species vocalizations to amplify the differences between the feature extractors' capabilities to structure the data.

Table 1. List of feature extractors compared in this study. Columns "abbrev." shows the an abbreviated name used in Fig. 1. "training" shows the training setup chosen during training, i.e. ssl for self-supervised learning, supl for supervised learning and ft for fine-tuning. The "architecture" column more specifically describes the model architecture used. "dimension" shows the output dimension of the feature extractor. "trained on" summarizes the training data of the model. "ref." provides the respective publication.

name	abbrev.	training	architecture	dimension	trained on	ref.
Animal2vec_XC	a2v_xc	ssl	d2v2.0	768	birds	[10]
Animal2vec_MK	a2v_mk	ssl + ft	d2v2.0	1024	meerkats	[10]
AudioMAE	aud_mae	ssl + ft	ViT	768	general	[8]
AVES_ESpecies	aves	ssl + ft	HuBERT	768	general + animals	[7]
AvesEcho_PaSST	aecho	supl	PaSST	768	birds	[16]
BioLingual	bioling	supl	CLAP	512	animals + birds	[17]
BirdAVES_ESpecies	birdaves	ssl + ft	HuBERT	1024	general + birds	[7]
BirdNET	brdnet	supl	EffNetB0	1024	birds	[9]
Google_Whale	g_whale	supl	EffNetB0	1280	whales	-
Insect459NET	i459	supl	EffNetv2s	1280	insects	-
Insect66NET	i66	supl	EffNetv2s	1280	insects	-
NonBioAVES_ESpecies	nonbioaves	ssl + ft	HuBERT	1024	general + non-bio	[7]
Perch_Bird	perch	supl	EffNetB0	1280	birds	-
ProtoCLR	p_clr	supl	CvT-13	384	birds	[18]
SurfPerch	s_perch	supl	EffNetB0	1280	coral reefs + birds	[19]

2.2 Data pipeline

For each of the feature extractors, the respective model code base was cloned, and the model was stripped of its classifier. For both animal2vec feature extractors, outputs from the attention heads and input lengths are averaged, resulting in one embedding per input segment (as is the case with all other feature extractors). Data are imported from the sound files, resampled to the model-specific sample rate, and padded to fit the model-specific input length. All the necessary code to reproduce the computations can be found in the repository **bacpipe** [1] (**bio**acoustic **c**ollection **pipe**line).

2.3 Methods for evaluating embedding spaces

Embedding spaces are evaluated using clustering and classification. Our primary focus is the comparison of the two paradigms: supervised learning and self-supervised learning. Furthermore, we explore how the data chosen for training affects the clustering capabilities of different feature extractors.

[1] `github.com/bioacoustic-ai/bacpipe`

The clustering is computed using K-Means with the same number of clusters as classes in the ground truth. Clustering performance is evaluated using Adjusted Mutual Information (AMI) [20] to compare the K-Means clustering with the ground truth.

Performance is also evaluated by training a simple kNN classifier on each of the embedding spaces with a nearest neighbor parameter of 15. The classifier is trained on the 11 and 18 classes for the bird and frog datasets respectively. Data are split into train, validation and test set in the ratio 0.65:0.15:0.2. Performance is evaluated using a balanced macro accuracy score [21] to handle the imbalance in class sizes.

Evaluations are computed in both the original embedding spaces and an embedding space reduced to 300 dimensions. This way the embedding dimension is standardized and performance can be compared while controlling for this factor. Uniform manifold approximation projection (UMAP) [22] is selected for the dimensionality reduction to 300 dimensions. UMAP is also used to visualize the embeddings in two dimensions in Fig. 2.

Table 2. Classification (macro accuracy) and clustering (AMI) performance of the original embeddings, and UMAP embeddings reduced to 300 dimensions. Values show the mean over all ssl, supl, bird and non-bird feature extractors, corresponding to the categories and colors in Fig. 1. Best values among all categories and dimensionalities are bold.

bird data	classification		clustering	
category	original	UMAP	original	UMAP
supl	0.695	0.711	0.418	0.476
ssl	0.617	0.619	0.256	0.405
bird	0.712	**0.723**	0.426	**0.479**
non-bird	0.658	0.618	0.271	0.413
frog data				
category	original	UMAP	original	UMAP
supl	0.668	0.655	0.488	0.546
ssl	0.682	0.679	0.414	0.508
bird	**0.705**	0.698	0.5	**0.558**
non-bird	0.638	0.627	0.414	0.5

3. RESULTS

Table 2 shows the averaged performances over all feature extractors, grouped into the different categories: supervised vs. self-supervised learning, and trained on bird data vs. non-bird data. Firstly, we want to point out the performance changes following dimensionality reduction using UMAP. For evaluation with bird and frog datasets, UMAP embeddings significantly improve clustering results for each category. For the classification performance, values are very similar between original and UMAP reduced embeddings, however, when applied to the bird data, UMAP yields performance increases for most categories, whereas for the frog data, the original embeddings yield better results.

Supervised feature extractors outperform self-supervised ones by a large margin for classification and clustering on the bird dataset. For the frog dataset, due to the improved performance of the AVES models (see Fig. 1), self-supervision outperforms supervised learning measured by kNN classification. When comparing the values between all categories, the bird-trained feature extractors outperform all other categories for both bird and frog evaluation sets.

Figure 1 shows the averaged performances for each of the feature extractors. First, we will focus on the feature extractors that are applied to the bird dataset, shown in blue. When focusing on the clustering (top), the six best performing feature extractors are trained using supervised learning, while all self-supervised learning feature extractors reach clustering performances under 0.31. Performance measured by kNN classification is more mixed, however again supervised learning feature extractors reach the three highest values. Furthermore, Animal2vec_XC, the only self-supervised learning feature extractor that was not fine-tuned, performs poorly for both clustering and kNN classification. Google_Whale represents the only supervised learning feature extractor performing very poorly by clustering and kNN classification.

Comparing by training data, feature extractors trained on only or including bird datasets (supl bird and ssl bird) outperform the other feature extractors by kNN classification and even more so by clustering, with the exception of Animal2vec_XC. Aside from ProtoCLR the supervised learning models that are also trained on birds (supl bird) vastly outperform all other models by clustering and with the exception of the AVES feature extractors also by kNN classification. Perch and BirdNET lead both in clustering and kNN classification by a large margin. Biolingual, which was trained on large bird databases using a multimodal approach performs well by clustering, but comparatively poorly by kNN classification.

In green we can see the performance when the feature extractors are applied to the frog data. Among supervised learning feature extractors, changes in both clustering and kNN classification performance are varied. Especially the three best performing models by clustering for the bird data, Perch, BirdNET and Biolingual, all decrease in performance when applied to the frog dataset. The non-bird trained supervised learning feature extractors (supl non-bird) all improve their clustering performance by a large margin. All self-supervised feature extractors vastly improve in clustering performance and aside from Animal2vec_MK also in kNN classification. The self-supervised AVES feature extractors (BirdAVES, AVES and NonBioAVES) drastically improve in both clustering and kNN classification on the frog data. So much so, that all three outperform all other feature extractors by kNN classification.

All non-bird trained feature extractors improve in clustering when applied to frog data. Again, when applied to the frog dataset, all bird trained feature extractors except for Animal2vec_XC outperform the rest by clustering and the top six models are the supervised learning

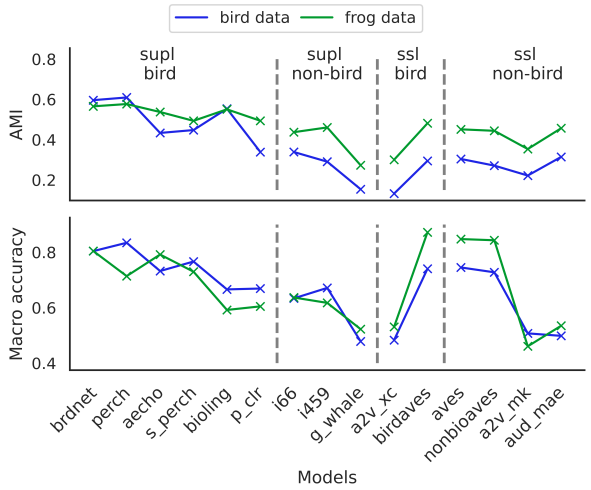


Figure 1. Comparison of feature extractor performance by learning paradigm, training data and application data. The top plot shows clustering results of AMI. The bottom plot shows macro accuracy results of kNN classification. Colors correspond to performance of the feature extractors when applied to bird data (blue) and frog data (green). The x-axis shows abbreviated model names, corresponding to "abbrev." column in Tab. 1. Models are grouped into categories along the x-axis by training paradigm (supervised learning (supl) and self-supervised learning (ssl)) and training data (bird data and non-bird data, see Table 1).

bird trained feature extractors. Among them, only AvesEcho improves in both clustering and kNN classification. However, by kNN classification, results are more mixed by both training paradigm and training domain.

For a more qualitative analysis of the different embedding spaces, two-dimensional UMAP embeddings of the feature extractors applied to the bird data are shown in Fig. 2. The worst-performing feature extractors produce large unstructured clouds of mixed color, indicating that no significant clustering is achieved. In the first and second row, feature extractors can be seen to separate the embeddings into meaningful clusters. It is noticeable that some feature extractors such as AvesEcho_PaSST and ProtoCLR seem to generate more subclusters than most other feature extractors. This, however does not reflect in their performance (Fig. 1). The seven best-performing feature extractors are all trained using supervised learning and the top three are additionally trained on bird vocalizations. All three of the AVES models (BirdAVES, AVES and NonBioAVES) reach similar performances in spite of big differences in their fine-tuning datasets [7]. Despite the embedding spaces of BirdAVES and Animal2vec_XC looking similarly cluttered, their performance varies by clustering and even more so by classification (see Fig. 1).

4. DISCUSSION

Although the self-supervised feature extractors represented in this study are trained on very large datasets, their clustering performance is inferior to most of the supervised learning feature extractors. Nonetheless, their lack of supervision benefits generalization: the majority of self-supervised feature extractors improve performance on the frog data, both for clustering and classification. Yet, as has been shown in previous studies [23], supervised learning and training data consisting of large bird song databases yield the best results, even for challenging PAM datasets. Perch and BirdNET [9], both of which are trained on thousands of classes of bird vocalizations, vastly outperform the other feature extractors by clustering and for the bird data also by classification. Despite the authors' claims [17], the multi-modal feature extractor Bilingual, which performs very well by clustering but comparably poor by classification, is outperformed by BirdNET and Perch. SurfPerch [19] and AvesEcho_PaSST [16], both of which have largely benefited from Perch or BirdNET pretraining, perform well for both clustering and classification tasks. Most notably, AvesEcho_PaSST is the only supervised learning feature extractor that demonstrates generalization by improving performance on the frog data. This could be attributed to the model's innovative transformer architecture using patchout, thereby selectively dropping patches of spectrograms during training, whilst having learned from the well-trained BirdNET embeddings through knowledge distillation [16].

As stated in the introduction, self-supervised learning models lack supervision and might therefore learn classes not meaningful to differentiate between species vocalizations. When comparing Figures 2 and 1 we observe poor clustering both in terms of AMI performance and by qualitative visual analysis of the embedding separation, which could be resulting from non-meaningful classes. However, for the three AVES feature extractors, the kNN classifier is nonetheless able to learn a meaningful differen-

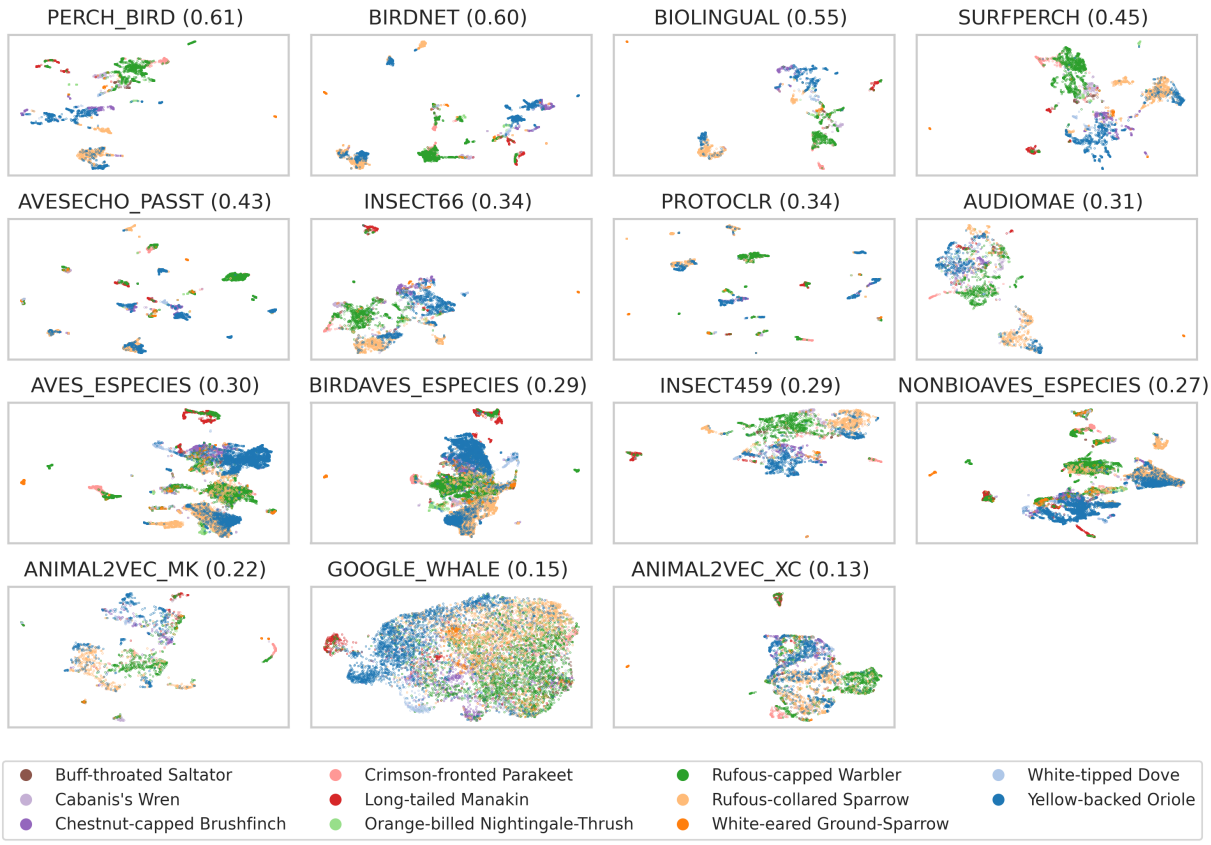


Figure 2. Two-dimensional embedding spaces of all feature extractors applied to bird data, sorted descending by their clustering performance of AMI values (indicated next to their name) from top left to bottom right. Colors correspond to the class labels, which are 11 different tropical bird species.

tiation between the classes. This could be attributed to the fact, that while they are self-supervised, the data used to train these models consisted of curated and non-sparse sound events, thereby increasing the likelihood that meaningful classes are learned. Furthermore, the HuBERT architecture used for the AVES models uses tokenization through acoustic unit discovery [7]. These acoustic units are generated during training based on 39-dimensional Mel-frequency ceptral coefficients (MFCC) features and labeled using a K-Means clustering. The transformer encoder then predicts these cluster labels. This differs fundamentally from the training procedure of the Animal2vec models and AudioMAE, both of which rely on masked prediction. In terms of classification, the results suggest that the MFCC features lead to more meaningful classes than the prediction of masked emebddings. This is supported by the drastic performance increase of all three AVES models when evaluated for the frog dataset.

For the self-supervised learning feature extractors, fine-tuning seems to only marginally improve performance. The three feature extractors based on the AVES models all share the same general audio pretraining and architecture but differ largely in fine-tuning. The similarity in performance indicates that the dominant influence on the structuring of embeddings is defined by either the pretraining or the architecture. Animal2vec_XC and Animal2vec_MK, the latter of which is fine-tuned, largely share the same architecture but were trained on very different datasets. Yet, both models reach similarly poor performance, this is especially surprising for the fine-tuned Animal2vec_MK.

While the dimensions of the feature extractors vary

greatly, performance does not correlate with dimensionality. When we used UMAP to standardize the embedding spaces, we saw performance improvements (Table 2). The observed improvements are more pronounced in clustering, likely because UMAP is an optimization algorithm that trains a neural network to find an optimized lower dimensional graph representation, which benefits K-Means.

Although the bird data were in-domain for BirdNET and Perch, the same applies for Biolingual, Animal2vec_XC and BirdAVES_ESpecies, none of which reached similar performance. The decrease in classification performance by Perch on the frog data raises the question whether this difference can be attributed to its training dataset. Perch's training data, which is comprised of solely xeno-canto recordings perhaps makes it less domain agnostic than BirdNET which was trained on selected curated bird datasets along with a large portion of xeno-canto.

This study presents a workflow for in-depth analysis of embedding spaces, which can be reproduced with the provided repository bacpipe. Evaluation through clustering and classification has shown to vary significantly when applied to the different evaluation sets, undermining the use of both metrics to better understand how training setup affects performance. While the results presented here allow for further discussion, we believe streamlining the process of evaluating and comparing such a wide variety of feature extractors can help to investigate performance differences as a function of training paradigm and training domain. By establishing a default analysis of feature extractors alongside the common classification benchmarks, bioacoustic research can accelerate towards a better understanding of what training characteristics are beneficial in this domain.

5. CONCLUSION

In this study we have compared a variety of different state-of-the-art bioacoustic deep learning models, representing different training paradigms and training domains. To compare the models, we have isolated their feature extractors and used them to generate embeddings of two curated evaluation datasets consisting of annotated bird and frog sounds. The aim of this study was to firstly present a large comparison of very different bioacoustic deep learning feature extractors and to evaluate how training setup affects performance. Performance was evaluated through clustering using an AMI score and through kNN classification using a macro accuracy score.

We have shown that bioacoustic feature extractors still struggle with polyphonic PAM datasets, especially if they are outside of the training domain. However, when comparing training paradigms, supervised learning remains a strong method to pretrain a feature extractor for general use, despite advances in self-supervised learning. This performance difference is visible in both kNN classification and even more in clustering. Furthermore, we have shown that alignment of training domain and target domain during pretraining impacts performance more than during fine-tuning. This study presents a roadmap for a more in-depth performance evaluation of bioacoustic deep learning models, allowing for a better understanding of how training setup impacts downstream performance.

6. ACKNOWLEDGMENTS

A lot of work went into developing each of the feature extractors presented here, and we highly appreciate that they are made publicly available. We would also like to acknowledge Álvaro Vega-Hidalgo as well as Juan Sebastian Cañas and their coauthors, who collected, assembled and annotated the datasets used to evaluate the feature extractors. This project is funded by the Marie Skłodowska-Curie doctoral network BioacousticAI.

7. REFERENCES

[1] F. Gosselin and J.-M. Callois, "Relationships between human activity and biodiversity in Europe at the national scale: Spatial density of human activity as a core driver of biodiversity erosion," *Ecological Indicators*, vol. 90, pp. 356–365, July 2018.

[2] D. S. Schmeller, M. Böhm, C. Arvanitidis, S. Barber-Meyer, N. Brummitt, M. Chandler, E. Chatzinikolaou, M. J. Costello, H. Ding, J. García-Moreno, M. Gill, P. Haase, M. Jones, R. Juillard, W. E. Magnusson, C. S. Martin, M. McGeoch, J.-B. Mihoub, N. Pettorelli, V. Proença, C. Peng, E. Regan, U. Schmiedel, J. P. Simaika, L. Weatherdon, C. Waterman, H. Xu, and J. Belnap, "Building capacity in biodiversity monitoring at the global scale," *Biodiversity and Conservation*, vol. 26, pp. 2765–2790, Nov. 2017.

[3] L. S. M. Sugai, T. S. F. Silva, J. W. Ribeiro, Jr, and D. Llusia, "Terrestrial Passive Acoustic Monitoring: Review and Perspectives," *BioScience*, vol. 69, pp. 15–25, Jan. 2019.

[4] D. Stowell, "Computational bioacoustics with deep learning: A review and roadmap," *PeerJ*, vol. 10, p. e13152, Mar. 2022.

[5] A. Cowans, X. Lambin, D. Hare, and C. Sutherland, "Improving the integration of artificial intelligence into existing ecological inference workflows," *Methods in Ecology and Evolution*, vol. n/a, Dec. 2024.

[6] S. Allen-Ankins, S. Hoefer, J. Bartholomew, S. Brodie, and L. Schwarzkopf, "The use of BirdNET embeddings as a fast solution to find novel sound classes in audio recordings," *Frontiers in Ecology and Evolution*, vol. 12, Jan. 2025.

[7] M. Hagiwara, "AVES: Animal Vocalization Encoder based on Self-Supervision," Oct. 2022.

[8] P.-Y. Huang, H. Xu, J. Li, A. Baevski, M. Auli, W. Galuba, F. Metze, and C. Feichtenhofer, "Masked Autoencoders that Listen," *Advances in Neural Information Processing Systems*, vol. 35, pp. 28708–28720, Dec. 2022.

[9] S. Kahl, C. M. Wood, M. Eibl, and H. Klinck, "BirdNET: A deep learning solution for avian diversity monitoring," *Ecological Informatics*, vol. 61, p. 101236, Mar. 2021.

[10] J. C. Schäfer-Zimmermann, V. Demartsev, B. Averly, K. Dhanjal-Adams, M. Duteil, G. Gall, M. Faiß, L. Johnson-Ulrich, D. Stowell, M. B. Manser, M. A. Roch, and A. Strandburg-Peshkin, "Animal2vec and MeerKAT: A self-supervised transformer for rare-event raw audio input and a large-scale reference dataset for bioacoustics," July 2024.

[11] J. Hamer, E. Triantafillou, B. van Merriënboer, S. Kahl, H. Klinck, T. Denton, and V. Dumoulin, "BIRB: A Generalization Benchmark for Information Retrieval in Bioacoustics," Dec. 2023.

[12] xeno-canto, "Xeno-canto :: Sharing wildlife sounds from around the world." https://xeno-canto.org/, 2025.

[13] C. Pérez-Granados, "BirdNET: Applications, performance, pitfalls and future opportunities," *Ibis*, vol. 165, no. 3, pp. 1068–1075, 2023.

[14] Á. Vega-Hidalgo, S. Kahl, L. B. Symes, V. Ruiz-Gutiérrez, I. Molina-Mora, F. Cediel, L. Sandoval, and H. Klinck, "A collection of fully-annotated soundscape recordings from neotropical coffee farms in Colombia and Costa Rica," Jan. 2023.

[15] J. S. Cañas, M. P. Toro-Gómez, L. S. M. Sugai, H. D. Benítez Restrepo, J. Rudas, B. Posso Bautista, L. F. Toledo, S. Dena, A. H. R. Domingos, F. L. de Souza, S. Neckel-Oliveira, A. da Rosa, V. Carvalho-Rocha, J. V. Bernardy, J. L. M. M. Sugai, C. E. dos Santos, R. P. Bastos, D. Llusia, and J. S. Ulloa, "A dataset for benchmarking Neotropical anuran calls identification in passive acoustic monitoring," *Scientific Data*, vol. 10, p. 771, Nov. 2023.

[16] B. Ghani, V. J. Kalkman, B. Planqué, W.-P. Vellinga, L. Gill, and D. Stowell, "Generalization in birdsong classification: Impact of transfer learning methods and dataset characteristics," Sept. 2024.

[17] D. Robinson, A. Robinson, and L. Akrapongpisak, "Transferable Models for Bioacoustics with Human Language Supervision," Aug. 2023.

[18] I. Moummad, R. Serizel, E. Benetos, and N. Farrugia, "Domain-Invariant Representation Learning of Bird Sounds," Sept. 2024.

[19] B. Williams, B. van Merriënboer, V. Dumoulin, J. Hamer, E. Triantafillou, A. B. Fleishman, M. McKown, J. E. Munger, A. N. Rice, A. Lillis, C. E. White, C. A. D. Hobbs, T. B. Razak, K. E. Jones, and T. Denton, "Leveraging tropical reef, bird and unrelated sounds for superior transfer learning in marine bioacoustics," May 2024.

[20] S. Romano, J. Bailey, V. Nguyen, and K. Verspoor, "Standardized Mutual Information for Clustering Comparisons: One Step Further in Adjustment for Chance," in *Proceedings of the 31st International Conference on Machine Learning*, pp. 1143–1151, PMLR, June 2014.

[21] K. H. Brodersen, C. S. Ong, K. E. Stephan, and J. M. Buhmann, "The Balanced Accuracy and Its Posterior Distribution," in *2010 20th International Conference on Pattern Recognition*, pp. 3121–3124, Aug. 2010.

[22] L. McInnes, J. Healy, and J. Melville, "UMAP: Uniform Manifold Approximation and Projection for Dimension Reduction," Sept. 2020.

[23] B. Ghani, T. Denton, S. Kahl, and H. Klinck, "Global birdsong embeddings enable superior transfer learning for bioacoustic classification," *Scientific Reports*, vol. 13, p. 22876, Dec. 2023.

DOI: 10.61782/fa.2025.0294



FORUM ACUSTICUM
EURONOISE 2025

Development of an Ear Tag System for Diagnosing Swine Respiratory Diseases Using Long Short-Term Memory Networks

Yuki Matoba[1] **Shunsuke Ishimitsu**[1*] **Seiji Yumoto**[1] **Osamu Mikami**[2]
Yosuke Ogawa[2] **Hiroaki Inoue**[2] **Mitsuyoshi Ishida**[2] **Daisuke Tanaka**[3]
[1] Graduate School of Information Sciences, Hiroshima City University, Hiroshima, Japan
[2] National Agriculture and Food Research Organization, Tsukuba, Japan
[3] Tohoku University, Sendai, Japan

ABSTRACT

In the Japanese livestock industry, while the number of pig farms is decreasing, the number of pigs raised per farm is increasing, leading to larger-scale operations. This scaling-up raises the risk of widespread damage from rapid infectious disease outbreaks. Furthermore, respiratory diseases such as pneumonia inhibit growth, delay shipments, and reduce cost-effectiveness for farmers. Consequently, there is a demand for systems that can detect illnesses early. Previous research constructed a disease diagnosis model using the cepstrum and Δ-cepstrum of body-conducted sounds from pigs as inputs, employing LSTM. However, variations among individual pigs were found to decrease the accuracy of the disease diagnosis model. Therefore, this study investigates the construction of machine learning models for individual subjects, aiming to eliminate the effects of individual differences by detecting abnormalities on a case-by-case basis.

Keywords: *Body conducted sound, Ear tag sensor, Disease detection, LSTM, Autoencoder*

1. INTRODUCTION

Porcine respiratory diseases cause significant economic damage in the livestock industry, with annual losses due to Porcine Reproductive and Respiratory Syndrome (PRRS) estimated at $664 million annually in the U.S. [1]. Hence, to prevent severe complications and widespread infections among individuals, the early detection of porkets afflicted with respiratory diseases is crucial. Furthermore, the recent trend towards large-scale porket farming has exacerbated labor shortages, highlighting the need for using technology for efficiently monitor the health status of pigs [2]. Mito et al. [3] proposed a system that utilizes a microphone array and cameras installed in pigpens to detect and locate the source of coughing and sneezing sounds, which are indicators of porcine respiratory diseases. However, environmental noise within pigpens hinders the accurate localization of these sounds. M. Guarino et al. [4] investigates the use of an intelligent alarm system for early disease detection in pigs through online monitoring of cough sounds. Initially developed in laboratory settings, the system was tested on 44 pigs in field conditions using close-range microphones. The classification accuracy was 85.5% for coughs and 86.6% for other sounds. However, the reliance on close-proximity microphones presents practical challenges for real-world application, as environmental noise impacts performance. Lagua et al. [5] discusses a commercially available AI system designed for monitoring respiratory health in swine, integrating temperature and humidity sensors with audio technologies. The system captures body-conducted sounds from individual pigs to detect respiratory diseases, employing machine learning algorithms for effective disease surveillance and management in livestock farming. However, the current system still faces limitations, particularly regarding accuracy and practical applicability in real-world settings. They suggest that further advancements in AI and sensor technology are necessary to create smarter, more reliable solutions for comprehensive health monitoring in livestock. To address this need, we are developing a system that

[*] ***Corresponding author***: *ishimitu@hiroshima-cu.ac.jp*
Copyright: *©2025 First author et al. This is an open-access article distributed under the terms of the Creative Commons Attribution 3.0 Unported License, which permits unrestricted use, distribution, and reproduction in any medium, provided the original author and source are credited.*

uses ear tag sensors to detect the body-conducted sounds of pigs, analyzes the biometric data in the cloud, and notifies farmers. Previously, models used cepstrum and Δcepstrum as inputs and employed Long Short-Term Memory (LSTM) networks for disease diagnosis [6]. However, individual differences among pigs caused a decrease in model accuracy. Therefore, this study has explored constructing individual machine learning models for each pig to mitigate the impact of these variations by detecting anomalies individually.

2. COLLECTION OF BODY-CONDUCTED SOUNDS

The animal experiment was approved by the Agricultural Research Organization's Expert Committee on Experiments. Pigs are often fitted with ear-tags for identification. In this context, our research group developed ear-tag sensors [7] that incorporated electronic circuits and miniature sensors to record body-conducted sounds. To collect data from pigs with respiratory diseases, we conducted animal experiments by intentionally infecting the animals with bacteria. Ear-tag sensors were attached to pigs at 5 w of age and data were collected during both healthy periods (2–3 d) and periods of illness (2 w).

3. CONSTRUCTION OF THE ANOMALY DETECTION MODEL

The autoencoder is a representative method for anomaly detection that compresses and reconstructs input data using an encoder and a decoder, respectively. Anomalies are detected by measuring the difference (reconstruction error) between the input and output. An LSTM model using a spectrogram of body-conducted sounds as input can accurately distinguish between pre- and post-illness states [8]. Building on these findings, the current study aimed to achieve high-precision anomaly detection using an LSTM autoencoder that used a spectrogram of body-conducted sounds as input.

3.1 LSTM Autoencoder

The LSTM autoencoder learns a vector representation of the time-series data in the encoder and reconstructs the time series in the decoder using the current hidden state and values predicted at the previous time step. The time-series data were denoted as $X = \{x^{(1)}, x^{(2)}, \ldots, x^{(L)}\}$, and the hidden state of the encoder at each time point $h_E^{(i)}$. Here, $i \in \{1, 2, \ldots, L\}$ and $h_E^{(i)} \in R^C$, where c represents the number of LSTM units in the encoder's hidden layer. In the LSTM autoencoder, the encoder compresses the data in chronological order, whereas the decoder reconstructs the data in reverse chronological order. Thus, the final state of the encoder, $h_E^{(L)}$, is used as the initial state for the decoder, $h_D^{(L)}$, and the time-series data are output in the order of $\{x^{(L)}, x^{(L-1)}, \ldots, x^{(1)}\}$[8].

3.2 Calculation of Reconstruction Error

Initially, the LSTM autoencoder model generated a 5-s output from a 5-s input. When calculating the reconstruction error, overlapping 5-s frames were used within data segments longer than 14 s. The mean and distribution differences of the reconstruction errors obtained in this manner were utilized as indicators to classify the states before and after disease onset.

3.3 Kullback-Leibler Divergence

In this study, the Kullback–Leibler (KL) divergence was used to measure the differences between probability distributions and served as a classification metric. KL divergence is a measure of how one probability distribution diverges from the second-expected probability distribution. When Q and P are discrete probability distributions, KL divergence is defined by Equation (1) [9]:

$$D(P \parallel Q) = \sum_{i=1}^{N} P(x_i) \log \frac{P(x_i)}{Q(x_i)} \quad (1)$$

For instance, if Q and P represent the probability distributions of the reconstruction errors for healthy data, the KL divergence value would be small due to the minimal difference between the distributions. However, if Q represents the reconstruction error distribution of data from healthy pigs and P represents data from diseased pigs, substantial differences in the distributions would lead to a larger KL divergence value. Therefore, by substituting reconstruction error with KL divergence, an improvement in accuracy was achieved.

3.4 Identification Results for Five Pigs

The process of training the model and detecting anomalies is described. Initially, approximately 50% of the data from a single healthy pig were used as training data and approximately 20% were used as validation data to build the model. Subsequently, the remaining data from healthy and diseased pigs were input into the built model as test data. The output results were used to calculate the

reconstruction error or KL divergence, and the anomalies in the pigs were detected based on predefined thresholds. In this study, the thresholds were set to the maximum values of the reconstruction error or KL divergence from the validation data.

To effectively implement an anomaly detection system on a real farm, it is imperative to classify all pigs with high accuracy, regardless of the presence of symptoms. Therefore, pigs A to E, showing a range of lung lesions from severe to mild, were used to validate the effectiveness of the LSTM autoencoder and KL divergence. Each pig had a machine learning model built specifically for it. The identification results for pigs A–E are shown in Figures 1–5. Except for pig D, the LSTM Autoencoder models using spectrograms as input could accurately distinguish between the pre-illness and illness states. Moreover, the use of KL divergence improved the accuracy of disease identification in pigs B –E. However, pig D showed a low identification accuracy of 0–20%. This was attributed to the presence of significant outliers in the reconstruction error or KL divergence of the 's validation data of pig D, which were set as thresholds. Consequently, the data that were actually diseased were incorrectly classified as healthy, leading to a decrease in accuracy.

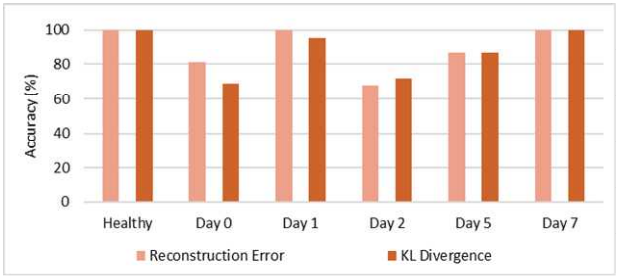


Figure 1. Results for Pig A (severe infection). The input was a spectrogram, with thresholds set for each method. 'Day' indicates the number of days post-infection.

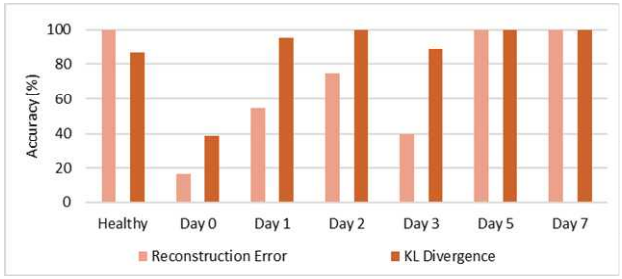


Figure 2. Results for Pig B (moderate severity infection). The input was a spectrogram with a threshold set for each method. 'Day' indicates the number of days post-infection.

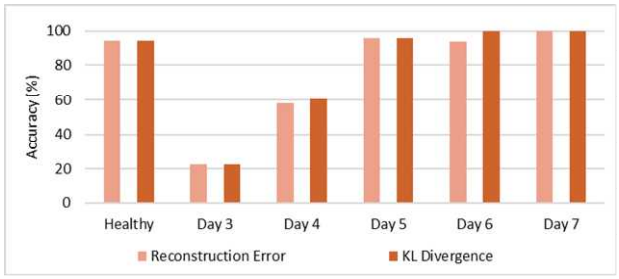


Figure 3. Results for Pig C (moderate severity infection). The input was a spectrogram with a threshold set for each method. 'Day' indicates the number of days post-infection.

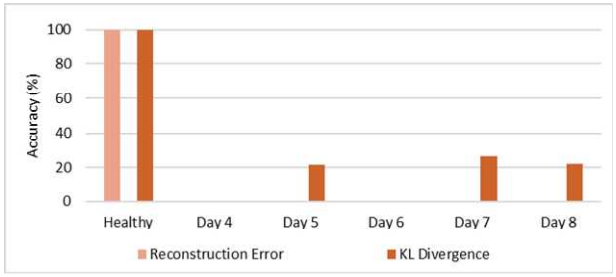


Figure 4. Results of Pig D (mild severity infection). The input was a spectrogram with a threshold set for each method. 'Day' indicates the number of days post-infection.

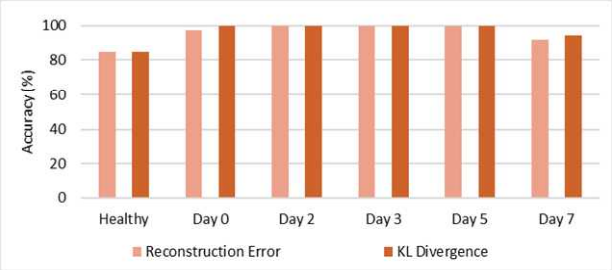


Figure 5. Results of Pig E (mild severity infection). The input was a spectrogram with a threshold set for each method. 'Day' indicates the number of days post-infection.

4. CONCLUSION

In this study, we addressed the issue of reduced identification accuracy due to individual differences by building a separate machine-learning model for each pig and detecting anomalies. Using an LSTM autoencoder with spectrogram inputs enabled highly accurate differentiation between healthy and diseased conditions, and incorporating the Kullback–Leibler divergence further improved the disease detection rates. However, for certain pigs, the classification accuracy declined substantially. Therefore, in future work, we plan to improve accuracy by using a different metric from the KL divergence and tuning the model hyperparameters through cross-validation.

5. ACKNOWLEDGMENTS

This research was supported by the Japan Racing and Livestock Promotion Foundation.

6. REFERENCES

[1] F. J. Pallarés, "Economic impact of respiratory diseases in pigs", Ceva Swine Health. Website. https://swinehealth.ceva.com/blog/economic-impact-of-respiratory-diseases-in-pigs, (Accessed on November 15, 2024)

[2] Ministry of Agriculture, Forestry and Fisheries, Livestock Statistics Survey, "Cumulative Statistics of the Number of Households and Pigs Nationwide (1960-2023)", https://www.maff.go.jp/j/tokei/kouhyou/tikusan/index.html, (accessed November 15, 2024).

[3] M. Mito, T. Aoki, K. Mizutani, K. Zempo, N. Wakatsuki, Y. Maeda, N. Takemae, R. Tsunekuni, T. Saito, "Frequency analysis of the sneeze caused by swine influenza virus strains: Automatic sneeze around-the-clock detection using a support vector machine." , Computers and Electronics in Agriculture, 179, 105789, (2020).

[4] M. Guarino, P. Jans, A. Costa, J. Aerts, D. Berckmans, "Field test of algorithm for automatic cough detection in pig houses", Computers and Electronics in Agriculture, 62, pp. 22-28, (2008).

[5] E. Lagua, H. Mun, K. AMPODE, V. Chem, Y. Kim, C. Yang, "Artificial Intelligence for Automatic Monitoring of Respiratory Health Conditions in Smart Swine Farming.", Animals: an Open Access Journal from MDPI, 13., (2023).

[6] Y. Matoba, S. Ishimitsu, S. Yumoto, O. Mikami, H. Inoue, M. Ishida, D. Tanaka, "Construction of LSTM Models for Detection of Respiratory Disease in Pigs", *in Proc. of the 30th International Congress on Sound and Vibration,* (Amsterdam), 8 pages, 2024

[7] K. Narusawa, Y. Cheng, S. Ishimitsu, M. Nakayama, S. Iijima, O. Mikami, M. Takagi and H. Inoue, " Analysis of body-conducted sound to identify infected pigs", *ICIC Express Letters Part B:Applications* vol. 11, no. 8, pp.735-741, 2020.

[8] Y. Matoba, S. Ishimitsu, N. Okada, S. Yumoto, O. Mikami, H. Inoue, M. Ishida, D.Tanaka, "Disease detection using machine learning techniques in time-frequency domain", Proceedings of 52nd International Congress and Exposition on Noise Control Engineering, Chiba, Japan on 20-23 August, 2023.

[9] Pankaj Malhotra, et al, LSTM-based Encoder-Decoder for Multi-sensor Anomaly Detection, The 33rd International Conference on Machine Learning, 2016

DOI: 10.61782/fa.2025.0164



FORUM ACUSTICUM
EURONOISE 2025

AUTOMATED DATA CURATION FOR SELF-SUPERVISED LEARNING IN UNDERWATER ACOUSTIC ANALYSIS

Hilde I Hummel[1*] **Sandjai Bhulai**[2] **Burooj Ghani**[3]
Rob van der Mei[1]
[1] Center of Mathematics and Computer Science, Amsterdam, Netherlands
[2] Vrije Universiteit, Amsterdam, Netherlands
[3] Naturalis Biodiversity Center, Leiden, Netherlands

ABSTRACT

The sustainability of the ocean ecosystem is threatened by increased levels of sound pollution, making monitoring crucial to understand its variability and impact. *Passive acoustic monitoring* (PAM) systems collect a large amount of underwater sound recordings, but the large volume of data makes manual analysis impossible, creating the need for automation. Although machine learning offers a potential solution, most underwater acoustic recordings are unlabeled. Self-supervised learning models have demonstrated success in learning from large-scale unlabeled data in various domains like computer vision, Natural Language Processing, and audio. However, these models require large, diverse, and balanced datasets for training in order to generalize well. To address this, a fully automated self-supervised data curation pipeline is proposed to create a diverse and balanced dataset from raw PAM data. It integrates *Automatic Identification System* (AIS) data with recordings from various hydrophones in the U.S. waters. Using hierarchical k-means clustering, the raw audio data is sampled and then combined with AIS samples to create a balanced and diverse dataset. The resulting curated dataset enables the development of self-supervised learning models, facilitating various tasks such as monitoring marine mammals and assessing sound pollution.

Keywords: *Data curation, Underwater Acoustics, Self-Supervised Learning*

**Corresponding author*: h.i.hummel@cwi.nl.

Copyright: *©2025 Hummel et al. This is an open-access article distributed under the terms of the Creative Commons Attribution 3.0 Unported License, which permits unrestricted use, distribution, and reproduction in any medium, provided the original author and source are credited.*

1. INTRODUCTION

The increasing levels of sound pollution threaten the preservation of ocean ecosystems, necessitating the monitoring of underwater sounds [1]. *Passive Acoustic Monitoring* (PAM) systems are globally deployed and collect a vast amount of diverse underwater sound recordings. The complexity of the marine environment, combined with the large volume of data, makes manual analysis impractical. As a result, annotating such data is time-consuming and expensive, leaving most PAM recordings unlabeled [1]. Although *machine learning* (ML) could potentially facilitate automatic analysis, the performance of supervised methods is limited by the scarce label availability. *Self-Supervised Learning* (SSL) has successfully handled large-scale unlabeled data in domains like computer vision, Natural Language Processing [2], and audio [3]. However, the performance of SSL models is reduced when they are optimized on uncurated data [4]. This makes balancing of the training data by data curation a key aspect for SSL models to generalize on downstream tasks. Despite the widespread availability of uncurated PAM data, no prior research has focused on curating these data to support the development of SSL-driven models for automatic underwater acoustic analysis. To address this gap, this article presents a fully automated pipeline for the curation of large-scale, freely accessible PAM recordings. This pipeline integrates *Automatic Identification System* (AIS) data with PAM data to balance both the ship distribution and the raw audio distributions. The key contributions of this paper are:

- A simple AIS curation method based on ship oc-

currence;

- An online hierarchical clustering approach for raw large-scale PAM data curation.

The curation method is evaluated by training an SSL algorithm on the curated dataset. The embedding space will be evaluated on a downstream task. The learned embeddings serve as input for the linear regression-based classification, to classify ship types from the reference datasets Deepship [5] and ShipsEar [6] containing underwater recordings of ships labeled by the type of ship.

2. RELATED WORK

2.1 SSL in underwater acoustics

Several previous studies have shown the potential of SSL in the automatic recognition of ship types [1]. With no large, curated underwater acoustic dataset publicly available yet, [7] and [8] proposed pretraining on AudioSet applying a mix-up strategy. Next, a Swin Transformer encoder is optimized with masked log-Melspectrogram, while a decoder is optimized to reconstruct the full spectrogram. A high masking rate was needed because of the limited contrast in these spectrograms. The fine-tuning on Deepship [5] yielded an accuracy of 80% - 86%. However, because of the complexity of the marine environment, tasks related to acoustics above the water may not be representative of the marine environment. To address this, [9] proposed a generative transformer model pretrained solely on underwater acoustic data. To reduce the GPU demand during training, they proposed hierarchical token-convolutions and masked these for reconstruction. Deepship model pre-training and fine-tuning on both Deepship and ShipsEar [6] improved performance over a supervised transformer baseline. However, their method is limited in real-world applications because of the lack of diversity of ocean environments in their training data. Our study overcomes this issue by representing a data curation pipeline to extract a diverse and balanced unlabeled dataset for SSL algorithms.

2.2 Data curation methods

SSL models need a balanced and diverse dataset to compete with supervised methods. The simple scraping of raw data from the web results in an unbalanced dataset, creating the need for data curation [4]. Previous research proposed an automatic data curation pipeline for data curation from images scraped from the web [10]. They suggested converting both a labeled curated dataset and an unlabeled uncurated dataset to the embedding space and performed deduplication by removing near-duplicate images in the uncurated dataset. Finally, they retrieved images from the uncurated dataset by calculating the relative distance to the curated samples. Although they state that this method is self-supervised, it still requires a large labeled dataset for matching. In a follow-up article, [11], they proposed a hierarchical KMeans algorithm to retrieve images from an uncurated dataset. Here, they overcome the problem that web-scraped big data is mostly long-tailed. Sampling from traditional KMeans does not encounter this, and therefore, hierarchical KMeans clustering and sampling are proposed. In addition, the DINOv2 algorithm was applied to text-image pairs [4]. In this paper, they performed data curation. Here, they aligned the images to the captions and sampled from the aligned captions to create the image dataset. The addition of metadata for data curation has also been proposed for audio-visual video representations in [12]. In this work, they tried to maximize the estimated mutual information between the video imagery and the corresponding audio. Both studies showed that the incorporation of metadata for data curation can improve the quality of the curated data.

3. METHODS

3.1 PAM data

The raw audio data is collected from NOAA [1], selecting hydrophones which started recording in 2023 or later. All these PAM audio recordings are combined into the resulting dataset $\mathcal{D}$. In total, this combination covers the duration of 8 years, 6 months, 9 days, 15 hours, 19 minutes, and 49 seconds from 11 individual hydrophones. These hydrophones are visualized in Figure 1.

3.2 AIS data

Track records of ships are recovered by AIS. This system captures information about ship characteristics, the location, and movements of almost all ships worldwide. The NOAA also provides freely accessible AIS data [2] covering the same regions as raw PAM data. The raw PAM data were aligned with the AIS data by drawing a 4 km

[1] https://console.cloud.google.com/storage/browser/noaa-passive-bioacoustic;tab=objects?inv=1&invt=AbnmXQ&prefix=&forceOnObjectsSortingFiltering=false

[2] https://marinecadastre.gov/accessais/



Figure 1. The locations of the hydrophones from the web scraped PAM data, indicated in red pointers.

$\times$ 4 km square with the hydrophone in the center (Figure 2). This square defines the range of the hydrophone, and therefore, every AIS pulse within this range was considered recorded. The data set containing the AIS pulses will be referred to as $\mathcal{A}$. All recordings, with AIS information, were gathered to create the dataset $\mathcal{D}_s$.

3.3 AIS data curation

The low contrast of radiated ship noise against background noise makes it difficult for simple machine learning methods to encounter ship noise in a large volume of data. To ensure a diverse representation of the acoustic profiles of the ships in the curated dataset, the AIS data $\mathcal{A}$ is also curated. A simple approach inspired by [4] is proposed. Here, they proposed to curate the aligned caption to curate an image dataset from a caption-image pair dataset. In this work, the AIS data are aligned with the PAM data, creating a dataset $\mathcal{D}_s$ holding the aligned PAM recordings and a dataset $\mathcal{A}$ holding the aligned AIS pulses. These pulses are then sampled based on the occurrence of individual ships, using a threshold value t. This threshold is defined based on the incidents of individual ships in the aligned PAM dataset $\mathcal{D}_s$. Ships with a lower incidence than t will not be sampled and kept complete in the curated dataset, while ships that exceed t are sampled according to their sample probability. This probability is inversely proportional to the occurrence of the ship in $\mathcal{D}_s$, the higher the occurrence, the lower the sampling probability and vice versa. Here, the objective is to balance the long-tailed distribution of $\mathcal{D}_s$ given $\mathcal{A}$, resulting in a more balanced dataset $\mathcal{D}_s^*$:

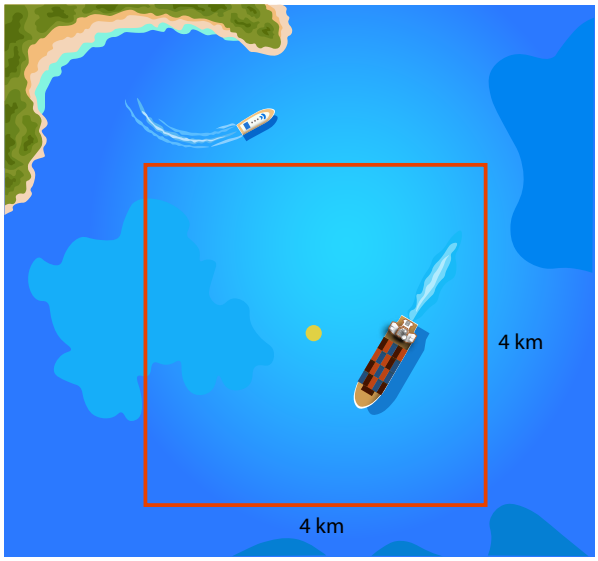


Figure 2. The defined range of the selected hydrophones to align raw PAM recordings with the AIS pulses.

$$\mathcal{D}_s^* \leftarrow f(\mathcal{D}_s; \mathcal{A}, t) \tag{1}$$

3.4 Audio preprocessing

First, the raw audio was resampled to a sample rate of 16 kHz to ensure a common sample rate for all recordings. Next, the audio was windowed using a 10-second window size without overlap. From this windowed audio, embeddings were generated using the model presented in [13]. In this research, they state that this model is optimized on a large quantity of unlabeled underwater acoustic data and generates generalized embeddings with dimension 2048.

3.5 PAM data curation

The objective of the PAM data curation method is to retrieve a dataset with the target distribution U. This distribution is defined as a uniform distribution with the support of the distribution P, where P represents the distribution of dataset $\mathcal{D}$. The data curation method is inspired by the method proposed by [11]. The entire dataset $\mathcal{D}$ is employed to optimize a hierarchical KMeans model using the resampling-clustering technique. This model consists of four levels with cluster sizes of $[6000, 400, 40, 10]$. Here, the lower cluster levels focus on detailed informa-

tion, while the upper levels capture global features. Audio samples of 10 seconds are then drawn from each hierarchical layer. Given the large size of the dataset $\mathcal{D}$, the hierarchical KMeans is optimized in a streaming manner, which approximates the optimal solution [14]. After training, the optimal HKmeans is utilized to sample the data from each cluster level. A maximum of target size N samples is selected from the first datastream based on the relative distance of the datapoints to the assigned cluster centers. As additional datastreams are processed, once the target number of N samples is exceeded, the samples with the greatest distance to the cluster center are replaced by those closer to the center.

3.6 SSL algorithm training and evaluation

The proposed method is evaluated by training the Data2vec base framework [15]. The base model pretrained on speech is completely fine-tuned using the curated dataset. This dataset is defined as:

$$\mathcal{D}^* = \mathcal{D}_a + \mathcal{D}_s^* \tag{2}$$

The model is optimized using a batch size of 64, where each input sample for the student model is masked for 15% while the teacher model receives the full audio. The teacher model weights Δ keep track of the student model weights θ by:

$$\Delta = \tau\Delta + (1-\tau)\theta \tag{3}$$

The parameter τ $(\tau_0 \leq \tau \leq \tau_e)$ is gradually increased from $\tau_0 = 0.999$ to $\tau_e = 0.9999$ over 20 updates. The performance of the model is compared by training the same framework on a randomly curated dataset of the same size. A simple logistic regression is optimized using the learned embeddings for the classification of the type of ships.

4. RESULTS

4.1 Data curation

For the AIS curation method, the optimal threshold value t is defined to correspond to the knee of the skewed distribution of $\mathcal{D}_s$ [4]. Figure 3 illustrates the number of 10-second audio windows per individual ship, revealing a skewed distribution. The optimal threshold, aligning with the knee of the distribution, is around 250. For this reason, the threshold value t was set to 250, resulting in a dataset $\mathcal{D}_s^*$ capturing 25,021 audio samples.

In addition to AIS samples, 323,532 samples were selected during PAM data curation. These samples were combined to create the dataset $\mathcal{D}^*$ holding roughly 970 hours of PAM recordings.

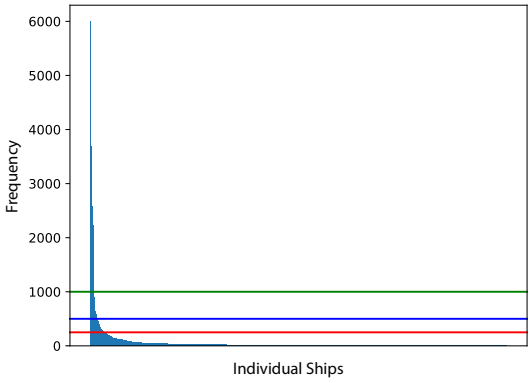


Figure 3. AIS distribution of individual ships in dataset $\mathcal{D}_s$ with threshold value $t = 250$ in red, $t = 500$ in blue, $t = 1000$ in green

4.2 SSL results curated dataset

The proposed method is evaluated using the labeled benchmark datasets Deepship [5] and ShipsEar [6]. Both datasets hold ship types recorded in two distinct regions. Table 1 presents the accuracy scores of the Data2Vec model trained on curated and random datasets. The results indicate that the curated model outperforms the random model on both benchmark datasets. However, the performance gain is smaller for ShipsEar, likely due to environmental factors. The ocean environment of ShipsEar is quite different from the environment of the hydrophones in the raw PAM data (Figure 1), making classification more challenging. In contrast, the ocean environment of Deepship is more comparable with the PAM data, leading to a performance increase of more than 7%.

Table 1. Accuracy scores ship type classification

	ShipsEar	Deepship
Random	51.98%	49.16%
Curated	53.11%	56.72%

5. CONCLUSION

This work describes the first automatic data curation pipeline to curate large web-scraped PAM data. The study demonstrates that curation is a key aspect in extracting accurate SSL model representations from unlabeled underwater recordings. Although this work focuses on data curation, more research is still required on SSL methods applied to underwater acoustics. Due to the stationarity of the data, the masking strategy may be suboptimal, and the results may benefit from a more contrastive approach. In addition to the raw web-scraped PAM data used in this study, more diverse data is publicly available. Expanding the diversity by incorporating more hydrophones from various regions would make the representations more robust for various other underwater acoustic-related tasks. This offers the possibility of training large-scale SSL models from scratch, enabling more advanced underwater acoustic applications.

6. REFERENCES

[1] H. I. Hummel, R. D. van der Mei, and S. Bhulai, "A survey on machine learning in ship radiated noise," *Ocean Engineering*, vol. 298, p. 117252, 2024.

[2] J. Gui, T. Chen, J. Zhang, Q. Cao, Z. Sun, H. Luo, and D. Tao, "A survey on self-supervised learning: Algorithms, applications, and future trends," *IEEE Trans. Pattern Anal. Mach. Intell.*, vol. 46, no. 12, p. 9052–9071, 2024.

[3] S. Liu, A. Mallol-Ragolta, E. Parada-Cabaleiro, K. Qian, X. Jing, A. Kathan, B. Hu, and B. W. Schuller, "Audio self-supervised learning: A survey," *Patterns*, vol. 3, no. 12, p. 100616, 2022.

[4] C. Jose, T. Moutakanni, D. Kang, F. Baldassarre, T. Darcet, H. Xu, D. Li, M. Szafraniec, M. Ramamonjisoa, M. Oquab, *et al.*, "Dinov2 meets text: A unified framework for image-and pixel-level vision-language alignment," *arXiv preprint arXiv:2412.16334*, 2024.

[5] M. Irfan, Z. Jiangbin, S. Ali, M. Iqbal, Z. Masood, and U. Hamid, "Deepship: An underwater acoustic benchmark dataset and a separable convolution based autoencoder for classification," *Expert Systems with Applications*, vol. 183, p. 115270, 2021.

[6] D. Santos-Domínguez, S. Torres-Guijarro, A. Cardenal-López, and A. Pena-Gimenez, "Shipsear: An underwater vessel noise database," *Applied Acoustics*, vol. 113, pp. 64–69, 2016.

[7] K. Xu, Q. Xu, K. You, B. Zhu, M. Feng, D. Feng, and B. Liu, "Self-supervised learning–based underwater acoustical signal classification via mask modeling," *The Journal of the Acoustical Society of America*, vol. 154, no. 1, pp. 5–15, 2023.

[8] Q. Xu, J. Jiang, K. Xu, Y. Dou, C. Gao, B. Zhu, K. You, and Q. Zhu, "Self-supervised learning-for underwater acoustic signal classification with mixup," *IEEE Journal of Selected Topics in Applied Earth Observations and Remote Sensing*, vol. 17, pp. 3530–3542, 2024.

[9] S. Feng, X. Zhu, and S. Ma, "Masking hierarchical tokens for underwater acoustic target recognition with self-supervised learning," *IEEE/ACM Transactions on Audio, Speech, and Language Processing*, vol. 32, pp. 1365–1379, 2024.

[10] M. Oquab, T. Darcet, T. Moutakanni, H. Vo, M. Szafraniec, V. Khalidov, P. Fernandez, D. Haziza, F. Massa, A. El-Nouby, M. Assran, N. Ballas, W. Galuba, R. Howes, P.-Y. Huang, S.-W. Li, I. Misra, M. Rabbat, V. Sharma, G. Synnaeve, H. Xu, H. Jegou, J. Mairal, P. Labatut, A. Joulin, and P. Bojanowski, "DINOv2: Learning Robust Visual Features without Supervision," *Transactions on Machine Learning Research Journal*, pp. 1–31, 2024.

[11] H. V. Vo, V. Khalidov, T. Darcet, T. Moutakanni, N. Smetanin, M. Szafraniec, H. Touvron, C. Couprie, M. Oquab, A. Joulin, *et al.*, "Automatic data curation for self-supervised learning: A clustering-based approach," *arXiv preprint arXiv:2405.15613*, 2024.

[12] S. Lee, J. Chung, Y. Yu, G. Kim, T. Breuel, G. Chechik, and Y. Song, "Acav100m: Automatic curation of large-scale datasets for audio-visual video representation learning," in *Proceedings of the IEEE/CVF International Conference on Computer Vision*, pp. 10274–10284, 2021.

[13] H. I. Hummel, A. Gansekoele, R. D. van der Mei, and S. Bhulai, "The computation of generalized embeddings for underwater acoustic target recognition using contrastive learning," *Available at SSRN: http://dx.doi.org/10.2139/ssrn.5112948*, 2025.

[14] D. Sculley, "Web-scale k-means clustering," in *Proceedings of the 19th international conference on World wide web*, (New York, NY, USA), pp. 1177–1178, 2010.

[15] A. Baevski, W.-N. Hsu, Q. Xu, A. Babu, J. Gu, and M. Auli, "Data2vec: A general framework for self-supervised learning in speech, vision and language," in *International conference on machine learning*, (Maryland, USA), pp. 1298–1312, 2022.

DOI: 10.61782/fa.2025.0157

FORUM ACUSTICUM EURONOISE 2025

PRELIMINARY RESULTS ON AUDIO EVENT CLASSIFICATION APPLIED TO A UNIVERSITY SQUARE IN MILAN (ITALY) BEFORE AN URBAN REGENERATION PROJECT

Andrea Potenza[1*] **Ester Vidaña-Vila**[2] **Andrea Afify**[3]
Roberto Benocci[1] **Rosa Ma. Alsina-Pagès**[2] **Giovanni Zambon**[1]
[1] Department of Earth and Environmental Sciences, University of Milano-Bicocca, Italy
[2] Human Environment Research (HER), La Salle Campus Barcelona – Ramon Llull University, Spain
[3] Department of Physics, University of Milan, Italy

ABSTRACT

Biophonies, anthropophonies and geophonies characterize and shape an environment and contribute to the human appreciation of that place. Thus, sound event classification can be a useful tool to assess its quality and detect changes affecting it. In this study, different machine-learning models for multilabel sound classification are tested to monitor the ante-opera situation of the renewed square "Piazza della Scienza" of the University of Milano-Bicocca (Italy). The one-week monitoring was performed in May 2023 using 7 Song-Meter-Micros. The recordings were equalized to correct the devices' nonlinear frequency response. The paper is structured to: (a) test two sets of features in the Piazza's polluted soundscape by constant ventilation noise and other anthropogenic sources: YAMNet embeddings and classic audio features (such as MFCCs), (b) find the best algorithm between: decision tree, random forest, k-nearest neighbor and support vector classifier and (c) evaluate their performance when filtering the background ventilation noise to increase the datasets size. Preliminary results are presented with the final aim of optimizing the detection and applying it to describe the Piazza's soundscape, investigate differences in events spatial distribution, and evaluate the effects of the urban regeneration plan on the soundscape.

*__Corresponding author__: a.potenza@campus.unimib.it.
__Copyright__: ©2025 Potenza et al. This is an open-access article distributed under the terms of the Creative Commons Attribution 3.0 Unported License, which permits unrestricted use, distribution, and reproduction in any medium, provided the original author and source are credited.

Keywords: *Sound event classification, YAMNet, MFCCs, soundscape, background noise.*

1. INTRODUCTION

Noise pollution is a major environmental health concern in Europe since noise made by traffic, trains and airplanes is the second most important cause of disease, behind air pollution caused by very fine particulate matter [1]. This issue is particularly impactful in urban areas where about 60% of the European population will live by 2050 [1, 2]. In urban centers there are multiple anthropogenic sound sources often overlapping with one another (e.g., engines idling, car horns, technical installations, sirens and alarms, nightlife) [3] and with biophonic sounds (e.g., birds vocalizations, dog barking, cicada sounds) and geophonic ones (e.g. wind, rain, thunder). The noise impact on humans does not depend solely on the overall sound pressure level but also on the typology of noise sources, the individual sensitivity and the social and cultural context [3–5]. This reasoning is also valid for faunal communities which are impacted by noise depending on its typology and on species' aural sensitivity [6, 7]. For these reasons, sound event classification is a topic that gained greater importance in these years and many studies have dealt with it. This technique applied to open environments is useful in many applications, from automatically discriminating against adverse meteorological conditions in large datasets [8,9], to detect specific noises [8] and to collect events for soundscape assessments [10] and bio/eco-acoustic analyses [8, 9, 11, 12]. Linked to urban settle-

ments, many works have been performed on event classification from real in-field recordings, focusing on single events or on overlapping multiple events [10–12]. In this work, sound event classification is applied to a university square in Milan (Italy) which is heavily impacted by constant technical installation noise. The study's final aim is to develop a classifier for different sound events (i.e., road traffic, tram passages, speech, sirens) which will be used to assess the changes in the square's sound environment after an architecture requalification [13] which will improve the public space usage and increase the surface occupied by trees, bushes and lawns instead of cement. Moreover, the classification will allow a better understanding of the ecoacoustic indices behavior in urban environments and of people's acoustic environment perception already carried out in the square. In this paper, the efficacy of two sets of features on the square recordings was tested: the YAMNet embeddings and more classical features, such as the Mel-frequency cepstral coefficients (MFCCs), using different machine learning classificators: Decision tree, Random forest, K-nearest neighbor e Support vector classifier.

2. MATERIALS AND METHODS

2.1 Study Area

The area under study is the main square of the University of Milano-Bicocca called "Piazza della Scienza". It is set in the Bicocca neighborhood in the north outskirts of Milan, an area which went through a renovation process in the last fifty years, shifting from an industrial site to a university and third sector district. The Piazza covers a surface area of 8590 m^2 and is surrounded by 6-floor buildings and arranged on two levels: a fully cemented ground level and four lowered courtyards, three of them with a lawn cover. In 2024, the Piazza underwent a regeneration process thanks to the MUSA project (Multilayer Urban Sustainability Action) [13]. This project is set into the framework of the National Recovery and Resilience Plan (NRRP) and aims at proposing management strategies to face the environmental, social, and economic sustainability challenges of the metropolitan city of Milan. The Piazza renovation aims to increase its environmental sustainability in terms of reducing the heat island effect, increasing the water descent into the aquifer, reducing local air pollution, and improving the area's biodiversity. Moreover, it will allow a better use of the public space and increase students' quality of life in the Piazza. These results will be achieved through the depaving and greening of the ground level and the renewal of the lowered courts (Figure 1).

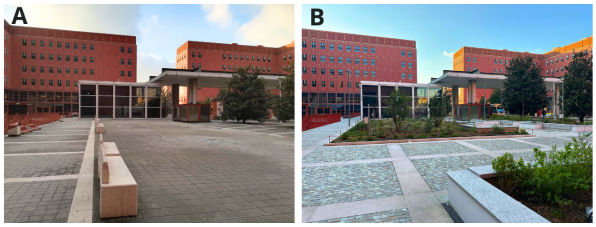


Figure 1. Piazza della Scienza before (A) and after (B) the regeneration process of MUSA.

2.2 Data collection and annotation

The monitoring campaign used to populate the database was performed in May 2023, from Monday 22th to Sunday 28th, in 7 sites of the Piazza (Figure 2). To capture the different sound sources present, 2 devices were placed at the ground level floor, 2 in the lowered courtyards and 3 at the first floor of the buildings.

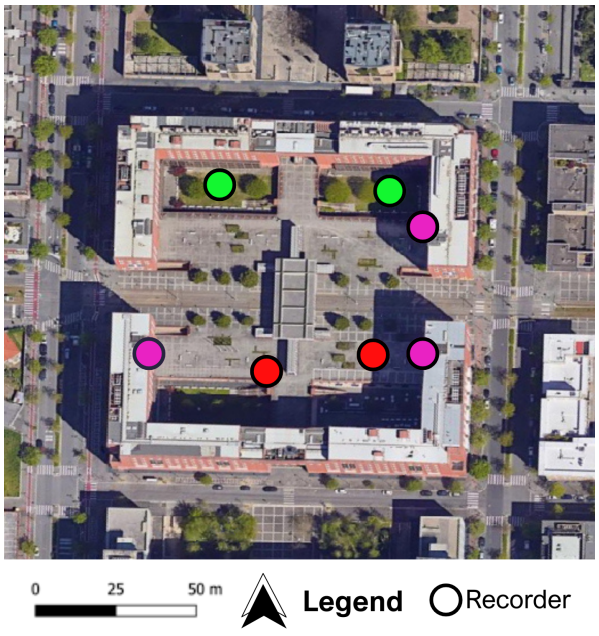


Figure 2. Piazza della Scienza (before the regeneration) and recording sites (pink: first floor, red: ground floor, green: lowered courtyards).

Table 1. Event labels present in the dataset, their description and total time duration.

Label	Description	Duration (min)
Road	Road traffic	17.55
Brake	Brake noise from vehicles and tram	5.65
Car horn	Car horn	0.24
Vpbor	Vehicle passing by on tram rails	0.89
Tram	Tram passing by, stopping and departing	12.41
Motorbike	Motorbike engine noise and passing by	3.79
Street cleaning	Street cleaning vehicles and operators	1.09
Siren	Ambulance and police sirens	6.10
SignalAlarm	Signals and Alarm noises	4.22
Construction	Noises from construction sites	3.29
TrolleyCart	Cart and trolley noises on pavimentation	5.39
Bird	Birds vocalizations	5.29
Dog	Dog barks	0.34
Insects	Insects sounds	4.33
Wind	Gusts of wind	1.66
Speech	Speech and human voices, exclamation, laughs	21.57
Ventilation	Technical installations noise	125.00
Complex	Unclassified sounds	3.23

The Song Meter Micros from Wildlife acoustic were used, set with a sampling rate of 48 kHz and an amplitude gain of +12 dB, recording for 1 minute and pausing for 1 minute. Furthermore, the recordings were equalized to correct the devices' nonlinear frequency response [14,15]. In the Supplementary Materials of [14] it is available the open source MATLAB script for equalizing the recordings and obtain linear-comparable audio files with other devices and between ecoacoustic studies. The recording campaign resulted in a total of 75 hours of acoustic data per sensor. The labelling process was performed on Audacity following previous works of coauthors [16]. Audacity is an audio recording and editing software which allows users to select part of an audio file and associate a text label with it. These labels can be exported in a text file (txt) as a list indicating the labels' name and their starting and ending time (time is expressed in seconds and calculated referencing to the audio beginning as the time zero). In this work, a single label was applied to each sound event independently of its time duration. The total labelled time is 2 hours and 5 minutes. The label taxonomy was adapted from [17] to fit the particular sound events present in the Piazza and discharge those not happening. In Table 1 are reported the 18 labels kept for this study area and their total time duration in the dataset. To be fed into the classifiers, the txt files from Audacity were converted into one-hot-encoded format.

2.3 Feature extraction

To detect the sound events in the Piazza two methods have been used to test their efficiency:

- YAMNET's embeddings.
- Features from the python package librosa.

2.3.1 YAMNet's embeddings

YAMNet is a pre-trained neural network model which has been used in many works in literature to perform sound event detection [9, 18] or to obtain features to be used as features for other algorithms [19]. The model relies on the MobileNet V1 architecture which consists of 27 convolutional layers, 1 global average pooling layer, and 1 fully connected layer; it employs ReLU activation functions, batch normalization and Softmax activation to obtain an

Table 2. Labels occurrences in each dataset.

Label	YAMNet OR	YAMNet filt	Librosa 1s OR	Librosa 1s filt	Librosa 20ms OR	Librosa 20ms filt
Road	2'211	6'633	1'115	3'345	5'435	16'305
Brake	738	2'214	397	1'191	1'866	5'598
Car horn	37	111	26	78	104	312
Vpbor	135	405	105	315	425	1'275
Tram	1'566	4'698	792	2'376	3'844	11'532
Motorbike	488	1'464	260	780	1'241	3'723
Street cleaning	137	411	67	201	334	1'002
Siren	761	2'283	373	1'119	1'842	5'526
SignalAlarm	536	1'608	285	855	1'384	4'044
Construction	426	1'278	235	705	1'095	3'285
TrolleyCart	692	2'076	368	1'104	1'760	5'280
Bird	755	2'265	467	1'401	2'074	6'222
Dog	51	153	37	111	158	474
Insect	556	1'668	279	837	1'370	4'110
Wind	240	720	143	429	640	1'920
Speech	2'750	4'864	1'457	2'733	6'931	12'649
Complex	487	1'461	347	1'041	1'430	4'290

output feature vector of size 1024 [20, 21]. The model predicts the 521 sound event classes of the AudioSet corpus [22]. Each audio file is first downsampled at 16 kHz and normalized to fit the AudioSet requirements before calculating the features (embeddings) on a time window of 0.96 seconds with a 50% overlap. The embeddings calculation is explained here [23] but, shortly, they are logarithmic Mels calculated in the range 0.125 - 7.5 kHz and fed to the MobileNet V1 model. As the final step, the model calculates the output scores for each of the 521 AudioSet classes. In our study, YAMNet was used as a feature extractor on each labelled audio file and each 0.96 seconds time frame is characterized by 1024 features.

2.3.2 *Features from the python package librosa*

To compare YAMNet's features performances, another set of features have been calculated. In particular, the python package librosa [24] was used. In this case, downsampling and normalization were not applied. The features were calculated on a 1-second time frame and a 20-millisecond time frame without overlapping; the double timeframes are kept to understand their influence on the classification. The following spectral features were calculated following previous works [25]:

- Mel-frequency cepstral coefficients (MFCCs), using a number of coefficients of 13.
- Spectral centroid (SC).
- Roll-off frequency, with a rollpercent of 10 and 90.
- Amplitude root-mean-square (RMS).
- Zero-crossing rate (ZCR).
- Static tempo.
- Flatness.
- Spectral bandwidth.

For each feature (except MFCCs and static tempo), 7 statistical descriptors were calculated: minimum, maximum, mean, median, standard deviation, skewness and kurtosis [25]. Thus, each 1-second time frame is characterized by 1272 values (of which 1222 are MFCCs), while each 20-millisecond time frame by 297 values (of which 247 are MFCCs).

2.4 Data filtering to increase the datasets

To increase the number of recordings populating the datasets, filtration of the ventilation noise (label "Ventilation") has been carried out. This operation have been achieved using the "Noise Reduction" function of Audacity. This function elaborates the noise profile of a recording and uses it to reduce that noise in other recordings.

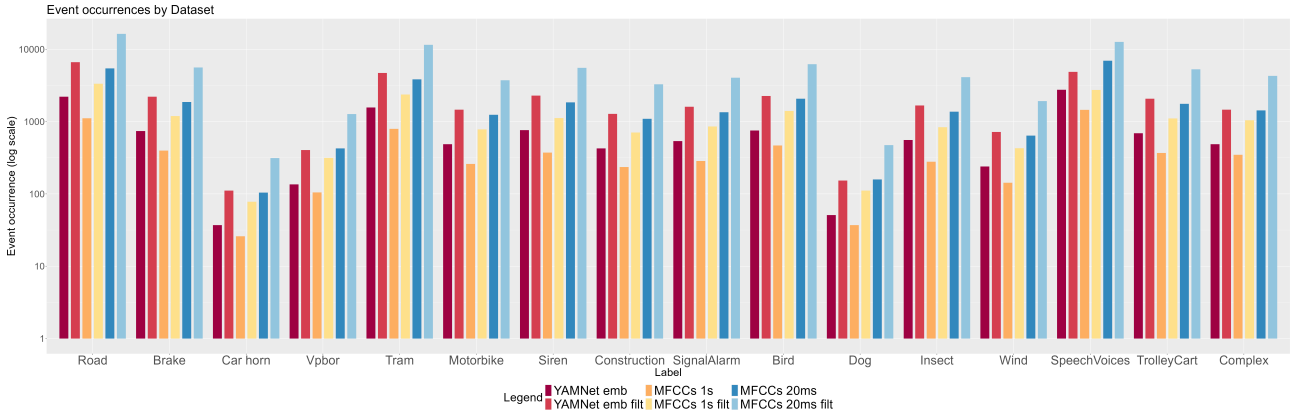


Figure 3. Labels occurrences in each dataset.

For each site, a midnight recording containing only ventilation noise was selected. Two settings were applied: T1 (Noise reduction: 6 dB, Sensitivity: 5, Frequency Smoothing = 4) and T2 (Noise reduction: 10 dB, Sensitivity: 10, Frequency Smoothing = 8). Furthermore, due to uneven occurrences of labels (see Table 2 and Figure 3), in the filtered recordings the label with the highest occurrence ("Speech") and the corresponding features were removed when the event was not overlapped with others. After these filtering and balancing processes, the datasets are shaped as reported in Table 2 and in Figure 3.

2.5 Detection

For the detection of sound events, different classification models have been implemented in the Python environment. A pipeline has been built to run the following classification models: decision tree (DT), random forest (RF), k-nearest neighbor (KNN), support vector classifier (SVC). These algorithms are executed to perform a multi-output classification to classify overlapping sound events. Different trials have been performed using three different scalers (standardscaler, minmaxscaler, robustscaler); standardscaler subtracts the mean and scales the data to unit variance, minmaxscaler uses the maximum and minimum values of the dataset to rescale the features in the range [0, 1], and robustscaler is based on the percentiles thus is less affected by outliers [26]. The datasets have been split into training (80%) and testing (20%) using the train_test_split command from sklearn. The best classifier will be chosen based on three metrics: Precision, Recall and F1-Score.

3. RESULTS AND DISCUSSION

In Table 3 and 4, the best values of Precision, Recall and F1-score are reported for each label and feature typology, indicating the relative dataset, classifier and scaler.

Looking at the "Dataset" columns of Table 3 and 4, we found that the classificators performed better with the augmented datasets (occurrences increased by filtering the Ventilation background noise). Regarding the librosa features timeframe, the 20-ms windowing allowed a better performance.

Focusing on the typology of Classifier and Scaler, the most frequent one are the Decision Tree (DT), followed by the Random Forest (RF), and the StandardScaler (Std).

In Table 3 (YAMNet embeddings), it is possible to notice that the majority of the F1-scores are above 60% with Street cleaning, Siren, Bird, Insect and Speech being over 70%. On the other hand, in Table 4 (Librosa features) events that have an F1-score higher than 70% are Street cleaning, Siren, Insect, Speech, Road, Tram, SignalAlarm, Construction and TrolleyCart. Dog barking obtained the lowest scores, probably due to its lower occurrence in the dataset (Table 2) and the masking caused by ventilation systems. Siren got the highest score, probably because of its marked distinguished spectrum.

When comparing the F1-score between the datasets, the librosa features received higher scores for the majority of labels. This trend is also visible for Precision and Recall, even if not for the same sound events.

Table 3. Best results using the YAMNet embeddings

Label	Precision	Recall	F1-score	Dataset	Classifier and scaler
Road	0.64	0.67	0.65	Filter	DT - Std
Brake	0.59	0.62	0.61	Filter	DT - Std
Car horn	1.00	0.45	0.62	Filter	RF - Std
Vpbor	0.56	0.71	0.63	Filter	DT - Std
Tram	0.59	0.65	0.62	Filter	DT - Std
Motorbike	0.53	0.64	0.58	Filter	DT - Std
Street cleaning	0.71	0.77	**0.74**	Filter	DT - Std
Siren	0.83	0.83	**0.83**	Filter	DT - Std
SignalAlarm	0.55	0.61	0.58	Filter	DT - Std
Construction	0.64	0.63	0.63	Filter	DT - Std
TrolleyCart	0.66	0.67	0.67	Filter	DT - Std
Bird	0.96	0.61	**0.74**	Filter	RF - Std
Dog	0.45	0.45	0.45	Filter	DT - Std
Insect	0.73	0.72	**0.72**	Filter	DT - Std
Wind	0.48	0.56	0.52	Filter	DT - Std
Speech	0.91	0.68	**0.78**	Filter	RF - Std
Complex	0.56	0.56	0.56	Filter	DT - Std

Table 4. Best results using the Librosa features

Label	Precision	Recall	F1-score	Dataset	Classifier and scaler
Road	0.97	0.61	**0.75**	20ms Filter	RF - Std
Brake	0.58	0.59	0.58	20ms Filter	DT - Std
Car horn	0.40	0.57	0.47	20ms Filter	DT - Std
Vpbor	0.50	0.60	0.55	20ms Filter	DT - Std
Tram	0.98	0.59	**0.74**	20ms Filter	RF - Std
Motorbike	0.60	0.64	0.60	20ms Filter	DT - Std
Street cleaning	0.95	0.88	**0.91**	20ms Filter	SVC - Std
Siren	0.98	0.86	**0.92**	20ms Filter	RF - Std
SignalAlarm	0.99	0.56	**0.72**	20ms Filter	RF - Std
Construction	0.97	0.65	**0.78**	20ms Filter	SVC - Std
TrolleyCart	0.99	0.70	**0.82**	20ms Filter	RF - Std
Bird	0.57	0.64	0.60	20ms Filter	DT - Std
Dog	0.44	0.51	0.47	20ms Filter	DT - Std
Insect	0.93	0.74	**0.82**	20ms Filter	RF - Std
Wind	0.61	0.61	0.61	20ms Filter	DT - Std
Speech	0.94	0.55	**0.70**	20ms Filter	RF - Std
Complex	0.54	0.58	0.56	20ms Filter	DT - Std

4. CONCLUSIONS

Sound classification is a rich and growing research field in various acoustic branches nowadays and has been applied to numerous case studies around the world. This paper is focused on classifying the sounds occurring in the Piazza della Scienza in Milan, Italy.

These preliminary results provide important insights which show the better performance of the models using the librosa features instead of the YAMNet embeddings and the usage of a shorter time frame. Future analyses will be implemented on the librosa features dataset. They will consist of different steps like the implementation of confusion matrices and the application of a cross validation. Moreover, the GridSearch algorithm will be applied for tuning the models' hyperparameters. Furthermore, other algorithms will be tested (i.e., CNN-models) and the effects of the time window size on the performances will be studied. Finally, transfer learning will be taken into account to increase the dataset size, alongside the addition of audios recorded outside the Piazza to bypass the ventilation background noise.

5. ACKNOWLEDGMENTS

Investigation performed within the MUSA – Multilayered Urban Sustainability Action – project, funded by the European Union – NextGenerationEU, under the National Recovery and Resilience Plan (NRRP) Mission 4 Component 2 Investment Line 1.5: Strengthening of research structures and creation of R&D "innovation ecosystems", set up of "territorial leaders in R&D".

6. REFERENCES

[1] B. Lex, *Burden of disease from environmental noise. Quantification of healthy life years lost in Europe*. City: World Health Organization, 2011.

[2] U. N. D. of Economic and S. Affairs, *World Urbanization Prospects: The 2018 Revision*. City: United Nations, 2019.

[3] M. Raimbault and D. Dubois, "Urban soundscapes: Experiences and knowledge," *Cities*, vol. 22, no. 5, pp. 339–350, 2005.

[4] S. Dreger, S. A. Schüle, L. K. Hilz, and G. Bolte, "Social inequalities in environmental noise exposure: a review of evidence in the who european region," *International journal of environmental research and public health*, vol. 16, no. 6, p. 1011, 2019.

[5] N. Singh and S. C. Davar, "Noise pollution-sources, effects and control," *Journal of Human ecology*, vol. 16, no. 3, pp. 181–187, 2004.

[6] R. J. Dooling and A. N. Popper, "The effects of highway noise on birds. report to the california. department of transportation, division of environmental analysis, sacramento, california," 2007.

[7] D. Waddington, M. Wood, B. Davies, and R. Young, "Habitats: Managing the ecological impacts of noise on wildlife habitats for sustainable development," in *INTER-NOISE and NOISE-CON Congress and Conference Proceedings*, vol. 265, pp. 5247–5251, Institute of Noise Control Engineering, 2023.

[8] A. Brown, S. Garg, and J. Montgomery, "Automatic rain and cicada chorus filtering of bird acoustic data," *Applied Soft Computing*, vol. 81, p. 105501, 2019.

[9] F. Terranova, L. Betti, V. Ferrario, O. Friard, K. Ludynia, G. S. Petersen, N. Mathevon, D. Reby, and L. Favaro, "Windy events detection in big bioacoustics datasets using a pre-trained convolutional neural network," *Science of the Total Environment*, vol. 949, p. 174868, 2024.

[10] D. Bonet-Solà, E. Vidaña-Vila, and R. M. Alsina-Pagès, "Prediction of the acoustic comfort of a dwelling based on automatic sound event detection," *Noise Mapping*, vol. 10, no. 1, p. 20220177, 2023.

[11] B. Swaminathan, M. Jagadeesh, and S. Vairavasundaram, "Multi-label classification for acoustic bird species detection using transfer learning approach," *Ecological Informatics*, vol. 80, p. 102471, 2024.

[12] Devos, Paul, "Birdsong of common birds in an urban soundscape as evaluated with recurrent neural networks," in *Forum Acusticum 2023 : 10th Convention of the European Acoustics Association, Proceedings*, p. 2, 2023.

[13] MUSA, "Multilayered urban sustainability action," 2023. Available at: `https://musascarl.it/`, Accessed on: 31-03-2025.

[14] A. Potenza, V. Zaffaroni-Caorsi, R. Benocci, G. Guagliumi, J. M. Fouani, A. Bisceglie, and G. Zambon, "Biases in ecoacoustics analysis: A protocol to equalize audio recorders," *Sensors (Basel, Switzerland)*, vol. 24, no. 14, p. 4642, 2024.

[15] T. Alvares-Sanches, P. E. Osborne, and P. R. White, "Impacts of the covid lockdown on the soundscape of an urban area: noise, psychoacoustic metrics and ecoacoustic indices," in *INTER-NOISE and NOISE-CON Congress and Conference Proceedings*, vol. 268, pp. 5700–5708, Institute of Noise Control Engineering, 2023.

[16] E. Vidaña-Vila, L. Duboc, R. M. Alsina-Pagès, F. Polls, and H. Vargas, "Bcndataset: Description and analysis of an annotated night urban leisure sound dataset," *Sustainability*, vol. 12, no. 19, p. 8140, 2020.

[17] J. Salamon, C. Jacoby, and J. P. Bello, "A dataset and taxonomy for urban sound research," in *Proceedings of the 22nd ACM international conference on Multimedia*, pp. 1041–1044, 2014.

[18] J. Mariscal-Harana, V. Alarcón, F. González, J. J. Calvente, F. J. Pérez-Grau, A. Viguria, and A. Ollero, "Audio-based aircraft detection system for safe rpas bvlos operations," *Electronics*, vol. 9, no. 12, p. 2076, 2020.

[19] N. H. Valliappan, S. D. Pande, and S. R. Vinta, "Enhancing gun detection with transfer learning and yamnet audio classification," *IEEE Access*, 2024.

[20] A. G. Howard, M. Zhu, B. Chen, D. Kalenichenko, W. Wang, T. Weyand, M. Andreetto, and H. Adam, "Mobilenets: Efficient convolutional neural networks for mobile vision applications," *arXiv preprint arXiv:1704.04861*, 2017.

[21] A. Avila and C. Pinzón, "Comparative analysis of vggish and yamnet models for welding defect detection," in *International Scientific-Technical Conference MANUFACTURING*, pp. 184–199, Springer, 2024.

[22] AudioSet, "Audioset, a large-scale dataset of manually annotated audio events." Available at: `https://research.google.com/audioset/index.html`, Accessed on: 31-03-2025.

[23] YAMNet, "Yamnet." Available at: `https://github.com/tensorflow/models/tree/master/research/audioset/yamnet`, Accessed on: 31-03-2025.

[24] B. McFee, C. Raffel, D. Liang, D. P. Ellis, M. McVicar, E. Battenberg, and O. Nieto, "librosa: Audio and music signal analysis in python.," *SciPy*, vol. 2015, pp. 18–24, 2015.

[25] R. Benocci, A. Afify, A. Potenza, H. E. Roman, and G. Zambon, "Toward the definition of a soundscape ranking index (sri) in an urban park using machine learning techniques," *Sensors*, vol. 23, no. 10, p. 4797, 2023.

[26] F. Pedregosa, G. Varoquaux, A. Gramfort, V. Michel, B. Thirion, O. Grisel, M. Blondel, P. Prettenhofer, R. Weiss, V. Dubourg, J. Vanderplas, A. Passos, D. Cournapeau, M. Brucher, M. Perrot, and E. Duchesnay, "Scikit-learn: Machine learning in Python," *Journal of Machine Learning Research*, vol. 12, pp. 2825–2830, 2011.

DOI: 10.61782/fa.2025.0426



FORUM ACUSTICUM
EURONOISE 2025

HARDWARE ACCELERATION OF CONVOLUTIONAL NEURAL NETWORK FOR LUNG ULTRASOUND SEGMENTATION

A. Rubio[1,2,*] **M. Muñoz**[1,2] **G. Cosarinsky**[1]
J. F. Cruza[1]

[1] Institute for Physical and Information Technologies, Spanish National Research Council, 28006 Madrid, Spain

[2] Electronic Department, Universidad de Alcalá, 28805 Alcalá de Henares, Spain

ABSTRACT

Lung Ultrasound (LUS) imaging is a valuable diagnostic technique for lung condition evaluation, due to its non-ionizing and portable nature. However, its complex interpretation can be enhanced by Machine Learning (ML) tools, yet traditional solutions often fail to meet the speed demands of real-time applications. This paper presents a Field Programmable Gate Array (FPGA)-based hardware solution for real-time segmentation of lung ultrasound images using a Convolutional Neural Network (CNN), achieving a throughput of 80 inferences per second.

Keywords: *Machine Learning (ML), Lung ultrasound (LUS), Field Programable Gate Array (FPGA), hardware acceleration, edge computing.*

1. INTRODUCTION

Artificial Intelligence (AI) has revolutionized many scientific fields. In medicine, AI tools have aided healthcare professionals in more accurate and effective patient diagnoses [1, 2].

LUS is a non-invasive imaging technique increasingly used for evaluating respiratory diseases [3]. Although its acquisition is fast, LUS interpretation requires expertise and can result challenging for less experienced clinicians [4] .

Muñoz et al. [5] developed a Machine Learning (ML) model based in the U-NET architecture [6], trained on a video dataset from 30 patients, acquired and labeled at video level by an expert physician. That manual tagging was extended to frame level by a semiautomatic labeling tool developed in the same work. The model processes the B-Scans and generates four outputs (pleura, consolidation, B-line, and A-line) representing the probability of each artifact per pixel. While achieving high performance, its GPU implementation (Mini-PC with integrated GTX-2060) limits its usability in low-power consumption portable devices and clinical enviroments.

Field Programmable Gate Arrays (FPGAs) are integrated circuits that can be reprogrammed after manufacturing, showing promising results in accelerating ML models [7], due to their versatility, low power consumption, and small size.

This work proposes a high-throughput implementation using Vitis-AI, an open source framework that provides the tools to implement AI models it a cost-effective FPGA real-time solution, demonstrating its viability for ML hardware acceleration.

2. METHODS

2.1 Neural Network

Convolutional Neural Networks (CNNs) are widely used for segmentation tasks due to their ability to identify both

*__Corresponding author__: adrian.rubio@csic.es.

__Copyright__: ©2025 A. Rubio et al. This is an open-access article distributed under the terms of the Creative Commons Attribution 3.0 Unported License, which permits unrestricted use, distribution, and reproduction in any medium, provided the original author and source are credited.

local features and global patterns. The U-Net architecture has skip connections that incorporate spatial information at different scales, thus preserving structural details. In this work, attention gates, used in the skip connections of [5] were removed from the implemented model due to limitations with Vitis-AI on FPGA fabric. One of the objectives of this work is to analyze how the performace is affected by this modification.

A simplified version of the architecture is shown in Fig. 1. The 256x128 input image first goes through the encoder, where increasingly abstract information is extracted, while spatial resolution is reduced. The decoder processes and upsamples the extracted features thanks to skip-connections, which help maintain crucial spatial information. This results in four 256x128 output images, each segmenting a relevant artifact (Pleura, consolidations, B-lines and A-lines).
This model underwent the same training as the original and serves as the baseline for comparing subsequent modifications.
Python implementations of ML are typically optimized for CPU or GPU architectures, which differ significantly from the architecture of FPGAs. The original model needs to go through some transformations to make it compatible with FPGA constraints. As a consequence, both model size and inference time decrease. The processes required to implement the model in FPGA are pruning (removal of weights with values close to zero and retraining to recover accuracy) and quantization (conversion of model parameters from floating-point to fixed-point representations). For this specific implementation only quantization was required.

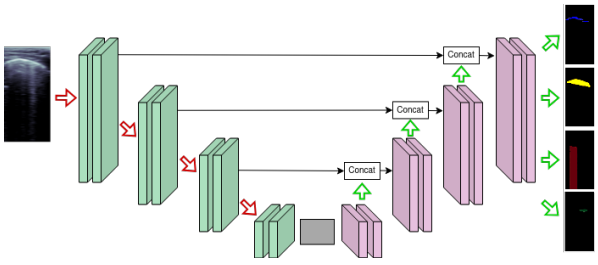


Figure 1. U-NET architecture. The first half encodes and reduces the dimensionality of the input, while the second half decodes and expands.

2.1.1 Training

The Python model was trained with 9624 images (70 % train, 30 % validation), using a learning rate of 0.0005. The loss function employed was binary cross-entropy, with a batch size of 64 images. Training was conducted for a maximum of 100 epochs, with early stopping activated if the validation loss did not decrease for 6 consecutive epochs. Upon completion of the training process, the model was prepared for quantization.

2.1.2 Quantization

FPGAs are not well-suited for the 32-bit floating-point precision commonly used in Python models. Instead, their computational capabilities are optimized for 8-bit fixed-point operations. This process, known as quantization, involves retraining the original model with a subset of the dataset, readjusting parameters and activations, and rounding decimals beyond a specific point (Fig. 2). The quantized model weighs less than a quarter of the original model.

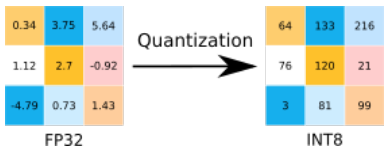


Figure 2. Quantization simple example.

2.2 FPGA architecture

The model is implemented on the Kria KV260 Vision AI Starter Kit, an FPGA particularly well-suited for real-time computer vision and edge computing applications. Its low cost and limited power consumption make it a suitable solution for a portable IA-assisted diagnosis tool.
The Deep Learning Processing Unit (DPU) is a programmable core for AMD FPGAs optimized for accelerating neural network computations through a specialized instruction set. The DPU processes the input data, provided with the correct dimensionality, performs the necessary computations (such as convolutions), and stores the segmentation results in the FPGA memory for further use.
Vitis-AI was used to retrain, modify, quantize, and tune the parameters of the model in an intuitive manner.

After successfully creating the hardware project, including the DPU and its bus connections with the embedded microprocessor and system memory, we generated a PetaLinux image configured to load the trained ML model and perform the segmentation process.
A dataset of 1358 validation images is transferred to the board. A Python script executed on the board processes the images to generate the segmentation masks. These masks are then transferred back to the host computer for analysis.

3. RESULTS

Fig. 3 and Fig. 4 show two segmentation examples. In each figure, the left image represents the tagged segmentation (ground truth) of the LUS artifacts, color-coded as follows: pleura (blue), consolidations (yellow), B-lines (red), and A-lines (green). The middle image shows the output of the original U-NET model (thresholded at 0.5), using the same color scheme. The right image shows the output of the FPGA-implemented model with the same threshold. Visually, the FPGA results are almost identical to the original model's.

Comparing the segmentations indicates that the model's performance was not significantly affected by the modifications required for FPGA implementation. Tab. 1 presents three evaluation metrics, calculated for all artifacts across the test dataset: the **Dice** coefficient (measuring the overlap between two sets), **precision** (the percentage of correctly identified positive pixels), and **recall** (the percentage of retrieved positive pixels). The FPGA-implemented model shows very similar performance to the original model in detecting all artifacts.

The model achieves a throughput of more than 80 inferences per second, compared to the the 50 per second reached in the previous GPU implementation.

4. DISCUSSION

This study successfully implemented a LUS segmentation model, originally developed in Python, onto an FPGA. The necessary modifications for FPGA compatibility were achieved with minimal impact on the model's performance. The results demonstrate that the FPGA-implemented model closely replicates the behavior of the original software model, as shown in Tab. 1.

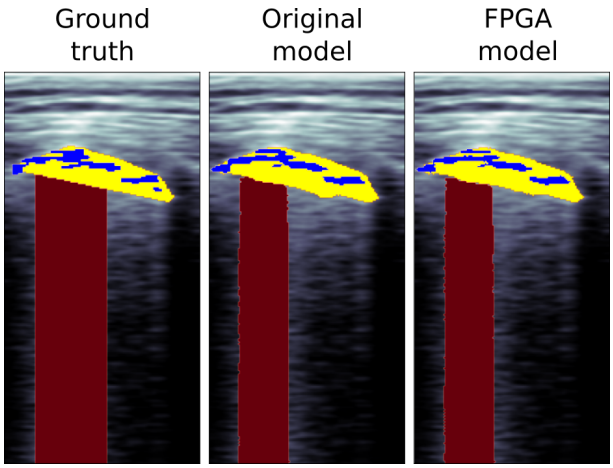


Figure 3. Pleura, B-line and Consolidation output example.

Table 1. Metrics for all artifacts and the two different models.

	Metric	Original	FPGA
Pleura	DICE	0.86	0.86
	Precision	0.85	0.88
	Recall	0.89	0.85
Consolidation	DICE	0.97	0.97
	Precision	0.97	0.98
	Recall	0.99	0.99
B-line	DICE	0.77	0.76
	Precision	0.90	0.90
	Recall	0.82	0.82
A-line	DICE	0.73	0.71
	Precision	0.78	0.77
	Recall	0.80	0.79

The achieved latency (12.5 ms), throughput, and power consumption demonstrate that FPGAs offer a viable alternative to traditional GPUs for hardware acceleration of AI-assisted LUS diagnostic tools. The compact size of the FPGA makes it particularly suitable for integration into small, portable ultrasound scanners.

The KV260 evaluation board (14cmx12cmx3.5cm) is smaller than the mini-PC with an integrated GPU

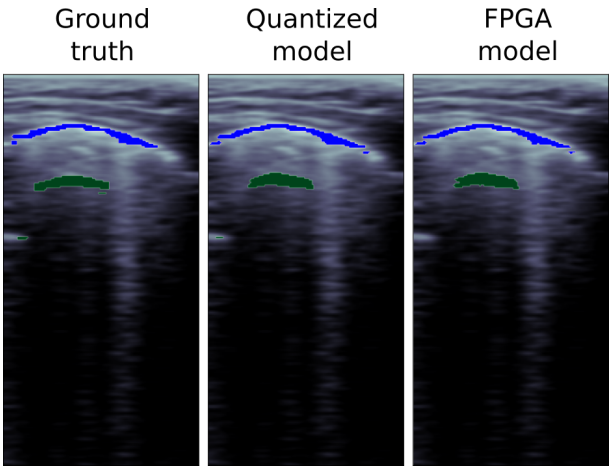


Figure 4. Pleura and A-line output example.

(21cmx19cmx5cm) employed in [5], and its use would eliminate the bottleneck caused by transferring the raw data to the PC for inference. Energy-wise, following the literature [8] FPGAs are more energy-efficient than GPUs, but a detailed study needs to be carried out to conclude that.

While the results are promising, this study was conducted using an offline test, processing all images in batch. Future work will focus on implementing frame-by-frame segmentation, integrating the neural network into the real-time data acquisition pipeline, and displaying the results to the physician on a screen.

5. CONCLUSIONS

Our findings demonstrate the suitability of FPGA acceleration for real-time LUS diagnosis due to its high inference speed, small size, and low power consumption with a cost-effective device. A key finding is that the quantization process bears almost no appreciable effect in the model performance, while reducing the size to a quarter of the original. Similarly, the removal of attention gates had neglible impact on the model's effectiveness.

The developed pipeline has been optimized for the specific characteristics of LUS segmentation. However, its core steps—model modification, quantization, and implementation—are adaptable and can be applied to other ML models and FPGA platforms. This underscores the potential of FPGAs in edge-computing by enabling rapid inference directly at the point of data acquisition.

6. ACKNOWLEDGEMENTS

Supported by the European Commission + NextGenerationEU, through Momentum CSIC Programme: Develop Your Digital Talent. The funding for these actions/grants and contracts comes from the European Union's Recovery and Resilience Facility-Next Generation, in the framework of the General Invitation of the Spanish Government's public business entity Red.es to participate in talent attraction and retention programmes within Investment 4 of Component 19 of the Recovery, Transformation and Resilience Plan. G. Cosarinsky staff is hired under the Generation D initiative, promoted by Red.es, an organisation attached to the Ministry for Digital Transformation and the Civil Service, for the attraction and retention of talent through grants and training contracts, financed by the Recovery, Transformation and Resilience Plan through the European Union's Next Generation funds.

Supported by the project PID2022-143271OB-I00, funded by MCIN/AEI /10.13039/501100011033/FEDER, UE.

7. REFERENCES

[1] M. L. Marinovich, E. Wylie, W. Lotter, H. Lund, A. Waddell, C. Madeley, G. Pereira, and N. Houssami, "Artificial intelligence (ai) for breast cancer screening: Breastscreen population-based cohort study of cancer detection," *eBioMedicine*, vol. 90, Apr 2023.

[2] J. Liao, X. Li, Y. Gan, S. Han, P. Rong, W. Wang, W. Li, and L. Zhou, "Artificial intelligence assists precision medicine in cancer treatment," *Frontiers in Oncology*, vol. 12, 2023.

[3] M. Beshara, E. A. Bittner, A. Goffi, L. Berra, and M. G. Chang, "Nuts and bolts of lung ultrasound: utility, scanning techniques, protocols, and findings in common pathologies," *Critical Care*, vol. 28, p. 328, Oct 2024.

[4] J. L. Herraiz, C. Freijo, J. Camacho, M. Muñoz, R. González, R. Alonso-Roca, J. Álvarez-Troncoso, L. M. Beltrán-Romero, M. Bernabeu-Wittel, R. Blancas, *et al.*, "Inter-rater variability in the evaluation of

lung ultrasound in videos acquired from covid-19 patients," *Applied Sciences*, vol. 13, no. 3, p. 1321, 2023.

[5] M. Muñoz, A. Rubio, G. Cosarinsky, J. F. Cruza, and J. Camacho, "Deep learning-based algorithms for real-time lung ultrasound assisted diagnosis," *Applied Sciences*, vol. 14, no. 24, 2024.

[6] O. Ronneberger, P. Fischer, and T. Brox, "U-net: Convolutional networks for biomedical image segmentation," 2015.

[7] A. Nechi, L. Groth, S. Mulhem, F. Merchant, R. Buchty, and M. Berekovic, "Fpga-based deep learning inference accelerators: Where are we standing?," *ACM Trans. Reconfigurable Technol. Syst.*, vol. 16, Oct. 2023.

[8] A. Reuther, P. Michaleas, M. Jones, V. Gadepally, S. Samsi, and J. Kepner, "Survey and benchmarking of machine learning accelerators," in *2019 IEEE High Performance Extreme Computing Conference (HPEC)*, pp. 1–9, 2019.

DOI: 10.61782/fa.2025.0255

FORUM ACUSTICUM EURONOISE 2025

CROSS-DOMAIN TRANSFER LEARNING FOR SEGMENTATION OF LUNG ULTRASOUND IMAGES

M. Muñoz[1,2*] **A. Rubio**[1,2] **G. Cosarinsky**[1]
J. Camacho[1]
[1] Institute for Physical and Information Technologies, Spanish National Research Council, Madrid, Spain
[2] Electronic Department, Universidad de Alcalá, Madrid, Spain

ABSTRACT

Developing deep learning models for lung ultrasound (LUS) segmentation is hindered by limited annotated data. This study demonstrates the effectiveness of cross-domain transfer learning (TL) using ImageNet pre-trained encoders (VGG16, ResNet50, MobileNetV2) within a U-Net architecture. Compared to training from scratch, TL with ResNet50 and VGG16 significantly improved segmentation Dice score (up to 30%). Furthermore, TL allowed reducing the training dataset to 45% while achieving performance comparable to the baseline trained on full data. These findings validate cross-domain TL as a valuable and data-efficient approach for LUS analysis.

Keywords: Artificial Intelligence (AI), Transfer Learning, Fine-tuning, Segmentation, Lung Ultrasound (LUS).

1. INTRODUCTION

Artificial Intelligence (AI) has emerged as a transformative technology with significant potential in medical imaging and diagnostics. In particular, AI-based approaches hold promise for improving the accuracy and efficiency of diagnostic procedures in various medical domains, including pulmonary imaging [1, 2, 3]. Lung ultrasound imaging plays an important role in diagnosing respiratory conditions, offering real-time visualization of pulmonary lesions [4]. However, the interpretation of lung ultrasound images can be challenging, and requires expertise to identify subtle features and abnormalities accurately [5].

AI-based Semantic segmentation, is a powerful approach for assessing LUS interpretation. However, a critical challenge in applying deep learning models for segmentation is the limited availability of large, annotated datasets. The process of acquiring LUS images and obtaining accurate annotations from expert radiologists is both time-consuming and expensive. To mitigate this bottleneck, some research efforts focus on developing automatic labeling tools [6]. While promising, transfer learning offers a complementary strategy by leveraging knowledge from pre-trained models, potentially reducing the amount of labeled data and training time required to achieve high performance.

Transfer learning has the potential to address the challenges associated with acquiring and labeling large datasets for comprehensive model training, making it a promising approach for enhancing the diagnostic utility of AI-based segmentation models in pulmonary ultrasound imaging [7].

The objective of this study is to investigate the application of cross-domain transfer learning techniques for lung ultrasound image segmentation, aiming to harness the power of pre-trained convolutional neural network (CNN) models for diagnostic assistance in pulmonary imaging and, to evaluate the impact of reduced training data on accuracy. Specifically, architectures such as VGG16, ResNet50 and MobileNetV2 are studied as pre-trained encoders within an Attention U-Net architecture.

[*] ***Corresponding author***: mario.munoz.prieto@csic.es.
Copyright: *©2025 M. Muñoz et al. This is an open-access article distributed under the terms of the Creative Commons Attribution 3.0 Unported License, which permits unrestricted use, distribution, and reproduction in any medium, provided the original author and source are credited.*

2. METHODS

2.1 CNN architectures

For semantic segmentation of LUS images, an Attention U-Net architecture [8] was employed. This network is based on the U-Net [9], which follows an autoencoder design (Figure 1). An autoencoder consists of two primary components: an encoder that progressively reduces the spatial dimensions of the input image while extracting increasingly abstract features, and a decoder that upsamples these features to reconstruct an output of the same size as the input. In U-Net based networks, skip connections between corresponding encoder and decoder layers facilitate the preservation of fine-grained details. The Attention U-Net incorporates spatial and channel attention modules [8] to further enhance feature discrimination.

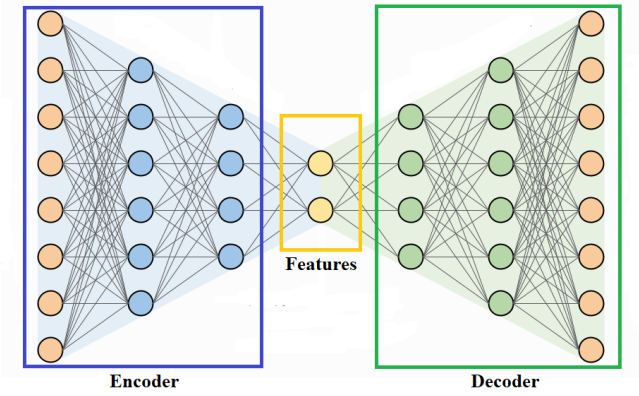


Figure 1. Schematic Autoencoder network architecture

To leverage transfer learning, the encoder portion of the Attention U-Net was replaced with pre-trained networks. Transfer learning is a technique where a model developed for a task is reused as the starting point for a model on a second task. In this case, models pre-trained on the large ImageNet dataset for image classification were utilized as encoder of the new architectures adapting them for LUS image segmentation. This study investigated three such pre-trained models: VGG16 [10], ResNet50 [11], and MobileNetV2 [12]. The classification layers of these models were removed, and feature maps were extracted from a specific layer of each encoder serving as input to the Attention U-Net decoder, which remained consistent across all configurations.

2.2 Dataset

This study utilized a dataset of 5131 lung ultrasound (LUS) images obtained from 30 patients diagnosed with COVID-19. The images were acquired as part of the clinical study described in [13]. The dataset exhibits typical LUS artifacts associated with pneumonia, including A-lines, B-lines, and consolidations.

Image annotation was performed using a semi-automatic labeling tool presented in [6]. This tool employs signal processing algorithms to generate initial segmentation masks. The results of this semiautomatic annotation tool were validated at the video level by a LUS expert physician. The annotations delineate the boundaries of artifacts such as pleura, A-lines, B-lines, and consolidations.

2.3 Methodology

This study evaluated cross-domain transfer learning for LUS image segmentation. An Attention U-Net, trained from scratch, was compared to three transfer learning configurations using pre-trained encoders (VGG16, ResNet50, MobileNetV2). Each configuration was trained four times with different random weight initializations to account for the inherent stochasticity of the training process. Performance was assessed using the mean and standard deviation of the Dice Similarity Coefficient (DSC) between the mean values on a reserved test set.

The dataset was divided into training (60%), validation (20%), and testing (20%) sets using a patient-wise split to provide a more realistic assessment of generalization performance. All models were trained with a learning rate of 3e-5, a batch size of 32, and the binary cross-entropy loss function. A two-stage transfer learning procedure was used: encoder layers were frozen for the first 60 epochs, then unfrozen for fine-tuning during the remaining 60 epochs. The reference model was trained from scratch for 120 epochs. Training was performed using TensorFlow 2.10 on two NVIDIA 2080 Ti GPUs.

The best-performing encoder (based on DSC) was then used in a data reduction experiment. Training set size was reduced 5% by 5% until the model achieved a validation DSC value below the reference model. The training procedure was repeated four times for each reduced dataset aiding consistency to the results. The model is stopped when the DSC is below the baseline model.

3. RESULTS

Table 1 shows the mean and standard deviation of the Dice Similarity Coefficient (DSC) for each model applying

Transfer learning (TL) and fine-tunning (FN) calculated on the test set.

Table 1. Segmentation performance.

Model Att-Unet	Dice (mean±std)
From Scratch	0.544 ± 0.034
VGG16 (TL+FN)	0.691 ± 0.033
MobileNetV2 (TL+FN)	0.516 ± 0.152
ResNet50 (TL+FN)	0.711 ± 0.043

Using ResNet50 as encoder with TL and FN achieved the highest mean DSC (0.71 ± 0.04), a statistically significant improvement over the baseline Attention U-Net (0.54 ± 0.03). With VGG16 as encoder (TL+FN) also significantly outperformed the baseline (0.69 ± 0.03). These results showed no statistically significant difference between Resnet50 and VGG16 encoders. MobileNetV2 (TL+FN) exhibited the lowest DSC (0.52 ± 0.15).
Figure 2 illustrates an example of the differences on segmentation performance between the Attention U-Net base model and the Resnet50-based Attention U-Net.



Figure 2. Segmentation performance comparison between the reference model (from scratch) and the Resnet50-Att. U-Net with TL and FN.

Following the initial comparison, the best-performing encoder (ResNet50) was used to investigate the impact of reduced training data. Models were trained on progressively smaller subsets of the training data, ranging from 95%. Figure 3 illustrates the mean DSC (± standard deviation) achieved modifying the percentage of training data used. The results indicate that leveraging transfer learning with the ResNet50 encoder allowed the training dataset size to be reduced to approximately 45% while still achieving a mean DSC comparable to the baseline Attention U-Net model trained from scratch on the full (100%) training dataset.

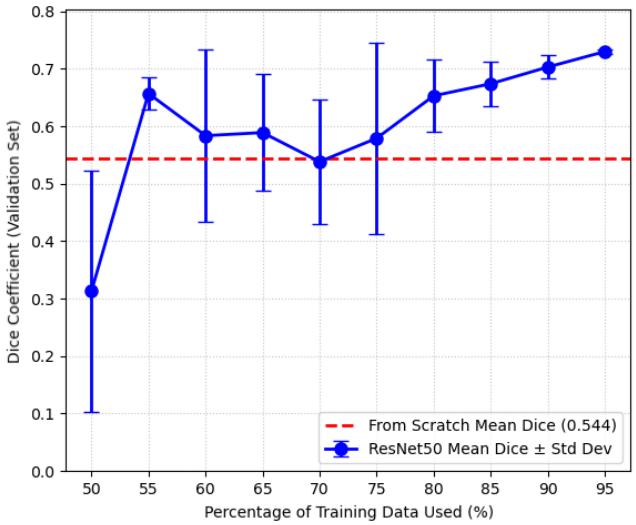


Figure 3. Data reduction results over Resnet50-based Attention U-Net fine-tuned.

4. DISCUSSION

This study investigated the effectiveness of cross-domain transfer learning for LUS image segmentation. The results demonstrate its advantages: pre-trained ResNet50 and VGG16 encoders significantly outperformed the baseline Attention U-Net trained from scratch. This suggests that, despite the significant domain difference between natural images (ImageNet) and medical ultrasound, features learned during pre-training are valuable for extracting relevant patterns in all type of images. While ResNet50 yielded the highest mean Dice score, VGG16's performance was comparable. On the contrary, MobileNetV2 performed worse, potentially because its design, focused on efficiency via parameter reduction, leads to lower representational capacity or features less transferable to this specific cross-domain task.

The data reduction study further highlights the value of transfer learning, with results quantitatively presented in Figure 3. This figure plots the validation Dice score of the ResNet50 transfer learning model against the percentage of training data used. It demonstrates that performance comparable to the baseline model (DSC ≈ 0.54) was maintained even when using only 55% of the original training data. This represents a substantial 45% reduction in the required annotated dataset, underscoring the practical benefit of cross-domain transfer learning in mitigating the need for extensive data annotation. Interestingly, the performance trend was not strictly constant; a noticeable dip

towards the baseline performance occurred around the 70% data mark where the mean performance approached or slightly fell below the baseline threshold. However, a sustained drop significantly below the baseline threshold was only observed for data levels below 55%. Furthermore, Figure 3 illustrates increased performance variability (larger standard deviations) at lower data percentages (particularly ≤75%), indicating greater training instability or sensitivity to data sampling when data becomes severely limited. Notably, while the standard deviation observed at the 55% data level appears comparatively low relative to surrounding data percentages in this experiment, this is likely to be due to the stochastic nature of training with only four runs, rather than an indication of particular stability at this specific data level.

It is important to acknowledge certain limitations of this study. Notably, exhaustive hyperparameter optimization was not performed for each encoder, potentially impacting individual model performance. Furthermore, results are based on a specific COVID-19 LUS dataset, which may limit generalizability. Future work should address these limitations by performing systematic hyperparameter tuning and evaluating performance on larger, more diverse LUS datasets encompassing various pathologies. Investigating more recent encoder architectures and comparing cross-domain pre-training with medical domain pre-training could also yield valuable insights.

Despite these limitations, this work provides evidence that cross-domain transfer learning, particularly with ResNet50 or VGG16, is a highly effective and data-efficient approach for LUS segmentation.

5. CONCLUSIONS

This study evaluated the application of cross-domain transfer learning techniques for the semantic segmentation of LUS images. The results conclusively demonstrate that using pre-trained architectures such as VGG16 and ResNet50 as encoders within an Attention U-Net network significantly improves segmentation performance compared to training from scratch. A marked increase in the Dice Similarity Coefficient (DSC) of approximately 30% was observed when employing transfer learning with the most effective encoders.

A key additional finding is the potential of transfer learning to mitigate the need for large annotated datasets. The data reduction analysis indicated that it is possible to decrease, in this specific example, the training dataset size to approximately 45% of its original size while still achieving segmentation performance comparable to the baseline model trained on the full dataset. This data efficiency considerably reduces the burden associated with manual labeling and model training, facilitating the development of AI tools in data-limited settings.

Finally, this work validates the utility of cross-domain transfer learning for medical imaging, and specifically for lung ultrasound. It confirms that features learned from large-scale natural image databases can be effectively transferred and adapted to improve analysis in specialized medical domains such as LUS, despite the inherent differences between the image types. Overall, transfer learning presents itself as a practical strategy for developing accurate and efficient LUS segmentation models.

6. ACKNOWLEDGMENTS

This research was partially supported by the project PID2022-143271OB-I00, funded by MCIN/AEI /10.13039/501100011033/FEDER, UE; and supported by the European Commission + NextGenerationEU, through Momentum CSIC Programme: Develop Your Digital Talent. The funding for these actions/grants and contracts comes from the European Union's Recovery and Resilience Facility-Next Generation, in the framework of the General Invitation of the Spanish Government's public business entity Red.es to participate in talent attraction and retention programmes within Investment 4 of Component 19 of the Recovery, Transformation and Resilience Plan. G. Cosarinsky staff is hired under the Generation D initiative, promoted by Red.es, an organisation attached to the Ministry for Digital Transformation and the Civil Service, for the attraction and retention of talent through grants and training contracts, financed by the Recovery, Transformation and Resilience Plan through the European Union's Next Generation funds.

7. REFERENCES

[1] Bajwa J, Munir U, Nori A, Williams B. Artificial intelligence in healthcare: transforming the practice of medicine. Future Healthc J. 2021 Jul;8(2): e188-e194. doi: 10.7861/fhj.2021-0095. PMID: 34286183; PMCID: PMC8285156.

[2] Zhao, L., & Lediju Bell, M. A. (2022). A review of deep learning applications in lung ultrasound imaging

of COVID-19 patients. BME Front., 2022, 9780173. https://doi.org/10.34133/2022/9780173X

[3] Mento F, Perrone T, Fiengo A, Smargiassi A, Inchingolo R, Soldati G, Demi L. Deep learning applied to lung ultrasound videos for scoring COVID-19 patients: A multicenter study. J Acoust Soc Am. 2021 May;149(5):3626. doi: 10.1121/10.0004855. PMID: 34241100.

[4] Tung-Chen Y, Martí de Gracia M, Díez-Tascón A, Alonso-González R, Agudo-Fernández S, Parra-Gordo ML, Ossaba-Vélez S, Rodríguez-Fuertes P, Llamas-Fuentes R. Correlation between Chest Computed Tomography and Lung Ultrasonography in Patients with Coronavirus Disease 2019 (COVID-19). Ultrasound Med Biol. 2020 Nov;46(11):2918-2926. doi: 10.1016/j.ultrasmedbio.2020.07.003. Epub 2020 Jul 13. PMID: 32771222; PMCID: PMC7357528.

[5] Herraiz JL, Freijo C, Camacho J, Muñoz M, González R, Alonso-Roca R, Álvarez-Troncoso J, Beltrán-Romero LM, Bernabeu-Wittel M, Blancas R, et al. Inter-Rater Variability in the Evaluation of Lung Ultrasound in Videos Acquired from COVID-19 Patients. Applied Sciences. 2023; 13(3):1321.

[6] Muñoz, M., Rubio, A., Cosarinsky, G., Cruza, J. F., & Camacho, J. (2024). Deep Learning-Based Algorithms for Real-Time Lung Ultrasound Assisted Diagnosis. Applied Sciences, 14(24), 11930. https://doi.org/10.3390/app142411930.

[7] Yu, X., Wang, J., Hong, Q.-Q., Teku, R., Wang, S.-H., & Zhang, Y.-D. (2022). Transfer learning for medical images analyses: A survey. Neurocomputing, 489, 230-254. https://doi.org/10.1016/j.neucom.2021.08.159.

[8] Oktay, O.; Schlemper, J.; Folgoc, L.L.; Lee, M.; Heinrich, M.; Misawa, K.; Mori, K.; McDonagh, S.; et al. Attention u-net: Learning where to look for the pancreas. arXiv 2018, arXiv:1804.03999.

[9] Ronneberger, O.; Fischer, P.; Brox, T. U-net: Convolutional networks for biomedical image segmentation. In Medical Image Computing and Computer-Assisted Intervention–MICCAI 2015, Proceedings of the 18th International Conference, Munich, Germany, 5–9 October 2015; Proc., Part III 18; Springer International Publishing: Berlin/Heidelberg, Germany, 2015; pp. 234–241.

[10] Simonyan, K., & Zisserman, A. (2014). Very deep convolutional networks for large-scale image recognition. arXiv preprint arXiv:1409.1556.

[11] He, K., Zhang, X., Ren, S., & Sun, J. (2016). Deep residual learning for image recognition. In Proc. of the IEEE conference on computer vision and pattern recognition (pp. 770-778).

[12] Sandler, M., Howard, A., Zhu, M., Zhmoginov, A., & Chen, L. C. (2018). Mobilenetv2: Inverted residuals and linear bottlenecks. In Proceedings of the IEEE conference on computer vision and pattern recognition (pp. 4510-4520).

[13] Camacho, J.; Muñoz, M.; Genovés, V.; Herraiz, J.L.; Ortega, I.; Belarra, A.; González, R.; Sánchez, D.; Giacchetta, R.C.; et al. Artificial Intelligence and Democratization of the Use of Lung Ultrasound in COVID-19: On the Feasibility of Automatic Calculation of Lung Ultrasound Score. Int. J. Transl. Med. 2022, 2, 17–25

DOI:

Main theme: A09 Machine learning and Artificial Intelligence in Acoustics

Session A09.05/A08.07 Artificial intelligence for industrial applications

Chair(s): R. M. Alsina-Pagès, G. Licitra

DOI: 10.61782/fa.2025.0737



FORUM ACUSTICUM
EURONOISE 2025

REINFORCEMENT LEARNING TO ENHANCE COMPUTATIONAL FLUID DYNAMIC SIMULATIONS WITH ACOUSTICS

David Huergo[1*] **Martín de Frutos**[1] **Óscar Mariño**[1]
Eduardo Jané[1] **Gonzalo Rubio**[1,2] **Esteban Ferrer**[1,2]
[1] ETSIAE-UPM-School of Aeronautics, Universidad Politécnica de Madrid,
Plaza Cardenal Cisneros 3, E-28040 Madrid, Spain.
[2] Center for Computational Simulation, Universidad Politécnica de Madrid,
Campus de Montegancedo, Boadilla del Monte, 28660 Madrid, Spain.

ABSTRACT

Reinforcement learning (RL) offers a powerful approach to automate decision-making in Computational Fluid Dynamic (CFD), improving accuracy and reducing human effort, leading to more efficient solvers.

In this work, we expand our RL-based polynomial adaptation technique for high-order solvers [1, 2] to capture acoustics. We improve aeroacoustic simulations employing RL to define a high-order acoustic path in the high-order solver HORSES3D [3], allowing precise wave capture from source to observer. Offline training eliminates the need for high-fidelity solutions, making the method versatile across various meshes and PDEs. This approach effectively addresses aeroacoustic challenges, focusing computational efforts where needed and ensuring accurate results at a reduced cost.

Keywords: *reinforcement learning, high-order discontinuous Galerkin, p-adaptation, adaptive mesh refinement, acoustics*

1. INTRODUCTION

The field of computational fluid dynamics (CFD) has undergone a paradigm change through the integration of machine learning techniques with classical numerical methods [4, 5]. In particular, reinforcement learning (RL) has been adopted as a valuable tool for a variety of fields, creating high-performing autonomous agents capable of making real-time decisions in complex environments [6]. In fluid dynamics, RL has been widely used to enable dynamic flow control [7–9], surpassing traditional approaches. Other applications in the field of numerical simulations for fluid dynamics include the selection of constants in turbulence models [10, 11], optimal parameters in high-order schemes [12, 13] or mesh adaptation.

Mesh adaptation or adaptive mesh refinement (AMR) allows to refine or coarsen the computational mesh based on sensors or metrics. Traditionally, this process has relied on manual intervention, heuristics or error estimators [14, 15], which is time-consuming and limits the ability to capture complex flow phenomena. The integration of RL for mesh adaptation offers a novel approach to automate the process, minimizing user intervention while providing a flexible and general framework applicable to a wide range of problems. RL has been successfully used for AMR (h-refinement) in recent works, where agents were trained to refine or coarsen the mesh, increasing the accuracy in critical regions and minimizing the computational cost [16]. Additionally, Yang et al. [17] consider new policy architectures which are trained from numerical simulations and are agnostic to the mesh size. These approaches provide accurate solutions and a reduced computational cost, surpassing traditional mesh refinement approaches.

This work extends our research presented in [1, 2], where

*__Corresponding author__: david.huergo.perea@upm.es.
__Copyright__: ©2025 David Huergo et al. This is an open-access article distributed under the terms of the Creative Commons Attribution 3.0 Unported License, which permits unrestricted use, distribution, and reproduction in any medium, provided the original author and source are credited.

we established the basis for applying reinforcement learning to p-adaptation in complex 3D turbulent problems. Furthermore, we provide an RL-based error estimator that can be used to estimate the order of magnitud of spatial errors inexpensively. Based on this original concept, we have developed a novel methodology to apply this approach to acoustic simulations. Here, we define an acoustic path, from a source to an observer, where the task of the p-adaptation algorithm is to accurately capture pressure waves; while outside of the acoustic path, the mesh is refined based on aerodynamic features. This hybrid adaptation strategy provides accurate solutions and results in a reduction of the required computational cost when running numerical simulations for acoustics.

2. METHODOLOGY

The methodology is implemented in the open source solver HORSES3D [3, 18, 19], developed at the ETSIAE-UPM School of Aeronautics in Madrid, and available on Github (`https://github.com/loganoz/horses3d`). This solver is a high-order discontinuous Galerkin (DG) tool capable of simulating compressible, incompressible, and multiphase flows with acoustics. HORSES3D allows for the use of high order polynomials in each element in the mesh, and shows exponential decay of the error when increasing the polynomial order but with only a linear increase in the cost, which results in very efficient computations.

The p-adaptation strategy [2] allows one to select the optimal polynomial order in each element of the mesh independently. As the proposed approach is anisotropic, three different polynomials are defined inside each element of the mesh. This methodology provides an automatic way of increasing the accuracy of the solver, by refining the mesh in regions with strong gradients, while keeping the computational cost down, as the polynomial order is reduced in the far field or other regions of less interest. The p-adaptation process is based on a set of *variables of interest* (e.g., momentum or pressure) that the user must provide. These variables will be used as a reference for the RL agent, resulting in an optimal adaptation for these specific variables.

When applied to acoustics, it is possible to define an *acoustic path* between a source and an observer. Within this acoustic path, the RL agent applies a pressure-based p-adaptation to accurately capture the acoustic waves; and outside the path, it applies a momentum/velocity-based adaptation to represent aerodynamic flow features. The acoustic path is defined along a straight line between the source and the observer. Then, the minimum distance from every high order Gauss node of the mesh to that line is calculated as depicted in Figure 1. All elements with at least one Gauss node whose distance d is below a threshold d_{th}, will be included inside the acoustic path. The definition of d_{th} is problem dependent and is an input provided by the user. Finally, in a real problem both the source and the observer could be defined as a surface (e.g., a boundary) instead of a single point. In this scenario, a different line is created from each node of the source to each node of the observer. Furthermore, since this step is performed only once, at the beginning of the simulation, the overhead in relation to the complete simulation time is negligible.

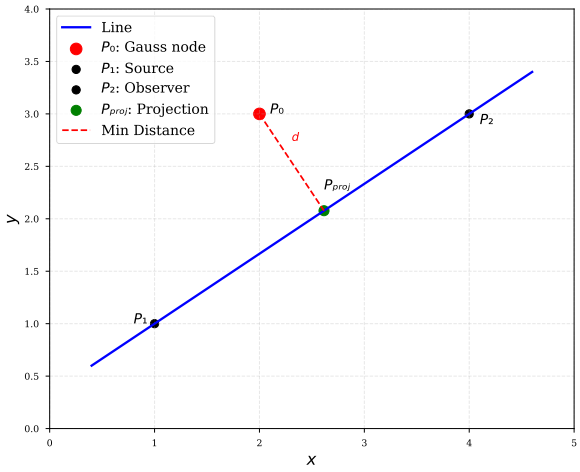


Figure 1. Example of the distance calculation from a high order Gauss node to the line that connects the acoustic source and the observer.

3. RESULTS

To test the proposed p-adaptation methodology for acoustics and the acoustic path, we simulate different problems, in increasing level of complexity. As the RL-based p-adaptation agent is agnostic to the computation mesh and the PDE being solved, only one agent is trained, which is used for every problem without modifications.

3.1 Monopole

First, to test the performance of the pressure-based p-adaptation against a momentum-based, a simple

monopole is simulated using the nonlinear Euler Equations (EE). The mesh is a square with 400×400 elements. In this test case, the acoustic path is not considered; instead, the polynomial order will be adapted by the RL agent in the whole mesh. A snapshot of the pressure field, once quasi-steady state conditions are achieved, is represented in Figure 2.

Additionally, to validate the proposed methodology, three simulations have been performed, with different p-adaptation strategies: an uniform $p = 6$ polynomial order (used as a reference), a pressure-based adaptation and a momentum-based adaptation. For the two p-adaptation strategies, the maximum polynomial order is limited to $p_{\max} = 6$; hence, the uniform $p = 6$ simulation will always be more accurate than the p-adaptation solutions, but also more costly. In Figure 3, we show the error between both p-adaptation strategies and the reference $p = 6$ solution for the pressure field. The solution computed with the pressure-based adaptation shows a significantly smaller error. Although momentum-based adaptation is appropriate to capture aerodynamic features [2], this problem highlights the importance of using pressure as the reference variable for acoustics.

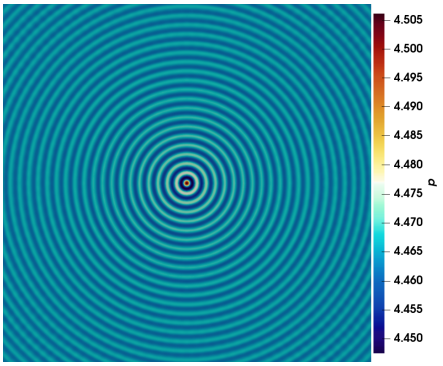
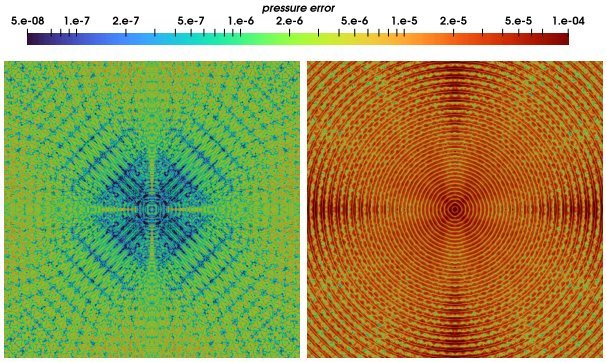


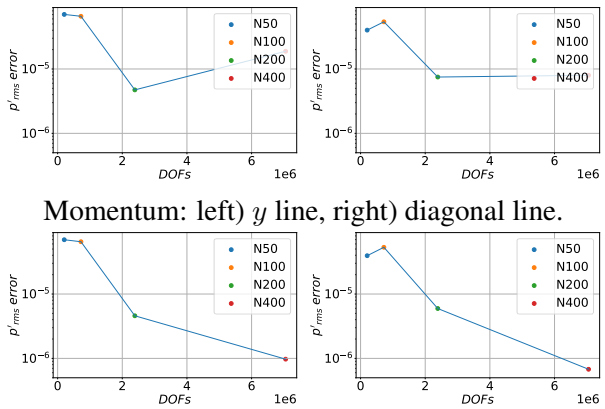
Figure 2. Snapshot of the pressure field.

Finally, in Figure 4 we show the rmse error of the pressure field, as a function of the degrees of freedom of the mesh, in a vertical line (from the source to the boundary at the top) and a diagonal line (from the source to the top-right corner) for both the momentum-based and the pressure-based simulations. As expected, the pressure-based adaptation shows a decreasing error with the number of degrees of freedom, while the momentum-based is not able to reduce the error below 10^{-5}, even if the mesh is refined. Therefore, the momentum field is not an appropriate reference variable to accurately capture acoustic waves.



a) Pressure-based. b) Momentum-based.

Figure 3. Comparison of the pressure error, in relation to the reference $p = 6$ simulation, between the pressure-based and the momentum-based adaptations.



Momentum: left) y line, right) diagonal line.

Pressure: left) y line, right) diagonal line.

Figure 4. Comparison of the pressure rmse error for four different meshes, computed in relation to the reference $p = 6$ simulation, for the pressure-based adaptation and the momentum-based adaptation.

3.2 Multiphase monopole

Once it is demonstrated that the pressure is the appropriate variable to adapt the polynomial order in acoustic problems, we simulate a multiphase problem with two fluids: air and water. In this problem, an acoustic source generates pressure waves in the air region, which are propagated to the water region through an interface. The problem is solved inside a square with a 100×100 Cartesian mesh. To avoid reflections at the boundaries, a sponge is defined near the boundaries to dampen the acoustic waves. This setup is shown schematically in Figure 5. As the wavelength of the pressure waves are different in air and water, the p-adaptation agent should be able to select the optimal polynomial order in each region accordingly. Then, as we want to focus on the propagation of the acoustic waves from the air to the water, we define the acoustic path from the source to the boundary at the bottom, as shown in Figure 6, with a threshold distance of $d_{th} = 2.5$. This way, the RL agent will adapt the polynomial order inside the acoustic path only, reducing the computational cost of the overall simulation.

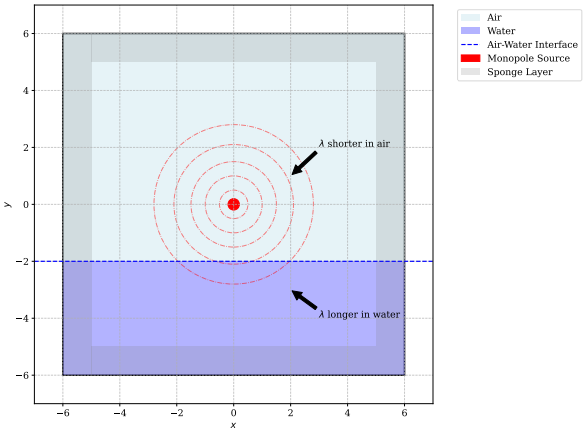


Figure 5. Setup of the multiphase problem.

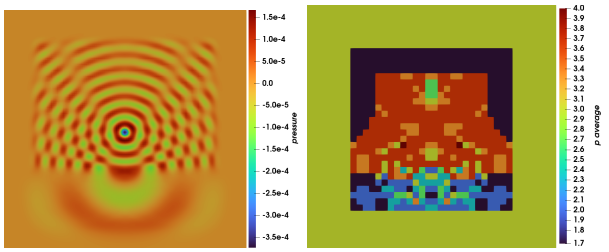
The pressure field, once the simulation is stable, is represented in Figure 7 a). As expected, the wavelength of the pressure waves is significantly longer in the water and, therefore, the polynomial order should be smaller in that region. The average polynomial order (among the three anisotropic polynomials p_x, p_y and p_z) in each element of the mesh is shown in Figure 7 b). In this figure, there are four regions of interest that should be analyzed:

1. Near the boundaries, inside the sponge layer, the polynomial order has been manually fixed to a constant value to avoid undesired reflections.
2. Above the source, in the air region, but outside the acoustic path, the polynomial order is set to the minimum to reduce the computational cost, as we are not interested in the acoustics there.
3. Inside the acoustic path, in the air region, the wavelengths are shorter, and strong pressure gradients can be found inside some elements. Hence, the RL agent selects high-order polynomials to accurately capture the pressure waves.
4. Inside the acoustic path, in the water region, the wavelengths are longer and low order polynomials are enough to represent the pressure waves.

In conclusion, the RL agent is capable of selecting the optimum polynomial order inside the acoustic path, discriminating between different regions, and adapting the polynomial order accordingly.



Figure 6. Acoustic path of the multiphase problem.



a) Pressure. b) Average polynomial.

Figure 7. Snapshot of the pressure field and the average polynomial order in each element of the mesh.

3.3 Cylinder at Reynolds 200

Finally, we propose a more challenging problem, the direct noise computation (DNC) produced by the flow around a cylinder at Reynolds 200, where the RL agent must consider two different adaptation strategies at the same time: inside the acoustic path, a pressure-based adaptation is performed to capture the acoustic waves, and outside the acoustic path, a momentum-based adaptation is used to represent aerodynamic flow features, such as vortices. For this problem we solve the full compressible Navier–Stokes (NS) equations, that accounts for both aerodynamics and acoustic physics. The acoustic path for this problem and the background mesh are depicted in Figure 8, where the acoustic source is the cylinder, the observer is defined 20 length units above the source and the threshold distance is $d_{th} = 1$. Also, it is necessary to define two tolerances to let the agent know when the fluctuations of the reference variable inside one element are negligible. In this case:

$$tol_m = 10^{-2} \qquad tol_p = 10^{-4}, \tag{1}$$

with tol_m as the momentum tolerance and tol_p as the pressure tolerance.

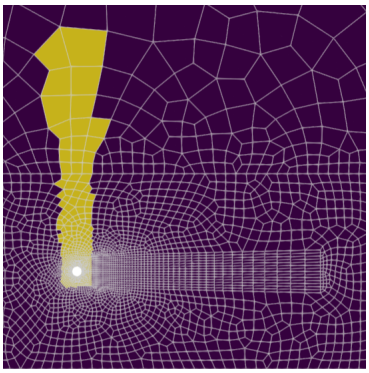


Figure 8. Acoustic path of the cylinder at $Re = 200$.

Once the flow field is stable, a snapshot of the average polynomial order in each element is represented in Figure 9, where there are three main regions:

1. The acoustic path: The polynomial order is increased to capture the pressure waves between the source and the observer.
2. The wake: The vortex shedding creates strong velocity gradients in this region, and high-order polynomials are required to accurately represent the flow field.
3. The far field: Although this region is also adapted based on momentums, the gradients are negligible, and the RL agent selects the minimum polynomial order available in each axis, as nothing of interest is happening.

Therefore, the RL agent, without additional information on this particular problem, is able to discriminate between different regions and to select the optimal polynomial order that provides an accurate solution while keeping the computational cost down.

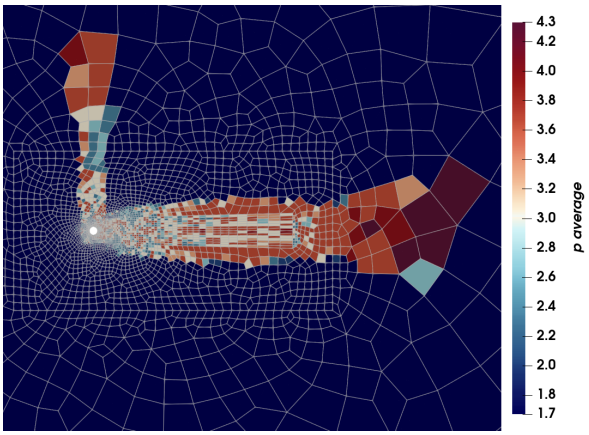


Figure 9. Snapshot of the average polynomial order of the cylinder at $Re = 200$.

Then, to check the accuracy of the proposed methodology, we compare the current results with two additional simulations with an uniform polynomial order of $p = 3$ and $p = 5$ in the whole mesh. First, in Figure 10 we show the root mean square pressure fluctuations along the acoustic path, from source to observer. Although the number of high-order elements in the p-adapted mesh is smaller, the results show a good agreement with the reference simulations. Furthermore, the reader may notice that the p-adapted solution is closer to the reference $p = 3$ simulation instead of $p = 5$, which is more accurate. The main reason behind this behavior is that, close to the cylinder, the aerodynamic pressure gradients are stronger than the acoustic fluctuations, but also very smooth. Therefore, near the cylinder a polynomial order $p = 2$ or $p = 3$ is enough to represent the pressure gradients, reducing the accuracy of the acoustic waves in that region, which are

propagated to the observer. To solve this issue, an uniform high-order polynomial order could be set around the body manually. Secondly, in Figure 11 we compare the SPL measured at the observer's location with different approaches, which highlights the accuracy of the current methodology.

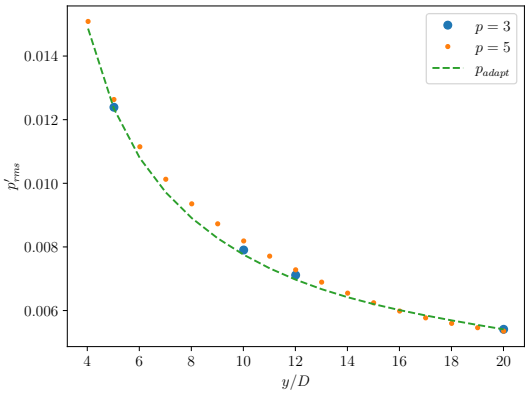


Figure 10. Comparison of the rms pressure fluctuations from the source to the observer.

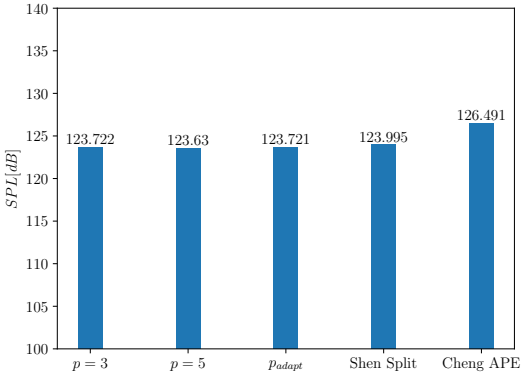


Figure 11. Comparison of the overall SPL at the observer's location.

Finally, for completeness, the u velocity field following the x axis is shown in Figure 12, where the vortex shedding is accurately represented, highlighting the effectiveness of the proposed p-adaptation strategy. In addition, this problem shows the flexibility of the p-adaptation RL agent, which can be applied in many different ways (to different problems, PDEs and meshes) and based on arbitrary reference variables, without retraining the agent. All these advantages make reinforcement learning for adaptive mesh refinement a good choice to solve aeroacoustic CFD problems, including DNC.

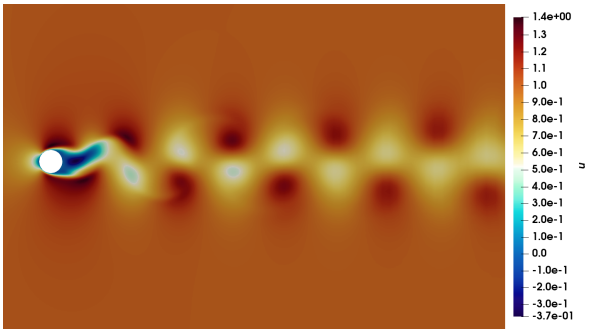


Figure 12. Snapshot of the velocity field of the cylinder at $Re = 200$.

4. CONCLUSIONS

In conclusion, this study presents a new approach to applying anisotropic p-adaptation for acoustics in high-order h/p solvers using reinforcement learning. The RL-based adaptation dynamically adjusts high-order polynomials based on the pressure field to capture acoustic fluctuations. Furthermore, it can handle different adaptation regions based on pressure, momentum, velocity, or other flow features. The proposed methodology is independent of the computational mesh and can be applied to any partial differential equation, illustrating its broad applicability and flexibility.

These findings open new avenues for further research in acoustics and other CFD applications using RL-based h/p-mesh adaptation.

5. ACKNOWLEDGMENTS

This research has received funding from the European Union (ERC, Off-coustics, project number 101086075). Views and opinions expressed are, however, those of the authors only and do not necessarily reflect those of the European Union or the European Research Council. Neither the European Union nor the granting authority can be held responsible for them.

EF and GR acknowledge the funding received by the Grant DeepCFD (Project No. PID2022-137899OB-I00) funded by MICIU/AEI/10.13039/501100011033 and by ERDF, EU.
DH and EF acknowledge the funding received by the Comunidad de Madrid according to Orden 5067/2023, of December 27th, issued by the Consejero de Educación, Ciencia y Universidades, which announces grants for the hiring of predoctoral research personnel in training for the year 2023.
Finally, all authors gratefully acknowledge the Universidad Politécnica de Madrid (www.upm.es) for providing computing resources on Magerit Supercomputer and the computer resources at MareNostrum and the technical support provided by Barcelona Supercomputing Center (RES-IM-2024-1-0003).

6. REFERENCES

[1] D. Huergo, G. Rubio, and E. Ferrer, "A reinforcement learning strategy for p-adaptation in high order solvers," *Results in Engineering*, vol. 21, p. 101693, 2024.

[2] D. Huergo, M. de Frutos, E. Jané, O. A. Marino, G. Rubio, and E. Ferrer, "Reinforcement learning for anisotropic p-adaptation and error estimation in high-order solvers," *arXiv preprint arXiv:2407.19000*, 2024.

[3] E. Ferrer, G. Rubio, G. Ntoukas, W. Laskowski, O. Mariño, S. Colombo, A. Mateo-Gabín, H. Marbona, F. Manrique de Lara, D. Huergo, J. Manzanero, A. Rueda-Ramírez, D. Kopriva, and E. Valero, "Horses3d: A high-order discontinuous galerkin solver for flow simulations and multi-physics applications," *Computer Physics Communications*, vol. 287, p. 108700, 2023.

[4] S. Le Clainche, E. Ferrer, S. Gibson, E. Cross, A. Parente, and R. Vinuesa, "Improving aircraft performance using machine learning: A review," *Aerospace Science and Technology*, vol. 138, p. 108354, 2023.

[5] R. Vinuesa and S. L. Brunton, "Enhancing computational fluid dynamics with machine learning," *Nature Computational Science*, vol. 2, p. 358–366, June 2022.

[6] R. S. Sutton and A. G. Barto, *Reinforcement Learning: An Introduction*. The MIT Press, 2^{nd} *ed.*, 2018.

[7] P. Garnier, J. Viquerat, J. Rabault, A. Larcher, A. Kuhnle, and E. Hachem, "A review on deep reinforcement learning for fluid mechanics," *Computers & Fluids*, vol. 225, p. 104973, 2021.

[8] C. Vignon, J. Rabault, and R. Vinuesa, "Recent advances in applying deep reinforcement learning for flow control: Perspectives and future directions," *Physics of Fluids*, vol. 35, no. 3, p. 031301, 2023.

[9] B. Font, F. Alcántara-Ávila, J. Rabault, R. Vinuesa, and O. Lehmkuhl, "Active flow control of a turbulent separation bubble through deep reinforcement learning," in *Journal of Physics: Conference Series*, vol. 2753, p. 012022, IOP Publishing, 2024.

[10] M. Kurz, P. Offenhäuser, and A. Beck, "Deep reinforcement learning for turbulence modeling in large eddy simulations," *International Journal of Heat and Fluid Flow*, vol. 99, p. 109094, 2023.

[11] A. Beck and M. Kurz, "Toward discretization-consistent closure schemes for large eddy simulation using reinforcement learning," *Physics of Fluids*, vol. 35, no. 12, 2023.

[12] Y. Feng, F. S. Schranner, J. Winter, and N. A. Adams, "A deep reinforcement learning framework for dynamic optimization of numerical schemes for compressible flow simulations," *Journal of Computational Physics*, vol. 493, p. 112436, 2023.

[13] D. Huergo, L. Alonso, S. Joshi, A. Juanicotena, G. Rubio, and E. Ferrer, "A reinforcement learning strategy to automate and accelerate h/p-multigrid solvers," *Results in Engineering*, p. 102949, 2024.

[14] M. Kompenhans, G. Rubio, E. Ferrer, and E. Valero, "Adaptation strategies for high order discontinuous Galerkin methods based on Tau-estimation," *Journal of Computational Physics*, vol. 306, pp. 216–236, 2016.

[15] M. Kompenhans, G. Rubio, E. Ferrer, and E. Valero, "Comparisons of p-adaptation strategies based on truncation- and discretisation-errors for high order discontinuous Galerkin methods," *Computers and Fluids*, vol. 139, pp. 36–46, 2016.

[16] C. Foucart, A. Charous, and P. F. Lermusiaux, "Deep reinforcement learning for adaptive mesh refinement," *Journal of Computational Physics*, vol. 491, p. 112381, 2023.

[17] J. Yang, T. Dzanic, B. Petersen, J. Kudo, K. Mittal, V. Tomov, J.-S. Camier, T. Zhao, H. Zha, T. Kolev, *et al.*, "Reinforcement learning for adaptive mesh refinement,"

in *International Conference on Artificial Intelligence and Statistics*, pp. 5997–6014, PMLR, 2023.

[18] L. Botero-Bolívar, O. A. Marino, C. H. Venner, L. D. de Santana, and E. Ferrer, "Low-cost wind turbine aeroacoustic predictions using actuator lines," *Renewable Energy*, vol. 227, p. 120476, 2024.

[19] O. A. Marino, R. Sanz, S. Colombo, A. Sivaramakrishnan, and E. Ferrer, "Modelling wind turbines via actuator lines in high-order h/p solvers," 2024.

DOI: 10.61782/fa.2025.0803



FORUM ACUSTICUM
EURONOISE 2025

SOUNDSCAPE SYSTEM BASED ON PASSENGER EMOTION AND CONVERSATION PERCEPTION OF AUTONOMOUS VEHICLES

Kyoung-Jin Chang[1*] **Jeonggoo Kang**[1] **Dong Chul Park**[1]
Gyumin Cho[2] **Chang Wook Ahn**[2]
[1] Hyundai Motor Company, Hyundai-ro 150, Namyang-eup, Hwaseong-si, Gyeonggi-do, 18280, Korea
[2] Graduate School of AI, Gwangju Institute of Science and Technology, Korea

ABSTRACT

When passengers of an autonomous vehicle have conversations or engage in various activities, the soundscape of the vehicle that suits the atmosphere can play an important role. This study introduces the results of developing a system that recognizes emotions and conversation states from passengers' face images in autonomous vehicles, selects music or the sounds of nature that match this atmosphere, and automatically adjusts the volume to not interfere with passengers' conversation. This study consists of the following process. First, algorithms for emotion classification and conversational state recognition using facial expressions are developed, and the program is lightened and implemented in the vehicle's deep learning control system. Second, a soundscape system is developed that matches and plays sound sources suitable for emotions and conversational states estimated in real time in vehicles. Third, the control and soundscape system are installed in an autonomous vehicle and the accuracy and satisfaction of the systems are evaluated by users. This technology is expected to provide new auditory experiences and increase satisfaction, especially for passengers of autonomous vehicles such as robotaxi.

Keywords: *artificial intelligence, soundscape, emotion recognition*

[*] ***Corresponding author***: changkj@hyundai.com.
Copyright: *©2025 Kyoung-Jin Chang et al. This is an open-access article distributed under the terms of the Creative Commons Attribution 3.0 Unported License, which permits unrestricted use, distribution, and reproduction in any medium, provided the original author and source are credited.*

1. INTRODUCTION

In recent years, automobiles are expanding from simple means of transportation to spaces that improve the quality of life, and at the same time, the technology to provide new experiences in accordance with the emotions of passengers in the vehicle is becoming more important. Particularly in autonomous vehicles, playing music that best suits the mood and emotions without disturbing the conversation of several passengers is expected to give high satisfaction.

Research on recognizing emotions from passengers' facial expressions using cameras in vehicles is an important technology for personalization, and many studies have been conducted so far [1-3]. For example, W. Li et al. [1] had a camera installed in a vehicle simulator and analyzed the driver's emotions into five categories: anger, happiness, sadness, fear, and surprise. Z. Chen et al. [2] developed a face recognition and emotion classification system for autonomous vehicles with a low latency of 2ms and high accuracy (F-score 96%) to enable real-time implementation in Internet of Things (IoT) systems. K.-J. Chang et al. [3] developed a new soundscape provision system that classifies emotions and provides customized driving sound using a multimodal analysis method that combines facial expressions, heart rate, and skin conductivity of vehicle drivers. These studies show that there is a growing interest in in-cabin camera utilization and emotion recognition technology to provide personalized entertainment services. However, when implemented in a vehicle controller, it is very necessary to design an efficient algorithm that can achieve high performance at a low capacity so as not to interfere with other control performance of a vehicle.

On the other hand, in terms of technology for recognizing the conversation state, only methods for measuring and analyzing users' voices have been mainly studied [4-5].

In contrast, this study introduces a technology that uses only an in-cabin camera to identify the passenger's emotions and conversation state from the passenger's facial image information and provides the most appropriate soundscape in the vehicle. In addition, an algorithm that operates with minimal capacity and calculation is produced and implemented in the AI controller of an autonomous vehicle for robotaxi.

2. AI ALGORITHMS

2.1 Emotion recognition

First, the face recognition model of this study uses Multi-task Cascaded Convolutional Neural Networks (MTCNNs) [6]. This is a cascade structure that sequentially passes through three lightweight convolutional neural networks (CNNs) called proposal network (P-Net), refinement network (R-Net), and output network (O-Net), so it is fast to process and accurate even in low-quality images. Fig. 1 shows the architecture of MTCNN. The face recognition model of this study has been designed with a small capacity of 600 KB and has achieved a high recognition rate of 98.02% for 24,111 images on the FER-2013 dataset. Next, the emotion classification model uses the Mini-Xception algorithm [7], which is a lightweight and efficient convolutional neural network (CNN) architecture. This is known for its depthwise separable convolutions that reduce computational cost while maintaining performance. In this study, the emotion classification model has been designed with a small capacity of 853 KB and has showed 74% accuracy for 10,767 images on the FER-2013 datasets. Table 1 shows the results of testing the accuracy of the emotion classification model used in this study. For use in vehicles, confidence for emotions such as Happy, Sad, and Neutral is extracted for each basic frame according to the passenger's facial expression, and the emotion with the greatest value is classified as a cumulative emotion by accumulating the confidence for 30 seconds. Here, 30 seconds is a cycle in which emotions are updated to change the soundscape, and as the emotion update time approaches, confidence is given a high weight so that the recent emotional state can be reflected more. When several passengers board, the above analysis is performed for each passenger, and the most common emotion is selected as the representative emotion.

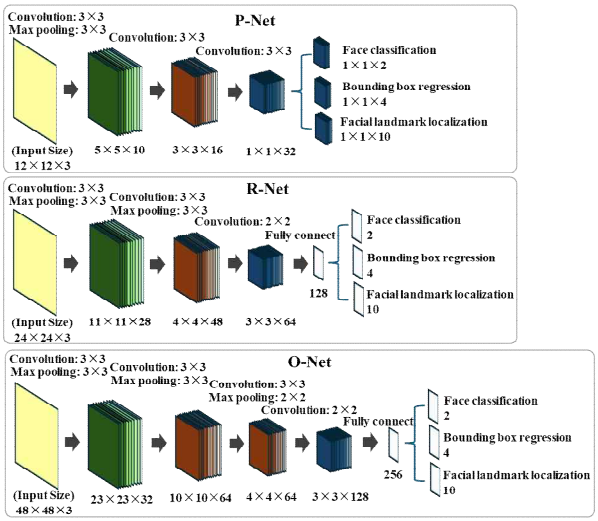


Figure 1. Architecture of MTCNN.

Table 1. Emotion classification test results using the Mini-Xception.

Predicted / Actual	Neutral	Happy	Sad
Neutral	5198	553	224
Happy	857	2257	75
Sad	912	209	482

2.2 Conversation state recognition

When several passengers talk to each other, it is important to select music suitable for the atmosphere and provide it at an appropriate volume so as not to interfere with the conversation. In this study, the conversational state of passengers is determined through CNN algorithm and calculation process from the passenger's facial image data, not the passenger's voice. This method has the advantage that it is not necessary to add a microphone and is not affected by various vehicle noises because it can be performed with an in-cabin camera. A model with 68 face landmarks from the passenger's face image is constructed, and the passenger's conversation state is determined by calculating the number of openings and the opening distance of the landmark around the mouth for a certain time. The above process is repeated for all passengers' mouths, and the conversational state is divided into three categories: No talk, Weak talk, and Strong talk from the calculation results. Fig. 2 shows an example of landmarks around the mouth estimated by facial images.

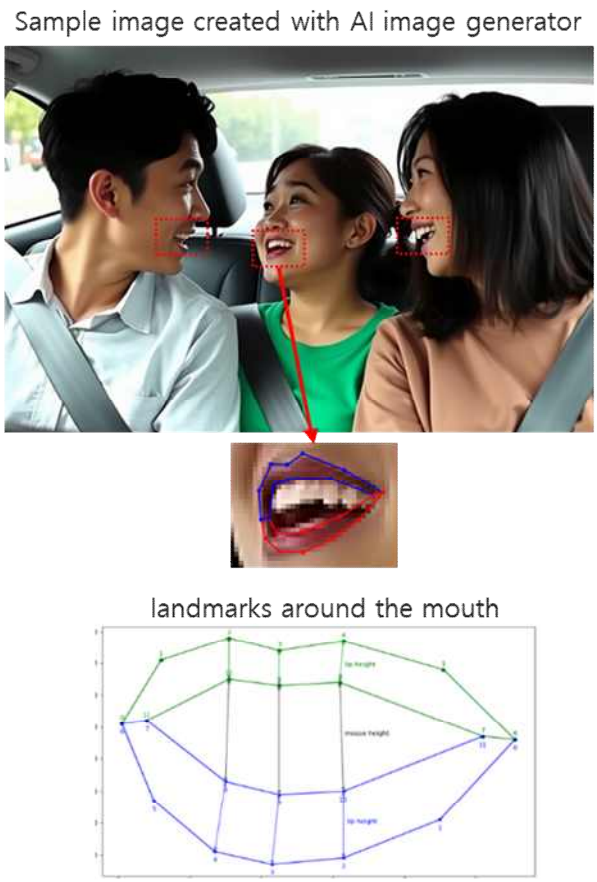


Figure 2. Examples of landmarks around the mouth for conversation state recognition.

3. SOUNDSCAPE

3.1 Soundscape library

Sound sources collected in the library of four concepts (i.e., Neutral, Happy, Sad, Talkative) are used to provide soundscape suitable for passengers' emotions and conversational states. These sound sources have been produced using an AI composition program and improved through correction by music experts. The Happy library contains bright and fast beat music, and the Sad library contains blue and melancholic music. The Neutral library contains comfortable and calm music, and the Talkative library contains simple music with the beats removed so as not to disturb the conversation.

3.2 Soundscape control logic

The Soundscape library selects the sound source that best matches the results of the passengers' representative emotions and conversational states analyzed in real-time in the vehicle. If multiple passengers show various emotions, four complex emotions can be selected as follows: Neutral + Happy (NH), Neutral + Sad (NS), Happy + Sad (HS), and Neutral + Happy + Sad (NHS). In the case of complex emotions, music that satisfies both or more emotions is matched, and if there is a dominant emotion (e.g., cumulative confidence of 80% or more), music that considers that emotion first is selected. Fig. 3 shows the distribution of sound sources matched according to the four complex emotions in this study. On the other hand, when the conversation of passengers is detected, music suitable for the conversation state is played. In addition, the automatic volume logic is applied to reduce the volume of music if it corresponds to Strong talk and increase the volume of music again if it corresponds to Weak talk by determining the stage of conversation with the method introduced in Section 2.2.

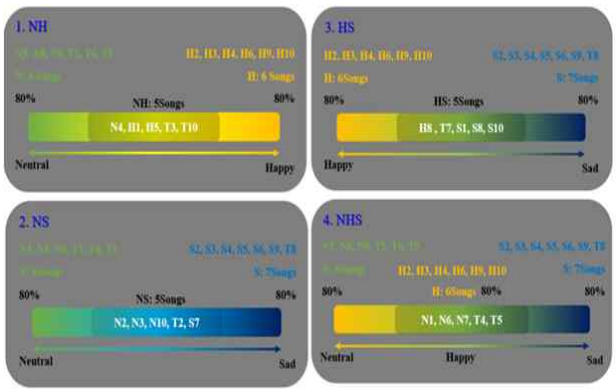


Figure 3. Distribution of sound sources according to the four complex emotions.

3.3 Jury test

Jury evaluation has been performed on 20 people with the camera, AI controller, and soundscape provision system developed in this study. The average age of the subjects is 26.3 years old, and they are organized to have various emotions while looking at various images in the listening room. At the same time, music suitable for the emotions recognized from the subjects' facial expressions is played, and the accuracy of emotion recognition, the accuracy of matching music and emotion, and auditory satisfaction are evaluated. The results of evaluating each item with a 10-

point Likert scale are shown in Fig. 4, and the average value is 7 points or more, showing relatively good results.

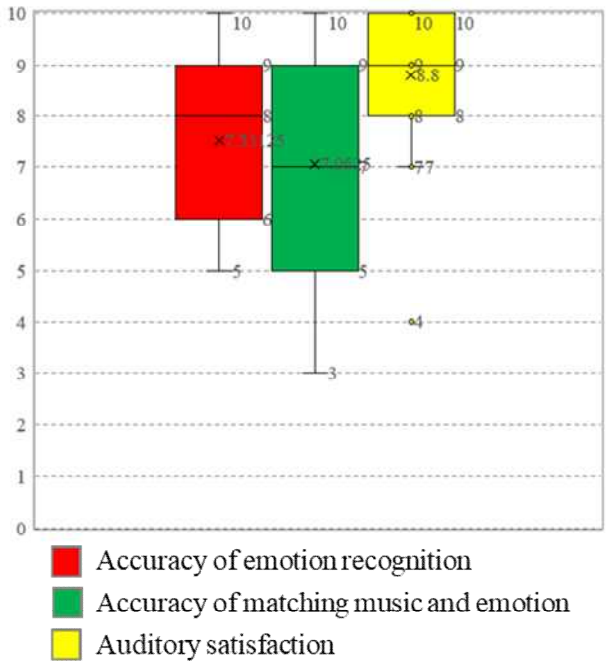


Figure 4. Jury test results for AI algorithms and soundscape.

4. IMPLEMEMTATION IN AUTONOMOUS VEHICLES

4.1 AI Controller

The AI model of this study has been programmed with TensorFlow and embedded in an Ambarella EVK board capable of AI image processing to operate in an autonomous vehicle. Fig. 5 shows the Ambarella EVK board used in this study, which is equipped with CV25, a system-on-chip that supports EasyAI libraries and provides a vector processor with instruction sets that handles a lot of data. The camera installed in the front center of the vehicle interior to capture images of passengers is the ON Semiconductor's AR0239, which is a 1/2.7-inch CMOS digital image sensor with an active-pixel array of 1936 × 1188.

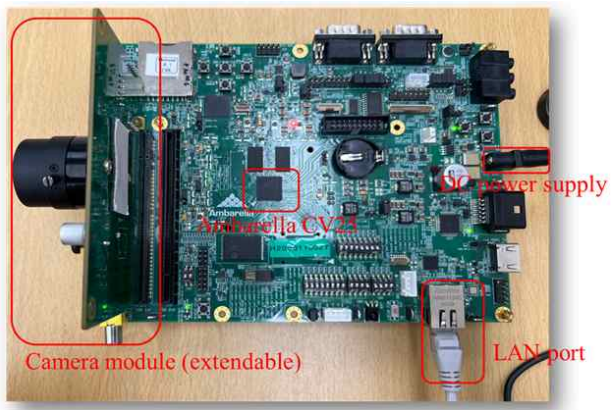


Figure 5. Ambarella EVK board.

4.2 User Interface system

An application for Microsoft Surface Pro tablets has been created to allow passengers to check the emotional and conversational status analyzed in real time, watch videos that fit well with the music determined by the proposed algorithm, and manually select an interface menu. Fig. 6 shows the screen image of this application, including the function of automatically adjusting the volume according to the conversation state. The determined music is played by the vehicle audio amplifier and speaker through the added external sound card. Fig. 7 shows a camera and tablet mounted inside the vehicle, an Ambarella controller mounted in the trunk room, and a sound card.

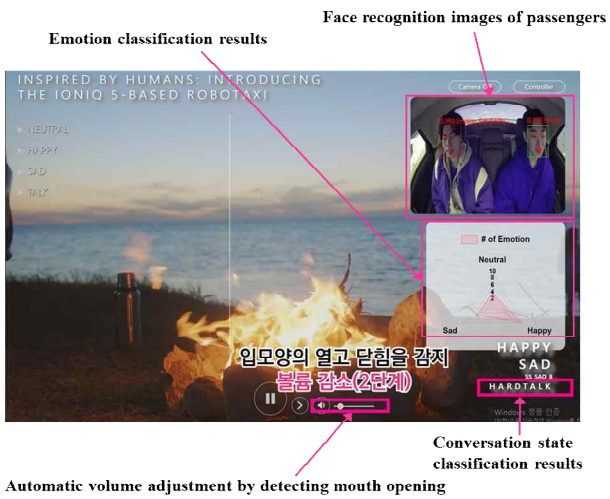


Figure 6. Screen image of an app running on a tablet.



Figure 7. AI controller and camera mounted on an autonomous vehicle.

4.3 Driving Demonstration

The control and soundscape system of this study has been mounted on an autonomous test vehicle and demonstrated while driving with several passengers on board. In the demonstration and evaluation involving a total of 16 people, the overall satisfaction score is 8.4 out of 10. Compared to Section 3.3 evaluated in the listening room, the vehicle evaluation result shows higher satisfaction. Many users are found to be satisfied with providing a soundscape suitable for customers' emotions and moods in the vehicle.

5. CONCLUSIONS

In this study, a lightweight emotion/conversation recognition and soundscape matching algorithm using face images that can be embedded in a deep learning controller of an autonomous vehicle has been proposed and implemented in a test vehicle. As a result of user evaluation, it has been confirmed that the accuracy of emotion recognition, the accuracy of matching music and emotions, auditory satisfaction, and user satisfaction in vehicles are all better than 70%. The results of this study can be used as important guidelines for designing autonomous vehicle services. That is, it is possible to provide a more personalized and immersive auditory experience to passengers through a soundscape suitable for the recognized emotion and conversation state. In addition, if the results of this study are used for self-driving taxis, it is expected to improve the service quality of self-driving taxis and secure a competitive advantage over other transportation methods by providing a personalized sound environment experience in the vehicle.

6. REFERENCES

[1] W. Li, Y. Cui, and et al: "A Spontaneous Driver Emotion Facial Expression Dataset for Intelligent Vehicles: Emotions Triggered by Video-Audio Clips in Driving Scenarios," *IEEE Transactions on Affective Computing*, vol. 14, no. 1, pp. 747-760, 2023.

[2] Z. Chen, X. Feng, and S. Zhang: "Emotion detection and face recognition of drivers in autonomous vehicles in IoT platform," *Image and Vision Computing*, vol. 128, no. 104569, pp. 1-11, 2022.

[3] K.-J. Chang, G. Cho, and et al: "Personalized EV Driving Sound Design Based on the Driver's Total Emotion Recognition," *SAE Int. Journal of Advances & Current Practices in Mobility*, vol. 5, no. 2, pp. 921-929, 2023.

[4] S. Chamishka, I. Madhavi, and et al: "A voice-based real-time emotion detection technique using recurrent neural network empowered feature modelling," *Multimedia Tools and Applications*, vol. 81, pp. 35173–35194, 2022.

[5] C. Gobl and A. Chasaide: "The role of voice quality in communicating emotion, mood and attitude," *Speech Communication*, vol. 40, no. 1–2, pp. 189-212, 2003.

[6] K. Zhang, Z. Zhang, and Z. Li: "Joint Face Detection and Alignment Using Multitask Cascaded Convolutional Networks," *IEEE Signal Proc. Letters*, vol. 23, no. 10, pp. 1499-1503, 2016.

[7] C. Dongyan and H. Shen: "Facial Expression Recognition Based on Mini-Xception Network," *Int. Journal of Computational Intelligence Systems and Applications*, vol. 11, no. 1, pp. 50-57, 2024.

DOI: 10.61782/fa.2025.0166

FORUM ACUSTICUM EURONOISE 2025

AUTOMATIC CLASSIFICATION OF PACKAGING WASTE AT SOURCE USING ACOUSTIC TECHNOLOGY

Marc Arnela* **Ester Vidaña-Vila** **Augusto Fantinelli** **Alejandro Moñux-Bernal**
Jesús Vaquerizo-Serrano **Sergi Rubio-Garcia** **Joan Claudi Socoró**
Human-Environment Research (HER) group, La Salle, Universitat Ramon Llull,
Barcelona, Calalonia, Spain

ABSTRACT

Sorting packaging waste at the source is key to effective recycling. Reverse vending machines (RVMs) can encourage recycling by offering incentives, but they rely on costly sensors like barcode scanners and computer vision, which face issues such as unreadable barcodes, high computational demands, and lighting sensitivity. This paper proposes an alternative approach using acoustic technology. The idea is to use a parametric array loudspeaker (PAL) to emit ultrasonic and audible sound waves towards the recyclable object, and by measuring its interaction, classify the item with the help of machine learning or deep learning. The exponential sine sweep method is used to measure the ultrasonic and audible impulse response of each item, creating a dataset for various containers. Classical and deep learning models are trained to classify items into categories like plastic, glass, cardboard, and metal. The system was tested in a controlled environment featuring a scaled replica of a reverberation chamber, with an omnidirectional parametric loudspeaker (OPL) serving as the sound source. Preliminary results demonstrate high classification accuracy, highlighting the potential of acoustic-based methods to improve the accessibility and efficiency of RVMs in promoting recycling initiatives.

Keywords: *ultrasounds, parametric arrays, machine learning, reverse vending machine, packaging waste classification*

**Corresponding author*: marc.arnela@salle.url.edu.
Copyright: *©2025 Arnela et al. This is an open-access article distributed under the terms of the Creative Commons Attribution 3.0 Unported License, which permits unrestricted use, distribution, and reproduction in any medium, provided the original author and source are credited.*

1. INTRODUCTION

Reverse vending machines (RVM) are devices used to recover recyclable packaging waste at source. These machines receive and identify the introduced package and give a reward in return to the customer. The idea is to motivate users' participation in the recycling chain while preventing this packaging waste from reaching waste deposits, incineration plants or nature itself —places where its impact can be problematic in varying degrees of severity. This goes in hand with a global trend towards sustainability and the implementation of circular economy [1–3].

The identification of the type of packaging waste in RVMs has been done by several means. Most commonly, barcode readers, infrared sensors and vision systems are used to classify the item. These are not without their challenges. Barcode readers are useless in cases where the barcode is damaged or missing [4], and infrared and vision systems depend on external factors such as illumination, item condition and fullness [5]. Other systems, such as magnetic separators and inductive sensors [4], are dependent on the material and cannot deal with glasses or cartons. Furthermore, these devices can be expensive, which limits the spread of RVMs that employ them in certain regions. Acoustic-based systems can circumvent the above limitations. The sensors they use, such as microphones, are typically more affordable than vision cameras or barcode sensors. Moreover, acoustic data is less computationally demanding to process than images and is not affected by lighting conditions. Most of the solutions are passive, that is, they classify the item according to the sound it produces when it is returned [5–8]. However, they are sensitive to environmental noise.

This work proposes to use an acoustic technology

based on an active approach. A sound is emitted with a loudspeaker and the recyclable item is detected by analysing the variations it produces in the acoustic field. Parametric acoustic loudspeakers (PAL) are used for this purpose. Based on the Parametric Acoustic Array (PAA) phenomenon [9], they generate ultrasonic waves and, thanks to the non-linear propagation in the air, audible waves are also produced. The packaging waste is then excited with ultrasonic and audible waves at the same time, covering a wide frequency range. The impulse response of the recyclable item is obtained in the ultrasonic and audible range simultaneously, following the exponential sine sweep (ESS) methodology presented in [10] and latter applied in [11] to measure the acoustic absorption coefficient of material samples in a reverberation chamber. The ultrasonic and audible impulse responses of various recyclable items are collected and used to train and test various machine learning algorithms, like support vector machines (SVM), k-nearest neighbours (KNN), random forests (RF), and others. The developed approach is tested under laboratory conditions using an omnidirectional parametric loudspeaker (OPL) as the sound source [12], and a highly reverberant enclosure designed specifically for these experiments. The experimental setup is located inside an anechoic chamber to minimize background noise. To train and test machine learning algorithms it is necessary to apply windows to post-process the impulse responses. This work also explores the sensitivity of the method to these windows by exploring various configurations.

This paper is structured as follows. Section 2 presents the dataset, the ESS method, the experimental setup and the machine learning techniques used. Section 3 displays the classification results based on the combination of the ultrasonic and audible data. Section 4 finishes the discussion and proposes potential explorations in future works.

2. METHODOLOGY

This section first explains the experimental setup used to gather data. Then, it describes the signal processing techniques and the feature extraction process. Finally, it presents the machine learning models used for the automatic classification of packaging waste.

2.1 Measurement of the ultrasonic and audible impulse responses

The experimental setup (see Figure 1) consisted of a mini-reverberation chamber made of cellular polycarbonate,

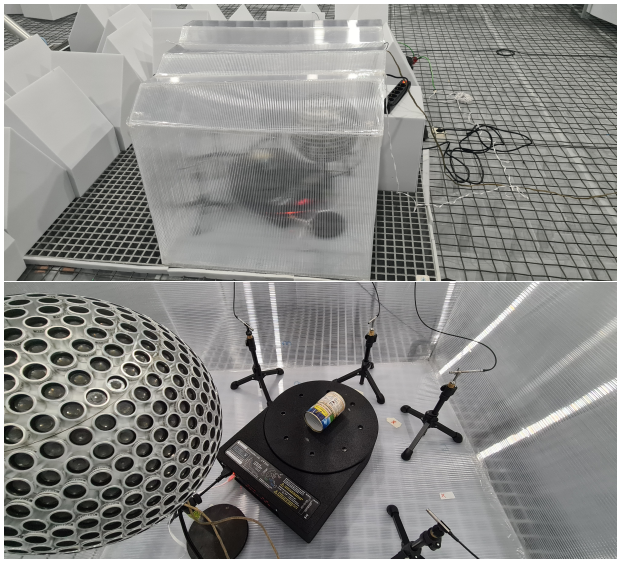


Figure 1: Experimental setup to measure the ultrasonic and audible impulse responses of packaging waste. It consists of a mini reverberation chamber located inside an anechoic chamber containing an omnidirectional parametric loudspeaker (OPL), four microphones and a turntable. An aluminium can in horizontal position is shown as an example.

following the shape of the reverberation chamber at La Salle - Universitat Ramon Llull (URL) and scaling it down by a factor of 1:70. Its irregular shape is expected to improve sound diffusion. To eliminate background noise, the mini-reverberation chamber was placed inside the anechoic chamber of La Salle - URL. Inside, we find the OPL described in [12], used to generate audible and ultrasonic waves through the PAA effect [9]. The recyclable item was put on a rotating table (Outline ET250R2-3D) that rotated every 30 degrees. Four 1/4" measurement microphones (two GRAS 40BF and two GRAS 46BF-1), located at about $0.22\,\mathrm{m}$ from the packaging waste, were used to record the generated sound field . The generation and acquisition of the signal were performed using a Brüel & Kjaer LAN-XI Type 3160-A-042 module with a UA-3102-041185 front-end. The generated signal was amplified up to $17\,\mathrm{V}$ peak-to-peak using an Ecler XPA3000 amplifier. A sampling frequency of $131\,072\,\mathrm{Hz}$ — the maximum available for the equipment — was used.

The Exponential Sine Sweep (ESS) methodology was used to measure impulse responses due to its robustness



(a) Glass wine bottle (item #24).



(b) Large plastic water bottle (item #29).



(c) Energy drink can (item #42).



(d) Almond milk carton (item #53).

Figure 2: Examples of items in the training dataset.

to noise and distortion [13–15]. It consists of emitting and recording a sinusoidal signal with exponentially increasing frequency. The recording is then convolved with the respective inverse filter of the sine sweep, resulting in the impulse response of the system. In the context of this work, the presence of a recyclable object inside the enclosure causes an impact on the sound field, which is reflected in the measured impulse response. This in turn is used to classify the different items. The utilisation of ESS in PALs was first proposed in [16] and extended in [10] to simultaneously measure audible and ultrasonic impulse responses. It requires that the sweep goes through an upper side-band amplitude modulation (USBAM) with a transmitted carrier component [17]. This strategy is adopted in this work, setting the carrier frequency for the OPL to 44.1 kHz [10].

The dataset comprises items that could potentially be introduced into a reverse vending machine. Fifty-one different containers were selected. In terms of material, we used 16 glass bottles, 11 metallic cans, 15 plastic bottles and 9 cardboard cartons. Figure 2 shows a representative

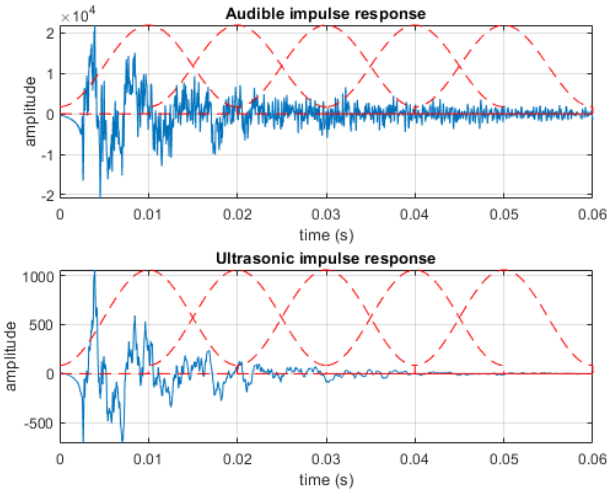


Figure 3: Audible and ultrasonic impulse response of a glass bottle. The red dashed lines indicate the five short windows used to extract the features.

item from each category. Each item was measured in horizontal and vertical position and rotated every 30 degrees. The sound field in the enclosure is measured at 4 different positions. This results in 96 different measurements per item, yielding a total of 4896 measurements that will be analysed by the machine learning algorithms.

2.2 Extraction of features

To evaluate the best way to characterize the impulse responses, a set of features was extracted from both audible and ultrasonic impulse responses. This set includes classical acoustic features such as 13 Mel Frequency Cepstral Coefficients (MFCC) and 13 GammaTone Cepstral Coefficients (GTCC), the spectral centroid, spectral entropy, spectral crest, spectral flatness, spectral flux, spectral kurtosis, spectral skewness, spectral spread and spectral rolloff point.

For each measurement, these features were first obtained from the audible impulse response and a post-processed version of the ultrasonic impulse response obtained by translating its frequency content to the audible range. Then, the features were merged to obtain a single vector of characteristics for each measurement.

The features were extracted from five separate windows of the original impulse response, using a window duration of 20 ms and 50% of overlap. From each of these windows, a set of the 35 aforementioned features were ex-

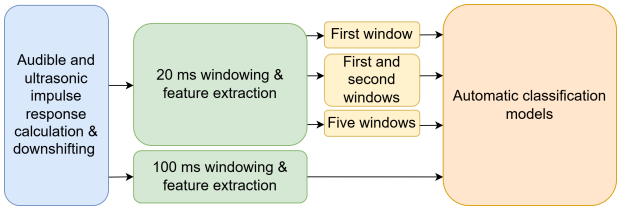


Figure 4: Block Diagram of the 4 different windowing modalities.

tracted, effectively multiplying the amount of total available features for both training and testing by five.

Figure 3 shows an example of audible and ultrasonic impulse responses from a glass bottle measurement, where the 5 windows are superimposed using red dashed lines. It can be observed that the audible impulse response has a slower decay compared to the ultrasonic one, and that both responses (audible and ultrasonic) show an exponential decrease over time. This typical behaviour, confirmed also in the whole set of measurements, suggested to us that the discriminative information between packaging waste is not equally distributed along the time axis. For this reason, four types of feature vector configurations have been explored in this work: i) using only the first window (first 20 ms); ii) using the first two windows (first 30 ms); iii) using all five windows (up to 60 ms); iv) using a single but wider time window that encompasses the same length that 5 windows (also 60 ms). The first and the fourth configurations use the same number of features (35) while the second option doubles this number (70) and the third compiles a total of $35 \times 5 = 175$ features.

In order to validate the amount of windows to be used, the training and testing of the models has been done separately for each of the four feature configurations, as shown in Figure 4.

2.3 Machine learning and deep learning models

The extracted features have been used to train and test six different models of both more traditional machine learning and deep learning models. Regarding machine learning, they can be categorized between those that make use of Decision Trees and those that are not. Specifically, Decision Trees (DT) were utilized directly, while Random Forest (RF) and Gradient Boosting (GB) were included to assess ensemble learning variations of Decision Trees for this task. Additionally, K-Nearest Neighbour (KNN) and Support Vector Machine (SVM) algorithms were employed to evaluate their performance on this type of data. For the deep learning models, a Multi-Layer Perceptron (MLP) was tested as the simplest deep learning approach to determine the viability of such algorithms for classification in this task. All models were evaluated using accuracy and F1-Score as performance metrics. To ensure result stability, a 5-fold cross-validation process was applied.

3. RESULTS

Table 1 presents the results for each experimental setting, incorporating the six machine learning and deep learning algorithms along with the four window configurations described in the previous section. The results bring a series of interesting insights to light. First, the best-performing model across all settings is the SVM, with a peak of 89% in both evaluation metrics. Ensemble models (RF and GB) have achieved a good score on both metrics (accuracy and F1), but they still fall short compared to the performance of both the KNN and SVM models. The same applies to the MLP model, which is the only one to benefit from the increased input feature size. Second, the use of five windows does not provide a significant increase in any of the evaluation metrics, despite this configuration is the one that uses the largest number of features. In fact, this configuration generally leads to a decline in performance. Notably, the best results are achieved when only the first two windows are used, indicating that the most relevant information from the impulse response is concentrated within the first 30 milliseconds. Looking at Figure 3, it can be confirmed that most of the energy is concentrated in this region, and beyond 30 ms we have almost no information. The use of a single window across the entire impulse response yields the lowest score. The features extracted from this large window fail to provide enough information for the models to effectively differentiate between classes. The number of features used in this setting is the same as in the first one, where only the first of the five windows is used. However, the latter contains much richer information, resulting in an accuracy increase of 4-19% depending on the model.

Table 2 shows the confusion matrix for the SVM model, using only the first two of the the five possible windows. This matrix presents the aggregated results of the five cross-validation folds. There is little confusion between classes, with the highest misclassification occurring between plastic and glass, the two most represented classes in our samples. These samples primarily consist

Table 1: Classification metrics obtained through cross-validation using the 4 different windowing modalities of impulse responses. The tested algorithms include classical machine learning techniques (DT, RF, GB, KNN, and SVM) and a deep neural network (MLP)

Algorithm	1st Window (of 5 of 20 ms)		1st-2nd Windows (of 5 of 20 ms)		1st-5th Windows (of 5 of 20 ms)		1 Window (of 60 ms)	
	Accuracy	F1	Accuracy	F1	Accuracy	F1	Accuracy	F1
DT	52%±2%	52%±2%	51%±2%	50%±2%	48%±1%	48%±1%	48%±2%	44%±2%
RF	79%±2%	78%±2%	81%±2%	81%±2%	76%±2%	76%±2%	69%±2%	66%±2%
GB	68%±1%	68%±1%	71%±1%	71%±1%	69%±2%	69%±2%	60%±1%	57%±1%
KNN	82%±1%	82%±1%	88%±1%	87%±1%	86%±1%	86%±1%	70%±1%	68%±1%
SVM	83%±1%	83%±1%	89%±1%	89%±1%	89%±0%	89%±0%	74%±1%	74%±1%
MLP	67%±1%	67%±1%	73%±0%	73%±0%	75%±1%	75%±1%	48%±1%	40%±1%

Table 2: Confusion matrix for the first two windows aggregating the results of all the cross-validation folds. The model used for the classification is the Support Vector Machine.

Metal	**974**	17	46	19
Cardboard	29	**735**	78	22
Plastic	38	66	**1244**	92
Glass	21	23	90	**1402**
	Metal	Cardboard	Plastic	Glass

of different types of bottles, jars, and similar containers. It is possible that the size and shape of the container influence on the classification and the ability of the model to differentiate between samples. However, this confusion accounts for only 6% of the total predictions, which is not a concerning amount of misclassified samples.

4. CONCLUSIONS

This work has proposed to use acoustic technology and machine learning to classify packaging waste in reverse vending machines (RVMs). The idea is to use a parametric array loudspeaker (PAL) to emit ultrasonic and audible sound waves towards the recyclable item, and by measuring the sound field, detect the recyclable item introduced with the help of machine learning or deep learning models. The exponential sine sweep method has been used to obtain the acoustic impulse response of the recyclable items in both the ultrasonic and audible range. Results have shown that the technology is viable, achieving a top evaluation metric of 89% in both Accuracy and F1-Score with a Support Vector Machine. Four window configurations were tested to extract the features, but the one that worked best used two windows for the first 30 ms. Incorporating more time generally led to a decrease in classifier performance.

The experimental setup used in this work was performed in a controlled environment using high-end measurement equipment, ensuring optimal input data conditions for the models. While this data does not fully replicate the environmental conditions of an RVM, it serves as a foundational testbed for future research. Future work will focus on conducting measurements in enclosures that more closely resemble an RVM, as well as developing new PALs designed to fit within these machines. It is worth mentioning that the best-performing model, the SVM, is lightweight enough to be deployed on lower-end hardware, enabling on-device processing and classification. This, in turn, will makes RVMs more stable and cost-effective to produce.

5. ACKNOWLEDGMENTS

This work has been funded by MCIN/AEI/10.13039/501100011033 and the European Union - NextGenerationEU through project Sonora (TED2021-132376A-I00). The authors thank the support of the Catalan Government (Departament de Recerca i Universitats) for the grant 2021 SGR 01396 given to the HER group.

6. REFERENCES

[1] EPA, "Sustainable materials management," 2023.

[2] EUROPEAN PARLIAMENT, "Circular economy," 2023.

[3] K. Kotyal, "Sustainable waste management in the circular economy: Challenges and opportunities," *Environmental Reports*, 2023.

[4] E. Watanyulertsakul, "The accuracy of sorting beverage cans and bottles for a reverse vending machine," *ECTI Transactions on Computer and Information Technology*, vol. 13, p. 11051, May 2019.

[5] G. Lu, Y. Wang, H. Yang, and J. Zou, "One-dimensional convolutional neural networks for acoustic waste sorting," *Journal of Cleaner Production*, vol. 271, p. 122393, 2020.

[6] O. I. Funch, R. Marhaug, S. Kohtala, and M. Steinert, "Detecting glass and metal in consumer trash bags during waste collection using convolutional neural networks," *Waste Management*, vol. 119, pp. 30–38, 2021.

[7] M. K. Korucu, Özgür Kaplan, O. Büyük, and M. K. Güllü, "An investigation of the usability of sound recognition for source separation of packaging wastes in reverse vending machines," *Waste Management*, vol. 565, pp. 46–52, 2016.

[8] T. Munaka, F. Samiea, L. Bauer, and J. Henkel, "Improved feature extraction method for sound recognition applied to automatic sorting of recycling wastes," *Journal of Information Processing*, vol. 28, pp. 658–665, 2020.

[9] P. J. Westervelt, "Parametric acoustic arrays," *J. Acoust. Soc. Am.*, vol. 35, no. 4, pp. 535–537, 1963.

[10] M. Arnela, C. Martínez-Suquía, and O. Guasch, "Carrier frequency influence on the audible and ultrasonic fields generated by an omnidirectional parametric loudspeaker excited with exponential sine sweeps," *Appl. Acoust.*, vol. 200, p. 109073, 2022.

[11] M. Arnela, R. Burbano-Escolà, R. S. Ribeiro, and O. Guasch, "Reverberation time and random-incidence sound absorption measured in the audible and ultrasonic ranges with an omnidirectional parametric loudspeaker," *Appl. Acoust.*, vol. 229, p. 110414, 2025.

[12] M. Arnela, O. Guasch, P. Sánchez-Martín, J. Camps, R. M. Alsina-Pagès, and C. Martínez-Suquía, "Construction of an omnidirectional parametric loudspeaker consisting in a spherical distribution of ultrasound transducers," *Sensors*, vol. 18, no. 12, p. 4317, 2018.

[13] A. Farina, "Simultaneous measurement of impulse response and distortion with a swept-sine technique," in *Audio Engineering Society Convention 108*, (Paris, France), pp. 1–24, Audio Engineering Society, 2000.

[14] S. Müller and P. Massarani, "Transfer-function measurement with sweeps," *Journal of the Audio Engineering Society*, vol. 49, pp. 443–471, 2001.

[15] A. Farina, "Advancements in impulse response measurements by sine sweeps," in *Audio Engineering Society Convention 122*, (Vienna, Austria), pp. 1–21, Audio Engineering Society, 2007.

[16] M. Arnela, C. Martínez-Suquía, and O. Guasch, "Characterization of an omnidirectional parametric loudspeaker with exponential sine sweeps," *Appl. Acoust.*, vol. 182, p. 108268, 2021.

[17] A. Fantinelli, M. Arnela, R. Burbano-Escolà, and J. Vaquerizo-Serrano, "A study of the ultrasonic and audible frequency response of commercial loudspeakers for use as parametric acoustic arrays," in *Internoise 2024*, (Nantes, France), International Institute of Noise Control Engineering, 2024.

DOI: 10.61782/fa.2025.0261



FORUM ACUSTICUM
EURONOISE 2025

DEEP LEARNING-AIDED DESIGN OF A BROADBAND LOW-FREQUENCY META-ABSORBER FOR ROOM ACOUSTIC APPLICATIONS

Oluwaseyi Ogun[1] **John Kennedy**[1*]
[1] School of Engineering, Trinity College Dublin, Ireland, D02 PN40

ABSTRACT

Designing acoustic metamaterials (AMMs) capable of achieving broadband low-frequency absorption remains a considerable challenge due to the physical limitations imposed by long wavelengths, which typically necessitate thick, voluminous structures. This paper introduces a data-driven approach that employs a pretrained deep learning (DL) model to generate optimized AMM geometries based on targeted absorption spectra, which are tailored to room-specific modal behavior and layout. The resulting designs aim to maximize absorption efficiency within the 100–250 [Hz] range while minimizing structural footprint and material usage. The proposed AMM absorbers are evaluated through finite element simulations and validated against experimental reverberation time (RT60) measurements in a partially evacuated office environment. Performance is benchmarked against a commercial 10 [cm] thick Spektra A10 absorber. Results reveal that the AMM, with only 3 [cm] thickness, achieves competitive performance in the targeted low-frequency range, offering moderate RT60 reduction. While the Spektra A10 exhibits better performance above 200 [Hz], the AMM's compact form factor and design flexibility provide compelling advantages for low-frequency room treatment. These results highlight the potential of integrating machine learning with acoustic design to develop lightweight, application-specific absorption solutions for modern architectural acoustics.

*__Corresponding author__: *jkenned5@tcd.ie.*

__Copyright__: *©2025 Ogun et al. This is an open-access article distributed under the terms of the Creative Commons Attribution 3.0 Unported License, which permits unrestricted use, distribution, and reproduction in any medium, provided the original author and source are credited.*

Keywords: *broadband absorption, deep learning, room acoustics, low-frequency.*

1. INTRODUCTION

The way sound is perceived within a room results from both direct sound—traveling straight from the source to the listener—and reflected sound, which bounces off various surfaces. Key contributors to these reflections include architectural features such as walls, floors, and ceilings, but other objects, including furniture and even people, can also influence sound propagation. How sound interacts with a surface depends on factors such as the material composition and the angle at which the sound wave strikes it. The acoustical analysis of a room is essential for understanding and optimizing the behavior of sound within enclosed spaces for optimal sound experience. The interaction of sound waves with surfaces, objects, and air affects how sound is perceived, making room acoustics a critical factor in designing environments such as concert halls, theaters, recording studios, classrooms, offices, and residential spaces [1]. Poor acoustic design can lead to issues such as excessive reverberation, speech intelligibility problems, and unwanted echoes, which degrade the quality of auditory experiences.

However, achieving a universally ideal acoustic environment for concerts and theaters for instance, is an idealization, as musical perception is influenced not only by objective sound characteristics, but also by individual perceptions and requirements. This inherent diversity in acoustic preferences leads to a wide range of successful concert hall designs, making room acoustics a continuously evolving field [2]. To navigate these complexities, acoustic modeling provides a structured approach to evaluate key sound characteristics within a space, and enables

auralization [3].

The two primary methods for modeling room acoustics are based either on solving the Helmholtz wave equation or its variants, or on the principles of geometrical acoustics which form the foundation of ray acoustics. Geometrical acoustics, a commonly used approach for room acoustic modeling [1, 4–6], treats sound propagation as rays and disregards its wave nature. This assumption is accurate at high frequencies where the sound wavelength is much smaller than the objects and room features (e.g., walls, furniture). However, at low frequencies, wave phenomena such as diffraction and interference become more pronounced, leading to significant small-scale effects that geometrical acoustics cannot account for, thus necessitating wave-based methods such as the finite element modeling (FEM) or a hybrid approach [7].

Konrad et al. [8] explores simulating room acoustics using the finite-difference time-domain (FDTD) method, focusing on boundary and medium modeling. Their findings suggest that the proposed 3D schemes outperform traditional methods like Yee's staggered grid [9], and the digital waveguide mesh while maintaining desirable boundary properties. Elzbieta et al. [10] explores the theoretical and practical approaches to optimizing the sound field through architectural design. The study provides guidelines for acoustic planning, focusing on sound absorption strategies, spatial and material solutions, aiding systems, and proper device implementation. Noting a gap between acoustics and architecture, the paper bridges these fields by highlighting their mutual influence on sound absorption and propagation in office spaces.

Noise control in open offices can be achieved through high room absorption, tall screens, bookcases, and sufficient masking sound. However, the interaction of these elements is complex, particularly at varying distances from a speaker. Jukka et al. [11] conducted room acoustic measurements in 15 open offices and developed a model using multivariable regression analysis of the measurement data. Their model predicts two key descriptors of open office acoustics: the A-weighted speech level per distance doubling and the radius of distraction. These predictions are then used for decision making, to improve speech privacy and overall acoustic conditions.

An optimization model to help office space designers select cost-effective noise control materials while meeting acoustic quality requirements was presented in Abdullah et al. [12]. The model follows five key stages: identifying designer decisions affecting cost, formulating an optimization function, defining constraints related to acoustic quality and material selection, implementing the model using genetic algorithms (GA), and evaluating its performance in a real-world office space. Their model determines the optimal type and area of acoustic materials for each surface in the room, ensuring both cost efficiency and acoustic performance.

Low-frequency noise is still a challenge that is practically difficult to deal with especially in communication spaces where sound quality is non-trivial. Fuchs et al. [13] highlights the often-overlooked issue of low-frequency noise (below 100–125 [Hz]) in communication spaces such as offices, conference rooms, and restaurants. Traditional building and room acoustic standards fail to address this frequency range, which significantly impacts speech intelligibility and sound quality. To tackle this, the development and consulting institute, IBP, developed slender compound panel absorbers (CPA), which can be mounted on walls or ceilings to dampen dominant room eigenfrequencies. Through extensive real-world testing, the study demonstrates substantial improvements in acoustic comfort. The paper serves as a call to recognize the limitations of conventional acoustic ratings and proactively address low-frequency issues rather than waiting for updated standards.

Artificial intelligence (AI) has emerged as a transformative tool in the field of acoustics, revolutionizing acoustic design by enabling advanced noise control solutions. With its ability to analyze vast amounts of data and predict sound behavior with high precision, AI allows for the creation of customized acoustic environments tailored to specific needs, empowering designers to achieve targeted sound control with greater efficiency, and achieving optimized acoustics in spaces ranging from open offices to concert halls, while reducing time and resources spent on traditional trial-and-error approaches. A machine learning-based approach to estimate room acoustic parameters using only geometrical information as input was employed in [14]. The work demonstrates that traditional methods often rely on geometrical models (which approximate high-frequency sound as rays but lack accuracy for wave effects) or wave-based models (which are more precise but computationally expensive). The study builds a dataset from real-world acoustical measurements, using microphone array encoding to extract room impulse responses and absorption area in multiple directions. A neural network model is then trained to predict key acoustic parameters like reverberation time (T60) and early decay time (EDT). Compared to the traditional Sabine method, the model achieves higher accuracy, particularly at low

frequencies.

In Ciaburro et al. [15], an automatic procedure for estimating the reverberation time of a room using artificial neural networks (ANNs) was developed. Traditionally, reverberation time measurement requires specialized equipment and exclusive access to the space. In contrast, their work proposed a method that uses simple audio recordings, from which acoustic features are extracted and labeled with corresponding reverberation time values in octave bands. The labeled dataset is then used to train an ANN model, enabling it to predict reverberation time in any closed space without the need for complex measurements or calculations. The approach simplifies and streamlines the process of estimating reverberation time, making it more accessible and efficient.

Low-frequency broadband noise is a common phenomenon in room acoustics, which is a challenge for traditional acoustic panels as they would need to be impractically bulky to absorb such frequencies. In this paper, a partially empty office space is considered for acoustic treatment. A wave-based numerical method based in COMSOL® Multiphysics is used to simulate the behavior of the room to sound, and the reverberation time measurements are compared with those from experiment. Next, a previously trained deep learning model of an acoustic metamaterial (AMM) absorber is used to predict broadband absorber geometries, with a user-specified subwavelength thickness, according to the experimentally determined room modes. This paper is structured as follows. Section 2 outlines the methodology, including the numerical modeling procedure, experimental setup, and the measurement metrics employed. Section 3 presents the results of the study, covering the validation of the numerical model and the performance comparison between the proposed AMM and a commercial-grade absorber based on RT60. Finally, Section 4 provides the conclusions and discusses key findings and potential improvements.

2. METHODOLOGY

2.1 Room description and numerical modeling

The considered office space is a rectangular room of dimensions 580 [cm] × 266 [cm] × 280 [cm], with a window of dimensions 130 [cm] × 54 [cm] × 180 [cm] as depicted in Fig. 1(a). The office is constructed with solid concrete and brick surfaces with reflective acoustic characteristics. The walls are made of exposed bricks, offering high mass and rigidity. This results in strong sound reflection, with minimal sound absorption at lower frequencies. The surface texture of the brick may introduce some diffusion at mid-to-high frequencies. The ceiling consists of a solid reinforced concrete slab, providing a highly reflective surface that contributes to sound reverberation within the room. The lack of absorption may lead to longer decay times for higher frequencies unless treated with acoustic materials. The floor is a polished concrete surface, which is both acoustically reflective and structurally robust. The smooth finish enhances high-frequency reflections, potentially increasing room brightness. The window is a rectangular opening with a shallow cavity ending in the glass backing. The glass pane, set at the rear of the cavity, influences both sound reflection and absorption characteristics.

The acoustic response of the room is modeled using the lossless Helmholtz wave equation within the Pressure Acoustics Module of COMSOL® Multiphysics. The medium is excited with a monopole domain source, applied through a spherical volumetric source. This configuration approximates an omnidirectional point source, which is representative of a typical loudspeaker or sound source in enclosed spaces. The spherical region ensures uniform radiation of acoustic energy in all directions, minimizing directional bias and better simulating diffuse field conditions assumed in statistical models such as the Sabine and Eyring formulas.

Boundary conditions are assigned to the room surfaces and furniture based on their respective material properties, as detailed in Tab. 1, and their absorptivities across octave band center frequencies are obtained from the literature [16, 17]. The computational domain is discretized using a tetrahedral mesh, with a maximum element size of $\lambda/7$, where λ represents the wavelength corresponding to the highest frequency of interest.

2.2 Reverberation time

Reverberation is a key acoustic parameter that defines how sound persists in a room after the source has stopped [18]. It significantly impacts both speech intelligibility and musical quality. Excessive reverberation can blur speech by masking short consonant sounds, while insufficient reverberation can make music sound lifeless and lacking in richness. The reverberation time, $RT60$, is the duration required for the sound level to decay by 60 dB after the source ceases. This metric provides insight into the room's acoustic properties and can be measured empirically by analyzing the sound pressure level over time. The RT60 in frequency domain is commonly computed

Table 1: Absorption coefficients of the surface materials in the investigated office space.

Surface		Absorptivities in Octave Bands					
Type	Material	125 [Hz]	250 [Hz]	500 [Hz]	1000 [Hz]	2000 [Hz]	4000 [Hz]
Window	Glass	0.18	0.06	0.04	0.03	0.02	0.02
Window frame	Plywood	0.28	0.22	0.17	0.09	0.1	0.11
Ceiling/floor	Concrete	0.01	0.01	0.015	0.02	0.02	0.02
Door	Wood	0.1	0.07	0.05	0.04	0.04	0.04
Side walls	Brick	0.03	0.03	0.03	0.04	0.05	0.07
Table	Wood	0.15	0.11	0.10	0.07	0.06	0.07

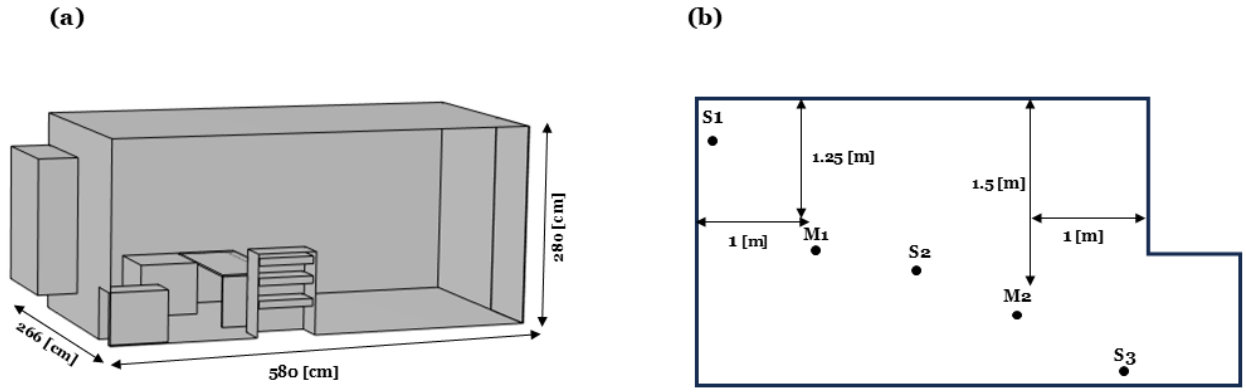


Figure 1: Illustration of the office space drawing simulated in COMSOL. (a) shows the CAD drawing of the room with a table, book shelve and a drawer, and (b) shows the map of the speaker-microphone positions during measurements.

according to the Sabine formula [19] in Eqn. (1)

$$RT60 = \frac{0.161V}{A}, \tag{1}$$

where V is the volume of the room, and A is the total equivalent absorption area given by

$$A = \sum(S_i.\alpha_i), \tag{2}$$

where S_i is the effective surface area of each material in the room, and α_i is the absorption coefficient of the material. The Sabine formula assumes that sound energy is uniformly distributed within the room, with minimal influence from objects and furniture on the overall acoustic response. However, in practice, perfect sound diffusion is rarely achieved, requiring adjustments in some cases to account for furniture or surfaces not accounted for due to the assumption.

2.3 Measurement setup

Reverberation time measurements are conducted in accordance with the ISO 3382-2:2008 standard. Two microphone positions, M_1 and M_2 are marked within the room, spaced at least 1 [m] from the nearest reflecting wall, and avoids symmetric positions. Three sound source positions are utilized: two located at opposite corners of the room (S_1 and S_3) and one at the center, S_2 (see schematic in Fig. 1(b). The excitation signal is a time-domain logarithmic sine sweep, providing a high signal-to-noise ratio and enabling deconvolution to extract the room impulse response from which RT60 is estimated via Schroeder integration. The sweep is generated at –12 [dBFS] with a sampling rate of 44.1 [kHz].

A total of ${}^3P_2$ (= 6) source-microphone combinations were measured, and the results were averaged to obtain a single representative reverberation time curve. The of-

fice measurement setup comprises a Genelec 8020B active monitoring loudspeaker and an omnidirectional microphone, connected to the output and input channels, respectively, of a Focusrite Scarlett 2i4 audio interface. The measurement signals are generated and analyzed using Room EQ Wizard (REW) V5.31.3, allowing for precise estimation of the decay characteristics of the room impulse response.

3. RESULTS AND DISCUSSION

3.1 Model validation

Fig. 2 shows the one-third octave RT60 of the office space without any acoustic treatment. The measurements at each speaker-microphone position are shown in gray, while the average response is indicated in red (refer to Fig. 1(b) for speaker-microphone positioning). It is noteworthy that the office space was already in use, meaning some items could not be removed during measurements, which may have impacted the room's response. Subsequently, the numerical RT60 is compared to the experimental results. Initial simulation shows that the numerical model tends to overestimate the reverberation time. This discrepancy is likely due to the presence of surfaces, crevices, cavities, and other elements within the office space that are not fully accounted for in the numerical model. To correct for this, the unknown absorption characteristics are estimated by calculating the absorption area required to match the difference between the numerical and experimental RT60 responses. This "deficit" in absorption area is used to generate frequency-dependent absorption data, which are subsequently applied to a section of the room's wall in the numerical model. The required absorption area is computed using Sabine's equation as

$$\Delta A(f) = A_{exp}(f) - A_{num}(f) = \frac{0.161.V}{RT_{60}^{exp}} - \frac{0.161.V}{RT_{60}^{num}}, \tag{3}$$

So that the correction absorption coefficient, $\Delta\alpha(f)$, is then obtained according to Eqn. (4)

$$\Delta\alpha(f) = \frac{\Delta A(f)}{A_{corr}}, \tag{4}$$

where A_{corr} is the correction absorption area. The result of this correction is shown in Fig. 3 which validates the numerical for subsequent analysis.

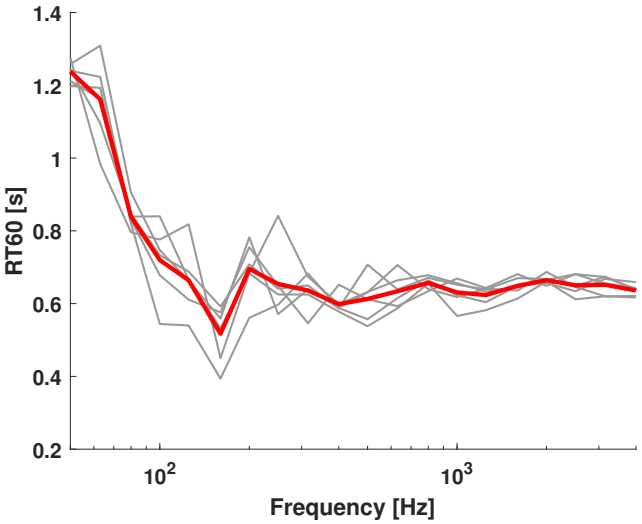


Figure 2: Acoustic response of the space measured using a logarithmic sine sweep excitation showing the reverberation time (RT60) and decay characteristics of the space.

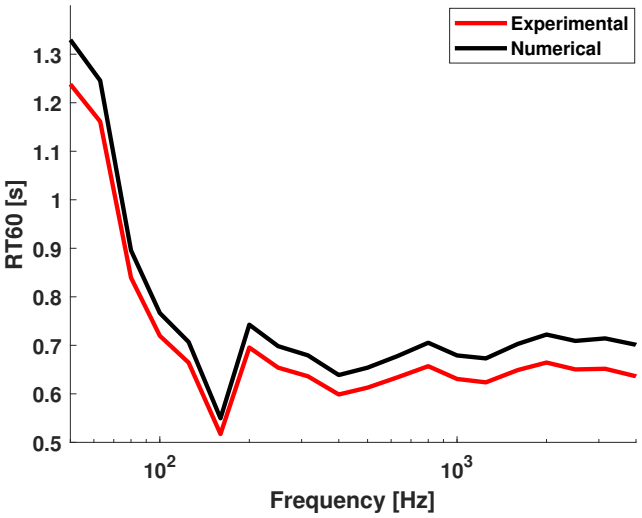


Figure 3: Comparison between experimental and numerical reverberation times after correcting for the unknown absorption area in the space.

3.2 AMM Application to Room Acoustics

Having validated the numerical room model against experimental measurements, a simulation study is conducted

to evaluate the performance of a deep learning-based AMM absorber in comparison to a conventional industrial absorber, the Spektrum A10, which consists of a fabric cover and mineral wool core, with dimensions 60[cm] $\times$ 60 [cm] $\times$ 10 [cm]. A pre-trained autoencoder model is employed for inference, enabling the prediction of AMM geometrical parameters based on a desired target absorption spectrum. Here, the target spectrum is informed from the room's reverberation response in Fig. 2. The decoder component of the network is used to reconstruct the original input spectrum, which is subsequently applied to the AMM panels in the numerical room model. A unit structure of the designed AMM absorber is shown in Fig. 4. Each unit is a supercell composed of four inhomogeneous cells, each tuned to a different target frequency. The supercells are periodically arranged in a 60 [cm] $\times$ 60 [cm] rectangular panel, which is then applied to the room surfaces and ceiling. Four panels each of 60 [cm] $\times$ 60 [cm] cross-section are used in the simulation. On the other hand, the industry-grade Spektrum A10, shown in Fig. 5 is of similar cross-section, but witha thickness of 10 [cm]

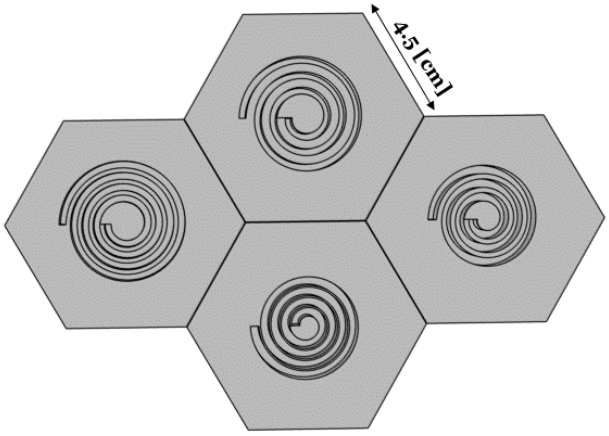


Figure 4: A unit structure of the designed broadband AMM absorber composed of a hexagonal cavity, a spiral inclusion and a top perforated plate.

For the private office space under consideration, it is desired to have RT60 between say $0.4 \leq \text{RT60} \leq 0.6$ [s] at low frequencies (< 200 [Hz]) to improve speech intelligibility and reduce listener fatigue from reflected noise. Thus, a broad range of 100 to 200 [Hz] with absorptivities higher than 0.8 is presented to the encoder for which the corresponding geometry is predicted, and the reconstructed absorption spectrum, $\alpha(f)$, is then applied to the

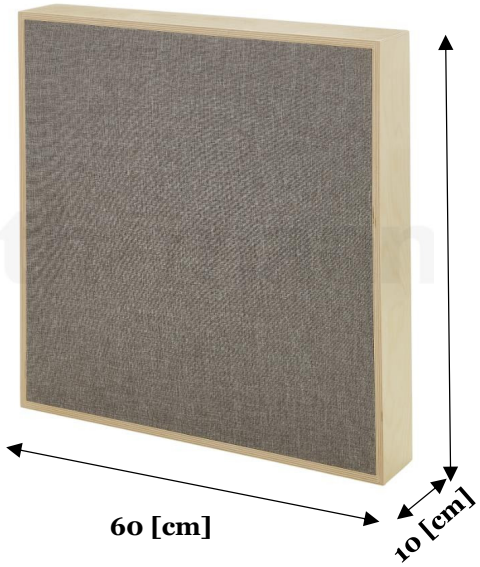


Figure 5: A 60 [cm] $\times$ 60 [cm] Spektrum A10 industrail panel used as a benchmark in this study

absorber surfaces in the room model. For fair comparison, the AMM absorber is also designed with the same 60[cm] $\times$ 60 [cm] cross-section, but with a thickness of 3 [cm]. Fig. 6 shows the performance comparisons of both absorbers. It can be observd that the AMM slighly improves the RT60 relative to the baseline in the range between 100 and 200 [Hz], but the effect at higher frequencies are very minimal. This is because the absorber is targeted for the low frequencies (≤ 200 [Hz]) and more so, the range of influence of the aborber can be increased by increasing the number of inhomogeneous unit that makes up each broadband absorber, as low frequencies are characterized by sharp narrow peaks. The Spektrum A10 on the other hand performs better at higher frequencies ($>$ 200 [Hz]) with lower RT60. Fig. 7 shows a bar plot of the reduction in RT60 relative to the baseline. It is clear that the AMM provides a superior performance in the targeted low-frequency range, and beyond this range, the Spektrum A10 provides the better performance.

4. CONCLUSIONS

This paper presents a deep learning-driven acoustic metamaterial (AMM) absorber aimed at mitigating low-frequency room acoustic issues, and compares its performance with a conventional industry-grade absorber. The

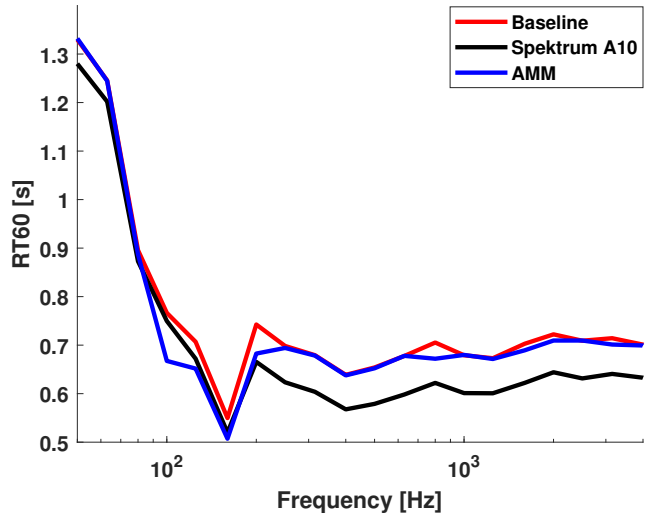


Figure 6: Performance comparison of RT60 curves from both absorbers relative to the baseline.

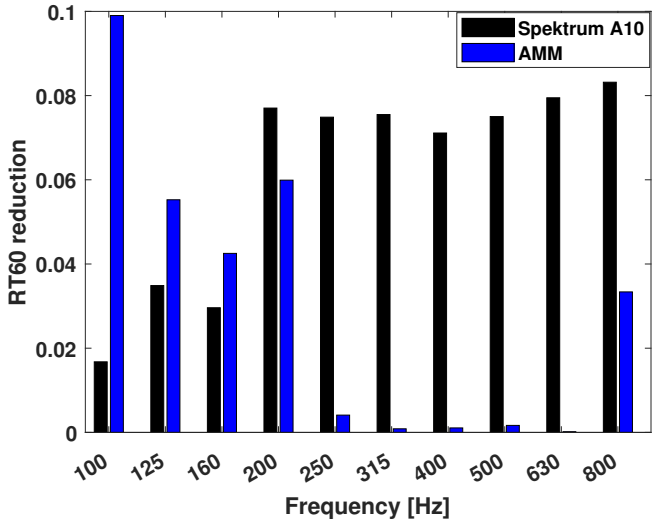


Figure 7: Relative difference in RT60 from the baseline from both absorbers in the targeted frequency range.

target environment is an existing office space that was partially evacuated and acoustically characterized using the RT60 metric.

To establish a baseline and validate the simulation framework, numerical modeling was carried out using the finite element method in COMSOL Multiphysics. Following validation, a pretrained autoencoder was employed to predict an optimal absorption spectrum in the 100–250 [Hz] frequency range. These frequency-dependent absorption coefficients were then applied to panel surfaces in the FEM model to simulate the corresponding reverberation times.

Simulation results demonstrate that the proposed AMM absorber shows promising performance within the targeted low-frequency range, with a modest reduction in RT60 compared to the untreated baseline response. However, the commercial Spektra A10 panel, with a thickness of 10 [cm], slightly outperforms the 3 [cm] thick AMM at higher frequencies above 200 [Hz]. This performance gap is primarily attributed to the limited number (four) of inhomogeneous unit cells used in constructing the broadband AMM absorber. It is anticipated that increasing the number of such units would broaden the effective bandwidth and enhance overall absorption performance over a wider operational range.

5. ACKNOWLEDGMENTS

The authors gratefully acknowledge the support of the Provost's awards of Trinity College Dublin.

6. REFERENCES

[1] L. Savioja and U. P. Svensson, "Overview of geometrical room acoustic modeling techniques," *The Journal of the Acoustical Society of America*, vol. 138, no. 2, pp. 708–730, 2015.

[2] H. Kuttruff, *Room acoustics*. Crc Press, 2016.

[3] M. Kleiner, B.-I. Dalenbäck, and P. Svensson, "Auralization-an overview," *Journal of the Audio Engineering Society*, vol. 41, no. 11, pp. 861–875, 1993.

[4] M. Vorländer, "Computer simulations in room acoustics: Concepts and uncertainties," *The Journal of the Acoustical Society of America*, vol. 133, no. 3, pp. 1203–1213, 2013.

[5] L. Aspöck and M. Vorländer, "Room geometry acquisition and processing methods for geometrical acoustics simulation models," *Proceedings of the EuroRegio*, 2016.

[6] A. Bassuet, D. Rife, and L. Dellatorre, "Computational and optimization design in geometric acoustics," *Building Acoustics*, vol. 21, no. 1, pp. 75–85, 2014.

[7] D. Murphy, M. Beeson, S. Shelley, A. Southern, and A. Moore, "Renderair – room acoustics simulation using a hybrid digital waveguide mesh," in *Proceedings of the 124th AES Convention*, (Amsterdam, The Netherlands), May 2008.

[8] K. Kowalczyk and M. van Walstijn, "Room acoustics simulation using 3-d compact explicit fdtd schemes," *IEEE Transactions on Audio, Speech, and Language Processing*, vol. 19, no. 1, pp. 34–46, 2011.

[9] K. Yee, "Numerical solution of initial boundary value problems involving maxwell's equations in isotropic media," *IEEE Transactions on antennas and propagation*, vol. 14, no. 3, pp. 302–307, 1966.

[10] E. Trocka-Leszczynska and J. Jablonska, "Contemporary architectural design of offices in respect of acoustics," *Applied Acoustics*, vol. 171, p. 107541, 2021.

[11] J. Keränen, P. Virjonen, D. Oliva Elorza, and O. V. Hongisto, "Design of room acoustics for open offices," *SJWEH Supplements*, no. 4, pp. 46–49, 2008.

[12] A. AlOmani, K. El-Rayes, and A. Altuwaim, "Optimizing the use of acoustic materials in office buildings," *Scientific reports*, vol. 11, no. 1, p. 20652, 2021.

[13] H. Fuchs, X. Zha, X. Zhou, and H. Drotleff, "Creating low-noise environments in communication rooms," *Applied Acoustics*, vol. 62, no. 12, pp. 1375–1396, 2001.

[14] R. Falcon Perez, "Machine-learning-based estimation of room acoustic parameters," 2018.

[15] G. Ciaburro and G. Iannace, "Acoustic characterization of rooms using reverberation time estimation based on supervised learning algorithm," *Applied Sciences*, vol. 11, no. 4, p. 1661, 2021.

[16] M. J. Crocker, F. M. Kessler, and A. J. Price, *Noise and Noise Control: Volume 1*. Crc Press, 2018.

[17] P. Jensen, C. R. Jokel, and L. N. Miller, "Industrial noise control manual," 1978.

[18] T. Rossing, *Springer handbook of acoustics*. Springer Science & Business Media, 2007.

[19] L. L. Beranek, "The notebooks of wallace c. sabine," *The Journal of the Acoustical Society of America*, vol. 61, no. 3, pp. 629–639, 1977.

DOI: 10.61782/fa.2025.0285

FORUM ACUSTICUM EURONOISE 2025

DETECTION OF OPERATIONAL REGIMERELATED FAULTS IN AIR COMPRESSOR SYSTEMS USING ACOUSTIC ANALYSIS AND MACHINE LEARNING

Andrej Hvastja **Jurij prezelj**
Faculty of Mechanical Engineering, University of Ljubljana, Slovenia

ABSTRACT

Compressed air systems are critical yet energy-intensive in industrial operations, making operational reliability essential for efficiency and safety. This study presents a novel approach using acoustic monitoring and machine learning to detect and classify operational regime-related faults in air compressor stations. Signal-processing and psychoacoustic features extracted from audio recordings enabled distinct regime identification through dimensionality reduction (autoencoders) and clustering (Gaussian Mixture Models). Regime duration analysis facilitated anomaly detection linked to operational inefficiencies. The proposed method effectively distinguished normal from abnormal patterns, highlighting regimes tied to compressed air consumption variability and equipment cycling, offering valuable improvements for predictive maintenance and reliability.

Keywords: *compressor station, acoustic monitoring, regime classification, anomaly detection*

1. INTRODUCTION

1.1 Compressed Air Systems in Industry

Compressed air is a versatile energy carrier widely used in various industrial sectors due to its applicability in numerous operational processes [1,2]. However, compressed air systems represent significant energy consumers within industrial facilities. According to [3], air compressors account for approximately 10% of industrial electricity consumption in the European Union and the USA, and up to 9.4% in China. According to [4], use of compressed air should be limited to scenarios involving safety improvements, substantial productivity improvements, or considerable labor reductions.

1.2 Economic and Operational Challenges

The operating costs of compressed air systems are predominantly due to their electricity consumption, which frequently exceeds the initial investment cost of the equipment [3, 4]. Furthermore, air compressor systems are prone to frequent faults and anomalies, making them expensive and inefficient, especially as the equipment ages [5]. Older compressors are notably susceptible to faults arising from wear and aging, highlighting the necessity for robust fault detection and diagnostic approaches [6]. In industries such as manufacturing, where machinery operates under extreme conditions and at high speeds, undetected faults can significantly disrupt production and compromise employee safety [7].

1.3 Fault Detection and Maintenance Strategies

Traditional preventive maintenance strategies, which rely on scheduled intervals, often result in premature component replacement, incurring unnecessary expenses [8].

Condition-Based Maintenance (CBM) addresses this inefficiency by monitoring the actual condition of the equipment to determine precise maintenance actions before failures occur. CBM involves tracking parameters such as vibration, acoustics, temperature, and pressure to detect early fault indicators [9].

1.4 Advantages of Acoustic Monitoring

Among various monitoring methods, acoustic sensors offer distinct advantages, including their non-contact nature, non-destructive implementation, and ease of integration into existing systems due to their compact size. The relatively low installation cost of microphones has encouraged widespread adoption for acoustic data collection in industrial environments. Despite these benefits, distinguishing

fault-related acoustic signals from background noise remains a challenge due to noisy industrial conditions [10]. Machine learning (ML) has emerged as an effective tool to address this challenge, enabling efficient analysis and interpretation of acoustic data.

1.5 Operational Regime Classification

While conventional fault detection techniques primarily address abnormalities linked to fluctuating loads and environmental factors [10], much less attention has been paid to systematically classifying operational regimes. Yet industrial performance depends not only on mechanical reliability, but also on precise scheduling and evaluation of task durations. By comparing expected task timelines with actual operational performance, discrepancies become evident, revealing potential workflow anomalies or inefficiencies. This paper tackles that gap by emphasizing the necessity of classifying operational regimes, particularly those underscored by deviations between standard task durations and real-world operational times.

2. MATERIALS AND METHODS

2.1 Data Acquisition and Preprocessing

An operating compressor station, responsible for supplying compressed air to the Faculty of Mechanical Engineering in Ljubljana, was monitored using a microphone. The sound was recorded in WAV format over several days, including both weekdays and weekends. To accurately capture continuous operating conditions, a custom Python script segmented the audio into 2-second intervals with a 50% overlap.

2.2 Feature Extraction

For each sound segment the folowing signal-processing features were computed: Root Mean Square (RMS), Zero Crossing Rate (ZCR), Crest Factor, Short-Time Energy (STE), Variance, Skewness, Kurtosis and Arc length of the signal and its derivative, effectively capturing dynamic variations in the acoustic signals.

In addition to signal-processing features, the following psychoacoustic features were also computed on the sound signal: Sharpness, roughness, tonality, loudness, fluctuation strength, as they have been shown to be effective in machine fault detection [11].

2.3 Data filtering

To ensure data quality for the unsupervised clustering of operating regimes, outlier detection was performed using Isolation Forest on the aggregated feature set. Detected outliers, representing atypical data, were removed, preserving only normal operational data for subsequent analysis.

2.4 Dimensionality Reduction with Autoencoder

A deep autoencoder neural network was used for feature set dimensionality reduction [12]. The autoencoder architecture consisted of 4 dense layers with progressively reduced dimensions leading to a latent space dimension of 3 neurons. The model was trained with mean squared error (MSE) loss, using early stopping to avoid overfitting.

2.5 Operational Regime Classification

Latent features obtained from the autoencoder were clustered using a Gaussian Mixture Model (GMM). This unsupervised clustering approach grouped similar compressor operating states based on their latent representations, effectively classifying distinct operating regimes. Model selection criteria (AIC and BIC) were used to determine the optimal number of clusters. An illustration of the GMM clustering is provided in Figure 1 below, clustering latent features into 6 classes.

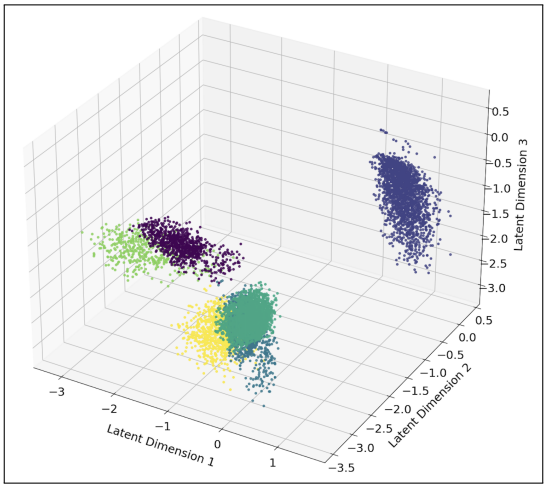


Figure 1. 6 clusters of operating regimes, based on GMM clustering.

2.6 Sequential Data Classification

The autoencoder and GMM were trained on randomly shuffled data to reduce overfitting and improve overall generality. In the second step, the same dataset was classified into identified operational regimes using the trained models. Whenever multiple consecutive sound recordings were assigned the same class, the event duration increased accordingly. However, to accurately evaluate the class or event duration, it is essential to process the recordings in their original sequence. This approach yields a feature that closely reflects the true duration of each event, and any deviation from this duration is flagged as an anomaly in the working regime.

3. RESULTS

This study examined a dataset of compressor station sound recordings spanning various operating regimes. Signal-processing features and psychoacoustic features, which capture human auditory perceptions and have been effective in machinery fault detection were derived from the sound recordings. The latent representation of the features was acquired using an autoencoder neural network and clustered using the Gaussian Mixture Model where the number of regime classes was selected using the AIC and BIC criteria.

Out of the six identified operating regimes, not all event durations are repeatable. As shown in Figure 2, the blue classes represent normal weekend operation and its typical duration range. Weekends serve as the baseline for "normal behavior" because of minimal compressed air usage. Through auditory inspection, Class 1—with its wider spread—was identified as the "working regime," as its duration varies with compressed air consumption. In contrast, Classes 0, 2, 3, 4, and 5 remain similar across weekend (normal) and weekday (test) datasets, suggesting they correspond to more repeatable operations (e.g., turning compressors on/off or switching between them). Their durations should therefore remain relatively constant, given that these transient events (start-up, shutdown, etc.) are not driven by air consumption. Consequently, any deviation from expected durations in these transient regimes may indicate abnormal behavior and signal changes in compressor station operation.

Meanwhile, the purple set of regimes was recorded when a series of tests were conducted following compressor station maintenance. These regimes, labeled "overloading" and "rest," demonstrated notably different durations, underscoring that the anomaly detection method successfully captured these unusual events.

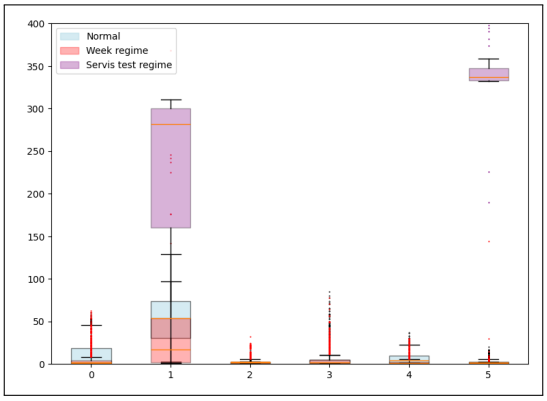


Figure 2. Event duration distribution of train (blue) and test (red) dataset.

The criteria for marking an event as an anomaly required its duration to fall below the 0.01 percentile or exceed the 0.99 percentile of the test dataset's event durations. This approach proved most effective, as it flags events that are significantly shorter or longer than expected.

Figure 3 highlights these anomalous events using golden rectangles with thin red outlines. Several anomalies occurred in Class 1, which corresponds to compressor operation tied directly to compressed air consumption, and is therefore naturally more variable. Additional anomalies appeared in Class 2, typically representing regimes expected to have consistent durations. Notably, anomalies in Class 1 diminished over time as the operational durations became shorter and returned to expected ranges.

As expected, Figure 4 illustrates that all events from the unusual "overloading" testing regime following compressor maintenance were marked as anomalies. This confirms the method's sensitivity and effectiveness in accurately detecting operational deviations.

4. CONCLUSION

This study demonstrated the effectiveness of acoustic monitoring combined with machine learning for detecting operational regime-related faults in air compressor systems. By extracting and analyzing signal-processing and psychoacoustic features from compressor sound recordings, distinct operational regimes were successfully iden-

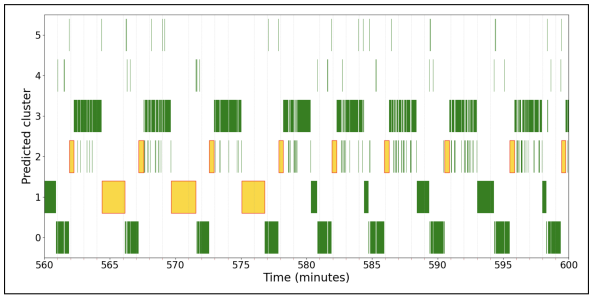


Figure 3. Work regime classes with corresponding durations.

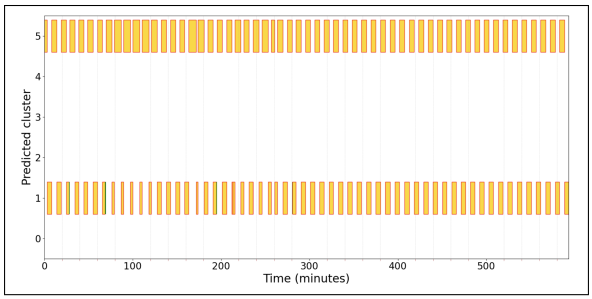


Figure 4. Overloading testing regime classes with corresponding durations.

tified using dimensionality reduction with autoencoders and clustering via Gaussian Mixture Models (GMM). The approach enabled the detection of anomalies based on deviations in regime durations, which were shown to correspond closely to actual operational events. Particularly, it was found that regimes associated with variable compressed air consumption exhibited significant variability in duration, whereas regimes related to equipment cycling and switching were highly consistent. Future work may focus on integrating this method into real-time monitoring systems to further enhance predictive maintenance and operational reliability in industrial compressor stations.

5. REFERENCES

[1] C. Y. Yuan, T. Zhang, A. Rangarajan, D. Dornfeld, B. Ziemba, and R. Whitbeck, "A decision-based analysis of compressed air usage patterns in automotive manufacturing," *Journal of Manufacturing Systems*, vol. 25, no. 4, pp. 293–300, 2006.

[2] J. J. Cabello Eras, A. Sagastume Gutiérrez, V. Sousa Santos, and M. J. Cabello Ulloa, "Energy management of compressed air systems. assessing the production and use of compressed air in industry," *Energy*, vol. 213, p. 118662, 2020.

[3] R. Saidur, N. Rahim, and M. Hasanuzzaman, "A review on compressed-air energy use and energy savings," *Renewable and Sustainable Energy Reviews*, vol. 14, no. 4, pp. 1135–1153, 2010.

[4] D. Kaya, P. Phelan, D. Chau, and H. saraç, "Energy conservation in compressed-air systems," *International Journal of Energy Research*, vol. 26, pp. 837 – 849, 07 2002.

[5] B. Elliott, *Compressed air operations manual*. McGraw Hill Professional, 2010.

[6] J. Ma and J. Jiang, "Applications of fault detection and diagnosis methods in nuclear power plants: A review," *Progress in Nuclear Energy - PROG NUCL ENERGY*, vol. 53, pp. 255–266, 04 2011.

[7] B. G. Joung, C. Nath, Z. Li, and J. Sutherland, "Bearing anomaly detection in an air compressor using an lstm and rnn-based machine learning model," *The International Journal of Advanced Manufacturing Technology*, vol. 134, pp. 3519–3530, 09 2024.

[8] J. J. Montero Jimenez, S. Schwartz, R. Vingerhoeds, B. Grabot, and M. Salaün, "Towards multi-model approaches to predictive maintenance: A systematic literature survey on diagnostics and prognostics," *Journal of Manufacturing Systems*, vol. 56, pp. 539–557, 2020.

[9] N. K. Verma, R. K. Sevakula, S. Dixit, and A. Salour, "Intelligent condition based monitoring using acoustic signals for air compressors," *IEEE Transactions on Reliability*, vol. 65, no. 1, pp. 291–309, 2016.

[10] Y. Tagawa, R. Maskeliunas, and R. Damaševičius, "Acoustic anomaly detection of mechanical failures in noisy real-life factory environments," *Electronics*, vol. 10, p. 2329, 09 2021.

[11] J. Murovec, L. Čurović, T. Novaković, and J. Prezelj, "Psychoacoustic approach for cavitation detection in centrifugal pumps," *Applied Acoustics*, vol. 165, p. 107323, 2020.

[12] Y. Wang, H. Yao, and S. Zhao, "Auto-encoder based dimensionality reduction," *Neurocomputing*, vol. 184, pp. 232–242, 2016. RoLoD: Robust Local Descriptors for Computer Vision 2014.

DOI: 10.61782/fa.2025.0585

FORUM ACUSTICUM EURONOISE 2025

MONITORING OF MANUFACTURING PROCESS USING UNSUPERVISED SOUND EVENT CLASSIFICATION WITH APPLICATION OF SOUND DIRECTIVITY

Jurij Prezelj[1*] **Andrej Hvastja**[1] **Tomaž Berlec**[1]
[1] University of Ljubljana, Faculty of Mechanical Engineering, Slovenia

ABSTRACT

This study explores the use of sound directionality (DOA) as a key feature for unsupervised classification of acoustic events in industrial environments. A novel methodology was developed, combining a custom microphone array with SubWindowing to extract directional, spectral, and statistical features from production noise. Acoustic events were clustered using the k-means algorithm, with the optimal number of clusters determined via the elbow and silhouette methods. Feature importance was evaluated using Principal Component Analysis (PCA), which consistently identified sound directionality as the most influential feature. The results showed that integrating DOA significantly improved clustering performance and enabled accurate identification of machine states. The detected clusters aligned well with manually recorded operational states, confirming the method's effectiveness. This approach offers a robust and interpretable framework for real-time monitoring and fault detection in industrial settings. Future work will focus on extending this method to predictive maintenance systems and broader manufacturing environments.

Keywords: *acoustic event classification, sound directionality, unsupervised learning, k-means clustering, industrial monitoring*

1. INTRODUCTION

Current machine learning approaches for acoustic event classification in industrial environments typically rely on spectral, statistical, and temporal features. Traditional supervised methods have been widely applied, but unsupervised techniques, such as k-means clustering, are gaining traction due to their ability to classify unlabeled data and reduce dimensionality in high-dimensional datasets [4]. For instance, Ding and Li [4] proposed a feature selection framework for k-means, while Sun and Wang [5] introduced improvements via an ADMM algorithm to enhance clustering performance. Coates and Ng [6] also emphasized the role of k-means in feature learning, particularly due to its simplicity and effectiveness.
In audio classification specifically, deep learning methods have been reviewed by Mesaros et al. [7], highlighting the importance of robust feature representation. However, these methods largely overlook spatial acoustic features, such as sound directionality, also known as Direction of Arrival (DOA). Despite its well-known role in human perception, evident in the "cocktail party effect", DOA remains underexplored in unsupervised learning pipelines for acoustic event classification [2]. Base on literature review and our expertise we identified a research gap, placed a hypothesis, detect challenges and placed objectives of this study.
Research Gap: Current machine learning approaches for acoustic event classification typically rely on spectral, statistical, and temporal features. However, the role of sound directionality has been underexplored as a key feature for classification. Despite the relevance of directionality in distinguishing sound sources, it remains inadequately studied within unsupervised learning models, such as k-means clustering, for acoustic event classification [2].

[*] ***Corresponding author**: jurij.prezelj@fs.uni-lj.si*
***Copyright**: ©2025 Jurij Prezelj et al. This is an open-access article distributed under the terms of the Creative Commons Attribution 3.0 Unported License, which permits unrestricted use, distribution, and reproduction in any medium, provided the original author and source are credited.*

Hypothesis: Incorporating DOA as a core feature can significantly improve clustering performance and enable more accurate detection of machine states and process deviations in industrial environments.
Challenges: Accurate measurement of DOA requires precise sensor arrays and fast-response algorithms (<50 ms). Another challenge lies in combining DOA with time–frequency features into a unified feature set and validating its impact using robust dimensionality reduction methods such as Principal Component Analysis (PCA).
Objective:
This study aims to investigate the role of DOA in the classification of acoustic events using unsupervised learning, specifically focusing on k-means clustering.

2. METHODOLOGICAL OVERVIEW

The classification system developed in this study consists of three main stages: (1) data acquisition using a custom-designed differential microphone array, (2) feature extraction incorporating both time–frequency and directionaly DOA, and (3) unsupervised classification using the k-means algorithm. To enhance temporal resolution, a SubWindowing technique was used to segment the acoustic data. Features were extracted from both time and frequency domains, including Direction of Arrival (DOA) information computed via beamforming algorithms. Dimensionality reduction techniques such as Principal Component Analysis (PCA) was employed to assess feature importance and ensure model interpretability. The proposed system enables precise spatial classification of acoustic events and supports real-time monitoring in industrial environments.

2.1 Feature Extraction

The feature extraction process is a critical step in the overall methodology, converting raw sound signals into meaningful descriptors that can be used for clustering and classification. Key features are extracted from both the time and frequency domains. Spectral features such as spectral centroid, spectral bandwidth, spectral flatness, and spectral roll-off are calculated for each SubWindow segment. Temporal features, including Zero-Crossing Rate (ZCR), Root Mean Square (RMS) energy, and Sound Pressure Level (SPL), are also extracted. Additionally, statistical features like skewness, kurtosis, and entropy are computed to capture distributional properties of the signal. A unique contribution of this study is the inclusion of sound directionality as a feature, which is derived from the microphone array's spatial configuration. This information is combined into a feature vector representing each time segment, enabling a comprehensive representation of the acoustic event.
The feature set is subsequently refined using dimensionality reduction techniques, including Principal Component Analysis (PCA), to identify and retain only the most influential features for clustering

2.2 Time Intervals of feature extraction and their integration

In industrial acoustic environments, sound signals are inherently complex. They are composed of a combination of impulsive, transient events, such as impacts, cutter engagements, or part drops, and longer lasting background or cyclical machine operations. Capturing this full acoustic landscape using a single fixed time resolution would either miss rapid changes or smooth over important long-term patterns. To address this, we implemented a dual-time-constant segmentation strategy, which enables the extraction of both fast-evolving and slowly varying features from the signal.

2.2.1 Motivation for the Approach

The main rationale behind this two-level segmentation was to construct a feature representation that simultaneously captures the detail of transient events and the consistency of long-term operational patterns. Many machine learning models fail to distinguish between these layers of acoustic behavior when using a single time scale, which leads to suboptimal clustering or misclassification of machine states. By layering feature extraction over both short and long intervals, we aimed to provide the unsupervised algorithm with richer and more distinguishable patterns for clustering.
This approach mirrors human auditory perception, where the brain reacts to sudden sounds immediately while also tracking longer sequences and rhythms over time. The short segments allow us to detect quick, local fluctuations in sound energy or frequency, while the longer segments offer context highlighting how those fluctuations develop over time.

2.2.2 Short-Term Segmentation (τ_z)

The sound signal was initially divided into short overlapping windows of duration τ_z. These segments were small enough to preserve detail on the time scale of tens of milliseconds, suitable for detecting tool strikes or abrupt machine transitions. For each τ_z segment, we applied a Short-Time Fourier Transform (STFT) to compute sound pressure level (SPL) values across multiple frequency bands. This frequency-domain representation was essential for identifying spectral structures linked to different

machine behaviors. The use of overlapping windows ensured smoother transitions between adjacent segments, preventing the loss of critical information at boundary points and improving temporal continuity in the feature space.

2.2.3 2.2.3 Long-Term Aggregation (τ_k)

To build a higher-level representation, we grouped i consecutive τ_z segments into a longer interval $\tau_k = i \cdot \tau_z$. Within each τ_k block, a set of statistical metrics was computed for every frequency band and acoustic feature:

- Mean: representing the average energy or behavior in the interval,
- Range: capturing variation or dynamics,
- Standard deviation and variance: indicating spread or instability,
- First-order temporal derivatives: highlighting changes and slopes.

This allowed us to extract a macro level picture of the evolving sound environment, revealing whether the machine operation was stable, variable, cyclic, or anomalous.

2.2.4 2.2.4 Temporal Derivatives and Spectral Dynamics

To further enrich the feature set, we computed temporal derivatives (differences between adjacent τz segments) for each SPL value, capturing short-term dynamics like rising or falling spectral power. These were aggregated in the same way as raw SPL values, maintaining the temporal structure of the sound while enabling detection of directional changes in signal characteristics.

We also calculated the spectral length for each frequency band, defined as the cumulative distance (or variation) between successive SPL values. This served as a descriptor of spectral "activity" or instability, providing a useful contrast between steady and fluctuating sounds.

2.2.5 2.2.5 Feature Matrix Construction

The final step involved concatenating all extracted descriptors—spectral, temporal, statistical, and derivative-based—within each τk interval into a composite feature vector. These vectors formed the rows of the feature matrix used for unsupervised clustering with the k-means algorithm. Importantly, we later appended the direction of arrival (DOA) features (see Section 2.3) to this same matrix, enabling the clustering to incorporate both spectral content and spatial origin.

This dual-time approach, illustrated in Figures 1 and 2, ensured that the model could effectively group acoustic events that were similar not only in sound quality, but also in time structure and directional behavior—essential for robust classification in complex industrial soundscapes.

$$L = \sum_{j=1}^{N-1} \sqrt{(\Delta f)^2 + (Lp_{j+1} - Lp_j)^2} \quad (1)$$

By using this methodology for the analysis of acoustic data, numerous features of the sound can be extracted from the frequency domain. Furthermore, by transforming the data into a new time constant, it is possible to derive features that also describe changes in the time domain. This dual-domain approach ensures that both rapid and gradual changes in sound are effectively captured, thereby improving the clustering and classification of acoustic events.

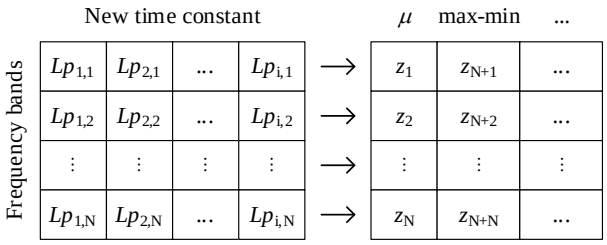


Figure 1: Grouping i[th] time steps into a time constant τk for each frequency band.

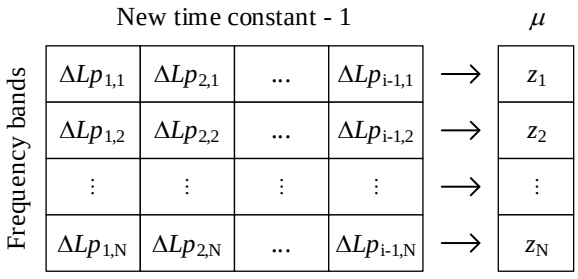


Figure 2: Grouping (i-1)[th] derivatives into a time constant τ_k for each frequency band.

2.3 Directionality (DOA) Estimation with SubWindow Beamforming

The process of measuring immission directivity necessitates the use of a microphone array and a beamforming algorithm, tools that aid in localizing sound sources or determining the Direction Of Arrival (DOA) of sound. Differential Microphone Arrays (DMAs), a distinct subset in sound localization, have emerged as the most appropriate beamforming method for a variety of applications that require speech recognition over the past decade. These applications include hands-free systems, mobile phones, and hearing aids. Circular DMAs have undergone extensive

examination for speech and audio applications, primarily due to their adaptability in control, the capacity to establish frequency-invariant directivity patterns, and superior directivity factor [8] Their inherent benefits include significant beam alignment, frequency independence, and a compact geometrical configuration Several models have been constructed where all the first-order DMA computations are conducted in the time domain. This approach offers a crucial advantage - the computations exhibit minimal latency. This feature is particularly vital and advantageous in real-time applications [9, 10, 11]. The principle of merging microphone signals from a circular array [12] sparked the development of our unique algorithm [13, 14, 15, 16, 17]. This algorithm, designed to compute the DOA, utilizes a simplified method based on timed delay cascading pairs, as depicted in figure 3 and given by Eq. (2). to form a DMA.

$$argminj = \|\sum_{i=0}^{D}\left[x_{\mathrm{mic1}}(n) - x_{\mathrm{mic2}}\left(n - \frac{D}{2} + i\right)\right]^2\|_{j=1}^{N} \quad (2)$$

The differential beamforming algorithm based on sub-windowing (SubW-DBA), is developed for this application and is described in our previous work [13] SubW-DBA has an advantage in that it is not limited to the low-frequency range, at least theoretically. In practice, the low-frequency limit is defined by the phase matching of the microphone pairs. The high-frequency limit depends on the nature of the sound. If the sound is random, there is no frequency limit. If the sound is harmonic, the boundary is at the distance between the microphone pairs, like the usage of sound intensity probes.

The algorithm defined in Eq. (2) was used to compute the instantaneous DOA to experimentally verify the hypothesis that the 2D immission directivity pattern can be obtained by associating the instantaneous total sound level (SPL) with the instantaneous dominant direction (DOA) during sub-windowing. The objective is to compile a collection of immission vectors from which an immission directivity pattern can be derived through consistent integration/averaging of the immission vectors. $x_{mic,1}(n)$ and $x_{mic,2}(n)$ in Eq. (2) represents the signals from microphone 1 and microphone 2 respectively. N denotes the number of directions. D is the number of samples in the observed window. The minimum value of D is defined by the speed of sound c, the sampling frequency f_s and the distance between two microphones, which determine the time resolution of direction detection. Index i represents the steering value, i.e., Δn, which is proportional to the time delay $\Delta\tau$.

$$D_{min} = \frac{X_{mic} f_s}{c} \quad (3)$$

For the fastest possible response of detecting the direction of arrival M = N.

$$\Delta t_{min} = \frac{D_{min}}{f_s} \quad (4)$$

Using a differential array with four microphones and a diameter/side length of 0.04 m, it is possible to shorten the length of the direction detection subwindow to 0.232 ms. Shortening the subwindow to 0.232 ms provides 44 signal values for calculating the DOA of the dominant sound source. If the signals from two microphones placed 40 mm apart are recorded at a sampling rate of 192 kHz, then 22 samples are needed to arrange the signals for the maximum delay for each direction, and thus the time resolution of detecting the dominant direction is 0.232 ms.

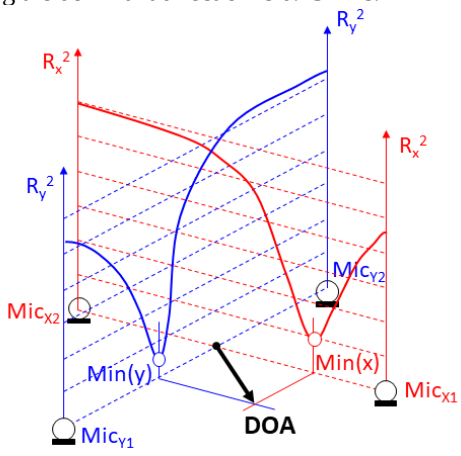


Figure 3: Differential microphone array of the first order, used during the experiment. Two pairs were used for the calculation of DOA on the immission plane.

2.4 Experimental setup

To optimize the quality of the acoustic data, a specific part of the production facility was selected, focusing primarily on the area where aluminum profiles are cut and processed using CNC (Computer Numerical Control) machinery. This decision assumed that these processes would produce distinguishable and characteristic sound signatures suitable for efficient clustering using the k-means algorithm.

The recording site was strategically positioned among seven cutting machines where incoming aluminum profiles are cut and mechanically processed before being automatically stacked into metal containers by handling robots. This location was chosen because it provided a rich source of distinctive mechanical sounds while being sufficiently

distant from the cluster of CNC machines, thereby reducing potential background noise interference.

To further minimize sound reflections and possible echo effects that could distort the acoustic data, the array of microphones was placed in an open area, as far away from wall surfaces as possible. The arrangement of microphones was carefully planned to avoid obstructing factory operations while ensuring the placement did not interfere with worker movement or the transit of forklifts. The selected recording site is depicted in figure. 5, where the observed machines are labeled from 1 to 7. The microphone array was oriented according to the layout shown in the figure.

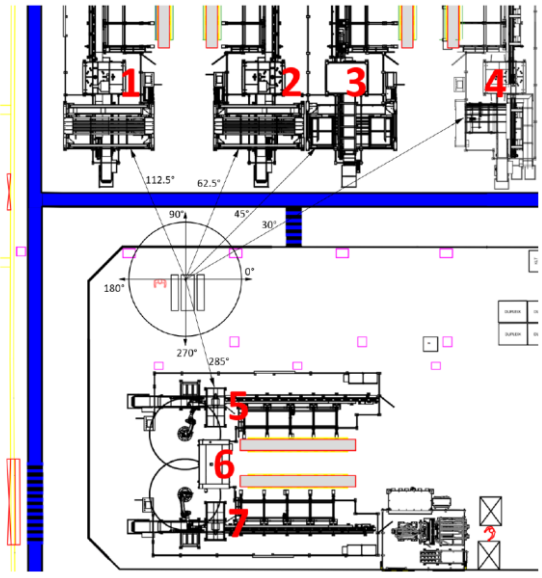


Figure 5: Recording site layout

Based on the microphone configuration, the expected orientation of the dominant sound during the operation of each machine was calculated. For machine 1, the sound direction was expected to be between 110° and 120°, for machine 2 it was estimated between 60° and 65°, and for machine 3, around 45°. Machine 4 was expected to have a dominant sound direction of around 30°, while machines 5, 6, and 7 had dominant sound directions expected to fall between 270° and 290°.

The machines being observed were expected to produce sharp, steady-frequency sounds caused by the milling cutter, as well as loud impulsive sounds generated when aluminum pieces were dropped into metal containers. To capture these sound events effectively, four omnidirectional microphones with polarized 6.35 mm condenser capsules were utilized. These microphones had a frequency range of 20 Hz to 20 kHz and a maximum sound pressure level (SPL) of 132 dB. The microphones were mechanically linked at equal distances to facilitate the calculation of the dominant sound direction.

The system also included a Behringer soundboard for initial pre-amplification and signal merging. For data storage, a simple signal acquisition program was developed using the LabVIEW software environment. This comprehensive setup ensured high-quality data acquisition, enabling the accurate capture of essential sound properties for subsequent feature extraction and clustering analysis.

3. RESULTS

Figure 6 presents a typical 30-second sound recording from the production environment. The upper panel shows the spectrogram, illustrating the spectral energy distribution over time. Several high-energy broadband events are visible, especially between seconds 4–6, 10–12, 17–18, and 23–25, which correspond to distinct mechanical actions such as cutting or part ejection.

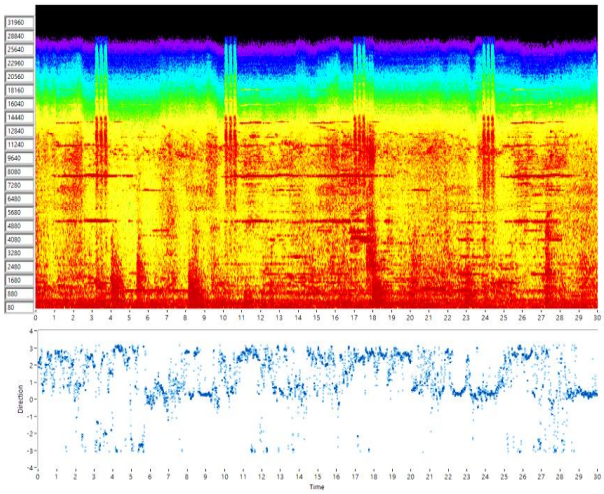


Figure 6. Spectrogram of a typical 30-second recording segment from the manufacturing process (top), with extracted dominant sound directions plotted below (bottom). The spectrogram displays energy distribution across frequencies, while the blue dots in the lower plot represent the instantaneous direction of arrival (DOA) of the sound.

The lower panel of the figure displays the corresponding instantaneous direction of arrival (DOA) of the dominant sound source, extracted using the SubWindow-DBA algorithm. The DOA estimates exhibit clustered patterns in both time and angular space, indicating repeated events

with consistent spatial origin, likely associated with recurring machine actions. Notably, transitions in DOA correspond well with changes in spectral content, affirming the relevance of including directionality as a classification feature.

This visualization supports the hypothesis that directionality provides an orthogonal, highly discriminative feature not captured by traditional spectral descriptors. The events clustered in the spectrogram are reinforced by clear directional patterns in the lower plot, validating the importance of sound directionality for distinguishing machine states. This correlation is consistent with the PCA results (Fig. 7), where DOA was identified as the most influential feature.

3.1 Identification of the Most Influential Features Using PCA

Typica spectrogram, together with extracted direction of Arival (DOA) in blue dots is presented in figure 6 above. To identify the most influential features in the dataset, a PCA analysis was employed. This process provided an assessment of the importance of each feature, which were then ranked according to their significance and the fifteen most important are displayed in Figure 7.

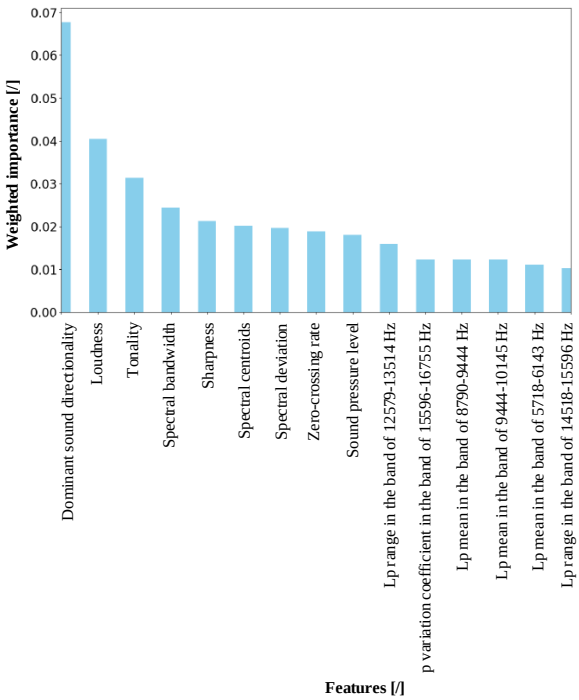


Figure 7: Weighted importance of the 15 most influential features below.

The graph reveals a decline in the weighted importance of features after the first few. This visualization serves as a useful tool for selecting and recognizing features. It helps to assess whether certain features contribute meaningfully to the quality of the data input or if they represent unnecessary noise. Figure 7 further allows for a clear understanding of which features contribute most significantly to the diversity of the data.

The analysis shows that the dominant feature is sound directionality. It has by far the highest weighted importance. This result is expected, as it is the only feature not directly derived from the sound signal itself and the only one that does not describe the characteristics or quality of the sound. Consequently, it has the lowest correlation with the other features, thereby contributing the most to the diversity of the data - a key aspect for successful classification. Following the dominant sound directionality, other key features calculated at the time constant τk=1 second, such as loudness, tonality, and spectral characteristics, also rank highly.

Next, a set of features derived from the frequency domain at a shorter time constant τ_z=50 milliseconds follow in terms of importance. Among these features, those describing higher frequency bands have the most significant influence. While these individual features do not possess high weighted importance on their own, together they still contribute significantly to the diversity of the data. This contribution underlines the relevance of combining features from different time scales and frequency ranges, ensuring the model captures both short-term and long-term acoustic patterns crucial for effective classification.

The optimal number of clusters for the k-means method can be determined in several ways. One common approach is an iterative trial-and-error method, where clustering begins with two clusters and gradually increases the number of clusters, observing changes in the classification results. The process continues until adding more clusters and no longer provides new information about the dataset. Another widely used approach involves the use of formal methods, such as the elbow method and the silhouette coefficient method, to identify the optimal number of clusters.

3.1.1 Elbow Method

The elbow method is visualized through a graph, as shown in Figure 8, which plots the sum of squared distances within each cluster as a function of the number of clusters *k*. The "elbow" of the curve is the point where the rate of decrease in the sum of squared distances slows down significantly, indicating that adding more clusters provides diminishing returns in reducing within-cluster variability. For this

particular study, the elbow can be observed around k=3 or k=4, as the addition of clusters beyond this point results in only marginal reductions in the total within-cluster sum of squares. This observation suggests that selecting 3 or 4 clusters would provide an optimal balance between simplicity and classification performance.

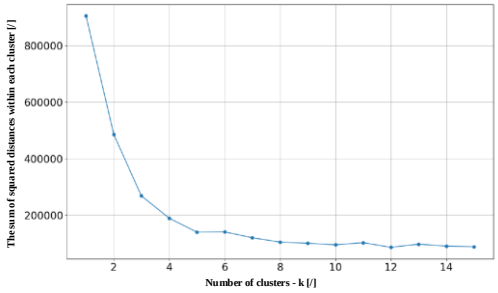


Figure 8. Elbow method graph for finding the optimal number of clusters - *k*.

3.1.2 Silhouette Coefficient Method

The silhouette coefficient method offers another perspective on selecting the optimal number of clusters. The silhouette coefficient measures how similar an object is to its own cluster compared to other clusters. A higher silhouette score indicates well-defined clusters. The silhouette graph for the data used in this study is presented in Figure 9. The peak of the graph is observed at k=2, indicating that, at this point, the clustering achieves the highest coherence of points within clusters. However, dividing the data into only two clusters limits the classification utility, as it would only distinguish between operational and non-operational states of the production process. This segmentation could still be useful for monitoring downtime, including pauses, breaks, and shift changes.

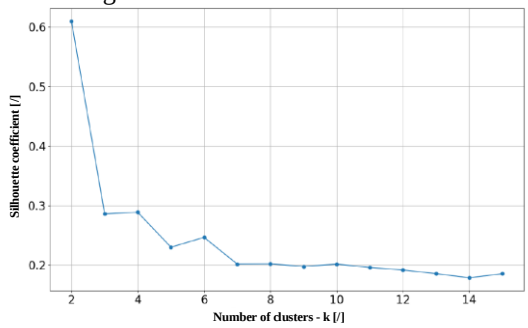


Figure 9. Silhouette coefficient graph for finding the optimal number of clusters - *k*.

As the number of clusters increases, the silhouette score gradually decreases, but it remains above zero, indicating that the cluster structure is still meaningful even with a larger number of clusters. Notably, local peaks are observed at k=4 and k=6, which correspond to improved clustering results relative to other values of k. Given that the elbow method also indicated a clear break at k=4, it can be inferred that selecting k=4 would provide the most interpretable and effective clustering solution for this dataset. This selection ensures a balance between model simplicity and classification accuracy, offering meaningful segmentation of acoustic events within the production process.

4. CONCLUSIONS

Based on the conducted research and the obtained results , the main findings can be summarized as follows:

1. We successfully classified acoustic signals using the k-means algorithm, effectively grouping the data into meaningful clusters based on their features. Initial classification was performed with k=4 clusters, followed by a refined analysis with k=6 clusters.
2. The feature extraction process was based on a methodology where frequency domain characteristics were derived at a lower time constant τ_0=50 ms. These features were then aggregated using various merging methods to form a higher time constant τ_k=1 second, thereby capturing time-domain properties as well.
3. Principal Component Analysis (PCA) was employed. A dimensionality reduction technique facilitated better organization of the data in a multidimensional space, ultimately improving the classification efficiency of the *k*-means algorithm.
4. It was found that the k-means algorithm was unable to capture all anticipated acoustic patterns, which can be attributed to the algorithm's limited generalization capabilities. Certain specific acoustic patterns, which are critical for a comprehensive understanding of machine operation, remain undetected.
5. The results indicate that the choice of the number of clusters *k* plays a crucial role in classification quality, but at the same time, it is challenging to determine objectively. The application of PCA to identify the most influential features revealed that the directionality of the dominant sound is the most important feature. This finding was expected since this is the only feature not directly derived from the sound signal and the only one that does not describe the sound's properties or quality. Consequently, it has the lowest correlation with other features and contributes the most to data variability, which is essential for successful classification. By implementing the PCA on the extracted features, we confirmed the hypothesis that the direction of the sound event is a significant feature that

should be included in classification algorithms for acoustic event detection.

The study demonstrated that the k-means algorithm is suitable for basic classification of acoustic signals in production environments, but it has limitations that require further investigation to achieve a more comprehensive capture of all acoustic patterns. Our study contributes to a better understanding of the applicability of classification algorithms in real-world industrial environments.

4.1 Suggestions for Future Work

Based on the findings of this study, it would be beneficial to explore the use of other unsupervised learning methods that were not considered in this research. While this study focused on the classification of specific acoustic patterns, future research could investigate longer periods of production operation and place greater emphasis on macro-level events. Additionally, efforts could be made to quantitatively assess the relative productivity of the production process over time. This broader perspective would provide a more comprehensive understanding of operational efficiency and help identify potential areas for optimization.

5. REFERENCES

[1] J.E.K. Foreman: *Sound Analysis and Noise Control*. New York: Van Nostrand Reinhold, 1990.

[2] J. Prezelj, L. Čurović, T. Novaković, and J. Murovec: "A novel approach to localization of environmental noise sources: Sub-windowing for time domain beamforming," *Applied Acoustics*, vol. 195, 2022.

[3] J. Prezelj, J. Murovec, S. Huemer-Kals, K. Häsler, and P. Fischer: "Identification of different manifestations of nonlinear stick–slip phenomena during creep groan braking noise by using the unsupervised learning algorithms k-means and self-organizing map," *Mechanical Systems and Signal Processing*, vol. 166, 2022.

[4] C. Ding and T. Li: "Unsupervised Feature Selection Ordering in High-Dimensional Data," *Proc. of the 25th International Conference on Machine Learning*, pp. 1033-1040, 2009.

[5] X. Sun, J. Wang: "Improved ADMM Algorithm for K-means-Based Unsupervised Feature Selection". arXiv preprint arXiv:2411.151972024

[6] A. Coates and A.Y. Ng: "Learning feature representations with k-means," In: *Neural Networks: Tricks of the trade*, Lecture Notes in Computer Science, vol. 7700. Springer, Berlin, Heidelberg, pp. 561-580, 2012

[7] A. Mesaros, T. Heittola, T. Virtanen, A review of deep learning methods for acoustic scene classification, *Applied Sciences*, Vol. 10, (6), 2020.

[8] G. Huang, J. Benesty, J. Chen, Design of robust concentric circular differential microphone arrays. J Acoust Soc Am, Vol.141(5), 2017, pp.3236–49. https://doi.org/10.1121/1.4983122.

[9] J. Benesty, C. Jingdong, Study and design of differential microphonearrays, Springer Science & Business Media; 2012. https://doi.org/10.1007/978-3-642-33753-6.

[10] Y. Buchris, I. Cohen, J. Benesty, First-order differential microphone arrays from a time-domain broadband perspective, In: 2016 IEEE international workshop on acoustic signal enhancement (IWAENC). IEEE; 2016. https://doi.org/10.1109/iwaenc.2016.7602886.

[11] Y. Buchris, I. Cohen, J. Benesty, On the design of time-domain differential microphone arrays, Appl Acoust, Vol.148, 2019, pp.212–22. https://doi.org/10.1016/j.apacoust.2018.12.013.

[12] G. Huang, J. Benesty, J. Chen, Design of robust concentric circular differential microphone arrays. J Acoust Soc Am, Vol.141(5), 2017, pp.3236–49. https://doi.org/10.1121/1.4983122.]

[13] J. Prezelj, L. Čurović, T. Novaković, J. Murovec, A novel approach to localization of environmental noise sources: Sub-windowing for time domain beamforming, Applied Acoustics, Volume 195, 30 June 2022, 108836

[14] J. Murovec, et al. Environmental noise event classification based on selforganizing map using psychoacoustic features and spatial filtering. Universitätsbibliothek der RWTH Aachen; 2019.

[15] I. Salom, et al. An implementation of beamforming algorithm on FPGA platform with digital microphone array. Audio Engineering Society Convention 138., Audio Engineering Society, 2015.

[16] D. Todorovic, et al. Implementation and application of FPGA platform with digital MEMS microphone array. Proceedings of the 4th international conference on electrical, electronics and computing engineering, 2017.

[17] J. Murovec, et.al, Microphone array based automated environmental noise measurement system. Appl Acoust Vol. 141, 2018, pp.106–14. https://doi.org/10.1016/j.apacoust.2018.07.004.].

DOI: 10.61782/fa.2025.0400

FORUM ACUSTICUM EURONOISE 2025

FAULT DETECTION IN C-EPS BEARINGS BASED ON UNSUPERVISED LEARNING

Hyeon-Cheol Jo[1*] **Jun-Seo Park**[1] **In-je Cho**[1] **Jae-Yong Seo**[1] **Seong-Sik Yoo**[1] **Sangkyeong Lee**[1]
Seung-Je Bang[2] **Jeong-Lyul Oh**[2] **Chol-Hwan Jung**[2] **Sung-Zoon Cho**[2]
[1] Hyundai Mobis, 17-2, Mabuk-ro 240beon-gil, Giheung-gu, Yongin-si, Republic of Korea
[2] Big Data AI Center, Seoul National University, Republic of Korea

ABSTRACT

The Column Type Electric Power Steering (C-EPS) system consists of a motor, a reduction gear, and bearings that ensure structural stability and minimize friction. Noise in rotating systems mainly arises from motor noise, component defects, and frictional sounds caused by rotational dynamics.

Operational noise defects are typically managed within regulatory thresholds. Recently, machine learning-based anomaly detection models have gained popularity, often relying on labeled datasets for training. However, this process demands substantial human and time resources for labeling, and distinguishing between noise types remains a significant challenge.

In response to these challenges, this study introduces a method that preprocesses noise input data using Short-Time Fourier Transform (STFT), utilizes unsupervised learning for data encoding, and applies clustering to generate labels. The effectiveness of the proposed approach is demonstrated through a validation process.

Commonly Mel-spectrogram and MFCC transformations are used for AI noise input, but bearing noise often exhibits distinct high-frequency features. STFT was chosen to preserve high-frequency characteristic without attenuation. Various unsupervised learning techniques were utilized to encode the noise data effectively. As the goal was clustering rather than generation, and C-EPS noise shows limited temporal variation, experiments identified Convolutional Autoencoder as the effective unsupervised learning method for mapping noise.

Keywords: *Convolutional Autoencoder, Column Type Electric Power Steering, Self-Labeling, Dimensionality Reduction, Anomaly Detection*

1. INTRODUCTION

As shown Fig. 1, the steering system required to steer in a vehicle is divided into three main parts: the steering gear system that changes the rotational force into linear force, the Column Type Electric Power Steering system (C-EPS) [1] that helps the driver to steer with the power of motor [2] and the universal joint that connects the steering gear system and C-EPS. Among them, as shown Fig. 2, the C-EPS which consist of motor and the reducing gear system causes a lot of noise problems. In general, these noises cause emotional quality degradation to customers who drive the vehicle, which incurs steady field claim costs to companies. [3] One of the consistently problematic noise issues in C-EPS originates from the bearings in the worm shaft system. This bearing-induced noise can be broadly classified into frictional noise and rotational noise. However, there are limitations in detecting it using conventional quantitative noise indicators such as overall level and order noise level. Recently, supervised learning-based machine learning models have been introduced for anomaly detection. However, these methods still rely on subjective human evaluations, and there are ambiguous cases where classification based on subjective assessment is challenging. As a result, the accuracy of labeling inherently suffers, and a significant human resource is required. In addition, conventional quantification methods such as overall level

[*] ***Corresponding author***: *clfclfdlsp@mobis.com.*
Copyright: *©2025 First author et al. This is an open-access article distributed under the terms of the Creative Commons Attribution 3.0 Unported License, which permits unrestricted use, distribution, and reproduction in any medium, provided the original author and source are credited.*

and order-based filtering are limited in effectively analyzing bearing noise in C-EPS systems.

Consequently, this study aims to identify an optimized model for detecting bearing noise defects in C-EPS using an unsupervised learning approach. In addition, the labeling of bearing noise based on unsupervised learning can be further utilized in combination with supervised learning and explainable AI (XAI) to establish new criteria. In other words, it enables the development of an end-to-end model capable of generating noise specifications even in the absence of prior knowledge about the noise characteristics.

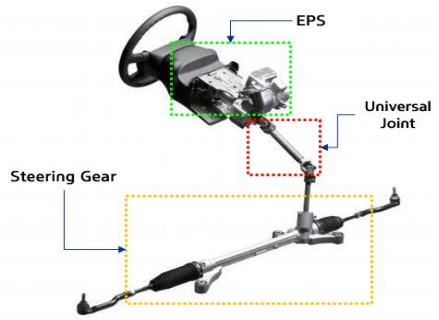


Figure 1. Composition of steering system of vehicle

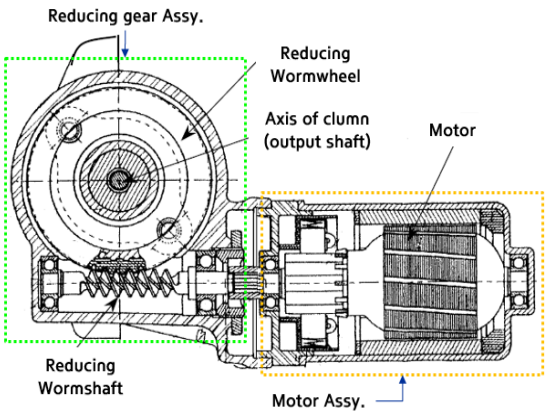


Figure 2. C-EPS Structure Diagram

2. EVALUATION OF NOISE AND VIBRATION

2.1 Evaluation Method

To measure the operational noise of the C-EPS, tests are conducted under constant velocity or constant acceleration conditions using equipment that controls the torque while considering the real vehicle conditions of the input and output, as shown in Fig. 3. As shown in the STFT colormap of the C-EPS operational noise in Fig.4, the advantage of constant acceleration evaluation is that it enables the identification of frequency characteristics across a range of rotational speeds in a single test. Reflecting this advantage, constant acceleration evaluation is commonly selected for assessing abnormal noise in rotating systems.

For the evaluation, both a microphone and multiple accelerometers were used to capture noise and vibration signals. The accelerometers were attached to the motor center, the motor lower area near the defective bearing, and the worm shaft. The reason for including accelerometer measurements was to ensure the applicability of the model not only during development but also in the production stage, where microphone-based measurements are often not feasible in End-of-Line environments.

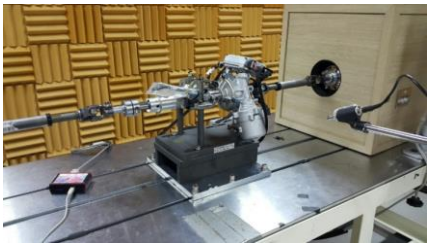


Figure 3. Evaluation setup for operational noise

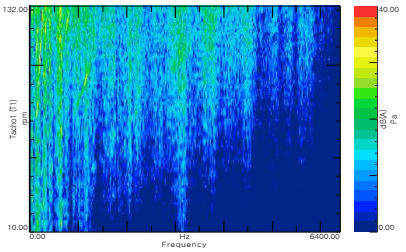


Figure 4. Colormap of the STFT Spectrogram

2.2 Description and analysis of noise

The bearing located at the upper end of the worm shaft, which is in contact with the motor, is subjected to a high load. Therefore, even minor defects can cause noise issues, which are generally classified into friction noise and rotational noise. Friction noise typically occurs when foreign substances such as aluminum particles or grease enter the bearing, whereas rotational noise is generated when there is damage to the raceway surface. Friction noise is characterized by broad-band frequency components that

are independent of rotational speed. In contrast, rotational noise exhibits prominent order components that vary with speed.

In general, noise regulation is based on problematic order components and overall level, and the operational noise of C-EPS systems is also quantified using these two criteria. As shown in Table 1, the detection performance based on the overall level indicates that the microphone sensor failed to capture more than 50% of the bearing noise cases. The accelerometer attached to the motor lower section detected rotational noise with an accuracy of 61%, but was less effective for frictional noise, detecting only around 34%. Notably, the accelerometer placed at the motor center detected less than 15%, which is likely due to strong reflections of motor-specific characteristics. Theses results suggest that proper sensor placement is critical for effectively detecting bearing noise. Additionally, detection rates based solely on order components were extremely low and therefore not included in the table.

Table 1. Detection performance according to Noise type based on overall RMS thresholding (O/A)

	detection rate [%]	
Sensor type and Location	Rotation	Friction
MIC O/A	54.3	33.1
Motor Center Acc O/A	20.4	9.2
Motor Lower Acc O/A	67.7	44.2
Worm Shaft Acc O/A	59.1	39.9

2.3 Data preprocessing

Although the STFT is commonly used for preprocessing bearing operational noise, various preprocessing techniques including Mel spectrogram, Mel Frequency Cepstral Coefficients (MFCC), and Continuous Wavelet Transform (CWT) were applied in this study to prepare the data as input for machine learning models.

Mel Spectrograms and MFCC are widely used feature representations in audio signal processing, particularly in machine learning-based approaches. Mel spectrograms provide a time-frequency representation based on Mel scale, which reflects the non-linear perception of pitch.[4] MFCC, in contrast, captures perceptually relevant characteristics by modelling the human auditory system and is effective for extracting timbral features.[5] Both techniques have been extensively applied in speech recognition, acoustic scene analysis, and environmental noise classification, serving as standard input features for various learning models.[6] As shown in Figure 5, the average colormaps of MFCC and Mel spectrogram for each noise type indicate that MFCC fails to reflect the timbral differences of bearing noise, and the Mel spectrogram similarly does not sufficiently highlight distinctive frequency characteristics compared to STFT. This is likely because both preprocessing methods apply scaling in the high-frequency range, resulting in dimensionality reduction that diminishes the high-frequency characteristics of bearing noise. Therefore, it was concluded that these methods offer no clear advantage over STFT in preserving the high-frequency characteristics of bearing noise.

And CWT is effective for preprocessing impulsive or transient signals due to its ability to capture localized time-frequency characteristics with high resolution. This makes it a suitable choice for fault detection tasks where short-duration, high-frequency components are critical.[7] As shown in the CWT colormaps for each noise type in Figure 5, the characteristic order components of rotational noise appear too be suppressed by the CWT representation. Considering these characteristics of CWT, it was concluded that STFT is more effective in capturing the features of both rotational and frictional noise.

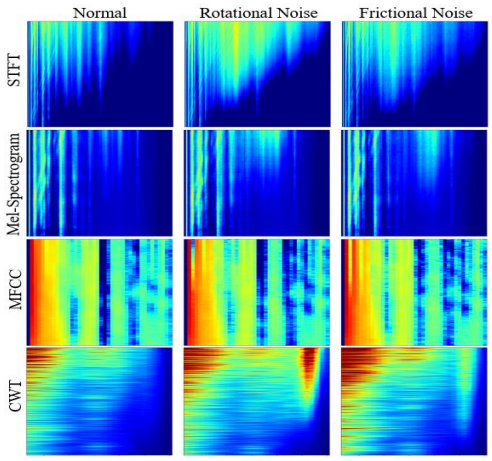


Figure 5. Average colormaps of each preprocessing method according to bearing noise defect types

3. UNSUPERVISED LEARNING

3.1 Unsupervised Learning

To embed the input data preprocessed using STFT through unsupervised learning, several models were employed, including Convolutional Autoencoder (CAE), Cluster GANs, Variational Autoencoder (VAE), ResNet-18 and LSTM-CNN Autoencoder. Since the primary objective of

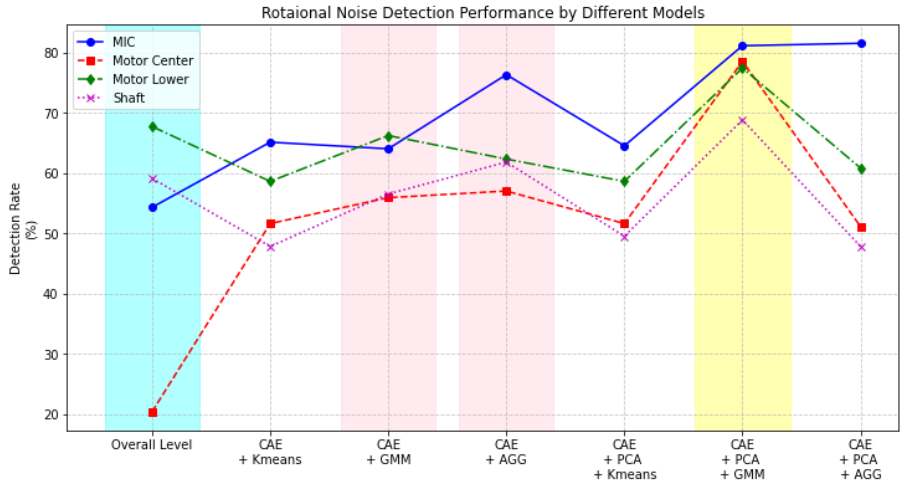
this study is clustering rather than generation, and the rotational noise signals exhibit minimal temporal variation, the experimental results suggest that the CAE is the most suitable architecture for unsupervised mapping of operational noise in C-EPS bearing.[8]

3.2 Clustering

For clustering the latent features extracted by the convolutional autoencoder (CAE), we utilized Gaussian Mixture Models (GMM), K-means, and Agglomerative Clustering (AGG). Among the clustering methods applied to the CAE-extracted embeddings, as shown Fig.6, the GMM and AGG achieved notably better separation of frictional and rotational anomalies compared to K-means. The improved performance of GMM and AGG can be attributed to their flexibility in modeling non-spherical clusters, robustness to boundary ambiguities, and ability to capture complex structure in high-dimensional acoustic feature spaces.[9] Furthermore, it was observed that applying Principal Component Analysis (PCA) to the latent representations extracted by the CAE further improved the detection performance when combined with GMM clustering.[10] These results are considered to stem from PCA's ability to reduce noise and redundancy in the CAE-derived embeddings, thereby improving the separability of clusters in the GMM process. In conclusion, the results in Table 2 demonstrate that GMM clustering, when applied after sequential embedding via CAE and PCA, substantially improves the detection rate compared to the baseline approach based on overall level. The calculated value represents the proportion assigned to the two clusters classified as defective products through clustering, rather than as normal ones. Although the detection performance of unsupervised learning does not surpass that of supervised approaches, it offers greater potential in capturing previously unseen frictional or rotational noise. This is particularly important in real-world applications, where ambiguous acoustic anomalies often lack clear boundaries, and the initial labeling process is prone to subjectivity. Therefore, the level of detection performance achieved in this study is considered highly meaningful and practically valuable. Accordingly, in situations where no alternative indicators beyond overall level or order level are available, the proposed model can be recommended for detecting bearing-related noise.

Table 2. Detection performance by noise type based on overall RMS thresholding (O/A) versus CAE-PCA-GMM (C.P.M)

		Detection rate [%]	
Sensor	Method	Rotation	Friction
MIC	O/A	54.3	33.1
	C.P.M	81.1	76.1
M. Center (Acc)	O/A	20.4	9.2
	C.P.M	78.5	54.6
M. Lower (Acc)	O/A	67.7	44.2
	C.P.M	77.4	63.8
Worm Shaft (Acc)	O/A	59.1	39.9
	C.P.M	68.8	52.8



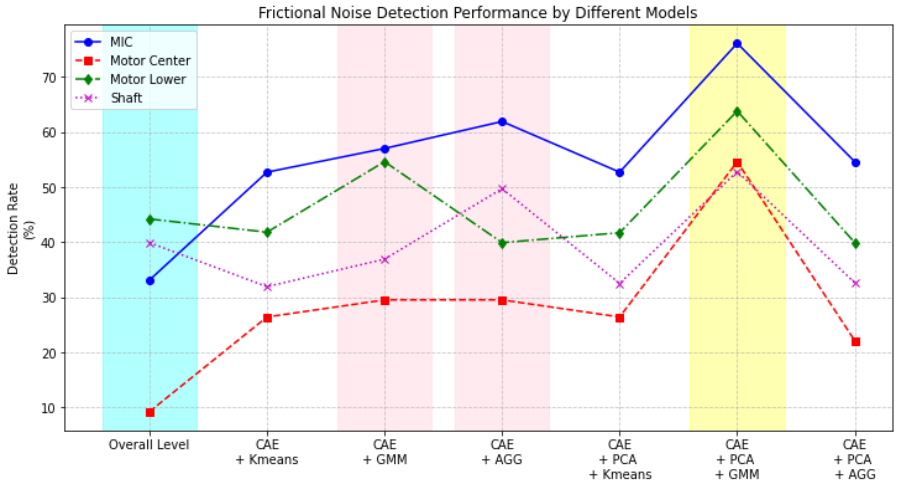


Figure 6. Detection rates for rotational and frictional noises using unsupervised learning with different clustering

3.3 End-to-End model for feature extraction

In addition to performing anomaly detection using unsupervised learning and clustering, the label sets obtained through these unsupervised approaches can further be utilized to enable supervised learning and XAI. This allows for the extraction of class-specific feature maps corresponding to different types of bearing noise. The overall framework can thus be the end-to-end model for extracting discriminative feature maps of bearing noise. As shown in Fig. 7, the process begins with STFT-based time frequency transformation, followed by dimensionality reduction through CAE and PCA. Unsupervised learning with GMM clustering yields label sets, which are then utilized to train a supervised classification model. Finally, XAI methods are applied to interpret the learned representations and extract feature maps associated with each noise type. Initially, both the ResNet18 and ResNet18 with Self-Attention models were applied for supervised learning. [11-12] Due to the lack of significant differences between the two, a classification model was developed using ResNet18. Subsequently, XAI tools such as Smooth Grad, Gradient-weighted Class Activation Mapping (Grad CAM), Score-Weighted Visual Explanations for Convolutional Neural Networks (Score CAM), and Local Interpretable Model-agnostic Explanations (LIME) were utilized to obtain the average heatmap of feature maps for each noise type. [13-15]

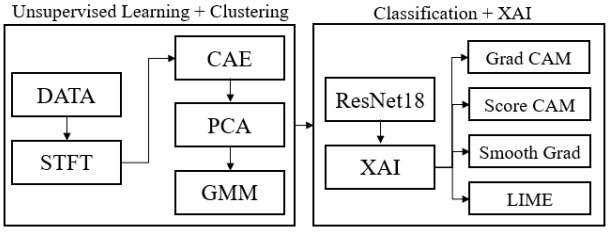


Figure 7. Diagram of end-to-end model

As shown Fig.8, the heatmaps generated by each XAI tool revealed that rotational noise primarily identifies the diagonal components of the order elements as key factors, while frictional noise is characterized by broad bands regardless of speed. In conclusion, an end-to-end process is established where labeling is performed through unsupervised learning and clustering. Subsequently, a classification model is developed based on the labeled data using unsupervised learning. Finally, XAI tools are employed to automatically extract features according to the characteristics of each noise type. If additional noise types are anticipated, unsupervised learning can be employed to add new classes. These feature maps can then be utilized as weighted filters for the specifications of noise and vibration. We believe that recalculating the noise using such feature maps and managing it through thresholding is significantly more effective than conventional overall-level-based approaches.

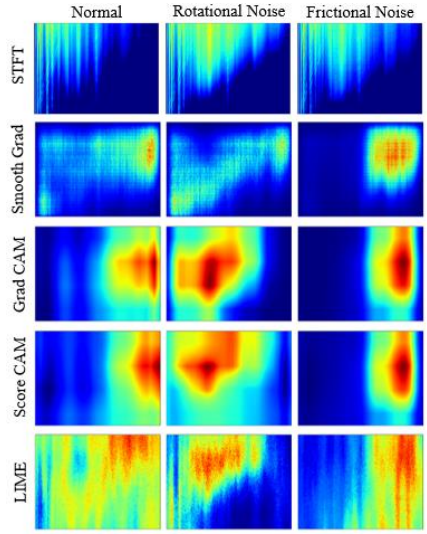


Figure 8. Average heatmaps of each XAI method according to bearing noise defect types

4. CONCLUSIONS

This study demonstrates the effectiveness of anomaly detection in diagnosing bearing defects in C-EPS systems by optimizing unsupervised learning and clustering methodologies. To preprocess the input data, STFT was employed to retain the high-frequency characteristics of bearing noise.

Unsupervised learning was conducted using CAE, with PCA applied to improve performance. The embedded features were clustered using GMM, resulting in superior detection capabilities compared to the traditional overall level metric for noise and vibration. Although both noise and vibration were analyzed, vibration was prioritized due to limitations of noise measurement in EOL environments.

Additionally, a classification model was developed using supervised learning based on noise-type labels derived from optimized unsupervised learning and clustering. This model integrates XAI to extract feature maps for each noise type, enabling identification of the speed and frequency at which anomalies occur. While the end-to-end model does not guarantee perfect detection, it offers a fast and practical auxiliary tool for EOL and early-stage development.

5. ACKNOWLEDGMENTS

This research was supported by Hyundai Mobis.

6. REFERENCES

[1] Y. Kozaki, G. Sekiya, and Y. Miyaura: “Electric power steering (EPS)”, *Motion & Control, vol.6*, pp. 9-15, 1999.

[2] Tanaka, Toshinori: "Motors for electric power steering," *Motor Technologies for Industry and Daily Life Edition*, 2003.

[3] Freund, Mary Kate, and Oumar Rafiou Barry: "Noise and vibration suppression of electric power steering systems: a survey" *International Journal of Vehicle Noise and Vibration*, 15.1, pp.68-88, 2019.

[4] Hong, G. and Suh, D.: “Mel Spectrogram-based advanced deep temporal clustering model with unsupervised data for fault diagnosis” *Expert Systems with Applications*, *217*, p.119551, 2023.

[5] Gupta, S., Jaafar, J., Ahmad, W.W. and Bansal, A.: “Feature extraction using MFCC” *Signal & Image Processing: An International Journal*, *4*(4), pp.101-108, 2013.

[6] Rawat, P., Bajaj, M., Vats, S. and Sharma, V.: “A comprehensive study based on MFCC and spectrogram for audio classification” *Journal of Information and Optimization Sciences*, *44*(6), pp.1057-1074, 2023.

[7] Rioul, O. and Duhamel, P.: “Fast algorithms for discrete and continuous wavelet transforms” *IEEE transactions on information theory*, *38*(2), pp.569-586, 1992.

[8] Guo, Xifeng, Xinwang Liu, En Zhu, and Jianping Yin, “Deep clustering with convolutional autoencoders." In *Neural Information Processing: 24th International Conference, ICONIP 2017, Guangzhou, China, November 14-18, 2017, Proceedings, Part II 24*, pp. 373-382. Springer International Publishing, 2017.

[9] Reynolds, Douglas A.: “Gaussian mixture models”. *Encyclopedia of biometrics*, *741*(659-663), p.3, 2009.

[10] Abdi, Herve and Lynne J., Williams: “Principal component analysis” *Wiley interdisciplinary reviews: computational statistics*, *2*(4), pp.433-459, 2010.

[11] Targ, S., Almeida, D. and Lyman, K., “Resnet in resnet: Generalizing residual architectures” *arXiv preprint arXiv:1603.08029*, 2016.

[12] Stephen, A., Punitha, A. and Chandrasekar, A.: “Designing self-attention-based ResNet architecture

for rice leaf disease classification" *Neural Computing and Applications*, *35*(9), pp.6737-6751, 2023.

[13] Panati, Chandana, Simon Wagner, and Stefan Brüggenwirth, "Feature relevance evaluation using grad-CAM, LIME and SHAP for deep learning SAR data classification." In *2022 23rd International Radar Symposium (IRS)*, pp. 457-462. IEEE, 2022.

[14] Wang, Haofan, Zifan Wang, Mengnan Du, Fan Yang, Zijian Zhang, Sirui Ding, Piotr Mardziel, and Xia Hu, "Score-CAM: Score-weighted visual explanations for convolutional neural networks." In *Proceedings of the IEEE/CVF conference on computer vision and pattern recognition workshops*, pp. 24-25. 2020.

[15] Smilkov, Daniel, Nikhil Thorat, Been Kim, Fernanda Viégas, and Martin Wattenberg, "Smoothgrad: removing noise by adding noise." *arXiv preprint arXiv:1706.03825*, 2017.

DOI: 10.61782/fa.2025.0260

FORUM ACUSTICUM EURONOISE 2025

DEEP LEARNING FOR ULTRASOUND SURFACE ECHO DETECTION WITH MATRIX ARRAYS

M. Larrea[1*] **M. Muñoz**[1,2] **A. Rubio**[1,2]
J.F. Cruza[1] **G.Cosarinsky**[1]
[1] Ultrasound Systems and Technology Group (GSTU), Institute for Physical and Information Technologies (ITEFI), Spanish National Research Council (CSIC),c/Serrano 144, 28006 Madrid, Spain
[2] Electronics Department, Escuela Politécnica, Universidad de Alcalá de Henares, Ctra.Madrid-Barcelona, Km. 33,600, 28805 Madrid, Spain

ABSTRACT

In Non-Destructive Testing (NDT), imaging with array probes is frequently performed in a two propagation medium scenario, where the first acts as a coupling medium, and the second is the object under test. Therefore, the position and shape of the refracting interface between the two mediums must be known in order to compute the imaging focal laws. This geometrical information can be inferred from the arrival times of echoes reflected on the object's surface, which must be identified within the signals. A common approach for detecting these surface echoes is the first-threshold crossing method; however, it is susceptible to outliers, and more robust alternatives are needed. In a recent work, we developed and trained a 3D Convolutional Neural Network (DeepEcho3D) using an 11x11 matrix array to accurately and reliably detect surface echoes. While effective, the model is tailored to the specific array used. In this study, we explore extending DeepEcho3D to other matrix arrays with varying shapes and frequencies. Our findings demonstrate that it is unnecessary to start from scratch for each new array; instead, we can leverage transfer learning from the initial model.

Keywords: *Time of Flight (TOF), Surface Detection, Non-Destructive Testing (NDT), Convolutional Neural Network (CNN), Probe Location and Orientation (PLO), Deep Learning, Fine-Tuning*

**Corresponding author*: marcelo.larrea@csic.es.

Copyright: ©2025 First author et al. This is an open-access article distributed under the terms of the Creative Commons Attribution 3.0 Unported License, which permits unrestricted use, distribution, and reproduction in any medium, provided the original author and source are credited.

1. INTRODUCTION

Ultrasonic Testing (UT) is a widely used Non-Destructive Testing (NDT) technique for internal imaging of industrial and structural components. It relies on proper coupling between the transducer and the test component, often achieved through immersion tests, that is, using water as coupling media.

The use of array probes [1] allows various imaging modes, including conventional Phased Array (PA), as well as more advanced techniques such as TFM (Total Focusing Method) [2] and PWI (Plane Wave Imaging) [3, 4], which offer improved resolution and versatility.

Inspection using the immersion technique presents difficulties in accurately calculating focal laws due to refracted rays. This, in turn, requires in-depth knowledge of both the test component surface and the probe location and orientation (PLO) relative to it.

The mentioned challenge has been addressed by adaptive imaging algorithms, which utilize ultrasonic signals to estimate the geometry before generating the final image, also referred to as auto-focusing techniques [5–7]. Among the various proposed algorithms for computing surface points, a subset of them relies on accurately detecting the time of flight (TOF) of surface echoes, making a robust TOF measurement method essential.

There are various methods for TOF detection [8, 9], being the simplest one the threshold crossing technique. Nevertheless, despite its efficiency, spurious echoes, as

those from water bubbles or probe surface waves, can cause measurement errors. Improving these methods is essential, as TOF measurements is widely used not only in UT but also in numerous other acoustic signals applications.

Given the strong capabilities of machine learning and deep learning for data classification and image segmentation, as well as their successful application in NDT research [10, 11], we leveraged this potential in a recent study to address the aforementioned measurement issues. The designed network (DeepEcho3D) was trained using data acquired from a 3 MHz, 1 mm pitch, 11×11 matrix array and a set of simple yet diverse surfaces [12]. The model demonstrated strong performance in detecting surface echoes across a sufficiently distinct set of test geometries, evaluated using two customized metrics: the percentage of outliers and a magnitude of error relative to the ground truth for the acquired data.

This study explores the adaptation of the DeepEcho3D model to a different array configuration using transfer learning and fine-tuning techniques. The model was adapted to a 5 MHz, 0.9 mm, 8×16 matrix array. The adaptation process consisted of three key stages: **(a)** transferring the pre-trained model to the new array dimensions, **(b)** fine-tuning selected layers to improve performance, and **(c)** evaluating the model's stability across multiple training runs.

2. METHODS

The adaptation process involved loading the pre-trained DeepEcho3D model, modifying its architecture to accommodate the new input shape (8×16), and transferring the original model's weights to the corresponding layers in the new network. To fine-tuning the transferred network, the dataset was obtained from a plane surface. The purpose is to use a single component instead of a set of different shapes, as in [12]. And finally, performance evaluation was conducted using customized metrics originally defined for the original net.

2.1 Data Acquisition

Data was generated through the Full Matrix Capture (FMC) [1] technique across 178 PLOs. For each PLO, a partial FMC was obtained using 9 elements as emitters, and all 128 elements as echo receivers, resulting in a total of 1602 (178 × 9) images. These images were then randomly divided into training (60%), testing (20%), and validation (20%) subsets

Essential for the network retraining stage, image labeling was automated during the post-processing of the acquired data. The Ground Truth (GT) is a binary mask, $GT(i,j)$, being i the time index and j the array element index. The theoretical TOF of the surface echo has time index $Idx_{true}(j)$, such that:

$$GT(i,j) = \begin{cases} 0, & i > Idx_{true}(j) \\ 1, & i < Idx_{true}(j) \end{cases} \quad (1)$$

$Idx_{true(j)}$ is computed using the law of specular reflection, as described in [13]. Fig. 1 shows an example of Idx_{true} in its upper graph (green line).

Three extra sets of data, two convex cylindrical surfaces (35 and 12 mm diameter), and one concave-shaped cylinder (40 mm diameter), were further acquired to assess the fine-tuned models performance under different geometries.

2.2 Experimental Setup

2.2.1 Preliminary Testing

The first dataset came from a plane surface, providing an initial test for the transferred model. The initial assessment revealed that, although the model generalized well, certain segmentation inaccuracies persisted. Fig. 1 and Fig. 2, illustrate, respectively, **1)** an example of satisfactory performance, where the model correctly segmented the image (lower plot) based on the ground truth shown in the upper graph; and **2)** a challenging case for the new model, with imprecise segmentation. Both images correspond to a single emitter element, and what is seen is the 2D representation of the 3D array acquisition (upper plot), and the transferred model segmentation output (lower plot). Now, to mitigate these segmentation inaccuracies, a fine-tuning strategy was implemented, retraining specific layers on the new dataset.

2.2.2 Section-Wise Exploration

DeepEcho3D consists of an *autoencoder* architecture, which can be divided into three main sections: (1) the encoder, which extracts hierarchical features and compresses input data into a lower-dimensional representation. It consists of two internal blocks, each containing

[1] FMC: Technique where each element in an ultrasound array transmits a pulse one at a time while all elements in the array record the returning echoes. This process is repeated for each element in the array.

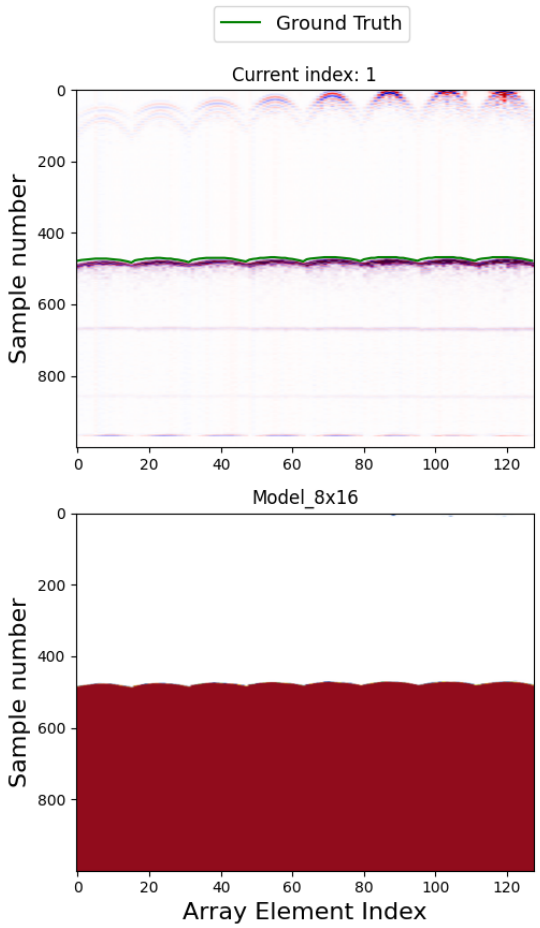


Figure 1: Instance of acceptable performance for initial model adaptation

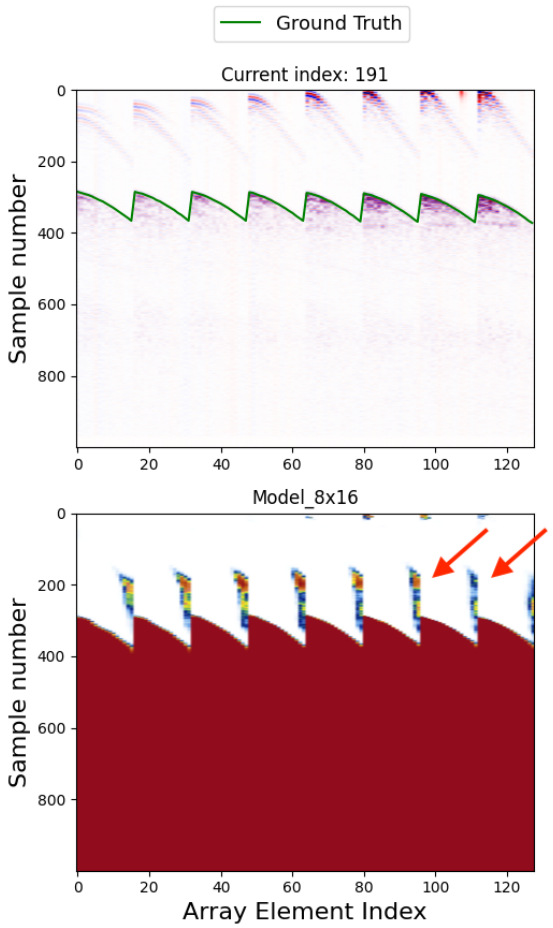


Figure 2: Instance of challenging case for initial model adaptation. Red arrows highlight the regions where the network's segmentation is inaccurate.

two convolutional layers. (2) The bottleneck, which incorporates a reduced set of features representing the most important information from the input; and (3) the decoder, that reconstructs the original data from the latent space, aiming to preserve essential spatial and feature details.

The exploration was structured into the network's three main sections: encoder, bottleneck, and decoder, with fine-tuning applied only to convolutional layers, excluding batch normalization and other layers. Additionally, the two internal encoder blocks were added as supplementary configurations to be explored. This led to five different fine-tuning setups. **1)** Encoder (4 convolutional layers); **2)** Bottleneck (2 convolutional layers); **3)** Decoder (5 convolutional layers); **4)** Encoder 1st block (2 convolutional layers); and **5)** Encoder 2nd block (2 convolutional layers)

Convolutional layers are primarily responsible for feature extraction and generalization across different datasets [14–16], which motivated the chosen approach.

2.2.3 *Fine-Tuning Implementation*

During the fine-tuning process, the following optimized hyperparameters were used (see Table 2), originally se-

lected as the best-performing ones for the 11×11 model [12]. This approach aimed to retain the effectiveness of the original model while allowing it to generalize to different array configurations.

Table 1: DeepEcho3D optimized hyperparameters.

Hyperparameter	**Value**
Number of filters	16
Number of layers	12
Convolutional kernel size	(3, 3, 12)
Pooling size	(1, 1, 8)
Epochs	10
Batch size	16
Learning rate	0.001
Steps per epoch	61
Loss function	Binary cross-entropy

2.3 Evaluation

Regarding the metrics used to assess the performance of the resulting models, two customized evaluation metrics were employed, defined as follows.

Index Error: This metric is defined as the maximum of the absolute value of the numerical difference between the predicted indexes and the true indexes, over the entire set of array elements [2], see Eqn. (2). Thus, for each A-scan within an FMC acquisition, a theoretical TOF index is determined and compared against the index predicted by the model.

$$Idx_{MaxError} = \max(|Idx_{pred} - Idx_{true}|) \quad (2)$$

Outlier Rate: This metric is particularly important for evaluating models reliability in practical applications. It is based on the computed error of indexes ((3))

$$Idx_{err} = |Idx_{pred} - Idx_{true}| \quad (3)$$

It measures how frequently the Idx_{err} exceeds a predefined threshold. The total count of such occurrences, relative to the dataset size (N), defines the outlier percentage.

[2] For instance, with 989 test images, this would correspond to $N = 989 \times 128 = 126592$ index-error values

Finally, given the stochastic nature of deep learning optimization, a stability assessment was carried out on each of the fine-tuned configurations, via multiple runs. Specifically, 10 runs per model were performed, and both evaluation metrics were computed for each, aiming to identify the configuration with the least deviation from its previous results. Therefore, the ideal models are those that exhibit minimal dispersion and remain close to the origin in the metric space.

Performance was assessed using data acquired from the three previously mentioned cylindrical components. These geometries were previously included in the test set for the original 11×11 model, making them suitable benchmarks to evaluate fine-tuned models. In particular, the concave-shaped 40 mm cylinder posed the greatest challenge, as it represents a complex case for the segmentation process.

3. RESULTS

Fig. 3 presents a comprehensive comparative analysis, not only between the fine-tuned models and the transferred network (Model_8x16) but also among themselves. It shows that the selective retraining of each set of convolutional layers enhances the capabilities, to a greater or lesser extent, of the transferred model, which has 14.43% outliers.

The most significant improvement correspond to the first block of the encoder section, highlighted in Fig. 3 (with 2.33% of outliers), followed by the full encoder (5.53 %); the bottleneck (6.56 %); the decoder (8.13 %); and finally the second block of the encoder (8.37 %).

Fig. 4 illustrates how fine-tuning enhances performance in a challenging case where the initial model encounters difficulties with image segmentation, where the test image exhibits low-amplitude surface echoes.

With the model using only the transferred weights, it fails to accurately identify and segment these surface echoes (Fig. 4a). However, in the encoder's first-block fine-tuned version, the model demonstrates a notable ability to capture very low-amplitude surface echoes while effectively suppressing superficial waves generated by the transducer (Fig. 4b). This highlights the efficacy of fine-tuning in improving the model's image segmentation performance.

Fig. 5 represents the results of the stability analysis described earlier. As observed, this analysis confirms that the first block of the encoder is the most consistent and stable configuration, exhibiting the least dispersion and

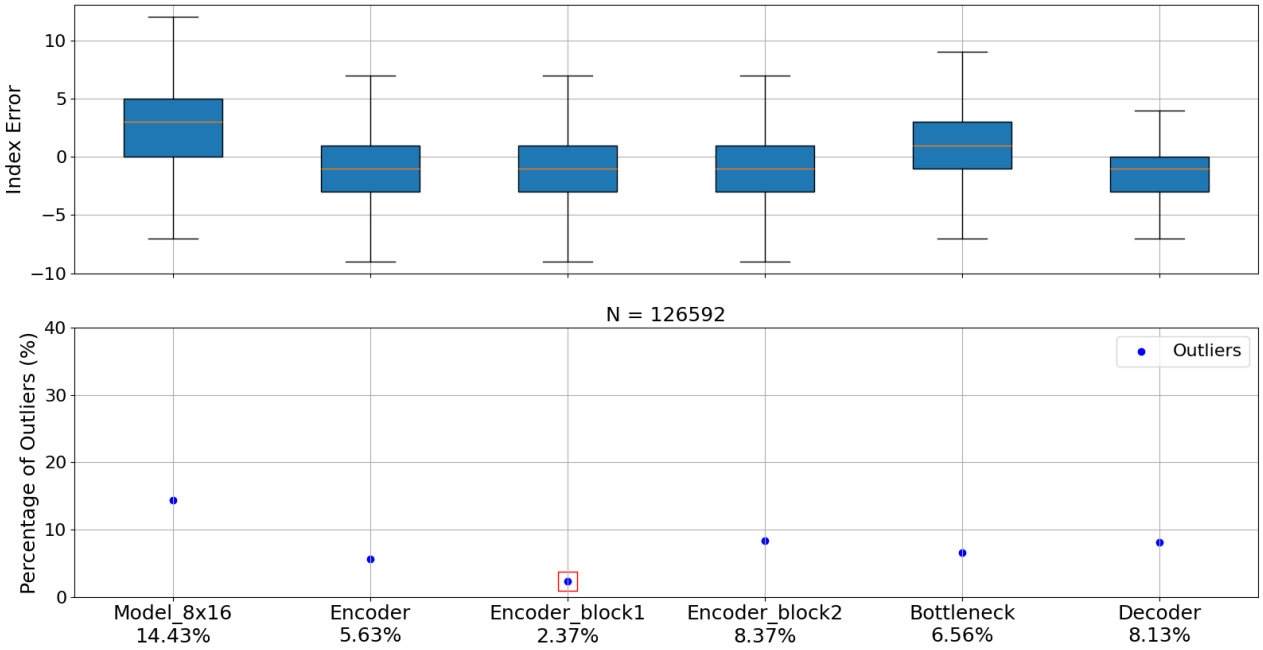


Figure 3: Comparison of Model Performance by customized metrics

the best performance in the metric space (with an average outlier rate of 2.6%, and an average $Idx_{MaxError}$ of 6.4%).

4. DISCUSSION

This study confirmed that knowledge learned from one array setup can be successfully leveraged for another, with fine-tuning improving segmentation accuracy. However, several aspects of this adaptation approach call for further discussion.

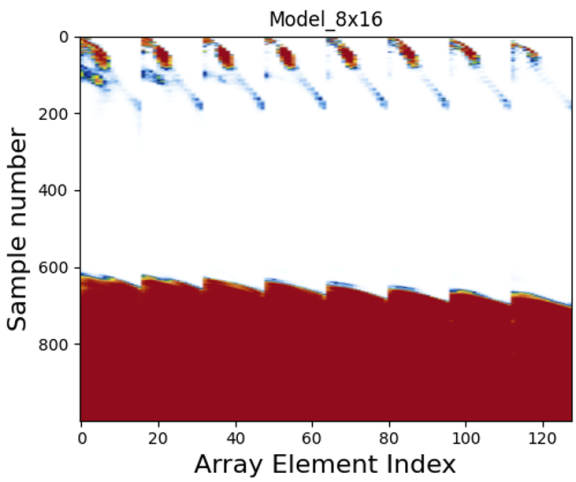
One of the key challenges in transfer learning is determining which layers should be fine-tuned to maximize performance while maintaining computational efficiency. This study evaluated various fine-tuning configurations, with results indicating that retraining the first encoder block yielded the most stable and accurate outcomes. However, the success of the first encoder block in this specific setting does not necessarily generalize to all ultrasound imaging problems, and a more thorough analysis could reveal alternative fine-tuning strategies with even better results. For instance, investigating the impact of fine-tuning different types of layers, beyond just convolutional ones, or employing techniques such as progressive fine-tuning [17], may further refine model adaptation.

While the study successfully adapted the model to an 8x16 array, the performance of this transfer learning approach could be explore further across different ultrasound imaging conditions, such as variations in material properties, noise levels, or different probe manufacturers.

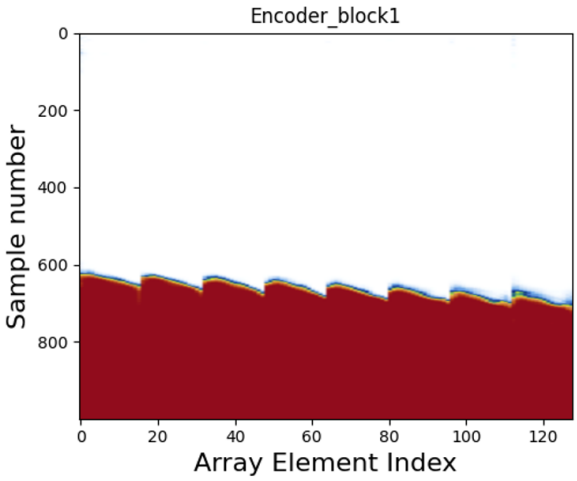
To enhance model adaptation even more, future research could explore adaptive fine-tuning strategies that automatically determines the optimal layer to update based on the dataset and task complexity [18]. Additionally, conducting experiments with a wider variety of geometries and different acquisitions conditions would help validate the robustness of the approach.

5. CONCLUSIONS

The results demonstrate that transfer learning plus fine-tuning was a viable approach for adapting the DeepEcho3D model for a different array configuration, without requiring a complete retraining process, and by utilizing only a single training component. The initial transferred model already showed promising performance, confirming that knowledge learned from one array setup can be effectively leveraged for another. Despite this, fine-tuning



(a) Segmentation for initial transferred model without fine-tuning



(b) Segmentation after fine-tuning the first block of the encoder

Figure 4: Comparison between Transfer learning vs Transfer learning + Fine-tuning

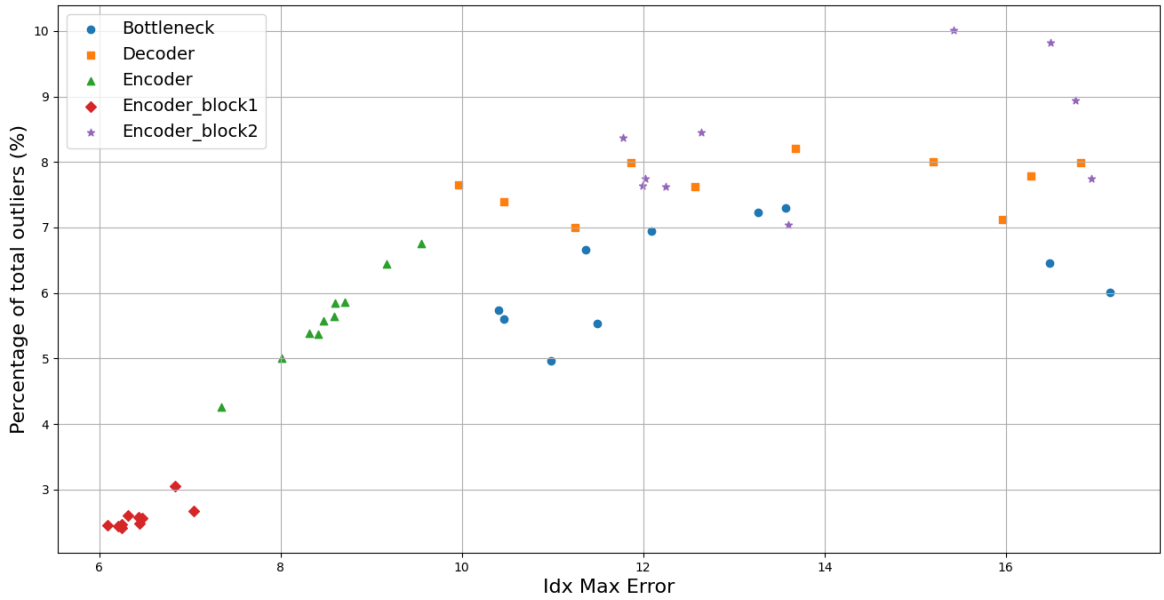


Figure 5: Stability Analysis

specific network sections enhanced segmentation accuracy.

The exploration of different fine-tuning strategies revealed that focusing on the first block of the encoder pro-

vides the most significant improvements, offering the best performance and greatest stability within the metric space. This suggests that early layers of the encoder, which capture more fundamental features, may be particularly critical for adapting the model to new array configurations.

6. ACKNOWLEDGMENTS

This research was supported by the project PID2022-143271OB-I00, funded by MCIN/AEI /10.13039/501100011033/FEDER, UE., the project PLEC2024-011165, funded by MICIU/AEI/10.13039/501100011033/ FEDER, UE, and by the European Commission – NextGenerationEU, through Momentum CSIC Programme: Develop Your Digital Talent. The funding for these actions/grants and contracts comes from the European Union's Recovery and Resilience Facility-Next Generation, in the framework of the General Invitation of the Spanish Government's public business entity Red.es to participate in talent attraction and retention programmes within Investment 4 of Component 19 of the Recovery, Transformation and Resilience Plan.

G. Cosarinsky staff is hired under the Generation D initiative, promoted by Red.es, an organisation attached to the Ministry for Digital Transformation and the Civil Service, for the attraction and retention of talent through grants and training contracts, financed by the Recovery, Transformation and Resilience Plan through the European Union's Next Generation funds.

7. REFERENCES

[1] B. W. Drinkwater and P. D. Wilcox, "Ultrasonic arrays for non-destructive evaluation: A review," *NDT & e International*, vol. 39, no. 7, pp. 525–541, 2006.

[2] C. Holmes, B. W. Drinkwater, and P. D. Wilcox, "Post-processing of the full matrix of ultrasonic transmit–receive array data for non-destructive evaluation," *NDT & e International*, vol. 38, no. 8, pp. 701–711, 2005.

[3] G. Montaldo, M. Tanter, J. Bercoff, N. Benech, and M. Fink, "Coherent plane-wave compounding for very high frame rate ultrasonography and transient elastography," *IEEE transactions on ultrasonics, ferroelectrics, and frequency control*, vol. 56, no. 3, pp. 489–506, 2009.

[4] L. Le Jeune, S. Robert, and C. Prada, "Plane wave imaging for ultrasonic inspection of irregular structures with high frame rates," in *AIP Conference Proceedings*, vol. 1706, AIP Publishing, 2016.

[5] Z.-b. Luo, Z.-h. Liu, F.-l. Li, and S.-j. Jin, "Defects imaging in corner part with surface adaptive ultrasonic and focusing in receiving (fir) strategy," *Journal of Nondestructive Evaluation*, vol. 43, no. 2, p. 49, 2024.

[6] J. Camacho, J. F. Cruza, J. Brizuela, and C. Fritsch, "Automatic dynamic depth focusing for ndt," *IEEE Transactions on Ultrasonics, Ferroelectrics, and Frequency Control*, vol. 61, no. 4, pp. 673–684, 2014.

[7] G. Cosarinsky, J. Cruza, M. Muñoz, and J. Camacho, "Optimized auto-focusing method for 3d ultrasound imaging in ndt," *NDT & E International*, vol. 134, p. 102779, 2023.

[8] F. Bai, D. Gagar, P. Foote, and Y. Zhao, "Comparison of alternatives to amplitude thresholding for onset detection of acoustic emission signals," *Mechanical Systems and Signal Processing*, vol. 84, pp. 717–730, 2017.

[9] S. Pan, Z. Qin, H. Lan, and J. Badal, "Automatic first-arrival picking method based on an image connectivity algorithm and multiple time windows," *Computers & Geosciences*, vol. 123, pp. 95–102, 2019.

[10] S. Cantero-Chinchilla, P. D. Wilcox, and A. J. Croxford, "Deep learning in automated ultrasonic nde–developments, axioms and opportunities," *Ndt & E International*, vol. 131, p. 102703, 2022.

[11] H. Hervé-Côte, F. Dupont-Marillia, and P. Bélanger, "Automatic flaw detection in sectoral scans using machine learning," *Ultrasonics*, vol. 141, p. 107316, 2024.

[12] M. Muñoz Prieto, A. Rubio Martínez, M. Larrea Álvarez, J. F Cruza, J. Camacho, and G. Cosarinsky, "Three-dimensional convolutional neural network for ultrasound surface echo detection," *Available at SSRN 4979182*.

[13] G. Cosarinsky, J. F. Cruza, M. Muñoz, and J. Camacho, "Automatic estimation of surface and probe location for 3d imaging with bidimensional arrays," *NDT & E International*, vol. 141, p. 102990, 2024.

[14] J. Yosinski, J. Clune, Y. Bengio, and H. Lipson, "How transferable are features in deep neural networks?,"

Advances in neural information processing systems, vol. 27, 2014.

[15] C. Linse, B. Brückner, and T. Martinetz, "Enhancing generalization in convolutional neural networks through regularization with edge and line features," in *International Conference on Artificial Neural Networks*, pp. 432–446, Springer, 2024.

[16] C.-L. Fan, "Multiscale feature extraction by using convolutional neural network: Extraction of objects from multiresolution images of urban areas," *ISPRS International Journal of Geo-Information*, vol. 13, no. 1, p. 5, 2023.

[17] T. Kadeethum, D. O'Malley, Y. Choi, H. S. Viswanathan, and H. Yoon, "Progressive transfer learning for advancing machine learning-based reduced-order modeling," *Scientific Reports*, vol. 14, no. 1, p. 15731, 2024.

[18] G. Vrbančič and V. Podgorelec, "Transfer learning with adaptive fine-tuning," *IEEE Access*, vol. 8, pp. 196197–196211, 2020.

DOI:

Main theme: A09 Machine learning and Artificial Intelligence in Acoustics

Session A09.06 Machine learning for array processing

Chair(s): M. Cobos, T. Abhayapala

DOI:

Main theme: A09 Machine learning and Artificial Intelligence in Acoustics

Session A09.07 Events detection and localization, and acoustic scenes, using ML techniques

Chair(s): P. Aumond, V. Lostanlen

DOI: 10.61782/fa.2025.0311

FORUM ACUSTICUM EURONOISE 2025

DOES SOURCE DIRECTIVITY INFLUENCE NEURAL NETWORK-BASED SPEECH POSITION ESTIMATION?

Rhoddy Viveros-Muñoz[1*] **Sebastián Guajardo**[1]
[1] Department of Electronics and Computer Sciences, Universidad Técnica Federico Santa María, Concepción, Chile

ABSTRACT

This study explores the ability of an artificial neural network (ANN) to estimate the position of speech sources—comprising both direction of arrival (DOA) and distance—by addressing the question: "Does the directivity of a speech source influence an ANN's position estimation?"
A comparative analysis was performed between omnidirectional and directional speech sources, with the latter simulating the natural directivity pattern of a human voice. Stimuli were generated using an acoustic virtual reality framework (RAVEN), encompassing multiple conditions: four reverberation times (0.1, 0.3, 0.6, and 0.9 seconds), 12 DOA angles (spaced at 30-degree intervals in azimuth), and two source types (omnidirectional vs. directional).
Findings from this analysis aim to shed light on the role of source directivity in shaping the performance of machine learning models for spatial audio tasks, such as sound source localization and enhancement in complex acoustic environments. The outcomes have promising implications for applications in spatial audio systems, hearing aids, and autonomous systems that rely on auditory information for navigation and interaction.

Keywords: *artificial neural network, direction of arrival, source directivity, acoustic virtual reality, source position estimation.*

[*] ***Corresponding author***: *rhoddy.viveros@usm.cl.*
Copyright: *©2025 First author et al. This is an open-access article distributed under the terms of the Creative Commons Attribution 3.0 Unported License, which permits unrestricted use, distribution, and reproduction in any medium, provided the original author and source are credited.*

1. INTRODUCTION

Sound source localization (SSL) refers to the process of estimating the spatial origin of an acoustic signal, specifically described in terms of direction of arrival (DoA) and distance relative to a listener or sensor array. Accurate SSL is critical for various applications, including surveillance, human-computer interaction, robotics, and auditory scene analysis [1-2]. In recent years, increasing attention has been paid to data-driven and learning-based approaches for solving SSL tasks, as traditional signal processing techniques such as time difference of arrival (TDOA), interaural level and time differences (ILD/ITD), and beamforming; often struggle in reverberant or noisy environments [3-4].
Machine learning (ML) methods, particularly deep neural networks (DNNs), have demonstrated considerable promise in overcoming the limitations of classical approaches by learning robust representations from complex acoustic scenes [5]. Interestingly, many of these models draw inspiration from human auditory processing mechanisms. For example, the use of mel-frequency cepstral coefficients (MFCCs) or mel-spectrograms as feature representations mimics the frequency selectivity of the human cochlea [6-7], embedding perceptual priors into the computational models.
Among the broad category of SSL tasks, the localization of speech sources is of particular importance, especially in the context of assistive hearing technologies. For hard-of-hearing individuals or users of hearing aids, the ability to spatially segregate and localize speech sources plays a critical role in auditory scene understanding and effective communication [8-10]. One key but often overlooked property of speech is its acoustic directivity, the way the voice radiates differently across directions depending on frequency and articulation. While traditional SSL models usually assume omnidirectional sources, human speech

exhibits strong directional patterns that can influence spatial cues, particularly under realistic reverberant conditions [11-12]. Despite its potential importance, the influence of source directivity on neural network-based SSL systems remains underexplored.

Therefore, the primary objective of this study is to investigate whether the directivity of speech sources has a measurable effect on the performance of deep neural network-based models for speech position estimation using binaural recordings. We aim to compare two types of spectral feature representations: (i) a Fourier-based spectrogram, which provides a general, physics-driven decomposition of the signal, and (ii) a mel-spectrogram, which mimics the frequency analysis performed by the human auditory system.

By training similar neural network architectures on both representations, we seek to isolate the role of biologically inspired features in learning to resolve spatial information, particularly under conditions that include speech signals with varying directivity patterns.

Understanding the interaction between acoustic directivity and feature representation is expected to provide theoretical insights into the interpretability of ML models for speech localization and inform future designs of assistive hearing technologies that operate in real-world acoustic environments.

2. METHOD

2.1 Dataset and Acoustic Simulation

To investigate the effect of speech source directivity on the performance of neural network-based position estimation, we used a dataset of speech recordings using a controlled simulation framework. The speech material consisted of 700 phonetically balanced sentences adapted from the SHARVARD corpus [13] into Chilean Spanish. These sentences were recorded by 20 native speakers (10 female), all of whom participated in a supervised recording session. The recordings were made in a sound-attenuated booth using a high-quality microphone at a sampling rate of 44.1 kHz.

Spatialization of the speech recordings was performed using the Room Acoustics for Virtual Environments (RAVEN) simulation framework [14], which allowed precise control over source characteristics, spatial configuration, and room acoustics. Two types of source directivity were modeled: an omnidirectional source, radiating energy uniformly in all directions, and a directional speech source, simulating the typical radiation pattern of the human voice. For the directional condition, two speaker orientations were simulated to reflect contrasting spatial alignments relative to the listener: (i) facing the listener, and (ii) facing directly away from the listener (i.e., 180° rotation). This manipulation aimed to capture the acoustic variability introduced by speech directivity and head orientation.

The directional speech source was modeled using a voice directivity pattern available in the RAVEN directivity database. Each selected utterance was rendered in multiple acoustic scenes, varying systematically across:

- Four reverberation times (T30): 0.1 s, 0.3 s, 0.6 s, and 0.9 s.
- Twelve DoA: 0°, 30°, 60°, 90°, 120°, 150°, 180°, 210°, 240°, 270°, 300°, and 330°.
- Three source conditions: omnidirectional, directional-facing, and directional-reversed.

Binaural renderings were generated using head-related transfer functions (HRTFs) obtained from the IHTA-indHARTF database, which contains high-resolution acoustic measurements from 30 adult participants recorded [15]. Their use ensured that the binaural stimuli reflected perceptually valid spatial information suitable for human-oriented localization models.

The final dataset comprised 144,000 binaural audio samples. The data were split into training (80%), validation (10%), and test (10%) sets.

2.2 Feature Extraction

To investigate the role of feature representation in speech source position estimation, we extracted two types of time-frequency features from the binaural audio signals: Short-Time Fourier Transform (STFT) spectrograms and mel-spectrograms.

For the STFT spectrograms, each audio signal was segmented using a Hamming window of 512 samples and a hop size of 256 samples. The STFT was independently applied to the left and right channels, yielding complex-valued spectrograms that were converted to magnitude representations. These were subsequently concatenated along the channel axis to form a two-channel input capturing the interaural spectral differences.

For the mel-spectrograms, a Hamming window of 1024 samples and a hop size of 512 samples were used to better align with perceptual frequency resolution. The resulting magnitude spectra were passed through a mel filterbank composed of 64 filters spaced according to the mel scale, approximating cochlear frequency selectivity. The resulting mel-spectrograms were log-compressed

(log-mel) to enhance dynamic range compression and facilitate neural network training.
Both representations were stored as input tensors of shape [C × F × T], where C = 2 (left and right channels), F corresponds to the number of frequency bins (129 for STFT, 64 for mel), and T denotes the number of time frames. This formulation allows for a consistent comparison of biologically inspired and physics-based spectral front-ends within the same deep learning framework.

2.3 Neural Network Architecture

We implemented a convolutional neural network (CNN) designed to estimate the position of speech sources—specifically, the DoA and distance—from binaural time-frequency representations. The network accepts as input either STFT spectrograms or mel-spectrograms, both formatted as two-channel tensors that encode spectral features from the left and right ears.
The architecture consists of the following components:

- **Input layer**: Accepts input tensors of shape [2×F×T], where F is the number of frequency bins, and T is the number of time frames, depending on the duration of the audio segment and the hop size used.
- **Convolutional blocks**: The feature extractor comprises four convolutional layers with increasing filter depths (64, 128, 256, 512), each followed by ReLU activation, 2D max-pooling, and dropout (rate = 0.1). These layers are responsible for learning hierarchical patterns across time and frequency.
- **Flattening and fully connected layers**: The output of the final convolutional block is flattened and passed through a series of dense layers with 64 and 32 hidden units, respectively. This stage maps the high-level feature representations to a compact encoding suitable for regression.
- **Output layer**: The final dense layer contains two units, corresponding to the predicted azimuth angle (in degrees) and distance (in meters).

The total number of trainable parameters was approximately 2 million, and the model was implemented using PyTorch version 2.4.1. To ensure a controlled comparison, both models were trained using the same neural network architecture and optimization procedure, although the input representations differed not only in perceptual scaling (mel vs. linear) but also in time-frequency resolution due to distinct window and hop size configurations.

2.4 Evaluation Metrics

The performance of the neural network models was evaluated using regression-based metrics for both spatial dimensions: DoA and distance. Given the continuous nature of these output variables, the Mean Absolute Error (MAE) was used as the evaluation metric on the test set. For both DoA and distance, MAE was computed as the average absolute difference between the predicted values and the ground truth. MAE in DoA was expressed in degrees, while MAE in distance was expressed in meters. This metric provides an intuitive measure of average estimation accuracy and is robust to outliers.
All metrics were computed independently for the STFT-based and mel-based models under each experimental condition. Performance was further analyzed by grouping the results according to source directivity (omnidirectional, directional-facing, directional-reversed) to assess whether speech radiation patterns affected localization accuracy.

3. RESULTS AND DISCUSSION

3.1 Effect of Source Directivity on Direction of Arrival (DoA) Estimation

The impact of source directivity on DoA estimation was analyzed for both STFT-based and mel-based models across the 12 tested azimuth angles. Figures 1 and 2 show polar plots of the Mean Absolute Error (MAE) in azimuth estimation as a function of angle, grouped by directivity condition (omnidirectional, directional-facing, and directional-reversed). Figure 1 corresponds to the mel-spectrogram-based model, while Figure 2 displays results from the STFT-based model.

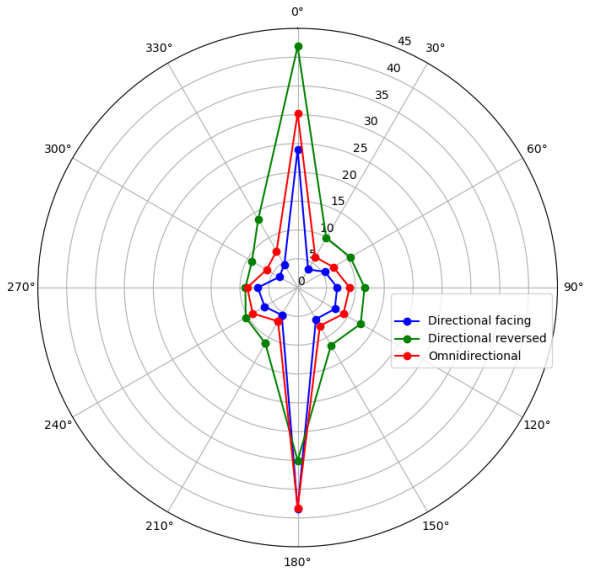


Figure 1: Mean Absolute Error (MAE) in DoA estimation for the mel-spectrogram-based model, plotted as a function of source azimuth angle. The polar plot shows results for three source directivity conditions: omnidirectional (red), directional-facing (blue), and directional-reversed (green).

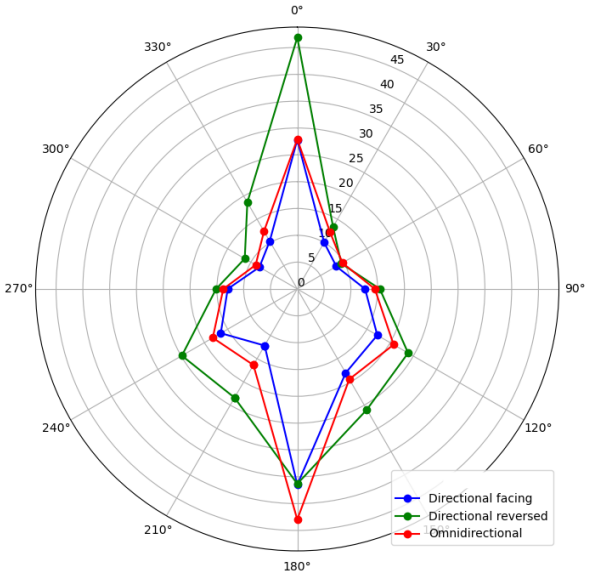


Figure 2: Mean Absolute Error (MAE) in DoA estimation for the STFT-based model, plotted as a function of source azimuth angle. The polar plot includes results for omnidirectional (red), directional-facing (blue), and directional-reversed (green) conditions.

For both feature types, source directivity strongly influenced DoA estimation accuracy. The lowest errors were consistently observed for the directional-facing condition, followed by the omnidirectional condition. In contrast, the directional-reversed configuration yielded the highest errors, especially at frontal (0°) and rear (180°) angles, suggesting a prominent front-back confusion effect.

When comparing the two feature representations, the mel-based model exhibited a more robust DoA estimation across all azimuth degrees and source directivity conditions. Specifically, mel features reduced angular MAE by up to 10 degrees in the most challenging reversed condition at 0° and 180°, relative to the STFT model. This suggests that the perceptually motivated mel scale better captures direction-dependent spectral variations, particularly under conditions of direct-path cues.

Overall, these results confirm that speech directivity patterns, especially when facing away from the listener, can impair azimuth estimation, and that mel-based models are more resilient to such degradations.

3.2 Effect of Source Directivity on Distance Estimation

Figures 3 and 4 show the Mean Absolute Error (MAE) in distance estimation as a function of distance bins (ranging from 1.0 to 4.0 meters), grouped by source directivity condition. Figure 3 presents results for the mel-spectrogram-based model, while Figure 4 displays results for the STFT-based model.

Both the STFT-based and mel-based models demonstrated clear performance degradation with increasing distance, consistent with the expected weakening of spatial cues at longer ranges.

In terms of directivity effects, the directional-facing condition yielded the most consistent and lowest distance errors across all bins, for both models. The omnidirectional source, in contrast, showed increasing error with distance, particularly above 2.5 meters, likely due to more uniform spatial energy distribution and reduced spectral asymmetries. The directional-reversed condition exhibited variable performance: at close distances, its error was relatively low, but it increased sharply beyond 3 meters, especially for the STFT model.

Again, mel-spectrograms provided superior distance estimation, with lower overall MAE in all distance bins and for all directivity types. The advantage of mel features was particularly pronounced for far-field estimation (>3 m), where STFT-based predictions showed significantly larger variance and error, especially for omnidirectional sources.

These findings reinforce the idea that biologically inspired spectral representations enhance robustness in challenging

acoustic conditions, especially when direct-path information is weak or distorted by reverberation and source radiation patterns.

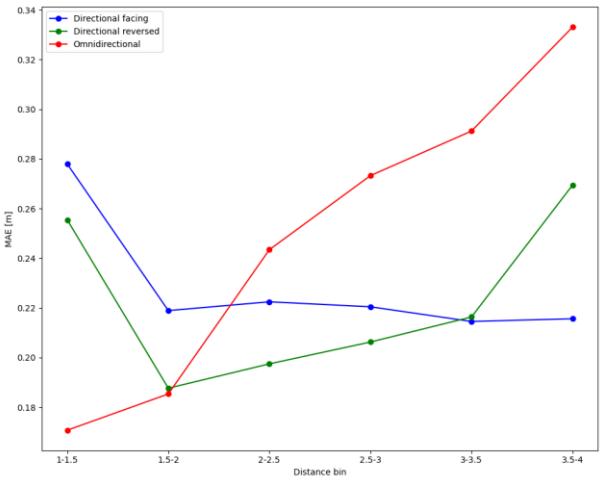


Figure 3: Mean Absolute Error (MAE) in distance estimation for the mel-spectrogram-based model, shown across distance bins from 1.0 to 4.0 meters. Each curve represents a different source directivity condition: omnidirectional (red), directional-facing (blue), and directional-reversed (green).

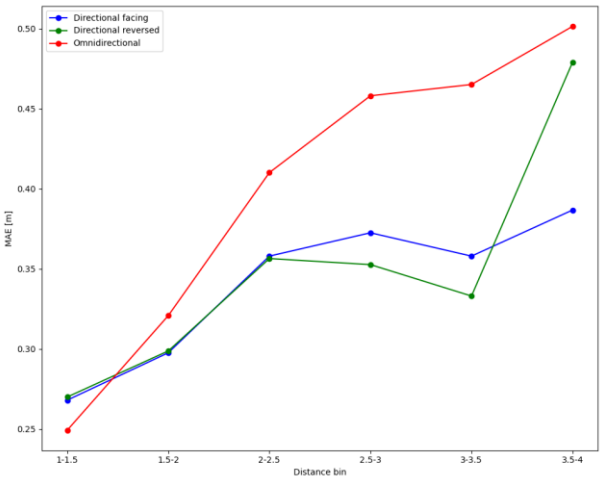


Figure 4: Mean Absolute Error (MAE) in distance estimation for the STFT-based model, plotted across distance bins from 1.0 to 4.0 meters. Results are shown for three source directivity conditions: omnidirectional (red), directional-facing (blue), and directional-reversed (green).

4. CONCLUSION

This study investigated whether the directivity of speech sources affects the performance of a deep neural network in estimating source position from binaural audio. The findings provide a clear affirmative answer to the central question: yes, source directivity significantly influences neural network-based speech position estimation.

Across both spatial dimensions, DoA and distance, models trained on signals from directional sources yielded different levels of accuracy depending on the orientation of the speaker. The directional-reversed condition, in which the source was facing away from the listener, consistently led to higher estimation errors, especially under reverberant conditions. This demonstrates that the directionality of speech radiation alters the availability and quality of spatial cues, which are crucial for both angular and distance localization.

Furthermore, models trained with mel-spectrogram features showed greater robustness to variations in source directivity and acoustic conditions compared to those using STFT-based representations. This suggests that biologically inspired, perceptually motivated features may better capture the spatial information encoded in directional speech signals.

Overall, the results emphasize that source directivity should not be neglected in the development and evaluation of spatial hearing models. Accounting for realistic radiation patterns is essential for building deep learning systems capable of generalizing complex and ecologically valid environments. These insights are particularly relevant for applications such as assistive hearing devices, speech enhancement systems, and auditory scene analysis in autonomous agents.

While the use of simulated environments allowed precise control over acoustic and spatial parameters, future work should explore real-world recordings and dynamic source behaviors—such as head movements—to further enhance model generalizability and ecological validity.

5. REFERENCES

[1] J. Blauert, *Spatial hearing: the psychophysics of human sound localization*. MIT press.

[2] D. Desai and N. Mehendale, 'A Review on Sound Source Localization Systems', *Arch. Comput. Methods Eng.*, vol. 29, no. 7, pp. 4631–4642, Nov. 2022, doi: 10.1007/s11831-022-09747-2.

[3] I. Dokmanić, R. Parhizkar, A. Walther, Y. M. Lu, and M. Vetterli, 'Acoustic echoes reveal room shape', *Proc. Natl. Acad. Sci.*, vol. 110, no. 30, pp.

12186–12191, Jul. 2013, doi: 10.1073/pnas.1221464110.
[4] P.-A. Grumiaux, S. Kitić, L. Girin, and A. Guérin, 'A survey of sound source localization with deep learning methods', *J. Acoust. Soc. Am.*, vol. 152, no. 1, pp. 107–151, Jul. 2022, doi: 10.1121/10.0011809.
[5] A. Carlini, C. Bordeau, and M. Ambard, 'Auditory localization: a comprehensive practical review', *Front. Psychol.*, vol. 15, p. 1408073, Jul. 2024, doi: 10.3389/fpsyg.2024.1408073.
[6] M. Slaney, 'Auditory toolbox: A MATLAB toolbox for auditory modeling work'. Interval Research Corporation, Tech. Rep, 1998.
[7] Y. Tokozume and T. Harada, 'Learning environmental sounds with end-to-end convolutional neural network', in *2017 IEEE International Conference on Acoustics, Speech and Signal Processing (ICASSP)*, New Orleans, LA: IEEE, Mar. 2017, pp. 2721–2725. doi: 10.1109/ICASSP.2017.7952651.
[8] V. Best, S. Carlile, C. Jin, and A. Van Schaik, 'The role of high frequencies in speech localization', *J. Acoust. Soc. Am.*, vol. 118, no. 1, pp. 353–363, Jul. 2005, doi: 10.1121/1.1926107.
[9] J. Zaar and L. H. Carney, 'Predicting speech intelligibility in hearing-impaired listeners using a physiologically inspired auditory model', *Hear. Res.*, vol. 426, p. 108553, Dec. 2022, doi: 10.1016/j.heares.2022.108553.
[10] A. Francl and J. H. McDermott, 'Deep neural network models of sound localization reveal how perception is adapted to real-world environments', *Nat. Hum. Behav.*, vol. 6, no. 1, pp. 111–133, 2022.
[11] B. B. Monson, E. J. Hunter, A. J. Lotto, and B. H. Story, 'The perceptual significance of high-frequency energy in the human voice', *Front. Psychol.*, vol. 5, Jun. 2014, doi: 10.3389/fpsyg.2014.00587.
[12] A. Ihlefeld and B. G. Shinn-Cunningham, 'Effect of source spectrum on sound localization in an everyday reverberant room', *J. Acoust. Soc. Am.*, vol. 130, no. 1, pp. 324–333, Jul. 2011, doi: 10.1121/1.3596476.
[13] V. Aubanel, M. L. G. Lecumberri, and M. Cooke, 'The Sharvard Corpus: A phonemically-balanced Spanish sentence resource for audiology', *Int. J. Audiol.*, vol. 53, no. 9, pp. 633–638, Sep. 2014, doi: 10.3109/14992027.2014.907507.
[14] D. Schröder and M. Vorländer, 'RAVEN: A real-time framework for the auralization of interactive virtual environments', *Forum Acusticum*, pp. 1541–1546, 2011.
[15] F. Pausch, S. Doma, and J. Fels, 'Hybrid multi-harmonic model for the prediction of interaural time differences in individual behind-the-ear hearing-aid-related transfer functions', *Acta Acust.*, vol. 6, p. 34, 2022, doi: 10.1051/aacus/2022020.

DOI: 10.61782/fa.2025.0823

FORUM ACUSTICUM EURONOISE 2025

SPEECH POSITION ESTIMATION USING NEURAL NETWORKS FROM ACOUSTIC SIGNALS OF HEARING AIDS

Sebastián Guajardo-Herrera[1*] **Rhoddy Viveros-Muñoz**[1]

[1] Department of Electronics and Computer Sciences, Universidad Técnica Federico Santa María, Concepción 4030000, Chile.

ABSTRACT

The localization of sound events, including speech, has evolved with the use of deep learning algorithms. The inclusion of distance in the task of estimating the direction of arrival allows us to obtain the spatial position of the sound source, which is a variable of interest for the improvement of auditory perception. This study addresses speech direction of arrival and distance estimation using signals generated by simulated hearing aid microphones in acoustic virtual reality environments.

The approach involves the collection of a dataset designed to represent various scenarios, with 96,000 samples distributed at 24 angular positions, varying distances between the source and the listener (ranging from 1 to 3 meters) and 4 reverberation times (0.1, 0.3, 0.6, and 0.9). These data are then used to evaluate the performance of a deep learning algorithm in simulated scenarios that replicate real conditions. The objective of this work is to contribute to the development of techniques that integrate direction of arrival and distance estimation in applications related to hearing aid systems and other acoustic support devices.

Keywords: Direction of Arribal Estimation, Distance Estimation, Deep Learning, Neural Networks, Hearing Aids

1. INTRODUCTION

The perception of the position of a sound event can be decomposed in the estimation of the direction of arrival (DoA), that refers to the angular direction of the event with respect to the listener, and the sound distance estimation (SDE) that is the relative distance between the source and the listener. These parameters allow to characterize spatially one or more sources, allowing to use them in different systems and applications. These parameters have been previously studied using different signal processing and deep learning (DL) techniques [1, 2].

Generally, implemented models for these tasks has been: convolutional neural networks (CNN) [3, 4], residuals networks (ResNet) [5], recurrent convolutional networks (CRNN) [6], Conformers [5, 7], and Transformers [8]. Among the input features used we can find magnitude and phase spectrograms, mel spectrograms, intensity vectors in the case of ambisonic microphones, interaural phase difference, generalized cross-correlation and Spatial Cue-Augmented Log-Spectrogram (SALSA) [9, 10] being particularly prevalent. These features have proven to be effective in obtaining spatial characteristics of sound sources.

A sound source of interest is the voice, which is crucial in communication processes, knowing the spatial position can improve the assistance systems as well as robotic applications [11].

In the case of hearing aids, they have been applied for the estimation of DoA [12], but distance estimation has not been incorporated. In this study we seek to test the effectiveness of deep learning algorithms for the estimation of both: DoA and distance.

The data used in this study have been generated in acoustic virtual reality [13], which enables faster data acquisition and fully accurate labels, avoiding the need for fully measured and controlled environments.

*__Corresponding author__: sguajardo@doctoradoia.cl.

__Copyright__: ©2025 First author et al. This is an open-access article distributed under the terms of the Creative Commons Attribution 3.0 Unported License, which permits unrestricted use, distribution, and reproduction in any medium, provided the original author and source are credited.

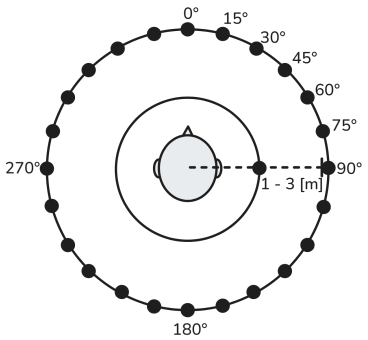


Figure 1. The positions of the simulated sources were configured in azimuth every 15°, elevation 0°, and distance between 1 and 3 meters.

2. METHODOLOGY

2.1 Dataset and Acoustic Simulation

Using a dataset of recorded speech and a controlled simulation framework, we investigated whether a neural network can learn the position of speech using hearing aid signals. The speech signals consisted of 700 sentences adapted to Chilean Spanish from the SHARVARD corpus [14]. These sentences were recorded with high quality microphones at a sampling rate of 44.1 kHz.

The speech signal was positioned at different distances and DoAs, varying in intensity, reverberation and source directivity using the simulation framework Room Acoustic for Virtual Environments (RAVEN) [15]. The listener was simulated as a 4 channel hearing aid. Hearing aid transfer functions (HATF) were obtained from the IHTA-indHARTF dataset [16]. This variability allows the models to generalize to different head shapes and sizes, avoiding the limitation of training to a single type.

The generated data contains the following spatial characteristics: 24 different azimuth angles between 0-360° every 15°, random distance between listener and event in the range of 1-3[m], random directivity of the source between 0-360° (see Figure 1).

The total data was generated is 96,000 samples of 4 channel audio, with a uniform distribution for both DoA and distance. For training the network, this was divided into training and validation sets with an 80-20 ratio.

2.2 Feature Extraction

The feature used for training and inference was a Mel Spectrogram obtained using Torchaudio library, to extract frequency and time features from the 4 microphones channels. We used a Hanning window with 1024 samples with a hop size of 512 samples, to get a magnitude spectrogram and applied a mel filterbank with 64 filters. The resulting input tensor has the shape [C x F x T], where C = 4 (left/right front and rear microphones), F corresponds the frequency bins (64) and T denotes the number of time frames.

2.3 Neural Network Model

The model used was a CNN designed to estimate the position (DoA + Distance) of a sound source, in this case speech, from a 4-channel time-frequency representation of the hearing aid. The architecture consists of:

1. **Input Layer**: Mel spectrogram per channel with shape [4 x F x T].
2. **Convs Layers**: Extract features from time-frequency representation, increasing filter depths (64, 128, 256, 512), each layer followed by ReLU activation function and 2D Max-Pooling. In the training process we used a Dropout (rate = 0.1).
3. **Flattening and Fully Connected Layer**: Flattened features passed through a dense layers with 64 and 32 hidden units.
4. **Output Layer**: Use a two neurons output, corresponding to azimuth angle (in scaled degree) and distance (in scaled meters).

The size of the network was approximately 2 million of parameters, and the model was implemented using PyTorch version 2.4.1.

3. RESULTS AND DISCUSSIONS

The overall results of the network for all validation data can be seen in Table 1, where we can observe the errors of the predictions in terms of DoA (in degrees) and Distance (in meters), measured in Mean Absolute Error (MAE) and Root Mean Square Error (RMSE).

The effect of the different reverberation times can be seen for DoA in Figure 2 and for Distance in Figure 3, in both cases we can observe an exponential increase of the error.

Table 1. MAE and RMSE calculated using the validation data set. Azimuth DoA is displayed in degrees and distance between listener and event is displayed in meters.

	MAE	RMSE
Distance [m]	0.40	0.49
DoA [°]	24.91	35.1

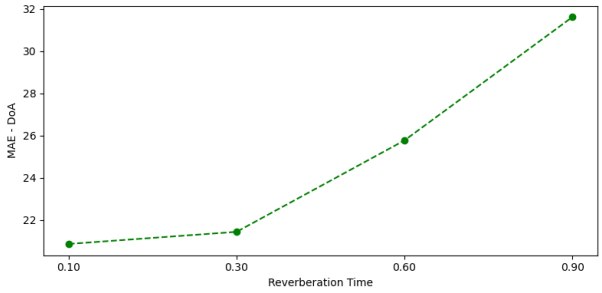


Figure 2. MAE of DoA estimation plotted as a function of reverberation time.

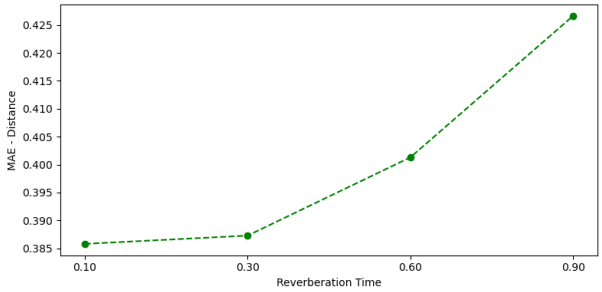


Figure 3. MAE of Distance estimation plotted as a function of reverberation time.

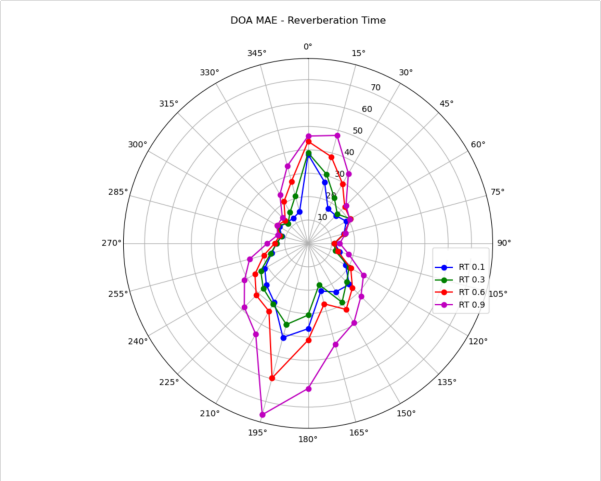


Figure 4. MAE of DoA plotted as a function of source azimuth angle. The polar plot includes the result for 4 reverberation times: 0.1(blue), 0.3(green), 0.6(red), 0.9(magenta).

Finally, the results of the error by DoA are presented in Figure 4 we can see an increase of the error in the rear zone of the listener, since the best estimation angles are the lateral ones.

4. CONCLUSIONS

This work investigate whether DL architectures, such as CNN, are capable of estimating the position of a speech sound source from signals coming from hearing aids. In this work, it is possible to demonstrate the architecture capability to perform this work from using only spectrograms of Mel as feature extraction, as well as characterize how the estimation varies according to the reverberation and position of the source.

Given the results, as future work we will analyze the possibility of incorporating more features and measure the impact that these have on improving the results, as well as incorporate improvements to the proposed model, thinking about applications in hearing aid systems or other acoustic support systems.

5. REFERENCES

[1] G. Jekateryńczuk and Z. Piotrowski, “A Survey of Sound Source Localization and Detection Methods

and Their Applications," *Sensors*, vol. 24, p. 68, Jan. 2024. Number: 1 Publisher: Multidisciplinary Digital Publishing Institute.

[2] M. U. Liaquat, H. S. Munawar, A. Rahman, Z. Qadir, A. Z. Kouzani, and M. A. P. Mahmud, "Localization of Sound Sources: A Systematic Review," *Energies*, vol. 14, p. 3910, Jan. 2021. Number: 13 Publisher: Multidisciplinary Digital Publishing Institute.

[3] K. Van Der Heijden and S. Mehrkanoon, "Goal-driven, neurobiological-inspired convolutional neural network models of human spatial hearing," *Neurocomputing*, vol. 470, pp. 432–442, Jan. 2022.

[4] H. Yu, "DOA AND EVENT GUIDANCE SYSTEM FOR SOUND EVENT LOCALIZATION AND DETECTION WITH SOURCE DISTANCE ESTIMATION," 2024.

[5] Q. Wang, Y. Dong, H. Hong, R. Wei, M. Hu, S. Cheng, Y. Jiang, M. Cai, X. Fang, and J. Du, "THE NERC-SLIP SYSTEM FOR SOUND EVENT LOCALIZATION AND DETECTION WITH SOURCE DISTANCE ESTIMATION OF DCASE 2024 CHALLENGE," 2024.

[6] S. Adavanne, A. Politis, and T. Virtanen, "A multi-room reverberant dataset for sound event localization and detection," May 2019. Issue: arXiv:1905.08546 arXiv:1905.08546.

[7] Q. Wang, Y. Jiang, S. Cheng, M. Hu, Z. Nian, P. Hu, Z. Liu, Y. Dong, M. Cai, J. Du, and C.-H. Lee, "THE NERC-SLIP SYSTEM FOR SOUND EVENT LOCALIZATION AND DETECTION OF DCASE2023 CHALLENGE," 2023.

[8] S. Kuang, J. Shi, K. v. d. Heijden, and S. Mehrkanoon, "BAST: Binaural Audio Spectrogram Transformer for Binaural Sound Localization," Aug. 2024. Issue: arXiv:2207.03927 arXiv:2207.03927.

[9] T. N. T. Nguyen, K. N. Watcharasupat, N. K. Nguyen, D. L. Jones, and W.-S. Gan, "SALSA: Spatial Cue-Augmented Log-Spectrogram Features for Polyphonic Sound Event Localization and Detection," *IEEE/ACM Transactions on Audio, Speech, and Language Processing*, vol. 30, pp. 1749–1762, 2022. Conference Name: IEEE/ACM Transactions on Audio, Speech, and Language Processing.

[10] T. N. Tho Nguyen, D. L. Jones, K. N. Watcharasupat, H. Phan, and W.-S. Gan, "SALSA-Lite: A Fast and Effective Feature for Polyphonic Sound Event Localization and Detection with Microphone Arrays," in *ICASSP 2022 - 2022 IEEE International Conference on Acoustics, Speech and Signal Processing (ICASSP)*, pp. 716–720, May 2022. ISSN: 2379-190X.

[11] C. Rascon and I. Meza, "Localization of sound sources in robotics: A review," *Robotics and Autonomous Systems*, vol. 96, pp. 184–210, Oct. 2017.

[12] P. Goli and S. van de Par, "Deep Learning-Based Speech Specific Source Localization by Using Binaural and Monaural Microphone Arrays in Hearing Aids," *IEEE/ACM Transactions on Audio, Speech, and Language Processing*, vol. 31, pp. 1652–1666, 2023. Conference Name: IEEE/ACM Transactions on Audio, Speech, and Language Processing.

[13] M. Vorländer, *Auralization*. Springer, 2020.

[14] V. Aubanel, M. L. G. Lecumberri, and M. Cooke, "The sharvard corpus: A phonemically-balanced spanish sentence resource for audiology," *International journal of audiology*, vol. 53, no. 9, pp. 633–638, 2014.

[15] D. Schröder and M. Vorlaender, *RAVEN: A real-time framework for the auralization of interactive virtual environments*. Jan. 2011.

[16] F. Pausch, S. Doma, and J. Fels, "Ihta-indhartf–database of individual behind-the-ear hearing-aid-related transfer functions with high spatial resolution," *Institute for Hearing Technology and Acoustics, RWTH Aachen*, 2022.

DOI: 10.61782/fa.2025.0518



FORUM ACUSTICUM
EURONOISE 2025

LEVERAGING PRE-TRAINED FOUNDATIONAL AUDIO MODELS FOR ACOUSTIC EVENT DETECTION IN DRIVING SCENARIOS

Mohammad Moghimi [1*] **Patrick Healy** [1] **Carlos Castorena** [2]
Francesc J. Ferri [2] **Maximo Cobos**[2]
[1] Department of Computer Science, University of Limerick, Ireland
[2] Department of Computer Science, University of Valencia, Spain

ABSTRACT

Smart vehicles are experiencing increasing adoption, driven by a growing demand for their applications. To facilitate widespread deployment, it is important to improve the security and trust of these vehicles. This paper focuses on improving smart car safety by developing an audio-based system for detecting important sound events, including emergency vehicle sirens, tire skidding, car crashes, horn types, drifting, and others. Our methodology involves a multifaceted approach to classifying a diverse range of driving-related audio events. We begin with a Convolutional Recurrent Neural Network (CRNN) as a baseline. Subsequently, we investigate the performance of pre-trained foundational models (e.g., BEATs, Audio Spectrogram Transformers) followed by a Recurrent Neural Network layer, aiming to leverage the pre-trained representations for improved event classification. Additionally, we explore the potential benefits of combining these approaches, considering as well the effect of introducing augmented data. We propose novel hybrid models that integrate features extracted by the convolutional layers of the CRNN with those directly obtained from the pre-trained models. Our experimental results demonstrate significant performance gains when combining these distinct approaches into a unified architecture.

Keywords: *Sound Event Detection, Deep learning Models, Smart Vehicles, Driver safety, Convolutional Recurrent Neural Network (CRNN), Audio Spectrogram Transformer (AST), BEATs, Data Augmentation.*

**Corresponding author*: mohammad.moghimi@ul.ie.
Copyright: *©2025 Mohammad Moghimi et al. This is an open-access article distributed under the terms of the Creative Commons Attribution 3.0 Unported License, which permits unrestricted use, distribution, and reproduction in any medium, provided the original author and source are credited.*

1. INTRODUCTION

Human senses, especially sight and hearing, play a major role in our perception, communication, and safety. Although sight is undoubtedly the most important sense, hearing helps humans absorb and analyze surrounding information and may even be the only reliable source in certain situations. Due to the importance of auditory information, integrating auditory sensing into smart devices and autonomous systems, which are increasingly prevalent, has become essential [1]. These systems, including smart cars, are now equipped with various sensors such as cameras, long and short-range radars, Light Detection and Ranging (LiDAR), ultrasonic transducers, and GPS receivers. However, these sensors have limitations [1]. For instance, cameras have blind spots and are sensitive to lighting and scene structure, making visual information unreliable. According to the National Highway Traffic Safety Administration, approximately 840,000 blind spot incidents occur annually in the United States, resulting in 300 fatalities [2]. Similarly, lasers are ineffective in extreme weather conditions.

To handle these challenges, researchers are increasingly focusing on the ability of devices to automatically detect and classify sound events through technological means known as sound event detection (SED) [3]. SED is the automatic process that detects and classifies events in audio streams and estimates the onset and offset of these events [4]. SED has many applications, including audio/video surveillance [5,6], healthcare monitoring, environmental monitoring [7], industrial machine fault mon-

itoring [8], human-computer interaction, and smart cars. By accurately detecting and timestamping sound events, SED systems can enhance the capability, security, and trust in smart devices and autonomous systems.

However, SED is still an evolving research topic due to several challenges, such as having enough data for training, ensuring performance in noisy environments, real-time processing, and modeling overlapping sounds [9]. Additionally, the development of robust SED systems is complicated by the need for sufficiently labeled datasets with accurate annotations for training purposes, making them more applicable in real-world scenarios [10]. Traditional SED methods relied on manual feature extraction (e.g., MFCC [11], Mel spectrograms) and classical machine learning techniques such as SVM [11], KNN, and HMM/GMM [12]. While these approaches provided initial insights, they often required extensive experimentation and struggled in complex, noisy environments. These limitations spurred the transition to deep learning, which has revolutionized sound event detection. Recent works have shown that through deep learning models, specifically Convolutional Neural Networks (CNNs) [13,14] and Recurrent Neural Networks (RNNs) [15], state-of-the-art performance is achieved on numerous tasks involving pattern recognition and learning data representations. These models reduce the dependency on manual feature extraction. This gave deep learning models the potential to handle the complexities of multiple concurrent and overlapped sound events; hence deep learning has become the state-of-the-art approach for SED with better accuracy and robustness.

More recently, pre-trained foundational audio models, such as BEATs [16] and the Audio Spectrogram Transformer (AST) [17], have emerged as powerful tools for capturing universal audio representations from large-scale datasets. These models offer enhanced feature extraction capabilities and have shown promise in various audio analysis tasks, making them particularly well-suited for addressing the challenges of SED in dynamic environments like driving scenarios.

There are, however, a few remaining research gaps. Despite many advances, current models still need to better consider temporal dependencies, contextual complexities, and rich feature extraction. Moreover, more generalized models that perform well under diverse acoustic environments [15] are needed, and the issue of computational efficiency—especially for deployment in resource-constrained setups—remains a challenge. The main objective of this paper is to address these gaps by investigating novel deep learning architectures and training strategies aimed at developing more robust, general, and efficient SED systems for driving scenarios. In particular, this paper promotes the sound event detection field by developing and evaluating novel deep learning models that combine the strengths of traditional CNN and RNN architectures with the enhanced representations obtained from pre-trained embedding models. The critical contributions from this work include presenting a novel hybrid model that integrates convolutional and recurrent layers with pre-trained audio representations to improve both performance and generalization. Comprehensive experimental results on data collected in driving environments, demonstrate the effectiveness and superior performance of the proposed methods.

Section 2 provides an overview of the data used in our study. Section 3 outlines a baseline system and different proposed SED models. Section 4 describes the experimental setup, including the preprocessing step, training details, and evaluation metrics. Section 5 provides the experimental results and discusses their implications, and Section 6 concludes the paper with suggestions for future research.

2. DATASET

The dataset used in this study was collected by [18], specifically designed to support the training and evaluation of sound event detection systems in driving environments. This dataset has sounds that originated from both internal sources within the vehicle, such as vehicle components, devices, and human interactions, as well as external sources like traffic, road conditions, and environmental factors (see Fig. 1).

2.1 Dataset overview and Sources

The dataset comprises 19,000 audio files, each with a duration of 10 seconds, resulting in a total duration of approximately 53 hours. To ensure a balanced representation of events, the dataset was split into training, validation, and test subsets: 15,000 audio samples for training, 2,000 for validation, and 2,000 for testing [18]. The sound events were sourced from various publicly available datasets with unrestricted usage rights, including: Musical Genre Classification of Audio Signals [19], UrbanSound [20], AudioSet [21], Old Phone Ringtones as MIDI [22], ASR-CabNois (Cabin Noise Dataset) [23], Freesound [24], A Singing Voice Dataset [25], DCASE



Figure 1. Internal (e.g. ring tone) and external (e.g. horn, siren) sounds while driving.

2020 Task 4 Dataset [26], Donate-A-Cry Corpus Features Dataset [27].

2.2 Synthetic Data Generation and Labeling

To simulate realistic driving conditions, the dataset was created using **Scaper** [28] with augmentation techniques such as time stretching and pitch shifting applied to improve diversity and model generalization. Table 1 provides a concise overview of our dataset, which comprises 41 classes. In our classification framework, we explicitly consider a problem with 41 distinct classes. These events are organized into nine primary distractor categories- horns, Sirens, Speech, Physiological, Pets, Notifications, Vibrating, RingTone, and Cry- each of which represents sounds most likely to divert a driver's attention. All other environmental sounds, such as rain, thunder, or microphone noise, are grouped under "Other", thus completing the broader driving environment. Each event was assigned **hard labels**, providing precise onset and offset timestamps within the 10-second clips. The event annotations followed a standardized format: The audio file name, the event type, the event onset and offset times. This structured labeling approach ensured the dataset was compatible with multiple machine learning frameworks and facilitated accurate model training. The dataset is openly accessible via `https://www.kaggle.com/datasets/ccastorena/sound-event-detection-for-driver-safety` and can be utilized by researchers and practitioners for benchmarking and further development in sound event detection [18].

Table 1. Dataset Summary

Class Groups	Classes	Appearances
Horns	4	11,693
Sirens	3	8,858
Speech	1	3,020
Physiological	3	8,639
Pets	2	5,843
Notifications	1	2,862
Vibrating	1	2,988
RingTone	1	2,835
Cry	1	2,950
Other	24	16,597
Total	**41**	**66,285**

3. SED MODELS

Sound Event Detection (SED) involves identifying and localizing sound events by capturing both their spectral details and temporal dynamics. We begin with a popular CRNN baseline from the DCASE framework, which uses convolutional layers to extract features from Log-Mel spectrograms and recurrent layers to model how these features evolve over time. To further enhance our model's performance, we also combine additional feature extraction from pretrained models like the Audio Spectrogram Transformer (AST) and BEATs, creating a richer representation of the audio signals for more robust detection.

3.1 CRNN model as a baseline

We employ the DCASE baseline architecture [29] based on Convolutional Recurrent Neural Networks (CRNNs), which are widely used in sound event detection. This architecture is used to detect patterns in complex audio signals (via convolutional layers) and interpret how those patterns evolve over time (via recurrent layers). We use the standardized CRNN architecture defined by the DCASE framework, ensuring compatibility with other studies. As illustrated in Figure 2, the CRNN starts by converting audio into a Log-Mel spectrogram. This spectrogram, sized [1, 626, 128] (1 is the channel dimension, 626 is the time dimension, and 128 is the number of Mel frequency bands), is processed through seven convolutional blocks.

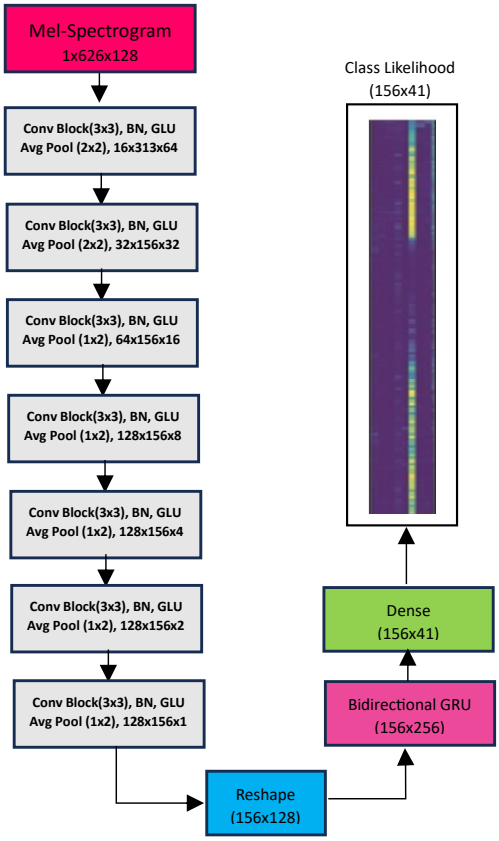


Figure 2. Baseline CRNN Architecture.

Each block uses a 2D convolution with a kernel size of 3×3, batch normalization, GLU activations, and average pooling. The number of filters in each layer is: 16, 32, 64, 128, 128, 128, 128, and the pooling operations has the specific dimensions of 2×2, 2×2, 1×2, 1×2, 1×2, 1×2, 1×2, respectively. This results in the convolutional output shape of [128, 156, 1]. To integrate with the bidirectional recurrent layers, the filter dimensions are transposed, and the extra dimension is removed. The bidirectional GRU layer produces an output of [156, 256], with 128 hidden units in both directions. Finally, a dense layer with softmax activation generates the final output with 156 frames and 41 distinct events.

3.2 Proposed models

Our proposed framework explores three distinct feature-extraction pathways for each audio clip, as illustrated in Figure 3. The first pathway, termed the *Baseline CNN Path*, uses Log-Mel spectrograms of size 1×626×128 as input to a convolutional neural network. This CNN processes the spectrograms to generate initial feature tensors with dimensions of [128, 156, 1].

The second pathway, referred to as the *AST Path*, leverages the frame-level version of the Audio Spectrogram Transformer (AST), specifically the ATST-Frame variant with a Base384 configuration. This model processes 10-second audio segments to produce a feature tensor of size 768×496 (representing the embedding dimension and time steps). An average pooling stage is applied to reduce the time dimension from 496 to match the CRNN's temporal resolution of 156, resulting in a pooled output of size [768, 156]. Features from this path are stored in HDF5 format for efficient loading.

The third pathway, known as the *BEATs Path*, utilizes BEATS_iter3_plus_AS2M.pt, a model pre-trained on AudioSet. Operating at a 16 kHz sampling rate with a 25 ms window (and a 10 ms hop length), this approach also outputs embeddings of size 768×496, which are similarly reduced via average pooling to produce a tensor of dimensions [768, 156]. Again, the features are stored in HDF5 format.

To harness the complementary strengths of these pathways, our framework investigates several fusion strategies. The simplest strategy is the CNN+RNN baseline, which relies solely on features extracted by the CNN. Alternatively, pretrained features from the BEATs and AST paths can be fed directly into recurrent layers (BEATs/AST Path + RNN). Another approach involves concatenating the CNN-extracted features with those from the AST or BEATs paths (CRNN + AST/BEATs), before inputting the combined representation into recurrent layers. Finally, a full integration strategy (CRNN + BEATs + AST) is proposed, combining all feature streams into a unified architecture. This multi-path fusion is designed to exploit the diverse and rich representations provided by each pathway, ultimately enhancing the robustness and accuracy of sound event detection in dynamic driving scenarios.

4. EXPERIMENTAL SETUP

4.1 Audio Pre-processing and Augmentation

All audio clips are first resampled to a 16 kHz sampling rate (mono) using Librosa. To ensure consistent input lengths, clips longer than 10 seconds are truncated, and those shorter than 10 seconds are zero-padded to reach

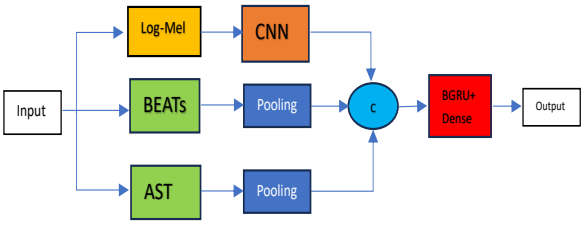


Figure 3. Proposed models.

the 10-second duration. For labeling, a frame-wise hard label format is used, where each frame corresponds to a discrete timestamp. Each frame has a value of 1 when an event is present and 0 otherwise. The output must predict 156 frames, corresponding to the chosen number of events. The model uses log-mel spectrograms as input features for the CNN model, using 128 mel-filters with a window length and FFT size of 2048, a Hamming windowing function, and a hope size of 256. The frequency range for the Mel spectrogram is from 0 Hz to 8000 Hz. The resulting Mel spectrogram has dimensions of 626 frames, 128 Mel bands, and a single channel. During training, we apply a combination of data augmentation techniques to enhance the robustness and generalization of our models. Specifically, we use the mixup technique and specaugment. Mixup is a widely adopted augmentation method in both machine listening and computer vision [30]. It creates synthetic training samples by linearly interpolating pairs of input spectrograms and their corresponding labels, thereby increasing the diversity of the training data and smoothing the decision boundaries. In addition, specaugment [31] is applied to the Log-Mel spectrograms, which involves randomly masking blocks of time and frequency bins. This perturbation forces the model to learn more invariant features and reduces sensitivity to noise, ultimately contributing to improved performance in dynamic and challenging driving scenarios.

4.2 Training Schedule

All experiments (CRNN-only, CRNN+AST, CRNN+BEATs, etc.) use the same overall training procedure: training continues for up to 200 epochs with early stopping triggered if no improvement is observed for 100 consecutive epochs, a dropout rate of 0.5 is applied, and the batch size is set to 48 for both training and validation. Additionally, the Adam optimizer is employed with a learning rate of 0.001 and a warm-up phase during the first 50 epochs.

4.3 Metrics

To comprehensively evaluate sound event detection systems, we employ a range of complementary metrics. While Accuracy is a common measure, relying on it exclusively can be misleading, especially for frame-by-frame detection and rare events. Thus, we complement it with more detailed metrics, such as the F1 score and the Polyphonic Sound Detection Score (PSDS).

The F1 score is widely used because it effectively balances Precision and Recall, thereby measuring the system's accuracy in detecting events without over- or under-detection. Meanwhile, the PSDS is computed using the `psds_eval` toolbox [32], which is a recognized standard within the DCASE community. PSDS values are derived from 50 operating points (linearly distributed from 0.01 to 0.99) and refer to the normalized area under the PSD-ROC (Receiver Operating Characteristic) curve up to a specified maximum effective false positive rate (eFPR).

In our experiments, we use PSDS1, where $DT_C = GT_C = 0.7$, in accordance with common practices in general SED tasks.

5. RESULTS AND DISCUSSION

Models	Augmentation	Accuracy	PSDS	F1
CRNN+ReLU	None	92	22.1	55.6
CRNN+ ReLU	Mixup+specaugment	94	23.5	56.3
CRNN+GLU(baseline)	Mixup+specaugment	95	28.1	58.1
AST+RNN	Non	96	30.1	59.9
BEATs+RNN	Non	98	31.5	60.6
CRNN+AST	Mixup+specaugment	97	37.4	61.2
CRNN+BEATs	Mixup+specaugment	97	39.7	61.6
BEATs+AST+RNN	Non	97	43.6	63.1
CRNN+BEATs+AST	Mixup+specaugment	97	44.3	63.4

Table 2. Comparison of models, augmentations, and their performance metrics.

Table 2 summarizes the performance of various sound event detection models. We begin with a CRNN+ReLU model without augmentation that achieved an accuracy of 92%, a PSDS of 22.1, and an F1 score of 55.6. When augmented with Mixup and specaugment, the CRNN+ReLU configuration improved slightly to 94% accuracy, 23.5 PSDS, and 56.3 F1. Replacing ReLU with GLU in the

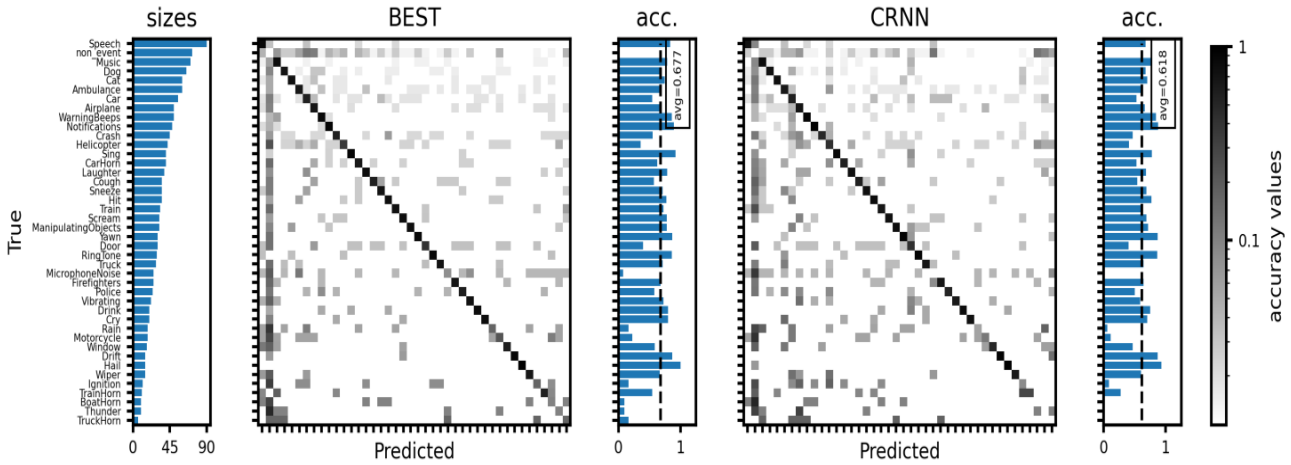


Figure 4. Confusion matrices comparing the best proposed model (left) and the CRNN+GLU baseline(right)

CRNN, while using the same augmentation, further enhanced performance to 95% accuracy, 28.1 PSDS, and 58.1 F1. This enhanced model not only serves as the baseline for the DCASE 2021-2023 editions [29], but it also becomes our reference point for comparing the performance of our proposed models, and forming the backbone of our hybrid approaches.

Models that integrate pre-trained audio features also showed notable improvements. The AST+RNN model, which does not use data augmentation, reached 96% accuracy, 30.1 PSDS, and 59.9 F1, while the Beats+RNN model outperformed it with 98% accuracy, 31.5 PSDS, and 60.6 F1.

The benefits of fusion strategies become even more evident in the hybrid models. The CRNN+AST and CRNN+Beats models, CNN employing Mixup and specaugment, achieved 97% accuracy with PSDS scores of 37.4 and 39.7, and F1 scores of 61.2 and 61.6, respectively. The Beats+AST+RNN configuration, without augmentation, reached 97% accuracy, 43.6 PSDS, and 63.1 F1. Finally, the fully integrated model CRNN+Beats+AST with Mixup and specaugment maintained 97% accuracy while achieving the highest PSDS (44.3) and F1 (63.4) scores.

To illustrate the behavior of the best model and the CRNN+GLU baseline on different classes, frame-based confusion matrices and associated accuracies are shown in Figure 4. The confusion matrices demonstrate that the BEST model has a stronger diagonal, reflecting a higher number of correct predictions, whereas the baseline shows more off-diagonal misclassifications. In Figure 4, we use a support-weighted per-class accuracy metric that differs from the frame-based accuracy presented in Table 2. The Table 2 metric is computed online using `torchmetrics`, evaluating the model's ability to correctly detect the presence or absence of sound events within fixed-length segments and capturing both active and inactive portions. By contrast, the metric in Figure 4 is derived post-hoc from a confusion matrix (often excluding the non-event class) by normalizing each class's counts and computing a weighted average based on class frequencies, effectively treating each class as a separate binary classification (one-vs-rest). These differences in aggregation, class inclusion, and weighting account for the observed discrepancies between the two accuracy values. Notably, for Figure 4, the BEST model achieves an average accuracy of 67.7% compared to the CRNN baseline's 61.8%, highlighting the benefits of integrating pre-trained audio features in driving scenarios.

These results indicate that leveraging pre-trained audio models substantially enhances the detection of complex, overlapping sound events in dynamic driving environments, with data augmentation further improving generalization. The superior performance of the hybrid models over the CRNN approaches underscores their potential for robust real-world sound event detection in challenging driving scenarios.

6. CONCLUSION

In this study, the integration of pre-trained models, specifically AST and BEATs, into a CRNN-based framework represents a significant breakthrough in sound event detection for driving scenarios. By leveraging the advanced feature extraction capabilities of models like AST and BEATs alongside the proven temporal modeling of CRNNs, our hybrid approach achieves superior performance—demonstrated by higher accuracy, PSDS, and F1 scores—compared to traditional methods. Data augmentation techniques such as mixup and specaugment further enhance model robustness in noisy, real-world environments, making the approach well-suited for the complex auditory landscapes encountered in smart vehicle applications.

Looking ahead, these findings open up promising avenues for future research, including real-time deployment optimizations, exploration of additional fusion strategies, and training on more diverse datasets. Overall, our work marks a significant step toward developing safer, more reliable autonomous systems by providing a robust framework for detecting critical sound events in dynamic driving conditions.

7. ACKNOWLEDGMENTS

This work has been supported by Science Foundation Ireland Grant No. 18/CRT/6223. Also, this work has been supported by Grant TED2021-131003B-C21 funded by MCIN/AEI/10.13039/501100011033 and by the "EU Union NextGenerationEU/PRTR", as well as by Grant PID2022-137048OB-C41 funded by MICIU/AEI/10.13039/501100011033 and "ERDF A way of making Europe".

8. REFERENCES

[1] E. G. Vidal, E. F. Zarricueta, and F. A. Cheein, "Human-inspired sound environment recognition system for assistive vehicles," *Journal of Neural Engineering*, vol. 12, no. 1, p. 016012, 2015.

[2] W. H. Organization, *Global status report on road safety 2018*. World Health Organization, 2019.

[3] Z. Islam and M. Abdel-Aty, "Real-time emergency vehicle event detection using audio data," 2022. arXiv preprint, arXiv:2202.01367.

[4] Z. Shuyang, T. Heittola, and T. Virtanen, "Active learning for sound event detection," *IEEE/ACM Transactions on Audio, Speech, and Language Processing*, vol. 28, pp. 2895–2905, 2020.

[5] K. Manikanta, K. P. Soman, and M. S. Manikandan, "Deep learning based effective baby crying recognition method under indoor background sound environments," in *Proceedings of the 2019 4th International Conference on Computational Systems and Information Technology for Sustainable Solution (CSITSS)*, pp. 1–6, IEEE, 2019.

[6] K. Deepak, S. Chandrakala, and C. K. Mohan, "Residual spatiotemporal autoencoder for unsupervised video anomaly detection," *SIViP*, vol. 15, pp. 215–222, 2021.

[7] K. Deepak, G. Srivathsan, S. Roshan, and S. Chandrakala, "Deep multi-view representation learning for video anomaly detection using spatiotemporal autoencoders," *Circuits, Systems and Signal Processing*, vol. 40, no. 3, pp. 1333–1349, 2021.

[8] M. Saimurugan and R. Ramprasad, "A dual sensor signal fusion approach for detection of faults in rotating machines," *Journal of Vibration Control*, vol. 24, no. 12, pp. 2621–2630, 2018.

[9] A. Mesaros, T. Heittola, T. Virtanen, and M. D. Plumbley, "Sound event detection: A tutorial," *IEEE Signal Processing Magazine*, vol. 38, no. 5, pp. 67–83, 2021.

[10] Q. Kong, Y. Xu, W. Wang, and M. D. Plumbley, "Sound event detection of weakly labelled data with cnn-transformer and automatic threshold optimization," *IEEE/ACM Transactions on Audio, Speech, and Language Processing*, vol. 28, pp. 2450–2460, 2020.

[11] S. E. Küçükbay and M. Sert, "Audio-based event detection in office live environments using optimized mfcc-svm approach," in *Proceedings of the 2015 IEEE 9th International Conference on Semantic Computing (IEEE ICSC 2015)*, pp. 475–480, IEEE, 2015.

[12] B. Elizalde, M. Ravanelli, K. Ni, D. Borth, and G. Friedland, "Audio-concept features and hidden markov models for multimedia event detection," in *SLAM@ INTERSPEECH*, pp. 3–8, 2014.

[13] H. C. Chu, Y. L. Zhang, and H. C. Chiang, "A cnn sound classification mechanism using data augmentation," *Sensors*, vol. 23, no. 15, p. 6972, 2023.

[14] J. K. Das, A. Ghosh, A. K. Pal, S. Dutta, and A. Chakrabarty, "Urban sound classification using convolutional neural network and long short term memory based on multiple features," in *Proceedings of the 2020 Fourth International Conference On Intelligent Computing in Data Sciences (ICDS)*, pp. 1–9, IEEE, 2020.

[15] S. V. Shanmukha and K. Deepak, "Sound event detection in constrained real-world environments using fine tuned cnns," in *Proceedings of the 2024 International Conference on Distributed Computing and Optimization Techniques (ICDCOT)*, pp. 1–6, IEEE, 2024.

[16] S. Chen, Y. Wu, C. Wang, S. Liu, D. Tompkins, Z. Chen, and F. Wei, "Beats: Audio pre-training with acoustic tokenizers," *arXiv preprint arXiv:2212.09058*, 2022.

[17] Y. Gong, Y.-A. Chung, and J. Glass, "Ast: Audio spectrogram transformer," *arXiv preprint arXiv:2104.01778*, 2021.

[18] C. Castorena, M. Cobos, J. Lopez-Ballester, and F. J. Ferri, "A safety-oriented framework for sound event detection in driving scenarios," *Applied Acoustics*, vol. 215, p. 109719, 2024.

[19] G. Tzanetakis and P. Cook, "Musical genre classification of audio signals," *IEEE Transactions on Speech and Audio Processing*, vol. 10, no. 5, pp. 293–302, 2002.

[20] J. Salamon, C. Jacoby, and J. P. Bello, "A dataset and taxonomy for urban sound research," in *Proceedings of the 22nd ACM International Conference on Multimedia*, pp. 1041–1044, ACM, 2014.

[21] J. F. Gemmeke, D. P. W. Ellis, *et al.*, "Audio set: An ontology and human-labeled dataset for audio events," *Proceedings of the IEEE International Conference on Acoustics, Speech and Signal Processing (ICASSP)*, pp. 776–780, 2017.

[22] V. Torosyan, "Old phone ringtones as midi dataset," 2019. Online dataset.

[23] A. R. Team, "Asr-cabnois: A dataset of vehicle cabin noises for audio analysis," *Journal of Acoustic Research*, vol. 15, pp. 105–115, 2023.

[24] Freesound, "Freesound database," 2023. Online dataset.

[25] J. Wilkins, I. Mcloughlin, and D. Howard, "A singing voice dataset for mir research," *Journal of the Acoustical Society of America*, vol. 144, no. 3, pp. 1452–1463, 2018.

[26] R. Serizel, A. P. Shah, and J. Salamon, "Sound event detection in domestic environments with weakly labeled data and soundscape synthesis," in *Workshop on Detection and Classification of Acoustic Scenes and Events (DCASE)*, 2020.

[27] A. Valani *et al.*, "Donate-a-cry corpus: A dataset of infant cries for sound classification," *Journal of Infant Research*, vol. 20, pp. 75–89, 2023.

[28] J. Salamon and J. P. Bello, "Scaper: A library for soundscape synthesis and augmentation," in *IEEE Workshop on Applications of Signal Processing to Audio and Acoustics (WASPAA)*, pp. 344–348, IEEE, 2017.

[29] R. Serizel, N. Turpault, H. Eghbal-Zadeh, and A. Parag Shah, "Large-scale weakly labeled semi-supervised sound event detection in domestic environments," in *Workshop on Detection and Classification of Acoustic Scenes and Events*, (Woking, United Kingdom), Nov 2018. Submitted to DCASE2018 Workshop.

[30] H. Zhang, M. Cisse, Y. N. Dauphin, and D. Lopez-Paz, "mixup: Beyond empirical risk minimization," *arXiv preprint arXiv:1710.09412*, 2017.

[31] D. S. Park, W. Chan, Y. Zhang, C.-C. Chiu, B. Zoph, E. D. Cubuk, and Q. V. Le, "Specaugment: A simple data augmentation method for automatic speech recognition," in *Interspeech 2019*, interspeech_2019, ISCA, sep 2019.

[32] Ç. Bilen, G. Ferroni, F. Tuveri, J. Azcarreta, and S. Krstulović, "A framework for the robust evaluation of sound event detection," in *ICASSP 2020 IEEE International Conference on Acoustics, Speech and Signal Processing (ICASSP)*, pp. 61–65, IEEE, 2020.

DOI: 10.61782/fa.2025.0397

FORUM ACUSTICUM EURONOISE 2025

EXPLORING THE POTENTIALITIES OF MACHINE LEARNING TECHNIQUES FOR THE ANALYSIS AND THE FORECAST OF ROAD TRAFFIC NOISE LEVELS

Domenico Rossi[1,*] **Aurora Mascolo**[1] **Daljeet Singh**[2]
Claudio Guarnaccia[1]
[1] Department of Civil Engineering, University of Salerno, Italy
[2] Department of Mechanical Engineering, Thapar Institute of Engineering & Technology, Patiala, India

ABSTRACT

Machine Learning (ML) techniques are gaining interest in many scientific applications, including analysing and forecasting road traffic noise. Many alternatives to the classic Road Traffic Noise Models (RTNMs) are then opened: ML provides ways for studying the traffic noise in urban and non-urban environments straightforwardly, using the same input data of the RTNMs. In this work, an analysis of road traffic noise equivalent levels by using ML regressors is described. Those regressors are calibrated on real data (coming from an experimental long-term monitoring station) using the well-known 80%/20% calibration/validation split rule. Splitting of data for calibration and validation is coupled with shuffling of the data themselves to evaluate possible output variations. Even with some differences, regressors exhibit promising potentialities in the simulation of the road traffic noise levels in the case under study. The mean error is very low and comparable with other models available in Literature. The comparison between the distribution of the measured data and the simulated one shows a general good agreement, and also underlines peculiarities of the single regressors.

Keywords: *machine learning, regression analysis, road traffic noise, modelling, computed data.*

[*] ***Corresponding author***: *drossi@unisa.it*
Copyright: *©2025 Rossi et al. This is an open-access article distributed under the terms of the Creative Commons Attribution 3.0 Unported License, which permits unrestricted use, distribution, and reproduction in any medium, provided the original author and source are credited.*

1. INTRODUCTION

Noise has a severe impact on urban environments since it is ubiquitous and its gravity is generally not perceived as other pollutants. People subjected to high noise levels, anyway, experience equal or even worse effects. Consequences of prolonged exposure to high noise levels are numerous: tiredness, lack of sleep, irritability and irascibility, problems in concentration, scarce intelligibility during conversations, tinnitus, and difficulty in conducting daily tasks like study or work [1]. Worse consequences may be related to transient or permanent hearing loss and, even if rarely, to hypertension and/or cardiovascular diseases [2]. Road traffic is responsible for the main part of the impact of noise in a given urban environment, and for this reason, governments are constantly trying to implement noise control and reduction strategies [3]. European Union, for example, aims at a 30% reduction in the number of people subjected to high noise levels before 2030 [4]. Due to this, the importance of monitoring and controlling noise in urban areas is clear, and the implementation of valid measuring strategies is decisive for a successful assessment of the problem. Noise can be directly measured, but when such a direct approach is not possible, modelling is an appropriate alternative. Many models, commonly known as Road Traffic Noise Models (RTNMs), exist since long time, and different RTNMs have been adopted in the past by different national institutions: the CoRTN model, used in the United Kingdom [5], the SonRoad model, used in Switzerland [6]; the NMBP model in France [7]; the ASJ in Japan [8]; the RLS90 in Germany [9] and the Harmonoise model [10]. A comprehensive review of the evolution of RTNMs can be found in [11]. Recently the European Union (EU) has realized and recommended the CNOSSOS-EU model, which is a common procedure for the evaluation and simulation of transportation and industrial noise levels in all European countries [12-13]. CNOSSOS-EU framework is

also used for the final development of noise maps. Together with the aforementioned methods, anyway, recently new procedures have recently been investigated and implemented for the assessment of noise. In particular, Machine Learning (ML) techniques have been more and more used for this scope. While RTNMs investigate the direct physical cause-effect relationships between noise emitters characteristics (number of vehicles running, vehicle category, speed) and noise levels at a sensible receiver, ML approaches evaluate such relationship from a statistical point otrof view. In such a way they open to their usability in the same contexts where traditional RTNMs are commonly applied, but also in unusual traffic conditions (presence of roundabouts and/or stops and traffic lights). This is very important considering that RTNMs typically presuppose free-flow conditions. Many examples can be found in the literature. In [14], as an example, Support Vector Machine and Multilinear Regression have been used to evaluate noise in relation to its annoyance to people, generating a final model that correlates noise perception, noise exposure levels, and demographics; in [15] a similar approach is reported, but with more details on the type and number of inputs to be used. An Extreme Gradient Boosting (XGB) approach has been used in [16] to properly relate the performances of the most common traffic noise models and validate them. A wide comparison of the efficiency of several ML approaches can be found in [17]. In the work of Singh et al. [18], a ML approach is used together with a Monte Carlo Simulation for the assessment of noise impact in India. In [19], together with the classic input road traffic parameters, the honking occurrences have been used as input for ML approaches, namely Decision Tree and Random Forest. In [20] the very same regressors have been calibrated by using pass-by noise. All these literature experiences, together with the high potentiality of such approaches, have led the authors to dedicate efforts to the production of a large and comprehensive study on three different ML regressors - Multilinear Regressor (MLR), Decision Tree (DT) and Random Forest (RF) to predict Road traffic noise equivalent levels. After a detailed hyperparameter tuning and calibration approach such models have been validated on a set of road traffic collected data. Specifically, data have been collected by French researchers in a specific extra-urban viaduct in Saint Berthevin, France, during an experimental campaign that lasted several years called "Long Term Monitoring Station" (LTMS). Such data are freely available for research use.

The here presented study stands out for the important aspects of the ML application to road traffic noise simulation. The experimental procedures have been developed using Python programming language. Outputs of the here presented models are provided as hourly continuous equivalent sound level $L_{eq,h}$. The result is a study on the potentiality of the application of such ML approaches on noise assessment and its impact on the environment of urban and extra-urban contexts.

2. MATERIALS AND METHODS

2.1 Workflow of the experimental procedure and used programming environment

Jupyter notebook, a Python environment, has been used to implement the Machine Learning analysis on a DELL personal computer (Intel® Xeon® CPU E3-1245 v5 @3.50 GHz) with 16 GB of RAM installed, 64-bit. The main packages used were: pandas, numpy, scikitlearn, matplotlib and seaborn. The whole experimental procedure consisted of three parts: a first part in which the three chosen regressors have been tuned with the best hyperparameters combination; a second part consisting in the calibration of the regressors, and a final part of validation of the regressor themselves. Figure 1 visually resumes the steps of the process.

2.2 Dataset used for calibration and validation of the regressors

The data used in this experiment to calibrate and validate the regressors come from a large road traffic noise dataset available in the literature, obtained from a large campaign of data collection pursued by the *Unité Mixte de Recherche en Acoustique Environnementale* (UMRAE), within Université Gustave Eiffel, Nantes. In this study, both meteorological and acoustic data were collected by different masts installed in the city of Saint-Berthevin (France) for a period of six years, from 2002 to 2007 [21]. Within this large dataset, the following data were used in this paper: sound equivalent levels, number of light and heavy vehicles, and average speeds for both vehicle categories. Specifically, all the above parameters were recorded in 15-minute intervals, but for this study, they were converted to 60-minute time ranges. To do this, equivalent levels based on 15 minutes were logarithmically summed to calculate the equivalent hourly level. When performing this procedure, authors removed the entries where, for some reasons, equivalent levels were missing. A detailed report of this procedure can be found in [22]. As a result, the dataset used for this contribution was reduced from the original 30347 entries (based on 15 minutes) to a filtered one of 3404 entries (based on 1 hour).

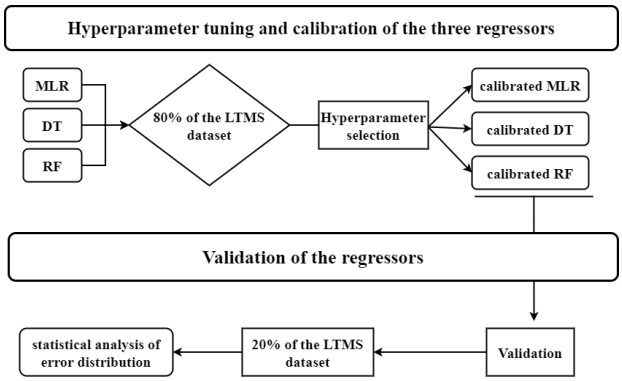


Figure 1: Workflow of the experimental procedure.

2.3 Hyperparameters tuning of the regressors

Hyperparameters tuning is a procedure aiming at finding the best combination possible of the hyperparameters of each regressor to get the best simulation results taking as input a given set of data. In this application, the tuning test has been performed on the same dataset used in the calibration described in subsection 2.4. Different nested cycles have been implemented to check the progressive advances of each test and to save the results. Please note that an in-built function for hyperparameter testing is present in the Scikit-learn package, but the authors preferred to build a personalized one, to have more control over the phases of each iteration. A description of the hyperparameters involved in the tuning procedure is reported below.

For Decision Tree (DT), the hyperparameters are: the criterion to measure the quality of the split, the strategy used to choose the split at each node, the maximum depth of the tree, the minimum number of samples required to split an internal node, the minimum number of samples required to be at a leaf node, the minimum weighted fraction of the sum of weights, the number of features to consider when looking for the best split, the function considering the randomness of the estimator, a maximum number of nodes for each leaf, the value inducing a decrease of the impurity at each node split, the hyperparameter used for Minimal Cost-Complexity Pruning and the monotonicity constraint to enforce on each feature.

For Random Forest (RF), the hyperparameters are: the number of trees in the forest, the function to measure the quality of a split, the maximum depth of the tree, the minimum number of samples required to split an internal node, the minimum number of samples required to be at a leaf node, the minimum weighted fraction of the sum total of weights, the number of features to consider when looking for the best split, a hyperparameter to grow trees with a maximum number of leaves in best-first fashion, the value inducing a decrease of the impurity at each node split, a hyperparameter to establish whether bootstrap samples are used when building trees, a hyperparameter to establish whether to use out-of-bag samples to estimate the generalization score, the number of jobs to run in parallel, a hyperparameter controlling both the randomness of the bootstrapping of the samples used when building trees, the hyperparameter controlling the verbosity when fitting and predicting, a hyperparameter establishing to reuse the solution of the previous call to fit and add more estimators to the ensemble, a complexity hyperparameter used for Minimal Cost-Complexity Pruning, the number of samples to draw to train each base estimator the monotonicity constraint to enforce on each feature.

Finally, for MultiLinear Regressor (MLR), the hyperparameters are: the hyperparameter controlling whether to calculate the intercept or not, the number of jobs to use for the computation, a hyperparameter forcing the coefficients to be all positive.

2.4 Calibration of the regressors

The calibration of the regressors is the process by which every single regressor involved in this experimental study has been trained with a section of the calibration dataset and then has been evaluated in a subsequent validation (test) phase. This process has been carried out following a standard procedure where a section of the data has been devoted to the training of the regressors and the remaining section to their validation. For this specific application 80% of the whole dataset has been used for training, and the remaining 20% for the validation. The train/test split of the dataset is randomly performed by an in-built method of the scikit-learn package that assigns a seed to assure the repeatability of the process. All the analyses reported in Section 3 have been pursued using the same seed, thus fixing the calibration and validation datasets.

2.5 Validation of the regressors

After the calibration of the model, the validation step has been performed by comparing the values simulated by each single regressor with the real one. The validation of the regressors took accounts of statistical analysis of the distribution of the simulated values and of the real ones (mean, standard deviation, skewness, kurtosis) and also a statistical evaluation of the distribution of the errors, where errors have been calculated as the difference of real data and the corresponding simulated ones.

3. RESULTS

3.1 Hyperparameters tuning and calibration results

The first step of evaluation of the work focused on the hyperparameters tuning of the four regressors. As described in subsection 2.3, MLR has been tuned by testing 4 hyperparameters, DT has been tuned by testing 11 hyperparameters and RF has been tuned by testing 17 hyperparameters. In Figure 2 the authors report the boxplots of the distributions of the MAE for the three regressors considered. MLR has a very narrow distribution of MAE values: the minimum value is 1.37 dBA, and the maximum one is 1.39 dBA. DT has a value of MAE ranging from 1.17 dBA to 1.49 dBA. RF has a minimum MAE value of 1.01 dBA and a maximum of 1.32 dBA.

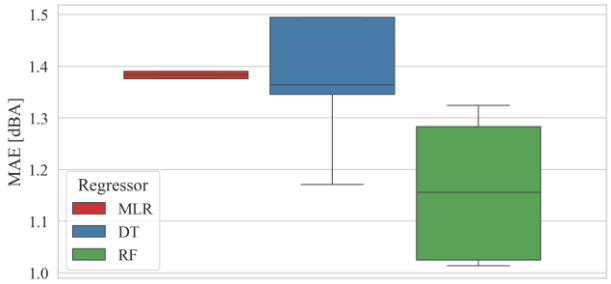


Figure 2: Boxplots of the MAE distributions of all the tested hyperparameters combinations, for all regressors. The solid line is the median of the distribution.

Figure 2 implies an important consideration to be done when calibrating a model since it clarifies how the accuracy of the regressors cannot be considered as a single value coming from a single procedure, but it must be interpreted after taking account of the hyperparameters' tuning. If working on RF, as an example, an output having MAE of 1.3 dBA could be considered as a good value since both MLR and DT have higher average values, but carefully analysing the results of hyperparameters' tuning, it's observed that the final result could be furtherly improved with a better hyperparameters' combination, having an even lower MAE value.

Table 1 reports the best hyperparameters' combination for each regressor as a function of the MAE and mean residuals. The residual is computed as the difference between the measured and the simulated noise levels in the tuning/calibration phase. Consequently, the negative values of the mean residuals found in Table 1 show a slight overestimation of all the models.

Since the tuning has been performed by testing the various hyperparameters' combinations on the same 80% of the overall dataset selected for the calibration, the results of this process provided the final calibration of each regressor.

Table 1: Results of the best hyperparameters' tuning combination for each regressor, in terms of mean error and MAE

Regressor	Mean Error [dBA]	MAE [dBA]
MLR	-0.05	1.38
DT	-0.04	1.17
RF	-0.08	1.01

3.2 Simulation outputs: validation and error analysis

After the regressors tuning and calibration phase, the validation step of the regressors themselves has been made. A due premise to this subsection is that until now authors used the MAE metric as the main indicator for the tuning and calibration phase. The strategy of using MAE as an indicator of the calibration phase has been used to drive the choice of the best hyperparameters setting for each calibration since it is a concise and easy-to-use indicator. In contrast, the validation process has been pursued more in detail, comparing the distributions of real and simulated data, and performing on them statistical investigations. Specifications of such analysis are presented below.

After the hyperparameters selection has been done, the regressors have been fed with input validation data and the final outputs have been collected and compared with the measured levels. Table 2 reports the main statistical descriptors of the measured and simulated equivalent sound level distributions for each regressor, which are plotted in Figure 3.

Table 2. Main statistical descriptors of measured and simulated levels distributions.

	Mean [dBA]	Median [dBA]	St.dev. [dBA]	Skew	Kurt
Measured	72.04	72.52	2.16	-2.13	4.87
MLR	72.09	72.03	0.88	0.49	0.06
DT	72.09	72.41	1.89	-1.50	4.42
RF	72.13	72.38	1.40	-1.79	5.09

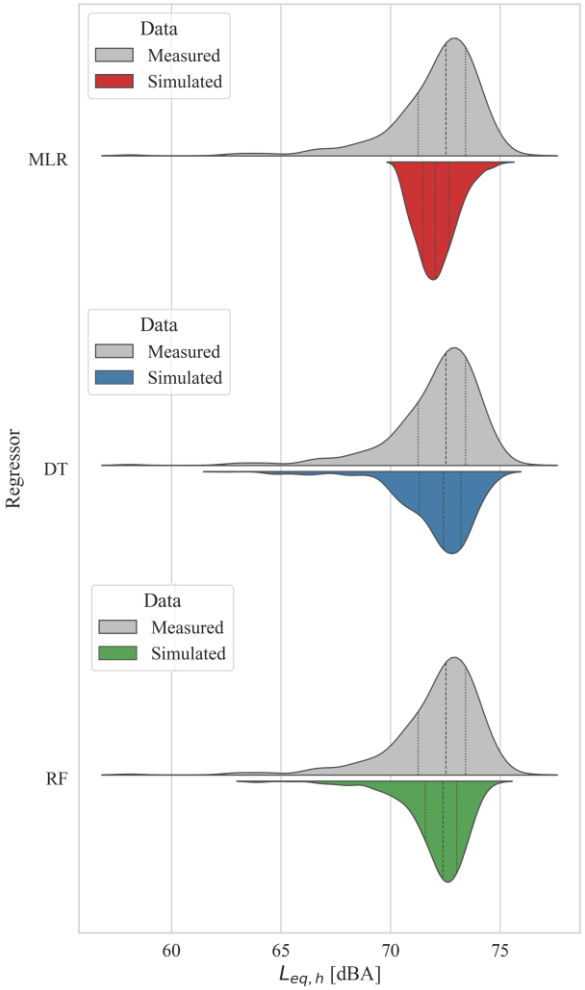


Figure 3. Distributions of measured and simulated equivalent sound levels, calculated by each regressor. The dashed line is the median and the dotted lines are the 1st and 3rd quartile.

At first glance, all the regressors give as output simulated data close to the measured ones, meaning that the hyperparameters' tuning process performed before the calibration indeed selected a good combination for each regressor. Validation data present a mean value of 72.04 dBA, a median of 72.52 dBA, a standard deviation of 2.16 dBA, a skewness of -2.13 (due to the equivalent levels on the left tail of the distribution), and a kurtosis index of 4.87. As for the central tendency metrics, all the regressors perform well, especially with the mean values of the distributions being very close to the measured ones. Median values show a small underestimation of MLR compared to the other regressors.

As for the standard deviations, it is interesting to note how the three regressors' distributions present a value lower than the measured levels one, meaning that no regressor can fully and properly simulate the dispersion of the real data, especially in the tails of the distribution. This behaviour reflects also on the skewness and kurtosis indexes for MLR, which are significantly different from those related to the distribution of the measured levels. More specifically, MLR tends to stabilize around zero skewness and kurtosis indexes. In contrast, DT and RF have higher values (in absolute) for both indexes, close to those of the distribution of the measured levels. MLR, then, can simulate data whose mean value is very close to the real one but misses the shape information of the simulated data distribution. DT and RF also catch the central tendency of the distribution but, in addition, they can also depict the left tail of the distribution, even if not perfectly.

A deeper analysis of the results comes from the investigations of the errors, defined as measured minus simulated equivalent levels in each entry of the dataset (each 1-hour slot), whose distributions are reported in Figure 4. The main statistical descriptors of error distributions for each regressor are resumed in Table 3.

Shapes of the error's distributions are very similar for the three regressors and all have mean values very close to zero (see Table 3). This aspect means that all the chosen regressors can simulate the equivalent noise levels in a good way and that the models aren't affected by any systematic underestimation or overestimation error. From Table 3 it also appears the Gaussian shape of the errors' distribution, since the Shapiro-Wilk index [23], measuring the normality of the distribution, is very high (0.91 for all the regressors).

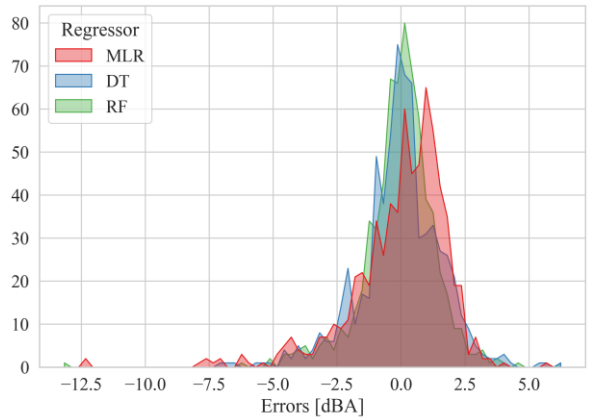


Figure 4. Distributions of the errors according to the regressor used for simulation.

Table 3. Main statistical descriptors of the error distributions for all the regressors.

	MLR	DT	RF
Mean [dBA]	-0.05	-0.04	-0.08
Median[dBA]	0.32	0.02	0.06
St. deviation [dBA]	1.92	1.62	1.48
Kurtosis index	6.32	2.10	10.72
Skewness index	-1.75	-0.42	-1.46
Shapiro-Wilk index	0.89	0.97	0.91
Bowley-Youle index	-0.15	0.00	-0.09

The Bowley-Yule test [24], used to estimate the symmetry of the distributions, is also good since it is very close to zero for all three regressors. Errors of the regressors, then, are peaked to zero and are symmetrically distributed on both negative and positive values, ensuring the stochastic nature of the errors themselves.

A final investigation comes from the visualization of Figure 5, where the scatterplots of measured (on *x*-axis) versus simulated (on *y*-axis) values of $L_{eq,h}$ for all the regressors are reported. The solid red diagonal line represents the ideal 1:1 agreement, whereas the red dashed lines indicate a ±2 dBA deviation, which does not have any statistical validity but it's a commonly accepted range in environmental noise modelling.

As for MLR (top plot), one of the most striking aspects of the model's behaviour is that it does not predict values lower than approximately 70 dBA. The same aspect was observed also in Figure 3, looking at the missing left tail. This result suggests a limitation in its ability to capture the full range of noise levels, possibly due to the linear nature of the model. If the dataset includes lower measured values, the model might be constrained by the way predictor variables interact, leading to an artificial threshold effect. Additionally, the data points are tightly clustered, with a tendency to underestimate higher values, as confirmed by the median simulated level in Table 2 and median error in Table 3, reinforcing the idea that MLR struggles with nonlinear relationships in the data.

The DT model (centre plot) exhibits a much wider scatter, with significant deviation from the 1:1 line. Unlike MLR, it does predict lower values but does so with higher dispersion. The large spread outside the ±2 dBA range reinforces the known tendency of decision trees to create rigid, locally optimized models that may not perform well on new data [25].

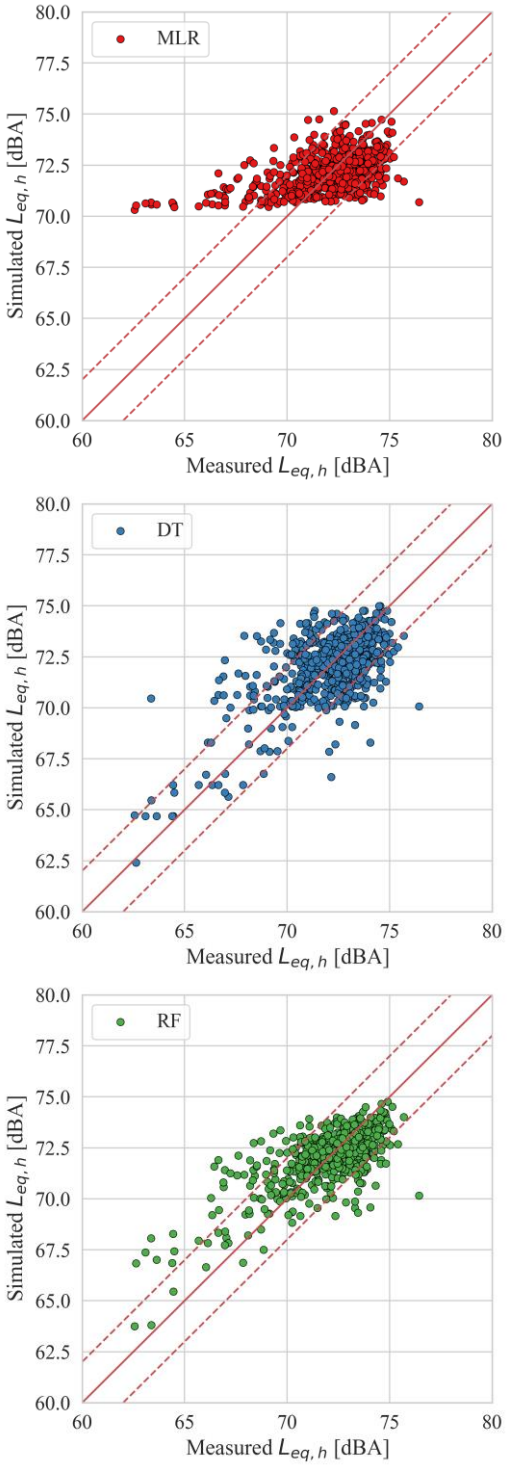


Figure 5. Scatterplots of simulated vs measured data for each regressor

As for the RF model (bottom plot), it provides a more balanced spread of predictions across the range of measured values, without the artificial cut-off seen in MLR. The alignment with the 1:1 line is generally better, although some dispersion is still evident, particularly at the extreme ends of the scale. This suggests that while RF effectively captures nonlinear dependencies, it may still struggle with rare or extreme cases. However, the lower variance compared to DT and the statistics resumed in Table 3 indicate a better ability to generalize.

From a comparative standpoint, the RF model appears to be the most robust, showing good predictive capability across the measured range while maintaining relatively low variability. The MLR model, despite being a simpler approach, fails to predict values below 70 dBA, which raises concerns about its suitability for datasets with a wider dynamic range. Meanwhile, the DT model, though flexible, introduces higher variability.

For a better understanding of such results, the authors calculated the amount of data lying between the ±2 dBA diagonal dashed lines. Table 4 resumes the percentage of data falling within and outside the mentioned interval. RF has the greater amount of data within the ±2 dBA interval, confirming the above comments about its performances.

Table 4. Percentage of data within the ± 2 dB area for each regressor.

	MLR	**DT**	**RF**
Data within ± 2 dBA lines	81.06%	80.91%	87.96%

4. CONCLUSIONS

In this paper three different regressors have been tuned, calibrated and validated on a measured dataset of equivalent continuous sound levels available in literature, to simulate the road traffic noise levels of an extra-urban road. The calibration approach of the regressor is a classical one, where a section of the whole dataset (80%) has been dedicated to the calibration and the remaining part (20%) to the validation of the models. Before the calibration, the regressors were tuned with fine hyperparameter tuning, which revealed the best combination of each regressor to get the lower MAE.

When validating on the dedicated portion of the dataset, outputs show how the simulated values with all regressors fall in a reasonable range of validity. The three regressors seem to get equivalent results when considering central tendency metrics. Anyway, differences exist and can be highlighted by looking at the shape of the distributions of the simulated data, which are slightly different from the measurements' distribution.

MLR is not able to depict the data on the tails, completely missing then noise situations far from the average ones and exhibiting an artificial threshold effect around 70 dBA. For this reason, concerns have been raised regarding its suitability for datasets exhibiting a broader dynamic range, even if the MLR model respects the parsimony principle, with a low number of parameters. DT, while sufficiently accurate, introduces slightly higher variability in the error. The RF model appears to be the most precise, exhibiting good performances in the entire range of measurements and keeping relatively low error mean and dispersion.

In conclusion, machine learning regressors seem to provide a valid option, besides the already existing models, to simulate noise traffic values, starting from the very same input parameters. The future steps of this work will be surely focused on improving the analyses performed on the regressors and including additional models, as well as testing all the regressors on new datasets, possibly related not only to highway road traffic noise data but also urban levels. This will shed light on the usability of such an approach in more complex scenarios, in which several sources may contribute to the environmental noise levels.

5. ACKNOWLEDGMENTS

This study was carried out within the MOST – Sustainable Mobility National Research Center and received funding from the European Union Next-GenerationEU (PIANO NAZIONALE DI RIPRESA E RESILIENZA (PNRR) – MISSIONE 4 COMPONENTE 2, INVESTIMENTO 1.4 – D.D. 1033 17/06/2022, CN00000023). This manuscript reflects only the authors' views and opinions, neither the European Union nor the European Commission can be considered responsible for them.

6. REFERENCES

[1] A. Mehrotra, S.P. Shukla, A.K. Shukla, M.K. Manar, S.K. Singh, and M. Mehrotra: "A Comprehensive Review of Auditory and Non-Auditory Effects of Noise on Human Health", *Noise and Health*, Vol 26. no. 121, pp. 59-69, 2024.

[2] D. Hugh, and I. Van Kamp: "Noise and cardiovascular disease: A review of the literature 2008-2011", *Noise and Health* 14.61 pp. 287-291, 2012.

[3] European Commission. Directive 2002/49/EC Relating to the Assessment and Management of

Environmental Noise; European Commission: Brussels, Belgium, 2002.
[4] World Health Organization. Environmental noise guidelines for the European region. Regional Office for Europe: World Health Organization; 2018.
[5] R.A. Hood: "Accuracy of calculation of road traffic noise". *Applied Acoustics*, vol. 21 no. 2, pp. 139-146, 1987.
[6] K. Heutschi: "SonRoad: New Swiss road traffic noise model", *Acta Acustica united with Acustica*, vol. 90, no. 3, pp. 548-554, 2004.
[7] G. Dutilleux, J. Defrance, D. Ecotière, B. Gauvreau, M. Bérengier, F. Besnard, and E.L. Duc: "NMPB-routes-2008: The revision of the french method for road traffic noise prediction", *Acta Acustica united with Acustica*, vol. 96, no. 3, pp. 452-462, 2010.
[8] S. Sakamoto: "Road traffic noise prediction model "ASJ RTN-Model 2013": Report of the Research Committee on Road Traffic Noise." *Acoustical Science and Technology* vol. 36, no. 2, pp. 49-108, 2015.
[9] Bundesminster FV., Wohnungswesen B.: "Richtlinien für den Lärmschutz an Straßen (RLS 90)", Verkehrsblatt: Amtsblatt des Bundesministers für Verkehr der Bundesrepublik Deutschland (VkBl) no. 7, 1990
[10] G. Watts: "Harmonoise prediction model for road traffic noise", Trans. Res Lab, 2005.
[11] C. Guarnaccia, A. Mascolo, P. Aumond, A. Can, and D. Rossi: "From early to recent models: A review of the evolution of road traffic and single vehicles noise emission modelling", *Current Pollution Reports*, vol. 10, no. 4, pp. 662-683, 2024.
[12] S. Kephalopoulos, M. Paviotti, F. Anfosso-Lédée, "Common noise assessment methods in Europe (CNOSSOS-EU)", *Publications Office of the European Union*, 2012.
[13] A. Kok, A. van Beek, "Amendments for CNOSSOS-EU: description of issues and proposed solutions", *RIVM Lett Rep*, 2019.
[14] L. Bravo-Moncayo, J. Lucio-Naranjo, M. Chávez, I. Pavón-García, and C. Garzón: "A machine learning approach for traffic-noise annoyance assessment", *Applied Acoustics*, vol. 156, pp. 262-270, 2019.
[15] M. Ali Khalil, K. Hamad, and A. Shanableh: "Developing machine learning models to predict roadway traffic noise: An opportunity to escape conventional techniques", *Transportation Research Record*, vol. 2673, no. 4, pp. 158-172, 2019.
[16] M. Fallah-Shorshani, X. Yin, R. McConnell, S. Fruin, and M. Franklin: "Estimating traffic noise over a large urban area: An evaluation of methods", *Environment International*, vol. 170, 107583, 2022.
[17] K. Marciniuk, and B. Kostek: "Machine learning applied to acoustic-based road traffic monitoring", *Procedia Computer Science*, vol. 207, pp. 1087-1095, 2022.
[18] D. Singh, P. Kaler, I. Lyall, A. Singh, and H. S. Pannu: "Traffic noise prediction using machine learning and Monte Carlo data augmentation: a case study on the Patiala city in India", *Journal of Physics: conference series*, vol. 2162, no. 1, 012021, 2022
[19] D. Singh, A.B. Francavilla, S. Mancini, and C. Guarnaccia: "Application of machine learning to include honking effect in vehicular traffic noise prediction", *Applied Sciences*, vol. 11, no. 13, 6030, 2021.
[20] X. Zhang, H. Kuehnelt, and W. De Roeck, "Pass-by noise modelling applying machine learning", in *Proc. of the Forum Acusticum*, pp. 2251-2258, 2020.
[21] B. Gauvreau: "Long-term experimental database for environmental acoustics", *Applied Acoustics*, vol. 74, no.7, pp. 958-967, 2013.
[22] D. Rossi, A. Mascolo, and C Guarnaccia: "Calibration and validation of a measurements-independent model for road traffic noise assessment", *Applied Sciences* vol. 13, no. 10, 6168, 2023.
[23] S.S. Shapiro, and M.B. Wilk: "An analysis of variance test for normality (complete samples)" *Biometrika*, vol. 52, no. 3/4, pp. 591-611, 1965.
[24] G. U. Yule: "Revision of "Elements of Statistics" by A. L. Bowley", *The Economic Journal*, vol. 31, no. 122, pp. 220-224, 1921.
[25] L. Breiman, J.H. Friedman, R.A. Olshen, C.J. Stone: *Classification and Regression Trees*. CRC Press, 1984.

DOI: 10.61782/fa.2025.0940

FORUM ACUSTICUM EURONOISE 2025

URBAN SOUND CLASSIFICATION ON THE EDGE: EXPLORING THE ACCURACY-EFFICIENCY TRADE-OFF

Lion Cassens[1*] **Maarten Kroesen**[1] **Simeon Calvert**[2]
Sander van Cranenburgh[1]
[1] Department of Engineering Systems & Services, Delft University of Technology, the Netherlands
[2] Department of Transport & Planning, Delft University of Technology, the Netherlands

ABSTRACT

Sound source classification is a valuable addition to noise monitoring, providing `further insights into local soundscapes. For privacy preservation, this classification often must be conducted on the edge, i.e., in real time on noise sensors. This puts constraints on the size and complexity of the classification models that can be used. Furthermore, there is a trade-off between accuracy and efficiency, which needs to be balanced on battery or solar powered sensors. However, little is known about this trade-off under consideration of constraints imposed by such sensors. In this paper, we explore the scope of sound classification models that can run efficiently on low-cost sound sensors. Specifically, we investigate the Pareto frontiers between model accuracy and computational complexity, providing insights into the trade-off necessary for deploying such models on very constrained hardware. Building on these findings, we train new classification models optimized for edge devices. The models are trained on publicly available audio samples and a new Dutch Urban Sounds dataset specifically collected to enhance the accuracy of sound source classification in urban environments. The models and implementation are open source, enabling researchers and practitioners to adopt, adapt, and build upon our work.

[*]***Corresponding author***: *l.cassens@tudelft.nl.*
Copyright: *©2025 Cassens et al. This is an open-access article distributed under the terms of the Creative Commons Attribution 3.0 Unported License, which permits unrestricted use, distribution, and reproduction in any medium, provided the original author and source are credited.*

Keywords: *environmental sound classification, edge AI, convolutional neural network*

1. INTRODUCTION

Various studies have shown the importance of perception to explain the human response to the urban soundscape[1]. Annoyance, as well as recreational effects of the sound environment, depend not only on loudness but also on various other indicators. One important factor is the presence or absence of different sound sources. Bird song may be perceived by most as pleasant, while traffic noise is more likely to create a negative stress response. Machine learning models can be used to predict the presence of such sources. For privacy purposes, it is often necessary to run such models on a sensor, which requires small and efficient models.

While various papers propose such small models, few consider the end-to-end performance on edge devices (e.g., execution time including preprocessing), and practical constraints of microprocessors (such as limited for certain deep learning architectures).

In this paper, we define various models and analyze the trade-off between predictive performance and on-device efficiency. This trade-off is very important for battery or solar-powered sensors, as more efficient models result in lower energy consumption. Lastly, three Pareto optimal models along this trade-off are identified.

2. METHODS

The study follows the following steps: potential model candidates are created based on constraints imposed by microcontrollers. Then, these models are pretrained on public datasets and finetuned to a new dataset on Urban

Dutch Sounds. This dataset is then used to measure the predictive performance of all models. The on-device execution time of all models is measured as a proxy for energy efficiency. Lastly, Pareto optimal models are identified along the trade-off of predictive performance and efficiency.

2.1 Microcontroller constraints

Microcontrollers are energy and cost-efficient and, therefore, well-suited for low-cost or energy-constraint noise sensors. Yet, these low-memory devices impose several hardware and software limitations for machine learning models on the edge.

One difference compared to a desktop computer is the limited memory. Microcontrollers typically have less than 8MB RAM, which needs to be shared between sound source classification and all other tasks. Therefore, the model weights and any intermediate results and variables must not occupy more than a few MB of memory. Another difference is the limited processing speed, which is important because edge AI requires sound to be processed in real time. Thus, the classification time for a 3-second audio sample must not exceed 3 seconds.

Besides hardware constraints, there are further limitations in the support and optimization of certain ML operations. While it is theoretically possible to implement and optimize all required operations from scratch, this requires extensive knowledge and effort, which is often ignored in literature proposing very small ESC models. For this analysis, we constrain the choice of machine learning models to those that are supported and optimized for microcontrollers by TensorFlow Lite Micro. This excludes Transformer models and Long Short-Term Memory models.

Lastly, resampling audio is computationally expensive on most microcontrollers. We assume that the proposed models will run alongside a dB(A) calculation, which benefits greatly from a high sample rate. Therefore, all proposed models process audio sampled at 48 kHz.

2.2 Model candidates

Based on the constraints imposed by hardware and software, a total of nine convolutional neural network (CNN) candidates are evaluated. Specifically, three CNN architectures with varying numbers of parameters are combined with three Mel spectrogram sizes: 32, 64, and 104 Mels. All Mel spectrogram sizes are computed from short-time furrier transforms (STFT) with a 1024 sample window and hop rate. Table 1 lists the three CNN architectures.

Table 1. Layers and number of filters for all three model architectures. MaxPooling2D (2x2) follow each Conv2D but were omitted. Flatten and Dropout layers were also omitted from the table.

	Number of filters in Conv2D and units in dense layer		
Layer	**Small**	**Medium**	**Large**
Conv2D (3x3)	16	32	64
Conv2D (3x3)	16	48	64
Conv2D (3x3)	32	64	64
Conv2D (3x3)	32	64	96
Conv2D (3x3)	48	64	128
Dense	64	128	128
Dense (output)	11	11	11

2.3 Datasets

All models were pretrained on public datasets and then finetuned and evaluated on recently collected sound samples from the Netherlands.

To cover a variety of sounds, samples from the following datasets have been combined for the pretraining of all models: Google's AudioSet[2], ESC-50[3], UrbanSound8K[4], SONYC-UST[5] and Amsterdam Sounds Serval[6].

Some samples do not contain any of the selected sound classes but have been included to ensure that other audio sources are not mistaken for the sources considered here (i.e., to reduce false positives).

2.3.1 Dutch Urban Sounds

In addition to the existing datasets, a novel dataset has been collected to improve the prediction performance of sound source classification in an urban context. These 3-second samples have been collected in the Dutch cities Amsterdam and Leiden. Ideally, the microphone used for training data collection should be the same microphone that will be used in a noise sensor running the model. Otherwise, differences in microphones might bias the model predictions. This dataset has been recorded with a TDK ICS-434 MEMS microphone, which is well-suited for noise sensors.

Finetuning the candidate models to these samples is expected to improve real world accuracy, as publicly available datasets such as Google AudioSet can have poor data quality and do not necessarily reflect real world conditions. Other datasets such as SONY-UST are collected in a realistic setting, but specific to the American context.

Table 2. Audio datasets and occurrences of relevant sound classes per dataset.

	AudioSet	SONY-UST	Urban Sound 8K	ESC-50	Amsterdam Serval	Dutch Urban Sounds	Total
Samples	33,220	18,509	8,730	2,000	1,629	1,727	65,815
Vehicle	7,790	10,025	1,000	40	863	405	20,123
Honking	2,043	2,382	428	40	132	18	5,043
Aircraft	2,811	-	-	80	-	40	2,931
Siren	2,443	1,502	929	40	-	190	5,104
Human	10,310	7,254	1,000	40	634	585	19,823
Bark	843	1,114	999	40	-	61	3,057
Bird song	2,485	-	-	40	-	271	2,796
Church Bell	1,089	-	-	40	-	52	1,181
Music	6,886	1,627	1,000	-	-	133	9,646
Wind	2,322	-	-	40	-	457	2,819
Rain	1,145	-	-	40	-	104	1,289

Table 2 shows the number of samples per sound class for each dataset. AudioSet, SONY-UST, and Dutch Urban Sounds are multilabel datasets, meaning each sound class can occur more than once per sample.

2.4 Evaluation procedure

All models are pretrained on the mentioned public datasets. Then, each model is finetuned with 5-fold cross-validation on our Dutch Urban Sounds dataset. This dataset is imbalanced (i.e., some sound classes are sparser than others). Therefore, we evaluate the prediction performance using macro precision, recall, and F1. Micro metrics consider all samples equally, while macro metrics consider all sound classes equally. The latter is more suitable for this imbalanced dataset because the real-world class distribution likely differs from the dataset's distribution. To balance precision and recall, the macro F1 score is used as the final indicator of model performance.

An optimal model not only needs to be accurate but also computationally efficient. Slower models with longer execution times require stronger hardware and lead to an increased energy consumption. Therefore, an optimal model is always a trade-off between prediction performance (e.g., accuracy or F1 score) and efficiency. We measure efficiency as the total time to run the prediction pipeline on the sensor (execution time). The pipeline contains preprocessing and the ML inference itself. The on-device execution time is also a good proxy for energy consumption.

Measuring both prediction performance and efficiency allows us to find models that are Pareto optimal. A model is considered Pareto optimal if no other model performs better in one metric (e.g., F1 score or efficiency) without performing worse in the other, meaning it offers an optimal trade-off between the two.

3. RESULTS AND DISCUSSION

Table 3 lists macro precision, recall and F1 scores over all classes. As discussed, the macro F1 scores are used to determine the best predicting model.

The medium and large 104 Mel models achieve the same macro F1 scores. This may be caused by the imbalanced and relatively small finetuning dataset, which may lead to overfitting of large models. The worst model based on macro F1 is the small 32 Mel model.

Table 3. Macro precision, recall, and F1 scores for all model candidates.

Model		Macro		
Architecture	**Mels**	**Precision**	**Recall**	**F1**
Small	**32**	74.41%	52.38%	59.96%
Small	**64**	76.89%	55.80%	63.41%
Small	**104**	73.34%	54.30%	61.38%
Medium	**32**	70.38%	55.82%	61.90%
Medium	**64**	73.30%	56.17%	62.52%
Medium	**104**	76.27%	58.46%	65.69%
Large	**32**	70.33%	55.99%	61.97%
Large	**64**	75.04%	58.23%	64.77%
Large	**104**	76.07%	59.05%	65.69%

Prediction performance alone, however, is not sufficient to identify an optimal model for resource constraint edge AI. Therefore, we now discuss the on-device speed of each model.

The execution time refers to the overall time required to make a sound source prediction on the sensor. In this case, time was measured on an ESP32-S3 running at 240 MHz. Continuous monitoring of soundscapes requires the execution time for processing of n-seconds audio to not surpass n-seconds. In this case, each audio sample is 3 seconds long. Table 4 shows that all but the Large 104 Mel models fulfill the real-time requirement. The table further shows that architecture size is more important than input size (which depends on the number of Mels) for the execution time of the candidate models. Preprocessing (creation of Mel spectrograms) poses a significant overhead for smaller models but less so for larger models. This is due to the computational expense of short-term furrier transforms (STFT), which is independent of the number of Mels. Only the conversion to Mels varies but is less computationally demanding than STFT.

Table 4. Execution time (including preprocessing and ML inference) for the model candidates.

Model		Execution time (ms)		
Architecture	**Mels**	**Preprocessing**	**Inference**	**Total**
Small	**32**	107	79	186
Small	**64**	113	155	268
Small	**104**	118	250	368
Medium	**32**	107	239	346
Medium	**64**	113	476	589
Medium	**104**	118	759	877
Large	**32**	107	1,040	1,147
Large	**64**	113	2,069	2,182
Large	**104**	118	3,844	3,962

After considering predictive performance and efficiency (represented by execution time) individually, we now discuss the trade-offs between both metrics.

The ideal trade-off depends on the specific use case and design requirements. Therefore, there is no universally best trade-off. Instead, we look at multiple Pareto optimal models along this trade-off, which form the Pareto front.

Figure 1 compares the total execution time and Macro F1 scores of all models. Three models are Pareto optimal, namely the small architecture with 32 Mels, the small architecture with 64 Mels, and the medium architecture with 104 Mels. The large architecture with 104 Mels does not fulfill the requirements of a Pareto optimal model because the medium architecture with 104 Mels has a better execution time for the same Macro F1 score. The remaining models are also inferior to at least one of the Pareto optimal models and can be rejected.

The three Pareto optimal models contain between 46,379 and 281,147 model weights and occupy between 58 and 296 KB of memory after quantization.

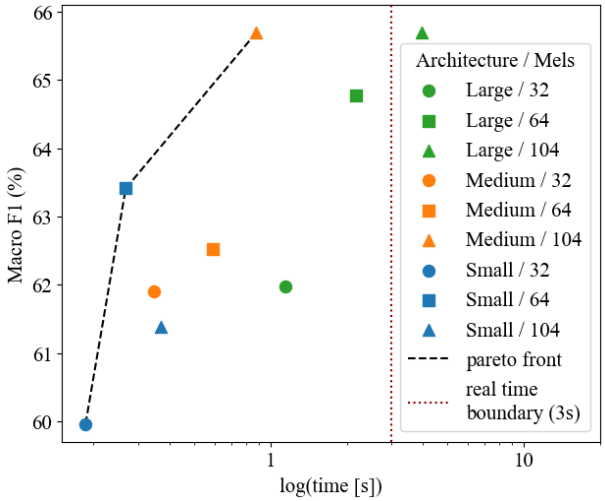


Figure 1. Total execution time and Macro F1 scores of all models and their Pareto front.

For training similar models on other datasets, it is recommended to repeat the Pareto analysis as the model candidates may perform differently depending on the dataset characteristics.

To provide a reference point for model performance, we compare the models with the state-of-the-art Audio Spectrogram Transformer[7] (AST) after also finetuning it on our Dutch Urban Sounds dataset. The AST reached a Macro F1 score of 74.87%. While this surpasses the best-performing model of this paper, the AST is also significantly larger (86,197,259 parameters). The finetuned AST is more than 300 times bigger than our largest Pareto optimal model and unsuitable for microprocessors.

Further research is necessary to compare our Pareto optimal models with other approaches, such as a training pipeline proposed by Mohaimenuzzaman[8].

4. CONCLUSION

Microprocessors impose various practical constraints on the choice of machine learning models due to hardware limitations or missing support and optimization for various deep learning architectures. This currently prohibits the use of Transformer and LSTM models with ML libraries such as TensorFlow Lite Micro.

Therefore, nine convolutional neural networks were compared regarding the trade-off between model performance (measured via Macro F1 scores) and efficiency (measured as total execution time). The most complex model did not fulfill real-time requirements but was also not found to be optimal. Instead, three Pareto-optimal models have been identified, each representing a different optimal trade-off between F1 score and efficiency.

The analysis shows the importance of considering efficiency in addition to model performance, as all six non-optimal models would lead to either more computational cost or less accurate sound source predictions. All three Pareto optimal models are openly available on GitHub[1] and can be used on microcontrollers supported by TensorFlow Lite Micro.

5. ACKNOWLEDGEMENTS

The research was funded by the TU Delft AI Initiative. The sound sample collection in Amsterdam was supported by the Responsible Sensing Lab of the Amsterdam Institute for Advanced Metropolitan Solutions.

6. REFERENCES

[1] Alvarsson, J.J., Wiens, S., Nilsson, M.E.: Stress Recovery during Exposure to Nature Sound and Environmental Noise. International Journal of Environmental Research and Public Health. 7, 1036–1046, 2010.

[2] Gemmeke, J.F., Ellis, D.P.W., Freedman, D., Jansen, A., Lawrence, W., Moore, R.C., Plakal, M., Ritter, M.: Audio Set: An ontology and human-labeled dataset for audio events. In: 2017 IEEE International Conference on Acoustics, Speech and Signal Processing (ICASSP). pp. 776–780, 2017.

[3] Piczak, K.J.: ESC: Dataset for Environmental Sound Classification. In: Proceedings of the 23rd ACM international conference on Multimedia. pp. 1015–1018. Association for Computing Machinery, New York, NY, USA, 2015.

[4] Salamon, J., Jacoby, C., Bello, J.P.: A Dataset and Taxonomy for Urban Sound Research. In: Proceedings of the 22nd ACM international conference on Multimedia. pp. 1041–1044. ACM, Orlando Florida USA, 2014.

[5] Cartwright, M., Cramer, J., Mendez, A.E.M., Wang, Y., Wu, H.-H., Lostanlen, V., Fuentes, M., Dove, G., Mydlarz, C., Salamon, J., Nov, O., Bello, J.P.: SONYC-UST-V2: An Urban Sound Tagging Dataset with Spatiotemporal Context, http://arxiv.org/abs/2009.05188, 2020.

[6] Amsterdam Sounds Serval on GitLab, https://gitlab.waag.org/lodewijk/amsterdam-sounds-serval/-/tree/master

[7] Gong, Y., Chung, Y.-A., Glass, J.: AST: Audio Spectrogram Transformer, 2021.

[8] Mohaimenuzzaman, M., Bergmeir, C., West, I., Meyer, B.: Environmental Sound Classification on the Edge: A Pipeline for Deep Acoustic Networks on Extremely Resource-Constrained Devices. Pattern Recognition, 2023.

[1] https://github.com/lioff/fa-euronoise-2025-urban-sound-classification

DOI: 10.61782/fa.2025.0167



FORUM ACUSTICUM
EURONOISE 2025

AUTOMATIC DETECTION OF ROADWAY NOISE USING AI CLASSIFIERS AND SOUND LEVEL FEATURES

Erwann Betton-Ployon[1,2*] **Abbes Kacem**[1] **Jérôme Mars**[2] **Nadine Martin**[3]
[1] ACOUSTB, Saint-Martin-d'Hères, 38400, France
[2] Universite Grenoble Alpes, CNRS, Grenoble-INP, GIPSA-Lab, Grenoble, 38000, France
[3] ASTRIIS, Chambery, 73000, France

ABSTRACT

Noise management has become a major public health issue over several decades. To initiate protective measures against noise overexposure, it is essential to accurately evaluate annoyance. This involves detecting sound sources, their emission durations and associated sound levels. Among commonly encountered sources, road traffic is a prominent contributor to noise pollution, according to health organisation reports. This paper presents an automatic roadway noise detection system. The proposed method combines event detection and classification through a multi-layer approach. Sound event detection is ensured by distinct units. First, a sliding window enables signal preclassification by identifying specific patterns on its mel-spectrogram. Simultaneously, sound level features are used to detect prominent periods, often marking off sound events. Both units combined and sharpened provide detection of the most relevant sound events over the acoustic signal. Precise classification is issued by an additional AI model, dedicated to recognising roadway noise among various vehicle types. Our system operates in diverse soundscapes while maintaining a high level of roadway noise detection accuracy. It permits an automatic estimation of roadway noise contribution, which corresponds to equivalent sound level when roadway noise prevails. This estimation closely aligns with manual assessments from experts, validating the proposed system relevance.

Keywords: *roadway noise, sound event detection, acoustic signal processing, noise monitoring*

***Corresponding author**: *erwann.betton-ployon@egis-group.com.*

***Copyright**: ©2025 Erwann Betton-Ployon et al. This is an open-access article distributed under the terms of the Creative Commons Attribution 3.0 Unported License, which permits unrestricted use, distribution, and reproduction in any medium, provided the original author and source are credited.*

1. INTRODUCTION

Over the past decades, noise from transportation has emerged as a significant public health issue. Several World Health Organization reports point at induced health issues [1]. The European Union indicates that "approximately 1 in 5 people [...] are exposed to unhealthy levels of road traffic noise" among European citizens [2]. In such context, it is essential to provide adequate solutions to reduce noise overexposure. This involves first, a precise diagnosis of the impacted areas, by estimating roadway noise contribution. Roadway noise contribution corresponds to the equivalent sound level during periods of roadway noise prevalence over other sound sources. It is often evaluated thanks to a manual detection of roadway noise over acoustic signals. However, this is a tedious and time-consuming task. With the advent of Machine Learning and automatic Sound Event Detection models, a new perspective appears to automate this process. In that context, an automatic approach is proposed in this paper, through a three-staged method designed to handle long-term acoustic signals and separate roadway from non-roadway noise periods. Its detailed functioning is presented (Section 2) before discussing its performances in several contexts (Section 3) and concluding on various development perspectives.

2. METHODOLOGY

The presented process addresses the issue of automatic roadway noise contribution estimation, which requires the identification of roadway noise prevalence periods over other sound sources. The proposed method relies on successive units, presented in Fig. 1. *YAMNet sound ensemble preclassification* and *Final classification* operate at different levels to classify sounds. They are enhanced by two processing units, refining event detection and boundary definition thanks to the evolution of sound level.

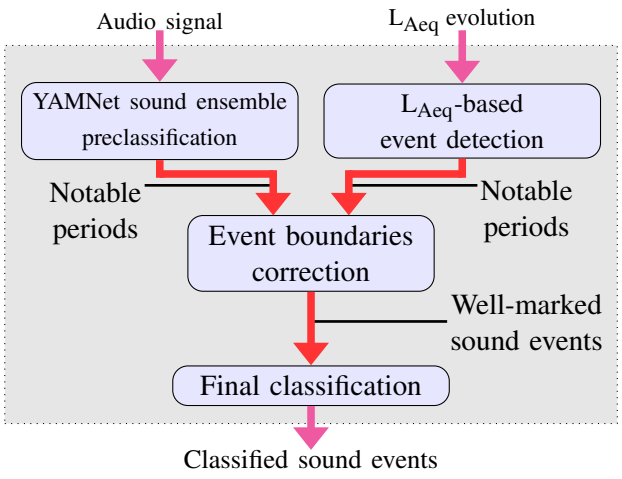


Figure 1. Description of the proposed automatic roadway noise detection method.

The first stage involves a coarse detection process, which utilizes two parallel analyses: one classification over the raw audio signal and another event detection system relying on sound level evolution. In the second stage, the *Event boundaries correction* algorithm processes the detected "Notable periods" from both units. This step provides a clear delimitation of each detected event, defining accurate start and end points, and identifying the monophonic or polyphonic nature of the event. In the last stage, a classifier processes each refined event to accurately classify the prominent sound source, determining whether it corresponds to roadway noise or not. These stages are now discussed in three dedicated subsections (2.1 to 2.3).

2.1 Long-term signal preclassification

This subsection details the two upper units of Fig. 1. The outcome of the open source environmental acoustic classifier YAMNet is exploited (section 2.1.1). In parallel, another algorithm uses A-weighted equivalent sound level (L_{Aeq}) evolution to detect singular events (section 2.1.2).

2.1.1 YAMNet sound ensemble preclassification

After the recording of a long-term acoustic signal, a broad preclassification stage helps understanding the various elements that form the complete soundscape. This analysis is carried out with a sliding window (0.96 s, 50%-overlap) over the full audio signal, to get an objective first view of the prevalent sources. Open-source environmental acoustic classifier YAMNet [3], developed by Google in 2020, was trained on more than 2 millions of audio segments, split into 521 labels [4]. As a CNN replicating MobileNet v1 architecture, it relies on mel-spectrogram representation of the audio signal [3]. Thus, characteristic spectral patterns are identified over the signal and associated with sound sources. However, data imbalance and label imprecision make the classifier unreliable in complex soundscapes. It is better to interpret its prediction as a hint on the involved sounds. Thus, several sound ensembles are defined: *Vehicles, Animals, Music or Speech, Alarms, Loud construction sounds* and *Background noise*. Each initial YAMNet class is associated with one of our sound ensembles. We look into the predicted sound ensembles instead of the YAMNet class, to prevent most misclassifications. This helps defining notable periods over the signal, where detected sounds clearly differ from background noise.

2.1.2 L_{Aeq}-based event detection

To complement sound ensemble preclassification, the equivalent sound level (L_{Aeq}, Eq. (1)) evolution is used to detect notable periods on the long-term signal. In this context, "notable periods" refer to energetic parts of the signal, having the most impact on the perceived nuisances.

$$L_{Aeq,T} = 10\log_{10}\left[\frac{1}{T}\int_0^T \frac{p_A^2(t)}{p_{ref}^2}\,dt\right] \qquad (1)$$

Two different properties or patterns are sought in the L_{Aeq} signal to detect these notable periods. Medium or long-term L_{Aeq} leaps signify the appearance of a loud sound source. Also, a high L_{Aeq} degree of variance is often inconsistent with roadway noise, and rather caused by speech, construction or animal sounds.

Two criteria are introduced to detect these two phenomena. For detecting medium and long-term L_{Aeq} leaps, we compare short-term $L_{Aeq,T=2\ min}$ to long-term $L_{Aeq,T=3\ hrs}$ (Eq. (1)) along the signal. Each time short-term exceeds long-term levels, a notable period is defined. On the other hand, detection of periods with a high degree of variance is performed with a threshold on $L_{Aeq,1s}$ standard deviation over a 20s-long sliding window.

2.2 Event boundaries correction

The stage role is to gather information from the initial preclassification and event detection stages (Notable periods in Fig. 1). Outcomes of both units are subject to sound emergence and duration criteria before they get merged. Thus, each event is defined with its starting time, ending time and one or several prevalent sound ensemble(s). These information are transmitted to the final classifier, aimed at improving the sound sources classifications.

2.3 Final classification

At this stage, a complete overview of the major sounds that prevail over the long-term acoustic recording is available. Nonetheless, numerous use cases require more precision than the defined sound ensembles (section 2.1.1).

For example, the *Vehicles* ensemble may refer to roadway noise as well as aircraft or railway noise. Therefore, we choose to use another classifier to bring in-depth sound source prediction. With such expectations, close attention should be paid to the chosen dataset and classifier model.

2.3.1 *Training dataset*

In order to build a performing supervised classifier, an appropriate training dataset is essential. It should cover most environmental sounds with few classes, while keeping consistency in defined classes. Our dataset architecture is inspired from other major environmental sounds datasets (AudioSet [4] and ESC-50 [5]). 13 classes are used, split into 4 categories, as depicted in Tab. 1.

Table 1. Categorisation of the classifier training dataset.

Roadway sounds	Human sounds, Animal & Music	Other vehicles sounds	Natural sounds
Dense road traffic noise	Human Voice	Airplanes & Helicopters	Wind
Cars	Music & Alarms	Railway	Rain
Motorcycles	Animals (Birds)	Construction machines	
Trucks & Buses	Animals (Insects)		

Internally collected signals, completed with few samples from ESC-50 [5] and Urbansound8k [6] make up for a total of 3500 files and around 10h of labelled data.

2.3.2 *Classifier model*

Regarding the classification model, the goal is to maximize the separation between roadway-related sounds and non-roadway noise. To build it, we drew inspiration from Contrastive Language-Audio Pretraining (CLAP) model, recently proposed in [7]. This model has already shown its effectiveness to encode audio waveforms and text signals. The same audio encoder architecture is trained on our data and used as input to a two-layer deep neural network. These last layers provide a 1D-classification vector corresponding to our dataset classes (Tab. 1).

3. DATASET AND RESULTS

3.1 Step-by-step application on a custom example

To ease the evaluation, a synthetic audio signal is built in mixing sound events from various sites over 30 minutes. Added sound events include train pass-bys, construction sounds, music, alarms, birds, insects and human voice, from 3 dB(A) to 30 dB(A) above residual sound level. L_{Aeq} evolution, reference labels and mel-spectrogram of this signal are shown in the three upper subplots of Fig. 2.

The detection part (2 preclassification stages and event boundaries correction) is first evaluated on its own. A 99 % recall and a 73 % precision are reached when comparing frames from reference and automatically detected events. This means that almost the entirety of reference events have been detected with proper boundaries. Meanwhile, some frames belonging to background noise were detected as sound events, explaining the 73 % precision.

Once the events are properly detected, the final classification unit is called. For each event, it predicts whether it belongs to roadway noise or not. This prediction is depicted in the last subplot of Fig. 2. To evaluate it, Average Precision (AP) [4] is computed regarding the *Roadway sounds* category. On this short example, a 0.92 AP is obtained. It shows that the detector recognizes various environmental sources emerging from background roadway noise. However, this small synthetic test sample is not large enough to conclude on the system performances.

3.2 Application on a large dataset

To carry on with the evaluation, real acoustic signals from 3 different locations were recorded and strongly labelled. Along each 24-hour long signal, roadway noise is manually detected and established as a reference. It permits the estimation of roadway noise contribution : equivalent sound level over all roadway noise-labelled periods. For each site, roadway noise contribution (denoted here as $L_{road,ref}$) is given in Tab. 2. It can be compared to $L_{glob,ref}$, equivalent sound level over the whole signal. The closer both indicators are, the more prevalent roadway noise is.

Table 2. Soundscapes and noise contribution of the 3 evaluation dataset sites.

Site	Major non-roadway source	$L_{road,ref}$	$L_{glob,ref}$
1	Construction machines	53.3 dB(A)	55.9 dB(A)
2	Birds	51.3 dB(A)	51.8 dB(A)
3	Railway	45.8 dB(A)	56.0 dB(A)

Chosen sites cover various use cases: prevalent roadway noise in sites 1 & 2, with disturbance from construction machines or birds. On site 3, railway noise prevails and road traffic is the secondary noise disturbance source.

Audio recordings from each site are supplied to our automatic detector, whose outcome is used to compute AP (Tab. 3). Also, automatic roadway noise contribution estimation ($L_{road,auto}$) is compared to the manual one ($L_{road,ref}$). This second comparison focuses on noisier periods, that matter most for noise contribution estimations.

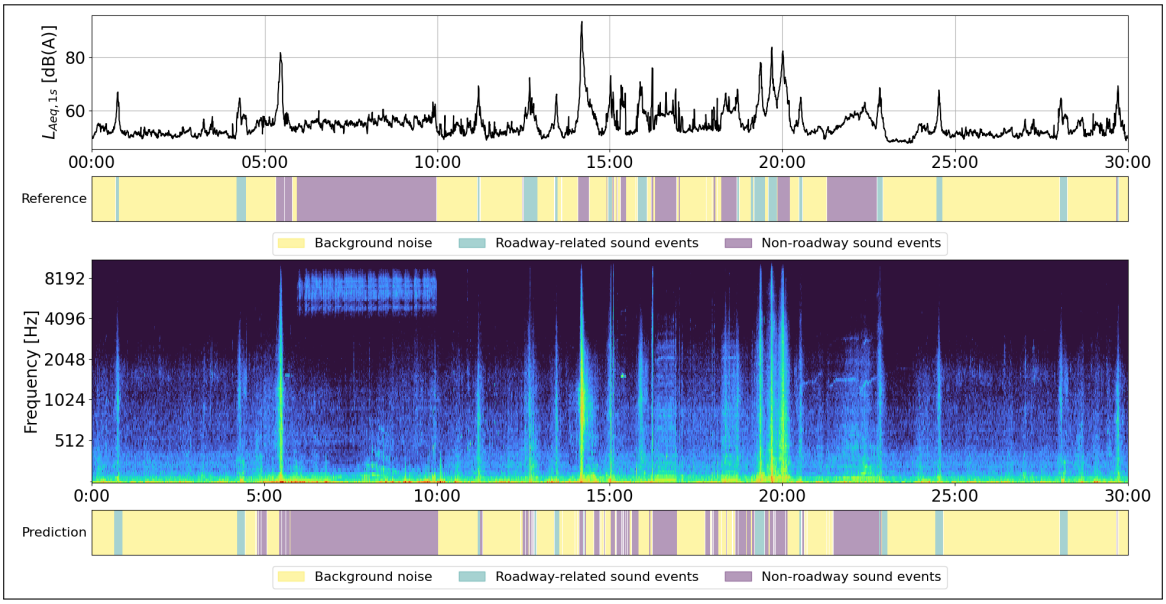


Figure 2. $L_{Aeq,1s}$ evolution, manually detected events, mel-spectrogram and predicted events for a 30-minute signal.

Table 3. Average Precision (AP) of the automated roadway noise detection and comparison between automated and manual roadway noise contributions.

Site	AP	$\lvert L_{\mathbf{road,auto}} - L_{\mathbf{road,ref}} \rvert$
1	0.88	0.1 dB(A)
2	0.91	0.1 dB(A)
3	0.96	0.7 dB(A)

On each site, AP stands above 0.88 and even reaches 0.96 for Site 3. Regarding automatic roadway noise contribution estimations, it also stands within a 0.7 dB(A) margin compared to the one obtained with manual labelling. Therefore, in three various contexts, our automatic achieves a high roadway noise detection rate, especially for noisier periods, allowing an accurate roadway noise contribution estimation.

4. CONCLUSION

In this paper, an automatic roadway noise detection method is proposed. With two classifiers enhanced by sound level analysis units, a robust sound event detection method is provided for road-impacted soundscapes. On 3 long-term signals from various recording sites, a minimum 0.88 Average Precision is reached. Above all, the proposed method aims at automating roadway noise contribution estimations. To this matter, it achieves satisfactory results on each site, with predictions standing within a 0.7 dB(A) margin compared to manual estimation. Future work on dataset or final model may improve accuracy. Still, this method already efficiently handles the automatic roadway noise detection tasks in various contexts.

5. REFERENCES

[1] World Health Organization *et al.*, "Burden of disease from environmental noise: Quantification of healthy life years lost in Europe," 2011.

[2] European Environment Agency, "Reported data on noise exposure covered by directive 2002/49/EC," 2024.

[3] E. Tsalera, A. Papadakis, and M. Samarakou, "Comparison of pre-trained CNNs for audio classification using transfer learning," *Journal of Sensor and Actuator Networks*, vol. 10, no. 4, p. 72, 2021.

[4] J. F. Gemmeke, D. P. Ellis, *et al.*, "Audio set: An ontology and human-labeled dataset for audio events," in *2017 IEEE international conference on acoustics, speech and signal processing*, pp. 776–780, 2017.

[5] K. J. Piczak, "ESC: Dataset for Environmental Sound Classification," in *Proceedings of the 23rd Annual ACM Conference on Multimedia*, pp. 1015–1018, 2015.

[6] J. Salamon, C. Jacoby, and J. P. Bello, "A dataset and taxonomy for urban sound research," in *Proceedings of the 22nd ACM International Conference on Multimedia*, p. 1041–1044, 2014.

[7] Y. Wu, K. Chen, *et al.*, "Large-scale contrastive language-audio pretraining with feature fusion and keyword-to-caption augmentation," in *IEEE International Conference on Acoustics, Speech and Signal Processing*, 2023.

DOI: 10.61782/fa.2025.0340

FORUM ACUSTICUM EURONOISE 2025

ENHANCED ENVIRONMENTAL SOUND EVENT CLASSIFICATION THROUGH TRANSFER LEARNING WITH CLAP MODEL

Francesco Artuso[1*] **Geremia Pompei**[2] **Andac Akbaba**[3]
Gino Iannace[3] **Francesco D'Alessandro**[4] **Francesco Fidecaro**[1]
Gaetano Licitra[2] **Luca Fredianelli**[2]
[1] Department of Physics, University of Pisa, Italy
[2] Institute for Chemical-Physical Processes of the Italian Research Council, Pisa, Italy
[3] Department of Architecture and Industrial Design, University of Campania, Aversa, Italy
[4] iPOOL S.r.l., Via Antonio Cocchi 3, 56121 Pisa, Italy

ABSTRACT

Long-term noise monitoring is essential to ensure compliance with regulations. This process requires the removal of spurious sounds unrelated to the target source or to the typical soundscape of the monitored area. Traditionally, such tasks relied on manual labelling by operators, but recent advancements in data-driven methodologies highlight that it is time to automate the process using cutting-edge machine learning techniques. Pre-trained models, widely available in literature, are trained on extensive datasets covering numerous classes and serve as a foundation for developing specialized machine learning models fine-tuned for specific tasks or subsets of classes. This study presents a Transfer Learning approach to leverage the knowledge of the Contrastive Language-Audio Pre-training (CLAP) model for a classification task focused on a subset of its original classes. Although the CLAP model has demonstrated adaptability across a broad range of classes with good results, the findings of this study suggest that the application of Transfer Learning can enhance classification accuracy for the selected subset of environmental sound classes.

Keywords: *environmental noise, sound event classification, pre-trained models, transfer learning, clap*

**Corresponding author*: *francesco.artuso@phd.unipi.it.*
***Copyright**: ©2025 Artuso et al. This is an open-access article distributed under the terms of the Creative Commons Attribution 3.0 Unported License, which permits unrestricted use, distribution, and reproduction in any medium, provided the original author and source are credited.*

1. INTRODUCTION

The evaluation of noise sources is essential for monitoring and mitigation of environmental noise levels in order to protect public health [1]. The primary contributors to environmental noise typically include road traffic [2–4], railways [5,6], airports [7], and industrial activities [8]. In real monitoring scenarios, however, in addition to the noise originating from the target source, a substantial number of unintended or anomalous events, referred to as spurious sounds, is also collected. In this context, accurately attributing the correct amount of responsibility to each source is crucial. Consequently, the identification and subsequent exclusion of spurious events from measurements becomes a key task. At present, this process is generally performed by acoustic experts through visual inspection of time histories and spectral representations. While effective in some cases, this method is highly time-consuming and susceptible to human error. These limitations are particularly evident in the case of wind turbine noise, where long-term measurements are necessary. To address these challenges, it can be useful to adopt new data-driven methodologies, capable of efficiently processing large volumes of data. In this regard, machine learning and deep learning offer promising potential to enhance and accelerate the detection of spurious events. The specific name of the task just described is Sound Event Detection (SED), which aims not only to identify the class of the event but also to determine its onset and offset within a longer audio recording. In this article, we address a preliminary step to this task, commonly referred to as Sound Event Classification (SEC), where audio segments are pre-

trimmed to contain only the sound event to be classified. This classification step serves as a foundation for building a model capable of accurately recognizing sound classes, which can then be integrated into a more complex pipeline to perform event detection.

One of the main difficulties related to this task lies in the highly heterogeneous nature of these anomalous occurrences, which makes their identification very complex. The principal categories of identifiable sources include anthropogenic sounds, transportation infrastructure noise, natural and animal-generated sounds, agricultural machinery, and industrial operations. Nevertheless, even this macro-level classification does not fully capture the variability found within individual categories, highlighting the need for adaptable classification approaches. The traditional strategy for addressing these tasks involves designing a neural network architecture and training it from scratch to differentiate among a fixed set of predefined target classes. While this method is effective in scenarios with a limited scope, it lacks generalization capability. Specifically, if the initial set of target classes were to be extended, the model would require complete retraining to accommodate the new classes. Moreover, in order to achieve good classification performance, especially on heterogeneous and complex datasets such as in this case, it is necessary to train the neural network on a very large amount of data. This ensures that the model can learn a comprehensive representation of the wide variability in data and scenarios it will be required to recognize. To address the need for a solution that is both adaptable to diverse contexts and trained on sufficiently varied data, the use of pre-trained models has recently become widespread. Pre-trained models already possess knowledge of the general features typical of the task they were designed for, such as image recognition, natural language processing, or audio classification. They can be used either directly or as a starting point to develop specialized models tailored to a specific set of classes or more targeted tasks. In this context, the Contrastive Language-Audio Pretraining (CLAP) [9, 10] model has been developed. It is a deep learning model designed to learn joint representations of audio and text. In order to achieve this, CLAP transforms both an audio measurements and its corresponding textual description into vectors of the same dimension, called embeddings. During training, the model pulls the embeddings of matching audio-text pairs closer together, while pushing apart those of unrelated pairs. This contrastive learning enables the model to capture semantic relationships, organizing the embedding space so that similar sounds and descriptions are near each other. To reinforce the selection of this model, it is worth mentioning that in [11] it has been demonstrated that, on a subset of five classes extracted from the ESC-50 dataset [12], the performances achieved using embeddings extracted by CLAP overcome the performances obtained using the classic features Mel-Frequency Cepstral Coefficients and Gammatone Frequency Cepstral Coefficients, both in clustering and classification task.

A more detailed description of the CLAP model will be provided in Section 2, along with an explanation of the transfer learning approach adopted in this study. Subsequently, in Section 3 the preliminary outcomes obtained with the fine-tuned model will be presented and compared with the results of the original CLAP model on the same dataset. Finally, Section 4 will briefly analyze these results and outline the main conclusions.

2. METHODOLOGY

2.1 CLAP model

The CLAP model consists of an audio encoder and a text encoder, designed to extract two embeddings of equal dimensionality d from the audio measurement and its corresponding textual description, respectively. The audio encoder is based on a Transformer architecture named Hierarchical Token-Semantic Audio Transformer (HTS-AT), introduced in [13]. The goal of CLAP is to compare these embeddings and optimize the representation space such that audio and text embeddings with similar semantic content are pulled closer together, while those with differing semantics are pushed farther apart. Analyzing the structure of the model in detail, the input of the audio encoder is the Mel-Spectrogram of the audio, that is the spectrogram computed using the Mel scale, designed to mimic human auditory perception, which is nonlinear. This scale converts frequencies so that equal distances on the scale correspond to equally perceived differences in sound, with greater sensitivity to lower frequencies and less to higher ones. The structure of CLAP model is depicted in Figures 1 and 2.

The Mel-Spectrogram of dimensions (T, F), where T is the temporal dimension and F is the number of frequency bins, is cut into different patches of dimensions $(P \times P)$, as it can be seen in Figure 1. Each element of the sequence is then passed to a module composed by a Convolutional Neural Network (CNN), to be transformed transformed in a so-called token of dimen-

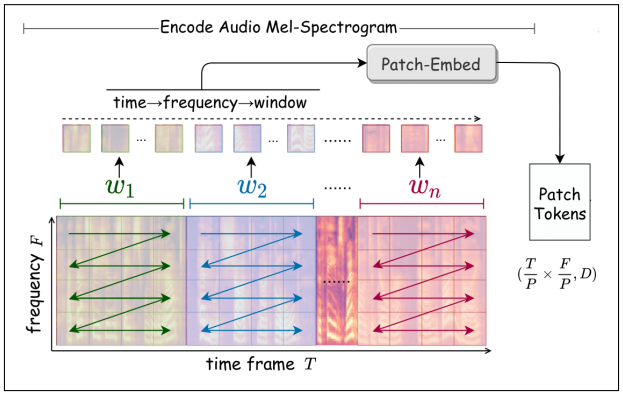


Figure 1. Mel-spectrogram encoding as input for HTS-AT. Architecture and Figure have been presented in [13].

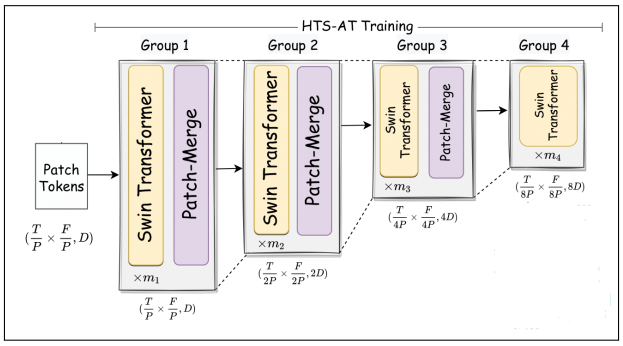


Figure 2. Sequence of SWIN Transformers and Patch-Merge in HTS-AT. Architecture and Figure have been presented in [13].

sions $(1, D)$. Then, all the tokens are arranged in a single structure of dimensions $\left(\frac{T}{P} \times \frac{F}{P}, D\right)$ where $\frac{T}{P} \times \frac{F}{P}$ is the number of tokens. The tokens are then fed into a sequence of transformer-encoder groups, as shown in Figure 2. The transformer architecture differs from previous models used in sequence analysis, like recurrent neural networks (RNNs) and long short-term memory networks (LSTMs), as it doesn't rely on recurrent structures. Instead, it uses a self-attention mechanism to dynamically adjust the relevance of different tokens based on their contextual dependencies, allowing the model to focus on the most relevant parts of the sequence and capture complex relationships within the data. After the Transformer, the patch-merge module is applied to decrease the number of patches and increase the dimension in the latent space, combining adjacent patches. This procedure is repeated sequentially for other groups of transformer-merger, until the i^{th} audio is transformed into the embedding E_a^i of dimension $d = 1024$. By means of an encoder also every textual descriptions is transformed into a d-dimensional embedding E_t^i. Assuming to have N pairs of audio and text, it is possible to arrange the embeddings into two matrices E_a and $E_t \in R^{N \times d}$. The audio and text embeddings obtained through this procedure are then used to compute a similarity measurement, namely a scalar product between the vectors as an estimate of their distance in the hyperspace created by the model. The similarity matrix is equal to

$$\text{SIM} = \tau(E_t \cdot E_a^\top) \,, \tag{1}$$

where τ is a scaling factor. The matrix contains the similarity between N matching pairs in the diagonal and between $N^2 - N$ non-matching pairs off-diagonal. The goal of the training stage is to bring closer matching pairs and separate non-matching ones. The loss function is therefore designed so that, by minimizing it, the similarity between matching pairs (i.e., along the diagonal) is increased, while the similarity between non-matching pairs (i.e., off-diagonal elements) is decreased. The two loss functions ℓ_{text} and ℓ_{audio} are equal to

$$\ell = -\frac{1}{N} \sum_{i=0}^{N} \log \text{diag}(\text{softmax}(\text{SIM})) \,. \tag{2}$$

The terms of the matrix softmax(SIM) can be interpreted as the probability of matching between the corresponding audio-text pairs. The total loss is equal to:

$$\mathcal{L} = 0.5(\ell_{text} + \ell_{audio}) \,. \tag{3}$$

In the latent hyperspace of the model, minimizing this loss function results in bringing closer audio and text embeddings concerning the same semantic area.

2.2 Transfer learning

The CLAP model, once trained, generates a latent space where elements are arranged based on their semantic relationships. This structure allows the model to be used for classification tasks without additional training. To classify a new sound using the original model, a set of candidate class labels must be provided. Since the pre-training

objective was to align audio and text embeddings that refer to the same concept, the model performs classification by evaluating the similarity between these embeddings. Specifically, it computes the similarity score between the audio embedding and each of the class label embeddings, selecting the class with the highest score as the predicted output. Directly employing the pre-trained model for classification offers clear advantages, including its ability to recognize a vast range of classes. However, performance on an arbitrary set of classes is not guaranteed to be optimal. Since the goal of this work is not to ensure applicability to an unlimited set of categories, but rather to achieve high performance on a well-defined subset, a transfer learning strategy was adopted. The idea is to leverage the robust foundational knowledge of the CLAP model and fine-tune it to specialize in the selected subset of classes. The goal is to enhance accuracy within a limited set of sound classes, compared to the broader but less specialized performance of the original model. To achieve this, only the initial portion of the CLAP architecture, specifically the component responsible for embedding extraction, was retained. A new linear layer was then trained to project the resulting embeddings of dimension $d = 1024$ into a lower-dimensional space corresponding to the number of target classes of dimension $n_{\text{classes}} = 21$. Each output value from this layer represents the predicted likelihood that the input sound belongs to one of the predefined categories. The linear transformation applied by the layer to map the input x into the output y is equal to:

$$y = xW^{\top} + b \,, \tag{4}$$

where W and b are the learnable weights and bias of the layer, of dimension (n_{classes}, d) and (n_{classes}) respectively.

2.3 Dataset

The dataset was constructed using both measurements collected online, primarily from the website freesound.org [14], and those recorded by the authors. The classes were selected based on the authors' experience with monitoring measurements, primarily conducted in non-urban or sparsely populated areas with some human presence. The classes belong to five main categories: anthropogenic sounds, transportation infrastructure noise, natural and animal-generated sounds, agricultural machinery, and industrial operations. The chosen classes are 21, and they are reported in Table 1. It has been observed that varying the segment lengths within the same dataset during classification can result in different accuracy outcomes. Consequently, multiple versions of the dataset were created, with measurements segmented into durations ranging from 1 to 10 seconds in 1-second increments. For each dataset version, four distinct sets were constructed: the training set, the validation set, the early stopping set, and the test set. The early stopping set is essential to prevent overfitting, as training is stopped when the accuracy on the early stopping set does not improve for 10 consecutive epochs. Each dataset version consisted of 500, 100, 100, and 100 measurements for the training, validation, early stopping, and test sets, respectively. In cases where the total duration of the dataset for a given segment length was insufficient to meet these numbers, data augmentation was applied through the addition of gaussian noise.

Table 1. Classes of sounds chosen for the dataset.

Classes of Sounds	
Airplane	Bells
Birds	Cats
Chicken coop	Cicadas and crickets
Clacson	Crows and seagulls
Dogs	Glass breaking
Helicopter	Lawn mower and brush cutter
Music	Sirens and alarms
Thunder, fireworks and gunshot	Train
Vacuum cleaner, fan and hairdryer	Vehicle idling
Vehicle pass-by	Voices
Workshop	

3. RESULTS

In this Section the results obtained using directly the pre-trained model are compared with the results obtained with the fine-tuned model. The length of the measurement in seconds plays a crucial role in classification performance. It has been observed that varying the lengths of the segments from the same dataset during classification can lead to different accuracy results. This variation is likely due to the structural differences in the spectrograms. To accurately capture recurring patterns in a sound's spectrogram,

a minimum duration may be required. Hyperparameters were tested with lengths ranging from 1 to 10 seconds, in 1-second increments. Table 2 shows the accuracy and loss of the original pre-trained model on the validation set, depending on the length of the input audio. Various experiments were then conducted using the fine-tuned model, with different hyperparameters adjusted during training. The best result is reported in Table 3.

Table 2. Accuracy and Loss results of the original CLAP model on the validation set at varying of the audio length hyperparameter.

Audio length	Accuracy	Loss
4 s	72.93 %	2.83
7 s	72.89 %	2.82
8 s	70.55 %	2.83
3 s	70.23 %	2.82
9 s	69.49 %	2.83
10 s	69.35 %	2.83
5 s	68.32 %	2.83
6 s	66.81 %	2.83
2 s	64.02 %	2.84
1 s	60.42 %	2.86

Table 3. Accuracy and Loss result of the fine-tuned model.

Audio length	Accuracy	Loss
4 s	91.83 %	0.28

4. DISCUSSION AND CONCLUSIONS

This study presents the Contrastive Language-Audio Pretraining (CLAP) model, which integrates inputs from different domains into a shared space where their vector representations can be compared and manipulated. The model was fine-tuned using a Transfer Learning approach to perform Sound Event Classification (SEC) on a specific dataset, focusing on key environmental sources relevant to noise monitoring. A linear layer was applied to the sound embeddings generated by the original model to adapt it for the classification task. The results demonstrate a significant improvement in accuracy, increasing from 72.93 % (the best performance achieved by the original model) to 91.83 % (the best performance achieved by the fine-tuned model) on the validation set. These findings highlight the effectiveness of the fine-tuned model in the classification task, showing a substantial performance gain over the original model. Further analysis and exploration of additional fine-tuning strategies are warranted to continue improving these results. The next step in this research will involve incorporating the fine-tuned model into a detection pipeline for Sound Event Detection (SED), which is the ultimate objective in real-world scenarios.

5. ACKNOWLEDGMENTS

The paper was supported by the PRIN 2022 project 20223LMSZN, COMBINE "Sustainable condition monitoring of wind turbines using acoustic signals and machine learning techniques" and by the Ministry of University and Research (MUR) as part of the PON 2014-2020 "Research and Innovation" resources – Green/Innovation Action – DM MUR 1061/2022.

6. REFERENCES

[1] European Environment Agency., *Environmental noise in Europe, 2020.* LU: Publications Office, 2020.

[2] E. M. Andersson, M. Ögren, P. Molnár, D. Segersson, A. Rosengren, and L. Stockfelt, "Road traffic noise, air pollution and cardiovascular events in a Swedish cohort," *Environmental Research*, vol. 185, p. 109446, June 2020.

[3] L. Fredianelli, S. Carpita, M. Bernardini, L. G. Del Pizzo, F. Brocchi, F. Bianco, and G. Licitra, "Traffic Flow Detection Using Camera Images and Machine Learning Methods in ITS for Noise Map and Action Plan Optimization," *Sensors*, vol. 22, p. 1929, Mar. 2022.

[4] G. Licitra, M. Bernardini, R. Moreno, F. Bianco, and L. Fredianelli, "CNOSSOS-EU coefficients for electric vehicle noise emission," *Applied Acoustics*, vol. 211, p. 109511, Aug. 2023.

[5] F. Bunn and P. H. T. Zannin, "Assessment of railway noise in an urban setting," *Applied Acoustics*, vol. 104, pp. 16–23, Mar. 2016.

[6] G. Licitra, L. Fredianelli, D. Petri, and M. A. Vigotti, "Annoyance evaluation due to overall railway noise and vibration in Pisa urban areas," *Science of The Total Environment*, vol. 568, pp. 1315–1325, Oct. 2016.

[7] M. Espey and H. Lopez, "The Impact of Airport Noise and Proximity on Residential Property Values," *Growth and Change*, vol. 31, pp. 408–419, Jan. 2000.

[8] P. C. Eleftheriou, "Industrial noise and its effects on human hearing," *Applied Acoustics*, vol. 63, pp. 35–42, Jan. 2002.

[9] B. Elizalde, S. Deshmukh, M. A. Ismail, and H. Wang, "CLAP Learning Audio Concepts from Natural Language Supervision," in *ICASSP 2023 - 2023 IEEE International Conference on Acoustics, Speech and Signal Processing (ICASSP)*, (Rhodes Island, Greece), pp. 1–5, IEEE, June 2023.

[10] B. Elizalde, S. Deshmukh, and H. Wang, "Natural Language Supervision for General-Purpose Audio Representations," Feb. 2024. arXiv:2309.05767 [cs, eess].

[11] F. Artuso, F. Fidecaro, F. D'Alessandro, G. Iannace, G. Licitra, G. Pompei, and L. Fredianelli, "Identifying optimal feature sets for acoustic signal classification in environmental noise measurements," in *INTER-NOISE and NOISE-CON Congress and Conference Proceedings*, vol. INTER-NOISE24, (Nantes, France), pp. 7540–7549, Institute of Noise Control Engineering, 2024.

[12] K. J. Piczak, "ESC: Dataset for Environmental Sound Classification," in *Proceedings of the 23rd ACM international conference on Multimedia*, (Brisbane Australia), pp. 1015–1018, ACM, Oct. 2015.

[13] K. Chen, X. Du, B. Zhu, Z. Ma, T. Berg-Kirkpatrick, and S. Dubnov, "HTS-AT: A Hierarchical Token-Semantic Audio Transformer for Sound Classification and Detection," Feb. 2022. arXiv:2202.00874 [cs, eess].

[14] Freesound Team, "Freesound." `https://freesound.org`, 2024.

DOI: 10.61782/fa.2025.0006



FORUM ACUSTICUM
EURONOISE 2025

A COMPARATIVE ANALYSIS OF INTERIOR VS. EXTERIOR VEHICLE MICROPHONE PLACEMENT FOR ACOUSTIC EVENT DETECTION IN DRIVING ENVIRONMENTS

Carlos Castorena[1*] **Lucas Banchero**[2] **Juan A. De Rus**[1] **Francisco Vacalebri**[2]
Sandra Roger[1] **Jose M. Mossi**[2] **Jose J. López**[2] **Francesc J. Ferri**[1] **Maximo Cobos**[1]
[1] Departament d'Informàtica, Universitat de València, Burjassot, Spain
[2] Institute of Telecommunications and Multimedia Applications,
Universitat Politecnica de Valencia, Valencia, Spain

ABSTRACT

Safe driving depends on both internal and external factors of the vehicle, including those manifested as acoustic signals. Sounds, whether external, such as sirens or horns, or internal, such as conversations between passengers or the sound system, provide critical information to identify events that could compromise safety. The placement of microphones used for monitoring and feeding into an artificial intelligence-based detection system plays a crucial role. Microphones placed externally are essential for capturing sounds like sirens or horns, but they face challenges such as wind noise and vibrations caused by the movement of the vehicle. On the other hand, detecting these external events from the interior presents difficulties due to attenuation or distortion caused by the acoustic insulation of the body of the vehicle. This work explores the relevance of microphone placement by comparing the performance of models when processing data captured separately from the interior and exterior of vehicles. The challenges associated with capture are also discussed.

Keywords: *sound detection, mic placement, road safety*

1. INTRODUCTION

Audio-based event detection systems offer distinct advantages over vision-based systems in vehicle safety and driver assistance, particularly in scenarios where a direct line of sight to the event source is obstructed [1]. The ability to recognize critical acoustic cues, such as emergency vehicle sirens or horn sounds, enhances situational awareness and supports timely decision-making while driving [2, 3]. However, the performance of such systems is highly sensitive to microphone placement and their robustness in dynamic, noisy environments.

Microphone positioning plays a critical role in determining the accuracy and reliability of audio-based detection systems. External microphones, mounted outside the vehicle, are well-suited to capturing environmental sounds, such as approaching emergency vehicles or honking cars. However, they are vulnerable to various interferences, including wind noise, road noise, and other environmental disturbances. To mitigate these issues, approaches such as physical filters [4], digital signal processing techniques [5], and deep learning-based noise reduction methods [6] have been proposed. While these methods enhance detection performance, they require careful optimization to remain effective under diverse real-world conditions.

In contrast, placing microphones inside the vehicle provides a more controlled acoustic environment, thereby reducing exposure to external noise. Nonetheless, this setup introduces its own challenges, such as sound attenuation caused by the vehicle's structure and interference from internal noise sources like conversations, infotainment systems, and engine vibrations. Additionally, capturing external acoustic events from within the cabin is complicated by the sound-insulating properties of modern vehicle designs. To address these challenges, advanced

*Corresponding author: carlos.castorena@uv.es.
Copyright: ©2025 Carlos Castorena et al. This is an open-access article distributed under the terms of the Creative Commons Attribution 3.0 Unported License, which permits unrestricted use, distribution, and reproduction in any medium, provided the original author and source are credited.

deep learning models capable of processing polyphonic sound events [7, 8]—where multiple overlapping sounds occur simultaneously—are increasingly employed. These models improve the system's ability to differentiate between relevant and irrelevant auditory signals within the complex acoustic environment of a vehicle interior.

Recent research has also explored multimodal approaches [9] that integrate both audio and visual data to improve event detection capabilities. By combining acoustic signals with visual cues, these systems can compensate for limitations in either modality, leading to improved overall detection accuracy. However, multimodal systems introduce additional complexities, including higher computational demands, synchronization requirements between audio and video streams, and sensitivity to adverse environmental conditions (e.g., poor lighting or occlusions) that may impair one or both modalities. These limitations highlight the need for thoughtful design and implementation when considering multimodal solutions.

This study evaluates the impact of microphone placement—inside versus outside the vehicle—on the performance of three state-of-the-art deep learning models: the Audio Spectrogram Transformer (AST) [4, 10], Convolutional Recurrent Neural Networks (CRNN) [11, 12], and a version of YOLO adapted for audio spectrogram inputs [8, 13]. Rather than focusing solely on performance comparisons, the primary objective is to investigate how microphone placement, ambient noise conditions, and overlapping sound events influence the ability of each model to detect key auditory events, such as sirens and horn sounds, under realistic driving scenarios. By examining detection accuracy across different microphone configurations, this work sheds light on the trade-offs inherent in each setup and contributes to the development of more robust and context-aware audio-based detection systems for intelligent vehicle applications.

2. METHODOLOGY

2.1 Data Collection

To evaluate model performance under different acoustic conditions, two distinct sets of audio recordings were collected. Recordings were made using WM-61A DIY and XYH-6 microphones connected to a Zoom H6 recorder to ensure synchronized multi-channel capture. Two channels were placed inside the vehicle, centrally positioned, while four were mounted externally—two on each side. The external microphones were installed on a stable base and fitted with physical wind filters, which have been shown in prior studies to effectively reduce wind interference. The microphone layout is shown in Figure 1.

In Scenario 1, recordings were conducted both inside and outside the vehicle under low-noise conditions . No additional sound sources from the inside—such as radio, mobile phones, or conversations—were present . This scenario represents an idealized environment with minimal internal interference. A total of 1245 seconds were recorded, which were segmented into 4-second clips using a 1-second sliding window, resulting in 23 horn and 94 siren events.

Scenario 2 was designed to simulate a realistic and noisy in-cabin environment. In this case, background sounds including conversations, radio playback, and mobile phone usage were deliberately introduced. The total duration of this recording was 877 seconds, yielding 29 horn and 179 siren events after segmentation using the same process as in Scenario 1.

Both datasets were segmented into overlapping 4-second clips using a 1-second stride to construct a continuous and structured dataset. Rather than adopting a traditional sound event detection (SED) framework, each segment was assigned a single label—*Horn*, *Siren*, or *No Event*—based on the presence of a target sound within the

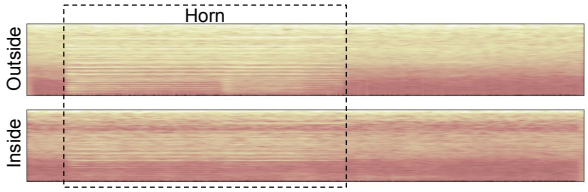


Figure 1: Microphone placement in the vehicle. Microphones M1–M4 (WM-61A DIY) are positioned externally, while microphone M5 (XYH-6, two channels) is located inside.

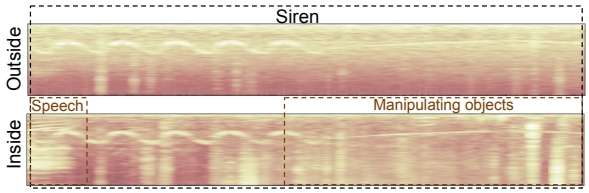
clip. This simplified labeling strategy was chosen to facilitate a direct and controlled comparison of model performance across different microphone placements, focusing on the detectability of key acoustic events rather than precise time event localization or boundary detection. While this approach does not capture the full temporal dynamics of sound events, it provides a practical and interpretable means of evaluating classification accuracy under varying acoustic conditions.

All recordings were conducted with the vehicle in a stationary state to minimize wind-induced noise, whose limited impact has been demonstrated in [4]. The recording site was selected to ensure consistent exposure to traffic-related sounds, resulting in a naturally high frequency of siren and horn events.

To illustrate the acoustic differences between scenarios, Figure 2 shows representative 4-second audio segments from both conditions: (a) a clean sample from Scenario 1, and (b) a more complex recording from Scenario 2, where overlapping internal sounds such as speech and object interaction are present.



(a) Scenario 1: 4-second audio segment with minimal background noise.



(b) Scenario 2: 4-second audio segment with overlapping in-cabin events (e.g., speech, object handling).

Figure 2: Representative audio samples from the two recording scenarios. Scenario 1 provides a low-noise baseline, while Scenario 2 reflects more realistic in-vehicle acoustic conditions.

2.2 Detection Models

To investigate how microphone placement affects the detection of relevant acoustic events in vehicular contexts, we implemented three deep learning-based models with distinct architectural characteristics: the Audio Spectrogram Transformer (AST), a Convolutional Recurrent Neural Network (CRNN), and a fully convolutional architecture based on YOLO. While the primary goal is not to compare absolute model performance, these architectures offer complementary perspectives on how different microphone configurations influence the perception and classification of acoustic signals. Each model was adapted to produce standardized outputs—three class probabilities for *Siren*, *Horn*, and *No Event*—to enable a consistent evaluation framework.

The AST model [14] leverages a Multihead Self-Attention mechanism to learn long-range dependencies within audio sequences. This capacity to capture global contextual information makes it particularly effective for identifying complex acoustic patterns, even in the presence of noise or temporal distortion. In this study, AST was trained using 4-second Mel spectrograms with 128 Mel bands, a 32 ms analysis window, and a 10 ms hop size. Unlike the other models, AST processes stereo audio by jointly analyzing two input channels. For in-cabin detection, the two interior microphones were used as stereo input; for exterior detection, the two side-mounted microphones were combined. To adapt the model for three-class classification, the pre-trained attention layers were frozen, and a dense layer with 768 neurons and PReLU activation was added, followed by a softmax output layer with three units [4].

The CRNN model [11,12] combines two-dimensional convolutional layers for spectral feature extraction with a bidirectional GRU layer to model the temporal evolution of sound events. Its frame-wise output allows for temporal localization of events within each segment. In contrast, the YOLO-based model [8] follows a fully convolutional approach adapted from object detection in computer vision. It produces predictions at multiple temporal resolutions using bounding-box-like structures, without relying on sequential modeling. Both CRNN and YOLO operate on single-channel audio, and were thus trained and tested on individual microphone signals. Input Mel spectrograms for these models were computed with 128 Mel bands, a 32 ms window, a 16 ms hop, a Hamming window function, and a 2048-point FFT, all sampled at 16 kHz.

The models were trained on a curated subset of open-

source datasets, primarily based on AudioSet [15], augmented with additional publicly available recordings of sirens, horns, and urban noise. Training procedures were customized for each architecture, ensuring that learned features aligned with the goal of robust acoustic event detection under real-world conditions.

While AST was trained using 4-second monophonic labels, both CRNN and YOLO were originally designed for polyphonic event detection across 10-second clips. For evaluation, however, all models were tested using 4-second segments to ensure consistency. Although AST does not support polyphony, this limitation had minimal impact in our experimental setting, where overlapping events were rare. Nevertheless, this distinction remains an important consideration when interpreting the models' capabilities in more complex acoustic environments.

2.3 Performance Metrics and Evaluation

The performance of each model was evaluated using standard classification metrics: precision (P), recall (R), and F1-score (F1), which are commonly used in classification tasks. These metrics provide a comprehensive assessment of model performance, particularly in scenarios with imbalanced class distributions. In such cases, it is essential to evaluate not only the quantity of correct predictions but also their relevance and consistency. This is especially important in the context of acoustic event detection, where the goal is to identify specific sounds (e.g., horns and sirens) amidst varying levels of background noise.

The recordings used in this study were segmented into 4-second clips with a 1-second sliding window. Each segment was assigned a single label—*Horn*, *Siren*, or *Nothing*—with events outside these categories discarded, particularly for the CRNN and YOLO models. These models generate hard predictions, meaning they provide precise timestamps for detected events within each 4-second segment. For consistency across all models, these timestamps were converted into weak labels, simplifying the task to a binary classification problem, i.e., determining whether an event was present or absent in each segment, without considering its exact duration or temporal position.

Each model was evaluated using both interior and exterior microphones, under two distinct recording conditions. Scenario 1, with minimal background noise, represents a controlled environment, allowing us to assess model performance in an ideal setting. In contrast, Scenario 2 introduces background noise from conversations, radio playback, and mobile phone use, simulating a more realistic in-vehicle environment. By analyzing the performance of the models in these scenarios, we can assess how the placement of the microphone affects the detection accuracy and robustness of the models under varying acoustic conditions.

3. RESULTS

The results presented in Table 1 highlight the impact of microphone placement and background noise on the performance of the three deep learning models—AST, YOLO, and CRNN—in detecting acoustic events. Overall, all models performed better with external microphones compared to internal ones. This effect was observed in both scenarios, but it was especially pronounced in Scenario 2, where background noise from conversations, radio playback, and mobile phone use inside the vehicle further degraded performance.

In Scenario 1, where external microphones captured clearer signals, AST achieved the highest F1-score (0.77), followed closely by YOLO (0.72) and CRNN (0.51). AST's superior performance in this controlled environment is largely attributed to its high recall values, particularly for horn detection (0.96). However, when evaluated inside the vehicle, all models experienced performance drops. AST, despite maintaining the highest F1-score (0.69), showed a notable decline in recall (0.63), while YOLO and CRNN also decreased to 0.50 and 0.34, respectively.

The performance degradation is even more evident in Scenario 2, where additional noise sources such as conversations, radio, and mobile phone sounds were present. AST exhibited the most pronounced decline, particularly for horn detection inside the vehicle, where its precision, recall, and F1-score dropped to zero. This suggests that AST, which assigns a single label per segment, struggles in polyphonic scenarios where multiple sound events overlap, leading to a total drop in performance for horn detection when other, more dominant sources are present. In contrast, while YOLO and CRNN also showed a considerable drop in performance, they retained some detection capability for horns, with F1-scores of 0.15 and 0.17, respectively. However, AST maintained a similar average F1-score inside the vehicle due to its stronger performance in siren detection, despite its inability to detect horns in this scenario.

Although the results of the experiment suggest that external microphone placement might be more effective for detecting sirens and horns, it is important to note that

		Transformer				YOLO				CRNN			
		Scenario 1		Scenario 2		Scenario 1		Scenario 2		Scenario 1		Scenario 2	
		Outside	Inside	Outside	Inside	Outside	Inside	Outside	Inside	Outside	Inside	Outside	Inside
Horn	P	0.58	**0.80**	**0.65**	0.00	**0.82**	0.36	**0.37**	0.16	**0.28**	0.14	**0.21**	0.10
	R	**0.96**	0.87	**0.38**	0.00	**0.78**	0.70	**0.45**	0.17	**1.00**	0.96	**0.76**	0.28
	F1	0.72	**0.83**	**0.48**	0.00	**0.80**	0.47	**0.41**	0.17	**0.44**	0.24	**0.33**	0.14
Siren	P	0.89	**1.00**	**1.00**	**1.00**	0.65	**0.76**	**0.97**	0.61	**0.47**	0.37	0.46	**0.76**
	R	**0.76**	0.38	**0.54**	0.18	**0.63**	0.41	**0.40**	0.08	**0.76**	0.52	**0.51**	0.11
	F1	**0.82**	0.55	**0.70**	0.30	**0.64**	0.54	**0.57**	0.14	**0.58**	0.44	**0.49**	0.19
Avg.	P	0.73	**0.90**	**0.82**	0.50	**0.73**	0.56	**0.67**	0.38	**0.38**	0.26	0.33	**0.43**
	R	**0.86**	0.63	**0.46**	0.09	**0.71**	0.56	**0.43**	0.13	**0.88**	0.74	**0.64**	0.19
	F1	**0.77**	0.69	**0.59**	0.15	**0.72**	0.50	**0.49**	0.15	**0.51**	0.34	**0.41**	0.17

Table 1: Performance metrics (Precision, Recall, and F1-score) for horn and siren detection using AST, YOLO, and CRNN models under two recording scenarios. Results are presented for both external and internal microphones.

this study has excluded certain variables that could influence monitoring effectiveness in real-world conditions. These variables include background noise from the external environment, weather conditions, microphone wear, among others. Additionally, for comprehensive monitoring of the vehicular environment, it is crucial to consider that monitoring the interior may be more complex from the outside due to the vehicle's inherent acoustic insulation, compared to detecting external events from the inside. This suggests that future research could explore the feasibility of implementing two microphone sources, each focused on detecting specific events from the interior and exterior, which could improve the accuracy and reliability of the system in more complex scenarios.

4. CONCLUSIONS

This study evaluated the performance of three deep learning models—AST, YOLO, and CRNN—for detecting external acoustic events (such as sirens and horns) in vehicular environments under various conditions. The results highlight the significant impact of microphone placement and background noise on detection accuracy. External microphones generally provided clearer signals, leading to better performance, while internal microphones were more susceptible to degradation, particularly in noisy conditions.

AST achieved the highest F1-score in controlled environments but struggled with overlapping sounds, resulting in a complete failure in horn detection inside the vehicle. In contrast, YOLO and CRNN maintained some detection ability in these challenging scenarios, although with lower overall accuracy.

Future work should explore the models' performance in more complex tasks, such as detecting the precise onset and duration of events, rather than merely classifying their presence within fixed segments. Additionally, investigating multi-microphone fusion strategies could help mitigate the limitations observed with single-channel inputs.

5. ACKNOWLEDGMENTS

This work has been supported by Grant TED2021-131003B-C21 funded by MCIN/AEI/10.13039/501100011033 and by the "EU Union NextGenerationEU/PRTR", as well as by Grant PID2022-137048OB-C41 funded by MICIU/AEI/10.13039/501100011033 and "ERDF A way of making Europe". Authors would like also to thank *Generalitat Valenciana-Santiago Grisolía* program for financing this work (GRISOLIAP/2021/060, CPI-21-232). Finally, the authors acknowledge as well the Artemisa computer resources funded by the EU ERDF and Comunitat Valenciana, and the technical support of IFIC (CSIC-UV).

6. REFERENCES

[1] K. Choudhury and D. Nandi, "Review of emergency vehicle detection techniques by acoustic signals," *Transactions of the Indian National Academy of Engineering*, vol. 8, 2023.

[2] L. Marchegiani and P. Newman, "Listening for sirens: Locating and classifying acoustic alarms in city scenes," *IEEE Transactions on Intelligent Transportation Systems*, vol. 23, 2022.

[3] M. Y. Shams, T. A. El-Hafeez, and E. Hassan, "Acoustic data detection in large-scale emergency vehicle sirens and road noise dataset," *Expert Systems with Applications*, vol. 249, 2024.

[4] L. Banchero, F. Vacalebri-Lloret, J. M. Mossi, and J. J. Lopez, "Enhancing road safety with AI-powered system for effective detection and localization of emergency vehicles by sound," *Sensors*, vol. 25, no. 3, 2025.

[5] S. Grimm and J. Freudenberger, "Wind noise reduction for a closely spaced microphone array in a car environment," *Eurasip Journal on Audio, Speech, and Music Processing*, vol. 2018, 2018.

[6] S. Braun, H. Gamper, C. K. Reddy, and I. Tashev, "Towards efficient models for real-time deep noise suppression," in *ICASSP, IEEE International Conference on Acoustics, Speech and Signal Processing - Proceedings*, vol. 2021-June, 2021.

[7] A. Mesaros, T. Heittola, T. Virtanen, and M. D. Plumbley, "Sound event detection: A tutorial," *IEEE Signal Processing Magazine*, vol. 38, 2021.

[8] C. Castorena, M. Cobos, J. Lopez-Ballester, and F. J. Ferri, "A safety-oriented framework for sound event detection in driving scenarios," *Applied Acoustics*, vol. 215, p. 109719, 2024.

[9] M. Zohaib, M. Asim, and M. ELAffendi, "Enhancing emergency vehicle detection: A deep learning approach with multimodal fusion," *Mathematics*, vol. 12, no. 10, 2024.

[10] Y. Gong, C.-I. Lai, Y.-A. Chung, and J. Glass, "SSAST: Self-Supervised Audio Spectrogram Transformer," *Proceedings of the AAAI Conference on Artificial Intelligence*, vol. 36, pp. 10699–10709, Jun. 2022.

[11] F. Ronchini, R. Serizel, N. Turpault, and S. Cornell, "The impact of non-target events in synthetic soundscapes for sound event detection," in *Proceedings of the 6th Detection and Classification of Acoustic Scenes and Events 2021 Workshop (DCASE2021)*, (Barcelona, Spain), pp. 115–119, 2021.

[12] N. Turpault, R. Serizel, A. P. Shah, and J. Salamon, "Sound event detection in domestic environments with weakly labeled data and soundscape synthesis," in *Workshop on Detection and Classification of Acoustic Scenes and Events*, p. 0, 2019.

[13] C. Castorena, J. Lopez-Ballester, J. A. D. Rus, M. Cobos, J. Lopez-Ballester, and F. J. Ferri, "Edge Computing for Driving Safety: Evaluating Deep Learning Models for Cost-Effective Sound Event Detection," *J Supercomput*, vol. 288, 2025.

[14] Y. Gong, Y. A. Chung, and J. Glass, "Ast: Audio spectrogram transformer," in *Proceedings of the Annual Conference of the International Speech Communication Association, INTERSPEECH*, vol. 1, 2021.

[15] J. F. Gemmeke, D. P. W. Ellis, D. Freedman, A. Jansen, W. Lawrence, R. C. Moore, M. Plakal, and M. Ritter, "Audio Set: An ontology and human-labeled dataset for audio events," in *2017 IEEE International Conference on Acoustics, Speech and Signal Processing (ICASSP)*, pp. 776–780, 2017.

DOI:

Main theme: A09 Machine learning and Artificial Intelligence in Acoustics

Session A09.08 Artificial intelligence in musical acoustics

Chair(s): M. Pezzoli, R. Russo

DOI:

Main theme: A10 Materials and Metamaterials

Session A10.02 Acoustic, vibroacoustic and elastic metamaterials

Chair(s): M. Malléjac, M. Miniaci, D. Torrent, B. Van Damme

DOI: 10.61782/fa.2025.0429



FORUM ACUSTICUM
EURONOISE 2025

HIGH BULK MODULUS PENTAMODES: THE THREE-DIMENSIONAL METAL WATER

Sebastiano Cominelli[1*] **Giacomo Brambilla**[1] **Marco Verbicaro**[1]
Matteo Pozzi[1] **Gabriele Cazzulani**[1] **Francesco Braghin**[1]
[1] Department of Mechanical Engineering, Politecnico di Milano, Italy

ABSTRACT

Pentamode metamaterials (PMs) mimic the acoustic properties of liquids and offer a powerful means of controlling sound propagation. However, their design and realisation remains an open challenge, especially in three dimensions. Existing PMs rely on thin junctions to simultaneously achieve high bulk modulus, low shear modulus and adequate density. This is successful in 2D but not in 3D, where an upper bound on the bulk modulus prevents efficient interaction with underwater sound waves. Hence, a fundamentally different geometry is needed.

We first apply topology optimisation to find different geometries and test it against the design of a two-dimensional Lüneburg lens. We show that it offers greater flexibility than conventional parametric optimisation approaches and the usual geometry based on effective pins is recovered. However, extending this method to three dimensions leads to geometries that are extremely difficult to manufacture. We show that simple pin-like kinematics are no longer sufficient in 3D, but that slider-like joints are required. Applying this paradigm, we propose the first 3D periodic lattice that successfully mimics the acoustic behaviour of water at low frequencies.

Keywords: *pentamode, underwater acoustics, cloaking, phononic crystal.*

1. INTRODUCTION

Pentamode metamaterials (PMs) have attracted considerable attention for their potential in underwater acoustics, enabling applications such as acoustic lenses, waveguides and invisibility cloaks [1]. PMs are solids in which the propagation of shear waves is prevented by a low shear-to-bulk modulus ratio, allowing them to behave like artificial fluids. It is common in the literature to present the concept in a two-dimensional approximation, where the so-called bimode metamaterials (BMs) are typically designed by parametric optimisation. All current designs are based on thin junctions that act as kinematic pins, making it possible to achieve a material with the same quasi-static properties as water. The same concept has been applied to the design of three-dimensional PMs [2, 3], and materials with the same sound speed as water and tunable anisotropy have been proposed to build acoustic devices [4]. However, the acoustic impedance of such materials is two orders of magnitude lower than that of water, preventing effective implementation. In this work, we first rely on topology optimisation to look for a new geometry of BMs. A unit cell shape similar to those existing in the literature is recovered, with the advantage of being a more efficient and versatile approach than the usual parametric optimisation. When aiming for a 3D PM, topology optimisation provides a geometry that is extremely difficult to realise [5], so we take a step back and focus on the kinematics of a PM. We show that the pin-like junctions are no longer sufficient to achieve the high bulk modulus of water and that a more complex topology is required [6]. We therefore propose slide-like junctions and design the first material whose mechanical properties are truly indistinguishable from water in the quasi-static limit.

2. TOPOLOGY OPTIMIZATION FOR BIMODE METAMATERIALS

To design a BM with a desired acoustic behaviour, we apply a density-based topology optimisation strategy to a

*__Corresponding author__: sebastiano.cominelli@polimi.it.
__Copyright__: ©2025 Sebastiano Cominelli et al. This is an open-access article distributed under the terms of the Creative Commons Attribution 3.0 Unported License, which permits unrestricted use, distribution, and reproduction in any medium, provided the original author and source are credited.

square unit cell. For simplicity, we focus on the design of an isotropic material, targeting only the effective bulk modulus and mass density, along with a low shear modulus. We define the inverse problem for a unit cell as:

$$\begin{aligned} &\min_{\rho} \mathbb{C}^{\mathrm{H}}_{33} + \alpha_T C_T \\ &\text{subject to :} \\ &\quad \mathbb{C}^{\mathrm{H}}_{11} < \kappa_L \\ &\quad \mathbb{C}^{\mathrm{H}}_{12} > 0.99\,\kappa_L \\ &\quad 0.99\,V_L < V < V_L \\ &\quad 0 \le \rho_k \le 1 \quad \forall k = 1, \dots, N \\ &\quad \text{Cell problem} \\ &\quad \text{Thermal problem} \end{aligned} \tag{1}$$

where the tensor $\mathbb{C}^{\mathrm{H}}$ is the homogenised elasticity tensor [7]. The objective function minimises a combination of the shear stiffness $\mathbb{C}^{\mathrm{H}}_{33}$ and the thermal compliance C_T, scaled by a weight factor α_T. The thermal compliance acts as a proxy for joint thickness, introduced following the virtual temperature method so that overly thin or disconnected regions are penalised [8]. The constraints enforce that the effective moduli $\mathbb{C}^{\mathrm{H}}_{11}$ and $\mathbb{C}^{\mathrm{H}}_{12}$ match the target bulk modulus κ_L, while a volume constraint ensures that the amount of solid material remains within bounds (V close to a prescribed value V_L). The design field $\rho \in [0, 1]$ describes the solid and void regions inside the cell. We apply this topology optimisation framework to design the unit cells of a 2D Lüneburg lens [9] for underwater acoustics. A circular Lüneburg lens is discretised into square unit cells that are optimised independently. The target properties for each cell are given by the local bulk modulus κ_L and density ρ_L, derived from the analytical profile of an impedance matched lens. The results demonstrate that the optimised structures provide accurate refractive index control, preserve constant impedance, and enable fluid-like wave propagation, making them ideal candidates for underwater metamaterial applications. Figure 1 shows that the effective properties of the cells are very close to the desired ones.

3. TRANSITION TO 3D: A NEW KINEMATIC APPROACH

The inverse design of a 3D PM can be solved by topology optimisation as before, but the solution is generally hard to realise, see for example [5]. In fact, while thin joints are sufficient for 2D metaliquids, applying this approach

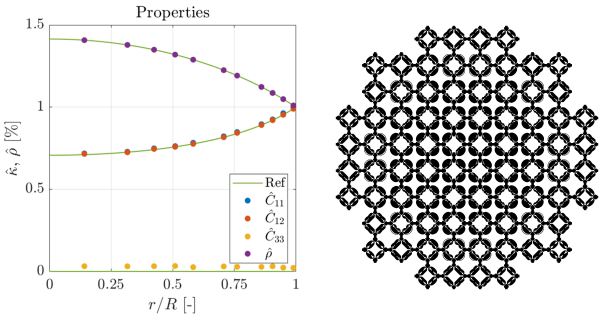


Figure 1: Left, properties of the optimised cells compared to the target; right, microstructure of the lens.

to three dimensions limits the bulk modulus to two orders of magnitude less than a liquid [6]. The effective stress tensor $\mathbb{C}^{\mathrm{H}}$ of an elastic network is computed as the summation over the boundary nodes of a cell as [10]

$$\mathbb{C}^{\mathrm{H}} = V^{-1} \sum_i \mathbf{r}_i \otimes \mathbf{f}_i, \tag{2}$$

where $\otimes$ is the outer product, $\mathbf{r}_i$ the position of the i^{th} node, and $\mathbf{f}_i$ the force applied to it. Note that the moments acting on the nodes have no effect. Therefore, we relax the hinge-hinge kinematics and instead design a link that acts as a slider, transferring not only axial forces but also momenta from one node to another. To address this, we propose a novel 3D pentamode metamaterial (PM) geometry inspired by the kinematics of ropes. Instead of relying on traditional pin-like junctions, our structure uses thin fibre links that behave like slider joints. This design enables the PM to replicate the acoustic properties of water in the low-frequency regime, achieving a near-perfect pentamode response. The proposed design is illustrated in Figure 2, where each titanium unit cell consists of massive nodes connected by multiple thin fibres acting as sliders. Repeating this unit cell results in a face-centred cubic lattice whose effective elastic tensor is:

$$\frac{\mathbb{C}^{\mathrm{H}}}{\kappa_{\mathrm{H_2O}}} = \begin{bmatrix} 1.04 & 1.01 & 1.01 & 1.4\times10^{-5} & -2.9\times10^{-5} & -2.1\times10^{-5} \\ & 1.04 & 1.01 & 1.9\times10^{-5} & -2.2\times10^{-5} & -1.9\times10^{-5} \\ & & 1.04 & 1.2\times10^{-5} & -2.3\times10^{-5} & -1.8\times10^{-5} \\ & & & 0.039 & -5.2\times10^{-6} & -5.8\times10^{-6} \\ & \text{sym} & & & 0.039 & 5.7\times10^{-6} \\ & & & & & 0.039 \end{bmatrix}, \tag{3}$$

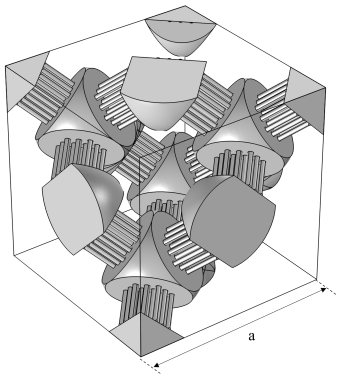


Figure 2: The PM lattice of the metal water.

where $\kappa_{H_20} = 2.2\,\mathrm{MPa}$ is the bulk modulus of water. The tensor $\mathbb{C}^{\mathrm{H}}$ is very close to that of water, with the terms in the upper left 3×3 matrix close to 1 and the remaining terms very small.

4. CONCLUSION AND FUTURE PERSPECTIVES

In this work, we propose two different approaches to the design of pentamode metamaterials aimed at replicating the acoustic properties of liquids. Topology optimisation has proven to be a flexible strategy for designing bimode materials for underwater applications, ensuring both manufacturability and precise control over the acoustic parameters.

When extending the design to three dimensions, a more complex topology is required. To address this, we introduce fibre-based slider-like connections that overcome the limitations of traditional pin-junction designs, achieving a nearly ideal pentamode material with a bulk modulus comparable to that of water. The proposed 3D structure exhibits a low shear modulus and impedance matching with water, making it a promising candidate for underwater acoustic applications such as invisibility cloaking. As a next step, we are preparing for experimental validation, which will include the fabrication of the proposed structures and their acoustic characterisation.

5. REFERENCES

[1] A. N. Norris, "Acoustic metafluids," *The Journal of the Acoustical Society of America*, vol. 125, no. 2, pp. 839–849, 2009.

[2] G. W. Milton and A. V. Cherkaev, "Which elasticity tensors are realizable?," *Journal of Engineering Materials and Technology*, vol. 117, pp. 483–493, 10 1995.

[3] M. Kadic, T. Bückmann, N. Stenger, M. Thiel, and M. Wegener, "On the practicability of pentamode mechanical metamaterials," *Applied Physics Letters*, vol. 100, p. 191901, 05 2012.

[4] Q. Li and J. S. Vipperman, "Three-dimensional pentamode acoustic metamaterials with hexagonal unit cells," *The Journal of the Acoustical Society of America*, vol. 145, pp. 1372–1377, 03 2019.

[5] D. Zhang, X. Zhai, L. Liu, and X.-M. Fu, "An optimized, easy-to-use, open-source gpu solver for large-scale inverse homogenization problems," *Structural and Multidisciplinary Optimization*, vol. 66, no. 9, p. 207, 2023.

[6] G. Brambilla, S. Cominelli, M. Verbicaro, G. Cazzulani, and F. Braghin, "High bulk modulus pentamodes: The three-dimensional metal water," *Extreme Mechanics Letters*, vol. 74, p. 102267, 2025.

[7] E. Andreassen and C. S. Andreasen, "How to determine composite material properties using numerical homogenization," *Computational Materials Science*, vol. 83, pp. 488–495, 2014.

[8] S. Liu, Q. Li, W. Chen, L. Tong, and G. Cheng, "An identification method for enclosed voids restriction in manufacturability design for additive manufacturing structures," *Frontiers of Mechanical Engineering*, vol. 10, pp. 126–137, 6 2015.

[9] R. K. Luneburg, *Mathematical theory of optics*. Univ of California Press, 1966.

[10] A. N. Norris, "Mechanics of elastic networks," *Proceedings of the Royal Society A: Mathematical, Physical and Engineering Sciences*, vol. 470, no. 2172, p. 20140522, 2014.

DOI: 10.61782/fa.2025.0464



FORUM ACUSTICUM
EURONOISE 2025

INCREASING HELMHOLTZ RESONATOR STABILITY AGAINST NON-LINEAR RESISTANCE INCREMENTS USING CHAMFERS

David Jun[1*] **Josef Plasek**[1] **Monika Rychtarikova**[2]
Zuzana Fisarova[1] **Christ Glorieux**[3]
[1] Brno University of Technology, Faculty of Civil Engineering, Brno, Czech Republic
[2] KU Leuven, Department of Architecture, Campus Brussels and Ghent, Brussels, Belgium
[3] KU Leuven, Department of Physics and Astronomy, Leuven, Belgium

ABSTRACT

Weakly damped Helmholtz resonators (WDHRs) are resonant devices with their surface resistance near resonance being substantially lower than the one of air and therefore the sound reflection at their resonance is out-of-phase. They are known for their absorption to increase with increasing in-neck velocities. This nonlinear effect is a consequence of turbulence and jets forming at the interfaces between the neck and the inner cavity and the exterior environment, causing increased acoustic resistance. In many cases, the level dependence of the behavior can be partially overcome by increasing the cavity or neck damping by enhanced increased level-independent resistance of an incorporated porous material, which leads to lower in-neck velocity magnitudes, but leads to at least partial loss of the WDHR-specific reflection characteristics. A WDHR with level-independent reflection characteristics would be beneficial for narrow-band room acoustic corrections such as damping of modes or their redistribution over the spectrum. In this work, chamfering of the resonator neck edges is used as a strategy to obtain a weakly damped resonator with sound pressure level independent behavior.

Keywords: *Helmholtz resonator, perforated board, neck shape, chamfer, impedance tube*

**Corresponding author*: *David.Jun@vut.cz.*
***Copyright**: ©2025 David Jun et al. This is an open-access article distributed under the terms of the Creative Commons Attribution 3.0 Unported License, which permits unrestricted use, distribution, and reproduction in any medium, provided the original author and source are credited.*

1. INTRODUCTION

Helmholtz resonators (HRs) are devices that can be used for acoustic applications by utilizing a compressible cavity with an open aperture (neck) in order to achieve subwavelength resonance. A weakly damped Helmholtz resonator (WDHR) is a variant of an HR, having its surface resistance near resonance substantially lower than that of air so that the sound reflection at its resonance is out-of-phase. Such behavior can be exploited for selective mode damping or manipulation [1–3] or scattering [4]. WDHRs are generally known for their characteristics being dependent on the in-neck velocity, which is also part of the focus of this contribution.

Ingard and Labate [5] studied the formation of vortices and jets on perforated boards and modeled the structure by defining four distinct regimes of nonlinear behavior in terms of the average particle velocity in the orifice. In the first region, vortices start to form around the orifice edges; in the fourth one, the turbulent jet is fully developed at least at one side of the orifice. It is worth noting that the authors pointed out that at resonance "nonlinear effects become of importance for sound pressure levels of about 65 dB for the incoming wave". The occurrence of nonlinear effects at this moderate sound pressure level makes the phenomenon relevant also for room acoustics. A few years later, Ingard [6] published his major work on Helmholtz resonator design, covering also the non-linear behavior. Ingard here introduced the following term for resonator resistance using neck end correction lengths:

$$\rho_0 c_0 \theta_{\text{total}} = \rho c(\theta_{\text{l}} + \theta_{\text{nl}}) = \frac{2R_s}{r_0}\left(t + \Delta_{\text{l}} + \Delta_{\text{nl}}\right) \quad (1)$$

where $\rho_0 c_0$ is the characteristic specific impedance

of air, ρ_0 the density, and c_0 the speed of sound in air. The dimensionless correction θ_{total} [-] accounts for both the linear θ_{l} [-] and non-linear θ_{nl} [-] end correction effects related to the apparent neck length in terms of losses. The surface resistance R_s is given by $R_s = 0.5\sqrt{2\mu\rho\omega}$ [kg·m^{-1}·s^{-1}], where μ is the dynamic viscosity, r_0 is the neck radius, and t is the plate thickness. Δ_{l} and Δ_{nl} are the linear and non-linear end correction lengths for the neck length. According to his work, the linear end correction is given by $\Delta_{\text{l}} = 2r_0 = d$, and the non-linear end correction Δ_{nl} can be expressed for sufficiently thick plates using the empirical equation:

$$\frac{\Delta_{\text{nl}}}{d} = C u_0^n \tag{2}$$

where C and n are parameters that might show some frequency dependence and u_0 [m/s] is the particle velocity magnitude in the aperture. The work of Blackman [7], however, reported experimental results that aligned rather poorly with the above model. Later, Ingard and Ising [8] further refined his findings, showing that at high pressure levels (in the 4th regime), the resistance of the orifice is approximately given by

$$R \approx \rho_0 u_0 \tag{3}$$

Melling [9] further extended this relation by invoking the particle velocity-dependent "orifice discharge coefficient", C_D [-], as part of the proportionality factor between R and ru_0. The discharge coefficient was known from fluid dynamics and had been studied already in a steady-state situation with constant flow by Johansen and Southwell [10]. While Melling [9] was mainly interested in the highest nonlinear regime, where C_D asymptotically reaches a constant value, the earlier steady flow-focused work of Johansen and Southwell [10] showed the potential of this parameter to identify and describe also the remaining regimes. Despite that, no model has been proposed for these lower regimes by any of the authors mentioned above.

More recently, the non-linear behavior in the orifice was exploited in micro-perforated panels (MPP) and was characterized via a non-linear impedance [11–14]. Investigations of non-linear HR behavior (or more generally, perforated plates) are still ongoing, mainly at high sound pressure levels [15] or for measurement applications [16].

In room acoustics-related applications, sound pressure level (SPL)-dependent damping characteristics are typically not considered or generally unwanted, since the most common room acoustic measures rely on linear acoustics assumptions. The objective of the current work is to reduce nonlinearities by shifting the transition from the first most weakly nonlinear regime to the other ones towards higher SPL levels. This approach is followed by chamfering the neck edges.

2. METHODS

The insight on the effect of chamfering was gained by analyzing the in-neck velocity, the in-neck Reynolds number, and the incident pressure, which were extracted from impedance tube measurements. The two-microphone impedance tube method was used according to ISO 10534-2 [17]. In this method, the pressure reflection factor of the WDHR resonator, r, is retrieved from the transfer function measured between two microphone positions, $H_{12} = \frac{p_2}{p_1}$, where p_1 and p_2 are the acoustic pressures measured at the respective microphone positions. The surface acoustic impedance was then obtained from the pressure reflection coefficient via

$$Z_s = R + jX = \frac{1+r}{1-r} \cdot Z_0, \tag{4}$$

where R, the real part of Z_s, is the surface resistance, X is the surface reactance, and $Z_0 = \rho_0 c_0$ is the characteristic impedance of air. The impedance tube used in this study was a next-generation version of the one used and validated in [18]. The tube in this study was made out of steel and had a square cross-section. The lateral dimensions were 102×102 mm^2, the steel wall thickness was 4 mm, and the rigid termination was 30 mm deep. The tube corners were rounded with a radius of 4 mm. The tube frequency range, given by its geometry, was 40 Hz to 1680 Hz. The acquisition chain consisted of two Behringer ECM8000 microphones, a Focusrite Scarlett 18i20 Gen3 sound card, and a Fedora Linux-powered mini PC running Python-based "imptube" software [18]. On the sound source side, a logarithmic sweep was played through a t.amp S75 MKII power amplifier and a low to medium frequency range 6.5" loudspeaker with a working frequency range of 40 to 4500 Hz.

At first, in the analysis phase, the instantaneous sound pressure $p_{m,\text{norm}}(f)$ in the tube was obtained according to Figure 1. The input sweep $y_{\text{in}}(t)$ was normalized to the full-scale range of -1 to 1, and its spectrum was used as a reference $y_{\text{in,norm}}(f)$ for calculating the instantaneous values relative to full scale $y_{m,\text{norm}}(f)$.

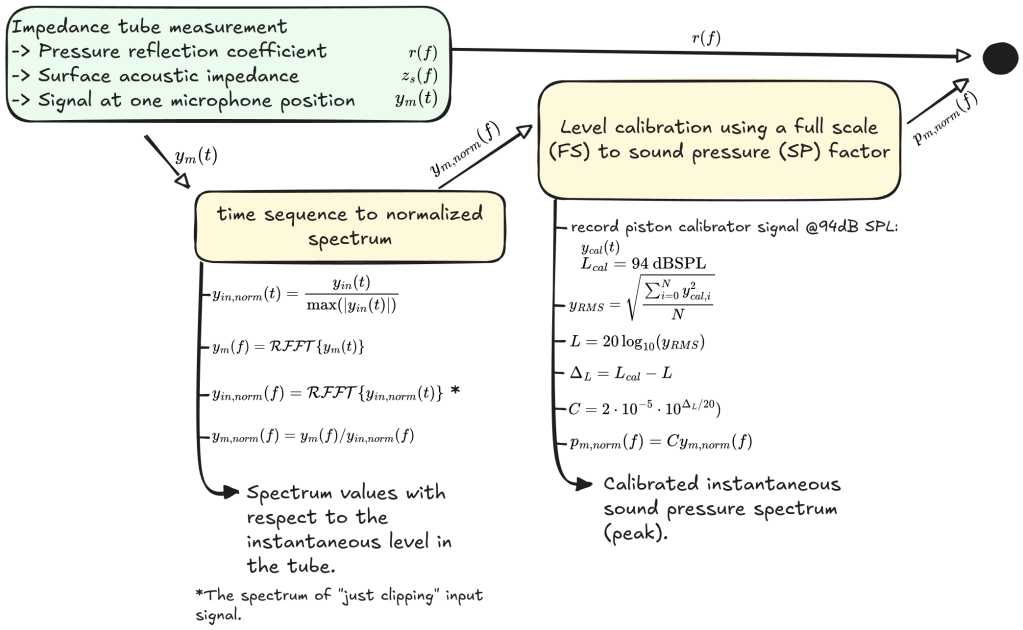


Figure 1. Procedure for obtaining the instantaneous sound pressure from an impedance tube measurement. The measured time sequence was first transformed to frequency domain and then divided by the "just-clipping" input sweep spectrum. That led to a spectrum expressing for each frequency its headroom towards clipping. Level calibration was based on a piston calibrator measurement, its RMS level and the subtraction of the calibrator level value (94 dB) and the recorded signal value. The latter was converted to a factor applied to the instantaneous pressure spectrum.

$$y_{m,\text{norm}}(f) = \frac{y_m(f)}{y_{\text{in,norm}}(f)} \tag{5}$$

This representation yields the spectrum with respect to the instantaneous level in the tube for each frequency bin. These values were converted to the physical pressure $p_{m,\text{norm}}(f)$ using a piston calibrator of known RMS SPL level.

Assuming plane wave propagation normal to the test specimen, the sound field can be decomposed into two opposing waves, and the homogeneous particle velocity can be obtained as a function of the acoustic pressure at a microphone position, $p(x_m)$, and the pressure reflection factor at the specimen surface r.

$$u(x=0) = \frac{p(x_m)\cdot(1-r)}{Z_0\left(e^{-jkx_m} + re^{jkx_m}\right)} \tag{6}$$

The average particle velocity in the neck of a plate perforation can be expressed as

$$u_0 = \frac{u(x=0)}{\phi} \tag{7}$$

where $\phi = \frac{A_n}{A}$ is the open plate porosity, i.e., the ratio between the neck cross-section surface A_0 and the total specimen surface A. The velocity can be used for calculating the in-neck Reynolds number Re:

$$\text{Re} = \frac{\rho_0 u_0 L}{\mu} \tag{8}$$

where L is the characteristic length (in this case, the perforation diameter d), $\mu = 1.84 \times 10^{-5}$ Pa·s is the dynamic viscosity of air, and u_0 is the particle velocity magnitude. Similarly, the in-neck displacement ξ [m] can be obtained:

$$\xi = \frac{u_0(f)}{i\omega} \tag{9}$$

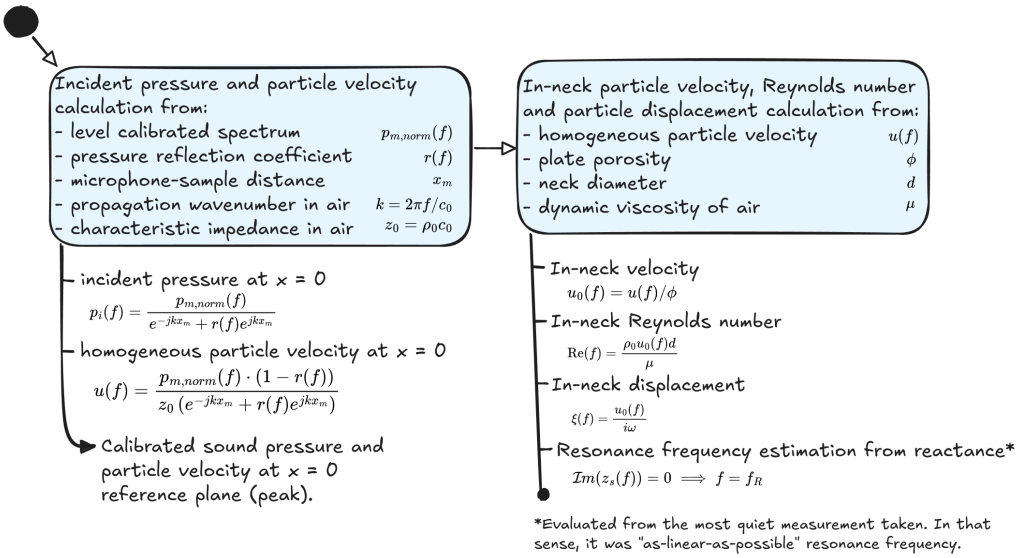


Figure 2. Calculation summary for the incident pressure, in-neck particle velocity, Reynolds number and displacement.

Similarly to the homogeneous velocity, also the incident pressure can be obtained from a plane wave reflection measurement as

$$p_i = \frac{p(x_m)}{e^{-jkx_m} + re^{jkx_m}}. \tag{10}$$

The calculation overview is shown in Figure 2.

3. RESULTS AND DISCUSSION

Two perforated plate variants were measured under different pressure levels in the tube. Both shared most of the geometrical parameters: the neck diameter $d = 12\,\mathrm{mm}$, the virtual neck spacing (the lateral dimension of the tube) $D = 102\,\mathrm{mm}$, the plate thickness $t = 9\,\mathrm{mm}$, and the cavity depth behind the plate $d_c = 200\,\mathrm{mm}$. The only changing parameter was the presence/absence of a 1 mm deep chamfer cut at 45° from both sides of the neck.

In the following, the quantities are presented only at the resonance frequency obtained from the acoustic reactance of the most quiet measurement. In that sense, it was the as-linear-as-possible resonant frequency obtained through measurements. This choice was done for two reasons, which appeared during the analysis: (a) At the resonance frequency, HRs show a rather simple behavior of either completely in- or out-of-phase response, leading to a pressure maximum or minimum directly in the neck. (b) The response at the resonance frequency seems to drive also the response in its vicinity. More precisely, a similar degree of nonlinearity is observed near the resonance, even though the calculated in-neck velocities differ.

Figure 3 shows the normal incidence absorption coefficient with respect to the incident pressure level. In both cases, the values started at about 0.5 for lower levels, reach a maximum, and start to decrease again. The decrease happens when the acoustic resistance crosses the characteristic impedance of air. Maximum absorption is reached for both cases at different levels, which are approximately 3.5 dB apart in incident SPL. The average difference for $0.5 < \alpha < 0.9$ between the two cases is $\Delta L_p = 10.6 \pm 3.2\,\mathrm{dB}$. Since the analysis does not account for the resonance frequency shift at high levels, the chamfered variant does not reach the $\alpha = 1$ point.

Figure 4 puts the findings in the context of in-neck velocity and Reynolds number. These results can be qualitatively compared to the previous studies. Johansen and Southwell [10] reported for low porosity plates that the transition between the weakly velocity-dependent regime 1 and the strongly velocity-dependent regime 4 happens at $10 < \sqrt{\mathrm{Re}_0} < 40$, which seems to align rather well with the presented results. For the chamfered variant, this transition is shifted towards higher Reynolds num-

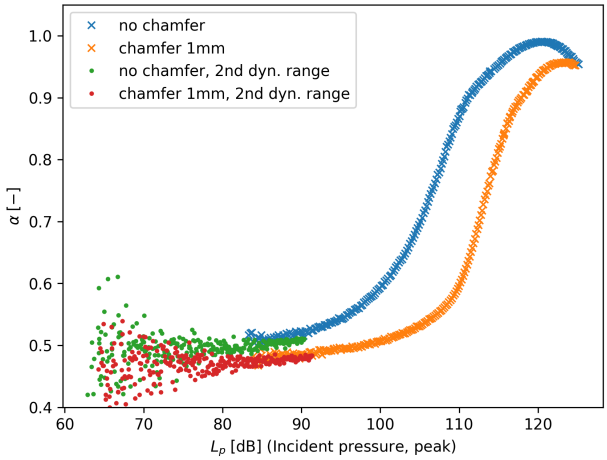


Figure 3. Normal incidence absorption coefficient at the resonance frequency as a function of incident SPL level (peak). Two dynamic ranges of measurements were tested for both orifice variants. In the first one (blue and orange), there is a minor offset between the levels of approx. 0.2 dB, in the second one 0.1 dB (green and red).

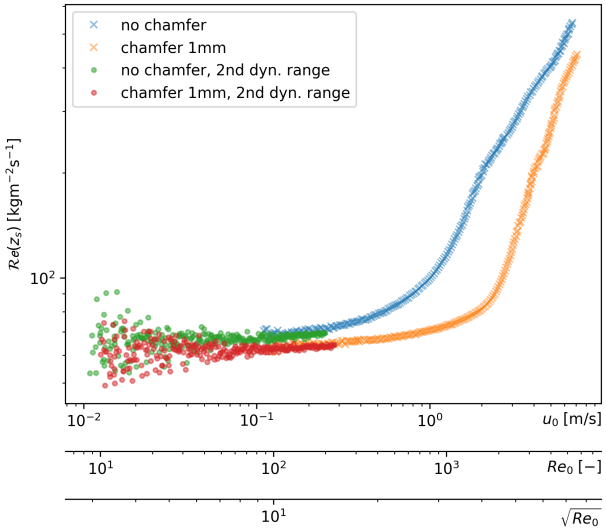


Figure 4. Normal incidence surface resistance as a function of in-neck velocity amplitude, Reynolds number and its square root. Two dynamic ranges of measurements were tested for both orifice variants. In the first one (blue and orange), input sweep level spacing is approx. 0.2 dB, in the second one 0.1 dB (green and red).

bers. When comparing to Ingard and Labate [5], we need to extrapolate their findings. At 224 Hz and for a plate thickness of 9 mm, they located the transition between $0.5 < u_0 < 2$ m/s. Based on their experiments and assumptions, both values of this range should decrease towards lower frequencies. In the present case, the transition roughly happens in the range originally assigned to $f = 224$ Hz.

It is important to note that it is not feasible to strictly connect the definitions of the different regimes between different authors, such as Ingard and Labate, Johansen, or Melling. For Labate and Ingard, regime 4 started when the turbulent jet appears at least on one side of the plate. In the view of Johansen's and Melling's discussions, no strict transition boundaries were mentioned, but a full turbulent jet was assumed as the limit at which the discharge coefficient stabilizes and which could be seen as the boundary of the final regime.

4. CONCLUSIONS

The objective of this study was to extend the weakly non-linear regime of a Helmholtz resonator reflection response towards higher incident sound pressures. The effect of neck chamfering was studied under normal incidence conditions in an impedance tube. The instantaneous sound pressure amplitude was used to calculate the in-neck velocity and the Reynolds number in order to allow for a more in-depth view of the problem. The results for the sharp-edge variant were found to be in good qualitative agreement with previous studies [5, 6, 10]. The chamfered variant showed an uplift of $\Delta L_p = 10.6 \pm 3.2$ dB in terms of the level difference at which the transition to more strongly non-linear regimes happens.

Future research should focus on a more parameter-rich and in-depth description of the different non-linear regimes as well as on the neck shape influence on them. For the sake of comparison, steady flow measurements should be conducted in a flow resistivity setup to further verify the discharge coefficients obtained acoustically and under steady flow.

5. ACKNOWLEDGMENTS

This project has received funding from the European Union's Horizon Europe research & innovation programme under the HORIZON-MSCA-2021-DN-01 grant agreement No. 101072598 – "ActaReBuild". The contribution was produced also with support for specific university research at Brno University of Technology, FAST-S-24-8572 and FAST-S-25-8768.

6. REFERENCES

[1] F. J. Fahy and C. Schofield, "A note on the interaction between a Helmholtz resonator and an acoustic mode of an enclosure," *Journal of Sound and Vibration*, vol. 72, pp. 365–378, Oct. 1980.

[2] J. Klaus, I. Bork, M. Graf, and G. P. Ostermeyer, "On the adjustment of Helmholtz resonators," *Applied Acoustics*, vol. 77, pp. 37–41, 2014.

[3] D. Jun, J. Plasek, M. Rychtarikova, and C. Glorieux, "Room modes in rectangular rooms with complex impedance boundaries," in *Juniorstav 2024: Proceedings 26th International Scientific Conference Of Civil Engineering*, (Brno, Czech republic), p. 8, Brno University of Technology, 2024.

[4] N. Jiménez, T. Cox, V. Romero-García, and J.-P. Groby, "Metadiffusers: Deep-subwavelength sound diffusers," *Scientific Reports*, vol. 7, Dec. 2017.

[5] U. Ingard and S. Labate, "Acoustic Circulation Effects and the Nonlinear Impedance of Orifices," *The Journal of the Acoustical Society of America*, vol. 22, pp. 211–218, Mar. 1950.

[6] U. Ingard, "On the theory and design of acoustic resonators," *Journal of the Acoustical Society of America*, vol. 25, no. 6, pp. 1037–1061, 1953.

[7] A. W. Blackman, "Effect of Nonlinear Losses on the Design of Absorbers for Combustion Instabilities," *ARS Journal*, vol. 30, pp. 1022–1028, Nov. 1960.

[8] U. Ingard and H. Ising, "Acoustic Nonlinearity of an Orifice," *The Journal of the Acoustical Society of America*, vol. 42, pp. 6–17, July 1967.

[9] T. H. Melling, "The acoustic impendance of perforates at medium and high sound pressure levels," *Journal of Sound and Vibration*, vol. 29, pp. 1–65, July 1973.

[10] F. C. Johansen and R. V. Southwell, "Flow through pipe orifices at low Reynolds numbers," *Proceedings of the Royal Society of London. Series A, Containing Papers of a Mathematical and Physical Character*, vol. 126, pp. 231–245, Jan. 1930.

[11] D.-Y. Maa, "Microperforated panel at high sound intensity," in *Proceedings of Inter Noise 94*, (Yokohama, Japan), pp. 1511–1514, 1994.

[12] D.-Y. Maa, "Potential of microperforated panel absorber," *The Journal of the Acoustical Society of America*, vol. 104, pp. 2861–2866, Nov. 1998.

[13] S.-H. Park, "A design method of micro-perforated panel absorber at high sound pressure environment in launcher fairings," *Journal of Sound and Vibration*, vol. 332, pp. 521–535, Feb. 2013.

[14] Z. Laly, N. Atalla, and S.-A. Meslioui, "Acoustical modeling of micro-perforated panel at high sound pressure levels using equivalent fluid approach," *Journal of Sound and Vibration*, vol. 427, pp. 134–158, Aug. 2018.

[15] A. Komkin, A. Bykov, and M. Mironov, "Experimental study of nonlinear acoustic impedance of circular orifices," *The Journal of the Acoustical Society of America*, vol. 148, pp. 1391–1403, Sept. 2020.

[16] E. Di Giulio, R. Di Leva, and R. Dragonetti, "Theoretical and Experimental Assessment of Nonlinear Acoustic Effects through an Orifice," *Acoustics*, vol. 6, pp. 818–833, Dec. 2024.

[17] "ISO 10534-2:1998, Acoustics-Determination of sound absorption coefficient and impedance in impedance tubes-Part 2: Transfer-function method," 1998.

[18] D. Jun and J. Plasek, "Impedance Tube Solution for Helmholtz Resonator Prototyping," *Acoustics Australia*, Jan. 2025.

DOI: 10.61782/fa.2025.0844

FORUM ACUSTICUM EURONOISE 2025

SWITCHING ROOM ACOUSTICS WITH CAUSALITY-DRIVEN DUAL-FUNCTION PASSIVE METAMATERIALS FOR BROADBAND SOUND ABSORPTION AND DIFFUSION

E. Ballestero [1*] **Y. Meng**[1] **P. Sheng**[2]
V. Tournat[1] **V. Romero-García**[3] **J.-P. Groby**[1]
[1] Laboratoire d'Acoustique de l'Université du Mans (LAUM),
Institut d'Acoustique - Graduate School (IA-GS), UMR CNRS 6613, Le Mans, France.
[2] Institute for Advanced Study, Hong Kong University of Science and Technology,
Clear Water Bay, Kowloon, Hong Kong, China.
[3] Instituto Universitario de Matemática Pura y Aplicada (IUMPA),
Universitat Politècnica de València, Spain.

ABSTRACT

Acoustic metamaterials offer unique capabilities for achieving exceptional performance at low frequencies with compact designs. However, many existing designs focus on single-function applications, leaving a need for multi-functional solutions. To address this, we propose a Dual-Function Passive Acoustic Metamaterial (DFPAM) that integrates sound absorption and diffusion within the same structure by applying principles of causality and passivity. The DFPAM delivers broadband performance with excellent sound absorption ($< \alpha >= 0.85$) and diffusion ($< \delta >= 0.8$) over 1 octave and a half each, i.e., 400-1100 Hz for absorption and 1000-2500 Hz for diffusion. With a compact thickness of 12 cm-nearly half the size of traditional treatments-it efficiently uses space (1/3 for absorption, 2/3 for diffusion) while optimizing the performance of each state. Importantly, it mitigates the trade-offs often associated with combining these two acoustic mechanisms. This solution offers significant potential for room acoustics and environments where space is at a premium. By addressing multi-functional requirements with dual efficiency, The DFPAM offers transformative possibilities for room acoustics and can be adapted to diverse environments where multi-functional acoustic solutions are in increasing demand.

Keywords: *absorption, diffusion, hybrid materials, metamaterial, passivity*

1. INTRODUCTION

Most existing acoustic metamaterial solutions remain configuration-dependent, addressing either sound absorption or diffusion, but rarely both. Hybrid solutions attempting to integrate these functions have often been constrained by physical and spatial trade-offs, leading to suboptimal performance.

In this work, we adopt a causality-driven approach to design a Dual-Function Passive Acoustic Metamaterial (DFPAM) that optimizes both absorption and diffusion within a single structure.

2. DESIGN PRINCIPLE

Absorption and diffusion of acoustic waves are contrastive effects as the former needs to dissipate the acoustic energy and the latter needs to scatter the waves with minimal dissipation. In the present case, we intend to use a strategy based on rigidly-backed slits loaded by an array of Helmholtz resonators as shown in Fig. 1(a).

**Corresponding author*: *Jean-Philippe.Groby@univ-lemans.fr.*

***Copyright**: ©2025 Ballestero et al. This is an open-access article distributed under the terms of the Creative Commons Attribution 3.0 Unported License, which permits unrestricted use, distribution, and reproduction in any medium, provided the original author and source are credited.*

By analyzing the sum rule given by the passivity/causality conditions of the acoustic system accounted for in this work, it is possible to evaluate the optimal value of the absorption-to-diffusion surface area ratio, $\phi_{\alpha|\delta}$, with a given target absorption spectrum. A depth of 12 cm is chosen in order to provide a solution that fits within dimensions similar to other metamaterial designs reported in the literature. It follows that $\min\left(\phi_{\alpha|\delta}\right) \approx 0.33$. Starting from a 3×3 square grid for the quarter of unit-cell with a combinatorial ratio of absorption cells to overall cells $\phi_\alpha = 1/3$, there are a total of 84 possible combinations. Due to mirror symmetries and further physical considerations regarding the choice of tesselation pattern and diffusion optimality, the rhombus depicted in Fig. 1(a) happens to be one of the best candidates available for sound diffusion. We finally make use of non-linear constrained minimization algorithms for maximizing both absorption and diffusion as well as determining their respective geometries. Figures 1(b-c) display the analytical, numerical and experimental sound diffusion and absorption coefficients obtained throughout this study. The DFPAM achieves high broadband sound absorption ($<\alpha>\approx 0.85$) and diffusion ($<\delta>\approx 0.8$), covering more than one octave in each configuration. For more details, the reader can refer to [1].

3. CONCLUSION

In this work, we present a dual-function metasurface capable of achieving high values of absorption, $<\alpha>= 0.85$, and diffusion, $<\delta>= 0.8$, for different broadband frequency ranges covering more than one octave in each configuration, i.e., $\Delta\alpha = [400, 1100]$ Hz, and $\Delta\delta = [1000, 2500]$ Hz, while still maintaining compact dimensions.

4. ACKNOWLEDGEMENTS

The authors gratefully acknowledge the ANR-RGC METARoom (No. ANR-18-CE08-0021) project. E.B. acknowledges N. Pajusco and B. Hamilton for their great help in the numerical room simulations.

5. REFERENCES

[1] E. Ballestero, Y. Meng, P. Sheng, V. Tournat, V. Romero-García, and J.-P. Groby, "Transforming room acoustics with causality-driven dual-function passive metamaterials," *Advanced Materials Technologies*, p. 2402082, 2025.

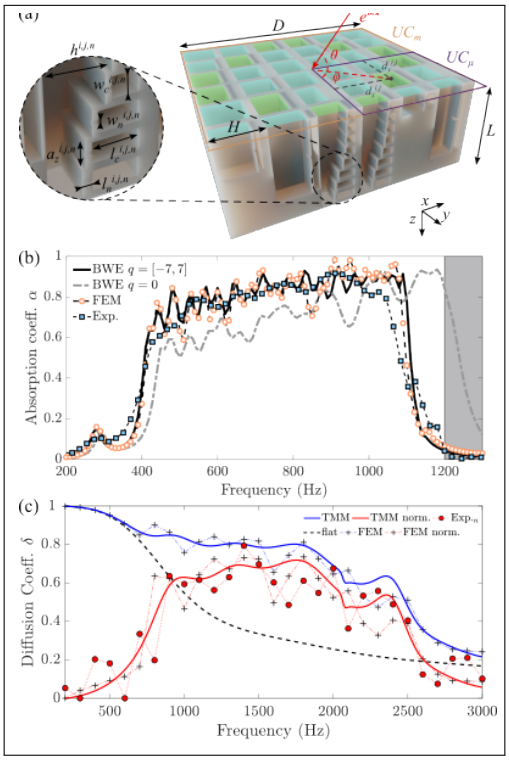


Figure 1. (a) 3D visualization of the DFPAM of side width $D = 30$ cm and depth $L = 12$ cm, with highlights on the micro unit cell (violet), used for absorption measurement in a square impedance tube and the overall macro unit cell (orange), which is formed by two-fold mirror symmetry. (inset) Geometrical parameters of the $(x, y) \rightarrow (i, j)$ slit for the n-th slit resonator section of height h and depth a_z. (b) Analytical, numerical and experimental absorption coefficients overlayed with those of each individual slits. (c) Analytical, numerical and experimental frequency-dependent diffusion coefficient $\delta(\omega)$.

DOI: 10.61782/fa.2025.0760

FORUM ACUSTICUM EURONOISE 2025

ROTATABLE PHONONIC CRYSTAL WITH MULTIRESONANT SCATTERERS FOR ACOUSTIC SWITCHING APPLICATIONS

David Ramírez-Solana[1,2,3,4*] **Valentino Sangiorgio**[2,3] **Rubén Picó**[2]
Javier Redondo[2] **Muhammad Gulzari**[1] **Maria Pia Fanti**[4]
[1] Structured Materials and Dynamics Lab, School of Civil Engineering, University College Dublin, Ireland
[2] Instituto de Investigación para la Gestión Integrada de Zonas Costeras, Universitat Politècnica de València, Gandía, Spain
[3] Department of Engineering and Geology (INGEO), D'Annunzio University of Chieti-Pescara, Pescara, Italy
[4] Department of Electrical and Information Engineering, Politecnico di Bari, Bari, Italy

ABSTRACT

This study presents an acoustic switch based on a sonic crystal (SC) with multiresonant scatterers arranged in a square 2D lattice. The scatterers feature Helmholtz resonators (HRs) tuned to different frequencies. A 90° rotation of all scatterers enables switching the interaction between Bragg bandgaps (Bragg- BGs) and Helmholtz resonator (HR) bandgaps, creating selective frequency filtering and wave propagation control. The research targets low to mid frequencies (500-2500 Hz), an underexplored range in current studies. The structure, made via cost-effective 3D printing without infill to reduce absorption, is both simple and practical. Tests in an anechoic chamber reveal a notable 20 dB contrast in acoustic insulation. This design offers potential applications in noise reduction for urban and industrial settings, adaptive acoustic systems, sensors, and acoustic energy harvesting.

Keywords: *Acoustic Switch, Helmholtz Resonators, Multiresonant Scatterer.*

**Corresponding author*: *david.ramirezsolana@ucd.ie.*
Copyright: *©2025 Ramírez-Solana et al. This is an open-access article distributed under the terms of the Creative Commons Attribution 3.0 Unported License, which permits unrestricted use, distribution, and reproduction in any medium, provided the original author and source are credited.*

1. INTRODUCTION

Phononic crystals are periodic structures composed of rigid scatterers embedded in a fluid. A particular case of phononic crystals is the so-called Sonic Crystals (SCs), where the fluid is air. They allow fluid and light passage while blocking specific acoustic frequencies due to multiple scattering effects [1]. These frequency gaps, known as Bragg Bandgaps (Bragg-BGs) [2], depend on the lattice periodicity. The first Bragg-BG for a square lattice under normal incidence occurs at $f_{\text{Bragg}} = c/2a$, where c is the sound speed in air and a is the lattice parameter [3].

SCs have been extensively studied since Kock and Harvey's pioneering work [1], enabling applications in waveguides [4], diffusers [5], noise barriers [6, 7], and switches [8]. Beyond Bragg scattering, local resonances, particularly from Helmholtz resonators (HRs) [9], create additional bandgaps (HRs-BGs). Their frequencies depend on the internal cavity and mouth orientation, offering enhanced wave control [10, 11].

Most acoustic metamaterials operate passively within fixed frequency ranges, limiting adaptability [12]. Phononic crystals with asymmetric scatterers have demonstrated switching capabilities in high-frequency regimes (around 300 kHz) by independently varying scatterer angles [13].

This study introduces a multiresonant SC-based acoustic switch. Each scatterer consists of two perpen-

dicular HRs, enabling two distinct configurations: 0° and 90°, relative to the incident wave. These orientations determine selective frequency filtering by tuning Bragg- and HRs-BGs. The switch functionality requires mechanical adjustment of all scatterers.

The paper is structured as follows: Section Fig. 2 details the methodology, covering numerical modeling (II.A), 3D printing (II.B), and experimental validation (II.C). Section Fig. 3 presents numerical and experimental comparisons, assessing the device's performance. Finally, Section Fig. 4 summarizes key findings and practical applications.

2. MATERIALS AND METHODS

We analyze a 2D sonic crystal (SC) composed of scatterers with Helmholtz resonators (HRs) arranged in an infinite periodic square lattice. The unit cell, illustrated in Fig. 1a, consists of a scatterer with an outer radius R and two apertures forming HRs with distinct resonant frequencies. Periodic boundary conditions are applied along the X and Y boundaries to model the infinite SC, characterized by a constant square lattice parameter a and the unit cell of the irreducible Brillouin zone in reciprocal space [14]. The HRs are defined by the neck length L (thickness and difference between outer and inner radii), mouth width w, and inner surface area S. The first resonant frequencies of the HRs oriented at 0° and 90° are given by [15]:

$$f_{HR}^{0°/90°} = \frac{c}{2\pi}\sqrt{\frac{w}{(L+\delta\frac{w}{2})S_{0°/90°}}} \tag{1}$$

where δ is the correction factor for the effective neck length, accounting for the neck-cavity junction effects due to sudden changes in circular cross-sections (typically between 1.6 and 1.8).

The first resonances of the HRs ($f_{\text{HR}}^{0°}$ and $f_{\text{HR}}^{90°}$) relative to the central frequency of the Bragg bandgap (f_{Bragg}) are critical in determining their interaction with the periodic structure. Notably, the inclusion of HRs in an SC does not inherently reduce transmission through the structure [11]. Therefore, careful attention must be given to the alignment of the HR mouths and their fundamental frequencies. Fig. 1a depicts a scatterer with two HRs aligned at 0° and 90°, with coupled surfaces and a 110° angle between the separation walls. The central frequency of the Bragg bandgap is $f_{\text{Bragg}} = 1400$ Hz, with the HRs' fundamental frequencies at the extremes of the first Bragg bandgap. The larger cavity (90°) has $f_{\text{HR}} = 760$ Hz $> f_{\text{Bragg}}$, while the smaller cavity (0°) has $f_{\text{HR}} = 1800$ Hz $< f_{\text{Bragg}}$. Both HRs share identical mouth dimensions ($w = 0.025$ m) and neck length ($L = 0.006$ m).

Thermoviscous losses in the medium are negligible in this study due to the dimensions of the multiresonant scatterers and the low frequency range of interest (see Appendix A in ref [11]). At a measurement temperature of 293 K and the lowest operational frequency of 500 Hz, the viscous and thermal boundary layers in air are calculated to be 116 μm and 97.8 μm, respectively. These values are 1.56% and 1.85% of the neck length $L = 0.006$ m, well below the 5% threshold known to affect acoustic performance in small cavities [16].

The band structure is calculated for different propagation directions (ΓX, XM, MX', $X'\Gamma$), as shown in the inset of Fig. 1a. These directions correspond to the unit cell of the SC and the irreducible Brillouin zone of the square lattice, based on Bloch-Floquet theory [14]. Numerical simulations evaluate transmission in two configurations: ΓX for the 0° orientation and $X'\Gamma$ for the 90° orientation. Periodic boundary conditions (PBC) are applied along the Y-direction to emulate an infinite SC, while the X-direction is limited to three rows of scatterers for practical modeling (see Fig. 1b and Fig. 1c).

Both transmission models use a lattice parameter $a = 0.12$ m. The geometric model of the SC and the unit cell represent the same periodic structure, a 2D square lattice. However, while the unit cell represents an infinite system, the transmission models consist of three-layer systems with infinite lateral extension. A harmonic plane wave with frequency f and acoustic pressure P_i propagates along the X-axis, aligned with the mouth of the higher-frequency HR in Fig. 1b and the lower-frequency HR in Fig. 1c (referred to as 0° and 90° alignments). Perfectly matched layers (PML) are placed at the ends of the X-axis to absorb outgoing waves.

Transmission is determined using pressure fields (P_t) evaluated at specific points (shown in Fig. 1b and Fig. 1c), positioned 1 m from the SC. Fig. 1d shows a numerical model simulating the experimental setup described in Section 2.2. This 2D simulation replicates expected experimental conditions, enabling direct comparison between numerical predictions and experimental results. The evaluation region is defined by a grid with points spaced at intervals of $a/4 = 0.03$ m, allowing accurate analysis of the transmitted pressure field in the frequency range of interest.

In Fig. 1d, the source is represented by a vertical line emitting an acoustic pressure of 1 Pa, located 0.5 m from the nearest scatterers. The evaluation region spans 0.5 m

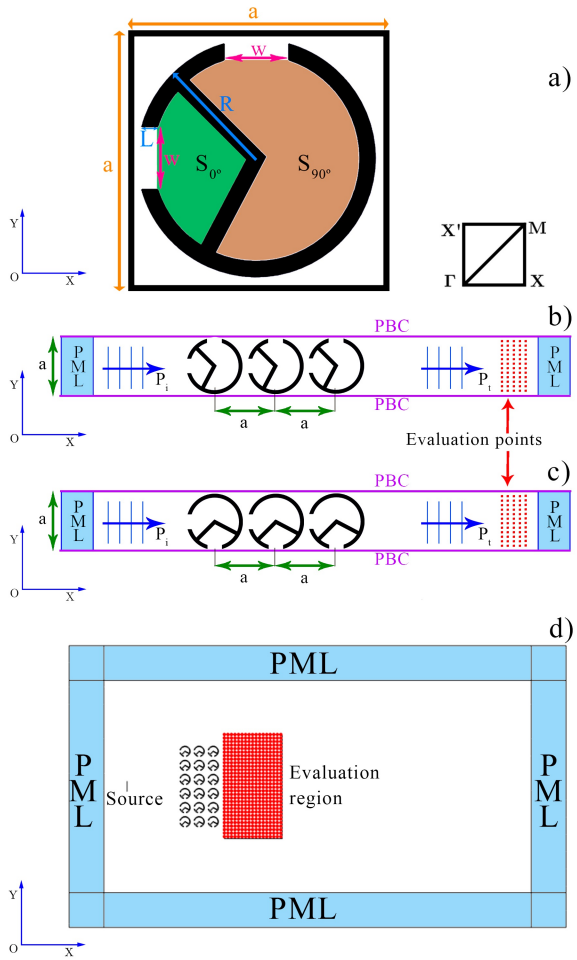


Figure 1. (a) Unit cell with two Helmholtz resonators; inset shows paths in the irreducible Brillouin zone. (b) and (c) Transmission models for 0° and 90° orientations. (d) Full numerical model corresponding to the experimental setup.

along the x-axis and 1.1 m along the y-axis, with the closest measurement points 0.05 m from the last scatterer row and the furthest points 0.55 m away. The y-axis evaluation region is centered relative to the SC array (3 columns by 6 rows), leaving 0.09 m between the evaluation region and the top and bottom edges of the SC structure.

Transmittance ($\mathbb{T}$) is defined as:

$$\mathbb{T} = \frac{\langle P_{t,with}^2 \rangle}{\langle P_{t,without}^2 \rangle} \tag{2}$$

where $\langle\rangle$ denotes the average over all evaluation points, $P_{t,without}$ is the acoustic pressure without the SC, and $P_{t,with}$ is the transmitted acoustic pressure with the SC. Insertion loss (IL) in decibels is derived from Eq. 2:

$$\text{IL} = -10 * \log_{10}(\mathbb{T}), \text{ [dB]} \tag{3}$$

This equation quantifies the change in sound pressure level (SPL) at the evaluation points when the SC is placed in the path of the incident acoustic wave.

The transmission coefficient $\mathbb{T}$ is used to compare the performance of the SC configurations across different frequency ranges. Asymmetric transmission, quantified by the Contrast Ratio (CR) [17, 18], measures the difference in transmission for waves incident from opposite directions. In this study, CR is evaluated based on the comparison of two scatterer orientations, with wave incidence from left to right along the x-axis. The 0° orientation corresponds to the ΓX direction in reciprocal space, while the 90° orientation corresponds to the $X'\Gamma$ direction. The CR is given by:

$$CR = \frac{|\mathbb{T}_{0^\circ} - \mathbb{T}_{90^\circ}|}{|\mathbb{T}_{0^\circ} + \mathbb{T}_{90^\circ}|}, \tag{4}$$

where $\mathbb{T}_{0^\circ}$ and $\mathbb{T}_{90^\circ}$ represent the transmission coefficients for the ΓX and $X'\Gamma$ directions, respectively. The CR quantifies the contrast in wave propagation between the two perpendicular orientations of the multiresonant scatterers, with a maximum value of 1 indicating complete suppression of transmission in one orientation and a minimum value of 0 indicating identical transmission in both orientations.

2.1 Numerical Analysis

This section explores the simulation results based on the geometry described in Section 2, focusing on the band structure and transmission of an incident plane wave. The interaction between the Bragg bandgap and HRs yields increased transmission, particularly due to the alignment of the resonators' mouths. The band structure, calculated using finite element analysis with Floquet periodicity conditions, is shown in Fig. 2. The complete Bragg bandgaps for all propagation directions (ΓX, XM, MX', $X'\Gamma$) are shown in gray, while partial bandgaps for 0° (ΓX) and 90° ($X'\Gamma$) are shown in blue and red, respectively.

The transmission ($\mathbb{T}$) is shown adjacent to the band structure. Transmission values close to zero occur at frequencies corresponding to the partial bandgaps for each orientation, highlighting the acoustic switching function

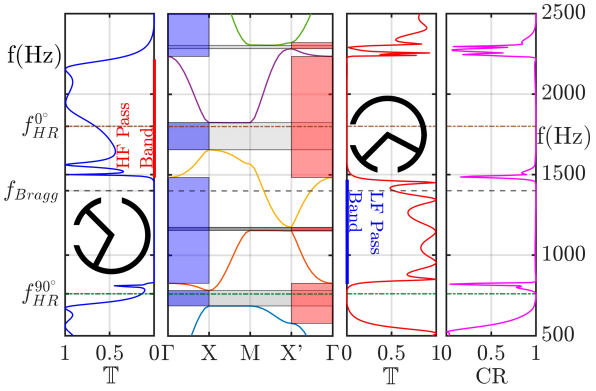


Figure 2. Band structure diagram and perpendicular transmission spectra.

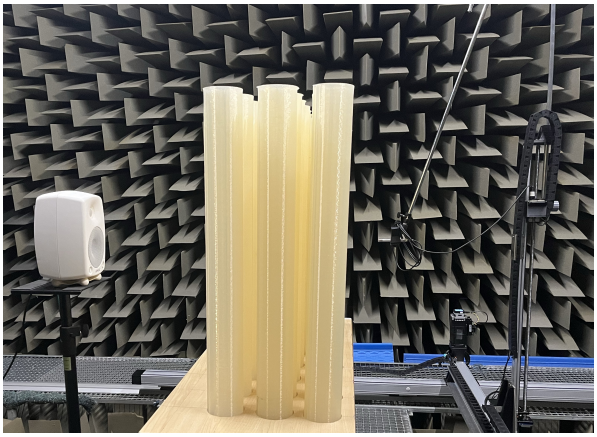


Figure 3. Side view of the experimental setup.

of the structure. The Low Frequency Pass Band (LFPB) spans 830-1500 Hz for the 0° orientation, while the High Frequency Pass Band (HFPB) spans 1500-2250 Hz for the 90° orientation. The first resonant frequencies of the HRs and the central Bragg bandgap frequency (f_{Bragg}) follow the order $f_{\text{HR}}^{90^\circ} < f_{\text{Bragg}} < f_{\text{HR}}^{0^\circ}$, enabling interactions that support the acoustic switch function.

Complete bandgaps, shown in gray, occur at frequencies close to the first resonant frequencies of the HRs ($f_{\text{HR}}^{90^\circ} = 760$ Hz and $f_{\text{HR}}^{0^\circ} = 1800$ Hz) and the Bragg frequency ($f_{\text{Bragg}} = 1400$ Hz). Despite their presence, the SC maintains effective transmission in both the LFPB and HFPB.

2.2 Experimental Assessment

A prototype SC device was manufactured using 3D printing and tested in the anechoic chamber of the Higher Polytechnic School of Gandia (Valencia, Spain). The experimental setup, shown in Fig. 3, included a Genelec 8030A loudspeaker as the sound source and a B&K Type 4189 microphone for acoustic field measurements. The SC was placed on a rigid wooden base, and measurements were taken using a 3D Robotised Acoustic Measurement System.

The frequency range of interest was 500-2500 Hz, with the source placed 0.5 m from the SC. Measurements were taken over a 1.1 m × 0.5 m grid with a spacing of $a/4 = 0.03$ m, resulting in 576 measurement points. The microphone was calibrated using a B&K Sound Calibrator Type 4231, and the robotized system ensured precise acoustic field mapping.

3. RESULTS

The experimental results are compared with numerical simulations in Fig. 4, which shows the transmittance ($\mathbb{T}$) and contrast ratio (CR) as functions of frequency. The top plot illustrates $\mathbb{T}$ for both 0° and 90° orientations, with numerical and experimental data showing strong agreement. The bottom plot depicts CR, highlighting the difference in transmittance between the two orientations. High CR values in the LFPB (830-1500 Hz) and HFPB (1500-2250 Hz) indicate effective acoustic switching behavior.

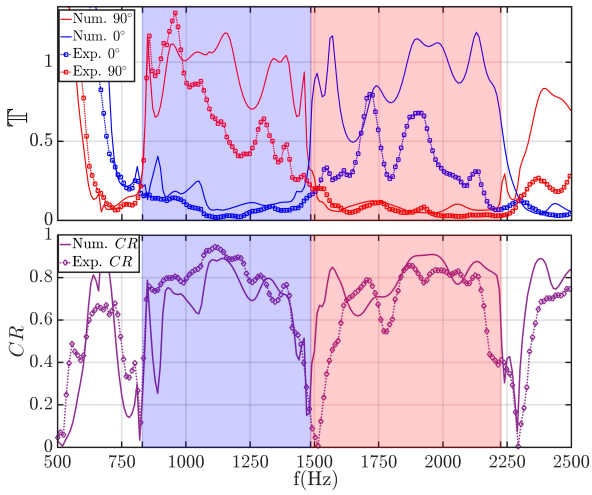


Figure 4. Transmittance, numerical and experimental (top); contrast ratio (CR), numerical and experimental (bottom).

The design functions as an effective acoustic filter, with the ability to control transmission based on scatterer orientation. The strong agreement between numerical and experimental results underscores the robustness of the design and experimental methodology. Fig. 5 shows insertion loss (IL) maps and CR maps for representative frequencies in the LFPB and HFPB, further illustrating the acoustic switching performance of the SC.

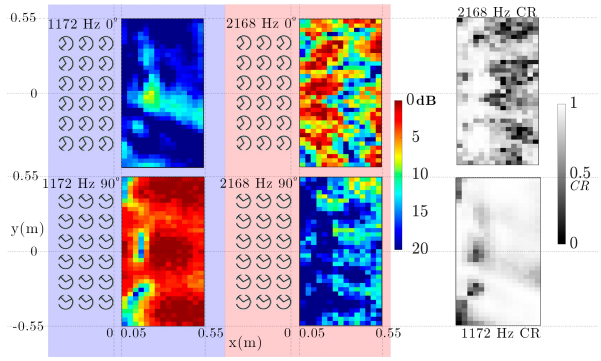


Figure 5. Experimental insertion loss maps with CR maps for two representative frequencies at 0° and 90°.

The results demonstrate the SC's potential as an effective acoustic switch, with tunable transmission properties based on scatterer orientation. This capability is promising for applications in acoustic control, passive filtering, and reconfigurable acoustic devices.

4. CONCLUSION

In conclusion, this paper introduces a novel multiresonant SC device that leverages the interaction between Bragg and Helmholtz resonator-based bandgaps in a simple 3D-printed structure. By varying the scatterer orientation, the device effectively switches between two distinct frequency passbands (830–1500 Hz and 1500–2250 Hz), overcoming limitations of existing acoustic switches that rely on complex geometries or operate at higher frequencies.

The device's performance was validated through numerical and experimental studies, demonstrating strong agreement. Transmission characteristics, contrast ratio (CR), and insertion loss (IL) confirmed its ability to control acoustic response based on scatterer orientation, achieving high contrast and effective attenuation.

Potential applications include urban and industrial noise reduction and adaptive acoustic environments in buildings and vehicles. This versatile and easy-to-implement design opens new possibilities for wave manipulation and acoustic metamaterials.

5. ACKNOWLEDGEMENT

This research was funded by grant PID2022-138321NB-C22 funded by MICIU/AEI/ 10.13039/501100011033 and ERDF/EU. This work was also supported by Construct Innovate, Ireland's National Research Centre for Construction Technology and Innovation (Enterprise Ireland TC-2022-0033, Seed Fund Call CISFC1-23_002). This research was also supported by project "MUD-MADE: MUlti-objective optimization of Digitally MAnufactureD Earth building components supported by neural networks (PRIN PNRR 2022)".

6. REFERENCES

[1] W. E. Kock and F. K. Harvey, "Refracting Sound Waves," *The Journal of the Acoustical Society of America*, vol. 21, pp. 471–481, Sept. 1949.

[2] E. Economou and M. M. Sigalas, "Elastic and acoustic wave band structure," *Journal of sound and vibration*, vol. 158, no. 2, pp. 377–382,, 1992.

[3] C. Kittel, *Introduction to Solid State Physics*. Hoboken, NJ: Wiley, 8th ed ed., 2005.

[4] T. Miyashita, "Sonic crystals and sonic wave-guides," *Measurement Science and Technology*, vol. 16, pp. R47–R63, May 2005.

[5] J. Redondo, R. Picó, V. Sánchez-Morcillo, and W. Woszczyk, "Sound diffusers based on sonic crystals," *The Journal of the Acoustical Society of America*, vol. 134, pp. 4412–4417, Dec. 2013.

[6] D. Ramírez-Solana, V. Sangiorgio, N. Parisi, J. Redondo, A. M. Mangini, and M. P. Fanti, "Parametric Design and Assessment of 3D Printable Open Noise Barrier: Device Customization to Protect Buildings from Train Brake Noise," *Journal of Architectural Engineering*, vol. 30, no. 2, 2024.

[7] J. V. Sanchez-Perez, C. Rubio, R. Martinez-Sala, R. Sanchez-Grandia, and V. Gomez, "Acoustic barriers based on periodic arrays of scatterers," *Applied Physics Letters*, vol. 81, pp. 5240–5242, Dec. 2002.

[8] S. Alagoz and B. Baykant Alagoz, "Sonic crystal acoustic switch device," *The Journal of the Acoustical Society of America*, vol. 133, no. 6, pp. EL485–EL490, 2013.

[9] Z. Liu, X. Zhang, Y. Mao, Y. Y. Zhu, Z. Yang, C. T. Chan, and P. Sheng, "Locally Resonant Sonic Materials," *Science*, vol. 289, pp. 1734–1736, Sept. 2000.

[10] A. Krynkin, O. Umnova, A. Y. B. Chong, S. Taherzadeh, and K. Attenborough, "Scattering by coupled resonating elements in air," *Journal of Physics D: Applied Physics*, vol. 44, p. 125501, Mar. 2011.

[11] J. Redondo, D. Ramírez-Solana, and R. Picó, "Increasing the Insertion Loss of Sonic Crystal Noise Barriers with Helmholtz Resonators," *Applied Sciences*, vol. 13, pp. 3662:1–3662:13, Mar. 2023.

[12] B. Wu, W. Jiang, J. Jiang, Z. Zhao, Y. Tang, W. Zhou, and W. Chen, "Wave Manipulation in Intelligent Metamaterials: Recent Progress and Prospects," *Advanced Functional Materials*, vol. 34, p. 2316745, July 2024.

[13] H. Heo, A. Krokhin, A. Neogi, Z. Cui, Z. Yuan, Y. Hua, J. Ju, and E. Walker, "Multifunctional Acoustic Device Based on a Phononic Crystal with Independently Controlled Asymmetric Rotating Rods," *Physical Review Applied*, vol. 19, p. 054008, May 2023.

[14] L. Brillouin, *Wave Propagation in Periodic Structures*. New York: Dover Publications inc., 1953.

[15] L. E. Kinsler, A. R. Frey, A. B. Coppens, and J. V. Sanders, *Fundamentals of Acoustics*, vol. 72. New York, US: John Wiley & Sons, 2000.

[16] G. P. Ward, R. K. Lovelock, A. R. J. Murray, A. P. Hibbins, J. R. Sambles, and J. D. Smith, "Boundary-Layer Effects on Acoustic Transmission Through Narrow Slit Cavities," *Physical Review Letters*, vol. 115, p. 044302, July 2015.

[17] X.-F. Li, X. Ni, L. Feng, M.-H. Lu, C. He, and Y.-F. Chen, "Tunable Unidirectional Sound Propagation through a Sonic-Crystal-Based Acoustic Diode," *Physical Review Letters*, vol. 106, p. 084301, Feb. 2011.

[18] A. Cicek, O. Adem Kaya, and B. Ulug, "Refraction-type sonic crystal junction diode," *Applied Physics Letters*, vol. 100, p. 111905, Mar. 2012.

[19] J. V. Sánchez-Pérez, D. Caballero, R. Mártinez-Sala, C. Rubio, J. Sánchez-Dehesa, F. Meseguer, J. Llinares, and F. Gálvez, "Sound Attenuation by a Two-Dimensional Array of Rigid Cylinders," *Physical Review Letters*, vol. 80, no. 24, pp. 5325–5328, 1998.

DOI: 10.61782/fa.2025.0103

FORUM ACUSTICUM EURONOISE 2025

ADDITIVE MANUFACTURE OF FLEXIBLE LATTICE ABSORBERS FOR ENHANCED LOW FREQUENCY PERFORMANCE

Conor Neill[1*] **John Kennedy**[1]

[1] Department of Mechanical, Manufacturing and Biomedical Engineering, Trinity College Dublin, Dublin, Ireland

ABSTRACT

Traditionally porous materials have been used to mitigate a range of noise problems with excellent performance in the mid to high-frequency range, but these materials struggle to attenuate low frequencies. Recently, additive manufacturing (AM), including stereolithography (SLA), has enabled the fabrication of engineered porous structures that can create tuneable acoustic materials. This research focuses on the further development of flexible lattice structures, with inclusions that can add local resonances as an additional dissipation mechanism. This study systematically designs, manufactures, and tests flexible lattice absorbers for low-frequency noise control. By controlling the print parameters and lattice geometry, the acoustic properties can be varied and evaluated through impedance tube testing. Numerical modelling is utilised to iteratively manufacture an optimised flexible lattice structure for low-frequency sound absorption. This study focuses on refining the relationship between printing parameters and acoustic properties to enhance sound absorption while also maintaining structural integrity. These flexible lattice structures provide a tuneable lightweight solution for low-frequency sound absorption while also progressing the fabrication process of engineered porous materials. This offers a novel solution that helps to broaden the scope of engineered porous materials, benefiting the field of noise control.

*__Corresponding author__: neillco@tcd.ie.

__Copyright__: ©2025 Conor Neill, et al. This is an open-access article distributed under the terms of the Creative Commons Attribution 3.0 Unported License, which permits unrestricted use, distribution, and reproduction in any medium, provided the original author and source are credited.

Keywords: *flexible lattices, additive manufacturing, low frequency absorption, local resonance, noise control*

1. INTRODUCTION

Noise pollution is a growing concern in urban and industrial environments, as exposure to excessive levels can lead to hearing impairment, psychophysiological distress, and cardiovascular diseases [1]. While mid to high-frequency noise is well addressed by conventional materials, low-frequency noise has remained difficult to attenuate [2]. This highlights the need for new engineered noise control solutions to innovate and solve these low-frequency issues. Engineered porous materials are a new area of study, made possible by the significant improvements in computing power and manufacturing techniques, which allow these complex shapes to be fabricated more easily [3]. Lattice structures have demonstrated potential for sound absorption similar to that of traditional materials but can allow increased tuneability by controlling their geometric parameters [4, 5]. The lattice structure attenuates the noise through viscous and thermal dissipation. This has been shown to be similar to traditional foam materials, with higher broadband absorption and shallow resonance peaks [3]. Tuned Helmholtz resonators (HR) can provide low-frequency noise absorption and can have high attenuation peaks, but they suffer from a narrow frequency range [6].

This work combines lattices for acoustic absorption with embedded resonators using a flexible material and demonstrates a new potential for noise control materials. This complex geometry has been enabled through increases to computational power required for both design and modelling. Additionally due to the introduction of

low-cost commercial 3D printers, such a structure is becoming more readily manufacturable at industrial scales. With the use of SLA, the two designs are merged to enable a single-step manufacturing process that incorporates tunable broadband and peak absorption, utilising local resonances through the embedded HR's. This combination allows for low-frequency noise absorption, while also maintaining broadband absorption at the mid and high frequencies of traditional materials. The use of a flexible material can allow for these lattices to be contoured and bent to fit a chosen profile under space constraints. The use of SLA allows for the flexible and precise lattice-Helmholtz resonators to be fabricated in a single step, and subsequently tested using ISO 10543-2 standard impedance tube testing to examine the noise absorption performance.

2. METHODOLOGY

The lattice structure's design was based on a Kelvin cell geometry for its isotropic and energy-absorbing qualities while remaining relatively simple to fabricate [5, 7]. The lattice parameters were determined using LattSAC, which is a software for the acoustic modelling of lattice sound absorbers [8]. The final design parameters included a cell size of 4.25 mm and a strut width of 0.66 mm. These values provided a good balance between what the LattSAC software could simulate, manufacturability, and testable acoustic properties. The HR design was based on Eqn. (1) [9]. The correction factor δ_R is $0.849r$, where r is the neck radius, and is based on the Rayleigh equation for the resonance frequency of a HR.

$$f = \frac{c}{2\pi}\sqrt{\frac{A_0}{V\left(l_0 + 2\,\delta_R\right)}}. \tag{1}$$

This was used to design both embedded HR's. The parameters used and the resulting resonance frequency can be seen in Tab. 1. The three final designs can be seen in figure Fig. 1 below, with a section view to show the embedded HR. The design features, (a) Bare Lattice, (b) Helmholtz resonator set at the middle for a low resonant frequency (LHL), and (c) Helmholtz resonator lowered to the bottom for a mid-resonant frequency (MHL).

The hexagonal shape of the unit structures was chosen for space-saving reasons and it allowed units to be easily combined in different arrangements. The dimensions for the individual hexagons were 50.95 mm tall and 33.43 mm from flat side to flat side. The included partition that created the HR was 1 mm with the neck wall thickness being 0.75 mm, this is highlighted in red in figure Fig. 1. Both experimental tests included a PLA holder that fit tightly around the hexagonal design and into the respective impedance tube. The large holder could accommodate seven hexagons and the smaller could fit a single unit.

Table 1: Helmholtz Resonators Equation Parameters

Parameter	**Large**	**Small**
Neck area, A_0 (m^2)	1.96×10^{-5}	2.83×10^{-5}
Cavity volume, V (m^3)	1.75×10^{-5}	1.70×10^{-6}
Neck length, l_0 (m)	5×10^{-3}	3×10^{-3}
Neck radius, r (m)	5×10^{-3}	6×10^{-3}
Res. frequency (Hz)	**601**	**2480**

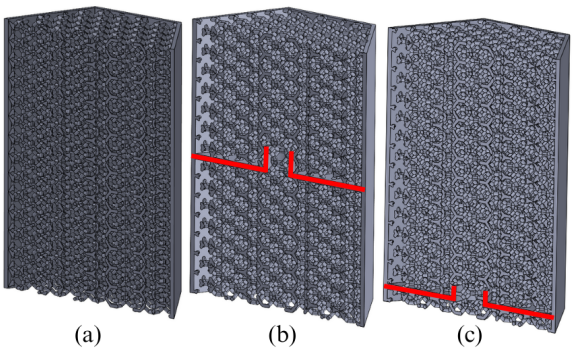


Figure 1: CAD designs, (a) Bare Lattice, (b) Low-Frequency Helmholtz-Lattice (LHL), (c) Mid-Frequency Helmholtz-Lattice (MHL)

The samples were made from Prusa Flex 80A and printed on a Prusa SL1S Speed. The relevant printing parameters for reliable fabrication can be seen in Tab. 2. These were the necessary changes from the default Prusa print settings. In total, 17 samples were made, seven Bare Lattices, seven LHL's, and three MHL's. This was to allow a mixture of the Bare Lattice and LHL designs to be tested in the larger impedance tube.

Absorption measurements were conducted in accordance with ISO 10534-2 using two impedance tubes, one low-frequency (50-1500 Hz), and one high-frequency (300-4500 Hz). The two tubes had respective internal diameters of 127 mm and 40 mm, where the schematic can be seen in Fig. 2. Acoustic measurements were taken using GRAS 40PH microphones (50 Hz - 5 kHz, ± 1.5

Table 2: Print Parameters

Parameter	Value
Layer height	0.05 mm
Exposure time	4 s
Initial exposure time	32 s
Support	Build plate only
– Pillar diameter	1.7 mm
– Base diameter	3.7 mm
– Base height	1.7 mm

dB). A National instruments DAQ, amplifier, and MATLAB GUI controlled the system. For sample testing in the high-frequency tube, each sample design was fabricated three times and tested three times, totalling to nine results per design. This ensured repeatability and reproducibility within the designs. The low-frequency tube tests, because they consisted of seven single samples, were tested three times to obtain an average.

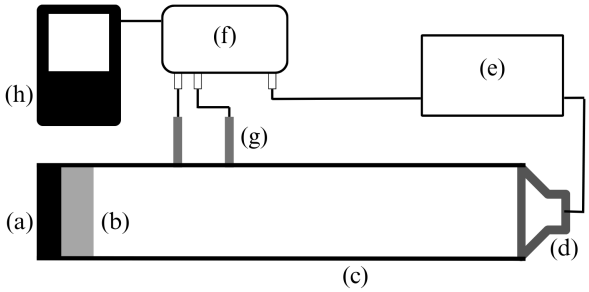


Figure 2: Impedance tube schematic (a) Hard end, (b) Sample, (c) Impedance tube, (d) Speaker, (e) Amplifier, (f) Data acquisition system, (g) Microphones, (h) Computer

3. RESULTS AND DISCUSSION

Fig. 3 shows the predicted absorption coefficients from the LattSAC model. The Bare Lattice (black line) shows 2 peaks at 1500 Hz and 4100 Hz, with absorption coefficients of 0.44 and 0.61 respectively. Once a HR is embedded in the lattice the effective thickness is reduced to the distance from the resonator division to the top of the sample. The two coloured dashed lines are calculated based on this reduced lattice thickness from Fig. 1. These thicknesses are 50% and 94% thickness of the LHL and MHL designs. As expected, the 94% lattice (MHL) is very similar to the bare design, with a small lowering and shift to

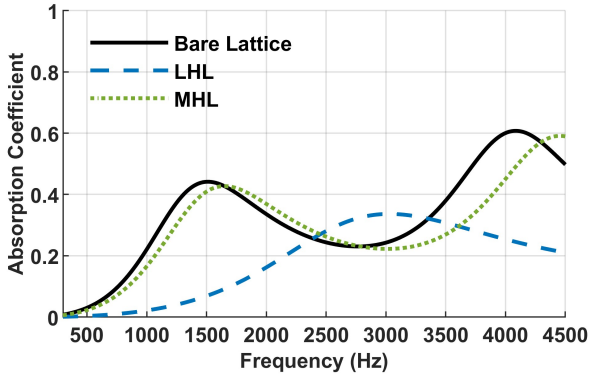


Figure 3: LattSAC numerical absorption coefficient tests

the right, due to the small decrease in available lattice. The 50% lattice (LHL) has its peak lowered to 0.34 and shifted considerably to the right at 3000 Hz.

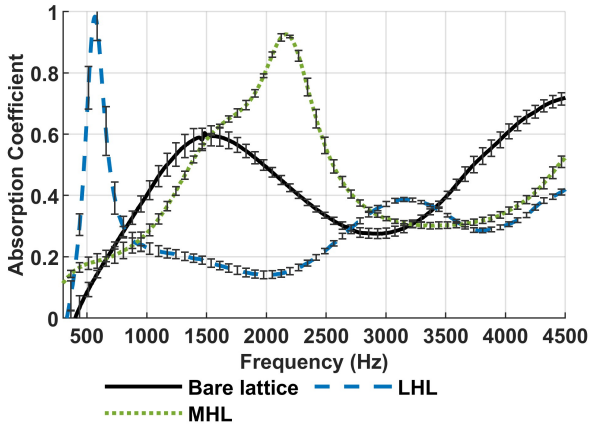


Figure 4: High-frequency impedance tube tests

Fig. 4 shows experimental results from the designs in Fig. 1. The bare lattice matched the LattSAC model with a peak absorption at 1500 Hz but has increased the absorption coefficient to 0.6. This is likely due to LattSAC's inability to take into account surface roughness which will increase the peak absorption [10, 11]. The MHL (green dotted) curve showed a similar peak shift to the right at the beginning. Then the peak from the HR occurs at 2170 Hz with an absorption coefficient of 0.92. This is lower than analytically expected due to the reduced accuracy of the Helmholtz model at higher frequencies. The LHL (dashed blue) curve showed an excellent absorption at 570 Hz with a peak absorption of 0.98. This aligned well with both the analytical and LattSAC models, with its lattice-only portion showing a peak at 3150 Hz and an absorption of 0.39.

Fig. 5 presents four tests where seven individual samples were configured as an array in a PLA holder. An example design of 4 LHL - 3 Bare Lattice can be seen within the figure. The Bare Lattice design (black line) matched well with the single test and LattSac by showing a rising peak up to around 1400 Hz. The LHL (blue dashed) curve agreed with the individual tests and had a peak of absorption of 0.91 at 570 Hz. The other two tests consisted of a blended array of the Bare lattice and LHL designs. The 4 LHL - 3 Bare Lattice array showed a lower peak at 560 Hz but maintained absorption above 0.43 over the 800 Hz to 1400 Hz range due to the increased lattice content. The standalone LHL design did not exceed 0.2 in the same range. To confirm this, the 3 LHL - 4 Bare Lattice array was also tested, which had a lower Helmholtz peak, as expected.

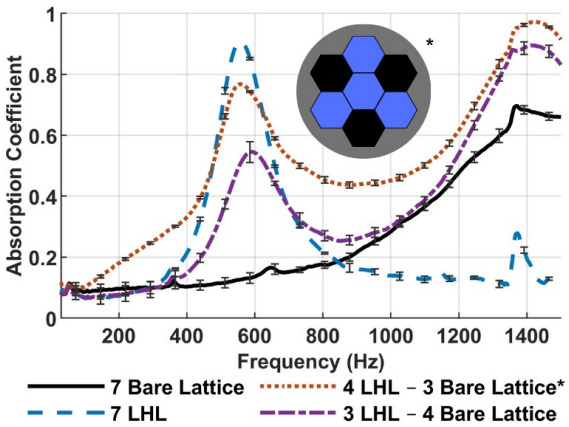


Figure 5: Low-frequency impedance tube tests

4. CONCLUSION

To summarise, an acoustic modelling software was used to design a lattice structure with enhanced performance through the inclusion of embedded Helmholtz resonators. The resonant frequencies were controlled through simple geometric modifications to the unit cells. The samples were manufactured in a flexible material with high precision. Repeatable and reproducible designs were successfully manufactured with the acoustic properties and printing parameters being optimised for enhanced mid and low-frequency sound absorption. The performance was validated through impedance tube testing of individual and grouped sample combination designs that demonstrated how a variety of unit cells can be combined to achieve a target performance. This work demonstrates that a tuneable, lightweight, and flexible material for low-frequency absorption can be designed and fabricated successfully. Future work on further design optimisation and the ability to fabricate larger-scale samples could see applications to real-world noise control.

5. REFERENCES

[1] World Health Organization, "Environmental Noise Guidelines for the European Region," technical report, World Health Organization, 2018.

[2] Y. I. Bobrovnitskii and T. M. Tomilina, "Sound Absorption and Metamaterials: A Review," *Acoustical Physics*, vol. 64, pp. 519–526, Sept. 2018.

[3] X. Li, J. W. Chua, X. Yu, Z. Li, M. Zhao, Z. Wang, and W. Zhai, "3D-Printed Lattice Structures for Sound Absorption: Current Progress, Mechanisms and Models, Structural-Property Relationships, and Future Outlook," *Advanced Science*, vol. 11, no. 4, p. 2305232, 2024.

[4] J. Zhang, X. Chen, Y. Sun, Y. Wang, and L. Bai, "Sound-absorption and mechanical properties of multisheet Gyroid lattice structures by stereolithography," *Composite Structures*, vol. 325, p. 117589, Dec. 2023.

[5] H. Rice, J. Kennedy, P. Göransson, L. Dowling, and D. Trimble, "Design of a kelvin cell acoustic metamaterial," *Journal of Sound and Vibration*, vol. 472, p. 115167, 2020.

[6] K. Mahesh, S. K. Ranjith, and R. S. Mini, "Recent Advancements in Helmholtz Resonator Based Low-Frequency Acoustic Absorbers: A Critical Review," *Archives of Computational Methods in Engineering*, vol. 31, pp. 2079–2107, May 2024.

[7] R. Daya Karthic, J. Joy, G. Sakthivel, and R. Nadimpalli, "Mechanical characterization of 3D-printed Kelvin cell with varying infill densities," *Materials Today: Proceedings*, vol. 84, pp. 41–46, Jan. 2023.

[8] J. W. Chua, Z. Lai, X. Li, and W. Zhai, "LattSAC: a software for the acoustic modelling of lattice sound absorbers," *Virtual and Physical Prototyping*, Dec. 2024. Publisher: Taylor & Francis.

[9] R. C. Chanaud, "Effects Of Geometry On The Resonance Frequency Of Helmholtz Resonators," *Journal of Sound and Vibration*, vol. 178, pp. 337–348, Dec. 1994.

[10] A. Ciochon, J. Kennedy, R. Leiba, L. Flanagan, and M. Culleton, "The impact of surface roughness on an additively manufactured acoustic material: An experimental and numerical investigation," *Journal of Sound and Vibration*, vol. 546, p. 117434, 2023.

[11] A. Ciochon and J. Kennedy, "Efficient modelling of surface roughness effects in additively manufactured materials," *Applied Acoustics*, vol. 220, p. 109953, 2024.

DOI: 10.61782/fa.2025.0919



FORUM ACUSTICUM
EURONOISE 2025

TUNABLE ENVELOPE SOLITONS IN A PIEZOELECTRIC METAMATERIAL OBEYING THE NONLINEAR SCHRÖDINGER EQUATION

Chongan Wang[1] **Alper Erturk**[1*]

[1] G. W. Woodruff School of Mechanical Engineering, Georgia Institute of Technology, USA

ABSTRACT

Nonlinear shunt circuits can substantially alter the dynamic response of piezoelectric structures, offering a great potential to use in metamaterials and metastructures for wave manipulation. These circuits, implemented as analog or digital shunts, offer tunable and programmable nonlinear characteristics. In this work, we investigate the solitary wave dynamics in a metamaterial beam with a periodic array of piezoelectric patches shunted to Duffing circuits. Our focus is placed on the tunability of the solitary wave propagation by varying the linear and nonlinear inductance values. The wave evolution in the proposed piezoelectric metamaterial beam follows the nonlinear Schrödinger equation (NLSE), where the dispersion and nonlinear coefficients are dependent on the inductance parameters. By adjusting the linear inductance, the dispersion curve can be tuned, enabling the generation of solitary waves with either softening nonlinearity or hardening nonlinearity. The amplitude and shape of the solitary wave can also be controlled through the variation of inductance values. These findings may open new avenues for programmable elastic/acoustic metamaterials, with potential applications in elastic wave control, targeted energy transfer, and physical intelligence.

Keywords: piezoelectric metamaterial, nonlinear dynamics, nonlinear Schrödinger equation, solitons

**Corresponding author*: alper.erturk@me.gatech.edu.

Copyright: *©2025 C. Wang and A. Erturk This is an open-access article distributed under the terms of the Creative Commons Attribution 3.0 Unported License, which permits unrestricted use, distribution, and reproduction in any medium, provided the original author and source are credited.*

1. INTRODUCTION

Shape-invariant solitary waves in nonlinear mechanical metamaterials attracted significant attention due to its ability to propagate without dispersion, making them valuable for energy and information transmission. While previous research on solitons in mechanical metamaterials have mainly focused on the structural design with geometric nonlinearity, recent advances in piezoelectric structures [1] highlight the potential for controlling structural responses by introducing the source of nonlinearity through cubic inductive shunts. Such nonlinear shunt circuits can be implemented using either analog circuits or digital signal processing-based synthetic impedance circuits. Compared to purely structural nonlinearity, these nonlinear circuits offer a great flexibility of wave manipulation by controlling mechanical responses through electric signals. In this work, we investigate the tunability of solitary wave motion in a piezoelectric metamaterial beam [2] with an array of piezoelectric patch pairs shunted to linear and cubic inductive circuits. We exclusively focus on how variations in linear and cubic nonlinear inductance influence soliton formation and propagation.

2. SYSTEM DESCRIPTION

We consider a piezoelectric metamaterial beam with unit cells made of two piezoelectric layers sandwiching a central substrate layer (i.e. bimorph setting) as shown in Fig. 1. The piezoelectric layers are oppositely poled in different directions and segmented periodically. The surface electrodes of each unit cell are connected to a nonlinear shunt circuit with a linear inductance and a cubic nonlinear inductance (Fig. 1). Based on the Euler-Bernoulli

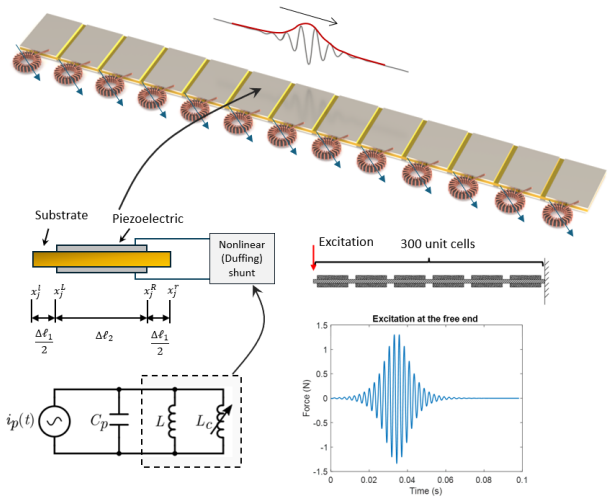


Figure 1. System overview depicting the metamaterial beam, unit cell detail, the excitation and its location on the beam with free-fixed boundary conditions.

beam theory, the undamped flexural wave equation of the beam with electromechanical coupling and circuit current balance equations are:

$$\frac{\partial^2}{\partial x^2}\left(EI(x)\frac{\partial^2 w}{\partial x^2}\right)+m(x)\frac{\partial^2 w}{\partial t^2} -\vartheta\frac{\partial^2}{\partial x^2}\sum_{j=1}^{N} v_j\left(t\right)\left[H\left(x-x_j^L\right)-H\left(x-x_j^R\right)\right]=0 \tag{1a}$$

$$C_{p,j}\dot{v}_j+\frac{1}{L_j}\int_0^t v_j\left(\tau\right)d\tau +\frac{1}{L_{cj}}\left(\int_0^t v_j\left(\tau\right)d\tau\right)^3+\vartheta\int_{x_j^L}^{x_j^R}\frac{\partial^3 w}{\partial x^2\partial t}dx=0 \tag{1b}$$

where the $j-$ th pair of piezoelectric patch spans the spatial positions x_j^L to x_j^R. The transverse deflection $w(x,t)$ and the voltage in the $j-th$ shunt circuit v_j are the unknown variables in Eq. (1). The distribution of mass $m(x)$, flexural rigidity $EI(x)$, electromechanical coupling ϑ and capacitance $C_{p,j}$ are dependent on the material and structural properties of the beam, while the linear and nonlinear inductance L_j and L_{cj}, can be independently designed on the circuit side, allowing tunability of the system's response.

Previous analysis in [2] has shown that a continuous and homogeneous approximation can be applied to the foregoing integro-differential equations, converting the governing equations to a simpler nonlinear partial differential equation in the long wavelength limit:

$$\bar{m}\frac{\partial^2\bar{w}}{\partial t^2}+\bar{EI}\frac{\partial^4\bar{w}}{\partial x^4}-\bar{\vartheta}\frac{\partial^3\bar{\lambda}}{\partial x^2\partial t}=0 \tag{2a}$$

$$\bar{C}_p\frac{\partial^2\bar{\lambda}}{\partial t^2}+\frac{1}{\bar{L}}\bar{\lambda}+\frac{1}{\bar{L}_c}\bar{\lambda}^3+\bar{\vartheta}\frac{\partial^3\bar{w}}{\partial x^2\partial t}=0 \tag{2b}$$

where an overbar represents homogenized variables, and $\bar{\lambda}$ denotes the flux linkage, defined as the time integral of voltage over time. $\bar{L}$ and $\bar{L}_c$ are the linear and cubic nonlinear inductance scaled over an entire piezoelectric patch given by:

$$\begin{aligned}\bar{L}=L_j\Delta\ell;\ \ \bar{L}_c=L_c\Delta\ell\\ \Delta\ell=x_j^R-x_{j-1}^R=x_j^L-x_{j-1}^L\end{aligned} \tag{3}$$

Under weakly nonlinear assumption, the method of multiple scales is introduced to solve the nonlinear partial differential equations given by Eq. (2):

$$t_i=\varepsilon^i t; x_i=\varepsilon^i x, i=0,1,2,... \tag{4}$$

where ε is a small bookkeeping parameter. The leading-order solution of Eq. (2) is the linearized plane wave solution:

$$\begin{pmatrix}\bar{w}\\ \bar{\lambda}\end{pmatrix}\approx\varepsilon A_1\left(x_1,t_1,x_2,t_2\right)\begin{pmatrix}C_{w1}\\ C_{\lambda1}\end{pmatrix}e^{i(kx_0-\omega t_0)}+c.c. \tag{5}$$

where $(C_{w1},C_{\lambda1})^T$ denote the mode shape, and c.c. denotes the complex conjugate. ω and k denote the frequency and wavenumber of the plane wave that obeys the dispersion relation. Past research [3] reveals that the linearized dispersion relation of the piezoelectric metamaterial exhibits a frequency bandgap near the resonant frequency of the shunt circuit.

The modulation equation of the envelope A_1 can be solved by substituting Eq. (5) back into Eq. (2). Perturbation analysis in [2] shows that the modulation of A_1 follows the nonlinear Schrödinger equation (NLSE) that is well known to support solitary wave solutions [4]:

$$i\frac{\partial A_1}{\partial\tau_2}+P\frac{\partial^2 A_1}{\partial\xi_1^2}+QA_1^2A_1^*=0 \tag{6}$$

where ξ_i and τ_i are coordinate variables in the frame moving at the group velocity v_g,

$$\xi_i=x_i-v_g t_i;\ \tau_i=t_i, \tag{7}$$

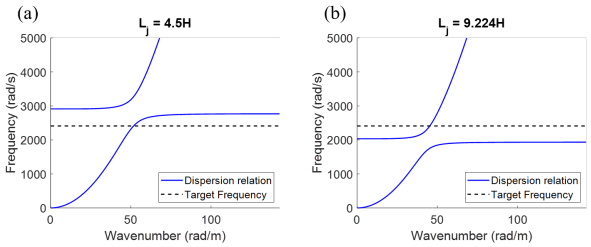


Figure 2. Linearized dispersion relation for different linear inductance values (a) $L_j = 4.5\text{H}$ where the excitation frequency hits the acoustic band and (c) $L_j = 9.224\text{H}$ where the excitation frequency hits the optical band.

Furthermore, P and Q quantify the effect of dispersion and nonlinearity:

$$P = \frac{1}{2}\frac{\mathrm{d}^2\omega}{\mathrm{d}k^2} \tag{8a}$$

$$Q = -\frac{3\left|C_{\lambda 1}\right|^4}{L_{\mathrm{c}}\begin{pmatrix} C_{w1}^* & C_{\lambda 1}^* \end{pmatrix}\begin{pmatrix} 2\bar{m}\omega & i\bar{\vartheta}k^2 \\ -i\bar{\vartheta}k^2 & 2\bar{C}_p\omega \end{pmatrix}\begin{pmatrix} C_{w1} \\ C_{\lambda 1} \end{pmatrix}}, \tag{8b}$$

where the superscript $*$ denotes the complex conjugate.

3. RESULTS AND DISCUSSIONS

We investigate the tunability of solitons by numerically simulating a cantilever beam with 300 pairs of piezoelectric patches as shown in Fig. 1 inset. The excitation is applied at the free end of the cantilever beam with the profile shown in Fig. 1. The pulse has a sech-shaped envelope, characteristic of NLSE soliton solutions, and oscillates at a frequency close to 2500 $\mathrm{rad/s}$.

We first examine the dispersion curves for different values of linear inductance, which influence the frequencies of the LC (inductive-capacitive) circuit dynamics. Since the frequency bandgap of the metamaterial beam is close to the circuit resonant frequency, varying the linear inductance shifts the bandgap accordingly. In Fig. 2, we present the linearized dispersion curves of the metamaterial beam, as developed in [5], for linear inductance values of 4.5H and 9.224H. The figure illustrates the tunability of the frequency bandgap, which can be shifted by varying the inductance—allowing the excitation frequency to lie within either the acoustic or the optical band.

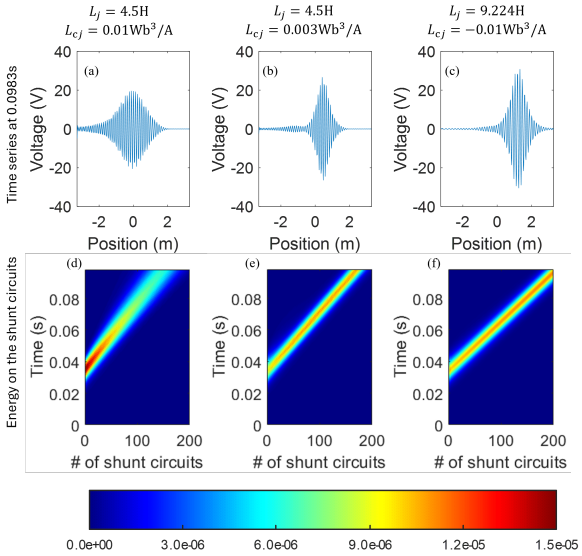


Figure 3. Distribution of the voltage across the metamaterial beam: (a,b,c) Time series of voltage across all entire shunt circuits at $t = 0.0983\text{s}$ and (d,e,f) Spatio-temporal variation of the energy in each shunt circuits. The linear and nonlinear inductances are given by, (a,d) $L_j = 4.5\text{H}$ and $L_{cj} = 0.01\text{Wb}^3/\text{A}$, (b,e) $L_j = 4.5\text{H}$ and $L_{cj} = 0.003\text{Wb}^3/\text{A}$ and (c,f) $L_j = 9.224\text{H}$ and $L_{cj} = -0.01\text{Wb}^3/\text{A}$.

The excitation frequency falls in different branches of the dispersion curve, resulting in distinct solitary wave solutions. As shown in [4], the NLSE supports solitary wave solution only with the focusing nonlinearity condition $PQ > 0$, where the nonlinearity counterbalance the effect of dispersion. Eq. (8) shows that P is proportional to the second derivative of the dispersion curve, while Q always has the opposite sign of the cubic inductance L_{cj}. To initiate a solitary wave, a softening nonlinear inductance is required in the acoustic band where the dispersion relation is concave upwards, whereas hardening nonlinear inductance is required in the optical band where the dispersion relation is concave downward.

To confirm our analysis, we present finite-element simulation results of the entire metamaterial beam, considering the linear inductances 4.5H, and 9.224H, combined with various nonlinear inductance values $L_{cj} = \pm 0.01\text{Wb}^3/\text{A}$, and $0.003\text{Wb}^3/\text{A}$. The voltage and energy distributions across the shunt circuits of the entire

metamaterial beam are presented in Fig. 3.

The simulation results confirm the theoretical analysis on soliton's tunability. Fig. 3a and 3d present the simulation results of $L_j = 4.5\text{H}$ and $L_{cj} = 0.01\text{Wb}^3/\text{A}$. With an excitation frequency in the acoustic branch and a hardening nonlinearity, the wavepacket maintains a solitary-like bell shape. However, from Fig. 3d, we note that the energy gradually disperses as the wavepacket propagates along the metamaterial beam. A stronger nonlinear focusing effect is observed with a larger nonlinear coefficient. As shown in Fig. 3e, reducing the nonlinear inductance to $L_{cj} = 0.003\text{Wb}^3/\text{A}$ enhances the nonlinearity, resulting in reduced energy dispersion during propagation. In Fig. 3b, the wavepacket is much narrower compared with the one in Fig. 3a as the nonlinear coefficients are increased.

In addition, Figs. 3c and 3f present simulation results for $L_j = 9.224\text{H}$ and a softening nonlinear inductance of $L_{cj} = -0.01\text{Wb}^3/\text{A}$. These results confirm the initiation of a solitary-like wavepacket when the excitation frequency lies within the optical branch and the system exhibits softening nonlinearity. Overall, the simulations highlight the high tunability of solitary wave responses—demonstrating that by varying the linear and nonlinear inductance, the frequency bandgap can be shifted and the nonlinearity can switch between hardening and softening, enabling the effective generation of solitons in both the acoustic and optical bands.

4. CONCLUDING REMARKS

To summarize, we propose a piezoelectric metamaterial beam coupled with nonlinear shunt Duffing circuits consisting of both linear and cubic nonlinear inductance. We investigate the effects of these inductance values on the solitary wave propagation within the metamaterial beam, demonstrating strong tunability of solitary waves. Specifically, varying the linear inductance shifts the linearized frequency bandgap, allowing excitation of either the acoustic band, optical band, or bandgap under identical external excitation. Since the dispersive effect is dependent on the second derivative of the dispersion curve, different types of nonlinearity supports distinct soliton solutions. In particular, hardening nonlinearity supports solitons in the acoustical band, whereas softening nonlinearity supports solitons in the optical band. Furthermore, since the soliton is formed due to the counterbalance of nonlinearity, we demonstrate that the steady-state profile of the soliton can be tuned by varying nonlinear inductance. With identical excitation, a larger nonlinear coefficient leads to stronger focusing effect, resulting in a narrower wavepacket. By tuning the linear and nonlinear inductance, solitons with varying amplitudes and widths can be achieved under the same excitation profile.

5. ACKNOWLEDGMENTS

The Carl Ring Family Chair endowment (for Prof. Alper Erturk) is gratefully acknowledged.

6. REFERENCES

[1] O. Alfahmi and A. Erturk, "Programmable hardening and softening cubic inductive shunts for piezoelectric structures: Harmonic balance analysis and experiments," *Journal of Sound and Vibration*, vol. 571, p. 118029, 2024.

[2] C. Wang and A. Erturk, "Solitons in piezoelectric metamaterials with nonlinear shunt circuits." Manuscript submitted to Journal of the Mechanics and Physics of Solids, 2024.

[3] C. Sugino, S. Leadenham, M. Ruzzene, and A. Erturk, "An investigation of electroelastic bandgap formation in locally resonant piezoelectric metastructures," *Smart Materials and Structures*, vol. 26, no. 5, p. 055029, 2017.

[4] T. Dauxois and M. Peyrard, *Physics of Solitons*. Cambridge University Press, 2006. ISBN: 0-521-85421-0.

[5] M. Alshaqaq, C. Sugino, and A. Erturk, "Programmable rainbow trapping and band-gap enhancement via spatial group-velocity tailoring in elastic metamaterials," *Physical Review Applied*, vol. 17, no. 2, p. L021003, 2022.

DOI: 10.61782/fa.2025.0666



FORUM ACUSTICUM
EURONOISE 2025

OPTIMIZING LOCALLY RESONANT ELEMENTS DISTRIBUTION ON ISOTROPIC PLATE FOR INCREASED SOUND INSULATION AND MASS REDUCTION

Klara Chojnacka[1*]

[1] AGH University of Krakow, Poland
Faculty of Mechanical Engineering and Robotics
Department of Mechanics and Vibroacoustics, al. Adama Mickiewicza 30, 30-059 Cracow

ABSTRACT

Locally resonant metamaterials enhance sound and vibration reduction within specific frequency ranges when attached to a base plate. Typically, these metamaterials are designed with periodically distributed elements across the surface, maintaining subwavelength spacing. Using periodic boundary conditions simplifies calculations and reduces the computational power needed compared to finite-sized models. However, no other practical background states that the elements should be distributed evenly in the whole available space for maximum metamaterial effectiveness. The effectiveness of each resonant element depends on the displacement amplitude of the base plate, making elements placed in areas with lower vibration amplitude less effective than those in higher vibration regions. This work presents a topological optimization of the distribution of locally resonant elements. The Method of Moving Asymptotes is employed to minimize the number of resonant elements while preserving the initial sound reduction achieved by periodic metamaterials. Calculations were conducted in COMSOL Multiphysics with MATLAB, using a combined analytical and numerical approach for sound insulation simulation. The results confirm that the number of resonant elements, and therefore the additional mass of the metamaterial on the base plate, can be reduced while maintaining the initial effectiveness of the solution.

Keywords: locally resonant structures, noise and vibration reduction, topological optimization, mass reduction

*__Corresponding author__: klara.chojnacka@agh.edu.pl.
__Copyright__: ©2025 Chojnacka This is an open-access article distributed under the terms of the Creative Commons Attribution 3.0 Unported License, which permits unrestricted use, distribution, and reproduction in any medium, provided the original author and source are credited.

1. INTRODUCTION

Locally resonant structures (LRS) are widely exploited in the literature in noise and vibration suppression problems. Resonant elements are based on a mass-spring-damper system and when attached to a base plate create a stopband effect. In the stopband frequency range, flexural waves cannot propagate in the base plate, causing vibration and noise mitigation. Typically, LRS consists of a periodical mesh of resonant elements distributed equally over the plate surface at sub-wavelength distances [1]. The periodic distribution is beneficial due to the simplification of manufacturing and the lower computational costs. In the literature, most of the LRS simulation examples are based on unit cell simulations with periodic boundary conditions, as a simplified model that gives information about the whole structure [2]. However, the periodicity is a proper solution in model simplification, and gives a good approximation of how the finite system will behave, it also narrows the possibility of creating quasi-periodic or non-periodic solution. It can be stated that the effectiveness of the resonant elements distributed on the plate depends on the displacement of the base plate at the attachment point [3, 4]. Therefore, in places where the base plate has lower displacement amplitude, resonant elements may have lower effectiveness.
In this paper a topological optimization procedure is pre-

sented, which allows for resonant element number minimization, while preserving the metamaterial effectiveness in noise and vibration reduction at specified level. This gives the possibility to create quasi-periodic element distribution on the base plate, by removing unnecessary mesh elements, which leads to mass reduction.

2. SOUND INSULATION FOR PLATE WITH RESONANT ELEMENTS

Sound reduction index is a logarithmic variable dependent on transmission coefficient τ_d and is given as

$$R = 10 \log_{10} \frac{1}{\tau_d}. \tag{1}$$

Coefficient τ_d for a diffuse field can be described in approximate form as

$$\tau_d \approx 8\rho_0 c_0 \int_0^{\pi/2} \frac{\Re(\overline{z}_{f,\text{fin}})}{|Z_{\text{eff}} + 2\rho_0 c_0 \overline{z}_{f,\text{fin}}|^2} \sin\theta \mathrm{d}\theta, \tag{2}$$

where ρ_0 is air density, c_0 is wave speed in the air, θ stands for elevation incident wave angle, $\overline{z}_{\text{fin}}$ is radiation impedance, and Z_{eff} is mechanical impedance of the structure [3]. In the analyzed case, the radiation impedance is calculated for a finite-size rectangular plate according to the equations given in [5] and [3]. The effectiveness of resonant elements can be determined based on the effective modal mass [6], calculated for the natural frequencies of the single resonant element. The effective modal mass can be used to calculate the effective parameters of the plate with LRS. One of the parameters is effective mechanical impedance Z_{eff} which can be calculated according to equation

$$Z_{\text{eff}} = \frac{B'}{i\omega}\left(k_x^2 + k_y^2\right)^2 + i\omega\left(m_p'' + \frac{m_z'' s_z''(1+i\eta_z)}{i m_z''(\omega_0^2 - \omega^2) + i\eta_z s_z''}\right). \tag{3}$$

In Eq. (3) B' stands for plate bending stiffness, m_p'' is the surface mass of the plate, m_z'', s_z'' and η_z are the surface mass, stiffness and damping of the resonant element with a resonant frequency ω_0. The variables k_x, k_y are wavenumber components, and ω is frequency. Based on these equations the effectiveness of the plate with LRS can be determined.

3. OPTIMIZATION OF THE RESONANT ELEMENTS DISTRIBUTION

The Method of Moving Asymptotes algorithm was selected for the topological optimization of the LRS distribution [7]. The problem solved in this chapter was defined as a constrained cost function. The cost function minimizes the number of resonant elements while constraining the mechanical impedance of the base plate. In this case, the constraint was defined as the smallest possible difference between the effective mechanical impedance of the optimized solution and the effective mechanical impedance of the reference solution with uniformly distributed resonant elements.

The contribution of each resonator in the model is determined by the variable ζ^e, which is assigned individually to each resonator. The variable ζ^e can be defined by the following equation

$$\zeta^e = \begin{cases} 0, \text{ dla } e \in P_r \\ 1, \text{ dla } e \notin P_r, \end{cases} \tag{4}$$

where P_r is a vector of resonant elements included in the model. When a resonant element is absent in the P_r vector, $\zeta^e = 0$. The optimization problem is meant to find the values of ζ^e through cost function f_c minimization, while fulfilling the constraint g at the same time, which can be described as [8]

$$\begin{aligned} \min_{\zeta} \quad & f_c(\zeta) \\ \text{s.t.} \quad & g \leq 0, \\ & 0 \leq \zeta_{min} \leq \zeta^e \leq 1. \end{aligned} \tag{5}$$

To minimize the number of resonant elements, the cost function was defined as follows

$$f_c(\zeta) = \frac{1}{N_{\text{rezo}}}\left(\sum_{\zeta=0}^{N_{\text{rezo}}} \zeta^e + \alpha \sum_{\zeta=0}^{N_{\text{rezo}}} \zeta^e(1-\zeta^e)\right), \tag{6}$$

where N_{rezo} is the overall number of resonant elements, and α is weighting factor forcing ζ^e to achieve values 0 or 1. The constraint function can be written as

$$g(\zeta, \Delta, P, f) = \frac{1}{\Delta}||\delta_Z||_P - 1, \tag{7}$$

where Δ is the target difference between the mechanical impedance level of the basic and optimized case, and δ_Z is the level difference in the current iteration.

4. HYBRID SIMULATION MODEL

In order to perform topological optimization of resonant elements distribution, a hybrid analytical-numerical model was created. Hybrid modeling allowed for a finite-size plate with resonant elements implementation with reduced time needed for a single calculation. Simulations were conducted using COMSOL Multiphysics with

MATLAB LiveLink. The numerical model created in COMSOL is shown in Fig. 1. 3D model consisted of a shell plate with finite dimensions $x_{\text{plate}} = 0.55$ [m], $y_{\text{plate}} = 0.45$ [m], and thickness 0.001 [m]. The plate material was steel with the material parameters: density $\rho = 7850$ [kg/m^3], Young's modulus $E = 205$ [GPa], and Poisson ratio $\nu = 0.33$ [−]. For the base plate, an excitation was defined in the form of a force per unit area, expressed in [N/m^2].

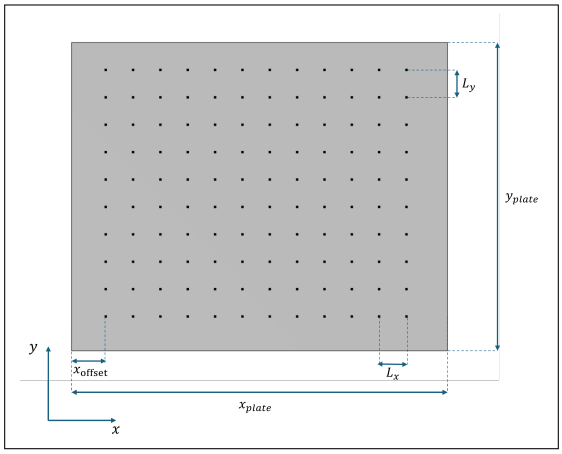


Figure 1. Base plate model with periodically distributed resonant elements, with dimensions.

On the surface of the base plate, a grid of points was created, in which resonant elements modeled as mass-spring-damper systems were placed. The distance between consecutive points is defined along the y axis as L_y and $L_y = L_x$. To model the resonant element, the *Lumped Parameter Modelling* module was used, which allows the parameters of a mass-spring-damper system to be expressed through mechanical parameters, without the need to model the geometry of the element. The effective parameters of the resonant element were determined using a hybrid model based on modal mass calculations [6].

For the developed base plate model, it was possible to determine the vibration velocity of the base plate and, on this basis, the mechanical impedance Z_{eff} of the plate with metamaterial. The mechanical impedance of the plate can subsequently be used to calculate the acoustic insulation of a plate with LRS according to equations presented in Sec. 2.

5. RESULTS

To determine the frequency range of interest, calculations were performed for frequencies in the range $100-300$ Hz. Resonant elements were tuned to one of the base plate resonant frequencies $f = 153$ Hz. The calculations were limited to the implementation of a resonant element with a natural frequency of $\omega_0 = 153$ Hz and effective mass in the z axis. For these elements, the effective mass was $m_r = 0.00051$. The loss factor was assumed to be $\eta = 0.05$ (as for polycarbonate).

For the optimization of the resonator distribution, the frequency range was narrowed to $f = \langle 140, 170 \rangle$ Hz with a step of 3 Hz to reduce the computation time per iteration. In optimization, a target error $\Delta = 3$ dB was assumed. The optimization was run for 600 iterations and the solution was obtained after 225 iterations. The error δ_Z achieved after optimization was 2.8 dB, which met the constraints defined by the constraint function.

In Fig. 2 optimized distribution of resonant elements is presented. In color, the base plate displacement amplitude for 153 Hz is presented. The positions of the resonant elements resulting from the optimization procedure are correlated with areas with larger displacement amplitudes. The acoustic insulation characteristics obtained from the simulation for an empty steel plate, a plate with a uniform distribution of resonant elements, and a plate with an optimized distribution of elements are shown in Fig.3. Despite a 35 % reduction in the number of resonant elements, the differences in the acoustic insulation values for individual frequencies do not exceed 1 dB.

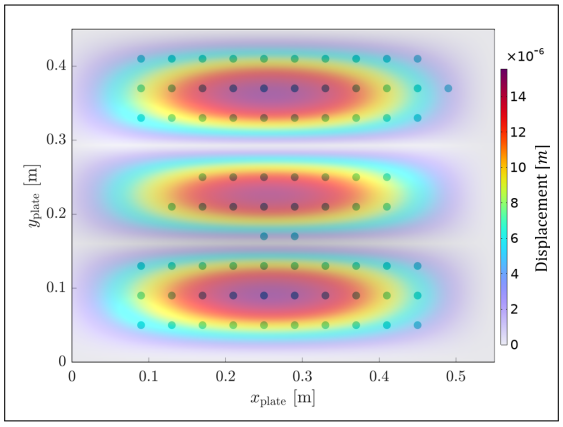


Figure 2. Displacement of the base plate at the frequency $f = 153$ Hz with the optimized distribution of resonant elements on the surface of the base plate.

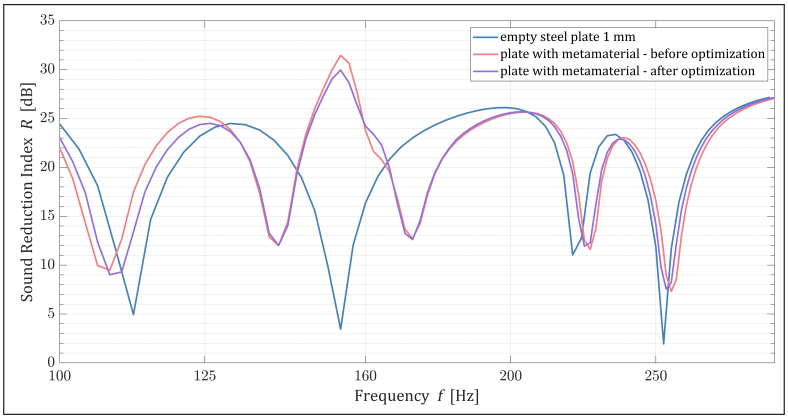


Figure 3. Comparison of the acoustic insulation simulation results for the empty steel plate, the plate with uniformly distributed resonant elements over the entire available surface, and the plate with the optimized distribution of resonant elements.

6. CONCLUSION

In this paper, an optimization procedure is presented, which allows for resonant elements number minimization while preserving the effectiveness of the solution in noise and vibration mitigation in specified frequency range. Thanks to the conducted optimization, the possibility of optimizing the distribution of resonant elements on the base plate in order to minimize the number of resonant elements was confirmed. The effectiveness of the optimization algorithm was validated for the case of a rectangular plate with fixed edges and excitation by a plane wave. The method of optimizing the distribution of elements can be extended, for example, by optimizing the distribution of elements in a three-dimensional machine casing. The developed optimization procedure, combined with algorithms based on hybrid models for LRS simulation, constitutes a solution that enables the improvement and extension of computational capabilities for vibroacoustic metamaterials.

7. REFERENCES

[1] C. C. Claeys, K. Vergote, P. Sas, and W. Desmet, "On the potential of tuned resonators to obtain low-frequency vibrational stop bands in periodic panels," *Journal of Sound and Vibration*, vol. 332, no. 6, pp. 1418–1436, 2013.

[2] M. Nouh, O. Aldraihem, and A. Baz, "Wave propagation in metamaterial plates with periodic local resonances," *Journal of Sound and Vibration*, vol. 341, pp. 53–73, 2015.

[3] J. H. Vazquez Torre, J. Brunskog, and V. Cutanda Henriquez, "An analytical model for broadband sound transmission loss of a Finite Single Leaf Wall using a two degree of freedom resonant Metamaterial," *Proceedings of the International Congress on Acoustics*, vol. 2019-Septe, no. June, pp. 2091–2098, 2019.

[4] A. Hall, E. Calius, G. Dodd, E. Wester, and K. Chan, "Development of locally resonant structures for sonic barriers," *Building Acoustics*, vol. 21, no. 3, pp. 199–220, 2014.

[5] J. Brunskog, "The forced sound transmission of finite single leaf walls using a variational technique," *The Journal of the Acoustical Society of America*, vol. 132, no. 3, pp. 1482–1493, 2012.

[6] D. Giannini, M. Schevenels, and E. P. B. Reynders, "Rotational and multimodal local resonators for broadband sound insulation of orthotropic metamaterial plates," *Journal of Sound and Vibration*, vol. 547, p. 117453, 2023.

[7] K. Svanberg, "The method of moving asymptotes—a new method for structural optimization," *International journal for numerical methods in engineering*, vol. 24, no. 2, pp. 359–373, 1987.

[8] J. Jung, J. S. Jensen, C. H. Jeong, O. Jeon, and S. Wang, "Optimizing a distribution of resonators on a thin plate for the desired sound radiation," *Journal of Sound and Vibration*, vol. 496, pp. 1–16, 2021.

DOI: 10.61782/fa.2025.0476

FORUM ACUSTICUM EURONOISE 2025

Initial Analytical Attempts to Handle the Sound Absorption using Segmented Oblique Perforations

Tommaso D'Orazio[1] **Denilson Ramos**[2] **Luís Godinho**[2]
Claudia Guattari[1] **Francesco Asdrubali**[3]
[1] Roma TRE University, Department of Philosophy, Communication and Performing Arts, Via Ostiense 139, 00154 Rome, Italy
[2] Universidade de Coimbra, ISISE, ARISE, Departamento de Engenharia Civil, Rua Luis Reis dos Santos,
3030-788 Coimbra, Portugal
[3] Department of International Human and Social Sciences, Perugia Foreigners' University, Piazza B. Fortebraccio 4, 06123 Perugia, Italy

ABSTRACT

This research presents a novel geometric configuration for acoustic metamaterials designed to optimize sound absorption, particularly at low frequencies. The design introduces a segmented pathway composed of two sections, creating an effective acoustic path longer than the linear distance between the sound wave entry point and the cavity access. This configuration maximizes absorption while maintaining a constant overall thickness.
The study explores various geometric configurations by adjusting the angles of the segmented pathway to enhance absorption at specific frequencies. The research integrates analytical analyses based on the transfer matrix method implemented in MATLAB. A prototype fabricated through 3D printing provides experimental validation of the findings. Preliminary results indicate that tuning the angles of the segmented pathway significantly improves acoustic absorption, offering new possibilities for applications in noise control and architectural acoustics.

*Corresponding author: tommaso.dorazio@uniroma3.it
Copyright: ©2025 Tommaso D'Orazio et al. This is an open-access article distributed under the terms of the Creative Commons Attribution 3.0 Unported License, which permits unrestricted use, distribution, and reproduction in any medium, provided the original author and source are credited.

Keywords: *fluid equivalent model, acoustic metamaterials, sound absorption.*

1. INTRODUCTION

Acoustic metamaterials (AMMs) are designed to optimize sound absorption, particularly at low frequencies. Traditional configurations consist of a flat rigid surface with circular holes or slits, where the neck is typically a single, linear, and straight segment [1]. Sound attenuation primarily occurs due to viscous friction within the pores, while the combination of the neck and the cavity allows for resonance phenomena to enhance absorption. For this reason, resonant absorbers are widely used in architectural acoustics. However, optimizing absorption at low frequencies remains a complex challenge, as the effectiveness of passive absorbers is constrained by the size required to interact with long acoustic wavelengths. Various strategies have been proposed to lower the resonance frequency, such as increasing panel thickness, reducing the diameter of the perforations, or decreasing the overall porosity [2,3]. Although these solutions are effective, they present limitations related to bulkiness, manufacturing costs, and compatibility with compact spaces.
Recent studies have demonstrated that tilting the perforations can shift the resonance frequency to lower values and increase the acoustic absorption coefficient [4,5]. To this end, this research investigates two different

approaches to predict the acoustic properties of materials with segmented pores divided into two inclined sections, contributing to the design of more efficient devices.
This study is structured as follows: Section 2.1 presents the modeling approach and discusses the geometric description of the acoustic metamaterial's unit cell. Section 2.2 describes the analytical method based on the transfer matrix method implemented in MATLAB. Section 2.3 details the experimental procedure, following ISO 10534-2 [6], to characterize the sound absorption properties of the proposed metamaterial. Subsequently, Section 3 presents a comparison of the preliminary results obtained. Finally, Section 4 discusses the main conclusions.

2. GENERAL DESCRIPTION

2.1 Unit Cell Description

The alternative studied in this article introduces a single neck, but divided into two inclined segments, creating a structured geometric configuration. In this design, the first segment forms an entry angle with the external surface, while the second segment, connected to the first, generates a transition angle that alters its direction. Finally, the neck terminates with an exit angle inside the resonant cavity. This configuration extends the effective length of the neck without increasing the overall system thickness, thereby optimizing absorption at low frequencies.
Figure 1 illustrates the geometric dimensions of the resonator in cross-section. Here, r and R_w represent the perforation radius and the impedance tube radius, respectively; L is the resonator thickness; D and R_c denote the cavity depth and radius, respectively; while θ_1 and θ_2 correspond to the inclination of the first segment relative to the incidence surface and the inclination of the second segment relative to the cavity surface. The linear lengths of the first and second segments, L_1 and L_2, are:

$$L_1 = \frac{L}{\frac{\cot(\theta_2)}{\cot(\theta_1)}+1}\frac{\cot(\theta_2)}{\cot(\theta_1)} \quad (1)$$

$$L_2 = \frac{L}{\frac{\cot(\theta_1)}{\cot(\theta_2)}+1}\frac{\cot(\theta_1)}{\cot(\theta_2)} \quad (2)$$

While the effective lengths of the first and second segments, d_1 and d_2, are:

$$d_1 = \frac{L\cos(\theta_2)}{\sin(\theta_1+\theta_2)} \quad (3)$$

$$d_2 = \frac{L\cos(\theta_1)}{\sin(\theta_1+\theta_2)} \quad (4)$$

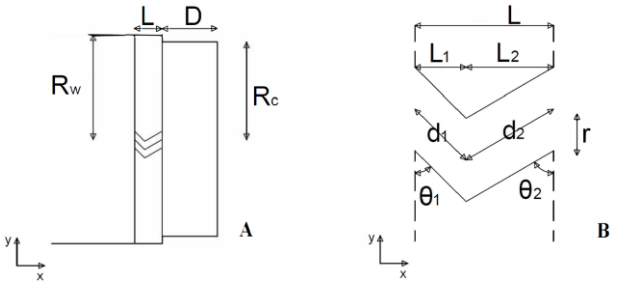


Figure 1. Schematic cross-sectional representation of the proposed resonator with the indication of the main geometric parameters. Figure 1a (left) illustrates the overall configuration of the resonator, highlighting the general geometry, the resonant cavity, and the impedance tube. Figure 1b (right) provides a detailed view of the resonator structure alone, emphasizing the configuration of the neck, which is divided into two inclined segments. Additionally, the total thickness (L), the perforation radius (r), and the angles (θ_1, θ_2) of the two neck segments are indicated.

2.2 Analytical model

The analytical model formulated in this study for characterizing the sound wave propagation in the acoustic metamaterial (AMM) employs the transfer matrix method [7] and the equivalent fluid approach of Johnson-Champoux-Allard (JCA) [8], with the analytical estimation of transport parameters adapted from Atalla and Sgard [3]. To investigate the acoustic properties of the proposed absorber, a theoretical model based on the equivalent fluid theory was developed, treating the perforated resonator as a homogeneous medium with fluid equivalent acoustic properties. This approach enables the characterization of the absorber's acoustic impedance and its behavior in terms of sound absorption.
The absorption coefficient is calculated as:

$$\alpha = 1 - \left|\frac{T(1,1) - Z_0\,T(2,1)/S_w}{T(1,1) + Z_0\,T(2,1)/S_w}\right|^2 \quad (5)$$

where $T=M_1M_2M_c$ is the transfer matrix, $Z_0=c_0\rho_0$ is the characteristic impedance of air, c_0 is the speed of sound propagation, ρ_0 is the air density, and $S_w=\pi R_w^2$ is the cross-section of the impedance tube.
M_1 and M_2 are the matrices describing the acoustic wave propagation through the first and second inclined segment of the resonator neck:

$$M_i = \begin{bmatrix} \cos(k_i L_i) & jZ_i \sin(k_i L_i) \\ \frac{j}{Z_i} \sin(k_i L_i) & \cos(k_i L_i) \end{bmatrix} \quad (6)$$

with $i=1,2$ where the characteristic impedance of the first and second segment of the neck is $z_i = \sqrt{\rho_i B_i}/\pi r^2$. The matrix describing the acoustic wave propagation through the air cavity of the resonator is:

$$M_c = \begin{bmatrix} \cos(k_0 D) & j\frac{Z_0}{S_c} \sin(k_0 D) \\ \frac{jS_c}{Z_0} \sin(k_0 D) & \cos(k_0 D) \end{bmatrix} \quad (7)$$

$S_c = \pi R_c^2$ is the cross-section of the cavity, the wavenumber of air is $k_0 = \omega/c_0$ and the wavenumber of the first and second segment is $k_i = \omega(\rho_i/B_i)^{\frac{1}{2}}$ where ω is the frequency. Initially, in the model herein developed, each region can be homogenized as function of equivalent density ρ_i [8]:

$$\rho_i = \rho_0 \alpha_{\infty i} \left(1 + \frac{\sigma_i \phi_i}{j\omega\rho_0 \alpha_{\infty i}} G_i\right) \quad (8)$$

$$G_i = \sqrt{1 + \frac{4j{\alpha_{\infty i}}^2 \rho_0 \omega}{\lambda^2 {\sigma_i}^2 {\phi_i}^2}} \quad (9)$$

with viscous and thermal characteristic length $\lambda = r/2$. The subscript i describe the effective density in the first and second perforation segments, respectively.

The geometric tortuosity $\alpha_{\infty,i}$ of the first and second neck segments [3]:

$$\alpha_{\infty i} = \frac{1}{\sin^2(\theta_i)} + 2\frac{\varepsilon_{ei}}{d_i} \quad (10)$$

with $\varepsilon_{ei} = 0.85 r F_{ei}$ and $F_{ei} = 1 - 1.4092\xi_i + 0.33818\xi_i^3 + 0.06793\xi_i^5 - 0.02287\xi_i^6 + 0.03015\xi_i^7 - 0.01641\xi_i^8$ with $\xi_i = (\Phi_i)^{1/2}$ is the Fork function [9]. The flow resistance of the first and second neck segments is described as [3]:

$$\sigma_i = \frac{(2d_i/r)sin^2(\theta_i)+4}{d_i \Phi_i} Rs + \frac{8\eta}{\phi_i \left(\frac{r}{2}\right)^2 \cos^2(\theta_i)} \quad (11)$$

where η is the dynamic viscosity of air and $Rs = \frac{\sqrt{2\eta\rho_0\omega}}{2}$. $\Phi_1 = S/S_w$ is the open porosity of the first segment of the neck, where $S = \pi r^2$ and the open porosity of the second segment is $\Phi_2 = 1$, since the radii of the first and second perforation are equal.

The effective compressibility in the first and second segments is [8]:

$$B_i = \frac{\gamma P_0}{\Phi_i} [\gamma - (\gamma - 1)(1 - HG')^{-1}]^{-1} \quad (12)$$

$$H = \frac{8\eta}{j\lambda^2 Pr\omega\rho_n} \quad (13)$$

$$G' = \sqrt{1 + \frac{jPr\omega\rho_0\lambda^2}{16\eta}} \quad (14)$$

where γ is the ratio of specific heats of air, P_0 is the static air pressure, and $Pr = 0.71$ is the Prandtl number for air.

2.3 Experimental Model

To validate the theoretical model introduced in this research, experimental tests were conducted in the laboratory using an impedance tube. The samples were manufactured through an additive manufacturing process at the *Institute for Sustainability and Innovation in Structural Engineering (ISISE)*, within the Department of Civil Engineering at the University of Coimbra. Considering recent advancements in 3D printing techniques for acoustic metamaterials (AMMs) [10], these acoustic metamaterials were designed using advanced computer-aided design (CAD) software and fabricated through a *Fused Deposition Modelling (FDM)* process. The 3D printing process was carried out using a *Blocks One MK2* printer. The *Fused Deposition Modelling (FDM)* method involves melting a thermoplastic filament composed of polylactic acid (PLA), with a diameter of 1.75 mm, at a temperature of 210°C. The molten filament is extruded through a heated 0.4 mm nozzle and systematically deposited layer by layer onto a print platform maintained at 50°C. The 3D-printed samples, shown in Fig. 2, feature a circular configuration with a nominal outer radius R_w of 18.75 mm (Fig. 2a), precisely designed to fit perfectly within a 37,5 mm impedance tube. The actual thicknesses of the specimens, with nominal values (L) of 5 mm and 10 mm, are shown in Fig. 2b and Fig. 2c, respectively.



Figure 2. Sample of the proposed AMM.

Table 1 summarizes the actual thickness (L) dimensions of the six tested samples.

Table 1. Thickness (L) measurements of the printed samples expressed in millimeters.

Sample	L
45°-45°	5,16
60°-45°	5,30
30°-60°	5,28
45°-45°	10,22
60°-45°	10,23
30°-60°	10,28

For this evaluation, the measurement procedure was carried out using the previously described small-scale samples under controlled conditions. The sound absorption and reflection coefficients were measured using the two-microphone technique, employing the transfer function method, in accordance with ISO 10534-2 [6]. The measurement apparatus consists of a closed tube with a sound source that emits a sine-sweep signal generated by a loudspeaker, thereby exciting the system within its operational frequency range. Specifically, for a circular tube with an internal radius of R_w = 18,75 mm, the operational frequency range is between 200 Hz and 4800 Hz. The measurement process of the acoustic pressure measured by microphones p_1 and p_2, positioned at points x_1 and x_2 inside the tube, can be described as follows:

$$P_1 = |p_i|e^{jkx_1} + |p_r|e^{-jkx_1} \quad (15)$$

$$P_2 = |p_i|e^{jkx_2} + |p_r|e^{-jkx_2} \quad (16)$$

where $|p_i|$ and $|p_r|$ represent the amplitudes of the incident and reflected wave pressures on the sample surface, respectively. The transfer functions H_i and H_r, considering each component of the total pressure, can be expressed as follows:

$$H_i = \frac{p_i e^{jkx_2}}{p_i e^{-jkx_1}} = e^{jks} \quad (17)$$

$$H_r = \frac{p_r e^{jkx_2}}{p_r e^{-jkx_1}} = e^{-jks} \quad (18)$$

where $s = x_2 - x_1$. Consequently, the transfer function between the two microphones, H_{12}, is defined as:

$$H_{12} = \frac{p_2}{p_1} = \frac{e^{jkx_2} + Re^{-jkx_2}}{e^{jkx_1} + Re^{-jkx_1}} \quad (19)$$

where R is the complex reflection coefficient, which, as a function of H_{12}, can be expressed as:

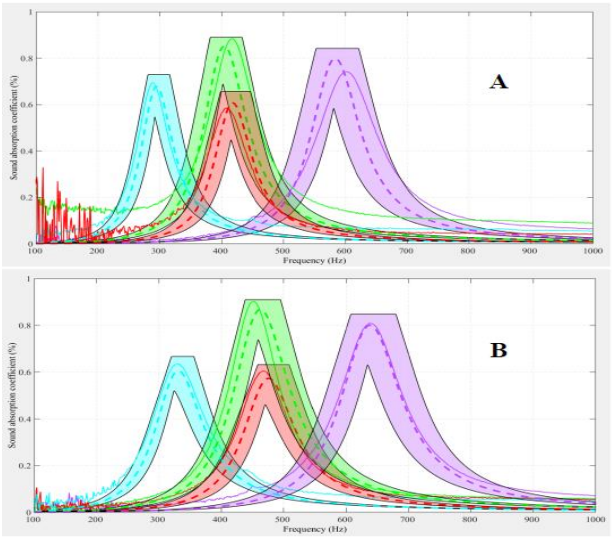
$$R = \frac{H_{12} + H_i}{H_r - H_{12}} e^{2jkx_1} \quad (20)$$

The sound absorption coefficient can then be calculated for normal incidence using the following relation: $\alpha = 1 - |R|^2$. This formulation allows for the determination of the sample's acoustic absorption based on the measurement of the transfer function between the two microphones, following the standardized method outlined in ISO 10534-2 [6].

3. PRELIMANARY RESULTS

In the experimental tests, three different unit cell geometries were analyzed, characterized by angles (θ_1 and θ_2) of 45°-45°, 60°-45°, and 30°-60°, respectively. For each configuration, two different variants of nominal thickness (L), 5 mm and 10 mm, and two nominal cavity depth (D) configurations, also 5 mm and 10 mm, were tested. The experimental results obtained in the laboratory were compared and validated using the analytical model. The latter was implemented using the (L) values measured directly from the samples, as reported in Table 1.

Figure 3 shows the comparison between the analytical predictions and the experimental data for the absorption coefficient as a function of frequency. The envelope observed in the analytical graphs is attributed to the uncertainty in the exact measurement of the sample neck radius r. To account for potential inaccuracies due to the printing process, an error margin of 0.05% of the nominal radius of 3 mm was introduced, allowing for possible variations in the actual radius.



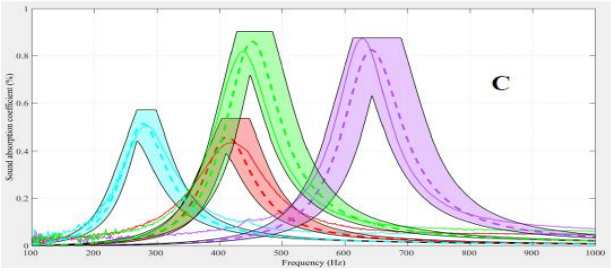


Figure 3. Comparison between experimental and analytical results for the acoustic absorption coefficient as a function of frequency with different geometric configurations of AMMs. Graph (A) corresponds to the configuration with angles 45°-45°, (B) to the 60°-45° configuration, and (C) to the 30°-60° configuration. The colored curves represent different combinations of thickness (L) and cavity depth (D): blue indicates L = 10 mm, D = 10 mm; red L = 10 mm, D = 5 mm; green L = 5 mm, D = 10 mm; and purple L = 5mm, D = 5 mm. Solid lines represent the experimental results, while dashed lines indicate the analytical results obtained for a perforation radius of r = 3 mm. The envelope accounts for a ±5% variation in the perforation radius.

4. CONCLUSIONS

The article explored the study of different unit cell geometries for an acoustic metamaterial resonator (AMM), examining the influence of variations in thickness (L), cavity depth (D), and angles (θ_1 and θ_2) on the geometric configuration of individual cells. The absorption values of the unit cells were validated both through an analytical model using the transfer matrix method [7] and the Johnson-Champoux-Allard (JCA) equivalent fluid approach [8] and through experimental measurements conducted according to the guidelines of ISO 10534-2 [6] on 3D-printed samples. The results demonstrated a significative agreement between the experimental data and analytical predictions, highlighting how variations in geometric characteristics influence both the resonance frequencies and the absorption coefficient amplitudes. This opens space to future investigations about optimised panels handling the segmented necks.

5. ACKNOWLEDGEMENTS

This work was partly financed by FCT / MCTES through national funds (PIDDAC) under the R&D Unit Institute for Sustainability and Innovation in Structural Engineering (ISISE), under reference UID/04029/Institute for Sustainability and Innovation in Structural Engineering (ISISE), and under the Associate Laboratory Advanced Production and Intelligent Systems ARISE under reference LA/P/0112/2020.

6. REFERENCES

[1] P. Ruggeri, F. Peron, N. Granzotto, and P. Bonfiglio, “Analisi sperimentale parametrica sull’assorbimento acustico di risonatori acustici a cavità,” in *Proc. of the 41st National Conference of the Italian Acoustical Association (AIA)*, Pisa, Italy, 2014.

[2] D. Y. Maa: “Noise control using perforated panel absorbers,” *Noise Control Eng. J.*, vol. 29, no. 3, pp. 77–84, 1987.

[3] N. Atalla and F. Sgard: “Acoustic modeling of porous materials,” *J. Sound Vib.*, vol. 303, pp. 195–208, 2007

[4] J. Carbajo, S. Ghaffari Mosanenzadeh, S. Kim, and N. X. Fang, “Sound absorption of acoustic resonators with oblique perforations,” *Appl. Phys. Lett.*, vol. 116, no. 5, pp. 054101, 2020.

[5] K. Attenborough: “Sound absorption in porous materials with inclined pores,” *Appl. Acoust.*, vol. 130, pp. 188–194, 2018.

[6] International Organization for Standardization: *ISO 10534-2:1998 Acoustics — Determination of sound absorption coefficient and impedance in impedance tubes — Part 2: Transfer-function method*. Geneva, Switzerland: ISO, 1998.

[7] M. Munjal: *Acoustics of Ducts and Mufflers*. New York: Wiley, 2014. ISBN: 978-1-118-44309-5.

[8] J. Allard and N. Atalla: *Propagation of Sound in Porous Media: Modelling Sound Absorbing Materials*. New York: Wiley, 2009. ISBN: 978-0-470-74734-6.

[9] Jaouen, L., Chevillotte, F. “Length correction of 2D discontinuities or perforations at large wavelengths and for linear acoustics”, *Acta Acustica United with Acustica*, vol. 104, pp. 243-250, 2018.

[10] T. G. Zieliński, N. Dauchez, T. Boutin, et al.: "Taking advantage of a 3D printing imperfection in the development of sound-absorbing materials," *Applied Acoustics*, vol. 197, pp. 108941, 2022. ISSN: 0003-682X. doi: 10.1016/j.apacoust.2022.108941.

DOI: 10.61782/fa.2025.0917

FORUM ACUSTICUM EURONOISE 2025

TRANSFER MATRIX MODELLING OF FOLDED QUARTER-WAVELENGTH RESONATORS WITH 90° BENDS

Femke De Bie[1,3*] **Hervé Denayer**[2,3] **Elke Deckers**[1,3]

[1] Department of Mechanical Engineering, campus Diepenbeek, KU Leuven, Belgium
[2] Department of Mechanical Engineering, campus Heverlee, KU Leuven, Belgium
[3] Flanders Make@KU Leuven

ABSTRACT

Acoustic metamaterials that consist of multiple folded quarter-wavelength resonators in parallel have the potential to realise high and broadband low-frequency sound absorption while maintaining a compact volume. In a previous study, it was shown that folding can alter the acoustic behaviour of a quarter-wavelength resonator significantly and a length correction factor was proposed to account for the effect of a single 90° bend in analytical models. In this paper, a transfer matrix approach to model quarter-wavelength resonators with multiple 90° bends is proposed. Firstly, the different steps of the transfer matrix method are discussed and the two-port matrix of a 90° bend is predicted as a function of the resonator width by applying a passive two-port characterisation technique to the result of numerical simulations. Then, the transfer matrix method is applied to determine the resonance frequency of a set of single-bend and two-bend quarter-wavelength resonators. Lastly, these results are verified against other modelling approaches and finite element simulations in COMSOL Multiphysics.

Keywords: *acoustic metamaterial, quarter-wavelength resonator, transfer matrix method, 90° bend*

*__Corresponding author__: *femke.debie@kuleuven.be.*

__Copyright__: *©2025 De Bie, F. et al. This is an open-access article distributed under the terms of the Creative Commons Attribution 3.0 Unported License, which permits unrestricted use, distribution, and reproduction in any medium, provided the original author and source are credited.*

1. INTRODUCTION

Sound absorbing panels made of porous material (e.g. mineral wool) offer a broadband solution to indoor noise problems, but since the needed layer thickness scales with the wavelength, issues might arise when targeting low-frequency sound in confined spaces. In such case, resonant acoustic metamaterials can be used instead, offering a compact and broadband solution to low-frequency sound problems [1–3].

This work focusses on quarter-wavelength ($\lambda/4$) acoustic metamaterials, which consist of multiple folded or coiled $\lambda/4$ resonators in parallel and/or series. In a previous study, it was shown that folding can affect the resonance frequency of a $\lambda/4$ resonator significantly [4]. Hence, an empirical length correction factor was derived to account for the effect of a 90° bend [5]. Although the proposed correction factor was successfully verified and validated [6], its use is limited to $\lambda/4$ resonators with a single 90° bend, whereas real-life resonators are often folded multiple times.

Hence, this paper investigates the use of a transfer matrix approach to determine the absorption coefficient and resonance frequency of a $\lambda/4$ resonator with multiple 90° bends. The remainder of this paper is structured as follows. In Section 2, the different steps of the proposed transfer matrix method are discussed and transfer matrices for straight and 90° corner elements are defined. Section 3 covers the numerical verification of the transfer matrix method against various single-bend and two-bend resonator configurations. Finally, the main conclusions are given in Section 4.

2. TRANSFER MATRIX METHOD

The transfer matrix method (TMM) is a well-established approach to determine the acoustic properties (e.g. the absorption coefficient) of a complex, multi-element structure [7]. In this work, the structure is a folded $\lambda/4$ resonator, which can be seen as a series arrangement of straight and 90° corner elements, embedded in a baffle. The different steps of the TMM are discussed in the following subsections.

2.1 Transfer matrix of an acoustic element

In order to apply the TMM, the transfer matrix $\underline{T}$ of each element must be known. This matrix relates the total pressure p and axial particle velocity v at the inlet and outlet of the element, as given by Eqn. (1) [7]:

$$\begin{Bmatrix} p \\ v \end{Bmatrix}_{out} = \underline{T} \begin{Bmatrix} p \\ v \end{Bmatrix}_{in}. \tag{1}$$

Depending on the type of element, $\underline{T}$ is calculated directly or derived from the scatter matrix $\underline{S}$, which relates the complex amplitudes of the left and right propagating pressure wave at the inlet and outlet of the element, as given by Eqn. (2) [8]:

$$\begin{Bmatrix} p^+_{out} \\ p^-_{in} \end{Bmatrix} = \underline{S} \begin{Bmatrix} p^+_{in} \\ p^-_{out} \end{Bmatrix}. \tag{2}$$

2.1.1 *Straight element*

For a straight element, $\underline{T}$ is given by Eqn. (3):

$$\underline{T} = \begin{bmatrix} \cos(kL) & -\mathrm{j}Z\sin(kL) \\ -\mathrm{j}\frac{1}{Z}\sin(kL) & \cos(kL) \end{bmatrix}, \tag{3}$$

with j the imaginary unit, L the length of the element, and k the wavenumber and Z the characteristic impedance of the equivalent fluid inside the element, respectively [7, 9].

2.1.2 *90° corner element*

For a 90° corner element, a direct representation of $\underline{T}$ like Eqn. (3) is not available in literature. Hence, $\underline{T}$ is calculated from $\underline{S}$ using Eqn. (4):

$$\underline{T} = \begin{bmatrix} \frac{1-S_{12}}{2} & \frac{Z(1+S_{12})}{2} \\ \frac{-S_{22}}{2} & \frac{ZS_{22}}{2} \end{bmatrix}^{-1} \begin{bmatrix} \frac{S_{11}}{2} & \frac{ZS_{11}}{2} \\ \frac{S_{21}-1}{2} & \frac{Z(1+S_{21})}{2} \end{bmatrix}. \tag{4}$$

The scatter matrix of a 90° corner element is derived by applying a passive two-port characterisation technique to the results of 2D finite element simulations in COMSOL Multiphysics [10]. In this work, only 90° corners with a square cross-section with side length b ranging from 1 to 6 mm are considered. It is found that, for each corner, $\underline{S}$ is symmetric (i.e. $S_{11} = S_{22}$ and $S_{12} = S_{21}$) and can be obtained using Eqn. (5)-(8):

$$\Re(S_{11}) = -0.287(k_0b)^2 - 0.013(k_0b) + 0.999, \tag{5}$$

$$\Im(S_{11}) = -0.783(k_0b) - 0.001, \tag{6}$$

$$\Re(S_{12}) = -0.161(k_0b)^2 - 0.004(k_0b) - 0.0002, \tag{7}$$

$$\Im(S_{12}) = -0.221(k_0b) - 0.0003. \tag{8}$$

The coefficients in the above equations are rounded to enhance readability. Eqn. (5)-(8) are valid for $k_0b \leq 0.16$, with k_0 the wavenumber of the lossless medium. The R^2-value of each fit is greater than 0.98.

2.2 Transfer matrix of the entire structure

Once the transfer matrix of each element is defined, the total transfer matrix $\underline{T}'$ of the $\lambda/4$ resonator can be calculated using Eqn. (9):

$$\underline{T}' = \left(\prod_{i=m}^{i=1} \underline{T}_i \right) \underline{T}_{EC} \underline{T}_{\phi}, \tag{9}$$

with $\underline{T}_i$ the transfer matrix of the i-th element, $\underline{T}_{EC}$ the end correction matrix and $\underline{T}_{\phi}$ the porosity matrix [11].

2.3 Absorption coefficient and resonance frequency

From $\underline{T}'$, the absorption coefficient α of the $\lambda/4$ resonator can be calculated using Eqn. (10):

$$\alpha = 1 - \left| \frac{T'_{21} + \frac{T'_{22}}{Z_0}}{\frac{T'_{22}}{Z_0} - T'_{21}} \right|^2, \tag{10}$$

with Z_0 the characteristic impedance of the lossless medium [7]. The resonance frequency f_R of the resonator is the frequency at which α reaches its maximum value.

3. NUMERICAL VERIFICATION

The use of Eqn. (3)-(10) is verified by comparing the results of the TMM to the results of 3D finite element simulations for a wide variety of folded $\lambda/4$ resonators.

3.1 Approach

To verify the formulas presented in Section 2, various single-bend and two-bend $\lambda/4$ resonators are modelled in 3D in COMSOL Multiphysics. Each resonator has a square cross-section and is embedded in a square baffle, as shown in Fig. 1.

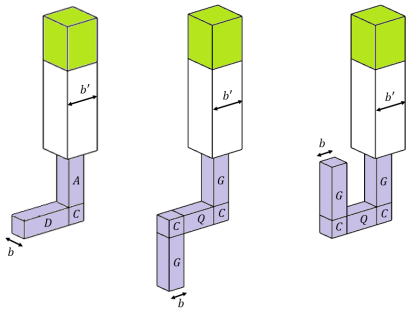


Figure 1. 3D model of a single-bend (left), Z-shaped two-bend (middle) and U-shaped two-bend (right) $\lambda/4$ resonator. Each capital letter indicates an acoustic element.

An overview of the modelled resonators is given in Tab. 1. In total, 54 unique single-bend and 192 unique two-bend resonators are modelled.

Table 1. Overview of the modelled $\lambda/4$ resonators. The porosity ϕ equals $(b/b')^2$.

Resonators with one 90° bend	
Porosity ϕ [-]	0.072
Centreline length L_{CL} [m]	0.06; 0.15; 0.35
Side length b [mm]	1; 2; 3; 4; 5; 6
L_A/L_{CL} [-]	0.1; 0.5; 0.75
L_D [m]	L_{CL} - b - L_A
Resonators with two 90° bends	
Folding shape [-]	U; Z
Porosity ϕ [-]	0.072
Centreline length L_{CL} [m]	0.06; 0.1; 0.25; 0.4
Side length b [mm]	1; 2; 3; 4; 5; 6
L_Q/b [-]	0.2; 0.6; 1; 5
L_G [m]	(L_{CL} - 2b - L_Q) / 2

For each resonator, the absolute relative error in predicted resonance frequency $|\Delta f_R|$ is calculated using Eqn. (11):

$$|\Delta f_R| = \left| \frac{f_R(T) - f_R(C)}{f_R(C)} \right| .100\%, \qquad (11)$$

with $f_R(C)$ the resonance frequency extracted from the finite element simulations and $f_R(T)$ the resonance frequency obtained using the TMM. For the single-bend resonators, the accuracy of the TMM is verified against the accuracy of two other modelling approaches: the length correction factor (LCF) and the model used to model unfolded resonators, which is from now on referred to as the basic analytical model (BAM) [4,6]. For the two-bend resonators, the accuracy of the TMM is only verified against the accuracy of the BAM since the LCF is not applicable.

3.2 Single-bend resonators

The results for the single-bend resonators are visualised in Fig. 2. In this figure, it is seen that the TMM yields similar accuracy values as the LCF. Since the latter was successfully validated in earlier work [6], the use of the formulas presented in Section 2 is justified. It can also be seen that both methods yield significantly higher accuracies than the BAM. The maximum value of $|\Delta f_R|$ when applying the TMM is 0.18%.

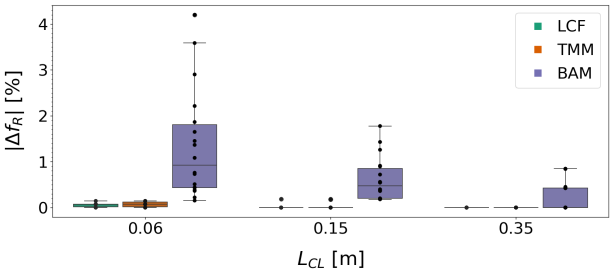


Figure 2. Results for the 54 single-bend resonators.

3.3 Two-bend resonators

The results for the two-bend resonators are visualised in Fig. 3. In this figure, it is seen that (i) the TMM yields significantly higher accuracies than the BAM and (ii) similar accuracy values are achieved for U- and Z-shaped resonators. The maximum value of $|\Delta f_R|$ when applying the TMM is 0.56%.

When looking into the values of $|\Delta f_R|$ in more detail, it is found that, for fixed values of b and L_{CL}, $|\Delta f_R|$ increases when the distance between the bends decreases. This holds for both U- and Z-shaped resonators and implies that interaction effects occur between closely spaced bends. However, since the TMM still yields accurate results, no additional correction is included to account for these effects.

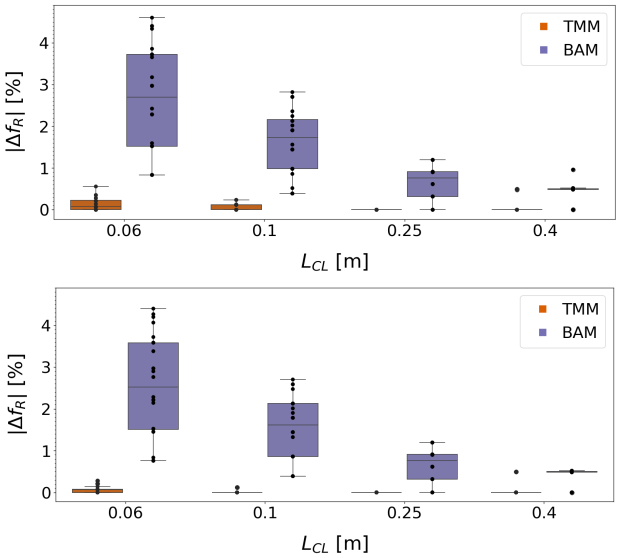


Figure 3. Results for the U-shaped (top) and Z-shaped (bottom) resonators.

4. CONCLUSIONS AND OUTLOOK

In this work, the TMM is applied to determine the resonance frequency of various square $\lambda/4$ resonators with one or two 90° bends and the results are verified against other modelling approaches and 3D finite element simulations in COMSOL Multiphysics. It is found that the TMM yields accurate results: the maximum absolute relative error in predicted resonance frequency is 0.18% and 0.56% for single-bend and two-bend resonators, respectively. In a next step, the use of the TMM will be verified for square $\lambda/4$ resonators with more than two 90° bends and experimental validation will be performed on 3D-printed samples.

5. ACKNOWLEDGMENTS

The research of F. De Bie (fellowship no. 1S17424N) is funded by a personal grant from the Research Foundation Flanders (FWO).

6. REFERENCES

[1] C. Chen et al. A low-frequency sound absorbing material with subwavelength thickness. *Applied Acoustics*, 110, 2017.

[2] Y. Wang et al. A tunable sound-absorbing metamaterial based on coiled-up space. *Journal of Applied Physics*, 123, 2018.

[3] L. Prasetiyo, E.N. Wongso and J. Sarwono. Developing sub-wavelength sound absorber based on coiled up tube resonator. *Journal of Engineering and Technological Sciences*, 51(3), 2019.

[4] Z. Zhang et al. Optimized metamaterial using quarter-wavelength resonators for broadband acoustic absorption. In *Proc. of DAGA2021* , pages 101–104, Vienna, Austria, 2021.

[5] F. De Bie et al. Quarter-wavelength acoustic metamaterials: the effect of folding on the resonance frequency. In *Proc. of ISMA2022-USD2022* , pages 3054–3065, Leuven, Belgium, 2022.

[6] F. De Bie et al. Experimental validation of the length correction factor for folded quarter-wavelength resonators. In *Proc. of Forum Acusticum* , pages 1969–1976, Turin, Italy, 2023.

[7] N. Jiménez, J.P. Groby and O. Umnova. *Acoustic Waves in Periodic Structures, Metamaterials, and Porous Media*. Springer, Cham, Switzerland, 2021.

[8] M. Åbom. Measurement of the scattering-matrix of acoustical two-ports. *Mechanical Systems and Signal Processing*, 5(2):89–104, 1991.

[9] J.F. Allard and N. Atalla. *Propagation of Sound in Porous Media: Modelling Sound Absorbing Materials, Second Edition*. Wiley, Chichester, UK, 2009

[10] L. Criscuolo et al. Experimental analysis of aeroacoustic instabilities in Helmholtz resonators. In *Proc. of ISMA2018-USD2018* , pages 601–611, Leuven, Belgium, 2018.

[11] A. Dell, A. Krynkin and K.V. Horoshenkov. The use of the transfer matrix method to predict the effective fluid properties of acoustical systems. *Applied Acoustics*, 182, 2021.

DOI:

Main theme: A10 Materials and Metamaterials

Session A10.03 Metamaterials for noise and vibration reduction: novel applications and experimental methods

Chair(s): E. Deckers, L. Van Belle, E. Shabalina, J. Cuenca

DOI: 10.61782/fa.2025.0734



FORUM ACUSTICUM
EURONOISE 2025

REDUCED-ORDER MODELING ANALYSIS OF RANDOM GEOMETRIC CHANGES ON THE VIBROACOUSTIC BEHAVIOR OF METAMATERIALS

Yves Pillot[1,3] **Régis Boukadia**[1,3] **Lucas Van Belle**[1,3]
Elke Deckers[2,3]

[1] Department of Mechanical Engineering, KU Leuven, Belgium
[2]Department of Mechanical Engineering, Campus Diepenbeek, KU Leuven, Belgium
[3] Flanders Make@KU Leuven, Belgium

ABSTRACT

As metamaterials are coming closer and closer to becoming a mature industrial solution, the question of manufacturing has started to gain importance. Indeed, variability related to industrial processes can cause geometric variability which might degrade the attenuation performance of manufactured samples. Hence, there is a strong need to quantify the impact of uncertainty on the behavior of vibroacoustic metamaterials. However, full-scale metamaterial models can require a relatively high computational time to solve. This makes uncertainty quantification methods like Monte-Carlo simulations either computationally intensive or infeasible due to the high number of model solves required. Hence, this paper proposes a parametric reduced-order model based on the Krylov subspace to predict the vibroacoustic response of a metamaterial structure due to geometric changes without requiring another solve of the full system. Derivation of the response statistics is then achieved by applying a Monte-Carlo simulation on the obtained reduced-order model.

Keywords: *Geometric Variability, Model-Order Reduction, Vibroacoustic Metamaterials.*

**Corresponding author*: *yves.pillot@kuleuven.be.*
***Copyright**: ©2025 Yves PILLOT et al. This is an open-access article distributed under the terms of the Creative Commons Attribution 3.0 Unported License, which permits unrestricted use, distribution, and reproduction in any medium, provided the original author and source are credited.*

1. INTRODUCTION

When it comes to lightweight solutions for sound and vibration attenuation, metamaterials are showing more and more potential for noise and vibration harnessing in different areas of the industry [1, 2]. The locally resonant nature of metamaterials allows them to create stopbands in which the vibration response is attenuated. However, the problem of variability in metamaterials and the prediction of its effects on their performance is currently a topic of interest. As metamaterials often rely on either in tune resonators or periodicity, imperfect manufacturing of metamaterial structures could lead to underperforming solutions. This is why, the impact of such uncertainty needs to be assessed.

Currently, few design procedures for metamaterials take into account the impact of uncertainties. At present, metamaterials are typically designed by Unit-Cell (UC) modeling [3]. This method takes advantage of the metamaterial translational symmetry to reduce the size of the problem, as only the smallest repeating period of the material is modeled. Some authors used this method to characterize the impact of uncertainty at the UC level [4, 5]. However, as this representation assumes perfect periodicity of the material between the UCs, it is not able to describe the random imperfections that occur when the material is actually manufactured. Still, to take into account these imperfections, different approaches were already proposed in current literature. Some authors suggest to take into account the impact of variability in a finite metamaterial model. Some references [6, 7] present studies of

metamaterial structures through uncertainty quantification techniques such as Gaussian process modeling to characterize e.g. the uncertainty bounds on its response metrics. In [8], a model-order reduction strategy is presented to improve the solving time of nearly periodic structure, based on periodic structure theory, which allows to partially overcome the computational limitations of statistical analysis for large metamaterial structures.

However, the study of uncertainty in metamaterials has been mostly limited to point scatterers or idealized resonators [9], and the study of geometric deviations in such structures has received less attention. Indeed, geometric perturbations of a structure leads to nonlinear changes in the finite element matrices, making model-order reduction more complex. Additionally, parametric model-order reduction schemes need to be developed for efficient sampling and uncertainty quantification of the system as the number of solves needed for convergence of the statistics under consideration might be high in some cases.

In this paper, a parametric model-order reduction scheme based on [9] is developed for finite-size metamaterials. The method is applied to a phononic crystal beam to obtain the statistics of its vibration response to a point excitation. The accuracy of the method is assessed by comparison with the full-order model for individual simulations, but also for the statistics of the system's response.

The rest of the paper is structured as follows: section 2 provides a description of the problem under consideration. Then, section 3 gives an overview of the parametric model-order reduction approach. A statistical analysis of the structure as well as a comparison with the full-order model are given in section 4. An extension of the proposed method by projection basis enrichment is proposed in 5. Finally, the results are summarized in section 6.

2. PROBLEM DEFINITION

In this paper, the phononic Euler-Bernoulli beam of [10] is considered as case study. A one-dimensional structure is considered, for which geometric changes are straightforwardly defined and have a direct effect on the stopband behavior of the metamaterial. The system also has the advantage of being practically manufacturable, allowing for possible experimental validation of the numerical study in future work.

The beam is composed of 9 UCs with subsequent thickness variations (Fig. 1). The UC has a length $L_{UC} = 40$ mm and is composed of two equal-sized parts with different heights $h_1 = 10$ mm and $h_2 = 3$ mm respectively. The material properties of the beam are described in table Tab. 1. Free-free boundary conditions are considered and a unit transverse point force is applied on the first node on the left side of the beam.

Table 1. Properties of the phononic beam.

Property	Symbol	Value
Width	b	10 mm
Mass density	ρ	1135 kg/m^3
Young's modulus	E	1.9 GPa
Structural damping	η	5 %

Due to the presence of variability, the position of each UC center is assumed to randomly deviate from its nominal value and is described by the parameters l_n. This choice is motivated by the fact that this phononic beam relies on periodicity to produce a stopband. Therefore, modifying l_n directly impacts the periodicity but also preserves its total length as well as the location of the forcing and response nodes. The length deviation of l_n is assumed to follow a uniform distribution with limits at $\pm 3\%$ of the nominal length. There is currently no justification for this choice as data in the metamaterial literature on such variation is rather limited. However, the statistical distribution of the l_n could be determined by production of a large enough series and statistical analysis of the dimensions of the system.

To conduct the numerical study, the beam is discretized using the Finite Element Method (FEM). Euler-Bernoulli beam elements are used to obtain a small, one-dimensional problem instead of a full elastodynamic model. 8 elements per UC are used, ensuring a minimum of 10 elements per wavelength in either of the sections of the beam. The FE-discretized, l_n-dependent equations of motion then write as

$$\mathrm{D}(l_n)\mathbf{u}(l_n) = \mathbf{F}, \tag{1}$$

where $\mathrm{D}(l_n)$ is the dynamic stiffness matrix, $\mathbf{u}(l_n)$ is the displacement vector and $\mathbf{F}$ is the force vector. The dependency with respect to the l_n is accounted for by moving the nodes of the structure in space such that the elements of the beam are either contracted or dilated by a small percentage compared to the case $l_n = 0$ to match the desired geometric variation. In general, metamaterial UCs can become quite intricate, and UC meshes rather large, making full structure models of the UC assembly even

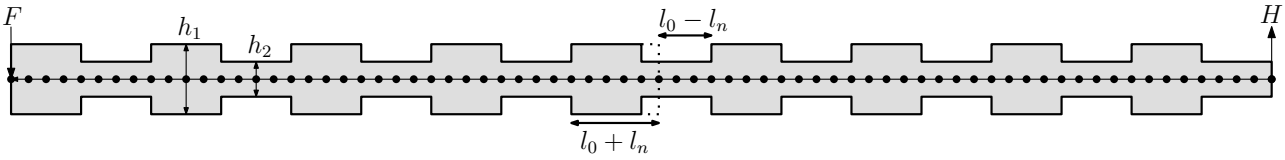


Figure 1. Phononic beam structure under consideration. F represents the forcing point, while H represent the velocity response point.

larger. Solving equation Eqn. (1) might then be too computationally expensive for full-order uncertainty propagation simulations requiring high amount of samples as the computational cost for one solve is already high. In the following section, a parametric model-order reduction scheme is developed to take into account the impact of geometrical uncertainties. The model under consideration is rather small and does not need to be reduced to perform uncertainty quantification. In principle, the method proposed is however generally valid, and in this paper it will be applied to this simple case as a first validation. The goal of the method is to obtain a parametric reduced-order model to quickly evaluate the response of a structure subject to geometric variations.

3. METHODOLOGY

3.1 Parametric Model-Order Reduction Scheme

As a first approach, one might consider expanding $\mathbf{u}$ as a first order perturbation series around $\mathbf{u}_0$:

$$\mathbf{u} \simeq \mathbf{u}_0 + \sum_{n=1}^{N_p} l_n \mathbf{u}_1^{(n)}, \tag{2}$$

with N_p the number of random parameters, equal to the number of UCs in this study, $\mathbf{u}_0 = \mathbf{u}(l_n = 0)$ and $\mathbf{u}_1^{(n)} = \mathrm{D}^{-1}(0)\frac{\partial \mathrm{D}}{\partial l_n}|_{l_n=0}\mathbf{F}$. The matrices $\frac{\partial \mathrm{D}}{\partial l_n}$ can be straightforwardly evaluated using the analytical expression of the Euler-Bernouilli beam element matrices

$$K_e^p = \frac{EI_p}{l_e^3}\begin{pmatrix} 12 & 6l_e & -12 & 6l_e \\ 6l_e & 4l_e^2 & -6l_e & 2l_e^2 \\ -12 & -6l_e & 12 & -6l_e \\ 6l_e & 2l_e^2 & -6l_e & 4l_e^2 \end{pmatrix}, \tag{3}$$

$$M_e^p = \frac{\rho S_p l_e}{420}\begin{pmatrix} 156 & 22l_e & 54 & -13l_e \\ 22l_e & 4l_e^2 & 13l_e & -3l_e^2 \\ 54 & 13l_e & 156 & -22l_e \\ -13l_e & -3l_e & -22l_e & 4l_e^2 \end{pmatrix}, \tag{4}$$

where K_e^p and M_e^p are respectively the Euler-Bernoulli beam element stiffness and mass matrices of the p-th cross section of the beam with $p = 1, 2$, S_p and I_p are the surface and quadratic moment of inertia of the p-th cross section of the beam and l_e is the element length.

Eqn. (2) usually suffers from accuracy and instability, especially in the presence of resonances, making it unsuitable for accurate computation of the frequency response of a vibrating structure in which many resonances are present [11].

This is why an alternative moment-matching approach [9, 12] is used instead in this paper. The moments of the first-order perturbation series $\mathbf{u}_0$ and $\mathbf{u}_1^{(n)}$ are multiplied by a set of coefficients for the chosen set of parameters by multiplying them by a correction contribution amplitude w_n.

$$\mathbf{u} \simeq w_0\mathbf{u}_0 + \sum_{n=1}^{N_p} w_n l_n \mathbf{u}_1^{(n)}. \tag{5}$$

These additional degrees of freedom will later allow for an optimal correction of the displacement vector. This is equivalent to taking the assumption that the solution $\mathbf{u}$ lies in the subspace

$$\mathrm{Q} = orth\left(\left[\mathbf{u}_0, \mathbf{u}_1^{(1)}, ..., \mathbf{u}_1^{(N_p)}\right]\right). \tag{6}$$

Projecting Eqn. (1) onto the basis Q, the following reduced-order problem is obtained

$$\tilde{\mathrm{D}}(l_n)\mathbf{w}(l_n) = \tilde{\mathbf{F}}, \tag{7}$$

with $\tilde{\mathrm{D}}(l_n) = \mathrm{Q}^*\mathrm{D}(l_n)\mathrm{Q}$, and $\tilde{\mathbf{F}} = \mathrm{Q}^*\mathbf{F}$. Eqn. (7) can then be used to quickly evaluate the changes of $\mathbf{u}$ to parametric variations, without the need to solve for the full-order problem once again, and only requiring a reassembly of the system matrices with a transformed mesh according to the l_n.

3.2 Monte-Carlo simulations

To quantify the random changes in the structure's response, Monte-Carlo simulations are used to propagate the uncertainty. For a sufficiently large number of samples $N_{samples}$, the set of l_n is drawn from a uniform distribution using a random number generator. In this study, the Python function from the *Numpy* library `numpy.random.uniform` is used.

For each set of l_n, and at each frequency the matrix $\mathrm{D}(l_n)$ is assembled. Then the system Eqn. (7) is derived and solved. Equation Eqn. (5) is finally used to obtain the displacement vector and the response. Once the procedure is repeated for the full set of l_n, statistical analysis can be run on the obtained set of responses.

In the following section, the previously derived reduction scheme and the Monte-Carlo simulation approach are used for statistical analysis of the phononic beam structure.

4. STATISTICAL ANALYSIS OF THE PHONONIC BEAM

In this section, the method of section 3 is validated on the structure from section 2. Then an error analysis is performed to verify the accuracy of the method.

4.1 Response analysis

In (Fig. 2), the endpoint velocity response of the beam is displayed in dashed lines for the nominal case, where $l_n = 0$. The nominal periodic phononic beam shows a frequency range of strong vibration reduction around 1050 Hz. As shown in [10], this is due to the presence of a Bragg stopband around this frequency. Destructive interference occurs, which prevents waves from propagating to the probing location at the other side of the beam. As this effect is linked to the periodicity of the structure, including disorder in the UC geometry through the l_n, and therefore breaking the periodicity of the systems is expected to have an impact on the stopband effect.

The median of the response (blue) as well as the confidence interval between its 5-th and the 95-th percentiles (light blue region) are also displayed. A total of 1000 Monte-Carlo sample are computed using the reduced-order model from Eqn. (7) method and used to obtain the statistics of the response. After 1000 samples, it was observed that the relative variation in the statistical indicators under consideration is less than 3% over the frequency range $50 - 2500$ Hz when increasing the number of iterations.

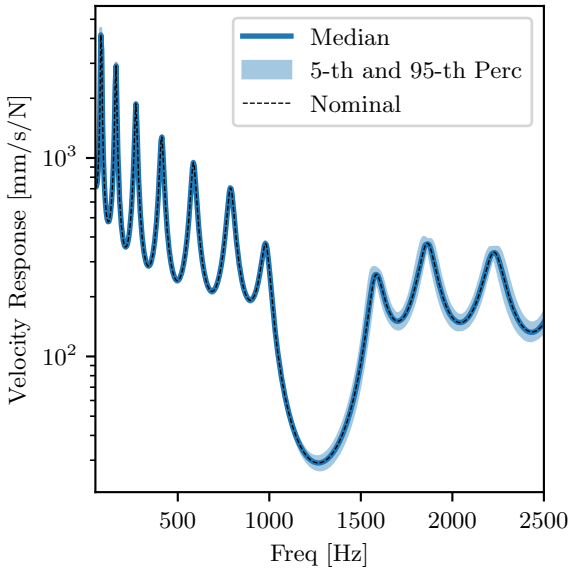


Figure 2. Endpoint velocity response of the phononic response in the nominal case, median, 5-th and the 95-th percentiles of the response.

Thanks to these response statistics, the effect of geometric variations on the vibration attenuation performance of the beam can be assessed. In the higher frequency part of the stopband region, as well as above it, the difference between the 95-th and 5-th percentile responses is seen to be bigger than in the lower part of the frequency range, meaning that the magnitude of the response is more uncertain in this frequency region. For the geometrical changes considered, small variations affect the response in the band gap. However, a clear attenuation region still persists for the disorder strength considered. This was also observed for locally resonant disordered beam metamaterial structures in the literature [6, 13, 14].

4.2 Error Analysis

Following computation of the response statistics, an analysis is conducted to compare how representative the reduced-order model is of the full-order model. After performing statistical computations with the reduced-order model, a Monte-Carlo simulation is run for the full-order model Eqn. (1) for the same set of l_n to conduct an error analysis. This is feasible since the model considered

here has a small number of degrees of freedom. To verify the accuracy of the reduced-order model, the maximum of the relative error between the reduced and full-order models across all realizations of the structure is evaluated. This error metric can serve as an estimate of the minimum degree of accuracy attained by the method in the desired frequency range.

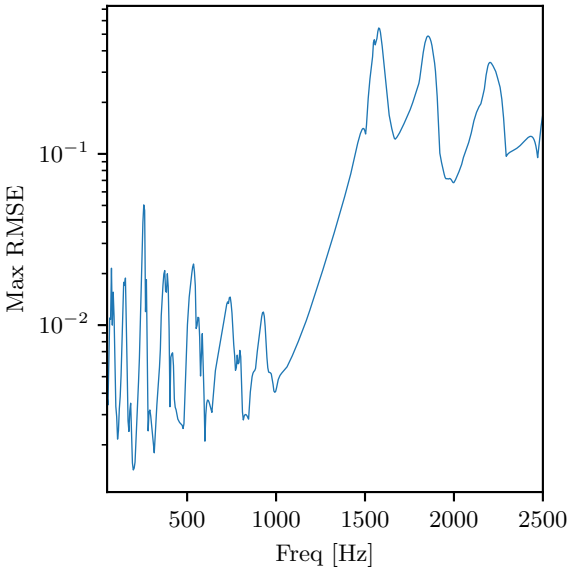


Figure 3. Maximum relative root mean square error between the reduced and full-order models observed across realizations of the system.

The results of this first analysis are displayed in Fig. 3. From the error curve across the frequency range, we can observe that the reduced-order model performs best up to 1000Hz, before the stopband region, with under 5% relative error. At higher this frequencies, the maximum error between the two models is higher, and can get as high as 40% near some resonances. Indeed, past the stopband, the dynamics of the phononic beam are different and could explain the difference in accuracy. Additionally, error peaks occur near resonances of the system.

To verify the accuracy of the method, the error on the statistical indicators is computed for this system, namely, the median, 5th and 95th percentiles of the response is computed compared to the full-order system in (Fig. 4).

The error does not exceed 15% for either of the statistical quantities over the frequency range of interest. How-

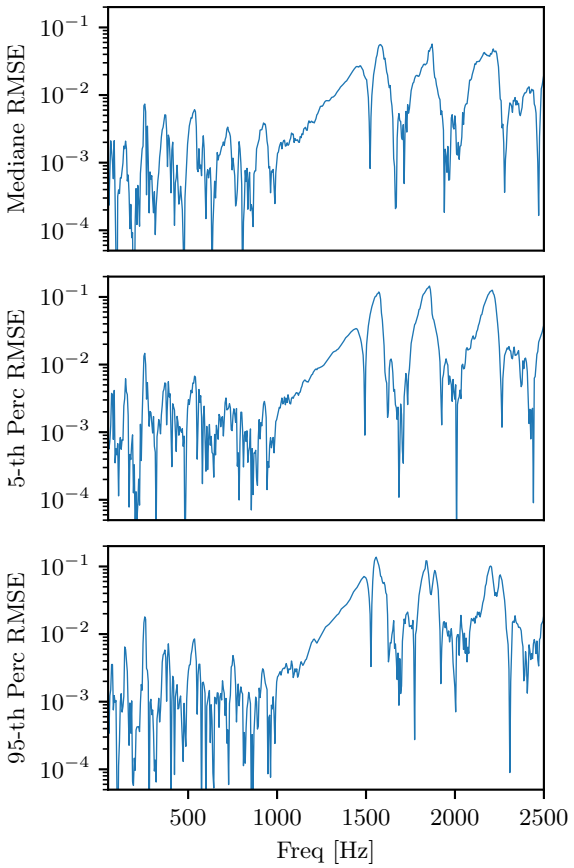


Figure 4. Relative root mean square error between the reduced and full-order models on the median, 5-th and 95-th percentiles of the endpoint velocity response.

ever, similarly to (Fig. 3), a much lower accuracy is obtained above the stopband region and error peaks are again notified near resonances of the system, confirming the inaccuracy problem notified earlier. The relative error on the statistics is seen to be much lower than the maximum error across realizations of the system. This is to be expected since the first error metric serves as a measure of the maximal error and single realizations of the system will have an error profile either lower or equal to the one of (Fig. 3).

If the desired accuracy of the reduced-order model is not acceptable for certain use cases. The origin for the error between the two models is that the subspace Q is not

of sufficient rank to describe effect of geometric variations with sufficient accuracy, especially in the regions of high error. A higher accuracy could be attained by enriching the projection basis with higher order moments of $\mathbf{u}$ and is the object of the following section.

5. SECOND ORDER PROJECTION SCHEME

To obtain additional accuracy, one may consider adding the second order terms of the perturbation series to the reduced-order basis. The subspace Q then becomes,

$$\mathrm{Q}_2 = orth\left(\left[\mathrm{Q}, \mathbf{u}_2^{(1,1)}, \mathbf{u}_2^{(1,2)}, ..., \mathbf{u}_2^{(N_p,N_p)}\right]\right), \quad (8)$$

where the $\mathbf{u}_2^{(m,n)}$ are defined as

$$\mathbf{u}_2^{(m,n)} = \mathrm{D}^{-1}(0)\left[2\frac{\partial \mathrm{D}}{\partial l_m}\mathbf{u}_1^{(n)} + \frac{\partial^2 \mathrm{D}}{\partial l_m \partial l_n}\mathbf{u}_0\right]_{l_m=0}. \quad (9)$$

The procedure from section 3 is then followed using Q_2 instead of Q. Monte-Carlo simulations are run on this enriched reduced-order model. The maximum error across realizations of the system is computed again and displayed in Fig. 5.

An increase of accuracy of about one to two orders of magnitude is observed compared to Fig. 3 for the whole frequency range. Error peaks are still observed but their magnitude is lower. However, this gain of accuracy comes at the cost of a higher need in computational resources as the size of the reduced-order model might increase significantly from $1 + N_p$ to $1 + N_p + N_p^2$ at most due to the number of correction vectors to be computed increasing.

6. CONCLUSION

In this paper, a parametric model-order reduction scheme was derived to analyze the effect of random geometric variations on the behavior of a phononic crystal beam. A comparison of the reduced-order model with the full-order model response and statistics was performed, verifying the accuracy of the method.

Statistical analysis of the structure was conducted through Monte-Carlo simulation of the reduced-order model. A statistical analysis of the metamaterial structure allowed for quantification of the effect of geometrical variations stopband behavior of the structure. The attenuation performance of the structure was observed to be impacted by the random length changes in some cases,

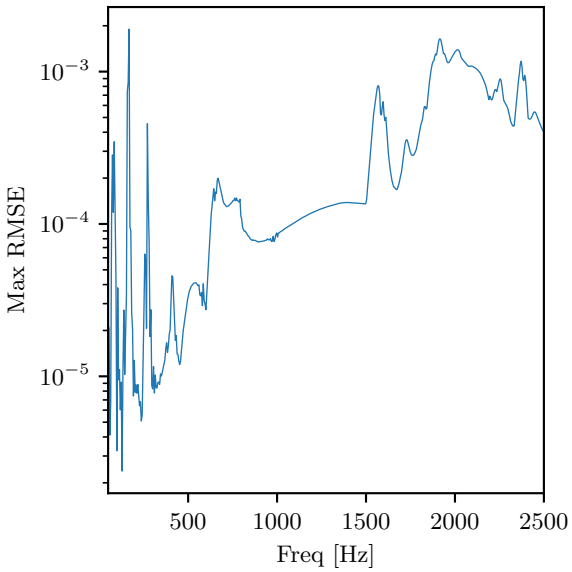


Figure 5. Maximum relative root mean square error between the reduced and second order full-order models observed across realizations of the system.

meaning that some samples of the beam might underperform compared to its target performance, which was observed in the literature for different structures. In this situation, the vibration attenuation region stays relatively close to the nominal case for the considered geometric perturbations.

In the specific case study of this paper, the full and reduced-order models take similar time to run. In the upcoming works, larger structures will to be analyzed as the computational cost reduction is expected and needs to be quantified. The impact of the number basis of correction vectors used in the model needs as well to be assessed in terms of accuracy gain and computational cost increase for a wider range metamaterial structures and problems, as it is important to verify that the accuracy is sufficient for the study under consideration. To do so in a different, specific case study, the analysis from (Fig. 3), using only a few realizations (say 10 to 50) of the system could serve as a benchmark.

7. ACKNOWLEDGMENTS

The European Union is gratefully acknowledged for their support of the METAVISION research project (GA

101072415). Views and opinions expressed are however those of the authors only and do not necessarily reflect those of the European Union. The European Union cannot be held responsible for them. The research of R. Boukadia (fellowship no. 12E2823N) and L. Van Belle (fellowship no. 1254325N) is funded by a grant from the Research Foundation – Flanders (FWO). Internal Funds KU Leuven are gratefully acknowledged for their support.

8. REFERENCES

[1] F. A. Pires, R. F. Boukadia, M. Wandel, C. Thomas, E. Deckers, W. Desmet, and C. Claeys, "Novel resonator concept for improved performance of locally resonant based metamaterials," *Thin-Walled Structures*, vol. 209, 4 2025.

[2] N. de Melo Filho, C. Claeys, E. Deckers, and W. Desmet, "Realisation of a thermoformed vibro-acoustic metamaterial for increased stl in acoustic resonance driven environments," *Applied Acoustics*, vol. 156, pp. 78–82, 2019.

[3] V. Cool, E. Deckers, L. Van Belle, and C. Claeys, "A guide to numerical dispersion curve calculations: Explanation, interpretation and basic matlab code," *Mechanical Systems and Signal Processing*, vol. 215, p. 111393, 2024.

[4] M. N. Ichchou, F. Bouchoucha, M. A. B. Souf, O. Dessombz, and M. Haddar, "Stochastic wave finite element for random periodic media through first-order perturbation," *Computer Methods in Applied Mechanics and Engineering*, vol. 200, pp. 2805–2813, 10 2011.

[5] J. Henneberg, J. S. G. Nieto, K. Sepahvand, A. Gerlach, H. Cebulla, and S. Marburg, "Periodically arranged acoustic metamaterial in industrial applications: The need for uncertainty quantification," *Applied Acoustics*, vol. 157, 1 2020.

[6] L. Van Belle, E. Deckers, and A. Cicirello, "Investigating and exploiting the impact of variability in resonator parameters on the vibration attenuation in locally resonant metamaterials," *Philosophical Transactions of the Royal Society A: Mathematical, Physical and Engineering Sciences*, vol. 382, 8 2024.

[7] R. Santoro, M. Mazzeo, and G. Failla, "A computational framework for uncertain locally resonant metamaterial structures," *Mechanical Systems and Signal Processing*, vol. 190, p. 110094, 2023.

[8] J.-M. Mencik, "Improved model reduction with basis enrichment for dynamic analysis of nearly periodic structures including substructures with geometric changes," *Journal of Computational and Applied Mathematics*, vol. 445, p. 115844, 8 2024.

[9] R. F. Boukadia, Y. Pillot, E. Deckers, W. Desmet, Y. Pillot, E. Deckers, and W. Desmet, "Quantifying the impact of variability on locally resonant metamaterial performance through reduced order modeling," 2024-08-02.

[10] B. Van Damme and A. Zemp, "Energy distribution and exchange between spatial harmonics in bending wave phononic crystals," *Physical Review Applied*, vol. 10, no. 1, p. 014001, 2018.

[11] P. B. Nair and A. J. Keane, "Stochastic reduced basis methods," *AIAA journal*, vol. 40, no. 8, pp. 1653–1664, 2002.

[12] P. Benner and L. Feng, "A robust algorithm for parametric model order reduction based on implicit moment matching," *Reduced order methods for modeling and computational reduction*, pp. 159–185, 2014.

[13] A. T. Fabro, "University of southampton faculty of engineering and the environment institute of sound and vibration research propagation in waveguides with slowly changing variability," 2014.

[14] A. T. Fabro, N. S. Ferguson, T. Jain, R. Halkyard, and B. R. Mace, "Wave propagation in one-dimensional waveguides with slowly varying random spatially correlated variability," *Journal of Sound and Vibration*, vol. 343, pp. 20–48, 5 2015.

DOI: 10.61782/fa.2025.0769



FORUM ACUSTICUM
EURONOISE 2025

SHAPE OPTIMIZATION OF INERTIA-AMPLIFIED MECHANICAL RESONATORS FOR VIBRATION DAMPING OF MOUNTED PLATE

L. Mardini[1*,2] **A.Bergamini**[1] **E. Deckers**[2,4]
C. Claeys[3,4] **B. Van Damme**[1]
[1] Empa, Laboratory for Acoustics/Noise Control, Switzerland
[2] Department of Mechanical Engineering campus Diepenbeek, KU Leuven, Belgium
[3] Department of Mechanical Engineering campus Heverlee, KU Leuven, Belgium
[4] Flanders Make@KU Leuven, Belgium

ABSTRACT

A well-known solution for suppressing undesired resonances in a vibrating structure is to place a tuned mass damper tuned to the frequency of the targeted mode. When a range of frequencies needs to be attenuated, vibroacoustic metamaterials are known as an effective solution. However, the periodic placement of resonators increases the added mass significantly, limiting its implementation in industrial applications. To address this, recent works have developed a methodology for optimizing the location and modal properties of a small number of resonators to achieve broadband attenuation in a desired frequency range. The aim of this study is to propose a practical implementation of this method for different mountings of a steel rectangular plate. Applying rotational inertia amplification for the local resonators offers a high dynamic to static mass ratio. The modal properties – mass and frequency - of the resonators are achieved by shape optimization to suit the target frequency range of a specific mounting case. This multi-objective optimization uses a practical data-driven generic design tool to avoid computationally heavy finite element models. The attenuation achieved by the rotational inertia amplifiers is then compared to the one achieved by mass-spring systems with equivalent modal properties.

Keywords: *vibration mitigation, shape optimization, inertia-amplified resonator.*

**Corresponding author*: line.mardini@empa.ch.

***Copyright**: ©2025 L. Mardini et al. This is an open-access article distributed under the terms of the Creative Commons Attribution 3.0 Unported License, which permits unrestricted use, distribution, and reproduction in any medium, provided the original author and source are credited.*

1. INTRODUCTION

Periodic placement of resonators on a host structure to mitigate vibrations, a solution known as locally resonant metamaterials, results in the attenuation of not a single frequency, but a range of frequencies known as a bandgap. This solution poses limitations for industrial applications, as it involves adding a significant amount of mass to the system. For this reason, methods for locally treating the host structure have been investigated [1, 2]. In [3], Dedoncker et al. propose to apply two algorithms, gradient based and simulated annealing, in order to simultaneously optimize the placement and modal properties of a finite number of tuned mass dampers on a plate to achieve broadband attenuation. Based on a defined frequency range to be attenuated, the algorithm converges on a solution that maximizes the vibration attenuation of the host plate and returns the position and mass, frequency and damping of the desired number of tuned mass dampers (TMDs). However, this method is based on the strong assumption that TMDs are ideal mass-spring-damper systems and can exhibit any combination of modal properties. The design of realistic resonators, on the other hand, limits the practical application of the method. Machine learning approaches have been investigated to relate design parameters to physical parameters [4–6]. In [7], the modal properties of a spiral-shaped resonator are tuned by optimizing the spiral's design parameters. This approach provides a rapid way of designing resonators according to required modal properties, both frequency and mass, using a conditional variational auto-encoder (cVAE). In this

work, we propose a practical implementation of these two methods to present an optimization routine for plate vibration treatment under different mounting scenarios. A gradient-based optimization routine calculates the optimal positions and modal properties of the resonators to be placed. These modal properties will be used by the cVAE-optimizer to design a series of complex-shaped mechanical resonators, a specific design which includes rotational inertia amplification. The vibration attenuation obtained by the set of rotational amplifier resonators, optimally placed on the plate, will be compared with the attenuation predicted by the gradient-based method using the set of ideal TMDs.

2. GRADIENT BASED METHOD FOR RESONATOR PLACEMENT AND MODAL PROPERTIES OPTIMIZATION

The following study considers a steel plate with a thickness of 3 mm and dimensions of 1,6 m (x-direction) by 1,2 m (y-direction). Two mounting conditions, shown in Figure 1, are investigated. In the first mounting scenario the plate is clamped on its left and right edges and excited by a force of 1 N (z-direction) at the center of the top edge. The second mounting scenario supposes that the plate is clamped on its bottom edge and excited by a force of 1 N (z-direction) on the top-right corner. The gradient based algorithm is used to optimize the placement and modal properties of 3 TMDs to maximize plate attenuation over the frequency range 150 Hz-200 Hz for these two mounting scenarios. The modal properties of the optimized TMDs are bounded by the distribution of the modal properties of the resonator dataset used to train the cVAE. Here, TMDs can take any frequency between 10 and 300 Hz, although their effective mass is constrained between 148 and 152 g. This high constraint on the effective mass is due to a narrow distribution of the modal properties of the resonator dataset considered. The modal properties of the 6 TMDs proposed by the algorithm are presented in Table 1. Figure 2 shows the average plate deformation with (blue) and without (black) TMDs. In both scenarios, we observe that 3 resonators are sufficient to achieve broadband attenuation over the frequency range specified: all resonance peaks are suppressed within this range.

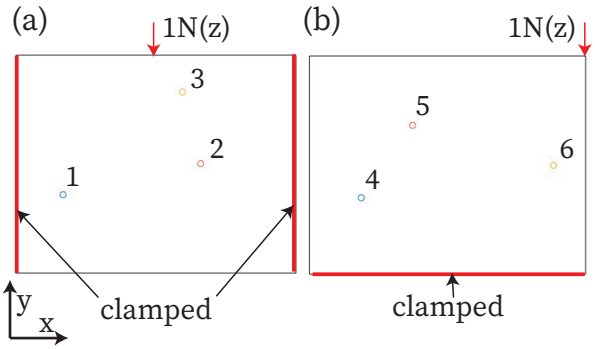


Figure 1. Mounting scenarios 1 (a) and 2 (b) and optimized positioning of the TMDs 1 to 6.

Table 1. Modal properties of the TMDs required by the gradient based optimization for the mounting scenario 1 (TMDs 1,2 and 3) and the mounting scenario 2 (TMDs 4,5 and 6).

	Frequency (Hz)	Effective mass (kg)
TMD 1	176	0.1506
TMD 2	165	0.1506
TMD 3	160	0.1505
TMD 4	177	0.1506
TMD 5	154	0.1504
TMD 6	163	0.1506

3. SHAPE OPTIMIZATION OF ROTATIONAL AMPLIFIERS USING CONDITIONAL VARIATIONAL AUTOENCODERS

The geometry of the resonator is chosen as follows: an hourglass shaped soft core is connected to two identical heavy disks at the bottom and top. The disks are connected by tilted struts with spherical joints as in [8]. The tilted struts allow the translation of the disks to be coupled to their rotation thereby inducing inertia amplification to the system as described in [9, 10]. As a consequence, the rotational amplifier achieves a high static-to-dynamic mass ratio, further minimizing the mass added to the host structure. The torsional and axial stiffnesses connecting the disks together are defined by the design of the hourglass-shaped core, which therefore influences the amplifier's modal properties. Realistic resonators are designed using the cVAE developed in [7] to achieve the modal properties given in Table 1. The geometry of the ro-

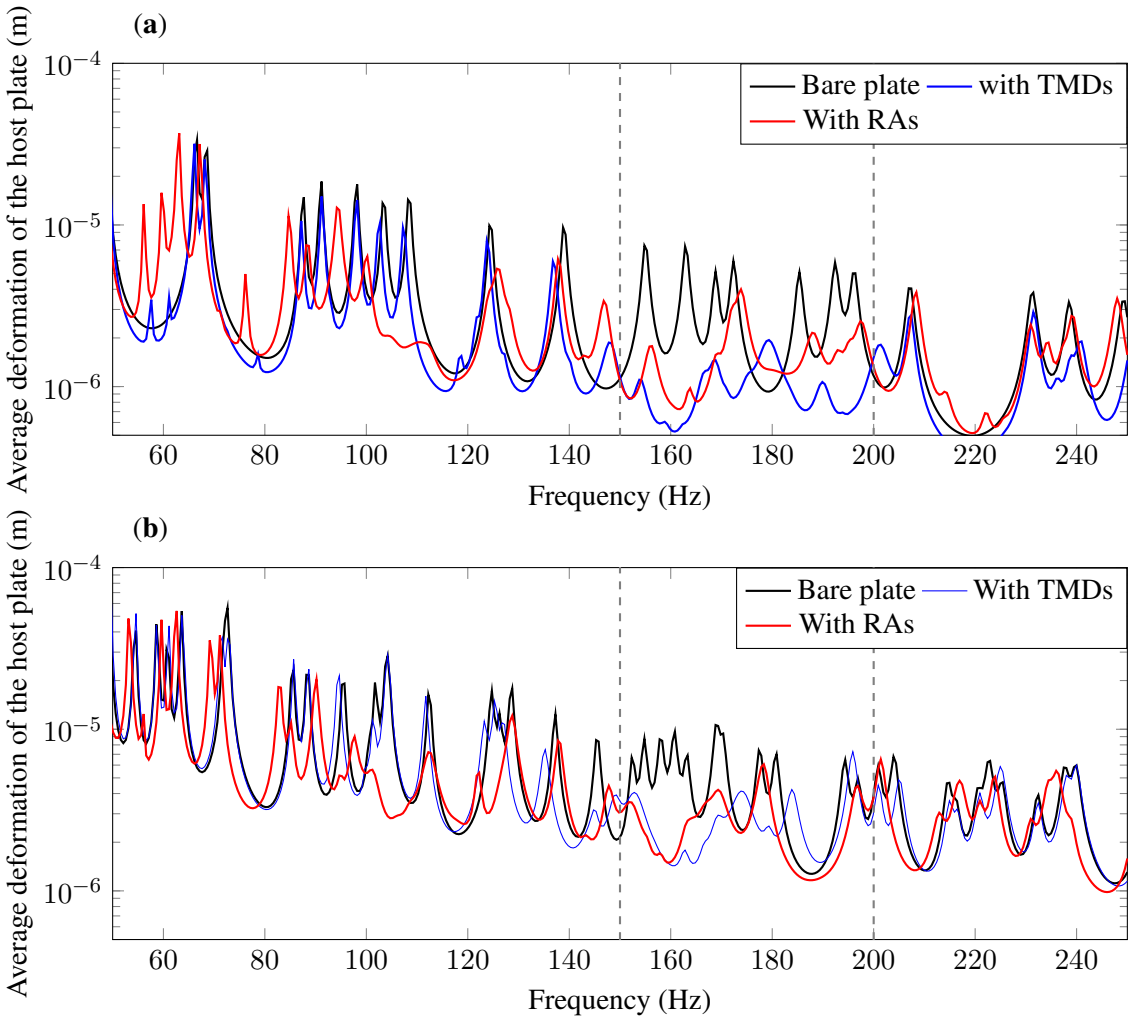


Figure 2. Average deformation of the mounted plate under mounting scenarios 1 (a) and 2 (b): bare plate in black, with ideal TMDs in blue and with RAs in red.

tational amplifier (RA) is parameterized according to the dimensions d1, d2, d3, d4 and angles a1 and a2 shown in Figure 3(a). 1100 designs are generated by Latin Hypercube sampling (LHS) of the resonator's geometrical parameters. The frequency and effective mass of the predominant axial vibration mode of each design, shown in Figure 3(b), are calculated performing a modal analysis in AnsysR2024V2. The conditional variational auto-encoder is then trained on the dataset created and finds the best designs to reach desired modal properties. The modal properties predicted for the best design given by the cVAE are compared with those required by the gradient-based algorithm. These latter modal properties are then compared to those observed on a FEM model of the suggested design. The geometric parameters of the 6 RAs best fitting the modal properties of the 6 TMDs required by the gradient based optimization are shown in Table 2. For the 6 ideal TMDs, Table 3 shows an error of less than 5% for all frequencies and effective masses.

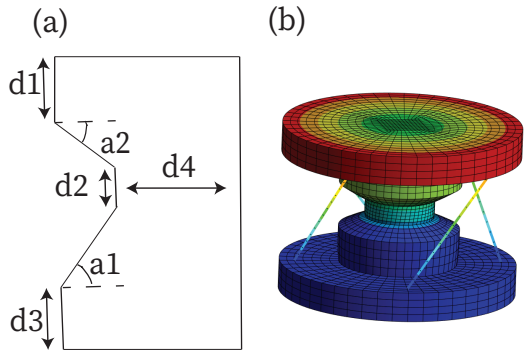


Figure 3. (a) Parametrized shape of the soft core. (b) First torsional mode of the rotational amplifier.

4. PRACTICAL IMPLEMENTATION OF THE DESIGNED ROTATIONAL AMPLIFIERS

An explicit FEM model created in ANSYS2024R2 couples the resonators designed with the cVAE to a plate with dimensions defined above at their optimized position as shown in Figure 4. The rotational amplifiers for the two considered mounting scenarios attenuate the targeted resonance peaks between 150 and 200 Hz. As an interesting side effect, the chosen resonators also attenuate the plate over unforeseen frequency ranges. A clear vibration reduction is noticeable near 100 Hz for both configurations: the resonators undergo a bending mode in this frequency range, and attenuate the motion of the plate. The approach presented in [3] allows the accurate placement of realistic resonators. However, the attenuation level achieved by the realistic resonators is lower than that achieved by ideally tuned mass dampers, as observed at 170 Hz for both mounting scenarios. This difference can be explained by two assumptions made by the gradient based optimization method. The optimized TMDs feature a single vibration mode, allowing only the predominant axial mode of the resonator to be modeled, and thus ignoring the more complex resonator dynamics. Moreover, this method assumes a point-wise contact between the resonator and the host plate, thus neglecting the local stiffening that can be observed at attachment points.

Table 2. Geometric parameters of the best design suggested by the cVAE fitting the modal properties of the 6 TMDs required.

	d1 (m)	d2 (m)	d3 (m)	d4 (m)	a1 (rad)	a2 (rad)
RA1	0.011	0.008	0.010	0.015	0.99	0.89
RA2	0.011	0.012	0.010	0.014	0.34	0.94
RA3	0.012	0.008	0.009	0.012	0.72	0.57
RA4	0.009	0.011	0.010	0.016	0.81	1.00
RA5	0.009	0.007	0.009	0.013	0.90	0.89
RA6	0.008	0.008	0.009	0.014	0.88	0.10

Table 3. Relative errors between the required (req), designed (cVAE) and observed (FEM model) modal properties (frequency f and modal mass m).

	f_{req} to f_{cVAE}	m_{req} to m_{cVAE}	f_{req} to f_{FEM}	m_{req} to m_{FEM}
TMD 1	0.3%	0.1%	0.9%	1.0%
TMD 2	0.3%	0.2%	0.8%	1.1%
TMD 3	0.0%	0.3%	4.4%	1.3%
TMD 4	0.1%	0.1%	1.5%	1.5%
TMD 5	0.1%	0.2%	2.4%	4.0%
TMD 6	0.3%	0.0%	2.6%	2.8%

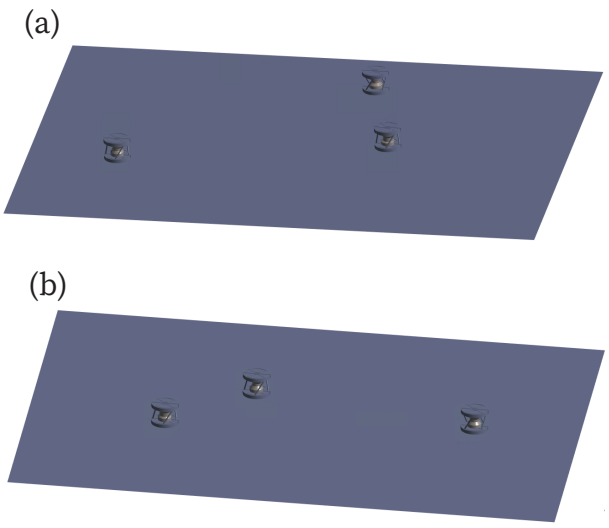


Figure 4. FEM model of the mounting scenarios 1 (a) and 2 (b) and optimized positioning of rotational amplifiers designed.

5. CONCLUSION

In this study, two optimization methods are combined to enable a fast routine for positioning and designing a small number of resonators to attenuate a mounted plate. This method allows the resonator design to be adapted to the different mountings and excitation points of the plate. Coupling the two methods results in a clear attenuation over the desired frequency range containing multiple resonance peaks. However, the fast optimization methods use simplifying assumptions, such as ideal, point-like mass-spring systems and the omission of multiple resonances of the resonators. The more complex dynamics of realistic resonators should be considered explicitly, by full harmonic simulations of the final setup.

6. ACKNOWLEDGMENTS

This work was done in the framework of the European Commission's Horizon Europe research and innovation programme under grant agreement No 101072415 and funded by the Swiss State Secretariat for Education, Research and Innovation (SERI), contract No 22.00225. Views and opinions expressed are however those of the authors only and do not necessarily reflect those of the European Union. The European Union cannot be held responsible for them. Internal Funds KU Leuven are gratefully acknowledged for their support.

7. REFERENCES

[1] J. Q. Sun, M. R. Jolly, and M. A. Norris, "Passive, Adaptive and Active Tuned Vibration Absorbers—A Survey," *Journal of Mechanical Design*, vol. 117, pp. 234–242, June 1995.

[2] B. Lossouarn, M. Aucejo, J.-F. Deü, and B. Multon, "Design of inductors with high inductance values for resonant piezoelectric damping," *Sensors and Actuators A: Physical*, vol. 259, pp. 68–76, June 2017.

[3] S. Dedoncker, C. Donner, L. Taenzer, and B. V. Damme, "Optimization of resonant absorbers for passive vibration control: a numerical approach and its experimental validation,"

[4] L. Zheng, S. Kumar, and D. M. Kochmann, "Data-driven topology optimization of spinodoid metamaterials with seamlessly tunable anisotropy," *Computer Methods in Applied Mechanics and Engineering*, vol. 383, p. 113894, Sept. 2021.

[5] W. Ma, F. Cheng, and Y. Liu, "Deep-Learning-Enabled On-Demand Design of Chiral Metamaterials," *ACS Nano*, vol. 12, pp. 6326–6334, June 2018.

[6] M. Filho and N. G. Rocha, "Design space exploration for resonant metamaterials using physics guided neural networks," *Proc of ISMA*, vol. 2020, 2020.

[7] S. Dedoncker, C. Donner, R. Bischof, L. Taenzer, and B. Van Damme, "Generative inverse design of multimodal resonant structures for locally resonant metamaterials," *Engineering with Computers*, Mar. 2025.

[8] W. Ding, R. Zhang, T. Chen, S. Qu, D. Yu, L. Dong, J. Zhu, Y. Yang, and B. Assouar, "Origin and tuning of bandgap in chiral phononic crystals," *Communications Physics*, vol. 7, p. 272, Aug. 2024.

[9] A. Bergamini, M. Miniaci, T. Delpero, D. Tallarico, B. Van Damme, G. Hannema, I. Leibacher, and A. Zemp, "Tacticity in chiral phononic crystals," *Nature Communications*, vol. 10, p. 4525, Oct. 2019.

[10] B. Zhao, H. R. Thomsen, X. Pu, S. Fang, Z. Lai, B. V. Damme, A. Bergamini, E. Chatzi, and A. Colombi, "A nonlinear damped metamaterial: Wideband attenuation with nonlinear bandgap and modal dissipation," *Mechanical Systems and Signal Processing*, vol. 208, p. 111079, Feb. 2024.

DOI: 10.61782/fa.2025.0271

FORUM ACUSTICUM EURONOISE 2025

DESIGN AND EXPERIMENTAL CHARACTERIZATION OF MULTI-MODAL METAMATERIAL PANELS ACHIEVING BROADBAND SOUND TRANSMISSION AND RADIATION REDUCTION

Daniele Giannini[1]* **Lucas Van Belle**[2,3] **Elke Deckers**[3,4]
Edwin P.B. Reynders[1]
[1] Department of Civil Engineering, KU Leuven, Belgium
[2] Department of Mechanical Engineering, KU Leuven, Belgium
[3] Flanders Make@KU Leuven, Belgium
[4] Department of Mechanical Engineering, Campus Diepenbeek, KU Leuven, Belgium

ABSTRACT

Resonant metamaterials are a promising approach to achieve vibroacoustic attenuation in partition panels. By adding subwavelength resonators to a host plate, free-travelling elastic waves in specific frequency bands, called bandgaps, are prohibited. While conventional resonant metamaterials typically exploit single-mode translational resonators resulting in narrowband attenuation, recent advancements have theoretically indicated that broader attenuation bands can be achieved by resonators with multiple translational and rotational modes. However, the effectiveness of this concept has not yet been experimentally demonstrated. In this study, we address this gap by designing, manufacturing and experimentally validating a multi-modal metamaterial panel aimed at mitigating broadband coincidence effects in orthotropic host plates. The proposed metamaterial panel integrates medium-density fiberboard resonators attached to an orthotropic cross-laminated timber plate. The resonator geometry is optimized to maximize the effect of two distinct directional bandgaps induced by two rotational resonator modes. Extensive vibroacoustic testing is performed to characterize the metamaterial performance. Laser vibrometry measurements under shaker-based excitation confirm the presence of these two resonance-based bandgaps. Sound transmission and radiation tests demonstrate significant attenuation within the bandgaps (by around 8-10 dB) compared to the host plate, as well as the suppression of the broad sound transmission loss dip due to coincidence effects.

Keywords: *locally resonant metamaterial panels, multi-modal resonators, sound transmission loss, sound radiation, experimental characterization*

1. INTRODUCTION

In the search for compact and lightweight solutions for vibroacoustic attenuation, locally resonant metamaterials have been introduced to achieve exceptional properties beyond those of conventional materials [1]. These metamaterials achieve enhanced wave control by small, local resonators added to a host structure on a subwavelength scale. As a result, an effective mass that varies with frequency is achieved, which shows a peak around the local resonance [2]. Around this frequency, the effective mass of the metamaterial structure surpasses its static mass, significantly improving sound insulation [3, 4]. Additionally, in the frequency range immediately above the peak, the effective mass becomes negative and a wave propagation bandgap emerges, which inhibits free-traveling mechanical waves [5].

Metamaterials have been successfully employed to enhance vibration attenuation and sound insulation in partition panels [6]. Conventional designs only utilize a single mode of the local resonators, typically associ-

*__Corresponding author__: daniele.giannini@kuleuven.be.
__Copyright__: ©2025 D. Giannini et al. This is an open-access article distributed under the terms of the Creative Commons Attribution 3.0 Unported License, which permits unrestricted use, distribution, and reproduction in any medium, provided the original author and source are credited.

ated with a transversal vibration to the host plate, therefore limiting the attenuation bandwidth. To achieve attenuation in a broader band, multiple mechanical resonators can be attached in series [7, 8] or in parallel [9, 10] to the host plate. More recently, theoretical studies have indicated that multi-modal metamaterial panels—featuring multiple local resonances within each resonating unit, and including both transversal and rotational modes—can generate a sequence of adjacent attenuation bands, which collectively span a broader frequency range [11, 12]. However, despite their potential, the experimental validation of metamaterial panels incorporating multi-modal and particularly rotational resonators remains an open challenge.

This study addresses this gap by designing, manufacturing and experimentally validating a metamaterial panel with multi-modal rotational resonators. The proposed metamaterial panel is specifically tailored to mitigate broadband coincidence effects in orthotropic host plates. It consists of a host orthotropic plate made of cross-laminated timber (CLT) to which local resonators made of medium-density fiberboard (MDF) are attached. The resonator geometry is optimized to suppress the broad sound transmission loss (STL) dip due to coincidence effects in the host panel, by leveraging two distinct directional bandgaps induced by two rotational resonator modes. Extensive vibroacoustic testing is conducted to assess the performance of the metamaterial panel, in terms of sound transmission loss, structural wave propagation, and sound radiation.

The paper is structured as follows. Section 2 describes the design of the proposed multi-modal metamaterial CLT panel. The experimental validation is presented in the following Sections, in terms of sound transmission loss (Section 3), flexural wave propagation (Section 4), and sound radiation (Section 5). Finally, Section 6 concludes the paper.

2. DESIGN OF THE MULTI-MODAL METAMATERIAL CLT PANEL

The proposed metamaterial panel, shown in Fig. 1, consists of an orthotropic CLT host plate with periodically attached multi-modal rotational resonators made of MDF. The orthotropic host CLT panel is composed of 3 spruce wood layers, crosswise glued together with alternating fiber directions [13], following a 0°/90°/0° stacking sequence relative to the global x-axis. The host CLT panel has an overall thickness of $t_{\mathrm{CLT}} = 0.027$ m

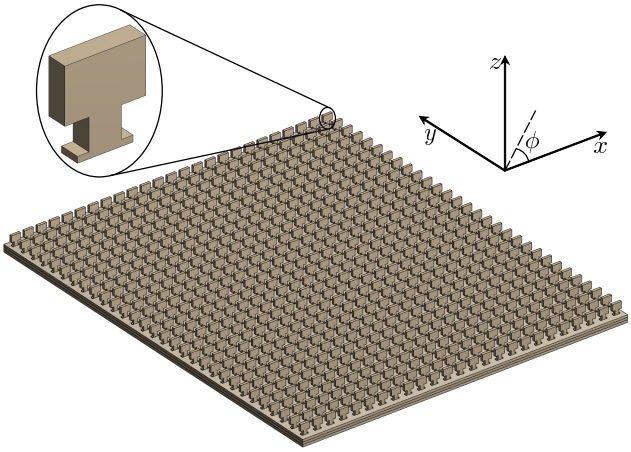


Figure 1: Designed metamaterial CLT panel with MDF multi-modal rotational resonators.

(each layer being 0.009 m thick), and has in-plane dimensions 1.235×1.485 m^2.

Due to its high degree of orthotropy, the host CLT panel exhibits broadband coincidence effects, leading to a broad dip in its diffuse STL curve. In orthotropic panels, the critical frequency f_{cr}, at which the flexural wave speed matches the speed of sound waves in the surrounding fluid, varies with the in-plane propagation direction defined by the azimuthal angle ϕ (see Fig. 1). Under diffuse sound incidence, this results in a broad coincidence STL dip spanning the range $\left[\min\left(f_{\mathrm{cr}}(\phi)\right), \max\left(f_{\mathrm{cr}}(\phi)\right)\right]$. To mitigate broadband coincidence effects, the metamaterial panel integrates multi-modal local resonators made of MDF. The resonators are laser-cut and periodically attached to the host panel using adhesive, with subwavelength unit cell dimensions 0.05×0.05 m^2. Each resonator includes a vertical cantilever beam, a mass at the top of the beam, and a broadened base for attachment to the host panel.

The material properties of the CLT layers and the MDF resonators are experimentally identified through dynamic testing [14] and summarized in Tab. 1. Both materials are modelled as orthotropic and characterized by the Young's moduli E_{x}, E_{y}, E_{z}, the shear moduli G_{xy}, G_{yz}, G_{xz}, the Poisson's ratios ν_{yx}, ν_{zy}, ν_{zx}, the mass density ρ, and the damping loss factor η.

The multi-modal local resonators are designed to suppress the broad STL dip of the host structure. This is performed by leveraging the first two bending modes of the vertical cantilever beam-mass structure (Fig. 2),

Table 1: Estimated material properties for CLT layers and MDF. CLT properties refer to the local reference system, with x-axis along the wood fibers, oriented at 0°/90°/0° to the global x-axis. MDF properties refer to the global reference system.

	CLT layers	MDF
$E_x = E_z$ [N/m^2]	$6.8 \cdot 10^8$	$3.67 \cdot 10^9$
E_y [N/m^2]	$1.202 \cdot 10^{10}$	$2.65 \cdot 10^8$
$G_{xy} = G_{yz}$ [N/m^2]	$8.3 \cdot 10^8$	$1.55 \cdot 10^8$
G_{xz} [N/m^2]	$7.12 \cdot 10^7$	$1.31 \cdot 10^9$
$\nu_{yx} = \nu_{zy}$ [-]	0.0189	0.0672
ν_{zx} [-]	0.03	0.25
ρ [kg/m^3]	468	616
η [-]	0.07	0.025

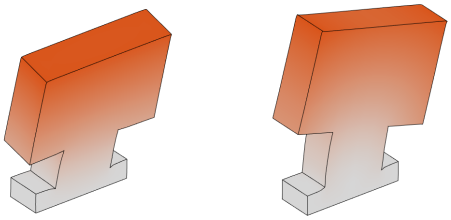


Figure 2: Eigenmodes of the local resonator at 1085 Hz and 1640 Hz.

in which the end mass rotates around the x and the y axis respectively. These rotational modes generate two directional bandgaps that inhibit flexural wave propagation in the directions perpendicular to the rotation axes, and are exploited to suppress coincidence effects along the two principal axes of the orthotropic host plate.

The resonator layout is numerically optimized by using the dimensions of its geometrical features as design variables. A genetic algorithm is employed to maximize the broadband diffuse STL in the frequency range 100-3150 Hz, while ensuring that the resonator mass does not exceed 20% of the host panel's mass [11]. The final optimized configuration exhibits local resonance frequencies at 1085 Hz and 1640 Hz (Fig. 2), strategically positioned to suppress the broad STL dip, and maximized participating mass in the modes of interest.



Figure 3: Fabricated multi-modal metamaterial panel, mounted in the transmission opening of the Laboratory of Acoustics of KU Leuven.

3. EXPERIMENTAL EVALUATION OF THE SOUND TRANSMISSION LOSS

The STL of both the bare CLT host panel and the metamaterial panel is experimentally measured in the transmission suite of the Laboratory of Acoustics of KU Leuven. The facility consists of two reverberation chambers, each with a volume of 87 m^3, and a transmission opening with dimensions 1.25 × 1.5 m^2, inside which the tested panel is installed (Fig. 3). The sound transmission loss R is measured according to the ISO 10140-2 standard [15].

The STL curves of the bare CLT panel (without resonators) and the metamaterial CLT panel are displayed in 1/48-octave bands in Fig. 4, along with numerical predictions obtained through an infinitely periodic finite element model [16, 17]. In this model, one single unit cell is discretized by solid finite elements, including a segment of the laminated CLT panel and one attached resonator. The STL is computed by analyzing the interaction between the panel and the surrounding diffuse acoustic fields, under appropriate periodicity boundary conditions. The numerical predictions are reported for the bare panel, for a bare panel with an equivalent

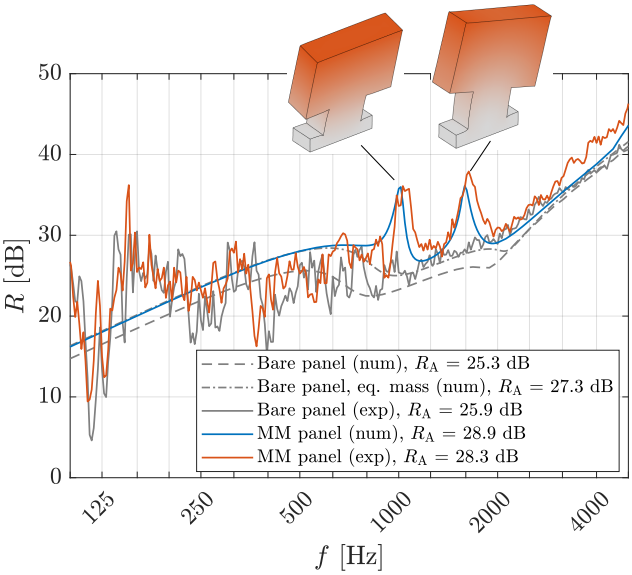


Figure 4: Comparison between the experimentally measured and numerically predicted diffuse STL of the bare and the metamaterial panel.

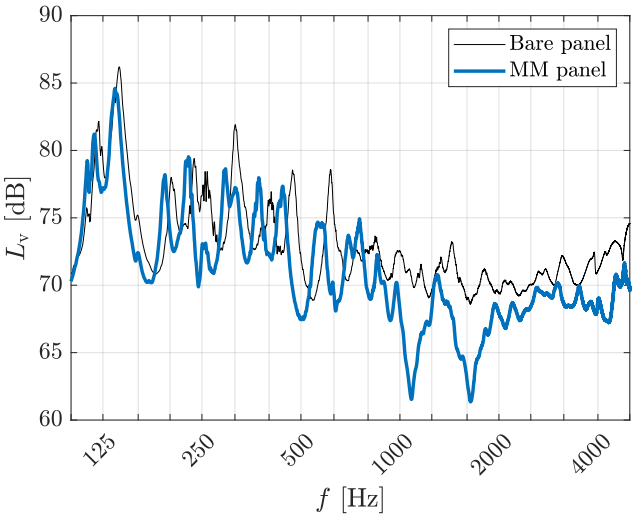


Figure 5: Comparison between the experimentally measured surface-averaged vibration velocity levels of the bare and the metamaterial panel under shaker-based excitation.

mass to the metamaterial panel, and for the metamaterial panel.

At low frequencies, the 20% added mass of the resonators shifts the numerical STL curve upwards by around 1.6 dB. In this range, besides mass effects, the measured STL is mainly dominated by the global modal behaviour of the panel, which is particularly prominent given its relatively compact dimensions. Since the periodic finite element model does not account for boundary effects and global panel resonances, some deviations between numerical and experimental results are observed.

Above 250 Hz, the influence of the individual panel modes becomes less significant, progressively leading to a good alignment between numerical predictions and experimental results. Within the broad coincidence range (760-1950 Hz), the STL dip observed in the bare panel is effectively suppressed by two distinct STL peaks, achieving STL improvements of about 8-10 dB around the local resonance frequencies. Interestingly, no STL dip is observed in the frequency ranges immediately above the resonance peaks, which constrasts with the usual behaviour seen when the local resonances are tuned below coincidence. By tuning the local resonances within the coincidence range, here no additional range of increased radiation efficiency is introduced, and the overall zone of efficient acoustic radiation is reduced [18].

To provide a standardized evaluation of the sound insulation performance, the single number rating R_A from ISO 717 [19] is also computed. This metric represents the A-weighted broadband diffuse sound insulation for pink noise excitation over the frequency range 100-3150 Hz, and is found as $R_A = R_w + C$, where R_w and C are defined by the ISO standard. Both numerical predictions and experimental results indicate that the metamaterial panel achieves an increase of R_A by around 3 dB compared to the bare CLT panel, while the R_A improvement with respect to the bare panel with equivalent mass is 1.6 dB. This confirms the effectiveness of the proposed multi-modal rotational resonator design in enhancing broadband sound insulation.

4. EXPERIMENTAL EVALUATION OF FLEXURAL WAVE PROPAGATION

To evaluate the impact of the metamaterial design on flexural wave dispersion, the vibration fields in both the bare CLT panel and the metamaterial panel are measured under shaker excitation. The shaker is attached to the panel (mounted in the transmission opening) via

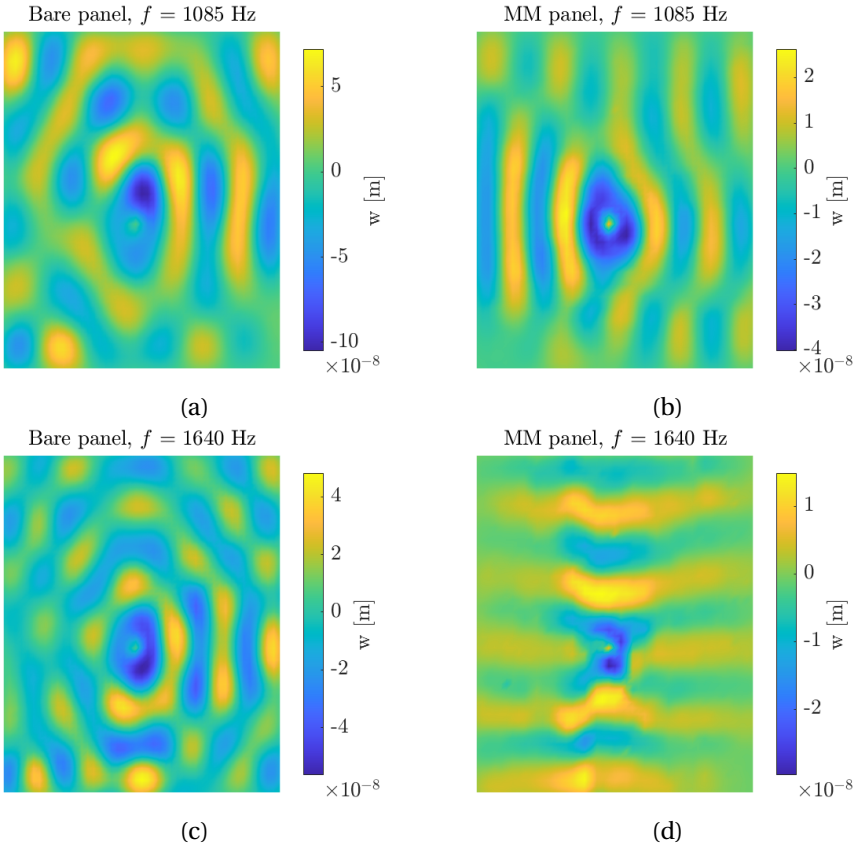


Figure 6: Measured vibration fields for (a, c) the bare and (b,d) the metamaterial panel at (a,b) 1085 Hz and (c,d) 1640 Hz, in terms of the out-of-plane displacement w.

an impedance head, which measures the input force. The shaker is positioned slightly off-centered with respect to the panel, and a white noise excitation signal is applied as input. The resulting out-of-plane vibration field is measured by a scanning laser Doppler vibrometer (SLDV), by evaluating the frequency response function (FRF) between the input force and the displacement responses. A Polytec PSV-Qtec Scanning Vibrometer is used to capture the vibration field at 2769 points on a rectangular grid, with a spatial resolution of 2.5 cm. Measurements are taken across the frequency range 0-6400 Hz with a frequency resolution of 0.5 Hz.

The measured vibration data are used to compute the surface-averaged velocity level L_v at each frequency, considering a reference velocity value of $5 \cdot 10^{-8}$ m/s. Fig. 5 compares the L_v curves for the bare panel and the metamaterial panel, in 1/48-octave bands. Across the entire frequency range, the added mass of the resonators causes a slight shift downwards in the L_v curve of the metamaterial panel compared to the bare CLT panel, along with a slight reduction of the resonance frequencies associated with the global panel modes. Most notably, two pronounced dips appear at 1085 Hz and 1640 Hz, corresponding to the directional bandgaps introduced by the local resonators. Around these frequencies, the vibration levels are effectively reduced by approximately 8 dB compared to the bare panel.

The impact of the directional bandgaps is further analyzed by comparing the measured vibration fields of the metamaterial panel against those of the bare panel. In the bare panel, flexural waves radiate uniformly in all directions from the excitation point (Figs. 6a and 6c). In the metamaterial panel, wave propagation is inhibited in specific directions due to the introduced directional

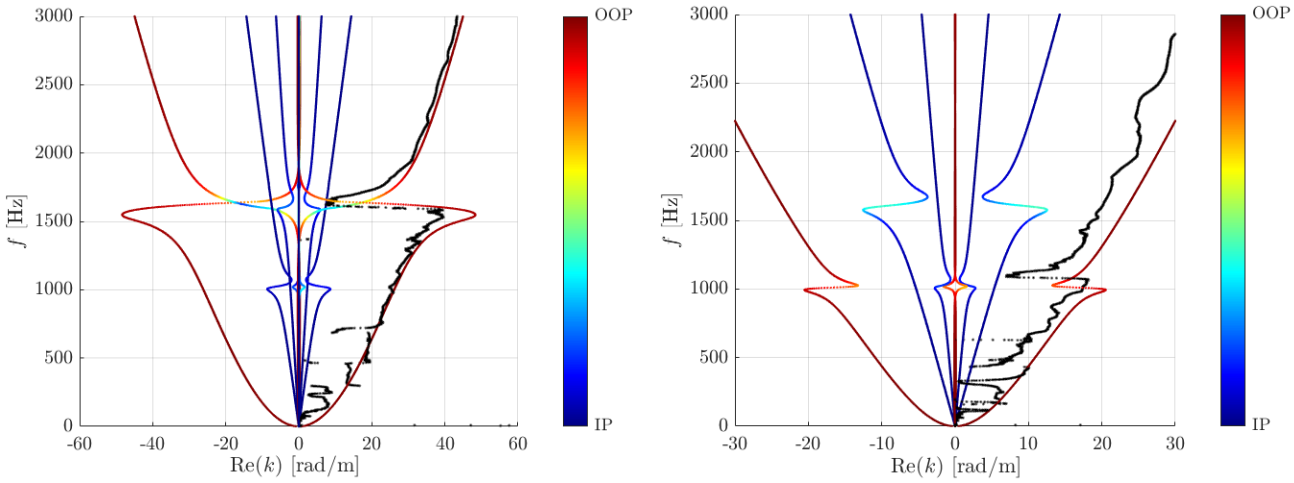


Figure 7: Experimental (black) and numerical (coloured) dispersion curves of the metamaterial panel for propagation along (a) the x axis and (b) the y axis. The numerical dispersion curves are coloured according to the out-of-plane (OOP) vs. in-plane (IP) nature of the wave modes.

bandgaps: at 1085 Hz, flexural wave propagation is suppressed along the vertical direction (Fig. 6b), while at 1640 Hz, flexural wave propagation is suppressed along the horizontal direction (Fig. 6d).

To further characterize the wave behaviour, the experimental dispersion curves are extracted using the Extended Inhomogeneous Wave Correlation approach [5], which correlates the measured vibration fields with analytical functions representing inhomogeneous plane waves. Fig. 7 presents the experimental dispersion curves (for real wavenumbers), along with numerical predictions through periodic finite element modelling. The numerical dispersion curves are coloured according to the out-of-plane nature of the wave modes, which is calculated using the ratio of surface-averaged out-of-plane to in-plane nodal displacements at the mid-plane of the plate: red indicates out-of-plane flexural waves and blue indicates in-plane waves. Both in-plane and out-of-plane (flexural) dispersion branches are numerically predicted, but since only out-of-plane displacement fields are measured, only the flexural wave dispersion is experimentally retrieved.

In the lower frequency range, the experimental estimation of the dispersion curves is strongly influenced by the global modal behaviour of the panel. Above 800 Hz, the modal behaviour of the panel becomes less pronounced, and a good agreement is observed between experimental and numerical results. A minor discrepancy is present in the slope of the dispersion curve for propagation along y, where the experimental panel appears slightly stiffer than predicted.

For both numerical and experimental results, two regions of significant flexural wave dispersion are identified: one around the first directional bandgap for propagation along y and another around the second directional bandgap for propagation along x. The observed bandgap behavior shows strong agreement between experimental measurements and numerical simulations.

Interestingly, the numerical model further predicts that the directional bandgaps also affect in-plane wave propagation, despite this effect not being captured by experiments. This highlights that the designed vertical cantilever beam-mass resonators transfer both bending moments and in-plane forces to the host structure, impacting both flexural and in-plane wave behavior.

5. EXPERIMENTAL ASSESSMENT OF SOUND RADIATION

To experimentally assess the reduction of acoustic radiation in the bandgap regions, the spatially averaged sound pressure in the receiver room of the transmission

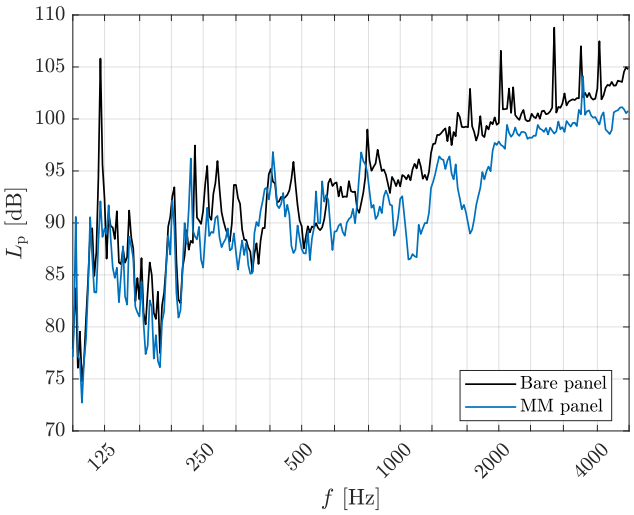


Figure 8: Comparison between the experimentally measured sound pressure levels in the receiver room when the bare and the metamaterial panel are subjected to structure-borne (point) excitation.

suite is measured, when the panel is mounted in the transmission opening and subjected to structure-borne (point) shaker excitation. The FRF between the input shaker force and the harmonic sound pressure in the receiver room is measured for 4 different excitation locations and 8 microphone locations. The sound pressure level L_p per unit of excitation force is then computed by energetically averaging the FRFs obtained for all excitation and measurement positions.

Fig. 8 compares the resulting sound pressure levels for the bare panel and the metamaterial panel, in 1/48-octave bands. In general, the metamaterial panel exhibits a slight reduction in overall sound radiation due to the additional mass of the resonators. More significantly, two distinct dips are observed around the local resonance frequencies (1085 Hz and 1640 Hz), where the metamaterial treatment achieves an 8–10 dB reduction in radiated sound pressure compared to the bare CLT panel.

6. CONCLUSIONS

In this work, we have experimentally demonstrated the effectiveness of multi-modal metamaterial panels in achieving broad attenuation bands. Specifically, a multi-modal metamaterial panel has been designed, manufactured and experimentally validated to mitigate broadband coincidence effects in orthotropic host plates. The proposed metamaterial panel integrates medium-density fiberboard resonators attached to an orthotropic cross-laminated timber plate. The resonators consist of a vertical cantilever beam-mass structure and their layout has been geometrically optimized to maximize the effect of two distinct directional bandgaps induced by two rotational modes.

The performance of the metamaterial panel has been characterized by extensive vibroacoustic testing. Laser vibrometry measurements under shaker-based excitation have confirmed the presence of two resonance-based bandgaps. Diffuse sound transmission and radiation tests have demonstrated significant attenuation within the bandgaps (by around 8-10 dB) compared to the host plate, as well as the suppression of the broad sound transmission loss dip caused by coincidence effects.

The results of the work represent a significant advancement towards lightweight insulating partitions with broadband enhanced vibroacoustic performance through metamaterials.

7. ACKNOWLEDGEMENTS

Daniele Giannini and Lucas Van belle gratefully acknowledge the financial support of Research Foundation - Flanders (FWO), respectively through the post-doctoral fellowships 12A3Q24N and 1254325N. Furthermore, this work was supported by KU Leuven internal funds under project C2E/24/031.

8. REFERENCES

[1] G. Ma and P. Sheng, "Acoustic metamaterials: From local resonances to broad horizons," *Science Advances*, vol. 2, no. 2, p. e1501595, 2016.

[2] P. Li, S. Yao, X. Zhou, G. Huang, and G. Hu, "Effective medium theory of thin-plate acoustic metamaterials," *Journal of the Acoustical Society of America*, vol. 135, no. 4, pp. 1844–1852, 2014.

[3] J. Vazquez Torre, J. Brunskog, and V. Cutanda Henriquez, "An analytical model for broadband sound transmission loss of a finite single leaf wall using a metamaterial," *Journal of the Acoustical Society of America*, vol. 147, no. 3, pp. 1697–1708, 2020.

[4] J. Vazquez Torre, J. Brunskog, V. Cutanda Henriquez, and J. Jung, "Hybrid analytical-numerical optimization design methodology of acoustic metamaterials for sound insulation," *Journal of the Acoustical Society of America*, vol. 149, no. 6, pp. 4398–4409, 2021.

[5] L. Van Belle, C. Claeys, E. Deckers, and W. Desmet, "On the impact of damping on the dispersion curves of a locally resonant metamaterial: Modelling and experimental validation," *Journal of Sound and Vibration*, vol. 409, pp. 1–23, 2017.

[6] L. Van Belle, C. Claeys, E. Deckers, and W. Desmet, "The impact of damping on the sound transmission loss of locally resonant metamaterial plates," *Journal of Sound and Vibration*, vol. 461, p. 114909, 2019.

[7] Y. Chen, M. Barnhart, J. Chen, G. Hu, C. Sun, and G. Huang, "Dissipative elastic metamaterials for broadband wave mitigation at subwavelength scale," *Composite Structures*, vol. 136, pp. 358–371, 2016.

[8] D. Roca, J. Cante, O. Lloberas-Valls, T. Pàmies, and J. Oliver, "Multiresonant layered acoustic metamaterial (MLAM) solution for broadband low-frequency noise attenuation through double-peak sound transmission loss response," *Extreme Mechanics Letters*, vol. 47, p. 101368, 2021.

[9] C. Claeys, N. Rocha de Melo Filho, L. Van Belle, E. Deckers, and W. Desmet, "Design and validation of metamaterials for multiple structural stop bands in waveguides," *Extreme Mechanics Letters*, vol. 12, pp. 7–22, 2017.

[10] S. Janssen, L. Van Belle, N. de Melo Filho, W. Desmet, C. Claeys, and E. Deckers, "Improving the noise insulation performance of vibro-acoustic metamaterial panels through multi-resonant design," *Applied Acoustics*, vol. 213, p. 109622, 2023.

[11] D. Giannini, M. Schevenels, and E. Reynders, "Rotational and multimodal local resonators for broadband sound insulation of orthotropic metamaterial plates," *Journal of Sound and Vibration*, vol. 547, no. 117453, pp. 1–17, 2023.

[12] D. Giannini and E. Reynders, "Effective medium modelling of real-world multi-modal metamaterial panels achieving broadband vibroacoustic attenuation," *Extreme Mechanics Letters*, vol. 69, p. 102161, 2024.

[13] A. Santoni, S. Schoenwald, B. Van Damme, and P. Fausti, "Determination of the elastic and stiffness characteristics of cross-laminated timber plates from flexural wave velocity measurements," *Journal of Sound and Vibration*, vol. 400, pp. 387–401, 2017.

[14] D. Giannini and E. P. B. Reynders, "Optimized multimodal rotational resonators for enhanced sound insulation in metamaterial cross-laminated timber panels," in *Proceedings of the 31st International Conference on Noise and Vibration Engineering, ISMA 2024* (W. Desmet, B. Pluymers, D. Moens, and S. Neeckx, eds.), (Leuven, Belgium), p. 261–274, September 2024.

[15] International Organization for Standardization, *ISO 10140-2: Acoustics – Laboratory measurement of sound insulation of building elements – Part 2: Measurement of airborne sound insulation*, 2021.

[16] Y. Yang, B. Mace, and M. Kingan, "Vibroacoustic analysis of periodic structures using a wave and finite element method," *Journal of Sound and Vibration*, vol. 457, pp. 333–353, 2019.

[17] Y. Yang, C. Fenemore, M. Kingan, and B. Mace, "Analysis of the vibroacoustic characteristics of cross laminated timber panels using a wave and finite element method," *Journal of Sound and Vibration*, vol. 494, no. 115842, pp. 1–20, 2021.

[18] C. Claeys, P. Sas, and W. Desmet, "On the acoustic radiation efficiency of local resonance based stop band materials," *Journal of Sound and Vibration*, vol. 333, no. 14, pp. 3203–3213, 2014.

[19] International Organization for Standardization, *ISO 717-1: Acoustics – Rating of sound insulation in buildings and of building elements – Part 1: Airborne sound insulation*, 2013.

DOI: 10.61782/fa.2025.0715

FORUM ACUSTICUM EURONOISE 2025

PSYCHOACOUSTICAL DESIGN OPTIMIZATION FOR ACOUSTIC METAMATERIALS USING GLOBAL SENSITIVITY ANALYSIS

Jiahua Zhang[1,2*] **Jacques Cuenca**[1] **Laurent De Ryck**[1]
Lucas Van Belle[2,3] **Elke Deckers**[3,4]
[1] Test Division, Siemens Digital Industry Software, Belgium
[2] Department of Mechanical Engineering, KU Leuven, Belgium
[3] Flanders Make@KU Leuven, Belgium
[4] Department of Mechanical Engineering, Campus Diepenbeek, KU Leuven, Belgium

ABSTRACT

While acoustic metamaterials have shown promising noise reduction capabilities, their design optimization has traditionally focused on physical acoustic properties rather than perceived sound quality. This research introduces a design methodology that integrates psychoacoustic metrics into the optimization of metamaterial architectures. The methodology uses a previously developed Global Sensitivity Analysis scheme as a basis for an optimization framework that specifically targets desired psychoacoustic outcomes while maintaining practical design constraints. Micro-perforated panels are used as a preliminary case study. The design optimization is validated with multiple prototypes and measured in an impedance tube, with results analyzed for both traditional acoustic measurements and psychoacoustic metrics including loudness and sharpness. The experimental validation demonstrates how optimized designs can achieve specific sound quality targets while remaining practically manufacturable.

Keywords: *sound quality, acoustic metamaterial, sensitivity analysis, micro perforated panel*

1. INTRODUCTION

Acoustic metamaterials have revolutionized the field of noise control with their ability to manipulate sound waves beyond conventional materials. Their unique structures enable exceptional sound absorption, transmission loss, and wavefront manipulation capabilities [1]. Traditionally, metamaterial design has been guided by physical acoustic properties such as absorption coefficients and transmission loss. However, these objective parameters do not fully correlate with human perception of sound quality. Previous research revealed that acoustic metamaterials can significantly alter psychoacoustic metrics, sometimes in directions contrary to what traditional acoustic measurements might suggest [2]. This potential disconnect between objective measurements and subjective perception creates a design challenge when optimizing metamaterials for human-centered acoustic environments.

This paper builds upon a recently developed sensitivity analysis approach for micro-perforated panels (MPPs) [3], extending the methodology into a full optimization workflow, and including an experimental validation of the psychoacoustic metrics. The research objective is to develop a framework for designing acoustic metamaterials with desired psychoacoustic features as targets, while maintaining practical design constraints. The focus is specifically on a simplified single-panel MPP configuration to establish the foundation for more complex systems.

The rest of the paper is structured as follows: Section 2 described the MPP model, design optimization and validation methodologies. In Section 3 the results are shown. Discussion of the results and a summary can be found in Section 4.

**Corresponding author*: *jiahua.zhang@siemens.com.*
***Copyright**: ©2025 Zhang et al. This is an open-access article distributed under the terms of the Creative Commons Attribution 3.0 Unported License, which permits unrestricted use, distribution, and reproduction in any medium, provided the original author and source are credited.*

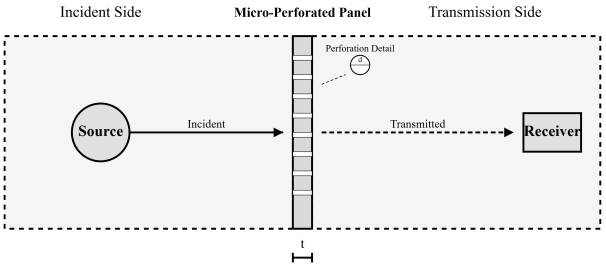


Figure 1. Overview of the problem configuration.

2. METHODS

2.1 Micro-Perforated Panel Modeling

The analysis is simplified to focus on a single MPP, 1-D transmission configuration, as shown in Figure 1, to establish a clear relationship between design parameters and sound quality metrics. For the MPP analysis, 3 key parameters are determined, with parameter bounds carefully defined by balancing theoretical acoustic principles, manufacturing feasibility constraints, and the desired transmission loss (TL) performance targets [4]:

- Perforation diameter (d): 0.03 to 3 mm,
- Porosity (ϕ): 0.2% to 3.14%,
- Panel thickness (t): 1.5 to 2.0 mm.

The acoustic behavior of the MPP was modeled using Atalla and Sgard's approach [5], where the surface impedance for transmission is calculated as:

$$Z_t = \left(\frac{4t}{d} + 4\right)\frac{R_s}{\phi} + \frac{1}{\phi}(2\epsilon + t)j\omega\rho_0 + \rho_0 c, \qquad (1)$$

where ω is the angular frequency, $\epsilon = 0.24\sqrt{\pi d^2}(1 - 1.14\sqrt{\phi})$ represents the end correction factor, R_s is the surface resistivity, ρ_0 is the air density, and c is the speed of sound. Then, with the characteristic acoustic impedance $Z_0 = \rho_0 c$, the transmission coefficient can be derived as:

$$\tau = \frac{1 + R_s}{Z_t/Z_0} = \frac{2\rho_0 c}{Z_t + \rho_0 c}. \qquad (2)$$

TL values in decibels (dB) can then be calculated as $\mathrm{TL} = 10\log(1/\tau)$.

2.2 Global Sensitivity Analysis Framework

The global sensitivity analysis (GSA) approach used in this study follows the Sobol method [6], which quantifies the contributions of individual parameters and their interactions to the variance in model outputs. This approach is particularly valuable for complex systems like metamaterials where multiple parameters may exhibit nonlinear and interdependent effects on acoustic performance. The GSA process preserves the quasi-random properties of Sobol sequences while ensuring that each parameter's individual and interactive effects can be isolated through variance decomposition.

In order to sufficiently explore the design space, a sampling method is needed. A sampling procedure was implemented through the SALib library's `saltelli.sample` function [7–10], resulting in 4096 distinct parameter combinations for the 3-parameter MPP system. With each parameter combination, a unique acoustic transmission coefficient is computed and documented, preparing for the sound quality metrics prediction.

2.3 Sound Quality Prediction and Design Optimization

For the design optimization phase, conventionally, MPP parameters are directly calculated from objective acoustic (sound absorption or transmission loss) behaviors. However, in this research, the general goal is to predict MPP parameters using psychoacoustic metrics (loudness and sharpness) as targets. The motivation for using these psychoacoustic metrics comes from their direct relation with human perception, offering an intuitive approach to acoustic design than traditional physical metrics alone. Loudness quantifies the subjective intensity of sound perceived by listeners, while sharpness characterizes the high-frequency content often contributing to annoyance. Hence, the sound quality prediction process follows this systematic workflow:

1. Generation of acoustic filters (impulse responses) based on transmission coefficients from MPP parameters;
2. Convolution with pre-recorded noise stimuli;
3. Calculation of psychoacoustic metrics: loudness from ISO 532-1:2017 C code [11] and sharpness using Python library MosQiTo [12].

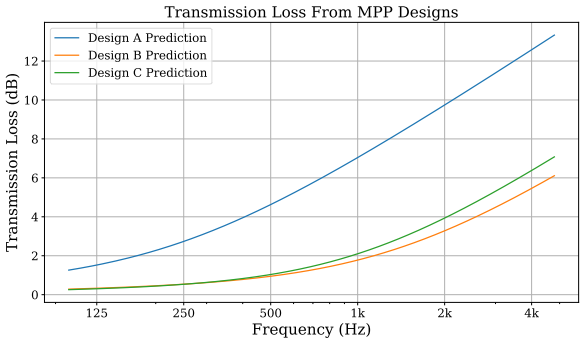


Figure 2. Predicted transmission loss curves for the MPP design A, B, and C.

Key parameters were predicted based on earlier GSA results and targeted toward specific sound quality goals:

- Design 1: Minimize loudness and sharpness.
- Design 2: Maximize loudness and sharpness.

2.4 Prototype Designs and Acoustic Performance

Based on the 4096 Satelli samples from GSA, three distinct MPP designs: Panel labels A, B, and C were manufactured with parameters shown in Table 1, and Figure 2 shows their predicted transmission loss performances. Panel A is designed to have in overall lowest loudness and sharpness metrics, panel B and C are designed to have high loudess and sharpness, but having parameters that differ enough. Hereby, panel samples are manufactured using a photomask laser cutter with a precision of 5 µm. With this tolarance, the TL deviation is maximally 0.04%, ensuring minimal impact from engineering errors.

Table 1. MPP design parameters for the three prototype configurations.

Design	Diameter (mm)	Porosity (%)	Thickness (mm)
A	0.94	0.594	2
B	0.47	2.99	2
C	0.73	1.94	1.5

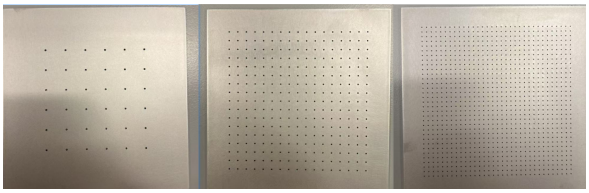


Figure 3. Stainless steel panels A, B, and C, laser cut with 0.005 mm precision.

2.5 Experimental Setup for Micro-Perforated Panel Measurements

The acoustic transmission characteristics of micro-perforated panels (MPPs) were experimentally investigated using an impedance tube configuration corresponding to the modeled 1-D setting described in Figure 1. The experimental apparatus consists of a Mecanum impedance tube, Siemens SCADAS Mobile data acquisition frontend with Simcenter Testlab 2406.0002 "Sound transmission loss using impedance tube," six G.R.A.S. 46BD quarter inch microphones, following the procedure in ASTM standard [13]. The manufactured panels are shown in Figure 3. The frequency range of this measurement is between 100 Hz and 5000Hz, with a resolusion of 5 Hz. Considering that the sharpness metric is greatly impacted by the contrast between high and low frequency content, sound stimuli in this research is designed not to contain much frequency information above 5000 Hz, minimizing potential impact when validating in the impedance tube.

3. RESULTS

Figure 4 shows the measured transmission loss (TL) curves for each design: Design A, B, and C from Table 1. Design A demonstrates higher TL values across all frequencies, especially in the mid to high-frequency range, while Design B and Design C offer moderate TL performance. The impulse responses corresponding to the simulation are then calculated from the transmission coefficients, shown in Figure 5.

The simulated and measured impulse responses are compared with normalized mean square error (NMSE) and normalized rood mean square error (NRMSE) over dynamic range. Panel B has the best overall match, with an NMSE of 0.176 and an NRMSE over the dynamic range of 0.016. Panel A has an NMSE of 0.457 and an NRMSE of 0.025, while Panel C has an NMSE of 0.425 and an NRMSE of 0.0212. These higher NMSE

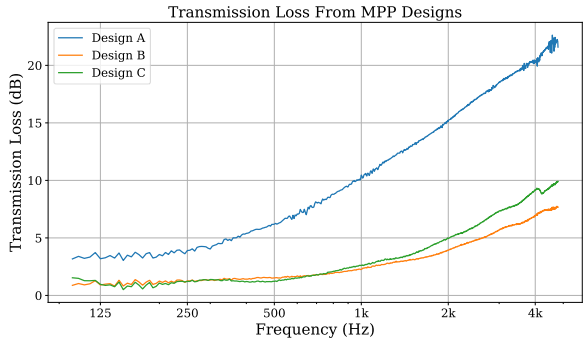


Figure 4. Measured transmission loss curves for the MPP design A, B, and C.

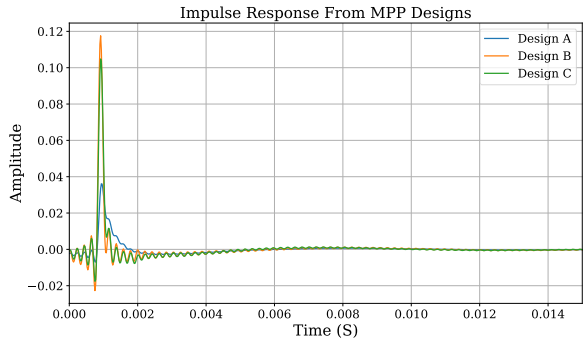


Figure 5. Impulse responses derived from the MPP design A, B, and C.

and NRMSE values for panel A and C indicate a moderate match between the simulated and measured impulse responses for these MPPs.

3.1 Psychoacoustic Performance

The predicted and measured psychoacoustic metrics for the three designs are presented in Table 2.

The results show agreement between predicted and measured psychoacoustic metrics, with deviations less than 6% for loudness and sharpness. Design A, with its smaller perforation rate and larger diameter, achieved the lowest loudness (22.2 sone) and sharpness (0.82 acum), aligning with our optimization target. Design B, featuring the average perforation diameter and perforation rate, resulted in the highest loudness (26.4 sone) and sharpness (0.97 acum), as expected from GSA predictions.

Table 2. Predicted vs. measured psychoacoustic metrics for the three designs.

Design	Loudness (sone)		Sharpness (acum)	
	Predicted	Measured	Predicted	Measured
A	23.5	22.2 (-5.5%)	0.87	0.82 (-2.0%)
B	27.0	26.4 (-5.7%)	0.99	0.97 (-4.5%)
C	26.8	25.6 (-2.2%)	0.99	0.94 (-5.1%)

4. DISCUSSION AND CONCLUSION

This study demonstrates the effectiveness of using global sensitivity analysis (GSA) as a framework for optimizing acoustic metamaterials based on psychoacoustic metrics. The findings confirm that this computational model can accurately predict complex relationships between psychoacoustic metrics such as loudness and sharpness, and the design parameters of the micro-perforated panels (MPP) such as thickness, hole diameter, and perforation rate.

The experimental validation of the theoretical predictions has yielded several important insights:

First, the disagreements between predicted and measured values are within 6% for both loudness and sharpness metrics. Considering the loudness parameter sone is on a relative scale, this deviation on loudness can be considered negligible. For instance, Design A has a loudness deviation from 23.5 sones predicted to 22.2 sones measured, which are correspondingly converted to 73.5 dB and 72.7 dB. This difference (0.8 dB) is within the just-noticeable difference (1 dB) of human hearing. This finding suggests the reliability of the prediction.

Second, this research provided a basis for design optimization. By establishing quantitative relationships between design parameters of MPP and sound quality metrics, it becomes possible to navigate the design space to achieve specific sound quality targets. Design B and C have distinct design parameters but share the same sharpness (0.99 acum predicted). This confirms that GSA-based design optimizations can be trusted for practical design applications.

Third, the workflow presented bridges the gap between objective acoustic properties to subjective auditory perception. It allows acousticians directly compare the

sound quality metrics derived from material parameters. These metrics represent perceptually relevant features that correlate with subjective impressions, providing a more intuitively valid assessment of acoustic performance compared to abstract measurements of TL numbers and IR curves across the spectral and temporal domains. This approach extends the material design range by incorporating human perception into the design process, which is valuable for applications where sound quality, rather than mere noise reduction, is the primary design goal.

While this study focused on a simplified MPP configuration to establish methodologies, the workflow can be extended to more complex setups. Future work may explore periodic media exhibiting metamaterial behavior, starting with periodic arrangements of MPPs.

In conclusion, this study validates the use of GSA as an effective tool for sound quality driven metamaterial design. The agreement between predicted and measured psychoacoustic metrics suggests that this approach can guide the design optimization using sound quality as targets. By integrating acoustic modeling with sound quality metrics, this methodology provides a framework for designing materials that address not only physical performance requirements but also human perceptual preferences.

5. ACKNOWLEDGMENTS

The European Commission is gratefully acknowledged for their support of the Horizon Europe DN METAVISION project (GA 101072415). Views and opinions expressed are however those of the authors only and do not necessarily reflect those of the European Union. The European Union cannot be held responsible for them. The research of L. Van Belle (fellowship no. 1254325) is funded by a grant from the Research Foundation – Flanders (FWO).

6. REFERENCES

[1] S. A. Cummer, J. Christensen, and A. Alù, "Controlling sound with acoustic metamaterials," *Nature Reviews Materials*, vol. 1, no. 16001, 2016.

[2] L. D. Ryck and J. Cuenca, "Perceptual evaluation of metamaterials as insulation partitions - a listening test within the cost action denorms ca15125," in *Proc. of Int. Conf. on Noise and Vibration Engineering (ISMA)*, (Leuven, Belgium), 2018.

[3] J. Zhang, L. D. Ryck, J. Cuenca, L. V. Belle, and E. Deckers, "Impact of design variations of micro-perforated panels on psychoacoustic metrics of transmitted sound," *Proc. Mtgs. Acoust.*, vol. 55, no. 1, 2024.

[4] R. Huysse, *Analysis of the micro-perforated panel parameters in a modal filter for tonal and broadband damping*. PhD thesis, KU Leuven, 2021.

[5] N. Atalla and F. Sgard, "Modeling of perforated plates and screens using rigid frame porous models," *J. Sound Vib.*, vol. 303, pp. 195–208, 2007.

[6] I. M. Sobol, "Global sensitivity indices for nonlinear mathematical models and their Monte Carlo estimates," *Math. Comput. Simul.*, vol. 55, pp. 271–280, 2001.

[7] J. Herman and W. Usher, "SALib: An open-source python library for sensitivity analysis," *The Journal of Open Source Software*, vol. 2, jan 2017.

[8] T. Iwanaga, W. Usher, and J. Herman, "Toward SALib 2.0: Advancing the accessibility and interpretability of global sensitivity analyses," *Socio-Environmental Systems Modelling*, vol. 4, p. 18155, May 2022.

[9] A. Saltelli, "Making best use of model evaluations to compute sensitivity indices," *Computer Physics Communications*, vol. 145, pp. 280–297, May 2002.

[10] A. Saltelli, P. Annoni, I. Azzini, F. Campolongo, M. Ratto, and S. Tarantola, "Variance based sensitivity analysis of model output. design and estimator for the total sensitivity index," *Computer Physics Communications*, vol. 181, pp. 259–270, 2 2010.

[11] "Acoustics – methods for calculating loudness – part 1: Zwicker method," standard, International Organization for Standardization, Geneva, Switzerland, 2017. Standard.

[12] G. F. Coop, "MOSQITO," Apr. 2024.

[13] ASTM International, "Standard test method for normal incidence determination of porous material acoustical properties based on the transfer matrix method," Standard E2611-19, ASTM International, West Conshohocken, PA, 2019.

DOI: 10.61782/fa.2025.0626

FORUM ACUSTICUM EURONOISE 2025

NUMERICAL AND EXPERIMENTAL STUDY OF ACOUSTIC PERFORMANCE OF PHONONIC CRYSTALS-BASED VENTILATED NOISE BARRIERS FOR TRAFFIC NOISE

Noman Ahsan[1,2*] **Nicolas Herrera**[2] **Luca Sangiuliano**[1]
Paulo Amado Mendes[2] **Luis Godinho**[2]
[1] Phononic Vibes SRL, Via Francesco Cherubini 6, 20145, Milan, Italy
[2] University of Coimbra, ISISE, ARISE, Department of Civil Engineering, Coimbra, Portugal

ABSTRACT

Phononic crystal-based noise barriers offer promising solutions for urban noise mitigation, particularly concerning traffic and highway noise, due to their capacity to efficiently attenuate sound while maintaining ventilation. This study advances the state of the art through two key contributions: first, by developing an experimental setup to analyze stopband frequencies and, second, by creating a numerical model that replicates real-world conditions for further validation. Unlike previous studies, which primarily assessed phononic crystal barriers in semi-anechoic chambers with single noise sources, this work introduces a more realistic experimental approach. The setup utilizes an Alpha cabin with a diffuse sound field, where a 4×6 array of cylindrical scatterers is mounted on the cabin door. Insertion Loss (IL) is measured using an external microphone array, capturing the barrier's performance in practical conditions. To account for production and assembly tolerances, slight variations in the scatterers' x and y coordinates are introduced into the numerical model. Results show peak attenuation values between 1 and 2 kHz, aligning with critical urban noise frequencies. This study presents a methodology for evaluating ventilated phononic crystals in real-world scenarios, providing valuable insights for designing efficient noise barriers tailored to traffic and highway applications.

Keywords: *Acoustic Metamaterials, Phononic Crystals, Ventilated Noise Barriers, Insertion Loss, Traffic Noise*

[*] ***Corresponding author***: *noman.ahsan@phononicvibes.com*
Copyright: *©2025 Noman Ahsan et al. This is an open-access article distributed under the terms of the Creative Commons Attribution 3.0 Unported License, which permits unrestricted use, distribution, and reproduction in any medium, provided the original author and source are credited.*

1. INTRODUCTION

Noise pollution is a growing concern in urban environments, impacting public health and well-being. Prolonged exposure to excessive noise levels can result in hearing loss, cardiovascular issues, sleep disturbances, and cognitive impairments, particularly in children. Conventional noise barriers, while effective in reducing sound transmission, tend to be bulky and visually intrusive, blocking natural airflow. These limitations have spurred the search for alternative solutions, with phononic crystal-based noise barriers emerging as a promising innovation.

Phononic crystals (PCs), a type of acoustic metamaterial, utilize periodic structures to control wave propagation, providing enhanced noise reduction while still allowing for ventilation. Recent studies have explored their ability to reduce traffic noise, but practical applications remain limited. PCs can create stopbands, which are frequency ranges where sound transmission is blocked, making them particularly effective for targeted noise reduction. However, further research is necessary to optimize their design for real-world applications.

Traffic noise is one of the primary sources of urban noise pollution, affecting large populations in cities due to the high volume of vehicles and continuous road traffic. Figure 1 illustrates the spectral energy contribution rate of traffic noise at various vehicle speeds, ranging from approximately 34 km/h to 93 km/h. Figure 2 displays the sound pressure levels (SPL), in dB(A), at ground level as a function of frequency. Both figures emphasize that traffic noise is most prominent between 500 Hz and 2 kHz, with a peak between 1 kHz and 1.6 kHz. This observation aligns with typical noise sources, including engine vibrations, tire-road interactions, and aerodynamic effects. The energy distribution increases significantly within this frequency

range, indicating that any effective noise mitigation strategy must focus on these frequency bands.

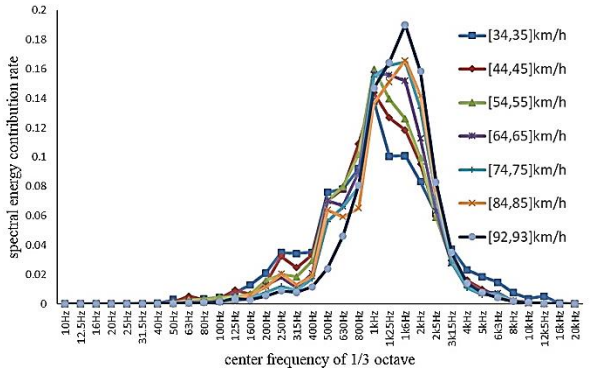


Figure 1. Traffic Noise Spectrum showing dominant frequencies [1]

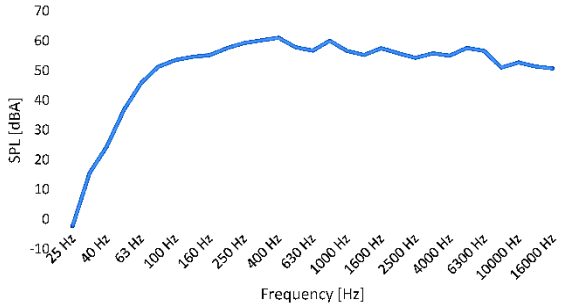


Figure 2. SPL versus frequency recorded in traffic-generated noise measurements [2]

In recent years, acoustic metamaterials have been increasingly utilized to mitigate traffic noise, capitalizing on their unique ability to manipulate sound waves. Sonic crystals and phononic crystals have garnered attention for their ability to control sound propagation, especially at frequencies where traffic noise is typically present. Sonic crystals use periodic arrays of scatterers to create band gaps that block specific frequencies of sound [3]. Phononic crystals, on the other hand, utilize periodic structures at the scale of acoustic wavelengths to prevent the transmission of sound, making them highly effective for controlling low-frequency noise [4]. Their tunable properties enable the precise targeting of problematic noise frequencies, making them highly adaptable for various applications in traffic noise control.

This study presents an integrated approach that combines numerical modeling with experimental validation to evaluate the performance of an array of phononic crystal-based noise barriers. A 4×6 array of cylindrical scatterers was tested in a diffuse sound field within an Alpha cabin, with Insertion Loss (IL) measurements taken externally. By incorporating production tolerances into numerical analysis, this research provides a more realistic evaluation of PC barriers. The findings demonstrate peak attenuation between 1 and 2 kHz, which aligns with the dominant frequencies of urban noise pollution. This work contributes to the advancement of sustainable, high-performance noise control solutions suitable for traffic and highway applications.

2. THEORY AND DESIGN

Phononic crystals (PCs) are artificially engineered periodic structures that manipulate the propagation of elastic and acoustic waves. These structures achieve sound attenuation by introducing bandgap frequency ranges where wave transmission is significantly suppressed. The attenuation mechanism primarily relies on Bragg scattering and local resonance effects [5].

The concept of sonic crystals was first introduced by Martinez [6] in 1995. They conducted sound attenuation experiments on a sculpture by Eusebio Sempere, which was displayed at the Juan March Foundation in Madrid. The team measured sound attenuation under outdoor conditions, focusing on sound wave vectors that were aligned perpendicularly to the vertical axis of the cylinder. They identified a sound attenuation peak at 1670 Hz, marking the emergence of the first band gap.



Figure 3: Different types of Sonic Crystals, also known as periodic structures

According to Bragg's law [7], the mechanism of sound attenuation involves the destructive interference of reflected sound waves with incident sound waves within the band gaps. If the interference is constructive, then the energy of the original wave gets transmitted through the sonic crystal, which forms the propagation bands. In Bragg scattering,

destructive interference occurs when the wavelength of an incident wave matches the periodicity of the structure. The Bragg condition for a 1D periodic structure is given by:

$$m\lambda = 2dsin\theta \quad (1)$$

Where m is the diffraction order (usually m = 1 for the first Bragg condition), λ is the wavelength of the incident wave, d is the lattice constant (the periodic spacing of the scatterers), θ is the angle of incidence of the wave relative to the structure. For a 2D phononic crystal, where periodicity is in two dimensions, the formation of a stopband is governed by the Bloch wave condition using the dispersion relation:

$$k = k0 + G \quad (2)$$

Where k is the wavevector in the phononic crystal, k_0 is the incident wavevector, and G is the reciprocal lattice vector. This equation describes the multiple scattering effect, where waves interfere constructively and destructively, leading to bandgap formation [8]. For periodic scatterers with a lattice constant a, the Bragg Bandgap frequency can be approximated as:

$$f_b = \frac{c}{2a} \quad (3)$$

Where c is the speed of sound in the background medium, this relation shows that the stopband shifts to lower frequencies as the lattice spacing increases, making it a crucial design parameter in phononic crystal barriers. In theory, band gaps should be at multiples of the above fundamental frequency.

Similarly, the filling fraction, a crucial property, influences the width of the band gap. It indicates the proportion of the structure filled by the cylinders [4]. For a square lattice arrangement with scatterers of radius r, the filling fraction is defined as

$$F = \frac{\pi r^2}{a^2} \quad (4)$$

The fundamental component of a phononic crystal is its unit cell, which can be a scatterer or multiple scatterers and can have shapes such as cylindrical, square, or spherical, organized in a periodic pattern. The selection of lattice configuration, whether square, hexagonal, or triangular, greatly influences wave propagation characteristics. A square lattice featuring cylindrical scatterers is frequently used in phononic crystal barriers due to its simplicity in production and the reliable creation of bandgaps.

In this study, we have modeled and tested a unit cell with a lattice constant of 15 cm, a scatterer diameter of 10 cm, and a height of 100 cm to investigate the effectiveness of sonic crystal-based noise barriers in attenuating traffic noise. Figure 4 illustrates the dimensions and geometry of a single unit cell. For the array configuration, we opted for four rows and six columns of scatterers, which was determined to provide an optimal trade-off between acoustic performance and structural efficiency. This array configuration ensures sufficient coverage of the target frequencies while minimizing material usage and production complexity.

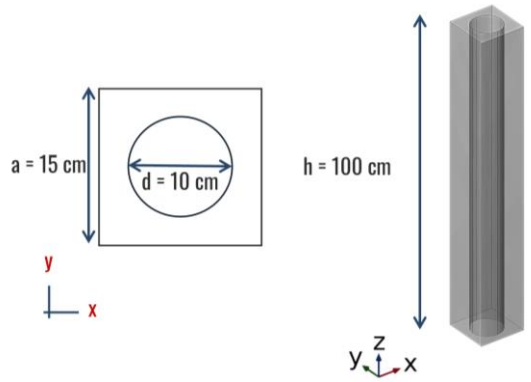


Figure 4: Unit Cell representing one barrier with a=lattice constant, d=diameter of scatterer, and h=height of scatterer

Using the designed unit cell, a numerical model was developed in COMSOL Multiphysics, complemented by an experimental setup, to study the acoustic performance of the unit cell and the array of barriers. The numerical simulations allowed for a detailed analysis of sound wave interactions with the scatterers, while the experimental setup provided empirical data for validation. This methodology enabled a comprehensive evaluation of the noise attenuation capabilities of the barriers, as detailed in Section 4, and the results are discussed in Section 5.

3. METHODOLOGY

3.1 Stopband Analysis

An eigenfrequency study is conducted on the unit cell shown in Figure 6 to determine its band structure and eigenmodes by analyzing the first five eigenfrequencies. A parametric sweep is performed for the wave vector kx along the wave propagation direction over the range $0 \leq kx \leq \pi/a$, which corresponds to the irreducible part of the Brillouin zone.

This analysis helps identify phononic bandgap frequency ranges where wave propagation is prohibited by observing gaps in the computed eigenfrequencies. The resulting dispersion curve provides insights into the wave propagation characteristics of the phononic crystal, enabling the optimization of its design for effective noise attenuation, particularly within the 500 Hz–2 kHz range, which is relevant to traffic noise.

3.2 Numerical Model

To evaluate the acoustic performance of a periodic sonic crystal array in a realistic setting, a comprehensive 3D finite element model was developed using COMSOL Multiphysics. The simulation focused on predicting the insertion loss (IL) and identifying the acoustic stopband behavior of a 4 × 6 array of scatterers, tailored to replicate a real-world prototype under diffuse field conditions. A conceptual diagram is illustrated in Figure 5.

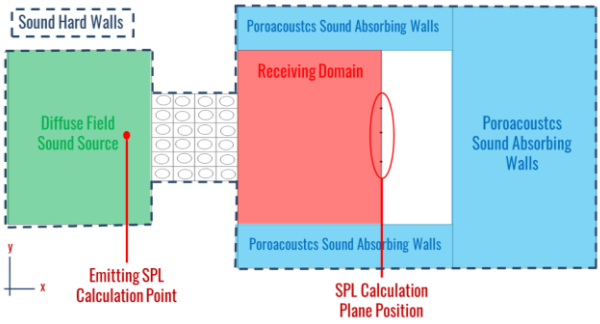


Figure 5: 2D Graphical representation of numerical model used in COMSOL to compute Insertion Loss

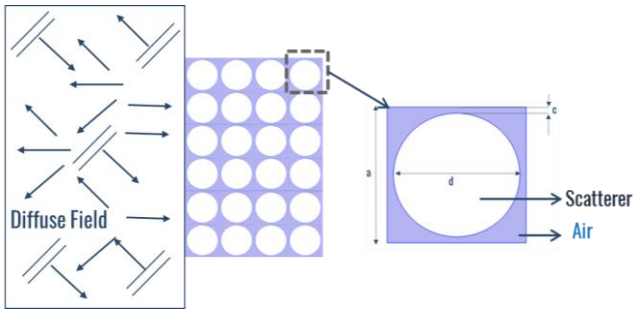


Figure 6: Air applied on surrounding domain of scatterer and random pressure in emitting domain

Table 1. Geometric Parameters of Unit Cell.

Parameter	Description	Value
a	Lattice Constant	15 cm
d	Diameter	10 cm
c	Gap	5 cm

The simulated geometry represents a 3D array of 24 cylindrical scatterers (4 rows × 6 columns) positioned in air, as illustrated in Figures 5 and 6. Scatterers are infinitely rigid and, on the source side, random pressure input diffuse field effects.
In the absence of flow and thermal effects, the Helmholtz equation governs the acoustic pressure field in the frequency domain:

$$\nabla \cdot \left(\frac{1}{\rho_0}\nabla p\right) + \frac{\omega^2}{\rho_0 c_0^2} p = 0 \qquad (6)$$

where:

- p is the complex acoustic pressure [Pa],
- ρ_0 is the air density [kg/m^3],
- c_0 is the speed of sound in air [m/s],
- $\omega = 2\pi f$ is the angular frequency [rad/s].

To replicate realistic boundary absorption (instead of using perfectly matched layers, PML), porous absorbing materials were modeled using the Johnson-Champoux-Allard (JCA) framework, valid for rigid-frame porous media. To replicate environmental excitation such as traffic noise, a diffuse acoustic field was approximated numerically by summing multiple

incident plane waves over an emitting domain. This mimics a random incidence angle distribution:

$$p_{\text{inc.}}(\mathbf{r}) = \sum_{n=1}^{N} A_n e^{-j\mathbf{k}_n \cdot \mathbf{r}} \quad (8)$$

where:

- r: position vector,
- k_n: incident wave vector for angle θ_n and ϕ_n
- A_n: complex amplitude (random phase),
- N: number of plane waves.

Considering geometric variations for realism, this model simulates prototype inaccuracies and production tolerances, precisely scatterer position offsets.

Insertion Loss (IL) measures the reduction in sound transmission that occurs when a barrier is inserted into the acoustic path. In the model, IL is calculated as the difference in Transmission Loss (TL) between the reference case (an empty domain) and the case with the present barrier. Sound pressure levels (SPL) were measured inside and outside the array, and the IL of the variety was computed in dB using TL with and without barriers as explained in the following relations:

$$TL_{empty} = SPL_{inside} - SPL_{outside}$$

$$TL_{barriers} = SPL_{inside} - SPL_{outside}$$

$$IL\ (dB) = TL_{barriers} - TL_{empty}$$

$$= SPL_{outside\ (Empty)} - SPL_{outside\ (Barriers)}$$

The difference in TL values isolates the acoustic effect of the barrier, effectively accounting for diffraction and scattering. This method ensures a reliable and realistic evaluation of the barrier's performance, consistent with established acoustic standards.

3.3 Experimental Setup

To experimentally validate the stop-band effect of the sonic crystal array due to Bragg scattering, measurements were conducted by installing a sonic crystal (SC) array on the door of an Alpha Cabin reverberant cabin, which serves as a diffuse-field sound source. Sound excitation was generated using six high-power loudspeakers capable of producing a sound power of up to 115 dB, thereby creating a diffuse sound field that simulates real-world noise conditions, as shown in Figures 7 and 8.

A 4×6 array of rigid PVC pipes, acting as sonic crystals, was installed on the door of the measurement cabin. Each scatterer has a diameter of 10 cm and is arranged in a square lattice with a 15 cm periodicity, resulting in an array with a width of 90 cm, a depth of 60 cm, and a height of 100 cm.

The pipes were filled to avoid any resonances and precisely arranged to maintain the desired periodicity required for Bragg scattering. To prevent unwanted sound leakage, the array was fully sealed with wooden panels on all four sides- top, bottom, left, and right- except for the side facing the microphone array.

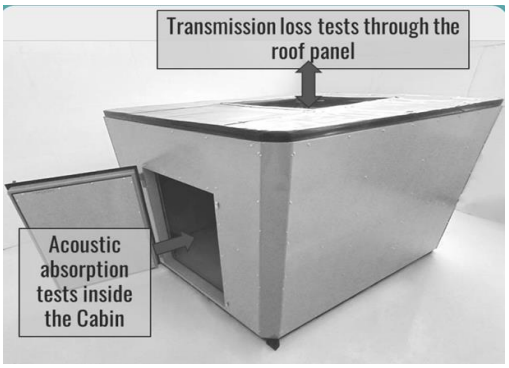


Figure 7: Phononic Vibes 9m^3 Alpha Cabin

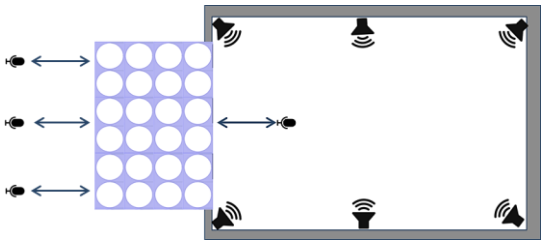


Figure 8: Schematics showing how source and receiving domain look in experimental setup

This configuration ensures that sound waves existing in the cabin must pass through the periodic structure, facilitating selective frequency attenuation via the bandgap effect.

A 2D array of seven microphones is positioned 60 cm from the last row of the SC array to capture transmitted sound levels. To accurately capture sound pressure levels (SPL), seven microphones were placed in front of the array,

and one microphone was positioned inside the cabin. This multi-point measurement approach enabled spatial logarithmic averaging, reducing position-dependent variations and providing a more representative assessment of the overall sound attenuation caused by the barrier.

Table 2. Description of Microphones and their distances.

Microphone no.	Position	Distance from Array
Mic1	Receiving	60 cm
Mic2	Receiving	60 cm
Mic3	Receiving	60 cm
Mic4	Receiving	60 cm
Mic5	Receiving	60 cm
Mic6	Receiving	60 cm
Mic7	Receiving	60 cm
Mic8	Emitting	60 cm

Sound pressure levels (SPL) were measured at multiple positions inside and outside the phononic crystal array to evaluate its noise attenuation performance. The microphone-facing walls of the Alpha cabin were covered with sound-absorbing material to minimize unwanted reflections and prevent any unnecessary resonances that could interfere with the accuracy of the measurements. Additionally, the wall behind the microphone array was also treated with absorbent material to eliminate back reflections, ensuring that the recorded sound levels accurately represent the transmitted sound without contamination from secondary reflections, as shown in Figures 9 and 10.

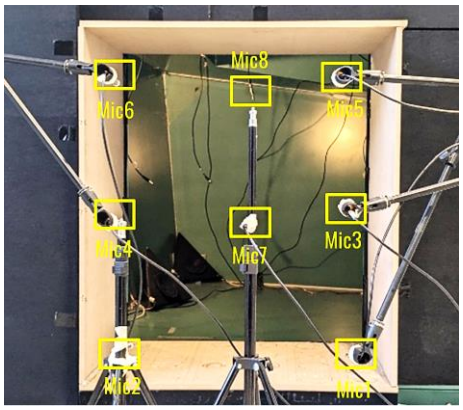


Figure 9: Baseline: No barriers installed and SPL_{empty} measured inside (Mic8) and outside (Mic1-7) to computed TL_{empty}

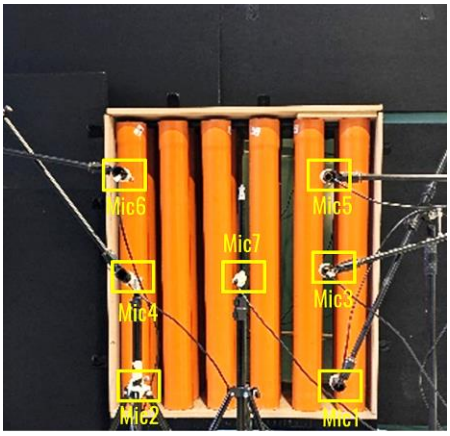


Figure 10: Barriers installed and $SPL_{barriers}$ measured inside (Mic8) and outside (Mic1-7) to computed $TL_{barriers}$

Given the periodic arrangement of the SC array, Bragg scattering effects are expected to cause significant attenuation in the 500–2 kHz range, which corresponds to the dominant frequencies of traffic noise. The measured IL data will validate the formation of a bandgap and assess the overall effectiveness of the SC array in noise mitigation applications.

4. RESULTS AND DISCUSSION

The numerical and experimental results indicate that the phononic crystal (PC) array exhibits strong attenuation characteristics within the designed frequency range. The dispersion analysis of the unit cell (Figure 11) confirms the presence of a complete stopband between 1300 Hz

and 1400 Hz, demonstrating the periodic arrangement's potential to suppress wave propagation effectively. This range aligns well with the observed peak insertion loss (IL) in the numerical simulations (Figure 13).

Figure 13 illustrates the insertion loss obtained for the 4x6 array of scatterers, comparing the ideal periodic arrangement with a structure incorporating random variations in scatterer positioning along the x- and y-coordinates. The results show that the perfectly periodic PC configuration achieves a maximum IL of approximately 16 dB at 1250 Hz, validating its effectiveness in mitigating noise in the mid-to-high-frequency range, with a grey-shaded envelope representing the range between maximum and minimum values.

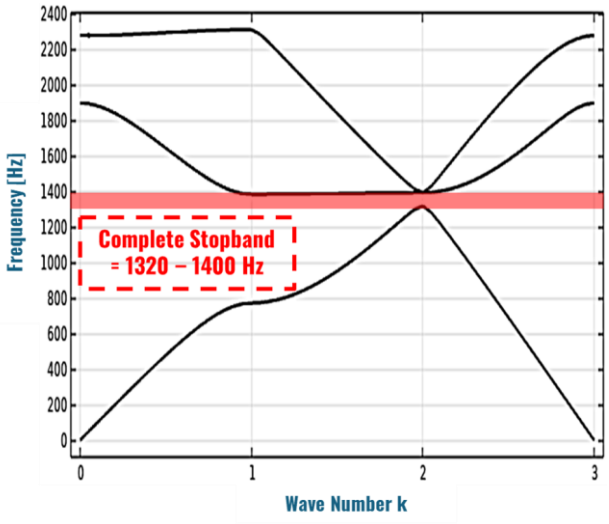


Figure 11: Dispersion Curve showing a complete stop band of designed unit cell between 1300-1400 Hz

The application of random variation along scatterers introduces some fluctuation in the insertion loss response yet maintains a strong attenuation band centered around 1250 Hz. The broadening of the attenuation peak suggests improved robustness and potential for practical deployment, where production imperfections and environmental conditions would otherwise degrade performance.

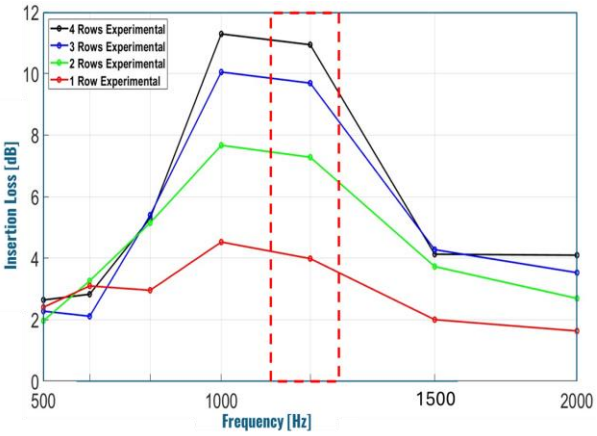


Figure 12: Experimentally measured IL showing the stopband between 1000-1500 Hz in 1/3 Octave bands

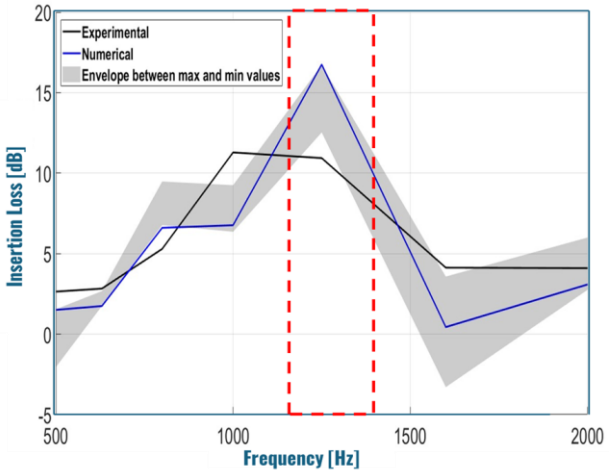


Figure 13: Experimental vs Numerical IL of 4x6 Array of Barriers

Figure 12 shows the experimentally computed IL with different numbers of rows of the barriers. The incremental increase in IL with additional rows suggests that multiple scattering and destructive interference significantly contribute to noise reduction. The experimental results demonstrate the effectiveness of the sonic crystal noise barrier in reducing sound transmission, particularly in the 1000–1400 Hz range, where the insertion loss (IL) reaches a peak of approximately 12 dB for the 4-row configuration.

Figure 13 shows a comparison between experimental and numerical IL for a 4x6 array of barriers, considering variation, and confirms the presence of a stopband between the desired frequencies. The deviations between experimental and numerical data could stem from imperfect boundary conditions (such as wooden panels), production tolerances, or edge diffraction effects.

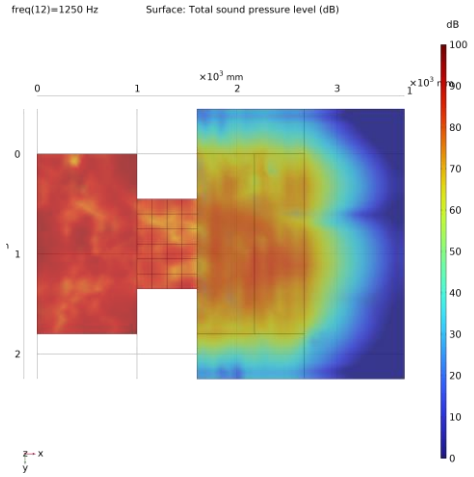


Figure 14: With no barriers, no apparent reduction in SPL

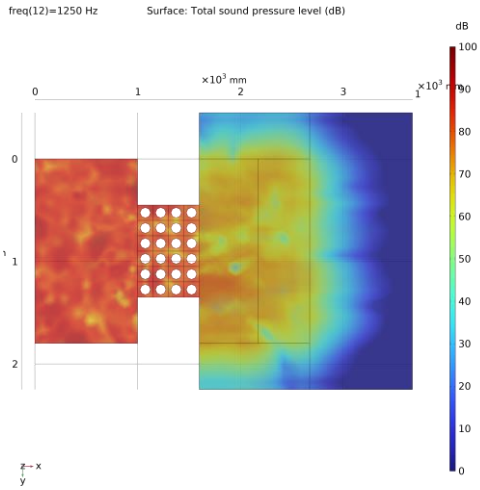


Figure 15: SPL reduced in receiving domain with barriers

Figure 14 shows the scenario without barriers, where SPL remains high and widespread, indicating minimal noise reduction. In contrast, Figure 15 presents the sound pressure level (SPL) distribution, demonstrating reduced SPL in the receiving domain when barriers are present, confirming their noise mitigation capability. These results highlight the effectiveness of the barrier array in controlling noise propagation within stopband frequencies.

5. ACKNOWLEDGMENTS

We gratefully acknowledge the European Commission for its support of the Marie Sklodowska Curie program through the Horizon Europe DN METAVISION project (GA 101072415).

This work was partly financed by FCT / MCTES through national funds (PIDDAC) under the R&D Unit Institute for Sustainability and Innovation in Structural Engineering (ISISE), under reference UID/04029/Institute for Sustainability and Innovation in Structural Engineering (ISISE), and under the Associate Laboratory Advanced Production and Intelligent Systems ARISE under reference LA/P/0112/2020.

6. REFERENCES

[1] Yang, Weijun, Ming Cai, and Peng Luo. "The calculation of road traffic noise spectrum based on the noise spectral characteristics of single vehicles." Applied Acoustics 160 (2020): 107128.

[2] Minea, Marius, and Cătălin Marian Dumitrescu. "Urban traffic noise analysis using uav-based array of microphones." *Sensors* 23.4 (2023): 1912.

[3] Chen, Qiqi, et al. "Review of Phononic crystals and acoustic metamaterials." *IOP Conference Series: Materials Science and Engineering*. Vol. 788. No. 1. IOP Publishing, 2020.

[4] Liu, Xiaohua, et al. "Pneumatic soft phononic crystals with tunable band gap." *International Journal of Mechanical Sciences* 240 (2023): 107906.

[5] Bragg WH, Bragg WL (1913) The reflexion of X-rays by crystals. Proc R Soc Lond A 88(605):428–438

[6] Martínez-Sala, Rosa, et al. "Sound attenuation by sculpture." nature 378.6554 (1995): 241.

[7] Page, John H., et al. "Phononic crystals." *physica status solidi (b)* 241.15 (2004): 3454-3462.

[8] Kittel C (1996) Introduction to solid state physics. Wiley, New York

DOI: 10.61782/fa.2025.0948

FORUM ACUSTICUM EURONOISE 2025

VALIDATING THE USE OF ACOUSTIC METAMATERIALS IN INDUSTRIAL APPLICATIONS FOR LOW-FREQUENCY NOISE REDUCTION

Ester Cierco[1*] **Marcel Janer**[2] **David Suárez**[2]
Pere V. Rodríguez[1]
[1] ICR, Ingeniería para el Control del Ruido, Berruguete 52, Barcelona, Spain
[2] Eurecat, Centre Tecnològic de Catalunya, Advanced Manufacturing Systems Unit, Spain

ABSTRACT

Vibroacoustic and acoustic metamaterials are promising technologies for noise and vibration reduction. However, their adoption in the industry is limited due to several factors, including a complex design process, industrialization challenges, and costly solutions that constrain their cost-benefit in real applications.
The present work focuses on the design and experimental validation of two types of metamaterials designed to address specific acoustic challenges in train interior noise. The first solution is a vibroacoustic metamaterial (VAMM) based on local resonance effect, designed to reduce the transmission of vibrations on a train panel around 160 Hz. The second solution is a ventilated acoustic metamaterial (AMM) for rectangular open ducts, conceived to reduce airborne noise at frequencies around 170 Hz without reducing the airflow. For both cases, a numerical model was developed and a prototype was built using additive manufacturing technologies.
Experimental validations showed vibration reductions greater than 30 dB in narrow-band and 17 dB in 1/3rd octave bands at the frequencies of interest for the VAMM. In addition, sound pressure level reductions up to 6 dB in narrow-band and 3 dB in 1/3rd octave bands were achieved for the AMM. These results demonstrate the potential of metamaterials for industrial and railways applications.

[*] ***Corresponding author***: ecierco@icrsl.com.
Copyright: *©2025 First author et al. This is an open-access article distributed under the terms of the Creative Commons Attribution 3.0 Unported License, which permits unrestricted use, distribution, and reproduction in any medium, provided the original author and source are credited.*

Keywords: *acoustic metamaterial, ventilated, additive manufacturing, railways.*

1. INTRODUCTION

Developing low frequency and broadband sound insulation solutions has always been a significant challenge in noise control engineering. In many sectors like aircraft and railways, solutions based on porous materials for low-frequency sound absorption are limited to the available space for their installation, as these require a significant thickness to be efficient. This challenge becomes even more critical when low frequency airborne sound attenuation is needed with minimal reduction of the air flow. To address this, acoustic metamaterials (AMMs) offer promising solutions.
AMMs are engineered materials that have unique properties, such as negative mass or negative bulk modulus, which arise from their periodic structure. The study of AMMs originated with research on phononic crystals in 1993. In recent decades, its use has expanded significantly, driven by advancements in additive manufacturing technologies that enable the fabrication complex geometries. One of the most compelling aspects of AMMs is their ability to manipulate sound, enabling the creation of barriers that selectively attenuate specific frequencies [1].
Recently considerable effort has been dedicated to developing AMM for low frequency broadband insulation. Some proposed solutions include the use of periodically aligned acoustic black holes [2], honeycomb sandwich structures with attached membranes [3]. Additionally, significant advances have been made to enhance the broadband attenuation capabilities of vibracoustic metamaterials (VAMM) [4] and ventilated acoustic

metamaterials [5], offering solutions that are both effective and easy to manufacture. In the railways sector, innovative solutions for interior noise reduction in trains, including AMMs, were explored in the TRANSIT project with promising results from simulation point of view [6] [7].

2. RESEARCH CONTEXT AND OBJECTIVES

The aim of this work is to propose innovative solutions, based on metamaterials, for potential application cases in railways and industry. Noise reduction based on conventional solutions faces limitations related to weight and space, particularly when dealing with low frequency. Train interior noise is a combination of airborne and structure-borne noise. The structure-borne part is low frequency, and it is transmitted from the main noise sources such as the bogie and auxiliary equipment through the train carbody to the interior. Vibroacoustic metamaterials can help to reduce vibration and thus the structure-borne noise contribution in this frequency range. In this context, a VAMM based on local resonance effect to cancel bending waves in a plate structure is proposed.

Besides, there are several acoustic sources related to ventilation systems, such as cooler fans of auxiliary equipment, or the HVAC supply fan. The latter might be a relevant noise source for train interior noise, especially at train low speeds and for certain passenger positions. The duct's system has often limitations in terms of space, so solutions based on AMM can be a smart alternative to reduce the fan's blade passing frequency. In this context a ventilated AMM is proposed, tuned at a typical frequency for this kind of fan.

The objective of this research is, based on previous works found on literature as a starting point, to adapt specific designs to the above-mentioned applications.

The VAMM solution and its validation are described in chapter 3. The ventilated AMM solution and its validation are described in chapter 4.

3. CASE STUDY 1: VIBROACOUSTIC METAMATERIAL

3.1 Proposed solution

The first solution proposed in this study is a resonator, based on the VAMM approach proposed in [4] but redesigned to achieve its eigenmode at lower frequencies (around 150 Hz). Additionally, the requirements for the solution included ease of manufacturing, the ability to be mounted vertically and the affordability of use in terms of cost. For this reason, a beam-like resonator made with polypropylene with a metallic tip mass was designed and simulated.

The resonator was attached to a 3mm thick aluminum 2024 T3 plate, which served as the base structure. A 3.6 g steel tip mass, representing 26% of the bare plate's mass, was used. According to the framework described in [4], this configuration is expected to produce a bandgap width of 15 Hz. COMSOL Multiphysics was used to fine-tune the resonator's geometry in order to achieve the desired eigenfrequency of around 160 Hz (Figure 1). The chosen material, Innovatefil© polypropylene used has a very low young modulus (390 MPa), making it suitable for this application. The VAMM was manufactured using Bambu X1 Carbon 3D printing machine and glued directly to the aluminum plate. To facilitate the placement of the samples, a 0.8 mm thick tape was also printed

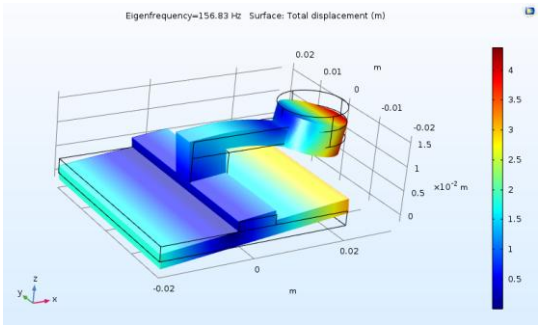


Figure 1. Modal analysis simulation of the beam-type VAMM resonator.

3.2 Experimental validation

The validation of the VAMM material performance was done by measuring averaged frequency response functions through impact testing. Results have been compared between 2 cases:

- The reference plate (bare plate)
- The reference plate + add-on VAMM

Validation has been done for two different configurations: a case where the VAMM has been installed over the whole plate area and a case where it has been installed only in the central part of the plate, occupying 22% of the total area.

Acceleration frequency response functions have been measured by averaging 5 impacts, performed at the lower edge of the plate. The response was measured at 4 different positions, at the upper edge of the plate. The impacts were performed with an instrumented hammer (PCB, model

086D05) with a nylon tip, and a set of piezoelectric accelerometers of 100mV/g.
The experiment performed with the solution added on the whole surface was done in free boundary conditions, by suspending the plates on an elastic rope, and in supported condition, with the plates supported on a table by means of foam pads (Figure 2). The evaluation of the partially applied solution has only been done in the supported condition.

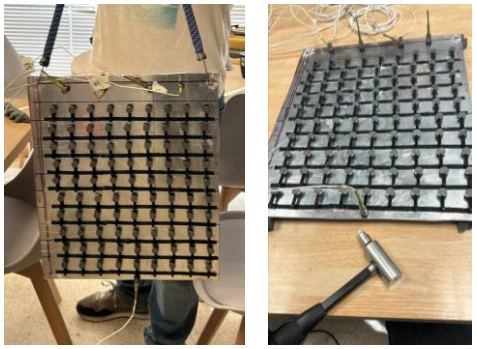


Figure 2. Experimental validation of the beam-like VAMM in free and supported boundary conditions.

3.3 Results

The comparison of the averaged frequency response functions of the bare plate and the bare plate with the VAMM are shown in Figure 3 and Figure 4 for free and supported boundary conditions respectively.

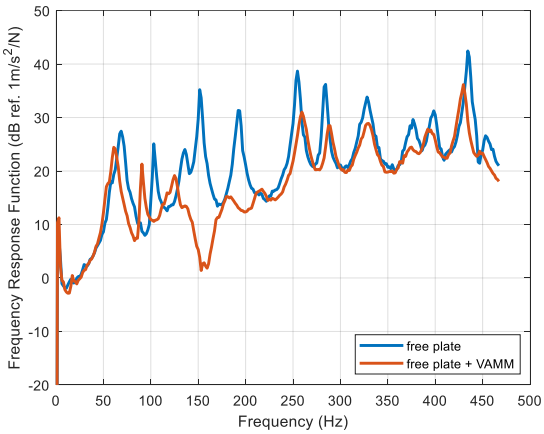


Figure 3. Magnitude of the averaged acceleration frequency response function with the VAMM solution applied in the whole plate surface (free boundary conditions).

Some differences are observed in the magnitude of the peaks between the free and supported cases. Despite the different boundary conditions, the same stop band is observed in both cases, in the range between 130 and 180 Hz, with a strong dip at 155 Hz (33 dB of reduction). Furthermore, a suppression of the peaks is observed up to 210 Hz. Besides, probably due to a significant amount of damping, peaks above 210 Hz are partially damped.

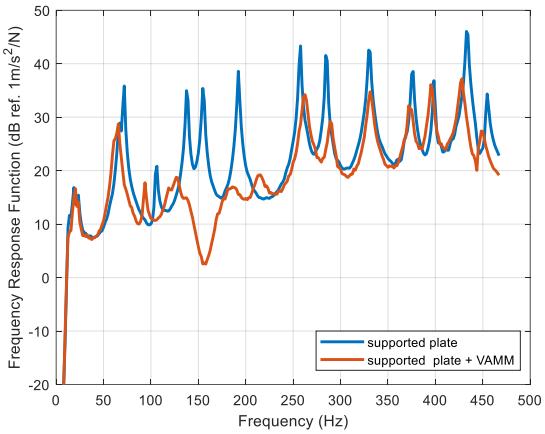


Figure 4. Magnitude of the averaged acceleration frequency response function with the VAMM solution applied in the whole plate surface (supported boundary conditions).

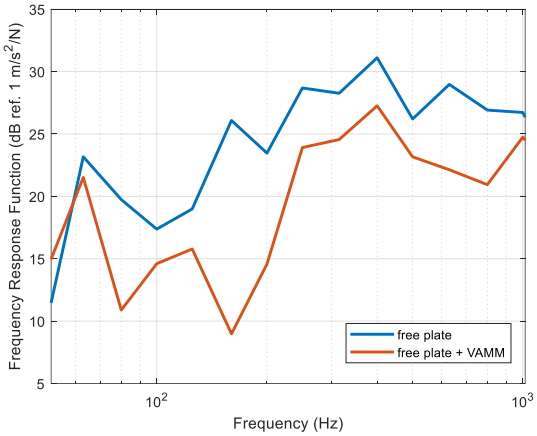


Figure 5. Averaged acceleration frequency response function in 1/3rd octave bands with the VAMM solution applied in the whole surface.

It is worth reading these results in one-third octave bands, as they are commonly used in noise control in industry. Reductions of 17 dB at 160 Hz band, and 9 dB at 200 Hz are achieved (Figure 5).
Results for the VAMM installed in 22% of the surface are shown in Figure 6. The stop-band behaviour is not observed in this case. A reduction in the amplitude of the peaks is achieved between 140 and 200 Hz. Above this frequency, only a very slight reduction in the amplitude of the peaks is observed. In one-third octave bands, the maximum reduction achieved is 11 dB at 160 Hz.

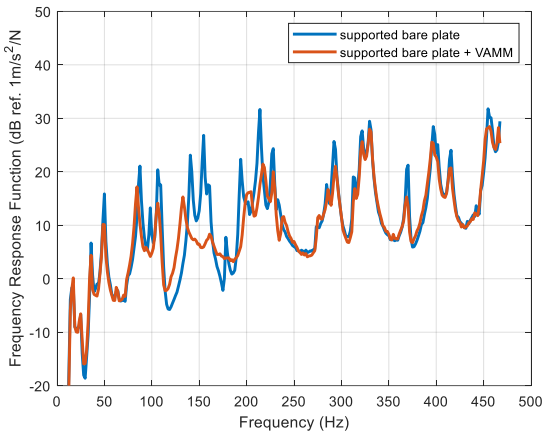


Figure 6. Magnitude of the averaged acceleration frequency response function with the VAMM solution applied in 22% of the plate surface.

4. CASE STUDY 2: VENTILATED ACOUSTIC METAMATERIAL

4.1 Proposed solution

The solution proposed to increase the absorption in an open-duct is a ventilated acoustic metamaterial, composed of multiple monopolar resonators arranged the same plane parallel to the section of the tube. The design features several Helmholtz resonators placed in a rectangular ring configuration. This design was based on the methodology proposed by Meng et al. [5], adapted to match the typical dimensions of a train's HVAC ducts (270 x 210 mm). A frequency domain analysis was performed using COMSOL Multiphysics to achieve an eigenfrequency at lower frequencies. The analysis involved creating a plane wave excitation in a Navier-Stokes linearized domain with perfect matching layers applied at the end of the ducts. The results show that the sound pressure levels (SPL) at Helmholtz resonator cavities are highest around 170 Hz (Figure 7).

The ventilated acoustic metamaterial was fabricated using PLA on a Prusa XL 3D printer. Due to the large sample size, the structure was subdivided into multiple sections and assembled using screws. To avoid the use of support materiel, the Helmholtz cavities were printed without the rear wall, which was glued in place after printing.

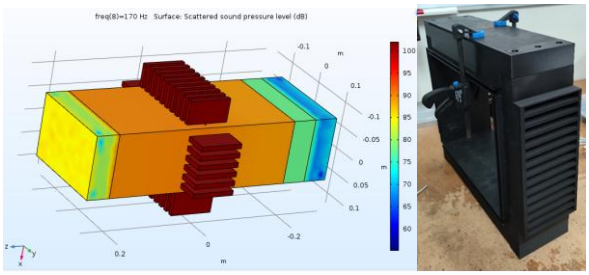


Figure 7. Scattered SPL obtained with finite element simulation of ventilated acoustic metamaterial (left), and process of assembling the metamaterial (right)

4.2 Experimental validation

Experimental validation has been done in a semi-anechoic chamber. A rectangular duct made of 4 mm thick PMMA material has been mounted and assembled, at one end, to a box containing a loudspeaker. To test the solution, the AMM has been assembled at the other end of the rectangular duct (Figure 8).
The validation has consisted in the comparison of the sound pressure level at a set of receiver positions between the case with the AMM installed and a reference case, where the duct has been assembled to a sample with the same dimensions than the ventilated AMM but without the Helmholtz resonators. Pink noise has been used as acoustic excitation.
The set of 15 receivers has been placed at 80 cm from the end of the sample, covering an area of 100 x 50 cm. Results have been calculated by averaging the sound pressure level at all positions.

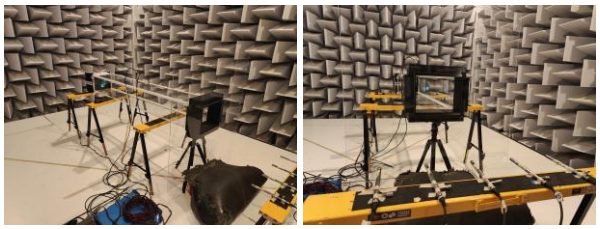


Figure 8. Images of the set-up in the semi-anechoic chamber.

4.3 Results

The comparison of the averaged sound pressure level results with and without the AMM solution is shown in Figure 9. In narrow band, a maximum reduction of 6 dB is found at 178 Hz and at 202 Hz. In one-third octave bands, this translates into a reduction of 3 dB at the band of 200 Hz and 1.4 dB at 160 Hz.

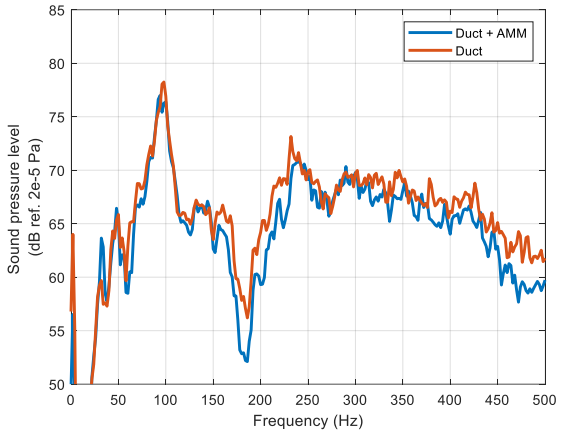


Figure 9. Comparison of the average sound pressure level results with and without the AMM solution installed.

5. CONCLUSIONS

In this work, two metamaterials have been designed, prototyped and experimentally evaluated for potential applications in the railway industry, based on the requirements and specifications of possible real-world cases. The proposed solutions are lightweight, easily manufacturable and easy to mount, with low production cost.

After the experimental evaluation of the beam-resonator based VAMM, a stop band has been clearly observed, with reductions up to 33 dB at 155 Hz. This corresponds to a reduction of 17 dB at 160 Hz one-third octave band. Thanks to these results, the solution appears promising. It has been observed that the total amount of resonators in the plate is relevant for the stop band performance. The next step to further develop this material would be, on the one hand, to move forward toward the industrialization phase. On the other hand, modifications could be explored to increase the stop-band frequency range without adding extra weight to the solution.

The results of the ventilated AMM solution have shown reductions of 6 dB in narrow band at frequencies near the target frequency, 170 Hz, which leads to a reduction of 3 dB at 200 Hz third-octave band. Discrepancies with the results of the literature may arise from defects in the design of the AMM, which is not completely optimized, or issues related to the assembly of its components. Further research is needed to improve the performance of the proposed solution.

6. ACKNOWLEDGMENTS

This work was funded by the European Union – Next Generation UE and the Recovery, Transformation, and Resilience Plan (PADIH); and supported by the Spanish Ministry of Industry and Tourism and EOI.

7. REFERENCES

[1] Aydın, G., & San, S. E. (2024). Breaking the limits of acoustic science: A review of acoustic metamaterials. Materials Science and Engineering: B, 305(April). https://doi.org/10.1016/j.mseb.2024.117384

[2] Li, L., Hu, H., & Wu, X. (2023). Ultra-Low-Frequency Acoustic Black Hole Radial Elastic Metamaterials. Applied Sciences, 13(20), 11542. https://doi.org/10.3390/app132011542

[3] Sui, N., Yan, X., Huang, T. Y., Xu, J., Yuan, F. G., & Jing, Y. (2015). A lightweight yet sound-proof honeycomb acoustic metamaterial. Applied Physics Letters, 106(17). https://doi.org/10.1063/1.4919235

[4] Atzrodt, H., Maniam, A., Droste, M., Rieß, S., & Hülsebrock, M. (2023). A Power-Based Framework for Quantifying Parameter Uncertainties in Finite Vibroacoustic Metamaterial Plates. Materials, 16(14). https://doi.org/10.3390/ma16145139

[5] Meng, Y., Romero-García, V., Gabard, G., Groby, J. P., Bricault, C., & Goudé, S. (2023). Subwavelength Broadband Perfect Absorption for Unidimensional Open-Duct Problems. Advanced Materials Technologies, 8(12). https://doi.org/10.1002/admt.202201909.

[6] I. Lopez, M. Abom, E. Cierco, FX. Magrans, R. Serra. Feasibility study of new concepts and approaches, TRANSIT Deliverable D4.1, December 2020

[7] E. Cierco, FX. Magrans, I. Lopez, A. Aulitto, D. Passato, M. Abom. Acoustic performance characterization of baseline and new design variants, TRANSIT Deliverable D4.2, June 2022.

DOI: 10.61782/fa.2025.0730



FORUM ACUSTICUM
EURONOISE 2025

RECIPROCITY DRIVEN OMNI-DIRECTIONAL ABSORPTION

Juan Pablo Escudero[1*] **Jean-Philippe Groby**[1] **Vincent Pagneux**[1]
[1] Laboratoire d'Acoustique de l'Université du Mans (LAUM), UMR 6613,
Institut d'Acoustique - Graduate School (IA-GS), CNRS,
Le Mans Université, France

ABSTRACT

In order to obtain a strong absorption over a large range of incidence angle, the reflection of an incident acoustic plane wave by a rigidly backed lossy architectured layer is studied numerically and theoretically. This layer is composed of a periodic arrangement of inclined resistive wiremeshes. Impedance matching is achieved when the angle of the incident wave corresponds to the angle of inclination of the wiremesh as well as its exact opposite angle, thanks to the reciprocity principle. The structure exhibits either large absorption over a broad frequency band for medium inclination angles or almost omnidirectional large absorption over a subwavelength frequency band for large inclination angles. This peculiar acoustic behavior provides another perspective for the design of perfect omnidirectional subwavelength sound absorbing devices.

Keywords: *wiremesh, effective medium, broadband absorption, omni-directional absorption.*

1. INTRODUCTION

Low frequency noise absorption is a challenging task which has been addressed in numerous studies this last decade [1–3]. The main difficulties to confront this problem are related with the large acoustic wavelength and the required space and amount of material for passive noise control solutions [4]. As an alternative, acoustic metamaterials developed under the slow sound propagation concept have been used to design broadband acoustic perfect absorbers leading to deep-subwavelength structure thicknesses [5]. The performance of these solutions is limited when the acoustic wave arrives from angles that are different from normal incidence or from grazing angles.
Among other metamaterials, layered metasurfaces based on the extraordinary reciprocity property [6, 7] exhibit a symmetric reflection coefficient providing very interesting absorption characteristics. From this property, the reflection coefficient of a structure with ultra thin resistive sheets, in a transmission problem, is zero when the incident field arrives with the same angle as the orientation of the layers. On the other hand, when the incident field arrives with the exact opposite angle, the reflection is again zero and the transmission is different to one. In consequence, impedance matching is produced at this exact opposite angle and the absorption coefficient is close to the unity.

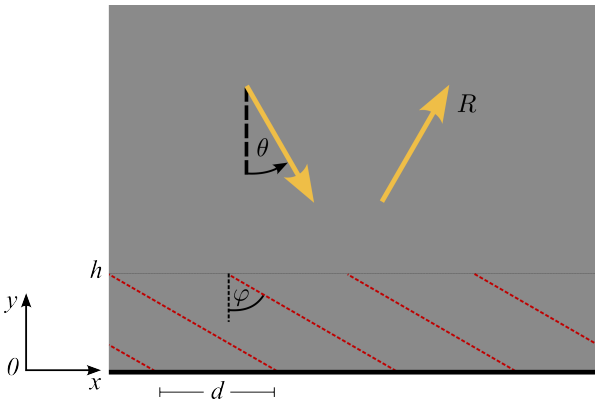


Figure 1. Reflection problem of a wiremesh (red dashed) grating with rigid backing.

Inspired by this reciprocity principle, we explore the reflection of an incident acoustic plane wave by a rigidly

**Corresponding author*: *juan_pablo.escudero_lopez@univ-lemans.fr.*
***Copyright**: ©2025 Juan Pablo Escudero et al. This is an open-access article distributed under the terms of the Creative Commons Attribution 3.0 Unported License, which permits unrestricted use, distribution, and reproduction in any medium, provided the original author and source are credited.*

backed lossy architectured layer composed of resistive wiremesh material. In this study, we compute the absorption coefficient numerically and theoretically. In addition, we show that the structure exhibits either large absorption over a broad frequency band for medium inclination angles or almost omni-directional large absorption over a subwavelength frequency band for large inclination angles. This document is organized as follows. Sec. 2 describes the wiremesh grating structure in a reflection problem. Sec. 3 presents the structure effective medium formulation and an explicit expression for the reflection coefficient. Finally, comparisons between the numerical computations with analytical results are shown in Sec. 4.

2. WIREMESH GRATING

Fig. 1 depicts a reflection problem of a rigid backing wiremesh grating. This problem is described by the Helmholtz equation, $(\Delta + k^2)p = 0$, using the time-harmonic convention $e^{-i\omega t}$. The structure is composed of inclined thin wiremesh units horizontally arranged with a periodicity d, a layer inclination angle φ and a height h. The boundary conditions that define the wiremesh, assuming that the layers does not vibrate, are a normal particle velocity continuous through the wiremesh and a pressure jump around the layer [8,9], as

$$[\![\partial_n p]\!] = 0 \;\; and \;\; [\![p]\!] = \frac{i\zeta}{k}\partial_n p. \tag{1}$$

In Eqn. (1), ζ is the purely resistive wiremesh impedance normalized by the characteristic impedance of the medium ρc. As the structure is d-periodic along the x-axis, the present study is focused only on the propagation of the fundamental mode, i.e. $kh/\pi \leq 1$ [10].

3. EFFECTIVE MEDIUM FORMULATION

According to the effective medium theory ($kd \ll 1$), a lossy wiremesh layered structure can be represented using an artificial homogeneous anisotropic medium slab, with principal directions of anisotropy (X, Y) [11], as it is represented in Fig. 2. This problem is described by the wave equation

$$\nabla \cdot [\mathbf{a}\nabla p(x,y)] + bk^2 p(x,y) = 0. \tag{2}$$

In this equation, $\mathbf{a}$ and b are the effective parameters related with the density and bulk modulus of the slab relative to a reference medium (where $a = 1$ and $b = 1$). The boundary conditions for the reflection problem are

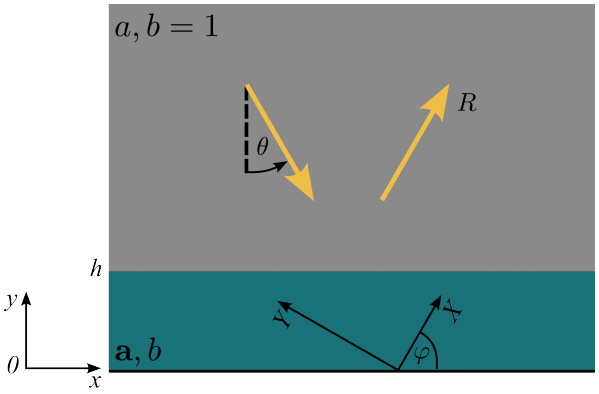


Figure 2. Reflection problem of a rigid backing wiremesh grating.

$$\begin{aligned} [\![p]\!] = 0 \quad and \quad [\![\mathbf{n}\cdot(\mathbf{a}\nabla p)]\!] = 0 \quad at \;\; y = h, \\ \mathbf{n}\cdot(\mathbf{a}\nabla p) = 0 \quad at \;\; y = 0. \end{aligned} \tag{3}$$

Considering that the principal directions of anisotropy (X, Y) coincides with the directions of the unit cell, the effective parameter $\mathbf{a}$ is a diagonal matrix defined as

$$\mathbf{a} = \begin{pmatrix} 1/\rho_{eff} & 0 \\ 0 & 1 \end{pmatrix}, \tag{4}$$

with an effective density [12]

$$\rho_{eff} = 1 + \frac{i}{kh}\left(\frac{\zeta h}{d\cos\varphi}\right). \tag{5}$$

Applying a rotation of the homogenized medium by an angle φ, the $\mathbf{a}$ matrix is mapped to the global components (x, y) in the form

$$\mathbf{a} = \begin{pmatrix} a_x & a_{xy} \\ a_{xy} & a_y \end{pmatrix}. \tag{6}$$

The reflection problem is solved using the wave fields solutions

$$\begin{aligned} p(x, y \geq h) &= e^{ik_x x}\left(e^{-ik_y(y-h)} + Re^{ik_y(y-h)}\right), \\ p(x, 0 \leq y \leq h) &= e^{ik_x x}\left(Ae^{i\kappa^+ y} + Be^{i\kappa^- y}\right), \end{aligned} \tag{7}$$

with $k_x = k\sin\theta$, $k_y = k\cos\theta$ and k the wave number in the reference medium. In Eqn. (7), $\kappa^{\pm}$ is the wave number of the anisotropic slab in the normal direction

$$\kappa^{\pm} = -\frac{a_{xy}k_x}{a_y} \pm \frac{k}{a_y}m', \tag{8}$$

with

$$m' = \sqrt{ba_y - (a_x a_y - a_{xy}^2)\sin^2\theta}.$$

Applying the boundary conditions of Eqn. (3), the reflection coefficient of the homogenized slab at $y = h$ is

$$R = \frac{\frac{\cos\theta}{m'} + i\tan\frac{kh}{a_y}m'}{\frac{\cos\theta}{m'} - i\tan\frac{kh}{a_y}m'}, \tag{9}$$

and the absorption coefficient is computed as

$$\alpha = 1 - |R|^2. \tag{10}$$

4. RESULTS

In order to compare the effective medium formulation, the absorption coefficient is calculated numerically using COMSOL Multiphysics and used as reference. In Fig. 3, the absorption coefficient is depicted. On the left-hand side numerical results using input parameters $\zeta = 2$ and $h = 2$ and on the right-hand side the effective medium results for dimensionless parameters $\varphi = 60$ and $\zeta h = 4$. In this figure, the effective medium results exhibit absorption deviations compared with numerical computation when kh/π increases. Furthermore, large absorption is obtained in both cases when the incident angle is exact the inclination angle of the layered structure ($\theta = \pm 60$), for frequencies above 0.4.

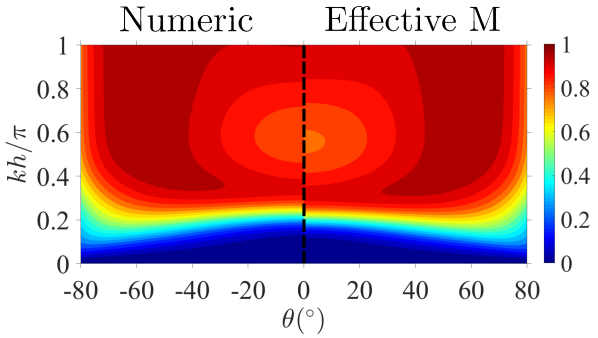


Figure 3. Absorption coefficient of the metasurface for $\varphi = 60$ and $\zeta h = 4$. Left side, numerical result using $\zeta = 2$ and $h = 2$, and at the right side the effective medium formulation.

The effect of varying φ for a fixed ζh value is presented in Fig. 4, for numeric ($\zeta = 2$ and $h = 2$) and effective medium computations. These results show that increasing the inclination angle of the layer structure larger absorption is achieved. A remarkable result is noticed for $\varphi = 75$, where impedance matching is achieved at the exact the inclination angle of the layered structure and broadband absorption is appreciable starting from low frequency ($kh/\pi \leq 0.2$). Furthermore, almost omnidirectional large absorption over a subwavelength frequency band is obtained for $\varphi = 75$ at a $kh/\pi = 0.14$. From the effective medium results, deviations appear as the frequency increase. Despite this, effective medium retains the subwavelength absorption and broadband at the same inclination angle of the structure.

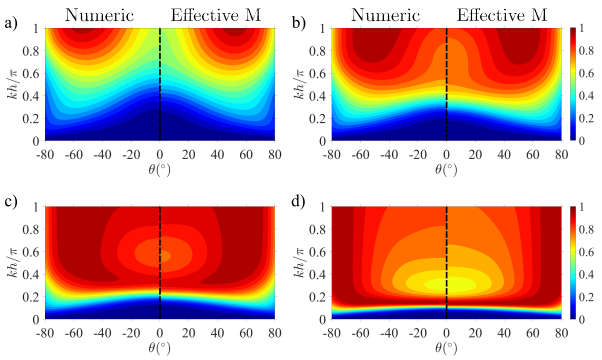


Figure 4. Effect of varying φ for $\zeta h = 4$ value. a) $\varphi = 30$, b) $\varphi = 45$, c) $\varphi = 60$ and d) $\varphi = 75$.

5. CONCLUSIONS

In this work, we studied the reflection problem of a rigidly backed lossy architectured layer composed of resistive wiremesh material. The understanding of the structure was performed using the effective medium formulation. From this procedure, we observed the dependency of the reflection coefficient on the dimensionless parameters kh and ζh. To compare the effective medium formulation, we used numerical computations as reference. We showed good correlation between numerical and effective medium results, and deviations where addressed at high frequencies. We observe good agreement between effective medium theory and full numerical solutions for a given ζh, as long as ζ is not large and h not too small. Additionally, we showed that the structure exhibits either large absorption over a broad frequency band for medium

inclination angles or almost omni-directional large absorption over a subwavelength frequency band for large inclination angles. This peculiar acoustic behavior provides another perspective for the design of perfect omni-directional subwavelength sound absorbing devices.

6. ACKNOWLEDGMENTS

The European Commission is gratefully acknowledged for their support of the Horizon Europe DN METAVISION project (GA 101072415). Views and opinions expressed are however those of the authors only and do not necessarily reflect those of the European Union. The European Union cannot be held responsible for them.

7. REFERENCES

[1] V. Romero-García, G. Theocharis, O. Richoux, A. Merkel, V. Tournat, and V. Pagneux, "Perfect and broadband acoustic absorption by critically coupled sub-wavelength resonators," *Scientific reports*, vol. 6, no. 1, p. 19519, 2016.

[2] C. Fu, M. Yang, and Z. H. Hang, "Ultra-broadband symmetrical acoustic coherent perfect absorbers designed by the causality principle," *Physical Review Research*, vol. 5, no. 4, p. L042020, 2023.

[3] Y. Duan, J. Luo, G. Wang, Z. H. Hang, B. Hou, J. Li, P. Sheng, and Y. Lai, "Theoretical requirements for broadband perfect absorption of acoustic waves by ultra-thin elastic meta-films," *Scientific Reports*, vol. 5, no. 1, p. 12139, 2015.

[4] J. Carbajo, S. Ghaffari Mosanenzadeh, S. Kim, and N. X. Fang, "Sound absorption of acoustic resonators with oblique perforations," *Applied Physics Letters*, vol. 116, no. 5, 2020.

[5] J.-P. Groby, N. Jiménez, and V. Romero-García, "Acoustic metamaterial absorbers," *Acoustic Waves in Periodic Structures, Metamaterials, and Porous Media: From Fundamentals to Industrial Applications*, pp. 167–204, 2021.

[6] J. Luo, H. Chu, R. Peng, M. Wang, J. Li, and Y. Lai, "Ultra-broadband reflectionless brewster absorber protected by reciprocity," *Light: Science & Applications*, vol. 10, no. 1, p. 89, 2021.

[7] H. Fan, J. Li, Y. Lai, and J. Luo, "Optical brewster metasurfaces exhibiting ultrabroadband reflectionless absorption and extreme angular asymmetry," *Physical Review Applied*, vol. 16, no. 4, p. 044064, 2021.

[8] M. Farooqui, Y. Aurégan, and V. Pagneux, "Ultrathin resistive sheets for broadband coherent absorption and symmetrization of acoustic waves," *Physical Review Applied*, vol. 18, no. 1, p. 014007, 2022.

[9] S. Kuznetsova, Y. Aurégan, and V. Pagneux, "Loss-induced modal selection by a resistive wiremesh," *The Journal of the Acoustical Society of America*, vol. 156, no. 1, pp. 369–377, 2024.

[10] N. Bonod and J. Neauport, "Diffraction gratings: from principles to applications in high-intensity lasers," *Advances in Optics and Photonics*, vol. 8, no. 1, pp. 156–199, 2016.

[11] O. A. Oleïnik, A. Shamaev, and G. Yosifian, *Mathematical problems in elasticity and homogenization*, vol. 26. Elsevier, 1992.

[12] J.-P. Groby, M. Mallejac, A. Merkel, V. Romero-García, V. Tournat, D. Torrent, and J. Li, "Analytical modeling of one-dimensional resonant asymmetric and reciprocal acoustic structures as willis materials," *New Journal of Physics*, vol. 23, no. 5, p. 053020, 2021.

DOI: 10.61782/fa.2025.0591

FORUM ACUSTICUM EURONOISE 2025

EXPERIMENTAL AND NUMERICAL ANALYSIS OF SONIC CRYSTAL NOISE BARRIERS WITH HYBRID SCATTERERS

Nicolas Herrera-Leon[1*] **Noman Ahsan**[1,2] **Luís Godinho**[1]
Luca Sangiuliano[2] **Paulo Amado-Mendes**[1]
[1] University of Coimbra, ISISE, ARISE, Department of Civil Engineering, Coimbra, Portugal
[2] Phononic Vibes SRL, Via Francesco Cherubini 6, 20145, Milan, Italy

ABSTRACT

Sonic crystals (SC) have emerged as a promising alternative to solid noise barriers, offering comparable attenuation properties with improved design flexibility. This study presents the design and analysis of a sonic crystal noise barrier covered with absorbing material to reduce urban traffic noise. The scatterers are designed to meet urban aesthetic requirements, with a maximum height of 1 m and a diameter of 8 cm.

Numerical simulations and experimental work were conducted to evaluate the sound absorption and insertion loss of the barrier. The results highlight the distinct roles of the rigid core and absorbing material layer, showing significant noise attenuation across a wide frequency range.

This research demonstrates the potential of combining absorbing material with rigid structures to develop effective noise barriers for urban environments. Furthermore, it details nonstandard methods to test the attenuation of the barrier. The findings contribute to advancing the practical application of sonic crystals in addressing traffic noise challenges while maintaining aesthetic and functional considerations

Keywords: Sonic crystal, urban noise, porous material, FEM, alpha cabin

*__Corresponding author__: uc2023166693@student.uc.pt.
__Copyright__: ©2025 Herrera-Leon et al. This is an open-access article distributed under the terms of the Creative Commons Attribution 3.0 Unported License, which permits unrestricted use, distribution, and reproduction in any medium, provided the original author and source are credited.

1. INTRODUCTION

Acoustic waves have been the focus of research for decades. Brillouin's classical work opened the field's possibilities with concepts like band gaps or the Brillouin zone, which can also be used in electromagnetic waves [1]. In 1987, the photonic crystal concept was first proposed to evaluate light's propagation inside a periodic structure [2]. Taking that work as inspiration, the concept of phononic crystal (PC) was born, with acoustic waves propagating inside periodic structures as well.

Phononic crystals are man-made composite materials consisting of periodically distributed scatterers in a matrix (fluid) with a high impedance, mass, and elastic moduli contrast to the host fluid, which can give rise to acoustic dispersions and band structures due to Bragg scattering [3]. Phononic crystals are mainly organized in three different distributions: one, two, and three dimensions (1D, 2D, 3D). The dimensions refer to the number of directions in which the crystal is periodic. Each of these tackles either pure or mixed transversal and longitudinal waves. [4]

The infinite repetition of the same unit cell or pattern constitutes a periodic system. This means that, at any location or portion of the system, the behavior is the same and is independent of its vicinity. The specific pattern that will be infinitely repeated is called a lattice. The space between individual unit cells in a lattice is called the *lattice constant* and is generally abbreviated with the symbol a. This is one of the most important things to consider when designing the SC. a will, in theory, determine the first Bragg band gap (BG) [5]. This means that the spacing between unit cells in rigid sonic crystals will establish the frequency range where acoustic waves are not able to propagate. a and the frequency relate to each other in the

equation:

$$f_c = \frac{c}{2a} \tag{1}$$

where f_c is the central frequency of the first Bragg-BG, and c is the speed of sound in the propagating medium.

Another important geometric parameter is the *filling fraction*, abbreviated with ff. This value is the amount of volume the scatterers occupy relative to the total volume of the sonic crystal. For a 2D sonic crystal with a rectangular lattice pattern, it can be calculated as:

$$ff = \frac{\pi r^2}{a^2} \tag{2}$$

where r is the radius of the scatterers, with a constant lattice constant a. If the filling fraction increases, it means that the scatterers occupy more of the total volume. As shown in equations 1 and 2, the effective frequency range that the noise barrier (NB) will attenuate is governed by the geometric parameters. Bevilacqua and her team [6] performed a study campaign to see the change in the insertion loss of a wooden SC when the radius and spacing of the unit cells are changed. They demonstrated that thinner scatterers shift the sound attenuation to higher frequencies. If the aim is to attenuate low frequencies in the unit cells, a larger diameter size should be considered.

While rigid sonic crystals offer promising noise reduction capabilities, further advancements can be achieved by incorporating additional functionalities into their design. There have been works that focus on changing the shape of the scatterer, like the one made by [7]. They found that by doing this, they have more versatility in changing the band gap without having to modify a or ff. Another option to enhance the acoustic response of the scatterers is to take advantage of its resonance. This means not only improving the spacing or the geometry of the inclusions but also taking advantage of another property. [8, 9] used a split ring resonator to enhance the properties of the sonic crystal. When the opening is carefully selected to have a resonance under or over the Bragg BG, the barrier in theory will have a wider bandgap. Another approach is to coat the scatterer with a porous material. Umnova et al. [10] Their findings show that covering the cylinders with a porous material makes the array insertion loss more uniform in frequency.

What these researchers can tell is that SC is an effective technique to combat railway and traffic noises. They are more aesthetically pleasing than solid NB and require less material to build. However, to have good attenuation properties in a wide frequency range using rigid scatterers is not enough. Early improvements to SC focused on geometric parameters, that are effective in some applications. For traffic use, it is necessary to combine multiple strategies in one inclusion in a way that guarantees the necessary properties.

This study focuses on the design and evaluation of a sonic crystal (SC) enhanced with an absorbing material to improve its performance against traffic noise. Given the intended outdoor application, porous concrete was selected as the preferred material due to its sound absorption properties and durability. To assess the effectiveness of the proposed configuration, a nonstandard experimental approach was employed. The methodology utilizes an alpha cabin as a controlled noise source, with the SC noise barrier mounted at the cabin door. An array of microphones is used to measure the attenuation induced by the scatterers, with focus on insertion loss. In addition to the experimental campaign, numerical models of the SC array are developed to compare with the measured results, providing further insight into the barrier's acoustic performance and the impact of the hybrid material composition.

The paper from this point forward is distributed as: Sec. 2 introduces the dimensions of the SC, materials used, and how they were characterized numerically and experimentally. Sec. 3 explains the experimental method to test the SC with the alpha cabin. Sec. 4 details the how the array was modeled using FEM. The experimental and numerical results are presented in sec. 5. Finally, sec.6 discusses the results.

2. SONIC CRYSTAL DESIGN AND MATERIAL CHARACTERIZATION

2.1 Sonic crystal unit cell and array dimensions

In this study, a square lattice sonic crystal (SC) was designed with scatterers consisting of a PVC pipe core (6 cm diameter) surrounded by a 1 cm thick polyester fiber absorbing layer, resulting in a total scatterer diameter of 8 cm. While the final SC design will use rigid and porous concrete, the polyester fiber layer was chosen for experimental testing in the alpha cabin as a proof of concept. Numerical simulations compare the acoustic behavior of both materials to assess their performance. In Fig. 1 the diagram of the scatterer is represented. In Tab. 1 the acoustic parameters of the configuration are given. The chosen lattice constant is because for traffic noise the most critical frequencies are close to 1000 [Hz], and to the ge-

ometric constraints of the experimental setup.

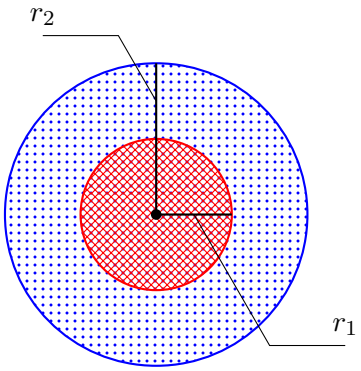


Figure 1: Top view of the scatterer

Table 1: Array geometric and acoustic parameters

Parameter	Value	Description
r_1	3 [cm]	radius rigid inner core
r_2	4 [cm]	radius complete scatterer (core + absorbing layer)
a	15 [cm]	lattice constant
f_c	1143 [Hz]	central Bragg frequency
ff	1.4	filling factor

2.2 Experimental material characterization

The characterization of the absorbing material was conducted in the Alpha cabin following ISO 354:2003 [11]. This standard specifies the use of a reverberation room and a 12 m² sample to determine a material's sound absorption coefficient (α) based on its reverberation time. Although the standard requires a large test sample, the polyester fiber layer was characterized inside the Alpha cabin, which also generates a diffuse sound field, ensuring the validity of the method. In this case, the sample size was reduced to 1.2 [m^2].

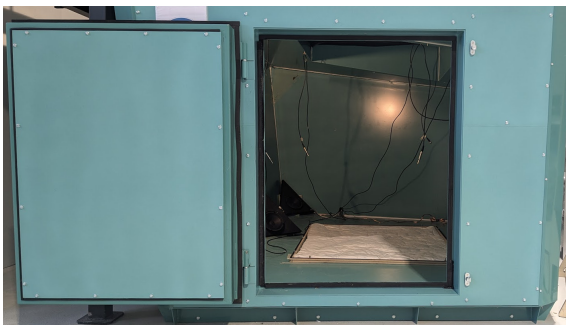


Figure 2: Polyester fiber sound absorption coefficient measures in an Alpha cabin using ISO 354:2003 standard.

To calculate α, two measurements were performed. First, the reverberation time was measured inside the empty Alpha cabin. Then, the test was repeated with the material inside. By comparing the reverberation times from both cases and applying Sabine's formula (Eq. 3), the absorption coefficient was determined.

$$TR_{60} = \frac{0.161 \times V}{S \times \alpha}. \tag{3}$$

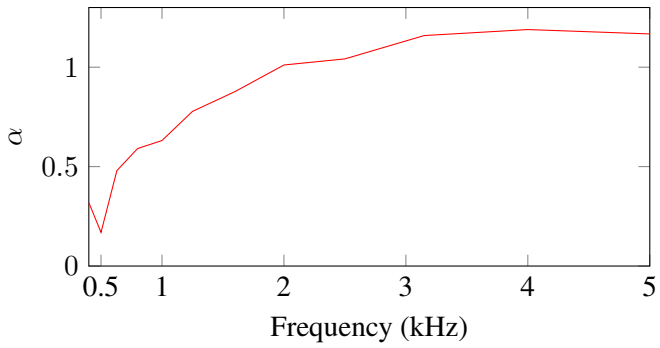


Figure 3: Polyester fiber sound absorption coefficient results obtained in an Alpha cabin using ISO 354:2003 standard.

2.3 Miki Equivalent fluid models

Miki's equivalent fluid model [12] are empirical relationships that estimate the characteristic impedance and propagation constant of porous materials. Those depend on porosity, tortuosity, and a pore shape factor.

Miki proposes to use the following expressions for the wave number (k) and characteristic impedance (Z_c):

$$Z_c = \rho_0 c_0 \left(1 + 5.5(\times 3\left(\frac{f}{\sigma}\right)^{-0.632} - i8.43(\times 3\left(\frac{f}{\sigma}\right)^{-0.632}\right) \tag{4}$$

$$k = \frac{\omega}{c_0}\left(1 + 7.81(\times 10^3\left(\frac{f}{\sigma}\right)^{-0.618} - i11.41(\times 10^3\left(\frac{f}{\sigma}\right)^{-0.618}\right) \tag{5}$$

The selected absorbing material can be accurately represented using this model.

3. EXPERIMENTAL METHOD

Noise barriers are typically tested *in situ* following the ISO 10847:1997 standard. However, since the current design is still under development, performing full-scale tests for every iteration would be impractical. Instead, a non-conventional method is proposed to obtain reliable data on noise attenuation rapidly. The key component, besides the sonic crystal (SC), is an Alpha cabin, whose characteristics are summarized in the following table and visible in Fig. 4.

Table 2: Alpha cabin characteristics

Parameter	Value
Internal volume	9 m^3
Maximum SPL	115 dB
Frequency range	400–10,000 Hz

To assess the effectiveness of the sonic crystal, insertion loss (IL) is selected as the performance metric, defined by:

$$IL = SPL_{\text{without}} - SPL_{\text{with}} \quad \text{[dB]} \tag{6}$$

This requires measuring the sound pressure level (SPL) in two configurations: (i) with the SC mounted on the Alpha cabin door and (ii) without it. The SPL is recorded using an array of seven PCB Piezotronics 130F20 microphones, positioned 60 cm from the outermost scatterer of the SC.

The system is controlled via a DEWESoft Sirius XHS LV, which generates a white noise signal for the speakers and processes input from the microphone array.

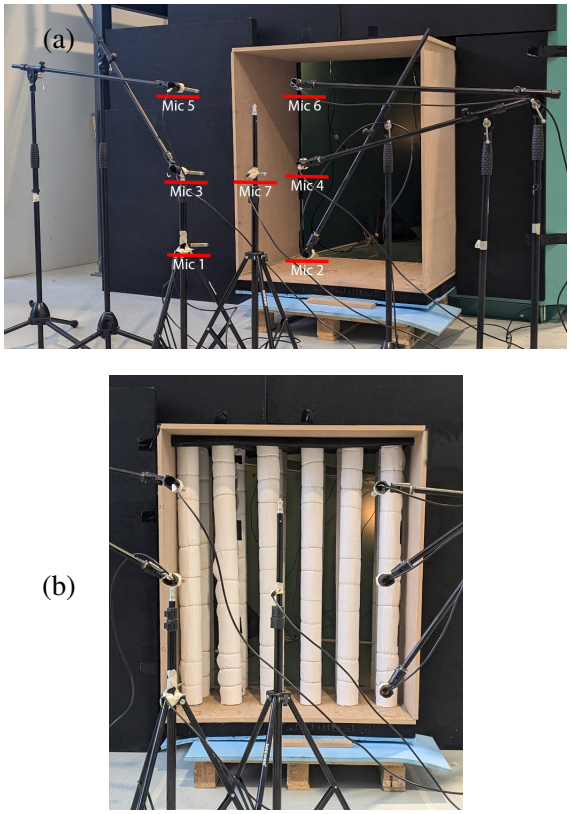


Figure 4: IL experimental setup: (a) Empty Alpha cabin with SC frame; (b) SC covered with polyester fiber absorbing material.

4. NUMERICAL MODELING

To validate and understand the behavior of 2D sonic crystals two-dimensional FEM simulations were employed. By using this technique, it is possible to test parameter changes quickly. The simulation setting for this section is relatively simple and is used with some adaptions for the studied cases.

Fig. 1 shows the geometries for the simulation. r_1 is the radius of the rigid cavity inside the scatterer, and r_2 is the radius of the full scatterer (core + absorbing material). Likewise, as with the experimental method, the analysis parameter to assess the barrier's performance is Insertion Loss (IL).

The modeled geometry is three scatterers in a row with infinite periodic conditions to the sides. The system is excited by a plane wave coming from the bottom edge of the model.

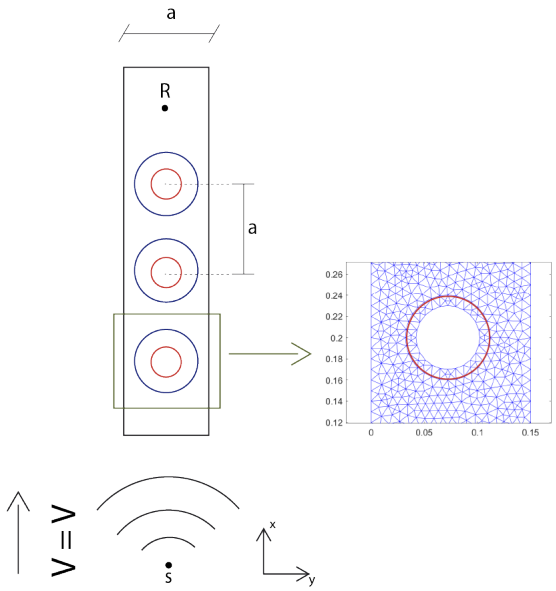


Figure 5: FEM model example for the numerical analysis.

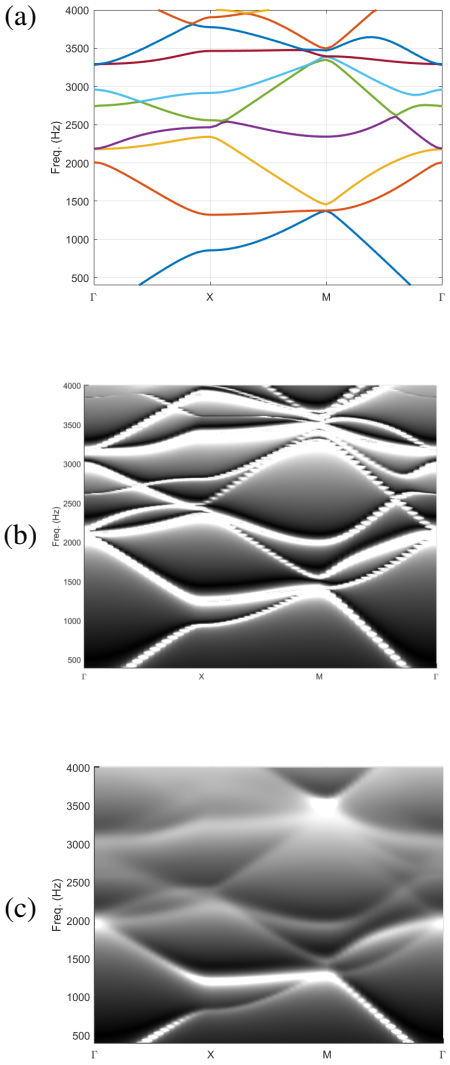


Figure 6: Dispersion relation curves for the different configurations: (a) normal eigen frequency analysis for a 8 cm rigid scatterer SC; (b) fine band analysis of a 8 cm rigid scatterer SC; (c) fine band analysis of a 6 cm rigid scatterer SC covered with 1 cm thick polyester layer.

5. RESULTS

Dispersion relation curves were obtained for both the rigid and porous cases to understand the wave propagation characteristics of the sonic crystal (SC) and identify the expected frequency range of the band gap. The rigid case was analyzed using eigenfrequency analysis, providing a direct calculation of the dispersion curves. In contrast, the porous case required a frequency-dependent approach, where each frequency was evaluated separately, and the contribution of the modes was analyzed independently.

Figure 6 presents the dispersion relation curves for both configurations. The results highlight differences in wave propagation characteristics between the two cases, with the introduction of porous material influencing the modal contributions, making them weaker. By this behavior, it is possible to expect a considerable energy reduction

starting around 600-700 Hz. These findings provide insight into the type of acoustic response expected from the SC and indicate the frequency range where attenuation effects should be most pronounced.

Experimental tests were conducted to measure the SC's acoustic attenuation performance. Figure 7 presents an overview of the microphone measurements collected during the experimental setup.

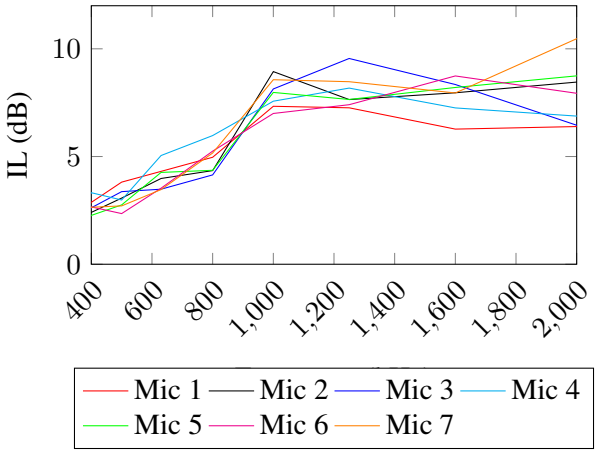


Figure 7: IL results per microphone for the absorbing layer configuration SC.

With these results, it is possible to see the contribution from both the Bragg scattering and the absorbing layer. As predicted, there is a peak of absorption between the 1000 to 1200 Hz 1/3 octave band, this is thanks to the interference caused by the rigid core. After the bandgap, the attenuation stagnates with a high value, which is approximately the same behavior as the experimental sound absorption coefficient curve visible in Fig. 3.

The IL experiments are then correlated with a FEM analysis. The results of the comparison are visible in Fig. 8

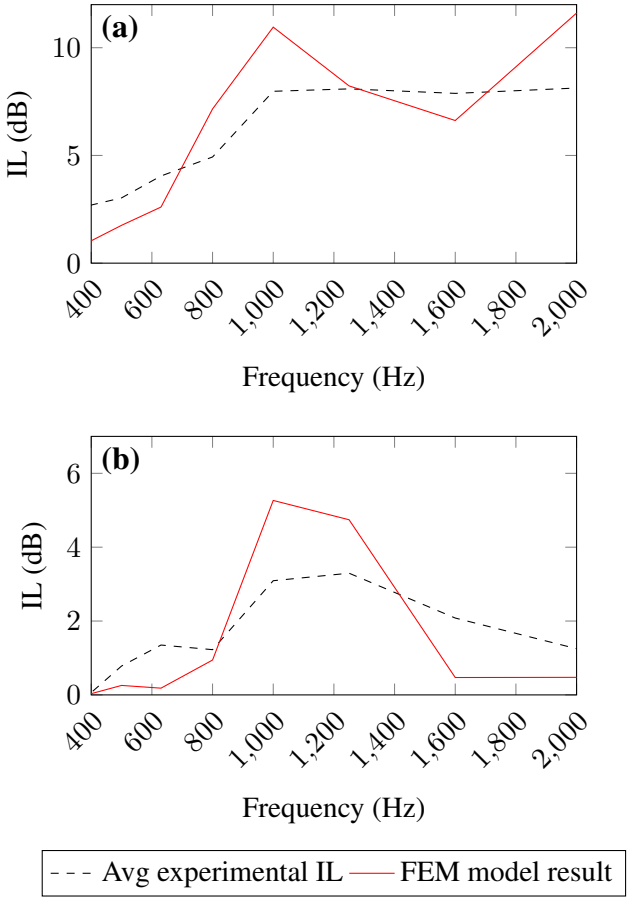


Figure 8: Average experimental IL results compared with numerical FEM results for the configurations: (a) 6 cm rigid core scatterer covered with 1 cm polyester fiber, and (b) 6 cm rigid scatterer.

The numerical results align with the experimental findings and the dispersion relation predictions, confirming the role of the porous material in enhancing sound attenuation. The simulations provide a detailed understanding of the SC's acoustic behavior, reinforcing the observed improvements in noise reduction.

The experimental results reveal key differences in insertion loss between the two cases, demonstrating the impact of the porous material on acoustic attenuation. The presence of the absorbing layer enhances attenuation, shifting and broadening the band gap, as anticipated from the dispersion analysis. These observations provide strong experimental support for the effectiveness of integrating

porous materials into the SC design.

6. FINAL REMARKS

The numerical results align closely with both the experimental findings and the dispersion relation predictions, confirming the role of the porous material in enhancing sound attenuation. The consistency of these results underscores the potential of combining porous materials with sonic crystal structures for effective noise control solutions. The simulations contribute to a detailed understanding of the SC's acoustic behavior, suggesting that this design approach could be a viable strategy for mitigating urban noise pollution, particularly from traffic sources.

7. ACKNOWLEDGMENTS

The European Commission is gratefully acknowledged for their support of the Horizon Europe DN METAVISION project (GA 101072415). Views and opinions expressed are however those of the authors only and do not necessarily reflect those of the European Union. The European Union cannot be held responsible for them.

This work was partly financed by FCT / MCTES through national funds (PIDDAC) under the R&D Unit Institute for Sustainability and Innovation in Structural Engineering (ISISE), under reference UID/04029/Institute for Sustainability and Innovation in Structural Engineering (ISISE), and under the Associate Laboratory Advanced Production and Intelligent Systems ARISE under reference LA/P/0112/2020.

8. REFERENCES

[1] L. Brillouin, "Wave propagation in periodic structures," 1946.

[2] S. John, "Strong localization of photons in certain disordered dielectric superlattices," *Phys. Rev. Lett.*, vol. 58, pp. 2486–2489, Jun 1987.

[3] M.-H. Lu, L. Feng, and Y.-F. Chen, "Phononic crystals and acoustic metamaterials," *Materials Today*, vol. 12, no. 12, pp. 34–42, 2009.

[4] B. Wan, L. Zhu, X. Ma, T. Li, and J. Zhang, "Characteristic analysis and structural design of hollow-core photonic crystal fibers with band gap cladding structures," *Sensors*, vol. 21, no. 1, 2021.

[5] J. Redondo, D. Ramírez-Solana, and R. Picó, "Increasing the insertion loss of sonic crystal noise barriers with helmholtz resonators," *Applied Sciences*, vol. 13, no. 6, 2023.

[6] A. Bevilacqua, G. Iannace, I. Lombardi, and A. Trematerra, "2d sonic acoustic barrier composed of multiple-row cylindrical scatterers: Analysis with 1:10 scaled wooden models," *Applied Sciences*, vol. 12, no. 13, 2022.

[7] V. Romero-García, C. Lagarrigue, J.-P. Groby, O. Richoux, and V. Tournat, "Tunable acoustic waveguides in periodic arrays made of rigid square-rod scatterers: theory and experimental realization," *Journal of Physics D: Applied Physics*, vol. 46, p. 305108, jul 2013.

[8] X. Hu, C. T. Chan, and J. Zi, "Two-dimensional sonic crystals with helmholtz resonators," *Phys. Rev. E*, vol. 71, p. 055601, May 2005.

[9] Y. B. Chong, *Sonic crystal noise barriers*. Open University (United Kingdom), 2012.

[10] O. Umnova, K. Attenborough, and C. M. Linton, "Effects of porous covering on sound attenuation by periodic arrays of cylinders," *The Journal of the Acoustical Society of America*, vol. 119, pp. 278–284, 01 2006.

[11] International Organization for Standardization, *ISO 355:2003*, 2003. Available at: `https://www.iso.org/standard/34545.html`.

[12] Y. Miki, "Acoustical properties of porous materials-generalizations of empirical models-," *Journal of the Acoustical Society of Japan (E)*, vol. 11, no. 1, pp. 25–28, 1990.

DOI: 10.61782/fa.2025.0219



FORUM ACUSTICUM
EURONOISE 2025

COMPARATIVE ANALYSIS OF LIGHTWEIGHT METAMATERIAL PARTITIONS FOR ENHANCED ACOUSTIC PERFORMANCE AND PERCEPTUAL SOUND EVALUATION

M. Ribera[1,2*] **B. Van Damme**[2] **A. Pereira**[1]
P. Amado Mendes[1] **J. Zhang**[3] **L. Godinho**[1]
[1] Universidade de Coimbra, ISISE, ARISE, Department of Civil Engineering, Portugal
[2] EMPA, Laboratory for Acoustics/Noise Control, Switzerland
[3] Test Division, Siemens Digital Industries Software, Leuven, Belgium

ABSTRACT

Locally resonant acoustic metamaterials have shown significant potential to enhance acoustic insulation in lightweight partitions, though typically only within narrow bands. We previously developed a highly efficient numerical model of a metamaterial partition to address the coincidence dip of a single panel using equally tuned resonators. This study introduces multiresonant configurations, optimized via a genetic multi-objective algorithm, to broaden the resonators' impact on diffuse transmission loss near the critical frequency while minimizing the added mass. Comparative analyses between equally tuned and multiresonant systems are performed, evaluating both acoustic and psychoacoustic metrics to investigate the relationship between varying mass ratios and perceptual features. The findings aim to inform the design of lightweight, high-performance acoustic partitions for diverse environments.

Keywords: *acoustic metamaterials, sound transmission loss, optimization, building acoustics, sound quality*

1. INTRODUCTION

Locally resonant metamaterials have emerged as a cutting-edge solution for lightweight, high-performance sound insulation, addressing challenges where traditional methods struggle to meet environmental and mass constraints [1]. Their unique ability to manipulate wave propagation through tailored resonant structures has drawn increasing attention from both academia and industry, leading to diverse applications across multiple sectors.

Multiresonant structures have been explored as a means to enhance sound transmission loss by extending the bandwidth of attenuation. This can be achieved through the incorporation of multiple resonators within a unit cell (UC) [2] or through multimodal optimized resonators [3]. Both approaches enable the formation of multiple band gaps within a target frequency range, effectively reducing structural vibrations and noise transmission. Given the complexity of designing such systems, advanced optimization techniques —particularly topology optimization and generative inverse methods— represent some of the most promising approaches for developing realizable multimodal metamaterials [4].

This study aims to compare the acoustic performance of metamaterial-based building partitions configured with either equally-tuned or multiresonant systems, represented as independent mechanical resonators. Leveraging an efficient hybrid modeling approach, we implement a genetic algorithm for multi-objective optimization, enabling to obtain a Pareto front or set of optimal solutions. Evaluation is then conducted using both objective acoustic metrics, such as the weighted sound reduction index, and psychoacoustic metrics to assess perceptual annoyance. For this case study, we focus on single-leaf building partitions and specifically target the critical frequency dip under diffuse sound incidence.

*Corresponding author: marco.ribera@empa.ch.
Copyright: ©2025 M. Ribera et al. This is an open-access article distributed under the terms of the Creative Commons Attribution 3.0 Unported License, which permits unrestricted use, distribution, and reproduction in any medium, provided the original author and source are credited.

2. MODELING AND OPTIMIZATION

To enable the optimization and psychoacoustic study of the metamaterial partition, a computationally efficient model is required. This section outlines the hybrid numerical-analytical modeling approach used to evaluate the sound transmission loss of the partition wall.

2.1 Sound Transmission Loss

The partition wall is modeled with beam elements using an efficient Finite Element (FE) model in 1D, as detailed in [5]. The host-structure consists of standard 1/2" Gypsum board panels with density $\rho = 820$ kgm^{-3}, Young's modulus $E = 3.2$GPa, Poisson's ratio $\nu = 0.262$ and loss factor $\eta = 0.1$.

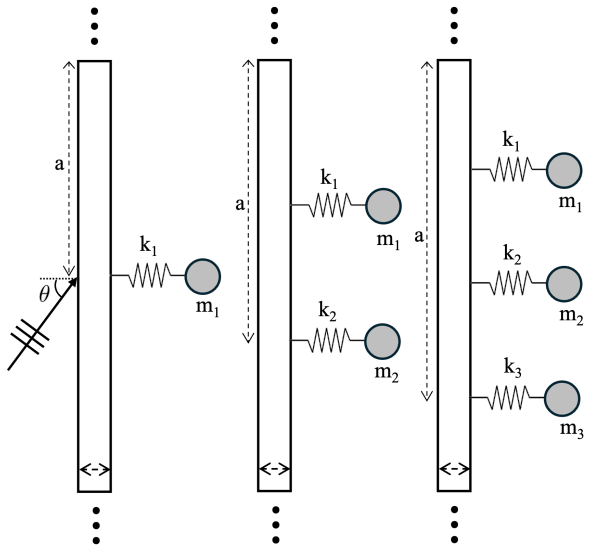


Figure 1. Representative scheme of modeled UCs.

A single unit cell (UC) is modeled using periodic Bloch-Floquet boundary conditions, which significantly reduce computational costs by limiting the domain to a representative repeating unit. Figure 1 presents a representation of the UC, illustrating three configurations: single, double, and triple resonator systems. Each resonator is represented as a vibrating spring-mass element with a single translational degree of freedom and massless attachment point.

The transmission coefficient of the periodic infinite structure, τ_∞, is determined as the ratio of radiated to incident sound pressure. The radiated pressure is approximated using the computed velocity of the vibrating panel, given by $|p_{\text{rad}}| = Z_0|v|$, where Z_0 is the air characteristic impedance and v is the velocity derived from nodal displacements. For a given plane wave incidence angle θ, the corresponding sound reduction index or sound transmission loss is obtained as $R_\theta = -10\log_{10}(\tau_\infty)$.

Although computationally efficient, R_θ is limited by its assumption of a single incidence angle and an infinitely extended structure, which does not accurately represent real-world conditions. In practical scenarios, sound waves arrive from multiple angles, interacting with a finite panel. To address this, additional analytical computations are performed to approximate a more realistic transmission loss, integrating the transmission coefficient over all incident angles

$$\tau_{\text{d}}(\omega) = \frac{\int_{\theta=0}^{\pi/2} \tau_f(\omega,\theta)\cos(\theta)\sin(\theta)\,\text{d}\theta}{\int_{\theta=0}^{\pi/2} \cos(\theta)\sin(\theta)\,\text{d}\theta}, \tag{1}$$

where $\tau_f = \tau_\infty(\sigma_R \cos\theta)$ is the transmission coefficient of the finite structure [6]. The acoustic domain is taken into account through the radiation efficiency σ_R, obtained from the real part of the normalized radiation impedance averaged over the azimuth angle [7]. A panel measuring 1.5 × 1.25 m is assumed for all computations, following ISO 10140 [8], which defines this size for laboratory measurements of sound insulation of building elements with a small test opening. Finally, the diffuse incidence sound transmission loss of the finite structure can be obtained by $R = -10\log_{10}(\tau_{\text{d}})$.

2.2 Multiobjective Optimization

Optimization is performed using a genetic algorithm with two cost functions: one aimed at maximizing the sound transmission loss R_θ around the critical frequency and another minimizing the added mass ratio M_{r}, given by the ratio between the added resonators m_r and the host structure's UC mass m_p, which can be defined as:

$$\varphi_1 = \frac{1}{\left(\int_{f_l}^{f_u} R_{\theta,\text{meta}}(f, f_{res}, M_{\text{r}}, \eta_{\text{r}}) - R_{\theta,\text{bare}}(f)\,\text{d}f\right)^2}, \tag{2}$$

$$\varphi_2 = M_{\text{r}} = m_r/m_p. \tag{3}$$

To prevent resonators from being tuned to the same resonance frequency f_{res}, constraints are imposed on the frequency range assigned to each resonator. This range is evenly subdivided based on the number of resonators in a given configuration. The optimization bounds for frequency, f_l and f_u, are set to 1500 Hz and 3500 Hz, respectively, corresponding to the typical coincidence range for gypsum board panels [5]. Additionally, the mass ratio is constrained between 0.01 and 0.5 to ensure lightweight solutions. A structural damping factor η_r of 5% is assumed for all resonators, implemented as a complex stiffness term. This value is chosen based on typical values obtained in realizable resonant elements [2].

To enhance the genetic algorithm's ability to explore the solution space thoroughly and avoid convergence to local minima, a population size of 500 is used in MATLAB's `gamultiobj` function. Optimization is performed at grazing incidence, as this approach has been shown to yield equivalent results with significantly reduced computation time in comparison to diffuse incidence optimization [5]. On average, a single run takes 45 seconds on a 10-core M1 Pro CPU. The resulting Pareto front consists of 175 solutions, as shown in Figure 2.

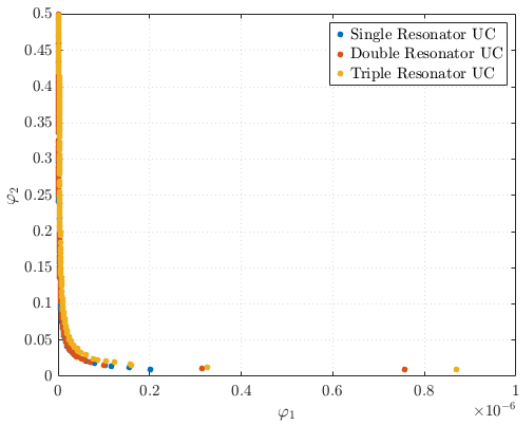


Figure 2. Pareto front of modeled UCs.

By computing the diffuse sound transmission loss for each solution point using Equation 1, the single-value rating R_w can be determined according to ISO 717-1 [9]. The resulting ratings can be then plotted as a function of the mass ratio (Figure 3) for each resonator configuration.

In terms of the weighted sound reduction index, sound insulation improves steadily with increasing mass ratio.

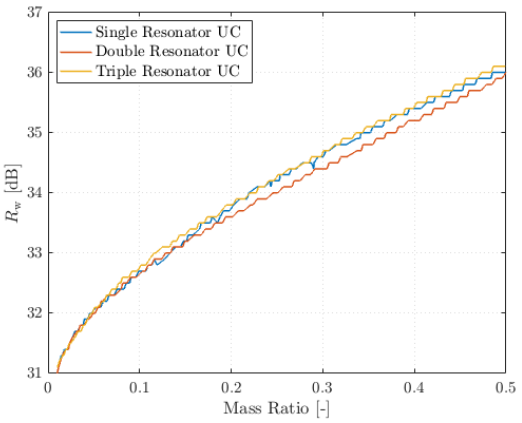


Figure 3. Weighted sound reduction index in function of mass ratio.

However, for the critical dip in gypsum board panels, the improvements achieved with multi-resonant configurations appear too small to be significant. This is because R_w accounts for the overall increase in sound insulation across one-third-octave frequency bands from 100 Hz to 3150 Hz and is not designed to capture narrowband improvements in R, such as those introduced by metamaterials. Taking the pareto optimal solution (i.e. the points of each pareto front closer to the origin) we can plot the optimal solution found for each resonator configuration (Figure 4).

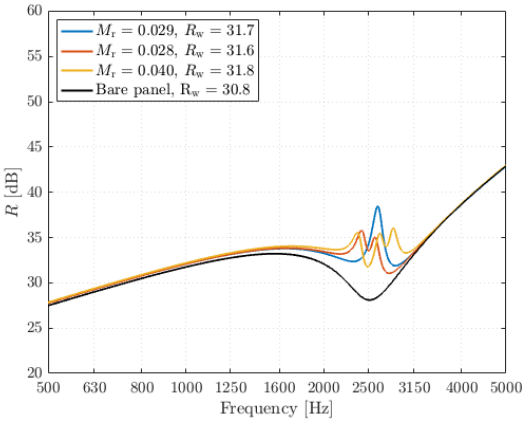


Figure 4. Sound reduction curves for pareto optimal solutions.

2.3 Sound quality evaluation

A sound quality evaluation, incorporating psychoacoustic metrics, was conducted to explore additional assessment criteria for the metamaterial partitions. The optimized Pareto front solutions were analyzed using their random incidence curves, computed across the complete audible range with a 10 Hz frequency resolution.

The impulse response for each solution point was obtained by applying an inverse Fourier transform to the transmission magnitude. A random phase spectrum, generated from precomputed values between 0 and 2π, was added to the transmission spectrum to ensure a more accurate translation of the signal into the time domain [10]. Finally, the impulse response was convolved with a pink noise signal.

For this study, the Psychoacoustic Annoyance (PA) metric was employed, as it integrates multiple perceptual attributes —including loudness, tonal characteristics, and temporal structure— into a single measure [11]. It is calculated as:

$$\mathrm{PA} = N_5 \left(1 + \sqrt{w_S^2 + w_{FR}^2}\right) \tag{4}$$

$$w_S = \begin{cases} (S - 1.75) \cdot 0.25 \log(N_5 + 10) & S > 1.75 \\ 0 & S \leq 1.75 \end{cases} \tag{5}$$

$$w_{FR} = \frac{2.18}{N_5^{0.4}}(0.4F + 0.6R) \tag{6}$$

where N_5 is the percentile loudness in sones, S is the sharpness metric, F the fluctuation ratio, and R the roughness metric. These psychoacoustic metrics were computed using MATLAB according to ISO 532-1 [12], and a virtual calibrated microphone with a 1 kHz reference signal assuming a SPL meter reading of 84 dB.

The computed annoyance values plotted against the mass ratio, are shown in Figure 5. Across all configurations, annoyance levels were lower than those of the bare panel. For mass ratios below 5%, the configurations exhibited similar annoyance values. However, as the mass ratio increased, differences became more pronounced. Notably, the triple-resonator configuration achieved the greatest reduction in annoyance, with its advantage becoming increasingly significant at higher mass ratios.

Beyond a 20% added mass ratio, perceived annoyance plateaued —unlike the single-value rating, which suggested a steady improvement in sound insulation with increasing M_r. This discrepancy can be attributed to the trend in loudness (Figure 6), as loudness carries the highest perceptual weighting in annoyance calculations. Additionally, higher M_r values lead to a more pronounced dip in insulation following the resonators' peak performance. This trend is reflected in the Sharpness metric, which consistently increases with M_r across all configurations.

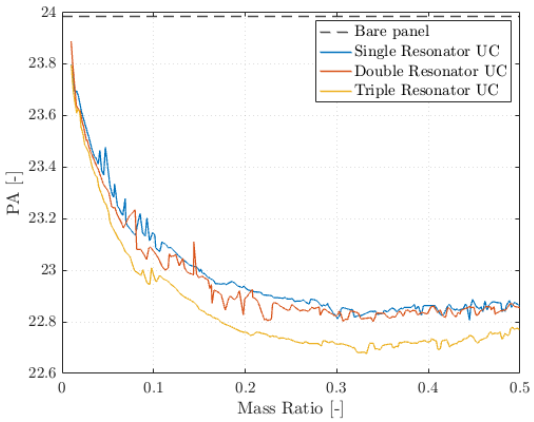


Figure 5. Zwicker's Annoyance metric of the optimized metamaterial panels.

3. CONCLUSION

This work presents an efficient modeling and optimization approach for a partition wall with multiple local resonators, designed to enhance sound insulation around the critical frequency while minimizing the added mass ratio. Additionally, psychoacoustic metrics are introduced as an evaluation tool, complementing traditional single-value ratings by providing deeper insights into specific configurations. This holistic approach is particularly relevant for applications where human acoustic comfort is a priority. Future research could explore additional psychoacoustic metrics and their integration into the optimization process.

4. ACKNOWLEDGMENTS

We gratefully acknowledge the European Commission for its support of the Marie Sklodowska Curie program through the Horizon Europe DN METAVISION project (GA 101072415).Views and opinions expressed are however those of the authors only and do not necessarily reflect those of the European Union. The European Union cannot be held responsible for them.

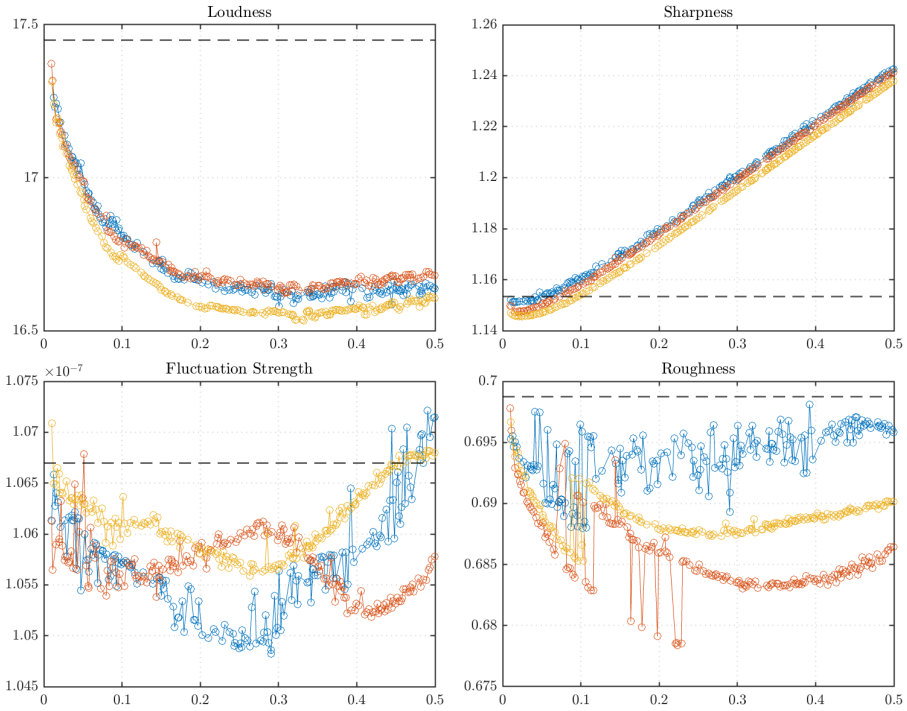


Figure 6. Psychoacoustic metrics computed in function of mass ratio.

This work was partly financed by FCT / MCTES through national funds (PIDDAC) under the R&D Unit Institute for Sustainability and Innovation in Structural Engineering (ISISE), under reference UID/04029/Institute for Sustainability and Innovation in Structural Engineering (ISISE), and under the Associate Laboratory Advanced Production and Intelligent Systems ARISE under reference LA/P/0112/2020.

5. REFERENCES

[1] Y. Zhang, J. Zhang, Y. Li, D. Yao, Y. Zhao, Y. Ai, W. Pan, and J. Li, "Research progress on thin-walled sound insulation metamaterial structures," in *Acoustics*, vol. 6, pp. 298–330, MDPI, 2024.

[2] F. Alves Pires, W. Desmet, and C. Claeys, "Design strategies for narrow and broadband noise and vibration reduction through distributed resonators," 2023.

[3] D. Giannini, M. Schevenels, and E. P. Reynders, "Topology optimization design of multi-modal resonators for metamaterial panels with maximized broadband vibroacoustic attenuation," *Journal of Sound and Vibration*, vol. 595, p. 118691, 2025.

[4] S. Dedoncker, C. Donner, R. Bischof, L. Taenzer, and B. Van Damme, "Generative inverse design of multimodal resonant structures for locally resonant metamaterials," *Engineering with Computers*, pp. 1–17, 2025.

[5] M. Ribera, B. Van Damme, A. Pereira, P. Amado Mendes, and L. Godinho, "Modeling and optimization of a lightweight metamaterial partition for improved sound transmission loss," in *Proc. of TecniAcustica 2024 Congress and Conference*, (Faro, Portugal), 2024.

[6] J. Allard and N. Atalla, *Propagation of sound in porous media: modelling sound absorbing materials*. John Wiley & Sons, 2009.

[7] J. Brunskog, "The forced sound transmission of finite single leaf walls using a variational technique," *The Journal of the Acoustical Society of America*, vol. 132, no. 3, pp. 1482–1493, 2012.

[8] ISO 10140-2: 2021, "Acoustics—laboratory measurement of sound insulation of building elements—part 2: Measurement of airborne sound insulation," 2021.

[9] ISO 717-1: 2013, "Acoustics—rating of sound insulation in buildings and of building elements—part 1: Airborne sound insulation," 2013.

[10] A. Moorhouse, "Virtual acoustic prototypes: Listening to machines that don't exist," *Acoustics Australia*, vol. 33, no. 3, p. 97, 2005.

[11] E. Zwicker and H. Fastl, *Psychoacoustics: Facts and models*, vol. 22. Springer Science & Business Media, 2013.

[12] ISO 532-1: 2017, "Acoustics—methods for calculating loudness—part 1: Zwicker method," 2017.

DOI: 10.61782/fa.2025.0428



FORUM ACUSTICUM
EURONOISE 2025

HIERARCHICAL LABYRINTHINE METAMATERIALS FOR LOW FREQUENCY NOISE ABSORPTION APPLICATIONS

Pérez Compte, Eloi[1*] **Nistri, Fabio**[1] **Zambila, Liviu**[2]
Bergamini, Andrea[2] **Gliozzi, Antonio**[1] **Shtrepi, Louena**[3] **Bosia, Federico**[1]
[1] Department of Applied Science and Technology, Politecnico di Torino, Turin, Italy
[2] Swiss Federal Laboratories for Materials Science and Technology, EMPA, Dübendorf, Switzerland
[3] Department of Energy, Politecnico di Torino, Turin, Italy

ABSTRACT

We present a proof-of-concept experiment demonstrating the efficient noise absorption of a 3-D printed metamaterial panel. The panel consists of an arrangement of unit cells designed using a fractal-inspired geometry from which a relation between the level of iteration and resonance frequency is derived. An analytical model and numerical simulations are used to study the absorption characteristics of the single labyrinthine units, and optimization methods derived from the causality principle are employed to find the optimal arrangement of unit cells to enhance the absorption performance in the low frequency range ($\sim$ 300 Hz). The performance of the panel is experimentally validated in fully anechoic room, using an impulsive sound source separation technique. Results show close to ideal values of absorption at the desired frequency of operation in a subwavelength regime with a wavelength to thickness ratio of 27.5 for a panel 50 mm thick. This work suggests a design procedure for noise-mitigation panel solutions and provides experimental evidence of the versatility and effectiveness of hierarchical coiled-up metamaterials in providing tunable low-frequency sound attenuation with relatively thin structures.

Keywords: *Hierarchical, Labyrinth, Broadband, Low frequency, Panel*

*__Corresponding author__: eloi.perezcompte@polito.it.
__Copyright__: ©2025 Pérez Compte et al. This is an open-access article distributed under the terms of the Creative Commons Attribution 3.0 Unported License, which permits unrestricted use, distribution, and reproduction in any medium, provided the original author and source are credited.

1. INTRODUCTION

Acoustic metamaterials (AMs) have gained growing attention because of their exotic properties, which are not found in naturally occurring materials. AMs design parameters offer the possibility of developing a new generation of acoustic absorbers and diffusers tailored for a desired frequency spectrum and with sub-wavelength sizes [1] and low-frequency absorption [2]. AMs are thus able to achieve high performance in terms of noise reduction, and simultaneously reduce the size and weight of structures [3], going beyond the limitations of conventional technologies based on porous absorbers or resonant structures coupled with air [4]. AMs are employed as acoustic sound absorbers with which perfect absorption can be obtained at their resonance frequency, by design. This occurs for a critical coupling condition: thermo-viscous losses are exactly balanced by energy leakage [5]. Thus, to extend the effect on a broader frequency range, the design concept of 'rainbow trapping' is exploited combining acoustic resonators with variable parameters, and hence working frequencies [6] or systems with asymmetric porous absorbers [7].

With the aim of reducing the volume occupied by these AM absorbers, 'labyrinthine' or 'coiled' structures were brought up [8, 9]. These are based on exploiting acoustic wave propagation in curved channels of sub-wavelength cross-section, giving rise to an extremely high effective refractive index (and thus to a decrease of the effective wave speed). Fractal inspired design with the aim of tuning the resonance frequency range, reducing the volume encumbrance have been investigated and experimentally characterized [9–11]. Thus, labyrinthine and space-filling AMs have provided a very

convenient and efficient way to achieve sound control in large frequency ranges, especially in the subwavelength regime, by tuning geometrical design parameters (e.g. channel tortuosity or elongation and cavity size). This kind of adaptability could largely benefit noise absorption applications at small to medium scale, in comparison with thick conventional acoustic absorbing materials. At present, few studies in the literature have presented detailed acoustic characterization studies on large structures such as metamaterial-based panels, and none on labyrinthine ones, to the best of our knowledge. Further, the need emerges to investigate labyrinthine AM performance on structures that are closer to potential operating conditions, i.e. in free field.

2. METHODS

2.1 Unit cell design

The design of the Unit Cell (UC) shown in fig. 1a corresponds to the second iteration of the Wunderlich curve. This system can be simplified to two connected waveguides of different cross section for the orifice and the coiled-up channel. While the orifice acts as a pore, the channel works as a quarter wavelength resonator and its resonance frequency can be computed as $f_0 = 4c/L_{eff}$, where $c = 343$ m/s is the speed of sound in air, and L_{eff} is the effective length of the tube. With the same design principle of [9], a 3D UC is designed (fig. 1b). Due to the narrower size of both the orifice and the channel compared to the wavelength, thermoviscous losses have to be taken into account. These physical dissipation mechanisms effectively absorb sound energy, leading to perfect absorption when they are balanced by the acoustic energy leakage by radiation from the UC: the matching of the two correponds to the critical coupling condition [5]. Thus combining the Stinson's and Johnson-Champoux-Allard models for the coiled-up channel and the orifice, respectively, we can compute the impedance Z_s at the aperture of the UC, from we which we can compute the absorption spectrum:

$$\alpha = 1 - \left| \frac{Z_s - Z_0}{Z_s + Z_0} \right|^2, \qquad (1)$$

where Z_0 is the characteristic impedance of air. A parametric study of the analytical model is carried out (fig.1c) to study the dependence of maximum sound absorption on the edge size a, ranging from $20-60$ mm, and the aperture cross section t from approximately $10-50$ mm. From this four-parameter map a UC of size $a = 20$ mm and $t = 15$ mm is selected and numerically characterized, showing good agreement with the analytical prediction (fig.1d).

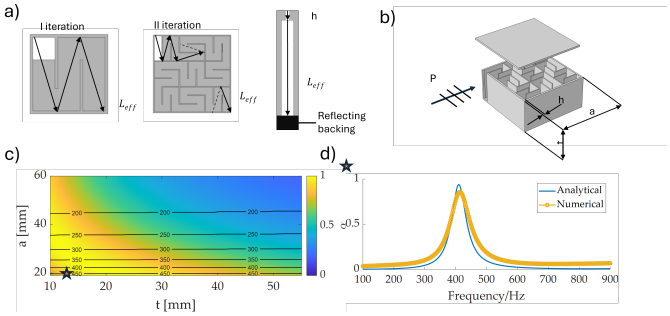


Figure 1. (a) Exploded view of the UC and its lid. (b, left) Top view of the coiled up structure and effective length path with (right) schematic of its equivalent model. (c) Four parameter map of absorption peak as a function of the UC cell size a and thickness t

2.2 Panel design and fabrication

Establishing the target frequency for sound absorption around 300 Hz, we use analytical data to design the sound absorption panel. This can be achieved by exploiting various UCs of different effective length, corresponding to different resonance frequencies arranged in a exponential progression, to maximize the absorption spectrum over the target frequency range [3]. An AM panel is thus designed, consisting of differently sized UCs. The internal wall thickness of each UC is 2 mm and their height of 20 mm. 6 UCs have been selected with edge size a ranging from 38.5 to 40.2 mm and assembled together in a row, as shown in fig. 2a. The complete panel consists of the combination of 87 macro-cells arranged in the plane (2b), to total size of $775 \times 640 \times 43$ mm. The UCs are selected so as to provide different absorption peaks, whose superposition provides a wider working frequency spectrum in the chosen target frequency range. The overall impedance of the panel can be calculated as the combination in parallel of the impedances of the single UCs. The polyamide panel is then manufactured through selective laser sintering (SLS), a technique where each level is sintered by a laser beam, directed by a scanning system. The process is repeated, and the prototype is built layer by layer.

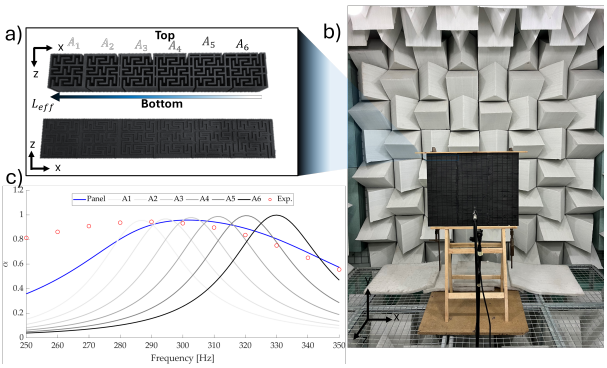


Figure 2. (a) Top and bottom view of the macrocell featured by 6 UCs of different edge size, i.e. L_{eff}. (b) Experimental setup in anechoic chamber. (c) Absorption spectra analytical prediction compared with the experimental result.

2.3 Experimental determination of sound reflection characteristics

In order to measure the performance of the hierarchical panel in a free field condition, all measurements were performed in a fully anechoic room. The setup consisted in placing the panel and the loudspeaker in front of each other and fixing their respective position. Then, between the panel and the loudspeaker, a grid of microphones should be placed, in order to measure the scattered field from different positions and take account of the boundary effects such as the diffraction by the edge of the panel. In our case, repeated measurements with a single microphone were made, placing it at each respective point of the grid, in order to have an equivalent system. The position of the panel and the microphone in the anechoic room can be seen in figure 2b. The measurement grid points were chosen along the horizontal and vertical middle line of the panel. The input signal sent to the loudspeaker consisted of three consecutive exponential sweeps, each generated according the the following function:

$$x(t) = \sin\left[2\pi f_1 \exp\left(\frac{N f_s \ln(f_2/f_1)}{T} t\right)\right] / f_s \,, \quad (2)$$

where f_s is the sampling rate, f_1 and f_2 are the start and end frequencies of the sweep, N is the length of the signal and T is the sweep duration.

2.4 Signal processing

Once the output signal $y(t)$ is measured, some processing must be done to get the reflection index of the panel.

First, for each microphone placement, three consecutive sweeps were sent. By performing a cross-correlation with the input signal, we could synchronize and cut the sweeps in order to perform an average, removing a significant amount of noise. The signal was then deconvoluted to obtain the impulse response $h(t)$ by means of a convolution with the inverse sweep defined as:

$$x_{\text{inv}} = x(-t) \exp\left[-\frac{t}{T} \ln\left(\frac{f_2}{f_1}\right)\right]. \quad (3)$$

For obtaining the reflected field without the contribution of the incident field, we used the signal subtraction technique. It consists in subtracting the free field impulse response to which an appropriate amplitude correction has been applied, to the scattered field impulse response.

In order to avoid unwanted reflections, an Adrienne window composed of a leading edge having a left Blackman-Harris shape, followed by a flat portion and closing with a trailing edge having a right Blackman-Harris shape was applied to the impulse response. With that, we were able to compute the Fast Fourier Transform (FFT) of both the incident and the reflected fields in order to get the Frequency Response Functions (FRF) $H_{i,k}(f)$ and $H_{r,k}(f)$ for each measurement point k of the incident and reflected fields respectively.

The reflection index is calculated as follows:

$$R(f) = \frac{1}{n} \sum_{k=1}^{n} \left[\frac{|H_{r,k}(f)|^2}{|H_{i,k}(f)|^2} C_{\text{geo},k}\right] \quad (4)$$

where the correction factor for geometrical divergence $C_{\text{geo},k}$ is:

$$C_{\text{geo},k} = \left(\frac{d_{r,k}}{d_{i,k}}\right)^2, \quad (5)$$

and $d_{i,k}$ is the distance from the front panel of the loudspeaker to the k-th measurement point and $d_{r,k}$ is the distance from the front panel of the loudspeaker to the source and microphone reference plane and back to the k-th measurement point following specular reflection.

Finally, he absorption coefficient of the panel is simply:

$$\alpha = 1 - |R|^2. \quad (6)$$

3. RESULTS

The absorption coefficient has been calculated analytically and measured experimentally in the range of frequencies where the largest absorption was expected. The length of the unit cells were tuned for the absorption peaks of the quarter-wavelength resonators to cover a the interval of 280 to 330 Hz as shown in figure 2c. Experimentally, the panel has a wide peak at the same interval with perfect absorption close to 290 Hz, shown by the red dots in figure 2c.

Indeed, the panel has a thickness of the order of 50 mm, and it can absorb acoustic waves of wavelength $\lambda = c/f$ of the order of one meter. With a wavelength to thickness ratio of ≈ 27.5 at the frequency for perfect absorption, the resonator shows sub-wavelength absorption properties, covering a range of about 50 Hz around the perfect absorption frequency before the absorption decays.

4. CONCLUSIONS

The present work shows the effectiveness of the designed panel in terms of broadband, low frequency, subwavelength absorption. The conception based in labyrinthine quarter-wavelength resonators optimizes their length to a limited surface area, allowing for low-frequency absorption capabilities in a limited space. The arranged design broadens the absorption spectrum while maintaining the width of the panel. Analytically, the design features of the panel were determined and tuned to achieve perfect absorption in the wanted frequency range. A polyamide panel was built, and, using a microphone measurement grid in an anechoic room and proper signal processing, we observed how the panel exhibits perfect absorption close to the analytical target frequency range, with a high wavelength to thickness ratio of about 27.5 confirming the subwavelength quality of the design.

5. REFERENCES

[1] X. Zhang, Z. Qu, and H. Wang, "Engineering acoustic metamaterials for sound absorption: from uniform to gradient structures," *Iscience*, vol. 23, no. 5, 2020.

[2] S. Kumar and H. P. Lee, "The present and future role of acoustic metamaterials for architectural and urban noise mitigations," in *Acoustics*, vol. 1, pp. 590–607, MDPI, 2019.

[3] J. Li, X. Wen, and P. Sheng, "Acoustic metamaterials," *Journal of Applied Physics*, vol. 129, no. 17, 2021.

[4] F. Langfeldt and W. Gleine, "Improved sound transmission loss of glass wool with acoustic metamaterials," *Proc 26th ICSV*, pp. 7–11, 2019.

[5] V. Romero-García, G. Theocharis, O. Richoux, and V. Pagneux, "Use of complex frequency plane to design broadband and sub-wavelength absorbers," *The Journal of the Acoustical Society of America*, vol. 139, no. 6, pp. 3395–3403, 2016.

[6] N. Jiménez, V. Romero-García, V. Pagneux, and J.-P. Groby, "Rainbow-trapping absorbers: Broadband, perfect and asymmetric sound absorption by subwavelength panels for transmission problems," *Scientific reports*, vol. 7, no. 1, p. 13595, 2017.

[7] J. Boulvert, T. Humbert, V. Romero-García, G. Gabard, E. R. Fotsing, A. Ross, J. Mardjono, and J.-P. Groby, "Perfect, broadband, and subwavelength absorption with asymmetric absorbers: Realization for duct acoustics with 3d printed porous resonators," *Journal of Sound and Vibration*, vol. 523, p. 116687, 2022.

[8] Z. Liang and J. Li, "Extreme acoustic metamaterial by coiling up space," *Physical review letters*, vol. 108, no. 11, p. 114301, 2012.

[9] F. Nistri, V. Kamrul, L. Bettini, E. Musso, D. Piciucco, M. Zemello, A. Gliozzi, A. Krushynska, N. Pugno, L. Sangiuliano, *et al.*, "Efficient broadband sound absorption exploiting rainbow labyrinthine metamaterials," *Journal of Physics D: Applied Physics*, vol. 57, no. 24, p. 245111, 2024.

[10] Y. Liu, W. Xu, M. Chen, T. Yang, K. Wang, X. Huang, H. Jiang, and Y. Wang, "Three-dimensional fractal structure with double negative and density-near-zero properties on a subwavelength scale," *Materials & Design*, vol. 188, p. 108470, 2020.

[11] A. O. Krushynska, F. Bosia, and N. M. Pugno, "Labyrinthine acoustic metamaterials with space-coiling channels for low-frequency sound control," *Acta Acustica United with Acustica*, vol. 104, no. 2, pp. 200–210, 2018.

DOI: 10.61782/fa.2025.0869

FORUM ACUSTICUM EURONOISE 2025

THE INFLUENCE OF SAMPLE SIZE ON THE RESULTS OF SOUND INSULATION MEASUREMENT CONDUCTED IN SMALL COUPLED REVERBERATION ROOMS

Dorota Młynarczyk[1*] **Katarzyna Baruch-Mazur**[1] **Agata Szeląg**[1]
[1] Cracow University of Technology, Poland

ABSTRACT

The paper presents the results of acoustic insulation measurements conducted in a unique small size coupled reverberation rooms. The volumes of the rooms are approximately 1.36 m³ each, which imply a lower measurement range limit of 400 Hz for the actual dimensions of the samples (and 50 Hz for 1:8 scale testing). Aim of the research was to evaluate the measurement setup and assess its suitability for studying the properties of various types of material including metamaterials. The influence of sample size and geometry on measurement outcomes was analyzed by comparing four square windows of side lengths equal 8.5, 17.5 cm, 35 cm and round 65 cm, and two rectangular windows of dimensions equal 12.5 × 25 cm and 25 × 50 cm. Five samples of different materials with various thicknesses selected to have diverse properties affecting wave propagation were studied: steel 0.6 and 1 mm thick, PMMA 3.8 mm thick, MDF 3.2 mm thick, Sylomer (HD 100) 12.5 mm thick and gypsum board 12.5 mm thick were measured. The analysis showed that the influence of the size and shape of the window on the obtained insulation coefficient dependent on the test frequency and the stiffness of the sample material.

Keywords: *sound insulation, small sized coupled reverberation rooms, acoustic insulation measurements, sample geometry*

[*] ***Corresponding author***: *dorota.mlynarczyk@pk.edu.pl*
Copyright: *©2025 First author et al. This is an open-access article distributed under the terms of the Creative Commons Attribution 3.0 Unported License, which permits unrestricted use, distribution, and reproduction in any medium, provided the original author and source are credited.*

1. INTRODUCTION

In laboratory acoustic testing of the sound insulation properties of materials and structures, three standardized methods can be used [1]. The first involves measuring the sound reduction index (R) of a sample placed between two reverberation rooms. The second method also uses the sound reduction index (R), where the sample separates a source room with a free-field condition from a receiving room with a reverberant field. The third approach is based on the measurement of transmission loss (TL) in an impedance tube. The article focuses on the research of the sound reduction index (R) using coupled reverberation rooms.

The measurement of the sound reduction index (R) using coupled reverberation rooms is described in the ISO 10140 series of standards, from part 1 to part 5. For material testing in full size reverberation rooms, the standard requires the use of a sample with a surface area of 10 m^2. Various methods of mounting the sample and sealing are also recommended [2]. In the literature, there is little information on the influence of sample size and shape on the results obtained. Wareing et al. demonstrated that sample size can significantly affect sound transmission loss, depending on the construction of the tested element [3]. In a subsequent study, the authors observed that smaller samples exhibited higher sound transmission loss at frequencies below the coincidence frequency [4]. On the other hand, study made by Mleczko remarked that small baffles have lower sound insulation compared to the large baffle [5]. The differences noted are more significant in the case of the square-shaped baffle. However, the author himself points out that the study should be expanded with more samples and repetitions. Therefore, the aim of this study is to address the gap in the literature by examining how different sample sizes and shapes affect the sound

reduction index measured in small size coupled reverberation rooms.

2. METHODS

The tests were performed on a unique small size coupled reverberation room [6, 7]. The stand consists of two reverberation rooms, each with a volume of 1.36 m³, designed as irregular hexagonal enclosures constructed from 20 mm thick plexiglass panels. The stand is a 1:8 scale of the coupled reverberation rooms located at AGH University of Science and Technology [8]. The rooms are connected by a shared wall that includes measurement windows for mounting test samples. The dimensions of the windows and corresponding measurement samples are summarized in Table 1.

Table 1. Measurement windows and samples shape and size.

Sample No.	Sample Shape	Sample Size [cm]
1	square	8.5 x 8.5
2	square	17.5 x 17.5
3	square	35.0 x 35.0
4	square	65.0 x 65.0
5	rectangular	12.5 × 25.0
6	rectangular	25.0 × 50.0

For investigating the influence of sample size on sound insulation measurement results in smallcoupled reverberation rooms, a selection of materials was made to encompass a wide range of thicknesses, internal structures, and, most importantly, diverse properties affecting wave propagation. The tested materials included:

- Steel – thicknesses: 0.6 mm;
- Steel – thicknesses: 1.0 mm;
- PMMA (Polymethyl methacrylate) – thickness: 3.8 mm;
- MDF (Medium-density fibreboard) – thickness: 3.2 mm;
- Sylomer (HD 100) – thickness: 12.5 mm;
- Gypsum board – thickness: 12.5 mm.

The sound reduction index (R) was measured in accordance with ISO 10140-4 [2] within the frequency range of 400–20,000 Hz. The test sample was mounted in the measurement window, securely pressed against the frame, and sealed with putty to prevent leakage.

3. RESULTS

This section presents the results of sound reduction index (R) measurements conducted for samples of various sizes and shapes. The aim was to evaluate how these parameters influence the measured acoustic insulation performance. Selected data sets are shown to illustrate the observed trends and differences. The full dataset was analyzed for consistency and repeatability across repeated measurements.

Each sample was measured three times. For each repetition, the sample was removed and reinserted into the measurement opening, then carefully resealed with putty. As part of the study, all results were compiled for each measurement opening and for each sample material across different opening sizes.

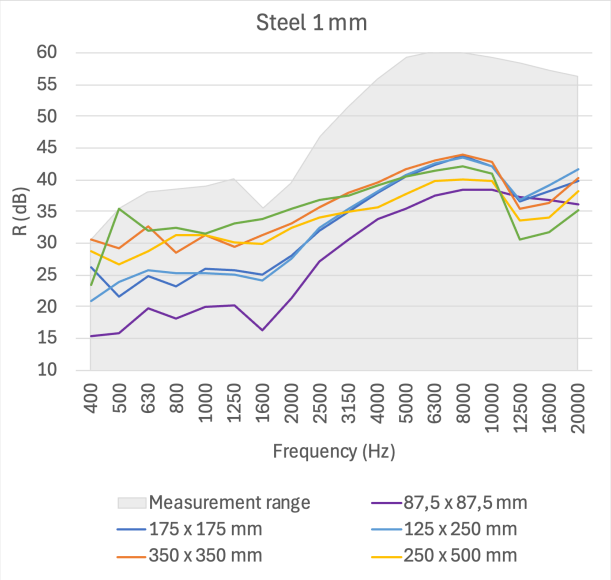


Figure 1. Sound reduction index (R) measured for a 1 mm thick steel sample of various shapes and sizes: 8.5 cm × 8.5 cm, 17.5 cm × 17.5 cm, 35cm × 35 cm, 65 cm × 65 cm, 12.5 cm × 25 cm and 25 cm × 50 cm.

This article presents selected sets of the test results. Figure 1 shows sound reduction index (R) measured for a 1 mm thick steel sample of various shapes and size.

The analysis of the sound reduction index (R) for steel samples with a thickness of 1 mm, tested in openings of varying sizes, revealed a significant influence of sample size on the measurement results. Above the coincidence frequency, an increase in sample size corresponds to a decrease in R, whereas below this frequency, larger samples exhibit higher R values. A similar trend was observed for the other tested materials, including steel samples with a thickness of 0.6 mm, PMMA with a thickness of 3.8 mm, MDF with a thickness of 3.2 mm, Sylomer HD 100 with a thickness of 12.5 mm, and gypsum board with a thickness of 12.5 mm. For clarity and conciseness, the results and analysis presented here are based on the 1 mm steel samples as a representative example.

4. CONCLUSIONS

The study demonstrated that the influence of window size and shape on the measured sound reduction index depends both on the test frequency and the stiffness of the sample material. In the case of the steel samples, a clear correlation was observed between sample size and R values, with the direction of this effect varying depending on whether the frequency was above or below the coincidence frequency.

These findings are more consistent with the observations made by Mleczko [5], who reported lower sound insulation for smaller baffles, particularly in square configurations. In contrast, the results diverge from those reported by Wareing et al. [4], especially in the context of frequencies below the coincidence frequency. This suggests that the relationship between sample size and sound insulation may be more complex than theoretical assumptions typically indicate and is likely influenced by factors such as boundary conditions and panel stiffness.

5. ACKNOWLEDGMENTS

This work is part of the project LIDER13/0030/2022 entitled “Innovative metamaterial cladding increasing the sound insulation of partitions by reducing resonance bands” funded by The National Centre for Research and Development (NCBR), Poland.

6. REFERENCES

[1] L. Weber, H. Schreier, Klaus-Dieter Brandstetter. "Measurement of sound insulation in laboratory-comparison of different methods," *Proc. of the International Conference on Acoustics*, (Rotterdam), pp. 701–704, 2009.

[2] International Organization for Standarization. ISO 10140-4 Acoustics—LaboratoryMeasurement of Sound Insulation of Building Elements— Part 4: Measurement Procedures and Requirements; International Organization for Standarization: Geneva, Switzerland, 2011.

[3] R. R. Wareing, J. L. Davy, J. R. Pearse, “Effects of sample construction, sample size and niche depth on measured sound transmission loss,” *Proc. of the INTER-NOISE and NOISE-CON Congress and Conference*, Vol. 249, No. 5, pp. 2641-2650, Institute of Noise Control Engineering, 2014.

[4] R. R. Wareing, J. L. Davy, J. R. Pearse, “Variations in measured sound transmission loss due to sample size and construction parameters,” *Applied Acoustics*, vol. 89, pp. 166-177, 2015.

[5] D. Mleczko, “Testing the airborne sound insulation of reduced size baffles with different dimensions,” *Vibrations in Physical Systems*, vol. 34, no. 2, 2023.

[6] A. Szeląg, K. Baruch-Mazur, K. Brawata, B. Przysucha, D. Mleczko: “Validation of a 1: 8 scale measurement stand for testing airborne sound insulation,” *Sensors*, vol. 21, no. 6663, 2021.

[7] K. Baruch, A. Majchrzak, B. Przysucha, A. Szeląg, T. Kamisiński: “The effect of changes in atmospheric conditions on the measured sound absorption coefficients of materials for scale model tests,” *Applied Acoustics*, vol. 141, pp. 250-260, 2018.

[8] D. Mleczko, T. Wszołek: „Effect of diffusing elements in a reverberation room on the results of airborne sound insulation laboratory measurements,” *Archives of Acoustics*, vol. 44, pp. 739–746, 2019.

DOI: 10.61782/fa.2025.0478

FORUM ACUSTICUM EURONOISE 2025

INJECTION MOULDED LOCALLY RESONANT RINGS FOR VIBRATION MITIGATION IN PIPES

K. Steijvers[*1,2] **U. Arasan**[1,2] **C. Claeys**[2,3]
L. Van Belle[2,3] **E. Deckers**[1,2]

[1.] KU Leuven, Campus Diepenbeek, Department of Mechanical Engineering, Wetenschapspark 27, 3590 Diepenbeek, Belgium
[2.] Flanders Make@KU Leuven
[3.] *KU Leuven, Department of Mechanical Engineering, Celestijnenlaan 300B box 2420, 3001 Heverlee, Belgium*

ABSTRACT

Locally resonant metamaterials (LRMs) are promising lightweight solutions for targeted vibration attenuation, achieved by incorporating resonant elements on a sub-wavelength scale into a host structure. However, manufacturability limitations form a major hurdle in their industrial adoption. Additive manufacturing offers design versatility but lacks industrial-scale throughput, while high-throughput techniques such as laser cutting or punching of resonators often require labor-intensive assembly steps to create the LRM. Furthermore, manufacturing-induced deviations in geometry and material properties can significantly impact the vibro-acoustic LRM performance, often necessitating multiple design iterations. This study addresses these challenges by proposing the high-throughput injection moulding process while accounting for process-induced influences on the LRM performance using a process simulation-informed design workflow. Injection moulding enables robust and large-scale manufacturing, whereas dedicated process simulations allow incorporating manufacturing process influences in the vibro-acoustic performance predictions. This work therefore presents the design, manufacturing and experimental validation of an injection moulded LRM demonstrator to treat a noise radiation problem around a targeted vibration mode of an aluminum pipe. The achieved vibration reduction and good agreement with the model-based predictions demonstrate the strong potential of injection moulding for the mass-manufacturing of LRMs with targeted performance.

Keywords: Locally resonant metamaterials, Injection moulding, Demonstrator

1. INTRODUCTION

The machine and transportation industries are increasingly adopting lightweight design to reduce material use, energy consumption and environmental impact. However, the resulting lightweight structures often come with deteriorated noise and vibration characteristics, impacting our health and well-being. As

[*] ***Corresponding author***: kristof.steijvers@kuleuven.be
Copyright: *©2025 K. Steijvers et al. This is an open-access article distributed under the terms of the Creative Commons Attribution 3.0 Unported License, which permits unrestricted use, distribution, and reproduction in any medium, provided the original author and source are credited.*

a solution, locally resonant metamaterials (LRMs) are currently investigated [1]. They allow for targeted frequency zones with strong vibration attenuation, so-called stop bands. These resonance-based stop bands result from the addition of resonant elements on or into a flexible host structure on a sub-wavelength scale [2].

LRMs are typically composed of periodic assemblies of identical unit cells (UC). Although periodicity is not strictly necessary for resonance-based stop bands, this facilitates the use of periodic structure modelling to predict wave propagation and stop bands early in the design stage. Dispersion curves are typically calculated from a finite element (FE) model of the representative periodic UC, combined with Bloch-Floquet periodicity boundary conditions [2].

Building upon these prediction tools, the potential of LRMs has been widely explored and demonstrated through many conceptual LRM realizations. Nevertheless, the manufacturing of LRMs is found to be challenging since the integration of resonant elements often leads to geometrically intricate geometries. Consequently, additive manufacturing (AM) has become a strong enabler in the manufacturing of LRMs. However, additive manufacturing techniques currently do not reach the throughput for commercial applications [3]. In attempts to transition towards more mass-manufacturing suited processes, laser cutting and milling have been used to produce separate resonators. Moreover, LRM structures have been manufactured using thermoforming and punching [4], requiring a post-production milling or bending step to realize the resonators. Recently, the injection moulding (IM) has been proposed for the manufacturing of resonators [5] [6]. This process comes with low costs when used for mass-manufacturing and allows achieving lower process variability in terms of dynamic LRM response compared to AM [5].

Besides the difficulties to manufacture LRM geometries, manufacturing processes also affect their geometry and material properties. Consequently, the final LRM geometry and material properties often deviate from the initial design, leading to off-design LRM performance. In case of AM, large deviations in the material properties together with anisotropy and geometric inaccuracies have led to off-design LRM stop bands [4]. In forming and bending processes, the stiffness and local density of the sheets is strongly affected by the difficult to control local thinning during forming. These effects significantly affect the resonator eigenfrequencies and, consequently, the resulting stop band. To achieve the desired LRM performance after manufacturing, design and material property updating is currently performed in iterative design steps. In case of the IM process, dedicated IM process simulations have been proposed to predict and account for process influences during the LRM design phase [7]. It is shown that for three different resonator geometries, manufactured in two materials, incorporating IM process simulations in the LRM design flow significantly improves the eigenfrequency predictions.

In view of practice-oriented solutions, LRMs have been often demonstrated as add-on resonators or resonator patches which can be applied to existing host structures. This is often more appealing to industry since it allows for LRM demonstration of existing products and machinery. For example, laser-cut resonators have been manufactured and manually glued to plates, and pipes [8] in academic demonstrators. Similar approaches have been reported to attach resonators manufactured with IM in [5].

Although successful IM mass-manufacturing of resonators with reduced off-design performance has been demonstrated, prior work has focused mainly on basic resonator geometries. This study advances the state-of-the-art by leveraging IM together with process simulation-informed LRM performance predictions to realize and validate a mass-manufacturable ready-to-use LRM solution for vibration mitigation in pipes. This allows to align the envisaged performance during LRM design and the as-manufactured performance and so reduces possible design iterations. As a demonstrator case, a aluminum tube similar to the one used in [8] is selected for targeted vibration attenuation around a dominant radiating mode. To facilitate LRM assembly, a snap-fit connection is integrated.

2. PROBLEM DESCRIPTION

The demonstrator targets an acoustically relevant ovalling mode in an aluminum pipe, inspired by [8]. An experimental modal analysis (EMA) is performed for modal identification and FE-model updating.

2.1 Experimental modal analysis

An impact hammer test is conducted to experimentally characterize the modal behavior of the pipe. To this end, the pipe is divided into a regular grid of 88 measurement points. The grid consists of 11 measurement points along the pipe's length, which are axially patterned 8 times around the circumference leading to a 45 degree shift between each measurement array. The pipe is suspended

in a free-free configuration and excited at each point using a PCB 086C03 modal hammer in a roving hammer sequence. The radial acceleration response is captured in measurement point 1 (0°, 0 mm length) and 29 (45°, 600 mm length) using two PCB ICP lightweight accelerometers. The point-to-point FRFs are calculated over 5 averages in Siemens Simcenter Testlab using the H_v approach. To avoid leakage, an exponential decaying window is applied to the excitation signal while a Hanning window is applied to the response signal.

2.2 Numerical eigenmode calculations

In order to accurately predict the LRM performance, a representative numerical host structure model is desired. To this end, a structural dynamic FE model of the host structure is created in Siemens Simcenter to calculate both the undamped eigenfrequencies and the acceleration response under force excitation. Specifically, a quadratic CQUAD8 shell mesh with an element size of 10 mm is applied to the pipe's midsurface. The pipe dimensions and mass are measured and listed Table 1. The pipe's real eigenfrequencies and forced response are calculated over a frequency range of 50-1200 Hz. For the latter, a normal unit force is applied at the first measurement point location, and the acceleration response is measured at all other measurement points. The predicted eigenfrequencies and forced response are compared to the experimentally determined modal frequencies and FRFs, whereafter the Young's modulus of the aluminum (69 GPa) is updated to the value of Table 1 to obtain good agreement between the numerical eigenfrequency of the first ovalling mode and the corresponding experimental value.

Table 1: Main dimensions and material properties of the targeted pipe host structure.

Length [mm]	1002	Young's Modulus [GPa]	81.8
Outer diameter [mm]	100.25	Density [kg/m^3]	2711
Wall thickness [mm]	2	Poisson ratio [/]	0.33
Mass [g]	1742.4		

Comparing the experimentally and numerically obtained FRFs (Figure 1a), three eigenfrequencies are identified in the frequency range under 1000 Hz. Figure *1*b, presents an overview of the FE-based real eigenmodes and the modal displacements obtained through the EMA at the peak frequencies. For the first frequency of 582 Hz, the ovalling and torsional mode are present, both of which were also identified from the EMA deformation pattern around 581 Hz. At 627 Hz, an ovalling pattern is observed, varying along the axial direction, in superposition with the first pipe bending mode. A similar modal deformation is observed in the EMA at approximately 620 Hz. Around 825 Hz, both the simulation and EMA show a similar out-of-plane behavior of higher order.

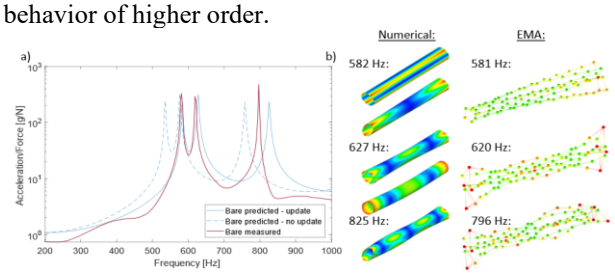


Figure 1: a) Comparison of the experimentally obtained and numerically predicted FRF of the bare pipe, b) numerically obtained real eigenfrequencies and experimentally obtained model displacement patterns at the determined resonance frequencies.

3. IDEALIZED METMAMATERIAL DESIGN

To design an LRM for targeting the first ovalling tube mode, both the LRM's vibro-acoustic performance and the IM manufacturability must be taken into account. Therefore, an idealized LRM design is optimized for a suitable eigenfrequency and hence stopband location, together with a maximized Modal Effective Mass (MEM) to increase the stop band width [2]. For three different designs resulting from the optimization, the IM manufacturability is assessed separately in Section 4.

3.1 Snap-fit ring concept

For the LRM design, eight resonant elements will be used, placed over each 45 degrees of the pipe circumference, in accordance with [8]. Whereas in this work the resonators have been manually glued to the host structure, a punched out add-on ring shaped concept has been shown in [4]. These rings allow to assemble multiple resonators simultaneously which reduces the risk op resonator misalignments, which potentially influence the final LRM performance. However, the resonator masses were still glued manually, hindering cost-effective series production. Building upon these studies, the proposed LRM in this work consists of two

identical ring sections with each four evenly distributed integrated resonators as illustrated in Fig. 2a. The ring sections can be assembled around the pipe using a snap-fit mechanism to form a closed ring. This simplifies LRM assembly by eliminating additional components. Furthermore, by moulding only half a ring at a time, the required mould size, melt volume and clamping force can be reduced, reducing the overall cost. As a result, the moulded product is ready-to-use, requiring no additional components for LRM assembly.

3.2 Resonator tuning and optimization

To create the resonance based stop band, an often-used cantilever beam type resonator is selected and adapted for integration on the ring base, targeting the first out-of-plane eigenmode. Fig. 2a,b show the design dimensions and the targeted first flexural eigenmode for a clamped ring circumference. The parameterized resonator dimensions are optimized towards a maximum MEM for the targeted eigenmode. The frequency tuning range was set around the ovalling frequency of the tube between 560-600 Hz, still allowing for a small misalignment to increase the design freedom. An exact tuning is in this stage redundant since the design will later still be tailored for IM manufacturing. Parameter ranges are set for the eight main resonator dimensions (Table 2). For these ranges, specific IM design rules are already accounted for. For example, wall thicknesses are kept under 4 mm to prevent voids caused by high shrinkage. Moreover, X_{Mass} is already set equal to X_{Leg} to facilitate filling during IM manufacturing. Lastly, the thickness of added ribs should not exceed 60% of the base structure thickness. In case the resonator is seen as a pure rib, the Y_{Leg} parameter would be highly restricted. However, the resonator is not a typical rib which is attached to the base structure over the entire rib length, therefore, this rule is not already incorporated. The selected material is ABS NOVODUR P2H-AT from INEOS (E = 2240 MPa, ρ = 1050 kg/m^3 , ν = 0.4). The optimization is performed using the hybrid adaptive SHERPA algorithm in Siemens Simcenter HEEDS across 400 designs. The objective function is formulated as follows:

Maximize MEM,

Subjected to:

$$560\ \text{Hz} \leq F_1 \leq 600\ \text{Hz}$$

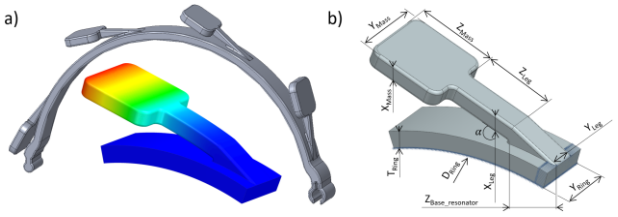


Figure 2: a) Conceptual LRM ring section with snap-fit mechanism, b) main dimensions of the LRM ring and resonator, c) targeted first out-of-plane eigenmode.

Three designs with high MEM are selected and will be evaluated for manufacturability in the following section. Table 2 lists the obtained dimensions, eigenfrequency and MEM for these designs. For all three designs, the resonator dimensions Y_{Mass} and Z_{mass} are maximized, as expected from the objective. The main differences between the designs relate to the resonator angle α, the cantilever beam length Z_{Leg} and the cantilever beam width Y_{Leg}. For design 2, the high MEM is obtained due to the high value of Y_{Leg}, whereas both the MEM and Y_{Leg} are smaller in design 3. Comparing design 2 to design 1, the steeper resonator angle in design 1 leads to only a minor difference in performance. Although design 2 offers the best MEM, it is the further away from the targeted ovalling eigenfrequency at 582 Hz.

Table 2: Baseline, min and max value of the design parameters for the optimization, followed by the obtained dimensions, eigenfrequency and MEM for the three selected designs.

Parameter	Baseline	Min	Max	Design 1	Design 2	Design 3
Y_{Ring}	8	4	10	10	10	10
$Z_{Base_resonator}$	7	3	10	7	10	8
α	95	85	100	95	85	95
Z_{Leg}	18	10	25	17	17	14
X_{Leg}	3	2	3.5	3	3	3
Y_{Leg}	6	3	Y_{Ring}-1	8	8	5
X_{Mass}	X_{Leg}	-	-	3	3	3
Y_{Mass}	9	Y_{Leg}+3	14	14	14	14
Z_{Mass}	8	8	14	14	14	14
D_{Ring}	100.5	-	-	100.5	100.5	100.5
T_{Ring}	3	-	-	3	3	3
			Mode 1 [Hz]	570.1	568.5	575.6
			MEM [g]	0.69	0.7	0.62

4. LRM MANUFACTURABILITY AND MOULD

In this section, the idealized design is further assessed and tailored for IM manufacturing by taking into account

IM related process effects such as the volumetric shrinkage. The optimal resonator design is selected and the mould design and LRM manufacturing are explained.

4.1 Manufacturability assessment of the resonator

The IM process requires specific design guidelines to enhance mouldability and avoid defects such as sink holes, part warpage and internal stresses. These effects relate to the filling, packing and cooling steps of the IM process. During the filling stage, a speed controlled forward motion of the screw ensures precise injection. When the mould cavity is almost filled, the process transitions from speed to pressure regulation at the switch-over point. From this point, a defined packing pressure is maintained at the back of the screw to fill the remainder of the cavity and compensate for material shrinkage during part solidification. Here, the available packing time strongly depends on the part solidification, thin sections like the resonator leg might solidify rapidly, hindering material entrance in thicker part sections such as the resonator mass. When the packing is finalized, the screw retracts, preparing the next shot of material while the part continues to cool.
To predict the filling, solidification and shrinkage of the resonator, commercial IM simulations are used [7]. The process settings are set to rule of thumb starting values. More specifically, the injection speed is set to 40 cm^3/s and a packing pressure is held for 10 seconds at a level of 80% of the maximum filling pressure. The melt and mould temperature are set to 240 °C and 60 °C, respectively, in accordance with the material datasheet. The resulting volumetric shrinkage and solidification time are assessed for the three resonator geometries. The volumetric shrinkage is used to compare the designs' sensitivity for sink marks, while the solidification time provides an estimate of the available packing time.

4.2 Resonator mouldability

Fig. 3 illustrates the maximum volumetric shrinkage and molten core at the time step that the first design has a fully solidified cross section, after 17 seconds of cooling. Design 1 and 2 exhibit higher volumetric shrinkage at the resonator base compared to design 3, which is attributed to the larger Y_{Leg}. This indicates a higher risk of sink marks after manufacturing. In design 3, the risk of sink marks is reduced at the expense of a lower MEM due to the lower $Y_{Resonator}$ parameter. From the molten core values, the resonator arm of design 3 freezes around 17 seconds, while design 1 and 2 still have a molten connection between the ring and the resonator mass. Therefore, design 1 and 2 allow for longer packing time, as compared to design 3. However, 17 seconds is already longer than the value used in practical moulding given the typical small gates used for the overall part melt entrance, causing the gate freezing time to be the main bottleneck for the packing phase. As a result, the difference in $Y_{Resonator}$ will not impact the filling of the resonator mass significantly, which can also be concluded from the similar shrinkage values in the resonator mass. Based on these considerations and outcomes, design 3 is selected as the final resonator geometry.

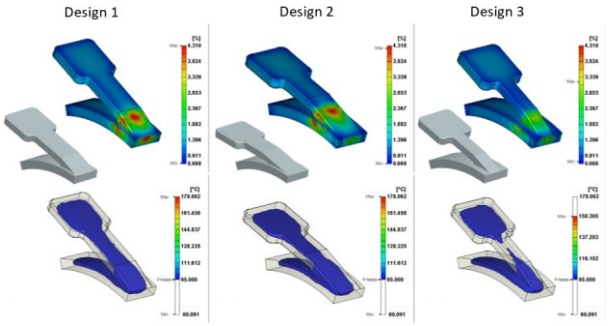


Figure 3: Volumetric shrinkage [%] (top) and molten core [°C] (bottom) after 17 seconds for the three selected designs.

4.3 Final LRM product and mould design

From the above ring filling calculations, the warpage after cooling resulted in 0.65 %, therefore, the entire design was scaled with this value to ensure a proper fit to the tube. With the resonator and ring dimensions in place, the design is further tailored for IM manufacturing. To this end, draft angles are incorporated in the entire design except for the inner diameter to facilitate demoulding while maintaining a large contact area with the pipe. Furthermore, all sharp corners are rounded to reduce internal stresses. Lastly, a cantilever-snap fit with a plug diameter of 4 mm is added and the LRM part design is further tailored for IM. These changes lead to the LRM design shown in Fig. 4a, for which a final resonator eigenfrequency of 571 Hz is obtained. To facilitate the moulding process, a 5 mm diameter runner is designed, and a submarine gate is selected. This gate type enables automatic part-gate separation during demoulding caused by the undercut which is present. The mould design includes two part

cavities, with the parting plane positioned at the product's center (Fig. 4b).

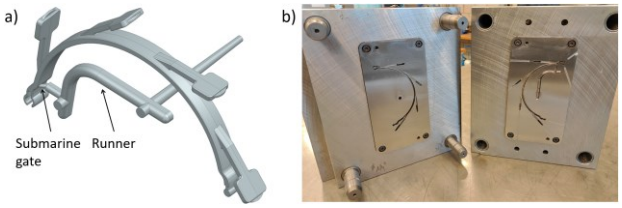


Figure 4: a) Final LRM and runner design, b) both cavity inserts positioned in the mould.

4.4 LRM manufacturing

The moulding is performed using a single screw electrical DEMAG ERGOTECH IntElect 50/330-100 IM machine. The maximal mould clamping force is 500 kN, while a 22 mm horizontal screw with a L/D ratio of 20 is used. The mould temperature is regulated using a EURO CHILLER 3FLOWS P 612/90 controller. The primary process parameters are listed in Table 3. During manufacturing, a cycle time of 21 seconds is maintained. To assemble the LRM, sixteen ring sections (Fig. 5a) are added to the tube (Fig. 5b), leading to 8 full ring additions with a intermediate spacing of 25 mm.

Table 3: Main IM process parameters.

Dosing volume [cm3]	16.3
Switch over point [cm3]	4.4
Melt temperature [°C]	240
Mould temperature [°C]	70
Packing pressure [MPa]	60
Packing time [s]	5
Cooling time [s]	20
Volumetric injection rate [cm3/s]	26.6

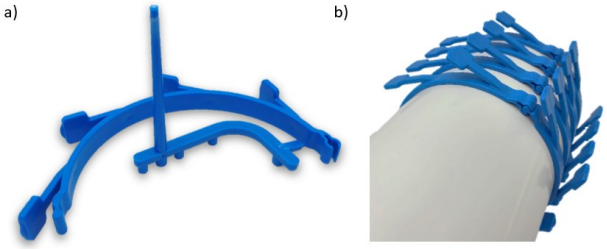


Figure 5: a) Manufactured LRM ring with runner, b) LRM rings assembled to the aluminium pipe.

5. RESONATOR AND LRM PERFORMANCE PREDICTIONS

The resonator eigenfrequencies and the LRM stop bands are predicted using the corresponding resonator and 25 mm UC FE-models. To this end, the manufacturing process-informed toolchain as proposed in [7] is used. This allows to account for process induced shrinkage and density during the predictions by transferring the deformed Boundary Layer Mesh (BLM) with distributed material density obtained from the IM simulation to structural FE. Therefore, an in-house material property mapping routine is used, in which the Scattered Interpolation [9] method is implemented in MATLAB. This method employs Delaunay triangulation to construct an interpolation function over the IM mesh. The material properties on the FE mesh are then computed using linear interpolation, ensuring smooth transitions. From the resonator FE model, the eigenfrequencies are calculated. Next, the resonator mesh is mated to host-structure for stop band calculation.

5.1 Deformed geometry and density distribution

With the final LRM, runner and gate design in place, a filling, packing and warpage simulation is conducted. Fig. 6 shows the resulting displacement of the base ring and resonators, along with the density distribution. The total displacement due to shrinkage and warpage consists of the displacement in the base ring and the displacement of the individual resonators. The ring inner diameter decreases which was already accounted for in the design to ensure a proper fit to the pipe. The resonator shrinkage is expected to lead to an increased eigenfrequency. Additionally, differences in shrinkage between the different resonators (res. 1-4) also result from the non-uniform shrinkage. The density distribution shows a decreased density at the resonator feet, in line with the shrinkage results from the manufacturability assessment in section 4.2. This density decrease at the

feet becomes more pronounced with increasing distance from the gate, as the extended flow length makes the shrinkage compensation during the packing phase more difficult. Overall, the resulting net density is 1030 kg/m^3, compared to the datasheet value of 1050 kg/m^3. The total predicted part mass is calculated to be 7.953 g.

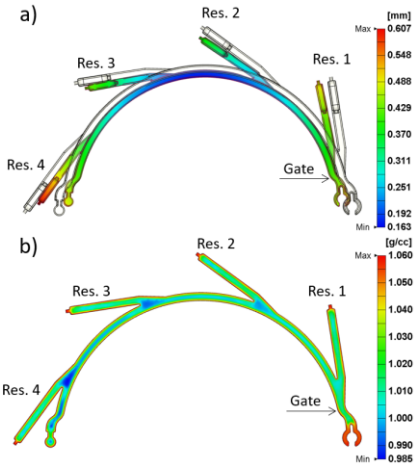


Figure 6: a) Displacement [mm] (deformation x10) and b) density distribution [g/cc] within the LRM ring obtained from IM simulation.

5.2 Eigenfrequency and stop band predictions

The resonator eigenfrequencies for an entire ring section are predicted in Siemens Simcenter using solution 103. A fixed boundary condition is applied on the inner and outer surfaces of the ring. Tab. 4 lists the predicted resonator eigenfrequencies in accordance with the numbering of Fig. 6.

Table 4: Resonator eigenfrequencies obtained form manufacturing-informed predictions.

Resonator 1 [Hz]	579.71
Resonator 2 [Hz]	579.71
Resonator 3 [Hz]	579.73
Resonator 4 [Hz]	580.60

As expected from the calculated model shrinkage and density distribution, all eigenfrequencies increase with respect to the original 571 Hz obtained after drafting. Again, only small differences appear among the resonators individually. This is expected, as the overall displacement and density distribution in the resonator cross-sections are uniform. Since the lower density of resonator 4 occurs in the resonator base, it does not significantly influence the resonator eigenfrequency.

Figure 2 compares the calculated dispersion curves for the bare and LRM case. For the bare tube, the cut-off frequency of the ovalling mode is at 582Hz. Due to the addition of the resonators and their interaction with the ovalling and bending wave, two new cut-on frequencies appear at 499.8 Hz and 665.9 Hz. The obtained stopband for the ovalling mode is (indicated in red) situated between 562.3 Hz and 665.9 Hz. A second bandgap is obtained in the bending wave branch between 562.3 Hz and 579.8 Hz result.

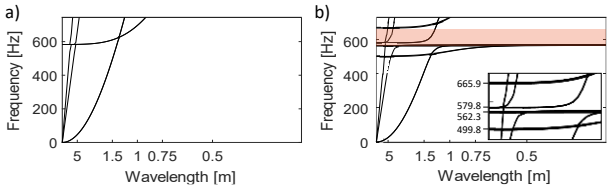


Figure 2: Obtained dispersion diagrams for the a) bare and b) LRM pipe.

6. LRM VALIDATION

For the LRM pipe with 8 fully assembled rings, the forced response is measured. The impact locations are chosen around the circumference, in front of the LRM rings while the response is captured behind the resonator ring additions (Fig. 13). To evaluate the influence of both the clamping and the mass of the rings on the pipe's response, both required to fasten the resonators to the pipe, an non-resonant ring case is created using the rings but removing the resonators, called the non-resonant ring case.

For the non-resonant ring case, the addition of the rings to the pipe clearly lowers the frequency of the first mode (ovalling) while only slightly influencing the second mode (bending). When adding the LRM rings, a clear decrease in the response between 553 Hz and 655 Hz is caused by the resonant effect of the LRM. This is in fair agreement with the predicted stop band between 562.3 Hz and 665.9 Hz. Furthermore, the first peak in the LRM curve around 500 Hz corresponds to the cut-on frequency of the ovalling mode in the LRM dispersion curve. Here the tube's and resonators' motion are in phase. After the stop band, a peak is observed in the FRF

around 655 Hz, which corresponds to the ovalling cut-on frequency after the stop band in the dispersion curve.

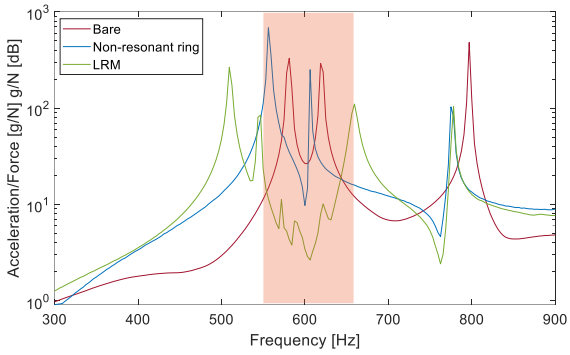


Figure 3: Measured vibration response of the bare, equivalent mass and LRM pipe.

7. CONCLUSION

IM allows for mass-manufacturing of LRM resonators whereas the incorporation of IM process simulation outcomes in the LRM performance predictions has been shown to reduce the off-design performance of resonators. This work builds upon these findings and demonstrates the design and manufacturing of a ready-to-use LRM solution. More specifically, the first ovalling mode of an aluminium pipe is experimentally determined, based on which an LRM ring with four resonators is designed for vibration treatment. To this end, three different resonator designs are found using parameter optimization, whereafter the manufacturability of the designs has been assessed using IM simulations. The final LRM is manufactured and experimentally characterized. The final LRM stop band is predicted using manufacturing-informed predictions, and good agreement is found with experimental pipe response measurements. The successful mass-manufacturing of a ready-to-use LRM with targeted as-manufactured performance facilitates the integration of LRMs in larger-scale designs and paves the way for mass-manufacturable lightweight products with superior NHV performance by design.

8. ACKNOWLEDGMENTS

The research of K. Steijvers (fellowship no. 1S63423N) and L. Van Belle (fellowship no. 1254325) is funded by a grant from the Research Foundation – Flanders (FWO). The Research Foundation Flanders (FWO) and São Paulo Research Foundation-Brazil (FAPESP) are gratefully acknowledged for their support through the bilateral research cooperation project (FWO no. G0F9922N, FAPESP no. 21/05510-3). This research was partially supported by Flanders Make, the strategic research centre for the manufacturing industry.

9. REFERENCES

[1] M. I. Hussein, et al., "Dynamics of phononic materials and structures: Historical origins, recent progress, and future outlook," *Appl. Mech. Rev.*, vol. 66, no. 4, Jul. 2014, doi: 10.1115/1.4026911.

[2] C. Claeys, et al., "On the potential of tuned resonators to obtain low-frequency vibrational stop bands in periodic panels," *J. Sound Vib.*, vol. 332, no. 6, pp. 1418–1436, Mar. 2013, doi: 10.1016/j.jsv.2012.09.047.

[3] X. Wu, et al., "Perspective of additive manufacturing for metamaterials development," Aug. 12, 2019, *Institute of Physics Publishing*. doi: 10.1088/1361-665X/ab2eb6.

[4] E. Deckers *et al.*, "Locally resonant vibro-acoustic metamaterials: applications at KU Leuven," in *DAGA 2021, (90-93)*,

[5] K. Steijvers, et al., "Injection moulding of resonators for locally resonant metamaterial production," in *AIP Conference Proceedings: The 2nd international symposium on plastics technology*, Aachen, Germany: American Institute of Physics, May 2024. doi: 10.1063/5.0192336.

[6] J. Yu, et al., "Mass production applicable locally resonant metamaterials for NVH applications," in *Proceedings of the 26th International Congress on Sound and Vibration, ICSV 2019*.

[7] K. Steijvers, et al., "Incorporating Manufacturing Process Simulations to Enhance Performance Predictions of Injection Moulded Metamaterials," *J. Vib. Eng. Technol. 2023*, vol. 1, pp. 1–13, Oct. 2023, doi: 10.1007/S42417-023-01159-1.

[8] A. Nateghi, et al., "Design and experimental validation of a metamaterial solution for improved noise and vibration behavior of pipes," *J. Sound Vib.*, vol. 455, pp. 96–117, Sep. 2019, doi: 10.1016/j.jsv.2019.05.009.

[9] I. Amidror, "Scattered data interpolation methods for electronic imaging systems: a survey," 2002, doi: 10.1117/1.1455013.

DOI: 10.61782/fa.2025.0495

FORUM ACUSTICUM EURONOISE 2025

ON THE RELATIONSHIPS BETWEEN MANUFACTURING PARAMETERS, GEOMETRICAL ACCURACY, AND VIBRATIONAL PROPERTIES OF SELECTIVE LASER SINTERED PA-12 BEAMS

Kryuchkov A.[1,2*] **Pavan M.**[1] **Claeys C.**[2,4] **Deckers E.**[3,4]

[1] Materialise NV, Leuven, Belgium
[2] Department of Mechanical Engineering, KU Leuven, Belgium
[3] Department of Mechanical Engineering, Diepenbeek, KU Leuven, Belgium
[4] Flanders Make @ KU Leuven, Belgium

ABSTRACT

Selective Laser Sintering (SLS) enables the production of complex structures, but ensuring their geometrical accuracy and material properties remains challenging due to many parameters that influence the final print quality. This study investigates the vibrational properties of PA-12 beams manufactured using SLS, focusing on the relationships between the manufacturing parameters, geometrical accuracy, and natural frequencies. The beams are evenly distributed across the build volume to investigate spatial and thermal effects on the quality of the part. Dimensional measurements are used to calculate the expected natural frequencies of the cantilever beams, which are then compared with the experimental results obtained using an automated impact hammer setup. The collected data visualizes the relationships between beam dimensions, resonant frequencies, and temperature of the printer bed. This data can further be used to optimize SLS manufacturing parameters for improved precision and mechanical performance of printed components, especially important in the design and reliable performance of produced metamaterials, where small deviations can significantly alter functional behavior.

*Corresponding author: alexander.kryuchkov@materialise.be.

Copyright: ©2025 Kryuchkov A. et al. This is an open-access article distributed under the terms of the Creative Commons Attribution 3.0 Unported License, which permits unrestricted use, distribution, and reproduction in any medium, provided the original author and source are credited.

Keywords: *Selective Laser Sintering, PA-12, Natural Frequencies, Additive Manufacturing Accuracy, Metamaterials*

1. INTRODUCTION

Selective Laser Sintering (SLS) is a powder bed additive manufacturing (AM) process that uses one or more lasers to selectively fuse polymer powder layer by layer, enabling the fabrication of complex self-supporting geometries without the need for molds or support structures [1, 2]. Polyamide-12 (PA-12) is a common SLS material valued for its mechanical properties. Achieving high dimensional accuracy in SLS parts is critical, as deviations can negatively impact both mechanical and functional performance [2].

However, maintaining this accuracy is challenging because of shrinkage and warping effects. These occur when the sintered layers cool and crystallize, resulting in geometric distortions [3]. Effective thermal management is therefore essential to mitigate these effects and ensure consistent replication of the intended design dimensions [3, 4]. Such precision becomes even more important in acoustically sensitive designs, where geometric inaccuracies can degrade performance. For example, a study of 3D printed air diffusers found that differences in surface quality and dimensional precision across AM methods significantly influenced acoustic performance [5]. Accurate part fabrication is therefore essential in acoustic applications that rely on tightly controlled geometries. An explicit link is made between the production accuracy of

SLS and the resulting vibro-acoustic properties in a study of a lightweight vibro-acoustic metamaterial demonstrator [6]. In another investigation focused on acoustic resonators, it is suggested that the deviation of the experimental results from the predicted peaks (theory and FEA) might have been caused by geometrical inaccuracies of the 3D-printing machine [7]. Additionally, surface roughness introduced during additive manufacturing has been shown to significantly affect acoustic performance [8]. There is also growing interest in using 3D printed structures for vibration and modal analysis [9].

This study investigates the vibrational performance of PA-12 cantilever beams fabricated across the SLS build volume. Specifically, it examines how dimensional variations and thermal history correlate with the natural frequencies of the beams. The objective is to determine whether certain process parameters significantly influence resonance behavior. This information could accelerate quality control processes in the future.

2. METHODS

2.1 Part Fabriction

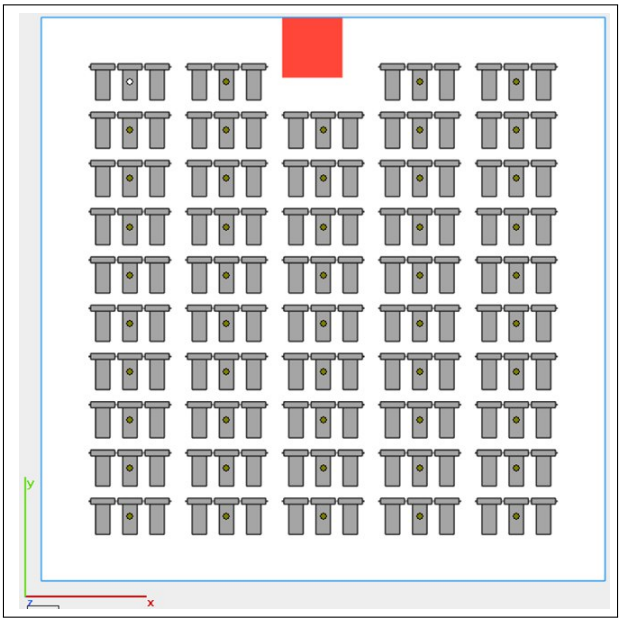


Figure 1. Top view of the printer bed beam layout.

The cantilever beam parts were manufactured using SLS on a Sindoh S100 laser sintering system. Each printed unit consists of three beam segments connected by a thin cylindrical bridge with a diameter of 1.5 mm. The base section of each beam is designed as a 5 × 5 × 20 mm³ block, while the beam portion extends 25 mm in length, 12 mm in width, and 2.5 mm in thickness. These dimensions are shown in millimeters in Figure 2.

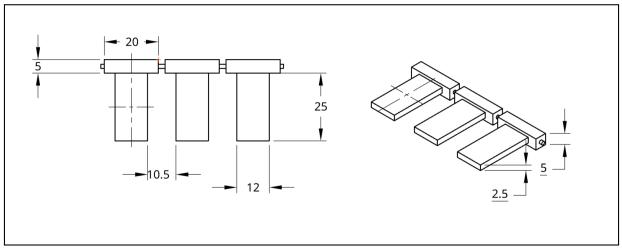


Figure 2. Dimensions of the beam set (mm).

To investigate spatial effects on part quality, the beam units were distributed evenly across the build volume. Individually, the beams form a 15 × 10 grid, which is stacked vertically for a total of 10 layers along the Z-axis. A margin of approximately 40 mm was maintained on all four sides of the print bed. Additionally, a 10 mm vertical offset was introduced below the first printed layer to help record thermal history. The spacing between adjacent parts was 12.5 mm in the X-direction, 10 mm in the Y-direction, and 20 mm in the Z-direction. Figure 1 illustrates the layout of the beam units on the printer bed. The red square in the rear region of the bed denotes a "no-build zone", designated for pyrometer temperature measurements.

All parts were printed in a single job using the same process parameters. A 1:1 mix of new and recycled PA-12 powder was used, with the bed preheat temperature maintained at 173°C. Although the print order reflects the digital label of a part, the actual scan pattern generally proceeded from the front-left to the back-right corner of the print bed, with the back row typically completed last within each layer. Upon completion, the build was allowed to cool gradually inside the chamber for four days.

All beams were labeled at the base, corresponding to their location. All three beam parts in one unit have the same X,Y, and Z label, and are distinguished by an additional number, i.e, X1Y2Z3B1, X1Y2Z3B2 and X1Y2Z3B3 with XYZ referring to the position of the unit in the build.

2.2 Geometrical Measurements

Only beams located in the odd-numbered Z-layers were measured. The primary dimensions — length, width, and thickness — were recorded using digital calipers. All measurements were taken at consistent locations across the parts. Length was measured once along the centerline of the beam (Figure 2, from base to tip. Additional measurements from the base to the left and right sides of the tip were also taken, however, only the central full-length measurement was used in the data analysis due to its greater reliability.

Width and thickness were each measured at three positions along the beam: near the base, at the midpoint, and near the tip. The centerline is shown as a dashed line in Figure 2. For data processing, the average of the midpoint and near-tip measurements was used. Measurements taken near the base were excluded from the average due to greater potential for deviation, as that region is influenced by proximity to the part's base feature.

2.3 Thermal Monitoring

The printer bed temperature was recorded using two instruments located inside the printer: the Optris CT LT pyrometer and the FLIR A655sc infrared (IR) camera. A custom script logged temperature data twice per layer: once before scanning and once before recoating the new layer. The pyrometer readings were used to correct the IR images, as the IR camera is more susceptible to heat deviations and artifacts. Each IR image was subsequently processed to determine the average temperature in the area surrounding each beam. Each beam had a square region positioned at its center, encompassing both the beam itself and the surrounding area on either side. The average temperature was then determined by averaging the pixel values within this selected square region. Certain spots were excluded from the analysis due to obstructions or dead pixels in the IR camera.

2.4 Vibrational Testing

Natural frequencies were extracted using the Grindosonic MK7 automatic impact hammer testing setup. Each beam was positioned on a piece of soft foam, placed directly above the microphone of the device. The impact hammer delivered a consistent tap to the part of the beam corresponding to the expected location of maximum displacement in the first natural frequency mode. The test was repeated three times per beam to ensure repeatability. Only the beams from the first printed layer were measured.

3. RESULTS

The SLS process yielded relatively small dimensional deviations in the length and width of the beams. However, thickness exhibited significantly larger deviations, primarily due to the small design value of 2.5 mm and the influence of shrinkage and warpage effects, as discussed in Section 1. This comparison is illustrated in Figure 3. While length and width deviations were generally centered around 0%, thickness deviations were consistently positive, ranging from approximately 9% to 20%.

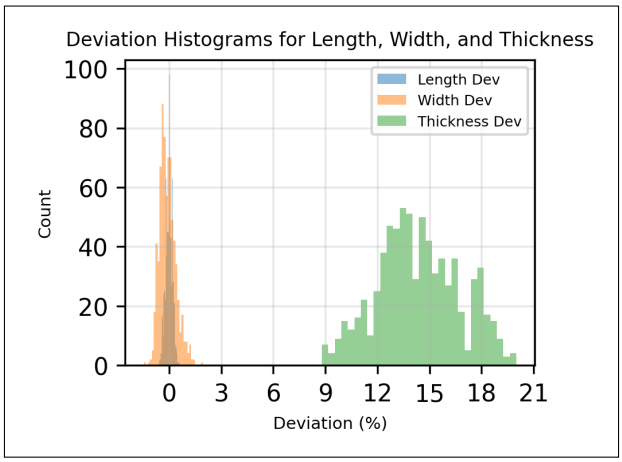


Figure 3. Percent deviation from the design values of beams' dimensions.

A closer look at the thickness distribution at layer Z3, shown in Figure 4, reveals that the thicker beams are concentrated on the right side, particularly near the back-right corner of the printer bed. This trend is also observable, to varying degrees, across the other measured layers.

Figure 5 shows the average temperature measured at each beam location. Uneven thermal distribution across the print bed is evident, with cooler temperatures concentrated near the center. In contrast, the highest recorded temperatures are observed near the back-right corner of the printer bed.

To compare thickness variations, Figures 6 and 7 display all thickness measurements plotted against their corresponding positions. Each data point is colored according to its print order. The front view in Figure 6 reveals an increase in thickness values from left to right, particularly noticeable in X indices 4 and 5. Figure 7 confirms

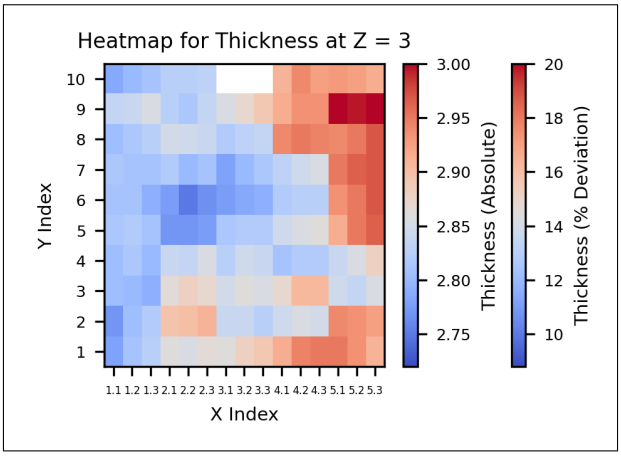


Figure 4. Heatmap of thickness measurements in layer Z3.

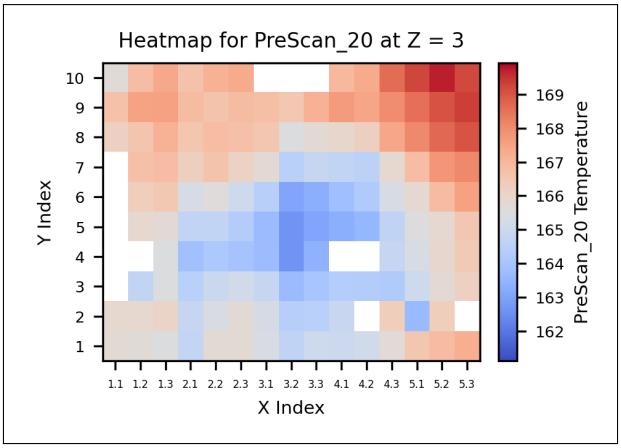


Figure 5. Heatmap of prescan temperature at the twentieth layer of parts at layer Z3 (obstructions and dead pixel measurements excluded).

that parts were generally printed from the front to the back of the bed and highlights a noticeable dip in thickness between Y indices 4 and 7.

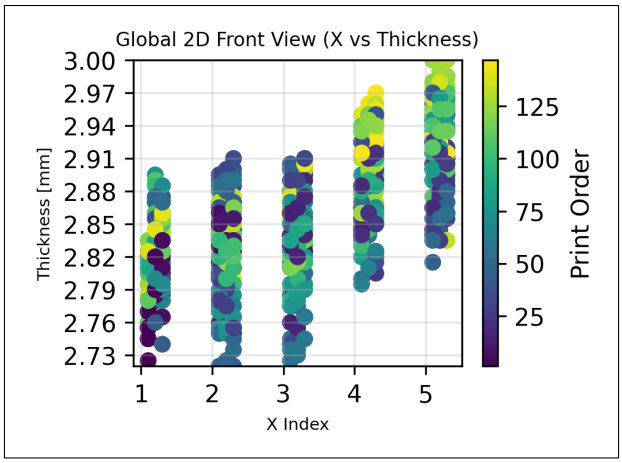


Figure 6. Front view of thickness measurements with print order in all measured layers.

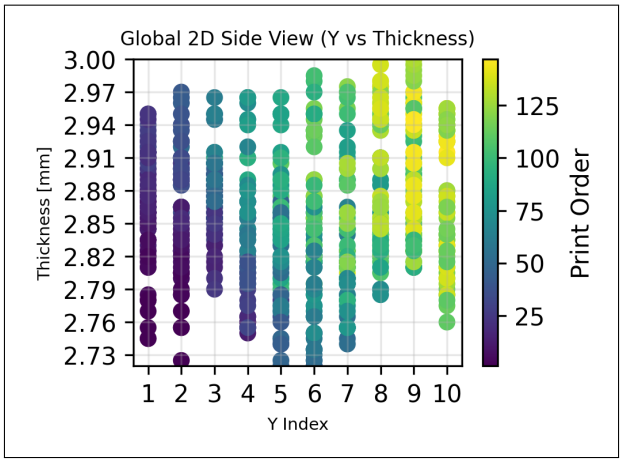


Figure 7. Side view of thickness measurements with print order in all measured layers.

Figure 8 presents the correlation matrix for all measured variables at layer Z1. In this figure, Interlayer T and Part T refer to the temperature measurements taken between layers and at the part layers, respectively. PR and PS denote the PreRecoat and PreScan processes. The numerical suffix indicates the layer number at the specific location: -1 corresponds to the layer just before the part is printed, while 20 indicates the twentieth layer of the

part. Strong correlations are observed between the different temperature measurements, as well as between frequency and both width and thickness. Moderate correlations are also evident between temperature variables and beam dimensions, as well as with the print order.

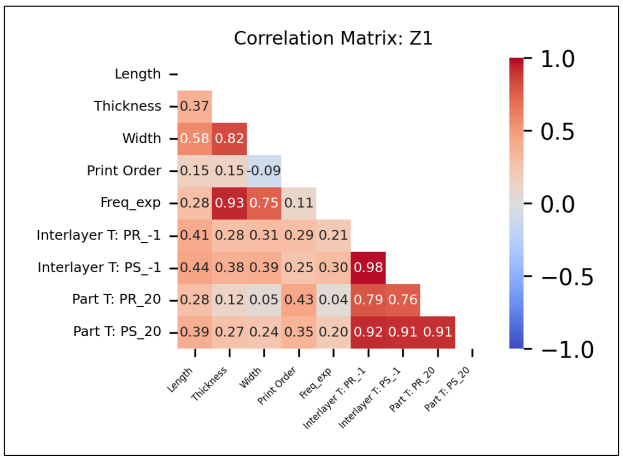


Figure 8. Correlation matrix of measurements in Z1.

The correlation matrix across all layers is shown in Figure 9, which excludes the frequency measurements. Compared to Figure 8, the correlations between the temperature variables, beam dimensions, and print order appear stronger when considering the full dataset. This suggests that the overall thermal history and printing sequence have a more pronounced effect on the geometry of the parts when aggregated across all layers.

4. DISCUSSION

The results of this study provide insights into the complex relationship between SLS manufacturing parameters, dimensional accuracy, and the vibrational properties of PA-12 parts.

4.1 Printer Bed Temperature

Goodridge et al. identified thermal management as one of the primary challenges in achieving consistent part quality in SLS processes [1]. The heatmap of the temperature distribution in Figure 5 shows a distinct thermal variation across the build platform: lower temperatures are observed near the center of the bed, while higher temperatures appear around this region, with the highest values recorded near the back-right corner. This uneven

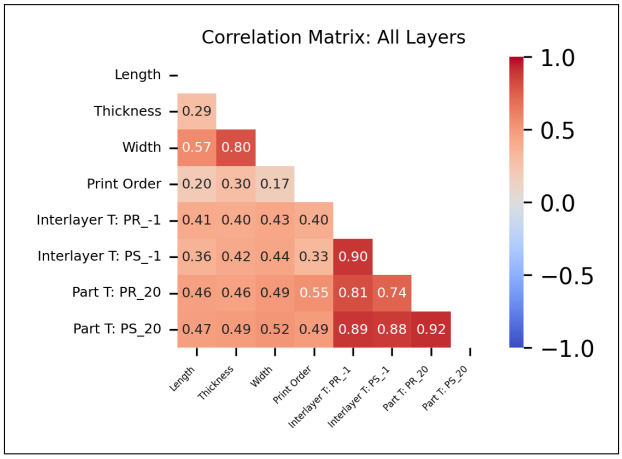


Figure 9. Correlation matrix of measurements in all measured layers.

heating correlates with observed variations in part dimensions. For instance, Figure 7 shows that beams located in the middle of the bed (Y5–Y7) tend to be thinner than those printed in surrounding regions. Likewise, Figure 4 indicates that the beams located in the back-right corner—where the temperatures are highest—are among the thickest in the build.

Despite this spatial trend, the correlation matrix in Figure 9 shows only moderate correlations between recorded temperatures and beam thickness. One explanation is that beams near the left edge of the build are also thinner, yet they experience similar temperature levels to those on the right. This suggests that additional factors, such as print order or local cooldown conditions, may play a role. As described in Section 2, the print order generally progresses from the front-left to the back-right corner, meaning the last-printed parts (often thicker) also correspond to areas with higher recorded temperatures. This may indicate a cumulative thermal effect, where successive laser passes raise the local bed temperature, influencing not only the printed layers but also the interlayers preceding them. However, if temperature were driven only by this effect, a stronger correlation with thickness would be expected. The moderate correlation observed likely arises because temperature is affected by both space and time factors. For instance, thin parts situated near the center of the bed may lie in regions with higher temperatures, but those parts are printed earlier within the layer sequence. As a result, the influence of geometry on temperature becomes entangled with location and print sequence,

weakening the direct correlation between thickness and recorded temperature.

Additionally, the absolute temperature values in Figure 5 are notably lower than the target preheat temperature of 173°C. While the powder bed reaches this temperature during the interlayer heating phase, it drops rapidly during the printing of each layer due to the time required for sintering. The internal heaters cannot compensate quickly enough, resulting in lower effective temperatures at the printed layers. This drop appears to be specific to the part layout of this particular print job and setup – too many small parts were evenly distributed throughout the printer bed, which is not common in typical builds.

4.2 Parameter Correlations

The global correlation matrix in Figure 9 reveals several key relationships between print parameters and part quality. As discussed in Section 1, shrinkage and warpage are known to affect dimensional accuracy. In this design, the width and thickness were more sensitive to these effects and thus exhibited a strong correlation with one another.

Moderate correlations were observed between all temperature variables and both the geometric dimensions and print order. These findings are consistent with the analysis presented in Section 4.1, which suggests that localized temperature changes and thermal history contribute to dimensional variability.

In the Z1 correlation matrix shown in Figure 8, the natural frequency variable was included and, as expected, showed strong correlations with both thickness and width. This is in line with theoretical predictions: the first mode of vibration in beams is a bending mode, which strongly depends on the beam's moment of inertia I, defined for a rectangular cross-section as shown in Equation 1. Here, w is the beam width and t is the beam thickness (height in the bending direction). Dimensional deviations in these parameters therefore have a direct and significant effect on the measured vibrational behavior.

$$I = \frac{wt^3}{12} \tag{1}$$

The strong correlation between natural frequency and thickness and width suggests that frequency testing can serve as an effective quality control method on its own. Rather than relying on multiple dimensional measurements, a streamlined quality control process could use automated frequency testing to flag parts that deviate from expected resonant behavior. Since the natural frequency is highly sensitive to small geometric variations, setting specific frequency thresholds would allow rapid identification of parts that may not meet the required geometrical criteria. This non-destructive testing approach could substantially reduce inspection time and costs, ensuring that only components with the proper vibrational characteristics proceed to final assembly or application in acoustically sensitive systems.

5. CONCLUSION

This study has investigated the relationships between SLS manufacturing parameters, dimensional accuracy, and vibrational properties of PA-12 cantilever beams. The findings reveal variations in thickness throughout the build volume that moderately correlate with temperature in the powder bed. Correlation analysis of the first layer of printed beams demonstrated consistent relationships between thermal conditions, dimensional deviations, print order, and natural frequencies. A strong correlation between natural frequency and part dimensions suggests the possibility of a faster, geometry-based quality control process for SLS-manufactured PA-12 parts. While only moderate correlations were found between frequency and temperature data in the first layer, measuring additional layers may reveal stronger associations.

Several areas for improvement and further investigation have emerged. First, the part design should be revised. A revised design could improve the reliability of frequency measurements and potentially reduce scan times — an important factor, as prolonged scanning was observed to lower the bed temperature during printing.

Additionally, increasing the preheating duration may help stabilize the thermal environment. Uncorrected IR camera data showed that the machine was still accumulating heat during the first two part layers of the build. A longer preheating phase could allow the system to reach thermal equilibrium before the actual printing begins. Furthermore, re-evaluating the heater orientation within the machine may help achieve a more uniform temperature distribution across the build surface.

Future work should focus on a more comprehensive analysis of the interactions between process parameters, dimensional accuracy, and vibrational response. This includes collecting data across all build layers, improving thermal management, and optimizing beam geometry. The application of compensation factors to address predictable dimensional deviations could lead to improved part consistency and performance.

6. ACKNOWLEDGMENTS

We gratefully acknowledge the European Commission for its support of the Marie Sklodowska Curie program through the Horizon Europe DN METAVISION project (GA 101072415). Views and opinions expressed are however those of the authors only and do not necessarily reflect those of the European Union. The European Union cannot be held responsible for them. The authors thank the Grindosonic team for their support in collecting the frequency data. The first author also thanks Ricardo Santander, Stefan Janssen, and Piet Van den Ecker for their invaluable help and patience. Materialise's MatGPT text-generator was used to debug parts of the code used for this study.

7. REFERENCES

[1] R. D. Goodridge, C. J. Tuck, and R. J. M. Hague, "Laser sintering of polyamides and other polymers," *Progress in Materials Science*, vol. 57, pp. 229–267, 2012.

[2] A. E. Magri, S. E. Bencaid, H. R. Vanaei, and S. Vaudreuil, "Effects of laser power and hatch orientation on final properties of pa12 parts produced by selective laser sintering," *Polymers, 14, 3674*, 2022.

[3] J. Li, S. Yuan, J. Zhu, S. Li, and W. Zhang, "Numerical model and experimental validation for laser sinterable semi-crystalline polymer: Shrinkage and warping," *Polymers, 12(6), 1373*, 2020.

[4] A. Pilipović, P. Ilinčić, M. Tujmer, and M. R. Havstad, "Impact of part positioning along chamber z-axis and processing parameters in selective laser sintering on polyamide properties," *Appl. Sci., 14, 976.*, 2024.

[5] T. O. Joldos, P. Danca, and A. Cernei, "Comparative acoustic analysis of standard and innovative air diffusers with enhanced mixing capabilities," in *E3S Web Conf.*, vol. 608, 2025.

[6] C. Claeys, E. Deckers, B. Pluymers, and W. Desmet, "A lightweight vibro-acoustic metamaterial demonstrator: Numerical and experimental investigation," *Mechanical Systems and Signal Processing*, vol. 70, pp. 853–880, 2016.

[7] A. C. de Sousa, E. Deckers, C. Claeys, and W. Desmet, "On the assembly of archimedean spiral cavities for sound absorption applications: Design, optimization and experimental validation," *Mechanical Systems and Signal Processing*, vol. 147, p. 107102, 2021.

[8] A. Ciochon and J. Kennedy, "Efficient modelling of surface roughness effects in additively manufactured materials," *Applied Acoustics*, vol. 220, p. 109953, 2024.

[9] P. Boron, J. Chelmecki, J. M. Dulinska, N. Jurkowska, B. Ratajewicz, P. Stecz, and T. Tatara, "On the possibility of using 3d printed polymer models for modal tests on shaking tables: Linking material properties investigations, field experiments, shaking table tests, and fem modeling," *Materials (Basel), 16(4):1471*, 2023.

DOI: 10.61782/fa.2025.0721



FORUM ACUSTICUM
EURONOISE 2025

QUANTIFYING THE IMPACT OF INJECTION MOLDING PROCESS PARAMETERS ON THE VIBROACOUSTIC PERFORMANCE OF MANUFACTURED LOCALLY RESONANT METAMATERIALS

Alara Karaman[1,2*] **Lucas Van Belle**[2,3] **Elke Deckers**[1,2]

[1] Department of Mechanical Engineering, Campus Diepenbeek, KU Leuven, Belgium
[2] Flanders Make@KU Leuven, Belgium
[3] Department of Mechanical Engineering, KU Leuven, Belgium

ABSTRACT

Locally resonant metamaterials (LRMs) have recently emerged as a promising solution which can combine lightweight design with effective noise and vibration control. These LRMs, typically consisting of a host structure with sub-wavelength added resonators, are often manufactured using additive manufacturing, which is unsuitable for mass production. Moreover, the manufacturing process can significantly affect the performance of LRMs, leading to differences between their intended design and actual results. Injection molding (IM) has been recently explored as an alternative that is suitable for mass manufacturing of LRMs though it still may affect performance.

This study focuses on how IM process parameters such as injection and packing pressure, mold and melt temperature, cooling and packing time, and injection speed influence the vibration attenuation in LRMs by investigating their impact on the effective modal parameters of the resonator and on the predicted stop band. A framework is proposed which iteratively calculates these objectives and uses single and multi-objective Bayesian approaches to determine its upper and lower bounds with respect to variation in the process parameters. These process parameters are found to have a significant impact on the vibroacoustic behavior of the LRMs, which may also be leveraged further in view of broadband vibration attenuation.

*__Corresponding author__: alara.karaman@kuleuven.be.
__Copyright__: ©2025 *This is an open-access article distributed under the terms of the Creative Commons Attribution 3.0 Unported License, which permits unrestricted use, distribution, and reproduction in any medium, provided the original author and source are credited.*

Keywords: *metamaterials, injection molding, uncertainty*

1. INTRODUCTION

Industry has a clear trend toward lightweight designs mainly due to economic and ecological reasons; however, traditional noise and vibration mitigation strategies typically rely on adding mass or volume, which leads to heavy and bulky solutions. This not only increases emissions during transport but also contradicts the trend towards lightweight design. In contrast, LRMs offer a lightweight and targeted approach to addressing noise and vibration issues.

In literature, LRMs have been manufactured using additive manufacturing [1–3], which has advantages like rapid prototyping but is not suitable for mass production. For metals, manufacturing techniques such as punching and bending [4], milling [5], and waterjet cutting [6] are utilized. Additionally, laser cutting [7] and thermoforming [8] are other alternatives. Some recent studies [9, 10] also investigated injection molding (IM) for LRM production, which is one of the most common techniques for mass manufacturing plastics. Manufacturing variability is inherent due to real-world engineering conditions [11], which may affect robustness.

In a previous study, it was shown that incorporating IM simulations during the design of an injection-molded metamaterial can improve the predicted performance [10]. It is also well known that the machine process variables in the IM process significantly impact product quality, particularly in terms of warpage and shrinkage deformations

[12], as well as part weight [13]. In particular, process parameters influence warpage, shrinkage, and material variability. In this study, we propose an approach to evaluate the potential influence of operational parameter ranges by combining a numerical prediction workflow [10] for the as-produced metamaterial performance with an interval uncertainty quantification approach.

In what follows, first in Sec. 2 a brief description of the metamaterial design is given. Sec. 3 outlines the approaches used to calculate the performance metrics and bounds. Sec. 4 introduces the model and presents the results. Finally, Sec. 5 discusses the main findings and gives the future perspectives.

2. THE METAMATERIAL DESIGN

An LRM plate is investigated, which consists of a 50 mm square aluminum (aluminum 6061) plate with a 1.5 mm thickness as the unit cell host structure and periodically added dual-cantilever polypropylene (PP) resonators. The resonator C [10] is chosen for analysis using the same geometric parameters employed in the study, with a first combined bending eigenfrequency tuned nominally around 1154 Hz.

3. METHODOLOGY

In this section, the numerical performance prediction flow is explained, the performance metrics to be used in this study are introduced, and approaches to find the performance bounds are briefly discussed.

3.1 Injection Molding Simulations

The machine process parameters to be varied are injection and packing pressure, mold and melt temperature, cooling and packing time, and injection speed. For the specific parameters, filling, packing, and warpage processes are simulated with MOLDEX3D 2023 using a boundary layer mesh (BLM) of the part. Then, this BLM mesh is exported, including the material cards that may differ in density across the elements in the mesh.

Two approaches have been studied for performance predictions: Approach 1 for modal parameter estimation and Approach 2 for stop-band predictions. These two approaches are summarized in Fig. 1.

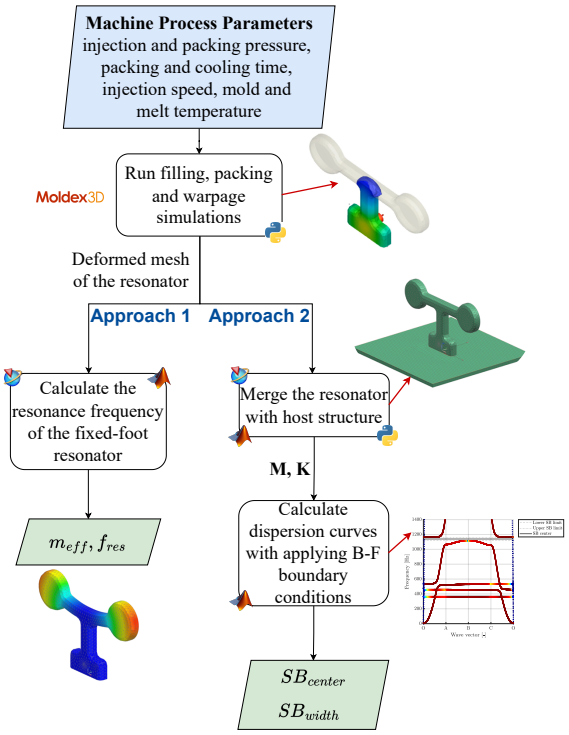


Figure 1: The flowchart of the performance prediction calculations for modal parameters (Approach 1) and stop-band predictions (Approach 2).

3.2 Approach 1: Modal Parameter Estimation

Two key modal parameters for LRM design are chosen as performance metrics: the resonator's eigenfrequency (f_{res}) and its modal effective mass (m_{eff}). The eigenfrequency of the resonator directly affects the stop-band center. On the other hand, as the m_{eff} of the resonator increases, larger stop-band widths can be achieved [14]. Hence, it is crucial to know how these metrics vary if the performance of LRMs is to be assessed.

These metrics will be computed for the resonator with clamped boundary conditions on its foot elements. The nodes corresponding to the resonator foot bottom are automatically selected and fixed for the deformed resonator mesh with variable density information exported from the injection molding simulations. Then, the f_{res} and m_{eff} are calculated by solving the corresponding eigenvalue problem. The automatization of this resonator performance prediction, Approach 1, was implemented using NX open scripts created in Python.

3.3 Approach 2: Stop-band Predictions

Ultimately, to evaluate the performance of the LRMs, m_{eff} and f_{res} may not provide the full story. Therefore, Approach 2 is employed for the stop-band predictions.

First, the deformed resonator is merged with the host structure using conformal meshes by projecting foot elements of the resonator to the unit cell of the plate host structure. Automation for this task is again done using an NX-open script created in Python. Then, applying Bloch-Floquet boundary conditions to the boundaries of the unit cell, the dispersion curves of the infinite periodic structure are calculated along the irreducible Brillouin contour (IBC). A reduced unit cell model technique known as Generalized Bloch Mode Synthesis (GBMS) [15] is used to save computational time. Finally, stop-band characteristics (SB_{center} and SB_{width}) are extracted using the resulting dispersion curves. For a more in-depth explanation of the stop-band calculation procedure, the reader is referred to [16].

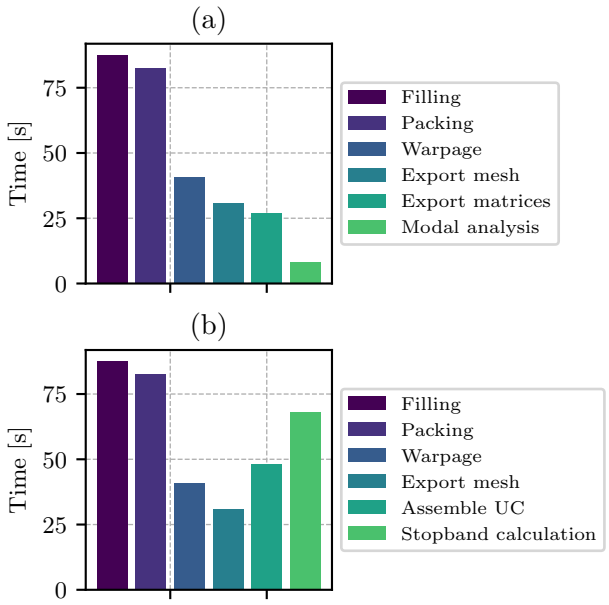


Figure 2: Overview of the time taken for (a) Approach 1, (b) Approach 2.

The steps in Sec. 3.1 and Sec. 3.2 for Approach 1, and Sec. 3.1 and Sec. 3.3 for Approach 2, are sequentially connected to formulate the objective (black-box) function that is to be iterated throughout the optimization step.

3.4 Calculating the Performance Bounds

Recently, Van Belle et al. [17] used interval descriptions of the uncertain resonator parameters to investigate the interval description of the performance metrics. A similar approach is applied here, but this time, instead of the resonator design parameters, the defined seven machine process parameters of IM are used as the bounded input parameters, which would lead to bounds to be found on the performance metrics. This has the advantage of not requiring knowledge of input distributions, allowing one to rely on ranges, tolerances, common sense, or physical constraints; however, the disadvantage is that this method results in only bounds on the performance metrics as output. Nevertheless, this method offers a useful first approximation of how significantly the process parameters influence the performance of LRMs. The objective function for this problem is defined as the calculation of the minimum and maximum values of the performance parameters (minimum and maximum of Approaches 1 and 2) according to the uncertain input interval.

The computation costs for one full evaluation using Approach 1 and Approach 2 are shown in Fig. 2. Due to these computational costs, performing a large number of evaluations for the 7-dimensional parameter space would rapidly become time-consuming. A sampling-based approach, such as quasi-random sampling, typically requires many samples, leading to numerous full simulations. Additionally, it may fail to effectively identify the performance bounds, as it may not cover the entire input space. On the other hand, given the small number of parameters, a similar surrogate modeling technique from the aforementioned study, based on Gaussian processes (GP) and Bayesian optimization (BO), can be leveraged, as it offers an efficient framework for propagating interval-uncertain parameters when there is limited number of uncertain parameters while effectively decreasing the number of simulations to be run.

The methodology of this combined BO and GP approach can be summarized as follows [18]: For a training set, based on a limited number of full simulations, a GP model of the objective function is created. This GP model acts as a hypersurface that approximates the objective function across the entire parameter space. Using this GP model, an acquisition function (AF) can be efficiently minimized to find the likely optimum, which is the potential minimum of the objective function. Depending on the AF used, the likely optimum might be based on local GP mean, uncertainty, or confidence bounds. After the most

promising parameter combination is identified with this AF, a new full simulation is run at that parameter combination. This new data point is then added to the training set, and the GP model is updated accordingly. The process then reiterates, with the updated GP model potentially suggesting even better optimals, until a stopping criterion is met, which is the maximum number of evaluations in this case.

3.4.1 Single Objective Bayesian Approach

For Approach 1, the bounds on the resulting performance metrics at the resonator level, f_{res} and m_{eff} can be computed by the following four optimization problems:

$$\begin{aligned} m_{eff,LB} &= \min\{m_{eff}(\mathbf{p}) \mid \mathbf{p}_{\min} \leq \mathbf{p} \leq \mathbf{p}_{\max}\} \\ m_{eff,UB} &= \max\{m_{eff}(\mathbf{p}) \mid \mathbf{p}_{\min} \leq \mathbf{p} \leq \mathbf{p}_{\max}\} \\ f_{res,LB} &= \min\{f_{res}(\mathbf{p}) \mid \mathbf{p}_{\min} \leq \mathbf{p} \leq \mathbf{p}_{\max}\} \\ f_{res,UB} &= \max\{f_{res}(\mathbf{p}) \mid \mathbf{p}_{\min} \leq \mathbf{p} \leq \mathbf{p}_{\max}\} \end{aligned} \tag{1}$$

where $\mathbf{p}_{\min} \leq \mathbf{p} \leq \mathbf{p}_{\max}$ denotes a vector inequality, i.e., $(p_{\min})_i \leq p_i \leq (p_{\max})_i$ for every $i = 1, 2, \ldots, 7$ defined for the input space for process parameters.

Single-objective BO with GP is applied separately to each objective function to determine the bounds for each modal performance parameter. The acquisition function is selected as the lower confidence bound. This is implemented using the *bayesopt* function in MATLAB, and a *bounding box* is created for the model performance metrics, which demarks the bounded region in the m_{eff}-f_{res} space. An initial training set of 27 full simulations is run, with the corresponding 27 parameter combinations generated through the Halton sequence using the MATLAB function *haltonset*. The stopping criterion is set at a total of 108 model evaluations for each corner of the *bounding box*.

3.4.2 Multi Objective Bayesian Approach

Instead of calculating the *bounding box*, the *bounding envelope* can be calculated if multiobjective optimization is used to calculate the Pareto optimal. Assuming a convex bounding envelope, the f_{res} and m_{eff} space is divided into four quadrants, and the Pareto front for each of these quadrants is sought by the following optimization problems:

$$\begin{aligned} f_{Q1} &= \min\{\begin{matrix}-m_{eff}(\mathbf{p}) \\ f_{res}(\mathbf{p})\end{matrix} \mid \mathbf{p}_{\min} \leq \mathbf{p} \leq \mathbf{p}_{\max}\} \\ f_{Q2} &= \min\{\begin{matrix}-m_{eff}(\mathbf{p}) \\ -f_{res}(\mathbf{p})\end{matrix} \mid \mathbf{p}_{\min} \leq \mathbf{p} \leq \mathbf{p}_{\max}\} \\ f_{Q3} &= \min\{\begin{matrix}m_{eff}(\mathbf{p}) \\ -f_{res}(\mathbf{p})\end{matrix} \mid \mathbf{p}_{\min} \leq \mathbf{p} \leq \mathbf{p}_{\max}\} \\ f_{Q4} &= \min\{\begin{matrix}m_{eff}(\mathbf{p}) \\ f_{res}(\mathbf{p})\end{matrix} \mid \mathbf{p}_{\min} \leq \mathbf{p} \leq \mathbf{p}_{\max}\} \end{aligned} \tag{2}$$

For this, a multiobjective Bayesian algorithm called TSEMO [19] is used. The stopping criteria is set to a total of 120 model evaluations per quarter, with a different set of 27 initial random data points generated through Latin hypercube sampling (LHS) for each quarter.

4. CASE STUDY

A BLM with 5 boundary layers with 1 mm node seed is used, resulting in 33949 elements. After the injection molding simulations, the mesh with variable material cards is exported using the dedicated finite element export option in MOLDEX3D. Similar to [10], density is reduced so that a minimum of 30 different material cards are exported to reduce computational time. The mesh of the resonator is given in Fig. 3.

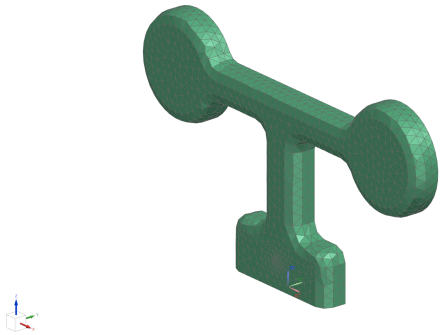


Figure 3: The resonator mesh

The machine process parameter ranges to be examined are listed in Tab. 1.

4.1 Resonator Performance Bounds

A prestudy is conducted using a random Halton dataset and an orthogonal Taguchi array with 14 levels. The total number of model evaluations is set to 196 for the Halton

Table 1: Machine process parameter ranges

Parameter	Low Bound	High Bound
Injection pressure [MPa]	100	180
Packing pressure [MPa]	100	170
Packing time [s]	1	20
Cooling time [s]	1	20
Injection speed [cm^3/s]	10	40
Mold temperature [°C]	40	70
Melt temperature [°C]	220	270

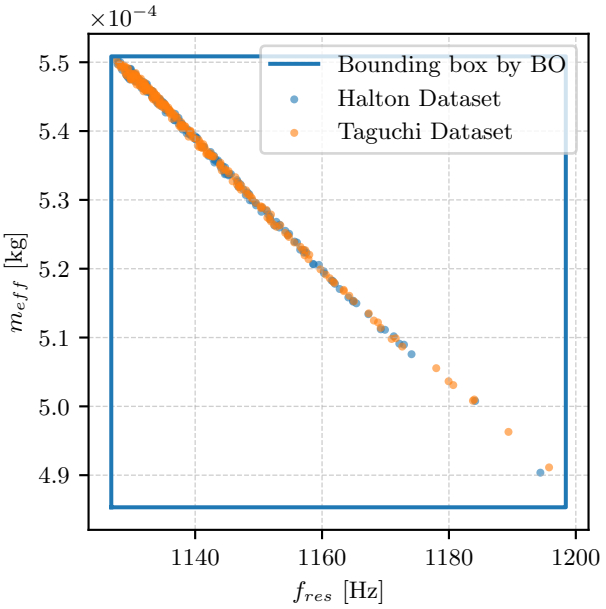


Figure 4: The bounding box calculated by single objective Bayesian optimization, together with 197 different data points calculated by Taguchi array and Halton Sequence.

dataset, based on the corresponding Taguchi array with 7 levels.

Fig. 4 gives the overview of single objective optimization and sampling results. The relationship between the resonator's eigenfrequency and modal effective mass appears to be quite linear, based on sampling. Finding the separate individual bounds shows that the samples are all within these bounds. However, the bounding box, which is now necessarily a rectangle, loses that clear trend. Thus, although interesting and promising, the multiobjective approach could give more insights.

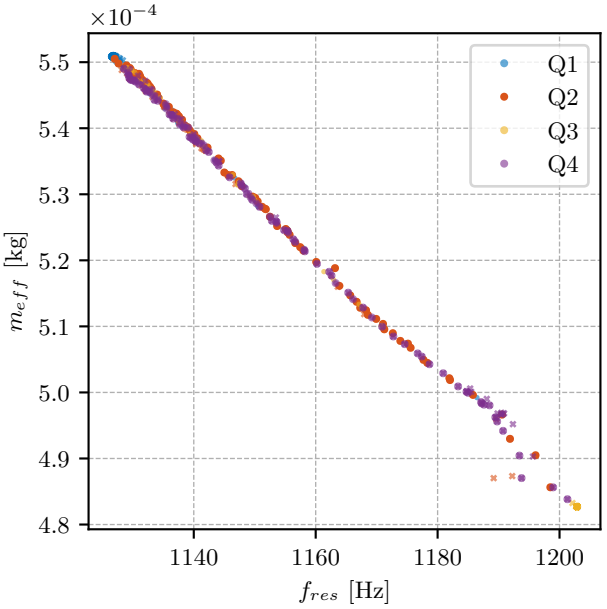


Figure 5: The bounding envelope calculated by multi-objective Bayesian optimization.

Fig. 5 gives an overview of the multi-objective optimization results. In comparison with Fig. 4, it shows that only a few samples are in the bottom-right corner, while most are clustered in the middle to top-left regions. This suggests that the parameter range leading to the bottom-right region is potentially narrow or scattered, making it harder to capture. While the BO algorithm performs well in the middle and top-left, refining the acquisition function, kernel, or objective function may help improve results in the bottom-right.

4.2 Stop-band Performance Bounds

A Taguchi sampling-based approach is done on the stop-band performance to present an initial impression in this paper. Fig. 6 shows an overview of the stop-band predictions. As is well-known from metamaterial design, the SB_{center} is highly correlated with f_{res}, which is also seen on Fig. 6, while the SB_{width} depends on the (effective) mass of the resonator. Moreover, a broader stop-band with increasing frequency is typically expected. However, in this case, the increasing frequency corresponds to, and may even be caused by, a reduced resonator ef-

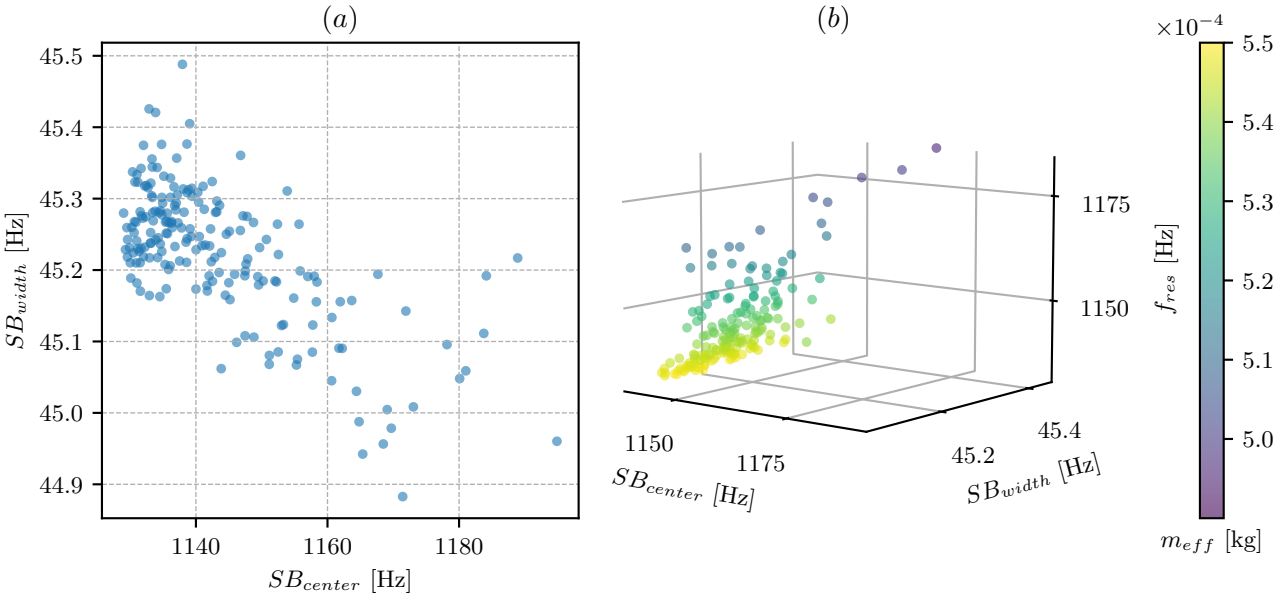


Figure 6: (a) Approach 2 metrics calculated with the Taguchi sample (b) combined resonator (Approach 1) and stop band (Approach 2) metrics plotted together.

fective mass. In Fig. 6, the stop-band width slightly decreases (yet remains almost constant), suggesting that, at the LRM level, both of these effects may, to some extent, counterbalance each other for this example.

5. CONCLUSIONS

In this paper, two approaches for assessing the IM variability are proposed for LRMs. These approaches iteratively calculate the LRM performance, either at the resonator level or at the unit cell level, to investigate the influence of manufacturing variability effects of IM.

The machine operation parameters of the IM process are shown to have a clear effect on the vibroacoustic performance of the LRMs and the targeted frequency range of the resonator. For the given case study, with the variation in process parameters shown in Tab. 1, an approximately 3% variation in frequency and 6% variation in effective mass of the resonator can be observed from Fig. 5. This variation could be utilized further for broadband attenuation.

Although the bounding box indicates bounds on individual performance metrics well, trends that may exist between dependent performance metrics are lost. Using a Pareto multi-objective BO optimization showed great potential in more accurately capturing the performance bounds in LRMs.

Further investigation is required for more definitive conclusions, as the results for Approach 1 need more analysis, and the results for Approach 2 are still very preliminary and indicative. However, this framework shows promising potential for investigating manufacturing variability. In future work,

- a qualitative study will be conducted on each parameter to assess the contribution and importance of individual machine parameters versus their combined impact.
- the analysis of resonator metrics will be further expanded, including stiffness, to explain frequency variation better.
- the scope will be extended to include material property variation besides purely manufacturing process settings.

6. ACKNOWLEDGMENTS

The European Commission is gratefully acknowledged for their support of the METAVISION research project (GA 101072415). Views and opinions expressed are,

however, those of the authors only and do not necessarily reflect those of the European Union. The European Union cannot be held responsible for them. The research of L. Van Belle (fellowship no. 1254325) is funded by a grant from the Research Foundation – Flanders (FWO). Internal Funds KU Leuven are gratefully acknowledged for their support.

7. REFERENCES

[1] C. Claeys, E. Deckers, B. Pluymers, and W. Desmet, "A lightweight vibro-acoustic metamaterial demonstrator: Numerical and experimental investigation," *Mechanical Systems and Signal Processing*, vol. 70–71, pp. 853–880, 2016.

[2] L. Sangiuliano, C. Claeys, E. Deckers, J. De Smet, B. Pluymers, and W. Desmet, "Reducing Vehicle Interior NVH by Means of Locally Resonant Metamaterial Patches on Rear Shock Towers," in *SAE Technical Paper*, pp. 2019–01–1502, 2019.

[3] S. Tomita, T. Masutani, and H. Sato, "Locally resonant metamaterials damped by particles embedded through additive manufacturing," *Journal of Sound and Vibration*, vol. 596, p. 118715, 2025.

[4] M. Droste, D. Manushyna, S. Rieß, H. Atzrodt, T. Druwe, S. Melzer, A. Struß, and A. Lühring, "Design and validation of production-suited vibroacoustic metamaterials for application in a vehicle door," in *Fortschritte der Akustik - DAGA 2021*, p. 1647, 2021.

[5] L. Sangiuliano, R. Boukadia, E. Deckers, W. Desmet, and C. Claeys, "Reduction of Structure-Borne Tyre/Road Noise through Rubber Resonant Metamaterials in Tyres," *SAE International Journal of Advances and Current Practices in Mobility*, vol. 5, no. 2, pp. 909–920, 2022.

[6] S. Rieß, R. Schmidt, W. Kaal, H. Atzrodt, and S. Herold, "Vibration Reduction on Circular Disks with Vibroacoustic Metamaterials," *Applied Sciences*, vol. 14, no. 11, p. 4637, 2024.

[7] L. Van Belle, C. Claeys, E. Deckers, and W. Desmet, "On the impact of damping on the dispersion curves of a locally resonant metamaterial: Modelling and experimental validation," *Journal of Sound and Vibration*, vol. 409, pp. 1–23, 2017.

[8] N. De Melo Filho, C. Claeys, E. Deckers, and W. Desmet, "Realisation of a thermoformed vibro-acoustic metamaterial for increased STL in acoustic resonance driven environments," *Applied Acoustics*, vol. 156, pp. 78–82, 2019.

[9] J. Yu, C. Nerse, G. Lee, S. Wang, and K.-j. Chang, "Mass Production Applicable Locally Resonant Metamaterials for NVH Applications," in *26th International Congress on Sound and Vibration*, 2019.

[10] K. Steijvers, C. Claeys, L. Van Belle, and E. Deckers, "Incorporating Manufacturing Process Simulations to Enhance Performance Predictions of Injection Moulded Metamaterials," *Journal of Vibration Engineering & Technologies*, vol. 11, no. 6, pp. 2617–2629, 2023.

[11] S. Cantero-Chinchilla, A. T. Fabro, H. Meng, W.-J. Yan, C. Papadimitriou, and D. Chronopoulos, "Robust optimised design of 3D printed elastic metastructures: A trade-off between complexity and vibration attenuation," *Journal of Sound and Vibration*, vol. 529, p. 116896, 2022.

[12] N.-y. Zhao, J.-y. Lian, P.-f. Wang, and Z.-b. Xu, "Recent progress in minimizing the warpage and shrinkage deformations by the optimization of process parameters in plastic injection molding: A review," *The International Journal of Advanced Manufacturing Technology*, vol. 120, no. 1-2, pp. 85–101, 2022.

[13] H. Hassan, "An experimental work on the effect of injection molding parameters on the cavity pressure and product weight," *The International Journal of Advanced Manufacturing Technology*, vol. 67, pp. 675–686, July 2013.

[14] F. Pires, R. Boukadia, M. Wandel, C. Thomas, E. Deckers, W. Desmet, and C. Claeys, "Novel resonator concept for improved performance of locally resonant based metamaterials," *Thin-Walled Structures*, vol. 209, p. 112866, 2025.

[15] D. Krattiger and M. I. Hussein, "Generalized Bloch mode synthesis for accelerated calculation of elastic band structures," *Journal of Computational Physics*, vol. 357, pp. 183–205, Mar. 2018.

[16] L. Van Belle, N. Filho, M. Clasing, C. Claeys, E. Deckers, F. Naets, and W. Desmet, "Fast metamaterial design optimization using reduced order unit cell modeling," in *Proceedings of ISMA 2020*, p. 2487–2501, 2020.

[17] L. Van Belle, E. Deckers, and A. Cicirello, "Investigating and exploiting the impact of variability in resonator parameters on the vibration attenuation in locally resonant metamaterials," *Philosophical Transactions of the Royal Society A: Mathematical, Physical and Engineering Sciences*, vol. 382, no. 2279, p. 20230364, 2024.

[18] A. Cicirello and F. Giunta, "Machine learning based optimization for interval uncertainty propagation," *Mechanical Systems and Signal Processing*, vol. 170, p. 108619, 2022.

[19] E. Bradford, A. M. Schweidtmann, and A. Lapkin, "Efficient multiobjective optimization employing Gaussian processes, spectral sampling and a genetic algorithm," *Journal of Global Optimization*, vol. 71, no. 2, pp. 407–438, 2018.

DOI: 10.61782/fa.2025.0942



FORUM ACUSTICUM
EURONOISE 2025

USING 3D PRINTED LABYRINTHINE INCLUSIONS TO IMPROVE THE LOW-FREQUENCY PERFORMANCE OF A THIN, CONVENTIONAL SOUND-ABSORBING PANEL

Michał Niedzielczyk **Tomasz G. Zieliński***
Institute of Fundamental Technological Research, Polish Academy of Sciences
ul. Pawińskiego 5B, 02-106 Warsaw, Poland

ABSTRACT

The development of acoustic materials with broad-spectrum efficiency remains a critical challenge, particularly for achieving effective low-frequency absorption. This study presents a composite sound absorber that combines a dense, conventional felt matrix with additively manufactured 3D printed inclusions designed to enhance low-frequency attenuation. These inclusions, fabricated using cost-effective Fused Filament Fabrication (FFF) technology, feature labyrinthine geometries with high tortuosity, designed to achieve subwavelength resonances. The combination of these elements results in a thin, lightweight, and scalable solution for sound attenuation. The design procedure developed for such composites is based on complex but fully analytical modelling. The composite material exhibits exceptional performance, achieving high levels of absorption at the designed low frequency due to inclusions, while maintaining efficient broadband characteristics of the matrix. The analytical predictions are confirmed experimentally by impedance tube measurements. By leveraging the advantages of additive manufacturing and conventional materials, this work paves the way for economically viable, tailored acoustic solutions.

Keywords: *Acoustic composites, Conventional porous matrix, 3D printed labyrinthine inclusions, Multiscale modelling, Sound absorption.*

Corresponding author: *tzielins@ippt.pan.pl.*

Copyright: *©2025 Michał Niedzielczyk and Tomasz G. Zieliński. This is an open-access article distributed under the terms of the Creative Commons Attribution 3.0 Unported License, which permits unrestricted use, distribution, and reproduction in any medium, provided the original author and source are credited.*

1. INTRODUCTION

Low-frequency sound absorption remains a major challenge in acoustic material design. Traditional porous absorbers, such as fibrous or foam-based materials, rely on viscous and thermal losses to dissipate acoustic energy [1]. While effective at mid-to-high frequencies, these materials require considerable thickness to achieve meaningful absorption at lower frequencies due to the inherent limitations of quarter-wavelength resonance. This constraint often conflicts with the practical need for thin, lightweight, and efficient sound absorbers, particularly in applications such as automotive interiors and aircraft structures.

To overcome this limitation, researchers have explored various approaches to enhance low-frequency sound absorption without excessively increasing material thickness. Acoustic metamaterials [2] have been developed to manipulate wave propagation in unconventional ways, enabling sub-wavelength sound absorption through engineered periodicity and resonance effects.

Many of these solutions are based on the use of resonant structures, such as Helmholtz resonators [3–5] of unconventional geometry, often in parallel arrangements, or micro-perforated panels [6, 7] backed by air cavities of various shapes. The aim is to exploit resonance effects in order to improve acoustic absorption in specific low-frequency bands. Impedance-matching techniques [8–10] are used for graded or hierarchical structures to help transfer sound energy more effectively into dissipative regions. Another way to approach the problem is to extend the effective propagation path of sound waves in the volume of the material, thereby improving the energy dissipation mechanisms without a substantial increase in the material thickness. Solutions based on this idea include coiled-

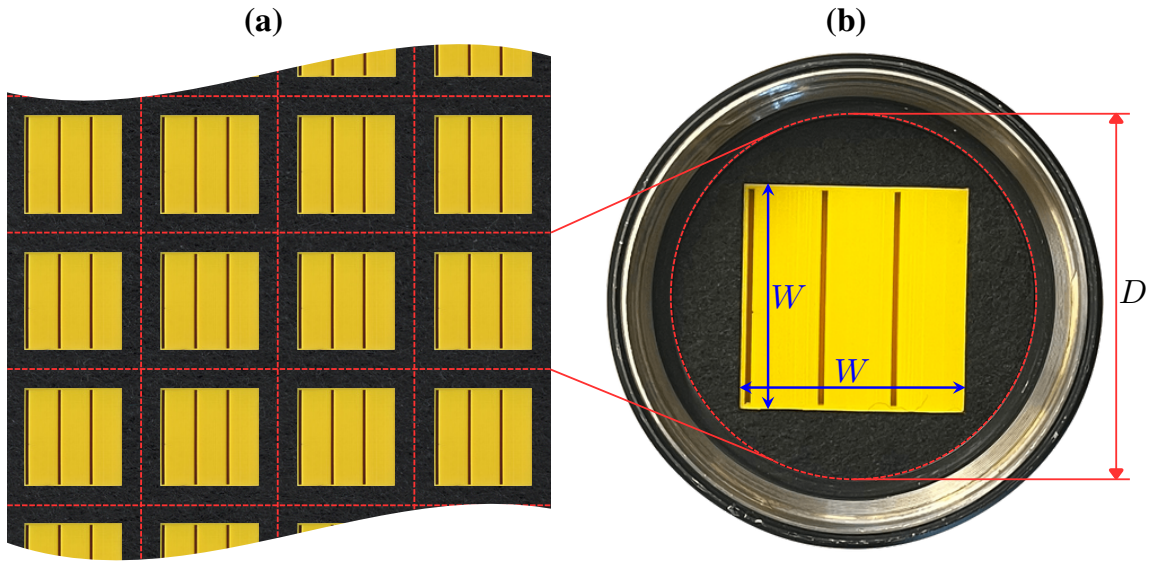


Figure 1. (a) Acoustic composite made of a black polyester felt panel with yellow 3D-printed inclusions embedded in a periodic arrangement; (b) sample of the composite panel inside a circular impedance tube.

up cavities and labyrinthine channels [11–14]. In parallel to the aforementioned strategies, the integration of engineered materials and metamaterials within composite absorbers [12, 15–17] has gained increasing attention. By embedding carefully tailored acoustic structures into conventional porous materials, it is possible to enhance energy dissipation mechanisms and extend the absorption to lower frequencies.

This study presents an experimentally validated analytical modelling of an acoustic composite to demonstrate how inexpensive and easy-to-3D-print inclusions can enhance the low-frequency sound absorption of conventional felt-based materials. The work addresses the above-mentioned critical limitation of traditional porous absorbers, which require significant thickness to achieve effective performance in the low frequency range.

The paper is structured as follows. Section 2 describes the composite material design and its components, including their fabrication and assembly. An acoustic modelling for predicting the performance of the composite absorber is discussed in Section 3. Section 4 discusses sound absorption results and provides experimental validation obtained through impedance tube measurements of a composite sample under normal incidence conditions. The key findings and conclusions are summarised in Section 5.

2. COMPOSITE PANEL

2.1 Design and components

Conventional polyester acoustic felt is known for its excellent sound absorption capacity in the mid- and high-frequency range. However, its relatively low tortuosity and high porosity limit its effectiveness at lower frequencies. To overcome this limitation, a composite structure is proposed in which labyrinthine metamaterial inclusions are embedded in a felt matrix.

Figure 1 (a) shows an example design of such a composite panel with a simple, periodic arrangement of identical inclusions. These inclusions have the shape of a cuboid with a square base and dimensions $W \times W \times H$, see Figure 2 (b) and Table 1 for the actual values of these and other dimensions. The inclusion thickness H is greater than the thickness H_F of the felt matrix, so an air gap is created behind the felt layer, which increases its absorption capacity. The proposed acoustic composite panel consists therefore of three materials: a conventional polyester felt, 3D-printed inclusions with labyrinthine channels, and air. The air fills the gap behind the felt layer, but also saturates the pores in the felt and the labyrinthine channels of the inclusions, thus acting as a medium for the propagation of sound waves.

Table 1. Useful dimensions (mm).

D	W	H	H_F	H_G	w	a	b
63.5	40	18	9	9	1.05	0.8	6.35

An important aspect of designing the composite panel is determining the appropriate ratio of the inclusion surface area to the surface area of the felt matrix. This ratio plays an important role in the composite modelling, as discussed in Section 3. In this study, this proportion was adopted so that a composite sample that is representative of the entire composite panel could be tested in a circular impedance tube with an internal diameter of $D = 63.5$ mm, see Figure 1 (b).

2.2 Composite sample

Figure 2 shows two components, i.e. (a) the felt matrix and (b) the metamaterial inclusion, of a circular sample of the composite panel, as well as (c) the assembled sample ready for testing in a circular impedance tube. The component manufacturing and sample assembly procedure are described below.

A circular matrix sample of diameter D, see Figure 2 (b), was cut from the felt panel of thickness H_F, using an optical laser cutter (Sculpfun S30 Pro Max). The cutting diameter was increased by the laser beam width of 0.3 mm. This dimensional compensation was applied to ensure precise fit of the sample inside the impedance tube. A similar compensation was applied when cutting the square hole with dimensions $W \times W$ for the inclusion.

The labyrinthine inclusion shown in Figure 2 (b) was designed to contain three identical labyrinthine slits (channels) characterised by very high tortuosity, see Figure 3, and optimised for low-frequency sound absorption. It was additively manufactured from the thermoplastic polymer acrylonitrile-butadiene-styrene (ABS), which was selected for its reliability, quality and good mechanical properties. The two-dimensional inclusion design (see Figure 3) was optimised to facilitate efficient 3D-printing via Fused Filament Fabrication, taking into account in particular the size of the printing nozzle.

To ensure proper integration within the polyester felt matrix and eliminate acoustic leakage, aluminium tape was glued to the back and side surfaces of the inclusion as shown in Figure 2 (b). The taped inclusion was tightly fitted into the square hole of the felt matrix during assembly of the composite sample, Figure 2 (c).

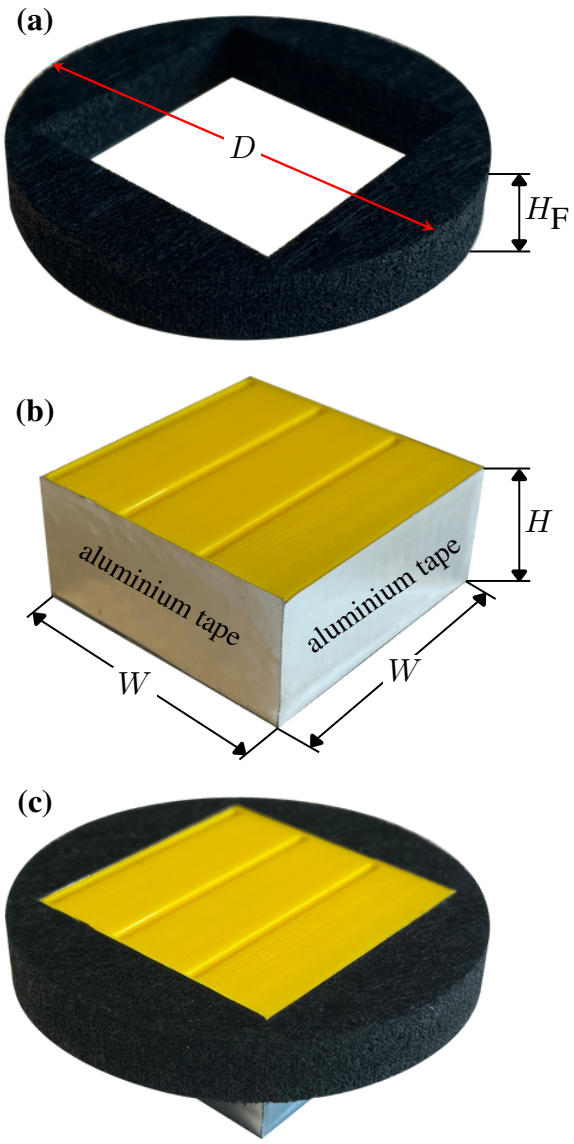


Figure 2. (a) Matrix cut from a polyester felt panel; (b) 3D printed labyrinthine inclusion with the bottom and side surfaces covered with aluminium tape; (c) assembled composite sample.

3. ACOUSTIC MODELLING

3.1 Equivalent fluid approach

Acoustic modelling of the composite is based on the equivalent-fluid approach [1]. This means that both com-

Table 2. JCAL parameters for the composite panel components.

Material	ϕ (%)	α_∞ (–)	Λ_v (10^{-6}m)	Λ_th (10^{-6}m)	$\mathcal{K}_0$ (10^{-10}m^2)	Θ_0 (10^{-10}m^2)
polyester felt	96	1.1	27.3	82.5	3.21	5.89
labyrinth	52.43	38.02	1050	1050	12.67	481.7

ponents, i.e the felt material and the labyrinth inclusion, are modelled as effective acoustic fluids equivalent to rigid materials with open porosity saturated with air.

The well-known Johnson-Champoux-Allard-Lafarge (JCAL) model [1] is employed for both equivalent fluids. This model requires six intrinsic parameters of a porous material to fully describe its acoustic behaviour. These parameters are: porosity (ϕ), tortuosity (α_∞), viscous characteristic length (Λ_v), thermal characteristic length (Λ_th), static viscous permeability ($\mathcal{K}_0$), and static thermal permeability (Θ_0). They are discussed below for both composite components.

Once the six parameters are known for a porous material, its two dynamic permeabilities – viscous and thermal – can be calculated using the scaling functions of the JCAL model. The scaling functions, and therefore both dynamic permeabilities, depend on the frequency f. The dynamic viscous permeability also depends on the kinematic viscosity of the air saturating the pores, while the dynamic thermal permeability depends on the thermal diffusivity of air. The dynamic permeabilities are used to calculate the effective properties of the equivalent fluid: firstly, the effective density and compressibility, and then also the effective speed of sound and characteristic impedance. For this purpose, the ambient mean pressure and some other air properties are also required. Details can be found in Refs. [1, 18].

3.2 Parameters for the conventional acoustic felt

For the acoustic polyester felt, the JCAL parameters were determined experimentally using inverse characterisation combined with gravimetric analysis. The Porosity was estimated directly by the gravimetric analysis, while the remaining five parameters were obtained by fitting theoretical predictions of the surface acoustic impedance and reflection coefficient to the corresponding experimental results measured in an impedance tube on a circular sample of the felt panel. This hybrid procedure ensured correct parameter estimation, enabling precise modelling of the acoustic behaviour of the felt. The parameters characterised for the felt material are given in Table 2.

3.3 Parameters for the labyrinthine inclusion

In contrast to the felt, all six JCAL parameters can be determined analytically for the 3D printed labyrinthine inclusion, because its microstructural geometry is relatively simple and well-defined. It is clearly visible in Figure 3 which shows a cross-section of the composite sample. The inclusion has three identical labyrinthine channels of constant width w, which along with the remaining two dimensions a and b (see Figure 3) uniquely define the two-dimensional microgeometry of the inclusion. The actual values of all necessary dimensions are given in Table 1. These dimensions allow for a direct calculation or estimation of the required JCAL parameters.

The porosity defined as the volume ratio of air in the three channels to the total volume of the inclusion can be determined from the microstructural geometry of its cross-section (see Figure 3), namely

$$\phi = \frac{3w\ell}{WH}\,, \tag{1}$$

where

$$\ell = 16a + 14b + 14w \tag{2}$$

is the length of each labyrinthine channel (calculated along its centreline with sharp corners at each bend).

Since the channels are identical and have a constant width, the kinematic tortuosity can be estimated using the definition of geometric tortuosity [13, 19, 20], i.e. as the squared ratio of the channel length ℓ to the material thickness H. Zielinski et al. [13] demonstrated that to make this estimation more accurate the channel length should be replaced by the estimated length of the flow path through the channel

$$\widetilde{\ell} \approx \ell - 24w + 24\frac{\pi}{2}\frac{w}{2}\,. \tag{3}$$

Here, the flow path is accurately approximated by the channel centreline with rounded corners (at each of

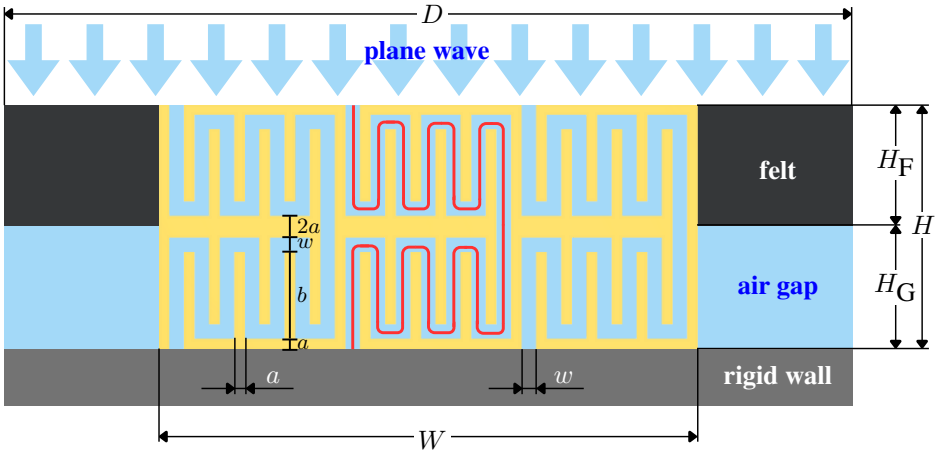


Figure 3. Cross-section of the composite panel (see Table 1 for the actual dimensions).

24 bends), marked with a red curve in Figure 3. Therefore, the tortuosity of the labyrinthine material is calculated as follows

$$\alpha_\infty \approx \left(\widetilde{\ell}/H\right)^2. \tag{4}$$

For a channel with constant width, the thermal characteristic length is equal to its width. This also applies to the characteristic viscous length if the channel is straight. When it is tortuous, as in the case of labyrinthine slits of this work, the channel width is still a very good approximation of the viscous length [1, 13]. Therefore,

$$\Lambda_\mathrm{v} \approx \Lambda_\mathrm{th} = w\,. \tag{5}$$

Based on the determined parameters, the viscous and static thermal permeabilities can be computed for the material with labyrinthine slits, using the following formulae

$$\mathcal{K}_0 \approx \frac{\phi\, w^2}{12\alpha_\infty}\,, \qquad \Theta_0 \approx \frac{\phi\, w^2}{12}\,. \tag{6}$$

The values of JCAL parameters calculated for the labyrinthine inclusion are listed in Table 2, where they can be confronted with those determined for the felt material.

3.4 Surface acoustic impedances

The JCAL parameters determined for the felt matrix and labyrinth inclusion (see Table 2) allowed the calculation of the effective properties for both equivalent fluids that represent these materials in acoustic modelling. In particular, the effective speed of sound for the felt material c_F and for the labyrinth c_L were calculated along with the corresponding characteristic impedances, Z_F and Z_L, respectively. Recall that all these effective properties are complex functions of frequency.

The effective properties can be used to determine sound wave propagation in fluids equivalent to porous materials. Important acoustic indicators such as surface acoustic impedance of a porous layer can be determined. The surface acoustic impedance $\mathcal{Z}_\mathrm{sF}$ of a hard-backed felt panel with thickness H_F and the surface impedance $\mathcal{Z}_\mathrm{sL}$ of a hard-backed labyrinthine material with thickness H_L are calculated as follows

$$\mathcal{Z}_\mathrm{sF} = Z_\mathrm{F} \coth\left(\mathrm{i}\omega H_\mathrm{F}/c_\mathrm{F}\right), \tag{7}$$

$$\mathcal{Z}_\mathrm{sL} = Z_\mathrm{L} \coth\left(\mathrm{i}\omega H/c_\mathrm{L}\right). \tag{8}$$

Here, $\omega = 2\pi f$ is the angular frequency and $\mathrm{i} = \sqrt{-1}$.

Recall that the felt matrix in the composite panel is backed by an air gap of thickness $H_\mathrm{G} = H - H_\mathrm{F}$, see Figure 3. Therefore, the surface acoustic impedance of such a two-layer system is required, i.e.

$$\mathcal{Z}_\mathrm{sFG} = \frac{\mathcal{Z}_\mathrm{sF}^2 + \mathcal{Z}_\mathrm{sF}\mathcal{Z}_\mathrm{sG}}{\mathcal{Z}_\mathrm{sF} + \mathcal{Z}_\mathrm{sG}}\,. \tag{9}$$

In the formula above

$$\mathcal{Z}_\mathrm{sG} = Z_0 \coth\left(\mathrm{i}\omega H_\mathrm{G}/c_0\right) \tag{10}$$

is the surface acoustic impedance of a hard-backed air gap with thickness H_G. Here, Z_0 and c_0 are the characteristic impedance and speed of sound in air, respectively.

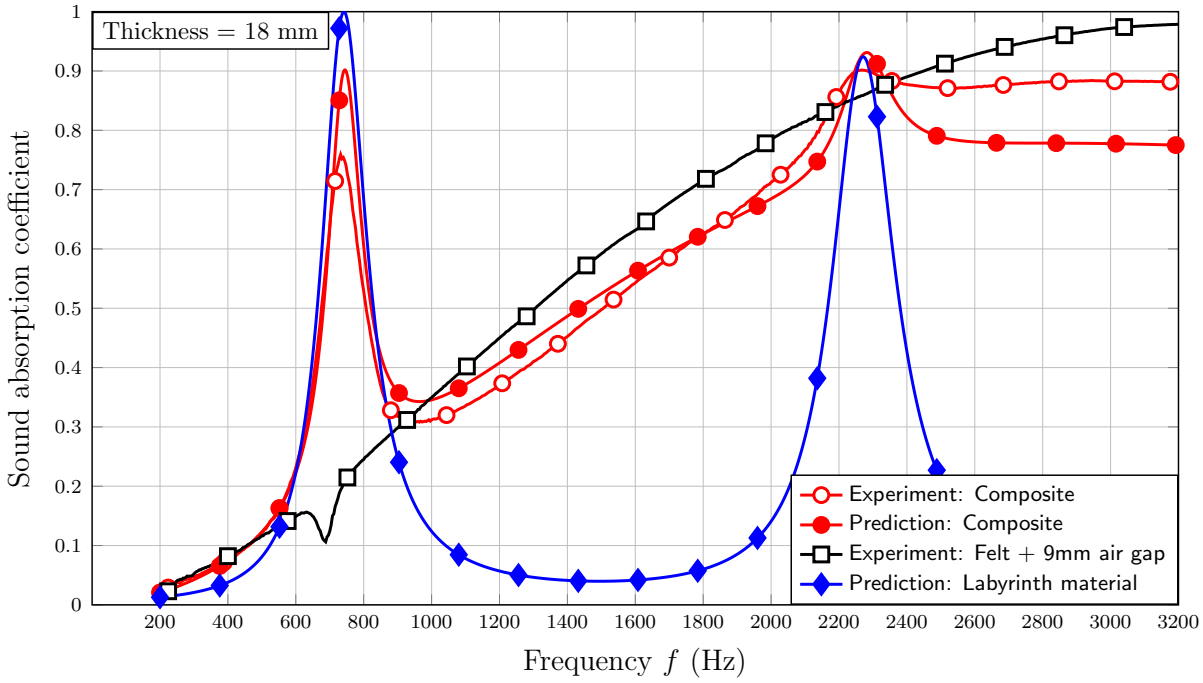


Figure 4. Sound absorption measured and predicted for the acoustic composite sample, measured for the felt panel backed by an air gap, and calculated for the labyrinthine material.

Finally, the surface acoustic impedance of the composite panel can be determined as

$$\mathcal{Z}_{\mathrm{sC}} = \frac{1}{\Phi_{\mathrm{L}}/\mathcal{Z}_{\mathrm{sL}} + (1-\Phi_{\mathrm{L}})/\mathcal{Z}_{\mathrm{sFG}}}\,, \tag{11}$$

where

$$\Phi_{\mathrm{L}} = \frac{W^2}{\pi D^2/4} \tag{12}$$

is the fraction of the inclusion face area relative to the front surface area of the composite sample, see Figure 1 (b). Formula (11) describes in fact the combined surface acoustic impedance of two components, i.e. the air-supported felt matrix and the labyrinthine inclusion arranged (acting) in parallel [21].

4. SOUND ABSORPTION

4.1 Predictions and measurements

This section presents the predictions and measurement results of sound absorption at normal incidence for the acoustic composite studied in this work. The predictions were calculated using the surface acoustic impedances defined in Section 3.4 and the well-known formulae for the reflection and sound absorption coefficients, see e.g. Ref. [1]. The experimental measurements were performed on the composite sample, see Figure 1 (c), using an impedance tube set-up according to ISO standard 10534-2 [22]. The impedance tube has an internal diameter of $D = 63.5\,\mathrm{mm}$, which ensures plane wave propagation within the frequency range of interest up to 3.2 kHz. The transfer function method with two microphones was used to determine the sound absorption coefficient under normal incidence conditions [22].

Figure 4 shows both the experimental and analytical results obtained for the composite sample. A prediction of sound absorption for the labyrinthine material itself is also presented, as well as the absorption curve measured for the homogenous felt panel backed by an air gap.

4.2 Comparison and discussion of the results

The sound absorption curves shown in Figure 4 can be compared, as they all correspond to configurations with the same total thickness of $H = 18\,\mathrm{mm}$.

The black curve with square markers represents the absorption coefficient measured for a reference configuration consisting of a 9 mm polyester felt backed by a 9 mm air gap. As expected, this material exhibits very good absorption capacity in the mid- and high-frequency ranges, but rather poor performance at lower frequencies, although the overall absorption is improved by the air gap. Furthermore, the undesirable effect related to the resonance of the elastic skeleton of the felt is clearly visible around 700 Hz. It locally reduces the already weak low-frequency absorption. Incidentally, such poroelastic behaviour occurs only around this resonant frequency of the skeleton, and the rigid-frame equivalent-fluid model is appropriate and valid for the entire frequency range beyond the elastic-skeleton resonance.

To overcome the limitations of the felt acoustic panel, a labyrinth inclusion was designed using the model described in Section 3 to introduce a subwavelength resonance with a frequency similar to the resonance frequency of the elastic skeleton of the felt. This is evidenced by the corresponding sound absorption calculated for the labyrinthine material, represented with the blue curve with diamond markers in Figure 4. This curve has two absorption peaks and perfect absorption is achieved with the first peak at about 750 Hz.

After embedding the labyrinthine inclusion in the polyester felt to form an acoustic composite panel, significant improvement in sound absorption was achieved in the targeted low frequency range. The predicted and measured acoustic absorption performance of the composite is shown in Figure 4 by two red curves marked with circles. These curves show good agreement with each other, which confirms the validity of the analytical model proposed in Section 3. It is easy to observe that incorporating the labyrinthine inclusion into the polyester felt does not degrade its good mid-to-high-frequency sound absorption. Instead, the combined acoustic absorption performance of a conventional porous matrix and a metamaterial inclusion is achieved.

5. CONCLUSIONS

An acoustic composite panel combining conventional acoustic felt with 3D-printed labyrinthine inclusions was researched and designed to enhance low-frequency sound absorption while retaining the natural ability of the felt to absorb mid- and high-frequency noise.

The impedance-tube measurements performed on a composite sample confirm that tailored labyrinthine inclusions can significantly increase the sound absorption at low frequencies through a quarter-wavelength resonance tuned in design. At the same time, embedding metamaterial inclusions into the felt matrix in the appropriate proportion does not significantly affect the good performance of the matrix material in the mid and high frequency range, offering a lightweight and space-saving solution for broadband sound absorption.

The good agreement of the measurement results with the predictions proved that the applied analytical modelling based on the equivalent fluid approach and the calculation of the surface impedance of the sound-absorbing elements working in parallel are correct and accurate.

Future work will focus on manufacturing larger composite samples and testing them in different configurations and noise conditions, e.g. as liners in a duct or in a diffuse field, to evaluate their performance under real-world conditions.

6. ACKNOWLEDGMENTS

This research was financially supported by the National Science Centre (NCN), Poland, under Grant Agreement No. 2021/41/B/ST8/04492.

7. REFERENCES

[1] J. F. Allard and N. Atalla, *Propagation of Sound in Porous Media: Modeling Sound Absorbing Materials, 2nd ed.* Chichester: John Wiley & Sons, 2009.

[2] J.-P. Groby, N. Jiménez, and V. Romero-García, "Acoustic metamaterial absorbers," in *Acoustic Waves in Periodic Structures, Metamaterials, and Porous Media: From Fundamentals to Industrial Applications* (N. Jiménez, O. Umnova, and J.-P. Groby, eds.), ch. 5, pp. 167–204, Cham: Springer International Publishing, 2021.

[3] J. Huang, J. Wang, T. Ma, H. Wei, S. Zhang, G. Wang, L. Wang, Q. Wang, W. Zhou, and Z. Zhang, "Composite structure with porous material and parallel resonators for broadband sound absorption at low-to-mid frequencies," *Applied Acoustics*, vol. 225, p. 110193, 2024.

[4] W. Kong and T. Fu, "A novel butterfly double-panel metastructure filled with porous materials for broadband low-frequency sound absorption," *Journal of Building Engineering*, vol. 97, p. 110935, 2024.

[5] S. Bi, E. Wang, X. Shen, F. Yang, X. Zhang, X. Yang, Q. Yin, C. Shen, M. Xu, and J. Wan, "Enhancement of sound absorption performance of Helmholtz resonators by space division and chamber grouping," *Applied Acoustics*, vol. 207, p. 109352, 2023.

[6] Y. Qian, B. Li, and J. Zhang, "Study of ultra-wideband acoustic metamaterial based on multi-order broadband resonance band coupling of ultra-micro perforated panel," *Applied Acoustics*, vol. 235, p. 110643, 2025.

[7] P.-F. Zhang, Z.-H. Li, Y.-J. Zhou, Q.-F. Zhang, B. Liu, F. Liu, S.-C. Pei, K. Shi, and P. kang Bai, "Improved sound absorption with 3D-printed micro-perforated sandwich structures," *Journal of Materials Research and Technology*, vol. 34, pp. 855–865, 2025.

[8] F. Wu, X. Zhang, Z. Ju, J. Zhao, M. Hu, M. Gao, J. Luo, and H. Pu, "Ultra-broadband sound absorbing materials based on periodic gradient impedance matching," *Frontiers in Materials*, vol. 9, 2022.

[9] Y. Liu, X. Zeng, S. Ren, W. Sun, H. Wang, and Y. Lei, "A broadband multi-resonant sound-absorbing metastructure based on impedance-matching nesting channels," *Applied Acoustics*, vol. 223, p. 110099, 2024.

[10] S. Ren, Y. Liu, W. Sun, H. Wang, Y. Lei, H. Wang, and X. Zeng, "Broadband low-frequency sound absorbing metastructures composed of impedance matching coiled-up cavity and porous materials," *Applied Acoustics*, vol. 200, p. 109061, 2022.

[11] G. do N. Almeida, E. F. Vergara, L. R. Barbosa, A. Lenzi, and R. S. Birch, "Sound absorption metasurface with symmetrical coiled spaces and micro slit of variable depth," *Applied Acoustics*, vol. 183, p. 108312, 2021.

[12] H. Zhao, Y. Wang, D. Yu, H. Yang, J. Zhong, F. Wu, and J. Wen, "A double porosity material for low frequency sound absorption," *Composite Structures*, vol. 239, p. 111978, 2020.

[13] T. G. Zieliński, K. C. Opiela, N. Dauchez, T. Boutin, M.-A. Galland, and K. Attenborough, "Extremely tortuous sound absorbers with labyrinthine channels in non-porous and microporous solid skeletons," *Applied Acoustics*, vol. 217, p. 109816, 2024.

[14] I. Lee, I. Han, and G. Yoon, "Compact acoustic metamaterials based on azimuthal labyrinthine channels for broadband low-frequency soundproofing and ventilation," *Applied Acoustics*, vol. 228, p. 110273, 2025.

[15] C. Lagarrigue, J. P. Groby, V. Tournat, O. Dazel, and O. Umnova, "Absorption of sound by porous layers with embedded periodic arrays of resonant inclusions," *The Journal of the Acoustical Society of America*, vol. 134, pp. 4670–4680, 12 2013.

[16] Y. Fang, X. Zhang, J. Zhou, J. Guo, and X. Huang, "Acoustic metaporous layer with composite structures for perfect and quasi-omnidirectional sound absorption," *Composite Structures*, vol. 223, p. 110948, 2019.

[17] Q. Xu, J. Qiao, Z. Ren, J. Sun, G. Zhang, and L. Li, "Multi synergistic coupling design for broadband sound absorption based on compact porous composite embedded with massless membrane resonator," *Composite Structures*, vol. 286, p. 115312, 2022.

[18] T. G. Zieliński, R. Venegas, C. Perrot, M. Červenka, F. Chevillotte, and K. Attenborough, "Benchmarks for microstructure-based modelling of sound absorbing rigid-frame porous media," *Journal of Sound and Vibration*, vol. 483, p. 115441, 2020.

[19] K. Attenborough, "Microstructures for lowering the quarter wavelength resonance frequency of a hard-backed rigid-porous layer," *Applied Acoustics*, vol. 130, pp. 188–194, 2018.

[20] B. Ghanbarian, A. G. Hunt, R. P. Ewing, and M. Sahimi, "Tortuosity in porous media: A critical review," *Soil Science Society of America Journal*, vol. 77, no. 5, pp. 1461–1477, 2013.

[21] K. Verdière, R. Panneton, S. Elkoun, T. Dupont, and P. Leclaire, "Transfer matrix method applied to the parallel assembly of sound absorbing materials," *The Journal of the Acoustical Society of America*, vol. 134, pp. 4648–4658, 12 2013.

[22] "ISO 10534-2: Determination of sound absorption coefficient and impedance in impedance tubes," 1998.

DOI: 10.61782/fa.2025.0724



FORUM ACUSTICUM
EURONOISE 2025

RAINBOW TRAPPING RESONATOR ARRAY FOR HIGH-LEVEL SOUND ABSORPTION

Adam Cavanagh[1*] **Olga Umnova**[1] **Deepak Akiwate**[1]
[1] University of Salford, Acoustics Research Centre, M5 4WT, Salford, UK

ABSTRACT

This study analyses a proof-of-concept ducted rainbow-trapping resonator array designed for high-level sound absorption. By tuning the dimensions of the array's resonators, it absorbs sound waves over a broad frequency range and with increasing efficiency with incident pressure amplitude. The arrays' acoustic behaviour was modelled numerically, where the greatest attenuation was observed at the highest level considered, 155 dB. The results show the potential applicability of absorber designs that exhibit rainbow-trapping behaviour to high-intensity environments.

Keywords: *high-amplitude sound, acoustic rainbow-trapping, resonator array, sound attenuation, resonator nonlinearity*

1. INTRODUCTION

Sound absorbers based on resonant cavities, i.e. those in perforated liners, can exhibit significant local nonlinear effects at high SPLs, impairing or enhancing absorption properties [1, 2]. The dominating nonlinear effect in resonant absorbers is the increased resistance with incident wave amplitude. A HR side-loaded to a principal waveguide can exhibit increased energy dissipation by converting the incident wave's energy to vortical kinetic energy at the sharp edges of the resonator's neck, i.e., at discontinuities. For instance, this increased dissipation can induce coherent perfect absorption at high SPLs [3]. The perforations in a liner's face sheet exhibit similar effects at high SPL. These effects have been extensively studied (see,e.g. [4, 5], and can significantly alter an absorber's intended performance.

Another approach to increase absorption is absorbers with graded spatial properties, i.e., "rainbow-trapping" structures. These are designed using arrays of critically coupled resonators with frequency-cascaded band gaps to target a broadband frequency range. This way the spatial grading results in a "slow sound" phenomenon where different frequency waves become confined to specific points along the array's length, resulting in highly efficient and even perfect absorption in transmission problems [6]. Moreover, [7] have studied in detail the acoustic properties of an acoustic black hole absorber, providing valuable insights into the effect of geometry on performance and behaviour.

Maintaining efficient broadband absorption at high SPLs remains challenging due to resonators' nonlinear effects at such levels. The works of [6, 7] highlight the effectiveness of spatially graded absorbers for broadband sound absorption, and those of [3–5] offer insights into the theory and design principles of effective high-level absorption. Together, these contributions provide a compelling foundation for designing superior broadband sound absorbers for high-intensity environments.

This work evaluates the sound absorption performance of rainbow-trapping resonator arrays (RTRAs) in linear and nonlinear acoustic regimes. Two designs are considered, the first optimised for maximum linear regime absorption and the second for maximum nonlinear regime absorption. These are respectively denoted RTRA_1 and RTRA_2 hereinafter. Notably that the present configurations and simulations are for the two-dimensional case and serve as a proof of concept for nonlinear-aware optimisation applied to rainbow-trapping absorbers. The geo-

*Corresponding author: a.a.cavanagh1@salford.ac.uk.
Copyright: ©2025 A. Cavanagh et al. This is an open-access article distributed under the terms of the Creative Commons Attribution 3.0 Unported License, which permits unrestricted use, distribution, and reproduction in any medium, provided the original author and source are credited.

metric configurations and modelling approach, results and discussion, and conclusions and further work are respectively presented in 2, 3, and 4.

2. METHODOLOGY

Both structures comprise an array of $N_1 = 8$ and $N_2 = 5$ differing HRs, respectively, each side-loaded to a principal waveguide of constant height arbitrarily set to 29 mm, see Fig. 1. The RTRAs' lengths and heights are constrained to a maximum length $L_t = 100$ mm and height $H_t = 30$ mm to ensure compactness and applicability to small ducts. Four parameters describe each HR's geometric configuration due to the two-dimensional setup. These parameters are the neck and cavity lengths and widths, respectively denoted $l_n^{[n]}$, $l_c^{[n]}$, $d_n^{[n]}$, and $d_c^{[n]}$ (superscript $[n]$ denotes the n^{th} HR). Each HR is designed such that its resonance frequency f_r is close to the n^{th} value in a set $\mathcal{F}$ of N_n equally spaced frequencies over the range $f_1 = 1$ kHz to $f_N = 2$ kHz. In this way, the resonances overlap to cover a broadband frequency range due to their moderate Q factors.

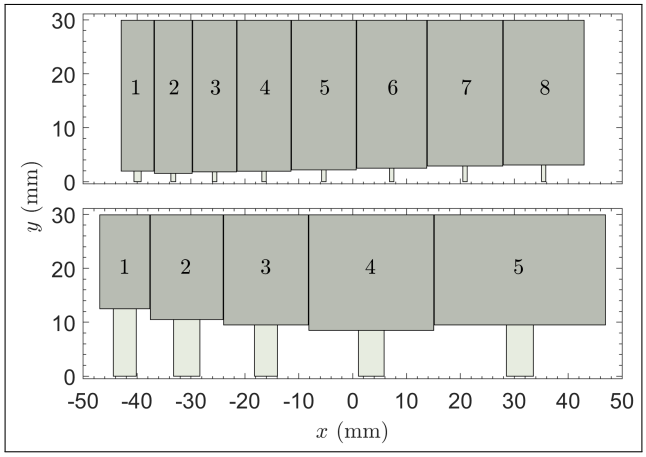


Figure 1. Linear (top) and nonlinear (bottom) optimised RTRA geometric configurations; principal waveguide is not illustrated for clarity, but is placed horizontally at $x = 0$. Geometry is in two-dimensions, meaning the structures extend infinitely into and out of the page.

2.1 Optimisation Scheme

The design process began with the development and numerical validation of an analytical model using the transfer matrix method (TMM) with effective complex and frequency-dependent density and compressibility obtained using the Johnson-Champoux-Allard equivalent fluid model [8, 9]. Then, an optimisation scheme similar to that in [6] was implemented to fine-tune the HRs dimensions. The scheme's genetic algorithm (GA) sought to minimise the cost function,

$$\mathcal{C} = \sum_{f \in \mathcal{F}} |R(f)|^2 + |T(f)|^2 + \varepsilon\,, \tag{1}$$

i.e., to minimise the system's leakage. The quantity ε denotes a conditional penalty applied if the RTRAs' length, L, exceeds L_t ($\varepsilon = |L - L_t|$), $\varepsilon = 0$ otherwise. It controlled $l_n^{[n]}$, $d_n^{[n]}$, and $d_c^{[n]}$ with 0.01 mm minimum step size, the remaining $l_c^{[n]}$ was implicitly defined in the cost function such that $l_c^{[n]} = Ht - l_n^{[n]} - h$, where $h = 0.1$mm is a realistically manufacturable wall thickness value.

2.2 Numerical Model

Nonlinear behaviour was approximated numerically using FEM in COMSOL Multiphysics 6.2™. More precisely, nonlinear effects were accounted for using the interior perforated plate boundary condition (BC) in the Frequency Domain Pressure Acoustics interface. The BC implements the model in [4] for circular micro- and macro-perforations. Although the present configurations are in two dimensions, meaning they have slit-shaped necks, this formulation is considered acceptable under this work's conceptual nature because the underlying theory is general and applies to realistic geometries. Furthermore, the TMM's equivalent fluid model does not account for the distinct flow behaviour in larger holes and hence will not agree with FEM results for the second design, RTRA_2, where the neck widths are not much less than the target wavelength (see Tab. 2). While the RTRA_1 neck widths are significantly smaller, the TMM results were used solely for optimisation and are omitted from this work.

2.3 RTRA_1 – Optimised for Linear Regime

RTRA_1, with $N_1 = 8$ HRs side-loaded to the principal waveguide (see Fig. 1), is optimised for maximum absorption in the linear regime. The resonator geometric parameters were constrained during the optimisation process to

ensure correct cascading of resonance bandgaps. See Tab. 1 for the resulting RTRA_1 resonator dimensions.

Table 1. Geometric parameters for RTRA_1. All dimensions are given in millimetres.

n	$l_n^{[n]}$	$d_n^{[n]}$	$l_c^{[n]}$	$d_c^{[n]}$
1	1.96	1.33	27.94	6.08
2	1.53	0.90	28.37	6.99
3	1.82	0.83	28.08	8.14
4	1.94	0.80	27.96	10.00
5	2.18	0.83	27.72	12.00
6	2.50	0.81	27.40	13.00
7	2.90	0.81	27.00	14.00
8	3.09	0.79	26.81	15.00

2.4 RTRA_2 – Optimised for Nonlinear Regime

RTRA_2 is designed with high SPL absorption in mind. Sound levels inside, e.g. an aeroengine can breach the nonlinear regime during flight conditions ($>$ 150 dB) [10]. Shock waves can form at such levels if the wave can propagate sufficiently far uninterrupted. The distance a shock wave will from its sound source, known as the shock formation distance, is given by [11],

$$\overline{x} = \frac{\rho_0 c_0^3}{\omega \beta p_0'}, \tag{2}$$

where ρ_0, c_0, ω, β, and p_0' denote the density of air in kg/m^3, sound speed in air in m/s, angular frequency in rad/s, coefficient of nonlinearity in air (dimensionless) equally approximately 1.2 , and the incident wave's amplitude in Pa, respectively. Shock formation distance is inversely related to f and p_0', meaning reduction in $\overline{x}$ with increased f or p_0'. The RTRA_2's L should remain minimum one magnitude smaller than $\overline{x}$ to suppress internal shock formation.

The design accounts for nonlinear effects like flow separation and vortex shedding in the necks. These effects are realised as the dependency of the neck's acoustic resistance on incident wave amplitude, increasing the conversion of the incident wave's energy into thermal and vortical kinetic energy. Typical micro-perforation sizes present flow resistivity values that are too high for the effective transfer of wave energy into the resonators due to the non-negligible inertial effects at high SPLs. HR neck widths in RTRA_2 were thus constrained to a minimum size of 4 mm during optimisation. In this way, the GA tuned the resonators close to their respective $f \in \mathcal{F}$ while ensuring sufficiently low flow resistivity. RTRA_2 optimised dimensions are tabulated in Tab. 2.

Table 2. Geometric parameters for RTRA_2. All dimensions are given in millimetres.

n	$l_n^{[n]}$	$d_n^{[n]}$	$l_c^{[n]}$	$d_c^{[n]}$
1	12.50	4.25	17.40	9.28
2	10.50	4.89	19.40	13.51
3	9.50	4.25	20.40	15.71
4	8.50	4.75	21.40	23.18
5	9.50	5.00	20.40	31.77

3. RESULTS

Both RTRAs' performance is analysed numerically at three increasing excitation levels (80, 130, and 155 dB) to understand linear and nonlinear regime behaviour.

3.1 Linear Regime Performance

Individual resonator α is illustrated in Fig. 2. The f_r cascade is clear for both RTRAs. RTRA_1's resonators (Fig. 2 [a]) exhibit α peaks approximately over the range 750 Hz to 1720 Hz, with a gradual reduction in f from the first to last HR. Although the n^{th} HR's f_r should approximately match the corresponding $f \in \mathcal{F}$, the first four HRs exhibit maxima below 1000 Hz. This discrepancy is not too problematic (see succeeding results) and is likely attributed to the optimisation process, where the GA does not strictly know to tune each HR to each f. Conversely, most of RTRA_2's HRs present α maxima inside the target range $\mathcal{F}$, excluding the final $n = N_2$ HR.

The frequency cascade effect becomes clear when comparing the individual resonator α peaks with the full RTRA α shown in Fig. 3 (a). RTRA_1 exhibits good broadband absorption across most of the target range. The best performance is between approximately 1000–1400 Hz, with consistent $\alpha \approx 0.9$ and minimal R and T. RTRA_2 shows adequate broadband α in the linear regime despite

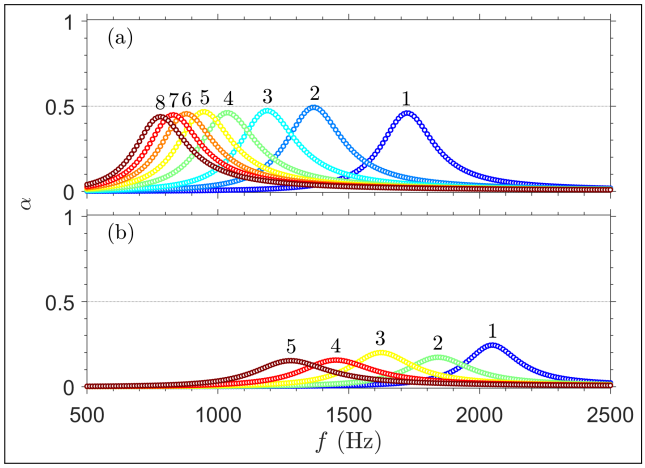


Figure 2. Sound absorption coefficients of each of the $N_1 = 8$ HRs in RTRA$_1$ (a), and for each of the $N_2 = 5$ HRs in RTRA$_2$ (b). The n^{th} HR's absorption curve is indicated by the numbers located at each of the maxima. Dotted horizontal line represents maximum possible α of a single side-loaded HR, i.e., coeherent perfect absorption.

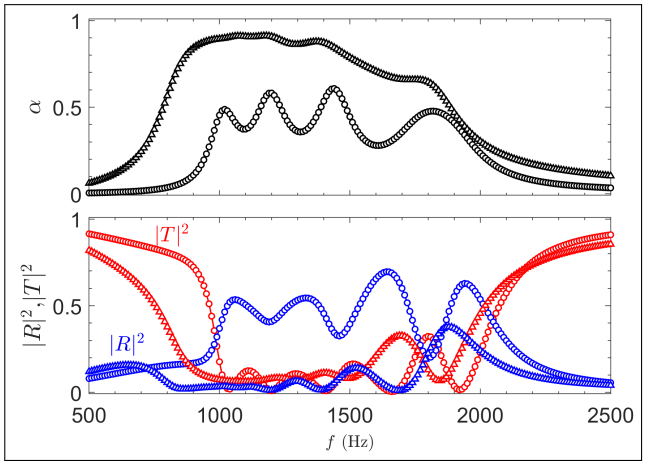


Figure 3. Sound absorption (top), reflection and transmission (bottom) coefficients obtained numerically with FEM model with 80 dB incident SPL. The coefficients for RTRA$_1$ and RTRA$_2$ are indicated by the triangle and circle markers. Red and blue curves represent reflection and transmission coefficients.

the geometric constraints. The four α peaks at approximately 1000, 1200, 1450, and 1820 Hz show the frequency cascade effect clearly, where the n^{th} and $n^{th}+1$ HR resonances accumulate [1], causing maxima between their individual resonances.

3.2 Nonlinear Regime Performance

Nonlinear regime α performance for both RTRAs is presented in Fig. 4. RTRA$_1$ (Fig. 4 [a]) shows a pronounced deterioration from the broadband $\alpha \approx 0.85$ at 80 dB to a broadband $\alpha \approx 0.75$ at 155 dB. This behaviour is mainly due to the neck's small widths, which increases flow resistivity at higher SPLs (i.e., reduced wall admittance in the neck). Notably, the first resonator ($f_r \approx 1720$ Hz) shows an increased α at 130 dB, which then deteriorates at 155 dB. This behaviour can be attributed mostly to the relatively large d_n^1 chosen by the GA, the perforation size is large enough to increase dissipation in the weakly nonlinear regime, but is too small to behave in the same way in the full nonlinear regime.

RTRA$_2$ (Fig. 4 [b]) exhibits significant α growth with incident SPL. The necks' larger widths (see Tab. 2) performed as intended and resulted in their flow resistivities having a weaker amplitude-dependency, resulting in increased dissipation and absorption as expected.

[1] All resonances accumulate in actuality.

4. CONCLUSIONS AND FURTHER WORK

This work investigated the design and optimisation of a conceptual rainbow-trapping resonator array for high-level sound absorption. The arrays' performance were analysed numerically. Results show that, depending on the intended usage, the absorbers are effective broadband sound absorbers in both linear and nonlinear acoustic regimes. The frequency-cascaded resonances of the arrays' resonators cause efficient targetted absorption of differing frequency waves along their lengths.

Further work will focus on realising a rainbow-trapping resonator array for small ducts, including realistic geometry (e.g., axial symmetry), comparisons with TMM results and experimental data.

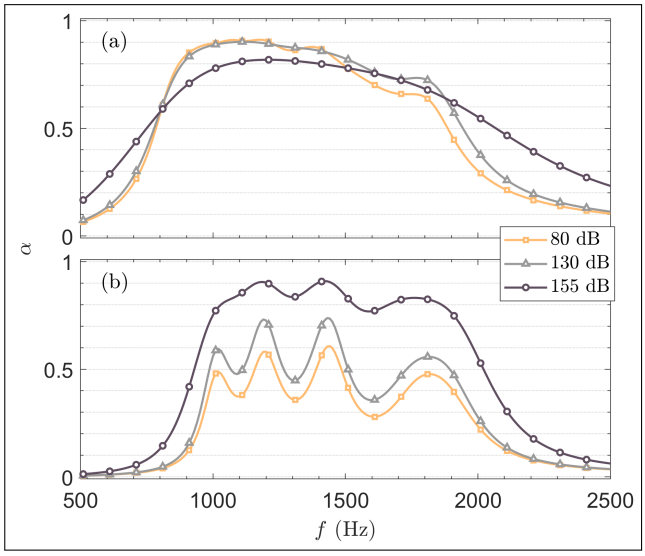


Figure 4. Sound absorption coefficients of the RTRAs at increasing incident SPLs obtained numerically with FEM model. (a) $RTRA_1$ (b) $RTRA_2$.

5. REFERENCES

[1] D. C. Brooke, O. Umnova, P. Leclaire, and T. Dupont, "Acoustic metamaterial for low frequency sound absorption in linear and nonlinear regimes," *Journal of Sound and Vibration*, vol. 485, 10 2020.

[2] M. Meissner, "The influence of acoustic nonlinearity on absorption properties of helmholtz resonators. part 1. theory," *Archives of Acoustics*, vol. 24, no. 2, pp. 179–190, 1999.

[3] V. Achilleos, O. Richoux, and G. Theocharis, "Coherent perfect absorption induced by the nonlinearity of a helmholtz resonator," *The Journal of the Acoustical Society of America*, vol. 140, pp. EL94–EL100, 07 2016.

[4] M. A. Temiz, J. Tournadre, I. L. Arteaga, and A. Hirschberg, "Non-linear acoustic transfer impedance of micro-perforated plates with circular orifices," *J. Sound Vib.*, vol. 366, pp. 418–428, 03 2016.

[5] Z. Laly, N. Atalla, and S.-A. Meslioui, "Acoustical modeling of micro-perforated panel at high sound pressure levels using equivalent fluid approach," *Journal of Sound and Vibration*, vol. 427, pp. 134–158, 08 2018.

[6] N. Jiménez, V. Romero-García, V. Pagneux, and J.-P. Groby, "Rainbow-trapping absorbers: Broadband, perfect and asymmetric sound absorption by subwavelength panels for transmission problems," *Scientific Reports*, vol. 7, 10 2017.

[7] G. Bezançon, O. Doutres, O. Umnova, P. Leclaire, and T. Dupont, "Thin metamaterial using acoustic black hole profiles for broadband sound absorption," *Applied Acoustics*, vol. 216, 01 2024.

[8] N. Jiménez, O. Umnova, and G. Jean-Philippe, eds., *Acoustic Waves in Periodic Structures, Metamaterials, and Porous Media: From Fundamentals to Industrial Applications*. Springer International Publishing, 2021.

[9] J. Allard and N. Atalla, *Propagation of sound in porous media*. Hoboken, NJ: Wiley-Blackwell, 10 2009.

[10] E. P. Ross, K. M. Figueroa-Ibrahim, S. C. Morris, D. L. Sutliff, and G. J. Bennett., "Evaluating an additive manufactured acoustic metamaterial using the advanced noise control fan," *AIAA Journal*, vol. 62, pp. 2783–2799, 07 2024.

[11] M. F. Hamilton and D. T. Blackstock, eds., *Nonlinear acoustics*. San Diego, CA: Academic Press, 11 1997.

DOI:

Main theme: A10 Materials and Metamaterials

Session A10.04 Materials and systems for noise and vibration reduction

Chair(s): F. Pompoli, J. Carbajo San Martín, J. Arenas

DOI:

Main theme: A23 Vibro-Acoustics

Session A10.05/A23.05 Metamaterials and acoustic black holes in vibro-acoustics

Chair(s): J. Deng, F. Gautier, W. Jeon

DOI: 10.61782/fa.2025.0102



FORUM ACUSTICUM
EURONOISE 2025

ADDITIVE ACOUSTIC BLACK HOLES TO SUPPRESS ACOUSTIC ENERGY IN A RESONANT CAVITY

Jie Deng[1,2*] **Oriol Guasch**[2] **Xu Chen**[3]

[1] Chongqing Industry Polytechnic College, 401120 Chongqing, China
[2] Human-Environment Research (HER) group, Department of Engineering, La Salle, Universitat Ramon Llull C/Quatre Camins 30, 08022 Barcelona, Catalonia, Spain
[3] Department of Mechanical Engineering, Tsinghua University, Beijing, 100084, China

ABSTRACT

Conventional acoustic black hole (ABH) periodic arrays have been extensively investigated for their effective vibration reduction performance. However, embedded ABHs are not suitable in many problems due to the loss of structural stiffness. That is avoided with additive ABHs, which have also proven to be very valuable in suppressing vibrations. In this paper, we explore their potential for noise reduction. An additive ABH plate is connected to a uniform base plate through the corners, and then coupled to a resonant cavity filled with air. In the first configuration, the base plate is facing the cavity, while in the second one, the ABH plate is oriented towards the cavity. It is shown that, in the first configuration, the vibrations in the base plate are significantly reduced and, consequently, the acoustic energy in the cavity decreases as well. For the second configuration, moreover, the coupling force at the fluid-structure interface diminishes, so that the acoustic energy in the cavity is even lower.

Keywords: *acoustic black hole, fluid-structure interaction, cavity*

Corresponding author: *jie.deng@salle.url.edu.*

Copyright: *©2025 Jie Deng This is an open-access article distributed under the terms of the Creative Commons Attribution 3.0 Unported License, which permits unrestricted use, distribution, and reproduction in any medium, provided the original author and source are credited.*

1. INTRODUCTION

Acoustic black holes (ABHs) are very efficient in reducing the vibration and noise from thin-walled structures. However, due to the thickness reduction, the structural stiffness may weaken, limiting its applicability in many situations. Recently, additive ABHs have become a promising method to avoid such limitation. The idea is to treat the ABH components as external vibration absorbers, as done in beams [1–3] and plates [4–6].

However, most existing studies on additive ABHs focus on vibration reduction in structures. In this paper, we explore their potential for suppressing noise within a closed sound cavity, which is interesting for applications such as high-speed trains and airplanes. We consider a periodic ABH plate, with the design proposed in [7], which can be easily connected to the host plate through the corners. When the composite plate is assembled, we can couple it to the resonant cavity. Here, we consider 2 cases: i) the host plate faces the cavity (Config. I) and ii) the ABH plate faces the cavity (Config. II). It will be shown how the acoustic energy in the cavity isreduced when an external force is applied to the plate.

2. MODELING

As shown in Fig. 1a, the composite plate in Fig. 1b is placed on the top surface of a rectangular cavity, with dimensions $L_x \times L_y \times L_x = 0.8 \times 0.6 \times 0.5$ m^3, filled with air with density $\rho_0 = 1.21$ kg/m^3 and sound speed $c_0 = 343$ m/s. The host plate (see Fig. 1b), is made of steel with Young modulus $E_p = 210$ GPa, density

$\rho_p = 7800$ kg/m^3, Poisson ratio $\nu_p = 0.3$, and a thickness of $h_p = 5$ mm. On the other hand, the geometry details of the additive ABH plate are depicted in Figs. 1c and 1d, where the thickness reduces from $h_a = 3$ mm to $h_c = 0.2$ mm following the power laws $h = \frac{h_a - h_c}{r_{abh}^m}|x|^m + h_c$ and $h = \frac{h_a - h_c}{r_{abh}^m}|y|^m + h_c$ in the x and y directions, respectively, where $r_{abh} = 9$ cm, and $m = 2$. The ABH plate is also made of steel. The yellow component in Figs. 1c and 1d is the damping layer, with thickness $h_d = 2$ mm, and half width $r_d = 4.5$ cm. The damping layer has Young modulus $E_d = 5$ GPa, density $\rho_d = 950$ kg/m^3, Poisson ratio $\nu_d = 0.33$, and loss factor $\eta_d = 0.5$.

To characterize the coupled system, we employ the Gaussian expansion method (GEM) [8, 9] to model the host plate, the ABH plate (plus the damping layer) and the resonant cavity, separately. This results in the uncoupled equation of motion,

$$(\boldsymbol{K} - \omega^2 \boldsymbol{M})\boldsymbol{A} = \boldsymbol{0}, \tag{1}$$

where $\boldsymbol{K} = \mathrm{diag}(\boldsymbol{K}_p, \boldsymbol{K}_a, \boldsymbol{K}_c)$ and $\boldsymbol{M} = \mathrm{diag}(\boldsymbol{M}_p, \boldsymbol{M}_a, \boldsymbol{M}_c)$ are respectively the stiffness and mass matrices, and $\boldsymbol{A}$ is the coefficent vector of Gaussian functions.

Next we consider the coupling between substructures, and discretize the constraints for $\boldsymbol{A}$ also with Gaussian functions. Finding the the nullspace basis of the constraint matrix we get $\boldsymbol{A} = \boldsymbol{Z}\boldsymbol{k}$, where $\boldsymbol{Z}$ contains the basis vectors and $\boldsymbol{k}$ is the superposition coefficient vector [10]. Taking this relation back to Eqn. (1) results in the following coupled equation of motion,

$$(\boldsymbol{Z}^\top \boldsymbol{K} \boldsymbol{Z} - \omega^2 \boldsymbol{Z}^\top \boldsymbol{M} \boldsymbol{Z})\boldsymbol{k} = \boldsymbol{0}. \tag{2}$$

To obtain Eqs. Eqn. (1) and Eqn. (1) we have used a displacement formulation to describe all problem unknowns. Details can be found in [9].

3. RESULTS

We apply a unitary force on the plate and compute the total acoustic energy of the cavity, $E_c = \frac{1}{2\rho_0\omega^2}\int \nabla^2 p \mathrm{d}V + \frac{1}{2\rho_0 c_0^2}\int p^2 \mathrm{d}V$, E_c (dB)$= 10\lg(E_c \times 10^{12})$. To better inspect the results, we have converted the spectrum into 1/3 octave bands, see Fig. 2. It can be observed that when the cavity is coupled to the bare plate (i.e., the host plate alone), the cavity energy remains the highest above 150 Hz. When the ABH plate is placed on the top of the host one (Config. I), the sound energy is substantially reduced over the entire frequency range of interest, particularly at high frequencies. The reason for that is that the vibration of the host plate is transferred to the ABH plate where it is efficiently dissipated by the damping layer, resulting in less energy transmitted into the cavity from the

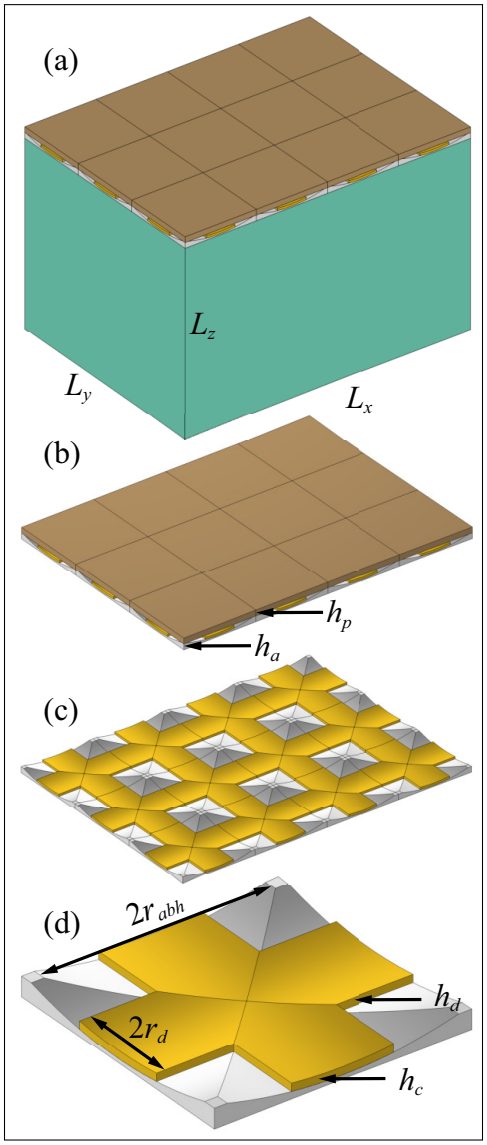


Figure 1. Geometry of the model. (a) The coupled system. (b) The composite plate. (c) The ABH plate with a damping layer (yellow region). (d) A single ABH cell.

host plate. If we change the situation and let the ABH plate face the cavity (Config. II) it is observed that the energy within the cavity is further reduced for $f > 200$ Hz. This is because the radiation efficiency of the ABH plate is lower than that of the uniform plate [11], resulting in a smaller coupling coefficient of the fluid-structure interaction [12]. .

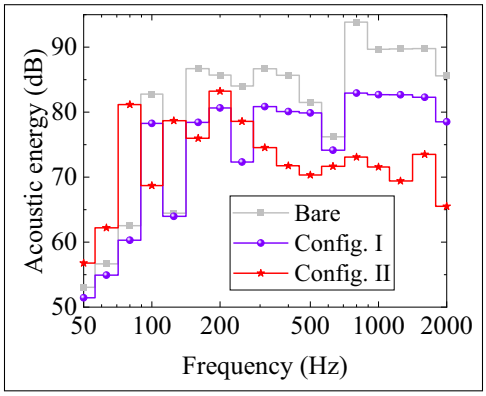


Figure 2. Comparison of the acoustic energy of the cavity of the bare host plate, and the composite plate. Config. I: The host plate is facing the cavity. Config. II: the ABH plate is facing the cavity.

4. CONCLUSIONS

In this paper, we have investigated the potential of additive acoustic black holes (ABHs) to reduce sound energy in resonant cavities. To this end, a semi-analytical model has been developed, incorporating coupling conditions using the nullspace method. Two configurations have been compared. When the uniform host plate faces the cavity, noise is efficiently suppressed due to vibration damping in the ABH plate. Alternatively, when the ABH plate faces the cavity, the sound energy inside the cavity is further reduced because the radiation efficiency decreases, leading to a lower coupling coefficient.

5. ACKNOWLEDGMENTS

J. Deng acknowledges the support received by the National Natural Science Foundation of China (52301386), and the support of the Beatriu de Pinós postdoctoral program of the Department of Research and Universities of the Generalitat of Catalonia (2022 BP 00027). O. Guasch acknowledges the support of the Generalitat de Catalunya (Departament de Recerca i Universitats) through grant 2021 SGR 1396 awarded to the HER group.

6. REFERENCES

[1] T. Zhou and L. Cheng, "A resonant beam damper tailored with acoustic black hole features for broadband vibration reduction," *Journal of Sound and Vibration*, vol. 430, pp. 174–184, 2018.

[2] J. Deng, J. Ma, X. Chen, Y. Yang, N. Gao, and J. Liu, "Vibration damping by periodic additive acoustic black holes," *Journal of Sound and Vibration*, vol. 574, p. 118235, 2024.

[3] J. Deng, N. Gao, X. Chen, B. Han, and H. Ji, "Evanescent waves in a metabeam attached with lossy acoustic black hole pillars," *Mechanical Systems and Signal Processing*, vol. 191, p. 110182, 2023.

[4] T. Zhou and L. Cheng, "Planar swirl-shaped acoustic black hole absorbers for multi-directional vibration suppression," *Journal of Sound and Vibration*, vol. 516, p. 116500, 2022.

[5] S. Park, J. Y. Lee, and W. Jeon, "Vibration damping of plates using waveguide absorbers based on spiral acoustic black holes," *Journal of Sound and Vibration*, vol. 521, p. 116685, 2022.

[6] J. Deng, X. Chen, Y. Yang, Z. Qin, and W. Guo, "Periodic additive acoustic black holes to absorb vibrations from plates," *International Journal of Mechanical Sciences*, vol. 267, p. 108990, 2024.

[7] J. Deng, L. Zheng, and N. Gao, "Broad band gaps for flexural wave manipulation in plates with embedded periodic strip acoustic black holes," *International Journal of Solids and Structures*, vol. 224, p. 111043, 2021.

[8] J. Deng, L. Zheng, O. Guasch, H. Wu, P. Zeng, and Y. Zuo, "Gaussian expansion for the vibration analysis of plates with multiple acoustic black holes indentations," *Mechanical Systems and Signal Processing*, vol. 131, pp. 317–334, 2019.

[9] J. Deng, O. Guasch, and L. Maxit, "A displacement formulation for coupled elastoacoustic problems that preserves flow irrotationality," *Journal of Sound and Vibration*, vol. 597, p. 118815, 2025.

[10] J. Deng, Y. Xu, O. Guasch, N. Gao, and L. Tang, "Nullspace technique for imposing constraints in the rayleigh–ritz method," *Journal of Sound and Vibration*, vol. 527, p. 116812, 2022.

[11] J. Deng and L. Zheng, "Noise reduction via three types of acoustic black holes," *Mechanical Systems and Signal Processing*, vol. 165, p. 108323, 2022.

[12] H. Ji, X. Wang, J. Qiu, L. Cheng, Y. Wu, and C. Zhang, "Noise reduction inside a cavity coupled to a flexible plate with embedded 2-d acoustic black holes," *Journal of Sound and Vibration*, vol. 455, pp. 324–338, 2019.

DOI: 10.61782/fa.2025.0689

FORUM ACUSTICUM EURONOISE 2025

PREDICTING THE ACOUSTIC RESPONSE OF A RESONANT CAVITY COUPLED TO SONIC BLACK HOLES BY MEANS OF PATCH TRANSFER FUNCTIONS

Pedro Cerântola[1,2*] **Laurent Maxit**[2] **Oriol Guasch**[1] **Jie Deng**[1,3]

[1] Human-Environment Research (HER) group, Department of Engineering, La Salle, Universitat Ramon Llull, C/ Quatre Camins 30, Barcelona, 08022, Catalonia, Spain
[2] Laboratoire Vibrations Acoustique (LVA), INSA Lyon, 25 bis Av. Jean Capelle O, Villeurbanne cedex, 69621, France
[3] Chongqing Industry Polytechnic College, Chongqing, 401120, China

ABSTRACT

Reducing broadband noise in enclosed spaces, such as rooms or the cabins of cars and airplanes, is a challenge for acoustic comfort. In recent years, sonic black holes (SBHs) have been investigated to achieve anechoic terminations in ducts, but their potential for room acoustics remains unexplored. A conventional SBH consists of a wave-guide with concentric inner rings of decreasing radius separated by cavities that are partially filled with absorbing material. This arrangement slows down and traps incident sound waves dissipating their energy, which results in very little reflection beyond the cut-on frequency of the SBH. In this work we study the acoustics of a resonant cavity with an array of SBHs coupled to one of its walls. The patch transfer function (PTF) method is applied to couple the cavity and the set of SBHs. For the former, an analytical modal model is used, while the response of the SBHs is characterized by means of the finite element method (FEM). This substructuring approach provides a low-cost numerical method to investigate how SBH design parameters influence the acoustic response of the cavity.

*__Corresponding author__: pedro.cerantola@salle.url.edu.
__Copyright__: ©2025 Pedro Cerântola et al. This is an open-access article distributed under the terms of the Creative Commons Attribution 3.0 Unported License, which permits unrestricted use, distribution, and reproduction in any medium, provided the original author and source are credited.

Keywords: *sonic black hole, substructuring method, patch transfer function method, room acoustics, coupled system.*

1. INTRODUCTION

In connection with the need to develop engineering solutions to control vibrations and noise, research in acoustic black holes (ABHs) has been increasing in recent years. In theory, these devices are capable of slowing down impinging elastic waves to a singularity point where the propagation and the reflection become impossible, delivering perfect energy focusing [1]. Two main classes of ABHs are investigated: the vibrational black holes (VBHs), which absorb mechanical vibrations [2, 3], and the sonic black holes (SBHs), that are intended to dissipate sound waves and which were first proposed in [4]. While VBHs consist of thin beams and plates with decreasing thickness profile indentations that can capture and dissipate bending waves, their acoustic counterpart, the SBHs, achieve the black hole effect by means of a waveguide whose inner radius decreases according to a power law profile and whose wall admittance has a specific spatial variation [5]. If a perfectly continuous SBH with a null final radius was possible, perfect absorption could be attained [4, 5].

The most common realization of an SBH is made of a homogeneous wave-guide equipped with various concentric rings of decreasing inner radii that follow the power profile and are separated by cavities. Manufacturing con-

straints such as the end truncation, number and dimensions of rings and cavities and damping mechanisms will limit the performance of the SBH (see e.g., [6–8]). To date, most works have been devoted to better characterize the SBH as a single system by using different numerical approaches [7, 9, 10] and to enhance its performance at low frequencies using microperforated panels for the cavities [11, 12] or periodic SBHs [13, 14]. Efforts have been also made to optimize the SBH design [15, 16] for a better performance, to find alternative approaches based on metafluid analogies [17, 18] and slow-down lattice absorbers [19], or to design SBH inspired mufflers [20].

However, none of the above works have considered coupling a set of SBHs to a cavity, which could be important for many industrial applications. That is the goal of this paper. Given that aiming at a full finite element method (FEM) simulation of the problem would be computationally very costly, it is herein proposed to resort to a substructuring technique. In this context, the so-called patch transfer function (PTF) is used, which has proven to be very effective in characterizing vibroacoustic systems [21–23]. This method offers a viable option to couple linear subsystems through transfer functions evaluated over patch surfaces at a very low computational cost. We will use the PTF to assess the acoustics of a homogeneous cavity when we couple a set of SBHs to it. The cavity and SBHs will be characterized separately and coupled using continuity conditions in the framework of the PTF [21]. The coupled model will be validated against a full FEM simulation of the complete model.

The main technical aspects of the modelling strategy of the proposed approach are presented in Section 2. The validation of the method is provided in Section 3. Conclusions and future research lines are drawn in Section 4.

2. PTF MODELLING PROCEDURE

2.1 PTF approach to describe the coupling between the cavity and the SBHs

As shown in Fig. 1, let us consider a rectangular cavity with dimensions $L_x \times L_y \times L_z$ coupled to N identical SBHs on face $y = 0$. For simplicity, it is assumed that there is no direct interaction between the SBHs. A monopole source is located inside the cavity at point S of coordinates (x_S, y_S, z_S). Our goal is to predict the mean quadratic pressure inside the cavity taking into account the effect of the SBHs. To this end, we use the PTF substructuring approach to partition the problem into two subsystems. The cavity constitutes one single subsystem whereas the N SBHs constitute the other one. There are N coupling surfaces between the cavity and the SBHs which compose the so-called "patches" in the PTF method (see Fig. 2). The following two conditions must be satisfied:

- the patches must be smaller than than half the acoustic wavelength to respect the PTF criterion, i.e., the frequencies of interest must be lower than a critical frequency corresponding to an acoustic wavelength equal to twice the size of the patch;
- the area of the patches must correspond to that of the opening of the SBHs, but their shapes do not need to be the same. For instance, the opening of the SBH may be in the form of a disk while the patch of the cavity in front of it may be square for convenience. It was shown in the past that this approximation is valid if the previous condition is respected.

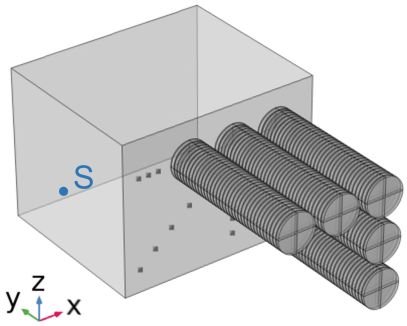


Figure 1. General case of a cavity coupled to N SBHs.

For acoustic domains, the PTFs can be defined as the acoustic impedance of each patch, that is, the ratio between its mean pressure and its mean velocity. The PTFs should be estimated for each subsystem separately (cavity and set of SBHs). For an acoustic subsystem m, the PTF between patches i and j corresponds to a cross-impedance and is defined by,

$$Z_{ij}^m = \frac{\langle p_j^m \rangle}{\langle u_i^m \rangle}, \tag{1}$$

where $\langle p_j^m \rangle$ is the mean pressure on patch j when a mean normal velocity is imposed on patch i and all other patches have zero normal velocity. For the sake of brevity, the

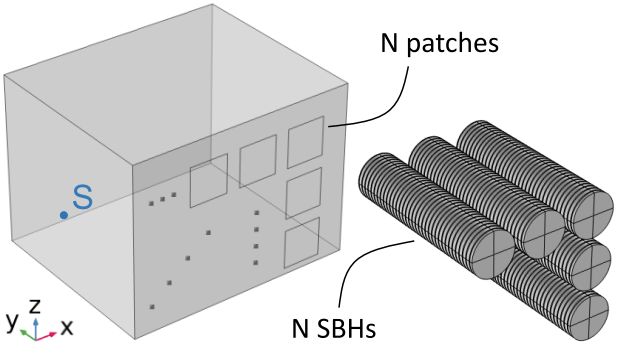


Figure 2. PTF sub-structuring of a cavity coupled to N SBHs.

brackets $\langle \quad \rangle$ will be hereby suppressed, and it is understood that all PTFs are defined from mean values.

Similarly, to account for an arbitrary receiver point R, the patch-to-point impedance is defined as

$$z_{Ri}^{m} = \frac{p\left(R\right)}{u_i^m}, \tag{2}$$

where $p\left(R\right)$ is the pressure at R when a mean normal velocity is imposed on patch i. Finally, the external source (i.e. the monopole at S in our case) is characterized by the patch blocked pressure p_{jS}^{m}, corresponding to the mean pressure on the patch j induced by the source when all other patches are rigid (null normal velocity), i.e.,

$$Z_{jS}^{m} = p_{jS}^{m}. \tag{3}$$

Once all the PTFs of interest for both subsystems have been calculated by any suitable method, we couple them to calculate the total system response by applying continuity conditions on the patches. In the following, we denote by $ss1$ the subsystem 1 (cavity) and by $ss2$ the subsystem 2 (N SBHs). Looking at Fig. 2, it is clear that the mean pressure in each patch will be the same for both the cavity and the SBHs, while the surface normal velocity will have opposite signs when pointing toward the cavity or toward the SBHs. Pressure and velocity continuity at each patch implies,

$$\begin{cases} p_j^{ss1} = p_j^{ss2} & \forall j = 1, ..., N \\ u_j^{ss1} = -u_j^{ss2} & \forall j = 1, ..., N. \end{cases} \tag{4}$$

The superposition principle allows one to compute the pressure at an arbitrary patch j of subsystem 1 as,

$$p_j^{ss1} = p_{jS}^{ss1} + \sum_{i=1}^{N} Z_{ij}^{ss1} u_i^{ss1} \quad \forall j = 1, ..., N, \tag{5}$$

and for subsystem 2 we have,

$$p_j^{ss2} = \sum_{i=1}^{N} Z_{ij}^{ss2} u_i^{ss2} \quad \forall j = 1, ..., N. \tag{6}$$

Applying the continuity condition of Eqn. 4 to Eqns. 5 and 6, we are left with the following matrix system that allows us to compute the coupling velocities in the patches from the impedances of subsystems 1 and 2 and the external pressure,

$$\left[u^{ss2}\right] = \left[Z^{ss1} + Z^{ss2}\right]^{-1} \left[p_S^{ss1}\right]. \tag{7}$$

2.2 Estimation of the PTFs of the cavity using the modal expansion method

The PTF method presents a substructuring strategy that does not depend on how the susbsytem impedances are calculated. Analytical, numerical or experimental approaches, or a mix of them, can be used [21]. In the present study, a modal expansion will be used for the cavity as it is rectangular and homogeneous.

The acoustic pressure inside the cavity admits a standard modal expansion,

$$p\left(x, y, z, \omega\right) = \sum_{q,r,s} \Gamma_{qrs}\left(\omega\right) \phi_{qrs}\left(x, y, z\right), \tag{8}$$

with eigenmodes,

$$\phi_{qrs}\left(x, y, z\right) = \cos\left(\frac{q\pi x}{L_x}\right) \cos\left(\frac{r\pi y}{L_y}\right) \cos\left(\frac{s\pi z}{L_z}\right), \tag{9}$$

and eigenfrequencies,

$$\omega_{qrs} = c_0 \sqrt{\left(\frac{q\pi}{L_x}\right)^2 + \left(\frac{r\pi}{L_y}\right)^2 + \left(\frac{s\pi}{L_z}\right)^2}. \tag{10}$$

The expansion coefficients $\Gamma_{qrs}\left(\omega\right)$ in Eqn. (8) are given by

$$\Gamma_{qrs} = \frac{\mathrm{j}\omega \int_{S_i} \phi_{qrs} dS}{\mu_{qrs}\left(-\omega^2 + \mathrm{j}\omega\eta_c\omega_{qrs} + \omega_{qrs}^2\right)}, \qquad \mu_{qrs} = \frac{L_x L_y L_z}{8\varepsilon_{qrs}\rho_0 c_0^2}. \tag{11}$$

In the above Equations c_0 is the speed of sound, $\mathrm{j} = \sqrt{-1}$, η_c is the modal damping factor and $\varepsilon_{qrs} = \left(\frac{1}{2}\right)^{\Xi}$, being Ξ the number of indices of the mode that equal zero.

From the modal expansion, we can compute the patch-to-patch impedance in Eqn. 1, needed to characterize the cavity (subsystem 1), as in Eqn. 12 below. Modal expressions from Eqns. 2 and 3 can be derived in a similar way,

$$Z_{ij}^{ss1} = -\sum_{q,r,s} \frac{\mathrm{j}\omega \int_{S_i} \phi_{qrs} dS \frac{1}{S_j} \int_{S_j} \phi_{qrs} dS}{\mu_{qrs}\left(-\omega^2 + \mathrm{j}\omega\eta_c\omega_{qrs} + \omega_{qrs}^2\right)}. \quad (12)$$

Note that, to ensure a reliable description of the cavity dynamics and considering that one patch is dedicated to each SBH, the number of vibration modes considered must be such that, for each propagation direction $q \geq N\frac{L_x}{L_x^{SBH}}$ and $r \geq N\frac{L_y}{L_y^{SBH}}$ [21].

2.3 Estimation of the SBH impedance using a FEM model

The SBH has been characterized by means of a FEM model to solve the wave equation using the commercial software COMSOL, see Fig. 3.

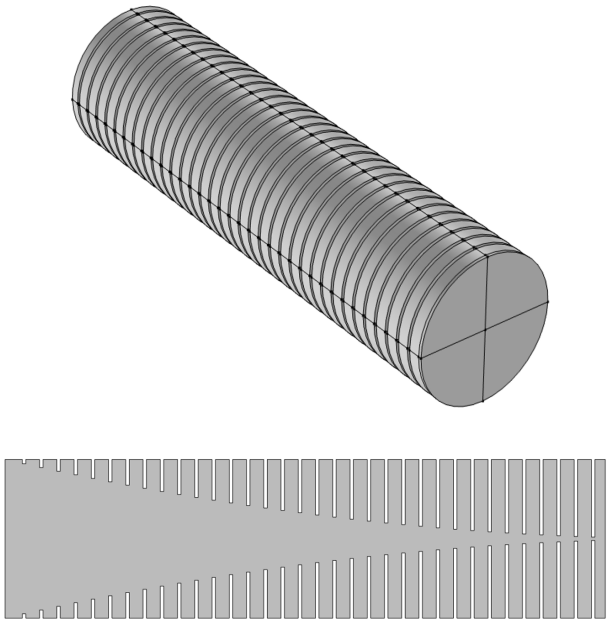


Figure 3. SBH model built in COMSOL: 3D and mid-plane cut view.

Given that we have neglected any interaction between the SBHs the impedance matrix of subsystem 2, Z^{ss2}, is diagonal. Furthermore, all the values on the diagonal will be equal to the impedance of a single SBH, Z_{SBH}, since we have considered all of them to be identical. Z_{SBH} is defined as the mean pressure on the SBH opening surface over the mean normal velocity prescribed at the opening. A unitary harmonic velocity is imposed at the entrance of the SBH FEM model, while the rings and external waveguide that comprises the SBH are considered rigid. By means of a direct FEM computation in the frequency domain, we obtain the pressure in the SBH aperture and get the impedance as,

$$Z_{SBH} = \frac{p_{SBH}}{u_{SBH}}. \quad (13)$$

Since the SBH has a retarding effect on the waves traveling through its interior, causing their effective wavelength λ_{eff} to diminish as the SBH termination is approached, a conservative criterion was established for the maximum mesh element size to be $h_{\max} \leq \lambda_{eff}/12$, where λ_{eff} is the minimum wavelength achieved inside the SBH. The SBH domain was meshed using tetrahedral elements.

2.4 Coupling of the subsystems and computation of the mean quadratic pressure

Having obtained the impedance matrices for subsystems 1 and 2 in the previous sections, we can now compute the mean velocities at the patches from Eqn. 7. Next, it is straightforward to calculate the acoustic pressure at any receiver point inside the cavity, $R \in \Omega_c$, as

$$p(R) = p_S^{ss1}(R) + \sum_{i=1}^{N} z_{Ri}^{ss1} u_i. \quad (14)$$

The mean square sound pressure inside the cavity is finally obtained by averaging over the cavity volume,

$$\langle p^2 \rangle^{ss1} = \frac{1}{\Omega_c} \int_{\Omega_c} p(R)\,\bar{p}(R)\ \mathrm{d}\Omega_c, \quad (15)$$

with $\Omega_c = L_x L_y L_z$ and the overbar denoting the complex conjugate.

3. VALIDATION OF THE PTF STRATEGY AGAINST FEM

To validate the proposed PTF method for the current cavity plus SBH problem, a first case study was conducted.

Fig. 4 shows the tested case. This comprises an air cavity of dimensions $0.24 \times 0.20 \times 0.18$ m^3 and a monopole source located at $(0.034,\ 0.16,\ 0.36)$ m with volume velocity 10^{-6} m^3/s. The air has density $\rho_0 = 1.297$ kg/m^3, sound speed $c_0 = 340$ m/s and damping $\eta_{ss1} = 0.01$. The two SBHs in the model are identical and have a quadratic profile with entrance radius $R_0 = 23$ mm, length $L = 0.175$ m, truncation $l = 1$ mm, 35 rings of thickness $h_r = 1$ mm and minimum radius at truncation $r_l = 0.5$ mm. Viscothermal losses inside the SBHs are accounted for by means of a constant damping factor $\eta_{ss2} = 0.05$. The two SBHs are positioned on the plane xz at coordinates $a = (0.192,\ 0.135)$ m and $b = (0.048,\ 0.045)$ m. The cut-on frequency of a quadratic SBH is given by $f_{\text{cut-on}} = c_0/\pi L \sim 618$ Hz [24] while the cut-off frequency of the duct, beyond which non-planar waves propagate, is extremely high in this case given the small radius of the duct $f = 1.84 c_0/R_0 \sim 27.4 \times 10^3$. Results will be presented for the frequency range between 600 and 2000 Hz.

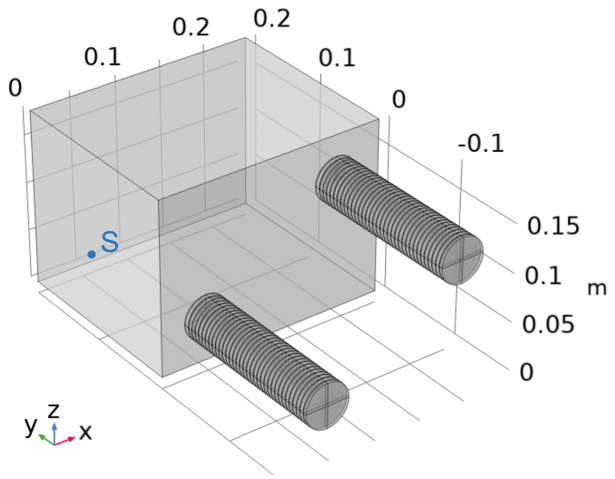


Figure 4. Nominal system to validate the proposed method.

From the SBH impedance obtained in Section 2.3, we can compute the reflection coefficient, R,

$$\mathrm{R} = \frac{Z_{SBH} - Z_0}{Z_{SBH} + Z_0}, \tag{16}$$

where $Z_0 = \rho_0 c_0$ is the characteristic impedance of air. The absorption coefficient, α, is given by,

$$\alpha = 1 - \left|\mathrm{R}^2\right|, \tag{17}$$

and has been represented in Fig. 5. As seen, its values are very close to 1 for the analyzed frequency range.

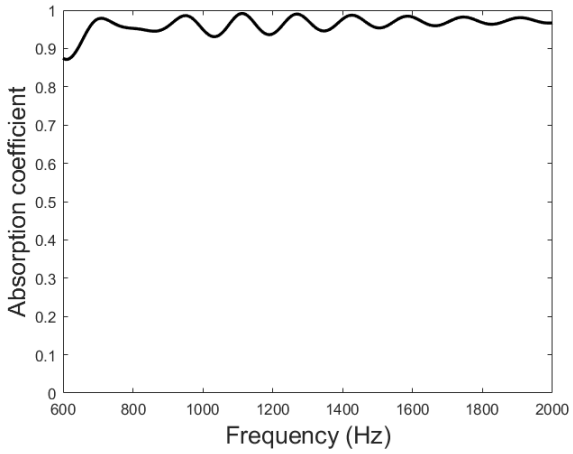


Figure 5. Absorption coefficient of the SBH.

Finally, the complete coupled system (subsystem 1 + subsystem 2) has been modelled using a FEM model and is taken as a reference for comparison with the proposed PTF substructuring methodology. In Fig. 6, we present the mean square sound pressure of the cavity (see Eqn. (15)) without SBHs (black line), with SBHs using the complete FEM model (dashed blue line) and with SBHs using the PTF approach (dashed orange line). The influence of the SBHs on the cavity is very significant for all modes, as it is clearly observed. Surprisingly, for higher frequencies, where the coefficient α remains very high, the influence of the SBHs seems to be less important than at lower frequencies. This is attributed to the fact that the SBHs are located close to the nodal planes of the involved modes.

As for the comparison between the proposed PTF method and the FEM complete model, it is seen that the mean error over the analyzed range is 0.58 dB and that the maximum observed error is $\sim$ 3 dB at 1400 Hz. The FEM model has 345579 elements and took 105 minutes to compute, while the PTF, coded and simulated in Matlab, took only 0.5 seconds.

4. CONCLUSIONS

In this work, a numerical procedure based on patch transfer functions (PTFs) was presented to calculate the response of a closed cavity coupled to sonic black holes (SBHs) when an inner sound source is excited. The cavity

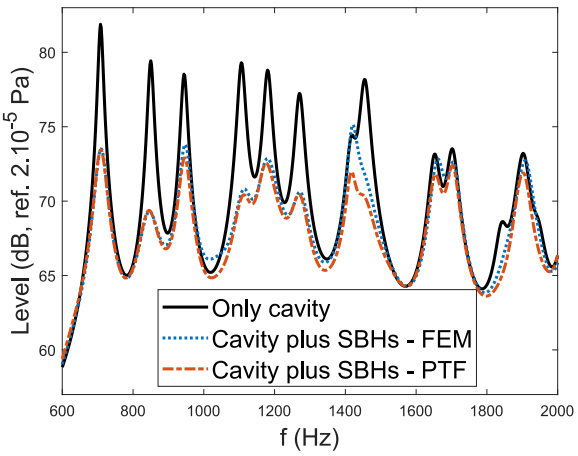


Figure 6. Mean quadratic pressure inside the cavity - Validation.

plus SBHs system was divided into a cavity subdomain and an SBHs subdomain. The former was characterized by means of a modal expansion while a FEM model was used for the SBHs. Also a FEM model of the complete system was built for comparison. The comparison between the latter and the proposed PTF approach shows a very good agreement, and that the PTF requires much less calculation time.

Given the efficiency of the presented approach, in future work it will be easy to test different and optimal distributions of SBHs in cavity walls, as well as to improve their modelling for better characterization. Different types of SBHs, such as those cited in the introduction with, for example, improved behavior at low frequency, could also be easily tested in the proposed framework.

5. REFERENCES

[1] A. Pelat, F. Gautier, S. Conlon, and F. Semperlotti, "The acoustic black hole: A review of theory and applications," *Journal of Sound and Vibration*, p. 115316, Mar 2020.

[2] M. Mironov, "Propagation of a flexural wave in a plate whose thickness decreases smoothly to zero in a finite interval," *Soviet Physics Acoustics*, vol. 34, no. 3, pp. 318–319, 1988.

[3] V. Krylov and F. Tilman, "Acoustic 'black holes' for flexural waves as effective vibration dampers," *Journal of Sound and Vibration*, vol. 274, no. 3, pp. 605–619, 2004.

[4] M. Mironov and V. Pislyakov, "One-dimensional acoustic waves in retarding structures with propagation velocity tending to zero," *Acoustical Physics*, vol. 48, 05 2002.

[5] J. Deng, O. Guasch, and D. Ghilardi, "Solution and analysis of a continuum model of sonic black hole for duct terminations," *Applied Mathematical Modelling*, vol. 129, pp. 191–206, 2024.

[6] O. Guasch, M. Arnela, and P. Sánchez-Martín, "Transfer matrices to characterize linear and quadratic acoustic black holes in duct terminations," *Journal of Sound and Vibration*, vol. 395, pp. 65–79, 2017.

[7] M. Červenka and M. Bednařík, "On the role of resonance and thermoviscous losses in an implementation of "acoustic black hole" for sound absorption in air," *Wave Motion*, vol. 114, p. 103039, 2022.

[8] S. Li, J. Xia, X. Yu, X. Zhang, and L. Cheng, "A sonic black hole structure with perforated boundary for slow wave generation," *Journal of Sound and Vibration*, vol. 559, p. 117781, 2023.

[9] A. Mousavi, M. Berggren, and E. Wadbro, "How the waveguide acoustic black hole works: A study of possible damping mechanisms," *The Journal of the Acoustical Society of America*, vol. 151, no. 6, pp. 4279–4290, 2022.

[10] O. Umnova, D. Brooke, P. Leclaire, and T. Dupont, "Multiple resonances in lossy acoustic black holes - theory and experiment," *Journal of Sound and Vibration*, vol. 543, p. 117377, 2023.

[11] X. Zhang and L. Cheng, "Broadband and low frequency sound absorption by sonic black holes with micro-perforated boundaries," *Journal of Sound and Vibration*, vol. 512, p. 116401, 2021.

[12] Y. Chen, K. Yu, Q. Fu, J. Zhang, X. Lu, X. Du, and X. Sun, "A broadband and low-frequency sound absorber of sonic black holes with multi-layered micro-perforated panels," *Applied Acoustics*, vol. 217, p. 109817, 2024.

[13] Y. Mi, L. Cheng, W. Zhai, and X. Yu, "Broadband low-frequency sound attenuation in duct with embedded periodic sonic black holes," *Journal of Sound and Vibration*, vol. 536, p. 117138, 2022.

[14] J. Deng and O. Guasch, "Sound waves in continuum models of periodic sonic black holes," *Mechanical Systems and Signal Processing*, vol. 205, p. 110853, 2023.

[15] G. Serra, O. Guasch, M. Arnela, and D. Miralles, "Optimization of the profile and distribution of absorption material in sonic black holes," *Mechanical Systems and Signal Processing*, vol. 202, p. 110707, 2023.

[16] A. Mousavi, M. Berggren, L. Hägg, and E. Wadbro, "Topology optimization of a waveguide acoustic black hole for enhanced wave focusing," *The Journal of the Acoustical Society of America*, vol. 155, no. 1, pp. 742–756, 2024.

[17] O. Guasch, P. Sánchez-Martín, and D. Ghilardi, "Application of the transfer matrix approximation for wave propagation in a metafluid representing an acoustic black hole duct termination," *Applied Mathematical Modelling*, vol. 77, pp. 1881–1893, 2020.

[18] M. Mironov and V. Pislyakov, "One-dimensional sonic black holes: Exact analytical solution and experiments," *Journal of Sound and Vibration*, vol. 473, p. 115223, 2020.

[19] J. W. Chua, X. Li, X. Yu, and W. Zhai, "Novel slow-sound lattice absorbers based on the sonic black hole," *Composite Structures*, vol. 304, p. 116434, 2023.

[20] T. Bravo and C. Maury, "Broadband sound attenuation and absorption by duct silencers based on the acoustic black hole effect: Simulations and experiments," *Journal of Sound and Vibration*, vol. 561, p. 117825, 2023.

[21] M. Ouisse, L. Maxit, C. Cacciolati, and J.-L. Guyader, "Patch transfer functions as a tool to couple linear acoustic problems," *Journal of Vibration and Acoustics*, vol. 127, 10 2005.

[22] L. Maxit, M. Aucejo, and J.-L. Guyader, "Improving the patch transfer function approach for fluid-structure modelling in heavy fluid," *Journal of Vibration and Acoustics*, vol. 134, p. 051011, 10 2012.

[23] T. Zhong and C. Yang, "Application of the patch transfer function method for predicting flow-induced cavity oscillations," *Journal of Sound and Vibration*, vol. 521, p. 116678, 2022.

[24] Y. Mi, W. Zhai, L. Cheng, C. Xi, and X. Yu, "Wave trapping by acoustic black hole: Simultaneous reduction of sound reflection and transmission," *Applied Physics Letters*, vol. 118, no. 11, 2021.

DOI: 10.61782/fa.2025.0929

FORUM ACUSTICUM EURONOISE 2025

ULTRA-THIN AND ULTRA-LIGHTWEIGHT META-PANEL FOR BROADBAND NOISE INSULATION

Jiwan Kim[1] **Wonju Jeon**[2*]
[1] Mechanical Engineering Research Institute,
Korea Advanced Institute of Science and Technology, Daejeon, Republic of Korea
[2] Department of Mechanical Engineering,
Korea Advanced Institute of Science and Technology, Daejeon, Republic of Korea

ABSTRACT

This study presents an ultra-thin and ultra-lightweight meta-panel for broadband noise insulation. The meta-panel consists of a multi-scale lattice structure sandwiched between two thin membranes, engineered to induce negative effective material properties for high sound transmission loss (STL) across a wide frequency range. A theoretical model is developed for fast and accurate prediction of the meta-panel's STL by integrating the effective impedances of membranes under elastic boundary restraints and wave propagation through the multi-scale lattice structure. This model facilitates a systematic inverse design process to maximize STL over the 100-1500 Hz range while simultaneously minimizing the meta-panel's thickness and weight. The meta-panel is fabricated via 3D printing, and its insulation performance is experimentally validated through impedance tube tests. Experimental results demonstrate an STL improvement of up to 30 dB compared to a same-weight plate, highlighting the meta-panel's superior weight-to-performance efficiency.

Keywords: *acoustic metamaterial, sound insulation, negative effective material properties, multi-scale lattice structure, meta-panel*

1. INTRODUCTION

The development of ultra-thin and ultra-lightweight soundproofing solutions for low-frequency broadband noise remains a important challenge across a range of industries, including transportation, home appliances, industrial machinery, and architectural structures. Conventional materials such as rubber sheets and gypsum boards are still widely used for noise insulation, but their effectiveness is limited by the mass law [1], which requires increased weight to achieve adequate sound insulation. To address this limitation, this study presents an ultra-thin and ultra-lightweight meta-panel designed to achieve low-frequency broadband noise insulation, by inducing negative effective material properties. The proposed meta-panel incorporates a multi-scale lattice structure sandwiched between two thin membranes, utilizing hierarchical design concepts to enhance broadband sound insulation. A theoretical model is developed to provide fast and accurate predictions of the meta-panel's sound transmission loss (STL), along with a systematic design approach aimed at achieving high STL performance over a broad frequency range of 100–1500 Hz. Finally, the sound insulation performance of the meta-panel is validated through fabrication and experimental testing.

2. THEORY AND EXPERIMENTS

The propagation behavior of sound waves is governed by the acoustic properties of a medium—mass density and bulk modulus. In conventional materials, both of those parameters are inherently positive. However, through the use of acoustic metamaterials, it is possible to engineer either the effective mass density or the effective bulk modulus to take on negative values, enabling significantly

*Corresponding author: wonju.jeon@kaist.ac.kr.
Copyright: ©2025 First author et al. This is an open-access article distributed under the terms of the Creative Commons Attribution 3.0 Unported License, which permits unrestricted use, distribution, and reproduction in any medium, provided the original author and source are credited.

enhanced sound insulation performance compared to traditional acoustic materials [2–5].

When an acoustic metamaterial exhibits a negative effective mass density ($\rho_{eff} < 0$) or a negative effective bulk modulus ($B_{eff} < 0$), the resulting speed of sound c and wavenumber k in the medium are given by:

$$c = \sqrt{\frac{B_{eff}}{\rho_{eff}}}, \quad (1)$$

$$k = \frac{\omega}{c} = \omega\sqrt{\frac{\rho_{eff}}{B_{eff}}}, \quad (2)$$

where the condition is:

$$\frac{\rho_{eff}}{B_{eff}} < 0. \quad (3)$$

Under this condition, the wavenumber k becomes purely imaginary (i.e., $k = i\alpha$ with $\alpha < 0$), leading to an exponential decay of the propagation energy E along the wave path x:

$$E \propto e^{-\alpha x}. \quad (4)$$

This relationship implies that as sound waves propagate through the medium, their energy diminishes exponentially, thereby enabling highly efficient sound insulation using thin and lightweight structures.

Expanding upon the theoretical foundation, this study presents a comprehensive methodology for both predicting and enhancing the sound insulation performance of the proposed meta-panel. To this end, a theoretical model is developed that rapidly and accurately predicts the STL by accounting for the effective acoustic impedance of the membranes and the wave propagation characteristics within the multi-scale lattice channels. Based on this model, a design framework is established to optimize STL performance across a wide frequency range of 100–1500 Hz, all while minimizing structural thickness and overall mass.

Compared to a previous design benchmark [6], the newly optimized meta-panel achieves a 64% reduction in thickness and a 26% decrease in weight. The meta-panel was fabricated via 3D printing, and its acoustic performance was validated experimentally using impedance tube testing. The results revealed that the meta-panel outperformed a reference plate with the same mass by approximately 30 dB in STL. Particularly in the low-frequency range of 100–500 Hz, the panel exhibited high broadband insulation capabilities. Within this range, its performance matched that of a 9 mm thick steel plate, despite weighing only 1/40 as much—demonstrating outstanding insulation performance relative to its weight.

3. CONCLUSION

This study presents an ultra-thin and ultra-lightweight meta-panel designed for broadband sound insulation in the low-frequency regime. The meta-panel features a multi-scale lattice structure sandwiched between two thin membranes, and it is tailored to exhibit negative effective material properties, enabling high STL across a wide frequency range of 100–1500 Hz. A theoretical model was formulated to predict STL, serving as the foundation for a systematic inverse design strategy aimed at maximizing STL while minimizing both thickness and mass. The meta-panel was fabricated using 3D printing techniques, and its sound insulation performance was experimentally evaluated through impedance tube measurements. Experimental results showed an STL improvement of approximately 30 dB compared to a plate of equal weight. These findings confirm that the proposed meta-panel delivers outstanding sound insulation despite its compact and lightweight form factor. Based on its excellent weight-to-performance ratio, the proposed meta-panel offers strong potential as a lightweight soundproofing solution for diverse applications, including electric vehicles, urban air mobility (UAM), drones, consumer electronics, and architectural acoustics.

4. REFERENCES

[1] L. M. Brekhovskikh: *Waves in layered media*. New York: Academic Press, 1980.

[2] Z. Liu, X. Zhang, Y. Mao, Y.Y. Zhu, Z. Yang, C.T. Chan, and P. Sheng: "Locally resonant sonic materials," *Science*, vol. 289(548), pp. 1734-1736, 2000.

[3] Z. Yang, J. Mei, M. Yang, N.H. Chan, and P. Sheng: "Membrane-type acoustic metamaterial with negative dynamic mass," *Physical Review Letters*, vol. 101(20), 204301, 2008

[4] M. Yang, G. Ma, Z. Yang, and P. Sheng: "Coupled membranes with doubly negative mass density and bulk modulus," *Physical Review Letters*, vol. 110(13), 134301, 2013.

[5] N. Sui, X. Yan, T.-Y. Huang, J. Xu, F.-G. Yuan, and Y. Jing: "A lightweight yet sound-proof honeycomb acoustic metamaterial," *Applied Physics Letters*, vol. 106(17), 171905, 2015.

[6] J. Kim, E. Choi, and W. Jeon: "Lightweight soundproofing meta-panel for separate wide frequency bands," *Mechanical Systems and Signal Processing*, vol. 184, 109647, 2023.

DOI: 10.61782/fa.2025.0950

FORUM ACUSTICUM EURONOISE 2025

VENTILATED ACOUSTIC METAMATERIAL FOR NOISE REDUCTION IN A DUCT WITH NON-UNIFORM CROSS SECTIONS

Dohaeng Kim[1] **Jiwan Kim**[2] **Wonju Jeon**[1*]

[1] Department of Mechanical Engineering, Korea Advanced Institute of Science and Technology, Republic of Korea

[2] Mechanical Engineering Research Institute, Korea Advanced Institute of Science and Technology, Republic of Korea

ABSTRACT

The mitigation of noise propagated along flow path while allowing airflow is crucial in mechanical systems including fluid-guiding structures. While metamaterials are being actively researched to overcome the limitations of conventional materials used for duct noise reduction, most studies have only focused on ducts with uniform cross-sections, limiting their range of application. In this study, we propose a ventilated acoustic metamaterial, called a metaliner, for noise reduction in a duct with non-uniform cross-sectional areas. The design considers the effects of variations in duct cross-sectional areas on noise reduction performance and the influence of locally varying velocity profiles along the direction of flow. In order to achieve this, our impedance model for effective impedance of the metaliner is established to incorporate locally different friction velocities. Using this theoretical model, we design metaliners that achieve high insertion loss and experimentally demonstrate their effectiveness at reducing noise in ducts with non-uniform cross-sections under the presence of flow.

Keywords: *acoustic metaliner, duct noise reduction, non-uniform cross section, friction velocity*

[*] ***Corresponding author***: *wonju.jeon@kaist.ac.kr*

Copyright: *©2025 D. Kim et al. This is an open-access article distributed under the terms of the Creative Commons Attribution 3.0 Unported License, which permits unrestricted use, distribution, and reproduction in any medium, provided the original author and source are credited.*

1. INTRODUCTION

Noise mitigation within ducts is crucial in many mechanical systems, including vehicle ventilation systems, building HVAC systems, and power plants. Conventional solutions, such as acoustic louvers [1] and mufflers [2], face limitations due to their bulky structures. Recently, acoustic metamaterials [3-6] have attracted significant attention due to their potential in noise control applications. However, existing studies mainly focused on ducts with constant cross sections, limiting their practical applicability. To address this, we propose an acoustic metaliner, a type of ventilated acoustic metamaterial, specifically designed to achieve high noise attenuation performance in ducts with non-uniform cross sections and validate its performance through experimental investigations.

2. THEORETICAL DEVELOPMENT AND EXPERIMENTAL VALIDATION

2.1 Theoretical development

The acoustic metaliner presented in this study features a thin structure relative to the target acoustic wavelength and is installed underneath the duct wall without obstructing the airflow as shown in Fig. 1. The primary challenge was accommodating the variation of cross-sectional area and associated locally varying flow velocity profiles along the duct length. To this end, a friction velocity-based analytical approach was formulated, enabling precise prediction of the metaliner's effective acoustic impedance under flow conditions in ducts with non-uniform cross-sections.

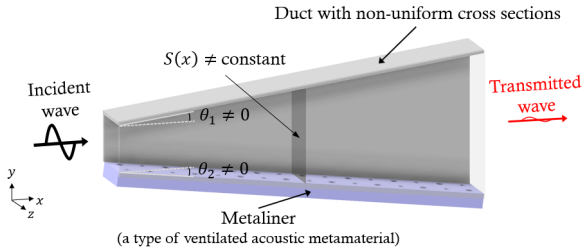


Figure 1. Schematic of an acoustic metaliner and a duct with non-uniform cross sections.

Using the developed impedance model, the metaliner was designed for a target frequency of 900 Hz. The designed metaliner exhibited an insertion loss of 45 dB at the target frequency for an inlet flow velocity (U_0) of 34 m/s, with a length of 408 mm and a thickness of λ/19. This result demonstrates a significant enhancement, exhibiting a 31 dB higher insertion loss compared to the metaliner designed using the methodology proposed in [6], which is suitable for ducts with constant cross sections.

2.2 Experimental validation

An experimental device, the Flow Grazing Incidence Tube (FGIT), was constructed to evaluate the metaliner's noise reduction performance under flow conditions in ducts with non-uniform cross sections. The designed metaliner was fabricated using 3D printing. Experimental measurement result is shown in Fig. 2. The measured insertion loss aligned with theoretical predictions, demonstrating the metaliner's effectiveness in reducing noise in ducts with non-uniform cross sections.

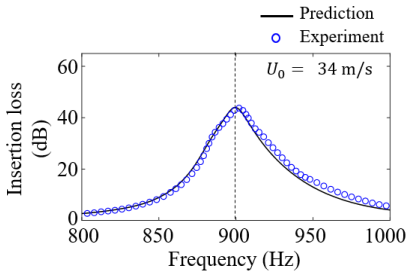


Figure 2. Insertion loss spectrum the designed metaliner. The blue circle indicates the measured results. For comparison, the predicted results are shown as the black solid line.

3. CONCLUSIONS

In summary, we demonstrated that the metaliner effectively reduces noise in ducts with non-uniform cross-sectional areas. To account for the effects of cross section's variation and locally varying flow velocity profiles, a theoretical model for the metaliner's impedance was established in terms of friction velocity. This model was employed to design the metaliner, which was subsequently fabricated using 3D printing. Experimental evaluations validated the impedance model's accuracy and showed the metaliner's effectiveness for noise reduction in ducts characterized by non-uniform cross sections.

4. REFERENCES

[1] E. B. Viveiros, B. M. Gibbs, and S. N. Y. Gerges: "Measurement of sound insulation of acoustic louvres by an impulse method," *Applied Acoustics*, vol. 63, no. 12, pp. 1301-1313, 2002.

[2] A. P. Dowling and J. E. Ffowcs Williams, *Sound and sources of sound*. London: Ellis Horwood, 1983.

[3] Z. Zhang, D. Yu, Y. Xiao, B. Hu, Y. Bai, and J. Wen: "Compact broadband acoustic meta-silencer based on synergy between reactive and resistive units," *Journal of Physics D: Applied Physics*, vol. 56, no. 1, 015303, 2023.

[4] J. Boulvert, G. Gabard, V. Romero-García, and J. P. Groby: "Compact resonant systems for perfect and broadband sound absorption in wide waveguides in transmission problems," *Scientific Reports*, vol. 12, 10031, 2022.

[5] T. S. Oh and W. Jeon: "Bandgap characteristics of phononic crystals in steady and unsteady flows," *The Journal of the Acoustical Society of America*, vol. 148, no. 3, pp. 1181–1192, 2020.

[6] T. S. Oh and W. Jeon: "Acoustic metaliners for sound insulation in a duct with little flow resistance," *Applied Physics Letters*, vol. 120, no. 4, 044103, 2022.

DOI: 10.61782/fa.2025.0275

FORUM ACUSTICUM EURONOISE 2025

DESIGN OF A METAMATERIAL PLATE WITH ACOUSTIC BLACK HOLE ABSORBERS AND ITS APPLICATION TO FLOATING RAFT SYSTEM

Siting Hao[1] **Haiqin Li**[1*] **Qian Ding**[1]
[1] Tianjin Key Laboratory of Nonlinear Dynamics and Control, Department of Mechanics, Tianjin University, China

ABSTRACT

Acoustic metamaterials have demonstrated great application potential in the fields of vibration and noise control. To suppress the broadband and low-frequency vibration in practical engineering, a novel design of the microunit is proposed, which uses a beam-type acoustic black hole (ABH) absorber as the resonator. By the coupling effects of ABH and the local resonance mechanism, a vibration attenuation band with relative bandwidth up to 0.93 can be generated. Furthermore, the microunit is used as the core layer embedded into a honeycomb raft plate, which is applied to the floating raft system. Due to the sandwich design, the stiffness of the novel metamaterial raft is improved. By analyzing the output vibration response of the foundation and the vibration level difference of the whole system, it shows a broadband and better vibration isolation performance, compared with the normal raft. In all, this study may provide a new idea for the design and application of vibration isolation meta-devices.

Keywords: acoustic metamaterial, acoustic black hole, floating raft system, vibration isolation.

1. INTRODUCTION

After the concept of acoustic black hole (ABH) was proposed by Mironov [1], the ABH-based structure has been studied extensively as a passive vibration control method [2]. Recent years, the idea of employing ABH-type structures as dynamic vibration absorbers (DVAs) has been emerged, proposed by Zhou and Cheng [3] first in the form of a unilateral ABH-DVA. Subsequently, various designs such as tree-shaped ABH-DVA [4] and two-dimensional circular ABH-DVA [5] are presented. Utilizing dynamic interaction with the host structure and damping enhancement as a result of ABH-specific energy trapping, resonant peaks can be reduced systematically over a broad frequency range, while the stiffness and strength of the host structure retain intact. Moreover, researchers introduce ABH-DVA into the concept of acoustic metamaterials, and demonstrate burgeoning potential in engineering vibration and noise reduction [6, 7]. For instance, the model and the corresponding calculation method of a host beam with distributed ABH-DVAs are proposed, achieving significant evanescent waves in a very broad frequency range [8, 9]. In research [10], discontinuous broadband vibration attenuation on a meta-beam is realized by using mistuning ABH-DVAs. However, studies for two-dimensional acoustic metamaterials with ABH-DVAs are not enough, and there is also a need for low-frequency vibration suppression.

Floating raft system is a typical vibration isolation technology used in ships and submarines, owing to its ability to inhibit the transmission of vibration generated by multiple equipment to the hull [11]. To further improve the vibration isolation performance of the system, various configurations have been added such as passive or active DVAs [12, 13], quasi-zero-stiffness (QZS) devices [14] and nonlinear energy sink (NES) cells [15]. However, the above studies either need complex structures or neglect the elastic deformation of the raft and foundation in modelling. Thus, some designs based on acoustic metamaterials have been proposed and focus on the substructures themselves in this coupled system. For example, a periodic structure is used to replace the isolators to suppress the disadvantageous effects

[*] ***Corresponding author***: lihaiqin1992@tju.edu.cn
Copyright: *©2025 Siting Hao et al. This is an open-access article distributed under the terms of the Creative Commons Attribution 3.0 Unported License, which permits unrestricted use, distribution, and reproduction in any medium, provided the original author and source are credited.*

of substructure resonances on vibration and noise radiation [16], while this may result in reduced stiffness which affects the practicability. Recent research designs a sandwich-plate-type raft with graded resonators, taking the advantage of light weight, high bending strength and high stiffness of sandwich structures [17]. Nevertheless, too much resonators may also add unnecessary load. Motivated by these studies, this paper aims to propose a light-weight sandwich raft plate to achieve low-frequency and broadband vibration isolation.

The rest of the paper is organized as follows. Section 2 presents the model of the metamaterial design based on ABH-DVA. Section 3 introduces both the numerical and experimental results of the vibration band gap, and the effect of ABH is analyzed. Section 4 illustrates the application of the proposed structure to the design of a sandwich raft, the static stiffness of which and the vibration isolation performance of the entire floating raft system are investigated. Finally, conclusions are drawn in Section 5.

2. MODELLING AND DESIGN

As depicted in Fig. 1, the proposed microunit is comprised of three parts: the inner ABH beam (the side view is shown in Fig. 1(c)), the outer frame, and the connectors in-between them. The whole structure is named as FC-ABH in the followings. The ABH beam is made of TPU (Thermoplastic Polyurethane), with width b (in the x direction) and assumed to undergo bending vibration in the z direction. Its layout in the y-z plane, see in Fig. 1(c), is symmetric about the horizontal line $y = 0$, as well as the mid-surface $z = 0$. As such, the ABH beam contains a plateau region of length $2l_0$ with uniform thickness and two thickness decreasing regions of length l_{ABH}, such that the overall thickness profile $h(y)$, as noted in Fig. 1(c), satisfying Eq. (1), where h_{min} and h_{uni} are respectively half of the thickness of the uniform region and the ABH terminal, and ε is the smooth parameter, defined by Eqn. (2).

$$h(y)=\begin{cases} 2h_{uni} & 0\le|y|\le l_0 \\ 2\left[h_{min}+\varepsilon\left(l_{ABH}+l_0-|y|^2\right)\right] & l_0\le|y|\le l_{ABH}+l_0 \end{cases} \quad (1)$$

$$\varepsilon=\frac{h_{uni}-h_{min}}{l_{ABH}^2} \quad (2)$$

Such an ABH beam is then embedded into a square frame through four identical connectors, each of whom is with thickness δ and with segment lengths l_1 (for segment ①), l_2 (for segment ②), and $(a\text{-}2\Delta a\text{-}b\text{-}2l_1\text{-}2\delta)/2$ (for segment ③). Both the frame and connectors are made of epoxy. All the geometric and material parameters are list in Tab. 1.

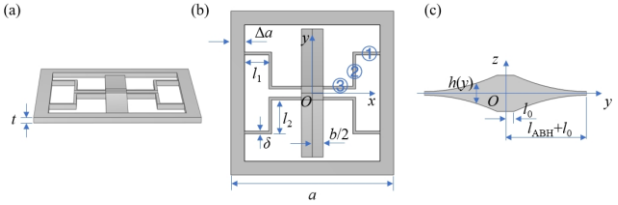


Figure 1. Schematic diagram of FC-ABH. (a) Stereogram of the microunit. (b) Top view. (c) Cross-section of the ABH portion.

Table 1. Structural parameters of FC-ABH. E_1, ρ_1, ν_1, E_2, ρ_2, ν_2 are elastic modulus, density and Poisson's ratio of epoxy and TPU respectively.

Parameters	Value[unit]	Parameters	Value[unit]
a	0.12[m]	h_{min}	0.5[mm]
Δa	0.01[m]	h_{uni}	0.002[m]
l_1	0.018[m]	l_{ABH}	0.042[m]
l_2	0.025[m]	l_0	0.005[m]
δ	0.002[m]	ε	0.85[m^{-1}]
t	0.003[m]	b	0.016[m]
E_1	2.6[GPa]	E_2	61[MPa]
ρ_1	1120[kg/m^3]	ρ_2	1100[kg/m^3]
ν_1	0.41	ν_2	0.47

3. VIBRATION ABSORPTION OF FC-ABH

3.1 Numerical simulation of bandgap

The Floquet-Bloch periodic boundary conditions are applied on the edges of the FC-ABH microunit as in Figs. (3) and (4), where $\boldsymbol{w}$ denotes the out-of-plane displacement vector, $\boldsymbol{k} = (k_x, k_y)$ is the wave vector and $i^2 = -1$[18].

$$\boldsymbol{w}\left(-\frac{a}{2},y\right)=\boldsymbol{w}\left(\frac{a}{2},y\right)e^{ik_x a} \quad (3)$$

$$\boldsymbol{w}\left(x,-\frac{a}{2}\right)=\boldsymbol{w}\left(x,\frac{a}{2}\right)e^{ik_y a} \quad (4)$$

The dispersion curve can be obtained by sweeping $\boldsymbol{k}$ along the boundaries of the irreducible Brillouin zone as shown in Fig. 2(a). The calculation process is carried out using the finite element method (FEM) via COMSOL, and the results are displayed by scatter points in Fig. 2(a). To manifest the dominant of flexural waves in vibration modes, the colors of these points are determined by Eqn. 5, where u and v are in-plane displacements along the x and y axes, and $\iiint$.dV

means that the integration is taken throughout the entire volume of the FC-ABH unit.

$$p = \frac{\iiint w^2 dV}{\iiint \left(u^2 + v^2 + w^2\right) dV} \tag{5}$$

It can be found that there is an omnidirectional bandgap within 61.29-68.78 Hz and several directional bandgaps within 68.78-90.82 Hz, 90.82-104.64 Hz and 119.3-167.12 Hz respectively.

To verify the predicted bandgaps by the dispersion curves, the vibration transmittance of a finite periodic plate consisting of 4 microunits is calculated. The model of the plate is shown in Fig. 2(b), with continuous periodicity boundary conditions applying in the y direction. Two specific points are noted: the bottom point EP denotes an excitation point where a unit harmonic force in the z direction is introduced into, while the top right point RP is the response point. By measuring the dynamic response of the two points, the transmittance is obtained as in Eqn. 6, where A_{out} and A_{in} are the acceleration amplitudes at RP and EP.

$$\text{Transmission} = 20\lg\frac{A_{out}}{A_{in}} \tag{6}$$

As presented in Fig. 2(b), there are three obvious vibration attenuation bands (named as VAB in the followings to distinguish from the bandgap), the frequency ranges of which are in good agreement with those of bandgaps in the dispersion curves. The relative bandwidth Ω of one VAB is defined as in Eqn. 7, where f_{upper} and f_{lower} represent the upper and lower boundary frequencies.

$$\Omega = \frac{2\left(f_{upper} - f_{lower}\right)}{f_{upper} + f_{lower}} \tag{7}$$

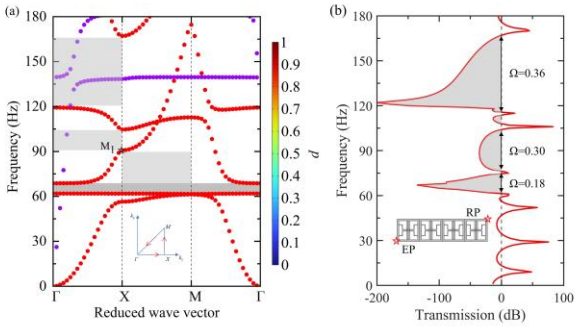


Figure 2. (a) Dispersion curves of the infinite periodic FC-ABH structure. (b) Transmittance of the finite periodic FC-ABH plate. The shaded areas indicate bandgaps or vibration attenuation bands (VABs).

3.2 Experimental validation

A vibration test is conducted to verify the transmittance results of numerical simulation. The 4×1 FC-ABH plate is manufactured by 3D printing, with the ABH portions printed using TPU while the others printed using polylactic acid (PLA). The experiment is carried out at room temperature, and it is noteworthy that the damping characteristics of the two materials are considered here. The material properties of PLA are E_3 = 1.98 GPa, ρ_3 = 1220 kg/m^3 and v_3 = 0.37, and the damping coefficients η of PLA and TPU are set as 0.1 and 0.15 respectively. Boundary conditions and the way of applying excitation are consistent with those set in the numerical simulation mentioned in subsection 3.1. Vibration signals are measured by the laser vibrometer (Ploytec PSV-500-3D).

Fig. 3 shows the experimental results, and the data is filtered using the moving average filter in MATLAB. It can be seen that there is a good agreement compared with the numerical results, especially for the frequency range of the VAB. Within the range of 0-150 Hz, a continuous VAB is generated beyond the third resonant frequency with Ω = 0.93, verifying the effective vibration suppression performance of the finite FC-ABH plate.

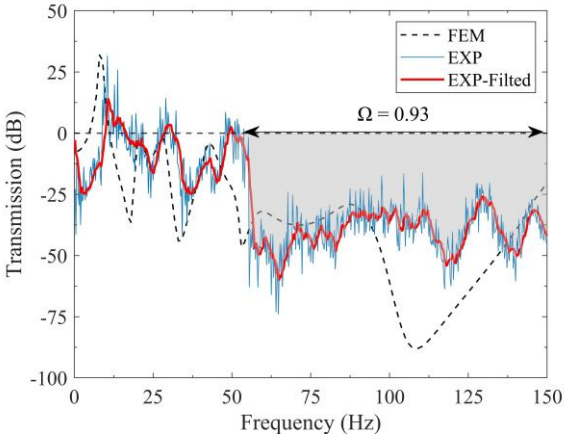


Figure 3. The experimental and simulation results of the transmittance of the finite periodic FC-ABH plate. The shaded area indicates the vibration attenuation band.

3.3 Effects of ABH

Since the bandgaps generated by FC-ABH are beyond the scope of conventional locally resonant bandgaps, one can deduce that the ABH beam acts a special role in the structure. In the view point of vibration absorption, ABH is generally proved to be effective beyond a certain cut-on frequency, which guarantees the tip to reduce the wave speed as well as the reflected energy. To make ABH perform sufficiently, the cut-on frequency is defined as in Eqn. (8) [19].

$$f_\varepsilon = \frac{\varepsilon}{\pi}\sqrt{\frac{3E_2}{4\rho_2}} = 55.17\text{Hz} \tag{8}$$

Therefore, for FC-ABH, ABH keeps absorbing vibration from the beginning of the first omnidirectional bandgap. This explains why the vibration can also be well attenuated at the frequency corresponding to M_1 marked in Fig. 2(a), although it is not within the bandgaps.

To illustrate this advantage more clearly, three frequency points are selected in the three VABs respectively, which are 65 Hz, 90 Hz and 130 Hz, and the displacement fields of the finite periodic plate at these frequencies are shown in Fig. 4. It can be observed that no matter inside or outside bandgaps, the displacement of the ABH portion is prominent, especially concentrated on the microunits near EP, thus reducing vibration at RP.

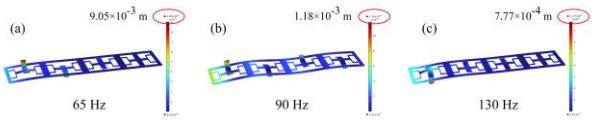


Figure 4. Displacement fields of the finite periodic FC-ABH plate at (a) 65 Hz, (b) 90 Hz and (c) 130 Hz.

4. APPLICATION TO FLOATING RAFT SYSTEM

Since the proposed FC-ABH can achieve broadband vibration suppression, in this section, it is used as the core layer embedded into a honeycomb plate. The periodic sandwich structure is then applied to the floating raft system, which can isolate the vibration transmitted by the machines to the hull effectively, under the premise of ensuring the load-bearing capacity.

4.1 Floating raft system based on FC-ABH

A typical model of the floating raft system is shown in Fig. 5(a), where the proposed FC-ABH is embedded into a conventional honeycomb plate-type raft periodically, forming a novel sandwich raft. The side length of the honeycomb microunit is equal to the lattice constant of the FC-ABH. Considering the practical application of this system, all parts of the raft and the foundation are made of structural steel. Parameters used in the calculation are depicted in Tab. 2.

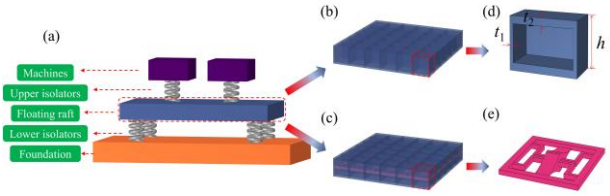


Figure 5. Schematic diagram of floating raft system with (b) honeycomb metamaterial raft and (c) sandwich metamaterial raft based on FC-ABH. (d) Cross-section of the honeycomb microunit. (e) Stereogram of FC-ABH.

Table 2. Structural parameters of the microunit of the raft. E_4, ρ_4, ν_4 are elastic modulus, density and Poisson's ratio of structural steel respectively.

Parameters	Value[unit]	Parameters	Value[unit]
h	0.026[m]	E_4	200[GPa]
t_1	1.05[mm]	ρ_4	7850[kg/m^3]
t_2	0.003[m]	ν_4	0.3

4.2 Load-bearing analysis

In this study, the equivalent elastic modulus of a sample consisting of 2×2 microunits is calculated to predict the mechanical properties of the two types of floating rafts. As we focus on the out-of-plane compression resistance of the proposed model, the elastic modulus E_z along the z direction is investigated as follows. As shown in Fig. 6(a), two rigid plates are connected with the top and bottom surface of the structure to simulate the test in practice. The bottom plate is fixed and a displacement with amplitude U_0 is applied to the top one in the negative direction of z axis. The stress-strain curve is obtained by sweeping U_0 from 0 to 0.3 mm, and the values of the stress and strain at a certain U_0 are derived as Eqns. (9) and (10), where F_r denotes the boundary reactive force at the surface that contact with the top rigid plate, and

∫.dS means that the integration is taken over the entire top surface.

$$\sigma = \frac{\int_S F_r dS}{\left[2(a+2t_1)\right]^2} \tag{9}$$

$$\varepsilon = \frac{U_0}{h} \tag{10}$$

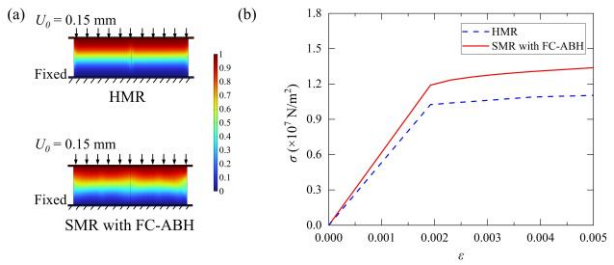


Figure 6. (a) Displacement fields of the sample of the raft in compression simulation when U_0 = 0.15 mm. (b) Stress-strain curves of the sample with and without embedding FC-ABH.

Fig. 6(b) exhibits the simulation results. It can be observed that the linear response for both samples is similar in the initial loading, while the compressive strength of the honeycomb one reaches the peak first, with the appearance of plastic buckling. The yield elastic moduli of the samples with and without FC-ABH calculated by $E_z = \sigma/\varepsilon$ are 5.33 GPa and 6.19 GPa respectively, indicating that the sandwich design improves the static stiffness of the ordinary raft. In addition, by analyzing the displacement fields of the cross-section at the linear segment, it can be observed that the presence of the interlayer changes the distribution of displacement, and partly improves the buckling resistance.

4.3 Vibration isolation of sandwich metamaterial raft

In this subsection, the simulation model of the floating raft system is simplified as shown in Fig. 7(a), where one machine is retained to provide the excitation and the raft is composed of 6×6 sandwich microunits. The side length of the simply-supported foundation is equal to that of the raft, with thickness 0.02 m. Moreover, the upper and lower isolators are substituted by the same 0.1 m×0.1 m×0.027 m rubber pads, with material properties E_5 = 0.02 GPa, ρ_5 = 1300 kg/m^3, ν_5 = 0.47 and η_5 = 0.1. The machine model is set as a rigid domain and a sinusoidal excitation with an amplitude of 20 N is applied to the top of it. To evaluate the vibration isolation performance of the system, the vibration level difference between the machine and the foundation is calculated via Eqn. (11), where A_m and A_f represent the acceleration amplitudes of the corresponding points output-1 and output-2.

$$L_D = 20\lg\frac{A_m}{A_f} \tag{11}$$

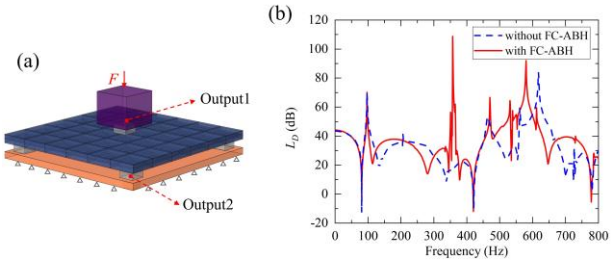


Figure 7. (a) Model of the floating raft system in simulation. (b) Vibration level differences of the floating raft system with honeycomb metamaterial raft and sandwich metamaterial raft based on FC-ABH.

Fig. 7 shows the vibration level difference results, compared with those of the system with honeycomb raft. It can be found that when using the sandwich raft, there is a more significant vibration isolation at 300-400 Hz, which is due to the locally resonant effect. In addition, beyond the locally resonant bandgap, the L_D of the system with the sandwich raft keeps higher than that with an ordinary one, especially at 480-600 Hz, which is because of the ABH absorbers. Due to the limitation of the length of the article, the vibration isolation mechanism of the sandwich raft is not analyzed in detail here. However, to reflect the vibration response of the entire system more comprehensively, the mean quadratic velocity (MQV) of the foundation and the raft surface are calculated, as in Eqn. 12, where ω is the angular frequency and ref = 1×10^{-18} m^2/s^2 [20].

$$\mathrm{MQV} = 10\lg\frac{\omega^2\iint_S w^2 dS}{\left[6(a+2t_1)\right]^2\cdot \mathrm{ref}} \tag{12}$$

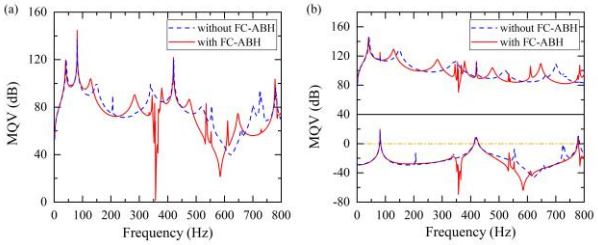


Figure 8. MQV curves of (a) the foundation plate, (b) the raft plate and the difference between them.

As displayed in Fig. 8, the sandwich raft operates at 300-600 Hz, which is consistent with the frequency band that the L_D increases significantly in Fig. 7(b). Furthermore, it can be found that the second peak of the MQV difference disappears in the system with the sandwich raft, presenting broadband vibration isolation performance.

5. CONCLUSION

This paper proposes a novel metamaterial design to achieve broadband and low-frequency vibration suppression, utilizing the coupling effects of local resonance and wave absorption of the acoustic black hole (ABH). The dispersion relation of the infinite periodic structure and the vibration bandgap of the finite periodic plate are calculated, verified by the experimental results. The ABH part acts as a vibration absorber as well as a resonator, allowing vibration to be well attenuated even beyond the bandgap.

After the monomer is analyzed, its application to the floating raft system is studied. The microunit is used as a core layer embedded into a honeycomb plate-type raft periodically. Out-of-plane compression process reveals that the sandwich raft exhibits improved static stiffness, which can meet the requirement of large load-bearing capacity in practical applications. Compared with the conventional floating raft system, the vibration level difference of the one with the proposed sandwich raft is significantly improved in vibration bandgaps, demonstrating low-frequency and broadband vibration isolation performance.

This study offers an effective design with superior static and dynamic properties. The proposed meta-structure may provide a new strategy for ship-vibration technologies.

6. ACKNOWLEDGMENTS

This work is supported by the National Natural Science Foundation of China (No. 12132010, No. 12202304), and S&T Program of Hebei (225676162GH).

7. REFERENCES

[1] M. A. Mironov: "Propagation of a flexural wave in a plate whose thickness decreases smoothly to zero in a finite interval," *Sov Phys Acoust*, vol. 34, no. 3, pp. 318-319, 1988.

[2] A. Pelat, F. Gautier, S. C. Conlon, et al.: "The acoustic black hole: A review of theory and applications," *Journal of Sound and Vibration*, vol. 476, no. 115316, 2020.

[3] T. Zhou and L. Cheng: "A resonant beam damper tailored with Acoustic Black Hole features for broadband vibration reduction," *Journal of Sound and Vibration*, vol. 430, pp. 174-184, 2018.

[4] K. X. Huang, Y. N. Zhang, X. T. Rui, et al.: "A multibody dynamics approach on a tree-shaped acoustic black hole vibration absorber," *Applied Acoustics*, vol. 210, no. 109439, 2023.

[5] H. L. Ji, N. Wang, C. Zhang, et al.: "A vibration absorber based on two-dimensional acoustic black holes," *Journal of Sound and Vibration*, vol. 500, no. 116024, 2021.

[6] H. Sheng, M. X. He and Q. Ding: "Vibration control and multifunctional design based the acoustic black hole structure: a state-of-the-art review," *International Journal of Dynamics and Control*, vol. 13, no. 25, pp. 1-20, 2025.

[7] S. T. Hao, H. Sheng, X. S. Liu, et al.: "Low-frequency and broadband vibration absorption of a metamaterial plate with acoustic black hole resonators," *Thin-Walled Structures*, vol. 202, no. 112073, 2024.

[8] J. Deng, J. F. Ma, X. Chen, et al.: "Vibration damping by periodic additive acoustic black holes," *Journal of Sound and Vibration*, vol. 574, no. 118235, 2024.

[9] J. Deng, N. S. Gao, X. Chen, et al.: "Evanescent waves in a metabeam attached with lossy acoustic black hole pillars," *Mechanical Systems and Signal Processing*, vol. 191, no. 110182, 2023.

[10] H. Sheng, M. X. He and Q. Ding: "Vibration suppression by mistuning acoustic black hole dynamic vibration absorbers," *Journal of Sound and Vibration*, vol. 542, no. 117370, 2022.

[11] L. L. Ren, Y. Li, X. C. Huang, et al.: "Dynamic Modeling and Characteristic Analysis of Floating Raft System with Attached Pipes," *Shock and Vibration*, vol. 2017, pp. 1-13, 2017.

[12] H. L. Sun, K. Zhang, P. Q. Zhang, et al.: "Application of dynamic vibration absorbers in floating raft system," *Applied Acoustics*, vol. 71, pp. 250-257, 2010.

[13] Z. Wang and C. M. Mak: "Application of a movable active vibration control system on a floating raft," *Journal of Sound and Vibration*, vol. 414, pp. 233-244, 2018.
[14] Y. L. Li and D. L. Xu: "Force transmissibility of floating raft systems with quasi-zero-stiffness isolators," *Journal of Vibration and Control*, vol. 24, no. 16, pp. 3608-3616, 2017.
[15] H. L. Wang, M. Li, Y. C. Zeng, et al.: "Experimental, theoretical and optimization studies on multimode vibration reduction of floating raft system based on NES cells," *Ocean Engineering*, vol. 311, no. 118897, 2024.
[16] Y. B. Song, J. H. Wen, D. L. Yu, et al.: "Suppression of vibration and noise radiation in a flexible floating raft system using periodic structures," *Journal of Vibration and Control*, vol. 21, no. 2, pp. 217-228, 2013.
[17] X. Y. An, X. F. Yuan, G. Q. Sun, et al.: "Sandwich plate-type metastructures with periodic graded resonators for low-frequency and broadband vibration attenuation," *Ocean Engineering*, vol. 298, no. 117229, 2024.
[18] J. Deng, L. Zheng and N. S. Gao: "Broad band gaps for flexural wave manipulation in plates with embedded periodic strip acoustic black holes," *International Journal of Solids and Structures*, vol. 224, no. 111043, 2021.
[19] J. Deng, O. Guasch and L. Zheng: "Ring-shaped acoustic black holes for broadband vibration isolation in plates," *Journal of Sound and Vibration*, vol. 458, pp. 109-122, 2019.
[20] S. T. Wen, M. X. Chen, Z. W. Zhou, et al.: "Analytical and experimental studies for the vibration transmission of the double-plated structure containing the inner fluid and elastic connections," *Thin-Walled Structures*, vol. 188, no. 110806, 2023.

DOI: 10.61782/fa.2025.0325



FORUM ACUSTICUM
EURONOISE 2025

EFFECTS OF ACOUSTIC BLACK HOLE PILLARS ON THE ACOUSTIC ENERGY OF A WATER-FILLED CAVITY

Junjun Li[1] **Jie Deng**[1,2*] **Oriol Guasch** [1*]
[1] Human-Environment Research (HER) group, Department of Engineering, La Salle, Universitat Ramon Llull C/ Quatre Camins 30, 08022 Barcelona, Catalonia, Spain
[2] Chongqing Industry Polytechnic College, 401120 Chongqing, China

ABSTRACT

Acoustic additive black hole (ABH) pillars are known to significantly reduce vibration energy from a host plate. However, little has been done to investigate their performance when the host plate partially encloses a water-filled resonant cavity, a problem that may be important for marine applications. In this work, the ability of ABH pillars to reduce the acoustic energy of the cavity is investigated and compared to that of standard uniform pillars. The elastoacoustic problem is solved using a displacement formulation and Gaussian basis functions are employed to expand all the unknowns of the problem. Boundary and coupling conditions are imposed using the null space method (NSM). The results show that ABH pillars can substantially reduce the acoustic energy of the cavity, outperforming uniform pillars despite their lower mass.

Keywords: *Acoustic black holes, Vibroacoustics, Heavy fluid, Nullspace method*

1. INTRODUCTION

In recent years, acoustic black hole (ABH) technology has garnered a great deal of attention for its effectiveness in mitigating noise in fluid systems. Bowyer and Krylov [1] pioneered experimental investigations into the acoustic radiation of ABH plates, demonstrating that rectangular plates with tapered indentations can effectively reduce acoustic power radiation. Subsequently, the vibroacoustic behavior of ABH plates coupled to air cavities but their connection to heavy fluids has only started recently. In [2], the fluid-structure interaction of ABHs with heavy fluids was addressed by showing the suppression potential of a composite plate-cavity ABH system under heavy fluid excitation, achieving sound pressure level reductions of 4-9 dB above 300 Hz. More recently, the underwater acoustic radiation characteristics of ABH plates were further examined demonstrating superior underwater sound power suppression between the cut-on and critical frequencies [3,4].

Although embedded ABH configurations are the most common, they compromise the original stiffness of the host plate due to thickness adjustment. To overcome these limitations different types of additive ABHs have been proposed. In [5], a dynamic vibration absorber with ABH features (ABH-RBD) was set on a uniform beam achieving effective vibration suppression without compromising structural integrity. Subsequently, symmetric [6] and eccentric [7] circular ABH dynamic vibration absorbers (2D ABH-DVA) were developed to reduce vibrations in uniform plates. Additional research has been conducted on spiral ABHs [8], curved ABHs [9], and ABH pillars [10] as additive structures.

In this study, we propose to place multiple ABH pillars on a uniform beam coupled to a cavity to reduce noise in a cavity filled with heavy fluid. The equations of motion for the fluid-structure coupling system are established from the displacement formulation in [11], using Gaussian basis functions (GEM expansion method in [12–14]) and the nullspace method (NSM) [15] to impose boundary coupling conditions. Finally, the noise reduction capability of the proposed configuration is computed.

***Corresponding author**: *oriol.guasch@salle.url.edu, jie.deng@salle.url.edu.*
Copyright: *©2025 First author et al. This is an open-access article distributed under the terms of the Creative Commons Attribution 3.0 Unported License, which permits unrestricted use, distribution, and reproduction in any medium, provided the original author and source are credited.*

2. THEORETICAL MODEL

2.1 Problem description

As illustrated in Fig. 1, to mitigate the noise inside a water-filled cavity with dimensions $L \times L_c$ (highlighted in the blue region), multiple ABH pillars are uniformly mounted on a uniform beam with thickness h_p. The thickness profile of each ABH pillar follows a power-law distribution given by $h_a(x) = \varepsilon x^m + h_c$, where $\varepsilon = (h_a - h_r)/r_{\text{abh}}^m$. At the ends of the ABHs, some damping layers $r_d \times h_d$ (highlighted in the brown region) have been attached to favor energy dissipation. The geometry and material parameters of the coupled system are detailed in Tab. 1.

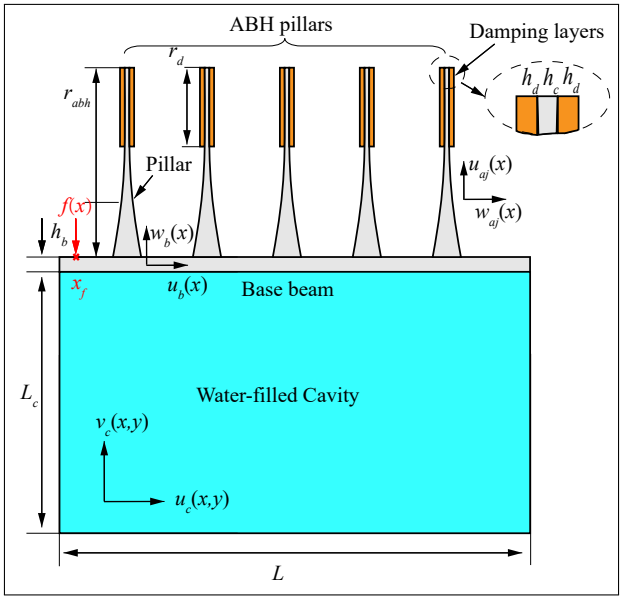


Figure 1. Illustration of the base beam with ABH pillars coupled to a cavity. The blue region indicates the cavity filled with water, while the brown regions represent the damping layers.

2.2 Fluid-Structure Interaction Model

The displacements are represented by variables $u_c(x, y)$, $v_c(x, y)$ for the fluid within the cavity and by $w_b(x, t)$, $u_b(x, t)$ for the uniform beam, respectively. Similarly, the flexural and longitudinal displacements of the ABH pillars can be expressed as $w_{aj}(x, t)$ and $u_{aj}(x, t)$, where $j = 1, 2, \ldots, 5$ denotes the index of the ABH pillars. They are

Table 1. Geometry and material parameters of the coupled system.

Geometry parameters	Material parameters
$L_{cx} = L_b = 0.8\,\text{m}$	$\rho_c = 1000\,\text{kg/m}^3$
$L_{cy} = 0.6\,\text{m}$	$c_c = 1500\,\text{m/s}$
$h_b = h_a = 5\,\text{mm}$	$\eta_c = 0.02$
$m = 2$	$\rho_b = \rho_a = 7800\,\text{kg/m}^3$
$r_{\text{abh}} = 0.4\,\text{m}$	$E_b = E_a = 210\,\text{GPa}$
$\varepsilon = 0.028\,\text{m}^{-1}$	$\eta_b = \eta_a = 0.005$
$h_r = 0.5\,\text{mm}$	$\rho_d = 950\,\text{kg/m}^3$
$r_d = 0.2\,\text{m}$	$E_d = 5\,\text{GPa}$
$h_d = 1\,\text{m}$	$\eta_d = 0.5$

expanded as

$$u_c = \boldsymbol{C}^\top(t)\partial_x\boldsymbol{\varphi}_c(x,y), v_c = \boldsymbol{C}^\top(t)\partial_y\boldsymbol{\varphi}_c(x,y), \quad (1)$$

$$w_b = \boldsymbol{B}_1^\top(t)\boldsymbol{\varphi}_{b1}(x), u_b = \boldsymbol{B}_2^\top(t)\boldsymbol{\varphi}_{b2}(x), \quad (2)$$

$$w_{aj} = \boldsymbol{A}_{j1}^\top(t)\boldsymbol{\varphi}_{aj1}(x), u_{aj} = \boldsymbol{A}_{j2}^\top(t)\boldsymbol{\varphi}_{aj2}(x), \quad (3)$$

where $\boldsymbol{\varphi}_c(x, y) = \boldsymbol{\alpha}(x) \otimes \boldsymbol{\beta}(y)$ are 2D Gaussian functions for the 2D cavity, $\boldsymbol{\varphi}_{b1}(x)$, $\boldsymbol{\varphi}_{b2}(x)$, and $\boldsymbol{\varphi}_{aj1}(x)$, $\boldsymbol{\varphi}_{aj2}(x)$ $(j = 1, 2, \ldots, 5)$ are the 1D Gaussian functions for the base beam and the five ABH pillars, respectively. $\boldsymbol{C}$, $\boldsymbol{B}_1$, $\boldsymbol{B}_2$, $\boldsymbol{A}_{j1}$, and $\boldsymbol{A}_{j2}$ are the coefficient vectors to be determined. The assembled coefficients are defined as $\boldsymbol{q} := [\boldsymbol{C}, \boldsymbol{B}_1, \boldsymbol{B}_2, \boldsymbol{A}_j]$, where $\boldsymbol{A}_j := [\boldsymbol{A}_{j1}, \boldsymbol{A}_{j2}]$.

The Lagrangian of the coupled system is the summation of the Lagrangians of its three components, namely, the cavity, the uniform beam, and the five ABH pillars. This leads to,

$$\mathcal{L} = T_c + T_b + T_a - U_c - U_b - U_a, \quad (4)$$

where T_i and U_i $(i = a, b, c)$ represent the kinetic energy and potential energy of each structure.

By substituting the above expressions into the Euler-Lagrange equations, we can derive the equations of motion,

$$(\boldsymbol{K} - \omega^2\boldsymbol{M})\boldsymbol{Q} = \boldsymbol{0}, \quad (5)$$

where $\boldsymbol{K}$ and $\boldsymbol{M}$ are the stiffness and mass matrices, respectively. However, the above derivation does not explicitly consider the essential boundary conditions of the cavity and the uniform beam, nor the coupling ones at the substructure interfaces. These are accounted for by means of the nullspace method.

The three walls of the cavity are rigid, which implies,

$$u_c(0,y)=0, \quad u_c(L_x,y)=0, \quad v_c(x,0)=0. \tag{6}$$

As for the base beam, it is simply supported on the cavity and coupled with its the upper boundary. The ABH pillars and the uniform beam are coupled at intervals of $d = L_b/6$. These conditions are described by the following equations:

$$w_b(0)=0, \quad w_b(L_x)=0, \tag{7}$$
$$u_b(0)=0, \quad u_b(L_x)=0, \tag{8}$$
$$w_b(x)=v_c(x,L_y), \tag{9}$$
$$w_b(x_j)=u_{aj}(0), \quad u_b(x_j)=w_{aj}(0), \tag{10}$$
$$\partial_x w_b(x_j)=-\partial_x w_{aj}(0), \tag{11}$$

where x_j denotes the connection points of the j-th ABH pillar on the base beam ($j = 1, 2, \ldots, 5$).

Substituting Eqn. (1) to Eqn. (3) into Eqn. (6) to Eqn. (11), we obtain,

$$\boldsymbol{\Xi Q} =: \boldsymbol{\Phi}^\top \boldsymbol{Q} = \boldsymbol{0}, \tag{12}$$

where $\boldsymbol{\Xi}$ is the matrix form of the above constraints.

To avoid numerical instabilities, we square and integrate Eqn. (12) over the interface domain, which yields,

$$\boldsymbol{Q}^\top \left[\int \boldsymbol{\Phi}^\top \boldsymbol{\Phi} \, \mathrm{d}x, \right] \boldsymbol{Q} =: \boldsymbol{Q}^\top \boldsymbol{\Psi} \boldsymbol{Q} \tag{13}$$

where, we have defined matrix $\boldsymbol{\Psi}$ is the constant constraint matrix. Finding a basis for the nullspace $\mathcal{N}(\boldsymbol{\Psi})$, we can express $\boldsymbol{Q}$ as $\boldsymbol{Q} = \boldsymbol{Z}\boldsymbol{k}$, with $\boldsymbol{Z}$ containing the nullspace eigenvectors and $\boldsymbol{k}$ being the coefficient vector. Substituting into the equation of motion, Eq. (5), we arrive at,

$$\left(\overline{\boldsymbol{K}} - \omega^2 \overline{\boldsymbol{M}}\right) \boldsymbol{k} = \boldsymbol{0}, \tag{14}$$

where $\overline{\boldsymbol{K}} = \boldsymbol{Z}^\top \boldsymbol{K} \boldsymbol{Z}$ and $\overline{\boldsymbol{M}} = \boldsymbol{Z}^\top \boldsymbol{M} \boldsymbol{Z}$, represent the coupled stiffness and mass matrices, respectively.

3. NUMERICAL RESULTS

To evaluate the performance of ABH pillars in reducing noise inside the cavity, a unit point force is applied at the left x_f of the uniform beam, see Fig. 1.

In Fig. 2, we first present the mean square velocity (MSV) of the host beam. It is observed that if ABH pillars are attached to it instead of uniform (UNI) pillars, the vibration becomes significantly reduced. On the other hand, Fig. 3 presents the acoustic energy ($E = T_c + U_c$) within the cavity. The results indicate again that ABH pillars are more effective than uniform pillars over almost the entire frequency range.

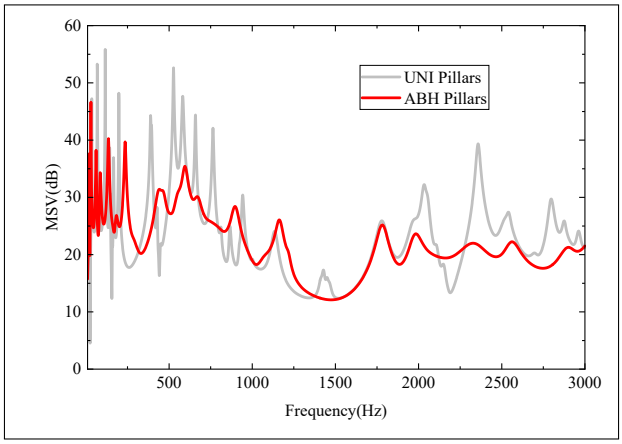


Figure 2. Mean square velocity (MSV) of the host beam.

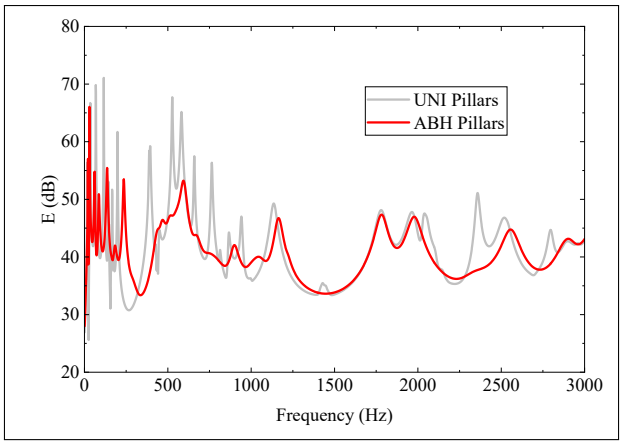


Figure 3. Acoustic energy in the water-filled cavity.

4. CONCLUSION

This paper proposes attaching ABH pillars to host plate to reduce noise transmission inside a heavy-fuid filled cavity. The displacements of the ABH pillars, the base beam, and the fluid have been represented using the Gaussian expansion method (GEM), while the nullspace method (NSM) has been employed to impose the essential boundary and

continuity conditions of the problem. The results indicate that ABH pillars can significantly dampen the vibrations of the uniform beam and reduce the energy transmission to the cavity, thus showing excellent noise reduction capability.

5. ACKNOWLEDGMENTS

The authors thank the fund by the China Scholarship Council (CSC No. 202406050053). J. Deng acknowledges the support received by the National Natural Science Foundation of China (52301386), and the support of the Beatriu de Pinós postdoctoral program of the Department of Research and Universities of the Generalitat of Catalonia (2022 BP 00027). O. Guasch acknowledges the support of the Generalitat de Catalunya (Departament de Recerca i Universitats) through grant 2021 SGR 1396 awarded to the HER group.

6. REFERENCES

[1] E. Bowyer and V. V. Krylov, "Experimental study of sound radiation by plates containing circular indentations of power-law profile," *Applied Acoustics*, vol. 88, pp. 30–37, 2015.

[2] D. Wu, M. Yu, Q. Shen, D. Li, and Z. Bai, "Investigation on the characteristics of flow-induced vibration and noise of acoustic window with embedded compound acoustic black holes," *Applied Acoustics*, vol. 228, p. 110376, 2025.

[3] J. Deng, N. Gao, X. Chen, H. Pu, and J. Guo, "Underwater sound radiation from a mindlin plate with an acoustic black hole," *Ocean Engineering*, vol. 278, p. 114376, 2023.

[4] L. Ma and L. Cheng, "Vibration and sound radiation of an acoustic black hole plate immersed in heavy fluid," *The Journal of the Acoustical Society of America*, vol. 154, no. 1, pp. 179–190, 2023.

[5] T. Zhou and L. Cheng, "A resonant beam damper tailored with acoustic black hole features for broadband vibration reduction," *Journal of Sound and Vibration*, vol. 430, pp. 174–184, 2018.

[6] H. Ji, N. Wang, C. Zhang, X. Wang, L. Cheng, and J. Qiu, "A vibration absorber based on two-dimensional acoustic black holes," *Journal of Sound and Vibration*, vol. 500, p. 116024, 2021.

[7] H. Ji, X. Zhao, N. Wang, W. Huang, J. Qiu, and L. Cheng, "A circular eccentric vibration absorber with circumferentially graded acoustic black hole features," *Journal of Vibration and Acoustics*, vol. 144, no. 2, p. 021014, 2022.

[8] S. Park, J. Y. Lee, and W. Jeon, "Vibration damping of plates using waveguide absorbers based on spiral acoustic black holes," *Journal of Sound and Vibration*, vol. 521, p. 116685, 2022.

[9] J. Deng and N. Gao, "Broadband vibroacoustic reduction for a circular beam coupled with a curved acoustic black hole via nullspace method," *International Journal of Mechanical Sciences*, vol. 233, p. 107641, 2022.

[10] J. Deng, N. Gao, and X. Chen, "Ultrawide attenuation bands in gradient metabeams with acoustic black hole pillars," *Thin-Walled Structures*, vol. 184, p. 110459, 2023.

[11] J. Deng, O. Guasch, and L. Maxit, "A displacement formulation for coupled elastoacoustic problems that preserves flow irrotationality," *Journal of Sound and Vibration*, vol. 597, p. 118815, 2025.

[12] J. Deng, L. Zheng, P. Zeng, Y. Zuo, and O. Guasch, "Passive constrained viscoelastic layers to improve the efficiency of truncated acoustic black holes in beams," *Mechanical Systems and Signal Processing*, vol. 118, pp. 461–476, 2019.

[13] J. Deng, L. Zheng, O. Guasch, H. Wu, P. Zeng, and Y. Zuo, "Gaussian expansion for the vibration analysis of plates with multiple acoustic black holes indentations," *Mechanical Systems and Signal Processing*, vol. 131, pp. 317–334, 2019.

[14] J. Deng, O. Guasch, and L. Zheng, "Ring-shaped acoustic black holes for broadband vibration isolation in plates," *Journal of Sound and Vibration*, vol. 458, pp. 109–122, 2019.

[15] J. Deng, Y. Xu, O. Guasch, N. Gao, and L. Tang, "Nullspace technique for imposing constraints in the Rayleigh–Ritz method," *Journal of Sound and Vibration*, vol. 527, p. 116812, 2022.

DOI: 10.61782/fa.2025.0955



FORUM ACUSTICUM
EURONOISE 2025

VIBRATION CONTROL IN A HONEYCOMB SANDWICH METAPANEL MADE UP OF PERIODIC CELLS WITH AN ABH-LIKE THICKNESS PROFILE.

S.Avetisov[1*] **F.Gautier** [1] **A.Pelat**[1]
S.Sorokin[2] **G.Gabard**[1] **M.Versaevel**[3] **J.Mardjono**[3]
[1] Laboratoire d'Acoustique de l'Université du Mans (LAUM), UMR CNRS 6613,
Institut d'Acoustique - Graduate School (IA-GS), Avenue Olivier Messiaen, 72085 Le Mans, France
[2] Department of Materials and Production,
Aalborg University Fibigerstraede 16, DK 9220 Aalborg, Denmark
[3] Safran Nacelles, Route du Pont VIII, 76700 Gonfreville-l'Orcher, France

ABSTRACT

Acoustic Black Holes (ABHs) have gained significant attention for their potential in vibration control by effectively trapping flexural waves within structures featuring gradually tapered thickness profiles. In this study, we investigate the wave propagation of bending waves in a honeycomb sandwich panel that integrates ABH effects to attenuate vibrations in a high broadband frequency band and also in a low tunable frequency band. By periodically modulating the thickness of the panel with an ABH-like thickness profile, the design leverages both Bragg band gaps and the ABH effect to enhance wave attenuation. The sandwich configuration offers a high stiffness-to-mass ratio, making it particularly attractive for lightweight structural applications. The band structure is analyzed using a plane wave expansion method based on Kirchhoff's assumptions, and finite element (FE) simulations are conducted to validate the theoretical predictions. The results confirm the existence of tunable low-frequency band gaps controlled by key geometric parameters. This approach provides an effective strategy for designing lightweight, stiff, and highly efficient vibration-damping panels, suitable for advanced engineering applications

*__Corresponding author__: *stepan.avetisov@univ-lemans.fr.*
__Copyright__: *©2025 First author et al. This is an open-access article distributed under the terms of the Creative Commons Attribution 3.0 Unported License, which permits unrestricted use, distribution, and reproduction in any medium, provided the original author and source are credited.*

Keywords: *acoustic black holes, phononic crystal plates, bragg scattering band gaps*

1. INTRODUCTION

In recent years, periodic materials and structures have garnered significant attention in physics and engineering due to their unique wave propagation characteristics and their ability to control vibrations [1]. One particularly promising approach is the integration of acoustic black holes (ABHs) into engineered structures. A particularly promising approach involves integrating acoustic black holes (ABHs) into engineered structures. The ABH effect, first introduced by Mironov in 1988 [2] and further developed by Krylov [3], employs a gradual reduction in structural thickness, typically following a power-law decreasing profile, to create a near-zero reflection condition for bending waves. This process results in a progressive reduction in wave velocity and the accumulation of vibrational energy, which, when paired with suitable damping layers, results in effective energy dissipation [4].

Combining ABHs with sandwich panels offers significant advantages in low-frequency vibration suppression. Sandwich structures, widely used in aerospace and automotive industries due to their high stiffness-to-weight ratio and efficient load-bearing capacity, often suffer from poor noise insulation and susceptibility to structural vibrations. To overcome these challenges, periodic thickness modulation has emerged as an effective strategy for enhancing wave attenuation. Recent studies [5] have demon-

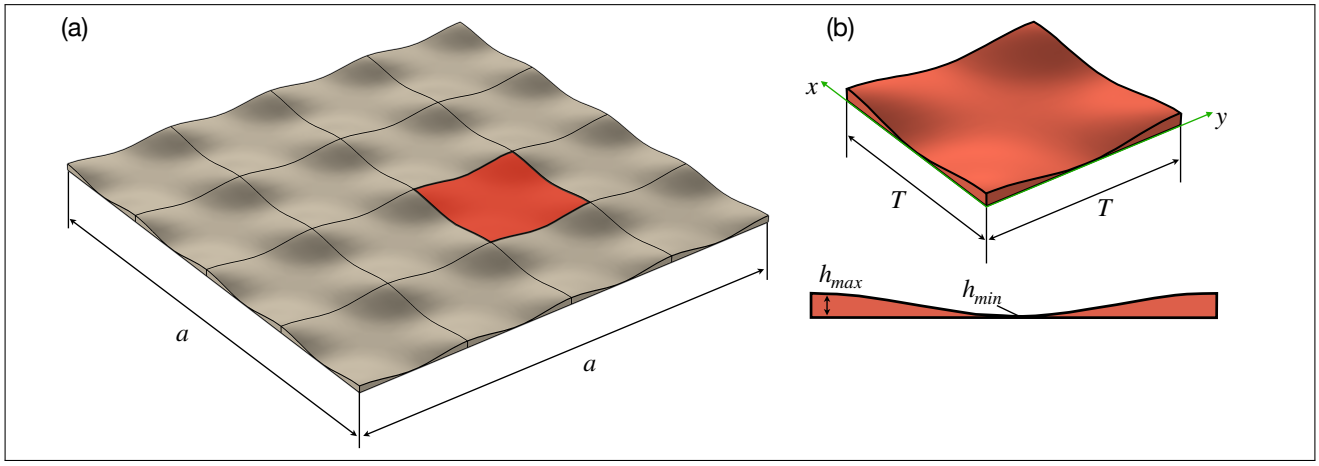


Figure 1. The proposed design of the ABH PC plate: (a) 3D view composed of a 4×4 array of identical rectangular unit cells, and (b) detailed layout of the rectangular unit cell defined in Eqn. (1).

strated that incorporating periodic effects, such as Bragg bandgaps (BGs), into solid panels can substantially reduce vibrations and sound transmission. By integrating ABHs with periodic structures, vibration control can extend beyond the traditional cut-on frequency limitations of ABHs, improving broadband performance. The same undulation periodicity design in plates was explored by G. Trainiti [6], where multiple scattering between the cells of an infinite periodic lattice leads to complete bandgaps. Geometrical undulations have proven to be effective design parameters that can be adjusted to achieve the desired dynamic characteristics.

This study aims to investigate the synergistic effects of ABHs and periodic modulation in sandwich panels for enhanced vibration and noise control. By combining the wave-trapping properties of ABHs with the bandgap effects of periodic structures, we seek to develop a novel approach for lightweight panels with improved acoustic performance. The plate is analyzed based on dispersion relations using the plane wave expansion (PWE) method, alongside the finite element (FE) method, both of which are employed to obtain the band structure. The FE method is also employed to compute the dynamic response of the acoustic black hole phononic crystal plate.

2. DESIGN AND GEOMETRY OF THE MODULATED PANEL

The acoustic black hole phononic crystals (ABH PCs) is shown in Fig.1. The geometry of the panel is characterized by a periodic variation in thickness, h, with a spatial period, T. For simplicity and to ensure an integer number of unit cells in the modulated panel, we consider a rectangular unit cell, as shown in Fig.1b. The curvature undulation is defined as a combination of cosine functions of the spatial coordinates (u, v) for the rectangular unit cell, as follows

$$h(u,v) = \alpha + \beta\Bigg[\cos\left(\frac{2\pi}{T}u\right) + \cos\left(\frac{2\pi}{T}v\right) + \gamma\cos\left(\frac{2\pi}{T}u\right)\cos\left(\frac{2\pi}{T}v\right)\Bigg], \quad (1)$$

where the average thickness of the plate, for the shape parameter $\gamma = -1$, is given by $\alpha = \dfrac{\gamma h_{max} + (\gamma - 2)h_{min}}{2\gamma - 2}$ and the contrast parameter is $\beta = \dfrac{h_{max} - h_{min}}{2\gamma - 2}$, which is defined in terms of the maximum and minimum thickness values. A diverse set of thickness distributions can be achieved by adjusting the shape parameter γ [5].

3. BAND DIAGRAMS AND VIBRATION ANALYSIS

3.1 PWE and FE modeling of a rectangular unit cell

We focus on an inhomogeneous thin plate based on Kirchhoff-Love theory. Using the PWE method, we analyze the band structure of an infinite periodic rectangular unit cell, as shown in Fig.1b. The equation of motion for

the PWE method, described by the flexural displacement $w(\mathbf{r})$, is given as follows:

$$
\begin{aligned}
&-\rho h(\mathbf{r})\omega^2 w(\mathbf{r}) + \Delta(D(\mathbf{r})\Delta w(\mathbf{r})) \\
&\quad = (1-\nu)\Bigg(\frac{\partial^2 D(\mathbf{r})}{\partial y^2}\frac{\partial^2 w(\mathbf{r})}{\partial x^2} - 2\frac{\partial^2 D(\mathbf{r})}{\partial x \partial y}\frac{\partial^2 w(\mathbf{r})}{\partial x \partial y} \\
&\qquad + \frac{\partial^2 D(\mathbf{r})}{\partial x^2}\frac{\partial^2 w(\mathbf{r})}{\partial y^2}\Bigg).
\end{aligned} \tag{2}
$$

where ρ is the mass density, ω is the angular frequency, $D(\mathbf{r}) = \dfrac{Eh(\mathbf{r})^3}{12(1-\nu^2)}$ is the bending stiffness of the plate, $\mathbf{r}$ is the spatial position vector, depending on the coordinates x and y, and ν is Poisson's ratio. Due to the periodicity of the ABH PC, these material parameters can be expanded as a Fourier series [5, 7]. According to Bloch's theorem, the Eqn. (2) can be used to compute the eigenvalue problem of $\omega(\mathbf{k})$, and the energy band structure can be obtained by solving this equation. The wave vector $\mathbf{k} = [k_x, k_y]$ can be taken at the boundary of the irreducible Brillouin zone (IBZ) of a two-dimensional rectangular unit cell. We can calculate energy band properties along the IBZ path ΓXM and obtain the corresponding dispersion curves. The Bloch wave vector $\mathbf{k}$ starts from Γ and moves along the x-direction to X, where $k_x \in (0, \pi/T)$ and $k_y = 0$. Next, the wave vector continues from X to M, where $k_x = \pi/T$ and $k_y \in (0, \pi/T)$. Finally, the wave vector returns to Γ from M, following the path where $k_x = k_y \in (0, \pi/T)$.

Since we are interested in the BGs at low frequencies and assume that the panel does not exhibit shear deformation or core compressibility, the total plate stiffness of the sandwich panel $D(\mathbf{r})$ is considered frequency-independent. The ABH PC is modeled using the following equivalent homogenized material properties: Young's modulus $E = 54 \cdot 10^8$Pa, $\nu = 0.3$, and $\rho = 126$kg/m^3.

The numerical simulations based on the finite element (FE) method are implemented using the commercial software COMSOL solid mechanics package to calculate the band structures. A Floquet periodic boundary condition is applied to both sides of the rectangular unit cell, as derived from the Bloch's theorem. A parametric sweep of the reduced wave vector $\mathbf{k}$ is performed over the first irreducible Brillouin zone. The model materials correspond to the equivalent homogenized material as indicated above, with no damping loss.

The frequency dependence on the wave number is plotted in Fig.2. The geometric parameters of the rectangular unit cell from Fig.1b were chosen as follows: the

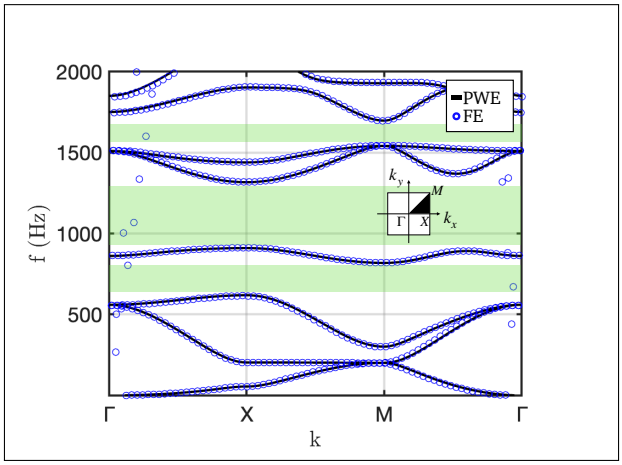


Figure 2. Dispersion curves with green-shaded areas denoting band gap distribution of the rectangular unit cell. The band structure along the IBZ path was computed using FE (blue circles) and PWE (black line) methods.

maximum and minimum thicknesses are $h_{max} = 12$mm and $h_{min} = 0.6$mm, with a length of $T = 200$mm. It is clearly observed that the FE (blue circles) and PWE (black line) results are highly consistent. The green-shaded area in the diagram represents the three generated BGs of the rectangular unit cell, where wave transmission is prohibited. The first band gap opens around 615Hz and continues up to 912Hz. The widest band gap spans the frequency range from 912Hz to 1318Hz. The third band gap appears in the frequency range from 1544Hz to 1696Hz.

3.2 Numerical results for the finite panel with multiple ABHs

We consider an ABH PC plate composed of 4×4 array of identical rectangular unit cells, as shown in Fig.1a, and analyze its response when subjected to an external point force of $F = 1$N. The excitation point is located at the center of the finite structure, and the plate is assumed to be clamped along its edges. The width of the ABH PC plate is $a = 800$mm, with other material and geometric characteristics are taken from the previous section. We focus on the spatial average squared mobility of this plate, defined as $10log_{10}(v/F)$, where v is the velocity.

Fig.3a compares the mobility of the ABH PC plate with a 4×4 array of identical rectangular unit cells (red line), an ABH PC plate with an 8×8 array of identical

unit cells (black line), and the reference plate (blue line), modeled as a uniform plate with a total thickness corresponding to the maximum thickness of the ABH PC plate, $h_{tot} = 12$mm. As shown in Fig.3a, the mobility of the ABH PC plates is significantly reduced, resulting in noticeable vibration attenuation at low frequencies, which is attributed to the formation of BGs.

Additionally, Figs.3b,c,d show the displacement field at 821Hz (green dashed line) for the different panels. These results demonstrate complete vibration isolation in the ABH PC plate, with the wave progressively attenuated as it passes through each unit cell. Furthermore, the mobility decreases substantially as the number of unit cells increases.

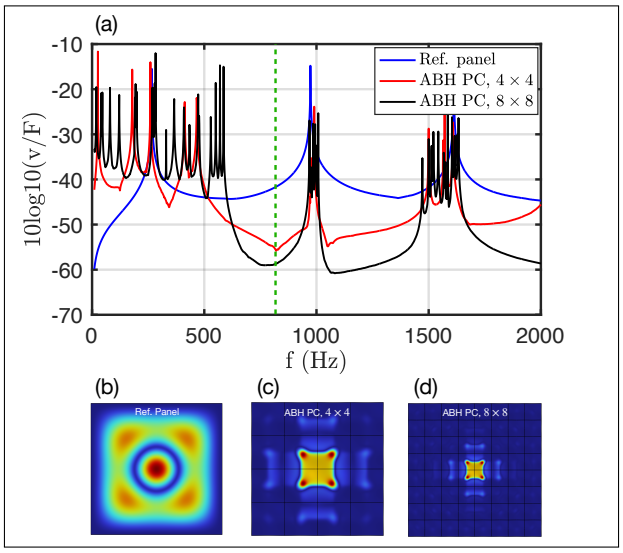


Figure 3. a) The spatial average squared mobility of the ABH PC plate composed of a 4×4 array of identical rectangular unit cells (red line), an 8×8 array of identical unit cells (black line), and the uniform plate (blue line). b,c,d) Corresponding displacement fields at 821Hz (green dashed line).

4. CONCLUSION

This study investigates the synergistic effects of ABHs and periodic modulation in sandwich panels for enhanced vibration and noise control. The band structure analysis using the PWE method and dynamic response evaluated through FE simulations revealed the presence of tunable low-frequency band gaps, which effectively attenuate mechanical waves and significantly reduce vibrational energy. The dynamic response analysis of the ABH PC plate, along with the effect of the number of unit cells, further confirmed a substantial reduction in the spatial average squared mobility compared to the uniform plate, demonstrating the efficiency of the proposed design. This work advances the understanding of acoustic metamaterials and offers a promising approach for developing lightweight materials for noise isolation and vibration suppression in various engineering applications.

5. ACKNOWLEDGMENTS

The authors acknowledge the financial support of the Safran Group and the Agence Nationale de la Recherche (France) through the Industrial Chair ASTRAL (grant ANR-20-CHIN-00050-01)

6. REFERENCES

[1] C. Kittel, Introduction to Solid State Physics, 8th ed. *Wiley, New York*, 2004.

[2] M.A Mironov, Propagation of a flexural wave in a plate whose thickness decreases smoothly to zero in a finite interval, *Sov.Phys.Acoust.*, 34(3) 318–319, 1988.

[3] V.V Krylov, Localized acoustic modes of a quadratic solid wedge, *Moscow University Physics Bulletin*, 45(6):65-69, 1990.

[4] A. Pelat, F. Gautier, S.C. Conlon, F. Semperlotti, The acoustic black hole: A review of theory and applications, *J. Sound Vib.*, 476, 115316, 2020.

[5] F. Gautier, A. Pelat, Broadband vibration mitigation using a two-dimensional acoustic black hole phononic crystal, *J. Acoust. Soc. Am.*, 155:3051–3059, 2024.

[6] G. Trainiti, J.J. Rimoli, M. Ruzzene, Wave propagation in periodically undulated beams and plates, *International Journal of Solids and Structures*, 75–76:260–276, 2015.

[7] Y. Zhang, L. Han, Z. Ni, L. Jiang, Flexural vibrations band gaps in phononic crystal Timoshenko beam by plane wave expansion method, *Optoelectronics and advanced materials-rapid communications*, 6(11-12):1049-1053, 2012.

DOI: 10.61782/fa.2025.0053

FORUM ACUSTICUM EURONOISE 2025

ABSORPTION AND SCATTERING OF BENDING WAVES BY AN ACOUSTIC BLACK HOLE EMBEDDED IN A HONEYCOMB SANDWICH PANEL

Alex Besse[1*] **Omar Aklouche**[2] **Frédéric Ablitzer**[1]
Adrien Pelat[1] **François Gautier**[1]
[1] Acoustic Laboratory of Le Mans University (LAUM), Le Mans University, France
[2] National Engineering school of Le Mans (ENSIM), Le Mans, France

ABSTRACT

Acoustic Black Hole (ABH) is a passive vibration control technique that involves introducing a local reduction in the thickness of a panel, combined with a thin viscoelastic coating in the weak area. This approach increases vibration damping with no additional mass, making it particularly attractive for lightweight structures such as honeycomb sandwich panels used in aerospace applications. The vibration field of ABH is mainly controlled by complex localised modes, classified according to their circumferential order. The reflection coefficient of an incident bending wave converging on the ABH, defined for each circumferential order, is analysed in the complex frequency plane. It is shown that each mode corresponds to a pair of poles and zeros symmetrical about the real frequency axis. The viscoelastic ABH coating allows the pairs to rotate about the origin, bringing the zeros closer to the real axis, creating interesting dips in the reflection coefficient as a function of real frequency. A wave-based model is used to identify local modes, study the role of the ABH profile and the effect of the damping layer. The approach provides a list of rules for optimal design of the ABH absorber.

Keywords: *sandwich panel, vibration mitigation, local modes, acoustic black hole, critical coupling*

**Corresponding author*: *alex.besse@univ-lemans.fr.*
***Copyright**: ©2025 Alex Besse et al. This is an open-access article distributed under the terms of the Creative Commons Attribution 3.0 Unported License, which permits unrestricted use, distribution, and reproduction in any medium, provided the original author and source are credited.*

1. INTRODUCTION

Acoustic Black Holes (ABHs) are an effective passive technique for vibration and noise reduction in engineering structures. An ABH consists of a tapered region within a beam or plate that traps and dissipates flexural waves. Introduced by Mironov and Krylov [1, 2], it relies on a power-law thickness profile with a thin viscoelastic layer for enhanced wave absorption. Initial studies on one-dimensional (1D) ABHs analysed wave trapping using geometrical acoustics [3, 4] and impedance models [5], highlighting the role of damping in ABH performance. Later research accounted for evanescent waves and imperfections [6]. More recently, ABHs have been integrated into sandwich structures to improve vibration attenuation despite challenges emerging from frequency-dependent bending stiffness [7–9]. The influence of local modes on ABH performance was first demonstrated in [10]. These modes create local minima in the reflection coefficient, with zeros aligning on the real frequency axis under optimal damping (critical coupling). This study extends the concept to 2D configurations, using a semi-analytical model of a honeycomb sandwich plate with a circular ABH to analyse local modes and reflection coefficients. Inspired by prior wave-based modelling [11, 12], the study compares identical ABHs in sandwich and solid panels to assess modal density effects. The ABH profile is then adjusted to examine effects of positioning of zeros and establish design guidelines for improved ABH performance.

2. EFFECT OF BENDING STIFFNESS FREQUENCY DEPENDANCE ON ABH PERFORMANCE

2.1 Configurations

In order to investigate the effect of the sandwich's bending stiffness decreasing with frequency, an adaptation of the wave based model, described in [9], of an ABH embedded in a infinite panel is used. The local behaviour is studied for two configurations. The first configuration corresponds to a sandwich panel modelled as an uniform Kirchhoff's panel based on Nilsson's sandwich theory [7]. This theory propose modelling of a sandwich structure composed of two identical skin as a uniform material panel with a bending stiffness dependent on frequency. The second configuration, corresponds to the "solid panel", which is identical to the sandwich panel, in geometry and material properties, except for a uniform bending stiffness set to the static bending stiffness of the sandwich panel. The mechanical properties of the skins and the core are given in table 1 with an identical loss factor $\eta = 0.04$. An ABH is embedded in these two configurations. This ABH is composed of 2 main zones, a tapered zone in which the honeycomb core of the sandwich is decreasing with the skins staying of constant thickness and a zone made of a central plateau of a single skin. At the connection of these zones, there is a small region where the two skins connect. The ABH can be characterised with $a = 0.05$m, the radius of the central plateau and $b = 0.15$m the radius of the ABH. A viscoelastic layer is added to the ABH using the RKU model [13]. The ABH placed in the two configurations lead to a bending stiffness profile depending on the radius as demonstrated in Figure1 (a) for the solid panel and in Figure 1(b) for the sandwich panel.

	ρ	ν	E	G
Skin	1541 kg/m^3	0.35	19.3 GPa	7.1 GPa
Core	37 kg/m^3	0.3	55 MPa	21 MPa

Table 1. Mechanical parameters of a honeycomb sandwich panel.

2.2 Reflection coefficient of ABH in sandwich and solid plates

The two configurations previously described are used to investigate the performance and local dynamics of an ABH embedded in an infinite panel composed of either a solid material or a sandwich material modelled with Nilsson theory. In order to do so, the value of the reflection coefficient, R, is evaluated in a complex frequency plane and plotted along the real frequency axis for the circumferential order $n = 0$ (Figure 1(c)). The results show a number of local minima identified by the zeros in the complex frequency plane. It appears that each zero corresponds to a local modes of the ABH. In the sandwich case, an increased number of zeros is observed due to the softening of the structure which increases the modal density of the ABH. When looking at the reflection coefficient value along the real axis, each zero corresponds to a dip, leading to an overall value of $|R|$ being lower in the case of a sandwich panel (for f=1500 Hz, $|R|_{sandwich} = 0.3$ while $|R|_{solid} = 0.5$. An increased number of zeros ,i.e number of local modes, leads to an ABH being more effective. When designing an ABH it is crucial to carefully consider the local dynamics of the scatterer.

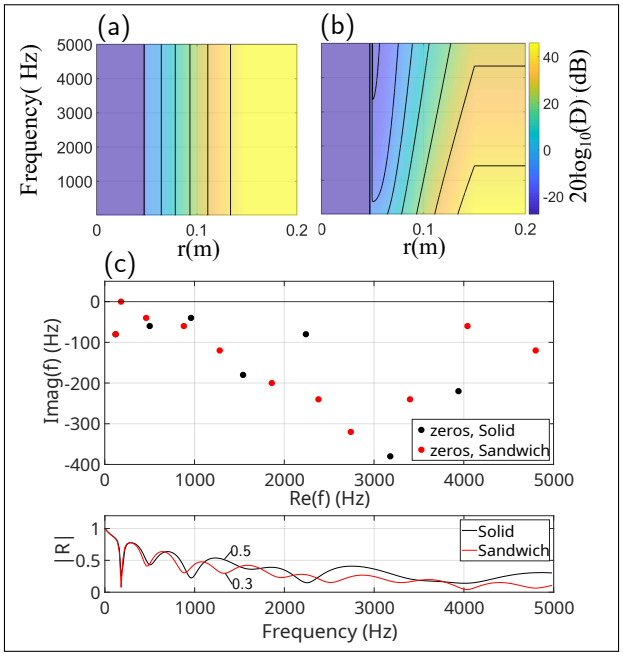


Figure 1. (a) Bending stiffness profile of an ABH placed in a solid panel. (b) Bending stiffness profile of an ABH placed in a sandwich panel panel. (c) Positions of zeros in the complex frequency plane and value of $|R|$ along the real frequency axis for the two configurations at circumferential order $n = 0$.

3. ZERO POSITIONING TO IMPROVE ABH PERFORMANCE

3.1 Selected ABH profiles

As previously shown in section 2, the performance of an ABH is dependent on local modes which create zeros in the reflection coefficient reducing its overall value. The aim of this section is to improve the performance of an ABH by modifying the placement of zeros through geometry variations. Two geometries are compared and correspond to an ABH placed in the same sandwich panel as the previous section with $\eta = 0.01$. In these panels, the two ABH geometries are placed. The first, called 'ABH-1', is identical to the one used in section 2 and its cross-section is shown in Figure 2(a). The second, named 'ABH-2', corresponds to an ABH of radius $b = 0.15$m, with the same power law profile as ABH-1 but with a central plateau twice as large, $a = 0.10$m, its cross section is visible in Figure 2(b).

3.2 ABH performance

These configurations are compared by studying the zeros of the reflection coefficient in the complex plane and the mobility values. The ratio $\chi = im(f)/re(f)$ describes the proximity of the zero to the real axis. The zeros of the reflection coefficient for ABH-1 and ABH-2 are shown in Figure 2(c) for $n = 0$. In this figure, it appears that the zeros of ABH-2 are closer to the real frequency axis ($\chi_{ABH-2} = 2\%$ vs $\chi_{ABH-1} = 10\%$). The proximity of the zeros to the real frequency axis leads to an improvement in the performance of an ABH due to deeper dips in the reflection coefficient value.

To confirm the improved absorption performance of ABH-2, the quadratic mobility averaged over a finite circular sandwich plate is computed using the model presented in [9] and is shown in third-octave band representation in Figure 2(d). In this figure, the mobility of a panel without ABH is compared to the mobility of the panel in the presence of ABH-1 and ABH-2. A mobility reduction of up to 5 dB is observed between the uniform panel and ABH-1, whereas ABH-2 achieves a reduction of up to 8 dB. It appears that the geometry of ABH-2 allows for a greater mobility reduction, particularly between 500 and 2000 Hz. This result correlate with the positions of zeros in the complex frequency plane. These results highlight the importance of the positioning of zeros in the complex plane to enhance the performance of an ABH.

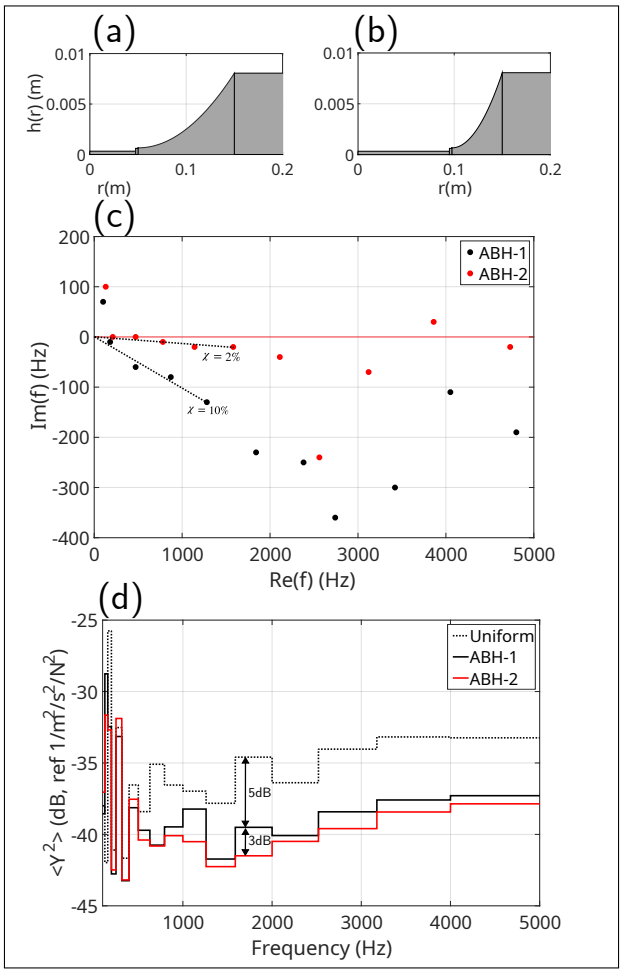


Figure 2. (a) ABH-1 profile with $a = 0.0475$m, $b = 0.05$m and $c = 0.15$m. (b) ABH-2 profile with $a = 0.095$m, $b = 0.0975$m and $c = 0.15$m. (c) Positions of zeros in the complex frequency plane for the two configurations at circumferential order $n = 0$. (d) Spatially averaged quadratic mobility for a plate with no ABH (Uniform), ABH-1 or ABH-2.

4. CONCLUSION

This study investigated the influence of local modes and their positioning in the complex frequency plane on the performance of Acoustic Black Holes (ABHs) embedded in sandwich panels. Using a semi-analytical wave-based model, the analysis demonstrated that an increase in modal density of the scatterer induces an increased number of zeros in the reflection coefficient. This leads, particularly when they are critically coupled, to enhance vibration attenuation. The comparison between ABH-1 and ABH-2 confirmed that a modified geometry can improve the absorption performance by increasing the proximity of the zeros to the real axis. These findings highlight the critical role of local dynamic behaviour in ABH design and provide key guidelines for optimising ABH performance. To create better ABH, careful consideration must be given to the study of local modes and the positioning of zeros, achieved through precise tuning of damping, geometry and materials when possible.

5. ACKNOWLEDGMENTS

This work is part of the MAMBO project, financially supported by the Direction Générale de l'Aviation Civile (DGAC), 2021-2025.

6. REFERENCES

[1] M. Mironov, "Propagation of a flexural wave in a plate whose thickness decreases smoothly to zero in a finite interval," *Sov. Phys. Acoust.*, vol. 34, pp. 318–319, 1988.

[2] V. V. Krylov, "Localized acoustic modes of a quadratic solid wedge," *Moscow University Physics Bulletin*, vol. 45, pp. 65–69, 1990.

[3] V. V. Krylov and R. E. T. B. Winward, "Experimental investigation of the acoustic black hole effect for flexural waves in tapered plates," *Journal of Sound and Vibration*, vol. 300, pp. 43–49, 2007.

[4] V. Krylov, "New type of vibration dampers utilising the effect of acoustic 'black holes'," *Acta Acustica united with Acustica*, vol. 90, pp. 830–837, 2004.

[5] V. B. Georgiev, J. Cuenca, F. Gautier, L. Simon, and V. V. Krylov, "Damping of structural vibrations in beams and elliptical plates using the acoustic black hole effect," *Journal of Sound and Vibration*, vol. 330, pp. 2497–2508, 2011.

[6] D. J. O'Boy, V. V. Krylov, and V. Kralovic, "Damping of flexural vibrations in rectangular plates using the acoustic black hole effect," *Journal of Sound and Vibration*, vol. 329, pp. 4672–4688, 2010.

[7] A. C. Nilsson and B. Liu, "Prediction of some vibroacoustic properties of sandwich plates with honeycomb and foam cores," *The Journal of the Acoustical Society of America*, vol. 144, pp. 1600–1614, 2018.

[8] K. Ege, N. Roozen, Q. Leclère, and R. Rinaldi, "Assessment of the apparent bending stiffness and damping of multilayer plates; modelling and experiment," *Journal of Sound and Vibration*, vol. 426, pp. 129–149, 2018.

[9] A. Besse, P. O'Donoughue, O. Aklouche, F. Ablitzer, A. Pelat, and F. Gautier, "Vibration damping of fiberglass honeycomb sandwich panels based on the acoustic black hole effect," *Journal of Sound and Vibration*, vol. 604, p. 118991, 2025.

[10] J. Leng, V. Romero-García, A. Pelat, R. Picó, J. P. Groby, and F. Gautier, "Interpretation of the Acoustic Black Hole effect based on the concept of critical coupling," *Journal of Sound and Vibration*, vol. 471, pp. 115–199, 2020.

[11] D. J. O'Boy and V. V. Krylov, "Damping of flexural vibrations in circular plates with tapered central holes," *Journal of Sound and Vibration*, vol. 330, pp. 2220–2236, 2011.

[12] O. Aklouche, A. Pelat, S. Maugeais, and F. Gautier, "Scattering of flexural waves by a pit of quadratic profile inserted in an infinite thin plate," *Journal of Sound and Vibration*, vol. 375, pp. 38–52, 2016.

[13] D. Ross, E. Ungar, and E. K. Jr., "Damping of plate flexural vibrations by means of viscoelastic laminae," *Structural damping*, pp. 49–97, 1959.

DOI: 10.61782/fa.2025.0332

FORUM ACUSTICUM EURONOISE 2025

EFFICIENCY OF AN ACOUSTIC BLACK HOLE EMBEDDED INTO A HONEYCOMB SANDWICH PANEL

Alex Besse[1*] **Omar Aklouche**[2] **Frédéric Ablitzer**[1]
Adrien Pelat[1] **François Gautier**[1]
[1] Acoustic Laboratory of Le Mans University (LAUM), Le Mans University, France
[2] National Engineering school of Le Mans (ENSIM), Le Mans, France

ABSTRACT

The Acoustic Black Hole (ABH) is a passive vibration control technique that enhances damping without increasing structural mass. This effect is achieved by reducing stiffness locally, such as tapering plate thickness following a power-law profile, and adding a viscoelastic coating for increased damping. In lightweight honeycomb sandwich panels, the shear effect significantly influences wave propagation, introducing unique ABH characteristics. This study investigates the behavior of an ABH embedded in a honeycomb sandwich panel (with glass fiber skins and a honeycomb core) in the vicinity of a point excitation force. Using models and experiments, the aim is to evaluate the ABH's ability to absorb vibrations generated by the source. Vibration fields of several samples panels (without ABH, with one and multiple) are measured using a scanning laser vibrometer. The absorption effect (reduction in the average mobility of the panel mobility) is compared with models predictions. Results reveal that the distance between the excitation point and the ABH is critical for good performance. This finding raises the possibility of seeing an ABH not only as a passive vibration absorber but also as a vibrations isolator to decouple the force entry point and the rest of the structure.

Keywords: *acoustic black hole, numerical model, experimental results, vibration isolation*

**Corresponding author*: *alex.besse@univ-lemans.fr.*
***Copyright**: ©2025 Alex Besse et al. This is an open-access article distributed under the terms of the Creative Commons Attribution 3.0 Unported License, which permits unrestricted use, distribution, and reproduction in any medium, provided the original author and source are credited.*

1. INTRODUCTION

The Acoustic Black Hole (ABH) is a passive vibration control technique that enhances damping without adding mass. This technique consists of locally reducing the thickness, through a tapered profile, and increasing local loss, with an added viscoelastic layer. Originally proposed by Mironov [1] and Krylov [2], the concept has been extensively studied in uniform panels [3, 4] and more recently in complex structures such as honeycomb sandwich panels [5]. These panels, commonly used in aerospace and automotive applications due to their low weight and relative stiffness, introduce additional challenges due to frequency-dependent bending stiffness induced by shear effects [6, 7].

Experimental studies have demonstrated the effectiveness of ABHs for reducing structural vibrations across various configurations. O'Boy et al. [8] and Georgiev et al. [9] validated the ABH effect through measurements on beams and plates. Recent work [10, 11] extended these findings to composite materials, highlighting the industrial relevance of ABH. In order to further develop the industrial applications of ABH, this study investigates the performance of an ABH embedded in a honeycomb sandwich panel under point excitation. Using experimental measurements and numerical models, the relevance of ABH positioning for performance is studied by comparing configurations with single and multiple ABHs. In highly damped structure, such as honeycomb sandwich panels, the proximity between the vibration source and the ABH is found to be crucial for effective vibration reduction. This finding suggest that ABHs can function not only as vibration absorbers but also as isolators, offering new possibilities for decoupling vibration sources from surround-

ing structures. These insights contribute to the ongoing development of ABH-based solutions for lightweight and high-performance engineering applications.

2. EXPERIMENTAL PROOF OF MOBILITY REDUCTION INDUCED BY ABHS

In order to evaluate the performance of an ABH placed inside a honeycomb sandwich panel, the spatially averaged squared mobility is evaluated outside of the ABH. Such quantity is proportional to the panel's kinematic energy and corresponds to the panel's overall vibratory level. This quantity is experimentally obtained on free boundary panels, using a scanning laser vibrometer (Polytec PSV500 Xtra), an impedance head (PCB 288D01) and an an electrodynamic shaker (Modal Shop 2075E). The excitation is placed close to one corner. A periodic chirp signal is used as excitation. Using this setup, three panel configurations are tested: a uniform reference panel (Figure 1 (a)), a panel with a central circular ABH (Figure 1 (b)), and a panel with four ABHs placed at each corner (Figure 1 (c)). The results of these measurements are shown in (Figure 1 (d)) in one third octave band representation. The single ABH panel shows a reduced mobility of 4dB up to 3500 Hz, demonstrating the effect of the ABH. Above this frequency, the reduction diminishes to less than 1dB . This is due to the highly damped nature of the reference panel. At low frequencies, the displacement field corresponds to a modal field while at higher frequencies, only the propagative field exists in the panel. The propagative field leads to sub-optimal interaction with the ABH leading to a limited mobility reduction effect. To counteract this issue, the ABH is placed closer to the excitation point, aiming to absorb the vibratory energy upon entry and decouple the rest of the panel before it can propagate. Based on this approach, a panel equipped with four ABHs is designed. This configuration offers enhanced low-frequency performance due to the simultaneous operation of all four ABHs, (7dB instead of 4 dB). However, at higher frequencies, 3 out of the 4 ABH are not interacting with the propagative displacement field, rendering them ineffective. This transition phase is observed from 2000 Hz onward leading to an improvement in mobility reduction from 2 dB, for the singular ABH, to 4 dB, for the 4 ABH. The proximity of an ABH to the excitation point ensures sustained efficiency over the entire frequency range for highly damped structures.

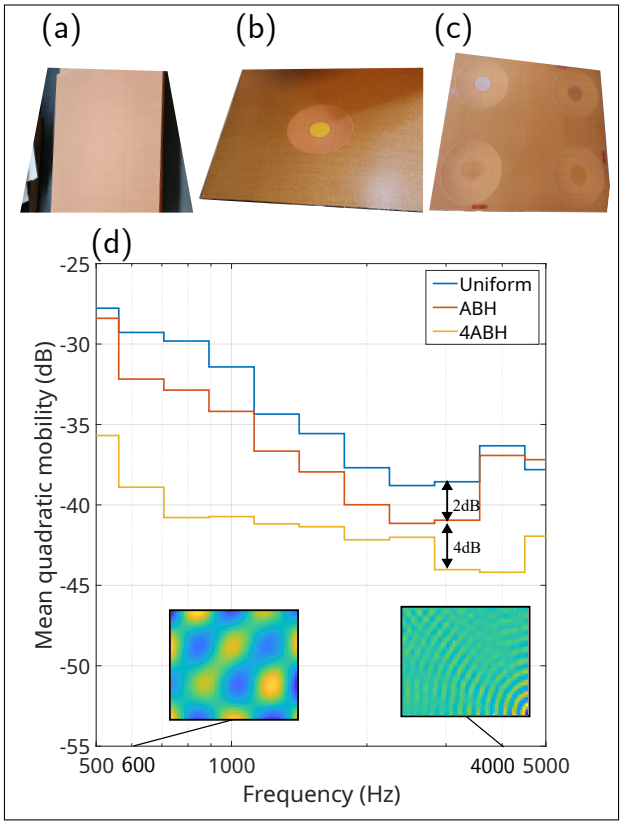


Figure 1. (a) Uniform honeycomb sandwich panel. (b) ABH embedded at the centre of a honeycomb sandwich panel. (c) 4 ABHs embedded at each corner of a honeycomb sandwich panel. (d) Comparison between the spatially averaged quadratic mobility outside of the ABHs for the three panels.

3. NUMERICAL INVESTIGATION OF THE EFFECT OF THE PROXIMITY OF AN ABH TO AN EXCITATION POINT

As stated previously, placing an ABH close to the excitation point of the structure is beneficial to ensure good performance of the device, in both low and high frequency. This is demonstrated by experimental results, under the assumption that ABHs placed too far from the excitation point are not active. In order to verify this assumption, finite element models are created, using the commercial software Comsol Multiphysics, to represent a sandwich panel, based on material properties from [5] with one or multiple ABHs embedded. These models are used to evaluate the spatially averaged quadratic mobility, outside of the ABHs, for different configurations. In total, five panel are tested with the first three being identical to the three experimental configuration (no ABH, centred ABH and 4 ABH) of Figure 1. The last two configurations correspond, respectively, to a single ABH placed next to the excitation point (corner ABH) and 3 ABH placed at the opposite corners of the excitation, (3 ABH) as represented in Figure 2 (a) and (b). The results, shown in one third octave band, are visible in Figure 1 (c). These curves highlight the importance of ABH positioning. The lowest mobility is observed in configurations where an ABH is close to the excitation point (e.g., 4 ABH or Corner ABH), highlighting the importance of proximity. However, the 3 ABH provide similar performance than the centred ABH due to the ABHs being further away from the excitation and them not being active. The models of ABH embedded in sandwich panel are still under development and are not yet giving results that can directly be compared to the experimental results. However, they still demonstrate the importance of ABH proximity and can be used to generate the hypothesis that an ABH can be used not just as a vibration absorber, but also as a vibration isolator, by decoupling an entire structure from a vibration source. This new application of the ABH is especially beneficial in specific scenarios, such as highly damped panels.

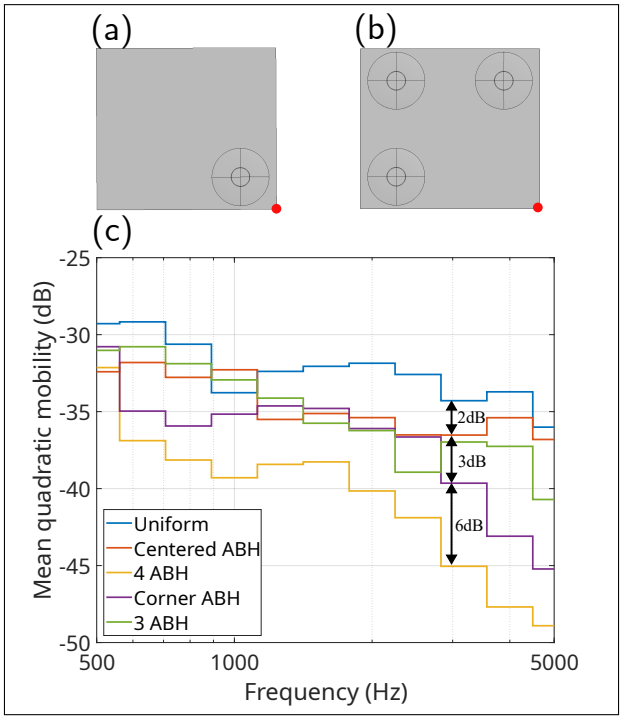


Figure 2. (a) Honeycomb sandwich panel equipped with an ABH placed in the corner next to the excitation. (b) 3 ABHs embedded at the opposites corners of the excitation of a honeycomb sandwich panel. (c) Comparison between the spatially averaged quadratic mobility outside of the ABHs for the five configurations.

4. CONCLUSION

This study explored the performance of an Acoustic Black Hole (ABH) embedded in a highly damped honeycomb sandwich panel using experimental samples and numerical models. The spatially averaged quadratic mobility of a uniform sandwich panel was compared to that of a panel equipped with a centrally located ABH and another with four ABHs positioned at the corners. Results revealed a 4 dB reduction in mobility at low frequencies, with diminished performance at higher frequencies. This decline is attributed to the transition of the displacement field from modal to propagative, which weakens the interaction with the scatterer. The findings highlight the importance of ABH placement, as demonstrated by the four-ABH panel, which achieves improved performance across both low and high frequencies. This insight suggests a novel application of ABHs as vibration isolators, capable of decoupling an entire structure from its excitation source. Ongoing Numerical simulations further confirm that strategic placement of a single ABH can outperform multiple poorly positioned ABHs, reinforcing the potential of this approach for advanced vibration control strategies.

5. ACKNOWLEDGMENTS

This work is part of the MAMBO project, financially supported by the Direction Générale de l'Aviation Civile (DGAC), 2021-2025. The authors sincerely thank F. Besluau, M. Roisin and S. Jegouzo for preparing and supplying the sandwich panels, and P. O'Donoughue, M. Sécail-Géraud and F. Foucart for their fruitful contributions to the experiments.

6. REFERENCES

[1] M. Mironov, "Propagation of a flexural wave in a plate whose thickness decreases smoothly to zero in a finite interval," *Sov. Phys. Acoust.*, vol. 34, pp. 318–319, 1988.

[2] V. V. Krylov, "Localized acoustic modes of a quadratic solid wedge," *Moscow University Physics Bulletin*, vol. 45, pp. 65–69, 1990.

[3] V. Krylov, "New type of vibration dampers utilising the effect of acoustic 'black holes'," *Acta Acustica united with Acustica*, vol. 90, pp. 830–837, 2004.

[4] V. V. Krylov and R. E. T. B. Winward, "Experimental investigation of the acoustic black hole effect for flexural waves in tapered plates," *Journal of Sound and Vibration*, vol. 300, pp. 43–49, 2007.

[5] A. Besse, P. O'Donoughue, O. Aklouche, F. Ablitzer, A. Pelat, and F. Gautier, "Vibration damping of fiberglass honeycomb sandwich panels based on the acoustic black hole effect," *Journal of Sound and Vibration*, vol. 604, p. 118991, 2025.

[6] A. C. Nilsson and B. Liu, "Prediction of some vibroacoustic properties of sandwich plates with honeycomb and foam cores," *The Journal of the Acoustical Society of America*, vol. 144, pp. 1600–1614, 2018.

[7] K. Ege, N. Roozen, Q. Leclère, and R. Rinaldi, "Assessment of the apparent bending stiffness and damping of multilayer plates; modelling and experiment," *Journal of Sound and Vibration*, vol. 426, pp. 129–149, 2018.

[8] D. J. O'Boy, V. V. Krylov, and V. Kralovic, "Damping of flexural vibrations in rectangular plates using the acoustic black hole effect," *Journal of Sound and Vibration*, vol. 329, pp. 4672–4688, 2010.

[9] V. B. Georgiev, J. Cuenca, F. Gautier, L. Simon, and V. V. Krylov, "Damping of structural vibrations in beams and elliptical plates using the acoustic black hole effect," *Journal of Sound and Vibration*, vol. 330, pp. 2497–2508, 2011.

[10] E. P. Bowyer and V. V. Krylov, "Experimental investigation of damping flexural vibrations in glass fibre composite plates containing one- and two-dimensional acoustic black holes," *Composite Structures*, vol. 107, pp. 406–415, 2014.

[11] J. Zhang, K. Fu, J. Qiu, X. Xia, H. Nie, and X. Wen, "Vibration characteristics of CFRP sandwich panels with acoustic black hole structures," *Mechanics of Advanced Materials and Structures*, vol. 0, pp. 1–11, 2024.

DOI:

Main theme: A10 Materials and Metamaterials

Session A10.06 Numerical methods for acoustic materials and metamaterials

Chair(s): L. Godinho, O. Dazel

DOI:

Main theme: A15 Room Acoustics

Session A10.07/A15.07 Characterization of acoustic materials

Chair(s): M. Nolan, F. Chevillotte, L. Jaouen

DOI: 10.61782/fa.2025.0932

FORUM ACUSTICUM EURONOISE 2025

UNCERTAINTIES IN PARAMETER ESTIMATION OF POROUS MEDIA IN TUBE MEASUREMENTS

Ziqi Chen[1*] **Ning Xiang**[1]
[1] Graduate Program in Architectural Acoustics, Rensselaer Polytechnic Institute, United States

ABSTRACT

Characteristic impedance is a critical parameter for porous media. This work discusses the performance of porous materials and how uncertainties in acoustic measurements affect porous material models over an extended frequency range. The three-mic method [Salissou & Panneton, J. Acoust. Soc. Am. 128, pp. 2868–2876 (2010)] is employed to measure the characteristic impedance of porous materials. Impulse responses experimentally measured in an empty impedance tube allow acoustic measurement calibration. Bayesian inference is applied to estimate the parameters in characteristic impedance models associated with the measured impulse response at high frequencies. The uncertainties and inaccuracies in the characteristic impedance of porous materials are analyzed. This paper also addresses challenges for an extended frequency range.

Keywords: *Impedance tube, Characteristic impedance, Bayesian inference*

1. INTRODUCTION

Characteristic impedance is one of the most critical parameters commonly used by the acoustic material community to describe the acoustical performance of porous materials. Multiple models have been established to describe the characteristic impedance, such as the Delany-Bazley-Miki model [1] and the Horoshenkov model [2]. This study combines the three-mic method [3] and cylindrical mode decomposition [4] to measure the characteristic impedance in an extended frequency range, and the measured characteristic impedance is compared to the theoretical values to see the performance of the model.

2. METHODOLOGY

2.1 Measurement

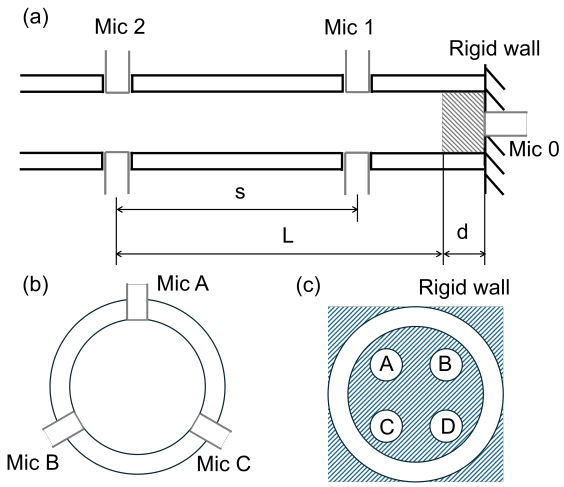


Figure 1. Impedance tube measurement for the characteristic impedance. (a) Arrangement for the measurement. (b) Arrangement of the circumferential position for position 1 and 2. (Arrangement of the Microphone position 0)

Figure 1 shows the impedance tube measurement setup in this work. We measure 3 impulse responses in the same plane for Position 1 and 2 and measure 4 im-

*Corresponding author: chenz33@rpi.edu.
Copyright: ©2025 Ziqi Chen et al. This is an open-access article distributed under the terms of the Creative Commons Attribution 3.0 Unported License, which permits unrestricted use, distribution, and reproduction in any medium, provided the original author and source are credited.

pulse responses at back of the testing material. To extend the frequency range of the impedance tube measurement, we distribute microphone positions evenly along the circumference. The surface reflectance measured is calculated from

$$\underline{R} = \frac{\underline{H}_{12} - \mathrm{e}^{-\underline{\gamma} s}}{\mathrm{e}^{\underline{\gamma} s} - \underline{H}_{12}} \mathrm{e}^{2\underline{\gamma} L}, \tag{1}$$

where γ is the propagation coefficient, s is the separation between position 1 and 2, L is the distance from position 2 to the front surface of the testing materials, and H_{12} is the ratio of the average sound pressures. The transfer function is

$$\underline{H}_{ij} = \frac{\overline{P}_i}{\overline{P}_j} \tag{2}$$

where $\overline{P}$ is defined as the average value of sound pressures measured at different circumferential positions and the same longitudinal position.

$$\overline{P}_i = \frac{1}{N} \sum_{n}^{N} P_{in} \tag{3}$$

(4)

Therefore the wave number and the characteristic impedance of the material is [3]

$$\underline{k} = \frac{1}{d} \cos^{-1} \left(\frac{1 + \underline{R}}{\mathrm{e}^{\underline{\gamma}(L-s)} + \underline{R} \mathrm{e}^{-\underline{\gamma}(L-s)}} H_{10} \right) \tag{5}$$

$$\underline{Z}_D = \mathrm{j} \frac{1 + \underline{R}}{1 - \underline{R}} \tan(\underline{k} d) \tag{6}$$

where d is the thickness of the material.

The cut-off frequency of the extended impedance tube measurement is [4]

$$f_{mn} = \frac{\alpha_{mn} c}{\pi d}, \tag{7}$$

where m is the circumferential modal number of the Bessel function, n is the radial modal number of the Bessel function, α_{mn} is the positive zeros of the Bessel function, c is the sound speed in the tube, and d is the diameter of the tube. With two microphones placed evenly along the circumference, the cutting-off frequency for a tube with a diameter of 1.4 inches (35.6 cm) is 9300 Hz. Note that the valid frequency range for a tube with a diameter of 1.4 inches is only up to 5600 Hz according to ASTM E1050 [5].

2.2 Model

Multiple models have been developed to describe the characteristic impedance of the porous material. In this work, we choose the Miki generalized model for the Bayesian inference to analyze the uncertainties and inaccuracies. According to the Miki generalized model, the characteristic impedance of porous materials can be approximated as a function of frequency and flow resistivity [1]

$$Z_M = \rho_0 c_0 \frac{\sqrt{\alpha_\infty}}{\phi} \left[1 + 0.07 \left(\frac{f}{\sigma_e} \right)^{-0.632} - \mathrm{j}\, 0.107 \left(\frac{f}{\sigma_e} \right)^{-0.632} \right], \tag{8}$$

where ρ_0 is the air density, c_0 is the sound speed in air, α_∞ is the tortuosity, and ϕ is the porosity. the effective flow resistivity σ_e is defined as

$$\sigma_e = \frac{\phi}{\alpha_\infty} \sigma \tag{9}$$

2.3 Bayesian framework

In this work, we estimate critical parameters using Bayesian inference. Bayes' theorem for the estimation is

$$\overbrace{p(\boldsymbol{\theta} | \underline{Z}_\mathrm{D}, \underline{Z}_\mathrm{M}, I)}^{\text{posterior}} = \frac{\overbrace{p(\underline{Z}_\mathrm{D} | \boldsymbol{\theta}, \underline{Z}_\mathrm{M}, I)}^{\text{likelihood}} \times \overbrace{p(\boldsymbol{\theta} | \underline{Z}_\mathrm{M}, I)}^{\text{prior}}}{p(\underline{Z}_\mathrm{D} | \underline{Z}_\mathrm{M}, I)}, \tag{10}$$

where θ collectively represents parameters for characteristic impedance models, and I is the background information, including that '*the prediction model is able to describe the data well*'. The likelihood distribution is assigned to

$$p(\underline{Z}_\mathrm{D} | \boldsymbol{\theta}, \underline{Z}_\mathrm{M}, I) = \frac{\Gamma(K/2)}{2} \left(\pi \sum_{k=1}^{K} \epsilon_k^2 \right)^{-K/2}, \tag{11}$$

where $\Gamma(\dots)$ is the standard Gamma function, and ϵ_k is the residual error. The residual error ϵ_k is defined as,

$$\epsilon_k^2 = \mathrm{Re}(\underline{Z}_\mathrm{D} - \underline{Z}_\mathrm{M})^2 + \mathrm{Im}(\underline{Z}_\mathrm{D} - \underline{Z}_\mathrm{M})^2. \tag{12}$$

3. RESULT

3.1 Air Characteristic Impedance

To eliminate the influence of tube dissipation on the accuracy of measurement [6], we measure the empty tube

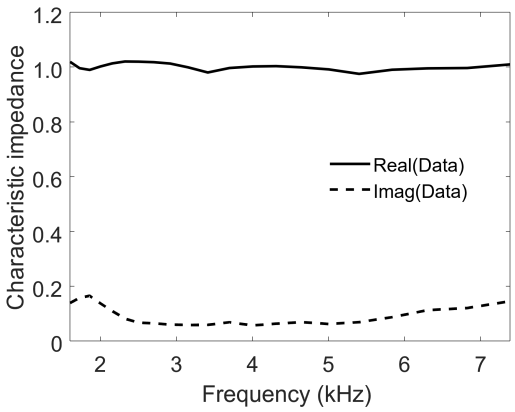


Figure 2. Normalized characteristic impedance of the hypothetical air layer.

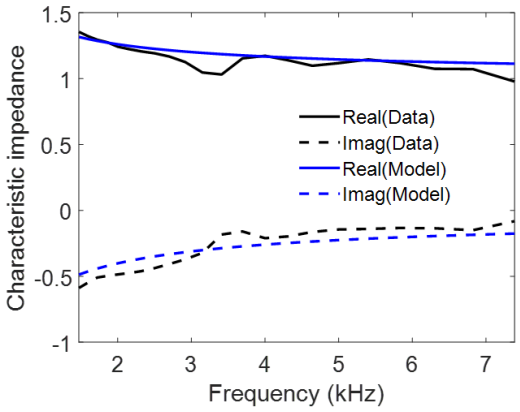


Figure 3. Estimated and measured normalized characteristic impedance.

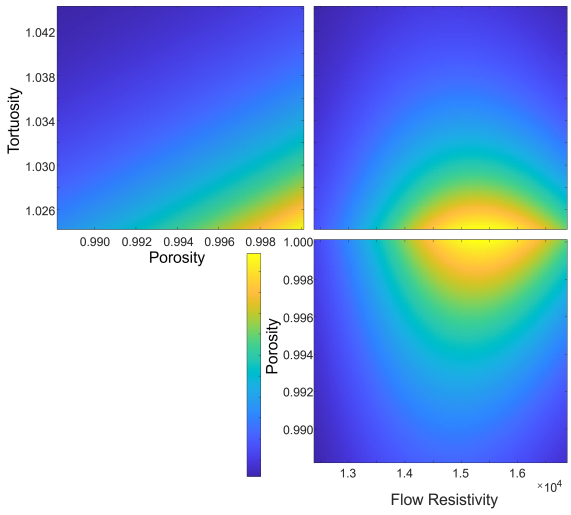


Figure 4. Posterior probability distributions over two-dimensional parameter space for the Miki generalized model.

and assume a hypothetical air layer in front of the rigid termination as the testing material. Figure 2 shows the normalized characteristic impedance of the hypothetical air layer after calibration. Although the calibrated characteristic impedance is not ideal, it is generally equal to the theoretical characteristic impedance of air.

3.2 Porous Material

With the estimated tube dissipation and sound speed after calibration, we are able to estimate the flow resistivity of the porous material. In this work, we used a piece of melamine foam as a test material. Bayesian inference is employed to inversely estimate the critical parameters in the Miki generalized model. Figure 3 demonstrates the estimated characteristic impedance of porous material. The roughness in the measured characteristic impedance may be due to energy leakage on the surface of the rigid termination and the ill-posedness of the testing material [7]. Without microphones evenly distributed along the circumference, the measurement is valid only up to 5600 Hz. Figure 4 shows the posterior probability distributions between parameters.

4. CONCLUSION

In this work, we combine the cylindrical mode decomposition and three-microphone impedance tube measurement to extend the frequency range of characteristic impedance measurements. Bayesian inference is applied to calibrate the impedance tube and estimate the critical parameters in the Miki generalized model based on the measured characteristic impedance. The melamine foam is used to validate the performance of the Miki generalized model at extended frequency.

5. REFERENCES

[1] Y. Miki, "Acoustical properties of porous materials-modifications of Delany-Bazley models," *J. Acoust. Soc. Japan*, vol. 11, no. 1, pp. 19–24, 1990.

[2] K. V. Horoshenkov, A. Hurrell, and J.-P. Groby, "A three-parameter analytical model for the acoustical properties of porous media," *The Journal of the Acoustical Society of America*, vol. 145, no. 4, pp. 2512–2517, 2019.

[3] Y. Salissou and R. Panneton, "Wideband characterization of the complex wave number and characteristic impedance of sound absorbers," *J. Acoust. Soc. Am.*, vol. 128, no. 5, pp. 2868–2876, 2010.

[4] J. Panzer, "Extracting the fundamental mode from sound pressure measurements in an acoustic tube," in *Audio Engineering Society Convention 147*, Audio Engineering Society, 2019.

[5] ASTM E1050-19, "Standard Test Method for Impedance and Absorption of Acoustical Materials Using a Tube, Two Microphones and a Digital Frequency Analysis System," 2019. (American Society for Testing and Materials, Philadelphia).

[6] Z. Chen and N. Xiang, "Bayesian estimation of dissipation and sound speed in tube measurements using a transfer-function model," *J. Acoust. Soc. Am.*, vol. 155, no. 4, pp. 2646–2658, 2024.

[7] R. Roncen, Z. E. A. Fellah, and E. Ogam, "Addressing the ill-posedness of multi-layer porous media characterization in impedance tubes through the addition of air gaps behind the sample: Numerical validation," *J. Sound & Vib.*, vol. 520, p. 116601, 2022.

DOI: 10.61782/fa.2025.0192

FORUM ACUSTICUM EURONOISE 2025

CHARACTERISATION OF ACOUSTIC METAMATERIALS ALLOWING AIRFLOW

Gianluca Memoli[1*] **Mark Puttock-Brown**[1] **Jonathan Eccles**[3]
Ben Pearce[4] **Emma Greenland**[4]
[1] Department of Informatics, University of Sussex, UK
[2] Department of Engineering, University of Sussex, UK
[3] Metasonixx Ltd, Brighton, UK
[3] Anderson Acoustics, Brighton, UK

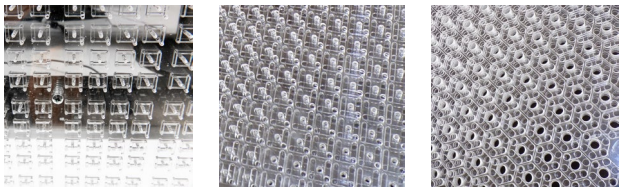
ABSTRACT

Managing noise and ventilation at the same time is one of the key challenges for acousticians worldwide. This is why, when a new type of solution – e.g. based on acoustic metamaterials – promises to manage both, it is important to have reliable acoustic and pressure measurements. In this study, we review the applicability of ISO 7235 to three different acoustic metamaterials, based on the principle of phase cancellation. We present acoustic measurements in the lab and benchmark them with measurements taken on a building façade, advocating for a potential revision of the standard. We discuss the challenges of measuring total pressure drop and present a dedicated measurement rig. Our work may be useful to any researcher or acoustician considering the placement of metamaterial-based products in their project.

Keywords: *metamaterials, noise, ventilation, measurements.*

1. INTRODUCTION

In a joint paper from 2022, the UK Association of Noise Consultants and the Institute of Acoustics highlighted the challenges of managing simultaneously noise and ventilation in the built environment [1]. This is because traditional solutions rely on absorbing materials, which are bulky and need to be cleaned periodically, or on mass, which opposes the passage of air, by definition. In this context, different research groups worldwide are looking at acoustic metamaterials as the next candidate for the simultaneous management of noise and ventilation.



(a) (b) (c)

Figure 1. The three perforated metamaterials of this study, in order of increasing perforated area (ß).

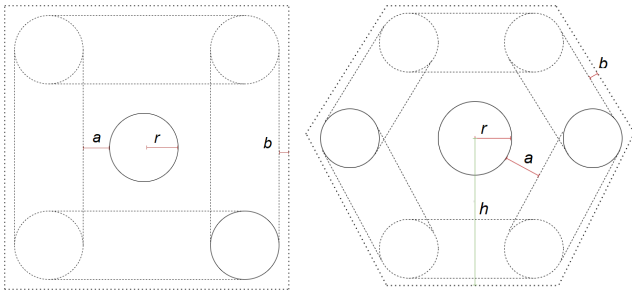
Acoustic metamaterials are a special class of materials, whose acoustic properties are determined by their sub-wavelength geometry, more than their chemical properties [2,3]. Supported by the development of advanced manufacturing, broadband acoustic metamaterials are quickly translating from laboratories to applications. One of the key challenges for acoustic metamaterials, however, is measuring their properties, so that their performance can be compared with more traditional solutions. This is because a solution based on metamaterials is often non-uniform and non-homogeneous: two hypotheses that underpin the most common measurement standards in acoustics (e.g. ISO 10534-2:2023, which relies on impedance tubes [5])

[*] ***Corresponding author***: g.memoli@sussex.ac.uk
Copyright: *©2025 Memoli et al. This is an open-access article distributed under the terms of the Creative Commons Attribution 3.0 Unported License, which permits unrestricted use, distribution, and reproduction in any medium, provided the original author and source are credited.*

Particularly important for ducted silencers and termination units is ISO 7235:2003 [6], which relies on a waveguide to establish flow and allows measurements behind the silencer either in a reverberation room or in a test duct (with anechoic termination) or in "essentially free field" conditions. In this work, we test the validity of this standard to characterize a family of three acoustic metamaterials optimized for transmission loss in the presence of airflow (see Figure 1). We discuss how the challenges of obtaining reliable measurements required dedicated testing rigs – both in acoustic and fluid dynamics – and the need to benchmark potential changes to measurement methods with existing ISO standards.

2. METAMATERIAL DESIGN

The three metamaterials in Figure 1 were fabricated assembling multiple layers. Each layer consists of a 3 mm acrylic sheet, on which unit cells have been excavated in a repetitive pattern (e.g. by laser cutting). Each 2D unit cell is designed to create two paths in the final 3D geometry: a pass-through hole (typically in the center) and a labyrinthine path (typically on the outside). Figure 2 shows the two cases used in this study (a square and a hexagon), both inspired by optical lattices .



(a) (b)

Figure 2. The unit cells at the base of the metamaterials used in this study.

Different values of the perforation rate ß can be obtained by varying the design parameters of these cells: the radius r of the holes, the spacing a between the central hole and the labyrinth, the radius R of the holes in the labyrinth and the spacing $2b$ between one labyrinthine unit cell and next one. For the square cell (Figure 2a), which has one channel in the center and one on the outside of the same radius (i.e. $R = r$) – the perforation rate $ß_{Square}$ is:

$$\beta_S = \frac{\pi}{2} \cdot \frac{1}{\left(3 + \frac{a+b}{r}\right)^2} \leq 17.4\% \qquad (1)$$

The maximum value in equation (1) is $ß_{Square} \sim \pi/18$, which is obtained when a and b are much smaller than r. In this study, we will be using $ß_1 = 2.5\%$ (two 2 mm diameter holes) and $ß_2 = 6.2\%$ (two 4 mm diameter holes).

The hexagonal unit cell (Figure 2b) has two channels on the outside, for a total of three holes. For even comparison with the square cell, in this study we required the holes in the labyrinth to have the same area as the central hole (i.e. $R = 0.71\ r$), so that the perforation rate is:

$$\beta_H = \frac{2\pi r^2}{\frac{1}{2} \cdot \frac{12}{\sqrt{3}} \cdot h^2} = \sqrt{3}\frac{\pi}{3} \frac{1}{\left(1 + \sqrt{2} + \frac{a+b}{r}\right)^2} \leq 31.1\% \qquad (2)$$

where h is the apothem of the external hexagon. In this study, we used $ß_3 = 12.6\%$ for the hexagon shaped plate.

The acoustic insertion-loss of a hole in a perforated plate, at normal incidence, is due to two contributions: one viscous and one inertial [7]. Using the formulae in [7] we calculated that, for 18 mm thick acrylic plates, the acoustic impedance due to the first term dominates for smaller holes (e.g. microperforated panels), while the second wins as the holes become bigger (∅≥2 mm here) or at larger frequencies (Figure 3).

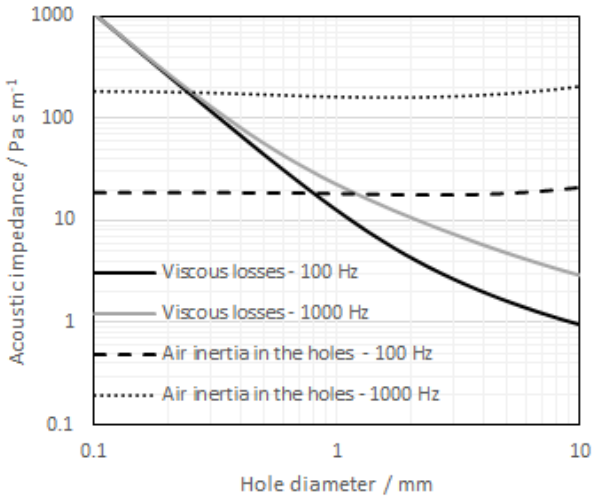


Figure 3. Acoustic impedance for a single hole in an 18 mm thick perforated plate of acrylic as a function of hole diameter and frequency.

(1)

According to Putra and Ismail [7], due to this complex interaction, a perforated plate allows through specific acoustic frequencies with a Lorentzian response, where the center frequency of the Lorentzian (i.e. the frequency with minimal insertion loss) is determined by the size of the holes, by the material of the plate (e.g. density ρ=1180 kg/m^3 and Young modulus E=3 GPa for acrylic) and by the thickness of the plate (t=18 mm for the square plates and t=24 mm for the hexagonal ones). For the 2D unit cells in Figure 2, the length of the (3D) labyrinthine path was designed to cancel the sound that would otherwise go through the central hole (i.e. like a half-wave plate in optics). At first approximation, therefore, the 3D structures originated by the unit cells in Figure 2 combine the broadband insertion loss given by the mass of the layered acrylic plates with the interferometric cancellation between the frequencies going through the two paths [8].

3. ACOUSTIC MEASUREMENTS

In the first instance, the transmission loss of each metamaterial plate was determined starting from the method described in ISO 7235 [6]. A speaker with a metamaterial casing (to remove back-emission – see [9]) was connected to a semi-open cylindrical tube, long enough to provide a planar wavefront for a propagating logarithminc sweep obtained using an arbitrary waveform generator (model RSDG2042X by RS-components) after amplification (model TPA3255 by Fosi audio). Both the speakers used in this part of the study (one for the range 80 Hz – 4000 Hz and one for the range 400Hz – 8000 Hz) had flat frequency response in the range used. ISO 7235 also prescribes to measure the insertion loss using an average over multiple microphone positions. When the measurements are taken in a test duct, the microphones need to be placed along the diagonal of the duct, so that their spacing is at least $\lambda/4$ for each 1/3rd-octave band. In the free-field case, ISO 7235 prescribes microphones to envelope the emission (like in ISO 3746).

In this study, we measured acoustic pressure in essentially free field conditions and calculated the insertion loss as the average over multiple measurements, taken at the exit of the tube with and without the metamaterial plate. The optimal number of microphones and their mutual positions were determined exploiting the traslational symmetry of the metasurface and the guidelines for reducing the number of microphones in acoustic holography (see [10] and references therein). We found that, while three positions were sufficient, they were not supposed to be along a line, so we took a) one measurement along the axis at distance X from the metasurface; b) one measurement off axis, also at a distance X; and c) one measurement off axis, at distance Y from the metasurface. While this method shows some similarities with ISO 7235:2003, a benchmark assessment of the transmission loss was needed.



Figure 3 The metamaterial panel mounted as secondary window by Anderson Acoustics, for the façade measurements.

This was performed by Anderson Acoustics, which used the procedure described in BS EN ISO 16283-3:2016 [11] tipically used for determine the acoustic properties of façade elements. The small square panel ($ß_1$=2.5%) was therefore mounted as secondary window in a standard frame, already containing a PVC window (see Figure 3) A hemi-dodecahedron loudspeaker (Norsonic 250) was used as pink-noise source outside, while a class I, calibrated microphone mounted on a tripod (Norsonic 140) was used to record inside. A potential sound flanking transmission path was identified, via the boiler outlet penetration (see Figure 3), but was neglected due to the mass of the external masonry wall. The window itself was standard thermal double glazing (28 dB Rw+Ctr estimated), with good perimeter seals. The measurement of sound reduction index $D_{ls,2m,nT}$ was performed in two conditions: with the PVC double glazed window open and with the PVC window partially open (i.e. with a 10 cm opening), with and without the metamaterial panel. The results of façade measurements (Figure 4) show a clear effect of the secondary window, whose impact increases with frequency, as expected from a mass-based solution. Once insertion loss was calculated, the results of façade measurements and laboratory tests were found to be similar for $ß_1$=2.5% (Figure 5). The laboratory method was then used for all the other plates (see Table 1).

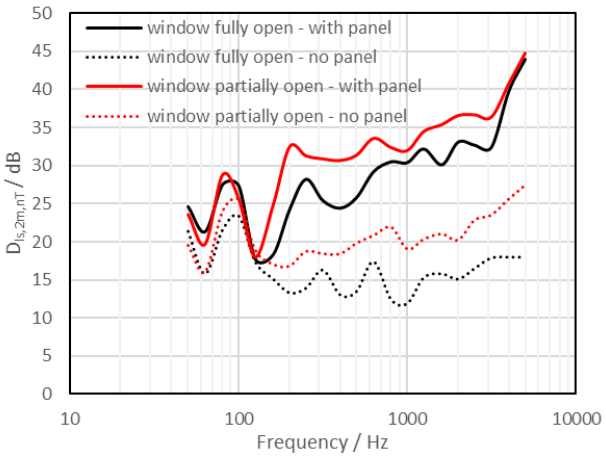


Figure 4 Results of the in-situ acoustic measurements made using the procedure in 16283-3:2016

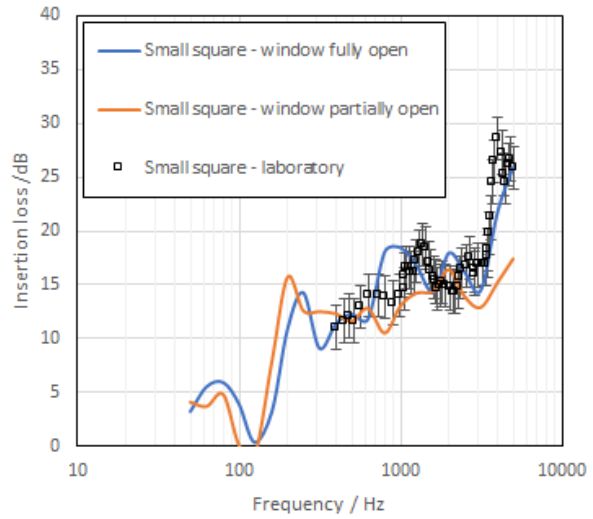


Figure 5 Results of the insertion loss measurements for the metamaterial plate with $ß_1$=2.5%: laboratory tests and façade measurements.

4. PRESSURE DROP MEASUREMENTS

These measurements were conducted using the procedure described in ISO 7235-2: each plate was inserted in the modified square section (hydraulic diameter: D_h = 200 mm) of a suction-type wind tunnel. As shown in Figure 6, each metamaterial plate was secured between two flanges with 12xM8 bolts with a central alignment pin to keep the individual layers in the correct relative orientation. A single-phase axial ventilation fan was positioned downstream of the plate, while upstream the section was extended for 12.2D_h with a square bell mouth to reduce entrance effects. For pressure drop measuring across the plate, two wall mounted pressure tapings were used, whose readings were acquired using an EvoScann P16-D differential pressure scanner. The reference pressure was taken as the ambient atmosphere and measured separately using a precision barometer.

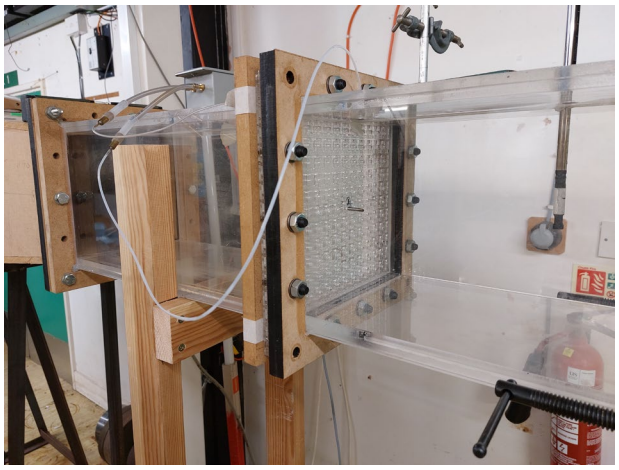


Figure 6 Measurement set-up at Sussex University.

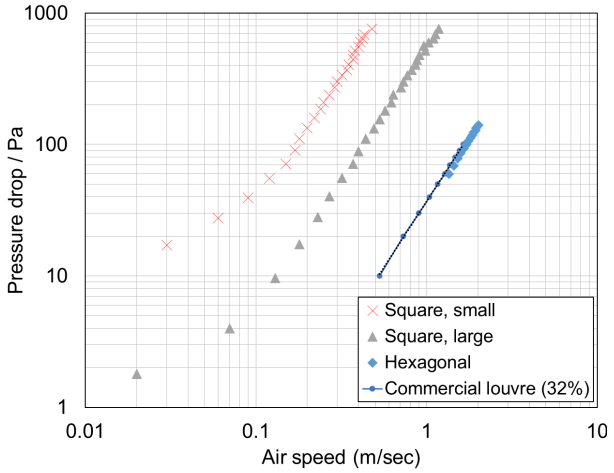


Figure 7 Pressure drop measurements for the three plates in this study and a commercial acoustic louvre.

Volumetric flow rate was measured using a Testo 405i thermal anemometer $10D_h$ from tunnel inlet perpendicular to the flow at the centre over a 30 second average. Given the low flow rate the calculated entrance length to develop a full laminar profile could be up to $1160D_h$ and so a uniform flow in the duct is assumed, and the volumetric flow rate calculated accordingly. Discrete measurement points of pressure drop were obtained by incrementing the fan speed by 100 rpm from 146 (min) to 2800 (max). Figure 7 reports the results of the pressure drop measurements, compared with the pressure drop from the datasheet of a commercial acoustic louvre (model: SlimShield SL-150 by IAC Acoustics, thickness: 150mm thick, weight: 30 kg m^{-2}, effective area: 32%).

5. DISCUSSION

The pressure drop curves in Figure 7 also show the result for a multi-linear fit., with the curve given by the power law:

$$\Delta P = K \cdot v^{\alpha} \tag{3}$$

A multi-linear fit (see Table 1) for velocities above 0.1 m/s gives $\alpha = 2.06 \pm 0.05$, in agreement with Bernoulli's expression which predicts $\alpha=2$ for purely inertial dependence. As shown in Figure 7, the trend deviates from the simple quadratic law for lower velocities, where viscous effects start to dominate, but above 0.1 m/s the constant K corresponds to the total pressure loss coefficient in ISO 7235. The fitting values – $K_1 = 3500 \pm 100$ kg m^{-2} s^{-1} (small squares) $K_2 = 560 \pm 60$ kg m^{-2} s^{-1} (large squares); and $K_3 = 32 \pm 4$ kg m^{-2} s^{-1} (hexagons) – also correspond to the value of the pressure drop at 1 m/s for the three panels. Figure 7 confirms that the pressure drop of the hexagonal panel corresponds to the one of the selected acoustic louvre.

The acoustic measurements show that, in the range 100 – 4000 Hz, the insertion loss of the three panels in Figure 1 follow a similar trend. In Figure 8, we fitted the data with the function [12]:

$$IL = 10 \cdot \log(1 + C \cdot (f - f_0)^{\gamma}) \tag{3}$$

and obtained a similar value for the power law $\gamma = 0.55 \pm 0.5$ where $\gamma = 1$ is expected for a standard mass-based insertion loss. The different values of the constants C (which is related to the surface density of the plate) and f_0 (which is related to the first vibrational thickness mode of each panel) can be found in Table 1.

Table 1. Fitting parameters for the metamaterial panels in Figure 1, as measured in laboratory.

	Small Square	Large square	Hexagon
α	2.02	2.02	2.12
K / kg m^{-2} s^{-1}	3500	560	32
ß / %	2.5	6.2	12.6
γ	0.60	0.50	0.55
C / $Hz^{-\gamma}$	0.38	0.30	0.05
f_0 / Hz	48	78	241
Thickness / mm	18	18	24
Density / kg m^{-2}	16.4	17.6	12.4

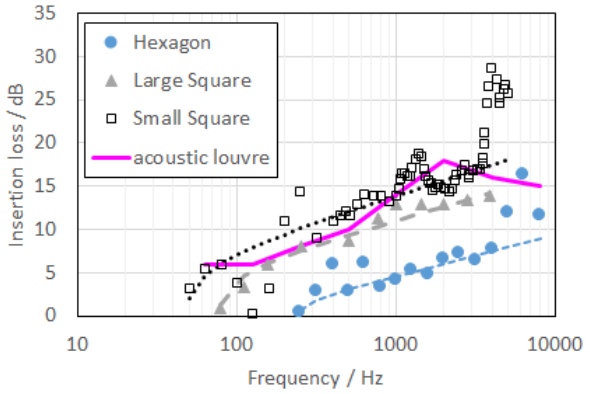


Figure 8 Insertion loss for the panels in Figure 1. The graph also reports the fitting curve from eq. (3) – see Table 1.

According to Figure 8, the acoustic performance of the louvre we selected for comparison falls within the insertion loss of the small square and of the large square. However, 3 dB are lost on average while passing from the Small Square to the large square panel and further 6 dB are lost – on average – while passing from the large square panel to the hexagonal one. This means that, while the hexagonal panel shows the same pressure drop as the selected acoustic louvre, its acoustic attenuation is lower. More work is therefore needed before this type of materials can substitute an acoustic louvre, adding superior acoustic performance to the advantages of less space occupied (24 mm instead of 150 mm) and lower weight (12.4 kg m^{-2} vs 30 kg m^{-2}).

6. CONCLUSIONS

In this work, we characterized three perforated labyrinthine metamaterials using ISO 7235-2. From the fluid dynamic point of view, we highlighted the challenges to run the prescribed measurements and described a dedicated experimental set-up that was built for this purpose at the University of Sussex. From the acoustic point of view, we described the modifications we applied to the standard for having reliable results and the benchmarking procedure followed by Anderson Acoustics using ISO 16283-3.

This study shows how acoustic metamaterials are approaching the performance of traditional solutions, using less space and weight. Like other studies focused on the application of acoustic metamaterials, this work highlighted a design space. Further studies, with more prototypes, will allow us to map the space ($ß$, ΔP, IL) and, consequently, to optimize the design of the panels presented here for specific needs in noise and ventilation management, like silencing heat pumps.

7. ACKNOWLEDGMENTS

The authors GM and MPB acknowledge funding from Research England through the Higher Education Impact Fund, managed by the University of Sussex.

8. REFERENCES

[1] Acoustic Noise Consultants & Institute of Acoustics, "Avoustic Ventilation and Overheating - Residential Design Guide," January 2020. [Online]. Available: https://www.association-of-noise-consultants.co.uk/wp-content/uploads/2019/12/ANC-AVO-Residential-Design-Guide-January-2020-v-1.1.pdf. [Accessed April 2025]

[2] S. Cummer, J. Christensen and A. Alù, "Controlling sound with acoustic metamaterials," *Nature Reviews Materials,* vol. 1, 2016. A. Putra and A. Ismail, "Normal Incidence of Sound Transmission Loss from Perforated Plates with Micro and Macro Size Holes," *Advances in Acoustic and Vibration,* p. article ID 534569, 2014.

[3] C. J. Naify, A. Titovich and M. R. Haberman, "What is an acoustic metamaterial?," in *184th Meeting of the Acoustical Society of America*, Chicago, 2023.

[4] A. A. El Ouahabi and G. Memoli, "A transfer matrix method for calculating the transmission and reflection coefficient of labyrinthine metamaterials," *Journal of the Acoustical Society of America,* vol. 151, p. 1022–1032, 2022.

[5] ISO, "ISO 10534-2: Determination of acoustic properties in impedance tubes. Part 2: Two-microphone technique for normal sound absorption coefficient and normal surface impedance," ISO, Geneva, 2023.

[6] International Standardisation Office, "ISO 7235:2003 - Laboratory measurement procedures for ducted silencers and air-terminal units — Insertion loss, flow noise and total pressure loss," ISO, Geneva, 2003.

[7] A. Putra and A. Ismail, "Normal Incidence of Sound Transmission Loss from Perforated Plates with Micro and Macro Size Holes," *Advances in Acoustic and Vibration,* p. article ID 534569, 2014.

[8] G. Memoli, M. Caleap, D. Sahoo, B. Drinkwater and S. Subramanian, "Acoustic Wave Manipulation". UK Patent WO2018146489A1, 2017.

[9] L. Chisari, P. Martignon, M. Di Cola and G. Memoli, "Preliminary studies for metamaterial based audio systems," in *Proceedings of Euronoise 2021*, 2021.

[10] D. Manwill and J. Blotter, "Nearfield Acoustic Holography Experiments on Variously Correlated Compound Sources," in *SpaceGrant conference*, Salt Lake City, 2009.

[11] ISO, "ISO 16283-3:2016 - Field measurement of sound insulation in buildings and of building elements - Part 3: Facade measurements," ISO, Geneva, 2016.

[12] D. Vigé, "13 - Vehicle interior noise refinement – cabin sound package design and development," in *Vehicle Noise and Vibration Refinement*, Woodhead, 2010, pp. 286-317.

DOI: 10.61782/fa.2025.0589



FORUM ACUSTICUM
EURONOISE 2025

MULTI-DENSITY INVERSION CHARACTERISATION METHOD FOR FIBROUS MATERIAL

Andrea Santoni[1*] **Francesco Pompoli**[1] **Cristina Marescotti**[1]
Patrizio Fausti[1]
[1] Department of Engineering – University of Ferrara, Ferrara, Italy

ABSTRACT

This paper describes a novel inversion methodology for determining the transport parameters of the Johnson-Champoux-Allard (JCA) equivalent fluid model, developed to provide a quick and easy-to-implement characterisation tool. The proposed approach, based on an optimisation algorithm, requires only the experimental evaluation of the normal incidence sound absorption coefficient on fibrous material samples, prepared from loose fibres, at various compression ratios. Unlike existing inversion methods, the proposed approach links the variation of transport parameters to changes in the material's apparent density. The validation presented in the paper considers experimental data measured on two types of fibres: hemp fibres and glass fibres. Validation of the proposed method shows good agreement with well-established techniques and demonstrates its effectiveness across a broad range of fibrous materials.

Keywords: *acoustic optimization, inversion approach, material characterisation, fibrous material, sound absorption*

1. INTRODUCTION

This paper presents a methodological approach for characterising the transport parameters necessary to describe the acoustic behaviour of fibrous materials, using measurements of the normal incidence sound absorption coefficient, in accordance with the transfer function method described in ISO 10534-2. The main objective of this study is to develop a simple and reliable procedure for characterising fibrous materials and optimizing their density. This allows for a significant reduction in the prototyping phases typically required during the design and optimization of sound-absorbing panels. Although several inversion techniques have already been developed for the same purpose, the proposed method is the only one capable of correlating variations in transport parameters with material density. Conventional inversion techniques perform separate minimisations for each material or sample, followed by a possible data interpolation [1]. The developed inversion methodology is based on the semi-phenomenological model of Johnson-Champoux-Allard (JCA) [2, 3], which requires five transport parameters as input data to compute the complex density and the dynamic bulk modulus of an equivalent dissipative fluid: airflow resistivity σ, porosity ϕ, tortuosity α_∞, and the viscous and thermal characteristic lengths Λ and Λ'. This paper presents the main validation results of the proposed methodology by considering two types of fibres: hemp fibres and glass fibres. However, the proposed methodology is also applicable for the characterization of various fibrous materials, including both natural fibres and those traditionally used in acoustic applications, as detailed in reference [4].

2. MATERIALS AND METHODS

The proposed inversion characterization approach requires the experimental measurement of the normal incidence sound absorption coefficient $\alpha_{n,\mathrm{exp}}$, in accordance, for example, with ISO 10534-2, on samples at different compression ratios, which implies different bulk densities of the fibrous material. This methodology is partic-

*Corresponding author: andrea.santoni@unife.it.
Copyright: ©2025 Andrea Santoni et al. This is an open-access article distributed under the terms of the Creative Commons Attribution 3.0 Unported License, which permits unrestricted use, distribution, and reproduction in any medium, provided the original author and source are credited.

ularly suitable for investigating loose fibres: the fibres are weighed and placed in the sample holder of an impedance tube, where they can be easily compressed using a movable rigid backing. An acoustically transparent mesh is used to restrain the sample and prevent sliding along the tube, as shown in Figure 1. The sound absorption coefficient $\alpha_{n,\mathrm{exp}}$ is then measured for different combinations of sample thickness h and density ρ of the samples. Increasing the compression ratio of the sample results in an increase in density and a reduction in open-cell porosity ϕ, which can be evaluated knowing the fibre's density ρ_s as:

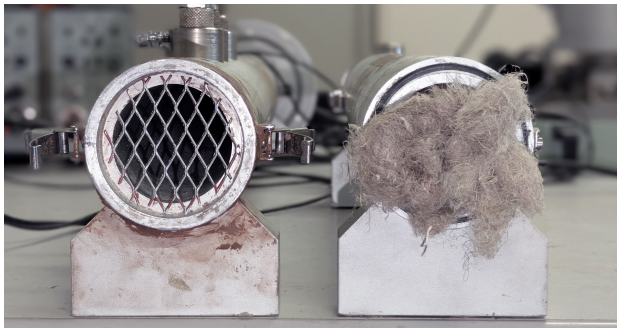


Figure 1. Loose hemp fibres and their installation in the plane wave impedance tube.

$$\phi = 1 - \frac{\rho}{\rho_s} \tag{1}$$

The material's airflow resistivity σ can be approximated as a function of porosity ϕ and the effective radius r_e of an equivalent 2D monodisperse fibrous medium [5]:

$$\sigma = \frac{\eta}{(2r_e)^2} \times \frac{\sqrt{1-(1-\phi)}}{0.21\left(\frac{0.71}{1-\phi} - 3\sqrt{\frac{0.71}{1-\phi}} + 3 - \sqrt{\frac{1-\phi}{0.71}}\right)} \tag{2}$$

The remaining transport parameters used in the JCA model can be expressed analytically as functions of porosity ϕ or the effective radius r_e. The latter is one of the design parameters of the multi-variable function to be optimized. The high-frequency limit of tortuosity α_∞ is computed using Archie's empirical law based on the material's porosity ϕ:

$$\alpha_\infty = \left(\frac{1}{\phi}\right)^{\beta} = \left(\frac{1}{\phi}\right)^{0.9574} \tag{3}$$

While the constant β could be generally treated as an additional design parameter of the multi-variable optimisation, dependent on the microstructural characteristics of the fibrous material, in this case a fixed value $\beta = 0.9574$ was adopted, independent of the fibres' effective radius r_e [5]. The scale-of-pores geometrical quantities representing viscous and thermal characteristic lengths are determined using empirical equations proposed by Pompoli [6]:

$$\Lambda = A_1 r_e (1-\phi)^{-A_2} \tag{4}$$

$$\Lambda' = A_3 r_e (1-\phi)^{-A_4} \tag{5}$$

The unknown coefficients A_i (with $i = 1, 2, 3, 4$) represent, along with the effective radius r_e, the optimisation design variables to be determined through a minimisation algorithm. This algorithm computes the normal incidence sound absorption coefficient using the JCA model $\alpha_{n,\mathrm{JCA}}$, expressing the transport parameters through Eqs. (1) to (5). The optimisation goal is to determine a set of design variables

$$x = \{r_e, A_1, A_2, A_3, A_4\},$$

that minimise an objective function $\mathcal{F}(x)$ defined in terms of the normalized difference between the experimental and JCA-predicted sound absorption coefficients:

$$\mathcal{F}(x) = \sum_{i=1}^{n} \frac{1}{n} \sum_{l=1}^{m} \frac{1}{m} \left|\alpha_{n,\mathrm{exp},i,l} - \alpha_{n,\mathrm{JCA},i,l}\right| \tag{6}$$

The minimisation of $\mathcal{F}(x)$ reduces the discrepancy between the experimental and JCA-predicted normal incidence sound absorption coefficients, summed over all the frequencies m and all the investigated densities n, by adjusting the design variables the transport parameters depend upon. The optimal solution can be computed using different solvers, while specifying search space boundaries, constraints of the optimization problem, and, in some cases, an initial guess for the design variables. The results presented in the following section were obtained using a MATLAB implementation of the proposed approach, employing a nonlinear programming solver. Further details on the implementation and the influence of different solvers are provided in reference [4].

3. EXPERIMENTAL RESULTS

This paragraph presents the main result validating the proposed methodology and assessing its reliability by analysing the accuracy of both the transport parameters obtained from the optimization process and the computed

normal incidence sound absorption coefficient. Two different types of fibres are considered: natural hemp fibres subjected to a carding process (HF_{car}) and traditional glass fibres (GF). The transport parameters obtained through the proposed approach, expressed as functions of material density, are compared with values derived from well-established inversion techniques based on measurements of a single sample [1]. Figure 2 compares the airflow resistivity curve $\sigma_{\text{opt.}}$, obtained using the proposed optimization methodology, with the target values σ_{target}, which are derived from the dynamic density of each sample, experimentally evaluated using the three-microphone transfer matrix method. This comparison follows the relationship proposed by Olny and Panneton [7]. The comparison highlights a good approximation of the target values within the investigated density range. The airflow resistivity curve evaluated for glass fibres (GF, shown on the right-hand side of Figure 2) interpolates the values determined at discrete densities considered in the experimental testing of the samples. For hemp fibres (HF_{car}, on the left-hand side of Figure 2), a slight deviation is observed between the airflow resistivity obtained as a function of density through the optimization algorithm and the discrete values derived from the measured complex density. The optimized airflow resistivity curve slightly overestimates the target values due to the simplifying assumptions in Eq. (2). The assumed condition of a two-dimensional unidirectional fibre orientation, with fibres aligned perpendicularly to the airflow, is generally met by traditional fibrous materials, where fibre dimensions and orientation can be designed, but it does not accurately represent the random distribution of natural fibres. Although tortuosity is not dependent on design variables,

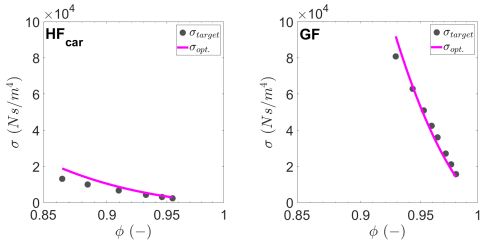


Figure 2. Comparison between the airflow resistivity curve obtained from the proposed method and the values derived from an experimental approach: left hemp fibres (HF_{car}), right glass fibres (GF).

since it is directly defined solely as a function of porosity, which varies with different compression ratios, Figure 3 compares the density-dependent curve $\alpha_{\infty,\text{opt.}}$, used in the adopted model, with the discrete values $\alpha_{\infty,\text{target}}$ obtained from a well-established inverse characterization approach. This comparison aims to demonstrate the reliability of Eq. (3) in estimating tortuosity as a function of porosity. For the HF_{car} material, the optimized tortuosity curve closely approximates the discrete tortuosity values. Although the two trends exhibit a slightly different slope, the values obtained from both approaches remain very close for any given porosity, especially considering the limited variation range of this parameter. For the GF material, the inverted values exhibit significant scatter, making it difficult to identify a clear trend. Nevertheless, the optimized curve remains within the range of scatter across the entire porosity range. Figure 4 presents sim-

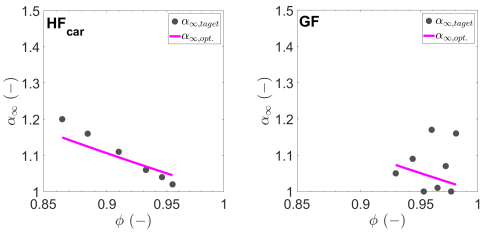


Figure 3. Comparison between the tortuosity curve obtained from the proposed method and the values derived from an experimental approach: left hemp fibres (HF_{car}), right glass fibres (GF).

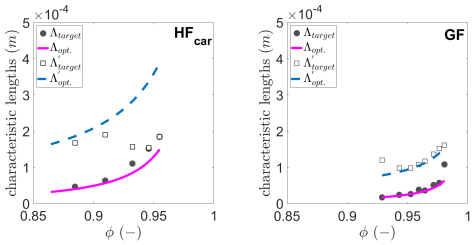


Figure 4. Comparison between the characteristic length curves obtained from the proposed method and the values derived from single inversions: left hemp fibres (HF_{car}), right glass fibres (GF).

ilar comparisons between the optimized $\Lambda_{\text{opt.}}$ and $\Lambda'_{\text{opt.}}$ curves obtained using the proposed methodology and the values of the characteristic lengths Λ_{target} and Λ'_{target} derived from traditional inversion methods. For both HF_{car}

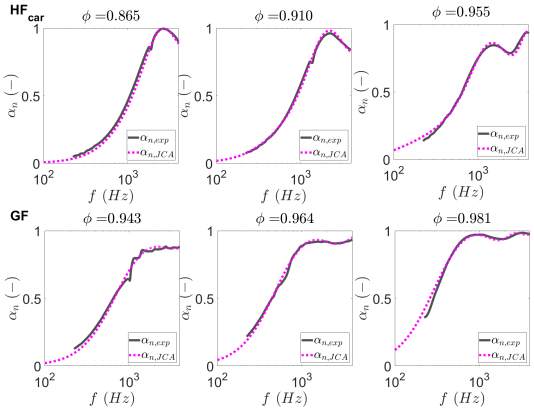


Figure 5. Comparison between the experimental and the JCA-predicted normal incidence sound absorption coefficients: top hemp fibres (HF_{car}), bottom glass fibres (GF).

and GF materials, the method provides results consistent with those obtained through single-sample inversion characterization. In general, with single inversions, the trend of the viscous characteristic length Λ as a function of porosity is more easily identifiable than that of the thermal characteristic length Λ'. Consequently, in the optimized curves, a higher consistency with the target values is observed for the viscous characteristic length Λ. Finally, the accuracy of the method is assessed by comparing the experimental normal incidence sound absorption coefficient with the frequency-dependent curves predicted through the JCA model by using the transport parameters characterized by the proposed methodology. Figure 5 illustrates this comparison for different porosity values, for both hemp and glass fibres. In both cases, the results highlight the high accuracy of the JCA model, confirming the reliability of the transport parameters determined using the proposed method.

4. CONCLUSIONS

This article presented an innovative, fast, and reliable methodology for characterising the macrostructural parameters of fibrous materials, providing a valuable tool for the design and optimisation of sound-absorbing panels while significantly reducing the prototyping phases. The proposed inverse characterization methodology integrates an optimization algorithm with the Johnson-Champoux-Allard (JCA) model and can be easily implemented in any acoustics laboratory, as it requires only the experimental measurement of the normal incidence sound absorption coefficient for samples with different densities. Unlike other inversion methods, the proposed approach allows for the correlation of transport parameter variations with the apparent density of the material. The results presented, referring to two different types of fibres, demonstrate that the methodology provides reliable estimates of the transport parameters essential for the acoustic optimisation of the material. The methodology can be applied to a wide range of fibrous materials used for acoustic applications and is particularly advantageous when working with loose fibres.

5. REFERENCES

[1] P. Bonfiglio and F. Pompoli, "Inversion problems for determining physical parameters of porous materials: Overview and comparison between different methods," *Acta Acustica united with Acustica*, vol. 99, no. 3, pp. 341–351, 2013.

[2] D. L. Johnson, J. Koplik, and R. Dashen, "Theory of dynamic permeability and tortuosity in fluid-saturated porous media," *Journal of fluid mechanics*, vol. 176, pp. 379–402, 1987.

[3] Y. Champoux and J.-F. Allard, "Dynamic tortuosity and bulk modulus in air-saturated porous media," *Journal of applied physics*, vol. 70, no. 4, pp. 1975–1979, 1991.

[4] A. Santoni, F. Pompoli, C. Marescotti, and P. Fausti, "Characterization of fibrous media transport parameters from multi-compression-ratio measurements of normal incidence sound absorption," *The Journal of the Acoustical Society of America*, vol. 157, no. 2, pp. 1185–1201, 2025.

[5] F. Pompoli and P. Bonfiglio, "Definition of analytical models of non-acoustical parameters for randomly-assembled symmetric and asymmetric radii distribution in parallel fiber structures," *Applied Acoustics*, vol. 159, p. 107091, 2020.

[6] F. Pompoli, "Acoustical characterization and modeling of sustainable posidonia fibers," *Applied Sciences*, vol. 13, no. 7, p. 4562, 2023.

[7] X. Olny and R. Panneton, "Acoustical determination of the parameters governing thermal dissipation in porous media," *The Journal of the Acoustical Society of America*, vol. 123, no. 2, pp. 814–824, 2008.

DOI: 10.61782/fa.2025.0551



FORUM ACUSTICUM
EURONOISE 2025

MEASUREMENTS AND SIMULATIONS OF A DOUBLE-POROSITY MATERIAL UNDER VARIATION OF PERFORATION PARAMETERS

Manuel Isenegger[1*] **Thomas Graf**[1] **Martin Sonderegger**[2]
Alexandre Bonnard[2] **Silja Fleischli**[2] **Armin Taghipour**[1]
[1] Institute of Electrical Engineering, Lucerne University of Applied Sciences and Arts, Switzerland
[2] ECHOJAZZ AG, Kriens, Switzerland

ABSTRACT

Porous materials are used for sound absorption, typically either without perforation or with an additional perforated faceplate for aesthetic, structural, or protective purposes. While the influence of perforated faceplates on sound absorption is well documented, the impact of perforations within the sound absorber itself on its acoustic performance remains insufficiently understood. The present study focuses on this research gap. The material used was made from recycled PET fibers. In a first step, the absorption coefficient of 41 small-scale samples ($20\,\mathrm{cm}$x$20\,\mathrm{cm}$) with varying perforation geometries, sizes, and percentages was measured in an impedance tube. Based on these results, the perforation parameters were selected for a set of larger panels: geometry (circles and triangles), perforation size ($1.13\,\mathrm{cm}^2$-$36.19\,\mathrm{cm}^2$), and perforation percentage (1-32%). The sound absorption coefficient of these panels was measured in a reverberation room. Statistical analysis showed that the absorption coefficient α primarily decreased with increasing perforation percentage. Secondary influences were also observed, such as perforation size. Additional numerical simulations with the boundary element method provided further insight into the acoustic performance of perforated sound-absorbing panels as room dividers. This research provides important insights into the role of double-porosity designs in creating effective acoustic absorber panels.

Keywords: *Poro-Elastic Materials, Double Porosity, Macroperforation, Sound Absorption*

***Corresponding author**: *manuel.isenegger@hslu.ch.*

***Copyright**: ©2025 Manuel Isenegger et al. This is an open-access article distributed under the terms of the Creative Commons Attribution 3.0 Unported License, which permits unrestricted use, distribution, and reproduction in any medium, provided the original author and source are credited.*

1. INTRODUCTION

There are several types of acoustic absorption, one important type being porous absorption [1]. This kind of absorber can be made from a plethora of materials with inherently different structural, and acoustic characteristics. Acoustic properties for most porous materials can be partially controlled in manufacturing, in its simplest form by varying the thickness of a panel.

The influence of additional perforations on the acoustic properties have been investigated analytically [2, 3], numerically [4, 5] and empirically [6, 7]. Investigations focused on the material near a rigid backing and in most cases under orthogonal sound incidence. Few publications have empirically analyzed the acoustic properties under diffuse sound incidence, and no publication was found addressing the behavior in the absence of a rigid backing. In addition, no publication investigating the acoustic separation performance of perforated sound absorber panels is known to the authors.

This publication investigates the effects of perforation parameters on acoustic properties of a $24\,\mathrm{mm}$ absorber material, made from polyethylene terephthalate (PET) fibers. A first measurement campaign was conducted in the impedance tube with 41 different sample configurations measured at two different heights. A second measurement campaign was conducted in the reverberation room with 16 different perforation configurations.

Furthermore, numerical analysis using the Boundary Element Method (BEM) compared the acoustic separation capabilities of a perforated and unperforated absorbing and reflective panels in a free-field environment.

2. METHODS

2.1 Material production and perforation

The absorber panel, EchoBoard® 24mm, is made out of 100% PET felt with a percentage of recycled fibers. The fibers are needled into a uniform fleece during production. Subsequent heat and pressure treatment creates a structurally stable sound absorber with a density of $3600\,\mathrm{g/m^2}$. The panels measure $2400\text{x}1800\text{x}24\,\mathrm{mm}^3$ and are available in various colors. They are further processed on a computerized numerical control (CNC) cutting plotter, which offers a wide range of design options with different knives and cutting angles. The perforations are precisely cut using vector data and an oscillating knife. After cutting, the parts are pushed out by hand. The choice of perforation designs is limited by the structural properties of the material and the production technique. Large perforation percentages reduce the structural stability of the panel. Another design limit comes from the CNC blades. The smallest cutting radius is $5\,\mathrm{mm}$ and the distance between individual cuts may not fall below $5\,\mathrm{mm}$.

2.2 Absorption measurements

2.2.1 Impedance tube

Absorption measurements in the impedance tube were conducted at Lucerne University of Applied Sciences and Arts in Horw, based on ISO 10534-2:2023 [8]. The available measurement device allows for a measurement range between $100\,\mathrm{Hz}$ and $3200\,\mathrm{Hz}$. Samples were cut to a size of $201\,\mathrm{mm}$ side length, so they could be mounted flush/snugly to the walls of the impedance tube with minimal compression of the material. The software m|abstube by Müller-BBM Acoustic Solutions GmbH (version 2.75.8515.38409) was used for measurement and evaluation. Temperature, atmospheric pressure and relative humidity were recorded before every measurement session. Only one sample per perforation configuration was measured.

An initial set of 41 perforations with varying perforation parameters (size, percentage, geometry, regularity) was chosen and samples produced (see Fig. 1). The choice of perforations was based on the results of prior research on double-porosity materials. Measurements of the samples were made with $0\,\mathrm{cm}$ and $4\,\mathrm{cm}$ distance to the rigid backing. In total, 84 different configurations were measured in the impedance tube.

Statistical analysis was implemented with the Pearson correlation coefficient (PCC) between numerical independent variables (total perforation area, individual perforation size) and dependent variables (absorption coefficient) per frequency bin. For categorical variables, analysis of covariance (ANCOVA) has been used with the Holm-Bonferroni correction method.

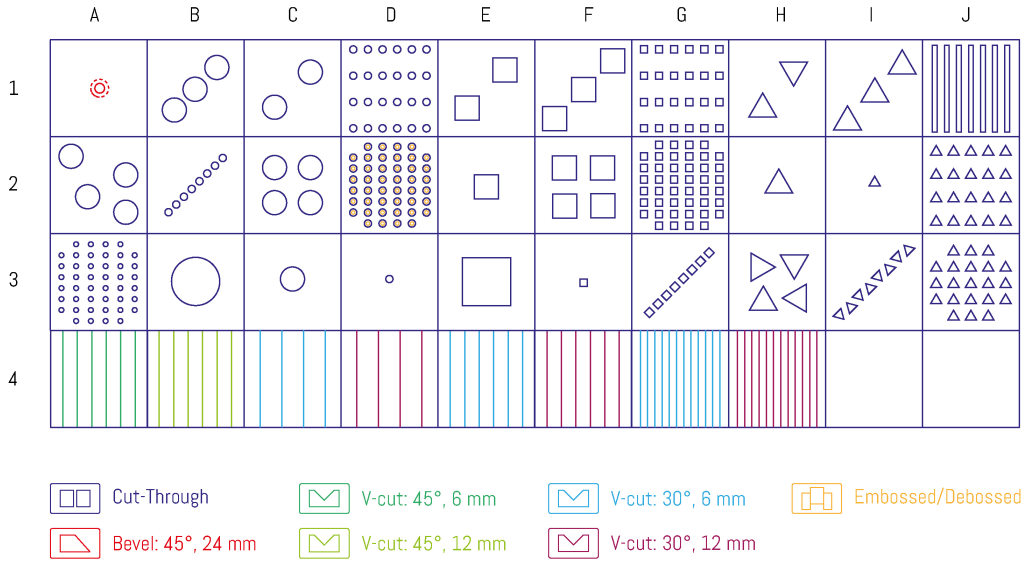


Figure 1: Perforation configurations for impedance tube measurements

2.2.2 *Reverberation room*

Absorption measurements in the reverberation room were conducted at Lucerne University of Applied Sciences and Arts in Horw, based on ISO 354:2003 [9]. The properties of the reverberation room conform to the requirements defined by the standard. The measured absorber panels, in their intended application as room dividers, were considered to be discrete objects, according to section 6.2.2.2 of the mentioned ISO standard. All panels were hung at a single position in the center of the reverberation room. Temperature and relative humidity were measured before both the measurement of the empty room and the measurement of the absorber panels. The interrupted noise method was applied using two loudspeaker positions and ten microphone positions. The software Nor850 measurement system by Norsonic (version 3.2) was used for measurement and evaluation.

The perforation parameters for this second measurement campaign were informed by the results of the impedance tube measurements and adapted dynamically after each measurement iteration. In addition, the availability of three panels resulted in restrictions on the amount and type of consecutive perforations. Ultimately, the three $2400\,\mathrm{mm}$ by $1800\,\mathrm{mm}$ panels were increasingly perforated in 5 consecutive steps before being measured, resulting in 16 configurations (including the unperforated panels). The parameter variation was on perforation geometry (circles, squares, and triangles), perforation size (S = 1.13-36.19 cm^2), and perforation percentage (ϕ_p = 1-32%). The scenarios measured in the reverberation room are visualized in Fig. 2. A description of the relevant perforation parameters can be found in Tab. 1.

For better comparability the sound absorption coefficient has been used, rather than the equivalent sound absorption area, as would be required by ISO 354 for discrete objects.

The following dependent variables have been used for the statistical analysis:

- Absorption coefficient according to ISO 11654 [10]
- Mean value of the (low-frequency) third-octave frequency bands $50-160\,\mathrm{Hz}$
- Mean value of the (mid-frequency) third-octave frequency bands $200-1250\,\mathrm{Hz}$
- Mean value of the (high-frequency) third-octave frequency bands $1600-5000\,\mathrm{Hz}$

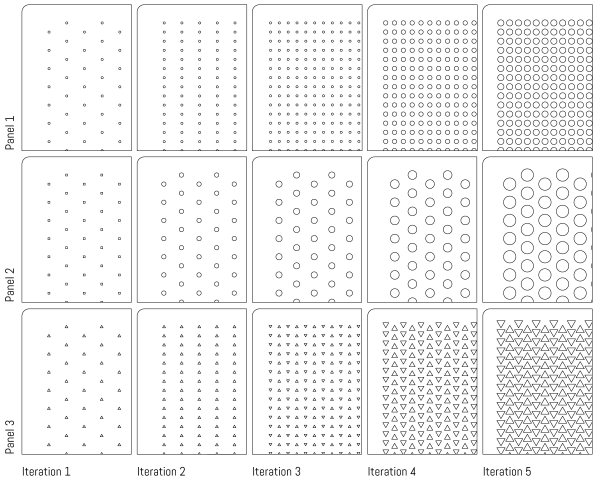


Figure 2: Enlarged view of the three panels' perforation configurations for the reverberation room measurements

Table 1: Parameters for the 15 perforation configurations measured in the reverberation room

	Panel 1	**Panel 2**	**Panel 3**
It. 1	$Geom. = \circ$ $S = 1.1\,\mathrm{cm}^2$ $n = 382$ $\phi_p = 1\%$	$Geom. = \square$ $S = 1.1\,\mathrm{cm}^2$ $n = 382$ $\phi_p = 1\%$	$Geom. = \triangle$ $S = 1.1\,\mathrm{cm}^2$ $n = 382$ $\phi_p = 1\%$
It. 2	$Geom. = \circ$ $S = 1.1\,\mathrm{cm}^2$ $n = 765$ $\phi_p = 2\%$	$Geom. = \circ$ $S = 4.5\,\mathrm{cm}^2$ $n = 382$ $\phi_p = 4\%$	$Geom. = \triangle$ $S = 1.1\,\mathrm{cm}^2$ $n = 765$ $\phi_p = 2\%$
It. 3	$Geom. = \circ$ $S = 1.1\,\mathrm{cm}^2$ $n = 1530$ $\phi_p = 4\%$	$Geom. = \circ$ $S = 9.0\,\mathrm{cm}^2$ $n = 382$ $\phi_p = 8\%$	$Geom. = \triangle$ $S = 1.1\,\mathrm{cm}^2$ $n = 1530$ $\phi_p = 4\%$
It. 4	$Geom. = \circ$ $S = 4.5\,\mathrm{cm}^2$ $n = 1530$ $\phi_p = 16\%$	$Geom. = \circ$ $S = 18.1\,\mathrm{cm}^2$ $n = 382$ $\phi_p = 16\%$	$Geom. = \triangle$ $S = 4.5\,\mathrm{cm}^2$ $n = 1530$ $\phi_p = 16\%$
It. 5	$Geom. = \circ$ $S = 9.0\,\mathrm{cm}^2$ $n = 1530$ $\phi_p = 32.1\%$	$Geom. = \circ$ $S = 36.2\,\mathrm{cm}^2$ $n = 382$ $\phi_p = 32.1\%$	$Geom. = \triangle$ $S = 9.0\,\mathrm{cm}^2$ $n = 1530$ $\phi_p = 32.1\%$

2.3 Numerical simulations

The software COMSOL Multiphysics® was used to compute the average sound pressure level (SPL) in a $1\,\mathrm{m}^3$ volume behind $2 \times 2\,\mathrm{m}^2$ panels in free space. The panels were $24\,\mathrm{mm}$ thick and modeled with infinite through-air resistance, enabling the use of surface impedance models. BEM-models were employed in the frequency domain to calculate the sound pressure distribution around the panels for both normal and $45°$ incident plane waves.

Two types of perforated panels were analyzed: one with 400 circular holes, each with a radius of $1.5\,\mathrm{cm}$, and another with 900 circular holes, each with a radius of $1.0\,\mathrm{cm}$. Both panels have the same front surface area of $3.72\,\mathrm{m}^2$ exposed to the incident plane wave in a free field environment. The perforated panels, including the boundary areas of the holes, were assigned an absorption coefficient of $\alpha = 0.8$ or 0.0 (sound-hard) across all frequencies. These two perforated panels were compared to a solid, non-perforated panel, which was also assigned an absorption coefficient of $\alpha = 0.8$ or 0.0.

The absorption coefficient α corresponds to a surface impedance Z for normal incidence, which is determined using the following equation:

$$Z = Z_0 \frac{1+R}{1-R} \tag{1}$$

where $Z_0 = \rho_A \cdot c_A = 413 Pa \frac{s}{m}$ is the characteristic acoustic impedance of air, and $R = \sqrt{1-\alpha}$ is the reflection factor of the panel. The impedance Z serves as the boundary condition in the numerical simulation of plane waves interacting with the panels.

3. RESULTS

3.1 Measurements

3.1.1 Impedance tube

The measurement result of the unperforated panel, as a reference, can be seen in Fig. 3.

The m|abstube software outputs 127 frequency bins from 85 to $3118 Hz$. Measuring 84 configurations, this results in 10'668 data points from the impedance tube measurements. For analysis, the delta between absorption coefficients of the perforated samples and the unperforated sample has been calculated.

Through statistical analysis, different trends could be detected. At $0\,\mathrm{mm}$ distance to the rigid backing, increasing the total perforation area significantly reduced the absorption coefficient across all frequencies. At high frequencies, a larger perforation size led to a significant reduction in absorption, while no such effect was observed below $1800\,\mathrm{Hz}$. The perforation geometry had only a minor impact: although all geometries reduced absorption, the "Circle" shape caused the least reduction and the "V-Cut" the most. The distribution of the perforations showed only weak effects on absorption.

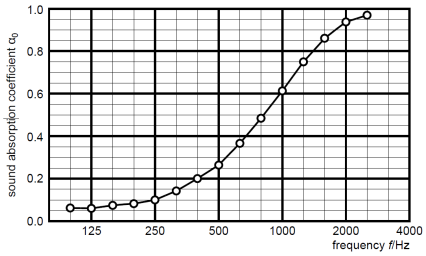


Figure 3: Sound absorption coefficient of the unperforated panel according to ISO 10534-2

At a distance of $40\,\mathrm{mm}$ to the rigid backing, a slight, non-significant increase in absorption was observed around $1\,\mathrm{kHz}$ with increasing total perforation area, while frequencies above and below exhibited a strong and significant reduction. For frequencies above $800\,\mathrm{Hz}$, an increase in perforation size resulted in significant, yet mixed effects depending on the frequency band. Above $170\,\mathrm{Hz}$, the geometry significantly affected absorption: in particular, "V-Cuts" and "Slits" caused the strongest reductions (-0.036 and -0.1, respectively). Once again, the perforation distribution had only weak effects.

3.1.2 Reverberation room

The measurement result of the unperforated panel, as a reference, can be seen in Fig. 4.

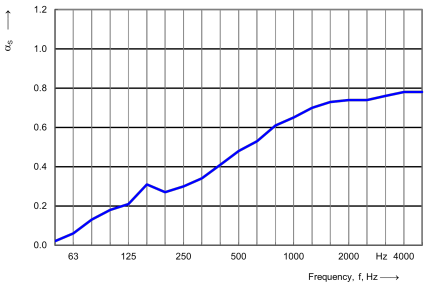


Figure 4: Sound absorption coefficient of the unperforated panel according to ISO 354

With the tested configurations, the primary dependence for all dependent (absorption) variables is the perforation percentage, where higher perforation percentages generally yield lower absorption values for all frequency regions. See Fig. 5 for detailed results.

Furthermore, the absorption dependency on perforation size was evaluated on a subset, including only perforation percentages $4, 16$ and 32% and the $circle$ perforation geometry. See Fig. 6 for detailed results.

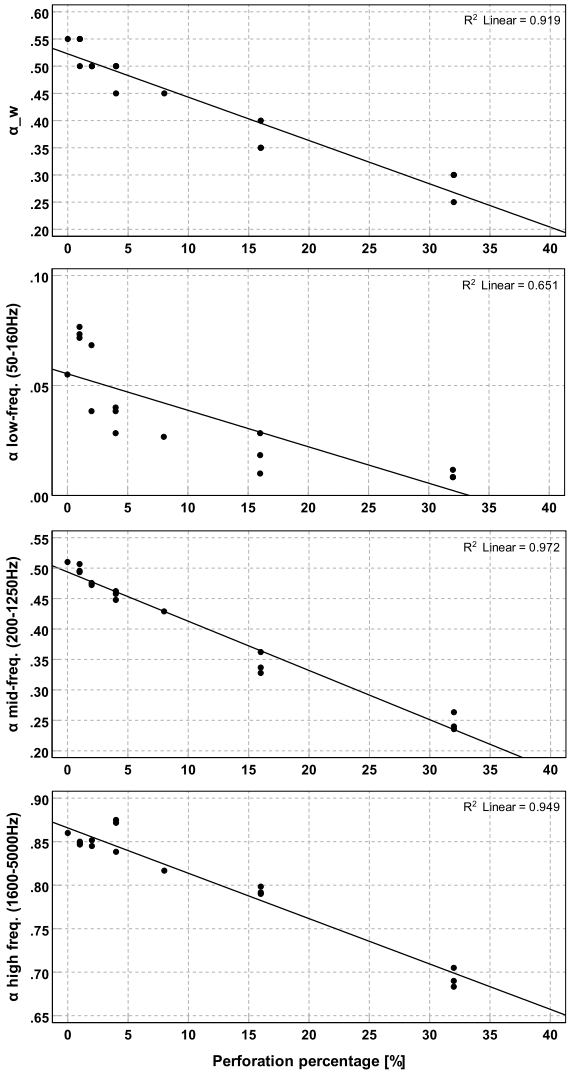


Figure 5: Absorption values plotted against perforation percentage with linear regression and R^2 values

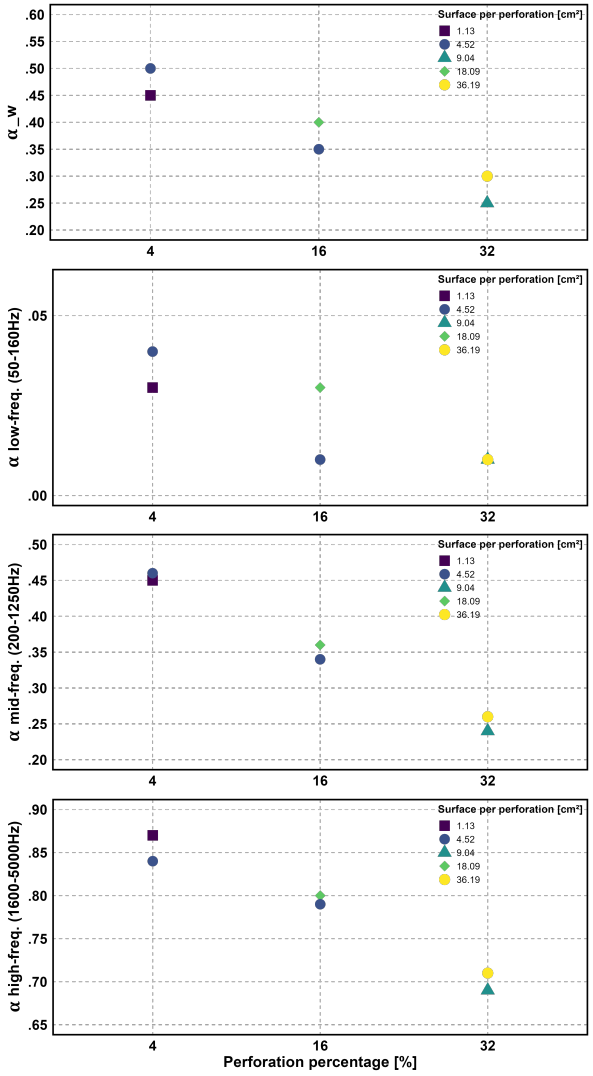


Figure 6: Absorption values plotted against perforation size

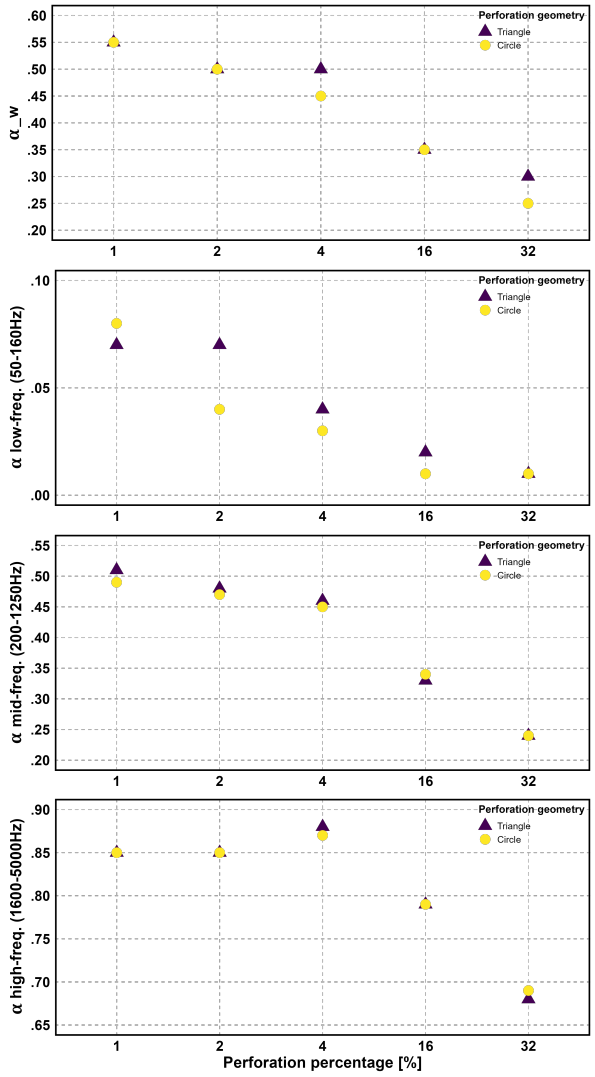


Figure 7: Absorption values plotted against perforation geometry

Finally, the trend influenced by the perforation geometry was analyzed on the subset, including perforation percentages $1, 2, 4, 16$ and 32% and the *circle* and *triangle* geometries. See Fig. 7 for detailed results.

3.2 Numerical simulations

Fig. 8 depicts the SPL at three frequencies in two planes orthogonal to the panel, centered at the panel's midpoints. A plane wave propagates under normal incidence from below. The figure highlights interference patterns resulting

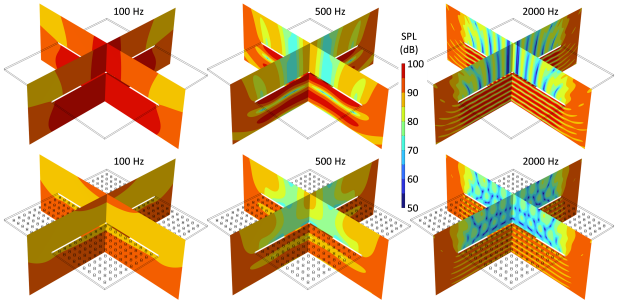


Figure 8: SPL around porous panels (200 x 200 x 2.4 cm^3) under normal incidence of a plane wave (93 dB) from below, at frequencies of 100, 500, and 2000 Hz. Top row: Unperforated panel with an overall absorption coefficient $\alpha = 0.0$. Bottom row: Perforated panel with 400 holes, each with a radius of 1.5 cm, and an overall absorption coefficient $\alpha = 0.8$.

from reflections below and diffraction above the panels. Sound attenuation is observed above both the unperforated, sound-hard panel (top row of Fig. 8) and the perforated panel with 400 holes, which has an absorption coefficient of $\alpha = 0.8$ (bottom row of Fig. 8). The average SPL values for both panels are summarized in Tab. 2. The perforated panel with 900 holes is not included in the table, as its values closely resemble those of the perforated panel with 400 holes.

Table 2: SPL averaged above the panels at three different frequencies. Row 1 and row 4 correspond to the settings of Fig. 8. Row 2 is an unperforated panel with $\alpha = 0.8$. Row 3 is a perforated, sound-hard panel with 400 holes.

SPL, averaged over $1m^3$ volume			
	$100Hz$	$500Hz$	$2000Hz$
unperforated, $\alpha = 0.0$	94.3 dB	80.7 dB	73.2 dB
unperforated, $\alpha = 0.8$	90.8 dB	77.5 dB	69.3 dB
perforated, $\alpha = 0.0$	91.8 dB	82.6 dB	75.9 dB
perforated, $\alpha = 0.8$	90.1 dB	78.5 dB	71.4 dB

At higher frequencies, both the perforated and unperforated panels exhibit greater sound attenuation compared to lower frequencies. This behavior is expected for the un-

perforated panel due to reduced diffraction at higher frequencies; however, it also applies to the perforated panel. Notably, the unperforated, sound-hard panel is less effective as a room divider across all frequency ranges compared to the perforated panel with an assigned absorption coefficient. Furthermore, the difference in sound attenuation between the perforated and unperforated panels, both with assigned absorption coefficients, is minimal. This finding indicates that a perforated, acoustically absorbing panel can serve as an effective alternative to an unperforated absorbing panel as a room divider, particularly when aesthetic design considerations are important.

4. DISCUSSION

The measurements both in the impedance tube and the reverberation room revealed a general dependence of the sound absorption coefficient on the perforation percentage, where the sound absorption decreases with a higher perforation percentage ϕ_p. This result is in accordance with results found in other research, which showed a decrease of absorption in macro-perforated materials with low flow resistivity.

The dependence of the absorption coefficient on perforation size S in the impedance tube is different from the observed dependence in the reverberation room. Especially with large perforations, high frequency sound waves were reflected from the rigid backing in the impedance tube. In the reverberation room, the opposite tendency occurred, where larger perforation sizes (under the same perforation percentage and geometry) showed better absorption. No explanation for this behavior in the diffuse sound field could be found by the authors.

Neither in the impedance tube, nor in the reverberation room, did the sound absorption reveal a strong dependence on perforation geometry.

Numerical simulations show, that for low frequencies (100 Hz) the perforated, sound-absorbing panel has the best sound reduction performance, followed by the unperforated, sound-absorbing panel, the perforated, sound-hard panel and the unperforated, sound-hard panel. For mid (500 Hz) and high (2000 Hz) frequencies, the best sound reduction is achieved by the unperforated, sound-absorbing panel, followed by the perforated, sound-absorbing panel, the unperforated, sound-hard panel and the perforated, sound-hard panel.

Intuitively, these simulation results are rather surprising. One might assume that a perforated panel allows more sound to pass through its openings, making it less effective at blocking sound compared to an unperforated panel, regardless of their sound absorption capabilities. However, the combination of diffracted sounds from the edges and the perforations, which are additionally dampened by the sound absorbing material, result in a lower SPL, compared to a sound-hard, unperforated panel. However, the best overall sound reduction capabilities are achieved by the sound absorbing, unperforated panel.

4.1 Limitations and further research

Measurements of the flow resistivity and further metrics of porous materials (porosity, tortuosity, viscous and thermal characteristic length, etc.) have not been carried out here, but would allow for analytical results to confirm and complement the empirical data and adjust the numerical simulations to the investigated material.

Different sample thicknesses or even different materials would complement the empirical data and allow for a more complete representation of the mechanisms governing the absorption behavior of double-porosity models.

The numerical simulations of double-porosity panels in a free-field environment give a first indication on their possible performance as room dividers. However, BEM-models do not account for sound transmission, which is typically higher for sound-absorbing, porous materials than for sound-hard, non-porous materials. Absorption values found in real materials should be used in further simulations. In addition, room dividers are typically used in rooms with reflective surfaces. Further simulations in typical office environments incorporating sound transmission of the simulated materials would yield a more accurate representation of the sound reduction possibilities of porous materials.

With regards to a demand for flexible room dividers in office environments, more research on the sound absorption behavior of free-standing panels and curtains, in general, and the potential of double-porosity materials, in particular, is needed. Especially, perforations with gradually varying size, as described in [3] and [11], are a promising approach to aesthetically pleasing and highly functional sound absorbers and room dividers.

5. CONCLUSIONS

This study provides valuable insights into the acoustic performance of double-porosity materials, specifically recycled PET fiber absorbers, under varying perforation parameters. Through a combination of impedance tube measurements, reverberation room testing, and numerical sim-

ulations, we observed that increasing the perforation percentage generally led to a reduction in sound absorption. Secondary effects, such as perforation size, also played a minor role in modifying the absorption coefficient.

The results suggest that careful tuning of perforation geometry, size, and percentage can help optimize the trade-off between aesthetic, structural, and acoustic performance in architectural applications.

Future research should explore the transfer of effects, which are well-known in impedance tube measurements, to free-standing configurations.

6. ACKNOWLEDGMENTS

The authors would like to thank the head and staff of the testing laboratory at HSLU for providing access to their measurement infrastructure.

Additional thanks go to Tobias Banz, Mario Rölli, Gregor Heini, Lél Bartha, and Samuel Ulrich for their help in transporting the large panels after each perforation step.

7. REFERENCES

[1] T. Cox and P. d'Antonio, *Acoustic absorbers and diffusers: theory, design and application*. CRC press, 2016.

[2] J. Auriault and C. Boutin, "Deformable porous media with double porosity. quasi-statics. i: Coupling effects," *Transport in porous media*, vol. 7, pp. 63–82, 1992.

[3] N. Atalla, R. Panneton, F. Sgard, and X. Olny, "Acoustic absorption of macro-perforated porous materials," *Journal of sound and vibration*, vol. 243, no. 4, pp. 659–678, 2001.

[4] N. Atalla, C. K. Amédin, R. Panneton, and F. Sgard, "Étude numérique et expérimentale de l'absorption acoustique et de la transparence acoustique des matériaux poreux hétérogènes en basses fréquences dans le but d'identifier des solutions à fort potentiel d'applicabilité," *Rapports de recherche scientifique IRSST*, 2001.

[5] F.-X. Bécot, L. Jaouen, and E. Gourdon, "Applications of the dual porosity theory to irregularly shaped porous materials," *Acta acustica united with Acustica*, vol. 94, no. 5, pp. 715–724, 2008.

[6] N. Atalla, C. K. Amédin, Y. Atalla, R. Panneton, and F. Sgard, "Développement de nouveaux matériaux absorbants à hautes performances acoustiques pour diminuer le bruit en basses fréquences," *Rapports de recherche scientifique IRSST*, 2004.

[7] F. Bécot, F. Sgard, and N. Amirouche, "Advanced heterogeneous materials for noise and vibration control," in *Symp. on the Acoustics of Poro-Elastic Materials*, pp. 287–294, 2005.

[8] ISO 10534-2:2023, "Acoustics — determination of acoustic properties in impedance tubes – part 2: Two-microphone technique for normal sound absorption coefficient and normal surface impedance," standard, International Organization for Standardization, Geneva, CH, 2023.

[9] ISO 354:2003, "Acoustics — measurement of sound absorption in a reverberation room," standard, International Organization for Standardization, Geneva, CH, 2003.

[10] ISO 11654:1997, "Acoustics — Sound absorbers for use in buildings — Rating of sound absorption," standard, International Organization for Standardization, Geneva, CH, 1997.

[11] X. Liu, X. Ma, C. Yu, and F. Xin, "Sound absorption of porous materials perforated with holes having gradually varying radii," *Aerospace Science and Technology*, vol. 120, p. 107229, 2022.

DOI: 10.61782/fa.2025.0023

FORUM ACUSTICUM EURONOISE 2025

A NOVEL ALGORITHM FOR ESTIMATING BIOT PARAMETERS IN ACOUSTIC SIMULATION OF FIBROUS MATERIALS BASED ON RAW MATERIAL COMPOSITION

Minh-Tan Hoang [1*] **Massimiliano Tiengo** [2] **Evan Harry** [2]
[1] Adler Pelzer Group, Acoustic TechCenter R&D, Z.I. François Sommer – BP13, 08210 Mouzon, France
[2] Adler Pelzer Group, C.so Savona 45, I 10029 Villastellone, Italy

ABSTRACT

For an automotive trim supplier, the production of material and component samples for certification and acceptance by vehicle manufacturers is an expensive and time-consuming task. Circumventing the need for these via pure simulation still requires the correct determination of Biot parameters, which can be carried out via batch samples. However, this is a complex task that is sensitive to both the measurement and the condition of the samples. Any discrepancies will propagate through the simulation and will create uncertainties in the results.
This paper describes a novel approach, called *Genetic*, in which the empirical calculation of Biot parameters of fibrous composites is based purely on the blended mixture of fibre types. This technique was the culmination of an extensive measurement and characterisation campaign on a wide selection of fibre types and is part of an ongoing investigation into the use of data science applications to enhance internal methodologies.
The next phase of the project is focused on porous media such as foams.

Keywords: *fibrous materials, fineness, composition, transport parameters, acoustic simulation, absorption, transmission loss.*

[*] ***Corresponding author***: *minh-tan.hoang@adlerpelzer.com.*
Copyright: *©2025 M. T. Hoang et al. This is an open-access article distributed under the terms of the Creative Commons Attribution 3.0 Unported License, which permits unrestricted use, distribution, and reproduction in any medium, provided the original author and source are credited.*

1. INTRODUCTION

Fibrous materials are increasingly used in automotive NVH (Noise, Vibration, and Harshness) packages due to their effective absorption and insulation properties. Their adoption by OEMs is also driven by sustainability concerns, such as the integration of recycled PET fibers. However, optimizing their acoustic performance requires a precise understanding of their physical properties, commonly referred to as Biot parameters. These parameters are divided into two groups: (i) transport parameters of an equivalent fluid model (e.g., JCA or JCAL), governing viscous and thermal dissipation within porous media, and (ii) solid-phase elastic parameters, which are more relevant for structural interactions but less critical for absorption-related applications [1].
As an automotive NVH trim supplier, it is essential to have access to accurate material properties, not only the Biot parameters but also key acoustic performance metrics such as normal incidence absorption, diffuse field absorption, and transmission loss of flat (planar) samples. These properties are crucial for material selection, simulation and validation. In practice, they are particularly relevant in (i) Request for Quotation (RFQ) phases to ensure compliance with OEM constraints (e.g., thickness, weight); (ii) acoustic simulations, for improved numerical models; and (iii) manufacturing and innovation, guiding material validation and optimization.
Currently, material properties of flat samples are obtained through two primary strategies:

- Material databases: These databases compile data for flat samples of various thicknesses (e.g., 5 to 30 mm), including Biot parameters, normal incidence and diffuse field absorption, as well as transmission loss. However, this approach is

constrained by predefined thicknesses and material types, requiring large-scale material manufacturing and extensive experimental campaigns, making it a less efficient solution.

- Acoustic simulation: Which are based on characterized Biot parameters for a given material composition. While simulations offer a way to estimate material performance, uncertainties may arise due to variations in sample conditions, material characterization methods, and acoustic models. These can be mitigated by validating simulation results against experimental data.

A more elegant approach is to estimate the so called composite "acoustic transport parameters" directly from fundamental raw material characteristics, such as fiber radius (µm) or fineness (dTex, mass in grams per 10 km of fiber), together with composition ratios, thereby enabling a predictive framework that reduces the dependency on costly experimental measurements.

Several methods have been proposed for computing the transport parameters of fibrous media from fiber properties. Publications relating to this computation are listed in the references [2] to [8] but can be categorized into:

- **Empirical regression models** – deriving parameters from experimental datasets (e.g., Biboud et *al.* (2024) on nylon fibers [4].
- **Analytical (or geometrical) models** – developing theoretical formulations based on fiber structures [5]-[6].
- **Hybrid numerical/semi-analytical models** – identifying transport parameters that best fit numerical simulations data [3].
- **Compression-based estimation models** – considering the effect of compression on initial material properties [7].

Pompoli and Bonfiglio [2] adapted existing analytical formulations and validated them through numerical simulations for parallel fiber structures. However, these formulations require the effective radius of the fibrous raw materials, which are typically not provided in manufacturing material data sheets. Santoni et *al.* [8] further utilized these formulations to study recycled fiber mixtures, but they required airflow resistivity and porosity of loose fibers as input parameters to inversely determine the effective radius of each kind of fiber in the composition.

While previous studies primarily focus on validating transport parameter estimations against normal incidence absorption measurements, automotive applications require a broader scope. Diffuse field absorption is an important parameter that must be considered for real-world applications.

In this paper, we propose a novel algorithm, developed through an extensive experimental campaign, to estimate JCA parameters from known manufacturing parameters: fineness in dTex and composition ratios. This algorithm provides reliable input data for simulating impedance tube absorption, diffuse field absorption, and sound transmission loss across a wide range of fibrous material densities and compositions.

Section (2) describes the materials and methods used, including fiber compositions and experimental approaches. Section (3) presents the results, validating the *Genetic* algorithms through various acoustic measurements. Finally, Section (4) concludes the paper, highlighting the practical applications of the proposed methods.

2. MATERIAL AND METHODS

2.1 Fiber Material

A group of fibrous flat samples were studied, each composed from five different mixtures. Each mixture consisted of a fixed number of fiber types with corresponding mass participation ratios. The raw loose fibers were classified as: PET (polyethylene terephthalate), Cotton fibers and PET-CoPET bicomponent fibers, where the core was PET and the surface was CoPET in a 1:1 ratio. The fineness of the input raw materials, expressed in dTex, was also known.

The fiber mixture compositions were selected based on several factors, including acoustic performance, mechanical requirements, processing constraints and cost. The chosen materials spanned a wide range of fiber fineness, with a variation factor of approximately 40 between the finest and coarsest fibers, depending on the mixture.

For each mixture, flat samples were fabricated with varying thicknesses and densities using the Hot Molding Process (HMP). During this process, the CoPET component melts, bonding the remaining fibers. The resulting samples, across all mixtures, have thicknesses ranging from 5 mm to 35 mm, with surface mass varying from approximately 490 to 2700 g/m².

2.2 Method

2.2.1 Experiment approaches

This study aims to define the transport parameters of fibrous materials through experimental data. Various tests were conducted on flat samples, including: (i) identification of transport parameters, (ii) measurement of Normal

Incidence Sound Absorption, (iii) measurement of Diffuse Field Absorption, and (iv) evaluation of Sound Transmission Loss.
From the identified transport parameters, linear or power curve fitting relationships were established. Once the transport parameters were determined, the acoustic performance of the materials were predicted using the "Johnson-Champoux-Allard" (JCA) equivalent fluid model, which requires five key parameters: open porosity ϕ, airflow resistivity σ, tortuosity α_∞ , viscous characteristic length Λ, thermal characteristic length Λ' [1].

2.2.2 Material characterization and acoustic measurements

Diffuse field sound absorption coefficient measurements were conducted on flat samples (1 m × 1.2 m) using a small reverberation room (6.44 m³), known as the Alpha Cabin. Ideally, according to ISO 354 [9], a large reverberation room (>180 m³) and a sample size of 12 m² are required. However, the reduced-size cabin allows for quick measurements with a 1.2 m² sample, which is commonly used in the automotive industry by both suppliers and OEMs.
Transmission Loss measurements were performed using the two-room method, where the flat sample was placed on a 0.9 mm-thick steel plate. Sound intensity and pressure measurements were taken in an anechoic room and a reverberation room, respectively [10].
For each flat sample (1.2 m²), three circular specimens (Ø100 mm) were extracted for airflow resistivity (AFR) measurements [11]. Subsequently, normal incidence sound absorption measurements [12] were carried out using Ø45 mm samples cut from the Ø100 mm specimens, ensuring that measurements were taken from the same locations, see Fig. 1.



Figure 1. Impedance tube samples (Ø45 mm) extracted from AFR samples (Ø100 mm) for different mixtures.

JCA transport parameters were identified for material samples with varying densities and thicknesses but the same raw material composition (i.e., the same mixture). For each given mixture, a minimization-based inversion was performed, simultaneously processing all samples of that mixture to fit the data from AFR and normal incidence sound absorption measurements [13]-[14].

3. RESULTS

3.1 Empirical regression models

Once the JCA parameters were identified for each sample, the datasets were used to develop empirical regression models. For each of the five transport parameters, a unique formulation was derived and validated for all mixtures. These algorithms, referred to as "*Genetic*", enable the calculation of transport parameters for any fibrous material using typical manufacturing inputs, based on linear or power-law relationships: fiber fineness (dT, in dTex), the mixing ratio (ω_i, the weight ratio of each fiber type to the total material weight) and the sample bulk density (ρ). The selection of these input parameters was physically justifiable, as the physical properties of fibrous materials depend on their microstructural characteristics [3]. Specifically, fiber diameters and their distribution can be represented by dT and ω_i, while the bulk density ρ or the open porosity ϕ represents the volume of solid or air within the material.
When the material density increases, the air volume inside decreases, leading to a linear relationship between porosity and density:

$$\phi = 1 - C_1\rho \quad (1)$$

The tortuosity can then be determined using Archie's law:

$$\alpha_\infty = (1/\phi)^\gamma \quad (2)$$

where γ is a constant depending on the material's microstructure [2]. Both constants, C_1 and γ, were determined to fit the identified porosity and tortuosity for the fibrous materials under study.
Previous work [3] has shown that at a fixed density ρ, the airflow resistivity σ is inversely related to fiber diameters. In other words, the thermal permeability k_0, which is linked to the airflow resistivity of porous material via the dynamic viscosity of air η, is inversely related to the total fiber length L_f per cubic meter. This can be formulated using dT,

ω_i and ρ. The thermal permeability can finally be computed as:

$$k_0 = \eta/(f_1 \sum_1^n(\omega_i/dT_i)) \quad (3)$$

where f_1 is a 4th-order polynomial function of density ρ and n is the number of fiber populations in the composition.
Fig. 2 shows a strong correlation between the *Genetic* algorithm (Eqn. 3) and the experimental results for static permeability, which is made non-dimensional using the standard fiber mean diameter d_{ref}.

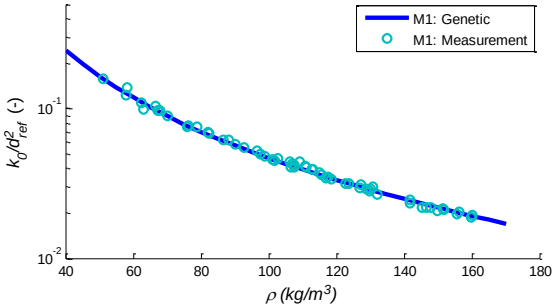


Figure 2. Static Permeability: Correlation between the experimental function (*Genetic* algorithm) and measurements for material mix M1.

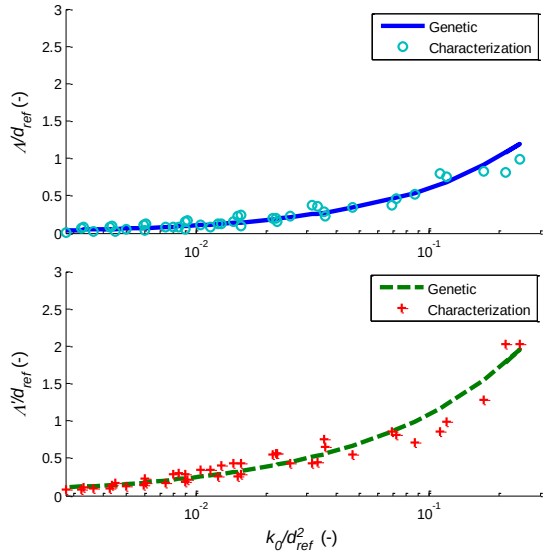


Figure 3. Characteristic Lengths: Correlation between the *Genetic* algorithm and material characterization through global minimization inversion for material mix M1.

As shown in the Eqn. 3, the static permeability k_0 (or airflow resistivity $\sigma = \eta/k_0$), one of the primary factors influencing porous media, contains all the material input parameter information. To put it another way, the two remaining parameters, the characteristic lengths, can be estimated from k_0 using power law functions of the following form:

$$\Lambda = C_2 {k_0}^{C_3}; \qquad \Lambda' = C_4 {k_0}^{C_5} \quad (4)$$

where the coefficients C_i can be easily identified to fit the characterized transport parameters. Using these formulations, good agreement is shown in Fig. 3, with a correlation factor R^2 greater than 0.93 for both characteristic lengths.
For user-friendliness, the *Genetic* functions have been integrated into a transfer matrix simulation tool (internally named PROTEIN), as shown in Fig. 4. Using basic raw material information (e.g., surface mass, thickness, and material composition), the acoustic properties of porous materials can be quickly estimated.

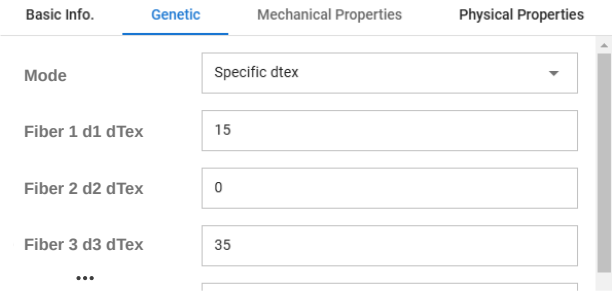


Figure 4. Implementation of a *Genetic* Algorithm model in a Transfer Matrix Simulation (TMM) tool called PROTEIN.

The *Genetic* functions were validated through material performance tests.
Firstly, normal incidence sound absorption, simulated using the Transfer Matrix Method (TMM), showed good correlation with the measurement results, as demonstrated in Fig. 5 for material Mix1. This strong correlation with impedance tube measurements was expected, as such results are commonly used as input for material characterization through inversion approaches. However, this study also presents a strong correlation with diffuse field sound absorption measurements using the Alpha Cabin, as shown in Fig. 6, providing a comprehensive evaluation of absorption performance.

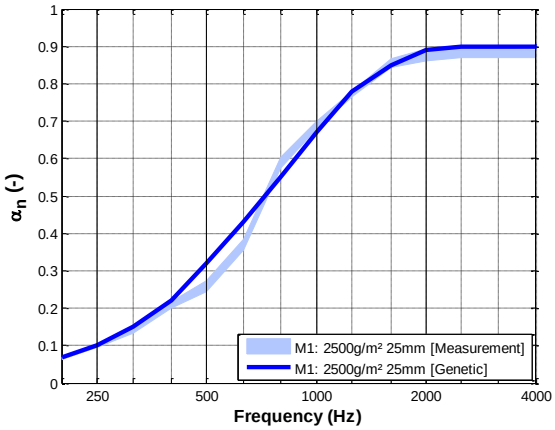


Figure 5. Normal Incidence Sound Absorption: Correlation between the *Genetic* algorithm and impedance tube measurements for material mix M1 at a thickness of 25 mm and density $\rho = 100$ kg/m^3.

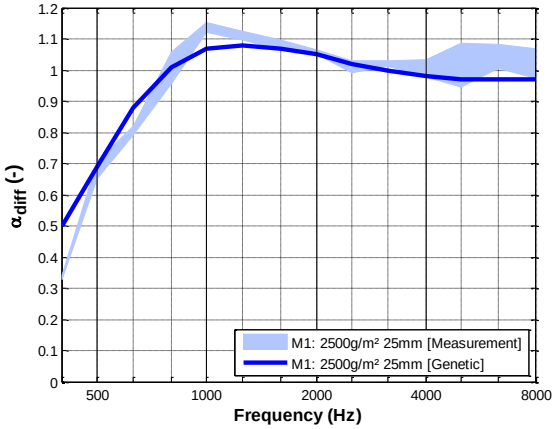


Figure 6. Diffuse Field Sound Absorption: Correlation between the *Genetic* algorithm and Alpha Cabin measurements.

Alpha Cabin measurements are typically problematic for their round robin reliability and the results were not as clear due to the more complex reverberant sound field. However, such a good level of correlation has not previously been reported.

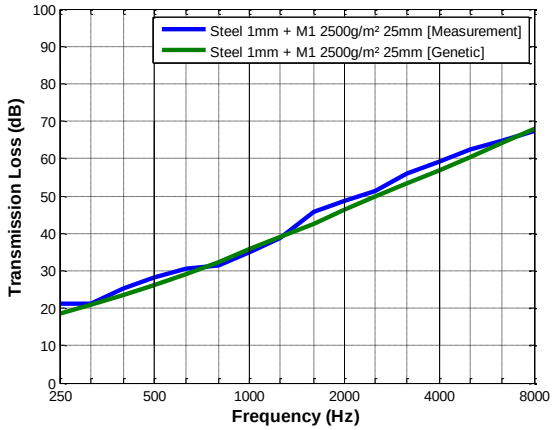


Figure 7. Sound Transmission Loss: Correlation between the *Genetic* algorithm and coupled reverberation/anechoic measurement results.

Additional validation of the *Genetic* algorithms was carried out through Sound Transmission Loss measurements in a simple system where the fibrous flat sample was placed on a steel plate. A good agreement was observed between the simulation and measurement results. Both the acoustic simulations for the Alpha Cabin and Transmission Loss were performed with diffuse field excitation using the Transfer Matrix Method [1].

4. CONCLUSIONS

In this paper, the JCA transport parameters of fibrous materials were computed from raw material information using functions derived from experimental results for various fibrous material compositions and a wide range of bulk densities. These algorithms, referred to as "*Genetic*" were validated, not only through normal incidence sound absorption, but also via diffuse field excitation for both sound absorption and transmission loss. The algorithms were implemented in an internal simulation tool, enabling rapid estimation of acoustic performance based on material typical inputs. This approach has proved useful for several applications, including RFQ responses, manufacturing support and innovation. Future work will involve extending this approach to polyurethane foam materials.

5. REFERENCES

[1] J. F. Allard and N. Atalla: *Propagation of Sound in Porous Media: modeling sound absorbing materials*. 2nd Ed., Wiley, Chichester, 2009.

[2] F. Pompoli and P. Bonfiglio: "Definition of analytical models of non-acoustical parameters for randomly-assembled symmetric and asymmetric radii distribution in parallel fiber structures," *Applied Acoustics*, vol. 159, 107091, 2020.

[3] Q. V. Tran, C. Perrot, R. Panneton, M.T. Hoang, L. Dejaeger, V. Marcel and M. Jouve: "Effect of polydispersity on the transport and sound absorbing properties of three-dimensional random fibrous structures," *International Journal of Solids and Structures*, vol. 296, 112840, 2024.

[4] J. Biboud, S. Elkoun and R. Panneton: "Optimization of sound absorption of recycled Nylon fibrous materials," *Frontiers in Acoustics*, 2:1478414, 2024.

[5] V. Tarnow: "Airflow resistivity of models of fibrous acoustic materials," *The Journal of the Acoustical Society of America*, vol. 100, 3706–3713, 1996.

[6] O. Umnova, D. Tsiklauri and R. Venegas: "Effect of boundary slip on the acoustical properties of microfibrous materials," *The Journal of the Acoustical Society of America*, vol. 126, 1850–1861, 2009.

[7] L. Lei, N. Dauchez and J. Chazot: "Prediction of the six parameters of an equivalent fluid model for thermocompressed glass wools and melamine foam," *Applied Acoustics*, vol. 139, 44–56, 2018.

[8] A. Santoni, P. Bonfiglio, A. Magnani, C. Marescotti, F. Pompoli, and P. Fausti: "A hybrid approach for modelling the acoustic properties of recycled fibre mixtures for automotive applications," *Applied Acoustics*, vol. 182, 108272, 2021.

[9] ISO 354:2003: *Acoustics — Measurement of sound absorption in a reverberation room*, 2003.

[10] ISO 15186-1:2000: *Acoustics — Measurement of sound insulation in buildings and of building elements using sound intensity — Part 1: Laboratory measurements*, 2000.

[11] ISO 9053-2:2020: *Acoustics — Determination of airflow resistance — Part 2: Alternating airflow method*, 2020.

[12] ISO 10534-2:2023: *Acoustics — Determination of acoustic properties in impedance tubes — Part 2: Two-microphone technique for normal sound absorption coefficient and normal surface impedance*. 2023.

[13] P. Bonfiglio and F. Pompoli, "Comparison of different inversion techniques for determining physical parameters of porous media," in Proc. of the 19th International Congress on Acoustics, (Madrid, Spain), 2007.

[14] P. Bonfiglio and F. Pompoli: "Inversion Problems for Determining Physical Parameters of Porous Materials: Overview and Comparison Between Different Methods," *Acta Acustica united with Acustica*, vol. 99, 2013.

6. ACKNOWLEDGMENTS

The authors would like to thank Rod Morris-Kirby from Adler Pelzer Group for his support in reviewing this paper.

7. DEFINITIONS / ABBREVIATIONS

OEM – Original Equipment Manufacturer
JCA – "Johnson-Champoux-Allard" (equivalent model)
RFQ – Request for Quotation
TMM – Transfer Matrix Method
AFR – Airflow Resistivity
PET – Polyethylene Terephthalate
CoPET – Copolyester
HMP – Hot Molding Process
dT– Fiber fineness (dTex)
ω_i – Fiber weight ratio
ρ – Material bulk density (kg/m^3)
σ – Airflow resistivity (Ns/m^4)
k_0 – Static thermal permeability (m^2)
ϕ – Open porosity (-)
α_∞ – Tortuosity (-)
Λ – Viscous characteristic length (μm)
Λ' – Thermal characteristic length (μm)
η – dynamic viscosity of air (Ns/m^2)
γ, C_i – "*Genetic*" algorithm constants

DOI: 10.61782/fa.2025.0020

FORUM ACUSTICUM EURONOISE 2025

A MULTI-MODAL ANALYSIS OF ANISOTROPY IN POROUS MEDIA

Mélanie Nolan[1*] **Simon Félix**[2] **Jean-Philippe Groby**[2]

[1] Departamento de Ingeniería Audiovisual y Comunicaciones, Universidad Politecnica de Madrid, Madrid, Spain
[2] Laboratoire d'Acoustique de l'Université du Mans, Le Mans Université, France

ABSTRACT

This paper introduces a modal decomposition method to retrieve the effective fluid parameters of a sample of anisotropic porous material from multi-modal reflection and transmission coefficients measured in a squared impedance tube. The approach extends on traditional impedance tube methods to include higher-order modes, allowing to characterize the test specimen for plane-wave and multi-modal reflection and transmission coefficients. The proposed formulation uses a modal expansion of the sound pressure and normal particle velocity in the tube, reducing the problem to a system of two differential equations for the components of the pressure and particle velocity projected over the normal modes. The system is solved analytically, which leads to an exact algebraic formulation of the reflection and transmission matrices. An inverse problem is further formulated to infer the bulk modulus and density tensor coefficients of the anisotropic specimen. The method is evaluated numerically on a synthetic anisotropic sample of known porous properties.

Keywords: *Anisotropic porous media, multi-modal analysis, impedance tube*

1. INTRODUCTION

Acoustic wave propagation and viscothermal dissipation of acoustic energy in porous media can be described macroscopically by an equivalent fluid model, which requires the knowledge of several pore parameters. Although some of the pore parameters can be measured directly, these methods require specialized equipment and are often difficult to perform. In this context, inverse characterization methods that are based on the inversion of the scattering matrix [1] are particularly interesting, as they allow to recover the dynamic density and bulk modulus of the equivalent fluid from simple measurements of the normal incidence reflection and transmission coefficients [2]. If the material is homogeneous and isotropic, these two frequency-dependent fluid parameters are also sufficient to determine the six Johnson-Champoux-Allard-Lafarge (JCAL) parameters [3] that control the dissipation of acoustic energy in the medium.

However, most porous materials are anisotropic and exhibit different properties along orthogonal directions known as the *principal directions*. Specifically, the influence of anisotropy translates into a full symmetric density tensor (in place of a scalar), drastically increasing the number of effective fluid parameters required to describe the medium.

Several studies extended the inversion procedure presented in [2] to characterize anisotropic materials. However, most of these studies are based on simplified assumptions on the nature of anisotropy; e.g., anisotropic materials with principal directions belonging to the layer plane interface [4, 5], or two-dimensional anisotropic materials with principal directions arbitrarily tilted with respect to the reference coordinate system [6–8]. To the authors' knowledge, the only study that characterizes fully anisotropic porous materials in three dimensions (i.e., anisotropic porous materials having principal axes tilted in *a priori* unknown directions) is due to Terroir et al.

*Corresponding author: melanie.nolan@upm.es.
Copyright: ©2025 First author et al. This is an open-access article distributed under the terms of the Creative Commons Attribution 3.0 Unported License, which permits unrestricted use, distribution, and reproduction in any medium, provided the original author and source are credited.

[9], who described a general method to recover the effective fluid parameters and the orientation of the material's principal directions from knowledge of the reflection and transmission coefficients at six angles of incidence. Experimental validation was recently achieved by Cavalieri et al. [10], who measured the normal incidence reflection and transmission coefficients of six samples of glass wool cut in six different orientations in an impedance tube.

Following a different approach, the present study exploits the concept of modal decomposition [11–14] to elicit higher order modes in the tube and characterize the test specimen for plane-wave and multimodal reflection and transmission coefficients. Such approach is significant in that it allows to retrieve the effective fluid parameters and the principal directions without changing the orientation of the sample in the tube.

2. THEORY

Consider a layer of homogeneous anisotropic porous material with thickness L, bulk modulus B and density tensor $\boldsymbol{\rho}$ mounted in a rectangular impedance tube with cross section $\mathcal{A} = [0, w_1]\times[0, w_2]$. In the reference coordinate system $(\mathrm{O}, \mathbf{e}_1, \mathbf{e}_2, \mathbf{e}_3)$ with position coordinates (x_1, x_2, x_3), its boundaries are defined by the equations $x_3 = 0$ and $x_3 = L$. We further assume that the density tensor $\boldsymbol{\rho}$ is symmetric; that is $\boldsymbol{\rho}^\top = \boldsymbol{\rho}$, where $^\top$ denotes non-conjugate transposition. In particular, the orthonormal coordinate system $(\mathbf{e}_\mathrm{I}, \mathbf{e}_\mathrm{II}, \mathbf{e}_\mathrm{III})$ of the principal directions of the layer can be defined so that the density tensor is diagonal in this system; that is $\boldsymbol{\rho} = \boldsymbol{\rho}^* = \mathbf{diag}(\rho_\mathrm{I}, \rho_\mathrm{II}, \rho_\mathrm{III})$, where ρ_I, ρ_II and ρ_III are the principal densities and the superscript * designates the diagonal tensor. In the reference coordinate system, the density tensor reads $\boldsymbol{\rho} = \mathbf{R}_{rot}\boldsymbol{\rho}^*\mathbf{R}_{rot}^\top$, where $\mathbf{R}_{rot} = \mathbf{R}_3(\theta_\mathrm{III})\mathbf{R}_2(\theta_\mathrm{II})\mathbf{R}_1(\theta_\mathrm{I})$ is the rotation matrix between the two coordinate systems, with $\mathbf{R}_1$, $\mathbf{R}_2$ and $\mathbf{R}_3$ being elementary rotation matrices and θ_I, θ_II and θ_III the roll, pitch, and yaw angles, respectively.

2.1 Formulation

Outside the layer (i.e., for $x_3 < 0$ and $x_3 > L$), the sound pressure and particle velocity fields $(p, \mathbf{v})$ are governed by the equations of mass and momentum conservation:

$$\mathrm{div}(\mathbf{v}) = \frac{\mathrm{i}\omega}{B_0}p, \tag{1a}$$

$$\mathrm{i}\omega\mathbf{v} = \frac{1}{\rho_0}\nabla p, \tag{1b}$$

where B_0 and ρ_0 are the bulk modulus and scalar density of air, respectively, $\omega = 2\pi f$ is the angular frequency and the time dependency $\mathrm{e}^{-\mathrm{i}\omega t}$ is omitted. Similarly, the sound pressure and particle velocity fields in the layer (i.e., for $0 < x_3 < L$) verify

$$\mathrm{div}(\mathbf{v}) = \frac{\mathrm{i}\omega}{B}p, \tag{2a}$$

$$\mathrm{i}\omega\mathbf{v} = \mathbf{h}\nabla p, \tag{2b}$$

where $\mathbf{h}$ is the symmetric inverse density tensor and reads

$$\mathbf{h} = \begin{pmatrix} h_{11} & h_{12} & h_{13} \\ h_{12} & h_{22} & h_{23} \\ h_{13} & h_{23} & h_{33} \end{pmatrix} = \begin{pmatrix} \mathbf{h}_\perp & \mathbf{h}_3 \\ \mathbf{h}_3^\top & h_{33} \end{pmatrix}, \tag{3}$$

where $(h_{11}, h_{12}, h_{13}, h_{22}, h_{23}, h_{33})$ are the individual inverse density tensor components, $\mathbf{h}_\perp$ is a 2×2 matrix, and the subscript $\perp$ designates the transverse components. This tensor is diagonal in the orthonormal coordinate system of the principal directions of the layer.

As the tube is of constant cross-section, the boundary condition at its walls read:

$$\mathbf{n}^\top\mathbf{v} = 0, \tag{4}$$

where $\mathbf{n} = [\mathbf{n}_\perp; 0]$ is the normal vector. The system of differential equations (2a) and (2b) can be rewritten as follows

$$\begin{cases} h_{33}\dfrac{\partial p}{\partial x_3} = -\mathbf{h}_3^\top\nabla_\perp p + \mathrm{i}\omega v_3, \\ \dfrac{\partial(\mathrm{i}\omega v_3)}{\partial x_3} = -\omega^2 B^{-1}p - \mathrm{div}_\perp(\mathbf{h}_\perp\nabla_\perp p + \mathbf{h}_3\dfrac{\partial p}{\partial x_3}), \end{cases} \tag{5}$$

with the boundary condition

$$\mathbf{n}_\perp^\top(\mathbf{h}_\perp\nabla_\perp p + \mathbf{h}_3\frac{\partial p}{\partial x_3}) = 0. \tag{6}$$

Outside the layer, the problem reads

$$\begin{cases} (\Delta + \omega^2\rho_0 B_0^{-1})p = 0 \\ \mathbf{n}_\perp^\top\nabla_\perp p = 0 \end{cases} \tag{7}$$

2.2 Modal decomposition

The pressure p and the axial particle velocity v_3 are now expressed as the superposition of an infinite number of transverse modes $\psi_b(x_1, x_2)$, $b \in \mathbb{N}$:

$$p(x_1, x_2, x_3) = \sum_{b\in\mathbb{N}} \psi_b(x_1, x_2)p_b(x_3), \tag{8a}$$

$$\mathrm{i}\omega v_3(x_1, x_2, x_3) = \sum_{b\in\mathbb{N}} \psi_b(x_1, x_2)U_b(x_3), \tag{8b}$$

where

$$\psi_b(x_1,x_2) = g_m^{(w_1)}(x_1) g_n^{(w_2)}(x_2), \tag{9}$$

with $g_m^{(w)}(x) = \sqrt{\varepsilon_m/w}\cos(m\pi x/w)$, $\varepsilon_0 = 1$ and $\varepsilon_{n>0} = 2$. The modal functions $\psi_b(x_1,x_2)$, $b \in \mathbb{N}$, are the eigenfunctions obeying the transverse eigenproblem $\mathrm{div}_\perp(\nabla_\perp\psi_b) = -\gamma_b^2\psi_b$, with the boundary condition $\mathbf{n}_\perp^\top\nabla_\perp\psi_b = 0$. They form a complete orthonormal basis for the inner product $(f|g) = \int_{\mathcal{A}} \overline{f} g \mathrm{d}S$; i.e., $(\psi_a|\psi_b) = \delta_{ab}$. The modal decompositions in Eqs (8a) and (8b) can also be written as [15]

$$p = \boldsymbol{\psi}^\top \mathbf{p}, \tag{10a}$$

$$\mathrm{i}\omega v_3 = \boldsymbol{\psi}^\top \mathbf{u}, \tag{10b}$$

where $\mathbf{p}$, $\mathbf{u}$ and $\boldsymbol{\psi}$ are column vectors.

Equation (5) is now projected on the orthonormal basis $(\psi_a)_{a\in\mathbb{N}}$

$$\begin{cases} h_{33}p_a' = -\sum_{b\in\mathbb{N}} C_{ab}p_b + U_a, \\ U_a' = -\omega^2 B^{-1} p_a - \sum_{b\in\mathbb{N}} (D_{ab}p_b + \tilde{C}_{ab}p_b'), \end{cases} \tag{11}$$

where $C_{ab} = (\psi_a|\mathbf{h}_3^\top\nabla_\perp\psi_b)$, $\tilde{C}_{ab} = (\nabla_\perp\psi_a|\mathbf{h}_3\psi_b)$ and $D_{ab} = (\nabla_\perp\psi_a|\mathbf{h}_\perp\nabla_\perp\psi_b)$. This yields a system of differential equations in $\mathbf{p}$ and $\mathbf{u}$

$$\begin{pmatrix} h_{33}\mathbb{1} & \mathbb{0} \\ -\tilde{\mathbf{C}} & \mathbb{1} \end{pmatrix} \begin{pmatrix} \mathbf{p}' \\ \mathbf{u}' \end{pmatrix} = \begin{pmatrix} -\mathbf{C} & \mathbb{1} \\ -\omega^2 B^{-1}\mathbb{1} + \mathbf{D} & \mathbb{0} \end{pmatrix} \begin{pmatrix} \mathbf{p} \\ \mathbf{u} \end{pmatrix}, \tag{12}$$

which can be solved using several numerical strategies [14]. Equation (12) can be rewritten as

$$\mathbf{p}'' + \frac{1}{h_{33}}(\mathbf{C} - \tilde{\mathbf{C}})\mathbf{p}' + \left(\frac{\omega^2}{h_{33}B}\mathbb{1} - \frac{1}{h_{33}}\mathbf{D}\right)\mathbf{p} = 0. \tag{13}$$

3. ANALYTICAL SOLUTION

In this study, we consider the particular case in which the principal directions are rotated only around the longitudinal axis $\mathbf{e}_3$ of the tube (i.e., in the transverse plane). In this case, $\mathbf{h}_3 = \mathbf{0}$ so that $\mathbf{C} = \tilde{\mathbf{C}} = \mathbb{0}$ and Eq. (13) reads

$$\mathbf{p}'' = \mathbf{M}\mathbf{p}, \tag{14}$$

where $\mathbf{M} = -h_{33}^{-1}(\omega^2 B^{-1}\mathbb{1} - \mathbf{D})$. The matrix $\mathbf{M}$ is diagonalized according to

$$\mathbf{M} = \mathbf{Q}\boldsymbol{\Gamma}^2\mathbf{Q}^{-1}, \tag{15}$$

where $\boldsymbol{\Gamma}^2$ is the diagonal matrix of eigenvalues and $\mathbf{Q}$ is the associated matrix of eigenvectors. This yields the general solution:

$$\mathbf{p}(x_3) = \mathbf{Q}\mathrm{e}^{\boldsymbol{\Gamma}x_3}\mathbf{Q}^{-1}\mathbf{c}^+ + \mathbf{Q}\mathrm{e}^{\boldsymbol{\Gamma}(L-x_3)}\mathbf{Q}^{-1}\mathbf{c}^-. \tag{16}$$

Let us now consider an incident plane wave propagating towards the layer from the left (i.e., in the region $x_3 < 0$). The multimodal solution to the differential equation (7) reads

$$\mathbf{p}(x_3 < 0) = \mathrm{e}^{\rho_0\mathbf{Y}_c x_3}\mathbf{p}^{(i)} + \mathrm{e}^{-\rho_0\mathbf{Y}_c x_3}\mathbf{p}^{(r)}, \tag{17}$$

where $\mathbf{p}^{(i)}$ is a vector containing the modal components of the incident wave at $x_3 = 0$, $\mathbf{p}^{(r)} = \mathbf{R}\mathbf{p}^{(i)}$ contains the modal components of the reflected wave with $\mathbf{R}$ the reflection matrix, and

$$\mathbf{Y}_{cab} = \frac{\mathrm{i}}{\rho_0}\sqrt{\omega^2\frac{\rho_0}{B_0} - \gamma_a^2}\delta_{ab} \tag{18}$$

is the characteristic admittance of the waveguide. In the region $x_3 > L$, the transmitted sound pressure reads

$$\mathbf{p}(x_3 > L) = \mathrm{e}^{\rho_0\mathbf{Y}_c(x_3-L)}\mathbf{p}^{(t)}, \tag{19}$$

where $\mathbf{p}^{(t)} = \mathbf{T}\mathbf{p}^{(i)}$ contains the modal components of the transmitted wave with $\mathbf{T}$ the transmission matrix.

The scattering matrix can be written as

$$\mathbf{S} = \begin{pmatrix} \mathbf{R} & \mathbf{T}' \\ \mathbf{T} & \mathbf{R}' \end{pmatrix}, \tag{20}$$

where $\mathbf{R}$ and $\mathbf{T}$ are the reflection and transmission matrices for a right-going incident wave (i.e., propagating towards the layer from the left), and $\mathbf{R}'$ and $\mathbf{T}'$ are the reflection and transmission matrices for a left-going incident wave (i.e., propagating towards the layer from the right). Since $\mathbf{h}_3 = \mathbf{0}$, we have $\mathbf{R} = \mathbf{R}'$ and $\mathbf{T} = \mathbf{T}'$. The matrices $\mathbf{R}$ and $\mathbf{T}$ are obtained from the continuity of the pressure and normal component of the particle velocity at $x_3 = 0$ and $x_3 = L$, and read:

$$\begin{cases} \mathbf{R} = (\mathbf{Y}_c + \mathbf{Y}_0)^{-1}(\mathbf{Y}_c - \mathbf{Y}_0), \\ \mathbf{T} = \mathbf{T}_r(\mathbb{1} - \mathbf{H}\mathbf{R}_l\mathbf{H}\mathbf{R}_r)^{-1}\mathbf{H}\mathbf{T}_l, \end{cases} \tag{21}$$

where $\mathbf{Y}_0 = \tilde{\mathbf{Y}}_c(\mathbb{1} - \mathbf{H}\mathbf{R}_r\mathbf{H})(\mathbb{1} + \mathbf{H}\mathbf{R}_r\mathbf{H})^{-1}$ is the admittance matrix at $x_3 = 0$, $\tilde{\mathbf{Y}}_c = h_{33}\mathbf{Q}\boldsymbol{\Gamma}\mathbf{Q}^{-1}$, $\mathbf{H} = \mathbf{Q}\mathrm{e}^{\boldsymbol{\Gamma}L}\mathbf{Q}^{-1}$, $\mathbf{R}_r = \mathbf{R}_l = (\tilde{\mathbf{Y}}_c + \mathbf{Y}_c)^{-1}(\tilde{\mathbf{Y}}_c - \mathbf{Y}_c)$, $\mathbf{T}_r = (\mathbf{Y}_c + \tilde{\mathbf{Y}}_c)2\tilde{\mathbf{Y}}_c$, and $\mathbf{T}_l = (\mathbf{Y}_c + \tilde{\mathbf{Y}}_c)2\mathbf{Y}_c$.

4. NUMERICAL RESULTS

The validity of the method is examined numerically on a synthetic anisotropic sample with known porous properties. Based on the reflection and transmission matrices derived in Sect. 3, the procedure described in [9] and [10] is applied to retrieve the bulk modulus B and the coefficients h_{11}, h_{12}, h_{22} and h_{33} of the inverse density tensor. The results were not available at the time of writing.

5. CONCLUSION

A multimodal method for the characterization of anisotropy in porous media has been formulated. The method is based on the inversion of the scattering matrix to retrieve the effective fluid parameters from multimodal reflection and transmission coefficients measured in an impedance tube.

6. ACKNOWLEDGMENTS

This work was funded by the Independent Research Fund Denmark under the DFF Individual International Postdoctoral Grant 1031-00012.

7. REFERENCES

[1] A. M. Nicolson and G. F. Ross, "Measurement of the intrinsic properties of materials by time-domain techniques," *IEEE Trans. Instrum. Meas.*, vol. 19, p. 377–382, 1970.

[2] B. H. Song and J. S. Bolton, "A transfer-matrix approach for estimating the characteristic impedance and wave numbers of limp and rigid porous materials," *J. Acoust. Soc. Am.*, vol. 107, no. 3, p. 1131–1152, 2000.

[3] D. L. Johnson, J. Koplik, and R. Dashen, "Theory of dynamic permeability and tortuosity in fluid saturated porous media," *J. Fluid Mech.*, vol. 176, p. 379–402, 1987.

[4] Z. Li, K. Aydin, and E. Ozbay, "Determination of the effective constitutive parameters of bi-anisotropic materials from reflection and transmission coefficients," *Phys. Rev. E*, vol. 79, p. 026610, 2009.

[5] A. H. Jiang, J. A. Bossard, X. Wang, and D. H. Werner, "Synthesizing metamaterials with angularly independent effective medium properties based on an anisotropic parameter retrieval technique coupled with a genetic algorithm," *J. Appl. Phys.*, vol. 109, p. 013515, 2011.

[6] A. Castanié, J.-F. Mercier, S. Félix, and A. Maurel, "Generalized method for retrieving effective parameters of anisotropic materials," *Opt. Express*, vol. 22, p. 2937–2953, 2014.

[7] J. H. Park, H. J. Lee, and Y. Y. Kim, "Characterization of anisotropic acoustic metamaterial slabs," *J. Appl. Phys.*, vol. 119, p. 034901, 2016.

[8] M. Berzborn and M. Vorländer, "Inference of the acoustic properties of transversely isotorpic porous materials," in *Proc. of Internoise 2024*, (Nantes, France), 2024.

[9] A. Terroir, L. Schwan, T. Cavalieri, V. Romero-García, G. Gabard, and J.-P. Groby, "General method to retrieve all effective acoustic properties of fully anisotropic fluid materials in three-dimensional space," *J. Appl. Phys.*, vol. 125, p. 025114, 2019.

[10] T. Cavalieri, M. Nolan, M. Gaborit, and J.-P. Groby, "Experimental characterization of fully-anisotropic equivalent fluids from normal incidence measurements," *J. Sound Vib.*, vol. 608, p. 119051, 2025.

[11] V. Pagneux, N. Amir, and J. Kergomard, "A study of wave propagation in varying cross-section waveguides by modal decomposition. part i. theory and validation," *J. Acoust. Soc. Am.*, vol. 100, no. 4, pp. 2034–2048, 1996.

[12] S. Félix and V. Pagneux, "Sound propagation in rigid bends: A multimodal approach," *J. Acoust. Soc. Am.*, vol. 110, no. 3, p. 1329–1337, 2001.

[13] J. Prisutova, K. Horoshenkov, J.-P. Groby, and B. Brouard, "A method to determine the acoustic reflection and absorption coefficients of porous media by using modal dispersion in a waveguide," *J. Acoust. Soc. Am.*, vol. 136, no. 6, pp. 2947–2958, 2014.

[14] A. Maurel, J.-F. Mercier, and S. Félix, "Modal method for the 2d wave propagation in heterogeneous anisotropic media," *J. Opt. Soc. Am. A*, vol. 32, no. 5, pp. 979–990, 2015.

[15] S. Félix and V. Pagneux, "Multimodal analysis of acoustic propagation in three-dimensional bends," *Wave Motion*, vol. 36, pp. 157–168, 2002.

DOI: 10.61782/fa.2025.0211

FORUM ACUSTICUM EURONOISE 2025

COMBINING ABSORPTION COEFFICIENT MEASUREMENTS IN REVERBERATION ROOMS WITH DIFFERENT VOLUMES

Heinrich Bietz[1*] **Volker Wittstock**[1]
[1]Physikalisch-Technische Bundesanstalt, Germany

ABSTRACT

One way to reduce the uncertainty of absorption coefficient measurements in reverberation rooms could be the combination of measurement results from rooms with different volumes. To investigate this, a round robin was conducted at PTB using two regular reverberation rooms and five rooms of 50 m³ volume which belong to the building acoustic test stands of PTB. The diffusivity was adjusted following the procedure described in ISO 345. Eight samples were measured in each room employing different staff and equipment, so the results can be regarded as statistically independent. The results show that the "50 m³" rooms deliver reasonable absorption coefficients over a wide frequency range, but in most cases fail at frequencies below 250 Hz. Furthermore, the approach taken to reduce the uncertainty by combining results from two rooms with different volumes provided promising results. One drawback certainly is the small database produced by the round robin; further research is necessary to support the findings presented in this article.

Keywords: *absorption coefficient, reverberation room, room volume, uncertainty, ISO 354.*

1. INTRODUCTION

The measurement of absorption coefficients α_s in reverberation rooms with a volume of at least 150 m³ (200 m³ for newly built rooms) is standardized in ISO 354 [1] at frequencies between 100 Hz and 5 kHz. ISO 12999-2 [2] describes a procedure to assess the uncertainty of these measurements. The uncertainty here is defined as the standard deviation of reproducibility σ_R, which is expressed as a linear relation:

$$\sigma_R = m\alpha_S + n \quad (1)$$

where the slope m and the offset n are frequency dependent constants which had been derived by evaluating a large amount of round robin data from the last decades [3]. The uncertainty can also be expressed as relative uncertainty in decibels, which may be useful for practical applications:

$$u(L_{\alpha s}) = 10\,\mathrm{lg}(1 + \sigma_R/\alpha_s)\ \mathrm{dB} \quad (2)$$

The resulting relative uncertainties are shown in Fig. 1 [4]. They increase at both ends of the frequency range, whereas the influence of the absorption coefficient is much more pronounced at higher frequencies.

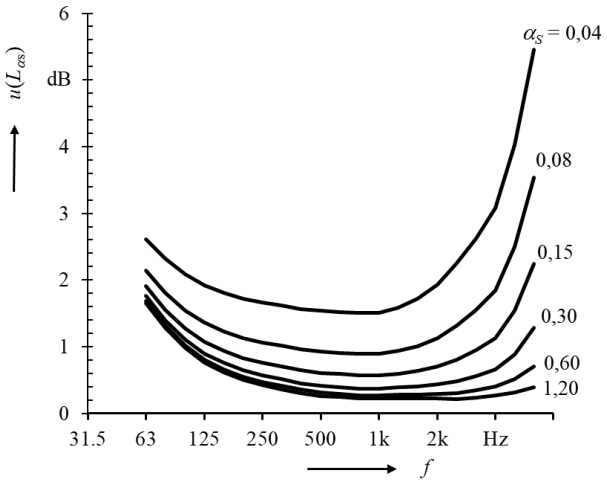


Figure 1. Relative uncertainty of α_s.

*Corresponding author: heinrich.bietz@ptb.de.
Copyright: ©2025 Heinrich Bietz et al. This is an open-access article distributed under the terms of the Creative Commons Attribution 3.0 Unported License, which permits unrestricted use, distribution, and reproduction in any medium, provided the original author and source are credited.

For certain applications, e.g. prediction of the speech transmission index (STI), an extension of the frequency range up to 10 kHz is sometimes desirable. As the large uncertainties at high frequencies are commonly attributed to air absorption, one possible way of improvement could be the use of a reverberation room with a smaller volume. If i.e. a room volume of 50 m³ is chosen, this would in theory cause a frequency shift of the figures *m* and *n* from Eqn. (1) and thus also of the relative uncertainty in Fig. 1. For low frequencies, modal density is assumed as the governing factor. We then get

$$\frac{f_2}{f_1} = \frac{\sqrt[3]{V_1}}{\sqrt[3]{V_2}} = 2^{2}/_{3} \text{ when } \frac{V_1}{V_2} = \frac{200}{50} = 2^2, \quad (3)$$

so *m* and *n* would be shifted upwards by two 1/3 octave bands. For high frequencies, air absorption is assumed as the dominant factor influencing the uncertainty. With

$$\frac{4m_1V_1}{\alpha_1 S_1} = \frac{4m_2V_2}{\alpha_2 S_2} \quad (4)$$

where $m_{1/2}$, are the air damping constants in rooms with volumes $V_{1/2}$, $\alpha_{1/2}$ the absorption coefficient of the samples of size $S_{1/2}$ to be measured and the assumption

$$\frac{m_1}{m_2} = \left(\frac{f_1}{f_2}\right)^2, \quad (5)$$

we finally get

$$\frac{f_2}{f_1} = 2^{1}/_{3} \quad (6)$$

under the assumption that the absorption coefficient α to be measured does not change at high frequencies. As a result, the uncertainty at high frequencies would be shifted by one 1/3 octave band to higher frequencies. It must be pointed out that these considerations include numerous simplifications, and the uncertainty is probably influenced by further effects. For the first investigation concerning these aspects, an internal round robin was conducted at PTB.

2. INTERNAL ROUND ROBIN

2.1 Scope

For the round robin, five rooms, all parts of building acoustics test stands, were used. The room volume ranged from 49 m³ to 58 m³. Eight different test samples were examined. In each room, these samples were measured by a different member of the working group staff with mostly different equipment. In addition, one member of the staff measured the samples in all test rooms, and in two reverberation rooms with 204 m³ and 237 m³ volume. For the measurements in the "50 m³" rooms, the area (or number) of the samples was scaled down accordingly, resulting in a sample area of about 4 m².

2.2 Test samples

As the uncertainty is directly dependent on the absorption coefficient, the samples were selected to cover a wide range of absorption coefficients. Tbl. 1 gives an overview of the employed samples. "Poly" refers to absorbers consisting of six rectangular metal frames with a thickness of 100 mm, and filled with a polyester fleece, which has absorbent properties like mineral wool. One side is open, and one side is covered with coated chipboard, which has a thickness of 8 mm for three boxes and 16 mm for the remaining boxes. These boxes were used to create six different absorber setups. For three setups, the boxes were laid out in a 2 x 3 configuration to create an absorber area. For the other three setups, three individual elements, each made of two boxes standing together upright, were realised.

Table 1. Absorbers used in internal round robin

Absorber	Description	Area in m²
WG 35	200 mm mineral wool with wooden frame, like reference absorber suggested by WG 35	4,3
Carpet	Carpeted floor 10 mm thick	3,9
Poly 1	Flat, all open sides upwards	4,3
Poly 2	Flat, 3 open sides and 3 8 mm chipboards upwards	4,3
Poly 3	Flat, all chipboard sides upwards	4,3
Poly 4	Single elements, both outward sides open	4,3
Poly 5	Single elements, 1 outward side open and 1 outward side 8 mm chipboard	4,3
Poly 6	Single elements, both outward sides chipboard	4,3

2.3 Preparation of the test rooms

The test rooms were fitted with diffusers following Annex A of ISO 354. Here, using a broadband absorber, an increasing number of diffusers is employed until a certain saturation of the absorption coefficient is realised. All absorbers that may have been present have been removed beforehand. Polycarbonate sheets with an area of 1,48 m x 0,9 m and 4 mm thickness were used as diffusers. A 100 mm thick, porous absorber with an area of 4,5 m² has been used for the diffusivity test. The rooms were finally fitted with five or 6 absorbers, making up (double-sided) between 15 % and 18 % of the room surface. An example for the qualification test is shown in Fig. 2.

ISO 354 specifies an upper limit for the equivalent absorption area A_1 of the empty room. Fig. 3 shows A_1 for rooms 1-5. The red line is the upper limit as specified by ISO 354 with frequency and magnitude adjusted for 50 m³ room volume. While three rooms stay well under the maximum limit, Room 3 exceeds the limits at some frequencies, and Room 1 is far beyond. Room 1 has some features different from all other rooms: The floor is fitted with a floating screed, the brickwork walls are not painted, and an opening to accommodate windows or glazings is covered with a chipboard laminated with lead. Room 2 and Room 3 are source and receiving room of a building acoustics test stand where a plastered lime brick wall (440 kg m²) was installed in the test opening. It could not be clarified why Room 3 has a significantly higher A_1. It was decided to nevertheless include all 5 rooms in the round robin for the moment to see if the results show noticeable deviations.

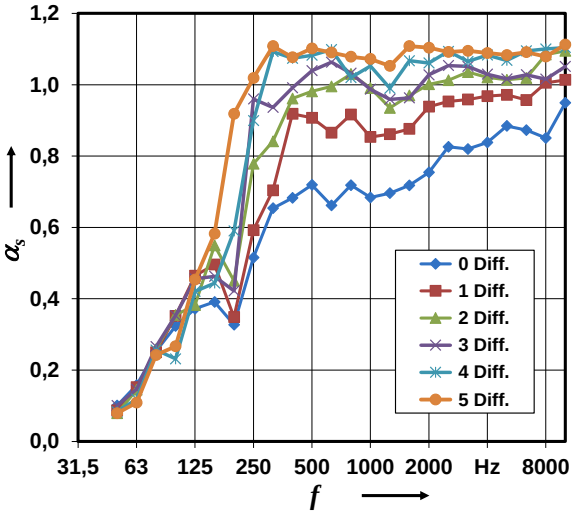


Figure 2. Example of a diffusivity test.

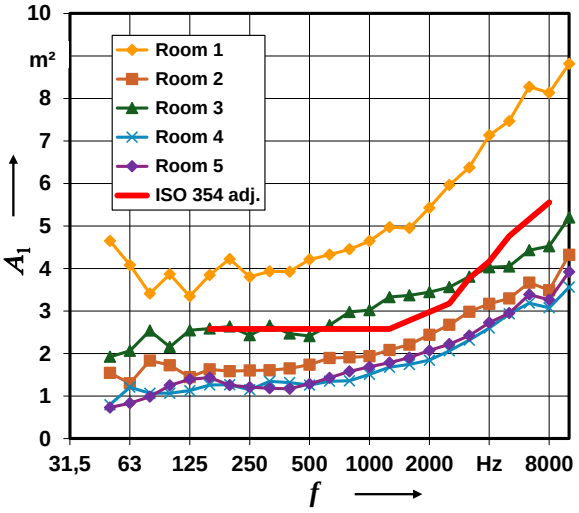


Figure 3. Equivalent absorption areas of empty rooms. ISO 354 specification adjusted for V = 50 m³.

2.4 Measurement results

The participants were requested to observe the specifications of ISO 354 as close as possible. In some cases, compromises were necessary due to the smaller room volume. Fig. 4 – Fig. 7 show some examples of the results.

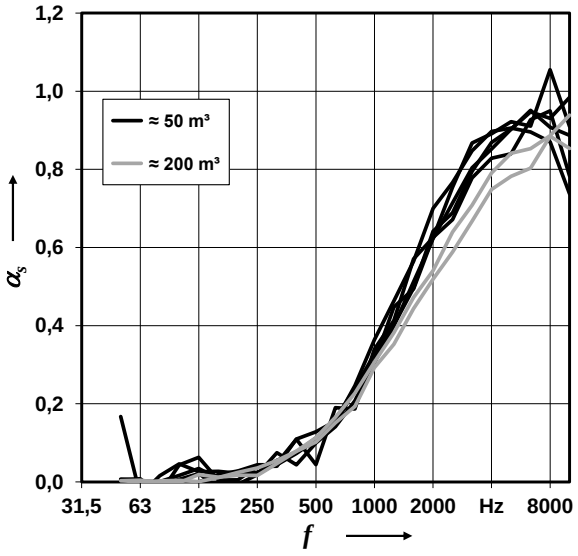


Figure 4. Absorption coefficients of carpet floor sample.

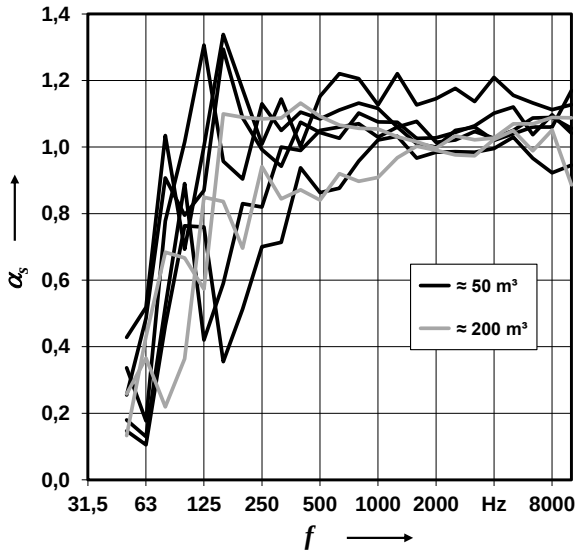


Figure 5. Absorption coefficients of 200 mm mineral wool absorber ("WG 35").

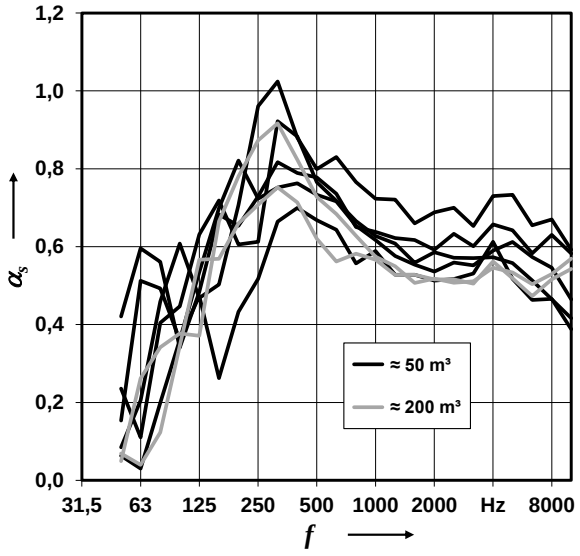


Figure 6. Absorption coefficients of Poly 2 sample.

It turned out that Room 1 delivered outlying results for the setups with individual elements ("Poly 4" – "Poly 6"). It was decided to not include these results for the statistical evaluation of the uncertainty coefficients, but to keep the data of the other absorber setups, because the data base is poor anyway.

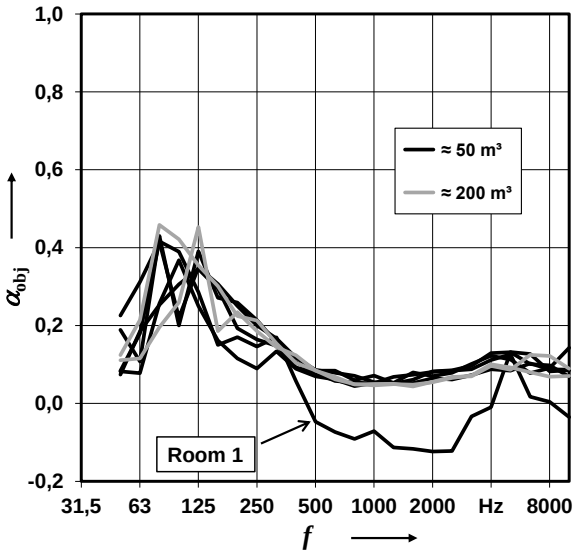


Figure 7. Absorption coefficients of Poly 6 sample.

3. EVALUATION OF RESULTS

3.1 Determination of coefficients *m* and *n*

The determination of the uncertainty coefficients follows the procedure described in [3], although the data base is much smaller. The average values for the individual samples and the respective standard deviations have been calculated and are shown in Fig. 8 and Fig. 9.

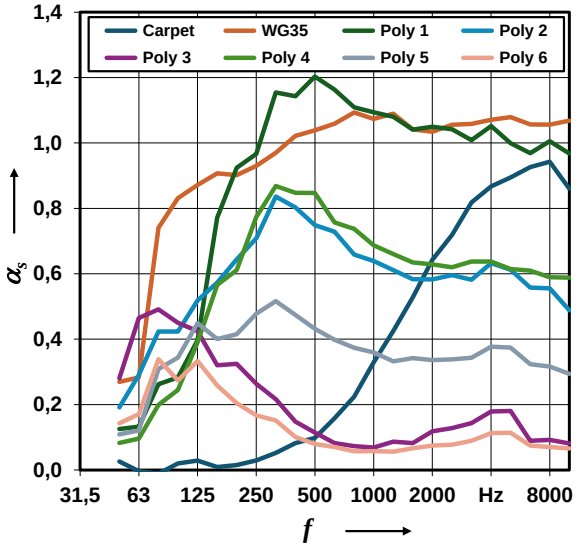


Figure 8. Average Absorption coefficients of individual samples.

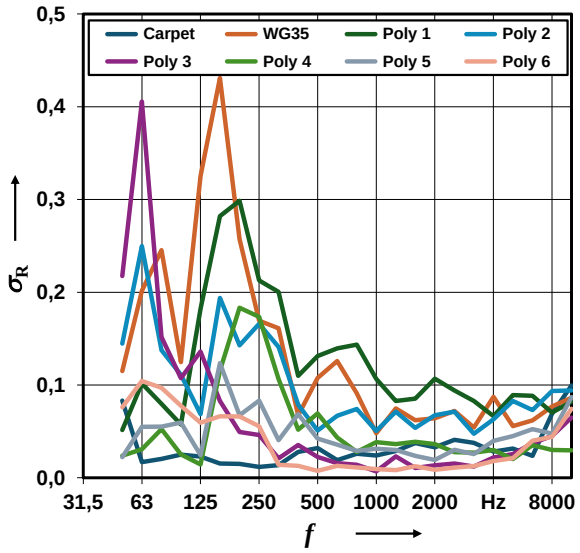


Figure 9. Standard deviation of reproducibility.

With this input data, it is now possible to determine the coefficients *m* and *n* from Eqn. (1) by linear regression. Fig. 10 gives an example for two one-third octave bands. For 125 Hz the correlation is quite low, as was to be expected regarding the small room volume and the low number of input data. For 1 kHz the correlation is much better. Finally, Fig. 11 and Fig. 12 show the coefficients obtained by the round robin data compared with those from [3], both in original form and shifted upwards by two one-third octave bands over the entire frequency range.

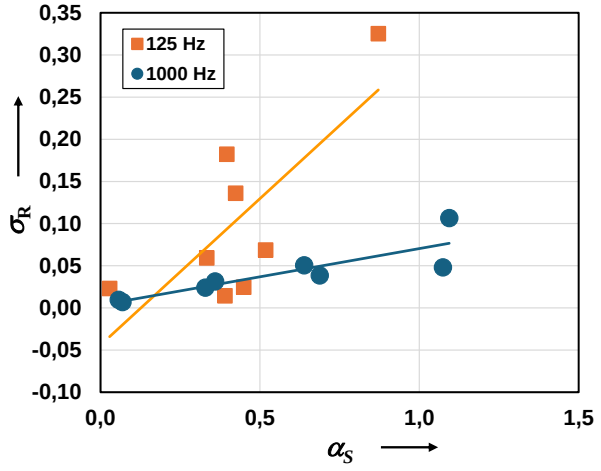


Figure 10. Obtaining *m* and *n* by linear regression.

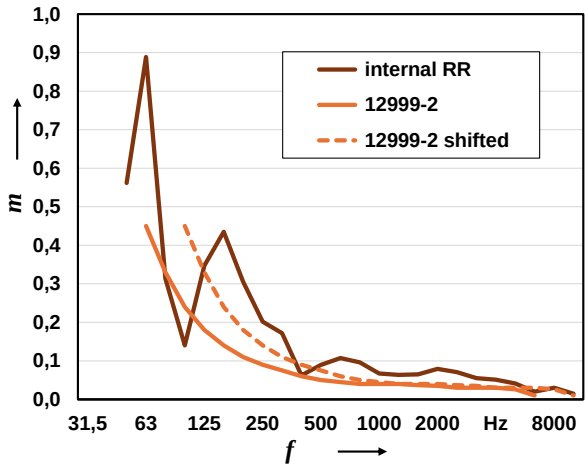


Figure 11. Results for coefficient *m*.

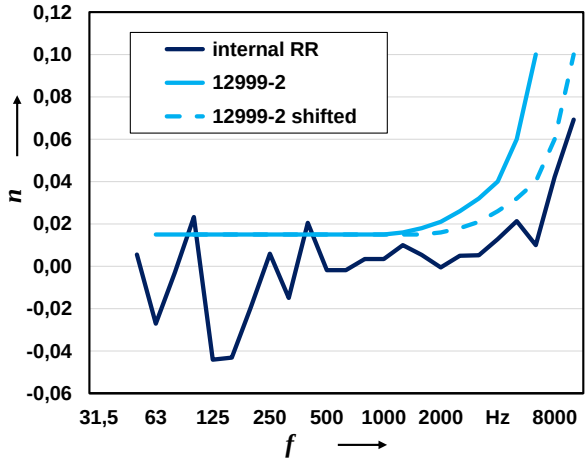


Figure 12. Results for coefficient *n*.

Regarding the low number of measurements considered, it seems to be reasonable to shift the values *m* and *n* from [3] by two one-third octave bands for a room size of 50 m³.

3.2 Combining results from different room volumes.

If the shifted values for *m* and *n* reasonably reflect the uncertainty for 50 m³ rooms, it should be possible to reduce the uncertainty by combining the results from two rooms of different size. In the frequency range where the original uncertainty $\sigma_{R,200}$ and the shifted uncertainty $\sigma_{R,50}$ are overlapping, the combined uncertainty is

$$\sigma_{R,\mathrm{comb}} = \frac{\sqrt{{\sigma_{R,200}}^2 + {\sigma_{R,50}}^2}}{2}. \qquad (7)$$

This would be possible at the one-third octave bands from 100 Hz to 6300 Hz. In the case that both individual uncertainties $\sigma_{R,200}$ and $\sigma_{R,50}$ are equal, $\sigma_{R,\mathrm{comb}}$ will be smaller than $\sigma_{R,200}$ and $\sigma_{R,50}$ by a factor of about 0,71 according to Eqn. (7). Fig. 13 and Fig. 14 illustrate the combination process. Fig. 13 shows the absorption coefficients for the "WG35" sample measured in both a "200 m³" room and a "50 m³" room, and the resulting average. The influence of the edge effect resulting from different sample sizes was not taken into account but should be considered in future research. The resulting uncertainties for the individual measurements and the combined uncertainty are shown in Fig. 14. For the calculation, the coefficients *m* and *n* from ISO 12999-2 were used shifted by two one-third octave bands for the 50 m³ room.

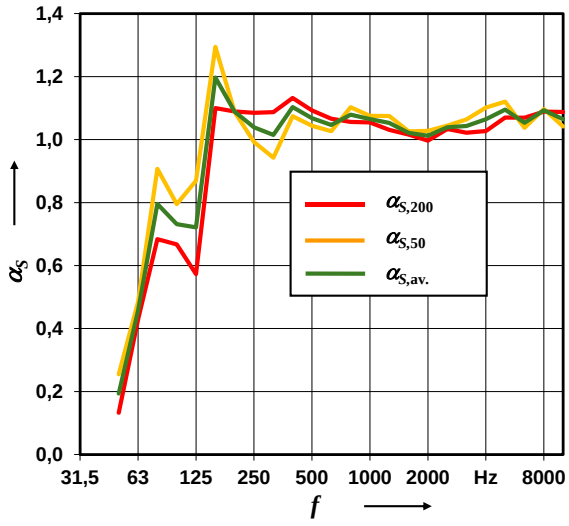


Figure 13: Example for individual and averaged absorption coefficient of "WG35" sample.

This example shows that for most one-third octave bands, the uncertainty of the reverberation room measurement is reduced. To get an idea of how the combination of uncertainties affects the overall uncertainty for all samples and room combinations, a stepwise evaluation procedure has been carried out. In a first step, for each sample the combined uncertainty was calculated for all ten possible combinations of "200 m³" and "50 m³" rooms (eight for the individual objects) using Eqn. (7), displayed in Fig. 15 as grey curves for the "WG35" sample.

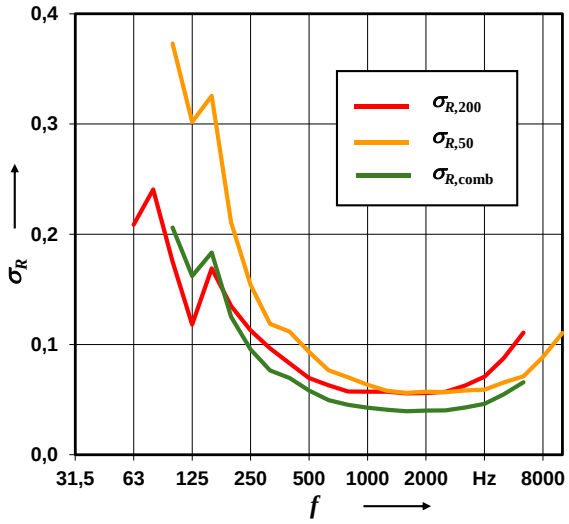


Figure 14: Respective individual and combined uncertainties for the absorption coefficients shown in Fig. 13.

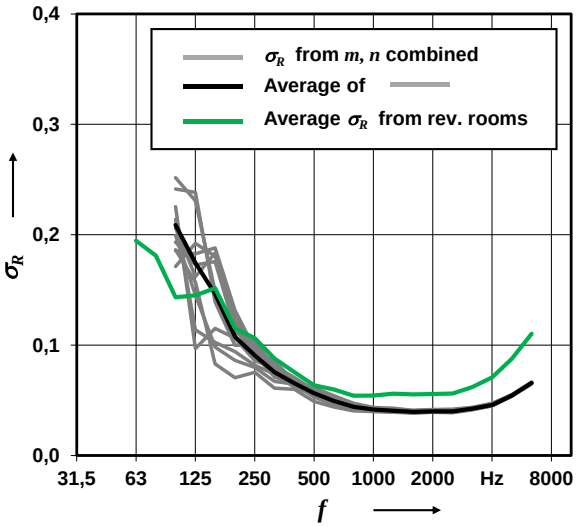


Figure 15: Combined uncertainties for "WG35" sample and average uncertainty of reverberation room measurements.

From these values the root mean square (black curve) was calculated, representing the average uncertainty $\sigma_{R,\mathrm{comb}}$ that can be achieved by combining the different room volumes.

The green curve shows the root mean square of the uncertainties $\sigma_{R,\text{rev rooms}}$ from the two reverberation room measurements which is our best estimate of the uncertainty of a single measurement in a reverberation room.

As a result, the ratio of $\sigma_{R,\text{comb}}$ to $\sigma_{R,\text{rev rooms}}$ expresses the average reduction (if < 1) or increase (if > 1) of the uncertainty that results from the combination of absorption coefficient measurements in two different (nominal 200 m³ and 50 m³) room volumes in relation to a single measurement in a standardized reverberation room. This is displayed in Fig. 16 for all eight samples.

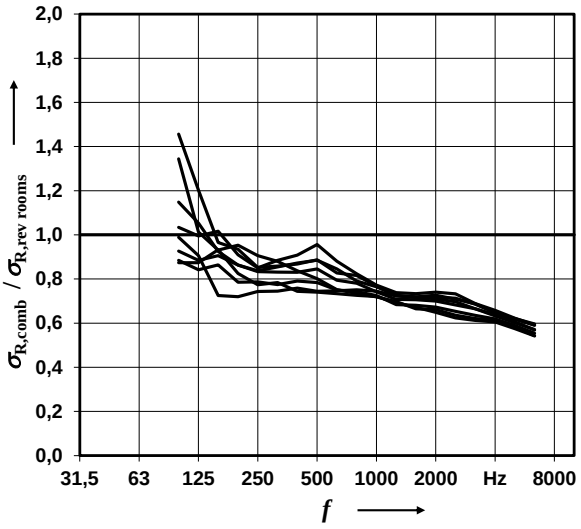


Figure 16: Ratio of $\sigma_{R,\text{comb}}$ to $\sigma_{R,\text{rev rooms}}$ for all samples.

A general reduction of the uncertainty is observed for all samples for all frequencies above 160 Hz. Above 1 kHz the results are quite uniform. A significant reduction of about a factor of 0,6 can be achieved at 6,3 kHz. Above this frequency, the combination is not possible because the coefficients *m* and *n* are not available. It should be mentioned again that of course all these considerations are based on a very small set of data, and further research on the topic is necessary.

4. CONCLUSION

An internal round robin conducted at PTB showed that measurement rooms with a volume in the range of 50 m³ deliver reasonable results for the absorption coefficient α_s, provided that the diffusivity of the rooms is adjusted properly. It was further shown that a combination of the results from the "50 m³" rooms with results from standardized reverberation rooms leads to a reduced uncertainty with respect to a single measurement in a reverberation room, especially at higher frequencies. However, given the very small amount of data this research is based on, further investigations are necessary to verify the presented findings. This also applies to the influence of the edge effect when results from different room sizes are compared.

5. ACKNOWLEDGMENTS

The authors gratefully acknowledge the contributions of all members of PTB's working group "Applied Acoustics", in particular Kevin Picker, Martin Schmelzer and Sylvia Stange-Kölling.

6. REFERENCES

[1] ISO 354: 2003: Acoustics – Measurement of sound absorption in a reverberation room.

[2] ISO 12999-2: 2020: Acoustics – Determination and application of measurement uncertainties in building acoustics – Part 2: Sound absorption.

[3] V. Wittstock: "Determination of Measurement Uncertainties in Building Acoustics by Interlaboratory Tests. Part 2: Sound Absorption Measured in Reverberation Rooms," *Acustica united with Acta Acustica*, vol. 104, pp. 999–1008, 2018.

[4] V. Wittstock: "How uncertain is the sound absorption measured in reverberation rooms compared to other acoustic measurements?" *Proc. DAGA 2022*, Stuttgart, pp. 747 - 750, 2022.

DOI: 10.61782/fa.2025.0133



FORUM ACUSTICUM
EURONOISE 2025

ANALYSIS OF THE RELATIONSHIP BETWEEN SOUND FIELD ISOTROPY AND ERRORS IN THE RESULTS OF SABINE'S ABSORPTION COEFFICIENT.

Marco Berzborn and Michael Vorländer
Institute for Hearing Technology and Acoustics, RWTH Aachen University, Germany

ABSTRACT

Sabine's absorption coefficient is measured in a reverberation rooms under the assumption of a diffuse sound field. Recently multiple authors presented experimentally approaches using microphone arrays to quantify sound field diffuseness within the context of absorption measurements, indeed highlighting the lack of a diffuse sound field for specific lab environments and frequency bands. This was found to be especially prominent when the absorbing test specimen is mounted in the room.
This work presents a combined factor analysis and linear regression model to investigate the relationship between the results of the aforementioned diffuseness quantification methods and the error in Sabine's absorption coefficient. A numerically predicted finite size absorption coefficient serves as ground truth to calculate the relative error in the absorption coefficient. Finally, the suitability of the model to correct the measurements of Sabine's absorption coefficient is analyzed.

Keywords: reverberation, directional energy decay, microphone array

1. INTRODUCTION

The measurement of Sabine's absorption coefficient according to ISO354:2003 [1] is performed in a reverberation room under the assumption of a diffuse sound field. While the method is widely used since the 1920s, it is well known to suffer from a poor reproducibility between laboratories. This has been shown in several inter-laboratory studies, see for example Refs. [2] and [3]. See Ref. [4] for a overview of the issues associated with the measurement of Sabine's absorption coefficient. Recent studies studies have indeed shown that the sound field in reverberation rooms is indeed not perfectly diffuse, or more precisely not isotropic [5], [6] This was found to be especially prominent when the absorbing specimen is mounted in the room.
To statistically investigate the relationship between the isotropy condition of the sound field in the laboratory and the error in Sabine's absorption coefficient which is calculated as per ISO354:2003 [1] a regression model is developed in this work. The input and output data-sets, as well as the regression model are derived in Section 2. The experimental setup consisting of three different laboratory conditions is described in Section 3. Section 4 and Section 5 present the implementation of the regression model and the results, respectively, followed by a conclusion in Section 6.

*__Corresponding author__: mbe@akustik.rwth-aachen.de.
__Copyright__: ©2025 Marco Berzborn et al. This is an open-access article distributed under the terms of the Creative Commons Attribution 3.0 Unported License, which permits unrestricted use, distribution, and reproduction in any medium, provided the original author and source are credited.

2. MODEL

2.1 Target Variables

As target variables for the regression model developed in this section, the relative error in Sabine's absorption coefficients are used. These are computed for the T_{20}, T_{30}, and T_{40} regression intervals

$$\varepsilon_j = \frac{\bar{\alpha}_j - \tilde{\alpha}}{\tilde{\alpha}}, \quad j \in \{20, 30, 40\}, \tag{1}$$

where $\tilde{\alpha}$ is a reference finite-size random-incidence absorption coefficient estimated using a combined finite element and boundary element method simulation similar to Ref. [7]. Material parameters were inferred from

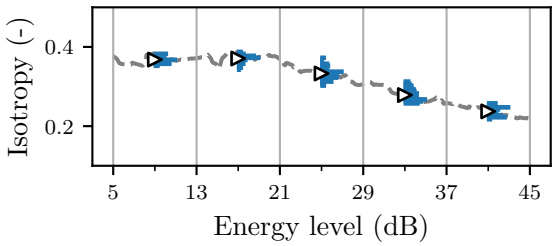


Figure 1: Isotropy evolution (- - -) as function of the decay level as well as the histogram (▬) of the indicated 8 dB intervals and their respective mean (▷).

impedance tube measurements using the method presented in Ref. [8]. Here, the relative error is chosen as it is independent from the absolute magnitude of the absorption coefficient.

2.2 Input Variables

The input data for the model is derived from the temporal evolution of estimators for sound field isotropy and axial symmetry. These estimators are calculated according to Berzborn *et al.* [9]. The isotropy estimator is based on Ref. [5] and the axial symmetry estimator is inspired by the work of Jammalamadaka and Terdik [10]. Both quantifiers are linearly interpolated to a common scale proportional to the decay level of the respective omnidirectional Energy Decay Curve (EDC). This normalization also aligns the evolution of the quantifiers with the reverberation time evaluation ranges. In addition to the estimator magnitude, their rate of change is of interest as well. This information is captured in the first derivative of the quantifiers with respect to the energy level.

The quantifiers are averaged over decay level intervals of 8 dB. The interval is chosen small enough such that the distributions of the data within the interval is uni-modal and is well represented by its mean. In agreement with ISO354:2003 [1], the initial 5 dB of the decay process are excluded from the analysis. The lowest energy level used is -45 dB due to the limited dynamic range of the Directional Energy Decay Curve (DEDC) measurements. An example of the process for the isotropy evolution is given in Fig. 1. Derivatives are typically sufficiently represented by averaging over the entire decay process.

This results in 12 input variables for each frequency band and room configuration. In the following, a matrix $\mathbf{\Gamma} \in \mathbb{R}^{12\times O}$ is constructed by stacking the vectors $\boldsymbol{\gamma}$ for all rooms and frequency bands. To ensure equal weighting of the symmetry quantifiers and their derivatives, the data are normalized to zero mean and unit variance Yong and Pearce [11].

2.3 Factor Analysis Regression

Since the symmetry quantifiers are derived from the same underlying data, they are expected to be correlated. The correlation is expected to be even stronger for cases where consecutive segmentation intervals show similar mean values, as is the case for configurations and frequency bands with uniform damping distribution. In order to identify a set of underlying latent variables and at the same time reduce the dimensionality of the input data vector a factor analysis is performed. The factor analysis is designed to explain the matrix of observations by a linear combination of the latent variables. In matrix notation, the factor analysis model can be written as [11]

$$\mathbf{\Gamma} = \mathbf{\Psi}\mathbf{Z} + \mathbf{N}, \tag{2}$$

where $\mathbf{\Psi} \in \mathbb{R}^{12\times Z}$ is the factor loading matrix, $\mathbf{Z} \in \mathbb{R}^{Z\times O}$ is the matrix of latent variables, and $\mathbf{N} \in \mathbb{R}^{12\times O}$ is an additive residual error matrix. The factor loading matrix is estimated iteratively from the correlation matrix of the input data using orthogonal *quartimax* rotations.

Assuming a linear relationship between the latent variables and the absorption coefficient error, a multiple linear regression model is used, which is expressed as

$$\boldsymbol{\varepsilon} = \boldsymbol{\beta}\hat{\mathbf{Z}} + \mathbf{n}_\varepsilon, \tag{3}$$

where $\boldsymbol{\varepsilon} \in \mathbb{R}^{3\times O}$ is the matrix containing the stacked vectors of absorption coefficient errors calculated for the three reverberation time intervals, $\boldsymbol{\beta} \in \mathbb{R}^{Z}$ is the vector of regression coefficients

$$\boldsymbol{\beta} = [\beta_0, \beta_1, \ldots, \beta_Z]^\mathsf{T}, \tag{4}$$

where β_0 is the intercept and $\mathbf{n}_\varepsilon \in \mathbb{R}^{O}$ represents the additive modeling error. The matrix $\hat{\mathbf{Z}}$ is obtained by adding a column of ones to the matrix of latent variables $\mathbf{Z}$ to account for the intercept term.

2.4 Absorption Coefficient Prediction

Once the factor loading matrix and the regression coefficients are identified, the model can re-arranged to predict a corrected version of Sabine's absorption coefficient based on the symmetry quantifiers. Replacing the reference absorption coefficient $\tilde{\alpha}$ in Eq. (1) with the predicted

absorption coefficient $\hat{\alpha}_j$, the corrected absorption coefficient can be computed as

$$\hat{\alpha}_j = \bar{\alpha}_j(1+\varepsilon_j) \quad j \in \{20, 30, 40\}. \tag{5}$$

Substituting Eq. (3) into Eq. (5) results in

$$\hat{\boldsymbol{\alpha}} = \bar{\boldsymbol{\alpha}} \odot \left(1 + \boldsymbol{\beta}\hat{\mathbf{Z}}\right), \tag{6}$$

where $\hat{\boldsymbol{\alpha}} \in \mathbb{R}^{3\times O}$ and $\bar{\boldsymbol{\alpha}} \in \mathbb{R}^{3\times O}$ are the matrices containing the corrected and measured absorption coefficients, respectively, and $\odot$ denotes the Hadamard product.

3. EXPERIMENTAL SETUP

The spherical and axial symmetry quantifiers were computed from experimental data captured in three different laboratory conditions: A rectangular reverberation room with volume $245\,\mathrm{m}^3$ in a configuration including 22 panel diffusers and a second configuration without any diffuser treatment – referred to as room no. 1 – and a second reverberation room with volume $215\,\mathrm{m}^3$ equipped with a combination of 12 panel and 85 boundary diffusers – referred to as room no. 2. The same glass-wool test specimen with $10.8\,\mathrm{m}^2$ was used in all laboratory conditions.

A Universal Robots UR5 scanning robotic arm was used to sequentially sample a dual-radius spherical microphone array. The sequential microphone array consists of a total of 310 sampling positions including interior points to stabilize the eigenfrequencies of the sphere. Their positions were calculated using the algorithm proposed by Chardon *et al.* [12]. Three different receiver positions were used in room no. 1, while only two receiver positions were used in room no. 2. For each condition, a single source position was used. The procedure to calculate the symmetry quantifiers is outlined in Ref. [9].

The reverberation time used to estimate the respective absorption coefficients was calculated from the omnidirectional EDC at the center position of the microphone array. Instead of using an additional measurement, the omnidirectional EDC was computed as the Schroeder [13] integral of the monopole moment of the omnidirectional response of the microphone array.

Note that while the setup is as similar to the procedure described in ISO354:2003 [1] as possible, it does not fully comply with the standard in the following aspects:

- The number of source and receiver positions per laboratory condition is far lower than the minimum number of 12 required by the standard.
- No frame was used to cover the specimen's sides, which is accounted for in the numerically calculated reference absorption coefficient.

4. MODEL IMPLEMENTATION

The factor analysis and multiple linear regression model were implemented based on the *scikit-learn* library, [14]. In order to later validate the model, a split of the data into a training and test set was performed, where the training set consisted of 75 % of the full dataset. The suitability of the input data for factor analysis was assessed using the Bartlett [15] test of sphericity and the Kaiser-Meyer-Olkin measure of sampling adequacy [11]. The number of latent variables used in the factor analysis was determined using a *scree* plot, and consecutively confirmed using a parallel analysis as suggested by Horn [16]. Estimation of the loading matrix was performed iteratively using the maximum likelihood approach. The linear regression based on the latent variables was performed using a standard least squares approach. A significance test of the regression coefficients was performed using an Analysis of Variances (ANOVA) on the regression models for the three reverberation time intervals. Additional significance tests of the individual regression coefficients were performed using *t*-tests.

5. RESULTS

The results presented in this chapter are based on the symmetry estimator input data derived for the occupied rooms. If not otherwise stated the presented results are based on the training data set.

5.1 Factor Analysis

The factor analysis indicated that the input data can be represented by three latent variables. Most prominently, the first latent variable represents the quantitative value of the isotropy and axial symmetry estimators, with high loadings for all respective intervals. Similarly, the second latent variable primarily represents the rate of change of the symmetry quantifiers. Interestingly, increased loading is also observed for the input variables representing the quantity of both estimators towards the late part of the decay process. This is most likely due to the fact that this part of the decay process shows the largest rate of change in the symmetry quantifiers in the case of non-uniform damping, see for example. Fig. 1. Such cross-loading of

input-variables on multiple latent factors indicates non-ideal separation of the latent variables. Nonetheless, the second latent variable may still be interpreted as the rate of change of the symmetry quantifiers.
In comparison, the third latent variable shows overall lower and slightly inconsistent loadings for all variables, and as a result is not clearly interpretable. As the next section will show, the third latent variable does not contribute significantly to the developed model.

5.2 Multiple Linear Regression

The ANOVA results indicate that the regression model is significant at a level $p < 0.001$ for all reverberation time intervals, with F-statistics of 44.9, 80.7, and 88.4, see Table 1. The individual t-tests of the regression coefficients indicate that all except β_3 are statistically significant with $p < 0.001$. For β_3, that is the third latent variable, the T-statistic is subject to low values while the p-values are between 0.12 and 0.41, indicating that the third latent variable does not significantly contribute to the model. As mentioned before, the third latent variable is consequently excluded from the model for the remaining analysis.

As a goodness of fit measure, the coefficient of determination R^2 was computed. For the training data set the coefficient of determination is found to increase with increasing dynamic range used for calculation of the reverberation time, showing values from 0.75 to 0.86, see Table 1. For the test data the R^2 and mean squared error are found to be slightly lower than for the training data, with R^2 values of 0.68 to 0.80, see Table 1. While the test data shows slightly lower accuracy, the results still indicate sufficient generalization capabilities of the model.

Figure 2 shows the regression lines for the individual latent variables separately, as well as the 95 % confidence interval, and the individually calculated R^2 measure. Each row corresponds to one of the reverberation time intervals. The increase of the reverberation time interval seemingly improves the accuracy of the model. In fact, Fig. 2 reveals that the increase in the goodness of fit is primarily due to the improved goodness of fit for the second latent variable. Interestingly, the R^2 measure obtained for the first latent variable is found to be similar for ε_{20}, ε_{30}, and ε_{40} with values between 0.64 to 0.68, while the R^2 measure for the second latent variable increases from 0.09 to 0.22. This may indicate two things: Firstly, the magnitude of the symmetry estimators is more indicative for the error in the absorption coefficient than their respective rate of change for the given model. Secondly, the rate of change in the symmetry quantifiers reflects the increase in the reverberation time estimation error – and hence increase in the absorption coefficient error – for larger evaluation intervals in the presence of multi-exponential energy decay. Note that the R^2 for the second latent variable is still low for all reverberation time intervals. This is also due to a number of distinct outliers. For the second latent variable outliers for $\Psi_2 > 0$ and $\varepsilon < -0.3$ are observed which result in an increased regression error for all reverberation time intervals, cf. Fig. 2. Similarly, outliers are observed for the first latent variable for $\varepsilon < -0.3$ and $\Psi_1 < 1$, cf. Fig. 2. While the outliers are not clearly interpretable, it is highly likely that they are due to insufficient separation of the input variables, which was already hinted at in the interpretation of the factor analysis.

Table 1: Results of the F-test, as well as the coefficient of determination R^2 for the multiple linear regression model. The F-test statistics are given for the training data only.

			R^2	
	F-statistic	p-value	Training	Test
ε_{20}	44.9	< 0.001	0.75	0.68
ε_{30}	80.7	< 0.001	0.85	0.81
ε_{40}	88.4	< 0.001	0.86	0.80

5.3 Absorption Coefficient Prediction

Figure 3 shows the corrected absorption coefficient (using Eq. (6)) without distinguishing between training and test data, as well as the measured absorption coefficient.Further, Fig. 3 shows the numerically computed finite size absorption coefficient. The depicted data for each frequency band corresponds to the average over three all laboratory rooms and receiver positions. The results indicate that the mean of the corrected absorption coefficient is in good agreement with the reference absorption coefficient for the T_{20}, T_{30}, and T_{40} intervals. Further, the $[2.5\,\%, 97.5\,\%]$ percentiles of the corrected absorption coefficient are smaller compared to the respective percentiles of the measured data. Interestingly, the agreement seems best for the T_{20} interval, and decreases with increasing

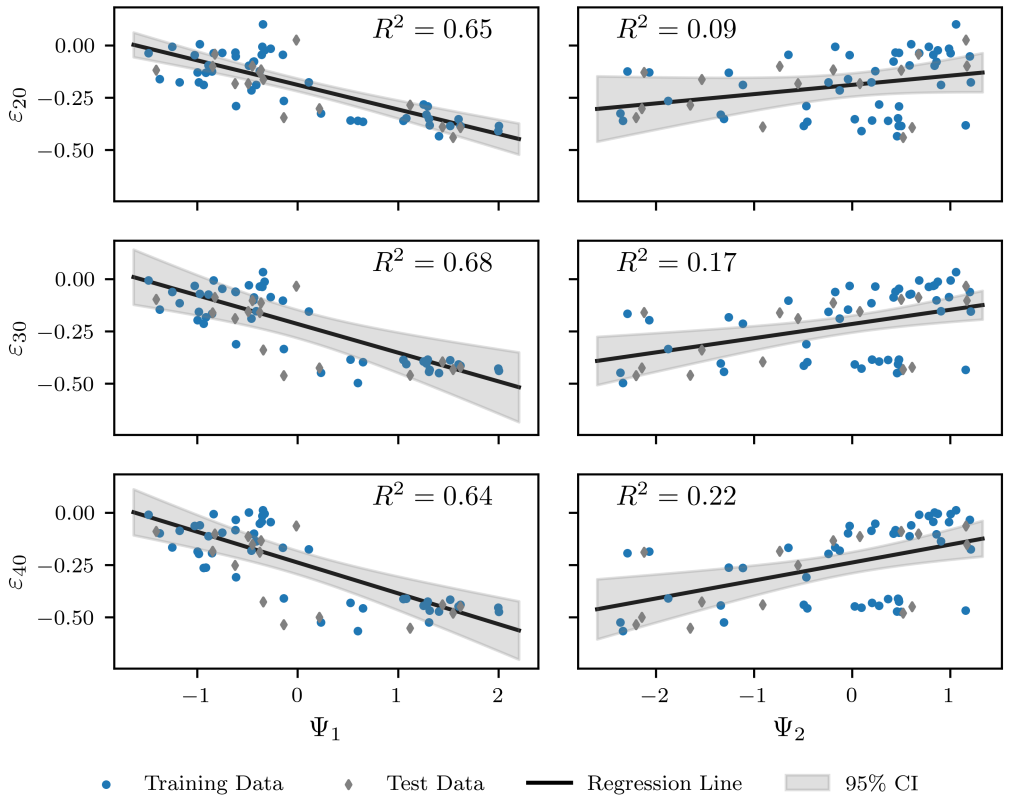


Figure 2: Regression lines for the two predicted relative absorption coefficient error based on the two latent variables. Shaded areas indicate the 95 % confidence interval.

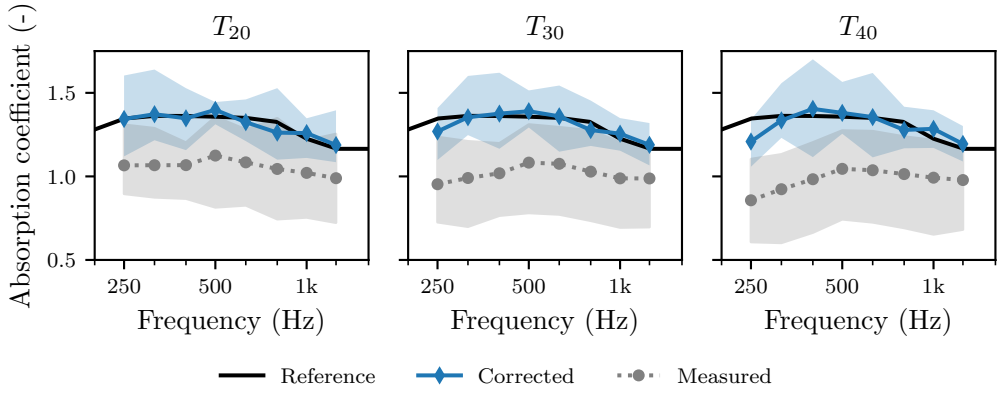


Figure 3: Mean of the corrected and measured absorption coefficient data averaged over all laboratory rooms. Shaded areas indicate the region spanning the 2.5 % and 97.5 % percentiles. The combined test and training data are used. The reference refers to the numerically computed absorption coefficient.

reverberation time evaluation interval which seems counterintuitive as the interval showed the lowest R^2 in the previous section.
An additional room by room analysis revealed that the high variance of the corrected absorption coefficient is primarily influenced by the room configuration without panel diffusers installed for most frequency bands.Similarly, the variance in the measured absorption coefficient is primarily influenced by the room configuration without panel diffusers installed.This observation is in agreement with the results of the previous section, which showed that the outliers in the regression model are primarily associated with the room configuration without panel diffusers installed.

6. CONCLUSION

This paper presented a stochastic model for the analysis between the uniformity of incident energy distributions – i.e. isotropy and axial symmetry – and the error in Sabine's absorption coefficient. The results indicate a statistically significant relationship. While the results of the regression model are promising, the analysis of the relationship between the latent variables and the absorption coefficient error revealed mismatches between the target data and the model. A number of distinct outliers were observed, which are most likely due to insufficient separation of the latent variables in the factor analysis. Future work should involve the development of an improving the identification of the latent variables. Especially a model-based parameterization of the symmetry quantifiers, is expected to improve the performance of the regression model. Nevertheless, initial results indicate that the model can be used to correct Sabine's absorption coefficient if data from multiple laboratory rooms are available to train the model.

7. ACKNOWLEDGMENTS

The authors would like to thank Melanie Nolan and Efren Fernandez Grande for the collaboration on the measurement campaign and Manuj Yadav for the fruitful discussions on the statistic model.
We would like to thank the Deutsche Forschungsgemeinschaft (DFG) for funding parts of this work under grant number 298797807.

8. REFERENCES

[1] ISO354:2003, *ISO 354:2003 - Measurement of sound absorption in a reverberation room*, 2003.

[2] R. E. Halliwell, "Inter-laboratory variability of sound absorption measurement," *J. Acoust. Soc. Am.*, vol. 73, no. 3, pp. 880–886, Mar. 1983. DOI: 10.1121/1.389011.

[3] C. Scrosati, F. Martellotta, F. Pompoli, *et al.*, "Towards more reliable measurements of sound absorption coefficient in reverberation rooms: An Inter-Laboratory Test," *Appl. Acoust.*, vol. 165, p. 107 298, Aug. 2020. DOI: 10.1016/j.apacoust.2020.107298.

[4] J. Balint, M. Berzborn, M. Nolan, and M. Vorländer, "Measuring Sound Absorption: The Hundred-Year Debate on the Reverberation Chamber Method," *Acoust. Today*, vol. 19, no. 3, p. 13, 2023. DOI: 10.1121/AT.2023.19.3.13.

[5] M. Nolan, M. Berzborn, and E. Fernandez-Grande, "Isotropy in decaying reverberant sound fields," *J. Acoust. Soc. Am.*, vol. 148, no. 2, pp. 1077–1088, Aug. 2020. DOI: 10.1121/10.0001769.

[6] M. Berzborn, M. Nolan, E. Fernandez-Grande, and M. Vorländer, "Comparison of Isotropy Estimators for the Analysis of Reverberation Rooms," in *E-Forum Acusticum*, e-Forum Acusticum 2020, 2020, pp. 139–146. DOI: 10/gqj4b9.

[7] M. Pereira, P. Mareze, L. Godinho, P. Amado-Mendes, and J. Ramis, "Proposal of numerical models to predict the diffuse field sound absorption of finite sized porous materials – BEM and FEM approaches," *Appl. Acoust.*, vol. 180, p. 108 092, Sep. 2021. DOI: 10.1016/j.apacoust.2021.108092.

[8] M. Berzborn and M. Vorländer, "Inference of the Acoustic Properties of Transversely Isotropic Porous Materials," in *Proceedings Of Internoise*, Nantes, 2024, pp. 1–6.

[9] M. Berzborn, M. Nolan, E. Fernandez-Grande, and M. Vorländer, "Directional sound field decay analysis in a reverberation room," *J. Acoust. Soc. Am.*, vol. under review, 2024.

[10] S. R. Jammalamadaka and G. H. Terdik, "Harmonic analysis and distribution-free inference for spherical distributions," *J. Multivar. Anal.*, vol. 171, no. 5, pp. 436–451, May 2019. DOI: 10.1016/j.jmva.2019.01.012.

[11] A. G. Yong and S. Pearce, "A Beginner's Guide to Factor Analysis: Focusing on Exploratory Factor Analysis," *TQMP*, vol. 9, no. 2, pp. 79–94, Oct. 12, 2013. DOI: 10.20982/tqmp.09.2.p079.

[12] G. Chardon, W. Kreuzer, and M. Noisternig, "Design of spatial microphone arrays for sound field interpolation," *IEEE J. Sel. Topics Signal Process.*, vol. 9, no. 5, pp. 780–790, 2015. DOI: 10.1109/JSTSP.2015.2412097.

[13] M. R. Schroeder, "New Method of Measuring Reverberation Time," *J. Acoust. Soc. Am.*, vol. 37, no. 6, pp. 1187–1187, 1965. DOI: 10.1121/1.1939454.

[14] F. Pedregosa, G. Varoquaux, A. Gramfort, *et al.*, "Scikit-learn: Machine Learning in Python," *J. Mach. Learn. Res.*, vol. 12, no. 85, pp. 2825–2830, 2011.

[15] M. S. Bartlett, "Properties of Sufficiency and Statistical Tests," *Proceedings of the Royal Society of London. Series A, Mathematical and Physical Sciences*, vol. 160, no. 901, pp. 268–282, 1937. JSTOR: 96803.

[16] J. L. Horn, "A rationale and test for the number of factors in factor analysis," *Psychometrika*, vol. 30, no. 2, pp. 179–185, Jun. 1, 1965. DOI: 10.1007/BF02289447.

DOI: 10.61782/fa.2025.0351

FORUM ACUSTICUM EURONOISE 2025

ESTIMATING THE IMPEDANCE OF A MATERIAL SAMPLE AT LOW FREQUENCIES

Albert G. Prinn[1*] **Rubén Maestro Vallejo**[2] **María Luisa López-Ibáñez**[2]
María Larrosa-Navarro[2] **Eduardo Latorre Iglesias**[2]
[1] Fraunhofer Institute for Integrated Circuits (IIS), Erlangen, Germany
[2] Grupo de Acústica Arquitectónica, Escuela Técnica Superior de Arquitectura, Universidad Politécnica de Madrid, 28040 Madrid, Spain

ABSTRACT

Reliable descriptions of a room's physical properties are essential for accurately simulating room acoustical fields. An important model input parameter is the impedance of the materials that comprise the boundaries of the room. However, the impedance information of commonly used sound-absorbing materials is generally unavailable. While databases of absorption coefficients are available for commonly used materials, these are of limited use for simulation tools that require impedance (or angle-dependent reflection coefficients) as input data, and it is uncommon to find absorption coefficients below 100 Hz. This study estimates the normal impedance of a sample of sound-absorbing material at frequencies below 100 Hz. An eigenvalue-based impedance estimation method is used to determine a sample's complex-valued, frequency-dependent impedance from measurements in a reverberation chamber. While the results are encouraging, the method is sensitive to model input parameters, and further refinement is required to make the method practical.

Keywords: *Reverberation chamber, Eigenvalue estimation, Impedance estimation.*

1. INTRODUCTION

Understanding the impedance characteristics of surfaces is crucial for accurately modeling room acoustical fields. However, obtaining this information can be challenging, particularly at low frequencies and for complex-valued impedance. Eigenvalue analysis has been suggested in the literature as a solution [1, 2]. This work employs eigenvalue analysis to estimate the normal impedance of an absorbing surface at low frequencies. In this report, the proposed method is used to estimate the normal impedance of the walls of an empty reverberation chamber and the impedance of a material sample placed in the same chamber. The approach is checked by comparing the measured and simulated reverberation times, absorption coefficients, and room transfer functions.

This paper is organized as follows. In Sec. 2, we provide background information by reviewing relevant literature and offer motivation for the work. Section 3 outlines the impedance estimation method. The measurements conducted in the reverberation chamber are described in Sec. 4, and the results of the impedance estimation are presented in Sec. 5. Finally, we discuss the findings of this study in Sec. 6 and conclude the paper in Sec. 7.

2. BACKGROUND

In general, the impedance of an absorbing material is best described by an extended reaction model. However, a local reaction model can be used to approximate the behavior of some commonly used materials. The local reaction model assumes that the surface impedance is independent of the angle of incidence, meaning it only models the impedance at normal incidence, yielding a normal impedance. Descriptions of absorbing materials based on normal impedance can be easily integrated into wave modeling tools. The normal impedance model is also advantageous for certain geometrical modeling tools, such

*__Corresponding author__: albert.prinn@iis.fraunhofer.de.
__Copyright__: ©2025 Prinn et al. *This is an open-access article distributed under the terms of the Creative Commons Attribution 3.0 Unported License, which permits unrestricted use, distribution, and reproduction in any medium, provided the original author and source are credited.*

as the image source method, because it allows practitioners to specify angle-dependent reflection and absorption coefficients (see, e.g., Ref. [3]).

In practice, absorption coefficient tables are often utilized in lieu of normal impedance values, a practice that has several disadvantages. The standard method for quantifying a material's sound-absorbing properties, known as the reverberation chamber method [4], provides absorption coefficients. In theory, these coefficients represent the sound absorption at all angles of incidence, but in practice, only a subset of all possible angles is represented in the data. This limitation leads to measured absorption coefficients that depend on the specific environment in which they were collected. The lack of angle-dependent information and the dependence of the data on the measurement room restrict the usefulness of these absorption coefficients. Therefore, having access to the normal impedances of commonly used materials would be highly beneficial for the room acoustics community.

The impedance tube method [5, 6] yields normal impedances of absorbing materials. The method is limited to small samples, which excludes edge effects and potentially includes unwanted installation effects. Depending on the physical dimensions of the tube being used, there is also a limited range of frequencies for which such a measurement is valid. Measurements at low frequencies typically require tubes of potentially impractical length. Due to these limitations, there are ongoing efforts within the community to develop in-situ impedance measurement methods. These usually depend on multi-microphone measurements and advanced signal processing techniques. The interested reader is directed towards Ref. [7] for a recent review of the work being done in this field. Long wavelengths and modal effects in the rooms under test complicate the in-situ measurement of surface impedance at low frequencies. An interesting approach is to use the room's modes to measure the surface impedance.

Hull and Radcliffe propose an eigenvalue-based impedance method [8]. They successfully demonstrate the method using one-dimensional analytical descriptions of the modes in an impedance tube. Nowakowski *et al.* [9] use the eigenmodes of a two-dimensional problem to estimate surface impedance. Prinn *et al.* [1, 2, 10] present an estimation method based on eigenvalue analysis of impulse responses simulated and measured in rooms containing a test sample. The proposed method is extended here to make the approach more robust and is used to estimate a sample's impedance in a reverberation chamber.

3. ESTIMATION METHOD

The eigenvalue-based estimator has two main steps: first, the reverberation chamber's eigenvalues are computed, and second, the measured eigenvalues are compared to the predicted eigenvalues obtained from a model, and an initial guess of the impedance is refined to obtain an impedance estimate. The following sections will describe these steps. For brevity, derivations are omitted, and the interested reader is directed towards Refs. [1, 2].

3.1 Chamber eigenvalues

The first step is to estimate the empty chamber's eigenvalues. We do this for a set of measured room impulse responses using the matrix pencil method [11], which provides a set of potential eigenvalues. The matrix pencil method can be written as follows: Solve the eigenvalue system

$$\det\left(\boldsymbol{H}_1^{\dagger}\boldsymbol{H}_2 - \gamma\boldsymbol{I}\right) = 0\,, \tag{1}$$

where superscript † indicates the Moore-Penrose pseudoinverse,

$$\boldsymbol{H}_1 = \begin{bmatrix} h_1 & h_2 & \cdots & h_p \\ h_2 & h_3 & & h_{p+1} \\ \vdots & & \ddots & \vdots \\ h_{N-p} & h_{N-p+1} & \cdots & h_{N-1} \end{bmatrix}_{(N-p)\times p}, \tag{2}$$

and

$$\boldsymbol{H}_2 = \begin{bmatrix} h_2 & \cdots & h_p & h_{p+1} \\ h_3 & & h_{p+1} & h_{p+2} \\ \vdots & \ddots & & \vdots \\ h_{N-p+1} & \cdots & h_{N-1} & h_N \end{bmatrix}_{(N-p)\times p}. \tag{3}$$

The entries of Hankel matrices (2) and (3) are samples from a measured impulse response, h_n, with $n = 1, 2, ..., N$, and pencil parameter $p = \text{round}(N/2)$. Solving (1) yields eigenvalues γ_m, which are used to compute the mth resonance frequency

$$f_m = f_\text{s}\arg(\gamma_m)/(2\pi)\,, \tag{4}$$

and the mth damping constant

$$\sigma_m = f_\text{s}\,\log(|\gamma_m|)\,, \tag{5}$$

where f_s is the sampling frequency. The mth measured chamber eigenvalue is then

$$\lambda_m = f_m + \text{i}\sigma_m/(2\pi)\,. \tag{6}$$

The matrix pencil method generates both valid and spurious eigenvalues (see, e.g., Ref. [12]). Given data from multiple measurement positions, the valid eigenvalues tend to form local clusters. From this clustering, the distance of each eigenvalue to its neighbors is calculated, and the eigenvalues with the smallest differences from one another are identified. Thus, in this work, k-means clustering (see, e.g., Friedman *et al.* [13]) is used to identify the valid eigenvalues. This provides us with a set of chamber eigenvalues that contain information on the resistance and reactance, i.e., the complex-valued impedance, of the surfaces in the chamber.

3.2 Impedance estimates

With a set of chamber eigenvalues, a numerical wave model of the chamber is used to find the unknown impedance. The finite element method is chosen to model the chamber since the method robustly models problems with arbitrary geometries. The Helmholtz equation-based eigenvalue problem is written as

$$\left[\boldsymbol{K} + (2\pi\mathrm{i})\frac{\hat{\lambda}}{c}\sum_{j=0}^{J}\hat{\zeta}_j^{-1}\boldsymbol{C}_j + (2\pi\mathrm{i})^2\frac{\hat{\lambda}^2}{c^2}\boldsymbol{M}\right]\boldsymbol{v} = \boldsymbol{0}\,, \quad (7)$$

where matrices $\boldsymbol{K}$, $\boldsymbol{C}$, and $\boldsymbol{M}$, are the usual finite element matrices (see, e.g., Ref. [14]). Here, $\hat{\zeta}_j$ is the impedance of the jth surface of the chamber, $\boldsymbol{v}$ is an eigenvector, and the mth simulated eigenvalue is given by

$$\hat{\lambda}_m = \hat{f}_m + \mathrm{i}\hat{\sigma}_m/(2\pi)\,. \quad (8)$$

For a given eigenvalue, the present method provides one impedance estimate. Therefore, to estimate the impedance of the jth surface for the mth resonance frequency, we assume that, either all impedances of the other surfaces in the chamber are known, or the impedance is spatially uniform ($J = 0$). To obtain an estimate, we refine an initial guess for $\hat{\zeta}_j$. This guess is refined using an optimization algorithm to minimize the differences between the chamber and simulated eigenvalues. Thus, we solve the problem

$$\hat{\zeta}_m = \min_{\hat{\zeta}\in\mathbb{C}}\left[\frac{\|\lambda_m - \hat{\lambda}_m\|_2}{\|\lambda_m\|_2}100\right]\,. \quad (9)$$

The cost function is a relative error. Estimates that fail to reach an upper bound on the error (in this case, 1%) are assumed to be erroneous and are removed from the frequency-dependent estimates set. This is necessary due to the sensitivity of the impedance estimation method.

A significant issue that can arise during optimization is when an eigenvalue is associated with an eigenvector that does not correspond to that eigenvalue. This situation occurs when eigenvalues are closely spaced in the frequency domain. As the impedance is varied, the eigenvalues can exchange their chronological order; for instance, an eigenvalue that was previously higher in frequency than its lower-frequency neighbor can become lower than that same neighbor after a change in impedance.

The consequence is that the impedance estimator may attempt to fit an impedance to the incorrect eigenvalue. To improve the method's robustness, we make use of measurements at multiple positions. We use the magnitude of the normalized transfer functions at the measurement positions to approximate the mth normalized eigenvector. This approach allows us to compare the error of the chosen eigenvector with the errors of its immediate neighbors (in terms of resonance frequency). If an eigenvalue with a lower eigenvector error is identified, it is assumed that the eigenvalues have exchanged their chronological order. The eigenvector with the lowest error is used for the estimation.

This work uses the commercially available finite element tool COMSOL [15] to solve the eigenvalue problem.

4. MEASUREMENT SETUP AND DATA

The reverberation chamber under test is shown in Fig. 1. The chamber is formed by two rooms with non-parallel walls joined by a large open window. The sound field produced by two sound sources is recorded at multiple positions within the room. One sound source is a full-range loudspeaker placed in a corner of the reverberation chamber, while the other is a low-frequency woofer placed in the same position. The measurements are taken in two chamber conditions: the empty chamber and the occupied chamber, in which two copies of a sound-absorbing material sample are placed on the chamber floor. This section outlines the experimental setup and presents the relevant data.

4.1 Empty chamber

The chamber is excited with a swept sine signal. An omnidirectional microphone receives the signal, emitted by either the loudspeaker or the woofer, at 12 evenly spaced receiver positions. These positions are reported in Tab. 1. The received signals are deconvolved to obtain a set of measured impulse responses. The speed of sound is estimated to be 343 m/s, and the medium density is 1.2 kg/m^3.

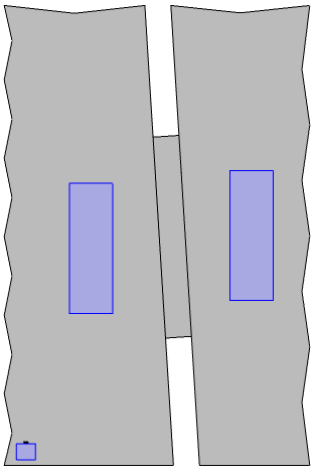


Figure 1: Top view of the reverberation chamber under test. The origin of the coordinate system is the bottom left-hand corner of the chamber. The highlighted rectangle close to the origin is the loudspeaker, facing in the y-dimension, and with the driver's center located at (0.5, 0.5, 0.2) [m]. The highlighted rectangles in the middle of each chamber section are two identical material samples.

Table 1: Measurement receiver positions.

id.	x	y	z
1	1.00	1.00	1.25
2	1.00	5.00	1.25
3	1.00	9.00	1.25
4	3.00	1.00	1.25
5	3.00	5.00	1.25
6	3.00	9.00	1.25
7	5.00	1.00	1.25
8	5.00	5.00	1.25
9	5.00	9.00	1.25
10	6.00	1.00	1.25
11	6.00	5.00	1.25
12	6.00	9.00	1.25

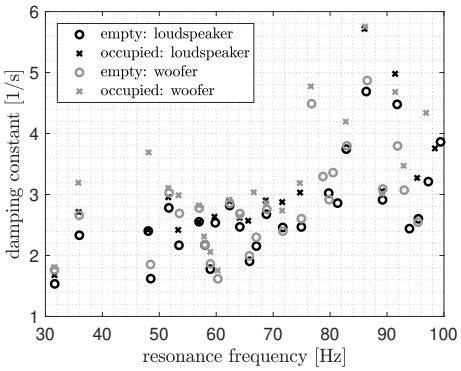


Figure 2: Comparison of empty and occupied chamber eigenvalues, for two sources of sound.

4.2 Chamber with sample

The absorbing material is a polyurethane foam with a porous foam top layer. It is divided into two parts (this is necessary due to the chamber construction; see Fig. 1). The two samples, each with dimensions $1.0 \times 3.0 \times 0.14$ m, are placed on the floor. The measurement procedure described above is repeated for the occupied chamber.

5. RESULTS

First, the unknown impedance of the chamber walls is estimated using the eigenvalues of the empty chamber. This impedance data is then used to estimate the sample's impedance using the eigenvalues of the occupied chamber. The empty and occupied chamber eigenvalues are presented in Fig. 2. Note the increase in damping with the introduction of the sample, and the unexpected damping offset between the sources. This section presents these data and compares the measured and simulated reverberation times, absorption coefficients, and transfer functions.

5.1 Impedance estimates

The estimated impedance of the chamber walls is shown in Fig. 3a for both the loudspeaker and the woofer. Although there are some differences between the two data sets, the general shape of the graphs is consistent. At low frequencies, the resistance of the chamber walls lies in the region between 100 and 250. It is important to note that the lower bound for the resistance optimization is 50, while the upper bound is 250. Thus, for the woofer data, the impedance estimate in the region of 60 Hz might not be correct. For the reactance, the lower and upper bound

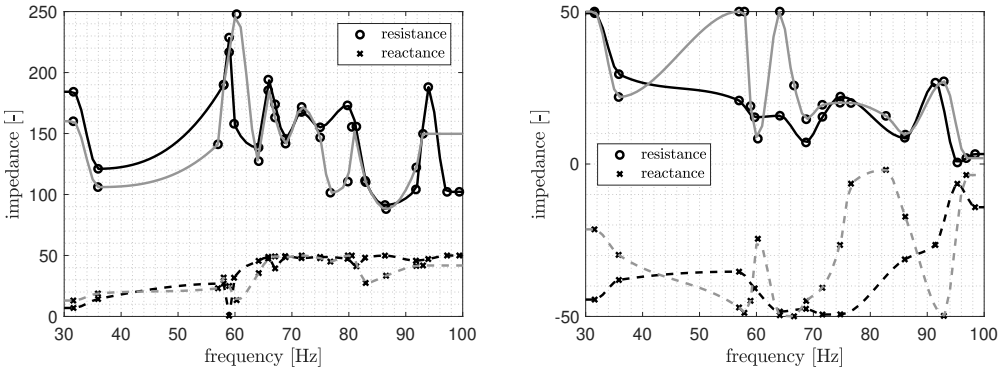


Figure 3: Impedance estimates for the loudspeaker (black lines) and the woofer (gray lines). (a) spatially uniform impedance of all surfaces of the empty chamber. (b) impedance of the material sample.

of the optimization are -50 and 50, respectively. The estimated reactance above approximately 65 Hz is close to the upper bound. It is important to note that this data likely does not represent the actual impedance of the chamber walls, as not all chamber surfaces may exhibit the same impedance (this is a necessary assumption in this work). Instead, this impedance estimate represents the spatially uniform complex-valued impedance.

The estimated impedance of the material sample is presented in Fig. 3b. As expected, the resistance of the sample is lower than that of the chamber walls. Upon comparison of the loudspeaker and woofer data, we see that while the data have similar trends, there are noticeable differences. It is expected that these differences appear due to inaccuracies at the eigenvalue estimation stage.

5.2 Reverberation time estimates

A set of spatially averaged reverberation times can be computed from the measured data. To simulate this quantity, the estimated impedance values are used to describe the boundary conditions of finite element models for both the empty and occupied chambers. A two-microphone method measures the velocity of the loudspeaker and woofer drivers during the measurements. The measured velocity is then post-processed to remove noise and is used to describe the source excitation in the models.

The measured and simulated reverberation times for third-octave bands are compared in Fig. 4. While there is some qualitative agreement between the two, noticeable differences exist. Notice also that the measured reverberation time depends on the source type. Since the same position was used for both sources, it is expected that these differences appear due to the changes in excitation levels as a function of frequency. The exact source of the differences between the measured and simulated data is unknown, but it is expected that improving the estimates of the sample impedance could help reduce them.

5.3 Absorption coefficients

The measured and simulated absorption coefficients are compared in Fig. 5. The measured absorption coefficients for the chamber walls were calculated from the reverberation times obtained in the empty chamber using Sabine's formula. The absorption coefficients for the sample were determined using the reverberation chamber method [4]. The random incidence absorption coefficients (see, e.g., Kuttruff [16]) were derived from the estimated impedances to obtain simulated absorption coefficients. We do not expect the measured and simulated absorption coefficients to be in perfect agreement since the random incidence assumption might not be fulfilled in this reverberation chamber at the low frequencies of interest.

Data for both the loudspeaker and the woofer are included. The results show that the absorption coefficients for the chamber walls are similar, which is reassuring. However, there are noticeable differences between the measured and estimated sample impedances. While improved impedance estimates are expected to yield better agreement for the woofer data, the loudspeaker absorption coefficients at 80 and 100 Hz are concerning.

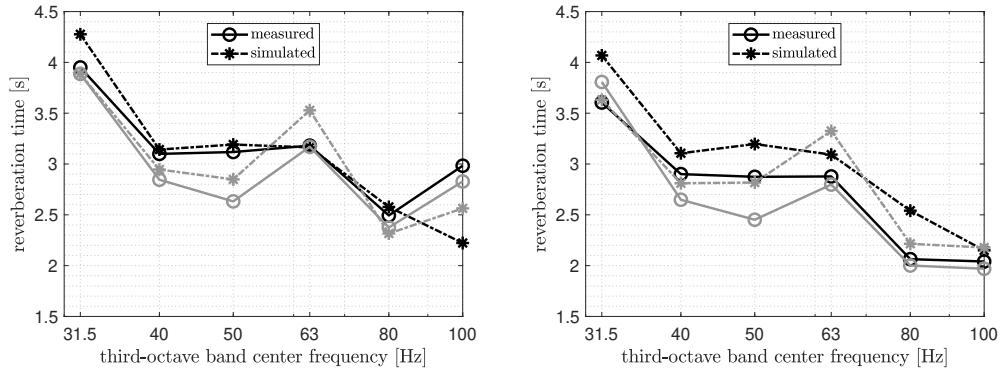


Figure 4: Comparison of measured and simulated spatially averaged reverberation times for the loudspeaker (black lines) and the woofer (gray lines). (a) empty chamber. (b) occupied chamber.

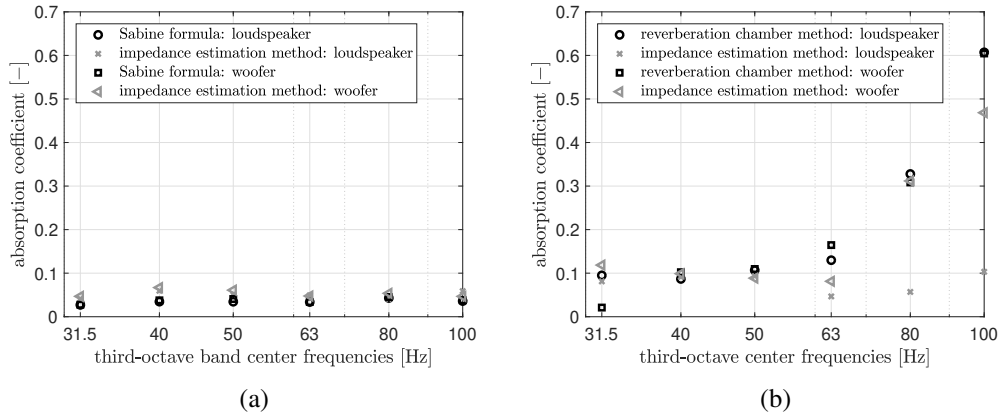
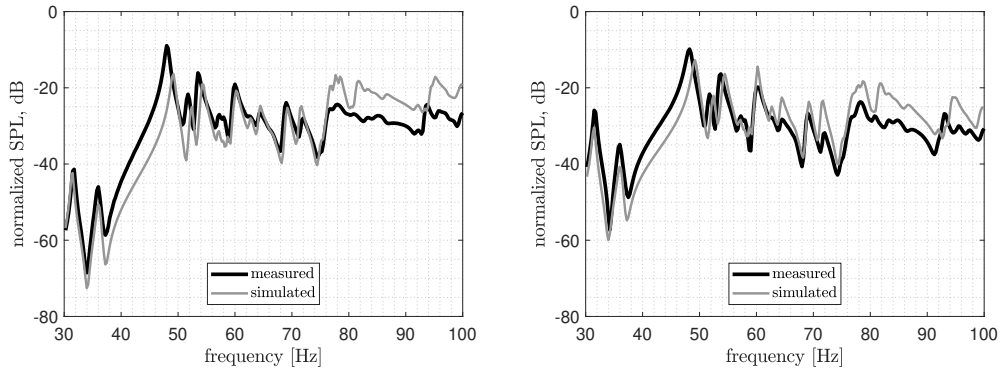


Figure 5: Comparison of the measured and simulated absorption coefficients. (a) chamber walls, (b) material sample.

5.4 Transfer functions

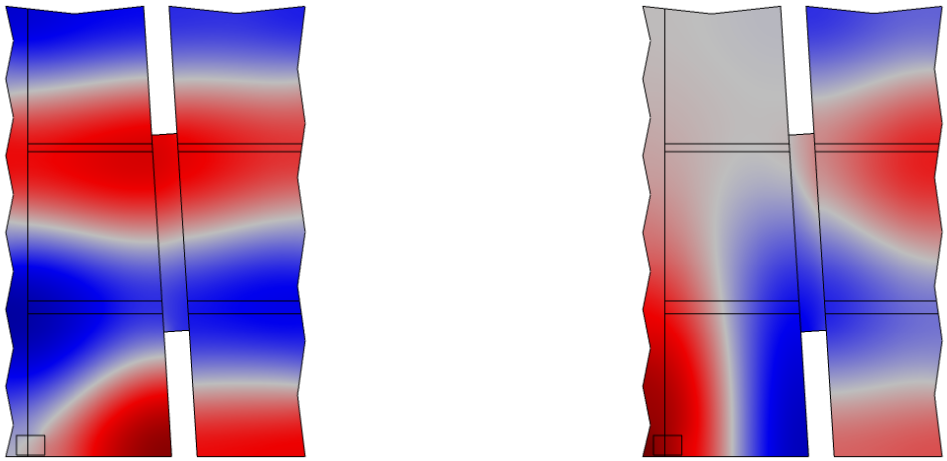
The empty chamber's measured and simulated transfer functions are compared in Fig. 6. In general, there is some agreement between the transfer functions; however, noticeable differences appear at certain frequencies. The cause of these discrepancies is not immediately apparent. It is possible that the positioning of the sources, or their acoustic centers, is not identical to those in the simulation.

For instance, at approximately 48 Hz, we observe a significant difference. An eigenvalue analysis of the chamber reveals two eigenvalues in this frequency range, with resonance frequencies around 48 Hz and 49 Hz. For the 48 Hz mode, there is a pressure minimum (a node) at the speaker location, whereas for the 49 Hz mode, there is a pressure maximum (an antinode). (Please refer to Fig. 7 for mode shapes.) One would expect that the 48 Hz mode would not be excited while the 49 Hz mode would be, but in the measured data the opposite seems to be true. Upon examining Fig. 6a and Fig. 6b, it appears that the 48 Hz mode is present in the measured data, while the 49 Hz mode is reflected in the simulations. Clearly, this study could be improved by increasing the precision of both the experimental and simulation setups.



(a) (b)

Figure 6: Comparison of empty chamber transfer functions at measurement position 1. (a) loudspeaker, (b) woofer.



(a) (b)

Figure 7: Modes of the empty chamber (a) 48 Hz, (b) 49 Hz.

6. DISCUSSION

While the results presented in this paper are promising, the comparisons between the measured and simulated data shown in Figs. 4, 5, and 6 indicate that further work is necessary for this method to be effectively used in impedance measurements. Some of the assumptions made to derive the impedance estimates may need to be modified. For example, we have assumed that the surface impedances of the floor, walls, and ceiling of the reverberation chamber are spatially uniform, which may be an oversight. Efforts should be made to quantify the impedances of all surfaces in the reverberation chamber, possibly including ventilation systems. The differences between the chamber eigenvalues computed for the two different sound sources, shown in Fig. 2, are concerning. In theory, since the chamber eigenvalues are global quantities, these should not depend on the sound source. The observed differences result in similar differences between the impedance estimates, shown in Fig. 3. The cause of the observed differences between the chamber eigenvalues is unknown. A detailed analysis of the measurement setup is needed to refine the input data for the impedance estimation method.

7. CONCLUSION

Measuring the normal impedance of a material sample at low frequencies can be challenging. In this study, we employed an eigenvalue-based method to estimate both the impedance of the walls of an empty reverberation chamber and that of a material sample at frequencies below 100 Hz. The impedance estimation method yielded two different results for two different sound sources, due to unexpected variations in the chamber's eigenvalues. The cause of the discrepancy remains unclear. Therefore, while the method is theoretically sound, it may produce unreliable impedance estimates due to measurement noise and uncertainties in the input parameters for the inverse model.

Future research should aim to minimize the uncertainties associated with this impedance estimation method. For example, more detailed descriptions of the chamber's geometry, the sound source, and the properties of the medium could improve the accuracy of the estimates. Additionally, reevaluating the assumption that a spatially uniform impedance adequately represents the impedance of the chamber walls may also lead to better estimations.

8. REFERENCES

[1] A. G. Prinn, A. Walther, and E. A. P. Habets, "Estimation of locally reacting surface impedance at modal frequencies using an eigenvalue approximation technique," *J. Acoust. Soc. Am.*, vol. 150, pp. 2921–2935, 2021.

[2] A. G. Prinn, P. Panter, A. Walther, and E. A. P. Habets, "Validation of an eigenvalue-based inverse method for estimating locally-reacting surface impedance," *Appl. Acoust.*, vol. 228, p. 110332, 2025.

[3] J. S. Suh and P. A. Nelson, "Measurement of transient response of rooms and comparison with geometrical acoustic models," *J. Acoust. Soc. Am.*, vol. 105, no. 4, pp. 2304–2317, 1999.

[4] ISO 354:2003, "Acoustics Measurement of sound absorption in a reverberation room," tech. rep., International Organization for Standardization, Geneva, CH, (2003).

[5] ISO 10534-1:1996, "Determination of sound absorption coefficient and impedance in impedance tubes Part 1: Method using standing wave ratio," tech. rep., International Organization for Standardization, Geneva, CH, (1996).

[6] ISO 10534-2:1998, "Determination of sound absorption coefficient and impedance in impedance tubes Part 2: Transfer-function method," tech. rep., International Organization for Standardization, Geneva, CH, (1998).

[7] E. Brandão, A. Lenzi, and S. Paul, "A review of the in situ impedance and sound absorption measurement techniques," *Acta Acust. United Ac.*, vol. 101, no. 3, pp. 443–463, 2015.

[8] A. J. Hull and C. J. Radcliffe, "An eigenvalue based acoustic impedance measurement technique," *J. Vib. Acoust.*, vol. 113, no. 2, pp. 250–254, 1991.

[9] T. Nowakowski, N. Bertin, R. Gribonval, J. de Rosny, and L. Daudet, "Membrane shape and boundary conditions estimation using eigenmode decomposition," in *IEEE International Conference on Acoustics, Speech and Signal Processing*, (Shanghai, China), Mar 2016.

[10] A. G. Prinn, "A finite element study of absorption coefficient measurement at low frequencies," in *INTER-NOISE and NOISE-CON Congress and Conference Proceedings*, vol. 268, (Chiba, Greater Tokyo, Japan), pp. 4996–5007, Institute of Noise Control Engineering, August 20 - 23 2023.

[11] Y. Hua and T. K. Sarkar, "Generalized pencil-of-function method for extracting poles of an EM system from its transient response," *IEEE Trans. Antennas Propag.*, vol. 37, no. 2, pp. 229–234, 1989.

[12] A. G. Prinn and E. A. P. Habets, "Acoustic eigenvalue estimation using rayleigh quotient iteration with a sparse matrix pencil," *Appl. Acoust.*, vol. 232, p. 110573, 2025.

[13] J. H. Friedman, J. L. Bentley, and R. A. Finkel, "An algorithm for finding best matches in logarithmic expected time," *ACM Trans. Math. Softw.*, vol. 3, p. 209226, Sept. 1977.

[14] A. G. Prinn, "A review of finite element methods for room acoustics," *Acoustics*, vol. 5, no. 2, pp. 367–395, 2023.

[15] COMSOL multiphysics®, "COMSOL AB, Stockholm, Sweden." v. 5.5.

[16] H. Kuttruff, *Room Acoustics*. Taylor & Francis, 6th ed., 2017.

DOI: 10.61782/fa.2025.0875

FORUM ACUSTICUM EURONOISE 2025

THE MEASUREMENT OF THE SOUND ABSORPTION OF AN ARRAY OF BAFFLES

Davy, John Laurence[1,2*] **Debevc, Mark**[3] **Truett, David**[1]
Payne, Jim[1] **Watson, John**[1]
[1] CSIRO Infrastructure Technologies, Melbourne, Australia
[2] School of Science, RMIT University, Australia
[3] Sontext Australia, Unit 2, 16 POA Court Craigieburn, Victoria, Australia, 3064

ABSTRACT

ASTM E795-23 specifies a Type J mounting WITHOUT A SURROUND for the measurement of the sound absorption of sound-absorbing units and requires that the measured sound absorption be reported. ISO 354:2003(E) specifies a Type J mounting WITH A SURROUND for the measurement of the sound absorption per unit of rectangular unit sound absorber pads or baffles. ISO 354:2003(E) also says that for a specified array of objects, the result is given as the sound absorption coefficient, and that in the case of a test specimen WITH A SURROUND, it is the area enclosed by the surround that is used. However, ISO 354:2003(E) also allows an array of objects to be measured WITHOUT A SURROUND and requires the sound absorption coefficient to be reported using the area covered by the test specimen. A baffle array could be regarded as being in a Type A mounting without covered edges. ISO 354:2003(E) says that if the edges are not covered, the area of the edges shall be included in calculating the test specimen area. Consultants want sound absorption coefficients so that they can enter in their ray tracing programs. The existence of different ways of measuring and/or reporting sound absorption is unacceptable.

[*]***Corresponding author***: *john.davy@rmit.edu.au*
Copyright: *©2025 john.davy@rmit.edu.au. This is an open-access article distributed under the terms of the Creative Commons Attribution 3.0 Unported License, which permits unrestricted use, distribution, and reproduction in any medium, provided the original author and source are credited.*

Keywords: *sound absorption coefficients, baffle arrays, reverberation rooms, sound absorption specimen mountings.*

1. INTRODUCTION

There appear to be a number of different ways in the current version of ISO 354:2003(E) [1] that the sound absorption of an array of baffles can be reported. 6.2.2.1 says "Rectangular unit sound absorber pads or baffles shall be installed in a Type J mounting as specified in Annex B." B.7 Type J mounting says "This mounting shall be used for the general specification of the sound absorption per unit of rectangular unit sound absorber pads or baffles." This means that the sound absorption per individual baffle and not the sound absorption coefficient needs to be reported. B.7 Type J mounting allows for the use of two different measurement methods, which are the well approach where “the height of the barrier shall be the same as the height of the baffles or pads”, and the deep well approach where “the barrier shall be 0,8 m higher than the baffles or pads, but the height of the barrier shall not exceed half of the height of the reverberation room”. It also says that “one or two walls of the reverberation room may be used as part of the barrier. This will probably lead to more possible different measurement results.
8.1.4 Calculation of equivalent sound absorption area of discrete absorbers says "For a specified array of objects, the result is given as the sound absorption coefficient." Thus, if the array of baffles is treated as a specified array of objects, the sound absorption coefficient needs to be reported. 3.8 Area of the test specimen NOTE 2 says "In the case of a test specimen surrounded by a structure (type E mounting or

type J mounting), it is the area enclosed by the structure." Thus, the floor area enclosed by the structure is used if an enclosure is used.

Baffle arrays are becoming much more complicated than was envisaged when the type J mounting in ISO 354:2003(E) [1] was written, as is shown in Figure 1 and Figure 2.

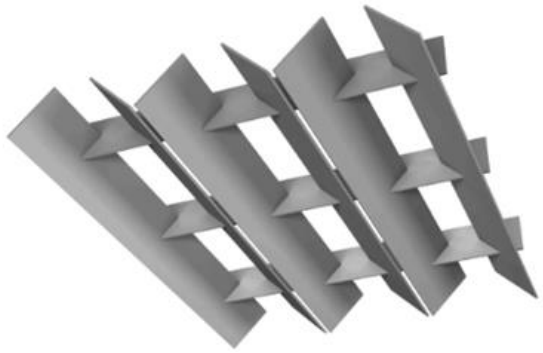


Figure 1. A baffle array with some baffles which are not vertical or horizontal, more than 3 rows of baffles in a measurement size specimen, and baffles running in two perpendicular directions.

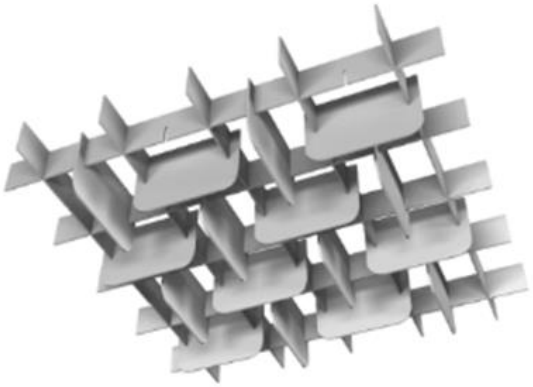


Figure 2. A baffle array with some baffles which are not continuous in their long dimension, more than 3 rows of baffles in a measurement size specimen, and baffles running in two perpendicular directions.

However, because 6.2.2.1 and B.7 Type J mounting only cover rectangular unit sound absorber pads or baffles where "The baffles shall be arranged in two or three parallel rows." most baffle arrays are probably not be covered by the type J mounting because there will usually be more than 2 or 3 parallel rows of baffles, and the baffles may not be rectangular or mounted vertically. In that case the baffle array should probably be tested without an enclosure as a specified array and the sound absorption coefficient should be reported as required by 8.1.4. 8.1.3 says that the area to be used for the calculation of the sound absorption coefficient "is the area, in square metres, covered by the test specimen (see 3.8)." Thus, just the covered floor area is used, and the area of the uncovered sides of the baffle array is not included.

Alternatively, the baffle array could be regarded as being in a Type A mounting without covered edges. B.2 Type A mounting says "If the edges of the test specimen are exposed when the material is normally installed in an actual application, then the edges of the test specimen shall not be sealed or covered during a test. If the edges are not covered, the area of the edges shall be included in calculating the test specimen area." In this case, the areas of sides as well as the area of the top of the cuboid containing the baffle array are used to calculate the sound absorption coefficient.

This possibility in ISO 354:2003(E) [1] to report the sound absorption of a baffle array in many ways is totally unacceptable. Examples of some of the possible different sound absorption coefficients are given later in this paper in Figure 5 and Figure 6 where the sound absorption coefficients differ by up to 0.45.

The Type J Mounting of ASTM E795-23 [2] does not surround the specimens with an enclosing non-absorptive barrier and its Note 13 says “The measured sound absorption is in square metres per unit.” This is because in the absence of an enclosing barrier to define the area, the use of a sound absorption coefficient is completely inappropriate. It is unfortunate that ISO 354:2003(E) [1] used the same Type J mounting name as ASTM E795-23 [2] when specifying a mounting type with a surrounding enclosure when the ASTM E795 Type J mounting is without a surrounding enclosure.

If Sabine’s equation is used, only the sound absorption added to the room by the arrays of baffles is needed. These days, most acoustic consultants use ray tracing programs for which they need the sound absorption coefficient. Also, it is difficult for measurement laboratories to have surrounds with many different lengths, widths and heights to cope with baffle arrays of different lengths, widths and heights. This has led to suppliers of baffle arrays having measurements made without a surround and quoting sound absorption coefficients calculated using only the area of the smallest rectangle covering or enveloping the projection on the nearest room surface of the installed baffle set. The authors of this paper are aware of sound absorption coefficients as high as 1.7 being advertised. This is much greater than the maximum that the edge effect could account for. Because the supplier would not release the

confidential test report, it was impossible to know the area of baffle arrays that had been tested and use that area to back calculate the sound absorption from the advertised sound absorption coefficient to calculate a more realistic sound absorption coefficient. In one case, a supplier advertised practical sound absorption coefficients which were greater than one, in contravention of ISO 11654:1997 [3].

Another complication when considering the best way to report the sound absorption of arrays of baffles, is that they may be installed in different ways. In a meeting room, only one or several baffle arrays may be installed, whereas in a factory or other large space, a large continuous area of baffle arrays may be installed. For a large area installation of baffle arrays, it is more appropriate to measure with a non-sound absorbing surround, because the reflections from the inside surface area of the surround simulate an infinite periodic array in two dimensions of the specimen inside the surround. However, if the installation area is small and the sides of the specimen volume and any airgap are not covered, testing without a non-sound absorbing surround may be more appropriate. If the sound absorption coefficients of the sides and the back side of the specimen volume are very different from the sound absorption coefficient of the front side of the specimen volume, then testing with a non-sound absorbing surround is probably more appropriate.

2. PROPOSED CHANGES TO ISO 354

ISO 354 should state that its primary measurement result is the amount of sound absorption added to the reverberation room by the addition of the specimen minus the sound absorption of any reverberation room surface area that the specimen covers (which is usually considered not to be significantly different from zero). It should require that the sound absorption in square metres be reported for all specimens.

3.8 of ISO 354 which defines the area of the test specimen as the “area of the floor or wall covered by the test specimen” needs to be changed. If a sound absorption coefficient is calculated, ISO 354 should require that any sound which hits the specimen must pass through an imaginary surface whose surface area is the area which is used to calculate the sound absorption coefficient. It should require that, as far as possible, any sound which passes through this imaginary surface hits the specimen, that this imaginary surface, possibly together with part of the room surface and the surface of any surrounding non-absorptive enclosure, encloses a relatively simple volume, and that the area of this imaginary surface is minimized. This enclosing simple volume would normally be expected to be a cuboid or occasionally a cylinder.

If the specimen consists of an array of elements separated by air gaps, the specimen shall consist of the smallest relatively simple volume which enclosures the array of elements. Again, this specimen volume would normally be expected to be a cuboid. This means that the specimen volume will be contained in, and maybe equal to, the enclosing volume used to determine the surface area to be used when calculating the sound absorption coefficient.

If the specimen consists of an array of elements which are placed periodically in a direction with a spacing of d, the specimen volume shall be extended by $d/2$ at each end of the specimen, as shown in Figures B.1 and B.2 of ISO 354:2003(E) [1]. This is because when larger areas of the specimen are installed, the periodic spacing of d would normally be continued in that direction. This extension could apply in two right-angled directions. This would be the case with the Type JV and JH mountings in ASTM E795-23 [2].

For a specimen which has an air gap between it and the room surface from which it is mounted, the enclosing volume will be the extension of the specimen volume to the room surface if the area of the surface of the enclosing volume, excluding the area of the surface of the enclosing volume which is a room surface, is smaller than the surface area of the specimen volume. Otherwise, the enclosing volume will be the specimen volume, and the specimen will be regarded as mounted in free space away from the room surface.

If the specimen volume is a cuboid whose length and width are L and W respectively, the area of the bottom surface of the specimen volume is LW. If the air gap has height H, the area of the skirt around it between the room surface and the specimen volume is $2H(L+W)$. Thus, the enclosing volume is the specimen volume if $H \geq LW/(2(L+W))$. For a specimen volume whose bottom is a square, the enclosing volume is the specimen volume if the height of the air gap is greater than or equal to one quarter of the length of the sides of the square. For a typical ISO 354:2003 specimen size of 3 by 3.6 m, the enclosing volume is the specimen volume if the height of the air gap is greater than or equal to 0.818 m. For a typical ASTM 423-22 [4] specimen size of 2.44 by 2.74 m, the enclosing volume is the specimen volume if the height of the air gap is greater than or equal to 0.645 m.

If a sound absorption coefficient is reported, the area used to calculate the sound absorption coefficient, and the surface used to calculate this area must both be reported.

For type A with a surround, Type B, Type E, Type G with a surround, Type I, and Type J mountings, the above

proposed rules mean that the area used to calculate the sound absorption coefficient is the area of the open top of the non-absorbing surround, as would be expected. For Type A and type G mountings without a surround, the above proposed rules mean that the area of the sides of the specimen volume and if an air gap exists, the area of sides of the air gap, or the area of the bottom of the specimen volume, are also included in the area used to calculate the sound absorption coefficient.

For individual objects which are “arranged randomly, spaced at least 2 m apart” and “mounted at least 1 m from any boundary or room diffusers and at least 1 m from any microphone”, the area of the surface of an enclosing volume should be calculated for each object.

The above proposed rules remove the problematic 8.1.3 which says that the area to be used for the calculation of the sound absorption coefficient "is the area, in square metres, covered by the test specimen (see 3.8)." They also remove the troublesome second sentence of 8.1.4 which says “For a specified array of objects, the result is given as the sound absorption coefficient” because the calculation of a sound absorption coefficient is optional. The proposed rules allow the basic type J mounting to be used for more general items than just two or three rows of rectangular unit sound absorber pads or baffles. In particular, the type J mounting could be used for baffle arrays or theatre seats. The proposed rules also cover functional sound absorbers because they require the sound absorption to always be reported.

In the field, the measured sound absorption coefficient should be applied to the surface calculated using the above proposed rules. This means that the effect of any uncovered sides becomes smaller as the area of the installation increases.

If non-absorbing enclosures are used, it is suggested that the enclosure be allowed to be between 0 and 12.5 mm higher than the object(s) that are being tested for practical reasons. This would enable the stacking of enclosure elements with heights of 12.5, 25, 50, 100, 200, 400 and 800 mm. It is suggested that for each enclosure element height, the enclosure elements consist of two 4.2 m lengths and two 3.6 m lengths so that they can be arranged by adjusting the junction overhangs at all 4 corners to enclose a rectangular area of any size complying with the area and aspect ratio specimen requirements of ISO 354. The areal density of the enclosure should be greater than 5 kg/m^2. The enclosure should not be constructed of gypsum plaster board.

The Type J mounting currently allows one or two of the room walls to be part of the non-absorbing enclosure. It is recommended that this no longer be allowed and that the non-absorbing enclosure be required to be away from all room surfaces except for the room surface that the non-absorbing enclosure is installed on. An exception to this rule would be for full length curtains or drapes and for absorbers that are to be mounted at room edges and corners.

The deep well approach [5] in the Type J mounting is designed to remove the edge effect. However, its use only with the Type J mounting is inconsistent with other mountings. It is recommended that its use be removed from ISO 354.

3. WITH AND WITHOUT AN ENCLOSURE

The sound absorption coefficients of two baffle arrays were measured with (Figure 3) and without (Figure 4) a surrounding enclosure.



Figure 3. The baffle array with 100 mm spacing with a surrounding enclosure.

Both baffle arrays were constructed from the same 12 mm thick polyester material with a density of 192 kg/m^3. The main vertical baffles were 300 mm deep and 3.6 m (2.4 and 1.2 m) long and were held in place by six 80 mm deep and 3 m (1.8 and 1.2 m) cross vertical baffles of the same 12 mm thick material between the floor of the reverberation room and the main baffles. 20 mm deep notches were cut into both types of baffles so that the main baffles and the support baffles could be interlocked together over a depth of 40 mm. This meant that the height of the baffle array was 340 mm.

In the first baffle array the centre planes of the main baffles were 200 mm (200) apart and in the second baffle array the centre planes of the main baffles were 100 mm (100) apart. The support baffle arrays extended half of the main baffle spacing beyond the centre planes of the main baffles at each end of the array. This was done to comply with the

requirement to have half of the main baffle spacing beyond the centre planes of the two outer baffles in the Type J mounting in ISO354:2003(E) [1]. Measurements were made with a 340 mm high non-absorbing surrounding enclosure (Yes) and without this enclosure (No). The enclosure consisted of 32 mm thick 300 mm high medium density fibreboard (MDF) with 1 mm thick 40 mm high steel on top. For the enclosure case, the sound absorption coefficients were calculated using the area of the top surface (Top) of the specimen volume (10.8 m^2). For the no enclosure case, the sound absorption coefficients were calculated using the area of the top surface (Top) of the specimen volume (10.8 m^2) and the area the top and side surfaces (Top+Sides) of the enclosing volume (15.288 m^2).The calculated sound absorption coefficients are shown in Figure 5 and Figure 6.



Figure 4. The baffle array with 100 mm spacing without a surrounding enclosure.

Above 200 Hz, the sound absorption coefficients calculated from the measurements made without a non-absorbing surrounding enclosure using the area of the top and sides of the enclosing volume are closer to those calculated from the measurements made with a non-absorbing surrounding enclosure using the area of the opening at the top of the enclosure, than those made using only the area of the top of the enclosing volume. This is a strong justification for adopting the changes to ISO 354:2003(E) [1] recommended in this paper.

However, there are still differences between sound absorption coefficients calculated with and without a non-absorbing surrounding enclosure. It is suggested that ISO:354 should recommend that sound absorption coefficients should normally be calculated from measurements made with a non-absorbing surrounding enclosure, unless there are very good reasons for measuring without a non-absorbing surrounding enclosure. If sound absorption coefficients are reported, it is further recommended that different names be given to sound absorption coefficients calculated using measurements made with or without a non-absorbing enclosure.

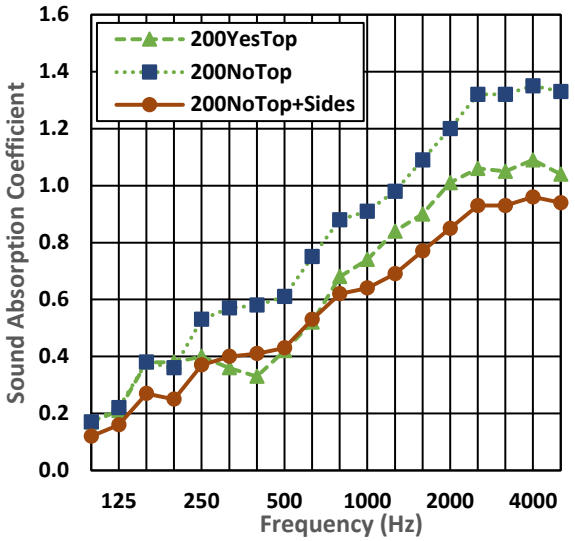


Figure 5. The calculated sound absorption coefficients of the baffle array with 200 mm spacing.

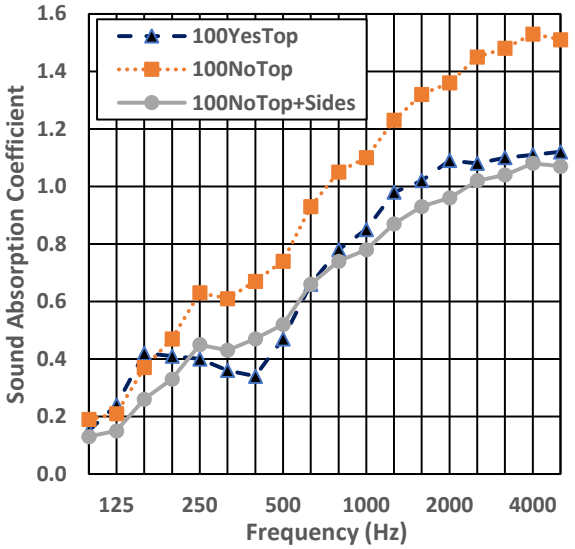


Figure 6. The calculated sound absorption coefficients of the baffle array with 100 mm spacing.

4. CONCLUSION

It is recommended that sound absorption be the fundamental result that is required to be given in ISO 354 reports. If sound absorption coefficients are reported, it is recommended that ISO 354 requires that they be calculated using the rules given in this paper. It is also recommended that different symbols be used for sound absorption coefficients calculated using measurements made with (α_e) or without (α_{ne}) a non-absorbing enclosure and that sound absorption coefficients calculated from measurements made with a non-absorbing enclosure are the preferred ones. These recommendations are made to stop suppliers advertising sound absorption coefficients as high as 1.7.
It is recommended that the room surfaces are not allowed to be part of a non-absorbing enclosure and that, in most circumstances, the only room surface close to a non-absorbing enclosure is the room surface that it is mounted on. It is recommended that the deep well approach be removed from ISO 354 for consistency.

5. REFERENCES

[1] ISO: "ISO 354:2003(E) Acoustics — Measurement of sound absorption in a reverberation room, Edition 2," International Organization for Standardization, Geneva, Switzerland, pp. 21, 2003.
[2] ASTM: "ASTM E795-23 Standard Practices for Mounting Test Specimens During Sound Absorption Tests ", ASTM International, West Conshohocken, United States, pp. 13, 2023.
[3] ISO: "ISO 11654:1997 Acoustics-Sound absorbers for use in buildings-Rating of sound absorption," International Organization for Standardization, Geneva, Switzerland, pp. 7, 1997.
[4] ASTM: "ASTM C423 − 22 Standard Test Method for Sound Absorption and Sound Absorption Coefficients by the Reverberation Room Method," ASTM International, West Conshohocken, United States, pp. 11, 2022.
[5] F. Kawakami, T. Sakai: "Deep-well approach for canceling the edge effect in random incident absorption measurements," *Journal of the Acoustical Society of Japan (E)*, vol. 19, no. 5, pp. 327-338, 1998.

DOI: 10.61782/fa.2025.0010



FORUM ACUSTICUM
EURONOISE 2025

A DATA-DRIVEN TWO-MICROPHONE METHOD FOR MEASURING THE SOUND ABSORPTION OF FINITE ABSORBERS

Leon Emmerich[1] **Patrik Aste**[2] **Eric Brandão**[3] **Mélanie Nolan**[4] **Jacques Cuenca**[5]
U. Peter Svensson[6] **Marcus Maeder**[1] **Steffen Marburg**[1] **Elias Zea**[2*]

[1] Chair of Vibro-Acoustics of Vehicles and Machines, Department of Engineering Physics and Computation, Technical University of Munich, Germany

[2] The Marcus Wallenberg Laboratory for Sound and Vibration Research, Department of Engineering Mechanics, KTH Royal Institute of Technology, Sweden

[3] Acoustical Engineering Program & Civil Engineering Graduate Program, Federal University of Santa Maria, Brazil

[4] Acoustic Technology, Department of Electrical and Photonics Engineering, Technical University of Denmark, Denmark

[5] Siemens Industry Software NV, Leuven, Belgium

[6] Department of Electronic Systems, Norwegian University of Science and Technology, Norway

ABSTRACT

A residual neural network is proposed to predict the sound absorption of an infinite rigidly-backed porous material from a classical two-microphone measurement above a finite porous sample. The network is trained using the microphones' transfer functions generated by a boundary element model (BEM), with a Delany-Bazley-Miki material model as a boundary condition. The network is validated numerically with BEM simulations and experimentally using two-microphone measurements of a baffled porous absorber of dimensions 60 cm×60 cm and 30 cm×60 cm, subject to various source locations. The results indicate that the network can significantly enhance the predictive capabilities of the classical two-microphone method. The suggested approach shows potential for accurately estimating the sound absorption coefficient of acoustic materials in realistic operational conditions.

**Corresponding author*: zea@kth.se.

Copyright: *©2025 L. Emmerich et al. This is an open-access article distributed under the terms of the Creative Commons Attribution 3.0 Unported License, which permits unrestricted use, distribution, and reproduction in any medium, provided the original author and source are credited.*

Keywords: *sound absorption estimation, finite porous materials, two-microphone method, neural networks.*

1. INTRODUCTION

The ability to characterize the absorption properties of absorbing materials is essential for a wide range of engineering applications. Standardized methods such as the impedance tube method [1, 2] or the reverberation chamber method [3] are limited to normal and random incidence, respectively. In contrast, angle-dependent absorption data can be obtained with *in situ* and free-field methods [4]. These methods typically rely on measurements of the sound pressure (and/or particle velocity) in the sample's vicinity [5–10] and on an analytical model of the sound field above the sample [4]. Existing models are based on plane-wave [5, 11, 12] or spherical-wave [6, 9, 10] assumptions and generally assume that the sample is infinite in extent. This assumption does not hold in measurements of realistic samples, and edge-diffraction effects result in erroneous absorption properties [13–19].

Several methods for modeling and mitigating edge diffraction effects have been proposed in the literature concerned with characterizing acoustic materials [18, 20–22]. In particular, a number of studies have employed

machine-learning approaches to mitigate the edge effect based on measurements with an array of microphones [23, 24]. Other work utilizes machine learning techniques for efficient work with the impedance tube [25] and physics-informed neural networks [26].

This study introduces a deep-learning-based two-microphone approach to predict the angle-dependent sound absorption coefficient of finite-sized acoustic samples. Such an approach is of interest in that it only requires common instrumentation and a straightforward measurement procedure (the well-established two-microphone method [5]), unlike the more cumbersome approach in [23]. The proposed method uses a 1D residual neural network trained to predict the angle-dependent sound absorption coefficient from transfer function measurements. The network is trained and validated based on BEM-generated data [18, 23]. The validity of the proposed approach is examined numerically and experimentally using fibrous samples of different sizes and orientations. The results are compared with impedance tube measurements and analytical predictions from the two-microphone measurements.

2. METHODOLOGY

2.1 Datasets

2.1.1 Numerical datasets

For training and validation purposes, a numerical dataset is generated with a boundary element method (BEM) [18], following a procedure similar to that of [23]. The two microphones are located at 1 cm and 3 cm above the sample, which is assumed to be flush-mounted on a rigid baffle. The material properties are described based on a Delany-Bazley-Miki model [27]. The remaining BEM parameters span relevant values commonly found in practical scenarios: the sample sizes span from 20×20 cm^2 to 1 m^2, the thicknesses $d \in [5, 200]$ mm, the flow resistivity $\sigma \in [5, 100]$ kNs/m^4, the source distance $\|\mathbf{r}_q\| \in [1.2, 1.8]$ m, the source azimuth $\phi \in [0, 360)$ deg, and the source elevation $\theta \in [0, 80]$ deg. The frequency range is $f \in [100 : 10 : 2000]$ Hz. 50 000 instances were generated and split into $80 : 20$ for training and validation, and an additional 3 000 unique instances (not seen during training) were generated to test the network. More details on sampling these parameters can be found in [28].

2.1.2 Experiental datasets

We also performed eight two-microphone measurements with glass wool samples, model Focus A2 by Saint-Gobain Ecophon, of two sizes (60×60 cm^2 and 30×60 cm^2) to validate the method experimentally for various source distances and incidence angles. The samples were flush-mounted in baffles of medium-density fiberboard (MDF) panels. As in the BEM-generated training set, the microphones (model G.R.A.S. 40 PH) were placed 1 and 3 cm above the sample, and an omnidirectional sound source (model Monacor KU-516) emitted a 10-second-long sine sweep. A Brüel & Kjær Type 2706 amplifier and a National Instruments NI eDAQ-9178 digital acquisition system were used to collect the relevant time signals for postprocessing. The reader is referred to [28] for more details on these experiments.

2.2 Proposed neural network

A 1D residual neural network is designed to take two input features: (i) the complex-valued transfer function between the two microphones, and (ii) the source elevation angle θ, to predict the frequency-dependent sound absorption coefficients. The real and imaginary parts of the transfer function are treated as separate feature channels. At the same time, the elevation angle is skip-connected and concatenated with the latent space resulting from the network's convolutional layers. For precise network design and architecture details, the reader is referred to [28].

The network is trained for 250 epochs, using the mean squared error (MSE) as the loss function. The optimization was performed using an Adam optimizer with mini-batches of 64 samples and a weight decay of 10^{-3} [29]. The learning rate was set to 10^{-3} in the first 10 epochs and reduced exponentially by 0.9 from the 11-th epoch onwards. An early stopping criterion was imposed to prevent overfitting. In general, it is shown in [28] that training converges around 125 epochs.

3. EXPERIMENTAL HIGHLIGHTS

The network predictions were first evaluated using only numerical data, that is, in the same form used for training. As mentioned in section 2.1, 3000 examples unseen by the network during training were used for testing the predictions. With an MSE of $8.42 \cdot 10^{-5}$, the network provides accurate predictions of the sound absorption coefficient in various scenarios.

Figure 1 shows the network's prediction for the two measured glass-wool samples. Figs. 1a and 1d show two example results for normal wave incidence, with the curves "Miki model" viewed as the reference results. The network predictions underestimate the absorption coefficient somewhat, by less than 0.05 for the larger sample (Fig. 1a) and by less than 0.10 for the smaller sample (Fig. 1d).

Physical absorber samples were measured in an impedance tube to offer typical experimental reference results. Results are shown in Figs. 1b and 1e, with predictions based on simulated measurements on a smaller sample, Fig. 1b, and a larger sample, Fig. 1e. Note that somewhat longer source distances were used in Figs. 1b and 1e, compared to Figs. 1a and 1d. Again, the predictions by the network seem to underestimate the absorption coefficient somewhat, but the agreement is very good for the larger sample. It is worth noting that the impedance tube measurement values deviate somewhat above 1.5 kHz and may not be considered as true reference results.

Finally, traditional two-microphone measurement results for a smaller and a larger sample are presented in Figs. 1c and 1f, together with network predictions. Slightly longer source distances were used for this final comparison. For such small samples as were tested here, the finite-size effects are substantial, and it is clear that the network predictions suppress these interference effects completely. For instance, owing to the intrinsic nature of the training of the network, the method inhibits the emergence of negative absorption values.

Finally, the consistency of the network predictions for varying source distances should be emphasized, as only marginal differences within the rows can be observed.

4. CONCLUSION

Based on a deep-learning-based two-microphone approach, we predict the angle-dependent sound absorption coefficient of finite-sized acoustic samples utilizing well-established measurement procedures and a one-dimensional residual neural network. More concretely, appropriate boundary element method simulations, assuming a Delany-Bazley-Miki material model, provide the necessary database for the network training and validation within a frequency range of interest between 100 Hz and 2 kHz. In addition, suitable measurements of fibrous samples of different sizes and orientations provide the transfer functions to validate the methodology. Comparing the results of the analytical model, the impedance tube measurements, and the prediction based on the neural network, one finds a high prediction quality concerning the analytical model and the impedance tube measurements. Furthermore, the neural network predictions toward the traditional two-microphone method are free from the typical edge diffraction effects, providing a suitable strategy for reliable absorption coefficient estimation. The proposed method aims to help engineers in room acoustics and material property identification accurately predict the sound absorption coefficients based on the well-known two-microphone measurement procedure without the common edge-diffraction errors.

5. ACKNOWLEDGMENTS

E.Z. acknowledges the financial support by the Swedish Research Council (Vetenskapprådet) under grant agreement No. 2020-04668. E.B. acknowledges the financial support by the National Research Council of Brazil (CNPq - Conselho Nacional de Desenvolvimento Científico e Tecnológico) under grant agreement No. 402633/2021-0. The authors would like to thank Saint-Gobain Ecophon (Hyllinge, Sweden) for providing the test samples and Stefan Jacob, Joakim Aste, and Charlotte Aste for supporting the work involved in the experimental setups.

6. REFERENCES

[1] ISO, "Acoustics - Determination of sound absorption coefficient and impedance in impedance tubes - Part 1: Method using standing wave ratio," International Standard ISO 10534–1, Geneva, Switzerland, 2001.

[2] ISO, "Acoustics - Determination of sound absorption coefficient and impedance in impedance tubes - Part 2: Transfer-function method," International Standard ISO 10534–2, Geneva, Switzerland, 2001.

[3] ISO, "Acoustics - measurement of sound absorption in a reverberation chamber," International Standard ISO 354, Geneva, Switzerland, 2003.

[4] E. Brandão, A. Lenzi, and S. Paul, "A review of the in situ impedance and sound absorption measurement techniques," *Acta Acustica United with Acustica*, vol. 101, no. 3, pp. 443–463, 2015.

[5] J. Allard and B. Sieben, "Measurements of acoustic impedance in a free field with two microphones and a spectrum analyzer," *The Journal of the Acoustical Society of America*, vol. 77, no. 4, pp. 1617–1618, 1985.

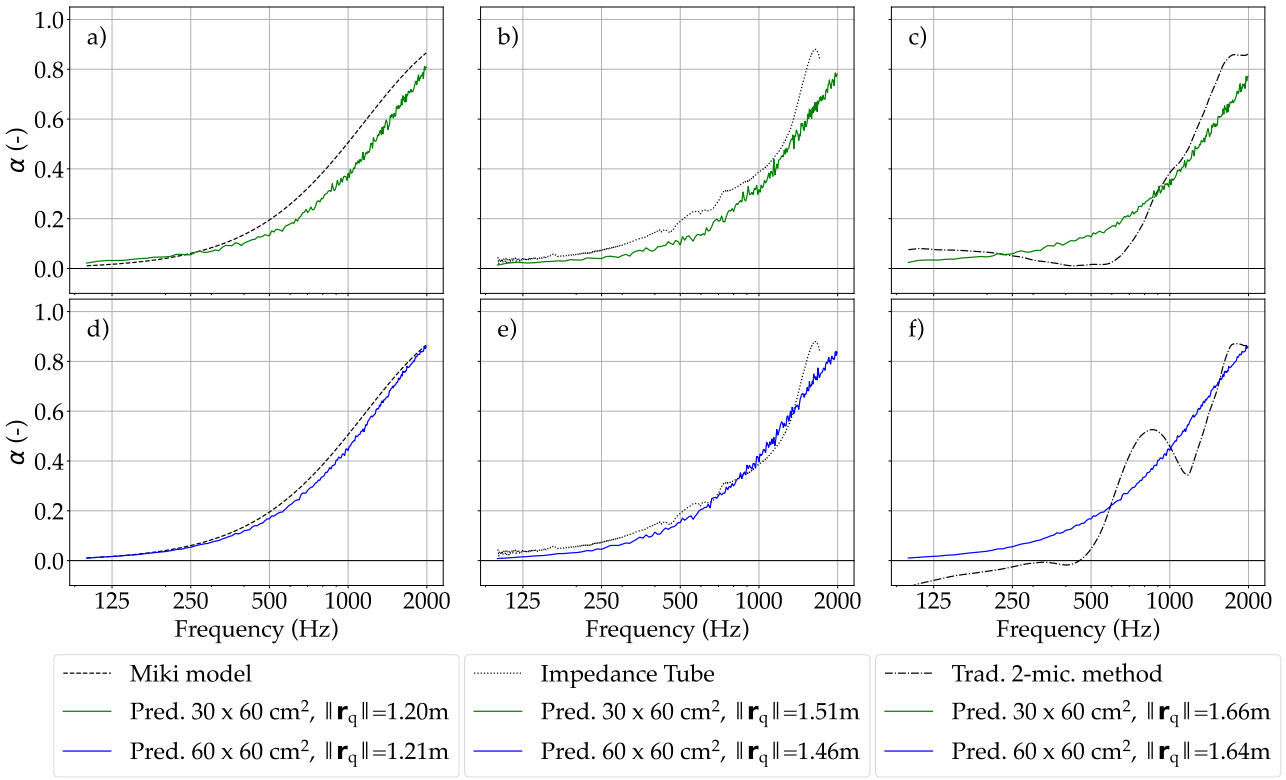


Figure 1. Predictions of the sound absorption coefficient for two samples at normal wave incidence and different source distances to the sample. Compared to Miki model with estimated flow resistivity of $54.7\,\mathrm{Nsm}^{-4}$ (a & d), impedance tube measurement (b & e) and the traditional two-microphone method (c & f).

[6] J.-F. Li and M. Hodgson, "Use of pseudo-random sequences and a single microphone to measure surface impedance at oblique incidence," *The Journal of the Acoustical Society of America*, vol. 102, no. 4, pp. 2200–2210, 1997.

[7] E. Mommertz, "Angle-dependent in-situ measurements of reflection coefficients using a subtraction technique," *Applied Acoustics*, vol. 46, no. 3, pp. 251–263, 1995.

[8] Y. Takahashi, T. Otsuru, and R. Tomiku, "In situ measurements of surface impedance and absorption coefficients of porous materials using two microphones and ambient noise," *Applied Acoustics*, vol. 66, no. 7, pp. 845–865, 2005.

[9] J. Hald, W. Song, K. Haddad, C.-H. Jeong, and A. Richard, "In-situ impedance and absorption coefficient measurements using a double-layer microphone array," *Applied Acoustics*, vol. 143, pp. 74–83, 2019.

[10] M. Alkmim, J. Cuenca, L. De Ryck, and W. Desmet, "Angle-dependent sound absorption estimation using a compact microphone array," *The Journal of the Acoustical Society of America*, vol. 150, no. 4, pp. 2388–2400, 2021.

[11] A. Richard, E. Fernandez-Grande, J. Brunskog, and C.-H. Jeong, "Estimation of surface impedance at oblique incidence based on sparse array processing," *The Journal of the Acoustical Society of America*, vol. 141, no. 6, pp. 4115–4125, 2017.

[12] M. Nolan, "Estimation of angle-dependent absorption coefficients from spatially distributed in situ measurements," *The Journal of the Acoustical Society of America*, vol. 147, no. 2, pp. EL119–EL124, 2020.

[13] A. De Bruijn, "A mathematical analysis concerning the edge effect of sound absorbing materials," *Acta Acustica United with Acustica*, vol. 28, no. 1, pp. 33–44, 1973.

[14] K. Kimura and K. Yamamoto, "The required sample size in measuring oblique incidence absorption coefficient experimental study," *Applied Acoustics*, vol. 63, no. 5, pp. 567–578, 2002.

[15] K. Hirosawa, K. Takashima, H. Nakagawa, M. Kon, A. Yamamoto, and W. Lauriks, "Comparison of three measurement techniques for the normal absorption coefficient of sound absorbing materials in the free field," *The Journal of the Acoustical Society of America*, vol. 126, no. 6, pp. 3020–3027, 2009.

[16] K. Hirosawa, H. Nakagawa, M. Kon, and A. Yamamoto, "Investigation of absorption coefficient measurement of acoustical materials by boundary element method using particle velocity and sound pressure sensor in free field," *Acoustical Science and Technology*, vol. 30, no. 6, pp. 442–445, 2009.

[17] T. Otsuru, R. Tomiku, N. B. C. Din, N. Okamoto, and M. Murakami, "Ensemble averaged surface normal impedance of material using an in-situ technique: Preliminary study using boundary element method," *The Journal of the Acoustical Society of America*, vol. 125, no. 6, pp. 3784–3791, 2009.

[18] E. Brandão, A. Lenzi, and J. Cordioli, "Estimation and minimization of errors caused by sample size effect in the measurement of the normal absorption coefficient of a locally reactive surface," *Applied Acoustics*, vol. 73, no. 6-7, pp. 543–556, 2012.

[19] M. Eser, S. Mannhardt, C. Gurbuz, E. Brandao, and S. Marburg, "Free-field characterization of locally reacting sound absorbers using bayesian inference with sequential frequency transfer," *Mechanical Systems and Signal Processing*, vol. 205, p. 110780, 2023.

[20] M. Ottink, J. Brunskog, C.-H. Jeong, E. Fernandez-Grande, P. Trojgaard, and E. Tiana-Roig, "In situ measurements of the oblique incidence sound absorption coefficient for finite sized absorbers," *The Journal of the Acoustical Society of America*, vol. 139, no. 1, pp. 41–52, 2016.

[21] E. Brandão and E. Fernandez-Grande, "Analysis of the sound field above finite absorbers in the wavenumber domain," *The Journal of the Acoustical Society of America*, vol. 151, no. 5, pp. 3019–3030, 2022.

[22] J. M. Schmid, M. Eser, and S. Marburg, "Bayesian approach for the in situ estimation of the acoustic boundary admittance," *Journal of Theoretical and Computational Acoustics*, vol. 31, no. 4, p. 2350013, 2023.

[23] E. Zea, E. Brandão, M. Nolan, J. Cuenca, J. Andén, and U. P. Svensson, "Sound absorption estimation of finite porous samples with deep residual learning," *The Journal of the Acoustical Society of America*, vol. 154, no. 4, pp. 2321–2332, 2023.

[24] M. Müller-Giebeler, M. Berzborn, and M. Vorländer, "Free-field method for inverse characterization of finite porous acoustic materials using feed forward neural networks," *The Journal of the Acoustical Society of America*, vol. 155, no. 6, pp. 3900–3914, 2024.

[25] M. Eser, L. Emmerich, C. Gurbuz, and S. Marburg, "Deep learning-assisted two-cavity method for estimating sound propagation characteristics in porous media," *Journal of Theoretical and Computational Acoustics*, vol. 33, p. 2440001, 2025.

[26] J. D. Schmid, P. Bauerschmidt, C. Gurbuz, M. Eser, and S. Marburg, "Physics-informed neural networks for acoustic boundary admittance estimation," *Mechanical Systems and Signal Processing*, vol. 215, p. 111405, 2024.

[27] Y. Miki, "Acoustical properties of porous materials-Modifications of Delany-Bazley models," *Journal of the Acoustical Society of Japan (E)*, vol. 11, no. 1, pp. 19–24, 1990.

[28] L. Emmerich, P. Aste, E. Brandão, M. Nolan, J. Cuenca, U. P. Svensson, M. Maeder, S. Marburg, and E. Zea, "A data-driven two-microphone method for in-situ sound absorption measurements," *arXiv:2502.04143*, 2025.

[29] A. Géron, *Hands-on Machine Learning with Scikit-Learn, Keras, and TensorFlow*. " O'Reilly Media, Inc.", 2022.

DOI: 10.61782/fa.2025.0300



FORUM ACUSTICUM
EURONOISE 2025

DIFFUSION EQUATION-BASED ESTIMATION OF SPATIALLY NON-UNIFORM SURFACE ABSORPTION COEFFICIENTS

Albert G. Prinn[1*] **Emanuël A. P. Habets**[2]
[1] Fraunhofer Institute for Integrated Circuits (IIS), Erlangen, Germany
[2] International Audio Laboratories Erlangen[†], Germany
[†]A joint institution of the Friedrich-Alexander-Universität Erlangen-Nürnberg (FAU) and Fraunhofer Institute for Integrated Circuits (IIS)

ABSTRACT

The acoustic diffusion equation provides a generalized statistical model of room acoustical fields, allowing for non-uniform distributions of sound energy and spatially varying surface absorption coefficients. Recent studies have shown that the diffusion equation can be used to estimate spatially uniform, frequency-dependent absorption coefficients from in situ measurements. In this work, we extend this approach to handle spatially non-uniform absorption by using the ratio of intensity to energy density. Numerical simulations demonstrate the feasibility of this method when used to estimate frequency-dependent, spatially non-uniform absorption coefficients in a room.

Keywords: *Acoustic diffusion equation, Non-uniform absorption coefficient estimation, Intensity - Energy density ratio, Field index.*

1. INTRODUCTION

Accurate descriptions of sound-absorbing materials are essential for reliable computer simulations of room acoustics [1]. While absorption coefficients can be measured in controlled environments, e.g., reverberation chambers [2], their applicability diminishes once materials are installed in a room. The angle-dependent nature of many sound-absorbing materials means that their absorption coefficients can depend on the room in which they are installed. Consequently, several in-situ measurement methods for measuring absorption coefficients can be found in the literature [3].

The diffusion equation has recently been used for in-situ estimation of spatially uniform, frequency-dependent absorption coefficients in a small room [4]. While the diffusion equation predicts a spatially uniform reverberation time (for an uncoupled room), it also predicts a non-uniform energy flux. The non-uniformity of the energy flux is utilized in this work to estimate spatially non-uniform absorption coefficients in a small room. The proposed inverse method employs eigenvalue analysis of a diffusion equation model of a room to estimate unknown surface absorption coefficients.

This paper is organized as follows: Section 2 provides background information relevant to the work. Section 3 presents the diffusion equation, a numerical implementation, and the post-processed solutions. The method for estimating the absorption coefficient is introduced in Sec. 4, and a simulated room with four different boundary conditions is presented as a test case in Sec. 5. The results of the absorption coefficient estimations are discussed in Sec. 6. Limitations and future studies of the proposed method are discussed in Sec 7, and Sec. 8 outlines the conclusions.

2. LITERATURE REVIEW

The normal incidence impedance of a material sample can be measured using an impedance tube [5], and a random incidence absorption coefficient can be computed from the normal impedance. However, measurements in an impedance tube preclude edge effects and may include unwanted installation effects. Thus, reverberation chambers are often used to measure the random incidence ab-

*__Corresponding author__: albert.prinn@iis.fraunhofer.de.
__Copyright__: ©2025 Prinn and Habets. *This is an open-access article distributed under the terms of the Creative Commons Attribution 3.0 Unported License, which permits unrestricted use, distribution, and reproduction in any medium, provided the original author and source are credited.*

sorption coefficients of large material samples [2]. Due to room and installation effects, the coefficients measured in a reverberation chamber may not reflect the actual absorption of a material placed in a room. Thus, in-situ methods can provide additional insight into the absorption characteristics of materials.

While many in-situ methods can be found in the literature [3], we limit our scope to those that consider intensity. Tijs and Druyvesteyn [6] propose and validate the use of several spatially distributed intensity measurements to determine the absorption coefficient of a material sample. Kuipers *et al.* [7] numerically verify a plane wave-based intensity method for measuring absorption coefficients of a material sample. Since the intensity over a sample can be non-uniform [8], intensity-based methods often require spatial averaging. Vigran [9] introduces a *field index*, which is the ratio of the intensity to the product of the energy density and the speed of sound. Wijnant *et al.* [10] note that the field index could be used as a measure of sound absorption. A review of the literature suggests that this observation has not been further explored.

Ollendorff [11] proposes a diffusion model of enclosed sound fields, and Picaut *et al.* [12] provide a mathematical derivation of the diffusion equation. Several researchers have developed and evaluated models based on the diffusion equation. For example, Foy *et al.* [13] compare predictions of reverberation time from two diffusion equation models to measured reverberation time data. Billon *et al.* [14] propose a boundary condition for the diffusion equation based on Eyring's absorption coefficient, and Jing and Xiang [15] propose a modified boundary condition for the diffusion equation. Prinn *et al.* [4] use the diffusion equation to estimate spatially uniform absorption coefficients of the surfaces of a measured room.

The diffusion equation allows for the incorporation of random incidence absorption coefficients that can vary spatially. By solving the diffusion equation, we can predict various parameters such as reverberation time, energy density, and intensity. This study utilizes the capability to model spatially non-uniform absorption along with predictions of reverberation time and field index to estimate absorption coefficients across multiple surfaces. The approach is demonstrated using low-frequency finite element simulations.

3. THEORY

In this section, we introduce the diffusion equation, a finite element method implementation, and the processing of the first eigenvalue and eigenvector of the diffusion equation.

3.1 Diffusion equation

Following the derivation by Picaut *et al.* [12], the homogeneous diffusion equation can be written as

$$\frac{\partial w(t,\mathbf{x})}{\partial t} - D\,\nabla^2 w(t,\mathbf{x}) = 0\,, \tag{1}$$

where $w(t,\mathbf{x})$ is the sound energy density, which depends on time t and spatial position $\mathbf{x}$. The diffusion coefficient $D = \bar{l}c/3$ is given in terms of the speed of sound c and mean free path $\bar{l}$. The mean free path is given by $\bar{l} = 4V/S$, where V is the room volume and S is the surface area. [1]

To complete the model, we make use of the sound absorption coefficient boundary condition proposed by Jing and Xiang [15]

$$D\,\frac{\partial w(t,\mathbf{x})}{\partial n} = \frac{-c\,\alpha}{2(2-\alpha)} w(t,\mathbf{x})\,, \tag{2}$$

where $\partial/\partial n$ is the normal derivative, and α is a random incidence absorption coefficient. Note that the absorption coefficient can be spatially dependent, a fact that forms the basis of this work.

Choosing a solution that decays exponentially, we write the sound energy density as [16, Eq. (5.6)]

$$w(t,\mathbf{x}) = \phi(\mathbf{x})\mathrm{e}^{-\lambda t}\,, \tag{3}$$

with amplitude (eigenvector) ϕ and damping constant (eigenvalue) λ.

3.2 Numerical implementation

Equations (2) and (3) are used in combination with the finite element method to reformulate Eq. (1), resulting in the eigenvalue problem

$$\left[D\,\mathbf{K} + \sum_{j=0}^{J} \frac{c\,\alpha_j}{2(2-\alpha_j)}\mathbf{C}_j - \lambda\mathbf{M}\right]\boldsymbol{\phi} = \mathbf{0}\,, \tag{4}$$

where $\mathbf{K}$, $\mathbf{C}$, and $\mathbf{M}$ are stiffness, damping, and mass matrices, respectively, j identifies an absorbing surface, λ is an eigenvalue, and $\boldsymbol{\phi}$ is a discretized eigenvector. The elemental stiffness, damping, and mass matrices are given by

$$\mathbf{K}_e = \int_e \nabla\mathbf{N}^T \cdot \nabla\mathbf{N}\,\mathrm{d}V\,, \tag{5}$$

[1] This mean free path is based on a diffuse field assumption.

$$\mathbf{C}_{e',j} = \int_{e'} \mathbf{N}^T \mathbf{N} \, \mathrm{d}S_j \,, \tag{6}$$

$$\mathbf{M}_e = \frac{1}{c^2} \int_e \mathbf{N}^T \mathbf{N} \, \mathrm{d}V \,, \tag{7}$$

where the subscript e represents an interior element, e' represents a boundary element, S_j is a sound absorbing surface, and $\mathbf{N}$ are interpolating shape functions. The elemental matrices are solved numerically and used to assemble $\mathbf{K}$, $\mathbf{C}$, and $\mathbf{M}$. (For details, see, e.g., Prinn [17]).

3.3 Post-processed quantities

The solution of Eq. (4) provides a set of eigenvalues and eigenvectors. We only concern ourselves with the first (smallest) eigenvalue, λ_0, and the first eigenvector, ϕ_0.

3.3.1 Reverberation time

An estimation of the reverberation time of an uncoupled room can be computed from the eigenvalue as follows:

$$\widehat{T}_{60} = \frac{2\log(1 \times 10^3)}{\lambda_0} \,. \tag{8}$$

3.3.2 Field index

A normalized energy flux, or intensity, can be computed from the eigenvector, as follows

$$\widehat{\mathbf{I}} = -D\nabla \cdot \phi_0(\mathbf{x}) \,. \tag{9}$$

The intensity normal to an absorbing surface is of interest in this work. This is given by

$$\widehat{\mathrm{I}}_n = \widehat{\mathbf{I}} \cdot \mathbf{n} \,, \tag{10}$$

where $\mathbf{n} = (n_x, n_y, n_z)$ is an outwardly pointing unit normal vector. Finally, for the absorption coefficient estimation, the (normalized) intensity to energy density ratio, or field index [9], is defined as

$$\widehat{\mathrm{F}} = \frac{\widehat{\mathrm{I}}_n}{\phi_0 \, c} \,. \tag{11}$$

Note that the field index can be related to the absorption coefficient (as observed in Ref. [10]). This can be shown by replacing the energy density in Eq. (2) with the eigenvector. Thus, for the boundary condition considered,

$$\widehat{\mathrm{F}} \sim \frac{\alpha}{2(2-\alpha)} \,. \tag{12}$$

4. ESTIMATION METHOD

The impedance estimation method consists of two main steps. First, measurements of sound pressure and normal velocity are taken at one or more positions within a room, but close to the surfaces at which we would like to estimate the absorption coefficient. This is because the intensity and energy density normal to the surface are required. The reverberation time, intensity, and energy density at these measured positions are calculated. A field index is then computed from the intensity and energy density.

Second, a diffusion equation model of the room is generated, which incorporates unknown absorption characteristics. For example, if the surfaces of a room have one impedance but an absorbing material with a different impedance is placed on the floor, two frequency-dependent absorption coefficients need to be estimated. An eigenvalue analysis of the diffusion equation model is performed, from which the reverberation time and field index at the measurement positions can be computed. An optimization algorithm is subsequently employed to minimize the differences between the observed and simulated values, allowing for the estimation of the absorption coefficients.

4.1 Reference data

An impulse response measurement is made at each surface of interest. The impulse response's energy decay curve is computed using backward Schroeder integration, and the reverberation time is estimated from a straight-line fit to the energy decay curve between -5 dB and -35 dB.

Using two microphones placed normal to the surface of interest, the normal velocity can be estimated from the conservation of momentum, approximated by a finite difference scheme. The frequency domain pressure, P, and normal velocity, V_n, are computed via Fourier transformation. For a given frequency, ω, the time-averaged active normal intensity is given by

$$\mathrm{I}_n(\omega) = \mathrm{Re}\left(\frac{P(\omega)V_n^*(\omega)}{2}\right) \,, \tag{13}$$

and the normal energy density is given by (see, e.g., [18])

$$\mathrm{E}_n(\omega) = \frac{|P(\omega)|^2}{2\rho c^2} + \frac{\rho |V_n(\omega)|^2}{2} \,. \tag{14}$$

A normal field index can be computed from these two quantities, as follows:

$$\mathrm{F}(\omega) = \frac{\mathrm{I}_n(\omega)}{\mathrm{E}_n(\omega) \, c} \,. \tag{15}$$

4.2 Absorption coefficient estimation

A diffusion equation model of the room under test is generated, and an optimization algorithm is used to refine initial guesses of the unknown absorption coefficients to arrive at final estimates. For the optimization, the reverberation times and field index are compared.

If the absorption coefficient sought is spatially uniform, the field index is not computed. The reason is that the field index will be the same on all surfaces. If two absorption coefficients are needed, an average of the reverberation times measured close to each of the surfaces of interest is compared to the diffusion equation prediction. Noting that the diffusion equation predicts a spatially uniform reverberation time, the averaging can lead to improved estimates. For two unknown impedances, two field indices are measured (one for each surface of interest). The ratio of the field indices is used as a measure of the amount of absorption at each surface. The ratio of field indices for two unknown absorption coefficients is given by

$$\mathrm{G}_{2,1} = \frac{\mathrm{F}_{n,2}}{\mathrm{F}_{n,1}}\,, \tag{16}$$

where the subscripts indicate the first and second surfaces. A similar expression is used for the ratio of the diffusion equation field indices. If three or more surfaces are considered, G will be a vector containing the ratios of the field indices with respect to one of the surfaces. Note that using the field index ratio results in a fully determined optimization problem.

To demonstrate the optimization routine, we consider a problem with three unknown absorption coefficients. An array that contains the reverberation time and two field index ratios is generated. For each frequency, or frequency band, considered, the optimization problem reads

$$\tilde{\boldsymbol{\alpha}}(\omega) = \underset{\hat{\alpha}_1,\hat{\alpha}_2,\hat{\alpha}_3}{\arg\min} \|\mathbf{C}(\omega) - \widehat{\mathbf{C}}(\hat{\alpha}_j(\omega))\|_2^2. \tag{17}$$

where $\mathbf{C} = [T_{60}\ \mathrm{G}_{2,1}\ \mathrm{G}_{3,1}]$ and $\widehat{\mathbf{C}} = [\widehat{T}_{60}\ \widehat{\mathrm{G}}_{2,1}\ \widehat{\mathrm{G}}_{3,1}]$. Using Sabine's formula [19], we obtain an initial estimate of the absorption coefficient from a measurement of the reverberation time, as follows:

$$\hat{\alpha}_j(\omega) = 0.161 \frac{V}{S\,T_{60}(\omega)}\,, \tag{18}$$

where V is the room volume, S is the total surface area, and T_{60} is the measured reverberation for a given frequency band. This value serves as an initial guess for all unknown absorption coefficients. A nonlinear least-squares solver is used to obtain the estimates.

5. SIMULATION TEST CASE

The test data is generated using a finite element model of a reverberant room. Details of the room, the simulation setup, and the post-processing applied to the simulation solutions are presented here.

5.1 Room and parameters

The room is a reverberant space with non-parallel surfaces. It may either be empty or contain a sample of material placed on the floor. A diagram of the room is provided in Fig. 1a, and the coordinates of the corners can be found in Tab. 1.

The air in the room has a speed of sound of 343 m/s, and a density of 1.2 kg/m³. A point source is located at the second corner of the room. Impedance boundary conditions are specified for the room's surfaces and the material sample. Four impedance conditions are considered; these are described below.

5.1.1 Case 0

A spatially uniform, frequency-independent, real-valued impedance is considered to demonstrate the inherent error of the diffusion equation-based estimation method. The room is empty, and all surfaces have a normalized impedance of 19.77, which results in a random incidence absorption coefficient of 0.3.

5.1.2 Case 1

In this case, a complex-valued, frequency-dependent impedance is specified on all surfaces of the empty room. The impedance is described using a Delany-Bazley-Miki model [20]. The impedance is given by:

$$\zeta = (R + \mathrm{i}X)\coth\left[(\gamma + \mathrm{i}\beta)l\right] \tag{19}$$

where

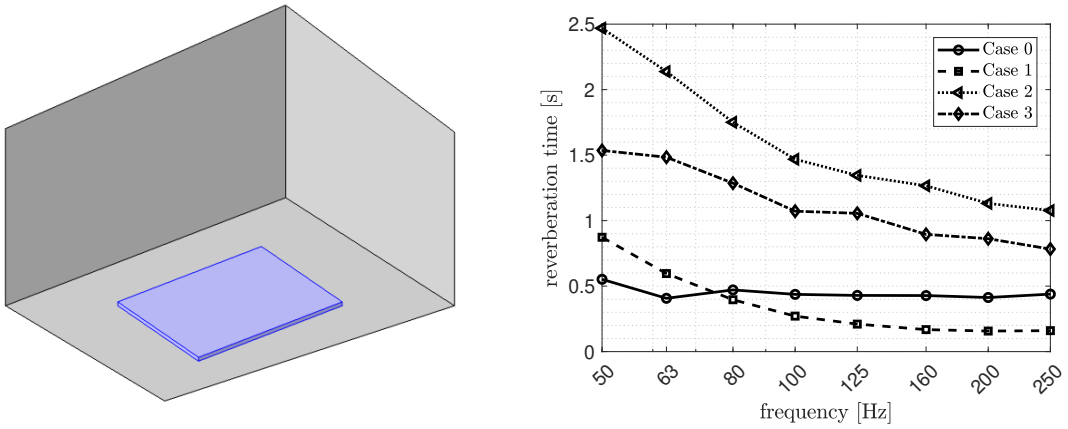
$$R = 1 + 0.070\left(\frac{f}{r}\right)^{-0.632}\,,$$

$$X = -0.107\left(\frac{f}{r}\right)^{-0.632}\,,$$

$$\gamma = \frac{2\pi f}{c}\left[0.160\left(\frac{f}{r}\right)^{-0.618}\right]\,,$$

$$\beta = \frac{2\pi f}{c}\left[1 + 0.109\left(\frac{f}{r}\right)^{-0.618}\right]\,,$$

f is frequency, $l = 0.1$ m, and $r = 41 \times 10^3$ rayl/m.



(a) (b)

Figure 1: Test case: (a) reverberant room with non-parallel absorbing walls and a material sample on the floor. (b) average reverberation time as a function of third-octave bands for four different boundary conditions.

Table 1: Coordinates of the corners of the simulated reverberation chamber. The corner at which the sound source is located is shown in bold.

corner	1	**2**	3	4	5	6	7	8
x [m]	0.36	**8**	7.8	0	0.36	8	7.8	0
y [m]	0.57	**0**	6	6	0.57	0	6	6
z [m]	0	**0**	0	0	4.17	4.51	5	4.6

Table 2: Coordinates of sample corners.

corner	1	2	3	4
x [m]	0.50	2.50	2.50	0.50
y [m]	0.50	0.50	2.00	2.00
z [m]	0.10	0.10	0.10	0.10

5.1.3 Case 2

The normalized impedance of the surfaces of the room is 100, which gives a random incidence absorption coefficient of 0.0734. A material sample with a height of 0.1 m is placed on the floor. The coordinates of four corners of the sample are given in Tab. 2. The impedance model described in Eq. (19) is specified on the sample's surface.

5.1.4 Case 3

The impedance of the walls is 100, while the impedance of the ceiling is 19.77. These values yield random incidence absorption coefficients of 0.0734 for the walls and 0.3 for the ceiling. The sample placed on the floor utilizes the Miki impedance model, as introduced in Eq. (19).

5.2 Simulation and post-processing

Finite element method simulations of the reverberation chamber are performed in the frequency domain to incorporate complex-valued, frequency-dependent boundary conditions in the impulse responses. Impulse responses are obtained via inverse Fourier transformation and filtered into third-octave frequency bands using a second-order Butterworth filter. Decay curves are then calculated from these responses using Schroeder integration [21]. The reverberation times, shown in Fig. 1b, are estimated by fitting straight lines to the energy decay curves between -5 dB and -35 dB, adjusting for offset, and determining the time at -60 dB. Field indices are computed from the pressure and normal velocity at the center of each surface of interest.

6. RESULTS

In this section, we compare the specified and estimated absorption coefficients for four test cases. It is important to note that the specified random incidence absorption coefficients are calculated from the specified impedances.

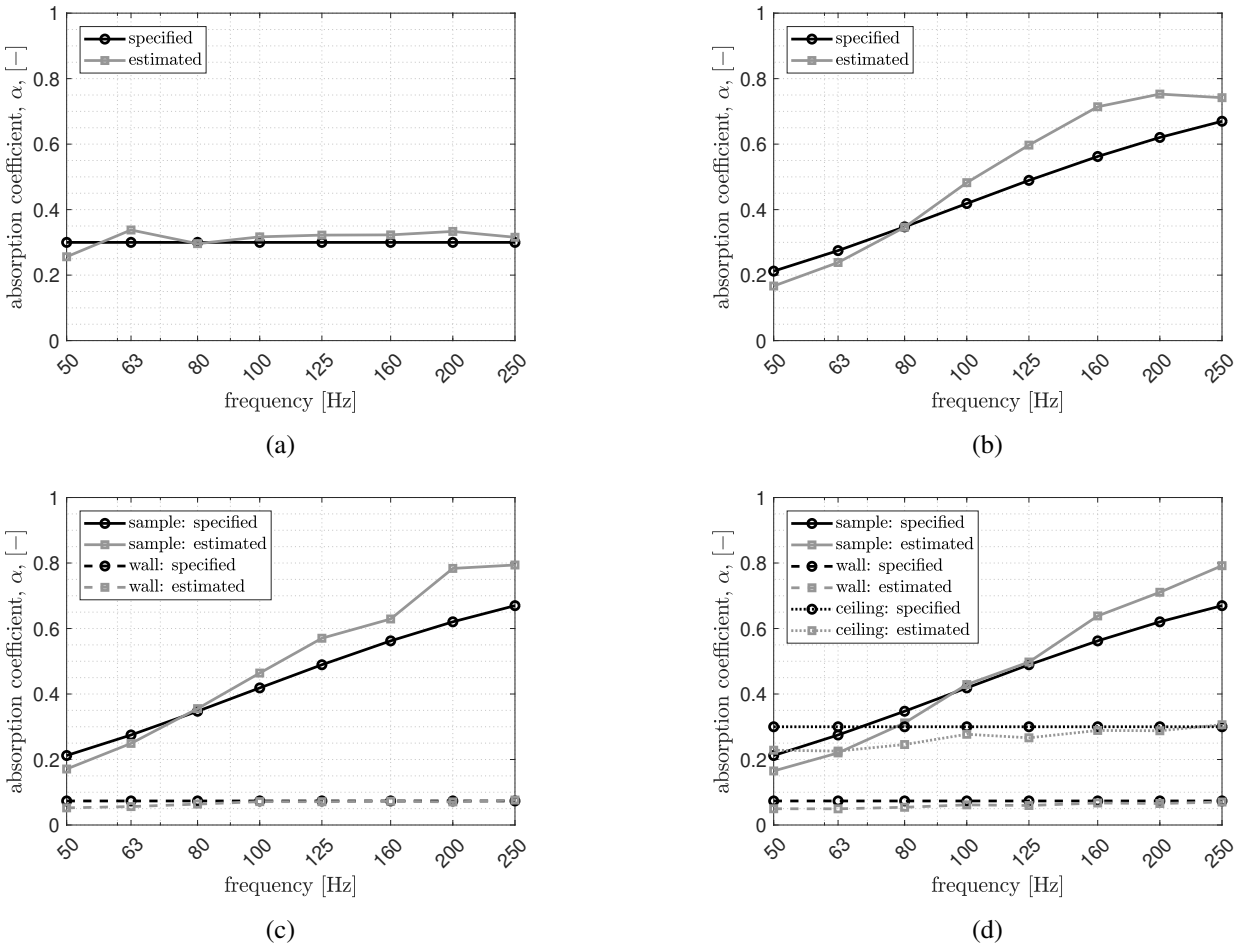


Figure 2: Comparison of specified and estimated absorption coefficients. (a) Case 0 (1 real-valued impedance), (b) Case 1 (1 complex-valued impedance), (c) Case 2 (2 impedances), and (d) Case 3 (3 impedances).

The absorption coefficients for Case 0 are shown in Fig. 2a. A reasonable level of agreement is found. Slight differences are caused by the inability of the diffusion equation to model the spatial non-uniformity of the reverberation time [22] and the assumption of a random incidence absorption coefficient in the diffusion equation, which is an idealization of sound absorption based on a perfectly diffuse field. In Fig. 2b, the spatially uniform absorption coefficients given by the Miki model are compared with the estimated values. The error in this comparison is larger than Case 0. Although the exact cause of this increased error is not fully known, it is believed that the reverberation time and the assumption of random incidence contribute to it. In Case 2, two unknown absorption coefficients are estimated: one for the room's walls and another for the sample itself. As can be seen in Fig. 2c, the absorption coefficient estimation method effectively captures both the frequency trends and the general levels of the unknown coefficients. For Case 3, three unknown absorption coefficients are estimated. This data is compared to the specified absorption coefficients in Fig. 2d. Once again, a reasonable level of agreement is found. We observe that, while there is some qualitative agreement, there are also differences between the specified and estimated absorption coefficients. We expect that these differences will diminish as the frequency increases; however, high-frequency models were not created for this study due to the high computational costs involved.

7. DISCUSSION

The present study has demonstrated that the proposed method can be used to estimate the unknown absorption coefficients of multiple surfaces. In this section, we address limitations and discuss possible future studies.

7.1 Reverberation time

The diffusion equation assumes a nearly diffuse field. Thus, the reverberation time predicted by the diffusion equation in an uncoupled room is spatially uniform. However, the reverberation time in a room tends to be spatially non-uniform. [2] Thus, more accurate measures of the average reverberation time may improve the estimates. While this might be reasonable in a dedicated measurement setting, a high number of measurements might be impractical for some audio applications, e.g., estimating the absorption coefficients of a listening environment using only a few microphones.

7.2 Normal velocity measurement

Accurately measuring the velocity normal to an absorbing surface can be challenging. The spacing of the microphones and their distance from the surface may affect the estimates. Errors in the measured velocity will lead to inaccuracies in the intensity and energy density, which will subsequently impact the estimates of the absorption coefficient.

7.3 Impedance estimation

In-situ absorption coefficients can be useful for certain simulation tools, but wave methods usually require boundary conditions based on impedance or admittance. Additionally, research has shown that using angle-dependent reflection coefficients at room boundaries enhances the accuracy of the image source method, which requires knowledge of the surface impedance. The absorption coefficients estimated in this study can be converted into real-valued impedances using theories like those from Kuttruff [16]. However, these values were calculated during the preparation of this paper but were deemed too inaccurate to be included. While literature exists on estimating complex-valued impedance from absorption coefficients, such as the work by Mondet *et al.* [23], this topic is outside the scope of the current study.

[2] This is well known in the community, evidenced by the need to average multiple reverberation time measurements in the reverberation chamber method [2], and recently demonstrated for low frequencies [22].

7.4 Modal field

This study has considered a range of frequencies that would generally be associated with the modal region of a sound field. While the diffusion equation is frequency-independent, by construction, it does not model modal fields. Some of the observed errors may be related to missing modal effects. While it is expected that the estimation method will perform better at frequencies above the Schroeder frequency, i.e., for frequencies at which the diffuse field assumption becomes reasonable, further testing is required to determine whether or not improved estimates might be found at higher frequencies.

7.5 Further studies

While the proposed method holds potential for real-world applications, several aspects still need to be investigated. These include the effects of the room geometry, source and receiver positions, measurement noise, and the diffusion coefficient, D, on the absorption coefficient estimates. Also, the impact of multiple complex-valued impedance surfaces and the method's performance for a broader range of frequencies should be investigated. Finally, extending the method to wave methods might also be interesting.

8. CONCLUSION

This paper presents an inverse method to estimate spatially non-uniform absorption coefficients in a room. The proposed method is based on the idea that field index ratios can identify areas of varying sound absorption in the room. An eigenvalue analysis of a diffusion equation model of the room is performed, from which the reverberation time and field index ratio(s) at the measurement positions are computed. An optimization algorithm is employed to minimize the differences between the observed and simulated values, allowing for the estimation of the unknown coefficients. The method is demonstrated using low-frequency finite element simulations. This proof-of-concept work has shown that, at least in principle, the diffusion equation can be used to estimate spatially non-uniform, frequency-dependent absorption coefficients. Future work should consider experimental validations of the proposed method.

9. REFERENCES

[1] M. Vorländer, "Computer simulations in room acoustics: Concepts and uncertainties," *J. Acoust. Soc. Am.*, vol. 133, no. 3, pp. 1203–1213, 2013.

[2] ISO 354:2003, "Acoustics — Measurement of sound absorption in a reverberation room," tech. rep., International Organization for Standardization, Geneva, CH, (2003).

[3] E. Brandao, A. Lenzi, and S. Paul, "A review of the in situ impedance and sound absorption measurement techniques," *Acta. Acust. united Ac.*, vol. 101, 06 2015.

[4] A. G. Prinn, C. Tuna, A. Walther, and E. A. P. Habets, "Estimating frequency-dependent absorption coefficients in small rooms using a diffusion model," in *156th AES Convention*, (Madrid, Spain), June 2024.

[5] ISO 10534-2:1998, "Determination of sound absorption coefficient and impedance in impedance tubes — Part 2: Transfer-function method," tech. rep., International Organization for Standardization, Geneva, CH, (1998).

[6] E. Tijs and E. Druyvesteyn, "An intensity method for measuring absorption properties in situ," *Acta Acust. united Ac.*, vol. 98, 03 2012.

[7] E. R. Kuipers, Y. H. Wijnant, and A. de Boer, "A numerical study of a method for measuring the effective in situ sound absorption coefficient," *J. Acoust. Soc. Am.*, vol. 132, pp. EL236–EL242, 08 2012.

[8] C.-H. Jeong, "Non-uniform sound intensity distributions when measuring absorption coefficients in reverberation chambers using a phased beam tracinga)," *J. Acoust. Soc. Am.*, vol. 127, pp. 3560–3568, 06 2010.

[9] T. Vigran, "Acoustic intensity-energy density ratio: An index for detecting deviations from ideal field conditions," *JSV*, vol. 127, no. 2, pp. 343–351, 1988.

[10] Y. Wijnant, E. Kuipers, and A. de Boer, "Development and application of a new method for the in-situ measurement of sound absorption," in *Proceedings of ISMA 2010 Conference*, pp. 1–14, Katholieke Universiteit Leuven, Sept. 2010.

[11] F. Ollendorff, "Statistical room-acoustics as a problem of diffusion (a proposal)," *Acustica*, vol. 21, pp. 236–245, 1969.

[12] J. Picaut, L. Simon, and J.-D. Polack, "A mathematical model of diffuse sound field based on a diffusion equation," *Acta Acust. united Ac.*, vol. 83, no. 4, pp. 614–621, 1997.

[13] C. Foy, A. Billon, V. Valeau, J. Picaut, A. Sakout, and G. Reigner, "Validation of a numerical diffusion-based modelling of the reverberated sound field in long rooms," in *ICSV*, 07 2005. Lisbon, Portugal.

[14] A. Billon, J. Picaut, and A. Sakout, "Prediction of the reverberation time in high absorbent room using a modified-diffusion model," *Appl. Acoust.*, vol. 69, no. 1, pp. 68–74, 2008.

[15] Y. Jing and N. Xiang, "On boundary conditions for the diffusion equation in room-acoustic prediction: Theory, simulations, and experiments," *J. Acoust. Soc. Am.*, vol. 123, pp. 145–153, 01 2008.

[16] H. Kuttruff, *Room Acoustics*. Taylor & Francis, 6th ed., 2017.

[17] A. G. Prinn, "A review of finite element methods for room acoustics," *Acoustics*, vol. 5, no. 2, pp. 367–395, 2023.

[18] J. Ghan, B. S. Cazzolato, and S. D. Snyder, "Expression for the estimation of time-averaged acoustic energy density using the two-microphone method (l)," *J. Acoust. Soc. Am.*, vol. 113, pp. 2404–2407, 05 2003.

[19] W. C. Sabine, *Collected papers on acoustics*. Cambridge: Harvard University Press, 1922.

[20] Y. Miki, "Acoustical properties of porous materials – modifications of delany-bazley models–," *J. Acoust. Soc. Jpn.*, vol. 11, no. 1, pp. 19–24, 1990.

[21] M. R. Schroeder, "New method of measuring reverberation time," *J. Acoust. Soc. Am.*, vol. 37, no. 6, pp. 1187–1188, 1965.

[22] A. G. Prinn, Çağdaş Tuna, A. Walther, and E. A. Habets, "A study of the spatial non-uniformity of reverberation time at low frequencies," *Appl. Acoust.*, vol. 227, p. 110220, 2025.

[23] B. Mondet, J. Brunskog, C.-H. Jeong, and J. H. Rindel, "From absorption to impedance: Enhancing boundary conditions in room acoustic simulations," *Appl. Acoust.*, vol. 157, p. 106884, 2020.

DOI: 10.61782/fa.2025.0217

FORUM ACUSTICUM EURONOISE 2025

COMPARATIVE ANALYSIS OF ACOUSTIC ABSORPTION TESTING METHODS FOR DIFFERENT LAYERS OF COTTON WADDING

Mehrangiz Mastoori[1*] **Ana Maria Lacasta**[2]
Inmaculada R. Cantalapiedra [2]**Francesca Merli**[3]
Cinzia Buratti[3]
[1] CIRIAF – University of Perugia, Perugia, Italy
[2] Universitat Politècnica de Catalunya, Barcelona, Spain
[3] University of Perugia, Perugia, Italy

ABSTRACT

Sound-absorbing materials play a crucial role in various applications, ranging from noise control to architectural acoustics, enabling us to enhance the acoustic environment and improve our quality of life. Cotton wadding samples with four thicknesses and dimensions were investigated in the present paper. They were assembled in panels, including cylindrical (29 mm and100-mm diameter) and square (400*400mm²) samples. A comprehensive investigation into the differences observed when evaluating the acoustic properties of a multi-layered material using two standardized methods was carried out. Through a series of experiments, including impedance tube and in-situ absorption measurements, this study investigates the complexities of accurately estimating sound absorption characteristics in multi-layered materials. The experimental findings highlight the importance of selecting an appropriate evaluation technique for multi-layered materials, particularly in applications where acoustic performance is critical at lower frequencies.

Keywords: *acoustic characterization, sound absorption, in-Situ absorption measurements, Kundt's impedance tube.*

***Corresponding author**: mehrangiz.mastoori@dottorandi.unipg.it*

***Copyright**: ©2025 M. Mastoori et al. This is an open-access article distributed under the terms of the Creative Commons Attribution 3.0 Unported License, which permits unrestricted use, distribution, and reproduction in any medium, provided the original author and source are credited.*

1. INTRODUCTION

Enhancing the sound absorption properties of materials is crucial in acoustical engineering and materials science, contributing to improved quality of life [1]. The growing trends of urbanization and industrial development have made effective noise mitigation strategies essential as the environments where we live, and work become increasingly noisy. Noise pollution is emerging as a significant environmental hazard to public health worldwide. The rising number of cars, trucks, and two-wheelers has significantly contributed to high levels of vehicular noise. Additionally, poor urban planning and limited city space have resulted in constructing homes near railway tracks, airports, industries, and busy traffic routes. This situation presents a serious risk of exposing the general population to noise-induced health hazards [2,3,4]. Noise reduction is a significant concern for both the government and scientists. Measures to reduce noise can be implemented in three ways: addressing the sound source, improving the transmission path, and enhancing the receiver. Passive control methods, such as sound absorption and sound insulation materials that diminish noise propagation, have been widely used and proven effective [5].

A significant issue in acoustic testing is the considerable discrepancies often observed between the results produced by different methodologies [6-8]. These discrepancies can significantly impact accurately characterizing a material's acoustic properties, resulting in challenges when predicting and optimizing its performance in real-world applications.

Over time, various methods have been developed to

measure sound absorption. Conventional techniques for measuring sound absorption include the impedance tube (or Kundt's tube) [9], and the in-situ surface impedance gun [10]. The impedance tube method is widely regarded as one of the most precise and repeatable techniques for measuring the standard incidence absorption coefficient, particularly on small samples. In contrast, the in-situ surface impedance technique has proven highly valuable, offering a complementary approach for characterizing acoustic absorption without requiring specialized testing facilities [11]. This method uses a sound intensity PU probe, providing a strong alternative to traditional microphone-based approaches. Its application across various industries, such as automotive [12], architecture [13], and road construction [14], demonstrates its versatility and effectiveness in assessing sound absorption.

Each of these techniques has specific strengths and weaknesses and combining results from multiple approaches is common. However, even for acoustic engineers, interpreting these results can be challenging, especially when different methods produce conflicting or inconclusive findings [11]. This section will discuss some well-known techniques. It is important to note that a thorough comparison of the two methods using various materials has not yet been conducted.

Studies [15-18] have demonstrated that, in some cases, the results from the in situ measurements can be quite similar to those obtained using Kundt's tube method, provided that the measurement conditions are consistent.

A sensitivity analysis was conducted by Maco et al. [19], on two different materials, rock wool, and melamine foam, with varying densities and sample thicknesses. The goal was to establish a set of guidelines for performing measurements with the in situ (PU probe) technique. The results obtained from both the in-situ impedance method and the impedance tube technique were compared at high frequencies. The findings indicated that the in-situ method (using a PU probe) provided more accurate results than the impedance tube method. A similar study was conducted in [20], which involved a comparative analysis of sound testing methodologies for multi-layered materials. This study revealed a significant discrepancy between the measurements taken with the impedance tube and those obtained from in situ methods, particularly at low frequencies. The alignment between the in-situ results and those from the reverberation chamber challenged prior assumptions, especially regarding the expected similarity between in-situ impedance measurements and those from the impedance tube for porous materials. Overall, the study underscores the importance of selecting appropriate evaluation techniques for multi-layered materials, as conventional methods may not adequately capture their complex acoustic behavior.

In another study by Peter Cats et al. [21], a preliminary comparison was made between PU probe-based in situ absorption methods and Kundt's tube method. It was found that similar results could be obtained for the examined samples using measurements from PU probes under normal incidence excitation as well as from Kundt's tube.

Despite advancements in the field, there is still a significant gap in understanding the most effective methods for evaluating the acoustic properties of complex, multi-layered materials, both porous and non-porous. This gap underscores a broader challenge: the need for a comprehensive approach that not only addresses the limitations of traditional methods, but also incorporates the strengths of newer techniques, such as the PU in-situ absorption method.

This study, a collaboration between Universitat Politècnica de Catalunya and University of Perugia, aims to try to fill this gap by conducting a comparative analysis of Cotton wadding with different layers. The evaluation will be carried out with two different measurement systems: an impedance tube (Kundt's tube, Brüel & Kjær model 4187) and an in-situ impedance measurement system from Microflown technologies. By comparing these methods directly, the research seeks to provide valuable insights into the selection of optimal tools for assessing acoustic properties, of different materials.

1. MATERIAL AND SAMPLES

The material used in this study is cotton wadding, a lightweight, fibrous textile primarily used in quilting and thermal insulation applications. This material consists of 100% cotton fibers, forming a porous and highly compressible structure, which makes it a potential material

for sound absorption applications. To evaluate its acoustic properties, samples were prepared with different layer configurations, ranging from one to eight layers. Each sample was cut into circular specimens with a diameter of 29 mm and 100 mm, following the standard requirements for impedance tube measurements 10534-2 Standard [22]. The thickness of each configuration was carefully measured to assess its impact on sound absorption performance. Figure 1 displays pictures of the measurement with impedance tube.

The characteristics of the different layers of cotton wadding used in the comparison are summarized in Table [1].

Table 1. Description of the samples for acoustic measurement.

Sample	Sample size (mm)	Thickness (mm)	Pictures
1 Layer	300 x 300 mm^2 Φ 29 mm Φ 100 mm	1.5	
2 Layers	300 x 300 mm^2 Φ 29 mm Φ 100 mm	3.0	
4Layers	300 x 300 mm^2 Φ 29 mm Φ 100 mm	6.0	
8 Layers	300 x 300 mm^2 Φ 29 mm Φ 100 mm	12	

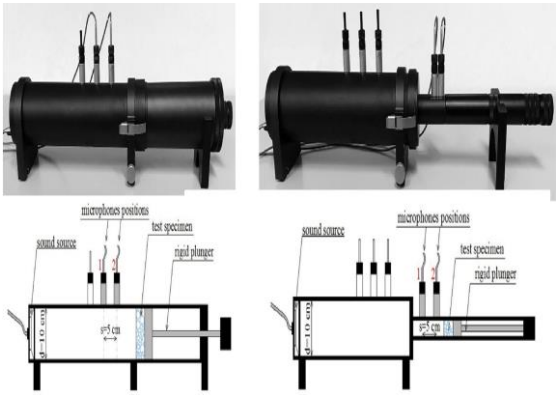


Figure 1. The Impedance tube: (a) absorption measurements configuration in large (left) and small (right) tube.

3. METHODOLOGY

3.1 Sound absorption testing methods

Over the years, several methods have been developed to measure sound absorption, each having its own unique strengths and limitations [23,24]. The results from these different techniques are often assessed from a broader perspective. However, interpreting these findings can be challenging for acoustic engineers, especially when different methods produce conflicting or inconclusive data. This section will provide a brief overview of the testing methods used in this paper.

An experimental investigation was conducted to characterize the sound absorption properties of a multi-layer sample consisting of 1 layer, 2 layers, 4 layers and 8 layers with an airflow resistivity 77600 Pa*s/m2. Different layers of this material were tested with different standardized methods, namely the Impedance Tube method (Brüel & Kjær, model 4206) [22]), as well as the in-situ PU method [11].

3.1.1 Impedance tube

The impedance tube method, commonly referred to as the Kundt tube, is widely used because it requires only small samples. The standard incidence absorption coefficient was measured using a two-microphone impedance tube (Brüel & Kjær, model 4206) and the transfer function method. This involved cylindrical samples with diameters of 29 mm, small tube for high frequencies between 5o Hz and 6400 Hz, and 100 mm, large tube for low frequencies covering a frequency range from 50 to 6400 Hz, in accordance with ISO 10534-2 standard [22].

In this method, the absorbed portion of the acoustic energy from a wave incident on the tested sample is evaluated in relation to the total incident energy; the unabsorbed portion is reflected back toward the source.

Despite its advantages, this method requires careful

sample preparation and manipulation at multiple sample diameters, which may be challenging for certain materials, such as low-density porous materials.

Moreover, differences between the sample and the actual implementation of the material may result in differences in acoustic properties, especially because in the impedance tube the measurements are carried out at normal incidence, whereas in situ the incidence is random end sometimes diffused.

3.1.2 In situ impedance

In this section, the in-situ absorption methods that will be used are briefly introduced. A more detailed description of the methods can be found in [11]. The measurements can be performed in a broad frequency range (typically from 300 Hz up to 10 kHz) on small samples (typically 0.03 m^2 to 0.38 m^2 or larger) while hardly being affected by background noise and reflections [18, 25-29].
The free-field methods originated from a generalization of the Impedance Tube method. Their purpose is to measure the acoustic impedance of ground surfaces by assessing both acoustic pressure and particle velocity above the target material. This approach allows for the capture of the specific impedance near the sample's surface [11,30-32]. Measurements of the sound absorption coefficient were conducted in both laboratory settings and in situ, utilizing an impedance gun provided by Microflown Technologies [11,18,19,33].
The user must specify the measurement range and frequency resolution at which results are displayed (e.g., octave bands, third-octave bands, or narrow frequency bands).

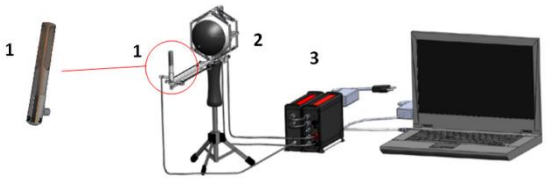


Figure 2. Measurement system assembly provided by Microflown Technologies.

While reflections from surrounding objects can potentially influence results, research has shown that in most relevant environments their impact on test outcomes is minimal, primarily due to the small distances between the sample and the P-U probe. Nevertheless, the impedance gun was calibrated [11] prior to conducting measurements. This calibration process involved pointing the impedance gun towards the best achievable free field conditions, far from any reflective surfaces.



Figure 3. Measurement systems used in the present investigation: in-situ PU method (Left), and impedance tube (right).

4. EXPERIMENTAL INVESTIGATION ON SOUND ABSORPTION

In the in-situ Absorption [19] measurements utilizing the Mirror Source model, each sample approximately is 0.4 m x 0.4 m in size. Measurements were taken by positioning a PU probe about 5mm above the sample's surface, at three arbitrary points (twelve total measurements).

The porosity and airflow resistivity and absorption coefficient of sound-absorb cotton were measured by equipment directly (Figure 4). Airflow resistance is also a powerful tool to characterize sound absorption properties. The airflow resistance has been determined with a Nor1517A airflow resistance measurement system which uses the alternating airflow method described in the standard ISO 9053-2:2020 [34].



Figure 4. Air flow resistance tool.

4.1 Results and discussion

Fiber type, material thickness, density, airflow resistance, and porosity are the key physical parameters influencing the sound absorption characteristics of nonwoven materials [35]. Figure 5 illustrates the specific airflow resistance (Rs) for samples with varying numbers of layers. The airflow resistivity, representing the specific airflow resistance per unit length, has been calculated as the slope of the linear fit, yielding a value of 77,600 Pa·s/m². This result indicates that as the material thickness increases, the resistance to specific airflow rises proportionally.

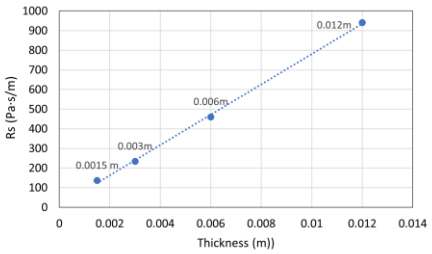


Figure 5. Specific airflow resistance as a function of thickness. The dotted line is a linear fit, the slope of which gives the value of the airflow resistivity of the material.

Sound absorption coefficient trends at normal incidence for the four samples vs. the frequency (range 100 - 6400 Hz), measured using the Impedance Tube and Impedance Gun, are shown in Figures 6 and 7, respectively. The small and a large Brüel & Kjær tube setup were used and later the measurements were combined to obtain sound absorption coefficient in the frequency range 50–6400 Hz.

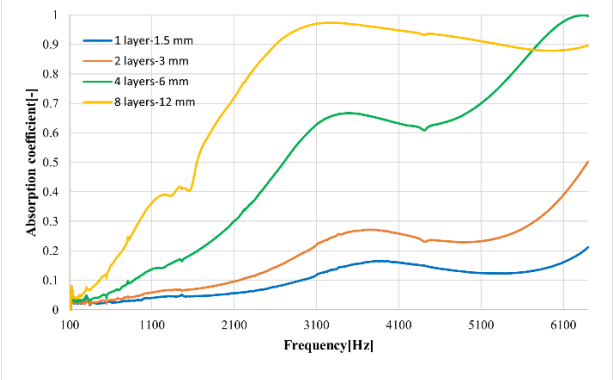


Figure 6. Sound absorption values of cotton wadding vs. frequency with Impedance tube.

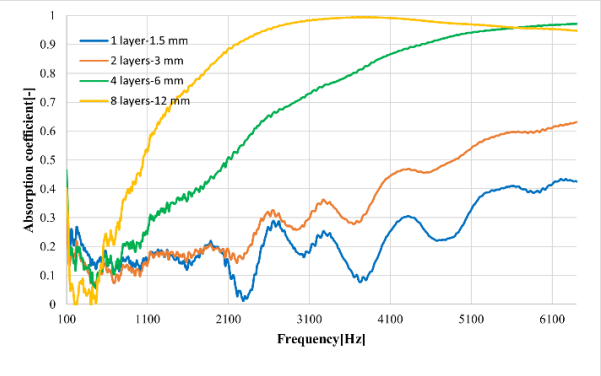


Figure 7. Sound absorption values of cotton wadding vs. frequency with Impedance gun.

Table 2. Values of sound absorption coefficient α, third octave bands with Impedance Tube.

Freguency (Hz)	1 layer	2 layers	4 layers	8 layers
200	0.05	0.08	0.04	0.06
251	0.00	0.01	0.02	0.02
316	0.04	0.04	0.05	0.09
398	0.03	0.03	0.04	0.09
501	0.03	0.04	0.06	0.13
630	0.04	0.05	0.07	0.18
794	0.04	0.05	0.09	0.22
1000	0.04	.06	0.11	0.29
1258	0.04	0.06	0.13	0.35
1600	0.05	0.08	0.19	0.46
2000	0.05	0.10	0.28	0.68
2500	0.07	0.16	0.44	0.87
3150	0.12	0.26	0.63	0.97
4000	0.16	0.29	0.64	0.95
5000	0.15	0.28	0.71	0.91
αavg	0.06	0.10	0.23	0.42

Table3. Values of sound absorption coefficient α, for third octave bands with Impedance Gun.

Freguency (Hz)	1 layer	2 layers	4 layers	8 layers
200	0.21	0.18	0.15	-0.01
251	0.23	0.18	0.19	0.05
316	0.19	0.14	0.14	0.06
398	0.14	0.9	0.10	0.03
501	0.14	0.10	0.11	0.19

630	0.14	0.11	0.14	0.23
794	0.13	0.12	0.18	0.34
1000	0.13	0.12	0.22	0.47
1258	0.16	0.17	0.32	0.64
1600	0.14	0.17	0.32	0.75
2000	0.14	0.12	0.47	0.86
2500	0.14	0.26	0.63	0.94
3150	0.18	0.37	0.74	0.98
4000	0.18	0.39	0.85	0.99
5000	0.32	0.55	0.94	0.97
αavg	0.17	0.27	0.37	0.49

Table 4. Noise Reduction Coefficient (NRC) index of the investigated materials using impedance tube and impedance gun.

Sample	NRC-Impedance Tube	NRC-Impedance Gun
1 layer	0.03	0.16
2 layers	0.05	0.15
4 layers	0.12	0.25
8 layers	0.22	0.37

As observed in Figure 6 and 7, an increase in the number of layers leads to a higher sound absorption coefficient across most frequencies, as expected. Cotton wadding 12 mm-thick (8layers), and 6 mm- thick (4 layers) demonstrate high absorption properties when compared to the 2 layers and 1 layer. This effect becomes more evident at higher frequencies (above 3000 Hz), where the increase in the number of layers leads to a significant improvement in sound absorption. Also, the first peak of the absorption curve increases with thickness, and it is moved to lower frequencies, according to [36], due to the higher tortuosity of the thicker sample. In order to better compare the acoustic behavior of different layers of cotton wadding, the Sound Absorption Average (SAA) index was calculated as the average of the absorption coefficients across the twelve 1/3 octave bands from 200 Hz to 5000 Hz (Table 1 and 2). As the number of layers increases, the sound absorption performance improves significantly both in the measurements carried out with the impedance tube and with the impedance gun. For example, the SAA value rises from 0.06 for a single-layer sample to 0.42 for the eight-layers with impedance tube. Similarly, with the impedance gun, the SAA rises from 0.17 for one layer to 0.49 for eight layers. The Noise Reduction Coefficient NRC (arithmetic average of the absorption coefficient values in the one third octave band at the frequencies of 250, 500, 1000, and 2000 Hz) of samples with impedance Gun is higher than the one of materials with impedance tube. Moreover, NRC increased when thickness increased (see data in Table 3).

5. CONCLUSION

In this research, we studied the sound absorption properties of a commercially available natural fiber material (cotton wadding). We investigated the effect of material thickness and used two different measurement tools to evaluate its acoustic performance. The results demonstrated that both material thickness and airflow resistance significantly affect sound absorption performance.

By utilizing two different tools, the study provided complementary insights, more reliable and accurate findings. It was found that increasing the thickness of the cotton wadding improved sound absorption, while airflow resistance also played a crucial role in optimizing the material's performance. These findings contribute to a better understanding of the key factors influencing sound absorption in cotton-based materials. Additionally, the use of multiple tools allowed for a more thorough analysis, ensuring strong results.

Further research could explore additional variables or alternative different types of materials to improve sound absorption measurements reliability in a variety of applications.

6. ACKNOWLEDGMENTS

This work was partially funded by MICIU/ AEI/10.13039/501100011033 through the project PID2020-117530RB-I00

7. REFERENCES

[1] L.E. Kinsler, A.F. Frey, A.B. Coppens, and J.V. Sanders, *Fundamentals of Acoustics*, 4th ed., John Wiley & Sons Inc., USA, 2000.

[2] L. Goines and L. Hagler, "*Noise pollution: a modern plague*," *South Med. J.*, vol. 100, no. 3, pp. 287–294, 2007.

[3] A. Muzet, "*Environmental noise, sleep and health*," *Sleep Med. Rev.*, vol. 11, no. 2, pp. 135–142, 2007.

[4] S.A. Stansfeld and M.P. Matheson, "*Noise pollution: nonauditory effects on health*," *Br. Med. Bull.*, vol. 68, no. 1, pp. 243–257, 2003.

[5] L. Cao, et al., "*Porous materials for sound absorption,"* Composites Communications, vol. 10, pp. 25–35, 2018.

[6] M.L.S. Vercammen, "*Improving the accuracy of*

sound absorption measurement according to ISO 354," in Proc. Int. Symp. Room Acoustics, 2010.

[7] K.V. Horoshenkov, A. Khan, F.-X. Bécot, L. Jaouen, F. Sgard, A. Renault, N. Amirouche, F. Pompoli, N. Prodi, P. Bonfiglio, G. Pispola, F. Asdrubali, J. Hübelt, N. Atalla, C.K. Amédin, W. Lauriks, and L. Boeckx, "*Reproducibility experiments on measuring acoustical properties of rigid-frame porous media (round-robin tests*," *J. Acoust. Soc. Am.*, vol. 122, no. 1, pp. 345–353, 2007.

[8] F. Pompoli, P. Bonfiglio, K.V. Horoshenkov, A. Khan, L. Jaouen, F.-X. Bécot, F. Sgard, F. Asdrubali, F. D'Alessandro, J. Hübelt, N. Atalla, C.K. Amédin, W. Lauriks, and L. Boeckx, "*How reproducible is the acoustical characterization of porous media?*" *J. Acoust. Soc. Am.*, vol. 141, no. 2, pp. 945–955, 2017.

[9] International Organization for Standardization, *ISO 10534-2:1998 Acoustics - Determination of sound absorption coefficient and impedance in impedance tubes - Part 2: Transfer-function method*, Geneva, Switzerland, 1998.

[10] F. Merli et al., "*Thermal and acoustic performance of gypsum plasters mixed with different additives: influence of bio-based, synthetic, and mineral fillers,"* Appl. Sci., vol. 13, no. 18, pp. 10480, 2023.

[11] E. Tijs, "Study and development of an in situ *acoustic absorption measurement method,"* Ph.D. dissertation, University of Twente, 2013.

[12] D. Siano, M. Viscardi, and M.A. Panza, *"Automotive materials: an experimental investigation of an engine bay acoustic performances," Energy Procedia*, vol. 101, pp. 1186–1193, 2016.

[13] M.A. Navacerrada, M.M. Barbero-Barrera, R. Fort, D. de la Prida, J.C. Núñez, and T.S. Gómez, *"Application of acoustic impedance gun to non-destructively monitor stone damage," Constr. Build. Mater.*, vol. 323, pp. 178–188, 2022.

[14] M. Li, W. van Keulen, E. Tijs, M. van de Ven, and A. Molenaar, *"Sound absorption measurement of road surface with in situ technology," Appl. Acoust.*, vol. 88, pp. 24–33, 2015.

[15] H.-E. de Bree, M. Nosko, and E. Tijs, "*A handheld device to measure the acoustic absorption in situ,"* in *Proc. 5th Int. Styrian Noise Vibration & Harshness Conf.*, Graz, Austria, 2008.

[16] H.-E. de Bree, E. Tijs, and T. Basten, *"Two complementary Microflown-based methods to determine the reflection coefficient in situ,"* in *Proc. ISMA Int. Conf. Noise Vibration Engineering*, Leuven, Belgium, 2006.

[17] E. Tijs, H.-E. de Bree, T. Basten, and M. Nosko, *"Non-destructive and in situ acoustic testing of inhomogeneous materials,"* in *Proc. 33rd Eur. Rotorcraft Forum*, Kazan, Russia, 2007.

[18] E. Tijs and E. Druyvesteyn, "*An intensity method for measuring absorption properties in situ," Acta Acustica united with Acustica*, vol. 98, no. 1, pp. 342–353, 2012.

[19] M.A. Ribera Tejeda, P.A. Mendes, R. S. Ribeiro, and P.T. Pinto, *"In-situ acoustic characterization of porous materials, using a PU-probe," Tecni Acustica*, Cuencia, 2023.

[20] M. Puljizević, T. Poljanšek, and A. Polak, *"Comparative analysis of acoustic testing methods of a multi-layered material: uncovering the membrane effect,"* in *Proc. Inter-Noise Conf.*, France, Aug. 2024.

[21] P. Cats, E. Tijs, and D.F. Comesana, *"Exploration of the differences between a pressure-velocity based in situ absorption measurement method and the standardized reverberant room method,"* J. Acoust. Soc. Am., vol. 133, no. 6, pp. 3956–3963, 2013.

[22] International Organization for Standardization, ISO 10534-2:2015 Acoustics—*Determination of sound absorption coefficient and impedance in impedance tubes*—Part 2: Transfer-Function Method, Geneva, Switzerland, 2015.

[23] E. Brandão, A. Lenzi, and S. Paul, *"A review of the in situ impedance and sound absorption measurement techniques," Acta Acustica united with Acustica*, vol. 101, pp. 1–14, 2015.

[24] N. Hiremath, V. Kumar, N. Motahari, and D. Shukla, *"An overview of acoustic impedance measurement techniques and future prospects," Metrology*, vol. 57, no. 5, pp. 791–808, 2021.

[25] E. Brandão, A. Lenzi, and J. Cordioli, *"Estimation and minimization of errors caused by sample size effect in the measurement of the normal absorption coefficient of a locally reacting surface," Appl. Acoust.*, vol. 73, no. 6–7, pp. 543–556, 2012.

[26] C. Kühnert, U. Figula, and J. Hübelt, "*Acoustical method for the non-destructive determination of the porosity of asphalts,"* in Proc. Euronoise 2009, Edinburgh, Scotland, 2009.

[27] E. Tijs, E. Brandão, and H.-E. de Bree, *"In situ PU surface impedance measurements for quality control at the end of an assembly line,"* in *Proc. SAE Noise and Vibration Conf.*, 2009, pp. 2142–2147.

[28] E. Tijs, H.-E. de Bree, and E. Brandão, *"Large scale in situ acoustic absorption measurements in a theatre,"* in *Proc. DAGA 2009*, Rotterdam, The Netherlands.

[29] P. Dickinson and P. Doak, *"Measurements of the normal acoustic impedance of ground surfaces," J. Sound Vib.*, vol. 13, no. 3, pp. 309–322, 1970.

[30] B.G.J. Briere de la Hosseraye, *"In situ PU-based characterization of sound absorbing materials for room acoustic modeling purposes,"* Ph.D. dissertation, Eindhoven University of Technology, 2023.

[31] K. Hirosawa, K. Takashima, H. Nakagawa, M. Kon, A. Yamamoto, and W. Lauriks, *"Comparison of three measurement techniques for the normal absorption coefficient of sound absorbing materials in the free field," J. Acoust. Soc. Am.*, vol. 126, 2009.

[32] H.-E. de Bree, E. Tijs, and T. Basten, *"An ultra-miniature measurement tool to measure the reflection coefficient of acoustic damping materials in situ,"* in *Proc. SAE 2007 Noise and Vibration Conf.*, St. Charles, IL, USA, May 15–17, 2007.

[33] E. Tijs and H.-E. de Bree, *"Recent developments in free field PU impedance technique,"* in Proc. SAPEM 2008, Bradford, UK, Dec. 17–19, 2008.

[34] ISO 9053-2:2020; *Acoustics—Determination of Airflow Resistance—Part 2: Alternating Airflow Method*. ISO: Geneva, Switzerland, 2020.

[35] M. Küçük and Y. Korkmaz, *"The effect of physical parameters on sound absorption properties of natural fiber mixed nonwoven composites,"* Textile Research Journal 2012 82: 2043 originally published online 15 May 2012.

[36] J.Turkiewicz and J. Sikora, *"Sound absorbing materials rubber products,"* MECHANICS AND CONTROL Vol. 32 No. 3 2013.

DOI: 10.61782/fa.2025.0125

FORUM ACUSTICUM EURONOISE 2025

AN EXPERIMENTAL DATA SET FOCUSED ON METHODOLOGIES FOR THE *IN SITU* CHARACTERIZATION OF ACOUSTIC MATERIALS

João Vitor Pontalti[1*] **Eric Brandão**[1] **William D'Andrea Fonseca**[1]
Paulo Henrique Mareze [1] **Gustavo Netto**[1] **Efren Fernandez-Grande**[2]
[1] Acoustical Engineering, Federal University of Santa Maria (UFSM), Brazil
[2] Technical University of Madrid (UPM), Spain

ABSTRACT

The *in situ* characterization of acoustic materials is used to assess material properties of installed devices. The use of sensor arrays guarantees access to spatio-temporal information about the scattered sound field that finite samples or diffusers create in realistic conditions. Such effects can be investigated by formulating suitable inverse problems, which incorporates the complexity of acoustic fields. Since this line of research is in constant evolution, this paper describes the construction of a database of impulse responses obtained with *in situ* measurement techniques and some of the results obtained with different techniques. A 3D scanner is used to move and position the microphone at the coordinates of a pre-established array geometry. The exploited measurement scenarios, the data organization, and post-processing strategies are described. Initial results considering the classical 2-microphone method, plane-wave expansion and the discrete complex image source methods are presented and compared.

Keywords: *in situ measurements, absorption coefficient, dataset, acoustic materials*

1. INTRODUCTION

The acoustic characterization of materials under *in situ* or free-field conditions is valuable for room acoustics and noise-control applications. The work of Brandão [1] extensively reviews such techniques for measurement scenarios with a few sensors. Usually, these methods rely on a mathematical sound field model above the material and assume the sample to be much larger than the wavelength [2]. Additionally, microphone array techniques for absorption measurements have been explored since the early works of Tamura in the 1990s [3, 4], as they provide information about the distribution of pressure and/or particle velocity in space. Recent approaches that seek to evaluate the acoustical absorption coefficient have benefited from the use of microphone arrays in conjunction with inverse problem theories that aim to reconstruct the sound field in the vicinity of the sample under evaluation [5–11].

In order to promote further advancement in this research area, constructing a well-structured experimental dataset is of interest. For instance, some datasets reported in the literature focus on simulations for room acoustics [12], Head-Related Transfer Function simulations [13], and environmental acoustics [14]. This paper outlines the methodology adopted for creating a dataset of *in situ* measurements of acoustical materials.

The experiments described in this study were carried out in a large reverberation chamber using relatively low-cost instrumentation. A time-windowing technique was applied to isolate the direct sound from the reflections caused by the chamber walls. A 3D scanner is employed to move the microphone throughout the spatial coordinates of a pre-defined array, and impulse responses are collected sequentially. A more comprehensive overview of the experimental setup and the routines implemented in the construction of the dataset can be found in Ref. [15]. This study investigates a double planar array topology, as in Ref. [6, 16]. The measured sound pressure serves as

**Corresponding author*: joao.pontalti@eac.ufsm.br.
Copyright: ©2025 Pontalti, J. V. et al. *This is an open-access article distributed under the terms of the Creative Commons Attribution 3.0 Unported License, which permits unrestricted use, distribution, and reproduction in any medium, provided the original author and source are credited.*

input for two inverse problems: a plane wave expansion (PWE) [9] and a novel approach called the Discrete Complex Image Source Method (DCISM) [11]. The first can be used to study effects like edge diffraction of the sample, and the second is a compact sound field model suitable for short source-receiver distances. The inverse problems results are compared to those obtained with the classical two-microphone technique [17, 18].

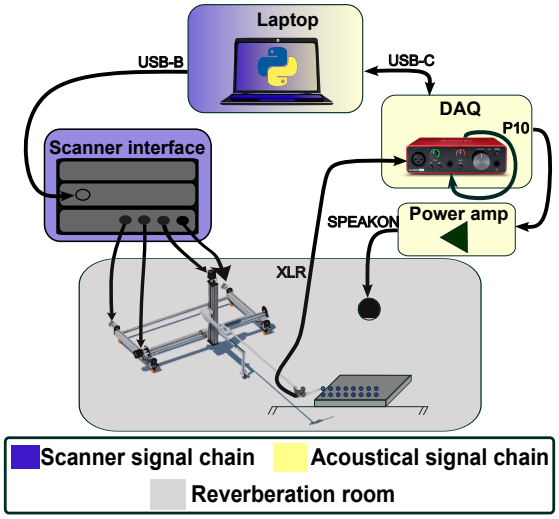
This paper is organized as follows: Section 2 outlines the experimental procedures, encompassing the instrumentation built and used, the measured samples evaluated, and the array's geometries. Section 3 presents the mathematical background necessary to understand the inverse problems. Section 4 presents the results and discussions, followed by the conclusions in Sec 5.

2. MATERIALS AND METHODS

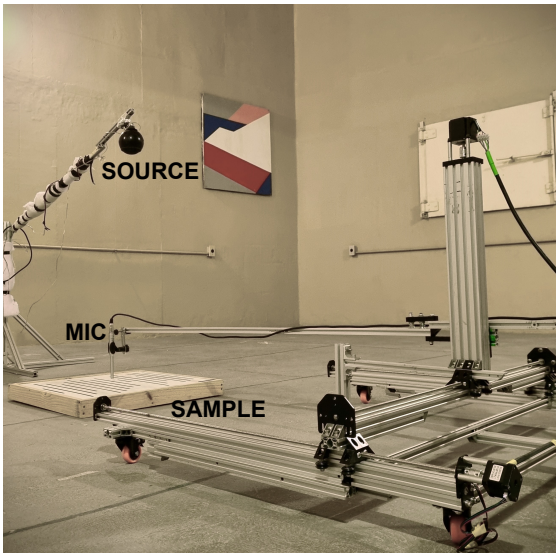
The experiments were conducted within a 207 m^3 reverberation chamber at the Acoustic Engineering Laboratory [19] of the Federal University of Santa Maria (UFSM - Brazil). The use of such a room was motivated by its controlled acoustic characteristics and by the fact that the walls can be substantially far from the sample and instrumentation [1]. The samples were positioned directly on the floor and in the center of the room. Figure 1b visually represents the experimental environment. This study presents results for 3 mounting conditions for 48×48 cm polyurethane (PU) foam with 25 mm of thickness. All evaluated scenarios consider the source positioned above the center of the sample at a distance of 1 m (normal incidence).

A 3D scanner, developed by the research team [10] was used to move a transducer through a set of predetermined spatial coordinates $\mathbf{r}_\mathrm{m} = (x, y, z)$. As the scanner operates, it sequentially measures the sound pressure at each coordinate. The scanner system, adapted from 3D printing technology, employs four NEMA stepper motors to move the microphone – two for the x axis (**M1** and **M2**), one for the y axis (**M3**), and another for z axis (**M4**) – providing three degrees of freedom. The scanner's control interface comprises an Arduino that handles the communication between the Python programming and the scanner, along with the drivers that operate the axis motors. A similar measurement system was envisioned and implemented by D'Antonio *et al.* [20]. Figure 1b illustrates the experimental setup mounted within the reverberation chamber, where it is possible to visualize the 3D scanner holding the microphone over the sample positioned directly below the sound source.

[1] Additionally, the laboratory does not have an anechoic room, unfortunately.



(a)



(b)

Figure 1: (a) Signal channeling with the cable connections. (b) Experimental setup within the reverberation chamber.

The acoustic signals reported herein were acquired using a Behringer ECM 8000 measurement microphone connected to a Focusrite Scarlett Solo audio interface

(ASIO driver). Other options were explored in the current dataset but are not reported here for the sake of brevity. The excitation signal consisted of an Exponential Sine Sweep (ESS) ranging from 100 Hz to 20 kHz, radiated from a full-range loudspeaker mounted on a spherical baffle with a diameter of 9 cm. A Brüel & Kjær 2716C power amplifier drives the loudspeaker. Both measurement and post-processing operate using Python, with object-oriented programming. The basic repositories primarily used in the work presented here are available on Github [21, 22]. Furthermore, the open-source library PyTTa Toolbox [23] was used extensively to create the excitation signals, record the responses, and compute the impulse responses. Atmospheric conditions, the name of the material under study, the hardware utilized, the Arduino setup, and the date and time of the measurements are stored as metadata on the measurement object and can be retrieved later.

The array explored in this paper is a double-layered microphone array, which evaluates the pressure above the sample's surface, $z > 0$. Its dimensions are 0.3×0.3 m^2, with 8 microphone positions along the x and y axis, resulting in 64 positions per layer and a total of $\mathcal{M} = 128$ measurement points. The vertical separation between the two layers was set to $\mathrm{z_r} = 0.02$ m, while the distance between the closest layer to the top of the sample was $\mathrm{z_0} = 0.02$ m.

3. THEORY OF INVERSE PROBLEMS

Many inverse problem formulations have been proposed over the years, aiming to reconstruct the sound field above finite or infinite samples. In this study, two approaches are considered: a plane wave expansion (PWE) model formulated as a set of propagating and evanescent plane waves [9] and the discrete complex image source method (DCISM), a novel method recently introduced in the literature by Brandao [11]. This paper briefly describes such methods, and more details can be found in the literature. In both cases, the inverse problem can be formulated as a matrix equation

$$\mathbf{p} = \mathbf{H}\mathbf{x} + \mathbf{n}\,, \tag{1}$$

where $\mathbf{p} \in \mathbb{C}^{\mathcal{M}}$ is the vector of measured sound pressures at $\mathrm{r_m}$, $\mathbf{x} \in \mathbb{C}^{l}$ contains the unknown amplitudes of interest, and $\mathbf{H} \in \mathbb{C}^{\mathcal{M}\mathrm{x}l}$ is the sensing matrix (Kernel), which models the acoustic field according to the method being implemented. Also, $\mathbf{n}$ is representative of noise that contaminates all measurements and model inconsistencies [6,9]. Typically, the dimensions of ℓ and $\mathcal{M}$ differ, and the inverse problem becomes ill-posed, requiring regularization. The main topics regarding the assembly of the sensing matrix for both PWE and DCISM are discussed in Secs. 3.1 and 3.2. Further notes on the reconstruction stage are given in Sec. 3.3.

3.1 Plane wave expansion

The basic formulation presented in this section if based on Refs. [6, 9]. It is assumed that the measured sound pressure can be represented as a superposition of ℓ propagating and evanescent plane waves, separated in an incident and a reflected sound field. Thus, the kernel matrix can be written as $\mathbf{H} = [\mathbf{H}_{\mathrm{inc}}, \mathbf{H}_{\mathrm{ref}}]$. For a given receiver at $\mathbf{r}_\mathrm{m} = (x, y, z)$ and a wave-number $\mathbf{k}_\ell$, the matrix elements are composed of

$$\begin{aligned} \psi_\ell^{\mathrm{inc}}\left(\mathbf{r}_\mathrm{m}\right) &= \mathrm{e}^{-\mathrm{j}\left(k_x x + k_y y + k_z\left(z - z^{+}\right)\right)}, \\ \psi_\ell^{\mathrm{ref}}\left(\mathbf{r}_\mathrm{m}\right) &= \mathrm{e}^{-\mathrm{j}\left(k_x x + k_y y - k_z\left(z - z^{-}\right)\right)}, \end{aligned} \tag{2}$$

with z^+ and z^- related to retracted virtual source planes that help to regularize the problem [6,9].

3.2 Discrete complex image source method

This formulation, proposed in Ref. [11] is based in Ref. [24]. It models the sound field as composed of a monopole (associated with the original source - incident sound field), a component associated with the image source, and a series of monopoles located along a complex line (reflected sound field). The matrix kernel is given by

$$G(\mathbf{r}_\mathrm{i}, \mathbf{r}_\mathrm{m}) = \frac{b}{2} w_\mathrm{i} \frac{\mathrm{e}^{-\mathrm{j}k|\mathbf{r}_\mathrm{i} - \mathbf{r}_\mathrm{m}|}}{|\mathbf{r}_\mathrm{i} - \mathbf{r}_\mathrm{m}|}\,. \tag{3}$$

For the original sound source, $\mathrm{i} = 1$, $\mathbf{r}_1 = (x_\mathrm{s}, y_\mathrm{s}, z_\mathrm{s})$. For the image source, $\mathrm{i} = 2$ and $\mathbf{r}_2 = (x_\mathrm{s}, y_\mathrm{s}, -z_\mathrm{s})$ ($\frac{b}{2} w_\mathrm{i} = 1$ in both cases). For the remaining complex sources $\mathrm{i} = 1, 2, \cdots, N$, $\mathbf{r}_\mathrm{i} = (x_\mathrm{s}, y_\mathrm{s}, -z_\mathrm{s} + \mathrm{j}q_\mathrm{i})$, with w_i and q_i given by the Gauss-Legendre quadrature rule, and b being a suitable truncation value for the integral [11, 24].

3.3 Inverse problem estimation and reconstruction

Given that the Kernel matrix $\mathbf{H}$ in Equation 1 leads to an ill-posed problem, an appropriate regularization technique is required to stabilize the inversion. This issue is addressed through Tikhonov regularization, which is formulated as

$$\tilde{\mathbf{x}} = \underset{\mathbf{x}}{\mathrm{argmin}} \left(\|\mathbf{H}\mathbf{x} - \mathbf{p}\|_2^2 + \lambda \|\mathbf{x}\|_2^2 \right), \tag{4}$$

with λ being the regularization parameter selected automatically by generalized cross-validation [25]. After finding $\tilde{\mathbf{x}}$, the sound pressure and the normal component of the particle velocity can be reconstructed over a set of K grid points located at the sample's surface. The reconstructed sound pressure is given by

$$\tilde{\mathbf{p}}_{\mathrm{re}} = \mathbf{H}_{\mathrm{re}}\tilde{\mathbf{x}}\,. \tag{5}$$

with $\tilde{\mathbf{p}}_{\mathrm{re}} \in \mathbb{C}^K$ being the reconstructed sound pressure vector and $\mathbf{H}_{\mathrm{re}} \in \mathbb{C}^{K\times\ell}$ the reconstruction matrix containing the wave functions evaluated at the reconstruction points. The particle velocity vector is retrieved by means of Euler's equation of motion, with $\tilde{\mathbf{u}}_{\mathrm{re}} = \frac{-1}{\mathrm{j}k\rho c}\nabla\mathbf{H}_{\mathrm{re}}\tilde{\mathbf{x}}$. Utilizing the reconstructed sound pressure and the particle velocity, an estimation of the surface impedance can be derived as either a point-wise impedance or the spatial average of a set of grid points used to compute the reconstructed surface impedance, where

$$\tilde{Z}_s\left(\mathbf{r}_s\right) = -\frac{1}{\rho c}\frac{\tilde{p}\left(\mathbf{r}_s\right)}{\tilde{u}_n\left(\mathbf{r}_s\right)}, \tag{6}$$

where ρ is the air density and c the sound velocity in the air. Subsequently, the sound absorption coefficient is inferred as

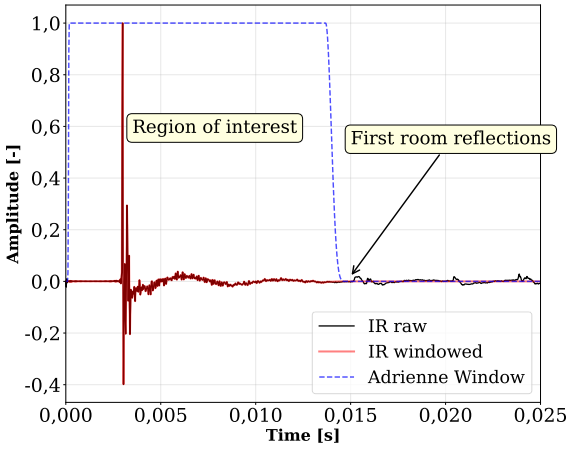
$$\alpha = 1 - \left|\frac{\bar{Z}_s\cos(\theta) - 1}{\bar{Z}_s\cos(\theta) + 1}\right|^2. \tag{7}$$

4. RESULTS

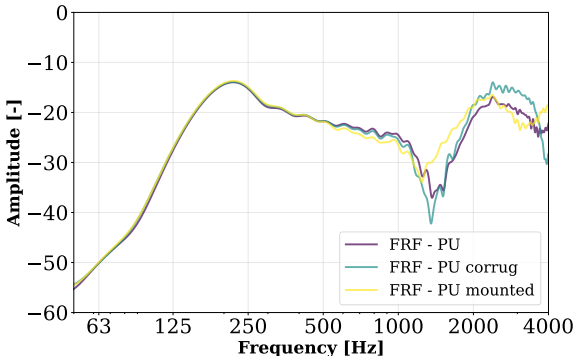
This section presents the main results and corresponding discussions from the experimental measurements. The acoustic sound field is analyzed in the wave number domain using the PWE introduced in Sec. 3.1, and the absorption coefficient is reconstructed using both proposed methodologies. For comparison purposes, the absorption coefficient (α) is also estimated using the conventional two-microphone technique [17] for each tested sample.

Three polyurethane (PU) foam configurations are evaluated: (i) a flat rectangular sample (25 mm thick); (ii) a corrugated sample with similar maximum thickness; and (iii) a composite configuration consisting of the corrugated foam mounted on the top of the flat sample.

The initial stage of the post-processing is the analysis of the impulse responses (IRs) and their corresponding frequency response functions (FRFs) to provide an initial assessment of the measurement quality. Figure 2 presents an IR obtained from the measurement of the flat PU foam,



(a)



(b)

Figure 2: (a) Measured impulse response alongside its windowed version and the applied window function. (b) FRF obtained from one measurement of each sample.

showing both the raw and windowed impulse responses, as well as the Adrienne window applied to the signal. The first reflections from the chamber walls reach the transducer at approximately 0,015 s after the direct sound. It is important to note that this time delay can vary depending on the spatial positioning of the microphone within the reverberation chamber.

Furthermore, Figure 2b displays the FRFs (windowed signal) obtained from the first measurement of each sample (near its center). The difference between the samples

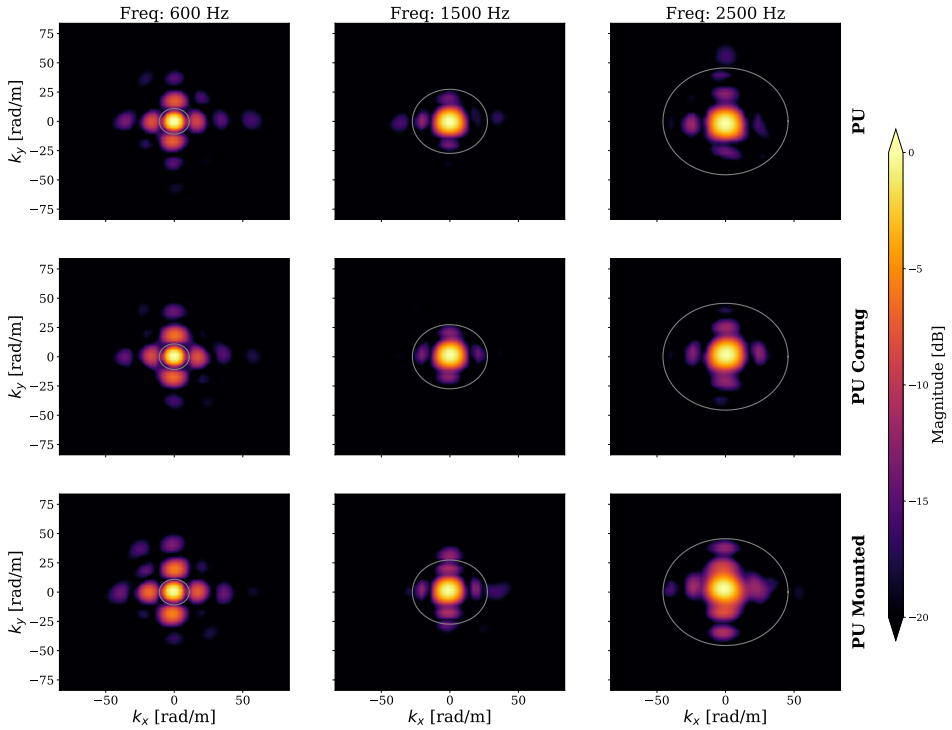


Figure 3: Wave-number spectrum for the PU sample estimated from the microphone array data.

is easier to be observed above 1000 Hz. Note that for the mounted sample, the magnitude of the FRF is significantly different than the others between 1 and 2 kHz.

Figure 3 shows the reflected components of the wave-number spectrum (k-space) at frequencies 500, 1500, and 2500 Hz for the PU flat, corrugated, and the mounted (corrugated + flat) situations. Each subfigure plots the radiation circle as a gray line to distinguish between propagating and evanescent plane waves. The source planes are located 1 cm below the lower layer of the microphone array and at 1 cm above the top layer. That ensures symmetry between the distances from the microphone array to the sample and to the source planes. In Fig. 3, the main lobe at the center of each subplot is associated with plane waves traveling in the direction of specular reflection, while the side lobes are likely due to the finite dimensions of the absorbers [9]. In all cases, at the frequency of 500 Hz, the wave-number spectra are similar and the evanescent components appear more prominent compared to the other spectra. This behavior is attributed to the fact that the wavelength of the incident wave is comparable to the size of the sample, which enhances the diffraction effects. The evanescent components tend to decrease in amplitude with increasing frequency, indicating a greater concentration of propagating waves at higher frequencies. It is interesting to note that the diffraction components for the corrugated samples seem to have slightly larger amplitudes when compared to the flat sample at 1500 and 2500 Hz, which can be attributed to a more irregular reflection pattern caused by the surface irregularities.

The absorption coefficient values for the three mounting configurations are shown in Fig. 4. The solid lines correspond to the results obtained using the DCISM method, while the dashed lines represent the values estimated using the PW approach. Dash-dotted lines are representative of the 2-mics technique. The three inference methods yield similar results across all configurations and mounting conditions. The DCISM and the plane-wave expansion methods show a closer agreement. Notably, the

DCISM tends to underestimate the absorption values below 500 Hz (compared to the plane-wave expansion). This discrepancy can be attributed to the different modeling assumptions. The absorption values for the stand-alone corrugated sample are relatively low because the average material thickness is small. For this reason, the estimates obtained using the two-microphone method show more erratic behavior above 1000 Hz. Note also that the absorption coefficient increases significantly for the mounted condition (corrugated on top of the flat sample). In both corrugated sample cases, it might be challenging to establish a surface to reconstruct the surface impedance on, which may contribute to the discrepancies between the DCISM and the plane-wave expansion models.

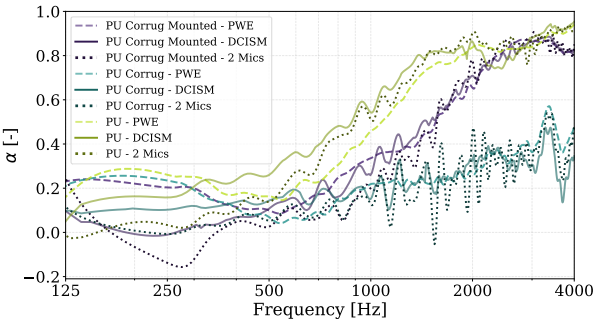


Figure 4: The sound absorption coefficient for 3 mounting conditions of finite PU samples measured with a double planar array.

5. CONCLUSIONS

The proposed experimental setup effectively measured impulse responses near three material configurations. The measurements performed with the double-layered array proved consistent, and the implemented inverse methods yielded satisfactory and insightful results regarding the behavior of the acoustic sound field. Additionally, both the PW method and the DCISM demonstrated consistency in reconstructing the absorption coefficient, with minor discrepancies aligned with predictions found in the literature. The two-microphone technique also proved to be a straightforward and reliable approach for establishing a a metric for comparison. The data presented herein will be included into the *in situ* acoustic database currently under development.

6. ACKNOWLEDGEMENTS

The authors would like to acknowledge the support and infrastructure of the Acoustic Engineering Department (EAC) at the Federal University of Santa Maria (UFSM), which made this work possible. This work is part of a research project into the spatial/temporal characterization of acoustic materials. The authors would like to thank the CNPQ universal project (No. 402633/2021-0) and PIBIC (Institutional Program for Scientific Initiation Scholarships) for their financial support.

7. REFERENCES

[1] E. Brandão, A. Lenzi, and S. Paul, "A review of the in situ impedance and sound absorption measurement techniques," *Acta Acustica united with Acustica*, vol. 101, no. 3, pp. 443–463(21), 2015.

[2] E. Zea, E. Brandao, M. Nolan, J. Cuenca, J. Andén, and U. Svensson, "Sound absorption estimation of finite porous samples with deep residual learning," 09 2023.

[3] M. Tamura, "Spatial fourier transform method of measuring reflection coefficients at oblique incidence. i: Theory and numerical examples," *The Journal of the Acoustical Society of America*, vol. 88, pp. 2259–2264, 11 1990.

[4] M. Tamura, J. Allard, and D. Lafarge, "Spatial fourier-transform method for measuring reflection coefficients at oblique incidence. ii. experimental results," *Journal of The Acoustical Society of America - J ACOUST SOC AMER*, vol. 97, pp. 2255–2262, 04 1995.

[5] M. Nolan, "Estimation of angle-dependent absorption coefficients from spatially distributed in situ measurements," *The Journal of the Acoustical Society of America*, vol. 147, pp. EL119–EL124, 02 2020.

[6] J. Hald, "Basic theory and properties of statistically optimized near-field acoustical holography," *The Journal of the Acoustical Society of America*, vol. 125, pp. 2105–2120, 04 2009.

[7] A. Richard and E. Fernandez-Grande, "Comparison of two microphone array geometries for surface impedance estimation," *The Journal of the Acoustical Society of America*, vol. 146, pp. 501–504, 07 2019.

[8] M. Alkmim, J. Cuenca, L. de Ryck, and W. Desmet, "Angle-dependent sound absorption estimation using a compact microphone array," *The Journal of the Acoustical Society of America*, vol. 150, pp. 2388–2400, 10 2021.

[9] E. Brandão and E. Fernandez-Grande, "Analysis of the sound field above finite absorbers in the wavenumber domain," *The Journal of the Acoustical Society of America*, vol. 151, no. 5, pp. 3019–3030, 2022.

[10] G. Souza, "Desenvolvimento de um escâner automatizado para medição sequencial e caracterização espaço-temporal de materiais acústicos." https://repositorio.ufsm.br/handle/1/27197, 2022.

[11] E. Brandão, W. D. Fonseca, P. H. Mareze, C. Resende, G. Azzuz, J. Pontalti, and E. Fernandez-Grande, "Sound absorption estimation using the discrete complex image source method and array processing," *Mechanical Systems and Signal Processing*, vol. 231, p. 112617, 2025.

[12] F. Brinkmann, L. Aspöck, D. Ackermann, R. Opdam, M. Vorländer, and S. Weinzierl, "A benchmark for room acoustical simulation. concept and database," *Applied Acoustics*, vol. 176, p. 107867, 2021.

[13] M. Marschall, J. G. Bolaños, S. T. Prepeliță, and V. Pulkki, "A database of near-field head-related transfer functions based on measurements with a laser spark source," *Applied Acoustics*, vol. 203, p. 109173, 2023.

[14] B. Gauvreau, "Long-term experimental database for environmental acoustics," *Applied Acoustics*, vol. 74, no. 7, pp. 958–967, 2013.

[15] J. V. Pontalti, E. Brandao, W. D'A. Fonseca, P. H. Mareze, and F. R. Mello, "Criação de um banco de dados de medições de materiais acústicos in situ," in *Actas del XIII Congreso Iberoamericano de Acústica FIA 2024*, (Santiago, Chile), pp. 867–877, Sociedad Chilena de Acústica (SOCHA), 2024.

[16] A. Richard and E. Fernandez-Grande, "Comparison of two microphone array geometries for surface impedance estimation," *The Journal of the Acoustical Society of America*, vol. 146, pp. 501–504, 07 2019.

[17] J. F. Allard and B. Sieben, "Meaurements of acoustic impedance in a free field with two microphones and a spectrum analyzer," *The Journal of the Acoustical Society of America*, vol. 77, no. 4, pp. 1617–1618, 1985.

[18] Y. Allard, J. F.; Champoux, "In situ two-microphone technique for the measurement of the acoustic surface impedance of materials," *Institute of Noise Control Engineering*, vol. 32, pp. 15–23, 1 1989.

[19] W. D'A. Fonseca, E. Brandão, P. H. Mareze, V. S. Melo, R. A. Tenenbaum, C. dos Santos, and D. X. da Paixão, "Acoustical engineering: a complete academic undergraduate program in Brazil," *The Journal of the Acoustical Society of America*, vol. 152, no. 2, pp. 1180–1191, 2022.

[20] P. D'Antonio, M. Nolan, and E. Fernandez Grande, "Design of a new sound field analysis recorder (sofar) for isotropy quantification in reverberation chambers," in *Proceedings of Inter-noise 2020*, (Lyon, France), 2020. 49¡sup¿th¡/sup¿ International Congress and Exposition on Noise Control Engineering, Inter-Noise 2020 ; Conference date: 23-08-2020 Through 26-08-2020.

[21] E. Brandão, "insitu_sim_python." https://github.com/eric-brandao/insitu_sim_python.

[22] E. Brandão, "scanner_meas." https://github.com/eric-brandao/scanner_meas.

[23] W. D'A. Fonseca, J. V. Paes, M. Lazarin, M. V. Reis, P. H. Mareze, and E. Brandao, "Pytta: Open source toolbox for acoustic measurement and signal processing," in *23rd International Congress on Acoustics - ICA 2019 (integrating 4th EAA Euroregio 2019)*, no. ISBN 978-3-939296-15-7, (Aachen, Alemanha), pp. 1–8, German Acoustical Society (DEGA), 2019.

[24] X. Di and K. E. Gilbert, "An exact laplace transform formulation for a point source above a ground surface," *The Journal of the Acoustical Society of America*, vol. 93, pp. 714–720, 02 1993.

[25] P. C. Hansen, *Discrete Inverse Problems*. Society for Industrial and Applied Mathematics, 2010.

DOI: 10.61782/fa.2025.0548

FORUM ACUSTICUM EURONOISE 2025

MEASUREMENT OF SOUND ABSORPTION OF WOOD CHIP-BASED MATERIALS FOR NOISE BARRIERS: EFFECTS OF TESTING AND CASTING CONDITIONS

Louena Shtrepi[1*] **Valentina Buggè**[1] **Sara Fasana**[2]
Marco Zerbinatti[2] **Arianna Astolfi**[1]
[1] Department of Energy, Politecnico di Torino, Italy
[2] Department of Structural, Geotechnical and Building Engineering , Politecnico di Torino, Italy

ABSTRACT*

The territories characterized by a large woodland area, offer considerable potential for the development of a wood supply chain based on principles of circular economy and sustainability. However, there are limited products and applications of virtuous processes for the valorization of local materials with an optimized acoustic performance. This work focuses on recycled and reused by-products as a secondary raw material for the implementation of acoustic materials for noise barriers applications. Different typologies based on the use of loose wood chips (WCh), stone sawing waste (SS) and their combination in mix designs (WChS), where the WCh has been used as an aggregate, have been investigated. Sound absorption measurements were conducted on cylindrical samples in an impedance tube and on larger samples in a small-scale reverberation room (SSRR). The work analyzed the variability of the sound absorption coefficients in terms of reproducibility due to the loose material selection, mix design casting and testing methods.
Experimental results demonstrated that the variability of the sound absorption of the WCh samples are affected mainly by the measurement method, while the WchS samples are significantly affected by the sample size, the mix design casting conditions, and measurement method.

*Corresponding author: louena.shtrepi@polito.it
Copyright: ©2025 Shtrepi et al. This is an open-access article distributed under the terms of the Creative Commons Attribution 3.0 Unported License, which permits unrestricted use, distribution, and reproduction in any medium, provided the original author and source are credited.

Keywords: *wood chips, sound absorption, stone waste, reuse.*

1. INTRODUCTION

This The development of a wood supply chain based on principles of circular economy and sustainability has gained interest and presents different opportunities [1]. However, there are limited products and applications of virtuous processes for the valorization of local materials with an optimized acoustic performance [2]. For example, Stradzas and Januševičius [3] showed in their review the performance potentials of acoustic barriers made using waste and plant-based materials. Many other applications could be explored through principles of circular economy, clean production and aesthetic integration [4]. The main goal of this research is to transform loose wood chips material obtained from sawmill wood waste into a high-value resource with an acoustic performance in noise barriers. This is further integrated with the use of stone sawing waste. Moreover, the work aims to analyze the variability of the sound absorption coefficients in terms of reproducibility due to the loose material selection, mix design casting and testing methods.
The loose material has been analyzed in a few studies. Lashgari et al. [5] presents a concise review of research on sound absorbers made from natural materials. Furthermore, they present measurements and prediction models for wood chip-based sound absorbers promoting the idea of the creation of sustainable sound-absorbing materials from wood chip wastes. Other studies have focused on specific plant varieties considering also leaves and wood in the mix design [6, 7]. Cottone et al. [4] highlights loose material are

completely recyclable once their service life concludes, unlike other mix designs that present limitations due to the binder characteristics.

Ornamental rock cutting wastes (sawing sludges) have been used in various applications; their function is to act as fine aggregates in conglomerate matrices, reacting by interaction with alkaline solutions [8-10]. However, their use as a binding matrix for wood chips in acoustic panels has been overlooked. The mix design between plant-based materials and stone sawing waste has been considered in [11]. To the author's knowledge, no previous studies have reported the variability of sound absorption due to the loose material selection, mix-design casting and testing methods. This is an important aspect to consider given its impact on the final material performance.

The objective of this work is to provide new perspectives of integration of wood waste material for acoustic applications by promoting the use of natural loose material. To this purpose, for a more sustainable approach, the loose material was used in different typologies based on the use of loose wood chips (WCh), stone sawing waste (SS) and their combination in mix designs (WChS), where the WCh has been used as large aggregate and the sawing stone (reacted with alkaline solutions) as a conglomerate matrix. It analyses the variability of the sound absorption coefficients in terms of reproducibility due to the sample mix design casting conditions, sample size and testing methods. Also, the fabrication place, i.e. laboratory or on-site, was considered as a variable in the analyses.

Table 1. Summary of the samples tested in IT and SSRR and their characteristics.

Sample		Thickness [mm]	Density [kg/m^3]	SSRR	IT
1	WCh	20	-		x (lab)
	WCh	100	-	x (site)	x (lab)
2	SS	60	1392-1415		x (lab)
3	WChS	20	752 -873		x (lab)
	WChS	40	752 -873	x (lab and site)	

2. MATERIALS AND METHODS

The work has been developed in two phases: first, the recycled and reused by-products have been studied in different mix designs and secondly, an acoustic characterization of their performance has been performed on cylindrical samples in an impedance tube and on larger samples in a small-scale reverberation room (SSRR).

The experimental work aims to analyze the variability of the sound absorption coefficient in terms of reproducibility of the samples and testing method given different a) loose material selection, b) mix design, c) sample size, and d) measurement method.

2.1 Materials

Three different typologies (Table 1) based on the use of loose wood chips (WCh), stone sawing waste (SS) and their combination in mix designs (WChS), where the WCh has been used as an aggregate, have been investigated. The wood chips were sorted into randomly mixed mesh sizes ranging from 0.5-25 mm, and it was found that stone sawing waste content of 2.7 times the weight of wood chips was suitable for the WChS samples to show both structural and acoustic performance.

Cylindrical samples with different thickness for measurements in the impedance tube and 50x50 cm sized samples for the small-scale reverberation room (SSRR) measurements were fabricated in the lab conditions and on site (building construction site). Table 1 provides a summary of all variables and characteristics of the samples.



Figure 1. Impedance tube sound absorption measurements: randomly mixed sizes of loose wood chips for samples WCh_20_1-4 and WCh_100_IT.

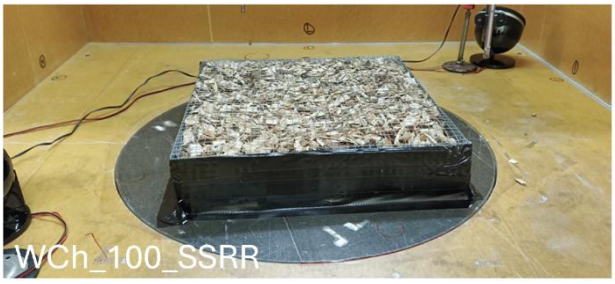


Figure 2. Small-scale reverberation room (SSRR) sound absorption measurements: WCh_100_SSRR.

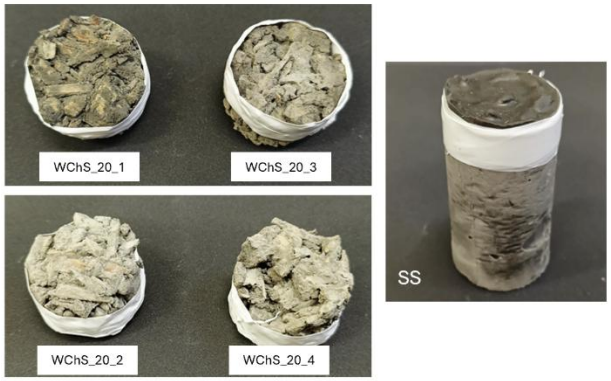


Figure 3. Impedance tube sound absorption measurements: samples WCh_20_ 1-4 and sample SS.

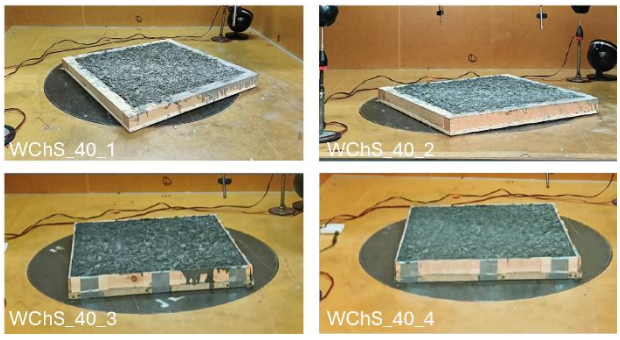


Figure 4. Small-scale reverberation room (SSRR) sound absorption measurements: samples in SSRR WChS_40_ 1-4.

1) Loose wood chips – WCh (Figure 1 and 2):
- 4 samples for impedance tube measurements; thickness 20 mm (WCh_20_1-4);
- 1 sample for impedance tube measurements; thickness 100 mm (WCh_100_IT);
- 1 sample for reverberation chamber measurements; dimensions 50x50 cm; thickness 100 mm (WCh_100_SSRR).

2) Sawing stone SS (Figure 3):
- 1 sample for impedance tube measurements; thickness 60 mm (SS). This sample has been considered as a reflective reference surface for the sawing stone waste material.

3) Mix design wood chips and sawing stone waste casting conditions – WChS (Figure 3 and 4):
- 2 (+2) samples for impedance tube measurements; thickness 20 mm (WChS_20_1-4). These samples were measured on both sides;
- 4 samples for reverberation room measurements; dimensions 50x50 cm; thickness 40 mm (WChS_40_1-4).

2.2 Measurement methods

Two different sound absorption measurements were conducted using cylindrical samples in an impedance tube and on larger samples (50x50 cm) in a small-scale reverberation room (SSRR).

2.2.1 Impedance tube

The acoustic measurements were performed on the three typologies in an ISO 10534-2 impedance tube [12] (two-microphone technique) to assess the normal-incidence sound absorption coefficient. An HW-ACT-TUBE impedance tube at the Applied Acoustics Laboratory (Department of Energy, Politecnico di Torino) was used for these measurements. This device has an internal diameter (ϕ) of 35 mm and is equipped with two ¼'' flush-mounted GRAS 46BD. The method allowed accurate sound pressure amplitude and phase measurements over the whole frequency range of interest, i.e., 100–5000 Hz [13].
The normal-incidence absorption coefficient (α_0) was measured for each composition. Figure 3 shows how the edges of the samples have been adequately sealed with a thin Teflon tape to even out the irregularities generated by the casting technique and to fill the gaps (<1 mm) between the sample and tube [13]. The loose material samples (WCh 20_1-4 and WCh_100_IT have been measured by filling in the tube considering both 20 and 100 mm depth of the rigid backing of the tube piston. The measurements were performed in vertical position for these samples.

2.2.2 Small-Scale Reverberation Room

For the measurement of the sound absorption coefficient in a reverberation room following the procedure of ISO 354:2003 [14] standard, the small-scaled reverberation room (SSRR) of the Department of Energy (DENERG) of Politecnico di Torino has been used. It has been thoroughly described and validated in [15]. The use of the SSRR allows the use of smaller sample sizes than 10-12 m^2 as required in the ISO 354, but maintains the diffuse field conditions of the method. However, this methodology has disadvantages such as the lack of field diffusivity in the mid to low frequencies and diffraction due to the finite size of the experimental samples, which generates so called edge effects. The SSRR measurement methodology specifically consists of an exponential sweep from 100 Hz to 25000 Hz generated through two omnidirectional dodecahedral sound sources. Six microphonic positions for a total of 12 measurements have been performed. To this aim, the measurement chain consists of six 1/400 BSWA Tech MPA451 microphones (BSWA Technology Co., Ltd., Beijing, China) and ICP104; two ITA High-Frequency Dodecahedron Loudspeakers with their specific ITA power amplifiers (ITA-RWTH, Aachen, Germany) and a sound card Roland Octa-Capture UA-1010 (Roland Corporation, Japan). For the measurement of the sound absorption coefficient Matlab software combined with the functions of the ITA-Toolbox (an opensource toolbox from RWTH-Aachen, Germany) [16] was used.
Figure 2 and 4 show the experimental setup and the sample with an area of 0.25 m^2.

3. RESULTS AND DISCUSSION

The sound absorption measurements results have been shown in Figure 5. It presents the variability of the sound absorption coefficient in terms of reproducibility of the samples given different a) loose material selection, b) measurement methods, c) mix design (IT), and d) mix design (SSRR). As shown in Figure 5. a) the SS sample shows a very low sound absorption coefficient similar to very reflective surfaces.

a) Loose material: The comparison of different measurements of four samples of randomly selected loose material shows a good reproducibility of the samples with a variation of the sound absorption of less than 0.2.

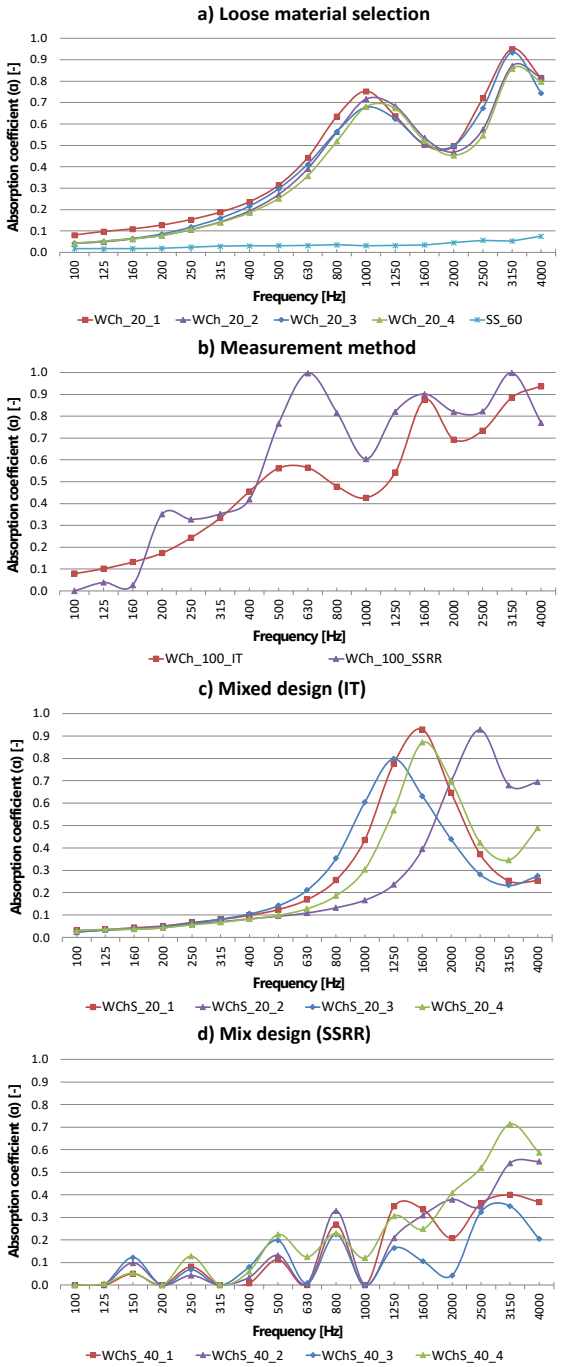


Figure 5. Sound absorption coefficient variation based on a) loose material selection, b) measurement method on loose material, c) mix design for small samples (IT) and d) mix design for larger samples (SSRR).

b) Measurement method: The comparison of the two different measurement methods (IT and SSRR) maintaining the same loose material sample thickness (10 cm) shows a high variability of the sound absorption curves suggesting that there might be significant differences between the distribution of the chips in a larger sample (50x50 cm) that would be complex to select in a representative way with small cylindrical (ϕ=35 mm) samples. The SSRR measurements show a peak at 630 Hz which is higher than the IT sample values of more than 0.4. The correspondence of the peaks with the characteristic geometrical dimensions of the sample patterns has been verified in relation to the thickness of the loose material d=100 mm which corresponds to the quarter-wavelength resonance frequency ($f_0 = c/4d$) of 857 Hz and falls within the 800 Hz third-octave band. This correspondence should be further verified since both curves show a peak at a lower third octave frequency band (630 Hz).

c) Mix design in the impedance tube: The results show significant differences between the two samples WChS_20_1 and _3 (front) presenting different frequency peaks and associated sound absorption at the peak values. Both sides of the same samples show significant differences with the tendency of the inverted samples WChS_20_2 and _4 (back) to shift the peak frequency at higher values. This suggests that the open porosity might be reduced for the back side of the samples which is used to place the samples on the casting plan. This difference was also highlighted in [17].

d) Mix design in the small-scale reverberation room: the curves show a high variability between the four samples, i.e. two fabricated in the lab and two fabricated on site. The variability is higher when comparing the two samples produced in the lab at two different moments. This is more evident at high frequencies above 1000 Hz suggesting that casting conditions may influence in a significant way the acoustic performance. The visual superficial inspection of the samples shows that open porosity could be one of the parameters that may be significantly affected by the casting and curing variables (e.g. operator, weather conditions, sample curing time etc).

4. CONCLUSION

The objective of this work was to provide new perspectives of integration of wood waste material for acoustic applications by promoting the use of natural loose material and stone sawing waste material from local quarries. To this purpose, for a more sustainable approach, the loose material was used in different typologies based on the use of loose wood chips (WCh), stone sawing waste (SS) and their combination in mix designs (WChS), where the WCh has been used as an aggregate. The variability of the sound absorption coefficients in terms of reproducibility due to the sample mix-design, size and testing methods has been presented. Furthermore, the fabrication place that may include the operator, environmental conditions, curing time etc., was considered as a variable in the analysis.

Overall, the work highlighted some of the variables that should be carefully monitored:

- The random selection of the loose material and measurements in the impedance tube samples may not affect or affect to a limited extent the sound absorption in the IT measurements.
- The two different measurement methods (IT and SSRR) showed significant differences suggesting that there might be significant differences between the distribution of the chips in a larger sample compared to smaller samples attempting to be representative of the larger ones.
- The mix-design in the impedance tube measurements showed significant differences in the two front and back oriented samples. This was mainly due to the casting conditions and material deposition on the casting plane.
- The mix-design in the small-scale reverberation room shows a high variability between the four samples, i.e. fabricated in the lab on the building site. In this case the sound absorption is significantly affected by the casting variables (e.g. operator, weather conditions, sample curing time etc.).

Further research could be conducted along this line of research to explore other mix-design and mounting method strategies for the application of sound absorbing porous loose wood chips and stone sawing waste in the frame of the sustainable architectural and urban design strategies. A more systematic study could be developed considering the variables explored in this work in order to build appropriate guidelines that would preserve optimized acoustic performance also in the fabrication/casting and curing phase on site and in lab conditions.

5. ACKNOWLEDGMENTS

The work has been financially supported by the Piedmont Region through the project LA.B. 23-24 – Laboratorio Bosco 2023-2024 (grant nr. 20201396791). The authors would like to thank Segheria Minetti Snc (Crodo, Italy), Pierpaolo Nuzzo, Andrea Bottega, Stefano Di Domenico and Franco Grindatto for their contribution to the sample construction.

6. REFERENCES

[1] M. Zbieć, J. Franc-Dąbrowska, and N. Drejerska: "Wood Waste Management in Europe through the Lens of the Circular Bioeconomy," Energies, vol. 15, no. 12, p. 4352, 2022.

[2] J.P. Arenas and K. Sakagami: "Sustainable Acoustic Materials," Sustainability, vol. 12, no. 16, p. 6540, 2020.

[3] E. Strazdas and T. Januševičius: "Evaluation and Analysis of Sound Absorption across Various Types of Hemp Fibre," *Environmental and Climate Technologies*, vol. 28, no. 1, p. 269–285, 2024.

[4] R. Cottone, L. Shtrepi, V. Serra, and S.L. Pagliolico: "The Recycling and Reuse of Natural Materials: Sound Absorbing Box Patterns That Use Waste from Olive Tree Pruning," Acoustics, vol. 5, no. 1, pp. 177–192, 2023.

[5] M. Lashgari, E. Taban, M.J. SheikhMozafari, P. Soltani, K. Attenborough, and A. Khavanin: "Wood chip sound absorbers: Measurements and models," Applied Acoustics, vol. 220, p. 109963, 2024.

[6] S. Bousshine, M. Ouakarrouch, A. Bybi, N. Laaroussi, M. Garoum, and A. Tilioua: "Acoustical and thermal characterization of sustainable materials derived from vegetable, agricultural, and animal fibers," Applied Acoustics, vol. 187, p. 108520, 2022.

[7] F. Martellotta, A. Cannavale, V. De Matteis, and U. Ayr: "Sustainable sound absorbers obtained from olive pruning wastes and chitosan binder," Applied Acoustics, vol. 141, pp. 71–78, 2018.

[8] M. Juenger, F. Winnefeld, J. Provis, J. Ideker: "Advances in alternative cementitious binders," Cem. Concr. Res. vol. 41, pp. 1232–1243, 2011.

[9] B. Coppola, J.-M. Tulliani, P. Antonaci, P. Palmero: "Role of Natural Stone Wastes and Minerals in the Alkali Activation Process: A Review," Materials, vol. 13, p. 2284, 2020.

[10] F. Vecchio, M. Zebinatti: "Alkali-activated mortars from rock muds. Experimental mix-design and tests for the prototyping of sustainable building products," Memoria Innovazione. Proceedings of Colloqui.AT.e. int. Congress, Genova (ITA), Sptember 07-10th 2022.

[11] A. Boubel, M. Garoum, S. Bousshine, and A. Bybi: "Investigation of loose wood chips and sawdust as alternative sustainable sound absorber materials," Applied Acoustics, vol. 172, p. 107639, 2021.

[12] ISO 10534-2: Acoustic – Determination of Sound Absorption Coefficient and Impedance in Impedance Tubes – Part 2: Transfer-Function Method. Geneva, Switzerland: International Organization for Standardization, 1998.

[13] N. Kino and T. Ueno: "Investigation of sample size effects in impedance tube measurements," Applied Acoustics, vol. 68, no. 12, pp. 1485–1493, 2007.

[14] ISO 354: Acoustics – Measurement of Sound Absorption in a Reverberation Room. Geneva, Switzerland: International Organization for Standardization, 2003.

[15] L. Shtrepi and A. Prato: "Towards a sustainable approach for sound absorption assessment of building materials: Validation of small-scale reverberation room measurements," Applied Acoustics, vol. 165, p. 107304, 2020.

[16] ITA-Toolbox for MATLAB. Developed at the Institute of Technical Acoustics, RWTH Aachen University.

[17] L. Shtrepi, A. Astolfi, E. Badino, G. Volpatti, and D. Zampini: "More Than Just Concrete: Acoustically Efficient Porous Concrete with Different Aggregate Shape and Gradation," Applied Sciences, vol. 11, no. 11, p. 4835, 2021.

DOI: 10.61782/fa.2025.0779



FORUM ACUSTICUM
EURONOISE 2025

SOUND ABSORPTION PREDICTION OF HIGH-DENSITY FOAM-FORMED SOFTWOOD FIBERS

Janis Heldmann[1*] **Jose Cucharero Moya**[2] **Tapio Lokki**[1]
[1] Acoustics Lab, Dept of Information and Communications Engineering, Aalto University, Finland
[2] Lumir Oy, Finland

ABSTRACT

Nowadays, porous absorption materials need to be environmentally sustainable. This concerns the sources of raw materials, low energy consumption in the manufacturing process, and options for recycling. Therefore, alternatives for mineral wools are needed and biomaterials offer an attractive solution. Some recently studied sustainable acoustic materials, such as foam-formed wood fibers, can be produced with a negative carbon footprint. However, sound absorption performance must match the less sustainable variants to ensure competitiveness. Therefore, the prediction of sound absorption is important because it supports the optimization of processes and functionality to achieve the best possible solution. In this study, foam-formed wood pulps of increasing density are produced, characterized, and modeled by semi-phenomenological and analytical models. Their density range exceeds an earlier study by choosing a non-ionic surfactant during synthesis and model accuracy across densities is evaluated against experimentally measured sound absorption. The aim is to create foam-formed fibers with maximal density and the possibility to predict sound absorption with accurate models. The results show that the JCAL model performs better than the analytical models, but the less tedious analytical models provide good approximations. The finding contributes to the optimization of foam-formed pulps by choosing feasible models for the aimed density.

Keywords: *foam-formed biomaterial, wood fibers, JCAl, analytic modeling, sound absorption*

**Corresponding author*: *janis.heldmann@aalto.fi.*

***Copyright**: ©2025 Heldmann et al. This is an open-access article distributed under the terms of the Creative Commons Attribution 3.0 Unported License, which permits unrestricted use, distribution, and reproduction in any medium, provided the original author and source are credited.*

1. INTRODUCTION

Density is a crucial factor in producing high performing acoustic absorbers. Increasing the density of a material also increases the low frequency absorption, which is often a key factor for the usability of acoustic absorbers. Usually, higher densities are related to more material per volume and therefore higher costs. However, in the light of biobased-absorbers more raw material used is a desired goal, as it allows to bind more carbon to the absorption material. This increases a negative carbon dioxide footprint, using more base material that is typically from side streams and leftovers from, e.g., the pulp and paper industry. Based on a previous study [1] that explored the prediction of foam formed wood pulp absorption with an analytical model, semi-phenomenological model, and further refined fitting, this study extends the maximum density range from 50 kg/m^3 to 64 kg/m^3. The necessary pore network stability is achieved with a non-ionic surfactant that is added during the material synthesis.

2. MATERIAL AND METHODOLOGY

Sound-absorbing foams were produced using a foam-forming process based on [2]. Pulp, water, and a non-ionic surfactant were mixed under axial agitation (3000 rpm) in a cylindrical vessel. Two pulp consistencies (3.5% and 4.5%) were used to vary foam density. The pulp was pre-soaked for one day, stirred for 10 minutes, then foamed after surfactant addition until the volume doubled.

The foam was poured into a 25 $\times$ 25 $\times$ 25 cm mold with stainless steel nets for drainage and structural support. Samples were dried at 40°C for two days. Denser foams were pre-conditioned at 99% relative humidity and

20°C before compression and final drying. Circular samples (100 mm and 29 mm diameter, 40 mm thick) were cut using a bench drill, and outer layers were trimmed to ensure uniform density. The non-ionic surfactant from the group of ethoxylated alcohol replaced sodium dodecyl sulfate (SDS) from the previous study to improve foam stability and allow higher densities. The density is controlled by air content, stability of the foam and the fibre type and dimensions. The choice of surfactant affects the interaction between bubbles and fibres and therefore the foam stability.

3. MEASUREMENT

The dynamic mass density $\widetilde{\rho}$ and dynamic bulk modulus $\widetilde{K}$ were measured using the three-microphone method in a 100 mm and 29 mm diameter B&K 4206 impedance tube. A broad-spectrum random signal of 50–2000 Hz for 100 mm samples and 50-6400 Hz for 29 mm samples was emitted from a loudspeaker, with the sample placed against a rigid termination. Measurements followed ISO-10534-2 [3], and each sample was tested on both sides to account for potential non-homogeneity. Reported values are averages from the measurements of both sides.

4. CHARACTERIZATION

The characterization of the JCAL parameters was performed with the RokCell software (Matelys, France). It estimates all six JCAL parameters based on measured dynamic mass density $\widetilde{\rho}$ and dynamic bulk modulus $\widetilde{K}$ [4]. The characterization was done for each measurement individually and the final estimated JCAL parameters are averages of parameters obtained from both sides. This is done to compensate for the possible non-homogeneous properties of the samples, even though the top and bottom layers of the materials were cut off.

5. MODELING AND ANALYTICAL FIT

The non-acoustic parameters determined during characterization allow modeling $\widetilde{\rho}$ and $\widetilde{K}$ and therefore the sound absorption coefficient [5]. The analytical model consists of six submodels which predict all JCAL parameters while assuming randomly oriented parallel fibers with a symmetric radius distribution, as described in [6], making it well-suited for naturally formed bio-based materials. The submodels are only based on the effective fiber radius and mass density $\widetilde{\rho}$, calculated from the sample mass and enclosing volume (values in Table 1). The effective fiber radius a = 12.7 μm for softwood pulp was obtained earlier from Kajaani FiberLab measurements on similar foam-formed pulps [7]. Non-acoustic parameters are derived using adapted equations to match the symmetric distribution assumption. Three related analytical models were employed. First, the original model proposed in [6], secondly an adaptation in which the equations for flow resistivity and viscous characteristic length were fitted to the characterized values of flow resistivity and viscous characteristic length of the produced materials. Third, an alternative model was used to fit the flow resistivity and viscous characteristic length to the characterized values. The procedure is equivalent to the preceding study of this work and the detailed equations can be found there [1].

In the original model, airflow resistivity is calculated according to Tamayol et al. [8] using the formula:

$$\sigma = \frac{\eta}{(2a)^2} \frac{\sqrt{1-(1-\phi)}}{c_1 \left(\frac{c_2}{1-\phi} - 3\sqrt{\frac{c_2}{1-\phi}} + 3 - \sqrt{\frac{1-\phi}{c_2}} \right)} \tag{1}$$

where a is the effective fiber radius and η is the viscosity of air. The fitting parameters $c_1 = 0.21$ and $c_2 = 0.71$ are validated for symmetric distributions of parallel fibers. The second model fits the parameters c_1 and c_2 to the characterized values of flow resistivity of the produced materials. The viscous characteristic length is according to the model of Umnova et al. [9]:

$$\Lambda = a \frac{(2-\phi)\phi^{c_3}}{2(1-\phi)} \tag{2}$$

with $c_3 = 2.732$ in the original model. In this study, the second analytical model fits also c_3 to the present set of values. The third model intends to further improve the modelling accuracy of the viscous characteristic length by using

$$\Lambda = b_1 (1-\phi)^{-b_2}, \tag{3}$$

for the viscous characteristic length.

6. RESULTS

Table 1 presents the characterized JCAL parameters in terms of their density and sample diameter. Flow resistivity shows a typical increase with increasing density. The smallest (29 mm) samples were quite tight in the tube and

it is possible that the material was a bit compressed when mounted, resulting in higher air flow resistivity than with 100 mm samples. Tortuosity grows slightly as material is denser but other parameters don't show very clear trends, however, all of them are reasonable.

Figure 1 shows the measured absorption curves across densities of 50-59 kg/m^3 for 100 mm samples and 59-64 kg/m^3 for 29 mm samples. For higher densities, the absorption curves shift towards lower frequencies. There are signs of elastic effects present such that the curves are not totally smooth. Such effects are often present when fitting in the impedance tube is tight. Figure 2 shows the comparison between JCAL, JCA, and the original and fitted analytical models. The original analytical model does not model the absorption precisely as it assumes parallel fibres resulting in lower flow resistivity and higher viscous characteristic length than in the actual randomly oriented fibre network. Fitting flow resistivity and viscous characteristic length of the analytical model improves its accuracy across densities. Unlike the results for lower densities in [1] a second step of fitting flow resistivity does not improve the accuracy further. JCAL and JCA models perform equally precisely. The elastic properties are not included in the model, therefore the curve omits the elastic modulation visible in the measured curve.

7. CONCLUSION

In this paper, the investigation of density dependent absorption and its prediction for foam-foamed fibers was extended towards higher densities by using a non-ionic surfactant instead of previously applied SDS. Sound absorption, dynamic mass density and bulk modulus were measured to characterize the JCAL parameters of the materials. An analytical model based on parallel fibres was adapted in terms of air flow resistivity and viscous characteristic length to improve its accuracy for the investigated randomly orientated fiber network. The JCAL model shows higher precision than the employed analytical models, while the analytical models give good approximations. The differences between measured and predicted sound absorption curves are due to elastic effects that appear by fitting the sample into the impedance tube, and are not included in the JCAL model.

8. ACKNOWLEDGEMENTS

This work was supported by the KAUTE foundation and by the Academy of Finland's Flagship Programme under Projects No. 318890 and 318891 (Competence Center for Materials Bioeconomy, FinnCERES)

9. REFERENCES

[1] J. Heldmann, J. Cucharero, and T. Lokki, "Characterization, modeling and prediction of foam-formed softwood fiber sound absorption," in *INTER-NOISE and NOISE-CON Congress and Conference Proceedings*, (Nantes, France), pp. 8745–8756, 2024.

[2] J. Cucharero, S. Ceccherini, T. Maloney, T. Lokki, and T. Hänninen, "Sound absorption properties of wood-based pulp fibre foams," *Cellulose*, vol. 28, no. 7, 2021.

[3] ISO, "10534-2:1998 - Acoustics - Determination of sound absorption coefficient and impedance in impedance tubes - Part 2: Transfer- function method.," *Ansi*, no. 1, 1998.

[4] L. Jaouen, E. Gourdon, and P. Glé, "Estimation of all six parameters of Johnson-Champoux-Allard-Lafarge model for acoustical porous materials from impedance tube measurements," *The Journal of the Acoustical Society of America*, vol. 148, no. 4, 2020.

[5] J.-F. Allard and G. Daigle, " Propagation of Sound in Porous Media: Modeling Sound Absorbing Materials," *The Journal of the Acoustical Society of America*, vol. 95, no. 5, 1994.

[6] F. Pompoli, "Acoustical Characterization and Modeling of Sustainable Posidonia Fibers," *Applied Sciences (Switzerland)*, vol. 13, no. 7, 2023.

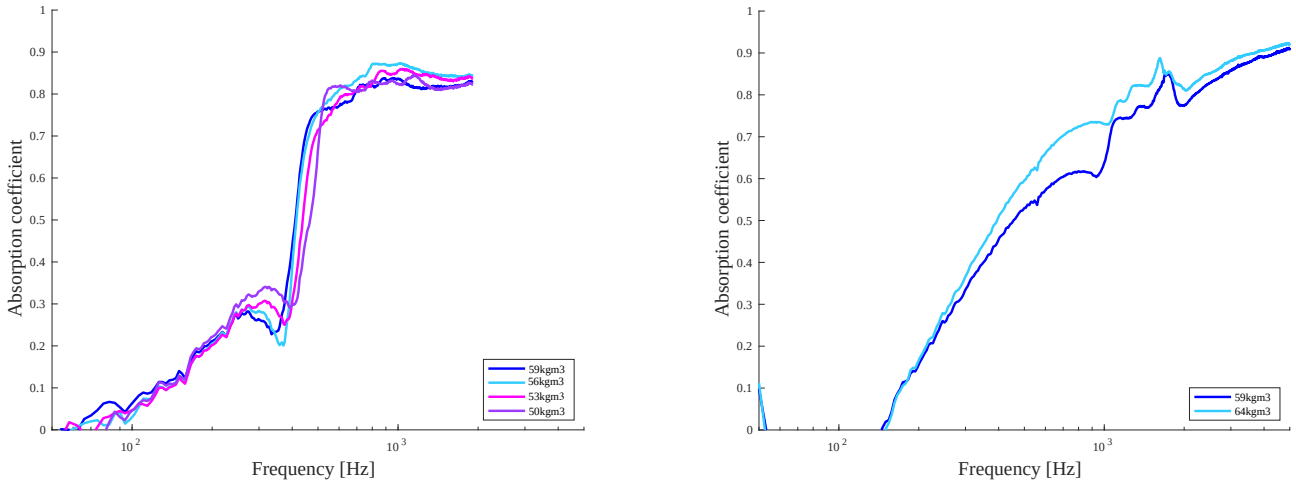
[7] J. Cucharero, S. Ceccherini, M. Awais, K. Kammiovirta, T. Maloney, L. Rautkari, T. Lokki, and T. Hänninen, "Studies on the sound absorption properties of wood-based pulp fibre foams," in *Proceedings of the International Congress on Acoustics*, 2022.

[8] A. Tamayol and M. Bahrami, "Transverse permeability of fibrous porous media," *Physical Review E - Statistical, Nonlinear, and Soft Matter Physics*, vol. 83, no. 4, 2011.

[9] O. Umnova, D. Tsiklauri, and R. Venegas, "Effect of boundary slip on the acoustical properties of microfibrous materials," *The Journal of the Acoustical Society of America*, vol. 126, no. 4, 2009.

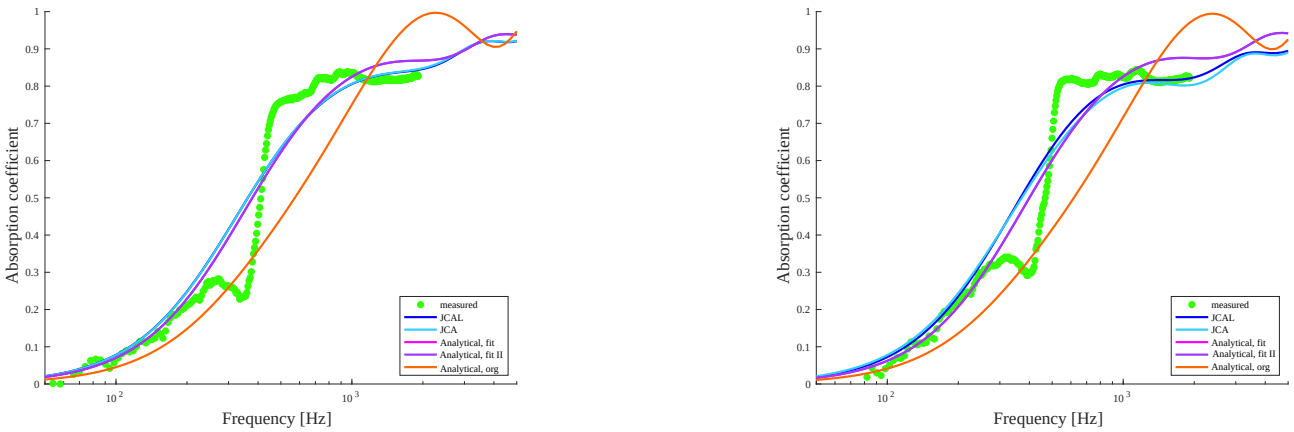
Table 1. Results for the characterization of flow resistivity, porosity, tortuosity, viscous characteristic length, thermal characteristic length, and thermal permeability of all samples in RokCell software.

Density (kg / m^3)	σ (Nsm^{-4})	ϕ (-)	α_∞ (-)	Λ (μm)	Λ' (μm)	k'0 (1e-10 m^2)	d_s (mm)
50	33400	0.97	1.38	32	124	16	100
53	43000	0.97	1.42	29	151	18	100
56	52200	0.97	1.57	31	178	18	100
59	49800	0.97	1.58	44	116	18	100
59	63600	0.97	1.45	33	104	14	29
64	81600	0.97	1.60	61	95	12	29



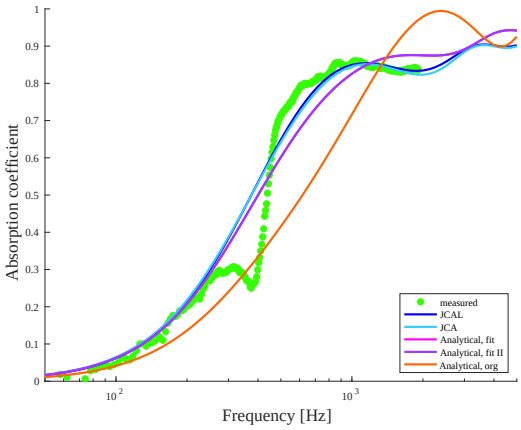
(a) Softwood, d$_s$ = 100mm (b) Softwood, d$_s$ = 29mm

Figure 1. Measured absorption curves for foam foamed bleached softwood pulps for two sample diameters and across increasing density.

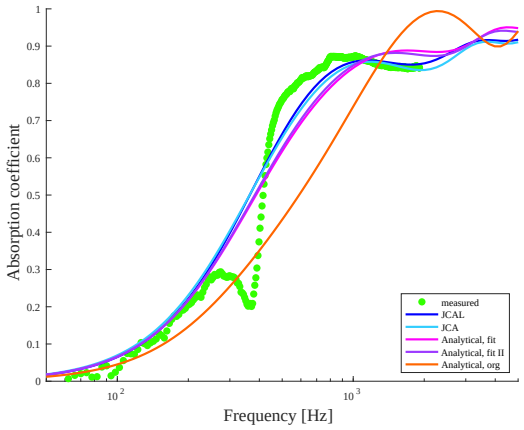


(a) 50 $\mathrm{kg/m^3}$, $\mathrm{d_s}$= 100mm

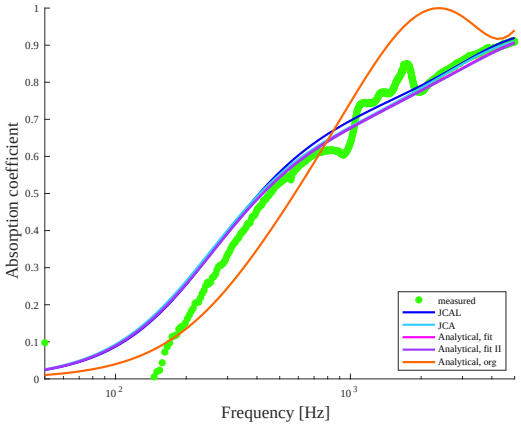
(b) 53 $\mathrm{kg/m^3}$, $\mathrm{d_s}$= 100mm



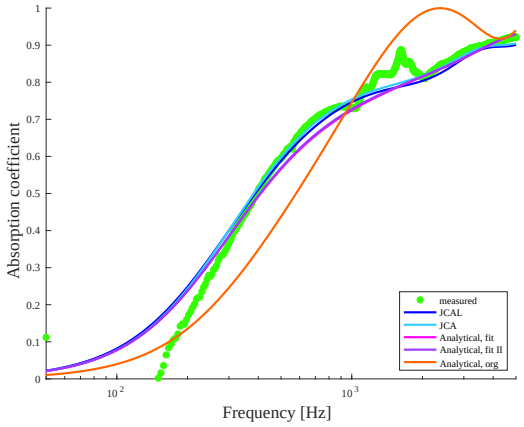
(c) 56 $\mathrm{kg/m^3}$, $\mathrm{d_s}$= 100mm



(d) 59 $\mathrm{kg/m^3}$, $\mathrm{d_s}$= 100mm



(e) 59 $\mathrm{kg/m^3}$, $\mathrm{d_s}$= 29mm



(f) 64 $\mathrm{kg/m^3}$, $\mathrm{d_s}$= 29mm

Figure 2. Sound absorption measurements and predictions at 50-5000 Hz for softwood foam-formed pulps that extend the density range from 50 - 64 $\mathrm{kg/m^3}$.

DOI: 10.61782/fa.2025.0198

FORUM ACUSTICUM EURONOISE 2025

CHARACTERIZATION OF THE SOUND ABSORPTION PROPERTIES OF A FIBROUS BIOMATERIAL: A KEY INPUT FOR ROOM ACOUSTIC SIMULATION SOFTWARE

Joaquin Garcia[1*] **Pablo Alloza**[2] **Edoardo Alessio Piana**[1]
[1] Applied Acoustics Laboratory, University of Brescia, via Branze 38, Brescia, Italy
[2] Track-Noise, Spain

ABSTRACT

In recent years, the search for sustainable materials has gained increasing importance in order to optimize resource use and reduce carbon emissions. In this context, bio-materials have emerged as an alternative due to their low environmental impact. In particular, those with a fibrous morphology, both vegetal or animal based, have proven effectiveness as sound absorbers in room acoustics applications. In this study, the acoustic absorption properties of a type of sheep wool are evaluated. The characterization of the acoustic absorption coefficient under normal incidence was carried out using the two-microphone impedance tube method and compared with the reverberant chamber method. Subsequently, the reverberation time of a selected room was measured before and after the implementation of two walls covered with the chosen material. The impulse response was also recorded using a spherical microphone array, which allowed the visualisation of early reflections applying beamforming algorithms. These measurements were used to validate the simulated impulse response of the room and to determine the most accurate absorption data for the model.

Keywords: *Sound absorption, impedance tube, biomaterials, acoustic camera, simulations.*

**Corresponding author*: *jorge.garcia@unibs.it.*
***Copyright**: ©2025 Garcia et al. This is an open-access article distributed under the terms of the Creative Commons Attribution 3.0 Unported License, which permits unrestricted use, distribution, and reproduction in any medium, provided the original author and source are credited.*

1. INTRODUCTION

The use of sustainable materials has become a significant trend in recent years, towards a strategy of zero-carbon emissions. Building materials typically come from non-renewable and synthetic resources. Porous materials are commonly derived from petrochemical products like polyester or polyurethane, which have a high environmental impact after use. Natural materials have emerged as a viable alternative, utilising renewable resources and generally exhibiting lower levels of environmental impact and embodied energy. Several studies have reported the acoustical properties of oil palm fibres [1], sugarcane bagasse [2], hemp fibres [3] and kenaf fibres [4].

Sheep wool is a natural material that has many advantages compared to others, such us their good thermal insulating performance and low flammability since it is self-extinguishing and does not ignite easily [2]. Furthermore it does not release any toxic particles or gases during combustion and, it is a renewable and recyclable material with a natural decomposition cycle. However, sheep wool is having less demand for applications in the textile industry and nowadays most of the surplus is burned or sent to landfill [5].

The sound absorbing properties of porous materials are normally linked to their porosity and flow resistivity. According to their structure, porous materials can be classified as cellular, fibrous and granular [6]. Fibrous materials are among the most widely used due to their high availability and origins from both animal and vegetable sources. The absorption properties can be measured through various methods. One of them is using an impedance tube. This method requires small samples and relatively inexpensive equipment. However it can only

characterise the absorption at normal incidence and up to the cut-on frequency of the impedance tube, that depends on the tube's diameter [7]. In contrast, the reverberation chamber method (ISO 354) implies the use of 10 m^2 samples, making it less convenient and more expensive. While the absorption coefficient obtained through this method is more representative of the material's behaviour in real world situations — reflecting conditions under a diffuse field — low reproducibility between laboratories can yield varying results [8]. Additionally, the placement of the material within the chamber can influence the measured absorption coefficient [9]. Within this context it can be not clear which values are more accurate to use when feeding computational models for room acoustic simulations in order to have results matching the reality.

In this paper the sound absorption properties of a sheep wool absorber was evaluated and used as an input material for feeding computational models for room acoustics. Furthermore the impulse response of a room was measured and the reverberation time deduced before and after covering the walls with sheep wool panels. Early reflections were observed by using a spherical microphone array and beamforming algorithms. These measurements were used to validate the computational model of the room and investigate which absorption data is more accurate to be used as input material in the model.

2. MATERIALS AND METHODS

The material selected was a sheep wool, wrapped in panels of 6 mm thickness. Three samples of 45 mm diameter were extracted as shown in 1 and their sound absorption properties were measured in an impedance tube. The material was provided by Farrás Home - Spain and in particular this model has also a coating of a series of natural resins that act as a catalytic converter. It absorbs the CO_2 and NOx, contributing to the ecological balance.



Figure 1: Samples of sheep wool.

2.1 Impedance tube measurements

The sound absorption coefficient was measured using a two microphones impedance tube according to the standard ISO 10534 [7]. The system was implemented with a cylindrical tube of 45 mm diameter allowing the characterisation of the sound absorption coefficient up to a cut-off frequency of 3800 Hz. The samples were mounted on a rigid back-end and two 1/4" microphones were spaced 45 mm from each other to measure the pressure field. On the other extreme of the tube a loudspeaker generated a broad band white noise as test signal. The transducers were connected to an OROS Type OR36 analyser, which measures the complex transfer functions between the microphones. The absorption coefficient was calculated given the sample thickness d as:

$$\alpha = 1 - |R|^2 \tag{1}$$

$$R = \frac{Z_s - \rho_0 c}{Z_s + \rho_0 c} \tag{2}$$

$$Z_s = -jZ_c cot(k_c d) \tag{3}$$

Where R is the sound pressure reflection coefficient, Z_s is the surface impedance of the sample, Z_c its characteristic impedance, and ρ_0 and c the density of air and speed of sound.

The results shown in section 3 are the average of three samples. The resulting curves are compared to the results of sound absorption measurements carried out in a reverberant room with the same material.

2.2 Impulse response measurements

The impulse response of a room with a volume of approximately 33 m^3 was measured with a NTi Audio XL2 sound level meter mounting a Type 1 microphone. The impulse was generated wiht a Delta Clapper. The sketch of the room with the measurement positions is presented in Figure 2 and the setup is shown in Figure 3. The reverberation time (RT) was measured in accordance with the guidelines established in ISO 3382-1:2009. According to this standard, the reverberation time T20 and T30 were calculated through the backward Schroeder integration in octave bands from 63 Hz to 8000 Hz. The results obtained from four microphone positions at 1.5 m height were averaged to obtain a representative reverberation time for the room as shown in Figure 2. The same measurement positions and procedures were repeated after applying the

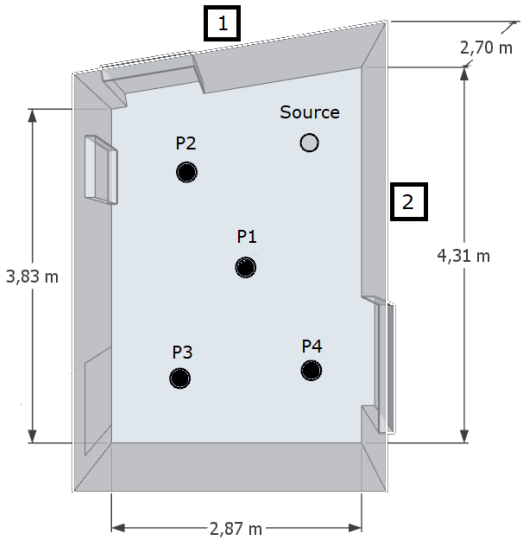


Figure 2: Top view of the room showing the positions of the sound source and microphones. The height is 2.7 m.



Figure 3: Sound level meter placed in the room.

acoustic treatment to the room. In what follows for all the measurements the absorptive material was installed covering walls 1 and 2 indicated in Figure 2.

2.3 Acoustic camera measurements

The measurement campaign was conducted using a Sphere48 AC Pro by gfai tech which is an advanced acoustic camera system designed specifically for 3D localization of sound sources in enclosed spaces. This spherical microphone array is equipped with 48 high-precision microphones arranged to capture sound from all directions, making it particularly suitable for indoor applications such as vehicle interiors, rooms, and architectural spaces. This tool represents a powerful and comprehensive solution for the localisation and visualisation of acoustic reflections in three dimensions. The array was positioned centrally within the room, mounted on a high-stability tripod, ensuring a clear line of sight to all major reflective surfaces (walls, ceiling, floor, furniture) (see Figure 4). The system was connected to a multi-channel data acquisition unit running the gfai tech NoiseImage software suite.

A series of impulsive sound stimuli were generated using a NTi Audio Delta Clapper placed at various locations within the room, mainly corners. Each impulse was recorded by the 48 microphones, capturing both the direct sound and the subsequent early and late reflections. To ensure spatial accuracy, the integrated Intel® RealSense™ depth camera was used to match the array position inside the 3D model captured by a laser-scanner, allowing beamforming results to be mapped directly onto the geometry of the room. The same measurement positions and procedure was repeated after the acoustic treatment.

2.4 Computational simulations

Room acoustics simulations were performed using the software Treble, which is a hybrid room acoustic simulation tool that combines wave-based simulations at low frequencies, to capture the important wave and modal behaviour up to a transition frequency (typically the Schroeder frequency), and geometrical acoustic simulations at high frequencies, to take advantage of the faster calculations. The geometry was first modelled in Sketchup and then imported into the software. The source and microphone positions were introduced according to those shown in Figure 2. After theat the materials and properties of the walls, roof and ceiling were defined according to the Table 1.

The transition frequency was set to 710 Hz and the number of rays for the geometrical solver was set to 20,000, considering up to 5th order reflection. The calcu-



Figure 4: Sphere acoustic camera inside the room.

lations, running on a dedicated server associated with the software, took around 3 minutes per complete simulation.

The measured sound absorption coefficients (both in impedance tube and reverberant chamber) of the sheep wool were entered as input to perform the simulations before after the acoustic treatment. The strategy was to combine the absorption values of the walls with those of the sheep wool, under the hypothesis that the wool panels are thin enough not to introduce significant damping, thus not change the low frequency absorption behaviour of the wall panels. For this purpose, the software allows for the introduction of combined sound absorption coefficients, and it calculates the surface impedance of the component using a fitting algorithm. In Figure 5 an example of the material generation window of the software is shown, where the inserted values (target) and the derived values (results) of sound absorption coefficient can be seen. Internally, during the fitting process, the software estimates the surface impedance, which is necessary to recover the phase information for the modal based solver.

3. RESULTS AND DISCUSSION

3.1 Absorption properties of the samples

The sound absorption coefficient in third-octave bands of the sheep wool is shown in Figure 6. As it can be seen, it has a typical behaviour of a fibrous material with a crescent absorption value towards the high frequency range crossing the 0.3 line at around 3000 Hz. On the same graph it is shown the absorption coefficient of the same material measured previously in reverberant room according to the ISO 354. As expected, the values are higher than the ones measured in impedance tube since in the last one only normal incidence behaviour of the sample is captured, while in the reverberant chamber a diffuse field condition is reached. However, the absorption coefficient in this last case can be overestimated due some drawbacks of the methods such us diffraction effects on the border of the sample. Consequently both curves are fed as input into the computational model and the impact on the reverberation time considering one or the other absorption curve is analysed in Section 3.2.

Table 1: Sound absorption properties of the materials used for the simulation

Frequency (Hz)	10 mm gypsum board + 100 mm mineral wool	Wooden flooring	Brick painted (ceiling)
63	0.39	0.16	0.05
125	0.27	0.15	0.04
250	0.14	0.13	0.04
500	0.08	0.1	0.03
1000	0.05	0.08	0.04
2000	0.05	0.07	0.05
4000	0.07	0.07	0.05
8000	0.07	0.07	0.05



Figure 5: Estimation of the absorption properties of the material after a fitting process inside Treble software.

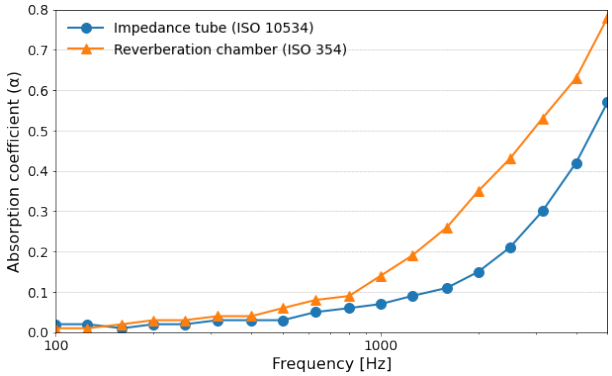


Figure 6: Sound absorption coefficient of the sheep wool measured in impedance tube and reverberant chamber

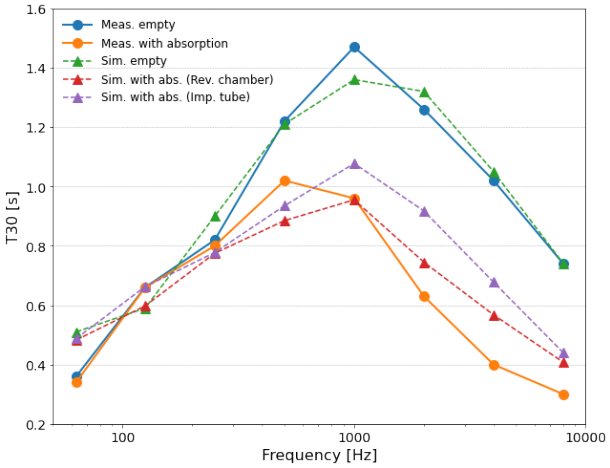


Figure 7: Reverberation time measured and simulated, with and without absorbing material.

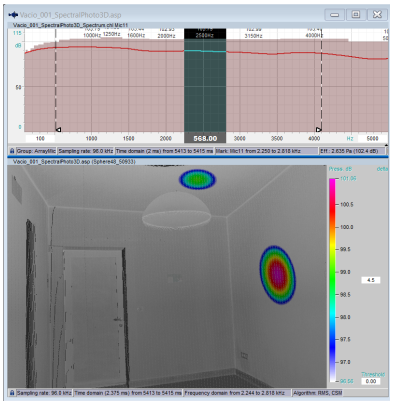
3.2 Impulse response of the room and simulations

The results obtained from the Reverberation Time (RT) measurements, indicate a significant reduction in RT values, particularly from the 500 Hz third-octave band onwards. The overall RT value decreased from 1.35 s to 0.99 s after the installation of the acoustic treatment as it can be seen in the solid line curves in Figure 7. On the same graph the results of the RT from the simulation can be seen. A very good agreement is observed between the measured and the simulated RT of the room without the porous material. When the absorption is applied, the RT curve considering the material measured in reverberation chamber is more close to the measured one than the case considering the absorption values from impedance tube. This might suggest that for non very high absorptive materials the reverberation chamber values potentially can give more accurate results in the model. The mismatch at 63 Hz can be attributed to a fitting difference in the material building module inside the software. For the rest of the frequency the curves follow the same tendency with slight differences.

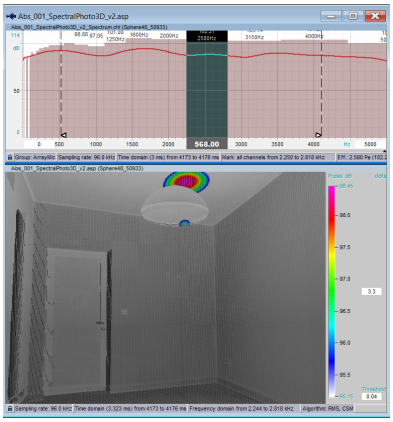
Additionally, the use of a 3D Acoustic Camera enabled the identification and analysis of early acoustic reflections within the room. This tool was instrumental in comparing the acoustic behaviour of the space before and after installing the absorptive material on two of the walls. The visual data clearly demonstrate the effectiveness of the material in attenuating acoustic reflections at its installed locations. This is particularly evident as shown in Figure 8 in the 2500 Hz third-octave band and with differences of about 5 dB at 1250 Hz and at 800 Hz third-octave bands, where the absorption performance aligns with the material's specified acoustic properties.

4. CONCLUSIONS

In this work a room acoustic study was conducted. First the acoustic absorption properties of a sheep wool material was assessed and used as input data to fed computational simulations. The same material was used to perform an acoustic correction of a room and the reverberation time before and after the acoustic treatment was measured to compare the situations. The acoustic camera was utilised to visualise the first reflections and verify the reduction of level in presence of the sheep wool materials. The room was simulated using a hybrid wave-based and geometrical acoustic software to investigate the response of the room. The model was validated using the experimental measurements. Sound absorption values of the same material measured in impedance tube and reverberation chamber were implemented in the software. It was shown that in the last case the values were closer to the measured ones. Despite normally the reverberation chamber method tends to overestimate the absorption coefficient, this might suggest that potentially for not very highly absorptive materials the most accurate option for use as input data in simulation models is the absorption coefficient measured in reverberant rooms.



(a) Without absorptive material.



(b) With absorptive material.

Figure 8: Visualisation of the first reflection on the walls at 2500 Hz third-octave band.

5. REFERENCES

[1] K. H. Or, A. Putra, and M. Z. Selamat, "Oil palm empty fruit bunch fibres as sustainable acoustic absorber," *Applied Acoustics*, vol. 119, pp. 9–16, 4 2017.

[2] M. H. Beheshti, A. Firoozi, M. Jafarizaveh, and A. Tabrizi, "Acoustical and thermal characterization of insulating materials made from wool and sugarcane bagasse," *Journal of Natural Fibers*, vol. 20, 2023.

[3] A. Santoni, P. Bonfiglio, P. Fausti, C. Marescotti, V. Mazzanti, F. Mollica, and F. Pompoli, "Improving the sound absorption performance of sustainable thermal insulation materials: Natural hemp fibres," *Applied Acoustics*, vol. 150, pp. 279–289, 7 2019.

[4] Z. Y. Lim, A. Putra, M. J. Nor, and M. Y. Yaakob, "Sound absorption performance of natural kenaf fibres," *Applied Acoustics*, vol. 130, pp. 107–114, 1 2018.

[5] B. Petek and R. M. Logar, "Management of waste sheep wool as valuable organic substrate in european union countries," 1 2021.

[6] J. P. Arenas and M. J. Crocker, "Recent trends in porous sound-absorbing materials," *Sound and Vibration*, vol. 44, no. 7, pp. 12–17, 2010.

[7] UNE-EN ISO 10534-2, "Determinación del coeficiente de absorción acústica y de la impedancia acústica en tubos de impedancia," 2002.

[8] C. Scrosati, F. Martellotta, F. Pompoli, A. Schiavi, A. Prato, D. D'Orazio, M. Garai, N. Granzotto, A. Di Bella, F. Scamoni, M. Depalma, C. Marescotti, F. Serpilli, V. Lori, P. Nataletti, D. Annesi, A. Moschetto, R. Baruffa, G. De Napoli, F. D'Angelo, and S. Di Filippo, "Towards more reliable measurements of sound absorption coefficient in reverberation rooms: An Inter-Laboratory Test," *Applied Acoustics*, vol. 165, p. 107298, 2020.

[9] J. Cucharero, T. Hänninen, and T. Lokki, "Influence of Sound-Absorbing Material Placement on Room Acoustical Parameters," *Acoustics*, vol. 1, no. 3, pp. 644–660, 2019.

DOI: 10.61782/fa.2025.0197



FORUM ACUSTICUM
EURONOISE 2025

CHARACTERIZATION OF THE ACOUSTIC BEHAVIOR OF RAW EARTH COATINGS

Mathias Ziapkoff[1*] **Philippe Glé**[1] **Arthur Hellouin de Menibus**[2]
Thibaut Blinet[3] **Catherine Guigou Carter**[3]
[1] UMRAE, CEREMA, Univ Gustave Eiffel, IFSTTAR, Strasbourg, France
[2] Matélow, Rennes, France
[3] Centre Scientifique et Technique du Bâtiment, Grenoble / Marne la Vallée, France

ABSTRACT

Raw earth systems are gaining increasing interest in civil engineering due to their low energy and carbon impact, particularly raw earth coatings, which are still underexplored compared to other types of coatings such as those using lime or cement. The objective of this article, which is part of the CarAc'Terre project, is to characterize the behavior of these coatings in terms of acoustic dissipation. The aim is to analyze whether these materials behave in a purely elastic manner or if visco-thermal phenomena need to be taken into account. Experiments have been conducted at material scale on different coatings prepared by masons, with different earths and fiber contents. Acoustical properties were determined with a Kundt Tube in normal incidence and resistivity, porosity, and elasticity of the materials were also measured. These results were then compared with specific models based on theoretical approaches. The analyses revealed that raw earth coatings exhibit complex behaviors that may require consideration of both elastic and visco-thermal dissipation mechanisms. This study contributes to a deeper understanding of the acoustic properties of these materials, opening up new avenues to model the acoustic behavior of a wide variability in earth coating formulation.

Keywords: *Acoustics, Raw earth coatings, Resistivity, Porosity, Elasticity*

**Corresponding author*: *mathias.ziapkoff@cerema.fr.*
***Copyright**: ©2025 Ziapkoff et al. This is an open-access article distributed under the terms of the Creative Commons Attribution 3.0 Unported License, which permits unrestricted use, distribution, and reproduction in any medium, provided the original author and source are credited.*

1. INTRODUCTION

The building sector is currently facing two major challenges: promoting the well-being of occupants [1] while minimizing the environmental impact of the materials and technical solutions used, which account for 40% of global energy consumption [2]. The use of sustainable materials, such as biosourced or geosourced materials, characterized by high thermal and acoustic performance, is an ideal solution in this context [3–5]. Among these materials, there is growing interest in raw earth systems, particularly hemp-earth concretes commonly referred to as "light earth".

Unlike other traditional hemp concretes, light earth concretes are biosourced granular materials produced by mixing hemp particles with clay. They can be used for construction work using formwork, projection, or block casting techniques, with or without wood. The use of a clay binder offers several advantages, including a carbon footprint around five times lower than that of hemp-lime, as the hardening of clay is reversible, unlike that of lime and cement. The hemp concrete family is valued both for its hygrothermal properties [6–9] and, as porous media, for their acoustic properties, which are crucial for guaranteeing a high level of safety and quality of life for inhabitants [10–13]. These studies have led to a better understanding of acoustic dissipation mechanisms within the material and have tested the applicability of traditional acoustic models such as Biot's poro-elastic approach [14] or the JCAL (Johnson-Champoux-Allard-Lafarge) model [15, 16].

However, analyzing the acoustic properties of light earth is not enough, as this material is rarely used alone at the wall or building scale by craftsmen. Indeed, it is com-

mon practice to add one or more layers of coating, a mixture of binder and additives (fibers, sand, aggregates) that provide better resistance but strongly limit sound absorption [13, 17]. Traditional lime or cement-based coatings are well known but are being questioned for their environmental impact. Raw earth coatings, on the other hand, although less studied, seem promising and are increasingly being considered [13,17–20]. However, there is still a lack of knowledge about the influence of coating formulation, such as its thickness or the nature of the binder employed.

The aim of this article, which is part of the CarAc'Terre project, is to characterize the acoustic behavior of different raw earth coating formulations applied to a layer of light earth, with a view to assessing the influence of formulation and initiating relevant numerical modeling. The aim is to determine whether the coating behaves purely elastically or whether visco-thermal phenomena need to be taken into account. This work is structured in three sections. The first section presents the study materials with the different coating formulations, as well as the experimental procedure for determining their acoustic and mechanical properties. Next, the first experimental results are analyzed, and initial trends are identified. Finally, the measurements are compared with numerical modeling proposals, considering the behavior of the two layers as purely isotropic elastic, as a porous-rigid, or as poro-elastic.

2. MATERIALS AND METHODS

2.1 Materials description

2.1.1 Raw materials

In the case of the light earth (i.e. "l-e"), the hemp particles are processed by the Planète Chanvre association, whose plant is located in Aulnoy (77). The earth used is betonite clay extracted from a single deposit in the commune of Le Buisson de Cadouin (24) and processed in the plant located in the commune of Mazeyrolles (24) by the Lafaure company.

For the coatings, two types of sifted re-employed clay, "Sygogne" and "Paix," were supplied by Totem Terre et Couleur, based in Saint-Gonlay (35). Two varieties of sand were also incorporated: 0/4 sand or 0/2 sand obtained from manual sieving of 0/4 sand using a 2,25 mesh sieve. Finally, four types of biosourced fibers were considered. Short-staple hemp wool was sourced from Agrochanvre (50), flax shiv from the Bosc Nouvel textile flax mill (76), Isocanna-type hemp shiv from Saint-Astier (24), and chopped straw fibers from a farm in Saint-Maden (94).

2.1.2 Samples manufacturing

The samples were made by Arthur Hellouin de Menibus from Matelow (35), a company specializing in light earth construction and training for professionals, Julia Cahour, Morgane Geffroy, Alice Lamy and Andra Varouchas. Moulds with a diameter of $100mm$ and different heights were prepared to form the samples into cylindrical shapes, while leaving a reserve of varying thickness for the coating. A total of 23 coating formulations were applied to the same light earth base. The light earth was applied with low compaction to avoid springback and guarantee a theoretical wet thickness of $30mm$. Four samples per formulation were prepared at the same time with three coatings and one uncoated as shown in Fig. 1.



Figure 1: Formulation example with three coated samples (A, C, D) and one uncoated sample (B).

Each formulation differs in terms of coating thickness, type of sand used, presence or absence of biosourced fibers, type of fibers, and finishes (trowel, sponge) during manufacture. To describe the formulation proposed, the samples are named according to a common nomenclature, $T_F_f_e_X$ or $T_S_f_e_X$, presented in Tab. 1. The dosages were carried out in proportion by volume, and the constituents were weighed each time to find the corresponding mass dosage.

Table 1: Sample nomenclature.

Symbol	Definition		Acronym
T	Type of earth	Earth "la Sygogne"	T1
		Earth "la Paix"	T2
F	Type of fiber	Short-staple hemp wool	L
		Flax shiv	A
		Hemp shiv	C
		Chopped straw fibers	P
		Lower fiber content used	min
S	Type of sand	0/2 sand	S02
		0/4 sand	S04
f	Type of finition	None	
		Trowelled surface	Tal
		Trowelled and sponged surface	TalEp
e	Thickness	$1mm$ thickness	1
		$2mm$ thickness	2
		$3mm$ thickness	3
		$2mm$ thickness	4
		$6mm$ thickness	6
		$10mm$ thickness	10
X	Sample index	N°1	A
		N°2	B
		N°3	C
		N°4	D

It is important to note that during the application of the coating, a certain amount of it penetrated into the microstructure of the light earth. Therefore, for the remainder of this work, it was necessary to estimate the actual thickness of the coating $e_{coating}$, presented in Tab. 2, from the coating density $\rho_{coating}$, the total mass of the sample m_{tot} and the mass of the light earth m_{l-e}. Considering a final coating volume that is always cylindrical, with R being the radius of the cylinder, we deduce $e_{coating}$ with Eqn. (1) below:

$$e_{coating} = \frac{\frac{m_{tot} - m_{l-e}}{\rho_{coating}}}{\pi R^2} \quad (1)$$

According to the results in Tab. 2 and the calculation of the relative deviation Δe between the theoretical and real coating thicknesses, the higher the theoretical coating thickness, the lower the relative deviation. This implies a lesser influence of its penetration into the microstructure of the light earth.

The samples were then stored at room temperature ($15 - 20°C$) and transported to the laboratory where they were weighed, their dimensions recorded, and then dried in an oven for 12 days at $50°C$ with a relative humidity maintained at 20% (Fig. 2a). Once this operation was complete, they were stored for a stabilization phase under the same conditions as in the experimental chamber ($\approx 20°C$, 50% RH) for at least 24 hours before the first tests (Fig. 2b). Once stabilized, the samples were weighed again and their dimensions were recorded to assess the absence of shrinkage after conditioning. The average thickness of the uncoated samples measured at $28,6mm$ with a coefficient of variation of 2% and an average density of $319kg/m^3$ with a coefficient of variation of 3% show that these samples can be considered comparable.



(a) (b)

Figure 2: Oven drying (a) and laboratory stabilisation (b) of the samples.

Table 2: General characteristics of coatings.

Nomenclature	$e_{theorical}$ (mm)	e_{real} (mm)	Δe (%)	$\rho\ (kg/m^3)$
$T1_L_1$	1	3,9	288	1369
$T1_L_2$	2	4,8	138	
$T1_L_3$	3	6,6	119	
$T1_L_4$	4	6,6	64	
$T1_L_6$	6	9,1	52	
$T1_L_10$	10	11,1	16	
$T1_S02_1$	1	3,6	259	2020
$T1_S02_2$	2	3,7	86	
$T1_S02_3$	3	4,2	39	
$T1_S02_4$	4	5,1	27	
$T1_S02_6$	6	7,1	18	
$T1_S02_10$	10	10,4	4	
$T1_S04_10$	10	11,5	15	1978
$T2_S04_10$	10	10,8	8	1977
$T1_A_6$	6	7,4	23	1473
$T1_A_10$	10	11,7	17	
$T1_A_min_6$	6	7,9	31	1802
$T1_A_min_10$	10	11,6	16	
$T2_A_10$	10	11,9	19	1423
$T1_P_10$	10	11,5	15	1606
$T1_C_10$	10	11,0	10	1375
$T1_C_Tal_10$	10	10,6	6	
$T1_C_TalEp_10$	10	10,4	4	

2.2 Experimental methods

2.2.1 *Kundt Tube*

Two main properties characterize the acoustic behavior of our samples at the material scale: insulation, represented by the transmission loss TL (dB), and acoustic correction, characterized by the absorption coefficient α $(-)$. In this work, we consider only the airborne transmission mode, thus not taking into account the so-called solid-borne noise.

The characterization methods used in this work are based on the use of a or Kundt Tube, shown in Fig. 3, at normal incidence. The same device can be used to determine sound absorption, the sound transmission loss, and the intrinsic properties of the material. To obtain the absorption coefficient, the three-position method without a cavity is used, while the transmission loss and intrinsic properties are measured by inducing an 18 mm plenum to free up the rear face of the samples. These two methods are presented in the thesis work of Philippe Glé [13].

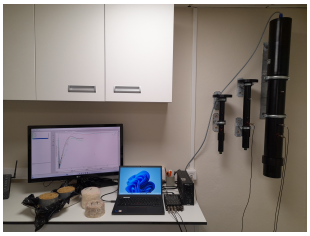


Figure 3: Kundt Tubes of different diameters and measurement acquisition device.

As mentioned in the introduction, taking inspiration from the work of Glé *et al.* [21] we can consider the two layers (light earth and coating) as having purely elastic behavior, with a rigid or poro-elastic skeleton. In the case of a purely elastic material, considered here as isotropic, only the mechanical contributions come into play. They are described by the density ρ, the Young's modulus E, the Poisson's ratio ν and the damping factor η, and can be identified using specific tests. The assumption of a rigid skeleton, considering only the porous phase of the material, is based on acoustic dissipations derived solely from visco-inertial and thermal effects. Advanced acoustic models such as the JCAL model characterize the porous behavior of a material based on six main parameters: porosity ϕ, resistivity σ, tortuosity α_∞, viscous and thermal characteristic lengths Λ and Λ', and static thermal permeability Θ_0. From these parameters, it is possible to derive the sound transmission loss and the sound absorption coefficient. It is generally common to determine the first three parameters (ϕ, σ, and α_∞) directly with experimental devices and to estimate the last three indirectly because they are more difficult to measure. When indirect estimation is also impossible, it is customary to simplify acoustic models, as we shall see in the last section. Finally, poro-elastic behavior combines the three dissipative effects based on the work of Biot [14, 22].

2.2.2 *Porosity*

Porosity ϕ $(\%)$, commonly considered to be open porosity in acoustics, is determined using the air volume comparison method mentioned by Leclaire *et al.* [23], illustrated in Fig. 4a. Conventional porosity measurements are used to characterize the porosity accessible to air. However, in the case of light earth, multi-scale behavior is also based on intra-particle porosity (Olny and Boutin [24]). In this case, an indirect assessment of porosity is required. Porosity can be estimated either from the asymptotic low or high-frequency limits of the dynamic incompressibility modulus, or from the low-frequency limit of the surface impedance. Where this is not possible, porosity can be inverted using a model such as Zwikker-Kosten [25].

2.2.3 *Resistivity*

The resistivity, denoted σ (Pas/m^2), can be measured directly using a resistivity device (Fig. 4b) as explained in [13]. Resistivity can also be characterized indirectly in a Kundt Tube under the same conditions as absorption and the transmission loss at normal incidence, as described by Jaouen et al. [26]. We refer the reader to Philippe Glé's thesis [13] for more information on direct or indirect estimation methods for other acoustic parameters. In the remainder of this study, we will prioritize data obtained directly, but in cases where it is impossible to obtain such data, we will use indirect estimates.



(a) (b)

Figure 4: Porosity (a) and resistivity (b) devices.

2.2.4 *Mechanical properties*

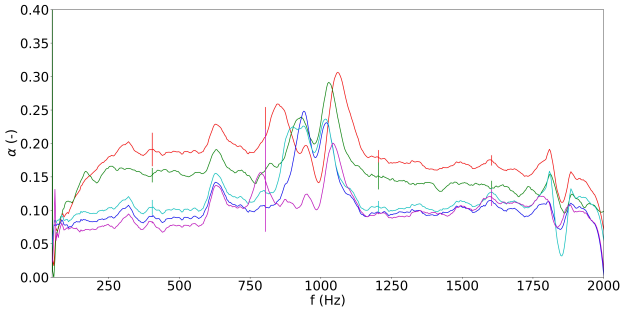
The apparent density ρ of a porous material can be measured directly by estimating its mass and volume. This work, presented in Tab. 2, was carried out for coatings by Catherine Guigou Carter and Thibaut Blinet at CSTB, a partner in the project, using bars with dimensions of $284mm \times 24mm \times 24mm$. They also estimated the Young's modulus E and the damping factor η of the coatings, according to the NF EN 14146 standard [27]. The density of the light earth was averaged at Cerema over all 23 uncoated sample measurements. The other parameters are taken from the work of Glé *et al.* [21] or the LOB+HIE project [18], pending future tests at the laboratory's quasistatic mechanical analyzer (QMA).

3. RESULTS

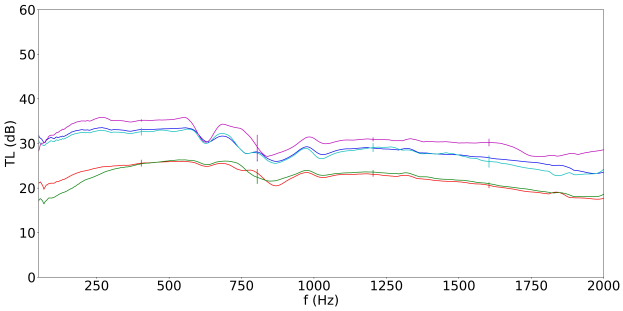
3.1 Experimental results : Influence of thickness

During this test campaign, 23 raw earth coating formulations were tested to observe the influence of the multiple factors mentioned above. In this article, we focus on the influence of coatings thickness with the study on $T1_L$ mixes (n°1 to 5), corresponding to coating thicknesses of 1, 2, 3, 4, and 6 mm. The mean data for the three coated samples, for each thickness, are plotted with their standard deviations as uncertainty bars in Fig. 5a and Fig. 5b.

Fig. 5a shows that the absorption coefficient decreases with increasing thickness. This observation can be explained by the fact that it is easier for the acoustic wave to penetrate the layer of light earth when the thickness of the coating is low. Because of its microstructure, the light earth layer allows more acoustic dissipation within the material, which increases acoustic absorption. However, according to Fig. 5b, and contrary to the absorption coefficient, as the thickness of the coating increases, so does the acoustic insulation of the sample. This finding, shared by [21], suggests that sound attenuation is not solely due to a mechanical contribution but involves other effects, such as viscous and thermal dissipation. Finally, we generally observe a stabilization of performance from a thickness of $4mm$.



(a)



(b)

Figure 5: Evolution of the absorption coefficient $\alpha\ (-)$ (a) and the transmission loss $TL\ (dB)$ (b) as a function of frequency $f\ (Hz)$ for a $T1_L$ sample of coating thickness $1mm$ (—), $2mm$ (—), $3mm$ (—), $4mm$ (—) or $6mm$ (—).

3.2 Numerical modeling

In this final section, we propose to model the acoustic behavior of one material using AlphaCell© software. We have chosen the $T1_L_10_D$ sample, which has the advantage of having a theoretical coating layer $10mm$ thick, meaning its penetration into the layer of light earth is less influential. It is also a formulation for which the porosity and resistivity have been determined directly.

We consider the behavior of the layers to be purely isotropic elastic, porous-rigid, or poro-elastic. As explained above, the mechanical properties of the two layers are derived from experimental measurements or from the literature. The modeling of the porous character of the light earth-layered layer is based on the thesis of [13], who suggests considering hemp concretes with the JCA models coupling those of Johnson et al. [15] and Zwikker-Kosten [25], and globally requiring four param-

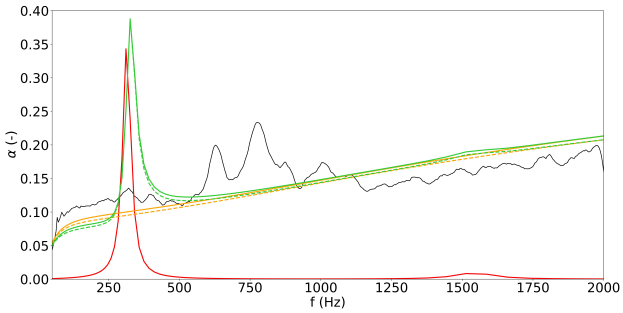
eters: porosity ϕ, resistivity σ, tortuosity α_∞, and viscous characteristic length Λ. The resistivity could be determined directly, whereas, due to the double-porosity phenomenon present in the material, the acoustic porosity had to be estimated indirectly, as well as the tortuosity and the viscous characteristic length.

On the other hand, for the porous nature of the coating, two rigid skeleton approaches are considered. Here, we use reduced models for the coating due to the relatively high resistivities of these materials, with other parameters having a more limited impact in this case. The first approach considers the coating with a JCAL model reduced to two parameters following the hypothesis of a perforated material geometry, σ and ϕ, considering the tortuosity equal to 1 and simplifying the relationships of the viscous and thermal characteristic lengths as well as the thermal static permeability. These relationships are shown in Tab. 3, which summarizes the mechanical and acoustic parameters of the two layers modeled, where r_1 is the radius of the pores considered to be cylindrical and μ is the shear viscosity of air, equal to $1,8 \times 10^{-5} Pa.s$. The second approach considers the coating with the Boutin-Geindreau granular model [28], requiring only two parameters, ϕ and r_2, the aggregates radius considered to be spherical, from which all the other acoustic parameters are deduced as described in Tab. 3. Note the closeness of the experimental values to those of [18], whether for light earth with, for example, a density of $295 kg/m^3$ and a porosity rate of 69%, or for earth coating with a density of $1500 kg/m^3$ or a Young's modulus of $2850 MPa$.

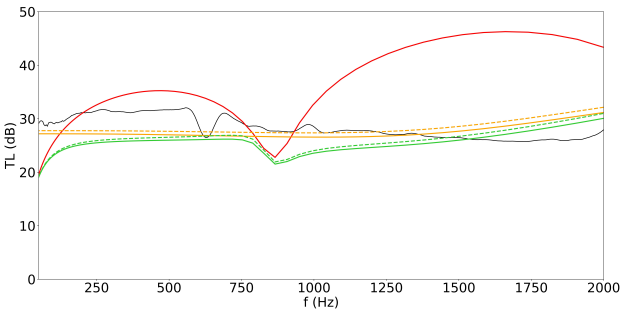
Table 3: Mechanical and acoustic parameters of the modelled layers. Data from [18] and [21] are shown as $^{[a]}$ and $^{[b]}$.

Parameters	Light earth	$T1_L_10_D$ sample	
	JZK Model	JCAL model reduced	Granular model
Thickness (mm)	27,3	12	
$\rho\ (kg/m^3)$	319	1369	
$E\ (MPa)$	$2^{[a]}$	1711	
$\nu\ (-)$	$0,1^{[a]}$	$0,2^{[a][b]}$	
$\eta\ (\%)$	$10^{[b]}$	3	
$\phi\ (\%)$	65	50	
$\sigma\ (Pa.s.m^2)$	1,6E+3	1,5E+6	
$\alpha_\infty\ (-)$	1,6E+3	1,5E+6	
$r_1\ (m)$	×	$r_1 = \sqrt{\frac{8\mu}{\phi\sigma}}$	×
$r_2\ (m)$	×	×	$r_2 = \sqrt{\frac{3\beta^2\mu}{\sigma\left(-1+\frac{2+3\beta^5}{\beta(3+2\beta^5)}\right)}}, \beta = (1-\phi)^{\frac{1}{3}}$
$\Lambda\ (m)$	2,6E-4	r_1	$\frac{4\phi\alpha_\infty}{9(1-\phi)} r_2$
$\Lambda'\ (m)$	×	r_1	$\frac{2\phi}{3(1-\phi)} r_2$
$\Theta_0\ (m^2)$	×	$\frac{\phi r_1^2}{8}$	$\frac{(5-9\beta+5\beta^3-\beta^6) r_2^2}{15(1-\beta^3)\beta^3}$

A total of five models are compared with the experimental absorption coefficient (Fig. 6a) and transmission loss (Fig. 6b).



(a)



(b)

Figure 6: Comparison of the evolution of the absorption coefficient $\alpha\ (-)$ (a) and the transmission loss $TL\ (dB)$ (b) as a function of the frequency $f\ (Hz)$ for the coated sample $T1_L_10_D$ between the experimental measurement (—), simulation of elastic bilayer behaviour (—), simulation of a porous-rigid bilayer behaviour using the reduced JCAL (—) or Boutin-Geindreau (- -) model and simulation of poro-elastic bilayer behaviour using the reduced JCAL (—) or Boutin-Geindreau (- -) model.

Analysis of Fig. 6a reveals that the assumption of purely elastic behavior of the two layers of the sample is insufficient to simulate its absorption behavior. On the other hand, the four other simulations, which take into account the porous character, seem to be closer to the experimental results. This suggests that the measured resistivity of the coating is fairly representative. The two categories of simulations have the advantage of being relatively simple, with few parameters, while providing a fairly relevant

prediction. This is particularly the case with poro-elastic behavior, which reproduces the resonance observed experimentally, although at lower frequencies. This resonance corresponds to that of the light eart layer, which is caused by the compression of its solid phase following acoustic stress. A second simulation later revealed that increasing the Young's modulus to $10MPa$ further improved the position of this resonance frequency. Finally, there was no major difference between the two approaches regarding the pore geometry of the coating.

The overall numerical prediction of the transmission loss by the five approaches is slightly poorer than that of the absorption coefficient, as shown in Fig. 6b. The hypothesis of purely elastic behavior of the sample should once again be ruled out, while the others seem to slightly underestimate the transmission loss at low frequencies and overestimate it at high frequencies. Overall, the simplified poro-elastic approach seems to be the most interesting, as it again reproduces the resonance of the lightened earth while providing a promising prediction regardless of the pore shape hypothesis.

4. CONCLUSION

This work, part of the CarAc'Terre project, focused on characterizing the acoustic behavior of different, as yet little-studied, raw earth coating formulations applied to light earth. We aimed to assess the influence of the formulation and propose an initial numerical modeling campaign for this two-layer material. After presenting the study materials with the different coating formulations, we described the methods for direct or indirect estimation of the acoustic and mechanical parameters required to characterize the acoustic performance of the samples. We then analyzed the initial experimental results, revealing the first trends. Among other things, it appeared that an increase in the thickness of the coating reduced the acoustic absorption of the bilayer, as opposed to the acoustic insulation. Finally, the measurements were compared with a proposal for numerical modeling, considering the behavior of the layers as purely elastic, porous-rigid, or poro-elastic. The poro-elastic approach appeared to be the most relevant, thanks to the simulation of mechanical and visco-thermal dissipation. This study raises a number of prospects for future work like improving the numerical approach by developing more accurate acoustic models or considering the scale of the wall and the entire building, which will be the subject of further studies as part of the project.

5. ACKNOWLEDGEMENTS

We would like to thank Julia Cahour, Morgane Geffroy, Alice Lamy and Andra Varouchas for their contribution to the coating samples. This project was funded by the French government as part of France Relance, now part of France 2030, and operated by ADEME.

6. REFERENCES

[1] S. Altomonte, J. Allen, P. M. Bluyssen, G. Brager, L. Heschong, A. Loder, S. Schiavon, J. A. Veitch, L. Wang, and P. Wargocki, "Ten questions concerning well-being in the built environment," *Building and Environment*, vol. 180, p. 106949, 2020.

[2] F. Pittau, F. Krause, G. Lumia, and G. Habert, "Fast-growing bio-based materials as an opportunity for storing carbon in exterior walls," *Building and Environment*, vol. 129, pp. 117–129, 2018.

[3] F. Asdrubali, "Green and sustainable porous materials for noise control in buildings: a state of the art," in *SAPEM-Symp. on the Acoustics of Poro-Elastic Materials*, 2011.

[4] N. H. Bhingare, S. Prakash, and V. S. Jatti, "A review on natural and waste material composite as acoustic material," *Polymer Testing*, vol. 80, p. 106142, 2019.

[5] M. Pedroso, J. de Brito, and J. Silvestre, "Characterization of eco-efficient acoustic insulation materials (traditional and innovative)," *Construction and Building Materials*, vol. 140, pp. 221–228, 2017.

[6] T. Colinart, T. Vinceslas, H. Lenormand, A. H. D. Menibus, E. Hamard, and T. Lecompte, "Hygrothermal properties of light-earth building materials," *Journal of Building Engineering*, vol. 29, pp. 2352–7102, 2020.

[7] F. Collet and S. Pretot, "Thermal conductivity of hemp concretes: Variation with formulation, density and water content," *Construction and Building Materials*, vol. 65, pp. 612–619, 2014.

[8] U. Dhakal, U. Berardi, M. Gorgolewski, and R. Richman, "Hygrothermal performance of hempcrete for ontario (canada) buildings," *Journal of Cleaner Production*, vol. 142, pp. 3655–3664, 2017.

[9] M. Sáez-Pérez, M. Brümmer, and J. Durán-Suárez, "A review of the factors affecting the properties and performance of hemp aggregate concretes," *Journal of Building Engineering*, vol. 31, pp. 2352–7102, 2020.

[10] M. Areias Trindade, *Propriétés mécaniques, thermiques et acoustiques d'un matériau a base de particules végétales: approche expérimentale et modélisation théorique*. Theses, Conservatoire national des arts et metiers - CNAM, 2005.

[11] P. Glé, E. Gourdon, and L. Arnaud, "Acoustical properties of materials made of vegetable particles with several scales of porosity," *Applied Acoustics*, vol. 72, pp. 249–259, 2011.

[12] P. Glé, E. Gourdon, and L. Arnaud, "Modelling of the acoustical properties of hemp particles," *Construction and Building Materials*, vol. 37, pp. 801–811, 2012.

[13] P. Glé, *Acoustique des matériaux du bâtiment à base de fibres et particules végétales-outils de caractérisation, modélisation et optimisation*. Theses, INSA de Lyon, 2013.

[14] M. A. Biot, "Theory of propagation of elastic waves in a fluid-saturated porous solid. i. low-frequency range," *The Journal of the Acoustical Society of America*, vol. 28, pp. 168–178, 1956.

[15] D. L. Johnson, J. Koplik, and R. Dashen, "Theory of dynamic permeability and tortuosity in fluid-saturated porous media," *Journal of fluid mechanics*, vol. 176, pp. 379–402, 1987.

[16] D. Lafarge, P. Lemarinier, J. F. Allard, and V. Tarnow, "Dynamic compressibility of air in porous structures at audible frequencies," *The Journal of the Acoustical Society of America*, vol. 102, pp. 1995–2006, 1997.

[17] O. Kinnane, A. Reilly, J. Grimes, S. Pavia, and R. Walker, "Acoustic absorption of hemp-lime construction," *Construction and Building Materials*, vol. 122, pp. 674–682, 2016.

[18] T. Blinet, T. Falwisanner, G. Philippe, C.-G. Catherine, K. Elias, and B. Farid, "Propriétés acoustiques des matériaux biosourcés," *Rapport final CSTB-Cerema-DHUP*, 2018.

[19] P. Glé, E. Gourdon, L. Arnaud, K.-V. Horoshenkov, and A. Khan, "The effect of particle shape and size distribution on the acoustical properties of mixtures of hemp particles," *The Journal of the Acoustical Society of America*, vol. 134, pp. 4698–4709, 2013.

[20] M. Miranda Santos, *La terre crue à l'épreuve des ambiances sonores: un dialogue entre la mesure physique et les expériences sensibles.* Theses, Universitat Politècnica de Catalunya, 2022.

[21] P. Glé, G. Massossa-Telo, A. Hellouin de Menibus, M. Degrave-Lemeurs, and E. Gourdon, "Characterization and modelling of the sound reduction of hemp-clay walls in buildings," *Journal of Building Engineering*, vol. 40, p. 102315, 2021.

[22] M. A. Biot, "Theory of propagation of elastic waves in a fluid-saturated porous solid. ii. higher frequency range," *The Journal of the Acoustical Society of America*, vol. 28, pp. 179–191, 1956.

[23] P. Leclaire, O. Umnova, K. V. Horoshenkov, and L. Maillet, "Porosity measurement by comparison of air volumes," *Review of Scientific Instruments*, vol. 73, pp. 1366–1370, 2003.

[24] X. Olny and C. Boutin, "Acoustic wave propagation in double porosity media," *The Journal of the Acoustical Society of America*, vol. 114, pp. 73–89, 2003.

[25] C. Zwikker and C. W. Kosten, *Sound absorbing materials*. New York: Elsevier, 1949.

[26] L. Jaouen, E. Gourdon, and P. Glé, "Estimation of all six parameters of johnson-champoux-allard-lafarge model for acoustical porous materials from impedance tube measurements," *The Journal of the Acoustical Society of America*, vol. 148, pp. 1998–200, 2020.

[27] Afnor Editions, "NF EN 14146 : Méthodes d'essai pour pierres naturelles - Détermination du module d'élasticité dynamique (par la mesure de la fréquence de résonance fondamentale)," 2004.

[28] C. Boutin and C. Geindreau, "Periodic homogenization and consistent estimates of transport parameters through sphere and polyhedron packings in the whole porosity range," *Physical Review E—Statistical, Nonlinear, and Soft Matter Physics*, vol. 82, p. 036313, 2010.

DOI: 10.61782/fa.2025.0831

FORUM ACUSTICUM EURONOISE 2025

STREAMING OVER MICRO-PERFORATED WALLS SUBMITTED TO ACOUSTIC PLANE WAVE

Daniel Mazzoni[1*] **Muriel Amielh**[1] **Loane Genevay**[1]
Teresa Bravo[2] **Cédric Maury**[3]
[1] Aix Marseille Univ, CNRS, Centrale Méditerranée, IRPHE UMR 7342, 13384, Marseille, France
[2] ITEFI, Consejo Superior de Investigaciones Cientificas, Madrid, 28006, Spain
[3] Aix Marseille Univ, CNRS, Centrale Méditerranée, LMA UMR 7031, 13013, Marseille, France

ABSTRACT

Micro-perforated panels (MPPs), lightweight structures, are investigated as alternatives to huge or active devices, to attenuate noise induced by external flow into the passenger compartment of automobile or aircraft cabins. Optimal sound absorption performance is achieved by appropriate selection of MPP geometry. The viscous losses through the apertures dissipate the acoustic energy around the Helmholtz resonance and provide high absorption efficiency over a wide bandwidth. Acoustically induced vorticity, due to streaming at the hole inlet/outlet, could also contribute. The experiment quantifies the flow induced by acoustic pressure fluctuations (”streaming”) in the vicinity of the perforations of an MPP placed on a cavity arranged on the wall of a closed tube. Three diameters of perforations ($1mm$, $0.6mm$ and $0.3mm$) are tested. The flow induced by an acoustic plane wave parallel to the surface of the MPP is characterized by TR-PIV (”Time Resolved Particle Image Velocimetry”), a laser optical diagnostics, synchronized with acoustic measurements by microphone. The dynamics of the jets emitted at the holes according to their relative position to the wavelength associated with different identified eigenmodes of the closed tube is highlighted. The objective is to estimate the viscous dissipation associated with these micro-jets and to link it to acoustic absorption.

Keywords: *micro-perforated panel, acoustic absorption, streaming, time resolved PIV.*

**Corresponding author*: muriel.amielh@univ-amu.fr.
***Copyright**: ©2025 First author et al. This is an open-access article distributed under the terms of the Creative Commons Attribution 3.0 Unported License, which permits unrestricted use, distribution, and reproduction in any medium, provided the original author and source are credited.*

1. INTRODUCTION

Under the influence of the development of noise standards, research is being conducted to propose passive and lightweight solutions whose fouling can be resolved in the case of industrial applications such as in the design of aeronautical engine walls and compatible with efforts in the field of sustainable development. Micro-perforated panels consisting simply of holes or based on walls made of metamaterials ([1, 2]) are interesting solutions whose performance must be evaluated. Perforated walls have been particularly studied by Maa [3], for the sizing of holes for optimal efficiency. More recent work by Laurens et al. [4] has proposed an introductory synthesis which describes the three contributions of perforations to the acoustic behavior of a perforated panel. The assumptions made are that the porosity is less than 4% so that the interactions between the holes are neglected, which also amounts to having a large spacing between holes and that the acoustic wavelength is large compared to the characteristic dimensions of the perforations. Among the three physical phenomena mentioned, the first one is a non-viscous effect related to that the flow inside the hole behaves like a small air piston. It induces that, due to inertia effects, one has to consider in the acoustic models a length correction on the depth of the perforations. Then, it is necessary to take into account the viscous effects in the boundary layers which develop on the internal wall of the hole which will participate in the absorption of acoustic energy. Finally, in the presence of high amplitude sound waves striking the opening, a vortex detachment, which converts the acoustic energy

into mechanical energy, then dissipated into heat, can occur.

The present study aims to investigate experimentally the space-time behavior of the flow induced when MPP is subject to such high amplitude sound waves without mean flow. In the experiment, the sound is generated by a plane wave whose wave vector is parallel to the surface of the perforated panel, placed in the bottom of a close tube. Section 2 gives the set-up that allows the measurements of the flow velocity in the vicinity of apertures by high-speed PIV and the acoustic pressure measurements by microphone. Section 3 specifies the acoustic conditions chosen for the study. Results presented in Section 4 highlight and quantify the structure of the flow induced by pressure fluctuations.

2. EXPERIMENTAL SETUP

The MPP (Micro-Perforated Panel) is a perforated metal plate of $D = 100mm$ diameter and $1mm$ thickness. Three types of MPP (Fig. 1) are studied, whose periodic perforation characteristics are summarized in Tab. 1. Each MPP is successively installed above the same cavity located in the center of the floor of the Kundt tube. The diameter of the cavity is $100mm$ and its depth is $30mm$. The Kundt tube (Fig. 2) is a parallelepipedic volume of length $L_x = 1.06m$ and of square cross-section of side $L_x = L_z = 150mm$. Lateral walls are in glass and an optical access is possible on the top wall where the laser sheet is passing.

High-speed PIV (Particle Image Velocimetry) images are acquired and post-processed by a Dantec Dynamics system (RapiDO) that includes one T4040 SpeedSense Phantom high-speed camera ($2560\times1664\,pixels$, 12 bits), and a double pulsed laser. The camera is equipped with a $200mm$ focal lens with a $f\#4$ aperture in order to obtain good resolution on a small field of view in the vicinity of the MPP's surface. The pulsed laser is a Photonics laser (527nm, $2 \times 30mJ$ at a nominal $1kHz$ repetition rate). The DynamicStudio software controls the synchronization of image acquisition. A laser sheet generator constituted of several adapted lenses is installed at the end of the optical arm to illuminate the field of view of interest ($24.3mm \times 15.7mm$). 7000 PIV images are acquired at the frequency $F_s = 6.4kHz$ when the laser is working in a single mode, which means that the delay between two pulses is $1/F_s = 156\mu s$. The volume of the Kundt tube is seeded with olive oil droplets of $2-3\mu m$ diameter injected by a hole located on the upper wall. During seeding, the small hole located in the bottom wall of the cavity is left open so that droplets can flee when also pervading the cavity volume. In order to let the seeding stay in suspension, it is preventively stopped a few minutes before experiments with sound and the small hole located in the bottom wall of the cavity is closed. Thanks to the RapiDO system, the sound pressure inside the Kundt tube is measured synchronously with PIV using a wall microphone GRAS SC40. The microphone is located on the top wall at $\delta X = 55mm$ from the extremity wall. A loudspeaker is mounted on the opposite side.

Table 1. MPP dimensions.

MPP	d (mm)	i (mm)	Porosity
MPP1.0mm	1.12	5.15	2.5%
MPP0.6mm	0.65	4.30	1.4%
MPP0.3mm	0.30	1.87	1.5%

The spatial resolution for PIV is $\delta_x = \delta_y = 154\mu m$. The (O, X, Y, Z) coordinate system is centered on the middle of tube floor where the investigation is focused. The two instantaneous components ($2C$) of velocity (U, V) are measured on the plane ($2D$) $Z = 0$ specified in (Fig. 2) by a green square. Statistics and other post-processing of the 6999 velocity fields and acoustic signals are performed by homemade codes developed in Matlab.

3. CHARACTERIZATION OF THE KUNDT TUBE ENCLOSING THE MPP

3.1 Eigen modes of the Kundt tube

In order to investigate the flow induced by pressure fluctuations through the holes of the MMP, one chooses to generate a pressure field of high SPL (Sound Pressure Level) inside the Kundt tube. For that, the first eigen modes of the Kundt tube volume are first calculated and then checked by acoustic pressure measurement by the microphone for a white noise excitation in the range $200 - 3000Hz$ delivered by the loudspeaker. For this experiment, the microphone signal is acquired with a sample frequency of $25.6kHz$ during $100s$. The experimental frequencies of the modes are obtained by spectral analysis as shown in Fig. 3. The agreement between both series of eigen mode frequencies is quite good (Tab. 2). The retained frequencies for the following

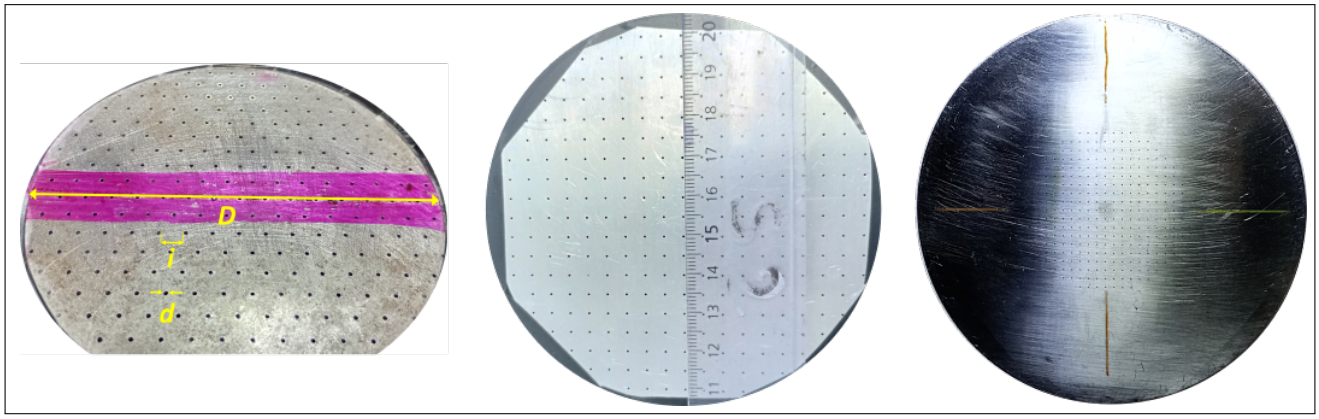


Figure 1. Disks of MPP, from left to right: MPP1.0mm, MPP0.6mm and MPP0.3mm.

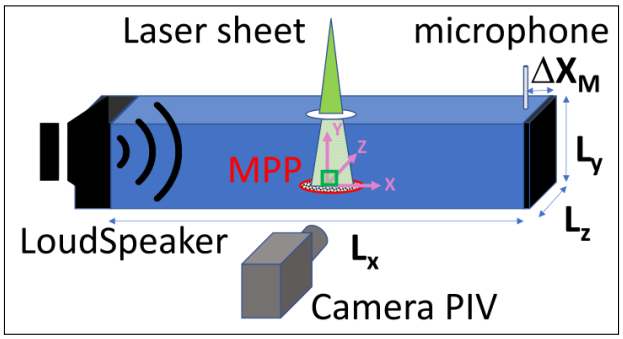


Figure 2. Setup of the high-speed PIV in the near field of MPP mentioned by the centered green square, the scheme is not scaled.

results correspond to the modes $(l, m, n) = (2, 0, 0)$ and $(3, 0, 0)$ along the respective direction (X, Y, Z). The associated frequencies will be named $F_2 = 324Hz$ and $F_3 = 486Hz$ hereafter. In this approach, the eigen modes of the cavity situated under the MPP, which are of higher frequencies, are not considered.

The two selected study frequencies allow to observe the behavior of the flow at the holes depending on whether the acoustic pressure is a node or an antinode. Fig. 4 gives a spatial representation of the amplitude of acoustic pressure in the Kundt tube. The scale of the geometry is respected and the PIV field of view is identified by a green rectangle above the red surface of the MPP centered on $(X = 0mm, Y = 0mm)$. For the long-wavelength $(2, 0, 0)$ and $(3, 0, 0)$ modes considered here, the microphone located at $\Delta X = 55mm$ from the closed end of the Kundt tube measures almost the maximum of the absolute value of the acoustic pressure amplitude.

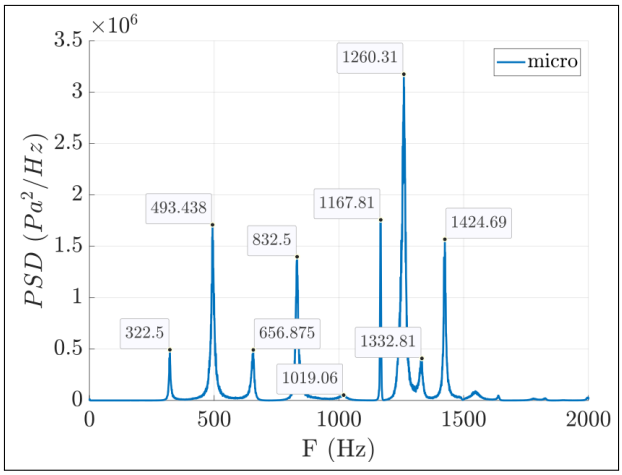


Figure 3. Spectral analysis of acoustic pressure measured by the microphone: experimental characterization of the first eigen modes of the Kundt tube by white noise excitation.

3.2 Measurement of the acoustic velocity by high-speed PIV

The case of the $(3, 0, 0)$ mode is investigated for a smooth wall for which the cavity is covered with a non-perforated

Table 2. Theoretical and experimental eigen modes of the Kundt tube.

l	m	n	$F_{l,m,n}$	F_{exp}
			(Hz)	(Hz)
1	0	0	162.1	-
2	0	0	324.2	322.50
3	0	0	486.29	493.44
4	0	0	648.39	656.88
5	0	0	810.49	832.50
6	0	0	972.59	1019.1
7	0	0	1134.7	1167.8
0	1 (0)	0 (1)	1143.3	-
1	1 (0)	0 (1)	1154.8	-
2	1 (0)	0 (1)	1188.4	-
3	1 (0)	0 (1)	1242.5	1260.3
8	0	0	1296.8	-
4	1 (0)	0 (1)	1314.4	1332.8
5	1 (0)	0 (1)	1401.5	-
9	0	0	1458.9	1424.7

metal plate. This configuration allows us to test whether we can measure the acoustic velocity with the PIV since for $F_3 = 486Hz$, the acoustic pressure is at a node above the MPP, but the amplitude of acoustic velocity is maximum. While measuring a standard deviation of $\sigma_P = 142.7Pa$ by microphone, a standard deviation σ_U of U velocity component, in the direction of plane wave vector generated by the loudspeaker, is measured by PIV. The spatial averaging of σ_U on the vertical direction Y at $X = 0mm$ gives $\sigma_U = 0.332m/s$ quite in a good agreement (4% error) with a theoretical estimation of the acoustic velocity by $\sigma_U = \sigma_P/(\rho c) = 0.347m/s$ with the sound speed $c = 343m/s$ and the air density $\rho = 1.2kg/m^3$. Similar measurements were made for $F_2 = 324Hz$ for which the theoretical acoustic velocity should be zero in the middle of the Kundt tube, one obtained a minimum of $\sigma_U = 0.013m/s$ on all the vertical line $X = -1.4mm$ in the PIV field of view.

Fig. 5 shows how the acoustic pressure signal measured at the Kundt tube end and the velocity components measured at X=0mm are timely synchronised. The signals of P, U and V are non-dimensionalized by their amplitude deduced from their standard deviation σ. All signals are harmonic. The V signal is of weak amplitude ($\sigma_V = 0.004m/s$) and very noisy comparatively to U signal for which $\sigma_U = 0.332m/s$. The phase shift between the velocity and the pressure is $\pi/2$ as it could be predict theoretically for a plane wave. These results indicate that PIV measurements give an applicable estimation of the acoustic velocity with the limitation of drag effects of seeding droplets.

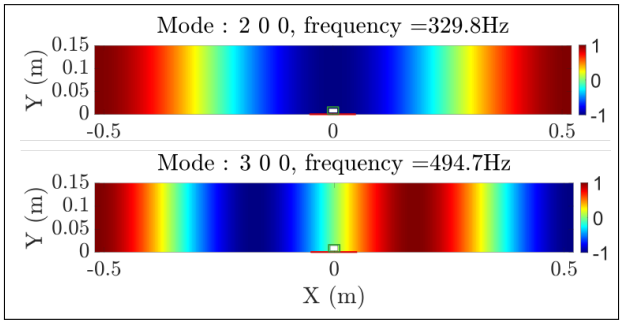


Figure 4. Theoretical acoustic pressure amplitudes for modes (l, m, n) = (2, 0, 0) and (3, 0, 0) of the Kundt tube.

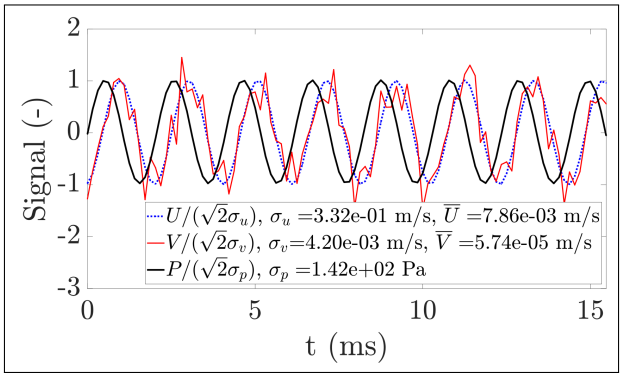


Figure 5. Time series of velocity components (U, V), extracted at position $(X = 0mm, Y = 5mm)$ in the PIV field of view for the smooth wall, and pressure signal measured synchronously by microphone, for $F_3 = 486Hz$ corresponding to a an acoustic pressure node at this place.

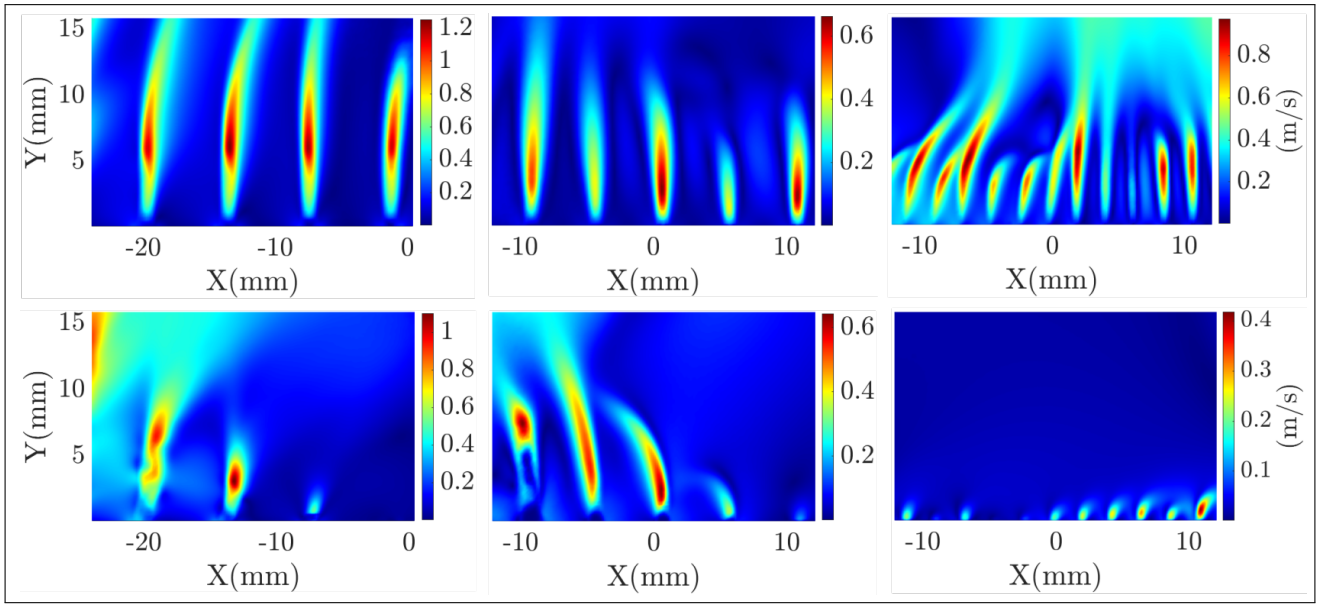


Figure 6. Mean velocity norm $\sqrt{\overline{U}^2 + \overline{V}^2}$ for MMP1.0mm, MPP0.6mm and MPP0.3mm from left to right. Top: for a antinode acoustic pressure (acoustic velocity node) over the MPPs, for $F_2 = 324Hz$. Bottom: for a acoustic pressure node (acoustic velocity antinode) over the MPPs , for $F_3 = 486Hz$.

4. EVIDENCE OF THE STREAMING

The mean velocity norm fields, obtained for all the MPPs, for both excitation frequencies $F_2 = 324Hz$ and $486Hz$, are presented in Fig. 6. The sound pressure levels associated to these PIV experiments are given in (Tab. 3). These results aim to compare the flow behaviour according to the existence of a node or antinode of acoustic pressure above the MPP. The influence of pressure is obvious. For conditions of pressure antinode ($F_2 = 324Hz$), the persistence of an average flow in the form of vertical jets escaping from the holes up to around $Y = 15d$ is an evidence of streaming. Contrariwise, for conditions of pressure antinode ($F_2 = 486Hz$), one observes an extinction of these jets in regions around $X = 0mm$. Remaining average jets have shorter vertical development than for $F_2 = 324Hz$ and seem to be submitted to transverse effects, possibly related to large scale streaming in the Kundt tube. At $F_2 = 324Hz$, the maxima of mean velocity norm occur at $Y/d = 5-6$ for MPP1.0mm and MPP0.6mm and rather at $Y/d = 15$ for MPP0.3mm. In this last case, the jets are not all active and those which have the greater vertical development interact in their far field. The standard deviation of V, not shown here, is maximum , respectively σ_v =0.46, 0.35, 0.49 m/s for the three MPPs, in the jet near field and becomes very weak in the region where the mean velocity norm becomes maximal. Beyond this region, the mean movement becomes predominant relatively to the fluctuating one.

Table 3. Sound Pressure Level (SPL) measured by the microphone with loudspeaker excitation.

SPL for	$F_2 = 324Hz$	$F_4 = 486Hz$
Smooth wall	133.7 dB	137.1 dB
MPP1.0mm	132.1 dB	140.2 dB
MPP0.6mm	129.2 dB	134.6 dB
MPP0.3mm	127.1 dB	133.9 dB

5. DYNAMICS OF THE FLOW

5.1 Spectral analysis

Fig. 7 presents a comparison of the spectral analyses of the acoustic pressure and the V velocity signal extracted

on the axis, in the near field, of one jet for the MPP1.0mm at $F_2 = 324Hz$. For the velocity signal, the excitation frequency and its harmonics are detected. However, the raw instantaneous PIV fields are noisy as shown by an extracted sample of V time series in Fig. 9, so a method is proposed herafter in order to fix the main contributions to the flow dynamics.

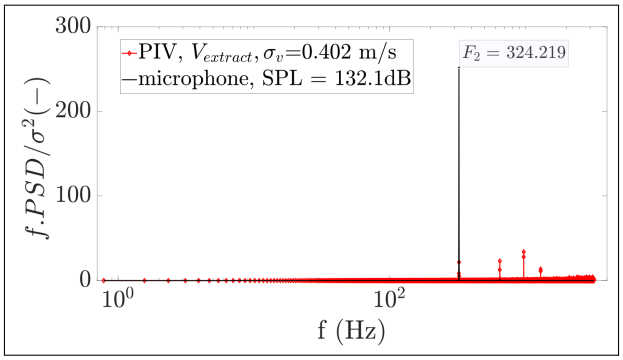


Figure 7. Spectral analysis of the pressure measured by microphone and V velocity components extracted from the PIV field at position $(X = 4.5mm, Y = 5mm)$ corresponding to an axial position on an ejected jet from a hole of MPP1.0mm at $F_2 = 324Hz$.

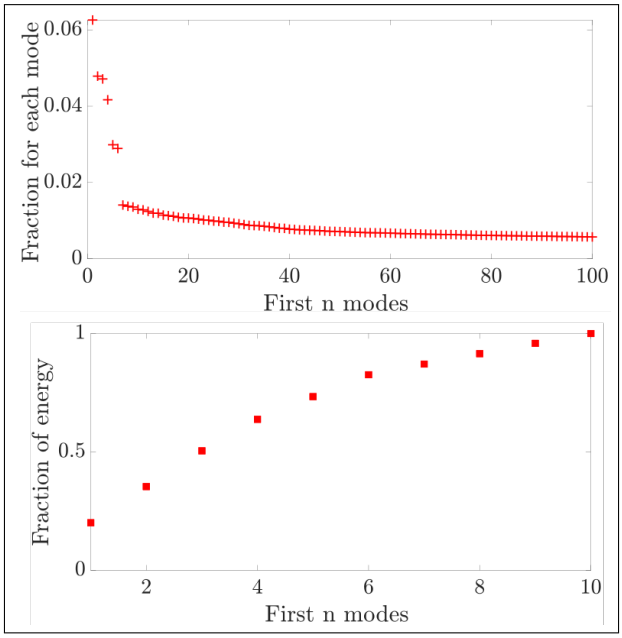


Figure 8. Fraction of energy associated to POD mode decomposition. Top: Ratio of energy for each considered mode to the cumulative energy of the first 100 modes. Bottom : Ratio of the cumulative energy for the n first modes to the cumulative for the first 10 modes.

5.2 POD of the velocity field

In order to highlight the space-time structure of the jets, one proposes to apply POD (Proper Orthogonal Decomposition, [5]) method which interest is to capitalize on the high amount of available fluctuating velocity fields. The principle of this method is to decompose the quantity of interest, here the velocity components, on a basis of eigen modes sorted by their energetic contribution. The decomposition is performed on 2000 uncorrelated snapshots of the two velocity components (U, V), which determines a number of modes equal to the number of realizations.

Fig. 8 illustrates how the energy is distributed according to the considered POD modes. The top figure shows the energetic contribution of each n mode to the cumulative energy of the first 100 modes. The first 6 modes are the main contributors comparatively to the all following ones. The ratio of the cumulative energy for n first modes to the cumulative for the first 10 modes presented in the bottom figure helps to specify that 64% or 83% cumulative energy is obtained by the contributions of the 4 or 6 first POD modes, respectively.

The space-time reconstruction of the instantaneous velocity field with the first 4 POD modes is proposed in Fig. 9 for a chosen jet ejected from one hole of the MPP1.0mm with the $F_2 = 324Hz$ excitation. The six snapshots presented in the top figure from the left to the right are associated to the instants $t_i = t_0, ..., t_5$ marked on the pressure time series plotted in the bottom figure for a duration covering at least one excitation period. According to the spatial representation of the theoretical mode (2,0,0) given in Fig. 4 the amplitude of the acoustic pressure over the MPP is of opposite sign to that can be measured by the microphone at Kundt tube end. So the non-dimensionalized signal of the velocity V extracted at the jet exit is plotted synchronously with the -P signal in order to analyse the flow dynamics in term of pressure fluctuations in the region of the MPP. When the acoustic pressure is negative, at t_1, a hemispherical flow burst is ejected from the hole. This burst continues to rise in the jet column and takes a spherical shape while, between t_2 and t_3,

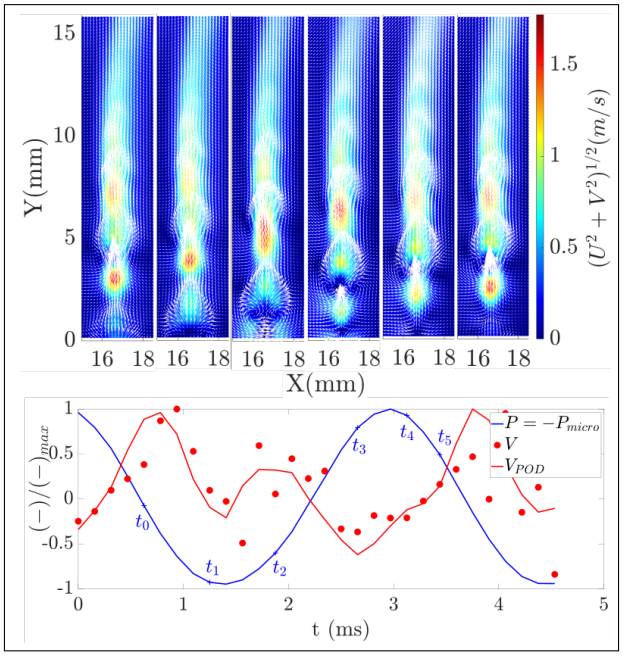


Figure 9. Top: Temporal evolution of the POD [1 2 3 4] velocity field for one jet ejected from a hole of the MPP1.0mm during a period for $F_2 = 324Hz$ excitation (acoustic pressure antinode over the MPP). The colorbar corresponds to the instantaneous velocity norm while the vectors are (U, V). Bottom : Times series of acoustic pressure measured by microphone synchronously with PIV. The vertical velocity component signal (V: raw PIV and V_{POD}: POD reconstruction) is extracted at the center of jet exit cross-section (position : $X = 16.6mm$, $Y = 0.15mm$)

pressure becomes zeros and flow stops moving at the hole exit. When the acoustic pressure is positive, the flow is reverse with negative V velocity in the hole near field and enters the hole as seen in velocity snapshots at t_3 and t_4. This behavior is repetitive over all pressure cycles.

The rotational aspect of the flow in the field of view suggests to calculate the vorticity using the POD reconstructed velocity vectors. Thanks to the high spatial resolution of (U, V) field, the out-plane instantaneous vorticity component:

$$\omega_z(X,Y,t) = \frac{\partial V(X,Y,t)}{\partial x} - \frac{\partial U(X,Y,t)}{\partial y} \qquad (1)$$

can be estimated. This is done with the first 6 POD mode reconstruction of (U, V) for the MPP1.0mm at $F_2 = 324Hz$.
Fig. 10 illustrates a snapshot of the fluctuating vorticity:

$$\omega'_z(X,Y,t) = \omega_z(X,Y,t) - \overline{\omega}_z(X,Y) \qquad (2)$$

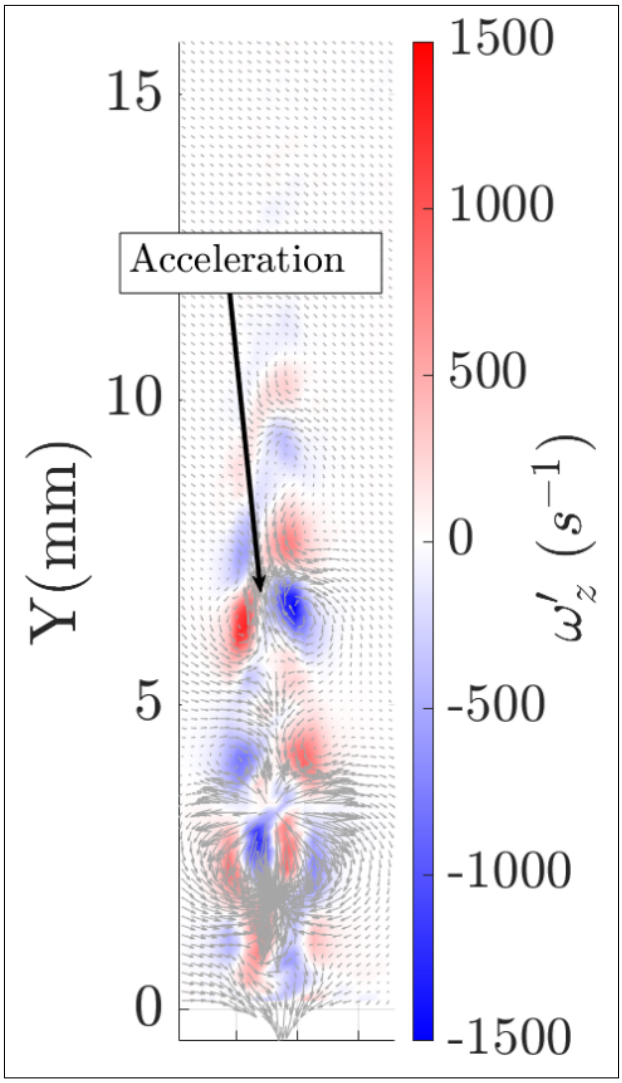


Figure 10. Snapshot of fluctuating vorticity component ω'_z and instantaneous velocity vectors (U,V) calculated from velocity field reconstructed with the six first POD modes for $F_2 = 324Hz$ excitation (acoustic pressure node over the MPP1.0mm).

This representation associated to the plotting of the

synchronous instantaneous velocity vectors underlines the symmetry of the flow on either side of the vertical axis of the jet. The snapshot is chosen for a positive acoustic pressure at the instant t_3 so that the flow entering the hole is clearly observable. Successive counter-rotating vortices are distributed along this symmetry axis. At $Y = 3.5mm$, it is clear that this $2D$ representation gives only a partial view of the $3D$ flow behavior. At $Y = 6mm$, two counter-rotating vortices with the largest magnitude of vorticity detected in the field of view induce an ascending vertical flow acceleration which could be the motor of the jet streaming since the maximum mean velocity is detected in this region as seen for the MPP1.0mm on the top figure of Fig. 6.

6. CONCLUSION AND PERSPECTIVES

The flow induced by high acoustic pressure levels at the apertures of MPP was investigated by measurements of velocity with high-speed PIV associated to synchronous measurements of acoustic pressure by microphone. When the MPP region is submitted to an acoustic pressure antinode, the flow is in the form of pulsated jets which could expand vertically above the aperture up to $Y/d = 15$. Thanks to a POD decomposition of the velocity field, the space-time structure of these jets is quantitatively characterized. The origin of a vertical streaming in the development region of the jet is guessed to be related to the presence of high vorticity counter-rotating vortices located at the end of the region above the apertures where the flow go out or in the perforation. The next step of the study is to quantify the loss of energy induced by this rotational aspect of the flow.

7. ACKNOWLEDGMENTS

The IRPHE technical staff is acknowledged for the design of the Kundt tube.
The high-speed stereo PIV system RapiDO is a funded project of A*Midex (Aix Marseille University).

8. REFERENCES

[1] C. Maury, T. Bravo, D. Mazzoni, M. Amielh, and L. Pietri, "Cost-efficient characterization of the aeroacoustic performance of micro-perforated wall-treatments in a wind tunne," in *Proc. of 179th Meeting of the Acoustical Society of America, POMA Volume 42*, (Virtually Everywhere), 2020.

[2] C. Maury and T. Bravo, "Vibrational effects on the acoustic performance of multi-layered micro-perforated metamaterials," *Vibration*, vol. 6, p. 695–712, 2023.

[3] D.-Y. Maa, "Potential of microperforated panel absorber," *Journal of the Acoustical Society of America*, vol. 104, no. 5, pp. 2861–2866, 2010.

[4] S. Laurens, E. Piot, A. Bendali, M. Fares, , and S. Tordeux, "Effective conditions for the reflection of an acoustic wave by low-porosity perforated plates," *Journal of Fluid Mechanics*, vol. 743, pp. 448–480, 2014.

[5] G. Berkooz, P. Holmes, and J. Lumley, "The proper orthogonal decomposition in the analysis of turbulent flows," *Annual Review of Fluid Mechanics*, vol. 25, p. 539–575, 1993.

DOI: 10.61782/fa.2025.0560

FORUM ACUSTICUM EURONOISE 2025

METHOD FOR ASSESSING THE IMPACT OF AGING OF SELECTED BUILDING MATERIALS ON THEIR ACOUSTIC PROPERTIES

Elzbieta Nowicka*
Department of Therma Physics, Acoustics and Environment, Instytut Techniki Budowlanej, Poland

ABSTRACT

The aim of the work is to assess the impact of aging on selected different building materials. Natural climatic exposures of building materials result in the deterioration of their acoustic properties. Laboratory tests performed on small samples, including acoustic tests correlated with climatic exposures in laboratory conditions, will allow for the assessment of the durability of the functional properties of building materials at the stage of introducing the product to the market. Assessment of the durability of acoustic properties of building materials is to consist in changes in acoustic parameters as a result of exposing samples to various weather conditions. This paper presents the results of preliminary tests carried out on small samples in an impedance tube. Based on the tests performed, an analysis of the results will be carried out in terms of the impact of exposure on the acoustic properties of the elements, mainly in terms of parameters specific to road screens..

Keywords: *aging, building materials, sound properties)*

1. INTRODUCTION

The assessment of the durability of the acoustic properties of road noise barriers is one of the elements in evaluating the functional performance of these structures. Currently, there are standards related to such assessment; however, they remain very general and describe the evaluation procedure in an ambiguous manner

Various approaches have been proposed in the existing literature, yet a clearly defined and standardized methodology is still lacking. Each of the considered proposals exhibits both advantages and shortcomings. To date, methods have primarily focused on testing elements already installed and exposed to natural environmental factors [1]. However, such methods are not suitable for application at the stage of product introduction to the market.

Large-scale sample testing has been undertaken, for instance, at the Silesian University of Technology, where the first assessments of the durability of road noise barriers were performed on samples with a surface area of approximately 5 m². This is the only study of this kind currently referenced in the literature [2].

Numerous publications address the ageing of construction materials and their impact on the acoustic properties of building components. Nonetheless, these studies do not concern road noise barriers and do not account for parameters directly related to this product – namely, the DL_R and DL_α indices [3,4].

The innovation of the proposed methodology lies in the use of small samples, approximately 15 cm² in size. This approach enables broader application, particularly under various environmental exposure conditions. Although previous literature indicates certain correlations between the absorption properties of large and small samples, the studies do not specifically address parameters associated with the evaluation of road noise barriers. [5,6]

2. EXPERIMENTAL WORK

The assessment of the durability of the acoustic properties of the barrier is to be based on the change in acoustic parameters resulting from exposing the samples to various atmospheric conditions: alternating UV radiation and rain, UV and condensation-based humidification, elevated temperature, heating–raining cycles and humid atmosphere.

The preliminary research were conducted on the simple samples: mineral wool with cover made of textile.

Based on the conducted tests, the results will be analyzed in terms of the impact of environmental exposure on the

*Corresponding author: e.nowicka@itb.pl

Copyright: ©2025 First author et al. This is an open-access article distributed under the terms of the Creative Commons Attribution 3.0 Unported License, which permits unrestricted use, distribution, and reproduction in any medium, provided the original author and source are credited.

acoustic performance of the elements – see the test cycle on the fig. 1.

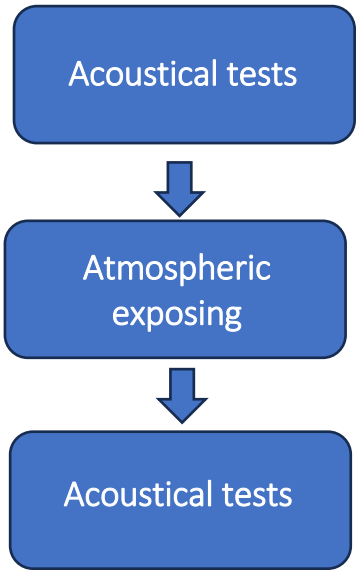


Figure 1. The cycle of test.

Sound absorption tests were carried out in accordance with PN-EN ISO 10534-2 [7], and airborne sound insulation was assessed based on ASTM E1050 [8] and ASTM E2611 [9] standards. Both tests were performed in the impedance tube (see Fig.2).



Figure 2. Impedance tube used for measurement of the acoustical parameters





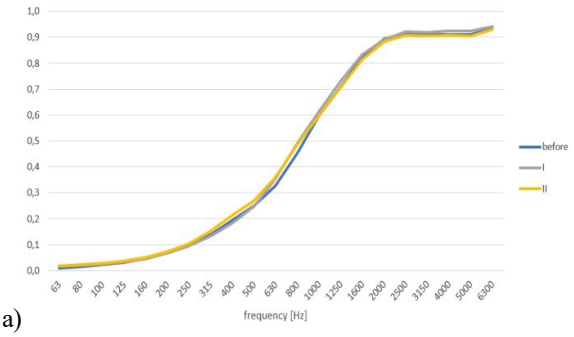


Figure 3. Atmospheric exposing

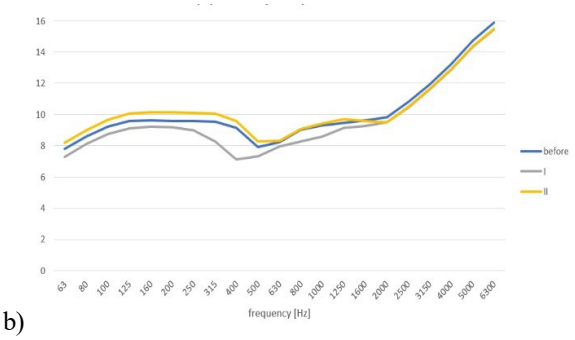
Atmospheric exposing was performed in the following setups:
Setup I – UV + rain: 336 cycles according to EN ISO 4892-3 [10],
Setup II – Temperature and humidity: 1008 hours according to TR024 [11].
Figure 3 presents the samples during atmospheric exposure.

3. RESULTS AND DISCUSSION

Figure 4 presents sound absorption and sound insulation of the samples before and after atmospheric exposing. It is seen, that applied exposing to the mineral wool doesn't change it's acoustical properties.



a)



b)

Figure 4. Sound absorption (a) and sound insulation (b) of samples before and after atmospheric expositions I and II

The results presented above are consistent with the findings reported by Nowoświat et al. [2]. They conducted similar tests on large samples with a surface area of 5 m², which were exposed to heat, cold, and rain. A total of 1000 exposure cycles were performed. Comparable changes in the parameters characterizing road noise barriers were observed — either no change or a decrease of 1 dB. These parameters are presented in Table 1. It means, that the sample size has no influence on this type of researches.

Table 1. Table captions should be placed above the table.

Acoustical parameter	ΔDL_R	ΔDL_α
Setup I	0 dB	0 dB
Setup II	0 dB	0 dB

4. SUMMARY

The method of assessing the impact of aging on selected different building materials and it's acoustical parameters. The preliminary research were conducted on the simple samples: mineral wool with cover made of textile. The applied cycle test included acoustical test of sound absorption and sound insulation with atmospheric exposing. Results confirm previous findings, that there is no influence despite of the sample size.

Future studies will involve samples made from different materials. It is also worth noting the duration of the exposure tests conducted so far, which correspond to approximately five years of natural environmental ageing. The standard requires data after 5, 10, 15, and 20 years of exposure. In the coming years, further research will be undertaken to address these timeframes.

5. REFERENCES

[1] CEDR Transnational Road Research Programme Call 2012: Noise: Integrating strategic noise management into the operation and maintenance of national road networks QUESTIM Assessing the acoustic durability of noise barriers on NRA road networks, 2014.

[2] A. Nowoświat, J. Bochen, L. Dulak, R. Żuchowski, Investigation studies involving sound absorbing parameters of roadside screen panels subjected to aging in simulated conditions, *Applied Acoustics* 111 (2016) 8–15. https://doi.org/https://doi.org/10.1016/j.apacoust.2016.04.001.

[3] A. Luciani, C. Todaro, D. Martinelli, D. Peila, Long-term durability assessment of PVC-P waterproofing geomembranes through laboratory tests, *Tunnelling and Underground Space Technology* 103 (2020) 103499. https://doi.org/10.1016/j.tust.2020.103499.

[4] M. Caniato, C. Schmid, A. Gasparella, A comprehensive analysis of time influence on floating floors: Effects on acoustic performance and occupants' comfort, *Applied Acoustics* 166 (2020) 107339. https://doi.org/10.1016/j.apacoust.2020.107339.

[5] L. Shtrepi, A. Prato, Towards a sustainable approach for sound absorption assessment of building materials: Validation of small-scale reverberation room measurements, *Applied Acoustics* 165 (2020) 107304. https://doi.org/10.1016/j.apacoust.2020.107304.

[6] H.M. Lee, Z. Wang, K.M. Lim, H.P. Lee, Investigation of the effects of sample size on sound absorption performance of noise barrier, *Applied Acoustics* 157 (2020) 106989. https://doi.org/10.1016/j.apacoust.2019.07.037.

[7] ISO 10534-2, Acoustics — Determination of acoustic properties in impedance tubes Part 2: Two-microphone technique for normal sound absorption coefficient and normal surface impedance, 2023.

[8] ASTM E1050, Standard Test Method for Impedance and Absorption of Acoustical Materials Using a Tube, Two Microphones and a Digital Frequency Analysis System, 2024.

[9] ASTM E2611, Standard Test Method for Normal Incidence Determination of Porous Material Acoustical Properties Based on the Transfer Matrix Method, 2019.

[10] EN ISO 4892-3, Plastics. Methods of exposure to laboratory light sources Fluorescent UV lamps, 2016.

[11] TR 024, Technical description and assessment of reactive products effective in case of fire, 2019.

DOI: 10.61782/fa.2025.0470

FORUM ACUSTICUM EURONOISE 2025

INFLUENCE OF MOISTURE CONTENT ON THE ACOUSTIC PROPERTIES OF TEXTILE MATERIALS

Luisa Euler[1] **Ahmed Mehrem**[1*] **Elena Shabalina**[1]

[1] German Institutes of Textile and Fiber Research Denkendorf, Germany

ABSTRACT

Moisture content in a material affects its ability to dissipate sound energy, particularly at mid to high frequencies. This effect has already been investigated for materials such as soil, perlite, or mineral wool, and trends appear to depend on the material. Therefore, acoustic models might not be accurate for hygroscopic materials in humid environments. Even though some explanations were suggested, underlying mechanisms remain unclear. Hence, in this study, fibrous absorbers (cotton and polyester) were analyzed in terms of their acoustic absorption behavior depending on the moisture content. Experimental methods were employed to measure the sound absorption coefficient with varied moisture contents reaching up to 20 wt-%. The results show an influence of the moisture content on the sound absorption, with an increased absorption coefficient for higher moisture contents. This means that changes in the relative humidity of the surroundings can affect the performance of fibrous sound absorbers. Further, when it comes to acoustic material characterization, conditioning of the test samples might be required to achieve reproducible and comparable results.

Keywords: *Absorption, Textile, Moisture, Humidity*

1. INTRODUCTION

Fibrous materials are effective sound absorbers due to their ability to dissipate acoustic energy within their pore structures. As sustainability is gaining importance, sound absorbers made from recycled and natural fibers are on the rise. However, most natural fibers are hygroscopic, which is why their physical properties are affected by humidity. Researchers have observed a strong correlation between relative humidity (RH) and moisture uptake for natural fibers such as cotton and wool. According to the review by [1], natural fibers exhibit increased swelling and weight gain under high RH conditions. As water molecules fill the voids, the pores are closed, and the airflow resistivity is increased, [2] thus potentially affecting the sound absorption. Here, [3] investigated wool-based materials and reported reduced sound absorption at high frequencies as moisture contents rose. On the other hand, most synthetic textile materials, such as polyester and polypropylene, show different behaviors under humid conditions due to their hydrophobic nature [2]. Therefore, the aim of this study is to determine how changes in moisture content impact the acoustic performance of fibrous sound absorbers, namely cotton and polyester nonwoven.

1.1 Effects of Moisture Content on Acoustic Performance of Materials

The effects of moisture content on the acoustic behavior have already been investigated for materials such as soil, perlite, or mineral wool, and trends appear to depend on the material. For soil, variations in moisture content were shown to affect the material's sound absorption, which can be related to changes in porosity ϕ and airflow resistivity σ. The moisture-dependent parameters are given by [4]:

$$\phi_{\text{wet}} = \phi_0 \cdot (1 - C_m M), \tag{1}$$

$$\sigma_{\text{wet}} = \sigma_0 \cdot (1 + C_r M), \tag{2}$$

*Corresponding author: ahmed.mehrem@ditf.de.

Copyright: ©2025 Euler et al. This is an open-access article distributed under the terms of the Creative Commons Attribution 3.0 Unported License, which permits unrestricted use, distribution, and reproduction in any medium, provided the original author and source are credited.

where ϕ_0 is the initial porosity, σ_0 is the dry resistivity, C_m describes the moisture-induced porosity factor and C_r describes the moisture-induced air resistivity factor. In Eqs. (1) and (2), some simplifying assumptions were made, such as linear relationships with moisture content and overlooks of material properties, along with a uniform moisture distribution.

1.2 Physical Effects of Moisture on Textile Materials

Many natural but also some synthetic fibers are hygroscopic to some extent, meaning they absorb moisture from air [5]. The amount of absorption depends on the fiber type and the environmental conditions, with natural fibers absorbing up to 30 % of their weight under high RH conditions, while most synthetic fibers usually take up less than 1 % [6–8]. For hygroscopic porous materials, water can be stored in the air voids either as vapor or in liquid form, or it may be bound inside the material itself [5]. Especially the latter can drastically affect fiber properties, including dimensional (mass, swelling), mechanical (tensile strength, extensibility), and electrical (resistance) properties [9]. The first study reporting structural changes in textiles from changes in moisture content can be found in [10]. Here, swelling of cotton fibers was found to affect a material's thickness and porosity [10]. Related to this, [2, 5] investigated the influence of moisture content on the air permeability of hygroscopic textiles and observed drastic changes at high RH caused by swelling, which reduced the free void space.

2. EXPERIMENT

As sound absorption is, among other factors, governed by porosity and airflow resistivity, this gives rise to the assumption that it might as well be affected by the moisture content in the fibrous material. Sustainable sound absorbers are often based on natural fibers (cotton). Cotton is hygroscopic and can bind moisture inside the fiber, whereas, for example, polyester can only store moisture in the voids formed by the fiber assembly. By testing these two types of fibrous absorber materials, namely a recycled cotton nonwoven and a recycled polyester nonwoven as reference material, we evaluate the influence of changes in moisture content on the acoustic properties of sustainable, fibrous sound absorbers.

2.1 Materials and Sample Characterization

The material under investigation is recycled nonwoven cotton, which is referred to as CO20. The material used as reference is a recycled polyester nonwoven (polyethylene terephthalate, PET), which is referred to as PET20. The sample properties are presented in Table 1. We estimated the porosity ϵ_0 of the samples based on the densities of the nonwoven structure ρ_n and the fiber densities ρ_f [11]:

$$\epsilon_0 = (1 - \frac{\rho_n}{\rho_f}) \times 100\ \% \tag{3}$$

The fiber densities from the literature are $\rho_f = 1.51 g/cm^3$ for cotton and $\rho_f = 1.38 g/cm^3$ for PET fibers. The air permeability κ was determined according to DIN EN ISO 9237:1995-12* at 200 Pa.

Name	ρ_n (kg/m³)	ϵ_0 (%)	t (mm)	κ (l/sm²)
CO20	45	97.0	20 ±0.2	538
PET20	40	97.1	20	1422

Table 1. Sample properties: ρ_n = density of structure; ϵ_0 = estimated porosity; t = sample thickness; κ = air permeability at 200 Pa

The recycled cotton samples did not only include loose fibers but also some smaller pieces of shredded fabric from the mechanical recycling process. On the other hand, the recycled polyester samples consisted of distinguishable fibers only. The microscopy and the SEM images of the samples are presented in Table 2.

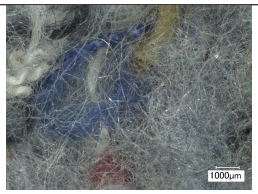
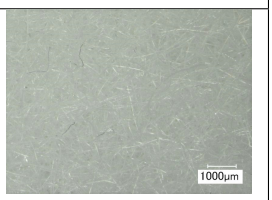
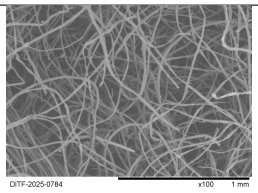
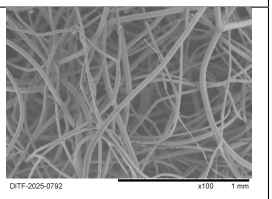
	CO20	PET20
top view		
SEM images		

Table 2. Microscopy images and SEM images of the samples

2.2 Sample Preparation

To imitate moisture contents in different RH surroundings, prior to measuring the acoustic properties, we steamed the specimens until reaching the desired amount of moisture, determined by the weight change. A moisture content of 0 % is not realistic for application scenarios. Therefore, the baseline for 0 % in this study is regarded as the moisture content in the specimen after being conditioned in a climate of T = 23 °C and RH = 40 % for at least 24 hours. The increase in moisture content M was calculated as a percentage increase in mass relative to the conditioned sample's mass m_{cond} and calculated as:

$$M = \frac{m_{\text{wet}} - m_{\text{cond}}}{m_{\text{cond}}} \times 100\ \%, \tag{4}$$

where m_{wet} is the weight after moisture absorption. We increased the moisture content gradually in increments of 5 % until reaching 20 %, while measuring the acoustic absorption coefficient at each step. We tested three specimens of PET20 and five specimens of CO20 (due to higher expected variations for this material arising from its inhomogeneous structure).

2.3 Measurement of Acoustic Properties

We measured the sound absorption coefficient α over a frequency range of 50 Hz to 1,600 Hz using the two-microphone impedance tube method based on ISO 10534-2 with a tube diameter of 100 mm (impedance tube Brüel & Kjær Type 4206-T). We monitored the climate over the entire testing duration to exclude errors from changing climate conditions. We used linear regression analysis to determine the significance (p-value) of the influence of M on the absorption coefficient α for the different materials.

2.4 Results and Discussion

As shown in Figures 1 and 2, there is an increase in sound absorption coefficient α with higher moisture levels for both materials, particularly at the higher frequencies (M = 15 % not pictured for visibility purposes). Even though the change is small and for cotton the standard deviations are partly overlapping, the regression analysis still found the influence of M to be statistically significant for both materials with p-values of p = 0.001 for cotton and p = 0.000 for the polyester samples. Further, the biggest change in α can be found when going from M = 0 % to M = 5 % for both materials. Hence, small amounts of moisture can already have a noticeable impact on the sound absorption behavior.

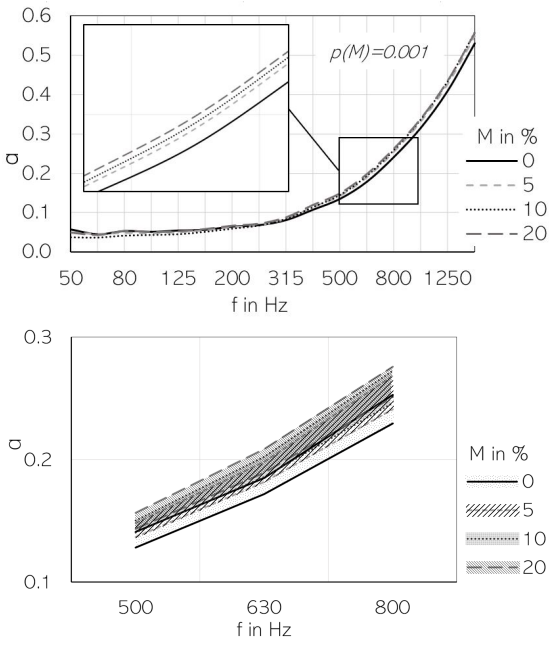


Figure 1. *TOP*: Average absorption coefficient α of CO20 for different moisture contents M; *BOTTOM*: Standard deviations for selected frequencies.

The increase in sound absorption can be attributed to several factors. One of the primary effects of moisture is the increase in airflow resistivity σ. As water fills the pores of the material, it creates additional resistance to airflow, which enhances the viscous damping of sound waves. The higher airflow resistivity in both CO20 and PET20 at elevated moisture levels likely increased sound absorption. Furthermore, thermal conductivity increases with water content, leading to enhanced dissipation of sound energy within the material.

The observed effect was more pronounced for PET than for cotton. This can be attributed to the (presumable) swelling of the cotton fibers in contrast to the PET fibers not swelling. While the water drops start filling the air voids, in the case of cotton, the fiber swelling further closes the pores. Hence, the porosity is reduced to a higher extent, thus counteracting the increase in sound absorption arising from the increase in air flow resistivity. In turn, the change in sound absorption is less dominant for cotton than for PET. Additionally, the inhomogeneous structure of the CO20 increased inter-sample variations, thus potentially overlaying some effects from moisture.

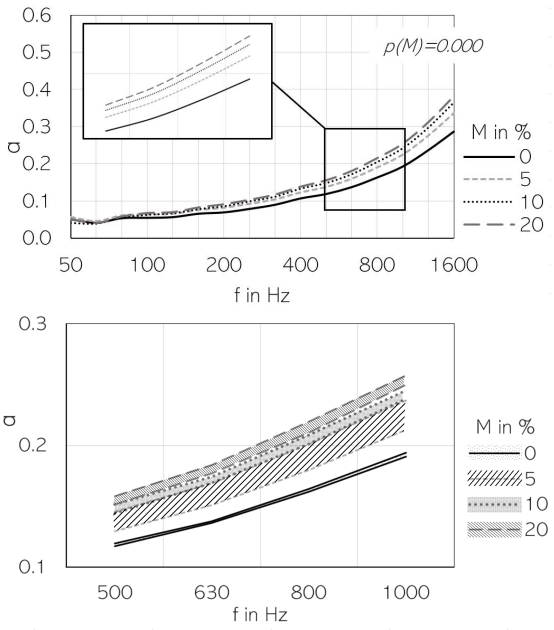


Figure 2. *TOP*: Averaged absorption coefficient α of PET20 for different moisture contents M; *BOTTOM*: Standard deviations for selected frequencies.

Nevertheless, it must be mentioned that the testing procedure not only increased the moisture content in the materials but also involved raised temperatures from the steaming process. Especially for PET this might be relevant as the glass transition temperature is in a similar region. We could not exclude this influence from the experiments, which is why this should be investigated in future work. Further, due to time constraints, we could only test a small number of samples. To increase statistical reliability, more repetitions should be performed.

Concluding we found that changes in the relative humidity of the surroundings can potentially affect the performance of fibrous sound absorbers. Further, when it comes to acoustic material characterization, conditioning of the test samples might be required to achieve reproducible and comparable results.

3. REFERENCES

[1] M. Musthaq, H. Dhakal, Z. Zhang, A. Barouni, and R. Zahari, "The effect of various environmental conditions on the impact damage behaviour of natural-fibre-reinforced composites (nfrcs)—a critical review," *Polymers*, vol. 15, no. 5, p. 1229, 2023.

[2] P. Gibson, D. Rivin, C. Kendrick, and H. Schreuder-Gibson, "Humidity-dependent air permeability of textile materials1," *Text. Res. J.*, vol. 69, no. 5, pp. 311–317, 1999.

[3] R. Del Rey, A. Uris, J. Alba, and P. Candelas, "Characterization of sheep wool as a sustainable material for acoustic applications," *Materials*, vol. 10, no. 11, p. 1277, 2017.

[4] D. Fredlund, *Soil mechanics for unsaturated soils*, vol. 517. John Wiley & Sons Inc, 1993.

[5] P. Gibson and M. Charmchi, "Modeling convection/diffusion processes in porous textiles with inclusion of humidity-dependent air permeability," *Commun. Heat Mass Transf.*, vol. 24, pp. 709–724, 09 1997.

[6] H. Dhakal, Z. Zhang, and M. Richardson, "Effect of water absorption on the mechanical properties of hemp fibre reinforced unsaturated polyester composites," *Compos. sci. and Technol.*, vol. 67, no. 7-8, pp. 1674–1683, 2007.

[7] T. Yang, L. Hu, X. Xiong, M. Petr, M. Noman, R. Mishra, and J. Militkỳ, "Sound absorption properties of natural fibers: A review," *Sustainability*, vol. 12, no. 20, p. 8477, 2020.

[8] A. Moudood, A. Rahman, A. Öchsner, M. Islam, and G. Francucci, "Flax fiber and its composites: An overview of water and moisture absorption impact on their performance," *J. Reinf. Plast.*, vol. 38, no. 7, pp. 323–339, 2019.

[9] B. Saville, "2 - textiles and moisture," in *Physical Testing of Textiles* (B. Saville, ed.), Woodhead Publishing Series in Textiles, pp. 26–43, Woodhead Publishing, 1999.

[10] J. Wehner, B. Miller, and L. Rebenfeld, "Moisture induced changes in fabric structure as evidenced by air permeability measurements," *Text. Res. J.*, vol. 57, pp. 247 – 256, 1987.

[11] G. Zhu, D. Kremenakova, Y. Wang, and J. Militky, "Air permeability of polyester nonwoven fabrics," *AUTEX Res. J.*, vol. 15, no. 1, pp. 8–12, 2015.

DOI: 10.61782/fa.2025.0835

FORUM ACUSTICUM EURONOISE 2025

STUDY OF SOME INFLUENCES ON THE ACOUSTIC BEHAVIOUR OF DISINTEGRATED SAMPLES OF USED CIGARETTES

Celia Moreno González[1*] **Valentín Gómez Escobar**[1] **Guillermo Rey-Gozalo**[1]

[1] Laboratorio de Acústica, Departamento de Física Aplicada & Instituto Universitario de Investigación para el Desarrollo Territorial Sostenible (INTERRA). Universidad de Extremadura. Avda. Universidad, s/n 10003 Cáceres, España.

ABSTRACT

Used cigarette butts are one of the most common types of waste in today's environment. However, there are not many proposals for its recycling, if we take into account the amount of waste generated annually.

Our research group has been working in recent years on the recycling of these wastes to give them an acoustic use. Thus, cigarette butts' samples are prepared by disaggregating the filter of used cigarettes, which, as shown in previous studies, presents promising properties as acoustic absorber. However, due to the heterogeneity of the filters and the disaggregation process, these samples tend to lack consistency and lose their shape when handled. Thus, the use of binders is advised in case of severe disaggregation.

This study examines the use of binders on cigarette butts' prepared samples for acoustic applications. Thus, some natural binders has been applied to enhance the structural strength of the samples and their effect onto the acoustic samples performance is analyzed.

The results indicate that samples treated with low binder concentrations retained their acoustic absorption properties while achieving a stronger and more durable structure.

Keywords: *acoustic absorption, impedance tube, binders, cigarette butts*

[*] ***Corresponding author***: *celiamg@unex.es*

Copyright: *©2025 First author et al. This is an open-access article distributed under the terms of the Creative Commons Attribution 3.0 Unported License, which permits unrestricted use, distribution, and reproduction in any medium, provided the original author and source are credited.*

1. INTRODUCTION

Cigarette butts are among the most prevalent forms of waste worldwide, raising significant environmental concerns due to their composition and the volume generated. It is estimated that approximately 4.55 trillion cigarettes are consumed annually [1], resulting in an equivalent number of discarded filters.

These filters are primarily composed of cellulose acetate, a non-biodegradable bioplastic that can take years to decompose in the environment. Moreover, cigarette butts contain various toxic compounds, including nicotine and heavy metals, which can leach into soil and water systems, contaminating ecosystems [2]. Despite the well-documented environmental impact of cigarette butts, few recycling solutions have been proposed to mitigate this problem [3].

Cellulose acetate, due to its fibrous and porous structure, has shown favorable acoustic properties. Recent studies have characterized and modeled the sound absorption behavior of cellulose acetate fibers from used cigarette filters, suggesting that this material could serve as a viable alternative to conventional acoustic absorbents in building materials [4,5]. This approach not only contributes to reducing the environmental impact of cigarette butt waste but also offers a sustainable solution for the development of construction materials.

The results obtained to date have been promising, indicating that samples fabricated from these residues can achieve sound absorption coefficients comparable to those of commercial products. However, one of the major

challenges identified has been the lack of structural consistency in the samples, which hinders their handling and potential commercialization.

To solve this issue, the use of binders has been proposed to improve structural integrity although their acoustic performance could be compromised [6,7,8]. The use of natural binders shows similar behavior to synthetics, potentially reducing environmental impact, as demonstrated by the study of Mirski et al. [9]

As an initial approach, white glue diluted in water at different concentrations has been used. The aim of this study is to develop a material that not only retains an effective sound absorption capabilities but also meets the mechanical and commercial requirements for real walls.

2. METHODOLOGY

2.1 Equipment used

To determine the absorption coefficient of samples, normal incidence wave measurements were conducted using the transfer function method, as established in ISO 10534-2 [11].

The equipment used for measuring the acoustic properties of the samples includes a Brüel & Kjaer 4206 T impedance tube, a Brüel & Kjaer PULSE multi-analyzer system with four channels (model 3560 C), a Brüel & Kjaer power amplifier (model 2716 C), Brüel & Kjaer ¼-inch microphones (model 4187), and Brüel & Kjaer Material Testing software for PULSE (model 7758).

The impedance tube features two sample holders with diameters of 100 mm and 29 mm, covering frequency ranges of 50–1600 Hz and 500–6400 Hz, respectively. However, for this study, only the 29 mm sample holder was used, limiting the results to the 500–6400 Hz frequency range.

Figure 1 presents a schematic of the experimental setup, while Figure 2 shows a photograph of the impedance tube with the 29 mm sample holder.

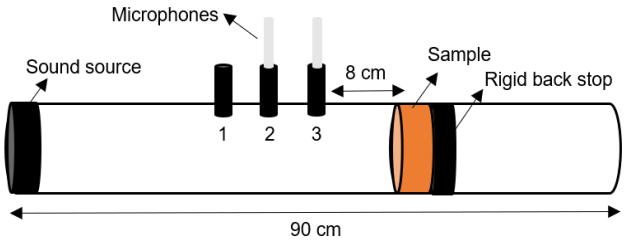


Figure 1. Diagram of sample placement for acoustic absorption measurements.

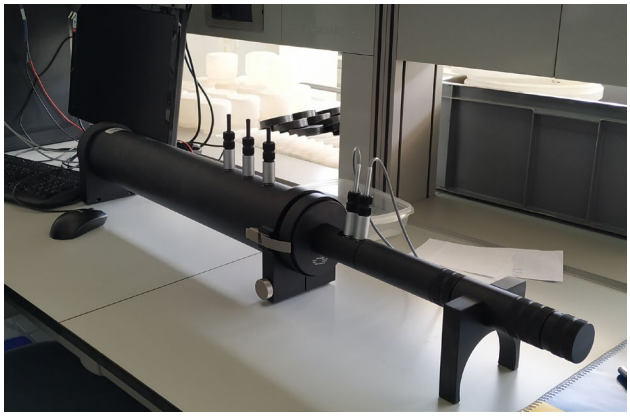


Figure 2. Impedance tube with the 29 mm diameter sample holder.

2.2 Materials

For this study, 30 samples composed of disaggregated cigarette butts were analyzed with the 29 mm diameter holder. Characteristics of the sample set are shown in Table 1.

Table 1. Characteristics of sample set.

Sample number	Thickness	Density
30	21-25 mm	71- 84 kg/m³

The acoustic behavior of the samples has been measured both before and after applying the binder. The binder used has been white glue diluted in water at different ratios (10%, 20%, 40%, 60%, and 80% glue to water ratio). Each combination was applied to six different samples to assess the reproducibility of the results.

Figure 3 shows one of the samples before applying the binder.



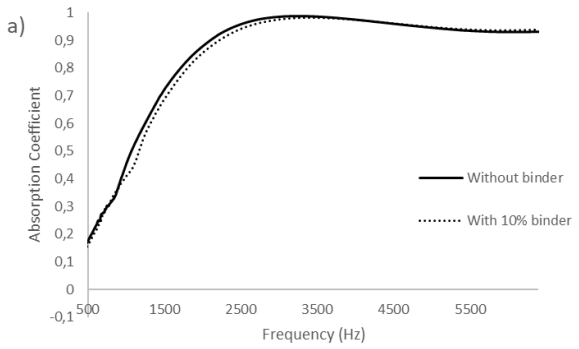
Figure 3. Initial sample before applying the binder.

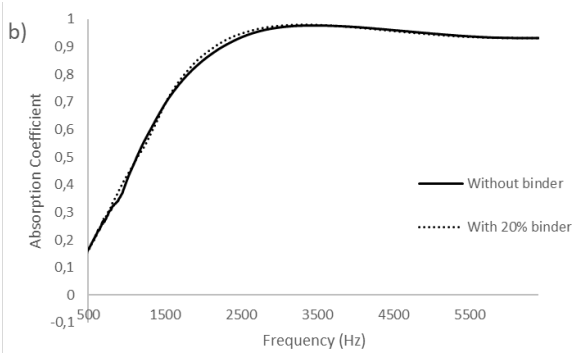
3. RESULTS AND DISCUSSION

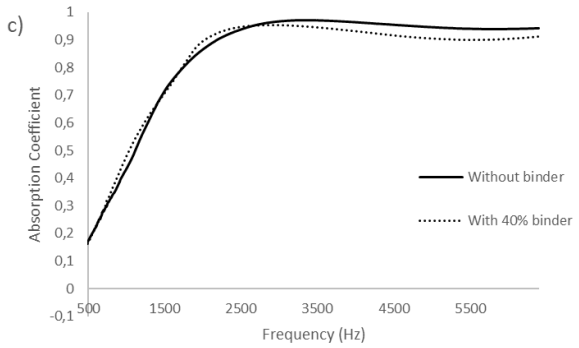
As mentioned earlier, 30 different samples were measured, all with similar characteristics. A different proportion of binder was applied to each six samples: 10%, 20%, 40%, 60%, and 80% white glue related to water. This approach allows us to evaluate how the binder application affects each sample (since measurements were taken before and after its application), how the amount of binder influences the acoustic behavior of the material, and whether these results are reproducible.

Figure 4 presents the average absorption coefficient values for sets of samples with the same binder concentration.

Figure 5 compares the behavior of the different sets, the green line represents the average value of all samples measured before the binder was applied, allowing for a comparison of the acoustic absorption before and after binder application.







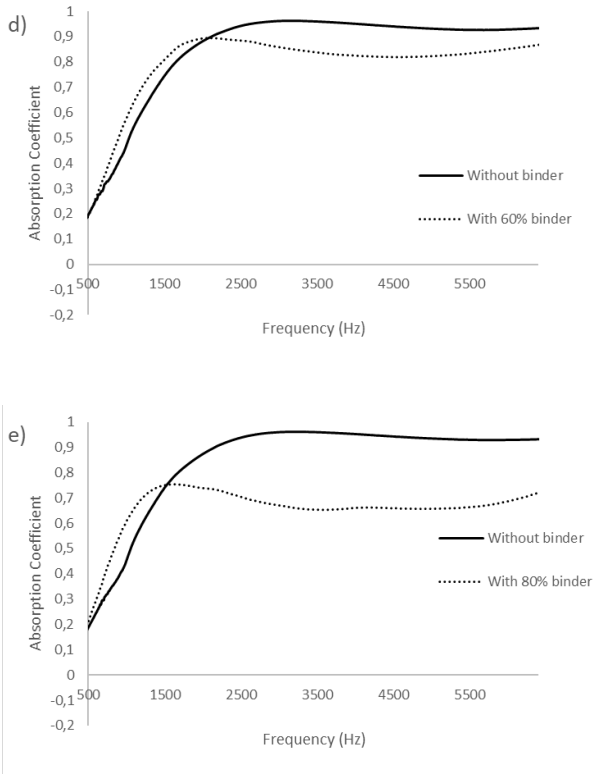


Figure 4. Comparison of samples with a without binder a) 10% b) 20% c) 40% d) 60% e) 80% glue respect water

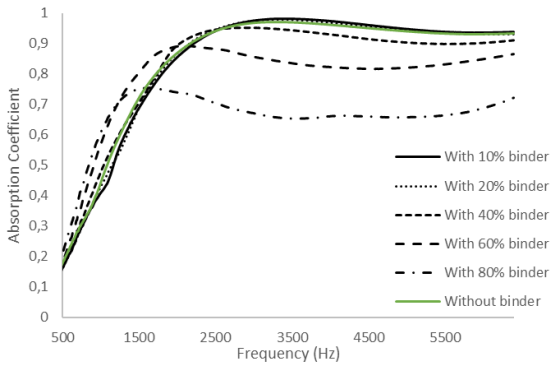


Figure 5. Average sound absorption coefficient before and after binder application

The results show that as the binder concentration in the solution increases, the difference in the measured absorption coefficient becomes more pronounced. Specifically, significantly lower values are observed for samples with solutions containing 60% (Figure 4.d) and 80% (Figure 4.e) of binder. On the contrary, samples treated with solutions with low binder content, such as 10% and 20% (Figure 4.a and Figure 4.b, respectively), show a minimal variation in acoustic behavior, particularly above 3000 Hz, where the difference becomes almost negligible. This decline in acoustic efficiency for high binder ratios can be attributed to a loss of porosity in the samples: the higher the binder content, the more compacted the material becomes, which has a negative impacts on acoustic absorption properties.

These results are corroborated by the data presented in Figure 6, which shows the average differences between each set of samples before and after binder application. It can be observed that, particularly above 3000 Hz, samples with 10% and 20% binder concentration show virtually no differences, while at lower frequencies, the differences remain below 5%. For samples with higher binder concentrations (60% and 80%), the difference increase, reaching a maximum of approximately 12% and 30%, respectively.

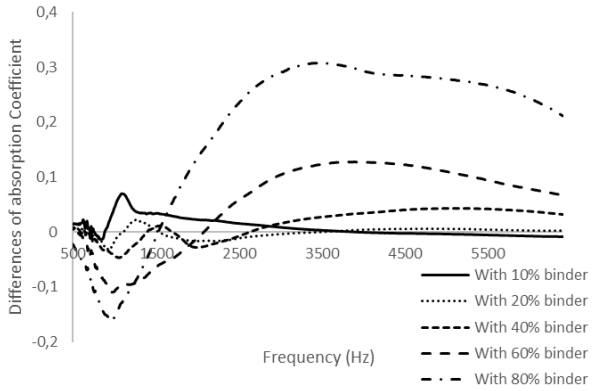


Figure 6. Average differences in sound absorption before and after binder application by concentration

The effect of the binder on the porosity of the samples is shown in Figure 7, which shows two samples: the one on the left was treated with a 10% binder-to-water ratio,

while the one on the right was treated with an 80% solution. At 80% binder concentration, the sample becomes completely rigid, resulting in a significant loss of surface porosity.



Figure 7. Effect of the binder on the samples: 10% concentration on the left, 80% on the right.

4. CONCLUSIONS

The use of white glue as a binder in samples composed of cigarette butts presents a valuable opportunity to enhance the structural integrity of the material, preventing deformation during handling.

When applying a low binder-to-water ratio—between 10% and 20%—the acoustic performance of the samples remains unaffected, with no significant reduction in the absorption coefficient upon the introduction of the binder. However, higher binder concentrations, ranging from 60% to 80%, have a notable impact on acoustic behavior, leading to absorption coefficient values up to 40% lower compared to samples without binder. This decrease is attributed to a loss of porosity in the material.

Therefore, it can be concluded that using low binder concentrations is beneficial, as it results in a more mechanically stable material without compromising its acoustic properties. This behavior will be further validated through an expanded sample set and the evaluation of alternative natural binders in future studies.

5. ACKNOWLEDGMENTS

This work is part of the agreement between the University of Extremadura and ALTADIS IMPERIAL BRANDS, titled “Development of the Research Line on Recycling Used Cigarette Filters as Acoustic Materials” (ref. 075/21). It is partially supported by “Ayudas para la contratación de personal investigador predoctoral en formación por el Sistema Extremeño de Ciencia, Tecnología e Innovación” funded by Junta de Extremadura and the European Social Fund Plus (PD23008). And partially supported by the European Regional Development Fund (ERDF) and by Junta de Extremadura, Consejería de Educación, Ciencia y Formación Profesional (Grant GR24069)

6. REFERENCES

[1] Euromonitor International, "Passport: Global Market Information Database," available online: https://tobaccoatlas.org (accessed on 7 April 2025)

[2] R. Maderuelo-Sanz: “Characterizing and modelling the sound absorption of the cellulose acetate fibers coming from cigarette butts,” *J. Environ. Health Sci. Eng.*, vol. 19, no. 1, pp. 1075–1086, 2021.

[3] K. R. Anapalli, H. B. Sharma, S. Anand, V. P. Ranjan, H. Singh, B. K. Dubey, and B. Mohanty: “Cigarettes butt littering: The story of the world’s most littered item from the perspective of pollution, remedial actions, and policy measures,” *J. Hazard. Mater.*, vol. 453, pp. 131387, 2023.

[4] V. Gómez Escobar, C. Moreno González, G. Rey Gozalo. “Analysis of the influence of thickness and density on acoustic absorption of material made form used cigarette butts”, Materials, 14, 4524 (16pp), 2021.

[5] V. Gómez Escobar, C. Moreno González, Mª J. Arévalo Caballero, Mª L. Durán Martín-Merás, G. Rey Gozalo, C. J. Pérez Sánchez. “Influencias en la absorción acústica de muestras preparadas a partir de colillas de cigarrillos usadas,” in Publicación del Congreso TecniÁcústica 2022 (Elche, Spain), pp 466, 473, 2022.

[6] F. Merli, E. Belloni, C. Buratti. “Eco-Sustainable Wood Waste Panels for Building Applications: Influence of Different Species and Assembling

Techniques on Thermal, Acoustic, and Environmental Performance", *Buildings*, 11, 361, 2021

[7] R. Belakroum, A. Gherfi, K. Bouchema, A. Gharbi, Y. Kerboua, M. Kadja, C. Maalouf, T.H. Mai, N. El Wakil, and M. Lachi: "Hygric buffer and acoustic absorption of new building insulation materials based on date palm fibers," *J. Build. Eng.*, vol. 12, pp. 132-139, 2017.

[8] N. El Hajj, R. M. Dheilly, A. Goullieux, Z. Aboura, M. L. Benzeggagh, and M. Quéneudec: "Innovant agromaterials formulated with flax shaves and proteinic binder: Process and characterization," *Composites Part B: Engineering*, vol. 43, no. 2, pp. 381-390, 2012.

[9] R. Mirski, D. Dziurka, M. Kuliński, and A. Derkowski: "Lightweight Insulation Boards Based on Lignocellulosic Particles Glued with Agents of Natural Origin," *Materials*, vol. 14, no. 12, p. 3219, 2021.

[10] ISO 10534-2:2023: "Acoustics—Determination of acoustic properties in impedance tubes—Part 2: Two-microphone technique for the determination of normal incidence sound absorption coefficient and normal surface impedance," International Organization for Standardization, 2023.

DOI: 10.61782/fa.2025.0027

FORUM ACUSTICUM EURONOISE 2025

A PRACTICAL APPROACH TO THE DETERMINATION OF REPRODUCIBILITY PRECISION (σ_{TARGET}) IN THE FIELD OF SOUND ABSORPTION MEASUREMENTS: EVALUATION OF PROFICIENCY TESTING DATA ACCORDING TO ISO 354:2003

Pedro Rosario[1*], José Luis Martínez[1]
[1] RPS-Qualitas, Madrid, Spain

ABSTRACT

ISO 354:2003 specifies a method of measuring the sound absorption coefficient of acoustical materials used as wall or ceiling treatments. The measured values in one-third octave bands of the sound absorption coefficient are converted to values in the corresponding octaves (practical and weighted sound absorption coefficients - ISO 11654). The adequacy of proficiency tests is guaranteed by means of the assessment of global precision criteria in compliance with the scope stipulated by the normative references in order to determine the reproducibility limits in a regulated measurement method. Unfortunately, the latest revision and endorsement of ISO 354 standard in 2024 does not include any information related precision data. From the experience acquired after seven rounds of the international interlaboratory comparison schemes for sound absorption measurements managed by RPS-Qualitas between 2012 and 2024, according to the methods specified in ISO 354:2003, and in this scenario, a practical approach is proposed to the determination of the reproducibility precision (σ_{target}) in the field of sound absorption measurements by means of the historical records evaluation of the relevant proficiency testing data obtained according to ISO 354:2003

The aim is to provide not only a reliable but also up-to-date criteria for the evaluation of repeatability and reproducibility limits in this field, particularly where there is not at all or very poor normative reference.

Keywords: *sound absorption tests, iso 354, target reproducibility precision. proficiency test.*

[*] ***Corresponding author***: *pedro.rosario@rpsqualitas.es*
Copyright: *©2025 Pedro Rosario et al. This is an open-**access** article distributed under the terms of the Creative Commons Attribution 3.0 Unported License, which permits unrestricted use, distribution, and reproduction in any medium, provided the original author and source are credited.*

1. INTRODUCTION

The standard ISO 354 ‘‘Acoustics. Measurement of sound absorption in a reverberation room’’ [1] specifies a method of measuring the sound absorption coefficient of acoustical materials used as wall or ceiling treatments, or the equivalent sound absorption area of objects, such as furniture, persons or space absorbers, in a reverberation room. The measured values in one-third octave bands of the sound absorption coefficient are converted to values in the corresponding octaves (practical and weighted sound absorption coefficients - ISO 11654) [2].
Since ISO/IEC 17025 [3] requires testing laboratories to put in place external quality control procedures for monitoring the reliability of their measurements, the participation in proficiency testing schemes is the main mechanism for assessing compliance.
In this context, RPS-Qualitas, as an independent consulting and technical advisory company, associated with the Universidad Politécnica de Madrid, has launched since 2012 a project called AQUS, with the aim of providing a

tool for the objective verification of technical competence, through the development of a biannual proficiency testing scheme in the field of acoustic absorption measurements, according to ISO 354 standard, in order to provide participating laboratories with a powerful tool to know the degree of adequacy in the said tests.

2. METHODOLOGY AND LIMITATIONS OF THE STANDARD

2.1 Proficiency test scheme

In order to satisfy this requirement, seven rounds of this proficiency testing scheme for sound absorption measurements have been conducted by RPS-Qualitas between 2012 and 2024, according to the methods specified in ISO 354 at international level. Since it is a proficiency test, the laboratories that were admitted had both a reverberation chamber and an alpha cabin, and the performance of the participating laboratories was also obtained from the results of measurements of the sound absorption coefficient in one-third octave bands. On the other hand, practical sound absorption coefficients were calculated in octaves and single weighted evaluation index was obtained according to the UNE - EN ISO 11654. All participating laboratories are accredited by ISO 17025. On the other hand, we would like to underline that in terms of the design of this proficiency testing programme, both the homogeneity and the stability of the samples have been duly checked throughout the proficiency test. Thus, we have achieved the goal of obtaining globally accurate results of high quality, so the requirements of ISO 17043 [4] have been taken into account from the outset and during the testing and data processing.

2.2 Stability and homogeneity of test item

In the AQUS project, the description of the proficiency testing (PT) scheme is well documented, considering a series of planned stages related to the monitoring, follow-up and control of the measurement items. This monitoring phase was designed to ensure both the stability and the homogeneity of the test item, which was evaluated and monitored by an accredited laboratory as a mandatory rule, allowing to declare that test item condition remain unchanged over time. It is important to mention that in each PT round, either a different type of material or a certain material with a range of thickness values were evaluated, with different absorption characteristics. These aspects are fully evaluated in order to guarantee the adequacy of the interlaboratory comparison through the evaluation of certain global precision guidelines in accordance with the current scope, since there are no regulatory or prescribed values for reproducibility verification in this scope.

2.3 Reproducibility precision

The precision goodness of the PT cannot be estimated via calculation of by the reproducibility of the test (measurement of acoustic absorption in reverberant chamber, according to ISO 354 standard), since there are no published data on this parameter in the corresponding standard. This standard has been recently revised and confirmed as unchanged until 2024. We have only been able to compare with previous data. Once the reproducibility data (SD_R of the revised ISO 354 standard) are available, these values will be selected as the appropriate SD_R value (σ_{target}) of the standardised test method for performance evaluation, adapted to the intended use of the participants.
This is the reason why the main objective of this paper is to propose a practical approach for the determination of the reproducibility precision (σtarget) in the field of sound absorption measurements by means of a proper evaluation of the experimental data obtained in the different proficiency test PT rounds.

3. STATISTICAL DESIGN AND PERFORMANCE EVALUATION

3.1 Statistical procedure

The protocol conducted in these proficiency test schemes outlines a statistical design not only intended for the analysis of the data but also for the evaluation of the proficiency testing results according to the standard ISO 5725-2, that describes the determination of the repeatability and reproducibility in a regulated measurement procedure using classical statistical methods with outlier elimination [5]. As regards the implementation of the PT scheme AQUS, the statistical parameters published for the

magnitudes object of study in the scope of the program are the following:

• assigned value (αs - sound absorption coefficient) in each frequency as consensus value from participants in the frequency range 100 - 5000 Hz

• estimate of the precision of the PT results in terms of repeatability and reproducibility limits

• standardized z-score taken as an assessment of the performance of the participation by each laboratory.

As for the determination of the assigned value, once discarded the outlier results, it is performed in accordance with the established protocol by first calculating the arithmetical average of the four results reported by each laboratory participants, taken as the consensus value for the number of non-excluded participants in each magnitude. This makes it possible to get the most appropriate measure of central tendency based on the distribution of the data of the participants, once verified the normality of them as mandatory previous rule. This condition of statistical normality of the test results allowed us to verify the results obtained with the ISO 13528 standard (robust statistical methods). Interestingly, they were quite similar and consistent in terms of the assigned value and reproducibility of the proficiency test that had been verified since the first round of the AQUS PT programme.Then, in order to define the variability of the proficiency test results, it is first necessary to estimate the values of both the standard deviation under conditions of repeatability (Sr) and the one under conditions of reproducibility (SD_R). These are applied to calculate the related parameters r and R according to ISO 5725-2.

$$r = 2{,}8\, S_r \tag{1}$$

$$R = 2{,}8\, S_R \tag{2}$$

The parameters r and R may be called ‘‘critical differences’’ or ‘‘limits,’’ as they describe the maximum difference of a pair of test results at which these can be considered equivalent at a probability level of 95 %.

3.2 Performance evaluation

The performance of each participant is evaluated by calculating the corresponding z-score, determined in accordance with:

$$z = (x_i - X_{PT})/\sigma_{PT} \tag{3}$$

where x_i is the laboratory result, X_{PT} is the assigned reference value and σ_{PT} is the estimate of the standard deviation of the proficiency test results. In this way, results with a value $|z| \leq 2$ are considered as satisfactory; results with $|z| \geq 3$ are unsatisfactory; results with $2 < |z| < 3$ are considered questionable.

4. PITFALLS TO ESTABLISH PRECISION GUIDELINES

4.1 Scope and purpose

Regarding the evaluation of the precision criteria for the proficiency test according to the recently revised ISO 354 standard, unfortunately there are no regulatory values available that can be used as a prescribed reference, unlike what happens in other standards in the field of acoustics tests. Therefore, it has not been possible to verify whether the reproducibility values obtained during these interlaboratory PT round comparisons following ISO 354 correspond to a normative reference in terms of significant differences.

In addition to the aim of supporting the participants in all proficiency tests conducted, we would like to broaden the understanding of the state-of-the-art regarding the precision of the results obtained with this method. Therefore, once the PT rounds have been completed and with the knowledge acquired during their development, our proposal is to provide some practical data guidance on the precision. Furthemore, these data will be specific for the application of this standard within the considered scope.

A practical approach has been applied to determine the reproducibility precision (σ_{target}) in the field of sound absorption measurements by evaluating historical records of the relevant proficiency test data according to ISO 354, by means of performing some operational steps leading to the prescription/formulation of provisional values of reproducibility precision. A similar approach has been proposed for the assessment of precision criteria in relation to the ISO 140-5 standard in 2015. [7]. The aim is to provide not only a reliable but also up-to-date criteria for the evaluation of repeatability and reproducibility limits in this field, particularly where there is not at all or very poor normative reference.

Table 1. Reproducibility Precision (SD_R), assigned values (AV) of sound absorption coefficient (αs) from AQUS-2012 – AQUS-2004 and values obtained for SD_R "pooled" (right column).

	AQUS-1- 2012		AQUS-2 - 2015		AQUS-3 - 2018		AQUS-4 - 2020		AQUS-5 - 2021		AQUS-6 - 2022		AQUS-7 - 2024		
Frequency	**p = 14**		**p = 13**		**p = 17**		**p = 15**		**p = 14**		**p = 16**		**p = 15**		
(Hz)	**SD_R**	**AV(α_s)**	**SD_R**	**AV(α_s)**	**SD_R**	**AV(α_s)**	**SD_R**	**AV(α_s)**	**SD_R**	**AV(α_s)**	**SD_R**	**AV(α_s)**	**SD_R**	**AV(α_s)**	**SD_R "pooled"**
100	0,027	0,10	0,022	0,04	0,028	0,06	0,024	0,12	0,018	0,03	0,026	0,06	0,014	0,04	**0,023**
125	0,067	0,19	0,024	0,07	0,033	0,09	0,038	0,20	0,018	0,05	0,024	0,07	0,019	0,05	**0,035**
160	0,068	0,33	0,021	0,10	0,025	0,11	0,026	0,29	0,020	0,08	0,022	0,11	0,016	0,08	**0,032**
200	0,053	0,52	0,024	0,14	0,032	0,16	0,037	0,39	0,022	0,15	0,023	0,14	0,025	0,13	**0,032**
250	0,075	0,76	0,020	0,20	0,041	0,22	0,045	0,49	0,022	0,23	0,018	0,17	0,033	0,19	**0,040**
315	0,079	0,89	0,030	0,30	0,035	0,31	0,040	0,59	0,025	0,36	0,029	0,24	0,048	0,28	**0,044**
400	0,095	0,99	0,044	0,48	0,049	0,42	0,044	0,67	0,034	0,51	0,049	0,30	0,081	0,40	**0,059**
500	0,060	1,06	0,054	0,63	0,039	0,55	0,037	0,76	0,037	0,69	0,034	0,38	0,075	0,61	**0,050**
630	0,074	1,09	0,051	0,74	0,052	0,67	0,043	0,82	0,049	0,83	0,047	0,47	0,078	0,83	**0,058**
800	0,062	1,07	0,051	0,84	0,049	0,76	0,050	0,85	0,062	0,92	0,036	0,56	0,060	1,00	**0,053**
1000	0,056	1,07	0,075	0,90	0,062	0,83	0,059	0,87	0,081	0,99	0,051	0,64	0,048	1,03	**0,062**
1250	0,055	1,03	0,063	0,94	0,055	0,86	0,048	0,87	0,075	0,98	0,065	0,70	0,045	0,96	**0,059**
1600	0,053	1,02	0,060	0,96	0,057	0,90	0,038	0,85	0,073	1,00	0,066	0,74	0,054	0,90	**0,058**
2000	0,057	1,01	0,052	0,97	0,043	0,90	0,052	0,85	0,079	1,01	0,070	0,79	0,056	0,87	**0,059**
2500	0,055	1,00	0,061	0,98	0,056	0,92	0,054	0,87	0,061	1,02	0,066	0,83	0,057	0,84	**0,059**
3150	0,055	0,99	0,064	0,98	0,059	0,93	0,076	0,89	0,057	1,01	0,057	0,86	0,061	0,84	**0,062**
4000	0,062	1,00	0,073	0,97	0,063	0,94	0,064	0,96	0,056	0,99	0,061	0,88	0,100	0,86	**0,070**
5000	0,073	0,99	0,076	0,97	0,066	0,96	0,047	1,00	0,075	1,01	0,061	0,89	0,061	0,87	**0,066**

5. RESULTS AND DISCUSSION

Once the seven rounds have been carried out (see Tab. 1), the assigned values obtained from the consensus of the participants, after rejection of the outliers, are presented for each frequency and each round, together with the corresponding standard deviation of reproducibility (SD_R), which shows a high consistency between the values of the measurable parameter over time. However, it should be noted that the sound absorption coefficient and the reproducibility precision seem to be strongly dependent on the type of material used as the PT test piece.

Therefore, after applying the statistical protocol for the calculation of PT results, the corresponding SD_R values were calculated, taken as an indication of the reliability of the interlaboratory comparison. A comparison of these SD_R values obtained at each measurement frequency for each PT round is presented to facilitate a graphical comparison over time (see Fig.1) with the estimated value of reproducibility precision (σ_{target}). The estimated value of reproducibility precision (σ_{target}) was calculated as a pooled standard deviation (SD_R" pooled") from the individual values of each independent PT round taking into account the number of participants (degrees of freedom) (see Tab.1) [8-9]. In addition, it is interesting to note that the SD_R values in the first (2012) and last (2024) round are more scattered at low and high frequencies compared to the majority of values in the remaining rounds, which are below the estimated target SD_R value (dark blue line). The causes of these higher SD_R values in the first PT Round (AQUS-1_2012) could be due to:

- Damage of PT ítems during transport
- Some participants did not fully comply with the instructions, in particular regarding the mounting of the sample in the reverberation room: the perimeter edge of the sample shall be sealed or covered with a acoustic reflective frame of rigid material according to Annex B point B.2 Type A mounting.

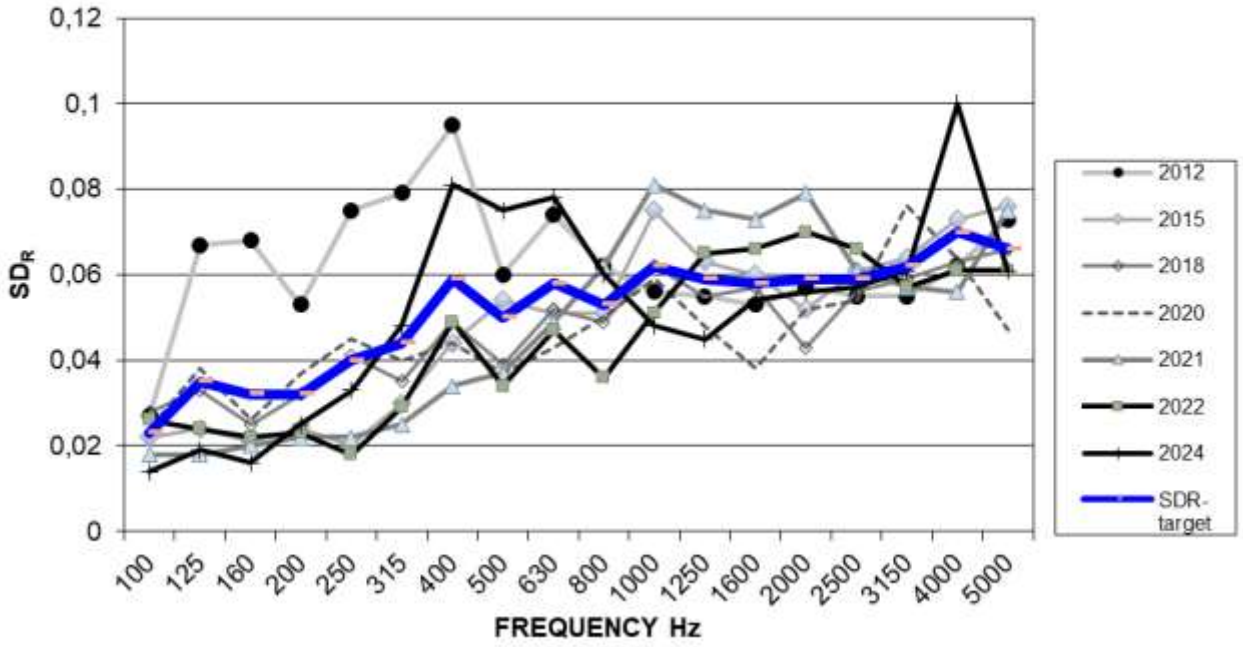


Figure 1. Comparison of standard deviation of reproducibility SD_R obtained in AQUS PT schemes (years 2012–2024) versus SD_R target (dark blue line)

The causes of these higher SD_R values in the last PT Round (AQUS-7_2024) could be due to:

- The material shows maximum absorption between the thirds of 630 and 1000 Hz. These absorption peaks are located differently by different laboratories and consequently there is maximum dispersion in this frequency range.
- Similarly, the material again shows a second absorption maximum around the 4000 Hz third, but not all laboratories clearly define this absorption peak. As a result, the dispersion in this octave third is very high. Some reverberation rooms, even if they meet the requirements of the standard, may lose sensitivity when measuring coefficient at high frequency.
- On the other hand, a slight permanent deformation may occur during transport due to crushing of the PT sample material plates. This crushing slightly alters the structure factor of the material, resulting in a slight change in the frequencies of maximum absorption in the range between 630 and 1000 Hz, and also at 4 kHz. This partly explains the higher dispersion of the SD_R values in the octave thirds shown.

6. CONCLUSIONS, PROPOSAL AND FUTURE OBJECTIVES

The next steps for the completion of the activities related to the present project should focus on developing of a collaborative study to assess the performance of the measurement method. This will allow for the establishment of precision guidelines based on the experience gained from

measurements conducted according to ISO 354. It is expected that the study will enable to assess if the proposed reproducibility values for each frequency (σ_{target}) are suitable in terms of minimum precision level to determine the standard deviation for proficiency assessment.
Furthermore, these prescribed values of precision should be verified regularly, as well as monitoring the practical conditions of application in such a way that the reproducibility values may also be used to verify the proper operation of test procedures of any laboratory involved in this scope of acoustic measurement.
Therefore, in this paper, we propose a practical approach to determine the reproducibility precision (σ_{target}) in the field of sound absorption measurements by evaluating historically relevant proficiency testing data according to ISO 354. Some points of interest that must be foreseen are related to both the applicability and practicability of the method since a collaborative trial requires substantial effort and should only be applied to methods that have received adequate prior testing. These values of the reproducibility precision (σ_{target}) will be used to assess the performance of participants in the next proficiency test AQUS-8 in 2026 for proving the goodness of this proposal.
It is honestly believed that this challenge is quite difficult to achieve, mainly because there are a large number of materials for acoustic testing with quite different characteristics and values of sound absorption coefficient (αs), without being able to make a suitable catalogue of SD_R target for each one. However, to the best of our knowledge, this is the first attempt to determine the reproducibility precision (σ_{target}) using a large experimental weight of data collected over a decade from 2012 to 2024.
The aim is to provide not only a reliable but also up-to-date criteria for the evaluation of repeatability and reproducibility limits in this field, particularly where there is not at all or very poor normative reference. In this way, future participants could have some kind of reference values for the evaluation of precision criteria in this field.

7. ACKNOWLEDGMENTS

We are very grateful to Prof. Juan Sancho of the Universidad Politécnica de Madrid for his technical and excellent support over the last few years, which we have greatly appreciated.

8. REFERENCES

[1] ISO 354:2003 - Acoustics — Measurement of sound absorption in a reverberation room. ISO, Geneva

[2] ISO 11654:1997 - Acoustics — Sound absorbers for use in buildings - Rating of sound absorption. ISO, Geneva

[3] ISO 17025:2017 - General requirements for the competence of testing and calibration laboratories. ISO, Geneva.

[4] ISO 17043:2023 - Conformity assessment — General requirements for the competence of proficiency testing providers. General requirements for the competence of testing and calibration laboratories. ISO, Geneva.

[5] ISO 5725-2:2019 - Accuracy (trueness and precision) of measurement methods and results—Part 2: Basic method for the determination of repeatability and reproducibility of a standard measurement method. ISO, Geneva

[6] ISO 13528:2022 - Statistical methods for use in proficiency testing by interlaboratory comparisons. ISO, Geneva

[7] Martinez, J.L., Trujillo, J.A., Silvan, J. Rosario, P, Sancho, J. "State of field measurement of facade sound insulation in buildings: evaluation of proficiency testing data according to ISO 140-5:1998", *Accred Qual Assur*. 20:297-303, 2015

[8] Miller JC, Miller JN (1988) - *Statistics and Chemometrics for analytical chemistry*. Ellis Horwood Limited, Chichester, 5th edition , 2005

[9] Coˆte´ I, Robouch P, Dumas P, Pedneault M et al. "Determination of the standard deviation for proficiency assessment from past participants performance". *Accred Qual Assur* 17:389–393, 2012

DOI: 10.61782/fa.2025.0060

FORUM ACUSTICUM EURONOISE 2025

ACOUSTIC CHARACTERISTICS OF AN HYDROPONIC MATERIAL

Gino Iannace [1*] **Antonella Bevilacqua**[2] **Amelia Trematerra** [1]
Giovanni Amadasi [3]
[1] Department of Architecture and Industrial Design, University of Campania L. Vanvitelli, Italy
[2] University of Parma, Italy
[3] SCS-ControlSys—Vibro-Acoustic, 35011 Padova, Italy

ABSTRACT

Green materials developed in recent decades have found numerous applications. These materials are designed to be recycled after their primary use, reducing waste and environmental impact. Hydroponic systems, widely used for growing plants without direct soil use, often employ alternative sublayers such as expanded clay, glass wool, perlite, paper, hemp and similar materials immersed in water. This study focuses on wheat grains planted on porous sublayers, including hemp, paper, wood chips, triturated sugarcanes from river water, oak leaves, layers of grass. As the wheat plants grew, their roots penetrated these porous materials, forming a single, compact material with a rigid skeleton. In the second stage, the resulting material was dried to thicknesses of 5 and 10 cm and tested using an impedance tube. Acoustic absorption at normal incidence was measured. The results indicate that hydroponic materials have excellent acoustic absorption properties, making them suitable for use in acoustic applications.

Keywords: *Hydroponic, acoustic measurements, absorption coefficient, impedance tube; sustainable constructions.*

1. INTRODUCTION

Hydroponics is a method of growing plants with minimal soil and water. Hydroponic systems enable plants cultivation without direct reliance on soil. This technique uses substrates made from alternative materials, such as expanded clay, rock wool, perlite, paper, hemp, wood chips and natural wool, combined with nutrient solutions or water [1]. Hydroponic cultivation is being studied as an alternative to traditional agricultural production, particularly for growing wheat or other crops while minimizing soil and water usage. One major advantage of hydroponic systems is their ability to produce crops in the absence of soil-borne diseases and pests, thereby reducing the need for chemical pesticides [2]. Additionally, hydroponic systems allow for significantly faster crop production compared to traditional soil-based farming. Today, hydroponic systems are mainly developed to provide animal feed as an alternative to synthetic or chemical processed options. Furthermore, hydroponic farming is being explored as a potential food source for future space missions [3]. In these contexts, plants are grown to provide food for space missions or for potential future colonies on the Moon or Mars. Studying hydroponic systems for human nutrition also offers a solution to challenges related to food production in the context of climate variability, population growth, and freshwater depletion. In the future, hydroponic crops could be used in regions with limited natural resources or extreme weather conditions. Since the Middle Ages, hydroponic cultivation has been a part of Christian Easter traditions. It has historically been used to grow plants for decorating church altars during Easter, as shown in Figure 1. During the Easter period, the faithful would prepare jute sheets on which they sowed wheat, watering them every evening. Within a few weeks, the wheat grew to about 20 cm in height, adorning church altars.

[*] ***Corresponding author***: gino.iannace@unicampania.it.
Copyright: *©2025 First author et al. This is an open-access article distributed under the terms of the Creative Commons Attribution 3.0 Unported License, which permits unrestricted use, distribution, and reproduction in any medium, provided the original author and source are credited.*



Figure 1. Plants used to decorate church altars during the Easter period.

2. MATERIALS AND METHODS

The hydroponic material model was designed to create layers of sound-absorbing materials. In this study, wheat was selected as the primary plant, although other grains such as corn, chickpeas, and beans could also be used. The germinating seed produces a plant above the surface, while the roots penetrate the underlying porous layer, forming a rigid network that compacts the material [4].

The objective of this research is to develop plant-based material layers using hydroponic systems. Layers of varying thicknesses were developed using different porous substrates, which served as growth media for wheat grains [5]. The grains were cultivated at room temperature and watered daily with small amounts of water. The material was housed in food-grade plastic containers and placed in an outdoor environment, where temperatures ranged from about 18°C at night to 35°C during the day.

The porous substrates used include hemp, shredded paper, wood chips, shredded river canes. Wheat grains were germinated on these porous layers, and over a two-week period, the plants grew to a height of 20 cm. During this process, the roots penetrated the porous substrates, forming a compact material with a rigid internal structure. Once dried, the water content was completely removed, yielding a material with promising acoustic properties. Various acoustic tests were performed on the resulting green tiles, which were composed of different porous sublayers [6]. Samples with thicknesses ranging from 5 cm to 10 cm were prepared for testing. The primary aim of this research is to assess the sound absorption coefficient of the tiles at different thicknesses. Measurements were performed using an impedance tube, which determines the sound absorption coefficient at normal incidence over a frequency range of 100 Hz to 2 kHz. The tests were conducted in accordance with the ISO 10534-2 standard [7]. The impedance tube used has the following features: internal diameter of 10 cm (corresponding to an upper frequency limit of 2 kHz), a length of 56 cm, as shown in Figure 2, and two microphones placed 10 cm apart, allowing measurements starting from 100 Hz.



Figure 2. Impedance tube used for measuring the absorption coefficient.

The wheat was sown on a layer of loose granular material. As the roots developed, they formed a rigid skeletal structure, which served as the basis for subsequent sound absorption measurements. Figure 3 shows the grain stalks that grow as the seeds on this material.



Figure 3. Germination of wheat grains.

Figure 4 shows the grain seeds that have grown on the loose granular material to give rise to the grain stalks.

Once the hydroponic material is fully grown, it is dried to create a new type of sound-absorbing material, whose acoustic characteristics are the focus of this study. The resulting material features a rigid skeletal structure formed by the roots, which have penetrated the loose granular substrate during growth. Figure 5 displays the final hydroponic material, showcasing its rigid root-based structure. This drying process results in a completely natural material suitable for acoustic applications.



Figure 4. Grain seeds were grown on the loose granular material, giving rise to grain stalks.

The sound absorption performance of the material varies depending on the type of porous substrate used. The following figures present the absorption coefficients for each material tested:

- Figure 6: absorption coefficient of hemp-based substrate.
- Figure 7: absorption coefficient of wood chips substrate.
- Figure 8: absorption coefficient of triturated paper substrate.
- Figure 9: absorption coefficient of triturated cane substrate.



Figure 5. New hydroponic material with a rigid substrate structure.

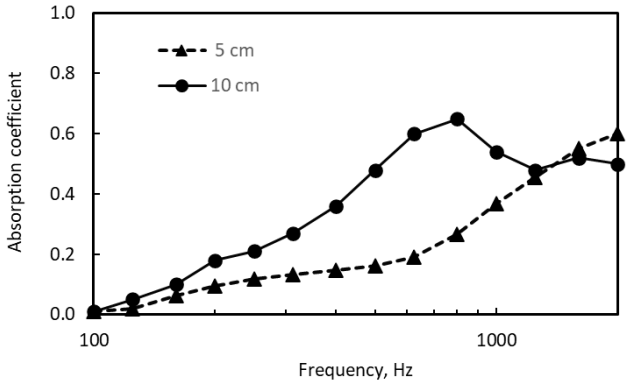


Figure 6. Absorption coefficient of hemp-based substrate.

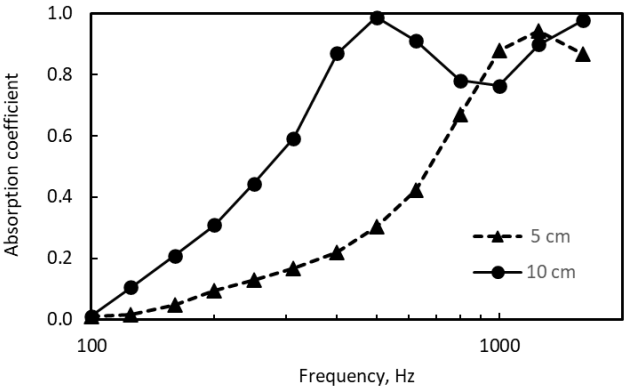


Figure 7. Absorption coefficient of wood chips substrate.

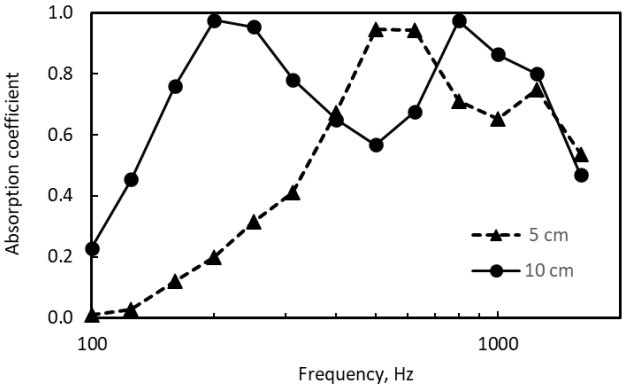


Figure 8. Absorption coefficient of triturated paper substrate.

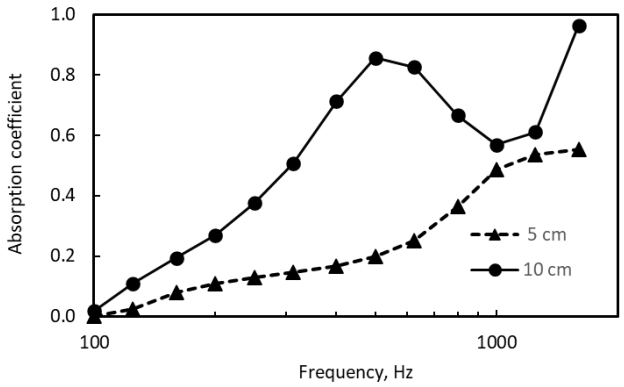


Figure 9. Absorption coefficient of triturated canes substrate.

3. DISCUSSION

For hemp-based substrate samples, when composed of 5 cm thickness, the highest values of absorption around 0.55-0.60 are observed at 2 kHz, while for 10 cm, the highest values are around 800 Hz of the same magnitude. However, the absorption performance at low frequencies remains close to zero [8]. In the case of wood chips, the maximum peak performance is centered on 1600 Hz for a 5 cm thickness and on 630 Hz for a 10 cm thickness. These peak values are around 0.95 and 1.0, which is the best performance. When the substrate consists solely of triturated paper, the absorption coefficients are highly effective, reaching a value of 1.0 at 500 Hz for a 5 cm thickness and at 250 Hz and 800 Hz for a 10 cm thickness. This is significantly remarkable since the absorption at low frequencies is always a challenge for commercial panels, unless their thickness is considerably high. When the substrate consists of triturated canes, the significant absorption is registered with the 10 cm sample, reaching peak values of 0.86 at 625 Hz and 0.96 at 2000 Hz.

4. CONCLUSIONS

The sustainable concept of preserving soil for agriculture can be effectively explored through hydroponic systems. Up to date, hydroponic systems have not been widely used for interior design or architectural finishes. However, this study demonstrates the functionality of green tiles in terms of absorption. A significant change in architectural design is possible by adopting strategies that reduce CO2 emissions and incorporate local, recycled materials aligned with the sustainability principles. Future research studies will focus on applying these green tiles to real case studies by measuring the reverberation before and after installation [9-10].

5. ACKNOWLEDGMENTS

This research was financially supported by the Bio-Acouis project. Bio-Acouis project has received funding through the European Union's Horizon 2021 research and innovation programme under grant agreement No: 101086325.

6. REFERENCES

[1] J.P. Arenas, M.J. Crocker: "Recent trends in porous sound absorbing materials for noise control", *Sound Vib*, 44(7), pp. 12–17, 2010.

[2] G. Iannace, G. Ciaburro, L. Guerriero, A. Trematerra, "Use of cork sheets for room acoustic correction". Journal of Green Building 2020; 15 (2). doi: https://doi.org/10.3992/1943-4618.15.2.45.

[3] K.H. Hasenstein, N.M. Miklave, "Hydroponics for plant cultivation in space – a white paper". Life Sciences in Space Research, (43), pp. 13-21, 2024.

[4] M. Pervaiz, M. Sain: "Carbon storage potential in natural fiber composites", Resour. Conserv. Recy., 39, pp. 325–340, 2003.

[5] Busra S, Giuseppe C, Gino I, Mustafa O. "Preparation of PPA based composite reinforcing with glass beads and clays: Investigation of sound absorbing". Building Acoustics. 2024; doi:10.1177/1351010X241254956.

[6] V. Puyana-Romero, J.S.A. Chuquín, S.I.M. Chicaiza, G. Ciaburro. "Characterization and Simulation of Acoustic Properties of Sugarcane Bagasse-Based Composite Using Artificial Neural Network Model". Fibers 2023 https://doi.org/10.3390/fib11020018.

[7] ISO 10534-2. Acoustics- Determination of Sound Absorption Coefficient and Impedance in Impedance Tubes Part 2: Transfer-function Method. Geneve, Switzerland, 1998.

[8] L. Tronchin, A. Farina, A. Bevilacqua, F. Merli, P. Fiumana, "Comparison failure and successful methodologies for diffusion measurements undertaken inside two different testing rooms", Appl. Sci., 11, 10523, 2021.

[9] G. Iannace, G. Ciaburro, A. Trematerra, "Modelling sound absorption properties of broom fibers using artificial neural networks", Applied Acoustics, https://doi.org/10.1016/j.apacoust.2020.107239.

DOI:

Main theme: A10 Materials and Metamaterials

Session A10.08 Modeling acoustic wave propagation in viscothermal structures, including porous materials

Chair(s): T. Bravo, M. Nolan, L. Jaouen, C. Maury

DOI: 10.61782/fa.2025.0180



FORUM ACUSTICUM
EURONOISE 2025

BOUNDARY ELEMENT METHOD WITH VISCO-THERMAL LOSSES: DEVELOPMENT, IMPROVEMENTS AND APPLICATIONS

Vicente Cutanda Henriquez[1*]
[1] Centre for Acoustic-Mechanical Microsystems
Department of Electrical and Photonics Engineering
Technical University of Denmark
Ørsteds Plads, Building 352, Kongens Lyngby, 2800 Denmark

ABSTRACT

Sound waves are affected by viscous and thermal losses, which manifest mainly inside a thin region close to the domain boundaries, the boundary layers [1,2]. Losses at boundaries cannot usually be neglected when modelling small or intricate devices, such as micro-transducers and metamaterials [3]. Over the last years, several numerical methods have been proposed and implemented to include viscothermal losses. Some methods assume restrictive hypotheses, as in the cases of the low reduced frequency (LRF) model by Beltman or the boundary layer impedance (BLI) reported by Berggren [4,5]. A full implementation using the Finite Element Method (FEM) was described by Malinen et al. and later included in commercial FEM software [6]. The Boundary Element Method (BEM) has also been adapted by Cutanda Henríquez and other authors as a full implementation of viscothermal losses, and it is employed as a research tool originally based on the open-source software OpenBEM [7,8,9]. This contribution summarizes the work done on the BEM with losses. Current work on the method will be described.

Keywords: *Boundary Element Method, Viscous and thermal losses.*

[*] ***Corresponding author***: *vcuhe@dtu.dk.*
Copyright: *©2025 Vicente Cutanda Henriquez. This is an open-access article distributed under the terms of the Creative Commons Attribution 3.0 Unported License, which permits unrestricted use, distribution, and reproduction in any medium, provided the original author and source are credited.*

1. INTRODUCTION

In the past two-three decades, the state of the art regarding the modeling of acoustics with viscous and thermal losses has seen a variety of new approaches, as described in the abstract. Several of these modeling techniques have been implemented in commercial software [10].
However, the user is left with a choice between methods with restrictive hypotheses such as the low reduced frequency model and the boundary layer impedance [4,5], or full methods with the only restrictions of linearity and no flow, existing in FEM and BEM [6,7,8,9]. The latter methods have the drawback of a heavy computational burden which places many relevant simulation problems almost or totally out of reach. Problems involving relatively large setups, high frequencies or intricate geometries with narrow passages cannot be treated with methods with restrictions [11,12].

2. BEM WITH LOSSES: REDUCED METHODS

There has been research in the past few years towards reducing the computational burden of the BEM with visco-thermal losses [13-14]. The BEM has the advantage of being based on a discretization of the domain boundary, not the domain itself as in FEM. This means that the very thin boundary layers do not need to be represented with tiny elements as is the case in the full FEM with losses. However, the BEM presents full, frequency dependent matrices that thwart its initial reduced nature. Ref. [13] presents an improved version of the BEM with losses in [7,9], where the coordinate changes have been simplified and the system of equations reduced to the same size of the lossless BEM. Ref. [14] introduces a Model Order Reduction (MOR) technique to a BEM implementation

with losses, this time based on the more simplified Boundary Layer Impedance.
New research is ongoing with the aim of extending MOR to full BEM with losses, possibly combining it with fast multipole methods.

3. CONCLUSIONS AND FUTURE TRENDS

There is a need for fast, reliable and not restricted modeling techniques that can deal with problems yet unreachable, such as intricate metalmaterials, minute transducers and acoustic devices such as hearing aids. Numerical optimization also needs such fast simulations to run and would open losses-controlled devices to numerical design.
The future probably belongs to a combination of advanced MOR methods and a yet more physics-oriented treatment of losses. Brute-force discretizations such as in the full FEM, or full BEM, with losses are inefficient. The BLI approach makes use of a simplified description of the boundary layers to reduce them to boundary condition. The LRF takes advantage of the behavior of the fluid within certain geometries. In this line, we need methods that cleverly employ the physical behavior of the fluid in an efficient description with less restrictive constraints [10].

4. REFERENCES

[1] G. Kirchhoff, (1868). Ann. d Phys. 134, 177.

[2] Pierce, A. D. (1981). Acoustics. An introduction to its physical principles and applications . McGraw-Hill.

[3] Cutanda Henriquez, V., García-Chocano, V. M., & Sánchez-Dehesa, J. (2017). Viscothermal Losses in Double-Negative Acoustic Metamaterials. Physical Review Applied, 8(1), 014029. https://doi.org/10.1103/PhysRevApplied.8.014029

[4] Beltman, W. M. (1999). Viscothermal wave propagation including acousto-elastic interaction, part I: Theory. Journal of Sound and Vibration, 227(3), 555–586. https://doi.org/10.1006/jsvi.1999.2355

[5] M. Berggren, A. Bernland, D. Noreland, Acoustic boundary layers as boundary conditions, J. Comput. Phys. 371 (2018) 633–650, http://dx.doi.org/10.1016/j.jcp.2018.06.005 .

[6] Malinen, M., Lyly, M., Råback, P., Kärkkäinent, A., & Kärkkäinen, L. (2004). A finite element method for the modeling of thermo-viscous effects in acoustics. Eccomas 2004 - European Congress on Computational Methods in Applied Sciences and Engineering.

[7] V. Cutanda Henriquez, P.M. Juhl, An axisymmetric boundary element formulation of sound wave propagation in fluids including viscous and thermal losses, J. Acoust. Soc. 134 (5) (2013) 3409–3418, http://dx.doi.org/10.1121/1.4823840 .

[8] V. Cutanda Henriquez, P.M. Juhl, OpenBEM – an open source Boundary Element Method software in acoustics, in: INTER-NOISE and NOISE-CON Congress and Conference Proceedings, 2010, pp. 5873–5882.

[9] V. Cutanda Henriquez, P. Risby Andersen, A three-dimensional acoustic boundary element method formulation with viscous and thermal losses based on shape function derivatives, J. Theor. Comput. Acoust. 26 (2018) 1850039, http://dx.doi.org/10.1142/S2591728518500391.

[10] Henriquez, V. C. (2024). Numerical modeling of acoustic visco-thermal losses: simplified implementations and their limitations. Proceedings of Inter-Noise 2024.

[11] M.J. Cops, J.G. McDaniel, E.A. Magliula, D.J. Bamford, M. Berggren, Estimation of acoustic absorption in porous materials based on visco-thermal boundary layers modeled as boundary conditions, J. Acoust. Soc. 148 (3) (2020) 1624–1635, http://dx.doi.org/10.1121/10.0001959 .

[12] P.R. Andersen, V. Cutanda Henriquez, N. Aage, On the validity of numerical models for viscothermal losses in structural optimization for micro-acoustics, Journal of Sound and Vibration, vol. 547 (2022), 117455. https://doi.org/10.1016/j.jsv.2022.117455 .

[13] Preuss, S., Paltorp, M., Blanc, A., Henríquez, V. C., & Marburg, S. (2023). Revising the Boundary Element Method for Thermoviscous Acoustics: An Iterative Approach via Schur Complement. *Journal of Theoretical and Computational Acoustics*, *31*(4), 2350015. https://doi.org/10.1142/S2591728523500159

[14] Paltorp, M., Henriquez, V. C., Aage, N., & Andersen, P. R. (2024). A Reduced Order Series Expansion for the BEM Incorporating the Boundary Layer Impedance Condition. *Journal of Theoretical and Computational Acoustics*, *32*(02), Article 2350012. https://doi.org/10.1142/S2591728523500123

DOI: 10.61782/fa.2025.0533

FORUM ACUSTICUM EURONOISE 2025

LOW-DRAG RAINBOW-TRAPPING FILTERS FOR BROADBAND SOUND DISSIPATION IN A LOW-SPEED DUCTED FLOW

Cedric Maury[1*] **Teresa Bravo**[2] **Fawad Ali**[1]
Daniel Mazzoni[3] **Muriel Amielh**[3]
[1] Laboratory of Mechanics and Acoustics (LMA CNRS), Marseille, France
[2] Institute for Physical and Information Technologies (ITEFI), Spanish National Research Council (CSIC), Madrid, Spain
[3] Institute of Research on Non-Equilibrium Phenomena (IRPHE CNRS), Marseille, France

ABSTRACT

Rainbow-trapping filters (RTFs) have mostly been designed with closed-end terminations to achieve near-unit broadband absorption under acoustic excitation, with applications as shallow wall-treatments in building acoustics or short anechoic terminations. The current study considers opened rib-designed RTFs being traversed by a low-speed grazing flow. The double objective is to design an enhanced silencer able to achieve broadband sound dissipation, e.g. with minute reflection and transmission of the incident wave, while ensuring a low friction factor. A key element is the lining of the interface between the RTF cavity mouths and the flow duct. Micro-perforated panels (MPP) have been chosen that provide holes diameter – holes pitch parameters optimized to determine maximal total dissipation or minimal friction factor. MPPs also contribute to enhance slow sound effects towards lower frequencies than unlined RTFs. Finite Elements (resp. Reynolds Averaged Navier Stokes k-ε) models have been developed to produce acoustic (resp. aerodynamic) design charts with respect to the MPP parameters. A set of MPP parameters has been found that maximizes the aeroacoustic performance of the MPP-RTF silencer. It has been validated against low-speed wind-tunnel experiments that showed an adverse effect of downstream propagation conditions on the wideband dissipative performance of the MPP-RTF.

Keywords: *broadband silencers, micro-perforated panels, aeroacoustic metamaterials, rainbow-trapping filters.*

1. INTRODUCTION

The emergence of acoustic metamaterials has led to the development of sub-wavelength perfect absorbers whose internal geometry can be tailored to achieve the required wideband and/or low-frequency performance [1]. Aeroacoustic, so-called ventilated, metamaterials have been much less studied [2] although their design is highly motivated by the development of soundproof natural ventilation systems or silencers for air-conditioning or automotive exhaust systems.

The current study focuses on the acoustic and aerodynamic properties of axially-graded fully-opened aeroacoustic metamaterials traversed by a low-speed grazing flow. One considers rib-designed rainbow trapping filters with progressive increase of the cavity depths whose mouth is shielded from the flow by (micro-)perforated panels. Insights into the acoustic and drag performance of such silencers under a low-speed flow are provided by analytical and numerical modellings in Sec. 2 and 3, respectively. Experimental verification of these effects are examined in Sec. 4 from low-speed wind-tunnel experiments.

[*] ***Corresponding author***: *cedric.maury@centrale-marseille.fr*

Copyright: *©2025 Maury et al. This is an open-access article distributed under the terms of the Creative Commons Attribution 3.0 Unported License, which permits unrestricted use, distribution, and reproduction in any medium, provided the original author and source are credited.*

2. AEROACOUSTIC MODELLING

2.1 MPP-shielded rainbow trapping filters

Rainbow trapping filters (RTF) are retarding silencers of rectangular or cylindrical cross-sections, made up of a set of N sidebranch outer cavities of increasing depths $D(x)$ such that

$$D(x)=\frac{H}{2}\left[1-\frac{(-x)^m}{L^m}\right], \qquad (1)$$

with $-L\le x\le 0$, L and H the duct length and height, respectively and $m>0$. One assumes that the RTF silencer is inserted in a duct with a square cross-section duct of height (and width) H. A cross-sectional view of the RTF is sketched in Fig. 1. m is the rate of increase of the cavity depths and is determinant to achieve impedance matching condition over a broad bandwidth at the inlet of the silencer. In the limit of $m\to\infty$, one gets a locally-reacting expansion chamber while $m=0$ corresponds to a rigid rectangular duct without silencer.

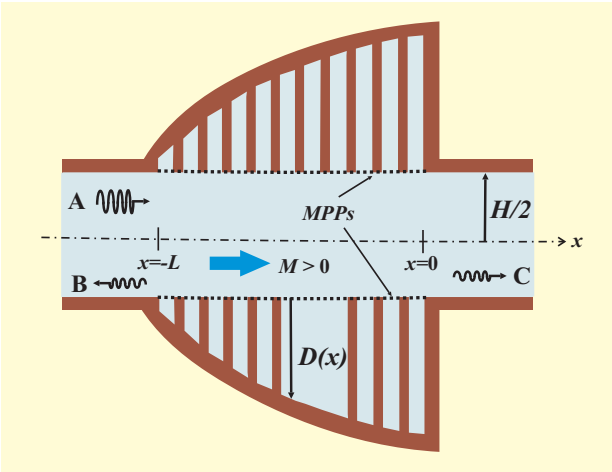


Figure 1. Sketch of a rib-designed rainbow trapping silencer shielded from a low-speed grazing flow of Mach number M (blue arrow) by a micro-perforated panel interface; an incident sound wave propagates along the axial flow.

The power-law increase of the cavity depths when x varies from $-L$ to 0 results in a progressive increase of the wall-admittance monitored by the air cavity stiffness. This produces a slow sound effect [3] with progressive decrease of the acoustic phase speed from c_0 at $x=-L$ down to $c_0/\sqrt{3}$ at $x=0$ where c_0 is the sound speed. The acoustic functionality of a RTF silencer is thus to trap the incident acoustic wave, whose amplitude is denoted A in Fig. 1, and fully dissipate its energy by visco-thermal effects along the inner walls of the cavities. It results in minute reflected and transmitted wave amplitudes, denoted B and C respectively, over the efficiency range of the RTF muffler. If used in transportation sectors, little reflection avoids the occurrence of thermo-acoustic instabilities triggered by acoustic waves back-reflected towards the combustion chamber [4] whereas small transmission contributes to lower noise emissions by thermal engines.

In practice, the entrances of the silencer cavities are shielded from the flow by a perforated or micro-perforated panel (MPP), as sketched in Fig. 1, to prevent clogging by dusts or particle residues, but also to limit the aerodynamic pressure drop when the flow traverses the fully-opened silencer. It will be seen in Sec. 3 that MPPs also have an acoustic functionality, namely to extend the efficiency range of RTF silencers towards the low frequency range.

2.2 Transfer matrix modelling

2.2.1 MPP transfer impedance

The overall transfer impedance, Z_{MPP}, for a MPP with circular holes of diameter d_h and thickness t_h is given by the following expression [5,6] in presence of a low-speed flow with grazing Mach number M

$$\frac{Z_{\text{MPP}}}{\sigma}=\frac{\mathrm{i}\omega\rho_0 t_h}{\sigma}\left[1-\frac{2}{k_h\sqrt{-\mathrm{i}}}\frac{J_1\left(k_h\sqrt{-\mathrm{i}}\right)}{J_0\left(k_h\sqrt{-\mathrm{i}}\right)}\right]^{-1} + \frac{\mathrm{i}\omega\rho_0}{\sigma}\frac{8d_h}{3\pi}F_M + \frac{4}{\sigma}\sqrt{\frac{\eta\rho_0\omega}{2}}+\frac{Z_0}{\sigma}K|M|, \qquad (2)$$

with σ the perforation ratio, η the dynamic viscosity of the air, $k_h=(d_h/2)/r_{\text{visc.}}(\omega)$, the perforate constant, e.g. the ratio of the MPP holes radius to the viscous boundary layer thickness, $r_{\text{visc.}}(\omega)=\sqrt{\eta/\rho_0\omega}$, ρ_0 the air density, ω the angular frequency and $Z_0=\rho_0 c_0$ the air

characteristic impedance. Eq. (2) is valid for linear acoustic regimes and for MPPs with a low perforation ratio, typically lower than 2%, for hole interaction effects to be negligible. Inner viscous dissipation and inertial effects within the MPP holes are accounted for within the first term of Eq. (2) where J_1 and J_0 are Bessel functions of the first kind and orders 1 and 0, respectively. The second term describes the added mass effect at the inlet/outlet of the MPP holes. It is reduced by grazing flow effects, all the more than the flow speed increases, by a correction factor $F_M = \left[1+\left(12.6\,|M|\right)^3\right]^{-1}$. The third term in Eq. (2) accounts for the added resistance at the MPP holes inlet and outlet while the fourth term describes the excess resistance induced at the MPP inlet by the grazing flow. It increases the MPP resistance by $K|M|Z_0/\sigma$, with the value $K=0.15$ educed for $|M|<0.15$ [6].

2.2.2 Transfer matrix model

Assuming plane wave propagation in the duct and in the cavities, an overall transfer matrix can be defined between the inlet ($x=-L$) and outlet ($x=0$) of the MPP-RTF silencer as the following product

$$\mathbf{T}=\prod_{n=1}^{N}\mathbf{T}_n=\begin{bmatrix}T_{11} & T_{12}\\ T_{21} & T_{22}\end{bmatrix}, \tag{3}$$

between the elementary transfer matrices $\mathbf{T}_n$ that relate the acoustic pressure and volume velocity fields [7] across the n$^{\text{th}}$ MPP-cavity-rib units. Each elementary transfer matrix results from the product, $\mathbf{T}_n=\mathbf{T}_d\,\mathbf{T}_t\,\mathbf{T}_{\text{cav},n}$, with $\mathbf{T}_d$ (resp. $\mathbf{T}_t$) the propagating matrices over the cavity width d (resp. the rib thickness t) and $\mathbf{T}_{\text{cav},n.}$ a matrix that describes the wall admittance effect of the n^{th} MPP-cavity. Assuming $\mathrm{e}^{\mathrm{j}\omega t}$ time-dependence, each propagating matrix $\mathbf{T}_w$ reads

$$\mathbf{T}_w=\mathrm{e}^{-\mathrm{j}Mkw}\begin{bmatrix}\cos(kw) & \mathrm{j}y_0^{-1}\sin(kw)\\ \mathrm{j}y_0\sin(kw) & \cos(kw)\end{bmatrix}, \tag{4}$$

with $w=d,t$ the length of each duct unit traversed by a flow with bulk Mach number M, $S=H^2$ the duct cross-sectional area and $y_0=S/Z_0$. The duct wavenumber k in presence of a uniform low-speed flow is given by $k=\left(k_0-\mathrm{j}\mathrm{Fr}M/2H\right)/\left(1-M^2\right)$ in which $k_0=\omega/c_0$. $\mathrm{Fr}=0.0072+0.612\,\mathrm{Re}^{-0.35}$ ($\mathrm{Re}<4.10^5$) is the Froude friction factor that accounts for the dispersion induced by the turbulent flow, and $\mathrm{Re}=MHZ_0/\eta$ is the flow duct Reynolds number.

Coupling between the ducted flow and the nth MPP-cavity is described by the transfer matrix [7]

$$\mathbf{T}_{\text{cav},n}=\frac{1}{1+2MY_{\text{cav},n}y_0}\times\begin{bmatrix}1+MY_{\text{cav},n}y_0 & M^2Y_{\text{cav},n}^2y_0^2\\ Y_{\text{cav},n} & 1+MY_{\text{cav},n}y_0\end{bmatrix}, \tag{5}$$

with $Y_{\text{cav},n}$ the local sidebranch volume admittance of the n^{th} MPP-cavity. It reads $Y_{\text{cav},n}=S_{\text{cav}}\,y(x_n)/Z_0$ with $S_{\text{cav}}=2Hd$ the cavities entrance area and x_n the axial location of the n^{th} sidebranch. The specific admittance is calculated as $y(x_n)=\left[Z_{\text{MPP}}/(Z_0\sigma)-\mathrm{j}\cot(k_0'x_n)\right]^{-1}$ with Z_{MPP}/σ given by Eq. (2) and k_0' a complex frequency-dependent wavenumber that accounts for visco-inertial and thermal effects over each cavity wall following the Johnson-Champoux-Allard-Lafarge model [8].

Assuming that the duct outlet ($x\to+\infty$) is infinite, e.g. there are no back-transmitted wave, as seen in Fig. 1, the following left reflection (resp. left-to-right transmission) coefficients r_{11} (resp. t_{12}) are obtained

$$\begin{cases}r_{11}=\dfrac{(T_{11}+y_0T_{12})-(T_{21}+y_0T_{22})}{(T_{11}+y_0T_{12})+(T_{21}+y_0T_{22})}\\ t_{12}=\dfrac{1+r_{11}}{T_{11}+y_0T_{12}}\end{cases}. \tag{6}$$

On can then deduce the power dissipated by the MPP-RTF silencer, namely $\eta=1-\rho-\tau$ with $\tau=|t_{12}|^2$ the transmission coefficient and $\rho=(1-M)^2|r_{11}|^2/(1+M)^2$ the convected reflection coefficient. The transmission loss (TL) is defined as $\mathrm{TL(dB)}=-10\log_{10}(\tau)$.

3. ACOUSTIC PROPERTIES OF A MPP-RTF

Simulations have been carried out to examine the influence of the MPP holes diameter and flow speed on the

acoustical performance of a MPP-RTF silencer. They have been achieved using the cost-efficient transfer matrix model presented in Sec. 2.2.2. This model has been validated in the no-flow case against finite element visco-thermal acoustic simulations [3], but also against experiments, as shown in Sec. 5.

One considers a MPP-RTF cubic silencer of length $L = 0.15$ m, of square cross-section of height and width $H = W = L$, composed of $N = 15$ cavities of width $d = 7$ mm separated by ribs of thickness $t = 3$ mm. Axial variations of the cavity depths follow Eq. (1). The cavity mouths are covered by a MPP of thickness $t_h = 0.5$ mm, of center-to-center separation $s_h = 5$ mm between the holes whose diameter has been varied to assess its effect on the silencer performance.

3.1 Influence of the MPP holes diameter

Figure 2 shows variations of the fraction of incident power dissipated, reflected and transmitted by MPP-RTF silencers when decreasing the MPP holes diameter from 0.9 mm down to 0.2 mm while keeping a constant holes pitch set to 5 mm. This corresponds to a decrease of the perforation ratio from 2.54% to 0.13%. The performance of the unshielded RTF silencer is also shown. It exhibits a near-unit dissipation plateau, minute reflection and little transmission as from 1 kHz up to the duct cut-on frequency 1140 Hz. Shielding the RTF by a MPP with 0.9 mm holes diameter significantly downshifts the onset of high performance from 1 kHz down to 650 Hz while enlarging by a factor 3.5 the efficiency range of the silencer, that now extends from 650 Hz to 1140 Hz. Over this range, the dissipation exceeds 0.9 and the reflection (resp. transmission) stays below 0.02 (resp. 0.08) respectively. This translates into a TL between 11dB and 18 dB, as shown in Fig. 3. This is due to increased reactance brought by the micro-perforations to the RTF cavity mouths whose resonances are still able to merge due to the added resistance.

Further decreasing the MPP holes diameter increases the extra inertial and resistive effects brought by the MPP holes to the silencer. As observed in Fig. 2, it results in a progressive downshift of the silencer efficiency range towards the low frequency range. It is accompanied by a decrease (resp. increase) of the maximum dissipation (resp. minimum transmission) values, as the holes diameter decreases.

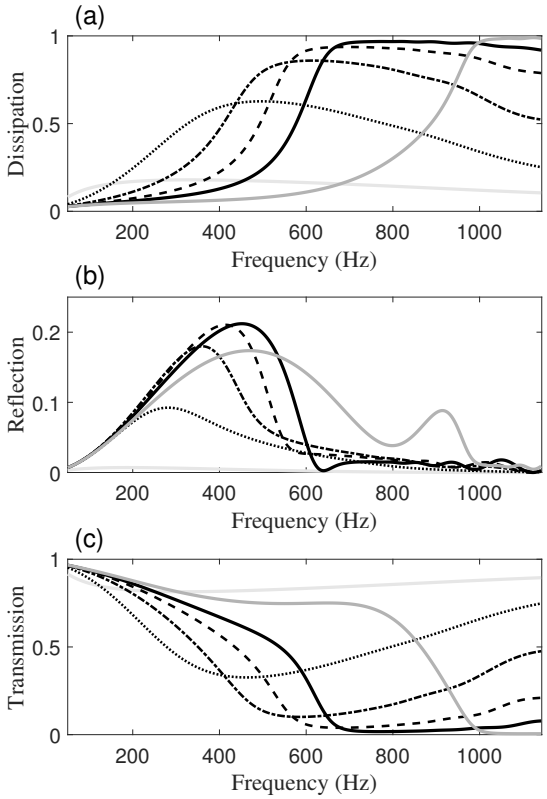


Figure 2. Influence of the MPP holes diameter on the dissipation (a), reflection (b) and transmission (c) coefficients of a MPP-RTF silencer in the no-flow case when decreasing the MPP holes diameter d_h (0.9 mm, plain black; 0.7 mm, dashed black, 0.5 mm, dash-dotted black; 0.4 mm, dotted; 0.2 mm, light grey) and without MPP (plain grey).

Note that variations of the MPP properties hardly influence the minute reflection properties of the MPP-RTF silencer. As for the largest holes diameter, low reflections are due to high dissipation within the cavities. They are due to increased transmission when the holes diameter increases. In the limit of very low perforation ratio (0.13%) with ultra-small holes diameters, almost full transmission is achieved with a TL lower than 1 dB.

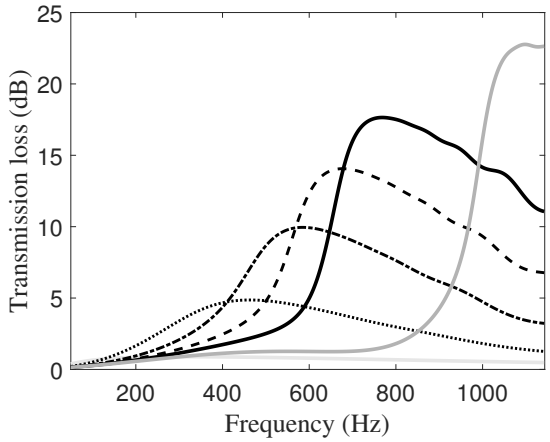


Figure 3. Influence of the MPP holes diameter on the Transmission loss (dB) spectra of a MPP-RTF silencer in the no-flow case when decreasing the MPP holes diameter d_h (0.9 mm, plain black; 0.7 mm, dashed black, 0.5 mm, dash-dotted black; 0.4 mm, dotted; 0.2 mm, light grey) and without MPP (plain grey).

3.2 Low-speed flow effects

In practice, a low-speed flow will travel within the MPP-RTF silencer, as would be the case in a ventilation or an automotive exhaust system. Assuming a discharge flow rate, the sound wave, which propagates from the shallowest to the deepest cavity, will also travel along the flow direction, e.g. under downstream propagation conditions (DPC). The effect of an increasing flow speed on the MPP-RTF acoustical performance has been simulated in Fig. 4. Simulations have been performed on a MPP-RTF silencer assuming a MPP with holes diameter $d_h = 0.9$ mm and holes pitch $s_h = 5$ mm . The main influence is a reduction of the efficiency bandwidth for the dissipation and the transmission loss towards higher frequencies as the flow speed increases. It is accompanied by a decrease of the maximum performance values. The onset of high dissipation values (greater than 0.9) and high TL (greater than 11 dB) is upshifted from 650 Hz (no-flow case) towards 880 Hz (flow at 30 m.s^{-1}). The TL dynamics, 11 dB – 18 dB without flow, reduces to 11 dB – 12 dB with flow at 30 m.s^{-1}. Note that the reflection coefficient is rather unaffected by low-speed flow effects as it stays below 2% over the range of flow speed variations.

Such adverse flow effects are due to an increase of the MPP resistance and a decrease of the MPP reactance, as seen from Eq. (1), when the flow speed or Mach number increases. Such over-resistive and under-reactive conditions could be overcome if integrated in an optimisation process that maximizes the total dissipation of the silencer.

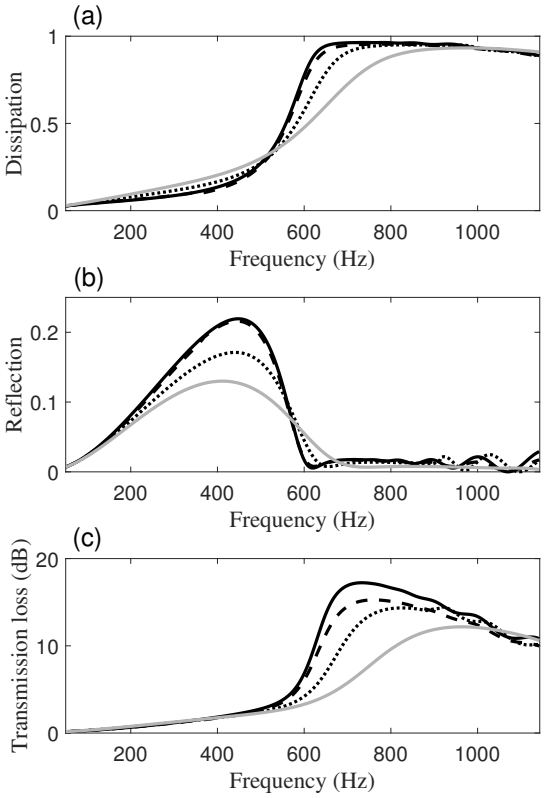


Figure 4. Influence of the flow velocity on the dissipation (a), reflection (b) and transmission loss (c) of a MPP-RTF silencer when traversed by a grazing flow of bulk velocity 10 m.s^{-1} (dashed black), 20 m.s^{-1} (dotted black) and 30 m.s^{-1} (grey); also shown the no-flow case (plain black).

4. AERODYNAMIC PERFORMANCE

Shielding the RTF silencer cavities from a grazing flow by using MPPs not only has an acoustic functionality, as seen in Sec. 3.1, but also limits the pressure drop that would be induced by interaction between the flow and the RTF cavity

mouths through detachment, vortex shedding and re-attachment at the cavity edges. A quantifier of this effect is the friction factor of the cubic MPP-RTF silencer that takes the following form, with $H = L$,

$$\varphi = \frac{H}{L}\frac{\Delta p}{\rho_0 U^2} = \frac{\Delta p}{\rho_0 U^2}, \qquad (7)$$

with Δp the pressure drop across the axial length L of the silencer and U the mean flow speed. These quantities have been calculated from Reynolds Averaged Navier Stokes k-ε model [9] solved by Finite Volume in Ansys Fluent imposing a fully-developed turbulent boundary layer profile at the silencer inlet with outer velocity 30 m.s^{-1} and turbulence rate 2%, typical of low-speed wind-tunnels.

Figure 5 shows a substantial decay of the friction factor when increasing the MPP holes pitch from 0.5 mm to 5 mm. It amounts to 17% for ultra small (0.2 mm) and 14.5% for near-millimetric (0.9 mm) holes diameters. This is associated to a decrease of the perforation ratio from 12.57% to 0.13% in the former case, and from 63.62% to 2.54% in the latter case. Moreover, the friction factor for $d_h = 0.9$ mm stays consistently higher than that for $d_h = 0.2$ mm, by 1 to 4%. As for $d_h = 0.9$ mm, holes pitch values lower than d_h have been excluded.

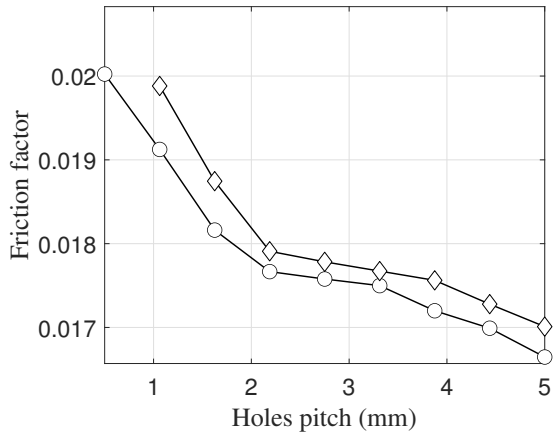


Figure 5. Influence of the MPP holes pitch on the friction factor of a MPP-RTF silencer traversed by a low-speed flow of bulk velocity 30 m.s^{-1} for two MPP holes diameters ($d_h = 0.2$ mm, circles; ($d_h = 0.9$ mm, diamonds).

It appears that the MPP with the lowest friction factor is the one with the smallest holes diameters and the largest holes pitch, e.g. with a very low perforation ratio. Back to Fig. 2 (light grey curves), it is associated to poor dissipation and transmission properties. A compromise thus has to be found to achieve both acceptable acoustical and aerodynamic performance. It can be seen from Fig. 5 that a MPP with holes pitch greater than 2 mm and holes diameter of 0.9 mm (for ease of manufacture) ensures a friction factor below 0.018. Assuming a holes pitch of 5 mm, Fig. 2 shows it provides excellent acoustical performance in the no-flow case, that should however be moderated by the results of Fig. 4 under a low-speed flow at 30 m.s^{-1}.

5. EXPERIMENTAL VERIFICATION

Low-speed wind-tunnel experiments have been performed to verify the simulated acoustical performance of a cubic RTF silencer of length, width and height $L = W = H = 0.15$ m, additively manufactured in ABS material. The silencer is shielded from a low-speed flow (30 m.s^{-1}) by a perforated panel of thickness 1.5 mm, holes diameter 2.6 mm and perforation ratio 2.8%. The RTF is composed of 20 cavities of width 3.5 mm separated by ribs of thickness 4 mm. Figure 6 shows that the silencer is plugged onto a low-speed wind-tunnel duct section. During the measurements, the inlet and outlet of the silencer are prolonged by 1 m length rigid square duct sections to ensure flow channeling. The airflow is generated by a centrifugal fan insulated with mufflers, straightened by honeycomb panels in a settling chamber, then accelerated through a convergent towards the test section. A transitional, almost turbulent, boundary layer has been characterized from hot-wire measurements at the silencer inlet location.

The test section is instrumented in order to measure the scattering matrix of the silencer [10]. Two sources and two pairs of three boundary layer microphones are located respectively in the 1 m duct sections upstream and downstream the silencer. The sources are sequentially driven by white noise to generate two independent states within the duct test section. The associated outgoing and ingoing plane wave amplitudes are deduced from the transfer functions measured between the microphones and the source drive signals after pseudo-inversion of the plane wave propagation matrix that accounts for convective effects and visco-thermal losses in presence of flow up to the duct cut-on frequency 1140 Hz. The scattering matrix

gathers the outgoing and ingoing wave amplitudes for each acoustic state from which the dissipation, reflection and transmission coefficients are readily deduced.

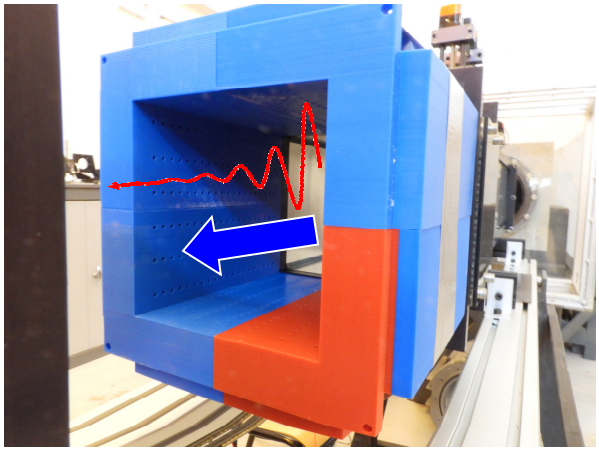


Figure 6. Photography of the outlet of a square RTF silencer mounted on a low-speed wind-tunnel and shielded from the grazing flow by perforated panels; the blue (resp. red) arrows represent the flow (resp. sound wave) travelling through the silencer.

It can be seen from Fig. 7 that the Finite Element simulations and the scattering matrix measurements closely correlate, showing high dissipation values of the perforated-RTF silencer exceeding 0.9 from 650 Hz to 950 Hz in the no-flow case. Over this range, merging occurs between the resonances of the activated perforate-RTF cavities. It is associated to very small values of the reflection coefficient, below 0.02, and a low transmission coefficient that stays below 0.2.

Without perforated coating, it is found from simulations (not shown) that the RTF silencer produces a high dissipation plateau only above 1400 Hz, beyond the plane wave regime that extends up to 1140 Hz. Adding the perforated coating over the RTF cavities thus downshifts by 750 Hz the onset of high acoustical performance. This is due to inertial effects added by the perforates with 2.8% wall porosity. Because of limitations on the minimum holes diameter that can be printed from fused deposition modelling using ABS polymer, such low-perforation ratio was achieved by increasing the perforate holes pitch, 7.5 mm along the streamwise direction and 25 mm along the spanwise direction, as seen from Fig. 6, rather than by decreasing the holes diameter to small sub-millimetric values. Due to the supra-millimetric holes diameters, visco-thermal dissipation occurs essentially within the RTF cavities. It well manages to balance the reflection and transmission leakages around 750 Hz, but slightly over-resistive conditions are observed above 900 Hz. They produce a progressive decrease of the dissipation down to 0.8 as well as an increase of the transmission up to 0.2 when the frequency raises up to 1100 Hz.

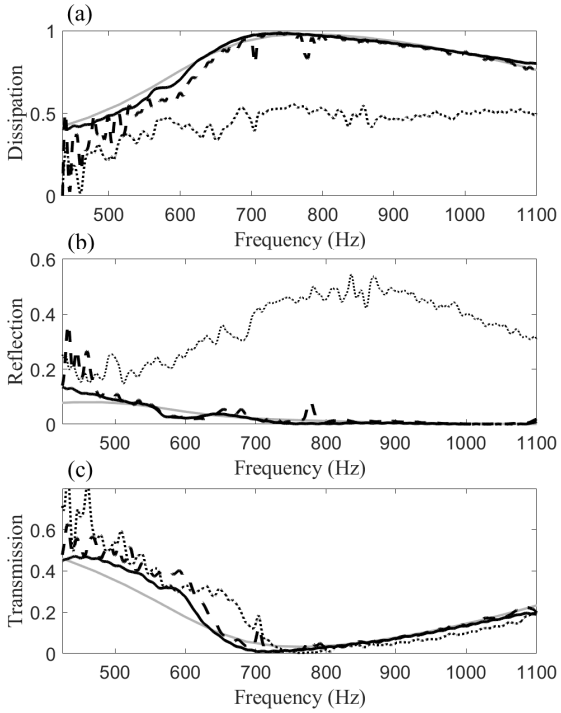


Figure 7. Dissipation (a), reflection (b) and transmission (c) spectra of the perforated RTF silencer simulated by Finite Element method (grey) and measured (black) in the no-flow case and under a low-speed flow at 30 m.s^{-1} assuming upstream (dashed) or downstream (dotted) plane wave excitations.

Under a low-speed flow (30 m.s^{-1}), one observes a slight upshift of the onset of high dissipation and transmission performance, from 650 Hz without flow to 690 Hz with flow, with almost unchanged reflection properties. This trend is in accordance with the low-speed flow effects simulated by the transfer matrix model in Fig. 4. These effects are due to the added resistance and deficit in wall

reactance caused by the flow. However, they appear to be less pronounced with respect to the effect of the same flow speed over a MPP-coated RTF silencer, as seen when comparing Fig. 7 and Fig. 4.

Assuming an incident wave propagating against the flow, e.g. impinging the silencer from the outlet side, Fig. 7 shows that it produces moderate broadband dissipation (that stays around 0.5) due to back reflections (up to 50% of the incident power). This is due to the wall admittance discontinuity encountered by the wave when entering the silencer flow outlet due to the low stiffness of the deepest cavity. This breaks the impedance matching condition that would be satisfied by the wave if it was entering the silencer flow inlet, due to the high stiffness of the shallowest cavity and progressive increase of the wall admittance. One also note from Fig. 7(c) the absence of reciprocity in transmission under grazing flow conditions.

6. CONCLUSIONS

The acoustic and aerodynamic effect of covering the cavities of RTF silencers by MPP or perforated panels has been examined under no-flow and low-speed grazing flow conditions, up to Mach 0.087. Transfer matrix modelling and measurements of the scattering matrix in a low-speed wind tunnel showed robustness of the broadband low-reflection and high dissipation performance to grazing flow effects, albeit over a bandwidth that reduces as the flow speed increases. The transmission loss of the coated RTF silencer is especially sensitive to this adverse flow effect.

A trade-off has to be found on the MPP parameters to ensure both high dissipation performance and low friction factor since either objective requires concurrent parameter sets. Further coupled acoustic and computational fluid dynamic simulations should be performed at the MPP holes local scale to investigate the geometrical parameters favoring visco-thermal dissipation in the acoustic/thermal boundary layers while limiting the occurrence of flow-induced vortex shedding over/within the holes and responsible of the drag. However, the analysis is not straightforward due to the interaction between the near-wall shear layers and the acoustic waves.

7. ACKNOWLEDGMENTS

This work is part of the project PID2022-139414OB-I00 funded by MCIN/AEI/10.13039/501100011033/ and by "ERDF A way of making Europe". It has also received support from the French government under the France 2030 investment plan, as part of the Initiative d'Excellence d'Aix-Marseille Université - A*MIDEX (AMX-22-RE-AB-157).

8. REFERENCES

[1] V. Romero-Garcia and A.-C. Hladky-Hennion (Editors): *Fundamentals and Applications of Acoustic Metamaterials: From Seismic to Radio Frequency*. London: ISTE Ltd, 2019.

[2] G. Palma, H. Mao, L. Burghignoli, P. Göransson and U. Iemma, "Acoustic Metamaterials in Aeronautics," *Applied Sciences*, 971, 8, 2018.

[3] T. Bravo and C. Maury: "Broadband sound attenuation and absorption by duct silencers based on the acoustic black hole effect: Simulations and experiments," *Journal of Sound and Vibration*, 561, 117825, 2023.

[4] T. Poinsot, "Prediction and control of combustion instabilities in real engines," *Proceedings of the Combustion Institute*, 36, 1–28, 2017.

[5] D. Y. Maa, "Potential of micro-perforated panel absorbers," *Journal of the Acoustical Society of America,* 104, 2861–2866, 1998.

[6] S. Allam and M. Åbom, "A new type of muffler based on microperforated tubes," *Journal of Vibration and Acoustics*, 133, 031005, 2011.

[7] M. L. Munjal, "Velocity ratio-cum-transfer matrix method for the evaluation of a muffler with mean flow," *Journal of Sound and Vibration*, vol. 39, pp. 105–119, 1975.

[8] J. F. Allard and N. Attala: *Propagation of Sound in Porous Media: Modelling Sound Absorbing Materials*, 2nd edn. Chichester: John Wiley & Sons Ltd, 2009.

[9] T.-H. Shi, W. W. Liou, A. Shabir, Z. Yang and J. Zhu, "A New k-ε Eddy-Viscosity Model for High Reynolds Number Turbulent Flows – Model Development and Validation," *Computers and Fluids*, 24, 227–238, 1995.

[10] E. Garnell, M. Åbom and G. Banwell, "The use of the two-port method to characterize high-speed small fans," *Applied Acoustics*, 146, 155–163, 2019.

DOI: 10.61782/fa.2025.0920

FORUM ACUSTICUM EURONOISE 2025

TUNABLE MICROPERFORATED PANEL ACOUSTIC ABSORBERS WITH COUPLING EFFECTS UNDER GRAZING FLOW

Ying Li[1] **and Yat Sze Choy**[1*]
[1] Department of Mechanical Engineering, The Hong Kong Polytechnic University, Hong Kong Special Administrative Region, People's Republic of China

ABSTRACT

Design for highly effective acoustic meta-liners with broadband sound attenuation under grazing flow is challenging due to performance degradation with high flow speeds and intricate internal structures involved. In this study, a tunable microperforated panel (MPP) acoustic absorber is proposed that leverages the coupling effects between its sub-components to achieve broadband sound absorption across static and flow conditions. A theoretical framework combining acoustic radiation theory with modal superposition principles is developed to predict the performance of the proposed absorber. The theoretical and numerical analysis clarifies how coupling effects enhance the absorption troughs in the proposed absorber. Finally, a broadband acoustic liner, composed of multiple optimized coupled MPP absorbers is proposed. Experimental investigations validate the sound absorption performance of the proposed acoustic liner under grazing flow, highlighting the potential of our theoretical model and coupled MPP absorbers to advance acoustic meta-liner design.

Keywords: *Flow and acoustic interactions, microperforated panel absorber; two-dimensional theoretical model; broadband sound absorption.*

1. INTRODUCTION

The highly effective broadband absorption of low-frequency sound is a growing and challenging topic for acoustic liners in aero-engines and ventilation ductwork systems [1]. Traditional porous materials and microperforated panels (MPPs) absorbers require sufficient thickness compared with the wavelength to control low-frequency sound, which hinders their wide application in practice. In recent years, acoustic metamaterials (AMMs) [2] that are artificial periodic structures with subwavelength building blocks provide a new idea for the design of low-frequency sound absorbers. A number of functionalities and applications have been proved and achieved based on AMMs. To enhance the sound absorption bandwidth, many metamaterial designs spatially stack resonators with varying cavity depths to connect all resonance frequency peaks. This approach, however, necessitates a surprisingly large number of units to effectively suppress noise. Inadequate numbers of resonant elements lead to unsatisfied absorption in the troughs, thereby limiting the applicability of AMMs in duct systems and room acoustics.

Building on these foundational principles and strategies, current advancements in AMM technology have led to their application in developing effective acoustic liners under flow conditions. However, increasing flow speeds trigger stronger coupling between grazing flows and acoustic waves, resulting in substantial degradation of meta-liner absorption performance [3-5]. To date, few metaliner designs have fully achieved simultaneous broadband noise reduction and stable absorption efficacy across varying flow velocities, representing a critical barrier to practical applications.

In this study, a coupled acoustic absorber (CAA) featuring inserted MPPs and shared cavities is proposed to achieve broadband sound absorption across static and flow conditions. The objectives of this study are as follows: (1) To propose a two-dimensional (2D) model for predicting the acoustic performance of the CAA based on sound radiation theory in a rigid-walled duct. (2) To design a coupled MPP absorbers that achieves broadband noise

[*] ***Corresponding author***: *mmyschoy@polyu.edu.hk.*
Copyright: *©2025 First author et al. This is an open-access article distributed under the terms of the Creative Commons Attribution 3.0 Unported License, which permits unrestricted use, distribution, and reproduction in any medium, provided the original author and source are credited.*

reduction while preserving effective broadband sound absorption performance under increasing flow velocities

2. THEORETICAL MODELLING

The proposed CAA comprised inserted MPPs and shared cavities, as shown in Fig. 1. The solid line denotes the rigid wall while the dashed line is the MPP in the TAA. The shaded region denotes the acoustically rigid block. We assumed that a normally incident wave p_{inc} impinged on the surface of the CAA. The acoustic pressure outside of the cavity is $p_a = 2p_{inc} + p_{rad_duct}$, where p_{rad_duct} denotes the pressure radiating from the surface. As shown in Fig. 1, the n-th MPP is located at surface S_{p_n} with a length of L_n. The particle velocity over the MPP surface S_{p_n} is expanded as a series of sine functions as

$$v_{p_n}(x) = \sum_{q=1}^{Q} V_{p_n,q}\phi_{p_n,q}(x), \tag{1}$$

with

$$\phi_{p_n,q}(x) = \sin\left(\frac{q\pi}{L_n}x\right) \tag{2}$$

where $V_{p_n,q}$ and $\varphi_{p_n,q}$ are the q-th modal amplitude and modal shape of the n-th MPP, respectively. q is the modal indices. With the proper truncation of the decomposition series, Eq. (1) can accurately represent the averaged particle velocity fields v_{p_n} except at the boundary edges. Subsequently, the pressure field in the duct above the meta-surface can be formally expressed as a superposition of plane wave modes [6]

$$p_{rad_duct}(x,0) = \rho_0 \sum_{g=0}^{G} \frac{\omega\psi_{d,g}(x)}{W\kappa_{d,g}} \int_{S_{p_1}} \psi_{d,g}(x')v_{p_1}(x')ds' \tag{3}$$

where, $\psi_{d,g}(x)$ is the g-th cross-sectional mode shape function of the duct, $\kappa_{d,g}$ is the propagation constant along the duct given by $-i\sqrt{k_{d,g}^2 - (k - i\alpha_{duct})^2}$, $k_{d,g}$ is the cross-sectional characteristic propagation constant, and k is the propagation constant without absorption. α_{duct} is the absorption coefficient of the duct defined in [7]. $\psi_{d,g}(x) = \sqrt{2-\delta_{0,g}}\cos(g\pi x/W)$ and $k_{d,g}^2 = (g\pi/W)^2$. $\delta_{0,g}$ is the Kronecker delta function, which is equal to zero when $g \neq 0$ and unity when $g = 0$. ρ_0 is the density of air and ω is the radial frequency. g is the modal index.

On the other hand, the acoustic pressure inside n-th channel excited by the velocity distribution on the adjacent r-th MPP ($r = n$ or n+1) can be separated into two parts: the sound radiated from the velocity distribution on the r-th MPP, and the corresponding reflected wave by the boundaries of the channel walls as $p_{MPP_r}^{ch_n} = p_{rad_r}^{ch_n} + p_{ref_r}^{ch_n}$. According to Doak's theory [6], the sound pressure radiated by a sound source distribution in r-th MPP in the n-th channel can be expressed as

$$p_{rad_r}^{ch_n}(x,y) = \rho_0 \sum_{m=0}^{M} \frac{\omega\psi_{n,m}(y)}{2D_n\kappa_{n,m}} \int_{S_{p_r}} \left[H(x-x')e^{-i\kappa_{n,m}(x-x')} + H(x'-x)e^{i\kappa_{n,m}(x-x')}\right]\psi_{n,m}(D_*)v_{p_r}(x')ds', \tag{4}$$

where H denotes the Heaviside function. $\psi_{n,m}(y)$ is the cross-section mode shape functions of the n-th channel, and $\kappa_{n,m}$ is the propagation constant along the n-th channel axis given by $-i\sqrt{k_{n,m}^2 - (k - i\alpha_{n,wall})^2}$, where $k_{n,m}$ is the cross-sectional characteristic propagation constant. $\alpha_{n,wall}$ is the absorption coefficient of the n-th channel, defined in ref [7]. $\psi_{n,m}(y) = \sqrt{2-\delta_{0,m}}\cos(m\pi y/D_n)$ and $k_{n,m}^2 = (m\pi/D_n)^2$. m is the modal index. $D_* = -D_n$ ($n < q$) or 0 ($n = q$).

The reflected wave induced by a sound source distribution in r-th MPP in the n-th channel is calculated in a manner similar to the radiation pressure in Eq. (4), except that the Heaviside functions are replaced by the unknown coefficients $C_{n,m}^+$ and $C_{n,m}^-$ as $C_{n,m}^+ = \frac{e^{ik_{n,m}(2W-2x')}+1}{e^{ik_{n,m}(2W)}-1}$ and $C_{n,m}^- = \frac{e^{ik_{n,m}(2W+2x')}+1}{e^{ik_{n,m}(2W)}-1}$, respectively.

2.1 Pressure gradient at the MPP

The acoustic boundary condition of the MPP mounted on the upper surface S_{p_1} can be described as

$$Z_{MPP_1}v_{p_1}(x,0) = \frac{1}{\rho_0 c_0}\left[p_{MPP_1}^{ch_1}(x,0) + p_{MPP_2}^{ch_1}(x,0) - 2p_{inc} - p_{rad_duct}(x,0)\right] \tag{5}$$

where c_0 is the sound speed of air. Substituting Eqs. (1-4) into Eq. (5), and meanwhile multiplying $\phi_{p_1,q'}(x)$ on both sides to apply the orthogonal property, and integrating over the MPP yields

$$(\boldsymbol{A}^{\mathrm{sur}}+\boldsymbol{A}^{\mathrm{radMPP_1}}+\boldsymbol{A}^{\mathrm{rad_11}}+\boldsymbol{A}^{\mathrm{ref_11}})\boldsymbol{V}_{\mathrm{p_1}} +(\boldsymbol{A}^{\mathrm{rad_12}}+\boldsymbol{A}^{\mathrm{ref_12}})\boldsymbol{V}_{\mathrm{p_2}}=\boldsymbol{A}^{\mathrm{inc}} \quad (6)$$

where $\boldsymbol{A}^{*}$ is the Q × Q matrix, and the $\boldsymbol{V}_{*}$ is the Q × 1 matrix. The acoustic impedance of the *n*-th MPP is determined using the acoustic impedance model (without flow) proposed by Maa [8]:

$$Z_{\mathrm{MPP_n}}=\frac{32\mu t_{\mathrm{MPP_n}}}{\sigma_{\mathrm{MPP_n}}d_{\mathrm{MPP_n}}^{2}}\left[\left(1+\frac{(K_{\mathrm{n}})^{2}}{32}\right)^{\frac{1}{2}}+\frac{\sqrt{2}}{8}K_{\mathrm{n}}\frac{d_{\mathrm{MPP_n}}}{t_{\mathrm{MPP_n}}}\right], +\mathrm{i}\frac{\rho_0\omega t_{\mathrm{MPP_n}}}{\sigma_{\mathrm{MPP_n}}}\left[1+\left(9+\frac{(K_{\mathrm{n}})^{2}}{2}\right)^{-1/2}+0.85\frac{d_{\mathrm{MPP_n}}}{t_{\mathrm{MPP_n}}}\right] \quad (7)$$

where $d_{\mathrm{MPP_n}}$, $t_{\mathrm{MPP_n}}$, and $\sigma_{\mathrm{MPP_n}}$ are the diameter, thickness, and porosity of the *n*-th MPP, respectively. μ are the density and viscosity of air. $K_{\mathrm{n}}=(d_{\mathrm{MPP_n}}/2)\sqrt{\rho_0\omega/\mu}$ is a parameter describing the ratio of the radius to the viscous boundary layer thickness inside the hole.

Analogously, by reorienting the reference axis to the left-hand side of the N-th (last) channel, the acoustic boundary condition on the MPP mounted at the surface $S_{\mathrm{p_n}}$ can be described as

$$Z_{\mathrm{MPP_n}}v_{\mathrm{p_n}}(x,0)=\frac{1}{\rho_0 c_0}\left[p_{\mathrm{MPP_n}}^{\mathrm{ch_n}}(x,0)-p_{\mathrm{MPP_n}}^{\mathrm{ch_n\text{-}1}}(x,0)-p_{\mathrm{MPP_n\text{-}1}}^{\mathrm{ch_n\text{-}1}}(x,0)\right]. \quad (8)$$

Substituting Eqs. (1-4) into Eq. (8), multiplying $\phi_{\mathrm{p_n,q}}(x)$ on both sides and integrating over the MPP yields

$$(\boldsymbol{A}^{\mathrm{rad_(N)(N\text{-}1)}}+\boldsymbol{A}^{\mathrm{ref_(N)(N\text{-}1)}})\boldsymbol{V}_{\mathrm{p_N\text{-}1}}+(\boldsymbol{A}^{\mathrm{radMPP_N}}+\boldsymbol{A}^{\mathrm{rad_NN}} +\boldsymbol{A}^{\mathrm{ref_NN}}+\boldsymbol{A}^{\mathrm{up_rad_NN}}+\boldsymbol{A}^{\mathrm{up_ref_NN}})\boldsymbol{V}_{\mathrm{p_N}}=\boldsymbol{0}, \quad (9)$$

where $\boldsymbol{A}^{*}$ is the Q × Q matrix, and the $\boldsymbol{V}_{*}$ is the Q × 1 matrix.

2.2 System matrix

Based on Eq. (8) and Eq. (9), the first and last row of the systematic matrix equation, considering the coupling of layers in CAA yields

$$\left[\boldsymbol{A}^{\mathrm{sur}}+\boldsymbol{A}^{\mathrm{radMPP_1}}+\boldsymbol{A}^{\mathrm{rad_11}}+\boldsymbol{A}^{\mathrm{ref_11}}\quad \boldsymbol{A}^{\mathrm{rad_12}}+\boldsymbol{A}^{\mathrm{ref_12}}\quad \cdots\quad \boldsymbol{0}\right]\left[\boldsymbol{V}_{\mathrm{p_1}}\right]=\left[\boldsymbol{A}^{\mathrm{inc}}\right], \quad (10)$$

and

$$\left[\boldsymbol{0}\quad \cdots\quad \boldsymbol{A}^{\mathrm{rad_(N)(N\text{-}1)}}+\boldsymbol{A}^{\mathrm{ref_(N)(N\text{-}1)}}\quad \boldsymbol{A}^{\mathrm{radMPP_N}}+\boldsymbol{A}^{\mathrm{rad_NN}}+\boldsymbol{A}^{\mathrm{ref_NN}}+\boldsymbol{A}^{\mathrm{up_rad_NN}}+\boldsymbol{A}^{\mathrm{up_ref_NN}}\right]\left[\boldsymbol{V}_{\mathrm{p_N}}\right]=\left[\boldsymbol{0}\right], \quad (11)$$

respectively.

Under a similar derivation, an equation that describes the *n*-th MPP (n = 2,3···N-1) of the CAA can be expressed as follows

$$(\boldsymbol{A}^{\mathrm{rad_(n)(n\text{-}1)}}+\boldsymbol{A}^{\mathrm{ref_(n)(n\text{-}1)}})\boldsymbol{V}_{\mathrm{p_n\text{-}1}}+(\boldsymbol{A}^{\mathrm{radMPP_n}}+\boldsymbol{A}^{\mathrm{rad_nn}}+\boldsymbol{A}^{\mathrm{ref_nn}} +\boldsymbol{A}^{\mathrm{up_rad_nn}}+\boldsymbol{A}^{\mathrm{up_ref_nn}})\boldsymbol{V}_{\mathrm{p_n}}+(\boldsymbol{A}^{\mathrm{rad_n(n+1)}}+\boldsymbol{A}^{\mathrm{ref_n(n+1)}})\boldsymbol{V}_{\mathrm{p_n+1}}=\boldsymbol{0}. \quad (12)$$

A more generalized systematic matrix for calculating the N-layer CAA is constructed by incorporating Eqs. (10-12). Any remaining entries in this generalized systematic matrix should be filled with zero matrices. For the sake of conciseness, the complete formulation of the generalized systematic matrix for the N-layer CAA is omitted here.

The unknown coefficient $\boldsymbol{V}_{\mathrm{p_n}}$ can be obtained after solving the generalized systematic matrix for the N-layer CAA. Thus, the sound pressures inside the duct and structure can be calculated. After obtaining the sound pressure field, the absorption coefficient of the CAA is calculated as follows [9]:

$$a=\frac{\rho_0 c_0\int_{S_{\mathrm{p_1}}}\mathrm{Re}\left(p_{\mathrm{a}}\cdot v_{\mathrm{p_1}}^{*}\right)ds}{W}, \quad (13)$$

where the asterisk denotes the complex conjugate.

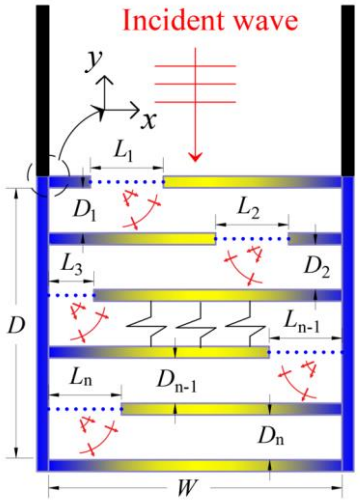


Figure 1. Two-dimensional schematic diagram of the CAA for theoretical modelling.

3. RESULTS AND DISCUSSION

To validate the proposed 2D theoretical model, the commercial software COMSOL Multiphysics and the finite element method (FEM) were used to calculate the absorption coefficients of the CAA. The predicted absorption coefficients for the two-layer coupled CAA are illustrated in. Fig. 2. The following structural parameters of the CAA were used: $W_1 = W_2 = 50$ mm, $D_1 = D_2 = 20$ mm. The diameter, thickness and porosity of the surface MPP are 1 mm, 1 mm, and 0.015. The diameter, thickness and porosity of the interior MPP are 0.15 mm, 1 mm, and

0.0123. As shown in Fig. 2, for the two-layer CAA calculated via the FEM, a near-total absorption peak appears at 600 Hz. The second peak occurs at 980 Hz. The outcome obtained by the proposed 2D model (solid line) is in good agreement with that calculated by the FEM (rhombus) for the two-layer CAA, both in terms of peak frequency and peak value. This demonstrates that the proposed 2D model accurately predicts the acoustic performance of CAA. The first peak is generated by the resonance of the right sub-resonator (star), while the second peak originates from the left sub-resonator (circle). Notably, a pronounced dip occurs at 780 Hz with an absorption value of approximately 0.86. This represents a significant enhancement compared to the case without the interior MPP (square), where the dip value is only 0.48.

To further investigate the enhancement mechanism induced by coupling effects, Fig. 3 presents the sound pressure and velocity distributions within the two-layer CAA at the first peak, dip, and second peak frequencies. As shown by the white arrows, at the dip frequency, a high acoustic velocity passes through the interior MPP, accompanied by high acoustic pressure in both left and right sub-resonators. This suggests that the superior sound absorption performance at the dip frequency arises from the synergistic effects of all MPPs. In contrast, at the peak frequencies, although only one sub-resonator dominates, the partial acoustic velocity through the interior MPP still contributes to a minor enhancement of the peak absorption value.

To further investigate the sound absorption mechanism and the role of the inserted MPPs in the proposed CAA, we conducted a modal analysis. Fig. 4 presents the modal amplitude ($|V_p|$) of particle velocity across each MPP interface in the two-layer CAA, as calculated by our theoretical model, focusing on the first peak (600 Hz), trough (780 Hz), and second peak (980 Hz). At the peak frequencies (Figs. 4a and 4c), while the dominant acoustic velocity occurs at the surface MPP, a non-negligible acoustic flow through the interior MPP is also observed, which can be absorbed by the interior MPP. In contrast, at the dip frequency (Fig. 4b), all MPPs exhibit significant acoustic velocity, further confirming that the enhanced sound absorption at this dip frequency stems from the collective contribution of all MPPs.

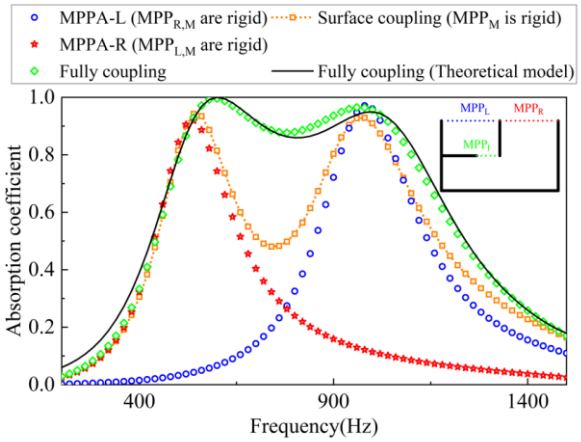


Figure 2. The predicted absorption coefficients for the two-layer CAA.

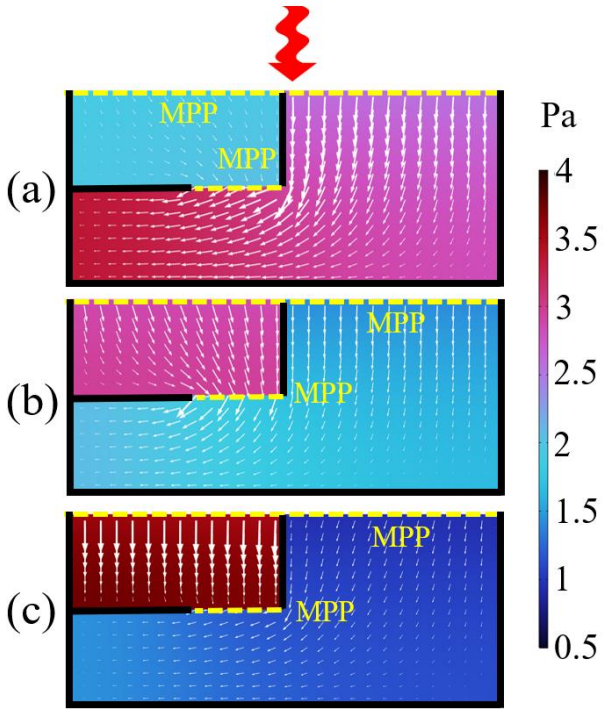


Figure 3. Distribution of sound pressure and velocity (arrow) at (a) 600 Hz, (b) 780 Hz and (c) 980 Hz. The direction of arrows denotes the intensity flow direction, and the size represents the velocity magnitude.

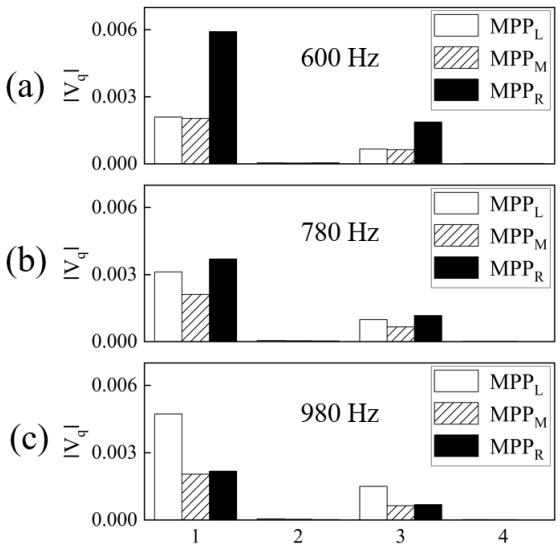


Figure 4. Modal amplitude of particle velocity over the MPP interface in the 2-layer CAA at (a) the first peak, (b) trough, and (c) second peak frequencies.

4. FLOW EFFECT ON THE CAA

Numerous efforts have been made to establish prediction formulas for the acoustic properties of orifices under various flow conditions. However, they have different assumptions for flow characteristics or do not consider the influence of shallow cavities behind the holes; thus, these formulae may forecast discrepant acoustic properties towards an orifice. To better understand the fluid dynamics when the flow passes over the proposed CAA, the flow patterns of the MPP (d = 1 mm) and four backed cavities with different cavity depths (2 mm and 6 mm) under grazing flow speeds of 34 m/s were investigated using the CFD method. In this study, the Reynolds averaged Navier–Stokes (RANS) simulations were applied to find the statistical average of the turbulent flow, and the shear stress transport (SST) k–ω turbulence model was utilized to account for the effects of turbulence on this averaged flow. The geometry of the computational model is shown in Fig. 5(a). The orifices and accompanying cavity were located on the underside of the duct. The cross-section of the main duct was 24 mm × 24 mm. The length of the upstream duct was set to 1000 mm, to generate a fully developed turbulent boundary layer in front of the orifice. The distance between the tested orifice and outlet (300 mm) was more than 50 times the orifice diameter. This ensured that any vorticity could be dissipated along this distance. The inlet of the duct was set as the mass-flow inlet boundary condition. A pressure-outlet boundary condition was imposed upon the duct outlet at standard atmospheric pressure (1 atm). The non-reflection boundary condition (NRBC) was applied to the inlet and outlet. The remaining walls of the main duct, orifice, and cavities were set as stationary and adiabatic walls, without any slip. Fig. 5(b) illustrates the vorticity distribution across the resonator surface. The consistent vorticity patterns observed at each surface orifice demonstrate that even under moderately high flow speeds (34 m/s), the hole spacing is sufficient to minimize inter-hole coupling effects. Notably, in the shallow-cavity configuration (left resonator), the injected flow through the surface MPP impinges on the second-layer MPP, effectively modulating its acoustic impedance through a mechanism analogous to bias flow. Conversely, in the deep-cavity configuration (right resonator), the injected flow dissipates before reaching the second MPP, thereby eliminating this interference.

Based on these observations for the absence of inter-hole coupling and backing cavity depths exceeding 10 mm, we adopt the flow-dependent MPP impedance model proposed by Li and Choy [10] in Eq. (9) to predict the acoustic liner's acoustic performance under grazing flow (Section 5).

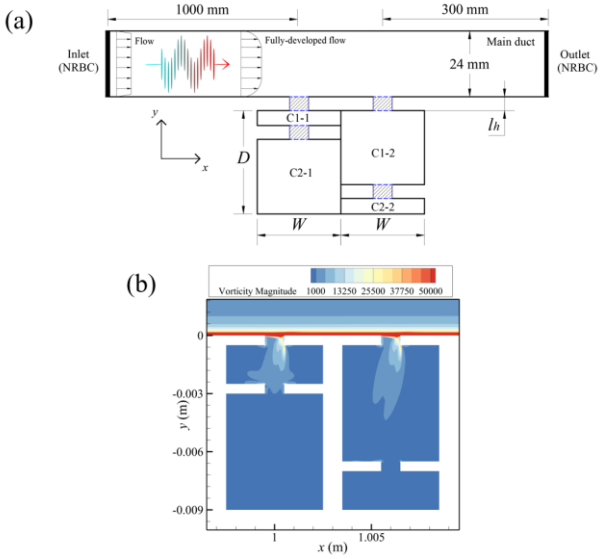


Figure 5. (a) Geometry of the computational model and (b) vorticity distribution.

5. EXPERIMENTAL INVESTIGATION

To test the sound absorption performance of the proposed acoustic liner and validate the proposed theoretical and numerical models under grazing flow, *TL* measurements of the acoustic liner consisting of four CAA were performed. Each CAA contains four layers. The following structural parameters of each CAA were used: $W = 100$ mm, $D_1 = D_2 = D_3 = D_4 = 20$ mm. The diameter, thickness and porosity of the surface MPP are 0.3 mm, 0.5 mm, and 0.022. The diameter, thickness and porosity of the interior MPPs are 0.5 mm, 0.5 mm, and 0.02. A photography of the test rig and tested acoustic liner are shown in Fig. 6(a). The experiment was conducted in a quiet mini-wind tunnel using a working section of dimensions 100 mm × 100 mm (cross-section) and 1.8 m (length). The first cut-on frequency of the duct was 1700 Hz, and the turbulence intensity of the fully developed grazing flow in the upstream sections was below 0.1%. The MPPs of the acoustic liner were fabricated from stainless steel via etching. Other components of the acoustic liner were 3D-printed. Two proposed acoustic liners were mounted on the two sides of the test section of the duct. Two pairs of B&K 1/2 in. condenser microphones (type no. 4187) were installed up- and down-stream of the tested absorber. The installments of four microphones are shown in Fig. 6(a) via the labels M1–4. The travelling wave components in the duct could be resolved by each pair of microphones. Using the approach of two independent sound sources at two positions to simulate physical anechoic termination, the *TL* of the acoustic liner was determined. The measured and predicted TL are present in Fig. 6(b). In general, the experimental results agree well with the predicted TL in terms of the tendency, under different flow speeds. Some discrepancy in peak values between experiments and prediction mainly results from the fabrication error of the 3D-printed model. As demonstrated in Fig. 6(b), the proposed acoustic liner achieves an average transmission loss of 18.92 dB across the 200-1700 Hz frequency range under static conditions (denoted by circles). When the flow speed increases to 25 m/s, the liner maintains an average transmission loss of 17.89 dB over the same bandwidth (square), representing only a 5.7% performance reduction. These experimental findings confirm that by localizing acoustic energy dissipation within embedded MPPs, the CAA significantly suppresses performance degradation caused by grazing-flow-induced aeroacoustic coupling. Our results provide new insights into the design of metamaterials for aero-noise control engineering and may promote the development of meta-liners for airflow applications.

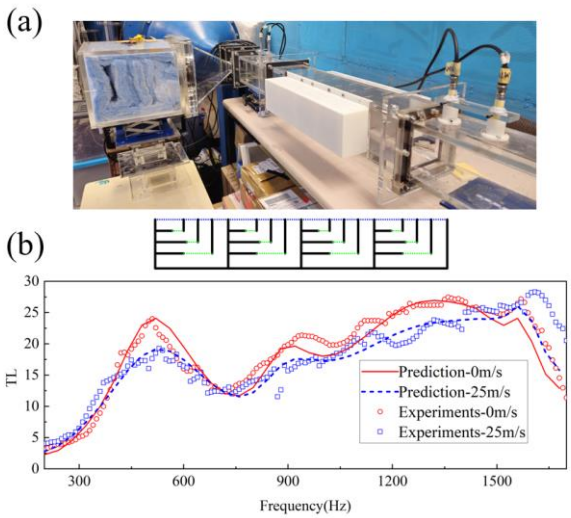


Figure 6. (a) photography of the test rig and tested acoustic liner and (c) TL obtained by prediction and experiments.

6. CONCLUSION

A coupled acoustic absorber (CAA) comprised inserted MPPs and shared cavities was proposed with broadband sound reduction under grazing flow. A two-dimensional model for predicting the acoustic performance of the CAA was proposed based on sound radiation theory in a rigid-walled duct. The sound absorption characteristics of the CAA was investigated via theoretical model and numerical model (finite element method). Consistent predicted results from both models manifested that the 2D theoretical model can accurately predict the acoustic performance of the CAA. In addition, the theoretical and numerical results revealed that the enhancement of the CAA's absorption troughs arises from the synergistic effects of all MPPs. Finally, experimental investigation was conducted and revealed that by localizing acoustic energy dissipation within embedded MPPs, the CAA significantly suppresses performance degradation caused by grazing-flow-induced aeroacoustic coupling. Our results provide new insights into the design of metamaterials for aero-noise control engineering and may promote the development of meta-liners for airflow applications.

7. ACKNOWLEDGMENTS

The authors would like to acknowledge the funding from The Hong Kong Polytechnic University and the Research Grants Council of the Hong Kong SAR (PolyU 15207221).

8. REFERENCES

[1] C. Lahiri, F. Bake, "A review of bias flow liners for acoustic damping in gas turbine combustors," *J. Sound Vib.*, 400 (2017) 564-605.

[2] Z. Liu, X. Zhang, Y. Mao, Y. Zhu, Z. Yang, C.T. Chan, P. Sheng, "Locally resonant sonic materials," *Science*, 289 (2000) 1734-1736.

[3] X. Zhang, L. Cheng, "Acoustic silencing in a flow duct with micro-perforated panel liners," *Appl. Acoust.*, 167 (2020) 107382.

[4] S. Huang, E. Zhou, Z. Huang, P. Lei, Z. Zhou, Y. Li, "Broadband sound attenuation by meta-liner under grazing flow," *Appl. Phys.* Lett., 118 (2021).

[5] J. Zhao, F. Wu, Z.-G. Ju, M. Hu, X. Zhang, D. Li, S.-L. Yan, K.-L. Liu, "Neck-embedded acoustic meta-liner for the broadband sound-absorbing under the grazing flow with a wide speed range," *J. Phys. D: Appl. Phys.*, 56 (2022) 045401.

[6] P. Doak, "Excitation, transmission and radiation of sound from source distributions in hard-walled ducts of finite length (I): The effects of duct cross-section geometry and source distribution space-time pattern," *J. Sound Vib.*, 31 (1973) 1-72.

[7] G. Yu, L. Cheng, D. Li, "A three-dimensional model for T-shaped acoustic resonators with sound absorption materials," *J. Acoust. Soc. Am.*, 129 (2011) 3000-3010.

[8] D.-Y. Maa, "Theory and design of microperforated panel sound-absorbing constructions," *Sci. Sin.*, 18 (1975) 55-71.

[9] W. Yang, Y. Choy, Y. Li, "Acoustical performance of a wavy micro-perforated panel absorber," *Mech. Syst. Signal Proc.*, 185 (2023) 109766.

[10] Y. Li, Y.S. Choy, "Acoustic behaviour of micro-perforated panel backed by shallow cavity under fully developed grazing flow," *J. Sound Vib.*, 569 (2024) 117985.

DOI: 10.61782/fa.2025.0581



FORUM ACUSTICUM
EURONOISE 2025

MODELLING SOUND ABSORPTION OF VEGETAL WOOLS : CONSIDERATION OF FIBRE POLYDISPERSITY

Lucien Mutel[1,2*] **Clément Piégay**[1] **Philippe Glé**[1]
Emmanuel Gourdon[2] **César Segovia**[3]
[1] CEREMA, Univ Gustave Eiffel, UMRAE, 11 rue Jean Mentelin, F-67035 Strasbourg, France
[2] ENTPE, Ecole Centrale de Lyon, CNRS, LTDS, UMR5513, 3 rue Maurice Audin, 69518 Vaulx-en-Velin Cedex, France
[3] CETELOR, Centre d'Essais Textile Lorrain, 27 Rue Philippe Séguin, F88000 Épinal, France

ABSTRACT

Vegetal wools are highly porous materials made of vegetal fibres and bicomponent polymer fibres. But despite their high-level multifunctional properties they suffer from poor low-frequency acoustic absorption for thin panels. A solution to this problem can be found in metamaterial methods and in particular double porosity. By using perforated multi-layered hemp wool panels, very good results have been obtained.

This promising use of double porosity has highlighted the necessity to accurately model the acoustic behaviour of vegetal wools in order to optimise their low-frequency sound absorption properties. However, unlike more conventional materials, vegetal wools don't have calibrated fibres, which poses a stalemate this work aims at answering.

Vegetal fibres exhibit high radius polydispersity. Most studies use a mean radius for simulations, and more recent works considered composite methods and used two mean radii (for vegetal and polymeric fibres). This work investigates weighted averaging methods with the aim of improving the estimation of the acoustic absorption for vegetal wools having large radius distribution.

Keywords: *acoustic, vegetal wools, polydispersity, optimisation*

**Corresponding author*: *lucien.mutel@cerema.fr.*

***Copyright**: ©2025 Mutel et al. This is an open-access article distributed under the terms of the Creative Commons Attribution 3.0 Unported License, which permits unrestricted use, distribution, and reproduction in any medium, provided the original author and source are credited.*

1. INTRODUCTION

From the growth of the plant from which the fibres come to the end of their life cycle, vegetal wools have many virtues that make them a very attractive insulation product for green buildings. These materials store atmospheric CO_2, have a low carbon footprint and reduced environmental impact [1–3]. They are hygroscopic, regulating humidity and temperature, contributing to the interior comfort of living spaces [4, 5], and offer good acoustic absorption thanks to their high porosity. Their main drawback is their low acoustic absorption at lower frequencies. To address this, it is first essential to accurately model their acoustic behaviour. Therefore, micro-macro modelling methods were investigated.

For this article, it seems relevant to use modelling methods to estimate static airflow resistivity (later referred as resistivity) from parameters such as porosity and fibre radii. Based on previous works [6, 7], which led to satisfactory results with monodisperse materials, the chosen formulas come from Tarnow's [8] and Umnova's [9] works.

However, vegetal wools are characterised by a large dimensional variability of their natural fibres [6]. Recent advances in the study of polydispersity in random fibrous materials demonstrated that optimised polydispersity can even lead to improved sound absorption at lower frequencies [10]. With this knowledge, this paper aims at investigating different analytical models for acoustic simulations taking these specificities into account.

To begin with, this paper introduce the materials involved in the study. Different vegetal wools, with different radius probability distributions, were experimented to in-

vestigate radius polydispersity as an optimisation method. To keep on, measurement protocols, methods, and analytical models used for this work are described. Eventually, measurement results on the radius probability distributions of the different wools are displayed. This is followed by analytical experiments to better understand how to implement materials with radius polydispersity in analytical models. As a conclusion, a promising path toward accurate estimation of airflow resistivity for these materials was found.

2. MATERIALS AND METHODS

2.1 Materials

For this work, the materials characterised are three vegetal wools : a wood wool (W), a hemp-flax wool (HF) and a wood-kenaf (WK) wool. The parameters used in the modelling of the resistivity, as well as the indirectly measured resistivity, are listed in Tab. 1.

Table 1: Characteristic parameters of the samples : mass proportion between vegetal and polymeric fibres, thickness (e), apparent density (ρ_a), porosity (ϕ) and resistivity (σ)

Material	W	HF	WK
Veg/pol	88/12	45/45/10	40/40/20
$\boldsymbol{e}$ (mm)	50	90	38
$\boldsymbol{\rho_a}$ $\left(kg \cdot m^{-3}\right)$	60	35	58
$\boldsymbol{\phi}$	0.96	0.98	0.96
$\boldsymbol{\sigma}$ $\left(N \cdot m^{-4} s\right)$	35000	3000	5500

2.2 Methods

2.2.1 *Measuring porosity and resistivity*

Porosity was estimated by weighing the samples and using known mass densities of the fibres. The airflow resistivity is obtained indirectly from measurements of an impedance tube with the 3 microphones methods originally developed by Iwase et al. [11] and adapted by Salissou and Panneton [12]. The cylindrical impedance tube used is the type I Acoustitube from Akustik Forschung, with a diameter of $100mm$. The analysis is done between $100Hz$ and $2000Hz$. Based on the work by Olny and Panneton [13, 14], we were able to indirectly estimate the resistivity with measures made on an impedance tube with the 3 microphones method [11].

2.2.2 *Radius distribution measurement*

To measure the radii of the fibres studied for this work, a Scanning Electronic Microscope (SEM) Hitachi TM3000 was used. Prior to their visualisation, the samples were metallised with a thin gold layer deposited in a plasma.

The images obtained are analysed on the software ImageJ, and after manual treatment the transversal profiles are measured. Vegetal fibres are not perfectly cylindrical, therefore an equivalent diameter is calculated by averaging the longest and shortest Ferret's diameters measurable [15, 16].

2.2.3 *Evaluation of the average radii*

Different ways of calculating an average fibre radius can be found in the literature. For this paper, four of them were selected.

- Piégay et al. [17] used a non weighted arithmetic average (NWA),
- Xue et al. [18] a non weighted quadratic average (NWQ).
- To predict the static viscous permeability of heterogeneous fibrous materials, Peyrega and Jeulin [19] preferred a volume weighted average (VW).
- For characteristic lengths, Tran et al. [10] chose an inverse volume weighted average (IVW).

The equations for these calculations are expressed in Eqn. (1) to (4). It is assumed in these calculations that the fibres all have an equal length L_f and are cylindrical. Therefore the volume and inverse volume weightings are simplified as square radius and square inverse radius weightings ($V_i \propto R_{f,i}^2$).

$$R_{f,NWQ} = \sqrt{\frac{1}{N_f}\sum_j R_{fj}^2} \tag{1}$$

$$R_{f,NWA} = \frac{1}{N_f}\sum_j R_{fj} \tag{2}$$

$$R_{f,VW} = \frac{\sum_j V_j R_{fj}}{\sum_j V_j} \approx \frac{\sum_j R_{fj}^3}{\sum_j R_{fj}^2} \tag{3}$$

$$R_{f,IVW} = \frac{\sum_j \frac{1}{V_j} R_{fj}}{\sum_j \frac{1}{V_j}} \approx \frac{\sum_j R_{fj}^{-1}}{\sum_j R_{fj}^{-2}} \tag{4}$$

2.2.4 *Estimation of airflow resistivity*

In order to evaluate the relationships presented in Eqn. (1) to (4), it was first decided to use the values obtained to determine the airflow resistivity of the materials, a key parameter in acoustic absorption modelling methods.

Two micro-macro modelling methods, proposing analytical relationships between a fibre radius value and characteristic pore network parameters, were selected for this work. These are the modelling approaches of Tarnow (Eqn. (5) for perpendicular incidence with random fibre arrangement) [8] and Umnova (Eqn. (6) for perpendicular incidence) [9] :

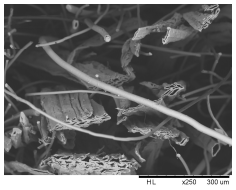
$$\sigma_{\perp} = 4\eta \frac{1-\phi}{R_f^2\left[0.64ln(1/(1-\phi)) - 0.737 + (1-\phi)\right]} \tag{5}$$

$$\sigma_{\perp} = \frac{16\eta}{R_f^2} \frac{(1-\phi)}{-2ln(1-\phi) - 2\phi - \phi^2} \tag{6}$$

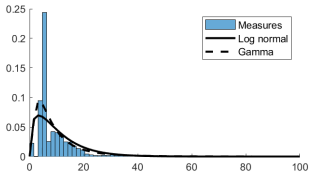
3. RESULTS

3.1 Measurements of fibre radius distributions

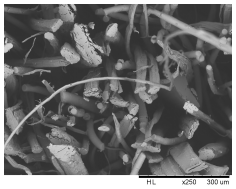
The images obtained with the SEM are displayed in Fig 1(a),(c) and (e). In Fig 1(b),(d) and (f) the resulting radius probability distributions calculated with the software ImageJ are presented.



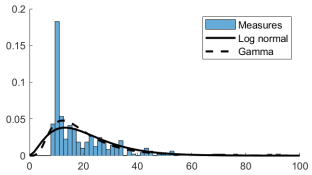
(a) Wood wool x250



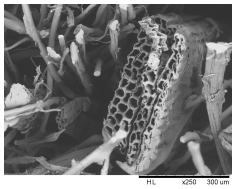
(b) Wood fibres radius distribution



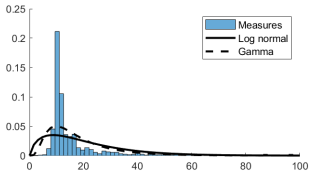
(c) Kenaf wool x250



(d) Hemp-Flax fibres radius distribution



(e) Hemp-Flax wool x250



(f) Wood-Kenaf fibres radius distribution

Figure 1: Photos of wood, wood-kenaf and hemp-flax wools with the SEM, with measured radius probability distributions.

3.2 Average radii

These distributions allowed the calculation of average radii following the methods in Eqn. (1) to (4). They are presented in Tab. 2.

3.3 Using the radii in the calculations

Using the average radii found for the global distribution and this formula, we can compare the predicted resistivity with the values obtained via indirect (Kundt tube) measurements.

The four averaging methods of the global distributions were considered. The results are displayed with the experimental values in Fig 2. To estimate the accuracy of our new analytical results, the ratios for every method was calculated relatively to these characterisation values, as presented in Tab. 3.

4. CONCLUSION AND PERSPECTIVES

All three of the material's radius distributions showcase a peak between $5\mu m$ and $10\mu m$. This is due to the presence of the polymeric fibres. Although they represent a low mass proportion of the fibres used, between 10% and 20%, thanks to their lower mean radius, they can represent between 34% and 77% of the total measured fibres.

When calculating the different average radii, what can be observed is that these calculations show very contrasted results. This is easily explainable due to the quadratic and cubic exponents augmenting the part played by the highest radii in the results. In ascending order, we have radii obtained with Inverse Volume Weight IVW, for which the lowest radii are more impactful, then arithmetic average NWA which is linear, quadratic average NWQ, and volume weight average VW, with quadratic and cubic exponents. The contrast can vary from almost equal for poly-

Table 2: R_f calculated with different averaging methods : Non Weighted Quadratic (NWQ), Non Weighted arithmetic (NWA), Volume Weighted (VW), Inverse Volume Weighted (IVW)

$R_f(\mu m)$		W	HF	WK
Global	NWA	10.8	20.7	20.7
	NWQ	21.0	26.3	34.0
	VW	210.9	54.7	139.3
	IVW	5.7	12.3	10.1
Vegetal	NWA	25.1	26.1	41.0
	NWQ	41.5	31.5	58.9
	VW	228.8	57.3	152.5
	IVW	13.6	15.7	13.3
Polymer	NWA	6.4	10.4	12.0
	NWQ	6.9	10.5	13.2
	VW	8.6	11.2	26.7
	IVW	5.4	10.1	10.8

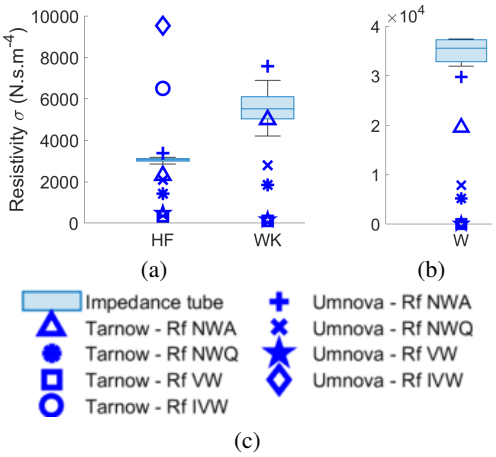


Figure 2: Predicted resistivity versus indirect measurements for the hemp-flax wool (HF), wood-kenaf wool (WK), and wood wool (W)

meric fibres, that have narrow distributions, to thirty-six times between the VW and IVW average radii of the wood wool.

We note that the two averaging methods producing the highest mean radii, NWQ and VW, systematically lead to a underestimation of the resistivity, whereas IVW, which gives the lowest mean radii, always leads to a great overestimation. In our case of our three materials made of mixed vegetal and polymeric fibres, the averaging method giving

Table 3: Resistivity relative error between measures and analytical estimations for the different averaging methods : Non Weighted Arithmetic (NWA), Non Weighted Quadratic (NWQ), Volume Weighted (VW), Inverse Volume Weighted (IVW)

		Resistivity relative error (%)			
		W	HF	WK	Mean
Tarnow	NWA	-44	-23	-9	-25
	NWQ	-85	-52	-66	-68
	VW	-99.9	-89	-98	-95
	IVW	+102	+117	+277	+166
Umnova	NWA	-15	+12	+38	+11
	NWQ	-77	-30	-49	-52
	VW	-99.8	-84	-97	-94
	IVW	+208	+219	+472	+300

the least error for the calculation of resistivity therefore seems to be a non weighted arithmetic average NWA. The mean error also seems to favour Umnova's formula for the calculation of resistivity. Further investigations will be lead in order to verify the current conclusion. Other vegetal wools will be studied to widen the database and have more statistically relevant results. Also, the biggest fibres measured may be wrongfully counted the same way as the others, because of the equal fibre length hypothesis used for this work. The widest fibres are, in fact, usually not as long as the others, and may need to be removed from the calculations. This would lead to a more precise use of the volume weighting in the calculation of resistivity, even though this method is not recommended. Another improvement could be brought with the use of a composite method [6], considering two or three parallel materials made of the types of fibres found in the wools, and in fine combining the results of the calculations.

The next step will then be to replicate this work for the modelling of sound absorption. Eventually, with knowledge on the fibre radius distributions for different vegetal fibres and having suitable analytical modelling methods, it will be possible to optimise the performances of a vegetal wool panel through its fibre radius distribution.

5. FUNDING

This research was funded, in whole or in part, by l'Agence Nationale de la Recherche (ANR), project ANR-23-CE22-0012.

6. ACKNOWLEDGEMENTS

I would like to acknowledge Melek Ayadi who first taught me how to use a Scanning Electronic Microscope, and Camille Chateau for sending me resources on image analysis with ImageJ.

7. REFERENCES

[1] F. Pittau, F. Krause, G. Lumia, and G. Habert, "Fast-growing bio-based materials as an opportunity for storing carbon in exterior walls," *Building and Environment*, vol. 129, pp. 117–129, Feb. 2018.

[2] F. Pittau, G. Habert, and G. Iannaccone, "The renovation of the building stock in Europe: an essential opportunity to store carbon in buildings," *TEMA: Technologies, Engineering, Materials and Architecture*, vol. 5, no. 2, pp. 147–157, 2019. Publisher: Ar. Tec.

[3] M. Schulte, I. Lewandowski, R. Pude, and M. Wagner, "Comparative life cycle assessment of bio-based insulation materials: Environmental and economic performances," *GCB Bioenergy*, vol. 13, pp. 979–998, June 2021. Publisher: John Wiley & Sons, Ltd.

[4] G. Almeida, R. Remond, and P. Perré, "Hygroscopic behaviour of lignocellulosic materials: Dataset at oscillating relative humidity variations," *Journal of Building Engineering*, vol. 19, pp. 320–333, 2018. Publisher: Elsevier.

[5] M. Lawrence, A. Shea, P. Walker, and P. De Wilde, "Hygrothermal performance of bio-based insulation materials," *Proceedings of the Institution of Civil Engineers - Construction Materials*, vol. 166, no. 4, pp. 257–263, 2013. _eprint: https://doi.org/10.1680/coma.12.00031.

[6] C. Piégay, P. Glé, E. Gourdon, E. Gourlay, and S. Marceau, "Acoustical model of vegetal wools including two types of fibers," *Applied Acoustics*, vol. 129, pp. 36–46, Jan. 2018.

[7] F. Pompoli, "Acoustical Characterization and Modeling of Sustainable Posidonia Fibers," *Applied Sciences*, vol. 13, no. 7, 2023.

[8] V. Tarnow, "Airflow resistivity of models of fibrous acoustic materials," *The Journal of the Acoustical Society of America*, vol. 100, pp. 3706–3713, Dec. 1996.

[9] O. Umnova, D. Tsiklauri, and R. Venegas, "Effect of boundary slip on the acoustical properties of microporous materials," *J. Acoust. Soc. Am*, vol. 126 (4), pp. 1850–1861, 2009.

[10] Q. V. Tran, C. Perrot, R. Panneton, M. T. Hoang, L. Dejaeger, V. Marcel, and M. Jouve, "Utilizing polydispersity in three-dimensional random fibrous based sound absorbing materials," *Materials & Design*, vol. 247, p. 113375, Nov. 2024.

[11] T. Iwase, Y. Izumi, and R. Kawabata, "A new measuring method for sound propagation constant by using sound tube without any air spaces back of a test material," Oct. 1998.

[12] Y. Salissou and R. Panneton, "Wideband characterization of the complex wave number and characteristic impedance of sound absorbers," *The Journal of the Acoustical Society of America*, vol. 128, pp. 2868–2876, Nov. 2010.

[13] X. Olny and R. Panneton, "Acoustical determination of the parameters governing thermal dissipation in porous media," *The Journal of the Acoustical Society of America*, vol. 123, pp. 814–824, Feb. 2008.

[14] R. Panneton and X. Olny, "Acoustical determination of the parameters governing viscous dissipation in porous media," *The Journal of the Acoustical Society of America*, vol. 119, pp. 2027–2040, Apr. 2006.

[15] H. G. Merkus, *Particle Size Measurements: Fundamentals, Practice, Quality*. Springer Science & Business Media, Jan. 2009.

[16] W. Garat, S. Corn, N. Le Moigne, J. Beaugrand, and A. Bergeret, "Analysis of the morphometric variations in natural fibres by automated laser scanning: Towards an efficient and reliable assessment of the cross-sectional area," *Composites Part A: Applied Science and Manufacturing*, vol. 108, pp. 114–123, May 2018.

[17] C. Piégay, P. Glé, E. Gourlay, E. Gourdon, and S. Marceau, "A self-consistent approach for the acoustical modeling of vegetal wools," *Journal of Sound and Vibration*, vol. 495, p. 115911, Mar. 2021.

[18] Y. Xue, J. S. Bolton, R. Gerdes, S. Lee, and T. Herdtle, "Prediction of airflow resistivity of fibrous acoustical media having two fiber components and a distribution of fiber radii," *Applied Acoustics*, vol. 134, pp. 145–153, May 2018.

[19] C. Peyrega and D. Jeulin, "Estimation of acoustic properties and of the representative volume element of random fibrous media," *Journal of Applied Physics*, vol. 113, p. 104901, Mar. 2013.

DOI: 10.61782/fa.2025.0365

FORUM ACUSTICUM EURONOISE 2025

EVALUATION OF METHODS FOR MODELLING THE IMPACT OF FLAME-RETARDANT TREATMENTS ON THE ACOUSTIC PERFORMANCE OF HEMP WOOLS

Clément Piégay[1*] **Thomas Schatzmayr Welp Sá**[1,2] **Hugo Bossert**[1]
Lucien Mutel[1] **Sandrine Marceau**[2] **Philippe Glé**[1] **César Segovia**[3]
[1] CEREMA, Univ Gustave Eiffel, UMRAE, 11 rue Jean Mentelin, F-67035 Strasbourg, France
[2] CPDM - Université Gustave Eiffel, 14-20 Boulevard Newton, 77454 Marne-la-Vallée, France
[3] CETELOR - Université de Lorraine, 27 Rue Philippe Seguin, 88051 Epinal, France

ABSTRACT

Hemp wools are bio-based insulating materials whose applications in green buildings are limited due to their flammable and flame-spreading nature. To overcome this problem while respecting their nature, an environmentally- friendly fire-retardant based on a mix of phosphorus and urea products has been identified. However, experimental characterizations using an impedance tube have shown that this treatment has an impact on the acoustic performance of vegetal wools and therefore on the microstructure of the materials. Until now, this type of impact has not really been studied in the literature. To better understand the effects of fire retardant treatments on the porous and fibrous structure characteristics of hemp wool samples, parameters related to the effects of visco-thermal dissipation such as porosity and airflow resistivity were determined and analyzed. Then, their evolution before and after treatment was evaluated. On the basis of these data, the acoustic absorption of hemp wools could be simulated using equivalent fluid modeling methods (JCAL) and compared with the experimental results for validation. In addition, the variation in fiber radii due to the fire-retardant treatment can be assessed indirectly using micro-macro homogenization methods.

Keywords: *Bio-based materials, Hemp wool, Fireproof treatment, Sound absorption, Homogenization modeling methods.*

**Corresponding author*: *clement.piegay@cerema.fr.*
Copyright: ©2025 Piégay et al. This is an open-access article distributed under the terms of the Creative Commons Attribution 3.0 Unported License, which permits unrestricted use, distribution, and reproduction in any medium, provided the original author and source are credited.

1. INTRODUCTION

On a global scale, according to one of the latest IPCC reports [1], the building field remains one of the main emitters of greenhouse gases (GHG) contributing to climate change. In Europe, with three quarters of the buildings built before 1980, often without thermal regulations [2], this sector has a decisive role to play in achieving European climate objectives. The building sector is also a key element in the fight against noise pollution. According to the EEA [3], in 2019, at least 20% of the European population was exposed to noise levels considered harmful to human health. In this context, acoustic and thermal insulation of both existing and new buildings is therefore a major issue in Europe as on a global scale. In order to respond to these problems, bio-based materials, such as vegetal wools, appear to be the type of insulation that offers the most climate-friendly solution [4, 5]. Indeed, their multifunctional performances, which are directly related to their fibrous and porous microstructure, and their hygroscopic nature contribute greatly to the improvement of acoustic and hygrothermal interior comfort. In addition, they contribute significantly to the storage of atmospheric carbon dioxide [6]. Nevertheless, a number of obstacles still limit their use, such as their flammable and flame-spreading nature [7]. So, to be used in public buildings or as apparent panels such as acoustic baffle or suspended ceiling tile, it is necessary to apply a fireproof treatment. Recent works [8] offer promising ways for

treatment with renewable bio-based compounds which are environmentally friendly and compatible with bio-based materials. However, there are very few studies in the literature concerning the impact of such flame retardants on vegetal wools [9]. As a first step, it would seem appropriate to quantify their impact on the acoustic properties at the wool scale. Then, it is therefore essential to better understand the effect of the selected flame retardant on the microstructure of materials. Indeed, acoustic properties, such as the sound absorption of vegetal wools, are directly related to the diameter of the fibers [10].

2. MATERIALS AND METHODS

2.1 Materials

The materials are hemp wools manufactured using a thermobonding process. A reference wool was manufactured without flame retardant treatment. For the other wools, the hemp fibers were treated before manufacture by a fireproof treatment consisting of a mixture of phytic acid and urea. This treatment is applied by spraying with two different formulations of fireproof treatment concentrations, 3% and 5% . An example of treated and untreated samples is shown in Fig. 1. The characteristics of the treated and untreated samples are referenced in Tab. 1. The samples used have thicknesses (e) and apparent densities (ρ_a) of the same order of magnitude in order to compare the sound absorption properties of the samples.



Figure 1. Reference sample on the left, treated sample on the right

Table 1. Characteristics of treated and untreated samples

Sample	Treatment (%)	e (mm)	ρ_a (kg.m-3)
Ref	-	34	63
T3%	3	36	63
T5%	5	35	61

2.2 Methods

2.2.1 Sound absorption

Characterization of sound absorption (α) was carried out using an impedance tube in accordance with standard ISO 10534-2 [11] at normal incidence. The characterization method is based on the use of the 3-microphones method originally developed by Iwase et al. [12] and adapted by Salissou and Panneton [13]. The diameter of the impedance tube (Akustik Forschung - AcoustiTube AFD 1000/1200) used in this work is 100 mm, allowing measurements over a frequency range from 100 to 2000 Hz.

2.2.2 Sound absorption modeling method

The JCAL approach based on the successive works of Johnson [14], Champoux and Allard [15], Lafarge [16] is used to simulate the acoustic performance of the treated and untreated materials. This is a proven semi-phenomenological approach for assessing the effect of the fireproofing treatment on pore geometry. This model is based on the use of 6 input parameters: porosity (ϕ), airflow resistivity (σ), tortuosity (α_∞), viscous characteristic length (Λ), thermal characteristic length (Λ') and static thermal permeability (k_0'). These parameters are characterized by indirect analytical methods presented in Panneton and Olny [17] and Olny and Panneton [18] as a function of the intrinsic parameters, dynamic density and bulk modulus, obtained from impedance tube measurements using the 3-microphone method.

2.2.3 Fiber size modeling method

As well as assessing the impact of fireproofing treatments on the pore network, it would also seem appropriate to evaluate their impact on fiber size. Indeed, the sound absorption properties of vegetal wools are directly related to the size of the fibers [10]. It is therefore possible to use

Tarnow's homogenization method [19], which has already been validated for hemp wools [20]. This method provides analytical relationships between an equivalent fiber radius value (R_f) and acoustic parameters such as porosity (ϕ) and airflow resistivity (σ). The relationship used in this paper, Eqn. (1), corresponds to the configuration of a random fiber distribution and a flow perpendicular to the longitudinal axis of the fibers.

$$R_f = \sqrt{4\mu \frac{(1-\phi)}{\sigma(0.640 \ln(\frac{1}{1-\phi}) - 0.737 + (1-\phi)}} \quad (1)$$

With $\mu = 1.8.10^{-5} Pa.s$ the dynamic viscosity of air.

3. RESULTS AND ANALYSIS

3.1 Sound absorption

As shown in Fig. 2, the experimental results obtained using the impedance tube clearly show a negative impact of fire retardant treatments on the sound absorption coefficient of hemp wool. In addition, there is a correlation between the percentage content of this treatment and the drop in the absorption level and the shift towards higher frequencies.

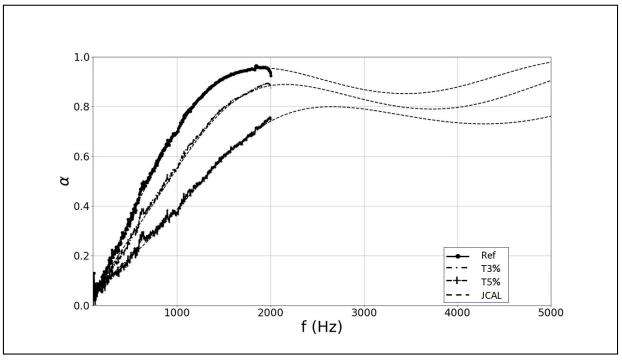


Figure 2. Sound absorption coefficient determined by experimental characterisation and JCAL modelling for reference plant wools, treated at 3% and 5%.

Fig. 2 also illustrates the good correlation between the experimental results and the JCAL modeling. Now, to understand the drop in sound absorption performance, it would seem appropriate to assess the impact of the treatment on the porosity and airflow resistivity of the materials, which are key parameters of the pore network.

3.2 Porosity

There is no significant impact of the fireproof treatment on the porosity of hemp wool. In fact, the porosity of the reference wool was evaluated at 95.8% and at 96.2% for treated wools. This minor difference cannot explain the drop in the sound absorption coefficient observed in Fig. 2. So, it is therefore important to assess the impact of treatment on airflow resistivity.

3.3 Airflow resistivity

The Fig. 3 shows the evolution of airflow resistivity values as a function of treatment concentration. A significant drop can be seen with values of 6257 $Nm^{-4}s$ for the reference hemp wool, 5150 $Nm^{-4}s$ for the wool treated with 3% and 3700 $Nm^{-4}s$ for the wool treated with 5%. Based on this result, we can expect that the fireproof treatment has a coating effect on the fibers, leading to a weakening of the airflow resistivity of the materials.

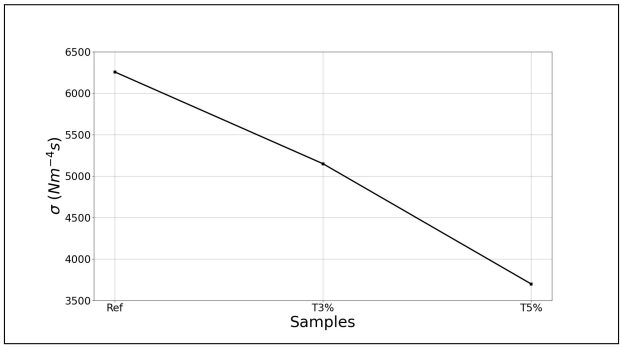


Figure 3. Airflow resistivity for reference hemp wool and treated hemp wools at 3% and 5%.

3.4 Fiber radius

From the above porosity (ϕ) and resistivity (σ) data, it is possible to estimate an effective fiber radius value using Eqn. (1) for each type of treated and untreated hemp wool. The values obtained are indicated in the Tab. 1. The value obtained for untreated hemp wool corresponds to the radius range generally determined from scanning electron microscope image analysis [10]. First of all, we can see higher values for treated wools. This can be explained by a coating effect on the fibers due to the use of the fireproof treatment. In addition, an increase in the value of the effective fiber radii is observed as a function of the concentration of the treatment.

Table 2. Effective fiber radii estimated using the Tarnow modelling method [19]

Sample	$R_f(\mu m)$
Ref	15.5
T3%	16.0
T5%	18.9

4. CONCLUSION

The identification of an effective fireproof treatment that respects the bio-based nature of hemp wool has opened up new prospects for the use of bio-based insulation in green buildings. However, the tests carried out using an impedance tube as part of this work show that the more concentrated the treatment is, the greater the impact both on the level of sound absorption of the wools and on the frequency range, with a shift towards high frequencies. It is shown that the treatment has a minor impact on the porosity of the wools. On the other hand, it has a much more significant effect on airflow resistivity, which helps to explain the impact on acoustic absorption. Tarnow's homogenization method was used to assess the effect of the fireproof treatment on fiber size. A correlation was observed between the concentration of the treatment and the increase in the effective radius of the fibers. This can be explained by a coating effect of the treatment on the fibers. In order to limit these impacts on sound absorption performance, the density of the wools could be considered as a lever for optimization. In addition, it may be appropriate to assess the behavior of materials by applying the treatment by spraying the surface instead of treating all the fibers.

5. FUNDING

This project has received funding from the European Union's Horizon 2020 research and innovation programme under the Marie Slkodowska-Curie COFUND grant agreement No 101034248 and from the French Agence Nationale de la Recherche (ANR) under grant ANR-23- CE22–0012 (Project BIOMETA).

6. REFERENCES

[1] Intergovernmental Panel On Climate Change (Ipcc), *Climate Change 2021 – The Physical Science Basis: Working Group I Contribution to the Sixth Assessment Report of the Intergovernmental Panel on Climate Change*. Cambridge University Press, 1 ed., July 2023.

[2] T. Häkkinen, "Systematic method for the sustainability analysis of refurbishment concepts of exterior walls," *Construction and Building Materials*, vol. 37, pp. 783–790, Dec. 2012.

[3] European Environment Agency., *Environmental noise in Europe, 2020*. LU: Publications Office, 2020.

[4] A. Galimshina, M. Moustapha, A. Hollberg, P. Padey, S. Lasvaux, B. Sudret, and G. Habert, "Bio-based materials as a robust solution for building renovation: A case study," *Applied Energy*, vol. 316, p. 119102, June 2022.

[5] V. Gumanová, L. Sobotová, T. Dzuro, M. Badida, and M. Moravec, "Experimental Survey of the Sound Absorption Performance of Natural Fibres in Comparison with Conventional Insulating Materials," *Sustainability*, vol. 14, p. 4258, Apr. 2022.

[6] G. Habert, G. Iannaccone, and F. Pittau, "The renovation of the building stock in Europe: an essential opportunity to store carbon in buildings," *Rivista Tema*, vol. 05, Oct. 2021.

[7] M. N. A. M. Taib, P. Antov, V. Savov, W. Fatriasari, E. W. Madyaratri, R. Wirawan, L. M. Osvaldová, L. S. Hua, M. A. A. Ghani, S. S. A. O. A. Edrus, L. W. Chen, D. Trache, and M. H. Hussin, "Current progress of biopolymer-based flame retardant," *Polymer Degradation and Stability*, vol. 205, p. 110153, Nov. 2022.

[8] T. Schatzmayr Welp Sá, S. Marceau, C. Piégay, P. Glé, F. Laoutid, C. Segovia, and E. Gourlay, "Comparison of two flame-retardant treatment methods on bulk hemp fibers: Towards a large-scale viability as a raw material for building insulation," *Industrial Crops and Products*, vol. 228, p. 120903, June 2025.

[9] J. Lazko, N. Landercy, F. Laoutid, L. Dangreau, M. Huguet, and O. Talon, "Flame retardant treatments of insulating agro-materials from flax short fibres," *Polymer Degradation and Stability*, vol. 98, pp. 1043–1051, May 2013.

[10] C. Piégay, P. Glé, E. Gourlay, E. Gourdon, and S. Marceau, "A self-consistent approach for the acoustical modeling of vegetal wools," *Journal of Sound and Vibration*, vol. 495, p. 115911, Mar. 2021.

[11] ISO 10534-2, "NF EN ISO 10534-2 Octobre 2023 - acoustics - determination of acoustic properties in impedance tubes - Part 2 : two-microphone technique for normal sound absorption coefficient and normal surface impedance," 2023.

[12] T. Iwase, "A NEW MESURING METHOD FOR SOUND PROPAGATION CONSTANT BY USING SOUND TUBE WITHOUT ANY AIR SPACES BACK OF A TEST MATERIAL,"

[13] Y. Salissou and R. Panneton, "Wideband characterization of the complex wave number and characteristic impedance of sound absorbers," *The Journal of the Acoustical Society of America*, vol. 128, pp. 2868–2876, Nov. 2010.

[14] D. L. Johnson, J. Koplik, and R. Dashen, "Theory of dynamic permeability and tortuosity in fluid-saturated porous media," *Journal of fluid mechanics*, vol. 176, pp. 379–402, 1987. Publisher: Cambridge University Press.

[15] Y. Champoux, M. R. Stinson, and G. A. Daigle, "Air-based system for the measurement of porosity," *The Journal of the Acoustical Society of America*, vol. 89, pp. 910–916, Feb. 1991.

[16] D. Lafarge, P. Lemarinier, J. F. Allard, and V. Tarnow, "Dynamic compressibility of air in porous structures at audible frequencies," *The Journal of the Acoustical Society of America*, vol. 102, pp. 1995–2006, Oct. 1997.

[17] R. Panneton and X. Olny, "Acoustical determination of the parameters governing viscous dissipation in porous media," *The Journal of the Acoustical Society of America*, vol. 119, pp. 2027–2040, Apr. 2006.

[18] X. Olny and R. Panneton, "Acoustical determination of the parameters governing thermal dissipation in porous media," *The Journal of the Acoustical Society of America*, vol. 123, pp. 814–824, Feb. 2008.

[19] V. Tarnow, "Calculation of the dynamic air flow resistivity of fiber materials," *The Journal of the Acoustical Society of America*, vol. 102, pp. 1680–1688, Sept. 1997.

[20] C. Piégay, P. Glé, E. Gourdon, E. Gourlay, and S. Marceau, "Acoustical model of vegetal wools including two types of fibers," *Applied Acoustics*, vol. 129, pp. 36–46, Jan. 2018.

DOI: 10.61782/fa.2025.0592

FORUM ACUSTICUM EURONOISE 2025

MULTI-FUNCTIONAL RAINBOW TRAPPING FILTERS FOR PARTICLE ACOUSTIC AGGLOMERATION

Teresa Bravo[1*] **Cédric Maury**[2] **Muriel Amielh**[3]
Daniel Mazzoni[3]
[1] Institute for Physical and Information Technologies (ITEFI), Spanish National Research Council (CSIC), Madrid, Spain
[2] Laboratory of Mechanics and Acoustics (LMA CNRS UMR 7031), Marseille, France
[3] Institute of Research on Non-Equilibrium Phenomena (IRPHE CNRS UMR 7342), Marseille, France

ABSTRACT

Moving towards global zero-emissions in transport and energy supply industries would enable to achieve a quieter, cleaner and healthier urban environment, more resilient to climate-change. The World Health Organisation has classified traffic noise as the second most important cause of ill health in Western Europe, behind only air pollution caused by very fine particulate matter. A leverage effect would be to enhance the agglomeration of the released ultrafine and fine particles into larger particles easily filtered out by classic clean air solutions. However, a major, still unsolved, challenge is to do it without requiring intense sound fields or high-drag flow mixing devices prone to increase flow-particle or particle-particle relative motion. Acoustic rainbow trapping filters (RTFs) have been shown to provide solutions for wideband low-frequency sound dissipation. In this work, we aim at exploiting the effective slow sound – small wavelength properties of acoustic metamaterials traversed by a low-speed flow to provoke mixing and nucleation of the convected ultrafine particles. We will explore conditions on the physical parameters of the RTFs and the seeded particles to produce simultaneous sound dissipation and particle agglomeration. The results open up multi-functional objectives to achieve simultaneous aerosol agglomeration, sound attenuation and low drag performance.

[*] ***Corresponding author***: teresa.bravo@csic.es.
Copyright: *©2025 Bravo et al. This is an open-access article distributed under the terms of the Creative Commons Attribution 3.0 Unported License, which permits unrestricted use, distribution, and reproduction in any medium, provided the original author and source are credited.*

Keywords: *rainbow trapping filters; particle agglomeration, sound dissipation.*

1. INTRODUCTION

Seven million persons in the world are estimated of being killed by air pollution every year [1]. The release of airborne particulate matters (PM) implies a range of adverse health effects. In particular, the growing concentration of fine particles of diameter lower than 2.5 µm per cubic meter in average per year [2] has a significant economic impact on public health system, and additional efforts have to be made to deeper cuts in emission.

Indoor concentration of particles originating inside or outside buildings relies on particle removal by ventilation filtering systems, that depends strongly on the particle sizes. There is a critical gap in the intermediate size range (0.2-1 µm) where classical filters present a pronounced dip for efficiency [3]. Agglomeration can force the smallest particles to aggregate and the filter can then efficiently capture the largest size components. Numerous applications have been tackled using preconditioning of PM agglomeration by generating ultrasonic standing wave fields. They have shown good performance but need very high levels of acoustic intensity to be efficient [4]. Electrostatic particle agglomerators [5] have also shown a great efficiency, but they also require significant electrical energy consumption to be performant.

In this work we propose a new approach based on the properties of acoustic metamaterials. In particular, we will make use of the "slow sound" generation when acoustic waves propagate in a ducted flow surrounded by a

metamuffler [6-9]. If the effective velocity of the incoming sound wave is progressively reduced to zero, sound waves can be eventually trapped in the meta-structure and the particles suspended in the fluid will oscillate and gradually should agglomerate and increase their sizes. The acoustic performance of the metasilencer is presented in Sec. 2, followed by fundamentals of particle agglomeration in Sec. 3. The simulated results will be analysed in Sec. 4 and we will finish with conclusions and some lines for future work in the last section.

2. ACOUSTICAL MODELLING

2.1 Rainbow trapping filters

Rainbow trapping filters (RTF) are composed of a set of outer cavities with increasing depths that are distributed between the inlet at $x=-L$ towards the outlet at $x=0$, as illustrated in Figure 1. One assumes that such acoustic metamufflers are axisymmetric cylindrical of radius R and length L. Progressive increase of the cavity depths ensures impedance matching and low reflection. It also provides axial variation of the wall impedance, resulting in slow sound and trapping of the incident wave.

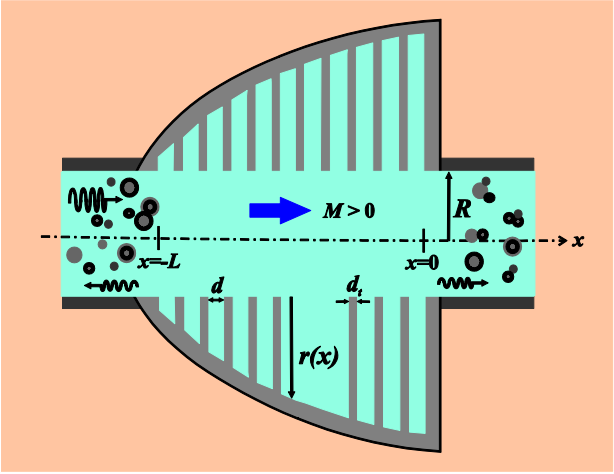


Figure 1. Sketch of a rib-designed rainbow trapping filter traversed by a low-speed flow of grazing Mach number M with an acoustic incident wave travelling along the flow.

A suitable choice of the cavity widths, that can be obtained from optimization of the total dissipation, enables to monitors the amount of visco-thermal losses required to fully dissipate the incident energy trapped within the RTFs.

An RTF with high acoustic performance is characterized by high broadband dissipation, minute reflection and transmission. These properties should be robust when traversed by a low-speed flow. Moreover, the excess friction factor should also be limited, but this aerodynamic constraint will not be considered in the current study. An uncommon design, but with high societal and health impact, is to develop acoustic RTFs that provoke the agglomeration of fine particles into coarser ones that can be readily filtered out by low pressure drop standard filters. The conditions required for these two functionalities will be simulated from transfer matrix modelling for the acoustic part, and from one-dimensional particle transport under drag viscous force for the agglomeration process.

2.2 Transfer matrix modelling

2.2.1 No-flow case

The Transfer Matrix Method (TMM) has been used for the analysis of the widely-opened muffler considering that this device is composed of a set of ring sections separated by air cavities and distributed over an overall length L along the axial dimension. The radii of the air cavities in the fully-opened silencer progressively increase from 0 to R following an expanding power law from the inlet situated at $x=-L$ towards the outlet at $x=0$. Assuming plane wave propagation, the local side-branch volume admittance at $x=x_i$ is given by $Y_{\text{cav},i}=S_{\text{cav}}y(x_i)/Z_0$, with $y(x_i)$ given by Eq. (4) in [6], $S_{\text{cav}}=2\pi Rd$ the cavities entrance area and d their width. Applying continuity of the acoustic pressure and acoustic flow rate across the i^{th} cavity-ring unit leads to the relationship, $[p_i\ u_i]^{\text{T}}=\mathbf{T}_i[p_{i+1}\ u_{i+1}]^{\text{T}}$, between the pressure and volume velocity fields at the input interface $[p_i\ u_i]^{\text{T}}$ and those at the output interface $[p_{i+1}\ u_{i+1}]^{\text{T}}$, with $\mathbf{T}_i$ the associated transfer matrix given by

$$\mathbf{T}_i=\begin{bmatrix}\cos(k_0d) & \mathrm{j}\dfrac{Z_0}{S}\sin(k_0d)\\ \mathrm{j}\dfrac{S}{Z_0}\sin(k_0d) & \cos(k_0d)\end{bmatrix}\times \begin{bmatrix}\cos(k_0d_t) & \mathrm{j}\dfrac{Z_0}{S}\sin(k_0d_t)\\ \mathrm{j}\dfrac{S}{Z_0}\sin(k_0d_t) & \cos(k_0d_t)\end{bmatrix}\times\begin{bmatrix}1 & 0\\ Y_{\text{cav},i} & 1\end{bmatrix} \tag{1}$$

The overall transfer matrix $\mathbf{T}$ between the inlet and the outlet satisfies $[p_1\ u_1]^{\mathrm{T}} = \mathbf{T}[p_{N+1}\ u_{N+1}]^{\mathrm{T}}$ and is expressed as the product of the transfer matrices, $\mathbf{T} = \prod_{i=1}^{N} \mathbf{T}_i = \begin{bmatrix} T_{11} & T_{12} \\ T_{21} & T_{22} \end{bmatrix}$. The expressions for the reflection and transmission coefficients are given by

$$\begin{cases} r = \dfrac{(T_{11} + z_0 T_{12}) - (T_{21} + z_0 T_{22})}{(T_{11} + z_0 T_{12}) + (T_{21} + z_0 T_{22})} \\ t = \dfrac{1 + r}{T_{11} + z_0 T_{12}} \end{cases}. \tag{2}$$

with $z_0 = S/Z_0$ and $S = \pi R^2$. The Johnson-Champoux-Allard-Lafarge model of visco-thermal losses inside the cavities has been used. The power dissipated by the ABH then reads $\eta = 1 - |r|^2 - |t|^2 = \alpha - \tau$ with α the absorption coefficient and τ the transmission coefficient. The transmission loss (TL) is defined as $\mathrm{TL(dB)} = -10\log_{10}(\tau)$.

2.2.2 Low-speed flow effects

The transfer matrix given by Eq. (1) for each cavity cell is extended to account for the convective and dissipative effects of the mean flow on the cell duct sections as well as for the grazing flow effect on the input impedance of the side-branch cavity [10]. It leads to the transfer matrix [11]

$$\widetilde{\mathbf{T}}_L = \mathrm{e}^{-\mathrm{j}M\tilde{k}L} \begin{bmatrix} \cos(\tilde{k}L) & \mathrm{j}\dfrac{Z_0}{S}\sin(\tilde{k}L) \\ \mathrm{j}\dfrac{S}{Z_0}\sin(\tilde{k}L) & \cos(\tilde{k}L) \end{bmatrix}, \tag{3}$$

for a section of length L traversed by a flow at Mach number $M = U/c_0$ with U the mean flow velocity. The duct wavenumber reads $\tilde{k} = (k_0' - \mathrm{j}FM/4R)/(1 - M^2)$ in which k_0' accounts for visco-thermal losses in the duct and $FM/4R$ for the dispersion induced by the turbulent flow, $F = 0.0072 + 0.612\,\mathrm{Re}^{-0.35}$ ($\mathrm{Re} < 4.10^5$) being the Froude's friction factor and $\mathrm{Re} = 2UR\rho_0/\eta$ the ducted flow Reynolds number. Eq. (3) generalizes the two first transfer matrices related in Eq. (1) to sections of length $L = d$ and d_t respectively. Coupling between the ducted flow and the *i*th sidebranch cavity is described by the transfer matrix [11]

$$\widetilde{\mathbf{T}}_{\mathrm{cav},i} = \frac{1}{1 + 2M\widetilde{Y}_{\mathrm{cav},i} z_0^{-1}} \times \begin{bmatrix} 1 + M\widetilde{Y}_{\mathrm{cav},i} z_0^{-1} & M^2 \widetilde{Y}_{\mathrm{cav},i}^2 z_0^{-2} \\ \widetilde{Y}_{\mathrm{cav},i} & 1 + M\widetilde{Y}_{\mathrm{cav},i} z_0^{-1} \end{bmatrix}, \tag{4}$$

so that $\mathbf{T}_i$ in Eq. (1) is replaced by $\widetilde{\mathbf{T}}_i = \widetilde{\mathbf{T}}_d \widetilde{\mathbf{T}}_{d_t} \widetilde{\mathbf{T}}_{\mathrm{cav},i}$. $\widetilde{Y}_{\mathrm{cav},i}$ accounts for the effects of grazing flow on the *i*th cavity input impedance. It can be expressed as [12]

$$\widetilde{Y}_{\mathrm{cav},i} = \frac{1 - M_c H(k_c s)}{Y_{\mathrm{cav},i}^{-1} - 2\dfrac{Z_0}{S_{\mathrm{cav}}} \dfrac{k_0 d}{\pi} \left(1 + \dfrac{\pi d}{4R_i}\right) \dfrac{H(k_c s)}{k_c s}}, \tag{5}$$

in terms of $H(x) = J_0(x)(J_0(x) - \mathrm{j}J_1(x))^{-1}$, $k_c = \omega/U_c$ being the convective wavenumber and $M_c = U_c/c_0$ the convective Mach number with $U_c \approx 0.23\,U$, $R_i = \sqrt{dr(x_i)/\pi}$ and $s = d/2$. The Bessel function terms in H account for the effect of vorticity shed from the cavity upstream edge. Note that Eq. (5) has been derived from linearized perturbation theory [12] assuming a low Mach number flow ($M < 0.3$) and a negligible mean shear across the cavity slit, thereby ruling out any shear layer instability effects.

3. PARTICLE AGGLOMERATION MODELLING

We consider a one-dimensional flow of mean velocity V_a along which propagates an acoustic wave that produces fluid oscillations given by $V_{ac}\sin(k_x x - \omega t)$, so that the total flow velocity reads

$$v_f(x,t) = V_a - V_{ac}\sin(k_x x - \omega t), \tag{6}$$

with $k_x = \omega/c_x$ the acoustic wavenumber and c_x the axial phase speed of the acoustic wave. Assuming that the particle density ρ_p is much greater than the fluid density ρ_0, the effects of inertial and added-mass forces are ignored and only the viscous drag force F_d holds. The equation for particle velocity v_p then reads [13]

$$\frac{dv_p}{dt} = F_d = \frac{1}{St}(v_f - v_p), \tag{7}$$

with $St = \dfrac{\rho_p \omega D_p^2}{18\eta}$ the Stokes number. D_p is the particle diameter. This equation is valid considering a small Stokes number, $St << 1$, meaning that the particles diameter should be small. The condition is achieved for fine ($D_p \leq 2.5\,\mu\text{m}$) and ultrafine ($D_p \leq 0.1\,\mu\text{m}$) particles. It is also required that the particle Reynolds number, $Re_p = \dfrac{2R_p\rho_0|v_f - v_p|}{\eta} \leq 2$. Eq. (7) can then be written in the form $dv_p/dt = (1/t_0)(v_f - v_p)$ with $t_0 = \dfrac{\rho_p D_p^2}{18\eta}$ the particle response time. We can also make the formulation in a moving frame of reference with the phase speed of the acoustic wave c, and in dimensionless form in the position and time by setting $X = kx_p$ and $\tau = \omega t$ [13, 14]. One gets

$$\frac{\mathrm{d}^2X}{\mathrm{d}\tau^2} + \frac{1}{St}\frac{\mathrm{d}X}{\mathrm{d}\tau} + \frac{U_{ac}}{St}\sin(X) = \frac{U_a - 1}{St}, \qquad (8)$$

with $U_a = V_a/c_x$ and $U_{ac} = V_{ac}/c_x$ the dimensionless acoustic and flow velocities. A change of variables can be done such as $\tau' = \tau\sqrt{U_{ac}/St}$, leading to the following equation,

$$\frac{\mathrm{d}^2X}{\mathrm{d}\tau'^2} + \alpha\frac{\mathrm{d}X}{\mathrm{d}\tau'} + \sin(X) = \beta, \qquad (9)$$

with $\alpha = 1/\sqrt{U_{ac}St}$ and $\beta = (U_a - 1)/U_a$. These two parameters control particle agglomeration. The second-order differential equation, Eq. (9), governing the transport of particles under a viscous drag force is solved by a finite-difference Runge-Kutta single-step scheme [15].

4. SIMULATION RESULTS

4.1 Acoustic performance

The acoustical performance of a RTF whose total dissipation has been optimized in plane wave regime [6] are now determined from the transfer matrix formulation presented in Sec. 2.2. It corresponds to a cylindrical rib-designed silencer of radius $R = 0.047\,\text{m}$ and length $L = 0.15\,\text{m}$, comprising a set of $N = 20$ annular cavities of axial width $d = 0.0035\,\text{m}$ separated by ring walls of thickness $d_t = 0.004\,\text{m}$, leading to a wall porosity $\sigma = d/(d + d_t) = 47\,\%$. The optimal rate of increase of the cavity depths is found to be $m = 1.8$. Figure 2 presents the simulated results for the dissipation, reflection and transmission loss power spectra up to the duct cut-on frequency 2142 Hz.

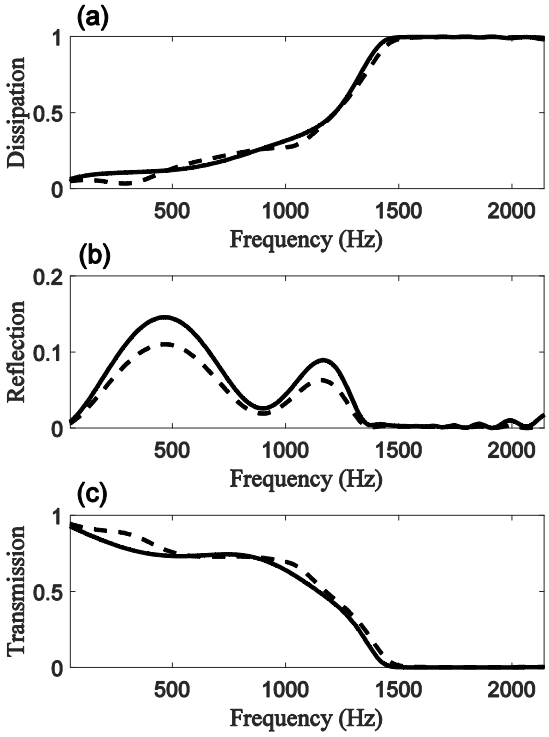


Figure 2. Dissipation (a), reflection (b) and transmission (c) coefficients of a rainbow trapping silencer in the no-flow case (plain) and when traversed by a low-speed grazing flow (dashed) with bulk velocity 20 m.s^{-1}.

Such optimized RTF silencer achieves near-unit dissipation as from 1500 Hz up to the duct cut-on frequency, as seen from Fig. 2(a). The optimization process led to cavity widths with a sufficient amount of visco-thermal losses so that the activated RTF cavity resonances are able to merge and fully dissipate the incident energy over this broad bandwidth. It is accompanied by near-zero reflection that stays below 0.1% over this efficiency range [Fig. 2(b)]. This is caused by the progressive increase of the cavity depths that ensures excellent impedance matching above 1500

Hz. The high dissipative performance result in a minute transmission coefficient above 1500 Hz [Fig. 2(c)]. Figure 3 shows that it translates into high TL values that stays above 27 dB as from 1500 Hz and with a maximum value of 32dB at 1700 Hz. The simulation performance of RTF silencers by the transfer matrix method has been validated against finite element simulations and impedance tube measurements in the no-flow case [6] and against wind-tunnel measurements when traversed by a low-speed flow [10]. The influence of a grazing flow on the acoustical performance of the optimized RTF silencer is also assessed in Figs. 2 and 3 assuming a low-speed bulk velocity of 20 m.s^{-1} (related to a Mach number of 0.06).

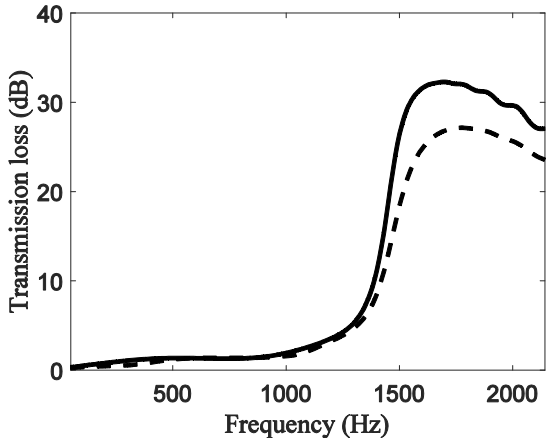


Figure 3. Transmission loss (dB) spectra of a rainbow trapping silencer in the no-flow case (plain) and when traversed by a low-speed grazing flow (dashed) with bulk velocity 20 m.s^{-1}.

As seen in Fig. 1, downstream propagation conditions (DPC) hold in which both the incident wave and the flow travel along the same direction from the inlet to the outlet of the silencer. Such low speed flows produce small effects on the acoustical performance, as seen in Fig. 2. From Fig. 2(a), one observes a moderate upshift (by 40 Hz) of the dissipation spectrum with the near-unit values above 1500 Hz hardly affected by the low-speed flow. The flow influence is mostly noticeable in Fig. 3 with a similar upshift by 40 Hz of the TL bump, but with a decrease by 5 dB of the maximum TL value. This is caused by a decrease of the wall-cavity reactance induced by the flow under DPC as the flow speed increases. A second flow effect is the increase of the wall-cavity resistance under DPC with the flow Mach number. Therefore, the cavity resonances activated over the RTF efficiency bandwidth become slightly over-damped due to the flow effect. This limits the ability of the sound wave to enter the wall cavities and results in a higher transmission and a lower TL. Note that the TL is very sensitive to small amounts of excess damping. Figure 2(b) shows that the impedance matching and reflection properties are weakly modified by the flow.

Of interest is to examine the axial variation of the acoustic velocity within the RTF at different frequencies in plane wave regime: out of the RTF efficiency range (600 Hz), at the onset (1400 Hz) and within (1800 Hz) the RTF high performance bandwidth. The results simulated by the transfer matrix model are illustrated in Fig. 4 with and without flow.

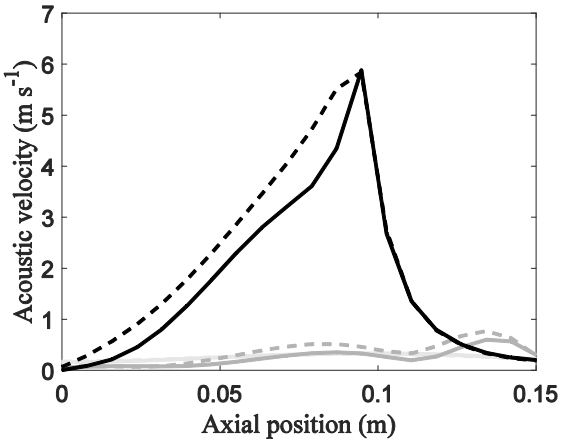


Figure 4. Axial variation of the acoustic velocity within a rainbow trapping filter at 600 Hz (light grey), 1400 Hz (grey) and 1800 Hz (black) in the no-flow case (plain) and when traversed by a low-speed grazing flow (dashed) with bulk velocity 20 m.s^{-1}.

At 600 Hz, the acoustic velocity weakly varies around 0.2 m.s^{-1} (132 dB) along the RTF which is rather inefficient at this frequency. At 1400 Hz, the deepest cavity is about to be activated. Therefore, Fig. 4 shows a slight bump of acoustic velocity around 0.6 m.s^{-1} towards the RTF outlet. At 1800 Hz, the twelfth acoustic cavity (numbered from one to twenty from the inlet to the outlet) is resonant. It results in a significant peak of acoustic velocity at its axial position with a steep (resp. smooth) decay towards the downstream (resp. upstream) cavities. The local rate of increase of the downstream

cavities is smaller than that of the upstream cavities, resulting in a greater density of the downstream resonances (with respect to the upstream resonances). The downstream cavities above order 12 are thus partially activated and also contribute to the dissipation of incident energy. This explains the steep decay of acoustic velocity above these cavities. Converting the acoustic velocity into sound pressure levels (SPLs) requires knowledge of the sound speed which, as seen in Sec. 4.2, varies within the RTF due to slow sound effects. The axial variations of the acoustic velocity in Fig. 4 are not drastically modified by the presence of a low-speed flow. The reactance decrease induced by the flow excites cavities with slightly higher resonance frequencies, e.g. the shallower cavities. This results in higher acoustic velocity for the upstream cavities.

4.2 Slow sound effective properties

Calculations of the axial phase speed $c_x(\omega)$ are achieved from analytical expression of the axial wavenumber $k_x(\omega)$ that appears in the linearized momentum conservation equation [6] that governs the propagation of a plane wave within a RTF with gradual axial variation of the wall impedance along the axial direction. It reads

$$\frac{\mathrm{d}^2 p}{\mathrm{d}x^2} + k_x^2 p = 0\,, \tag{10}$$

with

$$k_x = \frac{\omega}{c_x} = k_0\left[1 - j\frac{y(x)}{k_0 R}\right]^{1/2}, \tag{11}$$

and $y(x)$,defined in Sec. 2.2.1, the specific wall admittance associated to cylindrical cavities of axially increasing depth $r(x) = R\left(1-(-x)^m / L^m\right),\ m>0$.

Axial variations of the phase speed for the sound wave travelling through the RTF is shown in Fig. 5 for various frequencies out, at the onset and within the silencer efficiency range, e.g. at 600 Hz, 1400 Hz and 1800 Hz, respectively. As expected, whatever the frequencies, the axial phase speeds at the inlet of the RTF are equal to the sound speed c_0 of a plane wave travelling in a rigid duct. Within the RTF, the sound wave becomes dispersive and slow sound effects occur. At 600 Hz, $c_x(\omega)$ steadily decays down to 153 m.s^{-1} at the RTF outlet, which is $c_0/2$. At 1400 Hz, the phase speed further decreases and reaches 61 m.s^{-1}, e.g. $c_0/5.6$ at the location of the deepest activated cavity towards the RTF outlet. At 1800 Hz, slow sound effects are even more pronounced with a decay of the phase speed down to 20.5 m.s^{-1}, e.g. $c_0/16.7$, as from 0.09 m, the location of the twelfth activated cavity, until the RTF outlet. A low-speed flow of 20 m.s^{-1} under DPC, simulated by Eq. (5), has a minute effect on the slow sound curves tends to slightly decrease, with only a small uniform decrease of the axial phase speed, whatever the frequency.

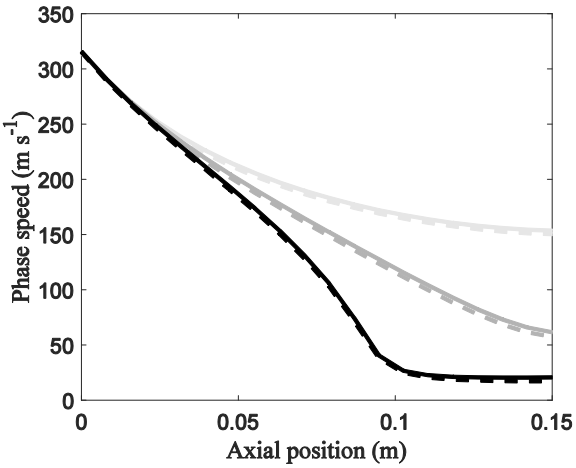


Figure 5. Slow sound effect of an acoustic wave propagating within a rainbow trapping filter at 600 Hz (light grey), 1400 Hz (grey) and 1800 Hz (black) in the no-flow case (plain) and when traversed by a low-speed grazing flow (dashed) with bulk velocity 20 m.s^{-1}.

4.3 Particle axial agglomeration

One considers fine particles of diameter 2µm and density 600 kg.m^{-3}, convected at a mean-flow speed V_a = 20 m.s^{-1} through the acoustically-optimized RTF silencer mounted on a duct. The particles also undergo an oscillatory motion of amplitude V_{ac} and phase speed $c_x(\omega_0)$ due to the slow sound propagation of the acoustic wave at frequency f_0 within the silencer. One assumes monodisperse spherical particles only experiencing viscous drag force induced by the air flow. This is valid for a small Stokes number, defined in Sec. 3, which does not exceed 0.1 at the duct cut-on frequency.

At the initial time, six particles are uniformly distributed over an axial distance of 0.015 m, separated by 3 mm, undergoing the same initial velocity V_a. Eq. (9) is solved using a finite-difference scheme [15]. A condition initially

derived by Sazhin *et al.* [13] for droplet grouping in oscillating flow field, later extended by Zhang *et al.* [14] for acoustic agglomeration in periodic metamaterials, requires that $|\beta| \leq 1$, e.g. $|V_a - c_x| \leq V_{ac}$ for the slow sound to provoke particle agglomeration in an acoustic field with particle velocity V_{ac} convected by mean flow velocity V_a. At 600 Hz, out of the RTF efficiency range, Fig. 6 shows that the trajectories of the particles stay parallel over the length of the silencer, clearly ruling out the occurrence of droplet grouping. Indeed, Fig. 4 showed that V_{ac} stays around 0.2 m.s^{-1} at 600 Hz and Fig. 5 indicates that the smallest phase speed is 153 m.s^{-1} at the RTF outlet. This leads to an agglomeration coefficient β that largely exceeds one, and prevent any grouping of the particles.

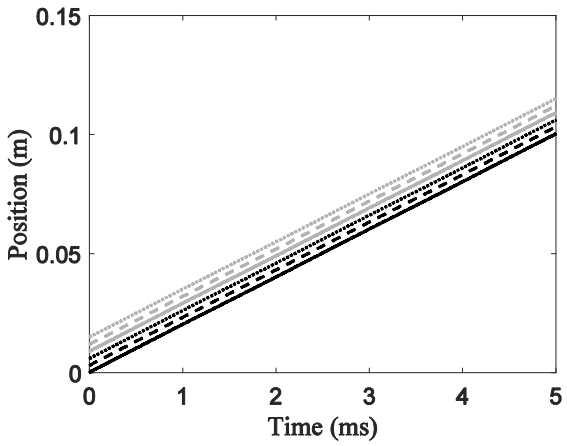


Figure 6. Trajectories of 6 fine particles convected by a low-speed grazing flow with bulk velocity 20 m.s^{-1} within a rainbow trapping filter at 600 Hz, assuming an acoustic phase speed of 153 m.s^{-1} and an acoustic velocity of 0.5 m.s^{-1}.

At 1800 Hz, within the RTF efficiency range, Fig. 7 shows grouping of the six particles into two coarser particles of 6µm diameter, over an axial distance at least 0.09 m apart from the inlet. In this region, at 0.11 m, V_{ac} reaches 2 m.s^{-1} (see Fig. 4) and slow sound effects are prominent with c_x = 20.5 m.s^{-1} (see Fig. 5), resulting in an agglomeration coefficient $\beta = 0.275$ lower than one, that complies with the grouping condition of particles. Figure 8 shows that, if the acoustic velocity is decreased to 0.5 m.s^{-1}, the agglomeration process is still ongoing, but requires a greater duration, and so a longer RTF to ensure slow sound.

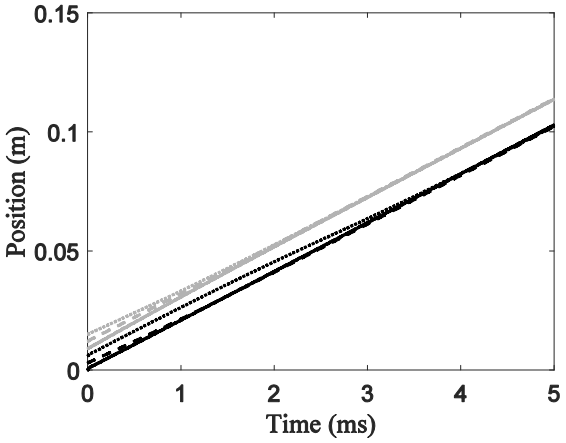


Figure 7. Trajectories of 6 fine particles convected by a low-speed grazing flow with bulk velocity 20 m.s^{-1} within a rainbow trapping filter at 1800 Hz, assuming an acoustic phase speed of 20.5 m.s^{-1} and an acoustic velocity of 2 m.s^{-1}.

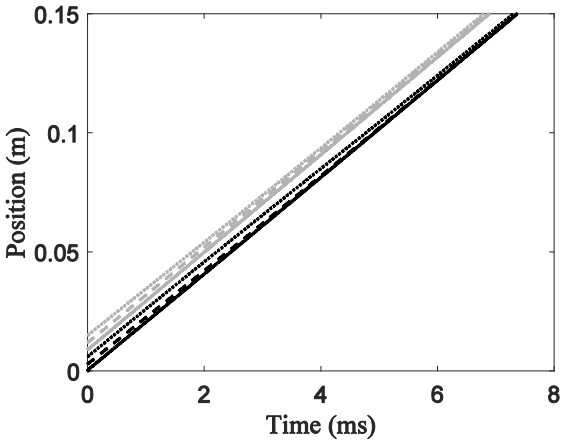


Figure 8. Trajectories of 6 fine particles convected by a low-speed grazing flow with bulk velocity 20 m.s^{-1} within a rainbow trapping filter at 1800 Hz, assuming an acoustic phase speed of 20.5 m.s^{-1} and an acoustic velocity of 0.5 m.s^{-1}.

5. CONCLUSIONS

Conditions under which RTF silencers can achieve multifunctional objectives, namely to fully dissipate the incident sound energy and to agglomerate fine particles into coarser ones, has been discussed in presence of a low-speed flow. Simulations have been carried out based on transfer matrix modelling of the RTF acoustical properties and axial particle transport under viscous drag. It was found that two conditions have to be met to fulfill these objectives. Slow-sound is a pre-requisite to achieve near-unit dissipation over a broad bandwidth, but also for the axial phase speed to get closer from the bulk flow velocity. Moreover, the acoustic velocity within the RTF should be sufficiently high for the agglomeration coefficient to be lower than one and particle grouping to occur at specific axial positions within the RTF. A trade-off should be delineated how to achieve both high attenuation, that creates low acoustic particle velocity, and particle grouping, that requires high particle velocity. This is the object of on-going study as well as the experimental validation of the acoustically-driven particle grouping properties within RTF silencers.

6. ACKNOWLEDGMENTS

This work is part of the project PID2022-139414OB-I00 funded by MCIN/AEI/10.13039/501100011033/ and by "ERDF A way of making Europe". It has also received support from the French government under the France 2030 investment plan, as part of the Initiative d'Excellence d'Aix-Marseille Université - A*MIDEX (AMX-22-RE-AB-157).

7. REFERENCES

[1] Sustainable Development Goal indicator 3.9.1: mortality attributed to air pollution. Geneva: World Health Organization; 2024.

[2] WHO. WHO Ambient Air Quality Database (update 2024). Version 6.1. Geneva, World Health Organization, 2024.

[3] J.T. Hanley, D.S. Ensor, D. D. Smith and L.E. Sparks, "Fractional Aerosol Filtration Efficiency of In-Duct Ventilation Air Cleaners," *Indoor Air,* vol. 4, pp. 169-178, 1994.

[4] G. Reethof, "Acoustic agglomeration of power plant fly ash for environmental and hot gas clean-up," *Noise Control Acoustics,* vol. 110, pp. 552-557, 1988.

[5] W.-Y. Lin, T.-C. Hsiao and B.-L. Hong, "Design and performance of an electrostatic aerosol particle agglomerator," *Journal of the Taiwan Institute of Chemical Engineers*, vol. 107, pp. 110-118, 2020.

[6] T. Bravo and C. Maury: "Broadband sound attenuation and absorption by duct silencers based on the acoustic black hole effect: Simulations and experiments," *Journal of Sound and Vibration*, 561, pp. 117825, 2023.

[7] G. Serra, O. Guasch, M. Arnella, D. Miralles, "Optimization of the profile and distribution of absorption material in sonic black holes," *Mechanical Systems and Signal Processing*, vol. 202, pp. 110707, 2023.

[8] X. Yu, Y. Mi, W. Zhai, L. Cheng, "Principles of progressive slow-sound and critical coupling condition in broadband sonic black hole absorber," *Journal of the Acoustical Society of America*, vol. 154, pp. 2988–3003, 2023.

[9] M. Červenka and M. Bednařík, "On the role of resonance and thermoviscous losses in an implementation of "acoustic black hole" for sound absorption in air," *Wave Motion*, vol. 114, pp. 103039, 2022.

[10] T. Bravo and C. Maury: "Converging rainbow trapping silencers for broadband sound dissipation in a low-speed ducted flow," *Journal of Sound and Vibration*, 589, pp. 118524, 2024.

[11] M. L. Munjal: *Acoustics of Ducts and Mufflers*. 2nd Ed., Hoboken: John Wiley & Sons, 2014.

[12] M. S. Howe, "The influence of grazing flow on the acoustic impedance of a cylindrical wall cavity," *Journal of Sound and Vibration* vol. 67, pp. 533–544, 1975.

[13] S. Sazhin, T, Shakked, V. Sobolev and C. Katoshevski, "Particle grouping in oscillating flows," *European Journal of Mechanics B/Fluids*, 27, pp. 131–149, 2008.

[14] Z. Zhang, M. Abom, H. Boden and M. Karlsson: "Particle Number Reduction in Automotive Exhausts Using Acoustic Metamaterials," *SAE Int. J. Engines* vol. 10 (4), pp. 1-8, 2017.

[15] J. R. Dormand and P. J. Prince, "A family of embedded Runge-Kutta formulae," *J. Comp. Appl. Math.*, Vol. 6, pp. 19–26, 1980.

DOI: 10.61782/fa.2025.0593

FORUM ACUSTICUM EURONOISE 2025

MULTI-RESONANT MATERIAL BASED ON CHANNELS WITH CONTRASTING TORTUOSITY

Tomasz G. Zieliński*
Institute of Fundamental Technological Research
Polish Academy of Sciences
ul. Pawińskiego 5B, 02-106 Warsaw, Poland

Marie-Annick Galland
Ecole Centrale de Lyon, CNRS
UCB Lyon 1, INSA Lyon, LMFA, UMR 5509
Ecully, France

ABSTRACT

The paper presents theoretical and experimental studies on the original multi-resonant sound-absorbing material. A representative geometry of the material contains several channels (disjoint pore networks) of contrasting tortuosity. For the assumed material thickness, one can estimate the quarter-wavelength resonance frequency of each channel based on its tortuosity. The proposed estimate is sufficiently accurate or can be systematically adjusted to eliminate the predictable error. It can therefore be used to design a very effective sound-absorbing layer by tuning the resonance frequencies. This is because the sound absorption peaks for such a layer backed by a rigid wall occur at the resonant frequencies. The tuning is performed by tailoring the shape of the channels to obtain contrasting tortuosities that should distribute their corresponding resonant frequencies over the desired, wide frequency range. In this way, broadband absorption can be achieved. An additional goal of tailoring the channels is to fit them tightly inside the representative space of the material while maintaining their separation. In the proposed material design, all shapes and characteristic sizes are suitable for additive manufacturing, so a sample of the material was 3D printed. It was tested in an impedance tube for sound absorption to validate the theoretical results.

Keywords: *sound absorption, separated pore networks, quarter-wavelength resonances, acoustic metamaterials.*

**Corresponding author*: *tzielins@ippt.pan.pl.*

***Copyright**: ©2025 T. G. Zieliński, M.-A. Galland. This is an open-access article distributed under the terms of the Creative Commons Attribution 3.0 Unported License, which permits unrestricted use, distribution, and reproduction in any medium, provided the original author and source are credited.*

1. INTRODUCTION

Conventional acoustic materials such as open-cell foams, felts, wools and other high-porosity fibrous materials are good sound absorbers, but only in the medium and high frequency range if their thickness is limited to a few centimetres. Broadband sound absorption, including lower frequencies, can be achieved by using very thick layers or almost equally thick multilayer arrangements of such materials [1]. Significant or even perfect sound absorption at individual lower frequencies can be obtained with tuned designs of Helmholtz resonators [2] or micro-perforated plates backed by air cavities with optimised depths [3]. However, these solutions are narrowband and their classical forms are bulky.

Desired sub-wavelength performance, i.e. significant attenuation of low-frequency sound waves by acoustic layers thinner than the wavelength in air, can be achieved using various recently-developed architected acoustic materials and metamaterials [4]. Such acoustic treatments are based on: coiled-up cavities of various geometries [5–8] often covered by micro-perforated plates, labyrinthine channels [9–12], coiled Helmholtz resonators [13], etc. Their performance is typically narrowband. To solve this problem, various multi-resonant solutions enabling broadband absorption of low-frequency sound have been recently proposed and intensively investigated. Representative examples are: parallel assemblies of coiled-up [14,15] or spiral cavities [16], nested networks [17], parallel or nested arrangements of Helmholtz resonators [18, 19].

This work presents a multi-resonant sound-absorbing material based on carefully designed, separated channels. Their shapes are tailored to ensure contrasting tortuosities and fit well into the limited space of the material without overlapping. By increasing (decreasing) the tortuosity, the

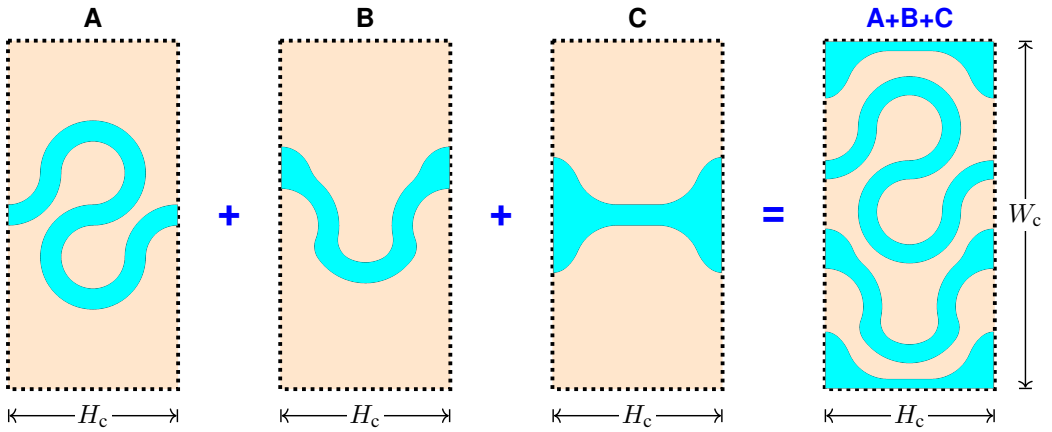


Figure 1. Periodic representative cells for three porous materials, each having a different pore network (A, B, or C), and for a multi-resonant material combining these three networks while keeping them separate.

associated quarter-wavelength resonance can be shifted to the desired lower (higher) frequency [20]. In this way, the resonances are spread over the required frequency range, which ensures broadband operation.

The outline of this paper is as follows. The tortuosity-based design of a multi-resonant material with three separated open-pore networks is discussed in Section 2.1. The main formulas necessary to model sound wave propagation and absorption in such materials are provided in Sections 2.2 and 2.3. Section 3.1 presents a 3D printed sample of the multi-resonant material and its testing configuration. The calculated and measured results of sound absorption by the multi-resonant material are confronted and discussed in Section 3.2. The main findings and conclusions are summarised is Section 4.

2. MATERIAL DESIGN AND MODELLING

2.1 Open-pore networks: designs based on tortuosity

Figure 1 shows four representative cells of periodic porous materials with an essentially two-dimensional structure. All cells are rectangular and have the same dimensions $W_c \times H_c = 16.5\,\text{mm} \times 8\,\text{mm}$. Each of the first three cells contains an open-pore network in the form of a single channel with a carefully designed shape. These networks and consequently the periodic cells and porous materials based on them will be referred to as network, cell or material A, B, and C.

The three networks were designed with the following two objectives in mind:

1. each network should have a designed tortuosity that is significantly different from the tortuosities of other pore networks to ensure different, desired quarter-wavelength resonance frequencies for a material layer of a specified, required thickness;

2. the network shapes should allow for a relatively tight fit within the limited space of a rectangular cell such that all the networks remain separated (i.e. do not overlap and ensure the required wall thickness between them) while providing the highest possible total porosity.

The realisation of the second objective resulted in the construction of the fourth representative cell shown in Figure 1, i.e. the periodic cell with three separated networks A+B+C. The total porosity of this cell (and of a periodic porous material composed of such cells) is the sum of the porosities of the three cells with one network, namely

$$\phi = \phi_A + \phi_B + \phi_C = 42.61\% \,. \tag{1}$$

Here and further in this work, ϕ_N (for N = A, B, and C) denotes the porosity of the periodic cell with a single open-pore network N. The values of these porosities are listed in Table 1.

As part of the design process to achieve the first objective, the Laplace problem for potential, i.e. inviscid flow was solved for each network N = A, B, C, to determine its kinematic tortuosity $\alpha_{\infty N}$ [21, 22]. The calculations were repeated every time the shape of the network was

Table 1. Main design parameters established for the designed networks and periodic representative cells, as well as the estimated and exact values (along with the estimation error) of the quarter-wavelength resonance (QWR) frequencies of the corresponding material layers with thickness $H = 40\,\text{mm}$.

Network N	Porosity ϕ_N [%]	Tortuosity $\alpha_{\infty N}$	QWR frequency* $\widetilde{f}_N$ [Hz]	f_N [Hz]	QWR est. error $\frac{\widetilde{f}_N - f_N}{f_N}$ [%]
A	17.14	9.71	694	645	7.60
B	11.43	3.33	1186	1126	5.33
C	14.04	1.69	1663	1610	3.29

*for $H = 40\,\text{mm}$

modified to tune its resonant behaviour, which was particularly the case for network B. The final tortuosity values are given in Table 1. It should be noted that they are very different from each other and as intended

$$\alpha_{\infty\text{A}} > \alpha_{\infty\text{B}} > \alpha_{\infty\text{C}}\,. \tag{2}$$

One should also notice that $\alpha_{\infty\text{A}}$ is much larger than the tortuosty of any conventional acoustic materials. Moreover, the geometric estimation of this tortuosity is possible and very accurate because network A is a narrow channel with constant width.

The proposed design method based on tortuosity was applied for each of the three networks to tune the respective quarter-wavelength resonance (QWR) frequency f_N of a porous layer with network N and thickness $H = 5H_\text{c} = 40\,\text{mm}$, i.e. containing five periodic cells per layer thickness. This is because, when the network tortuosity $\alpha_{\infty N}$ is known, the QWR frequency can be easily estimated by the upper-limit value $\widetilde{f}_N$, namely

$$f_N < \widetilde{f}_N = \frac{c_0}{4H\sqrt{\alpha_{\infty N}}}. \tag{3}$$

Here, c_0 is the speed of sound in air. The approach was simultaneously applied for all networks $N = \text{A}, \text{B}, \text{and C}$, to distribute the QWR frequencies more or less evenly over the desired frequency range. The upper estimates $\widetilde{f}_N$, listed in Table 1, prove to be very useful for this purpose.

2.2 Equivalent fluid model for sound-absorbing rigid-frame porous materials

The modelling of a multi-resonant acoustic material with multiple separated pore networks is based on the classical model of a porous material with a rigid frame and a single open-pore network. Time-harmonic wave propagation in such materials, with respect to the angular frequency $\omega = 2\pi f$ (f is the ordinary frequency), is determined by solving the Helmholtz equation of linear acoustics. For this purpose, it is first necessary to calculate the effective properties of the porous material modelled as an equivalent fluid, in particular, the effective speed of sound.

Homogenisation by the multi-scale asymptotic method (MAM) [23, 24] results in that the viscous and thermal effects are uncoupled at the micro-scale and the effective properties of a porous material depend on two dynamic permeabilities: one is related to the viscous oscillatory flow through a porous material and the other to the thermal diffusion in the pores. The dynamic viscous permeability $\mathcal{K}_N$ depends, in particular, on the kinematic viscosity ν of the air saturating the pores, while the dynamic thermal permeability Θ_N depends on the the thermal diffusivity of air ν'. Both are complex and frequency dependent functions that can be calculated using the well-known Johnson-Champoux-Allard-Lafarge-Pride (JCALP) model. The JACLP scaling functions depend on macro-parameters related to the structural geometry and static transport properties of the porous material. Therefore, for each porous material N, i.e. each periodic material with an open-pore network $N = \text{A}, \text{B}, \text{or C}$, the dynamic permeabilities are functions of the following parameters

$$\mathcal{K}_N = \mathcal{K}_N(\omega, \nu, \phi_N, \mathcal{K}_{0N}, \Lambda_N, \alpha_{0N}, \alpha_{\infty N}), \tag{4}$$

$$\Theta_N = \Theta_N(\omega, \nu', \phi_N, \Theta_{0N}, \Lambda'_N, \alpha'_{0N}). \tag{5}$$

See Refs. [1, 22] for the actual formulae of the JCALP model. Here, the porosity ϕ_N and the thermal charac-

teristic length Λ'_N are calculated from the geometry of the representative cell with network N, while the viscous characteristic length Λ'_N is determined from the aforementioned Laplace problem that is solved to calculate the kinematic tortuosity $\alpha_{\infty N}$. The static viscous permeability $\mathcal{K}_{0N}$ and the static viscous tortuosity α_{0N} are calculated from the solution of the Stokes flow through the periodic cell with network N, while the static thermal permeability Θ_{0N} and the static thermal tortuosity α'_{0N} are calculated from the solution of the Poisson problem defined on this periodic cell. See Refs. [21, 22, 24] for the details.

The dynamic permeabilities are used to calculate the effective density ϱ_N and the effective compressibility $\mathcal{C}_N$ for each material N, namely

$$\varrho_N = \frac{\nu \varrho_0}{\mathrm{i}\omega \mathcal{K}_N}, \quad \mathcal{C}_N = \frac{\phi_N}{P_0}\left(1 - \frac{\gamma - 1}{\gamma}\frac{\Theta_N}{\phi_N}\frac{\mathrm{i}\omega}{\nu'}\right). \quad (6)$$

where ϱ_0 and γ are the density and adiabatic index of air, respectively, P_0 is the ambient mean pressure, and i is the imaginary unit. Now, the effective speed of sound c_N, the effective wave number k_N, and the effective characteristic impedance Z_N can be calculated as follows

$$c_N = \frac{1}{\sqrt{\varrho_N \mathcal{C}_N}}, \quad k_N = \frac{\omega}{c_N}, \quad Z_N = \varrho_N c_N. \quad (7)$$

Note that not only the wave number but all effective properties are frequency dependent. In particular, $c_N = c_N(f)$ describes the dispersion in a porous material.

The QWR frequency f_N for a porous layer of thickness H can be determined by solving the following nonlinear equation

$$\frac{\mathrm{Re}\, c_N(f_N)}{4 f_N} = H, \quad (8)$$

where the real part of the effective speed of sound defines the acoustic wave velocity in the porous medium. Equation (8) was solved for the three materials N = A, B and C, assuming in each case the same layer thickness $H = 40\,\mathrm{mm}$. The resulting resonance frequencies f_N are compared in Table 1 with their upper-limit estimates $\widetilde{f}_N$, proving that the estimates are quite accurate. The typical expected accuracy is indicated by the relative errors shown in the last column of Table 1.

The surface acoustic impedance is an important acoustic indicator for sound absorbing and isolating materials. For a layer of porous material N and thickness H, it is calculated as

$$\mathcal{Z}_{\mathrm{s}N} = Z_N \coth(\mathrm{i}k_N H)\,. \quad (9)$$

It can be used to calculate other acoustic indicators such as the reflection coefficient $\mathcal{R}_N$ and the sound absorption coefficient $\mathcal{A}_N$, namely

$$\mathcal{R}_N = \frac{\mathcal{Z}_{\mathrm{s}N} - Z_0}{\mathcal{Z}_{\mathrm{s}N} + Z_0}, \quad \mathcal{A}_N = 1 - \left|\mathcal{R}_N\right|^2. \quad (10)$$

Here, $Z_0 = \varrho_0 c_0$ is the characteristic impedance of air.

2.3 Material with multiple, separated pore networks

The material with multiple open-pore networks that are separated from each other can be considered as an assembly of the corresponding single-network materials arranged in parallel, or rather independently occupying the same geometric space. Consequently, in the example investigated in this work, the triple-network periodic material marked as A+B+C (see Figure 1) can be modelled with three effective fluids that are acoustically equivalent to porous materials A, B and C, respectively. These equivalent fluids share the same computational domain, but the wave propagation in each of them is governed by an independent Helmholtz equation. There are therefore three acoustic pressures that are not coupled *within* the computational domain. However, they are coupled – which usually means that they are equalised – on some (or all) of its boundaries, so that wave propagation in the equivalent fluids corresponding to the individual networks is not completely independent. In the case when a layer of the material with multiple, separated networks is backed by a rigid wall, the coupling, i.e. pressure equalisation, occurs only on the front surface of the layer. It is easy to show that the surface acoustic impedance for such a hard-backed layer equals

$$\mathcal{Z}_{\mathrm{s}} = \frac{1}{\sum\limits_{N=\mathrm{A,B,C}} \mathcal{Z}_{\mathrm{s}N}^{-1}} = \frac{1}{1/\mathcal{Z}_{\mathrm{sA}} + 1/\mathcal{Z}_{\mathrm{sB}} + 1/\mathcal{Z}_{\mathrm{sC}}}. \quad (11)$$

This is the classic result for the impedance of a system of components N = A, B, C, set in parallel. It should be noted that the situation becomes much more complicated and dramatically different when the layer is supported by even a very thin air gap and not directly by a rigid wall. This is because in such a case the pressures in all networks also equalise on the back surface of the porous layer. Consequently, determining the surface acoustic impedance requires in this case much more complex calculations [25].

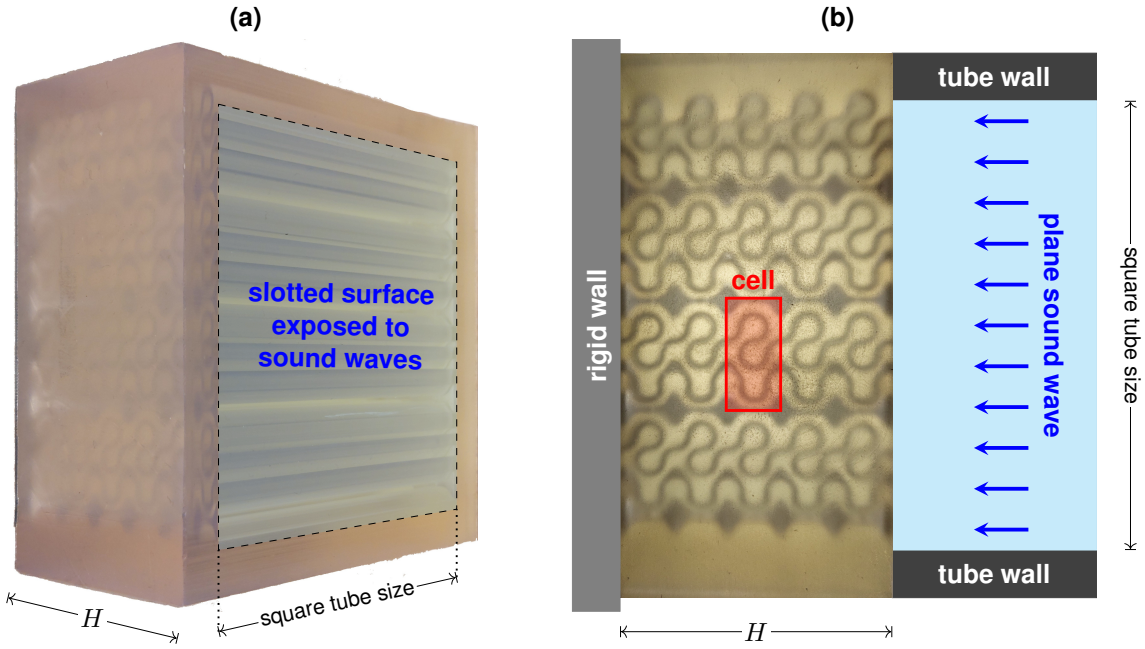


Figure 2. 3D printed sample of the multi-resonant material with three separated pore networks: (a) general view, (b) side view showing all pore networks (due to sample transparency) with one representative cell marked with a red rectangle. In the side view, the sample is placed inside the measurement scheme showing a fragment of a square impedance tube and a plane acoustic wave at normal incidence to the sample surface.

When the surface acoustic impedance $\mathcal{Z}_s$ is determined for the hard-backed multi-resonant material using Equation (11), the corresponding reflection coefficient $\mathcal{R}$ as well as the coefficient of sound absorption $\mathcal{A}$ are calculated using standard formulae, namely

$$\mathcal{R} = \frac{\mathcal{Z}_s - Z_0}{\mathcal{Z}_s + Z_0}, \quad \mathcal{A} = 1 - \left|\mathcal{R}\right|^2. \tag{12}$$

3. PROTOTYPING, TESTING AND VALIDATION OF MULTI-RESONANT MATERIAL

3.1 3D printed sample

Figure 2 (a) shows an additively manufactured sample of the designed multi-resonant material. The sample has a cuboid shape with a square base. Its thickness (height) is $H = 40$ mm. There are twelve slits on the front surface of the sample that lead to (four triplets of) separate networks. The corresponding twelve exit slits on the back side of the sample were sealed with an aluminium tape to prevent sound leakages when the sample was backed by a rigid wall and tested in a 66 mm square impedance tube. The testing configuration is depicted in Figure 2 (b).

The sample was 3D printed in the stereolithography (SLA) technology using a photopolymer resin of low viscosity so that its residues could be removed even from the most tortuous of the network channels. The resin is transparent, so that all the separate networks of the material can be seen in the photograph of one side of the sample shown in Figure 2 (b). The rectangular periodic cell is marked in red in this photograph, mirroring the design labelled as A+B+C in Figure 1. One should notice that there are five such cells per sample thickness. The configuration scheme shown in Figure 2 (b) illustrates how the sample is backed by a rigid wall and impinged at the front by a plane acoustic wave propagating in a square impedance tube.

3.2 Sound absorption: predictions and measurements

The modelling discussed in Section 2 was applied to predict the sound absorption by different material layers in a

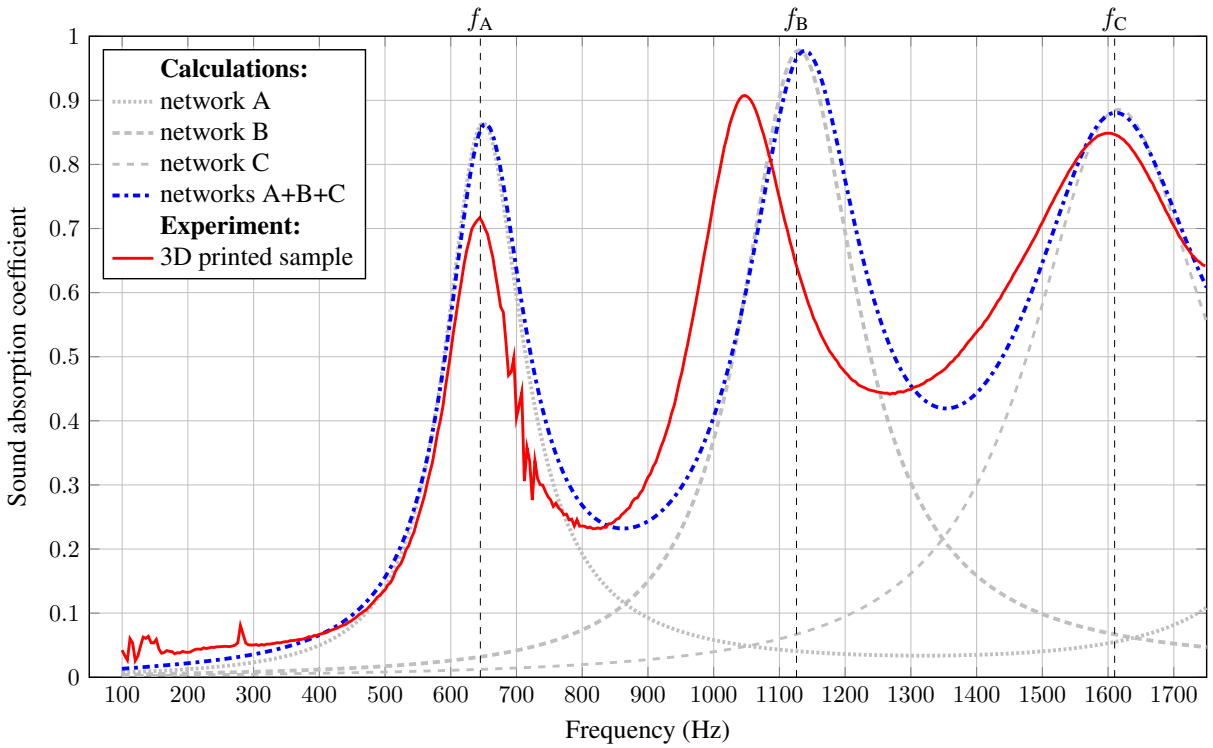


Figure 3. Sound absorption measured for a 3D printed sample of the mutli-resonant material with three pore networks (red curve) compared with the corresponding prediction (blue curve) and with the sound absorption curves calculated for single-network layers (grey curves) of the same thickness.

configuration where the layer under consideration is supported by a rigid wall, as illustrated in Figure 2 (b) for the 3D printed sample. Each material is based on one of the four periodic representative cells shown in Figure 1, which gives the four following cases:

1. a hard-backed porous layer with network A,
2. a hard-backed porous layer with network B,
3. a hard-backed porous layer with network C,
4. a hard-backed porous layer with three separated networks, arranged as in cell A+B+C, see Figure 1.

Each layer has five identical periodic cells along its thickness, which is therefore the same, i.e. $H = 40$ mm, as in the case of the 3D printed sample.

To predict sound absorption by hard-backed layers, the macro-parameters mentioned in Section 2.2 were first calculated for each of the three periodic cells with a single pore network N = A, B, C. In each case, the cell geometry used for calculations was *not exactly* the same as that used to 3D print the sample. However, the necessary geometric modification was minor and generally consisted of reducing the channel width by 0.1 mm to match the actual width of 3D printed channels. Incidentally, the values given in Table 1 were determined for such updated cell geometries. The macro-parameters were used to calculate the effective properties. Then, the sound absorption of each single-network layer was calculated using formulae (9) and (10). Equations (11) and (12) were used to calculate the sound absorption for the layer with three separated networks.

Sound absorption curves determined for the four materials are compared in Figure 3 within the frequency range up to 1.75 kHz. It should be observed that the absorption peak for the hard-backed layer with network A is almost at $f_A = 645$ Hz, which is the QWR frequency predicted for this layer by Equation (8). Similarly, the absorp-

tion peaks for the layer with network B and the layer with network C are close to their respective QWR frequencies. The sound absorption curve marked in blue was calculated for the layer with three separated networks A+B+C. It envelopes the three (grey) curves determined for the single-network layers. This curve envelope closely adheres to the absorption peaks, but not between them, where the sound absorption of the layer with three separate networks is noticeably higher than that of any single-network layer.

The blue sound absorption curve clearly demonstrates the multi-resonant acoustic behaviour of the material with multiple networks. This is confirmed by the experimental results, i.e. the red sound absorption curve in Figure 3, measured in an impedance tube for the 3D printed sample. Discrepancies between calculations and measurements are due to printing imperfections. They should be related to the geometric quality of each 3D printed network. It seems that the shape of the printed network B differs, albeit slightly but significantly, from the shape used to calculate its corresponding macro-parameters. One can expect that the actual tortuosity in this case is slightly larger than the calculated value, because the absorption peak associated with this network occurs at a frequency that is about 80 Hz lower than the predicted value of $f_B = 1126$ Hz.

4. CONCLUSIONS

Broadband low-frequency sound absorption can be achieved by porous materials with separate channels of contrasting tortuosity. Such materials exhibit multi-resonant behaviour and the individual resonant frequencies can be tuned during the design process to the desired values. To ensure overall broadband performance, they should be evenly distributed over the entire frequency range of interest.

In the proposed material design procedure, the main tailoring parameter is the tortuosity of each channel. Knowing this parameter and the material thickness, the quarter-wavelength resonance frequency associated with a given channel can be quickly estimated with acceptable accuracy. In the design process, this resonance can be shifted towards a lower frequency by increasing the tortuosity [20]. Even for a relatively thin material, this can be a very low frequency indeed, provided that the channel tortuosity is sufficiently high.

The design procedure is very efficient, especially for narrow channels of constant width because their tortuosity can be determined analytically with high accuracy based on the channel length [12, 26, 27]. Channel shapes should be designed simultaneously or at least taking into account the already constructed channels. This is because their tortuosities should be significantly different, and moreover, all channels should fit into the material space without overlapping but at the same time allow for the highest possible porosity. Optimised, three-dimensional design of channel shapes should lead to the creation of thin but very efficient and broadband, multi-resonant materials of this type.

5. ACKNOWLEDGMENTS

This research was financially supported by the National Science Centre (NCN), Poland, under Grant Agreement No. 2021/41/B/ST8/04492.

6. REFERENCES

[1] J. F. Allard and N. Atalla, *Propagation of Sound in Porous Media: Modeling Sound Absorbing Materials, 2nd ed.* Chichester: John Wiley & Sons, 2009.

[2] D. T. Blackstock, *Fundamentals of physical acoustics*. New York: Wiley, 2000.

[3] M. Yairi, K. Sakagami, K. Takebayashi, and M. Morimoto, "Excess sound absorption at normal incidence by two microperforated panel absorbers with different impedance," *Acoustical Science and Technology*, vol. 32, no. 5, pp. 194–200, 2011.

[4] J.-P. Groby, N. Jiménez, and V. Romero-García, "Acoustic metamaterial absorbers," in *Acoustic Waves in Periodic Structures, Metamaterials, and Porous Media: From Fundamentals to Industrial Applications* (N. Jiménez, O. Umnova, and J.-P. Groby, eds.), ch. 5, pp. 167–204, Cham: Springer International Publishing, 2021.

[5] X. Cai, Q. Guo, G. Hu, and J. Yang, "Ultrathin low frequency sound absorbing panels based on coplanar spiral tubes or coplanar Helmholtz resonators," *Applied Physics Letters*, vol. 105, p. 121901, 2014.

[6] Y. Li and B. M. Assouar, "Acoustic metasurface-based perfect absorber with deep subwavelength thickness," *Applied Physics Letters*, vol. 108, p. 063502, 2016.

[7] Y. Wang, H. Zhao, H. Yang, J. Zhong, D. Zhao, Z. Lu, and J. Wen, "A tunable sound-absorbing metamaterial based on coiled-up space," *Journal of Applied Physics*, vol. 123, p. 185109, 2018.

[8] G. Catapane, G. Petrone, O. Robin, and K. Verdière, "Coiled quarter wavelength resonators for low-frequency sound absorption under plane wave and diffuse acoustic field excitations," *Applied Acoustics*, vol. 209, p. 109402, 2023.

[9] K. Donda, Y. Zhu, S.-W. Fan, L. Cao, Y. Li, and B. Assouar, "Extreme low-frequency ultrathin acoustic absorbing metasurface," *Applied Physics Letters*, vol. 115, p. 173506, 2019.

[10] S. Kumar and H. P. Lee, "Labyrinthine acoustic metastructures enabling broadband sound absorption and ventilation," *Applied Physics Letters*, vol. 116, p. 134103, 2020.

[11] T. Yuan, X. Song, J. Xu, B. Pan, D. Sui, H. Xiao, and J. Zhou, "Tunable acoustic composite metasurface based porous material for broadband sound absorption," *Composite Structures*, vol. 298, p. 116014, 2022.

[12] T. G. Zieliński, K. C. Opiela, N. Dauchez, T. Boutin, M.-A. Galland, and K. Attenborough, "Extremely tortuous sound absorbers with labyrinthine channels in non-porous and microporous solid skeletons," *Applied Acoustics*, vol. 217, p. 109816, 2024.

[13] J.-S. Chen, Y.-B. Chen, Y.-H. Cheng, and L.-C. Chou, "A sound absorption panel containing coiled helmholtz resonators," *Physics Letters A*, vol. 384, no. 35, p. 126887, 2020.

[14] G. do N. Almeida, E. F. Vergara, L. R. Barbosa, and R. Brum, "Low-frequency sound absorption of a metamaterial with symmetrical-coiled-up spaces," *Applied Acoustics*, vol. 172, p. 107593, 2021.

[15] A. Magnani, C. Marescotti, and F. Pompoli, "Acoustic absorption modeling of single and multiple coiled-up resonators," *Applied Acoustics*, vol. 186, p. 108504, 2022.

[16] A. Carvalho de Sousa, E. Deckers, C. Claeys, and W. Desmet, "On the assembly of Archimedean spiral cavities for sound absorption applications: Design, optimization and experimental validation," *Mechanical Systems and Signal Processing*, vol. 147, p. 107102, 2021.

[17] A. Jamois, D. Dragna, T. G. Zieliński, and M.-A. Galland, "Acoustic absorption of 3D printed samples at normal incidence and as a duct liner," *Acta Acustica*, vol. 9, p. 12, 2025.

[18] X. Yang, X. Shen, F. Yang, Z. Yin, F. Yang, Q. Yang, C. Shen, M. Xu, and J. Wan, "Acoustic metamaterials of modular nested Helmholtz resonators with multiple tunable absorption peaks," *Applied Acoustics*, vol. 213, p. 109647, 2023.

[19] Z. Mei, Y. Lyu, X. Li, X. Cheng, and J. Yang, "Parallel-coupled hierarchical and reconfigurable structure for broadband sound absorption," *Applied Acoustics*, vol. 221, p. 109990, 2024.

[20] K. Attenborough, "Microstructures for lowering the quarter wavelength resonance frequency of a hard-backed rigid-porous layer," *Applied Acoustics*, vol. 130, pp. 188–194, 2018.

[21] C. Perrot, F. Chevillotte, and R. Panneton, "Bottom-up approach for microstructure optimization of sound absorbing materials," *The Journal of the Acoustical Society of America*, vol. 124, no. 2, pp. 940–948, 2008.

[22] T. G. Zieliński, R. Venegas, C. Perrot, M. Červenka, F. Chevillotte, and K. Attenborough, "Benchmarks for microstructure-based modelling of sound absorbing rigid-frame porous media," *Journal of Sound and Vibration*, vol. 483, p. 115441, 2020.

[23] E. Sanchez-Palencia, *Non-Homogenous Media and Vibration Theory*. Lecture Notes in Physics, Springer-Verlag, 1980.

[24] J.-L. Auriault, C. Boutin, and C. Geindreau, *Homogenization of Coupled Phenomena in Heterogenous Media*. ISTE Ltd., John Wiley & Sons, Inc., 2009.

[25] K. Verdière, R. Panneton, S. Elkoun, T. Dupont, and P. Leclaire, "Transfer matrix method applied to the parallel assembly of sound absorbing materials," *The Journal of the Acoustical Society of America*, vol. 134, pp. 4648–4658, 12 2013.

[26] K. Attenborough, "Macro- and micro-structure designs for porous sound absorbers," *Applied Acoustics*, vol. 145, pp. 349–357, 2019.

[27] B. Ghanbarian, A. G. Hunt, R. P. Ewing, and M. Sahimi, "Tortuosity in porous media: A critical review," *Soil Science Society of America Journal*, vol. 77, no. 5, pp. 1461–1477, 2013.

DOI:

Main theme: A10 Materials and Metamaterials

Session A10.09/A12.10 Acoustic wave propagation in complex media

Chair(s): V. Romero-García, T. Valier-Brasier

DOI: 10.61782/fa.2025.0635

FORUM ACUSTICUM EURONOISE 2025

NUMERICAL SIMULATIONS OF ELASTIC WAVE PROPAGATION IN SOLID MATERIALS CONTAINING A RANDOM DISTRIBUTION OF SPHERICAL SCATTERERS

Tanguy Bertels[1] **Tony Valier-Brasier**[1*] **Jean-Marc Conoir**[1]
[1] Sorbonne Université, CNRS, Institut Jean Le Rond d'Alembert, UMR 719,
4 Place Jussieu, Paris, F-75005, France

ABSTRACT

A numerical approach of multiple scattering based on the resolution of multiple scattering equations for elastic waves inside solid heteregenous media is presented. It is validated by extracting the effective velocity and attenuation of longitudinal and transverse coherent inside a dispersion of spherical scatterers embedded in a duralumin matrix.

Keywords: *multiple scattering, elastic waves, coherent wave, effective parameters, numerical approach.*

1. INTRODUCTION

The propagation of elastic waves in multiply scattering solid media is an old problem that has been less studied than the case of acoustic waves (in fluids) or electromagnetic waves. One of the reasons lies in the existence of conversions between longitudinal and transverse waves at the surface of each scatterer. This work presents a new method for simulating elastic wave propagation in heterogeneous media composed of spherical inclusions embedded in a solid matrix. The MuScat code, initially developed to simulate acoustic wave propagation in heterogeneous fluids [1], is adapted to take into account the vector nature of elastic waves in three dimensions. It is based on the analytical solution of the multiple scattering equations using the spherical harmonic expansion of the incident and scattered fields, which allows to consider very large dispersions of particles. In a first section, we describe this general principle behind the code. In a second section, we show the validation of the numerical approach on dispersions of spherical cavities filled with water embedded in a duralumin solid matrix. Note that a similar study has been performed in two dimensions (cylindrical cavities filled with water) in ref. [2].

***Corresponding author**: *tony.valier-brasier@sorbonne-universite.fr.*

Copyright: *©2025 Tanguy Bertels et al. This is an open-access article distributed under the terms of the Creative Commons Attribution 3.0 Unported License, which permits unrestricted use, distribution, and reproduction in any medium, provided the original author and source are credited.*

2. GENERAL PRINCIPLE OF THE MODELING

The modeling behind the MuScat code for elastic waves will be presented in details in a future work. In the following, we indicate the main principles behind it.

We consider an isotropic and homogeneous viscoelastic medium of Lamé parameters (λ, μ) and density ρ (we denote k_L the longitudinal wavenumber and k_T the transverse one) inside which are embedded N_p spheres of respective radii a_p, Lamé parameters (λ_p, μ_p) and densities ρ_p (fig. 2). There is no limitation on the polydisperisty either in size or elasticity.

We follow the T-matrix approach already used in electromagnetism [3, 4], adding the mode conversations between longitudinal and transverse waves that exist in the elastic case (details about this can be found in ref. [5]). Within this framework, the incident displacement field upon the distribution of scatterers is expanded upon the usual Vector Spherical Wavefunctions (VSWF) $\mathbf{L}_{nm}$, $\mathbf{M}_{nm}$ and $\mathbf{N}_{nm}$, that are solutions of the elastic wave equations in an homogeneous medium (see ref. [6] for their definition and properties), as

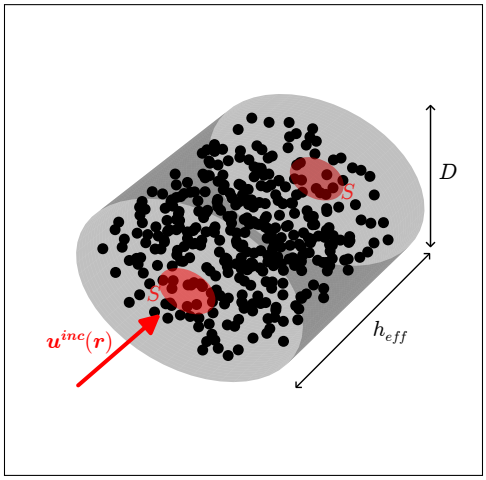


Figure 1. An incident displacement field (plane wave) is sent on a distribution of spherical scatterers placed in a cylindrical slab inside the solid matrix.

$$\mathbf{u}^{inc}(\mathbf{r}_0) = \sum_{n,m}(a_{nm}^{L}\mathbf{L}_{nm}^{(1)}(\mathbf{r}_0) + a_{nm}^{T}\mathbf{N}_{nm}^{(1)}(\mathbf{r}_0) + a_{nm}^{S}\mathbf{M}_{nm}^{(1)}(\mathbf{r}_0)). \quad (1)$$

This field is expressed in an arbitrary coordinates system R_0 ($\mathbf{r}_0$ denotes the position in this system), generally placed at the center of the distribution of scatterers. For convenience we have used the notation $\sum_{n,m} \equiv \sum_{n=0}^{+\infty}\sum_{m=-n}^{+n}$. The superscript (1) denotes the use of the spherical Bessel function of the first kind j_n in the definition of the VSWF. The coefficients a_{nm}^{M} are the amplitudes of the incident field and are known. The L part refers to longitudinal contributions to the displacement field whereas the T and S parts represent the transverse ones. The total field $\mathbf{u}$, which we seek to express, is

$$\mathbf{u} = \mathbf{u}^{inc}(\mathbf{r}_0) + \sum_{p=1}^{N_p}\mathbf{u}_p^{sc}(\mathbf{r}_p), \quad (2)$$

where $\mathbf{u}_p^{sc}(\mathbf{r}_p)$ is the scattered field of the p-th particule expressed in its local coordinates system R_p. Those fields are also expanded on the VSWF and are thus written

$$\mathbf{u}^{sc}(\mathbf{r}_p) = \sum_{n,m}(b_{nm}^{p,L}\mathbf{L}_{nm}^{(3)}(\mathbf{r}_p) + b_{nm}^{p,T}\mathbf{N}_{nm}^{(3)}(\mathbf{r}_p) + b_{nm}^{p,S}\mathbf{M}_{nm}^{(3)}(\mathbf{r}_p)). \quad (3)$$

The superscript (3) indicates here the use of the spherical Hankel function of the first kind $h_n^{(1)}$ in the definition of the VSWF. The coefficients $b_{nm}^{p,M}$ are the amplitudes of the mode $M = L, T, S$ of the scattered field of the p-th particle and are thus the unknowns of the problem. Using the addition theorems for VSWF [4, 7] we can express the excited field on the p-th particle $\mathbf{u}_p^{ex} = \mathbf{u}^{inc} + \sum_{q\neq p}\mathbf{u}_q^{sc}$ in its local coordinates system R_p. Knowing the T-matrix of the particle, we can eventually write a linear system that allows to find the coefficients $b_{nm}^{p,M}$ and then determine the total field. This system is solved numerically by introducing a modal truncature and using iterative methods.

3. EXTRACTION OF EFFECTIVE PARAMETERS OF A MULTIPLE SCATTERING MEDIUM

3.1 The coherent field

The validation of the numerical approach is here realized by comparison with a vector multiple scattering model (denoted as the LCVB model) giving the effective parameters of the coherent longitudinal and transverse waves [5]. Indeed, the displacement field for a realization of the disorder can be written $\mathbf{u} = \langle\mathbf{u}\rangle + \delta\mathbf{u}$, where $\langle\cdot\rangle$ denotes the configurational average. $\langle\mathbf{u}\rangle$ is thus the coherent field. It can be written

$$\langle\mathbf{u}\rangle = u_0 \mathrm{e}^{\mathrm{i}k_{eff}z}\hat{\mathbf{p}}, \quad (4)$$

where $\hat{\mathbf{p}}$ is the polarization of the incident wave and k_M^{eff} is the so-called effective wave number ($M = L$ for a longitudinal wave, $M = T$ for a transverse one). We have $k_M^{eff} = \omega/c_M^{eff} + \mathrm{i}\,\alpha_M^{eff}$, where c_M^{eff} is the effective velocity of the coherent wave and α_M^{eff} its effective attenuation. The propagation of the coherent wave is thus modeled as the propagation of an elastic wave of polarization $\hat{\mathbf{p}}$ inside an effective homogeneous medium. The two parameters c_M^{eff} and α_M^{eff} characterize the multiple scattering medium.

3.2 Results and discussion

We consider the propagation of an elastic wave inside a dispersion of spherical cavities (all with the same radius $a = 250$ µm) filled with water embedded inside a duralumin matrix ($\rho = 2800$ kg/m^3,$\lambda = 57.8$ GPa, $\mu = 28$ GPa). The spheres are put in a virtual volume of transverse diameter D and thickness h_{eff} (see fig. 2) and illu-

minated by a plane wave [1] . We measure the transmissions coefficients for N_{avg} dispersions of spheres. We denote $\mathcal{T}$ the configurationally averaged transmission coefficient [2] . The effective parameters are then extracted from the following expression

$$\mathcal{T} = \frac{e^{ik_{eff}h_{eff}}}{e^{ikh_{eff}}}, \tag{5}$$

with $k = k_L$ (resp. $k = k_T$) if the incident wave is longitudinal (resp. transverse).

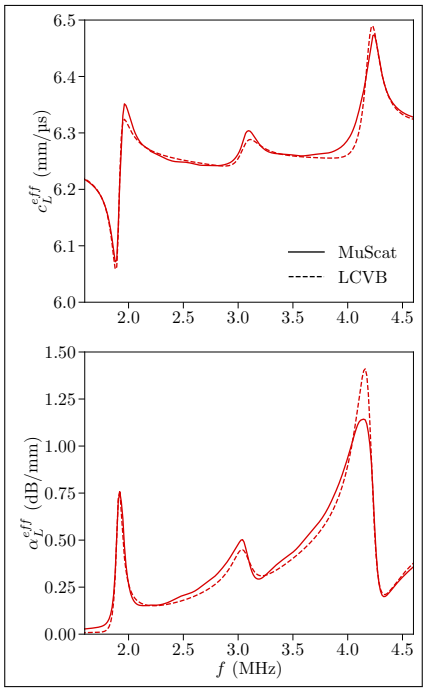


Figure 2. Frequency dependant effective velocity (top) and attenuation (bottom) of coherent longitudinal waves in a dispersion of cavities (filled with water) embedded inside a duralumin matrix ($\phi_v = 2\%$) around several resonances. Comparison between the LCVB model and numerical results obtained with MuScat.

[1] The number of modes to take into account for the truncature is determined from the scattering cross section of the scatterers. For an incident longitudinal (resp. transverse) wave, a maximum of 5 (resp. 6) modes has been taken.

[2] For each configuration of the disorder, we also perform spatial average (over a surface S as seen on fig. 2), as it is often do practically in experiments, to achieve a better averaging process.

Fig. 2 shows the effective velocity and attenuation of the coherent longitudinal wave in the dispersion of spherical cavities for a volume fraction $\phi_v = 2\%$. The spheres are placed inside the heteregenous medium with just a condition of non-overlaping, i.e. the distance between the centers of two scatterers shall be superior to $2a$. The figure shows a good agreement between the LCVB model and the numerical results obtained with MuScat. Several resonances can be observed, they are characterized by a strong dispersion on the effective velocity of the coherent wave and thus also by an effective attenuation peak.

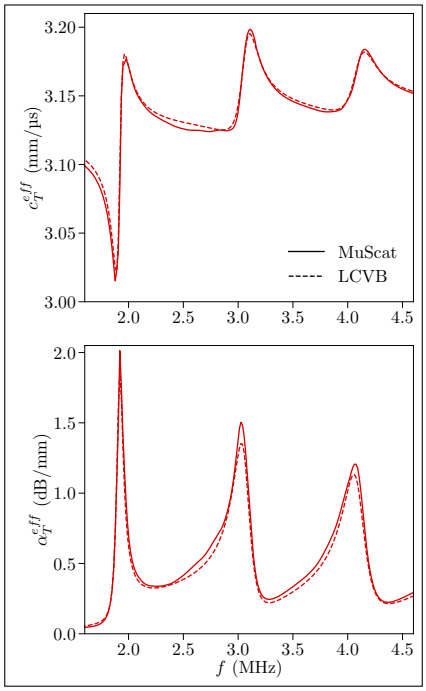


Figure 3. Frequency dependant effective velocity (top) and attenuation (bottom) of coherent shear waves in a dispersion of cavities (filled with water) embedded inside a duralumin matrix ($\phi_v = 2\%$) around several resonances. Comparison between the LCVB model and numerical results obtained with MuScat.

Fig. 3 shows the effective velocity and attenuation for the coherent shear waves in those dispersions. A good agreement can be seen between analytical and numerical results. Several resonances are also observed over the frequency band. In this kind of system, for both longitudinal and transverse waves, those resonances are linked to

the existence of whispering gallery waves and Rayleigh waves modes at the interface of the cavities [2].

4. CONCLUSION

We have presented a numerical approach, MuScat, aiming to study the propagation of elastic waves inside heterogeneous media. It has been validated here by comparison with a vectorial model of elastic wave multiple scattering. This numerical approach opens new perspectives for the study of elastic waves propagation inside dispersions of scatterers both on the coherent part of the field and on its fluctuations. Several types of incident waves can be used (point source, plane wave, Gaussian beam) and the distribution of scatterers can be polydisperse both in size and elasticity.

5. REFERENCES

[1] A. Rohfritsch, J.-M. Conoir, R. Marchiano, and T. Valier-Brasier, "Numerical simulation of two-dimensional multiple scattering of sound by a large number of circular cylinders," *The Journal of the Acoustical Society of America*, vol. 145, pp. 3320–3329, 06 2019.

[2] T. Valier-Brasier, A. Rohfritsch, J.-M. Conoir, and R. Marchiano, "Propagation of coherent longitudinal and shear waves in two-dimensional elastic media with randomly distributed resonant cavities," *Phys. Rev. B*, vol. 105, p. 054310, Feb 2022.

[3] L. Tsang, J. Kong, K. Ding, and O. Chi, *Scattering of Electromagnetic Waves, Numerical Simulations*. John Wiley & Sons, 2001.

[4] J. Fikioris and P. Waterman, "Multiple scattering of waves. iii. the electromagnetic case," *Journal of Quantitative Spectroscopy and Radiative Transfer*, vol. 123, pp. 8–16, 2013. Peter C. Waterman and his scientific legacy.

[5] F. Luppé, J.-M. Conoir, and T. Valier-Brasier, "Longitudinal and transverse coherent waves in media containing randomly distributed spheres," *Wave Motion*, vol. 115, p. 103082, 2022.

[6] P. Morse and H. Feshbach, *Methods of Theoretical Physics*. International series in pure and applied physics, McGraw-Hill, 1953.

[7] O. R. Cruzan, "Translational addition theorems for spherical vector wave functions," *Quarterly of Applied Mathematics*, vol. 20, pp. 33–40, 1962.

DOI: 10.61782/fa.2025.0317

FORUM ACUSTICUM EURONOISE 2025

DYNAMIC WAVE MANIPULATION IN SPATIOTEMPORAL INTERFACES AND SLABS FOR ACOUSTIC CONTROL

Rubén Picó[1*] **Jaime Galiana**[1] **Javier Redondo**[1]
Víctor J. Sánchez Morcillo[1]
[1] Institut d'Investigació per a la Gestió Integrada de les Zones Costaneres (IGIC), Universitat Politècnica de València (UPV), 46730 Gandia, Spain

ABSTRACT

Time-varying systems have emerged as a pivotal approach in wave physics, enabling unprecedented control over wave dynamics through the modulation of spatial and temporal properties. In this work, we analyze wave interactions at spatiotemporal interfaces, exploring the resulting scattering phenomena and their implications for acoustic wave manipulation. Building upon foundational principles, we classify interaction regimes—subsonic, supersonic, and intersonic—through a novel $\alpha - \gamma$ diagram, offering a comprehensive framework for understanding wave-interface dynamics. We extend this analysis to spatiotemporal slabs, which consist of two parallel interfaces moving with the same velocity. These structures combine spatial and temporal modulations, enabling intricate wave behaviors such as asymmetric interference patterns and dynamic frequency shifts. We demonstrate the scattering coefficients and frequency conversion characteristics within these slabs. The results highlight the transformative potential of spatiotemporal slabs for broadband acoustic wave control, paving the way for innovative applications in sound insulation, communications, and wave manipulation technologies.

Keywords: *Spatiotemporal, interface, slab, time-varying media, scattering*

**Corresponding author*: rpico@upv.edu.es.
Copyright: *©2025 This is an open-access article distributed under the terms of the Creative Commons Attribution 3.0 Unported License, which permits unrestricted use, distribution, and reproduction in any medium, provided the original author and source are credited.*

1. INTRODUCTION

Spatiotemporal modulation of acoustic media has opened new avenues for controlling wave propagation beyond the limitations of stationary systems. By dynamically varying properties such as sound speed or impedance, these systems allow for functionalities including frequency conversion, wave amplification, and nonreciprocal transmission [1–3]. Among the different strategies explored, the use of moving interfaces has proven particularly effective in generating new wave behaviors. When such interfaces propagate through the medium, they induce shifts in frequency and wavelength of the scattered waves, governed by the relative velocities of the interface and the acoustic media [4, 5].

Building upon these ideas, *spatiotemporal slabs*, structures defined by two parallel moving interfaces, represent a more complex configuration capable of producing rich scattering phenomena. Unlike a single interface, slabs introduce internal reflections and interference effects that depend on both the acoustic contrast and the motion of the slab. These configurations enable fine control over transmitted and reflected wave components, with potential applications in advanced sound control and acoustic metamaterials.

In this work, we present a study of wave scattering in spatiotemporal slabs. We peopoaw analytical expressions for the scattering coefficients in the subsonic and supersonic regimes, incorporating internal phase accumulation and frequency shifts due to the motion of the interfaces.

2. THE SPATIOTEMPORAL SLAB

A spatiotemporal slab is a dynamic structure defined by two parallel interfaces moving through an acoustic medium. It introduces a finite thickness region in which the wave speed changes from a background value c_1 to a new value $c_2 = \gamma c_1$, and then returns to c_1 after the slab has passed. Unlike single-interface systems, slabs support multiple internal reflections and wave interactions that significantly affect the overall scattering behavior.

These structures are the dynamic counterpart of classical spatial slabs used in layered media acoustics with additional complexity due to their motion. Conceptually, spatiotemporal slabs also generalize the idea of temporal slabs—media with time-varying properties studied in prior works [6, 7]—by combining both spatial and temporal discontinuities [8].

The interaction between an incident wave and the slab depends on the relative velocity of the interfaces ($v = \alpha c_1$) and the acoustic contrast γ. The first interface generates scattered components whose behavior is governed by the coefficient $\Gamma_f(\gamma, \alpha)$. Once the wave enters the slab, it travels in a medium with speed c_2, and the second interface must be analyzed with transformed parameters $1/\gamma$ and α/γ, effectively reversing the roles of the media.

In the subsonic regime, the slab moves slower than the wave, allowing multiple internal reflections that accumulate over time. In contrast, the supersonic regime occurs when the slab moves faster than the wave, leading to only a few distinct wave components without recursive reflections.

2.1 Subsonic regime

In the subsonic regime ($|\alpha| < \min(1, \gamma)$), the interface moves slower than both media. As shown in Fig. 1, an incident wave hits the first interface, producing a *reflected* wave and a *forward* wave that enters the slab. After traveling a distance L_A, the forward wave reaches the second interface, generating a new forward wave that exits the slab, and a reflected wave that remains within it. This process repeats, forming recursive internal reflections and building up multiple transmitted and reflected components. The final transmitted and reflected waves are superpositions of these components, each phase-shifted and frequency-modulated due to the slab motion.

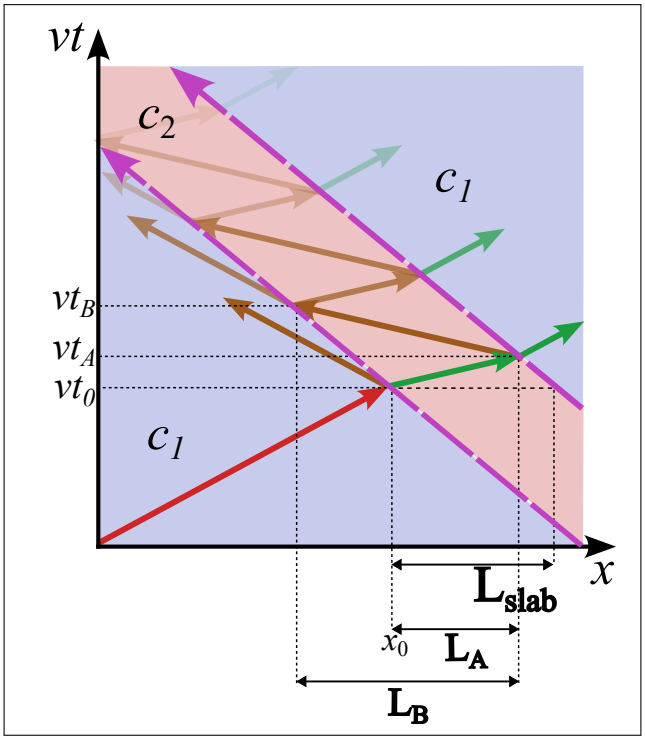


Figure 1. Subsonic slab: multiple internal reflections generate cumulative transmitted and reflected components.

2.2 Supersonic regime

In the supersonic regime ($|\alpha| > \max(1, \gamma)$), the interface moves faster than both media. Upon interaction with the first interface, the incident wave generates a *forward wave* and a *backward wave*, both propagating inside the slab in opposite directions as illustrated in Fig. 2. These components interact with the second interface, producing new forward and backward waves. Unlike in the subsonic case, no recursive reflections are generated.

3. SCATTERING COEFFICIENTS

The scattering response of a spatiotemporal slab is determined by the interference of the wave components that are generated through internal reflections. To compute the global scattering coefficients, three key aspects must be considered:

1. **Acoustic path lengths:** Each wave component travels a different distance inside the slab depend-

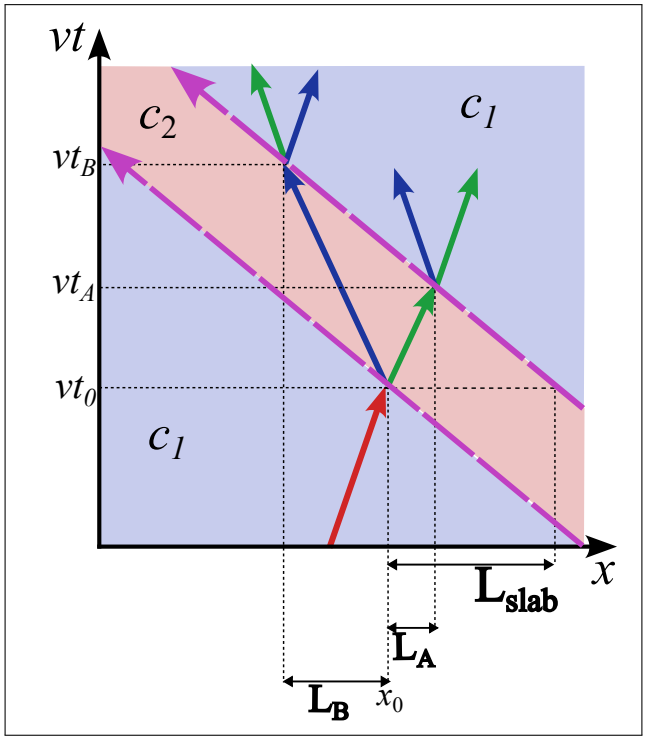


Figure 2. Supersonic slab: wave components interact only once at each interface, producing distinct forward and backward waves.

ing on its propagation direction. These distances are denoted as L_A for waves traveling in the same direction as the moving slab (copropagating), and L_B for waves traveling in the opposite direction (counterpropagating). In the subsonic regime, they are given by:

$$L_A = \frac{\gamma}{\gamma-\alpha}L_{\text{slab}}, \qquad L_B = \frac{\gamma}{\gamma+\alpha}L_{\text{slab}}. \quad (1)$$

2. **Frequency conversion:** Each interaction with a moving interface induces a frequency shift, modifying the phase evolution of the wave inside the slab. These shifts are described by frequency conversion factors.

3. **Interface scattering:** At each interface crossing, the wave amplitude is modified according to a scattering coefficient that depends on the propagation regime.

3.1 Forward Scattering Coefficient

The total forward wave transmitted through the slab is the sum of all forward components. In the subsonic regime, the closed-form expression is:

$$\mathbb{G}_F(\gamma,\alpha,L_{\text{slab}}) = \frac{4\gamma e^{\frac{j\alpha\gamma k_1 L_{\text{slab}} A_{1,F}}{\Phi_F}}}{(\gamma+1)^2 e^{\frac{j\gamma k_1 L_{\text{slab}} A_{2,F}}{\Phi_F}} - (\gamma-1)^2 e^{\frac{j\gamma^2 k_1 L_{\text{slab}} A_{1,F}}{\Phi_F}}}, \quad (2)$$

where:

$$\Phi_F = (\alpha^2-\gamma^2)^2,$$
$$A_{1,F} = \alpha^2+3\alpha\gamma+\alpha-\gamma,$$
$$A_{2,F} = \alpha^2(\gamma+2)-\alpha\gamma(\gamma-1)+\gamma^2.$$

3.2 Reflection Scattering Coefficient

The total reflected wave is composed of the direct reflection at the first interface and all components returning after internal reflections. Its final expression is:

$$\mathbb{G}_R(\gamma,\alpha,L_{\text{slab}}) = \frac{(\gamma^2-1)\left(1-e^{\frac{2jk_1 L_{\text{slab}} A_{1,R}}{\Phi_R}}\right)}{(\gamma+1)^2-(\gamma-1)^2 e^{\frac{2jk_1 L_{\text{slab}} A_{1,R}}{\Phi_R}}}, \quad (3)$$

where:

$$A_{1,R} = \gamma(\alpha-1)(2\alpha^3+\alpha^2+\gamma^2), \quad \Phi_R = (\alpha+1)(\alpha^2-\gamma^2)^2.$$

These analytical expressions capture the essential features of wave propagation through a moving slab, including internal phase accumulation, frequency shift, and multiple reflections.

The analytical results are illustrated in Fig. 3 and 4, which show the forward and reflected (or backward) scattering coefficients for both subsonic and supersonic regimes. The calculations are performed for a slab of thickness $L_{\text{slab}} = 0.1\,\text{m}$ and contrast $\gamma = 2$. The frequency at which the scattering coefficients reach their maxima and minima depends on the slab velocity. The motion of the slab changes the effective thickness that the waves experience as they propagate through it. The relative motion between the slab and the wave causes the wave to travel a longer or shorter distance inside the slab, depending on the direction of propagation. This change in effective thickness modifies the phase accumulation and, consequently, shifts the interference pattern that determines the scattering behavior.

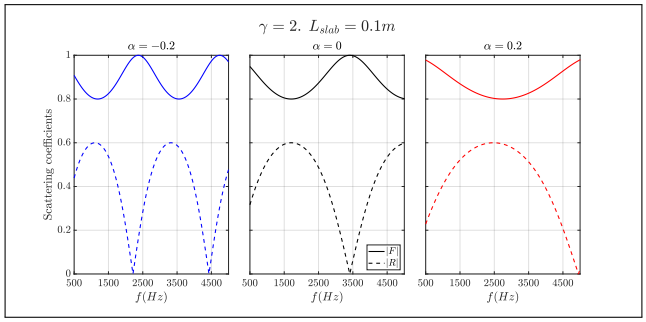


Figure 3. Scattering coefficients in the subsonic regime. Solid and dashed lines correspond to forward and reflected waves. Colors represent counterpropagating (blue), static (black), and copropagating (red) cases.

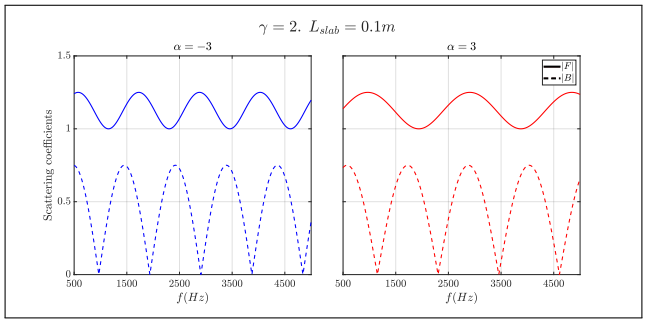


Figure 4. Scattering coefficients in the supersonic regime. Solid and dashed lines correspond to forward and backward waves. Colors represent counterpropagating (blue), static (black), and copropagating (red) cases.

4. CONCLUSIONS

We have presented a study of wave propagation through spatiotemporal acoustic slabs. By considering the combined effects of internal reflections, frequency conversion, and moving interface scattering, we derived closed-form expressions for the global scattering coefficients in subsonic regimes. The results show that slab motion introduces frequency-selective behavior and asymmetric transmission characteristics that are not present in static layered media. These findings provide a useful analytical framework for the design of spatiotemporally modulated acoustic devices for sound control, isolation, and filtering.

5. AKNOWLEDGEMENTS

This work was supported by the Spanish Ministry of Science and Innovation (MICINN) and the European Union FEDER (project PID2022-138321NB-C22).

6. REFERENCES

[1] Z. Chen, Y. Peng, H. Li, J. Liu, Y. Ding, B. Liang, A. Alù, "Nonreciprocal acoustic propagation via spatiotemporal modulation," *Science Advances*, 7(45), eabj1198 (2021).

[2] X. Wen et al., "Time-varying acoustic metamaterials with broadband nonreciprocal transmission," *Communications Physics*, 5(1), 18 (2022).

[3] M. H. Fakheri, H. Rajabalipanah, A. Abdolali, "Spatiotemporal coding acoustic metasurfaces," *Physical Review Applied*, 16(2), 024062 (2021).

[4] Z. L. Deck-Léger, C. Caloz, "Spacetime engineering: A new frontier for wave manipulation," *Advanced Photonics*, 1(5), 056002 (2019).

[5] Yuan, Y., Chen, W. Q. Journal of Sound and Vibration, 575, 118244, (2024).

[6] A. Bahrami, Z. L. Deck-Léger, C. Caloz, "Temporal slabs for wave engineering," *Physical Review Applied*, 19(5), 054044 (2023).

[7] D. Ramaccia, A. Alù, A. Toscano, F. Bilotti, "Temporal multilayer structures for higher-order transfer functions," *Applied Physics Letters*, 118(10), 101101 (2021).

[8] Y. Yu et al., "Spatiotemporal modulation in structured media," *Laser and Photonics Reviews*, 17(9), 2300130 (2023).

DOI: 10.61782/fa.2025.0924

FORUM ACUSTICUM
EURONOISE 2025

ULTRASONIC HOLOGRAM FOR BI-DIRECTIONAL DIFFUSION BY PHASE CONTROLLING THE SCATTERING COEFFICIENTS

Eric Ballestero[1*] **Josep Rodriguez-Sendra**[2] **Vicent Romero-García**[3]
Jean-Philippe Groby[1] **Noé Jiménez**[2]
[1] Laboratoire d'Acoustique de l'Université du Mans (LAUM),
Intitut d'Acoustique - Graduate School (IA-GS),
UMR CNRS 6613, Le Mans, France.
[2] Instituto de Instrumentación para Imagen Molecular,
Consejo Superior de Investigaciones Científicas (CSIC),
Universitat Politècnica de València, València, Spain.
[3] Instituto Universitario de Matemática Pura y Aplicada (IUMPA),
Universitat Politècnica de València, Spain.

ABSTRACT

In this work, we present a bi-directional asymmetric ultrasonic hologram that can simultaneously control both the reflected and transmitted wave-fields. To do that we design a surface made of a discrete spatial distribution of monolithic elements with different properties than the surrounding medium. This allows to compress two identical or different wavefield scattering patterns (for transmission and reflection) into a single monolithic object. We report an ultrasonic hologram based on Quadratic Residue sequences encoded with resonant building blocks behaving as an ideal Lambertian scatterer from both sides, with spatial autocorrelation coefficients of 0.7 each one, therefore diffusing waves in both transmission and reflection.

Keywords: *Acoustic hologram, Acoustic diffusers, Ultrasonic imaging, Acoustic scattering*

Research in ultrasounds covers a broad range of fields as non-destructive testing, underwater acoustics and imaging among others. Recently, there is an increasing interest in biomedical applications, such as non-destructive medical imaging [1, 2] and non-invasive controlled medical therapy [3, 4]. In this work we design of a bi-directional asymmetric ultrasonic hologram that works simultaneously in transmission and reflection. The design framework of such hologram follows a multi-objective optimization procedure which minimizes the difference in reflection and transmission phase values for a given length of polymer material, allowing the creation of a phase-space representing the total phase combinations between the two interfaces, the building blocks of which can be used to replicate any desired reflection and transmission phase profiles. In the work herein, the case of an ideal Lambertian scattering hologram made out of a Quadratic Residue sequence has been demonstrated, where high scattering values with a spatial auto-correlation coefficient around $\delta = 0.7$ have been reported [5].

We consider an ultrasonic hologram composed of a discrete spatial distribution of building blocks made of a monolithic polymer blocks with different height embedded in water. The working frequency is chosen at 1.1 MHz. An example layout can be seen through the artistic impressions in Figs. 1(a,b). We consider first a 1D problem for each constituting building block of the hologram. The building block is made of a monolithic polymer block of length l surrounded by two water blocks of length d_1 and d_2 respectively as shown in Fig. 1(c). The sound pressures, p, and normal particle velocities, v_z, at $z = 0$

*Corresponding author: eric.ballestero@univ-lemans.fr.
Copyright: ©2025 Eric Ballestero et al. This is an open-access article distributed under the terms of the Creative Commons Attribution 3.0 Unported License, which permits unrestricted use, distribution, and reproduction in any medium, provided the original author and source are credited.

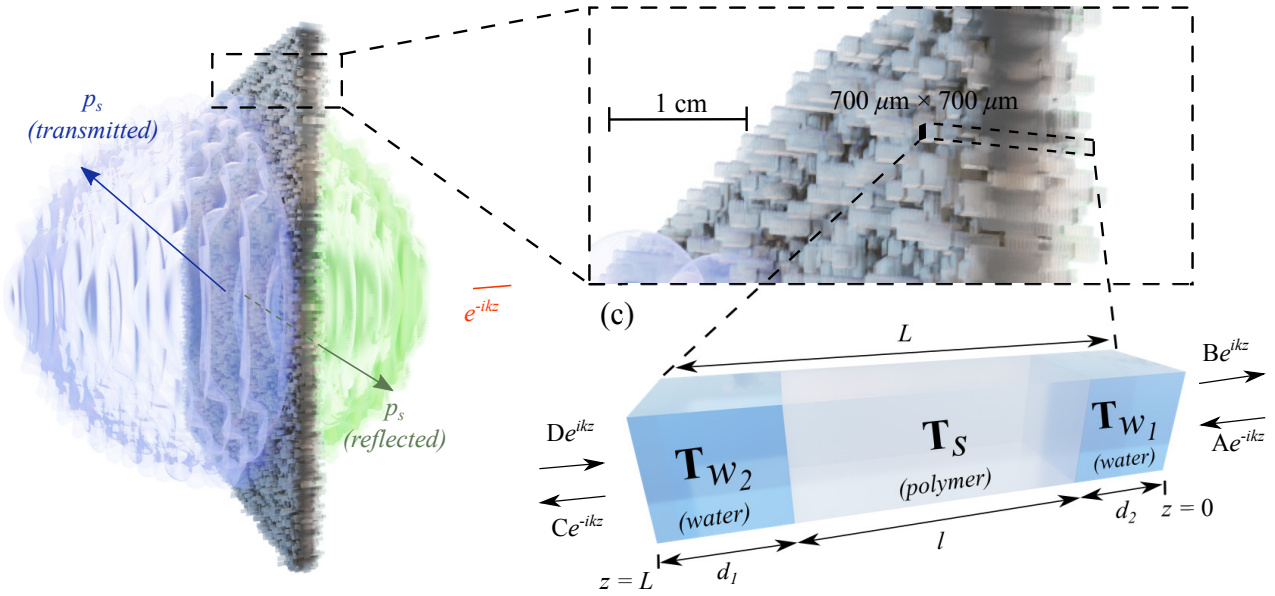


Figure 1. (a) Artistic impression of a 10 × 10 × 1 cm ultrasonic bi-directional hologram diffusing an incident plane wave in a uniform scattering profiles for each direction; reflection in green, transmission in blue. (b) Close-up of the lens; each monolithic block has a lateral size of $\Delta l_x \times \Delta l_y$=700$\mu$m×700$\mu$m. (c) Representative 1D Transfer Matrix diagram of a monolithic block of total length L composed of a solid element (e.g., polymer) and an exterior medium (here, water). The local phase and amplitude of the reflection and transmission coefficients depend on d_1, d_2 and l.

and at $z = L$ can be modelled by means of the Transfer Matrix Method (TMM). Due to the lateral dimensions of the building blocks ($\Delta l_x \times \Delta l_y$=700$\mu$m×700$\mu$m) we can assume plane wave propagation. Therefore, the transfer matrix **T** of the building block can be derived and the reflection, R, and transmission, T, coefficients calculated. This implies that we consider each building block is independent from each other in the structure and considered as an equivalent fluid. Such approximation can be made due to the low difference in impedance between the water and polymer media, with a polymer-to-water impedance ratio $Z_p/Z_w = 1.67$, coupled with the fact that shear waves can also be neglected due to the system being considered under normal incidence.

Following Fraunhofer's diffraction theory, the scattered sound pressure distribution over a surface with an anisotropic phase distribution, such as a reflection or transmission coefficient in this case, can usually be resumed as a spatial Fourier transform of the corresponding complex surface coefficient. In this case, the far-field pressure distribution, $p_s(\theta, \phi)$, where θ and ϕ are the azimuthal and elevational angles, respectively, of a radiating rectangular surface with a spatially dependent phase distribution coefficient, $\xi(x, y)$, of size $2a$ and $2b$ in the x and y directions respectively, can be calculated using the Fraunhofer integral [6]

$$p_s(\theta, \phi) = \int_{-a}^{a} \int_{-b}^{b} \xi(x, y) e^{ik(x \sin\phi \sin\theta + y \sin\phi \cos\theta)} \mathrm{d}x\mathrm{d}y. \quad (1)$$

The subindex $s = R, T$ represents the reflection and transmission problem respectively, and $\xi(x, y) = R(x, y)$ ($\xi(x, y) = T(x, y)$) for the reflection (transmission) problem.

In order to design a hologram that can behave as an ideal diffuser in both reflection and transmission sides, we look for a spatial phase distribution for the both the reflection and transmission coefficient such that the spatial Fourier transform of said distribution approximates a flat angular response. There are many number theoretic sequences that can help design such phase distribution, such as the maximum length or quadratic residue sequences [7].

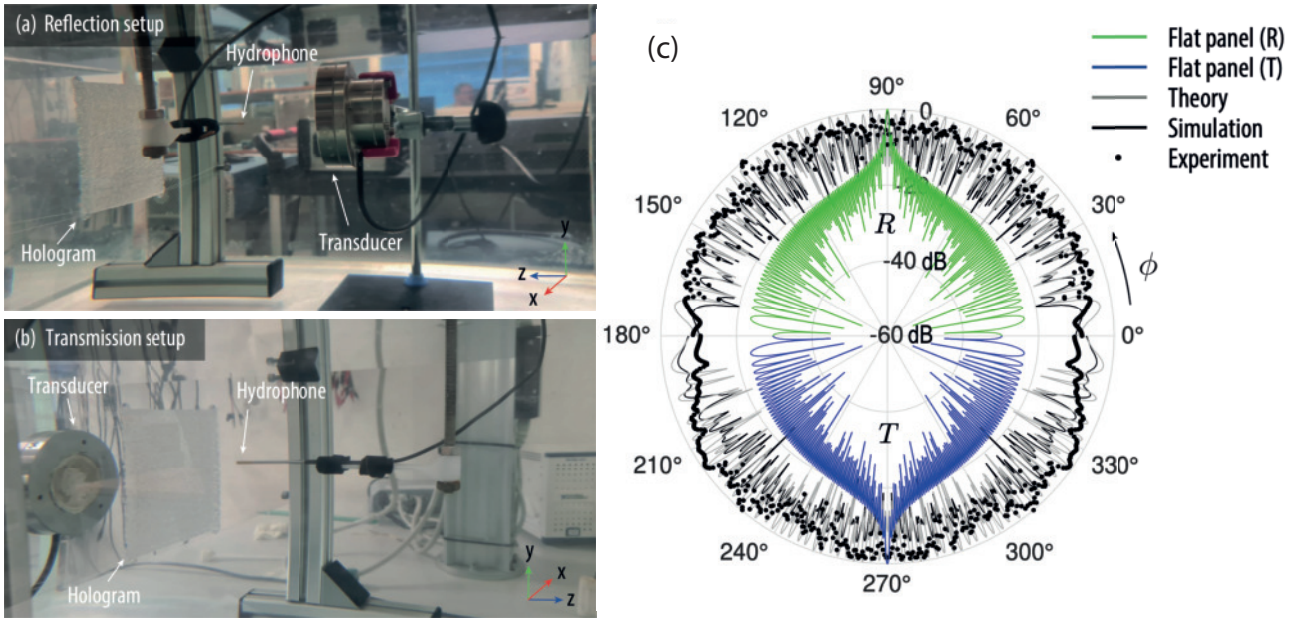


Figure 2. Experimental water tank measurement setup of the 3D-printed diffusing hologram in (a) reflection and (b) transmission situations. (c) Measured (dots) scattered polar pressure distribution in reflection (R) and transmission (T) compared to analytical (black line) values (QR) and the scattered field of a flat vibrating piston (blue and green lines).

Here, the quadratic residue (QR) sequence will be used, which when repeated in space, allows to generate evenly spaced diffraction lobes with even energy.

Experimental measurements of a 3D-printed hologram, with $N = 53$ repeated $M = 3$ times (see Fig. 1(a,b), were made in a water tank for the reflection and transmission configurations. Figures 2(c) show the polar scattered energy distributions measured from both sides of the hologram. It can be observed from Fig. 2(c) that both measured scattering fields are more uniform than the polar response of a planar vibrating piston, which outputs energy narrowly in the normal axis (0°), and are in good agreement with the predicted analytical curve. The Spatial Auto-Correlation Coefficient (SACC) of the polar distributions are $\delta^R = 0.65$ and $\delta^T = 0.71$ for the reflected and transmitted wave fields, respectively. Those can be considered quite high values due to the physical nature of the SACC where $\delta \to 0$ denotes a Dirac-like specular distribution and $\delta = 1$ a fully spherical one. Knowing than a SACC of unity is almost impossible to reach with traditional number theoretic sequences [8], there would be some diminishing returns in successfully increasing the SACC value when aiming closer to unity. A value around 0.7 thus already denotes a strong scattering behaviour, akin to one obtained through a Lambertian distribution.

In this work we have designed a bi-directional asymmetric ultrasonic hologram that can simultaneously control both the reflected and transmitted wave-fields. Depending on the applications, such hologram could be useful in situations where transmitted and reflected wave-fields need to be controlled at the same time, such as a bi-directional diffusing system emitting and receiving equally in and from all directions (equivalent of perfect optical diffusers in optics) or as a bi-directional beam directivity selector. Such hologram could also be used directly in reflection situations for minimizing unwanted specular reflections. This kind of tunable bidirectional hologram could be further optimized to create decollimating/collimating/focusing scattering wave fields for one or both directions, with potential applications ranging from ultrasound-guided medical procedures [9] to compressing sensing [10].

Acknowledgments

E.B would like to gratefully acknowledge the financial support from Institut d'Acoustique – Graduate School (IAGS ANR-17-EURE-0014) for granting mobility during this project. The collaboration between the authors of this article was made possible thanks to Institut d'Acoustique – Graduate School (IAGS) project (ANR-17-EURE-0014) from the Laboratoire d'Acoustique du l'Université du Mans (LAUM) for the support and mobility. The authors gratefully acknowledge the ANR-RGC METARoom (ANR-18-CE08-0021) project and N.J and V.R-G acknowledges financial support from Conselleria de Innovación, Universidades, Ciencia y Sociedad Digital de la Generalitat Valenciana through project CIAICO/2022/052 of the Programa para la promoción de la investigación científica, el desarrollo tecnológico y la innovación en la Comunitat Valenciana. This research has been supported by the Ministerio Español de Ciencia e Innovación grant RYC2021-034920-I and Agencia Estatal de Investigación grants PID2022-142719OB-C21 and CNS2023-145707 funded by MCIN/AEI/10.13039/501100011033 and grant PID2023-146237NB-I00 funded by MICIU/AEI/ 10.13039/501100011033.

Author contributions:

E.B, J-P.G, V.R-G, and N.J conceived the project, under the direction of N.J. E.B, V.R.-G and N.J wrote the code for the theoretical and numerical data. E.B performed the multi-objective optimization and provided the dimensions of the ultrasonic lens. J.R-S 3D-printed the sample and performed the experimental measurements along with N.J, as well as provided details on the experimental apparatus. N.J analyzed the experimental data. E.B, and N.J wrote the initial manuscript with input from all authors. E.B, V.R.-G and N.J prepared the revised version and the response to the referees with input from all authors. All authors have reviewed and commented on the final manuscript.

There are no competing interests to declare.

References

[1] G. Kossoff, "Basic physics and imaging characteristics of ultrasound," *World journal of surgery*, vol. 24, pp. 134–42, 03 2000.

[2] C. M. Otto, *Textbook of clinical echocardiography*, ch. Principles of echocardiographic image acquisition and Doppler analysis, pp. 1–29. Philadelphia, PA: WB Saunders, 2000.

[3] Y. Meng, Z. Shirzadi, B. MacIntosh, C. Heyn, G. Smith, I. Aubert, C. Hamani, S. Black, K. Hynynen, and N. Lipsman, "Blood-brain barrier opening in alzheimer's disease using mr-guided focused ultrasound," *Neurosurgery*, vol. 66, 09 2019.

[4] A. Battais, V. Barrère, W. A. N'Djin, A. Dupré, M. Rivoire, and D. Melodelima, "Fast and Selective Ablation of Liver Tumors by High-Intensity Focused Ultrasound Using a Toroidal Transducer Guided by Ultrasound Imaging: The Results of Animal Experiments," *Ultrasound in Medicine & Biology*, vol. 46, pp. 3286 – 3295, Dec. 2020.

[5] E. Ballestero, J. Rodriguez-Sendra, V. Romero-García, J.-P. Groby, and N. Jiménez, "Bidirectional lambertian scatterers using acoustic holograms for the simultaneous control of reflected and transmitted wavefronts," *Advanced Functional Materials*, p. 2423715, 2025.

[6] T. D. Rossing, F. Dunn, W. M. Hartmann, D. M. Campbell, and N. H. Fletcher, *Springer Handbook of Acoustics*. Springer Publishing Company, Incorporated, 1st ed., 2007.

[7] M. R. Schroeder, "Diffuse sound reflection by maximum length sequences," *The Journal of the Acoustical Society of America*, vol. 57, no. 1, pp. 149–150, 1975.

[8] E. Ballestero, N. Jiménez, J.-P. Groby, H. Aygun, S. Dance, and V. Romero-García, "Metadiffusers for quasi-perfect and broadband sound diffusion," *Applied Physics Letters*, vol. 119, 07 2021. 044101.

[9] S. Jiménez-Gambín, N. Jiménez, J. M. Benlloch, and F. Camarena, "Holograms to focus arbitrary ultrasonic fields through the skull," *Phys. Rev. Applied*, vol. 12, p. 014016, Jul 2019.

[10] P. Kruizinga, P. Meulen, A. Fedjajevs, F. Mastik, G. Springeling, N. Jong, J. Bosch, and G. Leus, "Compressive 3d ultrasound imaging using a single sensor," *Science Advances*, vol. 3, p. e1701423, 12 2017.

DOI: 10.61782/fa.2025.0249

FORUM ACUSTICUM EURONOISE 2025

CONDITIONS FOR WEAK SCATTERING AND THE BORN APPROXIMATION IN BEAMS WITH MULTIPLE RESONATORS

Mario Lázaro[1*] **Richard Wilsthaw**[2] **Richard Craster**[2] **Vicente Romero-García**[1]
[1] Instituto Universitario de Matemática Pura y Aplicada,
Universitat Politècnica de València, 46022 (Spain)
[2] Department of Mathematics, Imperial College London, London, SW7 2AZ, UK

ABSTRACT

We report the necessary conditions for weak scattering of longitudinal and flexural waves in a beam loaded by multiple resonators. The equations of motion of a one-dimensional elastic waveguide with several point resonators are derived by a Green's matrix approach, for any resonator with any number of natural frequencies and morphology modeled by the transfer matrix method. The multiple scattering theory is used to express the response os the system by an infinite series whose convergence is closely linked to the scattering intensity provided by the resonators. The spectral radius of the scattering matrix is used to study of the convergence. Furthermore, we show that the Born approximation is provided by the leading order of the multiple scattering expansion. The work offers approximate expressions for the spectral radius, providing a preliminary step to a clear physical interpretation of weak scattering.

Keywords: *Multiple Scattering, Locally resonant materials, Weak scattering, Born approximation*

Metamaterials are structured composites with engineered wave propagation properties. In elasticity and acoutstics, they offer advanced control over flexural waves, with applications in vibration isolation, energy harvesting, and cloaking [1–5]. The wave response in such systems is influenced by multiple scattering interactions between discrete resonators. When these interactions are weak, simplified models, such as the Born approximation, provide accurate solutions. However, a rigorous criterion for weak scattering in flexural wave systems is necessary.

We consider longitudinal and flexural waves propagating through a straight beam-rod waveguide of infinite length, and also assume that the reference axis x coincides with the centroid of the cross-section, so no coupling between both types of waves occurs if the medium is homogeneous [6]. In this paper, an arrangement of N scatterers with internal resonances distributed along the beam at locations $x_1 < x_2 < \cdots < x_N$, will also be considered. We do not make any restriction except that the motion of both beam and resonators is restricted to the xz–plane. This approximation, known as plane-strain, usually provides good representations of real-life problems.

Assuming time harmonic motion, the state vector can be written as $\mathbf{U}(x,t) = \mathbf{u}(x)\, e^{i\omega t}$ and hence the time dependence is understood and omitted hereafter, with

$$\mathbf{u}(x) = \{u(x),\ w(x),\ \theta(x),\ N(x),\ V(x),\ M(x)\}^T. \tag{1}$$

being $u(x)$ and $w(x)$ the displacements in x and z direction of the reference axis and $\theta(x)$ the cross section rotation; the functions $N_x(x), V_z(x), M_y(x)$ represent the generalized forces associated to the previous kinematics variables, i.e. the normal and shear forces, and bending moment at position x. The system of equations (**??**) is frequency–dependent and can be written in matrix form as

$$\frac{\mathrm{d}\mathbf{u}}{\mathrm{d}x} = \mathbf{A}\,\mathbf{u} + \mathbf{q}(x), \tag{2}$$

where

**Corresponding author*: malana@upv.es.

Copyright: ©2025 M. Lázaro et al. *This is an open-access article distributed under the terms of the Creative Commons Attribution 3.0 Unported License, which permits unrestricted use, distribution, and reproduction in any medium, provided the original author and source are credited.*

$$\mathbf{A} = \begin{bmatrix} 0 & 0 & 0 & 1/EA & 0 & 0 \\ 0 & 0 & 1 & 0 & 1/GA_z & 0 \\ 0 & 0 & 0 & 0 & 0 & 1/EI_y \\ -\rho A\omega^2 & 0 & 0 & 0 & 0 & 0 \\ 0 & -\rho A\omega^2 & 0 & 0 & 0 & 0 \\ 0 & 0 & -\rho I_y\omega^2 & 0 & -1 & 0 \end{bmatrix}, \qquad \mathbf{q}(x) = \begin{Bmatrix} 0 \\ 0 \\ 0 \\ -q_x \\ -q_z \\ -m_y \end{Bmatrix},$$

represents the constitutive matrix and the external forces, respectively.

The closed-form expression found for the matrix $\mathbf{K}_\alpha$, representing the response of the α-scatterer and that can be obtained by the Transfer Matrix Method [7], enables us to write Eq. (2) as follows

$$\frac{\mathrm{d}\mathbf{u}}{\mathrm{d}x} = \mathbf{A}\,\mathbf{u} + \sum_{\alpha=1}^{N} \mathbf{K}_\alpha \mathbf{u}(x_\alpha)\,\delta(x - x_\alpha) + \mathbf{q}_e(x)\,. \quad (3)$$

The total solution is written as

$$\mathbf{u}(x) = \boldsymbol{\psi}_0(x) + \mathbf{u}_s(x), \quad (4)$$

where $\boldsymbol{\psi}_0(x)$ denotes the state vector corresponding to the incident wave and is the solution of

$$\frac{\mathrm{d}\boldsymbol{\psi}_0}{\mathrm{d}x} = \mathbf{A}\,\boldsymbol{\psi}_0 + \mathbf{q}_e(x). \quad (5)$$

Moreover, $\mathbf{u}_s(x)$ represents the state vector of the scattered wave, which is solution of

$$\frac{\mathrm{d}\mathbf{u}_s}{\mathrm{d}x} = \mathbf{A}\,\mathbf{u}_s + \sum_{\alpha=1}^{N} \mathbf{K}_\alpha \mathbf{u}(x_\alpha)\,\delta(x - x_\alpha). \quad (6)$$

The solution will be presented in terms of the Green's matrix of the system, $\mathbf{G}(x)$, defined as the solution of

$$\left(\frac{\mathrm{d}}{\mathrm{d}x} - \mathbf{A}\right)\mathbf{G} = \mathbf{I}\,\delta(x). \quad (7)$$

The general solution of Eq. (3) can then be written as

$$\mathbf{u}(x) = \boldsymbol{\psi}_0(x) + \mathbf{u}_s(x) = \boldsymbol{\psi}_0(x) + \sum_{\beta=1}^{N} \mathbf{G}(x - x_\beta)\,\mathbf{K}_\beta\,\mathbf{u}(x_\beta). \quad (8)$$

After evaluating Eq. (8) at $x_1, \ldots, x_N$, the following system of linear equations arises

$$\mathbf{u}(x_\alpha) - \sum_{\beta=1}^{N} \mathbf{G}(x_\alpha - x_\beta)\,\mathbf{K}_\beta\,\mathbf{u}(x_\beta) = \boldsymbol{\psi}_0(x_\alpha) \quad , \quad 1 \le \alpha \le N. \quad (9)$$

Let us now introduce the following auxiliary variables associated with each resonator.

$$\boldsymbol{\phi}(x_\alpha) = \left[\mathbf{I} - \mathbf{G}(0^+)\mathbf{K}_\alpha\right]\,\mathbf{u}(x_\alpha). \quad (10)$$

After some rearrangements, the system of equations (9) is written in terms of the new variables defined above as

$$\begin{bmatrix} \mathbf{I} & -\mathbf{G}(x_1 - x_2)\mathbf{t}_2 & \cdots & -\mathbf{G}(x_1 - x_N)\mathbf{t}_N \\ -\mathbf{G}(x_2 - x_1)\mathbf{t}_1 & \mathbf{I} & \cdots & -\mathbf{G}(x_2 - x_N)\mathbf{t}_N \\ \vdots & \vdots & \ddots & \vdots \\ -\mathbf{G}(x_N - x_1)\mathbf{t}_1 & -\mathbf{G}(x_N - x_2)\mathbf{t}_2 & \cdots & \mathbf{I} \end{bmatrix} \begin{Bmatrix} \boldsymbol{\phi}(x_1) \\ \boldsymbol{\phi}(x_2) \\ \vdots \\ \boldsymbol{\phi}(x_N) \end{Bmatrix} = \begin{Bmatrix} \boldsymbol{\psi}_0(x_1) \\ \boldsymbol{\psi}_0(x_2) \\ \vdots \\ \boldsymbol{\psi}_0(x_N) \end{Bmatrix}, \quad (11)$$

where the new matrices $\mathbf{t}_\alpha$ are defined as

$$\mathbf{t}_\alpha = \mathbf{K}_\alpha\,\left[\mathbf{I} - \mathbf{G}(0^+)\mathbf{K}_\alpha\right]^{-1}. \quad (12)$$

This 6×6 matrix represents the dynamical impedance of each scatterer with respect to homogeneous parameters of the host beam. It contains the mechanical and inertia properties throughout the components of $\mathbf{K}_\alpha$ matrix, so fully described the resonant behavior of the scatterers. Eq. (11)

can be written in compact form as

$$[\mathbf{I} - \mathbf{g}]\ \mathbf{\Phi} = \mathbf{\Psi}_0, \tag{13}$$

where the matrix $\mathbf{g} = \hat{\mathbf{G}}\,\hat{\mathbf{T}}$ and

$$\hat{\mathbf{G}} = \begin{bmatrix} \mathbf{0} & \mathbf{G}(x_1 - x_2) & \cdots & \mathbf{G}(x_1 - x_N) \\ \mathbf{G}(x_2 - x_1) & \mathbf{0} & \cdots & \mathbf{G}(x_2 - x_N) \\ \vdots & \vdots & \ddots & \vdots \\ \mathbf{G}(x_N - x_1) & \mathbf{G}(x_N - x_2) & \cdots & \mathbf{0} \end{bmatrix}, \quad \hat{\mathbf{T}} = \begin{bmatrix} \mathbf{t_1} & \cdots & \mathbf{0} \\ \vdots & \ddots & \vdots \\ \mathbf{0} & \cdots & \mathbf{t}_N \end{bmatrix}. \tag{14}$$

The scattering coefficients $\mathbf{\Phi}$ are simply deduced from Eq. (13) as

$$\mathbf{\Phi} = [\mathbf{I} - \mathbf{g}]^{-1}\,\mathbf{\Psi}_0. \tag{15}$$

The state vector is obtained from

$$\mathbf{u}(x) = \boldsymbol{\psi}_0(x) + \sum_{\alpha=1}^{N} \mathbf{G}(x - x_\alpha)\,\mathbf{t}_\alpha\,\boldsymbol{\phi}(x_\alpha). \tag{16}$$

The solution of Eq. (15) and the state vector of Eq. (16) provide the exact approach to the problem for any frequency.

As shown above, the scattering coefficients are found from the solution of Eq. (15). If the elements of the *square* matrix $\mathbf{g}$ are sufficiently small, the inverse is efficiently evaluated by means of the Neumann series expansion, namely

$$[\mathbf{I} - \mathbf{g}]^{-1} = \mathbf{I} + \mathbf{g} + \mathbf{g}^2 + \cdots = \sum_{n=0}^{\infty} \mathbf{g}^n. \tag{17}$$

The necessary and sufficient condition to guarantee that the series converges is that the spectral radius $\rho(\mathbf{g})$, defined as the maximum of the absolute values of the eigenvalues of $\mathbf{g}$, is less than unity. When $\rho(\mathbf{g}) < 1$, the scattering induced by the N resonators can be considered as weak, meaning that a few terms of the series are necessary to accurately reproduce the scattering behavior of the system. In other situations for which $\rho(\mathbf{g}) > 1$ holds, the inverse matrix cannot be approximated by the expansion of Eq. (17).

By employing a Green's matrix approach, this work reports analytical derivations and approximations to effectively model the interaction between waves and resonators en beams [7]. Equations show that weak scattering conditions and the Born approximation depends on the spectral radius is sensitive to both local resonator properties and their spatial configuration, which influence scattering intensity. Future work could explore more complex arrangements and resonator types, potentially extending these findings to applications in structural health monitoring and wave-based material design.

Acknowledgments

M.L. and V.R.-G. are grateful for the partial support under Grant No. PID2020-112759GB-I00 funded by MCIN/AEI/10.13039/501100011033, and also for the partial support under Grant No. PID2023-146237NB-I00 funded by MICIU/AEI/10.13039/501100011033. V.R.-G. acknowledge support from Grant No. CIAICO/2022/052 of the "Programa para la promoción de la investigación científica, el desarrollo tecnológico y la innovación en la Comunitat Valenciana" funded by Generalitat Valenciana. M.L is grateful for support under the "Programa de Recualificación del Sistema Universitario Español para 2021-2023", (funded by "Instrumento Europeo de Recuperación (Next Generation EU) in the framework of the Plan de Recuperación, Transformación y Resiliencia de España", through the Ministerio de Universidades. R.W and R.V.C acknowledge financial support from the EU H2020FET-proactive project MetaVEH under grant agreement number 952039.

References

[1] P. Deymier, ed., *Acoustic Metamaterials and Phononic Crystals*. Springer-Verlag Berlin Heidelberg, 2013.

[2] R. Craster and S. Guenneau, *Acoustic Metamaterials, vol. 166 of Springer Series in Materials Science*. Springer, 2013.

[3] V. Romero-García and A. Hladky-Hennion, *Fundamentals and Applications of Acoustic Metamaterials: From Seismic to Radio Frequency*. ISTE Willey, 2019.

[4] N. Jiménez, O. Umnova, and J.-P. Groby, *Acoustic Waves in Periodic Structures, Metamaterials, and Porous Media*. Cham, Switzerland: Springer International Publishing, 2021.

[5] R. Craster and S. Guenneau, *Acoustic Metamaterials Absorption, Cloaking, Imaging, Time-Modulated Media, and Topological Crystals*. Springer Series in Materials Science, Springer, 2024.

[6] S. S. Rao, *Vibration of Continuous Systems*. John Wiley & Sons, 2007.

[7] M. Lázaro, R. Wiltshaw, R. Craster, and V. Romero-García, "Wave propagation in beams with multiple resonators: conditions for weak scattering and the born approximation," *arXiv:2410.00188*, 2025.

DOI:

Main theme: A10 Materials and Metamaterials

Session A10.10 Numerical methods for wave propagation in complex media

Chair(s): A. Prieto, P. Amado Mendes

DOI:

Main theme: A11 Musical Acoustics

Session A11.01 Musical acoustics - General

Chair(s): V. Chatziioannou, M. Ducceschi, V. Debut

DOI: 10.61782/fa.2025.0091

FORUM ACUSTICUM EURONOISE 2025

ACOUSTICAL BEHAVIOUR OF VENT HOLES ON BRASSWIND INSTRUMENTS

Marco Aragó Bishop [1*] **Arnold Myers**[2] **Murray Campbell**[1]

[1] School of Physics and Astronomy, The University of Edinburgh, Edinburgh, UK
[2] Royal Conservatoire of Scotland, Glasgow, UK

ABSTRACT

In most brass instruments, the acoustical resonator forms a cylindrically symmetric tube open at both ends. Sound is produced by the vibrations of the player's lips at the input end and radiates through the bell at the exit. Typically, these are the only two openings in brass instruments. However, in specific categories, such as the trumpets used in many modern performances by period orchestras, additional holes are drilled into the sides of the tube. The player can open or close these holes to improve the instrument's intonation and stability, particularly in baroque performances.

This paper studies the acoustical behaviour of two of the vent holes in a four-hole vented trumpet, for which the most notable behaviour is observed. The input impedance is measured using the BIAS system for all possible venting fingerings. These experimental results are compared with numerical simulations using the Openwind framework, with input data derived from mechanical measurements of the bore profile of the trumpet.

Keywords: *brass instruments, vented trumpet, input impedance, resonances, vent holes.*

1. INTRODUCTION

Brass instruments produce sound by modulating airflow through the player's vibrating lips at the mouthpiece, initiating oscillations in the air column within the instrument. This lip-driven excitation is what acoustically defines the family of brass instruments. Most modern examples, such as the trumpet, trombone, and tuba, are made of metal and incorporate valves or a slide mechanism to vary the effective tube length. By altering the tube's length, the player adjusts the instrument's resonant frequencies to match the lip vibration, allowing different notes to be played.

A notable exception is the natural trumpet, which lacks holes or valves, requiring players to rely solely on their embouchure and breath control to produce a range of pitches. The instrument's geometry is almost cylindrical, with an expanding bell at the end, requiring an appropriate mouthpiece to be played. With this configuration, the instrument can produce a series of pitched sounds close to that of a harmonic series, producing natural notes up to the 16th harmonic and beyond [1].

As with other brass instruments, the frequencies of the resonances of the natural trumpet form an approximately harmonic series. Nonetheless, even if they were perfectly harmonic, those pitches would not necessarily be considered "in tune" since neither the tempered scales nor the specific tuning requirements of a performance situation match a pure harmonic series. Consequently, natural trumpet players must be highly skilled to refine the pitch of the sound emitted by carefully adjusting embouchure, vocal tract, and breathing. Of particular difficulty is the high register, commonly known as the *clarino* register, which includes high-frequency notes that are closely spaced. This register is particularly challenging for players when performed at loud dynamics due to the instrument's resonances strongly dictating the pitches produced, which inherently limits the player's ability to control it with precision.

*__Corresponding author__: phyarago@gmail.com.
__Copyright__: ©2025 M. Aragó Bishop et al. This is an open-access article distributed under the terms of the Creative Commons Attribution 3.0 Unported License, which permits unrestricted use, distribution, and reproduction in any medium, provided the original author and source are credited.

The vented trumpet was invented in the second half of the twentieth century to facilitate stability and control of intonation in playing. Up to four vent holes were added, connecting the instrument's internal air column to the outside atmosphere, thereby reducing the amplitude of the pressure waves near the holes. This effect is comparable to cutting off the tubing portion below the hole for low frequencies. However, recent research has shown that the acoustical effects caused by opening the smaller vent holes are more subtle and require further analysis [2].

In this paper, the acoustical behaviour of two of the vent holes in an available four-hole vented trumpet crooked in D is presented. The analysis is restricted to the instrument's resonating air column, which is modelled in its linear regime through the input impedance Z_{in}, defined as the frequency-dependent ratio between the acoustic pressure and the volume flow at the instrument's entrance. The input impedance is measured using the BIAS system [3] for all possible venting fingerings. These experimental results are compared with simulations using the Openwind framework [4]. Input data for simulations is provided from mechanical measurements of the bore profile of the vented trumpet.

2. LINEAR ACOUSTICS OF RESONATOR

From a physical point of view, a wind instrument can be characterised by a non-linear excitation source coupled with a passive resonator, which is mainly reduced to its linear response. The latter provides a number of resonances, which interact with the non-linear source to produce the pitch and waveform of the played note [5]. In this study, the analysis is restricted to the linear acoustical response of the instrument.

To describe the system, we make use of the concept of acoustic impedance, which relates the acoustic pressure p to the particle velocity field $\underline{u}$. Since the velocity field is a vectorial quantity, the impedance is, in general, direction-dependent. However, in the case of tubular geometries and under the plane wave approximation, the particle velocity is assumed to be oriented along the longitudinal axis of the tube. As a result, the directional dependence of the impedance can be neglected. This approximation holds when the tube length is significantly larger than its radius, a condition satisfied by the vented trumpet examined.

In particular, the input impedance is of special interest, offering a convenient way to analyse brass instruments, as the magnitude of the input impedance explicitly shows the frequencies and amplitudes of the resonances on which the played notes are based [6]. It is, therefore, used as an invaluable way to characterise the instrument. Furthermore, it is possible to express the input impedance in terms of modal parameters [5],

$$Z_{in}(\omega) = i\omega \sum_m \frac{p_m^2(0)}{\omega_m^2 + i\omega\omega_m/Q_m - \omega^2}, \qquad (1)$$

where each linear term only depends on the angular frequency ω_m, amplitude $p_m^2(0)$ and quality factor Q_m of resonance m. This approach allows for efficient analysis of the resonator and hole effects, as specific resonances can be either boosted or suppressed depending on the playing requirements. In this framework, the behaviour of the vent holes can be analysed through the variation of the modal parameters associated with each resonance, providing a means to characterise their influence on the overall acoustical response.

2.1 Vent Holes

When opening a hole in an axially symmetric tube, the intended musical purpose must be taken into consideration. For vent holes, this corresponds to a strategically placed hole that is not used to define a new fundamental frequency but instead, when opened, helps with intonation correction, response improvement, or sound clarity.

The hole is studied by considering the component as an additional short tube in the instrument's geometry. In energetic terms, when a sinusoid travelling down the pipe encounters a hole, some of the energy is transmitted towards the bell end, some is radiated from the hole, and the remaining energy is reflected to the input. Therefore, the shape of the standing wave formed within the air column changes along the length of the instrument, even if the radius of the tube is constant throughout.

A proper parameter to characterise the energy in the system is the sound power transmission T, defined as the fraction of sound energy which is transmitted past the hole [7],

$$T = \frac{1}{1 + (cb^2/4\pi h_e r^2 f)^2}, \qquad (2)$$

where c is the speed of sound, f is the frequency of the sound wave, b is the hole radius, and h_e is the effective acoustic length of the side branch.

At low frequencies, the power transmission rapidly approaches zero, indicating an effective cutoff of the main

bore's right section. As the frequency increases, the transmission tends toward unity, with most of the sound propagating through the pipe, behaving as a high-pass filter. As a consequence, the effect of the hole on each resonance will vary depending on its frequency relative to this filtering behaviour. A useful parameter to characterise the hole is the cutoff frequency, defined as the frequency at which $T = \frac{1}{2}$. Resonances below the cutoff frequency will be significantly affected by the presence of the hole, while those above it will remain largely unaffected.

3. CALCULATING INPUT IMPEDANCE

The simulations performed on the vented trumpet rely on an accurate description of the instrument's bore profile, as well as ambient conditions matched to those of the experimental measurements. To maximise reproducibility between experiments and simulations, all relevant elements of the instrument were carefully measured. Assuming the main bore of the instrument is an axially symmetric tube, the geometry can be fully characterised by the radius as a function of the axial position. Accordingly, both the length of the pipe and the variation of its radius along the axis were measured mechanically using bore gauges. A three-dimensional reconstruction of the trumpet bore is shown in Fig. 1.

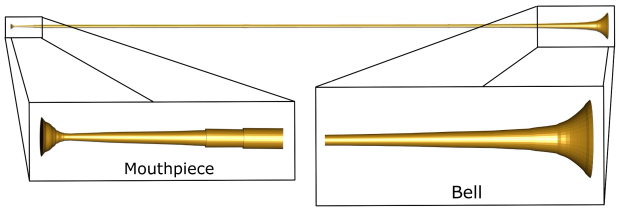


Figure 1. 3D model of vented trumpet geometry used in the Openwind simulation. A zoomed view of the shape of the mouthpiece and bell is shown. The total length of the bore is $L = 2.25\,\mathrm{m}$.

In this setup, following a systematic asymptotic analysis [8], the Webster horn equation, describing wave propagation in pipes of varying cross-sectional area, is reformulated as a pair of Telegrapher equations to model the system while accounting for viscothermal losses [9,10]. A Finite Element Method (FEM) approach, implemented in the Openwind framework, was employed to solve the system numerically. This method allows for the computation of the input impedance, as well as the pressure and volume flow fields along the bore, which were used to analyse the behaviour further.

The scheme enables the definition of the ambient conditions. For consistency with the experimental measurements, the temperature was set to $17\,^{\circ}\mathrm{C}$, and a radiation impedance for an infinitely flanged pipe was imposed as the boundary condition at the pipe end [11].

4. MEASURING INPUT IMPEDANCE

The input impedance was measured using the Brass Instrument Analysis System (BIAS), which offers a fast and accessible method to perform many successive measurements on the impedance of brass instruments [12]. It relies on a capillary-based technique, where two microphones are positioned on either side of a high-impedance capillary, which is then connected to the mouthpiece [3]. The experimental setup of the BIAS head mounted with a vented trumpet is shown in Fig. 2.



Figure 2. Experimental setup of the BIAS head mounted with the vented trumpet in the anechoic chamber.

Impedance data was collected using the Versatile Instrument Analysis System (VIAS) software, which allows for higher energy in the excitation signal and user-selected time and frequency range for each measurement. Measurements were performed using a logarithmic sweep from $20\,\mathrm{Hz}$ to $4\,\mathrm{kHz}$ with a period of $600\,\mathrm{s}$ using a sinusoidal excitation signal, ensuring adequate time for standing wave formation at lower frequencies.

Using this experimental configuration, the input impedance of the vented trumpet was measured systemat-

ically by opening one vent hole at a time. To replicate the opening and closing of holes as a player would with their fingers while ensuring consistency across measurements, all holes were appropriately sealed and maintained airtight closure except for tests when a single hole was opened. To ensure this was the case for all measurements, a reading of the impedance with all holes closed was taken at the beginning and end of the sessions, verifying the stability of the procedure.

5. RESULTS

The positions along the bore and dimensions of two vent holes on the vented trumpet are listed in Tab. 1, referred to as the thumb hole (hole 1) and octave hole (hole 4), with hole 1 having the larger radius. Due to the curved instrument surface, chimney height was defined as the maximum distance from the surface to the top edge of the hole, measured along the local normal and assumed constant across the hole.

Table 1. Position, radius, and chimney length of holes 1 and 4. Errors indicated in parentheses.

Hole	Position [m]	Radius [mm]	Chimney [mm]
Hole 1	1.1920(1)	3.72(5)	0.68(5)
Hole 4	1.0455(1)	1.75(5)	0.63(5)

Thus, opening hole 1 is expected to significantly alter the instrument's resonances. The measured input impedance in this configuration is shown in Fig. 3, where each peak corresponds to a resonance.

The large radius results in minimal energy transmission beyond the hole, leading to a general upward shift in resonance frequencies. In particular, the hole dimensions translate to a cutoff frequency of approximately 1913 Hz, which is well above the intended playing frequencies with the hole open. Consequently, the hole significantly alters the resonance structure in this frequency range. Moreover, Fig. 3 reveals a general trend in the impedance magnitude: odd resonances exhibit increased amplitude due to constructive interference of pressure waves upstream of the hole, whereas even resonances are attenuated as a result of destructive interference, leading to a reduction in the input impedance amplitude. These effects progressively diminish for resonances approaching the cutoff frequency.

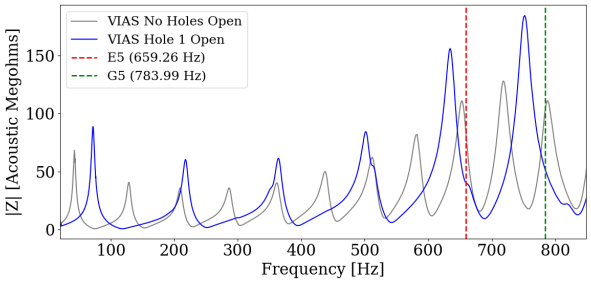


Figure 3. Input impedance magnitude measured for the vented trumpet with hole 1 opened (blue), and all holes closed (grey). The vertical dashed lines indicate the frequencies of the pitches for which the hole is opened, as indicated in the legend.

The intended playing frequencies with the hole open are occasionally E5 and, more importantly, G5, primarily improving playing security and intonation of the notes. However, in both cases, the nearest resonances (nine and eleven) undergo significant frequency shifts, reducing their amplitudes near the playing frequencies. At first glance, considering a simplistic approach in which the pitch is determined mainly by the closest resonance to the playing frequency, this suggests a negative impact on playability. Yet, analysis of the pressure and flow fields for the weak resonance just above G5 reveals a distinct acoustic effect which must be taken into account.

Fig. 4 shows the pressure and volume flow fields comparison between the large resonance with all holes closed at 790.30 Hz and the small resonance with hole 1 opened at 829.19 Hz, those closest to the G5 playing frequency. The apparent small pressure amplitude for the weak resonance with respect to the large resonance at the input is responsible for the small impedance magnitude observed previously.

A closer inspection of the pressure field reveals greater constructive interference occurring between the hole and the instrument's bell rather than between the input and the hole, thus increasing the amplitude of the standing wave pattern downstream of the hole. This suggests that the segment extending from the hole to the bell supports a robust resonance with pressure nodes at both boundaries near the resonance frequency. Consequently, a high flow amplitude is expected at the bell end, consistent with the bottom plot of Fig. 4. The intensified standing wave pattern downstream of the hole corresponds to an

increased energy concentration in that region. Given the relatively high flow amplitude at the bell compared to the overall wave amplitude, significant acoustic energy is radiated efficiently from the bell, facilitating the stable production of the G5 pitch despite the small amplitude of the associated resonance.

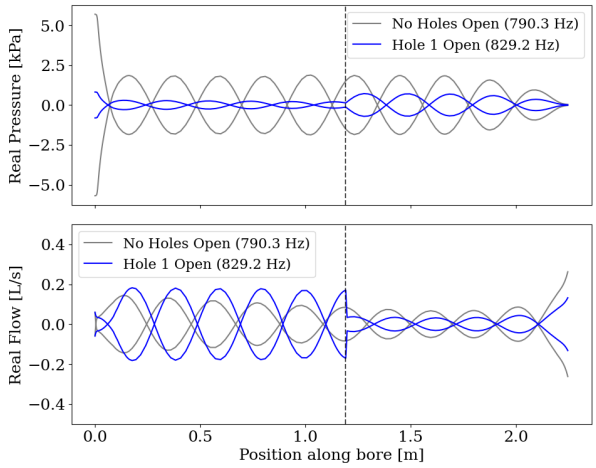


Figure 4. Top: Real part of complex pressure field along the bore for the resonance frequencies closest to G5. Bottom: Real part of the complex volume flow field along the bore is for the resonance frequencies closest to G5. The grey line indicates the closest resonance with all holes closed. The blue line indicates the closest resonance with hole 1 opened. The vertical dashed line indicates the hole position.

A similar behaviour was observed for hole 4. From Tab. 1, hole 4 has the lowest radius, thereby having the smallest cutoff frequency at 817 Hz. The qualitative behaviour of the fourth hole was found to be equivalent for both even and odd resonances. However, due to the small dimensions of the hole, these effects are drastically reduced as the resonances approach the cutoff frequency, giving a significantly different input impedance as compared to hole 1. For instance, the suppression of the even resonances is highly reduced near the cutoff frequency.

Hole 4 comprises the playing of notes corresponding to the even harmonics of D2. Fig. 5 shows three of these notes (D5, F♯5, A5) with their corresponding playing frequency to exemplify the acoustic behaviour of the hole. By opening hole 4, the resonances closest to the even harmonic playing frequencies have been shifted in frequency closer to these, notably improving the intonation of the notes. However, as for the case of hole 1, these resonances are somewhat suppressed by the hole. Therefore, the playability of the notes could be compromised.

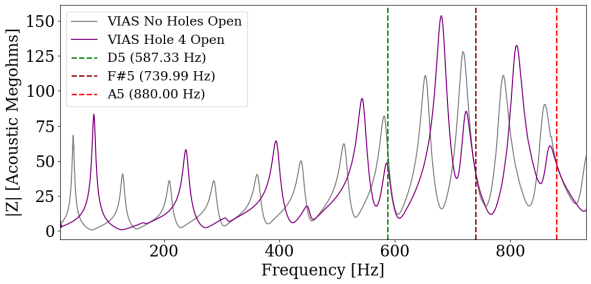


Figure 5. Input impedance magnitude measured for the vented trumpet with hole 4 opened (purple) and all holes closed (grey). The vertical dashed lines indicate the frequencies of the pitches for which the hole is opened, as indicated in the legend.

Nonetheless, the same reasoning applied to hole 1 extends to the acoustic pressure field and volume flow in this case. For the even resonances, a stronger standing wave pattern develops downstream of the hole, increasing flow amplitude at the bell and boosting sound radiation, thereby improving the stability of the even harmonics of D2.

6. CONCLUSION

The acoustical behaviour of the thumb and octave vent holes in an available four-hole vented trumpet has been examined. Under a linear approximation, the input impedance was used to determine the behaviour of the resonances of the system by observing variations in the amplitude, frequency and quality factors of each resonance when a hole was opened along the tube. The input impedance was measured experimentally using the BIAS system, and numerical simulations using the FEM were used to analyse the behaviour of each resonance in greater detail.

The opening of the thumb hole (hole 1) showed the nearest resonances to the intended playing frequencies to undergo a significant frequency shift and an evident reduction in their impedance amplitude, which suggested, at first instance, a negative impact on the playability. However, the acoustic pressure and volume flow fields calcu-

lated from the simulations on the instrument for these resonances showed a constructive interference occurring between the hole and the instrument's bell rather than across the input and the hole, thus increasing the amplitude of the standing wave pattern downstream the hole. The intensified standing wave pattern corresponds to an increased energy concentration in that region, and, as a result, significant energy is radiated efficiently from the bell, facilitating the stable production of the notes for which the closest resonances were observed to reduce their amplitude. A similar behaviour was observed for the octave hole (hole 4).

7. ACKNOWLEDGMENTS

The authors are grateful to Jim Woodhouse for his insightful discussions on modal parameter extraction, which have informed the analysis presented in this work. The authors also wish to thank Sandy McGrattan for sharing his expertise on the practical use of the vented trumpet and for testing the instrument, providing valuable feedback.

8. REFERENCES

[1] M. Campbell, A. Myers, and J. Gilbert, *Sounding Brass: Brasswind Instruments and How They Work*. New York: Springer, In Press.

[2] M. Campbell, A. Myers, and M. J. Newton, "Acoustical behaviour of "baroque" trumpets with vent holes," *J. Acoust. Soc. Am.*, vol. 155, no. 3, pp. A108–A109, 2024.

[3] W. Kausel, *A Musical Acoustician's Guide to Computational Physics: Concepts, algorithms and applications*. Vienna: Institute of Musical Acoustics, University of Music, 2003.

[4] Openwind, "Open wind instrument design." `https://openwind.inria.fr/`, 2022.

[5] J. Woodhouse, "Euphonics: The science of musical instruments." `https://euphonics.org/`, 2025.

[6] M. Campbell, J. Gilbert, and A. Myers, *The Science of Brass Instruments*. New York: Springer, 2021.

[7] L. E. Kinsler, A. R. Frey, A. B. Coppens, and J. V. Sanders, *Fundamentals of Acoustics*. New York: John Wiley & Sons, 2000.

[8] S. W. Rienstra, "Webster's horn equation revisited," *SIAM Journal on Applied Mathematics*, vol. 65, no. 6, pp. 1981–2004, 2005.

[9] J. Chabassier and R. Auvray, "Direct computation of modal parameters for musical wind instruments," *J. Sound Vib.*, vol. 528, p. 116775, 2022.

[10] R. Tournemenne and J. Chabassier, "A comparison of a one-dimensional finite element method and the transfer matrix method for the computation of wind music instrument impedance," *Acta Acust. United Ac.*, vol. 105, no. 2, pp. 356–369, 2019.

[11] A. R. da Silva and P. Guillemain, "Approximation formulae for the acoustic radiation impedance of a cylindrical pipe," *J. Sound Vib.*, vol. 320, no. 4–5, pp. 940–947, 2009.

[12] G. Widholm, "Brass wind instrument quality measured and evaluated by a new computer system," in *Proc. of the 15th International Congress on Acoustics*, vol. 3, pp. 517–520, 1995.

DOI: 10.61782/fa.2025.0336



FORUM ACUSTICUM
EURONOISE 2025

EMBOUCHURE PARAMETER VARIATIONS ACROSS BRASS MUSICIANS OF DIFFERENT LEVELS OF PROFICIENCY

Amann Paul[1*] **Chatziioannou Vasileios**[1]
Nicolay Pascal[2] **Willmann Roland**[2]
[1] Institute of Music Acoustics Wiener Klangstil, University of Music and Performing Arts Vienna
[2] Carinthia University of Applied Sciences, Austria

ABSTRACT

Sound production in brass instruments requires complex interactions between embouchure parameters such as blowing pressure, mouthpiece force, etc. This paper presents findings from the use of a custom-developed digital mouthpiece designed to efficiently acquire embouchure data. The digital mouthpiece is able to record the forces of the upper and lower lips separately, as well as air pressure both inside the oral cavity and inside the mouthpiece. Data from 31 trombonists of different levels of progress were recorded, including a wide range from beginners to experts. In this context, the study enhances and expands the existing understanding of forces exerted on the mouthpiece, by considering the forces of the upper and lower lip separately. The collected data demonstrate the widely-discussed pivoting movement during the performance of a brass instrument, and dominant types of playing can be seen with regard to the load conditions of the upper and lower lip.
In addition, data from the 31 participating musicians is shown, demonstrating the relationship between the mouthpiece force applied, the pitch, intensity and air pressure in the mouth under realistic playing conditions.

Keywords: *Brass Instrument Performance Variables, Mouthpiece Force, Embouchure*

**Corresponding author*: p.amann@fh-kaernten.at.
Copyright: *©2025 Amann, Paul et al. This is an open-access article distributed under the terms of the Creative Commons Attribution 3.0 Unported License, which permits unrestricted use, distribution, and reproduction in any medium, provided the original author and source are credited.*

1. INTRODUCTION

Embouchure parameters, such as mouthpiece force and blowing pressure, are featured in studies across various contexts, contributing to a better understanding of sound production for acousticians, educators, and brass musicians.
For example, the force exerted on the mouthpiece has been used to investigate the acoustical behaviour of brass players' lips with the aid of strain gauges placed between the lip and mouthpiece [1, 2]. The measured phase difference between the acoustic pressure in the lip-driven cylinder and the strain demonstrated the outward and upward striking movements of the lips in relation to the tone height. Other studies investigated the relationship between the mouthpiece force, pitch and sound pressure level, with the result that the force increases with pitch and intensity [3–5]. Besides the perspective of various pedagogical embouchure concepts regarding mouthpiece force [6, 7] and medical studies on the effect of mouthpiece force on tooth position [8], the relationship between the force applied and the level of proficiency was also examined [4, 9]. However, none of the experimental studies have separately examined the force exerted by the mouthpiece on the upper and lower lips. Observations of musicians indicate that a pivoting movement over the tone range is significant for the production of different pitches depending on the musician's embouchure technique [7]. The different angular positions of the mouthpiece of individual musicians and a pivoting movement were also observed in the MRI study on trumpet playing by Schumacher et al. [10]. Depending on the position of the jaw, this pivoting movement results in the mouthpiece being subjected to varying force distributions from the upper and lower lips.
The simultaneous measurement of multiple embouchure

parameters, as demonstrated by Bianco et al. [5], highlights that different combinations of input variables can result in the same output.
This paper gives insight into the data set of 31 trombonists of different levels of proficiency, in which the forces of the upper and lower lip, the oscillating air pressure in the mouthpiece, the air pressure in the oral cavity and the sound were recorded simultaneously. The study was approved by the ethics committee of the University of Music and Performing Arts Vienna.

2. STUDY DESIGN AND DATA AQUISITION

The study was conducted at music schools and music universities and lasted around 30 minutes per participant. After being informed about the study and giving their consent, the musicians had time to familiarise themselves with the measurement set-up. The musicians played a specified sequence of tones in two separate runs, which were recorded for analysis. Subsequently, they completed a detailed questionnaire. A set of sheet music, divided into three levels of difficulty and containing passages from contemporary literature, was developed as the specified sequence of tones. Each participant was required to play all sections corresponding to their level of proficiency.
An enhanced version of the measuring device described by Amann et al. [11, 12] was calibrated and employed for the data acquisition. This mouthpiece, equipped with four load cells and two air pressure sensors, among other components, allows for the recording of mouthpiece parameters without significantly affecting the playing experience. In addition, a clip microphone (Shure BETA98H/C) was attached to the bell to record the audio signal.
The recorded data from the measuring device with a sampling rate of approx. 1750Hz was then preprocessed using Matlab. For detailed analysis and comparability between musicians, it was necessary to assign individual data points to the corresponding notes played. To achieve this, the recorded audio signal was segmented into the individual tones of the .musicxml file of the sheet music using audio score alignment techniques [13]. Subsequent refinement of the segmentation using Sonic Visualiser was necessary. The continuously recorded time stamp from the measuring device with the segmentation enabled the assignment of all data points to their corresponding notes. Each note was labelled with specific attributes, such as articulation, note length, and other relevant characteristics.
For the statistical analysis, features were extracted from the extensive data set using the computing Software R.

3. STUDY RESULTS

A total of 31 individuals participated in the study, out of which 9 identified as female and 22 as male. Regarding age distribution, 20 participants were between 18 and 35 years old, and 11 participants were over 35 years old. To differentiate between various levels of proficiency, a single factor ”P” ranging from 0 to 6 was calculated based on responses from the survey and the musicians' ability to play part 1, parts 1 and 2, or parts 1, 2, and 3 of the music sheets. Although there is no clear distinction between beginners, intermediates, and experts, the differentiation based on the factor was defined as follows: a range of $0 \leq P \leq 2$ for beginners, $2 < P \leq 4.5$ for intermediates, and above 4.5 for experts. Accordingly, 14 beginners, 10 intermediate, and 9 experts participated in the study.

3.1 Upper and Lower Lip Mouthpiece Force

The forces referenced in this paper pertain to the mean force exerted by the upper and lower lips. For better comparability, the initial and final 25% of each note on a time scale were excluded from the calculation as they depend significantly on the articulation, which is not considered in this paper.
Figure 1 presents a box plot illustrating the forces exerted by the upper and lower lips, with each pair of boxes representing one participant. The lighter-coloured box indicates the force exerted by the upper lip, while the darker-coloured box represents the force exerted by the lower lip. In the plot, only those notes that are part of the easy excerpt and thus played by all participants are considered. The musicians are arranged from left to right according to their level of proficiency.
When considering the total mouthpiece force, no statistically significant differences between the applied forces and the level of proficiency can be observed. Although there are tendencies for higher mouthpiece forces and outliers among beginners, there are also musicians within this group who exert very low forces. The observed differences decrease when comparing the mouthpiece force of beginners in the easy excerpt with the mouthpiece force of experts in the hard excerpt.
After the data collection for beginners in music schools, the results were preliminarily discussed with their music teachers. Exceptionally high and very low forces exerted on the mouthpiece were not only revealed by the measurements but were also perceived by the teachers. High force values were commonly associated with the tense appearance of the student, while low force values were linked to

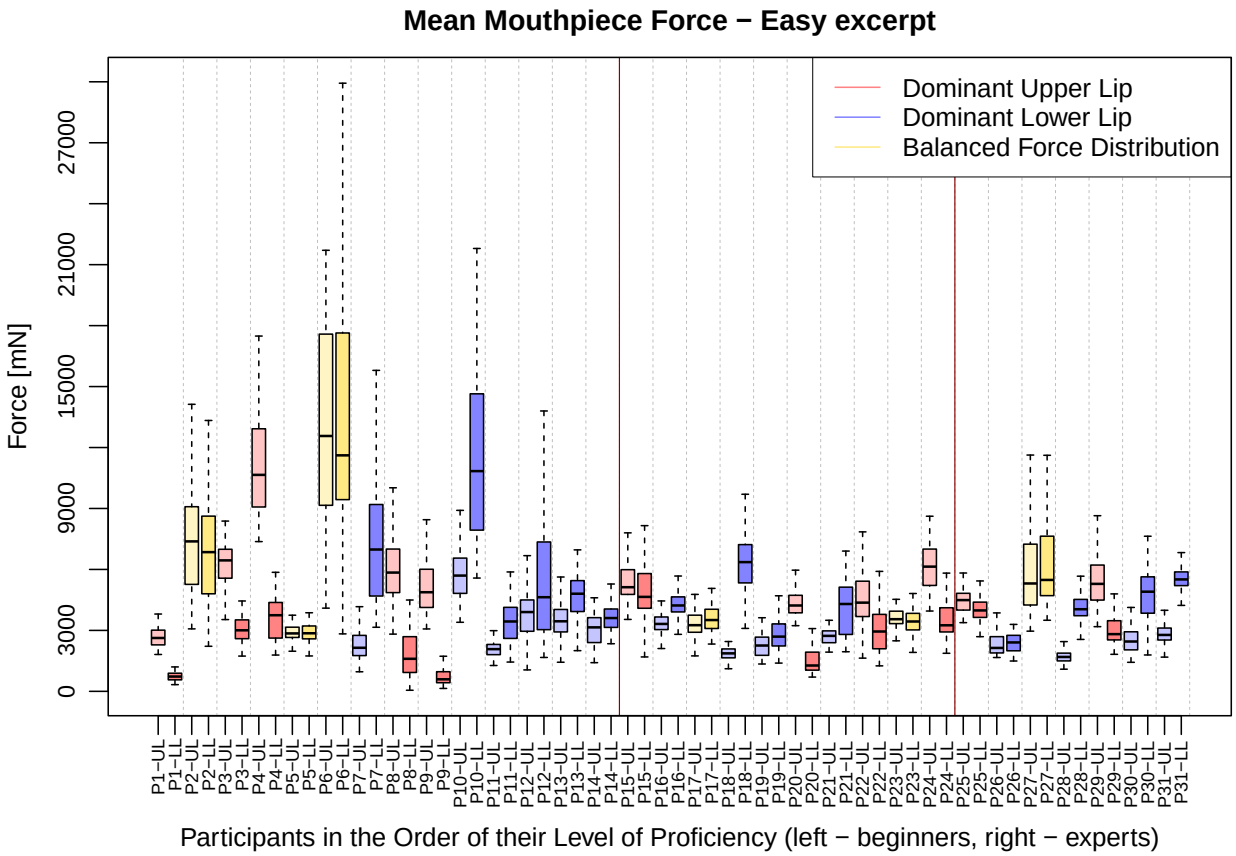


Figure 1. The Mouthpiece force of trombonists at different levels of proficiency is depicted, with UL and LL on the x-axis representing the force exerted by the upper and lower lips, respectively, for each individual. Participants 1 to 14 correspond to the beginner level, participants 15 to 24 correspond to the intermediate level, and participants 25 to 31 correspond to the expert level. The vertical lines separate the bars of the individuals (dashed) and the proficiency groups (red).

a lack of embouchure stability.

Different techniques and force distribution ratios are observed on average when comparing the forces exerted by the upper and lower lips. Musicians can be categorized based on their force distribution: those who apply more force to the upper lip (dominant upper lip, shown in red), those who apply more force to the lower lip (dominant lower lip, shown in blue), and those who maintain a balanced force distribution (shown in yellow). The distribution of forces can be caused both by a pivoting movement of the instrument relative to the head and by a displacement of the jaw. The ratio of the medians of the two forces is used as the threshold value to allow differentiation between the mentioned techniques. If the force exerted on the upper lip is 10% higher than that on the lower lip, the musician is classified as having a dominant upper lip embouchure. Conversely, if the force exerted on the lower lip is 10% higher than that on the upper lip, the musician is classified as having a dominant lower lip embouchure.

When examining the force distribution types in relation to pitch, some musicians exhibit a stable embouchure with minimal changes in force distribution. In contrast, others adjust their force ratios depending on the pitch significantly, resulting in noticeable variations. The change in embouchure when transitioning between different pitches, described by pedagogues as a tilting movement [7], can

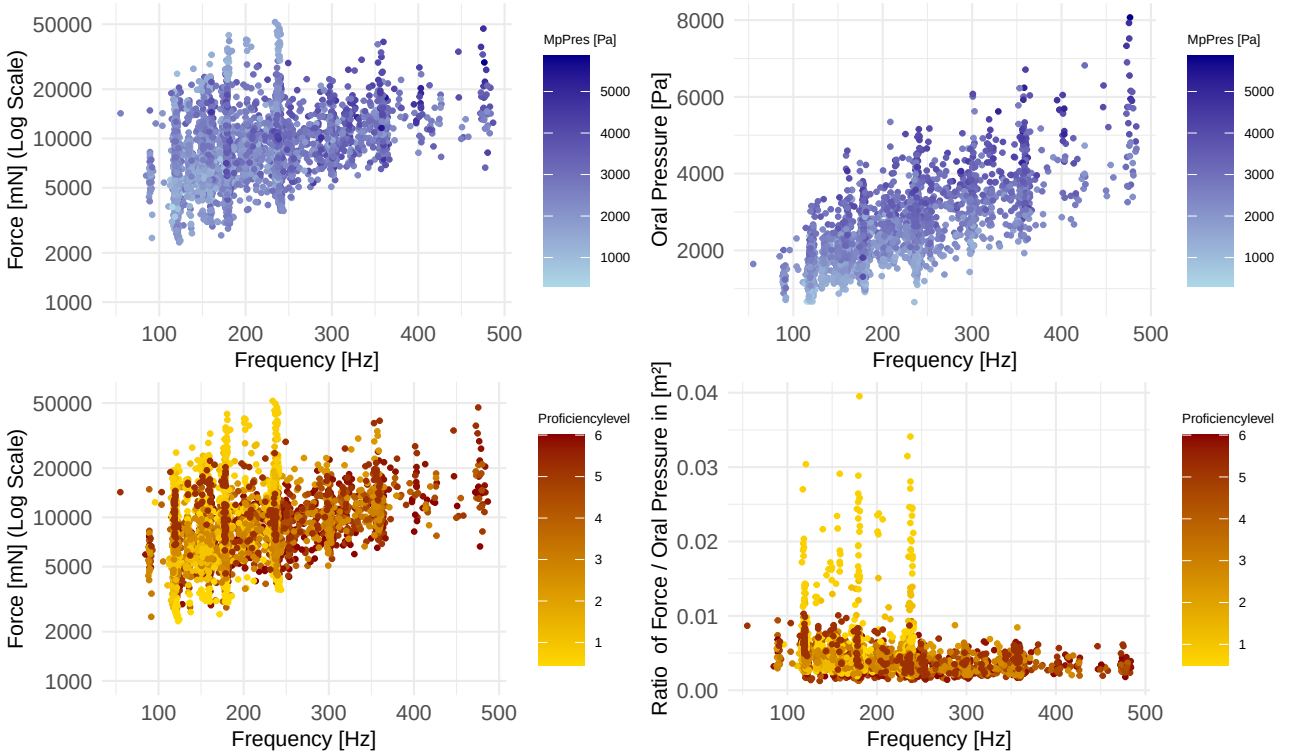


Figure 2. Relationships between force and frequency (top-left and bottom-left side), oral pressure and frequency (top-right side) and the ratio of force and oral pressure in relation to the frequency (bottom-right side) under realistic playing conditions. The colour of the upper plots indicates intensity: light blue for low RMS mouthpiece pressure values and dark blue for high RMS mouthpiece pressure values. The colour of the bottom plots correlates to the proficiency level of the musicians: yellow for beginners and red for experts.

be observed in the variations in the force distribution. The data do not support the popular assumption that certain embouchure techniques lead to increased success. Different force distribution types are observed across all levels of proficiency.

3.2 Interaction between Embouchure Parameters

The following section presents the results of the data analysis concerning the relationships between mouthpiece force, oral pressure, mouthpiece pressure, frequency, and proficiency level. Similar to the calculation of the shown force data, the oral pressure and root mean square (RMS) of the mouthpiece pressure values are derived from the middle 50% of the notes, thereby neglecting the note beginning and note ending.

As shown in Figure 2, the minimum mouthpiece force exerted by musicians to retain a note increases with frequency. When considering the data points of all musicians collectively, no relationship between intensity, represented by RMS mouthpiece pressure, can be discerned. Only by analyzing individual musicians separately does it become evident that, while some musicians maintain a constant force regardless of intensity, others increase their force as intensity rises.

When focusing on oral pressure, a clear positive correlation between frequency and oral pressure can be observed. The data in the lower frequency range align well with the results from brass instrument models regarding the minimum blowing pressure through linear stability analysis [14]. In the higher frequency range, however, the values achieved by musicians are significantly lower than predicted in [14].

The two bottom plots in Figure 2 pertain to the proficiency

level, ranging from 0 to 6, with red indicating high values and thus a high level of proficiency (experts). Since beginners were unable to achieve high notes, low levels of proficiency only extend up to the note Bb3 (approximately 233 Hz). It is notable that very low and very high mouthpiece forces in the lower pitch ranges are primarily utilized by beginners. Additionally, the maximum force values exerted by beginners when playing the note Bb3 are matched by expert musicians when playing Bb4.
In the bottom right plot, the ratio of force to oral pressure is shown as a function of frequency. What immediately stands out is that some beginners exert significantly more force on their lips relative to the corresponding air pressure in the oral cavity. Four individuals with a proficiency level between 0.5 and 1.2 (novice musicians) exceed a ratio of 0.11, while all others remain below this value.

4. CONCLUSIONS

In the paper, we examined the relationship between the embouchure parameters: mouthpiece force of the upper and lower lip, air pressure in the oral cavity, air pressure in the mouthpiece, in relation to pitch and proficiency level based on data from 31 trombonists. The separate examination of the forces of the upper and lower lip is a novelty and allows conclusions to be drawn about different playing techniques, with musicians exhibiting dominant upper lip force, dominant lower lip force, and balanced force distribution, similar to pedagogical methods regarding pivoting movements. A correlation between the dominant force distribution type and the level of proficiency cannot be established. It is also not statistically significant that beginners exert more force while playing than advanced and professional musicians. However, outliers among the beginners can be observed, who exert excessively high forces.
A limitation of this paper is that the force distribution between the upper and lower lip was not presented in relation to pitch and intensity. Musicians who tend to one of the three distribution types may change this distribution depending on the pitch, for example, through tilting. The detailed analysis will be presented in a future paper. Furthermore, the measurement system cannot record the placement of the mouthpiece and its changes during playing, which indirectly affects the force values of the upper and lower lip.
In relation to pitch, the data reveals a minimum necessary force and a minimum oral pressure required to sustain the notes (note initiation and note ending were not considered), which both increase with rising frequency. Additionally, the ratio of force to applied air pressure in the oral cavity is significantly higher for some novice participants. The presented data serve as a preliminary study for a larger study with more participants.

5. ACKNOWLEDGMENTS

We would like to express our sincere gratitude to the Austrian Research Promotion Agency (FFG) for funding the study. We also extend our heartfelt thanks to the musicians of Gustav Mahler Private University and the Carinthian Music Schools for their participation. Additionally, we are grateful to the Austrian mouthpiece manufacturer Breslmair for their crucial support in the development of the measuring device.

6. REFERENCES

[1] S. Yoshikawa, “On the modeling of self-oscillation in brass instruments,” *The Journal of The Acoustical Society of America*, vol. 84, 11 1988.

[2] S. Yoshikawa, “Acoustical behavior of brass player’s lips.,” *The Journal of the Acoustical Society of America*, vol. 97 3, pp. 1929–39, 1995.

[3] P. Farkas, *The Art of Brass Playing*. Bloomington: Brass Publications, 1962.

[4] J. F. Petiot, “Measurement of the force applied to the mouthpiece during brass instrument playing,” *Proceedings of the Stockholm Music Acoustics Conference*, 2003.

[5] T. Bianco, V. Freour, I. Cossette, F. Bevilacqua, and R. Causse, “Measures of facial muscle activation, intraoral pressure and mouthpiece force in trumpet playing,” *Journal of New Music Research*, vol. -, no. 0, pp. –, 2012.

[6] J. Ford III, *Scientific Characterization of Trumpet Mouthpiece Forces in the Context of Pedagogical Brass Literature*. PhD thesis, University of North Texas, University of North Texas, December 2007.

[7] S. J. Miles, *Dispelling the Myths of the Brass Wind Embouchure: Methods, Mechanics and Practices*. PhD thesis, University of Otago, 2019.

[8] L. Borchers, M. Gebert, and T. Jung, “Measurement of tooth displacements and mouthpiece forces during brass instrument playing,” *Medical Engineering & Physics*, vol. 17, no. 8, pp. 567–570, 1995.

[9] J. C. Barbenel, P. Kenny, and J. B. Davies, "Mouthpiece forces produced while playing the trumpet," *Journal of Biomechanics*, vol. 21, no. 5, pp. 417–424, 1988.

[10] M. Schumacher, C. Schmoor, A. Plog, R. Schwarzwald, C. Taschner, M. Echternach, B. Richter, and C. Spahn, "Motor functions in trumpet playing—a real-time mri analysis," *Neuroradiology*, vol. 55, no. 9, pp. 1171–1181, 2013.

[11] P. Amann, V. Chatziioannou, P. Nicolay, and R. Willmann, "On the capabilities of a 'digital mouthpiece' for real-time recording of embouchure parameters for brass musicians," *10th Convention of the European Acoustics Association*, 2023.

[12] P. Amann, P. Nicolay, V. Chatziioannou, and R. Willmann, "A "digital mouthpiece" for the autonomous analysis and improvement of brass musician performances," in *Fourth Vienna Talk on Music Acoustics*, Proceedings of Meetings on Acoustics, p. 035022, ASA, 2023.

[13] M. Müller and F. Zalkow, "libfmp: A Python package for fundamentals of music processing," *Journal of Open Source Software (JOSS)*, vol. 6, no. 63, pp. 3326:1–5, 2021.

[14] R. Mattéoli, J. Gilbert, C. Vergez, J.-P. Dalmont, S. Maugeais, S. Terrien, and F. Ablitzer, "Minimal blowing pressure allowing periodic oscillations in a model of bass brass instruments," *Acta Acustica*, vol. 5, p. 57, 2021.

DOI: 10.61782/fa.2025.0572

FORUM ACUSTICUM EURONOISE 2025

MODAL APPROACHES FOR MODELLING NONLINEAR ACOUSTICS IN 2D AXISYMMETRIC DOMAINS: APPLICATION TO BRASS INSTRUMENTS

Filipe Soares[1*] **Bruno Cochelin**[1] **Vincent Freour**[1,2]
Christophe Vergez[1] **Keita Arimoto**[2]

[1] Aix Marseille Univ, CNRS, Centrale Med, LMA UMR7031, Marseille, France
[2] Yamaha Corporation, Research and Development Division, 101 Nakazawa-cho, Naka-ku, Hamamatsu, Shizuoka 430-8650, Japan

ABSTRACT

The modelling approach presented here aims at developing accurate, yet computationally efficient, numerical models of brass instrument resonators including nonlinear propagation, viscothermal losses and 2D radiation effects. Firstly, we propose the use of the Blackstock equation to model the nonlinear acoustic propagation inside the resonator, a more appropriate choice when dealing with nonlinear standing wave patterns, compared to the commonly used Burger's equation. The initial step of the approach consists in obtaining a complex modal basis from a 2D-axisymmetric finite element model of the linearized equations. Here, we include a bounded domain outside the resonator with a nonreflecting boundary condition as well as the effect of viscothermal losses at the interior walls. The nonlinear Blackstock equation is then projected onto the resulting 2D complex modal basis, leading to a compact set of nonlinear ODEs. This leads to exploitable reduced formulations adapted to quick temporal simulations, bifurcation analysis or parametric studies, retaining nevertheless the accuracy of 2D models. The explicit account of the exterior acoustic field also allows for the calculation of radiated sound pressures as well as directivity patterns. Experimental validation and illustrative numerical results are presented for a simplified trumpet geometry in both linear and nonlinear scenarios.

Keywords: *nonlinear acoustic propagation, brass instruments, 2D axisymmetric modelling, complex modes*

[*] ***Corresponding author***: *filipedcsoares@gmail.com*
Copyright: *©2025 Soares et al. This is an open-access article distributed under the terms of the Creative Commons Attribution 3.0 Unported License, which permits unrestricted use, distribution, and reproduction in any medium, provided the original author and source are credited.*

1. INTRODUCTION

The physical modelling of brass wind instruments has received considerable attention in the last few decades [1]. These instruments constitute complex physical systems that, from the point of view of physical modelling, still present many challenging aspects. Here our focus is on the modelling of the instrument itself, i.e. without the influence of the lip vibration and the associated control by the musician.

Widely used and relatively simple models (typically in 1D frameworks) are able to qualitatively reproduce measured behavior. However, simplified models often present inherent limitations that prevent them from capturing the more subtle features of real instruments. For example, 1D models often rely on the assumption of plane wave propagation which, albeit reasonable in the narrower parts of the instrument bore, clearly breaks down at the exit of the instrument. Another important aspect is related to nonlinear acoustic propagation inside the resonator, a particularly relevant feature influencing the timbre of brass instruments [2]. Although some numerical studies have dealt with this topic, they almost exclusively rely on the Burgers equation [3][4]. However, this equation assumes only forward or backward propagating waves and its use in the context of brass instruments is questionable since standing waves are formed inside the instrument.

In commercial contexts, where manufacturers are interested in optimizing/fine-tuning certain aspects of their instruments, the accuracy provided by these simplified models often falls short of the desired goals. The motivation behind this work lies on the need to build a physical model that provides: (1) an accurate description of the pertinent acoustic phenomena, including an appropriate nonlinear acoustic propagation model, viscothermal losses at the walls as well as 2D propagation and radiation effects and

(2) an efficient and exploitable framework (low computational cost) that can be used for quick temporal simulations, parametric studies, optimization, bifurcation analysis, etc. The approach proposed here aims to bridge the accuracy provided by 2D-axisymmetric models and the efficiency of reduced-order modal approaches. The general idea consists in using a 2D finite element (FE) model of the linearized equations to obtain a suitable modal basis that can then be used to project the nonlinear equations, leading to exploitable reduced-order models (composed of a set of nonlinear ODEs). Due to the localized nature of the involved energy dissipation mechanisms (viscothermal and radiation losses), the eigenvalue problem stemming from the linearized 2D FE model leads to a complex modal basis [5]. In this particular context, the full potential of modal decomposition is highlighted. Firstly, the modal basis serves to spatially discretize the problem. Secondly, because modes have characteristic natural frequencies, they also serve to "discretize" the system in the frequency domain, i.e. modes whose natural frequencies fall outside the frequency bands of interest can generally be neglected. Thirdly, modes have characteristic damping ratios which encapsulate, in a simple manner, the often-times intricate dissipation mechanisms. For example, viscothermal losses are notably difficult to model in the time-domain since they give rise to fractional-order derivatives [6]. These can however be easily represented in a modal framework, suited for both frequency and time domain analysis. Finally, modal approaches have also been proven useful to treat nonlinear terms in an efficient manner [7] as well as for mitigating numerical dispersion, a common problem when solving stiff wave equations using finite difference or finite elements methods in the time domain [8].

2. MODEL DESCRIPTION

2.1 Nonlinear acoustics in 3D domains

In most applications, not involving explosions or other supersonic events, nonlinear acoustics are typically modelled through what are called weakly-nonlinear models. Starting from the set of irrotational compressible Euler equations and a state equation for the fluid, a wide variety of models have been proposed over the years, well documented in an historical review by Jordan [9]. Of particular interest to us, are the so-called wave equations, where the acoustic field is represented by a single scalar variable. In this work we propose the use of the Blackstock equation, written here in terms of the velocity potential $\phi(t, \mathbf{x})$

$$\ddot{\phi} - c^2\Delta\phi + 2(\nabla\dot{\phi})(\nabla\phi) + (\gamma-1)\dot{\phi}(\Delta\phi) = 0 \qquad (1)$$

where the over-dot denotes temporal derivatives, ∇ and Δ are the gradient and Laplacian operators, c is the speed of sound in the fluid and γ its adiabatic index. This second-order approximation of the more general Söderholm formulation is bound to be valid for acoustic Mach numbers up to $M < 0.1$. Note that this equation is equivalent to the more commonly used Kuznetsov equation [10].

Assuming the curved bents in typical brass instruments are acoustically negligible, Eq.(1) can be written in axisymmetric cylindrical coordinates (r, z) as

$$\begin{aligned}\ddot{\phi} - c^2\left[\frac{1}{r}\frac{\partial}{\partial r}\left(r\frac{\partial\phi}{\partial r}\right) + \frac{\partial^2\phi}{\partial z^2}\right] \cdots \\ +2\left(\frac{\partial\dot{\phi}}{\partial r} + \frac{\partial\dot{\phi}}{\partial z}\right)\left(\frac{\partial\phi}{\partial r} + \frac{\partial\phi}{\partial z}\right) \cdots \\ +(\gamma-1)\dot{\phi}\left[\frac{1}{r}\frac{\partial}{\partial r}\left(r\frac{\partial\phi}{\partial r}\right) + \frac{\partial^2\phi}{\partial z^2}\right] = 0\end{aligned} \qquad (2)$$

Additionally, because of the larger cross-section at the exit of the instrument, acoustic levels are relatively weaker. Hence, large amplitude acoustic perturbations and nonlinear propagation are known to occur primarily at the narrower parts of the horn [2], where the plane wave assumption is reasonable. This leads us to the conclusions that, in the context of brass instruments, the nonlinear terms in Eq.(2) involving the radial derivative $\partial\phi/\partial r$ can confidently be neglected, leading to

$$\begin{aligned}\ddot{\phi} - c^2\left[\frac{1}{r}\frac{\partial}{\partial r}\left(r\frac{\partial\phi}{\partial r}\right) + \frac{\partial^2\phi}{\partial z^2}\right] \cdots \\ +2\left(\frac{\partial\dot{\phi}}{\partial z}\right)\left(\frac{\partial\phi}{\partial z}\right) + (\gamma-1)\dot{\phi}\left(\frac{\partial^2\phi}{\partial z^2}\right) = 0\end{aligned} \qquad (3)$$

where only two quadratic nonlinear terms subsist.

2.2 Finite element axisymmetric model

As mentioned before, our first aim is to use a finite element discretization of the *linearized* model in order to obtain a suitable modal basis, which will serve as a basis of functions on which to subsequently project the nonlinear Blackstock equation. With regards to the acoustic domain then, we have simply the Helmholtz equation (linear wave equation in frequency domain). But furthermore, we need to consider two important dissipative boundary conditions representing: (1) radiation of energy towards the free-field and (2) the viscothermal losses occurring at the inner walls of the instrument. Concerning the former, we consider an exterior spherical domain whose outer boundary will

contain a nonreflecting condition, aimed at simulating an anechoic environment, as illustrated in Figure 1. For the viscothermal losses we have used the model proposed by Berggren et al. [11], which is based on the fact that, in air, viscothermal acoustic boundary layers (where losses take place) tend to be very small compared to reference dimensions/wavelengths and can hence be accurately approximated via an impedance boundary condition.

The complete linearized axisymmetric problem to be solved can then be written in the frequency domain as

$$\begin{aligned} k^2\phi - c_0^2\left[\frac{1}{r}\frac{\partial}{\partial r}\left(r\frac{\partial\phi}{\partial r}\right)+\frac{\partial^2\phi}{\partial z^2}\right] &= 0 \text{ in } \Omega \\ \left(\frac{1}{R}-ik\right)\phi+\frac{\partial\phi}{\partial n} &= 0 \text{ on } \Gamma_r \\ -\delta_v\frac{i-1}{2}\Delta\phi+\delta_t k^2\frac{(i-1)(\gamma-1)}{2}\phi+\frac{\partial\phi}{\partial n} &= 0 \text{ on } \Gamma_{vt} \\ \frac{\partial\phi}{\partial n} &= 0 \text{ on } \Gamma_w \end{aligned} \tag{4}$$

where the acoustic boundary layer lengths are given by

$$\delta_v=\sqrt{\frac{2\nu}{\omega}}\ , \quad \delta_t=\sqrt{\frac{2\kappa}{\omega\rho C_p}} \tag{5}$$

with ρ the fluid static density, ν its kinematic viscosity, κ its thermal conductivity and C_p the coefficient of specific heat at constant pressure.

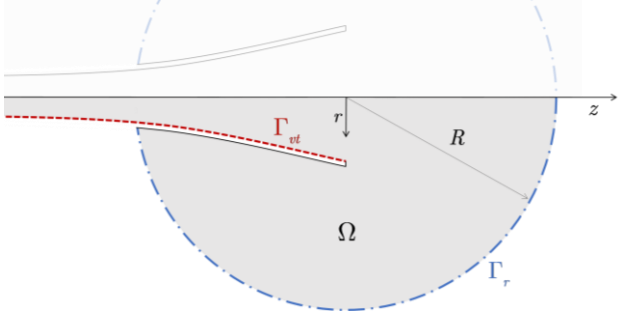


Figure 1. Diagram of the considered axisymmetric model. The dashed and dash-dotted lines correspond to the viscothermal Γ_{vt} and radiative Γ_r boundaries, respectively.

It is worth noting that the problem is here formulated in terms of acoustic velocity potential $\phi(r,z)$, but an equivalent formulation for the acoustic pressure can be obtained by replacing directly $\phi(r,z)$ by $p(r,z)$.

For compactness, we do not derive here the weak formulation or the FE discretization procedures, as these can be found in reference literature [12]. We simply note that second-order (6-node) triangular elements were used and the maximal size of each element $h_{\max}$ was set to at least one-fifth of the smallest considered wavelength.

2.3 Complex modal decomposition

After the FE spatial discretization, we obtain a dynamical system in the following form

$$\mathbf{M}\ddot{\boldsymbol{\phi}}(t)+\mathbf{C}\dot{\boldsymbol{\phi}}(t)+\mathbf{K}\boldsymbol{\phi}(t)=\mathbf{f}(t) \tag{6}$$

where $\boldsymbol{\phi}$ is a column vector of the velocity potential located at nodes of the FE discretized field and $\mathbf{f}(t)$ is a generic force vector that can represent external and/or nonlinear forces. Because of the localized nature of the modeled dissipative phenomena (radiation and viscothermal losses), our system belongs to a class of problems said to have non-classical damping. In practice, this prevents us from using typical modal approaches based on the real-valued modes shapes ($\mathbf{w}$), as these are not able to decouple the damped equations of motion. Here, we need to resort to complex modal analysis which is based around the state-space version of Eq.(6), arrived at by defining $\boldsymbol{\alpha}(t)=\dot{\boldsymbol{\phi}}(t)$, leading to

$$\mathbf{A}\dot{\mathbf{z}}(t)+\mathbf{B}\mathbf{z}(t)=\mathbf{F}(t) \tag{7}$$

with

$$\mathbf{A}=\begin{bmatrix}\mathbf{C} & \mathbf{M}\\ \mathbf{M} & 0\end{bmatrix}\ ;\ \mathbf{B}=\begin{bmatrix}\mathbf{K} & 0\\ 0 & -\mathbf{M}\end{bmatrix}\ ;\ \mathbf{z}(t)=\begin{Bmatrix}\boldsymbol{\phi}(t)\\ \boldsymbol{\alpha}(t)\end{Bmatrix}\ ;\ \mathbf{F}(t)=\begin{Bmatrix}\mathbf{f}(t)\\ 0\end{Bmatrix} \tag{8}$$

Solving the associated eigenvalue problem

$$(\lambda\mathbf{A}+\mathbf{B})\mathbf{u}=\mathbf{0} \tag{9}$$

leads us to the complex eigenvalues $\lambda_n\in\mathbb{C}$ and complex eigenvectors $\mathbf{u}_n\in\mathbb{C}$. Since $\mathbf{A}$ and $\mathbf{B}$ are symmetric, eigensolutions occur in pairs of complex conjugates

$$(\lambda_n,\ \bar{\lambda}_n)\ ;\ (\mathbf{u}_n,\bar{\mathbf{u}}_n)=\begin{Bmatrix}\mathbf{v}_n\\ \lambda_n\mathbf{v}_n\end{Bmatrix},\begin{Bmatrix}\bar{\mathbf{v}}_n\\ \bar{\lambda}_n\bar{\mathbf{v}}_n\end{Bmatrix} \tag{10}$$

where the overbar denotes complex conjugation. The full modal matrix of the first-order system is then

$$\hat{\mathbf{U}}=\begin{bmatrix}\mathbf{V} & \bar{\mathbf{V}}\\ \mathbf{V}\boldsymbol{\Lambda} & \bar{\mathbf{V}}\bar{\boldsymbol{\Lambda}}\end{bmatrix} \text{ with } \begin{cases}\mathbf{V}=\begin{bmatrix}\mathbf{v}_1,\dots\ \mathbf{v}_N\end{bmatrix}\\ \boldsymbol{\Lambda}=\text{diag}\ \lambda_1,\dots\ \lambda_N\end{cases} \tag{11}$$

Then, the complex modal transformation can be written in the following forms, due to its conjugate symmetry

$$\mathbf{z}(t)=\sum_{n=1}^{N}[\mathbf{u}_n q_n(t)+\bar{\mathbf{u}}_n\bar{q}_n(t)]=\mathbf{U}\mathbf{q}(t)+\bar{\mathbf{U}}\bar{\mathbf{q}}(t) \tag{12}$$

where $\mathbf{q}(t)$ are the modal coordinates and $\mathbf{U} = [\mathbf{V}\ \mathbf{V\Lambda}]^T$ is the reduced modal matrix of size $2N \times N$ pertaining to only one side of the conjugate pairs. Finally, replacing Eq.(12) in Eq.(7) and pre-multiplying by $\mathbf{U}^T$ leads to the reduced decoupled system

$$\dot{\mathbf{q}}(t) + \mathbf{\Lambda q}(t) = \mathbf{V}^T\mathbf{f}(t) \tag{13}$$

which is of size N (using only one mode of each conjugate pair), first-order in time and where coefficients and variables are complex-valued.

2.4 Projection of external forces and nonlinear terms

Since we can obtain an (approximate) continuous representation of modes shapes $\mathbf{v}_n$ from the FE model, the same procedure can be performed in a continuous framework where associated integrations (modal projections) can be performed numerically using Gaussian quadrature. With that said, the generic force terms presented in Eq.(13) can also be represented in continuous form

$$\mathbf{v}_n^T\mathbf{f}(t) \quad \Leftrightarrow \quad \int_\Omega f(r,z,t)V_n(r,z)drdz \tag{14}$$

where $f(r,z,t)$ is a generic force term and $V_n(r,z)$ is the continuous version of the n-th complex mode shape. If we now consider an expanded force term composed of a generic external force as well as the nonlinear terms in Eq.(3), expanded in modal coordinates, we obtain

$$\begin{aligned} f(r,z,t) = {} & g_{\text{ext}}(t)S(r,z) \\ & - \sum_{k,m}^{2N} \left[2V_m'V_k' + (\gamma-1)V_mV_k''\right]\dot{q}_m(t)q_k(t) \end{aligned} \tag{15}$$

where, to simplify notation, we use the over-dash represent the partial derivative $\partial\,/\,\partial z$. Note that we considered here an external force with separable spatial and temporal components, i.e. $g_{\text{ext}}(t)S(r,z)$. Finally, replacing the expansion (15) into (13) yields the final set of N nonlinear complex-valued ODEs

$$\dot{q}_n(t) + \lambda_n q_n(t) = g_{\text{ext}}(t)S_n + \sum_{k,m}^{2N} A_{kmn}\dot{q}_m(t)q_k(t) \tag{16}$$

for $n = 1,2...N$, where the constant terms associated with the modal projection are given by

$$A_{kmn} = \int_\Omega \left[2V_m'V_k' + (\gamma-1)V_mV_k''\right]V_n drdz \tag{17}$$

$$S_n = \int_\Omega S(r,z)V_n(r,z)drdz \tag{18}$$

At this point, there are a few important aspects of the derived system (16) that should be underlined. Firstly, the nonlinear tensor A_{kmn} is constant and is calculated "off-line", i.e. prior to any temporal integrations, nonlinear analysis, etc. Secondly, note that even though the original equations have two distinct nonlinear terms, these have the same temporal character. Therefore, when expanded in modal coordinates, they can be combined in a single nonlinear tensor A_{kmn}. On the other hand, because we are using a complex modal basis (as opposed to real modes), nonlinear terms need to be calculated using both modes in each conjugate pair, leading to a complex tensor A_{kmn} of size $2N \times 2N \times N$. Thirdly, by choosing an appropriate truncation N, we can build reduced models that are tailored to specific applications, e.g. large N (say 50-100) for strongly nonlinear scenarios or smaller N (say 10-20) for linear, or weakly-nonlinear ones.

2.5 Illustrative results: complex modes of a trumpet with simplified geometry

Complex mode shapes are awkward to illustrate in a static image. This is because, contrary to the motion of real modes where all points move in unison, complex modes contain phase shifts between different spatial regions. Hence, while real modes represent standing wave patterns, complex modes are a combination of standing and travelling waves. They are generally represented by their real $\text{Re}[V_n(r,z)]$ and imaginary $\text{Im}[V_n(r,z)]$ parts separately. Moreover, complex modes are defined up to a multiplicative complex factor. In this case, it is often useful to "rotate" the complex mode by an angle β (i.e. multiply by $e^{-i\beta}$) such that it maximizes its real part [13]. In this way, we can assess the "degree of complexity" of each mode by examining how large is its imaginary part. Examples of some complex mode shapes of a simplified trumpet model are shown in Figure 2. We note that lower order modes have a nearly null imaginary part, meaning that they represent almost perfect standing waves (i.e. real modes). Higher order modes however have much larger imaginary parts, representing their radiative character. That is, these modes reflect essentially waves travelling out of the horn towards the free-field.

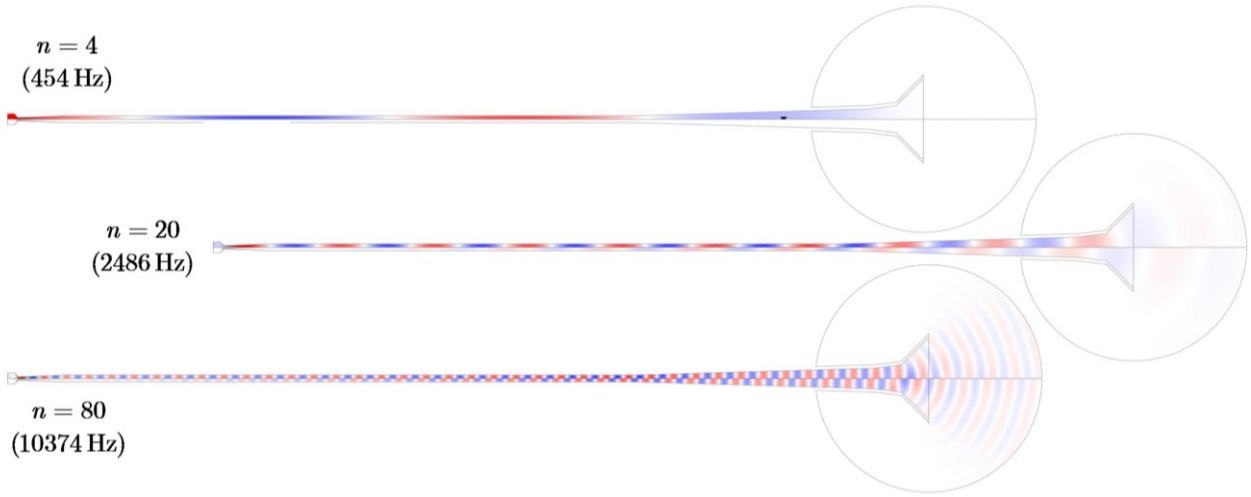


Figure 2. Some illustrative complex mode shapes $V_n(r, z)$ of the simplified trumpet. The real and imaginary parts are represented in the top and bottom of each plot, respectively. Note: modes shapes were rotated such that their real part is maximized (imaginary part minimized).

3. EXPERIMENTAL VALIDATION

To explore the effects of nonlinear propagation, an experimental set-up was prepared to excite the trumpet prototype harmonically. Acoustic excitation was provided by a BMS 4599 compression chamber placed at the entrance of the experimental prototype (without embouchure – i.e. only the cylindrical section plus the flaring horn section). Note however that this sort of set-up will inevitably influence the studied resonator since these drivers have an internal volume that is non-negligible. This volume was taken into account in the model, for validation purposes. However, naturally, the studied system in this case is not the same as that described in the previous section. The modal frequencies of the system were first identified via the exponential sine-sweep method. Subsequently, the system was excited at various modal frequencies at different amplitudes. A pressure sensor (Endevco 8507C-5) was placed iteratively on 40 locations along the resonator's length aimed at giving a spatial illustration of the nonlinear standing wave patterns. A second reference pressure sensor was fixed inside the cavity of the compression chamber to get a phase reference. The spatial distribution of the pressure inside the resonator when excited at the frequency of mode $n = 3$ (503 Hz) at different excitation amplitudes is shown in Figure 4. Analogous results from the model, obtained through temporal integrations using 100 complex modes are shown in Figure 5. Comparison of the experimental and modelled results are very satisfactory, with the model correctly representing the trends of the distorted standing wave patterns observed experimentally. Not only qualitatively, but also quantitatively, as the appearance and "level of distortion" appear to be congruent for the same values of the acoustic pressure. In a future work, different aspects of these results will be analyzed more thoroughly, as there are many more subtle aspects to be discussed.

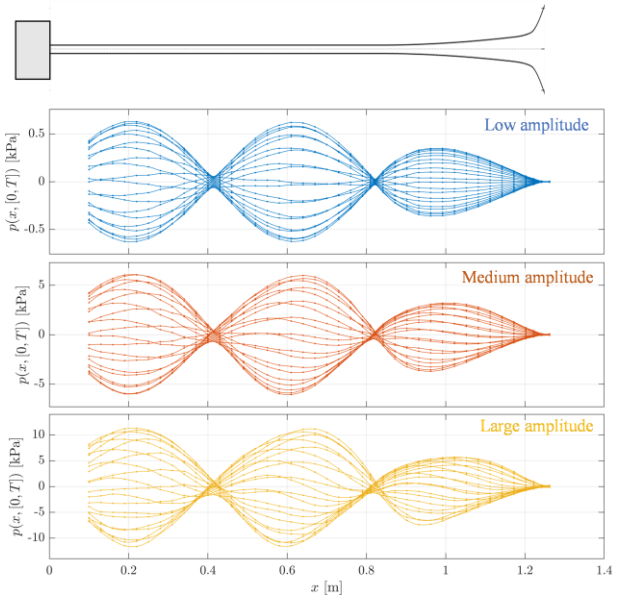


Figure 4. Experimental results: Snapshots of the measured pressure fields inside the trumpet at different amplitudes. Dots denotes the actual measurements while connecting lines were interpolated.

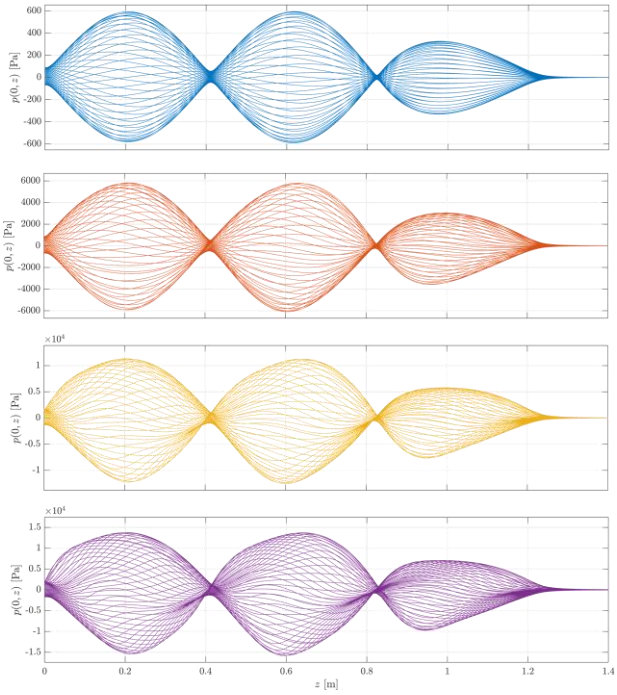


Figure 5. Modelling results: Snapshots of the modelled on-axis (r = 0) pressure fields inside the trumpet, excited harmonically at different amplitudes.

4. CONCLUSIONS

In this work we have shown how refined models of brass instruments, in a 2D axisymmetric framework, can be used to efficiently predict the behavior of real instruments, including a variety of complex physical phenomena like viscothermal losses at the walls, 2D radiation effects as well as nonlinear acoustic propagation. Within a reduced-order modal framework, these refined models convey essentially the same computational costs as the more typical 1D models used widely in the field. Moreover, the use of complex modes enables one to encapsulate intricate dissipative phenomena, like localized radiation or thermoviscous losses, in each modal component. This allows one to easily treat the problem in both the frequency and time domain, be that through temporal integrations, harmonic balance, numerical continuation, etc. The use of the Blackstock nonlinear acoustics equation instead of the more common Burger's equation allows us to calculate nonlinear standing wave patterns that can eventually be used to characterize brass instruments in terms of their capacity to produced "brassy" sounds. It is hoped that the developments shown here can stimulate a transition from descriptive towards predictive models of brass instruments.

5. REFERENCES

[1] A. Myers, J. Gilbert and M. Campbell, The Science of Brass Instruments, Springer, 2021.

[2] A. Myers, R. Pyle, J. Gilbert, M. Campbell, J. Chick and S. Logie, "Effects of nonlinear sound propagation on the characteristic timbres of brass instruments," *Journal of the Acoustical Society of America*, vol. 131, no. 1, pp. 678-688, 2012.

[3] S. Maugeais and J. Gilbert, "Nonlinear acoustic propagation applied to brassiness studies, a new simulation tool in the time domain," *Acta Acustica*, 2017.

[4] H. Berjamin, B. Lombart, C. Vergez and E. Cottanceau, "Time-domain numerical modeling of brass instruments including nonlinear wave propagation, viscothermal losses and lip vibration," *Acta Acustica united with Acustica*, vol. 103, no. 2, pp. 117-131, 2017.

[5] S. Krenk, "Complex modes and frequencies in damped structural vibrations," *Journal of Sound and Vibration*, pp. 981-996, 2004.

[6] N. Sugimoto, "Burgers equation with a fractional derivative: hereditary effects on nonlinear acoustic waves," *Journal of Fluid Mechanics*, vol. 225, no. 1, pp. 631-653, 1991.

[7] M. Ducceschi and C. Touzé, "Modal approach for nonlinear vibrations of damped impacted plates: Application to sound synthesis of gongs and cymbals," *Journal of Sound and Vibration*, vol. 344, pp. 313-331, 2015.

[8] C. Issanchou, S. Bilbao, J.-L. L. Carrou, C. Touzé and O. Doaré, "A modal-based approach to the nonlinear vibration of strings against a unilateral obstacle: Simulations and experiments in the pointwise case," *Journal of Sound and Vibration*, vol. 393, pp. 229-251, 2017.

[9] P. M. Jordan, "A survey of weakly-nonlinear acoustic models: 1910-2009," *Mechanics Research Communications*, vol. 73, pp. 127-139, 2016.

[10] B. Kaltenbacher and R. Brunnhuber, "Nonlinear Acoustics," Snapshots of modern mathematics from Oberwolfach , 2019.

[11] M. Berggren, A. Bernland and D. Noreland, "Acoustic boundary layers as boundary conditions," *Journal of Computational Physics*, vol. 371, pp. 633-650, 2018.

[12] L. Thompson, "A review of finite-element methods for time-harmonic acoustics," *Journal of the Acoustical Society of America*, vol. 119, no. 3, pp. 1315-1330, 2006.

[13] P. Vacher, B. Jacquier and A. Bucharles, "Extensions of the MAC criterion to complex modes," in *Proceedings of ISMA2010*, Leuven, Belgium, 2010.

[14] B. Cochelin, V. Freour and C. Vergez, "Exploiting the Use of Strong Nonlinearity in Dynamics and Acoustics: The Case of Musical Wind Instruments," in *Exploiting the Use of Strong Nonlinearity in Dynamics and Acoustics*, Springer Cham, 2024, pp. 121-149.

DOI: 10.61782/fa.2025.0350

FORUM ACUSTICUM EURONOISE 2025

ESTIMATING SOUND RADIATION CHARACTERISTICS OF COMPLEX-SHAPED PLATES USING REDUCED SETS OF ELEMENTARY SOURCES

Filipe Soares[1*] **Vincent Debut**[2,3]

[1] Aix-Marseille Université, CNRS, Centrale Marseille, LMA UMR7031, Marseille, France
[2] Instituto de Etnomusicologia, Centros de Estudos em Musica e Danca, Av. de Berna, Lisbon, Portugal
[3] Instituto Politecnico de Castelo Branco, Campus da Talagueira, Castelo Branco, Portugal

ABSTRACT

When calculating the acoustic radiation from vibrating planar structures, engineers are most often obliged to use computationally heavy approaches, like BEM or FEM. These are, however, largely unfit for parametric studies, optimizations, or real-time sound synthesis. The approach proposed here aims to approximate the acoustic fields produced by a vibrating plate via minimal sets of elementary sources. Based around a modal description of the plate vibration, each lobe region in a mode shape is to be represented by an equivalent punctual source. Aside from its evident computationally efficiency, the proposed approach is versatile since baffled and unbaffled cases can be treated using monopole and dipole arrays, respectively, and complex-shaped plates can be dealt with via automatic image segmentation techniques. Additionally, it enables the calculation of both modal radiation curves as well as forced multi-modal scenarios and transient responses. Because it is set in a modal framework, it can easily be combined with typical structural vibration models. The benefits of this reduced multipole approach are demonstrated through a series of illustrative examples, where approximate solutions are compared to reference results from either analytical or large-scale FEM models.

Keywords: *plate radiation, minimal models, equivalent sources, multi-modal radiation, monopoles and dipoles.*

[*] ***Corresponding author***: *filipedcsoares@gmail.com*
Copyright: *©2025 Soares et al. This is an open-access article distributed under the terms of the Creative Commons Attribution 3.0 Unported License, which permits unrestricted use, distribution, and reproduction in any medium, provided the original author and source are credited.*

1. INTRODUCTION

Whether driven by the need of understanding or of predicting sound radiation for control requirements, the radiation from plates has long been a topic of considerable relevance in engineering acoustics. The problem consists in predicting the sound field radiated by a planar structure of arbitrary shape, surrounded by a fluid and vibrating with a given surface velocity distribution. To provide useful insights, the analysis commonly proceeds on two approaches, addressing (1) the sound radiation from a specific mode, the so-called modal radiation, and/or (2) the overall radiation caused by unevenly forced excitation (e.g. point excitations), where many modes contribute to the vibrational response, the so-called multi-mode radiation.

Early works were mainly concerned modal radiation from simple analytical configurations and well-known results include asymptotic formulae and closed forms solutions for simply supported rectangular plates [1] [2] [3] [4]. One fact to emphasize is the difficulty of producing predictions for the unbaffled configuration, which considerably complicates the mathematical modelling and might lead to instabilities in the numerical implementations [5] [6]. In general, the radiation from more realistic complex-shaped plates typically requires the use of numerical approaches to solve the integral equations, for which finite element and/or boundary element methods are probably the most use techniques. Although precise solutions can usually be achieved by these techniques it is well known that the computation costs still represent a significant limitation particularly when dealing with optimization problems, parametric studies or real-time sound-synthesis.

Recently, a form of lumped model approach has been presented by Garcia et al. [7] by using combination of circular pistons that replicate modal radiation. In this model,

each lobe of a mode shape is viewed as a baffle piston that radiates the same amount of energy and with characteristics including size, amplitude, phase, and position, determined by the mode shape geometry. This concept, essentially a reduced form of the equivalent source method [8], is surely a powerful one, leading to very low computational cost and easily combined with modal-based structural vibration models. The authors have however dealt only with limited scenarios, namely, modal radiation in baffled configurations. It remains unclear how this could be extended to the unbaffled cases as well as the estimation of radiation patterns from unevenly excited plates (multi-modal).

In generic terms, the present formulation is a variant of the method proposed by Garcia et al. [7] as we use a spatial distribution of punctual sources to represent each lobe of a mode shape function. One major difference resides in considering monopoles and dipoles as the elementary radiators, which presents practical and conceptual advantages to deal with the problem. Monopole and dipole are the simplest acoustic sources and hence, are easy to model. Also, physically, it is well known that at low frequency, radiation from baffled plates can be represented by sets of monopoles and, similarly, unbaffled plates can be represented by sets of dipoles. In practice, the geometry of the mode shape directly determines the number of equivalent sources and the velocity distribution within each modal region defines the source strength and location of the equivalent point-source. Global measures of the pressure far-field, including total power and radiation efficiency, are then estimated using general analytical expressions derived for planar arrays of monopoles or dipoles. It is obvious that our formulation directly produces predictions for modal radiation but one practical advantage of the formalism is to deal easily with the forced multi-modal problem when one adopts a modal description for the plate dynamics. By doing so, the multi-modal problem is a natural extension of the modal case and hence can be addressed using the same expressions. This type of approach is obviously well adapted to programming and offers the possibility of efficient computations through solely one simple generic code for both baffled and unbaffled configurations. Other important feature of our work is the ability to deal with plates of arbitrary shape addressed by optimal and automatic positioning of the point sources achieved through techniques of image segmentation. Finally, note that by deriving the radiation model from the mode shape geometry, our formulation is readily well-suitable for integrating typical structural vibration models and could provide intuitive physical understanding and interpretation of the solutions.

2. MODAL RADIATION DESCRIBED BY A SET OF POINT SOURCES

The case of modal radiation is concerned with the vibration of a flexible plate animated by a simple harmonic motion in one of its natural modes. The velocity distribution of its surface is then written as

$$v(x,y) = v_m \phi_m(x,y) \tag{1}$$

where ϕ_m and v_m are the mode shape and modal velocity of mode m, respectively. The mode shape contains several local maxima/minima and its overall distribution can be then divided into a set of J convex regions containing one single minima or maxima (lobe). As illustrated in Figure 1, within the area of each region S_j, the location of an equivalent point source (x_j, y_j) will be defined by the weighted centroid of the mode shape, given by

$$x_j = \frac{\int_{S_j} x\phi(x,y)dxdy}{\int_{S_j} \phi(x,y)dxdy} \quad ; \quad y_j = \frac{\int_{S_j} y\phi(x,y)dxdy}{\int_{S_j} \phi(x,y)dxdy} \tag{2}$$

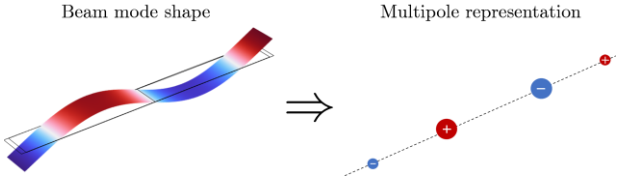


Figure 1. Illustration of the multipole method applied to a free-free beam mode.

2.1 Baffled case and monopoles

Assuming simple harmonic motion with frequency ω, the pressure field from a monopole may be expressed as

$$\hat{p}(r) = i\omega\rho\hat{U}\frac{e^{-ikr}}{4\pi r} = \hat{Q}\frac{e^{-ikr}}{4\pi r} \tag{3}$$

where $k = \omega / c$ is the wavenumber, i is the imaginary unit and quantities with a hat are complex amplitude containing phase information. The source strength $\hat{Q} = i\omega\rho\hat{U}$ represents the injection/suction of fluid into the region (a volume velocity). A generic representation of the source strength for plane radiators with continuous convex velocity distribution $v(x,y,t) = \hat{V}(x,y)e^{i\omega t}$ is given by

$$\hat{Q} = i\omega\rho\int \hat{V}(x,y)dxdy \tag{4}$$

The extension to account for N simple harmonic monopoles of complex source strength $Q_n = i\omega\rho U_n$ results from a direct application of the principle of linear superposition in acoustics. For such arrangement, the complex pressure at point $\mathbf{r}$ in the far-field is given by

$$p(\mathbf{r}) = \sum_{n=1}^{N} Q_n \frac{e^{-ikR_n}}{4\pi r} \tag{5}$$

where $R_n = |\mathbf{r} - \mathbf{r}_n|$ is the distance from the n-th source. Using Eq. (5), it can be shown that the acoustic power radiated by the set of monopoles is given by the sound intensity generated by

$$\Pi = \frac{\rho c k^2}{8\pi}\left(\sum_{n=1}^{N}|U_n|^2 + 2\sum_{n=1}^{N}\sum_{m>n}^{N}|U_n||U_n|\frac{\sin kl_{mn}}{kl_{mn}}\right) \tag{6}$$

where l_{mn} are the distance between source n and m. Eq.(6) states that the total acoustic power is determined by the power radiated by all individual sources when acting in isolation, and their mutual acoustic interaction, which is one of the most important mechanisms governing the effectiveness of sound radiation by vibrating surfaces [9] . It can also be written in the following compact matrix form

$$\Pi = \mathbf{u}^{\mathrm{H}}\mathbf{W}\mathbf{u} \tag{7}$$

where the superscript H is the complex conjugate transpose, $\mathbf{u}$ is the vector of the complex source volume velocities U_n and $\mathbf{W}$ is a matrix whose element (m,n) is

$$W_{mn} = \frac{\rho c k^2}{8\pi}\frac{\sin kl_{mn}}{kl_{mn}} \tag{8}$$

In this equivalent representation of modal radiation, the diagonal terms in $\mathbf{W}$ produce the "self" power radiated by the individual lobes whereas the off-diagonal terms, that clearly are symmetric, are associated to the "mutual" radiated power, i.e. the interference of the sound field radiated by the different lobes.

A useful measure of the effectiveness of sound radiation by vibrating surface, originally defined by Wallace [2], is the radiation efficiency, which is a normalized form of the radiated power. It is defined as

$$\sigma = \frac{\Pi}{\rho c S \langle |v(x,y)| \rangle} \tag{9}$$

where $\langle |v(x,y)| \rangle$ is the spatial and temporal average of the squared velocity distribution, which is defined by

$$\langle |v(x,y)| \rangle = \frac{v_n}{2S}\int_S |\phi(x,y)|^2 \, dxdy \tag{10}$$

Finally, note that all the previous derivations have been presented assuming monopole sources, hence radiating energy in free space. Adaptation to the baffle configuration implies to account for the fluid loading effects on a single side of the plate, so that expressions for the acoustic power must be multiplied by a factor of two.

2.2 Unbaffled case and dipoles

A dipole is typically an oscillating point source that can be conceptually modeled by two close monopoles of identical strength Q but opposite phase, and separated by a distance d . The pressure radiated by a dipole is given by

$$p(r,\theta) = -k^2\rho c\left(1 + \frac{1}{ikr}\right)Ud\left(\frac{e^{-ikr}}{4\pi r}\right)\cos\theta \tag{11}$$

where the dependence on the elevation angle θ evidences the directional character of the pressure field. Similarly with monopole source, a dipole source strength can be defined as

$$F = i\omega\rho Ud \tag{12}$$

where it is important to underline that here the source strength F has the units of a force. Contrary to generating a (unsteady) net volume outflow as in monopoles, a dipole source then exerts a force on the surrounding fluid and this renders their behavior physically and qualitatively different. If the establishment of a low-frequency equivalence between baffled plane radiators and monopoles is relatively straightforward by considering equivalent volume velocities, it becomes difficult to apply an equivalence between unbaffled plane radiators and dipoles. A simple example is that of a piston of area S and arbitrary shape, vibrating harmonically. If the piston is baffled, its volume velocity is independent of the piston shape. However, if the piston is unbaffled, difficulties arise because the same independence on the piston shape does not hold. That is, pistons with the same surface area but different shapes will not radiate the same amount of acoustic power, even at low frequencies. This is a consequence of localized inertial flows along the piston edges, which present large tangential velocities and significantly alter the force applied on the fluid by the vibrating piston. Analytical solutions for the low-frequency radiation of unbaffled circular [4] or elliptical [10] pistons are known, but deriving a generic expression for an arbitrary shaped piston is a more difficult task. However, in a recent work by the authors [11], a relatively generic approximation was proposed based on the piston compactness (ratio of area to perimeter). When looking at Eq.(12), the physical role of the equivalent distance d can be viewed as a correction factor $(d < 1)$ on

the volume velocity U, encapsulating the "edge effects", such that the equivalent force can be written as in (12). In the case of a circular disk for example, the equivalent distance is $d = (8 / 3\pi)a$. From a broad set of numerical results from a finite element model, the authors have proposed the following approximation for the equivalent distance, based on the piston compactness ratio

$$d = 2\left(\frac{8}{3\pi}\right)\frac{S}{P} \approx 1.7\,\frac{S}{P} \tag{13}$$

where P and S are the perimeter and area of the piston respectively. This expression is anchored on the known result for a circular disk, but also provides an excellent approximation for pistons of arbitrary shape. In our representation by means of equivalent modal radiators, Eq.(13) is used to estimate the equivalent dipole source strength F_j for each modal region j, using $d_j = 1.7\ S_j / P_j$ while the local volume velocity U_j is calculated as before (see Eq.(4)). Then, the pressure radiated in the far-field ($(kr \gg 1)$ by a set of N dipoles located arbitrary within a plane surface at position defined by vector $\mathbf{r}_n$ and pointed along the z-axis, is given by

$$p(\mathbf{r}) = -k^2\rho c\sum_{n=1}^{N} F_n\,\frac{e^{-ikR_n}}{4\pi r}\,\frac{\mathbf{r}_n\cdot\mathbf{d}_n}{r} \tag{14}$$

where $\mathbf{d}_n$ is the vector distance between the two dipoles. The total acoustic power radiated by the dipoles array is given by

$$\Pi = \mathbf{f}^{\mathrm{H}}\mathbf{D}\mathbf{f} \tag{15}$$

where $\mathbf{f}$ is a vector containing the dipole source strengths and the elements in the radiation matrix $\mathbf{D}$ are

$$D_{mn} = \frac{\rho c k^4}{8\pi}\left(\frac{\sin kl_{mn}}{(kl_{mn})^3} - \frac{\cos kl_{mn}}{(kl_{mn})^2}\right) \tag{16}$$

ILLUSTRATIVE RESULTS

2.3 Modal radiation of a baffled and unbaffled plate

The surface velocity of a rectangular baffled plate with dimensions L and w, with simply supported boundaries, vibrating at one of its natural modes is given by

$$v(x,y,t) = v_{mn}\phi_{mn}(x,y)e^{i\omega t}$$
$$\text{with}\quad \phi_{mn}(x,y) = \sin\left(\frac{m\pi x}{L}\right)\sin\left(\frac{n\pi y}{w}\right) \tag{17}$$

In this simple case, each mode (m,n) is divided into $J = m\times n$ regions with the same area

$$S_j = \frac{Lw}{mn}\ \forall j \tag{18}$$

The source strength of each equivalent monopole is the same for all sources

$$Q_j = \pm 2ik\rho c\left(\frac{Lw}{mn}\right)\frac{4}{\pi^2}v_{mn}\ \forall j \tag{19}$$

where a factor of two is present to account for the baffle. Note however that the sign of Q_j alternates between adjacent lobes. The weighted centroid of each modal region (monopole location) is located at the center of the lobe, define in a regular grid as

$$\mathbf{x}_j = \frac{L(p-1)}{2m}\ ;\ \mathbf{y}_j = \frac{w(q-1)}{2n}\ \text{for}\ \begin{cases} p = 1,2\ldots m \\ q = 1,2\ldots n \end{cases} \tag{20}$$

from which the inter-monopoles distance matrix l_{mn} can easily be obtained (as in Eq.(6)).

To illustrate the capability of the proposed method, Figure 2 shows the modal radiation efficiency of various modes of a simply supported square baffled plate calculated with the multipole approximation compared to the analytical solutions presented by Wallace [2]. The three plots shown pertain to the different modal families indexed: odd-odd, odd-even and even-even. The radiative behavior of these three modal families is characterized by their low-frequency behavior, which equates to a monopolar, dipolar or quadrupolar radiation efficiency, i.e. with σ_m proportional to $(kL)^2$, $(kL)^4$, $(kL)^6$, respectively. This simple example serves to underline the importance of symmetry in the radiation efficiency of vibrating structures. Here, much of the radiation from lobes of opposite phases, separated by a symmetry line, will cancel each other and severely reduce the amount of radiated power at low-frequencies. We also note, as expected, that the multipole formulation does not provide accurate results at high-frequencies. Since point sources have no characteristic dimension, a finite set of monopoles will not be able to reproduce the radiation of a physical structure when wavelengths λ exceed a critical length λ_c, related to the distance between the point sources (internodal distances).

Similarly, we illustrate the capacity of the dipole approximation considering modal radiation efficiency of a simply supported square unbaffled plate. Here, the dipolar equivalent distance can be easily calculated from Eq.(13)

$$d_j = 1.7\left(\frac{S}{P}\right) = 1.7\,\frac{2Lw}{Ln + wm}\ \forall j \tag{21}$$

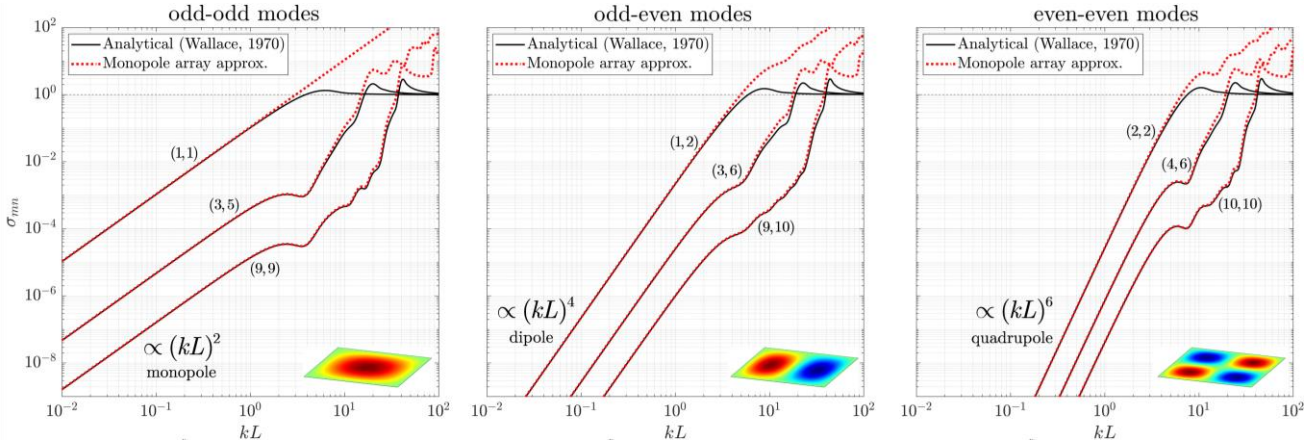


Figure 2. Modal radiation efficiency of square baffled plate with simply supported boundary conditions for odd-odd, odd-even and even-even modes as a function of the dimensionless frequency. The monopole approximations (red dotted lines) are compared to the analytical results (black lines) given by Wallace [2].

In this case, reference results were calculated using the method proposed by Laulagnet [5]. Figure 3 shows the modal radiation efficiency of some modes of an unbaffled plate from the three modal families. It shows that, at least for the case of a simply supported plate, the proposed formulation provides very reasonable approximations, almost as good as for the baffled case. We note however some minor quantitative differences, likely related to the validity of the approximate expression for the equivalent distance.

2.4 Watershed transform and automatic mode shape segmentation

The illustrative results shown in the previous section are simple to obtain since this case is simplified by the fact that all mode shapes have well-defined lobe regions, separated by the nodal lines of the mode shape. Hence, there is no ambiguity on the number and location of point sources to consider. However, this is not the general case and, particularly in complex-shaped plates, mode shapes often contain multiple local minima (representing multiple lobes) whose basins are not separated by nodal lines. Consider for example the well-known Matlab's "peaks" function (Figure 4). We note that this function contains three local minima and three local maxima. Hence, the proposed method would, in principle, require a minimal set of six-point sources to provide an approximation of its modal radiation efficiency. The three local minima (in blue) are indeed contained in regions bounded by nodal lines as opposed to the three local maxima (red/orange), which are in a single

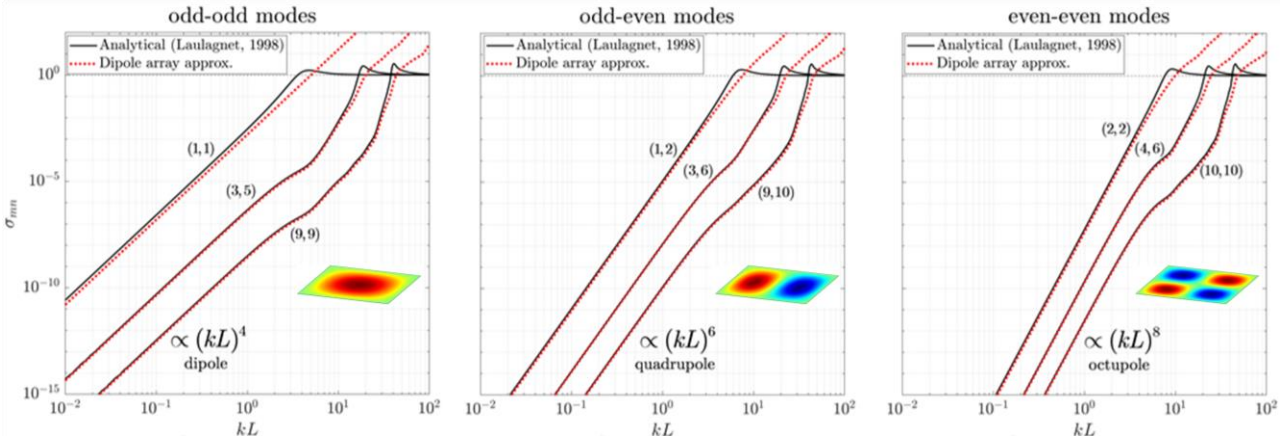


Figure 3. Modal radiation efficiency of square unbaffled plate with simply supported boundary conditions for odd-odd, odd-even and even-even modes as a function of the dimensionless frequency. The dipole approximations (red dotted lines) are compared to the analytical results (black lines) given by Laulagnet [5].

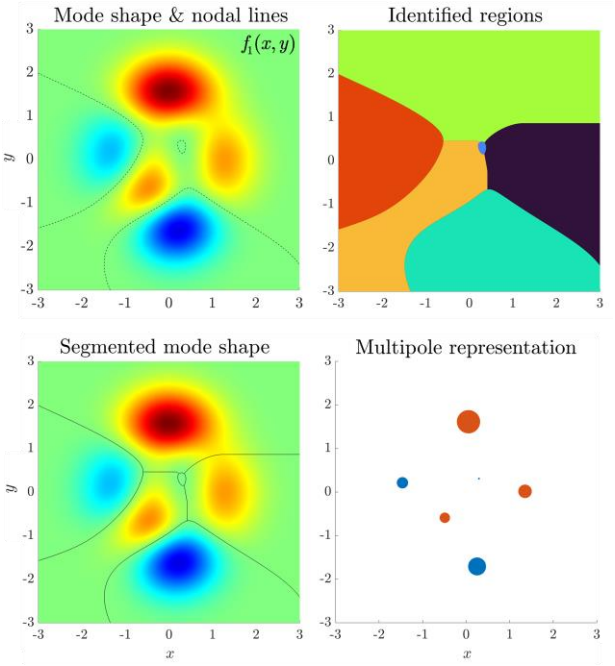


Figure 4. Illustration of the process of mode shape segmentation using the watershed transform on the "peaks" function, as well as the resulting point source representation.

"connected" region. We are then tasked to find lines that enable the segmentation of the three local maxima into different regions. This can be achieved in an automatic fashion using a variety of tailored algorithms. Here we suggest the use of the watershed transform [12] a widely used algorithm for image segmentation, which is simple, computationally efficient and perfectly fits the intended purpose. For brevity, we restrain from showing the details of the procedure here, but it essentially consists in performing the watershed transform on the modulus of the mode shape function $|f_1(x,y)|$. Figure 4 illustrates watershed transform on the peaks function and as well as the resulting multipole representation.

3. RADIATION DUE TO FORCED RESPONSE

3.1 Formulation for multi-modal scenarios

The natural extension of the previous formulation dealing with the sound power radiated by individual modes is to address the acoustic radiation from unevenly excited plates (e.g. from point force excitation), where many modes contribute to the vibratory and radiative responses. The difficulty in the multi-modal case stems from the fact that, although mode shapes are orthogonal from a vibratory point of view, the associated modal radiation fields are not. Hence, the total sound power is not equal to the sum of the sound powers generated by each mode separately but must also include the sound power produced by the radiative interaction between all modes [13]. Following our multipole representation of sound radiation, the total power radiated by a forced plate described by a set of N structural modes can be formulated by considering a large vector $\mathbf{Q}$ built by stacking a set of vectors $\mathbf{q}_n$, containing the source strengths of the point sources associated to each mode. Essentially, we aim to consider the interaction between all point sources in all modal sets. In view of such a structure, the radiation matrix $\mathbf{W}$ for a multimodal baffled plate is now a block matrix, in which the diagonal elements are square submatrices of modal radiation (as in Eq.(8)) and the off-diagonal blocks are submatrices of radiation stemming from inter-modal coupling, thus describing the production of acoustic power due to the interaction between all elementary sources pertaining to the different modes involved in the vibration. Knowing the modal response of the structure in terms of modal velocities u_n, the total acoustic power radiated for multimodal plates can thus be calculated from

$$\Pi = \begin{Bmatrix} q_1^1 \\ \vdots \\ q_1^{M_n} \\ \vdots \\ q_N^1 \\ \vdots \\ q_N^{M_n} \end{Bmatrix}^{\mathrm{H}} \begin{bmatrix} \mathbf{W}_{11} & \cdots & \mathbf{W}_{1N} \\ \vdots & \ddots & \vdots \\ \mathbf{W}_{11} & \cdots & \mathbf{W}_{NN} \end{bmatrix} \begin{Bmatrix} q_1^1 \\ \vdots \\ q_1^{M_n} \\ \vdots \\ q_N^1 \\ \vdots \\ q_N^{M_n} \end{Bmatrix} \quad (22)$$

where $\mathbf{W}_{pq}$ are full matrices whose elements $\mathrm{w}_{pq,rs}$ are given by

$$\mathrm{w}_{pq,rs} = \frac{\rho c k^2}{8\pi} \frac{\sin(kl_{pq,rs})}{kl_{pq,rs}} \quad (23)$$

in which we denote $p,q = 1,2\ldots N$ the modal index and r,s the index of elementary sources in each set, whose upper limit depends on the mode shape. For brevity, we present only the baffled case but the unbaffled case can similarly be formulated using an analogous procedure based on Eqs.(15)-(16) instead.

The local volume velocities q_n^m in Eq.(22) are calculated from the complex modal velocities v_n that can be calculated, when considering a point excitation at $\mathbf{r}_0 = (x_0, y_0)$ as

$$v_n = \frac{i\omega F_0\, \phi_n(\mathbf{r}_0)}{m_n(\omega_n^2 - \omega + 2i\omega\omega_n\zeta_n)} \tag{24}$$

where F_0 is the amplitude of the point force and m_n, ω_n and ζ_n are the modal mass, angular frequency and damping ratio of mode n, respectively.

3.2 Illustrative example on a rectangular plate

For illustrative purposes, we now consider a baffled simply supported rectangular plate with length $L = 0.6\,\mathrm{m}$, width $w = 0.5\,\mathrm{m}$ and thickness $h = 2\,\mathrm{mm}$, centered at $(0,0)$, such that it is defined in $x = [-0.3,\, 0.3]$ and $y = [-0.25,\, 0.25]$. Its natural frequencies and modal masses are given by

$$\omega_{mn} = \pi^2\sqrt{\frac{B}{\rho_s h}}\left[\left(\frac{m}{L}\right)^2 + \left(\frac{n}{w}\right)^2\right];\; m_{mn} = \frac{\rho_s L w h}{4} \tag{25}$$

where B is the bending stiffness and ρ_s is density. Modal damping was fixed uniformly at $\zeta_n = 0.01\ \forall n$.

For simplicity, we consider a unit force amplitude $F_0 = 1$ and two different locations for the excitation: $\mathbf{r}_1 = (0.19,\, 0.11)$ and $\mathbf{r}_2 = (0.24,\, 0)$. Reference results were calculated using an FEM model composed of a plate with prescribed velocity profile, surrounded by a hemisphere with non-reflecting boundaries (PMLs).

Figure 5 shows the vibratory response (collocated mobility), radiated power and radiation efficiency for excitation points $\mathbf{r}_1$, where results from the multipole method were calculated using $N = 100$ modes.

The results in Figures 5 show how the reduced set of point sources is clearly able to reproduce radiative properties of the plate in forced, multi-modal scenarios. At relatively low frequencies $(kL < \pi)$, the estimated radiated power and radiation efficiency are indistinguishable from the reference FEM results. Above $kL < \pi$, we note a drift of the estimated values, with the multipole method slightly overestimating radiated energy. Nevertheless, approximations are still reasonable even at these high frequencies. This is explained by the fact that the frequency limit of each modal approximation is related to the average distance between monopoles in each modal set, as seen in Figures 2 and 3. Hence, this frequency limit increases with

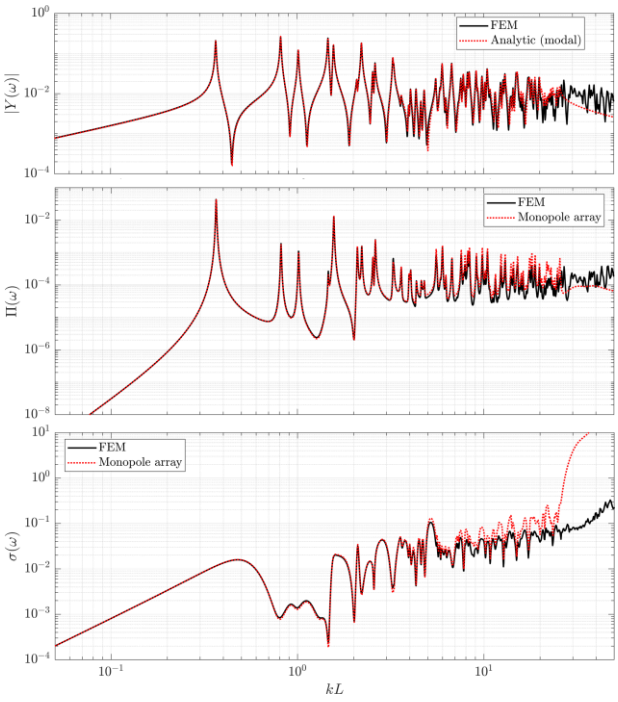


Figure 5. Magnitude of co-located mobility (top), total radiated power (center) and radiation efficiency (bottom) of the baffled rectangular plate excited at $\mathbf{r}_1 = (0.19,\, 0.11)$ as a function of the dimensionless frequency kL. Here, 100 modes were considered.

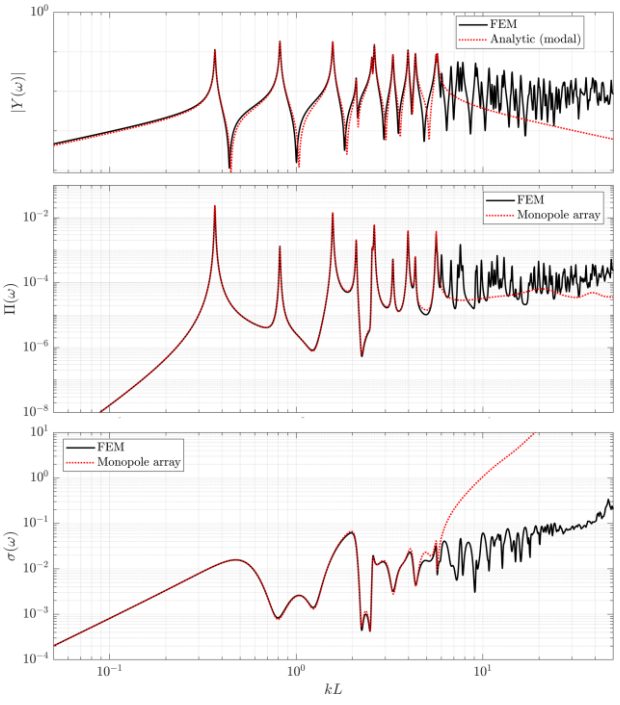


Figure 6. Magnitude of co-located mobility (top), total radiated power (center) and radiation efficiency (bottom) of the baffled rectangular plate excited at $\mathbf{r}_2 = (0.24,\, 0)$ as a function of the dimensionless frequency kL. Here 20 modes were considered.

modal order, as do the natural frequencies of the modes (!).

Figure 6 shows the analogous results for excitation point $\mathbf{r}_2$, and here, only $N = 20$ modes were used for the multipole method estimations. The responses in Figure 6 present less peaks since the excitation point is located on one of the symmetry lines and hence, some modes of the plate are not excited (those of even order in y-direction). Again, we clearly see a good approximation only limited in this case by the number of modes considered.

Finally, and most importantly, is it worth underlining that while the FEM model required approximately 1 to 5 seconds of computation time, per frequency bin, on a desktop computer, the reduced multipole model, with $N = 100$ (i.e. ~2500 sources) took approximately 30-40ms per frequency bin. Furthermore, when $N = 20$ (i.e. ~125 sources) it took about 0.3-0.4ms. Still, this computational time could be further reduced if one considers a threshold on the modal vibratory response. That is, for each frequency bin, considering only a limited set of modes whose vibratory response is dominant.

4. CONCLUSIONS

This paper shows how a method based on the distribution of point sources is able to recreate the radiation properties from vibrating plates, both from single mode excitation as well as multi-modal (unevenly forced) cases. Despite its simplicity, results show a relatively wide range of validity (not necessarily limited to low frequencies). Aside from the commonly treated baffled problem, we demonstrate how this approach can be generalized to unbaffled scenarios by using dipoles instead of monopoles. Also, to deal with complex-shaped plates, we propose an automatic mode-shape segmentation procedure that identifies the spatial distribution of the sources, based on the watershed transform. Illustrative results for the multi-modal case highlight the computational efficiency of the approach reaching acceptable approximations to reference results at computational costs that are several orders of magnitude below the analogous FE model.

An important feature of the formulation is the fact that it is built on a modal description of the plate vibration, which makes it readily integrable in standard structural models. This allows parametric studies and optimization strategies to be carried out for improving sound radiation of structural components, and gives the possibility to simulate very realistic sounds of bars and plates, even in real time.

5. REFERENCES

[1] G. Maidanik, "Response of ribbed panels to reverberant acoustic fields. J. Acoust. Soc. Am., pages," *Journal of the Acoustical Society of America*, pp. 809-826, 1962.

[2] C. Wallace, "Radiation resistance of a rectangular panel," *Journal of the Acoustical Society of America*, pp. 946-952, 1970.

[3] C. Oppenheimer and S. Dubowsky, "A radiation efficiency for unbaffled plates with experimental validation," *Journal of Sound and Vibration*, vol. 199, no. 3, pp. 473-489, 1997.

[4] T. Mellow and L. Karkkainen, "On the sound field of an oscillating disk in a finite open and closed back circular baffle," *Journal of the Acoustical Society of America*, vol. 118, no. 3, pp. 1311-1325, 2004.

[5] B. Laulagnet, "Sound radiation by a simply supported unbaffled plate," *Journal of the Acoustical Society of America*, vol. 103, no. 5, pp. 2451-2462, 1998.

[6] A. Putra and D. Thompson, "Sound radiation from rectangular baffled and unbaffled plates," *Applied Acoustics*, pp. 1113-1125, 2010.

[7] A. C. Garcia, N. Dauchez and G. Lefebvre, "Modeling the acoustic radiation of plates using circular pistons," *Journal of Sound and Vibration*, vol. 553, 2023.

[8] S. Lee, "Review: The Use of Equivalent Source Method in Computational Acoustics," *Journal of Computational Acoustics*, vol. 23, no. 1, 2017.

[9] F. J. Fahy and P. Gardonio, Sound and Structural Vibration: Radiation, Transmission and Response, Academic Press, 2006.

[10] A. Silbiger, "Radiation from circular pistons of elliptical profile," *Journal of the Acoustical Society of America*, vol. 33, no. 11, pp. 1515-1522, 1961.

[11] F. Soares and V. Debut, "On the radiation from unbaffled pistons and their dipole equivalent," in *Tecniacústica*, Cuenca, Spain, 2023.

[12] J. Roerdink and A. Meijster, "The watershed transform: definitions, algorithms and parallelization strategies," *Fundamenta Informaticae*, vol. 41, 2001.

[13] R. Keltie and H. Peng, "The effects of modal coupling on the acoustic power radiation from panels," *Journal of Vibration and Acoustics*, pp. 48-54, 1987.

DOI: 10.61782/fa.2025.0329



FORUM ACUSTICUM
EURONOISE 2025

EFFECTS OF DIFFERENT AUDITORY MONITORING CONDITIONS ON VOCAL INTONATION ACCURACY

Agnieszka Paula Pietrzak[1*]
[1] Institute of Radioelectronics and Multimedia Technology, Warsaw University of Technology, Poland

ABSTRACT

Precise intonation is crucial for ensemble singing performances, particularly when singers record their parts separately under varying monitoring conditions. This study investigated the intonation accuracy of five female choristers from an academic choir under three common feedback setups: speaker, open headphones, and closed headphones. Recordings were made in an anechoic chamber, where participants sang a perfect fifth (while the reference sound was still audible) and a major third (after the reference sound had ended). Intonation accuracy was measured in cents as the difference between the sung pitch and the expected frequency. Results showed that, for the perfect fifth (harmonic interval), using closed headphones resulted in the smallest median error (11 cents), suggesting that greater isolation may enhance pitch focus. However, for the major third (melodic interval), open headphones produced the lowest error (16 cents), indicating that too much isolation can lead to pitch overestimation when reference tones are no longer audible. Across both tasks, speaker monitoring exhibited the highest overall error values. Analysis of variance (ANOVA) confirmed statistically significant differences between these monitoring types. These findings suggest that selecting appropriate auditory feedback in both recording and rehearsal settings can optimize singers' intonation.

Keywords: *vocal intonation, auditory monitoring, headphones, pitch accuracy*

[*] ***Corresponding author***: *agnieszka.pietrzak@pw.edu.pl*
Copyright: *©2025 First author et al. This is an open-access article distributed under the terms of the Creative Commons Attribution 3.0 Unported License, which permits unrestricted use, distribution, and reproduction in any medium, provided the original author and source are credited.*

1. INTRODUCTION

The quality of ensemble or choir singing depends largely on the precise vocal intonation of its participants. Even small pitch discrepancies, initially below the threshold of casual perception, can accumulate and become audible tuning problem in vocal performances [1, 2].

While such issues can typically be resolved during in-person rehearsals, technological developments have expanded the contexts in which choral or ensemble recordings now take place, including situations where individual singers record their parts separately. From modern "virtual choir" projects to remote recording sessions, singers increasingly rely on various forms of auditory monitoring to maintain pitch accuracy with previously recorded tracks or external reference tones. Considering the advancements in modern recording techniques, understanding how auditory feedback mechanisms can influence pitch accuracy becomes important.

Research on vocal pitch control and intonation has long acknowledged the importance of auditory feedback [3]. Singers rely on both external cues (e.g., accompaniment, other vocal parts, or pre-recorded tracks) and internal cues (e.g., bone conduction, proprioceptive and tactile sensations) to guide their pitch production. When these cues are altered, the singer's ability to accurately judge and produce pitch can worsen [4,5]. Different types of headphones or speaker setups used as auditory monitoring can be a source of this kind of alteration. Previous studies have shown that closed-back headphones, for instance, can help isolate a vocal part and reduce external noise, thereby promoting more focused listening; however, they may also amplify the singer's own internal sounds (e.g., breathing, bone-conducted resonance), potentially leading to overestimation of one's pitch when an external reference is removed [6]. By contrast, open-back headphones allow for a more natural blend of external and internal sound, but they may also introduce ambient noise or bleed, which can

interfere with the clear perception of reference pitches. Speaker monitoring, while common in studio settings, can cause subtle pitch discrepancies depending on room acoustics or speaker placement, and may not offer the same level of isolation as headphones.

To objectively assess the impact of different monitoring methods on intonation, precise measurement metrics are necessary. Pitch accuracy in vocal performance is typically quantified in cents, with one semitone equivalent to 100 cents. Previous studies have shown that well-trained singers generally maintain intonation errors within the range of 10-20 cents [1,3]. In many cases, professional vocalists can achieve even lower error margins, often in the vicinity of 10–15 cents, reflecting their advanced auditory-motor control and extensive training. In contrast, less experienced singers or those operating in less controlled environments may exhibit errors exceeding 30 cents [6].

Based on these observations, this study aims to compare the effects of closed-back headphones, open-back headphones, and speaker monitoring on vocal intonation across both continuous (harmonic) and recalled (melodic) pitch tasks.

2. METHOD

This study investigated the influence of three monitoring conditions: open-back headphones (Beyerdynamic DT 990 Pro), closed-back headphones (Audio-Technica ATH-M50X), and speaker monitoring (JBL 4208), on singers' vocal intonation accuracy. The recordings were conducted with six female volunteers (aged 20–35) who were active members of the Warsaw University of Technology Academic Choir, but not professional vocalists. Of these six participants, one produced only the reference sounds, while the remaining five performed the target singing tasks. The small and homogeneous sample is a limitation of this study, which may restrict the generalizability of the findings, but only female voices were chosen, to limit the number of factors for analysis.

To generate reference material, one chorister recorded designated pitches that were initially presented by pure-tone sinusoids at known frequencies (e.g., 294 Hz, 392 Hz, 440 Hz). From these recordings, samples that demonstrated the most stable pitch and minimal errors were then selected for use as the reference stimuli. This approach was chosen over a fully synthesized tone to better reflect authentic vocal conditions.

All participants stood 15–20 cm from a Neumann U87 microphone, centrally placed in the anechoic chamber. The output level for each monitoring setup (open-back headphones, closed-back headphones, and speaker) was calibrated to 70 dB SPL at the participant's position. While the anechoic chamber was used to ensure experimental control, it may not appropriately represent the typical performance settings encountered in everyday practice.

The experiment comprised two tasks. In the first, singers performed a perfect fifth above a sung reference, thereby creating a harmonic interval. The perfect fifth was chosen for its high degree of consonance and harmonic stability. Three reference frequencies were used for this task (294 Hz, 349 Hz, and 392 Hz) and the singers were asked to sing the perfect fifths in just intonation (3:2 ratio). For each frequency there were five repetitions under each monitoring condition. In the second task, participants heard two sung notes forming a perfect fifth and were asked to sing a major third (5:4 ratio) after the reference tones ended, thus producing the interval melodically and in isolation. In contrast to a perfect fifth, which is a very stable consonant, the major third is generally more sensitive to intonation discrepancies, which could make the second task harder to perform. The reference fifths were sung from 330 Hz, 392 Hz, and 440 Hz and likewise repeated five times for each monitoring condition.

All resulting audio files were tracked in Cakewalk, exported as .wav files, and then analyzed in Python with the Librosa library. Fundamental frequency (F0) was extracted using the probabilistic YIN (pYIN) algorithm [7]. Given the typical pitch variability at note onsets and releases, only the 2-second portion deemed most stable, starting 0.5 seconds after the note attack, was used for subsequent measurements.

Intonation accuracy was assessed by calculating pitch error in cents, as the difference between the singer's average pitch and the expected frequency for the specified interval. Cents were used to compare pitch error at different absolute frequencies. Finally, a one-way analysis of variance (ANOVA) was performed to assess whether the selected monitoring condition exerted a statistically significant effect on intonation accuracy across both the harmonic (perfect fifth) and melodic (major third) intervals.

3. RESULTS

For both considered tasks: singing a perfect fifth while a reference tone was still audible (harmonic interval) and singing a complimentary major third after two reference tones had ceased (melodic interval) – performed analysis revealed statistically significant differences in performance across the three monitoring conditions.

For the harmonic interval of perfect fifth (Fig. 1), results showed the smallest median pitch error for closed

headphones (11 cents). Open-back headphones yielded a slightly higher but still relatively small median pitch error (13 cents), while speaker monitoring produced the largest pitch deviations (18 cents). Additionally, the distribution of individual values was most consistent (i.e., narrowest) under closed headphones, while speaker monitoring had the widest variability among participants.

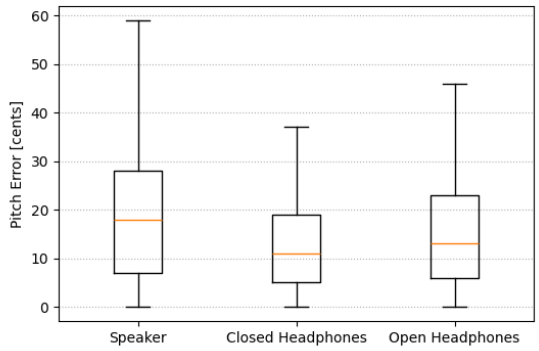


Figure 1. Box plot illustrating the pitch error (in cents) for a harmonic fifth sung under three different monitoring conditions (speaker, closed-back headphones, open-back headphones).

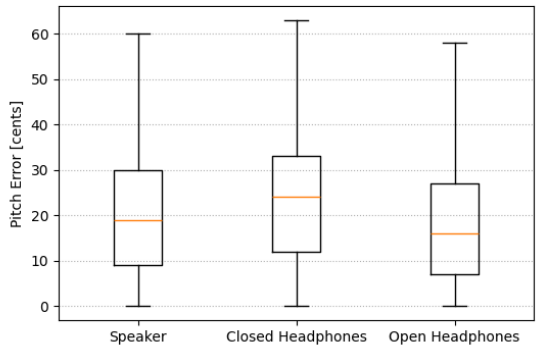


Figure 2. Box plot illustrating the pitch error (in cents) for a melodic third sung under three different monitoring conditions (speaker, closed-back headphones, open-back headphones).

When singing the major third without a continuously sounding reference, the patterns shifted (Fig. 2). Open-back headphones gave the lowest pitch error (16 cents), followed by the speaker setup (19 cents), and then closed headphones (24 cents). In this melodic context, the increased isolation provided by closed headphones appears to have contributed to overestimation of pitch, likely because participants relied primarily on their own vocal feedback once the reference was no longer audible.

A combined analysis of recorded intervals showed that the highest overall median error (19 cents) was observed for the speaker monitoring, followed by closed-back headphones (18 cents) and open-back headphones (16 cents). One-way analyses of variance (ANOVAs) for each interval type (perfect fifth: $F = 1243.4$, $p < 0.05$, major third: $F = 250.0$, $p < 0.05$), as well as for the combined data ($F = 343.4$, $p < 0.05$), confirmed that the differences between monitoring conditions were statistically significant.

Obtained results suggest that while closed-back headphones minimized pitch discrepancies for the harmonic (perfect fifth) interval, open-back headphones were more beneficial when singers had to recall pitch internally for the melodic (major third) task. Speaker monitoring consistently showed higher deviations in pitch accuracy compared to either headphone approach.

In addition to the statistically significant differences observed, the results may indicate, that even though the median differences between conditions are small, ranging from roughly 2 to 7 cents, they can be meaningful in professional contexts. Research indicates that trained musicians and critical listening environments can detect pitch differences as small as 2–5 cents [8]. Therefore, even these modest variations in pitch error may have practical implications for vocal performance quality, particularly in high-fidelity recording and live settings.

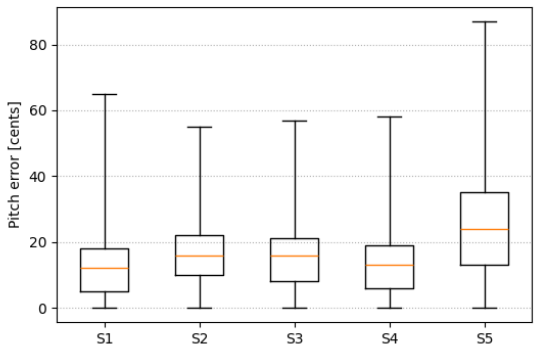


Figure 3. Box plot showing the combined pitch error distributions for singers S1–S5 across both intervals, highlighting individual variations in intonation accuracy.

Some insight can be also obtained by examination of individual singers performance. Figure 3 illustrates the singer-specific aggregated pitch error distributions, combined for both the harmonic (perfect fifth) and melodic (major third) tasks. Overall, S1, S2, S3, and S4 show moderate deviations, typically under 20 cents, indicating stable intonation. S5, however, displays a higher median error (24 cents) with the maximum exceeding 80 cents, suggesting greater difficulty controlling pitch. S5's broader error may suggest a tendency toward larger pitch mismatches, possibly due to individual factors such as technique, reliance on external cues, or comfort with recalling intervals.

4. CONCLUSIONS

This study demonstrates that the choice of monitoring method can affect choristers' ability to achieve precise intonation, especially when considering whether reference pitches are continuously present (harmonic tasks) or must be recalled (melodic tasks). Closed-back headphones produced the lowest intonation errors for a harmonic perfect fifth, suggesting that stronger isolation helps singers maintain focus on a reference pitch. However, for the melodic major third, sung without an ongoing reference, open-back headphones yielded the best results, implying that overly isolated conditions may lead to pitch overestimation once external cues are removed. Speaker monitoring, meanwhile, was associated with generally higher error values, showing its limitations for precise pitch accuracy during individual recordings.

These findings are in line with existing literature, which reports that well-trained singers typically maintain intonation errors in the range of 10–20 cents [1,4], with more experienced vocalists sometimes achieving errors as low as 10–15 cents [5,6]. In contrast, less-experienced singers may exhibit errors exceeding 30 cents. Trained musicians and professionals can detect pitch differences as small as 2–5 cents [8], therefore the pitch error differences observed in our study confirm that monitoring conditions can significantly influence pitch accuracy.

While this study offers some insight to the effects of monitoring conditions on intonation accuracy, it also has some limitations. The small, homogeneous sample, consisting only of non-professional, female choristers, and the controlled environment of an anechoic chamber may restrict the generalizability of these results to more natural performance settings. Moreover, the focus on only two intervals (perfect fifth and major third) simplifies the complex reality of vocal and choral singing. Future research should consider larger, more diverse participant groups and explore a broader range of intervals and musical contexts. Investigating alternative monitoring conditions (such as semi-open headphones or in-ear monitors) and testing in more acoustically realistic environments could give further information on how auditory feedback affects intonation.

5. REFERENCES

[1] S. Ternström and J. Sundberg, "Intonation precision of choir singers," *J. Acoust. Soc. Am.*, vol. 84, no. 1, pp. 59–69, 1988.

[2] H. Cuesta, E. Gómez Gutiérrez, A. Martorell Domínguez, and F. Loáiciga, "Analysis of intonation in unison choir singing," 2018.

[3] J. Sundberg, *The Science of the Singing Voice*, 1st ed. DeKalb, IL: Northern Illinois University Press, 1987.

[4] T. D. Rossing, J. Sundberg, and S. Ternström, "Acoustic comparison of voice use in solo and choir singing," *J. Acoust. Soc. Am.*, vol. 79, no. 6, pp. 1975-1981 (1986).

[5] D. Mürbe, F. Pabst, G. Hofmann, and J. Sundberg, "Significance of auditory and kinesthetic feedback to singers' pitch control," *Journal of Voice*, vol. 16, no. 1, pp. 44-51 (2002).

[6] D. Mürbe, F. Pabst, G. Hofmann, and J. Sundberg, "Effects of a professional solo singer education on auditory and kinesthetic feedback—a longitudinal study of singers' pitch control," *Journal of Voice*, vol. 18, no. 2, pp. 236–241, 2004.

[7] M. Mauch and S. M. Dixon, "pYIN: A Fundamental Frequency Estimator Using Probabilistic Inference," in *Proc. IEEE Int. Conf. Acoust., Speech, Signal Process.* (ICASSP), 2014, pp. 313–317.

[8] C. Micheyl, K. Delhommeau, X. Perrot, and A. J. Oxenham, "Influence of musical and psychoacoustical training on pitch discrimination," *Hearing Research*, vol. 219, no. 1–2, pp. 36–47, 2006.

DOI: 10.61782/fa.2025.0052

FORUM ACUSTICUM EURONOISE 2025

ABSOLUTE PITCH AMONG NON-GLOBAL POSSESSORS - TIMBRE AND CATEGORIZATION -

Ébano Resende de Souza[1*]

[1] Acoustics Research Institute, Austrian Academy of Sciences, Austria

ABSTRACT

Perfect or absolute pitch (AP) is typically considered to be an asset for any musician, however it is not well understood and may have some drawbacks. From a case study among students from the Musicology and Analysis Department of the Conservatoire National de Musique et Danse de Paris (CNSMDP), under direction of Dr. Adrien Mamou-Mani (CNSMDP/IRCAM) and Dr. Michèle Castellengo (LAM), we noted important issues raised by the students, in particular the relevance of timbre for AP categorization and identification. Among our findings we can highlight: 1) the strong relationship between AP identification and primary instrument; 2) the importance of the piano (pointed as the easiest timbre for recognition) and the voice (pointed among the hardest timbres for recognition) during AP identification and, 3) the loss of musical pleasure indicated by a considerable number of AP possessors. These highlights call for further research in Psychoacoustics and Cognition fields, including to understand to what extent AP perception can hinder RP perception and therefore the joy of music.

Keywords: *Absolute Pitch, Timbre, Categorization, Music and Cognition.*

1. INTRODUCTION

Built around several preconceived ideas, Absolute Pitch once held a distinguished position among musicians. Perceived as a rare and special phenomenon, it functions in many cases to legitimize a certain superiority in the hearing of its possessors. Currently, we are seeing a shift in this image, with a new understanding of the subject, and the idea of Absolute Pitch is gradually being better constructed. Regardless of this social relationship, the ability to hear specific frequencies remains an interesting tool for musical listening and can represent an important mechanism for learning and performing music. Understanding its role can contribute to a better understanding of musical activity and the relationship between the individual and music.

AP is defined in the literature as the ability to identify the pitch of isolated tones using musical pitch labels or to produce the pitch of any tones designated by note names without comparing to any reference pitch [1-11]. The incidence of AP is estimated to be around 0.1-1% of the population [7,12-14]. Among musicians this number can increase considerably, with estimates varying from between 5 to 50% [15, 16]. There is disagreement in the literature as to how AP is acquired. A more recent and now commonly supported hypothesis falls somewhere between the two previous hypotheses: some individuals have a genetic predisposition that is activated via a critical period during early musical training and it is strongly linked to our pitch categorization process [17-20].

Absolute Pitch remains a rich subject and represents an important part of the study of musicality. The increasing amount of research on this subject, and the exchange between researchers is fundamental in this context. For this research we ware particularly interested in aspects related to

[*] ***Corresponding author***: *ebano.resendedesouza(at)oeaw.ac.at*
Copyright: *©2025 E. Resende de Souza. This is an open-access article distributed under the terms of the Creative Commons Attribution 3.0 Unported License, which permits unrestricted use, distribution, and reproduction in any medium, provided the original author and source are credited.*

perception and the influence of timbre on pitch perception. Since music is composed mostly of complex sounds, timbre is a key attribute in this perception.

The discussion surrounding the definition of AP makes us reflect on the different aspects of this phenomenon. We can recognize different profiles depending on the type of difficulty encountered by individuals who possess it. We also find that musicians have a certain difficulty self-declaring that they possess this ability, given that, on the one hand, we have a certain lack of understanding of the definition and the different types of AP, and on the other hand, the difficulties encountered by these individuals can lead them to believe that they do not possess it or that they possess a so-called defective ear, given that it does not correspond to the common image of perfect AP. Research such as Bachem (1937) [5], and Takeuchi and Hulse (1993) [4] highlight already the different degrees of listening among those with Absolute Pitch. Differences in pitch perception depending on timbre and register, and difficulties related to singing or the accuracy of this identification lead us to classify them into categories or subgroups that can allow us to better analyze and understand this ability. We believe AP and RP (Relative Pitch) are not on the opposite ends of a continuum. Instead, AP and RP can both be present or absent in an individual.

2. THE CATEGORIZATION

The relationship between the individual and the environment in which they are located is marked by their interaction with objects and other individuals. In our understanding of the world, we need to find mechanisms that allow us to read this world and establish relationships between the different things that form it. We organize it in such a way as to separate and classify things in order to understand it. We classify them into large groups that both give rise to new subgroups and, in turn, form the basis for other subgroups depending on the degree of specialization we have in each concept. In this way, we classify objects, animals, colors, feelings, everything around us. Our perception is entirely based on these groups, which we build since childhood and which develop and subdivide throughout life according to the experiences and specific needs of each individual (in which language plays a fundamental role). In this sense, we can distinguish two types of categorization: prototypical categorization and perceptual categorization. The former refers to the type of categorization we construct based on our reading of the world, while the latter is more closely linked to established systems that individuals must assimilate. In prototypical categorization, two concepts are important: similarity aggregation (operated at the basic level) and pattern (or "typicality") [21].

The basic level encompasses the more general references we build since childhood and allows us, for example, to distinguish between the different objects that make up our environment. Throughout life, we create subcategories, as needed, to specify the differences between objects in the same group. The second type of categorization refers to specific learning, specific to a given culture. It is linked to a theory with fixed boundaries, based on measurements, and has a more scientific perspective, unlike the prototypical categorization, which relates to more variable phenomena and has a more psychological perspective.

3. THE TIMBRE

Among the various aspects of sound, one seems particularly interesting for musical listening and is also important in analyzing aspects of Absolute Pitch. Timbre can be defined as the fingerprint of sound. Each timbre is unique and results from the way the sound is produced. It can vary depending on the musician's playing style, the instrument used (such as a bow or fingers), and also depending on atmospheric conditions such as humidity and temperature, which modify the quality of the resonant materials [22]. We encounter a large number of possessors whose ability to label pitches is directly linked to timbre. The instruments they play have a fundamental role in this process and can even characterize the ability of the AP for a single instrument. This phenomenon is frequently observed in the case of the piano, widely used as a basic instrument in music theory courses [23]. This connection to specific timbre is relatively common and makes us reflect on the relationship between the perception of pitch and timbre. We also question the role of spectra in this context. In this sense, we may ask whether there are instruments that are more difficult to identify, as well as the relationship with their spectra, and also the role of formants and specific harmonics/partials in this process. The temporal envelope, also called ADSR, represents the four temporal stages of the sound: Attack, Decay, Sustain and Release, where the attack is very important for the timbre perception. Human perception does not evolve in a linear, additive relationship. It follows a logarithmic logic. The auditory system also does not behave the same way in different registers. Similarly, parameters such as intensity, duration, and timbre can also influence our perception of other musical elements.

4. CASE STUDY

4.1 Participants and Method

The research was conducted among students in the Department of Musicology and Analysis at the Conservatoire National de Musique et Danse de Paris (CNSMDP) after approval of the department's director, and the support of student representatives. The students enrolled in the department were between 18 and 30 years old and come from a variety of backgrounds and instrumental practices. Most enrolled at the National Conservatory between 2007 and 2014 and were currently pursuing programs such as Musicology, Musical Culture, Analysis, Pedagogy, Composition, Music Writing/Notation, Music History, and Aesthetics.

An electronic survey consisting of 25 questions was proposed to the 80 students of the department between November and December 2014, of whom 39 agreed to participate to this self declared research. Among the 39 participants, 36 were native French speakers, and the 3 foreign students were at an advanced level of language skills. The students began their music studies between the ages of 5 and 14 years old, and most followed the traditional curriculum of French conservatories (fixed do). The participant identification was not mandatory.

The questions we aimed to understand were: 1) the role of timbre in the students pitch identification; 2) aspects related to their auditory perception such as register, identification time, and vocal reproduction of notes; 3) the difficulties related to defining the term Absolute Pitch; and 4) the specificities and characteristics of the group that claims not to be sure if they have AP.

4.2 Results

4.2.1 Timbre

Participants were asked which timbres they found most difficult to identify. Of the twenty-five responses (five of which contained two answers), most (8) indicated the voice. Seven responded with wind instruments, with five specifying: English horn (2), oboe (1), clarinet (1), and brass (1). Lower register instruments were mentioned three times (one of which was the piano) and percussion three times (one of which was bells). The following instruments were mentioned once: piano, guitar, violin, viola, and organ. Two participants reported having no difficulties related to timbre, and one did not specify. Regarding the most easily identifiable timbres, we obtained twenty responses (three of which had two answers each). The highest number of responses was for the piano (6). The oboe and violin were mentioned three times. The harpsichord, voice, strings, and cello appeared once. Strings and woodwinds in general were also mentioned once each. Three participants did not report any particular timbres. We can see the most difficult and easiest timbres for pitch recognition in the Tab. 1.

Table 1. The most difficult and easiest timbres for pitch recognition.

The most difficult timbre		The easiest timbre	
Voice	8	Piano	6
Winds	7	Oboe	3
Percussion	3	Violin	3

Many students prefer the timbre of the instruments they practice when identifying pitches. However, this is not always the case. Other instruments may play an important role, as is the case with two pianists indicating the voice and the violin, or a bassist indicating the voice as the easiest timbre for pitch identification. The piano occupies an important position. Many instrumentalists consider it easier even if they do not practice it. This may be related to its use in theory lessons, leading to greater familiarity with its timbre and, in some cases, the development of what is called "absolute piano"(Instrument-Specific Absolute Pitch [24]). The difficulty in recognizing and notating vocal music with text was also mentioned. The voice occupies an important place among the hardest timbres for recognition, due, probably, to the overlap between AP label and the lyrics of the song during AP identification

We have cases where the instrument being practiced is cited as more difficult to identify than others, such as the case of a violinist who indicates the piano as the easiest and the violin as the most difficult, and that of a clarinetist for whom the piano comes first, unlike the clarinet, which occupies the ninth place, for which pitch identification is the easiest.

4.2.2 Time, Accuracy and Frequency range

Most of the participants (twenty) declared to recognize pitches instantly. Fourteen participants needed between 3

and 5 seconds, and two participants needed between 5 and 10 seconds. One student reported needing more than 10 seconds for recognition, and one reported not being able to do so (See Fig. 1).

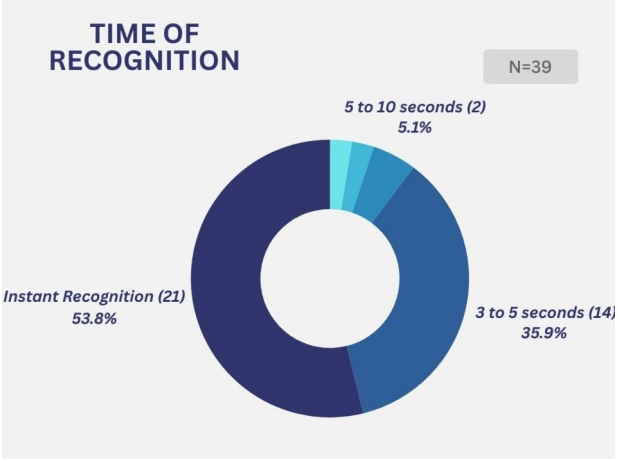


Figure 1. Time of recognition.

Regarding the accuracy of this identification, twelve participants reported always identifying the notes correctly. Twenty-two made errors of a semitone, and three were off by a whole tone or more. A half-tone error was quite common, and difficulties with atonalism and double-sharp or flat keys were also encountered (See Fig. 2).

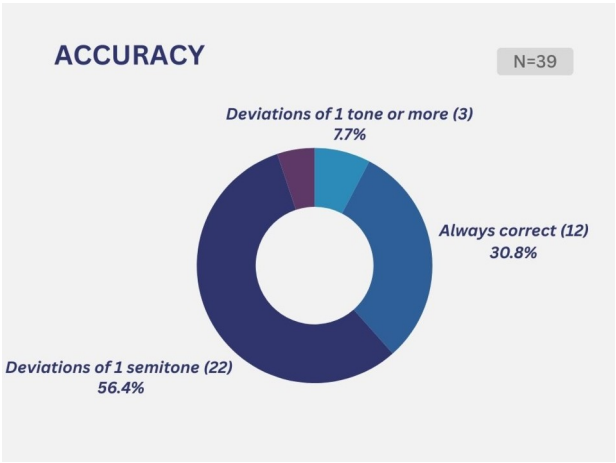


Figure 2. Accuracy of recognition.

Regarding the frequency range, 76.9% of the participants identified the middle register as the easiest register for pitch identification. Six participants (15.4%) identified the high register and two (5.1%) the low register - including one bassoonist (who started at the age of 14 after having previously played violin for six years) who stated he was unsure whether he had the AP, and the other, a pianist since the age of six, who stated he did not have the AP (See Fig. 3).

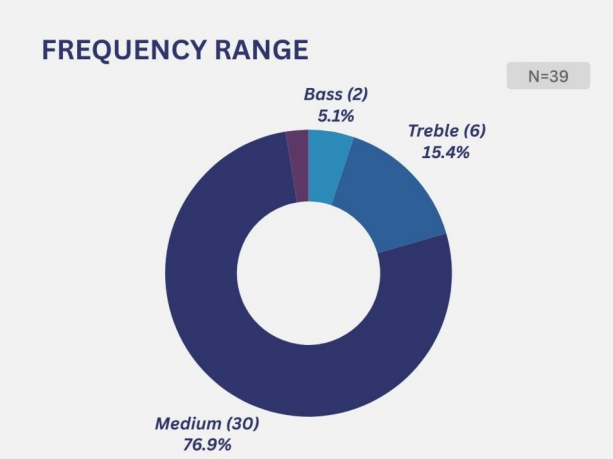


Figure 3. Preferred frequency range

5. DO I KNOW IF WE HAVE AP?

When asked how to recognize pitches, twenty-two participants (56.4%) said they did in the absolute way, compared to seventeen (43.6%) who declared the necessity of a reference note (such as A 440 Hz, for example).

Regarding the question of whether or not a participant has Perfect Pitch, an objective answer suggests some hesitation. Among the thirty-nine responses, eleven participants (28.2%) stated they have Absolute Pitch, seventeen (43.6%) stated they do not, and eleven participants were unsure. This last figure represents 28.2% of the responses and can tell us something about the difficulties in defining oneself as a possessor or not. A certain lack of understanding of the definition and the diversity of problems encountered (related to timbre or to the accuracy, for example) make the self identification as a possessor even more difficult. The preconceived ideas that arise from it, also plays an important role.

Eleven students made up the group who reported being unsure whether they had Absolute Pitch, including four pianists (one of whom is also a guitarist), three violinists,

two oboists, one bassoonist, and one clarinetist. The ages at which they began practicing ranged from 5 to 14 years old. Ten reported identifying pitches without the need for a reference note such as A 440 Hz, and only one relatively. Seven could do so instantly, and four did so after a 3 to 5 seconds of reflection. These ten participants (unsure if they have AP, but stated do not need a reference note for pitch identification) reported experiencing discrepancies of a semitone, while the one who do it relatively report always correct identification. Eight prefer the middle register, two the high register (the oboist—who also reports difficulty with all lower register instruments—and one violinist), and one student the lower register (the bassoonist). Regarding the reproduction of a required note for singing, nine report not needing reference notes (including the one who responded that they identify in relative form), and two report needing them. Three do it instantly, and eight need between 3 and 5 seconds to do it.

AP can appear in many forms. While there are some AP possessors with highly accurate AP across the board, some possessors have more limited AP capabilities. We refer to these groups as "global" and "non-global" AP possessors respectively. Possessors are also able to develop RP at different levels. It is not known how well RP develops among people with AP. As such, AP may actually be detrimental to some critical parts of the musical experience. The lack of understanding the definition and the different types of possessors we may encounter may be the source of this hesitation in declaring oneself a possessor. The group that hesitates to define itself as possessors is probably part of the non-global possessor group. One of the important aspects that differentiates possessors from non-possessors is the natural and intuitive nature of this pitch identification. AP is linked to "pitch memory," a labeling ability, to match a sound to a pre-established word or name. It is not a matter of just trying to identify a note. The sound heard and the associated name of the note (culturally chose) are, for most of these individuals, inseparable.

6. SUMMARY

Possessing AP can be a determining factor in the musical careers of many musicians. AP can be a very effective tool for success in music education in many countries. The importance given to identifying pitches in dictations and music theory lessons creates a favorable environment for those who possess it. In this case, this type of listening will always earn them good grades by giving the sensation of musical evolution. But this situation quickly changes when these musicians are confronted with other practices such as group music without the use of music scores when faced with improvisation within a piece. In some cases, possessors musicians may succeed in their path, but their approach and the relationship they establish with this type of piece are undoubtedly different. In this case, many players will rely on theoretical knowledge, such as tonality, the chords and the scales, rather than on the feeling of improvisation based on sound research. We also encounter cases where the players who hesitate to play in these conditions and remain completely dependent on the scores, and also situations where they change career paths, frustrated by not feeling comfortable playing in groups, either professionally or in informal settings, such as at friends' or family's houses, for example. During the course of this case study, we questioned ourselves a lot about the place of the individual player in the musical world. More than trying to understand how the AP works per se, we are also interested in understanding how these musicians relate to this skill and the relationship they establish with their musical practice.

The way possessors relate to music and code pitch are central to our understanding of music language and have clarified the extent and limits humans approach music, how we categorize acoustic stimuli, how the brain plasticity adapts to different ways of hearing and the impact it has in the music culture and the traditional music education. Some possessors, unlike those without AP, may have the tendency to lose the pleasure derived from music, which, in turn, negatively impacts their musical career. The study of the Non-global possessor subgroups can bring new knowledge to better understanding of AP ability and how humans and, musicians in particular, create different paths according to their abilities and limitations to make music. Despite the increasing number of studies and research about AP, a relatively small number of studies have been dedicated to non-global AP possessors. Studying the differences and the different levels possessors can present, we will be able to have a fine understanding about the categorization process in humans, the strategies non global possessors develop, and the influence of the musical pleasure in this process.

7. ACKNOWLEDGMENTS

I want to thank Dr. Adrien Mamou-Mani and Dr. Michèle Castellengo for guiding me in this research at the CNSMDP. I also thank Dr. Marisa Hoeschele, the supervisor of my current research, for the lecture and

discussions. This work is supported by The Seal of Excellence Post-Doctoral Fellowship at OeAW (Marie Skłodowska Curie Seal of Excellence Award) - OeAW Grant Service.

8. REFERENCES

[1] K. Miyazaki, K. "How well do we understand absolute pitch?". *Acoustical Science and Technology*, 2004.

[2] W. D. Ward, E. M. Burns. "Absolute pitch". *In*: D. Deutsch. *The Psychology of Music*, 1st ed. San Diego: Academic Press, pp. 431–451, 1982.

[3] D. Deutsch. "Absolute Pitch". *In*: D. Deutsch. *The Psychology of Music*. 3rd ed. San Diego: Academic Press, pp. 141–182, 2013.

[4] A. H. Takeuchi, S. H. Hulse. "Absolute pitch". *Psychol Bulletin*, pp. 345–361, 1993.

[5] A. Bachem, A. "Various types of Absolute Pitch". *Journal of the Acoustical Society of America*, pp. 146–151, 1937.

[6] J. Baggaley "Measurements of Absolute Pitch: A confused field". *Psychology of Music*, pp. 11–17, 1974.

[7] W. D. Ward. "Absolute Pitch". *In*: D. Deutsch. *The Psychology of Music*. 2nd ed. Academic Press, 1999.

[8] R. Parncutt and D. Levitin. "Absolute pitch". *Grove Music Online*. Oxford Music Online, 2013.

[9] N. G. Germano, H. C. Moreira, and G. Bortz. "Em Busca de uma Definição para o Fenômeno do Ouvido Absoluto". *Anais do SIMCAM 10*, Campinas, 2014.

[10] P. Loui. "Absolute pitch". *In*: S. Hallam, I. Cross, and M. Thaut *The Oxford Handbook of Music Psychology*. 2nded Oxford: Oxford University Press, pp. 81–94, 2016.

[11] D. Levitin. "L'Oreille absolue: Autoréférencement et mémoire". *L'Année Psychologique*, 2004.

[12] A. Bachem, A. "Absolute pitch". *Journal of the American Acoustical Society of America*, 27, pp. 1180–1185, 1955.

[13] H. M. Lenhoff, O. Perales, and G Hickok. "Absolute pitch in Williams syndrome". *Music Perception*. 18, pp. 491–503, 2001.

[14] D. Levitin and S. E. Rogers, S. E. "Absolute pitch: perception, coding, and controversies". *Trends Cogn. Sci*., 9, pp. 26–33, 2005.

[15] A. Wellek. "Musikpsychologie und Musikästhetik: Grundriss der systematischen Musikwissenschaft". *Akademische Verlagsgesellschaft*, Frankfurt, 1963.

[16] C. H. Chouard and R. Sposetti. "Environmental and electrophysiological study of absolute pitch". *Acta Otolaryngol*, 111, pp. 225-230, 1991.

[17] R. J. Zatorre. "Absolute pitch: a model for understanding the influence of genes and development on neural and cognitive function". *Nature Neuroscience,* 6 (7), pp. 692–695, 2003.

[18] D. Deutsch and K. Dooley. "Absolute pitch is associated with a large auditory digit span: A clue to its genesis". *Journal of the Acoustical Society of America*, p. 1859-1861, 2013.

[19] J. B. Crozier. Absolute pitch: Practice makes perfect, the earlier the better. *Psychology of Music*. 25, pp. 110–119, 1997.

[20] D. Levitin and R. J. Zatorre. "On the Nature of Early Music Training and Absolute Pitch: A Reply to Brown, Sachs, Cammuso, and Folstein". *Music Perception*. 21, pp. 105–110, 2003.

[21] M. Castellengo. "Écoute musicale et acoustique". Paris: *Eyrolles*, 2015.

[22] Z. Massida. "Étude de la perception de la voix chez le patient sourd post lingual implanté cochléaire unilatéral et le sujet normo-entendant en condition de simulation d'implant. Psychophysique et imagerie". *Thèse de Doctorat. Université de Toulouse* , 2010

[23] S. Vangenot. "L'énigme de l'oreille absolue". *In*: J. J. Nattiez (org). "Musiques, une encyclopédie pour le XXIème siècle. Les savoirs musicaux", Tome 2. Paris: *Actes Sud*, 2004.

[24] L. Reymore and N. C. Hansen. "A Theory of Instrument-Specific Absolute Pitch". *Front. Psychol*., 2020.

DOI: 10.61782/fa.2025.0015

FORUM ACUSTICUM EURONOISE 2025

A MEASUREMENT SYSTEM TO CAPTURE THE PLAYER'S CONTROL IN THE NATURAL PLAYING CONDITION OF SINGLE-REED MUSICAL INSTRUMENTS: APPLICATION TO THE PERFORMANCE LOG OF A BEGINNER PLAYER

Tetsuro Shoji[1*] **Yohei Wada**[1] **Yu Takahashi**[1] **Keita Arimoto**[1]
[1] Research & Development Division, Yamaha Corporation, Japan

ABSTRACT

It is well known that the control by players (e.g. embouchure, tonguing, respiration, and so on) gives significant effects on the sound generation of wind instruments. However, it is hard to measure them in actual playing conditions due to the difficulty in putting sensors without disturbing the performance. This paper proposes new devices for measuring the control induced by players of single-reed musical instruments. These devices are capable of acquiring various aspects of the player's control including blowing pressure, biting force, acoustic pressure inside a mouthpiece, abdominal motion, and chest wall motion. The devices are designed to minimize disturbance for players in order to realize measurements in a natural playing condition. A test measurement using the devices was conducted on a person who was completely new to playing the saxophone. The player was asked to engage in daily practice for three months under the supervision of an experienced player, while consistently measuring the control information. The analysis of the performance log reveals clear improvements in certain performance indicators such as loudness, spectral centroid, and respiratory motion.

Keywords: *gesture acquisition, performance log, wind instrument, embouchure, respiration*.

1. INTRODUCTION

There have been several studies on capturing the player's oral control when playing single-reed instruments. One of the pioneer works in this context is the study on the effect of vocal tract resonance by the measurement of the pressure in a player's mouth and the pressure in a mouthpiece [1]. This concept has been further explored in subsequent studies [2-4] and extended to the investigations on the role of player's control during the transient phase of the sound generation [5-6]. A completely different approach involved morphological analysis of vocal tract images obtained through MRI measurements for saxophone players [7].

On the other hand, there have been some studies on the measurement of respiratory motion while playing wind instruments [8-10]. These studies involve time series analysis of videos capturing the motion of optical markers placed on a player's body.

This paper proposes a measurement system to capture both oral control and respiratory motion, simultaneously. The system is expected to be utilized for pedagogical purposes, such as learning how to play musical instruments and understanding the advanced technique by skilled players. To achieve this goal, the measurement system is designed following the concept:

- minimize the disturbance to performance
- easy handling (easy setup, less special equipment)

2. MEASUREMENT SYSTEM

Fig. 1 illustrates a special mouthpiece designed to capture oral control. The mouthpiece is designed to measure similar information as [2][5-6] with introducing the concept of the tunnel employed by [1][3-4]. The tunnel enables a pressure sensor within the mouthpiece to measure the pressure inside

[*] ***Corresponding author***: keita.arimoto@music.yamaha.com.
Copyright: *©2025 First author et al. This is an open-access article distributed under the terms of the Creative Commons Attribution 3.0 Unported License, which permits unrestricted use, distribution, and reproduction in any medium, provided the original author and source are credited.*

the mouth cavity (Pcav). In addition to Pcav, the mouthpiece is also able to capture reed strain (Sreed) corresponding to the biting force and acoustic pressure inside the mouthpiece (Pmp).
The respiratory motions at abdomen (Abdominal) and chest (Chest) are captured by the belts that wrap around the player's body (Fig. 2). The belts are equipped with CNT sensors to capture the elongation of the belts induced by respiratory motion.

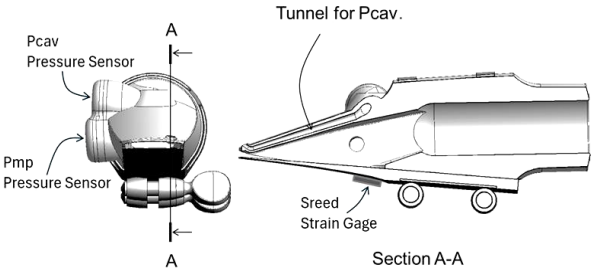


Figure 1. mouthpiece with sensors to capture the oral control.



Figure 2. belts with elongation sensors to measure the abdominal motion and chest motion.

3. EXPERIMENT

A long-term measurement test is conducted on a person who is completely new to playing the saxophone. The player is asked to engage in alto saxophone training under the supervision of an experienced amateur player. The signals from the 5 sensors are recorded throughout the training session, which typically lasts 30-60minnutes. The training is repeated every working day for three months. The player is obliged to play long tone (at Eb3, Eb4, and Eb5) and scale in Eb at least once in a daily training session.

4. RESULT

4.1 Analysis on acoustic pressure at mouthpiece

Fig. 3 and Fig. 4 are the results of the analysis on the Pmp signals (corresponding to acoustic pressure at mouthpiece). A long tone phrase in Eb4 is picked from each daily session and feature extraction is performed for the stable portion of the signal. Fig. 3 shows the median for rms amplitude of the waveform in linear scale. Fig. 4 shows the results on spectral centroid. The Comparison between the beginning (around the left end) and ending (around the right end) indicates that both the amplitude and spectral centroid gets approximately double. The result suggests that the player has improved one's playing skill through the daily training session. Note that there were no long tones in Eb4 observed on 0130 and 0202.

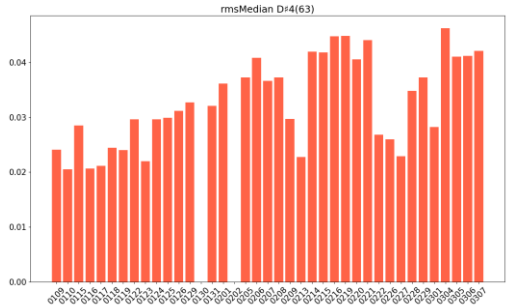


Figure 3. median for rms amplitude (in linear scale) on a Eb4 long tone over daily sessions.

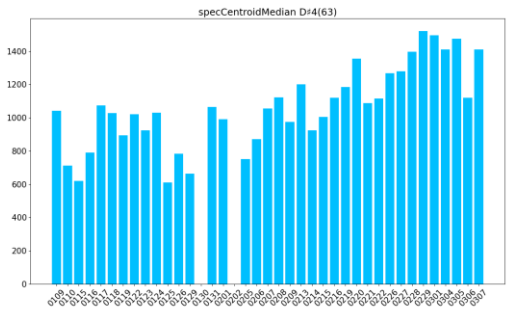


Figure 4. spectral centroid on a Eb4 long tone over daily sessions.

4.2 Analysis on the respiratory motion

From Fig. 5-a to Fig. 5-d show the analyses results of the respiratory sensors attached to the player's chest and abdomen. From the entire training period, data from distinctive four days were picked, and the figures depict the expansion and contraction of the respiratory sensors during the daily sessions. Throughout each daily session, the vertical axis plots the expansion and contraction of the band attached to the chest, and the horizontal axis plots that of the band attached to the abdomen. Comparing the plots, it is noticeable that at the very start of the training, the range of the sensor's expansion and contraction is small (Fig. 5-a). This indicates that breathing is not deep. However, in two weeks, the range of expansion and contraction for the chest sensor becomes larger, suggesting that the player is attempting to breathe more deeply using one's chest (Fig. 5-b). With further repetition of daily training, the range of expansion and contraction for the chest sensor gradually decreases (Fig. 5-c and Fig. 5-d). This suggests that the player has acquired more efficient control through training.

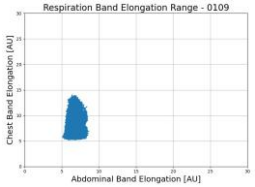


Figure 5-a. 01/09

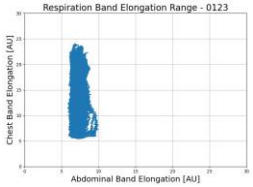


Figure 5-b. 01/23

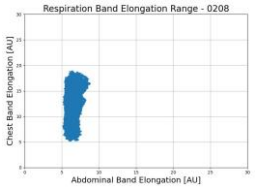


Figure 5-c. 02/08

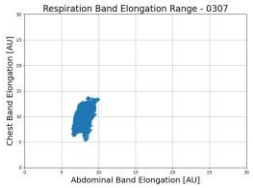


Figure 5-d. 03/07

Figure. 5 respiratory sensor elongations at four different daily sessions. Vertical and horizontal axes correspond to chest and abdomen motions, respectively.

5. FUTURE WORK

The preliminary results indicate that the measurement system has enough potential to assess the player's ability. However, the capability of the measurement system needs to be evaluated through the experiment involving players of different skill levels, from beginners to professionals. Additionally, intensive analysis of sensor signals also needs to be done in order to correlate the player's control and the resulting sound.

6. REFERENCES

[1] Garry. P. Scavone, Antoine Lefebvre, Andrey. R. da Silva: ''Measurement of vocal-tract influence during saxophone performance,'' *J. Acoust. Soc. Am.*, 123, pp. 2391–2400, 2008.

[2] Philippe Guillemain, Christophe Vergez, Didier Ferrand, Arnaud Farcy: "An instrumented saxophone mouthpiece and its use to understand how an experienced musician plays" *Acta Acustica United with Acustica* 96 pp. 622–634, 2010.

[3] Jer-Ming Chen, John Smith, Joe Wolfe: "Pitch bending and glissandi on the clarinet: roles of the vocal tract and partial tone hole closure" *J. Acoust. Soc. Am.,* vol 126, pp. 1511–1520, 2009.

[4] Jer-Ming Chen, John Smith, Joe Wolfe: "Saxophonists tune vocal tract resonances in advanced performance techniques" *J. Acoust. Soc. Am.,* vol 129, pp. 415–426, 2011.

[5] Weicong Li, André Almeida, John Smith, Joe Wolfe: "How clarinettists articulate: The effect of blowing pressure and tonguing on initial and final transients" *J. Acoust. Soc. Am.,* vol 139(2), pp. 825–838, 2016.

[6] Montserrat Pàmies-Vilà, Alex Hofmann, Vasileios Chatziioannou: "The influence of the vocal tract on the attack transients in clarinet playing" *J. New Music Res.* Vol 49(2), pp. 126–135, 2020.

[7] Tokihiko Kaburagi, Ayame Kato, Yuri Fukuda, Fumiaki Taguchi: "Control of the vocal tract when experienced saxophonists perform normal notes and overtones" *Acoust. Sci. & Tech.* 42, 2, pp. 83-92, 2021.

[8] Cossette I., Fabre B., Fréour V., Montgermont N., Monaco P. : "From Breath to Sound: Linking Respiratory Mechanics to Aeroacoustic Sound Production inFlutes" *Acta Acustica United with Acustica* 96, pp. 654–667, 2010.

[9] Vincent Fréour, René Caussé, Isabelle Csette: "Simultaneous Measurements of Pressure, Flow and Sound During Trumpet Playing" proc. *10eme Congres Francais d'Acoustique*, 2010.

[10] Camille Vauthrin, Benoît Fabre, Isabelle Cossette: "How Does a Flute Player Adapt His Breathing and Playing to Musical Tasks?" *Acta Acustica United with Acustica* 101, pp. 224–237, 2015.

DOI:

Main theme: A11 Musical Acoustics

Session A11.02/A09.08 Artificial intelligence in musical acoustics

Chair(s): M. Pezzoli, R. Russo

DOI: 10.61782/fa.2025.0029

FORUM ACUSTICUM EURONOISE 2025

A PROCEDURE FOR EVALUATING THE SOFTNESS OF SOUND PLAYED ON THE CLARINETS

Nozomiko Yasui[1*]
[1] National Institute of Technology, Kisarazu College, 2-11-1, Kiyomidaihigashi, Kisarazu City, Chiba, 292-0041, Japan

ABSTRACT

In wind ensembles, aligning not only pitch and timing but also the softness of the sound is said to be essential when multiple performers play the same piece. Particularly in clarinet performance, it is said that without the ability to control the softness, it becomes difficult to adapt to the wind ensemble's repertoire. While many instructional books provide basic exercises for aligning pitch and timing, there are very few that focus on exercises addressing the softness of sound, and there is little research that has investigated procedures for objectively evaluating softness. Therefore, this study proposes a procedure for evaluating the softness of the sound played on the clarinet. Specifically, this study conducted a subjective evaluation experiment by recording clarinet performance sounds and investigating whether listeners could perceive the softness intended by the performer in the same way. The acoustic characteristics of the performance sounds were extracted. The relationship between the characteristics and the softness was analyzed. Based on the results, a procedure for evaluating the softness of clarinet performance sounds was investigated. As a result, it was found that the softness in clarinet performance can be evaluated by three acoustic characteristics: slope of the attack, spectral centroid, and spectral flux.

Keywords: *clarinet, softness, slope of the attack, spectral centroid, spectral flux*

1. INTRODUCTION

In wind ensembles, it is considered important to match not only the pitch and timing, but also the softness of the sound when several musicians perform the same part together. Impressions such as "softness" are, however, difficult to quantify objectively and numerically, as they are subjective and depend on the listener's perception. As a result, there have been very few reports on practice systems designed to unify such sound impressions.

In a previous study [1], the visualization and analysis of reed vibrations in clarinets had been conducted, but the evaluation of softness had not been addressed. In another previous study [2], a prototype of performance support software was developed, which visually displays in real time the relative comparison between the parameters of a target sound and those of a performer's sound using radar charts and other visual tools. A trial evaluation conducted with clarinet players showed that the system was helpful in improving the "beauty" and "softness" of the sound. Specifically, "beauty" was evaluated based on the total power in the frequency spectrum, and "softness" was evaluated based on the slope of the spectral envelope. However, it had not yet been verified whether these parameters could appropriately assess impressions such as "beauty" or "softness."

This study proposes a method for appropriately evaluating softness from acoustic signals.

Based on previous research on the extraction of acoustic characteristics [3-5], three parameters were extracted to investigate the acoustic parameters associated with the perceived softness of sound and their relationship with subjective impressions of softness was analyzed. Based on the findings, a method for evaluating the softness of performance sounds is proposed.

[*] ***Nozomiko Yasui***: *yasui@j.kisarazu.ac.jp*
Copyright: *©2025 Nozomiko Yasui. This is an open-access article distributed under the terms of the Creative Commons Attribution 3.0 Unported License, which permits unrestricted use, distribution, and reproduction in any medium, provided the original author and source are credited.*

2. SUBJECTIVE EVALUATION EXPERIMENT ON THE SOFTNESS

2.1 Outline of experiment

A subjective evaluation experiment was conducted using recorded clarinet performances to assess the perceived softness of the sounds. The purpose of this experiment was to investigate whether listeners could consistently perceive the softness as intended by the performers. Only the recordings that showed agreement between performer intention and listener perception were selected for further analysis.

For the recordings, three clarinet players (P_1–P_3) with over 20 years of performance experience each were instructed to play both "hard" and "soft" tones five times each. A total of 30 audio samples were recorded: 15 "hard" tones and 15 "soft" tones. The instruments and components used in the recordings are summarized in Table 1. All samples were standardized to an open G note with a duration of approximately 6 seconds.

The recording setup included a C414 XLS microphone (AKG by HAEMAN) and a DR-680 recorder (TASCAM). Recordings were made in a soundproof room with a sampling rate of 48 kHz and a 16-bit quantization. A waveform example of the recorded performances is shown in Figure 1.

After the recordings, a subjective evaluation experiment was conducted with 20 student members of a wind ensemble. Each participant was randomly presented with the 30 recorded performances and asked to rate the perceived "softness" of each sound on a three-point scale: "soft," "neutral," or "hard."

Table 1. Instruments and components used in the recording.

Component	Manufacturer	Model/Specification
B ♭ Clarinet	Buffet Crampon	E13
Mouthpiece	Vandoren	5RV
Ligature	Buffet Crampon	SP
Reed	Vandoren	Traditional

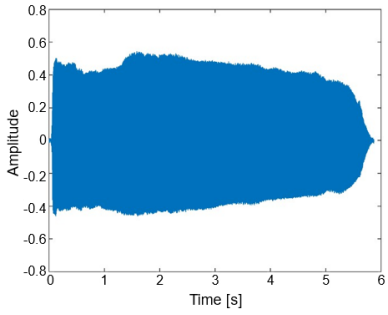
2.2 Experimental results

The accuracy rate was calculated based on the subjects' responses, where the "softness" intended by the performer was considered the correct answer. As a result, 23 of the recorded sounds achieved an accuracy rate of 60% or higher. The accuracy rate for the soft sounds was lower compared to that for the hard sounds.

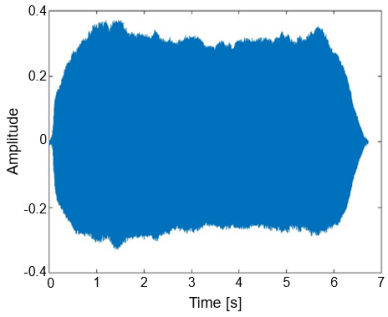
In this study, the 23 recorded sounds with an accuracy rate of 60% or higher were assumed to be the sounds where the listeners were able to correctly judge the "softness." These sounds were then subjected to further analysis.

3. ANALYSIS OF ACOUSTIC PARAMETERS IN RELATION TO THE SOFTNESS

Based on the results of the experiment described in Section 2, acoustic parameters were extracted from the recorded sounds that were correctly perceived by listeners in accordance with the performers' intended "softness." Among the 23 validated recordings, 12 samples—6 categorized as "hard" and 6 as "soft"—were selected for analysis. A decision boundary was then derived using the Nearest Neighbor (NN) classification method, based on the relationships among the three extracted acoustic parameters. To evaluate the classification performance of this boundary, it was applied to an additional set of 11 previously unused samples (7 hard tone and 4 soft tone) to assess their classification as unknown inputs.



(a) Hard tone



(b) Soft tone

Figure 1. Waveforms of the Recorded Clarinet Sounds.

3.1 Acoustic parameters used in this study

Among acoustic parameters, there are features such as loudness which represents the perceived intensity of a sound, and roughness which describes its perceived roughness. In this study, however, three specific acoustic parameters were extracted and analyzed: the slope of the attack, spectral centroid, and spectral flux.

The slope of the attack was calculated using Equation (1), which represents the gradient between the amplitude values at the onset and end points of the rising segment, as illustrated in Figure 2. Here, min_A and min_T denote the amplitude and time at the onset of the rise, while max_A and max_T represent the amplitude and time at the end of the rise.

The spectral centroid was computed using Equation (2), which defines the center of gravity of the power spectrum. In this equation, h denotes the analysis frame index, N represents the total number of frequency bins within the frame, and $L_h[n]$ refers to the power of the n-th frequency bin in the h-th frame.

The spectral flux was calculated using Equation (3), which expresses the variation in the power spectrum over time.

$$Slope = \frac{max_A - min_A}{max_T - min_T} \tag{1}$$

$$Centroid = \frac{\sum_{n=1}^{N} L_h[n] \times n}{\sum_{n=1}^{N} L_h[n]} \tag{2}$$

$$Flux = \sum_{n=1}^{N} (L_h[n] - L_{h-1}[n])^2 \tag{3}$$

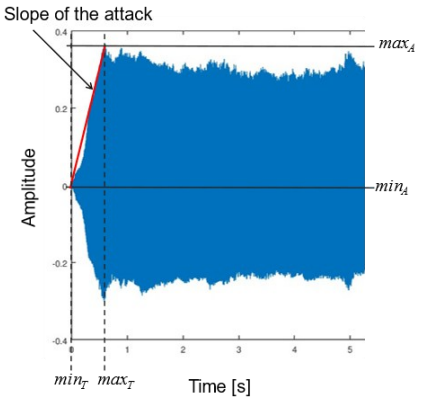


Figure 2. Outline of Slope of the attack.

3.2 Results

The relationships among the three acoustic parameters are illustrated in Fig. 3–5. Figure 3 shows the relationship between the slope of the attack and the spectral centroid. The line in the figure represents the perpendicular bisector connecting the centroids of the "hard" and "soft" tone clusters, which serves as the decision boundary derived using the NN method. This decision boundary is denoted as f_{SC}. Figure 4 shows the relationship between the spectral centroid and the spectral flux, along with the corresponding decision boundary, denoted as f_{CF}. Figure 5 presents the relationship between the spectral flux and the slope of the attack, and the resulting decision boundary is denoted as f_{SF}.

Next, it was examined whether the decision boundaries illustrated in Fig. 3-5 could be used to classify an additional set of 11 previously unused samples (7 hard tone and 4 soft tone). Table 2 shows the classification accuracy of "softness" based on the decision boundaries (f_{SC}, f_{CF}, f_{SF}) when the performer's intended softness is considered the ground truth. From the results in Table 2, f_{CF} and f_{SF} achieved relatively higher classification accuracy.

Table 2. Result of classification accuracy.

Decision boundary	f_{SC}	f_{CF}	f_{SF}
Classification accuracy[%]	73	82	82

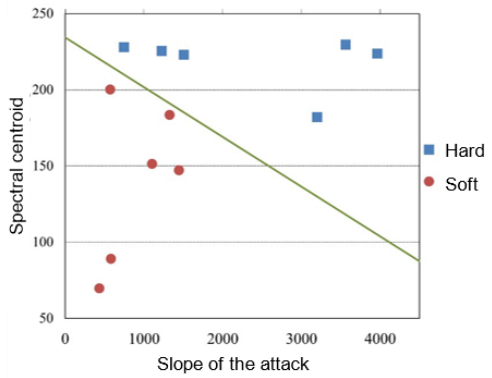


Figure 3. Outline of Slope of the attack.

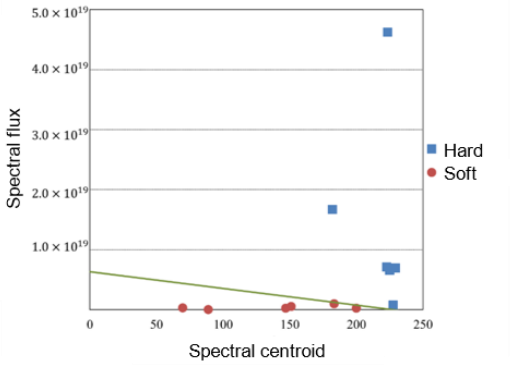


Figure 4. Outline of Slope of the attack.

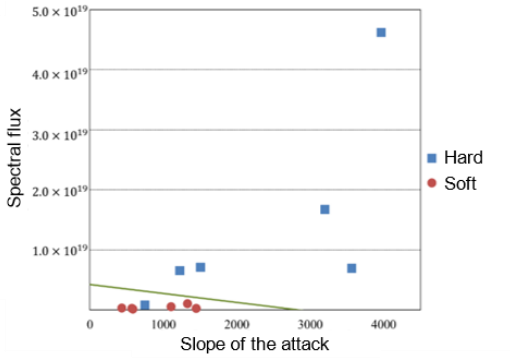


Figure 5. Outline of Slope of the attack.

4. DISCUSSION

From the experimental results shown in Fig. 3–5, it can be observed that data points plotted above the decision boundaries tend to correspond to hard sounds, whereas those below the boundaries are more frequently associated with soft sounds. These findings suggest that the proposed decision boundaries are effective in distinguishing the perceived softness of sound. In particular, the boundaries f_{CF} and f_{SF} appear to enable more accurate classification.

The classification accuracy of the decision boundary f_{SF}, based on the slope of the attack and spectral flux, was relatively low. As shown in Fig. 5, this appears to be due to certain "hard" sounds having spectral flux values similar to those of "soft" sounds, leading to misclassification. While the spectral flux values of "soft" sounds were generally consistent, those of "hard" sounds exhibited considerable variability. Since the value of spectral flux is affected by factors such as data length and frame shift during extraction, further investigation is required to assess the impact of these parameters and to determine whether spectral flux is a reliable feature for evaluating softness.

The findings suggest that clarinet sound "softness" can be evaluated using the slope of the attack, spectral centroid, and spectral flux. However, further validation with more samples and varied pitches is needed to generalize the results.

5. CONCLUSIONS

This study investigated a procedure for evaluating the softness of the sound played on the clarinet. The results showed that the highest classification accuracy was achieved when evaluating "softness" using spectral centroid, slope of the attack, and spectral flux. Therefore, it is suggested that these parameters can be effectively used for accurate evaluation of softness.

For future work, increasing the number of data samples used when constructing these boundaries will be necessary to obtain more accurate decision boundaries. Moreover, it will be important to investigate whether the same acoustic parameters can be used to evaluate "softness" when the pitch of the target sound is varied.

6. ACKNOWLEDGMENTS

The author is deeply grateful to clarinet musicians, Miyu Endo and the musicians from the National Institute of Technology, Matsue College brass band club for their valuable assistance for participating in the experiment.

7. REFERENCES

[1] K. Murao, “Visualization and Analysis of Reed Vibrations in Clarinets,” *IPSJ SIG Technical Reports*, vol. 2012-MUS-95, no. 11, pp. 1-5, 2012 (in Japanese).

[2] A. Yamaoka, Y. Bange, M. Wadamori, “Improvement of Performance Support Software for Wind Instruments Focusing on Tone Quality,” Tech. Rep. Musical Acoust. Acoust. Soc. Jpn., vol. 28, no. 8, pp. 25-28, 2010 (in Japanese).

[3] K.D. Martin, “Sound-Source Recognition: A Theory and Computational Model,” PhD Thesis, MIT, 1999.

[4] A. Eronen, and A. Klapuri, “Musical Instrument Recognition using Cepstral Coefficients and Temporal Features,” *Proc. of ICASSP*, pp.735–756, 2000.

[5] S. Essid, G. Richard and B. David, “Musical Instrument Recognition by Pairwise Classification Strategies,” *IEEE Trans. Audio, Speech, Lang. Process.*, vol.14, no.4, pp.1401-1412, 2006.

DOI: 10.61782/fa.2025.0708



FORUM ACUSTICUM
EURONOISE 2025

PSYCHOACOUSTIC ANALYSIS OF VISCOELLASTICALLY DAMPED MEMBRANES USING PHYSICS-INFORMED MACHINE LEARNING

Martínez Orellanos, Cristhiam Fidel[1*] **Bader, Rolf**[1]
[1] Institute for Systematic Musicology, University of Hamburg, Germany
Neue Rabenstr. 13, 20354 Hamburg, Germany

ABSTRACT

The perceived sound of percussion instruments is significantly influenced by Viscoelastic Damping (VD), a mechanism whereby damped energy is temporarily stored and released back into the system, modifying the frequency spectrum. Performers harness this influence by choosing different materials and damping additives to shape the sound of their instruments. However, this process is still not fully understood. To address this, we apply physics-informed machine learning within a psychoacoustically grounded framework to investigate how changes in VD parameters influence the perceived sound of musical membranes. By analyzing a physics-informed dataset, we track spectral centroid differences and spectral flux across time and frequency ranges. Results show that the perceptual influence of VD strongly depends on where along the frequency spectrum the damping occurs, particularly in relation to the fundamental frequency. A temporal drift of the affected spectral region toward lower frequencies was also observed. Self-organizing maps (SOMs), initialized with physically informed features, were used to explore these complex, high-dimensional relationships. This method offers new insights into how specific damping conditions shape perceived sound and provides a foundation for more detailed analyses using alternative time–frequency representations in future research.

Keywords: *viscoelastic damping, machine learning, psychoacoustics*

**Corresponding author*: *crismartinez@t-online.de.*
***Copyright**: ©2025 Martínez Orellanos et al. This is an open-access article distributed under the terms of the Creative Commons Attribution 3.0 Unported License, which permits unrestricted use, distribution, and reproduction in any medium, provided the original author and source are credited.*

1. INTRODUCTION

The sound of musical instruments is highly influenced by the physical properties of the materials with which they are constructed. For percussion instruments, membranes are typically made from materials like leather and polymers. The internal damping of these materials is largely determined by their viscoelastic properties, leading to what is known as Viscoelastic Damping (VD). VD is characterized by the interrelation between stress, strain and time; the present stress is the result of a finite history of previous strains [6]. Given that in viscoelastic materials there is a phase difference between stress and strain, the present stress is damped by the accumulated strain. If by the time the present stress is completely damped there is still energy stored in the history of strains, this energy is released back into the system, starting the cycle again. This is known as the memory effect and leads to a highly nonlinear relation between the parameters of VD and the resulting frequency spectrum [3].

Despite its complex behavior, musicians actively make use of VD either by exploring the diverse sonic possibilities that different materials offer (e.g., when selecting a membrane material), or by intentionally using VD to alter the instrument's original sound [2, 17]. Although this practice is widespread, little is known about how VD influences the perceived characteristics of sound. Specifically, how do modifications in VD parameters lead to particular changes in the perceived sound characteristics.

To investigate the relationship between perception and musical acoustics, different music information retrieval algorithms have been developed to analyze the frequency and temporal characteristics of musical instrument signals during the onset of the sound [4, 15]. Moreover, the development of such features, as well as the advent of data-driven methods have propelled the use of

machine learning and physical modeling in psychoacoustics [5, 14, 16]. Still, many of these approaches primarily target genre or instrument classification and transcription. With regard to damping in drums, an analysis of the influence of drumhead damping patterns in the perception of the sound using convolutional neural networks and physical modeling is presented in [1]. Nonetheless, mapping perceptible changes in the sound of a musical membrane to variations within the VD parameter space remains challenging. This is due to a lack of data reflecting consistent parameter changes in VD, as well as the need for tools capable of navigating a broad parameter space while flexibly and accurately analyzing transient dynamics from a psychoacoustic perspective. To address this, the authors introduced a method in [9], employing physics-informed machine learning to investigate the relationship between systematic variations in VD and the resulting frequency spectra, thereby revealing key characteristics of VD's physical behavior.

Still, a psychoacoustic analysis implies additional challenges. On the one hand, it requires flexible tools for analyzing the transient phase of percussive sounds, which is characterized by its high intricacy [11]—this being the time window during which VD primarily operates, as will be discussed in the next section. On the other hand, it demands a better understanding of which time and frequency features the auditory system extracts and integrates into perceptual categories such as timbre or pitch. Indeed, the fact that VD is embraced by musicians suggests that the auditory system is capable of detecting and extracting patterns from its complex relationships and behaviors. Still, this latter question remains under active investigation. Therefore, the present study is based on an analysis framework developed in previous work [10], which is based on findings from the existing literature related to important temporal cues for the perception of musical sounds—also outlined in the following section. However, a detailed analysis of the auditory cues underlying sound perception, lies beyond the scope of this work.

Accordingly, the aim of this study is twofold: (a) to employ physics-informed machine learning, grounded in a psychoacoustically relevant analysis framework, to identify underlying patterns and relationships between VD and measured features, in order to (b) investigate which changes in the frequency spectrum caused by VD modify the perceived characteristics of the sound—specifically, when, where, and how VD produces these modifications. Correspondingly, this article is structured as follows: Section 2 describes the methods, i.e. the analysis framework, physics-informed dataset data pipeline and experimental design. Sections 3 and 4 present the results and their interpretation, while Section 5 summarizes the conclusions of the study.

2. METHOD

2.1 Physics- and Psychoacoustics-Based Analysis Framework

Despite the highly nonlinear relation between the parametric modifications and the resulting frequency spectra, the musical application of VD points towards the ability of the brain to extract patterns from among these complex physical components. To understand this process, both the physical dynamics of VD and the brain's temporal cues for perceiving musical sounds must be considered. To this end, an analysis framework addressing this has been presented in previous research [10] and is summarized below.

Key physical characteristics of VD in musical membranes, identified in [3, 9], include: (1) the memory effect causes viscoelastically damped frequencies to decay non-exponentially, with a nonlinear amplitude behavior starting around 40-50 ms after an initial constant decrease; (2) modifications to the model parameters lead to nonlinear amplitude fluctuations in neighboring frequencies, with the width of the affected region yet to be determined; (3) VD influences sound most significantly during the first 120 ms, although this temporal interval may vary with frequency; (4) a noticeable increase in spectral fluctuation occurs around 25 ms [10]; (5) the FDTD model requires a minimum number of periods of the damped frequency for the damping to develop completely.

Concerning the perception of musical sounds, previous studies have highlighted relevant integration times for non-percussive and percussive-harmonic sounds [12, 15]. A time window of approximately 10 ms reflects the auditory system's state of inertia, as it requires around 10 ms to establish frequency filter widths on the basilar membrane. Auditory changes occurring above this threshold affect the envelope of the sound, while changes below it influence timbre perception [12]. The interval between 10 ms and 50 ms is closely associated with pitch perception; once the frequency filters are established, their sensitivity plays and important role [12]. For frequencies below 500 Hz, differences as small as 1.8 Hz can be perceived, whereas above this threshold, the detection limit increases with frequency [18]. Changes during this time window also shape timbral characteristics. A broader window of 100–150 ms

represents the upper bound beyond which sensitivity to frequency fluctuations remains relatively constant [12]. If such fluctuations persist up to 250 ms, the pitch percept tends to weaken, and the sound is perceived as more noise-like.

Although the influence of VD unfolds continuously over time, defining specific time points that are both physically and perceptually relevant serves as a starting point for understanding how VD affects the acoustic features upon which the auditory system forms perceived characteristics of a sound. These temporal cues therefore constitute the analytical framework of this study and are summarized in Table 1.

Table 1: Analysis framework.

Time (ms)	Description
10	Filter formation in the basilar membrane. Timbre and envelope perception
25	Increase in spectral flux
50	Non-linearities in amplitude of viscoelastically damped frequencies begin. Pitch and timbre perception. Sensitivity to frequency variations
100	Perception of harmonicity - noisiness
120	Influence of VD decreases

2.2 Physics-Informed Dataset

The behavior of viscoelastic damping can be systematically controlled and modified through four parameters defined in a Finite-Difference Time-Domain (FDTD) model of a viscoelastically damped membrane developed by the second author in [3] (see Table 2). By simulating a circular membrane with a tension of 2284 Pa, a density of 300 kg/m^3, a thickness of 3 mm, a radius of 10 cm, and fixed boundary conditions ($u_{\text{rim}} = 0$), and varying only the parameter space from Table 2, a physics-informed dataset was generated in [9]. For the present study, a subset of 220 time series was extracted from this dataset (see Table 3). Each sample has a duration of 500 ms and a sampling rate of 96 kHz. The selection of viscoelastically damped frequencies—hereafter referred to as VD$_{freq}$—is constrained by the FDTD model, which requires integer multiples of periodicity to maintain numerical stability. Furthermore, when $\Re\{E(s)\} = 0$, no viscoelastic damping is applied; this case is referred to as the *no-damping* condition.

Table 2: Parameters of the FDTD.

Parameter	Description
VD$_{freq}$	Viscoelastically damped frequency
T	Integration time. Length of memory effect
$\Re\{E(s)\}$	Damping coefficient
γ	Rate of decay

Table 3: Parameter space of the dataset.

Parameter	Fixed Value	Min. Value	Max. Value	Increase
VD$_{freq}$ (Hz)	700, 6400			
T (ms)	10			
$\Re\{E(s)\}$		0*	0.003	0.0003
γ		1/100	1/10	1/10

* $\Re\{E(s)\} = 0$ implies no VD (no-damping case).

2.3 Psychoacosutic Features

2.3.1 *Spectral Centroid Differences*

The spectral centroid has been shown to be strongly related to the sensation of brightness in a sound [13]. In accordance with the analysis framework described in Section 2.1, changes in spectral centroid caused by VD at discrete time points are investigated by calculating the difference between the centroid values of a data sample and those of the no-damping case at the same time points. Previous studies have found that the frequency range along which the spectral centroid varies can change considerably across different time points [10]. Therefore, the calculated differences are normalized to facilitate comparison across time. As a result, the centroid differences are calculated as:

$$CD_i(t) = \frac{C_i(t) - C_{\text{ref}}(t)}{CD_{max}(t) - CD_{min}(t)}, \qquad (1)$$

where $C_i(t)$ and $C_{\text{ref}}(t)$ denote the spectral centroids of sample i and the no-damping case, respectively, calculated at the discrete time point t. If $CD_{\text{max}}(t) = CD_{\text{min}}(t)$, then $CD_i(t) = 0$. The results are visualized as a heat map following the approach proposed in [10], with damping coefficients along the x-axis, decay rates along the y-axis, and centroid values mapped to color. This visualization enables a comprehensive overview of how changes in the parameter space of VD affect the spectral centroid at discrete time points.

2.3.2 *Spectral Flux per Mel Band*

Building on the approaches proposed in [11] and [4] to evaluate spectral dissimilarities in a logarithmically filtered Mel spectrogram between discrete time frames t and $t - \mu$, a measure of spectral dissimilarity based on the decibel scale and preserves values per Mel band was introduced in [10] and is calculated as:

$$SF(t, m) = X_{\text{dB,filt}}(t, m) - X_{\text{dB,filt}}(t - \mu, m), \quad (2)$$

where $X_{\text{dB,filt}}$ denotes the decibel-filtered Mel spectrogram, t the discrete time point, m the Mel band index, and $\mu = 1$. Quarter-tone Mel bands were employed in the present study. The objective of this approach is to investigate how and where VD affects the frequency spectrum, enabling the localization of spectral regions where VD-induced changes occur. This, in turn, provides insight into how the spectral centroid is affected and which frequency ranges are most impacted by the energy introduced through the memory effect.

2.4 Self-Organizing Maps (SOM)

Self-Organizing Maps (SOM) transform non-linear statistical relationships in high-dimensional data into geometric relations on a 2D $n \times n$ grid [8]. The dimensionality of each neuron in the SOM matches that of the feature vectors extracted from the dataset. Both neurons and data samples are normalized before training. During training, the Euclidean distance between each sample and neuron is computed to determine the Best Matching Unit (BMU). The BMU's weights and those of its neighboring neurons are updated iteratively using a Gaussian neighborhood function. This process continues for P iterations, refining the SOM structure. Cluster assessment is performed using a U-Matrix, with values ranging from 0 (complete similarity) to 1 (max. distance).

2.5 Data Pipeline and Experiments

Figure 1 depicts the data pipeline of the proposed method. For the frequency-domain transformation, a Short-Time Fourier Transform (STFT) was applied using a Bartlett window with a window size of 85.3 ms and a hop length of 1 ms. Since the highest simulated frequencies in the FDTD model reach approximately 15 kHz, only frequency bins up to this value were considered for the calculation of psychoacoustic features under each VD_{freq} condition.

At this stage, the pipeline branches into two processes. On one hand, the spectral centroid is calculated from the magnitude coefficients of the STFT frequency bins. Centroid differences at the discrete time points defined in the analysis framework are then computed and analyzed with respect to changes in the VD parameter space (Experiment 1). On the other hand, a decibel-scaled Mel spectrogram with quarter-tone Mel bands is computed, and spectral flux per Mel band is calculated, also at the time points t defined in the analysis framework.

Subsequently, the dissimilarity coefficients obtained from the spectral flux are segmented into three frequency ranges: (1) one octave below, (2) one octave around, and (3) one octave above VD_{freq}. For each range, a peak-picking algorithm is applied using minimum width and distance constraints to retain relevant information. The spectral dissimilarities corresponding to the extracted peaks are then isolated, normalized, and incorporated into the feature vector. Principal Component Analysis (PCA) is used to initialize the SOM's weights, and one SOM is trained per frequency range at each time point. Note that each SOM involves three stages of dimensionality reduction: frequency range selection, peak-picking, and PCA for initialization. The results are then analyzed with respect to both the VD parameters and the centroid differences (Experiment 2).

Each SOM is configured with $n = 20$ neurons, a Gaussian neighborhood radius $o = 1.5$, an initial learning rate $\eta(\ell) = 0.5$, and $P = 1000$ iterations. For visualization, the centroid difference coefficients and the parameter-space annotations of the FDTD dataset are used as metadata: the inner color of each data point represents the damping coefficient $\Re\{E(s)\}$ (darker = stronger damping), the outer color indicates the centroid difference (darker = higher difference), and the shape size encodes the rate of decay γ (larger = slower decay). The U-Matrix employs a black-to-white scale, where black denotes complete similarity and white indicates maximum dissimilarity. In this context, the term *physics-informed* refers to the principle of observational bias in physics-informed learning, where observational data inherently reflect the physical laws governing the system and thus serve to embed these laws into the machine learning model [7].

Both the analysis of centroid differences and the segmentation of the frequency spectrum into distinct ranges are key steps in the proposed method (see Fig. 1, rounded purple rectangles), as they directly address the central research question posed in the introduction—namely, where, when, and how VD influences the perceived char-

acteristics of a sound. Results are presented in the following section.

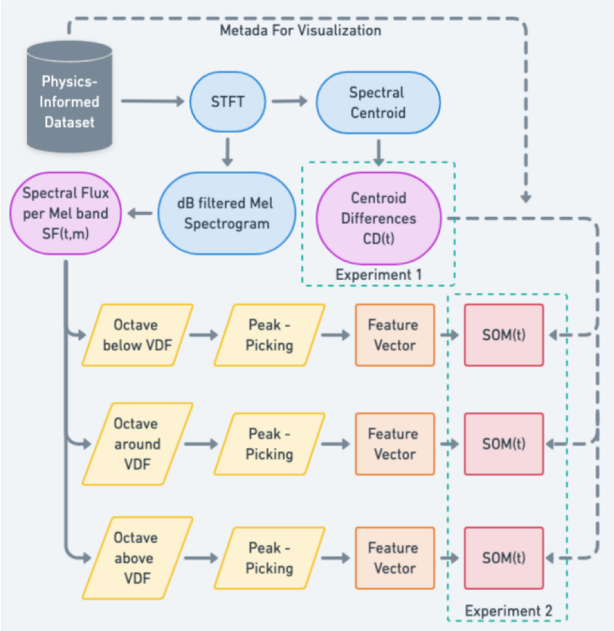


Figure 1: Overview of the data pipeline. An STFT with a Bartlett window (85.3 ms size, 1 ms hop) is applied. The pipeline branches into two processes: (1) spectral centroid, leading to centroid difference analysis (Experiment 1) and (2) computation of spectral flux per quarter-tone Mel band. Flux dissimilarities are segmented into frequency ranges relative to VD_{freq}, followed by peak picking, normalization, PCA initialization, and SOM training. Analysis is conducted in relation to VD parameters and spectral centroid differences (Experiment 2)

3. RESULTS

3.1 Experiment 1 - Centroid Differences

Figure 2 shows the analyses for the centroid differences for each VD_{freq} across the four time points defined in the analysis framework. For the 700 Hz case, at t =10 and 25 ms the centroid difference increases linearly with higher damping and slower decay, while at t = 50 and 100 ms the difference continues to grow with increasing damping but focuses towards $1/20 < \gamma < 1/70$. Moreover, at t = 50 ms some configurations of the parameter space of VD lead to a lower spectral centroid than that of the no-damping case (see Fig. 2 top row third column left to right, three first columns within the heat map).

In the 6400 Hz case, results show that at t = 10 and 25 ms the stronger the damping and the faster the decay the lower the spectral centroid. This trend persists at t = 50 ms, but the decrease is no longer linear throughout——for instance, the centroid decreases less at medium damping ($0.09 < \Re\{E(s)\} < 0.18$) than at higher damping values (≥ 0.21). At t = 100 ms, changes in the centroid become highly nonlinear; while medium damping values produce the greatest differences, this index varies with almost every decay rate. Since in both damped frequencies the 10 ms and 25 ms cases behave similarly, the 10 ms time point is discarded for the SOM analysis presented below.

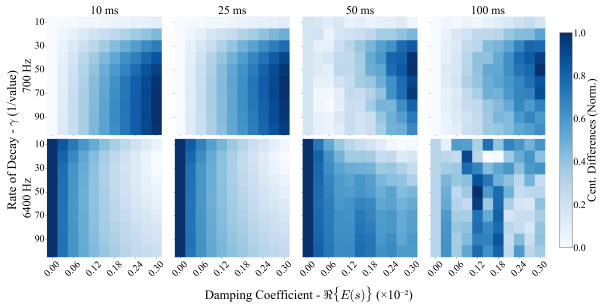


Figure 2: Centroid difference analysis for VD_{freq} = 700 and 6400 Hz. Each column, from left to right, represents one of the four time points defined in the analysis framework, increasing sequentially. Within each heat map, the damping coefficient increases left to right and the rate of decay decreases top to bottom. The darker the color, the higher the centroid difference. For the 700 Hz case, at t = 10 and 25 ms, centroid differences increase with higher damping and slower decay. At t = 50 and 100 ms, differences continue to rise but focus on damping values between $1/20 < \gamma < 1/70$. Notably, some configurations at t = 50 ms result in a lower spectral centroid than the no-damping case. For the 6400 Hz case, at t = 10 and 25 ms, stronger damping and faster decay lead to lower spectral centroids. This trend becomes nonlinear at t = 50 ms. At t = 100 ms, centroid changes become highly nonlinear. Based on these observations, the 10 ms time point is excluded from the SOM analysis.

3.2 Experiment 2 - Physics-Informed Self-Organizing Maps

Figure 3 shows the results for VD_{freq} = 700 Hz. In the octave below the VD_{freq} (first row top to bottom), at t = 25 ms data is distributed in three different regions following an increase in the damping coefficient. This distribution shows that an increase in both the damping coefficient and, in a lesser degree, the rate of decay lead to a higher centroid difference. At t = 50 ms, centroid values for low damping coefficients ($\Re\{E(s)\} < 0.12$) fall below those of the no-damping case represented by a lighter outer color, with the degree of reduction varying based on the decay rate. Furthermore, the gradual transition between clusters based on damping coefficients becomes

more diffuse, particularly separating data with a fast rate of decay. At t = 100 ms the gradual transition becomes even more fuzzy, still, centroid difference increases with increasing damping coefficient. In all three time points the clustering patterns of the SOM strongly match the centroid difference patterns found in Experiment 1 (see Fig. 2 top row). In the octave around the VD$_{freq}$ (Fig. 3 second row), at t = 25 ms the linear relation between the damping coefficients and the centroid differences remains. Moreover, the regions created by the U-Matrix group data according to their centroid difference values, although this distribution breaks the gradual transition found in the octave below the VD$_{freq}$. Small clusters based on damping coefficient are visible, but not clearly formed. At t = 50 ms, the overall data distribution aligns with the corresponding centroid differences heat map (see Fig. 2 center map). The U-Matrix groups data according to similar centroid difference values, clearly separating the two data samples with the highest difference. At t = 100 ms no pattern is found. In the octave above VD$_{freq}$, the previously observed clustering pattern related to the damping coefficient does not emerge at any of the three time points. However, small regions associated with centroid difference values are formed by the U-Matrix, particularly at t = 50 ms, where areas corresponding to low centroid differences (top left) and high centroid differences (top right) become noticeable. No distinct pattern is observed at t = 100 ms.

For the VD$_{freq}$ = 6400 Hz results are shown in Figure 4. At t = 25 ms, a gradual transition from low to high damping coefficients is displayed by the clustering pattern across all frequency ranges, which matches the trends found in Experiment 1 (see Fig. 2 bottom row). However, the octave above the damped frequency displays a clustering pattern that spans across both principal components of the SOM extensively, while the clustering from the octave below focuses only on one part of the map (bottom right), suggesting that its variance is mostly explained by only one of the principal components. Concerning the octave around the damped frequency, although it also coincides with the heat map, the SOM allocates some data points outside the overall pattern (see Fig. 4, second row, first column, top right), resulting in a decrease in how accurately the SOM matches the heat map. At t = 50 ms the octave below shows a general cluster distribution that matches the changes in centroid seen on the heat maps, while the octaves around and above cluster data mostly based on the damping coefficients with no pattern regarding the centroid, although the intra-cluster distance increases with lower rate of decay. This fuzzy clustering is also observed at t = 100 ms in the octave below the damped frequency.

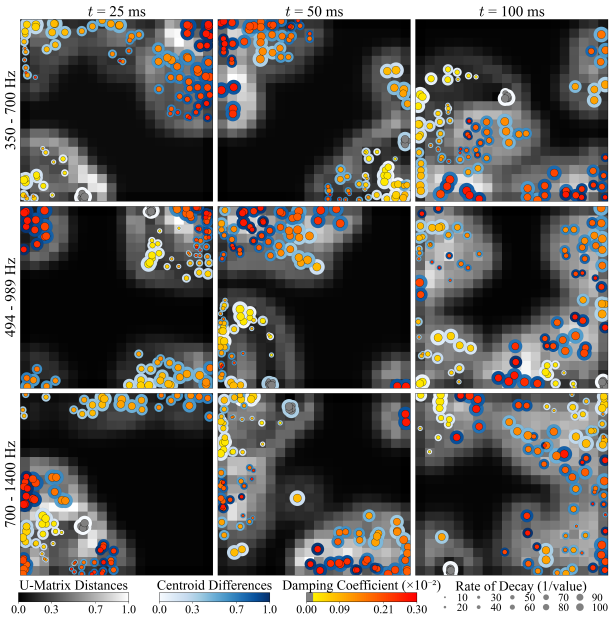


Figure 3: Physics-Informed SOM for VD$_{freq}$ = 700 Hz. Each row corresponds to a frequency range—one octave below (top), around (middle), and above (bottom) VD$_{freq}$—and each column to a time point (t = 25, 50, 100 ms). The U-Matrix displays local dissimilarities between neurons (lighter = more dissimilar). Outer color indicates spectral centroid difference (darker = higher difference), using the same color scale as in Fig. 2. Inner color shows the damping coefficient $\Re\{E(s)\}$ (redder = higher; gray = no damping). Point size reflects decay rate γ (larger = slower decay). In the octave below, a clear relationship emerges between damping coefficient, decay rate, and centroid difference—most evident at t = 25 and 50 ms—mirroring the patterns in Fig. 2. At t = 100 ms, patterns become more diffuse but the trend persists. In the octave around, data is grouped according to centroid differences, especially at t = 50 ms, though clustering is less consistent than in the lower octave. At t = 100 ms, no clear pattern emerges. In the octave above, no clustering by damping coefficient is observed, though at t = 50 ms, regions of low and high centroid difference are weakly distinguished.

4. DISCUSSION

Results suggest that how VD influences sound perception largely depends on the proximity of the viscoelastically damped frequency to the fundamental frequency. This proximity has consequences in the frequency domain that translate to the time domain and ultimately to the perception of the sound. In the frequency domain, when the damped frequency is close to the fundamental——as in the 700 Hz case—the influenced frequency region includes

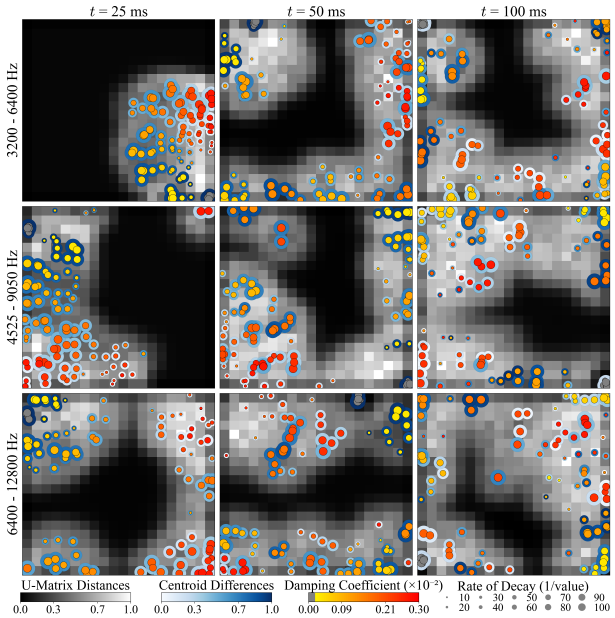


Figure 4: Physics-Informed SOM for VD$_{freq}$ = 6400 Hz. Visualization parameters (color and size coding) are consistent with those used in Fig. 3 for comparability. At t = 25 ms, clustering reflects a gradual increase in damping coefficient across all frequency ranges, aligning with centroid difference heat maps (Fig. 2). The lower octave shows compact clustering driven by the second principal component, while the upper octave spans both components. In the middle octave, some outliers reduce alignment with the heat map. At t = 50 ms, clustering in the lower octave matches trends observed in centroid differences, whereas middle and upper octaves group mainly by damping coefficient, with fuzzier patterns and greater intra-cluster distance for lower decay rates. At t = 100 ms, only the lower octave shows weak clustering; patterns in the higher ranges become increasingly ambiguous.

eigenmodes close to the fundamental frequency. Now, since lower eigenmodes carry more energy than higher ones, the memory effect stores and injects more energy in this frequency region than in a higher one. However, this is not a linear process due to the way the damping coefficient, which acts as both energy supplier and damper, and the rate of decay, which administrates the speed with which the stored energy is inserted back into the system, work together, specially when both have a middle to high value: the higher the damping coefficient, the more energy is available, but also the stronger this new injected energy is damped, on the other hand, if the stored energy decays slowly during the integration time of the memory effect, energy decays nonlinearly in the long run. According to the analysis framework, how long this decay lasts decides wether its the timbre, the pitch or the harmonicity/roughness of the sound what is influenced by the VD. In the 700 Hz case, results show that the spectral dissimilarities caused by VD may persist for 100 ms or more, affecting both the perception of pitch and the sensation of harmonicity. This phenomenon is observed in musical instruments such as the pat wain, where VD enhances pitch perception by influencing the lower modes [2]. Conversely, when the damped frequency is farther from the fundamental, as in the 6400 Hz case, the effect remains perceivable until approximately 50 ms, as shown by the clustering patterns found until this time point, sufficient to influence the timbre but unlikely to impact pitch perception or harmonicity.

Results also suggest that the size of the frequency region influenced by VD decreases over time, gradually shifting towards the region below the damped frequency. Although this size is still frequency dependent because of the different energy levels present in different parts of the spectrum as discussed above, this hypothesis is based on the absence of overall clustering patterns found in higher frequency ranges at longer time points as well as on the continuous decrease in spectral centroid found in the centroid analysis of 6400 Hz case. With regard to the clustering patterns, the clustering of data based on the damping coefficient aligns with the fact that, despite the nonlinear behavior, the damping coefficient is the driving parameter of VD [9].

In relation to the method, the proposed features (centroid differences and spectral flux per Mel band) offer a flexible tool for transient analysis in percussion instrumens. Together, they provide a framework for examining the impact of VD on perceived sound characteristics using psychoacoustically relevant metrics. Specifically, decibels measure the loudness of dissimilarities, determining whether they should be perceptible; quarter-tone Mel bands capture frequency changes that remain perceptible depending on the frequency range; and the spectral centroid serves as a well-established psychoacoustic metric for comparison. Furthermore, focusing on time intervals that are relevant to both the perception of musical instrument sounds and the physical evolution of VD provides insight into the research questions posed in the introduction—namely, how VD influences the perception of sounds produced by musical membranes, how the frequency spectrum evolves over time, and the psychoacoustic implications of the observed patterns. Additionally, each preprocessing step contributes to reduce the dimensionality of the feature vector based on psychoacoustics characteristics of the data, yielding clear results while preserving essential information.

5. CONCLUSSION

A method for analyzing the influence of viscoelastic damping on the perceived sound of musical membranes has been presented. This approach is grounded in the physical characteristics of viscoelastic damping and as well as in temporal cues relevant in the perception of musical sounds. The influence of viscoelastic damping was found to depend largely on the location along the frequency spectrum where damping occurs, specifically in relation to the distance from the fundamental frequency. A decrease in the size of the frequency region affected by viscoelastic damping was also found, with the region gradually shifting towards frequencies below the initially damped area over time. Further studies are needed to investigate additional parts of the spectrum beyond those addressed in the present work, as well as to examine scenarios involving simultaneous damping across multiple frequency regions. Also, future work should incorporate alternative time–frequency representations with higher frequency resolution—such as wavelet transforms—allowing for a more detailed analysis of both the extent and development of the affected regions. Finally, the results demonstrate that physics-informed self-organizing maps offer a powerful tool for analyzing viscoelastic damping given the complexity and high dimensionality of its parameter space.

6. REFERENCES

[1] Alexandraki, C., Starakis, M., Zervas, P., & Bader, R.: Inferring drumhead damping and tuning from sound using finite difference time domain (FDTD) models. *Acoustics* 5 (3) (2023), 798–816. https://doi.org/10.3390/acoustics5030047

[2] Bader, R.: Finite-Difference model of mode shape changes of the Myanmar pat wain drum circle using tuning paste. *Proc. Mtgs. Acoust.* 29 (1) (2016). https://doi.org/10.1121/2.0000450

[3] Bader, R.: Spectrally-Shaping Viscoelastic Finite-Difference Time Domain (FDTD) model of a membrane. *Int. J. Informatics Society* 12 (2) (2020), 81–93.

[4] Böck, S., & Widmer, G.: Maximum Filter Vibrato Suppression for Onset Detection. *Proc. 16th Int. Conf. Digital Audio Effects (DAFx)*, 55–61 (2013).

[5] Choi, K., & Cho, K.: Deep unsupervised drum transcription. *Proc. Int. Soc. Music Information Retrieval Conf. (ISMIR)* (2019), 183–191.

[6] Christensen, R. M.: Theory of viscoelasticity. An introduction. 2nd edition. Academic Press, New York, 1982.

[7] Karniadakis, G. E., Kevrekidis, I. G., Lu, L., Perdikaris, P., Wang, S., & Yang, L.: Physics-informed machine learning. *Nat. Rev. Phys.* 3 (6) (2021), 422–440. https://doi.org/10.1038/s42254-021-00314-5

[8] Kohonen, T.: *Self-Organizing Maps*. Vol. 30. Springer, Berlin Heidelberg, 2001. https://doi.org/10.1007/978-3-642-56927-2

[9] Martínez Orellanos, C. F., & Bader, R.: Analysis of nonlinear behavior of viscoelastic damping in musical membranes using physics-informed self-organizing maps. *APL Mach. Learn.* 3 (1) (2025). https://doi.org/10.1063/5.0242985

[10] Martínez, C. F., & Bader, R.: Physics- and Psychoacoustics-Based Analysis of Viscoelastically Damped Membranes. *Proc. Fortschritte Der Akustik – DAS DAGA*, to appear (2025).

[11] Masri, P.: Computer Modeling of Sound for Transformation and Synthesis of Musical Signals. Ph.D. thesis, University of Bristol, 1996.

[12] Reuter, C.: Der Einschwingvorgang nichtperkussiver Musikinstrumente. Vol. 148. Peter Lang, 1995.

[13] Schubert, E., Wolfe, J., Tarnopolsky, A., & others: Spectral centroid and timbre in complex, multiple instrumental textures. *Proc. Int. Conf. Music Perception Cognition*, Northwestern Univ., Illinois (2004), 112–116.

[14] Shete, S., & Deshmukh, S.: Automatic Tabla Stroke Source Separation Using Machine Learning. In *Adv. Signal Data Process.* (2021), 234–243. https://doi.org/10.1007/978-3-030-81462-5_22

[15] Siedenburg, K.: Specifying the perceptual relevance of onset transients for musical instrument identification. *J. Acoust. Soc. Am.* 145 (2) (2019), 1078–1087. https://doi.org/10.1121/1.5091778

[16] Vogl, R., Dorfer, M., Widmer, G., & Knees, P.: Drum transcription via joint beat and drum modeling using convolutional recurrent neural networks. *Proc. 18th Int. Soc. Music Information Retrieval Conf. (ISMIR)* (2017), 150–157.

[17] Worland, R., & Miyahira, W.: Physics of musical drum head damping using externally applied products. *Proc. Acoust. Soc. Am.* 35 (2019), 035004. https://doi.org/10.1121/2.0001011

[18] Zwicker, E., & Feldtkeller, R.: Das Ohr als Nachrichtenempfänger. 2nd edition. S. Hirzel, 1967.

DOI: 10.61782/fa.2025.0881



FORUM ACUSTICUM
EURONOISE 2025

THE REVOLUTION IS HERE: DEEP AUDIO PROCESSING REDEFINES OFFLINE AND REAL-TIME AUDIO EXPERIENCES

Bar-Yosef Yossi[1*] **Thor Yami**[1] **Fink Nir**[2,1]

[1] BETTEAR – Accessibility Technologies Development LTD, 33 HaBarzel, Tel-Aviv, Israel

[2] Department of Communication Disorders, Acoustics and Noise Research Lab in the Name of Laurent Levy, Ariel University, Ariel 40700, Israel.

ABSTRACT

Deep Audio Processing (DAP) introduces a novel approach to personalized audio optimization, bridging established techniques such as time stretching, remixing, and audio channel separation with a groundbreaking dual-mode application for offline and real-time scenarios. While traditional audio processing methods excel in specific domains, their adaptation to dynamic real-time environments or offline pre-processing with synchronization constraints has been limited. DAP addresses this gap by integrating adaptive latency management and user-specific audio adjustments to deliver an enhanced listening experience tailored to diverse hearing capabilities and preferences. Key innovations in DAP include latency reduction techniques leveraging silent or non-speech segments and extended temporal flexibility for optimizing speech rates, singer-to-instrument ratios, and dynamic loudness ranges. Additionally, machine learning–driven auditory scene classification dynamically adjusts acoustic weights and parameters, optimizing intelligibility and comfort. This unified framework supports applications ranging from live-streaming accessibility enhancements to personalized audio delivery in cinema, teleconferencing, and music playback.

Keywords: *deep audio processing, source separation, time scale modification, real-time processing, accessibility*

1. INTRODUCTION

Audio experiences are central to communication, entertainment, and education. Yet common consumer systems lack flexible, adaptive approaches to personalize audio for listeners with diverse hearing capabilities-particularly those requiring specialized real-time adjustments. Traditional settings such as "Movie Mode" or "Rock Mode" provide fixed equalization filters without dynamically adapting to listener needs or acoustic conditions.

Recent progress in deep learning has enhanced the ability to analyze and manipulate complex audio signals, particularly through advanced source separation [1,2] and non-uniform time scale modification [3]. However, fully deploying these technologies in everyday consumer applications remains challenging, as two main issues persist:

1. **User-specific personalization:** Beyond simple equalization, listeners may require adjustments of signal-to-noise ratio (SNR) and speech tempo that reflect their hearing needs or preferences.
2. **Synchronization constraints:** Maintaining accurate sync across events is essential in real-time or time-sensitive contexts (e.g., live streams or cinematic audio). Excessive time-stretching can introduce objectionable delays and user disapproval.

Deep Audio Processing (DAP) addresses these limitations by integrating classical audio methods (channel separation, time stretching, remixing) with modern machine learning algorithms for source separation and content recognition. A central contribution is DAP's non-uniform time scale modification (NU-TSM) procedure, which balances

[*] ***Corresponding author***: yossi@bettear.com.

Copyright: *©2025 Bar-Yosef et al. This is an open-access article distributed under the terms of the Creative Commons Attribution 3.0 Unported License, which permits unrestricted use, distribution, and reproduction in any medium, provided the original author and source are credited.*

the user's desired speech rate with the need to remain within allowable latency limits. The main contributions of this paper are:

1. **Personalized Deep Audio Processing System:** We propose an assistive architecture that seamlessly unifies audio source separation, content classification, and user-driven mixing/time-stretch control.
2. **Time-Scale Modification Under Latency Constraints:** We formulate a synchronization problem that constrains how speech segments can be stretched without violating lip-sync or real-time requirements.
3. **Speech Rate Preference Experiment:** We present an empirical user study measuring preferred speech rates in noisy backgrounds for listeners with varying degrees of hearing loss, informing the default target speech rates presets for our DAP system.

2. METHODS

2.1 System Architecture

Figure 1 provides a high-level depiction of the DAP system. The system operates in two layers:

- **Processing Pane (Upper):** Source separation, mixing, and time-scaling.
- **Analysis & Control Pane (Lower):** Content classification, user preference retrieval, and adaptive logic for mixing and stretching.

The input is an original audio signal plus user-specific settings (e.g., target SNR and preferred speech rate). The output is a newly reconstructed signal, where speech intelligibility or vocals are enhanced according to personalized criteria.

Next, we briefly describe the basic building blocks of the DAP system.

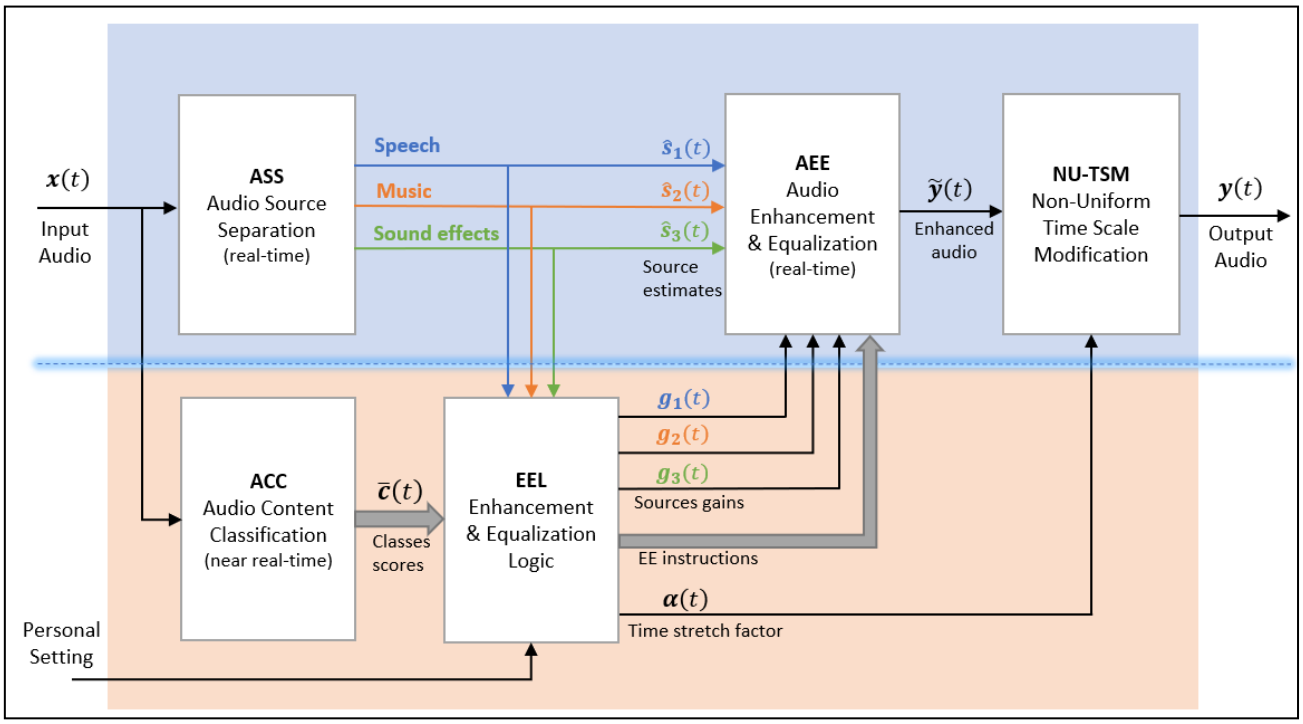


Figure 1. High level architecture of the Deep Audio Processing (DAP) system for assistive audio applications, illustrating the integration of audio capturing, source separation, content classification, enhancement logic, and audio enhancement modules. The upper pane is the "processing pane" and the lower is the "analysis & control pane".

2.1.1 Audio Source Separation (ASS)

The ASS module splits incoming audio into constituent sources such as speech/vocals, music, and sound effects. It uses a deep neural network architecture inspired by the MRX model [1]. Separated sources are crucial for fine-grained manipulation - particularly for adjusting gain or stretching specific elements (e.g., speech) without affecting background signals. Given an input signal $\boldsymbol{x}(t)$, the goal is to decompose it into constituent sources. This step is critical for enabling individualized control over each source's gain and temporal characteristics. Our current implementation follows the "cocktail-fork" concept [1], that separates the audio into three sources, speech, music, and sound effects (sfx). In the more general case, the output of the ASS module is a set of N source estimates,

$$\{\hat{\boldsymbol{s}}_1(t), \hat{\boldsymbol{s}}_2(t), \dots, \hat{\boldsymbol{s}}_N(t)\} \tag{1}$$

fed into subsequent processing blocks for enhancement and personalization.

2.1.2 Audio Content Classification (ACC)

In parallel, a convolutional neural network (CNN) classifies audio content into categories (inspired by [4]) (e.g., conversation, music, ambient noise). This "pseudo" real-time classification produces a time-varying score vector indicating the probability of each category.

$$\bar{\boldsymbol{c}}(t) = [\, c_1(t), \dots, c_K(t) \,]^T \tag{2}$$

where each component $c_k(t)$ reflects the likelihood of a specific content category k, and K is the total number of contents categories. These scores guide the system's adaptive mixing and time-scaling decisions. The index t refers to the corresponding audio frame starting time[1].

2.1.3 Personalized Targets

User preferences for (i) speech/vocal SNR relative to accompaniment and (ii) speech rate in various noise conditions is stored in an external module. These preferences can be specified manually (e.g., through an interface) or derived from user data. The system references these targets to dynamically apply mixing gains and stretching factors. These targets guide the subsequent processing steps within the EEL module.

[1] For simplicity we use the same notation for time indexing, while in all analysis modules and in most processing modules it applies to the index of the audio frame

2.1.4 Enhancement & Equalization Logic (EEL)

The EEL module interprets classification scores and user targets to generate control logic signals to subsequent processing blocks. It carries out:

2.1.4.1 Mixing Logic for SNR Target

In this module gains are computed for each source to match the desired speech-over-background ratio. The time-varying gain parameters are denoted as

$$\{\boldsymbol{g}_1(t), \boldsymbol{g}_2(t), \dots, \boldsymbol{g}_N(t)\}\,. \tag{3}$$

Practically, the SNR calculation is performed frame-by-frame. The calculated gain parameters are then passed to the mixer, which applies the adjustments to ensure that the desired SNR is maintained throughout the audio signal.

2.1.4.2 Speech Rate Estimation and Time Scale Logic

The time scale logic module focuses on the dynamic aspects of speech. It first estimates the local speech rate from the separated speech signal $\hat{\boldsymbol{s}}_1(t)$, to quantify the speech tempo in terms of phonemes-per-second (PPS). There are various approaches for approximating the PPS. The simple ones may consider spectral transition differences between time frames, while the more complicated may use a phonetic recognizer or speech recognition (more applicable to offline mode). This measurement is critical for determining how to adjust the audio timescale. Based on this estimation and the user's preferred speech rate, the module computes an adaptive time-scale factor $\boldsymbol{\alpha}(t)$ to achieve the desired speech rate,

$$\boldsymbol{\alpha}(t) = \boldsymbol{\alpha}\big(\bar{\boldsymbol{c}}(t), \mathrm{PPS}(t)\big)\,, \tag{4}$$

where $\bar{\boldsymbol{c}}(t)$ represents the classification scores from the ACC block, and $\mathrm{PPS}(t)$ represent the estimated momentary speech rate at time t. Eqn. 4, emphasizes that the scale factor is not only adjusted according to the momentary PPS, but is also oriented to the auditory scene, whether it contains merely speech (and may need to be stretched) or if it contains a sound effect (for instance the sound of a gunshot) that needs to maintain the same ratio (factor of 1 indicating no need for stretching), or whether it is a non-speech or a pause section that may be shortened.

The $\boldsymbol{\alpha}(t)$ factor guides the NU-TSM process, allowing for localized adjustments that slow down or speed up audio

segments while preserving the natural timing of non-speech elements.
Together, these two components enable the EEL module to output two sets of control signals: the gain parameters for achieving the desired SNR and the adaptive time-scale factor for targeted speech rate modification. This logic-based stage lays the groundwork for the subsequent re-mixing and time-stretching that occur in the Audio Enhancement & Equalization and NU-TSM modules respectively, ensuring that personalized audio processing meets user preferences.

2.1.5 Audio Enhancement & Equalization (AEE)

The AEE module rebuilds the final audio from the separated sources using the gains calculated by the EEL. Additional filters or effects may also be applied to each separated source as desired. The remixing is performed by:

$$\tilde{\boldsymbol{y}}(t) = \sum_{i=1}^{N} \boldsymbol{g}_i(t)\hat{\boldsymbol{s}}_i(t). \quad (5)$$

2.1.6 Non-Uniform Time Scale Modification (NU-TSM)

The final component, NU-TSM, applies the adaptive stretch factor to slow down high-rate speech segments and optionally compress silence or non-speech segments. A key challenge here is ensuring overall synchronization. Excessive stretching can cause noticeable latency or lip-sync mismatches, so the NU-TSM module operates within strict deviation bounds.

2.1.6.1 NU-TSM in Sync – Problem Derivation

Time scale modification in sync poses additional limitations on latency or on "run ahead" in offline scenarios. Typically, TSM algorithms relate to two parameters – the analysis frame step (which is a constant) and the synthesis frame step which is set according to the required stretch factor $\boldsymbol{\alpha}(t)$. when adding sync constraints, we wish to force the synthesis frames to be located inside a certain shift from the original location of the corresponding analysis frame, and this poses a new optimization problem, which is derived next. In the following derivation we use a discrete notation for the stretch factor $\alpha_t \equiv \boldsymbol{\alpha}(t)$, suggesting that t is a running frame index.

Problem derivation:
- Assume a given audio signal has T analysis steps, and a series of stretch factors (per frame) is given by $\{\alpha_0, \alpha_1, \dots, \alpha_t, \dots, \alpha_T\}$ where $\alpha_0 = 0$.
- Let $\boldsymbol{a}$ be the constant analysis step (samples or time units).
- Hence, a requested synthesis step at time t would be $\boldsymbol{a}\alpha_t$.
- The analysis frame position at time t is defined by:

$$x_t = x_0 + \boldsymbol{a}t \quad (6)$$

where x_0 is the initial position of the analysis.
- The "requested" synthesis position at time t follows the recursion

$$z_{t+1} = z_t + \boldsymbol{a}\,\alpha_{t+1} \quad , \quad (7)$$

where z_0 is the initial position of the synthesis (typically $x_0 = z_0$), and the momentary stretch time between two consecutive frames is defined by

$$z_{t+1} - z_t = \boldsymbol{a}\,\alpha_{t+1} \quad . \quad (8)$$

- The terms z_t are the requested synthesis positions without sync limitations. We seek a new set of synthesis positions, $\{y_0, \dots, y_t, \dots, y_T\}$ that aim to maintain the momentary stretch time of all steps, $z_{t+1} - z_t$, while satisfying strict sync conditions to the original analysis positions, defining L to be the allowed time deviation from the original position, the optimization problem is formulated as follows:

$$\begin{cases} \text{minimize} & \sum_{t=0}^{T-1} |(y_{t+1} - y_t) - (z_{t+1} - z_t)| \\ s.t. & |y_t - x_t| \le L \quad \forall \quad t \in \{0, \dots, T\} \\ & y_{t+1} - y_t \ge 0 \quad \forall \quad t \in \{0, \dots, T\} \end{cases} \quad (9)$$

Simplifying by replacing variables produces the following optimization problem,

$$\begin{cases} \text{minimize} & \sum_{t=0}^{T-1} |y_{t+1} - y_t - \boldsymbol{a}\alpha_{t+1}| \\ s.t. & |y_t - x_0 - \boldsymbol{a}t| \le L \quad \forall\ t \in \{0, \dots, T\} \\ & y_{t+1} - y_t \ge 0 \quad \forall\ t \in \{0, \dots, T\} \end{cases} \quad (10)$$

This formulation guarantees that the solution's time sync will not deviate from the preset boundaries however, the requested target scale is not guaranteed, it only tries to optimize it to the best effort.
Various real-time or offline approximation methods can solve this optimization efficiently. One approximation uses a greedy regressive procedure that may fit real-time scenarios due to its simplicity. In some conditions, the solution may be further simplified. For example, when assuming $\alpha_t \ge 1$ for all $t = 1, \dots, T$; the problem reduces to a convex problem with an analytical solution. In an offline scenario over an audio part of original length T_s where the requested total length is calculated by $z_T = \boldsymbol{a}\sum_{n=1}^{T} \alpha_n$ (following Eqn. (7)),

and the total margin is L before and after the speech part; setting $z_0 = x_0$, leads to a simple solution,

$$y_t = \begin{cases} z_t & \text{, if } z_T \le T_s + L \\ -L + z_t\left(\frac{T_s+2L}{z_T}\right) & \text{, if } z_T \ge T_s + 2L \\ -\left(\frac{z_T}{T_s} - 1\right) + z_t\left(\frac{T_s+L}{z_T}\right) & \text{else} \end{cases} \quad (11)$$

This offline solution obtains a "run ahead" time on y_0 (having a non-speech margin before the referenced part), allowing to compensate for the latency accumulated in the stretched part. This simplified result (Eqn. (11)) provides satisfactory outcomes in many situations.

2.2 User Experiment: Speech Rate Preferences Noise

2.2.1 Participants

A total of 44 participants with bilateral hearing impairment took part in the study. Participants were categorized by the severity of their hearing loss (HL) [5]; mild HL (n = 23), moderate HL (n = 8), severe HL (n = 6), and profound HL (n = 7). All provided informed consent and completed an online auditory profile questionnaire prior to testing, including hearing loss characteristics, onset, stability, and type of hearing impairment. The experiments were conducted remotely, with participants using their own listening devices in a quiet home environment. Stimuli and Equipment

2.2.2 Stimuli and Equipment

Speech stimuli consisted of recordings of a professional female narrator in a studio environment. The narrator read aloud multiple pages from a novel, ensuring natural prosody and articulation. The speech stimuli were presented simultaneously with a separately recorded police siren. The speech and siren were mixed to create a controlled background noise condition, ensuring consistency across all participants. All audio files were presented in MP3 format (44,100 Hz, 32-bit sampling rate). Participants were instructed to use headphones or their regular hearing aids/cochlear implants (if applicable) and to avoid adjusting device settings during the experiment. For further information, see [5].

2.2.3 Procedure

The experiment consisted of two phases. In the preliminary task, each participant determined their most comfortable level (MCL) for listening to speech in the presence of background noise. This was done using two pre-prepared audio files: one containing the narrated recordings and the other containing a constant-level police siren noise. The noise was played at a fixed intensity, while participants used a slider to adjust the intensity of the narrator's voice until they reached the minimal SNR that allowed for comfortable speech understanding.
Once the participant's individual SNR was determined, they proceeded to the main task, where they adjusted the speech rate of the narrator while listening under the same background noise conditions and using the SNR established in the preliminary phase. Participants used a sliding control to modify the recorded speech rate to the maximum speed at which they could still comprehend the story content.

2.2.4 Data Collection and Analysis

Data collection was conducted remotely via an online interface as described in [5]. Only participants who fully completed the experimental tasks were included in the analysis. An SPSS software was used for statistical analysis. Preferred speech rates (mean ± standard deviation) were calculated for each participant and group. A one-way analysis of variance (ANOVA) was conducted to assess whether speech rate preferences differed significantly between groups. Post hoc tests (Tukey's HSD) were performed to evaluate pairwise differences. Effect sizes (η^2) were calculated to quantify the magnitude of observed differences.

3. RESULTS

3.1 DAP System Outcomes

Figures 2 and 3 illustrate qualitative examples of how DAP adjusts SNR and speech tempo over time. Figure 2 presents a snapshot of the DAP system in the time domain, over a short audio example. It shows the speech SNR adjustment obtained through the mixing gains, the speech rate measurement and the time-scale modification in term of accumulated latency. It is observed that the NU-TSM algorithm stretches the speech section (during the first second of the audio), followed by shortening the non-speech segment of the audio.
Figure 3 presents an example of an audio recording containing a heated debate between two people. One can observe the time-scaling applied non-uniformly, where the pre-treated higher speech rates receive a larger stretch factor, while the pauses in the speech sections are shortened to compensate for the latency caused by the stretching process.

Thus, the maximum latency does not exceed a predefined limit of $L = 240$ msec. This parameter can be adjusted according to user needs or even according to the audio content classification.

Clearly, the effectiveness of NU-TSM is highly influenced by the allowable sync deviation and the structure of the speech segments. When a conversation or cinematic audio track includes sufficient pauses, users can experience improved intelligibility without perceiving noticeable synchronization issues.

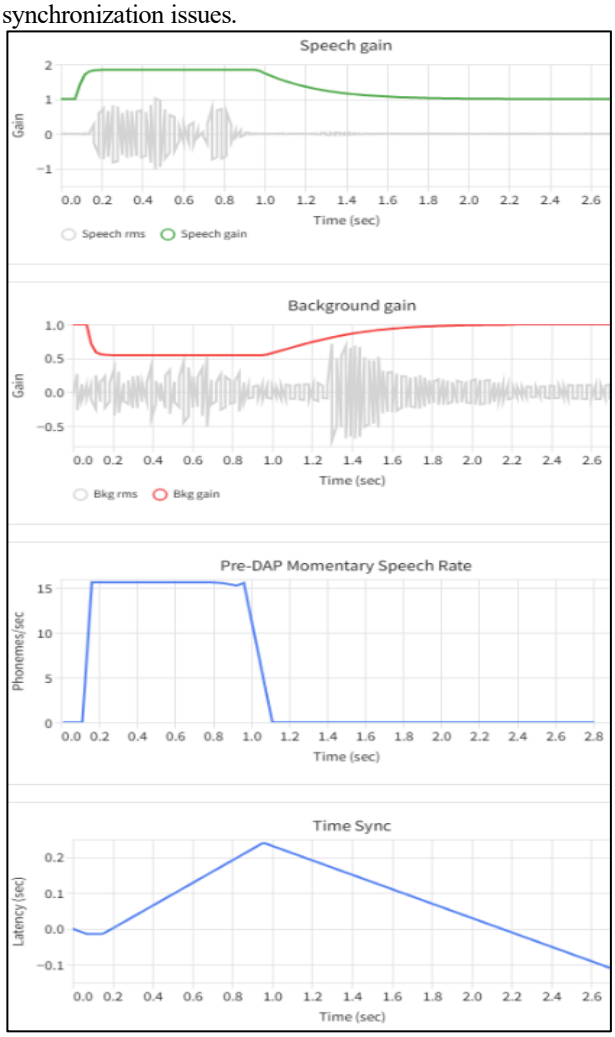


Figure 2. A snapshot of a processed audio example from the DAP system. The two upper plots describe the separated sources of 'speech' and 'background' (music and sound effects combined) with the gain factor (green and red gain curves) applied to emphasize speech. The third plot describes the approximated original speech rate, which is over 15 PPS, and the bottom plot describes the time scale modification in terms of latency. The speech part is stretched by almost 20%, allowing a latency of 240 msec, while the non-speech part is shortened to reduce the time latency. Notice that the line slope presents an effective scale factor.

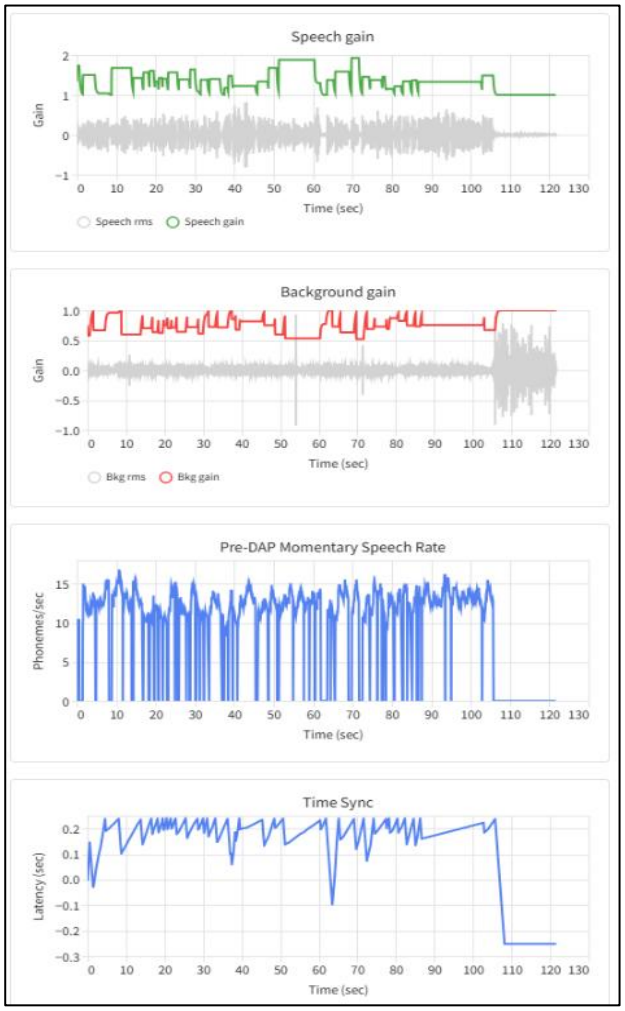


Figure 3. A snapshot of an audio recording of a heated debate. The target SNR is applied to most of the frames. Bursts of high speech rates exceed 15 PPS, and the time-scaling is applied non-uniformly. The maximum time deviation is 240 msec - as predefined in the system setting.

3.2 User Experiment Speech Rate Preference in Background Noise

Descriptive statistics for speech rate preferences in the presence of a background police siren are provided in Figure 4. Results show a general trend of decreasing preferred PPS with increasing hearing loss severity. Participants with mild HL preferred a mean PPS of 10.94, moderate HL preferred 10.42, severe HL preferred 9.30, whereas those with profound HL preferred a significantly slower rate of 8.51. On average, the preferred speech rate in background noise was 10.24 PPS.

A one-way ANOVA revealed a statistically significant effect of hearing loss severity on preferred PPS [$F(3,40) = 3.084$, $p = .038$, η^2=0.188]. Post hoc tests showed that the maximal preferred PPS for the perception of a female narrator speaking in background noise decreased significantly from mild to profound HL (-2.43 PPS, $p = 0.039$). No other significant group differences were observed.

These results suggest that individuals with greater hearing impairment prefer slower speech rates when background noise is present. Future studies should explore additional auditory factors influencing speech rate preference, such as spectral balance and dynamic range compression.

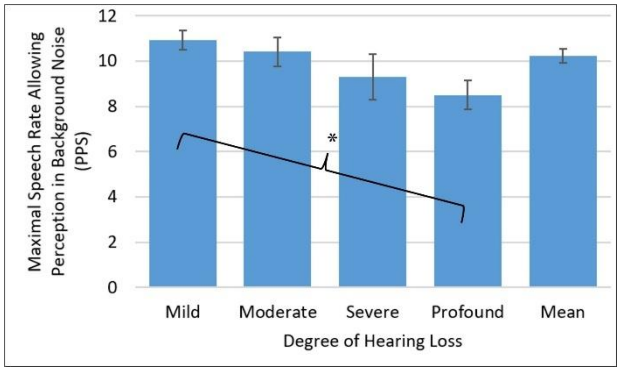


Figure 4. Maximal Speech Rate Allowing Perception (in PPS) of a female narrator in background noise across different hearing loss groups (Mild, Moderate, Severe, Profound and Mean). Error bars represent the standard error of the mean. ⋆ Indicates a statistically significant difference between the marked groups ($p < 0.05$).

4. DISCUSSION

This paper suggests a basic and general description for an assistive audio processing system. The practical system is more complicated and is not detailed here. Since the final output of the system depends on a series of different modules, source separator, content classification, auditory-scene oriented logic of time-scale modification, and time-constrained stretching algorithm, many independent variables may affect it. Because of this complexity, it is difficult to quantitatively validate the most influencing factors as they are entangled together. Future user experiments should address this issue. It also seems that to examine the quality of different algorithms, further comparative experiments should be conducted to provide empirical quantitative analysis.

While our study provides valuable primary insights about speech rate preferences in the presence of background noise, some limitations should be noted. First, hearing loss severity was self-reported rather than audiometrically verified, which may introduce variability in group classification. Future studies should incorporate objective hearing assessments to strengthen classification accuracy. Second, the experiment was limited to a single type of noise which in future experiments would be expanded to variable types of noise. The present study primarily examined speech intelligibility improvements. Additional research is needed to assess how DAP's strategies affect non-speech content such as music or sound effects, especially in scenarios where the artistic intent or emotional impact of the audio track must be preserved.

5. CONCLUSION

This paper has introduced a personalized DAP framework that combines advanced source separation, content-aware mixing, and NU-TSM to enhance audio in both offline and real-time contexts. By leveraging machine learning for audio content classification, DAP enables targeted improvements in speech intelligibility, adaptable speech-rate manipulation, and precise synchronization with visual media or other concurrent events. While the primary focus is on speech intelligibility, the underlying system can be adapted to enrich various user experiences - for example, by emphasizing a specific instrument or sound source.

Crucially, our NU-TSM approach shows how intelligibility can be improved without exceeding predefined latency constraints. We also introduced a user study on speech-rate preferences in noisy environments, establishing baseline presets that reflect listeners' auditory needs across different degrees of hearing loss. Although our findings suggest that DAP meets many user preferences, practical challenges persist - especially

regarding real-time processing demands and stringent latency requirements.
Moreover, fully understanding users' preferences and requirements necessitates subjective hearing experiments, due to the wide range of factors that shape listening experiences - hearing profiles, attention deficits, age, and content variability (e.g., music genres, cinematic audio, special effects). These complexities underscore the individualized nature of audio preferences and highlight the importance of extensive user-centric testing to capture diverse needs accurately.
Future research will address these constraints and further refine personalized audio processing by exploring more robust adaptation strategies, investigating broader content types, and incorporating formal audiometric evaluations. Ultimately, this work lays the groundwork for a versatile DAP system capable of serving a wide audience with varied listening preferences and challenges.

6. ACKNOWLEDGMENTS

The authors would like to express their gratitude to the participants who took part in this study and provided valuable insights and to Shaked Bigi for her assistance. This research was supported by a grant from The Israel Innovation Authority (Grant #83364) as part of the research and development project titled: "Development of Technology for the Accessibility of Auditory Content for Populations with Hearing Difficulties or Attention Deficit Disorders."

7. REFERENCES

[1] Y. Luo and N. Mesgarani, "Conv-TasNet: Surpassing ideal time–frequency magnitude masking for speech separation," in *IEEE/ACM Transactions on Audio, Speech, and Language Processing*, vol. 27, no. 8, pp. 1256–1266, Aug. 2019.

[2] D. Petermann, G. Wichern, Z.-Q. Wang, and J. Le Roux, "The cocktail fork problem: Three-stem audio separation for real-world soundtracks," in *Proceedings of the IEEE International Conference on Acoustics, Speech, and Signal Processing (ICASSP)*, pp. 876–880, 2022.

[3] A. Kupryjanow and A. Czyżewski, "A non-uniform real-time speech time-scale stretching method," in *Proceedings of the International Conference on Signal Processing and Multimedia Applications (SIGMAP)*, Seville, Spain, pp. 145–150, 2011.

[4] S. Soni, S. Dey, and M. S. Manikandan, "Automatic audio event recognition schemes for context-aware audio computing devices," in *2019 Seventh International Conference on Digital Information Processing and Communications (ICDIPC)*, pp. 23–28, 2019.

[5] Fink, Y. Thor, Y. Bar-Yosef. "Psychoacoustics of Remixing Music: Catering to Hard-of-Hearing and Normal-Hearing Audiences for Enhanced Experiences", in *Proceedings of Forum Acusticum (submitted). Malaga, Spain: European Acoustics Association (EAA),* 2025.

DOI: 10.61782/fa.2025.0466



FORUM ACUSTICUM
EURONOISE 2025

INDIVIDUAL VIOLIN SOUND IDENTIFICATION USING AUDIO FEATURES AND MACHINE LEARNING

Hugo Pauget Ballesteros[1*] **Philippe Lalitte**[2] **Claudia Fritz**[1]

[1] Institut d'Alembert, Sorbonne Université, France
[2] IReMus, Sorbonne Université, France

ABSTRACT

Identifying individual instruments of the same type from their recordings is a rarely addressed challenge. This paper explores violin sound identification using two datasets of recordings, featuring multiple violinists playing multiple violins. Several long-term audio features were compared, and their performance in violin classification was evaluated using classical machine learning algorithms. Among these features, long-term MFCCs demonstrated the ability to distinguish individual violins while taking into account player-induced variability, enabling reliable violin recognition. Additionally, the influence of key parameters – such as the number of violinists and choice of musical excerpts – on classification performance was analyzed. These findings offer guidelines for optimizing future data collection aimed at capturing a violin's unique sound signature.

Keywords: *violin identification, classification, features*

1. INTRODUCTION

Musical instrument classification is a key task in Musical Information Retrieval (MIR), aiming to identify the instruments present in a recording. This topic has been extensively studied in the literature, and for monophonic recordings (containing only one instrument), state-of-the-art models commonly reach accuracies of almost 100%. However, few articles have addressed the issue of identifying individual instruments of the same type, and even less so when focusing specifically on instruments from the violin family. Only a handful of studies ([1–3]) have tackled this challenge. These studies suggest that cepstral coefficients offer enough discriminative information about individual violin timbre for effective classification. Nevertheless, these studies relied on limited datasets, where not all violins were played by multiple violinists. This raises an important question: do these algorithms recognize the instruments themselves, or simply the unique playing styles of the performers?

This paper aims to address this challenge by reviewing and comparing various approaches to identify individual violins, from data collection to processing. It provides guidelines for recording sessions and introduces a long-term adaptation of MFCCs. The paper is organized as follows: section 2 describes the methodology, including data collection, feature extraction, data exploration, and classification using machine learning. The experimental results are presented and analyzed in section 3. Finally, section 4 provides concluding remarks and outlines potential directions for future work.

2. MATERIALS AND METHODS

2.1 Datasets

Two datasets were collected for this study, each consisting of recordings where a group of violinists played a set of violins. The violins and violinists sets were different in those two experiments. The first dataset includes a larger number of violins and violinists, while the second dataset comprises more recording time.

*__Corresponding author__: hugo.pauget@dalembert.upmc.fr.
__Copyright__: ©2025 Hugo Pauget Ballesteros et al. This is an open-access article distributed under the terms of the Creative Commons Attribution 3.0 Unported License, which permits unrestricted use, distribution, and reproduction in any medium, provided the original author and source are credited.

2.1.1 Bilbao Dataset

During the Bilbao Project, thirteen violins were built to relate their material and geometrical characteristics with their tonal quality [4]. These violins were played in 2019 by twenty-three professional violinists, each of them having recorded a 3-octave G chromatic scale on each violin and a short musical excerpt on a violin of their choice. The resulting dataset comprises 13×23 recordings of scales and 23 recordings of musical excerpts (one excerpt per violinist). The recordings were made under the same conditions in a large rehearsal room at the Bilbao conservatory, keeping a constant distance between the player and the microphone (Zoom H4n Pro) and using a sample rate of 48kHz.

2.1.2 CNSM Dataset

Another dataset was created at the Paris Conservatoire (CNSMDP), involving thirteen violinists and three violins. Participants were given time to familiarize themselves with each instrument before recording a chromatic scale and selected excerpts from the classical violin repertoire. These excerpts were taken from pieces by Bach, Mozart, Tchaikovsky, Sibelius, and Glazunov. The recordings were made under the same conditions in a large recording studio at the CNSM, keeping a constant distance between the player and the microphone (DPA 4006) and using a sample rate of 48kHz.

2.2 Features

2.2.1 Long-Term Average Spectra (LTAS)

The Long-Term Average Spectra (LTAS) of a recording is obtained by dividing the input signal into overlapping segments, then calculating the windowed DFT of each segment and finally averaging the power of those DFTs.
LTAS has been used in [5] to compare the tonal quality of violins. More specifically, the author compared the sound of old Italian violins (Stradivari/Guarneri) and modern violins. He concluded that differences between these two groups could be demonstrated using LTAS

2.2.2 Long-Term Cepstral Coefficients (LTCC)

LTCC were introduced in [1] for individual instrument identification. Their calculation is similar to that of MFCCs (see next section) except that a mel-filterbank is not applied and that the final step is given by an Inverse Discrete Fourier Transform.

2.2.3 Mel-Frequency Cepstral Coefficients (MFCC)

MFCCs are obtained by mapping the frequencies of a spectrum onto a nonlinear mel-scale (a perceptual scale of pitches judged by listeners to be equal in distance from one another), taking the logarithm, and then computing the Discrete Cosine Transform (DCT) of the result. Here, instead of calculating the MFCCs on overlapping segments, we use an LTAS as input spectrum as we want features with a long-term meaning.
MFCCs are a set of features that has been extensively used for Automatic Speaker Recognition and for Instrument Classification (e.g. [6, 7]).

2.3 Classifiers

We compare the results of three popular classification algorithms : K-Nearest Neighbours, Support Vector Machines and MultiLayer Perceptron. These three classifiers use different learning strategies and thus will give different results on our data.

3. RESULTS AND DISCUSSIONS

This section analyses classifier performance for violin identification. First, we provide an overview of the performance achieved by different features and classifiers, followed by the introduction of a fine-tuned baseline model. Subsequently, the influence of key hyperparameters on the performance of this baseline model is systematically examined. The results highlight the impact of dataset subsets and hyperparameter configurations on model effectiveness, offering insights into optimal settings for violin identification tasks.

3.1 Model performance

We first compare the performance of various features and classifiers. For each combination, we systematically tuned hyperparameters to determine optimal configurations. As our datasets are small, we use a repeated random subsampling cross-validation to compute the accuracy of each model. The best performing model is then selected as our baseline. The results of this comparative analysis are summarized in figure 1 for the Bilbao dataset and in figure 2 for the CNSM dataset. Note that the accuracies obtained for the two datatasets can not be compared as the number of violins involved is not the same.
On the CNSM dataset, all combinations of classifiers and features achieve comparable accuracy. In contrast, with the Bilbao dataset, which is both smaller and involves

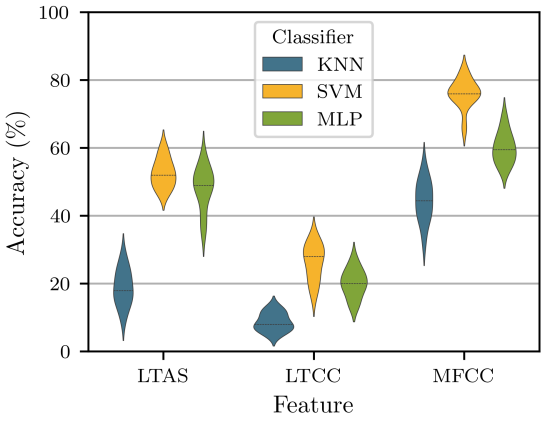


Figure 1. Cross-validation accuracy, Bilbao dataset.

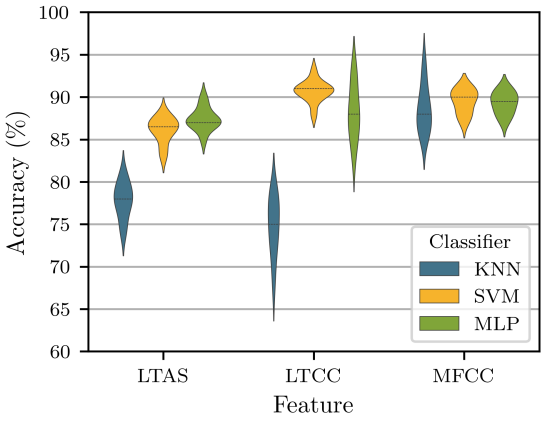


Figure 2. Cross-validation accuracy, CNSM dataset.

a larger number of classes, the selection of appropriate features and classifiers significantly impacts performance. We observe that MFCCs consistently deliver the best results, regardless of the classifier used. This suggests that MFCCs are the most effective features for distinguishing between violins, while taking into account variations in the playing styles of individual violinists. Optimal performance was observed when using MFCCs with an SVM classifier. This model utilized audio recordings downsampled to a 10kHz sampling rate, retained 60 MFCC coefficients, and employed a linear kernel in the SVM algorithm. In the rest of this paper, this model is referred to as "SVM-MFCC".

3.2 Influence of the training data

In this section, we use the fine-tuned SVM-MFCC model to assess the influence of training data on classification results. We focus solely on the CNSM dataset, better suited for this specific investigation due to the longer recording durations and the diversity of musical excerpts.

3.2.1 Influence of the number of players and excerpts per player

To understand the impact of both the number of violinists and the number of excerpts per violinist in the training data, we designed an experiment varying both parameters. First, 20% of the data was held out for testing. Next, for systematically varied numbers of violinists (n) and excerpts per violinist (m), we trained our SVM-MFCC model using randomly selected subsets. The performance of the model was then measured on the fixed test set. The resulting accuracy values, for different (n, m) pairs, are presented as a matrix in Figure 3.

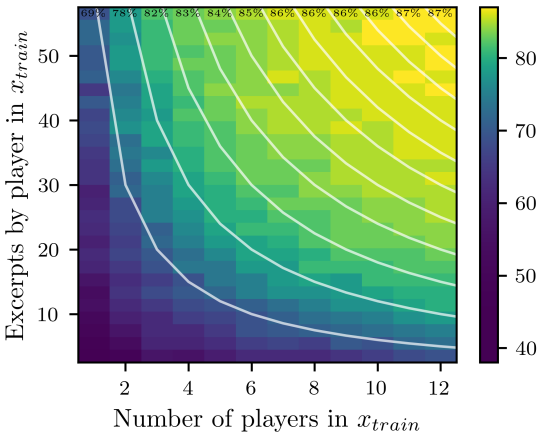


Figure 3. Test accuracy (%) of our baseline model for random training data subsets of n violinists and m excerpts per violinist. The white isolines represent fixed training-set sizes.

We observe that generally, accuracy increases with both the number of players and the number of excerpts per player. While optimal performance (87% accuracy) was achieved when both the number of players and the number of excerpts per player were high (more than 10 players, 50 excerpts per player), moderate performance (70% accuracy) could be reached with different trade-offs, such

as using data from many players with fewer excerpts each, or fewer players with many excerpts each (as shown by the accuracy along the white lines). If achieving moderate performance is sufficient, the specific balance between the number of players and excerpts per player can be chosen based on practical constraints.

3.2.2 Influence of the musical excerpt type

To assess the impact of different excerpts on the accuracy, we trained our SVM-MFCC model using only recordings of the same type for training, while keeping 20% of the data for testing. Figure 4 compares accuracy in two scenarios: (1) "same as training", where the model was tested only on data from the training set that corresponded to the same excerpt on which our model was trained, and (2) "different", where it was tested on all other excerpts.

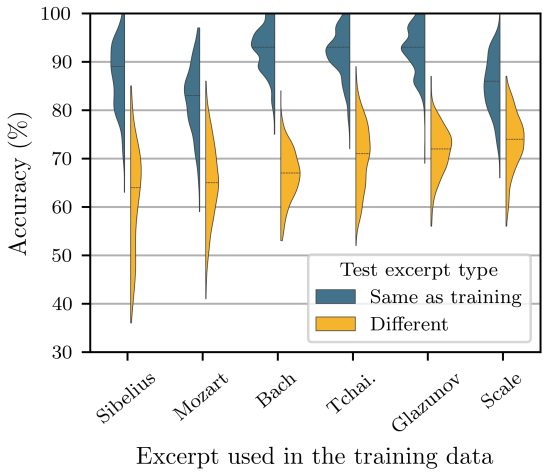


Figure 4. Violin plots of the test accuracy obtained with a SVM-MFCC model using different excerpts as training data. CNSM dataset.

Figure 4 shows that, unsurprisingly, the case "same" leads to better accuracy than the case "different". Moreover, while the accuracy is little influenced by the type of excerpt in average in both cases, the standard deviation is larger for Sibelius and Mozart, in particular for "different". This can be explained by the fact that these excerpts cover – mostly for Mozart and entirely for Sibelius – the upper-end of the register. It thus appears that using Scales, Glazunov, and Tchaikovsky recordings are better candidates for such classification task.

4. CONCLUSIONS

Few studies have addressed the problem of identifying individual violins based on their sound. Furthermore, the limited existing research often relies on datasets where not all violins are played by all musicians involved in the study. Utilizing two purpose-built datasets to address this limitation, and through comparison of various features and machine learning algorithms, this study confirms the feasibility of individual violin identification. Additionally, it provides practical guidelines for selecting the number of violinists and the types of excerpts to record. Future work will focus on exploring how MFCCs can explain perceptual evaluations of violin timbre by listeners.

5. ACKNOWLEDGEMENTS

We thank Collegium Musicæ for their support and Vincent Lostanlen for his valuable feedback.

6. REFERENCES

[1] E. Lukasik, "Long term cepstral coefficients for violin identification," *Journal of The Audio Engineering Society*, May 2010.

[2] Q. Wang and C. Bao, "Individual violin recognition method combining tonal and nontonal features," *Electronics*, vol. 9, p. 950, June 2020.

[3] M. Yokoyama and Y. Ishigaki, "Identification of violin timbre by neural network using acoustic features," *Proceedings of Meetings on Acoustics*, Dec. 2022.

[4] C. Fritz, G. Stoppani, U. Igartua, R. J. Rico, A. Arroitajauregi, and L. Artola, "The Bilbao project : How violin makers match backs and tops to produce particular sorts of violins," in *International Symposium on Musical Acoustics*, Sept. 2019.

[5] A. Buen, "Comparing the sound of golden age and modern violins: Long-time-average spectra," *VSA Papers*, vol. 1, July 2005.

[6] A. Eronen and A. Klapuri, "Musical instrument recognition using cepstral coefficients and temporal features," in *2000 IEEE International Conference on Acoustics, Speech, and Signal Processing. Proceedings*, June 2000.

[7] J. D. Deng, C. Simmermacher, and S. Cranefield, "A study on feature analysis for musical instrument classification," *IEEE Transactions on Systems, Man, and Cybernetics, Part B (Cybernetics)*, Apr. 2008.

DOI: 10.61782/fa.2025.0009

FORUM ACUSTICUM EURONOISE 2025

A DATA-DRIVEN TRANSFER MATRIX MODEL FOR THE DESIGN OF SAXOPHONE MOUTHPIECES

Gioele Greco[1*] **Xinmeng Luan**[2]
Alberto Bernardini[1] **Fabio Antonacci**[1] **Augusto Sarti**[1]
[1] Dipartimento di Elettronica, Informazione e Bioingegneria (DEIB), Politecnico di Milano
Piazza Leonardo Da Vinci 32, 20122 Milano, Italy
[2] Computational Acoustic Modeling Laboratory,
Center for Interdisciplinary Research in Music Media and Technology,
Schulich School of Music, McGill University, Canada

ABSTRACT

This study presents a data-driven methodology to estimate transfer matrices modeling saxophone mouthpieces based on their geometric parameters. A novel parametric model was developed to generate more than 1000 unique mouthpiece geometries. Key geometric features, such as chamber and throat cross-sections, shape radii, and baffle inclination angle, were varied to create the dataset. The training data are generated through Finite Element Method (FEM) simulations, from which transfer matrices were extracted and approximated using Chebyshev polynomials. Polynomial coefficients were then modeled using fully connected neural networks to enable efficient prediction. The results demonstrate the system's ability to accurately predict transfer matrix coefficients, highlighting the potential of computational methods to enhance the customization and design of specific elements of musical instruments, such as mouthpieces.

Keywords: *saxophone mouthpiece, acoustic modeling, finite element method, transfer matrix, data-driven design*

**Corresponding author*: *gioele.greco@polimi.it.*
***Copyright**: ©2025 Greco et al. This is an open-access article distributed under the terms of the Creative Commons Attribution 3.0 Unported License, which permits unrestricted use, distribution, and reproduction in any medium, provided the original author and source are credited.*

1. INTRODUCTION

The saxophone mouthpiece plays a crucial role in defining the tonal characteristics and playability of the instrument [1–3]. The design of a mouthpiece involves balancing complex geometric parameters that influence airflow dynamics and, consequently, sound production [4,5]. This study focuses on the internal geometry of the mouthpiece, particularly the throat, chamber, and baffle, which significantly affect its acoustic properties [6].

Traditional evaluation methods for mouthpiece designs often rely on physical prototypes and subjective auditory assessments. These approaches are inherently time-consuming and limited in their ability to explore large design spaces [7, 8]. Recent advances in computational modeling and data-driven techniques in musical acoustics [9, 10] present new opportunities to study and optimize mouthpiece designs systematically.

In this work, we propose a parametric modeling framework for saxophone mouthpieces, enabling the automated generation of a large dataset of internal cavity geometries. Finite Element Method (FEM) simulations are employed to compute the corresponding acoustic transfer matrices (TM) for each design [**?**, 11]. Subsequently, neural networks are trained to capture the complex relationships between geometric features and the resulting acoustic responses encoded in the transfer matrices.

Furthermore, the mouthpiece models are integrated with a simplified saxophone body representation to investigate the effects of estimation errors in the transfer matrices on the overall acoustic output. This analysis provides insights into the sensitivity of the saxophone acoustics to

the geometry of the mouthpiece and the accuracy of predictive models.

The insights gained from this study provide a foundation for the design of mouthpieces customized to specific acoustic preferences, paving the way for innovations in saxophone performance and personalization [12].

2. GEOMETRIC MOUTHPIECE PARAMETERS

To establish the geometric framework for the saxophone mouthpiece, we conducted a detailed analysis of a wide range of commercially available models. Drawing on the studies of [13] and [12, 14], we identified key geometric parameters that capture the essential variations among different mouthpiece designs. The primary objective was to define a minimal yet versatile set of parameters capable of approximating a broad spectrum of mouthpiece geometries, ensuring adaptability across various styles and manufacturers.

Although this study focuses specifically on the alto saxophone mouthpiece as a representative case, the proposed methodology is generalizable and can be extended to other saxophone families, including soprano, tenor, and baritone models.

Given the large number of variables that influence mouthpiece performance, our design strategy prioritizes parameters that directly affect internal airflow and acoustic response. Based on the acoustic modeling framework presented in [15], we intentionally excluded variables associated with the reed tip interface from the parametric space. Instead, the reed channel is simplified and approximated as a rectangular window to reduce complexity and computational cost.

A geometric schematic of the internal cavity of the mouthpiece model is shown in Fig. 1. To characterize the chamber and throat, we define parameters that describe their cross-sectional dimensions and shapes. Specifically:

- the heights of the cross-sections are denoted as s_c (chamber) and s_t (throat);
- the shape radii are denoted as r_c (chamber) and r_t(throat), which determine the curvature of the cross-sections by adjusting the fillets.

For the baffle, the parameter α is introduced to represent the angle of its inclination. A lower value of α corresponds to a narrower mouthpiece, and a larger baffle is typically associated with a brighter and more focused sound. In contrast, a larger α results in a wider mouthpiece and a lower baffle, often producing a darker and warmer tone.

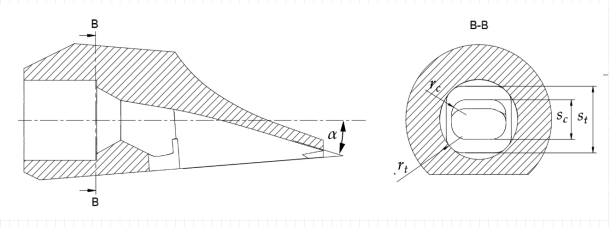


Figure 1: Scheme of the saxophone mouthpiece geometry. The left diagram shows a longitudinal cross-section highlighting the baffle angle α and internal cavity design, while the right diagram depicts the transverse cross-section (B-B plane) illustrating the chamber and throat dimensions s_c, s_t and their respective shape radii r_c, r_t.

It is important to recognize that the geometric parameters are constrained by the physical interfaces with other saxophone components, particularly the neck and the reed. Features such as the table, lay, tip opening, tip rail, and side rails must remain fixed to ensure compatibility with the wide variety of commercially available reeds. These constraints were explicitly integrated into the model to ensure that all generated geometries remain practical and compatible with standard saxophone configurations, preserving usability across a wide range of instruments and performance setups.

3. TRANSFER MATRIX METHOD

To describe the acoustic characteristics of the mouthpiece model, we employ the Transfer Matrix Method (TMM) introduced in [15]. The TMM is widely used in the study of wind instrument resonators (e.g., [11, 16, 17]), and is based on two-port acoustic theory. This theory models the reference acoustic system as a linear network with interconnected two-port elements, following the framework outlined in [15].

Specifically, a region between two ports is treated as a "black box" characterized by a 2×2 transfer matrix $\mathbf{T}(\omega)$, expressed as

$$\mathbf{T}(\omega) = \begin{bmatrix} T_{11}(\omega) & T_{12}(\omega) \\ T_{21}(\omega) & T_{22}(\omega) \end{bmatrix}, \tag{1}$$

such that the relationship between the input and output

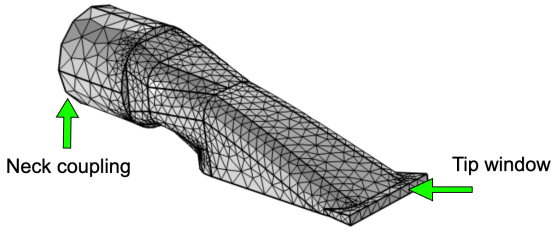


Figure 2: Finite element (FE) mesh of the saxophone mouthpiece used for acoustic analysis. The green arrows indicate the positions of the input and output ports, where acoustic pressure and volume velocity (P_i, U_i, P_o, U_o) are measured for transfer matrix derivation.

acoustic variables is given by:

$$\begin{bmatrix} P_o(\omega) \\ U_o(\omega) \end{bmatrix} = \mathbf{T}(\omega) \begin{bmatrix} P_i(\omega) \\ U_i(\omega) \end{bmatrix}. \tag{2}$$

Here, $\omega = 2\pi f$ is the angular frequency (in rad/s), while $P_i(\omega)$, $U_i(\omega)$ and $P_o(\omega)$, $U_o(\omega)$ represent the input and output acoustic pressure (in Pa) and volume velocity (in m³/s), respectively.

The transfer matrix of the mouthpiece is derived under the assumptions of linearity and passivity, which are valid when the sound source is decoupled from the mouthpiece. The reed's vibration is excluded, allowing the excitation and the nonlinearity to be modeled independently. Only propagating modes are considered, with a plane wave at the input and negligible output discontinuities. In addition, internal discontinuities are assumed to be far enough from the output plane to avoid interference. In Fig. 2 the positions of the input and output ports are shown in an example model. To derive $\mathbf{T}$, the two-load method proposed in [15] is employed. Then the following matrix equation can be solved to obtain the four terms of the TM

$$\begin{bmatrix} P_o^1 & Z_o^c U_0^1 & 0 & 0 \\ 0 & 0 & P_0^1 & Z_o^c U_o^1 \\ P_o^2 & Z_o^c U_o^2 & 0 & 0 \\ 0 & 0 & P_o^2 & Z_o^c U_o^2 \end{bmatrix} \begin{bmatrix} T_{11} \\ T_{12} \\ T_{21} \\ T_{22} \end{bmatrix} = \begin{bmatrix} P_i^1 \\ Z_i^c U_i^1 \\ P_i^2 \\ Z_i^c U_i^2 \end{bmatrix}, \tag{3}$$

where we dropped the argument ω for readability, and the superscripts 1 and 2 represent two different boundary conditions, with the loads set as a theoretical unflanged radiation impedance and the characteristic impedance, respectively.

4. DATASET CREATION

To generate a comprehensive dataset of mouthpiece parameters, we design the parametric model of the air cavity using COMSOL Multiphysics.

For our dataset, we generated five uniformly distributed values for each of s_c, s_t, and α within the predefined ranges shown in Table 1. To represent various cross-sectional shapes of the chamber, we computed three values for r_c and r_t relative to s_c and s_t using scaling factors that correspond to square, medium-smooth, and circular shapes. These parameter ranges and values, derived from [14], were informed by an analysis of the geometric characteristics of widely used commercial mouthpieces.

By combining these parameters, we obtained a dataset consisting of 1125 unique mouthpiece models. Each combination represents a plausible design variation in terms of throat and chamber shapes, as well as baffle inclinations. As an example, Fig. 3 illustrates four different mouthpiece models generated using this approach. These models demonstrate the impact of parameter variations on the throat and chamber cross-sections and the angle of the baffle.

Parameters	***Ranges Values***
s_c	[6.0 : 8.5] [mm]
s_t	[6.0 : 8.0] [mm]
α	[-5 : 25] [deg]
r_c	[0.05, 0.5, 1] $\times$ s_c
r_t	[0.05, 0.24, 0.49] $\times$ s_t

Table 1: The ranges or values of the selected geometric parameters. Five values in the ranges show in the table are randomly generated for s_c, s_t and α. Three different values with respect to each related cross section radii are generated for r_c and r_t.

4.1 Geometry Refinement

When musicians play the saxophone, it is common practice to adjust the depth of insertion of the mouthpiece into the neck to fine-tune the pitch. This mechanical coupling is critical for achieving proper intonation. To replicate this tuning behavior in our simulations, we adjust the length of

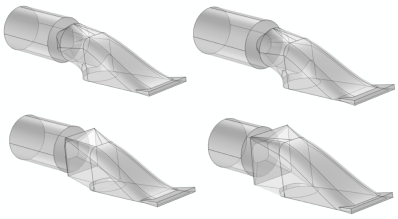


Figure 3: Four different parametric mouthpiece models obtained by different combinations of values of the selected parameters.

the coupling tube using a lumped acoustic model, ensuring that the system accurately reflects the tuning conditions.

The input impedance of the cylindrical equivalent of the mouthpiece is defined as $Z(\omega) = \frac{1}{\iota\omega\frac{\rho c^2}{V_m}}$ [15], where ι is the imaginary unit and V_m is the total volume. This relationship shows that maintaining a consistent volume of the mouthpiece in different models helps to preserve a similar resonance frequency. To match the neck diameter of the saxophone (1.7[cm] as measured on a Selmer Series III), the radius of the neck coupling's cross-section is fixed. Thus, to maintain the same volume of the mouthpiece, we adjust the length of the coupling tube accordingly.

4.2 FEM Simulation

Simulations are performed using COMSOL Multiphysics® software, employing the Pressure Acoustics, Frequency Domain finite element method (FEM) [18] to model the acoustic behavior of the air column within the saxophone mouthpiece. The accuracy and computational efficiency of this approach for wind instrument modeling have already been validated in previous studies [15].

As detailed in Section 3, two simulation scenarios are performed by applying distinct boundary conditions at the output: one with unflanged radiation impedance and the other with characteristic impedance. This setup enables the extraction of the elements of the transfer matrix necessary for subsequent acoustic analysis. A 1kPa pressure source is applied at the input tip window of the mouthpiece, depicted in Figure 2. The studied frequency range is [10,8000] Hz with a step of 50 Hz. The maximum mesh element size is $c/f_{max}/5$, with f_{max} the highest frequency.

We then extracted the TMs from the FEM simulations by solving (3), resulting in $\bar{\mathbf{T}} = [T_{ij}^{(\ell)}(\omega)] \in \mathcal{C}^{159\times1125\times4}$, where 159 is the number of sampled frequencies ω, 1125 is the number of geometry models ℓ, and we stacked them in 4 elements ij of TM $\mathbf{T}$ in (1). The obtained dataset is available at `https://kaggle.com/datasets/6c7d1b3c947d395b6d7954f9a628294e262baff0a7bee454bb119e8545ce9476`.

5. DATA-DRIVEN RECONSTRUCTION

5.1 Feedforward Neural Networks

We employed four Feedforward Neural Networks (FNN) to model the relationships between the geometric parameters and the four corresponding TM terms. The input consists of $\mathbf{x} = [s_c, s_t, \alpha, \frac{r_c}{s_c}, \frac{r_t}{s_t}]^\top \in \mathbb{R}^5$. To reduce the dimensionality of the neural network output, inspired by the approach discussed in [15], we used 10th-order Chebyshev polynomial coefficients for $\mathbf{T}$, resulting in 11 complex parameters arranged in a vector $\mathbf{p}_{ij}^{(\ell)}$. An example comparing $\mathbf{T}$ with its reconstruction from the polynomial approximation is presented in Fig. 4, demonstrating a good alignment and providing confidence in the accuracy of the polynomial fitting. For each neural network ij, the output is designed as $\mathbf{y}_{ij} = [\Re(\mathbf{p})^\top, \Im(\mathbf{p})^\top]^\top \in \mathcal{R}^{22}$, obtained by first converting $\mathbf{P}$ into a real-valued representation. The resulting vector is then normalized using the mean value across various mouthpiece models in the training dataset. Thus, given a set of geometric measurements $\mathbf{x}$, the ijth FNN must output a corresponding set of staked Chebyshev polynomial coefficients $\mathbf{y}_{ij}$ to define the ijth entry function of TM $\mathbf{T}(\omega)$.

Indeed, the dataset is divided into training, validation, and test sets with proportions of 70%, 15%, and 15%, respectively. This ensures that the model is not only trained effectively, but also evaluated for generalization on unseen data. The employed FNN architecture is shown in Fig. 5, featuring a single hidden layer with 10 neurons. The $\tanh$ activation function is used in the hidden layer to introduce nonlinearity, while no activation function is applied to the output layer. The loss function is defined as the mean squared error (MSE) between the neural network output and the exact target values $\mathbf{Y}$. The Levenberg-Marquardt backpropagation algorithm was utilized for optimization. The *MATLAB Deep Learning Toolbox* is used for the implementation.

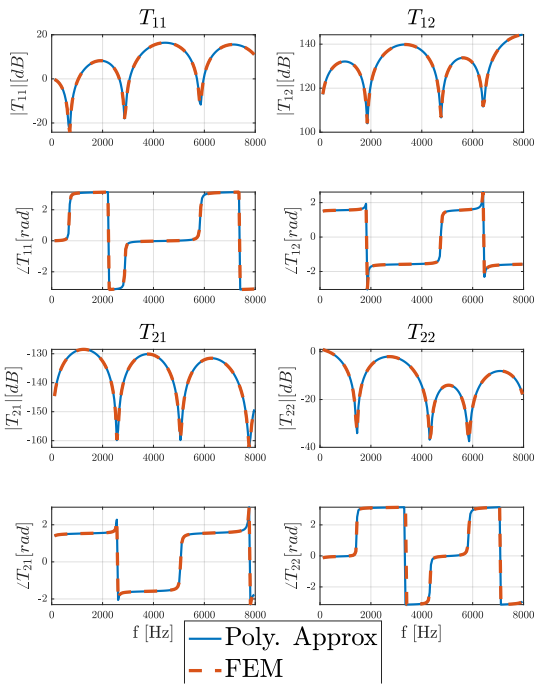


Figure 4: An example of magnitude and phase of TMs $\mathbf{T}$, comparing FEM and polynomial approximation results.

5.2 Linear Regression

As a comparison with the proposed data-driven method, we use a linear regressor. The linear regression assumes that the relationship between the dependent variable $\mathbf{Y}$ and the independent variable $\mathbf{X} = [\mathbf{x}]_\ell \; \forall \ell \in$ Training set (described in 5.1) can be expressed as

$$\mathbf{Y} = \mathbf{X}\beta + \varepsilon, \tag{4}$$

where β is the vector of regression coefficients; $\varepsilon \in \mathbb{R}^{n\times 1}$ is the vector of random errors, assumed to follow a normal distribution with zero mean and constant variance.

The vector of coefficients β can be estimated as

$$\hat{\beta} = (\mathbf{X}^T\boldsymbol{X})^{-1}\mathbf{X}^T\mathbf{Y}. \tag{5}$$

6. RESULTS

6.1 Closed Mouthpiece and Coupled System

The input impedance of the mouthpiece with a closed termination can be determined by setting the end impedance to infinity and evaluating it using the mouthpiece TM. Furthermore, to assess the influence of the mouthpiece on the saxophone body, we model the main bore of the saxophone as a truncated cone and couple it with the mouthpiece. The truncated conical resonator has an input radius of $8.05\,\mathrm{mm}$, which is equal to the radius of the mouthpiece neck coupling. The apex angle is $0.035\,\mathrm{rad}$, and the truncated cone length is $0.72\,\mathrm{m}$, which is aligned with the study in [19]. The input impedance is then derived accordingly with the unflanged radiation condition at the output. The elements of the transfer matrix for the truncated conical duct, $\mathbf{T}^{cone}$, are determined by Equation (5) in [20].

6.2 Metrics

To evaluate the performance of the proposed method, we employ three different metrics that are typically used in the literature [15]: the Normalized Mean Square Error (NMSE), the Frequency Shift (FS), and the coefficient of determination R^2.

Given a generic impedance Z_A and a ground truth impedance (i.e. Z_{FEM}) the NMSE of Z_A is defined as

$$\mathrm{NMSE}(Z_A) = ||Z_A - Z_{\mathrm{FEM}}||^2/||Z_{\mathrm{FEM}}||^2, \tag{6}$$

such that the discrepancy between estimated and reference impedance is quantified. FS expresses the deviation between the peak frequencies of two different functions and is defined as

$$\mathrm{FS}_k(Z_A) = |f_k(Z_A) - f_k(Z_{\mathrm{FEM}})|/f_k(Z_{\mathrm{FEM}}), \tag{7}$$

where k denotes the peak index and $f_k(\cdot)$ represents the resonance frequency of the magnitude peak of the given argument.

The coefficient of determination R^2 is used to evaluate the prediction accuracy. It is defined as

$$R^2 = 1 - \frac{\mathrm{SS}_{\mathrm{res}}}{\mathrm{SS}_{\mathrm{tot}}}, \tag{8}$$

where $SS_{\mathrm{res}} = \sum_{n=1}^{N}(y_n - \hat{y}_n)^2$, y_n is the value of the dependent variable for observation n, $\hat{y}_n$ is the predicted value from the model for observation n, $SS_{\mathrm{tot}} = \sum_{n=1}^{N}(y_n - \bar{y})^2$, and $\bar{y}$ is the mean of the observed values of y. R^2 values range from 0 to 1, with values closer to 1 indicating a better fit of the model to the data.

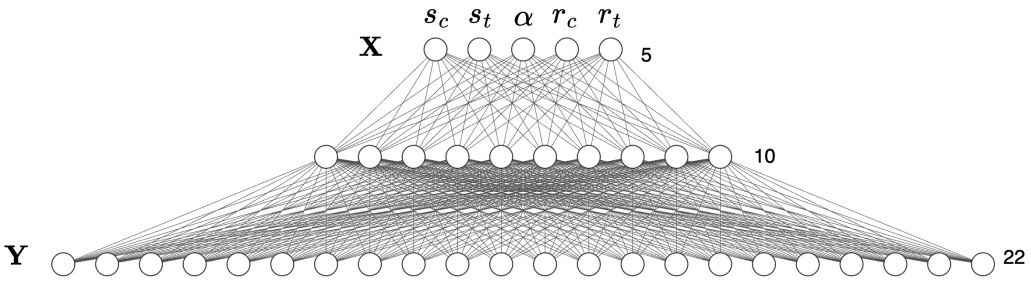


Figure 5: FNN architecture designed for modeling a single TM term.

6.3 Discussion

Performance metrics for input impedance predictions using both the FNN and linear regression models are summarized in Table 2. In all cases, the FNN consistently outperforms linear regression. Furthermore, Fig. 7 presents the coefficient of determination (R^2) for the input impedance of the coupled system, confirming the superior predictive accuracy of the FNN model.

An example of the input impedance comparison is shown in Fig. 6, where the FNN predictions closely match the FEM results, while linear regression exhibits notable deviations. These results reveal the presence of a nonlinear relationship between the mouthpiece geometric parameters and the corresponding TM elements. This underscores the importance of employing nonlinear models to adequately capture the relations between the geometric model parameters and the acoustic response.

	FNN	Linear
NMSE($\lvert Z_{in,\text{coupled}}\rvert$) [dB]	**-55.6**	-39.9
NMSE($\lvert Z_{in}\rvert$) [dB]	**-81.1**	-57.1
$\text{FS}_1(Z_{in})$ %	**0.36**	4.10
$\text{FS}_2(Z_{in})$ %	**0.24**	0.42
$\text{FS}_3(Z_{in})$ %	**0.36**	2.07
$\sum_{k=1}^{3} \text{FS}(Z_{in})/3$ %	**0.32**	2.19

Table 2: Comparison of performance metrics for FNN and Linear models, including NMSE and FS averaged for all the test dataset results.

7. CONCLUSION

In this study, we construct a synthetic dataset using a parametric model of saxophone mouthpieces that results in 1125 different designs. We consider the parameters related to the internal airflow cavity: the cross-section heights and radii of chamber and throat, and the angle of baffle inclination. The TMs of these models are then retrieved using the Finite Element Method (FEM). Additionally, a truncated cone is coupled with the parametric mouthpieces to serve as a simplified representation of the main bore of the saxophone. The acoustical influence of the mouthpiece is investigated on the basis of the input impedance spectra, which highlights the mouthpiece emphasis or modulation effect. Moreover, comparative analyses of the input impedance spectra reveal potential underlying relationships between the mouthpiece parameterization and the characteristics of the instrument. The presented dataset has significant potential for further research on the acoustic behavior of saxophone mouthpieces and sound generation. These studies can contribute to advances in the design of saxophone mouthpieces.

8. ACKNOWLEDGMENTS

We would like to acknowledge the Multilayered Urban Sustainability Action (MUSA) project, which is funded by the European Union, for their contributions to this work.

9. REFERENCES

[1] S. Carrala, V. Lorenzonib, and J. Verlindenc, "Influence of mouthpiece geometry on saxophone playing," *Proceedings of the Third Vienna Talk on Music Acoustics*, vol. 16, p. 19, 2015.

[2] A. H. Benade, *Fundamentals of musical acoustics*. Courier Corporation, 1990.

[3] V. R. Hasbrook, *Alto saxophone mouthpiece pitch and its relation to jazz and classical tone qualities*. PhD

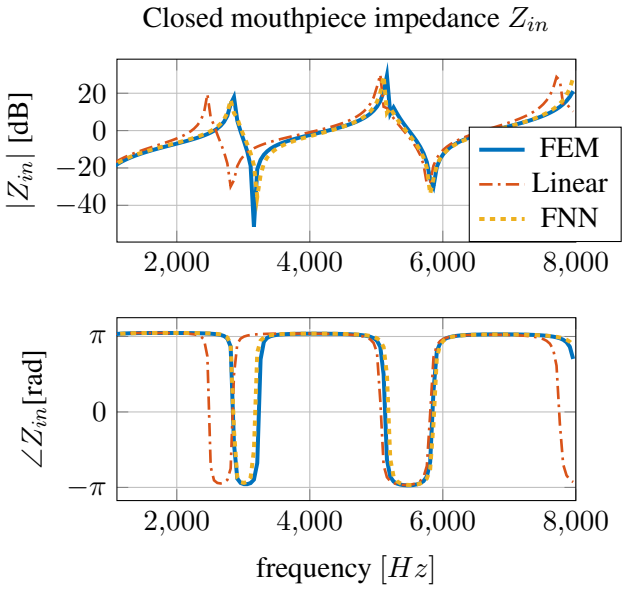


Figure 6: Example of input impedance magnitude (top) and phase (bottom) for the closed mouthpiece configuration. Results from the FEM simulation are shown alongside predictions from the linear regression model and the FNN. The FNN closely replicates the FEM results across the frequency range, while the linear model exhibits significant deviations, particularly around resonance and anti-resonance frequencies.

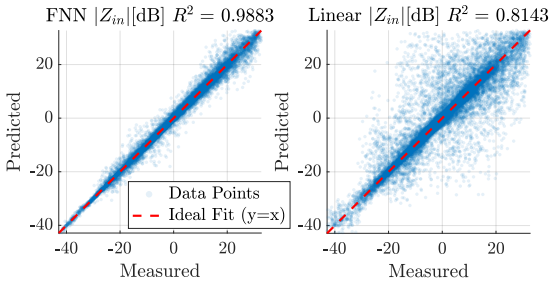


Figure 7: Comparison of predicted versus measured input impedance magnitudes (in dB) for the FNN, left and linear regression model (right) across all mouthpiece geometries. The FNN demonstrates a significantly higher coefficient of determination ($R^2 = 0.9883$), closely aligning with the ideal $y = x$ reference (red dashed line), while the linear model exhibits reduced accuracy ($R^2 = 0.8143$) and greater dispersion from the ideal fit.

thesis, University of Illinois at Urbana-Champaign, 2005.

[4] V. Lorenzoni and D. Ragni, "Experimental investigation of the flow inside a saxophone mouthpiece by particle image velocimetry," *The Journal of the Acoustical Society of America*, vol. 131, no. 1, pp. 715–721, 2012.

[5] S. Wang, G. Scavone, and E. Maestre, "Two methods for acoustic modeling of the saxophone mouthpiece," *The Journal of the Acoustical Society of America*, vol. 148, pp. 2611–2611, 10 2020.

[6] J. Kergomard, P. Guillemain, P. Sanchez, C. Vergez, J.-P. Dalmont, B. Gazengel, and S. Karkar, "Role of the resonator geometry on the pressure spectrum of reed conical instruments," 2019.

[7] A. Ricardo da Silva, G. P. Scavone, and M. van Walstijn, "Numerical simulations of fluid-structure interactions in single-reed mouthpieces," *The Journal of the Acoustical Society of America*, vol. 122, no. 3, pp. 1798–1809, 2007.

[8] T. Yoshinaga, H. Yokoyama, T. Shoji, A. Miki, and A. Iida, "Global numerical simulation of fluid-structure-acoustic interaction in a single-reed instrument," *The Journal of the Acoustical Society of America*, vol. 149, no. 3, pp. 1623–1632, 2021.

[9] D. G. Badiane, S. Gonzalez, R. Malvermi, F. Antonacci, and A. Sarti, "A neural network-based method for spruce tonewood characterization," *The Journal of the Acoustical Society of America*, vol. 154, no. 2, pp. 730–738, 2023.

[10] J.-F. Petiot, M. Roatta, V. Fréour, and K. Arimoto, "Contribution of machine learning and physics-based sound simulations for the characterization of brass instruments," in *Forum Acusticum 2023*, 2023.

[11] G. P. Scavone, "A tutorial on the transfer matrix

method for acoustic modeling," *Journal of the Acoustical Society of America*, vol. 149, 2021.

[12] V. Lorenzoni, E. Doubrovski, and J. Verlinden, "Embracing the digital in instrument making: Towards a musician-tailored mouthpiece by 3d printing," pp. 419–424, s.n., 2013.

[13] F. S. Wyman, *An acoustical study of alto saxophone mouthpiece chamber design*. University of Rochester, 1972.

[14] M. Ozdemir, V. Chatziioannou, J. Verlinden, G. Cascini, and M. Pàmies-Vilà, "Towards 3d printed saxophone mouthpiece personalization: Acoustical analysis of design variations," *Acta Acustica*, vol. 5, p. 46, 2021.

[15] S. Wang, E. Maestre, and G. Scavone, "Acoustical modeling of the saxophone mouthpiece as a transfer matrix," *The Journal of the Acoustical Society of America*, vol. 149, no. 3, pp. 1901–1912, 2021.

[16] A. Dell, A. Krynkin, and K. Horoshenkov, "The use of the transfer matrix method to predict the effective fluid properties of acoustical systems," *Applied Acoustics*, vol. 182, p. 108259, 2021.

[17] K. Verdière, R. Panneton, S. Elkoun, T. Dupont, and P. Leclaire, "Prediction of acoustic properties of parallel assemblies by means of transfer matrix method," *Proceedings of Meetings on Acoustics*, vol. 19, p. 065011, 05 2013.

[18] O. C. Zienkiewicz and P. Morice, *The finite element method in engineering science*, vol. 1977. McGraw-hill London, 1971.

[19] J.-B. Doc, C. Vergez, P. Guillemain, and J. Kergomard, "Sound production on a "coaxial saxophone"," *The Journal of the Acoustical Society of America*, vol. 140, no. 5, pp. 3917–3924, 2016.

[20] A. Lefebvre, G. P. Scavone, and J. Kergomard, "External tonehole interactions in woodwind instruments," *Acta Acustica united with Acustica*, vol. 99, no. 6, pp. 975–985, 2013.

DOI:

Main theme: A11 Musical Acoustics

Session A11.03 Consistency of musical instrument making

Chair(s): L. Ausiello, J.-P. Dalmont

DOI: 10.61782/fa.2025.0361

FORUM ACUSTICUM EURONOISE 2025

EVALUATING THE REPRODUCIBILITY OF IMPEDANCE MEASUREMENTS OF WIND INSTRUMENTS

Jean-Pierre Dalmont[1*] **Ernoult, Augustin**[2] **Cabaret, Jérémy**[3]
Boutin, Henri[4] **Colinot, Tom**[5] **Freour, Vincent**[6] **Viala, Romain**[7]
[1] Laboratoire d'Acoustique LAUM UMR CNRS, Le Mans Université, France
[2] Sorbonne Université and Inria Paris, CNRS, Institut Jean Le Rond d'Alembert, Lutheries-Acoustique-Musique team, Paris, France
[3] Itemm, 71 avenue Olivier Messiaen, Le Mans, France
[4] Sorbonne Université and IRCAM, STMS UMR CNRS, Paris, France
[5] Buffet Crampon, Mantes-la-Ville, France
[6] Yamaha Corporation, Research and Development Division, Hamamatsu, Japan
[7] Université Marie et Louis Pasteur, Femto-st UMR CNRS, Besançon, France

ABSTRACT

Input impedance is a physical quantity that allows the objective characterization of wind instruments. It is now a common measurement in research labs and wind instrument factories. To be relevant, these measurements must achieve a precision higher than what a musician can detect. Although the sensitivity of musicians to slight impedance variations is not known, it is important to have an idea of the precision of impedance measurements in realistic situations. In order to evaluate the accuracy and different type of variability (e.g.: intra- and inter-operator) of impedance measurements and to identify key sources of error in the process, a collaborative study has been conducted involving multiple operators using the experimental setups developed by the CTTM. Measurements were performed on simple pipe geometries, including cylindrical, with a focus on boundary conditions, material properties, and calibration procedures. Variability in experimental results is linked to the calibration steps, the pipes manipulation, and challenges with wall surfaces, particularly in wooden pipes. The study also revealed significant inter-operator variability and emphasizes the importance of rigorous calibration procedures and standardized measurement practices. These findings provide actionable insights for enhancing the reliability of experimental methods and support further research into more complex and realistic geometries.

Keywords: *wind instrument, input acoustic impedance, metrology.*

1. INTRODUCTION

Input impedance measurements of wind instruments are now commonly used tools in research laboratories and wind instrument manufacturing companies [1-3]. This tool can be used both during the prototyping phase of an instrument and for manufacturing control. However, the question of the accuracy that can be expected from such tools has rarely been asked. The objective of this work is therefore to provide quantitative elements on this accuracy and compare it with the accuracy that can be achieved in machining. This work focuses on the sensor developed jointly by LAUM and CTTM (now Almacoustic) [4].

To assess measurement uncertainty, standards are required. These standards are cylindrical tubes for which the errors related to the theoretical model are significantly lower than the uncertainties expected with the measurement. A number of tubes were manufactured in different materials and in multiple copies. Different operators with different sensors measured the different tubes several times, which allowed the repeatability uncertainty of each operator to be assessed,

[*] ***Corresponding author:*** *jean-pierre.dalmont@univ-lemans.fr.*

***Copyright**: ©2025 First author et al. This is an open-access article distributed under the terms of the Creative Commons Attribution 3.0 Unported License, which permits unrestricted use, distribution, and reproduction in any medium, provided the original author and source are credited.*

as well as the uncertainties related to the operators. Sample variability could also be assessed and compared with the measurement uncertainties.

2. THE SAMPLE PANEL

Tubes in different materials have been fabricated with a target length of 180mm and a target inner diameter of 14mm. Each sample consists of five specimens, so that measurements can be compared with simulations, taking into account manufacturing uncertainties. The three materials chosen for the cylinders are brass, boxwood, and Acrylonitrile Butadiene Styrene (ABS), a common polymer used in 3D printing.

After manufacturing, the actual geometrical parameters are measured with a ruler for the length and a telescopic gauge and caliper for the internal diameter (the wall thickness being deduced from internal and external diameters). The mean μ and standard deviation σ_{tot} of each dimension is given for each type of sample in Table 1. The standard deviations are estimated from the measurement tools resolutions (0.5 mm for the ruler and 0.1 mm for the caliper) and the measured variability. The same pipes are used for the open (O) and closed (C) conditions, using 3D-printed caps for the closed conditions and grease for the airtightness.

Table 1 Samples dimensions

Material	**Length** (mm)	**Diameter** (mm)
Brass	180.0 ± 0.3	13.92 ± 0.03
Wood	179.9 ± 0.65	13.97 ± 0.07
ABS	179.85 ± 0.3	14.03 ± 0.09

From Table 1, it appears that the brass tube sample is the most uniform. The boxwood sample, made by hand, has the largest length deviation, and the 3D printed samples have the largest wall thickness variation. The temperature (°C) and relative humidity (%) have been also measured to apply corrections on the speed of sound in the post processing step. The scientific sensors have generally a great precision (0.1°C and 1%), however due to possible air heterogeneity between the measured point and the air inside the tube the uncertainty on the speed of sound may remain large and might lead to rather large deviation between experiments made in different conditions.

3. MEASUREMENTS

The Measurements have been performed with impedance sensors produced by the CTTM [4]. This device necessitates one calibration step (measurement of a cap with an "infinite" impedance) and has a 16 mm output diameter. Logarithmic sine sweep which frequency range was 100-4000 Hz. Most of operators (2 to 4) attached the tubes to the impedance head with a connector printed in flexible material (thermoplastic polyurethane, TPU) to facilitate their alignment and to deal with small external diameter variations between specimens. Operator 5 preferred to place the tube by hand. The quality of the impedance measurement strongly depending on the air tightness at the contact between the impedance head and the sample, cork grease (for Wind instruments) has been used at this junction (or clay for O5). For a batch of five tubes, the measurements have been repeated five times for a given tube, the first one, to estimate the intra specimen variability for a given tube. Then, the four remaining tubes have been measured to estimate the inter specimen variability. Each batch has been measured this way for closed-closed and closed-opened boundary conditions. The complete protocol being time consuming, some experimenters have focused on some configurations (at least closed cylinders), but by measuring all the requested repetitions (intra + inter = 9). It is specified that operator 4 didn't measure the tube in the open configuration. Each operator was free to redo some measurements using his/her own criteria.

4. RESULTS

In this section, the reference values used to display the observables are taken from the calculation of the analytical solution for the closed cylinder [5-6]. All these simulations have been calculated for the average geometry of each sample (Table 1).

Both sound velocity and air density depend on air temperature T and relative humidity RH. This dependence affects the magnitude of the impedance and shifts the frequency axis. The calibration steps naturally scale the obtained data by the lossless characteristic impedance Z_c, removing the main magnitude dependence. However, in order to compare the data, it is necessary to correct the effect on the frequency axis, by applying to frequency a correction factor $c_{25}/c_{T,RH}$ where c_{25} is the speed of sound in dry air at 25°C and $c_{T,RH}$ is the speed of sound during the measurement taking into account temperature value and relative humidity.

Frequency and amplitude deviations from theory of first four maxima and minima of the input impedance are

analyzed. The deviations are expressed in cents for the frequencies, that is $1200\log_2(f_{meas}/f_{theo})$, and in dB for the amplitude, that is $20\log_{10}(Z_{meas}/Z_{theo})$.

4.1 Measurements of a single brass tube

In this section the modal characteristics of a single closed brass tube are analysed. Results are shown in Figure 1. For each operator and each configuration, the standard deviation of each observable is computed along the five measurements on the same specimen. These deviations do not seem to be related to the absolute frequency of the peak. For most operators, the deviations are even similar for all "resonances" (max amplitude) and for all "anti-resonances" (min amplitude). This suggest that deviation are related to small temperature or geometrical variations.

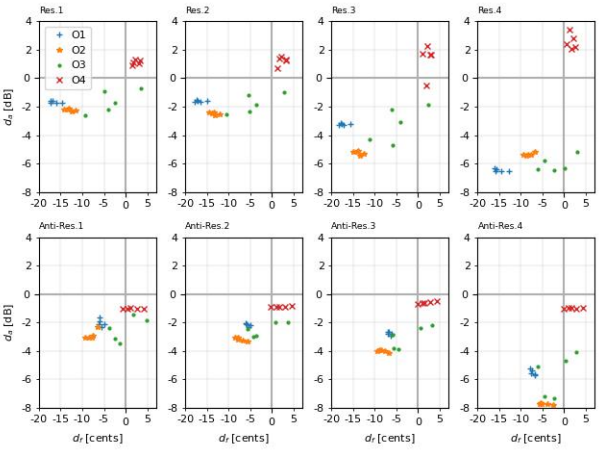


Figure 1. Deviation to the reference values of the frequency (d_f in cents) and magnitude (d_a in dB) of the 4 resonances and 4 anti-resonances, for the 5 repeated measurement of a given closed Brass cylinders. Each operator is associated to a marker shape and a color.

A result is that intra operator (same operator) deviations are much lower than inter operator deviations. Indeed, the standard deviation for all peaks and dips is less than 2 cents for operators 1, 2 and 4 and less than 4 cents for operator 3 for frequency and for amplitude it is 0.3 dB pour operator 1 et 2, 1 dB pour operator 4 et 1.5dB pour op. 3. This corresponds to the value obtained in previous studies [1-3]. The deviations between operators are much larger since it is around 10 cents in frequency and 2 dB in amplitude. The large difference for the amplitude is probably due to the difficulty to ensure a perfect closure of the tube since it is observed that the deviations are lower when the tube is open (1dB).

The origin of the inter-operator deviations is difficult to pinpoint. It can be due to a biased estimation of the temperature in the tube, a different placement of the sample on the sensor or differences between sensors. In practice to explain a 10 cents deviation a 3°C error on the temperature or a 1mm error on the tube length are needed. This deviation could also come from a deviation between sensors. To test this hypothesis, an operator measured the same pipe with five different sensors. This experiment being carried out a posteriori, a different tube has been used (about 1 m long and a 20 mm inner diameter). The obtained standard deviation between the sensors is about 3 cents and 0.5 dB. This is similar to the intra-specimen variability which suggests that the difference between the sensors cannot alone explain the inter-operator variability. The inter-operator variability is certainly due to the conjunction of multiples factors.

4.2 Measurements of various tubes

In order to compare the variability linked to manufacturing processes and the uncertainties of impedance measurement various tube have machined and their impedance measured (see table 1). It appears that the inter-specimen deviations are in the range or larger than the intra-operator variability. For 3D printed and brass tubes deviations in frequency cannot be assessed while for wooden tube significant deviation can be detected. Also, significant amplitude deviations can be detected for the wooden and 3D printed tubes. This validates the fact that the impedance measurement is capable of detecting small machining variations. However, this is only possible if measurements are performed by the same operator in the same experimental conditions.

Table 2 Median value over all operators of the inter-specimen standard deviation (open tubes)

Standard deviation	Brass	3D	Wood
Frequency (cents)	3	4	8
Amplitude (dB)	0.2	0.5	1.3

5. CONCLUSION

It appears that input impedance measurements – at least with the sensor we used - allow the determination of eigenfrequencies with a relative accuracy of about 3 cents

on frequency and 0.5 dB on amplitude. This means that it is possible to detect differences between two instruments as small as this provided that both instruments are measured under the same conditions. Measurements with different sensors and different operators suggest that below 10 cents and 1 dB it would be doubtful to conclude that the deviations betray a significant difference between the measured instruments. It can be estimated that the absolute accuracy of the measurements is of this same order of magnitude as long as the measured impedances are adapted to the sensor used. Here, the sensor has an input diameter of 16 mm and the measured tubes have a diameter of 14 mm. In the case of significantly narrower or wider tubes, the absolute errors will a priori be larger.

In another work, the sensor will be used to evaluate the accuracy obtained on the input impedance calculated from numerical models. It should be possible to assess if models can reach an accuracy of less than 5 cents on eigenfrequencies.

A question remains open: to what extent is a musician able to detect a difference between two similar instruments? This question has been little explored [2, 3] and the answer to this question will obviously depend on the instrument considered. We find an example in reference [2]: on saxophone necks, measurements were able to unambiguously highlight differences of the order of 8 cents on the first eigenfrequency. For his part, the musician tester was able to distinguish without difficulty the necks which had the lowest frequencies. Are musicians able to be more accurate than impedance measurements? The question remains open.

6. REFERENCES

[1] A. Guilloteau, Conception d'une clarinette logique. PhD thesis, Aix-Marseille Université, Marseille, France, 2015.

[2] M. Jeanneteau, Modélisation numérique d'un instrument de musique à vent réel et confrontation à la mesure expérimentale. PhD thesis, Université de Toulouse, France, 2025.

[3] V. Fréour, L. Guillot,H. Masuda, S. Usa,E. Tominaga, Y. Tohgi, Ch. Vergez and B. Cochelin. Numerical continuation of a physical model of brass instruments: Application to trumpet comparisons. J. Acoust. Soc. Am., 148(2), pp. 748–758, 2020.

[4] C. A. Macaluso and J. P. Dalmont, Trumpet with near-perfect harmonicity: Design and acoustic results. J. Acoust. Soc. Am. 129(1), pp 404–414, 2011.

[5] A. Chaigne and J. Kergomard, Acoustics of Musical Instruments. Modern Acoustics and Signal Processing, New York: Springer, 2016.

[6] D. H. Keefe, Acoustical wave propagation in cylindrical ducts: Transmission line parameter approximations for isothermal and non-isothermal boundary conditions. J. Acoust. Soc. Am., 75, pp. 58–62, 1984.

DOI: 10.61782/fa.2025.0150

FORUM ACUSTICUM EURONOISE 2025

ASSESSING THE CONSISTENCY OF NUMERICAL MODELS FOR WIND INSTRUMENT IMPEDANCE

Augustin Ernoult[1*] **Jérémy Cabaret**[2] **Juliette Chabassier**[3]
Tom Colinot[4] **Jean-Pierre Dalmont**[5] **Jean-Baptiste Doc**[6]
Vincent Fréour[7] **Romain Viala**[8]

[1] Sorbonne Université and Inria Paris, CNRS, Institut Jean Le Rond d'Alembert, LAM team, 75005 Paris, France
[2] Institut Technologique Européen des Métiers de la Musique, ITEMM, 71 avenue Olivier MESSIAEN, 72000 Le Mans, France
[3] Modartt, 9 avenue de l'Europe, Bâtiment B18, 31520 Ramonville Saint Agne, France
[4] Buffet Crampon, 5 Rue Maurice Berteaux, 78711 Mantes-la-Ville, France
[5] Laboratoire d'Acoustique de l'Université du Mans UMR CNRS 6613, Le Mans Université, 72085 Le Mans, France
[6] Conservatoire National des Arts et Métiers, 292 rue Saint-Martin, 75141 Paris Cedex 03, France
[7] YAMAHA Corporation, Research and Development Division, 10-1 Nakazawacho, Hamamatsu, 430-8650 Shizuoka
[8] Department of Applied Mechanics, Université de Franche-Comté, CNRS, Institut FEMTO-ST, F-25000 Besançon, France

ABSTRACT

Numerical simulation of the input impedance of wind instruments is the basis of much work in music acoustics. However, the accuracy and reproducibility of such simulations across different contributors remain little documented. This study aims to benchmark the reliability of numerical simulations for pipe impedance, focusing on simple geometries such as cylindrical and conical pipes, and to identify key factors influencing simulation variability. A collaborative approach was adopted, involving multiple contributors employing various numerical models, including TMM, FEM (1D or 3D), etc., and eventually different physical models for the propagation, the boundary conditions, and the thermo-viscous effects. Significant variability in simulation results was observed due to differences in implementation, numerical precision, and boundary condition modelling. Incomplete convergence in some methods also contributed to discrepancies. Despite these challenges, the collaborative work and exchanges reduced variability and improved consistency across contributors. The study highlights the importance of such benchmark and the interest to adopt good practices including verification of the numerical tools through comparative analysis and identification of convergence criteria. This work provides a framework for improving the reproducibility an accuracy of numerical simulations in musical acoustics context.

*__Corresponding author__: *augustin.ernoult@inria.fr.*
__Copyright__: *©2025 Ernoult et al. This is an open-access article distributed under the terms of the Creative Commons Attribution 3.0 Unported License, which permits unrestricted use, distribution, and reproduction in any medium, provided the original author and source are credited.*

Keywords: *wind instrument, impedance, simulation benchmark, linear acoustics*

1. INTRODUCTION

The input impedance of wind instruments is a fundamental quantity in musical acoustics. It serves as a basis for most physical modeling approaches, including sound synthesis, time-domain simulations, automatic design, etc. In practice, researchers often implement their own numerical models to compute this quantity, adapting them to the specific constraints of the studied objects or their research objectives.

However, the development of a new numerical model can introduce several sources of inaccuracy: the omission of physical phenomena that may significantly affect results (e.g. humidity rate), implementation errors, numerical approximations (e.g. rounding), and eventually artifacts due to spatial discretization. To address such issues, the scientific computing community has established the Verification and Validation (V&V) framework, particularly in fields such as Computational Fluid Dynamics (CFD) and Mechanical Engineering [1, 2].

Verification aims to ensure that the model accurately solves the underlying mathematical equations. This step typically involves comparisons with analytical solutions when available, or with results from independent numerical models in configurations where both are expected to be valid. Validation, on the other hand, focuses on assessing how well the model reproduces experimental data, accounting for uncertainties due to variability in geometry, material properties, boundary conditions, and measurement procedures.

In musical acoustics it is common to compare simulations and experiments (e.g. [3, 4]). However, the verification step is less systematically applied. Often, studies focus on validating new developments in configurations where existing models fail (e.g. [5]), without first verifying consistency between models on simpler, well-understood test cases.

This study specifically addresses the *verification* step, by comparing impedance results computed by different researchers using independent implementations. The focus is on simple geometries—closed or open cylindrical and conical tubes—for which reference or analytical solutions exist and for which numerical models are expected to agree. By identifying and resolving discrepancies in this controlled context, we aim to assess the robustness of current modeling practices and contribute to improving the reliability and reproducibility of impedance computations in musical acoustics.

2. CONSTRUCTION OF THE DATA SET

2.1 Configurations

The cases studied are 180 mm long pipes. This relatively short length gives the possibility to use heavy simulation methods (e.g. 3D-FEM) with a relatively low computation cost even at "high" frequency (5 kHz). A cylindrical pipe with a 14 mm internal diameter has been simulated with three radiation conditions: closed, open with infinitly thin wall (unflanged) and open with 7 mm wide wall (circular flanged). A closed conical pipe with an internal diameter from 10 mm to 22.6 mm (half angle: 2°) have been also simulated. For the latter, contributors assumed either plane or spherical wavefronts, which can be seen as different shapes of boundary conditions (plate or spherical caps). The wall material is assumed perfectly smooth, rigid, non-porous and a perfect conductor of heat.

The values of the physical quantities (speed of sound, air density, etc) are imposed. They are calculated, from [6, Chap.5.5.2], for a temperature of 25°C. For the lightest calculation methods, the recommended frequency axis for simulation is set to [0.2 Hz, 20 kHz] with a 0.2 Hz step. However, for methods necessitating high computation cost, a multiple of the frequency step could be used. Only 5 arbitrary frequencies was imposed for comparison ($f_{obs} \in [20, 100, 500, 1000, 5000]$ Hz) (see Sec.2.3).

2.2 Numerical methods

The input impedances of this set of configuration have been simulated by seven contributors, named A to F, using their own software or implementation of the models. For each simulation, the resulting impedance $\tilde{Z}$ is shared.

To simulate the wave propagation, contributors A to D use the one-dimensional (1D) telegrapher's equations including the visco-thermal losses with the Zwikker and Kosten expression (see e.g. [6, Chap.5]) or approximation proposed by Keefe [7]. The closed condition is modelled by an infinite impedance. For the open conditions, a radiation impedance computed with the expressions proposed by Silva [8] and Dalmont [9] are used. Contributors A, B and D used their own implementations of the Transfer Matrix Method (TMM). This technique combines solutions of the telegrapher's equation for cylinders (exact solution) or cones (approximation). For cone it is possible to refine the solution, by subdividing the geometry in small cones. Contributor C uses the software Openwind [10] given the possibility to solve the equations with TMM or 1D-finite elements method (1D-FEM) [11], which converges to the

exact solution if the mesh is refined enough.

Contributor E used its own implementation of the multi-modal (MM) approach [12]. The thermo-viscous effects are taken into account as a modification of each mode shapes through the expressions proposed by [13]. For open pipes, the radiation domain is modeled using a wider pipe surrounding the actual pipe studied [14].

Contributor F used the software Montjoie [15] to solve 3D (or 2D axi-symmetric when it is possible) acoustic propagation with FEM. The thermo-viscous effects are taken into account using a two steps simulation (sequential linearized Navier-Stokes model or SLNS) [16], or effective boundary conditions based on Cremer approach [17]. More detailed are given in [18]. For open pipes, a radiation domain bounded by perfectly-matched-layers condition (PML) is added.

In order to study the practical use of simulation, each contributor was responsible for choosing the spatial discretisation, making his/her own compromise between accuracy and computation time. This choice is strongly influenced by the scientific culture of the contributor (numerician, experimentalist, etc.) or by the intended application (model comparison, manufacturing application, etc.).

2.3 Distance quantification

In numerical studies, it is common to use the L2-norm to quantify the distance between two simulations. However, the presence of peaks in the impedance curve can lead to large deviations from small variations (e.g., a slight shift in a resonance peak). To mitigate this, the reflection function is used:

$$\mathcal{R} = \frac{Z-1}{Z+1}. \tag{1}$$

where $Z = \tilde{Z}S/(\rho c)$ is the input impedance scaled by the lossless characteristic impedance. The distance between two simulations (p, q) is then computed as the L2-norm at the five arbitrary imposed frequencies $f_{obs}^{(i)}$:

$$d_R^{(p,q)} = \frac{\sum_i^N |\mathcal{R}_p(f_{obs}^{(i)}) - \mathcal{R}_q(f_{obs}^{(i)})|^2}{\sum_i^N |\mathcal{R}_p(f_{obs}^{(i)})|^2}. \tag{2}$$

For two equivalent models, this distance should reach machine precision (here, 10^{-6}).

From a musical perspective, the "modal characteristics" are also analyzed for simulations with sufficiently fine frequency resolution. Both resonances and anti-resonances are characterized by their frequency and magnitude. For the i-th (anti-)resonance peak, the frequency $f^{(i)}$ is defined as the point where the impedance phase crosses zero, and the magnitude $a^{(i)}$ as the modulus of the impedance (or admittance) at that frequency. Simulations are compared through their deviation from a reference value, expressed in cents for frequencies:

$$d_f^{(i,p)} = 1200 \log_2 \left(\frac{f_p^{(i)}}{f_{ref}^{(i)}} \right) \tag{3}$$

and in decibels for amplitudes:

$$d_a^{(i,p)} = 20 \log_{10} \left(\frac{a_p^{(i)}}{a_{ref}^{(i)}} \right). \tag{4}$$

The reference values are taken from the analytical solution when available, or otherwise from the average across all simulations.

3. ANALYSIS

3.1 Closed cylinder

The first test case is a closed cylindrical tube. The "closed" condition is numerically defined by enforcing zero normal velocity at the cap wall, corresponding to zero flow in 1D, or equivalently, infinite acoustic impedance. This assumption neglects the thermo-viscous effects at the cap wall.

For this geometry, the telegrapher's equation admits an analytical solution including thermo-viscous losses. With the above boundary condition, the input impedance reads:

$$Z_{\text{closed cyl}} = Z_{cc} \coth(\Gamma L) \tag{5}$$

where L is the cylinder length, $Z_{cc} = \sqrt{Z_v/Y_t}$ is the complex characteristic impedance, and $\Gamma = \sqrt{Z_v Y_t}$ the complex wave number. This configuration is well suited for validation, as all TMM implementations should yield identical results, apart from the specific thermo-viscous formulations, since this method is formally similar to the analytical solution Eq. (5) in this configuration.

Contributors A, B, and C used the ZK formulation. C also tested the first- and second-order Keefe approximations (Keefe 1 and 2); D used Keefe 2. Contributor E implemented the multimodal (MM) model, and F used 3D FEM with 2D-axisymmetric SLNS resolution.

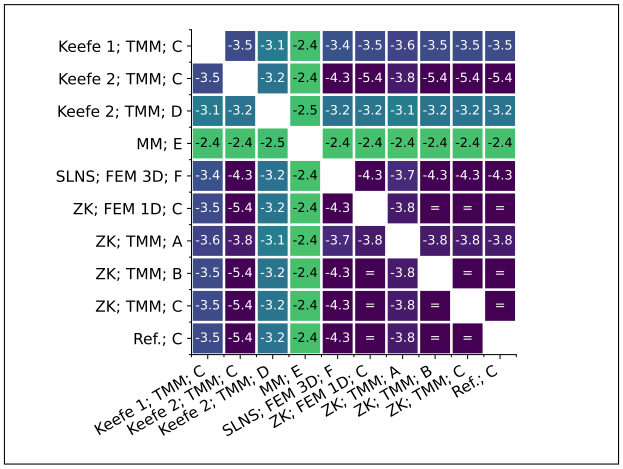


Figure 1. Closed cylinder. Relative distance matrix of the reflection function at reference frequencies ($f \in [20, 100, 500, 1000, 5000]$ Hz) in log scale ($\log_{10}(d_{\mathcal{R}})$). The symbol "=" denotes distances below machine precision (10^{-6}).

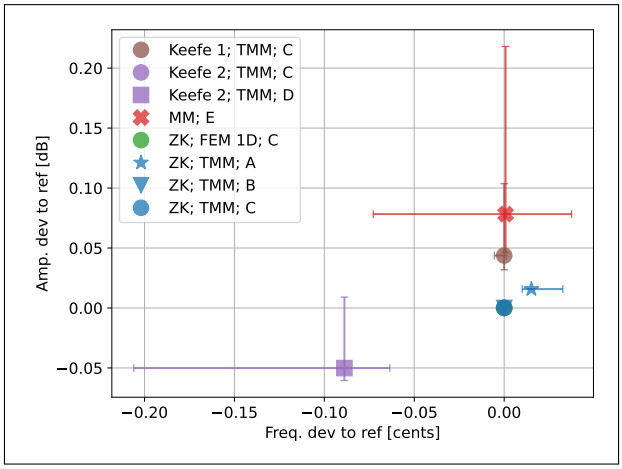


Figure 2. Closed cylinder. Deviation from the analytical modal characteristics (Eqs. 4, 3). Markers indicate median values; error bars denote the full range. Marker shapes identify contributors; colors indicate models and numerical methods.

Figure 1 presents the distance matrix for the reflection function (Eq. 2), and Figure 2 shows deviations in modal characteristics over 10 peaks (5 resonances, 5 anti-resonances). In this second Figure, the 3D FEM results are omitted due to insufficient frequency resolution for modal fitting.

From a musical point of view, all simulations exhibit good overall agreement, with frequency deviations remaining within ± 0.2 cents and amplitude deviations within ± 0.2 dB. The results provided by contributors B and C (ZK-TMM, 1D FEM and analytical solutions) are consistent to within machine precision across all metrics. Similarly, the 3D FEM results from contributor F and the second-order Keefe approximation from contributor C are nearly indistinguishable, with reflection distances below $10^{-4}\%$, frequency deviations below 10^{-3} cents and amplitude below 10^{-3} dB. Contributor A shows slightly larger but still minor discrepancies, attributed to a numerical issue in the implementation of physical quantities, after the sharing of the data.

The impact of thermo-viscous modeling choices is clearly visible. The multimodal (MM) model introduces more noticeable deviations, in reflection distance ($d_{\mathcal{R}} \approx 4 \cdot 10^{-3}$), in frequency ($d_f \approx 0.08$ cents) and amplitude ($d_a \approx 0.2$ dB). The first-order Keefe approximation also leads to moderate differences. By contrast, contributor D, who used the second-order Keefe approximation, exhibits unexpected deviations (-0.05 dB, -0.1 cents, $d_{\mathcal{R}} \approx 7 \cdot 10^{-4}$) not observed in C's results with the same model, suggesting a probable but yet-unidentified implementation issue.

3.2 Other geometries

Similar figures and analyses can be produced for other test cases. However, for clarity, the agreement between simulations is here assessed through statistical indicators.

Table 1. Mean and maximal values of the logarithm of the distance $d_{\mathcal{R}}$ between simulations for each configuration.

Case	Mean $\log_{10}(d_{\mathcal{R}})$	Max $\log_{10}(d_{\mathcal{R}})$
Cyl. C.	-4.0	-2.4
Cyl. Unfl.	-3.0	-2.4
Cyl. Wall	-2.7	-2.2
Cone Pl.	-2.1	-1.7
Cone Sph.	-3.3	-3.0

Table 1 shows the mean and maximal values of

Table 2. Root mean square (RMS) and maximal values of the deviations d_f (in cents) and d_a (in dB) between simulations for each configuration.

Case	RMS d_f	Max d_f	RMS d_a	Max d_a
Cyl. C.	0.05	0.24	0.05	0.22
Cyl. Unfl.	0.07	0.62	0.05	0.18
Cyl. Wall	0.20	0.60	0.11	0.32
Cone Pl.	0.8	5.7	0.4	2.2
Cone Sph.	0.04	0.17	0.04	0.07

$\log_{10}(d_{\mathcal{R}})$ for each configuration. Table 2 provides the root mean square (RMS) and maximal deviations of the modal characteristics between simulations.

Agreement between results decreases as the simulated configuration becomes more complex. The best match is observed for the closed cylinder (Cyl. C.), followed by the unflanged open cylinder (Cyl. Unfl.) and the open cylinder with finite wall width (Cyl. Wall). The largest deviations occur for the closed cone with plane wavefronts (Cone Pl.), with errors reaching a few cents, a few dB, and around 1% for $\mathcal{R}$. Conversely, the closed cone simulated with spherical wavefronts (Cone Sph.) shows excellent agreement, comparable to the closed cylinder. This may be due to the fact that this case was only simulated by contributors using software that had already been verified.

4. CONCLUSIONS

Even though simulations are generally consistent from a musical perspective ($d_f < 1$ cent, $d_a < 1$ dB), this study shows that achieving strict numerical consistency remains challenging. Variations arise when different researchers use distinct physical models and implementations, even for simple cases.

The presented values already reflect extensive discussions, data comparisons, and issue resolution. For instance, deviations for the conical pipe reached 20 cents in the initial dataset. Despite these efforts, increasing model complexity leads to growing discrepancies, highlighting the sensitivity to boundary conditions and the importance of careful numerical implementation. The most consistent results were observed for simple cases and by contributors with strong numerical skills.

Beyond the analyses of the presented implementations, this study emphasizes the importance of verification when developing new models or tools. This includes comparing results with existing tools on simple cases for which both are valid, identifying sources of discrepancies (e.g., convergence, simplifications), and quantifying deviations. In simulations requiring discretization (e.g. sliced conical pipes in TMM), the convergence behavior should be systematically evaluated and reported.

Promoting such practices is key to improving reproducibility and accuracy in simulations. A practical solution for sharing the numerical results of this study is under consideration, which should allow anyone to *verify* their tools by comparing them with this dataset and then to carry out validation with experiments.

5. REFERENCES

[1] Computational Fluid Dynamics Committee, ed., *Guide: Guide for the Verification and Validation of Computational Fluid Dynamics Simulations (AIAA G-077-1998(2002))*. Washington, DC: American Institute of Aeronautics and Astronautics, Inc., Jan. 1998.

[2] L. E. Schwer, "An overview of the ASME V&V-10 guide for verification and validation in computational solid mechanics," in *20th International Conference on Structural Mechanics in Reactor Technology*, pp. 1–10, 2009.

[3] A. Lefebvre, *Computational acoustic methods for the design of woodwind instruments*. PhD thesis, McGill University, 2010.

[4] P. Eveno, *L'impédance d'entrée pour l'aide à la facture des instruments de musique à vent : mesures, modèles et lien avec les fréquences de jeu*. PhD Thesis, Université Pierre et Marie Curie - Paris VI, Dec. 2012.

[5] T. Hélie, T. Hézard, R. Mignot, and D. Matignon, "One-Dimensional Acoustic Models of Horns and Comparison with Measurements," *Acta Acustica united with Acustica*, vol. 99, pp. 960–974, Nov. 2013.

[6] A. Chaigne and J. Kergomard, *Acoustics of Musical Instruments*. Modern Acoustics and Signal Processing, New York: Springer, 2016.

[7] D. H. Keefe, "Acoustical wave propagation in cylindrical ducts: Transmission line parameter approximations for isothermal and nonisothermal boundary

conditions," *The Journal of the Acoustical Society of America*, vol. 75, pp. 58–62, Jan. 1984.

[8] F. Silva, P. Guillemain, J. Kergomard, B. Mallaroni, and A. N. Norris, "Approximation formulae for the acoustic radiation impedance of a cylindrical pipe," *Journal of Sound and Vibration*, vol. 322, pp. 255–263, Apr. 2009.

[9] J.-P. Dalmont, C. Nederveen, and N. Joly, "Radiation impedance of tubes with different flanges: numerical and experimental investigations," *Journal of Sound and Vibration*, vol. 244, pp. 505–534, July 2001.

[10] J. Chabassier, A. Ernoult, O. Geber, A. Thibault, T. v. Baarsel, G. Castera, and R. Tournemenne, "openwind, https://openwind.inria.fr/," Feb. 2019.

[11] R. Tournemenne and J. Chabassier, "A Comparison of a One-Dimensional Finite Element Method and the Transfer Matrix Method for the Computation of Wind Music Instrument Impedance," *Acta Acustica united with Acustica*, vol. 105, pp. 838–849, July 2019.

[12] J.-B. Doc, B. Lihoreau, S. Félix, and V. Pagneux, "Bremmer series for the multimodal sound propagation in inhomogeneous waveguides," *Wave Motion*, vol. 67, pp. 55–67, Dec. 2016.

[13] A. Bruneau, M. Bruneau, P. Herzog, and J. Kergomard, "Boundary layer attenuation of higher order modes in waveguides," *Journal of Sound and Vibration*, vol. 119, no. 1, pp. 15–27, 1987.

[14] S. Félix, J.-B. Doc, and M. A. Boucher, "Modeling of the multimodal radiation from an open-ended waveguide," *The Journal of the Acoustical Society of America*, vol. 143, pp. 3520–3528, June 2018.

[15] M. Duruflé, *Intégration numérique et éléments finis d'ordre élevé appliqués aux équations de Maxwell en régime harmonique.* PhD thesis, Université Paris Dauphine, Paris, 2006.

[16] W. R. Kampinga, Y. H. Wijnant, and A. de Boer, "An Efficient Finite Element Model for Viscothermal Acoustics," *Acta Acustica united with Acustica*, vol. 97, pp. 618–631, July 2011.

[17] L. Cremer, "On the acoustic boundary layer outside a rigid wall.," *Arch. Elektr. Uebertr*, 1948.

[18] J. Chabassier and A. Thibault, "Viscothermal models for wind musical instruments.," Research Report 9356, Inria, Mar. 2020.

DOI: 10.61782/fa.2025.0509

FORUM ACUSTICUM EURONOISE 2025

IS IT POSSIBLE TO PREDICT SINGLE CANE REED MOUTHPIECE INTERACTION BY MEASURING THE REED ALONE?

Amélie Gaillard[1*] **Marie tahon**[2] **Camille Urban**[1,2]
Emmanuel Brasseur[1] **Bruno Gazengel**[1]
[1] Laboratoire d'Acoustique de l'Université du Mans (LAUM), UMR 6613
Institut d'Acoustique-Graduate School (IA-GS), CNRS, Le Mans Université
Avenue O. Messiaen, CEDEX 09, F-72085 Le Mans, France
[2] LIUM, Le Mans University

ABSTRACT

This paper deals with the experimental characterization of single cane reeds. According to some authors, the reed stiffness symmetry of the unmounted reed may explain it's perceived quality. Other studies show that the nonlinear stiffness of a reed mounted on a mouthpiece partially explains it's behavior in playing situations. According to these results, the aim of this work is to study the link between measurements performed on unmounted and mounted reeds.

We adapted two experimental test rigs to characterize 90 reeds with 3 different strengths. The first is dedicated to unmounted reeds. It enables to measure the local stiffness at a known distance from the reed tip by imposing a displacement and measuring the force. The second test rig focuses on the reed mouthpiece interaction. Using a force sensor and a camera, it enables to estimate the nonlinear characteristics between lip force and reed channel area.

Using these numerous measurements, we investigate the relation between the indicators by the use of statistical analysis and machine learning techniques. These methods enable to show several correlations between parameters obtained from unmounted and mounted reed measurements.

*__Corresponding author__: *amelie.gaillard@univ-lemans.fr.*
__Copyright__: *©2025 Amélie Gaillard et al. This is an open-access article distributed under the terms of the Creative Commons Attribution 3.0 Unported License, which permits unrestricted use, distribution, and reproduction in any medium, provided the original author and source are credited.*

Keywords: *clarinet, reed, measurements*

1. INTRODUCTION

Woodwinds instruments use a small piece of cane or synthetic material to produce a sound. According to musicians, this piece is very important for the control and the quality of sound and this was already said by Frederic Berr in 1836 [1] "Une bonne anche est un point capital pour l'exécutant, puisque la qualité du son dépend de sa confection et du choix du roseau ; aussi a-t-on dit qu'une bonne anche faisait la moitié du talent de l'exécutant" (A good reed is essential for the performer, since the quality of the sound depends on the way it is made and the choice of reed; it has been said that a good reed is half the talent of the performer.)

Today single reeds are made in an industrial manner so that the reed can be described by three parameters, its brand, its cut and its strength. However, even if the manufacturing process is very accurate, different reeds sold as identical (same brand, cut, strength) can be perceived as extremely different by musicians. This is even the case when the reed is chosen to be adapted to the mouthpiece tip opening [2]. Indeed the mouthpiece plays an important role in the ease of playing (linked to the oscillation threshold) and in the external sound pressure level and in the pitch variation [3].

According to previous results [4], the strength of the reed (obtained thanks to a measurement of the reed stiffness at a certain distance from the reed tip) is correlated with the subjective descriptor "ease of playing" but the strength does not enable to predict all musicians sensa-

tions. This explains the variability of musicians perception when they play identical reeds. The variability in the perception may be due to the reed symmetry [5,6] or to the interaction between the reed and the mouthpiece [7, 8].

For this reason, the work proposed in this paper aims at characterizing the reed thanks to two different experimental methods. First, measurements of the reed alone are conducted. They enable to estimate two different reed compliances (local and transfer compliance). Second, the interaction between the reed and the mouthpiece is analyzed by estimating the reed channel surface —the front surface between the mouthpiece tip and the reed— as a function of the force applied on the reed as described by Gaillard et al. [8]. Finally, relations between the two data sets are searched in order to investigate to what extend measurement on the reed alone can give information the reed-mouthpiece interaction.

The second half of this study covers measurement methods. Data analysis methodologies are discussed in Section 3, while Section 4 presents results obtained with 89 reeds before concluding and providing work perspectives.

2. MEASUREMENT TECHNIQUES

Two experimental set-ups were used. The first test rig uses a rod to apply a force on a clamped reed. It measures the local stiffness at various reed points and the deflection of the reed tip (figure 1). The second device (figure 6) consists of a mouthpiece, an artificial lip, and a reed. It allows to measure the nonlinear relationship between the opening of the reed channel and the force applied by the lip on the reed.

2.1 Measurements of the reed alone

The experimental set-up used to characterize the reed alone is described in figure 1. The thick part of the reed is clamped and its free length is set at ℓ = 2.7 cm. This length is controlled using a removable stop giving good repeatability during measurements. A camera (Imagine Source DMK 37BUX252) takes pictures of the reed tip, in order to capture the deflection $z_t(y_t)$ along y axis (tip displacement). A pointed rod that can move in the three directions in space imposes a known displacement z_p at the coordinates (x_p, y_p). The position of the rod in the reference frame linked to the reed is controlled in the y direction using a calibration procedure to compensate for any defects in the positioning of the reed on the bench. A sensor (Omega LCM703-5) measures the force F_p applied by the pointed rod to the reed for different positions along the z axis.

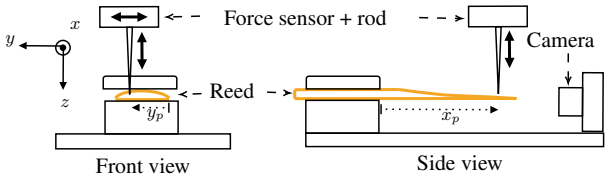


Figure 1. Schematic diagram of the bench used to measure the local stiffness and the tip deflection of a single reed.

Thanks to this test rig, two types of reed measurements are performed simultaneously : reed local stiffness (the compliance inverse) and reed tip deflection. The measurement procedure involves positioning the rod tip over the reed and then displacing it according to z. The force is recorded and a picture of reed tip is captured (as presented in figure 2.a). This automatic procedure is repeated for 4 positions along z and 9 points along y centered on the middle of the reed. This choice results from a compromise between the accuracy and the duration of the measurement. Indeed, as a large amount of reeds will be measured, the maximum measurement time for one reed is set to 10 minutes.

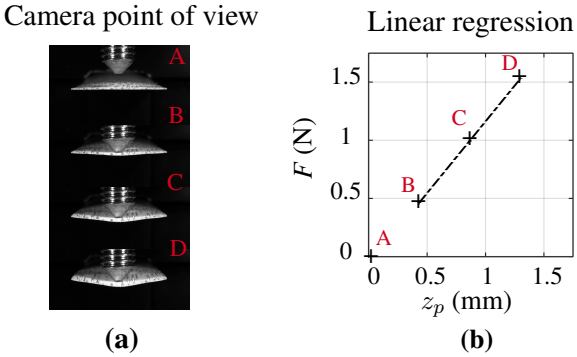


Figure 2. (a) Four rod positions and resulting in reed deflection (b) Estimation of local stiffness by linear regression between force and displacement imposed by the rod.

2.1.1 *Measurement of local stiffness*

For this measurement, a linear regression estimates the local stiffness K at coordinates (x_p, y_p) using the rod im-

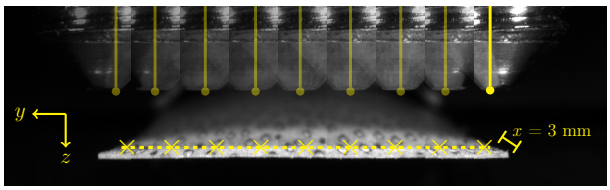


Figure 3. Nine points (yellow crosses) along the reed width y from y_0 (left) to y_8 (right) at $x = \ell - x_p = 3$ mm from the reed tip.

posed displacement and the measured force.

The local stiffness is measured for the nine y_p leading to the estimation of reed stiffness profile. The stiffness is modeled by a parabola described in a previous article [9] with three coefficients K_0, K_1 and y_0 leading to the theoretical stiffness $\hat{K} = K_0 + K_1(y_p - y_0)^2$. We also include $\Delta K = K(y_8) - K(y_0)$ to capture the symmetry of the reed.

2.1.2 Measurement of transfer compliance

In this measurement, only the force applied by the rod and the reed tip deflection are used as shown in figure 4. The reed tip deflection $z_t(y_t)$ is obtained with an image processing. For each z_p, the image is converted in black and white using a threshold value according to Almeida [10]. The contour between the white (reed) and dark zones (air) is obtained by thresholding the gradient of each y slice between the left and right side of the reed.

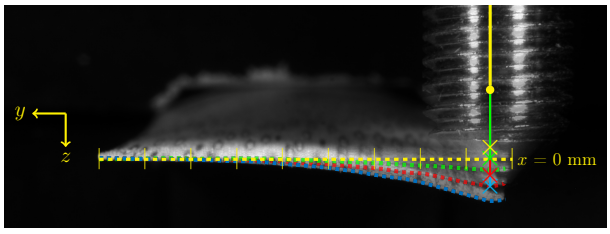


Figure 4. Four reed tip deflections (colored dotted lines) caused by four vertical displacements of the rod. The reed is at rest for the first displacement as in Figure 3, in yellow in both figures.

The full contour is interpolated to extract the reed tip deflection $z_t(y_t)$ at the nine segments between the small yellow vertical bars in Figure 4. Finally, these measurements result in a bunch of 4 z_p (rod displacements) $\times$ 9 y_p (rod positions) $\times$ 9 y_t (reed tip average deflection) $= 324$ deflection values for a reed. This enables to get first the reed tip profile at rest $z_r(y_t)$ (no force). Second it leads to the transfer compliance $c_{tp} = \frac{z_t}{F_p}$ at different rod positions y_p and tip positions y_t using a least mean square regression for 3 rod positions z_p. An example of such a transfer compliance matrix $\boldsymbol{C_{tp}}$ is given in figure 5.

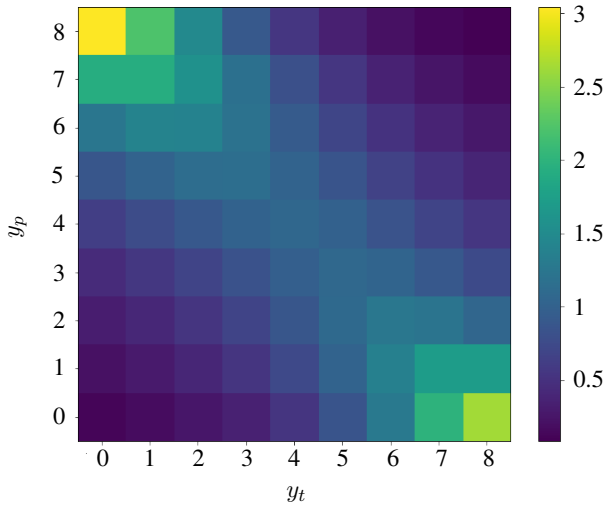


Figure 5. Example of compliance matrix $\boldsymbol{C_{tp}}$ (mm.N^{-1}) for reed 1.

2.2 Characterization of reed mouthpiece interaction

The second test rig (figure 6) is used to characterize the interaction between the mouthpiece and the reed. A mouthpiece (Vandoren BD4 - tip opening = 115.5 1/100 mm), on which a reed is held by a ligature (Vandoren Optimum), is fixed to the test rig. An artificial rectangular silicone lip (30 mm $\times$10 mm $\times$7 mm) moves along the x-axis (parallel to the height of the reed). In this case, the force F_L applied by the artificial lip is measured with a force sensor (Omega LCM703-5). A camera takes pictures of the reed channel for every lip force. This method of measurement is very similar to the one proposed by Taillard [7] but enables to measure the lip force (instead of lip position) automatically on a large number of reeds. It is the same as described in [8].

The lip is moved in steps of 0.2 mm along the z axis thanks to a manual micrometric screw leading to 31 force values. When the lip is in its first position, it does not touch the reed and the channel is fully opened. For each position of the lip until the channel is completely closed,

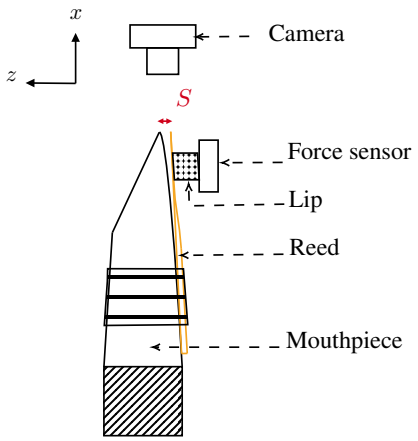


Figure 6. Test rig used to characterize the reed-mouthpiece interaction.

the force signal is recorded and a photo of the channel is taken. In this experiment, the presence of the artificial lip can create light reflections that make the processing more tricky than for the previous experiment. First, the image with the reed at rest is analyzed. The grayscale image is converted into a binary image choosing a threshold value which enables to get a reed contour having a width similar to the mouthpiece contour width, the contours being detected using the function *bwboundaries* of Octave software [11]. Then, for each force, each image is cropped such that the lip and the sides of the reed are not seen. Each image is converted into a binary image choosing a threshold value which enables to get a reed perimeter similar to the perimeter of the reed at rest. The contours of the mouthpiece and reed are detected and the height of the reed channel is estimated along the reed width. An example of a measurement obtained with this system is shown in Figure 7 (crosses). In addition to the total channel surface, the surface is also estimated for 9 different parts centered on y_t, distributed in a similar way to the reed alone.

As the lip positions are imposed, the lip forces are all distinct from all reeds, so it is not practical to study the raw data collected by image processing. Then, for every reed, the 10 (9 segments and total) surface area are modeled as proposed by Gazengel et al. [12]. Using this model, each characteristic is divided into three parts as shown in figure 7 (blue curve). For low lip forces, the linear part of the curve can be approximated by a straight line (in red in figure 7). Its y-intercept indicates the opening surface at rest S_{00} (without lip force). The x-intercept indicates the maximum closing force F_M. At intermediate forces, the reed bends on the curved rails of the mouthpiece. This part can be approximated by a parabola with length E (elbow). Finally, for high forces, the entire reed is in contact with the mouthpiece, leading to complete closure of the channel or to a residual leakage S_{inf}. If there is not any leakage, the measured area should be zero but because of lightning, sometimes the image processing can lead to a residual leakage which is not physical. This piece-wise function is defined by the 4 coefficients S_{00}, F_M, E and S_{inf}. It is of class C^1, and its derivative is continuous.

An example showing the 9 opening sections as a function of F_L is given in figure 8.

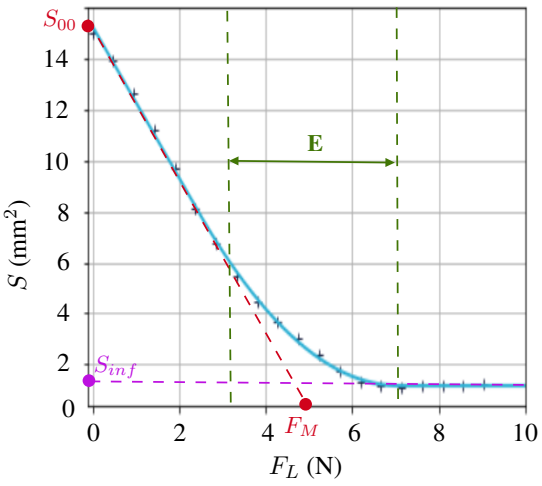


Figure 7. Total opening section of the channel with measurements (crosses), model (blue curve) and associated parameters.

3. DATA ANALYSIS

Eighty-nine reeds were randomly selected among commercial reeds. They are all of the same cut *V12* from the same manufacturer *Vandoren* but of three different strengths: 2 1/2 (29 reeds), 3 (30 reeds) and 3 1/2 (30 reeds). All the reeds were measured with the two test-rigs presented above.

The following data analysis has been realized to confirm and explore the relation between measurements on the reed alone and in interaction with the mouthpiece. All the code used to compute the different parameters and to

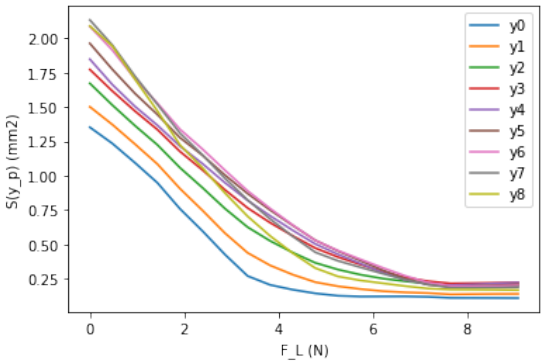


Figure 8. Example of nonlinear characteristics obtained by analyzing 9 opening sections $S(y_p)$ as a function of the lip force for reed 1.

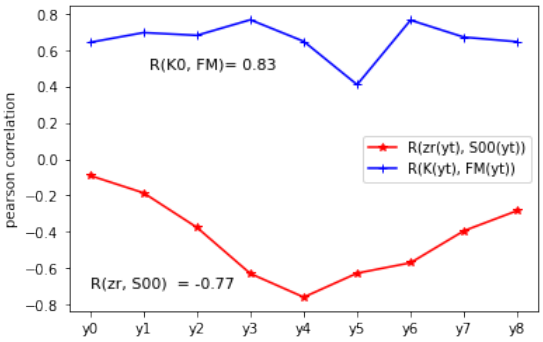


Figure 9. Red curve : $\rho(z_t(y_t), S_{00}(y_t))$ for the reed deflection at rest. Blue curve: Pearson correlation $\rho(K(y_t), F_m(y_t))$ between the reed local stiffness $K(y_t)$ and maximum force $F_M(y_t)$.

analyze the code is made available [1] . In this exploratory work, we mainly used correlations, however, more advanced techniques using mutual information or PCA are currently under investigation.

3.1 Reed tip position at rest

The reed tip position at rest is not supposed to vary according with the test rigs. Therefore we expect a high correlation between the reed tip deflection $z_r(y_t)$ of the reed alone, and the S_{00} parameter obtained in interaction with mouthpiece (segmented and total). We observe that the correlation between the mean rest deflection $\bar{z}_r$ of the reed and the S_{00} of the total opening section is high ($R = -0.77$). However, when comes to the local correlation, the highest correlations are found for the middle of the reed ($t = 4,\ y_t = 0$) which might due to the shape of the mouthpiece (red curve, figure 9).

3.2 Local stiffness

We first investigate how the reed stiffness parameters are correlated. We confirm that the correlation between stiffness K_0 and K_1 is high (0.953), and also the correlation between symmetry parameters y_0 and ΔK (0.867). However all other correlations are rather low (< 0.09). We also explore the relations between the local stiffness $K(y_t)$ (reed alone) and the maximum force $F_M(y_t)$ (reed is in contact with the mouthpiece). First, the Pearson correlation between K_0 and F_M associated to the total area is high (0.83). Then, the Pearson correlation for each position y_t is given by the blue curve in figure 9. We observe that the local stiffness $K(y_t)$ is strongly correlated with the force $F_M(y_t)$, thus confirming the consistency of the measures between the two rigs. Unfortunately, the correlation between y_0 or ΔK and E parameter are too low (< 0.17) to conclude to a relation between asymmetry of the reed alone and the bending of the reed on the mouthpiece.

3.3 Transfer compliance

Finally we analyze, the correlations between each of the 81 compliances c_{tp} (for a position of the rod y_p and a position of the reed tip y_t) and the equivalent parameters $S_{00},\ F_M,\ E,\ S_{inf}$ describing the total opening section between the reed and mouthpiece. Figure 10 shows the results.

We observe that S_{00} and S_{inf} are not correlated to the compliance at any position on the y axis. On the contrary, F_M and E are highly correlated with the 81 transfer compliance. Moreover, the correlation coefficient between F_M and E being 0.54, it suggests that the bending of the reed on the mouthpiece depends on the maximum force F_M. More precisely, the highest correlations between F_M and c_{tp} can be found when the rod is in the middle of the reed, for any position in the reed ($p = 3 \ldots 6,\ \forall t$). When the rod is applied at the edge of the reed ($p = 1, 2, 8, 9$), the correlation reaches its maximum value close to the rod position (2 to 3 segments around the rod position).

[1] https://git-lium.univ-lemans.fr/tahon/reedsml.git

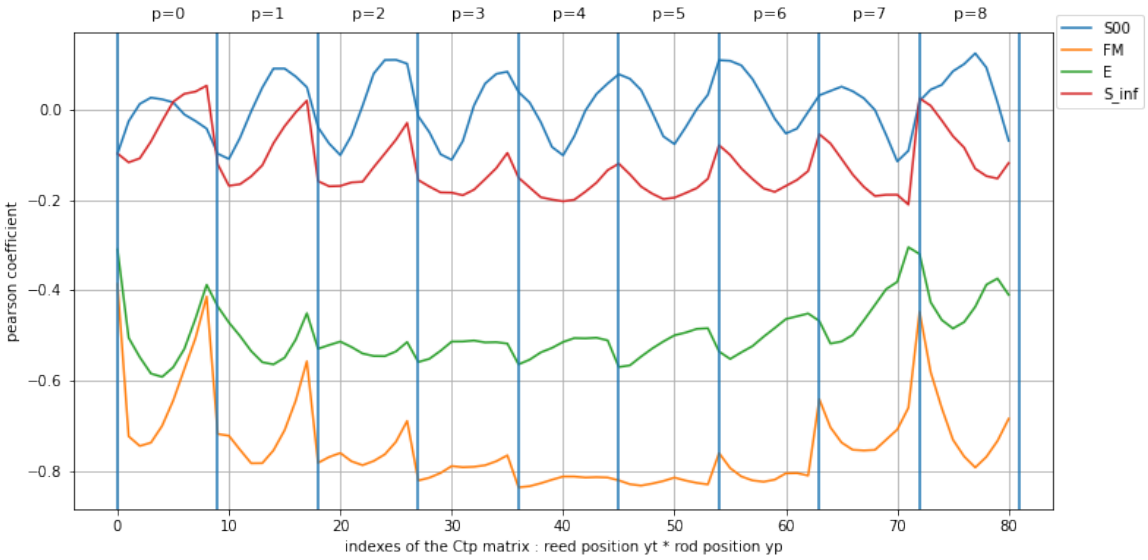


Figure 10. Pearson coefficient between the transfer compliance c_{tp} and the four mouthpiece-reed interaction parameters. The abscissa corresponds to the flatten matrix coordinates : $9 \times p + t$. For instance, if the rod position is at $p = 2$ and the observation of the reed deflection is at $t = 1$, the abscissa will be $2 \times 9 + 1$. Blue vertical lines indicates a change of position of the rod y_p.

4. CONCLUSION

This study used two different test rigs to experimentally characterize 89 clarinet reeds.

The first employs a clamped reed with a pointed tip that exerts force at a predetermined distance from the reed tip. First, it enables the measurement of local stiffness. Second, an image processing measures the reed tip displacement. This enables to get the reed tip position at rest and the transfer compliance matrix (ratio between the tip displacement and force at different coordinates). The local stiffness can be described by a parabola (3 parameters).

The second test rig employs a reed mounted on a clarinet mouthpiece, with an artificial lip exerting a force on the reed. It uses image processing to measure the height of the reed channel. This leads to the nonlinear characteristics (force-section) that are modeled using 4 parameters.

The analysis of the relation between the 2 data sets shows that the reed tip position at rest is consistent for both test rigs. The maximum local stiffness K_0 is strongly correlated to the maximum force F_M derived from the total opening section measured on the mouthpiece. At this stage, the asymmetry measured on the reed alone does not correlate with any parameter obtained with the reed + mouthpiece system. The transfer compliance is highly correlated with the maximum force F_M of the total opening section when the point force is applied in the middle of the reed, indicating that the force applied on the sides have a small effect on F_M. Finally, the correlation coefficient between F_M and the elbow E suggests that the bending of the reed on the mouthpiece depends on the maximum force F_M.

Deeper investigations will be conducted with more advanced data analysis such as Principal Components Analysis and entropy based approaches. Future work will use these two test rigs in parallel to perceptive tests in order to try to determine a link between physical parameters and subjective descriptors.

5. REFERENCES

[1] F. Berr, *Traité complet de la clarinette à quatorze clefs: manuel indispensable aux personnes qui professent cet instrument et à celles qui l'étudient*. Source gallica.bnf.fr BnF, 1836.

[2] "The saxophone mouthpiece tip opening." https://syos.co/en/blogs/news/

the-saxophone-mouthpiece-tip-opening. Accessed: 01-28-2025.

[3] M. Ozdemir, V. Chatziioannou, J. Verlinden, G. Cascini, and M. Pàmies-Vilà, "Towards 3d printed saxophone mouthpiece personalization: Acoustical analysis of design variations," *Acta Acustica*, vol. 5, p. 46, 2021.

[4] B. Gazengel, J. Dalmont, and J. Petiot, "Link between objective and subjective characterizations of Bb clarinet reeds," *Applied Acoustics*, vol. 106, 2016.

[5] C. Kemp and G. Scavone, "Mechanical, anatomical and modeling techniques for alto saxophone reed evaluation and classification," *Wood Science and Technology*, vol. 54, pp. 1677–1704, Nov. 2020.

[6] F. Pinard, B. Laine, and H. Vach, "Musical quality assessment of clarinet reeds using optical holography," *The Journal of the Acoustical Society of America*, vol. 113, no. 3, pp. 1736–1742, 2003.

[7] P.-A. Taillard, *Theoretical and experimental study of the role of the reed in clarinet playing*. PhD thesis, Le Mans Université, 2018.

[8] A. Gaillard, B. Gazengel, and V. Koehl, "Research of perceptual descriptors discriminating clarinet reeds of identical stiffness," in *INTER-NOISE and NOISE-CON Congress and Conference Proceedings*, vol. 270, pp. 2993–3000, Institute of Noise Control Engineering, 2024.

[9] A. Gaillard, V. Koehl, and B. Gazengel, "Link between stiffness symmetry and perceived quality of clarinet cane reeds," in *Forum Acusticum 2023, the 10th European Congress on Acoustics*, pp. 2729–2733, 2023.

[10] A. Almeida, C. Vergez, and R. Caussé, "Experimental investigation of reed instrument functioning through image analysis of reed opening," *Acta acustica united with acustica*, vol. 93, no. 4, pp. 645–658, 2007.

[11] J. W. Eaton, D. Bateman, S. Hauberg, and R. Wehbring, *GNU Octave version 8.4.0 manual: a high-level interactive language for numerical computations*, 2023.

[12] B. Gazengel, J.-P. Dalmont, A. Gaillard, E. Brasseur, and P.-A. Taillard, "Characterization of single reed mouthpiece interaction in quasi-static regime," *Acta Acustica*, vol. 9, p. 5, 2025.

DOI: 10.61782/fa.2025.0744

FORUM ACUSTICUM EURONOISE 2025

REPRODUCIBILITY IN THE CONSTRUCTION OF TRADITIONAL WOODEN AND 3D-PRINTED PLASTIC SOUNDBOARDS FOR STRING INSTRUMENTS

Labraña, Sebastián[1] **Correa, Víctor**[2] **Montoya, Aarón**[3]
Espinoza, Carolina[4*]

[1] Departamento de Física, Facultad de Ciencia, Universidad de Santiago de Chile, Santiago, Chile
[2] Universidad Academia de Humanismo Cristiano, Santiago, Chile
[3] Escuela de Diseño, Facultad de Arquitectura, Arte y Diseño, Universidad Diego Portales, Santiago, Chile
[4] Departamento de Sonido, Facultad de Artes, Universidad de Chile, Santiago, Chile

ABSTRACT

This study aims to quantify the reproducibility of 3D-printed soundboards for string musical instruments by comparing the frequency responses of ukulele tops made of three materials: Engelmann spruce (traditional tonewood), Chilean laurel (local tonewood), and PLA+ (3D printing material). Traditional Latin American luthiers fabricated the soundboards and the PLA+ plates were produced using FDM printing.

The frequency response of free soundboards and admittance measurements coupling the plates to printed bodies were performed. Pearson correlation coefficients assessed the similarity between free plates' responses within each material. As expected, the results show notable variability in the wooden plates: correlations between laurel plates range from 0.19 to 0.50, and between spruce plates, from 0.36 to 0.65. In contrast, the PLA-printed plates show high consistency, with correlations close to 0.94. Similar trends were obtained comparing admittance measurements in plates coupled to printed soundboxes, although the correlation values decrease significantly when compared to those of the free plates. These findings suggest that 3D printing offers promising consistency for the construction of reproducible musical instruments, which may benefit not only the commercial manufacturing of instruments but also research based on them.

Keywords: *3D-printing, 3D-printed guitar, guitar making consistency*

1. INTRODUCTION

One of the major challenges in the construction of string instruments is reproducibility. Even when working with wood from the same trees, using identical techniques and following parallel processes to ensure identical environmental conditions, the resulting instruments will still differ. This is due to the intrinsic variability of wood [1]. This difficulty in achieving consistent construction, combined with the rapid evolution of digital design and manufacturing techniques, has led to the proposal of 3D printing as an alternative to traditional fabrication methods [2-4]. This raises the question: how reproducible are instruments made using these techniques, and how does this reproducibility compare to traditional materials? To address this question, a vibroacoustic study of ukulele soundboards was conducted. The study involved comparing the frequency response of three sets of soundboards made from different tonewoods and 3D printing material. The response was measured under free boundary conditions and when coupled to 3D-printed resonance boxes, and the comparison was done using the Pearson correlation coefficient.

[1]***Corresponding author**: carolinaaespinozao@uchile.cl.*
***Copyright**: ©2025 Labraña et al. This is an open-access article distributed under the terms of the Creative Commons Attribution 3.0 Unported License, which permits unrestricted use, distribution, and reproduction in any medium, provided the original author and source are credited.*

2. METHODS

This study selected three materials to fabricate ukulele soundboards: Chilean laurel (*Laurelia sempervirens*), Engelmann spruce (*Picea engelmannii*), and PLA+. The three materials' density (ρ) and elastic constants (E_L and E_R) were measured. For the wooden samples, the elastic constants were obtained applying Caldersmith's equations [5], following the method proposed in [6]. For PLA+, tensile tests were conducted on specimens with the same orthotropic geometry as applied in the soundboard printing. The tensile tests followed the ASTM D638 standard, using a Type IV specimen. The equipment used was an Instron testing machine, and the tests were conducted at a speed of 50 mm/s. All tests were repeated on three different samples of each material.

The soundboards were fabricated once the materials were characterized, including the internal bracing structure. Fig. 1 shows (a) a printed soundboard, (b) a template for constructing the wooden soundboards and (c) a 3D-printed resonance box. The wooden soundboards were crafted by local luthiers. Unlike traditional construction, the ukulele soundboards were made from a single piece, rather than by joining two identical halves. The bracings were made using Spanish Cedar (*Cedrela odorata*). (see Fig. 2). The plates were printed with orthotropic geometries, with the direction of greatest stiffness aligned parallel to the string direction.

The frequency response of the soundboards was analyzed under free boundary conditions supported by elastic bands. A Stanford SR780 spectrum analyzer generated a swept sine from 20 Hz to 1 kHz. The signal was amplified using a Gemini XGA2000 amplifier and fed into a loudspeaker, which excited the plates. The response was recorded using a PCB 356A14 micro accelerometer connected to a PCB 408E09 signal conditioner. The signal was then returned to the spectrum analyzer, obtaining the frequency response spectrum for each plate. To quantify the degree of similarity, Pearson's correlation coefficient (r) was used [7]:

$$r = \frac{\Sigma(X_i-\bar{X})\Sigma(Y_i-\bar{Y})}{[\Sigma(X_i-\bar{X})^2\Sigma(Y_i-\bar{Y})^2]^{1/2}}, \quad (1)$$



Figure 1. (a) Printed soundboard, (b) Template for constructing the wooden soundboards and (c) 3D-printed resonance box.



Figure 2. Wooden soundboards.

where X and Y are the two datasets being compared, and $\overline{X}$ and $\overline{Y}$ are their respective means. This coefficient is a statistical measure that quantifies the linear relationship between two variables. It ranges from -1 to 1, where: (a) r = 1 means a perfect positive correlation (both variables increase together, (b) r = -1 means a perfect negative correlation (one variable increases while the other decreases), (c) r = 0 means no correlation (the variables are independent). The usefulness of this coefficient has been demonstrated in various studies where it was necessary to compare spectra obtained through different techniques as Raman Spectroscopy, Infrared Spectrometry, among others [8-10].

After characterizing the soundboards, they were glued to 3D-printed ukulele bodies. The assembled bodies were again supported on elastic bands, and their admittance was measured at the bridge position. This was done using a PCB 086C03 impact hammer and a PCB 356A14 micro accelerometer. The measurements were performed using the ObieApp software (see Fig. 4). The resulting spectra were again compared using Pearson's correlation coefficient.

3. RESULTS, ANALYSIS AND DISCUSSIONS

Table 1 presents the results of the measured properties for the different materials. Additionally, it indicates from which specific plates each soundboard plate was extracted.

Fig. 3 shows the spectra obtained for the printed plates, while Fig. 4 presents the spectra associated with the wooden plates. In each case, a zoomed-in view is included to observe the low-frequency behavior. It is possible to observe significant differences in the spectra of the wooden plates (Fig. 3a,b), while more similar behaviors are observed in the printed plates (Fig. 3c). The quantification of these similarities is shown in Fig. 4.

Table 1. Properties of the applied materials

Material	E_L (GPa)	E_R (GPa)	ρ (kg/m³)	Soundboard
Engelmann Spruce A	7.96 ± 0.66	0.70 ± 0.06	317 ± 11	1 - 2
Engelmann Spruce B	8.40 ± 0.47	0.59 ± 0.04	331 ± 8	3
Chilean Laurel A	16.23 ± 1.73	0.83 ± 0.09	505 ± 24	1 - 2
Chilean Laurel B	10.98 ± 1.17	0.77 ± 0.08	513 ± 24	3
PLA+	2.05 ± 0.03	1.83 ± 0.04	1039 ± 214	1 - 2 - 3

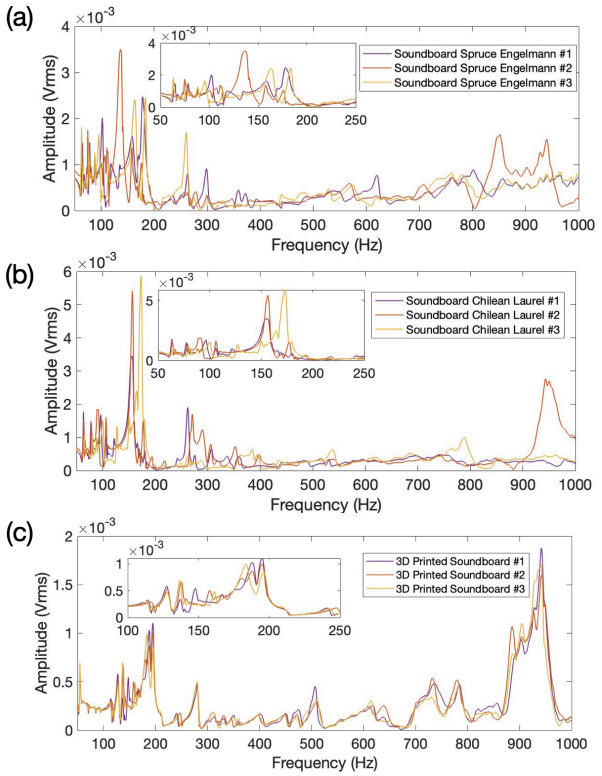


Figure 3. Measured spectra for (a) Spruce Engelmann soundboards, (b) Chilean Laurel soundboards, and (c) 3D-Printed soundboards.

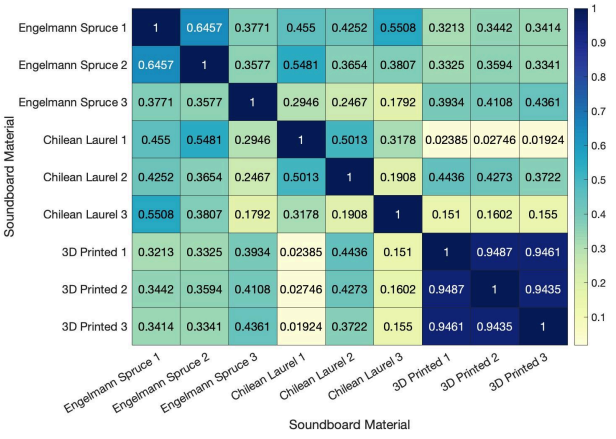


Figure 4. Pearson correlation coefficient obtained for each pair of plates.

Correlations between laurel plates range from 0.19 to 0.50, and between spruce plates, from 0.36 to 0.65. In contrast, the 3D-Printed plates show high consistency, with correlations close to 0.94. Similar trends were obtained comparing admittance measurements in plates coupled to printed soundboxes, although the correlation values decrease significantly when compared to those of the free plates (see Fig.5). In the case of the wooden soundboards, it can be observed that those made from the same plate have a higher correlation coefficient when compared to each other.

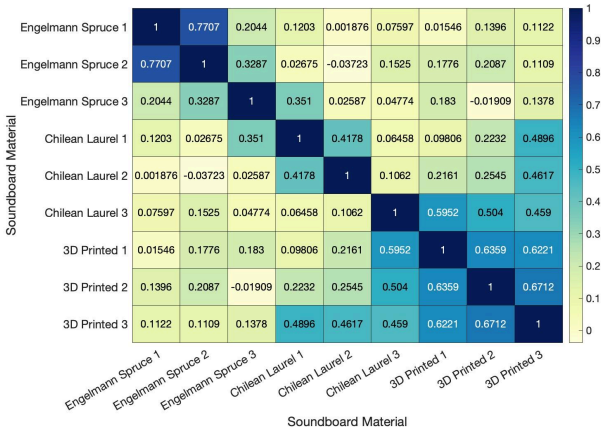


Figure 5. Pearson correlation coefficient obtained for each pair of plates coupled to 3D-Printed soundboxes.

4. CONCLUSIONS

Resonance plates for ukuleles have been made from different materials, including a traditionally used wood, a local wood, and PLA+ (a 3D printing material). The reproducibility of their vibratory behavior was assessed through acoustic response and admittance tests on both free plates and plates coupled to 3D-printed resonance boxes. The similarity between resonance spectra was measured using the Pearson Correlation Coefficient, showing that 3D-printed plates generally exhibit better reproducibility in their responses compared to wooden plates.

The fact that the Pearson Correlation Coefficient decreased with the coupled bodies (despite these being 3D printed and therefore expected to have the same level of reproducibility as the soundboards) highlights the relevance of the vibratory behavior of elements that are often overlooked, difficult to control, measure, and even model numerically, such as adhesives and joints between parts.

In any case, the consistency observed in the behavior of the printed parts could be useful for exploring other factors, such as how geometry affects the acoustic behavior of individual components from traditional instruments, while eliminating variability due to material differences.

These results highlight the potential of 3D printing as a manufacturing method that offers greater consistency in vibratory behavior, which could be advantageous for instrument design and production.

5. ACKNOWLEDGMENTS

This project was funded by Fondecyt Iniciación 2024 11240044, ANID, Chile. Special thanks to Maestro Luthier Roberto Hernández, and to Luthier and Researcher Claudio Carreño..

6. REFERENCES

[1] R. Viala, V. Placet and S. Cogan: “Simultaneous non-destructive identification of multiple elastic and damping properties of spruce tonewood to improve grading,” *Journal of Cultural Heritage*, vol. 42, pp. 108-116, 2020.

[2] A. Zoran: “The 3D Printed Flute: Digital Fabrication and Design of Musical Instruments,” *Journal of New Music Research*, vol. 40, no. 4, pp. 379-387, 2011.

[3] The Hovas, “Hovalin V5,” Hovalabs. [Online]. Available: https://www.hovalabs.com/blog/hovalin-five/. [Accessed: 11-Feb-2025].

[4] OpenFab PDX, “Modular Fiddle,” OpenFab PDX. [Online]. Available: https://openfabpdx.com/modular-fiddle/. [Accessed: 11-Feb-2025].

[5] G. Caldersmith and E. Freeman, ”Wood properties from sample plate measurements i,” J Catgut Acoust Soc, vol. 1, no. series II, pp. 8–12, 1990.

[6] S. Gonzalez, E. Chacra, C. Carreño, C. Espinoza, "Wooden mechanical metamaterials: Towards tunable wood plates," *Materials & Design*, vol. 221, p.110952, 2022

[7] J. Lee and A. Nicewander, "Thirteen Ways to Look at the Correlation Coefficient," *The American Statistician,* vol. 42, no. 1, pp. 59-66, 1988.

[8] P. Griffiths, and L. Shao, "Self-Weighted Correlation Coefficients and Their Application to Measure Spectral Similarity", *Applied Spectroscopy,* vol. 63, no. 8, pp. 916–919, 2009

[9] K. Lvova, A. Martínez-Arcos, A. López-Prieto, B. Pérez-Cid, X. Vecino, A.B. Moldes, and J.M. Cruz, "Correlation of Fourier transform infrared spectroscopy data for optimizing Gramicidin production in corn kernel aqueous stream," *Sustainable Chemistry and Pharmacy*, vol. 39, p. 101596, 2024.

[10] S. Ni, Q. Yang, J. Huang, M. Zhou, L. Wei, Y. Yang, J. Wen, W. Mo, W. Le, D. Qi, L. Jin, B. Li, Z. Zhao, and K. Du, "Constructing high-accuracy theoretical Raman spectra of SARS-CoV-2 spike proteins based on a large fragment method," *Chemical Physics Letters*, vol. 800, p. 139663, 2022.

DOI: 10.61782/fa.2025.0279

FORUM ACUSTICUM EURONOISE 2025

DESIGN, CONSTRUCTION, AND ACOUSTIC CHARACTERIZATION OF A FULLY FUNCTIONAL 3D-PRINTED GUITAR

Espinoza, Carolina[1*] **Adasme, Claudio**[1] **Correa, Víctor**[2]
Baeza, José[3]
[1] Departamento de Sonido, Facultad de Artes, Universidad de Chile, Santiago, Chile
[2] Universidad Academia de Humanismo Cristiano, Santiago, Chile
[3] Escuela de Diseño, Instituto DUOC UC, Santiago, Chile

ABSTRACT

Crafting a guitar demands expertise and skill from the artisan in selecting the appropriate tonewood and working with it. Despite these efforts, the outcome remains highly unpredictable. The above is due to inherent variability in material properties and manufacturing procedures. In contrast, 3D printing, coupled with parametric modeling, enables precise control over structural characteristics, replicability, and quick prototyping. Furthermore, the printing process offers potential benefits, including reduced waste generation and the use of bio-based materials.

In this work, an interdisciplinary team of luthiers, designers, and scientists designed, constructed, and characterized a scaled-down, fully functional guitar with a modular design, enabling its fabrication in desktop 3D printers. Acoustic measurements were conducted compared to a mass-produced guitar, highlighting the need to improve certain key aspects of the printed one, such as sustain and low-frequency response. Despite that, the results pave the way for future studies to optimize materials and techniques to enhance the acoustic quality of 3D-printed instruments.

Keywords: *luthiery, 3D-printing, 3D-printed guitar*

[1]***Corresponding author**: carolinaaespinozao@uchile.cl*
***Copyright**: ©2025 Espinoza et al. This is an open-access article distributed under the terms of the Creative Commons Attribution 3.0 Unported License, which permits unrestricted use, distribution, and reproduction in any medium, provided the original author and source are credited.*

1. INTRODUCTION

The variability of wood's mechanical properties has been a significant challenge in consistently building musical instruments such as the guitar [1]. Considering this, additive digital manufacturing techniques emerge as an alternative to traditional instrument-making, allowing not only the replication of conventional models but also the development of new design alternatives that would be impossible to achieve with subtractive or manual techniques [2]. Regarding string instruments, preliminary studies have explored the FDM printing of functional violins and ukuleles [3-5].

This work presents a functional 3D-printed guitar model, designed as an assemblable modular structure and manufacturable using desktop 3D printers. The model has undergone acoustic studies to compare specific timbral properties with those of a low-cost, mass-produced wooden guitar. The sound production when playing open strings has been analyzed, and the instruments' frequency content and time response have been compared.

2. GUITAR DESIGN

At the beginning of the research, specific fundamental characteristics were established for the 3D-printed guitar model:

1. It had to be manufactured using desktop 3D printers with an approximate build volume of 220 mm × 220 mm × 220 mm. This decision aims to facilitate the instrument's fabrication in different work environments.

2. IIt needed to be easily assembled, minimizing the use of adhesives.

3. It had to be functional and capable of standard tuning, like a traditional acoustic guitar.

All these characteristics align to create a replicable model in manufacturing and assembly, making it accessible to audiences interested in instrument fabrication. Based on these requirements, a modular, thread-assembled design was proposed, inspired by an 1886 Torres model [6] and Latin American instruments with a *golpeador*. In these traditional chordophones, the section of the soundboard that covers the upper bout is overlaid with a rigid and dense wood.

Given the limited printing dimensions, the proposed design corresponded to a 1/4-scale guitar with a vibrating string length of 480 mm (see Fig. 1).

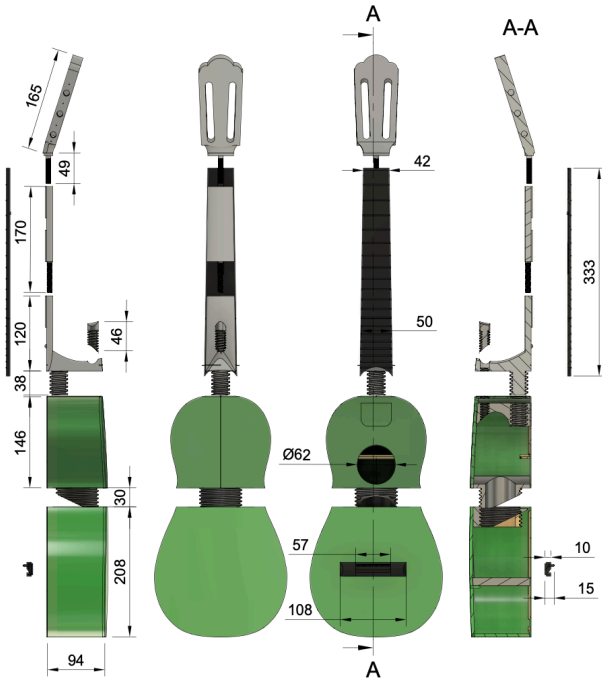
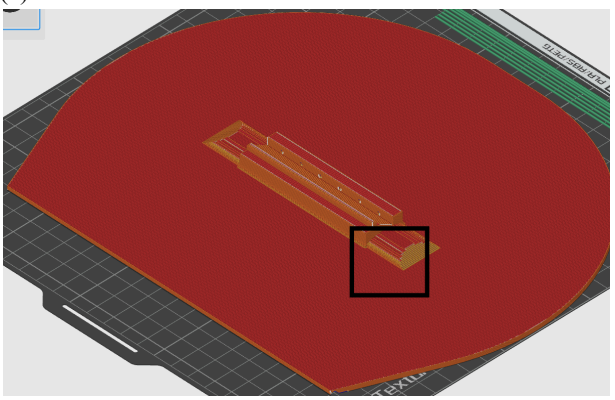


Figure 1. Main Dimensions of the Proposed 1/4 Guitar Model. The vibrating length is 480 mm.

3. MODEL SLICING

The slicing process was carried out using the open-source software Orca Slicer. The aim was to impart orthotropic properties to the printed components through specific printing parameters. To achieve these properties, printing directions were assigned following the grain orientation of the wood traditionally used in guitar making. For example, in the soundboard case, printing patterns were designed to align the primary strength direction to the strings, following the fiber orientation found in traditional soundboard construction. Fig. 2 shows details of the printing directions in the soundboard and bridge.

(a)



(b)

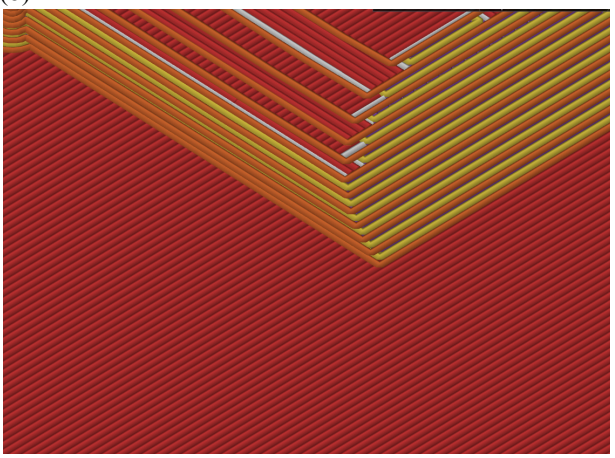


Figure 2. Printing orientation of the soundboard and bridge (a) View of the soundboard with the bridge attached. (b) Close-up showing details of the preferred orientations.

4. INSTRUMENT MANUFACTURING

PLA+ was used for manufacturing. Preliminary material characterizations were performed and elastic modulus measurements were conducted using tensile tests. The printing patterns corresponded to 100% infill of (a) longitudinal fibers "L" (aligned with the tensile direction) and (b) transverse fibers "T" (perpendicular to the tensile direction). Using a Type IV specimen, the tensile tests followed the ASTM D638 standard. The equipment used was an Instron testing machine, and the tests were conducted at a speed of 50 mm/s. The measured density was $\boldsymbol{\rho}$ = (1039 ± 214) kg/m³, with elastic moduli of $\mathbf{E_L}$ = (2.05 ± 0.03) GPa and $\mathbf{E_T}$ = (1.83 ± 0.04) GPa.

The printing time with a Bambu Lab X1 Carbon Combo printer was approximately 50 hours, while the assembly time was around 5 hours. The assembly process required post-processing of components, including support removal, thread cleaning, and minor adjustments.



Figure 3. 3D-Printed parts of guitars.

Finally, approximately 1 kg of filament was used. Fig. 3 shows various printed components. The tuning pegs and strings used are traditional. The guitar was strung with high-tension strings. Finally, Fig. 4 shows a fully assembled guitar.



Figure 4. Fully assembled printed guitar.

5. ACOUSTIC CHARACTERIZATION

For the acoustic characterization of the 3D-printed guitar, certain timbral attributes were compared with those of a reference guitar. The study involved recording the sound produced (a) when plucking each string individually in open position and (b) when strumming all strings open simultaneously.

The reference instrument was a 3/4 guitar (540 mm vibrating length), made of wood, mass-produced, and low-cost. This instrument was chosen for being the closest in price and size to the 3D-printed guitar.

The recordings were conducted in a semi-reverberant room, with the strings manually excited at L ~ (vibrating length)/3. A Dayton EMM-6 microphone was positioned 10 cm from the soundhole of each guitar, and a Focusrite Clarett interface was used for signal acquisition. The sound produced by each guitar was analyzed in both the time domain and the frequency domain.

In the time domain, the decay time was studied following the approach used in [7]. The RMS envelopes were obtained, and in the decay region, a function of the form $A_0e^{-t/\tau}$ was fitted. In this function, τ is the exponential time constant and corresponds to the time at which the signal amplitude has decayed to 36.8% of its maximum value. The results are shown in Fig. 5. It can be observed that while the decay constants for the strings tuned to E4 (~330 Hz) and D3 (~147 Hz) are practically the same, the strings tuned to A2 (~110 Hz) and E2 (~82 Hz) exhibit significantly longer decay times in the reference guitar. Despite the previous results, when evaluating the decay of the instruments when strummed with open strings, the decay times were practically identical.

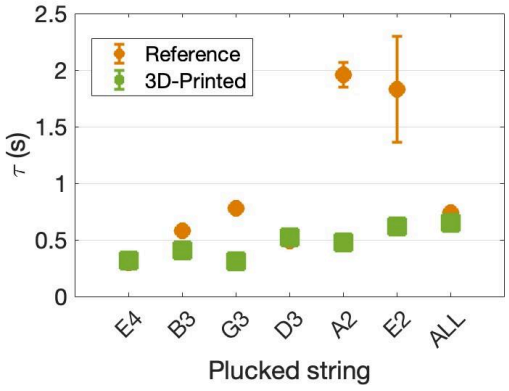


Figure 5. Time decay constant for open strings

In the frequency domain, the Power Spectral Density (PSD) was analyzed for each case. In general, the most significant differences appear in the low and mid-frequency ranges. In the low frequencies, the reference guitar exhibits a stronger response between 100 Hz and 200 Hz, whereas the 3D-printed guitar shows areas of greater response in the mid-frequency range. Figs. 6–8 show examples of the PSD obtained for the E2, E4, and all open strings cases.

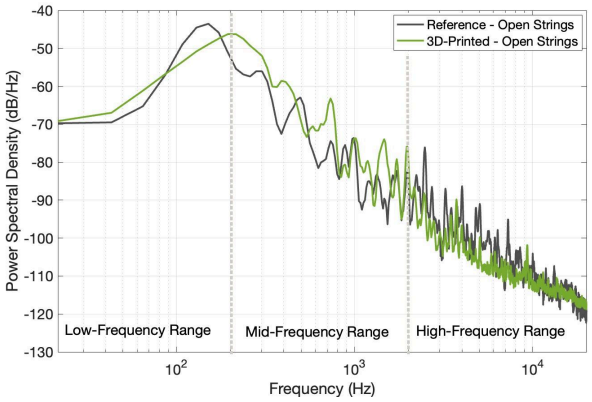


Figure 6. PSD for all open strings strummed.

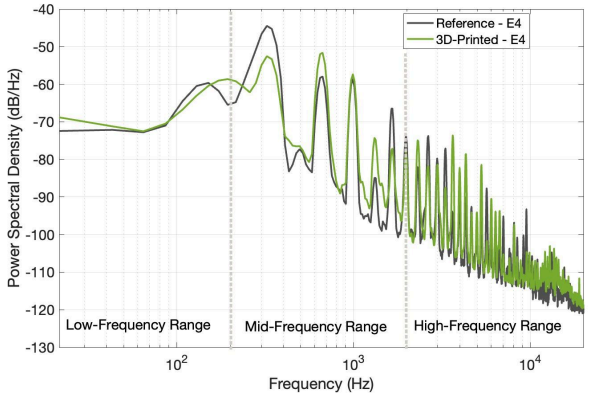


Figure 7. PSD for plucked E4 string.

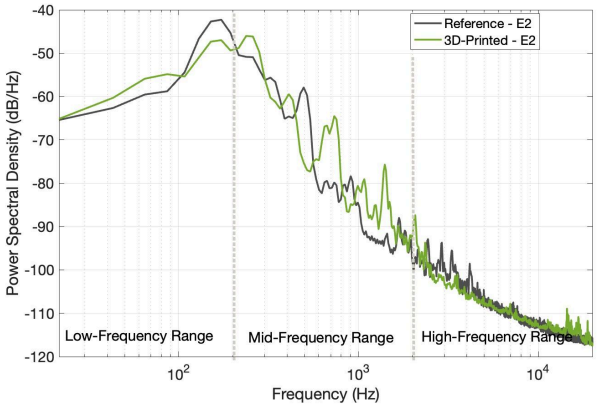


Figure 8. PSD for plucked E2 string.

6. CONCLUSIONS

Details on the design, slicing, and fabrication of a fully functional 3D-printed modular guitar were presented. The manufacturing time for the model is approximately 55 hours in a desktop machine, requiring around 1 kg of PLA+ filament.

The results demonstrate the feasibility of producing functional, low-cost instruments with rapid prototyping capabilities. This opens possibilities for both the construction of study guitars made from alternative, low-cost materials aimed at beginners and the development of scientific research using instruments built in a more controlled way compared to traditional wooden guitars.

Acoustic analyses generally show shorter decay times than those observed in wooden guitars, highlighting an area for improvement in future versions of the instrument. Additionally, a weaker low-frequency response is observed when compared to the reference instrument, which should also be addressed in the next stages of research.

7. ACKNOWLEDGMENTS

This project was funded by Fondecyt Iniciación 2024 11240044, ANID, Chile. Special thanks to Professor Héctor Sepúlveda, Maestro Luthier Roberto Hernández, and to the recording assistants Hakeen Mishea and Ignacio Rivera.

8. REFERENCES

[1] R. Viala, V. Placet and S. Cogan: "Simultaneous non-destructive identification of multiple elastic and damping properties of spruce tonewood to improve grading," *Journal of Cultural Heritage*, vol. 42, pp. 108-116, 2020.

[2] A. Zoran: "The 3D Printed Flute: Digital Fabrication and Design of Musical Instruments," *Journal of New Music Research*, vol. 40, no. 4, pp. 379-387, 2011.

[3] The Hovas, "Hovalin V5," Hovalabs. [Online]. Available: https://www.hovalabs.com/blog/hovalin-five/. [Accessed: 11-Feb-2025].

[4] OpenFab PDX, "Modular Fiddle," OpenFab PDX. [Online]. Available: https://openfabpdx.com/modular-fiddle/. [Accessed: 11-Feb-2025].

[5] P. Qian, N, Xiaoyu, L, Liangzhi, M. Junjie, Y. Shumeng, C. Zhuo, L. Jonghyun and F. Shengxue, "A comparison on sound quality of PLA 3-D printing ukulele and single board wooden ukulele," in *Proc. of Meetings on Acoustics*, (San Diego, California), p. 035007, 2019.

[6] R. Courtnall. *Making Master Guitars*. London: Robert Hale, 1993.

[7] S. Gonzales, M. Rau, C. Espinoza, G. Longo, F. Antonacci and A. Sarti, "Sound synthesis of geometric and material changes in archtop guitars: towards the timbral design of musical instruments" in *Proc. of Inter-Noise24*, (Nantes, France), pp. 6294-6303, 2024.

DOI: 10.61782/fa.2025.0676

FORUM ACUSTICUM EURONOISE 2025

PERCEPTUAL COMPARISON BETWEEN A LOW-COST GUITAR AND A 3D-PRINTED GUITAR

Espinoza, Carolina[1*] **Ibánez, Tania**[2] **Adasme, Claudio**[1]
Denzer, Milenko[2] **Díaz, Catalina**[2] **Moreno, Timoteo**[2]
[1] Departamento de Sonido, Facultad de Artes, Universidad de Chile, Santiago, Chile
[2] Departamento de Música, Facultad de Artes, Universidad de Chile, Santiago, Chile

ABSTRACT

This study evaluates perceptual and acoustic differences in timbral characteristics between two guitars: (1) a wooden, mass-produced, low-cost guitar designed for beginners and (2) a 3D-printed guitar. Blind listening tests were conducted with seven students specializing in musical performance, composition, and music theory. An experienced performer played identical musical pieces on both instruments—strumming, arpeggios, open strings, and harmonics—under controlled recording conditions. Participants rated the perceived timbral characteristics in low, mid, and high-frequency ranges and sustain for each recording using a five-point Likert scale.

Results showed considerable variability in participant responses, suggesting that the timbral differences between instruments were not easily distinguishable. The most significant difference was observed in the sustain rating, which was generally lower for the printed instrument. A preliminary acoustic analysis was conducted using the same evaluated recordings, and the results aligned with the perceptual findings. These results highlight the timbral characteristics of the 3D-printed guitar that require further development and demonstrate the potential of 3D printing in musical instrument manufacturing.

Keywords: *3D-printing, 3D-printed guitar, timbre*

[1]***Corresponding author**: carolinaaespinozao@uchile.cl*
***Copyright**: ©2025 Espinoza et al. This is an open-access article distributed under the terms of the Creative Commons Attribution 3.0 Unported License, which permits unrestricted use, distribution, and reproduction in any medium, provided the original author and source are credited.*

1. INTRODUCTION

The application of digital fabrication techniques, including 3D printing, has expanded into musical instrument manufacturing [1-3]. Given the increasing interest in 3D-printed instruments, it is important to assess how their timbral characteristics compare to those of traditional materials instruments. An example is presented in [4], where the sound quality of a 3D-printed ukulele and a wooden one is compared.

This work presents the results of perceptual evaluation and acoustic characterization of the timbre in two guitars: a mass-produced, low-cost acoustic guitar and a 3D-printed guitar made of PLA+. The evaluation was conducted through an acousmatic listening test, where participants evaluated pre-recorded performances of identical musical excerpts played on both instruments.

2. METHODS

The instrument under evaluation was a 1/4-scale 3D-printed guitar made of PLA+ with a vibrating string length of 480 mm. This instrument was designed to be a functional, low-cost alternative that could be produced quickly. The printing process required 50 hours using a Bambu Lab X1 Carbon Combo 3D printer, followed by approximately 5 hours of manual assembly. The total material consumption was 1 kg of PLA+ filament, with an estimated cost of 35 USD (see Fig. 1).

As a reference, we selected a 3/4-scale, mass-produced acoustic guitar designed for beginners, with a vibrating string length of 540 mm. This model was the smallest commercially available, and it had a price comparable to the manufacturing cost of the printed guitar (approximately 50 USD).

An acousmatic blind listening test was conducted with seven advanced music students to evaluate the sound of the printed guitar. A professional guitarist performed the same musical excerpts on both instruments, including strumming, arpeggios, open strings, and harmonics, which were referred to as 'categories' of playing. The recordings were made on the same day and location, using Dayton Audio EMM-6 microphones placed 50 cm from the instruments' soundholes. For each recording, participants used a five-point Likert scale to rate four perceived timbral characteristics: the frequency content in the low, mid, and high ranges, as well as sustain.

Each pair of recordings was presented twice consecutively for each category while maintaining the same order (e.g., for strumming, first the reference guitar, then the 3D-printed guitar). Across categories, the order was alternated randomly to reduce bias (e.g., a participant might hear the 3D-printed guitar first in the strumming category but the reference guitar first in the arpeggio category). The listening tests took place in a semi-reverberant room, where each participant was positioned approximately one meter in front of a pair of studio monitors. Example recordings of both guitars being strummed can be accessed at the following link.



Figure 1. Professional guitarist recording the 3D-Printed Guitar, Prof. Héctor Sepúlveda.

In order to compare the perceptual evaluations, acoustic analyses were conducted on the recorded audio samples. The spectral magnitude was obtained using the open software Audacity using a Hamming window of size 4096. The analysis was done for the complete audio recordings to provide a general assessment of their frequency content.

3. RESULTS, ANALYSIS, AND DISCUSSION

Tables I–IV show the means and standard deviations σ of the participants' evaluations. In the Strumming category (Table I), the most significant difference was observed in the sustain evaluation, where the 3D-printed guitar scored 3.0 ± 0.0, while the reference guitar scored 3.7 ± 0.5. These results suggest a clear perception of longer sustain in the reference guitar. The treble, midrange, and bass ratings were relatively close, with only minor differences.

For the Arpeggio category (Table II), the sustain rating again showed the most significant difference, with a mean of 2.4 for the 3D-printed guitar compared to 2.9 for the reference guitar. Although this suggests a perceptible difference, the higher standard deviation (0.9) for the reference guitar reduces the statistical significance of this result. Interestingly, although the difference is small, the bass frequencies were rated slightly higher for the 3D-printed guitar (3.1) than for the reference guitar (2.9).

In the Open Strings category (Table III), the most pronounced difference was observed in the sustain rating, with the reference guitar scoring 4.1 ± 0.9, compared to 3.1 ± 1.2 for the 3D-printed guitar. Additionally, the treble rating was noticeably lower for the 3D-printed guitar (2.7 ± 1.0) than for the reference guitar (3.3 ± 0.8), indicating that the printed instrument may have a perceived loss of brightness in open strings.

Finally, in the Harmonics category (Table IV), the most significant difference again appeared in the sustain rating, where the reference guitar scored 4.1 ± 0.7, while the 3D-printed guitar scored 3.4 ± 1.0. The ratings for treble, midrange, and bass, with minor variations, remained pretty close.

Overall, the results indicate a consistent trend of lower sustain ratings for the 3D-printed guitar across all categories. Additionally, the printed instrument's treble

ratings tend to be slightly lower, particularly in open strings. However, midrange and bass frequencies showed comparable ratings; in some cases, the 3D-printed guitar matched or slightly outperformed the reference instrument. Despite these tendencies, the large standard deviations in several evaluations suggest that individual perceptions varied significantly, making it difficult to establish definitive conclusions.

Table 1. Results for the Strumming category

Category: Strumming				
Frequency Range	3D-Printed guitar		Reference guitar	
	Mean	σ	Mean	σ
High	3,0	0,8	3,1	0,7
Mid	3,9	0,7	3,7	1,1
Low	3,4	0,8	3,4	0,5
Sustain	3,0	0,0	3,7	0,5

Table 2. Results for the Arpeggio category

Category: Arpeggio				
Frequency Range	3D-Printed guitar		Reference guitar	
	Mean	σ	Mean	σ
High	2,9	0,7	3,0	0,6
Mid	3,4	0,5	3,6	0,8
Low	3,1	0,7	2,9	0,9
Sustain	2,4	0,5	2,9	0,9

Table 3. Results for the Open Strings category

Category: Open Strings				
Frequency Range	3D-Printed guitar		Reference guitar	
	Mean	σ	Mean	σ
High	2,7	1,0	3,3	0,8
Mid	3,4	1,1	3,6	0,8
Low	3,3	0,8	3,7	0,5
Sustain	3,1	1,2	4,1	0,9

Table 4. Results for the Harmonics category

Category: Harmonics				
Frequency Range	3D-Printed guitar		Reference guitar	
	Mean	σ	Mean	σ
High	3,1	0,4	3,4	1,1
Mid	3,7	0,8	3,7	0,5
Low	3,0	0,8	3,0	0,8
Sustain	3,4	1,0	4,1	0,7

Regarding the acoustic analyses, Figs. 2-5 presents the results for the four categories. The graphs have been divided into three bands: the low range (20 Hz to 200 Hz), the mid-range (200 Hz to 2 kHz), and the high range (2 kHz to 20 kHz). In all categories, the overall response in the low range is similar, except around 100 Hz and 200 Hz, where the response of the reference guitar is greater. In the mid ranges, certain areas stand out for the 3D-printed guitar, particularly between 180 Hz and 1.2 kHz. In the high-frequency range, the response remains similar up to 4 kHz, after which the response of the 3D-printed guitar becomes more prominent.

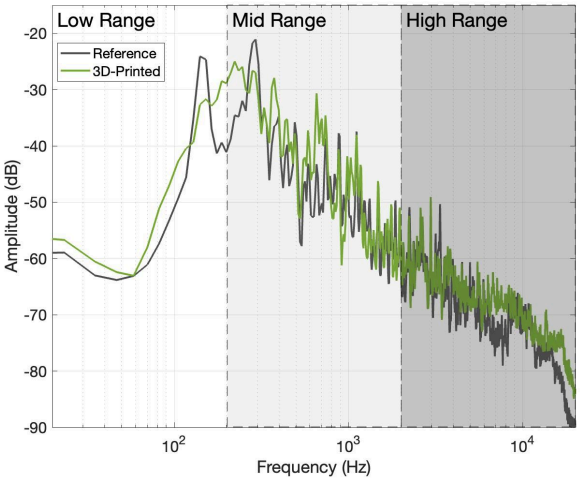


Figure 2. Spectral Magnitude for the Strumming category.

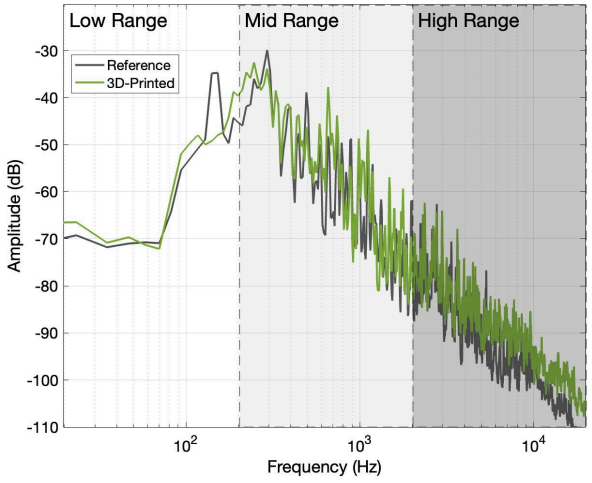


Figure 3. Spectral magnitude for the Arpeggio category.

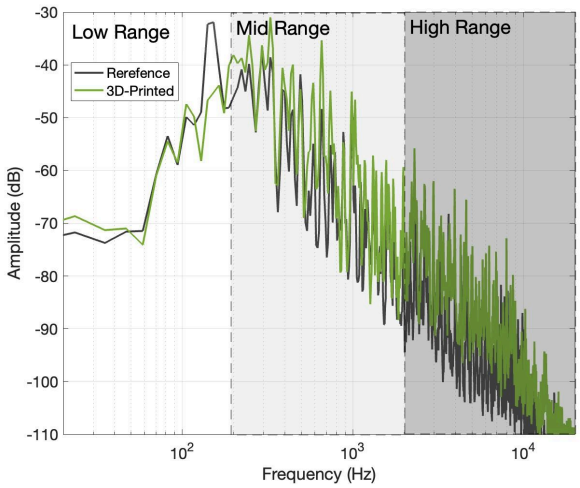


Figure 4. Spectral magnitude for the Open String category.

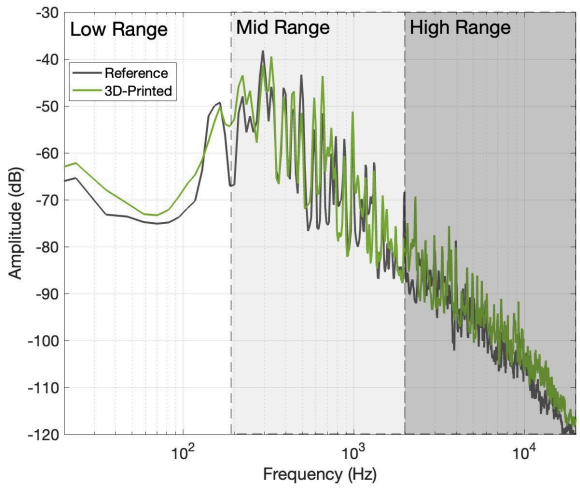


Figure 5. Spectral magnitude for the Harmonics category.

Certain correspondences can be observed between the perceptual and acoustic results. For instance, the spectral analysis showed that both guitars have similar low and middle-frequency responses, with localized differences (a greater response of the reference guitar between 100 Hz and 200 Hz and specific emphasized frequencies in the printed guitar). These results align with the perceptual results, where the ratings associated with bass and mid frequencies were similar across all categories.

The most significant difference is found in the treble response. Acoustic analyses showed that the printed guitar exhibits a more prominent response above 4 kHz. However, the printed guitar received lower treble ratings in the open strings category in the perceptual evaluation. This discrepancy, along with the perception of larger sustain in that category, could be because the perception of treble depends not only on spectral energy in the high-frequency range but also on other factors, such as the distribution of energy over time.

Regarding sustain, due to the characteristics of the playing style, it was impossible to study the strumming, arpeggio, and harmonics categories. However, frequency analysis was conducted for the open strings category. Fig. 6 shows spectrograms for both guitars. Both cases were plotted with the same time scale to facilitate the comparison. It can be observed that the reference guitar sounds for a longer time than the 3D-printed guitar. Although these results agree with the perceptual evaluation and serve for preliminary comparisons, it is necessary to conduct more measurements, focusing on the instrument's timbral properties.

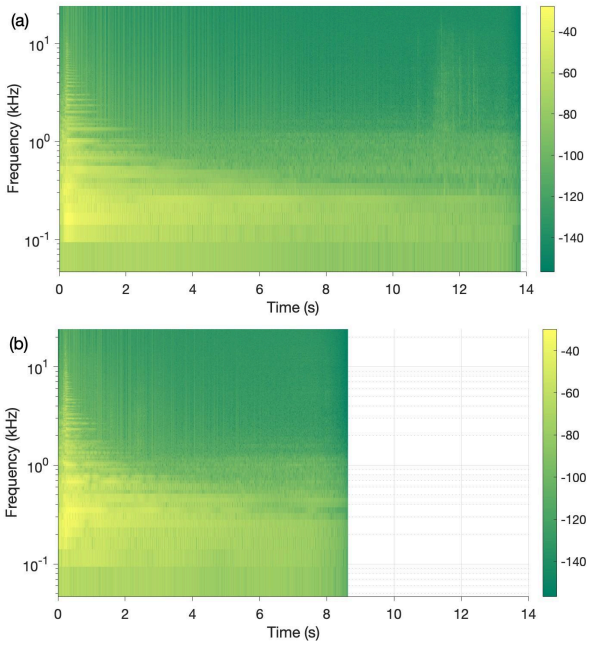


Figure 6. Spectrogram for the Open String category. (a) Reference guitar. (b) 3D-Printed guitar.

4. CONCLUSIONS

The results exhibited substantial variation in participant responses, indicating that the instrument's timbral differences were not easily perceived. Regarding the frequency content, no relevant perceptual differences were evaluated in the midrange and bass frequencies, while the high-frequency content was rated lower for the 3D-printed guitar. On the other hand, acoustic analyses showed differences only in specific frequencies in the low and mid ranges (which aligns with the perceptual evaluation). At the same time, the printed guitar displayed higher content in frequencies above 4 kHz (which differs from the general evaluation). This difference may be due to factors such as the listening conditions. For example, poor performance of the monitors above 4 kHz or background noise.

The most significant difference in the rating of the printed guitar compared to the reference instrument was observed in the sustain criterion, where the PLA+ instrument was evaluated lower in general. This could be solved by using materials with higher density or elastic moduli and optimizing the structural design, particularly of the soundboard and bridge. Although preliminary acoustic results were obtained that align with the perceptual results regarding the sustain, they should be repeated in future stages of the research.

For the perceptual study, several points for improvement were observed. In the future, the number of participants will be increased to improve the statistics. On the other hand, in addition to the evaluations conducted, discrimination tests will be added to assess the randomness of participants' responses. It has also been decided to improve the listening conditions for participants by replacing the studio monitors with hi-fi flat-response headphones so that the listening experience is not affected by the evaluator's position or background noise. Additionally, open-ended questions will be added to assess qualitative responses regarding the sound of each instrument.

Finally, more acoustic analyses remain pending to allow for a deeper study of the acoustic properties of the 3D-printed guitar, which, together with perceptual evaluations, will guide future versions of the instrument.

5. ACKNOWLEDGMENTS

This project was funded by Fondecyt Iniciación 2024 11240044, ANID, Chile. Special thanks to Professor Héctor Sepúlveda, and to the recording assistants Hakeen Mishea and Ignacio Rivera.

6. REFERENCES

[1] A. Zoran: "The 3D Printed Flute: Digital Fabrication and Design of Musical Instruments," *Journal of New Music Research*, vol. 40, no. 4, pp. 379-387, 2011.

[2] J. Savan and R. Simian: "CAD modelling and 3D printing for musical instrument research: the Renaissance cornett as a case study," *Early Music*, vol. 42, no. 4, pp. 537–544, 2014.

[3] R. Simian: "3D-Printed Musical Instruments: Lessons Learned from Five Case Studies," *Music & Science,* vol. 6, p. 20592043231210653, 2023.

[4] P. Qian, N, Xiaoyu, L, Liangzhi, M. Junjie, Y. Shumeng, C. Zhuo, L. Jonghyun and F. Shengxue, "A comparison on sound quality of PLA 3-D printing ukulele and single board wooden ukulele," in *Proc. of Meetings on Acoustics*, (San Diego, California), p. 035007, 2019.

DOI: 10.61782/fa.2025.0629



FORUM ACUSTICUM
EURONOISE 2025

NUMERICAL DESIGN OF A TRUMPET LEADPIPE: FROM THE NUMERICAL MODEL TO THE EVALUATION OF THE HARDWARE PROTOTYPE

Jean-François Petiot[1*] **Vincent Freour**[2,3] **Keita Arimoto**[3]
[1] Ecole Centrale de Nantes, LS2N UMR 6004, Nantes, France
[2] Aix Marseille University, CNRS, Centrale Marseille, LMA UMR 7031, Marseille, France
[3] Yamaha Corporation, Research and development Division, Hamamatsu, Japan

ABSTRACT

In a previous work, a machine learning model was trained using numerical simulations in order to predict intonation and playability descriptors of trumpets from the bore geometry [1]. Using this technology, a numerical design procedure was conducted where a new leadpipe geometry was proposed using a bi-objective optimization on the Equivalent Fundamental Pitch (*EFP*) and minimum blowing pressure (*Pth*), computed over five regimes. This recommendation led to a leadpipe numerical prototype that was manufactured by *Yamaha Corporation*, Japan. In this paper, we present recent investigations conducted on this hardware leadpipe prototype in order to compare the performances of the real instrument with the numerical expectations in the design phase. At first, impedance measurements of the prototype were performed, and sound simulations were computed from these measurements to assess the *EFP* and *Pth* descriptors. They were compared to the results of the numerical prototype. In a second step, playing tests with musicians were conducted in order to assess perceived differences between the original and prototyped leadpipe. These results are discussed in light of the potential sources of uncertainties through the whole procedure, from the model to the perception.

Keywords: *physics-based sound simulations, trumpet optimization, playing tests, instrument comparison.*

Corresponding author: *Jean-Francois.Petiot@ec-nantes.fr.*
Copyright: *©2025 Petiot et al.. This is an open-access article distributed under the terms of the Creative Commons Attribution 3.0 Unported License, which permits unrestricted use, distribution, and reproduction in any medium, provided the original author and source are credited.*

1. INTRODUCTION

An interesting mean to study the objective quality of musical instruments is to carry out sound simulations by physical modelling [1]. They constitute a very interesting approach because they allow, by working on a virtual prototype, the exploration of the design space, by the creation of a large number of virtual instruments. The main interest of these simulations is that the sound result is driven by the causes that create the sound, as for a real instrument: if the physical model used is accurate enough to generate simulations in agreement with the real behavior (such as it is perceived by the musician), then the simulations can constitute a predictive tool for the development of the instrument (virtual acoustics) [2].
In recent years, machine learning (ML) has become an essential approach for the modeling of systems. Using this technique, we have developed in previous works [1,4] a procedure for optimizing the leadpipe of a trumpet. Two criteria were considered for the optimization: the Equivalent Fundamental Pitch (*EFP*), which may represent the global intonation of the instrument, and the minimum blowing pressure (*Pth*), which may represent the ease of emission of the note. The procedure led to the definition of an "optimized leadpipe", that was manufactured by *Yamaha Corporation of Japan*.
The objective of this paper is to give the first results about this new leadpipe, mainly by comparing the performances of the real prototype to the theoretical expectations in the design phases, and to compare it to the standard leadpipe.

Section 2 presents the background on the project, mainly the procedure defined to lead to the "optimal" leadpipe. A reminder of the physical model and the bore reconstruction process is proposed. In section 3, the first results are presented. They concern the simulation of instruments from measured or calculated impedances, and the analysis of differences between instruments when played by musicians.

2. BACKGROUND: OPTMIZATION OF THE TRUMPET LEADPIPE

2.1 Sound simulations

In this study, we use a classical elementary model of a brass instrument under playing conditions, described in [2]. The vibrating lips are modeled as a one-degree-of-freedom (1-DOF) outward-striking valve, non-linearly coupled to the air column of the brass instrument. From the input impedance *Ze* of the instrument (calculated or measured), different regimes of the trumpet can be simulated using different virtual musicians. The parameters used for the simulations are described in [1, 4]. Five regimes of the instrument were considered (regime 2 to 6), corresponding to the notes Bb3, F4, Bb4, D5 and F5 (concert-pitch) (Fig. 1).

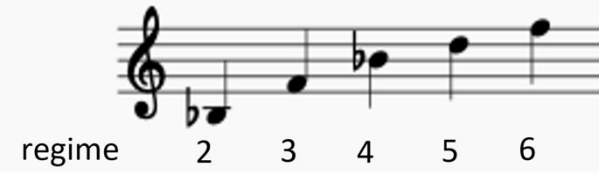


Figure 1. Notes corresponding to the five different regimes simulated on a Bb trumpet (concert pitch)

To characterize the intonation of each regime of a virtual instrument, the Equivalent Fundamental Pitch (*EFP* – Eqn. 1), that represents the deviation in cent of the average playing frequency f_n from a reference frequency f_R, according to natural intervals, was calculated. The reference frequency was chosen arbitrarily according to the common tuning note of the instrument (the regime 4, Bb4) (with $f_R = f_4 /4$, the *EFP* of the regime 4 is then necessarily equal to "0").

$$\overline{EFP_n} = 1200.log_2(\frac{\overline{f_n}}{n.\overline{f_R}}) \quad (1)$$

To characterize the global intonation of each virtual instrument, the global average *EFP* was computed. It corresponds simply to the average value of the absolute values of the *EFP* of all the regimes (2 to 6) (Eqn. 2).

$$\overline{EFP} = \frac{1}{5}.\sum_{k=2}^{6}|\overline{EFP_k}| \quad (2)$$

To characterize the global ease of playing of the instrument, the threshold pressure $P_{th,k}$ of each regime k was obtained by Linear Stability Analysis (LSA) [5]. The sum of the threshold pressure P_{th} for all the regimes was calculated (Eqn. 3).

$$\overline{P_{th}} = \sum_{k=2}^{6}\overline{P_{th,k}} \quad (3)$$

2.2 Optimization of the impedance

The general approach for the optimization of the impedance of a trumpet based on simulations and ML models consists of the following three stages:

Stage 1: Generation of sounds (section 2.1). Sound simulations by physical model are used to create a database of sounds (1000 trumpet samples), with the input impedance of the instrument as an input (modal parameters), and the sound signal as an output. Two descriptors are considered to characterize a virtual instrument: the global average *EFP* (Eqn. 2) and the threshold pressure P_{th} (Eqn. 3),

Stage 2: Supervised learning. ML models are fitted to the database, with the characterization of the impedance Z as an input (modal parameters) and the 9 different features as outputs (EFP_n (n =2, 3, 5, 6) and $P_{th,n}$ (n=2, 3, 4, 5, 6)),

Stage 3: Optimization. Using the previous ML models, the input impedance is optimized by a minimization of two descriptors: global average *EFP* and the threshold pressure P_{th}. A bi-objective optimization is considered, leading to a Pareto front, using a gradient-free method (Genetic Algorithms). An optimal target Z_{opt} was selected.

In addition to these stages, 2 more steps are necessary to obtain a real optimized instrument:

Stage 4: Bore reconstruction (section 2.3). The objective of this stage is to obtain the geometry of the bore that corresponds to the optimal impedance Z_{opt} identified in stage 3 (optimization),

Stage 5: Manufacture of the optimal instrument (section 2.4). Given the geometry of the bore (stage 4), a real instrument can be manufactured and tested with musicians, to assess the efficiency of the approach. Before manufacturing, a smoothing of the initial profile of the leadpipe was applied, to obtain a class C^1 profile (manufacturing of the trumpet leadpipe with a mandrel) Details of stages 1 to 4 are available in [1, 4].

2.3 Bore reconstruction

Instead of optimizing the whole bore of the trumpet (difficult to manufacture), it has been decided to focus only on an important part of the bore: the leadpipe. The leadpipe of a trumpet, located after the mouthpiece and before the tuning slide, plays an important role in the intonation. Its shape is evolutive, generally divergent. At the end of the process, only the leadpipe will need to be manufactured, resulting in a cost-effective and faster solution. The rest of the instrument corresponds to a Yamaha trumpet model for which accurate impedance measurements are available, and called in the next the "S" trumpet.

Six optimization variables were defined in the leadpipe, 5 diameters and one length (Fig. 2). The leadpipe is considered as a juxtaposition of truncated cones. The design variables are defined by vector X=(d_1, d_2, d_3, d_4, d_5, L).

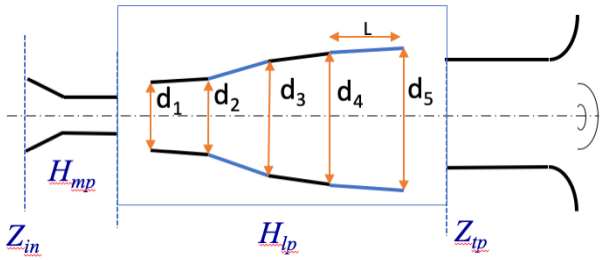


Figure 2. Overview of the bore of the trumpet (from the mouthpiece to the bell), with the definition of the design variables. The optimized part corresponds to the leadpipe, with the diameters d_1 to d_5 and the length L

To obtain the current input impedance of the trumpet, a transmission line model of the impedance has been used [6]. The input impedance of the instrument is a result of a calculation that involves three terms:

- The transfer matrix of the mouthpiece (Yamaha model), denoted as H_{mp}
- The transfer matrix of the four sections of the leadpipe, denoted as H_{lp}
- The input impedance Z_{tp} of the rest of the trumpet (a Yamaha model, S), measured with the CTTM impedance sensor at the entrance of the tuning slide.

Finally, the overall input impedance Z of the whole instrument is calculated as follows (Eq. 4):

$$\begin{aligned} H &= H_{mp}.H_{lp} \\ [P_{in}\ U_{in}] &= H.[Z_{tp}\ 1] \\ Z &= \frac{P_{in}}{U_{in}} \end{aligned} \tag{4}$$

The bore optimization problem of an instrument can be formulated as the search for the optimal geometry X* whose impedance Z fits as best as possible the target impedance Z_{opt}. A Genetic algorithm, NSGAII [7], with 300 individuals per generation, and a budget of 500 generations was used to solve this problem. From the Pareto front obtained at **stage 3**, which provides a range of optimal impedances that promote either a significantly lower *EFP* or a lower P_{th} than the training set and than the commercial trumpets, different target candidates were considered.

Nevertheless, one difficulty we have to face is to find, through bore reconstruction, leadpipe geometries that precisely produce the impedances of the Pareto front (or at least one impedance selected). Indeed, there is no guarantee that a solution to this inverse problem exists or can be easily reached, given the chosen design variables X=(d_1, d_2, d_3, d_4, d_5, L).

In this context, we could only obtain satisfactory bore reconstruction results by selecting a Z_{opt} with a lower *EFP* and P_{th} than commercial trumpets (namely the S trumpet), but located within the training set.

Different target instruments were considered for bore reconstruction. The optimal instrument $Z_{opt\text{-}rec}$ considered for the continuation of the study is presented in Fig. 3. Compared to instrument S, it presents a slight improvement of *EFP* and a decrease of P_{th} of around 70 Pa.

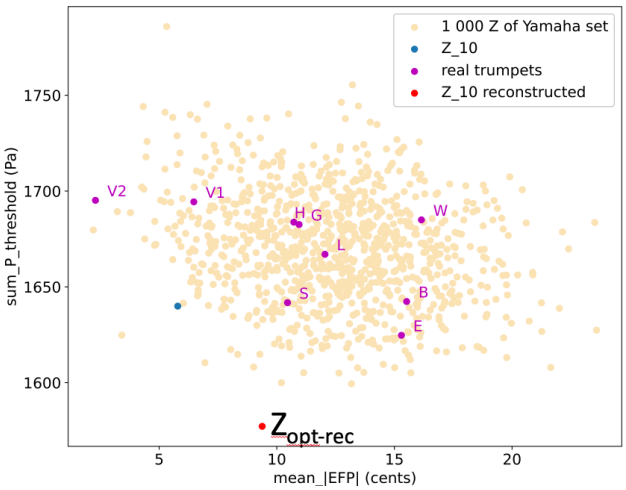


Figure 3. Position of different instruments in the plane of the two descriptors *EFP* and P_{th}: in particular, the Yamaha S trumpet, the reconstructed instrument $Z_{opt\text{-}rec}$ after re-simulation from the input impedance parameters. The training set counts 1000 instruments, corresponding to the beige colored points. The magenta points correspond to measured commercial instruments.

In perspective, one way to overcome this issue of "bore reconstruction" would be to compute a ML model of the descriptors directly from the design data (geometry of the leadpipe), and not from the modal parameters. We actually followed that strategy in another study not reported here, and that we conducted after this first phase of the project [9].

2.4 Manufacturing of the new leadpipe NL

The optimal leadpipe X* =(d_1, d_2, d_3, d_4, d_5, L)*, called NL, was communicated to *Yamaha Corporation* for the manufacturing (after a smoothing of the shape with a degree 4 polynom to have a class C^1 profile). A picture of the NL leadpipe is presented in Fig. 4, together with the current S leadpipe.



Figure 4. Picture of the NL new leadpipe and the S leadpipe

3. RESULTS: COMPARISON OF THE INSTRUMENTS

3.1 Simulations of S and NL

Impedance measurements of the NL prototype were performed, and sound simulations were computed from these measurements to assess the *EFP* and *Pth* descriptors.
Fig. 5 presents the results of the simulations for different versions of the instruments:

- S_{meas} corresponds to the S instrument, from the impedance measured on the real instrument,
- NL_{meas} corresponds to the NL instrument, from the impedance measured on the prototype,
- NL_{th} corresponds to the NL instrument, from the impedance calculated ($Z_{opt\text{-}rec}$) after bore reconstruction,
- $NL_{th\text{-}ycj}$ corresponds to the NL instrument, from the impedance calculated after a degree 4 smoothing of the optimal bore X* =(d_1, d_2, d_3, d_4, d_5, L)*.

Except for regime 6 (note F4), there is a remarkable degree of agreement between the position of the NL instruments resulting from impedance calculations and impedance measurements. This observation gives a good level of confidence in the quality of the Z models and the quality of the leadpipe manufacturing. The only difference is for regime 6, for which the P_{th} of the measured instrument NL_{meas} is slightly larger (+20Pa) than that of the theoretical instruments.
The agreement between the theoretical leadpipe NL_{th} and its version with a degree 4 smoothing $NL_{th\text{-}ycj}$ is excellent, indicating that this regularization has no

visible effect (in fact, it only changes the geometry of the leadpipe by a few hundredths of a millimeter).
The comparison between the S and the NL leadpipes leads to the following comments:

- The pitch of the Bb3 note is slightly higher for the S leadpipe (+30 cents), so the octave Bb3-Bb4 is closer to a theoretical octave (Ratio 2) for the NL instrument than for S. For the other notes, the EFP are very similar for the 2 leadpipes,
- For the note D5, the threshold pressure is higher for the S instrument than for the NL (+ 50Pa). For the other notes, pressures are comparable (lower than 30 Pa).

These results provide indications on the nature of the differences between the S and NL instruments, which must be confirmed by tests in playing conditions.

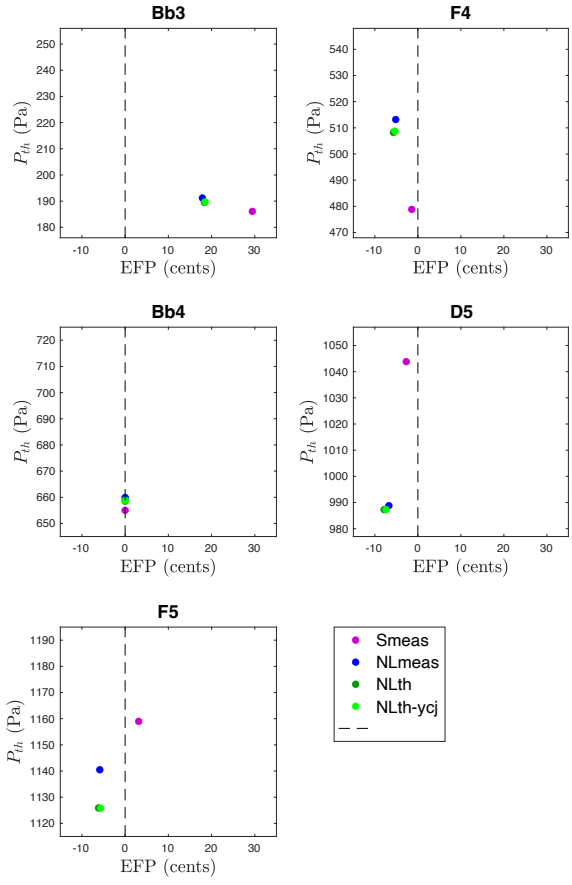


Figure 5. comparisons of the NL and S instruments for the different regimes. Different versions of the NL instruments are considered to estimate the deviation between theoretical and real instruments.

Fig. 6 presents a comparison of the input impedance of instrument NL, measured (NL_{meas}) or calculated ($NL_{th\text{-}ycj}$).

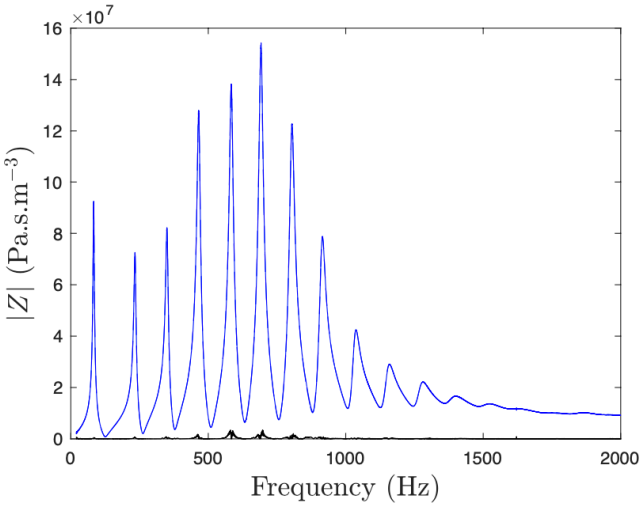


Figure 6. comparisons of the magnitude of the impedance of instrument NL, either measured or calculated. The difference between the 2 curves is presented in black lines.

Results show that the two impedance are very close and that the model agreement between the calculation and the measurements is large.

3.2 Recordings of the instruments and first analysis

The two instruments S and NL were played and recorded by 5 musicians. A series of five notes was recorded, in an ascending then descending arpeggio (Fig 7).

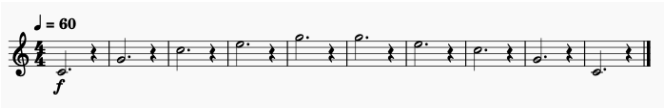


Figure 7. Sequence of notes played be the musicians (Bb writing)

Players were instructed to play as naturally as possible (without pitch corrections). The sounds were recorded with a Zoom H4 recorder (48kHz, 24 bits). Three repetitions of each sequence were performed, for each instrument S and NL.
From the audio recordings, the playing frequency of each note was estimated with the YIN algorithm [7], and similarly to the *EFP*, the deviation (in cent) from natural intervals was computed.

The intonation diagrams of the different notes are presented in Fig. 8, with the error bars corresponding to the 95% confidence interval calculated on the sample size of 3*2*5 = 30 observations.

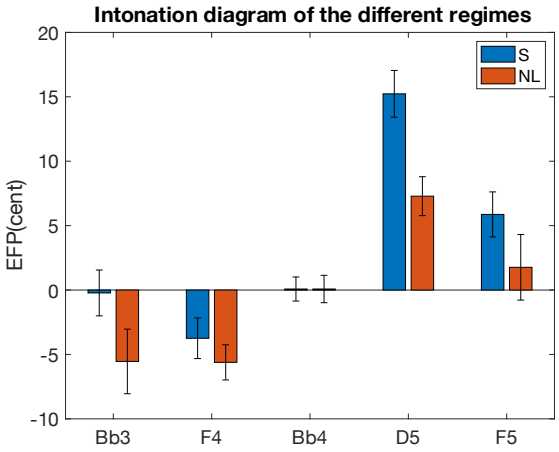


Figure 8. Intonation diagram for the different notes of the trumpet (in cent), with the 95% confidence intervals – Bb4 is the reference note (tuning note).

There are slight differences in intonation between the two instruments:

- Octave Bb3-Bb4 is larger with NL than with S
- Notes D4 and F4 are slightly higher with S than with NL

It is interesting to mention that this relative position of the played notes is in agreement with the relative positioning of the simulated sounds (Fig. 5): simulations can make interesting predictions of the pitch, at least from a relative point of view.

To characterize the spectrum of each instrument, the spectral centroid Sc_n of each regime n was considered, calculated as the power-weighted average spectral frequency (Eqn. 5).

$$\overline{Sc_n} = \frac{\int_0^\infty f.\left|\overline{S(F)_n}\right|^2 df}{\int_0^\infty \left|\overline{S(F)_n}\right|^2 df} \qquad (5)$$

The diagrams of the spectral centroid for the different notes are presented in Fig. 9, with the error bars.

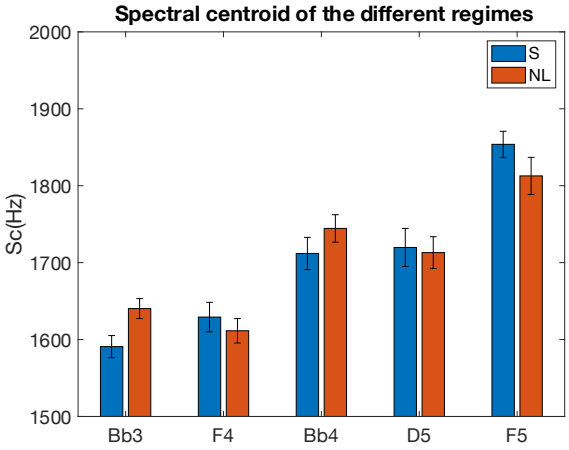


Figure 9. Spectral centroid of the different notes of the trumpet (in Hz), with the 95% confidence intervals.

Concerning the spectral centroid, instruments S and NL are extremely similar and no clear difference can be highlighted. Further investigations are needed to determine whether timbre differences are significant.

4. CONCLUSIONS

The work carried out in this article allows us to study to what extent theoretical differences, observed on a prototype of a virtual instrument, remain valid when the instrument is actually built. A trumpet leadpipe, developed and optimized using physical model simulations, was produced and mounted on an instrument. It should be noted that it is extremely rare in musical acoustics to be able to compare performances on virtual instruments to performances on a real instrument, as instrument manufacturing requires extensive resources and advanced know-how. This work constitutes a pioneering contribution. The first results show that the performances between virtual instruments and real instruments are rather in agreement, in particular with regard to playing frequencies. The continuation of this work will consist of determining whether the differences between the initial instrument and its optimized version are actually noticeable in playing conditions.

5. ACKNOWLEDGMENTS

We thank Yamaha trumpet designers for the manufacturing of the leadpipe prototype, and the

students of the specialization “Science et Musique” at Ecole Centrale de Nantes for their participation in the project.

6. REFERENCES

[1] J-F. Petiot, M. Roatta, V. Freour, K. Arimoto. “Contribution of machine learning and physics-based sound simulations for the characterization of brass instruments”, in *Proc. of Forum Acusticum 2023*, Politecnico di Torino, (Torino, Italy), September 2023.

[2] J-F. Petiot, J. Gilbert. “Comparison of trumpets' sounds played by a musician or simulated by physical modeling”. *Acta Acustica united with Acustica*. Vol. 99, 629-641, 2013

[3] S. Adachi and M. Sato. “Time domain simulation of sound production in the brass instruments”. *The Journal of the Acoustical Society of America*, 97(6): 3850-3861, June 1995.

[4] Petiot J-F., Roatta M., Freour V., Arimoto K. “Contribution of machine learning and physics-based sound simulations for the optimization of brass instruments”. *Proc. of INTER-NOISE24*, (Nantes, France), 25-29 August 2024.

[5] L. Velut, C. Vergez, J. Gilbert, M. Djahanbani. « How well can linear stability analysis predict the behaviour of an outward-striking valve brass instrument model?” In: *Acta Acustica united with Acustica* 103.1, pp. 132–148, 2017.

[6] A. Chaigne and J. Kergomard. *Acoustics of musical instruments*, Springer, 2016.

[7] K. Deb, A. Pratap, S. Agarwal and T. Meyarivan. “A fast and elitist multiobjective genetic algorithm: NSGA-II”. *IEEE Transactions on Evolutionary Computation*, 6(2), 182–197, 2002.

[8] A. De Cheveigné and H. Kawahara. “YIN, a fundamental frequency estimator for speech and music”. *The Journal of the Acoustical Society of America,* 111(4): 1917-1930, April 2002.

[9] Petiot J-F., Hamelin G., Freour V., Arimoto K. “Contribution of sound simulations by physical model and machine learning for the optimization of the bore of a brass instrument”. *Proc. of CFA 2025*, (Paris, France), 27-30 April 2025.

DOI:

Main theme: A11 Musical Acoustics

Session A11.04 Articulated musical instrument modelling

Chair(s): M. Van Walstijn, V. Chatziioannou

DOI: 10.61782/fa.2025.0726



FORUM ACUSTICUM
EURONOISE 2025

REAL-TIME BOWING PARAMETER SENSING METHODS FOR ARTICULATED BOW-STRING PHYSICAL MODELLING

Eoghan Ó Néill* **Maarten van Walstijn** **Miguel Ortiz**
SARC: Centre for Interdisciplinary Research in Music and Sound
Queens University Belfast

ABSTRACT

This paper presents bowing parameter estimation techniques developed specifically for real-time control of bowed-string physical models. By placing the sensors on the resonator instead of on the bow, the ability to seamlessly employ traditional bowing techniques is preserved. The sensing methods presented here are part of a larger project that aims to design and develop stage-ready virtual-acoustic bowed-string instruments.

The proposed approach utilizes load cells mounted beneath the string supports to sense bowing force and position in real time. An automatic offset adjustment algorithm is implemented to counter sensor drift, which enhances accuracy and long-term reliability. A Kalman-like feedback loop that implements level-dependent adaption of the bowing position was designed to avoid noisy estimates at small bowing forces. Experimental validation shows that this approach provides robust, usable estimates of bowing force and position with minimal calibration.

Bow velocity is inferred from string velocity data captured by an electromagnetic pickup system, utilising an approximation of the short-time probability density function. Preliminary bow velocity estimation results were obtained with an offline algorithm, showing promising capability for real-time application.

Keywords: Instrument Design, Physical Modelling, Sensor-Based Interface Design, Bowing Parameter Sensing

**Corresponding author*: eoneill65@qub.ac.uk.

Copyright: *©2025 Ó Néill et al. This is an open-access article distributed under the terms of the Creative Commons Attribution 3.0 Unported License, which permits unrestricted use, distribution, and reproduction in any medium, provided the original author and source are credited.*

1. INTRODUCTION

Among sound synthesis methodologies, physical modelling stands out for its distinctive advantage: its control parameters bear a direct physical correspondence to those of the acoustic instrument being simulated [1]. Recent advances in bow-string interaction modelling have yielded significant progress, including improved alignment with measurements [2, 3], guaranteed passivity [4, 5], and enhanced computational efficiency [6]. Although the accurate modelling of frictional dynamics at the bow-string interface remains an open challenge (see, e.g., [7]), these ongoing developments are steadily advancing toward real-time implementations that faithfully reproduce the salient acoustic characteristics of bowed-string interaction. Realising the full potential of such models, however, also requires the development of robust, real-time estimation techniques for bowing control parameters.

The excitation of a bowed-string physical model requires the specification of several key control parameters. This study concentrates on three primary bowing parameters: bowing force, bowing position, and bow velocity. Bowing force denotes the normal force applied by the bow at the point of contact with the string; bowing position specifies the location along the string where this contact occurs; and bow velocity corresponds to the relative tangential speed of the bow perpendicular to the string. Together, these parameters capture the dynamics at the bow-string interface, where frictional interaction gives rise to sound production. Although secondary factors such as bow tilt and inclination angle can influence the character of the interaction, the aforementioned primary parameters are generally sufficient to drive physically based bowed-string models with high fidelity [8].

Bowing parameter estimation has been the subject of

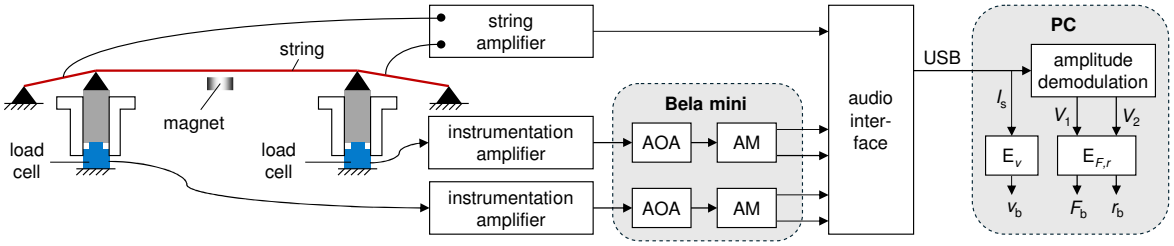


Figure 1: Bowing parameter estimation apparatus - system schematic.

extensive research for the past 40 years, driven by different motivations across disciplines. Researchers studying musical acoustics and gesture analysis aim to understand and quantify the mechanics of bowing, often prioritizing accuracy to capture the nuances of the bow-string interaction [3, 9–11]. In these areas of study, bowing parameter estimation is usually performed offline to achieve greater accuracy [3, 10, 11]. In the realm of pedagogy, bowing parameter estimation is pursued to enhance learning and teaching methods for string players. By analysing bowing techniques in real-time, educators and students can receive immediate feedback, fostering more effective practice and skill development [12–14]. Accuracy remains important in this context, but the primary concern is ensuring that the system is relatively non-intrusive and that the instrument retains familiarity with the traditional acoustic instrument being learned. The same holds for studies focused on instrument innovation, with additional emphasis on developing systems that are robust and capable of functioning in diverse performance environments. While precision is important, these systems do not require the same level of accuracy as those used in musical acoustics or gestural studies. They must be designed to accommodate different playing styles and instrument variations without requiring extensive calibration or modifications to the bow, allowing musicians to leverage their existing bowing techniques seamlessly [15, 16]. This paper is concerned with the latter research area, and as such, the methodology presented here reflects the priorities of developing a stage-ready bowed-string physical model interface.

2. METHODOLOGY

2.1 Selected Sensing Systems

Figure 1 provides an overview of the sensing system for bowing parameter estimation presented in this paper, illustrating the bowed-string interface and how the sensors are arranged, as well as the signal processing and routing.

In prior work, Lampis et al. [11] employed two load cells positioned beneath one of the string boundaries to estimate both the normal and transverse components of bowing force in controlled musical acoustics experiments. Building on this approach, we introduce a modified configuration in which a single load cell is placed beneath each of the string's boundaries (Figure 1). This arrangement enables simultaneous estimation of the normal bowing force and inference of the bowing position. Each load cell is mechanically coupled to its respective string boundary via a cylindrical shaft guided by a linear ball bushing, which constrains motion to a single plane – parallel to the shaft and perpendicular to the string. This mechanical design ensures accurate transmission of the normal component of bowing force while maintaining consistent coupling between the string and the sensing elements. The full assembly is mounted onto a 20×20, 55 cm-long aluminium profile using custom-designed, 3D-printed fixtures (Figure 6). While the current setup does not capture the transverse component of the bowing force – potentially leading to a slight underestimation when the bow is applied at an angle – this trade-off enhances structural rigidity and ensures robust sensor-string coupling, with the introduced difference being minor enough for musicians to adapt to comfortably. Each load cell operates on the Wheatstone bridge principle, producing millivolt-range output signals proportional to the applied force, which are subsequently amplified using AD620 instrumentation amplifiers.

In contrast to many existing methods for bowing parameter estimation, our approach eliminates the need for sensors to be mounted directly on the bow, thereby preserving the natural feel and freedom of motion familiar to string players. This design choice ensures that performance remains as unencumbered and authentic as possible. Although alternative bridge-force sensors – such as

piezoelectric discs – have been employed in prior studies, their AC-coupled nature renders them ineffective for capturing low-frequency or quasi-static variations in bowing force. Load cells, by contrast, provide DC-coupled measurements, enabling the accurate detection of both rapid transients and slow, gradual changes in applied force [11].

For bow velocity estimation, we propose a sensing methodology inspired by the work of Pardue et al. [16], which employs an electromagnetic pickup system to measure string velocity. This method again offers a non-intrusive means of acquiring bowing data without requiring direct modification of the bow. A neodymium magnet is positioned beneath the string at a fixed location, with one end of the string connected to the analogue input of a low-noise string amplifier, and the other end of the string connected to ground. In accordance with Lorentz force principles, the induced current in the string is directly proportional to its velocity at the location of the magnet. This string velocity information can then be used to infer the bow velocity at the point on the string directly above the magnet (see Section 2.5).

Alternatives to the above sensing techniques include the indirect estimation of parameters from AC-coupled sensor signals, which for example has been successfully applied to the estimation of plucking position in plucked-string instruments [17–21] and to tracking bowing parameters [15, 16]. However, all these methods share the disadvantage of relying on a particular structure in the waveform or spectrum, which may not be generally present under playing conditions. For estimating bowing parameters, machine learning techniques have been applied successfully for a specific set of notes [22], but with no follow-ups demonstrating more general estimation robustness covering a wide range of oscillation regimes.

Also worth noting here is that fully external sensing solutions such as camera-based motion tracking systems [8] offer high-resolution data in controlled laboratory settings, but their reliance on line-of-sight, controlled lighting, and computational overhead make them less suitable for real-time applications and live performance contexts – the target scenarios for our system.

Despite the advantages offered by the chosen sensing methodologies, several challenges must be addressed to ensure reliable and accurate parameter estimation. Although load cells are capable of capturing both rapid transients and slow variations in force, they are susceptible to signal drift over time, potentially compromising long-term measurement stability. Moreover, fluctuations in string tension and shifts in the string's equilibrium position introduce variability into the measured force signals, thereby affecting the accuracy of both bowing force and position estimations. Potential non-linearities in the load cell response further complicate matters and necessitate rigorous calibration procedures to ensure measurement fidelity.

The signal quality is also constrained by the limitations of the amplification stage. The employed load cell amplifiers exhibit a relatively poor signal-to-noise ratio, particularly at small force levels, where reliable data acquisition becomes more difficult. Electromagnetic pickups are particularly vulnerable to noise and interference from external electromagnetic sources. Mitigation strategies – such as the low-noise string amplifier developed by Pardue et al. [12] – have proven effective in reducing such interference, and as such has been implemented in the system presented here.

A further challenge arises due to the semi-chaotic nature of bowed-string interaction – particularly under expressive or unsteady bowing – which complicates the use of typical indirect sensing methods. This unpredictability demands a system that is robust across a wide range of performance conditions.

To address these challenges, a series of compensatory strategies have been implemented, detailed in the following sections.

2.2 Automatic Offset Adjustment

The load cell output, $V(n)$, represents the instantaneous voltage reading at time $t = n\Delta_t$, reflecting the combined effect of all forces acting on the system, including string tension and any external load. During startup, a calibration period occurs in which no external forces are applied, and the offset voltage $V_0(n)$ is calculated as an average over $M = 4410$ samples. This value serves as the baseline for adjusting the estimated applied force by subtracting $V_0(n)$ from $V(n)$. Ideally, $V_0(n)$ would remain constant; however, in practice, $V(n)$ does not always return to the same value upon bow release due to sensor drift, changes in string tension, and changes to the string's equilibrium state.

To counteract this artifact, an Automatic Offset Adjustment (AOA) algorithm is implemented. This Kalman-filter-like algorithm, illustrated in Figure 2, employs a feedback loop to update the offset voltage during periods of inactivity. Inactivity is defined as periods where the variance of both load cells falls below a threshold – set at 5% above a calibration-period variance reading taken

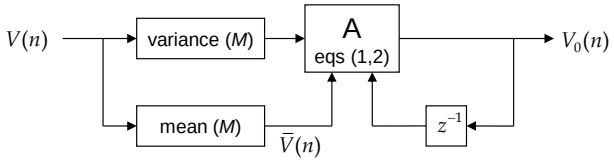


Figure 2: Schematic diagram of the automatic offset adjustment (AOA) algorithm. The variance and mean are calculated over M samples.

when the system is left undisturbed.

During these periods of inactivity, the following adaptation calculation is performed:

$$V_0(n) = V_0(n-1) + \Delta_V(n) \underbrace{g\,\Delta_t\,W(\Delta_V(n))}_{\gamma(n)}, \quad (1)$$

where:

$$\Delta_V(n) = \bar{V}(n) - V_0(n-1) \quad (2)$$

The term $\gamma(n)$ represents the effective adaptation rate at each step, and is composed of the scaling factor g – which statically determines the overall responsiveness of the adaptation, the time step Δ_t – ensuring proper temporal scaling, and the weight function $W(\Delta_V(n))$ – which dynamically modulates the adaptation rate based on the magnitude of $\Delta_V(n)$. This weight function is defined as:

$$W(\Delta_V(n)) = e^{-\psi\,|\Delta_V(n)|}, \quad (3)$$

where ψ is a tunable weight control factor. This formulation ensures that adaptation occurs more quickly for small deviations and more gradually for large deviations, preventing instability while still allowing for long-term drift correction.

2.3 Signal Routing

As illustrated in Figure 1, a Bela Mini is used to sample the amplified load cell signals at audio rate, maintaining high temporal resolution. To preserve this fidelity, the signals are transmitted at audio rate to a laptop via the Bela mini's audio outputs. This method leverages the Bela mini's low-latency audio path rather than relying on USB communication. Since many standard audio interfaces AC-couple their inputs – effectively filtering out DC components – an amplitude modulation (AM) scheme is used to encode the signals within the audio band. To mitigate phase misalignment issues that can arise between modulation and demodulation stages, each load cell signal modulates two carrier signals in quadrature. This approach enables robust demodulation in Max/MSP, ensuring accurate signal reconstruction for real-time bowing parameter estimation.

2.4 Bowing Force and Bowing Position Estimation

Equations for bowing force and bow position estimation are derived from heavily simplified acoustics of the string- assuming constant string tension, small string vibration, ideal string behaviour, and simplified boundary conditions. Under these assumptions, the force exerted on the string by the bow at the point of contact, $\tilde{F}_\mathrm{b}(n)$, is equal to the sum of the forces exerted by the string on the string's fixed boundaries, $\tilde{F}_1(n)$ and $\tilde{F}_2(n)$:

$$\tilde{F}_\mathrm{b}(n) = \tilde{F}_1(n) + \tilde{F}_2(n), \quad (4)$$

and these forces are distributed in such a way that:

$$\hat{r}_\mathrm{b}(n) = \frac{x_\mathrm{b}(n)}{L} = \frac{\tilde{F}_2(n)}{\tilde{F}_\mathrm{b}(n)}, \quad (5)$$

where $r_\mathrm{b}(n)$ is the relative bowing position, $x_\mathrm{b}(n)$ is the distance from the left string boundary to the bowing position, and L is the distance from one string boundary to the other-the effective length of the string.

Simulations were used to verify that these equations remain valid in the presence of stiffness and with different boundary conditions. However, it is less straightforward to predict whether they remain accurate under larger bowing forces, which induce large string deflections and significant increases in tension. In such cases, the resulting string slopes at the supports mean that the applied force is no longer purely parallel to the shafts, and thus is not fully captured by the load cells.

More importantly, the reliability of the estimates resulting from applying equation (5) deteriorates for small bowing forces, in which case the sensitivity to noise becomes extremely high, leading to large estimation errors. In practice, this can result in significant drift from the true position, occasionally producing values outside the expected range. To address these challenges, a feedback loop-similar in structure to the AOA algorithm is introduced. This adaptive mechanism improves stability when bowing forces are small and ensures that, in the absence of force input, the system retains the last reliable position estimate.

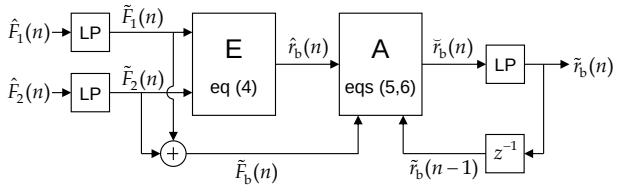


Figure 3: Bowing force and position estimation block diagram.

The following adaptation calculation is performed within the adaptation block A shown in Figure 3:

$$\breve{r}_b(n) = \tilde{r}_b(n-1) + \Delta_r(n) \underbrace{g\,\Delta_t\,W(\tilde{F}_b(n))}_{\gamma(n)}, \quad (6)$$

where,

$$\Delta_r(n) = \hat{r}_b(n) - \tilde{r}_b(n-1). \quad (7)$$

Here the term $\gamma(n)$ once again represents the effective adaptation rate at each step, only in this case the weight function $W(\tilde{F}_b(n))$ dynamically modulates the adaptation rate based on the magnitude of $\tilde{F}_b(n)$. The weight function is defined as:

$$W(\tilde{F}_b(n)) = 1 - e^{-\psi\,\tilde{F}_b(n)^2}, \quad (8)$$

where ψ is again a tunable weight control factor. This formulation ensures that adaptation occurs more quickly for large bowing forces and more gradually for small bowing forces, preventing wild fluctuation at small bowing forces where the noise can begin to affect the accuracy of the bowing position estimation.

2.5 Bow Velocity Estimation

The characteristic sound of a bowed string arises from a periodic cycle of 'sticking' and 'slipping.' The bow hairs grip the string momentarily, pulling it in one direction until friction is overcome, causing the string to slip back – only to stick again. This repeating motion, known as the Helmholtz motion, produces the characteristic sound of a bowed string [23]. Even when a periodic Helmholtz motion is not established, the bowed string's sound still results from instances of sticking and slipping. Our envisaged bow velocity estimation methodology relies upon the fact that the string velocity and the bow velocity are equal to each other during periods in which the bow hairs stick to the string. By measuring the string velocity, the bow velocity can be extrapolated by way of a probability density function – under the assumption that the sticking velocity is the dominant velocity in the signal, while slipping plays out over a more distributed range of velocities.

3. EXPERIMENTAL PROCEDURES AND RESULTS

A series of experiments were conducted to evaluate the efficacy of the proposed bowing parameter estimation methods.

3.1 Calibration and Validation with Static Forces

A bench experiment was devised to record load cell signals for various forces and positions along a 20cm string. A series of weights were suspended from the string using a 3D printed cradle to apply known static forces. The cradle was suspended in 5 known locations along the length of the string, limited to the middle 40% of the string due to the physical dimensions of the cradle and the strings supports.

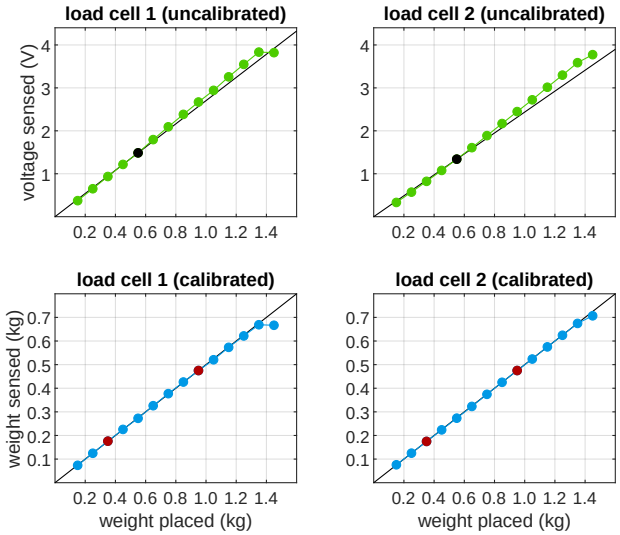


Figure 4: Load cell signals before and after logarithmic scaling calibration procedure. Black dots represent an arbitrary reference reading through which the linear black line is drawn. Red dots represent the calibration reference weights.

The load cell signals were recorded post-demodulation in Max/MSP. They were then rescaled to match the voltage read by the Bela mini, and a calibration scheme was devised to estimate the applied weight, as illustrated in Figure 4.

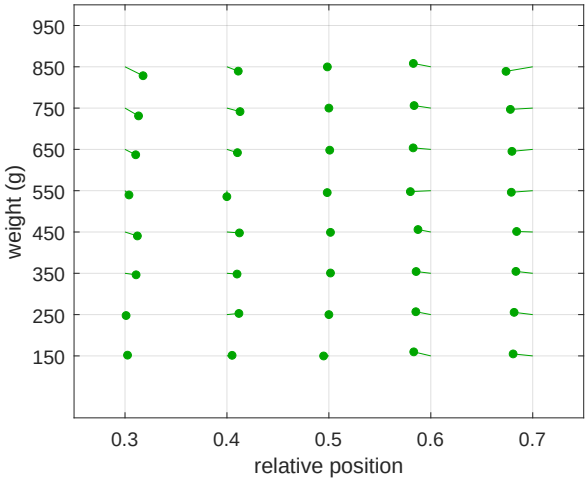


Figure 5: Estimation results for a known set of static weights and positions. Green dots show how estimation compares to nominal values at the grid line intersections.

Two reference weights are selected at the midpoint of the string, plotted as red points, upon which to scale the data logarithmically to correct for the slight nonlinearity observed in the uncalibrated data. In accordance with the project's overall goal of musical instrument implementation, the calibration procedure is intended to be practical and time efficient, so using as few calibration weights as possible is preferred. In this particular arrangement, we observe the beginning of saturation occurring in the upper region of the plot around 650g for load cell 1, or roughly 6.5N. As these plots represent the readings at the midpoint of the string, we can expect to measure a maximum of 6.5N at all points along the string, while larger forces can be measured the closer one bows to the centre of the string, up to 13N at the centre – double the maximum bowing forces measurable at the ends of the string.

The position estimation data is then calculated using equation (5) with the calibrated force data. Figure 5 illustrates the general accuracy of the bowing force and position estimation across a range of the string. As observed in Figure 5, the estimation errors can be largely described by an inward trend indicating lower accuracy for positions nearer the string ends. This can be attributed to the simplifications underlying equations (4) and (5), as discussed in section 2.4. While our calibration process ensures precise results at the center of the string, part of the total force remains unaccounted for when weights are hung away from the center, as variations in slope angles affect the proportion of the total force captured by the load cell. Consequently, the position estimation is less accurate when applying a load nearer to the string ends.



Figure 6: Monochord in cello orientation.

3.2 Bowing Experiment

In order to observe how the proposed estimation methods perform in the context of bowing practices, the third author, who is a cellist, bowed the experimental rig in an upright angled cello orientation using an *NS Design* electric cello stand, as shown in Figure 6.

Four short passages were recorded, where the cellist used four different cello bow strokes. As illustrated in Figure 7, the signal from a contact microphone placed on the monochord (green), bowing force estimation (blue), and bowing position estimation (red) were recorded in real-time. In these examples, the bowing force peaks at around 4N during *martelé* playing, well away from our saturation range of 6.5N, indicating that this will be enough headroom to capture most typical bowing techniques. We can also observe the slight inertia in bowing position estimation – for example, at around 7.5 seconds – when force is applied to the string and the bowing position estimation takes a few milliseconds to reach the new bowing position.

3.3 Preliminary Bow Velocity Sensing Results

In order to observe and validate the dominance of the sticking velocity in the string velocity signal, string velocity measurements were taken at a fixed position along the string using the apparatus detailed in Section 2.1 and illustrated in Figure 1. These measurements, as shown in Figure 8, illustrate that even when bowing away from the location of the magnet, the sticking velocity – and therefore the bowing velocity – can be estimated by finding the

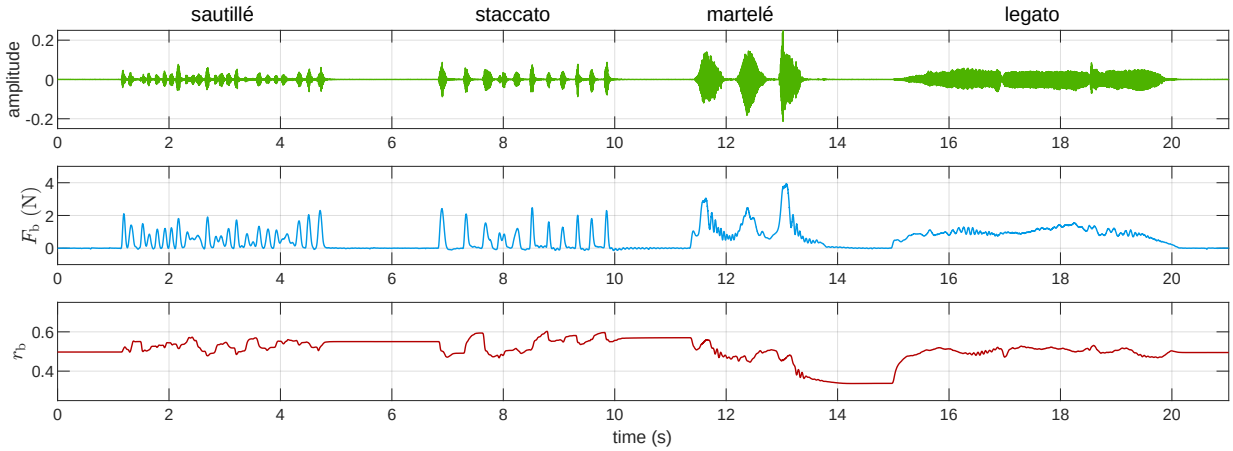


Figure 7: Real-time bowing force and bow-bridge distance estimation for four short cello bowing techniques performed on experimental rig.

peak of a probability density function. These preliminary results were calculated offline.

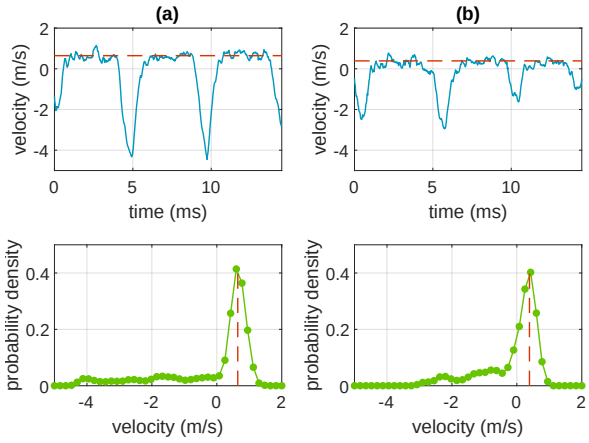


Figure 8: Bow velocity estimation - preliminary offline results. (a) - bowing above the magnet. (b) - bowing 2cm away from the magnet. Dashed red lines represent the estimated bow velocity.

4. CONCLUSION

This study contributes to the ongoing development of a sensing methodology for bowed-string instruments that avoids the limitations of on-bow sensing by positioning all sensors at the string interface. By eliminating the need for sensors on the bow itself, this approach preserves natural bowing technique and ergonomics – key considerations for integration into robust, stage-ready digital musical instruments with minimal calibration overhead. Our results demonstrate that load cells, when appropriately configured, can reliably estimate bowing force and position in real time within a compact, instrument-compatible design.

Experimental results indicate that accurate bowing force estimation can be achieved using only two calibration weights, offering a practical and time-efficient setup. Bowing position can be accurately tracked in the region around the string midpoint, with small errors arising for bowing nearer to the string ends. Preliminary investigations into bow velocity estimation via the string's sticking velocity – extracted using a probability density function – show promising potential.

Future work will focus on improving the calibration procedure to enhance relative bowing position estimation while preserving short setup times. Robust real-time estimation of the bow velocity for a wide range of bow-string interaction regimes remains an open challenge. Success in these areas would enable full real-time control of bowed-string physical models, unlocking new possibilities for expressive digital instrument design and performance-oriented applications in computer music.

5. ACKNOWLEDGEMENTS

The authors would like to thank Alessio Lampis, Adam Schmidt, Laurel Pardue, and Andrew McPherson for their discussions and advice. Special thanks to Andrew McPherson for supplying the string amplifier used in this

project. This research is supported by the Northern Ireland Department for the Economy (DFE)

6. REFERENCES

[1] M. Demoucron, *On the control of virtual violins: physical modelling and control of bowed string instruments*. PhD thesis, KTH Computer Science and Communication, 2008.

[2] E. Matusiak and V. Chatziioannou, "Elasto-plastic friction modeling toward reconstructing measured bowed-string transients," *The Journal of the Acoustical Society of America*, vol. 156(2), p. 1135–1147, August 2024.

[3] A. Lampis, A. Mayer, and V. Chatziioannou, "Assessing playability limits of bowed-string transients using experimental measurements," *Acta Acoustica*, vol. 8, September 2024.

[4] A. Falaize and D. Roze, "Generic passive-guaranteed nonlinear interaction model and structure-preserving spatial discretization procedure with applications in musical acoustics," *Nonlinear Dynamics*, pp. 3249–3275, October 2024.

[5] E. Matusiak, V. Chatziioannou, and M. van Walstijn, "Numerical modelling of elasto-plastic friction in bow-string interaction with guaranteed passivity," *Frontiers in Signal Processing*, 2025.

[6] R. Russo, M. Ducceschi, and S. Bilbao, "Efficient simulation of the bowed string in modal form," in *Proc. of the 25th International Conference on Digital Audio Effects DAFx2022*, 2022.

[7] J. Woodhouse, "Bowed string transients: Enhanced modeling of friction and finite-width bows," in *Proc. of the Stockholm Music Acoustics Conference SMAC 2023*, 2023.

[8] E. Schoonderwaldt, *Mechanics and acoustics of violin bowing: Freedom, constraints and control in performance*. PhD thesis, KTH Computer Science and Communication, 2009.

[9] E. Maestre, J. Bonada, M. Blaauw, A. Perez, and E. Guaus, "Acquisition of violin instrumental gestures using a commercial EMF tracking device," in *Proc. of the International Computer Music Conference*, 2007.

[10] E. Schoonderwaldt and M. Demoucron, "Extraction of bowing parameters from violin performance combining motion capture and sensors," *The Journal of the Acoustical Society of America*, vol. 126, pp. 2695–2708, November 2009.

[11] A. Lampis, A. Mayer, M. Pàmies-Vilà, and V. Chatziioannou, "Examination of the static and dynamic bridge force components of a bowed string," in *Proc. of Meetings on Acoustics*, 2023.

[12] L. S. Pardue, C. Harte, and A. P. McPherson, "A Low-Cost Real-Time Tracking System for Violin," *Journal of New Music Research*, vol. 44, pp. 305–323, Oct. 2015.

[13] Y. Mizuho, R. Kitamura, and Y. Sugiura, "Estimation of Violin Bow Pressure Using Photo-Reflective Sensors," in *Proc. of the International Conference on Multimodal Interaction*, 2023.

[14] Y. Mizuho and Y. Sugiura, "A Comparison of Violin Bowing Pressure and Position among Expert Players and Beginners," in *Proc. of the 6th International Conference AsiaHaptics*, 2024.

[15] K. Buys and A. McPherson, "Real-time bowed string feature extraction for performance applications," in *Proc. of the 15th Sound and Music Computing Conference*, 2018.

[16] L. S. Pardue, K. Buys, M. Edinger, D. Overholt, and A. P. McPherson, "Separating sound from source: sonic transformation of the violin through electrodynamic pickups and acoustic actuation," in *Proc. of the International Conference on New Interfaces for Musical Expression*, 2019.

[17] H. Penttinen and V. Välimäki, "A time-domain approach to estimating the plucking point of guitar tones obtained with an under-saddle pickup," *Applied Acoustics*, vol. 65, pp. 1207–1220, Dec. 2004.

[18] H. Penttinen, J. Siiskonen, and V. Valimaki, "Acoustic Guitar Plucking Point Estimation in Real Time," in *Proc. of the International Conference on Acoustics, Speech, and Signal Processing, ICASSP*, IEEE, 2005.

[19] Z. Mohamad, S. Dixon, and C. Harte, "Pickup position and plucking point estimation on an electric guitar," in *Proc. of the International Conference on Acoustics, Speech, and Signal Processing, ICASSP*, IEEE, 2017.

[20] J. M. Hjerrild, S. Willemsen, and M. G. Christensen, "Physical Models For Fast Estimation Of Guitar String, Fret And Plucking Position," in *Workshop on Applications of Signal Processing to Audio and Acoustics (WASPAA)*, IEEE, 2019.

[21] J.-L. Le Carrou and G. O. Paiva, "Numerical investigation of a plucking position estimation method in the time domain," in *Proc. of the Stockholm Music Acoustics Conference SMAC 2023*, 2023.

[22] A. Perez-Carrillo and M. M. Wanderley, "Indirect Acquisition of Violin Instrumental Controls from Audio Signal with Hidden Markov Models," *IEEE/ACM Transactions on Audio, Speech, and Language Processing*, vol. 23, pp. 932–940, May 2015.

[23] J. Woodhouse and P. M. Galluzzo, "The Bowed String As We Know It Today," *Acta Acustica united with Acustica*, vol. 90, 2004.

DOI: 10.61782/fa.2025.0046



FORUM ACUSTICUM
EURONOISE 2025

A TWO-REGISTER HAPTIC INTERFACE FOR ARTICULATED CONTROL OF HARPSICHORD PHYSICAL MODELS

Matthew Hamilton* **Riccardo Russo** **Craig J. Webb**
Michele Ducceschi
NEMUS Lab, Dept. of Industrial Engineering, University of Bologna

ABSTRACT

A two-register haptic interface is presented for the articulated control of physically modelled harpsichord sounds. While physical modelling synthesis affords realism and nuance, standard MIDI-based controllers lack the resolution to capture the fine temporal detail required for historically informed keyboard performance. A custom three-key harpsichord mechanism was commissioned from an expert builder, and augmented with optical and force-sensitive sensors to track independent jack displacements per register. These data inform a real-time nonlinear string synthesis engine, enabling control over subtle inter-register plucking delays characteristic of historical instruments. The interface supports velocity-sensitive articulation across registers and integrates with a real-time software model employing modal energy-preserving techniques. The system reintroduces key expressive features absent from sample-based approaches, offering a viable solution for high-fidelity digital reconstruction of early keyboard gestures.

Keywords: *physical modelling, harpsichord, musical interface, MIDI controller, Virtual Studio Technology*

1. INTRODUCTION

The evolution of digital sound synthesis has transformed the relationship between human gesture, performance, and sound production. Early digital instruments offered sonic flexibility but introduced a degree of abstraction, primarily due to reliance on indirect parameter manipulation rather than direct physical interaction [1, 2]. With advances in computational power, real-time processing and expressive controllers have reintroduced immediacy to digital performance, allowing musicians to interact with sound more intuitively [3–5]. Nevertheless, the fundamental challenge of expressive control remains central across domains such as live electronic music and interactive performance systems, where continued exploration has led to the creation of complex multimodal interfaces [6].

The challenge of control remains open and becomes relevant when applied to historical musical instruments, where physical fragility often precludes direct interaction [7–9]. Physical modelling synthesis presents a promising solution by enabling real-time simulation of an instrument's behaviour [10, 11]. However, digital reconstructions often struggle to capture the fine-grained control and responsiveness required for historically informed performance practices.

The harpsichord exemplifies this difficulty. Characterised by its distinctive articulation and multiple registers, it requires nuanced control to produce its characteristic sound [12]. In traditional harpsichords, jack staggering creates intentional time offsets between multiple plucks triggered by the same key [13]. This prevents the player from engaging multiple strings with excessive force simultaneously. Yet, such subtle timing is often overlooked in sample-based libraries, where a single MIDI note triggers all registers simultaneously. Standard MIDI keyboards compound the issue, lacking the tactile feedback and mechanical complexity necessary to replicate historical instruments' expressive intricacies—especially the delayed plucks across registers. Previous work has

**Corresponding author*: matthew.hamilton2@unibo.it.
Copyright: *©2025 Matthew Hamilton et al. This is an open-access article distributed under the terms of the Creative Commons Attribution 3.0 Unported License, which permits unrestricted use, distribution, and reproduction in any medium, provided the original author and source are credited.*

enhanced a museum-based keyboard replica with a sensor system [14] to control a commercial sample library, but sample-based implementations remain fundamentally limited. The core issue lies in their one-to-one mapping of MIDI events to sound triggers.

This paper introduces a novel control interface designed to overcome these constraints. By incorporating a custom sensing system that independently tracks the movement of each register, the proposed design enables precise articulation and timing control. This restores essential performance characteristics of historical harpsichords and strengthens the link between digital synthesis and authentic historical expression. A public repository containing supplementary material is available [1]. In particular, videos demonstrating the pluck detection mechanism are relevant for supporting the results discussed in the following section.

2. DETECTION MECHANISM AND INTERFACE PROTOTYPING

Rather than relying on commercial weighted-key MIDI controllers—which fail to replicate the mechanical resistance profile of a harpsichord [7]—a physical prototype of the harpsichord mechanism was commissioned from a professional instrument maker. The prototype includes three keys, each coupled to two jacks tuned in unison (Figure 1). While scaled down and unpitched, the string selection and mechanical dimensions were informed by a luthier to approximate the C2–D2 register with comparable tension and gauge. Each key acts as a class-1 lever, lifting jacks from different points along its length. This staggered design results in varying jack velocities, influencing the timing of plucks. Two complementary sensor types, QRE1113 reflective optical sensors and Interlink Electronics FSR 400 force-sensitive resistors (FRS), were employed to track gestures. The optical sensors—selected for their precision in short-range applications and prior success in musical interfaces—were directed at greyscale gradient tags attached to the sides of each jack. This setup largely draws from the original design by McPherson [15]. Mounted on custom PCBs (one per register), the sensors output voltage (`V_OUT`) in proportion to reflected infrared light, feeding analogue data into the microcontroller's ADC inputs (Figure 2(a)). Signal integrity was improved by shielding the open prototype construction against ambient light and power line interference through

[1] https://github.com/Nemus-Project/modal-harpsichord

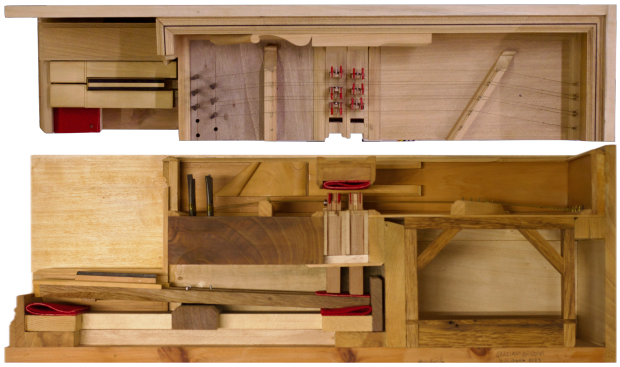
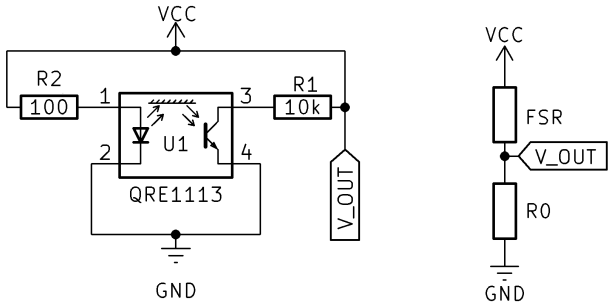


Figure 1: Top and side views of the three-key model built to prototype harpsichord key mechanisms and sensing system.



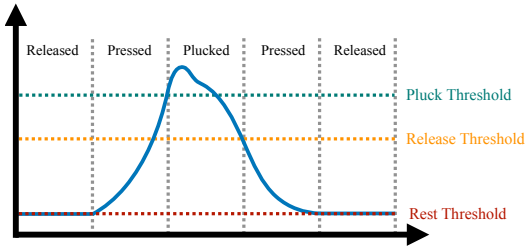
(a) QRE1113 (b) FSR

Figure 2: Sensor voltage divider circuits. In each case `V_OUT` connects to an ADC channel of the microcontroller.

both physical means (3D-printed cover plates) and software calibration (4-point moving average).

In a previous project involving the augmentation of a full-scale keyboard for the San Colombano Museum exhibition [14], a single-threshold detection system was implemented using only optical sensors. Although functional, it was prone to both false positives and missed events due to sensor noise, as occasional spikes led to unreliable threshold crossings during expressive play. Furthermore, artificially dragging the string with the plectrum, without producing an actual pluck, resulted in a series of false positives, as the detection system was unable to distinguish true plucks using simple thresholding alone.

A two-register pluck mechanism is reliable only if such false detections can be removed altogether. To




```
if(value > pluck_threshold AND state != PLUCKED)
   send_note_on(channel, note_number, velocity);
   state = PLUCKED;
else if(value < release_threshold AND state == PLUCKED)
   send_note_off(channel, note_number, velocity);
   state = PRESSED;
else if(value < rest_threshold)
   state = RELEASED;
```

Figure 3: Diagram of optical sensor signal transitioning through each state, and corresponding pseudocode.

achieve this, the current system uses a two-threshold hysteresis mechanism implemented as a finite state machine with three states: `RELEASED`, `PLUCKED`, and `PRESSED`. A MIDI `Note_ON` is triggered only when the sensor reading exceeds the `pluck_threshold` and the system is in the `RELEASED` state. Conversely, a `Note_OFF` is issued when the value falls below a lower `release_threshold`, and the system is in the `PLUCKED` state. This avoids instability from minor fluctuations near a single threshold and prevents rapid state toggling. Figure 3 presents a diagram of the hysteresis setup, and the corresponding pseudocode is given. Figure 4 presents snapshots of the plectrum-string interaction during a pluck, and the reflective sticker used by the optical sensing mechanism.

In the current design, FSR signals complement optical data by indicating actual force application. FSRs were installed beneath each jack to detect actual string excitation. Connected in a voltage divider circuit (Figure 2b), the output voltage reads:

$$V_{OUT} = \frac{R_0}{R_0 + R_{FSR}} V_{CC}, \tag{1}$$

from which the varying sensor's resistance R_{FSR} can be estimated. Such varying resistance can ultimately be converted to a force signal measured in Newton's via a conversion table from the supplier.

In addition to measuring force magnitudes, the FSR signal functions as a validation layer. When the optical



Figure 4: (Top): Snapshots of the plectrum-string interaction during a pluck. Note how the plectrum initially pushes the string but is eventually pushed back by the string before release. (Bottom): side view of a jack showcasing the colour gradient in the reflecting sticker used by the optical sensing mechanism.

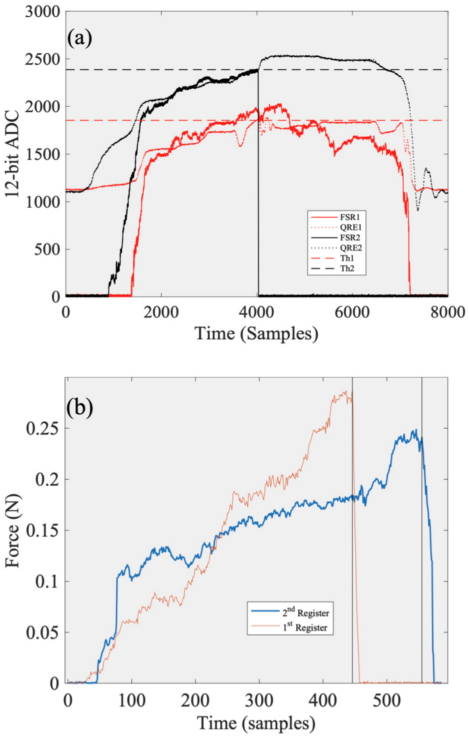


Figure 5: (a) FSR and optical sensor data for both registers of a key, as recorded by the ADC. **Th1** and **Th2** lines are the thresholds for the first and second set of optical sensors. (b) FSR data at 8 kHz sample rate. Black lines show the pluck point for each register. Time difference between plucks: 14 ms (110 samples).

sensor reading exceeds the pluck threshold, the system verifies whether a corresponding rate of change is present in the FSR signal. If no such drop is detected—indicating an absence of string contact—the event is disregarded. As a result, only deliberate plucking gestures lead to sound output, while unintended movements are effectively disregarded. Figure 5(a) displays the four signals captured from a single key gesture—two per register, representing the optical and force-sensitive sensors. It can be observed that one string is correctly identified as plucked, evidenced by a sharp drop in the force signal (black solid curve), while the second string (red curves), despite the optical threshold being crossed, is not plucked.

Figure 5(b) shows a time series from both sensors on a single key, sampled at 8 kHz and converted to Newtons. The onset of key motion is marked by displacement without resistance, followed by a sharp drop in the FSR signal that corresponds to the pluck. Together, the optical and force signals show strong temporal alignment across gestures. Based on recordings and sensor data, the delay between register plucks during normal performance ranged from 12ms to 30ms.

The current configuration supports per-register velocity assignment at note onset, with `Note_ON` velocities derived from the peak force measured by the FSR prior to its decay. Since FSRs are insensitive to key release, `Note_OFF` velocity is instead estimated from the rate of downward motion, as captured by the optical sensor when crossing the release threshold.

3. PHYSICAL MODELS AND IMPLEMENTATION

The control interface drives a nonlinear, two-register string model emulating the physical response of early Italian harpsichords. These instruments typically employed yellow brass strings, which, being relatively soft and unable to withstand high tension, contributed—together with the flexible soundboard and thin case sides—to a characteristically bright and sustained tone. For a digital reconstruction to sound convincing, it must account for behaviours like pitch glides, modal coupling, and amplitude modulation. Such features lie beyond the reach of linear string models and require the inclusion of geometric nonlinearities. Consider the following nonlinear model:

$$\rho A \partial_t^2 u(x,t) = \mathcal{L}u(x,t) + \partial_x \phi'_{nl}(\partial_x u) + \delta^{(x_f)} f(t), \quad (2)$$

where $u(x,t)$ denotes the transverse displacement; ρ is the material density; $A = \pi r^2$ is the cross-sectional area of a circular string; $\delta^{(x_f)} = \delta(x - x_f)$ is a Dirac delta representing the point of external excitation. The notation ∂_z^n denotes the n^{th} partial derivative along z, and primes ($'$) denote total differentiation. The operator $\mathcal{L}$ models linear dynamics:

$$\mathcal{L} := T_0 \partial_x^2 - EI \partial_x^4, \quad (3)$$

with T_0 the string tension, E Young's modulus, and $I = \pi r^4/4$ the area moment of inertia. The nonlinear potential function ϕ_{nl} governs the geometric nonlinearity:

$$\phi_{nl}(\partial_x u) := \frac{EA - T_0}{8} (\partial_x u)^4. \quad (4)$$

This expression approximates a low-order expansion of the geometrically exact string model (for the full model and a discretisation employing finite elements, see [16]), sufficient to produce perceptually relevant nonlinear effects such as pitch glides and modal coupling [17]. Note that the interactions with the soundboard and the radiation into the surrounding medium, whilst important for sound synthesis, are neglected at this stage, as they do not influence the structure of the control data stream of this proof-of-concept.

Boundary conditions are taken as simply supported: $u = \partial_x^2 u = 0$ at $x = \{0, L\}$. Applying modal decomposition:

$$u(x,t) := \sum_{m=1}^{M} X_m(x) q_m(t) = \mathbf{X}^\intercal(x)\, \mathbf{q}(t), \quad (5)$$

with $X_m := \sqrt{2/L} \sin\left(\frac{m\pi x}{L}\right)$ and $\mathbf{q}(t)$ the vector of modal coordinates, results in the following projected system:

$$\ddot{\mathbf{q}} = -\boldsymbol{\Omega}^2 \mathbf{q} - \mathbf{C}\dot{\mathbf{q}} - \int_{\mathcal{I}} \mathbf{X}' \phi'_{nl}\, dx + \boldsymbol{\eta} f(t), \quad (6)$$

where $\boldsymbol{\Omega} := \text{diag}[\Omega_1, ..., \Omega_M]$ is a diagonal matrix of eigenfrequencies defined as:

$$\Omega_m = \sqrt{\frac{T_0}{\rho A}\left(\frac{m\pi}{L}\right)^2 + \frac{EI}{\rho A}\left(\frac{m\pi}{L}\right)^4}. \quad (7)$$

The diagonal damping matrix $\mathbf{C} := \text{diag}[2\sigma_1, ..., 2\sigma_M]$ was arbitrarily added after modal projection, and it approximates the light, uncoupled modal losses. The damping coefficients σ_m can be estimated experimentally or be derived from a model such as Cuesta and Vallette's [18].

3.1 Energy quadratisation and time stepping scheme

The modal system is passive and satisfies the energy balance:

$$\frac{\mathrm{d}H}{\mathrm{d}t} = -\dot{\mathbf{q}}^\intercal \mathbf{C}\dot{\mathbf{q}} + \dot{\mathbf{q}}^\intercal \boldsymbol{\eta} f(t), \tag{8}$$

with total energy:

$$H = \frac{1}{2}\dot{\mathbf{q}}^\intercal\dot{\mathbf{q}} + \frac{1}{2}\mathbf{q}^\intercal\boldsymbol{\Omega}^2\mathbf{q} + \int_{\mathcal{I}} \phi_{nl}\,\mathrm{d}x, \tag{9}$$

and note that the energy is strictly decreasing when the source is inactive ($f(t) = 0$). To ensure numerical stability in the presence of nonlinear terms, the system is reformulated using the Scalar Auxiliary Variable (SAV) method [19, 20]:

$$\psi := \sqrt{2\int_{\mathcal{I}} \phi_{nl}\,\mathrm{d}x}, \tag{10}$$

yielding:

$$\ddot{\mathbf{q}} = -\boldsymbol{\Omega}^2\mathbf{q} - \mathbf{C}\dot{\mathbf{q}} - \psi\nabla_{\mathbf{q}}\psi + \boldsymbol{\eta} f(t), \tag{11a}$$

$$\dot{\psi} = (\nabla_{\mathbf{q}}\psi)^\intercal\dot{\mathbf{q}}. \tag{11b}$$

System (11) is discretised using staggered time series for $\mathbf{q}$ and ψ. Let $\mathbf{q}^n \approx \mathbf{q}(Tn)$ and $\psi^{n-\frac{1}{2}} \approx \psi(T(n-\frac{1}{2}))$ at time step n and with sampling period T. Discrete-time operators are defined as:

$$\delta_2\mathbf{q}^n := \frac{\mathbf{q}^{n+1} - 2\mathbf{q}^n + \mathbf{q}^{n-1}}{T^2}, \tag{12a}$$

$$\mu_2\mathbf{q}^n := \frac{\mathbf{q}^{n+1} + 2\mathbf{q}^n + \mathbf{q}^{n-1}}{4}, \tag{12b}$$

$$\delta_\cdot\mathbf{q}^n := \frac{\mathbf{q}^{n+1} - \mathbf{q}^{n-1}}{2T}, \tag{12c}$$

$$\delta_+\psi^{n-\frac{1}{2}} := \frac{\psi^{n+\frac{1}{2}} - \psi^{n-\frac{1}{2}}}{T}, \tag{12d}$$

$$\mu_+\psi^{n-\frac{1}{2}} := \frac{\psi^{n+\frac{1}{2}} + \psi^{n-\frac{1}{2}}}{2}. \tag{12e}$$

Using these, the time-stepping scheme employed here is:

$$\delta_2\mathbf{q}^n = -\tilde{\boldsymbol{\Omega}}^2\mu_2\mathbf{q}^n - \tilde{\mathbf{C}}\delta_\cdot\mathbf{q}^n - \mu_+\psi^{n-\frac{1}{2}}\mathbf{g}^n + \boldsymbol{\eta} f^n,$$

$$\delta_+\psi^{n-\frac{1}{2}} = (\mathbf{g}^n)^\intercal\delta_\cdot\mathbf{q}^n,$$

$$\mathbf{g}^n := (\nabla_{\mathbf{q}}\psi)\big|_{t=Tn},$$

where:

$$\tilde{\Omega}_m^2 := \frac{4}{T^2}\frac{1 - 2e^{-\sigma_m T}\cos(T\sqrt{\Omega_m^2 - \sigma_m^2}) + 2e^{-2\sigma_m T}}{1 + 2e^{-\sigma_m T}\cos(T\sqrt{\Omega_m^2 - \sigma_m^2}) + 2e^{-2\sigma_m T}},$$

$$\tilde{\sigma}_m := \frac{2}{T}\frac{1 - e^{-\sigma_m T}}{1 + 2e^{-\sigma_m T}\cos(T\sqrt{\Omega_m^2 - \sigma_m^2}) + 2e^{-2\sigma_m T}}.$$

This discretisation has several desirable properties. First, it ensures that the linear part is discretised exactly [21], as it appears in previous works employing modal synthesis [20, 22]. Second, it is unconditionally stable. Finally, the system's update -not shown here for brevity- is performed explicitly via the Sherman-Morrison formula [17, 19, 23], avoiding nonlinear root finding algorithms -often requiring several iterations per time step- or large matrix inversions.

To manage computational complexity further, full nonlinearity is applied only to modes below 3 kHz; higher modes are treated linearly. This hybrid approach preserves perceptual features while reducing floating-point cost. Additionally, a constrained version of the SAV method, adapted from [20], is employed to enforce the non-negativity of $\mu_+\psi^{n-\frac{1}{2}}$, preventing spurious numerical artefacts from appearing in the solution and allowing the auxiliary variable to decay toward zero. A detailed description can be found in [24, 25].

4. REAL-TIME SOFTWARE IMPLEMENTATION

The software component of the prototype system consists of a real-time instrument plug-in (VST3/Audio Unit), designed for integration with standard Digital Audio Workstations (DAWs). The selected DAW must support the transmission of MIDI channel information to the active track, enabling multi-channel polyphonic expression (MPE)-style communication.

4.1 System Overview

The software simulates a pair of nonlinear strings, forming a single voice whose pitch is determined by the mechanically actuated key. For the purposes of computational benchmarking, low-pitched notes were selected: specifically, C2 (65 Hz), along with the adjacent C#2 and D2. Each string is modelled with a length of 2 m and a radius of 0.3 mm, employing appropriate material parameters for brass.

The system processes `Note_ON` and `Note_OFF` events received over two independent MIDI channels, supporting individual excitation and damping of each

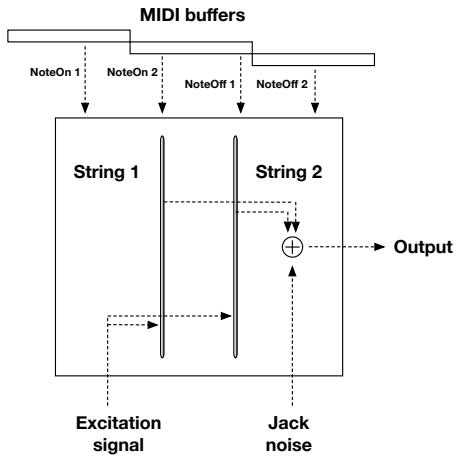


Figure 6: Real-time system implementation comprising a pair of nonlinear strings triggered by MIDI signals distributed across multiple buffers.

string and preserving temporal offsets between the associated jacks. These MIDI events may span multiple processing buffers; therefore, each is timestamped and rendered within the correct frame. Additional components include an excitation signal and jack noise, as illustrated in Figure 6.

Excitation is applied as a time-limited forcing term at a designated point along each string, informed by the pressure sensor beneath the mechanical key. The excitation signal, approximately 50 ms in duration, is selected via linear interpolation between two stored waveforms, based on the MIDI `Note_ON` velocity. Additionally, the sound of the jack returning to its rest position is incorporated via a pre-recorded noise sample. The `Note_OFF` velocity is used to modulate the amplitude of this signal prior to mixing with the output audio.

4.2 Computational Challenges

The use of nonlinear modal string synthesis in a real-time audio environment is computationally demanding, both at the model initialisation phase (`Note_ON`) and during continuous audio rendering at each time step. In contrast to a linear string model—which requires a single vector update and dot product per time step—the nonlinear system entails substantially more operations. For instance, the C2 note requires a modal resolution of 150 modes. Each time step involves two matrix-vector multiplications, seven vector updates, and six dot products. When matrices are square, multiplication accounts for over 80% of the total computational load.

To attain viable single-core CPU performance, both algorithmic and low-level code optimisations were implemented. As mentioned previously, one effective strategy involved partitioning the modal range into two segments: a low-to-mid frequency band up to approximately 3 kHz, and a higher frequency band extending to the upper modal limit. The lower segment (approximately 50 modes for C2) is computed using the full nonlinear model, whereas the higher modes are updated using a simplified linear routine. This segmentation reduces matrix dimensionality and lowers the cost of associated vector operations. With this approach, CPU usage per string was reduced to approximately 10%. Further optimisation is anticipated through under-sampling of the nonlinear modal segment.

Beyond real-time rendering, the initialisation of each string model introduces additional processing overhead. Specifically, the computation of modal shapes—involving thousands of trigonometric evaluations at each `Note_ON` event—can lead to transient CPU load spikes, potentially causing buffer under-runs. To mitigate this, a caching system for precomputed modal matrices is recommended for scalable polyphonic implementation.

5. DISCUSSION AND CONCLUSION

The system presented in this paper builds upon previous work on sensor-augmented harpsichord interfaces—most notably the San Colombano project [14]—by introducing substantial refinements in both gesture detection and synthesis integration. While earlier designs relied solely on optical displacement tracking, the present system introduces a dual-sensor architecture, combining reflective optical sensors with force-sensitive resistors (FSRs). This hybrid approach enables robust pluck detection through velocity-sensitive hysteresis and force validation, reducing false positives, particularly during complex or expressive gestural input. These developments address known shortcomings of threshold-based detection and allow for a more reliable mapping between mechanical gestures and sonic outcomes. The current prototype setup is visible in Figure 7.

Conventional digital control of plucked keyboard instruments suffers from several shortcomings, namely: the lack of control resolution in standard MIDI devices, the inability to articulate register-specific timing offsets, and the absence of mechanical feedback needed for histori-



Figure 7: The prototype setup, showing the three-key harpsichord model connected to a 2023 MacBook Pro. The prototype VST is visible, along with a list of triggered MIDI messages.

cally informed performance. The proposed system addresses these challenges through a custom-built harpsichord mechanism with staggered dual-register jacks, paired with real-time gesture tracking and nonlinear physical modelling. The resulting interface supports temporally resolved articulation across registers, required for expressive control.

From the perspective of sound synthesis, the system incorporates a physically realistic, nonlinear string model that supports two independently plucked registers per key. By constraining nonlinear computations to low-order modes (below 3 kHz), and employing a modal energy quadratisation scheme with a constrained Scalar Auxiliary Variable (SAV), the model achieves a balance between physical fidelity and computational tractability. As a result, real-time synthesis is attained on consumer-grade hardware with a CPU footprint of approximately 10% per voice on the most computationally demanding strings in the bass register, while preserving key nonlinear characteristics such as pitch glides and modal coupling.

The prototype shows that a high level of expressivity can be achieved through targeted hardware augmentation and physics-informed synthesis. It reaffirms the value of context-specific interfaces when coupled with physically grounded models, particularly in the domain of historically informed digital instrument design. Future work will extend the current architecture to a full keyboard, explore enhanced mapping strategies for velocity and dynamics, and incorporate more detailed models of soundboard interaction and acoustic radiation.

6. ACKNOWLEDGMENTS

This work was supported by the European Research Council (ERC) within the Horizon 2020 framework, with grant NEMUS-StG-950084.

7. REFERENCES

[1] C. Roads, *The Computer Music Tutorial*. MIT Press, 1996.

[2] F. R. Moore, *Elements of Computer Music*. Prentice Hall, 1990.

[3] S. Trolland, A. Ilsar, C. Frame, J. McCormack, and E. Wilson, "Airsticks 2.0: Instrument design for expressive gestural interaction," in *Proceedings of the International Conference on New Interfaces for Musical Expression*, (Auckland, New Zealand), pp. 16–21, 2022.

[4] M. Caren, R. Michon, and M. Wright, "The keywi: An expressive and accessible electronic wind instrument," in *Proceedings of the International Conference on New Interfaces for Musical Expression*, (Birmingham, United Kingdom), pp. 604–609, 2020.

[5] A. McPherson, "The space between the notes: Adding expressive pitch control to the piano," in *Proceedings of the International Conference on New Interfaces for Musical Expression*, (Daejeon, Republic of Korea), pp. 181–184, 2013.

[6] A. Tanaka and R. B. Knapp, "Multimodal interaction in music using the electromyogram and relative position sensing," in *Proceedings of the International Conference on New Interfaces for Musical Expression*, (Dublin, Ireland), pp. 171–176, 2002.

[7] K. B. McAlpine, "Sampling the past: A tactile approach to interactive musical instrument exhibits in the heritage sector," in *Innovation in Music 2013* (R. Hepworth-Sawyer, J. Hodgson, R. Toulson, and J. L. Paterson, eds.), KES Transactions on Innovation in Music, (York, United Kingdom), pp. 110–125, Future Technology Press, 2014.

[8] A. Baldwin, T. Hammer, E. Pechiulis, P. Williams, D. Overholt, and S. Serafin, "Tromba moderna: A digitally augmented medieval instrument," in *Proceedings of the International Conference on New Interfaces for Musical Expression*, (Brisbane, Australia), pp. 14–19, 2016.

[9] ERC, "NEMUS project." https://cordis.europa.eu/project/id/950084. Grant No. 950084, accessed 2025.

[10] J. O. Smith, "Physical modeling synthesis update," *Computer Music Journal*, vol. 34, no. 2, pp. 87–93, 2010.

[11] S. Bilbao, *Numerical Sound Synthesis: Finite Difference Schemes and Simulation in Musical Acoustics*. Chichester, UK: John Wiley & Sons, Ltd, 2009.

[12] E. L. Kottick, K. D. Marshall, and T. J. Hendrickson, "The acoustics of the harpsichord," *Scientific American*, vol. 264, no. 2, pp. 110–115, 1991.

[13] C. D. Veroli, "Optimising harpsichord staggering," *Harpsichord and Fortepiano*, vol. 16, pp. 8–13, 2012.

[14] M. Hamilton, M. Ducceschi, R. Livi, C. Vicens, and A. McPherson, "Augmentation of a historical harpsichord keyboard replica for haptic-enabled interaction in museum exhibitions," in *Proceedings of the International Conference on New Interfaces for Musical Expression*, (Canberra, Australia), 2025. Under review.

[15] A. McPherson, "Portable measurement and mapping of continuous piano gesture," in *Proceedings of the International Conference on New Interfaces for Musical Expression*, pp. 152–157, 2013.

[16] J. Chabassier and P. Joly, "Energy preserving schemes for nonlinear hamiltonian systems of wave equations: Application to the vibrating piano string," *Computer Methods in Applied Mechanics and Engineering*, vol. 199, no. 45-48, pp. 2779–2795, 2010.

[17] R. Russo, S. Bilbao, and M. Duccheschi, "Scalar auxiliary variable techniques for nonlinear transverse string vibration," in *Proceedings of the IFAC Workshop on Lagrangian and Hamiltonian Methods for Non Linear Control (IFAC)*, (Besançon, France), pp. 160–165, Apr. 2024.

[18] H. Cuesta and C. Vallette, "Nonlinear damping in musical string models," *Acta Acustica united with Acustica*, vol. 82, no. 4, pp. 657–664, 1996.

[19] S. Bilbao, M. Ducceschi, and F. Zama, "Explicit exactly energy-conserving methods for hamiltonian systems," *Journal of Computational Physics*, vol. 472, p. 111697, 2023.

[20] M. van Walstijn, V. Chatziioannou, and A. Bhanuprakash, "Implicit and explicit schemes for energy-stable simulation of string vibrations with collisions: Refinement, analysis, and comparison," *Journal of Sound and Vibration*, vol. 569, p. 117968, 2024.

[21] J. L. Cieśliński, "On the exact discretization of the classical harmonic oscillator equation," *Journal of Difference Equations and Applications*, vol. 17, no. 11, pp. 1673–1694, 2011.

[22] M. Van Walstijn, J. Bridges, and S. Mehes, "A real-time synthesis oriented tanpura model," in *Proceedings of the International Conference on Digital Audio Effects (DAFx)*, (Brno, Czech Republic), pp. 175–182, 2016.

[23] J. Sherman and W. J. Morrison, "Adjustment of an inverse matrix corresponding to a change in one element of a given matrix," *Annals of Mathematical Statistics*, vol. 21, pp. 124–127, 1950.

[24] S. Bilbao, R. Russo, C. Webb, and M. Ducceschi, "Real-time guitar synthesis," in *Proceedings of the International Conference on Digital Audio Effects (DAFx)*, (Guildford, UK), pp. 163–170, Sept. 2024.

[25] R. Russo, *Non-Iterative Numerical Simulation Techniques for Nonlinear String Vibration in Musical Acoustics*. Ph.d. dissertation, University of Bologna, Bologna, Italy, April 2025.

DOI: 10.61782/fa.2025.0727



FORUM ACUSTICUM
EURONOISE 2025

REAL-TIME DEMONSTRATORS TO EXHIBIT, INVESTIGATE AND TEACH TRANSIENT BEHAVIORS IN NONLINEAR DYNAMICS, FOCUSED ON MUSICAL INSTRUMENTS

Tom Colinot[1,2*]
[1] Buffet Crampon, Mantes-la-Ville, France
[2] Aix Marseille Univ, CNRS, Centrale Marseille, LMA, Marseille, France

ABSTRACT

Nonlinear dynamical systems exhibit various transient behaviors, whose understanding is required to fully apprehend how the system responds to sollicitations. This work focuses on multistable systems, where several stable solutions coexist for a given value of the system's parameters. In these settings, transients condition which solution actually appears during time integration. Then, a comprehensive description of the system's behavior entails mapping out the infinite possibilities of variations of the system's parameters with respect to time. This is impractical for models whose phase space is of high dimension, or in limited timescales such as practical activities for students. This work proposes real-time demonstrators of dynamical systems as a way to still investigate these phenomena. The construction of such demonstrators is detailed, including a display outlining the zones of stability of the solutions, and control inputs mimicking a musical instrument (such as a MIDI controller). We show how these elements coupled with audio and visual feedback enables users to quickly gauge a large variety of transient behaviors, for academic proofs of concept or pedagogical activities. A demonstrator for a Van der Pol toy model and one for a woodwind model used for a lab in a master's degree are used as examples.

Keywords: *musical acoustics, nonlinear dynamics, real-time synthesis, bifurcations*

**Corresponding author*: *tom.colinot@buffetcrampon.com.*
***Copyright**: ©2025 Tom Colinot This is an open-access article distributed under the terms of the Creative Commons Attribution 3.0 Unported License, which permits unrestricted use, distribution, and reproduction in any medium, provided the original author and source are credited.*

1 INTRODUCTION

It is very rarely possible to exhaustively predict the behavior of a nonlinear dynamical systems. Therefore, a lot of work in the dynamical systems community is descriptive: one observes, documents and explains the various behaviors that the system displays in its different configurations [1]. This leads to graphical representations such as bifurcation diagrams that represent behavior as a function of one parameter, or cartographies when two or three parameters are taken into account. This work presents two real-time construction of bifurcation diagrams. In a pedagogical context, the real-time audio and graphical representation tool allows impactful and flexible demonstrations, in which the students and the professor can decide to investigate a specific point and do so immediately. The audio feedback is especially interesting for music-related curriculums, where students want to interpreted dynamical system behaviors in terms relevant to music as often as possible.

2 A TOY OSCILLATOR ILLUSTRATES DIRECT, INVERSE AND DYNAMICAL HOPF BIFURCATIONS

A fifth order Van der Pol model [2], close to the normal form of a Bautin bifurcation [3], displays a Hopf bifurcation [4] that can be either direct or inverse. Its toy model nature makes it easy to write with a single equation

$$\ddot{x} + (\mu + \sigma(\dot{x}^2 + x^2) + \nu(\dot{x}^2 + x^2)^2)\dot{x} + x = 0 \quad (1)$$

Its solutions as well as the locus of its bifurcations are both completely described analytically. This good *a priori* knowledge of the system's steady states means the demonstration can focus on transient aspects such as hysteresis

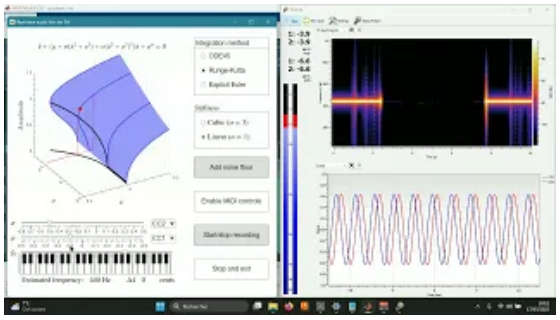


Figure 1. Snapshot from the demonstration video linked at https://youtu.be/a0S7l7Hjl1s.

and dynamical bifurcations. Figure 1 links to a video capture of such a demonstration. The full demonstrator is available online [5].

Negative values of σ lead to an inverse Hopf bifurcation at $\mu = 0$, which is followed by a saddle-node bifurcation [6]. In the region between these two bifurcations, the system is multistable. Therefore, the system displays a hysteresis cycle (0:00 timestamp) wherein the existing stable solution (constant or periodic) is maintained until the parameter leave the multistability region. When demonstrating this phenomenon, another feature is immediately apparent : the oscillations start and stop brutally. For music-oriented students, this observation is very interesting as it means that self-oscillating instruments that have an inverse Hopf bifurcation will likely be difficult to play at a *pianissimo* nuance. To the contrary, the Hopf bifurcation is direct for positive σ values. The user can experience that a fine adjustment of parameter μ enables arbitrarily low amplitude oscillations (0:23 timestamp).

Dynamical bifurcations are a phenomenon whereby the system's parameter cross a bifurcation point, but the effect of that bifurcation is only felt some time after the crossing [7]. For a Hopf bifurcation, this can mean that the oscillations only appear after a certain delay after μ crosses 0. This delay can be rather long, especially when the system is allowed to converge very close to the equilibrium. When the system is near the equilibrium and it becomes unstable, the distance between it and the position of the system is amplified exponentially. If this distance is very small, the time needed for it to become big enough for oscillations to be heard can be long. In the case of our real-time Van der Pol oscillator, 0:52 timestamp showcases a long bifurcation delay (of about 1 s). In a musical context, this duration is not negligible at all

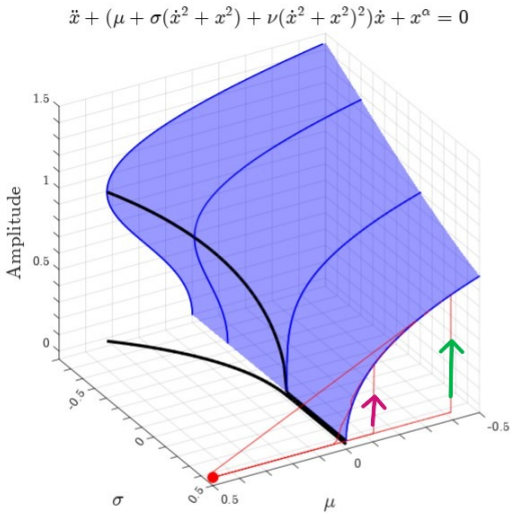


Figure 2. Bifurcation diagram: theoretical static solution amplitudes in blue, and time-integration trajectories in red for two increases in parameter μ from -0.5 to 0.4: first without added noise (green arrow) and then with added white noise (pink arrow).

(half a bar at 120 bpm). Then, a small white noise of standard deviation 10^{-5} is added to the variables of the system at the 1:04 timestamp. By preventing the system to approach the equilibrium too much, this modification greatly shortens the bifurcation delay. Figure 2 compares the two trajectories : compared to a short bifurcation delay, the long bifurcation delay also entails that oscillations appear when μ is larger and thus with a greater amplitude – which translates to a more sudden attack.

This demonstration shows the importance of the nature of the bifurcation in a musical context, as well as the more subtle phenomenon that is bifurcation delay.

3 A CLARINET MODEL SHOWS SIMPLE AND COMPLEX MULTISTABLE BEHAVIOR, AS WELL AS CHAOTIC REGIMES

A more applicative example, used in a lab for a master's degree, puts the student with a real-time integration of a woodwind model, whose modal parameters can be fixed by the user. The two variable control parameters are the

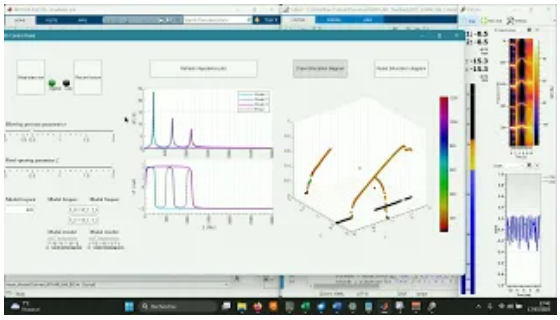


Figure 3. Snapshot from the demonstration video linked at https://youtu.be/D8AUCYr-XXg.

pressure in the mouth and the opening of the reed at rest. Although it is more involved than the previous toy model, this woodwind model writes rather simply as

$$\begin{cases} \dot{p_1} &= s_1 p_1 + C_1 u \\ \dot{p_2} &= s_2 p_2 + C_2 u \\ \dot{p_3} &= s_3 p_3 + C_3 u \\ p &= 2\Re(p_1 + p_2 + p_3) \\ u &= \zeta \max(p - \gamma + 1, 0)\text{sign}(\gamma - p)\sqrt{|\gamma - p|} \end{cases} . \tag{2}$$

where p_1, p_2 and p_3 are complex modal pressures associated with the three modes whose complex residues and poles are C_i and s_i, and ζ and γ are reed opening and blowing pressure dimensionless parameters [8].

Figure 3 shows the time integration results for this model, when the user manipulates sliders to control the parameters of the system.

The video first showcases the apparition of oscillations through direct Hopf bifurcations when increasing the blowing pressure γ (0:00 timestamp). This is explained as the system only producing sound if the musician blows into it sufficiently hard. Another Hopf bifurcation with respect to the reed opening parameter ζ (1:25 timestamp) is interpreted as the clarinet only producing sound if the reed is open enough at rest. A large multistability zone is explored through a hysteresis cycle at timestamp 0:35 timestamp. Then, the system's ability to produce chaos for a large reed opening is showcased though intermittent regimes (1:55 and 2:35 timestamps). A real-time sound synthesis model enables direct comments of the produced sounds. This parameter region also displays subharmonic regimes (2:21 timestamp). This subharmonic regime produces a note that is unexpected when looking at the resonances of the instrument, as it is lower than the lowest resonance frequency. Then (3:20 timestamp), it is shown that through chaos the system can transition from the first register (regime associated with the first resonance) to the second register (regime associated with the second resonance). These two registers are actually multistable for a large portion of the parameter space : when the second register is obtained it can then be easily maintained.

4 ACKNOWLEDGMENTS

This study has been supported by the French ANR LabCom LIAMFI (ANR-16-LCV2-007-01).

5 References

[1] N. M. Krylov and N. N. Bogoliubov, *Introduction to non-linear mechanics*. Princeton University Press, 1949.

[2] D. Dessi, F. Mastroddi, and L. Morino, "A fifth-order multiple-scale solution for hopf bifurcations," *Computers & structures*, vol. 82, no. 31-32, pp. 2723–2731, 2004.

[3] J. Guckenheimer and Y. A. Kuznetsov, "Bautin bifurcation," *Scholarpedia*, vol. 2, no. 5, p. 1853, 2007.

[4] Y. A. Kuznetsov, "Andronov-hopf bifurcation," *Scholarpedia*, vol. 1, no. 10, p. 1858, 2006.

[5] T. Colinot and C. Vergez, "Dynamical system audio demonstrator," 2023.

[6] Y. A. Kuznetsov, "Saddle-node bifurcation," *Scholarpedia*, vol. 1, no. 10, p. 1859, 2006.

[7] B. Bergeot, A. Almeida, C. Vergez, and B. Gazengel, "Prediction of the dynamic oscillation threshold in a clarinet model with a linearly increasing blowing pressure," *Nonlinear Dynamics*, vol. 73, no. 1-2, pp. 521–534, 2013.

[8] T. A. Wilson and G. S. Beavers, "Operating modes of the clarinet," *The Journal of the Acoustical Society of America*, vol. 56, no. 2, pp. 653–658, 1974.

DOI: 10.61782/fa.2025.0473

FORUM ACUSTICUM EURONOISE 2025

INFLUENCE OF THE BASINS OF ATTRACTION IN THE REGISTER JUMPS OF THE CLARINET

Nathan Szwarcberg[1,2*] **Tom Colinot**[1] **Christophe Vergez**[2]
Michaël Jousserand[1]
[1] Buffet Crampon, 5 Rue Maurice Berteaux, 78711 Mantes-la-Ville, France
[2] Aix Marseille Univ, CNRS, Centrale Med, LMA, Marseille, France

ABSTRACT

When playing the clarinet, opening the register hole allows for a transition from the first to the second register, producing a twelfth interval. On an artificial mouth, the blowing pressure range where the second register remains stable can be determined by gradually varying the blowing pressure while keeping the register hole open. However, when the register hole is opened while the instrument is already producing the first register, the range of blowing pressures that lead to a stable second register is narrower than the full stability zone of the second register.

This phenomenon is investigated numerically by performing multiple hole openings at different times for each blowing pressure value. The evolution of the probability of reaching the second register is computed, and its relationship with the structure of the basin of attraction of the second register is analyzed.

Keywords: *clarinet, multistability, basins of attraction, nonlinear losses, phase tipping*

1. INTRODUCTION

When characterizing a clarinet fingering, one of the first steps consists in measuring the minimum and maximum blowing pressure that play a note, for a fixed embouchure. The artificial mouth [1–4] is commonly used to determine these limits, known as the oscillation and extinction thresholds [5–7], by gradually increasing the blowing pressure. Above the extinction threshold, the reed is pressed against the mouthpiece and stops vibrating. When the pressure is then reduced, the reed starts oscillating again at a lower pressure, sometimes called the "inverse threshold" [6]. This difference between the extinction and inverse thresholds creates a hysteresis cycle, where the equilibrium (no sound) and the oscillating regime are multistable [8, 9].

The basin of attraction of a regime defines the set of initial conditions that lead to it. In a multistable system, knowing these basins helps predict which regime a musician is most likely to play [10]. However, calculating the full basin of attraction is highly time-consuming due to the high dimension of the phase space. Additionally, it is unclear whether a chosen initial condition accurately represents a musician's playing.

This study addresses these challenges by focusing on transitions between two notes. In this case, all initial conditions lie on the limit cycle of the regime of the first note.

A well-known transition on the clarinet happens when pressing the register key, which shifts from the first register to the second by an ascending interval of a twelfth. For beginner clarinetists, practicing this transition is important to avoid unintended notes when opening the hole.

This paper investigates a physical model of a cylindrical clarinet with a register hole. To allow the model to reproduce the register transition, nonlinear losses in the register hole are included [11, 12]. The model is introduced in Section 2. Time-domain simulations, similar to artificial mouth experiments, are then conducted. First, blowing pressure ramps are tested with the register hole both closed and open (Section 3.1) to identify stable and multistable regions. Next, for blowing pressure values in the multistability range between the second register and

*Corresponding author: nathan.szwarcberg@buffetcrampon.com.
Copyright: ©2025 Szwarcberg et al. This is an open-access article distributed under the terms of the Creative Commons Attribution 3.0 Unported License, which permits unrestricted use, distribution, and reproduction in any medium, provided the original author and source are credited.

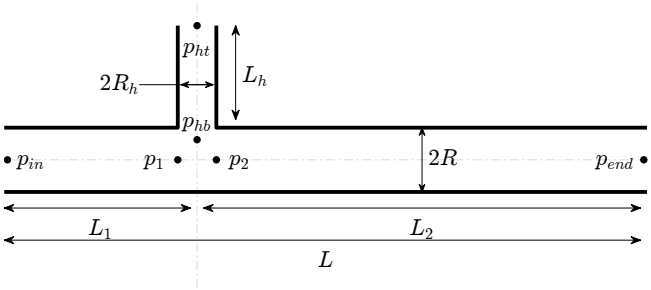


Figure 1. Definition of the digital resonators studied.

the equilibrium, several hole openings are performed to observe how the first register's limit cycle interacts with the attraction basins of the two competing regimes (Section 3.2). Finally, basin stability is investigated by introducing random perturbations when opening the register hole [13].

2. NUMERICAL MODEL

2.1 Digital resonators

The digital resonator is presented on Figure 1. It is composed of a first tube of length $L_1 = 132$ mm, radius $R = 7.5$ mm and cross-section $S = \pi R^2$. The characteristic impedance of plane waves propagating through the tube is $Z_c = \rho_0 c_0 / S$ where $\rho_0 = 1.23\ \mathrm{kg \cdot m^{-3}}$ and $c_0 = 343\ \mathrm{m \cdot s^{-1}}$. The acoustic field in the first tube is described by the pressure at the left extremity p_{in}, and at the right extremity p_1.

The tube is branched to a side hole of length $L_h = 12.7$ mm, radius $R_h = 1.5$ mm, cross-section $S_h = \pi R_h^2$, and characteristic impedance $Z_{ch} = \rho_0 c_0 / S_h$. The acoustic field in the side hole is described by the pressure at the bottom of the hole p_{hb} and at the top of the hole p_{ht}.

A second tube of length $L_2 = 166$ mm and cross-section S is branched downstream from the side hole. The acoustic field in this tube is described by the pressure at the left extremity p_2 and by the pressure at the right extremity p_{end}.

2.2 Viscothermal losses

Viscothermal losses are introduced through the complex wavenumber $\Gamma_i(s)$, where s is the Laplace variable and $i = \{1, 2, h\}$ refers to the index of the tube considered.

The function $G_i(s)$ is defined, such that

$$G_i(s) = e^{-\Gamma_i(s) L_i} = \lambda_i e^{-\epsilon_i \sqrt{s}} e^{-\tau_i s},$$

with

$$\lambda_i = e^{-(\alpha_2 \ell_v L_i)/R_i^2}, \quad \epsilon_i = \frac{\alpha_1 L_i}{R_i} \sqrt{\frac{2\ell_v}{c_0}}, \quad \tau_i = \frac{L_i}{c_0},$$

where $\alpha_1 = 1.044$, $\alpha_2 = 1.080$, and $\ell_v = 4 \cdot 10^{-8}$ m (Chap. 5.5 of [14]).

In practice, $G_i(s)$ are approximated by a first-order low-pass filter and a delay $\tilde{G}_i(s)$, following the work from [15]. Fractional delays are also accounted for through the order 1 filters proposed by [16].

2.3 Forward and backward-propagating pressure waves

In the following, time-domain variables are written in small letters (e.g. $p_2^+(t)$), and frequency-domain variables are written in capital letters (e.g. $P_2^+(s)$).

The propagation of the acoustic waves in the resonator is described through the forward and backward-propagating acoustic pressures p^+ and p^-. They are related to the acoustic pressure and flow (p, u) through the relationships:

$$p = p^+ + p^-, \qquad u = \frac{p^+ - p^-}{Z},$$

where $Z = Z_c$ in the main tube of cross-section S, and $Z = Z_{ch}$ in the side hole.

Since the tubes L_1, L_2 and L_h are all cylindrical, the acoustic field can be described as transmission lines equations in the frequency domain. For the tube of length L_1:

$$P_1^+ = G_1 P_{in}^+, \qquad P_{in}^- = G_1 P_1^-. \tag{1}$$

For the tube of length L_2:

$$P_{end}^+ = G_2 P_2^+, \qquad P_2^- = G_2 P_{end}^-. \tag{2}$$

For the tube of length L_h:

$$P_{ht}^+ = G_h P_{hb}^+, \qquad P_{hb}^- = G_h P_{ht}^-. \tag{3}$$

2.4 Boundary conditions

The boundary conditions in the tube are described hereafter.

2.4.1 Radiation

First, radiation from the open end is neglected: the pressure p_{end} is written consequently as

$$p_{end} = 0. \tag{4}$$

2.4.2 Hole junction

Secondly, since the register hole has a small diameter and a long chimney length, the series impedances of the hole can be neglected (section 3.3.2.2 of [17]). The boundary conditions at the bottom of the hole are therefore given by:

$$p_1 = p_2, \tag{5}$$
$$p_2 = p_{hb}, \tag{6}$$
$$u_1 = u_2 + u_{hb}. \tag{7}$$

2.4.3 Flow crossing the reed channel

The next boundary condition involves p_{in} and comes from the nonlinear characteristics of the flow entering the resonator. In this relationship, the acoustic flow u_{in} depends on the difference between the blowing pressure of the musician p_m and the pressure at the input of the instrument p_{in}. By assuming that the jet experiences total turbulent dissipation [18] and modeling the reed as a massless, undamped spring [19], the nonlinear characteristics is defined as [20]:

$$\hat{u}_{in} = \zeta[\hat{p}_{in} - \gamma + 1]^{+}\mathrm{sgn}(\gamma - \hat{p}_{in})\sqrt{|\gamma - \hat{p}_{in}|}, \tag{8}$$

where the function $[x]^+$ returns the positive-part of x, i.e. $[x]^+ = (x + |x|)/2$. The dimensionless blowing pressure is given by $\gamma = p_m/P_M$, where P_M is the minimum pressure needed to close the reed channel in a quasi-static regime. Typical values of P_M are in the range $P_M \in [4, 8]$ kPa, according to [6, 7]. The parameter ζ represents the embouchure, with common values for the clarinet between 0.05 and 0.4 [6]. The dimensionless quantities are defined as

$$\hat{p}_{in} = p_{in}/P_M, \qquad \hat{u}_{in} = u_{in}Z_c/P_M.$$

In Eq. (8), the dynamics of the reed are neglected to obtain a direct relationship between p_{in}^+ and p_{in}^-. This relationship is given in [21] and is detailed in the Appendix of [22]. It is expressed as:

$$\hat{p}_{in}^+ = f_{\gamma\zeta}(\hat{p}_{in}^-) = \gamma - X[\gamma - 2\hat{p}_{in}^-] - \hat{p}_{in}^-, \tag{9}$$

where the function X is defined in Appendix A of [21].

2.4.4 Localized nonlinear losses in the register hole

Localized nonlinear losses in the register hole are modeled using the following boundary condition for p_{ht}:

$$p_{ht}(t) = \rho_0 C_{\mathrm{nl}} v_{ht}(t)|v_{ht}(t)|, \tag{10}$$

where $C_{\mathrm{nl}} > 0$ is the nonlinear losses coefficient, which depends on the roundness of the edges of the hole [7], and v_{ht} is the acoustic speed at the top of the side hole. An explicit relationship between p_{ht}^+ and p_{ht}^- is given in [12]:

$$p_{ht}^-(t) = r_{\mathrm{nl}}\left[p_{ht}^+(t)\right], \tag{11}$$

where

$$r_{\mathrm{nl}}(x) = x\left(1 - \frac{4}{1 + \sqrt{1 + K_{\mathrm{nl}}|x|}}\right), \tag{12}$$

with $K_{\mathrm{nl}} = 8C_{\mathrm{nl}}/(\rho_0 c_0^2)$. For $K_{\mathrm{nl}} = 0$, we get $r_{\mathrm{nl}}(x) = -x$, which corresponds to an open hole boundary condition. As $K_{\mathrm{nl}} \to \infty$, $r_{\mathrm{nl}}(x) = x$, meaning the hole is closed.

In a dimensionless form, r_{nl} is rewritten as $\hat{p}_{ht}^- = \hat{r}_{\mathrm{nl}}\left[\hat{p}_{ht}^+\right]$, where

$$\hat{r}_{\mathrm{nl}}(x) = x\left(1 - \frac{4}{1 + \sqrt{1 + \hat{K}_{\mathrm{nl}}|x|}}\right), \tag{13}$$

with $\hat{K}_{\mathrm{nl}} = P_M K_{\mathrm{nl}} = 0.2$, assuming a moderate P_M and a hole with sharp edges.

2.5 Extraction of the modal acoustic pressure

Modal acoustic pressures are useful to visualize the limit cycles of the different oscillating regimes. However, they are not directly accessible through waveguide modeling. Filtering is applied *a posteriori*, using the modal decomposition of the input impedance $Z_{in} = P_{in}/U_{in}$:

$$Z_{in} = Z_c \sum_n \frac{C_n}{s - s_n} + \frac{\mathrm{conj}(C_n)}{s - \mathrm{conj}(s_n)}, \tag{14}$$

where C_n and s_n are the complex residues and poles, computed through the residues theorem from the analytic definition of the input impedance. In particular, the modal frequencies are given by $f_n = \Im(s_n)/(2\pi)$. The n-th modal acoustic pressure at the input p_n is defined through the following ODE:

$$\dot{p}_n(t) = Z_c C_n u_{in}(t) + s_n p_n(t), \tag{15}$$

where $\dot{p}_n = \partial_t p_n$ and $u_{in} = (p_{in}^+ - p_{in}^-)/Z_c$. Modal acoustic pressures can then be computed by filtering u_{in} with an IIR filter.

3. SIMULATIONS

Blowing pressure ramps are first carried out to find the ranges for which the first register is stable when the hole is closed, as well as the range for which the second register is stable when the hole is open.

Multiple hole openings are then performed for constant control parameters to assess the playability of the register jumps.

3.1 Blowing pressure ramps

The embouchure parameter is fixed at $\zeta = 0.3$ (average value for clarinet playing [6]) throughout the simulations. First, two blowing pressure ramps (*crescendi*) are performed: one for the hole closed ($\hat{K}_{\text{nl}} \to \infty$), one for the hole open ($\hat{K}_{\text{nl}} = 0.2$). For both cases, the values of the blowing pressure for which oscillations start ($\gamma_{\text{osc}}^{(c)}, \gamma_{\text{osc}}^{(o)}$) and stop ($\gamma_{\text{ext}}^{(c)}, \gamma_{\text{ext}}^{(o)}$) are noted. Multistability zones are then determined, knowing as an inner-property of reed instruments, that the equilibrium (no sound, noted R0) is stable when $\gamma > 1$ [5].

3.2 Hole openings

From a constant blowing pressure γ, the hole is instantaneously opened. The frequency of p_{in} is computed before the opening of the hole ($f^{(c)}$), and after ($f^{(o)}$). The ratio $f^{(o)}/f^{(c)}$ determines the register obtained. In particular, if $f^{(o)}/f^{(c)} \approx 3$, the second register is played.

For one value of the blowing pressure, $N_o = 200$ hole openings are performed at different times distributed over a time window $T^{(c)} = 1.5/f_1^{(c)}$, where $f_1^{(c)}$ is the first modal frequency for the closed hole. The value of $T^{(c)}$ is chosen to ensure that all limit cycles can be fully sampled. The proportion of the second register obtained for the N_o openings is computed.

Four thresholds are measured through this procedure: $\gamma_{\text{min}}^{(0\%)}, \gamma_{\text{min}}^{(100\%)}, \gamma_{\text{max}}^{(100\%)}, \gamma_{\text{max}}^{(0\%)}$. Thresholds $\gamma_{\text{min}}^{(100\%)}$ and $\gamma_{\text{max}}^{(100\%)}$ denote the minimum and maximum blowing pressures that always lead to the second register (R2) when the hole is opened. $\gamma_{\text{min}}^{(0\%)}$ is the maximum blowing pressure lower than $\gamma_{\text{min}}^{(100\%)}$ that never leads to R2, and $\gamma_{\text{max}}^{(0\%)}$ is the minimum blowing pressure greater than $\gamma_{\text{max}}^{(100\%)}$ that never leads to R2.

To explore if the initial conditions that lead to a specific regime are sensitive to a small perturbation, a random impulsion is added to $\hat{p}_{in}^{+}$ when the hole is opened. Different amplitudes of perturbation are tested, between 0.0 and 0.50.

Table 1. Values of the four thresholds characterizing the probability of playing the second register when opening the hole.

Threshold	$\gamma_{\text{min}}^{(0\%)}$	$\gamma_{\text{min}}^{(100\%)}$	$\gamma_{\text{max}}^{(100\%)}$	$\gamma_{\text{max}}^{(0\%)}$
Value	0.383	0.386	1.32	1.36

4. RESULTS

4.1 Blowing pressure ramps

Figure 2 shows the evolution of the amplitude of the acoustic pressure in the mouthpiece $\hat{p}_{\text{RMS}}$, as the blowing pressure increases linearly from $\gamma = 0$ to $\gamma = 3$ over 20 s. The blue and yellow curves represent the cases with the hole closed and open, respectively. The color mapping corresponds to the oscillation frequency: for the closed hole, the playing frequency is near the first modal frequency $f_1^{(c)}$ (first register R1), while for the open hole, it is close to the second modal frequency $f_2^{(o)}$ (second register R2).

For each case, the minimum ($\gamma_{\text{osc}}^{(c)}, \gamma_{\text{osc}}^{(o)}$) and maximum blowing pressures ($\gamma_{\text{ext}}^{(c)}, \gamma_{\text{ext}}^{(o)}$) that sustain oscillations are measured. The thick black lines at the bottom of the graph indicate values of γ where the equilibrium (no sound, R0) is stable. Note that the values of ($\gamma_{\text{osc}}^{(c)}$ and $\gamma_{\text{osc}}^{(o)}$) are overestimated due to bifurcation delay [23].

For the open hole, when $\gamma \in [1, \gamma_{\text{ext}}^{(o)}]$ R0 and R2 are both stable. In this range, if a musician plays in the first register with the hole closed and then opens the register hole, they may end up in either R2 or R0. The hole opening procedure described in Section 3.2 is used to evaluate how the probability of playing R2 evolves with γ. The four threshold values characterizing this probability are listed in Table 1.

Within the green region, R2 is always reached. In the blue region around $\gamma = 1.3$, the probability of playing R2 depends on the timing of the register hole opening. In the red region, the system always lands on the R0. Hence, the range of γ in which R2 can be played after opening the register hole from R1 is narrower than the range of γ where R2 is stable.

To characterize the transition regions, $\gamma \in [\gamma_{\text{min}}^{(0\%)}, \gamma_{\text{min}}^{(100\%)}]$ and $\gamma \in [\gamma_{\text{max}}^{(100\%)}, \gamma_{\text{max}}^{(0\%)}]$, multiple hole openings at different times are needed to determine which

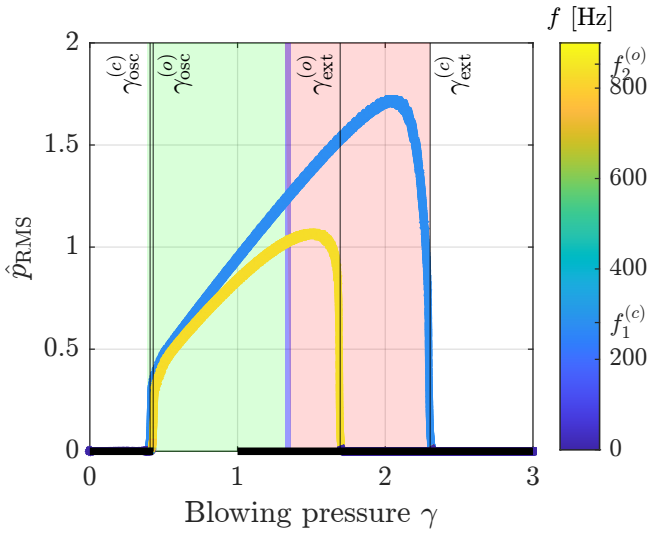


Figure 2. Evolution of the amplitude of the acoustic pressure into the mouthpiece when the blowing pressure γ increases linearly , for a constant embouchure $\zeta = 0.3$. Two *crescendi* are represented: one for the hole closed (blue curve), and one for the hole open (yellow curve). Colored surfaces in the background show the ranges of γ where the second register is reached with a given probability when the hole is opened. Green: 100 %. Blue: between 0 % and 100 %. Red: 0 %.

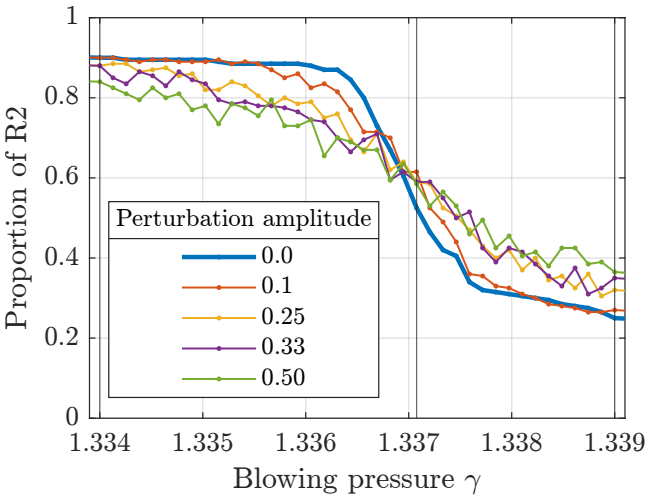


Figure 3. Evolution of the proportion of the second register (R2) when opening the register hole, for $\gamma \in [1.334, 1.339]$. The red, yellow, purple and green curves show the evolution of the proportion of R2 when random perturbations are added to $\hat{p}_{in}^{+}$ when the register hole is opened.

regime the model will predominantly converge to. Compared to the green or red regions, characterizing the blue region requires N_o times more simulations. For instrument makers studying the playability of twelfths in a clarinet model, the narrowness of these transition regions is an encouraging result.

A closer look at the transition from $\gamma_{\max}^{(100\%)}$ to $\gamma_{\max}^{(0\%)}$ is carried out in the next section.

4.2 Evolution of the probability of playing the second register

Figure 3 shows how the probability of playing the second register evolves within $\gamma \in [\gamma_{\max}^{(100\%)}, \gamma_{\max}^{(0\%)}]$. The probability follows negative sigmoid curve: it decreases gradually from 100 % to 90 %, then drops sharply between $\gamma = 1.336$ and $\gamma = 1.338$.

In the projection of the phase space on the variables $(\hat{p}_1, \dot{\hat{p}}_1)$, Figure 4 illustrates how the system converges to either R0 or R2 depending on the position of the initial condition on the R1 limit cycle. For instance, for $\gamma = 1.334$ (top left panel), only initial conditions within a small section of the cycle (around an angle of $3\pi/4$) are attracted to R0 (black dots). Opening the hole at a different time, corresponding to another position on the limit cycle, leads to R2 (red dots). This behavior is an instance of phase-tipping [24], where the result of a transition depends not only on the perturbation but also on the phase at which it is applied. As γ increases and the probability of playing R2 decreases, the set of initial conditions leading to R0 expands.

The top-center panel of Figure 4 shows that the set of initial conditions leading to R0 is not necessarily connected, highlighting the complex structure of the basin of attraction of the equilibrium in the $(\hat{p}_1, \dot{\hat{p}}_1)$ plane. At $\gamma = 1.339$ (top right panel), only a small portion of the limit cycle, around an angle of $-\pi/3$, leads to R2.

This visualization suggests that opening the register hole at the same time in every simulation is not ideal. Within $\gamma \in [\gamma_{\max}^{(100\%)}, \gamma_{\max}^{(0\%)}]$, if the hole were always opened when $(\hat{p}_1, \dot{\hat{p}}_1) \approx (0, -1200)$, the model would consistently produce R2. However, at $\gamma = 1.339$ (top right panel) there are few occurrences of R2.

Introducing a small random perturbation to $\hat{p}_{in}^{+}$ when opening the register hole results in smoother sigmoid curves in Figure 3, indicating that the basins of attraction of R0 and R2 remain stable under perturbations below 0.1. The second row of Figure 4 supports this, revealing additional regions belonging to R2's basin, such as the red dots around $\pi/2$ for $\gamma = 1.339$. Larger perturbations blur the basin boundaries in the $(\hat{p}_1, \dot{\hat{p}}_1)$ plane, as seen in the third row of Figure 4.

To better assess the basin stability of R0 and R2 when opening the register hole, alternative methods could be explored. Since perturbing p_{in}^{+} primarily affects $\dot{\hat{p}}_1$, adding white noise to the blowing pressure γ and the embouchure parameter ζ could provide a more balanced perturbation across the phase space.

5. CONCLUSION

A waveguide model of a clarinet with a register hole is studied. The blowing pressure ranges for which the first and the second registers are stable are determined. In particular, for the open hole configuration, the multistability regions of the second register and the equilibrium are quantified.

Results indicate that within this multistability range, repeatedly opening the register hole from the first register can lead the system to either the equilibrium or the second register. The probability of reaching a given register follows a sigmoid-shaped evolution as the blowing pressure increases. This behavior is reflected in phase space by the structure of the basins of attraction, which progressively enclose the limit cycle of the first register. The shifting probability of convergence to a given regime directly corresponds to changes in the shape of these basins.

Finally, the robustness of the basins of attraction is assessed by introducing random perturbations to the initial conditions. Preliminary results suggest that the basins remain robust under perturbations of p_{in}^{+} smaller than 0.1.

6. ACKNOWLEDGMENTS

This study has been supported by the French ANR LabCom LIAMFI (ANR-16-LCV2-007-01).

7. REFERENCES

[1] J. Backus, "Vibrations of the reed and the air column in the clarinet," *The Journal of the Acoustical Society of America*, vol. 33, no. 6, pp. 806–809, 1961.

[2] C. McGinnis, H. Hawkins, and N. Sher, "An experimental study of the tone quality of the boehm clarinet," *The Journal of the Acoustical Society of America*, vol. 14, no. 4, pp. 228–237, 1943.

[3] W. Li, A. Almeida, J. Smith, and J. Wolfe, "The effect of blowing pressure, lip force and tonguing on transients: A study using a clarinet-playing machine," *The Journal of the Acoustical Society of America*, vol. 140, no. 2, pp. 1089–1100, 2016.

[4] V. Chatziioannou, S. Schmutzhard, M. Pàmies-Vilà, and A. Hofmann, "Investigating clarinet articulation using a physical model and an artificial blowing machine," *Acta Acustica united with Acustica*, vol. 105, no. 4, pp. 682–694, 2019.

[5] J.-P. Dalmont, J. Gilbert, J. Kergomard, and S. Ollivier, "An analytical prediction of the oscillation and extinction thresholds of a clarinet," *The Journal of the Acoustical Society of America*, vol. 118, no. 5, pp. 3294–3305, 2005.

[6] J.-P. Dalmont and C. Frappé, "Oscillation and extinction thresholds of the clarinet: comparison of analytical results and experiments," *The Journal of the Acoustical Society of America*, vol. 122, pp. 1173–1179, Aug. 2007.

[7] M. Atig, J.-P. Dalmont, and J. Gilbert, "Saturation mechanism in clarinet-like instruments, the effect of the localised non-linear losses," *Applied Acoustics*, vol. 65, pp. 1133–1154, Sept. 2004.

[8] T. Colinot, C. Vergez, P. Guillemain, and J.-B. Doc, "Multistability of saxophone oscillation regimes and its influence on sound production," *Acta Acustica*, vol. 5, p. 33, 2021.

[9] T. Colinot, N. Szwarcberg, C. Vergez, and S. Missoum, "Cartography of a multistable system using support vector machines, applied to a clarinet model," *Nonlinear Dynamics*, pp. 1–12, 2025.

[10] A. H. Benade and D. H. Keefe, "The physics of a new clarinet design," *The Galpin Society Journal*, vol. 49, pp. 113–142, 1996.

[11] N. Szwarcberg, T. Colinot, C. Vergez, and M. Jousserand, "Second register production on the clarinet: nonlinear losses in the register hole as the decisive physical phenomenon," *arXiv preprint arXiv:2404.07540*, 2024.

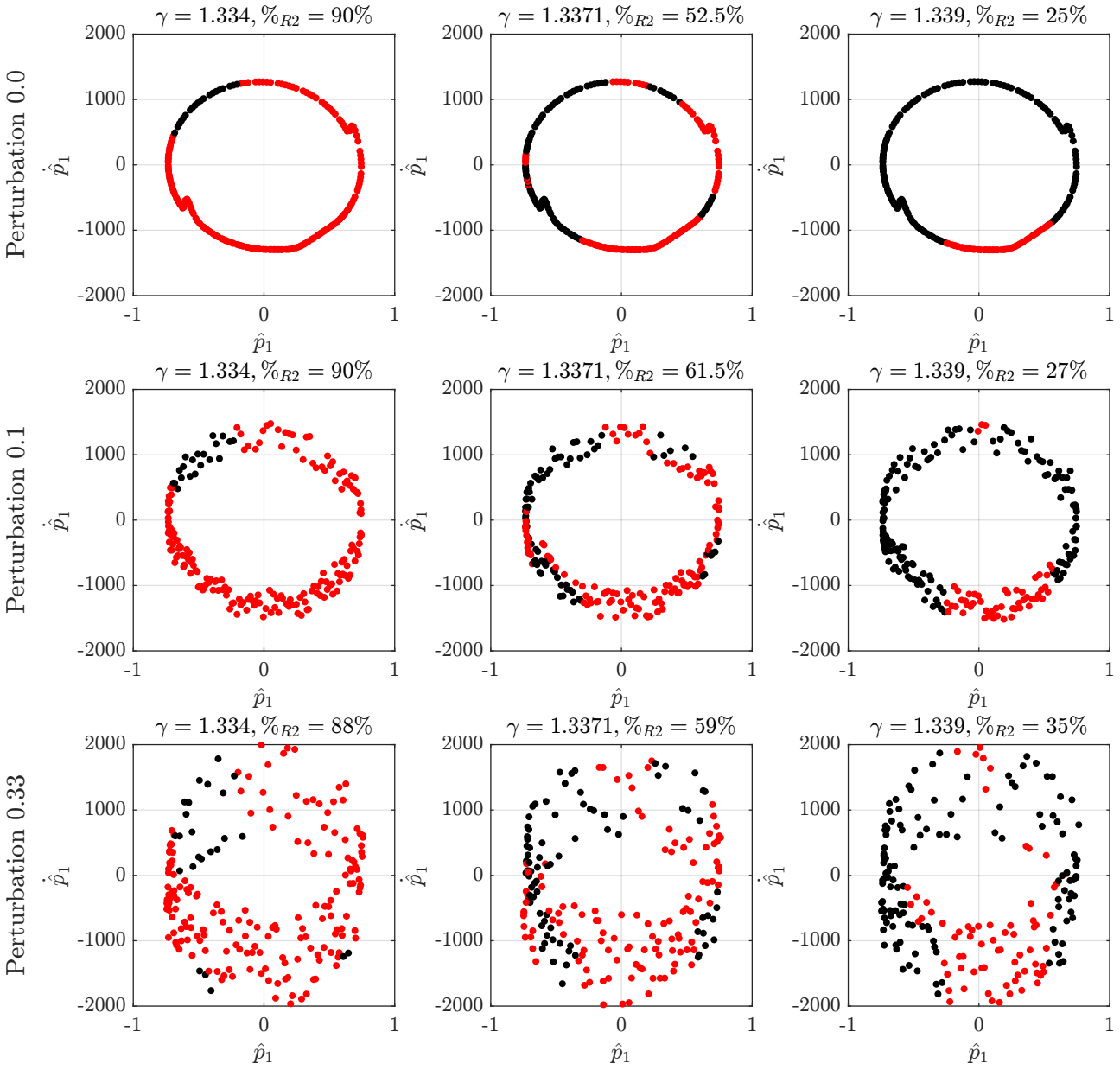


Figure 4. Positions on the limit cycle of the first register leading, when the hole is opened, to the second register (in red), and to the equilibrium (in black). Limit cycles are represented in the $(\hat{p}_1, \dot{\hat{p}}_1)$ space. Three different values of γ are displayed on each row. On the second row, a random perturbation of ± 0.1 is added to $\hat{p}_{in}^{+}$ when the hole is opened; on the third row the amplitude is 0.33.

[12] N. Szwarcberg, C. Vergez, T. Colinot, and M. Jousserand, "Oscillation threshold of a raman clarinet with localized nonlinear losses at the open end," *arXiv preprint arXiv:2411.18185*, 2024.

[13] P. J. Menck, J. Heitzig, N. Marwan, and J. Kurths, "How basin stability complements the linear-stability paradigm," *Nature physics*, vol. 9, no. 2, pp. 89–92, 2013.

[14] A. Chaigne and J. Kergomard, *Acoustics of musical instruments*. Springer, 2016.

[15] P. Guillemain, J. Kergomard, and T. Voinier, "Real-time synthesis of clarinet-like instruments using digital impedance models," *The Journal of the Acoustical Society of America*, vol. 118, no. 1, pp. 483–494, 2005.

[16] T. I. Laakso, V. Valimaki, M. Karjalainen, and U. K. Laine, "Splitting the unit delay [fir/all pass filters design]," *IEEE Signal Processing Magazine*, vol. 13, no. 1, pp. 30–60, 1996.

[17] V. Debut, J. Kergomard, and F. Laloë, "Analysis and optimisation of the tuning of the twelfths for a clarinet resonator," *Applied Acoustics*, vol. 66, pp. 365–409, Apr. 2005.

[18] T. A. Wilson and G. S. Beavers, "Operating modes of the clarinet," *The Journal of the Acoustical Society of America*, vol. 56, no. 2, pp. 653–658, 1974.

[19] S. Ollivier, J. Kergomard, and J.-P. Dalmont, "Idealized models of reed woodwinds. part ii: On the stability of," *Acta acustica united with acustica*, vol. 91, no. 1, pp. 166–179, 2005.

[20] J.-P. Dalmont, J. Gilbert, and S. Ollivier, "Nonlinear characteristics of single-reed instruments: Quasistatic volume flow and reed opening measurements," *The Journal of the Acoustical Society of America*, vol. 114, no. 4, pp. 2253–2262, 2003.

[21] P.-A. Taillard, J. Kergomard, and F. Laloë, "Iterated maps for clarinet-like systems," *Nonlinear dynamics*, vol. 62, pp. 253–271, 2010.

[22] B. Bergeot, A. Almeida, B. Gazengel, C. Vergez, and D. Ferrand, "Response of an artificially blown clarinet to different blowing pressure profiles," *The Journal of the Acoustical Society of America*, vol. 135, no. 1, pp. 479–490, 2014.

[23] B. Bergeot, A. Almeida, C. Vergez, and B. Gazengel, "Prediction of the dynamic oscillation threshold in a clarinet model with a linearly increasing blowing pressure," *Nonlinear Dynamics*, vol. 73, pp. 521–534, 2013.

[24] H. Alkhayuon, R. C. Tyson, and S. Wieczorek, "Phase tipping: how cyclic ecosystems respond to contemporary climate," *Proceedings of the Royal Society A*, vol. 477, no. 2254, p. 20210059, 2021.

DOI: 10.61782/fa.2025.0442



FORUM ACUSTICUM
EURONOISE 2025

IMAGING-BASED SAXOPHONE REED MODELLING

Diego Tonetti[1*] **Edoardo Piana**[1]

[1] Department of Mechanical Engineering, University of Brescia, Italy

ABSTRACT

Accurate sound synthesis of reed instruments based on physical models is of primary importance in the development and prediction of the sound produced by such devices. Since the sound is produced by reed oscillation, correct modelling of this part is mandatory. Several attempts have been explored in literature both by direct and inverse modelling. Here an imaging-based approach for characterising the reed dynamic behaviour is presented, using a high-speed camera and a Digital Image Correlation technique that allows the measurement of the reed vibrations under exponential sine sweeps pressure excitation signals. The transfer function between the reed and the driving pressure is estimated at different jaw forces using an artificial lip. This approach allows for direct modelling of the reed as a single-degree-of-freedom oscillator that can be implemented in sound synthesis.

Keywords: *reed, computer vision, high-speed camera, saxophone*

1. INTRODUCTION

The saxophone reed is responsible for the sound the instrument generates since its vibration generates a pressure variation over time that the instrument's body amplifies. Its oscillating frequency differs from its natural frequency, and it is imposed by the resonance frequency of the instrument in a feedback mechanism. Modelling the instrument-reed interaction has been first studied for a clarinet-like instrument (such as the saxophone) in [1], where the reed is assumed to behave as a single-degree-of-freedom oscillator, with the oscillations forced by the pressure difference across its surface. The same assumption on the reed dynamics is the most common approach in literature and is used by many authors [2–6]. Others simplify the reed model by assuming that the resonance frequency is much higher than the instrument's one, leading to a quasi-static model of the reed where the displacement is directly proportional to the pressure difference [7, 8]. This simplification is no longer valid as the instrument resonance frequency gets closer to the reed resonance frequency, thus, it is of mandatory importance to estimate its frequency response. Here, the reed transfer function that relates the reed motion to the acoustic pressure is estimated with a high-speed camera and a microphone. Digital Image Correlation is used as an image tracking algorithm to measure the reed displacement. Lip influence is considered, and the transfer function is measured at different biting forces. At last, least-squares optimization is used to fit a numerical model of the reed with experimental data, retrieving the reed stiffness, resonance frequency and damping for each lip force.

2. MATHERIALS AND METHODS

Following the acousto-mechanical modelling of the reed from the literature, the transfer function defined in Eq. (1) that relates the reed displacement $y(t)$ with the acoustic pressure $p(t)$ is estimated to retrieve the resonance frequency ω_r, the stiffness k_r and the damping ξ of the reed.

$$\ddot{y}(t) + 2\xi\omega_r\dot{y}(t) + \omega_r^2 y(t) = \frac{\omega_r^2}{k_r}p(t) \qquad (1)$$

A synthetic reed (Legere 3 tenor saxophone reed) is measured with a high-speed camera Mikrotron Cube7 and

*Corresponding author: diego.tonetti@unibs.it.

Copyright: ©2025 Diego Tonetti et al. This is an open-access article distributed under the terms of the Creative Commons Attribution 3.0 Unported License, which permits unrestricted use, distribution, and reproduction in any medium, provided the original author and source are credited.

a Bruel & Kjaer 4170 microphone inserted in the mouthpiece via a lateral hole placed 2 mm away from the reed tip. The microphone pressure is acquired with a Bruel & Kjaer Pulse acquisition system. Calibration of the image system is performed with a calibration sheet, which is used to compute the pixel-to-millimeter ratio, while the microphone is calibrated with a pistonphone Bruel & Kjaer type 4228. The chosen reed is made of a synthetic material, allowing us to discard the humidity's effect on the reed's flexibility, leading to more constrained boundary conditions. The reed is mounted on a saxophone mouthpiece, with a speaker connected to the mouthpiece through the hole where the saxophone neck is usually fitted. The effect of the player's lip biting on the reed is simulated with a soft foam of 10mm by 20mm and 5mm thick, with a hanging mass that determines the jaw force applied. The mass is varied from 0g to 1000g with steps of 250g, to simulate different biting forces on the reed. The 0g condition is achieved by removing the artificial lip, which means that the reed is simply clamped to the mouthpiece via the ligature. A constant light source is placed behind the reed, acting as a bright background in the recorded images and allowing for higher contrast in images, which is mandatory for image analysis. The experimental setup is schematized in Figure 1.

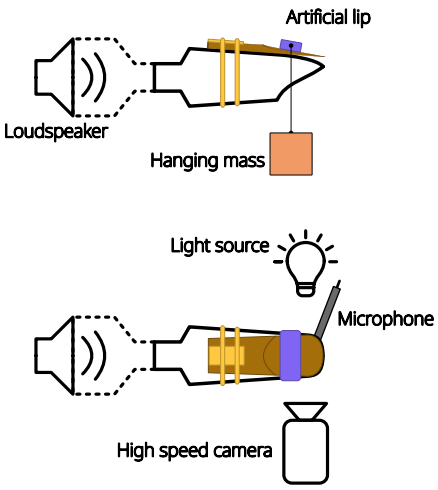


Figure 1. Scheamtic lateral and top view of the experimental setup.

The chosen signal is an exponential sine sweep generated with the plugin Aurora for Audacity [9], which also computes the inverse filter that will be used to remove all the harmonic distortions of the measured signals, allowing the retrieval of the linear response of the reed. For a signal $s(t)$, this is achieved by computing the convolution between the signal and the inverse filter as in Eq. (2):

$$r(t) = s(t) * x^{-1}(t) \tag{2}$$

where $x^{-1}(t)$ is the inverse filter of the exponential sine sweep $x(t)$. Looking at the time series of the convolution result $r(t)$, a series of peaks that correspond to the impulse responses of each harmonic is visible [10]. The linear response is the last impulse response visible in the series and can be isolated by taking a time window around it. An example of the convolution result is presented in Figure 2.

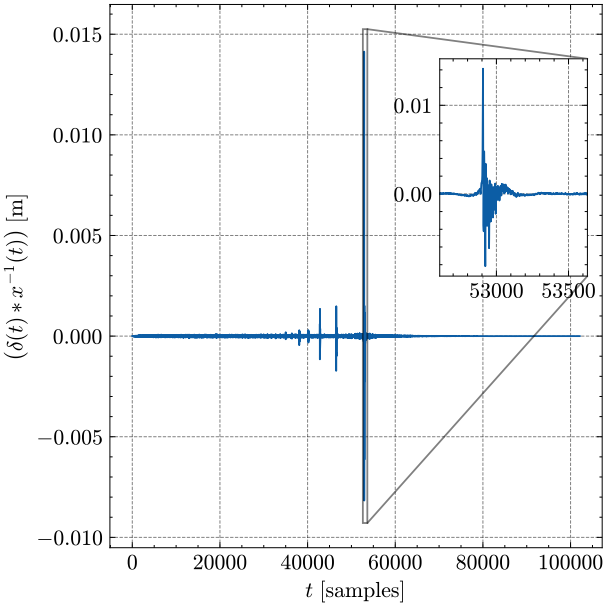


Figure 2. Convolution result of the measured displacement with a load of 0 g. A zoom is performed on the linear response.

Once the linear impulse responses of the pressure and displacement are retrieved, the measured transfer function of the reed $H_m(f)$ is evaluated in Eq. (3) as the ratio of the FFTs of the windowed impulse responses of the displacement $\delta'(t)$ and the pressure $p'(t)$.

$$H_m(f) = \frac{\mathcal{F}(\delta'(t))}{\mathcal{F}(p'(t))} \tag{3}$$

Performing the Laplace transform of Eq. (1) using the operator $s = j\omega = 2j\pi f$ leads to Eq. (4).

$$H(s) = \frac{Y(s)}{P(s)} = \frac{1}{k_r} \frac{\omega_r^2}{s^2 + 2\xi\omega_r s + \omega_r^2} \quad (4)$$

The measured transfer function can then be used to estimate the resonance frequency ω_r, the damping ξ and the elastic coefficient k_r of Eq. (1) by fitting the analytical transfer function $H(s)$ with the experimental transfer function $H_m(f)$. This can be done with least-squares optimization that aims at finding ω_r, ξ and k_r as in Eq. (5).

$$(\omega_r, \xi, k_r) = \arg\min_{\mathbf{b}} \| |H(f, \mathbf{b})| - |H_m(f)| \|, \quad \forall f \quad (5)$$

2.1 Image tracking

Tracking the reed's movement can be trivial, but the choice of image-tracking algorithm is crucial for the correctness of the obtained results. Digital image correlation (DIC) [11] is used here to track the movement of the reed; this procedure allows for computing the image shift between two different frames by computing the cross-correlation function between them, similar to the technique used to calculate the time-lag between two audio signals. The technique can be easily applied due to the image setup constraint, as it is possible to isolate the reed movement entirely from the surrounding ambient, as can be observed in Figure 3, where the only moving object is the reed.



Figure 3. Reed tip acquired by the camera.

The cross-correlation between two images can be computed efficiently with the discrete Fourier transform (DFT) as

$$r = \mathcal{F}^{-1} \left(G_a \circ G_b^* \right) \quad (6)$$

where $\circ$ is the element-wise multiplication of the DFT G_a and G_b of the image I_a at time t and the reference image I_b. The displacement is then equal to the position of the maximum correlation coefficient and can be retrieved as

$$(\Delta x, \Delta y) = \arg\max_{(i,j)}(r) \quad (7)$$

This approach is limited to discrete displacements of 1 pixel, while sub-pixel precision is required due to the small movements of the reed. A straightforward solution is to interpolate the cross-correlation function and find the new maximum given by that interpolation [12], thus achieving sub-pixel accuracy. Here, a 3rd order interpolation is used from the Python [13] library Scipy [14] by performing a zoom with an enlargement factor $Z = 10$, which leads to a sub-pixel accuracy of 0.1 pixel. To save computational costs, interpolation is performed on a small window around the pixel-level peak. The overall displacement due to the pixel displacement plus the sub-pixel displacement is then given by Eq. (8) as

$$(\Delta x, \Delta y) = \arg\max_{(i,j)}(r) + \frac{1}{Z} \arg\max_{(i,j)}(r') \quad (8)$$

where r' is the interpolated cross-correlation. To avoid problems at the borders that could cause aliasing, the images are multiplied by a two-dimensional Hann window. Also, contrast is enhanced via histogram stretching and noise is reduced with a Gaussian blur using OpenCV [15]. The algorithm steps are reported here:

1. Compute the FFT of the reference image multiplied by the Hann window.
2. Compute the FFT of the image at time instant t.
3. Compute the cross-correlation with Eq. (6).
4. Find the pixel-precision displacement with equation 7.
5. Crop the cross-correlation around the peak found in the previous step.
6. Interpolate the cross-correlation and retrieve the sub-pixel displacement again with 7.
7. Scale the sub-pixel displacement by the zoom factor and add it to the pixel-level displacement.

3. RESULTS

All the measurements are performed with a sine sweep that goes from 50 Hz up to 5 kHz with a duration of 5 s, and the sampling frequency is chosen equal to the framerate of the camera, i.e. 10 kHz. The window used around the peak is of 1024 samples, with a sampling frequency of 10 kHz, thus leading to a frequency resolution of 9.77 Hz. The experimental transfer function of the reed measured for all the lip loads is presented in Figure 4, where both the amplitude and the phase are shown.

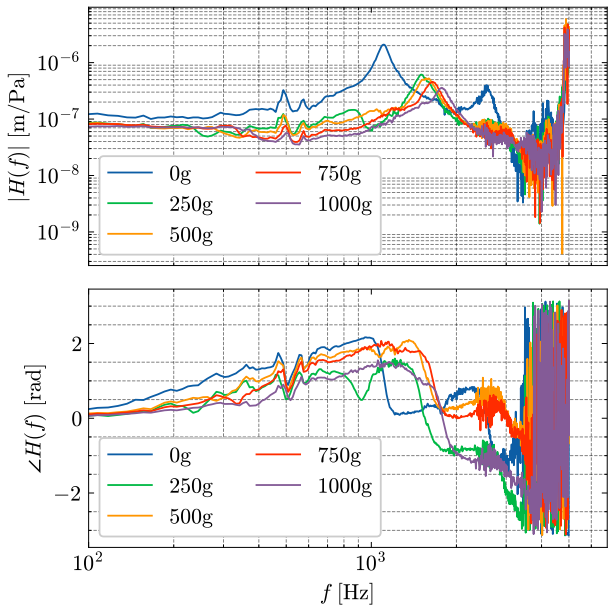


Figure 4. Reed measured transfer functions at different loads.

Comparisons between the measured and least-squares transfer functions are reported for various lip loads in Figure 5. Only the modules of the transfer functions are considered during the least-squares method, as the phase at low frequency presents a drift that makes the single DOF oscillator unfit. Following the control theory of Linear Time Invariant systems in the Laplace domain, the phase shift could be modelled by adding a zero (i.e. a derivative term) at low frequency in the transfer function of Eq.(4), which would increase the phase by 90 deg in agreement with the results, but it would also increase the module by 20 dB/dec which is not visible in the measures. Thus, following the literature, Eq. (4) is considered valid, the phase is discarded, and only the module is used for fitting the transfer function with experimental data. The data is fitted on the frequencies that range from 50 Hz to 2500 Hz to avoid noise at high frequency and at the low frequencies where the reed isn't excited by the ESS.

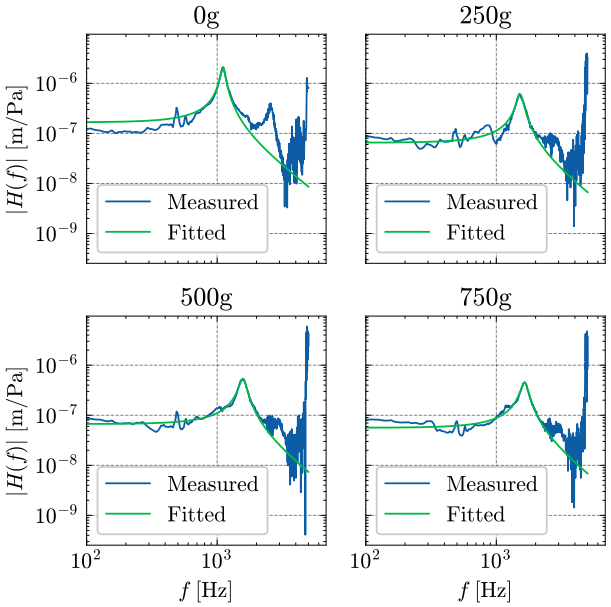


Figure 5. Measured and least-squares optimization results for 4 different lip loads.

The fitted transfer functions are reported in Figure 6, while the estimated coefficients derived from the least-squares optimization are summarized in Table 1.

load [g]	k_r [Pa/m]	ω_r [rad/s]	ξ [1]
0	6.01×10^6	6.97×10^3	3.95×10^{-2}
250	1.54×10^7	9.59×10^3	5.40×10^{-2}
500	1.50×10^7	9.92×10^3	6.24×10^{-2}
750	1.78×10^7	1.04×10^4	6.27×10^{-2}
1000	1.95×10^7	1.12×10^4	7.71×10^{-2}

Table 1. Caption

4. DISCUSSIONS

From the measured reed transfer function with no lip force applied, two resonance peaks are visible, one at 1104 Hz and one at 2549 Hz. The presence of two resonances is not visible when a lip load is applied; this could be a limitation

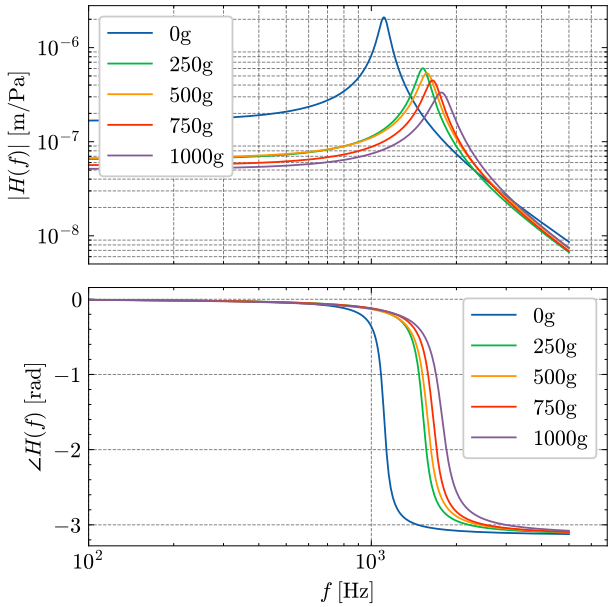


Figure 6. Fitted transfer function of the reeds at all lip loads.

of the experimental setup used, as it presents considerable noise above 3 kHz. A better signal-to-noise ratio can be achieved using a brighter light source, enhancing the image contrast. The reed's first resonance in the absence of lip influence is in agreement with the one measured in [16] for a tenor saxophone cane reed. The first resonance peak is shifted up in frequency as the lip load increases, which is in contrast with the measurements obtained in [5]. This behaviour of the reed increasing its resonance frequency is indirectly observed in [17] and is well known by players, where higher biting forces increase the pitch of the note. In [17], this is justified by stating that the reed is bent against the mouthpiece, thus shortening the reed portion that is allowed to vibrate. The measured resonance frequency and reed stiffness are close to the results obtained by inverse modelling of a clarinet reed in [6], and the reed stiffness is also comparable with the results found for a quasi-static clarinet reed [8]. Significant discrepancies are found with the resonance frequency, stiffness and damping with [18], where inverse modeling similar to [6] was performed on a tenor saxophone reed.

5. CONCLUSIONS

The transfer function of a reed was directly measured at different lip forces via a high-speed camera and Digital Image Correlation. This technique allowed non-contact measures of the reed displacement, representing an alternative to Laser Doppler Vibrometry. The performed measurements were compared with the literature, finding mixed results. These discrepancies could be due to the experimental setups, artificial lips and reed materials. The resonance frequency of the reed is found to be around 20 times greater than the instrument's lowest resonance frequency, while about only 3 times larger than the highest. A quasi-static model of the reed could thus be insufficient to model the reed as the note of interest moves up along the saxophone register.

6. ACKNOWLEDGMENTS

The authors thank Prof. Pietro Poesio and Prof. Davide Picchi (Fisica Tecnica Industriale Laboratory, the University of Brescia) and Dr. Simone Pasinetti (Misure Meccaniche e Termiche Laboratory, the University of Brescia) for lending the high-speed camera and the lens, respectively.

7. REFERENCES

[1] R. T. Schumacher, "Ab initio calculations of the oscillations of a clarinet," *The Journal of the Acoustical Society of America*, vol. 65, pp. S73–S73, 08 2005.

[2] A. Chaigne and J. Kergomard, *Acoustics of Musical Instruments*. Modern Acoustics and Signal Processing, Springer New York.

[3] S. Wang, E. Maestre, and G. Scavone, "Acoustical modeling of the saxophone mouthpiece as a transfer matrix," *The Journal of the Acoustical Society of America*, vol. 149, pp. 1901–1912, 03 2021.

[4] S. Bilbao, "Direct Simulation of Reed Wind Instruments," *Computer Music Journal*, vol. 33, pp. 43–55, Dec. 2009.

[5] J. Dalmont, B. Gazengel, J. Gilbert, and J. Kergomard, "Some aspects of tuning and clean intonation in reed instruments," *Applied Acoustics*, vol. 46, no. 1, pp. 19–60, 1995. Musical Instrument Acoustics.

[6] V. Chatziioannou and M. Van Walstijn, "Estimation of clarinet reed parameters by inverse modelling," *Acta*

Acustica united with Acustica, vol. 98, pp. 629–639, 07 2012.

[7] J. Gilbert, S. Maugeais, and C. Vergez, "Minimal blowing pressure allowing periodic oscillations in a simplified reed musical instrument model: Bouasse-Benade prescription assessed through numerical continuation," *Acta Acustica*, vol. 4, no. 6, p. 27, 2020.

[8] J.-P. Dalmont, J. Gilbert, and S. Ollivier, "Nonlinear characteristics of single-reed instruments: Quasistatic volume flow and reed opening measurements," *The Journal of the Acoustical Society of America*, vol. 114, pp. 2253–2262, 10 2003.

[9] Angelo Farina, "Aurora for audacity."

[10] farina angelo, "advancements in impulse response measurements by sine sweeps," *journal of the audio engineering society*, may 2007.

[11] P. E. Anuta, "Spatial Registration of Multispectral and Multitemporal Digital Imagery Using Fast Fourier Transform Techniques," *IEEE Transactions on Geoscience Electronics*, vol. 8, pp. 353–368, Oct. 1970.

[12] B. Xiong, Q. Zhang, and V. Baltazart, "On Quadratic Interpolation of Image Cross-Correlation for Subpixel Motion Extraction," *Sensors*, vol. 22, p. 1274, Feb. 2022.

[13] G. Van Rossum and F. L. Drake, *Python 3 Reference Manual*. Scotts Valley, CA: CreateSpace, 2009.

[14] P. Virtanen, R. Gommers, T. E. Oliphant, M. Haberland, T. Reddy, D. Cournapeau, E. Burovski, P. Peterson, W. Weckesser, J. Bright, S. J. van der Walt, M. Brett, J. Wilson, K. J. Millman, N. Mayorov, A. R. J. Nelson, E. Jones, R. Kern, E. Larson, C. J. Carey, İ. Polat, Y. Feng, E. W. Moore, J. VanderPlas, D. Laxalde, J. Perktold, R. Cimrman, I. Henriksen, E. A. Quintero, C. R. Harris, A. M. Archibald, A. H. Ribeiro, F. Pedregosa, P. van Mulbregt, and SciPy 1.0 Contributors, "SciPy 1.0: Fundamental Algorithms for Scientific Computing in Python," *Nature Methods*, vol. 17, pp. 261–272, 2020.

[15] G. Bradski, "The OpenCV Library," *Dr. Dobb's Journal of Software Tools*, 2000.

[16] B. Gazengel and J.-P. Dalmont, "Mechanical response characterization of saxophone reeds," in *Proceedings of "Forum Acusticum"*, (Aalborg, Denmark), p. 000124, June 2011.

[17] A. Almeida, D. George, J. Smith, and J. Wolfe, "The clarinet: How blowing pressure, lip force, lip position and reed "hardness" affect pitch, sound level, and spectrum," *The Journal of the Acoustical Society of America*, vol. 134, pp. 2247–2255, Sept. 2013.

[18] A. Muñoz Arancón, B. Gazengel, J.-P. Dalmont, and E. Conan, "Estimation of saxophone reed parameters during playing," *The Journal of the Acoustical Society of America*, vol. 139, pp. 2754–2765, 05 2016.

DOI: 10.61782/fa.2025.0964

FORUM ACUSTICUM EURONOISE 2025

VOCAL TRACT TURBULENCE AND RECORDER SOUND – A CFD APPROACH

Naomi Nordblom[1*] **Rolf Bader**[1]
[1] Institute for Systematic Musicology, University of Hamburg, Germany

ABSTRACT

Whether it is possible to change the timbre during recorder playing is a much debated question among recorder players. Chen et al. (2007) showed that it is indeed possible to alter the timbre of the recorder as a player. As the underlying mechanism is not clear, a large eddy fluid simulation in two dimensions of four different vocal tract shapes has been carried out. One vocal tract is straight, the second one has a constriction in the back, the third one has a constriction in the front and the last one is a short reference model. The velocities and the pressure point to the hypothesis that turbulence created in the front of the mouth cavity is associated with lesser correlated velocities in the jet region and reduced harmonics.

Keywords: *recorder, flue instrument, turbulence, vocal tract*

1. INTRODUCTION

Although the recorder is present in European culture at least since the middle ages [1], there is still no theoretical framework how to elicit different timbres as a player for a given pitch. Colorful recorder playing has first documented about 70 years ago by Frans Brüggen but until today, players struggle to reproduce this except very few virtuosi. A better understanding of virtuoso recorder techniques could make them accessible for more people. From a physical perspective, the recorder consists of an edge tone which is additionally enslaved by a resonator [2], [3]. This means, that the frequency of the recorder is strongly coupled to the blowing speed which guides the oscillation frequency of the jet [4]. However, there are some loopholes that have the potential to alter the timbre without changing the pitch (for an overview see [5]).

The most researched one sees the windway as the neck of a Helmholtz resonator sitting on the volume of the mouth cavity [6], [7]. This effect has also been examined with fluid simulations on an organ pipe with its chamber [8], [9]. Depending whether the frequency of the Helmholtz resonator is above or below the fundamental of the flue instrument, in-phase or anti-phase oscillations are elicited in the jet. The anti-phase oscillation leads to a more stable tone when the frequency of the Helmholtz is below the fundamental of the instrument [8], [9]. Moreover, possible alterations of the harmonics are discussed [6], [7]. Further in this paper this, will be called the Helmholtz effect. Another mechanism is the production of turbulence in the vocal tract. A spectral analysis revealed different timbres of a virtuoso recorder player when playing the same instrument [10]. After some hypotheses [10] as well as a first fluid simulation [5], it is still unclear, how the turbulence finds its way from the mouth to the sound. This is the scope of this paper.

Transient fluid simulations are well suited as a major contribution to tackle this problem because of their ability to deliver values of all relevant physical quantities at every point in time and space. Due to the 3D nature of turbulence and the different energy cascades [11], a thorough investigation would require several 3D Large-Eddy-Simulations (LES). This would ask for an enormous amount of calculation time and careful selection which data to write out. To facilitate this decision, 2D-simulations have been carried out to develop a qualitative hypothesis for more detailed testing e.g. a possible 3D-simulation.

**Corresponding author*: naomi.nordblom@studium.uni-hamburg.de.
***Copyright**: ©2025 Nordblom et al. This is an open-access article distributed under the terms of the Creative Commons Attribution 3.0 Unported License, which permits unrestricted use, distribution, and reproduction in any medium, provided the original author and source are credited.*

2. METHOD

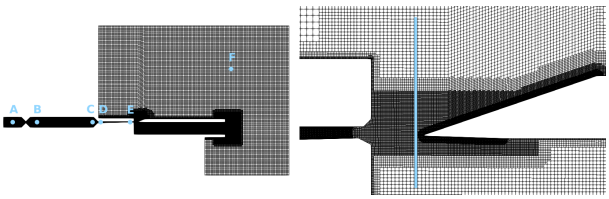


Figure 1: Mesh with sample locations in blue.

To investigate the influence of turbulence in the mouth cavity on the recorder sound, LES-simulations have been carried out. Four different shapes of "mouth cavities" have been tested (fig. 2): The first one is a straight tube. The second one has a constriction in the back and the third one in the front. It is expected, that the flow separates after the constriction to create shear turbulence. Moreover, a short model has been created to distinguish the influence of turbulence from the Helmholtz effect. The dimensions of the mouth cavities are very roughly estimated after [12] with a length of $14.8\,\mathrm{cm}$ and a diameter of $1.63\,\mathrm{cm}$ for the straight vocal tract and the ones with the constrictions in the front. The short vocal tract has the same volume as the front chamber of the mouth cavity with the constriction in the front. The simulations are run with OpenFOAM v2406 and its compressible solver rhoPimpleFoam. The numerics mostly follow [13] because the source code is online and some of his results have been confirmed by experiments [13] and a 3D simulation [14]. The turbulence is modelled with a one-equation-eddy model. The spacial derivatives are discretized with a filtered version of the central differencing scheme to obtain sharp gradients for the jet and suppress oscillations. The temperature is set to $293\,\mathrm{K}$ while the pressure is set to $101\,325\,\mathrm{Pa}$. The boundary conditions consist inter alia of an inlet with constant velocity of $1.17\,\mathrm{m\,s^{-1}}$, acoustically hard walls, a wave transmissive outlet for the pressure combined with an outlet velocity condition with a zero gradient outflow velocity for the air leaving the domain and a calculated inflow velocity for reverse flow into the domain.

The windway and labium of the recorder are built after an f-alto recorder by Johann Pörschmann (about 1680–1757) at the Musikhistorisk Museum in Copenhagen, inventory number CL 417 [15]. The measurements of the chamfers and the position of the labium's tip are lacking in this plan and estimated following the advice of recorder maker Geri Bollinger. The resonator consists of a straight tube with a length of $14.3\,\mathrm{cm}$ and a diameter of $1.93\,\mathrm{cm}$. When creating the mesh, emphasis has been given to a fine grid in the windway, the jet region, around the labium and at the walls (fig. 1). This results in grid sizes between 197 057 cells for the short vocal tract and 219 384 cells for the straight vocal tract. The simulations are run for $0.1\,\mathrm{s}$ with a time-step of $2.5 \times 10^{-6}\,\mathrm{s}$.

3. RESULTS AND DISCUSSION

In this section, we follow the flow from the vocal tract over the windway and the jet to the sound spectra.

3.1 Creation of Turbulence in the Vocal Tract

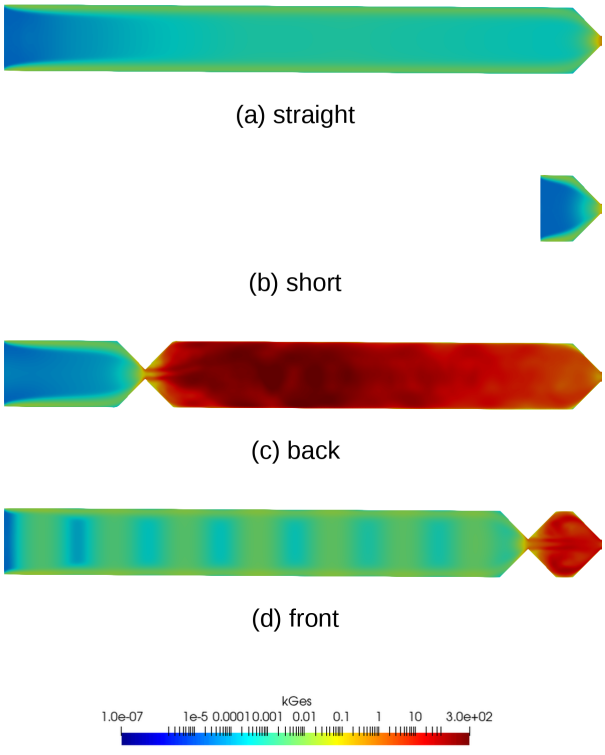


Figure 2: Logarithmically scaled turbulent kinetic energy in the vocal tract after $0.1\,\mathrm{s}$. The constrictions lead to boundary layer separation and create shear turbulence.

As we can see in fig. 2 taken after 0.1 s, the constriction creates shear turbulence by boundary layer separation. The image of the constriction in the back shows the typical growth and the decay of shear turbulence without extra energy supply in the direction of the flow. The energy spectra obtained from the autocorrelation of the velocity component in the mean flow direction show a clear periodicity for the straight and short vocal tracts while there is a typical line at the turbulent locations after the constrictions. The decay of the turbulence of the constriction in the back is also reflected on the spectrum, as harmonic components begin to reappear. This can be seen for example on the energy spectrum of the flow direction velocity in fig. 3 compared to the similar spectra of the straight vocal tract.

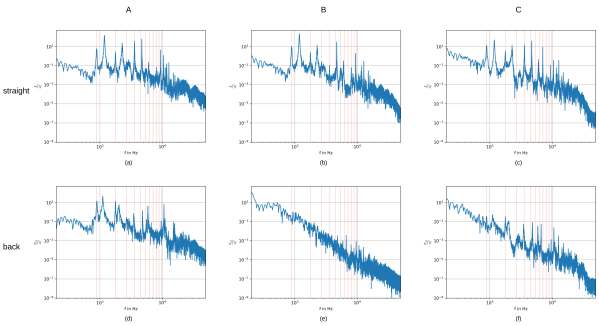


Figure 3: Energy spectra of the velocity fluctuations in the mean flow direction in the vocal tract. The first line shows the straight vocal tract as a comparison while the second line shows the spectra of the constriction in the back before (A), after (B) and long after the constriction (C).

3.2 Turbulence in the Windway

The energy spectrum in the direction along the windway can be seen in fig. 4. The first probe point, D, lies 1.428 57 mm after its entrance while the second probe point is located at 55.98 mm from the entrance, right above the lower chamfer, E (fig. 1). The spectra in fig. 4 show a blend of the acoustic and the flow field. The pink lines show multiples of the fundamental of 891 Hz while the dark red lines show multiples of the resonance frequency of the windway around 2858 Hz up to 10 000 Hz. The gray area shows the minimum eddy frequencies stemming from the turbulence in the windway between 7400 and 60 000 Hz. They are estimated by Taylor's hypothesis with a windway diameter of 9 mm at its entrance and 23 mm at its narrowest point where the flow separates from the lower chamfer to form the jet.

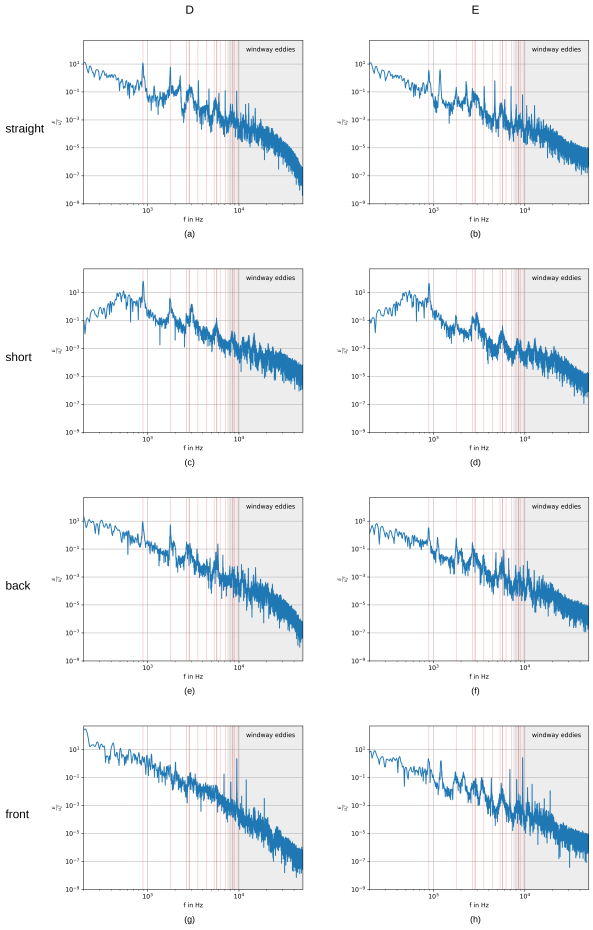


Figure 4: Energy spectrum of the velocity fluctuations in the x-direction from 0.02 to 0.1 s at the windway entrance and at the separation point at its exit.

In general, the spectra show some harmonic peaks associated with the sound field, a more or less logarithmically declining noise floor as well as some inharmonic peaks. Some of them are multiples of the estimated resonance frequency of the windway while others could descend from the flow field as documented by [16] and [9] for the sound pressure levels. The straight vocal tract has the clearest and best aligned harmonics. The spectra of the short vocal tract show less harmonics with broader peaks

and very clear windway resonances. The spectra of constriction in the back shows less aligned higher harmonics than the spectrum of straight vocal tract particularly above 4000 Hz. At the entrance, there are almost no harmonics discernible for the spectrum of the constriction in the front while they reappear with broad peaks and reduced amplitudes at the windway exit. Next, we are looking closer into the gray regions of fig. 4 which would allow for isotropic eddies in the windway. Except for the short vocal tract, all spectra show more energy at these frequencies at the exit of the windway compared to its entrance possibly because of the wall boundary layer of the windway. The reason for the exception of the short vocal tract is not known. The two vocal tracts with constrictions exhibit slightly enhanced amplitudes above 30 000 Hz. All in all, the different geometries show already different turbulence structures when leaving the windway with the straight vocal tract being the most harmonic and the constriction in front showing the most high-frequency peaks. A detailed analysis in this region has to be used with great caution because of the convection in the windway, the different energy cascade between 2D and 3D could play a major role.

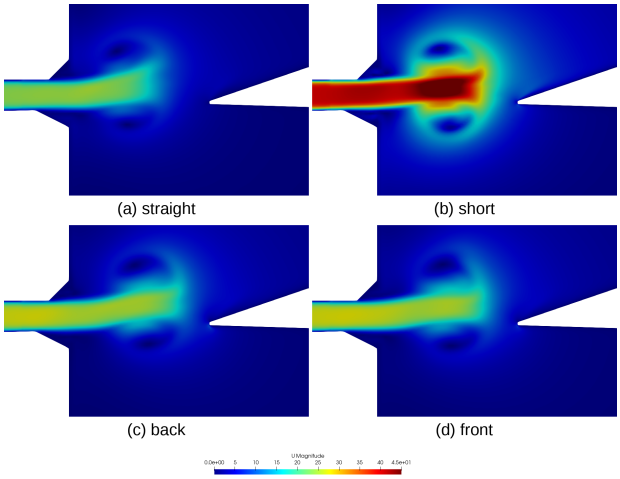


Figure 5: Jet velocity magnitude after 0.001 68 s for the straight, front and back condition and after 0.0008 s for the short vocal tract. The different histories of the jet are amplified by the Kelvin-Helmholtz instability.

3.3 Jet Velocities

The development of the jet velocities can be analyzed in two consecutive time windows. When the flow enters the cutup as a jet for the first time, it is mainly influenced by the Kelvin-Helmholtz instability (KHI) reflecting its aerodynamic history. After the resonator delivers its feedback over the time, interesting correlations of the jet velocities can be spotted and it seems more to behave like a complex system.

3.3.1 Initial Kelvin-Helmholtz Instability

Fig. 5 shows the Kelvin-Helmholtz instability of the velocity magnitude of the jet after 0.001 68 s for the straight, front and back condition and after 0.0008 s for the short vocal tract. At this moment, the initial shockwave [13] has already been reflected on the jet and it might also pertain to the perturbations of the jet amplified by the KHI.

The differences between the images reflect the different histories of the jets before arriving at the cut-up. The straight vocal tract shows the biggest upward bending of the jet. This initial upward-bending is clearly reduced for the short vocal tract due to its higher momentum. This condition shows a higher velocity at this initial stage because the air is more compressed in the mouth cavity before entering the windway due to the proximity of the inlet to the windway entrance. However, this enourmous velocity difference disappears in the steady-state. The constrictions show lower velocity gradients especially when the constriction is in front and thus flatter velocity profiles due to the upstream turbulence in accordance with [17].

3.3.2 Velocity Correlations During the Steady-State

To capture the vertically oscillating jet, a line sample of the velocities has been drawn perpendicularly through it 2.6364 mm away from the windway exit as shown in fig. 1. At this location, the vertical oscillation of the jet is well developed, but it is not yet highly asymmetrical due to the labium. The x-component of the velocity in the mean flow direction shows the position of the jet over time until 0.1 s (fig. 6).

The time development of the jet position is mirrored by the pressure evolution at 17 cm away from the labium above the foot as we can see at the example of the straight vocal tract. At first, an oscillation forms until 0.005 s and grows up to 0.023 s. During the growth, the velocities around the jet align their movement with the jet. The steady-state is temporarily disturbed between 0.042 s and 0.05 s by an exception in the velocities with a simulta-

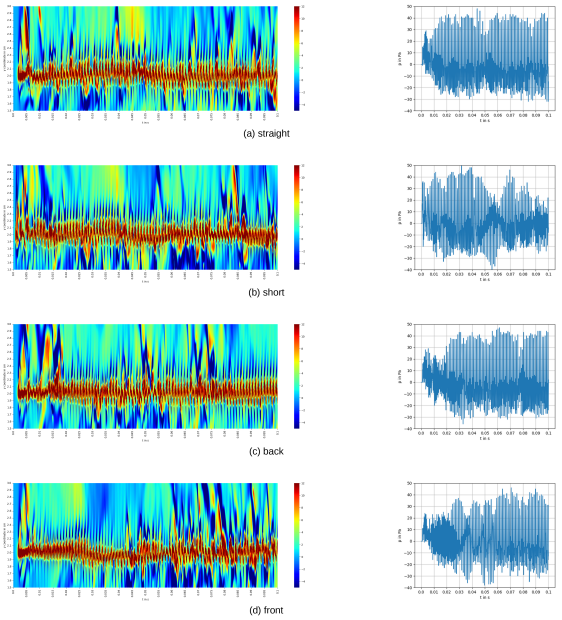


Figure 6: Left: Horizontal velocity component of a sample line perpendicular to the jet plotted over the time until 0.1 s. Right: corresponding pressure amplitudes 17 cm away from the labium above the foot at point F.

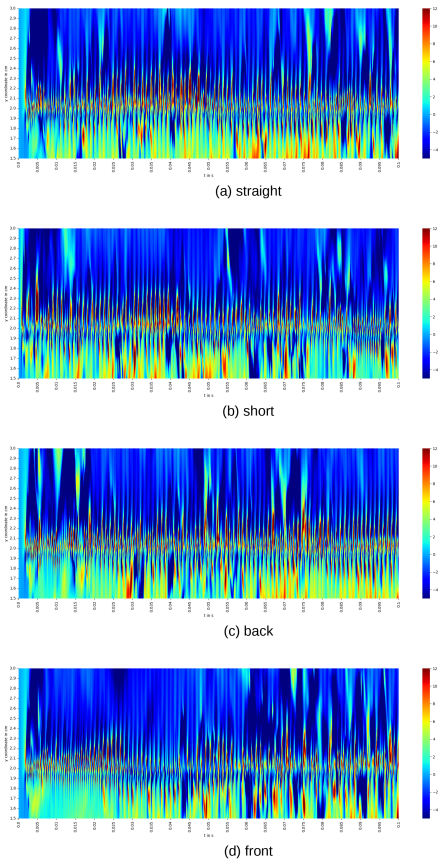


Figure 7: Vertical velocity component of a sample line perpendicular to the jet plotted over the time until 0.1 s.

neous reduction in sound pressure. The short vocal tract has a shorter initial transient and a less stable steady-state. From 0.0885 s and 0.096 s, the recorder overblows. This dependence of the overblowing on the geometry of the vocal tract could hint to [4] who have shown that trained recorder players can enlarge the hysteresis of their instrument with respect to overblowing. The constriction in the back exhibits a longer transient up until 0.038 s. Here, we can also watch the oscillations around the jet and the pressure amplitude grow together. The constriction in the front has a very long transient and growth until 0.028 s with very regular movements although it has some difficulties to take along as much air around the jet as the other conditions. Then, the the jet gets more irregular up to 0.028 s settling into a steady-state with a varying amplitude and surrounded by some quite far-reaching non-periodic velocity fluctuations.

While the x-component reveals the position of the jet, the y-component tells us something about its vertical movement (fig. 7).

During the steady-state, the heatmaps show different levels of variability of the vertical jet movement over time. Moreover, this jet movement influences the air around it up to different distances. To obtain a numerical value associated with these effects, the correlation function of the time evolutions of each sample point with a point in the middle of the jet has been taken. Fig. 8 shows the L1-norm of each correlation function depending on the y-coordinate.

The correlations are the highest inside the resonator. The reflection of the sound waves in this region could support the strong correlation. A second peak can be observed in the jet and a third one above the jet in the cut-up and slightly outside of the instrument. The image shows an

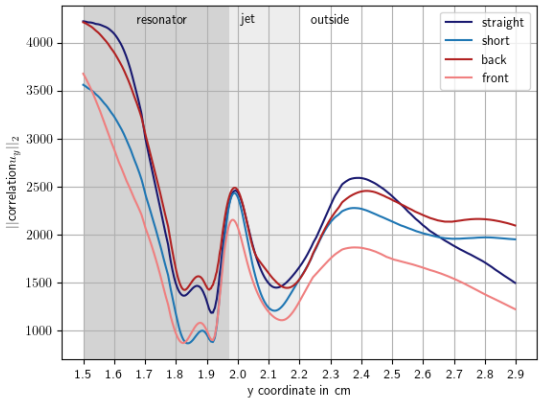


Figure 8: Correlation norm of the time evolution of each sample point with a point in the jet.

interaction between the size of the mouth cavity and the turbulence with enhanced correlations for a larger vocal tract and less turbulence. This is most prominent in in the cut-up peak outside of the jet and the resonator. Moreover, the difference between the front and the short condition suggest a second possibility to alter the sound next to the proposed Helmholtz effect.

3.4 Radiated Sound Spectra

The radiated sound spectra in fig.9 are taken 17 cm away from the labium above the foot from 0.02 to 0.1 s during the quasi-stationary state with a sample rate of 10^5 Hz. This gives a frequency resolution of 12.07 Hz. All the fundamentals are at 891 Hz. The spectrum of the straight vocal tract shows the clearest harmonics with the narrowest peaks. In this, the first and second harmonic are most prominent. In comparison, the spectra of the short vocal tract and the constriction in the back differ slightly while the spectrum in the front shows clear changes. The spectrum of the short vocal tract shows slightly wider peaks and tightened octaves as overtones. The first and second harmonic are a little bit weaker. The sound spectrum of the constriction in the back also displays slightly wider harmonics. In this case, the first and second harmonic are as strong as in the spectrum of the straight vocal tract with weakened third and fourth harmonics. In general, these changes are rather small and it would be interesting if they can be perceived. In contrast, the spectrum with the constriction in the front only shows a strong first harmonic with a weaker second and higher harmonics not discernible from the background. The first and second harmonic are considerably broader. Moreover, it displays some extra energy in the frequencies around the second harmonic and between 6000 and 7000 Hz. This rich fundamental and the enhanced noise floor between 6000 and 7000 Hz match with the virtuoso recorder technique described and recorded by [10] although the slightly enhanced noise could be just by chance. However, they report altering the position of the soft palate, a different body movement that is not necessarily associated with creating shear turbulence, so additional effects such as the Helmholtz effect could also play a role.

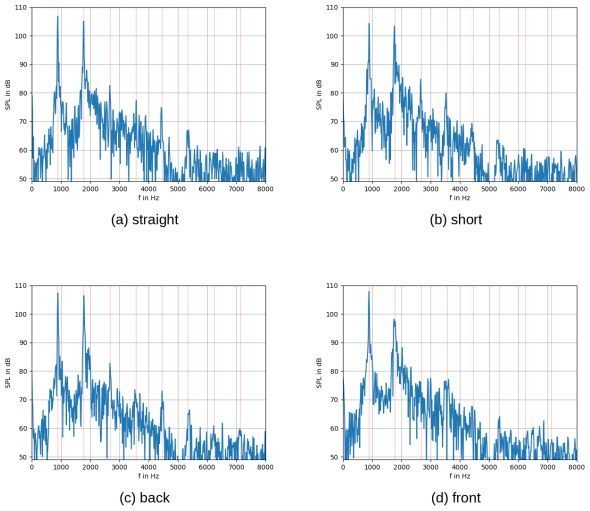


Figure 9: Pressure spectra during the quasi-stationary state from 0.02 to 0.1 s. The constrictions are associated with less clear harmonics in the sound spectrum.

In general, these results raise the questions whether the feedback between the jet and the resonator or the KHI plays the leading role for a timbre change with turbulence in the mouth cavity.

4. CONCLUSION

The results show changes throughout the instrument in the flow and the radiated sound pressure with the geometry in

the vocal tract. The data from the short vocal tract differ clearly from the changes seen in the vocal tract with a constriction in the front. This points to a second possibility to alter the sound for a given pitch next to the Helmholtz effect. We propose that this could work in two steps: First, the shear turbulence in the mouth influences the initial KHI by mostly by aerodynamic effects. In the second step, the instrument behaves like a complex system with the feedback between the jet and the resonator additionally altering resulting sound pressure. Moreover, the comparison between the constrictions in the front and in the back suggest that turbulence might be most efficient to alter the sound when created at the right spot in the mouth. These effects are associated with reduced harmonics when the constriction is in the front. However, this is only a first dip into the mechanism behind a possible vocal tract influence on the sound of a flue instrument. 2D turbulence has a different energy cascade which is also not accounted for by the used turbulence model. Therefore, the results need to be checked with a more resource consuming 3D simulation and experiments now that we have some better idea, which data could be useful to write out. Further simulations would also require a mesh quality study. In the meanwhile, recorder players could test whether this concept and some basic knowledge about turbulence could be artistically useful.

5. ACKNOWLEDGMENTS

Thank you to Dan Laurin and Han Tol for their support from a recorder players' perspective, Jost Fischer for his skillful introduction to openfoam, Bernd Leitl for sharing his knowledge about turbulence and asking good questions, Martin Stieben as an exceptionally motivated HPC admin and the acoustics group of our institute for many helpful discussions. Thank you also to Johann Joachim Quantz for demonstrating the importance of written transmission of flue instrument playing techniques.

6. REFERENCES

[1] M. H. Harras, "Blockflöte," in *MGG Online* (L. Lütteken, ed.), New York, Kassel, Stuttgart, 2016. zuerst veröffentlicht 1994, online veröffentlicht 2016.

[2] R. Bader, *Nonlinearities and Synchronization in Musical Acoustics and Music Psychology*. Current Research in Systematic Musicology, Vol. 2, Springer, 2013.

[3] J. L. Fischer, *On Turbulent Coherent Structures in Transient Processes of Aerophones–Principles of Sound Generation*. Staats-und Universitätsbibliothek Hamburg Carl von Ossietzky, 2022.

[4] R. Auvray, B. Fabre, and P.-Y. Lagrée, "Regime change and oscillation thresholds in recorder-like instruments," *The Journal of the Acoustical Society of America*, vol. 131, pp. 1574–1585, 02 2012.

[5] N. Nordblom, "Influence of vocal tract constrictions on the recorder sound," in *DAGA 2023 - 49. Jahrestagung für Akustik (2023)*, pp. 919–922, 2023.

[6] R. Auvray, B. Fabre, P.-Y. Lagree, S. Terrien, and C. Vergez, "Influence of the fluctuations of the control pressure on the sound production in flute-like instruments," *Acoustics 2012*, no. April, 2012.

[7] R. Auvray, A. Ernoult, S. Terrien, P. Y. Lagrée, B. Fabre, and C. Vergez, "Effect of Changing the Vocal Tract Shape on the Sound Production of the Recorder: An Experimental and Theoretical Study," *Acta Acustica united with Acustica*, vol. 101, pp. 317–330, mar 2015.

[8] S. Tateishi, S. Iwagami, G. Tsutsumi, T. Kobayashi, T. Takami, and K. Takahashi, "Role of the foot chamber in the sounding mechanism of a flue organ pipe," *Acoustical Science and Technology*, vol. 40, no. 1, 2019.

[9] Ikoga, Shiryu, Onomata, Tatsuki, Tabata, Ryoya, Iwagami, Sho, Kobayashi, Taizo, and Takahashi, Kin'ya, "Numerical study on role of foot of a flue organ pipe: relative phases in oscillations among pipe, foot and jet," *Acta Acust.*, vol. 8, p. 50, 2024.

[10] J.-M. Chen, D. Laurin, J. Smith, and J. Wolfe, "Vocal tract interactions in recorder performance," 2007.

[11] M. Miyamoto, Y. Ito, T. Iwasaki, T. Akamura, K. Takahashi, T. Takami, T. Kobayashi, A. Nishida, and M. Aoyagi, "Numerical Study on Acoustic Oscillations of 2D and 3D Flue Organ Pipe Like Instruments with Compressible LES," *Acta Acustica united with Acustica*, vol. 99, pp. 154–171, jan 2013.

[12] M. Arnela and O. Guasch, "Two-dimensional vocal tracts with three-dimensional behavior in the numerical generation of vowels," *The Journal of the Acoustical Society of America*, vol. 135, no. 1, 2014.

[13] J. L. Fischer, *Nichtlineare Kopplungsmechanismen akustischer Oszillatoren am Beispiel der Synchronisation von Orgelpfeifen*. PhD thesis, Universität Potsdam, Potsdam, 2014.

[14] O. M. Diaz, "Aeroacoustic characterization of a 3d organ pipe," 2022.

[15] T. Bergstrom, "Instrument drawings — Ture Bergstrøms Instrumentbyggeri."

[16] N. Giordano and K. L. Saenger, "Study of "half-integer" harmonics in recorder tones and some speculations about their origin," *The Journal of the Acoustical Society of America*, vol. 154, pp. 2917–2927, 11 2023.

[17] M. Kamruzzaman, O. Rømcke, and R. J. Hearst, "The impact of upstream turbulence on a plane jet," *Experiments in Fluids*, vol. 62, p. 18, 1 2021.

DOI: 10.61782/fa.2025.0595



FORUM ACUSTICUM
EURONOISE 2025

DYNAMICAL BEHAVIOR OF A BRASS INSTRUMENT AROUND A DOUBLE HOPF BIFURCATION

Martin Pégeot[1*] **Tom Colinot**[2] **Jean-Baptiste Doc**[3]
Vincent Fréour[4] **Christophe Vergez**[1]

[1] Aix Marseille Univ, CNRS, Centrale Med, LMA UMR7031, 4 impasse Nikola Tesla, CS 40006, 13453 Marseille Cedex 13, France

[2] Buffet Crampon, 5 rue Maurice Berteaux, 78711 Mantes-La-Ville, France

[3] Laboratoire de Mécanique des Structures et Systèmes Couplés, Conservatoire des arts et métiers, 75003 Paris, France

[4] Yamaha Corporation, Research and Development Division, 10-1 Nakazawa-cho, Chuo-ku, Hamamatsu, Shizuoka 430-8650, Japan

ABSTRACT

Self-sustained musical instruments, such as wind or bowed string instruments, are capable of producing sustained sounds from a continuous supply of energy. These instruments exhibit transient regimes when the sound appears and during note changes. In this study, we focus on certain transient behaviors of a soprano trombone around a double Hopf bifurcation, induced by a slide displacement. To numerically study these transients on a model, the input impedance of the instrument is interpolated between different slide positions. Linear stability analysis and time integration are applied to a brass model for this situation. These simulations show that around a double Hopf bifurcation and at constant blowing pressure, it is possible to select the equilibrium or two different periodic regimes by only controlling the slide position.

Keywords: *Double Hopf bifurcation, transients, multistability, self-sustained musical instruments, trombone impedance*

**Corresponding author*: *pegeot@lma.cnrs-mrs.fr.*

***Copyright**: ©2025 Martin Pégeot et al. This is an open-access article distributed under the terms of the Creative Commons Attribution 3.0 Unported License, which permits unrestricted use, distribution, and reproduction in any medium, provided the original author and source are credited.*

1. INTRODUCTION

Brass instrument are self-oscillating systems whose functioning regimes depend on the resonator parameters and on the playing parameters, such as the blowing pressure or the lips resonance frequency. In the scope of dynamical systems, the oscillations of a self-sustained musical instrument usually arise from Hopf bifurcations, where a periodic solution appears and the stability of an equilibrium solution changes. The study of the Hopf bifurcations and the dynamics of a brass instrument around these bifurcations is a common approach [1]. In most works concerning this subject, the considered sets of parameters foster one specific periodic regime at a time [2]. Nevertheless, these instruments exhibit double Hopf bifurcations where two Hopf bifurcations appear for the same values of parameters. Around those double Hopf bifurcations, two different periodic regimes may appear which results in rich transients and multistability issues. In this article, we focus on the transient behavior of a soprano trombone around a double Hopf bifurcation. The model is presented in Sec. 2 along with the input impedance interpolation of a slide instrument. Linear Stability Analysis (LSA) and time integration are then applied to the model in Sec. 3 to study a moving slide scenario. Conclusions are drawn in Sec. 4.

2. BRASS INSTRUMENT MODEL

2.1 Equations of the model

We use the same model as in [3]. The lips are represented by a one degree-of-freedom linear oscillator and the resonator by a modal decomposition of its input impedance. The air flow passing through the lips is modeled by the Bernoulli equation. Overall, the the model writes:

$$\begin{cases} \ddot{x} + \frac{\omega_L}{Q_L}\dot{x} + \omega_L^2(x - x_0) = \frac{p_0 - p}{\mu_L}, \\ \dot{p}_n - s_n p_n = Z_c C_n u \quad \forall n \in [1, N_m], \\ p = 2\sum_{n=1}^{N_m} \Re(p_n), \\ u = W\sqrt{\frac{2|p_0 - p|}{\rho}} \cdot \text{sign}(p_0 - p) \cdot \max(x, 0), \end{cases} \tag{1}$$

where x is the lip position, p_n are the modal pressures, u is the air flow and p_0 is the blowing pressure. ω_L, Q_L and μ_L are the angular frequency, the quality factor and the surface mass of the lips. N_m is the number of modes used to describe the input impedance and C_n and s_n are its residues and poles. Z_c is the characteristic impedance at the input of the resonator, W is the width of the lip channel, x_0 is the lip position at rest and ρ is the air density. In the remainder, we set the following parameters:

$$\begin{cases} f_L = 500 \text{ Hz}, \\ \mu_L = 2 \text{ kg.m}^{-2}, \\ Q_L = 4, \\ x_0 = 1 \cdot 10^{-4} \text{ m}, \\ W = 8 \cdot 10^{-3} \text{ m}, \\ Z_c = 1.83 \cdot 10^6 \text{ kg.s}^{-1}.\text{m}^{-4}. \end{cases} \tag{2}$$

2.2 Studying slide instruments

To explore the behavior of a brass instrument around a double Hopf bifurcation, we choose to fix the lip parameters and to vary continuously the resonator modal parameters using a slide. Indeed, it is difficult to control and estimate the lip parameters on an experimental setup whereas it is much easier to do so with a slide position. That is why we study a soprano trombone.

In order to simulate its behavior at any slide position or with a time evolving slide position, we interpolate the modal coefficients (poles C_n and residues s_n) of the input impedance measured at various slide positions. The input impedance is measured at each slide centimeter (the resonator length modification is twice as long as the slide displacement since the pipe is 180° curved) and its modal decomposition is computed with the peak-picking toolbox [4]. As a result, the resonator is entirely described by only one control parameter d_{slide}, which facilitates numerical implementation.

Using the peak-picking toolbox [4], the input impedance can be decomposed with at least $N_m = 11$ modes at any slide position without having spurious modes. However, in the following, we will only keep two of these modes which is sufficient to highlight a double Hopf bifurcation.

3. NUMERICAL ANALYSIS

3.1 Linear Stability Analysis (LSA)

We consider two control parameters (p_0, d_{slide}) since all other parameters are fixed according to (2). Usually, Linear Stability Analysis (LSA) is used to find threshold pressures and fundamental playing frequencies at the onset of the oscillations. This corresponds to finding Hopf bifurcations in the plane (p_0, f_L). Such a representation is given in Fig. 1 for $d_{slide} = 15$ cm. The intersection of two Hopf curves corresponds to a double Hopf bifurcation (marked with stars on Fig. 1, 2 and 3). In the remainder, we keep only modes 5 and 6 which are associated with the two Hopf bifurcations that cross around $f_L = 500$ Hz. The LSA of the two modes model is plotted in Fig. 2. Reducing the model to only two modes slightly changes the location of the Hopf bifurcations, but they still cross around $f_L = 500$ Hz.

Here, we consider a fixed $f_L = 500$ Hz and a variable d_{slide}. Consequently, the Hopf curves are rather plotted with respect to d_{slide} in Fig. 3. We limit the study to $p_0 \in [0, 5]$ kPa and $d_{slide} \in [10, 16]$ cm. In this region of interest, only two periodic solutions exist along with the equilibrium, and they show a double Hopf bifurcation at $p_{0,DH} = 2.8$ kPa and $d_{slide,DH} = 14.6$ cm.

Additionally, we use Manlab and the Hill-Floquet stability analysis [5] to compute the periodic branches and their stability. In this configuration, all Hopf bifurcations are direct. For a given d_{slide}, the first Hopf bifurcation (i.e. with the lowest p_0) leads to a stable regime whereas the second Hopf bifurcation (i.e. with the highest p_0) leads to an unstable regime. For p_0 higher than the second Hopf bifurcation, this second regime becomes stable through a torus bifurcation represented by dashed lines in Fig. 3.

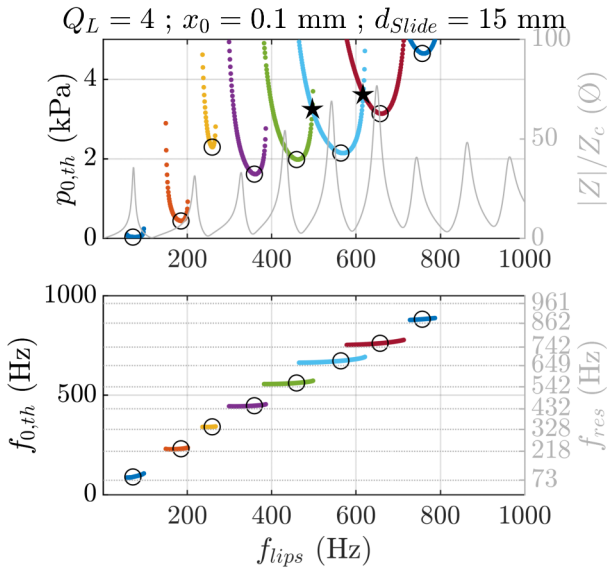


Figure 1: LSA with respect to f_L considering $N_m = 11$ modes. Pressure thresholds (top pane) and playing fundamental frequency at the onset of the oscillations (bottom pane). Double Hopf bifurcations are represented by stars. The dimensionless input impedance modulus is superimposed on the top pane whereas the resonance frequencies are represented as horizontal gray lines on the bottom pane. Each color corresponds to a different playing regime. The local minimum of $p_{0,th}$ are marked with a circle.

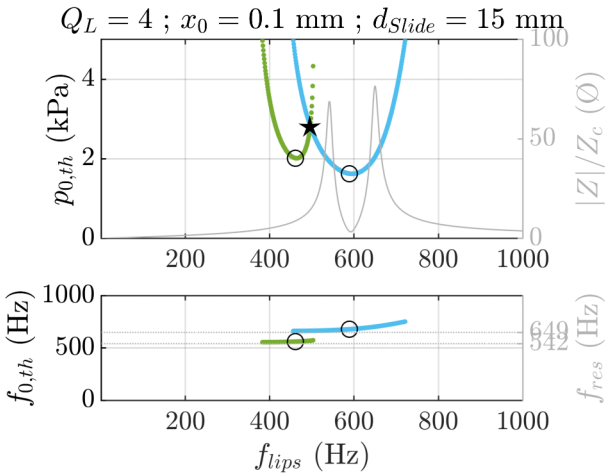


Figure 2: LSA with respect to f_L considering only modes 5 and 6. The double Hopf bifurcation is indicated by a star.

The regions where the second periodic regime is unstable are shaded.

3.2 Time simulation

According to Fig. 3, for p_0 slightly below the double Hopf $p_{0,DH}$, one can switch from one periodic regime to another passing through the equilibrium by varying only the slide position. We study this kind of scenario with time integration. The considered parameter trajectory is drawn in black in Fig. 3, with $p_0 = 2.6$ kPa and $d_{slide} \in [14, 16]$ cm. In Fig. 4, the time evolution of the mouthpiece pressure p computed with time integration is plotted along with the control parameters p_0 and d_{slide}, as well as its spectrogram.

Firstly, the brass model indeed passes through both periodic regimes and the equilibrium. Secondly, the system transients last few seconds after both parameters are fixed. This observation is consistent with the fact that the system is close to its Hopf bifurcations. Indeed, in this region, leading LSA eigenvalues (i.e. with the highest real part) are close to zero, which corresponds to slow exponential growth or decrease and therefore, long transients. Finally, the amplitude of the oscillations decreases for both periodic regimes as the slide position moves toward the double Hopf bifurcation, until oscillations disappear when the system reaches the equilibrium. Since d_{slide} varies dynamically, silence appears with some delay after the slide position crossed the static Hopf bifurcation predicted by LSA [6].

This type of behavior has been observed on preliminary experiments using artificial lips and a controlled air supply which suggests that the real system also exhibits double Hopf bifurcations for some sets of parameters.

4. CONCLUSION

In this short paper, we show that brass instruments may exhibit double Hopf bifurcations for some sets of parameters. Around such a bifurcation, two periodic regimes exist and the system has a rich behavior especially regarding transients. Here, we only focus on one specific

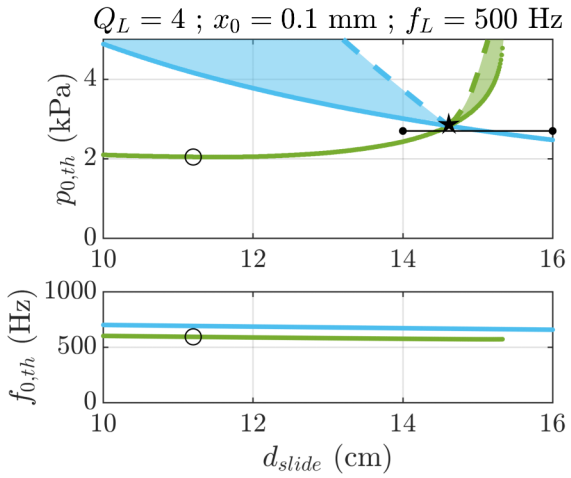


Figure 3: LSA with respect to d_{slide} considering only modes 5 and 6. Continuous lines represent Hopf bifurcations whereas dashed lines represent torus bifurcations. The double Hopf bifurcation is indicated with a star. The solution coming from the second Hopf bifurcation is unstable between its Hopf and its torus bifurcations. This is represented by shaded regions of the corresponding color. The horizontal black line represents the parameter trajectory considered for time integration in Sec. 3.2.

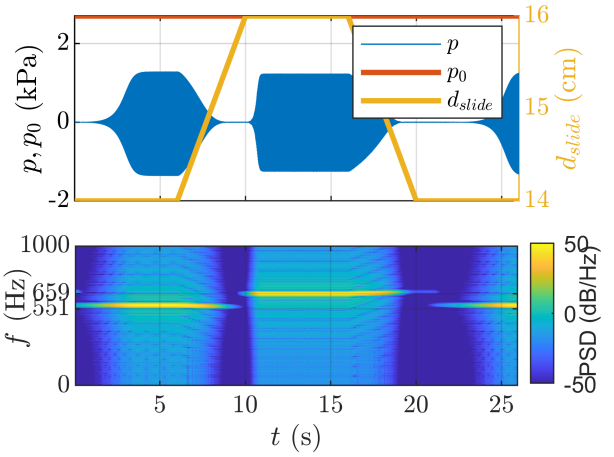


Figure 4: Top pane: time evolution of the control parameters p_0 and d_{slide} and of the resulting mouthpiece pressure p computed with time integration. Bottom pane: Corresponding spectrogram of p in terms of Power Spectral Density (PSD).

scenario where the slide position varies continuously. This scenario highlights the interest of studying the slide position as a bifurcation parameter since it induces interesting behaviors while remaining easy to control and to measure in an experimental context. To compute time integrations with a varying slide position, we propose to describe the input impedance with only one parameter by use of interpolations of the modal parameters. The multistability intrinsic to double Hopf bifurcations, as well as the associated transient behaviors, will be further explored in experimental and numerical studies.

5. REFERENCES

[1] L. Velut, C. Vergez, J. Gilbert, and M. Djahanbani, "How well can linear stability analysis predict the behaviour of an outward-striking valve brass instrument model?," *Acta Acustica united with Acustica*, vol. 103, no. 1, pp. 132–148, 2017.

[2] J.-B. Doc, C. Vergez, and J. Hannebicq, "Inverse problem to estimate lips parameters values of outward-striking trumpet model for successive playing registers," *The Journal of the Acoustical Society of America*, vol. 153, no. 1, pp. 168–178, 2023.

[3] M. Pégeot, T. Colinot, J.-B. Doc, V. Fréour, and C. Vergez, "Playability of self-sustained musical instrument models: statistical approaches," *Acta Acustica*, vol. 8, p. 74, 2024.

[4] F. Ablitzer, "Peak-picking identification technique for modal expansion of input impedance of brass instruments," *Acta Acustica*, vol. 5, p. 53, 2021.

[5] L. Guillot, A. Lazarus, O. Thomas, C. Vergez, and B. Cochelin, "A purely frequency based floquet-hill formulation for the efficient stability computation of periodic solutions of ordinary differential systems," *Journal of Computational Physics*, vol. 416, p. 109477, 2020.

[6] B. Bergeot, S. Terrien, and C. Vergez, "Predicting transient dynamics in a model of reed musical instrument with slowly time-varying control parameter," *Chaos: An Interdisciplinary Journal of Nonlinear Science*, vol. 34, no. 7, 2024.

DOI:

Main theme: A11 Musical Acoustics

Session A11.05 Instruments, hyperinstruments and beyond

Chair(s): A. M. Barbancho, S. Guillén

DOI: 10.61782/fa.2025.0597



FORUM ACUSTICUM
EURONOISE 2025

MUSICAL ACOUSTICS STUDENTS FACED WITH THE CHALLENGE OF BUILDING NEW MUSICAL INSTRUMENTS

Ana M. Barbancho* **Isabel Barbancho** **Lorenzo J. Tardón**

ATIC Research Group, ITIS Software, ETSI Telecomunicación,
University of Málaga, 29071 Málaga, Spain

ABSTRACT

One of the most difficult aspects to assess in university students is their level of initiative and creativity: teaching usually focuses on learning techniques for practical problem solving, mostly with systematic solutions. For this reason, in the subject Musical Acoustics, an optional subject in the fourth year of the Degree in Sound and Image Engineering at the School of Telecommunications Engineering of the University of Malaga, since the 2015-2016 academic year, students have been asked to make a new musical instrument as part of the assessment of the subject. The only condition that the instrument must meet is that it must produce three musical sounds of different frequencies. In this article, a brief compilation of all instruments is made in order to focus on the most original and creative ones. It should be noted that over the years, the pupils have made better and more creative instruments.

Keywords: *Musical Acoustics, Creativity, Musical Instruments, Higher Education*

1. INTRODUCTION

Nowadays, the job market is becoming increasingly competitive, and holding a university degree in engineering, while a necessary condition for accessing a qualified job, is no longer sufficient. For this reason, both students and professors must make a significant effort to ensure that the skills acquired during academic studies align with industry demands and provide students with a high degree of versatility. Among these skills, soft skills are gaining increasing importance. One of the most relevant soft skills is creativity. Traditionally associated with humanities and arts-related studies, creativity is now being increasingly recognized as a key competence in engineering education [1]. Furthermore, it is essential to acknowledge that engineering curricula are continuously evolving to adapt to the ever-changing technological landscape and to ensure that students acquire the necessary competencies for the professional world [2].

For this reason, elective courses such as Musical Acoustics [3], offered at the School of Telecommunications Engineering of the University of Málaga (UMA), must be in constant evolution to integrate competencies that are particularly relevant for the job market or that, despite their importance, may not have been adequately covered in other courses within the degree program. Musical Acoustics is a fourth-year elective course (final year of the program) in the Bachelor's Degree in Sound and Image Engineering. Due to the nature of its syllabus, its elective status, and its position in the final year of the degree—where the number of students enrolled is typically lower—it allows for more creative activities compared to mandatory courses from earlier years. For this reason, since the 2015-2016 academic year, the practical component of the course has included the construction and acoustic characterization of a musical instrument. However, since the 2022-2023 academic year, traditional lab practices have been replaced by personal projects, many of which still involve the creation of musical instruments [4]. The only requirement for the musical instrument is that it must be capable of producing at least three dis-

**Corresponding author*: abp@uma.es.

Copyright: *©2025 Ana M. Barbancho et al. This is an open-access article distributed under the terms of the Creative Commons Attribution 3.0 Unported License, which permits unrestricted use, distribution, and reproduction in any medium, provided the original author and source are credited.*

tinct musical sounds. This practical assignment replaced the classical sound characterization practice based on pre-recorded sounds, which did not allow for any form of creativity from students.

This paper presents the various instruments built by students and analyzes the level of creativity demonstrated across different academic years.

The structure of this paper is as follows: Section 2 describes the context in which students engage in this creative activity. Section 3 details the process of constructing and measuring a musical instrument, along with a list of the instruments created in each academic year. Section 4 presents the results of the creativity analysis conducted on students' projects over multiple academic years. Finally, Section 5 outlines the main conclusions drawn from this study.

2. CONTEXT

The University of Málaga has 21 faculties and schools, with an annual student population of approximately 33,000, although this number fluctuates slightly depending on the academic year [5]. Fig. 1 illustrates the evolution of student enrollment at UMA.

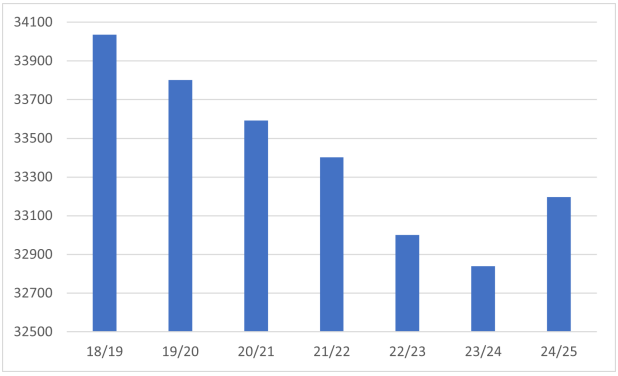


Figure 1. Evolution of the number of student enrolled at the UMA.

The students considered in this study are enrolled in the School of Telecommunications Engineering (ETSIT) within the Bachelor's Degree in Sound and Image Engineering (GISI). Specifically, they are students taking Musical Acoustics, a fourth-year elective course offered in the first semester. This subject has a teaching load of 6 ECTS, equivalent to 60 hours of classroom instruction, distributed as follows: 30 hours of theoretical lectures, 18 hours of laboratory sessions, 6 hours of problem-solving classes, 2 hours of student presentations, and 4 hours dedicated to other activities (such as visits to recording studios and theaters, as well as attendance at conferences). Fig. 2 compares the number of students enrolled at the ETSI of Telecommunications of UMA over the past five years with those enrolled in the Sound and Image Engineering degree. This figure shows that enrollment rates have remained quite stable, although a slight increase in total student numbers can be observed in recent academic years.

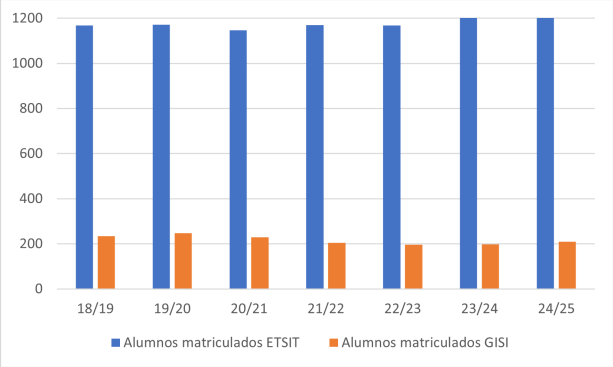


Figure 2. Evolution of student enrolled at the ETSI of Telecommunications of the UMA together with those enrolled in the Sound and Image Engineering degree (GISI).

Fig. 3 presents the evolution of student enrollment in Musical Acoustics, as well as the ratio between students who successfully complete the course and those who drop out. Notably, after the increase in enrollment in the academic year following the COVID-19 pandemic (2020-2021), the number of students taking the course has remained stable. More importantly, the number of students failing the subject has decreased. This suggests that students find the course appealing, both in terms of its description in the official syllabus [3] and through their experiences in class. Considering that overall student enrollment at UMA, and consequently across all degree programs, is declining, the sustained interest in Musical Acoustics, despite being an elective course, can be considered a success. Regarding the gender distribution of enrolled students, the percentage of male and female students is consistent with the average enrollment figures at the ETSI of Telecommunications of UMA [6].

The typical profile of students enrolled in this elec-

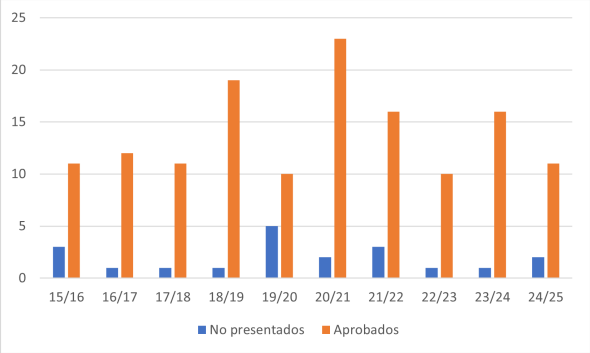


Figure 3. Evolution of students enrolled in Musical Acoustics, as well as the ratio between students who pass and student who drop out of the subject.

tive course includes those with a strong interest in music—either because they have formal conservatory training or because they seek to acquire musical concepts to apply them professionally, given their future careers as sound and image engineers. Additionally, students are often drawn to the course because of its distinctive pedagogical approach [4].

3. MUSICAL INSTRUMENTS DESIGNED IN MUSICAL ACOUSTICS

This section first outlines the required characteristics of the musical instruments to be constructed (subsection 3.1), followed by a summary of the instruments created in each academic year (subsection 3.2).

3.1 Required characteristics of the musical instrument

On the first day of the Musical Acoustics course, students are introduced to the syllabus and the various activities associated with the subject. Among these activities is the practical assignment of constructing a musical instrument, which was incorporated into the curriculum in the 2015-16 academic year. The specifications for this assignment are as follows: students must construct an analog musical instrument capable of producing at least three distinct, tuned musical notes. Additionally, they must record and acoustically characterize these sounds in both the time and frequency domains. A technical report must be submitted detailing the instrument's design, the materials used, the construction process, and the acoustic analysis of the sounds it produces.

Since the 2022-23 academic year, students have been given the option to replace traditional laboratory practices with a personal project. The theme of this personal project must be related to the subject matter of the course and aligned with the student's personal interests and future professional aspirations. Several project ideas are proposed to the students, including the construction of musical instruments, with an emphasis on integrating digital components into their design. The personal project requires the submission of a project report, which may take the form of a direct link to a website or an Instructable [7].

Furthermore, whether students choose to undertake the instrument construction assignment or a personal project, they must deliver an in-class presentation in the format of a masterclass, allowing their peers to learn the fundamental concepts underlying each project. The instrument or personal project may be completed individually or in teams of up to two students, depending on the scope of the work.

3.2 Revision de los instrumentos construidos

Tab. 1 presents a summary of the musical instruments constructed across different academic years. In the first year of implementation (2015-16), the instrument construction activity was highly structured, requiring all students to build an electronic monochord (Fig. 4). This guided workshop proved to be highly successful, leading to the continuation of the activity in subsequent years with greater flexibility granted to students.

In the 2016-17 academic year, students were encouraged to design instruments based on the golden ratio, which led to the development of the UMA-registered Auralófono® [8]. In the following years, students were given complete creative freedom in the design of their instruments (examples of analog instruments created in different academic years are shown in Fig. 5). A review of the constructed instruments reveals that most of them are pan flutes or recorders, although some academic years exhibit a higher degree of creativity than others.

Additionally, the activity has become increasingly consolidated, with a growing number of students incorporating electronic components into their designs. Fig. 6 showcases examples of such electronic instruments. Finally, it is worth noting that with the introduction of personal projects, the number of musical instruments constructed has decreased. However, the quality of the instruments has significantly improved, with most of them

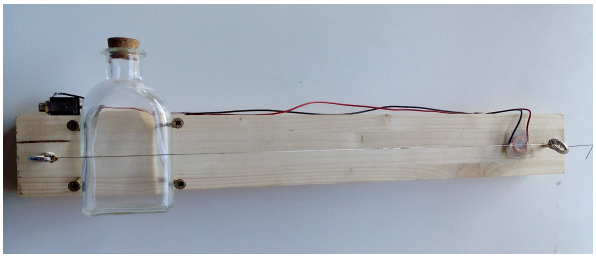


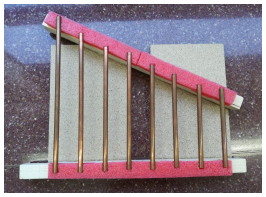
Figure 4. Electronic Monochord (15/16).



(a) 8-string lyre (17/18).



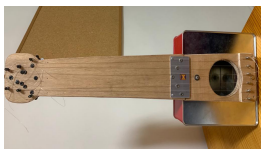
(b) Bicycle Spoke Kalimba (18/19).



(c) Xylophone copper (19/20).



(d) Cafelófono (21/22).



(e) Metal can guitar (21/22).

Figure 5. Examples of some of the analogue instruments built by the students of musical acoustics.

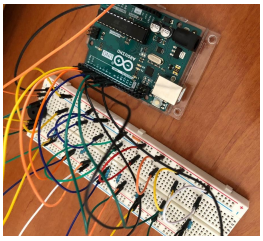
now featuring electronic components.

Conducting an analysis of students' creativity is a complex task, as defining creativity itself is challenging. However, by closely examining the instruments constructed along with the presentations given in class, some key observations can be made.

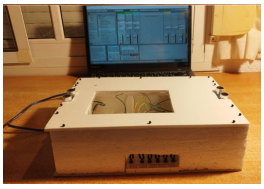
- Students generally struggle to be creative and to take risks with innovative proposals. Interestingly,

Table 1. List of musical instruments created by academic year

Academic Year	Musical Instruments
2015-16	Electronic Monochord (5 groups)
2016-17	Auralófono® (2 groups) Electric Guitar with Frying Pan
2017-18	8-String Lyre PVC Flute Pipe Organ with Cardboard Tubes
2018-19	Bicycle Spoke Kalimba Irish Flute Xylophone with PVC Tubes Cookie Tin Ukulele PVC Trombone Acoustic Bass
2019-20	Pan Flute PVC Flute 7-String Lyre Xylophone with Copper Pipes
2020-21	Pan Flute (10 groups) Recorder (4 groups) Rubber Band Lyre (3 groups) Clarinet with Rubber Bands Xylophone with Copper Pipes
2021-22	*Cafelófono*: Coffee Kalimba Xylophone with PVC Tubes Piano with Arduino and Sensors Guitar with Metal Can 3-String Monochord
2022-23	*Tubophone*: 3 Percussion Tubes Synthesizer with Arduino Clarinet with Rubber Bands
2023-24	Electromagnetic Microphone Ultrasonic MIDI Theremin 3D-Printed Violin Bela Synthesizer
2024-25	Banjo: Cookie Tin Banjo: 3D-Printed Body



(a) Piano with Arduino and sensors (21/22).



(b) Ultrasonic MIDI Theremin (22/23).



(c) Arduino synthesiser (22/23).

Figure 6. Examples of some of the electronic instruments built by the students of musical acoustics.

the most innovative proposals—precisely because they do not conform to traditional musical instruments—are those suggested by the course instructor (electronic monochord and Auralófono®).

- The level of creativity in the instruments built varies significantly depending on the student group. A noteworthy example is the instruments from the 2018-19 academic year, all of which were distinct and made from novel recycled materials, in contrast to those from the 2019-20 and 2020-21 cohorts, which were more conventional and similar in design. Interestingly, these student groups also differed in terms of academic performance and interpersonal dynamics.
- During the 2020-21 academic year, due to the COVID-19 pandemic, classes were held online, and projects were completed individually. This clearly influenced the students' level of creativity and effort in constructing their musical instruments.
- Although students in the Sound and Image Engineering program have a foundational knowledge of electronics, it is clearly insufficient for them to independently undertake projects requiring circuit construction. Students acknowledge their interest in creating electronically integrated instruments but do not feel adequately prepared to do so.
- The introduction of personal projects has resulted in the creation of instruments with an electronic component and increased complexity in terms of functionality, assembly, and capabilities. These instruments have proven to be more satisfying, even for the students themselves.
- Despite some highly developed instrument proposals, there is still significant progress to be made in fostering students' creativity.

4. CONCLUSIONS

This study has explored the implementation of a creative pedagogical approach within the Musical Acoustics course, an elective in the final year of the Bachelor's Degree in Sound and Image Engineering. The primary objective was to engage students in the construction of musical instruments that generate at least three distinct tuned pitches. The findings derived from this study offer valuable insights into the intersection of engineering education and creative practice:

- The integration of creative tasks within a traditionally technical curriculum is well-received by students, who demonstrate enthusiasm for hands-on, innovative learning experiences beyond conventional laboratory exercises.
- Over the years, as the activity has become institutionalized within the course, the diversity and complexity of the musical instruments produced have increased, reflecting a growing engagement with the creative process.
- The introduction of personal projects has led to fewer instrument constructions overall; however, the complexity, originality, and inclusion of electronic components in these projects have significantly improved. Students report a heightened sense of achievement and deeper conceptual understanding as a result.
- The choice of instrument type, level of innovation, and overall difficulty of construction are strongly influenced by the particular cohort of students. This suggests that group dynamics, peer collaboration, and prior experience play a crucial role in determining creative outcomes.

- A noticeable trend is the recurrence of simpler designs, particularly pan flutes and recorders. These choices are often associated with students who demonstrate lower engagement, possibly due to the abundance of readily available online instructions, reducing the necessity for independent problem-solving and innovation.
- While some students exhibit significant creativity in their projects, many struggle with the concept of innovation. The root causes of this reluctance remain unclear—whether due to a lack of intrinsic creativity, a hesitancy to invest additional effort, or a pervasive fear of failure in an academic setting.
- These findings highlight the urgent need to systematically incorporate creativity-enhancing methodologies within engineering education. By integrating more open-ended, interdisciplinary, and exploratory tasks into curricula, students can be encouraged to develop critical thinking, adaptability, and problem-solving skills essential for their future professional careers.

5. ACKNOWLEDGMENTS

This publication is part of project PID2021-123207NB-I00, funded by MCIN/AEI/10.13039/501100011033/FEDER, UE. This work was done at Universidad de Málaga, Research Group TIC208, Campus de Excelencia Internacional Andalucia Tech.

6. REFERENCES

[1] D. Bairaktarova and M. Eodice, eds., *Creative ways of knowing in engineering*. Springer, 2017.

[2] J. Mitchell, A. Nyamapfene, K. Roach, and E. Tilley, "Faculty wide curriculum reform: the integrated engineering programme," *European Journal of Engineering Education*, vol. 46, no. 1, pp. 48–66, 2001.

[3] E.T.S.I. de Telecomunicación, *Programación docente. Curso académico 2024-25*. Málaga: E.T.S. de Ingeniería de Telecomunicación, 2024.

[4] A. M. Barbancho, A. Peinado, I. Barbancho, L. J. Tardón, and S. Guillén, "Musical acoustics: Students facing the challenge of carrying out a personal project," in *2024 XVI Congreso de Tecnología, Aprendizaje y Enseñanza de la Electrónica (TAEE)*, pp. 1–6, 2024.

[5] Universidad de Málaga, "UMA, portal de transparencia. https://www.uma.es/portal-de-transparencia-universidad-de-malaga/info/120015/datos-de-matriculacion/," 2024. Accessed: March 6, 2025.

[6] A. M. Barbancho, I. Barbancho, L. J. Tardón, and A. Peinado, "Women in telecommunication engineering: Case studies," *IEEE Revista Iberoamericana de Tecnologias del Aprendizaje*, vol. 19, pp. 61–70, 2024.

[7] Instructable, "Instructables, colección musical acoustic student projects. https://www.instructables.com/musical-acoustic-student-projects/," 2025. Accessed: March 6, 2025.

[8] Universidad de Málaga, "Auralofono®. https://www.oepm.es/es/," 2016. Accessed: March 6, 2025.

DOI: 10.61782/fa.2025.0969



FORUM ACUSTICUM
EURONOISE 2025

WHAT DO BELLS MADE FROM LUNAR REGOLITHS SOUND LIKE?

Ana M. Barbancho[1*] **Isabel Barbancho**[1] **Lorenzo J. Tardón**[1] **Carlos Traginer**[2]

[1] ATIC Research Group, ITIS Software, ETSI Telecomunicación,
University of Málaga, 29071 Málaga, Spain
[2] Traginer Music Research LAB, Zaragoza, Spain

ABSTRACT

Building permanent bases for human life on both the moon and Mars is one of the greatest challenges facing humanity. All civilisations, from the most ancient to the present, have had their own music. This music has been conditioned, among other factors, by the material means that were naturally available. Moreover, the initial musical instruments of all civilisations have been percussion instruments. Therefore, if in the future humans are to inhabit the moon or Mars, they must be able to make musical instruments with the materials available in their environment. This article presents the design and the acoustic characterisation of bells made from lunar regolith. This will make it possible to analyse the ability to create music with the materials available on the moon and thus to improve the adaptation of humans.

Keywords: *bell, moon sound, lunar regolith, acoustic characterization*

1. INTRODUCTION

The origins of music are closely intertwined with the origins of humanity [1]. Both archaeological excavations and cave paintings depict music in its simplest forms—percussion and wind instruments. Music has always played a vital role in human communication, from warning of dangers to expressing emotions and serving as a form of entertainment.

*__Corresponding author__: abp@uma.es.

__Copyright__: ©2025 Ana M. Barbancho et al. This is an open-access article distributed under the terms of the Creative Commons Attribution 3.0 Unported License, which permits unrestricted use, distribution, and reproduction in any medium, provided the original author and source are credited.

Among all percussion instruments, bells have been present in every civilization, and they continue to be studied and constructed today, both as instruments for classical orchestras, church carillons, and as auditory signaling elements on ships, among other uses [2], [3].

Therefore, in a future—whether near or distant—where humanity may establish colonies on other planets or even in other galaxies [4], [5], music must remain an essential part of human life. Moreover, humans will need to build musical instruments using the materials available in the places where they live.

This article presents the design and acoustic characterization of bells made from lunar regolith. This will enable an analysis of the potential to create music using materials found on the Moon, thereby improving human adaptation to extraterrestrial environments.

The article is structured as follows. Chapter 2 presents the design of the bells. Chapter 3 details the data acquisition system used for capturing the sounds of the bells. Chapter 4 describes the bell sound database that has been created. Chapters 5 and 6 present the tools used for characterizing the bell sounds and the results obtained from their analysis, respectively. Finally, Chapter 7 provides the conclusions drawn from this study.

2. BELLS DESIGNS

The design of bells has been a task to which considerable time and effort have been devoted over the centuries across numerous civilizations. Through the analysis of bells and percussion instruments from various cultures, such as Japanese wind bells, Tibetan singing bowls, Japanese-style dopamine bells, the town hall bell of Brihuega (Guadalajara, Spain), wind chimes, and others, it was concluded that a cylindrical geometry provides an effective foundation for bell design. Moreover, considering

the nature of the materials to be used, as described in subsection 2.1, the size should be kept compact. Figure 1 presents the dimensioned plans of the bells that were designed and manufactured.

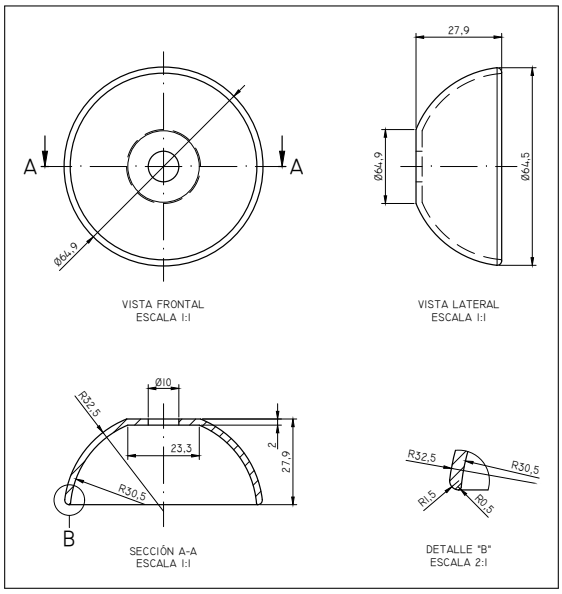


Figure 1: Plan, profile and elevation with dimensions of bells to be measured.

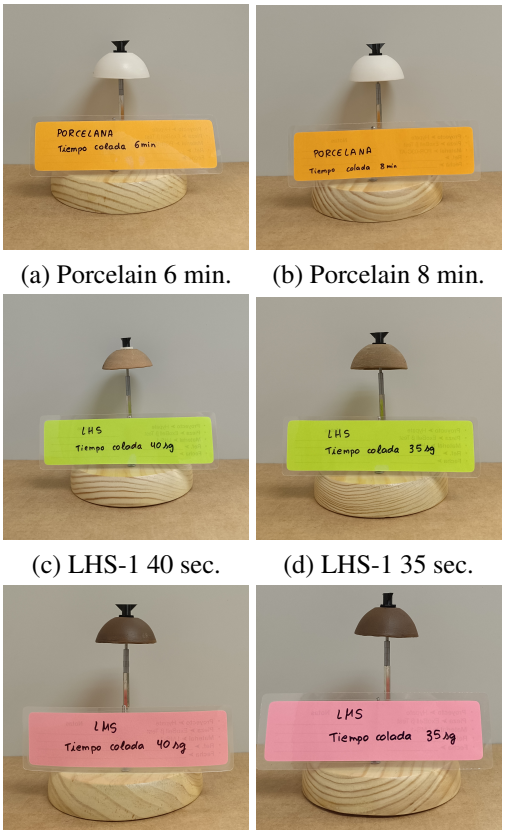
2.1 Bell manufacturing materials

In the present study, the acoustics of bells made from three different materials, each with two casting times, have been measured, resulting in a total of six bells to be measured and characterized. Figure 2 shows the six bells to be acoustically characterized, labeled with their respective material and casting time.

The three materials used are as follows:

- Porcelain (POR-03C-AT): A ceramic made from varying proportions of clay, kaolin, feldspar, and quartz. It is a material with good plasticity, being a casting porcelain suitable for general use [6].
- LHS-1: The Lunar Highlands Simulant (LHS-1) is a high-fidelity, mineral-based simulant designed to represent a generic or average highland location on the Moon. The highlands are considered the "lighter" regions of the Moon's surface, primarily composed of plagioclase, often referred to as Anorthosite. This simulant is not made from a single terrestrial lithology, but accurately replicates the texture of lunar regolith by combining both mineral and rock fragments in precise proportions based on the Apollo mission regolith samples [7].
- LMS-1: Lunar Mare Simulant (LMS-1) simulates the lunar mare regions, which are the darker portions of the Moon's surface. LMS-1 is a high-fidelity, mineral-based analog commonly used for educational and research purposes. This formula was designed based on data from the Apollo Lunar Soil samples [7].

It is noteworthy that due to the fragility and handling difficulties of the materials used, especially the porcelain, the 8-minute porcelain bell presents a small crack on its edge, which could lead to changes in its acoustics.



(a) Porcelain 6 min. (b) Porcelain 8 min.

(c) LHS-1 40 sec. (d) LHS-1 35 sec.

(e) LMS-1 40 sec. (f) LMS-1 35 sg.

Figure 2: Bells to be acoustically characterised labelled with material and casting time (a) Porcelain and casting time 6 min. (b) Porcelain and casting time 8 min. (c) LHS-1 and casting time 40 sec. (d) LHS-1 and casting time 35 sec. (e) LMS-1 and casting time 40 sec. (f) LMS-1 and casting time 35 sg.

2.2 Bell holders and mallets

In addition to the three types of manufacturing materials, three mallets made of different materials were used: wood, metal with a wooden head, and metal. These were used to assess how the type of mallet affects the sound produced by the bells. Figure 3 shows the three mallets used for the acoustic characterization.

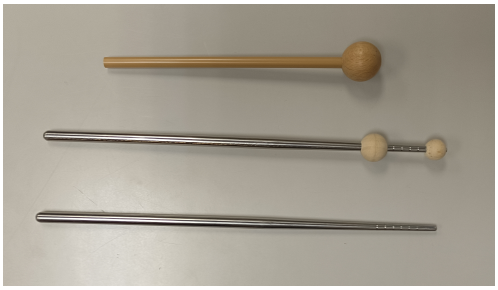
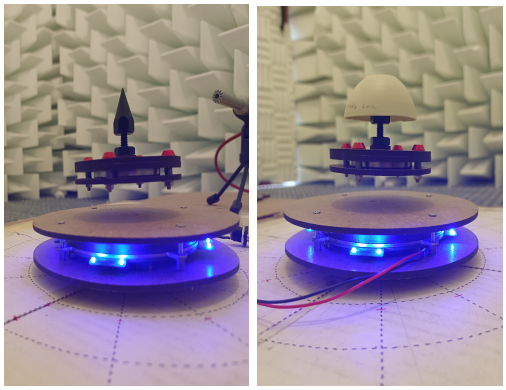


Figure 3: Mallets used for acoustic characterisation, from top to bottom: wooden mallet, metal mallet with shaped head and metal mallet.

Furthermore, to analyze the effect of the bell support, two types of supports were used: a fixed-base support (Fig. 2) and a support using a magnetic levitator (Fig. 4).



(a) Empty (b) With a bell

Figure 4: Magnetic levitator holder. (a) Empty. (b) With 6 min porcelain casting bell.

3. ACOUSTIC DATA ACQUISITION SYSTEM

In order to perform the acoustic characterization of the bells, it is essential to obtain sound recordings that are as pure and clear as possible, minimizing any external noise and interference from the recording environment. To achieve this, the recordings were made in the anechoic chamber at the E.T.S.I. de Telecomunicación, University of Málaga [8]. Figure 5 shows an image of the anechoic chamber at the E.T.S.I. de Telecomunicación, University of Málaga.

The anechoic chamber at the E.T.S.I. de Telecomunicación is specifically designed to eliminate acoustic wave reflections. Both the floor and the interior walls are lined with pyramidal wedges made of sound-absorbing materials, which further enhance the dispersion of any sound that is not absorbed. Additionally, the chamber is fully isolated from external noise sources.

For the recordings, two Behringer ECM8000 microphones [9] were employed. These are ultra-linear condenser microphones with a flat frequency response ranging from 20 Hz to 20 kHz, offering high sound resolution and an omnidirectional pickup pattern, making them ideal for precise acoustic measurements.

The bells were positioned in the center of the anechoic chamber, with the microphones placed at 90° and 180° relative to the striking point, as shown in Figure 6.

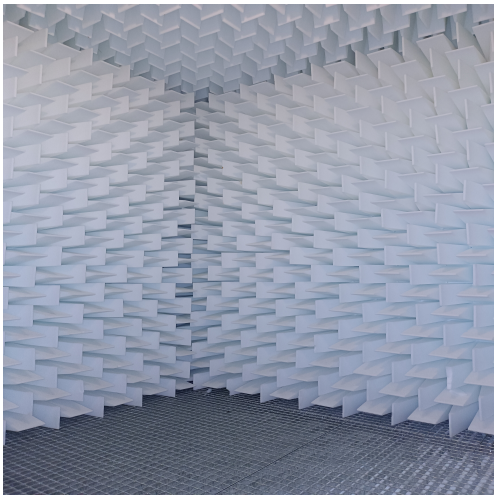


Figure 5: Anechoic chamber of the E.T.S.I. de Telecomunicacion of the University of Malaga [8].

To carry out the recordings, the output signal from the microphones was connected to the Roland QUAD-CAPTURE sound card [10], which allows for the recording of two independent audio channels. The sound card was configured to record at a resolution of 24 bits and a sampling rate of 44.1 kHz.

Regarding the software used, Audacity [11], a free

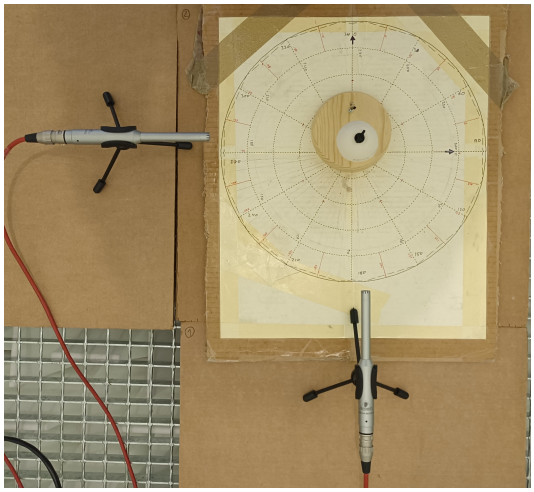


Figure 6: Positioning of the measuring microphones [9] in relation to the bells.

software application for recording and editing audio, was employed for the audio recording. For the analysis and characterization of the recordings, Matlab [12] was utilized due to its computational power and the existing libraries for audio signal processing.

4. DATABASE OF BELLS MADE WITH LUNAR REGOLITH AND PORCELAIN

This study has resulted in a database of bell sounds made from lunar regolith and porcelain. Each of the six bells (Fig. 2) was recorded with both types of supports, fixed and magnetic levitator, using the three types of mallets (Fig. 3), striking the bell twice—once on the lower half and once on the upper half—with two microphones positioned at 90° and 180° relative to the striking point (Fig. 6). This process has generated a database of 144 *.wav files, sampled at 24 bits and 44.1 kHz.

5. TIME AND FREQUENCY TOOLS FOR THE CHARACTERIZATION OF BELL SOUNDS

In this section, the time and frequency tools employed to characterize the bells sounds are described.

5.1 Time domain characterization

The study of the sounds produced by the bells in the time domain aims to determine if there are notable differences in the duration, amplitude, and waveform of the signals between the different bells, so that the influence of the material can be assessed.

A classic parameter for studying the signal in the time domain is the envelope. For this study, the classic envelope model for isolated musical sounds proposed by Jensen [13] will be used. To obtain the envelope, a 5th-order Butterworth filter with a cutoff frequency of 11 Hz was applied. The result was then normalized to a maximum value of 1. The attack time (T_a) is defined as the time between the first sample that exceeds 10% of the maximum value and the first sample that reaches 85% of the maximum amplitude. The release time (T_r) is calculated as the time between the last sample at 70% of the maximum amplitude and the last sample that exceeds 10%. The time between T_a and T_r is called the sustain time (T_s). It is expected that, depending on the material the bell is made from, and under equal excitation conditions, these times will differ.

5.2 Frequency Domain Characterization

To characterize the bell sounds in the frequency domain, both the FFT and the spectrogram will be used. In both cases, the frequency axis will be expressed in MIDI number (eq. 1).

$$MIDI = 69 + 12log_2(f/440) \quad (1)$$

The FFT calculation will be performed using the entire sound length of each recording. For the calculation of the spectrogram, a window size of 1024 will be used, with an overlap of 512, a Hamming window, and a DFT length of 4096. To determine the fundamental frequency, the algorithm proposed by Yin [14] will be employed. Additionally, for the characterization of the harmonic part of the signal relative to the residual, the model presented in [15] will be used.

6. RESULTS

This section characterizes the different bells and analyzes the influence of the supports, mallets used, and striking point, based on the time and frequency characteristics presented in section 5.

6.1 Analysis of the Envelope, Attack Time, and Decay Time

To perform the analysis of the envelope along with its attack and decay times, the first step was to evaluate whether there were significant differences between using recordings made with the microphones at 90° or 180°. As shown in Fig. 9, the envelopes are similar. Therefore, this section will focus on the recordings made with the microphone positioned at 90°.

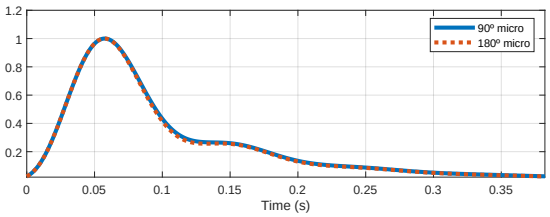


Figure 7: Envelope LHS-35s bell, wooden mallet, low impact and fixed support, for 90º and 180º microphone.

The attack and decay times were calculated as the average of the attack and decay times computed for each bell, with both types of supports, three types of mallets, and two striking positions (12 recordings in total per bell). It is noteworthy that the support and the method of excitation of the bell do not have a significant influence on the attack and decay times.

Table 1: Comparison of bells according to their time attack (T_a) and time release (T_r) (ms) and fundamental frequency ($F0$) in MIDI number and the distance from the fundamental to the first overtone (ΔF) also in MIDI.

Bell type	T_a	T_r	$F0$	ΔF
LHS-35s	31.5 ms	139.2 ms	108	14.80
LHS-40s	31.3 ms	179.0 ms	107	16.02
LMS-35s	30.7 ms	93.9 ms	108	14.18
LMS-40s	31.1 ms	113.9 ms	107	14.64
Por-6min	30.3 ms	81.7 ms	96	19.25
Por-8min	31.6 ms	134.6 ms	101	16.03

Table 1 shows the average attack and release times for each type of bell. The following observations can be made from this table:

- The attack and release times are similar across all bells, showing no significant differences according to the material type.
- The attack times are much shorter than the release times, which aligns with the typical characteristics of small-sized percussion instruments, such as the bells being characterized [16].

Regarding the shape of the envelope, when analyzing all the recordings based on the type of support, mallet, and striking position, it was observed that there are differences depending on whether a fixed support or a levitator support is used (Fig. 8). It was found that the levitator support, which allows the bell to move from its position, causes the envelope to decay uniformly. However, the fixed support, which provides rigid attachment at the top, results in some cases where the envelope does not decay uniformly.

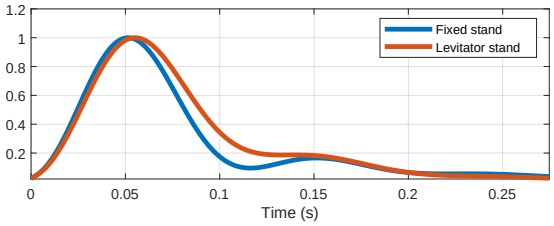


Figure 8: Comparison of envelope between fixed and levitator stand for LMS-40s bell, high stroke with wooden mallet.

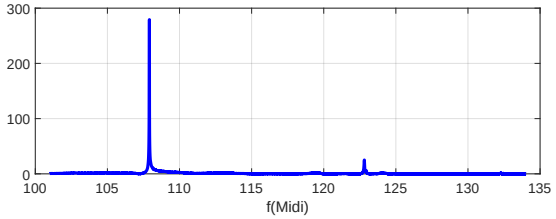
6.2 Analysis of the fundamental frequency

One of the most interesting parameters to study is the fundamental frequency of each bell, as well as the number of overtones they exhibit and the intervals between them.

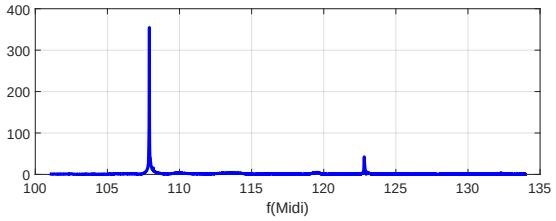
First, it was evaluated whether there were any differences in the frequency analysis when using recordings made with microphones placed at 90º or 18º0 degrees. It was observed that the microphone placement had no significant effect on the analysis, as shown in Fig. **??**. Therefore, it was decided to use the recordings from the microphone placed at 90º degrees.

The fundamental frequency was calculated as the average of the fundamental frequencies calculated for each bell, with both types of supports, the three types of mallets, and the two striking positions (12 recordings in total per bell). It is worth noting that the support type and the excitation method of the sound in the bell do not have a significant influence on the fundamental frequency. Similarly, the difference between the fundamental frequency and the first overtone was also calculated.

Table 1 shows the fundamental frequency of each bell in MIDI number, as well as the distance between the fundamental frequency and the first overtone, in MIDI number. The following observations can be made from this table:



(a) 90º microphone

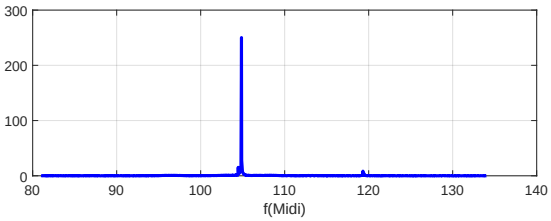


(b) 180º microphone

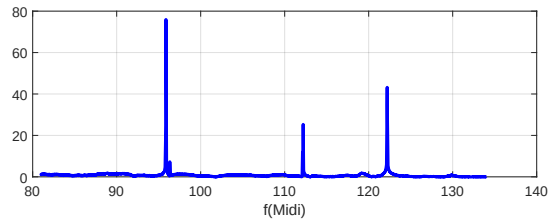
Figure 9: Spectrum of LMS-35s bell, mixed mallet, low stroke, fixed stand for (a) 90º and (b) 180º microphone.

- The fundamental frequencies of the bells made from lunar regolith (LHS and LMS) are higher than those of the porcelain bell.
- The fundamental frequencies of the bells made from lunar regolith are identical for the same pouring time, with those of shorter pouring times being higher. However, for the porcelain bell, the one with the longer pouring time exhibits a higher fundamental frequency.
- The distance between the fundamental frequency and the first overtone is significantly greater for the porcelain bells than for the lunar regolith bells. The harmonic distances in the lunar regolith bells are quite similar, except for the LHS bell with a pouring time of 40s, which shows a greater distance.
- None of the bells exhibit harmonic frequencies, as the distance between the fundamental frequency and the first overtone is not an integer multiple of the fundamental frequency (in Hertz).
- The fundamental frequencies are relatively high, given the small size of the bells.

Another parameter that has been analyzed is the number of overtones present in the recorded sounds of the bells. Upon analyzing all the recorded sounds of the bells, it was observed that the bells made from porcelain exhibit three peaks in the spectrum (fundamental frequency and two overtones), whereas the bells made from lunar regolith only show two peaks (fundamental frequency and one overtone). Clearly, porcelain behaves differently from lunar regolith in this regard. Fig. 10 shows an example of the spectrum of a lunar regolith bell and a porcelain bell, highlighting the difference in the number of overtones. To conduct a more in-depth study of the overtones produced by each material, it would be necessary to manufacture larger bells, as the ones available, having such high fundamental frequencies, result in any additional overtones falling outside the range of human hearing.



(a) LHS-40s bell



(b) Porcelain 6 min bell

Figure 10: Spectrum for (a) LHS-40s bell and (b) porcelain 6 min bell, mixed mallet, low stroke and fixed stand.

6.3 Influence of the type of support and striking location

As outlined in section 2.2, two distinct types of supports were used, fixed and magnetic levitation, to characterize the bell sounds. The magnetic levitation support, being a magnetic system, attracted the metal mallet, which led to the recordings being made with lower-force strikes and very light impacts.

The comparative acoustic evaluation of the recordings made with the fixed support versus the levitation support reveals that the recordings with the fixed support exhibit higher volume and richer tonal quality. This can be attributed to two factors: firstly, with the levitation system, the force applied had to be reduced to prevent excessive movement of the bell, which could cause the levitation point to be lost and the bell to fall. Secondly, because the

bell was levitating, some of the mallet's energy was dissipated in moving the bell and its support off its axis, which does not contribute to sound production.

This evaluation is evident in the calculation of harmonic energy relative to residual energy from the recordings of all the bells, considering the initial 20% of the total sound duration (from the attack time to the onset of the sustain phase). Table 2 displays the mean harmonic energy relative to residual energy for the six bells, across the three mallet types. It is clear that the higher striking point of the bell generates less harmonic richness than the lower striking point, and that the fixed support also contributes to a richer tonal output, as confirmed by the sound evaluation.

Table 2: Harmonic energy with respect to the residual for comparison of bells according to striking location and the type of support (Striking location-type of support): High-Levitator (H-L), High-Fixed (H-F), Low-Levitator (L-Lev) ando Low-Fixed (L-F).

Bell type	H-Lev	H-F	L-Lev	L-F
LHS-35s	1.37	1.81	1.97	2.52
LHS-40s	0.87	2.97	0.60	2.85
LMS-35s	1.60	2.91	1.10	5.12
LMS-40s	0.28	1.30	0.93	1.78
Por-6min	0.27	0.34	0.67	0.42
Por-8min	0.92	3.22	1.61	1.36

6.4 Influence of the type of mallet

As shown in Fig. 3, three different types of mallets were used. The choice of mallet type has been sonically proven to have an impact on the sound. In general, the sounds produced with the wooden mallet were louder and more resonant than those with the mixed mallet, while the metal mallet yielded the most limited volume and sonority. Clearly, more than the material, the larger striking surface of the mallet excites more movement in the bells (note that the wooden mallet has the largest surface, while the metal tip has the smallest).

In Table 3, the average harmonic energy relative to the residual energy is shown (considering the initial 20% of the total sound duration, which includes the attack time and the start of the sustain time) for the six bells, across both supports, both striking positions, and all three types of mallets (wooden, metal, and mixed). It is evident that the wooden mallet produces the greatest sound output of the three, followed by the mixed mallet.

Table 3: Harmonic energy with respect to the residual for comparison of bells according to evaluate the influence of the type of mallet.

Bell type	Wood	Metal	Mixed
LHS-35s	2.98	0.85	1.83
LHS-40s	4.47	0.55	3.68
LMS-35s	3.74	0.84	3.76
LMS-40s	1.79	0.83	0.68
Por-6min	0.76	0.49	0.41
Por-8min	1.40	1.46	2.52

7. CONCLUSIONS

This paper presents a study of the sound produced by bells made from lunar regolith. For this purpose, recordings were made of six different bells: four made from two types of lunar regolith (LHS and LMS), and two made from porcelain. The goal was to assess the differences between bells made from Earth materials. Additionally, three types of mallets and two support types—fixed and levitation—were employed.

The key conclusions drawn from this study are as follows:

- The sound of the bells made from lunar regolith shows strong similarities both among them and with the porcelain bells. Thus, it is possible to obtain instruments with similar tonal qualities even when using different starting materials.
- Due to their small size, the attack and decay times are relatively short. However, this is consistent with all percussion instruments of similar dimensions.
- Similarly, the fundamental frequencies are relatively high (ranging from 96 to 108 in MIDI number), as expected for small bells.
- The envelopes of the bells are similar across all samples, with the type of support having the greatest influence on their shape. The levitation support, by allowing free movement in all directions, results in smoother envelopes. This behavior could be representative of how such instruments would function

in environments with lower gravity than Earth's.

- The harmonic content of bells made from lunar regolith exhibits fewer overtones compared to porcelain bells. This indicates that the ability of lunar material to vibrate is slightly inferior.
- The study of support type and strike point revealed that striking the bell at a higher point produces fewer harmonic overtones than striking it lower. Furthermore, a fixed support produces a richer sound.
- The influence of mallet type showed that the wooden mallet generates the highest sound production, followed by the mixed mallet. It is evident that the size of the striking surface is the most significant factor influencing the sound, as the wooden mallet has the largest striking surface.

Given that the bells manufactured are very small and thus produce very high fundamental frequencies with short sound durations, it would be beneficial to have larger bells to continue advancing in the acoustic characterization of different materials.

In conclusion, this study demonstrates that it is possible to manufacture musical instruments similar to those used on Earth using materials from other celestial bodies. Thus, this research represents a significant step forward in the possibilities of supporting human life on other parts of the universe.

8. ACKNOWLEDGMENTS

This publication is part of the project PID2021-123207NB-I00 funded by MCIN/AEI/10.13039/501100011033/FEDER,UE.
This work was done at Universidad de Málaga, Research Group TIC208, Campus de Excelencia Internacional Andalucia Tech. Acknowledge the work of Miguel Jesús Ruiz González who helped with the acoustic measurements of the bells. We would like to thank M. Amparo Borrell and Rut Benavente from Instituto de Tecnología de Materiales (ITM), Universitat Politécnica de València, Spain, Carmen Alcázar, Paloma Recio and Rodrigo Moreno from Instituto de Cerámica y Vidrio (ICV), Consejo Superior de Investigaciones Científicas, Madrid, Spain Jesús Enrique Martínez-Martín from Facultad de Educación, Universidad Camilo José Cela, Spain, and Jesús Martinez-Frías from Instituto de Geociencias, IGEO (SIC-UCM), Madrid, Spain. It is because of all of them that the bells exist in such a real and meaningful way.

9. REFERENCES

[1] B. Lawergren, "The origin of musical instruments and sounds," *Anthropos*, pp. 31–45, 1988.

[2] T. D. Rossing, "The acoustics of bells: Studying the vibrations of large and small bells helps us understand the sounds of one of the world's oldest musical instruments," *American Scientist*, vol. 72, no. 5, pp. 440–447, 1984.

[3] J. Glixon, "Music and urban history: Twenty years later," *Journal of Urban History*, vol. 0, no. 0, p. 00961442251319012, 0.

[4] J. Tkemaladze, "Concept to the living space. longevity horizons," 2025.

[5] T. M. R. Lab, "Proyecto hypate, https://www.tmrl.org/hypate," 2020. Accessed on March 6, 2025.

[6] Vicar, "Vicar, https://vicar-sa.es/pastas-tradicionales," 2018.

[7] SRT, "Space resource tech, https://spaceresourcetech.com/collections/lunar-simulants/products/lhs-1-lunar-highlands-simulant," 2018. Accessed on February 14, 2025.

[8] E.T.S.I.Telecomunicación, "E.T.S.I. Telecomunicación, https://www.uma.es/etsi-de-telecomunicacion," 2025. Accessed on February 14, 2025.

[9] Behringer, "Measurement conderser microphone ecm8000 technical specifications," 2025.

[10] Roland, "Quad-capture audio interface," 2025.

[11] Audacity, "Audacity, free audio editor, recorder, music making and more!," 2025.

[12] Matlab, "Matlab r2023b," 2025.

[13] K. Jensen, "Envelope model of isolated musical sounds," in *Proc. of Digityal Audio Effects (DAFx99)*, (Trondheim, Nordway), pp. 1–5, 1999.

[14] A. de Cheveigne and H. Kawahara, "Yin, a fundamental frequency estimator for speech and music," *Journal of Acoustical Society of America*, vol. 111, no. 4, pp. 1917–1930, 2002.

[15] U. Zölzer, *DAFX: Digital Audio Effects*. Wiley, 2011.

[16] N. H. H. Fletcher and T. D. Rossing, *The Physics of Musical Instrumnets*. Springer, 2010.

DOI: 10.61782/fa.2025.0069



FORUM ACUSTICUM
EURONOISE 2025

ACOUSTIC DESIGN OF A DUAL-PURPOSE SOUND TUBE ORGAN

Elisa Pérez[1] **Sergio Guillén**[1] **Ana M. Barbancho**[1*]
Isabel Barbancho[1] **Lorenzo J. Tardón**[1]
[1] ATIC Research Group, ITIS Software, ETSI Telecomunicación,
University of Malaga, 29071 Málaga, Spain

ABSTRACT

This paper presents the design and construction of a homemade sound tube demonstrator that doubles as a functional musical instrument. Developed as a pedagogical tool, the prototype aims to introduce children to fundamental musical concepts such as sound production, pitch, and scales. The design process involved validating the instrument's operation as both an open and closed tube, with special attention given to determining the precise tube lengths required for accurate tuning. The study addresses theoretical challenges, such as material selection and tuning techniques, alongside practical considerations to ensure the prototype is both accessible and durable. Acoustic measurements were conducted to validate the theoretical predictions and ensure accurate tuning of the instrument. To assess its educational impact, the demonstrator was tested in a public educational setting, where children engaged with it through guided activities. The results show that the tool helps inspire musical curiosity and makes learning more engaging through hands-on activities. This work highlights the potential of simple, low-cost instruments as educational resources, contributing to both acoustic design and music. The sound tube demonstrator exemplifies how functional hyper-instruments can bridge science and art, inspiring future generations to explore music and acoustics.

Keywords: *Sound tube organ, demonstrator, study, vibrations, education*

**Corresponding author*: abp@ic.uma.es.

***Copyright**: ©2025 Elisa Pérez et al. This is an open-access article distributed under the terms of the Creative Commons Attribution 3.0 Unported License, which permits unrestricted use, distribution, and reproduction in any medium, provided the original author and source are credited.*

1. INTRODUCTION

From an early age, children develop the ability to quickly identify, differentiate, and reproduce a wide range of sound sequences, including melodies [1]. This is further supported by studies [2–4], which demonstrate that children show a stronger attraction to a more melodic, song-like maternal speech compared to standard speech, showing toddlers to be naturally attracted to music. There is a substantial body of research affirming the importance of musical education in early childhood, highlighting its role in activating essential cognitive processes: music learning engages the mental operations required for young children to perceive and analyze auditory stimuli effectively [5]. It has been shown to enhance memory [6], improve attention and concentration [7], and serve as a powerful means of expression while stimulating imagination in children space [8]. Previous research has demonstrated that rhythmic abilities not only develop rapidly during early childhood but are also closely linked to the development of non-musical skills in cognitive and motor domains [9].

Music has numerous positive effects on a child's development, making it essential to integrate it into their education, with the majority of early childhood educators acknowledging how children prefer music-related activities over non-musical ones [5].

There are many musical instruments suitable for introducing children to the world of music, allowing them to learn in a simple and engaging way. To this end, percussion instruments such as bells, maracas, and triangles are commonly used to teach basic rhythmic patterns, while the recorder (flute) serves as a tool for developing breath control and learning simple melodies.

For this purpose, this work presents a musical instrument designed for children with no prior musical experience. The goal is to introduce them to basic musical concepts such as sound production, scale creation, and

the distinction between low and high-pitched tones. For this purpose, a sound tube demonstrator is designed as a simplified pipe organ with eight tubes spanning the octave from C5 to C6. Its intuitive design ensures that anyone, regardless of their musical background, can easily use it to play and explore musical concepts interactively.

The novelty of this work lies in the integration of acoustic design and music education into a single, accessible instrument. The development process involved studying the fabrication of organ pipes, and selecting suitable materials and tuning system. Once constructed, the demonstrator's performance is evaluated by comparing its acoustic output with theoretical expectations. The effectiveness of the tool was demonstrated through an educational session with toddlers, during which various activities and new concepts were introduced and successfully understood by them.

This approach not only bridges the gap between theoretical and practical knowledge, but also provides an innovative tool that fosters creativity and learning in young children, making it a valuable contribution to music pedagogy and acoustic research.

This manuscript is organized as follows: Sec. 2 provides detailed information on the design and construction of the organ tube-like instrument, including the materials, tools required, and budget. Section 3 evaluates the instrument's performance and describes the educational activity conducted with children, demonstrating its effectiveness as a teaching tool. Finally, Section 4 presents the conclusions derived from this work.

2. DEMONSTRATION SYSTEM CONSTRUCTION

This section outlines the design details, materials, and tools used in construction, along with the budget considerations, as well as the challenges encountered during the process and the measures implemented to overcome them.

2.1 Materials and methods

The demonstrator is inspired by the mechanics of a pipe organ. This type of instrument produces sound by channeling pressurized air, or wind, through organ pipes, with each pipe generating a single pitch, typically controlled by one or more keyboards.

Unlike wind instruments powered by lung capacity, pipe organs require significantly higher air pressure and volume [10]. According to [11], an organ consists of several key components, all enclosed within a chest (resonance box), whose design varies based on historical period, craftsmanship, and register size.

- **Windchest with pipes:** The pipes are arranged by note and timbre. A rank consists of pipes that produce the same timbre across all notes. Each key corresponds to a note and can activate different ranks individually or in combination.
- **Wind system:** This includes the blower (air supply), reservoirs, regulators, and wind ducts that maintain stable airflow to the pipes.
- **Control system:** Comprising the keyboard, action mechanism (tracker, pneumatic, or electric), drawstops, and the pallet box, which connects keys to valves, allowing air to flow into the pipes.

Note that our demonstrator is designed as an educational tool to teach toddlers how sound is produced, using this simplified instrument as an example. Several adaptations have been made to achieve this goal:

- The pipes used in this demonstrator are indirect embouchure pipes. In this design, airflow passes through a narrow windway before striking the edge of the embouchure, ensuring sufficient pressure to produce sound. The demonstrator includes only one rank of eight tubes, covering the C5 to C6 scale. This limited size is intentional to suit toddlers' height and interaction ease. Note that not accidentals notes were considered to ease difficulty.
- The wind system replaces a traditional blower with a large balloon. This choice enhances usability for children while making the instrument visually engaging and intuitive to operate.
- The control system omits the keyboard, eliminating the need for a tracker action. Instead, airflow is managed manually via removable washers and a tap, which allow children to open specific pipes directly, fostering hands-on interaction.
- To enhance its educational value, the instrument does not include a resonance chest, leaving all components visible. This transparency helps young learners observe and understand the mechanisms behind sound production.

For the construction of the instrument, the following materials were considered:

- Polyvinyl chloride (PVC) was chosen for constructing the tubes of the instrument due to its affordability, ease of handling, availability in various diameters and rigidities, and the presence of prefabricated connection pieces further on the market.
- PVC was also used to create custom washers for sealing the tube bezels and fabricating the end caps of each tube with an eva sheet.
- The instrument is mounted on a handmade wooden plank with openings for each tube, enabling easy assembly and disassembly. This design keeps all components visible, enhancing its educational value.
- Recycled cork stoppers were repurposed to address windcap role.
- An adjustable tap was integrated to control the airflow through the tubes.
- A large balloon was employed as the air source to supply the instrument with consistent airflow.

The tools used to work with these materials included a PVC pipe cutter, a drill with a 8mm bit for creating the beveled hole, scissors for trimming the rest of the bevel, and sandpaper to smooth out imperfections and sharpen the beveled edge. Fig. 1 ilustrates the key components considered in the instrument functioning.

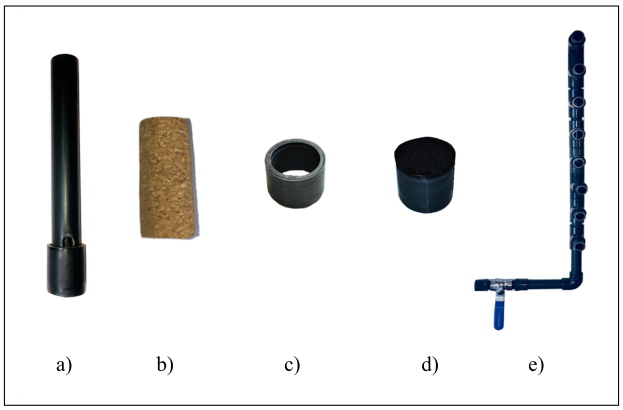


Figure 1. Instrument components, including a tube example (a), cork stopper (b), custom washer (c), tube end cap (d), and wind system with full assembly and tap (e).

When assembled, these parts are configured as depicted in Fig. 2, creating the complete instrument. This setup includes the custom wooden plank, which serves as an "open resonance chest" enabling both structural support and an educationally transparent view of the system.



Figure 2. Organ tube-like demonstrator constructed using the previously presented materials.

Tab. 1 presents a detailed breakdown of the budget required for the construction of the instrument.

Table 1. Detailed budget breakdown for components used in instrument construction

Component	Quantity	Unit price (€)
PVC tube 20mm (3m)	2	2.40
PVC tube 24mm (1m)	1	1.60
L connection	3	0.62
T connection	8	0.62
Nap	1	5.20
Eva rubber	1	0.90
Wood Plank	1	14.00
Balloon	1	2.00
	Total	35.32 €

The affordability of the selected materials and components highlights the accessibility of this solution, ensuring that the demonstrator can be easily reproduced and integrated by educators to introduce musical concepts to children in an engaging and practical manner.

2.2 Instrument Tuning

Pythagorean tuning, attributed to the sixth-century B.C. philosopher Pythagoras, was used as tuning system. It is based solely on the pure fifth (3:2 ratio) found in the harmonic series. This system prioritizes the purity of the fifths, over other intervals, such as seconds and thirds, which become noticeably compromised, which results in harmonically pleasing intervals [12].

To determine the intervals of each note relative to the tonic in Pythagorean tuning, successive additions of pure fifths are calculated within the limits of a single octave. Fig. 3 illustrates the final interval values derived from this method.

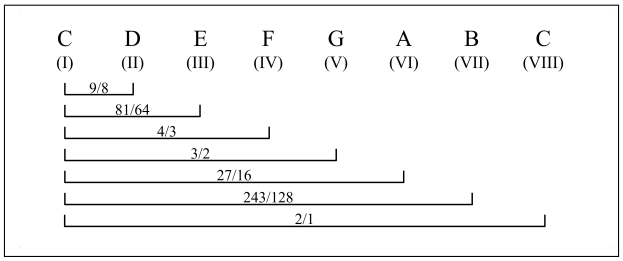


Figure 3. Intervals from each pitch to the tonic in the Pythagorean tuning system.

From this point, using these intervals to the tonic as a reference, the intervals between consecutive pitches are calculated and presented in Fig. 4.

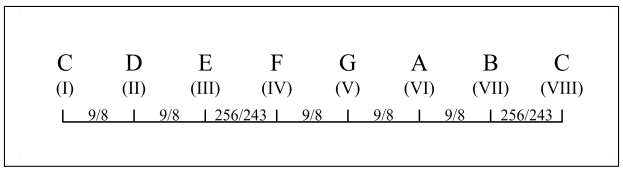


Figure 4. Intervals between consecutive pitches in the Pythagorean tuning system.

This figure illustrates how the Pythagorean scale is constructed using a single type of whole tone (9/8) and a single type of diatonic semitone (256/243).

First, the theoretical frequencies of the eight notes forming the demonstrator were calculated. The chosen system encompasses the octave from C5 to C6, with A5 (880 Hz) serving as the reference point, being the octave above the standard tuning note A4 (440 Hz). Using this reference, the frequency of each remaining tone is determined according to the following (1):

$$f_{\text{note}} = f_{\text{ref}} \cdot \left(\left(\frac{9}{8} \right)^{n_{\text{tones}}} \cdot \left(\frac{256}{243} \right)^{n_{\text{semitones}}} \right) \quad (1)$$

where f_{ref} corresponds to A5 frequency, and n_{tones} and $n_{\text{semitones}}$ represent the number of tones and semitones between the two notes. Note that if the new pitch is lower than A5, both n_{tones} and $n_{\text{semitones}}$ must be negative.

Tab. 2 presents the theoretical frequencies of the notes in the octave from C5 to C6, calculated using the expression outlined earlier.

Table 2. Theoretical frequencies calculated using the Pythagorean tuning system

Tune	Frequency (Hz)	Tune	Frequency (Hz)
C5	521.48	G5	782.22
D5	586.67	A5	880.00
E5	660.00	B5	990.00
F5	695.31	C6	1042.96

Now, tube design is assessed to obtain the target frequencies shown in the previous table. For this purpose, several assumptions are considered [13]:

- The tube diameter is sufficiently large to neglect the effects due to viscosity.
- The tube diameter is small compared to the tube length and the wavelength, λ, produced.
- The surfaces forming the tubes are rigid.

In pipe organs, sound is generated through longitudinal wave motion, where sound waves reflect at the tube ends. The air column is excited by the windway, transferring vibrational energy to the air. The point of excitation is neither a perfect node nor an antinode, leading to a slight inaccuracy in the frequency, which we aimed to adjust through design corrections.

In the tube's length, L, a half wavelength, λ, is produced [14]. The frequency of the harmonic can be calculated knowing the relationship between the frequency of the sound produced, the speed of propagation, and the wavelength using the following expression (2):

$$f_n = \frac{n \cdot c}{2L} \quad (2)$$

where f_n is the frequency of the $n-th$ harmonic, $c = 340m/s$ is the speed of sound in air, and L is the tube length.

Based on this expression, the first sound tube was constructed with a length of 12.7 cm to achieve a frequency of 880 Hz (A5 tune). The tube's length is measured from the end of the bevel to the open end (see Fig. 1.a). Fig. 5 displays the frequency response of the tube when excited.

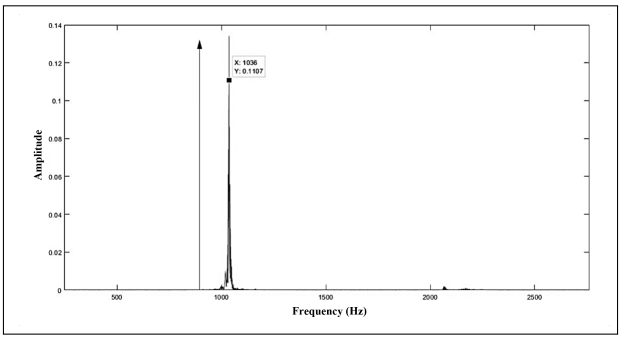


Figure 5. Spectrum obtained from a tube with $L = 12.72$ cm. An arrow is used to indicated the expected frequency of 880 Hz.

In this figure it can be observed the up-cited deviation from the theoretical expected frequency, with an obtained frequency of 1036 Hz when designing the tube to produce a sound of 880 Hz. Therefore, in practice it is observed how tube's length must be slightly lower than the theoretical value computed. This was already assesses in [15] where an approximation of the real length needed L_R is obtained by applying the following expression (3):

$$L_R = L - 3.3r \tag{3}$$

where L is the tube length and r stands for the intern ratio of the tube.

However, an adjustment to the formula is made based on the observed differences. This involves modifying the correction factor in the ratio according to the difference between the measured and expected values, as calculated by the following equations (4)(5):

$$L = \frac{c}{2 \cdot f} \tag{4}$$

$$L - L_R = c_{factor} \cdot r \tag{5}$$

where L is the tube length, L_R is the previously calculated real tube length, r represents the internal ratio of the tube, and c_{factor} is the new correction factor to be applied.

With this in mind, the new corrected tube length L'_R is computed as (6):

$$L'_R = L - 4.6 \cdot r \tag{6}$$

Following the calculations for all the desired frequencies, the resulting length values are presented in Tab. 3.

Table 3. New tube lengths obtained using the fixed equation previously presented.

Tune	Frequency (Hz)	Tube Length L'_R (cm)
C5	521.48	28.90
D5	586.67	25.30
E5	660.00	22.10
F5	695.31	20.80
G5	782.22	18.00
A5	880.00	15.60
B5	990.00	13.50
C6	1042.96	12.60

3. RESULTS AND EVALUATION

This section presents the actual measurements of each of the tubes, providing insight into the performance of the instrument and the details of the educational activity in which the demonstrator was tested with toddlers, illustrating its effectiveness as a pedagogical tool.

3.1 Instrument performance analysis

To test the instrument's alignment with theoretical values, three different types of measurements were considered: individual measurements for each pitch (tube), the intervals with the tonic, and the analysis of the closed tubes (lower octave). For the sound recordings and analysis, MATLAB software [16] was used, with a sampling frequency of 44100 Hz and a bit depth of 16 bits in a mono-channel configuration. Each sound was recorded for approximately 5 seconds to ensure that all relevant details of each sound were captured effectively.

3.1.1 Individual tubes measures

The first set of measurements involved assessing each tube individually to examine their fundamental frequency in relation to their length. This approach aimed to validate the

accuracy of the expression (6). Fig. 6 presents the spectrum obtained from the Fast Fourier Transform of the audio corresponding to the $C5$ tune.

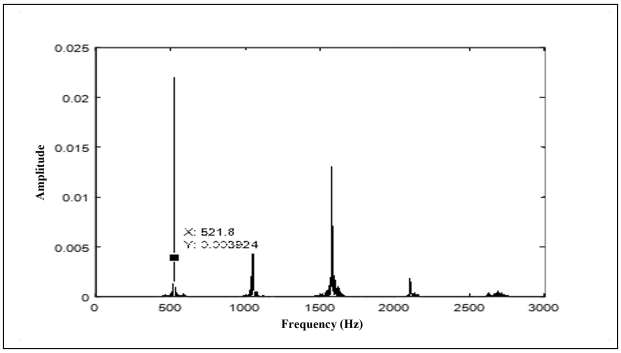


Figure 6. Spectrum obtained from a tube with $L = 28.90$ cm aiming to produce C5 tune ($f = 521.48$ Hz). The fundamental frequency is marked with a pointer.

This figure depicts that the fundamental frequency closely aligns with the theoretical frequency expected. Additionally, three harmonics are present at frequencies of 1044 Hz, 1571 Hz, and 2095 Hz, which correspond approximately to harmonics second to fourth harmonics ($2f$, $3f$ and $4f$). Their amplitudes are significantly lower than that of the fundamental frequency and diminishes as the frequency rises. At higher frequencies, the presence of harmonics becomes more difficult to discern, as expected from a wind instrument.

With this in mind, Tab. 4 presents a comparison between the obtained frequencies and the theoretical values, along with the absolute error in Hertz between them.

Table 4. Theoretical and obtained frequencies comparison, including the frequency error observed.

Tune	Expected frequency (Hz)	Obtained frequency (Hz)	Abs. Error (Hz)
C5	521.48	521.80	0.32
D5	586.67	585.90	0.77
E5	660.00	656.30	3.70
F5	695.31	695.60	0.29
G5	782.22	781.90	0.32
A5	880.00	881.00	1.00
B5	990.00	987.50	2.50
C6	1042.96	1042.00	0.69
		Mean Error	1.23

This table shows that the obtained results closely align with the expected frequencies, with a mean error below 1.25 Hz.

3.1.2 Intervals with tonic measures

The second set of measurements focused on analyzing each interval with the tonic. To present the results, graphs were created to display both the spectrum of the two sounds comprising the interval played simultaneously and each sound individually. This approach seeks to highlight the differences between a chord and the mere addition of two tones. An example is provided in Fig. 7, illustrating the major third interval formed between the notes C5 and E5.

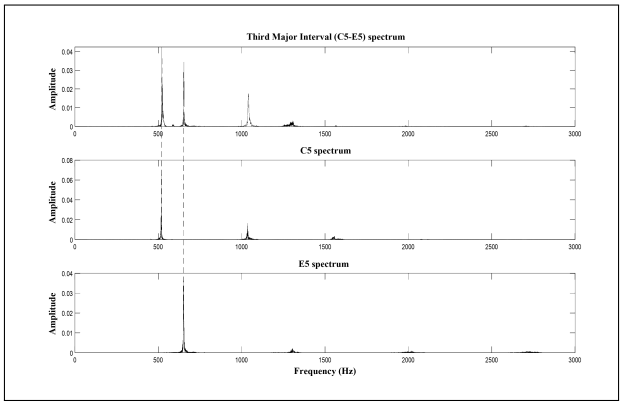


Figure 7. Frequency spectrums of C5 and E5 notes along with the spectrum of the interval formed between them.

The analysis confirms that the excited frequencies correspond to those of each individual tone in the interval. Additionally, alongside the fundamental frequencies, their respective harmonics are also excited. This behavior is consistent across all intervals, showing a similar trend to the findings in the previous section: as frequency increases, the number of generated harmonics decreases.

Furthermore, the spectral analysis reveals that the spectrum of an interval played as a chord is nearly identical to the sum of the spectra of its constituent tones. It was also observed that, depending on the interval, some harmonics of the individual tones may overlap in frequency, resulting in an additive effect. These findings highlight the predictable harmonic structure of the instrument and its intervals.

3.1.3 Closed tubes measures

Unlike open pipes, in a closed pipe, a node is formed at the closed end while an antinode occurs at the open end. Consequently, the wavelength in a closed pipe is twice that of an open pipe [14]. From the relationship between λ and f, the harmonics in a closed pipe are given by expression (7):

$$f_n = \frac{(2n-1)\cdot c}{4L} \tag{7}$$

where c is the speed of sound, L is the length of the pipe, and n represents the harmonic order. Note that only odd harmonics are present in closed pipes due to the boundary conditions at the ends.

However, since the tubes were specifically constructed to meet the design criteria for open pipes, the frequencies obtained through this method deviate significantly (mean value error of 4.85 Hz) from the ideal values, which should correspond to half the fundamental frequencies of the previous measurements (lower octave). Given the instrument's intended use as an educational tool, these deviations in frequency are considered acceptable. To achieve more conclusive results, the tube design would need to be adjusted to align with these new frequency requirements.

3.2 Educational activity

The ultimate purpose of constructing this demonstrator is its pedagogical use. It aims to help children understand how air is transformed into sound and how this sound depends on the size of the tubes. To evaluate its effectiveness, the demonstrator was presented at Colegio Enrique Tierno Galván in La Zubia (Granada) to a group of 5-year-old students.

The demonstration started by discussing musical instrument families—percussion, string, and wind—with examples like a tambourine, guitar, and recorder. Students then categorized other instruments and learned about the musical scale, writing and singing an octave from C5 to C6. Concepts like "low" (thick sound) and "high" (thin sound) were introduced.

The demonstrator was used to show how air turns into sound, starting with inflating a large balloon to capture toddler's attention. Playing the scale on the demonstrator, students observed that lower pitches came from larger tubes and higher pitches from smaller ones. They then took turns playing the demonstrator themselves, reinforcing the relationship between tube size and pitch.

The activity concluded with a recap of the concepts and another group performance of the scale. Fig. 8 shows three students interacting with the demonstrator.



Figure 8. Photograph taken during the musical instrument demonstration, showing students interacting with the demonstrator.

This activity was evaluated by the class tutor, who validated the tool's effectiveness and the achievement of its intended objectives. The demonstration proved its value as an educational resource for introducing young children to the physics of sound.

4. CONCLUSIONS AND DISCUSSION

This work presented a pipe organ demonstrator designed to illustrate sound production in open and closed pipes, enabling the study of vibration modes and the frequencies they produce. A comprehensive analysis of potential materials was undertaken, with PVC ultimately selected for its cost-effectiveness, availability, and recyclability, making the demonstrator an affordable tool for educational use.

The Pythagorean tuning system proved effective in demonstrating harmonic relationships in tuned intervals (2nd, 4th, 5th, and 8th) and inharmonicities in untuned intervals (3rd, 6th, and 7th). Adjustments were made to the tube length formula based on experimental data, improving the design's accuracy.

A thorough validation process was conducted to confirm the instrument's performance, with frequencies aligning closely with expectations for open pipes. While

discrepancies in the closed-pipe configuration were observed, they were deemed acceptable for educational purposes, with a redesign necessary for precise implementation.

The demonstrator's effectiveness as a pedagogical tool was validated through a hands-on activity with 5-year-old students. Despite no prior musical knowledge, students successfully learned the musical scale and the relationship between pitch and pipe size. While the demonstrator could benefit from further refinement in certain areas, it has proven to be an effective and valuable tool for educators to introducing young learners to the basic principles of music and acoustics.

5. ACKNOWLEDGMENTS

This publication is part of project PID2021-123207NB-I00, funded by MCIN/AEI/10.13039/501100011033/ FEDER, UE. This work was done at Universidad de Málaga, Research Group TIC208, Campus de Excelencia Internacional Andalucía Tech.

6. REFERENCES

[1] L. J. Trainor, "Predictive information processing is a fundamental learning mechanism present in early development: Evidence from infants," *International Journal of Psychophysiology*, vol. 83, no. 2, pp. 256–258, 2012.

[2] R. P. Cooper and R. N. Aslin, "Preference for infant-directed speech in the first month after birth," *Child Development*, vol. 61, no. 5, pp. 1584–1595, 1990.

[3] J. Vannatta-Hall, "Music education in early childhood teacher education: The impact of a music methods course on pre-service teachers' perceived confidence and competence to teach music," *ProQuest Dissertations and Theses*, p. 226, 2010.

[4] S. E. Trehub and H. R. Gudmundsdottir, "Mothers as singing mentors for infants," in *The Oxford Handbook of Singing*, Oxford Library of Psychology, 2015.

[5] J. Bolduc and M. Evrad, "Music education from birth to five: An examination of early childhood educator's music teaching practices," *" Research & Issues in Music Education*, vol. 13, no. 1, 2017.

[6] M. S. Franklin, K. S. Moore, C.-Y. Yip, J. Jonides, K. Rattray, and J. Moher, "The effects of musical training on verbal memory," *Psychology of Music*, vol. 36, no. 3, pp. 353–365, 2008.

[7] Y. Kasuya-Ueba, S. Zhao, and M. Toichi, "The effect of music intervention on attention in children: Experimental evidence," *Frontiers in Neuroscience*, vol. 14, no. 757, 2020.

[8] Y. Liu, "The influence of music activities on children's creative thinking development," *SHS Web of Conf.*, vol. 180, p. 04001, 2023.

[9] U. Frischen, F. Degé, and G. Schwarzer, "The relation between rhythm processing and cognitive abilities during child development: The role of prediction," *Frontiers in Psychology*, vol. 13, 2022.

[10] C. F. A. Williams, "Evolution of the organ," *Music & Letters*, vol. 5, no. 3, pp. 253–263, 1924.

[11] J. Angster, P. Rucz, and A. Miklós, "Acoustics of organ pipes and future trends in the research," *Acoustics Today*, vol. 13, pp. 12–20, 03 2017.

[12] B. Benward and M. Saker, *Music in Theory and Practice*. McGraw-Hill, 2008.

[13] M. Recuero, *Ingeniería Acústica*. Ediciones Paraningo, S.A, 1995.

[14] L. Azzaroni, *Canone infinito: lineamenti di teoria della musica (Manuali e antologie*. CLUEB, 2001.

[15] A. Calvo-Manzano, *Acústica físico-musical*. Real Musical, 1991.

[16] The MathWorks Inc., "MATLAB version: 9.4.0 (r2018a)," 2018.

DOI: 10.61782/fa.2025.0344



FORUM ACUSTICUM
EURONOISE 2025

ENHANCING MUSIC VISUALIZATION WITH HAPTIC FEEDBACK TO EASE PERCEPTION FOR DHH LISTENERS

Noemi Mauri[1] **Matteo Sacchetto**[1*] **Piera Bagnus**[2] **Chiara Nicora**[3]
Massimiliano Zanoni[4] **Andrea Bianco**[1] **Cristina Rottondi**[1]
[1] Dept. of Electronics and Telecommunications, Politecnico di Torino, Italy
[2] Conservatorio Giuseppe Verdi, Como, Italy
[3] Conservatorio Guido Cantelli, Novara, Italy
[4] Dept. of Electronics, Information and Bioengineering, Politecnico di Milano, Italy

ABSTRACT

This study introduces a novel integration of visual and haptic feedback to improve music perception for Deaf and Hard-of-Hearing (DHH) individuals. The proposed prototype, named MusicTanvas, leverages a touchscreen augmented with electroadhesion-based haptic technology, enabling dynamic overlay of tactile textures on visual content. The system processes pre-recorded audio tracks to extract spectral, harmonic, and rhythmic features, which are mapped to both visual and haptic representations. More in detail, key features such as chroma, Mel-Frequency Cepstral Coefficients (MFCCs), and rhythmic figures, are translated into corresponding visual attributes (e.g., color, shape, and size) and tactile textures. Users can explore music in real-time through these multisensory outputs, which evolve synchronously with the audio playback. A preliminary user assessment demonstrates the system's potential to enhance musical interaction by combining visual-haptic feedback.

Keywords: *Music Visualization; Haptic Feedback; DHH Listeners.*

**Corresponding author*: matteo.sacchetto@polito.it.
***Copyright**: ©2025 M. Sacchetto et al. This is an open-access article distributed under the terms of the Creative Commons Attribution 3.0 Unported License, which permits unrestricted use, distribution, and reproduction in any medium, provided the original author and source are credited.*

1. INTRODUCTION

Music perception for Deaf and Hard-of-Hearing (DHH) subjects is challenging due to the unavoidable involvement of auditory perception. Hence, the reliance on extra-auditory cues is essential to ease music conveyance to DHH listeners. Among those, visual representations [1] and tactile feedback [2] are the most widely adopted ones.

Various visual techniques exist (see [3] for a thorough overview), including color coding (i.e., the association of musical elements such as notes, scales, and chords with specific colors) and graphical notation (i.e., the use of symbols, shapes, and patterns to represent musical concepts such as rhythm, dynamics, and phrasing). Meanwhile, tactile feedback has been provided through wearables (e.g., vibrating wristbands) synchronized with musical events [4], to convey to DHH users the sense of rhythm, beat, and dynamics. Moreover, tactile graphics can be exploited to create representations of musical scores using raised textures or embossed materials, to be explored while listening to a recording of the pieces.

The joint adoption of visual representations and tactile feedback can be supported by programmable touchscreens enhanced with electroadhesion-based haptic technology. Such hardware has already been explored for the conveyance of the notion of "sonic grain", i.e., a form of "tactilization" that allows for a cross-modal connection between the texture of sound and material surfaces, thus bridging tactile and sonic experiences [5].

In this paper, we adopt the TanvasTouch [1] hardware

[1] Tanvas. Surface Haptics. https://tanvas.co/

support to offer a time-varying visual and tactile representation of one or multiple audio tracks [2] constituting a musical piece. Our developed prototype, named MusicTanvas, processes pre-recorded audio files to extract the evolution over time of their spectral characterization in terms of Mel-Frequency Cepstral Coefficients (MFCCs), chromas, spectral bands, entropy, their rhythmical content, and timbral features. Once the pre-processing phase is completed, a mapping between the above-mentioned features and the choice of colors, shapes, luminosity, and haptic textures to be associated to each track is identified and proposed to the listener during the audio reproduction [3] .

Results acquired through a preliminary usage assessment of MusicTanvas by a pool of 20 subjects testify to the usefulness of joint visual-tactile stimuli in enhancing music perception.

The remainder of the paper is organized as follows: Sec. 2 provides a review of the related literature. Sec. 3 introduces the TanvasTouch technology, describing its principles. Sec. 4 describes the characteristics and functionalities of our proposed implementation. The chosen visual and haptic representations are discussed in Sec. 5. The performance assessment of MusicTanvas is discussed in Sec. 6. Finally, Sec. 7 ends the paper.

2. RELATED WORK

2.1 Visual Representations

Visual representations of music play a crucial role in translating auditory information into visual stimuli for DHH individuals. Historically, Aristotle [6], Newton [7], Graves [8], Garner [9], and Kandinsky [10] explored correlations between colors and sounds. These insights have shaped interdisciplinary research, suggesting the use of color and shapes to convey musical tones and rhythmic elements [11]. From these studies, it emerges that the most common approach is to associate pitch or timbre with colors and shapes, whereas the intensity of the sound is often represented through the variation of shapes' sizes.

Smith and Williams [12] introduced a visualization technique in which the velocity of a single tone designates its loudness or softness. Velocity is represented by the relative size of a displayed sphere, with its radius ranging from 0 to 127, reflecting the minimum and maximum MIDI velocity values. Moreover, instruments with similar timbres are grouped and differentiated by color, according to the MIDI specification. Other, more recent options, such as the one proposed by Lima et al. [13], include a visualization prototype called *SongVis* that uses emojis, colors, lines, and shapes to represent different features such as danceability, mood, tempo, music genre, and instrument.

Malandrino et al. [14] proposed *VisualHarmony*, a visualization tool able to represent harmonic structures. It provides a music editor for the composition of 4-voices music with the possibility to highlight the harmonic structure with different colors, based on the circle of fifths. Furthermore, special attention is given to inclusiveness and accessibility, since VisualHarmony gives users the possibility to customize the circle of fifths to be discernible also by people with color perception deficiencies.

Deja et al. [2] introduced *ViTune*, a visualizer prototype built to allow DHH individuals to experience music by displaying a real-time visual representation of the played sound. ViTune performs a harmonic and percussive source separation once users upload their music files. The harmonic part is divided into four ranges, each one visually represented through bars and stars, with size changing based on the signal strength. Conversely, saturation, brightness, and opacity of the visualized components depend on the extracted chromagram. In our prototype, we will leverage a similar approach to visualize either chromagrams or MFCCs.

Another approach to visually representing musical features involves using shapes and sizes: Cruz et al. [15] use polygons, where the number of sides corresponds to different octaves. Higher octaves, representing treble sounds, are associated with polygons with more sides, whereas lower octaves, associated with bass sounds, are associated with polygons having fewer sides. Moreover, the volume (or velocity) of the note affects the size of the polygon: larger polygons indicate higher velocities. Our prototype adopts the same approach to visualize sound loudness.

2.2 Haptic Representations

In recent years, vibrotactile stimuli have gained attention as a method to convey musical elements, such as rhythm and melody, to DHH individuals. Research has increasingly explored how tactile feedback can enhance musical experience by converting audio signals into vibrations per-

technology

[2] A track is a single audio recording that may contain one or multiple musical stems (e.g., vocals, melody, bass, drumset).

[3] A video demonstrating the prototype usage is available on YouTube: https://youtu.be/HEz74yxcOZ8

ceived through the skin. Most research has focused on vibrating stimuli rather than more advanced haptic technologies, such as those based on the variation of electroadhesivity properties of surfaces [16], to create tactile sensations. Our prototype is based on the latter technique.

Furthermore, researchers have investigated how the tactile sense can convey information about a stimulus's roughness. Brown et al. [17] characterized roughness using a sinusoidal stimulus modulated by another signal, demonstrating that increasing the modulation frequency results in a rougher perceived signal. It is worth mentioning that auditory and tactile perceptions have significantly different dynamic ranges [4]. Hearing can perceive a dynamic range of approximately 130 dB, whereas tactile perception can discriminate only about 50 dB. Furthermore, audible sounds for humans range from about 20 to 20,000 Hz, with peak sensitivity between 500 and 4,000 Hz. In contrast, tactile sensitivity ranges from 1 to 1,000 Hz, with peak sensitivity around 200–300 Hz, depending on the body part. Despite these disparities, both auditory and vibrotactile senses exhibit high temporal resolution, enabling accurate perception of rhythm.

Alves Araujo et al. [18] conceived the *Auris System* to enable subjects with hearing loss to experience music through other senses. Musical features such as melody, rhythm, and harmony are reproduced by the combination of two different devices, the *Auris Chair* and the *Auris Bracelet*. Furthermore, Fontana et al. [19] examined how vibrations can be leveraged to experience musical harmony through vibrotactile stimuli.

3. BACKGROUND ON TANVASTOUCH

The TanvasTouch device leverages *electroadhesion* [20], a technique that uses an electric field to create friction between surfaces. It can produce friction at 256 distinct intensity levels, enabling users to feel a wide range of textures on a 2D surface [16] [21].

The TanvasTouch device is composed of two parts: hardware and software [22]. The hardware includes a specialized touchscreen that dynamically adjusts its surface friction in response to user interaction. Custom electronics detects touch input and modifies friction forces in real time, creating tactile sensations as users slide their fingers across the screen.

The software part is composed of the TanvasTouch Engine, which controls the electrostatic forces by interpreting finger movements on the screen and adjusting the electrostatic field to provide tactile feedback. Furthermore, the TanvasTouch API allows developers to develop touch-based applications that simulate various textures and tactile sensations.

When developing an application that utilizes TanvasTouch, developers can align the graphical and haptic representations with the corresponding displayed figures to ensure that tactile feedback is delivered in the correct area of the screen. However, there could be scenarios where haptic feedback is used to offer multiple textures within a single visual representation.

The images used for haptic feedback generation need to be in gray scale with values 0-255 per pixel and in .png file format. Essentially, the Tanvas device lets users perceive different textures through the contrast between black and white images: white areas represent high friction, creating a rough sensation, while black areas represent low friction, resulting in a smooth feel. As users slide their finger across the screen, the differences in friction between the black and white areas allow them to feel varying textures.

4. PROTOTYPE IMPLEMENTATION

Our prototype [4] was created using the C# language, within the Windows Presentation Foundation (WPF) User Interface (UI) framework, part of the .NET framework. To incorporate haptic feedback, we employed the TanvasTouch API from the TanvasTouch Software Development Kit [5]. The WPF framework uses XAML (Extensible Application Markup Language) for the declarative specification of UI components, while C# is used to implement their corresponding functionalities. In our implementation, the XAML script specifies the collection of UI components such as buttons, images, and layout configurations. Conversely, the C# script manages the display state of these UI elements, toggling image visibility, facilitating page navigation, initiating audio playback, extracting audio features, and handling haptic feedback. Within the XAML document, images are integrated using the `Image` tag, and haptic feedback functionality is achieved through the `TSprite` tag, a component of the TanvasTouch API.

Besides managing UI components and haptic feedback, the application also incorporates advanced audio

[4] The source code, along with audio clips, is publicly available in the following GitHub repository: `https://github.com/moeni27/MusicTanvas`

[5] Related documentation can be found at `https://api-docs.tanvas.co/tanvastouch/dotnet/5.0.1/api/index.html`

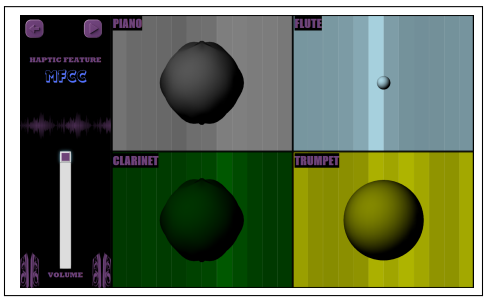


Figure 1: MusicTanvas UI, with 4 sections and MFCC values associated to background stripes.

feature extraction. This functionality is essential for providing meaningful audio analysis and improving user interactions based on audio content. The NAudio library [6], integrated into the .NET framework, facilitates audio playback, stop, and amplitude retrieval across multiple audio files concurrently. Meanwhile, feature extraction is achieved through Python and various libraries such as librosa [7] and numpy, specifically via the pythonnet library [8]. Key features extracted include spectral centroid, MFCCs, chromagram, and onset detection, which are crucial for analysis and interaction with the audio content.

5. VISUAL AND HAPTIC REPRESENTATIONS

5.1 Graphical User Interface Structure

The MusicTanvas UI is structured into up to four distinct sections, each representing a prominent instrument group (see Fig. 1). Users can explore the app in two modes: *Multi-Track Mode* and *Single-Track Mode*. In Multi-Track Mode, the user can upload up to four audio tracks (i.e., files) simultaneously. The UI dynamically adjusts based on the number of tracks uploaded, displaying a distinct section per track. All tracks must have the same duration to be reproduced or stopped simultaneously. Conversely, the Single-Track Mode utilizes Artificial Intelligence (AI) for audio processing. By uploading a single audio track, the app uses *Spleeter* [23] [9] to split it into four stems: vocals, bass, percussion, and other instruments. Different studies [24] [23] evaluated Spleeter's performance by comparing it with other state-of-the-art systems, showcasing its high-quality source separation capabilities.

5.2 Audio Processing Algorithms

To offer meaningful visualization of audio content, our application relies on a number of audio processing algorithms. More in detail, we implemented a window-based extraction procedure for chromagram, MFCC, spectral centroid (a descriptor of the perceived brightness of a sound [25]) and loudness. Such window-based extraction process is applied separately to each track. This ensures that the features are computed independently for each audio source, maintaining the integrity of the individual tracks. Chromagrams, MFCCs, spectral centroids, and onsets are extracted using the *librosa* Python library and stored in NumPy arrays. The extraction uses a window length of 1024 samples with an overlap of 512 samples. Given a sample rate of 44.1 kHz, this setup results in an update time for feature extraction of $512/44100 = 0.0116 \simeq 0.012$ seconds per frame, where each frame represents a brief time interval used for feature extraction and analysis. Furthermore, the application uses the NAudio stream properties to extract the amplitude values from audio segments. Furtermore, the application employs two complementary algorithms: as previously mentioned, in Single-track mode it uses *Spleeter* to segment the audio track into four predefined stems, whereas in Multi-track mode it implements an instrument recognition algorithm. This algorithm leverages a Convolutional Neural Network (CNN) and a K-Nearest Neighbors (KNN) classifier based on MFCCs, chroma, and spectral centroid acoustic features, to identify and categorize the primary musical instrument present in each uploaded audio track [26]. Based on the classification output, each track is then assigned to the corresponding section and color according to the associations proposed by Kandinsky [10] (see Table 1).

Finally, to quantify rhythmic complexity, we use an onset extraction algorithm [27], that starts by transforming the audio signal into a time-frequency representation using the Short-time Fourier Transform (STFT). This process breaks down the audio signal into overlapping frames (with a 50% overlap) and derives the spectral characterization for each frame, capturing the energy distribution of the signal. The overlapping frames are crucial to enhance the temporal resolution of the analysis, as they ensure that each frame shares information with adjacent frames, capturing smooth transitions, preserving temporal relationships in the audio signal, and reducing the influence of

[6] https://github.com/naudio/NAudio
[7] https://github.com/librosa/librosa
[8] https://github.com/pythonnet/pythonnet
[9] An AI source separation tool that uses pre-trained models to extract individual stems from audio tracks, where each stem corresponds to a specific instrument

Table 1: Musical Instrument and Color Mapping

Musical Instrument	Color Name	Visual Representation
Cello	Deep Blue	
Clarinet	Dark Green	
Flute	Light Blue	
Acoustic Guitar	Orange	
Electric Guitar	Violet	
Organ	Deep Purple	
Piano	Grey	
Saxophone	Brown	
Trumpet	Light Yellow	
Violin	Light Violet	
Vocals	Gold	
Bass	Blue	
Drum	Red	
Other	Green	

windowing artifacts.

From the STFT output, the spectrogram of the audio track is computed, which represents the magnitude of the audio signal over time. We apply a logarithmic compression to the spectrogram's magnitude, which enhances weak spectral components and simulates human perception, highlighting smaller variations that might otherwise be overlooked. Subsequently, a novelty spectrum is derived from the spectrogram, highlighting abrupt energy changes between consecutive frames. This spectrum is obtained by computing the difference between adjacent columns of the spectrogram: a positive difference indicates significant changes in the audio signal, hinting to potential onsets. The novelty spectrum represents such energy changes and helps detect new events. To enhance detection accuracy and minimize noise, a local average is computed across the spectrum. This smoothing process helps differentiate genuine onsets from minor signal fluctuations. In the final onset detection stage, each spectrum value is adjusted by subtracting its respective local average. Values surpassing a predefined threshold are identified as significant onset indications.

5.3 Mappings of Audio Features to Visual and Haptic Representations

Tab. 2 shows how specific audio features are mapped to their corresponding visual and haptic representation in our interface. More in detail, a sphere (i.e., the shape chosen to represent musical features) is visually represented in the foreground of each section (as in [12]). The sphere's radius dynamically adjusts based on the loudness of the corresponding audio track. This adjustment reflects amplitude variations within the track and is influenced by a volume slider controlling the overall audio output of the application (located on the left side of Fig. 1). If the tracks have different initial audio levels, the application performs normalization to ensure consistent volume output. The sphere's color brightness is linked to the spectral centroid feature. As the spectral centroid shifts across the audio track, the sphere's color brightness dynamically adapts, visually reflecting changes in tonal brightness. Moreover, the output of the onset detection algorithm influences the surface of the sphere, visually accentuating event changes in the audio content (Fig. 2). This representation gives users the possibility of visually appreciating the temporal structure and intensity variation within the musical composition. Spherical representations were chosen for their smooth visual appearance, complemented by dynamic changes to their surfaces to reflect audio characteristics effectively.

Table 2: Mapping of Audio Features to Visual Representations

Audio Feature	Visual Representation	Haptic Representation
MFCC or Chromagram	Color brightness of background stripes	Texture roughness of background stripes
Rhythmic complexity	Sphere's surface	-
Spectral centroid	Sphere's color brightness	-
Loudness	Sphere's radius	-

Regarding the background, inspired by [10], each section is adorned with a specific color palette, chosen according to the instrument automatically detected in the corresponding audio track. Moreover, in each section, the background is divided into several vertical stripes. Each stripe symbolizes either one of the 7 MFCCs derived from the feature extraction process or one of the 12 pitch classes of the chromagram. The choice between 7 and 12 stripes is determined by the feature being represented. The stripes' colors dynamically transition from lighter to darker hues, reflecting the normalized values of the corresponding MFCCs/chromas within a specific temporal context. Besides the visual representation, each

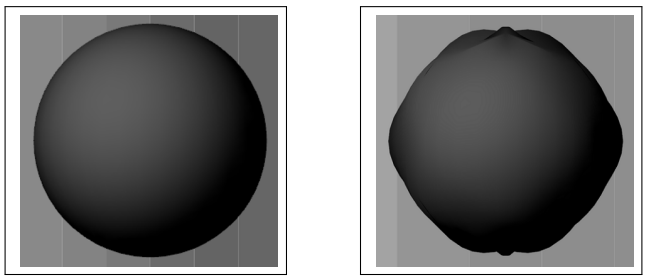


Figure 2: MusicTanvas GUI showing onset detection: smooth surface indicates no onset (left), non-smooth surface indicates onset detection (right).

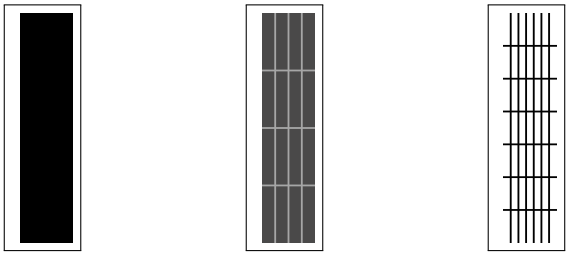


Figure 3: Haptic images representing feature value ranges: $0 \leq x < 0.1$ (left), $0.4 \leq x < 0.5$ (center) and $0.9 \leq x \leq 1$ (right).

stripe also features a corresponding haptic feedback representation. This haptic representation consists of a gradient stripe, transitioning from black to white through various shades of gray. Specifically, ten distinct haptic images are generated, ranging from black to white via 8 intermediate shades of gray.

Furthermore, vertical and horizontal lines are added, forming a grid-like pattern. For darker shades of gray, the grid consists of a few horizontal and vertical lines. As the shade lightens, more lines are progressively added, increasing the density of the grid. This granularity variation enhances the haptic experience, allowing users to better distinguish between different values through tactile feedback. These shades correspond to MFCC/chroma values ranging from 0 to 1. For instance, an MFCC value between 0 and 0.1 triggers a black haptic image, a value between 0.1 and 0.2 triggers a dark gray image, whereas a white image is associated with values between 0.9 and 1 (see Fig. 3). This approach allows users to perceive tactile feedback corresponding to the MFCC/chromagram variations by swiping their fingers over the screen. MFCC and chroma values are generated approximately every 12 milliseconds, but this interval is too brief for users to perceive the tactile feedback effectively. To overcome this issue, the system aggregates the values over a 5-second window and computes their average, thereby smoothing the tactile feedback into a more coherent and perceptible signal.

Table 3: Validation Accuracy vs. Number of Categories.

Number of Categories	2	3	11
Validation Accuracy	90%	75%	60%

Table 4: Processing Times for Feature Extraction and Source Separation

Audio Length (s)	10	40	120
Extraction Time (s)	0.17	0.68	2.17
Separation Time (s)	25.93	31.28	51.60

6. PERFORMANCE ASSESSMENT

The performance assessment of MusicTanvas evaluates instrument recognition accuracy, computational efficiency and user experience.

The IRMAS dataset [28] was used to train and test the instrument recognition model. The dataset includes 6705 audio recordings from 11 instrument classes. The dataset was split into 80% for training and 20% for testing. Moreover, a 5-fold cross-validation approach was performed to ensure robustness evaluation of the model. As shown in Tab. 3, the accuracy drops from 90% when classifying two instruments to 60.70% for 11 categories. This highlights the challenge of distinguishing between instruments with simlar audio features.

The system's computational efficiency was evaluated by measuring processing times for audio feature extraction and source separation on tracks of varying lengths, using *Spleeter*. As summarized in Tab. 4, feature extraction time and source separation time grow approximately linearly with the track length.

Due to the difficulty of recruiting DHH participants, a preliminary user assessment study was conducted with 20 non-impaired participants aged between 20 and 60 (see Tab. 5 for an overview of the participants' musical experience level). To simulate deafness, participants interacted with MusicTanvas without any auditory feedback, and all tasks were evaluated without sound. Participants were given a brief training session before the evaluation.

The user experience assessment evaluated the color-

Table 5: Musical Experience Level (scale from 1 = beginner to 5 = expert)

Experience Level	1	2	3	4	5
Frequency	2	4	10	4	0
Percentage	10%	20%	50%	20%	0%

Table 6: Enjoyment of MusicTanvas (scale from 1 = not enjoyable to 5 = very enjoyable)

Enjoyment	1	2	3	4	5
Frequency	0	0	0	12	8
Percentage	0%	0%	0%	60%	40%

instrument mapping and the impact of tactile and visual feedback on musical perception. Results show that color-instrument associations proposed by participants largely aligned with the MusicTanvas mapping. Furthermore, 85% of users preferred the multi-quadrant display for multi-instrument recognition, citing improved instrument differentiation.

Tactile and visual feedback were appreciated for enhancing the perception of individual musical parts, although the tactile feedback alone received mixed ratings regarding its effectiveness. Moreover, participants reported no negative experiences with tactile feedback, and all of them found the visualization helpful for instrument recognition. MusicTanvas was also appreciated for its ease of use (see Tab. 6). All participants agreed that it has great potential to help DHH subjects.

7. CONCLUSIONS

This paper presented MusicTanvas, a prototype application that utilizes a touchscreen enhanced with electroadhesion haptic technology, which enables the overlay of tactile textures onto displayed content that dynamically changes over time. The prototype incorporates a set of algorithms that pre-process single or multiple pre-recorded audio tracks to extract key spectral, harmonic, and rhythmic elements within set time intervals. These extracted musical features are stored as arrays or lists. During playback, the system retrieves the pre-extracted feature values, ensuring that they evolve synchronously with the audio. These values are then used to control both visual and haptic feedback, to ease music perception for DHH individuals with a multisensory interaction that matches the auditory playback.

As future work, we aim to develop a customizable feature mapping that will allow each user to define the sensory feedback that suits them best to perceive a given musical characteristic. Moreover, enhancing the system to process live audio in real-time would allow users to experience music as it is being performed.

Finally, this technology may prove useful also for blind and visually impaired individuals, if all visual elements are properly replaced with a haptic overlay, thus conveying a wider variety of musical features exclusively via tactile feedback.

8. ACKNOWLEDGMENTS

We acknowledge the support of the “Musical Metaverse: an inclusive Extended Reality platform for networked musical interactions” project (grant n. 2022CZWWKP) – funded by European Union – Next Generation EU within the PRIN 2022 program (D.D. 104 - 02/02/2022 Ministero dell’Università e della Ricerca) and of the MUSMET project funded by the EIC Pathfinder Open scheme of the European Commission (grant agreement n. 101184379). This manuscript reflects only the authors’ views and opinions and the Ministry, the European Union or the European Innovation Council cannot be considered responsible for them.

9. REFERENCES

[1] M. D. Fletcher, “Can haptic stimulation enhance music perception in hearing-impaired listeners?,” *Frontiers in Neuroscience*, vol. 15, p. 723877, 2021.

[2] J. A. Deja, A. Dela Torre, H. J. Lee, J. F. Ciriaco IV, and C. M. Eroles, “Vitune: A visualizer tool to allow the deaf and hard of hearing to see music with their eyes,” in *Extended Abstracts of the 2020 CHI Conference on Human Factors in Computing Systems*, pp. 1–8, 2020.

[3] H. B. Lima, C. G. D. Santos, and B. S. Meiguins, “A survey of music visualization techniques,” *ACM Computing Surveys (CSUR)*, vol. 54, no. 7, pp. 1–29, 2021.

[4] S. Papetti and C. Saitis, *Musical haptics*. Springer Nature, 2018.

[5] M. Sacchetto, M. Sangüesa, P. Bagnus, C. Nicora, and C. Rottondi, “Collection of design directions for the realization of a visual interface with haptic feedback to convey the notion of sonic grain to dhh students,” in *2023 4th International Symposium on the Internet of Sounds*, pp. 1–7, IEEE, 2023.

[6] A. Platt, J. A. Smith, W. D. Ross, *et al.*, *The Works of Aristotle*. Clarendon Press, 1912.

[7] R. Shamey, "Newton,(sir) isaac," in *Encyclopedia of Color Science and Technology*, pp. 1225–1230, Springer, 2023.

[8] M. Graves, *The Art of Color and Design*. McGraw-Hill Book Company, Incorporated, 1941.

[9] B. Hero and W. Garner, "On the relationship between color and music," *Leonardo*, vol. 12, no. 1, pp. 87–88, 1979.

[10] W. Kandinsky and M. Sadleir, *The Art of Spiritual Harmony*. Constable limited, 1914.

[11] J. L. Caivano, "Color and sound: Physical and psychophysical relations," *Color Research & Application*, vol. 19, no. 2, pp. 126–133, 1994.

[12] S. M. Smith and G. N. Williams, "A visualization of music," in *Proceedings. Visualization'97 (Cat. No. 97CB36155)*, pp. 499–503, IEEE, 1997.

[13] H. Lima, C. Santos, and B. Meiguins, "Visualizing the semantics of music," in *2019 23rd International Conference Information Visualisation (IV)*, pp. 352–357, IEEE, 2019.

[14] D. Malandrino, D. Pirozzi, and R. Zaccagnino, "Visualization and music harmony: Design, implementation, and evaluation," in *2018 22nd International Conference Information Visualisation (IV)*, pp. 498–503, IEEE, 2018.

[15] L. Cruz, V. Rolla, J. Kestenberg, and L. Velho, "Visual representations for music understanding improvement," in *Proceeedings of Music Technology with Swing: 13th International Symposium, CMMR 2017*, pp. 468–476, Springer, 2018.

[16] S. Feitl, J. Kreimeier, and T. Götzelmann, "Accessible electrostatic surface haptics: towards an interactive audiotactile map interface for people with visual impairments," in *Proceedings of the 15th International Conference on PErvasive Technologies Related to Assistive Environments*, pp. 522–531, 2022.

[17] L. M. Brown, S. A. Brewster, and H. C. Purchase, "A first investigation into the effectiveness of tactons," in *First joint eurohaptics conference and symposium on haptic interfaces for virtual environment and teleoperator systems. world haptics conference*, pp. 167–176, IEEE, 2005.

[18] F. Alves Araujo, F. Lima Brasil, A. Candido Lima Santos, L. de Sousa Batista Junior, S. Pereira Fonseca Dutra, and C. Eduardo Coelho Freire Batista, "Auris system: Providing vibrotactile feedback for hearing impaired population," *BioMed research international*, vol. 2017, no. 1, p. 2181380, 2017.

[19] F. Fontana, I. Camponogara, M. Vallicella, M. Ruzzenente, P. Cesari, *et al.*, "An exploration on whole-body and foot-based vibrotactile sensitivity to melodic consonance," in *Proceedings of the 13th International Conference in Sound and Music Computing, SMC 2016*, pp. 143–150, 2016.

[20] Tanvas, "Tanvastouch technology," 2024. Accessed: 2025-01-11. Available at `https://tanvas.co/technology`.

[21] A. Krishna, A. W. Luangrath, and J. Peck, "A review of touch research in consumer psychology," *Journal of Consumer Psychology*, vol. 34, no. 2, pp. 359–381, 2024.

[22] Tanvas, "Tanvastouch engine," 2024. Accessed: 2025-01-10. Available at `https://tanvas.co/resources/tanvastouch-basics`.

[23] R. Hennequin, A. Khlif, F. Voituret, and M. Moussallam, "Spleeter: a fast and efficient music source separation tool with pre-trained models," *Journal of Open Source Software*, vol. 5, no. 50, p. 2154, 2020.

[24] L. A. CA and C. Ancy, "Research on dnn methods in music source separation tools with emphasis to spleeter," *International Research Journal on Advanced Science Hub*, vol. 3, no. 6S, pp. 24–28, 2021.

[25] E. Schubert and J. Wolfe, "Does timbral brightness scale with frequency and spectral centroid?," *Acta acustica united with acustica*, vol. 92, no. 5, pp. 820–825, 2006.

[26] S. Prabavathy, V. Rathikarani, and P. Dhanalakshmi, "Classification of musical instruments using SVM and KNN," *International Journal of Innovative Technology and Exploring Engineering*, vol. 9, no. 7, pp. 1186–1190, 2020.

[27] M. Müller, *Fundamentals of music processing: Audio, analysis, algorithms, applications*, vol. 5. Springer, 2015.

[28] Irmas, "Irmasdataset," 2024. Accessed: 2025-01-07. Available at: `https://zenodo.org/records/1290750#.WzCwSRyxXMU`.

DOI: 10.61782/fa.2025.0558

FORUM ACUSTICUM EURONOISE 2025

MELOPAD, A PORTABLE DEVICE FOR MUSIC COMPOSITION BASED ON THE BELA AUDIO AND INTERACTION PLATFORM

Jasmin Thieme [1*] **Luis Molina-Tanco** [2]
[1] Shure DACH, Eppingen, Germany
[2] Telecommunication Research Institute (TELMA), Universidad de Málaga, Málaga, Spain

ABSTRACT

MeloPad is a prototype of a portable device designed for recording short musical annotations. Portability is key, allowing users to create music in any situation without requiring an external power source. The device includes interchangeable physical covers that simulate different instrument families. *MeloPad* detects the attached cover and dynamically adjusts its menu to offer sounds corresponding to the selected instrument family. It features an OLED display and buttons for selecting options. Users can practice a melody, record it, listen to it through headphones, and store it in the device's memory. When no cover is attached, previously recorded melodies can be accessed. The interaction and audio processing are managed using Bela, an open-source embedded computing platform designed for real-time audio and sensor-based applications. MeloPad is inspired by a MIDI peripheral developed by the French company Joué Play.

Keywords: *portable synth, Bela audio, i2c interface, 3d prototyping*

1. INTRODUCTION

The primary goal of this project, part of a bachelor's degree in Sound and Image Engineering (a four-year program), is to develop *MeloPad*, a fully functional prototype of an interactive electronic device that integrates knowledge in audio signal processing, digital circuit design, programming, and 3D modelling.

MeloPad is designed to capture spontaneous musical ideas anytime, anywhere, without relying on a mobile phone or the limitations of voice recording. Musical inspiration often strikes at inconvenient moments -on a train, while walking, or travelling- when there is no easy way to record a melody. While a phone's notepad or voice recorder can help, humming a tune rarely does justice to how it sounds in one's mind. *MeloPad* provides an intuitive alternative, offering a selection of virtual instruments and adjustable frequency ranges to accurately capture musical ideas. It features interchangeable physical covers called "*sábanas*" (sheets) which mimic different instrument interfaces. The device detects the placed sheet and adjusts its sound accordingly. Users can record, play back, and save their melodies for later use.

MeloPad draws inspiration from the *Joué Play* MIDI controller by the French company *Joué Music Instruments* [1]. Similar to Joué Play, which uses swappable, velocity-sensitive silicone pads to represent different instrument layouts, *MeloPad* employs interchangeable sheets to simulate different instrument interfaces such as a piano, string instrument, or percussion set. This physical interaction enhances the user experience, making the device more intuitive. Unlike Joué Play, which requires external power and must be connected to a tablet or similar device, *MeloPad* is fully autonomous, running on a rechargeable battery. A small OLED screen and three buttons allow for intuitive navigation and selection of options.

MeloPad is built around *Bela* [2], a real-time audio processing platform with low-latency and a user-friendly development environment, designed for musicians and

[*] ***Corresponding author***: *Jasmin Thieme, jasminth168@gmail.com*
Copyright: *©2025 First author et al. This is an open-access article distributed under the terms of the Creative Commons Attribution 3.0 Unported License, which permits unrestricted use, distribution, and reproduction in any medium, provided the original author and source are credited.*

developers with intermediate programming skills. To keep the device compact and portable, we chose *Bela Mini* [3], a smaller version that retains all essential functionality while reducing the overall size.

2. USE CASE ANALYSIS

To define the functionality of *MeloPad*, we have identified three main use cases that ensure a complete user experience: recording melodies, accessing stored recordings, and transferring them to an external device. Additionally, we analyse the operational context in which users interact with the system, detailing the different modes of operation and the interfaces involved. Finally, we outline the key functional requirements that *MeloPad* must meet to ensure seamless recording, playback, and file transfer, as well as an intuitive and portable user experience.

2.1 Use cases

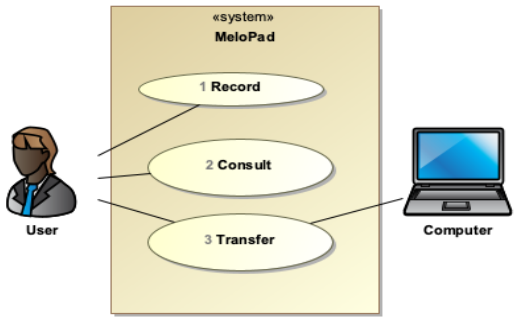


Figure 1. *MeloPad* Use Cases.

The system supports the core use cases shown in Figure 1 and explained as follows:
1. **Record:** The user selects an instrument and an octave range, practices the melody, and starts recording. The system captures the played notes and stores them as a .wav file in *MeloPad*'s memory.
2. **Consult:** Users can access previously stored melodies, play them back through headphones, and delete them if desired.
3. **Transfer:** By connecting *MeloPad* to a computer via USB, users can access the stored .wav files, copy them, and delete them using a file explorer interface.

Each use case has specific preconditions. For recording, a capacitive sheet must be correctly placed, and headphones must be connected. For accessing stored recordings, the sheet must be removed. Transferring files requires a USB connection to a computer.

2.2 Operational Context

MeloPad interacts with the user through various interfaces. The capacitive sheet detects touch input, while buttons allow navigation through menus and function selection. The system provides feedback through an integrated display and audio output via a 3.5mm headphone jack.
Key system interactions include:
• **User inputs**: Touching the capacitive sheet (note input), pressing buttons (navigation and controls), and adjusting the volume potentiometer.
• **System outputs:** Displaying information on the screen, playing audio through headphones, and allowing USB file transfer.
• **External connections:** The system connects to a computer for transferring recordings and supports battery charging via micro-USB.

MeloPad automatically detects whether a capacitive fabric is installed or not. If present, it enters Record Mode, allowing users to generate and record melodies. If no fabric is detected, the system switches to Consult Mode, where users can browse and play stored recordings. When connected to a computer, it enters Transfer Mode, enabling file management via micro-USB.

2.3 Functional and nonfunctional requirements

MeloPad's functionality is defined by the following core requirements:
• R1: **Audio Output** – The system must generate and play sound through headphones.
• R2: **Sound Configuration** – Users should be able to adjust volume (R2.1), select virtual instrument sounds (R2.2), and define a frequency range (R2.3).
• R3: **Portability** – The system must be portable, including a rechargeable battery (R3.1), weighing no more than 1kg (R3.2), and having a maximum dimension of 30 cm (R3.3).
• R4: **Capacitive Sensing** – *MeloPad* must detect user interactions through capacitive sensors.
• R5: **Recording Functionality** – Users should be able to start (R5.1) and stop (R5.2) recordings via button presses.
• R6: **Playback and Management** – The system must support playback (R6.1), deletion of a recent recording (R6.2), browsing stored files (R6.3), and removal of saved recordings (R6.4).
• R7: **Display Interface** – A screen must provide visual feedback and system status information.
• R8: **File Transfer** – *MeloPad* should allow users to transfer recordings to a computer via an integrated file management application.

These requirements have guided the development and verification of the prototype to ensure it meets the needs of the end user.

3. TECHNOLOGY AND DESIGN CHOICES

The *MeloPad*'s functionality is achieved through a combination of hardware components and developed software. The core of the device is the Bela Mini platform, chosen for its low-latency audio processing and compact size. Bela Mini runs Linux and is well-suited for the creation of interactive musical applications. Its development is supported by a user-friendly Integrated Development Environment (IDE) [4] accessible via the web, offering tools for coding, file management, and real-time audio visualization through a virtual oscilloscope.

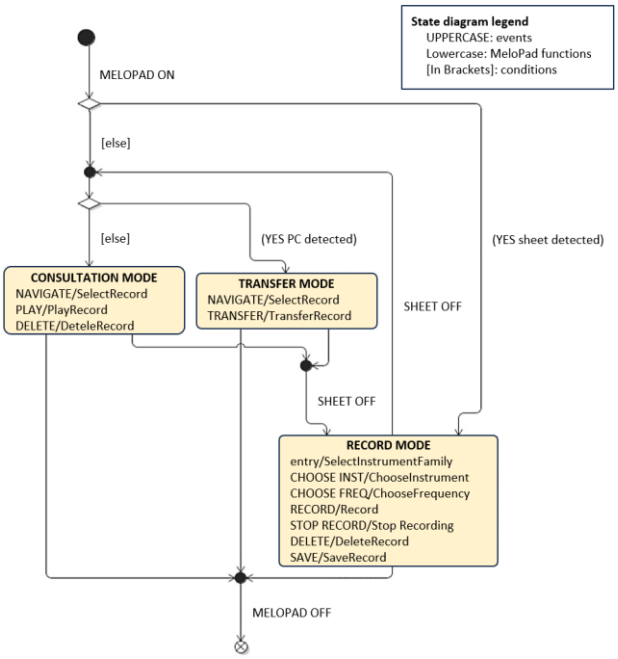


Figure 2. *Melopad*'s state diagram.

The whole hardware and software design was started after completing the first phase of this project, where the use cases and the system states were specified. Based on Figure 2 the next step was to start with the hardware and software design following the chosen requirements.

3.1 Hardware design

For user interaction and sound generation, *MeloPad* utilizes several key hardware elements:

• Trill Craft Sensor: The device employs a Trill Craft capacitive sensor [5]. This sensor, developed by Bela, features thirty inputs, allowing for the connection of conductive materials to detect variations in capacitance caused by touch. In *MeloPad*, this sensor is crucial for interpreting the user's input on the interchangeable "sábanas".
• Interchangeable "sábanas" (Sheets): A key innovative aspect of *MeloPad* is the use of physically interchangeable covers called "sábanas". These sheets are designed to simulate the interfaces of different musical instruments, such as a piano. *MeloPad* can detect the placed sheet through a detector circuit, and the software then offers corresponding instrument sounds in a menu. For example, a "sábanas" simulating an electronic piano was created to validate the concept. The connection of the "sábanas" is detected by the Bela, which then determines the appropriate instrument.
• OLED Screen and Buttons: A small OLED screen is integrated into the device to display basic options related to the placed "sábanas" and general information. Navigation through menus and selection of functions are facilitated by three buttons.
• Potentiometer: A potentiometer is included to allow the user to adjust the volume level of the audio output.
• Audio Output: Audio generated by *MeloPad* is outputted through a 3.5mm mini-jack stereo connector for headphones.

The communication between the Bela Mini and peripherals like the OLED screen and the Trill Craft sensor relies on the I2C (Inter-Integrated Circuit) serial communication protocol. I2C uses only two signal lines (SDA and SCL) for data transmission and synchronization. Each I2C device on the bus has a unique address, allowing the Bela (as the master device) to communicate with each peripheral individually. In *MeloPad*, the OLED screen has an address of 0x3c, and the Trill Craft sensor's address is 0x30.

For the physical design of *MeloPad*, the 3D modelling programme Blender was used to find the appropriate design and create the 3D printable model.

3.2 Software design

On the software side, the project is primarily developed using C++ within the Bela IDE. The software structure follows the standard Bela program flow with setup(), render(), and cleanup() functions. Several Bela-specific libraries are utilized, including:
• Bela.h: Provides access to core audio settings and input/output buffers.

• Trill.h: Enables communication with and control of the Trill Craft sensor.
• AudioFile.h: Facilitates the reading and writing of audio files to the device's memory, using the AudioFileUtilities namespace with functions like load() and write(). The setSamples() function is used for saving the generated melody, and loadMono() is used for reading from memory.

The project incorporates the Synthesis ToolKit (STK) [6], an external C++ library for real-time audio synthesis and processing. STK provides a wide range of virtual instruments, which are utilized in *MeloPad* to generate the different instrument sounds selectable by the user. Integrating STK required installing the library via the Bela's Ethernet connection (on a regular Bela board, as Bela Mini lacks Ethernet) and learning its API. The general structure for using STK involves creating instrument objects, setting their sample rate (Stk::setSampleRate(BelaSampleRate)) and frequency (instrument->setFrequency(frequency)), and using the sound generating functions: noteOn(frequency, amplitude) which generates a note but does no send it to the output; tick() to enable real-time audio production by advancing a sample on each call; and noteOff(amplitude) to turn off the generated note adjusting the fade out.

The software architecture also includes custom-developed classes like Display and Teclado (Keyboard) to organize the code for screen updates and sound generation, respectively. A Debouncer class, adapted from an open-source Bela resource, is used to handle button presses and prevent misreading due to bouncing. The U8g2 library is employed for controlling the OLED display via I2C. The entire software is configured to run automatically upon Bela Mini startup. It is possible to find the whole software on a Github repository[1].

This combination of Bela Mini's real-time audio capabilities, the Trill Craft sensor, interchangeable "sábanas" for varied user interfaces, and the STK library for sound synthesis forms the technological foundation of the *MeloPad* prototype.

4. DEVELOPMENT CHOICES AND PROTOTYPE

This project has involved a major development effort as it is a complete prototype of a software-hardware product. It was inspired by the Joué device [1], the first of the class of synthesisers whose keyboard is not fixed but interchangeable.

[1]Github Repository of *MeloPad*'s Software: https://github.com/JasminThieme/MeloPad

4.1 Mechanical design decisions

To minimize the size of *MeloPad*, the Bela Mini was chosen, which is more compact compared to the standard Bela version (56 x 35 x 21 mm vs. 87 x 54 x 27 mm). The Bela Mini is suitable for this project as no analogue outputs (such as those for speakers) are needed, which are exclusive to the standard Bela.

Initially, a touchscreen was considered for menu navigation, but it was quickly replaced with buttons due to the complexity and cost involved. Nevertheless, a screen was kept to display information and show the options activated by the buttons. After researching various screen sizes, the first version of *MeloPad* was created, which initially featured a small screen around one inch in size. This option would have required many push buttons, which would have made the design bulky. As a result, a design without a screen was proposed, using an LED for each button. However, this idea was soon discarded as one of the goals of the project was to implement a visual interface.
After extensive searching, a suitable 2.42-inch screen was found, leading to the second design version: five buttons with individual functions. Finally, the number of buttons was reduced to three and their functionality would change depending on the options displayed on the screen. This resulted in a complete implementation of both the screen and buttons.



Figure 3. *MeloPad* final 3D-design.

The choice of buttons and the potentiometer was based on a compromise between three factors: usability, space, and design, as the goal was to minimize the size while achieving an elegant, simple and intuitive prototype. After acquiring the chosen screen and buttons, the final design was adjusted as shown in Figure 3. The 3D model created in Blender has

been shared on a Github repository[2] as well to complete the design and for future consultation.

[2]Github Repository of *MeloPad*'s 3D Model:
https://github.com/JasminThieme/MeloPad-3D

4.2 Tests and implementation of "sábanas" (sheets)

The Trill Craft capacitive sensor from Bela was chosen due to its ability to create and customize sensors. With 30 capacitive inputs, it allows for the development of a wide range of projects in various sizes and applications. To ensure the proper operation of *MeloPad*, tests were carried out with different conductive materials, and the best option was to use a wire without the insulating plastic, as it has a bigger conductive surface and would be more sensitive to touch.

Two types of sheets were planned to be created: one to mimic a string instrument and another for a keyboard. The keyboard design was the simpler of the two, requiring one position per note. However, the string instrument design was more complicated due to the number of notes involved. Initially, multiplexing the strings to generate tones based on the combination of cables touched was considered, but it was discarded due to the limited position detection capability of the Trill Craft sensor. Eventually, one idea was to assign each guitar tone to an input on the sensor, this allowed for five frets to be covered with a single sensor, and by combining two sensors, a complete guitar neck could be built. The final test for the guitar sheet was based on three frets and three strings, with the sensitivity adjusted to ensure proper response. Due to time constraints, the guitar sheet implementation was discarded, and only the piano sheet was completed.

For the piano sheet, a simple design was used, with one cable per key to detect the capacitance variations. The software implementation utilized the equal temperament chromatic scale, where each semitone is calculated based on the twelfth root of two to calculate the frequencies of the two octaves of notes as in Eqn. (1):

$$f_n = f_0 * (\sqrt[12]{2})^n \quad (1)$$

where n is the note number relative to the fundamental, f_0.

4.3 Power supply for *MeloPad*

One challenge in designing *MeloPad* was that the same USB-micro connector of Bela Mini would be used for both power and connection to external devices. This means that the rechargeable battery and the USB-micro connector for connecting to a computer needed to share the same USB-micro port on the Bela.

The solution was to implement a sliding switch. In one position, the switch connects the Vcc input of the Bela to the Vcc of the rechargeable battery. In the second position, it connects the Vcc input from the external USB-micro connector, to connect an external device. For data transmission, the cable connected to the Bela needs to have four wires: GND, Vcc, Data+, and Data-, therefore the cable connected to Bela is a 4-wired one. For powering the device, only the first two wires are used as shown in Figure 4.

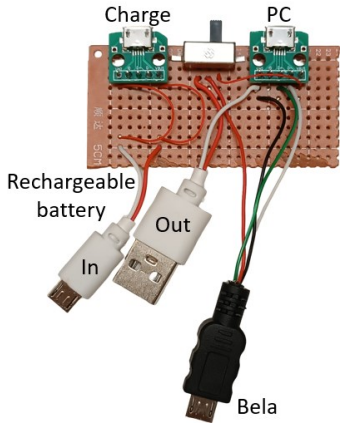


Figure 4. Power and connections piece.

The solution was to implement a power and connection piece which includes two USB-micro female connectors exposed to the outside, one micro-USB male connector with 2 wires for powering the external battery, one with 4 wires to connect the Bela, and a USB-A connector for charging the external battery. This set of components is housed inside the case.

4.4 Implementation of the display

The *MeloPad* features a 2.42-inch OLED display with a resolution of 128x64 pixels, offering a high contrast with white text on a black background. OLED technology provides individual pixel illumination, resulting in clearer visuals compared to LCD screens. The display serves as the main interface for user interaction, where information is displayed, and options are selected.

The screen shows various states depending on the action being performed. For the use case Record these software states include:

- **INITIAL**: Displayed when the device is powered on.

- **CHOOSE_INST**: The user selects an instrument (e.g., Rhodes, Hammond, Wurley) for the piano sheet.
- **CHOOSE_OCT**: The user chooses the octave for the selected instrument, adjusting the frequency range.
- **INFO**: Displays the current settings. Audio output is generated.
- **RECORD**: Activated when the user starts recording their melody.
- **STOP_REC**: Shown after recording ends, with options to save or retry.
- **SAVE_MEL**: Displays a confirmation message when the melody is saved.

In the Consultation use case (when no sheet is detected), the display shows a file list where users can play, navigate, or delete recordings. Screens for this process include:

- **LISTA**: The file list. One file per screen. Options to choose *next*, *play*, *previous*.
- **PLAY**: Displays the playback state. Option to delete the record.
- **ELIMINADO**: Confirms deletion of a recording.

This OLED display is crucial for guiding the user through different interaction stages, ensuring a seamless user experience while maximizing visual clarity.

4.5 Final prototype design

The distribution of the components inside the *MeloPad* case has been challenging as the components almost entirely occupy the available volume of the case, resulting in a very compact space, see **Figure 5**.

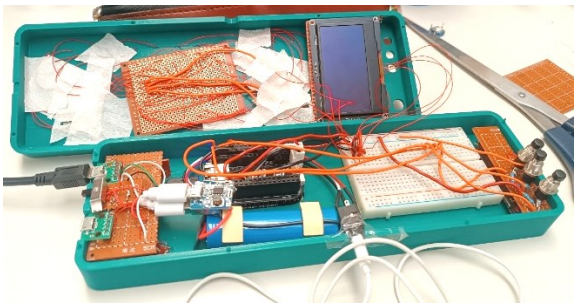


Figure 5. Components distribution in *MeloPad*'s case.

In the upper half of the case, the screen, capacitive sensor, and the cables connected to the sensor are placed. These wires are exposed to the outside through small holes visible in the 3D model, Figure 3. The cables for the sensor needed to be organized in such a way to avoid contact between them and minimize potential interference. The use of rigid cables made the ideal arrangement challenging. However, by maintaining the insulating plastic, interference was kept to a minimum, even when the wires were in contact.



Figure 6. Final look of the *MeloPad* prototype.

The final prototype looked compact and clean as shown in Figure 6. The piano sheet fit on the sensors area and the buttons would let one interact with the menu shown on the screen. Through the headphones the notes would sound when a position is being touched on the piano.

5. RESULTS AND DISCUSSION

5.1 Functionality and performance of the prototype

The *MeloPad* prototype demonstrated satisfactory functionality in its Record and Consultation modes, allowing the generation, recording and playback of sounds through an intuitive screen-based interface and buttons. The portability of the device, thanks to its compact design and rechargeable battery, meets the stated requirements. However, limitations were identified in the file deletion function and data transfer, which led to omitting the implementation of the third use case, Transfer.

5.1.1 Validation of implemented use cases

Verification tests showed that the *MeloPad* prototype largely meets the functional requirements set. In Record mode, the user interface based on the OLED display and buttons allowed an intuitive selection of instruments and octave ranges. Interaction with the capacitive sensors via the piano "sheet" generated accurate sounds and the recording function worked properly, allowing melodies of up to 20 seconds to be captured, played back and stored in Bela's memory.

In Consultation mode, navigation through the list of recordings was seamless, with options for playing and deleting files. However, a limitation was identified in the file deletion function, as files persisted in memory despite confirmation of deletion. This aspect requires improvement of the software.

5.1.2 Performance and Portability

The prototype demonstrated excellent transportability. Its compact (24.5 cm x 8 cm x 3.5 cm) and lightweight (350 grams) design makes it easy to carry and use in different environments. The internal rechargeable battery provides autonomy, eliminating the need for an external power supply.

5.2 Areas of improvement

The *MeloPad* project succeeded in developing a portable, self-standing device with an innovative design, fulfilling the main idea of creating a modular synthesiser with interchangeable "sheets" to simulate different instrument families. The intuitive interface and the ability to record and playback melodies enhance the user experience.

However, areas for improvement and future work were identified:

- **String Sheet**: Study of the layout of the sensors and optimisation of the design to accommodate as many inputs as necessary.
- **Sheet Material**: Explore more durable and tactile materials for the sheets.
- **Hardware Size**: Explore smaller microcontrollers to reduce the volume of the prototype.
- **Internal Cables**: Replace the internal rigid cables with flexible cables to improve durability and avoid disconnections.
- **Safe Shutdown**: Implement a safe shutdown button to protect Bela's operating system, avoiding data corruption.
- **Record Deletion**: Implement a record deletion function that allows users to delete files.
- **Transfer**: Develop a desktop application that allows users to transfer, consult and delete files from *MeloPad*.

5.3 Conclusion

The *MeloPad* project represents a progress in the creation of portable and modular digital musical instruments. Proposed improvements in future work could make *MeloPad* an even more versatile and accessible instrument for musicians and sound experimentation enthusiasts.

6. REFERENCES

[1] A. Douglas, "Joué Play MIDI controller review: Free your fingers and format", Popular Science, Sep. 30, 2022. [Online]. Available: https://www.popsci.com/gear/joue-play-midi-controller-review/. Accessed: Mar. 2025.

[2] Bela.io, "Craft beautiful interaction". Available: https://bela.io/. Accessed: Mar. 2025.

[3] Bela.io. "Bela Mini". Available: https://learn.bela.io/products/bela-boards/bela-mini/. Accessed: Mar. 2025.

[4] Bela.io. "Get to know the IDE". Available: https://learn.bela.io/get-started-guide/get-to-know-the-ide/. Accessed: Mar. 2025.

[5] Bela.io. "Working with Trill Craft". Available: https://learn.bela.io/tutorials/trill-sensors/working-with-trill-craft/#connecting-to-trill-craft. Accessed: Mar. 2025.

[6] Perry R. Cook and Gary P. Scavone, "The Synthesis ToolKit in C++ (STK)", 1995-2023. Available: https://ccrma.stanford.edu/software/stk/. Accessed: Apr. 2025.

DOI: 10.61782/fa.2025.0114

FORUM ACUSTICUM EURONOISE 2025

ALFONSO AND THERESA: MERGING TRADITIONAL LUTHERIE WITH MODERN ELECTRONICS IN THE DESIGN OF AN EXPANDED LUTE AND CONTRABASS

Celeste Betancur Gutiérrez[1*] **Luna Valentin**[1]
[1] CCRMA, Stanford University, USA

ABSTRACT

This paper details the parallel engineering and building processes for an electric and extended lute (Alfonso) and an electric and extended contrabass (Theresa). We illustrate how the fusion of craftsmanship, acoustic tradition, and modern electronic design can redefine the sonic possibilities of heritage instruments and traditional lutherie. We begin by discussing the initial concept and design phases, where musical and aesthetic considerations guided the instruments' form, function, and ergonomics. This step also relied on acoustical measurements made on a traditional lute from the Stanford collection and a traditional European contrabass. Next, we delve into the woodworking and carving techniques used to shape each instrument's body, discussing the role of material choice in achieving desired tonal and structural properties, and the accessibility of such techniques for novice instrument makers. Finally, we examine our approach to integrating pickup systems of various types, real-time signal processing, and onboard electronics. The instruments can produce a variety of signals that then can be remapped into control, audio, or both, ultimately making them hyperinstruments.

Keywords: *lutherie, expanded instruments, electric instruments*

**Corresponding author*: celeste@ccrma.stanford.edu.
Copyright: *©2025 Celeste Betancur Gutiérrez et al. This is an open-access article distributed under the terms of the Creative Commons Attribution 3.0 Unported License, which permits unrestricted use, distribution, and reproduction in any medium, provided the original author and source are credited.*

1. INTRODUCTION

The contrabass originates from the creation of both the Violone and the Violin/Cello, which designs merged during the 16th century into the modern contrabass we know today [1]. In the case of the lute, there are multiple stories and traditions, but the instruments we still call lutes today are from the same era, and were made in Europe too. These two instruments kept their basic shape almost unmodified for centuries.

We found ourselves playing traditional instruments in contemporary ensembles, improvisations, and jams with many other players with different tools, from traditional instruments like ours to modern midi controllers and new instruments. Being computer musicians with knowledge in acoustics, hardware and software development, we felt our practice was fragmented into multiple compartments. On one hand, we were using cutting edge algorithms in our own research for DSP or AI research and on the other hand we were playing traditional instruments, although expanded techniques on the instruments were fully incorporated in our practice already.

2. CONCEPT AND DESIGN

The project of building expanded instruments began as a conversation between the two authors, where we realized that our musical practice could benefit from instruments that combined traditional playing techniques with digital skills like software and hardware design. Luna was exploring archeo-acoustics, and Celeste was taking a graduate course in musical acoustics as part of her research. With guidance from Prof. Marc Rau (Musical Acoustics) and Prof. Sasha Leitman (Physical Interaction Design for Music), we started by measuring a lute made by a Belgian

luthier from the Harry R. Lange Collection of Musical Instruments and Bows at Stanford University.

2.1 The Lute, Celeste

I conducted a two-hour interview with Herbert W. Myers, the collection's curator, to learn more and discuss initial ideas. This conversation helped me choose this particular lute from the collection, which also includes several others. The choice was based on mainly two reasons: the quality and good sound of the selected lute and the more standardized shape that is not a common denominator for this family of instruments.

The design kept the lute's traditional L-shaped head while modifying other aspects for practicality and playability. The scale was shortened early on to accommodate metal strings, which introduced extra tension while maintaining a tuning similar to the original lute. For the body, I chose a more modern, ergonomic shape inspired by electric guitars, balancing tradition with contemporary aesthetics and functionality, also the resonant box was replaced by a solid body architecture.

It is important to note that modern lute construction is relatively rare, as the instrument has largely been replaced in contemporary musical practice. While some luthiers continue to refine traditional techniques and make improvements ([2]), our approach differed in that we aimed to introduce fundamental structural changes rather than merely refine existing methods.

2.2 The Contrabass, Luna

My goal was to design an electric contrabass that preserves key acoustic properties while improving transportability and ergonomics. I wanted to integrate a resonant cavity to maintain the fundamental response of an acoustic instrument, allowing natural amplification while reducing the instrument's physical volume for easier transport.

Unlike most commercial electric and custom upright basses [3], which lack sides and compromise bowing technique and upper-register access, this design includes a detachable side structure for improved ergonomics. Inspired by models like, this custom made bass and the Yamaha electric contrabass [4]—but with a more open, documented approach—this instrument balances classical playability with modular expandability.

The design process began with precise documentation of my own classical contrabass, a versatile instrument built in the 1950s in Southeastern Europe for traditional music playing and reworked for classical performance 15 years ago approximately. Its adaptable design, suited for both classical and jazz settings, served as a foundation for ensuring this new instrument retained traditional playability while enabling extended modifications.

3. CONSTRUCTION

3.1 The Contrabass, Luna

To streamline the process and accommodate my lack of prior luthiery experience, I started with a kit for certain key components, Fig. 1. The neck and fingerboard, both crucial for playability and precision, remained unmodified. The ebony fingerboard, included in the kit, was a cost-effective choice and avoided the challenge of carving a perfectly regular surface. The bridge also came precarved in a rough form, requiring additional thinning and height adjustments.

The hardwoods used for the rest of the instrument pieces were bought in a hardwood store in Oakland, CA, and selected under Dr. Mark Rau's guidance [5].

Please, note the contrabass that served as a model is a 5/8 sized contrabass, fitting my relatively short stature. The resulting electric contrabass is also between 5/8 and 3/4 sized.

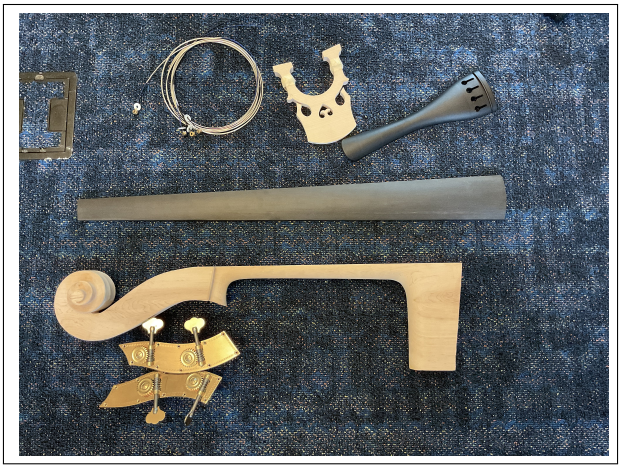


Figure 1. Pieces bought for the construction.

3.1.1 Designing and Carving the Body

The body was built as a minimalist resonant cavity, often designated as "the coffin", see Fig. 2. Its length was reduced to the bare minimum— just enough to maintain

string vibrating length and accommodate a shortened tailpiece. Although my traditional contrabass cavity measures 110 cm, I determined that a functional version could be reduced to 88 cm.

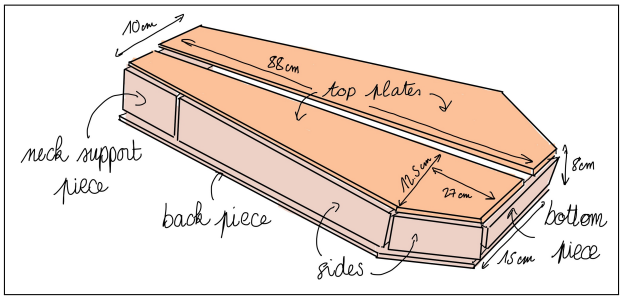


Figure 2. Schematics of the body of the electric contrabass.

I drew the shape of the coffin-looking resonnant cavity by projecting a scaled image of my acoustic contrabass on a piece of paper and then drawing the resonnant cavity, respecting minimum dimension previously calculated. The maximum width of the body is 25 cm, at the height of the bridge (27cm from the bottom of body) and fits the bridge wideness (16cm) plus extra centimeters to allow the top plate to vibrate with the bridge.



Figure 3. Photo of the body of the electric contrabass before final closure.

3.1.2 Neck Attachment

Joining the neck to the body was one of the most delicate steps, see Fig. 5. The neck insert has a highly specific shape, and my design choices reduced the contact area between the neck and body. To compensate, the neck was secured with a thick lag bolt after insertion, see Fig. 4.

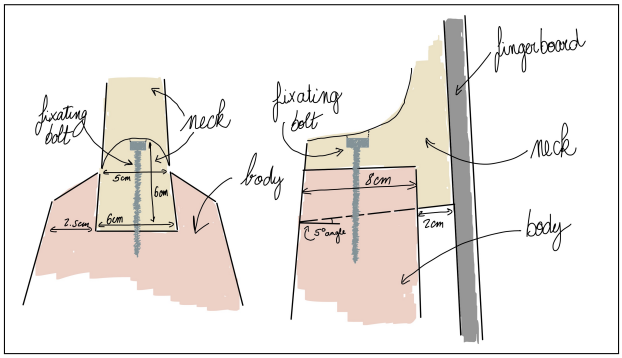


Figure 4. Schematics of the neck attachment.



Figure 5. Photo of the neck attachment hole.

A key structural parameter was the neck angle, critical for achieving the correct fingerboard elevation. Based on measurements from my classical contrabass, I determined that the neck needed a +5° angle between its base and the top plate. This was derived from a 2 cm clearance between the top plate and the fingerboard at its highest point and an 8 cm clearance at the lowest end, ensuring the right setup for bowing and playability. Recarving a hole in the body to create the space for the neck ended up being a complicated task that took over 6 hours to fit the shape of the neck nicely. This process could have been anticipated.

3.1.3 *Crafting the Tailpiece and Sides*

After assembling the main structure, the tailpiece and sides became more of an artistic handcrafting process than strict engineering. The tailpiece, based on my model contrabass but shortened to 14 cm, was hand-carved from zebrawood, repurposed from leftover lute-making materials, Fig. 6. The sides, cut from maple, were designed as a copy of the shape of my acoustic contrabass, in order to maintain ergonomic capacity. Retrospectively, this design poses functional issues and could be improved:



Figure 6. Tailpiece.

- Attachment system: The bolts and inserts are sturdy but impractical for quick assembly/disassembly.
- Weight issues: The maple shoulders are almost as heavy as the entire contrabass, suggesting the need for lighter materials (e.g., carbon fiber) to optimize portability.

These pieces were not the most time consuming but represented 4 days of work including cutting, times of setting for pieces glued together, shaping and sanding.

3.1.4 *Final Assembly and Adjustments*

The last steps—adding tuners, gluing the fingerboard, shaping the bridge, installing the nut, and fitting the endpin support—were relatively straightforward (6 extra days). The wood was finished with shellac varnish. While a professional luthier could refine certain aspects to improve playability, Theresa meets my envisioned design goals, balancing acoustic integrity, transportability, and modularity in my first instrument-making venture, Fig. 7



Figure 7. Final instrument

3.2 The Lute, Celeste

Unlike Luna, who had no experience in luthiery, I had prior knowledge from previous projects, including building electric bass guitars and electric guitars of various scales, shapes, and budgets. Additionally, I had some experience with general woodworking and carpentry, skills I acquired from my grandfather, a master carpenter with over 70 years of experience in Medellín, Colombia. From him, I learned numerous techniques and refined my craftsmanship so much so that I even named the lute in his honor.

3.2.1 *Measurements*

To initiate the process, I carefully measured the dimensions of the reference lute, focusing particularly on its scale length which is the critical distance between the nut and the saddle that determines fret spacing along the neck. The acoustic lute follows an international standard scale of 62 centimeters. Notably, despite its total length of 74 cm, its neck is relatively short, measuring only 24 cm, which allows for just 12 frets. Wanting to accommodate more frets, I opted for a longer neck and a greater neck-to-body ratio, ultimately designing an instrument that could fit 18 fret spacings.

When adapting the instrument to an electric version, I made a deliberate choice to shorten the scale length and reduce the overall dimensions. This decision was primarily influenced by the weight of the solid wood body in an electric lute and the tension of the metal string compared to the gut or nylon ones. Unlike its acoustic counterpart,

the denser construction significantly increases the instrument's mass, making it necessary to shorten the overall length for ergonomic playability.

Table 1. *Comparison between both lutes.*

Measure	*Acoustic*	*Electric*
Scale	$62cm$	$23 - 1/4in$
Tracks	$9(8*2, 1*1)$	$7(5*2, 2*1)$
Frets	12	18
Lenght	$74cm$	$69cm$
Neck	$24cm$	$37cm$
Shape	*Pear*	*Telecaster*

However, despite the reduced scale and total length, the neck of my electric lute extends to 37 cm—longer than that of the acoustic version. This extended neck allows for additional frets, aligning with the design principles commonly found in modern electric guitars.

By extending the fretboard, I aimed to enhance the instrument's versatility and provide a familiar playing experience for musicians accustomed to contemporary electric guitar designs, which is my personal experience although I also play the traditional lute.

3.3 Wood and first cuts

I chose zebra wood for the body, flamed maple for the bridge and fingerboard, mahogany for the head and neck, and ebony for the nut. The hardwoods, sourced from Oakland, CA, were selected with Dr. Mark Rau's guidance, balancing weight, stiffness, aesthetics, and cost.

Since the body wood wasn't the right size, I cut it into four pieces to create a mirrored pattern, planed them down, and hand-finished the seams for symmetry, Fig. 8

For the neck and head, I measured a 19-degree angle to achieve the L-shaped head, cut the pieces with a band saw, and glued them together—taking about two hours for prep and 24 hours for setting. I then routed the truss rod channel and finished with extensive sanding and planing, Fig. 9

3.4 Shaping

Once all the wood pieces were ready, I hand-drew designs directly onto the surface of the body wood, using the natural zebra wood patterns as inspiration. The flowing, wavy lines mirrored my own tattoos, giving the head and body a unique, organic aesthetic. Ultimately, the body shape took

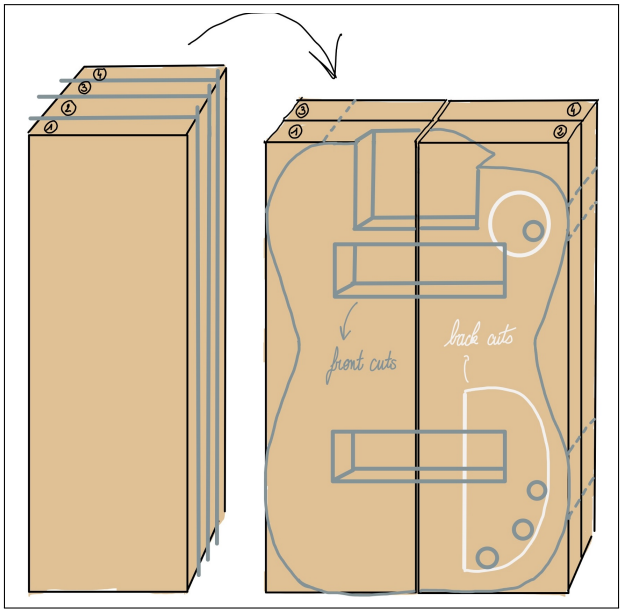


Figure 8. Crafting of Alfonso's body.

on a form reminiscent of Fender Telecasters, blending traditional craftsmanship with a modern touch.

Shaping the instrument required a jigsaw, electric sander, chisel, and hand router, making it the most labor-intensive stage—over 16 hours across four sessions, plus two full days dedicated to carving the neck's back arc. The fingerboard radius was carefully shaped by hand using a 3D-printed template from my instructor and sandpaper, a process that took two continuous hours. The bridge, crafted from flamed maple, was reinforced with epoxy resin due to minor imperfections, while the nut and saddle were shaped with an electric sander, using the same radius template for precision.

3.5 Assembly process and all related to strings

With all components prepared, I routed the channel for the saddle while considering the best way to attach the neck to the body. After weighing the options—adhesive bonding or screws—I chose screws for easier disassembly, making transportation, especially by plane, more practical.

Once this step was complete, I carefully calculated the string positioning, ensuring proper spacing and height relative to the fingerboard. Gradually tuning the strings helped apply the correct tension to the structure, preparing the lute for its final shape Fig. 10.

At this stage, the instrument was not yet fully com-

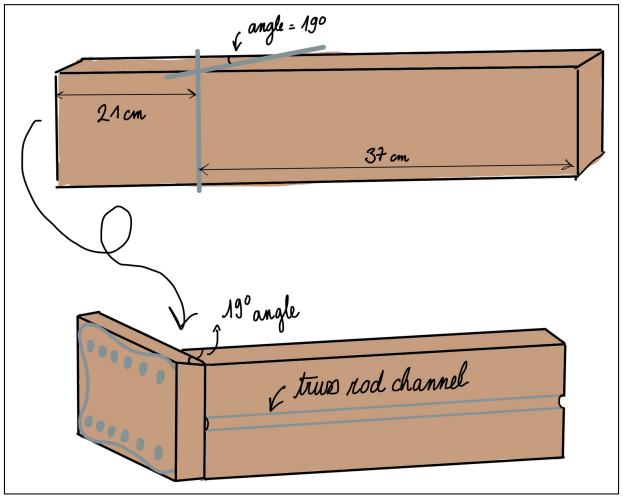


Figure 9. Crafting of Alfonso's body.



Figure 10. Final Lute Instrument

plete; the electromagnetic pickup and other essential components still needed installation, and no finishing had been applied.

4. ELECTRONICS - EXPANDED INSTRUMENTS

4.1 The Contrabass

Theresa was conceived not merely as an electric contrabass, but as an extended instrument—one that expands the performer's expressive and gestural vocabulary by integrating digital sensing and real-time sound processing. While retaining the tactile and acoustic qualities of a traditional instrument, the instrument enables a hybrid mode of performance that merges the physical gestures of instrumental playing with programmable interaction [6], [7], [8].

To support a broad spectrum of sonic characteristics, Theresa is equipped with two complementary pickup systems. An electromagnetic pickup, positioned at the end of the fingerboard, offers a focused, traditional amplified bass tone. In parallel, piezo pickups mounted at the bridge capture a richer dynamic and spectral response. These signals are compatible with standard bass amplification setups. Future iterations may include the addition of a condenser microphone inside the resonant cavity, inspired by systems like the Yamaha Silent Bass, to further recover the instrument's natural resonance and spatial depth.

Beyond this conventional amplification, the instrument integrates a modular electronic system designed to augment performer interaction and sound control. Installed on the left shoulder, the mounting platform hosts a range of swappable sensor modules and microcontrollers, configured to be easily accessed by the performer's right hand during performance (Fig. 11). The platform itself is designed for quick removal and interchangeability, reinforcing the concept of a reconfigurable and adaptive instrument.

The first implementation of this system includes buttons, rotary knobs, capacitive touch sensors, and motion-sensing elements such as accelerometers, gyroscopes, and compasses, all interfaced through an Arduino Uno [9]. These sensors communicate with a Max/MSP patch, allowing real-time mapping of gestural input to a variety of audio processing functions, including filtering, modulation, spatialization, and granular effects. In some cases, control parameters may also drive higher-level compositional structures, enabling a performative blending of instrumental play and live electronics.

This approach positions the instrument within the lineage of extended instruments—tools that transcend traditional definitions by embedding computational and gestural responsiveness within their design. For example, subtle tilts of the instrument can control spatial diffusion, while touch gestures on capacitive sensors may trigger or morph effects such as tremolo, distortion, or grain-based textures, extending the timbral range far beyond what is physically possible on an acoustic contrabass.

Importantly, this modular and expandable architecture supports ongoing development. While currently deployed on a single shoulder, the system is structurally pre-

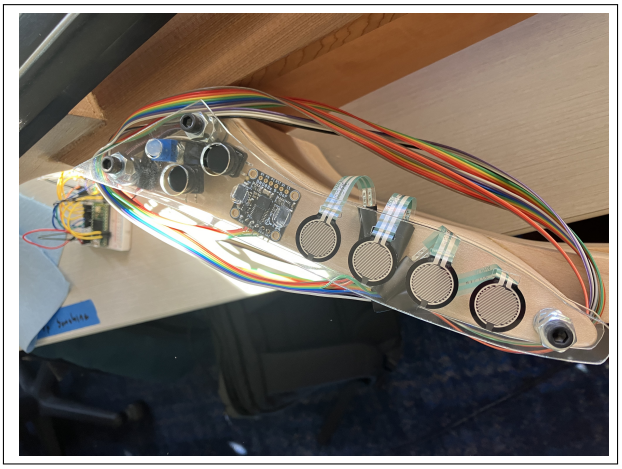


Figure 11. Modular electronics with capacitive touch sensors, an accelerometer, a gyroscope, a compass, knobs, and buttons, interfaced through an Arduino Uno

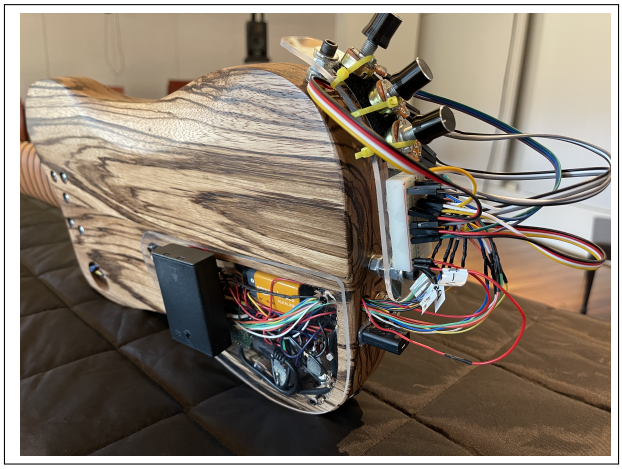


Figure 12. Electronics seen from the back

pared for extension to other parts of the instrument. Potential future additions include wireless communication, more compact or high-resolution sensors, and haptic feedback systems for bidirectional interaction—a feature that could fundamentally reshape the tactile experience of performance. Here, we exemplified an extended instrument paradigm: a hybrid of acoustic tradition and digital innovation, where gesture, sound, and spatial interaction coalesce [10]. It preserves classical technique while radically expanding the instrument's expressive scope, offering performers an adaptable and evolving tool for musical creation.

4.2 The Lute

The lute features an active microphone circuit based on the widely used Fishman Fluence pickup system. This system is designed to effectively capture the sound of the metal strings with high fidelity and minimal coloration. The Fluence circuit does not require any additional signal conditioning or processing within the instrument body: it outputs a clean, high-quality signal directly to a standard 1/4-inch female jack mounted on the instrument's side Fig. 12.

In addition to this, there is a second pickup system installed beneath the bridge. This is a Fishman piezoelectric acoustic pickup, optimized to capture the resonance and body vibrations of the lute. Unlike the Fluence system, the piezo signal is not sent directly to an output jack. Instead, it is routed into an embedded digital signal processor located inside the instrument. This processor runs a series of custom signal processing algorithms, allowing for advanced manipulation of the acoustic input before it is sent to a second 1/4-inch output jack, positioned just above the first one. Like the first, this circuit is also active, meaning it includes preamplification and requires power to operate. Both batteries live inside the circuit cavity inside the lute.

To manage the Fluence system, the instrument includes a pull-up potentiometer for switching between configuration presets, along with two additional rotary potentiometers that control tone, blend (mix), and overall output volume.

For the piezo and signal processing system, control is managed via a modular, custom-designed acrylic interface mounted on the side of the lute. This module houses four dedicated potentiometers, two Bela sensors (which could include touch, pressure, or motion sensors) [11], and a multifunction control board featuring eight general-purpose I/O pins. These I/O pins are directly connected to a Teensy microcontroller board embedded inside the lute [12], allowing for real-time interaction with the signal processing algorithms or for sending control data externally via USB or serial communication protocols.

The first iteration of the system's internal processor came preloaded with several essential audio effects modules: a high-pass filter, a resonant filter, a reverb effect based on the well-known Freeverb algorithm, and a custom-designed digital feedback circuit. These components work together to create a vivid and dynamic sonic

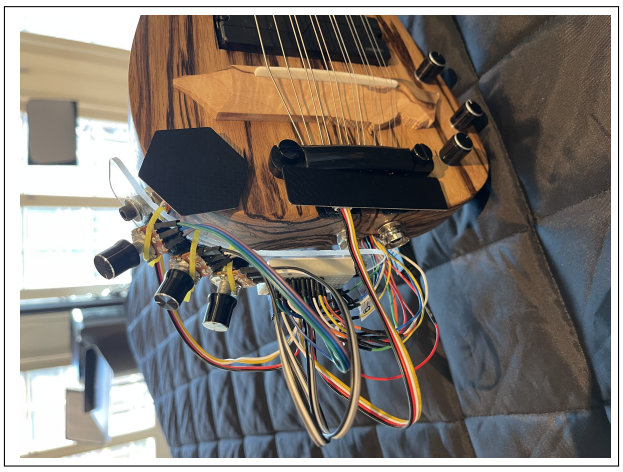


Figure 13. Electronics on the Lute

environment, enabling the performer to shape real-time feedback and texture in musically expressive ways. The digital feedback engine, in particular, is highly sensitive to changes in the input signal and spatial characteristics, making it ideal for gestural control. It is fully responsive to the BELA sensors, allowing the performer to modulate parameters such as filter cutoff, resonance, feedback depth, or reverb size using touch, motion, or pressure.

To enable both system updates and external data communication, a USB female connector is mounted just above the output jacks. This port provides direct access to the Teensy microcontroller, allowing the user to reprogram the internal firmware, upload new processing algorithms, or retrieve real-time digital data generated by the onboard sensors and control interfacesFig. 13.

5. CONCLUSIONS

Designing and building a musical instrument is an intensive, time-consuming, and deeply personal process—one that demands not only technical skill but also emotional endurance. As detailed throughout this paper, the construction of these particular instruments required fluency in a broad range of competencies: the use of hand and power tools, precise measuring, and a strong foundation in electronics, acoustics, and embedded systems. However, beyond the technical challenges, this process also proved to be profoundly gratifying and creatively rewarding.

In Celeste's case, the approach was unapologetically improvisational. Rather than following a strict plan from the outset, Celeste allowed intuition, spontaneity, and situational problem-solving to shape the development path. This wasn't a lack of structure but rather a fluid methodology rooted in her prior experience with instrument design and building. That experience acted as a compass, allowing her to make informed, responsive decisions in real time.

This hybrid of expertise and improvisation extended even to the integration of complex electronics: an active dual-circuit pickup system, real-time digital signal processing, and a rich sensor array. These components were not simply installed: they were curated, adjusted, and adapted according to the needs and affordances of the instrument as it evolved in her hands. From the sculpting of the sound through digital feedback and reverb to the custom interface for expressive control, each element reflects a balance between pragmatism and play.

Luna, by contrast, began with a clear and deliberate vision for both the aesthetic and functional dimensions of the instrument. Her goal was to create a lightweight, transportable electric contrabass that preserved the tactile and acoustic sensibilities of a traditional instrument, while offering modular expandability for live electronic performance. With little prior experience in luthiery, much of the process involved improvising practical solutions to realize that vision—from carving a resonant cavity inspired by classical proportions, to adapting hardware components for ergonomic assembly, and solving unforeseen mechanical issues with hands-on experimentation. The integration of a modular sensor platform and real-time processing system further expanded the instrument's expressive scope, enabling an embodied mode of performance where gesture, space, and sound are intricately linked.

Ultimately, building these instruments was not only about achieving functional tools; it was about crafting living systems, each capable of interaction, surprise, and sonic depth. They stand as reflections of both meticulous labor and creative joy, of structure and improvisation, and of a personal, evolving practice that values both precision and poetic expression.

6. ACKNOWLEDGMENTS

Special thanks to Mark Rau, Sasha Leitman, CCRMA Max Lab, Matt Wright, Nette Worthey.

7. REFERENCES

[1] R. Slatford and A. Shipton, "Double bass," 2001.

[2] L. Emmet, "Traditional lute making, with one hand occasionally on the mouse," *The Journal of Modern Craft*, vol. 11, no. 3, pp. 249–262, 2018.

[3] J. Roberts, *How the Fender Bass Changed the World*.

[4] E. Enright, "Yamaha silent bass slb300sk," 2020.

[5] M. G. Rau, *Vibration and Acoustic Measurements of Guitars with Applications to Luthiery Synthesis and Audio Effects*. PhD thesis, 2023. Copyright - Database copyright ProQuest LLC; ProQuest does not claim copyright in the individual underlying works; Last updated - 2025-01-27.

[6] A. Tanaka, "Musical performance practice on sensor-based instruments," in *Trends in Gestural Control of Music* (M. M. Wanderley and M. Battier, eds.), pp. 389–406, IRCAM - Centre Pompidou, 2000.

[7] E. R. Miranda and M. M. Wanderley, *New Digital Musical Instruments: Control and Interaction Beyond the Keyboard*, vol. 21 of *Computer Music and Digital Audio Series*. A-R Editions, 2006.

[8] M. M. Wanderley and M. Battier, eds., *Trends in Gestural Control of Music*. IRCAM - Centre Pompidou, 2000.

[9] D. Overholt, "The overtone violin," in *Proceedings of the International Conference on New Interfaces for Musical Expression (NIME)*, (Vancouver, BC, Canada), pp. 42–46, 2005.

[10] M. Gurevich and A. Fyans, "Digital musical interactions: Performer–system relationships and their perception by spectators," *Organised Sound*, vol. 19, no. 1, pp. 31–39, 2014.

[11] V. E. Gonzalez Sanchez, C. P. Martin, A. Zelechowska, K. A. V. Bjerkestrand, V. Johnson, and A. R. Jensenius, "Bela-based augmented acoustic guitars for sonic microinteraction," in *Proceedings of the International Conference on New Interfaces for Musical Expression*, pp. 324–327, Virginia Tech, 2018.

[12] Y. SULTANA, *Open-Source Audio Platform for Embedded Systems*. PhD thesis, UNIVERSITY OF APPLIED SCIENCES KIEL, 2018.

DOI:

Main theme: A11 Musical Acoustics

Session A11.06 Networked music performances and virtual environments

Chair(s): J. Sastre, S. Willemsen

DOI:

Main theme: A12 Physical Acoustics and Ultrasound

Session A12.01 Physical acoustics and ultrasound - General

Chair(s): N. Declercq, N. Jiménez

DOI: 10.61782/fa.2025.0925



FORUM ACUSTICUM
EURONOISE 2025

ULTRASONIC IMAGING FOR QUANTIFYING MICROPLASTIC CONCENTRATIONS IN LIQUIDS

Óscar Martínez-Graullera[1*] **Paula Moreno**[1] **Carlos Pinillos Boralla**[1] **Jorge Huecas**[1]
Ruslan Shaporin[1] **Montserrat Parrilla**[1] **Luis Elvira**[1]
[1] Instituto de Tecnologías Físicas y de la Información (ITEFI), CSIC, Spain

ABSTRACT

In recent decades, the uncontrolled disposal of plastic waste into the environment has caused widespread contamination, infiltrating even the food chain. The issue of microplastics, particularly in oceans, poses significant challenges with negative implications for marine ecosystems, human health, and the economy. Furthermore, emerging contaminants and their interactions with climate change exacerbate these impacts. To address this problem, active monitoring programs are being developed to detect contaminants such as microplastics, antibiotics, and chemicals in coastal waters. Advancing technologies to implement these strategies effectively is essential. This study aims to develop an analytical procedure to quantify microplastic concentrations in liquids (5–50 microns), optimized for onboard instrumentation. A system has been designed to channel the flow through a 1 mm diameter pathway, utilizing high-frequency ultrasonic imaging (20–50 MHz). Ultrasonic image processing enables the measurement of reflected energy to estimate microplastic concentrations. This method is calibrated using controlled monodispersive polystyrene particle concentrations, establishing a relationship between reflected energy and particle concentration. The proposed approach provides a pathway for real-time, accurate microplastic detection, supporting environmental monitoring and mitigation efforts. This paper presents a preliminary study, employing a 20 MHz transducer and an experimental setup with monodispersive polystyrene particles in continuous flow.

*__Corresponding author__: oscar.martinez@csic.es.

__Copyright__: ©2025 Óscar Martínez-graullera et al. This is an open-access article distributed under the terms of the Creative Commons Attribution 3.0 Unported License, which permits unrestricted use, distribution, and reproduction in any medium, provided the original author and source are credited.

Keywords: *microplastic, high frequncy ultrasonic, ultrasonic image*

1. INTRODUCTION

Nowadays, the presence of micro-scale contaminants in the food chain remains a significant uncertainty for human well-being. Studies have detected both chemical and physical pollutants at various points in the chain, with particular concern in the oceans, which serve as humanity's primary food reservoir [1,2]. To assess the severity of this issue, the European Union has launched research initiatives to establish monitoring protocols. These efforts are accompanied by technological developments that could be integrated into early warning systems in critical areas. This study is framed within that context.

Microplastic concentrations (5–50 microns) can be measured using various high-precision optical and spectroscopic methods [3–5]. However, ultrasound offers key advantages: it can detect particles in suspension, enables real-time marker-free detection, and allows for in situ application. These features are essential for developing an autonomous monitoring system. As a first step, this study proposes a measurement procedure using optical methods as a reference. The objective is to obtain an image of the sample—ultrasonic in this case—on which processing can be performed to quantify the number of particles.

Although this procedure does not allow for chemical identification and faces significant challenges, such as nanoparticle detection and the influence of factors like salinity, temperature, and turbidity on the ultrasonic signal, it is nonetheless more robust and applicable than other solutions. Additionally, since certain polymers absorb more ultrasonic energy, it offers some potential for discrimination.

2. EXPERIMENTAL SET-UP

2.1 Image Generation

Given the range of particle sizes to be detected, the decision was made to use high-frequency ultrasound and focused transducers (20 MHz, focal position at 13 mm, beam diameter of .1mm) operating in pulsed wave mode to generate the ultrasonic image. Due to the characteristics of the medium, a peristaltic pump (Watson-Marlow 120U/D1 pump 200rpm) and a 1 mm-section tube were used to create a closed circulating system for the sample. At a specific point, the transducer was integrated into a specially designed device that provides a flat interface with the sample flow. The transducer is positioned at an inclination angle of 30^o to increase the measurement area within the flow, as shown in Figure 1. However, the measurement section is limited to the beam section that covers only part of the tube (see Figure 1 right).

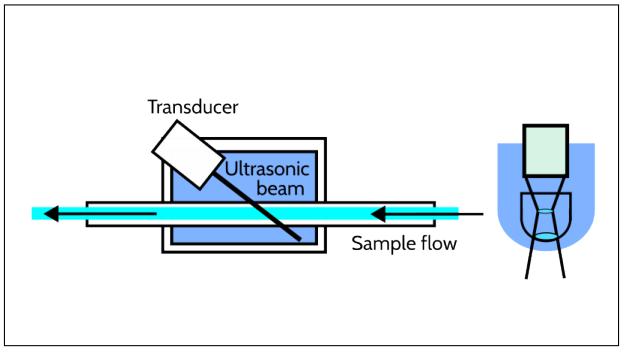


Figure 1. Transducer position in the measurement device.

In this setup, the image is composed by assembling a sequence of consecutive acquisitions. The image size is determined by the acquisition system's ability to maintain a constant data flow to the processing system. In this case, with a sampling rate of 80 MS/s, echoes are captured for 20 microseconds, and the analysis image consists of 5000 consecutive lines acquired every 500 milliseconds.

2.2 Sample Preparation

In order to develop an experimental system for the detection and quantification of particles in water samples, we have generated several calibrated samples based on spherical monodisperse polystyrene particles ranging from 2 to 12 microns in diameter. We calculated the concentrations by counting the particles in a Neubauer chamber under a microscope or using the ImageJ program. In Figure 2, we can see an optical image of the sample.

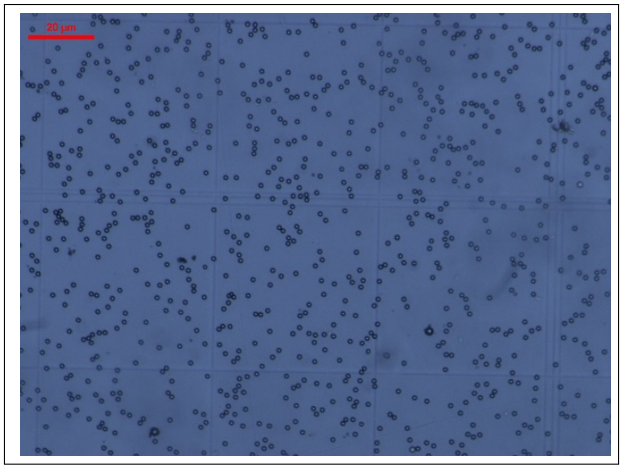


Figure 2. Spherical monodisperse polystyrene particles ranging 10 microns in diameter

To obtain polydisperse samples, with particles of different sizes and irregular shapes, we used polystyrene shavings. In these samples, we used the same methods to determine the concentration, but the irregular shape of the particles makes it difficult to distinguish whether we are observing large particles or several smaller particles agglomerated together (figure 3).

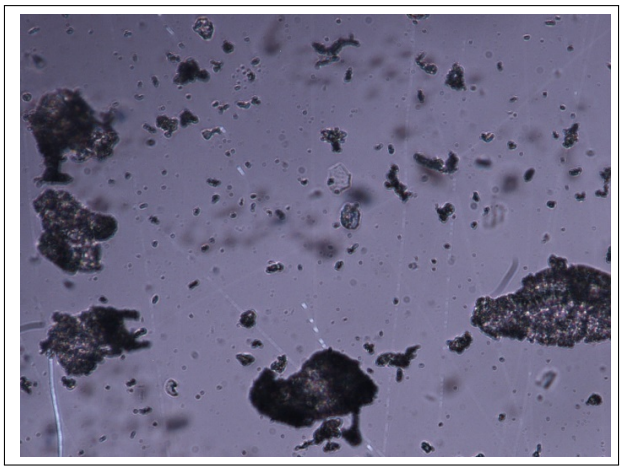


Figure 3. Polydisperse samples

2.3 Measurement Procedure

The measurement system is configured in two stages. The first, instrumental stage consists of the transducer, its support system, and an ultrasonic Difrascope system (DASEL Sistemas S.L.) responsible for signal acquisition. The second stage is a processing stage, at this moment developed in MATLAB, which handles signal preprocessing and reflector counting.

Ultrasonic imaging is composed of the assembly of consecutive A-scan lines (see figure 4). The image shows microplastic particles, artifacts due to multiple reflections in the measurement tube, and thermal noise. With a transducer frequency of 20 MHz, the preprocessing stage includes band-pass filtering and a spatial filter designed to eliminate the effect of multiple reflections within the tube. Once the structural elements are removed, image processing is performed. After applying a two-dimensional low-pass filter to reduce noise, dilation and erosion operations are used to differentiate reflectors from the background, eliminating spurious values. Then, a statistical analysis of the data is conducted to determine the threshold value that enables segmentation and reflector counting.

In the case of monodisperse spherical particles, the reflectors appear in a characteristic pattern as oblique lines following the flow direction (Figure 5). Other shapes, such as arcs and symmetrical forms, also appear, caused by flow variations induced by the peristaltic pump. The periodicity of these artifacts indicates their artificial nature.

Finally, it is important to note that the ultrasonic beam only covers a section of the tube, meaning that the measurement represents a sample-based estimate of the particle concentration. Calibration is necessary to adjust the measurement to the actual concentration value.

3. CALIBRATION

In order to assess the ability to distinguish between concentrations and calibrate the system, three concentration levels were used: 10 particles per μL, 26 particles per μL, and 50 particles per μL (sample composed by spherical monodisperse polystyrene particles ranging 10 microns in diameter). Each concentration was evaluated with the pump operating at different speeds: 4, 8, 12, and 16 rpm.

For each measurement, 3000 images were acquired, each consisting of 5000 lines. The number of circulating particles was counted in each image, and to eliminate outliers, the complete dataset was averaged using a sliding window of 32 samples. This value was empirically determined. Finally, the histogram is calculated to statistically characterize each distribution. Given the nature of the data—positive values with a significant mean—we have chosen the Rice distribution as the basis.

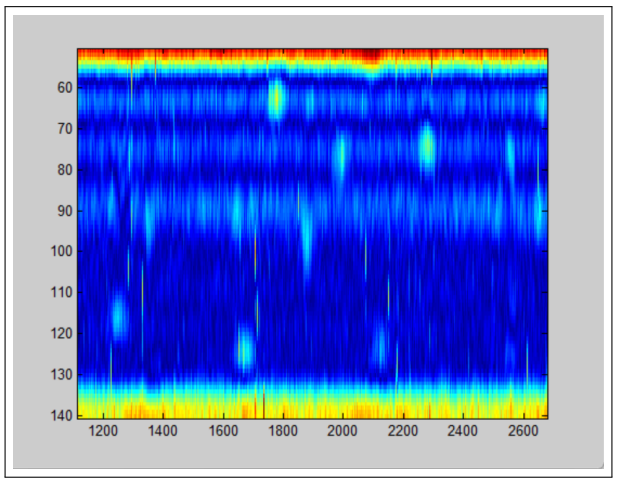


Figure 4. Ultrasonic image obtained at 20 MHz by assembling consecutive A-scan lines.

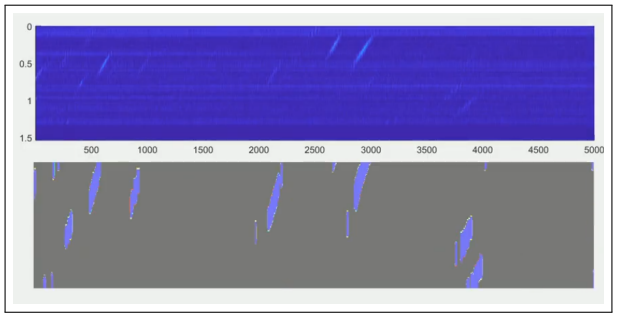


Figure 5. At the top, the ultrasonic image is presented after preprocessing. At the bottom, segmentation shows the reflectors.

To evaluate the results, the histograms of the three concentrations are compared at each speed, and Rice distribuions are estimated.

In Figure 6, we can see the result of circulating the liquid at the lowest speed. The number of detected particles is low, and the results are imprecise for all three concentrations, as the histograms overlap.

In Figure 7, we can see the result of circulating the liquid at speed 8rpm. The number of detected particles is higher, and the highest concentration becomes significant

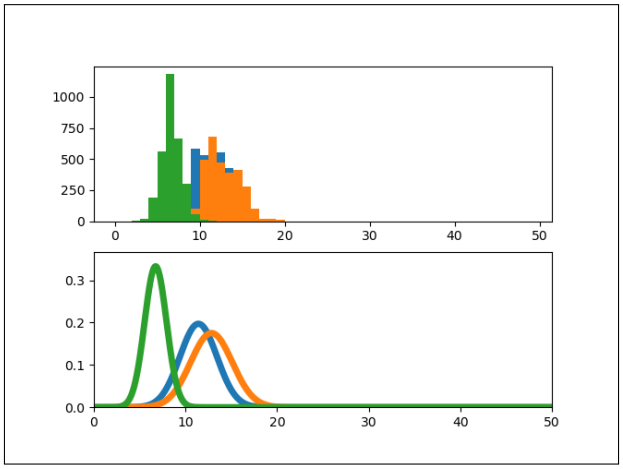


Figure 6. At the top, the histograms of the concentrations of 10 pp/μL (green), 26 pp/μL (blue), and 50 pp/μL (orange) at 4 rpm. At the bottom, the estimated Rice distributions (same color code).

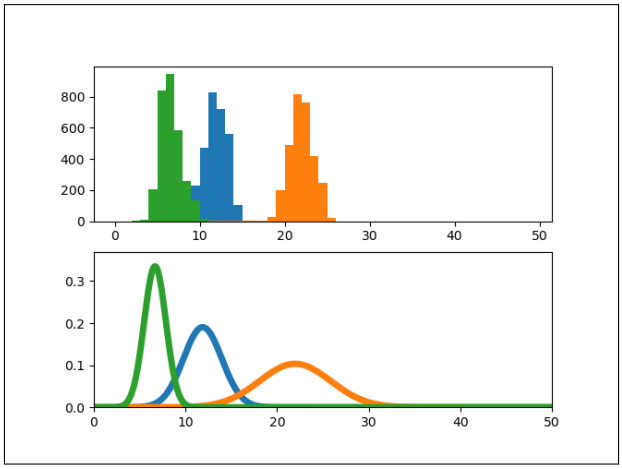


Figure 7. At the top, the histograms of the concentrations of 10 pp/μL (green), 26 pp/μL (blue), and 50 pp/μL (orange) at 8 rpm. At the bottom, the estimated Rice distributions (same color code).

and distinguishable from the other two. The 26 pp/μL and 10 pp/μL concentration remains consistent with the previous measurement.

In Figure 8, we can see the result of circulating the liquid at speed 12rpm. The concentrations can now be distinguished, and we can characterize them using the corresponding distribution functions. Although there is slight overlap between the 50 pp/μL and 26 pp/μL concentrations, the spread of the distributions allows for the calibration of intermediate concentrations.

In Figure 9, we can see the result of circulating the liquid at a speed of 16rpm. At this speed, the number of particles in the image increases, having opposite effects on the particle count. On one hand, the 26 pp/μL concentration increases in value and yields more consistent results, improving detection capability. On the other hand, the 50 pp/μL concentration decreases in value, contrary to expectations. This occurs because, as the number of particles under the beam increases, they cluster in such a way that, during the image binarization process, they may be counted as a single particle when, in reality, they could be two or more. In the case of 10 pp/μL, there is no substantial change in the mean. Despite the increase in speed, the particle density remains low, which means it cannot be ensured that the particles pass directly under the beam.

The results indicate that the pump exhibits an optimal operating speed at which measurement discrimination improves and histogram distributions become more concentrated. However, two key limitations were identified. At high concentrations, discrete particle counting is hindered by clustering effects, which compromise both the accuracy and precision of the measurements. This limitation necessitates the use of complementary descriptors to refine concentration assessment. Conversely, at low concentrations, it becomes essential to control the trajectory of microplastics to ensure their passage through the transducer beam, as their random motion can result in inconsistent or missed detections.

On a positive note, the measurement distributions can be statistically characterized using Rice distributions, which opens the possibility of developing a framework to manage measurement uncertainty based on the likelihood of belonging to a calibrated set of reference distributions.

4. CONCLUSIONS AND FUTURE WORK

This study has demonstrated the viability of using high-frequency ultrasound to quantify the concentration of microplastics in liquid media. The measurement protocol, while exhibiting a degree of flow dependence, has proven to be both reliable and reproducible and incorporates a defined margin to address uncertainty. Current research efforts are directed toward identifying the optimal flow velocity to enhance measurement resolution and extend the detection range toward lower concentrations. In parallel,

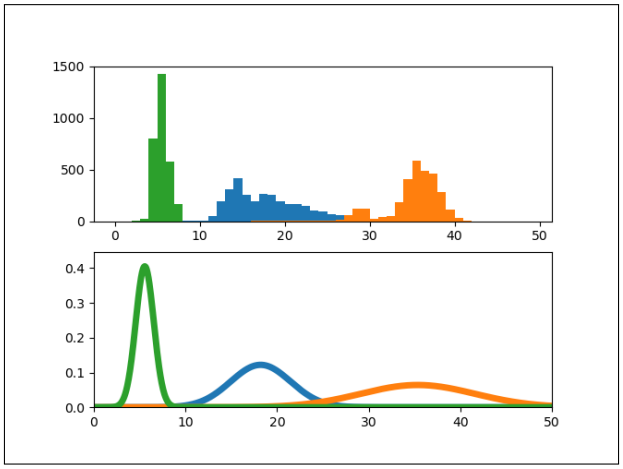


Figure 8. At the top, the histograms of the concentrations of 10 pp/μL (green), 26 pp/μL (blue), and 50 pp/μL (orange) at 12 rpm. At the bottom, the estimated Rice distributions (same color code).

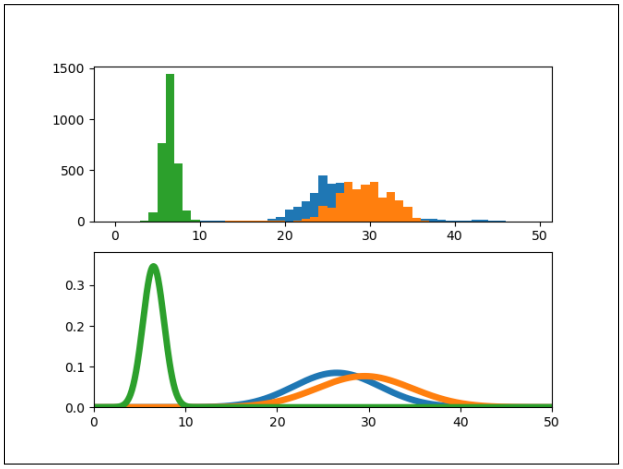


Figure 9. At the top, the histograms of the concentrations of 10 pp/μL (green), 26 pp/μL (blue), and 50 pp/μL (orange) at 16 rpm. At the bottom, the estimated Rice distributions (same color code).

alternative signal descriptors, such as energy density, are being evaluated to complement particle counting, with the aim of improving concentration estimation and resolving ambiguities that arise at elevated flow speeds.

Nonetheless, the methodology has thus far been validated only to a limited extent using polydisperse samples, and the potential impact of naturally occurring microorganisms in water has yet to be addressed. These considerations will introduce future refinements to the signal processing pipeline.

Despite these limitations, the results obtained thus far provide a solid foundation for the development of a next-generation measurement prototype, advancing the system toward eventual deployment on a lightweight computational platform.

5. ACKNOWLEDGMENTS

Carlos Pinillos, Staff hired under JAE-ICU, *Scholarships for starting a research career* cofunded by the Max-CSIC Program. ITEFI. CSIC.

Paula Moreno, Staff hired under PEJ-2021-AI/TIC-21647, AYUDAS PARA LA CONTRATACIÓN DE AYUDANTES DE INVESTIGACIÓN Y TÉCNICOS DE LABORATORIO (Orden 2839/2021, de 24 de septiembre, BOCM núm. 245, de 14 de octubre de 2021). Comunidad Autonoma de Madrid.

Jorge Huecas, Staff hired under the Generation D initiative, promoted by Red.es, an organisation attached to the Ministry for Digital Transformation and the Civil Service, for the attraction and retention of talent through grants and training contracts, financed by the Recovery, Transformation and Resilience Plan through the European Union's Next Generation funds.

This research work was funded by the European Commission – NextGenerationEU, through Momentum CSIC Programme: Develop Your Digital Talent

This work has been funded by the EU HORIZON-CL6-2023-ZEROPOLLUTION-01 project ONE-BLUE (Ref No. 101134929).

This work has been funded by the PID2022 - 138013OB -I00 /MCIN /AEI /10.13039/ 501100011033/ FEDER, UE

6. REFERENCES

[1] Mikaël KedzierskiMikaël KedzierskiDominique FrèreDominique FrèreGwénaël Le MaguerStéphane BruzaudStéphane Bruzaud. Why is there plastic packaging in the natural environment? Understanding the roots of our individual plastic waste management behaviours. The Science of The Total Environment 740:139985. DOI: 10.1016/j.scitotenv.2020.139985. June 2020

[2] Albert Vega-Herrera, Maria Garcia-Torné, Xavier Borrell-Diaz, Esteban Abad, Marta Llorca, Cristina M. Villanueva, Marinella Farré. Exposure to micro(nano)plastics polymers in water stored in single-use plastic bottles. Chemosphere (2023): doi.org/10.1016/j.chemosphere.2023.140106

[3] Renjith VishnuRadhanRenjith VishnuRadhanAnil LonappanAnil LonappanT.I. EldhoT.I. Eldho. A microwave-based technique as a feasible method to detect plastic pollutants in experimental samples. Journal of Hazardous Materials 428(5):128224. DOI: 10.1016/j.jhazmat.2022.128224. January 2022

[4] Tobias Kleinke and Finn-Frederik Stiewe and Tristan Winkel and Norman Geist and Ulrike Martens and Mihaela Delcea and Jakob Walowski and Markus Münzenberg. Identification and characterization of various plastics using THz-spectroscopy. arXiv. https://arxiv.org/abs/2212.04157. 2022

[5] Albert Vega-Herrera, Marta Llorca, Xavier Borrell-Diaz, Paula E. Redondo-Hasselerharm, Esteban Abad, Cristina M. Villanueva, Marinella Farré. Polymers of micro(nano) plastic in household tap water of the Barcelona Metropolitan Area. Water Research (2022): doi.org/10.1016/j.watres.2022.118645

DOI: 10.61782/fa.2025.0926

FORUM ACUSTICUM EURONOISE 2025

ULTRASONIC INTENSIFICATION REACTOR APPLIED TO THE AGRI-FOOD AND PHARMACEUTICAL INDUSTRY

Raúl Fernández-Clement[1*] **Francisco J. Pastor-Rodríguez**[1] **Francisco J. Navarro-Brull**[1]
Pedro Poveda-Martínez[2] **Roberto Gómez**[1]
[1] Department of Physical Chemistry, University of Alicante, Spain
[2] Department of Physics, Systems Engineering and Signal Theory, University of Alicante, Spain

ABSTRACT

Ultrasound has a wide range of applications in fields such as medicine, architecture, or chemistry. In particular, ultrasound-intensified reactors (where chemical and/or physical reactions take place) have proven to be more efficient than traditional reactors in multiple situations, offering a benefit to the industry. This is due to the increased control over the conditions in the mixture, helping to accelerate reactions and replace solvents, among other things. Two examples of this are the agri-food and pharmaceutical sectors. In the first case, ultrasound reactors can improve continuous production, product stability, and allergen removal. In the second, issues such as capillary blockages and crystallization treatments can be mitigated through this technology. This paper presents a preliminary design of an ultrasonic reactor aimed at these applications. The device utilizes a long sonotrode to enhance energy transmission to a continuous flow. This sonotrode consists of a solid cylinder with a machined helical groove along its surface, into which a tube is inserted through which the sample to be treated is passed. Analytical and numerical methods have been used for its design, which have subsequently been reflected at the experimental level for the agri-food and pharmaceutical industry applications.

Keywords: *ultrasound, flow reactor, agri-food industry, pharmaceutical industry*

*__Corresponding author__: *raulfer.clement@ua.es.*

__Copyright__: *©2025 Raúl Fernández-Clement et al. This is an open-access article distributed under the terms of the Creative Commons Attribution 3.0 Unported License, which permits unrestricted use, distribution, and reproduction in any medium, provided the original author and source are credited.*

1. INTRODUCTION

Ultrasound technology has emerged as a powerful tool across various scientific and industrial sectors, including medicine, chemistry, and engineering. Its application in reactors, particularly ultrasound-intensified reactors, has shown significant advantages over conventional methods [1,2]. These reactors enhance reaction efficiency by providing precise control over the conditions within the mixture, leading to faster reaction rates and the potential for solvent-free processes. Such benefits have been demonstrated in industries such as agri-food and pharmaceuticals, where ultrasound-assisted techniques improve production stability and mitigate common challenges like crystallization and capillary blockages [1,3].

The synthesis of particles with controlled properties at the nanoscale and microscale has garnered significant attention due to their diverse applications in fields such as adsorption, ceramics, catalysis, and drug delivery [4]. Among various fabrication methods, continuous flow approaches utilizing microreactors have emerged as powerful tools, offering advantages like enhanced mass and heat transfer, precise control over reaction conditions, and improved reproducibility [5]. However, a critical challenge in continuous flow systems, particularly when synthesizing particles or performing crystallization, is the potential for clogging of the microchannels by solid formation, including the aggregation or precipitation of products or by-products [1,3,6].

To address the issue of clogging in continuous flow reactors, several strategies have been explored. These include modifying the wettability of the channel surface, adjusting the viscosity of the solution [7], and employing multiphase flow [1,5,7]. Another promising technique in-

volves the application of ultrasound irradiation within the microreactor [1,2]. Ultrasound has demonstrated its effectiveness in preventing and even removing clogging in capillary systems, attributed to the strong cavitation effects it induces [1,3]. Furthermore, ultrasound can enhance mass transfer rates at gas-liquid or liquid-solid interfaces and promote mixing, which can be particularly beneficial in processes like continuous crystallization and nanoparticle synthesis [3,5,6].

In this context, a significant need exists for robust and scalable continuous flow reactors. Particularly, they can be applied to the agri-food and pharmaceutical industries as they can effectively handle solids and prevent clogging [3]. While continuous flow reactors offer numerous advantages, such as precise control and enhanced mass transfer [4, 6], their widespread adoption is hindered by challenges related to solid handling, including clogging from precipitate formation, solid catalysts, or insoluble byproducts [3].

To address these limitations, the design of a large-scale flow reactor should incorporate strategies for efficient solid management. Ultrasound irradiation emerges as a particularly promising technique for both preventing and clearing blockages in continuous flow capillary systems [3]. Ultrasound can induce cavitation, which provides a mechanical means to disrupt particle aggregation and resuspend settled solids [5, 8].

Notably, even low-power acoustics without cavitation has been shown to effectively unclog and prevent blockages [3].

The fabrication of such a reactor should consider several key aspects. The choice of materials must ensure chemical compatibility with the intended applications in the agri-food and pharmaceutical sectors. For efficient ultrasound transmission, materials such as glass can be advantageous [5]. The reactor design should incorporate optimized sonotrode geometries, such as blade, block, cylindrical, or even helicoidal shapes, to achieve wider and more uniform sonication areas suitable for larger reactor volumes and longer capillary lengths [3]. Acoustic design principles are crucial to ensure that the applied frequency resonates effectively with the reactor system, maximizing the conversion of electrical power into acoustic energy focused on the reaction channels. Finite element analysis (FEA) can be a valuable tool in the design process to simulate and optimize the acoustic field distribution within the reactor [6].

Validation of the large-scale flow reactor will be essential to confirm its efficacy in handling solids and preventing clogging while maintaining process performance. This should include characterizing the hydrodynamics of the reactor using residence time distribution (RTD) measurements to ensure predictable flow behavior, potentially approaching plug flow to minimize dispersion [8]. Techniques like high-speed microscopic imaging can visualize flow patterns and the behavior of solid particles under different operating conditions and with the application of ultrasound [3]. The reactor's ability to handle multiphase flow and maintain suspension of solid catalysts or reagents should be rigorously evaluated [5]. Furthermore, the performance of the reactor should be tested in relevant applications, such as continuous crystallization of pharmaceutical compounds with control over particle size and polymorph [9], and continuous catalytic reactions involving solid catalysts [5], demonstrating sustained, clog-free operation and desired product quality.

By focusing on integrated design, incorporating effective solid handling strategies like ultrasound, and thorough validation, the development of large-scale continuous flow reactors can be significantly advanced for the benefit of the agri-food and pharmaceutical industries. Nonetheless, their widespread adoption is hindered by challenges related to solid handling, including clogging from precipitate formation, solid catalysts, or insoluble byproducts [3].

Thus, ultrasound-intensified flux reactors serve as a tool to study the effects of ultrasound irradiation on substances of interest. Flux reactors, in contrast to ultrasonic batch reactors, allow continuous operation, which is beneficial at the industry level.

The reactors that will be studied consist of a system which contains a Langevin transducer (or two) coupled to a long sonotrode. This sonotrode consists of a solid aluminum cylinder with a helical machining along its surface, into which a tube is inserted through which the sample to be treated is passed by means of a peristaltic pump. The objective of this study is to design, build and experimentally test this kind of reactors.

The first section will be dedicated to the analytical and numerical design of the reactor. The second section will treat the experimental part, in which the experimental setup will be described, as well as the methodology and results.

2. DESIGN OF THE SONOTRODE

The system will consist of a Langevin transducer coupled to a cylindrical sonotrode, which will be an aluminum cylinder with a length of 630 mm, with a machined helical

groove on its surface to locate the tube. The first design was developed considering a 60 W Langevin transducer with two piezoelectric ceramics PZT8. The scheme of the system with its dimensions is shown in Fig. 1.

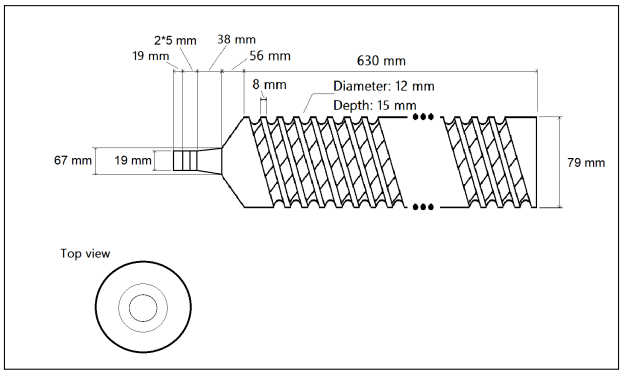


Figure 1. Initial scheme of the system.

Nonetheless, new high-power Langevin transducers were bought (with 4 piezoceramics PZT8), with dimensions different from those of the original Langevin transducer. Thus, the final scheme of the system has a step between the cone and the Langevin transducer, as shown in Fig. 2.

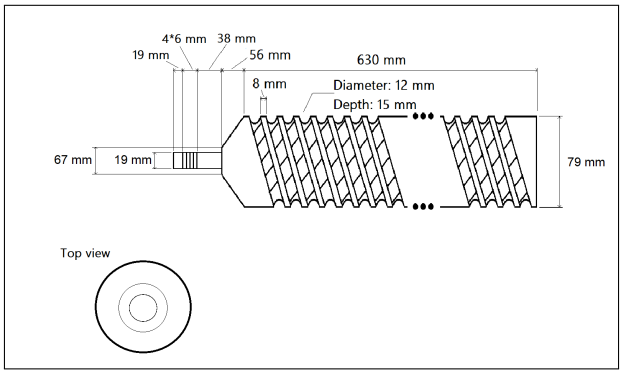


Figure 2. Initial scheme of the system.

2.1 Analytical design

The design of the system was made through the Mason model. The system was modeled to be resonant at 28 kHz. The equivalent circuit of the system can be seen in Fig. 3. An approximation has been used for the analytical solution. It has been considered that there is not a helical slit but a separated transversal ring slit sequence, in a way that there are maximum and minimum radius variations for the section. The part of the circuit corresponding to this ring sequence (the sonotrode) is shown in Fig. 4.

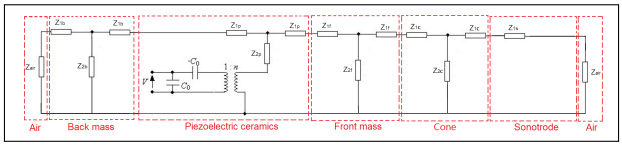


Figure 3. Equivalent circuit for the entire system. The sonotrode part is indicated as an equivalent impedance.

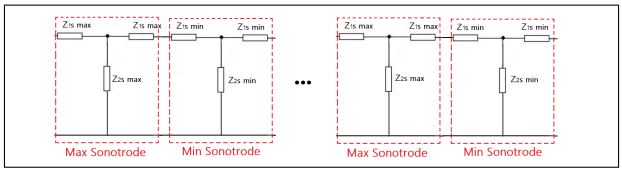


Figure 4. Equivalent circuit for the sonotrode part, where it is considered the sequence of maximum and minimum radius section of the sonotrode as if they were coupled blocks of different sections.

The result of the impedance of the system as a function of the frequency according to this method was solved using Python. The result is shown in Fig. 5, where it can be seen that the resonance of the system is approximately 28 kHz.

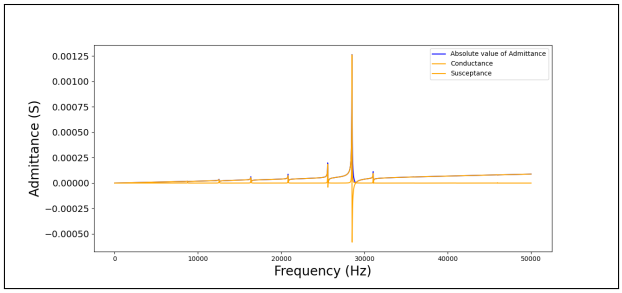


Figure 5. Absolute value of admittance, as well as conductance and susceptance of the system according to Mason model.

2.2 Numerical design

The system has also been numerically simulated in order to obtain the optimum design. The first attempt was to optimize the system at a frequency of 28 kHz. The software COMSOL Multyphysics has been used. The libraries used for this model have been "Solid mechanics", "Electrostatics" and "Piezoelectric effect". The result of this first attempt can be seen in Fig. 6, in which the transducer coupling to the sonotrode has been enlarged for better visualization.

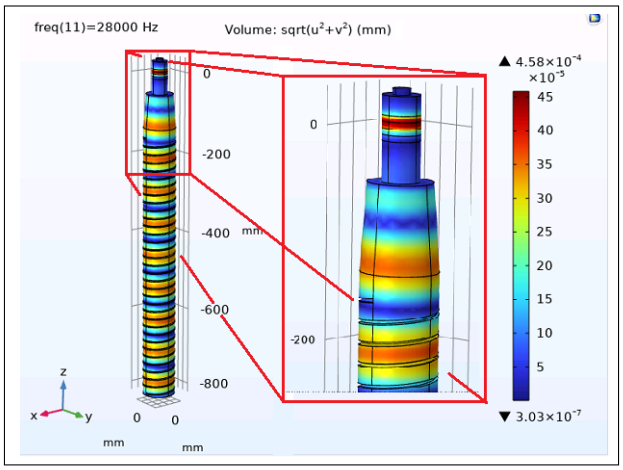


Figure 6. Numerical result of 28 kHz frequency response of the system. The parameters u and v correspond to the displacement on the x-axis and on the y-axis, respectively. Thus, $\sqrt{u^2+v^2}$ gives the total radial displacement of the system.

The absolute value of admittance, the conductance and the susceptance of the system has been computed from the numerical model by COMSOL Multphysics. The result is shown in Fig. 7.

Later, more designs were developed in order to increase the acoustic power. Thus, the new designs were mainly symmetric with two transducers of different resonant frequencies (20 kHz and 28 kHz), one in each side of the cylinder, as shown in Fig. 8, in which the transducer coupling to the sonotrode has also been enlarged for better visualization. Symmetric systems were modeled in 2D axisymmetric because they require less computational power and, due to the symmetry of the problem, the desired vibration modes can be studied in this way. In Fig. 9 the built sonotrodes are shown.

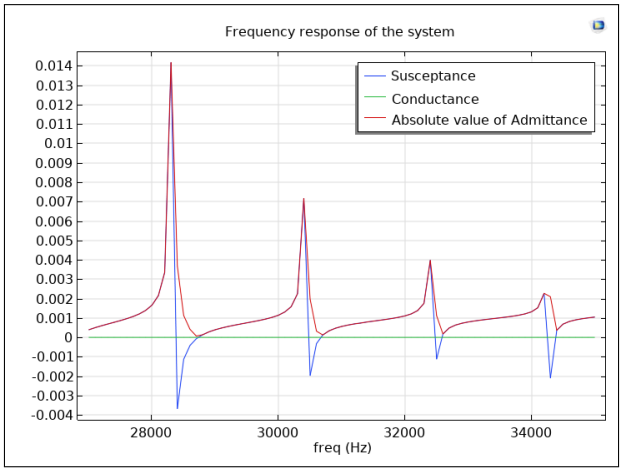


Figure 7. Numerical result of the absolute value of admittance, the conductance and the susceptance of the system. The result is not exactly the same as the one shown in Fig. 5, because that was an approximation.

3. EXPERIMENTS

The scheme of the experimental setup is shown in Fig. 10. The sample is forced to pass through the PFA tube by a peristaltic pump.

In order to control the experimental system, a LabVIEW program has been created. This program consists of a system of 3 tabs, each one in charge of a specific task. In the first tab, frequency sweep is performed in order to find the resonant frequencies of the system experimentally. In the second tab, the emission at the optimum frequencies can be controlled, making it possible to emit only at the desired frequency or at multi-frequency, with a continuous or totally customized pulsed signal. The third tab provides basic control of the pumps and monitoring of the potential pressure sensors and flow meters that can be added to the system.

Once the experimental setup has been completed (Fig. 11), tests can be started. The methodology is the same for all the experiments: the sample is passed through a tube coiled around the sonotrode, driven by a peristaltic pump. The pump flow rate and the type of ultrasound treatment (continuous or pulsed) can be changed depending on the sample and the purpose of the experiment.

In the laboratory, it has only been possible to perform preliminary studies which need to be systematically repeated in order to obtain more accurate and solid conclu-

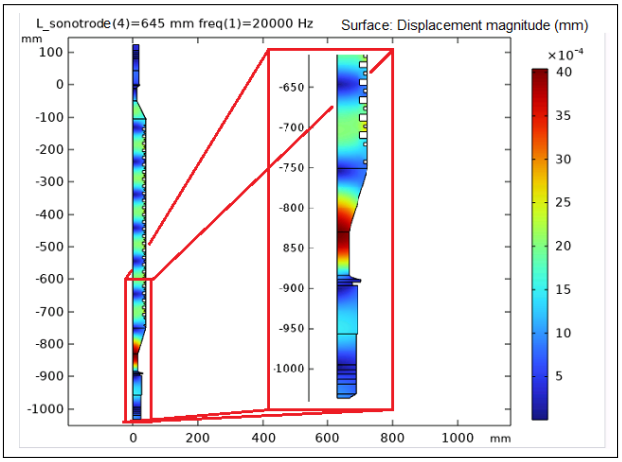


Figure 8. Numerical result of 20 kHz frequency response of the symmetric system.

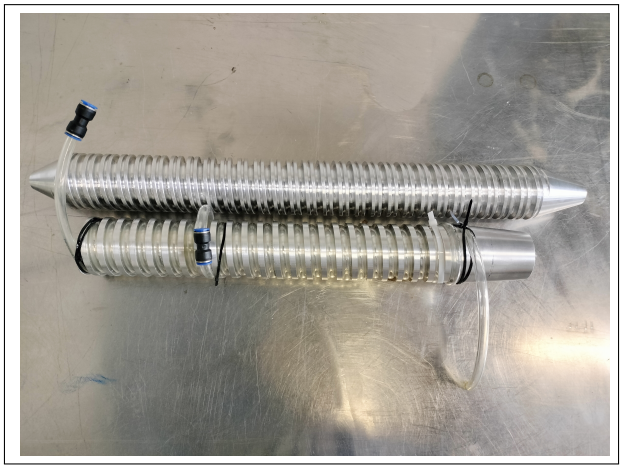


Figure 9. Built sonotrodes.

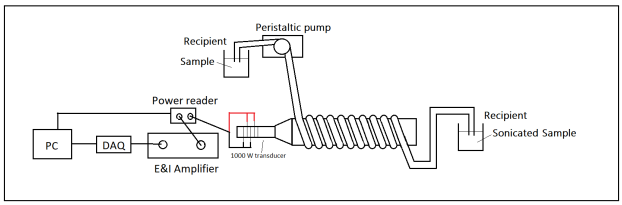


Figure 10. Experimental scheme (not to scale).

sions. Thus, only qualitative results can be summarized in this work.

The experiments performed coincide with the main problems found in continuous production in the industry, which are mentioned earlier. Thus, each experiment is a test to verify if the built device is able to solve the corresponding problem.

3.1 Antifoaming capacity

To check if the system is able to remove the foam, first it has to be generated. To create foam, the sample for the liquid-gas system was beer. When ultrasounds were applied some effects on the bubbles were observed, mainly the reduction of the large ones.

3.2 Unclogging capacity

The purpose of this experiment is to create a clog, and check if the ultrasound application can remove it. The sample for the liquid-solid system was water with sand.

The generation of the clog is made by means of a 3D printed tube reducer. The inner diameter of the tube goes from 2.5 mm to 1 mm in one single step.

When ultrasounds are applied, the effectiveness of removing and preventing clogs was qualitatively observed.

3.3 Homogenization of dispersed systems

The objective of this experiment is to increase the homogeneity of dispersed systems.

The sample for the dispersed system was pineapple juice. When ultrasounds are applied, a slight reduction of the juice pulp was observed.

More experiments are needed in order to prove the actual reduction of the juice dispersion.

3.4 Viscous systems

The objective of this experiment is to reduce the viscosity of the sample, in order to make it easier to transport. This is the case of sauces, for example. The sample in this case was mayonnaise.

When ultrasound is applied, a clear reduction in viscosity (slight liquefaction) was observed.

Another objective of this experiment is to test whether the device is capable of generating stable emulsions. This has not been made yet in the laboratory.

More quantitative, replicable and representative experiments are needed in order to properly test the proposed ultrasonic flux reactor in an industry context.

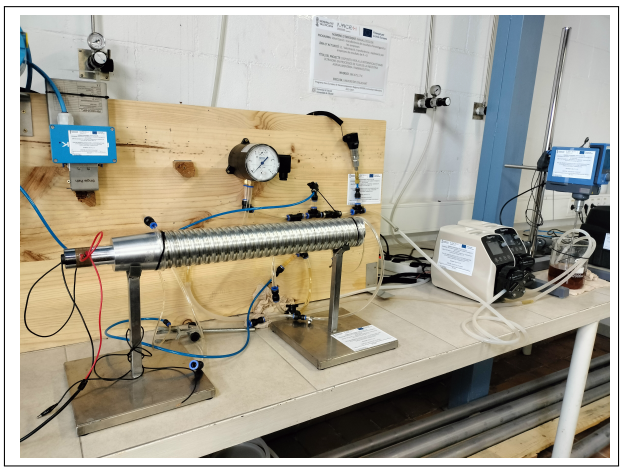


Figure 11. Experimental setup.

4. CONCLUSION

The application of ultrasonic reactors in the agri-food and pharmaceutical industries is explored, highlighting their advantages in enhancing reaction efficiency, preventing clogging, and improving product quality. The study presents the design and testing of a novel ultrasonic reactor, featuring a solid cylindrical sonotrode with helical slit for optimized energy transmission. The potential of the reactor has been experimentally suggested in terms of foam reduction, unclogging capacity, and liquefaction of sauces, although there are limitations in dispersion improvements. The results suggest that ultrasound-assisted reactors could be a valuable tool for industrial processes, offering potential scalable and effective solutions for continuous flow applications.

5. ACKNOWLEDGMENTS

This project (INNVA1/2022/36) was financed by the Agència Valenciana de la Innovació (IVACE)/Programa Fondo Europeo de Desarrollo Regional (FEDER) Comunitat Valenciana 2021-2027.

6. REFERENCES

[1] S. Fei, Y. Zhang, J. Zhang, Z. Tang, and Q. Wu, "Continuous synthesis of monodisperse silica microspheres over 1 μm size," *Journal of Flow Chemistry*, pp. 1–12, 2021.

[2] M. N. Hussain, S. Baeten, J. Jordens, L. Braeken, and T. Van Gerven, "Process intensified anti-solvent crystallization of o-aminobenzoic acid via sonication and flow," *Chemical Engineering and Processing-Process Intensification*, vol. 149, p. 107823, 2020.

[3] F. J. Navarro-Brull, A. R. Teixeira, G. Giri, and R. Gómez, "Enabling low power acoustics for capillary sonoreactors," *Ultrasonics Sonochemistry*, vol. 56, pp. 105–113, 2019.

[4] P. P. Ghimire and M. Jaroniec, "Renaissance of stöber method for synthesis of colloidal particles: New developments and opportunities," *Journal of Colloid and Interface Science*, vol. 584, pp. 838–865, 2021.

[5] Z. Dong, S. D. Zondag, M. Schmid, Z. Wen, and T. Noël, "A meso-scale ultrasonic milli-reactor enables gas–liquid-solid photocatalytic reactions in flow," *Chemical engineering journal*, vol. 428, p. 130968, 2022.

[6] F. J. Navarro-Brull, P. Poveda, R. Ruiz-Femenia, P. Bonete, J. Ramis, and R. Gómez, "Guidelines for the design of efficient sono-microreactors," *Green Processing and Synthesis*, vol. 3, no. 5, pp. 311–320, 2014.

[7] W. Cailly, K. Mc Carogher, H. Bolze, J. Yin, and S. Kuhn, "Analysis of dynamic acoustic resonance effects in a sonicated gas–liquid flow microreactor," *Ultrasonics Sonochemistry*, vol. 93, p. 106300, 2023.

[8] F. J. Navarro-Brull, A. R. Teixeira, J. Zhang, R. Gómez, and K. F. Jensen, "Reduction of dispersion in ultrasonically-enhanced micropacked beds," *Industrial & Engineering Chemistry Research*, vol. 57, no. 1, pp. 122–128, 2018.

[9] Y. Ma, S. Wu, E. G. J. Macaringue, T. Zhang, J. Gong, and J. Wang, "Recent progress in continuous crystallization of pharmaceutical products: precise preparation and control," *Organic Process Research & Development*, vol. 24, no. 10, pp. 1785–1801, 2020.

DOI: 10.61782/fa.2025.0698



FORUM ACUSTICUM
EURONOISE 2025

PRELIMINARY STUDY ON THEORETICAL CORRECTIONS TO THE EQUATION OF STATE IN SINGLE-BUBBLE SONOLUMINESCENCE AND EXTENSION OF THE MINIMUM RADIUS STAGE

Raúl Fernández-Clement[1*] **Pedro Poveda-Martínez**[2] **Roberto Gómez**[1]

[1] Department of Physical Chemistry, University of Alicante, Spain
[2] Department of Physics, Systems Engineering and Signal Theory, University of Alicante, Spain

ABSTRACT

Single bubble sonoluminescence (SBSL) involves the emission of very short flashes of light by bubbles subjected to a periodic ultrasonic acoustic field in a liquid medium, which slowly expand and rapidly contract, emitting light at the minimum radius stage. Several theories have been proposed to model the behavior and thermodynamic conditions inside the bubble, and most of them treat the gas inside as an ideal gas. Nonetheless, the experimental results obtained to date show conditions that deviate from the range of applicability of the ideal gas equation. This paper proposes a first approach to the study of the SBSL phenomenon through the application of an equation of state corresponding to real gases, and even to plasmas, in order to obtain theoretical corrections to the dynamics and thermodynamic conditions (mainly pressure and temperature) inside the bubble. In addition, the possibility of prolonging the minimum radius stage of the bubble by modifying the applied acoustic field will be analyzed, in order to examine whether the thermodynamic conditions inside the bubble vary or not in this case, and whether these conditions are stable in time.

Keywords: *sonoluminescence, equation of state, collapse prolongation*

**Corresponding author*: raulfer.clement@ua.es.

Copyright: *©2025 Raúl Fernández-Clement et al. This is an open-access article distributed under the terms of the Creative Commons Attribution 3.0 Unported License, which permits unrestricted use, distribution, and reproduction in any medium, provided the original author and source are credited.*

1. INTRODUCTION

Single bubble sonoluminescence (SBSL) refers to the phenomenon in which a gas bubble, when exposed to a periodic ultrasonic acoustic field within a liquid, emits brief but intense flashes of light. This occurs as the bubble undergoes a process of gradual expansion followed by rapid contraction, with the emission of light occurring precisely at the point of minimum bubble radius [1]. The role of the acoustic field is paramount, as the rapid oscillations induced by the ultrasonic waves are critical in driving the bubble dynamics that lead to the high-energy light emission observed during the bubble's collapse. Understanding the acoustics involved is essential, as the precise control of the ultrasonic field influences both the intensity and the characteristics of the emitted sonoluminescent light.

The equation of state (EOS) also plays a crucial role in understanding the extreme conditions reached inside a collapsing bubble in SBSL. During the collapse, the gas within the bubble is subject to rapid compression, leading to extreme temperatures and pressures characteristic of the warm dense matter (WDM) regime. Accurately modeling these conditions is essential for predicting key parameters such as density, temperature, and the subsequent light emission [2].

Different EOS models have been proposed to describe the thermodynamic behavior of the gas inside the bubble. Early approaches relied on the ideal gas law [3], but as experimental and numerical studies revealed significant deviations from ideal behavior [4], more sophisticated models, such as that based on the van der Waals equation [5] and high-complexity real gas models [6], have been introduced. These models incorporate non-ideal gas effects,

phase transitions, and even plasma formation [7] at the final stage of collapse.

The theoretical sensitivity of SBSL light emission to the choice of EOS suggests that sonoluminescence could serve as a unique experimental platform for testing and refining EOS models relevant to WDM physics [2].

On the other hand, the applied acoustic field can be modified in such a way that there is a point in space where a very high pressure is reached. In this context, if the bubble is located in that point, its behavior is different from that of normal SBSL. The bubble collapse is prolonged in time and it loses its stability.

The first section will be dedicated to the corrections to the equation of state for the gas in a sonoluminescing bubble. The main objective of this part is to perform a review of the current models which aim to apply realistic EOS in SBSL.

The second section will treat the conditions and numerical results for the prolongation of bubble collapse. The objective of this part is to find theoretical conditions for the bubble to keep collapsed more time.

2. EQUATION OF STATE FOR THE GAS IN THE BUBBLE

During the collapse, the gas inside the bubble in SBSL undergoes rapid compression, reaching temperatures and pressures characteristic of the warm dense matter (WDM) regime. The choice of EOS directly influences the predicted density, temperature, and light emission behavior, making it a key factor in SBSL modeling [2, 8].

First, it is necessary to define the theoretical model that will be used in order to describe the time evolution of the bubble radius. Rayleigh-Plesset model will be used, for which the time evolution of the bubble radius reads:

$$R\ddot{R} + \frac{3}{2}\dot{R}^2 = \frac{1}{\rho}\left(P - P_\infty - P(t)\right) \tag{1}$$

$$P = p_{\text{gas}} - 4\mu\frac{\dot{R}}{R} - 2\frac{S}{R} \tag{2}$$

where R is the bubble radius; ρ, the liquid density, p_{gas}, the pressure of gas inside the bubble (given by the chosen equation of state); P_∞, the ambient pressure of the liquid; $P(t) = P_A \sin(\omega t)$, the pressure due to the acoustic field of an angular frequency ω and amplitude P_A; μ, the liquid viscosity; S, the surface tension of the liquid; and the dot indicates time derivative. This is an approximation valid up to the order of $\dot{R}/c$ [9].

This section will review the different EOS used to model the gas inside the bubble in SBSL, including considerations of ideal gas behavior, non-ideal gas effects, and plasma formation, which is poorly studied.

2.1 Early Approaches: Ideal Gas Models

The simplest EOS used in SBSL studies is the ideal gas law, which assumes non-interacting particles [10]. It provides a useful first approximation, particularly in non-collapse conditions when the bubble follows an adiabatic process. The mean pressure of the gas is given by:

$$p = \frac{NkT}{V} = \frac{nRT}{V} \tag{3}$$

where N is the number of molecules; k, is the Boltzmann constant; T, the mean temperature of the gas; and V, the total volume occupied by the gas. For the second equation, n is the number of moles of the substance and R is the ideal gas constant.

The collapse of the bubble is very short-lived (thus, the collapse is considered to be adiabatic). Therefore, the bubble is most of the time (almost the whole cycle) outside the collapse range [11]. Thus, in non-collapse conditions, it can be assumed that the gas inside the bubble obeys the ideal gas law, for simplicity and because through this approach it is possible to extract a lot of information, making it a good first approximation for the study of this phenomenon.

The adiabatic equation applied to SBSL in this case reads [12]:

$$P = P_0\left(\frac{R_0}{R}\right)^{3\gamma} \tag{4}$$

where γ is the adiabatic index.

However, as the bubble collapses, pressure and temperature increase significantly [13], leading to ionization and strong deviations from ideal gas behavior [14].

2.2 Moderate Complexity Models: Van der Waals Equation

Real gases deviate from ideal behavior due to intermolecular interactions [15]. The van der Waals equation introduces correction terms:

$$p + \frac{a}{v^2} = \frac{RT}{v - b} \tag{5}$$

where $v = V/n$ is the molar volume of the gas (n is the number of moles of the substance). In this equation,

a and b are two constants, which are characteristic of the particular type of molecules that it describes [5].

This model predicts higher temperatures and pressures than the ideal gas law and provides a better approximation for SBSL conditions [16]. The adiabatic equation for this case is as follows [17]:

$$p = \left(P_0 + \frac{2S}{R_0}\right)\left(\frac{R_0^3 - h^3}{R^3 - h^3}\right)^{\gamma} \tag{6}$$

Where h is the characteristic van der Waals hard-core radius of the gas inside the bubble.

Despite its improvements, this model still falls short under extreme SBSL conditions.

2.3 Higher complexity models for real gases

Despite improving the ideal gas model, the Van der Waals model is also unsuccessful because of the extreme conditions reached in the collapse. Thus, more advanced EOS models, such as the Peng–Robinson equation, have been developed to improve accuracy under high pressures and temperatures [6]. These models refine SBSL predictions but do not fully account for plasma formation.

2.4 Warm Dense Matter regime

Warm dense matter (WDM) is a branch of plasma physics. Its importance lies in its influence in the structure and formation of giant planets and other astrophysical objects, such as brown dwarfs, as well as in the implosion trajectories of proposed laser fusion capsules [18, 19]. It is characterized by pressures of above a million atmospheres (100 GPa), and with temperatures between 1 and 100 eV (where 1 eV = 11600 K) [20], and its density is sufficiently high to render the ions strongly coupled [21].

In the laboratory, WDM can be created through lasers [22, 23], using a magnetic anvil cell [24], employing extreme ultraviolet radiation [25], or even utilizing a pulsed-power driver [26]. It is hard to obtain, so it is difficult to obtain a theoretical model to describe it [27–29]. Many attempts have been done to obtain an equation of state (EOS) for WDM [30–33].

In this context, SBSL is presented as a phenomenon in which it could be possible to generate WDM in a relatively simple way, given the extreme conditions of pressure, density and temperature inside the bubble in the collapse. Therefore, SBSL can be used to test EOS in WDM regime [2].

2.5 Plasma Formation and Ionization: The Role of Plasma in the Collapse

At extreme temperatures, the gas transitions into plasma, requiring a plasma-specific EOS. While early models relied on the Saha equation, experimental data suggest much higher opacity, pointing to strong Coulomb interactions [34]. Some models incorporate magnetohydrodynamic effects to explain plasma behavior during collapse [35].

Despite significant advances, a universally accurate EOS for all SBSL stages remains elusive, highlighting the need for hybrid approaches that combine different models.

3. COLLAPSE PROLONGATION IN SBSL

In SBSL, the final stage of the collapse (the time the bubble remains contracted at its minimum radius) lasts picoseconds [36], as the pulse width of the emitted light. In this context, some questions may arise: is the emitted light directly related to the minimum radius stage? Can the bubble stay contracted for longer? In that case, would the light pulse widths be longer? Would the light emitted have different characteristics?

In this section, the prolongation of the time the bubble remains collapsed will be numerically studied. In order to achieve that, modifications in the applied acoustic field will be analyzed. Specifically, the application of two excitation sources will be numerically studied.

The numerical model is as follows. A parallelepiped container full of water will be considered, with dimensions a = 10 cm, b = 20 cm and c = 30 cm (referring to the x, y and z coordinates respectively). The two sound sources are located on the same face of the container (one centered and one eccentric source) radiating at 25 kHz in phase, as can be seen in Fig. 1 . This simulation has been performed with ANSYS software. The sound pressure level inside the container can be seen in Fig. 2, where the point of maximum pressure is indicated in red, and the point of minimum pressure is indicated in blue.

In this context, a numerical study will be performed to analyze what is the time evolution of the bubble radius, as well as of the pressure and temperature inside the bubble if it is located at the point of maximum pressure level. The numerical model will consist of solving the Raylegih-Plesset equation using Python. In order to achieve that, a change of variable

$$u = \dot{R} \tag{7}$$

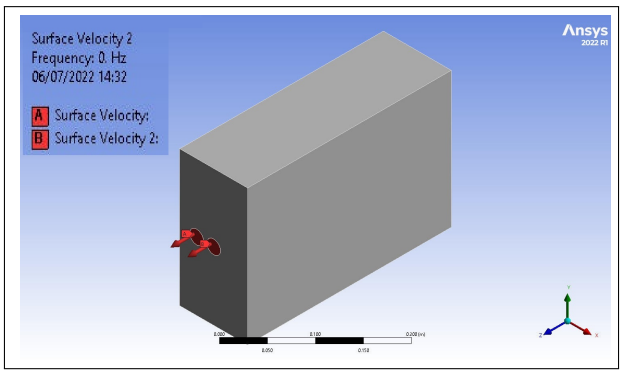


Figure 1. Problem statement of a parallelepiped with two excitation sources.

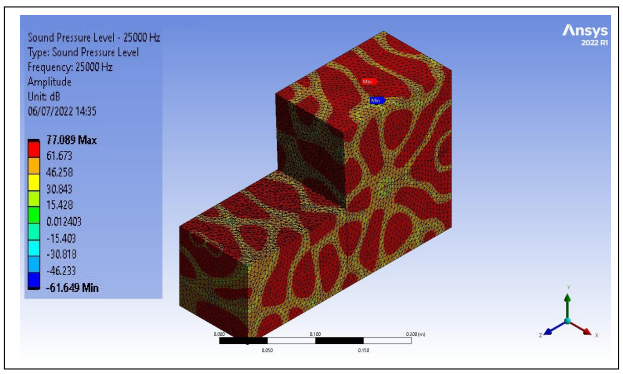


Figure 2. Sound pressure level in a parallelepiped with two excitation sources.

will be used. In this way, it is possible to obtain the following system of equations for the bubble:

$$\left.\begin{aligned} u &= \dot{R} \\ \dot{u} = \tfrac{1}{R\rho}\Big[\Big(P_0 + \tfrac{2\sigma}{R_0} - P_v\Big)\big(\tfrac{R_0}{R}\big)^{3\gamma}\big(1 - \tfrac{3\gamma u}{c}\big) - \\ -\tfrac{2\sigma}{R} - \tfrac{4\mu u}{R} - P_A\sin(\omega t) + \\ +P_v - P_0 - \tfrac{2\sigma}{R_0}\Big] - \tfrac{3u^2}{2R} \end{aligned}\right\} \tag{8}$$

where P_v is the vapor pressure; and σ, the surface (interfacial) tension of water. The pressure and temperature will be modeled as:

$$P(t) = \left(P_0 + \frac{2\sigma}{R_0} - P_v\right)\left(\frac{R_0}{R}\right)^{3\gamma} \tag{9}$$

$$T(t) = T_0\left(\frac{R_0}{R}\right)^{3(\gamma-1)} \tag{10}$$

Numerical results using Python suggest that the radius increases to a disproportionate and meaningless value, as shown in Fig. 3. This means that the movement of the bubble is not stable, i.e. the bubble disappears (explodes). This can also be deduced from the pressure and temperature graphs (Fig. 4), in which their value cancels out after a certain instant. These plots allow us to know the moment when the bubble explodes (from the moment when its value is zero), which is at approximately 20 microseconds. In addition, it should be noted that the pressure and temperature peaks are smoother (the changes are more progressive) than in the case of SBSL, where they are more similar to a Dirac delta, as shown in Figure 5a of [37]. This could mean that, due to the high pressure that the bubble undergoes, it stays longer in the minimum radius stage during the first 20 microseconds.

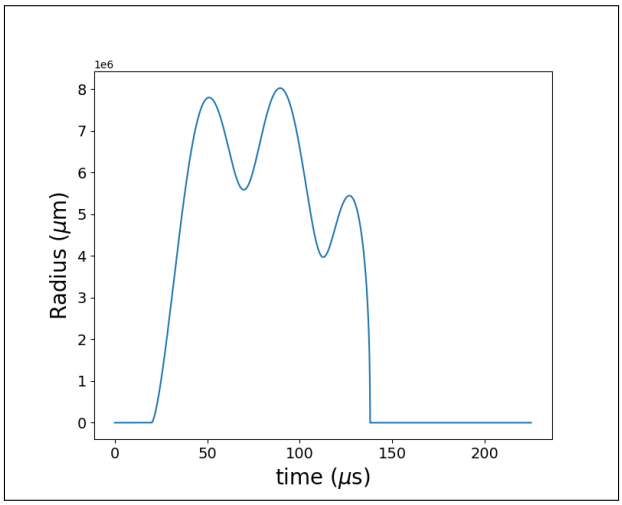


Figure 3. Time evolution of the bubble radius with two excitation sources.

If Fig. 3 is enlarged to see the initial instants, Fig. 5 is obtained, where it can be seen that the bubble remains collapsed almost 20 microseconds. Normal conditions in SBSL experiments show that the bubble collapse lasts a few picoseconds. That means a prolongation of six orders of magnitude for the time in which the bubble remains collapsed.

4. CONCLUSION

Numerical simulations suggest that modifying the acoustic field can prolong the collapse stage six orders of magnitude in time, though this may lead to instability. Addi-

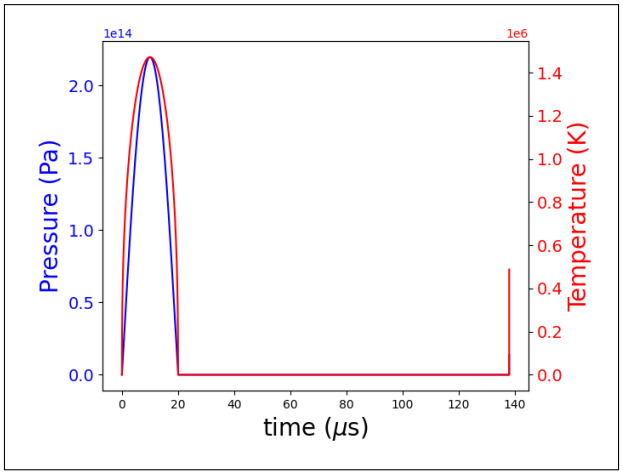


Figure 4. Time evolution of the pressure and temperature in the bubble with two excitation sources.

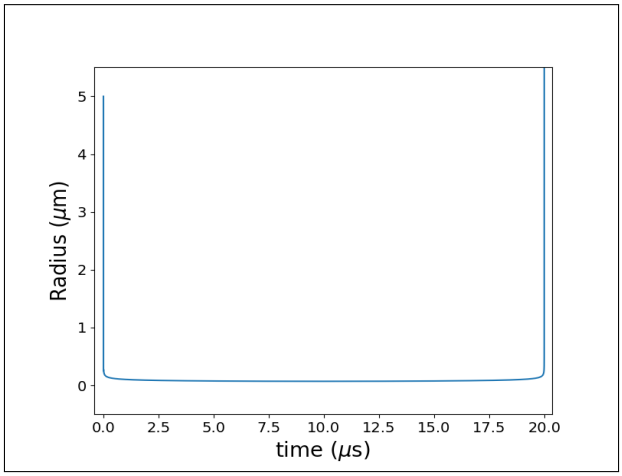


Figure 5. Time evolution of the bubble radius at the first instants of the motion.

tionally, none of the current theoretical models can explain exactly the experimental observations of SBSL, and one of the properties to be corrected is the considered EOS. The application of an EOS for real gases could more accurately model the thermodynamic properties inside a sonoluminescing bubble. This would lead to improved accuracy in fitting theoretical simulations with experimental data, as well as to a more complete explanation of the phenomenon. Although ideal gas models provide a useful starting point, deviations at high pressures and temperatures necessitate more complex approaches, including van der Waals corrections and plasma-based models. The application of these models, or even a combination of them, should give more accurate results that better fit the experimental data. Thus, the need for hybrid EOS models tailored to different SBSL phases is suggested, and also the possibility of collapse prolongation. The use of an appropriate EOS in SBSL, as well as finding conditions for stable prolongation of bubble collapse, is left for future research.

5. ACKNOWLEDGMENTS

The part of this article dedicated to the time prolongation of bubble collapse was first studied by the author in his Master's Thesis with the help of professors Jaime Ramis Soriano (University of Alicante) and Alessandro Fabbri (University of Valencia). The author thanks them for their help and enlightening comments and explanations. Professors Enrique Segovia and Jaime Ramis are also acknowledged by their work on the definition of the numerical model for the container.

6. REFERENCES

[1] M. A. Maiga, "Particle model of single bubble sonoluminescence," *International Journal of Physical Sciences*, vol. 11, no. 19, pp. 252–261, 2016.

[2] S.-F. Ng, J. Barnard, P. Leung, and S. Yu, "Sonoluminescence test for equation of state in warm dense matter," *Nuclear Instruments and Methods in Physics Research Section A: Accelerators, Spectrometers, Detectors and Associated Equipment*, vol. 606, no. 1-2, pp. 172–176, 2009.

[3] J. A. Ketterling and R. E. Apfel, "Extensive experimental mapping of sonoluminescence parameter space," *Physical Review E*, vol. 61, no. 4, p. 3832, 2000.

[4] H.-Y. Kwak and H. Yang, "An aspect of sonoluminescence from hydrodynamic theory," *Journal of the Physical Society of Japan*, vol. 64, pp. 1980–1992, 1994.

[5] K. L. R. O. Pohl, *Pohl's Introduction to Physics*. Springer, 2017.

[6] D. Qin, S. Lei, B. Chen, Z. Li, W. Wang, and X. Ji, "Numerical investigation on acoustic cavitation characteristics of an air-vapor bubble: Effect of equation

of state for interior gases," *Ultrasonics sonochemistry*, vol. 97, p. 106456, 2023.

[7] F. Bemani and R. Sadighi-Bonabi, "Plasma core at the center of a sonoluminescing bubble," *Physical Review E—Statistical, Nonlinear, and Soft Matter Physics*, vol. 87, no. 1, p. 013004, 2013.

[8] V. Kamath, A. Prosperetti, and F. Egolfopoulos, "A theoretical study of sonoluminescence," *The Journal of the Acoustical Society of America*, vol. 94, no. 1, pp. 248–260, 1993.

[9] S. Hilgenfeldt, M. P. Brenner, S. Grossmann, and D. Lohse, "Analysis of rayleigh–plesset dynamics for sonoluminescing bubbles," *Journal of fluid mechanics*, vol. 365, pp. 171–204, 1998.

[10] W. Greiner, L. Neise, and H. Stöcker, *Thermodynamics and statistical mechanics*. Springer Science & Business Media, 2012.

[11] K. S. Suslick and D. J. Flannigan, "Inside a collapsing bubble: sonoluminescence and the conditions during cavitation," *Annu. Rev. Phys. Chem.*, vol. 59, no. 1, pp. 659–683, 2008.

[12] T. Leighton, "Derivation of the rayleigh-plesset equation in terms of volume," 2007.

[13] B. Zeiger, *Bubbles and crystals: Time-resolved sonoluminescence, sonocrystallization, and sonofragmentation*. University of Illinois at Urbana-Champaign, 2012.

[14] B. Kappus, A. Bataller, and S. Putterman, "Energy balance for a sonoluminescence bubble yields a measure¡? format?¿ of ionization potential lowering," *Physical review letters*, vol. 111, no. 23, p. 234301, 2013.

[15] C. Wu and P. H. Roberts, "A model of sonoluminescence," *Proceedings of the Royal Society of London. Series A: Mathematical and Physical Sciences*, vol. 445, no. 1924, pp. 323–349, 1994.

[16] K. Kerboua and O. Hamdaoui, "Computational study of state equation effect on single acoustic cavitation bubble's phenomenon," *Ultrasonics Sonochemistry*, vol. 38, pp. 174–188, 2017.

[17] L. L. Vignoli, A. L. De Barros, R. C. Thomé, A. Nogueira, R. C. Paschoal, and H. Rodrigues, "Modeling the dynamics of single-bubble sonoluminescence," *European Journal of Physics*, vol. 34, no. 3, p. 679, 2013.

[18] D. Alfè, M. Gillan, and G. D. Price, "Composition and temperature of the earth's core constrained by combining ab initio calculations and seismic data," *Earth and Planetary Science Letters*, vol. 195, no. 1-2, pp. 91–98, 2002.

[19] T. Guillot, "A comparison of the interiors of jupiter and saturn," *Planetary and Space Science*, vol. 47, no. 10-11, pp. 1183–1200, 1999.

[20] D. Riley, *Warm dense matter: laboratory generation and diagnosis*. IOP Publishing, 2021.

[21] A. Ng, "Warm dense matter: The missing link between condensed matter and plasma," in *2012 Abstracts IEEE International Conference on Plasma Science*, pp. PL3–1, IEEE, 2012.

[22] D. Riley, "Generation and characterisation of warm dense matter with intense lasers," *Plasma Physics and Controlled Fusion*, vol. 60, no. 1, p. 014033, 2017.

[23] S. White, B. Kettle, J. Vorberger, C. L. Lewis, S. Glenzer, E. Gamboa, B. Nagler, F. Tavella, H. J. Lee, C. Murphy, *et al.*, "Time-dependent effects in melting and phase change for laser-shocked iron," *Physical Review Research*, vol. 2, no. 3, p. 033366, 2020.

[24] P.-A. Gourdain, A. Sefkow, and C. Seyler, "The generation of warm dense matter using a magnetic anvil cell," *IEEE Transactions on Plasma Science*, vol. 46, no. 11, pp. 3968–3972, 2018.

[25] C. Hyland, S. White, B. Kettle, R. Irwin, D. Bailie, M. Yeung, G. Williams, R. Heathcote, I. East, C. Spindloe, *et al.*, "Measurements of free-free absorption in warm dense aluminium," *Plasma Physics and Controlled Fusion*, vol. 63, no. 7, p. 074003, 2021.

[26] P.-A. Gourdain and C. Seyler, "The impact of three dimensional mhd instabilities on the generation of warm dense matter using a ma-class linear transformer driver," *High Energy Density Physics*, vol. 24, pp. 50–55, 2017.

[27] M. Laraia, C. Hansen, N. Shaffer, D. Saumon, D. Kilcrease, and C. Starrett, "Real-space green's functions for warm dense matter," *High energy density physics*, vol. 40, p. 100940, 2021.

[28] Z. Moldabekov, T. Dornheim, M. Böhme, J. Vorberger, and A. Cangi, "The relevance of electronic perturbations in the warm dense electron gas," *The Journal of Chemical Physics*, vol. 155, no. 12, 2021.

[29] V. V. Karasiev, D. Mihaylov, and S. Hu, "Meta-gga exchange-correlation free energy density functional to increase the accuracy of warm dense matter simulations," *Physical Review B*, vol. 105, no. 8, p. L081109, 2022.

[30] G. M. Petrov and A. D. Davidson, "The ion equation of state of plasmas in the warm dense matter regime," *AIP Advances*, vol. 13, no. 3, 2023.

[31] M. P. Böhme, L. B. Fletcher, T. Döppner, D. Kraus, A. D. Baczewski, T. R. Preston, M. J. MacDonald, F. R. Graziani, Z. A. Moldabekov, J. Vorberger, *et al.*, "Evidence of free-bound transitions in warm dense matter and their impact on equation-of-state measurements," *arXiv preprint arXiv:2306.17653*, 2023.

[32] C. Ma, M. Chen, Y. Xie, Q. Xu, W. Mi, Y. Wang, and Y. Ma, "Nonlocal free-energy density functional for warm dense matter," *arXiv preprint arXiv:2405.12527*, 2024.

[33] B. Militzer, F. González-Cataldo, S. Zhang, K. P. Driver, and F. Soubiran, "First-principles equation of state database for warm dense matter computation," *Physical Review E*, vol. 103, no. 1, p. 013203, 2021.

[34] S. Khalid, B. Kappus, K. Weninger, and S. Putterman, "Opacity and transport measurements reveal that dilute plasma models¡? format?¿ of sonoluminescence are not valid," *Physical review letters*, vol. 108, no. 10, p. 104302, 2012.

[35] S. Hu, B. Militzer, V. Goncharov, and S. Skupsky, "First-principles equation-of-state table of deuterium for inertial confinement fusion applications," *Physical Review B—Condensed Matter and Materials Physics*, vol. 84, no. 22, p. 224109, 2011.

[36] J.-S. Jeon, K.-M. Kang, C. Lim, I. Ko, and H.-Y. Kwak, "Pulse width measurement of sonoluminescing air bubbles in various solutions using a time-correlated single photon counting technique," *Journal of Fluid Science and Technology*, vol. 5, no. 1, pp. 2–13, 2010.

[37] G. Lee and M. Law, "Numerical modelling of single-bubble acoustic cavitation in water at saturation temperature," *Chemical Engineering Journal*, vol. 430, p. 133051, 2022.

DOI:

Main theme: A12 Physical Acoustics and Ultrasound

Session A12.02 NDT & SHM Applications

Chair(s): L. Chehami, M. Ben Tahar, M. Ech-Cherif El-Kettani, G. Cosarinsky

DOI: 10.61782/fa.2025.0580

FORUM ACUSTICUM EURONOISE 2025

MODELLING OF THE ACOUSTIC EMISSION (AE) WAVE PROPAGATION USING THE AE TRANSMITTING SENSORS' RESPONSES

Van-Duong LE [1, 2*] **Marianne PERRIN** [1, 3] **Luis ESPINOSA** [1, 3]
Marie-Laetitia PASTOR [1, 3] **Yannick LE MAOULT** [4]
[1] University of Toulouse, Institut Clément Ader, CNRS 5312, IMT Mines Albi, INSA, ISAE-SUPAERO, UPS, 1 rue Lautréamont, 65000 Tarbes, France.
[2] The University of Danang - University of Science and Technology, 54 Nguyen Luong Bang, 550000 Danang, Viet Nam.
[3] Institut Universitaire de Technologie of Tarbes, Université de Technologie Tarbes Occitanie Pyrénées UTTOP, 65000 Tarbes, France.
[4] University of Toulouse, Institut Clément Ader, CNRS 5312, IMT Mines Albi, INSA, ISAE-SUPAERO, UPS, Campus Jarlard, Albi Cedex 09, 81013, France.

ABSTRACT*

Acoustic Emission (AE) testing is a non-destructive evaluation technique widely used in numerous fields providing ongoing monitoring to detect and track early signs of damage within structures. To ensure an effective interpretation of AE signatures in relation to damage mechanisms, a combination of numerical and experimental approaches is crucial for a comprehensive study of the measurement chain, including excitation sources, propagation mediums, sensors, acquisition systems and signal processing. This study aims to model the AE measurement chain using highly reproducible and reliably characterized emission waves from a piezoelectric sensor. To achieve this, the first step was to calibrate the source using a laser vibrometer. The aperture effect and several parameters of the sensor responses were investigated. Then, 3D models incorporating these source mechanisms within a metallic material were developed simultaneously by experiment and simulation to analyze AE wave propagation and measurement chain effects. Validated results in time and frequency domains showed good agreement, demonstrating the accuracy of the numerical approaches. These findings are crucial for gaining a significant understanding of AE sensors, contributing to sensor calibration processes, modelling of the entire measurement chain to enhance the interpretation of damage mechanisms.

Keywords: *Non-Destructive Evaluation (NDE), Acoustic Emission (AE), AE simulation, AE transmitting sensor, Aperture effect.*

1. INTRODUCTION

Non-Destructive Evaluation (NDE) techniques are widely used in numerous industrial fields to assess structural health and detect early damage without causing permanent harm of components and structures. These techniques provide inspections that are both safe and reliable, while remaining cost-effective and able to be conducted without interrupting ongoing operations. Acoustic Emission (AE) method is one of the most frequently employed NDE methods to detect and track early signs of damage in mechanically loaded structures and components. In such cases, the AE waves are generated by the sudden releasing of energy under the form of elastic waves and propagating in all directions within the material. The source of AE events may come from natural phenomena (earthquakes, rock bursts) [1], deformation

* ***Corresponding author***: *vanduong.le@iut-tarbes.fr*
Copyright: *©2025 First author et al. This is an open-access article distributed under the terms of the Creative Commons Attribution 3.0 Unported License, which permits unrestricted use, distribution, and reproduction in any medium, provided the original author and source are credited.*

processes [2], crack propagation [3], damage mechanisms in composite structure [4], etc. These AE waves are usually captured by sensors which convert the mechanical disturbance on the contact surface into a voltage-time waveform signal, providing information about the location and characteristics of AE events. The detection process of AE signals is described by the measurement chain illustrated in Figure 1. According to this, an AE signal in time domain S(t) is obtained by the convolution (⊗) of the characteristics of all elements in the measurement chain, from excitation source F(t), propagation medium G(t), coupling conditions C(t) and sensor transfer function H(t), and acquisition system A(t) as Eqn. (1):

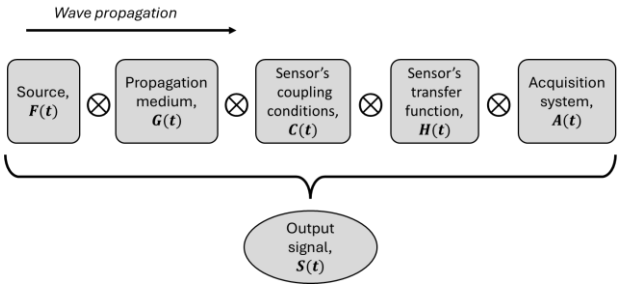


Figure 1. Measurement chain used for detection of AE waves.

$$S(t) = F(t) \otimes G(t) \otimes C(t) \otimes H(t) \otimes A(t) \quad (1)$$

The main scientific obstacles in enhancing our understanding of AE results lies in comprehending how the signal evolves from the excitation source to the obtained signal that highly dependent on the measurement chain configurations, such as excitation source mechanisms [5-6], structure and material properties, observation distance and direction [12-14], and sensors characteristics and its coupling conditions [15]. Piezoelectric sensors are widely used in AE testing due to their high sensitivity and affordability; however, their transfer function varies significantly based on sensor type, structure, and operating frequency [16-17]. These significant influences of the measurement chain configuration lead greater challenges when determining a robust correlation between AE signal characteristics and their respective actual excitation mechanisms. Addressing these challenges requires a well-defined characterization of each element in the measurement chain, which can be achieved through an effective combination of numerical and experimental approaches. For this purpose, studies should be carried out with configurations that include well-defined source mechanisms and propagation medium properties, facilitating a more straightforward analysis of the other elements in the measurement chain. With the rapid advancements in science and technology, numerical simulation tools have become essential and widely used by researchers to analyze the complex interactions and propagation of AE waves. Several mechanisms, simplified from AE events, have been used in simulations involving changes in applied force, displacement, or released energy over a very short excitation time. For instance, pencil-lead breaks sources are used to validate numerical results against experimental data, supporting the modeling of conical sensors, and considering the influence of geometrical specimen on AE signal characteristics [8, 18]. Moreover, glass tube fracture sources have been modeled and applied in research calibration processes for AE sensors [10, 16]. The mechanical impact sources are used to investigate the boundary reflection conditions and sensor characteristics in detecting AE wave propagation [19]. Another AE source mechanism consists of using a laser to generate an ultrasonic excitation that was used to obtain the calibration curve of piezoelectric sensors [20]. Furthermore, an artificial source generated by an AE sensor directly excited by an electrical pulse is also used in numerical research to study the complex behavior of piezoelectric conversion in AE sensors, as well as the influence of factors related to the propagation mediums of AE waves [14, 21]. Compared to other sources, the one generated by transmitting sensors offers higher reproducibility through control of the electrical pulse configuration, while also facilitating a better understanding of the electrical-mechanical conversion process, known as the sensor's response, thus contributing to successful sensor modeling in numerical approaches. The sensor's response is influenced not only by the sensor's geometry and the spatial variations across the sensor surface but also on the operating frequency, known as aperture effect [7, 21-22]. To the best of our knowledge, there has been limited exploration in literature regarding the precise determination of the response of transmitting sensors and its application in numerical studies to examine the influence of the AE measurement chain.

In this study, the source mechanism from AE sensors in terms of the normal velocity response was first characterized by using a laser vibrometer. Two types of sensors were used, including a resonant sensor, R15α, and a wideband sensor, F15α (from Physical Acoustics, USA). The influences of aperture effect on the response

of each sensor were investigated. Next, 3D models incorporating these mechanisms were developed to study the wave propagation and the influence of the measurement chain. The simulation results were validated with experiments to verify the accuracy of the modelling parameters and setup. Finally, the impact of contact surface conditions on the amplitude of the sensor response was taken into account to enhance the accuracy of the simulation results.

2. MEASUREMENT OF THE SENSOR'S RESPONSE

The vibration velocity responses across the active surface of sensors are non-uniform due to the aperture effect. To demonstrate this, a simplified model of the velocity response assumes that the variation across different positions on the sensor surface can be represented by the maximal velocity response usually measured at the center region of the surface, $v_{center}(t)$, multiplied by a k parameter as shown in Eqn. (2) [7].

$$v(t) = \frac{1}{S}\iint_S k(r).v_{center}(t)\,dS \quad (2)$$

Where S denotes the contact surface area of sensor, $k(r)$ is called the aperture effect function of the sensor and is a real number ranging from 0 to 1. This parameter represents the sensitivity of the normal vibration velocity at a position located at radius r, relative to its value at the center region of the sensor surface. In this study, two types of AE sensors were utilized: the narrowband resonance sensor, type R15α, with an operating frequency range from 50 kHz to 400 kHz, and the wideband flat frequency sensor, type F15α, with an operating frequency range from 100 kHz to 450 kHz.

Figure 2 shows the setup of the testing for measuring AE sensor response in terms of normal vibration velocity on its active surface. The acquisition includes an OFV-505 sensor head connected to an OFV-5000 vibrometer controller which was set with a VD-09 decoder board, and bandpass filter from 100 Hz to 1 MHz adapted to AE wave characteristics [1]. Ultrasonic excitation was obtained using a UTC110 system (MISTRAS, France), controlled through the EuroScan V software. AE sensors were fixed on a displacement system by plastic clamping units. The measurements on the active surface of the sensors were conducted along the centerline with a spacing of 200 µm between each point. The experimental data from the tests were processed using MATLAB® with a 4th-order Butterworth low-pass filter as in [18], with a cutoff frequency of 500 kHz adapted to operating frequency ranges of used sensors.

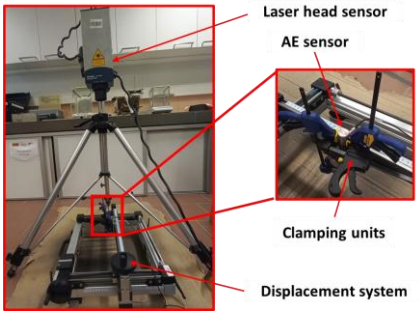


Figure 2. Test layout for measuring sensor's response in term of normal vibration velocity.

3. 3D MODELS OF WAVE PROPAGATION

3D models incorporating source mechanisms generated by transmitting sensors' response were established simultaneously by experiment and simulation as shown in Figure 3 a, and b, respectively. In the case of experiment, the same acquisition system as previous measurements were used to capture normal velocity of AE waves within an aluminum plate of dimensions 500 mm x 500 mm x 2mm. The AE sensor was mounted on the specimen surface by a thin layer of silicon glue. After several tests to determine the optimal excitation parameters, an excitation pulse with 100 volts and a rise time of 700 ns was applied to the AE sensor. The signals were obtained at two positions located at 30 mm and 90 mm as distances from sensors. A finite element approach was conducted by using the software COMSOL Multiphysics® through module "Solid Mechanics (Elastic waves)". The setup includes a 3D aluminum plate dimensioning 250 x 300 x 2 mm with its properties referred to [8]. The low-reflection conditions were applied to minimize the effects of reflected waves adapted to free conditions of wave propagation in larger geometry as experimental condition. The source from transmitting sensors were set on its contact surface using velocity response according to Eqn. (2) based on experimental results. Several tests were performed to determine the convergence of mesh element size and critical timestep. Based on these findings, the element size of 1 mm, corresponding timestep of 0.15 µs were chosen, offering a good compromise with computational time. On the other hand, a linear combination of mass and stiffness matrices were applied considering the attenuation of wave amplitude during propagating. Here, α and β are the mass

and stiffness proportionality coefficients, as known as Rayleigh damping coefficients. Both AE sensors used with operating frequency range less than 500 kHz, so the impact of β (mostly in high frequency) is neglected. Only α is applied (in low frequency), set to 30000, adapting with a damping factor of 0.002 at maximum frequency of 1 MHz based on experimental results.

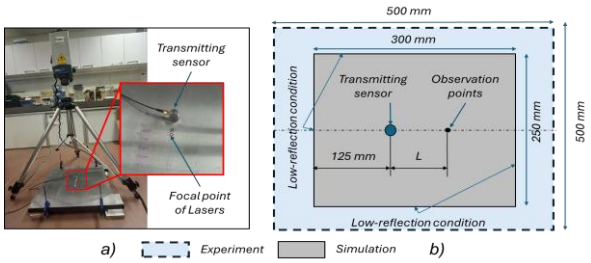


Figure 3. 3D models of wave propagation used for experiment (a) and simulation (b).

4. RESULTS AND DISCUSSION

4.1 Sensor surface velocity response and aperture effects

4.1.1 Sensor velocity response of sensors

The results in the response of two sensors at the surface center in terms of normal vibration velocity are illustrated in Figure 4. The normal velocity response varies significantly depending on the sensor type, affecting both waveform and its amplitude. The R15α resonant sensor shows higher sensitivity in peak velocity compared to the F15α wideband sensor, measuring 4.5 mm/s and 3.4 mm/s, respectively. Due to the inherent characteristics of resonant sensors, the R15α can maintain oscillations with minimal excitation energy, resulting in extended signal retention and higher amplitude responses compared to the F15α sensor.

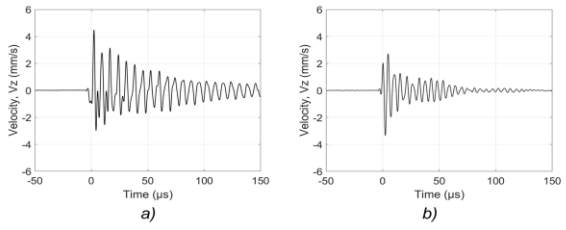


Figure 4. The velocity response measured at the center of surface for R15α (a) and F15α (b) sensors.

4.1.2 Peak velocity response across entire sensor surface

Figure 5 shows the results of peak velocity response across full measured diameter on active surface of both sensors. The standard deviation of peak velocity across 32 consecutive measurements remained below 0.1 mm/s (less than 3% of the max values) in most cases, demonstrating high reliability of tests. It can observe that the obtained peak velocity tends to exhibit symmetry along the centerline of the sensor's active surface. The results indicate that the peak velocity response varies with position on the sensor's contact surface, with higher values at the central region and decreasing towards the edges, depending on the sensor type. This is consistent with previous tests conducted on the μ80 sensor [22]. These findings highlight the influence of the aperture effect on the response of the AE sensors.

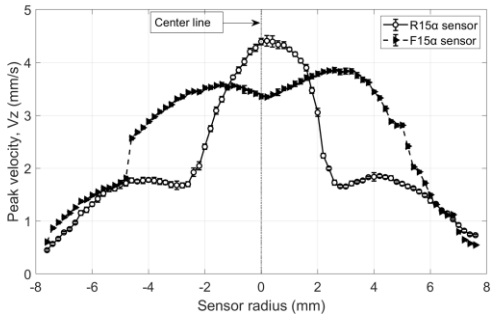


Figure 5. Peak normal velocity of the sensor response measured by laser vibrometer.

4.1.3 Aperture effect function of sensors

The *k(r)* factor, representing the influence of the aperture effect (Eqn. (2)), is illustrated in Figure 6. The analysis focuses on half of the sensor surface, taking into account its symmetrical response along the centerline. Here, the *k(r)* values were determined by normalizing the peak velocity at a given position *r* with respect to the maximum peak velocity response measured at the central region, followed by smoothing using a Savitzky-Golay filter [23]. For the R15α sensor, the highest *k(r)* value was found at the center, gradually decreasing toward edges of the sensor. Conversely, the F15α sensor exhibited a more uniform distribution, with *k(r)* values ranging between 0.93 and 1 over a central region extending up to 4 mm. These findings indicate that the peak amplitude variation across the sensor surface does not follow a simple uniform decay, as previously

assumed [7], but rather depends on both sensor characteristics and radial position *r*. The observed variations can be attributed to the aperture effect, which influences the sensor's transmitting transfer function, with dependencies on spatial positioning and operating frequency [7, 21-22]. This study enhances the understanding of how AE sensors convert electrical excitation into mechanical vibrations, providing valuable insights into source identification using transmitting sensors, contributing directly to accurate numerical sensor modeling, and the characterization of AE sensor transfer functions.

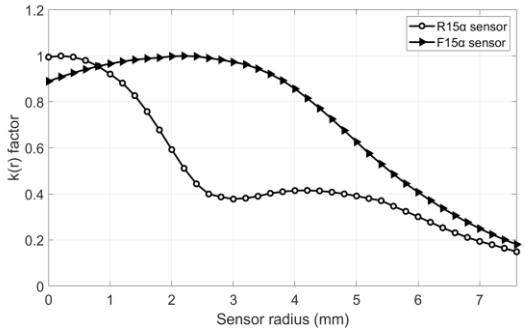


Figure 6. The values of *k(r)* as aperture effect function for both sensors.

4.2 AE wave propagation modelling

4.2.1 Excitation source mechanisms caused by AE sensors

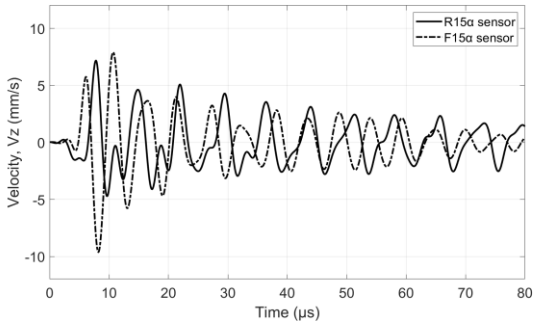


Figure 7. Source mechanisms generated by AE sensor response applying to numerical models.

The excitation source mechanisms generated by the transmitting sensor response for the R15α and F15α sensors are illustrated in Figure 7. These results were calculated using Eqn. (2), considering the sensor response at the center of the surface and its aperture function, which were applied for simulation.

4.2.2 Comparison of experimental and numerical results in both time and frequency domains

To match the configuration of the laser vibrometer in the testing setup, a 4th-order Butterworth bandpass filter (100 Hz – 1 MHz) was applied to the numerical results. Validation was performed by comparing the simulated and experimental normal velocity waveforms in the time domain and their corresponding FFTs, as shown in Figures 8 and 9, respectively, at observation points 30 mm and 90 mm away. Overall, the results show strong agreement across both domains. In order to quantify this agreement, the Pearson's correlation coefficient [24-25] was calculated for the full signal duration, a 30 μs window from the onset (limited between two vertical dash line), and the FFT results, summarized in Table 1. It is noted that a maximum correlation coefficient of 1 indicates a perfect positive correlation, -1 represents a perfect negative correlation, and 0 indicates no correlation. In all cases, the correlation coefficient ranged from 0.61 to 0.8 for the full signal, from 0.56 to 0.78 for the 30 μs window, and remained around 0.85 for the FFT results. These values align well with previous studies on AE wave modeling from pencil-lead breaks [9, 43]. A slight discrepancy in peak velocity was observed for the F15α sensor, with a difference of 1.3 mm/s at 30 mm and 0.3 mm/s at 90 mm, while for R15α sensor it is negligible. In the frequency domain, the R15α sensor results closely matched in both peak frequency and magnitude, while the F15α sensor showed a deviation of approximately 35 kHz and 10 dB, respectively. These differences might be caused by variations in sensor contact conditions during measurements and validation, as previously discussed in [21] and further discussions in the final section. A strong agreement between the experimental and simulation results validated the accuracy of the proposed numerical model, the calibrated excitation source mechanism from the transmitting sensors' responses and its aperture effect, and its application to AE wave propagation.

Table 1. Summary of the correlation coefficients of validated results.

Sensors	R15α		F15α	
Positions	30 mm	90 mm	30 mm	90 mm
Full duration	0.61	0.8	0.63	0.62
Within 30 μs	0.56	0.78	0.73	0.72
FFT	0.86	0.86	0.85	0.84

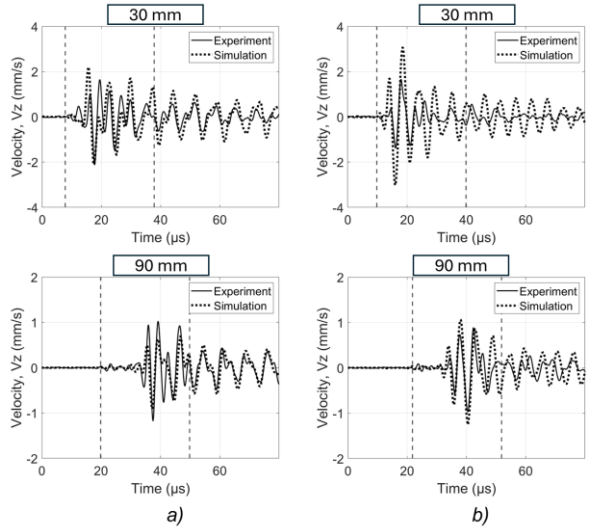


Figure 8. Validated results for the normal velocity of AE wave propagation generated by the response of R15α (a) and F15α (b) sensors.

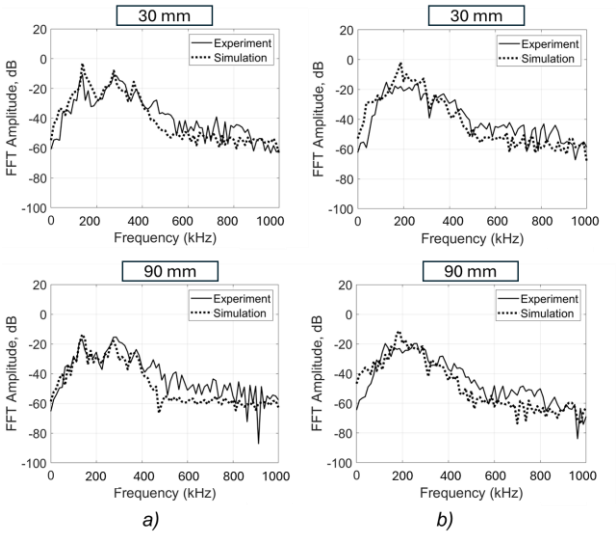


Figure 9. Validated results for FFT transformation of the AE wave propagation generated by response of R15α (a) and F15α (b) sensors. For vertical axis, 0 dB is referenced at 1 V/(mm/s).

4.2.3 . Consideration of the influence of sensor contact conditions

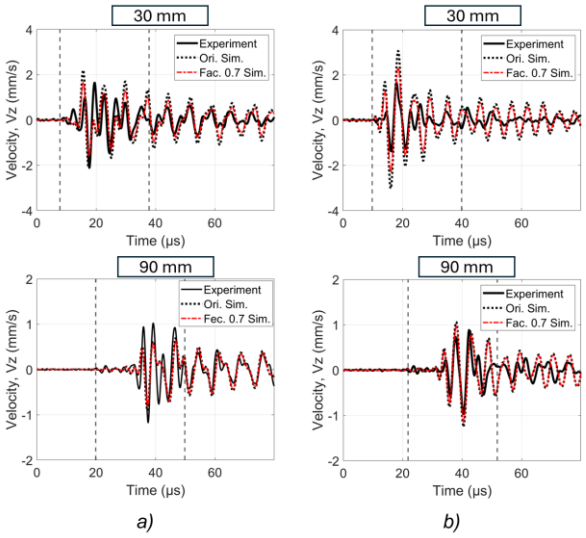


Figure 10. Validated results of normal velocity signals, accounting for the influence of the loss factor due to different sensor surface contact conditions, for R15α (a) and F15α (b) sensors.

As mentioned previously, differences in sensor's contact conditions may explain the slightly higher peak velocity and FFT magnitude observed in the simulation compared to the experiment in the near field. In sensor response measurements, the transmitting sensor's active surface was in free contact with air, whereas in the validation tests, it was in loaded contact with the specimen surface through a thin layer of silicon glue. In free contact conditions, the large impedance mismatch between the sensor and air could lead to increased oscillation energy at the surface, potentially enhancing resonance effects. In contrast, under loaded contact conditions, the smaller impedance mismatch, along with the applied pressure and coupling, resulted in smoother vibrations with lower amplitudes [21]. To account for the reduction in sensor response amplitude due to contact condition changes, a constant correction factor was introduced to improve simulation accuracy. Numerical simulations were conducted to evaluate the impact of different amplitude loss factors on the velocity response of transmitting sensors. The findings indicate that applying a loss factor of 0.7 improves agreement between simulated and experimental results. The damping coefficient α was recalculated and set to 12000 corresponding to the incorporating losing factor and its impact on the excitation

source's maximum amplitude. The final normal velocity signals are presented in Figure 10, comparing the original simulation (black dotted line), the simulation with a 0.7 loss factor (red line), and the experimental results (solid black line). Applying the loss factor improved the alignment between simulation and experiment, with a maximum error below 0.5 mm/s for the F15α sensor, while maintaining similar accuracy for the R15α sensor.

5. CONCLUSION

In this study, the normal velocity response on the active surface of two types of piezoelectric AE sensors was analyzed: the R15α, a narrowband resonant sensor, and the F15α, a wideband sensor with a flat frequency response. Additionally, 3D models were developed to simulate AE wave propagation generated by the response of transmitting sensors within an aluminum plate. To begin with, the results indicated that the normal velocity response is not uniform across the sensor surface and decreases toward the edges of the surface. Resonant sensors exhibited higher energy, with maximum sensitivity concentrated in a small central region of the surface, whereas wideband sensors showed lower energy but distributed peak sensitivity over a broader area. The study further examined *k(r)* as a function of the aperture effect, emphasizing the effects of sensor geometry, spatial variations, and operating frequency in shaping the peak normal velocity response. These findings provide valuable insights into AE sensor behavior, enabling improved sensor modeling in numerical methods without requiring detailed physical geometry. On the other hand, a very good agreement was observed between simulation and experimental results in both time and frequency domains, validating the accuracy of the numerical approach. To address variations in sensor response amplitude due to different coupling conditions, a loss factor was introduced, refining the simulation accuracy by accounting for changes from free contact (air) to loaded contact (specimen surface). These results contribute to a more comprehensive understanding of signal transformation from the source mechanism through wave propagation to the acquisition system, supporting the development of an improved AE measurement framework.

6. REFERENCES

[1] P. Kundu, "Review of rotating machinery elements condition monitoring using acoustic emission signal," *Expert Systems with Applications*, vol. 252, pp. 124169, 2024.

[2] C. K. Tan, P. Irving, and D. Mba, "A comparative experimental study on the diagnostic and prognostic capabilities of acoustics emission, vibration and spectrometric oil analysis for spur gears," *Mechanical Systems and Signal Processing*, vol. 21, no. 1, pp. 208–233, 2007.

[3] M. Chai, X. Hou, Z. Zhang, and Q. Duan, "Identification and prediction of fatigue crack growth under different stress ratios using acoustic emission data," *International Journal of Fatigue*, vol. 160, p. 106860, 2022.

[4] P. J. de Groot, P. A. M. Wijnen, and R. B. F. Janssen, "Real-time frequency determination of acoustic emission for different fracture mechanisms in carbon/epoxy composites," *Composites Science and Technology*, vol. 55, no. 4, pp. 405–412, 1995.

[5] W. Roundi, A. El Mahi, A. El Gharad, and J.-L. Rebiere, "Acoustic emission monitoring of damage progression in Glass/Epoxy composites during static and fatigue tensile tests," *Applied Acoustics*, vol. 132, pp. 124–134, 2018.

[6] S. Masmoudi, A. El Mahi, and S. Turki, "Use of piezoelectric as acoustic emission sensor for in situ monitoring of composite structures," *Composites Part B: Engineering*, vol. 80, pp. 307–320, 2015.

[7] Z. Hamam, N. Godin, C. Fusco, and T. Monnier, "Modelling of Acoustic Emission Signals Due to Fiber Break in a Model Composite Carbon/Epoxy: Experimental Validation and Parametric Study," *Applied Sciences*, vol. 9, no. 23, 2019.

[8] T. Le Gall, T. Monnier, C. Fusco, N. Godin, and S.-E. Hebaz, "Towards Quantitative Acoustic Emission by Finite Element Modelling: Contribution of Modal Analysis and Identification of Pertinent Descriptors," *Applied Sciences*, vol. 8, no. 12, p. 2557, 2018.

[9] Z. Hamam, N. Godin, C. Fusco, A. Doitrand, and T. Monnier, "Acoustic Emission Signal Due to Fiber Break and Fiber Matrix Debonding in Model Composite: A Computational Study," *Applied Sciences*, vol. 11, no. 18, 2021.

[10] M. G. R. Sause and M. A. Hamstad, "Numerical modeling of existing acoustic emission sensor absolute calibration approaches," *Sensors and Actuators A: Physical*, vol. 269, pp. 294–307, 2018.

[11] R.-R. Naber and H. Bahai, "Analytical and experimental validations of a numerical band-limited Green's function approach for modelling

acoustic emission waves," *Advances in Engineering Software*, vol. 38, no. 11, pp. 876–885, 2007.
[12] Y. Wu, M. Perrin, M.-L. Pastor, P. Casari, and X. Gong, "On the determination of acoustic emission wave propagation velocity in composite sandwich structures," *Composite Structures*, vol. 259, pp. 113231, 2021.
[13] Y. Wu, M. Perrin, M.-L. Pastor, P. Casari, and X. Gong, "Moisture Effects on Acoustic Emission Characteristics and Damage Mechanisms of Balsa Wood Core Composite Sandwich under 4-Point Bending," *Materials*, vol. 17, no. 5, pp. 1044, 2024,
[14] T. I. Khan, A. A. Rashid, and T. Nanami, "Theoretical and experimental analysis of acoustic emission signal for resonant sensor on homogenous material," *Sensing and Bio-Sensing Research*, vol. 39, pp. 100550, 2023.
[15] C. Hellier, *Handbook of nondestructive evaluation*. New York: McGraw-Hill, 2003.
[16] G. C. McLaskey and S. D. Glaser, "Acoustic Emission Sensor Calibration for Absolute Source Measurements," *Journal of Nondestructive Evaluation*, vol. 31, no. 2, pp. 157–168, 2012.
[17] K. Ono, "Rayleigh Wave Calibration of Acoustic Emission Sensors and Ultrasonic Transducers," *Sensors*, vol. 19, no. 14, pp. 3129, 2019.
[18] M. G. R. Sause, M. A. Hamstad, and S. Horn, "Finite element modeling of conical acoustic emission sensors and corresponding experiments," *Sensors and Actuators A: Physical*, vol. 184, pp. 64–71, Sep. 2012.
[19] Z. Heidary and D. Ozevin, "On the Influences of Boundary Reflections and Piezoelectric Sensors to the Characteristics of Elastic Waves for Pattern Recognition Methods," *Journal of Nondestructive Evaluation*, vol. 34, no. 1, pp. 271, 2014.
[20] L. Zhang, H. Yalcinkaya, and D. Ozevin, "Numerical approach to absolute calibration of piezoelectric acoustic emission sensors using multiphysics simulations," *Sensors and Actuators A: Physical*, vol. 256, pp. 12–23, 2017.
[21] N. Boulay, A. Lhémery, and F. Zhang, "Simulation of the spatial frequency-dependent sensitivities of Acoustic Emission sensors," *Journal of Physics: Conference Series*, vol. 1017, pp. 012008, 2018.
[22] T. Monnier, S. Dia, N. Godin, and F. Zhang, "Primary Calibration of Acoustic Emission Sensors by the Method of Reciprocity, Theoretical and Experimental Considerations," *Journal of Acoustic Emission*, vol. 30, pp. 152–166, 2012.
[23] Abraham. Savitzky and M. J. E. Golay, "Smoothing and Differentiation of Data by Simplified Least Squares Procedures.," *Analytical Chemistry Journal*, vol. 36, no. 8, pp. 1627–1639, 1964.
[24] N. Godin, P. Reynaud, and G. Fantozzi, "Challenges and Limitations in the Identification of Acoustic Emission Signature of Damage Mechanisms in Composites Materials," *Applied Sciences*, vol. 8, no. 8, pp. 1267, 2018.
[25] T. Le Gall, "Simulation de l'émission acoustique : Aide à l'identification de la signature acoustique des mécanismes d'endommagement," These de doctorat, Lyon, 2016.

DOI: 10.61782/fa.2025.0100



FORUM ACUSTICUM
EURONOISE 2025

ADAPTIVE 3D PLANE WAVE IMAGING THROUGH INTERFACES

Guillermo Cosarinsky[1*] **Adrián Rubio**[1,2] **Mario Muñoz**[1,2]
Jorge F. Cruza[1] **Jorge Camacho**[1]

[1] Ultrasound Systems and Technology Group (GSTU), Institute for Physical and Information Technologies (ITEFI), Spanish National Research Council (CSIC), c/Serrano 144, 28006 Madrid, Spain

[2] Electronics Department, Escuela Politécnica, Universidad de Alcalá de Henares, Ctra.Madrid-Barcelona, Km. 33,600, 28805 Madrid, Spain

ABSTRACT

Plane Wave Imaging (PWI) with ultrasonic arrays, initially developed for fast medical imaging, is nowadays being applied in Ultrasonic Testing (UT) for Non-Destructive Testing (NDT). In NDT, the Total Focusing Method (TFM) is regarded as the gold standard for image quality. However, TFM requires multiple transmission events (one for each array element), which can be slow for applications demanding very fast image acquisition. Since PWI can generate images of comparable quality with fewer transmissions, it presents a promising solution for such high-speed applications. This study demonstrates how volumetric PWI can be achieved using matrix arrays for testing arbitrarily shaped components, where a coupling medium is required and ultrasound waves are refracted on the component surface. This introduces complexity in calculating the time delays required to generate a plane wave within the component, a process that is straightforward in a single propagation medium scenario. Additionally, since the computation of those delays requires knowledge of the surface shape, we also explore how plane waves can be utilized for fast estimation of the surface shape.

Keywords: *non-destructive testing, plane wave imaging, adaptive imaging, matrix arrays*

**Corresponding author*: *g.cosarinsky@csic.es.*

Copyright: *©2025 First author et al. This is an open-access article distributed under the terms of the Creative Commons Attribution 3.0 Unported License, which permits unrestricted use, distribution, and reproduction in any medium, provided the original author and source are credited.*

1. INTRODUCTION

Non-Destructive Testing (NDT) plays a crucial role in ensuring the safety and integrity of critical infrastructure. In recent years, Plane Wave Imaging (PWI) has emerged as a promising technique for ultrasonic testing, offering significant advantages over traditional methods in terms of speed and image quality. Originally developed for medical imaging applications [1], PWI has found increasing relevance in industrial NDT scenarios, where rapid inspection and high-resolution imaging are fundamental [2].

In the field of NDT, the Total Focusing Method (TFM) has long been considered the gold standard for image quality [3]. However, TFM's requirement for multiple transmission events—one for each array element—can be a limiting factor in applications that demand very fast image acquisition. This limitation becomes significant when image reconstruction is performed by software and RF signals must be transferred to a computer, creating a bottleneck. Plane Wave Imaging (PWI) addresses this issue by reducing the amount of data that needs to be transferred and processed, generating images of comparable quality to TFM.

The application of PWI in industrial settings, particularly for testing components with complex geometries, presents unique challenges. Unlike medical applications where ultrasound typically propagates through a single medium, industrial NDT often involves coupling media and refraction at component surfaces. This introduces complexity in calculating the time delays required to generate a plane wave within the inspected component, a process that is relatively straightforward in single-medium

scenarios.

These challenges were addressed for the case of linear arrays and 2D imaging by various works [4–6]. In the context of railway inspection, Chang et al. [7] demonstrated a wavenumber-domain PWI technique capable of real-time dynamic imaging in vibrating environments, achieving frame rates of up to 83.3 fps. These developments highlight the potential of PWI to revolutionize NDT practices in the railway industry and beyond.

This study aims to further advance the application PWI using matrix arrays to perform 3D imaging of arbitrarily shaped components. We present a method for computing delay laws in 3D, which introduces additional challenges compared to the 2D case. Furthermore, we explore the use of plane waves for the rapid estimation of surface shape, a crucial step in accurately calculating time delays for wave generation within the component. The proposed methods are demonstrated through an example involving the testing of a cylindrical test piece using a 3 MHz 11x11 array.

2. METHODS

In this section we derive the emission focal laws to generate a three-dimensional plane wave across any given surface using a two-dimensional array. The approach begins by identifying a central ray originating from the array's center and refracting it in the desired plane wave direction, determined via Snell's law. For the remaining array elements, Fermat's principle is employed to compute rays that converge to a far-field focus positioned along the previously calculated central ray. A step-by-step derivation is provided below.

Figure 1 illustrates the geometry involved. A plane wave can be defined by a unit direction vector $\hat{k}$. For each array element E a ray must be found that refracts in the plane wave direction. To this end, the corresponding entry point G must be found (Figure 1.a). Snell's law states that the incident ray, the surface normal $\hat{n}$ at G, and the refracted ray are contained in a plane called the incidence plane. The directions of the incident and refracted rays are given by the unit vectors $\hat{v}_1$ and $\hat{v}_2$ respectively (Figure 1.b). According to Snell's law:

$$c_2 \sin(\theta_1) = c_1 \sin(\theta_2) \tag{1}$$

where θ_1 is the incidence angle, θ_2 the refraction angle, and c_1, c_2 the wave propagation velocities of the two media.

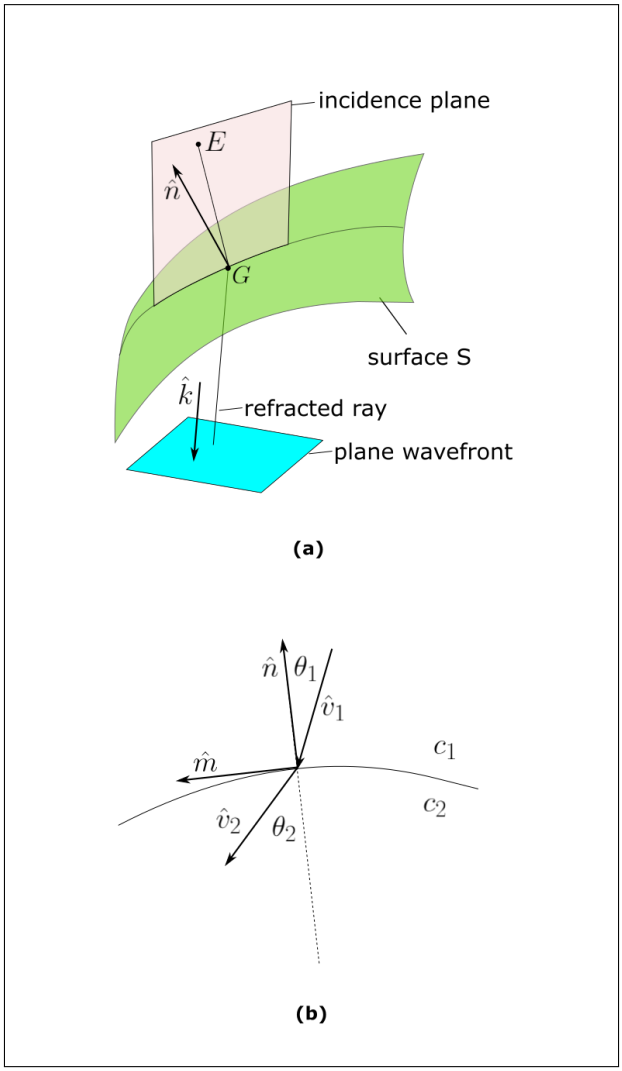


Figure 1. Geometry involved in the generation of a 3D plane wave through refraction. (a) Test piece surface, incidence plane and wavefront. (b) Vectors for Snell's law calculations

Given an element E and an entry point G, the incident unit vector is $\hat{v}_1 = \frac{\overline{EG}}{\|\overline{EG}\|}$. We need to compute $\hat{v}_2$ as a function of G, and solve the equation $\hat{v}_2 = \hat{k}$. From Figure 1.b we can see that:

$$\hat{v}_2 = \sin(\theta_2)\hat{m} - \cos(\theta_2)\hat{n} \tag{2}$$

where $\hat{m}$ is a tangent vector contained in the incidence

plane, which is given by:

$$\hat{m} = \hat{v_1} - \hat{v}_1 \cdot \hat{n} \tag{3}$$

The incidence angle cosine is given by the dot product:

$$\cos(\theta_1) = -\hat{v}_1 \cdot \hat{n} \tag{4}$$

Using equations (1) and (4) we get:

$$\sin(\theta_2) = \frac{c_2}{c_1}\sqrt{1 - (\hat{v}_1 \cdot \hat{n})^2} \tag{5}$$

Equations (2) and (5) along with the relation $\cos(\theta_2) = \sqrt{1 - \sin^2(\theta_2)}$ gives us $\hat{v}_2$ as a function of $\hat{v_1}$ and $\hat{n}$:

$$\hat{v}_2 = \frac{c_2}{c_1}\sqrt{1 - (\hat{v}_1 \cdot \hat{n})^2}\,(\hat{v_1} - \hat{v}_1 \cdot \hat{n}) - \sqrt{1 - \left(\frac{c_2}{c_1}\sqrt{1 - (\hat{v}_1 \cdot \hat{n})^2}\right)^2}\,\hat{n} \tag{6}$$

As was said before, to find the entry point coordinates (x, y, z) we should solve $\hat{v}_2 = \hat{k}$, which is a system of three non-linear equations. However, the z coordinate is a dependent variable. We suppose the surface is represented by a function $z = f(x, y)$. Additionally, vectors $\hat{v}_2$ and $\hat{k}$ have unit norm and thus one of its three coordinates is dependent on the other two. Therefore, we have a system of two equations with the two unknowns (x, y). Equation (6) does not show explicitly the dependence on (x, y). In order to make it explicit we should express the coordinates of $\hat{v_1}$ and $\hat{n}$ in terms of (x, y) as:

$$\hat{v}_1 = \frac{(x - E_x, y - E_y, f(x, y) - E_z)}{\sqrt{(x - E_x)^2 + (y - E_y)^2 + (f(x, y) - E_z)^2}} \tag{7}$$

$$\hat{n} = \frac{(-\frac{\partial f}{\partial x}, -\frac{\partial f}{\partial y}, 1)}{\sqrt{1 + \frac{\partial f}{\partial x}^2 + \frac{\partial f}{\partial y}^2}} \tag{8}$$

where (E_x, E_y, E_z) are the array element coordinates. Replacing (7) and (8) in (6) to solve $\hat{v}_2 = \hat{k}$ results in a complex and cumbersome system of equations with no analytical solution. As in the 2D case, numerical methods are needed to solve it. Newton-Raphson method might be used, but it required the calculation expression (6) partial derivatives which gives lengthy and impractical formulae. Thus, we implemented a brute force grid search approach, which is inefficient but easy to implement. We will call this method of computing the entry point Brute Force Snell (BFS). If it has to be applied to all the array elements, the overall computation time would be very high.

An alternative method for the computations of the entry points can be derived by following this idea: a plane wave emission is equivalent to an emission focused to a point in infinity. This is illustrated in Figure 2.a, where a bunch of rays from array elements is refracted and focused to a point F_{far} very distant to the array and surface. Figure 2.b shows the bunch of rays is close to a bunch of parallel rays. Rays from the array elements to F_{far} can be computed using Fermat's principle. But first we need to find the appropriate F_{far} for a given plane wave direction $\hat{k}$. As show in Figure 2.b, the far away focus must be located on the ray coming from the array center O_P, that is refracted at the point G_P. Thus $\overline{G_P F_{far}} = s\hat{k}$ with $s >> W$, where W is the aperture size ($s = 100 * W$ for example). Entry point G_P must be computed by Snell's law. In our case that was done using BFS, which is a slow algorithm but its only applied once per plane wave.

The emission time delay $\Delta t(E)$ for an array element E is finally computed as:

$$\Delta t(E) = t(E, F_{far}) - t(O_P, F_{far}) \tag{9}$$

where $t(E, A)$ is the TOF from E to a point A. With these delays a plane wave is created such that it goes through the array center at time $t = 0$. The TOF $t_{PW}(\hat{k}, \vec{r})$ of the plane wave to a point A is finally computed as:

$$t_{PW}(\hat{k}, A) = t_{far} + \frac{1}{c_2}\overline{F_{far}A} \cdot \hat{k} \tag{10}$$

$$t_{far} = t(O_P, F_{far}) \tag{11}$$

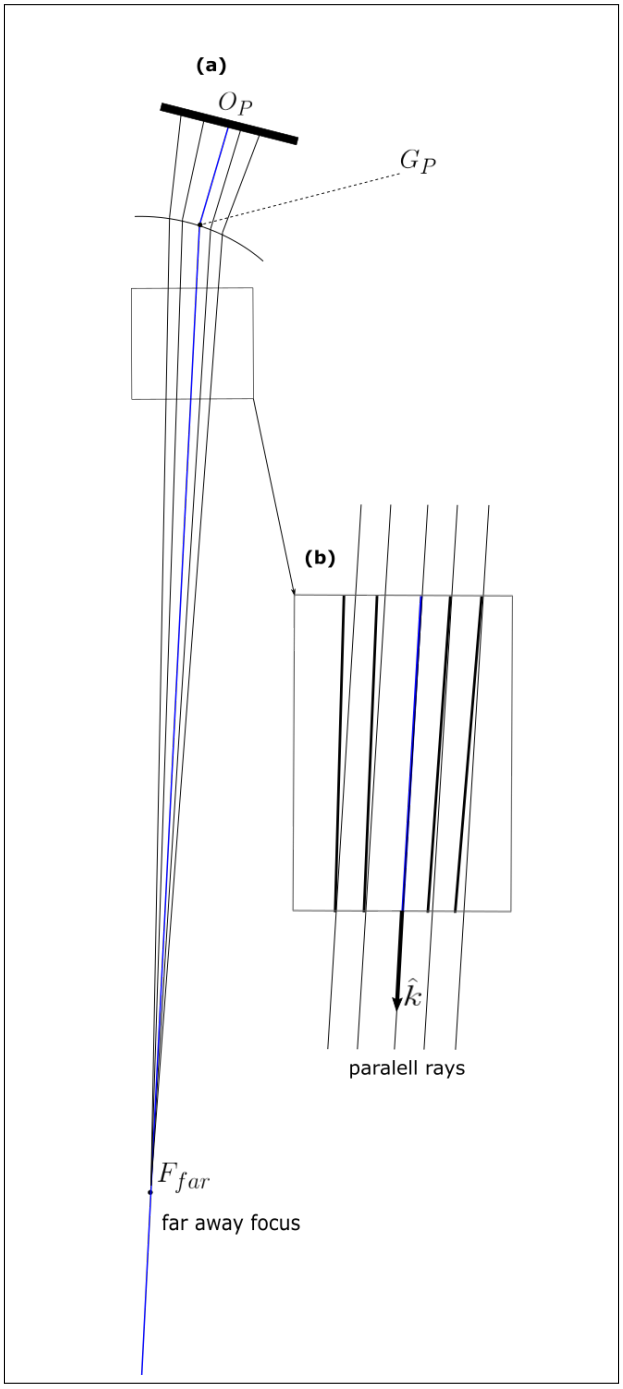


Figure 2. Geometry involved in the generation of a 3D plane wave through refraction. (a) Test piece surface, incidence plane and wavefront. (b) Vectors for Snell's law calculations

To compute the total TOF, we must calculate the ray path from the point $\vec{r}$ to each array element. This process typically requires an iterative calculation using Fermat's principle, which is computationally intensive. To optimize this procedure, we employ the 3D Virtual Array method, which we developed in our previous work [8].

As previously mentioned, TOF computations require a surface representation in the form $z = f(x, y)$. This representation can be obtained using ultrasound echoes reflected from the component's surface. In our previous work [9], we proposed several methods to achieve this for basic geometries, such as cylinders, planes and spheres.

One approach involves using a single plane wave directed along the array normal. This method has the advantage of requiring only a single firing, making it very fast. However, this method may fail if the probe's normal is at a significant angle to the surface, so it is best used in scenarios where such angular deviations are avoided.

For more complex or general geometries, alternative methods should be employed. Techniques such as those described in [10, 11] are promising candidates but would need to be extended to three-dimensional cases, as demonstrated in [12].

3. EXPERIMENTAL VALIDATION

In this section, we present an experimental example using a cylindrical aluminum test component with a 10 mm radius, featuring two Flat Bottom Holes (FBHs) in its midplane. The probe used was a 3 MHz, 11x11 matrix array with a 1 mm pitch. Data acquisition was performed using the SITAU II 128 full-parallel ultrasound system by DASEL S.L. (Spain).

TFM and PWI techniques were applied to generate images within a volume of 88x80x80 voxels. PWI was performed using nine plane waves, with an additional wave dedicated to surface detection. Lateral views of the resulting volumetric images are shown in Figure 3. It is observed in Figures 3 a and b that both methods produce similar results, where the 2 FBHs (H1 and H2 in Figure 3.a) are clearly imaged. A detailed comparison is presented in Figure 3.c, which displays the lateral amplitude profiles of H1 and H2, revealing that the contrast of H1 is slightly better in TFM. However, the acquisition efficiency difference between TFM and PWI is significant. TFM requires 121 individual firings, corresponding to each element in the 11x11 matrix array. In contrast, PWI in this experiment utilizes only 9 plane wave firings. Consequently, the RF signals collected for TFM contain ap-

proximately 14 times more data than those acquired for PWI. This substantial reduction in data volume for PWI highlights its potential for faster acquisition and processing times, which can be crucial in real-time imaging applications.

The main drawback of PWI is the requirement for an additional acquisition step to detect and reconstruct the surface, as well as the need to compute the emission focal laws—tasks that are unnecessary in the Full Matrix Capture (FMC) mode used for TFM, as they don't depend on the surface shape. However, in some cases, surface detection can be accomplished with just a single firing, and the computation of the delays, using the method described in Section 2, is highly efficient. In the example presented, this computation takes approximately 1 millisecond.

Regarding the software beamforming execution time, our current GPU implementation using an Nvidia GeForce RTX 3090 card demonstrates significant performance improvements for PWI compared to TFM: 68 ms for TFM and 15 ms for PWI. This represents more than a 4-fold speed increase for PWI over TFM in terms of image reconstruction. However, the most substantial advantage lies in the reduced data transfer time associated with PWI, coarsely 14 times less data in PWI than in TFM.

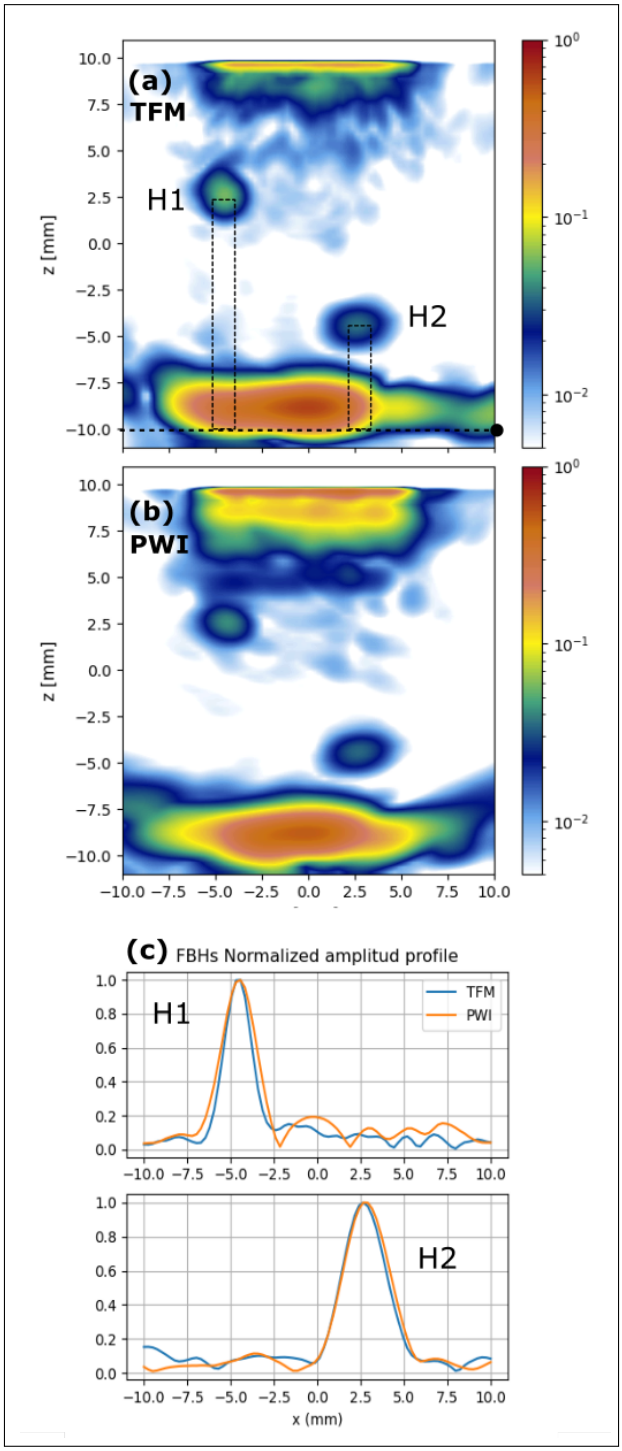


Figure 3. TFM and PWI images (lateral view). The cylinder axis is coincident with the X-axis. (a) TFM image; FBHs are represented by dashed lines in the schematic overlay (b) PWI image with 9 plane waves, (c) Amplitude profiles of the FBHs for the two imaging methods.

4. CONCLUSIONS

This study has demonstrated the feasibility and advantages of using 3D PWI with matrix arrays for non-destructive testing of components with arbitrarily shaped surfaces. By addressing the challenges associated with wave refraction at interfaces, we have presented a method for computing the delay laws required for the generation of plane waves within the inspected component. The use of a surface representation derived from ultrasound echoes makes the proposed method adaptive.

Experimental validation using a cylindrical test component with flat-bottom holes confirmed the effectiveness of the 3D PWI technique. The results demonstrate that PWI can achieve comparable image quality to the Total Focusing Method (TFM) while significantly reducing the number of transmission events.

Future work will focus on refining the surface detection and reconstruction algorithms and conducting comprehensive comparisons with TFM across a wider range of component geometries and defect types. Ultimately, the advancements in 3D PWI presented in this study contribute to the ongoing evolution of NDT techniques, paving the way for more efficient and reliable inspection of critical infrastructure components.

5. ACKNOWLEDGMENTS

This research was supported by the project PID2022-143271OB-I00, funded by MCIN/AEI /10.13039/501100011033/FEDER, UE., the project PLEC2024-011165, funded by MICIU/AEI/10.13039/501100011033/ FEDER, UE, and by the European Commission – NextGenerationEU, through Momentum CSIC Programme: Develop Your Digital Talent. The funding for these actions/grants and contracts comes from the European Union's Recovery and Resilience Facility-Next Generation, in the framework of the General Invitation of the Spanish Government's public business entity Red.es to participate in talent attraction and retention programmes within Investment 4 of Component 19 of the Recovery, Transformation and Resilience Plan.

G. Cosarinsky staff is hired under the Generation D initiative, promoted by Red.es, an organisation attached to the Ministry for Digital Transformation and the Civil Service, for the attraction and retention of talent through grants and training contracts, financed by the Recovery, Transformation and Resilience Plan through the European Union's Next Generation funds.

6. REFERENCES

[1] G. Montaldo, M. Tanter, J. Bercoff, N. Benech, and M. Fink, "Coherent plane-wave compounding for very high frame rate ultraso- nography and transient elastography," *IEEE Trans. Ultrason. Ferroelectr. Freq. Control*, vol. 56, pp. 489–506, 2009.

[2] L. Le Jeune, S. Robert, and C. Prada, "Plane wave imaging for ultrasonic inspection of irregular structures with high frame rates," in *AIP Conference Proc.*, vol. 1706, (Melville, NY, USA), p. 020010, AIP Publishing LLC, 2016.

[3] C. Holmes, B. Drinkwater, and P. Wilcox, "The post-processing of ultrasonic array data using the total focusing method," *Insight: Non-Destructive Testing and Condition Monitoring*, vol. 46, no. 11, pp. 677–680, 2004.

[4] G. Cosarinsky, J. F. Cruza, and J. Camacho, "Plane wave imaging through interfaces," *Sensors*, vol. 21, no. 15, 2021.

[5] R. Rachev, P. Wilcox, A. Velichko, and K. McAughey, "Plane wave imaging techniques for immersion testing of components with nonplanar surfaces," *IEEE Trans. Ultrason. Ferroelectr. Freq. Control*, vol. 67, pp. 1303–1316, 2020.

[6] H. Sui, P. Xu, J. Huang, and H. Zhu, "Space optimized plane wave imaging for fast ultrasonic inspection with small active aperture: Simulation and experiment," *Sensors (Switzerland)*, vol. 21, no. 1, pp. 1–11, 2021.

[7] Z. Chang, X. Xu, S. Wu, E. Wu, K. Yang, J. Chen, and H. Jin, "Ultrasonic dynamic plane wave imaging for high-speed railway inspection," *Mechanical Systems and Signal Processing*, vol. 220, p. 111672, 2024.

[8] G. Cosarinsky, J. F. Cruza, M. Muñoz, and J. Camacho, "Optimized auto-focusing method for 3d ultrasound imaging in ndt," *NDT and E International*, vol. 134, no. November 2022, 2023.

[9] G. Cosarinsky, J. F. Cruza, M. Muñoz, and J. Camacho, "Automatic estimation of surface and probe location for 3d imaging with bidimensional arrays," *NDT and E International*, vol. 141, p. 102990, 2024.

[10] J. Camacho, F. Cruza, J. Brizuela, and C. Fritsch, "Automatic dynamic depth focusing for ndt," *IEEE Trans. Ultrason. Ferroelectr. Freq. Control*, vol. 61, pp. 673–684, 2014.

[11] R. E. Malkin, A. C. Franklin, R. L. Bevan, H. Kikura, and B. W. Drinkwater, "Surface reconstruction accuracy using ultrasonic arrays: Application to non-destructive testing," *NDT and E International*, vol. 96, no. February, pp. 26–34, 2018.

[12] J. G. McKee, R. L. T. Bevan, P. D. Wilcox, and R. E. Malkin, "Volumetric imaging through a doubly-curved surface using a 2d phased array," *NDT E International*, vol. 113, no. August, p. 102260, 2020.

DOI: 10.61782/fa.2025.0928

FORUM ACUSTICUM EURONOISE 2025

ULTRASONIC PULSE-ECHO SYSTEM FOR MEASURING THE INTER-PLATE DISTANCE OF AN IRRADIATED FUEL ELEMENT

R. Mrabti[1] E. Le Clézio[1] T. Delaunay[1]

Y. Calzavara[2] G. Despaux[1]

[1] [a] IES, Univ Montpellier, CNRS, Montpellier, France

[2] Institut Laue Langevin – ILL, 71 Avenue des Martyrs, 38000 Grenoble, France

ABSTRACT

The High Flux Reactor at the Laue Langevin Institute produces the most intense neutron flux in the world, with a thermal power of 58 MW. As part of the global non-proliferation initiative, the Laue Langevin Institute aims to convert highly enriched fuel into low enriched uranium. This conversion is a challenging process, requiring strict compliance with safety standards and the preservation of the same performance quality for the new fuel element. During an irradiation cycle of the fuel element, multiple microstructural and physicochemical transformations occur, depending on the specific irradiation history of the fuel element, leading to a swelling phenomenon of the fuel plates and a decrease in the inter-plate distance. The Perseus project therefore aims to develop new evaluation tools, particularly a measurement of the inter-plate distance using an ultrasonic pulse-echo system with a frequency of 100 MHz. In this article, we will present the system developed over the course of three theses, the different solutions implemented to measure the inter-plate distance on an irradiated fuel element. The radiation-resistant transducer, custom-built along with its instrumentation, and the associated signal processing will be detailed to present measurements on irradiated fuel elements.

Keywords: *ultrasonic sensors, distance measurement, high-flux reactor.*

[*] ***Corresponding author***: *gilles.despaux@umontpellier.fr*

Copyright: *©2025 First author et al. This is an open-access article distributed under the terms of the Creative Commons Attribution 3.0 Unported License, which permits unrestricted use, distribution, and reproduction in any medium, provided the original author and source are credited.*

1. INTRODUCTION

The High-Flux Reactor (RHF) at the Institute Laue Langevin (ILL) generates the world's most intense neutron flux with a thermal power of about 58 MW [1-2]. As part of a global nonproliferation initiative, ILL aims to convert the RHF from high enriched uranium to low enriched uranium, a challenging process that must maintain safety standards and performance quality [3-5].

High Performance Research Reactors (HPRR) produce neutrons for material testing or science through fission in the reactor's fuel. During an irradiation cycle, various micro-structural and physical-chemical transformations occur in the fuel element. Post-irradiation examinations are essential to assess new fuel elements, identify structural modifications, and control irradiation histories [6]. Post-irradiation examinations activities, conducted in highly radioactive environments, require specialized infrastructure such as visual examination, radiography, and ultrasonic testing. Ultrasonic measurements are particularly valuable for nondestructive evaluation in the nuclear industry [7-10].

The Institut Laue Langevin and the University of Montpellier's Institute of Electronics and Systems launched the PERSEUS project to estimate the inter-plate distance within an ILL HPRR spent fuel element, linked to the RHF irradiation history. An ultrasonic device with a double element transducer was engineered and tested in the lab for in-situ measurements [11]. A mechanical system was developed to control the device underwater during testing. The paper discusses experimental constraints, the ultrasonic device and mechanical holder's structure and behavior, the instrumentation, and the time of flight estimation process. Section 4 covers in-laboratory measurement and calibration, and Section 5 presents the main result: an in-situ estimation

of the water-channel profile along 50 cm. The paper concludes with future perspectives.

2. EXPERIMENTAL CONSTRAINTS

To evaluate the irradiation history of the ILL RHF fuel element, several experimental constraints must be considered. First, non-destructive post-irradiation examinations are necessary to ensure the integrity of the fuel element. High precision measurements are required despite the challenging access to the element, which is submerged in a moderating water pool at a depth of 12 meters for cooling after use. Additionally, the fuel plates have involute shapes to maintain a constant nominal inter-plate distance of 1.8 mm, limiting the ultrasonic device's thickness to 1 mm. The desired measurements need micrometric resolution to detect expected microscopic structural modifications of around 25 µm, necessitating high-frequency operation to achieve resolutions of about 1 µm. The ultrasonic device must be carefully designed, as the wavelengths are comparable to its microstructure, significantly affecting the device's ultrasonic response. Finally, since the measurements are conducted in a highly radioactive environment, special attention must be given to the materials used in the ultrasonic device to ensure its performance when introduced into a spent fuel element. The following section details how we addressed these constraints through the design of the ultrasonic device and its integration into a measurement system.

3. EXPERIMENTAL SETUP

3.1 Measurement principle

Nondestructive testing has become crucial in the nuclear industry for assessing the efficiency and safety of nuclear power generation, especially in complex geometries like the High-Flux Reactor (RHF) at the Laue Langevin Institute [12]. Previous research led to the development of a measurement system to estimate the RHF fuel element's water-channel thickness (Fig. 1) [11-15]. This system, requiring expertise in electronics, high-frequency acoustics, and mechanics, has now been optimized to measure the inter-plate distance, known as the water-channel thickness.
The measurement system uses a waterproof dual piezoelectric transducer, which acts as both an emitter and receiver, integrated at the end of a 1 mm steel blade. When the blade is inserted into the nominal 1.8 mm inter-plate distance, (Fig. 2) the transducers are connected to a pulser/receiver to transmit and receive ultrasonic waves. These waves undergo specific signal processing to evaluate the inter-plate distance.

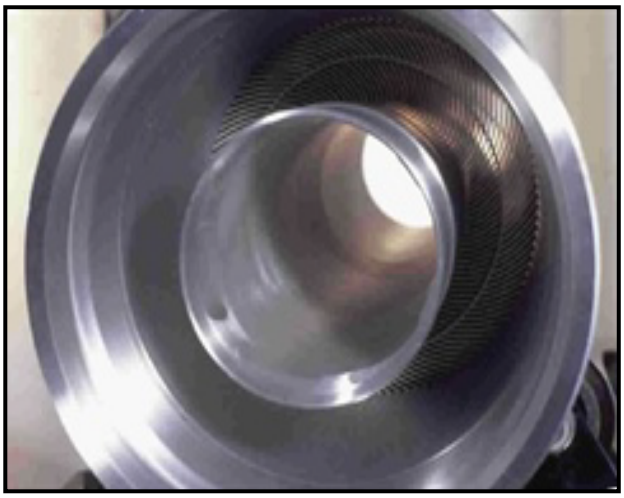


Figure 1. Bottom view of an RHF fuel element.

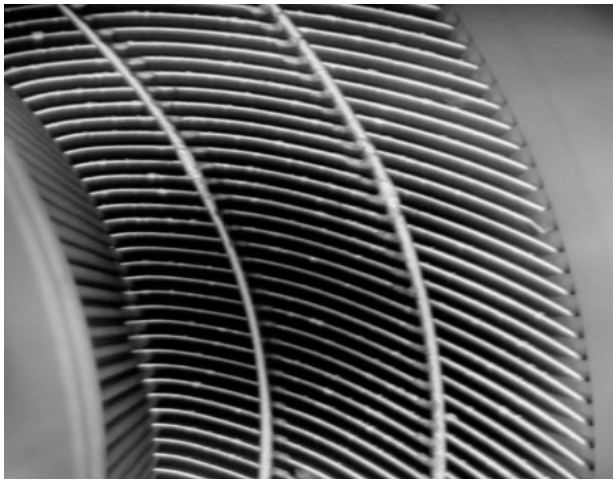


Figure 2. Enlarged top view of the plates of a fuel element with the channels whose distance needs to be measured.

The measurement principle involves two piezoelectric elements bonded to both faces of a silica support, mounted on one end of a 1 mm thick, 10 mm wide, and 1500 mm long stainless-steel blade (Fig. 3). After the blade is introduced into the water channel, the inter-plate distance is measured using ultrasonic waves emitted and received by a

dual transmitter/receiver system. The pulse echo method quantifies the time of flight t between reflections on the silica support and the fuel plates. Based on the ultrasonic velocity c in the propagation medium, the distance d is calculated using the formula in Eqn. (1).

$$d = (c*t) / 2. \quad (1)$$

By summing the distances d_1 and d_2 and adding the thickness d_s of the silica (Fig. 3), the measurement of the water channel thickness d_{wc} can be calculated using the following formula, with d_1 being the distance between the silica and the right plate, d_2 being the distance between the silica and the left plate, and d_s being the thickness of the silica Eqn. (2).

$$d_{wc} = d_1 + ds + d_2. \quad (1)$$

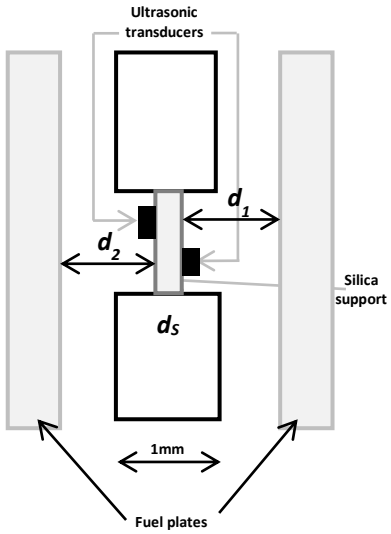


Figure 3. Schematic diagram of the measurement of a channel's thickness.

3.2 High-frequency ultrasonic device

A high-frequency ultrasonic transducer is a multi-layered device comprising a piezoelectric element disk, backing material, matching layer, and coaxial cables for transmission and reception. Fig. 4 illustrates the manufactured transducers. To meet experimental constraints and achieve the desired resolution, LiNbO3 ceramic was chosen for its excellent radiation resistance and vibration properties. The piezoelectric elements were carefully thinned to 35 µm, enabling operating frequencies of around 100 MHz. These elements were then attached to a 400 µm thick high-purity silica support, serving as the delay line. Special care was taken during the bonding process to ensure proper alignment of the transducers [16-17].

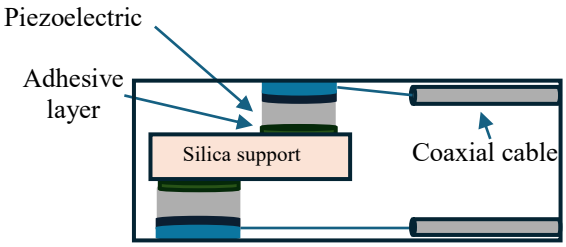


Figure 4. Transducer architecture.

To facilitate the insertion of transducers into the inter-plate distance, they were mounted on one end of a stainless-steel blade, as shown in Figure 5. This blade was meticulously manufactured, adhering to nuclear procedures to ensure material quality, cleanliness, and precise dimensions. The blade used in this study had specific dimensions: 1 mm thickness, 10 mm width, and 1500 mm length. The silica support, including the two active elements, was designed to fit into a hole at the blade's end. Grooves were drilled on both faces of the blade to facilitate cable connections for the transducers. Once mounted, the transducers were connected to a 20 m cable, allowing remote measurements.

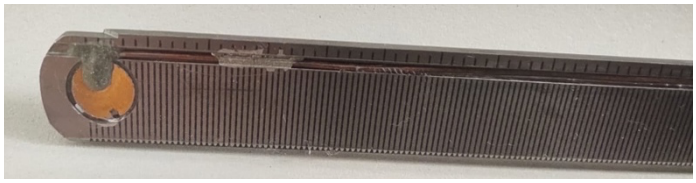


Figure 5. Ultrasonic transducer.

3.3 Instruments

The acquisition system begins with a dual transmitter/receiver electronic board (PXI) designed and manufactured at the University of Montpellier's Institute of Electronics and Systems. This dual pulse generator is optimized to produce high-frequency pulses compatible with transducers operating up to 400 MHz. Additionally, specific electronics enable the excitation of piezoelectric elements after a 20-meter cable.

Electric signals are transmitted through coaxial cables, and the received signals are then sent to a filtering system and a programmable gain amplifier. These signals are captured and converted into digital format using a NI PXIe-5162 acquisition card, chosen for its 2*2.5 GS/s sampling frequency and 10-bit resolution. Subsequently, digital signal processing is performed, with further details provided later.
All electronic board and the control computer are housed in a NI PXI rack, creating a compact and practical system for in-situ measurements. This setup not only ensures convenience but also facilitates procedures required for use in controlled nuclear zones.

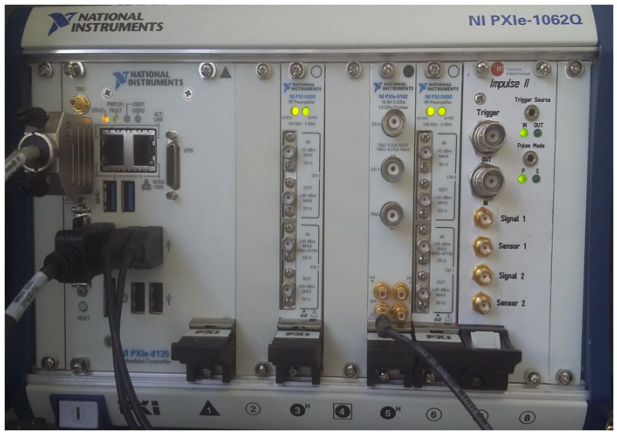


Figure 6. PXI controller with all electronic boards used for the generation, acquisition and processing of high-frequency ultrasonic signals.

3.4 Mechanical holder

Positioning the blade within the water channel is a crucial step in in-situ measurements, especially since the fuel element is stored in a 12-meter deep cooling pool. This experimental constraint necessitates high flexibility in aligning the ultrasonic device. To control and identify the device's position, ILL developed an automatic system. As shown in Fig. 7, this system includes a mechanism that allows translations along two axes to align the ultrasonic device with the fuel plates. It also utilizes motorized reels powered by a variable speed drive to control movement along the z-axis. Additionally, the reel can be operated manually for fine-tuning adjustments and situations requiring manual control.
A wire encoder is also used to determine the vertical position of the blade during measurements. This sensor is directly connected to the PXI rack computer, enabling synchronized ultrasonic measurements with the blade's height in the water channel being measured.

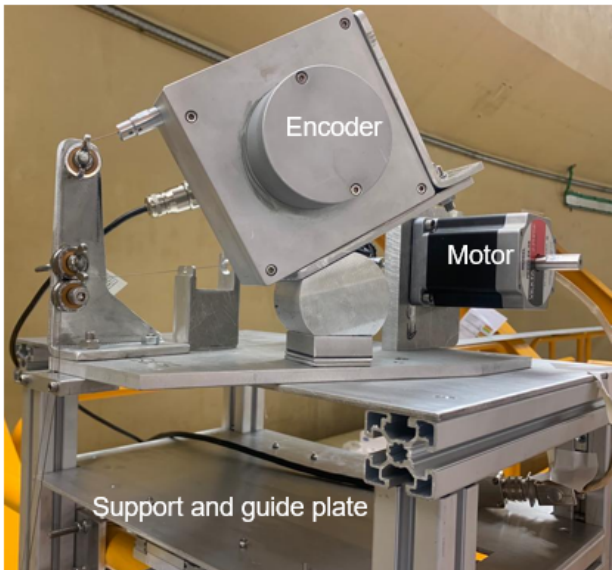


Figure 7. Mechanical holder.

3.5 Measurement principle

The distance measurement is based on a pulse/echo method [18]. The time of flight (ToF) of an ultrasonic wave corresponds to the interval between the emission and reception of an ultrasonic pulse reflected by an object or surface. To determine the distance d to the object, the echo time t is multiplied by the velocity c at which the ultrasonic wave propagates through the medium (Eq. 1).
Due to the transducer structure shown in Fig. 3, two series coexist in the signal. The first series, shown on the left side of the signal in Fig. 8, corresponds to the signature of a transducer positioned in water. This composite signal includes both the electrical excitation of the transducer and the multiple reflections of the initial pulse at the silica/water interface.
The complementary part of this signal is transmitted through the water and received after reflecting off the surface of the fuel plates. The resulting signal corresponds to the right side of the signal in Fig. 8.
To identify the time of flight, an inter-correlation is performed between the two parts of the signal in Fig 8, as indicated in [11]. To achieve this inter-correlation, the two overlapping zones must be separated. This is resolved by

point-by-point subtraction of the first zone with an acquisition made without a plate echo.

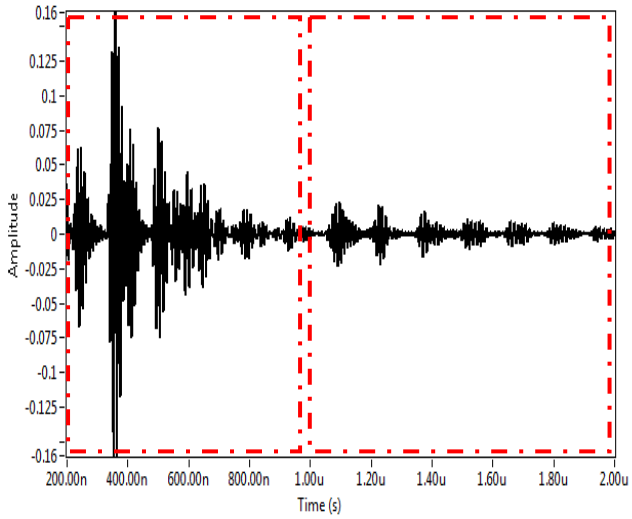


Figure 8. Experimental signal highlighting two series of echoes.

Using a silica delay line that produces multiple reflections allows for inter-correlation with a series of echoes rather than a single echo. This complicates signal processing due to the saturation of the initial echoes but facilitates the detection of the actual time of flight value, as the inter-correlation is performed over a large number of periodic echoes.

The inter-plate distance d_{wc} is then defined by Eq. (2), where d_s is the thickness of the silica layer and d_1 and d_2 are the thicknesses of the water layers on both sides of the blade. A statistical treatment for a given position can also be performed to reduce measurement noise.

4. IN-LAB MEASUREMENT

After introducing the principle of inter-plate distance measurement, we conducted an in-depth evaluation of the complete system to assess the transducer performance and signal processing accuracy for in-situ measurements.

4.1 Experimental bench in the laboratory

We built a motorized test bench with 8 degrees of freedom to ensure parallel motion of the blade to the plates. We first performed tests on a piece of fictitious fuel element, as shown in Figure 9. This allowed us to develop the measurement protocol and verify that the movements measured with the wire encoder, which will be used during on-site measurements, gave satisfactory results.

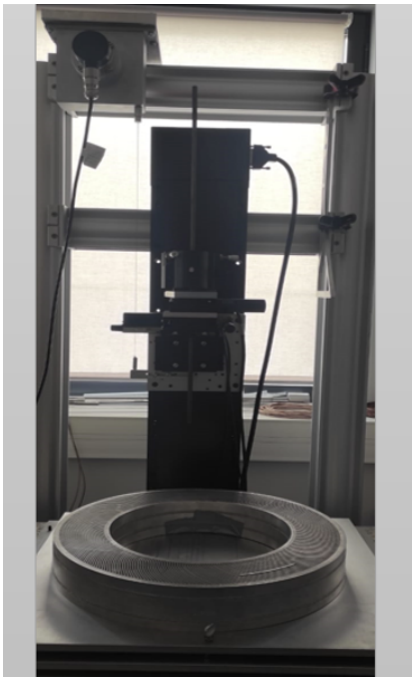


Figure 9. Experimental bench in the laboratory.

4.2 Measurements on a reference sample

This involved creating samples with faces as flat as possible and spaced 1.8 mm apart. To control this inter-plate distance, identical standard shims were machined to micron precision, ensuring the inter-plate distance was as close to 1.8 mm as possible. During a series of measurements, four ascending and descending movements of the device were performed to assess the distance between the plates along the height of this sample. The results of these measurements are displayed in Figure 10, indicating reproducible measurements at each position on a micrometric scale. The average thickness value for the 1.8 mm samples was determined to be 1.82 mm, with local standard deviations of 0.8 µm. There is a global variation of 1.4 µm across the sample's height, attributed to the fabrication process in the laboratory. These laboratory experiments clearly validate the reproducibility and quality of the measurements

performed with the designed devices and allow us to consider in-situ measurements.

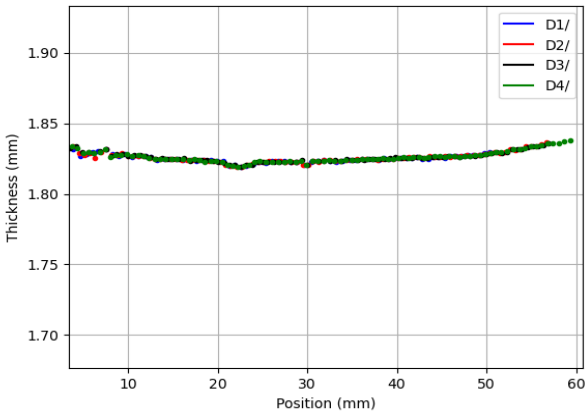


Figure 10. Measurement on a 1.8 mm reference sample.

5. IN-SITU MEASUREMENT

The RHF fuel element at the ILL, produced by CERCA, consists of 280 curved plates welded to two concentric aluminum tubes Fig.11. The fixed distance between two fuel plates, known as the water-channel thickness, is nominally 1.8 mm, allowing cooling water to pass through the reactor structure [19].

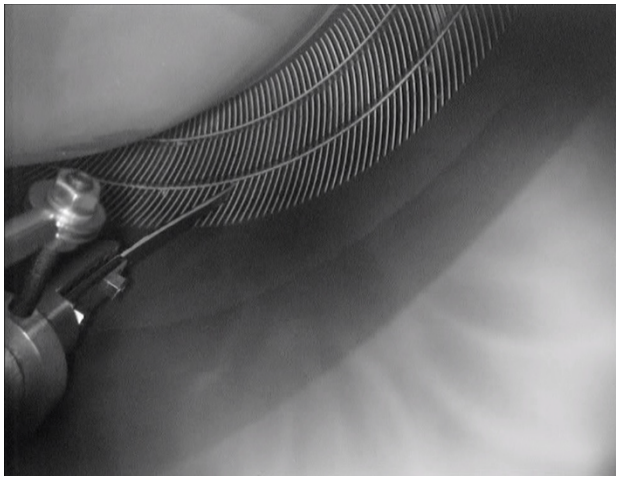


Figure 11. Photo of the insertion of a blade into a channel of the RHF fuel element in the pool.

An in-situ experiment was conducted at the ILL, where a spent fuel element is stored. A radiation-resistant camera was submerged in the pool above the fuel element to observe and control the blade's displacement. The ultrasonic device, equipped with instruments, was attached to a 12-meter support above the water pool. The blade was connected to a supporting system that ensured attachment, alignment, and synchronization with the wire encoder for real-time feedback.

Inter-plate distance measurements were performed on a single channel of the fuel element. Ultrasonic signals were recorded as the blade ascended along the water channel, with signals acquired every 50 ms. Post-treatment extracted high-confidence signals with good SNR from the data, corresponding to accurate estimations of the water-channel thickness. The results, presented in Fig. 12, show thickness estimations over 50 cm along the fuel element depth.

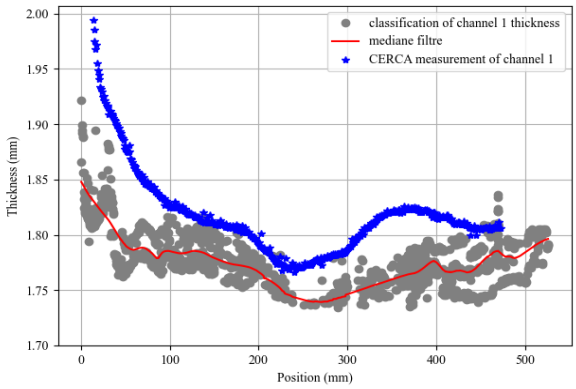


Figure 12. Results of ultrasonic measurements in gray, average in red, and comparison with pre-irradiation measurements conducted by CERCA in blue.

Due to the fuel element's position at the bottom of the cooling pool, alignment of the transducer with the plate surfaces cannot be guaranteed, leading to dispersion in thicknesses. The results, however, provide a good estimation of the water-channel thickness behavior, showing a curved shape with a local minimum between 200 mm and 300 mm.

The thickness estimation is presented as a red straight line along with gray measurement points. This mean behavior confirms a local minimum of 1739 µm in the water-channel thickness at 270 mm from the plate top. Furthermore, the

blue curve represents the measurement values provided by CERCA, estimating the inter-plate distance before irradiation, with an average of about 1796 µm. The global profiles for the two sets of measurements were found to be generally consistent. The mean thickness reduction in the first 50 mm is estimated to be around 40 µm.

6. CONCLUSIONS

To summarize, this extensive study outlined the design and application of a specialized ultrasonic transducer for examining the irradiation history of the RHF fuel element. The non-destructive control system utilized the pulse-echo method, enabling the estimation of the inter-plate distance within a fuel element through time-of-flight measurements.
Following the presentation of the system and the signal processing techniques for ToF estimation, various tests and evaluations were performed to verify the transducer's performance and accuracy in measuring this crucial parameter. These assessments helped validate the ultrasonic device and confirm its dependability for in-situ measurements under challenging access conditions.
A dedicated mechanical system was subsequently developed to efficiently transport and position the ultrasonic device in an underwater environment. This system facilitates flexible and agile movements, allowing the remote insertion of the ultrasonic transducer into water channels at a depth of 12 meters. Developed by ILL, this innovative mechanical system provides a solid foundation for inspections, offering more insights into the integrity of the fuel element and enabling measurements in different water channels of the fuel element.
In an initial experiment demonstrating the device's relevance, measurements were taken in one channel of the RHF fuel element. Post-processing was carried out to select signals with a high signal-to-noise ratio. The results presented in the final section were compared to water-channel thicknesses measured by CERCA prior to irradiation. The strong correlation between the two sets of results in the water-channel shape clearly demonstrates the quality of the proposed ultrasonic device and its suitability for future in-situ remote control in radiative environments.
Additionally, this device provided an initial estimation of one water-channel profile of a spent fuel element along 50 cm from the top of the element. The results indicate an average reduction in water-channel thickness of approximately 40 µm.
Since it is not possible to measure elements before irradiation, and to truly compare the measurements taken by CERCA with the ultrasonic measurements, it is proposed to create a demonstration sample that could be measured by both methods to confirm or refute the existing discrepancy between the two methods. Additionally, a further measurement campaign on other channels, compared with pre-irradiation measurements, could help enrich these conclusions.

7. ACKNOWLEDGMENTS

The authors would like to thank Y. Launay, O. Guillemard and A. Fournier for their strong contribution to the manufacture of the ultrasonic device and the associated mechanical bench and electronics.

8. REFERENCES

[1] http ://www.ill.eu.

[2] S. van den Berghe, A. Leenaers, E. Koonen, and L. Sannen, "From High to Low Enriched Uranium Fuel in Research Reactors", 5th Forum on new materials Part B, Advances in Science and Technology, vol. 73, no. 1, p. 78-90, 2011.

[3] A. Leenaers and S. Van den Berghe and E. Koonen and C. Jarousse and F. Huet and M. Trotabas and M. Boyard and S. Guillot and L. Sannen and M. Verwerft, "Post-irradiation examination of uranium- 7wt% molybdenum atomized dispersion fuel", Journal of Nuclear Materials, vol. 335, no. 1, p. 39-47, 2004.

[4] S. Van den Berghe and W. Van Renterghem and A. Leenaers, "Transmission electron microscopy investigation of irradiated U-7wt%Mo dispersion fuel", Journal of Nuclear Materials, vol. 375, no. 3, p. 340- 346, 2008.

[5] M. Sitek, C. Bojanowski, A. Bergeron, J. Licht, ”Involute Working Group - FSI Analysis of Fuel Plates Using Finite Volume and Finite Element Methods”, Nuclear Science & Engineering Division, Argonne National Laboratory, Tech. Rep. ANL/RTR/TM-21/30, 2021.

[6] M. K. Meyer, J. Gan, J. F. Jue, D. D. Keiser, E. Perez, A. Robinson, D. M. Wachs, N. Woolstenhulme, G. L. Hofman, Y. S. Kim "Irradiation performance of U-Mo Monolithic Fuel", Nuclear Engineering and Technology, Vol .45, no. 2, pp 169-182, 2014.

[7] W. A. Hanson, A. B. Robinson, N. J. Lybeck, J. W. Nielsen, B. Ye, Z. G. Mei, D. D. Keiser, L. M. Jamison, G. L. Hofman, A. M. Yacout, A. Leenaers, B. Stepnik and I. Y. Glagolenko, "Non-destructive analysis of swelling in the EMPIrE fuel test", Journal of Nuclear Materials, vol. 564, p. 153683, 2022.

[8] S. Park and N. Park and S. Baik and Y. Kang. "Visualization of internal defects in plate-type nucelar fuel by using noncontat optical interferometry", Nuclear Engineering and Technology, vol. 45, no. 3, p. 361-366, 2013.

[9] D. Baron, and D. Laux, and G. Despaux, "Mechanical characterization of irradiated fuel materials with local ultrasonic methods", Pellet-clad Interaction in Water Reactor Fuels : Seminar Proceedings, p. 169, 2005.

[10] J.-A. Smith, C.-J. Jesse, W.-A. Hanson, C.-L. Scott, D.- L. Cottle. "Channel Gap Measurements of Irradiated Plate Fuel and Comparison with Post-Irradiation Plate Thickness", Nuclear Engineering and Technology, vol. 55, no. 6, p. 2195-2205, 2023.

[11] G. Zaz, E. Le Clézio, A. Dekious, M. Alaoui Chrifi, Y. Calzavara and D. Gilles. "High-Resolution Measurement of HFR Nuclear Fuel Plates' Spacing", IEEE Transactions on Nuclear Science, vol. 65, no. 11, p. 2776-2783, 2018.

[12] S. Bakhtiari, H-T. Chien, A. Heifetz, and TW. Elmer. "Nondestructive testing research and development efforts at Argonne National Laboratory: An overview", Materials evaluation, vol. 76, no. 7, p. 911-920, 2018.

[13] G. Zaz, "Post Examination of a High Flux Reactor Single Element with Ultra-Sounds", Ph.D. dissertation, University of Montpellier, France, 2015.

[14] M. Chrifi Alaoui, "High Frequency Ultrasonic Device development for Non-Destructive Post-Irradiation Examination of the RHF Fuel Element", Ph.D. dissertation, University of Montpellier, France, 2018.

[15] R. Mrabti, "High frequency ultrasonic device for water channel measurement", Ph.D. dissertation, University of Montpellier, France, 2024.

[16] J. Chen, C. Fei, D. Lin, P. Gao, J. Zhang, Y. Quan, D. Chen, D. Li and Y. Yang, "A Review of UltraHigh Frequency Ultrasonic Transducers", Frontiers in Materials vol. 8, art. 733358, 2022.

[17] M. Guanbing, D. Hui, W. Weiqiang, M. Chao, Y. Jingli, Z. Chuanyu and T. Jianbang, "Compact MultiElement Ultrasonic Transducer for Inspecting Split Pins in Nuclear Power Plants," Frontiers in Materials, vol. 8, art. 643703, 2021.

[18] D. Marioli, C. Narduzzi, C. Offelli, D. Petri, E. Sardini, et A. Taroni, "Digital time of-flight measurement for ultrasonic sensors", IEEE Trans. Instrum. Meas., vol. 41, no. 1, p. 93-97, 1992.

[19] A. Bergeron, A. Tentner, and J.G. Stevens. "Feasability Analyses for HEU to LEU Fuel Conversion of the Laue Langevin Institute (ILL) High Flux Reactor (RHF)", Nuclear Science & Engineering Division, Argonne National Laboratory, Tech. Rep. ANL/RERTR/TM-10- 21, 2010.

DOI: 10.61782/fa.2025.0450



FORUM ACUSTICUM
EURONOISE 2025

IMPACT OF PHASE ANISOTROPY-RELATED SHIFTS ON THE CONTRAST OF DEFECT LOCALIZATION IMAGES IN REVERBERANT PLATES

Lynda Chehami* **Omar Bouchakour** **Emmanuel Moulin** **Elie Farha**

UPHF, CNRS, univ. Lille, UMR 8520-IEMN, F-59313, Valenciennes, France

ABSTRACT

Ultrasonic imaging based on beamforming relies generally on the precise synchronization of signals within a sensor network. Time shifts in these signals—often caused by sensor clock drifts—can be estimated and corrected during post-processing, prior to applying the backpropagation algorithm, using methods like the Peak Correlation Technique (PCT). However, in certain situations, particularly when defects exhibit anisotropy effects, additional time shifts can distort the backpropagated signals, undermining the accuracy of defect localization. This study focuses on statistically quantifying the impact of anisotropy-induced time shifts the contrast of defect localization images. The analysis is conducted in a thin reverberating plate, where covariance matrices are recorded in Full Matrix Capture (FMC) mode under two conditions: with and without a defect. Numerical simulations using A0 Lamb mode propagation are performed to validate the theoretical predictions.

Keywords: *Ultrasonic imaging, beamforming, Peak Correlation Technique, anisotropy-related shifts.*

1. INTRODUCTION

The demand for monitoring the structural integrity of infrastructures with minimal energy and hardware resources has led to the development of ”passive” imaging techniques. These methods leverage ambient noise to detect defects in reverberant media, eliminating the need for controlled emissions and ensuring substantial energy savings throughout the monitoring process. Studies such as [1, 2] have demonstrated that the Green’s function of a given medium can be reconstructed by cross-correlating ambient noise recordings from a network of sensors.

Structural Health Monitoring (SHM) has recently evolved with the increasing integration of autonomous sensor networks directly into infrastructures [3, 4]. This advancement revolutionizes integrity assessment by enabling continuous, real-time monitoring. Embedded sensors simplify traditional systems while enhancing efficiency, providing precise, instant data that supports swift, informed decisions, reducing failure risks and extending structural lifespan.

The use of autonomous sensor networks for SHM has significantly reduced costs and complexity, but signal resynchronization remains a major challenge. Each sensor relies on its own internal clock, leading to signal drift. Although various synchronization methods have been proposed, the most accurate ones require additional hardware, contradicting the goal of low-resource networks. The Peak Correlation Technique (PCT) [5–7] is a promising method for resynchronization, detecting time shifts by correlating the cross-correlation between signals. However, we have shown in previous works [8, 9] that noise in the measurement process can impair resynchronization and hinder defect localization.

In our previous studies, we assumed that the de-

*Corresponding author: lynda.chehami@uphf.fr.

Copyright: ©2025 Chehami et al. This is an open-access article distributed under the terms of the Creative Commons Attribution 3.0 Unported License, which permits unrestricted use, distribution, and reproduction in any medium, provided the original author and source are credited.

fect scattered isotropically in all directions (constant scattering amplitude in all directions). However, in a more realistic scenario, the defect may exhibit preferred directions [10–12], which can also introduce shifts that overlap with resynchronization errors, further degrading the accuracy of defect localization. In this paper, we will conduct a statistical study of the shifts related to the anisotropy of the defect to quantify their impact on the contrast of defect localization images.

This work is structured as follows: we begin by theoretically quantifying the impact of shifts induced by defect anisotropy on its detection in elastic reverberating plates. Subsequently, we perform numerical simulations to validate the theoretical results.

2. THEORETICAL DEVELOPMENTS

We consider an array of N sensors placed on the surface of a plate subjected to ambient noise. As explained in [13], detecting a possible defect in a plate consists of calculating the cross-correlations between all pairs of sensors, both in the presence and absence of the defect, and then taking the difference to isolate the signature of the latter. We recall that for a pair n of sensors, in order to compensate for the propagation distance from the first sensor to the defect and then from the defect to the second sensor, we backpropagate the resynchronized differential cross-correlation in post-processing $\Delta C_n^{res+}(\omega)$ by multiplying it by a dispersion compensation term as follows:

$$BPF_n(\omega) = \Delta C_n^{res+}(\omega)\, e^{jk(\omega)d_n}, \tag{1}$$

with $BPF_n(\omega)$ the backpropagation of $\Delta C_n^{res+}(\omega)$ to the pixel corresponding to the position of the defect, $k(\omega)$ the wave number of the bending mode A_0 and d_n the sum of the distances from the first sensor to the defect and from the defect to the second sensor.

The inverse Fourier transform of $BPF_n(\omega)$ allows to find the backpropagated signals on the position of the defect in the time domain. We note that, these backpropagated signals correspond, ideally, to the autocorrelation of the emission signal. In the case of an isotropic defect, and if the signals are perfectly synchronized, the typical shape of these signals is as shown in Fig. 1. However, in the case of an anisotropic defect, the anisotropy influences both the amplitude and the phase of the backpropagated signals. As illustrated in Fig. 2, this results in time shifts and amplitude variations observable in the backpropagated signals.

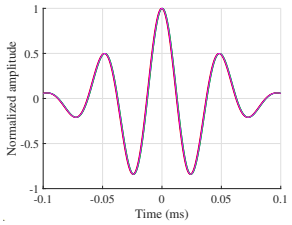


Figure 1. Example of back-propagated signals, on the defect position, in the case of an isotropic defect.

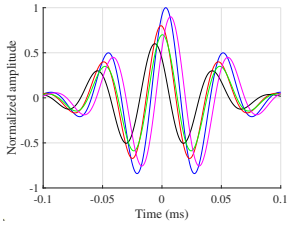


Figure 2. Example of back-propagated signals, on the defect position, in the case of an anisotropic defect ($\mathcal{E}_n = 0$ et $\tau_n \neq 0$).

In the remainder of this paper, we are interested in quantifying the contrast ratio defined in [8] as a function of the standard deviation of the initial shifts due to the phase anisotropy of the defect. To do this, we assume that back-propagated signals are affected both by the initial shifts and by the errors resulting from the imperfect resynchronization. As a result, the resynchronized version of the differential cross-correlation function becomes as follows:

$$\Delta C_n^{res+}(t) = \Delta C_n^{+}(t + \mathcal{E}_n + \tau_n), \tag{2}$$

with τ_n the initial shift due to the anisotropy of the defect and $\mathcal{E}_n$ the resynchronization error.

Which is equivalent, in the frequency domain, to:

$$\Delta C_n^{res+}(\omega) = \Delta C_n^{+}(\omega)\, e^{j\omega\mathcal{E}_n}\, e^{j\omega\tau_n}. \tag{3}$$

In a similar way to [8], we can express $\Delta C_n^{res+}(\omega)$ as follows:

$$\Delta C_n^{res+}(\omega) = f(\theta_n, \omega)\chi_n\, e^{-jk(\omega)d_n}\, U_0(\omega)\, e^{j\omega\mathcal{E}_n}\, e^{j\omega\tau_n}, \tag{4}$$

with $U_0(\omega)$ a term defined in [8].

Substituting Eq. 4 into Eq. 1 we obtain:

$$BPF_n(\omega) = f(\theta_n, \omega)\chi_n \, U_0(\omega) \, e^{j\omega\mathcal{E}_n} \, e^{j\omega\tau_n}. \quad (5)$$

Thus, the sum over the N_c pairs can be written as follows:

$$BPF(\omega) = \sum_{n=1}^{N_c} f(\theta_n, \omega)\chi_n \, U_0(\omega) \, e^{j\omega\mathcal{E}_n} \, e^{j\omega\tau_n}. \quad (6)$$

Returning to time domain and integrating the square of the modulus of $bpf(t)$, the inverse Fourier transform of $BPF(\omega)$, over an interval $[-T_0/2, T_0/2]$ containing the first wave packets, yields the intensity of the pixel corresponding to the defect position as follows:

$$I_{res} = \int_{-\frac{T_0}{2}}^{\frac{T_0}{2}} |bpf(t)|^2 \, \mathrm{d}t. \quad (7)$$

Replacing $bpf(t)$ with its expression (inverse Fourier transform of the Eq. 6) we obtain:

$$I_{res} = \int_{-\frac{T_0}{2}}^{\frac{T_0}{2}} \left(\sum_{n=1}^{N_c} f(\theta_n, \omega)\chi_n \tilde{u}_n(t) \right)^2 \mathrm{d}t, \quad (8)$$

with $\tilde{u}_n(t) = u_0(t + \mathcal{E}_n + \tau_n)$.

Similarly to [8], Eq. 8 becomes:

$$I_{res} = \frac{\sigma_0}{2\pi} \int_{-\frac{T_0}{2}}^{\frac{T_0}{2}} \left[\sum_{n=1}^{N_c} \chi_n^2 u_n^2 + \sum_{n=1}^{N_c} \sum_{m \neq n}^{N_c} \chi_n \chi_m \tilde{u}_n(t) \tilde{u}_m(t) \right] \mathrm{d}t. \quad (9)$$

Which can be written as follows :

$$I_{res} = \frac{\sigma_0}{2\pi} \left[E_0 \sum_{n=1}^{N_c} \chi_n^2 + \sum_{n=1}^{N_c} \sum_{m \neq n}^{N_c} \chi_n \chi_m \int_{-\frac{T_0}{2}}^{\frac{T_0}{2}} \tilde{u}_n(t) \tilde{u}_m(t) \, \mathrm{d}t \right]. \quad (10)$$

with $E_0 = \int_{-\frac{T_0}{2}}^{\frac{T_0}{2}} u_0^2(t) \, \mathrm{d}t$.

Since we are interested in an average behavior of the intensity on the position of the defect, we introduce the statistical average (denoted $\langle . \rangle$) on I_{res} for a set of random realizations on $\mathcal{E}_n$ and τ_n, and knowing that $\tilde{u}_n(t)$ and $\tilde{u}_m(t)$ are independent (because $\mathcal{E}_n$ and τ_n are assumed to be independent for $n \neq m$) we obtain:

$$\langle I_{res} \rangle = \frac{\sigma_0}{2\pi} \left(E_0 \sum_{n=1}^{N_c} \chi_n^2 + E_1 \sum_{n=1}^{N_c} \sum_{m \neq n}^{N_c} \chi_n \chi_m \right), \quad (11)$$

where $E_1 = \int_{-\frac{T_0}{2}}^{\frac{T_0}{2}} \langle \tilde{u}_n(t) \rangle^2 \, \mathrm{d}t$.

Then, Eq. 10 becomes:

$$\langle I_{res} \rangle = \frac{\sigma_0 N_c^2}{2\pi} \left[E_1 \, \bar{\chi}^2 + \frac{E_0 - E_1}{N_c} \bar{\chi^2} \right]. \quad (12)$$

Just like [8,9] , to quantify the degradation of the contrast ratio in the case of imperfect resynchronization, the definition of the contrast ratio consists of dividing the intensity of the Eq. 12 by a reference intensity calculated when the signals are perfectly resynchronized. This reference intensity can be expressed, by replacing E_1 with $E_0^{'}$ in the Eq. 12, as follows:

$$\langle I \rangle = \frac{\sigma_0 N_c^2}{2\pi} \left[E_0^{'} \, \bar{\chi}^2 + \frac{E_0 - E_0^{'}}{N_c} \bar{\chi^2} \right], \quad (13)$$

with $E_0^{'} = \int_{-\frac{T_0}{2}}^{\frac{T_0}{2}} \langle u_0(t + \tau_n) \rangle^2 \, \mathrm{d}t$.

Thus, under the assumption of a circular network around the defect, the contrast ratio defined in [8] can be written :

$$C_r = \frac{E_0 + (N_c - 1)E_1}{E_0 + (N_c - 1)E_0^{'}}. \quad (14)$$

Using Parseval's theorem and the transfer theorem in the same way as in [8], we can show that E_1 can be written:

$$E_1 = 4\pi^2 \int |U_0(\omega)|^2 \, |p_{\mathcal{E}}(\omega)|^2 \, |p_\tau(\omega)|^2 \, \mathrm{d}\omega, \quad (15)$$

with $p_{\mathcal{E}}(\omega)$ and $p_\tau(\omega)$ are the Fourier transforms of the probability density of the resynchronization errors and that of the initial shifts, respectively.

Similarly, we can easily show that:

$$E_0^{'} = 2\pi \int |U_0(\omega)|^2 \, |p_\tau(\omega)|^2 \, \mathrm{d}\omega. \quad (16)$$

As for E_0, its expression can be found in [8].

Finally, the Eq. 14 becomes:

$$C_r = \frac{\int |U_0(\omega)|^2 \, \mathrm{d}\omega + 4\pi^2 (N_c - 1) \int |U_0(\omega)|^2 |p_{\mathcal{E}}(\omega)|^2 |p_\tau(\omega)|^2 \, \mathrm{d}\omega}{\int |U_0(\omega)|^2 \, \mathrm{d}\omega + 2\pi (N_c - 1) \int |U_0(\omega)|^2 |p_\tau(\omega)|^2 \, \mathrm{d}\omega}. \tag{17}$$

This expression, which generalizes the expression developed in [8] for the case where the defect is anisotropic, shows that resynchronization errors affect the numerator of the contrast ratio, while initial shifts influence both the numerator and the denominator of this ratio. We will explore and confirm this relationship through a numerical simulation in the next section.

3. NUMERICAL VALIDATION

To validate the theoretical results obtained in the previous section, a numerical simulation is performed here using a finite element code ELMER. This code models acoustic wave propagation in a finite plate based on the Reissner-Mindlin plate theory.

The configuration tested (see Fig. 3) consists of an aluminum plate of dimensions 1×0.5 m^2 and thickness 3 mm. On the surface of this plate, we place an array of 8 sensors at known positions and a distribution of 600 sources uniformly distributed around the sensors. A defect is modeled by a zero normal displacement imposed at the position (53, 26) cm on the surface of the plate.

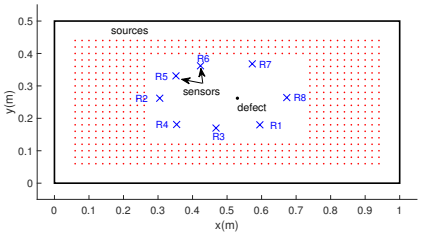


Figure 3. Simulated configuration: aluminum plate 1×0.5 m^2 and 3 mm thick. 8 sensors (blue crosses). 600 sources uniformly distributed around the sensors (red dots). A point defect at position (53, 26) cm.

The emission signal is a Gaussian-windowed sine of frequency $f_0 = 20$ kHz. The sampling frequency is 2.5 MS/s. For each pair of receivers, the summed cross-correlation over all sources is computed.

We whiten the simulated signals between 1 kHz and 30 kHz and then calculate the cross-correlations for all sensor pairs in the cases with and without defects. Next, we introduce initial shifts according to a Gaussian distribution with zero mean and variable standard deviation, denoted σ_τ. For each value of σ_τ, we add to these cross-correlations resynchronization errors modeled by a normal distribution with zero mean and variable standard deviation σ. We then apply the localization algorithm [13] to the obtained cross-correlations. Finally, we calculate the contrast ratio averaged over 100 draws of the initial shifts and 100 draws of the resynchronization errors. This numerical contrast ratio can be compared to the theoretical curve of the Eq. 17.

The curves showing the evolution of the contrast ratio as a function of σ for different values of σ_τ are shown in Fig. 4.

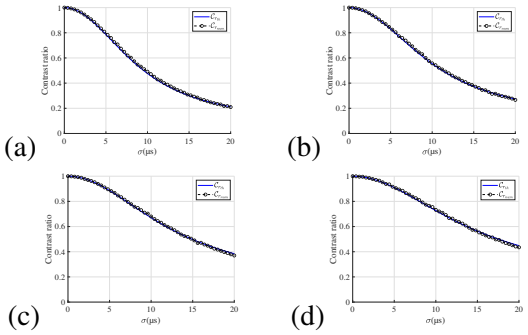


Figure 4. Comparison between the variation of the theoretical (blue line) and numerical (black circles) contrast ratio, as a function of σ, the standard deviation of the resynchronization errors, for different values of the standard deviation of the initial shifts : (a) $\sigma_\tau = 2$ µs, (b) $\sigma_\tau = 6$ µs, (c) $\sigma_\tau = 10$ µs, (d) $\sigma_\tau = 12$ µs.

On the one hand, we observe that the numerical results are in excellent agreement with the theory. On the other hand, it is clear that an increase in σ_τ causes a significant change in the shape of the curves.

4. CONCLUSION

In this paper, we have explored the impact of defect scattering anisotropy on the signals used for localization. We demonstrated that phase anisotropy leads to initial shifts in

the signals. These shifts can overlap with resynchronization errors and significantly affect the contrast in defect localization images. In future works, the results presented in this paper could be used to classify defects by conducting a detailed analysis of the initial shifts. This classification could be further refined by incorporating the defect's scattering cross section into the contrast ratio calculation.

5. REFERENCES

[1] O. I. Lobkis and R. L. Weaver, "On the emergence of the Green's function in the correlations of a diffuse field," *J. Acoust. Soc. Am.*, vol. **110**, pp. 3011–3017, 2001.

[2] A. Colombi, L. Boschi, P. Roux, and M. Campillo, "Green's function retrieval through cross-correlations in a two-dimensional complex reverberating medium," *J. Acoust. Soc. Am.*, vol. **135**, no. 3, pp. 1034–1043, 2014.

[3] T. Buckley, B. Ghosh, and V. Pakrashi, "Edge structural health monitoring (e-shm) using low-power wireless sensing," *Sensors*, vol. 21, no. 20, p. 6760, 2021.

[4] A. Sofi, J. Regita, B. Rane, and H. H. Lau, "Structural health monitoring using wireless smart sensor network–an overview," *Mech. Syst. Signal Process.*, vol. 163, p. 108113, 2022.

[5] K. G. Sabra, P. Roux, A. M. Thode, G. L. D'Spain, W. Hodgkiss, and W. Kuperman, "Using ocean ambient noise for array self-localization and self-synchronization," *IEEE Journal of Oceanic Engineering*, vol. **30**, no. 2, pp. 338–347, 2005.

[6] C. Sens-Schönfelder, "Synchronizing seismic networks with ambient noise," *Geophys. J. Int.*, vol. **174**, no. 3, pp. 966–970, 2008.

[7] L. Tenorio-Hallé, A. M. Thode, S. L. Swartz, and J. U. R, "Using anisotropic and narrowband ambient noise for continuous measurements of relative clock drift between independent acoustic recorders," *J. Acoust. Soc. Am.*, vol. **149**, no. 6, pp. 4094–4105, 2021.

[8] O. Bouchakour, E. Moulin, L. Chehami, and N. Smagin, "Quantification and mitigation of the effect of resynchronization errors in ultrasound sensor network for passive imaging in elastic plates," *J. Acoust. Soc. Am.*, vol. **155**, no. 5, pp. 3283–3290, 2024.

[9] O. Bouchakour, E. Moulin, and L. Chehami, "Impact of resynchronization errors on the localization quality of defects in reverberant plates," in *Journal of Physics: Conference Series*, vol. **2904**, p. 012006, IOP Publishing, 2024.

[10] U. Cicekli, G. Z. Voyiadjis, and R. K. A. Al-Rub, "A plasticity and anisotropic damage model for plain concrete," *Int. J. Plast.*, vol. **23**, no. 10-11, pp. 1874–1900, 2007.

[11] T. R. Jebieshia, D. K. Maiti, and D. Maity, "Vibration characteristics and damage detection of composite structures with anisotropic damage using unified particle swarm optimization technique," in *Proceedings of the American Society for Composites, 13th Technical Conference, Michigan State University, East Lansing, MI*, pp. 28–30, 2015.

[12] R. Desmorat, "Anisotropic damage modeling of concrete materials," *Int. J. Damage Mech.*, vol. **25**, no. 6, pp. 818–852, 2016.

[13] L. Chehami, E. Moulin, J. de Rosny, C. Prada, O. B. Matar, F. Benmeddour, and J. Assaad, "Detection and localization of a defect in a reverberant plate using acoustic field correlation," *J. Appl. Phys.*, vol. **115**, no. 10, p. 104901, 2014.

DOI: 10.61782/fa.2025.0961

FORUM ACUSTICUM EURONOISE 2025

VISCOELASTIC MODEL: THE MEMORY OF CEMENT

J. Gosalbez[1*] **V.J. Ruiz**[1] **J. Madrigal**[1]
R. Miralle[1] **I. Bosch** [1] **J. Quiroga**[3] **J. Payá**[1]
[1] Inst. de Telecomunicaciones y Aplicaciones Multimedia. Universitat Politècnica de València. Spain
[2] Instituto de Ciencia y Tecnología del Hormigón, Universitat Politècnica de València. Spain
[3] Universidad Industrial de Santander, Colombia

ABSTRACT

The high sensitivity of nonlinear terms in the elastic response of materials to the early appearance of damage has led to the emergence of the so-called NEWS methods (Non-linear Elastic Wave Spectroscopy). These NDE (Non-Destructive Evaluation) methods exploit the increase in the material's nonlinear behaviour as damage increases. In particular, the NIRAS technique (Non-linear Impact Resonance Acoustic Spectroscopy) detects changes in the resonance of a material (frequency, damping factor, etc.) as a function of impact intensity.
In this work, the NIRAS technique has been employed to characterize concrete using different sensing methods (accelerometers and FBG - Fiber Bragg Grating). Additionally, this study presents the conditioning process, along with a viscoelastic model of the Maxwell and Kelvin-Voigt types, to understand the effects of conditioning on the specimens during testing.

Keywords: *nonlinear acoustics, conditioning effect, fiber Bragg grating (FBG), NIRAS technique*

1. INTRODUCTION

Geomaterials—such as rocks, sand, soil, and combinations thereof like concrete—are classified within a specific group known as Non-Linear Mesoscopic Elastic (NME) materials [1]. These materials are characterized by their heterogeneous internal makeup, with a complex non-linear response strongly influenced by various microstructural elements, including micro-cracks, grain contacts, and voids. Compared to traditional atomic elastic materials, this response is significantly more pronounced. Due to these unique properties, the non-linear behavior of NME materials cannot be adequately described by Landau's classical non-linear elasticity theory [2].

One of the most effective methodologies for evaluating damage in concrete and other cementitious materials is the non-destructive technique known as Nonlinear Elastic Wave Spectroscopy (NEWS). This method focuses on analyzing various nonlinear phenomena [3], including the generation of higher-order harmonics, wave cross-modulation, shifts in resonance frequency, and amplitude-dependent attenuation. Despite variations in technique, all NEWS approaches share a common goal: to quantify non-linear material behaviors through dynamic responses.

Concrete degradation has been extensively studied over time, with research highlighting that different deterioration mechanisms alter their dynamic properties in distinct ways [5][6]. Concrete exposed to thermal shock (rapid temperature changes) can suffer significant internal damage due to the differential expansion and contraction of its constituent materials. This abrupt thermal gradient induces high tensile stresses, particularly at the interfaces between aggregates and the cement paste, often leading to microcracking, debonding, and eventual loss of mechanical integrity. Repeated thermal shocks can accelerate degradation, reducing stiffness, strength, and durability over time [7]. Investigations have applied NEWS techniques to evaluate thermal shock effects on concrete across various compositions and number of cycles [8][9] and changes in

[*] ***Corresponding author***: jorgocas@dcom.upv.es
Copyright: *©2025 First author et al. This is an open-access article distributed under the terms of the Creative Commons Attribution 3.0 Unported License, which permits unrestricted use, distribution, and reproduction in any medium, provided the original author and source are credited.*

acoustic non-linearity under thermal stress [10][11][12] [13].

A notable example is the Non-linear Impact Resonance Acoustic Spectroscopy (NIRAS) technique. NIRAS operates by monitoring how the material's resonance frequency varies with different levels of impact force (see Figure 1), providing insights into internal structural changes.

However, the use of NEWS techniques, and NIRAS in particular, also implies that, under certain conditions, the specimen may undergo a conditioning process as a result of material hysteresis. This leads to observable differences in the results between the first time the material is tested (i.e., non-conditioned state) and subsequent repetitions of the test (conditioned state). This phenomenon can be referred to as discrete memory or material conditioning, and it arises from a combination of slow dynamics and fast dynamics. It is worth noting that the material may or may not return to its relaxed or non-conditioned state over time [4].

In this study, the authors focus on two key aspects. First, they aim to demonstrate the conditioning effect that mortar specimens undergo when subjected to the NIRAS technique. To this end, results from the first (not conditioned status) and second tests (conditioned status) are compared. This conditioning becomes more pronounced in damaged specimens, as non-linear phenomena are more evident in these cases. Therefore, the study specifically considers specimens that have been damaged through thermal shock. Moreover, experiments are conducted using both traditional piezoelectric accelerometers and fiber Bragg grating (FBG) sensors, which are embedded into the specimens during the manufacturing process.

Thanks to the integration of embedded FBG sensors during specimen fabrication, the second objective of this work is to investigate the relaxation behavior of the specimens after being tested. The use of FBG technology allows for internal strain monitoring, offering valuable insight into the time-dependent recovery process that occurs as a result of mechanical conditioning.

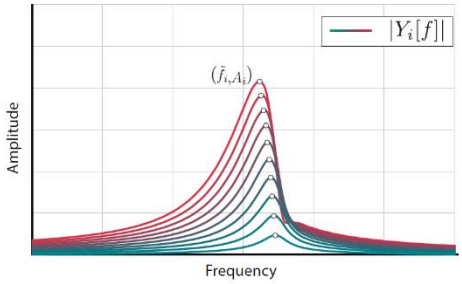


Figure 1. Received frequential response for the different impact levels ($Y_i(f)$)

2. MATHEMATICAL BACKGROUND

NIRAS is a method used for impact assessment and damage detection and involves impacting the material with different strength levels and analyzing the resulting acoustic frequency responses. The different reverberation signals are denoted by $y_i(t)$ where i denotes the different impacts and $Y_i(f)$ is the Fourier Transform of $y_i(t)$ (Figure 1). The non-linear parameters related to the resonance frequency shift α is obtained from a simple linear regression fit (Figure 2):

$$\frac{\tilde{f}_0 - \tilde{f}_i}{\tilde{f}_0} = \alpha \cdot A_i \tag{1}$$

$$A_i = \max|Y_i(f)| \tag{2}$$

$$\tilde{f}_i = \max_f|Y_i(f)| \tag{3}$$

Where A_i is the is the peak amplitude of the spectrum, $\tilde{f}_i$ is the peak frequency and $\tilde{f}_0$ denotes the intersection with y-axis of the linear relationship between the peak amplitudes A_i (x-axis) and the peak frequencies $\tilde{f}_i$ (y-axis).

The NIRAS technique obtains the parameter α_f^{NIRAS}, among others, as an indicator of the no linear behavior of the material: the greater the damage, the greater the no-linear behavior and the greater α_f^{NIRAS}.

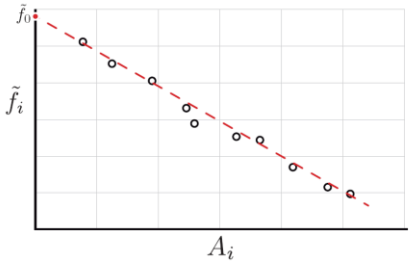


Figure 2. Linear regression from the different resonance signals.

The Maxwell model may be more suitable for describing the dynamic behavior of the specimen during fast mechanical responses, while the Kelvin-Voigt model is more appropriate for representing the slow dynamics effects, such as those associated with conditioning and material relaxation over time. However, experimental observations in this study suggest that both behaviors coexist in the tested specimens. The act of testing itself induces a conditioning state—often referred to as slow dynamics—which subsequently alters the specimen's mechanical response in follow-up impacts, which are governed by fast dynamics.

In this context, the Zener model, derived from a combination or modification of the Maxwell and Voigt models, provides a more comprehensive framework. It effectively captures both the immediate elastic response and the time-dependent relaxation behavior of the tested specimens. Although traditionally used to model fast relaxation phenomena, the results presented in this study and those in [4]demonstrate that damaged specimens, exhibiting stronger non-linear responses, undergo a measurable conditioning process simply as a result of being tested. This effect is clearly reflected in the evolution of the non-linear parameter α reinforcing the connection between mechanical damage, slow dynamics, and non-linear acoustic response.

3. EXPERIMENTAL

3.1 Manufacturing and damage induction of mortar specimens

Three mortar specimens (A, B and C) were prepared by mixing Portland cement (EN 197-1-CEM I 52.5 R) [14], sand (quartz) and water in the 1:3:0.5 ratio. After mixing the components, following the procedure described in UNE-EN 196-1 [15], the fresh mortar was placed in a prismatic mold of 50x60x240 mm size. Because prior to pouring the mortar, several optic fibers were settled according to Figure 4. Due to the fragility of the fibers, the mortar was poured in three layers, avoiding damaging the fibers. For this, the fresh mortar was dropped in a zone free of fiber and then the mold was vibrated (Vibrating Table ToniVIB Tonitechnic) for 30 seconds (vibration frequency 50 Hz, amplitude 1 mm). This procedure was twice repeated and finally the superior part was flattened using a spatula. Additionally, metallic capillary sheath (Figure 3a) was used to protect each optical fiber during the pouring and vibration process and was removed immediately after the surface leveling.

The mold was put in a humid chamber (20 ºC, RH>90%) for 24 hours. After this period, the specimens were carefully demolded and were covered with a plastic film, to avoid water evaporation. The wrapped specimens were stored in the same humid chamber for 46 days, to complete the hydration of the Portland cement.

After 88 days from mixing the mortar components, two of the specimens were subjected to thermal shock (B and C): the specimens were immersed in hot water (80ºC) for 1 hour and then immediately submerged in cold water (4ºC) for 10 minutes, tank of 0.01 m3.

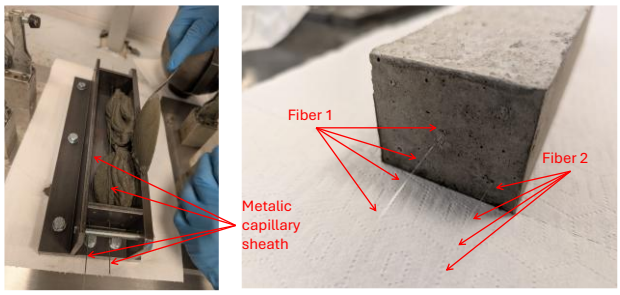


Figure 3. a) Manufacturing process b) Demolded specimen showing the optical fiber emerging from the mortar.

3.2 Embedded Instrumentation

Two of the three specimens (A and B) were internally instrumented during the fabrication process with two optical fibers aligned along the longitudinal axis of the specimen: one positioned at the center and the other near a corner (Figure 4). Each optical fiber contained two integrated Fiber Bragg Gratings (FBGs), which were located at the center and at one end of the fiber.

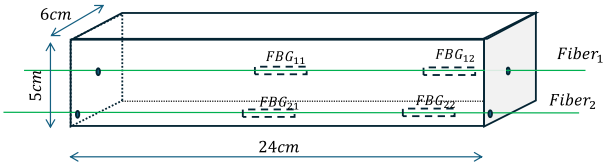


Figure 4. Representación de las fibras embebidas.

The FBGs were primarily tuned to the wavelengths listed in Table 1 and illustrated in Figure 5. Fiber 2 of Mortar A was damaged during the demolding process, therefore no measurements were obtained from this fiber.

Table 1. Wavelengths of the FBGs (nm)

Specimens	$\boldsymbol{Fiber_1}$		$\boldsymbol{Fiber_2}$	
	FBG_{11}	FBG_{12}	FBG_{21}	FBG_{22}
Mortar A	1533.98	1544.05	-	-
Mortar B	1534.07	1543.94	1553.95	1563.80

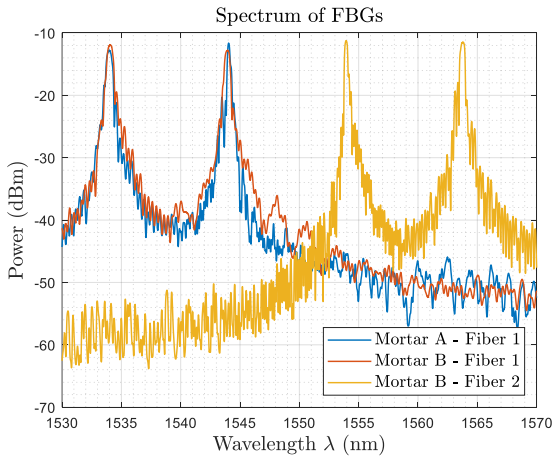


Figure 5. Spectrum of embebed fibers

3.3 Measurement setup

Two distinct experimental configurations were employed in the development of this study. In the first experimental, multiple impacts were applied to different specimens with the objective of analyzing the mechanical conditioning process induced by repeated excitation.

The second setup was designed to perform long-duration measurements, spanning a period of several days. In this case, the specimen was initially subjected to controlled impacts to induce a conditioned state, after which continuous monitoring was carried out with the aim of evaluating the temporal evolution of the material. The main objective was to observe the potential residual effects of the conditioning, as well as the gradual recovery of the specimen's original state once the excitation had ceased.

Both experiments were structured into three functional stages: an initial excitation phase using impact, a second sensing phase, and finally, a data acquisition system responsible for recording and storing the signals obtained.

In the first experiment, the excitation stage consisted of an instrumented hammer and a clamping system designed to immobilize the specimen during measurements, thereby ensuring consistent conditions for each impact. The hammer's attachment to the support allowed for an almost constant impact force across all repetitions, ensuring the repeatability of the conditioning process.

In the second experiment, aimed at studying the temporal evolution of the material, excitation was carried out solely using a conventional hammer, employed to induce the initial conditioning of the specimen prior to the start of prolonged monitoring. In this case, impact uniformity was not critical, as the primary interest lay in observing the post-conditioning effects over time.

During the sensing phase, two types of sensors were used: accelerometers and optical fibers with embedded Fiber Bragg Gratings (FBGs) within the specimens.

In the first experiment, both types of sensors were employed. One accelerometer was placed on the hammer to capture the impact during striking, and another was mounted on the specimen to monitor the material's dynamic response and evaluate the effect of the conditioning induced by repeated impacts. In addition, FBG optical sensors embedded within the specimen were used to

record both the impacts and the structural changes in the material resulting from the conditioning process.

In the second experiment, only FBG optical sensors were used, as the main objective was to analyze how the specimen, after being conditioned by the impacts, returned to its initial state or, alternatively, experienced a progressive loss of the properties induced by the conditioning. In this context, the use of accelerometers was not necessary, since the focus was on observing the temporal evolution of the material properties under resting conditions following the initial impacts.

The final stage of the experiment corresponds to data acquisition, for which two specific devices were used, each responsible for capturing data from the different sensors.

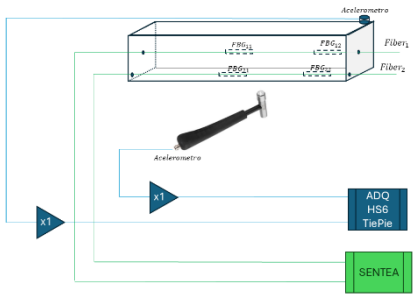


Figure 6. Esquema del montage.

In the first experiment, both devices were used. For the capture of accelerometer data, the TiePie HS6 data acquisition system was employed, which has four input channels. However, in this measurement, only two of these channels were used, dedicating one to each accelerometer (one for the hammer and the other for the specimen).

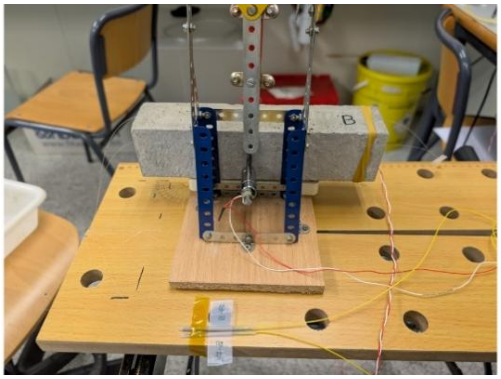


Figure 7. Photograph of the experiment

The second device used was the SENTEA optical interrogator, specifically designed for reading Fiber Bragg Gratings (FBGs). This device also has four channels, allowing for the simultaneous interrogation of multiple FBGs per channel. In the context of this experiment, each channel was used to interrogate a set of FBGs embedded within the specimen, enabling the capture of relevant data on the material's behavior.

In the second experiment, only the SENTEA interrogator was used, as the objective of the measurement focused exclusively on monitoring the FBGs, without the need to record data from the accelerometers.

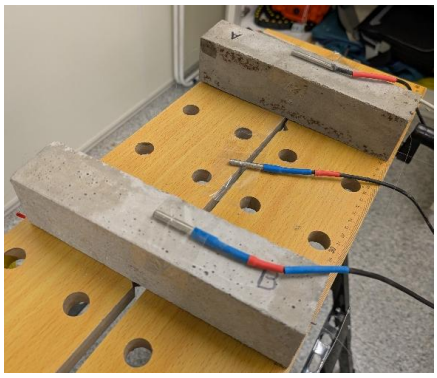


Figure 8. Overview of the long-term experimental setup

In the first experiment, the specimen was placed on a rigid support to prevent any displacement during the measurements (Figure 7). Ten consecutive impacts were applied using the instrumented hammer, with an increasing force in each strike. This process was repeated after the initial ten impacts, allowing for a comparison between measurements obtained under two conditions: one with the specimen in its initial (resting) state, and the other after it had been conditioned by the repeated impacts.

In the second experiment (Figure 8), the specimen was subjected to ten initial impacts in order to induce conditioning. Afterwards, it was left at rest for several days to observe its behavior over time, allowing for the evaluation of whether the specimen gradually returned to its original state or remained in a partially conditioned state. The main objective of this experiment was to analyze the temporal evolution of the material's properties, observing either a return to normality or a progressive loss of the conditioning induced by the impacts.

4. TESTS DESCRIPTION AND RESULTS

As described, two types of tests were conducted on the mortar specimens: the NIRAS acoustic spectroscopy test and the long-term conditioning evolution test. These tests were performed on both undamaged and damaged specimens, using embedded fiber Bragg gratings (FBGs) and piezoelectric accelerometers for strain and vibration measurement. Specifically, three specimens were studied: one undamaged specimen (A) and two thermally shock damaged specimens (B and C). Specimens A and B were instrumented with embedded FBG sensors. The complete experimental matrix is summarized in Table 2.

Table 2. List of damaged and undamaged mortar samples tested with accelerometers and FBGs, non-conditioned (M1) and conditioned (M2) and long-term monitoring

Sample	Status	Acc.		FBG		
		NIRAS				Long-term
		M1	M2	M1	M2	
A	Sound	√	√	√	√	√
	Damage	Reference sample – no damage applied				
B	Sound	√	√	√	√	-
	Damage	√	√	√	√	√
C	Sound	√	√	Not instrumented		
	Damage	√	√			

The first test, the NIRAS procedure, consisted of applying ten controlled impacts to the specimen using an instrumented hammer. The impacts were progressively stronger, modulated by increasing the striking angle. A second identical series of ten impacts was then performed. The first measurement set (M1) corresponds to the non-conditioned state, while the second (M2) corresponds to the conditioned state. This protocol enabled a direct comparison of the specimen's dynamic response before and after conditioning, allowing for the assessment of non-linear and hysteretic behavior resulting from damage. As shown in Figure 9 and Figure 10 the relationship between peak frequency and amplitude, exhibits a consistent variation between the first and second series. While the absolute change may be small, the trend is systematic. Since α is associated with the degree of non-linear behavior, this conditioning effect becomes more evident in the damaged specimens, where non-linearities are more pronounced.

Table 3 and Table 4 summarize the values of both α and f_0 for undamaged and damaged specimens, as well as for the first and second measurement series. For undamaged samples, α is close to zero, indicating an essentially linear material response within the applied impact range (i.e., resonance frequency does not depend on impact amplitude). As damage increases, the absolute value of α also increases, reflecting stronger non-linear behavior. The trend is consistent across both sensing technologies. Additionally, a decrease in f_0 is observed as damage progresses, consistent with a loss of mechanical stiffness. A systematic shift in both α and f_0 is also evident when comparing results from the first impact series (non-conditioned state) with subsequent impacts (conditioned state). This shift is more significant in damaged specimens, which display a more prominent hysteretic response.

Moreover, as shown in Table 3 and Table 4, the parameter α also varies consistently not only between the two damaged specimens but also between the two sensing technologies, reinforcing the robustness of the observed trends.

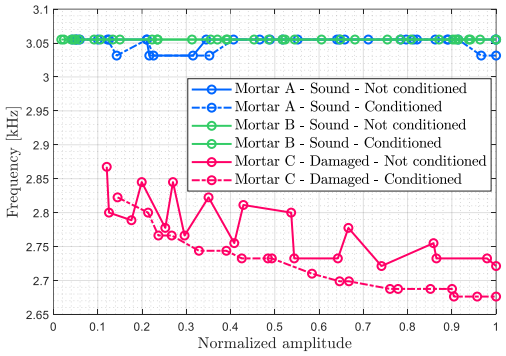


Figure 9. Amplitude vs. frequency curves measured with the accelerometer for conditioned and unconditioned specimens, with and without damage

Table 3. NIRAS parameters (α and f_0) for the samples A, B and C, between "Not conditioned" and "Conditioned" for the accelerometer sensor

Accel.		Not conditioned			Conditioned		
		$-\alpha$	f_0	R^2	$-\alpha$	f_0	R^2
A	Sound	5.77	3.04	0.06	1.14	3.0	0.01
B	Sound	0	3.05	-	0	3.05	-
	Dam.	94	2.78	0.7	106	2.8	0.70
C	Dam.	119	2.8	0.8	148	2.83	0.89

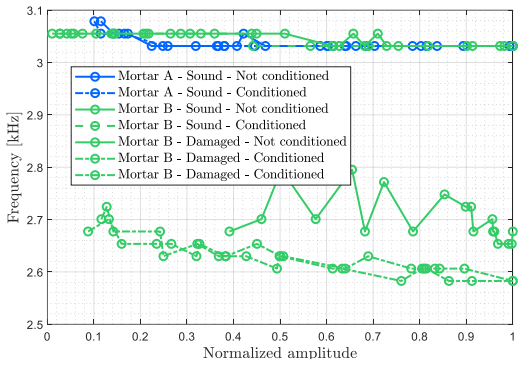


Figure 10. Amplitude vs. frequency curves measured with the FBG for conditioned and unconditioned specimens, with and without damage

Table 4. NIRAS parameters (α and f_0) for the samples A, B and C, between "Not conditioned" and "Conditioned" for one of the FBG sensor

FBG		Not Conditioned			Conditioned		
		$-\alpha$	f_0	R^2	$-\alpha$	f_0	R^2
A	Sound	30.0	3.05	0.37	30.5	3.05	0.38
B	Sound	27	-	0.58	32	3.07	0.77
	Dam.	-	-	-	109	2.68	0.85
C	Dam.	-	-	-	-	-	-

Thanks to the embedded nature of the FBG sensors, it was possible to perform a long-term strain monitoring following the NIRAS impact testing. This second experimental phase involved continuous tracking of the FBG wavelength shift for three days after the initial test. The post-impact wavelength evolution differed significantly between the undamaged and damaged specimens. In the undamaged sample, the wavelength showed a specific temporal trend which correlates with temperature changes, while in the damaged sample, the evolution also followed the temperature changes but with a distinct pattern. This difference can serve as an indicator of two key aspects: the first one the thermal response, since Figure 11 shows that the major wavelength variations coincide with temperature fluctuations; and second one , mechanical relaxation, given that both samples were kept in the same ambient conditions (temperature, humidity, and pressure), allowing the observed trend differences to be attributed to differences of material relaxation dynamics.

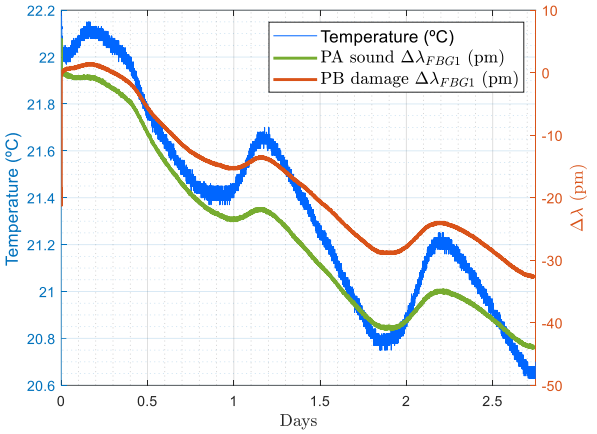


Figure 11. Temperature (blue line), wavelength of sound probe (A) (green line) and wavelength of damaged probe (B) (red line) along several days.

5. CONCLUSIONS

The ability to inspect instrumented specimens, with multiple sensing points along the same fiber, represents a valuable advancement in non-destructive evaluation techniques. The NIRAS technique has proven to be a highly sensitive method for detecting generalized damage. In this study, it was successfully applied to evaluate mortar specimens subjected to thermal shock damage and the comparison between undamaged and damaged samples confirmed the technique's sensitivity.

Furthermore, the study has revealed the presence of a conditioning effect, where specimens exhibit a distinct change in their dynamic response simply as a result of being tested. This was evidenced by systematic differences in the extracted parameters between the first test (non-conditioned state) and subsequent tests (conditioned state). In essence, the material exhibits a form of mechanical memory, which becomes increasingly prominent as damage severity increases.

Two distinct sensing technologies were utilized: traditional piezoelectric accelerometers and embedded fiber Bragg gratings (FBGs). Both demonstrated consistent trends. The accelerometers provided precise results with low variance and high repeatability but required surface attachment. On

the other hand, embedded FBGs, despite being more challenging to measure, allowed for similar results while offering the unique capability of long-term internal monitoring.

Thanks to this capability, the FBG sensors enabled the observation of post-test relaxation behavior, highlighting significant differences in the relaxation dynamics between damaged and undamaged specimens. This suggests that FBGs not only replicate conventional measurements but also provide additional insight into the temporal evolution of mechanical conditioning.

6. ACKNOWLEDGMENTS

Grant PID2020-120262GB-I00 funded by MCIN/AEI/ 10.13039/501100011033
2

7. REFERENCES

[1] R. A. Guyer, P. A. Johnson, Nonlinear Mesoscopic Elasticity: Evidence for a New Class of Materials, *Physics Today* 52 (4), 30, 1999.

[2] L. D. Landau, E. M. Lifshitz, "Theory of Elasticity, Pergamon", Oxford, England, 3rd edn., 1986.

[3] L. Ostrovsky, P. A. Johnson, "Dynamic nonlinear elasticity in geomaterials", *Rivista del Nuovo Cimento 24,* 1–46, 2001

[4] A. Carrión, V. Genovés, G. Pérez, J. Bittner, J.S. Popovics, J. Payá, J. Gosálbez, Effects of slow dynamics and conditioning on non-linear hysteretic material assessment using impact resonance acoustic spectroscopy, Mechanical Systems and Signal Processing, 150 (2021)

[5] P. C. Aïtcin, "Binders for durable and sustainable concrete", *CRC Press*, 2014.

[6] M. Alexander, S. Mindess, "Aggregates in concrete", *CRC Press*, 2010.

[7] Neville, A. M., "Properties of Concrete" (5th ed.). *Pearson Education*, 2011

[8] Eiras, J. N., et al., "Nonlinear Ultrasonic Evaluation of Thermal Damage in Concrete." Cement and Concrete Research, 80, 31–39, 2016

[9] Payan, C., Garnier, V., Moysan, J., & Johnson, P. A.. "Applying Nonlinear Resonant Ultrasound Spectroscopy to Improve Thermal Damage Assessment in Concrete." *Journal of the Acoustical Society of America*, 121(4), EL125–EL130, 2007

[10] C. Payan, et. al., "Probing material nonlinearity at various depths by time reversal mirrors", *Applied Physics Letters* 104 (14), 144102, 2014.

[11] C. Payan, T. J. Ulrich, P.-Y. Le Bas, T. Saleh, M. Guimaraes, "Quantitative linear and nonlinear resonance inspection techniques and analysis for material characterization: Application to concrete thermal damage", *The Journal of the Acoustical Society of America* 136 (2), 537–546, 2014.

[12] H. J. Yim, J. H. Kim, S.-J. Park, H.-G. Kwak, "Characterization of thermally damaged concrete using a nonlinear ultrasonic method", *Cement and Concrete Research* 42 (11), 1438–1446, 2012.

[13] Chen, J., Bharata, R., Yin, T. et al. "Assessment of sulfate attack and freeze–thaw cycle damage of cement-based materials by a nonlinear acoustic technique". *Mater Struct* 50, 105, 2017.

[14] AENOR, "UNE-EN 197-1. Cement. Part 1: Composition, specifications and conformity criteria for common cements.," 2011. [Online]. Available: www.aenor.es

[15] AENOR, "UNE-EN 196-1. Methods of testing cement. Part 1: Determination of strength.," 2018.

DOI: 10.61782/fa.2025.0088

FORUM ACUSTICUM EURONOISE 2025

ACOUSTIC RESONANCE SPECTROSCOPY USING FBG SENSORS EMBEDDED IN MORTARS

J. Gosalbez [1*] **V. J. Ruiz** [1] **J. Madrigal** [1]
A. M. Macián [2] **J. E. Carcel**[1] **J. Payá**[2]

[1] Inst. de Telecomunicaciones y Aplicaciones Multimedia. Universitat Politècnica de València. Spain
[2] Instituto de Ciencia y Tecnología del Hormigón, Universitat Politècnica de València. Spain

ABSTRACT

The high sensitivity of nonlinear terms in the elastic response of materials to the early appearance of damage has led to the emergence of the so-called NEWS methods (Non-linear Elastic Wave Spectroscopy). These NDE (Non-Destructive Evaluation) methods exploit the increase in the material's nonlinear behaviour as damage increases. In particular, the NIRAS technique (Non-linear Impact Resonance Acoustic Spectroscopy) detects changes in the resonance of a material (frequency, damping factor, etc.) as a function of impact intensity.
In this work, the NIRAS technique was employed to characterize damage in mortar concrete samples embedded with FBG (Fiber Bragg Grating) sensors. The advantage of this technique lies in the fact that these sensors can be integrated during the fabrication process, spatially distributed, share the same optical fiber, and be interrogated remotely.

Keywords: *impact resonance acoustic spectroscopy, thermal shock damage, fiber bragg grating sensors, thermal shock mortar degradation*

1. INTRODUCTION

Geomaterials—such as rocks, sand, soil, and combinations thereof like concrete—are classified within a specific group known as Non-Linear Mesoscopic Elastic (NME) materials [1]. These materials are characterized by their heterogeneous internal makeup, with a complex non-linear response strongly influenced by various microstructural elements, including micro-cracks, grain contacts, and voids. Compared to traditional atomic elastic materials, this response is significantly more pronounced. Due to these unique properties, the non-linear behavior of NME materials cannot be adequately described by Landau's classical non-linear elasticity theory [2].

One of the most effective methodologies for evaluating damage in concrete and other cementitious materials is the non-destructive technique known as Nonlinear Elastic Wave Spectroscopy (NEWS). This method focuses on analyzing various nonlinear phenomena [3], including the generation of higher-order harmonics, wave cross-modulation, shifts in resonance frequency, and amplitude-dependent attenuation. Despite variations in technique, all NEWS approaches share a common goal: to quantify non-linear material behaviors through dynamic responses.

Within the field of NEWS, impact spectroscopy has gained traction due to its straightforward excitation requirements and high sensitivity to non-linear effects. A notable example is the Non-linear Impact Resonance Acoustic Spectroscopy (NIRAS) technique. NIRAS operates by monitoring how the material's resonance frequency varies with different levels of impact force (see Figure 1), providing insights into internal structural changes.

Concrete degradation has been extensively studied over time, with research highlighting that different deterioration mechanisms alter their dynamic properties in distinct ways [4][5]. Concrete exposed to thermal shock (rapid

*Corresponding author: jorgocas@dcom.upv.es
Copyright: ©2025 First author et al. This is an open-access article distributed under the terms of the Creative Commons Attribution 3.0 Unported License, which permits unrestricted use, distribution, and reproduction in any medium, provided the original author and source are credited.

temperature changes) can suffer significant internal damage due to the differential expansion and contraction of its constituent materials. This abrupt thermal gradient induces high tensile stresses, particularly at the interfaces between aggregates and the cement paste, often leading to microcracking, debonding, and eventual loss of mechanical integrity. Repeated thermal shocks can accelerate degradation, reducing stiffness, strength, and durability over time [6]. Investigations have applied NEWS techniques to evaluate thermal shock effects on concrete across various compositions and number of cycles [7][8] and changes in acoustic non-lineartity ybder thermal stress [9][10][11] [12].

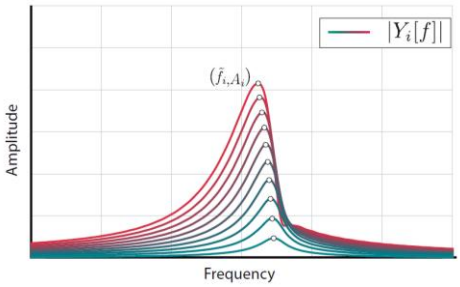


Figure 1. Received frequential response for the different impact levels ($Y_i(f)$)

In this study, the authors focus on the application of the NIRAS technique to evaluate thermal shock damage in mortar specimens, using embedded Fiber Bragg Gratings (FBGs) as sensors during the fabrication process. A key innovation lies in the simultaneous interrogation of multiple spatially separated FBG sensors inscribed along the same optical fiber. The performance of these FBG sensors is compared against that of surface-mounted accelerometers. While accelerometers are effective for measuring acceleration and vibration during impact events, FBGs offer precise strain and displacement measurements. Additionally, FBGs can be embedded within the material for long-term, remote monitoring and allow for the integration of multiple sensing points on a single fiber, enhancing spatial resolution.

2. MATHEMATICAL BACKGROUND

NIRAS is a method used for impact assessment and damage detection and involves impacting the material with different strength levels and analyzing the resulting acoustic frequency responses. The different reverberation signals are denoted by $y_i(t)$ where i denotes the different impacts and $Y_i(f)$ is the Fourier Transform of $y_i(t)$ (Figure 1). The non-linear parameters related to the resonance frequency shift α is obtained from a simple linear regression fit (Figure 2):

$$\frac{\tilde{f}_0 - \tilde{f}_i}{\tilde{f}_0} = \alpha \cdot A_i \quad (1)$$

$$A_i = \max|Y_i(f)| \quad (2)$$

$$\tilde{f}_i = \max_f|Y_i(f)| \quad (3)$$

Where A_i is the is the peak amplitude of the spectrum, $\tilde{f}_i$ is the peak frequency and $\tilde{f}_0$ denotes the intersection with y-axis of the linear relationship between the peak amplitudes A_i (x-axis) and the peak frequencies $\tilde{f}_i$ (y-axis).

The NIRAS technique obtains the parameter α_f^{NIRAS}, among others, as an indicator of the no linear behavior of the material: the greater the damage, the greater the no-linear behavior and the greater α_f^{NIRAS}.

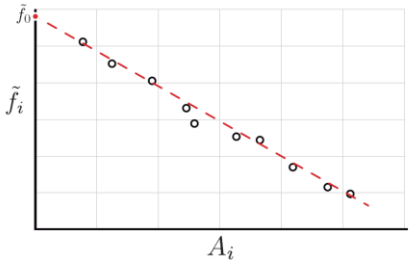


Figure 2. Linear regression from the different resonance signals.

3. EXPERIMENTAL

3.1 Manufacturing and damage induction of mortar specimens

Three mortar specimens (A, B and C) were prepared by mixing Portland cement (EN 197-1-CEM I 52.5 R) [13], sand (quartz) and water in the 1:3:0.5 ratio. After mixing the components, following the procedure described in UNE-EN 196-1 [13], the fresh mortar was placed in a prismatic mold of 50x60x240 mm size. Because prior to pouring the mortar, several optic fibers were settled according to Figure 4. Due to the fragility of the fibers, the mortar was poured in three layers,

avoiding damaging the fibers. For this, the fresh mortar was dropped in a zone free of fiber and then the mold was vibrated (Vibrating Table ToniVIB Tonitechnic) for 30 seconds (vibration frequency 50 Hz, amplitude 1 mm). This procedure was twice repeated and finally the superior part was flattened using a spatula. Additionally, metallic capillary sheath (Figure 3a) was used to protect each optical fiber during the pouring and vibration process and was removed immediately after the surface leveling.

The mold was put in a humid chamber (20 ºC, RH>90%) for 24 hours. After this period, the specimens were carefully demoulded and were covered with a plastic film, to avoid water evaporation. The wrapped specimens were stored in the same humid chamber for 46 days, to complete the hydration of the Portland cement.

After 88 days from mixing the mortar components, two of the specimens were subjected to thermal shock (B and C): the specimens were immersed in hot water (80ºC) for 1 hour and then immediately submerged in cold water (4ºC) for 10 minutes, tank of 0.01 m3.

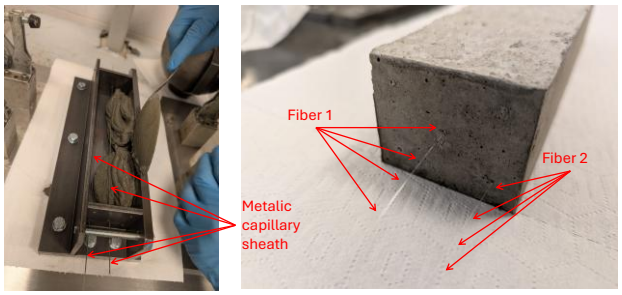


Figure 3. a) Manufacturing process b) Demolded specimen showing the optical fiber emerging from the mortar.

3.2 Embedded Instrumentation

Two of the three specimens (A and B) were internally instrumented during the fabrication process with two optical fibers aligned along the longitudinal axis of the specimen: one positioned at the center and the other near a corner (Figure 4). Each optical fiber contained two integrated Fiber Bragg Gratings (FBGs), which were located at the center and at one end of the fiber.

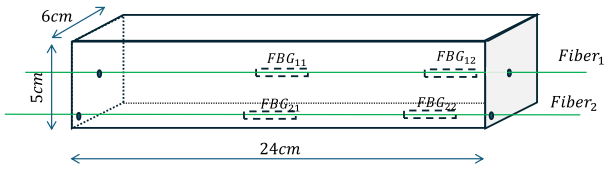


Figure 4. Representación de las fibras embebidas.

The FBGs were primarily tuned to the wavelengths listed in Table 1 and illustrated in Figure 5. Fiber 2 of Mortar A was damaged during the demolding process, therefore no measurements were obtained from this fiber.

Table 1. Wavelengths of the FBGs (nm)

Specimens	$Fiber_1$		$Fiber_2$	
	FBG_{11}	FBG_{12}	FBG_{21}	FBG_{22}
Mortar A	1533.98	1544.05	-	-
Mortar B	1534.07	1543.94	1553.95	1563.80

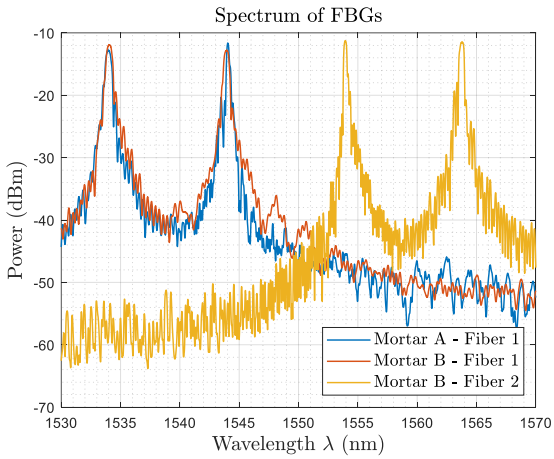


Figure 5. Spectrum of embebed fibers

3.3 Measurement setup

The experimental system employed for the execution of the test comprises three main subsystems: the excitation stage, the sensing stage, and the data acquisition stage.

In the excitation stage, an instrumented hammer was employed to apply controlled impacts to the specimen. The specimen was securely fixed using a custom-designed

support structure. As the hammer remained coupled to the support, multiple measurements could be performed without significant variation in the direction of the impacts, thereby ensuring the repeatability of the excitation conditions.

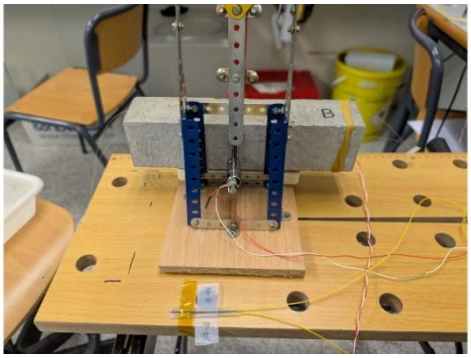


Figure 6. Photograph of the experiment

During the sensing stage, two accelerometers were utilized: one integrated into the instrumented hammer and another attached to the specimen. These devices were employed to record the accelerations induced in both the excitation element (Figure 8 - Column 1) and the tested specimen (Figure 8 - Column 2) . Additionally, two optical fibers were embedded within the specimen. Each fiber contained two Fiber Bragg Gratings (FBGs): one positioned at the center of the embedded section and the other at one of its ends. This configuration enabled the simultaneous monitoring of strain at various critical points of the specimen, with high sensitivity and spatial resolution (Figure 8 - Column 3 and 4). While two optical fibers (fiber 1 and fiber 2) were embedded into the mortar specimens, the present work reports results from only one of them.

The data acquisition stage was performed using two specialized instruments. Accelerometer signals from both the impact hammer and the specimen were recorded using a TiePie HS6 data acquisition system, noted for its high resolution and real-time capture capabilities. For the signals originating from the embedded optical fibers, an optical interrogator manufactured by SENTEA was used. This device features four independent channels and a maximum sampling frequency of 23 kHz. This configuration enabled the simultaneous interrogation of all the Fiber Bragg Gratings (FBGs), with one channel allocated per optical fiber. Each channel allows concurrent reading of multiple FBGs, thereby enabling synchronized acquisition of the two FBGs embedded in each fiber. This is illustrated in Figure 8, where the simultaneous signals from the accelerometers and spatially separated FBGs are plotted.

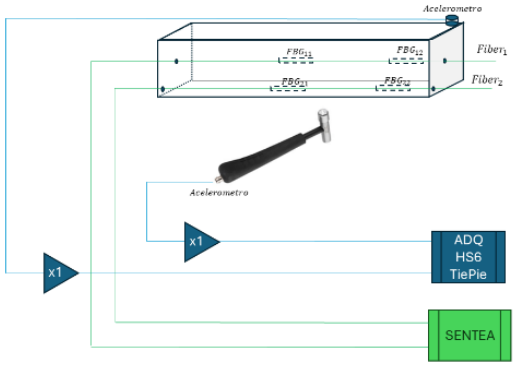


Figure 7. Experimental setup diagram

3.4 Tests description

The tests consisted of applying a series of controlled impacts to the specimen using the instrumented hammer. Each series involved ten consecutive impacts, with increasing force determined by the progressive increase of the striking angle. Upon completion of the first series, the procedure was repeated under similar conditions, applying an additional ten impacts to assess the repeatability of the specimen's dynamic response in its initial (undamaged) state.

As an illustrative example, Figure 8 displays a series of five impacts, showing the signals captured by both the hammer-mounted accelerometer and the surface-mounted accelerometer, as well as the signals recorded by the embedded FBGs in specimen B. The figure clearly shows the proper synchronization and simultaneous acquisition across the different sensor types. The FBG signals exhibit a baseline offset related to the specific wavelength at which each grating is fabricated. This baseline is inherent to the interrogation process itself and this mean value was subtracted from the FBG signals to ensure accurate analysis.

Subsequently, the specimen was subjected to a damage-inducing process via thermal shock. Once its structural properties had been altered, the two-testing series were repeated: ten impacts with the specimen in a non-conditioned state (i.e., without post-damage adjustments), followed by another ten impacts after conditioning. This procedure enabled a comparative analysis of the specimen's

dynamic behavior before and after thermal damage. The experiments are summarized in Table 2.

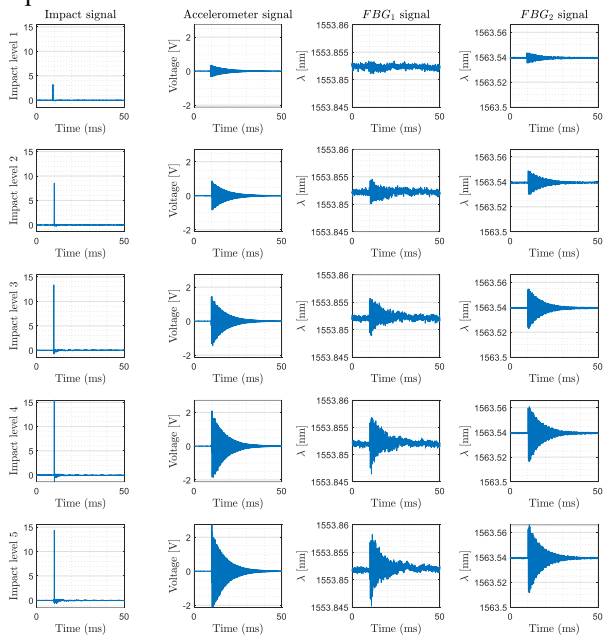


Figure 8. Temporal signals corresponding to different impact levels (displayed in rows) and different sensors (displayed in columns). The signals were acquired from Mortar B - Fiber 2, in its sound state.

Table 2. List of damaged and undamaged mortar samples tested with accelerometers and FBGs.

Sample	Status	Accelerometer	FBG
A	Sound	√	√
	Damage	Reference sample - no damage applied	
B	Sound	√	√
	Damage	√	√
C	Sound	√	No instrumented
	Damage	√	

4. RESULTS

Each experiment comprises ten different impact levels. For each impact signal, a Fourier transform was applied, resulting in a dataset of ten pairs of maximum amplitudes and their corresponding frequencies per experiment.

As an example, Figure 9 presents the normalized amplitudes versus the associated frequencies for specimen B under different conditions (sound and damaged) and using different types of sensors (accelerometers and FBGs). The figure reveals similar trends between the measurements obtained from the accelerometers and the FBGs for the same damage state.

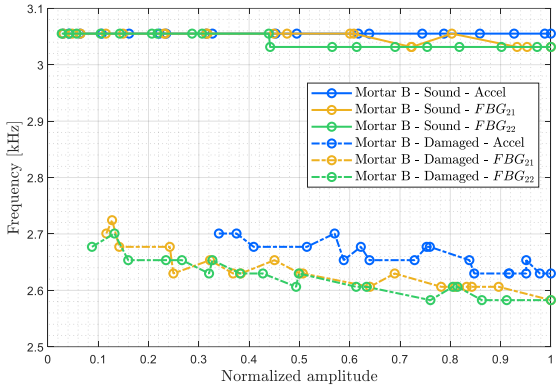


Figure 9. Normalized amplitudes vs frequencies for different conditions (sound and damaged) and different sensor types (accelerometers and embedded sensors FBGs) of specimen B.

From these curves, the NIRAS parameters α_f^{NIRAS} and f_0 were extracted for all the cases, as shown in Table 3. When available, the coefficient of determination R^2 is also reported to assess the goodness of fit. As observed, in the absence of damage, the frequency variation with impact level is negligible, resulting in a very small α parameter as expected for a horizontal line. Additionally, the estimation shows considerable variability, as reflected in the corresponding R^2 values in Table 3.

As damage increases, the nonlinearity in the system's response also increases, which is reflected by a higher α value. In such cases, the linear fit improves significantly. Notably, there is a strong correlation between the results from the accelerometers and the FBG sensors. The advantage of FBGs lies in their ability to accommodate multiple sensing points along the same optical fiber and enable simultaneous interrogation.

In this context, the parameter f_0 serves as a reliable damage indicator because all specimens share the same composition. However, for specimens with different mix proportions (and consequently different f_0 values), the variation in α becomes a more effective indicator of damage presence.

Table 3. NIRAS parameters obtained for different conditions (sound and damaged samples) and different sensor types (accelerometers and embedded sensors (FBG))

	Sound	Damaged
Accel.	**Probes A + B**	**Probes B+C**
$-\alpha$	1.15 ± 3.12	119 ± 20
$f_0\ [kHz]$	3.05 ± 0.003	2.78 ± 0.05
R^2	-	0.72 ± 0.13
$\boldsymbol{FBG_1}$	**Probes A + B**	**Probes B**
$-\alpha$	12.4 ± 17	112 ± 1.4
$f_0\ [kHz]$	3.06 ± 0.003	2.69 ± 0.002
R^2	-	0.76 ± 0.0006
$\boldsymbol{FBG_2}$	**Probes A + B**	**Probes B**
$-\alpha$	29.92 ± 2.1	112 ± 4.40
$f_0\ [kHz]$	3.05 ± 0.003	2.68 ± 0.05
R^2	0.53 ± 0.18	0.80 ± 0.07

5. CONCLUSIONS

This study highlights the potential of embedded sensor technologies as a reliable and effective approach for structural health monitoring in cement materials. In this case, thermal shock has been applied to mortar samples to generate damaged samples. The results indicate that the obtained values from the embedded Fiber Bragg Gratings (FBGs) sensors are similar to piezoelectric sensors. But embedded sensing systems offer numerous advantages, including real-time monitoring capabilities, high sensitivity to damage evolution, and the possibility of spatial and remote operation over the same optical fiber. Despite these benefits, several challenges remain, including sensor protection during the manufacturing process, ensuring long-term durability of the sensors within harsh environments, and reducing implementation cost.

Overall, embedded sensors represent a promising and evolving solution for advancing the reliability and efficiency of structural health monitoring systems in composite structures.

6. Acknowledgments

Grant PID2020-120262GB-I00 funded by MCIN/AEI/ 10.13039/501100011033

7. REFERENCES

[1] R. A. Guyer, P. A. Johnson, Nonlinear Mesoscopic Elasticity: Evidence for a New Class of Materials, *Physics Today* 52 (4), 30, 1999.

[2] L. D. Landau, E. M. Lifshitz, "Theory of Elasticity, Pergamon", Oxford, England, 3rd edn., 1986.

[3] L. Ostrovsky, P. A. Johnson, "Dynamic nonlinear elasticity in geomaterials", *Rivista del Nuovo Cimento 24,* 1–46, 2001

[4] P. C. Aïtcin, "Binders for durable and sustainable concrete", *CRC Press*, 2014.

[5] M. Alexander, S. Mindess, "Aggregates in concrete", *CRC Press*, 2010.

[6] Neville, A. M., "Properties of Concrete" (5th ed.). *Pearson Education*, 2011

[7] Eiras, J. N., et al., "Nonlinear Ultrasonic Evaluation of Thermal Damage in Concrete." Cement and Concrete Research, 80, 31–39, 2016

[8] Payan, C., Garnier, V., Moysan, J., & Johnson, P. A.. "Applying Nonlinear Resonant Ultrasound Spectroscopy to Improve Thermal Damage Assessment in Concrete." *Journal of the Acoustical Society of America*, 121(4), EL125–EL130, 2007

[9] C. Payan, et. al., "Probing material nonlinearity at various depths by time reversal mirrors", *Applied Physics Letters* 104 (14), 144102, 2014.

[10] C. Payan, T. J. Ulrich, P.-Y. Le Bas, T. Saleh, M. Guimaraes, "Quantitative linear and nonlinear resonance inspection techniques and analysis for material characterization: Application to concrete thermal damage", *The Journal of the Acoustical Society of America* 136 (2), 537–546, 2014.

[11] H. J. Yim, J. H. Kim, S.-J. Park, H.-G. Kwak, "Characterization of thermally damaged concrete using a nonlinear ultrasonic method", *Cement and Concrete Research* 42 (11), 1438–1446, 2012.

[12] Chen, J., Bharata, R., Yin, T. et al. "Assessment of sulfate attack and freeze–thaw cycle damage of cement-based materials by a nonlinear acoustic technique". *Mater Struct* 50, 105, 2017.

[13] AENOR, "UNE-EN 197-1. Cement. Part 1: Composition, specifications and conformity criteria for common cements.," 2011. [Online]. Available: www.aenor.es

[14] AENOR, "UNE-EN 196-1. Methods of testing cement. Part 1: Determination of strength.," 2018.

DOI: 10.61782/fa.2025.0196

FORUM ACUSTICUM EURONOISE 2025

Characterization of the adhesion quality in an aeronautical assembly by acoustic microscopy

Youness Ezziani[1], Damien Leduc[1], Pierre Maréchal[1], Mounsif Ech-Cherif El-Kettani[1*]
Mathieu Ducousso[2], Nicolas Cuvillier[2]
[1] LOMC, UMR 6294 CNRS, University of Le Havre Normandy, 75 Rue de Bellot, 76600 Le Havre, France.
[2] Safran Tech, Rue des Jeunes Bois, Chateaufort, 78772 Magny-les-Hameaux, France.

ABSTRACT

This work deals with the characterization of the adhesion quality and of the adhesive film properties in Titanium/Epoxy adhesive film/3D Composite aeronautical assemblies. Due to the thickness of the adhesive film in the different samples, between 80 µm and 200 µm, the study is carried out with a scanning acoustic microscope (SAM) in pulse-echo mode, at high frequencies (20 and 50 MHz). The difficulties expected and that are challenged are due both to the acoustic impedance contrast between the materials and to the high frequency of the study, which should render the reflected echo at the Epoxy film/Composite undetectable or very low. These conditions mean that the experiment must be carried out carefully and with high accuracy.
Nevertheless, the observation of the low amplitude reflected echo at the adhesive film/Composite interface in the different samples was possible thanks to the good signal-to-noise ratio (SNR) of the experimental set up instrumentation. The properties of the adhesive film are determined using the A-scan method with a planar transducer. Moreover, SAM images are obtained using a focused transducer, confirming the adhesion quantification and providing a fast estimation of the adhesive film thickness.

Keywords: *ultrasound characterization, scanning acoustic microscope (SAM), composite material, adhesive, high frequency transducer.*

[*] ***Corresponding author***: *echcherm@univ-lehavre.fr*
Copyright: *©2025 First author et al. This is an open-access article distributed under the terms of the Creative Commons Attribution 3.0 Unported License, which permits unrestricted use, distribution, and reproduction in any medium, provided the original author and source are credited.*

1. INTRODUCTION

Reducing the weight of aeronautical structures is essential to reduce fuel consumption and emissions. Adhesive bonding, which offers several advantages over traditional methods such as welding or riveting, plays a key role in achieving this weight reduction. Consequently, non-destructive evaluation (NDE) [1, 2] is required to assess the quality of the adhesion in the assemblies. Various NDE techniques are used to detect defects such as porosity or delamination [3]. This study focuses on samples representative of the Leap engine fan blade, provided by Safran Tech, which consists of a titanium alloy TA6V {Ti} bonded to a thick 3D woven Composite {Comp} with a thin layer of Epoxy resin AF191K {Epo} in the range of a hundred microns. The resulting structure is a trilayer stack {Ti/Epo/Comp}. Its properties are given on Table 1. Due to the thickness and properties of the Composite, it is considered as a semi-infinite medium in the frequency range of the study. To achieve effective echo separation, the axial resolution of the selected transducer must be appropriately matched to the adhesive layer thickness, typically ensured by maintaining a sufficient thickness-to-wavelength ratio. As a result, thin adhesive layers require a transducer with a center frequency in the tens of MHz range. Until now, obtaining reliable information on adhesion levels has been challenging, as it is highly dependent on the adhesive thickness and on the acoustic impedance ratios. The difficulty in performing ultrasonic evaluations with a favorable signal-to-noise ratio stems from the significant acoustic impedance contrast between TA6V and the Epoxy resin, and the relatively low contrast between the Epoxy resin and the Composite. This contrast, together with the attenuation introduced by the high frequency of the study, make the detection of the reflected echo at the Epoxy/Composite interface particularly

challenging. It is therefore crucial to find a balance: a frequency high enough to match the wavelength to the adhesive's thickness, but not too high (as the attenuation increases with the frequency) to detect background echoes, particularly the background echo at the Adhesive/Composite interface, with a sufficiently exploitable amplitude. The theoretical energy reflection and transmission coefficients for each interface in the assembly at normal incidence are as follows:

R_1 and T_1 (eq. (1)) correspond to the {Water/Ti} interface, R_2 and T_2 (eq. (2)) to the {Ti/Epoxy} interface, and finally R_3 and T_3 (eq. (3)) to the {Epo/Comp} interface.

$$\begin{cases} R_1 = \left(\dfrac{Z_{Ti} - Z_{Water}}{Z_{Ti} + Z_{Water}} \right)^2 \approx 0.8025 \\ T_1 = \dfrac{4 Z_{Ti} Z_{Water}}{\left(Z_{Ti} + Z_{Water} \right)^2} \approx 0.1975 \end{cases} \quad (1)$$

$$\begin{cases} R_2 = \left(\dfrac{Z_{Epo} - Z_{Ti}}{Z_{Epo} + Z_{Ti}} \right)^2 \approx 0.6393 \\ T_2 = \dfrac{4 Z_{Epo} Z_{Ti}}{\left(Z_{Epo} + Z_{Ti} \right)^2} \approx 0.3607 \end{cases} \quad (2)$$

$$\begin{cases} R_3 = \left(\dfrac{Z_{Comp} - Z_{Epo}}{Z_{Comp} + Z_{Epo}} \right)^2 \approx 0.0452 \\ T_3 = \dfrac{4 Z_{Comp} Z_{Epo}}{\left(Z_{Comp} + Z_{Epo} \right)^2} \approx 0.9548 \end{cases} \quad (3)$$

At the {Water/Ti} interface, approximately 80.25% of the energy is reflected, and only 19.75% is transmitted to the Ti layer. At the {Ti/Epo} interface, 63.93% of T_1 is reflected due to the significant impedance contrast between the two materials, while only 4.52% of the product T_1T_2 is reflected at the {Epo/Comp} interface. As a result, very small quantity of energy reaches the {Epo/Comp} interface, and then the reflection at the {Epo/Comp} interface is very weak due to the low impedance contrast between Epoxy and Composite.

2. EXPERIMENT

2.1 Studied samples

The samples studied are representative of the Leap engine fan blade and were provided by Safran Tech. They consist of three materials: a titanium alloy TA6V {Ti} bonded to a thick 3D woven Composite {Comp} using an Epoxy resin AF191K {Epo}. The Epoxy bonding process involves cleaning the interfaces with ethanol. Strips of the chosen material and specific thickness are then placed along the edges of the surfaces between the two materials to control the Epoxy layer thickness and prevent adhesive leakage during polymerization [1]. The polymerization process is carried out in a pressure-controlled oven, where four calibrated spring clamps apply a constant force of 65 N. Under standard conditions, the bonded sample is fully polymerized at 150°C for 3 h [1]. The adhesive thickness was estimated by in a first-hand simply by measuring the entire assembly with a caliper and subtracting the thickness of the titanium alloy and the Composite, as these are relatively thick. The parameters of the samples are given in Table 1, as supplied by the manufacturer.

Table 1. Properties of the studied trilayer assemblies.

Layer	TA6V	Epoxy	Composite
ρ [kg/m^3]	4430	1300	1590
E [GPa]	113	5.12	10.5
ν	0.34	0.30	0.29
c_L [m/s]	6060	2300	2920
c_T [m/s]	3120	1230	1600
h [µm]	180	80 to 200	13600

ρ [kg/m^3]: density; E [GPa]: Young's modulus; ν: Poisson's ratio; c_L [m/s]: Longitudinal wave velocity; c_T [m/s]: Transversal wave velocity; h [µm]: layer thickness.

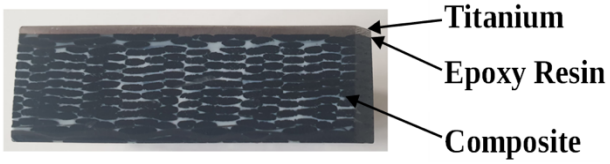


Figure 1. Cross-section view of the studied trilayer.

2.2 Scanning Acoustic Microscope (SAM)

The experimental study uses the PVA TEPLA Scanning Acoustic Microscope (SAM 301 - pulse-echo mode), which is based on the reflection of acoustic waves at interfaces due to changes in acoustic impedance. It is a sequential representation system in which a piezoelectric transducer emits a beam of ultrasonic waves which propagate through a coupling liquid, which is water in this case. The beam is scattered by the sample, and the signal is received by the same transducer [4, 5, 6]. As shown in Figure 2, the SAM consists of three main functional units: the acoustic sensor,

the electronic unit, the mechanical scanning system, and the display unit [7].

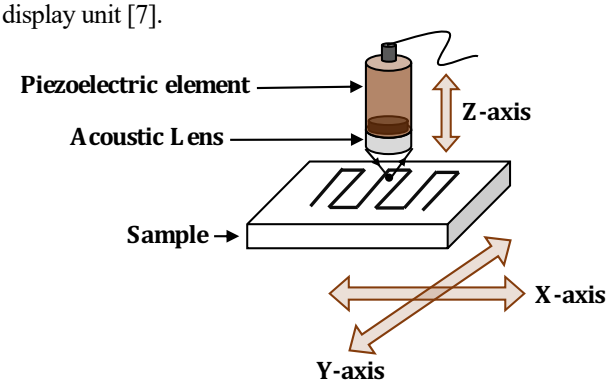


Figure 2. Scanning axes of the SAM.

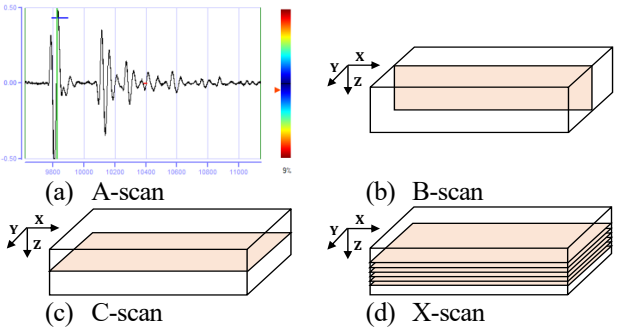


Figure 3. Types of scans for the visualization of ultrasound signals.

It also provides a variety of imaging options, as shown in Figure 3. Different types of scans are available, each offering a unique method of visualizing and assessing the material under examination. The four most commonly used scan types with SAM are A-scan, B-scan, C-scan, and X-scan [8].

3. CHARACTERISATION OF THE SAMPLES

Using the planar and focusing transducers available in the laboratory, background echoes from the adhesive were observed in samples with an Epoxy film thickness of less than 200 µm. This observation aligns with the fact that the adhesive is highly attenuating, and the energy of the echo at the Epoxy-Composite interface decreases with increasing Epoxy thickness. In this study, two samples with significant differences in the Epoxy film are examined: Sample 1 has a significantly thicker Epoxy film compared to Sample 2, as shown in Table 2.

3.1 Axial resolution consideration

The axial resolution (eq. 4) of the selected transducer must be adequate in relation to the thickness of the adhesive film being measured. This requirement is often expressed in terms of the thickness-to-wavelength ratio, which must be sufficient to allow effective echo separation. For a Gaussian echo envelope, the axial resolution is given by [9, 10]:

$$\Delta z_6 = \frac{t_6}{2T_0}\lambda_0 \approx \frac{0.88}{BW_{6,r}}\lambda_0 \qquad (4)$$

where Δz_6, t_6 and $BW_{6,r}$, represent respectively the axial resolution along the propagation axis, the round-trip signal duration, and the bandwidth at −6 dB, λ_0 and T_0 are the wavelength and the time period associated with the center frequency f_0. Consequently, the center frequency f_0 can be chosen so as to satisfy the following criterion:

$$f_0 \geq \frac{0.88}{BW_{6,r}} \max_{1\leq n\leq 3}\left\{\frac{c_{L,n}}{h_n}\right\} \qquad (5)$$

where $c_{L,n}$ is the longitudinal wave velocity and h_n is the thickness of the considered layer indexed n. In the studied case, with an estimated relative bandwidth of the transducer around $BW_{6,r} = 50\%$, the theoretical axial resolution limit at −6 dB is $\Delta z_6 = 1.76\ \lambda_0$. Thus, taking into account the thin adhesive layer into consideration, with a wave velocity of 2300 m/s in the Epoxy and a minimum thickness of 80 µm, eq. (5) gives a minimum center frequency f_0 of the transducer at 50 MHz.

A-scan characterizations are therefore performed using a planar transducer (Olympus V358-SU, SN: 1466080) with a center frequency of 50 MHz. As a result of eq. (4), the axial resolution of the system at 50 MHz is estimated at $\Delta z_6 \approx 81$ µm in the Epoxy layer. As an illustration, Figure 4 shows the A-scans obtained on samples 1 and 2.

3.2 A-scan

As a preliminary step, the caliper measurements of the thicknesses of the three constitutive layers are summarized in the following Table 2:

Table 2. Caliper measurements of thicknesses [µm].

Sample	TA6V	Epoxy	Composite
1	994	135	13540
2	981	86	13610

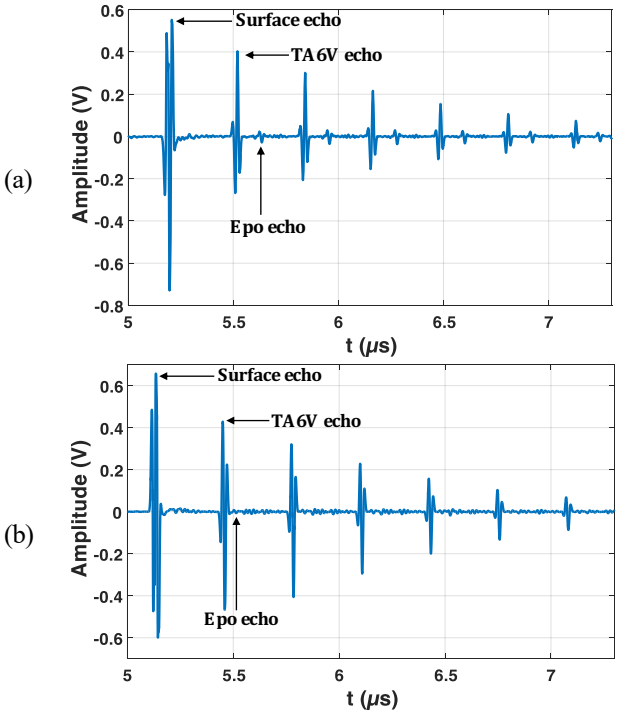


Figure 4. A-scan for 50 MHz center frequency excitation.: (a) Sample 1 and (b) Sample 2.

Upon examining the obtained signals in Fig.4, it can be observed: the echo reflected at the {Water/T} interface (first interface) labelled "Surface echo"; the echo reflected at the {Ti/Epo} film interface (second interface) labelled "TA6V echo"; a very small reflected echo at the {Epo/Comp} interface (third interface) labelled "Epo echo". Then are following periodically delayed multiple reflections from the TA6V layer, *i.e.* the {Ti/Epo} interface (second interface), as well as the associated small echoes from the {Epo/Comp} interface (third interface). The thickness of the adhesive film is then deduced by evaluating the time-of-flight between the background echo of TA6V (labelled "TA6V echo" on Fig.4) and the background echo of the Epoxy resin (labelled "Epo echo" on Fig.4), corresponding to the wave path within the Epoxy resin.

3.3 Determination of the Epoxy film thickness

This time-of-flight is estimated using the cross-correlation [11] between the Hilbert transform (HT) of the considered echoes indexed $n = \{1, 2\}$. The cross-correlation $cor_{e1,e2}(t)$ results from an integral between the envelopes $e_1(t)$ and $e_2(t)$ of the considered echoes $s_1(t)$ and $s_2(t)$, respectively:

$$cor_{e1,e2}(t) = \int_{-\infty}^{+\infty} e_1(\tau).e_2(t-\tau).d\tau \qquad (6)$$

with $$e_n(t) = \left|s_n(t) + i.HT\{s_n(t)\}\right| \qquad (7)$$

This envelope calculation (eq. 7) requires to pay a special attention of the studied echoes, as well as careful identification of the cutting boundaries of the echoes and a smooth windowing. The cross-correlation (eq. 6) shows a maximum at the date Δt_{max} which corresponds to the time-of-flight between the considered echoes $e_1(t)$ and $e_2(t)$.

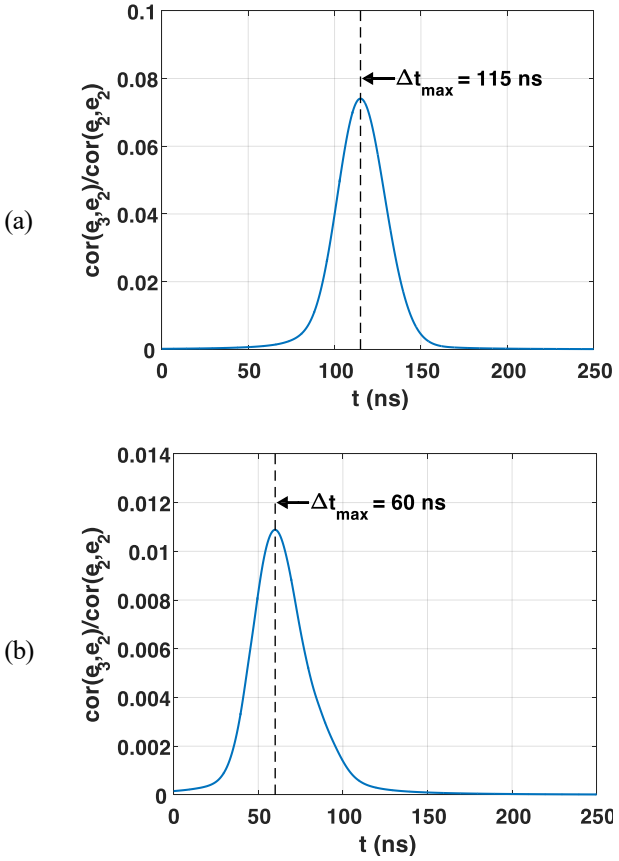


Figure 5. Cross-correlation of the Hilbert envelopes of the considered echoes of TA6V and Epoxy layers: (a) Sample 1 and (b) Sample 2.

As shown in Fig. 5, the calculated cross-correlation (eq. 6) of the Hilbert transform envelopes (eq. 7) of the relevant echoes, gives an evaluated cross-correlation time-of-flight Δt_{max} at 115 and 60 ns for samples 1 and 2, respectively. The thickness of the adhesive layer (Epoxy layer) is therefore estimated from the time-of-flight relationship: $e_{Epoxy} = c_L \times \Delta t_{max}/2$, giving in 132 µm and 69 µm for samples 1 and 2, respectively. These measurements are more accurate and more relevant than the subtraction estimation given in Table 2.

3.4 Hypothesis on the quality of the adhesion

Knowing that the samples were assembled with an Epoxy resin cured under the same conditions, it induces the same attenuation in the adhesive film. It can be seen that the background echo at the {Epo/Comp} interface is significantly higher for the thicker sample (sample 1, 132 µm), whereas the background echo at the {Ti/Epo} interface is almost the same for both samples. This amplitude difference between the two samples is assumed to be related to the quality of the adhesion at the {Epo/Comp} interface: a low level of adhesion in sample 1 leads to low transmission into the Composite and a high reflected echo, whereas a high level of adhesion in sample 2 results in higher transmission into the Composite and a lower reflected echo, as observed for this second sample. A series of C-scans, *i.e.* X-scans (Figure 3), are then performed to confirm this assumption.

3.5 X-scan

Using a 20 MHz focusing transducer, an X-scan is initiated to obtain 2D images (C-scans) reflecting the subsurface condition. Initially, it is essential to configure the experimental conditions, including setting the correct focal distance (with a fixed focus on the Epoxy background echo), calibration, and establishing the protocol for horizontal adjustment. The result will be C-scans at different depths within the sample. In addition, the focus was set on the Epoxy/Composite interface.

For all X-scan in this study, the gate size of each C-scan is 20 ns, corresponding to a distance of 23 µm in the Epoxy and 29.2 µm in the Composite. The axial resolution of the system at 20 MHz is 202 µm in the Epoxy.

A data window was selected and then divided into C-scan windows of 20 ns each. The scan area is 2 cm × 1.5 cm^2 with a pixel resolution of 200 µm/Pixel for sample 1 and 2×2 cm^2, with a pixel resolution of 100 µm/Pixel for Sample 2.

Analysing the images resulting from the X-scan starting from the TA6V-Epoxy interface (Figure 6a) for Sample 1, uniform colours are observed over most of the image, with some contrast at the edges, possibly indicating a slight misalignment of the sample. This colour homogeneity suggests that the medium remains unchanged, meaning we are still within the Epoxy layer. As we progress through the images, we reach C-scan n°7 where we can confirm the transition from the Epoxy to the Composite layer by the presence of carbon fibre bundles. By measuring the time shift between C-scan n°1 and C-scan n°7, corresponding to six windows of 20 ns each, the thickness of the Epoxy layer can be estimated as follows: $e_{epoxy} = 6 \times 23 = 138$ µm.

For Sample 2 (Figure 6b), a similar pattern is observed. The image shows a uniform color distribution, indicating that we are still within the Epoxy layer. As we analyze the successive images, C-scan n°4 shows the presence of carbon fibre bundles in light blue, mixed with the Epoxy in dark blue. This marks the transition from the Epoxy layer to the Composite zone, as the fiber bundles become clearly visible across several image windows. The thickness of the Epoxy layer is then estimated from the time shift between C-scan n°1 and C-scan n°4, corresponding to three windows of 20 ns each: $e_{Epoxy} = 3 \times 23 = 69$ µm.

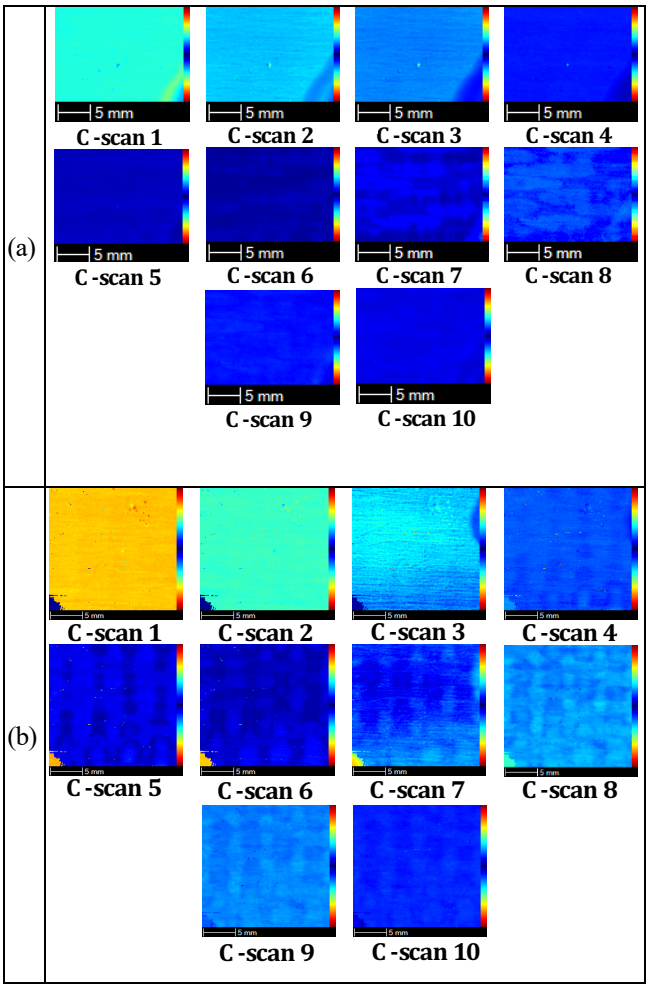


Figure 6. X-scan starting from the TA6V/Epoxy interface: (a) Sample 1 and (b) Sample 2.

Table 3 summarizes the measured thickness of the adhesive film by the three methods: the basic measure by the calipper, by X-Scan and A-Scan.

Table 3. Epoxy film thickness [µm] according to measurement method.

Method	Sample 1	Sample 2
Calliper	135	86
X-scan	138	69
A-scan	132	69

The A-scan measurement estimates it to be 132 µm, while the X-scan imaging gives a thickness of 138 µm. For sample 2, both methods give a thickness of 69 µm for the Epoxy layer. The A-scan method is the most accurate, but the X-scan can provide a quick estimate of the thickness of the Epoxy, although it is highly dependent on the time gate size and its initial starting position.

As shown in Figure 6, in terms of bond quality, the Composite is detected in several X-scan imaging windows of the same duration (20 ns): in sample 2 (spanning six C-scan windows, from C-scan n°4 to n°9). In contrast, it appears in only two X-scan imaging windows for sample 1 (C-scans n°7 and n°8) and is less distinct. These observations show how the transmitted echoes propagate through the Composite and allow the carbon fibers to be distinguished from the Epoxy. The number of detected C-scan images, which reflects the depth of the signal penetration into the Composite, confirms that the adhesion is stronger in Sample 2 than in Sample 1.

4. DISCUSSION

Initially, several samples with different adhesive film thicknesses were tested using either planar or focused transducers. Pulse-echo measurements showed that only samples with an adhesive film thickness of less than 200 µm exhibited round-trip echoes. This finding is consistent with the fact that the adhesive is highly attenuating, causing a further reduction in the energy reaching the {Epo/Comp} interface as its thickness increases. Two samples made of the studied trilayer structure {Ti/Epo/Comp} have been studied (see Table 2).

Accurate precise measurement of the Epoxy film thickness is essential to ensure the mechanical properties of the adhesive. In practice, strips of material placed on the edges of the surfaces between the two materials during the bonding process allow the thickness to be controlled. However, this thickness can change during polymerization. Therefore, the thickness measurement after the bonding operation is only an estimate that must be validated by acoustic methods. The measurement of the Epoxy film thickness for Sample 1 was 132 µm with the A-scan compared to 138 µm with the X-scan. However, for Sample 2, the thickness is 69 µm with A-scan and 69 µm with X-scan, compared to an estimate of 86 µm, indicating that the estimate is inaccurate and that the thickness to be taken into account is that obtained by acoustic method.

In terms of adhesion quality and comparing the results of the two samples, it can be seen that for Sample 2, with an Epoxy film thickness of 69 µm, the background echo amplitude is low. Conversely, for Sample 1, with an Epoxy film thickness of 132 µm, approximately double of that of Sample 2, the background echo amplitude is significant. This difference in amplitude cannot be attributed to the attenuation due to the viscosity of the adhesive but rather to interface conditions. This leads to the hypothesis that the adhesion quality of sample 2 is better than that of sample 1, the cohesive properties of the adhesive being identical.

In X-scan imaging, the Composite fibers are visible in several C-scan windows of the same duration (20 ns). For sample 2, the Composite fibers can be observed in 6 consecutive C-scan windows, whereas for sample 1, they are less visible, appearing in only 2 C-scan windows. This can be interpreted as a better energy transmission from the adhesive film to the Composite, suggesting a degraded adhesion quality in sample 1 compared to sample 2. These observations highlight the energy transmission within the Composite and allow the differentiation of the carbon fibers, with different levels of clarity in the different windows. As a result, the X-scan imaging supports the hypotheses derived from the A-scan analysis regarding adhesion quality.

Thus, regarding the background echo amplitude of the Epoxy film which depends on the {Epo/Comp} interface and the related adhesion quality, it can be concluded that the adhesion quality of Sample 2 is better than that of Sample 1.

5. CONCLUSION

The challenge of the ultrasound investigation lies in the very contrasting impedance discontinuities in the studied trilayer {Ti/Epo/Comp} structure: strong between the titanium and the adhesive, and weak between the adhesive and the Composite. These samples were characterized using the scanning acoustic microscope PVA TEPLA SAM 301. One of the objectives was to evaluate the thickness of the Epoxy film. Quantification using X-scan imaging was also carried out to obtain different C-scans in depth, particularly

from the Epoxy to the Composite, allowing the thickness of the epoxy film to be measured by imaging. The different levels of adhesion in the samples were identified by analyzing the background echo of the Epoxy film relative to its thickness, and by examining the amount of energy transmitted to the Composite layer through the X-scan imaging.

6. ACKNOWLEDGMENTS

The authors would like to thank the Le Havre Seine Metropole (LHSM) and the Normandy region for supporting the funding of this PhD work.

7. REFERENCES

[1] R. Hodé, S. Raetz, J. Blondeau, N. Chigarev, N. Cuvillier, V. Tournat and M. Ducousso, "Nondestructive evaluation of structural adhesive bonding using the attenuation of zero-group-velocity Lamb modes", Applied Physics Letters, vol. 116, p. 104101, 2020 (https://doi.org/10.1063/1.5143215).

[2] M. Ducousso, S. Bardy, Y. Rouchausse, T. Bergara, F. Jenson, L. Berthe, L. Videau and N. Cuvillier, "Quantitative evaluation of the mechanical strength of titanium/composite bonding using laser-generated shock waves", Applied Physics Letters, vol. 112, p. 111904, 2018 (https://doi.org/10.1063/1.5020352).

[3] L. Attar, M. Ech Cherif El Kettani, D. Leduc, M. V. Predoi and J. Galy, "Detection of kissing bond type defects and evaluation of the bonding quality in metal/adhesive/composite structures by a wavenumber-frequency insensitive SH mode", NDT & E International, vol. 137, p. 102841, 2023 (https://doi.org/10.1016/j.ndteint.2023.102841).

[4] R. A. Lemons and C. F. Quate, "Acoustic microscope - Scanning version", Applied Physics Letters, vol. 24, p. 163–165, 1974 (https://doi.org/10.1063/1.1655136).

[5] R. A. Lemons and C. F. Quate, "Integrated circuits as viewed with an acoustic microscope", Applied Physics Letters, vol. 25, p. 251–253, 1974 (https://doi.org/10.1063/1.1655459).

[6] V. Jipson and C. F. Quate, "Acoustic microscopy at optical wavelengths", Applied Physics Letters, vol. 32, p. 789–791, 1978 (https://doi.org/10.1063/1.89931).

[7] F. Hamdi, S. Bouhedja and H. Amrani, "Theoretical study of different attenuation measurement by acoustic microscopy", Journal of Applied Physics, vol. 114, p. 133501, 2013 (https://doi.org/10.1063/1.4823850).

[8] F. Bertocci, A. Grandoni and T. Djuric-Rissner, "Scanning Acoustic Microscopy (SAM): A robust method for defect detection during the manufacturing process of ultrasound probes for medical imaging", Sensors, vol. 19, p. 4868, 2019 (https://doi.org/10.3390/s19224868).

[9] N. Samet, P. Maréchal and H. Duflo, "Ultrasonic characterization of a fluid layer using a broadband transducer", Ultrasonics, vol. 52, pp. 427-434, 2012 (https://doi.org/10.1016/j.ultras.2011.10.004).

[10] N. Samet, P. Marechal and H. Duflo, "Ultrasonic imaging of bubble motion in a fiber preform", in Proceedings of the Acoustics 2012 Conference, pp. 2601-2606, 2012 (https://hal.science/hal-00810855).

[11] N. Ghodhbani, P. Marechal and H. Duflo, "Ultrasonic broadband characterization of a viscous liquid", Ultrasonics, vol. 56, pp. 308-317, 2015 (https://doi.org/10.1016/j.ultras.2014.08.013).

DOI: 10.61782/fa.2025.0927



FORUM ACUSTICUM
EURONOISE 2025

ULTRASONIC MAGING OF LAYER ON SUBSTRATE STRUCTURES USING HIGH-FREQUENCY ACOUSTIC FIELD CORRELATION

Nada Ben Jafela Lynda Chehami* Marc Duquennoy Emmanuel Moulin
Nikolay Smagin Dame Fall Zakariae Oumekloul

UPHF, CNRS, univ. Lille, UMR 8520-IEMN, F-59313, Valenciennes, France

ABSTRACT

Layer on substrate structures are often subject to various types of defects, particularly those resulting from manufacturing process during thin-film growth. Currently, one method of inspecting such structures involves the use of IDT transducers for excitation and laser vibrometry for reception. In this work, we propose a complementary approach inspired by passive noise correlation imaging methods initially developed in geophysics. This technique is applied here to image layered structures on substrates by exploiting the correlation of diffuse acoustic waves and the associated principle of passive Green's function reconstruction, enabling the detection and imaging of defects. The analysis was performed using numerical simulations and preliminary experiments on silicon wafers (3 mm thick). IDTs (10-25) MHz were used to generate surface waves, and the resulting displacement field was captured using laser vibrometry. Simulations and measurements were carried out on both defect-free and defect-containing cases. Correlation matrices were calculated on Full Matrix Capture mode. Finally, a beamforming algorithm was applied to localize defects, taking into account silicon's anisotropy.

Keywords: *Ultrasonic imaging, beamforming, anisotropy, Noise correlation, SAW, IDT.*

1. INTRODUCTION

Layer-On-Substrate (LOS) structures are subject to numerous degradations related to: manufacturing defects during thin film growth (thickness gradient), the quality of layer adhesion to the substrate (surface roughness), cracks, and delaminations. For these reasons, the microelectronics industry is increasingly interested in non-destructive evaluation methods, particularly for characterizing bonding quality in wafer assemblies. The work presented here proposes an alternative method based on the correlation of diffuse surface acoustic waves generated by inter-digital transducers (IDTs) operating in the frequency band between 10 and 25 MHz.

Typically, LOS characterization using IDT is performed by emitting a short (broadband) pulse onto the sample to be inspected, whose vibrational displacement amplitudes are then measured by a laser vibrometer. At high frequencies, this procedure must be performed with high precision, making automation a challenge. This so-called active method has yielded very promising results for the characterization of thin layers such as sol-gels [1, 2].

Meanwhile, the acoustic field correlation approach, initially used in geophysical applications [3–6] or in underwater acoustics [7–9], provides a relevant theoretical basis for the passive reconstruction of the medium's impulse response known as the Green's function (GF). Generally, GF estimation by noise correlation is based on the principle that waves emitted by random noise sources, when recorded at two points in the medium, can be used to retrieve the impulse response of the medium between these points sensing. In other words, the cross-correlation $C_{AB}(t)$ of the signals recorded at these two points A and B makes it possible to reconstruct the impulse response of the medium :

$$\frac{\partial}{\partial t} C_{AB}(t) = K\,[G_{AB}(t) - G_{AB}(-t)] + n_{AB}(t) \quad (1)$$

where C_{AB} is the cross-correlation between points A and B of the medium, G_{AB} is the Green's function (GF) between the same points, K is a constant depending on the

properties of the medium and the noise source, and n_{AB} is the residual error of the GF reconstruction.

This method is particularly useful in situations where it is difficult to generate controlled signals, such as in seismology, aeronautics, etc. However, the reconstruction quality is particularly influenced by the way the sources are distributed (localized or not), the number of sources, and the nature of the medium (absorption, attenuation, scattering, reverberation) [10]. In NDT/SHM, this method has been successfully validated at low frequencies (10, 30) kHz (Lamb waves) on aluminum damaged plates (cracks, holes, etc.) [11, 12].

In this work, we propose to extend this method to high frequencies (5-25) MHz by exploiting surface waves to probe microstructures (silicon wafers). Although complex (due to anisotropy), we first propose a simple numerical study to validate the approach on an anisotropic medium, and then it was attempted experimentally by developing suitable instrumentation using IDTs. Although promising, IDTs have rather poor reception capabilities; we therefore propose to use them here as a source of diffuse surface acoustic waves. IDTs are fabricated to focus the energy of surface acoustic waves onto the entire wafer [13]. To take full advantage of this method, optical detection is used and correlation functions are calculated. Figure 1 illustrates this principle.

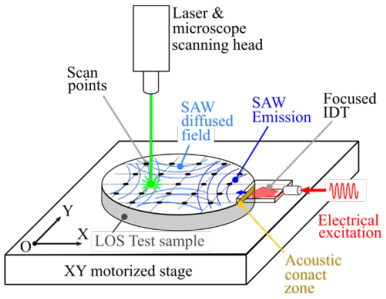


Figure 1. Schematic representation of the proposed characterization method based on the diffuse acoustic wave correlation.

The paper is divided into three parts: Section (1) is dedicated to the imaging in silicon (100); Section (2) is dedicated to numerical validation; and Section (3) is dedicated to the development of the instrumentation and preliminary tests on the GF reconstruction. Finally, a conclusion and perspectives.

2. IMAGING IN ANISOTROPIC MEDIA USING SURFACE WAVES

2.1 SAW propgation in Silicon (100)

Surface Acoustic Waves (SAW) propagate parallel to the surface of an elastic material, and their amplitude decreases rapidly, often exponentially, through the depth of the material. The penetration depth is of the order of the wavelength, providing high sensitivity to surface defects, voids, cracks, coatings, films, and nano/microparticles adhering to the surface. These waves are currently attracting increasing interest, particularly for miniaturization aspects. However, the acoustic propagation of these waves in anisotropic media is complex, where velocities depend on the propagation direction. Several theoretical studies [14, 15] are devoted to determining an analytical formulation of velocity profiles in anisotropic materials. In this paper, the velocities are calculated numerically using the analytical equation proposed by Teransako et al. [16].

On can recall here the Hooke's law extended to anisotropic materials using a tensor formulation that includes orientation:

$$\sigma_{ij} = c_{ijkl}\,\epsilon_{kl}; \quad i,j,k,l = 1,2,3 \tag{2}$$

where σ and ϵ are the stress and strain tensors.

The general case of a fourth-rank tensor requires 81 terms. By exploiting the cubic symmetry properties (silicon (100) has a face-centered diamond cubic crystallographic structure), the anisotropic properties of a cubic crystal can be described with a 6×6 matrix using a simplified tensor notation, which requires only three independent values: $c_{11} = 165.7$ GPa, $c_{12} = 63.9$ GPa, and $c_{44} = 79.56$ GPa.

The physical properties of silicon (100) are: Poisson's ratio $\nu = \frac{c_{12}}{c_{11}+c_{12}} = 0.278$; Young's modulus $E = c_{11} - 2\nu c_{12} = 130$ GPa; density $\rho = 2330$ kg/m^3; and the Zener coefficient $Z = \frac{2c_{44}}{c_{11}-c_{12}} = 1.56$.

In our case, the material under test is considered as a semi-infinite volume. Fig. 2 shows the estimated speed profile.

Two modes are observed for surface waves (regular mode and pseudo-mode) over a velocity range of 4500 to 5500 m/s.

In the following subsection, to perform defect imaging, an interpolation was performed on the two observed modes.

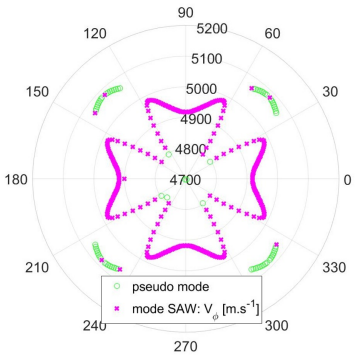


Figure 2. Theoretical (background) and experimental (red dots) velocity profiles.

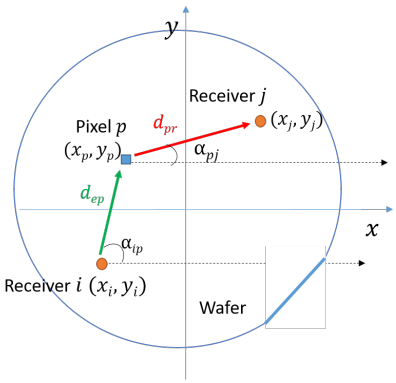


Figure 3. Illustration of the beamforming algorithm in anisotropic medium (backpropagation).

2.2 Imaging in anisotropic material

Considering two receivers R_i and R_j, the cross-correlation of the recorded signals across N_s noise sources can be expressed as follows:

$$C_{ijN_{Ns}}(\omega) = N_s\, D_{ij}(\omega) + n_{ijN_s}(\omega) \tag{3}$$

where D_{ij} represents a deterministic term containing the causal and anti-causal parts of the Green's function between the two receiver positions, and n_{ijN_s} is a term related to the residual noise from the reconstruction of the Green's function. As in [17], we adopt the differential beamforming algorithm to extract the defect signature, i.e., $\Delta\mathbf{C} = \mathbf{C}^{def} - \mathbf{C}^{ref}$, where "def" and "ref" refer to the cases with and without defects, respectively.

The principle consists of taking the image element index (i,j) of the matrix $\Delta\varphi$ and backpropagating it according to the current position of the pixel (x_p, y_p) and for each propagation direction (see Fig. 3). Concretely, this consists of multiplying the differential matrix by a phase function involving the wave number k depending on the surface wave direction, i.e.

$$bpf_{(}x_p, y_p)(\omega) = \sum_{i=1,\, j=1}^{N,N} \Delta\mathbf{C_{ij}}(\omega)\, e^{[+j\, k(\omega,\alpha_{ip})\, d_{ip} + k(\omega,\alpha_{pj})\, d_{pj}]} \tag{4}$$

with $\alpha_{ip} = atan\left|\frac{y_p - y_i}{x_p - x_i}\right|$ and $\alpha_{pj} = \arctan\left|\frac{y_j - y_p}{x_j - x_p}\right|$. The terms d_{ip} and d_{pj} are the distances from receiver i to pixel and from pixel to receiver j, respectively.

After returning to the time domain using an inverse Fourier transform, the pixel intensity is obtained by summing the resulting waveforms for each index value $(i,\, j)$ and calculating the energy of this sum over a time window T_0 (typically the inverse of the bandwidth):

$$I(x,y) = \int_0^{T_0} [bpf_{(x_p,y_p)}(t)]^2, dt, \tag{5}$$

where $bpf(t)$ is the FT of $bpf(\omega)$.

For pixels located on the defect, this amounts to a constructive sum and therefore to a maximum intensity at the defect position.

In Section 3, a numerical validation was proposed.

3. NUMERICAL VALIDATION

To validate the imaging algorithm proposed for anisotropic media, a simplified numerical simulation is proposed.

We consider the propagation of surface waves in an infinite plate without absorption. In the frequency domain, this propagation between a source and a receiver R_i at positions $\vec{r_s}$ and $\vec{r_i}$, respectively, can be modeled in the far field using the propagation function defined as follows:

$$P(\vec{r_s}, \vec{r_i}, \omega) = \frac{1}{\sqrt{(\vec{r_s} - \vec{r_i})}}\, e^{[-j\, k(\omega,\alpha_{ip})\, d_{ip} + k(\omega,\alpha_{pj})\, d_{pj}.]} \tag{6}$$

Therefore, the signal received at R_i can be expressed as follows:

$$u(\vec{r_s}, \vec{r_i}, \omega) = P(\vec{r_s}, \vec{r_i}, \omega)\, u_e(\omega), \quad (7)$$

where $u_e(\omega)$ is the Fourier transform of the transmitted signal.

In the presence of a defect, the signal received at R_i can be written as follows:

$$u_d(\vec{r_s}, \vec{r_i}, \omega) = u(\vec{r_s}, \vec{r_i}, \omega) + \Delta u(\vec{r_s}, \vec{r_i}, \omega), \quad (8)$$

with $\Delta u(\omega) = f_d(\omega)\, P(\omega)\, u(\omega)$. Here f_d represents the defect scattering amplitude and $\vec{r_d}$ is the defect position.

Using the inverse Fourier transform, we return to the time domain to obtain the signals $u_d(t)$ and $u(t)$ received by R_i in both cases: with and without a defect, respectively.

The tested configuration consists of an infinite silicon wafer whose properties are implicitly introduced in the previously estimated dispersion curves. Twelve receivers (crosses) are placed at known positions on its surface. The origin is taken at the low left corner of the wafer. At the center of the imaging array, a defect is modeled by a point scatterer of constant f_d (isotropic scatterer). A set of 361 sources (red dots) are randomly distributed around the receivers.

The transmission signal is a sinusoidal cycle weighted by a Hanning window at a center frequency of 7 MHz. The sampling rate is 300 MS/s. The signals are acquired for 28 μs. For each pair of receivers, the summed cross-correlation across all sources is calculated. The back-propagation-based imaging algorithm discussed above is then applied to the positive-time correlations. The localization image obtained for an area of (45 $\times$ 45) cm2 around the defect is shown in Fig. 4 for active and passive cases.

Pixel intensities are normalized relative to the maximum intensity. As observed, the defect location is correctly localized in passive mode compared to active result.

In what follows, we propose a suitable instrumentation to validate these numerical results.

4. EXPERIMENTAL VALIDATION: ESTIMATION OF GREEN'S FUNCTIONS

Here, we initially focused on studying correlation functions in a "defect-free" case. The experiments were performed on a silicon wafer of 7 cm in diameter and 2 mm thick. Surface acoustic waves were generated using a 7 to 25 MHz IDT transducer designed for this study [13], oriented at 45 degrees to favor the radiation of Rayleigh waves and minimize their conversion into bulk waves radiating into the substrate (cf Fig. 5). Since the transducer aperture is approximately 2 mm, the measurement points were chosen within the IDT's radiation zone. The measurement step size was approximately 10 mm, and a measurement grid of N = 25 points was created. Each Ascan is averaged 350 times and recorded over 2 ms. This corresponds to approximately 1000 times the reverberation time in the wafer.

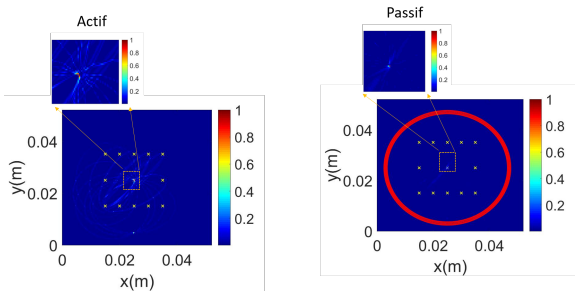


Figure 4. Defect localization image in active (raw signals in FMC mode) and passive (correlation functions, red circles indicate source positions) configurations.

The correlation functions are then calculated, and we obtain N$\times$ N impulse responses. Figure 6 shows a seismogram of cross-correlations between measurement point 3 of the grid and the other points on the same line.

As can be seen, the correlation functions are not symmetrical at zero. This demonstrates poor reconstruction quality of the Green's function (generally, when the correlation function is symmetrical between positive and negative times, it is a good indicator of convergence towards the Green's function). This can be explained by the fact that surface waves are not sufficiently reverberant at these operating frequencies. Another phenomenon may also occur, such as the conversion of surface wave modes into bulk waves. This work is in progress.

5. CONCLUSION

In conclusion, this study has shown the interest of the passive approach by correlation of diffuse waves to image silicon wafers. The results obtained by the numerical simulation are promising and have allowed to validate the

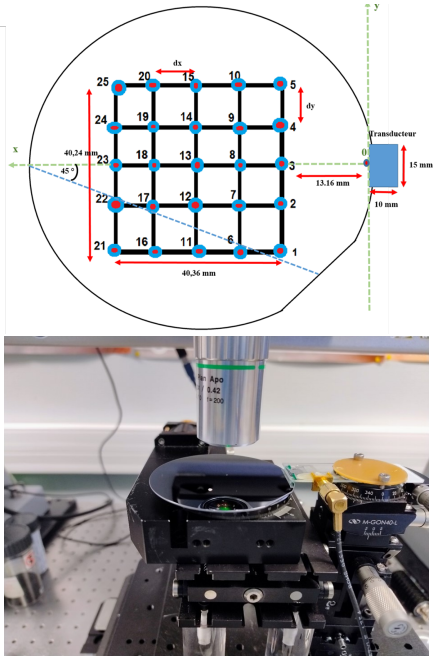


Figure 5. Experimental setup.

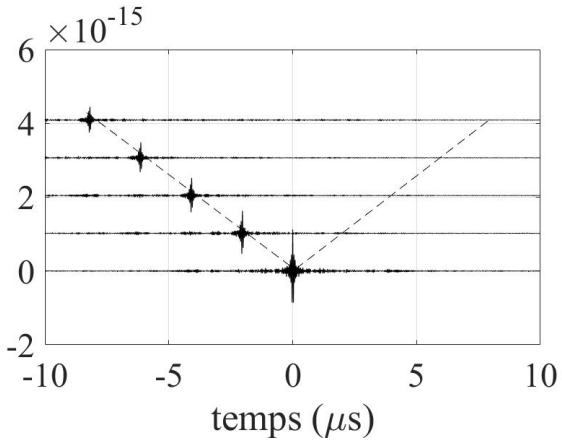


Figure 6. Seismogram of cross-correlations between measurement point 3 and the other points on the same line (see Fig. 5).

imaging algorithm in anisotropic medium. An experimental study was also conducted where an instrumentation adapted to generate a high frequency diffuse field by interdigital transducers was proposed. A preliminary study was first carried out on the estimation of the Green functions on a healthy wafer (without defect). The first results clearly show that surface waves are not very reverberant at these frequency ranges. To image micro-structures it is necessary to consider lower frequencies while remaining at the MHz scale, which can be particularly interesting in particular to image bonding defects in wafers. This approach certainly has a strong potential in the field of microelectronics.

6. ACKNOWLEDGMENTS

This project is funded by the French National Research Agency (ANR): DACLOS N^0:ANR-21-CE42-0002-01.

7. REFERENCES

[1] D. Fall, M. Duquennoy, M. Ouaftouh, N. Smagin, B. Piwakowski, and F. Jenot, "Non-destructive characterization of surfaces and thin coatings using a large-bandwidth interdigital transducer," *Review of Scientific Instruments*, vol. 89, Dec. 2018.

[2] D. Fall, F. Compoint, M. Duquennoy, H. Piombini, M. Ouaftouh, F. Jenot, B. Piwakowski, P. Belleville, and C. Ambard, "Surface acoustic wave characterization of optical sol-gel thin layers," *Ultrasonics*, vol. 68, pp. 102–107, may 2016.

[3] N. Shapiro, M. Campillo, L. Stehly, and M. Ritzwoller, "High-resolution surface-wave tomography from ambient seismic noise," *Science*, vol. 29, pp. 1615–1617, 2005.

[4] Y. Zheng, "Retrieving the exact Green's function by wavefield crosscorrelation," *The Journal of the Acoustical Society of America*, vol. 127, pp. EL93–EL98, mar 2010.

[5] K. Wapenaar, D. Draganov, R. Snieder, X. Campman, and A. Verdel, "Tutorial on seismic interferometry: Part 1 — basic principles and applications," *GEOPHYSICS*, vol. 75, pp. 75A195–75A209, sep 2010.

[6] Y. Chen and E. Saygin, "Green's function retrieval from deterministic seismic wavefield using higher-order cross-correlation," *ASEG Extended Abstracts*, vol. 2019, pp. 1–5, nov 2019.

[7] P. Roux and M. Fink, "Green's function estimation using secondary sources in a shallow water environment," *The Journal of the Acoustical Society of America*, vol. 113, pp. 1406–1416, mar 2003.

[8] V. V. Goncharov, Y. A. Chepurin, and O. A. Godin, "Passive acoustic tomography of the ocean using arrays of unknown shape," *Acoustical Physics*, vol. 59, pp. 170–178, mar 2013.

[9] M. G. Brown, O. A. Godin, N. J. Williams, N. A. Zabotin, L. Zabotina, and G. J. Banker, "Acoustic Green's function extraction from ambient noise in a coastal ocean environment," *Geophysical Research Letters*, vol. 41, pp. 5555–5562, aug 2014.

[10] L. Chehami, E. Moulin, J. de Rosny, and C. Prada, "Accuracy of green's function estimation from correlation of diffuse elastic waves on thin plates," *The Journal of the Acoustical Society of America*, vol. 146, pp. 3505–3511, nov 2019.

[11] L. Chehami, J. de Rosny, C. Prada, E. Moulin, and J. Assaad, "Experimental study of passive defect localization in plates using ambient noise," *IEEE Transactions on Ultrasonics, Ferroelectrics, and Frequency Control*, vol. 62, pp. 1544–1553, aug 2015.

[12] L. Chehami, E. Moulin, J. de Rosny, C. Prada, E. Chatelet, G. Lacerra, K. Gryllias, and F. Massi, "Nonlinear secondary noise sources for passive defect detection using ultrasound sensors," *Journal of Sound and Vibration*, vol. 386, pp. 283–294, jan 2017.

[13] M. Duquennoy, D. Fall, N. Ben Jafela, N. Smagin, Z. Oumekloul, L. Chehami, E. Moulin, and M. Ouaftouh, "A comparative study of divergent surface acoustic wave beams' generation on an y128° lithium niobate using various types of interdigital transducers," *Sensors*, vol. 25, p. 1067, Feb. 2025.

[14] G. Farnell, *Properties of elastic surface waves*. McGille University, 1969.

[15] Y. L. Y. X. D. Q. B. W. C. H. Guorong Song, Guangfu Hong, "Inversion of elastic constants of anisotropic (100) silicon based on surfacewave velocity by acoustic microscopy using particle swarm-based-simulated annealing optimization," *J Nondestruct Eval*, p. 34:43, 2015.

[16] A. T. R. C. nd Radim Kudelka, "Theoretical and experimental revision of surface acoustic waves on the (100) plane of silicon," *Scientific Reports*, vol. 11, no. 1, p. 2845, 2021.

[17] L. Chehami, E. Moulin, J. de Rosny, C. Prada, O. B. Matar, F. Benmeddour, and J. Assaad, "Detection and localization of a defect in a reverberant plate using acoustic field correlation," *Journal of Applied Physics*, vol. 115, p. 104901, mar 2014.

DOI:

Main theme: A12 Physical Acoustics and Ultrasound

Session A12.03 Biomedical ultrasound

Chair(s): O. Martinez-Graullera, G. Rus, J. Camacho, M. Pérez-Liva

DOI: 10.61782/fa.2025.0185

FORUM ACUSTICUM EURONOISE 2025

CAN ACOUSTIC VORTICES FRAGMENT KIDNEY STONES?

Sergio Maldonado-Ortega[1*], **Enrique González-Mateo**[1], **Alejandro Cebrecos**[1], **Cesar D. Vera-Donoso**[2], **Alicia Carrión**[1], **Francisco Camarena**[1], **Noé Jiménez**[1]
[1] Instituto de Instrumentación para Imagen Molecular (i3M), Universitat Politècnica de València (UPV) –Consejo Superior de Investigaciones Científicas (CSIC), Camino de Vera S/N, 46022 València, Spain
[2] Department of Urology, La Fe University and Polytechnic Hospital and Health Research Institute, Hospital La Fe, 46026 Valencia, Spain

ABSTRACT

Burst wave lithotripsy (BWL) is an ultrasound-based technique used to fragment kidney stones. In this proof-of-concept, we test a novel approach based on acoustic vortices to improve the efficiency of stone fragmentation. Acoustic vortices are wavefronts containing phase dislocations which carry pseudo-orbital angular momentum. These beams can be synthesized and focused by spherical phased-arrays which also enable beam steering and control the topological charge of vortices. Experiments were conducted using real and artificial kidney stones in water using a 128-channel therapeutic ultrasound phased-array transducer with 1.1-MHz central frequency. Sinusoidal-pulsed bursts of 20 cycles at 200-Hz pulse repetition frequency were generated. A confocal 128-element imaging probe monitored stones, while a camera recorded the fragmentation. Conventional BWL and single-topological-charge vortices were compared using same rarefaction pressure and, additionally, same energy. Artificial stones (Bego-stone) and real stones (calcium-oxalate-monohydrate and brushite) were tested. We observe that fragmentation speed is enhanced in a factor of two using vortices in artificial and real stones. Furthermore, vortices are a kind of defocused beams. Therefore, the mechanical index using vortices is lower than using BWL, resulting in a potentially less injurious therapy for surrounding tissues. These results demonstrate that acoustic vortices can enhance fragmentation using low-amplitude focused ultrasound.

Keywords: Acoustic vortices, Burst Wave Lithotripsy, Kidney stones

1. INTRODUCTION

Nephrolithiasis, or kidney stone disease, is a common and recurrent pathology affecting approximately up to a 20% of the population in some regions [1, 2]. It is characterized by the formation of solid crystalline deposits in the renal system [3]. Currently, shock wave lithotripsy (SWL) [4] remains a first-line, non-invasive treatment for renal calculi. SWL is an ultrasound-based technique used to eliminate these calculi based on high-energy acoustic pulses to fragment stones into smaller particles. However, SWL is associated with several limitations, including incomplete stone fragmentation, healthy tissue injury, and reduced efficacy [5, 6].

In recent years, burst wave lithotripsy (BWL) has emerged as a promising alternative to SWL [7]. This ultrasound-based technique, designed to fragment kidney stones using high-intensity and short-duration ultrasound bursts with low pressure amplitudes, improves precision and potentially reduces tissue damage. Preclinical and early clinical studies suggest that BWL may offer enhanced fragmentation efficiency and better patient outcomes compared to SWL [8-10].

Acoustic vortices are wavefronts with phase dislocations that carry pseudo-orbital angular momentum [11-13]. These specialized beams can be synthesized and precisely focused

*Corresponding author: smalort@upv.es
Copyright: ©2025 First author et al. This is an open-access article distributed under the terms of the Creative Commons Attribution 3.0 Unported License, which permits unrestricted use, distribution, and reproduction in any medium, provided the original author and source are credited.

using spherical phased-array transducers, which also allow beam steering and the control of vortex topological charge.

In this proof-of-concept study, we explore a novel approach to improve conventional BWL which leverages acoustic vortices to enhance fragmentation efficiency [14] as shown in Fig. 1.

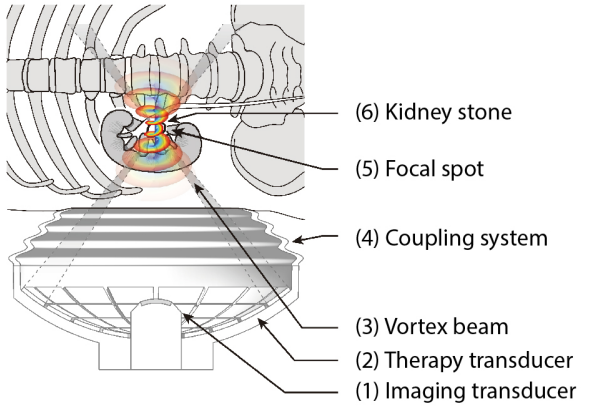


Figure 1. Schematic diagram of the proposed technique.

2. METHODS

Experiments were conducted to evaluate the feasibility of vortex-induced fragmentation using real and artificial kidney stones in a degassed-distilled water tank under controlled conditions. A 128-channel therapeutic ultrasound phased-array transducer, operating at a central frequency of 1.1 MHz, was used to deliver precise acoustic energy. The piezoelectric elements, arranged on a 150-mm diameter and 150-mm aperture bowl, generated sinusoidal pulsed bursts of 20 cycles at a 200-Hz pulse repetition frequency. Lower frequency and pulse repetition frequency are typically used in BWL experiments [15, 16].

A confocal 128-element ultrasound imaging probe enabled real-time monitoring of the stone and its progressive destruction, while a water-proof video camera recorded the fragmentation process enabling us to capture the fragmentation rates and patterns. The video of the experiment, once saved, was used for post-processing, in which the stone was segmented using a binary mask. This allowed us to determine the percentage of remaining stone.
The study compared conventional BWL with BWL enhanced by single-topological-charge acoustic vortices under identical rarefaction pressure conditions (8 MPa for both techniques) and at equal energy levels (8 MPa with vortex and 14 MPa with conventional BWL). Note that, since the focal spot volume is larger when using vortices, at similar energy values the mechanical index is reduced with vortices due to the lower applied pressure.

Artificial kidney stones were fabricated using cylindrical BegoStone [17, 18] samples of 2 mm radius and 10 mm height, with variations in the concrete-to-water ratio to replicate different mechanical properties of real kidney stones [19]. Concentrations of 3:1 and 5:1 were used in the experiments conducted with artificial stones. These two types of concentrations replicate Uric Acid and Calcium Oxalate Monohydrate (COM) real stones respectively. Experiments with real stones included the use of COM and Brushite samples, which were obtained from patients.

Both artificial and real stones were glued to a transparent film, ensuring they remained fixed to a non-rigid surface to enable the correct treatment without the displacement of the stone. This film was placed in 3D-printed structure designed to capture any fragments expelled from the surface of the stones.

3. RESULTS

We observed that acoustic vortices enhance fragmentation speed by a factor of two in artificial kidney stones and most real stones, with some exceptions. Fig. 2 illustrates the average fragmentation speed achieved across all experiments conducted with 3:1 artificial stones, which have similar properties to Uric Acid stones. The blue line represents experiments performed with acoustic vortices, while orange and gray lines correspond to experiments conducted without vortices. The orange line represents cases using the same rarefaction pressure as the vortex experiments. In contrast, gray line represents cases with the same energy levels as the vortex experiments, i.e., a much larger rarefaction pressure. Note that the fragmentation speed using conventional BWL is always slower, both for the same pressure and same energy levels, ensuring that the key factor leading to a more efficient fragmentation is the use of vortices.

In addition to the results presented in this work, similar experiments were conducted with 5:1 artificial stones, as well as with COM and Brushite real stones. Results obtained using real stones show a similar enhancement in fragmentation speed, with some exceptions that

showed no enhancement. These may be attributed to variations in the size and shape of the treated stones, which can influence the fragmentation process. However, for all artificial stones, results remained consistent, doubling the fragmentation speed when using vortices.

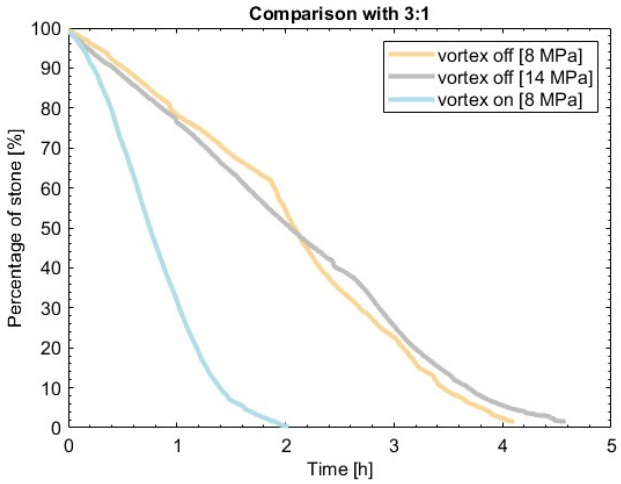


Figure 2. Evolution of the fragmentation as recorded by the video for the artificial stones of concentration 3:1.

4. CONCLUSION

The results indicate that acoustic vortices significantly enhance fragmentation speed, approximately doubling it in artificial kidney stones and in most real kidney stones. Additionally, due to the defocused nature of vortices, the mechanical index is reduced, suggesting potentially safer treatment for surrounding healthy tissue compared to conventional BWL. These findings demonstrate that acoustic vortices can effectively improve kidney stone fragmentation using low-amplitude focused ultrasound, offering a promising avenue for more efficient and less invasive lithotripsy techniques.

5. REFERENCES

[1] K. Stamatelou and D.S. Goldfarb: "Epidemiology of Kidney Stones," Healthcare, vol. 11, no. 3, pp. 424, 2023.

[2] J. Li, Y. Zhao, Z. Xiong and G. Yang: "Global, Regional, and National Incidence and Disability-Adjusted Life-Years for Urolithiasis in 195 Countries and Territories, 1990–2019: Results from the Global Burden of Disease Study 2019," *Journal of Clinical Medicine*, vol. 12, no. 3, pp. 1048, 2023.

[3] F. Grases, A. Costa-Bauza and R.M. Prieto: "Renal lithiasis and nutrition," *Nutrition Journal*, vol. 5, no. 23, 2006.

[4] C.H. Chaussy, W. Brendel and E. Schmiedt: "Extracorporeally induced destruction of kidney stones by shock waves," *The lancet*, vol 316, no. 8207, pp. 1265-1268, 1980.

[5] Y.A. Pishchalnikov, J.A. McAteer, J.C. Williams, I.V. Pishchalnikova and R.J. Vonderhaar: "Why stones break better at slow shockwave rates than at fast rates: in vitro study with a research electrohydraulic lithotripter," *Journal of endourology*, vol. 20, no. 8, pp. 537–541, 2006.

[6] A.A. Al Bazroon, A.A. Albassri, T. Swellam and I. Al Basha: "Vertebral Fracture Associated With Extracorporeal Shock Wave Lithotripsy: A Case Report," *Cureus*, vol. 16, no. 4, pp. 57900, 2024.

[7] A.D. Maxwell, B.W. Cunitz, W. Kreider, O.A. Sapozhnikov, R.S. Hsi, J.D. Harper, M.R. Bailey and M.D. Sorensen: "Fragmentation of Urinary Calculi In Vitro by Burst Wave Lithotripsy," *Journal of Urology*, vol. 193, no. 1, pp. 338–44, 2015.

[8] A.D. Maxwell, B. MacConaghy, M.R. Bailey and O.A. Sapozhnikov: "An investigation of elastic waves producing stone fracture in burst wave lithotripsy," *Journal of the Acoustical Society of America*, vol. 147, no. 3, pp. 1607–1622, 2020.

[9] M.R. Bailey, A.D. Maxwell, S. Cao, S. Ramesh, Z. Liu, J.C. Williams, J. Thiel, B. Dunmire, T. Colonius, E. Kuznetsova, W. Kreider, M. D. Sorensen, J.E. Lingeman, and O.A. Sapozhnikov: "Improving Burst Wave Lithotripsy Effectiveness for Small Stones and Fragments by Increasing Frequency: Theoretical Modeling and Ex Vivo Study," *Journal of endourology*, vol. 36, no. 7, pp. 996–1003, 2022.

[10] J.D. Harper, J.E. Lingeman, R.M. Sweet, I.S. Metzler, P.L. Sunaryo, J.C. Williams, A.D. Maxwell, J. Thiel, B.W. Cunitz, B. Dunmire, M.R. Bailey and M.D. Sorensen: "Fragmentation of Stones by Burst Wave Lithotripsy in the First 19 Humans," *The Journal of urology*, vol. 207, no. 5, pp. 1067–1076, 2022.

[11] N. Jiménez, R. Picó, V. Sánchez-Morcillo, V. Romero-García, L.M. García-Raffi and K. Staliunas: "Formation of high-order acoustic Bessel beams by spiral diffraction gratings," *American Physical Society*, vol. 94, no. 5, pp. 054027, 2016.

[12] N. Jiménez, J. Ealo, R.D. Muelas-Hurtado, A. Duclos and V. Romero-García: "Subwavelength Acoustic Vortex Beams Using Self-Demodulation," *American Physical Society*, vol. 15, no. 5, pp. 053004, 2021.

[13] M.A. Ghanem, A.D. Maxwell, Y. Wang, B.W. Cunitz, V.A. Khokhlova, O.A. Sapozhnikov and M.R. Bailey: "Noninvasive acoustic manipulation of objects in a living body," *Proceedings of the National Academy of Sciences*, vol. 117, no. 29, pp. 16848-16855, 2020.

[14] A. Randad, M.A. Ghanem, M.R. Bailey and A.D. Maxwell: "Design, fabrication, and characterization of broad beam transducers for fragmenting large renal calculi with burst wave lithotripsy," *Journal of the Acoustical Society of America*, vol. 148, no. 1, pp. 44–50, 2020.

[15] P.C. May, W. Kreider, A.D. Maxwell, Y.N. Wang, B.W. Cunitz, P.M. Blomgren, C.D. Johnson, J.S. Park, M.R. Bailey, D. Lee, J.D. Harper, and M.D. Sorensen: "Detection and Evaluation of Renal Injury in Burst Wave Lithotripsy Using Ultrasound and Magnetic Resonance Imaging," *Journal of endourology*, vol. 31, no. 8, pp. 786–792, 2017.

[16] A.D. Maxwell, C. Hunter, B.W. Cunitz, W. Kreider, S. Totten and Y.N. Wang: "Factors Affecting Tissue Cavitation during Burst Wave Lithotripsy," *Ultrasound in Medicine & Biology*, vol. 47, no. 8, pp. 2286-2295, 2021.

[17] E. Esch, W.N. Simmons, G. Sankin, H.F. Cocks, G.M. Preminger and P. Zhong: "A simple method for fabricating artificial kidney stones of different physical properties," in *Proc. of the 3rd International Urolithiasis Research Symp.*, (Indianapolis, USA), pp. 315–319, 2010.

[18] Y. Liu and P. Zhong: "BegoStone—a new stone phantom for shock wave lithotripsy research (L)," *Journal of the Acoustical Society of America*, vol. 112, no. 4, pp. 1265–1268, 2002.

[19] Kumarpranawa, I. Khan, D. Saranya and R. Arunai Nambi: "Preparation and characterization of kidney stone phantoms with compression strength and dielectric property studies," *International Journal of ChemTech Research*, vol. 8, no. 5, pp. 153-157, 2015

DOI: 10.61782/fa.2025.0179

FORUM ACUSTICUM EURONOISE 2025

BLOOD-BRAIN BARRIER OPENING IN SMALL ANIMALS USING FOCUSED ULTRASOUND

Jesús Limens-Pinaque[2*] **Josep Rodríguez-Sendra**[1] **Juan J. Rodríguez-García**[1]
Adrián Arándiga[1] **Jose L. Alonso-Ramos**[1] **Daniel Panadero-Soler**[2]
Noé Jiménez[1] **Patricia Rico**[3,4] **Santiago Canals**[2] **Francisco Camarena**[1*]

[1] Instituto de Instrumentación para Imagen Molecular (I3M), Universitat Politècnica de València (UPV) - Consejo Superior de Investigaciones Científicas (CSIC), Spain
[2] Instituto de Neurociencias (IN), Universidad Miguel Hernández (UMH) - Consejo Superior de Investigaciones Científicas (CSIC), Spain
[3] Centre for Biomaterials and Tissue Engineering (CBIT), Universitat Politècnica de València (UPV), Spain
[4] Biomedical Research Networking Center in Bioengineering, Biomaterials and Nanomedicine (CIBER-BBN), Spain

ABSTRACT

Focused ultrasound combined with microbubbles can locally and transiently open the blood-brain barrier (BBB) in a non-invasive and safe manner, providing a potential strategy for drug delivery into the brain. The technique is currently being used to test drugs for the treatment of different pathologies; however, the BBB opening dimensions depends on several characteristics of the ultrasonic beam. In this work we characterize the BBB opening in small animals produced by a manufactured transducer operating at frequencies 1.05 MHz (fundamental; $FWHM_{3dB}$ = 1.5 mm | DOF_{3dB} = 6 mm) and 3.25 MHz (first harmonic; $FWHM_{3dB}$ = 0.5 mm | DOF_{3dB} = 2 mm). The transducer has been tested in 11 mice, demonstrating its capability for different BBB opening dimensions with gadolinium (Gd) signal detected in contrast-enhanced T1-weighted MRI.

Keywords: *ultrasound, blood-brain barrier opening, preclinical research, neuromodulation, drug delivery*

[*] ***Corresponding authors***: *jlimens@umh.es fracafe@fis.upv.es*
Copyright: *©2025 Jesús Limens-Pinaque et al. This is an open-access article distributed under the terms of the Creative Commons Attribution 3.0 Unported License, which permits unrestricted use, distribution, and reproduction in any medium, provided the original author and source are credited.*

1. INTRODUCTION

The blood-brain barrier is a highly selective structure that regulates the passage of substances from the blood into the central nervous system (CNS). It is composed mainly of specialized endothelial cells, linked by tight junctions, which limit the diffusion of molecules larger than 400-500 Da and maintain brain homeostasis. However, this protective barrier also restricts the passage of most therapeutic compounds, posing a significant challenge for drug delivery in both preclinical animal models and clinical applications in humans.

Focused ultrasound (FUS) combined with microbubbles has been proven to transiently, non-invasively, and safely open the BBB in a localized manner [1]. This technique has been successfully demonstrated in various species, including rodents [2,3], macaques [4,5], and humans [6,7], enabling targeted drug delivery to the brain. Moreover, BBB opening has been explored for various applications, including enhanced chemotherapy delivery, gene therapy, and the treatment of neurodegenerative disorders [8].

In this study, we will use a manufactured FUS transducer operating at frequencies 1.05 (fundamental) and 3.25 MHz (first harmonic) together with microbubbles to open the

BBB in n = 20 mice. By employing T1-weighted FLASH magnetic resonance imaging (MRI) with gadolinium contrast, we will verify and analyze the openings.

2. MATERIALS AND METHODS

2.1 Acoustic simulation

Acoustic simulation was performed using the k-Wave MATLAB toolbox to model ultrasound wave propagation and quantify pressure distribution, focal spot localization, and transmission efficiency through the skull [9]. The transducer utilized in the simulation was identical to the one employed in the experiment, operating in two modes: at its fundamental frequency of 1.05 MHz and at its first harmonic frequency of 3.25 MHz. It had a diameter of 65 mm, a focal length of 50 mm, an inner aperture of 4 mm and a thickness of 2 mm.

For the acoustic simulations, we used an isotropic numerical grid with a spatial step of Δh = 292 µm for simulations at 1.05 MHz and Δh = 74 µm for simulations at 3.25 MHz, corresponding to a spatial resolution of 6 grid points per wavelength at each frequency. The numerical time step was chosen to ensure a Courant-Friedrichs-Lewy (CFL) number of 0.25. The CT data of the mouse used for the simulation were identical to [10]. The density and speed of sound for each voxel were derived from converting the corresponding Hounsfield Units (HU) to acoustic impedance [11,12]. Acoustic absorption coefficients were obtained from [10] and were 0.0023, 0.4374, and 17.6946 dB/cm for water, brain, and bone, respectively, at 1.05 MHz, and 0.0072, 1.3540, and 54.7469 dB/cm for water, brain, and bone, respectively, at 3.25 MHz.

Figure 1 presents the normalized acoustic fields obtained from simulations, illustrating the acoustic field for both frequencies.

2.2 Acoustic characterization

Acoustic characterization was performed in a water tank filled with degassed water to characterize the ultrasound field parameters. The transducer was positioned using a motorized stage (15 µm resolution, PI miCos GmbH, Germany) to ensure precise alignment. A calibrated hydrophone (HNA-400, Onda Corporation, USA) with a preamplifier (AG-2010, Onda Corporation, USA) was used to measure pressure waveforms at various spatial locations inside the skull cavity. The experimental measurements taken in the pool were compared with the simulations to verify the consistency and validity of the results (Figure 1 Bottom subplots).

Measurements performed in the water tank using ex vivo tissue revealed that the attenuation of the mouse skull was 21% at 1.05 MHz and 52% at 3.25 MHz. At 1.05 MHz, an input signal of 150 mV was required to obtain a pressure of 0.5 MPa, while at 3.25 MHz, an input signal of 315 mV was required to achieve a pressure of 0.6 MPa. For all measurements, the exact system used in the in vivo experiments was employed (Figure 2).

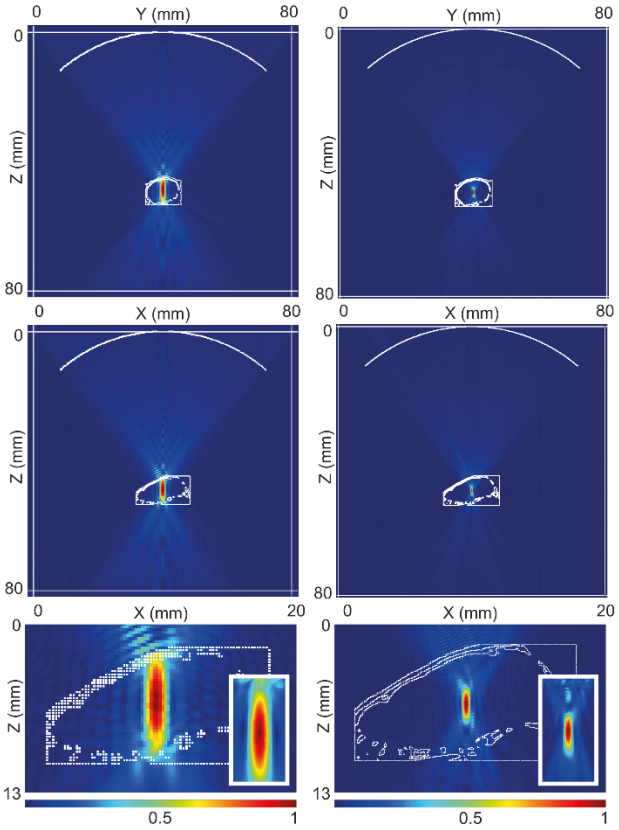


Figure 1. Ultrasound field simulated at 1.05 MHz (left), and 3.25 MHz (right). Images at the bottom show a zoom view of the focal point along with a subplot with the experimental results.

2.3 Animals

A total of 20 female swiss mice (age: 8 weeks, weight: 20 g) (SN-SWISS-F, JANVIER LABS, France) were used in this study. The animals were housed in standard conditions with a 12-hour light/dark cycle, temperature between 20 and 24°C and ad libitum access to food and water. When needed during the experiment, mice were anesthetized with 1-2% isoflurane and their body temperature was maintained at 37°C using a heating pad.

All procedures were conducted in accordance with European Directive 2010/63/EU on the protection of animals used for scientific purposes and approved by the Conselleria de Agricultura, Ganadería y Pesca of the Generalitat Valenciana (Approval ID: 2022 VSC PEA 0254 tipo 2).

2.4 Sonication

The sonication was performed using a custom ultrasound system based on a piezoelectric focal bowl, an arbitrary waveform generator (Red Pitaya 125-14, Red Pitaya US, USA) and an amplifier (OPAMP PA119, Apex Microtechnology, USA) specifically designed for the experiment (Figure 2). Prior to sonification, the animal was shaved in the head area and placed on the stretcher. Intravenous 1 µl/g microbubble injection (Definity, Lantheus Medical, USA) was administered immediately before the sonification.

Two sonification protocols were applied. The first involved f = 1.05 MHz, P = 0.5 MPa, PRF = 5 Hz, DC = 3%, and t = 120 s, and was applied to 10 mice. The second utilized f = 3.25 MHz, P = 0.6 MPa, PRF = 5 Hz, DC = 3%, and t = 120 s, and was applied to 10 mice. Following the sonification, an intraperitoneal injection of 200 µl Gd (Dotarem, Guerbet, France) was administered.

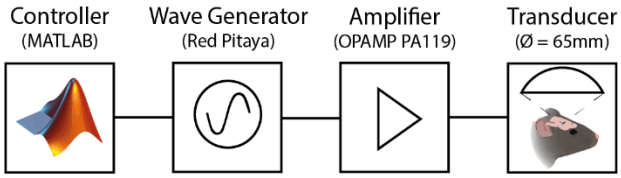


Figure 2. Ultrasound system diagram.

2.5 MRI

Mice were transferred to the MRI (BioSpec 70/30, Bruker, Germany) and anesthetized with isoflurane. A contrast-enhanced T1-weighted FLASH scan (TR/TE of 230/3.3 ms, flip angle of 70°, number of excitations of 18, inplane resolution of 85 µm × 85 µm, slice thickness of 500 µm and receiver bandwidth of 50 kHz.) was acquired 60 minutes after gadolinium injection. Scans were performed in both coronal and horizontal planes (Figure 3).

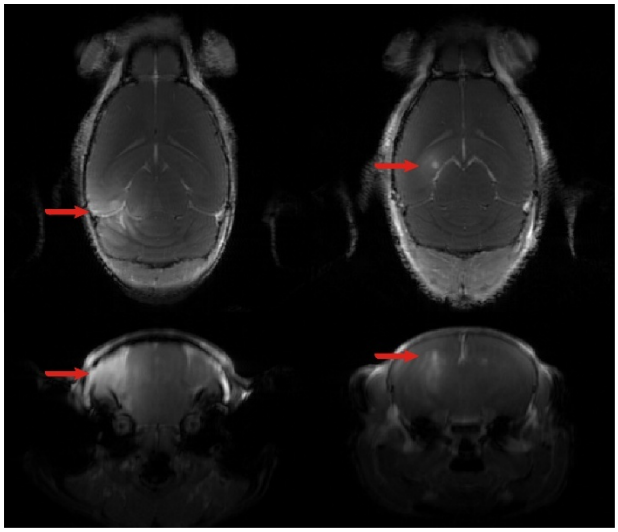


Figure 3. T1-weighted MRI images showing gadolinium due to blood-brain barrier opening. On the left, images obtained with the first protocol (f = 1.05 MHz), and on the right, with the second (f = 3.25 MHz).

2.6 BBB opening analysis

The analysis of the Gd signal in the T1-weighted MRI images aimed to obtain the centroid coordinates and the total volume of the BBB openings. For this analysis, *SAMson* was used to automatically segment the brain from the surrounding tissue in coronal planes [13]. Once isolated, all brains were segmented with *MATLAB* [14] using the same intensity threshold, resulting in a binary matrix. The *regionprops* function was then applied, which considers only the nonzero values in the matrix to extract the centroid coordinates (y and z coordinates). Additionally, the *nnz* function was used to count all nonzero voxels in the matrix. The total volume was then obtained by multiplying this

voxel count by the dimensions of a single voxel (85 µm × 85 µm × 500 µm). Since the *SAMson* tool is only applicable to coronal MRI studies, an additional manual segmentation was performed using *ITK-SNAP* [15] on the horizontal plane MRI study to obtain the *x* coordinates.

Finally, the centroid coordinates of each opening were referenced to the center of the generated matrix, as the matrix size had been adjusted to match the exact dimensions of the brain. This reference is robust across our different MRI studies, allowing for a reliable comparison of the locations of the openings.

3. RESULTS

Successful BBB opening was achieved in 11 mice. 9 mice did not show any opening. All of them had difficulty injecting the microbubbles. BBB disruption was observed in 6 mice using the 1.05 MHz protocol and in 5 mice using the 3.25 MHz protocol. For the first 7 openings (6 at 1.05 MHz and one at 3.25 MHz), the transducer was positioned in a specific brain region and kept fixed while the animals were placed accordingly to evaluate targeting precision. Subsequently, the transducer was shifted 3 mm forward to perform the remaining four openings at 3.25 MHz. The average BBB opening volume was 19.85 ± 6.20 mm³ for the 1.05 MHz condition and 12.41 ± 3.66 mm³ for the 3.25 MHz condition.

Regarding targeting precision, the displacement of the centroid of the BBB opening respect to the mean value per sonication event was 0.23 ± 0.18 mm, 0.20 ± 0.11 mm, and 0.07 ± 0.03 mm along the X, Y, and Z axes, respectively, for 1.05 MHz, and 0.08 ± 0.05 mm, 0.16 ± 0.13 mm, and 0.12 ± 0.06 mm along the X, Y, and Z axes, respectively, for 3.25 MHz (Figure 4). The total displacement of the centroid of all the BBB openings was 0.18 ± 0.16 mm, 0.17 ± 0.12 mm, and 0.11 ± 0.08 mm along the X, Y, and Z axes, respectively.

For the 1.05 MHz frequency, the positional analysis included all 6 mice with successful BBB openings. However, for the 3.25 MHz case, only three mice were considered for positional analysis. One of the remaining two was sonicated at the same location as the 1.05 MHz condition to confirm successful opening, while the other exhibited an opening significantly displaced from the intended area due to an animal positioning error. For the total displacement error, all BBB openings were included except the one with positioning error.

Additionally, for the 3.25 MHz case, all three openings were performed by physically shifting the target 3 mm forward to assess the system's targeting precision. The measured distances between these openings and the previous ones resulted in an average separation of 3.16 ± 0.11 mm.

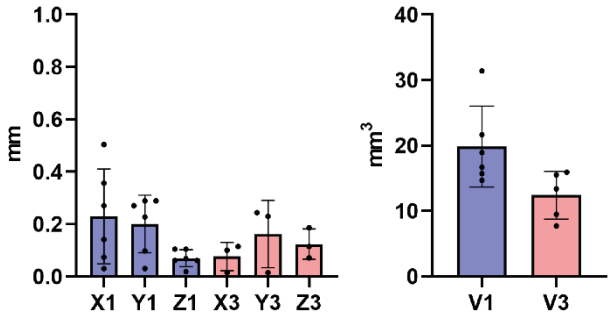


Figure 4. (Left) Mean and standard deviation of the absolute centroid displacement of the BBB opening along the X, Y, and Z axes. (Right) Mean and standard deviation of the volume of the BBB opening. Blue bars represent data acquired at 1.05 MHz, while red bars correspond to 3.25 MHz.

4. CONCLUSIONS

Twenty BBB opening procedures have been performed in mice using two different protocols in order to evaluate the capability of an FUS system to perform precise openings.

The average BBB opening volume was larger for the 1.05 MHz condition (19.85 ± 6.20 mm³) compared to the 3.25 MHz condition (12.41 ± 3.66 mm³), indicating a frequency-dependent effect on opening dimensions. Targeting precision analysis showed small centroid displacements per sonication event, with mean deviations of 0.23 ± 0.18 mm, 0.20 ± 0.11 mm, and 0.07 ± 0.03 mm along the X, Y, and Z axes, respectively, for 1.05 MHz, and 0.08 ± 0.05 mm, 0.16 ± 0.13 mm, and 0.12 ± 0.06 mm along the X, Y, and Z axes, respectively for 3.25 MHz. These results obtained are consistent and reliable, as they align with those described in

similar studies [10,16] and suggest that the manufactured transducer can achieve precise and reproducible targeting.

Furthermore, for the 3.25 MHz condition, the physical shift of the sonication target by 3 mm resulted in an observed average displacement of 3.16 ± 0.11 mm, confirming the system's targeting accuracy. This level of precision is particularly relevant for procedures requiring multiple BBB openings at different locations within the same experiment.

However, a significant portion of the variability in both volume and spatial distribution can be attributed to the initial target placement. Since the first sonications were performed at a randomly assigned location within the cerebellum due to errors in mice positioning, the irregular and smaller geometry of this brain region (compared to the hemispheres) led to Gd leakage spreading beyond the intended area, resulting in less well-defined openings. Quality of microbubble injections also played a crucial role in defining BBB opening volume, as incomplete administration of the microbubble dose frequently led to reduced opening sizes. Additionally, one case of significant displacement due to positioning error highlights the importance of accurate animal alignment in sonication experiments to ensure reproducibility and precise targeting across multiple sonication sites.

These findings demonstrate the feasibility of using the manufactured transducer for frequency-dependent BBB opening in small animals, providing valuable insights for future preclinical applications in drug delivery studies.

5. ACKNOWLEDGMENTS

This research has been funded by the Ministerio Español de Ciencia e Innovación y el Ministerio de Universidades with grant RYC2021-034920-I, PID2022-142719OB-C21 funded by MCIN/AEI/10.13039/501100011033/ and FEDER Una manera de hacer Europa and CNS2023-145707 and PRE2022-102801 funded by MCIN/AEI/10.13039/501100011033 and FSE+.

We would like to thank Juan José Manclús for providing us with a space in his laboratory to practice before the experiments, Juan González Valdivieso for his continuous assistance, Luis Tuset Sanchís for his technical support with the MRI, and Analía Rico Rodríguez for her assistance during the preliminary experiments. We also thank Sergio Jiménez Gambín for providing the mouse CT scan and Antonios Pouliopoulos for his advice on the execution of the blood-brain barrier opening.

6. REFERENCES

[1] Hynynen K, McDannold N, Vykhodtseva N, Jolesz FA. Noninvasive MR imaging-guided focal opening of the blood-brain barrier in rabbits. Radiology. 2001 Sep;220(3):640-6. doi: 10.1148/radiol.2202001804. PMID: 11526261.

[2] Kinoshita M, McDannold N, Jolesz FA, Hynynen K. Noninvasive localized delivery of Herceptin to the mouse brain by MRI-guided focused ultrasound-induced blood-brain barrier disruption. Proc Natl Acad Sci U S A. 2006 Aug 1;103(31):11719-23. doi: 10.1073/pnas.0604318103. Epub 2006 Jul 25. PMID: 16868082; PMCID: PMC1544236.

[3] Choi JJ, Pernot M, Small SA, Konofagou EE. Noninvasive, transcranial and localized opening of the blood-brain barrier using focused ultrasound in mice. Ultrasound Med Biol. 2007 Jan;33(1):95-104. doi: 10.1016/j.ultrasmedbio.2006.07.018. PMID: 17189051.

[4] Tung YS, Marquet F, Teichert T, Ferrera V, Konofagou EE. Feasibility of noninvasive cavitation-guided blood-brain barrier opening using focused ultrasound and microbubbles in nonhuman primates. Appl Phys Lett. 2011 Apr 18;98(16):163704. doi: 10.1063/1.3580763. Epub 2011 Apr 20. PMID: 21580802; PMCID: PMC3094460.

[5] McDannold N, Arvanitis CD, Vykhodtseva N, Livingstone MS. Temporary disruption of the blood-brain barrier by use of ultrasound and microbubbles: safety and efficacy evaluation in rhesus macaques. Cancer Res. 2012 Jul 15;72(14):3652-63. doi: 10.1158/0008-5472.CAN-12-0128. Epub 2012 May 2. PMID: 22552291; PMCID: PMC3533365.

[6] Carpentier A, Canney M, Vignot A, Reina V, Beccaria K, Horodyckid C, Karachi C, Leclercq D, Lafon C, Chapelon JY, Capelle L, Cornu P, Sanson M, Hoang-Xuan K, Delattre JY, Idbaih A. Clinical trial of blood-brain barrier disruption by pulsed ultrasound. Sci Transl Med. 2016 Jun 15;8(343):343re2. doi: 10.1126/scitranslmed.aaf6086. PMID: 27306666.

[7] Lipsman N, Meng Y, Bethune AJ, Huang Y, Lam B, Masellis M, Herrmann N, Heyn C, Aubert I, Boutet A, Smith GS, Hynynen K, Black SE. Blood-brain barrier opening in Alzheimer's disease using MR-guided focused ultrasound. Nat Commun. 2018 Jul 25;9(1):2336. doi: 10.1038/s41467-018-04529-6. PMID: 30046032; PMCID: PMC6060168.

[8] Gorick CM, Breza VR, Nowak KM, Cheng VWT, Fisher DG, Debski AC, Hoch MR, Demir ZEF, Tran NM, Schwartz MR, Sheybani ND, Price RJ. Applications of focused ultrasound-mediated blood-brain barrier opening. Adv Drug Deliv Rev. 2022 Dec;191:114583. doi: 10.1016/j.addr.2022.114583. Epub 2022 Oct 19. PMID: 36272635; PMCID: PMC9712235.

[9] Treeby BE, Cox BT. k-Wave: MATLAB toolbox for the simulation and reconstruction of photoacoustic wave fields. J Biomed Opt. 2010 Mar-Apr;15(2):021314. doi: 10.1117/1.3360308. PMID: 20459236.

[10] Jimenez-Gambin S, Jimenez N, Pouliopoulos A, Benlloch JM, Konofagou E, Camarena F. Acoustic Holograms for Bilateral Blood-Brain Barrier Opening in a Mouse Model. IEEE Trans Biomed Eng. 2022 Apr;69(4):1359-1368. doi: 10.1109/TBME.2021.3115553. Epub 2022 Mar 18. PMID: 34570701; PMCID: PMC9058858.

[11] Schneider U, Pedroni E, Lomax A. The calibration of CT Hounsfield units for radiotherapy treatment planning. Phys Med Biol. 1996 Jan;41(1):111-24. doi: 10.1088/0031-9155/41/1/009. PMID: 8685250.

[12] Mast, T.D. (2000). Empirical relationships between acoustic parameters in human soft tissues. *Acoustics Research Letters Online*, 1(2), 37–42.

[13] Panadero-Soler D, Kotb Selim M, Martínez-Tazo P, Muñoz-Moreno E, Ramos-Cabrer P, López-Larrubia P, De Santis S, Canals S, Pertusa, A. SAMson: an automated brain extraction tool for rodents using SAM. bioRxiv. 2025 Jan. doi: 10.1101/2024.03.07.583982

[14] The MathWorks, Inc. (2024). MATLAB (Version R2024b) https://www.mathworks.com

[15] Yushkevich PA, Piven J, Hazlett HC, Smith RG, Ho S, Gee JC, Gerig G. User-guided 3D active contour segmentation of anatomical structures: significantly improved efficiency and reliability. Neuroimage. 2006 Jul 1;31(3):1116-28. doi: 10.1016/j.neuroimage.2006.01.015. Epub 2006 Mar 20. PMID: 16545965.

[16] Hu Z, Chen S, Yang Y, Gong Y, Chen H. An Affordable and Easy-to-Use Focused Ultrasound Device for Noninvasive and High Precision Drug Delivery to the Mouse Brain. IEEE Trans Biomed Eng. 2022 Sep;69(9):2723-2732. doi: 10.1109/TBME.2022.3150781. Epub 2022 Aug 19. PMID: 35157574; PMCID: PMC9443669.

DOI: 10.61782/fa.2025.0623

FORUM ACUSTICUM EURONOISE 2025

NON-INVASIVE AND LOW-COST PHOTOACOUSTIC/ULTRASOUND DUAL-MODAL IMAGING SYSTEM FOR CAROTID PLAQUE IMAGING

Alejandro Ariza-Carrasco[1,2] **Javier G. Muñoz**[1,2] **Jorge Cruza**[3]
Luis Elvira[3] **Joaquín L. Herraíz**[1,2] **José M. Udías**[1,2]
María Alonso de Laciñana[4] **Jorge Rodríguez-Pardo**[4] **Paula Ibáñez García**[1,2]
Mailyn Pérez-Liva[1,2*]

[1] Department of Matter Structure, Thermal and Electronic Physics and IPARCOS, Complutense University of Madrid, Madrid, Spain
[2] Departamento de Estructura de la Materia, Física Térmica y Electrónica, Facultad de Ciencias Físicas, Universidad Complutense de Madrid (UCM); IdISSC, España.
[3] Ultrasound Systems and Technology Group (GSTU), Institute for Physical and Information, Spanish National Research Council (CSIC), Madrid, Spain
[4] Department of Neurology and Stroke Centre, Neurological Sciences and Cerebrovascular Research Laboratory, Neurology and Cerebrovascular Disease Group, Neuroscience Area Hospital La Paz Institute for Health Research, IdiPAZ (La Paz University Hospital, Universidad Autónoma de Madrid), Madrid, Spain

ABSTRACT

Carotid plaque rupture causes most ischemic strokes, yet current diagnostics focus on arterial stenosis, overlooking 80–90% of vulnerable plaques. This highlights the need for affordable, precise, and non-invasive imaging to assess plaque vulnerability. To address this, we developed a low-cost, dual Ultrasound/Photoacoustic system integrating a Vermon L7.5-MHz ultrasound probe, a 128-channel programmable phased array Ultrasound scanner (Dasel, Spain), and pannels of pulsed semiconductor lasers diodes of 5W emitting 100 ns pulses at 447 nm. Synchronization was managed via external pulse generators, with laser light delivered through optical fibers. Validation utilised phantoms of black nylon threads. GPU-accelerated delay-and-sum beamforming was used for image recontruction. The system achieved 530 μm lateral and 360 μm axial resolution. This system offers a cost-effective, non-invasive approach for high-resolution multiparametric tissue characterization. Future aims will be to improve in vivo assessment of plaque vulnerability.

Keywords: *photoacoustic, delay-and-sum, lateral and axial resolution, signal-to-noise ratio, low-cost*

**Corresponding author*: *mailyn01@ucm.es.*

***Copyright**: ©2025 Alejandro Ariza-Carrasco et al. This is an open-access article distributed under the terms of the Creative Commons Attribution 3.0 Unported License, which permits unrestricted use, distribution, and reproduction in any medium, provided the original author and source are credited.*

1. INTRODUCTION

Stroke causes over 11.6% of all deaths, with ischaemic stroke alone responsible for more than 6 million deaths annually, making it the second leading cause of death worldwide. It is primarily triggered by plaques in the carotid artery—mainly composed of lipids, blood, and collagen—that obstruct blood flow and rupture suddenly. While our understanding of plaque evolution has advanced, current diagnostics still focus mainly on detecting arterial stenosis. This approach only identifies 10-20% of cases, thereby missing crucial indicators of plaque vulnerability [1]. Consequently, there is an urgent need for non-invasive, simple, and low-cost imaging techniques that can assess carotid plaques' composition, stability and vulnerability.

Photoacoustic imaging (PAI) is a promising technique that combines the contrast and spectral benefits of optical imaging with the deep penetration and high spatial resolution of ultrasound, taking advantage of the low scattering of ultrasound in biological tissue and relying on the photoacoustic (PA) effect [2]. This effect is produced by illuminating the tissue with pulsed light of very short duration (around a few nanoseconds), which causes the molecules present, whether endogenous or exogenous (such as haemoglobin or melanin), to absorb the incident energy. This absorption generates a local increase in temperature and pressure, which in turn causes a thermoelastic expansion of the tissue, giving rise to acoustic waves that propagate and are picked up by ultrasound transducers. In this way, the technique complements ultrasound information by providing functional data on tissue oxygenation and vascular dynamics. The study aims to characterize a low-cost, portable ultrasound-photoacoustic system using semiconductor laser diodes, which are more affordable and portable than traditional lasers.

2. METHODOLOGY

2.1 System description

We developed a low-cost, non-invasive dual Ultrasound/Photoacoustic system. This system consists of a clinical ultrasound probe (Vermon L7.5 MHz) with 128 elements, a centre frequency of 7.5 MHz and a bandwidth of 60%. For the photoacoustic part, the system consists of two panels of five pulsed semiconductor laser diodes (SLD) with a wavelength of 447 nm and 5W of power, placed on each side of the clinical probe. The illumination from each diode is delivered uniformly to the transducer's acquisition plane via optical fibers attached to each diode on the panels (Fig. 1). The delivered pulse width is 100 ns with a pulse repetition rate of 1 kHz. This pulse generated by the diodes is regulated by an Arduino signal generator (Arduino Uno) and a controller (SLD Picolas LDP-V 240-100 V3.3 Driver) that is responsible for activating and synchronising the illumination and ultrasound detection. The images are acquired by a programmable ultrasound scanner provided by the company Dasel (Spain), with a sampling frequency of 62.5 MHz and 128 transmission and reception channels. This scanner can perform multiple acquisitions, allowing the use of different types of averaging to minimise the noise characteristic of photoacoustic images. The acquired photoacoustic images have a depth of 20 mm, since this depth marks the practical limit of imaging in the current photoacoustic configuration, since from that point the intensity of the fluence is 20% lower than its maximum value.

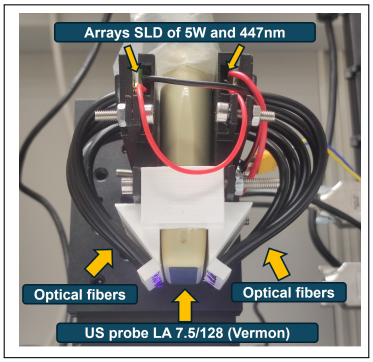


Figure 1. Photoacoustic system that combines a clinical ultrasound probe with two arrays of five 5W SLD (447 nm). These diodes are attached to the sides of the probe, and their light is delivered to the transducer's acquisition plane through optical fibers.

2.2 Image reconstruction

After the photoacoustic signal is captured by the ultrasound detectors, reconstruction algorithms are employed to convert the temporal variations in pressure into final photoacoustic images. Numerous reconstruction methods are now available to achieve this, and the GPU-accelerated delay and summation (DAS) method was used in this study [3].

2.3 Lateral and axial resolution

To evaluate spatial resolution, a home-made phantom of 0.26 mm diameter black nylon threads spaced 4 mm apart both laterally and axially (Fig 3A.), immersed in water, was scanned with our experimental setup. The following expressions were used to calculate the theoretical and lateral resolution [4]:

$$R_l = 0.71 \cdot \frac{c_0}{NA \cdot f_0} \qquad R_a = 0.88 \cdot \frac{c_0}{\Delta f} \tag{1}$$

with c_0 the velocity of sound in the medium, NA is the numerical acoustic aperture, f_0 and Δf the centre frequency and bandwidth of the transducer signal, respectively. To characterise the spatial resolution of our system we reconstructed the image of a point target, in this case

the black nylon thread, and used the Point Spread Function (PSF) method [4]. The Full Width at Half Maximum (FWHM) of the PSF determines our experimental spatial resolution.

2.4 Signal-to-noise ratio (SNR) and amplitude correction map

Several photoacoustic image acquisitions were performed to test the dependence of signal-to-noise ratio (SNR) on the number of averaged signals. Finally, an amplitude correction of the reconstructed PA image with DAS of the black nylon phantom was performed. For this purpose, the reconstructed image was divided into blocks and, for each block, the maximum amplitude value is extracted. This generates a 'correction map' representing the local variation of the signal in the image. This map is used to normalise the original image by dividing the reconstructed image by the correction map, thus compensating for acoustic and optical attenuations and local variations in amplitude, resulting in a more homogeneous representation of the signal. Finally, a median filter was applied, reducing residual noise and improving the visual quality of the corrected image.

3. RESULTS

3.1 Lateral and axial resolution evaluation

The theoretical lateral and axial resolution of the system were obtained to be 0.23 mm and 0.29 mm, respectively. However, these theoretical resolutions are not taking into account in their expressions the characteristics of the piezoelectric elements of the transducer such as kerf or pitch. On the other hand, Fig. 2B shows the photoacoustic image reconstructed with the delay-and-sum algorithm of the black nylon thread (Fig. 2A) immersed in water. From the PSF method, we extracted the FWHM of the reconstructed signal, previously performing a Gaussian fit to it and establishing that if the signal did not exceed a threshold of -6 dB then the system is not able to correctly resolve the point object. By analysing both the lateral and axial profiles of the signal, we obtained a lateral resolution of $R_L = 0.53$ mm and an axial resolution of $R_A = 0.36$ mm (Fig. 2C).

3.2 SNR vs number of signal averages and correction amplitude of the reconstructed images

To determine the optimal number of image averages for our acquisitions, we analyzed the SNR as a function of

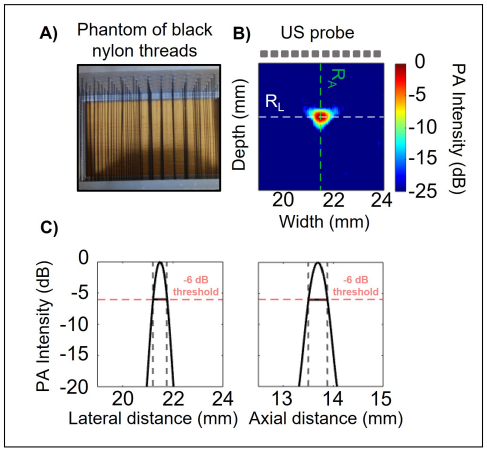


Figure 2. A) A phantom with 0.26 mm diameter black nylon threads spaced 4 mm apart laterally and axially. B) A PA image of the threads is reconstructed using DAS to assess the lateral and axial signal profiles. C) The lateral and axial resolutions are determined via the PSF method, using a -6 dB threshold as the resolvability limit.

the number of averaged frames. As shown in Fig. 3, the SNR progressively improves with the number of acquisitions. A noticeable increase is observed around 3000 averages, where the SNR reaches approximately 54%, indicating a significant enhancement in signal clarity. At 5000 and 10000 averages, the SNR further improves by roughly 30%. Based on these results, we selected 5000 averages as a suitable trade-off, providing a robust SNR of 72% while keeping the acquisition time within 5 seconds, making the system more suitable for time-sensitive applications.

Finally, a photoacoustic image of the phantom composed of black nylon threads was reconstructed using the DAS algorithm (Fig. 4A). An amplitude correction was subsequently applied to account for signal attenuation with depth and laterally (Fig. 4B). As illustrated in Fig. 4C, the corresponding amplitude profiles show a marked improvement, exhibiting a more homogeneous signal distribution across all the image. This indicates that the amplitude correction effectively compensates for intensity decay, enhancing the overall image uniformity and interpretability.

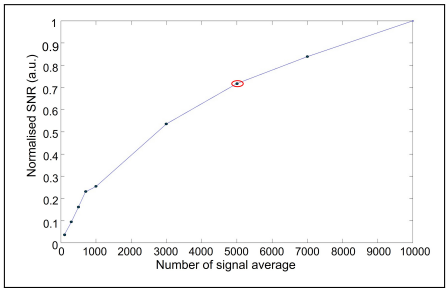


Figure 3. Normalised Signal-to-noise ratio (SNR) as a function of the number of signal averages. The red circle indicates the averaged signal number we chose to perform the rest of the measurements, since it represents 0.72 SNR, indicating a good signal-to-noise ratio.

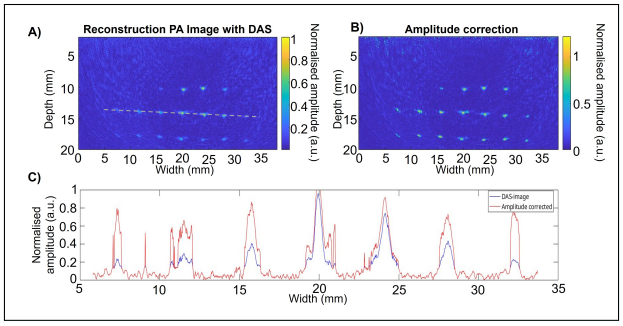


Figure 4. A) Normalized PA image of the black nylon threads phantom reconstructed with DAS. B) The image after amplitude correction. C) Amplitude profiles showing the original image in blue and the corrected image in red, with the dotted line indicating the DAS-extracted profile.

4. CONCLUSIONS AND FUTURE WORK

We developed a low-cost, non-invasive dual ultrasound/photoacoustic imaging system capable of delivering high-quality imaging performance, validated using black-wire phantom experiments. The system achieved a lateral resolution of 0.53 mm and an axial resolution of 0.36 mm, with a signal-to-noise ratio (SNR) of 0.72 obtained from 5000 averaged acquisitions. These results confirm the system's robustness and suitability for high-contrast, depth-resolved imaging.

Future work will focus on the ex vivo characterization of resected human atherosclerotic plaques under the ethical approval PI-6157 (La Paz University Hospital of Madrid, Spain). This next step aims to assess the system's ability to differentiate plaque composition and support the identification of features related to vulnerability, ultimately advancing its potential for clinical vascular imaging applications.

5. ACKNOWLEDGMENTS

This work received support from the European Union's Horizon 2020 research and Innovation Programme under the Marie Sklodowska-Curie Grant Agreement no.101030046, and the Programme Ramón y Cajal RYC2021-032739-I, funded by MCIN/AEI/10.13039/501100011033 and by the European Union "NextGenerationEU"/PRTR". Also, we acknowledge support from grants FASCINA (PID2021-126998OB-I00/), 3PET (PDC2022-133057-I00) from the Spanish Ministry of Science and Innovation (MCIN) AEI/10.13039/501100011033/Unión Europea Next GenerationEU/PRTR, Prototwin Project (TED2021-349 130592B-I00) and Tecnologías Avanzadas para la Exploración del Universo y sus Componentes" (PR47/21 TAU-CM TAU- PRTR), funded by EU Resilient and NextGeneration funds. This work was supported by Knowledge Generation Projects 2022 Type A Oriented Research, Government of Spain INVENTOR (PID2022-137114OA-I00).

6. REFERENCES

[1] G. . S. Collaborators, "Global, regional, and national burden of stroke and its risk factors, 1990–2019: a systematic analysis for the global burden of disease study 2019.," *The Lancet. Neurology*, vol. 20, no. 10, p. 795, 2021.

[2] M. Xu and L. V. Wang, "Photoacoustic imaging in biomedicine.," *Review of scientific instruments*, vol. 77, no. 4, p. 041101, 2006.

[3] V. Perrot, M. Polichetti, F. Varray, and D. Garcia, "So you think you can das? a viewpoint on delay-and-sum beamforming.," *Ultrasonics*, vol. 111, p. 106309, 2021.

[4] I. Pi-Martín, A. Cebrecos, J. J. García-Garrigós, N. Jiménez, and F. Camarena, "Spatial resolution and reconstructed size accuracy using advanced beamformers in linear array-based pat systems.," *Photoacoustics*, vol. 34, p. 100576, 2023.

DOI: 10.61782/fa.2025.0455

FORUM ACUSTICUM EURONOISE 2025

IMPACT OF SPATIOTEMPORAL EXCITATION PARAMETERS IN LASER DIODE-BASED PHOTOACOUSTIC MICROSCOPY

Javier A. Navarro-Calvo[1*] **Irene Pi-Martín**[1] **Víctor Company-Rubio**[1]
Adrián Arándiga[1] **Alejandro Cebrecos**[1] **Juan J. García-Garrigós**[1]
[1] Instituto de Instrumentación para Imagen Molecular, Universitat Politècnica de València – Consejo Superior de Investigaciones Científicas, Valencia, Spain

ABSTRACT

Photoacoustic (PA) microscopy provides high-resolution images with optical-selective contrast at greater depths than conventional optical techniques by detecting acoustic waves generated from the absorption of pulsed light. To increase the applicability of the technique, cost-effective, compact laser diodes (LDs) have emerged as a promising alternative to expensive and bulky solid-state lasers (SSLs). Due to their low peak power, widened temporal pulses are generally used to obtain more pulse energy and achieve acceptable PA signal levels. Additionally, the multimode, low-quality beams emitted by LDs hinder the focusing capabilities, resulting in larger focal spots, i.e., lower image lateral resolutions. The generated signal characteristics will thus differ from the well-known broadband photoacoustic waves of several MHz produced by SSL-based systems. In this work, we conducted an experimental study to analyze the impact of the pulse duration, pulse shape, and focal spot size on the generated PA signals, using a laser diode-based photoacoustic microscope. The analysis shows that the pulse durations and focal spot sizes of LDs produce narrowband PA signals shifted towards lower frequencies. This is important for improving the design of efficient transducers, which will eventually allow the implementation of cost-effective photoacoustic imaging systems in clinical practice.

Keywords: *photoacoustic microscopy, laser diode, ultrasound, cost-effective, frequency spectrum*

[*] ***Corresponding author***: *janacal@i3m.upv.es*
Copyright: *©2025 Javier A. Navarro-Calvo et al. This is an open-access article distributed under the terms of the Creative Commons Attribution 3.0 Unported License, which permits unrestricted use, distribution, and reproduction in any medium, provided the original author and source are credited.*

1. INTRODUCTION

Biomedical photoacoustic (PA) imaging combines optical and ultrasound technologies to offer high-resolution, non-invasive images with enhanced penetration and contrast. It relies on the photoacoustic effect, where endogenous chromophores such as melanin or haemoglobin absorb laser pulses, generating ultrasound waves that can be detected and used to reconstruct the absorption distribution [1].

The generation of PA pressure waves is based on the compliance of both stress and thermal confinements. This means that the excitation pulse duration must be shorter than the time that acoustic waves and heat require to travel through the excited volume [2]. Consequently, short pulses of a few nanoseconds coming from high-quality solid-state lasers (SSLs) are the preferred choice to efficiently generate PA signals. Moreover, the emitted acoustic waveform is proportional to the first derivative of the laser intensity temporal profile [2], [3]. Hence, short pulses generate sharp, bipolar pressure waves, allowing for high-contrast and high-resolution acoustic imaging [4].

The utilization of cost-effective laser diodes (LDs) in photoacoustic imaging (PAI) is gaining attention due to their affordability and compact size, which make them an attractive alternative to bulky and costly SSLs [5], [6]. However, these low-cost sources typically emit low-energy, low-quality laser beams, hindering their use in clinical-oriented systems [7]. The current drivers that pulse the LDs grant these sources with pulse tuning capabilities. For this reason, usually widened pulses are chosen to increase the per-pulse energy and, therefore, the image signal-to-noise ratio (SNR). However, longer pulses generate narrowband PA signals shifted to lower frequencies, which highly affects the image resolution [8], [9]. Moreover, stress confinement may be violated if the excited absorber is too small, reducing the generation efficiency.

Here, an experimental study has been carried out to study the impact of the pulse duration, pulse shape and source size in the generation of PA signals using a low-cost laser. With this work, we aim to offer novel and useful information about the generated frequency spectrum, which will eventually help the optimization of cost-effective PAI systems, aiding its implantation in clinical practice.

2. MATERIALS AND METHODS

2.1 Photoacoustic microscopy system

In this study, we used a custom photoacoustic microscope based on a cost-effective pulsed laser diode (905D2S3JT09X, Laser Components, Germany), which emits 235 W laser pulses at a PRF of up to 10 kHz in the NIR range (905 nm). The low-quality laser beam emitted by the PLD is reshaped and homogenized by coupling it into a multimode fiber. This fiber-coupled configuration allows to vary the focal spot size by simply placing a spatial filter, or pinhole, at the fiber output without decreasing the laser fluence or working distance. The current pulses are delivered by a pulse current driver (LDP-V 80–100, PicoLAS GmbH, Germany) controlled by a programmable pulse generator (Stemlab 125, RedPitaya). A commercial spherically focused sensor (focal length of 64 mm) made of polyvinylidene difluoride (PVdF) was aligned with the excitation in reflection mode with a 60º angle (Y-107, Sonic Concepts, USA), ensuring high sensitivity detection within 0.01-15 MHz. The detected PA waves are pre-amplified (ZFL-500LN, MiniCircuits, USA) and digitalized at a sampling rate of 150 MHz (ADQ14, Teledyne SP Devices, Sweden).

2.2 Experimental set-up

In optical-resolution photoacoustic microscopy, a tightly focused laser spot is used as the excitation beam, thus generating point-like acoustic sources. In this study, a USAF resolution target (R3L3S1P, Thorlabs, USA) made of a 120 nm-thin chromium film was used as absorber. To analyze the impact of the acoustic source size on the generated PA spectrum, tests were made without and with a 50 µm pinhole, having two focal spots of 150 and 50 µm, respectively. For each case, PA signals were acquired using laser pulse widths of 15, 35, 60, 80 and 100 ns, measured at their Full Width at Half Maximum. It is worth noting that low-cost pulse drivers usually generate asymmetric pulses with long rise times, which can affect the generated signals. To compensate for the poor SNR with shortened pulses, 5000 averages were done for fair comparison between cases.

3. RESULTS

The results are depicted in Figure 1. First (Fig. 1a), the larger source generates PA frequency spectra concentrated below 10 MHz, centered between 4-5 MHz depending on the pulse width. As expected, longer pulse widths result in less high frequency content in comparison with the shorter pulse, indicated by the 18 and 10 dB difference between the 10-15 MHz range and the main lobe, respectively. Similarly, for the smaller source of 50 µm (Fig. 1b), longer pulses generate PA signals with a reduced frequency content than the shorter ones. However, the small source size critically contributes to enlarging the bandwidth. While the 100 ns pulse generates PA signals with differences of around 10 dB in the 10-15 MHz range with respect to the main lobe, the 15 ns pulse generates a wideband signal, with differences below 6 dB in the 1-16 MHz range. In this case, the amplitude decrease beyond 15 MHz can also be influenced by the limited detection bandwidth of the ultrasound detector.

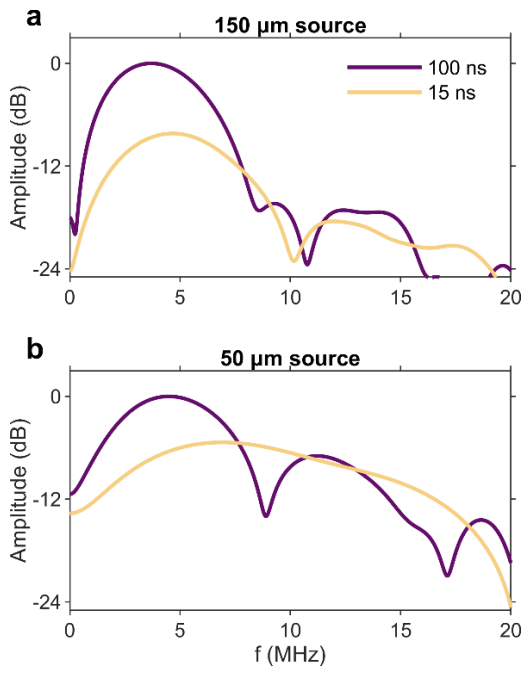


Figure 1. Comparison of the generated PA signal spectrum using pulse widths of 15 and 100 ns, for both (a) 150 µm and (b) 50 µm laser focal spots. Amplitude is normalized for each source size.

A more exhaustive analysis for all the laser pulse widths is shown in Figure 2. For the larger source of 150 µm (Fig. 2(a)), the generated PA amplitude increases with optical energy, which is proportional to the pulse width. However, for the smaller source of 50 µm (Fig. 2(b)),

that trend is not observed. This discrepancy is explained by considering the confinement time, estimated to be around 33 ns for the latter. In this way, shorter pulses (60 ns) produce higher amplitude signals than wider ones (100 ns), despite having 55% less optical energy. Hence, within this range, the effects of higher PA conversion efficiency and optical energy deposition are combined.

It is noteworthy how the asymmetric laser pulse, due to the slow rise time of the low-cost current driver, induces a different PA signal morphology compared with the well-known N-shaped waveform generated with a short laser pulse with fast and symmetric flanks. In this case, the slow rise time generates a short positive lobe, followed by a sharp negative lobe coming from the fast-falling edge of the laser pulse, which highlights the influence of the selected pulse driver and the excitation pulse shape.

Regarding the generated spectrum, center frequency and bandwidth at -6 dB was calculated for each case (Fig. 2 (a, b)). As observed, both source sizes show a similar tendency, reducing the bandwidth and center frequency as the pulse size increases. However, it is visible how these variations are more noticeable for the smaller source, which shows a clearly broader spectrum for the shorter pulses.

4. CONCLUSION

An experimental study to evaluate the impact of the spatiotemporal excitation parameters (pulse width, shape, and source size) on the generated photoacoustic spectrum has been carried out. By varying the pulse width from 15 to 100 ns, with two different excitation source sizes of 150 and 50 µm, we showed that the pulse width is highly correlated with the generated PA spectrum, and that this impact is also strongly dependent on the excited absorber size, i.e., the laser spot size in an optical-resolution photoacoustic microscopy system as the one used in this study. The experimental spectra show how typical LD excitation generates narrower bandwidths, shifted to central frequencies around 5 to 10 MHz, which highly differs from the PA signals generated with high-quality SSLs. Moreover, we have provided experimental evidence of the stress confinement time violation, indicated by the reduced amplitude of PA signals generated with longer pulse widths that, despite having more energy, result in a less efficient conversion. These results show the relevance of considering both the source size and the pulse width for selecting an appropriate detection bandwidth. Also, they highlight the necessary compromise between optical pulse energy and conversion efficiency in LD-based photoacoustic microscopy systems, associated with a plausible violation of the stress confinement time.

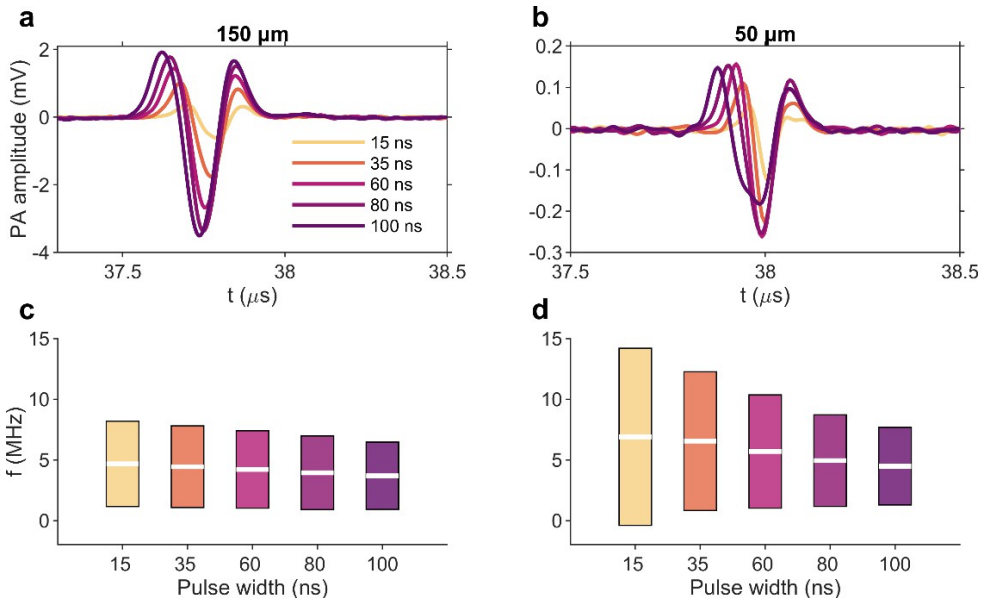


Figure 2. Experimental PA signals and their frequency content spread (center frequency and bandwidth at -6 dB) using laser pulse widths from 15 to 100 ns, for laser spots of 150 µm (a,c) and 50 µm (b,d).

We believe that these findings can provide useful insights to develop optimized PAI systems using low-cost components, thereby facilitating their integration into clinical practice.

ACKNOWLEDGEMENTS

We are grateful for the funding support through competitive call programs: Agència Valenciana de la Innovació (AVI) through the INNVA1/2022/50 project, Investigo INVEST/2022/171 Program of the European Union Next Generation EU funds.

REFERENCES

[1] J. Yao and L. V. Wang: "Sensitivity of photoacoustic microscopy", *Photoacoustics*, vol. 2, no. 2, pp. 87-101, 2014.

[2] L. V. Wang: *Photoacoustic Imaging and Spectroscopy*. Boca Raton: CRC Press, 2009.

[3] M. Pérez-Liva *et al.*: "Dual photoacoustic / ultrasound technologies for preclinical research: current status and future trends", *Phys Med Biol*, vol. 70, no. 7, p. 07TR01, 2025.

[4] P. Beard: "Biomedical photoacoustic imaging", *Interface focus*, vol. 1, no. 4, pp. 602-631, 2011.

[5] P. Kalitsounakis, G. Zacharakis, and G. J. Tserevelakis: "Towards affordable biomedical imaging: Recent advances in low-cost, high-resolution optoacoustic microscopy", *John Wiley and Sons Inc.*, vol. 298, no. 1, pp. 3-9, 2024.

[6] B. Huang and T. T. W. Wong: "Review of low-cost light sources and miniaturized designs in photoacoustic microscopy", *J Biomed Opt*, vol. 29, no. S1, 2023.

[7] J. J. García-Garrigós, A. Cebrecos, J. A. Navarro-Calvo, and F. Camarena: "A fiber-coupled laser diode design for reflection mode optical resolution photoacoustic microscopy", *Ultrasonics*, vol. 132, pp. 107008, 2023.

[8] P. K. Upputuri and M. Pramanik: "Pulsed laser diode based optoacoustic imaging of biological tissues", *Biomed Phys Eng Express*, vol. 1, no. 4, p. 045010, 2015.

[9] T. A. K. Agano: "Effect of light pulse width on frequency characteristics of photoacoustic signal - an experimental study using a pulse-width tunable LED-based photoacoustic system", *International Journal of Engineering and Technology(UAE)*, vol. 7, no. 4, pp. 3835–3842, 2018.

DOI: 10.61782/fa.2025.0281

FORUM ACUSTICUM EURONOISE 2025

DESIGNING ACOUSTIC HOLOGRAMS WITHOUT IONISING RADIATION FOR WEARABLE TRANSCRANIAL ULTRASOUND THERAPY DEVICES

Alba Eroles-Simó[1*] **Víctor Vegas-Luque**[1] **Alicia Carrión**[1]
José A. Pineda-Pardo[2] **Juan J. Rodríguez-García**[1] **José L. Alonso-Ramos**[1]
Francisco Camarena[1] **Noé Jiménez**[1]

[1] Instituto de Instrumentación para Imagen Molecular (i3M), Universitat Politècnica de València (UPV) – Consejo Superior de Investigaciones Científicas (CSIC), Camino de Vera S/N, 46022 València, Spain

[2] HM CINAC (Centro Integral de Neurociencias Abarca Campal), Hospital Universitario HM Puerta del Sur, HM Hospitales, Madrid, 28938, Spain

ABSTRACT

Acoustic holograms are used in transcranial ultrasound to tailor the acoustic wavefront generated by a single-element transducer compensating skull aberrations and focusing the beam over brain structures. However, current hologram design relies on full-wave simulations where acoustic properties are known by computed tomography (CT). Since exposing patients to ionizing radiation is undesirable, we propose the use of zero echo time (ZTE) magnetic resonance images (MRI) to construct the patient-specific lens. This MRI sequence enables the visualization of tissues with short T2 values, such as bone. By establishing a linear correlation between CT Hounsfield Units (HU) and ZTE intensity values, pseudo-CT images are generated. Furthermore, transducer positioning has been optimised. Temporal bone window is established as a suitable surface for propagating acoustic waves, due to its reduced thickness and flat morphology. Results show that peak pressure at the focus is reduced by 5.38% when using pseudo-CT holograms respect to CT-holograms. The obtained treated volumes considering acoustic properties of the pseudo-CT and those of the CT show a difference of 0.18%. This approach can be applied in holographic wearable devices for transcranial ultrasound therapies such as blood-brain barrier opening or neuromodulation to avoid the use of ionising radiation during the therapeutic treatment.

Keywords: *therapeutic ultrasound, magnetic resonance imaging, neuromodulation, acoustic holograms, transtemporal window.*

1. INTRODUCTION

Therapeutic ultrasound is an emerging modality to treat diseases affecting the central nervous system. It represents a minimally invasive technique with high spatial resolution, which allows targeting even the innermost structures of the brain [1-3]. In those therapies, precise targeting accuracy is required to focus ultrasound energy on the desired structures inside the brain. However, the skull bones present high acoustic impedance, absorption, heterogeneity, and irregular thickness. These produce aberrations and defocusing of the acoustic beam due to strong scattering, reflection, refraction and attenuation effects [2,3]. To

[*] ***Corresponding author***: *aerosim@i3m.upv.es.*
Copyright: *©2025 Alba Eroles-Simó et al. This is an open-access article distributed under the terms of the Creative Commons Attribution 3.0 Unported License, which permits unrestricted use, distribution, and reproduction in any medium, provided the original author and source are credited.*

mitigate these effects, acoustic holograms were proposed [4-6]. Acoustic holograms are passive lenses, commonly 3D printed, placed over a single-element transducer surface. They locally modulate the phase of the ultrasound beam, correcting skull aberrations and enabling the focalization over the desired structures inside the brain.

To design a lens for transcranial applications, full-wave acoustic simulations are performed, modelling wave propagation through the different media constituting the human head. These simulations require the acoustic properties of both soft tissues and cranial bones, which are commonly obtained from computed tomography (CT) images [7]. However, exposing patients to ionizing radiation is undesirable.

In this study, we propose the use of zero echo time (ZTE) magnetic resonance images (MRI) to avoid the use of X-ray CT images for hologram design. This imaging protocol enables the visualization of tissues with short T2 values, such as bone. Previous studies have obtained different linear correlations that enable ZTE intensity values conversion into Hounsfield Units (HU) measured on CT images. As a result, pseudo-CT images are obtained [8-11]. In addition, these pseudo-CT are used to optimize transducer location over the temporal bone window. With this approach, its flat morphology and reduced thickness are exploited, enabling higher pressure values at the focus, while reducing the remaining pressure over the skull [12,13]. This contributes to the optimal sonication of the desired structures inside the brain, allowing the generalisation and reproducibility of patient-specific positioning. It can be implemented in holographic wearable devices used in transcranial ultrasound therapies, eliminating the need for ionizing radiation.

2. METHODS

2.1 CT and ZTE Images

CT and ZTE images used in this work were obtained and provided by the Centro Integral de Neurociencias A.C. (HM CINAC) in Hospital Universitario HM Puerta del Sur and all patients provided written consent for data collection. The co-registration of both images is performed using 3DSlicer software. Density and sound velocity of hard and soft tissues are obtained from CT image values and the linear relationship between X-ray attenuation values.

2.1.1 Pseudo-CT Generation

To generate the pseudo-CT images, we have followed the steps presented by Miscouridou *et al.* [11]. ZTE images undergo a bias-field correction filter. Analysing the histogram of the resulting intensity values, two peaks can be identified. The first one, placed at lower intensity values, corresponds to the backward noise of the image. The second one, at higher intensity values, belongs to head soft tissues. Regarding this last peak, all voxel intensities are normalized to the soft tissue peak value. Intensity values between these two peaks are considered skull. By applying a threshold to the normalised ZTE image, a binary mask identifying the skull is generated. Morphological operations are used to fill the generated binary mask. Finally, the linear model defined in Eq. (1) is used in the voxels defined as skull, converting ZTE intensities values into HU [11].

$$CT = -2085\, ZTE + 2329. \qquad (1)$$

Fig. 1 shows the original HU values from the CT image and the HU values obtained from the transformation of the ZTE image into pseudo-CT for the same patient.

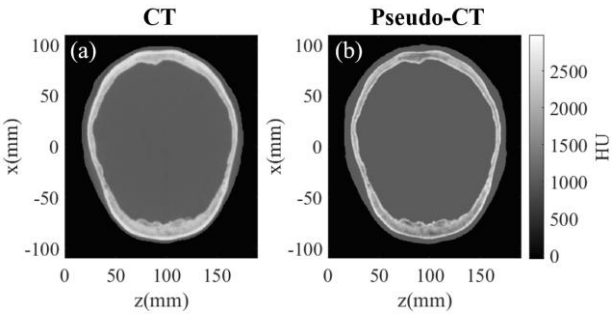


Figure 1. Representation of the HU values defined in (a) CT image, and the equivalent values obtained in (b) pseudo-CT.

2.2 Temporal Bone Window Positioning

An optimization algorithm has been developed to automate the positioning of the ultrasound transducer over the area of minimum thickness in the temporal window using the pseudo-CT [12,13]. In the sagittal view analysis of the generated skull mask, a local maximum in thickness can be identified in the temporomandibular joint (TMJ). Using the TMJ as a reference point, the algorithm automatically positions the transducer over the area of minimum thickness. To achieve normal orientation of the transducer with respect to the skin surface, it is necessary to ensure that there is no overlap with the ear structure [13].

2.3 Acoustic simulations

A flat transducer, with a diameter of 65 mm, excited at a central frequency of 650 kHz, is used. Skull, soft tissues and the transducer are considered to be immersed in water at a temperature of 37º C. Different acoustic simulations are performed in the time domain using MATLAB k-wave toolbox. It implements a pseudo-spectral method in k-space that allows the propagation of ultrasound in heterogeneous media to be modelled, considering the attenuation of the biological tissues considered. The defined workspace corresponds to a homogeneous medium, water, characterized as a cubic grid with a resolution of λ/6, where λ = 2.3 mm is the wavelength in water at the central frequency.

The holographic lens is designed performing a time-reversal simulation, known as *backward* simulation. A virtual source is placed at the centre of the therapeutic structure targeted for neuromodulation, the ventralis intermedius nucleus (Vim) of the thalamus. The segmented structure is corregistered for each analyzed patient. The virtual source emits a train of 100-cycle sinusoidal pulses at the central frequency. As the wavefront propagates through the skull, it is distorted due to differences in sound speed, density and attenuation, relative to those of soft tissues. The resulting wavefront is recorded over the holographic plane to design the geometry of the acoustic lens. Two different backward simulations are performed. The first one uses acoustic properties obtained from the CT image, while in the second one, the acoustic properties are extracted from the pseudo-CT image. As a result, two sets of holographic acoustic lenses are designed for each patient. An example of the recorded phase distribution over the holographic plane used to construct them is shown in Fig. 2.

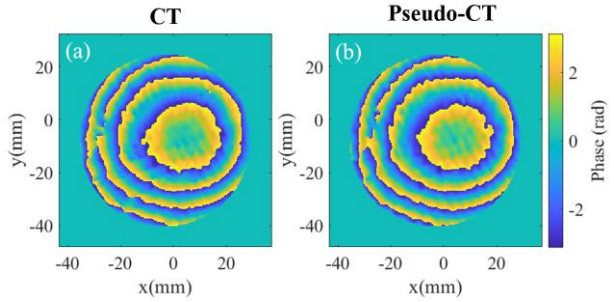


Figure 2. Phase distribution of the wavefront recorded in the holographic plane coming from the virtual source, taking into account the acoustic properties of (a) the CT image and (b) the pseudo-CT image.

In the numerical model, the material used for constructing the lens is a photoreactive resin Clear (Formlabs, USA) with the following acoustic properties: c_L = 2599.31 m/s, ρ_L = 1185.78 kg/m^3. The absorption value was set at α_L = 3.13 dB/(cm·MHz^y) at 650kHz, where y = 1.3, in agreement with values reported for photopolymers with similar properties [4].

A second acoustic simulation is then conducted, known as *forward* simulation. The same acoustic pulse is now emitted from the previously defined transducer. The wave passes through the holographic lens, which modulates it in phase, then through the skull, enabling the focalization over the desired structure. The maximum pressure acoustic field in the volume of interest is recorded for analysis. Three different situations are considered. First, the holographic lens designed using CT-derived acoustic properties is evaluated under matching conditions (CT-CT). Second, pseudo-CT based lens is measured under consistent acoustic conditions (pCT-pCT). Third, the pseudo-CT based lens performance is evaluated under CT acoustic properties in an effort to approximate the most realistic clinical scenario (pCT-CT).

3. RESULTS

The acoustic fields simulated under the specified conditions are evaluated in 5 anonymised patients. The differences between the resulting acoustic fields are quantified in terms of variations in focal position, volume of the sonicated therapeutic target, and peak pressures. In Fig. 3, the resulting acoustic fields obtained in the different considered situations are analysed, being (a) and (b) XZ and YZ planes for CT-CT, respectively, (c) and (d) for pCT-pCT, (e) and (f) for pCT-CT.

Fig. 4. (a) illustrates the deviation along the axial axis with respect to the coordinates of the virtual source defined for the holographic lens design, establishing that there is no significant difference between simulation conditions. A deviation of (-0.31 ± 1.80) mm along the beam propagation axis is observed between the pCT-CT and pCT-pCT simulations, while the deviation respect to CT-CT simulations is (1.02 ± 1.97) mm. Along the lateral axes, the deviation is not significantly distinguishable.

With respect to the sonicated target volume, the mean volume of the therapeutic target is (371.46 ± 5.20) mm^3. The results of the simulated fields show a reduction of 0.17% in the sonicated target volume when comparing the

pCT-CT to the pCT-pCT field. When comparing the treated volume between pCT-CT and CT-CT, the reduction is 0.18%.

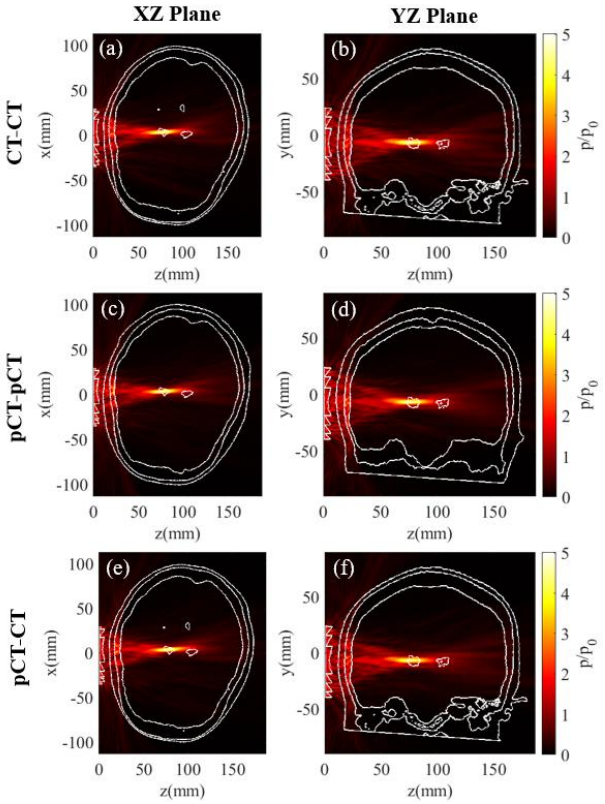


Figure 3. XY and YZ planes amplitude distribution of the acoustic field. (a) and (b) for the CT-CT simulation conditions, (c) and (d) for pCT-pCT conditions and (e) and (f) for the pCT-CT simulation conditions.

Regarding pressure values, a decrease of 3.74% in the maximum focal pressure is observed in pCT-CT field compared to the pCT-pCT field. When this same parameter is compared to the CT-CT field, the reduction reaches 5.38%. Fig. 4. (b) presents the mean maximum pressure measured at the focus for the 5 analysed patients under each simulation condition. Furthermore, the mean pressure over the analysed target volume is also evaluated. In the pCT-CT field, a decrease of 5.47% is measured relative to the pCT-pCT field, while a 5.57% reduction is observed when compared to CT-CT field. When optimizing transducer positioning, the remaining pressure over the skull is minimized. It can be seen that the maximum pressure on the skull in the pCT-CT field is reduced by 0.31%, yielding equivalent values to those obtained in the CT-CT field.

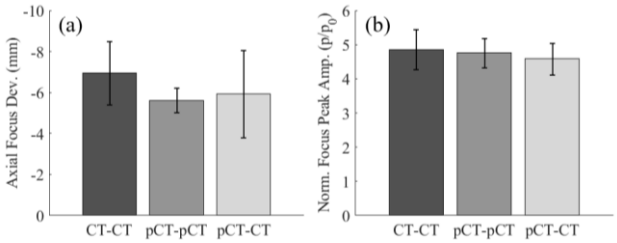


Figure 4. (a) Mean focus deviation in the beam propagation axis. (b) Mean normalized peak pressure measured at the beam focus. Kolmogorov-Smirnov test ($p>0.05$), establishes that there is no significant difference between pCT-pCT and pCT-CT, neither between CT-CT and pCT-CT.

4. CONCLUSION

By employing ZTE images, we generate pseudo-CT images that enable accurate estimation of skull acoustic properties. This study demonstrates that such images can be used as a suitable substitute for CT images in the design and fabrication of holographic lenses. They also allow the precise positioning over the temporal bone window.

Comparative analyses between the generated acoustic fields obtained using CT-based and pseudo-CT-based holographic lenses revealed that the treated volume remains constant. However, although not significant, differences in focal positioning and a reduction in the maximum pressure are observed. Future research will focus on correcting these variations by analyzing the potential underestimation of the skull HU values in pseudo-CT images.

These findings support the use of ZTE images as a non-ionizing alternative for the development of patient-specific acoustic holograms. Their integration into wearable transcranial ultrasound therapy devices opens a new path for non-invasive clinical applications, including neuromodulation and blood-brain barrier opening, while ensuring patient safety and the precision of the treatment.

5. ACKNOWLEDGMENTS

This research has been funded by Generalitat Valencia through grants INVEST/2023/553, EDGJID/2021/189, INNEST/2022/345 and CIAICO/2023/052. This research has been funded by the Minsterio Español de Ciencia e Innovación y el Ministerio de Universidades with grants PREP2022-000156 by the Agencia Estatal de Investigación,

PID2022-142719OB-C21 and CNS2023-145707 funded by MCIN/AEI/10.13039/501100011033 and by the FSE+.

6. REFERENCES

[1] J. Kubanek: "Neuromodulation with transcranial focused ultrasound," *Neurosurgical Focus*, vol. 44, no. 2, 2018.

[2] A. Fomenko and A.M. Lozano: "Neuromodulation and ablation with focused ultrasound – toward the future of noninvasive brain therapy," *Neural Regeneration Research*, vol. 14, no. 9, pp. 1509–1510, 2019.

[3] K. Lee, T.Y. Park, W. Lee and H. Kim: "A review of functional neuromodulation in humans using low intensity transcranial focused ultrasound," *Biomedical Engineering Letters*, vol. 14, pp. 407-438, 2024.

[4] K. Melde, A.G., Mark, T. Qiu and P. Fischer: "Holograms for acoustics," *Nature*, vol. 537, pp. 518-522, 2016.

[5] S. Jiménez-Gambín, N. Jiménez, J.M. Benlloch and F. Camarena: "Holograms to Focus Arbitrary Ultrasonic Fields through the Skull," *Physical Review Applied*, vol. 12, no. 1, 2019.

[6] D. Andrés, A. Carrión, F. Camarena and N. Jiménez: "Methods to design and evaluate transcranial ultrasonic lens using acoustic holography," *Physical Review Applied*, vol. 20, no. 4, 2023.

[7] J.F. Aubry, M. Tanter, M. Pernot, JL. Thomas and M. Fink: "Experimental demonstration of noninvasive transskull adaptive focusing based on prior computed tomography scans," *The Journal of the Acoustical Society of America*., vol. 113, no. 1, pp. 84-93, 2003.

[8] F. Wiesinger, L.I. Sacolick, A. Menini, S.S. Kaushik, S. Ahn, P. Veit-Haibach, G. Delso, D.D. Shanbhag: "Zero TE MR Bone Imaging in the Head," *Magnetic Resonance in Medicine*, vol. 75, pp. 107-114, 2016.

[9] F. Wiesinger, M. Bylund, J. Yang, S.S. Kaushik, D.D. Shanbhag, S. Ahn, J.H. Jonsson, J.A. Lundman, T. Hope, T. Nyholm, P. Larson, C. Cozzini: "Zero TE-based pseudo-CT image conversion in the head and its application in PET/MR attenuation correction and MR-guided radiation therapy planning," Magnetic Resonance in Medicine, vol. 80, pp. 1440-1451, 2018.

[10] J. Caballero-Insaurriaga, R. Rodríguez-Rojas, R. Martínez-Fernández, M. Del-Alamo, L. Díaz-Jiménez, M. Ávila, M. Martínez-Rodrígo, P. García-Polo and J.A. Pineda-Pardo: "Zero TE MRI Applications to Transcranial MR-Guided Focused Ultrasound: Patient Screening and Treatment Efficiency Estimation," *Journal of Magnetic Resonance Imaging*, vol. 50, no. 5, pp. 1583-1592, 2019.

[11] M. Miscouridou, J.A. Pineda-Pardo, C.J. Stagg, B.E. Treeby and A. Stanziola: "Classical and Learned MR to Pseudo-CT Mappings for Accurate Transcranial Ultasound Simulation," *IEEE Transactions on Ultrasonics, Ferroelectrics, and Frequency Control*, vol. 69, no. 10, pp.2896-2905, 2022.

[12] D. Andrés, N. Jiménez, J.M. Benlloch and F. Camarena: "Numerical Study of Acoustic Holograms for Deep-Brain Targeting through the Temporal Bone Window," *Ultrasound in Medicine & Biology*, vol. 48, no. 5, pp. 872-886, 2022.

[13] A. Eroles-Simó, D. Andrés, A. Carrión, J.J. Rodríguez-García, J.L. Alonso-Ramos, J.A. Pineda-Pardo, N. Jiménez and F. Camarena, "Optimización del posicionamiento de transductores de ultrasonidos sobre la ventana del hueso temporal," in *Conf. Proc. of Tecniacústica 2024-55º Congreso Español de Acústica y XIII Congreso Ibérico de Acústica*, (Faro, Portugal), pp. 637-645, 2024.

DOI: 10.61782/fa.2025.0420

FORUM ACUSTICUM EURONOISE 2025

GENERATING ACOUSTIC HOLOGRAMS BEYOND THE HYPERBOLIC APPROXIMATION

Víctor Vegas-Luque[1*] **Diana Andrés**[1] **Alba Eroles-Simó**[1]
Juan J. Rodríguez-García[1] **Francisco Camarena**[1] **Noé Jiménez**[1]
[1] Instituto de Instrumentación para Imagen Molecular (i3M), Universitat Politècnica de València (UPV) – Consejo Superior de Investigaciones Científicas (CSIC), Spain

ABSTRACT

Transcranial focused ultrasound has proven to be an effective method for the treatment of neurological disorders, offering a non-invasive and highly precise approach for the targeting of specific brain regions. In this context, ultrasound holograms have been shown to be capable of focusing through the human skull using low-cost 3D-printed acoustic holographic lenses, where a wavefront is encoded into the height of the pixels of a lens. When the coding is performed at the holographic plane, i.e., a planar surface in front of the transducer, the reconstructed wavefront is approximated by a hyperbolic phase profile in the thin lens approximation. However, as the thickness of the physical lens is beyond the thin lens approximation, this results in aberrations. In this work, a new strategy is proposed matching the phase of the field produced at the exit of the lens to the target phase in a whole holographic volume. The method is validated using analytic and simulations techniques. Results show that this phase-matching approach provides better focusing performance over traditional methods and, therefore, might be used for accurate hologram synthesis in practical applications.

Keywords: *Acoustic holograms, transcranial ultrasound, phase-matching*

**Corresponding author*: *vvegluq@i3m.upv.es.*
***Copyright**: ©2025 Víctor Vegas-Luque et al. This is an open-access article distributed under the terms of the Creative Commons Attribution 3.0 Unported License, which permits unrestricted use, distribution, and reproduction in any medium, provided the original author and source are credited.*

1. INTRODUCTION

Acoustic holograms are intricate lenses designed to encode customized phase distributions onto their surface, enabling the formation of specific acoustic pressure patterns within a medium [1]. Essentially, an acoustic hologram produces a three-dimensional acoustic field, providing precise control over pressure waves at a target region [1, 2]. It operates on the principles of interference and diffraction, akin to optical holograms, but adapted for sound waves. This technology has gained prominence for its versatility, finding applications in many fields such as in acoustics [3, 4], biomedical ultrasound [5, 6] and advanced techniques such as contactless micromanipulation or biofabrication [7, 8].

In particular, acoustic holograms hold significant promise in ultrasound therapy, particularly in transcranial ultrasound [6], where they have demonstrated great potential to enhance treatment effectiveness. Applications include improving hyperthermia treatments [9, 10], facilitating targeted drug delivery by opening the blood-brain barrier [11, 12], neuromodulation [5, 13] or the creation of customized cavitation patterns [14]. Beyond therapy, acoustic holograms can also be utilized for imaging and monitoring therapeutic ultrasound treatments [15].

Current holographic methods are based on the recording of a phase and/or amplitude of the desired wavefront [1]. In particular, phase-only acoustic holograms aim to build a *holographic lens* that allows the phase of the wavefront coming out of the lens to match that of the recorded wavefront. However, existing lens design methods fail to precisely encode the target phase distribution, primarily

due to the complex topology of these lenses, which introduces intricate wave physics often overlooked in the design process [16]. As a result, physical lenses generate suboptimal acoustic images. In this work, we propose a method for designing acoustic holograms and lenses that accurately reproduce a desired target field. This approach uses a *phase-matching* strategy to ensure that the phase of the field produced at the exit of the lens matches the target phase across the entire holographic volume. We validate this method through analytical and simulation techniques, demonstrating its superior performance in focusing acoustic waves compared to traditional methods.

2. METHODS

In current hologram design methods, the target field is defined in a transverse plane and it is assumed that the lens produces a phase shift at the transverse plane location [6]. This results in a simple linear relationship between the lens height and the phase of the field. However, this approach assumes plane wave propagation, and thus, does not account for other wave phenomena such as refraction and diffraction at discontinuities. To address these limitations, we propose a *phase-matching* strategy to match the field at the exit of the lens to better match that of the target field.

In contrast with conventional single plane methods, where the phase of the field is matched at a holographic plane at a set distance from the transducer, our proposed phase-matching method matches the phase of the field produced at the exit of the lens to the target phase in a whole holographic volume, that is, in successive planes parallel from the transducer location up to a desired distance. The height of each pixel in the lens is determined such that its transmission coefficient phase aligns with the recorded phase originating from the virtual sources at some point in the holographic volume.

The proposed method is validated through analytical mean and simulations using a 1.1-MHz circular 50-mm aperture transducer. Simulations were performed using k-Wave toolbox (MATLAB) for simulating acoustic wave propagation [17]. The transducer was modeled as a circular piston with a Gaussian distribution of the amplitude and a uniform phase distribution. Simulation are performed in a uniform water medium at a temperature of 25 °C with a resolution of $\lambda/6$, where $\lambda \approx 1.4\,\mathrm{mm}$ is the wavelength water at the working frequency; in which the lens is placed on top of the planar source.

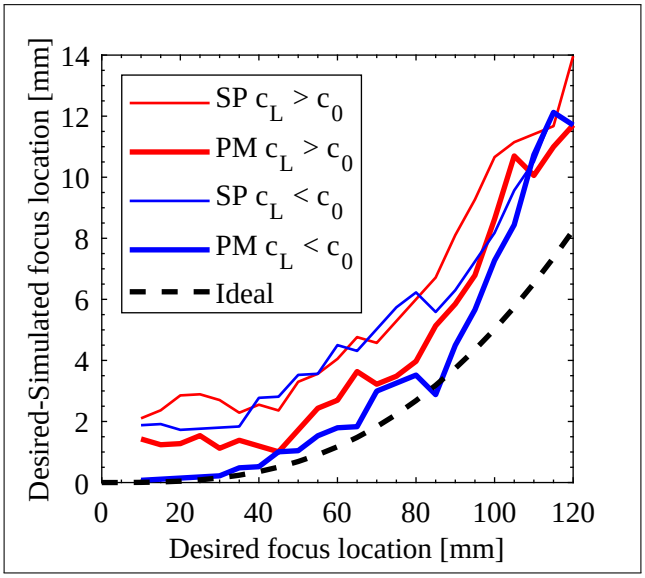


Figure 1. Simulated focus for single plane (SP) and phase matching (PM) lenses for rigid and soft materials.

The performance of the phase-matching approach is compared to traditional methods, comparing its focusing capabilities at multiple distances and its hability to create complex acoustic images at different depths via the estimation of their structural similarity index measure (SSIM) of the obtained acoustic fields for MNIST number images one to five [1]. The fields obtained via propagation through the lens will be compared againts the ideal pattern obtained via the Rayleigh-Sommerfeld integral using a back and forth propagation of the original MNIST images.

3. RESULTS

Simulation results in Fig. 1 in which both methods were compared against an ideal focused transducer. It can be observed that phase-matching hologram lenses outperform traditional methods for both rigid ($c_L > c_0$) and soft ($c_L < c_0$) lenses, producing focal spots closer to the ideal case for all studied focal distances. In particular, soft

[1] The SSIM index is a perceptual metric that quantifies the similarity between two images, ranging from 0 to 1, with 1 indicating perfect similarity [18].

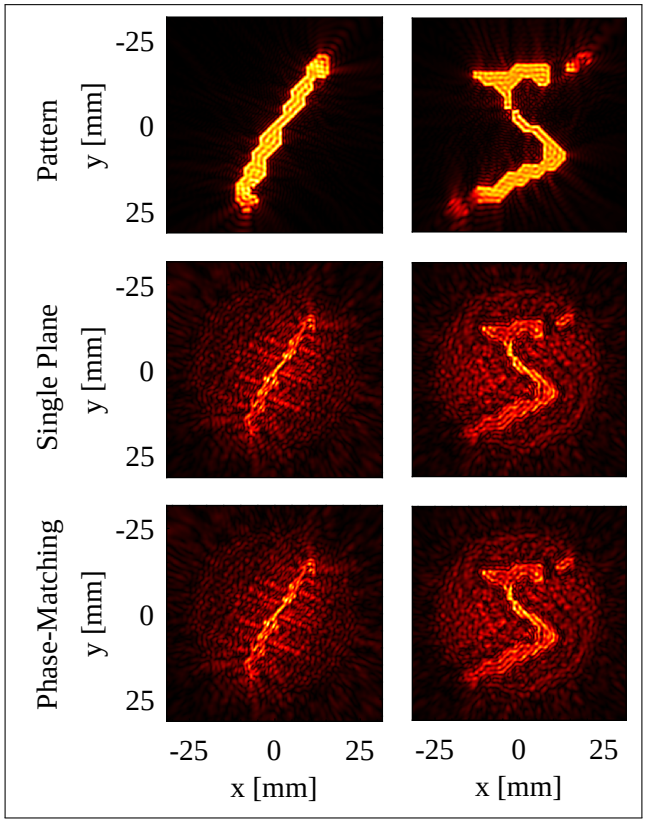


Figure 2. Acoustic patterns for MNIST iamges one and five obtained through Rayleigh-Sommerfeld propagation, traditional and phase-matching methods.

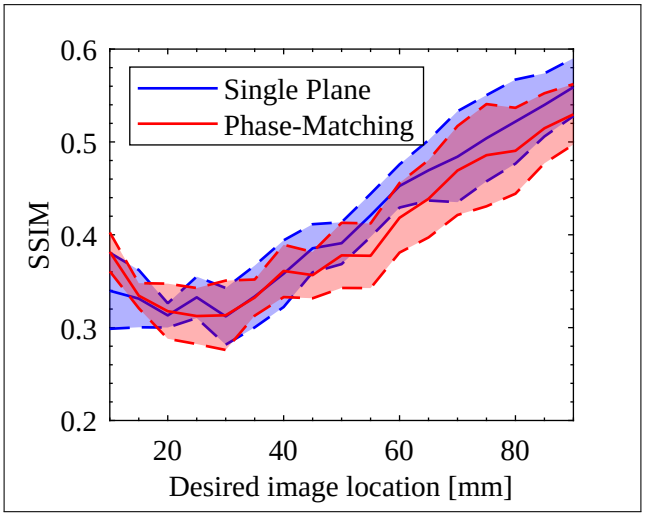


Figure 3. Average Structural Similarity Index Method (SSIM) for MNIST number images one to five obtained through traditional and phase-matching methods.

phase matching lenses appear to perform very close to an ideal focused transducer for nearer focus locations.

To study the performance of the phase-matching approach in creating complex acoustic images, we generated holograms to get the acoustic patterns for numbers one to five from the MNIST dataset. Due to the excelent focusing capabilities shown for soft lenses in Fig. 1 we have decided to work with soft lenses for this trial. An extract of theses images are shown in Fig. 2 for a focal distance of 15 mm. Since the prevalence of one method over the other cannot be easily ruled out, we evaluated the performance of these holograms at different focusing distances ranging from 10 to 90 mm in 5-mm steps using the Structural Similarity Index Method (SSIM), as shown in Fig. 3. The shaded error plot shows that both methods are pretty similar for this application, although we believe this may be to the existance of a critical angle that hinder the performance of the phase-matching approach. Still, for low focusing distances we can observe that the phase matching approach seems to outperform traditional methods.

4. CONCLUSIONS

In this work, we proposed a novel phase-matching approach for designing acoustic holograms that accurately reproduce the desired target field. This method aligns the phase of the field produced at the exit of the lens with the target phase across the entire holographic volume, resulting in superior focusing performance compared to traditional methods. We validated this approach through analytical and simulation techniques, demonstrating its effectiveness in focusing acoustic waves and creating complex acoustic images. Via simulations, we demonstrated that our approach outperfermorms traditional methods in terms of focusing capabilities at multiple distances, specially for soft lenses. The method also shows promise in generating complex acoustic images, with a slight advantage over traditional methods at lower focusing distances.

5. ACKNOWLEDGMENTS

This research has been supported thanks to grants RYC2021-034920-I, PID2022-142719OB-C21, and CNS2023-145707 funded by MCIN/AEI/10.13039/501100011033; Agencia Valenciana de la Innovació grants INNVA2/2022/11, INNVA1/2022/37, INNEST/2022/345, Generalitat Valenciana grant INVEST/2023/553 and Universitat Politècnica de València PAID-01-24.

6. REFERENCES

[1] K. Melde, A. G. Mark, T. Qiu, and P. Fischer, "Holograms for acoustics," *Nature*, vol. 537, pp. 518–522, 9 2016.

[2] D. Gabor, W. E. Kock, and G. W. Stroke, "Holography," *Science*, vol. 173, no. 3991, pp. 11–23, 1971.

[3] Y. Xie, C. Shen, W. Wang, J. Li, D. Suo, B. I. Popa, Y. Jing, and S. A. Cummer, "Acoustic holographic rendering with two-dimensional metamaterial-based passive phased array," *Scientific Reports*, vol. 6, 10 2016.

[4] S. Peng, A. Song, Y. Bai, C. Sun, and Y. Xiang, "Reconfigurable frequency-selective acoustic coding metasurface for multifunctional wavefront manipulation," *Applied Acoustics*, vol. 235, p. 110658, 5 2025.

[5] S. S. Yoo, A. Bystritsky, J. H. Lee, Y. Zhang, K. Fischer, B. K. Min, N. J. McDannold, A. Pascual-Leone, and F. A. Jolesz, "Focused ultrasound modulates region-specific brain activity," *NeuroImage*, vol. 56, pp. 1267–1275, 6 2011.

[6] S. Jiménez-Gambín, N. Jiménez, J. M. Benlloch, and F. Camarena, "Holograms to focus arbitrary ultrasonic fields through the skull," *Physical Review Applied*, vol. 12, 7 2019.

[7] Z. Ma, A. W. Holle, K. Melde, T. Qiu, K. Poeppel, V. M. Kadiri, and P. Fischer, "Acoustic holographic cell patterning in a biocompatible hydrogel," *Advanced Materials*, vol. 32, 1 2020.

[8] K. Melde, H. Kremer, M. Shi, S. Seneca, C. Frey, I. Platzman, C. Degel, D. Schmitt, B. Schölkopf, and P. Fischer, "Compact holographic sound fields enable rapid one-step assembly of matter in 3d," *Science Advances*, vol. 9, 2 2023.

[9] D. Andrés, J. Vappou, N. Jiménez, and F. Camarena, "Thermal holographic patterns for ultrasound hyperthermia," *Applied Physics Letters*, vol. 120, 2 2022.

[10] D. Andrés, I. Rivens, P. Mouratidis, N. Jiménez, F. Camarena, and G. ter Haar, "Holographic focused ultrasound hyperthermia system for uniform simultaneous thermal exposure of multiple tumor spheroids," *Cancers*, vol. 15, 5 2023.

[11] N. McDannold, C. D. Arvanitis, N. Vykhodtseva, and M. S. Livingstone, "Temporary disruption of the blood-brain barrier by use of ultrasound and microbubbles: Safety and efficacy evaluation in rhesus macaques," *Cancer Research*, vol. 72, pp. 3652–3663, 7 2012.

[12] S. Jiménez-Gambín, N. Jiménez, and F. Camarena, "Transcranial focusing of ultrasonic vortices by acoustic holograms," *Physical Review Applied*, vol. 14, 11 2020.

[13] K. Lee, T. Y. Park, W. Lee, and H. Kim, "A review of functional neuromodulation in humans using low-intensity transcranial focused ultrasound," 5 2024.

[14] J. Kim, S. Kasoji, P. G. Durham, and P. A. Dayton, "Acoustic holograms for directing arbitrary cavitation patterns," *Applied Physics Letters*, vol. 118, 2 2021.

[15] N. Lamothe, D. Andrés, A. Carrión, F. Camarena, J. A. Pineda-Pardo, and N. Jiménez, "Monitoring holograms for therapeutic ultrasound using passive cavitation beamforming," *Applied Acoustics*, vol. 224, 9 2024.

[16] D. Andrés, A. Carrión, F. Camarena, and N. Jiménez, "Methods to design and evaluate transcranial ultrasonic lenses using acoustic holography," *Physical Review Applied*, vol. 20, 10 2023.

[17] B. E. Treeby and B. T. Cox, "k-wave: Matlab toolbox for the simulation and reconstruction of photoacoustic wave fields," *Journal of Biomedical Optics*, vol. 15, p. 021314, 2010.

[18] Z. Wang, A. C. Bovik, H. R. Sheikh, and E. P. Simoncelli, "Image quality assessment: From error visibility to structural similarity," *IEEE Transactions on Image Processing*, vol. 13, pp. 600–612, 4 2004.

DOI: 10.61782/fa.2025.0807

FORUM ACUSTICUM EURONOISE 2025

SPARSE ARRAYS FOR 3D ULTRASOUND MICROSTRUCTURE IMAGING

Óscar Martínez-Graullera[1*] **Jorge Camacho**[1] **Jorge Huecas**[1]
Guillermo Cosarinsky[1] **Luis Elvira**[1] **Alberto Ibañez**[1]
[1] Instituto de Tecnologías Físicas y de la Información (ITEFI), CSIC, Spain

ABSTRACT

In the last decade, plane-wave-based volumetric ultrasonic imaging has become a promising research tool in preclinical neuroscience. Its high-speed imaging capability at a high operating frequency allows the observation of microvascular structures and the acquisition of functional ultrasound (fUS) images. However, achieving high-quality 3D super-resolution images requires fully functional full apertures supported by many independent channels, as well as high data transmission rates and processing capacity. Based on current technology, which emulates full array performance through multiplexing, this technique is far from reaching full maturity. This study investigates the potential of sparse arrays to achieve a trade-off in designing 3D imaging systems for fUS. Starting with a 32x32-element aperture, sparse array configurations with up to 256 elements for transmission and reception are explored. The study examines the requirements and opportunities of this approach during pre-beamforming and beamforming stages, focusing on system architecture.

Keywords: *plane wave, sparse array, ultrasonic imaging, volumetric imaging.*

1. INTRODUCTION

The plane-wave imaging technique involves emitting a plane wavefront and forming the image during reception by compensating for both the distance to the receivers and the distance traveled by the wavefront during transmission [1, 2]. Because the imaging region is very close to the aperture, the plane wave itself—during its formation process—primarily generates the acoustic noise responsible for the artifacts. Although this technique produces significant sidelobes and lower-quality images, it offers the advantage of very fast acquisition, thereby enabling new applications such as functional imaging [3,4]. To improve image quality, multiple images acquired at different transmission angles are combined. The diversity in the sidelobe distribution leads to their cancellation when combined, enhancing the overall image quality. In this way, a balance between image quality and acquisition speed can be sought.

In linear arrays, the number of angles used varies depending on the required image quality, with typical values ranging from 3 to 30 angles [1]. For two-dimensional arrays, these values range from 5×5 to 11×11 angles [2]. Determining the optimal number of angles requires prior experimental validation or a simulation model to balance image quality and acquisition complexity.

Volumetric imaging remains a technological challenge [5, 6]. One major limitation is the difficulty in achieving apertures with sufficient dimensions to provide high resolution. Current models in the literature typically assume a (32×32) element array (1024 elements) with inter-element spacing exceeding $\lambda/2$. Another critical challenge is the parallel control of a large number of elements. Only recently have systems been developed that support up to 256 elements in parallel, often relying on complex setups with multiple systems to reach that number.

The quality of plane-wave imaging is achieved through diversity. A set of images where the prevalence

*__Corresponding author__: oscar.martinez@csic.es.
__Copyright__: ©2025 Óscar Martínez-graullera et al. This is an open-access article distributed under the terms of the Creative Commons Attribution 3.0 Unported License, which permits unrestricted use, distribution, and reproduction in any medium, provided the original author and source are credited.

of reflectors against a background of varying noise from image to image enhances their presence and smooths out the sidelobes. This always occurs within a space primarily limited to the projection of the aperture—the region insonified by the plane wave—where the main contribution to the image comes from the 0-degree angle transmission, while the remaining angles provide diversity.

From the system's perspective, the ability to generate high-speed imaging depends not only on the time of flight but also on how quickly the acquisition buffers become available again (i.e., the time required to transmit the data to the storage unit). This time depends on the communication interface, for example, for an acquisition time of 14 microseconds and 256 parallel channels, it can be 150 microseconds (with a high-speed 3GBps interface) or 6.4 milliseconds (with a more common Gigabit Ethernet interface).

2. SPARSE ARRAYS FOR PLANEWAVE

For this work, we take as a reference the problem of operating a two-dimensional aperture of 1024 elements (32×32) spaced at λ at a central frequency of 15 MHz, using no more than 256 elements. This represents a 4-to-1 reduction, which can be implemented in various ways. However, when designing a sparse aperture, it is necessary to take into account the constraints imposed by the associated imaging modality. The volumetric imaging space considered ranges from 3 to 7 mm in depth, with a maximum size of 4 mm per side.

Therefore, it is important to analyze how the transmitted wavefront contributes to the generation of sidelobes in the near-field region of the aperture [7]. Figure 1 shows a representation of the wavefront generated by our reference aperture at $Z = 6mm$ in the fully populated case. The projection of the array, which is the area where the image is intended to be obtained, is marked by the two black lines. The complexity of the global wavefront pattern arises from the two-dimensional distribution of the elements, which leads to the formation of multiple secondary wavefronts, resulting in imaging artifacts. One way to mitigate these interfering wavefronts is by deactivating the outer elements.

In this case, the aperture is reduced to 256 elements—specifically, by limiting the emitting aperture to the central (16×16) elements. However, secondary lobes remain high due to the boxcar aperture shape. To reduce them, we can apply an apodization scheme based on element distribution.

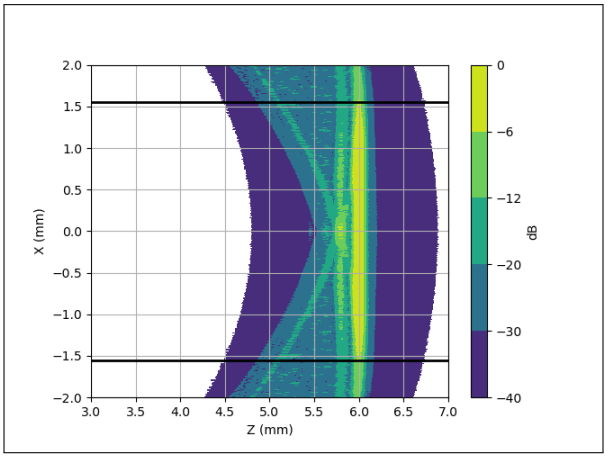


Figure 1. Emission waveform in $Y = 0$, fully populated case.

If we consider a sparse element distribution, such as a binned array, configured using a density scheme that implements a low-sidelobe window (in this case, a Taylor window), it is possible—at the cost of reducing the main wavefront size to one-third of that of the fully populated aperture—to suppress the main secondary wavefronts and reduce parasitic wavefronts to an irregular structure with very low intensity (figure 2). It is worth to mention that this apodization scheme avoids changing the emission voltage for each array element, a feature that is not available in all ultrasound systems.

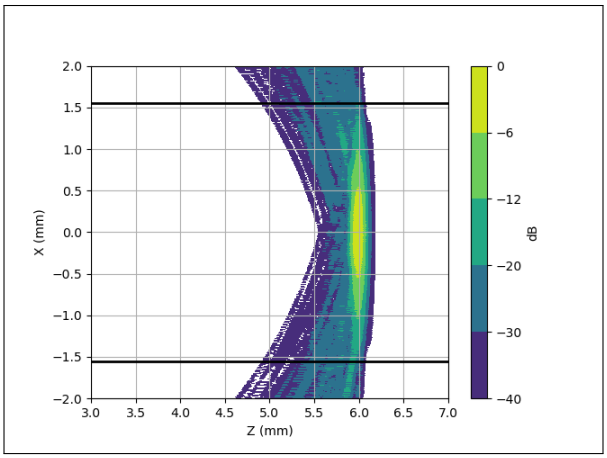


Figure 2. Emission waveform in $Y = 0$, 256 sparse case following a density apodization based on Taylor window

In reception, on the other hand, it is necessary to choose a solution that implements narrow beams to provide high-resolution imaging. In this regard, we have opted for a ring-shaped distribution. In both cases, we start by dividing the aperture into 4×4 bins, allowing us to select between 1 and 16 active elements per bin, depending on the desired density function across the aperture. In each transmission-reception process, both apertures are randomly selected according to their respective density function, thereby increasing the diversity of the diffraction pattern. Figure 3 presents an example of the solutions adopted for transmission (left) and reception (right) and the corresponding element density distributions.

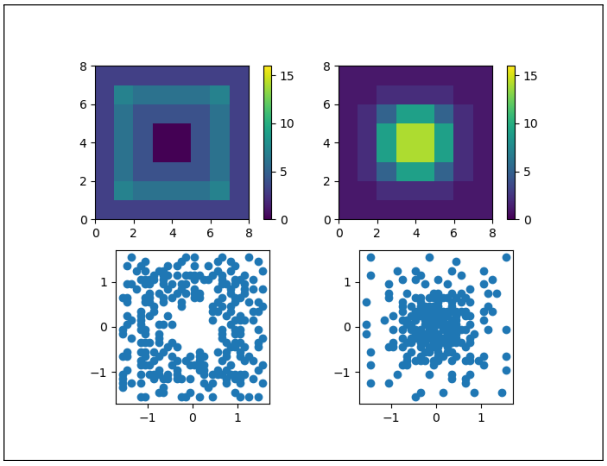


Figure 3. The 256 sparse array distribution. Top: In the left, element density for reception aperture. In the right, element density for transmission aperture. Bottom: In the left, example of reception aperture. In the right, example of transmission aperture.

For analyzing the process of generating an image for a single deflection angle (0^o) and compare the image from the full array with the one obtained using the sparse aperture, we have simulated the position of a line of scatterers along the Z-axis, separated by $0.25mm$. To assess the effect caused by diffraction, no white noise has been introduced into the model.

In Figure 4, we present the result of the full aperture. The image exhibits a large number of lobes and artifacts. To generate the final image, this image is combined with others obtained at different transmission angles, thereby reducing the interference pattern.

In Figure 5, we present the result of the sparse aperture. The image exhibits a significant reduction in artifacts, a lateral resolution comparable to that of the full aperture, and a secondary lobe pattern characteristic of the ring-shaped aperture.

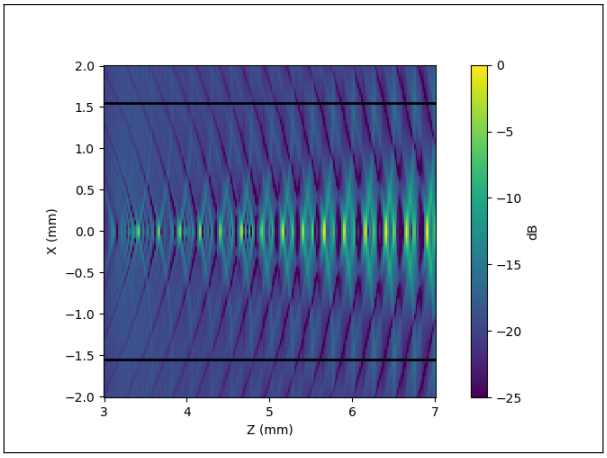


Figure 4. Image produced in the plane of interest ($Y = 0$) by the full aperture.

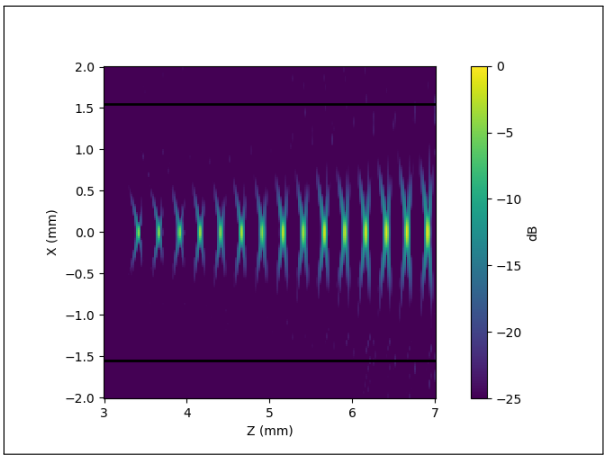


Figure 5. Image produced in the plane of interest ($Y = 0$) by the sparse aperture configuration.

To understand how the complete process works, we designed a sampling scheme with up to 32 emission shots, oriented to cover the entire reference volume. The scanning strategy follows a Fermat distribution based on the golden angle [8]. For the conventional plane-wave image, where emission superposition occurs in the illuminated scene, the final image is obtained by averaging the

32 steered images. To evaluate this process, we considered a more complex scene composed of a set of reflectors distributed in the XZ plane, maintaining the distribution along Z and a constant angular distribution along X. Figure 6 illustrates this in the case of a full aperture. The image can capture the presence of the reflectors but exhibits very low contrast.

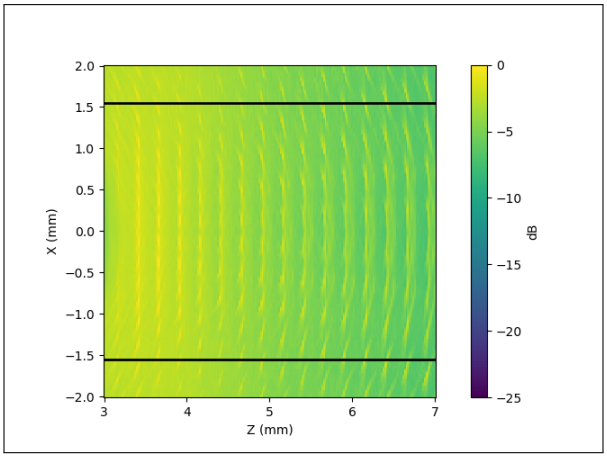


Figure 6. Image produced in the plane of interest ($Y = 0$) by the full aperture.

In the case of the proposed technique based on sparse apodized apertures, averaging between images cannot be applied since the emission beams are narrower and the images have minimal overlap. Therefore, the contribution of each image must be weighted according to the degree of influence that the emission beam has on the point under study. As explained earlier, while maintaining each aperture's respective density function for each shot, two new apertures are randomly generated—one for transmission and one for reception.

This operating approach, using sparse apertures and plane waves, offers an interesting alternative for integrating signal averaging. For a given angle, once a reception aperture has been selected, we could perform multiple consecutive transmissions with different sparse transmission apertures. By maintaining the same transmit lens and the same reception aperture, the signals can be directly averaged in the acquisition buffer.

By considering multiple sparse apertures for transmission that share the same main wavefront but produce different interfering secondary wavefronts, we can reinforce the main wavefront while generating destructive interference for the secondary wavefronts, thus minimizing their contribution to image artifacts (see figure 7). By adjusting the interference based on the relationship between transmission timing and time-of-flight, it is possible to make these variations "transparent" to the system, especially if a dual-buffer system is implemented.

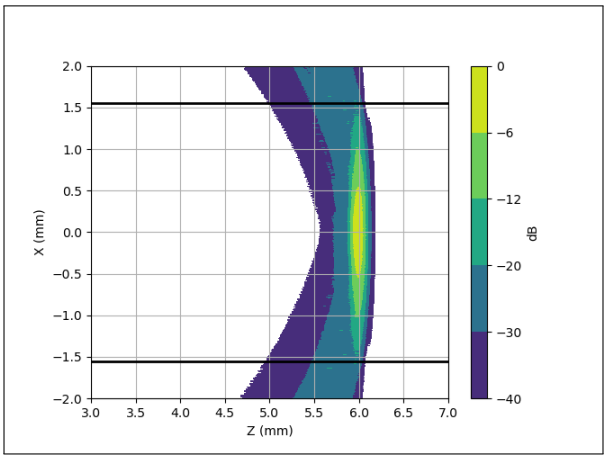


Figure 7. Emission waveform in $Y = 0$ averaged by 16 sparse apertures with 256 elements, following a density apodization based on Taylor window

Therefore, during the emission time of 32 shots required to obtain these 32 images, a total of 544 dispersed apertures were generated (32 for reception and 32×16 for transmission). The image produced by this configuration for the proposed imaging region is shown in Figure 8. Compared to the full-aperture image, the sparse array image improves contrast while maintaining lateral resolution. Residual secondary lobes are still present, but they are not significant enough to degrade image quality.

2.1 Volumetric imaging

We now consider a three-dimensional scene in which the reflectors are distributed along a spiral cone, with its vertex located at the center of the aperture. In this configuration, the reflectors are positioned at varying angles in both elevation and azimuth, as well as at different radial distances within the scanning volume. This setup allows us to compare the imaging performance of a full array versus a sparse array. In both apertures, the 32-angle sampling strategy based on the Fermat spiral was used. The figures display isosurfaces at -12 dB levels. To enhance the interpretability of the scene, the maximum intensities have been projected onto the XY, XZ, and YZ planes.

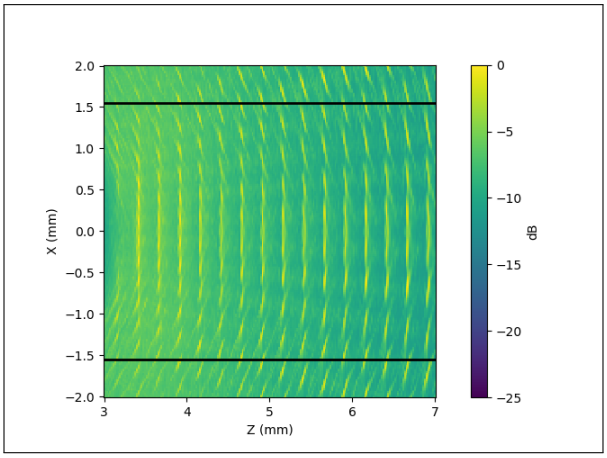


Figure 8. Image produced by the sparse aperture in the plane of interest ($Y = 0$). 16 averaged emissions performed.

The image obtained using the full aperture (Figure 9) exhibits limited dynamic range and resolution, indicating that the proposed scan is not sufficiently dense to produce a high-quality image. In contrast, the image generated using the sparse aperture—by introducing averaging and performing 16 transmissions (each with a different sparse emission aperture) per reception aperture—shows a significant improvement in dynamic range, along with a slight enhancement in lateral resolution compared to the non-averaged approach (Figure 10).

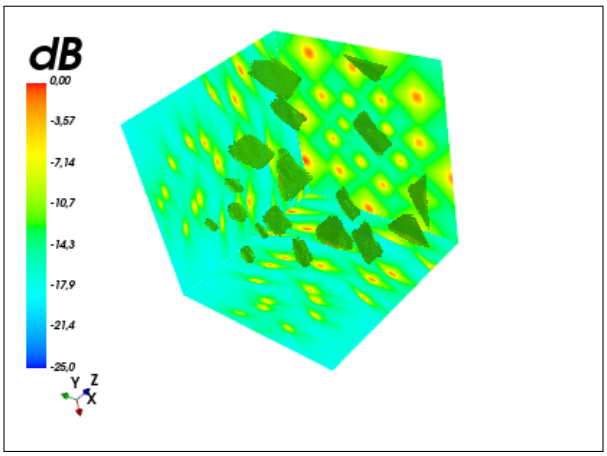


Figure 9. Volumetric image produced by the Full aperture.

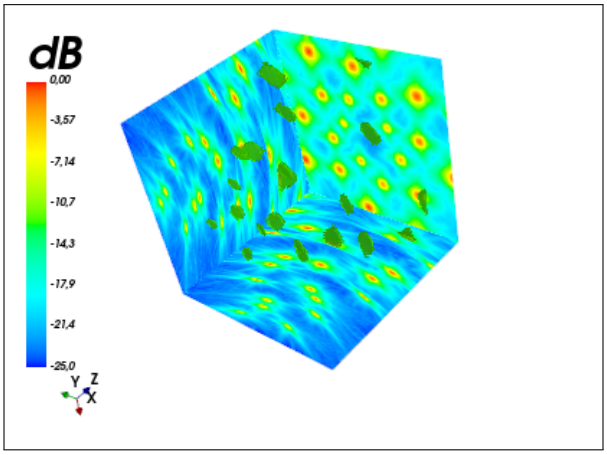


Figure 10. Volumetric image produced by the sparse aperture. 16 averaged emissions performed

The comparison between both apertures demonstrates that, when properly organized, sparsity can be effectively exploited to enhance near-field aperture performance and yield high-quality images. Averaging over the acquisition channels enables this process without incurring additional data flow costs. Furthermore, if the system supports double buffering for acquisitions and allows synchronization of the averaging transmissions with the transmit timing, the process can be rendered effectively transparent in terms of acquisition time. Within this imaging range and under plane wave illumination, the full aperture introduces a substantial number of artifacts and requires greater angular diversity and a higher number of transmissions to achieve comparable image quality.

3. CONCLUSIONS AND FUTURE WORK

The work has proposed a strategy for using sparse apertures in a plane-wave imaging system. Instead of proposing an exhaustive search for a solution, an open approach has been taken, where dozens of apertures are utilized to exploit the diversity they offer in order to improve the overall image result, according to a spatial distribution pattern designed to achieve a specific apodization response. In a way, the apodization used narrows the beam during emission, which nonetheless remains wide enough to allow for a sweep with a narrow beam during reception, generating a type of multi-beam focusing. It has been demonstrated how we can use several sparse apertures in transmission for the same reception to improve the signal-

to-noise ratio, and it has been suggested how this process can be integrated into the system as an averaging operation, parallelizing its activity with data transmission to maintain the acquisition rate at the desired values.

To evaluate this, three possible scenarios were designed in which we could compare the improvement relative to the flat aperture case. On one hand, the reduction of the artifact pattern caused by multiple wavefronts generated in the near field. On the other hand, the improvement in dynamic range when the interfering pattern becomes more complicated due to the regularity of the reflectors. And finally, when the volumetric image as a whole is considered. In all of these scenarios, the sparse aperture image has maintained an excellent response in terms of lateral resolution, even improving upon that of the full aperture.

The proposal is aligned with the objectives of the project, which seek to enhance the detection of microstructures using plane wave high-frame-rate imaging, while simultaneously reducing computational complexity and adapting the sensor to the available hardware resources. The forthcoming development of this work is directed toward the experimental phase, with the aim of assessing the performance of this technique when applied to functional imaging.

4. ACKNOWLEDGMENTS

Jorge Huecas, Staff hired under the Generation D initiative, promoted by Red.es, an organisation attached to the Ministry for Digital Transformation and the Civil Service, for the attraction and retention of talent through grants and training contracts, financed by the Recovery, Transformation and Resilience Plan through the European Union's Next Generation funds.

This research work was funded by the European Commission – NextGenerationEU, through Momentum CSIC Programme: Develop Your Digital Talent

This research work was funded by: PID2022 - 138013OB -I00 /MCIN /AEI /10.13039/ 501100011033/ FEDER, UE

This work has been developed within the framework of the LUNABRAIN-CM project, funded with €1,026 million by the Community of Madrid through the R&D activities program in technologies, granted by Order 5696/2024

5. REFERENCES

[1] Montaldo, G., Tanter, M., Bercoff, J., Benech, P., and Fink, M. Coherent plane-wave compounding for very high frame rate ultrasonography and transient elastography. In *IEEE Transactions on Ultrasonics, Ferroelectrics, and Frequency Control*, 56(3), 489–506, 2009.

[2] Heiles B, Correia M, Hingot V, Pernot M, Provost J, Tanter M, Couture O. Ultrafast 3D Ultrasound Localization Microscopy Using a 32 × 32 Matrix Array *IEEE Trans Med Imaging*, 38(9):2005-2015. doi: 10.1109/TMI.2018.2890358. 2019.

[3] Chavignon A, Heiles B, Hingot V, Orset C, Vivien D, Couture O. 3D Transcranial Ultrasound Localization Microscopy in the Rat Brain With a Multiplexed Matrix Probe. *IEEE Trans Biomed Eng*. 69(7):2132-2142. doi: 10.1109/TBME.2021.3137265. 2022.

[4] Zhang C, Lei S, Ma A, Wang B, Wang S, Liu J, Shang D, Zhang Q, Li Y, Zheng H, Ma T. Evaluation of tumor microvasculature with 3D ultrasound localization microscopy based on 2D matrix array. *Eur Radiol*. 34(8):5250-5259. doi: 10.1007/s00330-023-10039-x. 2024.

[5] Li X, Gachagan A, Murray P. Design of 2D Sparse Array Transducers for Anomaly Detection in Medical Phantoms. *Sensors*. 20(18):5370. doi: 10.3390/s20185370. 2020

[6] Martínez-Graullera Ó, de Souza JCE, Parrilla Romero M, Higuti RT. Design of 2D Planar Sparse Binned Arrays Based on the Coarray Analysis. *Sensors*. 21(23):8018. doi: 10.3390/s21238018. 2021

[7] Maffett R, Boni E, Chee AJY, Yiu BYS, Savoia AS, Ramalli A, Tortoli P, Yu ACH. Unfocused Field Analysis of a Density-Tapered Spiral Array for High-Volume-Rate 3-D Ultrasound Imaging. *IEEE Trans Ultrason Ferroelectr Freq Control*. 69(10):2810-2822. doi: 10.1109/TUFFC.2022.3188245. 2022

[8] J.N. Ridley, Packing efficiency in sunflower heads, *Mathematical Biosciences,* Volume 58, Issue 1, Pages 129-139, ISSN 0025-5564, https://doi.org/10.1016/0025-5564(82)90056-6. 1982,

DOI: 10.61782/fa.2025.0583

FORUM ACUSTICUM EURONOISE 2025

MODULAR AND FLEXIBLE HARDWARE ARCHITECTURE FOR REAL-TIME 3D ULTRASOUND IMAGING

Cruza, Jorge F.[1*] **Mateos, Raul**[2] **Bueno, Ricardo**[3]
Montaldo, Gabriel[4] **Camacho, Jorge**[1]
[1] Department of Sensors and Ultrasonics Systems, ITEFI (CSIC), Spain
[2] Department of Electronics, University of Alcalá, Spain
[3]DASEL SL Avda del Cañal 44, Nave 3 - 28500 Arganda del Rey (Madrid), Spain
[4]Neuro-Electronics Research Flanders, Leuven, Belgium

ABSTRACT

Ultrasound 3D imaging with arrays usually requires hardware systems with more active channels than for conventional 2D imaging, which increases systems complexity. Furthermore, it increases the beamforming difficulty, as more image lines have to be generated (3D volume) using more acquired raw signals (A-Scans). Typical approaches to this problem can be divided in hardware and software solutions. In the first, the beamforming process is carried out by a specialized hardware (FPGA, ASIC's, etc.), with lower power consumption, but also with lower flexibility. On the other hand, software beamformers are very flexible in terms of programming, but they require a much larger bandwidth with the acquisition system. This work presents a modular and flexible hardware architecture for 2D and 3D ultrasound imaging, which combines hardware beamforming capabilities with high-speed links with a processing computer. This approach enables to work with both hardware and software beamformers, taking full advantage of each one of them. A description of the architecture is given, along with the expected performance in terms of hardware processing power and data transfer rate. Finally, application examples are given: Total Focusing Method imaging in non-destructive-testing, and functional ultrasound imaging in the brain for pre-clinical models.

Keywords: *ultrasound, beamforming, 3D imaging*

1. INTRODUCTION

Ultrasound systems have evolved in the last years from hardware processing with highly specialized electronics, to software beamforming by high capacity computers, mainly because of the availability of powerful Graphical Processor Units (GPU), which are very efficient for the implementation of typical ultrasound imaging algorithms, and are easy to develop with than hardware architectures. Nevertheless, the software approach has limitations with regard to power consumption and integration for the development of industrial and medical devices, which prevents to completely abandon the specialized hardware approach.

This work presents a flexible and modular architecture able to fulfill the requirements of both, hardware and software beamformers. The idea behind that is to provide a platform were new developments can be performed faster and at lower cost by software programming, mainly oriented to scientific research and early stages of final product R&D, while it still have the capacity of implementing the more demanding parts in hardware, at higher processing rates with less power consumption, for final deployment.

A description of the architecture is presented, along with practical examples in two application fields: pre-clinical imaging and non-destructive-testing.

[*]***Corresponding author:*** *jorge.f.cruza@csic.es*
Copyright*: ©2025 Jorge F, Cruza et al. This is an open-access article distributed under the terms of the Creative Commons Attribution 3.0 Unported License, which permits unrestricted use, distribution, and reproduction in any medium, provided the original author and source are credited.*

2. HARDWARE ARCHITECTURE

The philosophy of this system is a flexible architecture to work in two different scenarios:

1. Hardware beamforming (HWBF): Whole beamforming and post-procesing is performed by the ultrasonic system and the host PC just displays the image.
2. Software beamforming (SWBF): System sends in real time the raw acquisition data in order to be processed by a high performance computer.

The architecture of the system is scalable, in order to build systems from 32 channels to 512 active channels, keeping the ability of real time beamforming the image in real time.

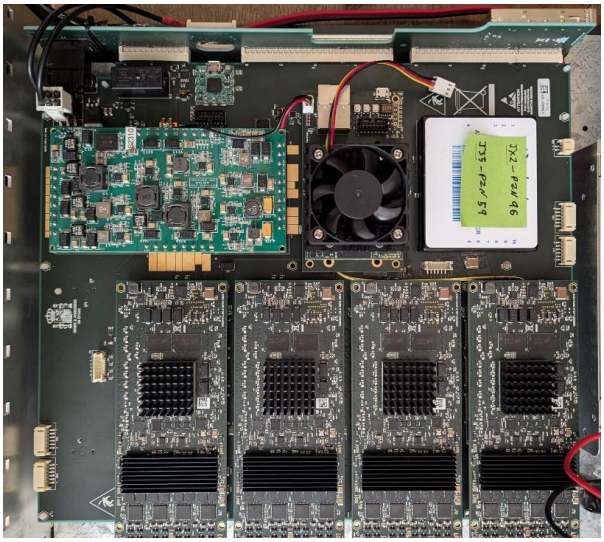


Figure 1. Motherboard of a 128 channels system, with 4x32 channels USMOD32 modules and FPGA SoC control unit.

2.1 System architecture

The control of the emission circuits, the digitalization of the received signals and the beamforming of the image are carried out in a distributed way in the system's FPGAs, transferring the final image to a host computer. The system also has the enough output bandwidth to send raw data to a remote system to be processed in real time. An FPGA SoC with embedded ARM processors performs the control of the system, and also implements the algorithms that are not too intensive but whose execution on the host PC can be a disadvantage due to larger latency.

The main design goals of the architecture are scalability, distributed processing and flexibility. Scalability is important to cover applications that require different numbers of channels, which is common in NDT. On the other hand, distributed processing is essential to handle the large volume of generated data. The third goal is flexibility, i.e. to be able to easily implement different imaging techniques, which is not only achieved by the reprogrammable nature of the FPGAs, but also by being able to evacuate the raw data in real time to an external processing system, e.g. a high-performance PC with GPUs.

The system is based on modules (USMOD32) capable of controlling, digitalizing and processing 32 ultrasound channels. The modules are connected together via a high-speed segmented bus to make possible systems with any number of channels in blocks of 32. **Figure 1** shows an implementation with 128-channels. Each module contains the pulsers, protection circuits and analog front-end (amplifier, filter and A/D converter) for 32 channels and 1 GB of DDR memory to store the beamforming results or the received signals. The selected FPGA is the XC7K160T, from Advanced Micro Devices (AMD, formerly Xilinx) Kintex series. The footprint is fully compatible with the higher-capacity XC7K325T and XC7K410T models for systems that require more hardware processing power.

Two segmented buses connect the FPGAs of the processing modules. The first, based on 10 LVDS pairs (1 Gb/s per pair), is used for programming acquisition and processing parameters and sending the images already conformed to the FPGA-SoC, which can carry out additional processing prior to sending them to the host PC.

The second bus is based on AMD GTX 7-series transceivers, which provide up to 10 Gbps full duplex communication in each direction. The FPGAs integrate 8 GTX transceivers, that are used to connect each module with the previous one with 4 GTX and to the next module with the remaining 4. Thus, closing the circuit (**Figure 2**) results in two circular buses of 40 Gbps each, with data flowing in opposite directions, allowing data transfer between any two FPGAs in the system at 80 Gb/s if both directions are used. This high-speed bus is used to transmit the partially beamformed images between the FPGAs of the modules, since each image line requires information from all channels.

In the HWBF mode, each module beamforms the image lines with the information acquired by its 32 channels, and sends them over one of the two 40 Gbps buses to the next FPGA. This one adds the results of beamforming its own channels with the data received from the previous one and sends the result to the next module.

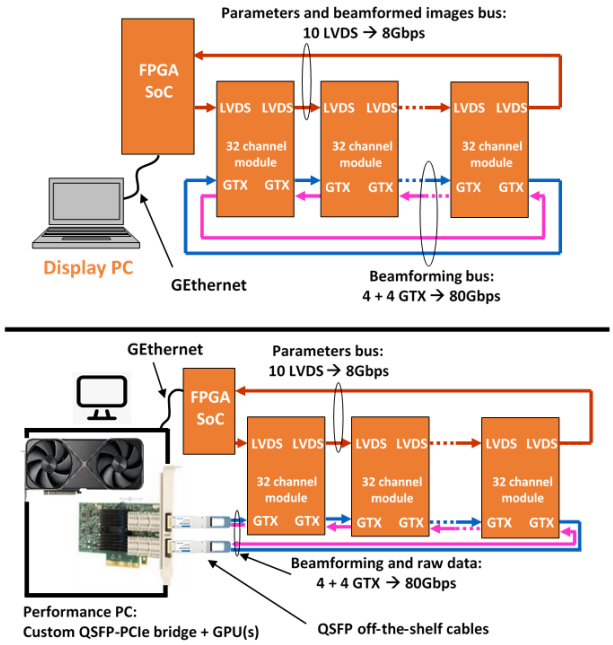


Figure 2. *Top*: configuration for hardware FPGA beamforming, host PC only for display. *Bottom*: configuration with a high performance PC, where beamforming process can be done by software.

When the data has travelled through all the FPGAs, the image is fully formed.

The image is stored in the dynamic memory (DDR), and it is divided into as many parts as USMOD32 are present in the system. This leverages not only the processing power of all the FPGAs, but also the memory bandwidth of all the modules, making the system a high-speed distributed processing architecture. This is the main difference with regard to previously proposed centralized architectures, where a central node requires a large memory bandwidth to store the result. This is particularly important in TFM and PWI image modes, since this kind of image modes have to sum many sub-images obtained with different emission, previous results has to be loaded from memory, summed with current ones and stored back to memory.

For the SWBF, the high bandwidth bus is used to send raw acquisition previously stored in the DDR of the USMOD32 through 2 QSFP cables. These cables are connected to a custom FPGA design implemented in a FPGA based PCIe board with 2 QSFP sockets, mounted in 8-lane PCIe 3.0 slot in a PC. The data from ultrasound system is stored in the PCI board DDR, and then is sent via DMA to PC main memory for the software processing of the ultrasonic data.

2.2 FPGA architecture

Figure 3 shows the representation of the receiving datapath. Other necessary subsystems, such as the emission beamformer, have been omitted in the figure for clarity. In general, the connections shown in this image follow the AXI4-Stream protocol, except for the connection to the DDR which is AXI4 and the 'register access bus' which is a 'custom' register access protocol similar to AXI4-Lite [1]. For the sake of clarity, the data width and operating frequencies of the buses have not been made explicit, but as a guide, they have been drawn with the width in relation to the total bus capacity. For example, the wider buses are capable simultaneously acquiring 32 signals and transmitting the beamforming result, therefore, they have a capacity of at least 28Gb/s. The narrower busses are sized to be transmitted over the LVDS links and, therefore, they have a maximum capacity of 8 Gbps (typically 32 bits at 250 MHz). The element named 'AXI-infrastructure' in Figure 3 consists of several elements of varying complexity such as multiplexers, DMAs, switches, clock domain changes, to name a few.

The datapath starts with the signals of the 32 channels being amplified, filtered and digitalized by the Analog Front End (AFE). Once inside the FPGA, the signals are filtered with a symmetrical FIR filter with 63 coefficients, followed by optional decimation. Afterwards, an adder with a high-capacity FIFO can perform averaging of up to 16 acquisitions. At this point, the acquisition can take two paths: it can either go into the beamformer or it can be stored in the module's DDR as raw data.

In the case of a remote PC performs the beamforming, the connection shown in red is used to dump the data from the DDR to the QSFP links. The protocol used to connect both the FPGAs to each other and the FPGAs to the PCIe card is the AURORA 64/66 protocol [2].

In case of hardware beamforming, the acquired signals can be input directly from the output of the averaged signals or can be loaded from the DDR memory. This is particularly useful if the same acquisition is to be beamformed several times by modifying the parameters (Multi-beamforming).

The beamformed data is summed with that of the precedent FPGAs, which are received from the GTX links. The sum is forwarded to the next FPGA, however, part of this sum has to be accumulated to the previous sub-images. Each FPGA is allocated a part of the image, in order to distribute the memory bandwidth usage among all modules.

2.3 Hardware beamforming

The beamforming operation is performed by a delay sum beamformer with a novel architecture previously developed

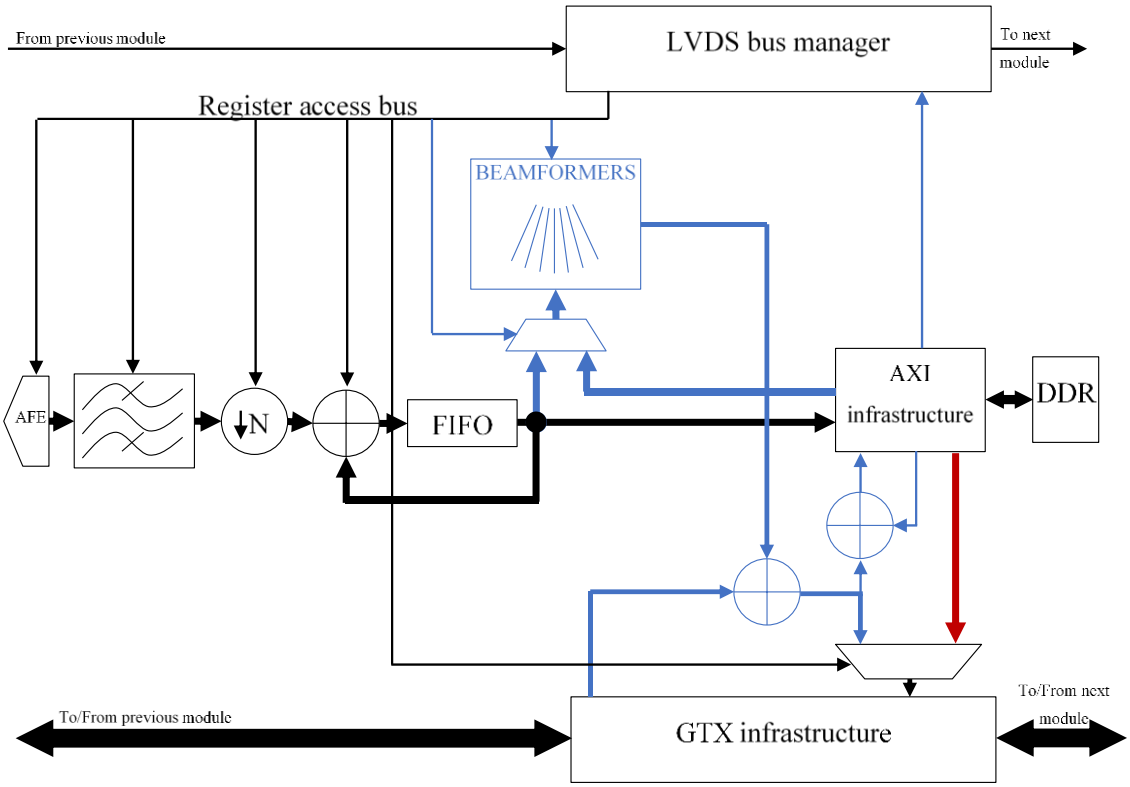


Figure 3. Schematic representation of the datapath inside each FPGA. Elements in black are utilized in both hardware and software beamforming. Blue elements are necessary for hardware beamforming while red connection is only used to dump raw acquisitions to the PC for a software beamforming.

by our group [3]. The delays are performed by using fractional delay filters [4] in order to get time resolution above the sampling frequency [5]. This design features a systolic and parallel architecture for interpolation and beamforming where fractional filtering and the process of sum are imbricated in the same hardware. Besides, this architecture makes an extensive use of the DSP tiles present in FPGAs [6]. These tiles are "hardwired" inside FPGA and therefore are less power consuming and can switch at higher frequencies than circuits implemented with regular FPGA resources, allowing time-multiplexing of these resources. Another key of the design are the delay calculators. Unlike other beamformers [7] where the delays are pre-calculated and loaded in FPGA memory, this beamformers uses a circuit to calculate iteratively the time delay that only needs parameters with a total of 80 bits wide. The delay calculator circuit is a pipelined version of the presented in [8] and a key part of the patent [9]. The pipelining, allows this logic switch at 250MHz using FPGA fabric resources.

Figure 4 shows the schematic of the beamformer. The samples coming from ADCs are stored in a 16 bit wide, 2048 deep circular buffer (one 32Kb Block RAM per channel). Simultaneously, the delay calculator output is used in this way: the integer part of the delay corresponds to index of the sample that is the input of the fractional filter, and the fractional part of the delay, chooses the set of coefficients used to apply the desired fractional delay (0, 1/4, 2/4 or 3/4). The delayed sample is automatically summed to the delayed sample of the other channels since delay filters are cascaded. Whole structure switches at 250MHz, so, we can time multiplex it in order to calculate more than one scan line at once. For example, with a broadband array of 15MHz center frequency where the sampling frequency can be 62.5 MHz, 4 scan lines can be obtained in parallel, while, in a 3MHz center frequency with 15.125MHz sampling frequency, 16 scan lines can simultaneously obtained. This can be useful in the conventional phased array technique if the emission focus is broad enough to beamform multiple scan lines of the image

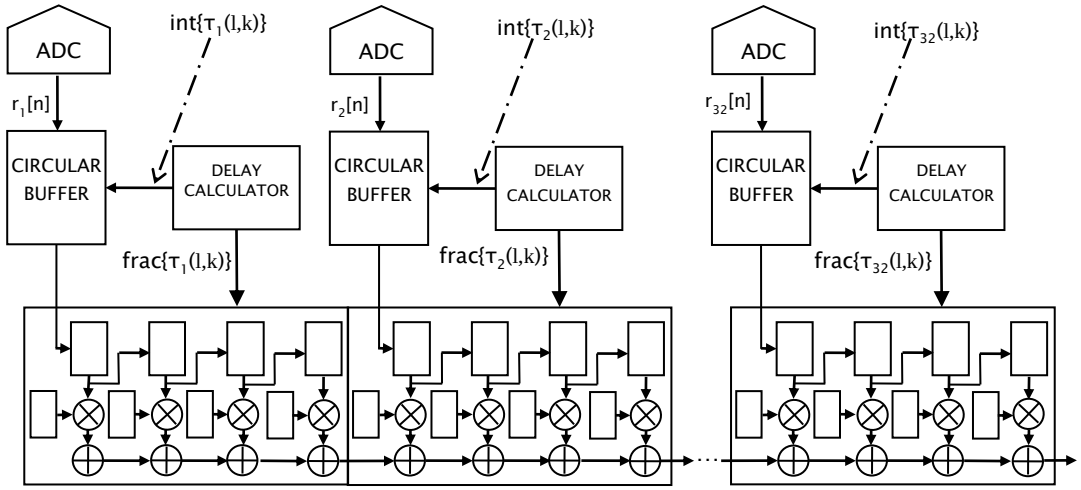


Figure 4. Beamformer architecture: fractional delay and the sum are performed by same FPGA resources, the DSP tiles.

in every emission. But is even much more interesting in plane wave image (PWI) or total focussing method (TFM) where emission is unfocussed and whole image have to be beamformed after every emission event (sometimes called "sub-image"). The ability of implement PWI or TFM in real time depends in the capacity to beamform all scan lines of the sub-image before next emission event. In this work we want to analyze three examples:

A PWI for functional ultrasound (fUS) for rat brain: c=1.5 mm/us, 15MHz center frequency (F_s=62.5 MSPS), L=128 lines of d=15mm depth, 500 beamformed images per second, each one compounded by 7 plane waves (PRF=3500Hz).

B Total Focusing Method: steel c=6.25 mm/us, 3MHz center frequency (15.125MSPS), 128 lines of 50mm depth, 25 images/s compounded by 128 sub-images, one per array element (PRF=1920Hz).

C 3D Total Focusing Method: 16x16 array (256 elements), steel c=6.25 mm/us, 5MHz center frequency (31.25MSPS), 256 lines of 50mm depth, 25 volumes/s compounded by 256 sub volumes, one per array element (PRF=6400Hz).

To determinate if the hardware is able to implement these examples in real time we have to define the next figures: $\mathbf{T_{PRF}}$ (1 / PRF) is the between different acquisitions. $\mathbf{T_A}$ is the time it takes acquiring necessary samples for the image, **L** is number of image lines, **M** is the relationship between switching frequency of the beamformer and acquisition sampling frequency and defines the number of lines in parallel can process in the acquisition time ($\mathbf{T_a}$). **N** is Number of beamformers (the structure shown in Figure 3 can be replicated inside FPGA). **R** is the times the beamformers have to reprocess the same acquisition data in order to beamform all the L lines of the image.

$$R = \left\lceil \frac{L}{M \cdot N} \right\rceil$$

Furthermore, to operate in strict real time, the time that takes to beamform the image (or sub-image) has to be lower than the time between different acquisitions:

$$R_{MAX} = \left\lfloor \frac{T_{PRF}}{T_A} \right\rfloor$$

Using these definitions, **Table 1** shows the number of beamformers needed for the three examples presented, employing this equation:

$$N = \left\lceil \frac{L}{M \cdot R_{MAX}} \right\rceil = \left\lceil \frac{L}{M \cdot \lfloor T_{PRF}/T_A \rfloor} \right\rceil$$

As **Table 1** reveals, the more exigent image mode, the more beamformer structures that have to fit in the FPGA to operate in real time. **Table 2** shows the resource used for the beamforming, taking into account that there are also other subsystems that have to fit in FPGA. Furthermore, the total resource consumption should be below 80% in some critical resources (LUTs

particularly) in order to allow place-and-route tool to reach timing closure.

Table 2~~2~~1. Number of beamformers needed for each acquisition mode

	A	B	C
c (mm/µs)	1,5	6,25	6,25
D (mm)	15	50	50
Ta (µs)	20	16	16
L (lines)	128	128	256
M (lines/beamformer)	4	16	8
FPS (images/s)	500	25	25
Sub-images (angles or elements)	7	128	256
PRF (Hz)	3500	3200	6400
T_{PRF} (µs)	285,71	312,50	156,25
Rmax	15	19	9
N (beamformers)	**3**	**1**	**4**

As can be appreciated with **Table 1** and **Table 2**, the mid-range FPGA XC7K160 can implement complex types of image like example B, but is unable to perform fUS in real time (example A)[10]. However, a system which features high range FPGAs can perform fUS or 3D TFM in strict real time without need a powerful external computer. Despite high-end FPGAs have a higher cost, their lower power consumption and size than a solution based on an external PC, could justify their use for industrial developments.

3. RESULTS

Three application examples with a 128 channels system developed with the proposed architecture are presented. **Figure 5** shows a functional ultrasound image of a rat brain, obtained with a 15 MHZ phased-array transducer, while a visual stimulus is applied to the animal. The Doppler image was generated by the ultrafast plane-wave technique [10] with 5 angles between -6º and 6º, 2 emitted pulses, 8 kHz PRF, 4 averages and a total of 8.000 consecutive images (20 seconds continuous acquisition). The output trigger of the system was received by the visual stimulus system and delayed 10 seconds before emitting a vertical lines pattern to the right eye of the mouse. This way, a base-line reference of 10 seconds can be compared with a stimulus of 10 seconds to detect the activated brain zones. The experiment was repeated 10 times and the response was averaged for better signal-to-noise ratio. Figure 8 shows the functional image in color, overprinted on a single Doppler image in black and white. The activated zone corresponds with that expected for the given stimulus, and the spatial resolution and SNR are in accordance with the experiment set-up.

A second experiment is presented, in this case, for a non-destructive-testing application (**Figure 6**). An 11x11 matrix array of 3.5 MHz was used for imaging inside a calibration block with several flat-bottom holes at different depths. The virtual array method was used [11] to obtain, in real time, the focusing delays inside the material, accounting for the refraction at the interface. The high-speed links were used to transfer data to a PC with an NVidia RTX4080 GPU, where the beamforming algorithms achieved an imaging rate of 10 volumes per second, automatically detecting the component surface location and shape (3D auto-focus).

Figure 7 shows the HWBF performance of the system, by acquiring a TFM image with a 15 MHz 128 elements array, in real-time. The beamformed region is 36mm wide (probe has an aperture of 32 mm) and 50mm depth. The beamformed image size has 256 lines wide and 700 points per line depth. With this configuration, it took 230ms to generate that image (4 frames per second). The system used for this experiment ships the smallest compatible FPGA (XC7K160), so this frame rate can be multiplied by 4 using higher range FPGAs.

Table 3~~3~~2. Number of beamformers that can fit in the 3 different pin compatible FPGAs. In bold, the limiting resource.

	one beamformer	XC7K160		XC7K325		XC7K410	
# BEAMFORMERS	1	2		4		8	
LUTs	10778	21556	21,26%	43112	21,15%	86224	33,92%
64-bit distributed RAM	6149	12298	35,13%	24596	38,43%	49192	**54,29%**
36Kb Block RAM	32	64	19,69%	128	28,76%	256	32,20%
DSPs	128	388	**64,67%**	512	**60,95%**	1024	**66,49%**

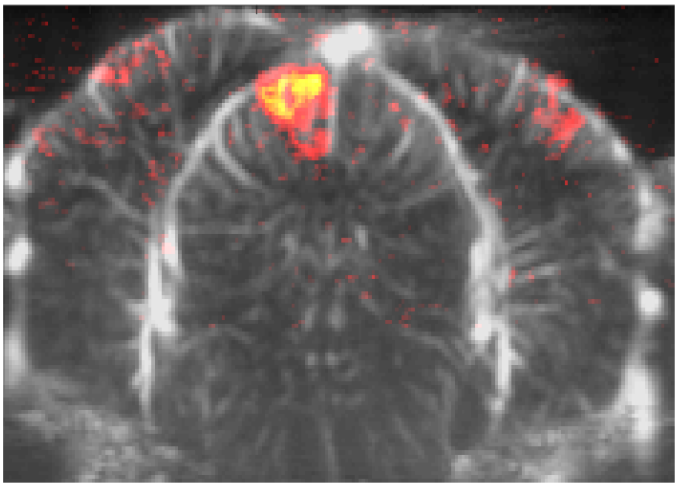


Figure 5. Hardware beamformed TFM with imasonic 128 elements 15MHz center frequency, 0.25 pitch probe, 36x50mm, 256 x 750pixels.

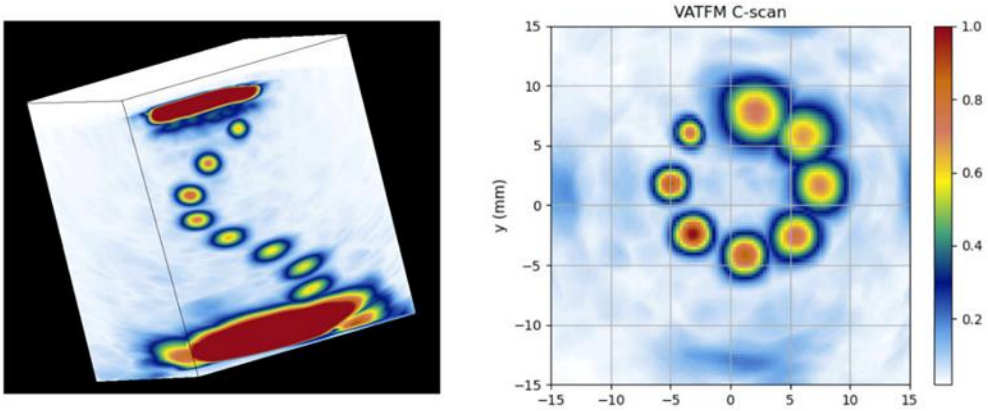


Figure 6. Left: 11x11 matrix array TFM image3D image SW processed with CUDA. Rigth: C-scan of the image.



Figure ~~5~~57. Hardware beamformed TFM with imasonic 128 elements 15MHz center frequency, 0.25 pitch probe, 36x50mm, 256 x 750pixels.

4. CONCLUSION

This work presents a high-end flexible and scalable hardware architecture for ultrasound imaging systems, able to operate in real-time by hardware beamforming, or transferring the raw data to a high-end processing computer for software beamforming. A 128 channel was built and tested in three demanding applications: Pre-clinical functional ultrasound brain imaging, 3D autofocused imaging in non-destructive testing, and real-time inspection with TFM technique. Future work includes extending the system channel count in a new prototype, able to work with 1024 elements matrix arrays for 3D functional ultrasound.

5. ACKNOWLEDGMENTS

Supported by the projects PID2022-143271OB-I00, funded by MCIN/AEI /10.13039/501100011033/FEDER, UE, PLEC2024-011165, funded by MICIU/AEI/10.13039/501100011033/ FEDER, UE, and by TEC-2024/TEC-43, LUNABRAIN-CM, funded by Comunidad de Madrid.

6. REFERENCES

[1] "*AMBA® AXI™ and ACE™ Protocol Specification AXI3™, AXI4™, and AXI4-Lite™ ACE and ACE-Lite™*", Arm Holdings plc, Cambridge, United Kingdom

[2] "*SP011Aurora 64B/66B Protocol Specification*", Advanced Micro Devices, Inc., Santa Clara, California, United States of America

[3] J. F. Cruza, "Design a real time beamformer", *Trabajo Fin de Maestría*, Dpto. de Electrónica, Esc. Politécnica Superior, Univ. Alcalá de Henares, Sep. 2011.

[4] T. I. Laakso, V. Valimaki, M. Karjalainen, U.K.Laine, "Splitting the Unit Delay", *IEEE Sig. Proc. Magazine*, pp. 30-58, Jan. 1996.

[5] G. S. Kino, D. Corl, S. Bennett, K. Peterson, "Real time synthetic aperture imaging system", *Proc. IEEE Ultrason. Symp.*, pp. 722-731, 1980.

[6] "*UG479- 7 Series DSP48E1 Slice*", Advanced Micro Devices, Inc., Santa Clara, California, United States of America

[7] M. Njiki, S. Bouaziz, A. Elouardi, O. Casula, O. Roy, "A Multi-FPGA implementation of real-time reconstruction using total focusing method", *Proc. 2013 IEEE Int'l Conf. on Cyber Technology in Automation, Control and Intelligent systems* , pp. 468-473, May 26-29, Nanjing, China, 2013.

[8] J. F. Cruza, J. Camacho, L. Serrano, C. Fritsch, "New Method for Real-time Focusing through Interfaces", *IEEE Trans. on Ultrason. Ferroelectr. Freq. Control*, **60,** 4, pp. 739-751, 2013.

[9] C. Fritsch, J. F. Cruza, J. Camacho, J. M. Moreno, J. Brizuela, L. Medina, "Controlador de enfoque dinámico para sistemas de imagen ultrasónica", *Pat. ES P201230799*, 25 May 2012.

[10] G. Montaldo, M. Tanter, J. Bercoff, N. Benech, and M. Fink, "Coherent plane-wave compounding for very high frame rate ultrasonography and transient elastography," *IEEE Trans. Ultrason. Ferroelectr. Freq. Control*, 56, 3, pp. 489–506, 2009.

[11] G. Cosarinsky, J.F. Cruza, M. Muñoz, J. Camacho, "Optimized auto-focusing method for 3D ultrasound imaging in NDT", *NDT & E International*, Volume 134, 2023, 102779, ISSN 0963-8695, https://doi.org/10.1016/j.ndteint.2022.102779.

DOI: 10.61782/fa.2025.0630



FORUM ACUSTICUM
EURONOISE 2025

NUMERICAL FRAMEWORK FOR DEEP LEARNING PHOTOACOUSTICS IMAGE RECONSTRUCTION

Javier G. Muñoz[1,2] **Alejandro Ariza-Carrasco**[1,2] **Jorge Cruza**[3]
Luis Elvira[3] **Jorge Camacho**[3] **José M. Udías**[1,2]
María Alonso de Laciñana[4] **Jorge Rodriguez-Pardo**[4]
Paula Ibáñez García[1,2*] **Mailyn Pérez-Liva**[1,2*]

[1] Nuclear Physics Group and IPARCOS, Department of Structure of Matter, Thermal Physics and Electronics, Universidad Complutense de Madrid, Spain

[2] Departamento de Estructura de la Materia, Física Térmica y Electrónica, Facultad de Ciencias Físicas, Universidad Complutense de Madrid (UCM); IdISSC, España.

[3] Ultrasound Systems and Technology Group (GSTU), Institute for Physical and Information, Spanish National Research Council (CSIC), Spain

[4] Department of Neurology and Stroke Centre, Neurological Sciences and Cerebrovascular Research Laboratory, Neurology and Cerebrovascular Disease Group, Neuroscience Area Hospital La Paz Institute for Health Research - IdiPAZ, Spain

ABSTRACT

Photoacoustic Imaging (PAI) combines optical excitation with ultrasound detection to produce high-quality molecular images of intact biological tissues. Conventional systems rely on Class IV [1] pulsed lasers, which limits clinical translation. This work explores the use of pulsed semiconductor diodes for their portability, versatility, and low-cost. However, their lower peak power decreases PAI signal amplitude. Implementing deep learning techniques trained with realistic synthetic data is a promising technique to increase PAI image quality [2]. Here we create a framework which simulates real scenarios taking into account acoustics and optical properties, ultrasound transducer characteristics and fiber bundles features, crucial to optimize reconstruction performance with a Neural Network. The simulated experimental setup included an array of optical fibers connected to semiconductor diodes parallel to a 128-element transducer array which registers the signal generated by the absorbed light. Optical properties were simulated in MCX Monte Carlo software using GPU parallelization. k-Wave software was used for acoustic simulations and Time-Reversal (TR) image reconstruction. Finally, a Neural Network model implemented using Tensorflow enhanced the reconstruction, recovering up to 3 cm depth and 200 µm of resolution, delivering exceptional vascular imaging quality.

Keywords: *Photoacoustic Imaging, Ultrasound, Medical Physics*

***Corresponding author**: mailyn01@ucm.es and pbibanez@ucm.es .*

***Copyright**: ©2025 Javier G. Muñoz et al. This is an open-access article distributed under the terms of the Creative Commons Attribution 3.0 Unported License, which permits unrestricted use, distribution, and reproduction in any medium, provided the original author and source are credited.*

1. INTRODUCTION

Photoacoustic imaging (PAI) is an emerging biomedical imaging modality that combines optical excitation and ultrasound detection to generate high-contrast structural and molecular images of biological tissues. Its underlying mechanism relies on the thermo-acoustic effect, mathematically represented by:

$$p_0 = \Gamma \mu_a \phi, \tag{1}$$

Where p_0 is the initial pressure rise, Γ is the

Grüneisen parameter, μ_a is the tissue absorption coefficient, and ϕ is the local optical fluence.

State-of-the-art PAI systems typically utilize Class IV pulsed lasers, which, despite providing sufficient optical power, present substantial drawbacks such as high costs, large size, and significant regulatory restrictions, limiting clinical translation. To overcome these challenges, semiconductor diode lasers have emerged as a compact and cost-effective alternative. However, their lower optical output power substantially reduces fluence, negatively impacting image quality and clinical applicability.

Recent advances in computational imaging, specifically deep learning techniques integrated with conventional reconstruction algorithms, offer promising pathways to compensate for reduced fluence and improve reconstruction accuracy. In this study, we develop and evaluate a neural network model trained using realistic numerical simulations of our experimental setup, meticulously accounting for relevant acoustic and optical properties of biological tissues. By improving image reconstruction quality, this approach aims to mitigate the intrinsic limitations associated with diode-based illumination, thereby enabling the development of clinically viable, handheld PAI systems.

2. METHODOLOGY

Training neural networks effectively requires extensive datasets. To meet this requirement, we developed a computational framework to generate realistic synthetic data closely replicating our experimental setup. This framework integrates acoustic and optical simulations using accurate physical parameters, thereby producing synthetic pressure distributions that closely mimic real-world scenarios. The resulting data is subsequently used to enhance the quality and effectiveness of signal post-processing and reconstruction.

2.1 Optical simulations

An array comprising five semiconductor diodes is arranged to uniformly illuminate the acoustic transducer acquisition plane, as illustrated in Fig. 1A. Optical simulations were conducted using MCX Monte Carlo software [3] to calculate the two-dimensional fluence distribution at the transducer acquisition plane. The simulated medium was water, selected due to its low scattering and absorption coefficients [4], facilitating clear evaluation of the optical fluence pattern.

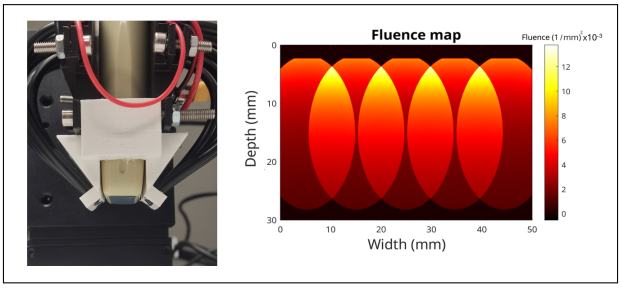


Figure 1. a) Experimental setup simulated. b) Fluence map in the transducer plane corresponding to the acquisition area.

2.2 Phantom generation

Phantoms with realistic vessel structures were generated using a 3D stochastic algorithm informed by real vessel data from coronary arteries [5]. Three distinct projections were created for each generated phantom, producing a comprehensive set of 2D images. By applying various geometric transformations and deformations, a diverse dataset comprising 2000 phantom images was compiled. Each phantom image was subsequently combined with the simulated fluence map to yield the corresponding initial pressure distribution. The ground truth used for neural network training was defined by an ideal, uniform fluence map, representing optimal illumination conditions with a perfectly homogeneous light source.

2.3 Acoustic simulations

Acoustic simulations were conducted using the k-Wave software [6], which addresses both the forward and inverse acoustic propagation problems. The forward simulation involved propagating the initial pressure distribution through water by solving the acoustic wave propagation equation. Signals were captured using a simulated 128-element ultrasound transducer array with a central frequency of 7.5 MHz, considering the acoustic properties of the medium and the geometric arrangement of the transducer elements [7].

Subsequently, the inverse acoustic problem was solved using the classical Time-Reversal (TR) reconstruction algorithm. This method reconstructs the initial pressure distribution by temporally reversing and re-emitting the recorded signals from each transducer element, effectively back-propagating the acoustic waves to their original spatial locations.

2.4 Neural network

The neural network framework developed for this study employs two distinct architectures, as depicted in Fig. 2. The first network is a U-Net designed to process the raw signals simulated with k-Wave under realistic fluence conditions and output signals corresponding to an ideal uniform fluence scenario. This step effectively corrects for fluence heterogeneities inherent in diode illumination.

Subsequently, a Y-Net architecture is utilized, receiving as inputs both the fluence-corrected signals from the U-Net and the initial reconstruction produced by the TR algorithm. The Y-Net generates an enhanced reconstructed image by combining the preliminary reconstruction information (TR) with additional data contained in the fluence-corrected signals, capturing potentially lost details during the initial reconstruction phase. All pressure maps and signals were normalized to their respective maximum values before neural network processing to ensure consistent training conditions and optimize network performance.

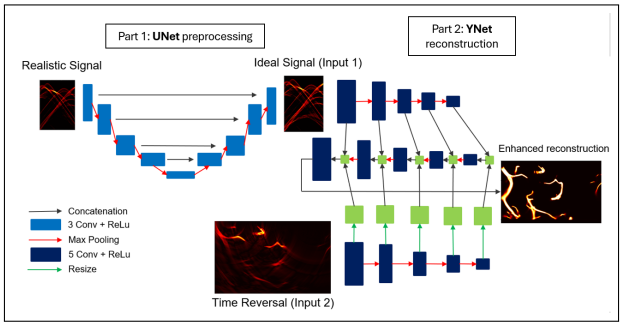


Figure 2. Neural Network workflow scheme.

3. RESULTS

3.1 Image reconstruction

The semiconductor diode illumination setup generates a non-uniform fluence distribution, as depicted in Fig.1, achieving a maximum imaging depth of approximately 30 mm. This depth represents the practical imaging limit for the current photoacoustic configuration, beyond which the fluence intensity decreases by 20% compared to the maximum. When comparing reconstruction techniques, the TR algorithm achieves effective reconstruction only up to approximately 20 mm, beyond which the image quality significantly deteriorates due to insufficient fluence and limitations in the algorithm, with the reconstruction pressure dropping to less than 20% of the maximum peak. In contrast, the combined approach utilizing the TR algorithm followed by the neural network (TR + Neural Network) successfully reconstructs images across the entire depth range enabled by the fluence distribution, demonstrating superior capability in compensating for the non-uniform illumination inherent in diode-based setups.

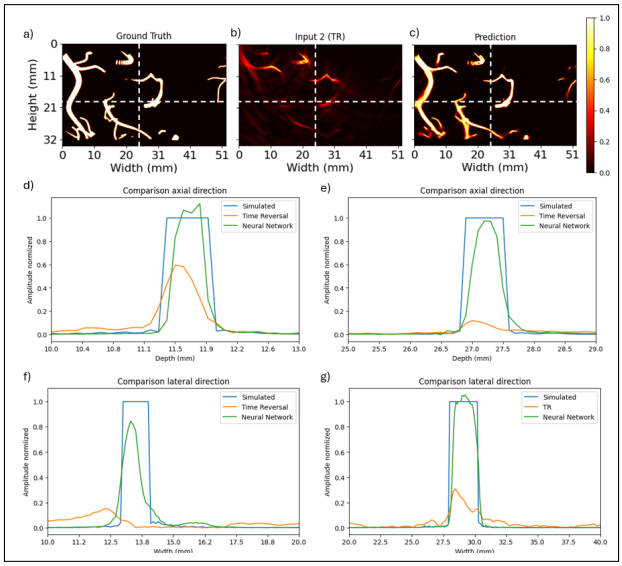


Figure 3. Enhanced image analysis. a) Ground truth. b) TR reconstruction. c) Neural Network reconstruction. d,e) Axial profiles. f,g) Lateral profiles.

3.2 Image enhancement and artifact reduction

Further evaluation of axial and lateral profiles in the reconstructed images provides insights into the effectiveness of signal recovery and artifact mitigation, as illustrated in Fig. 3. Axial profiles demonstrate the neural network's capability to compensate for fluence-induced signal loss at increased depths, effectively maintaining higher contrast compared to the TR reconstruction (Figs. 3d and 3e). Lateral profiles highlight the neural network's proficiency in reducing limited-view artifacts present in the TR method, which typically manifest as data loss along axial vessel structures. The neural network enhances the contrast and clarity of these structures, significantly improving overall image quality (Figs. 3f and 3g).

However, despite notable improvements, the neural network occasionally reconstructs vessel-like structures

absent from the ground truth, introducing artifacts. This phenomenon likely arises from model overfitting due to limited variability in the training dataset. Expanding the training set size and diversifying case scenarios could mitigate such artifacts and further enhance reconstruction accuracy.

4. CONCLUSIONS

The integration of classical reconstruction algorithms with neural network-based approaches demonstrates significant potential for improving the image quality of low-cost, handheld photoacoustic imaging systems. This combined methodology effectively compensates for the inherent limitations of semiconductor diode-based illumination, such as reduced and non-uniform fluence, by enhancing both image depth and contrast. Crucially, accurate and realistic simulation environments are essential for the successful training and performance optimization of neural networks. By employing meticulously characterized synthetic datasets that closely replicate experimental conditions, neural networks can achieve reliable reconstruction capabilities, leading to improved clinical viability and diagnostic utility of compact photoacoustic devices. Future efforts should focus on expanding the variability and size of training datasets, addressing artifacts introduced during reconstruction, and validating performance against experimental data to ensure robust clinical translation.

5. ACKNOWLEDGMENTS

This work received support from the European Union's Horizon 2020 research and Innovation Programme under the Marie Sklodowska-Curie Grant Agreement no.101030046, and the Programme Ramón y Cajal RYC2021-032739-I, funded by MCIN/AEI/10.13039/501100011033 and by the European Union "NextGenerationEU"/PRTR". Also, we acknowledge support from grants FASCINA (PID2021-126998OB-I00/), 3PET (PDC2022-133057-I00) from the Spanish Ministry of Science and Innovation (MCIN) AEI/10.13039/501100011033/Unión Europea Next GenerationEU/PRTR, Prototwin Project (TED2021-349 130592B-I00) and Tecnologías Avanzadas para la Exploración del Universo y sus Componentes" (PR47/21 TAU-CM TAU- PRTR), funded by EU Resilient and NextGeneration funds. This work was supported by Knowledge Generation Projects 2022 Type A Oriented Research, Government of Spain INVENTOR (PID2022-137114OA-I00).

6. REFERENCES

[1] P. Beard, "Biomedical photoacoustic imaging," *Interface Focus*, vol. 1(4), p. 602–631, 2011.

[2] A. B. E. Attia, G. Balasundaram, M. Moothanchery, U. S. Dinish, R. Bi, V. Ntziachristos, and M. Olivo, "A review of clinical photoacoustic imaging: Current and future trends," *Photoacoustics*, vol. 16, pp. 100–144, 2019.

[3] Q. Fang and D. Boas, "Monte carlo simulation of photon migration in 3d turbid media accelerated by graphics processing unit," *Opt. Express*, vol. 17, pp. 20178–20190, 2009.

[4] G. M. Hale and M. R. Querry, "Optical constants of water in the 200nm to 200 micron wavelength region," *Appl. Opt.*, vol. 12, pp. 555–563, 1973.

[5] K. Iyer, B. Nallamothu, C. Figueroa, and R. Nadakuditi, "A multi-stage neural network approach for coronary 3d reconstruction from uncalibrated x-ray angiography images," *Sci Rep*, vol. 13, 17603, 2023.

[6] B. E. Treeby and B. T. Cox, "k-wave: Matlab toolbox for the simulation and reconstruction of photoacoustic wave-fields," *J. Biomed. Opt.*, vol. 15, no. 2, p. 021314, 2010.

[7] C. Baumgartner, P. A. Hasgall, F. D. Gennaro, E. Neufeld, B. Lloyd, M. C. Gosselin, D. Payne, A. Klingenböck, and N. Kuster., "It'is database for thermal and electromagnetic parameters of biological tissues, version 4.2.," *IT'IS Database for Thermal and Electromagnetic Parameters of Biological Tissues, Version 4.2.*, 2024.

DOI:

Main theme: A12 Physical Acoustics and Ultrasound

Session A12.07 Acousto-optics

Chair(s): S. Dupont, J. Vanhamel, M. Duocastella

DOI: 10.61782/fa.2025.0903

FORUM ACUSTICUM EURONOISE 2025

TOWARDS BROADBAND LATERAL BAW EXCITATION IN A LOW-VELOCITY ANISOTROPIC SUBSTRATE

Konstantin B. Yushkov[1*] **Natalya F. Naumenko**[1] **Vladimir Ya. Molchanov**[1]
[1] Acousto-Optical Research Center, University MISIS, 119049 Moscow, Russia

ABSTRACT

We investigate a novel transducer structure that combines the thin plate lithium niobate (LN) and interdigital transducer (IDT) technologies. We simulated an anisotropic LN-on-TeO_2 structure with an IDT atop, in which shear horizontal (SH) bulk acoustic wave (BAW) excitation was considered. X-cut LN plate is bonded to the substrate, and the IDT electrodes are aligned with $Z + 41°$ direction of pure SH displacement. The transducer was aligned with (110) plane of the TeO_2 substrate having the SH BAW velocity in the range from 0.62 to 0.80 km/s depending on the cut angle α. Frequency dependencies of the resulting BAW polarization in the substrate were retrieved and analyzed. With a fixed-pitch IDT, SH BAW excitation can be achieved in the relative bandwidth of $\sim 20\%$ at various central frequencies depending on the LN plate thickness. At the boundaries of the excitation band, we observed transformation of the BAW mode from SH to longitudinal polarization. Owing to periodic IDT structure, the beam steering effect is observed for the excited SH BAW in TeO_2 that helps to extend the bandwidth of light-to-ultrasound coupling in photonic applications.

Keywords: *acousto-optics, beam steering, interdigital transducer, anisotropic multilayer structure*

1. INTRODUCTION

Broadband excitation of bulk acoustic waves (BAWs) is of great demand in various applications including acousto-optics and photonic integrated circuits. The golden standard of BAW transducers up to 1 GHz is thin plate lithium niobate (LN), which allows for longitudinal/shear mode excitation in solids with high electromechanical coupling. Interdigital transducer (IDT) technology is an effective method for surface and hybrid wave launching, but its applications in BAW domain are still limited. Commonly, leakage of acoustic waves into bulk modes is considered as a drawback and a source of undesired losses in high-frequency ultrasonic devices. To eliminate leakage, high-velocity substrates or membrane structures are commonly used in sufrace acoustic wave devices.

We analyze the possibility of applying IDT techniques for purposeful shear horizontal (SH) BAW excitation in a low-velocity TeO_2 crystal substrate (Fig. 1). Periodical out-of-phase excitation of ultrasound enables the effect of beam steering in the substrate crystal, which can be used to extend the phase-matching band of acousto-optic deflectors and tunable filters [1]. Radiation pattern of a periodically poled transducer depends on the ultrasound frequency that results in effective wavefront tilt and readjustment of acousto-optic phase matching. In this report, we numerically analyze excitation bandwidth and acoustic modal structure created by the said transducer.

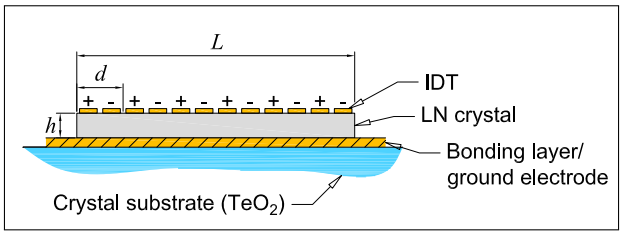


Figure 1. Piezoelectric transducer with an IDT atop of anisotropic LN-on-TeO_2 structure.

*Corresponding author: konstantin.yushkov@misis.ru.
Copyright: ©2025 K.B. Yushkov et al. *This is an open-access article distributed under the terms of the Creative Commons Attribution 3.0 Unported License, which permits unrestricted use, distribution, and reproduction in any medium, provided the original author and source are credited.*

2. METHODS

The proposed transducer structure combines the thin plate LN and IDT technologies. We simulated an anisotropic LN-on-TeO_2 structure with an IDT atop, in which SH BAW excitation was considered (panel A in Fig. 2). X-cut LN plate is bonded to the substrate, and the IDT electrodes are aligned with $Z + 41°$ direction of pure SH displacement. The transducer was aligned with (110) plane of the TeO_2 substrate having the SH BAW velocity in the range from 0.62 to 0.80 km/s depending on the cut angle α.

The transducer's performance was modelled with a semi-analytical SDA-FEM-SDA method developed for arbitrary anisotropic multilayered structures excited by an IDT: plane wave decomposition (spectral domain analysis, SDA) is used in homogeneous layers and finite-elements-method (FEM) is used in the electrode layer [2]. Periodic boundary conditions are applied. Frequency dependencies of the resulting BAW polarization in the substrate were retrieved and analyzed.

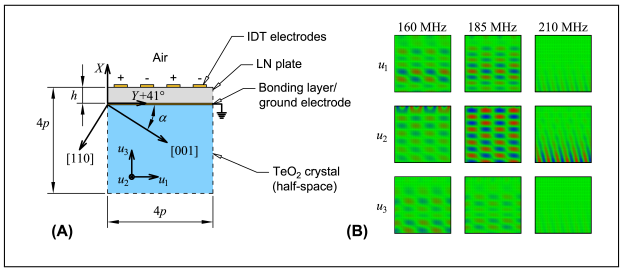


Figure 2. Numerical modelling of the piezoelectric transducer: (A) elementary cell for SDA-FEM-SDA modelling; (B) BAW structure (u_1, u_2 and u_3 mode amplitudes) at various frequencies.

3. RESULTS AND DISCUSSION

The transducer structure (Fig. 1) has several independent parameters, each of them affecting the performance and mode structure of the BAW fields in the substrate. In our simulations, the thickness and the fill factor of the IDT electrodes were fixed. The LN plate orientation corresponded to a standard homogeneous SH BAW transducer (see Fig. 2, A).

The TeO_2 substrate cut angle was $\alpha = 6°$ in $(1\bar{1}0)$ plane, which is a typical crystal orientation for acousto-optic deflectors and filters using slow SH BAW. The optimal IDT pitch $d = 58$ μm was derived from acousto-optic phase matching conditions for a broadband tunable filter design [1].

Admittance of the transducer was computed for different LN plate thickness values. With a fixed-pitch IDT, SH BAW excitation can be achieved in the relative bandwidth of $\sim 20\%$ at various central frequencies depending on the LN plate thickness h. At the boundaries of the excitation band, we observed transformation of the BAW mode from SH to longitudinal polarization. Simulated displacement maps are shown in Fig. 2 (B) for the IDT pitch of $2p = 58$ μm and LN thickness of $h = 5.6$ μm. The SH mode corresponds to u_2 component of the acoustic displacement vector. Owing to periodic IDT structure, the beam steering effect is observed for the excited BAW in TeO_2 that helps to extend the bandwidth of light-to-ultrasound coupling in photonic applications.

From the modelling results we concluded that the optimal LN thickness of h is much smaller than that for a homogeneous SH BAW transducer at the same resonance frequency. That proves a different mechanism of BAW excitation with an IDT: a plate mode is excited in the top layer of the substrate, which is converted into a non-homogeneous BAW mode owing to effective leakage to the low-velocity substrate.

4. CONCLUSIONS

Numerical modelling demonstrated that IDT-on-LN transducer structures are capable of effective excitation of SH BAW in TeO_2 crystal for acousto-optic applications. Resonance frequency can be adjusted by choosing a proper LN plate thickness h provided the IDT pitch d is fixed. Extension of the excitation bandwidth can be achieved using s stair-step LN plate with several segments corresponding to different resonance frequencies.

5. REFERENCES

[1] K.B. Yushkov, N.F. Naumenko, and V.Ya. Molchanov, "Design of a broadband acousto-optic filter using bulk acoustic wave beam steering with an interdigital transducer," *Results in Physics*, vol. 59, p. 107575, 2024.

[2] N.F. Naumenko, "Advanced numerical technique for analysis of surface and bulk acoustic waves in resonators using periodic metal gratings," *Journal of Applied Physics*, vol. 116, no. 10, p. 104503, 2014.

DOI: 10.61782/fa.2025.0933



FORUM ACUSTICUM
EURONOISE 2025

UNCERTAINTY RELATIONS FOR BROADBAND ULTRASONIC WAVEFORMS: THE CASE OF ACOUSTO-OPTIC FEMTOSECOND LASER PULSE SHAPING

Konstantin B. Yushkov[1*] **Vladimir Ya. Molchanov**[1]
[1] Acousto-Optical Research Center, University MISIS, 119049 Moscow, Russia

ABSTRACT

Broadband acoustic waveforms with phase modulation and complex-valued spectra are widely used for femtosecond laser pulse shaping in acousto-optic dispersive delay lines (AODDLs). Arbitrary transmission functions of quasi-collinear AODDLs can be achieved using the method of dispersive Fourier synthesis (DFS). Being a fast and efficient tool for generation different transmission functions with both phase-and-amplitude spectral modulation, the DFS method also provides the insight on fundamental limitations ultrasound signal performances. In particular, we demonstrate that there is an uncertainty relation between spectral resolution and modulation contrast for chirped ultrasonic waveforms with finite time window. More precisely, the product of spectral resolution by contrast is maximized when total frequency bandwidth equals twofold carrier frequency modulation range of the chirped ultrasonic signal. Experimental validation of the uncertainty principle is demonstrated with a high-resolution AODDL and 12 fs laser pulses at 800 nm. The applications of the DFS method with optimized parameters include programmable generation of arbitrary ultrashort pulse trains.

Keywords: *acousto-optics, femtosecond laser pulse, waveform synthesis, Fresnel transform*

***Corresponding author**: *konstantin.yushkov@misis.ru.*
Copyright: *©2025 K.B. Yushkov et al. This is an open-access article distributed under the terms of the Creative Commons Attribution 3.0 Unported License, which permits unrestricted use, distribution, and reproduction in any medium, provided the original author and source are credited.*

1. INTRODUCTION

Ultrasonic digital waveform synthesis has become a powerful tool for providing arbitrary transmission functions of acousto-optic tunable filters [1]. It enables creating the complex-valued transmission functions with predefined dispersion that is necessary for compression of ultrashort laser pulses [2]. Optimal parameters for synthesis of acoustic waveforms were investigated in this research.

2. ANALYSIS

To compute a chirped ultrasound waveform with given spectrum $S_{\mathrm{ac}}(\omega)$, we use the Fresnel transform:

$$S(t) = \mathrm{FT}_{(\omega,t)}\left\{S_{\mathrm{ac}}(\omega)\exp\left[iD_2(\omega-\omega_0)^2\right]\right\}, \quad (1)$$

where D_2 in the second order dispersion coefficient, and FT is the Fourier transform operator in (ω, t) domain. The resulting waveform duration T_{eff} is proportional to the frequency modulation band $\Delta\omega$:

$$T_{\mathrm{eff}} = D_2\Delta\omega. \quad (2)$$

A chirped waveform (1) can be decomposed as a sum of elementary signals each having a duration of τ. According to Gabor's uncertainty relation [3], the required bandwidth $\delta\omega$ is reciprocal to τ. Thus, we can define $\delta\omega = 4\pi\rho/\tau$, where the dimensionless parameter ρ that determines the signal contrast. Full bandwidth that is required for a chirped modulated signal is

$$B_\omega = \Delta\omega + 4\pi\rho/\tau, \quad (3)$$

the first term being the frequency modulation band.

The number of resolvable elements in the waveform defined as

$$N = T_{\mathrm{eff}}/\tau = D_2\Delta\omega/\tau. \quad (4)$$

Thus we can derive the information capacity of the chirped ultrasonic waveform as

$$N\rho = \frac{D_2}{4\pi}\Delta\omega(B_\omega - \Delta\omega) \le \frac{D_2\Delta\omega^2}{4\pi} \qquad (5)$$

The quantity $N\rho$ is maximized when $B_\omega = 2\Delta\omega$ that corresponds to the optimal signal bandwidth. This inequality represents the uncertainty principle for chirped pulses with arbitrary spectral modulation [4], which is illustrated in Fig. 1.

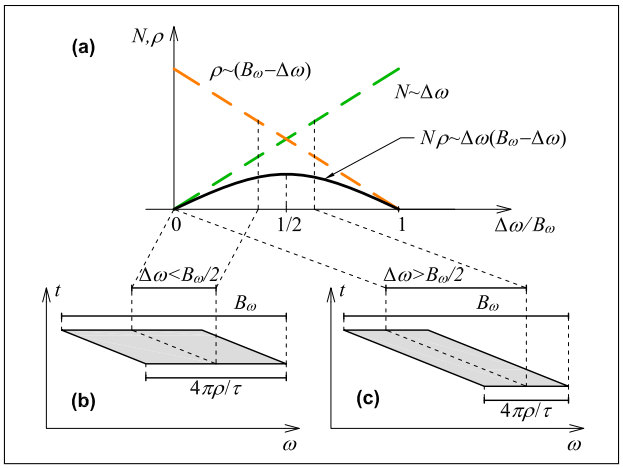


Figure 1. Graphical representation of the uncertainty relations for chirped pulses: (a) number of channels N and available channel bandwidth ρ; (b,c) spectrograms of a chirped pulse.

In the case of acousto-optic pulse shaping and synthesis of arbitrary transmission functions, the frequency modulation band $\Delta\omega$ is defined by the instantaneous bandwidth of processed light, and the full waveform duration is limited by the time aperture of the acousto-optic filter T_a. This allows one to find the optimal acoustic second order dispersion coefficient used in the Fresnel transform (1):

$$D_2 = T_\mathrm{a}/(4\Delta\omega). \qquad (6)$$

3. RESULTS AND DISCUSSION

The effect of optimal bandwidth selection was verified experimentally. The spectrum $S_\mathrm{ac}(\omega)$ was defined as a meander with the full width $\Delta\omega/2\pi = 20$ MHz and modulation period of 0.2 MHz; the waveforms were calculated with the signal's time aperture $T_\mathrm{a} = 50$ μs. The resulting spectra in Fig. 2 illustrate two cases: (a) in the case of minimum bandwidth $B_\omega = \Delta\omega$ the effective waveform duration is $T_\mathrm{eff} = T_\mathrm{a}$; (b) in the case of optimal bandwidth $B_\omega = 2\Delta\omega$ the effective waveform duration is $T_\mathrm{eff} = 0.5T_\mathrm{a}$, and 6 dB enhancement in modulation contrast is observed.

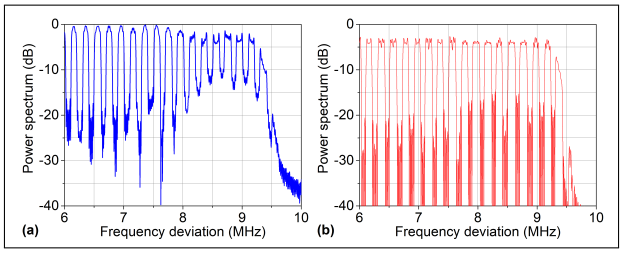


Figure 2. Numerical experiment on binary modulated chirped pulse spectrum: (a) minimal bandwidth $B_\omega = \Delta\omega$ causes contrast degradation near the window boundaries; (b) optimal bandwidth $B_\omega = 2\Delta\omega$ results in maximized contrast.

Similar contrast enhancement was obtained experimentally using broadband femtosecond laser radiation as a probe for arbitrary transmission function of a high-resolution quasi-collinear acousto-optic filter [4]. An original software package based on the Fresnel transform with optimized parameters was developed for controlling programmable acousto-optic filters [2].

4. REFERENCES

[1] V.Ya. Molchanov and K.B. Yushkov, "Advanced spectral processing of broadband light using acousto-optic devices with arbitrary transmission functions," *Optics Express*, vol. 22, no. 13, pp. 15668–15678, 2014.

[2] K.B. Yushkov *et al.*, "Dispersive Fourier Synthesis: Universal method and MATLAB tool for acousto-optic arbitrary femtosecond laser pulse shaping," *Optica Open*, p. 115346, 2024.

[3] D. Gabor, "Theory of communication. Part 1: The analysis of information," *Journal of the Institution of Electrical Engineers – Part III: Radio and Communication Engineering*, vol. 93, no. 26, pp. 429–441, 1946.

[4] K.B. Yushkov, V.Ya. Molchanov, and E.A. Khazanov, "Uncertainty relation in broadband laser pulse shaping," *Physics – Uspekhi*, vol. 64, no. 8, pp. 828–835, 2021.

DOI: 10.61782/fa.2025.0194



FORUM ACUSTICUM
EURONOISE 2025

CHARACTERIZATION OF OPTOELECTRONIC OSCILLATOR BASED ON COLLINEAR ACOUSTO-OPTIC CELL

Ekaterina Kostyleva[1*] **Sergey Mantsevich**[1] **Nataliya Polikarpova**[1]
Evgeniy Dyakonov[1]
[1] Department of Physics, M.V. Lomonosov Moscow State University, Russia

ABSTRACT

Optoelectronic oscillators (OEO) - the class of physical systems characterized by the presence of a nonlinear element and feedback loop (FL). Feedback allows controlling the nonlinear element operation and makes it possible to implement various OEO operating regimes - from stationary to chaotic. The presence of a FL time delay is fundamental. We present the results of OEO operation characterization, when the nonlinear element is the collinear acousto-optic (AO) filter. The AO filter provides the time delay existence due to the acoustic wave propagation time through the AO crystal. The fulfilled experiments have shown that the collinear AO filter OEO gives the possibility to adjust the time delay between input and output optical pulses by changing the FL gain. It was also found that changing the electrical signal phase shift in the FL allows OEO multistable states observation, characterized by a difference in the amplitude and frequency of the electrical signal in the FL and, accordingly, the intensity and structure of the light beam at the system optical output.

Keywords: *acousto-optics, feedback, time delay, collinear diffraction*

1. INTRODUCTION

This paper represents the results of the acousto-optic (AO) system with hybrid feedback the examination. The system is operating above the self-excitation threshold, we investigate the feedback loop (FL) parameters influence on its time characteristics and operation frequency.

The examined system is based on the collinear AO diffraction implemented with $CaMoO_4$ AO tunable filter (AOTF) [1]. The hybrid FL connects the AOTF optical output and its piezoelectric transducer [2–8].

The system may be attributed to the so-called optoelectronic oscillators (OEO) [9] - the class of optoelectronic systems that combine the nonlinear element with FL that controls the operating parameters of this nonlinear element. Here the role of a nonlinear element is assigned to the collinear AOTF [7, 8, 10, 11]. The FL is hybrid as it implements the conversion of the part of AOTF output optical signal into an electrical one and controls the parameters of the AO diffraction.

As the examined system operates above the self-excitation threshold, it does not require an external RF generator to arouse ultrasound in the AOTF, and can be treated as AO generator, providing both optical and RF output signals [12, 13].

It is known that the behavior of AO systems that include FL is extremely diverse as well as other OEOs architectures. Various types of oscillations may be observed in such systems, including harmonic, self-modulation, multistable and chaotic [4]. The multistable operation is characterized by the existence of several stable states differing in amplitude, frequency, and direction of diffracted light waves propagation [3, 6, 14].

It is shown that the FL gain variation allows to control the time delay between the optical seeding input optical pulse and the system output optical pulse. It is also shown that the FL time delay and phase shift variation allow one to manage the system operation frequency and,

*Corresponding author: kostyleva.ei16@physics.msu.ru.
Copyright: ©2025 Kostyleva et al. This is an open-access article distributed under the terms of the Creative Commons Attribution 3.0 Unported License, which permits unrestricted use, distribution, and reproduction in any medium, provided the original author and source are credited.

consequently, the output optical beam intensity and transmission function.

2. EXAMINED SYSTEM DESCRIPTION

The scheme of the examined AO OEO is shown in Fig.1. The collinear AOTF [1], placed between polarizers (α, β, γ), and providing 4 cm AO interaction length, is the main element. The FL operation is based on the AO heterodyning effect implemented with collinear AO diffraction optical radiation polarization peculiarities [15]. The interference between diffracted and non-diffracted optical beams after the output polarizer β makes it possible to obtain the optical radiation amplitude modulation with the frequency of ultrasound aroused in the AOTF for a certain mutual orientation of the input α and output β polarizers polarization planes [15] (α should be along Z or Y $CaMoO_4$ crystallographic planes and angle between α and β should be $45°$).

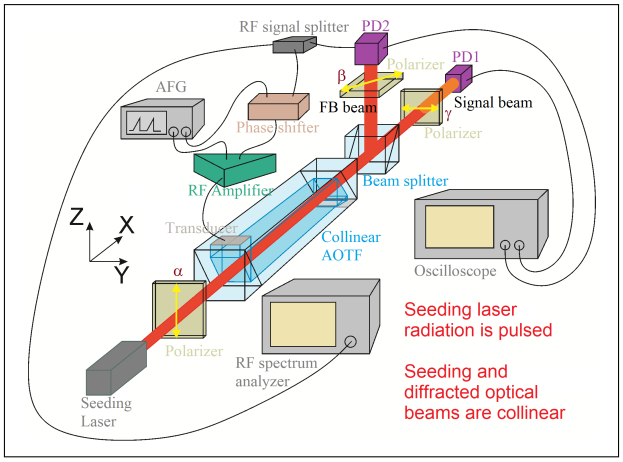


Figure 1. The examined AO OEO scheme.

The amplitude modulation is registered with the photodetector (PD2) that forms the FL input signal. The RF signal in the FL is amplified and phase shifted. Both amplifier gain and phase shifter operation are controlled by bias voltage fed from arbitrary function generator (AFG). The RF signal in FL is analyzed in time domain with a digital oscilloscope and in frequency domain - by the RF signal spectrum analyzer. The FL output feeds into the AOTF piezoelectric transducer.

The AO OEO optical output is organized as follows. The beam splitter is displaced at the AOTF output. It splits the output optical radiation (containing orthogonally polarized incident and diffracted light) into two beams - feedback beam and signal beam. The feedback beam passes through β polarizer and goes to PD2. The signal beam passes through γ polarizer with polarization plane orthogonal to α. This polarizer transmits only diffracted optical radiation. The signal beam intensity is registered by PD1 connected to the oscilloscope.

3. SYSTEM TIME DELAY DEFINITION

By the delay time τ_d we mean the time between the appearance of a laser pulse at the optical input of the system and the registration of diffracted optical pulse by the PD1. There is also another delay time characterized by the signal propagation time throughout the system τ_{fb}, including the FL and the propagation time of the acoustic wave along the entire length of the AOTF. Further, we will show that the τ_d delay time for high FL gain tends to the τ_{fb}.

Figure 2 represents the diffracted pulse intensity on time measurements obtained for FL gain μ values varying from 650 to 100 and optical seeding pulse with 1.3 ms duration.

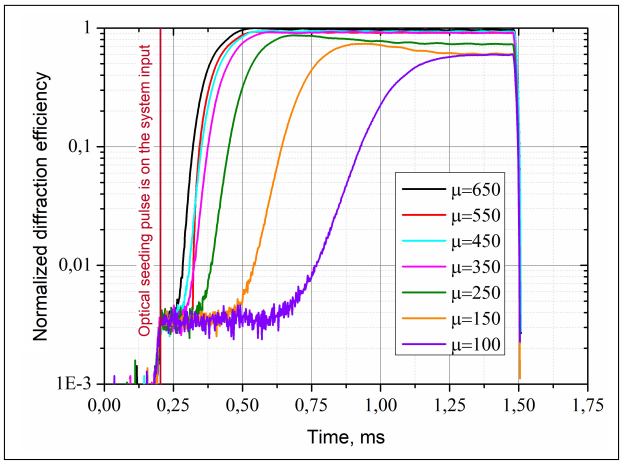


Figure 2. System response for 1.3 ms optical seeding pulse, observed for various FL gain μ magnitudes.

The analysis of the dependencies represented in Fig.2 allows to determine AO OEO time characteristics and follow the AO diffraction efficiency dependence on FL gain.

The obtained results show that the delay time τ_d depends on μ strongly. For the gain variation from 100 to 700, the τ_d decreases from 70 μs to 12 μs while the system time delay $\tau_{fb} \approx 14$ ms. The signal beam AO diffraction efficiency increases by 40%. The minimum τ_d value

is close to the acoustic wave propagation time along the entire AO cell, which seems to be a natural result.

Thus, we have shown that tuning the FL parameters allows one to vary the time characteristics of the examined system in a broad range.

Further we will show that FL phase shift variation, implemented by changing the phase shifter bias voltage, makes it possible to control the AO OEO operating frequency f and, consequently, the output signal beam intensity.

4. MULTISTABILITY OBSERVATION

Another feature of the examined system is the dependence of its operation on the phase shift χ introduced by the phase shifter. The χ magnitude is controlled by bias voltage fed from the AFG.

Figure 4 illustrates the dependence of the signal beam intensity I_s registered by PD1 on the AFG signal magnitude. It can be seen that the intensity (PD1 signal) variation has a rather complex shape. The reason for this is the dependence of the system operating frequency f on phase shift χ magnitude.

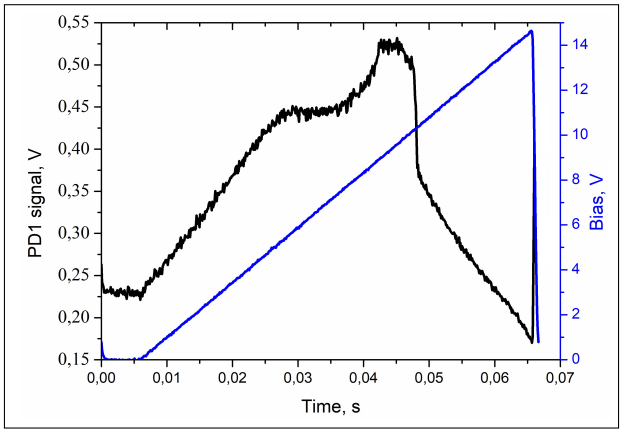


Figure 3. PD1 signal variation in time for varying phase shifter bias voltage.

To obtain the $I_s(\chi)$ dependence in explicit form, it is necessary to measure the χ dependence introduced by the phase shifter on the bias voltage for the AO OEO operating frequency (about 43.5 MHz). This dependence is shown in Fig.4a. It shows that the bias voltage variation from 0 to 15 V provides the χ/π variation from 0.2 to -0.9. It is interesting that the maximum absolute value is achieved for the bias voltage of about 12 V. Thus, the bias voltage variation may be limited by the range 0–12 V.

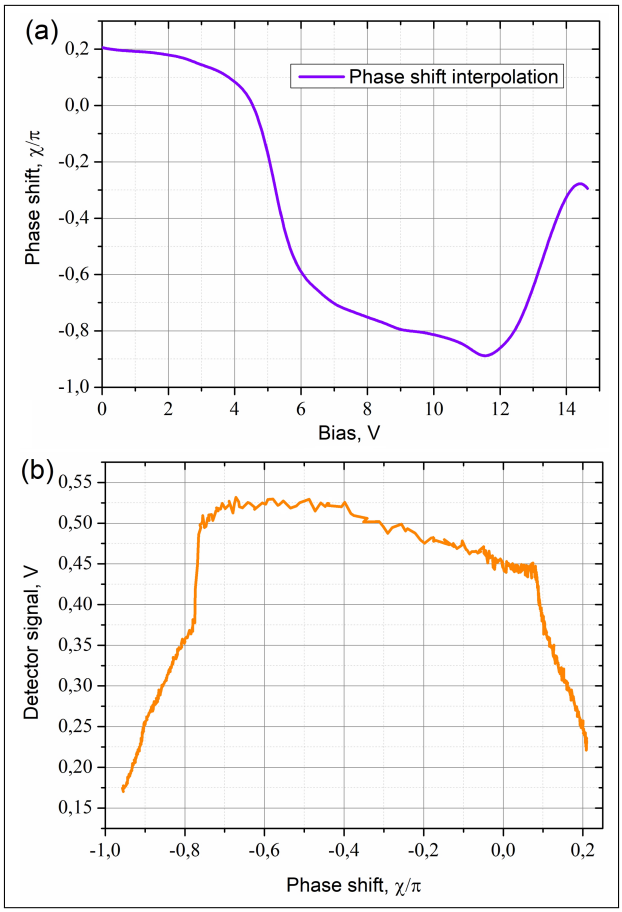


Figure 4. The dependence of normalized phase shift introduced by FL on bias voltage (a) and signal beam intensity dependence on the normalized phase shift magnitude (b).

Finally, the $I_s(\chi)$ dependence (in the form of PD1 signal magnitude) is shown in Fig.4b. It can be divided into three areas: 1 – signal growth between -0.95 and -0.75; 2 – a sharp leap and the second area where the signal beam intensity does not change much ($-0.75 < \chi/\pi < 0.1$); 3 – another leap follows and the third area is observed where the intensity drops significantly ($\chi/\pi > 0.1$).

The I_s variation is caused by the f tuning . Therefore, the leaps in intensity correspond to the frequency ones, and the slow intensity variation is caused by its smooth change.

The mechanism of f tuning with χ variation was considered previously [16]. It is based on the phase balance condition for the examined AO OEO, acting in conjunction with the amplitude balance condition - the frequency dependence of the system transmission coefficient (the feedback beam AO diffraction efficiency dependence on the ultrasound frequency).

The broadest band of f tuning may achieve 200 kHz, while the tuning band for the case shown in Fig. 4 is approximately 100 kHz.

5. CONCLUSION

We have examined the influence of FL parameters (introduced phase shift, time delay,gain) on the collinear AOTF OEO functioning.

The FL phase shift variation may cause a smooth change in the operating frequency and the output radiation intensity and the abrupt one. The operating frequency variation magnitude may exceed 200 kHz.

It was discovered that the FL gain variation allows one to control the AO OEO delay time. In the studied range of gain magnitudes, the delay time varies by about 6 times. It was found that the minimum delay time approximately equals the time required for an acoustic wave to propagate along the entire length of the AO cell.

6. ACKNOWLEDGMENTS

The work has been supported by the Russian Science Foundation (RSF), grant 23-12-00057.

7. REFERENCES

[1] S.E. Harris, S.T.K. Nieh, and R.S. Feigelson, "$CaMoO_4$ electronically tunable optical filter," *Appl. Phys. Lett.*, vol. 17, no. 5, pp. 223–225, 1970.

[2] J. Chrostowski and C. Delisle, "Bistable optical switching based on bragg diffraction," *Opt. Commun.*, vol. 41, no. 2, pp. 71–74, 1982.

[3] V.I. Balakshy, A.V. Kazaryan, V.Ya. Molchanov, and Hai Ming, "Bistable acousto-optic devices for optical information processing systems," *Proc. SPIE*, vol. 1731, pp. 303 – 312, 1992.

[4] M.R. Chatterjee and E. Sonmez, "Overview of acousto-optic bistability, chaos, and logical applications," *SPIE*, vol. 4514, pp. 41 – 60, 2001.

[5] V.I. Balakshy, Yu.I. Kuznetsov, and S.N. Mantsevich, "Effect of optoelectronic feedback on the characteristics of acousto-optical collinear filtering," *Quantum Electron.*, vol. 46, no. 2, pp. 181–184, 2016.

[6] V. Balakshy, Y. Kuznetsov, S. Mantsevich, and N. Polikarpova, "Dynamic processes in an acousto-optic laser beam intensity stabilization system," *Opt. Laser Technol.*, vol. 62, pp. 89 – 94, 2014.

[7] S.N. Mantsevich and V.I. Balakshy, "Experimental examination of frequency locking effect in acousto-optic system," *Appl. Phys. B*, vol. 124, no. 4, p. 54, 2018.

[8] S. Mantsevich, A. Voloshin, G. Slinkov, E. Kostyleva, and V. Balakshy, "Multiple-band frequency locking in an acousto-optic system with optoelectronic feedback," *J. Opt. Soc. Am. B*, vol. 37, no. 2, pp. 513–522, 2020.

[9] Y. K. Chembo, D. Brunner, M. Jacquot, and L. Larger, "Optoelectronic oscillators with time-delayed feedback," *Rev. Mod. Phys.*, vol. 91, p. 035006, 2019.

[10] S.N. Mantsevich and V.I. Balakshy, "Collinear acousto-optic filtration with electronically adjustable transmission function," *IEPJ*, vol. 11, no. 2, p. 7800315, 2019.

[11] S. Mantsevich, E. Kostyleva, V. Balakshy, and N. Polikarpova, "Collinear acousto-optic filtering of divergent optical beams in the presence of optoelectronic feedback," *Optics Communications*, vol. 552, p. 130114, 2024.

[12] V.I. Balakshy and I.M. Sinev, "Competition of modes in an optically heterodyned acoustooptic generator," *Quantum Electron.*, vol. 34, no. 3, pp. 277–282, 2004.

[13] S.N. Mantsevich and V.I. Balakshy, "Applications of frequency locking effect in acousto-optic systems for control of optical radiation composition," *J. Opt. Soc. Am. B*, vol. 36, no. 3, pp. 728–735, 2019.

[14] V.I. Balakshy and A.V. Kazaryan, "Laser beam direction stabilization by means of bragg diffraction," *Optical Engineering*, vol. 38, no. 7, pp. 1154 – 1159, 1999.

[15] V.I. Balakshy and S.N. Mantsevich, "Acousto-optic collinear diffraction of arbitrarily polarized light," *Tech. Phys.*, vol. 56, no. 11, pp. 1646–1651, 2011.

[16] S. Mantsevich, V. Balakshy, and E. Dyakonov, "Diffraction based optoelectronic oscillator," *SSRN Preprint*, p. 5163485, 2025.

DOI: 10.61782/fa.2025.0094

FORUM ACUSTICUM
EURONOISE 2025

ACOUSTO-OPTIC SPATIAL FREQUENCY FILTER WITH PHASE CONTROL FOR RECONFIGURABLE DARK OPTICAL TRAPS

Vladimir Ya. Molchanov[1]* **Alexander I. Chizhikov**[1] **Dmitry V. Obydennov**[1]
Konstantin B. Yushkov[1]
[1] Acousto-Optical Research Center, University MISIS, 119049 Moscow, Russia

ABSTRACT

We have developed an original acousto-optic spatial filter (AOSF) of laser beam angular frequencies for dynamically forming cylindrical laser beams with two walls advanced optical trap configurations. To expand the functionality of AOSFs, independent phase control should be added to frequency control, thereby transforming the filter's two-dimensional transfer function (2DTF) from a function of one variable into a function of two independent variables. The 2DTF is controlled by a variable phase of radio-frequency signal at a constant frequency. The peculiarity of the AOSF with phase control is based on the tilt of the acoustic wave front, which compensates for the asymmetry of the two-dimensional transfer function and makes it possible to create pairs of concentric intensity maxima separated by a dark region. An experimental AOSF on paratellurite has been designed and fabricated. This modification of the filter's annular 2DTF has made it possible for the first time to create double cylindrical beams ("thermos beams") that have direct application for optical trapping and microparticle manipulation. This configuration of the laser potential is in demand in dark optical traps, in which resonant particles are repulsed by the laser field and their trapping occurs in areas with minimum field intensity.

Keywords: *acousto-optics, laser beam shaping, optical trapping*

**Corresponding author*: v.ya.molchanov@gmail.com.
Copyright: ©2025 V.Ya. Molchanov et al. This is an open-access article distributed under the terms of the Creative Commons Attribution 3.0 Unported License, which permits unrestricted use, distribution, and reproduction in any medium, provided the original author and source are credited.

1. METHODS

Acousto-optic filters are tunable photonic devices based on anisotropic Bragg diffraction, which are used in spectroscopy, hyperspectral imaging, phase imaging, femtosecond pulse shaping, and laser beam shaping (LBS). The latter application utilizes angular dependence of phase matching, which enables direct filtering of the angular spectrum. Accurate analysis of the AOSF's two-dimensional transfer function can be performed using the curvature tensor of the acousto-optic crystal's refractive index surface [1].

In this work, we report design and fabrication of two AOSF prototypes and their commissioning in LBS systems and optical traps. The basic setup for bottle beam generation is shown in Fig. 1. A laser beam is focused onto the AOSF so that different components of its angular spectrum are diffracted with different efficiencies. The diffracted beam (p-polarization) is polarized orthogonally to the input one (s-polarization), and the first diffraction order is selected by a polarizer at the AOSF output. Relay optics is used for scaling the beam size, and the second Fourier lens converts a conical beam into a bottle beam in its back focal plane.

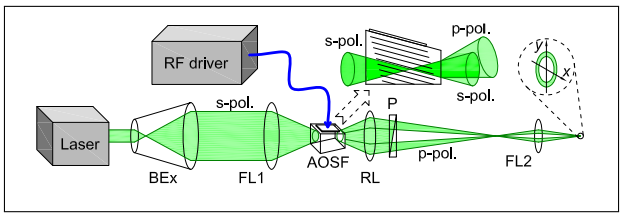


Figure 1. Schematic LBS setup based on an AOSF: BEx — beam expander; FL1, FL2 — Fourier lenses; RL – relay lens; P — polarizer.

The AOSF of configuration #1 was a single-transducer AOSF, which was driven by a radio-frequency (RF) arbitrary waveform generator either in single-frequency or in multi-frequency mode. This AOSF was commissioned with monochromatic radiation at the wavelength of 532 nm and femtosecond radiation at the wavelength near 800 nm. The AOSF of configuration #2 was a dual-transducer AOSF, which was driven by a two channel RF generator with programmable phase delay between the channels [2].

2. RESULTS

Various LBS modes are demonstrated in Fig. 2. Simple annular beam shaping is obtained with monochromatic light and single-frequency RF signal [3]. The phase matching locus is a ring whose radius changes with ultrasound frequency, Fig. 2 (a), that allows creating dynamic annular traps for dielectric particles. In the multi-frequency operation mode, different components of the laser beam's angular spectrum can be diffracted simultaneously with different efficiencies that enables beam profile tailoring. A flat-top beam obtained from a Gaussian beam is shown in Fig. 2 (b). In the case of multi-wavelength laser beam, each spectral component can be controlled independently. Fig. 2 (c) shows a two-color beam obtained from a femtosecond Ti:sapphire laser [4]. The central spot has the wavelength of 800 nm and the outer ring of the laser field has the wavelength of 790 nm.

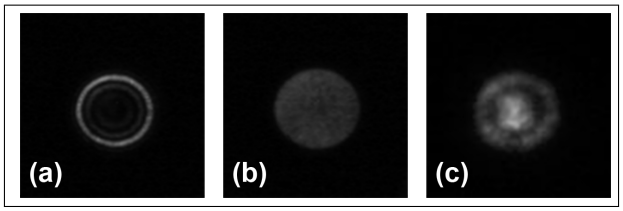


Figure 2. Experimental measurement of laser field distributions at the AOSF #1 output: (a) annular beam shaping of monochromatic light; (b) flat-top beam shaping at multifrequency AOSF operation; (c) multi-color femtosecond beam shaping by AOSF.

Figure 3 demonstrates operation of the phase-controlled AOSF #2 [2]. The RF signal in this case has two independent parameters, the frequency and the phase delay between two channels, which are both used to adjust the transfer function parameters. Owing to the effect of acoustic beam steering, splitting of the transfer function can be achieved. Two-dimensional transfer functions of this type can be used for creating dark optical traps, i.e. volumes with low laser beam intensity enclosed within volumes with higher intensity.

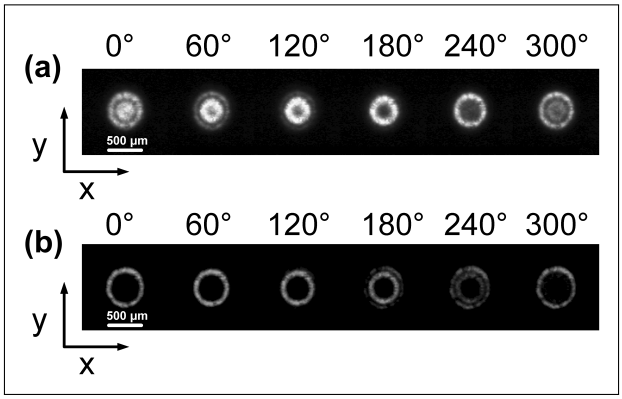


Figure 3. Tunable double-bottle-beam generation with the AOSF #2: (a) dark bottle beam mode; (b) thermos beam having dual cylindrical structure.

3. FUNDING

The research was supported by the Russian Science Foundation under project 20-12-00348.

4. REFERENCES

[1] K.B. Yushkov and N.F. Naumenko, "Optical beam diffraction tensor in birefringent crystals," *Journal of Optics*, vol. 23, no. 9, p. 095602, 2021.

[2] K.B. Yushkov, A.I. Chizhikov, D.V. Obydennov, and V.Ya. Molchanov, "Phase-tuned acousto-optic spatial filter," *Optics Letters*, vol. 49, no. 14, pp. 3866–3869, 2024.

[3] D.V. Obydennov, K.B. Yushkov, and V.Ya. Molchanov, "Ring-shaped optical trap based on acousto-optic tunable spatial filter," *Optics Letters*, vol. 46, no. 18, pp. 4494–4497, 2021.

[4] D.V. Obydennov, K.B. Yushkov, and V.Ya. Molchanov, "Independent multicolored bottle beam generation using acousto-optic spatial shaping of a femtosecond laser beam," *Optics Letters*, vol. 48, no. 20, pp. 5320–5323, 2023.

DOI: 10.61782/fa.2025.0845

FORUM ACUSTICUM EURONOISE 2025

TAILORED ULTRASOUND FIELDS FOR ACOUSTO-OPTIC LIGHT CONTROL DIRECTLY WITHIN A SAMPLE

Jordi Torres-Durall[1*] **Martí Duocastella**[1,2]
[1] Departament de Física Aplicada, Universitat de Barcelona, Spain
[2] Institut de Nanociència i Nanotecnologia (IN2UB), Barcelona, Spain

ABSTRACT

One of the main challenges in optics is to rapidly deflect, focus or guide light directly inside a sample. As of today, the only widely accepted method to achieve this is using endoscopes, that is, optical fibers that are inserted into the sample. However, this approach is intrinsically invasive and highly sample dependent. A recently developed strategy consists of using ultrasound for light control. The idea is to exploit the acousto-optic effect to generate virtual ultrasonic endoscopes, allowing fast and targeted deep light delivery while remaining non-invasive. Nonetheless, realistic applications of this technique still require further research on the optimal acoustic generation process and the subsequent light-coupling. Here, we discuss different hybrid ultrasound-light implementations designed for light control inside samples, highlighting optimal design features and current challenges. In particular, we present the development of a piezoelectric transducer that obviates the need for acoustic cavities and provides micrometric light guiding at MHz frequencies. We also show how ultrasound can be used to enhance imaging depth in a two-photon microscope.

Keywords: *acousto-optics, ultrasound transducer, remote scanning, scattering mitigation, two-photon microscopy*

1. INTRODUCTION

Light control technologies are a key tool for our society, enabling a wide range of medical and industrial applications such as confocal microscopy [1], optical topography [2] or laser surgery [3]. A paramount challenge in modern optics is to non-invasively extend current light-based techniques to deeper within scattering samples, such as biological tissue, as this would allow a paradigm change in light-based biomedical methods. One of the main ways to tackle this challenge is by controlling light directly within the samples.

Traditionally, light control within samples is achieved by inserting optical fibers [4] into the sample, as in traditional endoscopies [5]. Despite allowing operation at arbitrary depths, these methods are invasive and can produce relevant damage to the studied samples or tissues, and thus are not possible or not optimal for many applications. A promising non-invasive alternative is to generate acoustic lenses or waveguides within these samples [6], allowing fast light control while re-directing scattered photons to target locations. Previous studies show the applicability of this method to enhance a range of optical techniques. Despite these promising results, further research is still needed to circumvent geometrical constraints of current ultrasound generation implementations, and to prove the applicability of these methods in real world scenarios.

Here, we propose the use of acousto-optic scattering mitigation for Two-photon excitation fluorescence microscopy (TPEF). We also present the development of an ultrasound transducer geometry that allows the generation of an acoustic lens without the need of an acoustic cavity, circumventing a key restriction of most current implementations. We expect these advances to be a step forward in acousto-optic light control within samples and scattering-mitigation within biological tissues.

[*] ***Corresponding author***: jordi.torres.durall@ub.edu
Copyright: *©2025 Jordi Torres-Durall et al. This is an open-access article distributed under the terms of the Creative Commons Attribution 3.0 Unported License, which permits unrestricted use, distribution, and reproduction in any medium, provided the original author and source are credited.*

2. ACOUSTO-OPTIC DEEP LIGHT CONTROL

Light control within a sample is usually restricted by its absorption and scattering. While in deep light techniques light absorption is usually minimized by selecting a proper wavelength, scattering remains the main challenge that prevents controlling and focusing deep within samples. This scattering is caused by micrometric inhomogeneities within samples, that cause it to lose its initial phase and direction. Intensity I of not-scattered light (ballistic photons) within a sample can be expressed as: [7]

$$I = I_0(z)\cdot e^{-\mu z} = I_0(z)\cdot e^{-\tau}, \quad (1)$$

where $I_0(z)$ is the intensity expected in free propagation, z is the propagation distance within the sample and μ is the scattering coefficient of the sample. The total amount of scattering can be measured through the optical thickness τ, a dimensionless magnitude that can be interpreted as the average number of scattering events that photons have experienced to reach depth z.

The acousto-optic effect allows us to control light through pressure waves [8]. This is because a local change in pressure $\Delta P(\mathbf{r},t)$ leads to a local change in density, causing a local change in refractive index $\Delta n(\mathbf{r},t)$. For water-based materials, at pressure differences below 100 MPa, the acousto-optic effect can be expressed as: [9]

$$\Delta n(\mathbf{r},t) = C_{PO}\cdot \Delta P(\mathbf{r},t), \quad (2)$$

where C_{PO} is the piezo-optic constant of water, at room temperature $C_{PO} = 1.51\cdot 10^{-4}$ MPa^{-1}. This change in refractive index creates a change in light phase, allowing us to remotely focus or redirect light. Thus, exploiting this effect we can generate an acoustic lens within a sample, redirecting scattered photons to desired locations and thus enhancing light-based methods that require light to reach deep within scattering tissues or materials. Using this same principle, we can redirect light to focus it on target locations, allowing fast and dynamic light delivery within samples. [10]

3. ACOUSTIC CAVITIES FOR ACOUSTO-OPTIC SCATTERING MITIGATION

Recent advances in acousto-optics have described how to create acoustic lenses within samples, enabling scattering mitigation by redirecting scattered photons [11]. The usual method to create these acoustic lenses inside a sample is by placing the sample inside a cylindrical piezoelectric transducer, which acts as an acoustic cavity. Using this implementation, past work has shown applications in direct point-scanning imaging [6], light-pattern formation for imaging [12] and virtual waveguide creation for direct imaging [10].

Here, we propose that acousto-optic scattering mitigation can be used to enhance Two-photon excitation fluorescence microscopy (TPEF), synergically combining two state-of-the-art techniques for deep imaging within samples. In TPEF microscopy, the obtained image signal depends on the focal intensity squared. Thus, signal enhancement obtained using acousto-optic scattering mitigation becomes quadratically more relevant when combining it with TPEF microscopy. We exemplify this synergy in Fig. 1, using a waveguide generated with an acoustic cavity at 2.2 MHz frequency and 2 MPa peak pressure. Furthermore, TPEF microscopy usually relies on a near-infrared wavelength for excitation light, minimizing absorption and scattering in biological tissues and thus enhancing imaging depth.

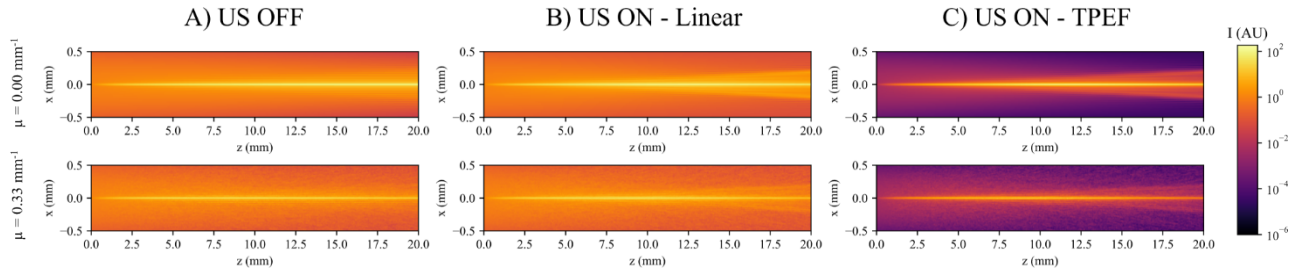


Figure 1. Signal intensity when using a Bessel Beam in different scenarios. (A) Simulated intensity of a Bessel beam, in a homogeneous or scattering medium. (B) Simulated intensity when using the same beam in conjunction with an ultrasound (US) waveguide within a cylindrical acoustic cavity. (C) Simulated intensity when using two photon excitation fluorescence microscopy (TPEF) combined with the same ultrasound waveguide, normalized to show the same peak intensity as (B). As TPEF signal depends on the intensity squared, ultrasound-induced intensity enhancements become quadratically more relevant in the proposed experiment. Note that thresholding effects have not been included in (C), despite potentially offering a substantial increase in resolution.

4. BEYOND ACOUSTIC CAVITIES

Despite generating an acoustic pressure profile optimal for light focusing and scattering mitigation, cylindrical piezoelectric transducers present the great disadvantage that the sample must be confined inside of them for direct deep light control. This means that big samples, including many relevant biological tissues, should be cut for the method to be applied, compromising the non-invasiveness of these techniques. Thus, this restriction often limits the applicability of these methods to phantom samples, far from real-world problems. For this reason, recent research is focusing on finding cavity-free ultrasound generation methods that allow direct deep light control. To this end, past studies have proposed using the photoacoustic-effect [13], two flat transducers [10], or acoustic holograms [14]. However, these implementations can be quite complex and often produce acoustic pressure profiles not optimal for direct light control within samples.

There are two main features that make the acoustic field generated by cylindrical transducers optimal for internal light control. First, it features highly focalized peak pressures, which maximize the change in refractive index. Second, it allows phase differences suffered by light to accumulate over the transducer's length, thus maximizing light focusing (see Fig. 2 A-C). In our recent research [15], we propose to use the angular section of a cylindrical transducer instead (see Fig. 2 D-E). This geometry maintains the key features needed for direct deep light control while allowing the generation of a cavity-free acoustic lens, obviating the need of confining the sample inside an acoustic cavity and thus expanding the applicability of acousto-optic lenses for direct light control within samples.

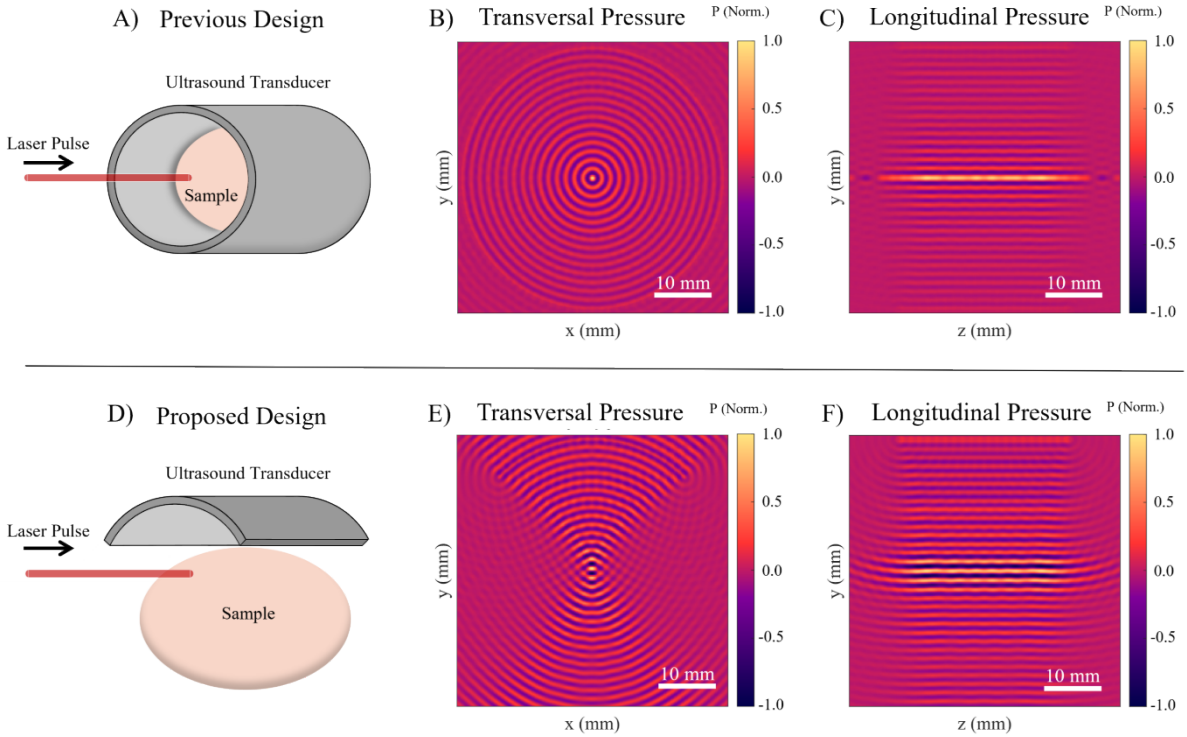


Figure 2. Comparison between acoustic field generation with a cylindrical piezoelectric transducer and our proposed geometry. (A) Scheme of a cylindrical transducer and corresponding simulated transversal (B) and longitudinal (C) normalized instantaneous pressure profiles at 1 MHz (transducer radius 23 mm). (D) Scheme of our proposed 90° cylindrical angular section transducer and simulated transversal (E) and longitudinal (F) instantaneous pressure profiles at 1 MHz. Our design is much less restrictive regarding sample geometry, while maintaining a highly intense elongated acoustic focus.

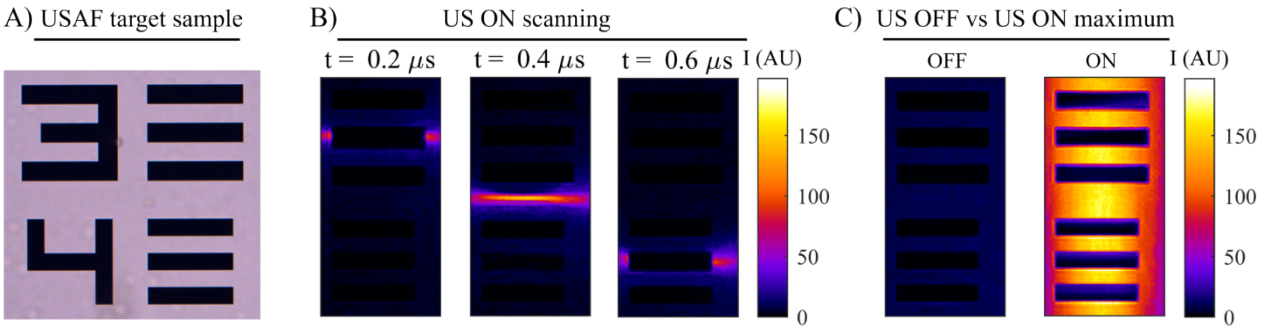


Figure 1. Fast light scanning using an ultrasound-induced lens. (A) Optical microscopy image of the USAF target elements imaged. (B) Captured image when ultrasound is applied, at different time delays between the ultrasound and the light pulse. (C) Maximum intensity detected at each pixel when scanning the light pulse across the whole sample.

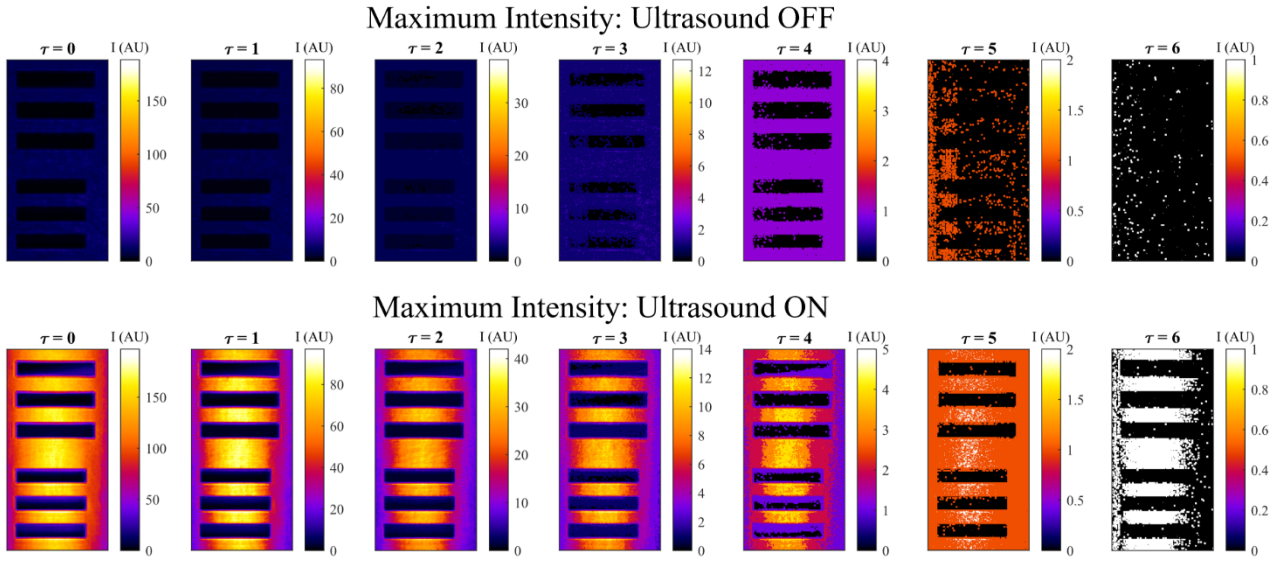


Figure 4. Maximum intensity detected at each pixel with and without ultrasound. We show the maximum intensity detected at each pixel in a 2000 frames video with and without scanning ultrasound. We can observe a huge increase in maximum intensity when using the ultrasound.

By using the proposed transducer geometry and a pulsed laser light source, a focal light line could be rapidly scanned through the sample, allowing fast targeted light delivery at MHz frequency rates over a millimetric region (See Fig. 3). By exploiting the stroboscopic effect, a sample was scanned for different scattering conditions, showing a factor 10 enhancement in light intensity when the ultrasound lens was used. Note that this allowed to reconstruct the sample structure even at scattering conditions where without the acoustic lens, only noise was detected (see Fig. 4). Furthermore, a single photon detector could be used to measure the transmitted intensity profiles, allowing to obtain a 1D profile of the 1.2 mm long sample in just 0.8 μs.

5. CONCLUSIONS

The acousto-optic effect can be used to control light directly within samples, enabling scattering mitigation for deep microscopy and fast light delivery to target locations. As our simulations demonstrate, the combination of Two-photon microscopy and acousto-optic scattering mitigation shows great potential for deep microscopy within scattering samples. Meanwhile, using a piezoelectric transducer consisting in the angular section of a cylinder allows to generate an acoustic profile substantially optimal for internal light control without the need of an acoustic cavity. The proposed geometry can remotely generate an acoustic lens that can be embedded inside a sample non-invasively, allowing targeted light delivery even in the case of large samples. We anticipate that these results will be a step towards non-invasive acousto-optic light control within a variety of materials, including biological tissues.

6. ACKNOWLEDGMENTS

The autors thank Dr. Mateu Colom, Dr. Pietro Ricci and Blanca Mestre-Torà for insights on the experimental implementation and computational simulations. Prof. Martí Duocastella acknowledges funding from the European Research Council (ERC) under the European Union's Horizon 2020 research and innovation programme (Grant Agreement No. 101002460). Prof. Martí Duocastella is a Serra Húnter professor. Jordi Torres-Durall is an FPU predoctoral researcher, with a contract funded by the Ministry of Science, Innovation and Universities of Spain.

7. REFERENCES

[1] M. Duocastella, G. Vicidomini, and A. Diaspro, "Simultaneous multiplane confocal microscopy using acoustic tunable lenses," *Opt Express*, vol. 22, no. 16, p. 19293, 2014.

[2] N. Vilar, R. Artigas, M. Duocastella, and G. Carles, "Fast topographic optical imaging using encoded search focal scan," *Nature Communications* 2024 15:1, vol. 15, no. 1, pp. 1–9, 2024.

[3] M. A. Kosoglu et al., "Fiberoptic microneedles: Novel optical diffusers for interstitial delivery of therapeutic light," *Lasers Surg Med*, vol. 43, no. 9, pp. 914–920, 2011.

[4] X. Yu, S. Zhang, N. Li, and M. Olivo, "Micro- and nano-fiber probes for optical sensing, imaging, and stimulation in biomedical applications," *Photonics Research*, Vol. 8, Issue 11, pp. 1703-1724, vol. 8, no. 11, pp. 1703–1724, 2020.

[5] V. Kučikas, M. P. Werner, T. Schmitz-Rode, F. Louradour, and M. A. M. J. van Zandvoort, "Two-Photon Endoscopy: State of the Art and Perspectives," *Mol Imaging Biol*, vol. 25, no. 1, pp. 3–17, 2023.

[6] B. Mestre-Torà and M. Duocastella, "Enhanced light focusing inside scattering media with shaped ultrasound," *Sci Rep*, vol. 13, no. 1, p. 11511, 2023.

[7] S. L. Jacques, "Optical properties of biological tissues: a review," Phys Med Biol, vol. 58, no. 11, p. R37, 2013.

[8] M. Duocastella, S. Surdo, A. Zunino, A. Diaspro, and P. Saggau, "Acousto-optic systems for advanced microscopy," *Journal of Physics: Photonics*, vol. 3, no. 1, p. 012004, 2021.

[9] M. Colom, P. Ricci, and M. Duocastella, "Rapid quantification of 3D ultrasound fields with wavefront sensing and Schlieren tomography," *Ultrasonics*, vol. 135, p. 107115, 2023.

[10] B. Mestre-Torà and M. Duocastella, "Parallelized Ultrasound-Guiding for Enhanced Light Delivery within Scattering Media," *ACS Photonics*, vol. 11, pp. 5161–5169, 2024.

[11] A. Pediredla, M. G. Scopelliti, S. Narasimhan, M. Chamanzar, and I. Gkioulekas, "Optimized virtual optical waveguides enhance light throughput in scattering media," *Nat Commun*, vol. 14, no. 1, 2023.

[12] M. Chamanzar et al., "Ultrasonic sculpting of virtual optical waveguides in tissue," *Nat Commun*, vol. 10, no. 1, p. 92, 2019.

[13] P. Ricci, M. Colom, B. Mestre-Torà, and M. Duocastella, "Photoacoustics for Direct Light-Guiding Inside Transparent and Scattering Media," *Laser Photon Rev*, p. 2401122, 2025.

[14] Q. Lin et al., "Acoustic hologram–induced virtual in vivo enhanced waveguide (AH-VIEW)," *Sci Adv*, vol. 10, no. 7, p. 2232, 2024.

[15] J. Torres-Durall and M. Duocastella, "Non-conventional ultrasound transducer geometry facilitates remote light control within samples," *Journal of Physics: Photonics*, vol. 7, no. 2, p. 025011, 2025.

DOI: 10.61782/fa.2025.0342

FORUM ACUSTICUM
EURONOISE 2025

ENHANCING EYE IMAGING MODALITIES WITH ACOUSTO-OPTIC INTERACTION

Ireneusz Grulkowski[1*] **Daniel Ruminski**[1]
[1] Institute of Physics, Faculty of Physics, Astronomy and Informatics, Nicolaus Copernicus University, Toruń, Poland

ABSTRACT

Optical imaging of the eye is a common clinical procedure in the diagnosis and management of the ocular disorders. Rapid advances in photonics technologies enabled development of optical modalities for diagnostics and management of ocular pathologies. Confocal Scanning Laser Ophthalmoscopy (cSLO) is a confocal microscope modality for visualization of the fundus of the eye. Optical coherence tomography (OCT) is a non-invasive imaging modality enabling generation of micrometer resolution, two-dimensional cross-sectional images and three-dimensional volumetric data presenting internal structure of ocular structures. Acousto-optic interaction facilitates ultrafast manipulation of the optical beam through precise shaping (modulation) of the wavefront. In particular, focus tunable lenses are active optical components that enable engineering of light delivery in optical imaging systems. Acousto-optic devices allow for enhancement of the performance of eye imaging instrumentation. Integration of acousto-optic lenses into OCT and cSLO systems enable improved in vivo imaging of the human eye.

Keywords: *acousto-optics, tunable focus, acousto-optic lens, imaging, ophthalmology, optical coherence tomography.*

[*] ***Corresponding author**: igrulkowski @fizyka.umk.pl*
***Copyright**: ©2025 I. Grulkowski et al. This is an open-access article distributed under the terms of the Creative Commons Attribution 3.0 Unported License, which permits unrestricted use, distribution, and reproduction in any medium, provided the original author and source are credited.*

1. INTRODUCTION

Acousto-optics is a branch of physics devoted to fundamental and applied studies of interaction of light with ultrasound. When an acoustic wave travels through an optically transparent material, periodic variations in the refractive index are generated—a phenomenon known as the photoelastic effect. This modulation appears as a dynamic diffraction grating, allowing the light to be modulated, deflected, or shifted in frequency depending on the acoustic signal. By leveraging the interaction between acoustic waves and light within a medium, acousto-optic devices such as modulators (AOMs), deflectors (AODs), tunable filters (AOTFs) and tunable lenses (AOLs) can dynamically alter the intensity, frequency, and direction of light beams in real time with high speed and precision [1]. Those components are currently widely used in imaging, telecommunications, spectroscopy, and laser systems. The advantages of acousto-optic technologies such as non-mechanical operation and rapid response times, make them especially valuable in modern optical and biomedical applications [2].

Eye imaging has become a standard procedure in modern ophthalmic diagnostics, offering visualization of ocular structures essential for early disease detection and monitoring. Advances of optical imaging modalities observed in last few decades provided tools for non-invasive and high-resolution assessment of subtle changes in tissue architecture and functionality, which are crucial for early diagnosis of the conditions like glaucoma, cataract, diabetic retinopathy, macular degeneration, and retinal vascular diseases.

As an important family of photonics industry, acousto-optic devices have been employed in ophthalmology related techniques, offering precise, high-speed control of light. Although we concentrate on imaging modalities, non-imaging applications of acousto-optics in ophthalmology

include also modulation of the intensity and duration of laser pulses, thus enabling precise targeting of ocular tissue during laser surgical procedures while minimizing damage to surrounding healthy structures.

2. ACOUSTO-OPTICS IN OPTICAL COHERENCE TOMOGRAPHY

Optical Coherence Tomography (OCT) is an interferometric modality that detects light that is back-scattered or back-reflected from the internal structures of the object. High-sensitivity and high axial resolution independent on numerical aperture of the objective lens enable OCT to generate cross-sectional or three-dimensional (volumetric) images of the semi-transparent objects such as ocular tissues. OCT has become an indispensable tool in ophthalmology, particularly for high-resolution imaging of the retina and the anterior segment. In recent years, the incorporation of acousto-optic (AO) technology into OCT systems has introduced substantial improvements in imaging speed, precision, and system adaptability.

One of the key contributions of acousto-optics to OCT is the implementation of acousto-optic deflectors (AODs). These devices allow for fast, inertialess beam steering by changing the frequency of the acoustic wave propagating through the crystal. In contrast to traditional mechanical scanning systems, AODs provide high-speed lateral beam scanning across the eye without moving parts. This non-mechanical approach significantly reduces motion artifacts through minimization of the examination time, which translates into improvement of patient comfort during imaging procedures [3].

Furthermore, acousto-optic tunable filters (AOTFs) are widely used in swept-source OCT systems, where rapid and precise wavelength selection is required in wavelength-tunable laser technology [4, 5]. AOTFs enable dynamic control over the central wavelength and bandwidth of the swept laser, facilitating fast tuning speeds (and high axial scan rates) essential for real-time imaging. Additionally, the flexibility of AOTFs supports advanced imaging techniques such as spectroscopic OCT, where wavelength-dependent tissue contrast can provide further diagnostic insights.

The integration of acousto-optic modulation also improves signal processing in OCT systems. For example, acousto-optic modulators (AOMs) can be employed for frequency shifting in interferometric detection schemes, helping to separate signal from noise and enhancing image contrast. This is particularly useful when the tissue is characterized by low scatter.

In addition, acousto-optics facilities enhancement of OCT image quality in terms of scan depth. Acousto-optic lenses enable fast focus tuning. When a series of OCT images is acquired at instances corresponding to different focusing depths, appropriate averaging of OCT scans results in effective extension of the depth of focus of scanning beam, which in turn improves signal in OCT image [6].

3. ACOUSTO-OPTICS IN CONFOCAL SCANNING LASER OPHTHALMOSCOPY

Confocal Scanning Laser Ophthalmoscopy (cSLO) constitutes another retinal imaging technique that enables high-resolution, real-time visualization of the retina and optic nerve head. Unlike traditional fundus photography, which captures a wide-field static image, cSLO uses a focused laser beam that scans across the retina. Like in confocal microscopy, a confocal pinhole is used to block out-of-focus light, allowing for sharp and high-contrast images of specific retinal layers. cSLO is widely used in ophthalmology for diagnosing and monitoring diseases such as glaucoma, macular degeneration, and diabetic retinopathy. Confocal SLO systems can be integrated with acousto-optic lenses to enable high-speed, inertialess axial scanning (z-scanning). Those approaches allow for rapid volumetric imaging of ocular structures.

4. CONCLUSIONS

Overall, acousto-optic technologies have contributed to the development of more compact, faster, and more stable OCT systems for ophthalmic applications. The advantages of acousto-optic devices allow for elimination of mechanical components, facilitate better image quality by high-speed scanning and support real-time visualization of ocular structures. As research advances, further integration of acousto-optic components is expected to enable even more powerful imaging systems.

5. REFERENCES

[1] K. Szulzycki, V. Savaryn, and I. Grulkowski, "Generation of dynamic Bessel beams and dynamic bottle beams using acousto-optic effect," Opt. Express **24**, 23977-23991 (2016).

[2] M. Jang, H. Ko, J. H. Hong, W. K. Lee, J.-S. Lee, and W. Choi, "Deep tissue space-gated microscopy via acousto-optic interaction," Nat. Commun. **11**, 710 (2020).

[3] M. Zurauskas, J. Rogers, and A. G. Podoleanu, "Simultaneous multiple-depths en-face optical coherence tomography using multiple signal excitation of acousto-optic deflectors," Opt. Express **21**, 1925-1936 (2013).
[4] Z. Hu, B. He, Y. Shi, C. Wang, Z. Chen, Z. Yin, X. Liu, X. Zhang, N. Zhang, L. Jing, G. Wang, and P. Xue, "High-speed k-linear swept laser using acousto-optic deflectors with Doppler shift compensation for optical coherence tomography," Opt. Lett. **49**, 101-104 (2024).
[5] T. Suzuki, Y. Kaneko, S. Choi, and O. Sasaki, "External-cavity laser diode using acousto-optic deflector as tunable grating," Opt. Lett. **47**, 1871-1874 (2022).
[6] I. Grulkowski, K. Szulzycki, and M. Wojtkowski, "Microscopic OCT imaging with focus extension by ultrahigh-speed acousto-optic tunable lens and stroboscopic illumination," Opt. Express **22**, 31746-31760 (2014).

DOI: 10.61782/fa.2025.0732

FORUM ACUSTICUM EURONOISE 2025

Recording neuronal activity in 3D using calcium and voltage genetically encoded indicators

Walther Akemann[1] **Joséphine Morizet**[1] **Laurent Bourdieu**[1*]
[1] IBENS, CNRS UMR 8197, INSERM U1024, Ecole Normale Supérieure, Paris.

ABSTRACT

We have developed a non-linear optical microscope for recording 3D neuronal activity in a cortical column, from awake head fixed behaving mice, with unrivalled temporal resolution. This new technique, called Custom-Address Serial Holography (CASH), uses acousto-optic deflectors (AODs) synchronized with a regenerative amplifier operating at 40 kHz. In this configuration, we have shown that the AODs function as ultrafast phase and amplitude modulators, enabling each laser pulse to be spatially shaped at 40kHz. Spatial modulation of laser pulses enables digital holography of extended volumes in the microscope's focal plane for fluorescence excitation. We will demonstrate the possibility of recording the activity of neurons labeled with Genetically Encoded Calcium Indicators (GECIs) such as GCaMP6f with holographic volumes covering their cell bodies. Using holographic volumes covering only cell membranes, we will demonstrate the possibility of using Genetically Encoded Voltage Indicators (GEVIs) to record the activity of 3D neuronal networks. By updating aberration and diffusion correction synchronously with the scanning, we have also performed trans-cranial imaging over fields of view that go beyond the scattering memory effect. Finally, we will discuss the implementation of temporal focusing to improve the optical sectioning of the 3D-CASH holographic microscope.

Keywords: *Two-photon microscopy; acousto-optic deflectors; random access scanning; Genetically Encoded Calcium and Voltage Indicators; holography; 3D scanning.*

[*] ***Corresponding author***: *laurent.bourdieu@ens.fr.*
Copyright: *©2025 Akemann et al. This is an open-access article distributed under the terms of the Creative Commons Attribution 3.0 Unported License, which permits unrestricted use, distribution, and reproduction in any medium, provided the original author and source are credited.*

1. INTRODUCTION

The brain is a complex 3D meshwork of circuits, neurons and micron-scale neuronal processes, which processes information in a distributed way within milliseconds. Understanding brain function therefore requires, ideally, to be able to record brain activity in 3D, at high spatial and temporal resolution. Optical methods, which allow to target neurons in a flexible and minimally-invasive way, offer bright promises and have considerably developed in the last decades. However, recording large numbers of neurons at millisecond temporal resolution, with micron-scale spatial resolution in depth and 3D access remains an unmet challenge.

Non-linear microscopy permits submicron resolution over a depth of a millimeter in the brain. However, because of the need to concentrate light spatially to achieve non-linear effects, it is fundamentally a sequential method, in which the signal arising from a single focal excitation volume (voxel) is collected at each time-point. This imparts a trade-off between the dwell-time (D_t) at each voxel, the number of voxels recorded (N_v) and the frame rate (R) of the recording ($R=1/N_vD_t$). The dwell-time itself determines the total number of photons collected by voxel (N_p) and thus the signal to noise ratio of the recording, at best $\sqrt{N_p}$ when reaching shot noise limit. The total number of photons per time unit is really what matters to discriminate a change in signal in a given object.

A solution to the signal/frame rate trade-off is to keep the dwell-time high but to reduce the number of apparent pixels. While a typical image contains from 250 to 1000 kilo-pixels, the number of identifiable neurons or neuronal parts in the field of view is generally 3 orders of magnitude lower, less than a thousand. Pointing each laser pulse only at one of these objects of interest and recording the signal produced would therefore constitute the optimal solution to record at both high temporal resolution and high signal levels. This "Random-Access" strategy cannot be implemented efficiently with mechanical scanning devices

such as mirrors, because their inertia imparts millisecond-scale switch times between random voxels in the field of view. A technique allowing fast addressing of cells of interest in 3D, with millisecond sampling rate is thus needed. This Random-Access technique should also be compatible with in vivo recordings in head-fixed animal, where brain motion due to breathing, heart beat and muscle contraction will prevent stable recording if not severely mitigated.

2. METHODS

Random-Access scanning has been pioneered in the late 90s by the team of Peter Saggau using Acousto-Optic Deflectors (AODs) [1]. In their standard application as angular deflectors, an AOD used in the Bragg mode efficiently deflects light into the first diffraction order at an angle θ given by :

$$\theta = \lambda.F/v \qquad \text{Eq. 1}$$

where λ is the wavelength of the light, F (~100MHz) the acoustic frequency and v (~650m/s) the velocity of the steady-state acoustic wave inside the crystal. An AOD is working at a central frequency F_0 over a bandwidth $+/-\Delta F/2$ (15 to 20 MHz). The maximum scan angle $\Delta\theta$ is given by $\Delta\theta = \lambda.\Delta F/v$ (~40mrad). The use of an AOD with femtosecond lasers having a broad spectrum $\delta\lambda$ (~10-15nm) raises however issues of temporal and spatial dispersion, that can be compensated at the center of the FOV using diffractive elements [2,3,4]. A crossed AOD pair allows then Random-Access sampling of the FOV at an unmatched speed. The time to establish an acoustic wave in an AOD is given by t_s=L/v, where L is the AOD active aperture. Using large AOD with 13mm aperture to achieve larger FOV give t_s= 20µs. As the dwell time $D_t \sim t_s$, sampling of up 50 000 objects per second (or 50 per ms) can be implemented.

AODs have initially been used as pure deflectors, where the same acoustic frequency occupies the whole profile of the laser beam and where all light is thus deflected to a given angle with a flat wavefront (Eq. 1). However, an AOD can also be used in a non-steady state mode, where it acts as single axis wavefront shapers. We have shown that an AOD that is filled with an ultrasonic pattern of frequency $f_{AOD}(x)$ and amplitude $a_{AOD}(x)$ at a position x in the AOD provides a complex spatial modulation consisting of an amplitude modulation $T(a_{AOD}(x))$, where T is the characteristic amplitude transfer function of the AOD, and a phase modulation $\varphi_{AOD}(x)$, which is related to the frequency modulation $f_{AOD}(x)$ [5]. This shows that an AOD is more than just a deflector, but is in fact a real beam shaping device, acting both as a simultaneous amplitude and phase modulator. Therefore tilt (2D scan) and defocus (3D scan) stands as straightforward applications, while more complex 2D beam spatial modulations can also be achieved and used e.g. in microscopy for digital holography applications.

However, this hides a major difficulty and subtlety. Indeed, a spatially-varying frequency pattern in the AOD cannot be established in a steady-state mode, as an ultrasonic wave is a propagating wave. As the repetition rate of standard lasers in non-linear microscopy (~100MHz) is 3 orders of magnitude larger than the refresh rate of an AOD (~100kHz), consecutive laser pulses interact thus each with different wave patterns in the AOD. To solve this issue, we proposed to use AODs in a "synchronous mode", where the laser pulses are synchronized with the AODs using a low-repetition rate laser, such that the propagating ultrasound pattern is somehow frozen [5]. In this mode, complex phase and amplitude patterns can be generated by the AODs. It includes defocus modulation to achieve fast 3D scans. It allows also to generate complex intensity patterns in the FOV using digital holography [6,7].

3. RESULTS

We have developed a non-linear optical microscope for recording 3D neuronal activity in a cortical column, from awake head fixed behaving mice, with unrivalled temporal resolution. It can indeed address typically 20 cells at 1 kHz or 200 cells at 100Hz. This new optical technique, called Custom-Address Serial Holography (CASH), uses acousto-optic deflectors (AODs) with a regenerative amplifier operating at 40 kHz in the synchronous mode described above. In this configuration, we took advantage of the fact that the AODs function as ultrafast phase and amplitude modulators, to spatially shaped at 40kHz each laser pulse. Spatial modulation of laser pulses enables 3D addressing of neurons but also synchronous digital holography of extended volumes in the microscope's image plane for fluorescence excitation. Whereas defocus modulation allows thus fast 3D scanning at kHz sampling rate, complex shaping of the microscope PSF by wavefront modulation provide 3 key features : 1) it allows to maximize the fluorescence signal by collecting it from an extended cell volume and preventing fluorescence saturation in a diffraction limited spot; 2) it minimizes accordingly photobleaching and photodamage; 3) it allows to minimize motion artifacts. We have generated a library of 2D patterns consisting of 2D arrays of diffraction limited spots or of short segments. To this aim, we have designed different algorithms to determine optimal phase only or complex

patterns in the AODs to achieve the desired intensity patterns in the microscope FOV. These patterns can be adapted to the recording type as e.g. the cell dimension or the amplitude of the motion artifacts that is e.g. larger at large imaging depth. They are also adapted to the cell labeling. In the case of Genetically Encoded Calcium Indicators (GECIs), 2D square arrays of spots were optimal, while 2 line of spots positioned next to the cells can be used to estimate the neuropil contamination. In the case of Genetically Encoded Voltage Indicators (GEVIs), patterns consisting of several small parallel segments positioned near the plasma membrane on each side of the cell were found optimal in terms of SNR and motion artifact mitigation.

3D-CASH recordings of GCaMP6f expressing neurons in layer 2/3 and 5 of mouse primary visual cortex in response to moving contrast gratings reveal the layered organization of the cortex, in the structure of the neuron pairwise correlation matrix. 3D-CASH provides also the possibility of using Genetically Encoded Voltage Indicators (GEVIs) to record the activity of 3D neuronal networks at millisecond timescale, taking advantage of the most recent GEVIs optimized for spike detection. 3D-CASH also allows performing trans-cranial imaging over fields of view that go beyond the scattering memory effect by updating aberration and diffusion correction synchronously with the scanning, Finally, 3D-CASH is limited currently to samples sparsely labeled due to the reduced optical sectioning associated to the holographic illumination, an effect that we aim at reducing by implementing temporal focusing.

4. ACKNOWLEDGMENTS

Funding was provided by NIH BRAIN Initiative (1U01NS133971-01), program Investissements d'Avenir, Memolife (ANR-10-LABX-54), Université PSL (ANR-11-IDEX-0001-02), and France Bioimaging Infrastructure (ANR-10-INSB-04-01).

5. REFERENCES

[1] Duemani Reddy, G., Kelleher, K., Fink, R., and Saggau, P. (2008). Three-dimensional random access multiphoton microscopy for functional imaging of neuronal activity. *Nature neuroscience*, *11*(6), 713–720.

[2] Iyer, V., Losavio, B. E., and Saggau, P. (2003). Compensation of spatial and temporal dispersion for acousto-optic multiphoton laser-scanning microscopy. *Journal of biomedical optics*, *8*(3), 460–471.

[3] Salomé, R., Kremer, Y., Dieudonné, S., Léger, J. F., Krichevsky, O., Wyart, C., Chatenay, D., and Bourdieu, L. (2006). Ultrafast random-access scanning in two-photon microscopy using acousto-optic deflectors. *Journal of neuroscience methods*, *154*(1-2), 161–174.

[4] Kremer, Y., Léger, J. F., Lapole, R., Honnorat, N., Candela, Y., Dieudonné, S., and Bourdieu, L. (2008). A spatio-temporally compensated acousto-optic scanner for two-photon microscopy providing large field of view. *Optics express*, *16*(14), 10066–10076.

[5] Akemann, W., Léger, J. F., Ventalon, C., Mathieu, B., Dieudonné, S., and Bourdieu, L. (2015). Fast spatial beam shaping by acousto-optic diffraction for 3D non-linear microscopy. *Optics express*, *23*(22), 28191–28205.

[6] Akemann, W., Wolf, S., Villette, V., Mathieu, B., Tangara, A., Fodor, J., Ventalon, C., Léger, J. F., Dieudonné, S., and Bourdieu, L. (2022). Fast optical recording of neuronal activity by three-dimensional custom-access serial holography. *Nature methods* *19*(1), 100–110.

[7] Akemann, W., and Bourdieu, L. (2024). Acousto-optic holography for pseudo-two-dimensional dynamic light patterning. *APL photonics*, *9*(4), 046103.

[8] Blochet, B., Akemann, W., Gigan, S., and Bourdieu, L. (2023). Fast wavefront shaping for two-photon brain imaging with multipatch correction. *Proceedings of the National Academy of Sciences of the United States of America*, *120*(51), e2305593120.

DOI: 10.61782/fa.2025.0274



FORUM ACUSTICUM
EURONOISE 2025

DESIGN AND VALIDATION OF AN ACOUSTO-OPTIC TUNABLE FILTER FOR SPECTRO-POLARIMETRY ANALYSIS

Samuel Dupont[1*] **Jurgen Vanhamel**[2,3] **Jean-Claude Kastelik** [1]
[1] Université Polytechnique Hauts-de-France (UPHF), IEMN – Campus Mont Houy – Cedex 9, 59313 Valenciennes, France
[2] TU Delft - Faculty of Aerospace Engineering, Kluyverweg 1, 2629 HS Delft, The Netherlands
[3] Electronic Circuits and Systems, KU Leuven, Kleinhoefstraat 4, 2440 Geel, Belgium

ABSTRACT

Acousto-Optic Tunable Filters (AOTF) are versatile devices with a range of applications in modern optics. Their technology has reached a mature industrialability. They are particularly valuable in fields requiring precise wavelength selection and fast switching capabilities, making them essential tools in various applications. The generalisation of their use has led to new applications still requiring specific developments.
We present the design and validation of an AOTF for spectro-polarimetry analysis which provides a constant spectral resolution over a wide spectral band. The variation of the spectral resolution is made possible by the manufacture of a transducer divided into multiple electrodes allowing to play on the interaction length easily by activating and deactivating the electrodes. In addition, the power distribution supplying the electrodes can be modulated, which offers the possibility of finely controlling the spectral template.
The device developed has an acoustic cut of 5°, operating from 450 to 800 nm. We opted for a transducer equipped with 5 electrodes. This strategy makes it possible, depending on the power supply conditions, to modulate the selectivity of the filter by a factor of 4 for a given wavelength and to maintain a constant selectivity of the order of 10 nm over the entire operating range.

Keywords: *AOTF, multi-electrodes, spectro-polarimetry.*

1. INTRODUCTION

Optical filters are essential components in various applications, including telecommunications, sensing, imaging, and spectroscopy [1]. Among these technologies, AOTF have emerged as an useful tool, allowing for precise control over the spectral characteristics of light [2]. Those devices have attracted a great interest, for example, the use of AOTF in imaging applications is under constant development [3-7].
Like all acousto-optic components, the design of the filters is subject to compromise depending on the intended use. For example, some applications require a large angular aperture, others require a large spectral band, while others require large rejection. The optical spectral filter function of an AOTF is a cardinal sine: it has a main lobe and adjacent secondary lobes. The side lobes reduce the performance of the filters by creating diaphony. This is a secondary aspect when filtering monochromatic signals, but it becomes an issue when we are in the presence of a wide spectral band signal. In this case, when tuning the filter for a given wavelength, it is possible to achieve a diffraction efficiency for a neighboring wavelength of up to 10%. In imaging, these secondary lobes are unwanted because they make the image blurry [6]. It is then necessary to reduce the adjacent lobes by implementing an apodization technique. Also, emerging applications drive advancements developments in spectro-polarimetry optical technologies. Spectro-polarimetry combines spectral and polarization information and becomes essential for various scientific fields, including materials science, biology, and remote sensing. The ability to tune the

[*] ***Corresponding author***: Samuel.dupont@uphf.fr
Copyright: *©2025 Samuel Dupont et al. This is an open-access article distributed under the terms of the Creative Commons Attribution 3.0 Unported License, which permits unrestricted use, distribution, and reproduction in any medium, provided the original author and source are credited.*

filter dynamically, as offered by acousto-optic technologies, enhances the versatility and efficiency of spectro-polarimetric measurements, allowing for real-time analysis of complex samples.
This study centers on the development of an apodised AOTF specifically tailored for spectro-polarimetry applications. We present the development of the AOTF, detailing the operational principle, the design parameters and the experimental validation.

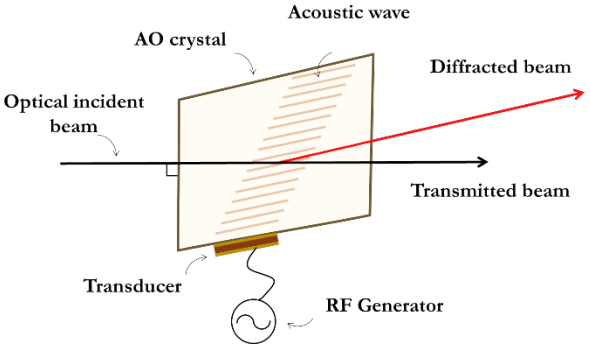


Figure 1. AOTF cell schematic view.

2. AOTF DESIGN

AOTFs are compact and efficient devices able to filter specific optical wavelengths with precision by the application of an appropriate Radio-Frequency (RF) signal that is tuned to satisfy the Bragg matching conditions for diffraction. In order to operate the AOTF, a piezoelectric transducer is mounted onto the side of a photoelastic crystal, such as in our case Tellurium Dioxide (TeO_2), figure 1. This transducer operates by converting RF signals into corresponding sound waves. By applying the appropriate frequency and power level to the transducer, the Bragg matching condition can be successfully satisfied: two first-order diffracted light beams are then separated at the output of the crystal for light with a precisely defined optical wavelength.

2.1 Bragg diffraction

Under Bragg phase matching conditions, the incident and diffracted optical wave vectors (k_i, k_d) and the acoustic wavevector (K) satisfy the exact momentum conservation:

$$\overrightarrow{k_d} = \vec{K} + \overrightarrow{k_i} \quad (1)$$

When the conditions exit the exact conditions (figure 2), a phase mismatch appears, it corresponds to a momentum offset Δk_d:

$$\overrightarrow{k_d} = \vec{K} + \overrightarrow{k_i} + \overrightarrow{\Delta k_d} \quad (2)$$

The study of these conditions allows to obtain information on the angles (incident and diffracted), the wavelength and the acoustic frequency of the interaction, since these parameters are related. With $\Delta\Phi = \Delta k_d . W_{eff}$ the phase mismatch and W_{eff} the effective interaction length that is given by:

$$W_{eff} = \frac{W\cos(\psi)}{\cos(\psi - \theta_i + \theta_a)} \quad (3)$$

Phase mismatch can come from several parameters: a variation in the wavelength $\Delta\lambda$ (spectral bandwidth); a variation in frequency Δf (frequency bandwidth); a variation of the incident angle (angular acceptance): $\Delta\theta$.

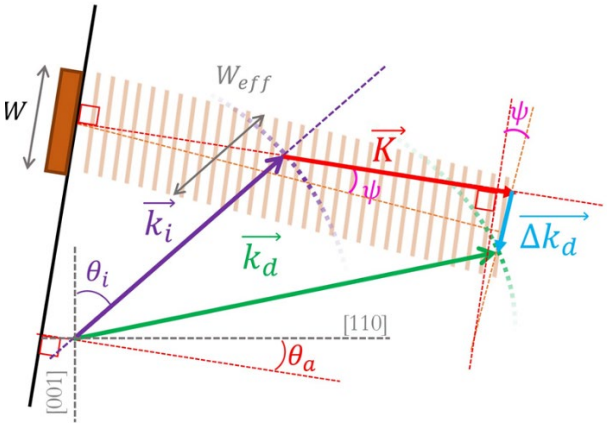


Figure 2. Wave vector diagram.

2.2 AOTF diffraction efficiency

The diffraction efficiency η of an acousto-optic component is expressed by:

$$\eta = \frac{P}{P_0}\frac{\sin^2\left(\frac{\pi}{2}\sqrt{\frac{P}{P_0}+\left(\frac{\Delta\Phi}{\pi}\right)^2}\right)}{\frac{P}{P_0}+\left(\frac{\Delta\Phi}{\pi}\right)^2} \quad (4)$$

The efficiency depends on the sound power P and the phase mismatch $\Delta\Phi$. As we are talking about a filter here, we are interested in the impact of the parameters on the filter optical spectral characteristics.
The analysis of the evolution of the diffraction efficiency as a function of wavelength, angle of incidence or acoustic frequency makes it possible to determine, respectively: an optical (or spectral), angular or acoustic bandwidth (Figure 3). The secondary lobes that characterize the rise in diffraction efficiency on either side of the main lobe can be determined in each of these cases.

An example of the typical diffraction efficiency evolution is shown in Fig. 3.

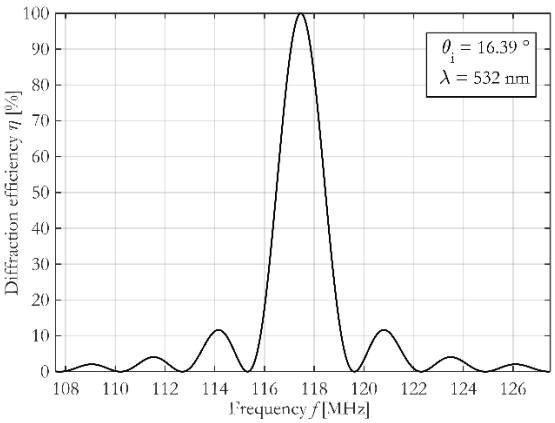


Figure 3. AOTF diffraction efficiency as a function of acoustic frequency.

The diffraction efficiency curves have a recognizable profile: a main lobe and side lobes for representation as a function of acoustic frequency or optical wavelength.
By exploiting the vector relation, it is possible to determine the expression of the acoustic frequency. If the interaction is from ordinary to extraordinary mode, it is expressed by [3]:

$$f_S = \frac{V}{\lambda}\sigma\left(n_i(\theta_i)\sin(\theta_i - \theta_a) - \sqrt{{n_d}^2(\theta_d) - {n_i}^2(\theta_i)\cos^2(\theta_i - \theta_a)}\right) \quad (5)$$

The frequency equation is a function of the parameters of the component and the interaction configuration: angle of incidence θ_i, acoustic cut θ_a, optical wavelength λ, acoustic velocity V, refractive indices ${n_i}^2$ and ${n_d}^2$.

It can be seen in Figure 4, which shows the different acoustic frequencies for extraordinary to ordinary (e-o) and ordinary to extraordinary (o-e) cases as a function of the angle of incidence, that the interaction frequency has some interesting particularities:
-It increases non-linearly if the wavelength decreases; -the two curves intercept.
-There is an incident angle for each frequency curve for which the variation around that angle does not cause a large frequency variation. This angle is the angle necessary to be in a particular case: the case of parallel tangents.
-The curves representing the two modes of interaction intersect at a single point, this is the point of the double interaction, where 100% of the polarizations are diffracted.
Also, it should be noted that the coordinate of the double interaction increases if the acoustic cut increases.

2.3 Apodisation of AOTF transfer function

Figure 3 clearly demonstrates that secondary lobes can be a limiting factor when monochromaticity of the filter is required. This is particularly relevant in the field of spectral imaging [6]. An interesting technic consists in the fabrication of a phased array transducer to control the acousto-optic transfer function [8, 9].
The principle of apodization in AOTFs with arrayed transducers involves the shaping of the acoustic wave's amplitude distribution to influence the diffraction pattern of light. By feeding the array transducer with a Gaussian power distribution, the acoustic wave's intensity generated tapers off gradually towards the edges, reducing abrupt transitions that cause side lobes in the optical output. Indeed, the acoustic wave generates the modulation of the refractive index of the medium, which acts as a diffraction grating for the incident light. The Gaussian power distribution across the transducers ensures that the acoustic wave's amplitude decreases symmetrically from the centre to the edges, so does the diffraction grating strength, minimizing the side lobes in the resulting optical transmission function.
There is of course a tradeoff between system complexity and the achievable filtering characteristics: using a large number of elements allows for a finely tuned filter transfer function with significant side lobe reduction, but it requires a more complex radiofrequency generator capable of producing as many radiofrequency tones as there are elements. We have established that even three elements can enhance the filtering characteristics of an AOTF [10]. To further improve these characteristics while keeping system complexity at an acceptable level, we have developed a device with five transducer elements.
The 5 electrodes can be activated independently, which allows the interaction length W_{eff} to be varied and therefore the optical spectral resolution $\Delta\lambda$ to be varied. This also allows for an apodization functionality.
To design the filter, it is useful to understand how the spectral and frequency bandwidths vary with different parameters. These variations depend on the acoustic cut, which is the first element we examine.

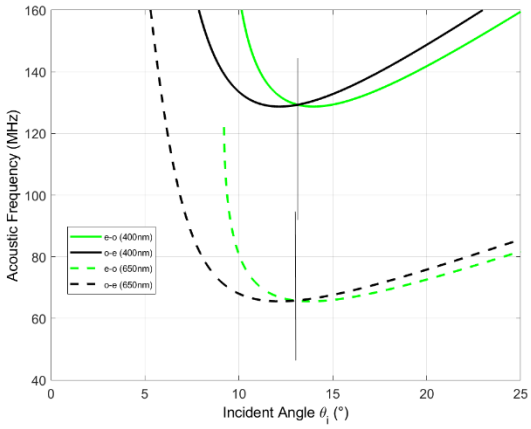


Figure 4. Evolution of the acoustic frequency at synchronism as a function of incident angle (acoustic cut considered for illustration: 6°).

3. DESIGN OF THE AOTF

Here, we present the design considerations for an AOTF operating in the visible light range, hence targeting an operational bandwidth from 400 nm to 900 nm at the design stage. Due to its high efficiency, paratellurite is chosen as the acousto-optic material.

3.1 Analysis of AOTF parameters

Figure 5 shows the variation of acoustic frequency across the reference spectral band for several acoustic cuts ranging from 3° to 9°. It can be observed that the frequency decreases as the wavelength increases, and this effect becomes more pronounced with larger acoustic cuts. High acoustic cuts necessitate higher radiofrequency operation, while low acoustic cuts are known to be more susceptible to unwanted gyrotropy effects [11].

Spectral resolution is a key criterion when selecting the acoustic cut for an AOTF. Figure 6 illustrates how spectral resolution varies with wavelength for several acoustic cut angles, assuming an effective acoustic column width of 7 mm. As can be seen, higher acoustic cuts result in lower spectral resolution. Moreover, a strong variation in spectral resolution is observed for small acoustic cuts; therefore, cuts of 4° or less were excluded, as they correspond to filters with optical resolution profiles that can reach up to 35 nm. However, a filter that would be too selective would result in low diffracted power. Hence, the higher cuts are neither favorable.

We have selected a 5° acoustic cut, which is sufficient to prevent gyrotropy effects while keeping the radiofrequency range confined within a single octave for a practical operation range from 450 nm to 800 nm and offer acceptable spectral resolution.

Then the choice of the number and the width of the electrodes should be considered. We first consider a single electrode of width comprised between 2 to 11 mm. Figure 7 illustrates the variation of spectral resolution with wavelength for various transducer lengths W. It can be observed that this electrode width enable a spectral resolution of approximately 10 nm across the entire operating band, with operation ranging from a 2 mm electrode at 450 nm to an 11 mm electrode at 800 nm. Since the number of electrodes is limited to five to enable spectral tunability while keeping system complexity at an acceptable level, we selected a central electrode larger than the others: 3 mm compared to 2 mm for the rest. This configuration allows, by activating adjacent electrodes, the formation of total transducer lengths of 2, 3, 4, 5, 7, 9, and 11 mm. By selecting, for example, only the 3 to 11 mm configurations, the spectral resolution varies by just a few nanometers across the entire optical band, ranging from approximately 8 to 11 nm, resulting in a variation factor of only 1.4 between the highest and lowest wavelengths.

Finally, considering the double operation point, an incident angle of 10.83° is required. A picture of the device is shown figure 8 and the parameters are summarized in table 1.

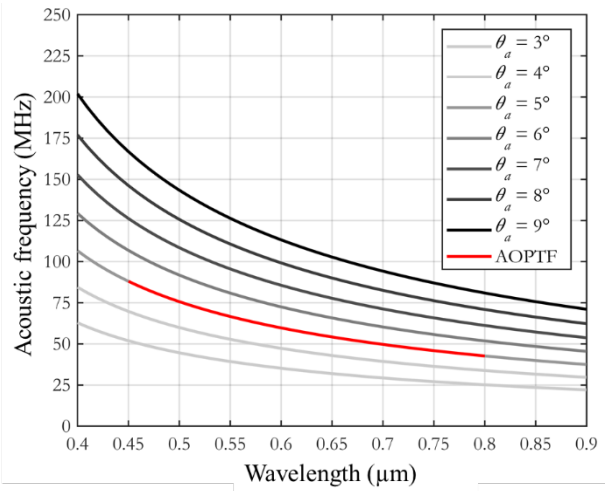


Figure 5. Evolution of acoustic Bragg frequency as a function of wavelength for acoustic cuts from 3° to 9°.

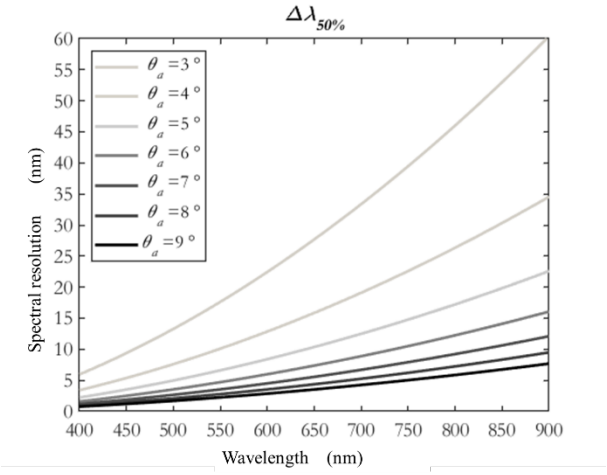


Figure 6. Evolution of AOTF spectral resolution as a function of wavelength for different acoustic cuts.

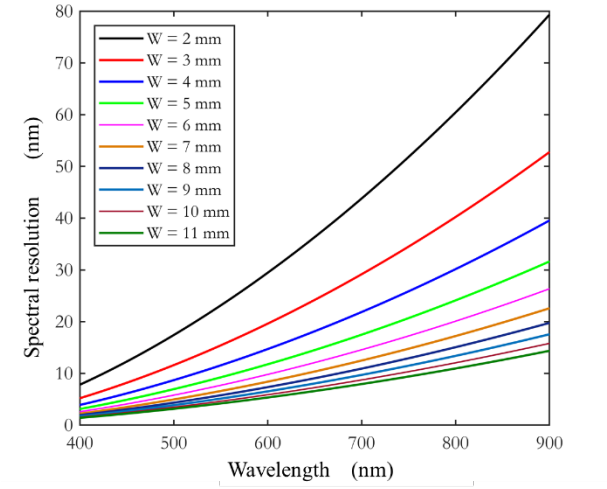


Figure 7. Evolution of spectral resolution for various transducer length.

Table 1. AOTF parameters.

Variable	Value	Unit
Acoustic cut θ_a	5	Degrees
Incident angle θ_i	10.83	Degrees
Transducer length	2 to 11	mm
Transducer number	5	

3.2 AOTF experimental validation

An experimental characterization of the AOTF was performed using the 514 nm line from an argon-ion laser. The same RF signal is coupled to all electrodes. Note that a phase shifter is introduced on the central electrode to compensate for its different behavior, due to its wider width compared to the other transducers. The AOTF's transfer function was estimated by scanning the RF signal across the Bragg frequency, a method known to approximate the optical transfer function shape. Figure 9 shows the relative efficiency of the AOTF for electrode widths ranging from 3 to 11 mm. As expected, a longer grating results in a reduced spectral bandwidth.
The apodization capability was then tested using a 5-channel RF generator developed in house, and an illustration of the apodized filter response is shown in Figure 10.

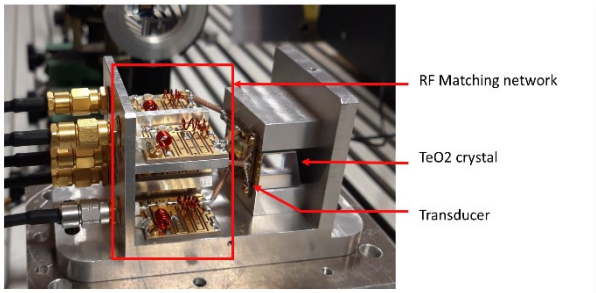


Figure 8. View of the AOTF.

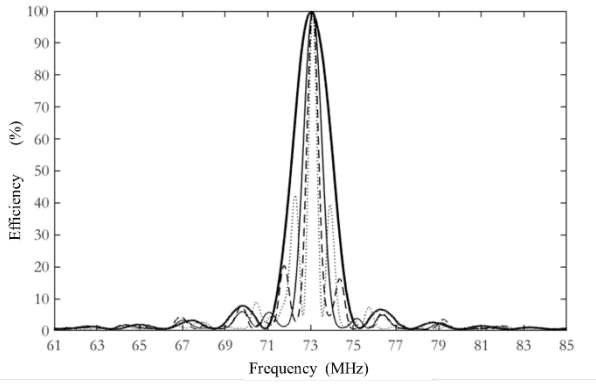


Figure 9. AOTF relative efficiency measured at 514 nm as a function of rf frequency for transducer width activated from 3 to 11 mm.

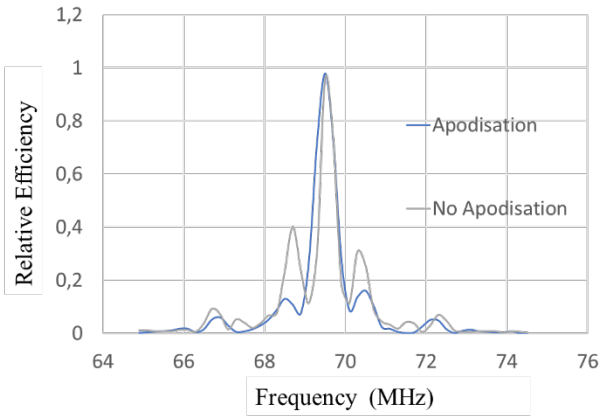


Figure 10. Test of apodisation capability at 532 nm.

During the apodization test, the power distribution across the five electrodes follows a Gaussian-like pattern, while the relative phase between the electrodes is adjusted to compensate for differences between the channels.

4. CONCLUSIONS

In this paper, we have outlined the key steps involved in the design and validation of an acousto-optic tunable filter capable of functioning as a spectropolarimeter. Simulation results were analysed to assess efficiency variations as a function of several parameters. Based on this analysis, an AOTF was designed and implemented to operate within the visible spectrum, from 450 nm to 800 nm. The device features five electrodes, enabling control of spectral resolution as a function of wavelength to achieve a nearly constant resolution across the entire operating range. Characterization and validation confirmed that the component met performance expectations, demonstrating that spectral resolution can be easily adjusted by activating multiple electrodes. With a resolution of approximately 10 nm, the system can distinguish up to 35 discrete spectral bands.

5. ACKNOWLEDGMENTS

The authors would like to thank F. Rivart for the fabrication of R.F. generator and the Delft University of Technology (TU Delft) and the Université Polytechnique Hauts-de-France (UPHF), to accommodate this collaboration and experimental work.

6. REFERENCES

[1] CHANG, I. C. Acousto-optic devices and applications. *Handbook of optics*, 1995, vol. 2, p. 12.1-12.54.

[2] GUPTA, Neelam. Acousto-optic tunable filters. *optics and Photonics News*, 1997, vol. 8, no 11, p. 23-27.

[3] V. B. Voloshinov, V. Y. Molchanov, and J. C. Mosquera, "Spectral and polarization analysis of optical images by means of acousto-optics," *Optics & Laser Technology*, vol. 28, no. 2, pp. 119–127, 1996.

[4] E. Dekemper, J. Vanhamel, B. Van Opstal, and D. Fussen, "The AOTF-based NO2 camera," *Atmospheric Measurement Techniques*, vol. 9, no. 12, pp. 6025-6034, 2016.

[5] Dan R. Lobb "Wide-angle optical systems with moderate spectral resolution, for monitoring the oceans from low Earth orbit", Proc. SPIE 5962, Optical Design and Engineering II, 59621K (14 October 2005)

[6] GUPTA, Neelam et SUHRE, Dennis R. Effects of sidelobes on acousto-optic tunable filter imaging. *Optical Engineering*, 2017, vol. 56, no 7, p. 073106-073106.

[7] POLIAKOV, M. P., BATSHEV, V. I., MACHIKHIN, A. S., et al. Unified optical scheme of an acousto-optical imaging spectrometer for the visible spectrum. *Journal of Optical Technology*, 2024, vol. 90, no 11, p. 674-678.

[8] Pieper, R.; Korpel, A.; Hereman, W. Extension of the acousto-optic Bragg regime through Hamming apodization of the sound field. *J. Opt. Soc. Am. A,* 3, 1608–1619, 1986.

[9] YUSHKOV, Konstantin B., CHIZHIKOV, Alexander I., et MOLCHANOV, Vladimir Ya. Acousto-optic transfer function control by a phased-array piezoelectric transducer. *Photonics*, vol. 10, no. 10, p. 1167, 2023.

[10] DUPONT, Samuel, KASTELIK, Jean-Claude, et VANHAMEL, Jurgen. Design and testing of a multi-electrode apodized acousto-optic filter for arbitrary polarized light. *Applied optics*, 2024, vol. 63, no 10, p. 2487-2493.

[11] KASTELIK, J.-C., DUPONT, Samuel, YUSHKOV, Konstantin B., *et al.* Double acousto-optic deflector system for increased scanning range of laser beams. *Ultrasonics*, 2017, vol. 80, p. 62-65.

DOI: 10.61782/fa.2025.0941



FORUM ACUSTICUM
EURONOISE 2025

OPTIMIZATION ALGORITHM FOR AOTF PARAMETER CHARACTERIZATION

Jurgen Vanhamel[1,2*] **Aleksandr Pavlov**[1] **Samuel Dupont**[3]
[1] TU Delft - Faculty of Aerospace Engineering, Kluyverweg 1, 2629 HS Delft, The Netherlands
[2] Electronic Circuits and Systems, KU Leuven, Kleinhoefstraat 4, 2440 Geel, Belgium
[3] l'Université Polytechnique Hauts-de-France (UPHF), IEMN – Campus Mont Houy – Cedex 9, 59313 Valenciennes, France

ABSTRACT

One of the main challenges for users applying an AOTF as a commercial off-the-shelf component for optical wavelength filtering, is the lack of detailed manufacturing information on critical parameters. Information such as diffraction angles, the precise RF driving frequencies required for momentum-matching conditions, as well as the data for each wavelength across a certain optical spectrum is not always easily available. To obtain this information, users must perform physical tests to configure the optimal frequencies, diffraction angles, and incidence angles for each wavelength of interest which is labor-intensive and costly.
This research uses an optimization algorithm applied to an analytical model which can characterize key angles related to the AOTF's crystallographic axis, such as the crystallographic axis angle θ_c, the tilt-angle α, as well as facet inclination angles β and γ. First, diffraction testing on an AOTF is done, by recording both output ray angles and the momentum-matching frequency. Then the optimization algorithm is chosen and applied to the analytical model to determine the optimal parameters for θ_c, α, γ, and β. With these parameters, the AOTF's behavior can be extrapolated to multiple wavelengths, which not only saves time, but also enables more versatile planning of optical setups..

Keywords: *AOTF, optimization model, analytical model.*

1. INTRODUCTION

Acousto-Optic Tunable Filters (AOTFs) make use of acoustic waves to manipulate the diffraction of light within a transparent crystal. These versatile devices are employed in various fields, such as ground- and space-based spectroscopy [1, 2] and network applications [3]. AOTFs are compact solid-state devices that filter desired optical wavelengths by applying an appropriate Radio-Frequency (RF) signal. Their compactness, robustness and quick tunability enables fast, efficient, and precise control over the spectral properties of light. AOTFs allow for the selective transmission or blocking of specific optical wavelengths, which makes them particularly appealing for space-based missions [4].
To operate AOTFs and regulate light diffraction at a specific optical wavelength, a transducer is mounted to the side of a transparent crystal, such as TeO_2 or quartz. This transducer converts RF signals of a designated frequency and power into sound waves [5]. Applying the appropriate frequency and power level, the Bragg matching condition can be satisfied, enabling two first-order diffracted light beams emitting at the crystal's output [6].
Using commercial off-the-shelf (COTS) AOTFs in an optical setup comes with certain challenges. Mostly the information provided on critical parameters in order to have an optimal functioning AOTF, is limited.
The aim of this paper is to present an optimization algorithm, using an analytical model, in order to characterize the AOTF's crystallographic axis angle θ_c, the tilt-angle α, as well as facet inclination angles β and γ (Fig. 1). Therefore, first a diffraction testing is done using

[*] ***Corresponding author***: *j.a.m.vanhamel@tudelft.nl*
Copyright: *©2025 Jurgen Vanhamel et al. This is an open-access article distributed under the terms of the Creative Commons Attribution 3.0 Unported License, which permits unrestricted use, distribution, and reproduction in any medium, provided the original author and source are credited.*

a COTS AOTF working in the optical visible domain. Both output ray angles are recorded, together with the momentum-matching frequency. Additionally, a developed optimization algorithm is applied to the analytical model, providing the parameters θ_c, α, γ, and β.

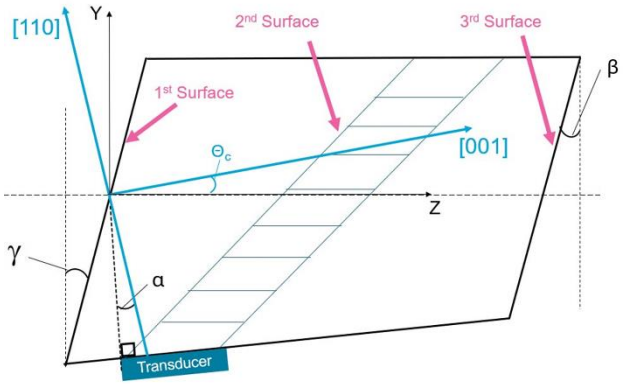


Figure 1. AOTF setup and positioning of the global (black) and crystallographic (blue) coordinate systems.

2. AOTF PARAMETER CHARACTERIZATION APPROACH

The optimization algorithm requires the analytical model's outputs in order to find optimal values that can characterize the main AOTF angles.. First, this model is briefly explained, followed by experimental diffraction tests. Consequently, the algorithm is applied to the model and the AOTF characterization parameters are obtained.

2.1 Analytical model

The goal of the analytical model is to provide as an output the undiffracted ray's optical path through the AOTF, as well as ray tracing of the diffracted ray, accompanied with the frequency signal required for the momentum-matching condition.

The model is based on the approach proposed by Zhao et al. [7], where the AOTF is split into three different surfaces, namely the AOTF entrance surface, the acoustic field and the exit surface (see Fig. 1). Using Directional Cosine Matrices (DCM) in 3D provides the baseline for the Python-based analytical model used in this research. This model has been broken down into more substages and uses adapted mathematical expressions in comparison to Zhao et al. [7], allowing a broad range of optical wavelengths in which the model is applicable.

2.2 Experimental diffraction tests

In this section, diffraction testing on a TeO_2 COTS AOTF (550 – 1000 nm) was carried out by recording both output ray angles, the rotational angle of the AOTF and the momentum-matching frequency. A vertically polarized 635 nm laser light is applied to the AOTF via a polarizer and an iris (Fig. 2). The diffraction occurred only when a vertically polarized light was shone, using a 145 MHz RF signal applied to the AOTF transducer. This RF signal was generated using a lab RF generator and amplifier setup.

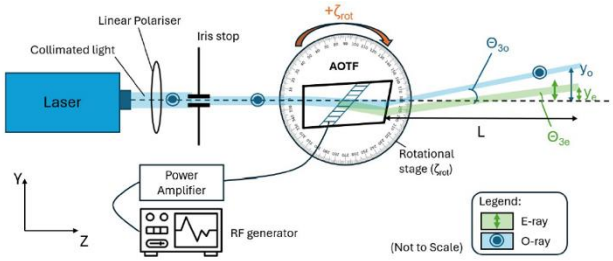


Figure 2. AOTF diffraction test setup with ζ_{rot} is the rotational angle, θ_{3o} is the ordinary undiffracted ray angle and θ_{3e} is the extraordinary diffracted ray.

An example of this diffraction is shown in Fig. 3, where the diffracted light appears faint to the left of the undiffracted light. The dimness of the diffracted light is due to the RF power being set at 100 mW.

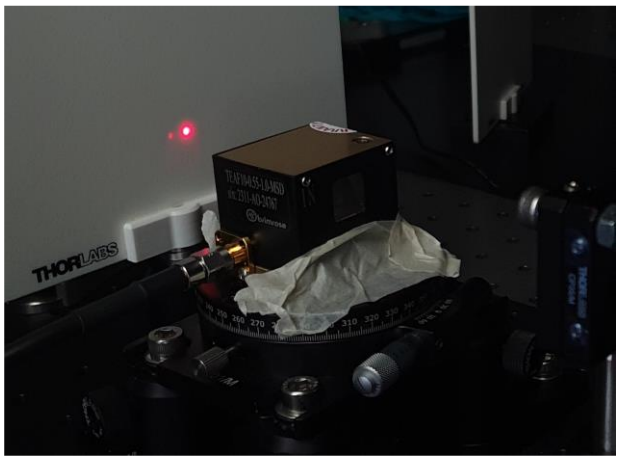


Figure 3. AOTF diffraction when a vertically polarised light is shone onto the AOTF.

The momentum-matching frequency was determined, by rotating the AOTF over a limited range (from -2 degrees

to 8 degrees, compared to the incoming light beam) using the rotational stage (Fig. 2 and 3). The accompanying diffracted and undiffracted rays angles θ_{3o} and θ_{3e} were also recorded by detecting the peak diffracted ray intensity.

2.3 Algorithm selection

To integrate the developed analytical model with an optimization algorithm, the first step was to identify a suitable algorithm. The approach involved selecting an existing method and adapt the analytical model accordingly. Given that the model was implemented in Python and involved multiple variables influencing the results, the selection was limited to multi-variable optimization algorithms available in SciPy. The "L-BFGS-B" algorithm (Limited-memory Broyden-Fletcher-Goldfarb-Shanno) was chosen due to its suitability for multi-variable nonlinear problems and its computational efficiency compared to other quasi-Newton methods [8]. Moreover, this algorithm supports box constraints, allowing for straightforward boundary conditions on variables (θ_c, α, γ, β).

Quasi-Newton methods aim to find a local minimum by approximating the curvature of the objective function, focusing on values where the function approaches a local minimum [8]. To determine the curvatures for each search variable, these methods typically rely on an inverse Hessian matrix [9], containing the second-order partial derivatives. However, calculating a full Hessian becomes increasingly time-consuming as the number of variables (n) grows [10]. To address this, the limited-memory approach estimates the Hessian matrix using only recent search iterations, rather than each time recalculating it from scratch [10]. A detailed mathematical explanation of how this algorithm works is beyond the scope of this research. The primary reason for selecting this algorithm is its computational efficiency in solving multi-variable problems and its ease of implementation in Python through the SciPy library, which also supports simplified variable constraints. Furthermore, the algorithm is relatively effective in finding a global minimum (optimal value) of the objective function [10].

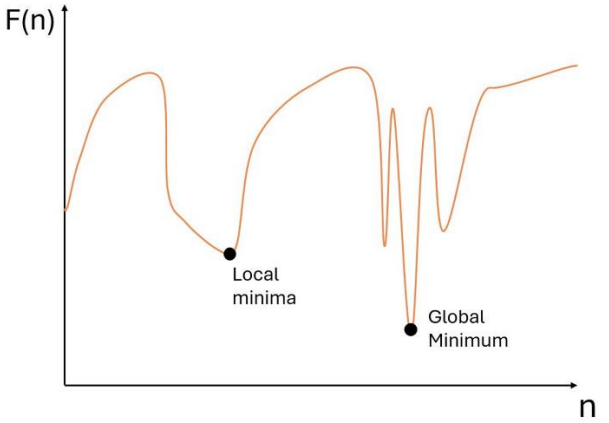


Figure 4. Simplified multimodal example where finding global minimum is challenging for Newton methods.

However, L-BFGS-B can become trapped in local minima, as shown in Fig. 4. This is an example of an objective function with a single variable n demonstrating this limitation [10]. To address this, running the algorithm multiple times with different initial guesses can improve the chances of finding the global minimum.

In contrast, genetic algorithms are generally more effective at locating the global minimum in such cases. Nevertheless, they are more complex to implement, requiring constraints within the objective function, and often come with higher computational costs [11, 12]. Due to these factors, genetic algorithms were not considered in this study but are recommended for future research.

2.4 Objective function and bounds selection

With the L-BFGS-B algorithm selected, the next step is to define its input for optimization. The primary input is the objective function — a scalar function that the algorithm seeks to minimize [10]. The objective is to reduce the discrepancy between the experimental measurements from the COTS AOTF diffraction testing and the predictions from the analytical model. This discrepancy is quantified as a total error, formulated in Eqn. 1 as the objective function. This represents the sum of squared errors for momentum-matching frequency and diffracted/undiffracted angles.

$$E_{tot} = E_{freq} + E_{diff} + E_{undiff} \quad (1)$$

Where each term is defined as follows:

$$E_{freq} = \sum_{i=1}^{n} \left(f_i^{exp} - f_i^{sim} \right)^2 \quad (2)$$

$$E_{diff} = \sum_{i=1}^{n} \left(\theta_{e,i}^{exp} - \theta_{e,i}^{sim}\right)^2 \quad (3)$$

$$E_{undiff} = \sum_{i=1}^{n} \left(\theta_{o,i}^{exp} - \theta_{o,i}^{sim}\right)^2 \quad (4)$$

In Eqn. 2, 3 and 4, *n* represents the number of data points in the experimental results array f^{exp} (momentum-matching frequency), obtained from the diffraction testing, with each point corresponding to a different ζ_{rot} angle. f^{sim} represents the simulated values of the momentum-matching frequency generated by the optimization algorithm. The squared difference is selected because it assigns greater weight to larger errors, ensuring the optimization algorithm to prioritize reducing significant discrepancies.

During each iteration, the algorithm tests different configurations of the variables θ_c, α, γ and β, aiming to minimize the cumulative error across all three equations, thus optimizing the objective function.

To ensure the search remains within realistic AOTF parameter ranges, bounds were set for θ_c, α, γ and β. The selected bounds for the COTS AOTF are listed in Tab. 1, where the left is the lower bound, and the right is the upper bound.

Table 1. Optimization variables and their bounds.

Variable	Bounds	Unit
θ_c	[10; 55]	Degrees
α	[5; 16]	Degrees
γ	[-0.1; 0.1]	Degrees
β	[5; 12]	Degrees

3. EVALUATION OF THE OPTIMIZATION RESULTS

After setting the objective function and bounds for the L-BFGS algorithm, the optimization was executed multiple times with varying initial guesses to avoid the algorithm from becoming stuck in a local minimum. Each optimization run converged to the optimized parameters listed in Tab. 2.

Table 2. Optimized parameters.

Variable	Optimized value	Unit
θ_c	25.92	Degrees
α	11.97	Degrees
γ	-0.1	Degrees
β	7.2	Degrees

The optimized values were subsequently applied to the analytical model. A frequency matching graph is shown in Fig. 5, indicating the match between the predictions (in green) and the experimentally obtained data (in blue). It can be seen that the frequency remains relatively consistent as the rotational angle increases.

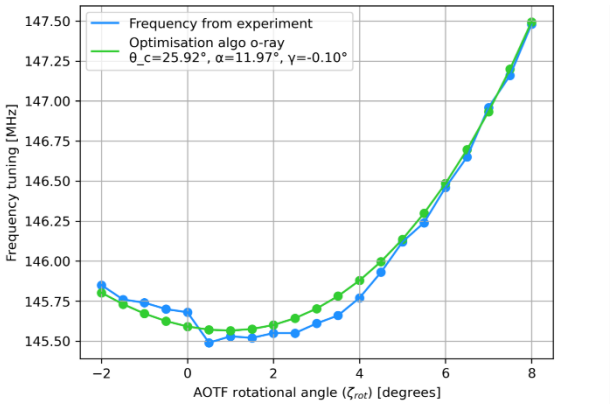


Figure 5. Momentum-matching frequencies as a function of AOTF rotational angle for the ordinary ray diffraction test.

The undiffracted and diffracted angle results are considered together. For the undiffracted rays presented in Fig. 6, in which β plays a key role, the optimization algorithm slightly overestimates the experimental curve.

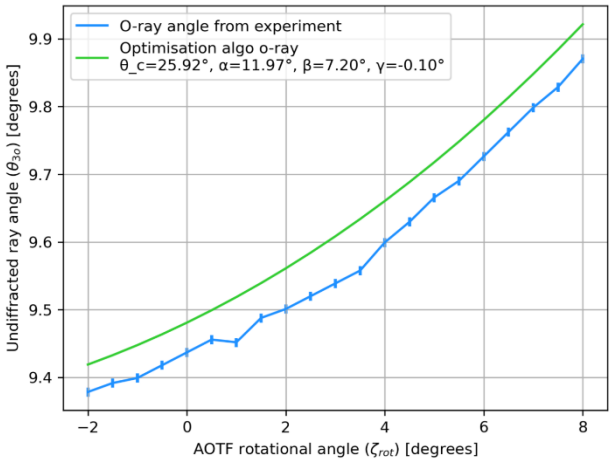


Figure 6. Undiffracted ray angles (θ_{3o}) as a function of AOTF rotational angle for the o-ray diffraction test.

Notably, the angles of the diffracted rays remain extremely stable for this AOTF, consistently ranging between 2.65° and 2.70° (Fig. 7). This stability is an advantage for the optical design, enabling precise predictions of the diffracted ray's path and accurate CCD placement. However, this stability also creates a challenge for the optimization algorithm. When the algorithm attempts to reduce the simulated undiffracted angle by lowering β, it inadvertently shifts the diffracted angle values downward, which penalizes the algorithm if β is reduced too much.

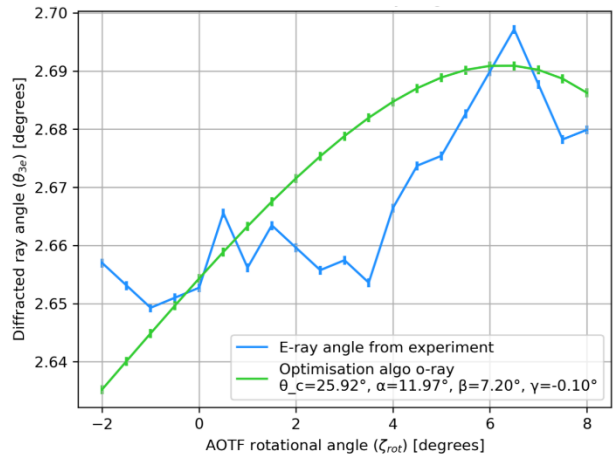


Figure 7. Diffracted ray angles (θ_{3e}) as a function of AOTF rotational angle for the o-ray diffraction test.

In general, the optimization algorithm shows good results, with all simulation curves aligning closely with the experimental data with a discrepancy between experimental and calculated values below 0,02° (Fig. 7). These frequency mismatches could arise from small deviations in the crystal's material properties, such as the acoustic velocity or refractive indices, compared to the values used in the analytical model.

4. CONCLUSIONS

In this research, a dedicated optimization algorithm is explored, in combination with an analytical model. The goal is to find characterization parameters linked to the practical build of the AOTF. The results show that the unknown parameters θ_c, α, γ, and β can be determined.
The L-BFGS optimization algorithm was selected due to its efficiency in handling multiple variables, its computational speed, and its enhanced capability in locating global minima compared to simpler optimization methods. To direct the optimization, an objective function was defined in order to minimize the difference between the simulated and measured values. Additionally, search bounds were set for the AOTF parameters θ_c, α, γ, and β, constraining the algorithm's variable adjustments within these limits.
The optimized values for these four parameters generated curves that closely matched the experimental results. Further improvements could be achieved by either adjusting the penalty in the objective function to refine frequency-matching curves or by incorporating additional variables, such as the material's acoustic velocity. These changes would increase computational time due to the added search variables, but could enhance the characterization process.

5. ACKNOWLEDGMENTS

The authors would like to thank the Delft University of Technology (TU Delft) and the l'Université Polytechnique Hauts-de-France (UPHF), to accommodate this collaboration and experimental work.

6. REFERENCES

[1] E. Dekemper, J. Vanhamel, B. Van Opstal, and D. Fussen, "The AOTF-based NO2 camera," *Atmospheric Measurement Techniques*, vol. 9, no. 12, pp. 6025-6034, 2016.

[2] J. Li, Y. Gui, R. Xu, Z. Zhang, W. Liu, G. Lv, M. Wang, C. Li,and Z. He: "Applications of Aotf

Spectrometers in in Situ Lunar Measurements," *Materials*, vol. 14, no. 13, pp. 3454-, 2021.

[3] C.S. Sobrinho, M.V.N. De Oliveira, M.G. Da Silva, J.L.S. Lima, E.F. De Almeida, and A.S.B. Sombra: "Numerical Analysis of the Crosstalk on an Integrated Acousto-Optic Tunable Filter (AOTF) for Network Applications," *Fiber and Integrated Optics*, vol. 23, no. 5, pp. 345–363, 2004.

[4] O.I. Korablev, A.Yu. Trokhimovskiy, Yu.K. Kalinnikov, "AOTF spectrometers in space missions and their imaging capabilities," in *International Conference on Space Optics ICSO 2016*, (Biarritz, France), pp. 105621M-1-8, 2016.

[5] A.P. Goutzoulis and D.R. Pape: *Design and Fabrication of Acousto-Optic Devices*, New York-Basel-Hong Kong: Marcel Dekker, Inc., 1994.

[6] T. Yano, and A. Watanabe: "Acoustooptic TeO_2 tunable filter using far-off-axis anisotropic Bragg diffraction," *Appl. Opt.*, vol. 15, pp. 2250-2258, 1976.

[7] H. Zhao, C. Li, and Y. Zhang: "Three-surface model for the ray tracing of an imaging acousto-optic tunable filter," *Appl. Opt.*, vol. 53, no. 32, pp. 7684–7690, 2014.

[8] K. Kumar, D. Ghosh, A. Upadhayay, J. Yao, X. Zhao, and A. Upadhyay: "Quasi-newton methods for multiobjective optimization problems: A systematic review," *Applied Set-Valued Analysis and Optimization*, vol. 5, no. 2, pp. 291–321, 2023.

[9] A. Sadeghi-Lotfabadi, and K. Ghiasi-Shirazi, "Speeding up L-BFGS by Direct Approximation of the Inverse Hessian Matrix," *Computational Optimization and Applications*, 2025.

[10] T.V. Mikosch, S.I. Resnick, and S.M. Robinson: *Numerical Optimization*, Springer Series in Operations Research and Financial Engineering. New York, Springer Science+Business Media, LLC, 2006.

[11] G.G. Wang and A.H. Alavi: *Evolutionary Computation*. Basel: MDPI, 2019.

[12] T.E.B. Davies, D.P. Mehta, J.L. Rodríguez-López, G.H. Gilmer, and C. V. Ciobanu: "A Variable-Number Genetic Algorithm for Growth of 1-Dimensional Nanostructures into Their Global Minimum Configuration Under Radial Confinement," *Materials and Manufacturing Processes*, vol. 24, no. 3, pp. 265-273, 2009.

DOI: 10.61782/fa.2025.0382

FORUM ACUSTICUM EURONOISE 2025

EXPLOITING THE ACOUSTO-OPTIC EFFECT FOR ADVANCED OPTICAL MICROSCOPY

Martí Duocastella[1*] **Christos Alexandropoulos**[1] **Jordi Torres-Durall**[2]
Blanca Mestre-Torà[1] **Laura Rodríguez-Suñé**[1] **Mateu Colom**[1]
[1] Department of Applied Physics, Universitat de Barcelona, C/Martí i Franquès 1, 08028 Barcelona, Spain

ABSTRACT

Optical microscopy is a key tool for investigating the structure and dynamics of biological systems at sub-cellular resolution. However, most conventional microscopy setups are designed to capture two-dimensional (2D) data from moderately thin samples labeled with fluorophores. Due to limitations imposed by light scattering and the need for mechanical focus adjustments, these systems struggle with deep tissue penetration and label-free imaging, making them insufficient for non-invasively studying biological complexity in medium-sized organisms such as organoids. Here, we survey our efforts to address these challenges and achieve label-free sub-millisecond imaging at potential depths of up to millimeters. Our approach leverages the acousto-optic effect – specifically, ultrasound-induced refractive index gradients – to focus, modulate, and guide light. The unique interaction between light and ultrasound enables rapid 3D control of light, making it ideal for developing inertia-free microscopes with no moving parts while achieving label-free imaging at hundreds of frames per second. Additionally, shaped ultrasound waves in a medium can act as an instantaneous waveguide, redirecting light toward a focus deeper than conventional optics. The synergistic integration of acousto-optics with advanced microscopy paves the way for an unprecedented in-situ characterization of dynamic processes.

Keywords: *acousto-optics, optical microscopy, deep imaging, light scattering, illumination encoding*

[*] ***Corresponding author***: *marti.duocastella@ub.edu.*
Copyright: *©2025 M. Duocastella et al. This is an open-access article distributed under the terms of the Creative Commons Attribution 3.0 Unported License, which permits unrestricted use, distribution, and reproduction in any medium, provided the original author and source are credited.*

1. INTRODUCTION

A key frontier in optical microscopy is achieving non-invasive, real-time, label-free imaging of biological samples at sub-cellular resolution. However, current microscopes are primarily optimized for acquiring 2D images at tens of frames per second from fluorescently labeled samples that are only a few hundred microns thick [*1*]. Deeper imaging, which is central for studying complex biological specimens such as organoids, remains limited by light scattering to depths of less than 1 mm [*2*]. Similarly, enhancing image contrast and specificity typically requires fluorescent dyes, introducing additional complexity and potential invasiveness to microscopy systems.

Several strategies have been developed to address these issues and advance toward deeper, faster, and label-free microscopes. Among them, exploiting the acousto-optic effect has proved effective in achieving unprecedented control of light outside and inside biological samples [*3*]. In this short paper, we present an overview of our work in this area. Specifically, we highlight the use of acousto-optics in two important microscopy scenarios: rapid axial focus control in quantitative phase imaging [*4*], and light guiding to enhance deep imaging [*5*].

2. PRINCIPLE OF ACOUSTO-OPTICS

The essence of the acousto-optic effect is to induce refractive index gradients within a medium using ultrasound. By sending ultrasound waves (pressure waves) within a medium, it is possible to locally and rapidly modify its density – and consequently, its refractive index. This enables dynamic control of the medium's optical properties, allowing light to be split, focused, or even guided on microsecond time scales. While acousto-optics has long been used in traditional microscopy – particularly

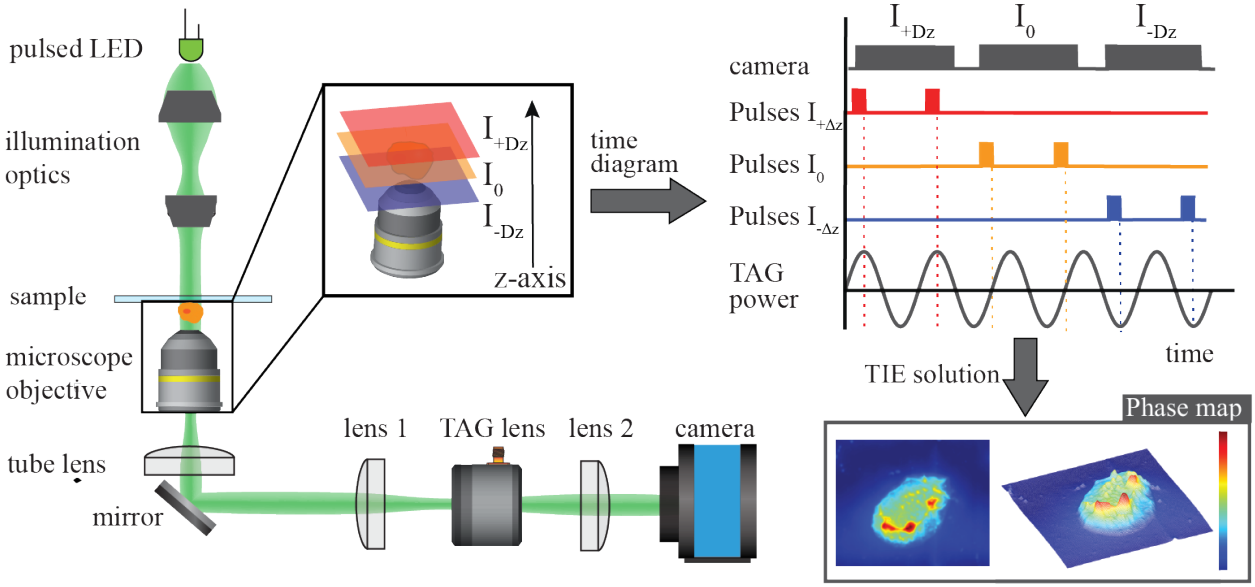


Figure 1. Schematic of the setup for rapid label-free imaging using acousto-optics. An acousto-optic liquid lens (TAG lens), synchronized with pulsed illumination, enables rapid selection of the three focal planes required to solve the Transport of Intensity Equation and retrieve a phase map of the sample. Quantitative phase imaging is thus be achieved at rates only limited by the camera frame rate.

through acousto-optic modulators and deflectors for beam conditioning – our focus here is on two more recent implementations. They have in common the use of non-traditional ultrasound geometries, which have opened new avenues for advancing microscopy.

3. QUANTITATIVE PHASE IMAGING WITH RAPID FOCUS CONROL

The use of fluorescent dyes for high-contrast microscopy can be obviated by measuring the phase shifts that light undergoes as it passes through a specimen – a technique known as phase imaging. Traditionally used as a qualitative method for contrast enhancement, phase imaging has evolved over recent decades into a quantitative approach. This advancement, known as Quantitative Phase Imaging (QPI), not only enhances contrast but also enables the extraction of physical properties such as the refractive index and thickness of the sample [*6*]. Among the various QPI techniques, the Transport of Intensity Equation (TIE) stands out for its simplicity and non-interferometric nature [*7*]. In fact, only two or three brightfield images acquired at known, distinct focal planes are sufficient to retrieve phase information. Unfortunately, precise axial movement of the sample relative to the microscope – often requiring fine adjustments for each specimen – is typically implemented with mechanical actuators, drastically reducing imaging speed in practice.

A promising solution toward real-time TIE imaging is the use of an acousto-optics liquid lens known as the TAG lens [*8*, *9*]. When synchronized with pulsed illumination, it enables remote focus control without any mechanically moving parts. This inertia-free approach allows for microsecond-scale focusing [*10*]. As shown in Figure 1, the sequential capture of three images – each at a different time delay relative to the TAG lens oscillation – allows for the retrieval of a phase map at a speed only limited by the camera's frame rate [*4*]. This high speed enables phase imaging of dynamic events. and, when combined with image stitching, facilitates large field-of-view imaging. This capability is particularly important for the label-free characterization of histopathology samples

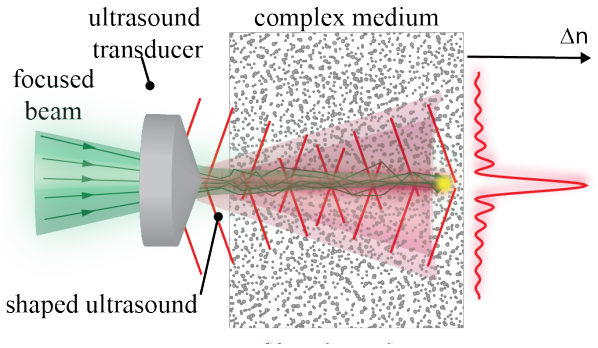


Figure 2. Principle of acousto-optic light guiding within scattering (complex) media. The refractive-index gradients induced by ultrasound act as an embedded waveguide directly inside the medium, helping light reach a deeper focus in analogy to an endoscope.

4. ULTRASONIC ENDOSCOPES

The acousto-optic effect has recently emerged as an effective strategy for mitigating light-scattering inside inhomogeneous media such as biological tissue [*5*, *11–13*]. In this case, shaped ultrasound – ultrasound waves with tailored spatial profiles – are directly sent into the medium of interest. The so-induced refractive index gradients act as effective lenses or waveguides embedded within the medium, helping light reach a deeper focus. In other words, ultrasound acts as a virtual endoscope, as shown in Figure 2. While promising, most implementations primarily rely on resonant acoustic cavities, which require the sample to be placed within the cavity – making the method inherently invasive.

Recent efforts to eliminate the need for resonant cavities include using specially designed ultrasound transducers [*14*, *15]* and specific geometries [*16*]. These methods have reached significant enhancements in the amount of light delivered within scattering media. For example, in samples with an optical thickness of 2.5 – where light is scattered an average of 2.5 times within the medium – the use of two parallel piezoelectric plates resulted in a 700% gain in delivered light [*16*]. This impressive result can be transformative for microscopy applications that rely on light delivery over large areas, such as photoacoustic microscopy.

5. CONCLUSIONS

Acousto-optics offers a promising path toward rapid, deep, and label-free microscopy. By combining innovative ultrasound geometries with new concepts – such as using ultrasonic endoscopes – there has been a recent surge in the potential applications of acousto-optics. We believe that ongoing progress in this area will significantly transform the microscopy landscape, bringing us closer to the coveted goal of a real-time, non-invasive, and deep optical tool.

6. ACKNOWLEDGMENTS

This work has received funding from the European Research Council (ERC) under the European Union's Horizon 2020 research and innovation programme (grant agreement No. 101002460), and the EU-funded OrganVision Horizon 2020 project (grant agreement number 964800). M.D. is a Serra Hunter Professor.

REFERENCES

[1] J. Pawley, *Handbook of Biological Confocal Microscopy* (Springer, 2006).

[2] V. Ntziachristos, "Going deeper than microscopy: The optical imaging frontier in biology", *Nat. Methods* **7**, 603–614 (2010).

[3] M. Duocastella, S. Surdo, A. Zunino, A. Diaspro, P. Saggau, "Acousto-optic systems for advanced microscopy", *JPhys Photonics* **3**, 012004 (2021).

[4] C. Alexandropoulos, M. Duocastella, "Video-rate quantitative phase imaging with dynamic acousto-optic defocusing", *Opt. Lasers Eng.* **169**, 107692 (2023).

[5] B. M. Torà, M. Duocastella, "Enhanced light focusing inside scattering media with shaped ultrasound", *Sci. Rep.*,**13,** 11511 (2023).

[6] Y. K. Park, C. Depeursinge, G. Popescu, "Quantitative phase imaging in biomedicine", *Nat. Photonics* **12**, 578–589 (2018).

[7] C. Zuo, J. Li, J. Sun, Y. Fan, J. Zhang, L. Lu, R. Zhang, B. Wang, L. Huang, Q. Chen, "Transport of intensity equation: a tutorial", *Opt. Lasers Eng.* **135**, 106187 (2020).

[8] A. Mermillod-Blondin, E. McLeod, C. B. Arnold, "High-speed varifocal imaging with a tunable

acoustic gradient index of refraction lens", *Opt. Lett.* **33**, 2146–2148 (2008).

[9] M. Duocastella, G. Vicidomini, A. Diaspro, "Simultaneous multiplane confocal microscopy using acoustic tunable lenses", *Opt. Express* **22,** 19293-19301 (2014).

[10] S. K. Kang, M. Duocastella, C. B. Arnold, "Variable Optical Elements for Fast Focus Control", *Nat Phot.* **14**, 533–542 (2020).

[11] M. Chamanzar, M. G. Scopelliti, J. Bloch, N. Do, M. Huh, D. Seo, J. Iafrati, V. S. Sohal, M. R. Alam, M. M. Maharbiz, "Ultrasonic sculpting of virtual optical waveguides in tissue", *Nat. Commun.* **10**, 1–10 (2019).

[12] M. G. Scopelliti, M. Chamanzar, "Ultrasonically sculpted virtual relay lens for in situ microimaging", *Light Sci. Appl.* **8**, 65 (2019).

[13] M. N. Cherkashin, C. Brenner, G. Schmitz, M. R. Hofmann, "Transversally travelling ultrasound for light guiding deep into scattering media", *Commun. Phys.* **3**, 180 (2020).

[14] Q. Lin, Z. Li, B. Wang, M. Zhou, Y. Xie, D. Wang, C. Hou, R. Wang, X. Liu, X. Sun, H. Shan, Z. Chen, H. Wu, Y. Yang, C. Fei, Z. Chen, "Acoustic hologram–induced virtual in vivo enhanced waveguide (AH-VIEW)", *Sci. Adv.* **10**, 22 (2024).

[15] J. Torres-durall, M. Duocastella, "Non-conventional ultrasound transducer geometry facilitates remote light control within samples", *J. Phys. Photon*, **7**, 025011 (2025).

[16] B. Mestre-Torà, M. Duocastella, "Parallelized Ultrasound-Guiding for Enhanced Light Delivery within Scattering Media", *ACS Photonics*, 11, 5161–5169 (2024).

DOI:

Main theme: A12 Physical Acoustics and Ultrasound

Session A12.10 Acoustic wave propagation in complex media

Chair(s): V. Romero-García, T. Valier-Brasier

DOI:

Main theme: A13 Physiological Acoustics and Audiology

Session A13.04 Advancements and challenges in military acoustics: physiological and audiological perspectives

Chair(s): F. Nir, M. Weger

DOI: 10.61782/fa.2025.0922

FORUM ACUSTICUM EURONOISE 2025

TWO HYBRID DIRECTIVITY MODELS OF MUZZLE BLASTS TO DESCRIBE THE FREQUENCY AND DISTANCE DEPENDENCY

Philipp Bechtel* **Christian Kleinhenrich** **Karl-Wilhelm Hirsch**
Cervus Consult GmbH, Germany

ABSTRACT

The muzzle blast is an auditory risk if the shooter or other personnel are exposed close to the weapon. To evaluate the risk, the signature of the blast must be measured or synthesized for simulation purposes. Muzzle blasts are highly directional. A common approach for simulation is to assume a source model with scalar directivity. This approach neglects the angle- and distance-dependent changes in the frequency spectrum of the blast. Hence, significant discrepancies occur between synthesized and measured shooting signals. This paper presents two alternative approaches to describe the distance- and frequency-dependent directivity of a muzzle blast. The first approach is based on the ANX model by Salomons. In contrast to the scalar directivity of the latter, here a separate source energy is determined for each exit angle using cosine transformation. This model synthesizes the blasts with only a few parameters. For the second model, a transfer function is given by the ANX model and a spherical harmonic source describes the angle and frequency dependency of the blast signature. Depending on the input data, this model provides very detailed reconstructions of measured muzzle blasts even close to the muzzle.

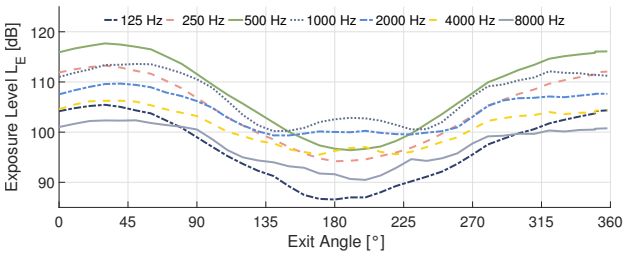
Keywords: *Muzzle blasts, nonlinear, directivity, ANX*

1 INTRODUCTION

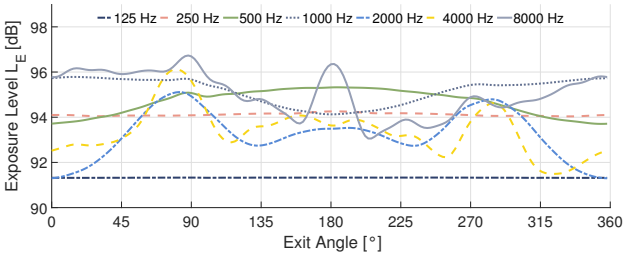
The hearing load of the shooter when firing handguns is primarily caused by the muzzle blast. The decisive input variable of models for assessing the exposure and the risk of hearing damage is the sound pressure time curve at the ear. For the investigation of such exposure models, reliable source models of the muzzle blast are required, which provide the sound pressure time signal. In addition to the pronounced frequency-dependent directivity of the muzzle blast, nonlinear effects in sound propagation must be taken into account in the near field of the weapon.

2 FUNDAMENTELS: DIRECTIVITY OF A MUZZLE BLAST

First, the special features of the directivity of a muzzle blast are discussed.



(a) Gun muzzle blast



(b) Loudspeaker

Figure 1: Level of octave bands as a function of the exit angle in the transversal plane for a gun muzzle blast and a loudspeaker (Genelec 8020c)

The level deviations of the octave bands over the azimuth

**Corresponding author*: bechtel@cervus.de
Copyright: *©2025 Philipp Bechtel et al. This is an open-access article distributed under the terms of the Creative Commons Attribution 3.0 Unported License, which permits unrestricted use, distribution, and reproduction in any medium, provided the original author and source are credited.*

angle in the transversal plane of a rifle muzzle blast and a loudspeaker are shown in Figure 1. Measurement data from the Genelec 8020c from the BRAS project was used for the loudspeaker directivity[1]. The following aspects become clear from the comparison of the level deviations of the octave bands.

- The octave band-dependent level deviation of the muzzle blast is up to 20 dB depending on the angle of exit and is therefore many times greater than that of the loudspeaker
- The eccentricity - the level difference between the front (firing direction) and the rear - of the muzzle blast is most pronounced in the low frequency bands of 125 Hz to 500 Hz and decreases towards high frequencies from approximate 20 dB to 10 dB
- Most of the energy of this rifle is emitted between 500 Hz and 1 kHz

The propellant gases escaping from the tube during the muzzle blast resemble a massively deformed sphere, as indicated in the schlieren photography from Figure 2.

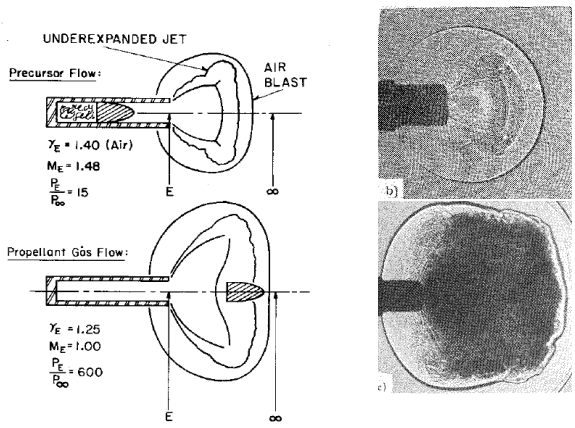


Figure 2: Flows occurring during the muzzle blast[2]

The first spherical sound front recognizable in the schlieren photography is the so-called *precursor*, which originates from the air pushed out by the projectile at supersonic speed. The actual muzzle blast is formed by the propellant gases behind the projectile. These also emerge from the pipe at supersonic speed and flow into the still air. This forms a so-called Mach plate, a well-known phenomenon in fluid dynamics[2]. The muzzle blast is therefore emitted neither from the muzzle itself nor from a sphere around it, but from a disk[3]. This explains why the directional effect is also directed forwards at longer wavelengths, while it tends to remain round at shorter wavelengths.

3 RAW AND REFERENCE DATA

In Figure 3 the 36 measuring points are outlined in the horizontal plane.

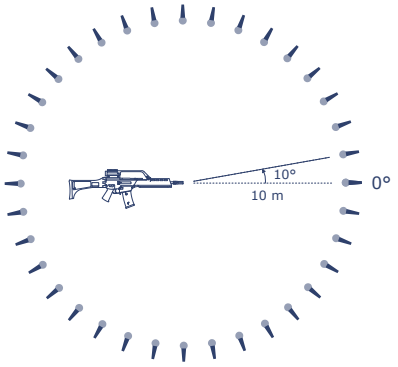


Figure 3: Sketch of the 360° measurement

There are three recorded shot signals per measuring point. The distance between the microphones and the muzzle is 10 m. The weapon used is a rifle on a fixture with a muzzle brake [1] . Both the muzzle and the respective measuring points are positioned 2 m above the approximately reverberant grass ground. This means that the ground reflection hits approximate 2.1 ms after the direct sound. For the investigations presented here, only the direct sound component windowed out using Hamming windows is considered. The full metal jacket ammunition corresponds to the caliber 5.56 mm × 45 mm. In the calculations, an exit velocity $v_0 = 1200\ m/s$ and a projectile mass $m_p = 3.7$ g were assumed for this ammunition.

A total of six additional measurement points from another measurement campaign were used to investigate the propagation models. There, the same rifle type with identical ammunition was measured on an open shooting range. In contrast to the 360° measurement, the ground here consisted of gravel and a shooter was used instead of a fixture. Four of the six reference points are outlined in Figure 4.

[1] According to the current state of the investigation, the muzzle brake influences the emitted sound from an angle of ≈ 140°, so that no clean blast is measured there.

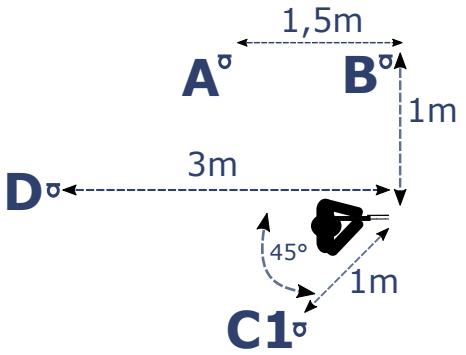


Figure 4: Sketch of reference measuring points

The two remaining measuring points C5 and C10 are in the propagation path of measuring point C1 at a distance of 5 m and 10 m from the muzzle.

4 ANX SOURCE MODEL

This model was introduced in 2024 by Salomons[4] under the title: *Analytical model for sound of explosives and firearms (ANX)*. It is based on a Friedlander blast[5], which has two characteristic values with the peak sound pressure P and the positive transit time T. The characteristic values and the resulting sound pressure time curve are sketched in Figure 5.

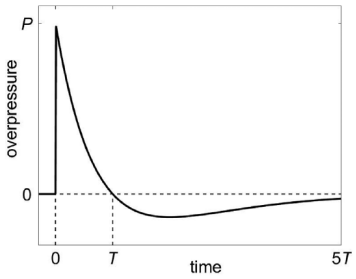


Figure 5: Friedlander waveform, with peak sound pressure P and positive transit time T[4]

The special feature of the ANX model is the nonlinear sound propagation. Here, the peak sound pressure $P(r)$ and the duration of the positive N-wave flank $T(r)$ are distance-dependent variables that are determined according to Equations (2) and (3). As the spectral energy of a signal moves increasingly towards low frequencies with increasing $T(r)$, a blast becomes more low-frequency with increasing distance from the muzzle according to the ANX model.

Table 1: Relevant constants and reference values

K	β	ρ	c	t_0	p_0
0.38	1.2	1.2 kg/m^3	340 m/s	1 s	20 µPa

The auxiliary variable r_*, which depends on the source energy E, limits the application range of the model with $r > 1.6\,r_*$ and can be determined according to Equation (4) with the values from Table 1. The source energy of handguns is usually less than 20 kJ which corresponds to a maximum r_* of 367 mm. This means that the model is suitable for most handguns from a distance of approximately 0.6 m applicable.

$$p(t) = P(r)\left(1 - \frac{t}{T(r)}\right) e^{-t/T(r)} \tag{1}$$

$$P(r) = K\rho c^2 \frac{r_*}{r}\sqrt{\frac{1}{\ln(r/r_*)}} \tag{2}$$

$$T(r) = K\beta \frac{r_*}{c}\sqrt{\ln(\frac{r}{r_*})} \tag{3}$$

$$r_* = 0.7\sqrt[3]{\frac{E}{\rho c^2}} \tag{4}$$

4.1 Scalar directivity

Salomons[4] uses a scalar approach with the directivity D. This value can be calculated with the reference quantity $m_0 = 75$ g according to Equation (5). For small arms, the propellant mass m is only a few grams, so that $m \ll m_0$ applies and the directivity is approximately 17.5 dB. The directional correction term C_{dir} can be determined according to Equation (6) and is for $m \ll m_0$ approximately 11 dB.

The scalar, exit angle-dependent correction level $\Delta L(\phi)$ thus results in Equation (7).

$$D = \frac{17.5}{1 + (m/m_0)^{1.5}} \tag{5}$$

$$C_{\text{dir}} = 10 \log \left(\frac{10}{D} \frac{10^{D/10}}{\ln(10)} \left[1 - 10^{-D/10} \right] \right) \quad (6)$$

$$\Delta L(\phi) = D \left(1 - \frac{\phi}{180} \right) - C_{\text{dir}} \quad (7)$$

For the rifle considered here, the source energy $E = 2500\,\text{J}$ is assumed.

4.2 Source energy-dependent directivity by cosine transformation

In this approach, an angle-dependent source energy $E(\phi)$ is determined. Using the coefficients of a rifle of 5.56 mm × 45 mm caliber from Table 2, the angle-dependent source energy can be determined by cosine transformation according to Equation (8). The angle-dependent source energy can then be used to calculate the distance-dependent signal parameters according to Equations (2) and (3) from which the final signals at the receiver result.

Table 2: Coefficients for determining the direction-dependent source energy of a rifle muzzle blast using the 5th order cosine transformation

Index i	1	2	3	4	5
c_i / J	2521	1908	557	79	52

$$E(\phi) = \sum_{i=1}^{N} c_i \cdot cos(\phi \cdot (i-1)) \quad (8)$$

5 SPHERICAL HARMONICS (SH) SOURCE

As a further source model, a transformation of the measurement data into the spherical frequency domain is considered. This was carried out with a 15th order spherical harmonics decomposition, resulting in 256 complex coefficients for each frequency support point. The method is described in more detail by Williams[6], among others. The reconstructed signals of this source model naturally only represent this type of rifle with the corresponding ammunition.

6 PROPAGATION MODELS

This chapter deals with two different propagation models. Both deal exclusively with distance-dependent attenuation. For example, atmospheric attenuation components that also occur during sound propagation are not taken into account in these models.

The reference distance r_0 was used for the spherical harmonics 10 m, as the data used for the decomposition was available at this distance. For the ANX source model, $r_0 = 1\,\text{m}$ was selected as the reference distance.

6.1 Linear sound propagation model

The linear propagation model uses the $1/r$ approach commonly used in acoustics. The calculation of the sound pressure time curve $p_r(t, \phi)$ at a distance r is shown in Equation (9), neglecting the phase and other attenuation effects.

$$p_r(t, \phi) = p_{r_0}(t, \phi) \cdot \frac{r_0}{r} \quad (9)$$

6.2 Nonlinear sound propagation model

This model describes the nonlinear sound propagation of an N-wave with spherical expansion in a homogeneous environment according to Pierce[7] [2]. The implementation of this model is based on the ANX model according to Section 4.

To determine the distance-dependent transfer function, the angle-dependent energy $E(\phi)$ of the sound source is first required. If this is not available, but for example sound pressure time curves at the known source distance r, the energy of these signals can be estimated. To do this, the exposure level L_E of the signal must be calculated. From this level, the auxiliary variable r_* can then be estimated according to Equation (10) [3]. With the constants and reference quantities from Table 1, the source energy can finally be determined with Equation (11).

$$L_E = 10 \log \left(\frac{\pi K^3 \beta \rho^2 c^3 r_*^3}{p_0^2 r_0^2 t_0} \frac{r_0^2}{4\pi r^2} \sqrt{\frac{1}{\ln(r/r_*)}} \right) \quad (10)$$

[2] Chapter 11.9

[3] According to Salomons[4], the deviation is less than 1 dB

$$E = \rho c^2 \left(\frac{r_*}{0.7}\right)^3 \tag{11}$$

In the next step, the creation of the transfer function is outlined. The angle-dependent source energy $E(\phi)$ is used to generate an ANX signal $p_{r_0}(t, \phi)$ for the reference distance r_0 and a second signal $p_r(t, \phi)$ for the desired source distance r. Using Fourier transformation, these two signals are transferred to the frequency domain and the quotient is formed, which corresponds to the transfer function.

By multiplying the source signal, which has also been transformed into the frequency domain, with the transfer function, the frequency response of the signal at a distance r at the angle of exit ϕ can be determined. The back transformation into the time domain results in the shot signal at the observation point with nonlinear sound propagation.

7 INVESTIGATION

In this section, the source models presented are examined with regard to their applicability in the vicinity of the muzzle. For this purpose, the predicted hearing load as well as the sound pressure time curves and frequency responses are considered.

Table 3: Nomenclature of the abbreviations

Scalar Directivity	scalar directivity according to Section 4.1
Cosine Trans.	energetic directivity according to Section 4.2
Linear	linear propagation model according to Section 6.1
NL	nonlinear propagation according to Section 6.2

The abbreviations used in the following can be taken from Table 3.

7.1 Predicted hearing load

The AHAAH model[8] used to determine the hearing load was developed explicitly for shooting noise. It is an appropriate hearing damage prediction method and is currently used by the US military[9], among others. The AHAAH settings unwarned, no hearing protection and frontal sound incidence were used consistently for all calculations.

The following statements can be derived from the hearing loads presented in Figure 6 over the angle of exit at a distance of 10 m.

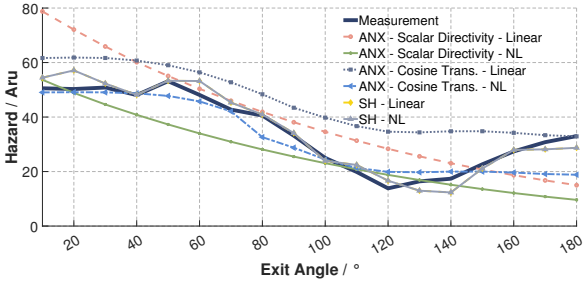


Figure 6: Hearing load over the angle of exit in 10 m muzzle distance

- The predicted hearing load of the measurement signals decreases with increasing angle until the influence of the muzzle brake from $\approx 140°$ causes it to increase again
- The curves of the spherical harmonics reconstructions with linear and nonlinear sound propagation are identical due to the reference distance $r_0 = 10\,\text{m}$ and deviate only slightly from the target values
- The hearing loads according to the ANX models with scalar directivity decrease approximately linearly over the angle of exit. As expected, the values are higher with the linear propagation model, as both the stronger additional level drop and the shift in the spectrum are neglected. The correlation with the values of the measurement are only low for the ANX source models with scalar directivity
- The ANX source model with cosine transformation directivity significantly overestimates the target values in a linear propagation calculation. In combination with the nonlinear propagation model, the method provides appropriate hearing exposure predictions for angles $< 140°$

Next, the models are analysed on the reference data according to Figure 4. For this purpose, Figure 7 shows the hearing loads at the reference measuring points removed in 1 m to 10 m and the following statements can be derived.

- The predicted hearing load of the measurement signals tends to decrease with increasing distance to the muzzle
- At the measurement points B and C1 near the muzzle, the spherical harmonics values deviate significantly from each other depending on which propagation

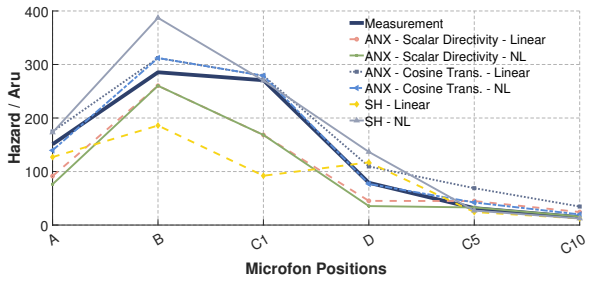


Figure 7: Hearing load at the reference measuring points according to Figure 4

method was used. The deviations with the nonlinear propagation model are significantly lower compared to the target values

- The ANX model with scalar directivity significantly underestimates the actual hearing load for the most part, regardless of the propagation model
- The ANX source model with the cosine transformation directivity and nonlinear sound propagation provides almost identical hearing damage risk as the measurement data When using the linear propagation model, the overestimation of the hearing load increases with the distance to the muzzle

7.2 Reconstructed shot signals

For further investigation, the measured and reconstructed signals at two measuring points on the circle after Figure 3 as well as two relevant positions at 1 m muzzle distance are considered in more detail.

In Figures 8 and 9 the sound pressure time curves and frequency responses at two representative measurement points of the circular measurement are discussed. This shows that, as expected, the spherical harmonics signals are identical to each other and show hardly any deviations from the measurement signals. The ANX approaches with linear sound propagation significantly overestimate the peak levels, in some cases by more than 6 dB. With the nonlinear propagation model, the differences to the target values are significantly smaller. With regard to the frequency responses, all the source models considered provide reasonable reconstructions.

In Figures 10 and 11 the sound pressure time curves and frequency responses are discussed in 1 m distance at different exit angles. For the spherical harmonics signals, the

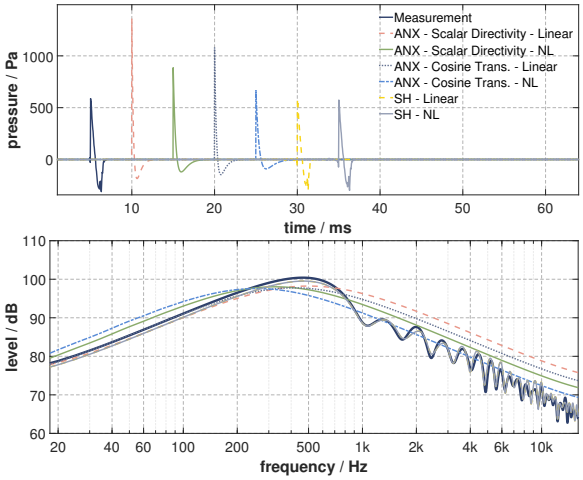


Figure 8: Sound pressure time curve and frequency response under 10° at 10 m distance

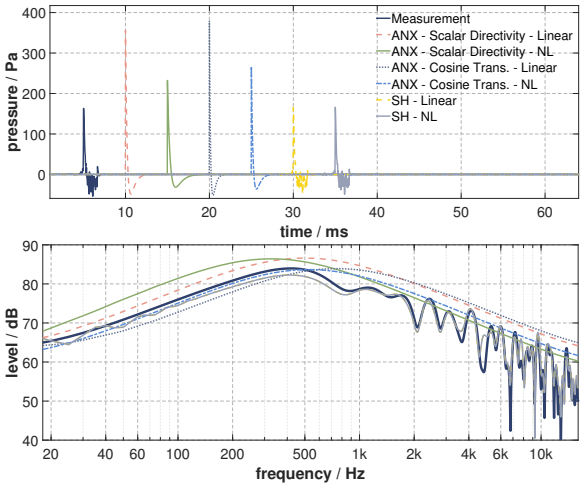


Figure 9: Sound pressure time curve and frequency response under 130° at 10 m distance

difference between them is 3 dB to 4 dB. The sound pressure time curves with nonlinear propagation tend to show higher similarities with the measured data. For the spectra, the model with nonlinear sound propagation also depicts the frequency responses above approx. 500 Hz better. Due to the short useful signal length of 7 ms, the curves below 500 Hz are only partially reliable.

As expected, the ANX source models show no differences at this distance with regard to the sound propagation method. In terms of directivity, the peak levels of the

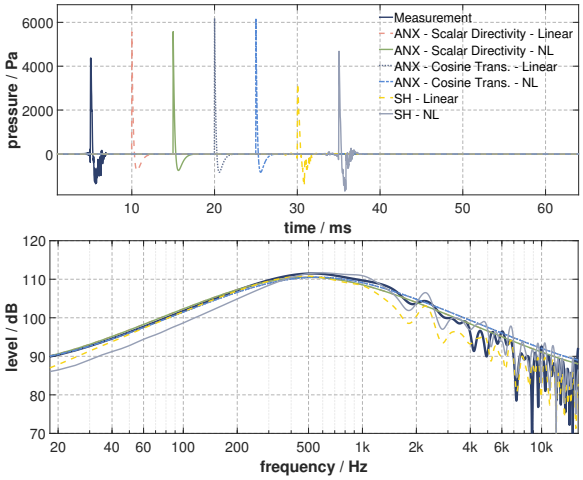


Figure 10: Sound pressure time curve and frequency response under 90° at 1 m distance (reference measuring point B)

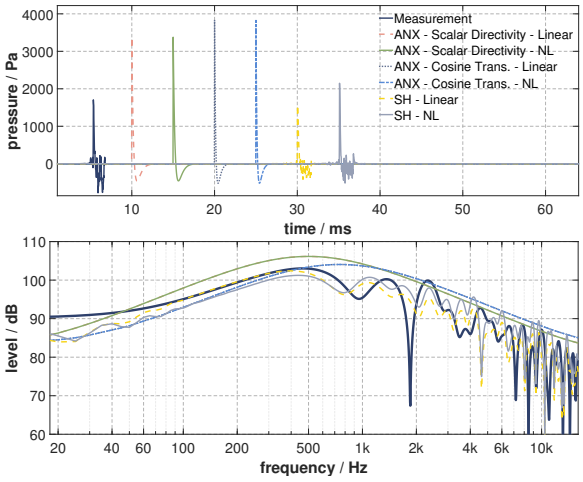


Figure 11: Sound pressure time curve and frequency response under 135° at 1 m distance (reference measuring point C1)

cosine transform method are slightly higher than those of the scalar approach. In addition, the spectra of the scalar ANX model are lower-frequency than those of the cosine transformation. Both ANX source models overestimate the peak level of the measurement signals with 3 dB to 8 dB, in some cases enormously. On closer inspection of the spectra, this difference results primarily from the overestimation of the frequency components above ≈ 3 kHz. The sound pressure time curves at measurement point B shown in Figure 12 were filtered low-pass [4] at 4 kHz for illustration purposes. A comparison with Figure 10 shows that the peak level differences of the ANX models compared to the measurement signal have fallen from above 3 dB to less than 1 dB.

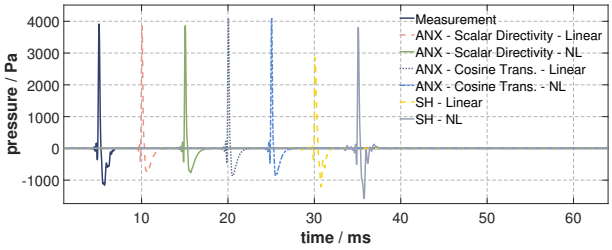


Figure 12: Low-pass [4] filtered sound pressure time curve under 90° at 1 m distance (reference measuring point B)

This aspect explains the high agreement of the AHAAH hearing damage predictions by the ANX model with cosine transformation and nonlinear propagation, despite the marked level differences. The reason for this lies in the way the AHAAH model works. This model calculates the auditory risk units for individual bark bands, whereby the maximum value is decisive. For the gunshot signals analysed here, the maximum ARU value is always in the frequency range between 1 kHz to 2.5 kHz. The lower and higher frequency signal components are therefore less significant when predicting the risk of hearing damage. Regardless of this, the ANX model tends to overestimate the energy of the high-frequency signal components of this gun muzzle blast, which requires further investigation.

8 CONCLUSION

It was shown that the ANX source model with cosine transformation as the directivity generates more realistic signals than the scalar approach, particularly with regard to the predicted hearing load. The reason for this lies in the oversimplified modelling approach of the frequency-dependent directivity of a muzzle blast. The attempt to model this with a single scalar factor logically results in higher deviations than with the more complex cosine transformation approach.

It also became clear that the quality of the shot signals generated close to the muzzle increases when nonlinear transfer functions are used instead of linear sound propa-

[4] 10th order Butterworth filter with 4 kHz cut-off frequency

gation. For example, the ANX model with cosine transform directivity and nonlinear propagation can be used to properly predict the hearing load of the direct sound component of the rifle muzzle blast, considered here as a function of both the angle of exit and the muzzle distance.

The results presented here are subject to some limitations. For example, only the direct sound components of gun blasts were considered. Investigations into the quality of the source and propagation models in combination with multiple reflections in closed systems are still pending. The fact that only one gun was considered here represents a further limitation. For further evaluation, the methods must be applied to other weapons and validated. As an alternative to the methods considered here, the Weber model is another source model to which the nonlinear sound propagation can be applied as a transfer function. Initial investigations into this appear promising.

9 ACKNOWLEDGMENTS

The work is supported by BAIUDBw GS II 2 and IUD I 5 of the German Ministry of Defense.

10 REFERENCES

[1] L. Aspöck, F. Brinkmann, D. Ackermann, S. Weinzierl, and M. Vorländer. *BRAS - Benchmark for Room Acoustical Simulation*. en. 2020. DOI: 10.14279/DEPOSITONCE-6726.3.

[2] E. M. Schmidt and D. D. Shearf. "Optical Measurements of Muzzle Blast". In: *AIAA Journal* 13.8 (1975), pp. 1086–1091.

[3] J. Zhang, G. Liu, W. Han, L. Liu, and Z. Wang. "Numerical research on the muzzle multiphase flow field produced by gas curtain launch". In: *Scientific Reports* 14.1 (Nov. 2024). ISSN: 2045-2322. DOI: 10.1038/s41598-024-81216-1.

[4] E. M. Salomons. "Analytical model for sound of explosives and firearms". In: *The Journal of the Acoustical Society of America* 156.3 (Sept. 2024), pp. 2034–2044. ISSN: 0001-4966. DOI: 10.1121/10.0030301.

[5] F. G. Friedlander. "The diffraction of sound pulses I. Diffraction by a semi-infinite plane". In: *Proceedings of the Royal Society of London. Series A. Mathematical and Physical Sciences* 186.1006 (Sept. 1946), pp. 322–344. ISSN: 2053-9169. DOI: 10.1098/rspa.1946.0046.

[6] E. G. Williams. *Fourier acoustics - Sound radiation and nearfield acoustical holography*. Academic Press, 1999. DOI: 10.1016/B978-0-12-753960-7.X5000-1.

[7] A. D. Pierce. *Acoustics: An Introduction to Its Physical Principles and Applications*. Springer International Publishing, 2019. ISBN: 9783030112141. DOI: 10.1007/978-3-030-11214-1.

[8] P. D. Fedele, M. S. Binseel, J. T. Kalb, and G. R. Price. *Using the Auditory Hazard Assessment Algorithm for Humans (AHAAH) With Hearing Protection Software, Release MIL-STD-1474E*. Tech. rep. ARL-TR-6748. Army Research Laboratory, 2013.

[9] US Department of Defense. *MIL-STD-1474E: Design Criteria Standard Noise Limits*. Military Standard. 2015.

DOI: 10.61782/fa.2025.0958

FORUM ACUSTICUM EURONOISE 2025

VIRTUAL AND EXPERIMENTAL ACOUSTICAL COMFORT TESTERS FOR EARPLUGS

Franck Sgard[1*] **Kevin Carillo**[2] **Simon Kersten**[3]
Robin Richert[2] **Olivier Doutres**[2]
[1] Department of Research, Institut de recherche Robert-Sauvé en santé et en sécurité du travail IRSST, Montreal, Canada
[2] Department of Mechanical Engineering, Ecole de Technologie Supérieure, Montreal, Canada
[3] Institute for Hearing Technology and Acoustics, RWTH Aachen University, Aachen, Germany

ABSTRACT*

Earplugs are widely used to prevent noise-induced hearing loss, but discomfort can reduce their effectiveness by affecting their consistent and proper use. Earplug comfort can be described by four dimensions: physical (biomechanical and thermal interactions with the earcanal), acoustical (noise/useful sound perception), functional (usability and efficiency), and psychological (well-being and satisfaction). (Dis)comfort results from the interplay within the user/earplug/work environment triad. The components of this triad and their interactions across multiple phases, ultimately shape the comfort judgment and are defined by various physical and psychological characteristics that must be assessed to fully understand comfort. This paper targets acoustical characteristics of both disposable and reusable earplugs when inserted in the earcanal, focusing on indicators such as sound attenuation and occlusion effect. It presents a synthesis of various acoustic comfort testers developed by the authors' research team to assess these characteristics. Virtual and physical truncated realistic artificial ears and whole head are explored. This research aims to provide manufacturers with comfort-driven design methods for earplugs.

Keywords: *earplugs, comfort, sound attenuation, occlusion effect*

* ***Corresponding author***: franck.sgard@irsst.qc.ca.
Copyright: *©2025 Sgard et al. This is an open-access article distributed under the terms of the Creative Commons Attribution 3.0 Unported License, which permits unrestricted use, distribution, and reproduction in any medium, provided the original author and source are credited.*

1. INTRODUCTION

Earplugs are commonly used to prevent noise-induced hearing loss, but their effectiveness can be compromised by discomfort, which affects consistent and proper usage. Comfort is a complex concept that encompasses multiple dimensions, including physical (biomechanical and thermal interactions), acoustical (related to noise perception), functional (usability and efficiency), and psychological (well-being and satisfaction) aspects [1].

The perceived (dis)comfort of earplugs results from the interplay between the user, the earplug, and the work environment—an interaction framework known as the "triad" [2]. Various intrinsic physical and psychological characteristics associated with each triad component, interact across several phases (fitting, interaction, internal human body effects, and perceived effects), ultimately shaping the comfort judgment [3]. Examples of physical factors include the earplug's design parameters (shape and material properties), the user's earcanal (EC) morphology, hand dominance and hearing loss condition, and the work environmental conditions. Examples of psychological characteristics involve the earplug's attractiveness or aesthetic design, the user's sex, age and prior experience with earplugs, as well as the nature of the work environment and required physical activity. During the interaction phase of the comfort model, the earplug interacts with the user's EC, leading to additional physical characteristics of the EC/earplug system, that can influence comfort [4]. Examples of such characteristics are the static mechanical pressure exerted by the earplug on the EC and the sound pressure field in the EC.

Understanding these physical and psychosocial influences is essential for enhancing earplug effectiveness in noise

protection. Incorporating comfort considerations into earplug design and selection can help ensure better compliance and protection for individual workers in different occupational settings. However, measuring comfort-related characteristics presents challenges, as objective and quantifiable indicators must be established for laboratory and field assessments.

This paper specifically explores the acoustical comfort of earplugs, focusing on the determination of key physical characteristics of the "EC/earplug" system in the interaction phase.

Acoustical discomfort from earplugs is primarily characterized by two conceptual acoustic sub-dimensions associated with the perception of “External Noises” (i.e. intelligibility of useful sounds) and “Internal Noises” (i.e. occlusion effect) [5]. Physical objective characteristics of the system “EC/earplug” that can impact these two sub-dimensions are the sound attenuation and the occlusion effect (OE) of the earplug [6,7]. The sound attenuation refers to the ability to block the incident noise and can be quantified by the insertion loss (IL). The OE is often described as an amplified and distorted perception of physiological noises, such as one’s own voice, which may sound boomy or cavernous, particularly at low frequencies, when the EC entrance is obstructed. This effect results from both an increase in sound transmission through tissues (skin, cartilage, bone), primarily at frequencies below 1 kHz, and a decrease in air-conducted sound transmission due to the presence of the occlusion device. The OE can be objectively measured by calculating the difference between the sound pressure levels in the open ear and the ear occluded by the earplug when stimulated by tissue conduction, either through physiological noises or a bone conduction transducer.

The sound attenuation and OE can be measured directly on human subjects or using original laboratory tools, called "comfort testers". These testers are intended to help manufacturers improve the comfort of their earplugs by knowing the objective characteristics that influence comfort, but by freeing themselves from participants. This is similar to what is done to estimate the acoustic performance of the protector by measuring its acoustic attenuation in the laboratory on artificial heads (also called ATF for "Acoustic Test Fixture" in English), equipped with an ear simulator. These earplug comfort testers can operate in the real world using physical sensors — we then speak of an "experimental" tester — or in an idealization of the real world using virtual sensors — we then speak of a "virtual" tester. In the latter case, we refer to an analytical or numerical model capable of predicting the physical characteristics of interest. A virtual tester can be useful to (i) better understand the physical mechanisms involved in the triad, (ii) study the effect of various factors on the quantity of interest (acoustic or mechanical), (iii) help design real-world testers.

Commercially available ATFs fail to assess key physical characteristics related to acoustic comfort, as they do not account for essential features such as realistic EC geometry and various tissue conduction paths that influence the sound pressure field in the EC induced by external or internal sound sources [8,9]. As a result, they are unable to capture intra- and inter-individual variability in these characteristics. These reasons make them unsuitable for evaluating sound attenuation and OE from a comfort perspective [10]. Therefore, developing more realistic testers is crucial to accurately replicating the EC/earplug system under both acoustic and mechanical excitations.

This paper provides a comprehensive synthesis of various virtual and experimental testers developed by the authors’ research team to assess sound attenuation and OE, both of which could influence acoustical comfort. These testers can be classified into two categories, distinguished by the level of geometric simplification they consider: (i) truncated ears of various anatomical complexity that consider a region of tissues surrounding a simplified or realistically shaped EC, including or not the pinna and (ii) whole head.

The synthesis presents key principles, selected example results, and limitations of each comfort testing method, starting with experimental and virtual testers for sound attenuation and followed by an analysis of those for the OE.

2. EXPERIMENTAL AND VIRTUAL TESTERS FOR SOUND ATTENUATION

2.1 Realistic truncated ears (Fig.1(a), (b) and (c))

The first tester, shown in Fig.1(a), includes an experimental version and its virtual counterpart. It features a realistic EC and surrounding tissues [11] reconstructed from medical images of a participant. The synthetic materials were selected for their mechanical properties, close to those of biological tissues. The experimental tester, manufactured by a company specializing in anatomical phantoms, includes an embedded microphone positioned at the eardrum but lacks an eardrum simulator. The tester evaluation was based on comparing the predictions provided by the virtual tester with those obtained using the associated experimental tester, both in the open ear and in the ear occluded by a cylindrical steel earplug. The latter has the advantage of being non-deformable and having well-characterized mechanical properties. Although the numerical model generally reproduces the trends observed experimentally,

particularly in terms of pressure levels in the open and occluded ear as well as attenuation (not shown here), some differences persist in certain frequency bands. A calibration of the material properties in the finite element model could improve this correspondence. Furthermore, the steel earplug poses challenges related to the contact conditions with the surrounding tissues. The use of a more conventional earplug, such as a molded silicone earplug, could facilitate the evaluation of the tester. Finally, the simulated IL follows a similar evolution to the attenuation curves measured on human subjects: an increase in attenuation up to the resonance frequency of the open canal, followed by a decrease.

The experimental tester was also evaluated against a reference participant who served as a model of the artificial ear and a commercial ATF. Attenuation measurements for 2 types of earplugs were conducted using the 3M E-A-Rfit system at 3 insertion depths. Results (not shown here) show that the artificial ear better replicate attenuation for roll-down foam earplugs than commercial ATF. However, for push-to-fit earplugs this remains challenging for both. Discrepancies between the virtual tester, the experimental tester, and participant measurements may be attributed to several issues with the experimental tester. These include: (i) material defects—such as degradation of the soft-tissue analogs in the EC due to overly thin walls and irregular surface conditions—that can induce acoustic leaks (ii) insufficient self-IL of the artificial ear, (iii) the fact that synthetic materials at room temperature mimic biological tissues at body temperature, leading to potential deviations (iv) the absence of a heating system which may affect the earplug's behavior and the lack of a eardrum simulator.

To circumvent some of the issues associated with the previous truncated artificial ear (manufacturing defects and self-IL), a simplified version, devoid of cartilage was considered (see Fig.1(c)). It was designed based on a different participant and manufactured at the ICAR laboratory using 3D printing and a soft tissue molding technique. This artificial ear is integrated into a cylindrical metal housing, simulating an artificial head, to limit parasitic transmissions through the side and rear walls of the artificial ear. Preliminary results (see Fig.2) show that the attenuation of the earplugs measured with the artificial ear is lower at low frequencies than that observed on the corresponding human participant, regardless of the insertion depth. At higher frequencies, the results are closer but may be higher or lower depending on the insertion depth. These discrepancies may arise from (i) an overestimation of tissue conduction due to the use of a single homogeneous, overly soft material to represent soft tissues, (ii) the absence of a heating system, (iii) the fact that artificial materials at room temperature mimic biological tissues at body temperature, and (iv) the lack of cartilage and an eardrum simulator.

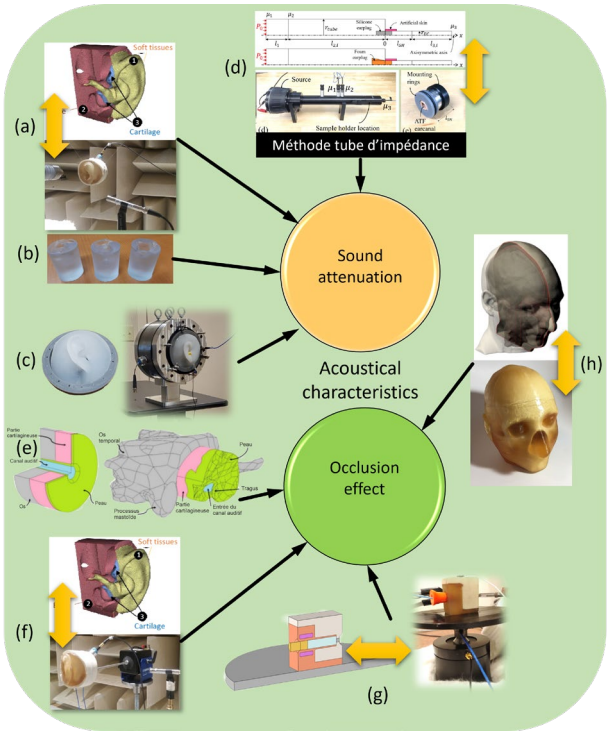


Figure 1. Experimental and virtual testers to assess acoustical physical characteristics of the coupled system EC/earplug

The testers of Fig.1(a) and (c) replicate the artificial ear of a specific individual. In contrast, the experimental tester in Fig.1(b) was designed to incorporate multiple artificial ears with realistic EC geometries but a simplified anatomical structure, adapted to the measurement of sound attenuation and representative of a sample of workers. An anthropometric analysis of a sample of ECs made it possible to identify three groups characterized by distinct morphologies [12]. For each group, the EC closest to the barycenter was selected as a representative model. Three artificial ears were thus manufactured using 3D printing, using a soft elastic resin of Shore 00 = 90 at room temperature. Heated to 37 ° C, these ears were evaluated for several earplugs using the 3M E-A-Rfit system, comparing them to measurements taken on participants during field training sessions. For each earplug, eight measurements were made, with insertions varying between standard depth and deeper insertion. The results (not displayed here) show that the ranking of sound attenuation obtained with these artificial ears is generally consistent with that observed in

participants. However, while these testers satisfactorily represent the attenuation variability measured for pre-molded earplugs, they have limitations for roll-down foam earplugs and pre-molded foam with stems, where significant amplitude differences occur. These differences could be attributed to the excessive rigidity of the artificial tissue, the absence of cartilage and artificial eardrum, and potential parasitic transmissions through the lateral and rear sides of the truncated ears.

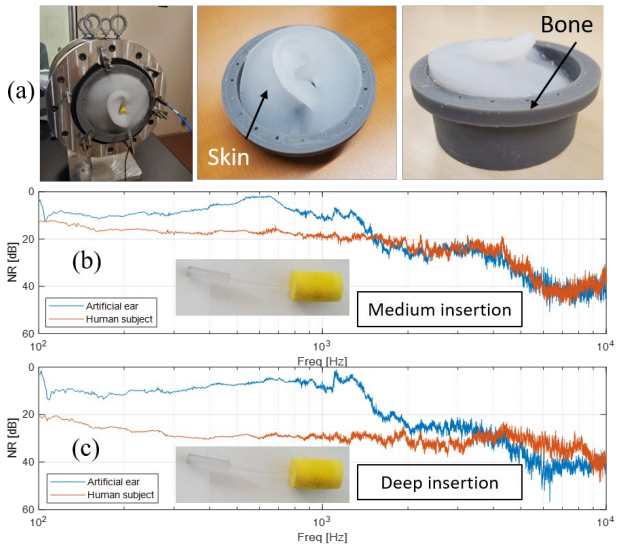


Figure 2. (a) Zoom on tester, noise reduction of a surrogate roll-down foam earplug measured with artificial ear and participant for (b) medium and (c) deep insertion.

2.2 Simplified truncated ear and the use of an impedance tube (Fig.1(d))

Although commercial ATFs are useful for assessing the sound attenuation of earplugs, they have drawbacks. They are costly and require expensive and bulky experimental setups, such as reverberation or anechoic chambers; they typically use a single-size EC, which does not account for variations in EC morphology between individuals and can result in significant differences in personal attenuation. Finally, commercial ATF measurements provide limited understanding of how the intrinsic acoustic properties of earplugs influence attenuation.

To address these challenges, a method for estimating earplug sound attenuation has been developed along with an associated experimental tester [13]. The technique allows to determine the acoustic properties of an earplug (transmission and reflection) inserted in a simplified truncated ear, consisting of a cylindrical artificial EC with a skin layer, all placed in an impedance tube. These acoustic properties are obtained from acoustic measurements upstream and downstream of the truncated ear, as well as using two separate acoustic loads. The measured earplug acoustic properties are then used as inputs to a one-dimensional analytical model to calculate the IL of the earplug. The latter is decomposed into two terms: the transmission loss (TL), which depends only on the physical objective characteristics of the "EC/earplug" system namely, mechanical properties of the inserted earplug and surrounding soft tissues as well as insertion depth, and a correction term, which depends on the reflection coefficients of the earplug medial face, the entrance to the EC and the medial termination of the EC.

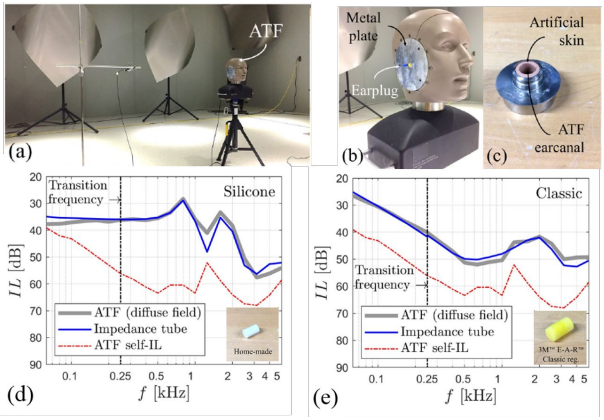


Figure 3. (a) ATF placed in the reverberant room, (b) zoomed-in view of the ATF, (c) ATF EC, Third octave band IL measured on ATF and estimated using the proposed impedance tube method for a silicone earplug (d) and roll-down foam earplug (e). The self-IL of the ATF is also displayed.

In parallel, two virtual testers (not shown here), based on numerical FE models of the experimental tester and an ATF, were developed to test the approach. The first simulated measurements to estimate the earplug's acoustic properties, which were then used in the one-dimensional analytical model to calculate the IL. The second simulated the IL on the ATF, allowing numerical evaluation of how the excitation field (normal incidence plane wave versus diffuse field) affects sound attenuation. The one-dimensional analytical model used to calculate the IL from the acoustic properties of the earplug was verified using the results provided by the previous virtual tester, which acted as a reference. The results obtained with the two testers agree and indicate that the attenuation of an earplug obtained in the tube is representative of that measured in a more realistic acoustic field. Furthermore, experimental

comparisons, on various types of earplugs, between the results obtained with the proposed measurement technique and those from a commercial ATF (see Fig.3) further validates the method. The main limitation of the method concerns its working frequency range determined by the tube diameter (about 6.5 kHz for a diameter of 29mm).
This impedance tube method offers several advantages over ATFs: (i) the technique uses a commercially available impedance tube, thus eliminating the need for an ATF (including the ear simulator) and an acoustic chamber, (ii) the method allows easy integration of different EC geometries using different sample holders, (iii) the method decomposes the earplug's IL into two a TL and a factor influenced by the acoustical characteristics of both open and occluded ear canals, providing deeper insight into sound attenuation and enabling more effective control, and (iv) the method enables the direct incorporation of eardrum impedance variability during post-processing by allowing the calculation of earplug attenuation for any tympanic acoustic impedance once its transmission and reflection properties have been determined.

3. EXPERIMENTAL AND VIRTUAL TESTERS FOR THE OCCLUSION EFFECT

3.1 Truncated ears (Fig.1 (e-g))

Virtual truncated ear testers, shown in Fig.1(e) and consisting of both lumped and FE models, were used to gain deeper insight into the fundamental physical phenomena underlying OE. These two modeling approaches are complementary. FE models supply input parameters for lumped models, while the latter offer a practical framework for interpreting FE simulations. For the FE testers, the set of mechanical boundary conditions and applied excitations was adjusted to reproduce a plausible vibration pattern of the EC wall [14] or to obtain simulation results consistent with experimental data from the literature on OE measured on groups of human subjects [15,16]. The virtual testers showed that OE occurs because blocking the EC creates a closed air cavity between the occlusion device and the eardrum, making it harder for the EC walls to compress it, which increases the acoustic pressure generated in the occluded EC. These models also allowed to revisit and clarify the interpretation commonly adopted in the literature of the OE—notably the influence of the high-pass filter of the open EC and the way in which this effect is modified by its occlusion—an interpretation which, although widespread, suffers from several ambiguities [17]. The first 3D numerical models of truncated cadaveric ears made it possible to highlight the influence of the vibration distribution of the EC wall on the OE [14]. The spatial distribution of the normal vibration of the open EC was characterized, at low frequencies, by the position of its barycenter along the curvilinear axis of the EC [18]. The axisymmetric 2D FE models then made it possible to study the mechanisms of contribution of earplugs to the OE [15,16]. Two mechanisms were highlighted: (i) a Poisson effect induced by the normal component of the parietal vibration of the EC and (ii) a longitudinal movement caused by the tangential component of this vibration.

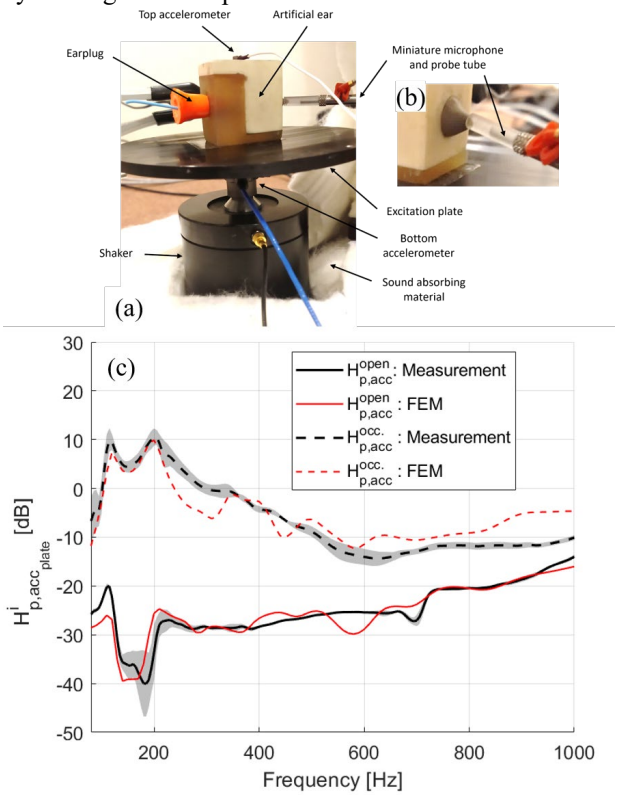


Figure 4. (a) View of tester of Fig.1(g), (b) rear view of the tester, (c) comparison between virtual and experimental tester - transfer functions between eardrum sound pressure and acceleration of excitation plate for open and occluded ears

The virtual tester presented in Fig.1(f) has been partially validated against its experimental counterpart [8,16] in the case of the steel earplug also used in section 2.1. The simulation of the objective OE approximately reproduces the slope of the measured data. However, significant deviations remain in some frequency bands. These discrepancies are attributed to differences in material properties, boundary conditions, coupling conditions or applied loads, between the experimental setup and the

simulation. For other types of earplugs, the validation of the virtual tester was not successful. Furthermore, the evaluations of the experimental tester against groups of participants did not give satisfactory results. Finally, the experimental tester was not directly confronted with the human subject from which it was designed.

To address the challenges associated with the tester shown in Fig.1(f), a new tester based on it and illustrated in Fig.1(g) was designed to simplify the validation process [9]. A virtual tester was developed first, followed by the manufacturing of its experimental counterpart (without artificial eardrum and heating system). The ear canal was reshaped into a straight cylinder with a circular cross-section, and the external boundaries of the truncated ear were modified into a parallelepiped form. The proportions of soft tissue, bone, and cartilage volumes were preserved relative to the realistic 3D artificial ear. Careful material selection and precise manufacturing ensured the faithful reproduction of key features essential for studying the OE. It also integrates excitation and boundary conditions that are more easily mimicked in the virtual tester. Its parallelepiped shape also facilitates experimental manipulations.

After rigorous calibration, the virtual tester was successfully validated against the experimental tester, in particular by comparing the transfer functions between eardrum sound pressure and acceleration of excitation plate for open ear and ear occluded by a silicone earplug (see Fig.4 (c)). The experimental tester was also successfully evaluated against measurements made on a group of participants. This device was shown to reproduce the main effects observed in OE measurements of several earplug types on participants, including (i) significant OE at low frequencies, decreasing with increasing frequency, (ii) reduced OE for deeper earplug insertion, and (iii) differences in OE between earplug types, particularly marked for deep versus shallow insertions. A numerical study also highlighted that the absence of cartilage significantly amplifies OE at low frequencies. Furthermore, the position of the cartilage influences OE, particularly when the artificial ear upper part is fixed. This tester was notably used to validate an innovative metamaterial earplug with reduced OE [19,20] which was then tested regarding perception and comfort judgment on human subjects [7].

The main limitations of this tester are the presence of parasitic structural resonances, which are not representative of what happens in a real head and the dominance of the air-conducted path over the bone conducted one when the EC is open in some frequency bands, potentially leading to an underestimation of OE compared to measurements on participants using a bone transducer.

3.2 Whole head (Fig.1 (h))

Two virtual testers based on the FE method and one experimental tester were developed from magnetic resonance images and computed tomography scans of a participant's entire head. The medical images were segmented using image processing software to reconstruct various anatomical structures of the head, namely soft tissues, auricular cartilage, bone, brain and cerebrospinal fluid, excluding middle and inner ears.

The first virtual tester, representing the participant (Virtual Participant), integrates tissue properties based on scientific literature and accounts for the acoustic effect of the middle and inner ear via an acoustic impedance boundary condition at the eardrum. The second, called Virtual AP-ATF is the counterpart to an experimental tester called augmented physical ATF (AP-ATF) made of artificial materials of known mechanical properties that mimic biological tissues. Unlike the Virtual Participant, neither the Virtual AP-ATF nor the experimental AP-ATF account for the acoustic effect of the middle and inner ear. Based on these testers, rigorous calibration and validation of the FE models used to simulate the physics are possible, as the simulations can be compared to measurements performed on the corresponding participant and on the associated AP-ATF [16].

The Virtual Participant tester was validated against experimental data from the literature on participant groups, as well as measurements on the participant used for its development (see Fig.5). It satisfactorily reproduces known effects, such as the reduction of OE with increasing earplug insertion depth and the influence of the earplug type on OE, particularly for deep insertions.

The Virtual AP-ATF tester was validated by comparing the simulated results with experimental data from the AP-ATF (see Fig.6). Although both testers were not calibrated, comparisons showed generally satisfactory results, with deviations of less than 5 dB. However, the results obtained with the AP-ATF show discrepancies compared to the measurements made on the participant. These differences could be due to the inadequacy of the synthetic materials used to reproduce biological tissues.

During the development of the virtual testers, several significant advances in modeling have been made [21,22] (i) the use of a perfectly matched layer improves the agreement of simulated results with experimental data, compared to a classical radiation impedance condition, (ii) the boundary conditions at the base of the head mainly influence the OE at very low frequencies (< 0.25 kHz), and (iii) modeling the external fluid and tympanic membrane's influence on the EC acoustic field using an impedance condition requires adaptation to account for the global

motion of both the EC entrance and the tympanic membrane. Otherwise, errors in the eardrum sound pressure can occur, especially when the EC is occluded.

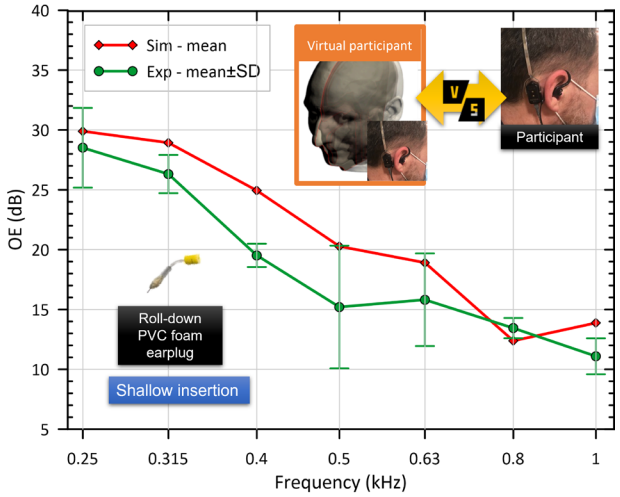


Figure 5. OE simulated using the Virtual participant and measured on the participant

The Virtual Participant tester was used to examine the effect of uncertainties related to several factors on the OE at low frequencies [21]:

• Position of stimulation on the head: the OE is not very sensitive to the global position of the stimulation (ipsilateral mastoid, contralateral mastoid, forehead). However, subtle variations in the stimulation position on the ipsilateral mastoid can contribute to the variability of the OE.

• Position of the measurement point in the EC: OE is little influenced by the exact position of the measurement point in the EC, especially for common earplug insertion depths. Differences between assessments performed at the medial surface of the earplug and at the eardrum are minimal, especially for medium or deep insertions. From an experimental point of view, these results suggest that OE, which is often measured at the medial surface of the earplug for safety and comfort reasons, is a good approximation of measurements performed at the eardrum.

• Mechanical properties of tissues: The stiffness of soft tissues and cartilage is a major factor influencing OE. This effect depends on the frequency band studied, with OE being more affected by the mechanical properties of soft tissues than by those of cartilage. At low frequencies, OE is sensitive to the skull bone Young's modulus, while the soft tissues Poisson's ratio also plays a key role.

Whole-head virtual testers provide more realistic FE simulations of EC vibration and sound pressure field than truncated ear models by accounting for full-head tissue conduction and eliminating boundary condition issues. Unlike other artificial ears used to assess the OE of earplugs [9], the whole-head tester allows for OE evaluation across different stimulation positions and can also be used for other hearing protection devices like earmuffs. However, the initial experimental prototype requires further refinement to better match participants' measurements.

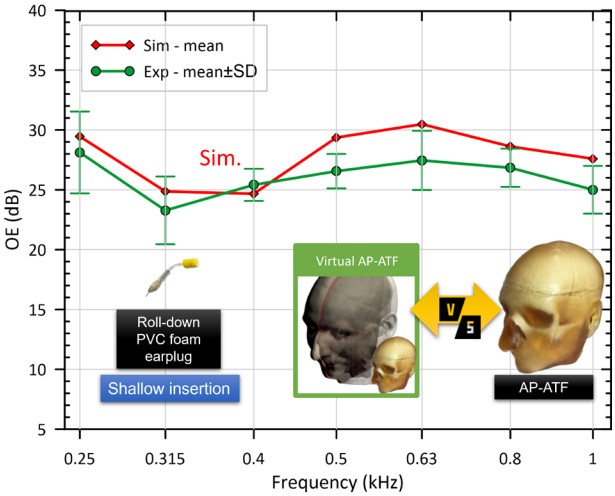


Figure 6. OE simulated using the Virtual AP-ATF and measured on the AP-ATF

4. CONCLUSIONS

This paper presented a synthesis of various virtual and experimental acoustic comfort testers developed by the authors' research team, designed to assess the sound attenuation and the OE of earplugs. While some testers are more advanced than others, they have collectively yielded promising results. Future work will focus on (i) optimizing synthetic materials to better replicate the EC/earplug interactions and tissue conduction, (ii) systematically integrating instrumentation (microphones, heating system and eardrum simulator), (iii) improve the knowledge about tissues and earplugs material properties, (iv) calibrating and validating sound attenuation and OE virtual testers, accounting for uncertainties, (v) incorporating inter-individual variability into both experimental setups and models and (vi) use whole-head virtual testers including middle and inner components to predict the differential intracochlear pressure and the subjective OE.

5. ACKNOWLEDGMENTS

We gratefully acknowledge IRSST (2015-0014), Mitacs (IT10643) and NSERC (RGPIN-2016-04926, RGPIN-2016–06795, I2IPJ 586099-2023), for funding this work.

6. REFERENCES

[1] O. Doutres et al., "A critical review of the literature on comfort of hearing protection devices: definition of comfort and identification of its main attributes for earplug types," *Int. J. Audiol*, 58, pp. 824–833, 2019.

[2] O. Doutres et al., "A critical review of the literature on comfort of hearing protection devices: Analysis of the comfort measurement variability," *Int. J. Occup. Saf. Ergon.*, pp. 1–12, 2020.

[3] O. Doutres et al., "Towards a Holistic Model Explaining Hearing Protection Device Use among Workers," *Int. J. Environ. Res. Public Health*, 19, p. 5578, 2022.

[4] B. Poissenot-Arrigoni et al., "Analysis of the physical discomfort of earplugs experienced by a population of Canadian workers and identification of the influencing variables," *Int. J. Ind. Ergon*, 98, p. 103508, 2023.

[5] A. Negrini et al., "Multidimensional comfort of earplugs – Development and validation of the North American COmfort of hearing PROtection Device questionnaire," *Saf. Sci.*, 181, p. 106688, 2025.

[6] C. Giguère, C. Laroche, V. Vaillancourt, and S.D. Soli, "Modelling speech intelligibility in the noisy workplace for normal-hearing and hearing-impaired listeners using hearing protectors," Int. J. Acoust. Vib., 15, pp. 156–167, 2010.

[7] K. Carillo, F. Sgard, O. Dazel, and O. Doutres, "Enhancing Acoustic Comfort for Earplug Users: Subjective Evaluation of Bone-Conducted Sound with Meta-Earplugs Incorporating Helmholtz Resonators," *Appl. Acoust (submitted)*, 2025.

[8] S. Benacchio, O. Doutres, E. Wagnac, and F. Sgard, *Design of realistic artificial ears dedicated to the study of the acoustic and physical comfort of in-ear hearing protectors R1106*, Montréal, IRSST, p. 104, 2020.

[9] O. Doutres et al., "On the design of an acoustical test fixture for assessing the objective occlusion effect," *Appl. Acoust.*, 228, p. 110295, 2025.

[10] B. Poissenot-Arrigoni et al., "Analysis of the functional and acoustical comfort of earplugs experienced by a group of workers in Canadian companies and identification of the influencing variables," *Int. J. Ind. Ergon (in preparation)*, 2025.

[11] S. Benacchio, F. Sgard, and O. Doutres, "Numerical modeling of the vibro-acoustic behavior of an artificial ear dedicated to the study of hearing protectors," *Proc. of Forum Acusticum* 2020, (Lyon, France), pp. 1–3, 2020.

[12] B. Poissenot-Arrigoni et al., "Morphologic clustering of earcanals using deep learning algorithm to design artificial ears dedicated to earplugs attenuation measurement," *J.A.S.A.*, 152, pp. 3155–3169, 2022.

[13] K. Carillo, O. Doutres, and F. Sgard, "An impedance tube technique for estimating the insertion loss of earplugs," *J.A.S.A.*, vol. 156, pp. 898–911, 2024.

[14] K. Carillo, O. Doutres, and F. Sgard, "Theoretical investigation of the low frequency fundamental mechanism of the objective occlusion effect induced by bone-conducted stimulation," *J.A.S.A.*, 147, pp. 3476–3489, 2020.

[15] K. Carillo, O. Doutres, and F. Sgard, "Numerical investigation of the earplug contribution to the low frequency occlusion effect induced by bone-conducted stimulation," *J.A.S.A.*, 150, pp. 2006–2023, 2021.

[16] K. Carillo et al., "On the modeling of the objective occlusion effect induced by earplugs: Recent advances, challenges and perspectives," *NHCA Spectr.,* vol. 38, pp. 15–22, 2021.

[17] K. Carillo, O. Doutres, and F. Sgard, "On the removal of the open earcanal high-pass filter effect due to its occlusion: A bone-conduction occlusion effect theory," *Acta Acust.*, vol. 5, pp. 1–6, 2021.

[18] K. Carillo, O. Doutres, and F. Sgard, "Principle of an acoustical method for estimating the centroid position of the earcanal wall normal velocity induced by bone-conducted stimulation: Numerical evaluation," *Appl. Acoust.*, 182, pp. 1–13, 2021.

[19] K. Carillo, F. Sgard, O. Dazel, and O. Doutres, "Reduction of the occlusion effect induced by earplugs using quasi perfect broadband absorption," *Sci. Rep.*, 12, p. 15336, 2022.

[20] K. Carillo, F. Sgard, O. Dazel, and O. Doutres, "Passive earplug including Helmholtz resonators arranged in series to achieve broadband near zero occlusion effect at low frequencies," *J.A.S.A.*, 154, pp. 2099–2111, 2023.

[21] H. Xu et al., "Simulation of the objective occlusion effect induced by bone-conducted stimulation using a three-dimensional finite-element model of a human head," J.A.S.A, 150, pp. 4018–4030, 2021.

[22] S. Kersten, F. Sgard, and M. Vorlander, "Impact of the ear canal motion on the impedance boundary conditions in models of the occlusion effect," J.A.S.A., 155, pp. 56–67, 2024.

DOI: 10.61782/fa.2025.0160

FORUM ACUSTICUM
EURONOISE 2025

AUDITORY DAMAGE RISK DUE TO INDOOR AND OUTDOOR SHOOTING

Frits van der Eerden* **Elisabeth van Pruissen** **Erik Salomons**
Paul de Krom **Ad van Heijningen**
TNO - Defense, Safety & Security, The Hague, The Netherlands

ABSTRACT

Many different weapons can be used for military training. For a safe working environment, the maximum permissible exposure needs to be predicted, taking into account the use of hearing protection. In the ISO 17201 standard part 6, 'Sound pressure measurements close to the source for determining exposure to sound', it is described how to capture the time history of the sound pressure at locations of interest, such as for an instructor or shooter. This time-history is the basis for further assessment, like the calculation of an auditory damage risk criterium. The objective of this research is to compare the measurement results using the ISO standard without a person present, with measurements using a microphone close to the head of the shooter or instructor. The A-weighted sound exposure is calculated (ASEL) as well as the Auditory Risk Unit (ARU) using the AHAAH model. Both indoor and outdoor measurement have been conducted for several small fire arms. It was seen that the tail of the time history has a large effect on the results for the ARUs. In addition, tests were carried out with small portable sound absorbing screens to reduce the muzzle blast towards the shooter, instructor and the environment.

Keywords: *shooting noise measurements, auditory damage risk, muzzle blast mitigation*

1. INTRODUCTION

To determine the auditory damage risk for shooting noise during military training, sound pressure measurements are needed close to the muzzle blast. Based on the time history of the sound pressure, the risk can be determined by applying an assessment method. This can be done by using the peak and time duration, the energy (such as the A-weighted sound exposure level: ASEL), or a physical model of the ear (such as the electroacoustic AHAAH model [2]). Each method yields different exposure variables, such as ASEL or Auditory Risk Units (ARU from the AHAAH model) [3].

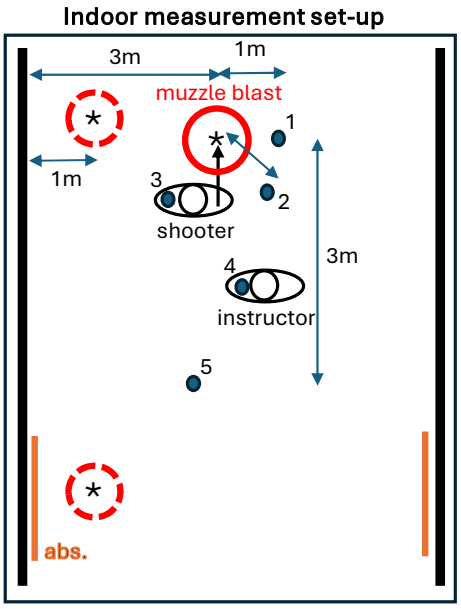


Figure 1. Measurement set-up using 5 microphones (blue markers) near the muzzle blast using 3 different firing positions (red circles).

*Corresponding author: frits.vandereerdenr@tno.nl
Copyright: ©2025 First author et al. This is an open-access article distributed under the terms of the Creative Commons Attribution 3.0 Unported License, which permits unrestricted use, distribution, and reproduction in any medium, provided the original author and source are credited.

In this paper measurement results are presented for different small caliber weapons, in an indoor and outdoor setting. The aim of these measurements is to compare the results for two different set-ups; one with a shooter present and one without a shooter; instead a weapon fixture is used. For the latter case the ISO 17201-6:2022 standard [1] is followed, in order to obtain measurements that are less dependent on the influences of the shooter and the microphone position close to the head of the shooter or instructor.

In Section 2 the ISO standard is introduced and in Section 3 the indoor and outdoor measurements are described. Section 4 discusses the results, with and without a shooter, using ASEL and AHAAH results.

Additional outdoor measurements were done, introducing two portable lightweight and sound absorbing screens, to reduce the muzzle blast exposure towards the environment and towards the shooter and instructor. The results for several positions of these screens are presented in Section 5.

2. ISO 17201-6 ON MEASUREMENTS

The ISO 17201 series 'Noise from shooting ranges' consist of 6 parts. The first part of ISO 17201 describes the measurement method to obtain the sound source energy and directivity of the muzzle blast or an explosive charge. The spectral levels can be used for the prediction of sound levels around shooting ranges (this is described in *part 3*). The standard is applicable to calibers of less than 20 mm or an explosive weight of less than 50 g TNT equivalent.

An important aspect for *part 1* of this standard is that the microphones are located at a distance where the peak levels are lower than 154 dB, so that the calculation of the source strength can be done with linear acoustic sound propagation models. As a result this standard cannot be used to determine the sound exposure levels close to the weapon (this is addressed in part 6).

ISO 17201 *part 6* is titled "Sound pressure measurements close to the source for determining exposure to sound" [1]. This part was added to the series to allow for sound exposure measurements at a short distance. It describes how to capture the time history of the sound pressure at the locations of interest, such as for an instructor or shooter. This time history is the basis for further assessment. The assessment itself is not within the scope of the standard.

The standard describes the requirements for a measurement system and the measurement set-up. A special case is described for the microphone position at the center of the head of the shooter. For a better reproducibility and comparison, the shooter should be removed and a weapons fixture should be used. The fixture shall be constructed in a way that minimizes reflections.

For part 6 the measured peak sound pressure levels can be higher than 154 dB, in contrast to the requirement for microphone positions used in *part 1* of ISO 17201, as (non-linear) propagation of the shockwave is not used in *part 6*.



Figure 2. Measurement set-up using 5 microphones close to hard walls (upper) and absorbing walls & ceiling (lower).

3. MEASUREMENT SET-UP

For the measurements, five microphones were used near the muzzle, see Figure 1. Microphones 1 and 2 are at 1 meter distance at the same height as the muzzle, at 90 and 135 degrees with respect to the firing direction. Microphone 3 and 4 are near the ear of the shooter and instructor,

respectively, or at the center of the head when there is no person present. Microphone 5 is at 3 meters distance to the back and was added for a comparison with German measurements.

Figure 1 shows the set-up for the position in the center of the indoor shooting range. It also shows two other positions: close to the reflecting walls and close to the absorbing walls and ceiling.



Figure 3. Outdoor measurement set-up using 5 microphones.

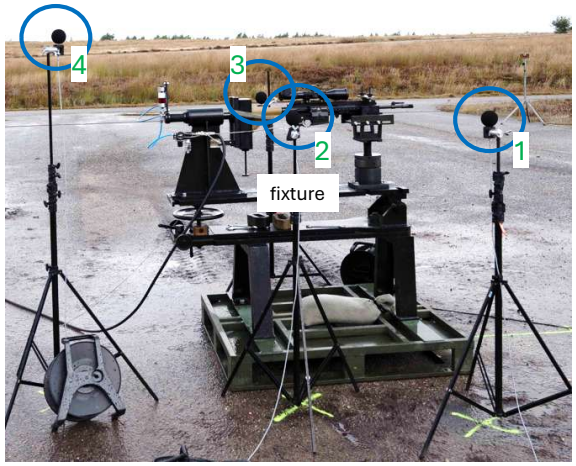


Figure 4. Outdoor measurement using a weapon fixture.

The photos in Figure 2, 3 and 4 give an impression of the indoor and outdoor measurements. Figure 2 shows two shooting positions: near the reflecting walls and ceiling as well as near the absorbing walls and ceiling. Figure 3 shows the outdoor set-up for a standing shooter (a prone position was also used), while Figure 4 shows the rifle in the weapons fixture. In this case the rifle was operated from a distance using a rope.

For the indoor measurements a 5.56 and 8.6 mm caliber rifle was used. For the outdoor measurements an additional 7.62 mm rifle was used. Standing and prone position were measured for both the 5.56 and 7.62 mm rifles. The 8.6 mm rifle was only used in a prone position. Also, a second shooter was included for 5.56 mm to capture possible differences.

At each position a series of 12 shots was measured. The average of these shots are presented in the next section.

4. RESULTS & COMPARISON

4.1 Indoor shooting

Figure 5 shows the (unweighted) sound exposure levels in octave bands for the 5.56 mm rifle, at the 5 microphone positions and for 4 different positions: 1) in the center of the indoor range using a shooter, 2) idem, using a fixture, 3) close to the fully reflecting walls using a shooter, and 4) close to the absorbing walls using a shooter.

Comparing the results for using a shooter (black line) and a fixture (blue line) shows that there is not a significant difference for the sound levels.

When moving the muzzle closer to the hard walls the sound levels are about the same, compared to the center position. The main difference can be seen in the interference pattern (due to the reflection) around 32 and 63 Hz. This can be seen best for the microphone at the shooter position (mic 3).

As expected, by using absorbing walls and ceiling the sound levels are reduced; the multiple reflections are damped. The largest reductions are for the instructor position and the microphone position that is 3 m to the back (mic 5).

On the right-hand side of the figures the results from the AHAAH model are given (in ARU). The results are calculated for 23 frequency bands and the maximum value is reported as the auditory risk. For microphones 3 and 4, at the shooter and instructor positions, a maximum value around 1500 ARU is obtained. Note that a dose above 500 ARU is unsafe, and that a daily limit of 200 ARU is recommended. In that case no temporary threshold shift is expected.

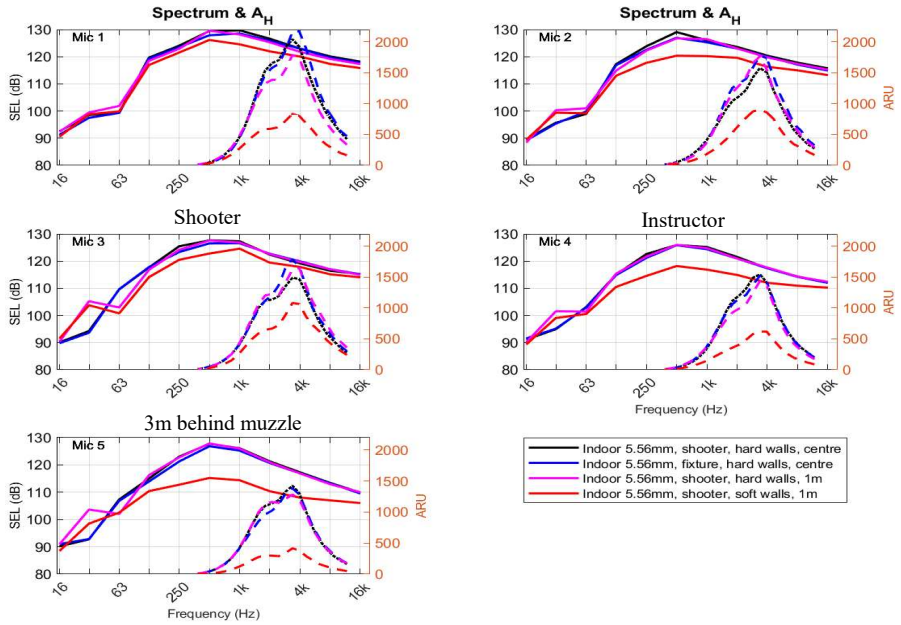


Figure 5. Indoor measurement results for a 5.56 mm rifle at 5 microphone positions and 4 different situations (see legend).

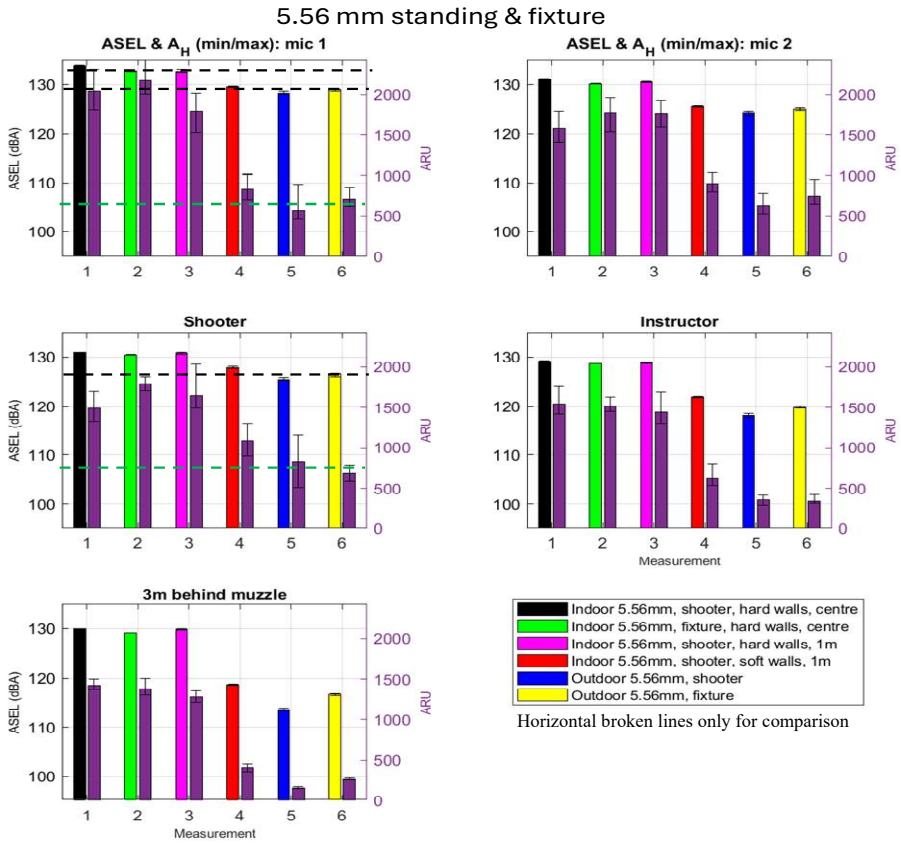


Figure 6. Indoor (& outdoor) measurement results for a 5.56 mm rifle at 5 microphone positions and 6 situations (see legend).

Comparing the ARU for the shooter position (mic 3) with and without a shooter shows a difference of about 200 ARU, while for the instructor position the difference is very small. Remember that the difference in sound levels is small when comparing the shooter and fixture (mic 3).

Figure 6 shows the single value results for the 5.56 mm rifle: the A-weighted sound exposure levels ASEL in dB(A) and the AHAAH (or A_H) results in ARU. Also included are the results for the outdoor measurements (blue & yellow bars), which only include the direct muzzle blast and the ground reflection.

For both the ASEL and ARU also the maximum and minimum values within a series are shown in black. Especially for the ARU the variation can be more than 20%. The ASEL variations are much smaller than 1 dB(A) (note that 1 dB = 26%).

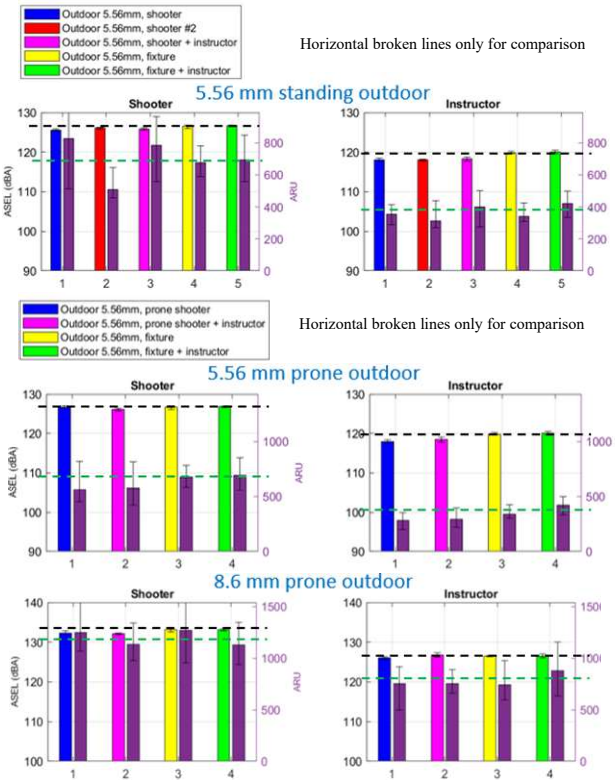


Figure 7. Outdoor measurements results for 5.56 and 8.6 mm weapons at shooter & instructor positions and for different situations (see legends).

The difference in dB(A) between using a shooter or a fixture is small. The ARU results are also in the same range; they can be higher, compared to a fixture, but also lower.

The indoor sound levels are around 6 dB(A) higher compared to outdoors (factor of 4). The ARU results can be up to 3 times higher, compared to outdoors.

4.2 Outdoor shooting

A selection of the outdoor results is given in Figure 7, at the shooter and instructor positions. In the upper figure there are five situations given for the 5.56 mm rifle: 1) with a shooter and no instructor present, 2) with another shooter (smaller), 3) with an instructor present, 4) with a fixture, and 5) with a fixture and an instructor present. It can be seen that the sound levels are within 1 dB(A), while the ARU show larger differences; 100 ARU or more. It is remarkable that for shooter #2 the ARU is substantially lower.

When using the prone position the differences when using a fixture (with a larger muzzle height) are small. The ARU results are a bit lower when using a shooter. The variation within a series is larger when using a shooter compared to using a fixture.

For the 8.6 mm rifle, used in the prone position, the results are similar, when comparing the shooter with the fixture.

4.3 Conclusions

To summarize the results for the indoor and outdoor measurements:

- Using a fixture instead of a shooter gives the same results in dB(A).
- The prone position gives slightly lower levels in dB(A) compared to using a fixture, around 1 dB(A).
- Within a series of 12 shots the ARU can differ up to a factor of two.
- The ARU results when using a shooter or a fixture are in the same range:
  - They can be higher, compared to a fixture, but also lower.
  - For the 7.62 mm standing position only, the ARU results with a shooter are more than a factor of 2 higher compared to using a fixture.

4.4 ARU growth as a function of time

With the AHAAH model one can visualize the ARU growth as a function of time, for example to see the differences between two situations. This is shown in Figure 8 for the 5.56 mm rifle, near the hard and near the absorbing walls, displaying a 1000 ms signal length. Figure 9 shows the corresponding time-pressure history, only for the first 30 ms. This shows that the reflections in the tail of the signal from the hard walls results in an ARU that is three times higher compared to the absorbing walls, where these reflections are much smaller (indicated with the green ellipse).

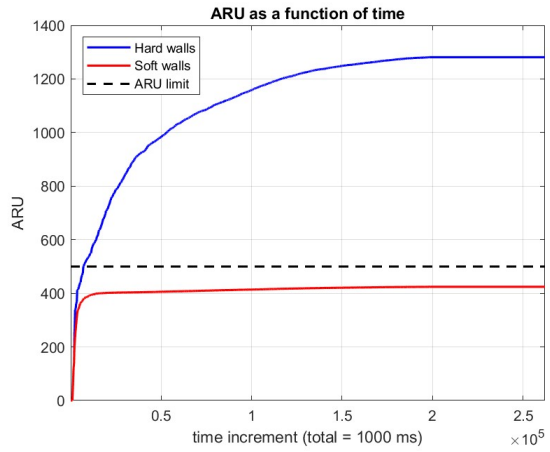


Figure 8. Growth of ARU as a function of time.

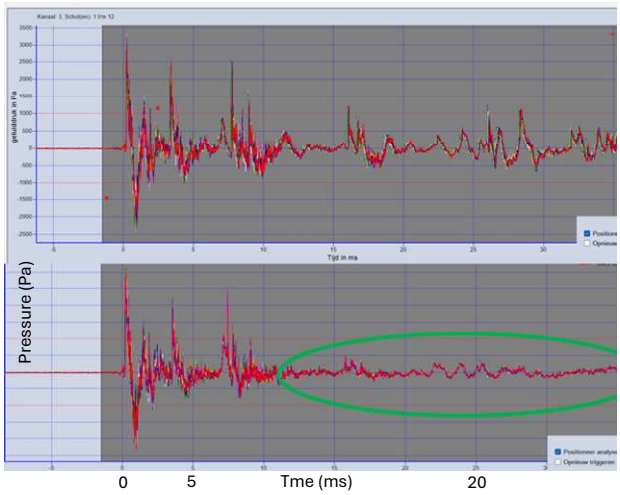


Figure 9. Muzzle blast and reflections (5.56 mm) for hard walls (upper) and absorbing walls & ceiling (lower).

5. OUTDOOR ABSORBING SCREENS

To reduce the contributions of the muzzle blast towards the environment, the performance of closely positioned screens was investigated. The screens are lightweight, so easy to move, and have absorbing panels on the side facing the muzzle blast. In addition the sound levels and auditory risk for the shooter and instructor were measured and compared to the situations without screens.

Two different rifles were used, with a 7.62 and 12.7 mm caliber. The 7.62 mm was used in kneeling and prone position. The 12.7 mm produces a very strong muzzle blast. It was seen that the thin surface layer covering the absorbing material did not remain intact when used close to the muzzle.

The absorbing panels (60 x 120 cm) consist of glass fiber core with a thickness of 5 cm. The are covered by a polyester film, so no gunpowder residue can penetrate the material.

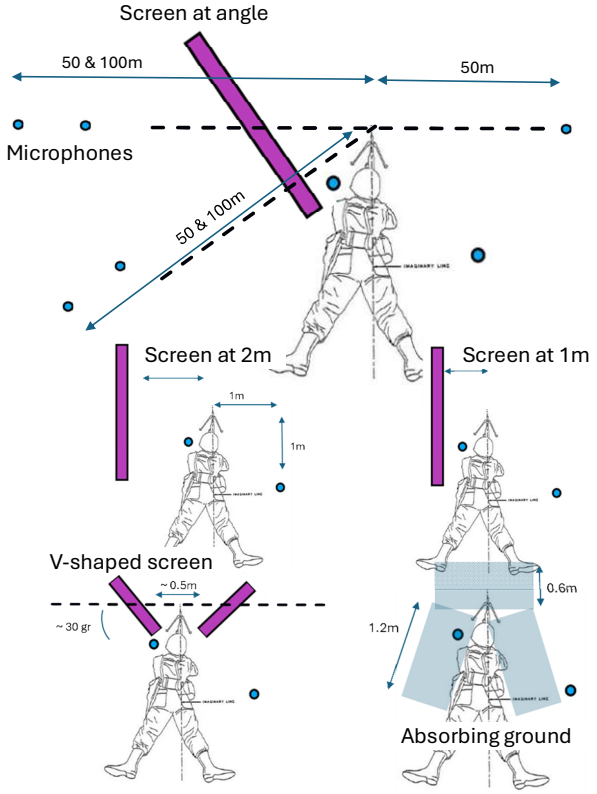


Figure 10. Four different positions of the absorbing screens and absorbing panels (in purple). One position with absorbing panels on the ground (in gray).

5.1 Measurement set-up

Figure 10 shows four positions for the absorbing screens. In fact, there are two screens each with a height of 180 cm and 120 cm wide. The upper figure shows the screen with an angle of 30 degrees w.r.t. the firing direction. The middle figures shows the screen at a distance of 2 and 1 meter from the muzzle. The lower figure shows the two screens in a V-shape (left) and using only the absorbing panels on the ground (right), to suppress the ground reflection. The photos in Figure 11 and Figure 12 further illustrate these set-ups.



Figure 11. Absorbing screen at 2m distance (upper) and at 1m distance (lower).



Figure 12. V-shaped absorbing screens.

As indicated in Figure 10, seven microphones were used: two for the shooter and instructor positions, four behind the screen at 50 and 100 meter from the muzzle (right-hand side, and one in the opposite direction (left-hand side).

5.2 Results

Single value results in dB(A) for the 7.62 mm caliber rifle in prone position are presented in Figure 13. The black bar results are for the situation without a screen and the colored ones for using a screen or an absorbing ground. The upper picture is for the shooter and instructor microphones, and also show the ARU results. It can be seen that using a screen has a small effect in dB(A), while the ARU can either be higher or lower (see also Table 1).

The middle picture shows the microphone position 50 m to the right, where a contribution due to a reflection may exist. This is not the case, the levels are the same or lower (especially for the V-shaped screens, shown in red)

For the microphones behind the screens larger reductions can be seen up to 10 dB(A).

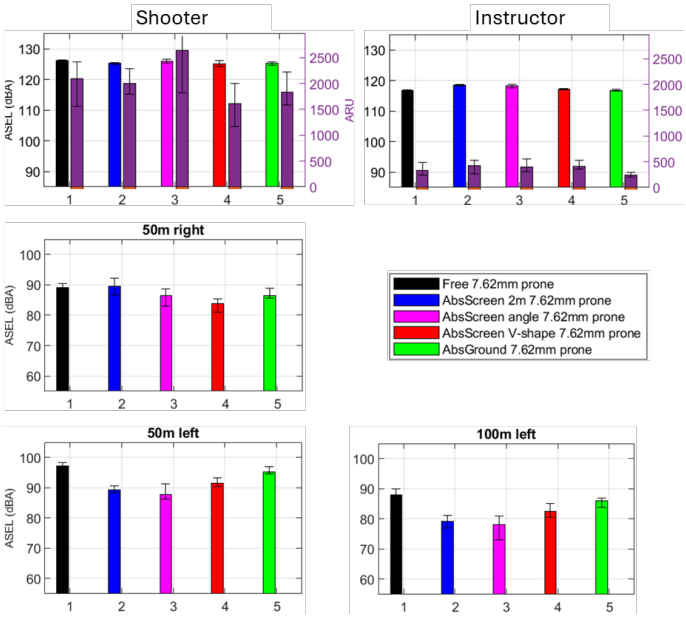


Figure 13. Measurement results in dB(A) and ARU without (black) and with absorbing screen/panels (color).

The differences, compared to the situation without a screen, are summarized in Table 1. The upper section lists the results in ARU for the shooter and instructor positions. The lower sections is in dB(A) for the microphones at 50 and 100 meters distance. When there is an increase the values are shaded in red.

The ARUs show quite a mixed result. For the shooter with a 7.62 mm rifle the results are positive, in general. While for the 12.7 mm rifle it is more negative in general. The instructor results are mostly negative as well. This is a bit surprising, as the other persons that were present behind the weapon observed a noticeable reduction, especially for the 12.7 mm rifle. Further investigation of these results is ongoing.

The reductions in dB(A) for the environment are more consistent. At 50 and 100 meter to the left, the reduction with a screen at 2 or 1 meter ranges between 6 to 10 dB for the 240 cm long and 180 cm high screen, both for the 7.62 and 12.7 mm rifles. While the reflection to the opposite side is between 0 and 1 dB.

The V-shaped barrier also provides a reduction to the left-hand side, between 5 and 6 dB.

The use of absorbing panels on the ground can reduce both the auditory risk in ARU and the sound exposure in dB(A). Only for the 12.7 mm rifle at the instructor an increase in ARU is measured, but this caliber produces a too strong muzzle blast for the absorbing panels to last.

Table 1. Reduction in ARU and dB(A) compared to the unscreened situation. Increase is shown in red.

Reduction w.r.t. unscreened				
Person (ARU)	Shooter	Instructor	Shooter	Instructor
	7.62mm	7.62mm	12.7mm	12.7mm
Abs. screen at 2m	94	-100	62	-229
Abs. screen at 1m	150	-96	-747	-155
Abs. screen at angle	-545	-73	-439	-134
V-shape screen	485	-83	-407	30
V-shape screen (hard)			-698	-90
Abs. ground	260	87	670	-167
Environment (dB(A))	50m right	50 & 100m left	50m right	50 & 100m left
	7.62mm		12.7mm	
Abs. screen at 2m	-1	8, 9	-1	8, 6
Abs. screen at 1m	0	8, 9	-1	9, 7
Abs. screen at angle	2	9, 10	0	9, 7
V-shape screen	5	5	6	8, 7
V-shape screen (hard)			2	5, 5
Abs. ground	2	2	1	1, 0

6. DISCUSSION AND CONCLUSIONS

Sound pressure measurements close to the muzzle blast of small caliber weapons have been carried out for an indoor and outdoor shooting range. The A-weighted sound exposure and the auditory risk units (ARU) from the AHAAH model have been calculated. A comparison of measurements with a shooter and with a weapon fixture have been made, showing a good correspondence for the sound exposure levels in dB(A). For the ARU results larger variations were seen though. The AHAAH model shows a sensitivity for variations in the pressure-time history that is not seen for the A-weighted sound exposure level. Note that a similar observation was made for the measured dose-response relation functions in tactical training environments; for the $L_{Aeq,8h}$ levels a better prediction for the temporary threshold shifts (TTS) was found then when using the AHAAH model [4].

In addition, tests were carried out with small portable sound absorbing screens to reduce the muzzle blast towards the shooter, instructor and the environment. For the environment reductions up to 10 dB(A) were obtained, behind the screen. For the opposite direction the contribution due to reflection is between 0 and 1 dB(A). Again, the ARU results show large variations, with either a reduction or an increase for the shooter and instructor positions.

7. ACKNOWLEDGMENTS

This work is done for The Netherlands Ministry of Defense (MoD-NL), within the BMW4-35 project for MoD-NL CEAG. The measurements were carried out by the MoD-NL KCWM department and this cooperation is gratefully acknowledged.

8. REFERENCES

[1] ISO 17201-6:2022 *Acoustics - Noise from shooting ranges - Part 6: Sound pressure measurements close to the source for determining exposure to sound.*

[2] G. R. Price and J. T. Kalb, "*The Philosophy, Theoretical Bases, and Implementation of the AHAAH Model for Evaluation of Hazard from Exposure to Intense Sounds*", United States Army Research Laboratory, ARL-TR-8333, Apr. 2018.

[3] F. van der Eerden, E. van Pruissen, E. Salomons, "Different exposure prediction methods for a wide range of impulsive noises: do they correlate?", *Proc. of Forum Acusticum 2023*, (Turin, Italy), 2023

[4] D. Kulinski et al, 'Estimated dose–response relationship between impulse noise exposure and temporary threshold shift in tactical training environments', *J. Acoust. Soc. Am.* 157 (3), March 2025

DOI: 10.61782/fa.2025.0172

FORUM ACUSTICUM EURONOISE 2025

BEYOND THE STANDARD AUDIOGRAM: THE NEED FOR COMPREHENSIVE ASSESSMENT OF COMBAT NOISE AUDITORY TRAUMA

Shai Chordekar[1], Devora Brand[2,3], Cahtia Adelman[2,3], Rachel Fraenkel[2,3], Nitza Horev[4,5], and Nir Fink[1]

[1] Department of Communication Disorders, Acoustics and Noise Research Lab in the Name of Laurent Levy, Ariel University, Ariel 40700, Israel.

[2] Department of Communication Disorders, Jerusalem Multidisciplinary College, Jerusalem 9101001, Israel.

[3] Speech and Hearing Clinic, Hadassah University Medical Center, Jerusalem 9112001, Israel.

[4] Institute for Hearing, Speech and Balance, Department of Otolaryngology, Head and Neck Surgery, Tel-Aviv Sourasky Medical Center, Tel-Aviv 6423906, Israel.

[5] Communication Sciences and Disorders, Ono Academic College, Kiryat Ono 5545001, Israel.

ABSTRACT

Combat noise exposure poses significant risks to auditory health, including high-frequency sensorineural hearing loss, synaptopathy, and central auditory processing deficits. However, sometimes, combat noise acoustic trauma results in undetectable damage using standard audiometric evaluations. Such impairments, frequently caused by blast-related injuries, may manifest as difficulty in understanding speech in noise, tinnitus, or other auditory complaints, even when conventional audiograms indicate normal thresholds. This work emphasizes the need for comprehensive audiological protocol designed to address these diagnostic limitations. The protocol should integrate conventional and extended high-frequency audiometry, otoacoustic emissions, speech-in-noise testing, and immittance measures while incorporating patient-reported outcomes and detailed noise exposure histories. Utilizing a multifaceted approach, this protocol aims to identify subtle auditory dysfunctions and provide clinicians with robust tools for early diagnosis and targeted management. Clinical examples highlight the necessity of each of these auditory tests. The diagnostic protocol should emphasize the clinical importance of thorough auditory evaluations. It should enable the detection of subclinical impairment and supports tailored rehabilitation strategies. It also highlights the need for continuous monitoring of at-risk populations. These suggestions advocate for a shift in the clinical perspective in evaluating and caring for individuals exposed to combat, with implications for clinical and operational settings.

Keywords: *combat noise, auditory complaints, hearing loss, diagnostic protocol.*

INTRODUCTION

Combat noise exposure, particularly from blasts, firearms, and explosions, is a distinct form of acoustic trauma that can result in complex and multifactorial auditory damage. Unlike continuous industrial or environmental noise, combat noise often involves short-duration, high-intensity pressure waves that may lead to both peripheral and central auditory injuries. These include, cochlear damage, disruptions at the level of the auditory nerve or brainstem, and if blast is involved tympanic membrane perforation and ossicular chain disarticulation [1]. Additionally, exposure to blast waves may also result in vestibular dysfunction and

*Corresponding author: Shaic@ariel.ac.il.

Copyright: ©2025 Fink et al. This is an open-access article distributed under the terms of the Creative Commons Attribution 3.0 Unported License, which permits unrestricted use, distribution, and reproduction in any medium, provided the original author and source are credited.

concomitant mild traumatic brain injury (mTBI), further complicating the clinical presentation [2–4].
Individuals exposed to such noise frequently report a range of auditory symptoms: tinnitus, hyperacusis, decreased sound tolerance, auditory fatigue, and difficulty understanding speech in noisy environments. While some may present with measurable hearing loss, others show normal audiograms despite persistent functional difficulties. This has given rise to the concept of "hidden hearing loss," referring to synaptic or neural damage undetected by standard pure-tone testing [5,6]. Understanding the full range of potential auditory pathologies resulting from combat noise is essential to developing appropriate diagnostic and rehabilitation strategies.

CLINICAL GAP AND DIAGNOSTIC CHALLENGE

Current clinical practices remain heavily reliant on pure-tone audiometry as the primary diagnostic tool. This creates a substantial gap in care: individuals who report persistent auditory difficulties, such as difficulty understanding speech in noise, sensitivity to sound, or auditory fatigue, are told their hearing is "normal" based solely on standard thresholds. As a result, they are often left without diagnosis, treatment, or acknowledgment of their difficulties [3,4].
This diagnostic limitation has important clinical implications. In current practice, medical treatment for acoustic auditory trauma and the subsequent eligibility for treatment and compensation, is typically contingent upon the demonstration of hearing loss in standard audiometry [7,8]. However, individuals who report significant auditory symptoms following combat noise exposure, such as difficulty hearing in noise or tinnitus, may show normal pure-tone thresholds [9,10]. As a result, these individuals are often not diagnosed with hearing damage and do not receive appropriate treatment or rehabilitation services. This reliance on the audiogram as the primary diagnostic criterion creates a gap in care for patients with functional auditory impairments that remain "invisible" to conventional testing.
A shift in clinical perspective is urgently needed. Rather than relying exclusively on audiometric thresholds, clinicians should adopt a more functional, patient-centered approach that validates subjective complaints and incorporates a broader range of diagnostic tools. Only by acknowledging the limitations of conventional testing can we begin to close the gap between patient auditory complaints and clinical action.

TOWARD A STRUCTURED ASSESSMENT APPROACH

To effectively identify and manage the spectrum of auditory dysfunctions associated with combat noise exposure, a more comprehensive and structured assessment protocol is needed. While pure-tone audiometry provides valuable information about threshold sensitivity, it fails to detect many of the suprathreshold deficits that impact real-world communication, particularly in noisy or cognitively demanding environments. Clinical evidence supports the need for advanced diagnostic tools such as extended high-frequency audiometry (EHF), speech-in-noise tests and distortion product otoacoustic emissions (DPOAEs) which offer critical insights into auditory integrity.
An essential component of such protocols is the use of a dedicated case history (structured auditory anamnesis) designed specifically for individuals exposed to combat noise. Unlike general intake forms, this targeted anamnesis includes questions about the acoustic characteristics of the exposure (e.g., blast proximity, use of hearing protection), timing and progression of symptoms, co-occurring complaints such as tinnitus or sound intolerance, and contextual factors like post-exposure stress or cognitive fatigue. It also considers prior auditory health and service-related functional impairments. This information is vital for tailoring the diagnostic approach and for differentiating between peripheral, central, and non-auditory contributors to the patient's complaints.
This suggested protocol integrates traditional and advanced audiological measures, along with the dedicated anamnesis, in a tiered manner. It guides clinicians through the diagnostic process while validating patient complaints that may otherwise be overlooked. Importantly, the protocol is designed not only to improve diagnostic accuracy but also to inform rehabilitative planning, ensuring that patients with normal audiograms but real functional deficits receive appropriate care.
Implementing such models represents a critical evolution in clinical audiology—one that aligns diagnostic strategies with the complexity of auditory trauma and bridges the longstanding gap between subjective experience and objective findings.

REFERENCES

[1] C. B. Paik, M. Pei, and J. S. Oghalai. Review of blast noise and the auditory system. *Hearing Research*, vol. 425, p. 108459, 2022.

[2] S. A. Fausti, D. J. Wilmington, F. J. Gallun, P. J. Myers, and J. A. Henry. Auditory and vestibular dysfunction associated with blast-related traumatic brain injury. *Journal of Rehabilitation Research and Development*, vol. 46, no. 6, pp. 797–812, 2009.

[3] F. J. Gallun, A. C. Diedesch, L. R. Kubli, T. C. Walden, R. L. Folmer, M. S. Lewis, J. A. Henry, and D. T. Walden. Performance on tests of central auditory processing by individuals exposed to high-intensity blasts. *Journal of Rehabilitation Research and Development*, vol. 49, no. 7, pp. 1005–1024, 2012.

[4] G. H. Saunders, M. T. Frederick, M. Arnold, S. Silverman, T. H. Chisolm, and P. Myers. Auditory difficulties in blast-exposed veterans with clinically normal hearing. *Journal of Rehabilitation Research and Development*, vol. 52, no. 3, pp. 343–360, 2015.

[5] S. G. Kujawa and M. C. Liberman. Adding insult to injury: Cochlear nerve degeneration after 'temporary' noise-induced hearing loss. *Journal of Neuroscience*, vol. 29, no. 45, pp. 14077–14085, 2009.

[6] V. Tepe, L. Guillory, A. Boudin-George, T. Cantelmo, and S. Murphy, Central auditory processing dysfunction in service members and veterans: Treatment considerations and strategies. *Journal of Speech, Language, and Hearing Research*, vol. 66, no. 8, pp. 2922–2949, 2023.

[7] N. Yehudai, N. Fink, M. Shpriz, and T. Marom. Acute acoustic trauma among soldiers during an intense combat. *Journal of the American Academy of Audiology*, vol. 28, no. 5, pp. 436–443, 2017.

[8] E. Zloczower, N. Tsur, S. Hershkovich, N. Fink, and T. Marom. Efficacy of oral steroids for acute acoustic trauma, Audiology *and Neurotology*, vol. 27, no. 4, pp. 312–320, 2022.

[9] J. A. Henry, S. Griest, K. M. Reavis, L. Grush, S. M. Theodoroff, S. Young, E. J. Thielman, and K. F. Carlson. Noise Outcomes in Servicemembers Epidemiology (NOISE) Study: Design, methods, and baseline results. *Ear and Hearing*, vol. 42, no. 4, pp. 870–885, 2021.

[10] K. M. Reavis, J. M. Snowden, J. A. Henry, F. J. Gallun, M. S. Lewis, and K. F. Carlson. Blast exposure and self-reported hearing difficulty in service members and veterans who have normal pure-tone hearing sensitivity: The mediating role of posttraumatic stress disorder. *Journal of Speech, Language, and Hearing Research*, vol. 64, no. 11, pp. 4458–4467, 2021.

DOI: 10.61782/fa.2025.0825

FORUM ACUSTICUM EURONOISE 2025

SQUAD-LEVEL OPERATIONAL PERFORMANCE UNDER VARYING HEARING PROTECTION DEVICES AND SIMULATED HEARING LOSS

Benjamin Sheffield[1,2*] **Rebecca E. Bieber**[2] **Stephanie Turcios**[2] **Douglas Brungart**[2]
[1] Defense Health Agency Public Health, Aberdeen, MD, USA
[2] Walter Reed National Military Medical Center, Bethesda, MD, USA

ABSTRACT

Noise-induced hearing loss continues to be an issue for military personnel, who rely on their hearing to maintain situational awareness and maximize operational effectiveness. Methodological advancements in measuring performance in dismounted combat are paving the way to examine the impact of hearing in these complex environments. In this study, squads from the US Army's 4th Infantry Division conducted standard combat training exercises under different hearing conditions using hearing protection devices (HPDs; passive, active) and hearing loss simulation (normal hearing, moderate-to-severe loss) while outfitted with audiovisual recorders, GPS trackers, laser engagement systems and inertial measurement units on the helmet and weapon. This allowed all squad movement, communication, and engagements to be captured. In addition, performance ratings were collected from observer-controllers (OCs) and participating Soldiers after each drill. Results show a clear advantage of active HPDs compared to the other conditions tested for both Soldier and OC ratings of squad performance. Soldiers also reported low frustration while wearing active HPDs and suffered less casualties on average, whereas a moderate-to-severe hearing loss resulted in higher mental demand and frustration and the highest number of casualties incurred. These findings can help inform Military leaders of the importance of wearing effective hearing protection in combat.

[*]***Corresponding author***: benjamin.m.sheffield.civ@health.mil
Copyright: *©2025 First author et al. This is an open-access article distributed under the terms of the Creative Commons Attribution 3.0 Unported License, which permits unrestricted use, distribution, and reproduction in any medium, provided the original author and source are credited.*
Disclaimer: *The views expressed in this abstract are those of the authors and do not necessarily reflect the official policy of the Department of Defense or the U.S. Government.*

Keywords: *hearing protection, hearing loss simulation, combat, performance*

1. INTRODUCTION

A Warfighter's hearing is critical for combat effectiveness, particularly in dismounted combat operations where Soldiers rely on their hearing to detect enemy movements, identify threats, and coordinate with their unit. In environments with limited visibility, such as dense forests or urban battlefields, auditory cues like distant gunfire, footsteps, or radio transmissions provide critical information for survival. The ability to process these sounds quickly allows soldiers to react effectively, enhancing their situational awareness (SA) and tactical decision-making.

Unfortunately, the battlefield is also filled with hazardous noise (e.g. explosions, gunfire, aircraft, vehicle engines) that can cause temporary or permanent hearing damage (e.g. hearing loss, tinnitus) and auditory fatigue. Even brief exposure to these sounds without protection can impair a soldier's ability to detect threats, potentially reducing combat effectiveness in both the short and long term.

Despite these risks, many soldiers are reluctant to wear traditional hearing protection because they fear it will diminish their SA. Standard passive earplugs or earmuffs can muffle critical battlefield sounds, making it harder to detect enemy movements or communicate effectively with teammates. In high-stakes combat situations, soldiers may prioritize immediate survival and effectiveness over long-term health, leading them to forgo hearing protection altogether.

To address this challenge, advanced HPDs have been developed that can both safeguard hearing and enhance

communication [1]. Modern tactical headsets and electronic earplugs filter out harmful noise levels while amplifying essential sounds, such as voices and quiet enemy movements. These devices can allow soldiers to maintain SA without sacrificing their hearing health. Ultimately, Soldiers must balance the tradeoff between hearing protection and SA. While advanced devices offer significant improvements, they are not always available or practical in every situation. Troops often have to decide whether to risk hearing damage for enhanced SA or rely on protection that may slightly reduce their ability to perceive battlefield cues. As technology continues to evolve, finding the optimal balance between hearing safety and operational effectiveness remains a crucial challenge for modern militaries.

In battlefield environments, degraded hearing can occur as a result of hearing protector use, but it can also occur as a result of acute hearing impairment from unprotected exposures during the current engagement or chronic hearing loss from a lifetime of noise exposure prior to the current engagement. In order to make decisions about when, how, and what kind of hearing protection to wear in combat, and also about who might have an acute or chronic hearing loss that is severe enough to interfere with combat operations, it would be extremely helpful to collect information that might allow a prediction of the impacts that different levels of hearing impairment might have on operational performance, regardless of the source.

Traditionally, testing the impacts of hearing loss or HPDs on combat operations has been limited to laboratory measures or carefully controlled field studies that focus on isolated tasks. However, the battlefield is a dynamic environment and the factors that influence combat effectiveness are extremely complex, so it has been difficult to translate these findings to lethality, survivability, or mission success in actual operational environments. Some studies have begun to examine the impact of hearing acuity on combat performance in more comprehensive environments using simulated sound sources [2] or realistic sound sources combined with hearing loss simulation [3-5]. However, in the infantry realm, this has been limited to the individual or fire team level, whereas the fundamental fighting element is the infantry squad.

Beyond logistical considerations, one challenge of expanding to the squad-level has been the lack of validated measures of operational performance in dismounted combat. Thankfully, recent methodological advancements in measuring performance in these environments [6-7] provide a framework to now explore the impact of hearing acuity at the squad level. Interestingly, the initial findings from those studies indicate that the most important contributing factor to combat performance is effective communication within the squad, further emphasizing the need to better understand this issue [7].

In the present study, we utilized the methodologies mentioned above for measuring/analyzing squad performance while varying each squad's hearing acuity across drills using hearing loss simulators and HPDs to examine their impact on performance, providing critical information for our Warfighters.

2. MATERIALS AND METHODS

2.1 Combat Exercise

The combat exercise used for the study was closely modeled after Battle Drill 2A: Conduct a Squad Assault, which is a fundamental infantry exercise that trains soldiers to close upon and destroy an enemy position through coordinated fire and movement. The drill involves a squad maneuvering against an opposition force (OPFOR), typically starting with suppressive fire to fix the enemy in place while an assaulting element moves forward to secure an objective. Soldiers execute bounding movements, alternating between providing covering fire and advancing under protection. The exercise emphasizes teamwork, communication, and aggressive action to overwhelm the enemy.

Data collection took place at a designated training area in Ft. Carson, CO consisting of primarily wooded terrain and grassland with slight elevation changes incorporating hills, meadows, and gulches. There were two Situational Training Exercise (STX) lanes setup on the range, each with differing movements toward their objective. In both cases, the primary objective was to secure a bunker manned by two members of the OPFOR. A third OPFOR member served as a Listening Post/Observation Post (LPOP) a few hundred yards forward of the bunker, where he was concealed in the brush to provide a surprise attack element. Each member of the OPFOR was outfitted with an M4 Carbine rifle.

2.2 Participants and Squad Composition

A total of 86 Soldiers, all male, aged 18-34 years, were recruited from the US Army's 4th Infantry Division to participate as part of their Squad Table III training

program. They ranged in rank from E-1 to E-6 and were assigned to remain within their normal squad and role for the duration of the exercises. Each 9 to 11-man squad consisted of a Squad Leader, a two-man gun team (Gunner and Assistant Gunner), and two fire teams (Alpha and Bravo). Each fire team consisted of 3-4 members depending on the squad size. Each had a Fire Team Leader, an Automatic Rifleman, and either a Grenadier or Rifleman (or in some cases both). The Gunner was outfitted with an M240 machine gun, the Automatic Rifleman with an M249 SAW (Squad Automatic Weapon), and the Grenadier with an M203 grenade launcher mounted on an M4 Carbine rifle. All other squad positions carried M4 Carbine rifles and all weapons were loaded with blank ammunition.

Table 1. Audiogram used for the Simulated Hearing Loss Condition.

Frequency (kHz)	0.25	0.5	1	2	4	8
Level (dB)	50	50	55	65	85	95

2.3 Hearing Conditions

Four hearing conditions were tested in the study, including two HPD conditions and two hearing simulation conditions. The active HPD (Peltor condition) tested was the Peltor ComTac XIII (3M Corp.), which encompasses downleads for participants outfitted with radio communications (Squad Leader and Fire Team Leaders). The other HPD tested was a standard foam earplug (Foam condition), which differed depending on the size for each participant, as determined by an audiologist (3M EAR Classic SuperFit 30 and 33 for small and large, respectively, and Sound Guard 2-color for medium). The two hearing simulation conditions were administered via a custom-designed helmet-mounted hearing loss simulator known as the HL Sims (Sensimetrics Corp.). The HL uses earphones outfitted with small microphones to pass through sound unfiltered when in the normal hearing setting (Simulated Open Ear condition). To simulate hearing loss, a combination of attenuation from the earplug and additive masking noise elevates the detection thresholds at certain frequencies, depending on the audiogram simulated (see [5] for more details). For this study, we chose a moderate-to-severe hearing loss using the values shown in Tab. 1 (Simulated Hearing Loss condition). The Simulated Open Ear condition served as a stand-in control condition since operating with a truly open ear would put the participants at risk of hearing damage from weapons fire.

2.4 Additional Equipment and Measurements

In addition to donning hearing loss simulators and HPDs, participants were outfitted with digital audio recorders (Evida Corp.) and GoPro cameras (GoPro, Inc) to capture communication. Soldiers' helmets and weapons were also equipped with inertial measurement units (IMUs; ADPM, Inc) to track acceleration, angular movement, and orientation of the head and weapon, and to count the number of rounds fired by each participant. Their weapons were also equipped with the Instrumentable-Multiple Integrated Laser Engagement System (I-MILES) lasers and they wore vests and halos with I-MILES sensors. Fig. 1 shows an example of a fully-equipped Soldier.



Figure 1. Fully equipped Soldier with red circles highlighting from left to right: helmet IMU, audio recorder mounted on the HL Sim, GoPro, and weapon IMU.

I-MILES data were routed to a central control tower using a body worn radio frequency transmitter that doubled as a Global Positioning System (GPS) tracker as part of the Homestation Instrumentation Training System. This system allows all movement and engagements to be captured for visualization in real time and to be saved for after action reporting and data analysis (Fig. 2).

2.5 Procedures

In total, there were six squads that each ran through four drills of the exercise alternating between the two STX lanes (two drills per lane) for a total of 24 drills. Each drill was conducted with all squad members in one of the four hearing conditions and conditions were switched between drills to achieve a balance within each squad.



Figure 2. Homestation Instrumentation Training System screenshot showing Bravo team engaging with OPFOR while Alpha team flanks left to assault. The red line indicates a pairing line between the OPFOR and Gunner and the red hat indicates the OPFOR as the shooter. The LPOP can be seen in the bottom left corner.

Before the start of the exercise, participants completed a hearing exam and filled out an intake questionnaire about their demographics, military and combat history, and experience using HPDs. They were also fit with appropriately-sized hearing protection and trained on how to operate the Peltors. After each drill, Soldiers rated their own performance and communication ability and completed the NASA Taskload Index (TLX) [8] via a tablet PC running a custom TabSINT [9] protocol. In addition, unit commanders (Platoon and Company) acted as OCs throughout the exercise and provided ratings of squad performance on two scales assessing Battle Drill task steps and tactical performance principles

2.6 Data Analysis

2.6.1 Observer-Controller Ratings

OC ratings were modeled using linear mixed effects regression in R version 4.4.1 [10]; the buildmer package version 2.11 [11] was used for model selection, using backwards selection and likelihood ratio testing to compare nested models; the effects package was used for visualization of model fitted values. The maximal fixed effects structure evaluated included two-way interactions between condition and each of the following squad-level measures: drill number (4 levels), mean years of service among squad members, mean length of time since the most recent live fire event, the mode value for length of time with the current squad, and mode value for the number of squad leaders during their current assignments, as well as non-interacting fixed effects of platoon (3 levels), lane (2 levels), and mean squad member age (continuous). The maximal random effects structure evaluated included interacting by-OC intercepts and slopes for condition and lane, as well as a random intercept of drill.

2.6.2 NASA Taskload Index

Responses to the NASA TLX were modeled using linear mixed effects regression using the methods described in the above section. The maximal fixed effects structure evaluated included an interaction of TLX subscale (categorical; 6 levels) and condition (categorical; 4 levels), along with non-interacting fixed effects of drill number (categorical; 4 levels), number of years of military service (continuous), age (continuous), and duration of time since the most recent live fire event (continuous). The maximum random effects structure evaluated included by-participant intercepts and slopes for condition and drill number, as well as a random intercept of date.

3. RESULTS

3.1 Observer-Controller Ratings

The final model selected included non-interacting main effects of condition and drill number, as well as a random intercept of OC grader. The main effect of condition is visualized in Fig. 3 and shows that performance was consistently rated higher when squad members were in the Peltor condition as compared to the Foam plugs (b=-12.56, SE=4.89, t=-2.57, p=.01) and Simulated Hearing Loss conditions (b=-19.2, SE=5.26, t=-3.65, p=.001). OC ratings did not differ significantly between Peltor and Simulated Open Ear conditions (b=-10.13, SE=5.2, t=-1.95, p=.06).

The non-interacting fixed effect of drill number indicates a pattern of improved ratings over the course of four drills. Ratings for Drill 4 were significantly higher than those for Drill 1 (b=17.7, SE=5.07, t=3.49, p=.001) and Drill 2 (b=11.97, SE=4.87, t=2.46, p=.02). Ratings did not differ between Drills 1 and 2 (b=5.73, SE=4.89,

t=1.17, p=.25) nor between Drills 3 and 4 (b=4.41, SE=5.12, t=-.86, p=.39).

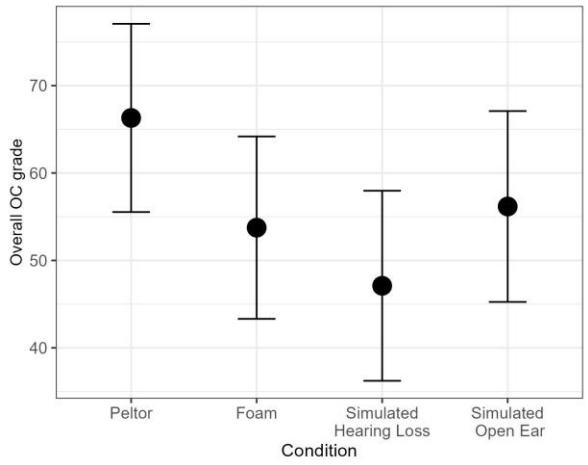


Figure 3. Model-fitted values for OC grade visualized as a function of hearing condition. Error bars reflect the 95% confidence interval. Higher values reflect better performance.

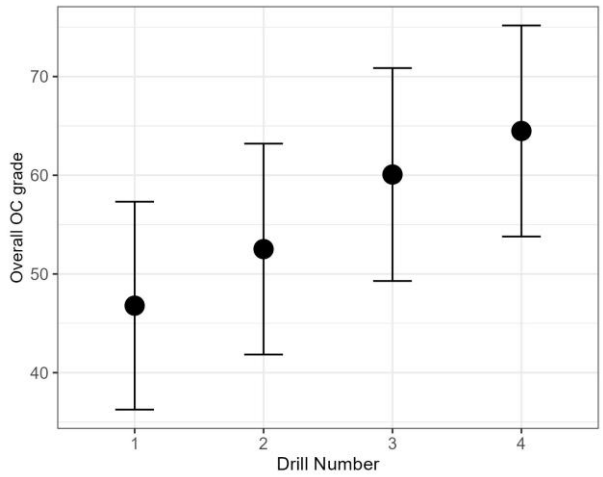


Figure 4. Model-fitted values for OC grade visualized as a function of hearing condition. Error bars reflect the 95% confidence interval. Higher values reflect better performance.

3.2 NASA Taskload Index

The final model selected to describe the NASA TLX data included an interaction of TLX subscale and condition, a non-interacting fixed effect of age, and a by-participant slope and intercept of condition. Significant interactions were examined by re-leveling and re-fitting the model to obtain estimates at all levels; see Fig 5.

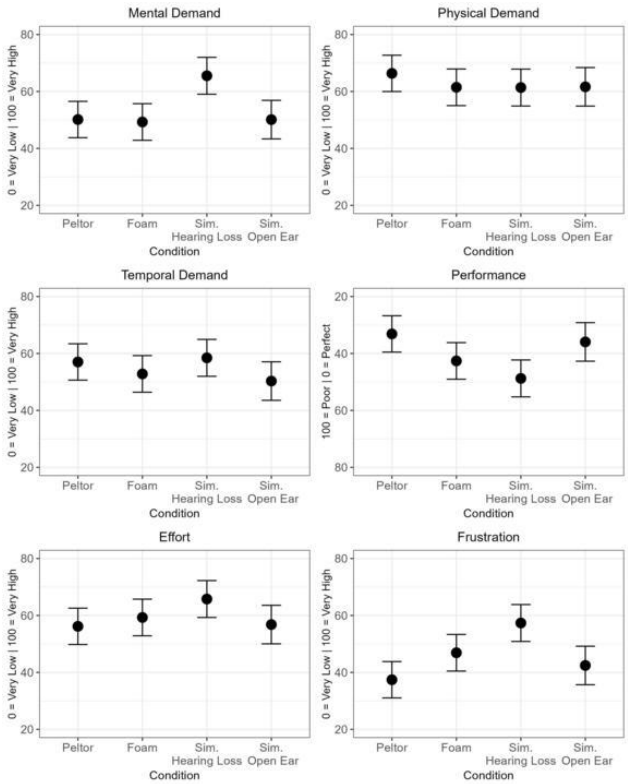


Figure 5. Model-fitted values for NASA Taskload Index subscales visualized as a function of hearing condition. Error bars reflect the 95% confidence interval.

Examination of the significant interaction between hearing condition and TLX subscale reveals the following: When rating levels of Mental Demand, Performance, Effort, and Frustration, participants consistently gave poorer ratings to the Simulated Hearing Loss condition as compared to all other conditions (p<.05, all comparisons). There were no significant differences between Simulated Hearing Loss and any of the other hearing conditions for ratings of Physical Demand or Temporal demand. Ratings of Frustration were significantly lower when using Peltors than either Foam plugs (b=9.48, SE=4.05, t=2.34, p=.02) or Simulated Hearing Loss (b=19.94, SE=4.37, t=270.92, p<.001), and were similar between Peltors and the Simulated Open Ear condition (b=5.02, SE=4.03,

t=1.24, *p*=.21). The same pattern was found for ratings of Performance (Peltor vs Foam: *b*=9.48, SE=4.05, *t*=2.34, *p*=.02; Peltor vs Simulated Hearing Loss: *b*=15.63, SE=4.36, *t*=3.58, *p*<.001; Peltor vs Simulated Open Ear: *b*=2.81, SE=4.04, *t*=0.7, *p*=.49).

3.3 I-MILES Engagement

Preliminary analysis of the I-MILES engagement data indicates no significant effect of hearing condition. However, squads did suffer the highest number of Blue Force (BLUFOR; i.e., friendly or allied forces) casualties on average when operating with a moderate-to-severe hearing loss and the least amount when operating with the Peltors (Fig. 6). Note that all participants were resurrected in HITS by the training operators any time they were indicated as killed until the Squad conducted their final assault on the bunker to maximize the training and keep everyone in play, which is why the number of casualties often exceeds the size of the squad. Fig. 6 also illustrates that the data collected to date are highly underpowered for this analysis with only 6 observations for each condition.

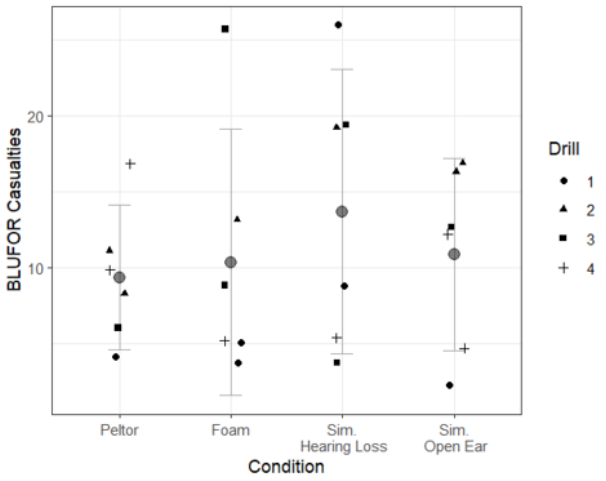


Figure 6. BLUFOR casualties as a function of hearing condition for each drill number. Large circles indicate mean casualties and error bars represent standard error of the mean.

3.4 Inertial Measurement Unit and GPS Analysis

Preliminary analysis of the IMU and GPS data is ongoing, but the early indications are that squads moved faster and spent less time in contact on average when operating with the Peltors and moved slower and spent more time in contact when operating with a moderate-to-severe hearing loss. However, these trends are not statistically significant and the data are currently underpowered for drill-level analyses.

4. DISCUSSION

4.1 Summary of Findings

The findings from this study highlight the operational advantages of advanced hearing protection devices for Soldiers in combat environments. Results indicate that Soldiers perform more effectively when equipped with these devices compared to passive foam earplugs. This underscores the critical importance of providing Soldiers with advanced hearing protection technology to enhance battlefield effectiveness.

Furthermore, the fact that the Peltor condition resulted in numerically higher OC ratings of performance than the Simulated Open Ear condition (though not statistically significant) and that Soldiers' self-ratings of performance were similar across both conditions suggests that wearing advanced hearing protection does not impose a performance cost. These findings may help alleviate concerns about potential trade-offs between hearing protection and operational effectiveness when wearing these types of advanced HPDs.

The study also demonstrates that simulated moderate-to-severe hearing loss significantly degrades performance while increasing mental demand, frustration, and effort. These factors indicate the potential for critical errors in complex operational environments if Soldiers are operating with a hearing impairment. This, too, highlights the importance of wearing effective hearing protection in combat to prevent temporary or permanent hearing loss.

Lastly, squad performance improved over time, reinforcing the effectiveness of the training exercises and underlining value of continued training and adaptation in dynamic combat scenarios.

4.2 Limitations and Future Directions

While these results provide valuable insights, several limitations should be acknowledged. This study represents the initial phase of data collection. Future research will expand the sample size to improve statistical power which will allow for a formal analysis of engagement data (e.g., casualties suffered). However, engagement data alone may

not capture the full scope of objective performance differences, warranting a more in-depth analysis of IMU and GPS data as conducted in [6]. Furthermore, communication data analysis has yet to be conducted, and given the importance of verbal coordination in combat operations, this will be a critical area for further investigation.

A key limitation is the impracticality of blinding the OCs or participants to the hearing condition, which may have introduced bias in performance evaluations. Another limitation is the inability to test a truly open ear condition due to ethical considerations from the risk of hearing damage to the participants, which may impact some of the comparisons involving the Simulated Open Ear condition. Also, the present results evaluate only one type of advanced HPD and only one type of hearing loss. Future research will incorporate other devices and investigate some of the subtleties related to hearing impairment to provide a more comprehensive understanding of the impact of hearing acuity on Soldier performance.

5. CONCLUSIONS

The findings from this study can help inform Military leaders of the importance of wearing effective HPDs in combat to preserve the hearing of our Warfighters, who rely on their hearing to maintain SA and maximize operational effectiveness. The methods employed can be replicated to provide a standardized and ecologically valid assessment of other advanced HPDs and their impact on the Warfighter performance.

6. ACKNOWLEDGMENTS

The authors would like to thank Andrea Brzuska, Briana Biel, Jessica Lanning-Baker, Tammie Taylor, Julianna Voelker, and CPT Dooho Kim for their assistance with data collection; COL Jillyen Curry-Mathis for coordination with the 4th ID; 3M for loaning us the Peltor Comtac XIIIs; and members of the 4th ID for their participation in the study. This study was partially-funded by a grant from the Military Operational Medicine Research Program.

7. REFERENCES

[1] Giguère, C., Laroche, C., Brammer, A. J., Vaillancourt, V., & Yu, G. (2011). Advanced hearing protection and communication: Progress and challenges. In *Proceedings of the 11th International Congress on Noise as a Public Health Problem* (pp. 24-28).

[2] Clasing, J. E., & Casali, J. G. (2014). Warfighter auditory situation awareness: effects of augmented hearing protection/enhancement devices and TCAPS for military ground combat applications. *International journal of audiology*, *53*(sup2), S43-S52.

[3] Sheffield, B., Brungart, D., Blank, A. (2016). The Effects of Hearing Impairment on Fire Team Performance in Dismounted Combat. In *Proceedings of the Human Factors and Ergonomics Society Annual Meeting*, *60*(1), 1509-1513.

[4] Keller, M.D., Ziriax, J.M., Barns, W., Sheffield, B., Brungart, D., Thomas, T., Jaeger, B. and Yankaskas, K. (2017). Performance in noise: Impact of reduced speech intelligibility on Sailor performance in a Navy command and control environment. *Hearing Research*, *349*, 55-66.

[5] Sheffield, B., Brungart, D., Tufts, J., & Ness, J. (2017). The effects of elevated hearing thresholds on performance in a paintball simulation of individual dismounted combat. *International Journal of Audiology*, *56*(sup1), 34-40.

[6] O'Donovan, M. P., Hancock, C. L., Coyne, M. E., Racicot, K., & Goodwin, G. A. (2023). Assessing the impact of dismounted infantry small unit proficiency on quantitative measures of collective military performance Part 1: Recommended test methodologies. NATICK/TR-23/013.

[7] Hancock, C. L., Teo, G. W., King, M. J., Goodwin, G. A., Pitts, K. P., Coyne, M. E., ... & O'Donovan, M. P. (2025). Quantitative team performance metrics for dismounted infantry battle drill analysis. *Applied Ergonomics*, *125*, 104473.

[8] Hart, S. G., & Staveland, L. E. (1988). Development of NASA-TLX (Task Load Index): Results of empirical and theoretical research. In *Advances in psychology*, *52*, 139-183. North-Holland.

[9] Shapiro, M. L., Norris, J. A., Wilbur, J. C., Brungart, D. S., & Clavier, O. H. (2020). TabSINT: Open-source mobile software for distributed studies of hearing. *International Journal of Audiology*, *59*(sup1), S12-S19.

[10] R Project, & Development Core Team. (2024). R Version 4.4. 1. R Project for Statistical Computing Vienna, Austria.

[11] Voeten, C. C. (2022). buildmer: Stepwise elimination and term reordering for mixed-effects regression. R package version, 2(11).

DOI: 10.61782/fa.2025.0446

FORUM ACUSTICUM EURONOISE 2025

IMPACT OF ACOUSTIC TEST FIXTURE EAR STIFFNESS ON EARPLUG ATTENUATION OF IMPULSIVE SOUNDS.

Christophe Ruzyla[1,2*] **Cyril Blondé-Weinmann**[1] **Pascal Hamery**[1]
Franck Sgard[3] **Sébastien Roth**[2]
[1] Department Acoustics and Soldier Protection, French-German Research Institute of Saint-Louis, 68300 Saint-Louis, France
[2] Laboratoire Interdisciplinaire Carnot de Bourgogne, site UTBM, UMR 6303 CNRS / Université de Technologie de Belfort-Montbéliard, France.
[3] Institut de Recherche Robert-Sauvé en Santé et Sécurité du Travail, Montréal (QC), Canada.

ABSTRACT

Acoustic Test Fixtures (ATFs) are physical substitutes designed to evaluate the attenuation provided by Hearing Protection Devices (HPD). These devices are particularly useful for measurements, where human testing is not feasible, such as high-level impulse noises exposure. However, challenges arise in integrating the mechanical elements required to mimic the response of the human head. The material properties of commercially available ATFs vary, potentially leading to different coupling with HPDs. This study aims to investigate the behavior of a rigid earplug and the resulting acoustic pressure in the ear canal when the stiffness of the ATF ear is modified. An experimental setup was developed, involving a custom laboratory-developed ATF to estimate a rigid earplug attenuation for three simplified ear materials of increasing stiffness. Additionally, a time-domain numerical model using finite element method was created to study the wave propagation in the simplified ATF ear. This study shows experimentally and numerically that the stiffness of the ATF ear significantly influences earplug attenuation measurements by modifying the contribution of tissular conduction in the wave propagation behind the protector. This study paves the way for improving ATF biofidelity by more accurately accounting for the behavior of the human outer ear mechanical properties.

[*]***Corresponding author***: christophe.ruzyla@isl.eu.
Copyright: *©2025 First author et al. This is an open-access article distributed under the terms of the Creative Commons Attribution 3.0 Unported License, which permits unrestricted use, distribution, and reproduction in any medium, provided the original author and source are credited.*

Keywords: *Hearing protection, acoustic test fixture, impulsive noise, finite element method.*

1. INTRODUCTION

Impulse noises are characterized by a high amplitude, a sudden onset, and a brief duration [1]. These noises can be encountered on the battlefield, where soldiers are exposed to impulsive noise levels ranging from 145 dB-peak to 190 dB-peak [1-2]. To ensure adequate protection, it is necessary to accurately assess the performance of Hearing Protection Devices (HPD). Acoustic Test Fixtures (ATF) are commonly used to estimate the attenuation allowed by HPD facing very high-level impulse noises. Nevertheless, the ATF correspond only to an approximation of the human auditory system, whether it concerns the eardrum, the Ear Canal (EC) anatomy, or the material properties [3]. More specifically, the interactions between the very high-level impulse wave and the HPD, as well as the transmission paths through the outer ear's tissues and the HPD, still need to be fully assessed for the current ATF. These transmissions strongly depend on the materials used in the ATF [4], but a clear relationship is not yet fully understood and requires further investigation.
This paper aims to investigate the relation between artificial ear material properties and earplug sound attenuation. An experimental setup was developed, involving a custom laboratory-developed ATF to estimate a rigid earplug attenuation for three geometrically simplified ear materials of increasing stiffness. Additionally, a time-domain numerical model using finite element method was created to study the wave propagation in the simplified ATF ear.

2. EXPERIMENTAL STUDY

2.1 Material and method

The laboratory-designed ATF used in this study, shown in Figure 1, is a modification of the ISL standard ATF that complies with the S.12.42 standard [5]. This laboratory-developed artificial head incorporates the electronics and measuring devices of the standard ISL head. It is modified to allow the installation of an ear flange (diameter 100 mm, thickness 8.5 mm) made from a single homogeneous material. This ear is held in position on the artificial head by an aluminum ring secured by 6 screws.

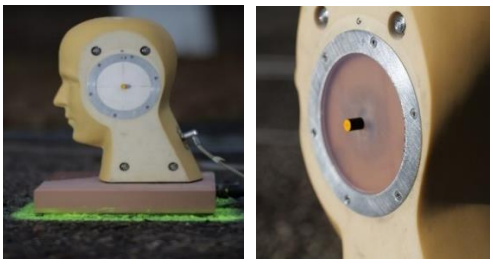


Figure 1 : View of the custom-made ATF (left) and a close-up of the ear flange (right).

For this study, three different ear materials of variable stiffness were considered. Their mechanical properties were measured through a compression test compliant with ASTM D575 and are shown in Table 1. The RTV 3325 ear was produced by molding. The other two ears were fabricated using 3D printing (Formlabs Form 3L).

Table 1. Average mechanical properties of the ears tested in the study with standard deviations.

Name	Young modulus [MPa]	Density [g/m^3]	Poisson's ratio [-]
RTV 3325	0.71 ± 0.02	1.21 ± 0.01	0.38 ± 0.03
Formlabs 50A	4.76 ± 0.16	1.09 ± 0.01	0.47 ± 0.01
Formlabs Draft	(1.40 ± 0.06) ×10^3	1.19 ± 0.01	0.47 ± 0.01

The measurements were conducted in an anechoic chamber. The source of impulsive noise was a laboratory shock tube [6] placed 4 meters from the ATF. A reference microphone was positioned at equidistance from the source to measure the external pressure (Brüel & Kjær ½"). The pressure in the EC was recorded by an ear simulator compliant with IEC 60318-3 standard. In this configuration, the head was subjected in a reproducible manner to an impulse noise of 136 ± 1 dB-peak.

The tests presented in this paper were carried out at normal incidence to the ear. The earplugs used are 3D printed with a cylindrical shape (diameter: 8 mm, length 20 mm) and are made of Acrylonitrile Butadiene Styrene (ABS). They were inserted 10 mm into the ears. The external pressure and the pressure under the earplug were recorded simultaneously with a TEAC LX10 data recorder. Measurements on each ear were conducted five times, to verify the repeatability.

2.2 Results

The average acoustic pressure history measured inside the occluded EC is shown in Figure 2.

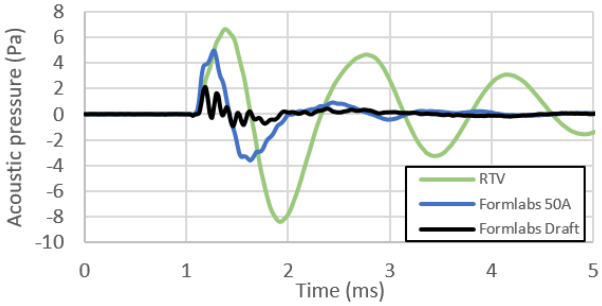


Figure 2. Average acoustic pressure measured inside the occluded EC.

Noise reduction (NR), i.e., the difference in peak levels between the pressure in front of the ear and the pressure in the occluded EC, has been determined for each configuration and is presented in Table 2.

Table 2. NR for the three ear materials tested.

Name	NR peak [dB]
RTV 3325	23.6
Formlabs 50A	28.7
Formlabs Draft	36.3

As shown in Table 2, peak noise reduction decreases with increasing rigidity of the ear flange. The three ears Insertion Losses (IL) were determined for the previously described impulse stimulation. From 100 to 400 Hz, an increase in IL of 12.9 dB per octave and 13.6 dB per octave was observed for the Formlabs 50A and Draft ears, respectively. From 200 Hz to 1 kHz, insertion loss was higher with increasing rigidity. In particular, at 700 Hz, we observe the largest deviations in IL. At this frequency, the IL was 17 dB, 30 dB, and 42 dB for the ear made of RTV, Formlabs 50A, and Draft, respectively. After 1 kHz, there are no marked differences between the different flanges.

3. NUMERICAL MODEL

To complete the experimental study, a numerical model of the laboratory-developed artificial head described in section 2.1 was developed. It allows for a more comprehensive analysis by estimating, in addition, the displacements of the protector and ear canal walls or the effect of potential micro-leaks. This time-domain finite element model is solved using COMSOL Multiphysics® (Stockholm, Sweden).

3.1 Methods

The 2D-axisymmetric numerical model developed comply with the ear flange geometry and is composed of four domains, represented in Figure 3. The earplug (labelled 2 in Fig. 3) and ear flange are considered as elastic solid materials, while the external air domain and the air in the EC (labelled 3 in Fig. 3) are modeled as fluid domains, satisfying the lossless Helmholtz equation. The mechanical properties applied to the three ear flanges correspond to the data determined experimentally in Table 1. The air fluid is defined by a density of 1.2 kg/m^3 and a sound speed of 343 m/s at 20°C. The earplug is made of ABS with a Young's modulus of 2200 MPa, a Poisson's ratio of 0.35 and a density of 1040 kg/m^3 [6]. No damping is applied in the solid domains.

The averaged incident sound pressure measured experimentally is used as input to a plane wave radiation condition applied at the bottom of the inlet air domain. The lateral sides of the ear flange are fixed boundary conditions (black lines in Fig.3) and constrained displacement conditions (green lines in Fig.3). These conditions were chosen based on practical insights into the integration of the ear flange with the ATF. An ear simulator consists of a main cavity and two slits to simulate the impedance of the middle ear. To evaluate the acoustic pressure at the ATF microphone position, the main cavity of the coupler has been represented along its entire length. The equivalent impedance of the two slits has been applied by a frequency-dependent impedance condition [7] at the ATF microphone position (purple line in Fig. 3). A fluid-structural coupling exists between EC and ear flange (yellow line labelled 1 in Fig. 3).

The equations in the air and solid domains are solved using at least five quadratic elements per wavelength (maximal resolution frequency was set to 10 kHz) ensuring solution convergence. The time-stepping method generalized-alpha is used to solve the problem. Both acoustic pressure in the EC and inlet air domain, as well as earplug and ear structural displacement fields are computed.

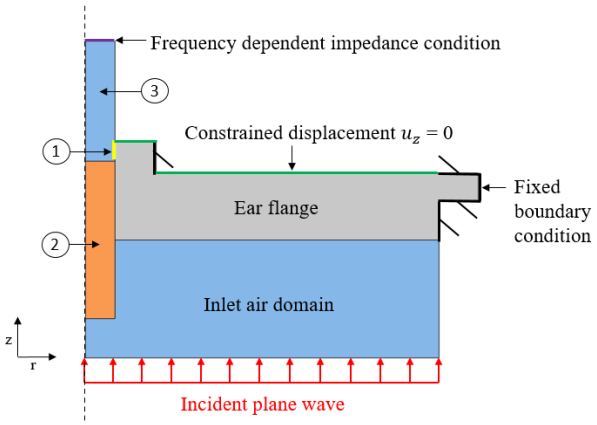
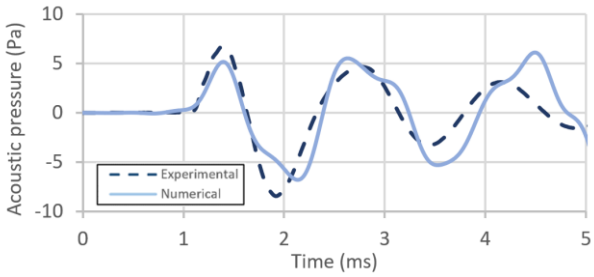


Figure 3. Geometry and boundary conditions of the FE model. The symmetry axis is shown as a dotted line. (1) interface between EC air domain and the ear flange, (2) earplug, (3) EC air domain.

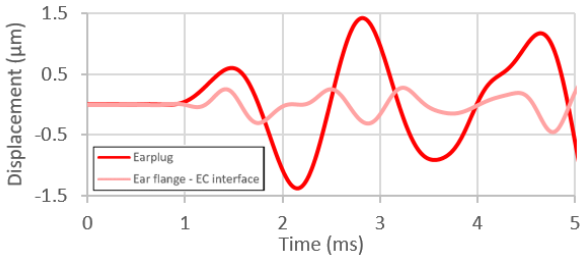
3.2 Results

Figure 4 shows the comparison between experimentally and numerically evaluated acoustic pressure time history in the occluded EC for the RTV ear. The numerical model yields a good pressure estimate, but exhibits undamped oscillations and combined contribution effects. Comparisons of the numerical simulations with the experimental results for the Formlabs 50A and Draft ear (not shown here for the sake of conciseness) indicate notably the presence of leakage during the experiment.

The displacement time history of the earplug (labelled 2 in Fig. 3) in longitudinal direction and of the EC air domain/ear flange interface (boundary 1 in Fig. 3) in radial direction are also represented. These undamped oscillating displacements present a first peak amplitude of 0.60 µm and 0.25 µm for the earplug and the ear canal/ear flange interface, respectively.



(a) Average acoustic pressure in the EC, (3) in Fig.3



(b) Simulated surface-average displacement of the earplug's domain (in z-direction), (1) in Fig.3, and of ear flange EC/interface (in r-direction), (2) in Fig.3.

Figure 4. Average acoustic pressure and displacements for the artificial ear in RTV.

4. DISCUSSION

The mechanical properties of the artificial ear significantly influence the attenuation provided by earplugs. Specifically, the peak noise reduction is enhanced as the stiffness of the outer ear increases. A previous experimental study has demonstrated the impact of outer ear hardness on the earplug "piston effect" [4]. This effect is characterized by a resonant, back-and-forth rigid body motion of the earplug coupled with the external auditory canal wall, typically occurring at frequencies below 2 kHz. The piston effect may account for some of the discrepancies observed at low-frequency for the earplug insertion loss among the three tested ears.

Analytically, the contribution of the piston effect to variations in ear canal sound pressure can be estimated by considering the relative equivalent occluded ear canal volume change and the adiabatic bulk modulus of air. Estimations based on numerically determined displacements reveal that for the softer ear made with RTV, 63% of the first peak acoustic pressure is attributable to the piston effect and 37% to the ear canal wall vibrations. For higher hardness (displacements curves omitted in this article), this second contribution rises to 38% for the Formlabs 50A ear and 44% for the Draft ear. Thus, the earplug piston effect contribution is predominant for the three ears tested but decreases with the ear's stiffness. The relative importance of these contributions to the human ear remains to be clarified.

Besides, stiffer materials induce additional effects. A low IL can be observed at lower frequencies, especially for the Formlabs 50A and the Formlabs Draft, indicating leakage during experimental measurements. These leakages can be attributed to improper seals between earplugs and EC walls due to the surface's conditions. Indeed, slight grooves could be seen on the earplug (3D printed) and EC surfaces.

5. CONCLUSION

Experimental measurements have quantified the impact of a modification in the stiffness of the ear on the attenuation of a protector. Specifically, peak noise reduction increases with ear stiffness. For the various ear materials, the protector and the EC wall displacements have been estimated numerically and discussed. This study shows that the earplug displacement is the main contribution to the pressure in the EC. The vibration of the interface EC / ear flange has a non-negligible effect, with a contribution increasing with ear stiffness. Finally, these results pave the way for improving ATFs by better reproducing the behavior of earplugs in human ears.

6. REFERENCES

[1] D. Smeatham and P. D. Wheeler, "On the Performance of Hearing Protectors in Impulsive Noise," *Appl. Acoust.*, vol. 54, no. 2, pp. 165-181, 1998.

[2] L. Humes, L. M. Joellenbeck and J. S. Durch, "Noise and Military Service : Implications for Hearing Loss and Tinnitus.," The National Academies Press, 2006.

[3] E. H. Berger, "Preferred Methods for Measuring Hearing Protector Attenuation,," *INTER-NOISE conference*, 2005.

[4] C. Blondé-Weinmann, P. Hamery, V. Zimpfer and S. De Mezzo, "Effects of the earplug and external ear hardness of the direct transmissions induced by high-level impulse noises," in *INTER-NOISE conference*, Nantes, 2024.

[5] P. Hamery, V. Zimpfer, K. Buck and S. De Mezzo, "Very high level impulse noises and hearing protection," in *Euronoise conference*, Maastricht, 2015.

[6] C. Blondé-Weinmann, "Description et caractérisation des phénomènes impliqués dans la limitation des protections auditives lors d'impulsions de fort niveau.," *Ph.D. thesis*, 2023.

[7] H. Wang and M. Hornikx, "Time-domain impedance boundary condition modeling with the discontinuous Galerkin method for room acoustics simulations," *J. Acoust. Soc. Am.*, vol. 147, no. 4, p. 2534–2546, 2020.

DOI: 10.61782/fa.2025.0781

FORUM ACUSTICUM EURONOISE 2025

SOUND ATTENUATION WITH DOUBLE HEARING PROTECTION: A COMPARISON OF REAL-EAR AND BEHAVIORAL HEARING THRESHOLD MEASUREMENTS

Hauptman Alon[1*] **Chordekar Shai**[1] **Dirks Coral**[2] **Fostick Leah**[3] **Fink Nir**[1]

[1] Department of Communication Disorders, Acoustics and Noise Research Lab in the Name of Laurent Levy, Ariel University, Ariel 40700, Israel.
[2] Department of Communication Sciences and Disorders, University of South Dakota, Vermillion, SD, USA
[3] Department of Communication Disorders, Auditory Perception Lab in the Name of Laurent Levy, Ariel University, Ariel 40700, Israel.

ABSTRACT

This study explores the relationship between objective sound measurements and subjective hearing thresholds under double hearing protection. Both Real-Ear Measurement (REM) and subjective testing were used to examine attenuation with EasyView Otoblock earplugs and Optime 105 earmuff. Stimuli were delivered from a fixed frontal source (0° azimuth) across a frequency range of 500 to 12,000 Hz, allowing observation of attenuation patterns at both low and high frequencies.

Descriptive analysis suggested consistent trends across participants. At higher frequencies (above 4 kHz), subjective results indicated more attenuation than objective REM values, whereas the opposite was observed at lower frequencies (below 4 kHz), where REM showed more attenuation. These patterns may reflect the contribution of bone conduction (BC) when air conduction (AC) is significantly reduced.

While the sample size limits statistical generalization, the findings highlight the value of integrating subjective data alongside objective measurements in evaluating hearing protection performance. The use of a realistic protection configuration and fixed sound direction offers practical insights into how auditory information is transmitted under high-attenuation conditions. These insights may support the development of more effective hearing protection devices for environments with hazardous noise exposure.

Keywords: *hearing protection devices, bone conduction, sound attenuation, real-ear measurements*

1. INTRODUCTION

1.1 Air Conduction and Bone Conduction Hearing

Hearing occurs through air conduction (AC), bone conduction (BC), and to a lesser extent, body conduction - which is often considered a subset of BC due to its indistinct boundaries [1]. AC is the dominant auditory pathway, transmitting sound via the ear canal, eardrum, and ossicles to the cochlea. In contrast, BC transmits sound through skull vibrations directly to the cochlea, bypassing the outer and middle ear entirely [2-3]. Under typical listening conditions, AC predominates, but when AC is obstructed,such as through the use of double hearing protection when combining insert earplugs and an earmuff,BC becomes increasingly relevant in auditory perception [4].

The AC pathway depends on the integrity and openness of the outer and middle ear structures. When these are sealed off by hearing protection, the transmission of sound via AC is significantly reduced. BC, however, is relatively unaffected by such occlusion and can become the primary pathway through which sound is perceived, particularly at lower frequencies (<1 kHz). This increased contribution of BC under occluded conditions is known as the occlusion effect, and it leads to measurable differences between physical (objective) and perceptual (subjective) assessments of sound attenuation [5].

*Corresponding author: Alonha@ariel.ac.il.

Copyright: ©2025 Hauptman et al. This is an open-access article distributed under the terms of the Creative Commons Attribution 3.0 Unported License, which permits unrestricted use, distribution, and reproduction in any medium, provided the original author and source are credited

These discrepancies are especially evident when comparing results from Real-Ear Measurement (REM) systems, used to objectively quantify sound levels in the ear canal, with behavioral threshold testing, which reflects the listener's perceptual experience. Under double hearing protection, where the AC path is highly attenuated, REM results tend to overestimate attenuation at low frequencies, while subjective tests reveal residual perception via BC [6].
In this study, we examine sound attenuation under a single, fixed condition of double hearing protection, using EasyView Otoblock earplugs in combination with Optime 105 earmuff. All sound stimuli were presented from the frontal direction (0° azimuth) to ensure consistent spatial input and to eliminate directional variability. This controlled setup allows us to focus specifically on how sound is conducted and perceived under maximum realistic occlusion, providing insight into the interplay between AC and BC under these conditions.
By understanding how the auditory system responds when AC is relatively blocked and BC dominates, especially in the context of real-world double hearing protection,we can better interpret the limitations of standard objective testing and develop more effective hearing protection strategies for high-noise environments.

AC is the most commonly utilized hearing pathway but is significantly reduced when hearing protection is applied. BC offers an alternative route, transmitting sound through bone and soft tissue [2]. Under double hearing protection, where both earplugs and earmuff are used, the attenuation of AC is high, and thus, the relative contribution of BC becomes more prominent. Understanding this shift in auditory pathways is essential for interpreting attenuation outcomes under such conditions.

1.2 Sound Attenuation Under Double Hearing Protection

Earplugs and earmuffs have different frequency-specific attenuation profiles, and their combination (i.e., double hearing protection) increases overall attenuation, particularly in the mid-to-high frequencies. However, the gains in attenuation are limited at low frequencies due to BC transmission, typically plateauing around 40–60 dB [4]. In this study, only the double protection configuration was evaluated using both objective and subjective measurements to assess how AC and BC interact under realistic high-attenuation conditions.
Subjective tests, which are based on perceptual thresholds, provide insight into the listener's experience and are influenced by BC. In contrast, objective methods such as REM offer consistent measurement of sound pressure levels in the ear canal but may underestimate BC effects [5]. This study compares both approaches to provide a more comprehensive eexplanation of attenuation under double protection.

1.3 Objective vs. Subjective Measures

Objective measures (e.g., REM) quantify sound levels in the ear canal using probe microphones, offering repeatable data that reflects the performance of the protection device [7]. However, they overlook the contribution of BC. Subjective thresholds, while more variable across individuals, are sensitive to BC influence. This study integrates both methods to evaluate the perceptual and physical aspects of attenuation under double protection and frontal sound presentation (0°).

1.4 Current Study Focus

This study investigates how double hearing protection affects auditory thresholds via both AC and BC, using a combination of objective (REM) and subjective (behavioral threshold of hearing) methods. The goal is to clarify the extent to which BC contributes to residual auditory perception when AC is substantially attenuated.
By focusing on a realistic protection configuration, earplugs combined with earmuff, the study enables a controlled and focused evaluation of auditory processing under high-attenuation conditions. This approach reduces variability related to directional hearing and protection level, allowing for a detailed analysis of the interaction between frequency, measurement modality, and the dominance of BC versus AC.
Through this design, the study aims to assess how effectively current measurement techniques capture attenuation, and to provide practical insights into the real-world performance of double hearing protection in high-noise environments.

1.5 Research Questions

1. How do objective real-ear measurements compare with subjective behavioral hearing thresholds when attenuation is assessed under double hearing protection?
2. Does the discrepancy between objective and subjective attenuation vary across frequencies?

1.6 Hypotheses

1. Subjective hearing thresholds will demonstrate less attenuation than objective REM measurements at low frequencies due to the contribution of BC pathways.
2. The gap between the subjective level of attenuation and the objective one will be most pronounced at low frequencies and will decrease at higher frequencies.

2. METHODS

2.1 Participants

Ten participants (6 female, 4 male), aged 18 to 28, with confirmed normal hearing, took part in the study. Testing was conducted at the Acoustics and Noise Research Laboratory at Ariel University. Inclusion criteria was air-conduction hearing thresholds of ≤20 dB HL between 500 and 8000 Hz. Exclusion criteria included any history of hearing loss, prolonged exposure to loud noise, or the use of ototoxic medications. The research protocol was approved by the university's ethical review board. All participants signed an informed consent before beginning the experiment.

2.2 Stimuli and Equipment

All measurements were conducted using the Interacoustics Affinity Compact system.

Objective measurements were carried out using Real-Ear Measurement (REM) module with 90 dB SPL pure-tone sweeps ranging from 250 Hz to 16,000 Hz. Sound pressure levels were recorded at the eardrum using a probe tube microphone.

Subjective hearing thresholds were obtained with the audiometer module using warble tones at 500, 1000, 2000, and 4000 Hz, as well as 1/12-octave intervals from 4000 to 12,000 Hz. Participants responded by pressing a button.

Calibration of all equipment was performed using a Brüel & Kjær Type 2250 Sound Level Meter.

All testing was performed in unoccluded condition and under double hearing protection, consisting of EasyView Otoblock earplugs and Optime 105 earmuff (see Figure 1).
Attenuation was calculated by comparing the protected condition to an unoccluded baseline for each participant, using both objective and subjective data.



Figure 1. EasyView Otoblocks by PHONAK, used as insert earplugs (left side), and Optime 105 earmuff by 3M (right side), comprising the double hearing protection configuration evaluated in the study.

2.3 Procedure

Participants completed both objective and subjective tests in a single session lasting approximately 1.5 to 2 hours. REM measurements were passive and required no response from the participant. During subjective testing, participants responded when they heard a tone, and thresholds were established using a manual audiometry protocol.
All stimuli for both objective and subjective tests were presented from a fixed sound source at 0° azimuth, positioned 50 cm infront of the participant's head.
Only the right ear was tested, while in the subjective testing, the left ear was masked at 50 dB HL using narrowband noise to eliminate cross-hearing.

2.4 Data Analysis

Due to the limited sample size, only descriptive statistical analysis was conducted. Attenuation (in dB) was examined across frequency and measurement method (objective vs. subjective). The analysis focused on identifying trends and patterns reflecting the contribution of BC under conditions of significant AC attenuation.

3. RESULTS

Mean attenuation values were analyzed across the tested frequency range, comparing objective measurements obtained through REM with subjective auditory hearing thresholds. The results depicted in Figure 2 revealed clear frequency-dependent patterns in both measurement methods, as well as systematic differences between them. Objective attenuation measurements peaked at approximately 36 dB near 3000 Hz, then gradually declined with increasing frequency, reaching a minimum of 18 dB at 12,000 Hz. Subjective attenuation showed a slightly deeper peak of around 38 dB near 4000 Hz, followed by a decrease

in attenuation to 33-40 dB at the upper end of the frequency range. At frequencies below 3000 Hz, objective attenuation exceeded subjective attenuation, whereas at higher frequencies, this pattern reversed, and subjective attenuation became greater.
This crossover pattern suggests that while objective measurements capture the attenuation of AC sound effectively, they may underestimate the perceptual influence of BC sound, particularly at higher frequencies. The divergence in attenuation levels between methods above 3000 Hz likely reflects the perceptual contributions of BC and the interaction with individual auditory sensitivity and occlusion effects.

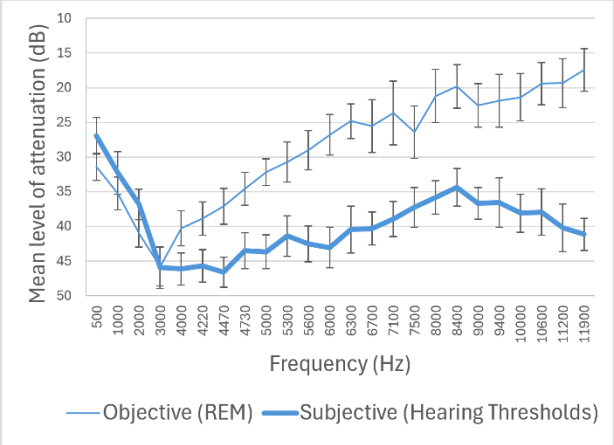


Figure 2. Mean attenuation (in dB) across frequencies, comparing objective REM (thin line) and subjective hearing thresholds (thick line). Measurements were conducted under double hearing protection. Error bars represent standard errors of the mean for each data point. (n=10)

4. DISCUSSION

The results of this study demonstrate clear differences between objective and subjective measurements of sound attenuation, with distinct frequency-dependent patterns. Objective attenuation levels peaked around 3000 Hz and decreased at higher frequencies, while subjective attenuation remained elevated beyond that frequency. This crossover at 3000 Hz may reflect the combined contributions of AC and BC to auditory perception under occluded conditions and aligns with earlier findings [4] showing that the limits of attenuation are set by the BC pathway even under maximal occlusion.

4.1 Dominant Sound Conduction Pathway

In conditions of high attenuation, such as those created by double hearing protection, the AC pathway is substantially reduced, allowing BC to play a more dominant role in perception. While objective REM primarily capture sound pressure levels in the ear canal and are largely AC-dependent [7], subjective thresholds reflect the listener's full perceptual experience, including the effects of BC transmission [23-]. The relatively higher objective attenuation at low frequencies, as compared to the lower subjective thresholds, supports the interpretation that BC continues to transmit sound effectively in this range. These findings are consistent with previous work showing that sound transmission via BC becomes the primary pathway under occluded conditions [3]. At higher frequencies, where subjective attenuation surpasses objective values, individual variability in skull vibration transmission or the auditory system's non-linear characteristics may contribute to perceptual differences not captured by physical measurements [2].
Moreover, it is well established that REM may underestimate BC influence, particularly under conditions involving strong occlusion and internal physiological noise [5]. This limitation underscores the value of using both objective and subjective measures to fully characterize hearing protection performance.

4.2 Stimulus Type Effects

The observed discrepancies between measurement modalities may also stem from differences in stimulus characteristics. Warble tones, used for subjective testing, minimize standing wave formation and provide a more perceptually stable signal, whereas the pure-tone frequency sweeps used in REM are more prone to standing waves and acoustic leakage artifacts [6]. These differences may partly explain the crossover effect between objective and subjective data observed in the present study.
Similar concerns have been raised in clinical hearing aid studies, where REM did not always predict perceptual performance, particularly when complex acoustic interactions were present [7]. Aligning the acoustic properties of the stimuli used in both measurement methods could help isolate the effect of stimulus type on attenuation results and improve the comparability between modalities in future work.

4.3 Limitations and Future Work

As a preliminary study, several limitations should be acknowledged. The sample size was modest, limiting the generalizability of the findings. Additionally, while the study design intentionally focused on a single hearing protection configuration and a fixed sound source direction to allow for controlled analysis, this necessarily reduced ecological variability. Future research should expand the sample population, explore additional hearing protection configurations, and investigate multiple azimuth angles to better simulate real-world listening environments. It is also recommended to further investigate the separate contributions of AC and BC. Finally, standardizing the stimulus type across both objective and subjective measurements could reduce methodological variance and improve the comparability of findings across modalities.

5. CONCLUSION

This study demonstrated clear, frequency-dependent differences between objective (REM) and subjective (threshold-based) measurements of sound attenuation under occluded conditions. A crossover pattern was observed around 3000 Hz, where objective attenuation peaked and then declined, while subjective attenuation remained elevated. These findings highlight the dominant role of bone conduction when air conduction is suppressed and underscore the limitations of relying solely on objective physical measures. Differences in stimulus type also contributed to the divergence between methods, reinforcing the need for methodological alignment. Overall, the integration of both objective and subjective assessments is essential for accurately evaluating hearing protection performance in high-attenuation environments.

6. ACKNOWLEDGMENTS

We extend our gratitude to the undergraduate students from the Department of Communication Disorders at Ariel University for their dedication and effort in data collection.

7. REFERENCES

[1] J. Ashmore, Hearing, *Novartis Foundation Symposium*, vol. 213, pp. 133–141, 1998.

[2] S. Stenfelt and R. Goode, Bone-conducted sound: Physiological and clinical aspects, *Otology and Neurotology*, vol. 26, pp. 1245–1261, 2005.

[3] S. Reinfeldt, S. Stenfelt, R. Goode, and B. Håkansson, Examination of bone-conducted transmission from sound field excitation measured by thresholds, ear-canal sound pressure, and skull vibrations, *The Journal of the Acoustical Society of America*, vol. 121, no. 3, pp. 1576–1587, 2007.

[4] E. H. Berger, R. W. Kieper, and D. Gauger, Hearing protection: Surpassing the limits to attenuation imposed by the bone-conduction pathways, *The Journal of the Acoustical Society of America*, vol. 114, no. 4, pp. 1955–1967, 2003.

[5] E. H. Berger and J. E. Kerivan, Influence of physiological noise and the occlusion effect on the measurement of real-ear attenuation at threshold, *The Journal of the Acoustical Society of America*, vol. 74, no. 1, pp. 81–94, 1983.

[6] E. T. Doherty, A comparison of real-ear subjective, real-ear objective, and an artificial head measurement method for determining the attenuation characteristics of hearing protectors, *Ear and Hearing*, vol. 8, no. 5 Suppl, pp. 127–133, 1987.

[7] H. G. Mueller, Probe microphone measurements: 20 years of progress, *Trends in Amplification*, vol. 5, no. 2, pp. 35–68, 2001.

DOI: 10.61782/fa.2025.0362

FORUM ACUSTICUM EURONOISE 2025

EVALUATION OF A NOVEL SOUND ENHANCING CONNECTING TUBE APPARATUS FOR IMPROVING SOUND LOCALIZATION OF OCCLUDED EARS

Aaron Benn[1*] **Liron Grushko**[1] **Gregory Banta**[2]
Nir Fink[1]
[1] Department of Communication Disorders, Acoustics and Noise Research Lab in the Name of Laurent Levy, Ariel University, Ariel 40700, Israel.
[2] Department of National Defence, Canada

ABSTRACT

Noise-induced hearing loss (NIHL) poses a serious risk to individuals exposed to high-intensity sounds, particularly military personnel and industrial workers. While hearing protection devices (HPDs) like foam earplugs mitigate NIHL, they often impair sound localization and speech intelligibility. This study investigates the sound-enhancing-connection-tube (SECT), a prototype perforated tube connected to the opening of two vented earplugs, designed to adjust attenuation across frequencies for improving sound localization while preserving protective benefits. Using head-related transfer functions (HRTF) to measure sound pressure at the position of the eardrum, the study evaluated SECT effects on the 1–4 kHz range, critical for speech and environmental sounds.

The research involved three experiments: HRTF-based optimization of SECT design using a head-and-torso-simulator (HATS) and two human trials to assess localization performance. HATS results demonstrated up to 15 dB less attenuation for frequencies above 800 Hz when the SECT was used with vented earplugs compared to just earplugs. However, human trials showed no significant localization improvement. Differences may stem from how the human brain processes complex auditory cues, bone and tissue conduction effects absent in HATS, and potential sound loss through SECT connectors. Future research should prioritize live-subject guided training to address these limitations.

Keywords: *hearing protection, sound source localization, noise induced hearing loss*

[*] ***Corresponding author***: *aaron.benn9@gmail.com*
Copyright: *©2025 Benn et al. This is an open-access article distributed under the terms of the Creative Commons Attribution 3.0 Unported License, which permits unrestricted use, distribution, and reproduction in any medium, provided the original author and source are credited.*

1. INTRODUCTION

Noise-induced hearing loss (NIHL) results from exposure to high-intensity sound, with prolonged noise above 85 dB posing significant risks [1]. Military personnel are especially vulnerable due to exposure to loud engine noise, gunfire, and explosions [2; 3]. Other at-risk populations include construction workers and factory laborers. NIHL can develop gradually, impairing communication and necessitating assistive devices like hearing aids [4; 5].

Hearing protection devices (HPDs) help mitigate NIHL by attenuating harmful noise levels. Linear HPDs, such as foam earplugs, reduce sound evenly across frequencies but may impair speech intelligibility and sound localization [6; 7]. Non-linear HPDs, in contrast, adjust attenuation based on intensity, allowing softer sounds to pass through while blocking louder noises [8]. However, even non-linear HPDs can interfere with localization cues by altering ear acoustics or blocking pinna effects, leading to degraded spatial hearing and increased cognitive effort for speech comprehension [9; 10; 11].

To address these limitations, this study examines a prototype sound-enhancing connection tube (SECT), designed to improve localization while maintaining noise attenuation. The SECT consists of a perforated tube

integrated with non-linear earplugs, allowing controlled attenuation similar to a woodwind instrument. Pilot studies [12; 13; 14] suggest SECT may improve speech intelligibility while retaining noise-blocking properties, though optimal design parameters remain unclear.

A head-related transfer function (HRTF) was used to assess how SECT impacts sound transmission. Initial HRTF measurements on a head and torso simulator (HATS) established baseline effects of occlusion. This study aims to determine SECT parameters that minimize attenuation in the 1-4 kHz range, critical for speech and firearm sounds.

This study's objectives were:

1. To determine which combination of SECT parameters, such as the number and spacing of perforations, leads to a significant difference in the HRTF with an earplug with the tube compared to an earplug without the tube.
2. To test whether individuals demonstrate improved sound localization when using the SECT with a non-linear HPD compared to using the non-linear HPD alone.

We hypothesized that

1. The HRTF measurements for ears occluded with the SECT will show less attenuation in the 1-4 kHz range compared to the occluded condition without the SECT.
2. Individuals using the SECT in combination with two perforated earplugs will show improved sound localization compared to the perforated earplugs alone but will still perform worse than in the unoccluded condition.

Study Overview

The research consists of three experiments:

- Experiment 1: HRTF measurements to analyze SECT design variations.
- Experiment 2: Wideband sound localization tests.
- Experiment 3: Narrowband sound localization tests.

Results will be discussed with implications for future HPD development.

2. EXPERIMENT 1

2.1 Introduction

A HATS is a system designed to replicate the acoustic properties of the human head, torso, and ear canals. It consists of an artificial head and torso with microphones embedded at the eardrum position, allowing researchers to analyze how sound is perceived in different conditions. HATS are widely used in audio research, particularly for testing hearing protection devices (HPDs) [15].

This experiment aimed to optimize the design of the SECT by identifying a configuration that minimizes attenuation in the critical 1-4 kHz frequency range. This range is important for speech perception and identifying key sounds such as rifle fire. Using a HATS setup, we tested various SECT designs to determine the combination of perforation spacing that would allow the best preservation of these frequencies.

2.2 Method

2.2.1 Tools

The experiment was conducted using a GRAS 45BC KEMAR HATS equipped with GRAS 46BD ¼" microphones at the ear canal positions. The HATS was powered by a GRAS 12AX 4-Channel CCP Power Module. Sound was generated using Sinus Samurai software and transmitted through an RCF Ayra 5 monitor, while measurements were analyzed using the same software. A GRAS 146AE rugged ½" reference microphone was placed near the tragus to record the original signal before it reached the ear.

2.2.2 Process

A pure tone sweep (100-12,800 Hz) was played from a monitor positioned 1 meter in front of the HATS at 0° azimuth. The sound level was set to 54 dB[A] at the reference microphone. The sound pressure level (SPL) recorded by the eardrum microphones was compared to the reference microphone to calculate the HRTF. This process was repeated using different SECT designs, with variations in perforation spacing, until a configuration was identified that minimized attenuation in the 1-4 kHz range. The setup we used for this stage of the study can be seen in Figure 1.

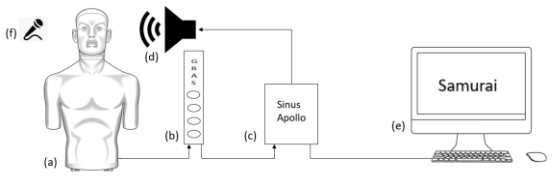


Figure 1. The setup used in Experiment One consisted of (a) KEMAR HATS with embedded microphones in ear canals, (b) Power module (c) Sinus Apollo Light, (d) monitor, (e) laptop with Sinus Samurai software, (f) reference microphone.

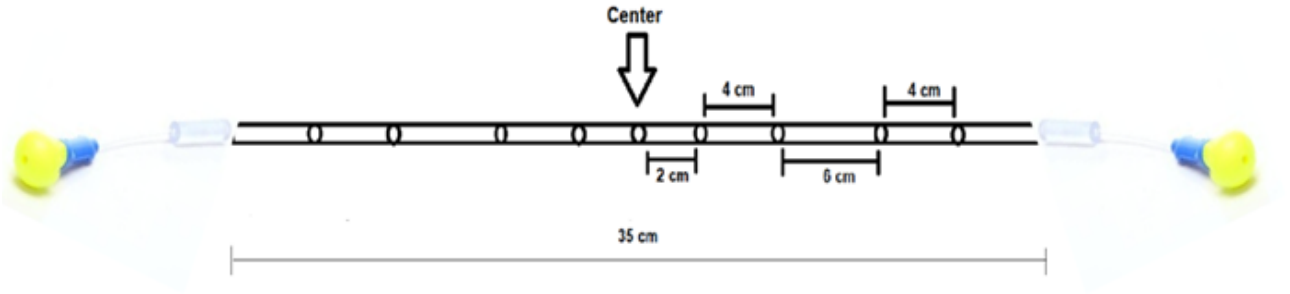


Figure 2. An illustration of the dimensions of the final SECT design used in this study. Earplugs are attached to either side of the SECT

2.3 Results

The optimal SECT design was determined by evaluating the effects of perforation spacing across three prototype tubes (2 cm, 4 cm, and 6 cm spacing). Each design produced frequency-specific attenuation reductions, with the 6 cm spacing showing the least attenuation at 1200 Hz, the 4 cm spacing at 2000 Hz, and the 2 cm spacing at 3000 and 5000 Hz. To incorporate the benefits of all three designs, a final SECT model was developed with perforations at progressively increasing distances from the tube's center (2 cm, 4 cm, and 6 cm), as seen in Figure 2.

2.4 Discussion

The results indicate that incorporating a perforated tube into earplugs alters the HRTF in a way that may enhance sound localization. By reducing attenuation in the 1-4 kHz range, the SECT allows more auditory cues to reach the ear, potentially improving the perception of speech and other critical sounds. This suggests that a properly configured SECT could provide a balance between hearing protection and environmental awareness. This hypothesis was further tested in subsequent human experiments, which assessed whether these modifications led to actual improvements in sound localization performance.



Figure 3. The SECT affixed to a helmet and connected to earplugs.

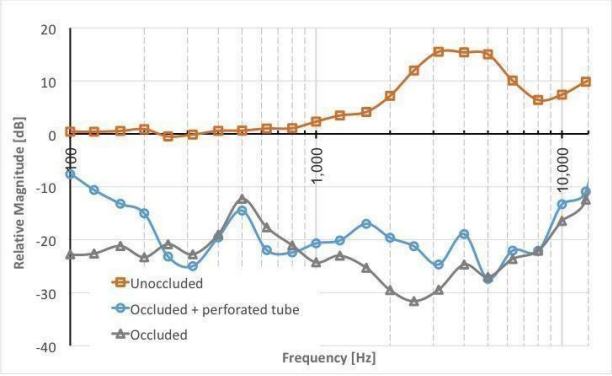


Figure 4. HRTF of the unoccluded condition (orange squares), the occluded condition (gray triangles) and the occluded + perforated tube (blue circles) condition.

3. EXPERIMENT 2

3.1 Introduction

Following the selection of the final SECT design, the next phase of the study tested its effect on human sound localization ability. Soldiers frequently report avoiding the use of HPDs in combat due to their negative impact on localizing sounds such as gunfire and spoken commands [16; 17]. To address this issue, we assessed localization performance using stimuli relevant to combat scenarios. It was hypothesized that the SECT would improve localization compared to standard push-in earplugs but would still perform worse than an unoccluded condition.

3.2 Method

3.2.1 Participants

Fourteen university-aged participants (9 female, 5 male; aged 21–29, mean = 23.9) took part in the study. All had normal hearing and no history of learning or attention disorders. Participants were compensated either monetarily or with course credit.

3.2.2 Tools

Sound stimuli were presented through eight RCF Ayra 5 monitors arranged in a circle around a central chair at a 1.8-meter radius. The speakers were positioned at azimuths of 22.5º, 67.5º, 112.5º, 157.5º, 202.5º, 247.5º, 292.5º, and 337.5º, with 0º representing directly in front of the participant. Responses were recorded via a touchscreen tablet displaying a circular interface, where participants tapped their perceived sound source location. More information about the tools can be found in Fostick and Fink (2021) [10].

3.2.3 Stimuli

Four stimuli were used: the Hebrew word “esh” (fire), a pink noise burst, a single M16 rifle shot, and three M16 shots fired in quick succession. All stimuli were presented at 75 dB SPL.

3.2.4 Procedure

Each participant sat in the center of the speaker array with a tablet on their lap. Each stimulus was presented ten times per speaker for a total of 320 trials (4 stimuli × 8 speakers × 10 repetitions). Stimulus order and speaker presentation were randomized. Each participant completed the experiment under three conditions:

1. Unoccluded (no HPD)
2. Occluded (3M™ E-A-R™ Push-Ins™ Earplugs)
3. SECT condition (SECT attached to 3M™ E-A-R™ Push-Ins™ Probed Test Plugs)

The order of conditions was randomized to prevent fatigue or learning effects. After each stimulus, participants tapped on the tablet to indicate the perceived sound source location. Regular breaks were provided. The research protocol was approved by the university’s ethical review board. All participants signed an informed consent before beginning the experiment.

3.3 Results

Root Mean Square Error (RMSE) was used to assess localization accuracy by measuring the difference between perceived and actual sound azimuths. A three-way ANOVA revealed a significant main effect for condition (unoccluded, occluded, occluded + SECT) ($F(2, 26) = 27.06$, $p < 0.001$, $\eta^2 = 0.675$), stimulus type ($F(3, 39) = 3.38$, $p = 0.028$, $\eta^2 = 0.206$), and speaker position ($F(1.49, 19.33) = 21.06$, $p < 0.001$, $\eta^2 = 0.618$).

Post hoc comparisons revealed that localization accuracy was best in the unoccluded condition, followed by the occluded condition, with the SECT condition yielding the highest RMSE (poorest localization). No significant differences were found between stimuli. RMSE was highest for stimuli from the rear (157.5° and 202.5°) and lowest for front-hemifield locations (22.5° and 337.5°).

A significant interaction was found for condition × speaker position ($F(14, 182) = 8.518$, $p < 0.001$, $\eta^2 = 0.396$) (Figure 5), but no significant interactions were observed for condition × stimulus ($p = 0.072$) or stimulus × speaker ($p = 0.179$).

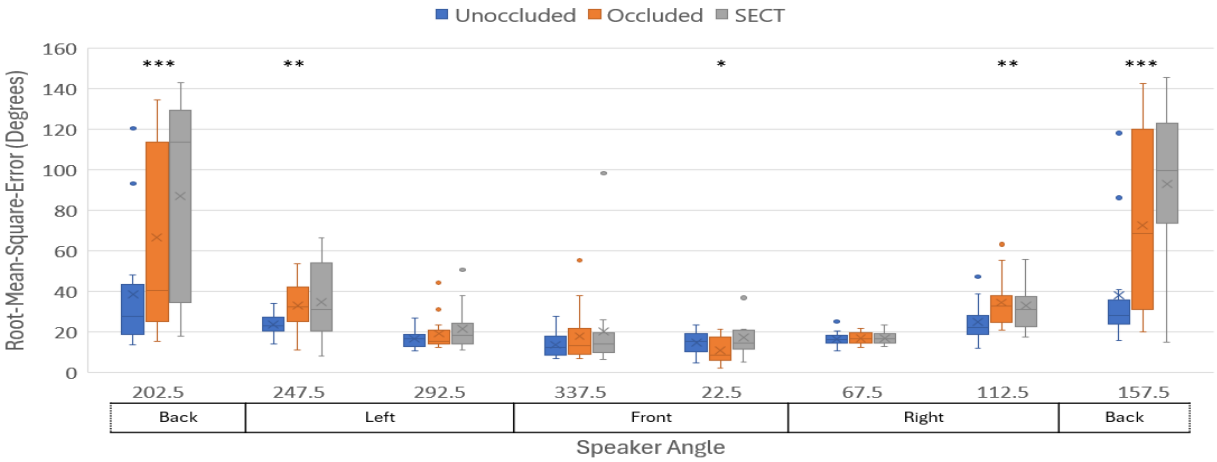


Figure 5. Interaction between condition and speaker angle for RMSE. *p<0.05 between (unoccluded, occluded); (occluded, SECT). **p<0.05 between (unoccluded, occluded); (unoccluded, SECT). ***p<0.05 between (unoccluded, occluded); (unoccluded, SECT); (occluded, SECT).

3.4 Discussion

After testing 14 participants, data analysis revealed no localization advantage for the SECT over standard occluded conditions. While speaker angle effects were consistent with previous findings [10], the SECT failed to enhance localization across the tested stimuli.

One possible explanation is the complexity of the stimuli's frequency content. The SECT was designed to reduce attenuation in the 100–250 Hz and 900–5000 Hz ranges, but its performance was initially measured at a 0° angle. Given that the localization task involved stimuli from multiple angles, SECT's effectiveness may not have translated across all directions, leading to its underperformance compared to expectations.

4. EXPERIMENT 3

4.1 Introduction

Experiment 3 aimed to simplify the stimuli from Experiment 2 in order to more accurately assess the SECT's effectiveness. Additional HRTF measurements were taken from a wider range of sound source angles (22.5°, 67.5°, 112.5°, and 157.5°) to identify which frequencies would most benefit from the SECT apparatus. Based on these measurements, two narrow-band stimuli were selected: a low-frequency stimulus (500-600 Hz) and a higher-frequency stimulus (1200-1600 Hz). These new stimuli are represented visually in Figure 6. The hypothesis was that the SECT would improve sound localization performance for the higher-frequency stimulus, but not for the lower-frequency stimulus. It was also expected that the unoccluded condition would outperform the other conditions for both stimuli.

4.2 Methods

4.2.1 *Participants*

Twenty participants (10 female, 10 male, aged 21-32, mean age 25.7) were recruited for this experiment, with inclusion and exclusion criteria identical to Experiment 2.

4.2.2 *Tools*

The same equipment used in Experiment 2 was employed for this stage of the study.

4.2.3 *Stimuli*

Two narrow-band noise bursts were used as stimuli: a low-frequency stimulus (500-600 Hz) and a high-frequency stimulus (1200-1600 Hz). Each burst lasted 250 ms and was presented at 75 dB SPL. The stimuli were delivered from 8 speakers at randomized positions around the participant.

4.2.4 *Procedure*

The experiment followed the same procedure as Experiment 2, with participants seated in front of 8 monitors. Each stimulus was presented 10 times from each speaker, totalling 160 presentations. The experiment

included the same three conditions: unoccluded, occluded, and SECT. The research protocol was approved by the university's ethical review board. All participants signed an informed consent before beginning the experiment.

4.2.5 *Data Analysis*

A three-way ANOVA was performed to assess the effects of condition, stimulus, and speaker on Root Mean Square Error (RMSE). Main effects and interactions were analyzed to determine how these variables influenced sound localization accuracy.

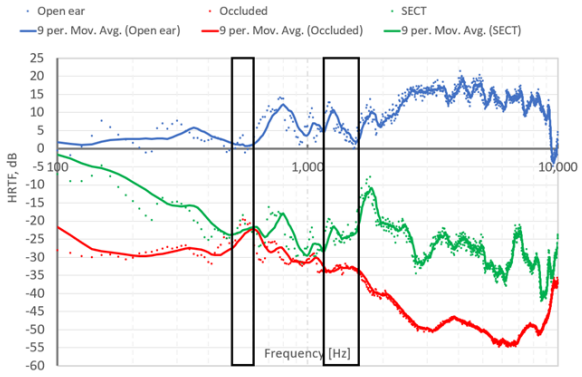


Figure 6. HRTF measurements averaged for stimuli presented from angles of 22.5º, 67.5º, 112.5º, and 157.5º for the unoccluded (blue), occluded (orange), and occluded with SECT (green) conditions. The areas encompassed by the black rectangles indicate the frequency ranges contained in the low-frequency narrow-band stimulus (500-600 Hz) and the high-frequency narrow-band stimulus (1200-1600 Hz) that were used to derive the two narrow sound burst stimuli for Experiment 3.

4.3 Results

A three-way ANOVA revealed significant main effects for both the condition ($F(2, 38) = 42.3$, $p < 0.001$, $\eta^2 = 0.69$) and speaker ($F(1.8, 34.18) = 41.14$, $p < 0.001$, $\eta^2 = 0.684$). There were also significant interactions between condition and stimulus ($F(2, 38) = 4.493$, $p = 0.018$, $\eta^2 = 0.191$), condition and speaker ($F(3.442, 65.39) = 10.867$, $p < 0.001$, $\eta^2 = 0.364$) (Figure 7), and stimulus and speaker ($F(3.905, 74.187) = 2.906$, $p = 0.028$, $\eta^2 = 0.133$). These results highlight that the experimental condition, speaker position, and stimulus type all influenced the RMSE in sound localization accuracy.

4.4 Discussion

The results from Experiment 3 showed that altering the stimuli to focus on low- and high-frequency ranges did not improve performance with the SECT, as hypothesized. While the high-frequency stimulus was expected to benefit from the SECT, no significant difference was found between the SECT and occluded conditions. These findings diverged from those of Villian & Cement (2020) [12], who observed better localization performance with SECT designs compared to standard earplugs. The discrepancy may be due to differences in earplug types used between the two studies (3M Ear Classic vs. 3M™ E-A-R™ Push-In™), and the different methods of performance analysis (RMSE vs. average angle error).

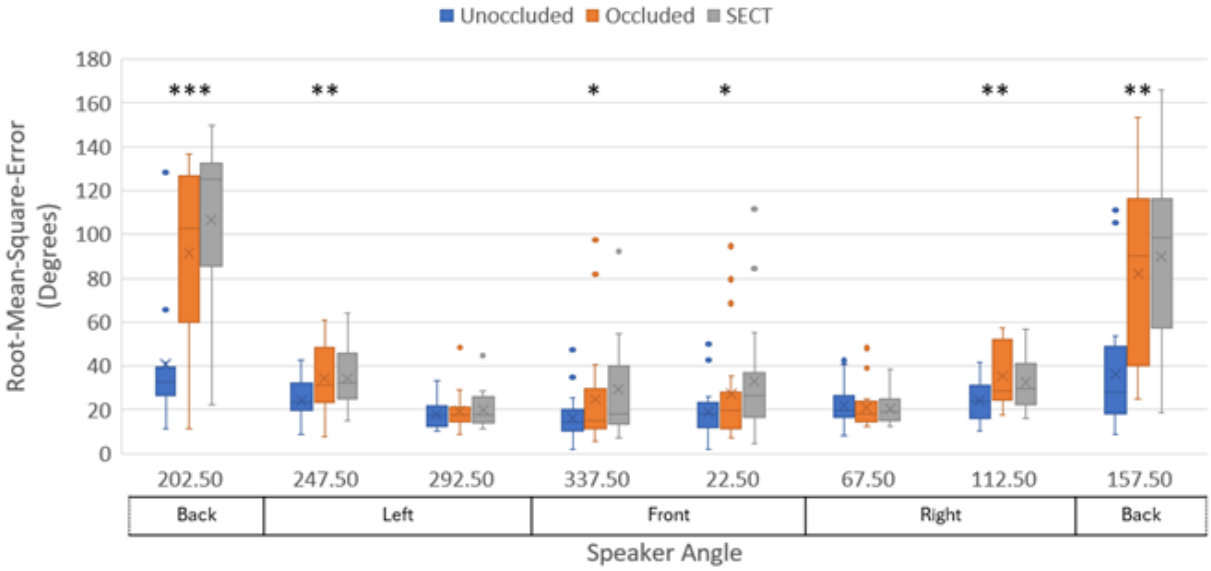


Figure 7. Interaction between condition and speaker angle for RMSE. *p<0.05 between (unoccluded, SECT). **p<0.05 between (unoccluded, occluded); (unoccluded, SECT). ***p<0.05 between (unoccluded, occluded); (unoccluded, SECT); (occluded, SECT).

5. GENERAL DISCUSSION

This study was conducted to create the SECT, a perforated air tube connected to two non-linear perforated earplugs, that would allow for improved sound localization abilities when compared to standard Push-Ins earplugs. HRTF measurements were performed on a HATS to determine which tube parameters allowed for the least amount of attenuation at the 1-4 kHz frequency range, chosen for its inclusion in spoken language as well as dominance in gunfire sound. This design was then tested on human subjects in a sound localization task. Upon analyzing the results, we found no significant statistical difference between the occluded condition and the SECT condition, contrary to our hypothesis. However, as predicted, the unoccluded condition displayed better performance than both occluded conditions.

There are several possible explanations for the discrepancy between the HATS results and the results received in experiments with human subjects. One possibility is based on how the human brain processes and interprets incoming stimuli. Whereas none of these occur within the HATS, typically, the brain processes two sound signals, one reaching each ear, and uses the interaural time and intensity differences to aid in localization, as well as acoustic factors such as the pinna effect [18]. However, the addition of the SECT introduces numerous sound signals to both ears through each of the perforations along the length of the SECT. The arrival of multiple similar stimuli simultaneously may inhibit the brain's ability to differentiate between them effectively [19]. Supervised training using the SECT followed by retesting the sound localization capabilities may lead to improved results. Indeed, Casali & Robinette (2015) [20] showed that training sessions can lead to improved performance in sound source localization tasks while wearing HPDs.

It is also possible that the passage of sound waves through the T-connectors and into the thinner probe tubes located within the perforated ear plugs may weaken sound levels at certain frequencies that would otherwise provide critical information.

Another possible cause for this study's results is the impact of bone and tissue conduction (BTC). The HRTF measurements obtained in the first stage of this study possess only air conduction pathway capabilities. However, the human cochlea also receives sound waves that propagate to the cochlea through the subject's body tissues and bones, which are not measured on the HATS. When HPDs are used, such as those used in conjunction with the SECT, sounds arriving through air conduction are attenuated, thus allowing BTC sounds to dominate the auditory experience. Thus, it may be necessary to

reconsider the way in which the SECT's final design was created. Instead of using a HATS, the HRTF measurements should be performed on a human subject so that the influence of the BTC can be taken into consideration.

6. CONCLUSIONS, LIMITATIONS AND FURTHER RESEARCH

In conclusion, this study explored the potential of the SECT, a perforated air tube connected to non-linear earplugs, to improve sound localization while providing adequate noise attenuation. The SECT design was based on HRTF measurements obtained from a HATS, with the goal of preserving frequencies essential for speech recognition and sound localization in the 1-4 kHz range. However, human trials did not confirm a significant improvement in localization with the SECT compared to standard occluded conditions, despite successful attenuation characteristics in HATS testing. This suggests that while the SECT concept is feasible, the current design may require further optimization to align with natural hearing cues and individual auditory processing mechanisms.

A few limitations may have influenced these outcomes. The study relied on HATS for initial HRTF measurements, which, while precise for acoustic modeling, cannot fully replicate the nuances of human auditory processing. Specifically, the HATS cannot simulate binaural processing and other brain functions that aid in sound localization, such as interaural time differences and the pinna effect. Moreover, the SECT design might introduce competing sound signals due to its perforations, potentially causing interference that limits sound source differentiation. Another important factor is the effect of BTC on hearing perception, which the HATS model does not capture. Human listeners experience BTC in conjunction with air-conducted sound, and the lack of BTC in testing could mean that significant aspects of sound transmission and localization were overlooked.

Future research could benefit from HRTF measurements conducted directly on human subjects to incorporate BTC effects, as well as from additional training protocols to help participants adapt to the SECT's unique signal presentation. These adaptations may enhance the SECT's effectiveness and provide clearer insights into its potential benefits for hearing protection and sound localization.

7. REFERENCES

[1] T. Ding, A. Yan, and K. Liu, "What is noise-induced hearing loss?" Br. J. Hosp. Med., vol. 80, no. 9, pp. 525–529, 2019.

[2] Lie et al., "Occupational noise exposure and hearing: A systematic review," Int. Arch. Occup. Environ. Health, vol. 89, pp. 351–372, 2016.S. M. Abel and J. S. Paik, "Sound source identification with ANR earmuffs," *Noise Health*, vol. 7, no. 27, p. 1, 2005.

[3] C. Moore, "Diagnosis and quantification of military noise-induced hearing loss," J. Acoust. Soc. Am., vol. 148, no. 2, pp. 884–894, 2020.

[4] E. Daniel, "Noise and hearing loss: A review," J. Sch. Health, vol. 77, no. 5, pp. 225–231, 2007.

[5] O. Hong, M. J. Kerr, G. L. Poling, and S. Dhar, "Understanding and preventing noise-induced hearing loss," Dis. Month, vol. 59, no. 4, pp. 110–118, 2013.

[6] Brown, B. T. Beemer, N. T. Greene, T. I. V. Argo, G. D. Meegan, and D. J. Tollin, "Effects of active and passive hearing protection devices on sound source localization, speech recognition, and tone detection," PLoS One, vol. 10, no. 8, p. e0136568, 2015.

[7] Audet, W. Gray, and A. Brown, "Audiovisual training rapidly reduces potentially hazardous perceptual errors caused by earplugs," *Hear. Res.*, vol. 414, p. 108394, 2022.

[8] G. L. Wilde and L. E. Humes, "Measurement of the attenuation characteristics of nonlinear hearing protective devices using the auditory brain stem response," J. Acoust. Soc. Am., vol. 81, no. 3, pp. 730–733, 1987.

[9] S. A. Gelfand, Hearing: An Introduction to Psychological and Physiological Acoustics, 4th ed., CRC Press, 2004.

[10] L. Fostick and N. Fink, "Situational awareness: The effect of stimulus type and hearing protection on sound localization," Sensors, vol. 21, no. 21, p. 7044, 2021.

[11] C. Kwak and W. Han, "The effectiveness of hearing protection devices: A systematic review and meta-analysis," Int. J. Environ. Res. Public Health, vol. 18, no. 21, p. 11693, 2021.

[12] N. Vilian and H. Cement, "Earplugs connected by an air tube to improve localization capability," Seminar, Ariel Univ., 2020.

[13] Nof and A. Yosef, "Earplugs connected by an air tube to improve speech-in-noise intelligibility," Seminar, Ariel Univ., 2021.
[14] R. Kaplan and M. Adjayeb, "Attenuation levels of earplugs connected by an air tube with varying numbers of perforations and their effect on speech-in-noise intelligibility," Seminar, Ariel Univ., 2022.
[15] V. Bruschi, A. Terenzi, N. A. Dourou, S. Spinsante, and S. Cecchi, "Comparative analysis of HRTFs measurement using in-ear microphones," Sensors, vol. 23, no. 13, p. 6016, 2023.
[16] C. J. Smalt et al., "The effect of hearing-protection devices on auditory situational awareness and listening effort," Ear Hear., vol. 41, no. 1, pp. 82–94, 2020.
[17] L. Fostick and N. Fink, "Measuring 'where': A comparative analysis of methods measuring spatial perception," Sensors, vol. 23, no. 23, p. 9434, 2023.
[18] M. Risoud et al., "Sound source localization," Eur. Ann. Otorhinolaryngol. Head Neck Dis., vol. 135, no. 4, pp. 259–264, 2018.
[19] M. D. Rugg and M. G. H. Coles, Eds., Electrophysiology of Mind: Event-Related Brain Potentials and Cognition, Oxford Univ. Press, 1995.
[20] J. G. Casali and M. B. Robinette, "Effects of user training with electronically modulated sound transmission hearing protectors and the open ear on horizontal localization ability," Int. J. Audiol., vol. 54, sup. 1, pp. S37–S45, 2015.

DOI: 10.61782/fa.2025.0269

FORUM ACUSTICUM EURONOISE 2025

DESIGN AND ANALYSIS OF MOBILE MICROPHONE ARRAYS FOR ACOUSTIC DRONE TRACKING

Martin Blass* **Franz Graf**
JOANNEUM RESEARCH Forschungsgesellschaft mbH
DIGITAL – Institute for Digital Technologies

ABSTRACT

The growing security threat posed by hostile drones (UAVs) highlights the urgent need for effective detection systems. Besides optical, radar or radio frequency systems, the acoustic domain offers significant but underutilized capabilities. Since human hearing is inherently limited in detecting and localizing weak or high-frequency sounds in noisy or dynamic environments, microphone arrays represent a significant improvement in tracking drone noise. In the literature, most of the existing acoustic systems are stationary and focus on the detection or localization of individual drones. The integration of mobile microphone arrays on vehicle roofs or soldier helmets can enhance military capabilities by enabling real-time tracking of drones in diverse and challenging scenarios. In this paper, we present the design criteria and development of a practical microphone array system capable of detecting and tracking multiple drones. First, we describe the implementation of a hemispherical array of 32 microphones. Then, we consider possible adaptations, e.g. in terms of reducing the number of microphones by selecting subarrays to address low-power consumption considerations and real-time processing for sound source localization. Finally, we show experimental results of a dataset recorded in a fixed and mobile scenario where the microphone array was mounted on a vehicle roof.

Keywords: *microphone, array, tracking, mobile, drone*

**Corresponding author*: martin.blass@joanneum.at.
Copyright: *©2025 Blass et al. This is an open-access article distributed under the terms of the Creative Commons Attribution 3.0 Unported License, which permits unrestricted use, distribution, and reproduction in any medium, provided the original author and source are credited.*

1. INTRODUCTION

Within the recent years, drones and other UAVs have become an established technology in the fields of industrial surveillance, disaster management, public safety, logistics, agriculture and smart cities, to name a few. As commercial drones are available at low cost and do not require explicit expertise, they can also easily be used to intentionally or accidentally violate privacy, cause public nuisance through noise, or even pose a threat to society or public institutions when used as a means of attack. Recent military conflicts, such as those in Ukraine and the Middle East, along with increasing drone-related incidents, highlight the need for effective countermeasures against UAV threats. To enhance civilian security and military defense, numerous research projects and counter-UAV technologies have emerged, employing multi-sensor approaches that integrate radar, computer vision, radio frequency, and acoustic detection [1,2]. While often overlooked due to range limitations, acoustic sensing provides a cost-effective and essential tool for UAV detection, especially in scenarios where other modalities face challenges. Microphone arrays, in particular, offer a practical and low-cost solution for determining the incident angles of sound sources, e.g. drones, within a limited range and hemispheric coverage [3].

In order to localize drone sounds in terms of their incident direction, microphone arrays enable the use of direction-of-arrival estimation (DOAE) and beamforming (BF) methods [4]. In addition, sound source tracking algorithms may be applied to process frame-based DOA estimates and to reconstruct movements of multiple sound sources. In [5] a large microphone array with 64 microphones and 4 m diameter was placed on the ground and used to compare three DOAE algorithms: GCC-PHAT, conventional delay-and-sum BF and differential evolu-

tion. Successful localization results were obtained within 80 m. In [6] a 16-channel L-shaped array was chosen together with MUSIC as DOAE method for narrowband, broadband and proposed harmonic focus (2-6 kHz) scenarios. The authors of [7] investigated DOAE using incoherent and proposed coherent BF performed with a 64-channel MEMS microphone array in simulations and outdoor experiments within a range of 200 m. Similar contributions were published in [8, 9].

There is only a limited amount of publications combining both detection and localization to address the sound source association problem to successfully track UAVs while rejecting other sound sources. One promising example is described [10], where UAV noise recorded with a spherical microphone array is used to train a so called *BeamLearning-ID* network to mimic the BF process. Another joint detection and localization approach is described in [11]. In our previous works [12, 13] we presented a framework that enables the joint detection and localization of sound emitted by multiple UAVs in real-time. Similar to [11] we proposed a track-before-detect approach, where multiple hypotheses are generated using a GMM-based sound source tracking algorithm together with a classical ML model relying on drone specific audio features. To the best of our knowledge, our latest paper [13] is one of the first to address mobile UAV tracking, which is of great importance for military applications in view of the global geopolitical situation.

Wearable microphone arrays have been explored for various applications, including sniper detection, situational awareness, and sound event localization. [14] developed a helmet-mounted array for sniper detection, capable of real-time localization by analyzing Mach and muzzle waves from rifle shots. Their system demonstrated robust performance in urban environments with low false alarm rates. [15] presents a similar system with focus on determining the optimum number and position of microphones on a helmet by taking into account diffraction paths and intensity differences. [16] introduced a conformal helmet-mounted array designed to enhance auditory situational awareness while providing hearing protection. Their system integrates BF with head-related transfer functions to maintain spatial hearing and natural localization of sound sources despite protective headgear. [17] focused on a wearable sound event localization and detection (SELD) dataset, using 24 microphones placed on head-worn accessories like glasses and earphones. They evaluated deep learning-based SELD methods, showing that microphone positioning significantly impacts localization accuracy.

In this paper, we want to explore ways to enhance the efficiency of acoustic drone tracking for mobile applications in terms of reducing energy and computational requirements by tuning the number of sensors and the geometry of microphone arrays. First, we present the design and development of *JR-IcoDome32*, a hemispherical 32-channel microphone array that can be deployed in fixed or mobile scenarios, e.g. on vehicle roofs. Second, we analyze a scaled version that could be suitable as a human-worn sensor, e.g. integrated into a soldier's helmet. Then, we derive sub-arrays from the *JR-IcoDome32* to compare their DOAE performance. Finally, we evaluate these array configurations using a dataset collected during measurement campaigns for a fixed and a mobile scenario where the microphone array was placed on the ground and mounted on the roof of a vehicle.

The remainder of this paper is organized as follows: Section 2 explains the microphone array design process including sub-array configurations and the methods used for DOAE and sound source tracking, Section 3 describes the sensor system development and hardware integration, Section 4 presents the experimental setup and results, and Section 5 concludes the work with a future outlook.

2. METHODOLOGY

2.1 Microphone Array Design

Based on the existing knowledge of typical drone sounds and the requirements for mobile application [12, 13], we designed a microphone array suitable for the task of UAV localization: The array should have a rotationally symmetrical directional characteristic, be rigid, lightweight and weatherproof. In addition, a high directivity in the frequency range below 3 kHz and an attenuation of noise below the array in mobile operation (e.g. car engine, rolling noise) should be achieved, which led to a 3D geometry in the design process. The result is a geodesic dome of the type *Icosahedron V2* with a diameter d of 1 m and 26 microphones. By adding 6 more sensors in the base plane, 5 as a pentagon and one in the center, we obtain a 32-channel configuration, of which 16 sensors are placed in 2D and 3D, respectively. In the following we refer to this microphone array as *JR-IcoDome32*. Figure 1 shows the proposed array geometry with microphone positions as connected icosahedron edges and Figure 2 the resulting simulated spatial response given as point spread functions (PSF) for selected octave-band center frequencies and summed over the total frequency range up to 16 kHz.

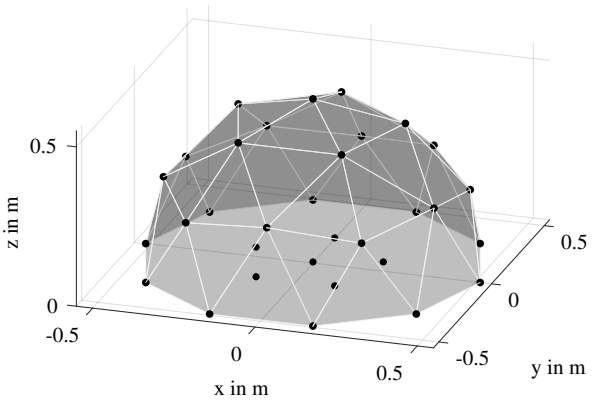


Figure 1: Array geometry of *JR-IcoDome32*.

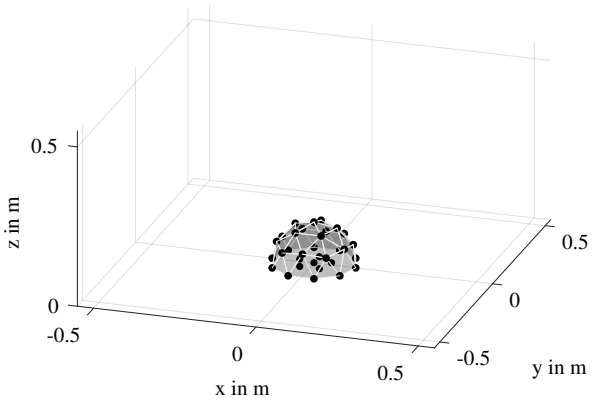


Figure 3: Array geometry of *JR-IcoDome32S*.

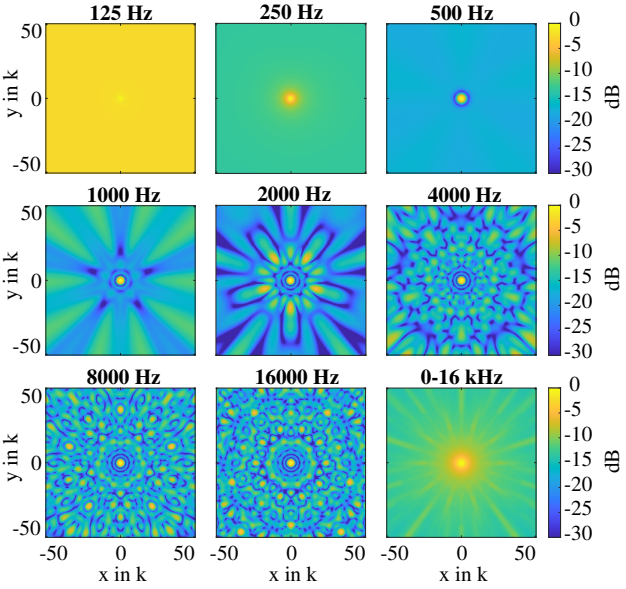


Figure 2: Spatial response as point spread function (PSF) of *JR-IcoDome32* for selected frequencies.

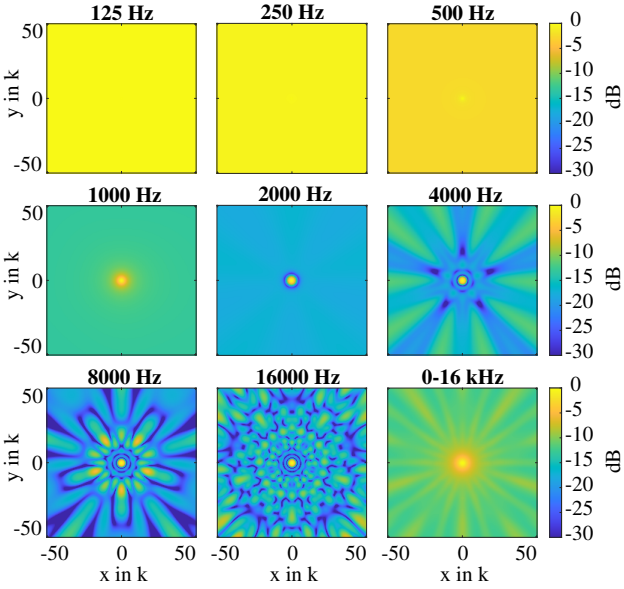


Figure 4: Spatial response of *JR-IcoDome32S* as a scaled version of *JR-IcoDome32* by a factor of 1/4.

In order to visually focus on the inspection of sidelobe levels while maintaining a constant mainlobe width, spatial grids of the simulated beam patterns are normalized by the wavenumber k, defined as $k = 2\pi/\lambda$, where λ denotes the wavelength. We choose a grid size of $k = 100$ in the scanned xy-plane at $z = d/2$, i.e. 0.5 m, over the array for evaluated frequencies. This leads to effective elevation angles of 1° and 71° for 125 Hz and 16 kHz, respectively.

Since we are not only interested in mobile applications for vehicles but also in portable and wearable sensor solutions, e.g. helmet arrays, we explore the spatial characteristics of a smaller scaled version of the *JR-IcoDome32*. For this purpose, we scale the array by a factor of 1/4 to obtain an aperture of $d = 0.25$ m, *JR-IcoDome32S*, which fulfills the requirements of being easily portable and fitting on a helmet. To make a fair com-

parison, we leave the geometry as it is and do not remove the six sensors inside the dome structure, which would be necessary when mounting the array on a helmet. Figures 3 and 4 show the geometry and spatial response results of *JR-IcoDome32S* for the same frequencies as shown for the original array configuration in Figure 2. Due to the scaling process, we observe that the same PSF patterns reappear at four times the frequency compared to *JR-IcoDome32*.

The rotational symmetry of the array allows us to easily derive sub-arrays from the original *JR-IcoDome32* geometry, called *dome32* for short: *base16* (2D) and *dome06*, *dome11*, *dome16* (3D). These configurations are shown in Figure 6 and are evaluated in terms of common array performance metrics in Table 1: f_{min} and f_{max} denote the theoretical, aliasing-free frequency range based on $\lambda/2$, HPBW is the half-power beamwidth, MSL and ASL are the maximum and average sidelobe levels, resp., and DI stands for the directivity index [4]. For this evaluation we use 201x201 points in k and average metrics over third-octave band center frequencies in 100-20000 Hz.

Table 1: Array metrics of *JR-IcoDome32* sub-arrays averaged over third-octave band center frequencies.

Metric	*dome06*	*dome11*	*dome16*	*base16*	*dome32*
f_{min} (Hz)	333	206	191	167	167
f_{max} (kHz)	2.80	3.68	5.28	7.21	19.73
HPBW (°)	25.94	21.49	22.89	21.13	21.80
MSL (dB)	-3.02	-3.95	-5.54	-7.95	-7.86
ASL (dB)	-5.53	-7.94	-9.64	-11.96	-13.02
DI (dB)	6.24	8.56	9.88	10.04	12.25

2.2 Direction-of-Arrival Estimation

As a DOAE algorithm we adapted a Gaussian Mixture Model (GMM)-based approach for clustering steered response power (SRP) estimates of a delay-and-sum beamformer with custom FFT frequency and spatial scanning grid settings as proposed in our previous work [12]. This enables probabilistic modeling, tracking of an unknown number of sound sources and source extraction using masked BF signal outputs. The algorithm provides good localization accuracy even with coarse scanning grids and the computational load enables real-time application. Details about the original algorithm can be found in [18].

2.3 Sound Source Tracking

To track potential sound source candidates based on DOA estimates, we use a simple but effective tracking approach to propagate GMM parameters over time as described in [18]: Since the number of active sources may change from frame to frame, each source candidate is assigned a time-to-live (TTL) as soon as it appears. The tracking algorithm then handles the three cases of birth, update and death of up to Q active sources. The birth of a source is controlled by a predefined source confidence threshold γ derived from the GMM parameters $\mathbf{\Sigma}$ and P, as well as by the shrink threshold Υ, i.e. the minimum angular separation between two sources. By using an age-token-based temporal smoothing method, the source locations $\hat{\boldsymbol{\theta}}$, the covariances $\mathbf{\Sigma}$ and the weights P are updated over time.

3. SENSOR SYSTEM

3.1 Microphone Array and Audio Hardware

The implementation of the array design *JR-IcoDome32* as described in Section 2 uses a rigid construction with a 6 mm solid plastic base plate and aluminum struts with 3D-printed corner connectors. ICP electret microphones with suitable signal conditioning and A/D converters were preferred over MEMS microphones due to better signal quality and less development effort in the hardware design. All components provide an IP67-rating to protect the sensors from water and dust. Figure 1 shows the final implementation of *JR-IcoDome32*.

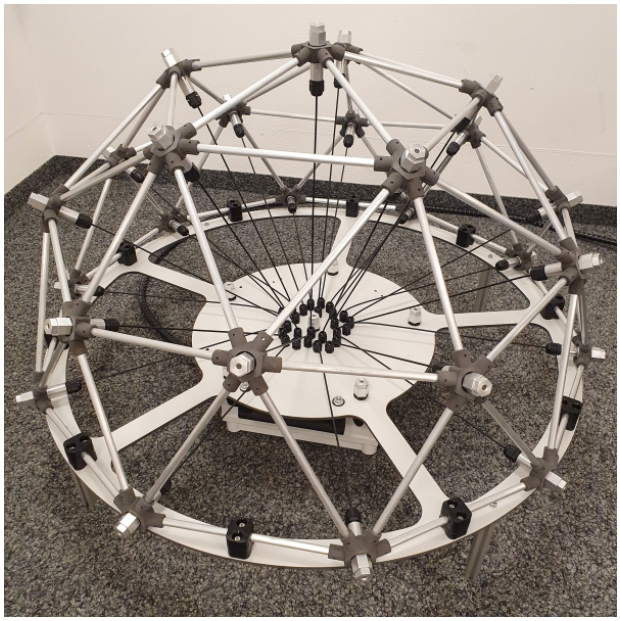
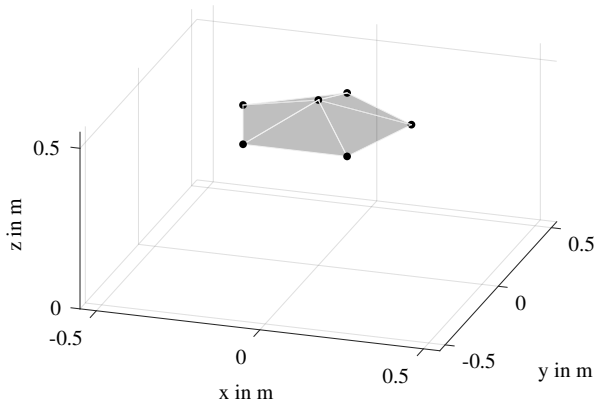
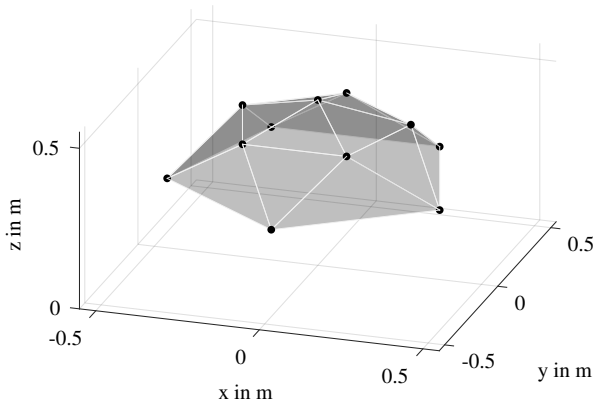


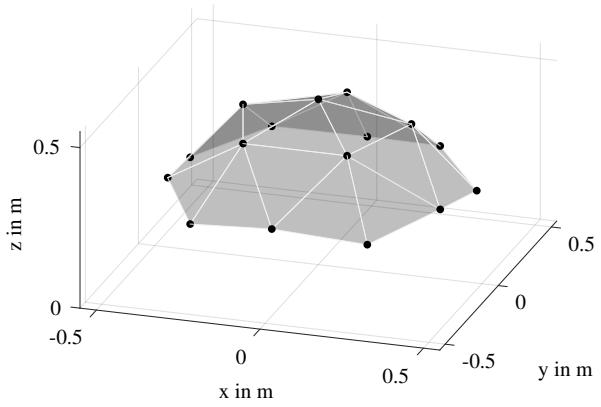
Figure 5: 3D microphone array *JR-IcoDome32*.



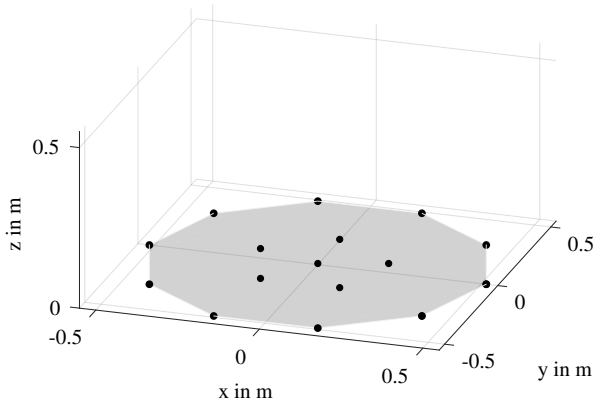
(a) Sub-array geometry of *dome06*.



(b) Sub-array geometry of *dome11*.



(c) Sub-array geometry of *dome16*.



(d) Sub-array geometry of *base16*.

Figure 6: Sub-array configurations derived from *JR-IcoDome32*.

3.2 Position and Orientation Sensors

The mobile use of a microphone array makes it necessary to determine the sensor position (GNSS) and orientation (IMU). This information is needed to transform DOA estimates from a relative to an absolute coordinate system in order to evaluate DOAE w.r.t. the position reference of a UAV. The following commercial sensors were procured:

- GNSS: *u-blox NEO-6M* with integrated antenna ,
- IMU: *Adafruit ADA2472* with *Bosch BNO055*.

The fusion and integration of these sensors was carried out using an *ESP32* micro-controller and a Python module as a serial interface with real-time data processing.

3.3 Vehicle Integration and Processing Hardware

The complete system consists of the *JR-IcoDome32* with spherical windshields, a suspension system of wire rope springs for a roof rack mount to dampen vibrations, the GNSS-IMU module mounted on the array base plate and an in-vehicle hardware rack. 32 BNC cables are routed as three DB-25 cables via a cable pass-through into the vehicle interior where they are connected to a rack containing USB audio interfaces synchronized via an AVB network and an *Intel NUC7i5DNK* processing unit. The system is powered using a portable power station and consumes approximately 120 W in operation. The integration into a vehicle is shown in Figure 7.



Figure 7: *JR-IcoDome32* with GNSS-IMU module mounted onto the rack roof of a car for mobile use.



Figure 8: Multicopter UAVs used for measurements.

Dataset	UAVs	Runs	Patterns	Duration
Fixed	3	11	3	1.5 h
Mobile	3	31	4	1.0 h

Table 2: Recordings of UAV flights conducted with *JR-IcoDome32* and resulting datasets for evaluation.

4. RESULTS

4.1 Experimental Setup

Audio data was recorded at 48 kHz sampling rate and 24 bit together with GNSS-IMU data logs for fixed and mobile setups at *UMFC Stocking* airfield in 2023. Three UAVs (*DJI Mini 2 SE*, *DJI Mavic 2 Pro*, *twinFOLD KAT*) were chosen for both scenarios, representing small, medium and large multicopters as shown in Figure 8. For the fixed setup, the *JR-IcoDome32* was placed on the ground, while the UAVs flew programmed and manual patterns (*hover*, *circle*, *free*) in distances up to 500 m from the array. In the mobile setup, the array was mounted on the car (Figure 7) and the UAVs performed manually controlled patterns (*hover*, *approach*, *follow*, *circle*) while the car drove at different speeds (10, 20, 30 km/h) in fixed gear on a dirt road. Each UAV was flown separately. Table 3 summarizes the recordings of fixed and mobile datasets.

4.2 System Parameters

For STFT processing, we resample the recorded audio signals to 24 kHz and set the window (Hann) and the FFT size to 2048, with a frame overlap of 50%. Considering the predominant characteristics of drone sound and the array metrics, we choose a frequency range of [300 2300] Hz resulting in 171 processed FFT bins. For the DOA scanning grid we choose a unit hemisphere of 200 quasi-uniformly distributed points [19]. The number of initial sound sources in each frame is 3. For source tracking we limit the maximum number of sources to 16 and set an initial and a maximum TTL for each source of 1.5 s, the minimum angular separation $\Upsilon = 30°$, the confidence threshold $\gamma = 0.3$ and specify an exponential smoothing constant of 0.9 corresponding to a time constant of 0.4 s.

4.3 Performance Evaluation

We present the DOAE results in terms of an exemplary run and a statistical evaluation of the DOAE error for all sub-array configurations. For each run and dataset, we compare the DOA estimates of three sound source tracks (SRC1-3) against the position reference (TRUE) obtained from GPS as azimuth and elevation angles. The opacity of each track represents the confidence output of the algorithm. Figures 9 and 10 show the results of a flight of *DJI Mavic Pro 2* in the fixed scenario for *dome06* and *dome32*, resp. In this run, the UAV took off next to the array and

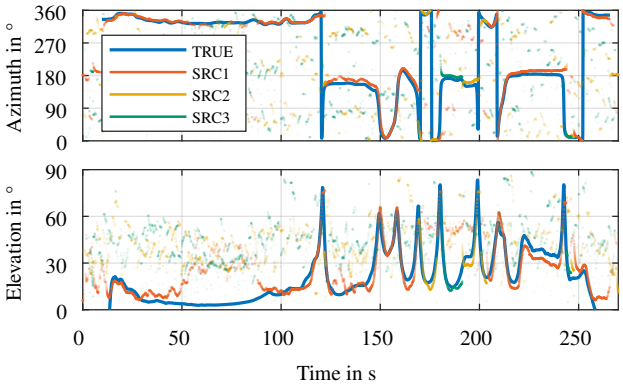


Figure 9: DOAE example with sub-array *dome06*.

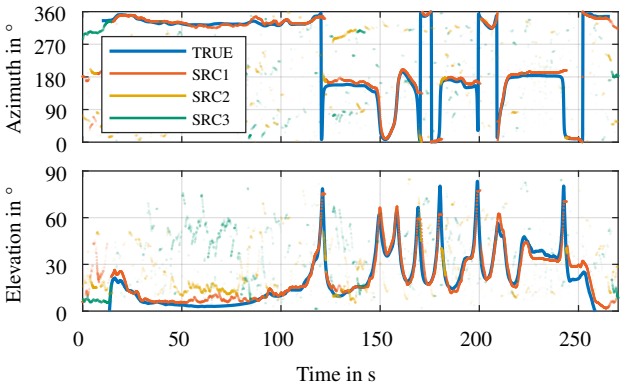


Figure 10: DOAE example with baseline *dome32*.

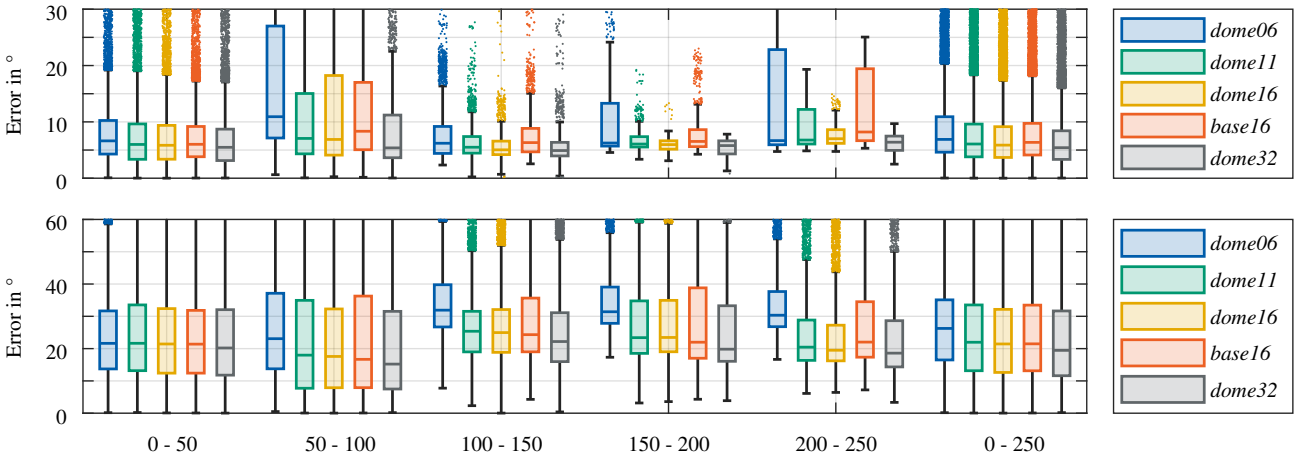


Figure 11: Absolute DOAE error over distance ranges for sub-arrays in fixed (top) and mobile (bottom) setup.

reached a distance of 100 m after 45 s and 260 m after 55 s. It then approached the array and passed 100 m at 90 s and 40 m at 100 s. For the rest of the run, the UAV flew within 80 m and performed overflights. It can be seen that *dome06* lost the UAV from 55-90 s, while *dome32* was able to keep the track (SRC1). In addition, this track is more stable, i.e. fewer changes between track hypotheses.

For each sub-array configuration, we assess the DOAE performance in terms of the absolute angle error for distance ranges in blocks of 50 m and up to 250 m in total. To provide a meaningful summary, we use boxplots to examine the median and interquartile ranges for each sub-array and dataset. Figure 11 presents median errors lower than 10° and 30°, except for *dome06*, for fixed and mobile datasets, respectively. It must be noted that GPS/IMU data may be inaccurate, as we use commercial systems without any enhancement, e.g. DGPS or RTK.

5. CONCLUSION

In this paper, we have presented a 3D microphone array design with possible sub-array configurations and experimental results for acoustic UAV tracking in a fixed and a mobile scenario. Our evaluations show similar results for sub-arrays with 11 or more sensors compared to the 32-channel baseline with 5° and 20° median DOAE error, resp. We argue that *JR-IcoDome32* is a suitable geometry for UAV tracking that also provides good accuracy in elevation. With sufficient drone noise content in the 1-4 kHz range, the proposed scaled version *JR-IcoDome32S* could provide similar performance. Possible future work lies in improving the DOAE and tracking algorithms, e.g. considering SRP amplitudes for weighted GMMs as proposed in [20], JIPDAF with Kalman filters [21], together with extensive evaluations using larger datasets.

6. REFERENCES

[1] M. A. Khan, H. Menouar, A. Eldeeb, A. Abu-Dayya, and F. D. Salim, "On the detection of unauthorized drones — techniques and future perspectives: A review," *IEEE Sensors Journal*, vol. 22, no. 12, pp. 11439–11455, 2022.

[2] A. Famili, A. Stavrou, H. Wang, J.-M. Park, and R. Gerdes, "Securing your airspace: Detection of drones trespassing protected areas," *Sensors*, vol. 24, no. 7, p. 2028, 2024.

[3] X. Yan, T. Fu, H. Lin, F. Xuan, Y. Huang, Y. Cao, H. Hu, and P. Liu, "Uav detection and tracking in urban environments using passive sensors: A survey," *Applied Sciences*, vol. 13, no. 20, p. 11320, 2023.

[4] H. L. Van Trees, *Optimum Array Processing*. John Wiley & Sons, 2002.

[5] A. Altena, S. Luesutthiviboon, G. de Croon, M. Snellen, and M. Voskuijl, "Comparison of acoustic localisation techniques for drone position estimation using real-world experimental data," in *Proc. of the 29th Int. Congress on Sound and Vibration*, 2023.

[6] Y. Chen, Y. Chen, P. Chen, and W. Wang, "Acoustic localization using an l-shape microphone array for multirotor drones," in *IEEE 6th Int. Conference on Information Communication and Signal Processing*, pp. 1168–1172, 2023.

[7] M. Varela, W.-D. Wirth, and M. Oispuu, "Wideband direction-of-arrival estimation using microphone arrays," in *Symp. Sensor Data Fusion & Int. Conference on Multisensor Fusion Integration*, pp. 1–6, 2023.

[8] N. Itare, J.-H. Thomas, K. Raoof, and T. Blanchard, "Acoustic estimation of the direction of arrival of an unmanned aerial vehicle based on frequency tracking in the time-frequency plane," *Sensors*, vol. 22, no. 11, p. 4021, 2022.

[9] S. Wu, Y. Zheng, K. Ye, H. Cao, X. Zhang, and H. Sun, "Sound source localization for unmanned aerial vehicles in low signal-to-noise ratio environments," *Remote Sensing*, vol. 16, no. 11, p. 1847, 2024.

[10] É. Bavu, H. Pujol, A. Garcia, C. Langrenne, S. Hengy, O. Rassy, N. Thome, Y. Karmim, S. Schertzer, and A. Matwyschuk, "Deeplomatics: A deep-learning based multimodal approach for aerial drone detection and localization," in *Quiet Drones*, 2022.

[11] Y. Sun, J. Li, L. Wang, J. Xv, and Y. Liu, "Deep learning-based drone acoustic event detection system for microphone arrays," *Multimedia Tools and Applications*, pp. 1–23, 2023.

[12] M. Blass and F. Graf, "A Real-Time System for Joint Acoustic Detection and Localization of UAVs," in *Quiet Drones*, 2020.

[13] M. Blass, S. Grebien, and F. Graf, "Experimental Evaluation of Acoustic Drone Tracking using Mobile Microphone Arrays," in *Quiet Drones*, 2024.

[14] S. Hengy, S. DeMezzo, and P. Hamery, "Sniper detection using a helmet array: first tests in urban environment," in *Unattended Ground, Sea, and Air Sensor Technologies and Applications IX*, vol. 6562, pp. 269–278, SPIE, 2007.

[15] H. O. Park, A. A. Dibazar, and T. W. Berger, "Design of a helmet-mounted microphone array for sound localization," in *IEEE Int. Conference on Acoustics, Speech and Signal Processing*, pp. 1478–1481, 2010.

[16] P. Calamia, S. Davis, C. Smalt, and C. Weston, "A conformal, helmet-mounted microphone array for auditory situational awareness and hearing protection," in *IEEE Workshop on Applications of Signal Processing to Audio and Acoustics*, pp. 96–100, 2017.

[17] K. Nagatomo, M. Yasuda, K. Yatabe, S. Saito, and Y. Oikawa, "Wearable seld dataset: Dataset for sound event localization and detection using wearable devices around head," in *IEEE Int. Conference on Acoustics, Speech and Signal Processing*, pp. 156–160, 2022.

[18] N. Madhu and R. Martin, "A Scalable Framework For Multiple Speaker Localization And Tracking," *Proc. of the International Workshop for Acoustic Echo Cancellation and Noise Control*, 2008.

[19] M. Deserno, "How to generate equidistributed points on the surface of a sphere," tech. rep., Max-Planck-Institut fuer Polymerforschung, Mainz, 2004.

[20] D. Frisch and U. D. Hanebeck, "Gaussian mixture estimation from weighted samples," in *IEEE International Conference on Multisensor Fusion and Integration for Intelligent Systems*, pp. 1–5, 2021.

[21] D. Musicki and R. Evans, "Joint integrated probabilistic data association: Jipda," *IEEE transactions on Aerospace and Electronic Systems*, vol. 40, no. 3, pp. 1093–1099, 2004.

DOI: 10.61782/fa.2025.0072



FORUM ACUSTICUM
EURONOISE 2025

ACOUSTIC DETECTION OF DRONES: A MACHINE LEARNING AND PSYCHOACOUSTIC APPROACH

Diana Tejera-Berengue[1*] **Gonzalo Corral-García**[1] **Fangfang Zhu-Zhou**[1]
Manuel Rosa-Zurera[1*] **Roberto Gil-Pita**[1] **Manuel Utrilla-Manso**[1]
[1] Department of Signal Theory and Communications, University of Alcalá, Spain

ABSTRACT

This study presents a detailed analysis of how acoustic signals generated by drones are perceived by humans compared to their detection by advanced microphone-based systems. The research includes various types of drones and employs a psychoacoustic model to evaluate the perceptual sound power of these signals. This model is used to estimate the maximum distance at which UAV noise remains audible, as a function of frequency. Additionally, a detection system incorporating machine learning techniques and the YAMNet neural network is implemented to investigate how drone acoustic signals are influenced by factors such as distance, frequency, and surface reflections during propagation. The results show that even the most basic acoustic detection systems significantly outperform human hearing in identifying drones. These findings underscore the effectiveness and versatility of such systems, highlighting their potential as valuable tools for enhancing security and surveillance in real-world scenarios.

Keywords: UAV, drone audibility, psyschoacoustic model, distance, masking threshold, comparison

1. INTRODUCTION

The acoustic detection and localization of drones might initially seem ineffective due to the low signal-to-noise ratio (SNR) typically associated with the sound emitted by small unmanned aerial vehicles (UAVs) at the receiver. Additionally, it is sometimes assumed that an acoustic surveillance system cannot outperform the human auditory system. In response to these assumptions, this study investigates the limits of the human auditory system's ability to detect drones, using MPEG Psychoacoustic Model 1 [1], originally developed for audio encoding. The goal is to determine the maximum distance at which a drone remains perceptible to the human ear and to compare this threshold with the detection capabilities of existing automated systems.

In the field of environmental acoustics, several works have evaluated the perceptual impact of drone noise using psychoacoustic sound quality metrics (SQMs), such as loudness, sharpness, and fluctuation strength. For instance, the study in [2] analyzes the perceived annoyance of UAV noise under varying altitudes and flight conditions, concluding that heavier drones flying at low altitudes generate greater discomfort, with loudness emerging as the dominant factor. Similarly, the authors of [3] compare the sounds of drones, helicopters, and lawnmowers, again identifying loudness as the main predictor of annoyance. In a related study [4], multirotor drones are reported to be more annoying than civil aircraft, with sharpness and fluctuation strength playing a key role in perceived disturbance.

However, there is still a lack of systematic analysis regarding the maximum distance at which drone sound remains perceptible to humans. This paper aims to address that gap by estimating the distance beyond which drone sound becomes fully masked by environmental noise and, therefore, no longer causes audible annoyance, or can be detected by humans beings. The analysis is carried out using the MPEG Psychoacoustic Model 1, which enables

*Corresponding author: diana.tejera@uah.es; manuel.rosa@uah.es.
Copyright: ©2025 D. Tejera-Berengue et al. This is an open-access article distributed under the terms of the Creative Commons Attribution 3.0 Unported License, which permits unrestricted use, distribution, and reproduction in any medium, provided the original author and source are credited.

the calculation of individual and global masking thresholds, to determine the audibility of signals emitted at a given distance from the listener and affected by propagation losses. This study also reinforces the relevance of acoustic localization and detection systems, demonstrating their ability to detect drones even at distances beyond human auditory capabilities.

To contextualize the comparison, a state-of-the-art acoustic detection system is used as a benchmark. Many modern detection systems rely on machine learning (ML) and deep learning (DL) methods applied to features such as the short-time Fourier transform (STFT) or Mel-frequency cepstral coefficients (MFCC) extracted from drone-specific acoustic patterns. These techniques have shown high classification accuracy and effective range under certain conditions [5–7]. Among these, the YAMNet neural network, used in a previous study by the authors [8], serves here as a reference to evaluate the performance of an automatic system. Rather than providing a detailed assessment of detection systems, this paper focuses on quantifying the audibility of drone noise using a perceptual model, and comparing it with the response of an automatic classifier.

This paper is structured as follows. Section 2 presents the theoretical background of the psychoacoustic model and describes the acoustic characteristics of sound produced by drones. Section 3 analyzes the audibility of a drone at varying distances and compares these findings with the performance of the YAMNet-based detection system. Finally, Section 4 presents the main conclusions of the study.

2. THEORETICAL BACKGROUND

This section introduces the main concepts about psychoacoustics and signal characteristics relevant to the perceptual analysis of UAV sound.

2.1 Psychoacoustic Model

A psychoacoustic model is a quantitative framework that approximates the behavior of the human auditory system [9]. It computes the global masking threshold, which defines the sound pressure level below which acoustic signals are no longer perceived by the human ear. This threshold varies dynamically across both frequency and level, depending on the energy distribution in adjacent spectral components [10].

Human auditory perception is primarily determined by the threshold in quiet and by masking effects produced

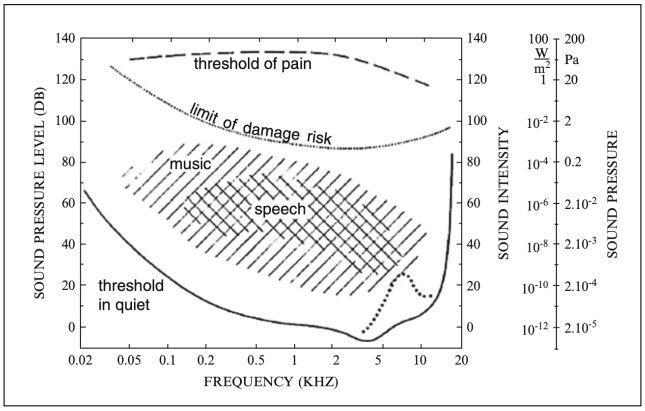


Figure 1: Hearing range [11].

by other sounds. The threshold in quiet refers to the minimum sound pressure level required to detect a pure tone in the absence of any background noise. This threshold is illustrated in Fig. 1, which shows the human hearing range using Sound Pressure Level (SPL) curves. As shown, human hearing ranges from approximately 20 Hz to nearly 20 kHz, with frequency-dependent thresholds for both hearing and pain. The threshold in quiet can be approximated by the frequency-dependent function provided in Eqn. (1).

$$T_Q(f) = 3.64\left(\frac{f}{1000}\right)^{-0.8} - 6.5 \cdot \exp\left[-0.6\left(\frac{f}{1000} - 3.3\right)^2\right] + 10^{-3}\left(\frac{f}{1000}\right)^4 \quad (1)$$

Masking effects at a given frequency depend solely on the signal energy within a limited bandwidth surrounding that frequency [12]. Due to the structure of the cochlea, which converts frequency information into spatial displacement along the basilar membrane, each position on the membrane responds to a specific range of frequencies. As a result, the peripheral auditory system functions as a spectral analyzer and can be modeled as a bank of partially overlapping band-pass filters. The audible range, approximately from 20 Hz to 16 kHz, is divided into 24 non-overlapping critical bands, each corresponding to a unit known as the Bark. Given the nonlinear distribution of resonant frequencies along the membrane, the bandwidths of these critical bands are not uniform and vary with frequency [9]. An analytical expression derived from experimental data is used to approximate the critical bandwidth

Δf as a function of the center frequency f_c:

$$\Delta f = 25 + 75 \left(1 + 1.4 \left(\frac{f_c}{1000}\right)^2\right)^{0.69} \quad (2)$$

The concept of critical bandwidth around a masker defines the frequency region in which masking effects are most pronounced. Consequently, the perception of a sound depends not only on its own frequency and intensity, but also on the presence of nearby spectral components. Masking phenomena are typically classified as either simultaneous or non-simultaneous. Simultaneous masking occurs when a sound becomes inaudible due to the concurrent presence of another sound with nearby frequencies, which raises the auditory threshold in that band. This can occur under several conditions: when narrowband noise masks tones within the same critical band, when tones mask other tones, or when narrowband noise masks other narrowband noise components within the same critical band. In contrast, non-simultaneous masking refers to the phenomenon where the audibility of a sound is affected by a masker that occurs immediately before or after it in time, due to the temporal dynamics of auditory masking.

In this work, perceptual analysis is based on Model 1 of the ISO/IEC MPEG-1 Audio Standard [1, 13]. This model divides the audio signal into subbands that approximate critical bands and estimates the masking threshold, to be used to quantize each subband signal according to the audibility of quantization noise [12].

To apply Model 1, the following steps are carried out:

1. Computation of the FFT and the SPL in each subband.
2. Determination of the absolute threshold of hearing.
3. Identification of tonal and non-tonal components in the input signal.
4. Decimation of invalid tonal and non-tonal maskers.
5. Calculation of individual masking thresholds.
6. Determination of the global masking threshold.
7. Estimation of the minimum masking threshold in each subband.
8. Calculation of the Signal-to-Mask Ratio (SMR).

In the final step, the SMR is computed as the difference between the signal level and the corresponding masking threshold. This value indicates, for each subband or frequency bin, whether a given sound is perceptible or masked by other components. If the SMR is low (i.e., negative in dB), the human ear cannot perceive the sound, even though it is physically present in the signal.

2.2 UAV signal Characterization

The acoustic signal generated by a drone originates primarily from the rotation of its propellers and motors, resulting in a sound with harmonic content when the rotational speed remains constant. However, during flight, this speed continuously varies in response to aerodynamic forces and control adjustments, leading to a non-stationary signal in the time domain. Consequently, frequency-domain analysis is more suitable, as the signal exhibits a spectral pattern characterized by peaks and valleys (as shown in Fig. 2), with energy concentrated in specific frequency bands associated with the rotational speeds of different components.

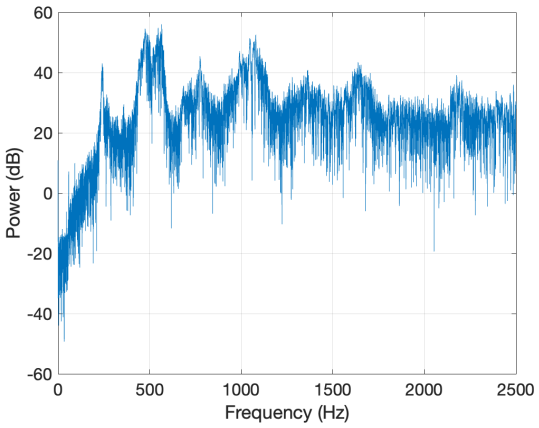


Figure 2: Power Spectrum of Hobbyking FPV250 drone.

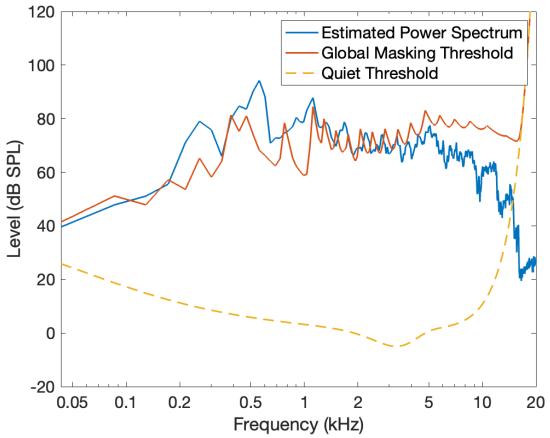
In particular, drone acoustic signals contain tonal components in the low-frequency range, corresponding to the blade pass frequency (BPF) and its harmonics [14]. These tonal components are linked to variations in rotor speed and are clearly reflected in Fig. 2. According to the study by Torija et al. [15], drones exhibit an average tonality of 0.36 tonality units (tu), indicating a moderately prominent tonal component in their acoustic signature. This characteristic has the potential to influence auditory masking effects and, therefore, human perception. These spectral characteristics highlight the suitability of drone noise for perceptual analysis based on auditory masking principles, which will be explored in the next section.

3. RESULTS

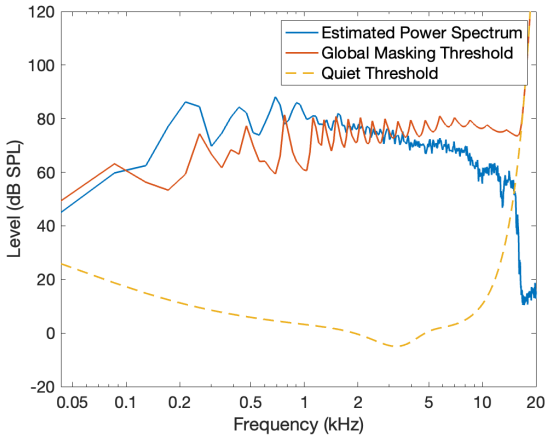
This section presents the results of the psychoacoustic analysis applied to UAV acoustic signals using the MPEG Psychoacoustic Model 1. The goal is to determine the maximum distance at which drone noise remains perceptible to the human ear, considering both ideal conditions and more realistic scenarios with propagation losses and environmental noise. In addition, results are also compared against a state-of-the-art detection system to highlight the limitations of human hearing.

As a first step, the analysis was performed on an in-flight recording of the Hobbyking FPV250 quadcopter. This UAV was selected as a representative example of a small and lightweight drone, typically classified in the C0 or C1 category according to current UAV classification standards. To complement this analysis, the DJI Phantom 3 was also evaluated, representing a larger and more robust drone classified within the C2 category. These two UAVs differ significantly in weight, physical dimensions, and structural design, providing a broader perspective on how human auditory perception responds to UAVs with different spectral and operational characteristics. Although some variations are expected between drones, most quadcopters share common tonal and non-tonal features in their acoustic signatures. Therefore, the perceptual results presented here are expected to generalize well to similar UAV configurations.

The initial analysis was conducted at a reference distance of 1 meter, without considering attenuation or background noise. Fig. 3 shows the estimated power spectrum, the global masking threshold calculated using the MPEG model, and the absolute threshold of hearing, for both UAV models. In both cases, the drone signals exhibit prominent energy in the low-frequency range, especially around the BPF and its harmonics. These tonal components result in masking thresholds that closely follow the spectrum shape, particularly where tonal maskers dominate. However, it can be observed that above approximately 1 kHz, the power spectrum begins to fall below the global masking threshold due to the progressive decline in signal energy with increasing frequency, combined with the accumulation of masking contributions from lower-frequency components. As a result, the perceptual significance of high-frequency components is reduced, and only the lower-frequency bands of the signal remain clearly audible. As observed in Fig. 3, both UAVs exhibit comparable spectral distributions and global masking thresholds under ideal conditions, with the signal remaining well above the masking threshold for frequencies below approximately 2 kHz. This confirms that both drones are clearly audible in quiet scenarios, although high-frequency information appears to be imperceptible. Given the similarity of their acoustic profiles, only the results of one of the two UAVs are presented in this paper for the subsequent analyses involving distance-based attenuation and ambient noise.



(a) Hobbyking FPV250



(b) DJI Phantom 3

Figure 3: Estimated power spectrum and masking threshold without considering noise or attenuation.

To evaluate auditory perception as a function of distance, an attenuation model was applied to estimate the frequency-dependent degradation of the acoustic signal over propagation. For this purpose, the standardized mod-

els defined in ISO 9613-1 [16] and ISO 9613-2 [17] were used, which account for effects such as atmospheric absorption or geometric spreading to simulate realistic propagation losses across different frequency bands. Based on this model, the next scenario considers the effect of distance alone, without introducing ambient noise.

As shown in Fig. 4, which corresponds to the DJI Phantom 3 at a distance of 100 meters, the signal spectrum shows a noticeable overall attenuation, particularly at high frequencies. This behaviour is expected due to the frequency-dependent nature of atmospheric absorption. However, in the frequency range where the signal was previously audible—primarily below 1 kHz—the spectral shape remains largely preserved, but with a lower dependence on the energy level. As a result, the masking threshold maintains the shape of the signal spectrum, and the signal-to-mask ratio (SMR) remains positive across most of the low-frequency bands. This indicates that, in the absence of ambient noise, increasing distance alone has the effect of reducing the signal power, but the SMR in the dominant low-frequency range remains almost unchanged.

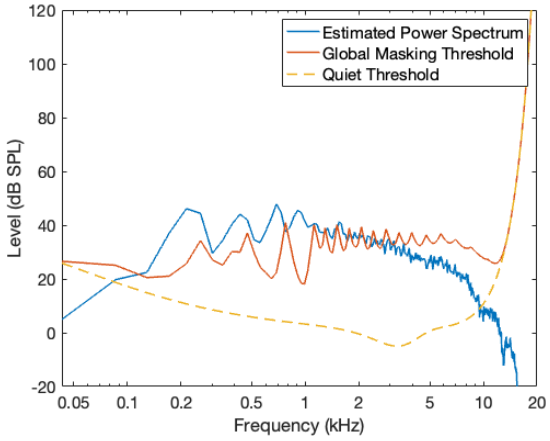


Figure 4: Estimated power spectrum and masking threshold at 100 meters without noise.

To assess the impact of environmental noise on auditory perception, an additional analysis was conducted by introducing Additive White Gaussian Noise (AWGN) at a level of 40 dB SPL. Fig. 5 shows the resulting power spectrum and global masking threshold for the DJI Phantom 3 at a distance of 100 meters under these conditions. Compared to the previous case, the masking threshold is significantly elevated across the entire spectrum, particularly in the mid and high-frequency bands due to the effect of noise.

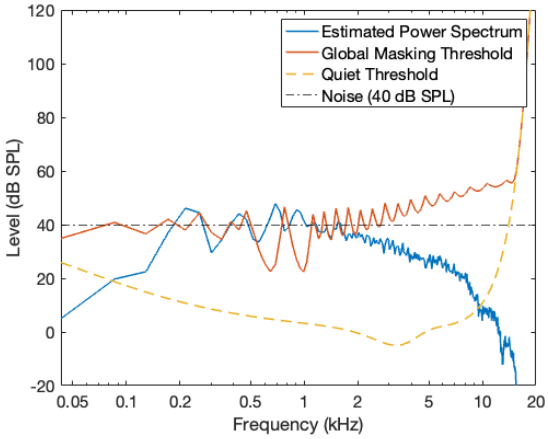


Figure 5: Estimated power spectrum and masking threshold at 100 meters with 40 dB SPL noise.

In this scenario, the estimated power spectrum of the drone signal falls below the masking threshold in most frequency regions, including parts of the low-frequency range. This is mainly due to the combined effects of attenuation and background noise, which increases the masking contributions and reduces the SMR. While a few low-frequency components—particularly some between approximately 100-1000 Hz—may remain marginally audible, their perceptibility is highly uncertain and depends on the local contribution of noise and the local masking level.

Fig. 6 shows the average Signal to Mask Ratio computed for the first 13 Bark bands, plotted at the center frequency of each band. This analysis was performed to assess how far the drone signal remains perceptible under varying propagation conditions. Two horizontal reference lines are included at 0 dB and 3 dB SMR. While an SMR above 0 dB indicates that the signal's spectral energy surpasses the global masking threshold, suggesting potential audibility, a margin of at least 3 dB is commonly adopted to ensure robust perceptual detection. The figure includes SMR curves obtained for multiple distances ranging from 1 meter to 500 meters for the DJI Phantom 3. The analysis is limited to the first 13 Bark bands (approximately up to 2 kHz), since previous results have shown that signal components beyond this frequency range are completely masked and thus perceptually irrelevant.

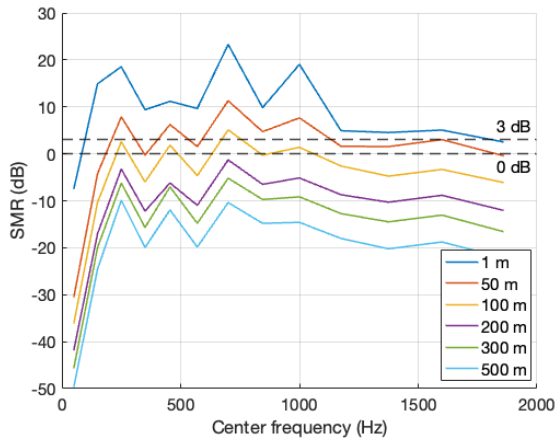


Figure 6: SMR degradation with distance across the first 13 Bark bands.

As illustrated, the drone signal is clearly audible at 1 meter, with all SMR values in the analyzed frequency range exceeding the 3 dB threshold. At 50 meters, the SMR remains above 0 dB in all bark bands, and although several bands still exceed the 3 dB margin, the perceptibility of the signal begins to decrease. At 100 meters, only a few low-frequency bands remain above the 0 dB threshold, while the majority of the spectrum falls below it, indicating that the signal is becoming increasingly masked. Beyond this distance, the SMR continues to decrease, confirming that drone audibility deteriorates rapidly due to the combined effects of frequency-dependent attenuation and ambient noise. Consequently, auditory detection by a human observer becomes extremely limited, or even entirely unfeasible, at distances exceeding 100 meters under typical outdoor conditions.

While the SMR-based analysis illustrates the limitations of human hearing, the following evaluation examines the capabilities of an automatic system under the same acoustic conditions. To compare the human auditory perception with a state-of-the-art acoustic detection system, the YAMNet neural network was evaluated under the same conditions used in the perceptual analysis, that is, with an ambient noise level of 40 dB SPL and propagation-induced attenuation applied according to outdoor transmission models. This deep learning architecture, specifically designed for audio event classification, was previously analyzed by the authors in [8], and the results are reused here to enable a direct comparison between human and machine-based detection performance.

Fig. 7 shows the Receiver Operating Characteristic (ROC) curves obtained for distances ranging from 1 to 500 meters. These curves represent the probability of detection (P_D) vs. the probability of false alarm (P_{FA}), serving as a standard performance metric in detection theory. In general, a larger area under the ROC curve indicates a more reliable detector. As shown, YAMNet maintains high detection performance even at 500 meters, significantly outperforming human auditory capabilities under the same acoustic conditions. These findings reinforce the importance of automated systems for reliable UAV detection over long distances.

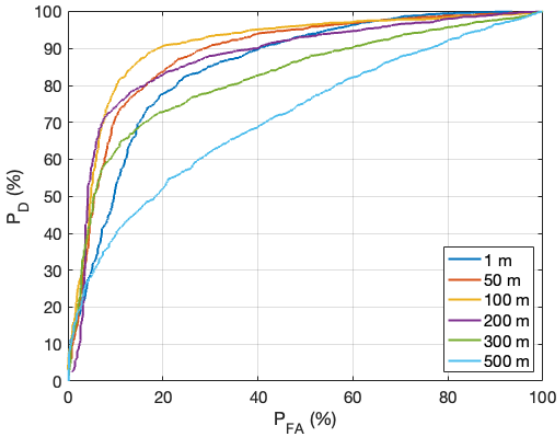


Figure 7: ROC curve for the YAMNet-based detector, at different distances [8].

As demonstrated in the previous analysis, human auditory perception of drone noise significantly deteriorates beyond 100 meters, mainly due to propagation losses and ambient noise. In contrast, state-of-the-art acoustic systems, such as the YAMNet-based model evaluated, can reliably detect drones at distances up to 500 meters. This highlights the critical importance of automated detection technologies, especially in surveillance and security applications, where relying on human hearing alone would severely limit detection capabilities and operational effectiveness. Furthermore, in line with findings from the literature on psychoacoustic sound quality metrics, it can be inferred that in order to avoid any perceptual disturbance to the population, drones should ideally operate at distances of at least 100 meters from inhabited areas, ensuring that their acoustic signature remains below the threshold of audibility and therefore does not cause annoyance.

4. CONCLUSION

In this work, the audibility of UAV noise was evaluated using the MPEG Psychoacoustic Model 1, with the objective of estimating the maximum distance at which a drone can be perceived by a human listener. Under ideal conditions, the acoustic signature of the drone remains clearly audible up to several hundred meters. However, when more realistic scenarios are considered, including propagation-induced attenuation and a moderate ambient noise level of 40 dB SPL, audibility declines significantly, becoming nearly null beyond 100 meters.

The analysis of the global masking threshold and the power spectrum revealed that the perceptible content of the drone signal is mainly concentrated in low-frequency components, particularly below 1 kHz. By calculating the Signal-to-Mask Ratio (SMR) across Bark bands and examining its variation with distance, it was observed that beyond 100 meters, the signal becomes largely masked by environmental conditions, resulting imperceptible to the human auditory system. This threshold naturally depends on ambient noise levels, and more adverse conditions would further reduce detectability.

In contrast, an automatic detection system based on the YAMNet neural network demonstrated robust performance under the same acoustic conditions, achieving reliable drone detection at distances up to 500 meters. These results highlight both the limitations of human auditory perception and the practical viability of acoustic detection systems for surveillance, security, and environmental monitoring applications, even in scenarios characterized by low signal-to-noise ratios.

Finally, the findings are consistent with prior research on psychoacoustic annoyance and support the recommendation that small UAVs should operate at least 100 meters away from populated areas under these conditions. At this range, the acoustic signature remains below the threshold of audibility, minimizing both detectability and potential disturbance.

5. ACKNOWLEDGMENTS

This work was funded by the Spanish Ministry of Science and Innovation under Project PID2021-129043OB-I00 (funded by MCIN/AEI/10.13039/501100011033/FEDER, EU).

6. REFERENCES

[1] K. Brandenburg and G. Stoll, "Iso/mpeg-1 audio: A generic standard for coding of high-quality digital audio," *Journal of the Audio Engineering Society*, vol. 42, no. 10, pp. 780–792, 1994.

[2] C. J. Hui, M. J. Kingan, Y. Hioka, G. Schmid, G. Dodd, K. N. Dirks, S. Edlin, S. Mascarenhas, and Y.-M. Shim, "Quantification of the psychoacoustic effect of noise from small unmanned aerial vehicles," *International Journal of Environmental Research and Public Health*, vol. 18, no. 17, p. 8893, 2021.

[3] N. Sieben, R. Aalmoes, and V. Vos, "A deeper understanding in the psychoacoustic characterization of drone noise," in *Forum Acusticum*, 2023.

[4] D. Y. Gwak, D. Han, and S. Lee, "Sound quality factors influencing annoyance from hovering uav," *Journal of sound and vibration*, vol. 489, p. 115651, 2020.

[5] J. Yousaf, H. Zia, M. Alhalabi, M. Yaghi, T. Basmaji, E. A. Shehhi, A. Gad, M. Alkhedher, and M. Ghazal, "Drone and controller detection and localization: Trends and challenges," *Applied Sciences*, vol. 12, no. 24, p. 12612, 2022.

[6] M. H. Rahman, M. A. S. Sejan, M. A. Aziz, R. Tabassum, J.-I. Baik, and H.-K. Song, "A comprehensive survey of unmanned aerial vehicles detection and classification using machine learning approach: Challenges, solutions, and future directions," *Remote Sensing*, vol. 16, no. 5, p. 879, 2024.

[7] V. Semenyuk, I. Kurmashev, A. Lupidi, D. Alyoshin, L. Kurmasheva, and A. Cantelli-Forti, "Advance and refinement: The evolution of uav detection and classification technologies," *arXiv preprint arXiv:2409.05985*, 2024.

[8] D. Tejera-Berengue, F. Zhu-Zhou, M. Utrilla-Manso, R. Gil-Pita, and M. Rosa-Zurera, "Analysis of distance and environmental impact on uav acoustic detection," *Electronics*, vol. 13, no. 3, p. 643, 2024.

[9] Y. Lin, W. H. Abdulla, *et al.*, "Audio watermark," *Audio Watermark A Comprehensive Foundation Using MATLAB*, 2015.

[10] R. Arelhi and D. Campbell, "A matlab simulink implementation of speech masking based on the mpeg psychoacoustic model 1," in *3rd International Symp. on Image and Signal Processing and Analysis, 2003. ISPA 2003*, vol. 1, pp. 543–548, IEEE, 2003.

[11] E. Zwicker and H. Fastl, *Psychoacoustics: Facts and models*, vol. 22. Springer Science & Business Media, 2013.

[12] D. Pan, "A tutorial on mpeg/audio compression," *IEEE multimedia*, vol. 2, no. 2, pp. 60–74, 1995.

[13] I. O. for Standardization/International Electrotechnical Commission *et al.*, "Information technology - coding of moving pictures and associated audio for digital storage media at up to about 1.5 mbit/s: Part 3: Audio," *ISO/IEC 11172-3*, 1993.

[14] D. Y. Gwak, D. Han, and S. Lee, "Sound quality factors influencing annoyance from hovering uav," *Journal of Sound and Vibration*, vol. 489, p. 115651, 2020.

[15] A. J. Torija, R. H. Self, and J. L. Lawrence, "Psychoacoustic characterisation of a small fixed-pitch quadcopter," in *Inter-Noise and Noise-Con Congress and Conference Proc.*, vol. 259, pp. 1884–1894, Institute of Noise Control Engineering, 2019.

[16] I. O. for Standardization, "Acoustics: Attenuation of sound during propagation outdoors," *ISO Standard 9613-1*, 1993.

[17] I. O. for Standardization, "Acoustics – attenuation of sound during propagation outdoors: Part 2: General method of calculation," *ISO Standard 9613-2*, 1996.

DOI: 10.61782/fa.2025.0501



FORUM ACUSTICUM
EURONOISE 2025

INVESTIGATING THE IMPACTS OF COCKPIT NOISE EXPOSURE ON HUMAN DECISION-MAKING

Elizabeth L. Fox[1*] **Ashley D. Cook**[1] **Frank Mobley**[1]
Gregory Bowers[2] **Hilary Gallagher**[1] **Zachariah Ennis**[2]
[1] Air Force Research Laboratory, WPAFB, OH 45433 USA
[2] BAE Systems, Inc., Space & Mission Systems, Dayton, OH 45435 USA

ABSTRACT

A large amount of research focuses on protecting military personnel from over exposure to noise, but little research has focused on the cognitive impacts. As such, Air Force Research Laboratory researchers have conducted a study to explore how cockpit noise influences decision-making. Fifteen participants were placed within a chamber with communication ear plugs (daily attenuation collected) and exposed to noise previously recorded within the cockpit of a fifth-generation fighter jet generated at levels of L_A= 60, 70 and 80 dB under protection. Participants completed a series of auditory working memory and visual search tasks in both single- and dual-task paradigms. Performance changes were observed across individual participants depending on differing noise level and task difficulty; additionally, individual fit variances led to differences in room (full body) sound pressure levels that require further investigating. Overall, the results of this study offer a better understanding of how high-level cockpit noise impacts multitasking and working memory performance involved in decision-making. From this work, recommendations can be made on how to manage cognitive load in these complex military operations.

Keywords: *F-35 cockpit noise, multitask efficiency, decision-making, noise sensitivity, valence-arousal*

**Corresponding author*: *elizabeth.fox.9@us.af.mil.*
***Copyright**: ©2025 Fox et al. This is an open-access article distributed under the terms of the Creative Commons Attribution 3.0 Unported License, which permits unrestricted use, distribution, and reproduction in any medium, provided the original author and source are credited.*

1. INTRODUCTION

Several studies have reliably captured cross-modal demand effects and have found task difficulty modulates the cross-modal impact on performance. More specifically, in a dual-task context, the task load in a primary task of one modality influences the performance on a second task presented in a different modality [1, 2]. However, the literature linking the deleterious effect of prolonged and continuous environmental acoustic noise on intra- or cross-modal attentional resources and cognitive functioning is limited. This is especially true when considering key mechanisms such as working memory (e.g., phonological loop) and higher-order executive functioning (e.g., multitask management). Limited studies have shown that acoustic noise can either enhance or degrade performance. For example, Awada and colleagues demonstrated that incorporation of low levels of white noise improved performance in creative tasks, but increased levels of noise only improved working memory tasks [3]. Overall level of noise influences some aspects of cognitive performance, but some studies have demonstrated that other characteristics (features) of the noise may also be critical indicators [4–6].

In a within-subjects experiment, we systematically investigated the relationship between the level (amplitude) of aircraft noise that F-35 pilots are exposed to and the cognitive processes most relevant for them to achieve mission success. We tested working memory through a standard auditory n-back task and decision-making through a visual multi-object search task. While many environmental stressors exist, this research focused on the impact of acoustic stressors, specifically the level of noise, on cognitive processing and decision-making under various

single- and dual-task loads. We factorially manipulated single- (n-back OR decision-task) and dual-tasks, 3 levels of n-back difficulty (n-back), and F-35 cockpit noise recordings presented at 4 A-weighted levels (quiet, L_A = 60, 70, and 80 dB as measured under hearing protection [UHP]). We assessed response times and accuracy to respond to task stimuli, mathematical modeling coefficients (efficiency cost of multitasking [2]), subjective assessments of affect and arousal (HAAS, [7]), and how one's sensitivity to noise (Noise Sensitivity Scale [NSS]; [8]) impacts performance in, and subjective assessments of, different levels of steady-state F-35 cockpit noise.

Unique to our lab task, participants placed hearing protection on before undergoing a measurement of hearing protection fit, which was used to individualize the external level of sound and properly control noise dose UHP. This was completed immediately prior to all three sessions where noise was administered. As such, the variation within- and between-people using communication earplugs (CEPs) will be reported. In addition to our primary research questions described above (and hypotheses below), these data are also useful for evaluating operational guidelines for use of CEPs as a form of hearing protection in the field.

1.1 Hypotheses

We have three hypotheses in regards to research questions of interest.

Hypothesis 1 (H1). Performance and efficiency will decrease when multitasking compared to isolated completion, and higher decrements will be observed with increasing working memory load.

Hypothesis 2 (H2). Performance and efficiency will decrease under noise, compared to quiet, and more decrements will be observed as the level of noise increases.

Hypothesis 3 (H3). Higher noise exposure will result in higher negative affect and lower positive affect in post session affect state assessment, compared to pre session assessment, moderated by the individuals' degree of noise sensitivity.

2. METHOD

2.1 Participants

Participants included 18 (N = 15 after exclusions) US citizens, 60/40 split between female/male, recruited from the Dayton, Ohio area, who received monetary compensation (20 USD/hour) for their time. All participants completed the task in a controlled laboratory setting on Wright-Patterson Air Force Base.

2.2 Surveys

Noise sensitivity is generally defined as "an individual's internal state which increases their degree of reactivity to noise [9]." It is measured using a 6-item noise sensitivity scale (NSS), where participants agree/disagree with each statement [8]. We measured participants' noise sensitivity prior to the experiment.

The Hedonic Arousal Affect Scale (HAAS) is a survey based on the valence-arousal model of affect. Valence is the hedonic tone or (dis)pleasure of the situation, and arousal is the amount of activation associated with their personal state [10]. The abbreviated 12-item HAAS [7] is well-suited for repeated measure designs, such as the experiment described here, and can be summarized to capture overall positive/negative effects of each noise level on one's relative change in valence and arousal. Participants rated each adjective (e.g., Active, Calm, Irritable, Tired) on a scale from 1 (very slight/not at all) to 5 (extremely) before and after each session. For noise sessions (2-4), participants completed the post-session survey after all trials were complete, but prior to terminating the room noise to obtain a reflection of their state in noise.

2.3 Procedure

Participants completed 4 sessions (each 2.5 hours; total time 10 hours) in the Voice Communication Research and Evaluation System (VOCRES) facility, which is a acoustically diffuse room (down to 500 Hz) and capable of continuous 125 dB A-weighted sound pressure level (SPL) w/ bandwidth 20-20k Hz. Session 1 was the quiet day and required participants to complete the informed consent, the NSS, an Ishihara Color Blindness test, and a baseline hearing assessment. Additionally, prior to and post sessions 1-4, the participant completed the HAAS survey. For sessions 2-4, participants completed daily attenuation measurements for their CEPs using the Michael & Associates FitCheck Solo System. Individuals' attenuation results were used to adaptively filter the noise in octave bands to control for any variance in fit across participants and sessions (noise level was randomized after session 1; noise exposure $<$ 2 hrs/session). Next, participants were tasked with completing the visual search (VS), the working memory (WM), or dual-task, depending on the assigned order. All conditions were completed in each session; participants completed practice trials each session.

Participants were given mandatory 30 second breaks approximately every 5 minutes. After the completion of all conditions and surveys, participants completed a post session hearing assessment to check for any threshold shifts (noise sessions) then were thanked and paid for their time (all sessions).

2.4 Tasks

Order of task presentation was pseudo-randomized. Session 1 required participants to complete the VS and WM tasks in isolation prior to completing the dual-task. All other sessions had randomized order of tasks.

2.4.1 Visual Search Task

Participants were asked to complete a visual discrimination task that had two simultaneous 2-alternative-forced-choice (2AFC) responses, where participants had to decide between two response options in each (see Figure 1 for stimuli). The first 2AFC was to determine whether a dog (left arrow key) or lion (right arrow key) was presented on screen; the second was to determine whether a car was present (up arrow key) or not (down arrow key) – each trial demanded two key presses; participants used their right hand to complete this task.

Six fixations were presented in a half-circle (above center), and one in the center for 500 ms at the start of each trial. Following a short, 0-300 ms blank screen, each fixation was replaced with either a target or distractor icon. The center fixation did not remain. Either a dog/lion was present every trial. On car present and absent trials, four and five distractors filled in the remaining locations, respectively. Stimuli were presented for 1000 ms, and participants had 3000 ms (from the onset of stimuli) to make both the animal and car responses.

Each participant completed a minimum of 15 practice trials (dependent on their understanding of the task) before moving onto data collection. Trials lasted 4600 ms for a total of 336 trials across 6 blocks which amounted to 56 trials/block. The task was presented in isolation and a dual-task context, both of which were completed with the participant at a 60 cm viewing distance from the screen.

2.4.2 Auditory Working Memory Task

Participants were also instructed to complete an auditory working memory task, in this case, an n-back task [11, 12] of varying difficulty (1, 2, 3-back). Responses were given in a Go/No-Go format, meaning that participants pressed a key (F; left hand) when the spoken letters matched the

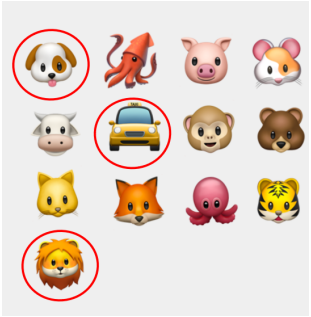


Figure 1. All possible visual stimuli. The red circle represents the target stimuli; all others served as distractors.

letter presented N-ago and withheld a response if the letters did not match, see Figure 2. Letters were prerecorded and took approximately 500 ms to transit aurally via the CEPs; letters C, H, and X were excluded due to idiosyncratic details for this particular experimental design. All letters were presented 6 dB above the level of noise under hearing protection (66, 76, and 86 dB, respectively) to ensure adequate intelligibility (via pilot testing); in the quiet condition, stimuli were presented at 66 dB.

Each participant completed a minimum of 16 practice trials at each difficulty level (dependent on task understanding) before moving onto data collection. Trials lasted 2300 ms with a 1500 ms response window for a total of 672 trials across 6 blocks, which amounted to 112 trials/block. The task was presented in isolation prior to a dual-task context in the first session.

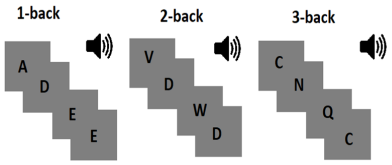


Figure 2. Example of how the n-back task was presented to participants. For these examples, the participant should press the 'F' key following the most recent letter (E, D, C, respectively).

2.4.3 *Dual-Task*

The dual-task consisted of all combinations of n-back paired with the search task. To maintain pacing, there were 2 auditory trials (2300 ms/trial) per 1 visual trial (4600 ms/trial). Each participant completed a minimum of 16 practice trials at each working memory difficulty before moving onto data collection.

2.5 Equipment

Participants used a desktop computer and the Michael & Associates FitCheck Solo System to collect attenuation data; the experimenter used the same computer to administer aircraft noise at the desired level for the duration of the experiment. Participants used a 10.5in Microsoft Surface Go 3 to complete the experiment (fixed location). Participants used CEP 508-SR w/ comply tips (Memory Foam P-Series) to both hear the audio stimuli and as hearing protection in the experiment, see Figure 3. Hearing threshold measurements were conducted using an AudioStar Pro.



Figure 3. Example of CEPs used by participants for noise protection and presentation of audio task.

3. RESULTS

3.1 Data Cleaning

For the visual search task, reaction times (RTs) quicker than 100 ms were removed to eliminate anticipatory responses. Three participants were removed due to any of the following: lack of responses within an isolated task, less than 60% accuracy when completing the visual task, or willingly excluding themselves from the experiment. Two auditory blocks, each in different sessions, were removed from one participant due to a lack of responses. Block one of the visual search task in isolation was removed due to training effects for all participants.

3.2 Auditory Health

Auditory thresholds, noted as hearing level (dB HL), were measured across nine frequencies in each ear (e.g., 125, 250, 500, 1k, 2k, 3k, 4k, 6k, 8k Hz). Baseline thresholds were taken during session 1 and any participant that had $>= 25$ dB HL in two+ frequencies in one ear were excluded, $M = 2.98$ dB HL, $Max = 25$ dB HL. No participants presented with greater than a 10 dB HL threshold shift averaging across 2-4k Hz after noise exposure (Threshold shift: $M = 1.05$ dB HL, $Max = 10$ dB HL) collected less than 5 minutes post-noise exposure.

Due to individual differences in inserting the CEPs, participants had changes in personal attenuation rating (PAR) each session. Nonetheless, due to the adaptive filtering used, the UHP levels remained balanced across participants. However, this necessitated different external room levels based on the individual fit differences, see Table 1.

Table 1. A table summarizing auditory differences among participants across noise levels.

	Desired Noise Exposure	$M(SD)$
CEP Fit	60	30.66 (3.88)
	70	31.85 (4.95)
	80	31.64 (4.08)
Room Levels	60	94.86 (3.86)
	70	107.24 (3.48)
	80	114.34 (3.28)
UHP Levels	60	58.35 (0.53)
	70	68.72 (0.59)
	80	78.15 (0.99)

3.3 Performance

To test H1 and H2, we assessed how VS and WM (n-back) task accuracy and efficiency changed as a function of WM task load and single- v. dual-task (H1), and as a function of noise (H2). We applied z-score and t-tests to assess post hoc differences between conditions for accuracy and Cost, respectively. We applied a Bonferroni p-value correction for all post hoc analyses.

3.3.1 *Accuracy*

First, we used two repeated-measured ANOVAs to assess the accuracy of the VS and WM tasks across single- and

dual-task conditions, and various WM loads and noise levels. z-score statistics are presented for single test or a [range] to summarize multiple tests.

VS task. We found significant main effects of WM load, $F(3, 38309) = 25.06$, $p < 0.05$ (supporting H1) and noise level, $F(3, 38309) = 2.82$, $p < 0.05$ (supporting H2), and their interaction, $F(9, 38309) = 2.71$, $p < 0.05$, on VS accuracy. Post hoc assessments revealed that the isolated VS task in 60 dB, $M = 98.84\%$, $SD = 10.72\%$ and 70 dB, $M = 98.52\%$, $SD = 12.08\%$, were more accurate than the VS task paired with the 3-back in 60 dB, $M = 96.78\%$, $SD = 17.65\%$, $z = 5.22$, $p < 0.05$ and 70 dB, $M = 97.30\%$, $SD = 16.22\%$, $z = 3.29$, $p < 0.05$, respectively. Lastly, the isolated VS task in 80 dB, $M = 99.11\%$, $SD = 9.38\%$, was more accurate than the VS task paired with the 2-back in 80 dB, $M = 96.53\%$, $SD = 18.30\%$, $z = 6.69$, $p < 0.05$. Alternative to our hypothesis, the isolated VS task in quiet, $M = 98.14\%$, $SD = 13.52\%$, is less accurate than the isolated VS task in 80 dB, $z = -3.64$, $p < 0.05$.

WM task. We found significant main effects of context (single- v. dual-tasking), $F(1, 19012) = 111.37$, $p < 0.05$, WM load (n-back), $F(2, 19012) = 1089.44$, $p < 0.05$, supporting H1, and noise level $F(3, 19012) = 11.16$, $p < 0.05$, supporting H2, on WM task hit rate. Additionally, there was an interaction between noise level and WM load on the WM task (n-back) hit rate, $F(6, 19012) = 10.51$, $p < 0.05$. Post hoc assessments revealed that in all noise levels, the 1-back, $M = [92.88\%, 93.85\%]$, $SD = [24.02\%, 25.72\%]$, was more accurate than the 2-back, $M = [83.21\%, 87.93\%]$, $SD = [32.59\%, 37.39\%]$, $z = [4.35, 7.56]$, $p < 0.05$, and the 3-back, $M = [57.47\%, 68.55\%]$, $SD = [46.45\%, 49.46\%], z = [19.38, 28.14]$, $p < 0.05$. In all noise conditions, participants had higher accuracy in the 2-back condition than the 3-back, $z = [13.83, 22.27]$, $p < 0.05$, collapsed across single- and dual-tasking. Participants' 2-back accuracy was higher in 70 dB noise, $M = 87.93\%$, $SD = 32.59\%$, compared to 80 dB, $M = 83.21\%$, $SD = 37.39\%$, $z = 3.62$, $p < 0.05$, partially supporting H2. Alternative to H2, the 3-back in quiet had lower accuracy than when completed in any noise level, $z = [-8.47, -6.22]$, $p < 0.05$.

3.3.2 Multitasking Cost

As a reminder, cost controls for how well individuals perform the task in an "unlimited capacity" environment (i.e., no second task, desired noise level). For each individual, a baseline (single-task) performance was collected in each noise level. These baselines were then compared to their dual-task performance in each level of noise, respectively. If the resulting cost score is equal to 0 and thus unlimited, processing efficiency remains consistent, while a score < 0 denotes a limited capacity and slower processing efficiency, and a score of > 0 demonstrates an increase in processing efficiency and super capacity (for reference see [2, 13]).

VS task. There was a main effect of WM load on VS cost, $F(2, 154) = 11.81$, $p < .05$ (see Figure 4). Specifically, VS paired with the auditory 1-back, $M_{cost} = -0.13$, $SD_{cost} = 3.49$, was more efficient than with 2-back, $M_{cost} = -1.91$, $SD_{cost} = 3.68$; $t(154) = 3.49$, $p < 0.05$, and 3-back, $M_{cost} = -2.51$, $SD_{cost} = 3.87$; $t(154) = 4.67$, $p < 0.05$, supporting H1. Additionally, there was a main effect of noise level on VS cost, $F(3, 154) = 11.66, p < .05$ (see Figure 4). Specifically, VS cost in quiet, $M_{cost} = 0.60$, $SD_{cost} = 4.30$, was higher (i.e., more efficient) than in 60 dB, $M_{cost} = -2.02$, $SD_{cost} = 4.17$; $t(154) = 4.46$, $p < 0.05$, 70 dB, $M_{cost} = -2.24$, $SD_{cost} = 3.16$; $t(154) = 4.83$, $p < 0.05$, and 80 dB, $M_{cost} = -2.41$, $SD_{cost} = 2.57$; $t(154) = 5.12$, $p < 0.05$, partially supporting H2.

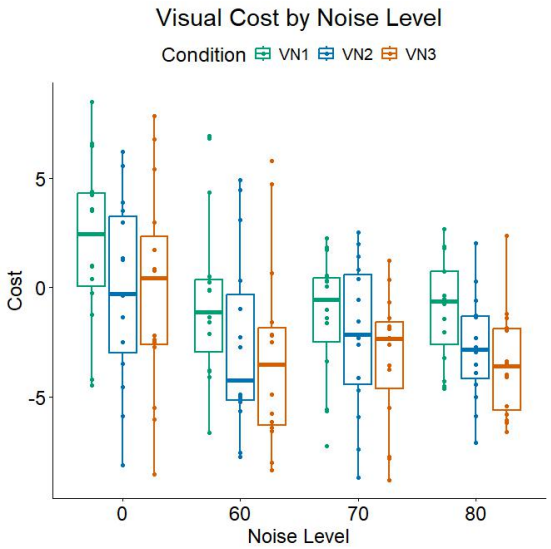


Figure 4. Visual search (VS) cost by noise level and condition. VN1 is an auditory 1-back, VN2 is 2-back, and VN3 is 3-back. All were paired with the VS task.

WM task. There were no main effects of difficulty

(n-back) or noise level (quiet, 60, 70, 80 dB), or their interaction, on WM task cost.

3.4 Survey Analyses

NSS scores were computed from individuals' survey answers at the start of the experiment. HAAS surveys were filled out prior to and after completion of tasks in each session; the difference in the scores was used to detect changes in affect due to the noise level, see Table 2.

NSS and HAAS. Using a simple linear regression model, we found a significant main effect of NSS score on degree of change in negative affect, $F(1, 13) = 6.08$, $p < 0.05$, see Figure 5. Post hoc simple slopes analyses revealed that the greater one's NSS score, the more their negative affect increased due to quiet, $t(32.57) = 2.47$, $p < 0.05$, and 70 dB noise, $t(32.57) = 2.34$, $p < 0.05$, partially supporting H3.

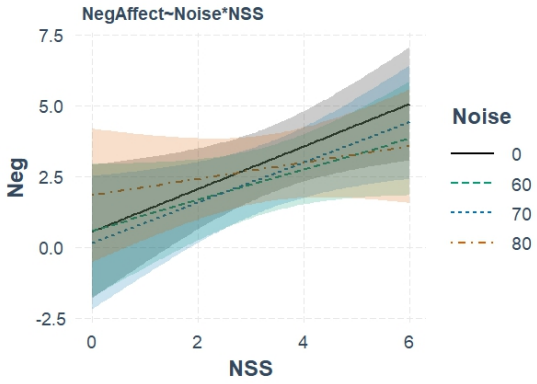


Figure 5. Change in negative affect (NegAffect) by noise level and Noise Sensitivity Scale (NSS) score.

Table 2. Means (standard deviations) for changes (Δ) in positive (Pos) and negative (Neg) affect across noise levels.

Noise Level	Δ Pos	Δ Neg
0	-3.6 (3.70)	3.07 (2.81)
60	-3.00 (2.59)	2.40 (2.47)
70	-2.33 (2.29)	2.53 (2.74)
80	-3.13 (2.77)	2.80 (1.78)

We found no significant main effect of Noise and NSS, or their interaction, to predict changes in positive affect.

VS task. Our results indicated a significant interaction between NSS score and noise level on VS task cost, $F(3, 159) = 3.48$, $p < 0.05$, see Figure 6, partially supporting H3. Post hoc paired-samples analyses revealed that for both low and moderate NSS scores, peoples' VS task efficiency decreased in all noise levels compared to quiet, $t(159) = [-5.42, -3.21]$, $p < 0.05$. Alternatively, those with high NSS scores are only less efficient in 60 dB noise, $t(159) = -2.91$, $p < 0.05$, compared to quiet.

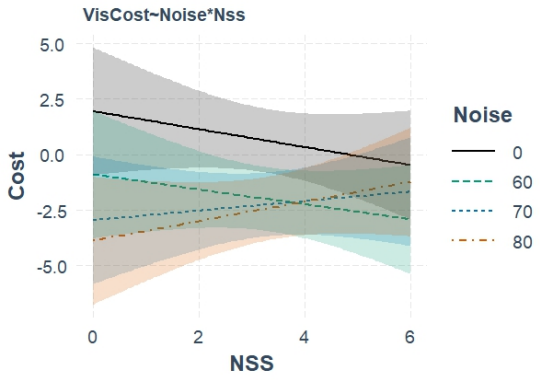


Figure 6. Visual search task cost (VisCost) by noise level and Noise Sensitivity Scale (NSS) score.

WM task. Our results indicated a significant interaction between NSS score and noise level on WM task cost, $F(3, 339) = 7.42$, $p < 0.05$, see Figure 7, partially supporting H3. Specifically, post hoc paired-samples analyses revealed that when participants had a lower NSS score, they were more efficient in the WM task in 60 dB noise, $t(339) = 3.13$, $p < 0.05$, compared to quiet. Alternatively, participants with a higher NSS score had lower efficiency in the WM task in 60 dB, $t(339) = -2.35$, $p < 0.05$, compared to quiet.

4. DISCUSSION

We investigated the relationship of three levels of steady-state F-35 noise and performance in concurrent VS and auditory WM tasks of varying difficulty levels. Importantly, we found no notable shifts in auditory thresholds due to noise exposure and CEP fit improved across session.

First, we found multitasking and WM load influenced performance in both tasks, supporting H1. In particular, VS task accuracy decreased due to multitasking and

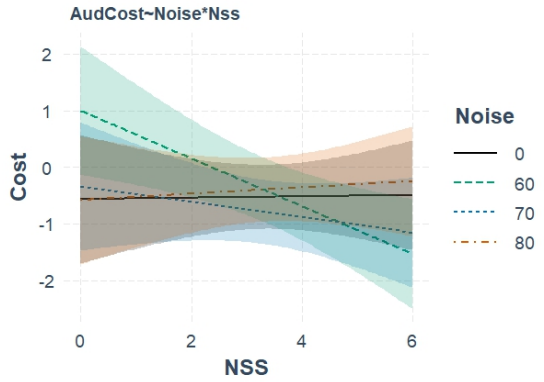


Figure 7. Working memory (WM) task cost (AudCost) by noise level and Noise Sensitivity Scale (NSS) score.

cross-modal WM load. In addition, participants' accuracy in both tasks significantly differed as a function of noise condition, partially supporting H2. Contrary to H2, 80 dB noise increased single VS accuracy; all noise levels led to higher WM accuracy when multitasking under a high load. Lastly, we found multitask efficiency (VS but not WM) decreased in noise, providing partial support for H2.

To investigate how one's sensitivity and emotional response to noise moderates our findings, we first assessed if one's noise sensitivity, as measured by a 6-item scale [8], predicted their degree of change (Δ) in positive and negative affect, as measured by a 12-item scale [7] after noise exposure. We found those with higher sensitivity to noise experienced significantly more negative affect following the quiet and the 70 dB noise conditions. However, no significant differences were found after 60 or 80 dB noise, and no shifts in positive affect were observed for any of the noise levels.

Then, we assessed noise sensitivity as a moderator of our findings and found those with low and moderate sensitivity performed the VS with an unlimited capacity in quiet, but with a limited capacity when exposed to any level of noise. Alternatively, those with high sensitivity to noise performed with an unlimited capacity in quiet, or 70 dB and 80 dB noise, but with a limited capacity in 60 dB noise. Interestingly, those with low sensitivity performed the WM task more efficiently with 60 dB noise than quiet, but those with high sensitivity performed with a more limited capacity in 60 dB noise.

These data suggest that one's degree of noise sensitivity plays a role in the degree of impact and type of interference that steady-state F-35 cockpit noise has on negative affect, and visual (VS task) and auditory (WM task) efficiency, when attempting to multitask. Our study results may indicate that those who are highly sensitive to noise actively work to ignore the noise and focus on maintaining adequate performance in a task of another modality (visual). Alternatively, those with low sensitivity had a within-modality (auditory) boost from the low level of noise, while highly sensitive individuals performed worse in the auditory (WM) task with the same 60 dB noise. Interestingly, those with high sensitivity performed the worst in both tasks when exposed to the low level of noise.

4.1 Limitations and future research

This research has its limitations, but these serve to highlight the importance of future work. First, we chose to control for the level of noise exposure UHP, which necessarily made the level of noise in the room vary across people. The room level may change the degree to which one receives aural information via bone conduction, and the degree to which the sound vibrations may alter effects of physical and cognitive fatigue. Future work should investigate the impact of room level on cognitive performance and use a type of hearing protection that has little variability in the degree of protection between people.

We also chose that Session 1 would always be quiet to mitigate potential harm should participants unknowingly engage in risky behavior (e.g., adjusting their CEPs mid-session). However, future work should fully randomize session order to validate our results.

Our tasks jointly differed in modality and cognitive resource demands so the two cannot be disentangled regarding the impact of noise on cognitive processes. Future work should replicate this study and systematically manipulate perceptual and cognitive resources. While [14] found that distractions that cause higher executive and WM load impacts real-world VS performance, regardless of the source, future research should investigate the moderator of noise sensitivity.

Lastly, we necessarily chose a single source of steady-state aircraft noise, and controlled for the potential effects of fatigue from extended noise exposure. Future work should investigate how variable noise and other types of noise sources may differentially impact cognitive processing and decision-making of single- and multitask demands, and the effects of prolonged exposures that often occur in operational environments [4].

5. CONCLUSIONS

This study provides valuable insights into the effects of aircraft noise on cognitive processes involved in multitasking contexts. We found that noise exposure led to shifts in visual and auditory task performance, especially in multitasking contexts. Additionally, noise sensitivity influenced peoples' cognitive efficiency and emotional impact of noise exposure. Overall, these results underscore the importance of considering individual noise sensitivity when assessing the impact of noise on cognitive and emotional functioning, especially in environments where multitasking is prevalent, such as in aviation or other high-stress operational settings. Future research should build on these findings to further explore how different noise types and individual differences in sensitivity influence cognitive performance across various task demands.

6. DECLARATIONS

6.1 Disclaimer

Distribution A. Approved for public release; distribution unlimited. AFRL-2024-6367; Cleared 15 Nov 2024. This research was supported in part by an appointment to the DOD Research Participation Program administered by the Oak Ridge Institute for Science and Education (ORISE) through an interagency agreement between the U.S. DOE and the DOD. ORISE is managed by ORAU under DOE contract number DE-SC0014664. The views expressed are those of the author and do not necessarily reflect the official policy or position of the AF, DOD, U.S. government, or ORISE.

7. REFERENCES

[1] J. S. Macdonald and N. Lavie, "Visual perceptual load induces inattentional deafness," *Attention, Perception, & Psychophysics*, vol. 73, pp. 1780–1789, 2011.

[2] E. L. Fox, J. W. Houpt, and P. S. Tsang, "Derivation and demonstration of a new metric for multitasking performance," *Human Factors*, vol. 63, pp. 833–853, 2021.

[3] M. Awada, B. Becerik-Gerber, G. Lucas, and S. Roll, "Cognitive performance, creativity and stress levels of neurotypical young adults under different white noise levels," *Scientific Reports*, vol. 12, no. 1, p. 14566, 2022.

[4] J. L. Szalma and P. A. Hancock, "Noise effects on human performance: a meta-analytic synthesis.," *Psychological bulletin*, vol. 137, no. 4, p. 682, 2011.

[5] C. Yang, L. Pang, J. Liang, X. Cao, Y. Fan, and J. Zhang, "Experimental investigation of task performance and human vigilance in different noise environments," *Applied Sciences*, vol. 12, no. 22, p. 11376, 2022.

[6] Y. Fan, J. Liang, X. Cao, L. Pang, and J. Zhang, "Effects of noise exposure and mental workload on physiological responses during task execution," *International Journal of Environmental Research and Public Health*, vol. 19, no. 19, p. 12434, 2022.

[7] P. Roca, C. Vázquez, and D. Ondé, "The hedonic and arousal affect scale (haas): A brief adjective checklist to assess affect states," *Personality and Individual Differences*, vol. 207, p. 112151, 2023.

[8] H. Kishikawa, T. Matsui, I. Uchiyama, M. Miyakawa, K. Hiramatsu, and S. A. Stansfeld, "The development of weinstein's noise sensitivity scale," *Noise and Health*, vol. 8, no. 33, pp. 154–160, 2006.

[9] R. S. Job, "Noise sensitivity as a factor influencing human reaction to noise," *Noise and Health*, vol. 1, no. 3, pp. 57–68, 1999.

[10] J. A. Russell, "A circumplex model of affect.," *Journal of personality and social psychology*, vol. 39, no. 6, p. 1161, 1980.

[11] W. K. Kirchner, "Age differences in short-term retention of rapidly changing information.," *Journal of experimental psychology*, vol. 55, no. 4, p. 352, 1958.

[12] P. Stróżak, P. Francuz, R. Lewkowicz, P. Augustynowicz, A. Fudali-Czyż, B. Bałaj, and O. Truszczyński, "Selective attention and working memory under spatial disorientation in a flight simulator," *The International Journal of Aerospace Psychology*, vol. 28, no. 1-2, pp. 31–45, 2018.

[13] L. M. Blaha and J. W. Houpt, "An extension of workload capacity space for systems with more than two channels," *Journal of mathematical psychology*, vol. 66, pp. 1–5, 2015.

[14] S. J. Nachtnebel, A. J. Cambronero-Delgadillo, L. Helmers, A. Ischebeck, and M. Höfler, "The impact of different distractions on outdoor visual search and object memory," *Scientific Reports*, vol. 13, no. 1, p. 16700, 2023.

DOI: 10.61782/fa.2025.0240

FORUM ACUSTICUM EURONOISE 2025

Comparison of REAT and insertion loss measurements using headphone audiometry

Zimpfer Véronique[1*] **Hamery Pascal**[1] **Blondé-Weinmann Cyril**[1]
[1] French-German Research Institut of Saint-Louis (ISL), France

ABSTRACT

Under the current standard, hearing protector performance is assessed using the REAT (Real-Ear Attenuation at Threshold) method. This method involves measuring hearing thresholds with and without hearing protection in free-field conditions. The insertion loss of the hearing protection corresponds to the difference between these thresholds. REAT requires a highly sound-isolated audiometry room with minimal background noise and a diffuse field to ensure that both ears receive identical sound exposure. This study aims to compare REAT results with those obtained through headphone audiometry. Unlike REAT, headphone audiometry measures thresholds separately for each ear, allowing the detection of minor asymmetry between ears. Furthermore, this technique requires only an isolated cabin rather than a free-field environment. This study measured the insertion loss of two different types of earplugs on 13 subjects: a foam earplug and a custom-molded earplug in hard acrylic. These values show some differences between the two methods, with small variations at high frequency for foam earplugs and slightly greater variation at low frequency for custom molded earplugs. In addition, the standard deviation is significantly higher, especially for custom-molded earplugs.

Keywords: Earplug performance, REAT, Headphone audiometry.

1. INTRODUCTION

Every day, we are exposed to continuous and/or impulsive noise that can damage our hearing. In Europe, legislation prescribes a maximum noise exposure level of 87 dB(A) for 8 hours with hearing protection [1]. The best-known solution is using individual Hearing Protection Devices (HPDs), as it is often complicated to reduce the noise level of the sound sources. Adequate protection requires accurate knowledge of the HPD's performances.

Currently, the European and American industries consider the REAT (Real-Ear Attenuation at Threshold) method as the reference for assessing the performance of hearing protectors worn by an individual [2-5]. The REAT method corresponds to a hearing threshold evaluation performed in a diffuse sound field, with and without an HPD. Although the ANSI/ASA S12.6 and ISO 4869 standards describe a detailed protocol to measure the attenuation provided by a given device, the described procedure is generally uneasy to implement on a large scale.
Key difficulties include:

- Acoustic environment: Requires a very well-insulated anechoic room with low background noise and a diffuse sound field so that the two ears perceive the same sound.
- Participant hearing symmetry: participants must have symmetrical hearing in both ears, as threshold is measured with both ears together.
- An additionnnal issue is that Brueck (2009) has shown that the actual attenuation performance of earplugs is often different from that claimed by the manufacturer [8], which limits the relevance of this subjective method.

Alternatively, an objective method is also described in the ANSI Standard [6]. This method is based on the estimation of the HPD insertion loss using a microphone inserted in

[*] ***Corresponding author***: veronique.zimpfer@isl.eu.
Copyright: *©2025 First author et al. This is an open-access article distributed under the terms of the Creative Commons Attribution 3.0 Unported License, which permits unrestricted use, distribution, and reproduction in any medium, provided the original author and source are credited.*

the ear canal: it is the MIRE (Microphone In Real Ear) method. Installing a microphone in earplugs is difficult as it could damage them or create an acoustic leak. A study by Berger [7] showed that it is possible to use this method with earplugs specially designed for insertion of a microphone probe, but these earplugs can only be used to measure attenuation.

In this context, fit-test systems have been developed to measure the effectiveness of HPDs in situ. These systems have been used in the literature to measure the attenuation of earplugs [9,10].The aim of this study is to find a method for estimating the effectiveness of earplugs in the laboratory that is easier to implement than the REAT method and less intrusive than the MIRE method. We therefore propose to estimate insertion loss by measuring hearing thresholds with and without earplugs using headphone audiometry. Measuring threshold with headphones rather than in the open field has a number of advantages:

- the headphones isolate the subject, which simplifies the environmental conditions of the measurement,
- participants can present auditory asymmetry between the two ears as each ear is measured separately,
- there are two attenuation values for each subject (one for each ear).

2. MATERIAL AND METHOD

In this study, we performed a comparison between the results obtained with headphone audiometry and data provided by the earplug manufacturers, which were obtained by the approved laboratories using the REAT method.

2.1 Earplugs used

Two different earplugs have been evaluated (Figure 1) :

- A custom earplug in Crylit® manufactured by 3D printing, with a specific geometry for each ear tested,
- A classic foam earplug.



Figure 1. Photographs of the two earplugs used.

2.2 Headphone audiometry

The audiometer used was an Otometrics audiometer with TDH39 headphones. We used the Békésy method at fixed frequencies to measure hearing thresholds. With our equipment, we were able to measure the center frequency of octaves from 125 Hz to 8 kHz. The audiometer cannot measure frequencies below 125 Hz.

2.3 Participants

Thirteen voluntary subjects (nine males and four females) participated in the tests. Each participant has their custom earplug with the same filter from the same manufacturer.

2.4 Measurement protocol

Each participant sat in an audiometry booth in front of the audiometer. They each performed 4 audiometry, each time starting with the left ear:

- the first without an earplug;
- the second with the custom earplug;
- the third with the foam earplug;
- the fourth without the earplug.

The last test was used to check whether the participants were still focused. The measurements were validated if the difference between the first and last measurements did not exceed 5 dB for each frequency tested. The test lasted no longer than 20 minutes.

2.5 Estimated acoustic quantities

We determined the average attenuation per central octave frequency for each earplug between 125 Hz and 8 kHz over the 26 measurements (13 participants times 2 ears). For each frequency, the Assumed Protection Value (APV) was calculated. This APV corresponds to the mean value minus one standard deviation.

To calculate the SNR (Single Number Rating as described in ISO 4869-2 [5]) and the H, M, and L values, the earplug's attenuation at 63 Hz had to be estimated. It is proposed that the attenuation at 63 Hz be taken as the attenuation at 125 Hz minus 1 dB. The standard deviation is the same as at 125 Hz.

3. RESULTS

Figure 2 shows the average insertion loss values obtained for the 26 ears for the two types of earplug. These values are compared with the data provided by the earplug manufacturers. There was little difference except for the results at 125 Hz for the custom earplugs.

Figure 3 shows the APVs for the two types of earplugs. For the foam earplugs, there was a good correlation between our results and those provided by the manufacturer.

On the other hand, for the custom earplugs, where the standard deviation was significant, the APVs were lower than the manufacturer's data, especially at low frequencies. This discrepancy, caused by a very high standard deviation at low frequencies, cannot be explained at present.

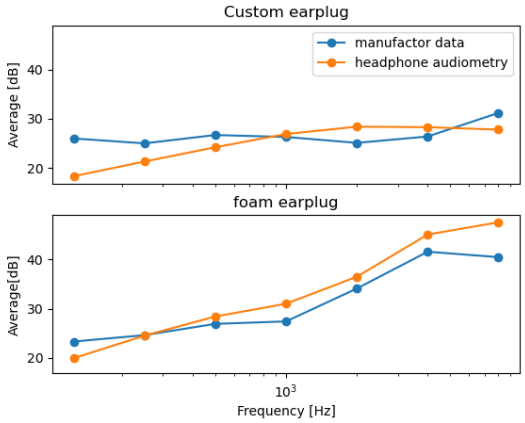


Figure 2. Average insertion loss for the two earplug.

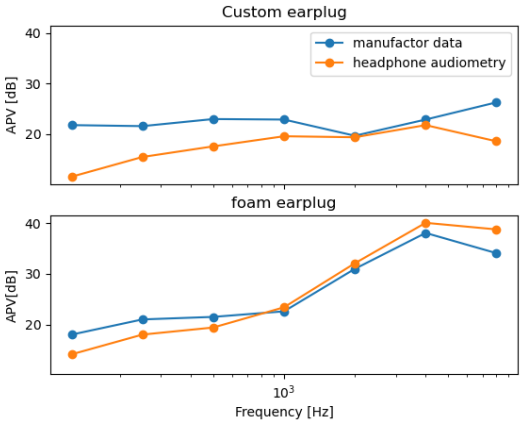


Figure 3. APV for the two earplugs.

Table 1 gives the two earplugs' SNR, H, M, and L values. As with the APV measurements for the foam earplug, the values for the custom earplugs are equivalent but slightly lower.

Table 1. SNR, H, M and L values for each earplug in dB.

	Custom earplug			
	SNR	H	M	L
Manufacturers data	27,7	30	24	22
Headphone audiometry	27	31	23	19
	Foam earplugs			
	SNR	H	M	L
Manufacturers data	23	21	22	22
Headphone audiometry	21	20	19	17

4. DISCUSSION

A method of assessing HPD that is simpler to implement than the REAT and MIRE methods was investigated. This approach consists of determining hearing thresholds with and without hearing protection using headphone audiometry.

In this preliminary assessment, the method gave promising results for foam earplugs, showing good agreement with the manufacturer's data. However, for custom earplugs, the method gave lower insertion loss and APV estimates than the manufacturer's data, especially at low frequencies.

One hypothesis to explain this difference could be that the static pressure exerted by the helmet on the auricle slightly affects the positioning of the protector, possibly reducing its performance. Indeed, the performance of custom earplugs can be more easily affected by deformation of the hearing canal than that of foam earplugs.

5. CONCLUSION & PESPECTIVE

Headphone audiometry method gives results that are consistent with the manufacturer's REAT measurements for foam earplugs. Nevertheless, this method warrants further study to verify whether the observations made with custom earplugs are valid. Given the difficulty of implementing this method, it could be used to verify whether or not the performance of earplugs is stable during prolonged wear. Indeed, Gong et al (2023) [10] reported a very slight loss after two hours of use. This new method could therefore be extended to assess changes in the performance of protectors over time, without the biases of conventional methods.

6. ACKNOWLEDGMENTS

We thank all the volunteers who participated in this test.

7. REFERENCES

[1] Buck, K., P. Hamery, and V. Zimpfer. The European Regulation 2003/10/EC and the Impact of its Application to the Military Noise Exposure. in International Congress on Acoustics, ICA. 2010

[2] American National Standards Institute (ANSI). 2008. ANSI/ ASA S12.6. American National Standard Methods for the measuring the real-ear attenuation of hearing protectors. New York (NY): ANSI.

[3] American National Standards Institute (ANSI). 2018. ANSI/ ASA S12.71. American National Standard performance criteria for systems that estimate the attenuation of passive hearing protectors for individual users. New York (NY): ANSI.

[4] ISO 4869-1:2018 (en) -Acoustics — Hearing protectors — Part 1: Subjective method for the measurement of sound attenuation

[5] ISO, B., 4869-2 Acoustics-Hearing protectors. Part 2: Estimation of effective A-weighted sound pressure levels when hearing protectors are worn. 1994, British Standards Institution, London

[6] American National Standards Institute (ANSI). 2008. ANSI/ ASA S12.42-2010. Methods for the measurement of insertion loss of hearing protection devices in continuous or impulse noise using microphone in-real-ear or acoustic test fixture procedures. New York (NY): ANSI.

[7] Berger, E. H., Voix, J., Kieper, R. W., & Le Cocq, C. (2011). Development and validation of a field microphone-in-real-ear approach for measuring hearing protector attenuation. Noise and Health, 13(51), 163-175.

[8] Brueck, L., *Real world use and performance of hearing protection.* Health Saf Lab, 2009: p. 37-8

[9] Karch, S. J., Federman, J., Ginsberg, J. T., & Qureshi, I. (2024). Measuring earplug noise attenuation: A comparison of laboratory and field methods. Journal of Occupational and Environmental Hygiene, 21(1), 68-76.

[10] Gong, W., Murphy, W. J., Meinke, D. K., Feng, H. A., & Stephenson, M. R. (2023, November). Evaluating earplug performance over a 2-hour work period with a fit-test system. In Seminars in Hearing (Vol. 44, No. 04, pp. 470-484). Thieme Medical Publishers, Inc.

DOI: 10.61782/fa.2025.0880

FORUM ACUSTICUM EURONOISE 2025

THE RELATIONSHIP BETWEEN DAMAGE RISK CRITERIA FOR IMPULSE NOISE EXPLAINED BY SIMPLE ACOUSTICAL DESCRIPTORS

Marian Weger*
French-German Research Institute of Saint-Louis (ISL), Saint-Louis, France

ABSTRACT

Hazardous impulse noise is still a major problem for personnel in industry and construction work, and particularly in the military. The allowed maximum permissible exposures per day for a certain combination of noise and hearing protection differ across countries, depending on the applicable criterion for predicting auditory hazard. Such Damage Risk Criteria (DRC) for impulse noise may take into account signal extrema, zero-crossings, amplitude/energy statistics, or physical ear models. Consequently their reactions to environmental and source characteristics diverge. We evaluated the differences between DRC and their correlations with acoustical descriptors. Most of the variance between hazard predictions by DRC could be explained by linear regression using only a few descriptors that cover certain key sound characteristics or peculiarities of the hearing system. This relationship allows us to better understand how certain sound characteristics translate to the risk of hearing damage and contributes to the ongoing discussion on future DRC standards. As the data comprised only a subset of soldiers' noise exposure, follow-up studies should include larger caliber weapons and complex noise combined with hearing protection, in order to draw more general conclusions.

Keywords: *impulse noise, damage risk criteria, weapon noise, auditory hazard, hearing injury*

1. INTRODUCTION

Despite all efforts and advances in noise control and Hearing Protection Devices (HPD), loud impulse noise still constitutes a major health risk for personnel in industry, construction work, and within the military. Especially during military training, noise exposures from firearms can induce hearing injury among soldiers. In order to quantify a soldier's individual risk of hearing injury, several objective Damage Risk Criteria (DRC) have been proposed. Their predictions, however, diverge, especially for ecologically valid scenarios comprising both continuous noise (from vehicles) and impulse noise (from weapon systems). Even within the EU, several national standards are in use; e.g., Pfander criterion in Germany, LAeq in France, or the Auditory Hazard Assessment Algorithm for Humans (AHAAH) in The Netherlands, and also the thresholds for the maximum admissible daily noise dose vary. At the time of writing, no currently available standard is sufficiently validated in order to cover all relevant aspects of auditory hazard. In addition, the differences between DRC as well as their individual qualities and restrictions are not yet entirely understood. The topic is therefore still subject to extensive civilian and military research worldwide. Various studies have compared existing DRC against each other, with respect to the predicted hazard or the resulting Maximum Permissible Exposures (MPE) per day (and per weapon/HPD combination).

For example, van der Eerden et al. [1] compared the A-weighted Sound Exposure Level (ASEL) to the risk predicted by the AHAAH. They concluded that there is no simple correlation between the two, especially due to the AHAAH's non-monotonic behavior. In particular, with growing impulse strength in terms of increasing Weber radius of synthesized Friedlander waves, ASEL grows monotonically, while the hazard predicted by the AHAAH decreases again, after having reached its maximum at an ASEL of around 140 dBA. In addition, the authors found that the AHAAH was disproportionately sensitive to additive continuous noise in comparison to ASEL. This can also be interpreted as low robustness against SNR [2].

***Corresponding author**: marian.weger@isl.eu.
***Copyright**: ©2025 Marian Weger. This is an open-access article distributed under the terms of the Creative Commons Attribution 3.0 Unported License, which permits unrestricted use, distribution, and reproduction in any medium, provided the original author and source are credited.*

The Pfander criterion ignores any sound below −10 dB with respect to the peak [3]. A major difference between Pfander and AHAAH thus concerns the inclusion of room reflections. Furthermore, their relationship shows the same non-monotonic behavior as between ASEL and AHAAH [3]. Pfander and ASEL were assumed to be too different to be converted into one another [4].

As ASEL also covers continuous noise, it is widely used in any context. For complex noise that exhibits both impulsive and continuous components, however, an adjustment in terms of "impulsiveness" (quantified by statistical kurtosis) correlated better with medical data than ASEL alone [5]. Likewise, the US military standard 1474E [6] includes an adjustment by the duration of the impulse in order to correct ASEL's assumed overestimation of large-caliber weapon noises.

As most of the mentioned studies were based on synthesized sounds, they provide valuable insights into the direct relationship between DRC and certain controlled parameters. However, these results cannot be easily transferred to actual weapon usage under realistic training conditions. We therefore compared hazard predictions by several DRC based on real recordings of shooting noise with different weapon configurations and under different ecologically valid environmental conditions (indoor and outdoor). The dataset is briefly described in Sec. 2, while the evaluated DRC are summarized in Sec. 3.

We further tried to predict the differences between DRC by selected acoustical descriptors that are supposed to cover sound qualities which might cause the respective differences. These descriptors are summarized in Sec. 4. In Sec. 5, correlations between DRC are analyzed and discussed in terms of their prediction by acoustical descriptors using multiple linear regression. Finally, general conclusions are drawn in Sec. 6.

2. DATASET & PREPROCESSING

The evaluation is based on the same dataset as described in [2]. It comprises impulsive noise events that were recorded within the multinational measurement campaign NATO RTG SET-286 carried out in 2023. These included 10 single shots with 9 weapon configurations reaching from pistol to anti-material rifle (some with silencer) using live ammunition in 8 environmental conditions (4 outdoor, 4 indoor) as well as 4 explosive configurations (stun grenade and 3 different door breaching charges) with 4 repetitions. Cleaned from defective items, the dataset includes 731 impulses. The stimuli are assumed to cover a majority of infantry soldiers' noise exposure. Recordings were made in 1 m distance at 90° left to the muzzle, with respect to shooting direction, at 1.6 m height or approximate ear level (for explosive, distances were only approximate between 1 m and 3 m).

For the calibrated recordings, the phase was occasionally flipped to always positive peak, DC offset was removed, and noise events were cut to 1 s duration, with the onset (where the amplitude first reaches −3 dB resp. peak) aligned to 5 ms. Signals were low-pass filtered by an 8th-order Bessel filter at 22 kHz cutoff frequency, as recommended by [7].

3. DAMAGE RISK CRITERIA

For each noise event of the above-described dataset, the auditory hazard was predicted by 6 different DRC: Pfander, Leq, LAeq, LIAeq, LAeq-Kurtosis, and AHAAH. Irrespective of the applicable limit, each of these DRC includes a hazard prediction function that we express in the form of hazard level L_H in dB for allowing meaningful comparisons. As the exact definitions used in this work may differ from other publications or national standards, we briefly summarize them below.

The Pfander criterion expresses auditory hazard by the Pfander level $L_\mathrm{H}^\mathrm{Pfander}$, see Eqn. (1), which depends on the unweighted (or Z-weighted) peak Sound Pressure Level (SPL) $\hat{L}_\mathrm{p}$ and C-duration T_C which is the sum of all time periods during which the waveform exceeds −10 dB below $\hat{L}_\mathrm{p}$ [8].

$$L_\mathrm{H}^\mathrm{Pfander} = \hat{L}_\mathrm{p} + 10\log_{10}(T_\mathrm{C}) \tag{1}$$

Leq predicts hazard based on sound energy. Sound exposure within a certain period of time is $E = \int p(t)^2 \mathrm{d}t$. The unweighted Sound Exposure Level (SEL) or L_E with respect to $E_0 = 400\,\mu\mathrm{Pa}^2\mathrm{s}$ is then interpreted as hazard level $L_\mathrm{H}^\mathrm{SEL}$:

$$L_\mathrm{H}^\mathrm{Leq} = \mathrm{SEL} = L_\mathrm{E} = 10\log_{10}(E/E_0) \tag{2}$$

LAeq extends Leq by incorporating the A-weighted sound exposure E_A:

$$L_\mathrm{H}^\mathrm{LAeq} = \mathrm{ASEL} = L_\mathrm{A,E} = 10\log_{10}(E_\mathrm{A}/E_0) \tag{3}$$

LIAeq is an extension to LAeq that adjusts ASEL through the A-duration T_A, i.e., the duration between the last zero crossing before and the first zero crossing after the peak, as given in Eqn. (4). In the actual standard, T_A is restricted between 0.2 ms and 2.5 ms [6]; however, as no other DRC includes such hard parameter clipping, we

leave T_A unrestricted for the current evaluation. Note that we use the alternative version for 1 s window length [6].

$$L_\mathrm{H}^\mathrm{LIAeq} = L_\mathrm{A,E} - 1.5 \cdot 10 \log_{10} \left(T_\mathrm{A}/0.2\,\mathrm{ms}\right) \quad (4)$$

LAeq-Kurtosis, originally developed for complex factory noise [9], adjusts ASEL by the statistical measure of kurtosis β, as given in Eqn. (5). A $\beta > 3$ (larger than kurtosis of Gaussian noise) means stronger tails of the probability distribution, i.e., more extreme values due to impulses. The amount of adjustment is set to $\lambda = 4.02$ [9]. Kurtosis is computed for the entire 1 s analysis window.

$$L_\mathrm{H}^\mathrm{LAeq\text{-}K} = L_\mathrm{A,E} + \lambda \log_{10} \left(\beta/3\right) \quad (5)$$

The AHAAH implements a physical model of the hearing system. It interprets the maximum basilar membrane displacement due to noise exposure as potential hazard H^AHA, expressed in Auditory Risk Units (ARU) and hazard level after (6). Note that we consider only the unwarned mode, meaning that the acoustic reflex is initially deactivated and gets triggered by the impulse [10, 3]. The acoustic reflex ramps in with a time constant of $\tau = 11.7$ ms, starting at 9 ms after the 134 dB threshold is exceeded for the first time. For consistent results with lower levels, we use an adaptive threshold at -3 dB below the peak. Due to the sharp rising edge of weapon noises, in theory following a Friedlander wave, the resulting error in trigger time is considered negligible.

$$L_\mathrm{H}^\mathrm{AHA} = 10 \log_{10} \left(H^\mathrm{AHA}/10^{-10}\,\mathrm{ARU}\right) \quad (6)$$

4. ACOUSTICAL DESCRIPTORS

In order to better understand the differences between DRC, we tried to predict their results by different combinations of acoustical descriptors. These are briefly summarized below.

4.1 Peak, action times, and energy

Most of the examined DRC themselves are already constructed from a couple of descriptors which we include into the analysis: peak SPL $\hat{L}_\mathrm{p}$, C-duration T_C, A-duration T_A, SEL L_E, ASEL $L_\mathrm{A,E}$, kurtosis k. In addition to these, we add common variants using A- and C-weighting that are not yet contained: $\hat{L}_\mathrm{A,p}$, $\hat{L}_\mathrm{C,p}$, and CSEL ($L_\mathrm{C,E}$) To account for spectral differences, we use the Spectral Centroid (SC) that is the frequency-weighted sum of spectral bins normalized by their unweighted sum.

4.2 Diffuseness

An important sound characteristic that is not yet covered by the above descriptors is diffuseness, i.e., the amount of reflections or reverberation that is defined by the environment in which the noise is perceived. A simple statistical descriptor for diffuseness is the Direct-to-Reverberant energy Ratio (DRR), i.e., the ratio between direct and reverberant sound energy. In practice, a Room Impulse Response (RIR) is split at an arbitrary time, typically 2.5 ms after the onset, into the direct and the reverberant part. For impulse noise, the recordings can already be interpreted as impulse responses, which allows us to directly obtain DRR according to Eqn. (7):

$$\mathrm{DRR} = 10 \log_{10} \left(\frac{\int_{t=0}^{2.5\,\mathrm{ms}} p(t)^2 \mathrm{d}t}{\int_{t=2.5\,\mathrm{ms}}^{\infty} p(t)^2 \mathrm{d}t} \right) \quad (7)$$

4.3 Psychoacoustical descriptors

If the frequency weighting curves that are so commonly used in noise assessment actually reflect anything, then that is sound perception.

Using A- and C-weighting curves for predicting auditory hazard implies the assumption that there is a relationship between auditory perception and the risk of hearing injury. We might therefore assume that psychoacoustical sound quality metrics correlate with that risk as well. Using the Sound Quality Analysis Toolbox (SQAT) [11], we computed Perceptual Loudness (PL) in sone [12], Perceptual Sharpness (PS) in acum [13], and Perceptual Roughness (PR) in asper [14]. Note that we used the time-variant (non-stationary) definition in free field and skipped the first 4 ms of the analysis window, i.e., starting 1 ms before the onset. As we seek single predictor values instead of block- or band-wise results, we used averages as well the maximum values as descriptors: $\mathrm{PL}_\mathrm{mean}$, PL_max, $\mathrm{PS}_\mathrm{mean}$, PS_max, $\mathrm{PR}_\mathrm{mean}$, PR_max.

4.4 Acoustic reflex and banded energy

The AHAAH incorporates several non-linear effects that are surely not covered by the acoustical descriptors that have been introduced in this section so far. Two of these are the acoustic reflex and the maximum basilar membrane displacement. Below, we derive very simplified signal processing models for both aspects, in order to obtain acoustical descriptors that may express similar information.

4.4.1 *Acoustic reflex*

As the activation of the acoustic reflex is a binary decision (triggered when the instantaneous sound pressure passes a threshold of 134 dB) its activation function equals a step function $u_\mathrm{A}(t)$ that is 0 before the onset, and 1 afterwards. In the AHAAH model, activation is smoothed by a 1st-order low-pass RC filter with time constant $\tau = 11.7$ ms, which we implement as leaky integrator whose output $s_\mathrm{A}(t)$ is the smoothed activation function:

$$s_\mathrm{A}[n] = (1-\alpha)u_\mathrm{A}[n] + \alpha u_\mathrm{A}[n-1] \quad (8)$$

$$\text{where} \quad \alpha = e^{-1/(\tau F_\mathrm{s})} \quad (9)$$

Once the acoustic reflex is fully activated, its effect can be regarded as a shelving filter that attenuates frequencies below 3 kHz by up to -21 dB (gain $g_\mathrm{S,min} = 0.089$) [15, 21]. Assuming that the filter attenuation is directly controlled by $s_\mathrm{A}(t)$, the dynamic filter gain becomes:

$$g_\mathrm{S}(t) = 1 - (1 - g_\mathrm{S,min})\, s_\mathrm{A}(t) \quad (10)$$

The applied filter uses a constant cutoff frequency at 3 kHz and a slope of 1, combined with the dynamic gain $g_\mathrm{S}(t)$. The application of this simple filter model of the acoustic reflex on a noise measurement is now defined as "unwarned"- or uw-weighting. For the already-included sound energy predictors SEL, ASEL, and CSEL, we add their respective variants $L_\mathrm{E,uw}$, $L_\mathrm{A,E,uw}$, and $L_\mathrm{C,E,uw}$ to the analysis.

4.4.2 *Maximum banded sound exposure*

Within the AHAAH, the displacement of the basilar membrane is analyzed at 23 discrete locations of equal spacing across its length from the oval window to the round window [16, 15]. These locations are attributed to equally-spaced frequencies on a logarithmic scale, from 11.76 kHz down to 0.38 kHz. A rough approximation of this excitation pattern can be achieved by a gammatone filterbank (GTFB), a widely used model for the auditory filters [17]. For modeling auditory perception, their center frequencies are typically tuned to equal spacing on the ERB-rate scale, with constant bandwidth in parts of the Equivalent Rectangular Bandwidth. In order to match the AHAAH model, we tune them to the same 23 center frequencies, with bandwidths set accordingly so that neighboring bands overlap at their -4 dB cutoff frequency (e.g., as done in [18]). The exposure within the 23 frequency bands b is computed with Z-, A-, and C-weighting, in order to obtain banded exposure levels L^b_E, $L^\mathrm{b}_\mathrm{A,E}$, and $L^\mathrm{b}_\mathrm{C,E}$, respectively. As the AHAAH evaluates the maximum across locations, we likewise compute the maximum across bands, $L^\mathrm{max}_\mathrm{E}$, $L^\mathrm{max}_\mathrm{A,E}$, and $L^\mathrm{max}_\mathrm{C,E}$, respectively, as acoustical predictors of auditory hazard. In addition, we also consider their uw-weighed variants: $L^\mathrm{max}_\mathrm{E,uw}$, $L^\mathrm{max}_\mathrm{A,E,uw}$, and $L^\mathrm{max}_\mathrm{C,E,uw}$.

5. CORRELATIONS BETWEEN DRC AND ACOUSTICAL DESCRIPTORS

Based on the acoustical descriptors that were derived above, we aimed at explaining differences between DRC and at predicting the respective hazard level by other means. We investigated all possible and meaningful combinations of 1-, 2-, and 3-way linear prediction models (without and with interactions) made from the above descriptors, for predicting the hazard levels of the evaluated DRC. Combinations are considered as meaningful if the predictors are either more robust with regard to technical parameters of the measurement (as of [2]) or more computationally efficient in view of an implementation on embedded platforms. Best fitting models are selected with respect to the Akaike Information Criterion (AIC) in order to avoid overfitting.

5.1 Pfander and Leq

The Pfander level is known for being a good predictor of signal energy, yet avoiding actual integration. The correlation between L_E and $L^\mathrm{Pfander}_\mathrm{H}$ is shown in Fig. 1 for outdoor and indoor recordings, respectively. Outdoors, we observe almost perfect correlation ($L^\mathrm{Pfander}_\mathrm{H} \approx L_\mathrm{E} + 3$ dB, $R^2 = 0.989$). If analyzing the difference between target ($L^\mathrm{Pfander}_\mathrm{H}$) and the linear model based on SEL, the resulting Probability Density Function (PDF) is a superposition of two almost normal distributions (Fig. 2, $R^2 = 0.955$). In Fig. 2 and all following figures, marker colors correspond to weapon categories (Pistols P, Assault Rifles AR, Battle Rifles BR, Sniper Rifles SR, and Explosive E), while marker shapes depict specific models/configurations; filled/unfilled markers represent outdoor/indoor settings, respectively. As the difference between Pfander and Leq primarily concerns diffuseness, the best performing two-way model uses SEL in combination with the DRR ($R^2 = 0.973$), resulting in a PDF more close to normal (Fig.3). Individual weapon configurations now spread along straight lines, which suggests that the majority of the remaining variance is within weapon conditions. The remaining variance could not be explained without the Pfander descriptors $\hat{L}_\mathrm{p}$ or T_A themselves.

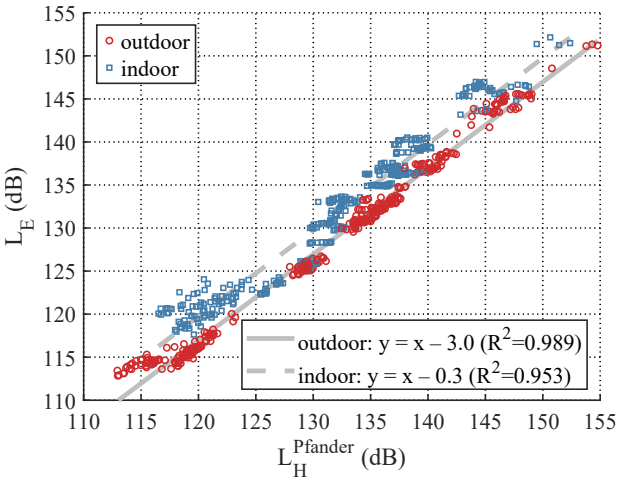


Figure 1. L_E as a function of $L_\mathrm{H}^\mathrm{Pfander}$.

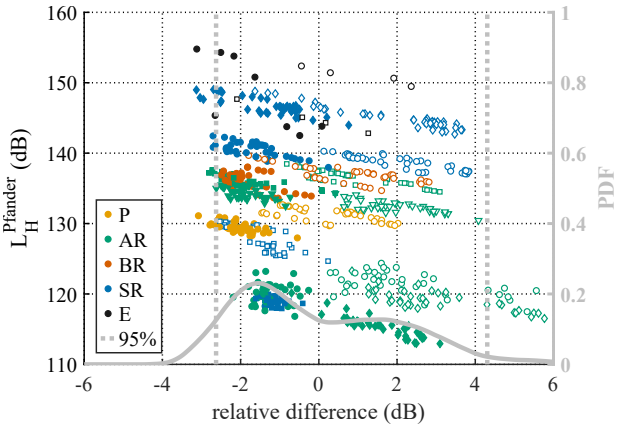


Figure 2. $L_\mathrm{H}^\mathrm{Pfander}$ predicted L_E ($R^2 = 0.955$). Marker coding: color = weapon category, shape = weapon model, filled/unfilled = outdoor/indoor.

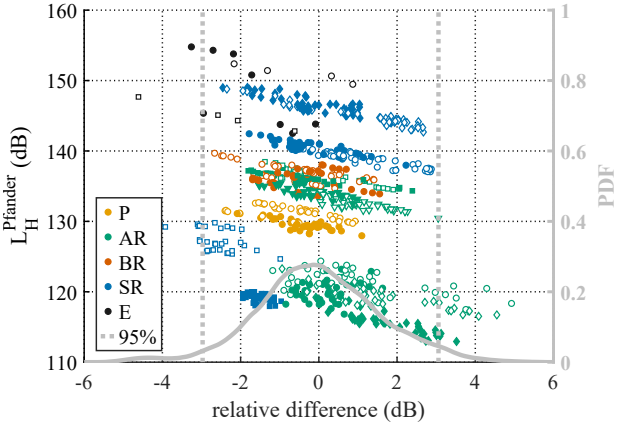


Figure 3. $L_\mathrm{H}^\mathrm{Pfander}$ predicted by L_E and DRR ($R^2 = 0.973$).

5.2 LAeq

The difference between LAeq and Leq is shown in Fig. 4. It follows a characteristic curved shape due to the interplay between A-weighting and noise level. As all tested noises originate from explosions (firearms or explosive charges), the resulting sounds are band-limited, in theory exhibiting a Weber spectrum. Its center frequency decreases with increasing Weber radius, i.e., increasing intensity. Maximum sound energy is thus passed for ASEL ≈ 130 dBA, when A-weighting and Weber spectrum maximally overlap, i.e., when their center frequencies match. The center frequency can be expressed by SC. An interaction between SEL and SC is thus supposed to account for the difference between ASEL and SEL. The best-performing two-way linear model with interactions, however, combined SEL directly with the A-weighted peak, as shown in Fig. 5 ($R^2 = 0.997$). It must be noted that the interaction model of $\hat{L}_\mathrm{C,p}$ and k_A was almost as good ($R^2 = 0.996$).

5.3 LIAeq

As LIAeq depends on A-duration, it is extremely sensitive to the exact measurement specifications and signal preprocessing, which makes it almost impossible to obtain consistent results [2]. Figure 6 shows the difference between LIAeq and LAeq, thus the effect of A-duration. Note the sniper rifle with silencer (blue squares) for which the A-duration is not meaningful and thus leads to extreme variance. Although a more robust equivalent to T_A might be interesting, no useful predictor could be found within the tested acoustical descriptors including their combination. The best-performing descriptor was $\hat{L}_\mathrm{p}$ with only moderate correlation ($R^2 = 0.420$).

5.4 LAeq-Kurtosis

The difference between LAeq-Kurtosis and LAeq (i.e., the contribution of kurtosis adjustment) is shown in Fig. 7. Similar as for the difference between Pfander and Leq, the difference is mainly due to diffuseness. While ASEL alone increases with higher diffuseness due to the added energy of reflections, the resulting difference between indoor and outdoor that is visible in Fig. 7 is effectively minimized through kurtosis adjustment, leading to similar $L_\mathrm{H}^\mathrm{LAeq\text{-}K}$ indoor and outdoor. $L_\mathrm{H}^\mathrm{LAeq\text{-}K}$ could be well predicted by

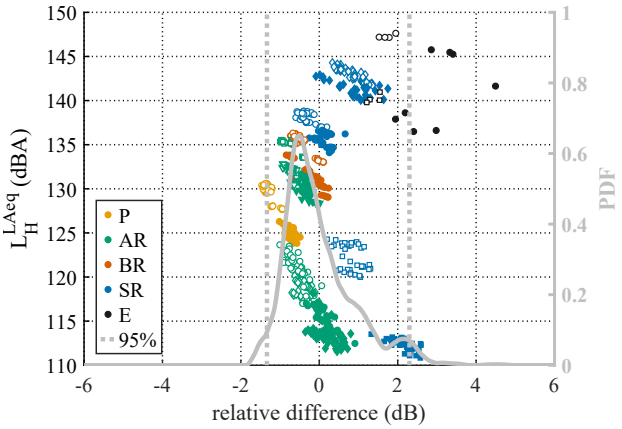


Figure 4. $L_{A,E}$ predicted by L_E ($R^2 = 0.991$).

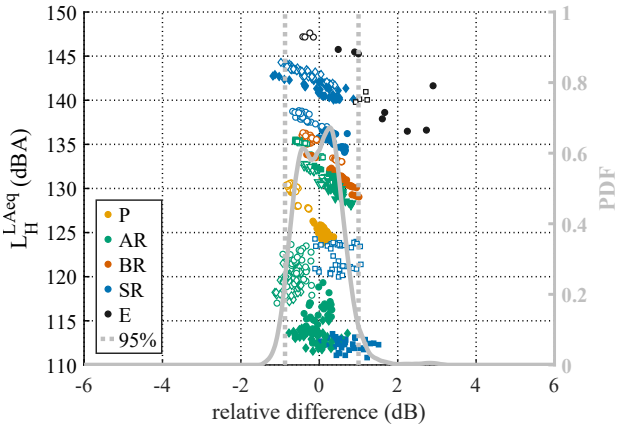


Figure 5. $L_{A,E}$ predicted by L_E and $\hat{L}_p$ (with interaction, $R^2 = 0.997$).

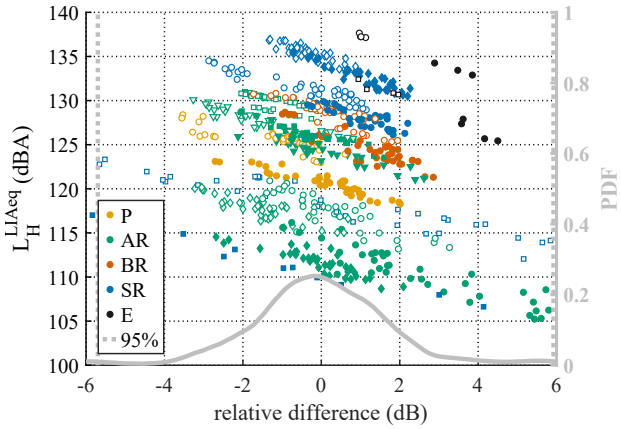


Figure 6. L_H^{LIAeq} predicted by $L_{A,E}$ ($R^2 = 0.897$).

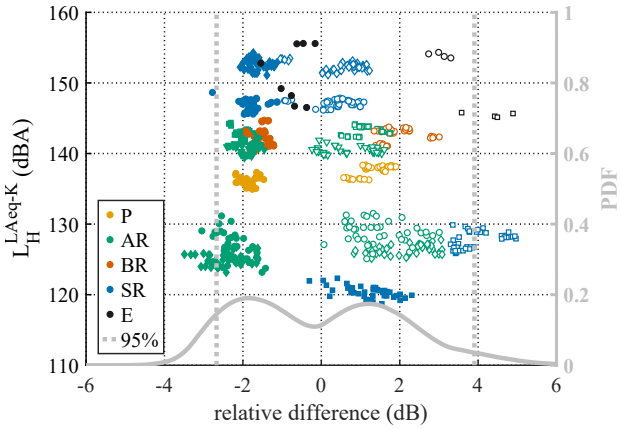


Figure 7. L_H^{LAeq-K} predicted by $L_{A,E}$ ($R^2 = 0.960$).

$\hat{L}_{C,p}$ alone ($R^2 = 0.986$), as shown in Fig. 8, even better by an interaction model of $\hat{L}_{C,p}$ and CSEL ($R^2 = 0.998$) or best (in terms of lowest AIC) by DRR_A, $\hat{L}_{A,p}$ and $L_{A,E}$ ($R^2 = 0.999$, see Fig. 9). The best single predictor for kurtosis alone was DRR_A ($R^2 = 0.822$).

5.5 AHAAH

The best-performing single linear predictor of L_H^{AHA} was the maximum banded ASEL, $L_{A,E}^{max}$ (Fig. 10); however, the AHAAH is too complex for being predicted by such a simple signal model and thus only moderate correlation was achieved ($R^2 = 0.640$), on par with ASEL ($R^2 = 0.624$). The unwarned version of banded ASEL with simplified acoustic reflex was no improvement, as the reflections are anyway underrated due to other mechanisms within the AHAAH. The best-fitting two-way model is therefore a linear combination of $L_{A,E}^{max}$ in conjunction with DRR, as shown in Fig. 11 ($R^2 = 0.904$).

6. CONCLUSIONS AND OUTLOOK

We compared 6 DRC for impulse noise in terms of their respective prediction of auditory hazard. Comparisons were based on a dataset that covers a majority of the impulsive noise exposure of infantry soldiers.

In order to explain the differences between hazard predictions, we tested different kinds of acoustical descriptors based on the unweighted, A-weighted, and C-weighted sound recording. Classical descriptors included action times, SEL, and peak SPL. Statistical descriptors included kurtosis and DRR. Psychoacoustical descriptors included perceptual loudness, sharpness, and roughness. Additional

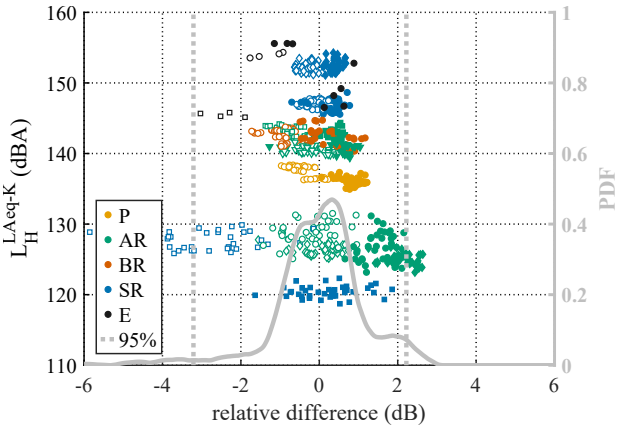


Figure 8. $L_{\mathrm{H}}^{\mathrm{LAeq\text{-}K}}$ predicted by $\hat{L}_{\mathrm{C,p}}$ ($R^2 = 0.986$).

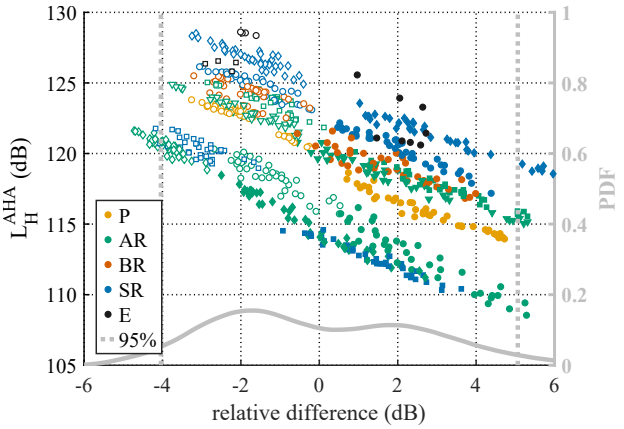


Figure 10. AHAAH ($L_{\mathrm{H}}^{\mathrm{AHA}}$) predicted by $L_{\mathrm{A,E}}^{\mathrm{max}}$ ($R^2 = 0.640$).

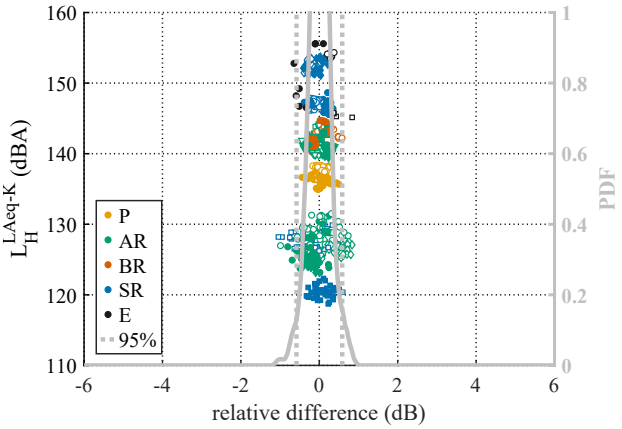


Figure 9. $L_{\mathrm{H}}^{\mathrm{LAeq\text{-}K}}$ predicted by $\mathrm{DRR_A}$, $\hat{L}_{\mathrm{A,p}}$, and $L_{\mathrm{A,E}}$ ($R^2 = 0.999$).

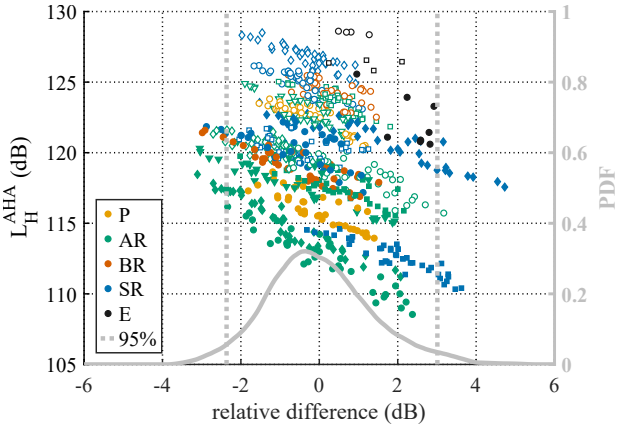


Figure 11. AHAAH ($L_{\mathrm{H}}^{\mathrm{AHA}}$) predicted by $L_{\mathrm{A,E}}^{\mathrm{max}}$ and DRR ($R^2 = 0.904$).

descriptors were derived in order to account for specific characteristics of the AHAAH model. These include a simple filter model of the acoustic reflex as well as a rough approximation of the maximum basilar membrane displacement across fixed positions by taking the maximum exposure across auditory filters.

Most variance between the examined DRC could be explained by linear models of one or multiple descriptors. The difference between Pfander and Leq is mainly due to reflections and thus well expressed by the DRR. The difference between LAeq and Leq, i.e., the effect of A-weighting, could be explained by the interaction between SEL and either peak or SC. LAeq-Kurtosis could be almost perfectly predicted by a combination of C-weighted peak and CSEL. Finally, the auditory hazard predicted by the AHAAH model was best modeled by the maximum of banded ASEL in combination with DRR. The difference between LIAeq and LAeq, i.e., the A-duration, however, could not be sufficiently modeled by any of the tested descriptors. Loudness, sharpness, and roughness did not perform well in predicting the examined DRC. However, this does not exclude a possible correlation with the actual risk of hearing injury, as the examined DRC themselves are insufficiently validated in this concern. We can further conclude that a major aspect of the AHAAH model can be replicated by banded energy. We suppose that similar results could even be obtained from ASEL in $1/3$-octave bands. The simple acoustic reflex model was not useful in this concern, presumably because its effect is concealed by an even stronger effect of diffuseness that is better

covered by the DRR. For specific applications such as mobile noise dosimetry, it might be beneficial to use such an alternative computation that is either more robust or less computationally expensive.

The DRR generally proved to be a good predictor of differences between DRC that emerge from diffuseness. As the Pfander criterion exhibits low robustness against measurement specifications due to dependency on peak and zero crossings [2], it might be tempting to replace its computation by a more robust prediction model using SEL and DRR. However, the DRR was found to be equally sensitive as C-duration and is therefore no useful substitute. Other measures of diffuseness should therefore be evaluated in the future. A major shortcoming of this evaluation is the restriction to impulse noise, although some of the DRC were designed for complex noise that includes continuous sound by vehicles or machinery. As the data included only a subset of soldiers' noise exposure, future studies should also include complex noise and heavier weapons in order to draw more general conclusions.

7. ACKNOWLEDGMENTS

This work was done in collaboration with the TA-38 between MoD-NL and MoD-DE on "Hearing damage risk of shooting noise to personnel & underlying damage risk criteria". The cooperation with TNO, WTD91, and Cervus Consult is acknowledged.

8. REFERENCES

[1] F. van der Eerden, E. van Pruissen, and E. Salomons, "Different exposure prediction methods for a wide range of impulsive noises: do they correlate," in *Forum Acusticum, Turin, IT*, 2023.

[2] M. Weger, "Damage risk criteria for impulse noise: How robust are they against measurement specifications?," in *DAGA*, (Copenhagen, DK), 2025.

[3] C. Hudasch, P. Bechtel, K.-W. Hirsch, C. Kleinhenrich, and T. Langenbucher, "Das Pfander-Kriterium im Vergleich zum Gehörgefährdungsindex des AHAAH-Modells," in *DAGA*, (Hannover, DE), 2020.

[4] S. Dantscher and A. Wolff, "Beurteilung der Gehörgefährdung durch Schießlärm: Pfander- oder LAE-Verfahren?," in *DAGA*, (Rostock, DE), 2019.

[5] W. Qiu, W. J. Murphy, and A. Suter, "Kurtosis: a new tool for noise analysis," *Acoust Today*, vol. 16, no. 4, 2020.

[6] "MIL-STD 1474E: Design criteria standard: Noise limits," 2015.

[7] ISL, DGA, and WTD91, "Vorschriften und Richtlinien zur Registrierung und Auswertung von Waffen- und Detonationsknallen," 1995.

[8] F. Pfander, *Das Schalltrauma*. 1994.

[9] G. Goley, W. J. Song, and J. H. Kim, "Kurtosis corrected sound pressure level as a noise metric for risk assessment of occupational noises," *JASA*, vol. 129, no. 3, 2011.

[10] C. Kleinhenrich, P. Bechtel, C. Hudasch, and T. Langenbucher, "Einfluss des Stapediusreflexes auf den Gehörschadensindex des AHAAH-Modells," in *DAGA*, (Hannover, DE), 2020.

[11] G. F. Greco, R. Merino-Martínez, A. Osses, and S. C. Langer, "SQAT: a MATLAB-based toolbox for quantitative sound quality analysis," in *Inter-Noise*, vol. 268, 2023. https://doi.org/10.5281/zenodo.14641811.

[12] ISO, "Standard no. 532-1: Acoustics - methods for calculating loudness - part 1: Zwicker method," 2017.

[13] DIN, "Standard no. 45692: Measurement technique for the simulation of the auditory sensation of sharpness," 2009.

[14] P. Daniel and R. Weber, "Psychoacoustical roughness: Implementation of an optimized model," *Acta Acustica united with Acustica*, vol. 83, no. 1, 1997.

[15] G. Price and J. Kalb, "The philosophy, theoretical bases, and implementation of the ahaah model for evaluation of hazard from exposure to intense sounds," *ARL-TR-8333*, 2018.

[16] P. D. Fedele, M. S. Binseel, J. T. Kalb, and G. R. Price, "Using the auditory hazard assessment algorithm for humans (AHAAH) with hearing protection software, release MIL-STD-1474E," *ARL-TR-6748*, 2013.

[17] V. Hohmann, "Frequency analysis and synthesis using a gammatone filterbank," *Acta Acustica united with Acustica*, vol. 88, 2002. https://github.com/LeoVarnet/Hohmann_Gammatone.

[18] M. Weger, T. Hermann, and R. Höldrich, "Real-time auditory contrast enhancement," in *ICAD*, 2019.

DOI:

Main theme: A13 Physiological Acoustics and Audiology

Session A13.05 Asymmetric hearing loss - clinical solutions and functionality

Chair(s): B. Williges, S. Zirn

DOI: 10.61782/fa.2025.0820

FORUM ACUSTICUM EURONOISE 2025

SPEECH INTELLIGIBILITY IN NOISE OF SINGLE-SIDED DEAF COCHLEAR IMPLANT USERS FOR NEAR AND DISTANT TALKERS

Thomas Wesarg[1*]
[1] Department of Otorhinolaryngology, Medical Center – University of Freiburg, Germany

ABSTRACT

People with single-sided deafness (SSD) encounter hearing problems particularly related to speech perception in noise. Among the different treatment options, only the cochlear implant (CI) allows for a (re)habilitation of binaural hearing. Various studies with SSD CI users have shown binaural benefits of CI in speech intelligibility in noise (SIN) for near target talkers including the summation effect, and benefits of the application of remote microphone technology in SIN for distant talkers both on group level.
The aim of this paper is to evaluate the relations between the speech intelligibility in quiet (SIQ) with the CI only and the benefit of a CI in SIN for near talkers on the one hand, and the benefit of remote microphone technology in SIN for distant talkers on the other hand, in adult SSD CI users. The analysis revealed that the SIQ with the CI only was positively correlated with the benefit of remote microphone technology in SIN for distant talkers, while it was not correlated with the benefit of a CI in SIN for near talkers.

Keywords: *cochlear implant, remote microphone, speech intelligibility, summation effect*

1. INTRODUCTION

People with single-sided deafness (SSD) have difficulty understanding speech in challenging listening situations, particularly in noisy environments [1,2]. According to [3], SSD is defined as having a four-frequency (0.5, 1.0, 2.0, and 4.0 kHz) pure-tone threshold average (4PTA) of at least 70 dB HL, i.e. a severe to profound hearing loss in the poorer ear, a 4PTA of at most 30 dB HL, i.e. normal or nearly-normal hearing (NH) in the better ear, and an interaural threshold gap of at least 40 dB HL. Treatment options for SSD include conventional contralateral routing of signal hearing aid, bone conduction device, and cochlear implant (CI). However, (re)habilitation of hearing in the poorer ear and restoration of binaural hearing can only be achieved with a CI.
Several studies have shown CI treatment of people with SSD to enable significant improvements of speech intelligibility in noise (SIN) when binaurally listening with the NH ear and the CI compared to monaural listening with the NH ear only. These studies investigated SIN for near target talkers, i.e. talker-to-listener distances of at most 1.5 meters, and revealed various binaural effects with CI, particularly head shadow and summation [4-7]. For bilateral CI users, the summation effect, which is assessed for frontal presentation of target speech in quiet or collocated noise, has been shown to relate negatively to the interaural asymmetry in SIN, i.e. the difference in monaural SIN between the better and poorer CI [8,9]. In SSD CI users, the summation effect may also be negatively related to the interaural asymmetry in monaural speech intelligibility (SI), i.e. the difference in SI between the NH ear and the CI, and positively related to the SI with the CI only. The first aim of this paper is to evaluate the relation between the binaural summation effect for speech in noise and the monaural speech performance in quiet with the CI in SSD CI users.
SI for distant talkers in multi-source noise environments with medium and higher noise levels such as frontal teaching in a noisy classroom is poor in unilateral, bimodal and bilateral CI users, and is significantly improved by the application of remote microphones (RMs) [10,11]. RMs pick-up the target speech with a high signal to noise ratio (SNR) and transmit it wirelessly to a receiver connected to or built in a hearing device, e.g. CI sound processor or hearing aid (HA). RMs have also been shown to improve

[*] ***Corresponding author***: thomas.wesarg@uniklinik-freiburg.de.
Copyright: *©2025 Thomas Wesarg. This is an open-access article distributed under the terms of the Creative Commons Attribution 3.0 Unported License, which permits unrestricted use, distribution, and reproduction in any medium, provided the original author and source are credited.*

SIN for distant talkers in multi-source classroom noise in SSD CI users, when used with the CI, NH ear or bilaterally [12]. In SSD CI users, the benefit of RMs, when used with the CI, in SIN may be positively related to the SIQ or SIN with the CI only, respectively. The second aim of this paper is to investigate this relation with regard to the monaural speech performance in quiet with the CI.

2. BENEFIT OF A COCHLEAR IMPLANT

2.1 Methods

To assess the relation between the summation effect with a CI for speech in noise and the monaural speech performance in quiet with the CI, the SIN data of the twelve adult subjects with SSD who participated in a prospective hearing device comparison study at our department and received a cochlear implant during this study [7] were analyzed. In this study, the summation effect was calculated as the difference in speech reception threshold (SRT) between listening in unaided condition preoperatively and binaural listening with the NH ear and CI at six months post activation, and this summation effect is referred to in the present paper. The SRTs were measured for presentation of sentences of the Oldenburg sentence test (OLSA, German matrix test) in collocated speech-shaped noise at 65 dB SPL from a frontal speaker one meter apart from the participants. The Freiburg monosyllabic word recognition score (WRS) in quiet obtained with the CI only at six months post activation within clinical routine was used to describe the monaural SIQ with the CI. To analyze the relation between the summation effect and the monaural SIQ with the CI, the Spearman's rank correlation coefficient is calculated.

2.2 Results

The twelve SSD CI participants showed median SRTs in speech-shaped noise of -4.7 dB SNR (-6.2 dB SNR – 3.1 dB SNR) preoperatively unaided and -5.8 dB SNR (-8.2 dB SNR – -4.7 dB SNR) binaural at six months post activation resulting in a significant median summation effect of 1.4 dB (0.2 dB – 2.8 dB; p = 0.013) [7]. At six months with CI, their median monaural WRSs were 100% (90% – 100%) with the NH ear and 25% (0% – 40%) with the CI resulting in a median interaural difference in monaural WRS of 72.5% (60% – 90%). Figure 1 presents a scatterplot of the individual summation effects versus the individual monaural WRSs with the CI. Between these measures, there was no significant correlation (p = 0.615).

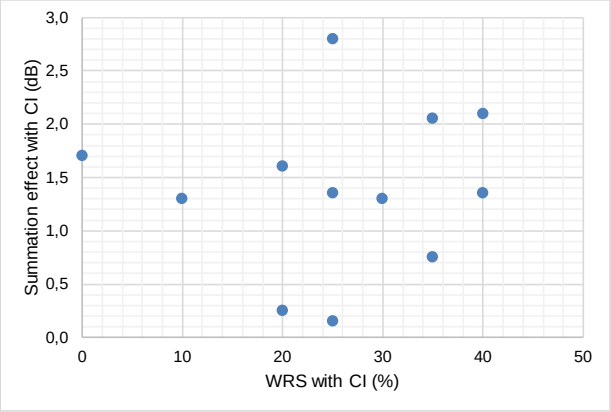


Figure 1. Scatterplot of summation effect versus monaural word recognition score (WRS) with CI.

2.3 Discussion

Contrary to our expectation, there was no significant correlation between the binaural summation effect with the CI for speech in noise and the monaural SIQ with the CI in the twelve SSD CI participants. The missing correlation might be due to the application of a speech in quiet instead of a speech in noise measure to assess the monaural speech performance with the CI, and/or the small sample size and thus low statistical analysis power. Therefore, future studies should include more SSD CI users and use speech in noise measures for both the summation effect and the monaural speech performance to investigate the relation between these measures.

3. BENEFIT OF A REMOTE MICROPHONE

3.1 Methods

The relation between the benefit of a RM in speech performance in noise and speech performance in quiet with the CI is assessed using the SIQ and SIN data of the eleven adult SSD CI users who participated in a prospective remote microphone technology study at our department [12]. In this study, the participants had a CI experience of ten to 122 months at the time of testing. For monaural listening with the NH ear as well as binaural listening with the NH ear and the CI (condition NH+CI), and, amongst other RM conditions, for binaural listening with the NH ear and the CI with a RM (transmitter Roger Pen, receiver Roger X; Phonak AG, Stäfa, Switzerland) connected with the CI (NH+CI/RM), the speech recognition score (SRS) for presentation of OLSA sentences from a loudspeaker 5.5 meters in front of the participants in a multi-source

classroom noise established by Schafer and Thibodeau [13] was measured. At the position of the participants, the speech level was 60.3 dB(A) and the noise level was 65 dB(A) yielding an SNR of -4.7 dB.
For each participant, the benefit of the RM used with the CI, is calculated as the difference in speech recognition score (SRS) between the NH+CI/RM and NH+CI listening conditions. The present paper refers to this RM benefit and to the Freiburg monosyllabic WRS with the CI only obtained at the time of testing in this study, and the Spearman's rank correlation coefficient is calculated to analyze the relation between these measures.

3.2 Results

In multi-source classroom noise, the eleven SSD CI participants yielded median SRSs of 16.0% (0.7% – 39.3%) with the NH ear, 18.0% (4.0% – 36.7%) in the NH+CI condition, and 87.3% (27.3% – 95.3%) in the NH+CI/RM condition. Compared to binaural listening with the NH ear and CI, binaural listening and using a RM with the CI enabled a significant median improvement in SRS, i.e. a significant median benefit of the RM of 57.3% (16.0% – 91.3%). At the time of testing, the participants' median monaural WRS with the CI was 55% (50% – 95%). A scatterplot of the individual benefits of the RM used with the CI versus the individual monaural WRSs with the CI is illustrated in Figure 2. The rank correlation analysis revealed a significant positive correlation between these measures (*rho* = 0.5456, *p* = 0.082).

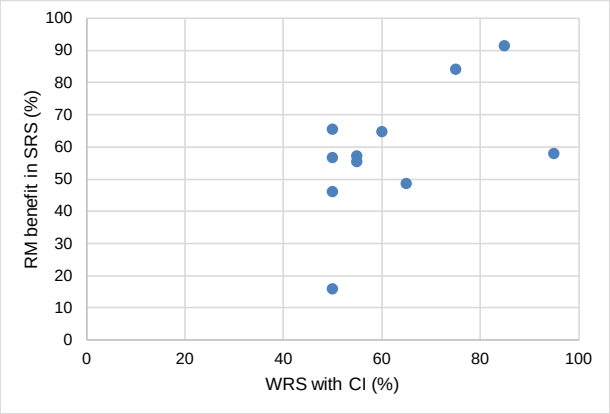


Figure 2. Scatterplot of benefit of a remote microphone (RM) used with CI in speech recognition score (SRS) versus monaural word recognition score (WRS) with CI.

3.3 Discussion

According to our expectation, there was a significant positive correlation between the benefit of the remote microphone (transmitter Roger Pen, receiver Roger X) used with the CI in SIN for a frontal talker in a multi-source noise classroom environment and the SIQ with the CI only in the eleven SSD CI participants. This result suggests that SSD CI users showing a good monaural SIQ with the CI should use RMs with the receiver attached to their CI, while SSD CI users with poor SIQ with the CI only should use RMs with the receiver Roger Focus attached to their NH ear, to obtain a considerable improvement in speech performance for distant talkers in multisource-noise environments. The benefit of the RM in SIN assessed in the eleven SSD CI users in the remote microphone technology study [12] is due to the improvement of the SNR of the target speech at the listener's position, which is based on both overcoming the spatial decay of target speech-level over the distance between the talker and the listener and the application of an adaptive beamformer in the RM transmitter. However, the contributions of both effects were not investigated separately in this study, and thus cannot be disentangled.

4. REFERENCES

[1] T. G. Giolas, D. J. Wark: "Communication problems associated with unilateral hearing loss", *Journal of Speech and Hearing Disorders*, 32(4), pp. 336-343, 1967.

[2] O. B. Wie, A. H. Pripp, O. Tvete: "Unilateral deafness in adults: effects on communication and social interaction", *Annals of Otology, Rhinology and Laryngology*, 119(11), pp. 772-781, 2010.

[3] P. Van de Heyning, D. Távora-Vieira, G. Mertens, V. Van Rompaey, G. P. Rajan, J. Müller, et al.: "Towards a Unified Testing Framework for Single-Sided Deafness Studies: A Consensus Paper", *Audiology and Neurotology*, 21(6), pp. 391-398, 2016.

[4] S. Arndt, R. Laszig, A. Aschendorff, F. Hassepass, R. Beck, T. Wesarg: "Cochlear implant treatment of patients with single-sided deafness or asymmetric hearing loss", *HNO*, 65(Suppl 2), pp. 98-108, 2017.

[5] G. Mertens, M. De Bodt, P. Van de Heyning: "Evaluation of long-term cochlear implant use in subjects with acquired unilateral profound hearing

loss: focus on binaural auditory outcomes", *Ear and Hearing*, 38(1), pp. 117-125, 2017.

[6] J. P. M. Peters, J. A. A. van Heteren, A. W. Wendrich, G. A. van Zanten, W. Grolman, R. J. Stokroos, et al.: "Short-term outcomes of cochlear implantation for single-sided deafness compared to bone conduction devices and contralateral routing of sound hearing aids-Results of a Randomised controlled trial (CINGLE-trial)", *PLoS One*, 16(10), e0257447, 2021.

[7] T. Wesarg, I. Kuntz, L. Jung, K. Wiebe, R. Schatzer, S. Brill, et al.: "Masked Speech Perception with Bone Conduction Device, Contralateral Routing of Signals Hearing Aid, and Cochlear Implant Use in Adults with Single-Sided Deafness: A Prospective Hearing Device Comparison using a Unified Testing Framework", *Audiology and Neurotology*, 29(4), pp. 271-289, 2024.

[8] R. Litovsky, A. Parkinson, J. Arcaroli, C. Sammeth: "Simultaneous bilateral cochlear implantation in adults: a multicenter clinical study", *Ear and Hearing*, 27(6), pp. 714-731, 2006.

[9] Y. S. Yoon, Y. Li, H. Y. Kang, Q. J. Fu: "The relationship between binaural benefit and difference in unilateral speech recognition performance for bilateral cochlear implant users", *International Journal of Audiology*, 50(8), pp. 554-565, 2011.

[10] J. Wolfe, E. Schafer, A. Parkinson, A. John, M. Hudson, J. Wheeler, et al.: "Effects of input processing and type of personal frequency modulation system on speech-recognition performance of adults with cochlear implants", *Journal of the American Academy of Audiol*ogy, 26(6), pp. 532-539, 2015.

[11] G. De Ceulaer, D. Pascoal, F. Vanpoucke, P. J. Govaerts: "The use of cochlear's SCAN and wireless microphones to improve speech understanding in noise with the Nucleus6® CP900 processor", *International Journal of Audiology*, 56(11), pp.837-843, 2017.

[12] T. Wesarg, Y. Stelzig, D. Hilgert-Becker, B. Kathage, K. Wiebe, A. Aschendorff, et al.: "Application of Digital Remote Wireless Microphone Technology in Single-Sided Deaf Cochlear Implant Recipients", *Journal of the American Academy of Audiology*, 31(4), pp. 246-256, 2020.

[13] E. C. Schafer, L. M. Thibodeau: "Speech recognition in noise in children with cochlear implants while listening in bilateral, bimodal, and FM system arrangements", *American Journal of Audiology*, 15(02), pp. 114-126, 2006.

DOI: 10.61782/fa.2025.0323

FORUM ACUSTICUM EURONOISE 2025

EFFECT OF REDUCING THE STATIC INTERAURAL TIME DIFFERENCE IN BIMODAL LISTENERS

Zirn, S.[1], Roth, S. [1,2], Mueller, F.-U. [1,2], Hemmert, W.[2], Angermeier, J. [1,3]
[1]University of Applied Sciences Offenburg, Peter Osypka Institute of Medical Engineering, Offenburg, Germany
[2] Technical University of Munich, Munich, Germany
[3]Osypka AG, Rheinfelden, Germany

ABSTRACT

Previous work has shown that the ability to localize sound signals in the horizontal plane can be improved in listeners provided with a cochlear implant (CI) in one ear and a hearing aid (HA) in the contralateral ear (bimodal listeners) when the static interaural time delay between the modalities is technically reduced. The timing mismatch is caused by differences in the processing latencies of CI and HA and by different stimulation sites (CI: auditory nerve; HA: external auditory canal). In 2020 the CI manufacturer MED-EL has made the technical reduction of the timing mismatch available by a programmable across-frequency CI stimulation delay.
To reduce the timing mismatch even further, we now use frequency-dependent delays to minimize the timing mismatch in every frequency band. Results show that the rms and the signed bias of sound localization can be further reduced in most bimodal study participants when using frequency-specific delays compared to an across-frequency delay. However, it is methodically complex to determine appropriate delays for different frequency bands. It is therefore questionable whether frequency-specific delays are useful in clinical practice.

Keywords: *bimodal hearing, sound localization, timing*

1. INTRODUCTION

Bimodal hearing refers to the use of two different types of hearing devices in opposite ears: a cochlear implant in one ear and a hearing aid in the other. This approach leverages the distinct advantages of each device to enhance overall auditory perception, particularly for individuals with asymmetric hearing loss or those who receive limited benefit from hearing aids alone.

A cochlear implant bypasses damaged parts of the inner ear by directly stimulating the auditory nerve with electrical signals, providing access to sound for individuals with severe to profound sensorineural hearing loss [7]. On the other hand, a hearing aid amplifies sound acoustically and is suited for individuals who have some residual hearing capability [3]. When used together in a bimodal configuration, these devices can complement each other, with the cochlear implant providing clear access to speech and the hearing aid enriching sound quality and providing additional auditory cues, such as pitch and timbre, that enhance music perception and spatial awareness [4].

Research and clinical experience show that bimodal hearing can significantly improve speech understanding in noise, localization of sound, and overall quality of life for individuals with hearing loss. This synergistic effect capitalizes on the brain's ability to integrate complex signals from both devices, fostering a more natural and comprehensive listening experience [5, 6]. Despite the synergistic effect and its potential benefits, sound localization is usually significantly worse in bimodal listeners compared to bilateral HA users or even bilateral CI

*Corresponding author: stefan.zirn@hs-offenburg.de.
Copyright: ©2025 Zirn et al. This is an open-access article distributed under the terms of the Creative Commons Attribution 3.0 Unported License, which permits unrestricted use, distribution, and reproduction in any medium, provided the original author and source are credited.

users [8]. One reason for this are interaural mismatches in bimodal stimulation.

2. INTERAURAL MISMATCHES IN BIMODAL HEARING

Bimodal hearing presents unique challenges, primarily due to potential interaural mismatches in loudness, frequency, and timing. These mismatches can affect the integration of auditory information and the overall hearing experience.

Loudness Mismatches: Loudness perception can differ significantly between the electrically-stimulated ear with a cochlear implant and the acoustically-amplified ear with a hearing aid. The dynamic range of a cochlear implant is typically smaller than that of normal acoustic hearing, requiring careful adjustment to match loudness levels across ears [3]. This discrepancy can lead to difficulty in balancing sound perception, affecting binaural cues necessary for localization and speech understanding in noise [7].

Frequency Mismatches: Frequency mismatches occur because cochlear implants often provide less precise frequency resolution compared to acoustic hearing aids. Cochlear implants convey sound via a limited number of electrodes, each stimulating a broad frequency band, which might not align perfectly with the natural cochlear tonotopy that hearing aids aim to preserve [4]. This can impact the quality of sound perception, especially for complex sounds like music, which rely heavily on fine frequency discrimination [6].

Timing Mismatches: Temporal processing differences between the ears can also pose challenges. Cochlear implants process sound with manufacturer dependent delays due to differences in signal processing and stimulate the auditory nerve directly. However, acoustic hearing aids process sounds in front of the ear and input the amplified sound into the outer ear canal. From there on the natural middle and cochlear delays apply [2]. The resulting timing differences can impair sound localization [1].

Addressing these interaural mismatches involves personalized device programming and fitting strategies to better align the loudness [10], frequency [9], and timing [1] cues offered by each device, thereby enhancing the benefits of bimodal hearing.

3. METHODS

Bimodal hearing test subjects were seated in an audiometric booth equipped with a sound localization setup designed to assess auditory spatial awareness, 11 loudspeakers were positioned in a horizontal arc at ear level in front of the subject, each spaced 15° apart, covering a total span from -75° to +75° relative to the forward-facing position. A central loudspeaker is positioned at 0°, with others extending symmetrically in both directions. Correspondingly, an LED array with 180 LEDs mirrored this setup, each LED representing a loudspeaker position for response indication. The test began with the subject seated, facing the 0° speaker. During the test, pulsed noise with level an spectral roving was randomly played from the loudspeakers. Subjects then indicated perceived sound locations by activating the corresponding LED. These responses are recorded for analysis.
Before the test started loudness between ears/devices was balanced. Subjects were then tested in three different conditions in a randomized order. Condition 1: No compensation of timing nor frequency mismatch. Condition 2: Compensation of timing mismatch by an across-frequency delay applied to CI stimulation. Condition 3: Compensation of the interaural timing mismatch together with the frequency mismatch. In this condition frequency-specific delays were applied to CI stimulation.

4. RESULTS

Figure 1 illustrates the rms error of sound localization of 8 bimodal hearing test subjects.

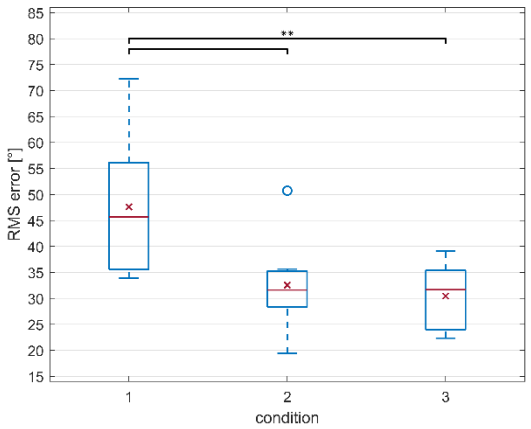


Figure 1. RMS error of sound localization of 8 bimodal listeners in three different listening conditions. Condition 1: Without compensation; condition 2: with timing

compensation; condition 3: with timing & frequency compensation.

Activating the across-frequency delay had no significant effect on the rms error (difference between condition 1 and 2). But we think that including more test subjects will lead to a significant reduction comparable to the results in [1]. Frequency-specific delays (condition 3) further reduced the rms error in some subjects, but in others there was no difference, resulting in a non-significant difference between condition 2 and 3.

5. CONCLUSION

This paper presents results of an ongoing study aiming at reducing the interaural stimulation mismatches in bimodal listening. Results show that the rms of sound localization can be further reduced in some bimodal study participants when using frequency-specific delays compared to an across-frequency delay. However, only a slight further improvement has been achieved in the 8 test subjects tested so far. The approach for combined time and frequency adjustment is methodologically complex, especially the determination of suitable delays for different CI frequency bands. Up to this point, it is questionable whether frequency-specific delays are useful in clinical practice.

6. ACKNOWLEDGMENTS

We thank the test subjects who participated in our study. We would also like to thank MED-EL for their continued support of our research.

7. REFERENCES

[1] Angermeier, J., Hemmert, W. and Zirn, S. (2023). Clinical Feasibility and Familiarization Effects of Device Delay Mismatch Compensation in Bimodal CI/HA Users. Trends in Hearing, 27, https://doi.org/10.1177/23312165231171987

[2] Zirn, S. et al. (2015). Interaural stimulation timing in single sided deaf cochlear implant users. Hearing Research, 328, pp. 148–156. https://doi.org/10.1016/j.heares.2015.08.010

[3] Ching, T. Y., Dillon, H., & Byrne, D. (2004). Speech recognition of hearing-impaired listeners: Predictions from audibility and the limited role of high-frequency amplification. *Journal of the Acoustical Society of America, 116*(1), 467–477.

[4] Dorman, M. F., & Gifford, R. H. (2010). Combining acoustic and electric hearing. *Laryngoscope, 120*(S4), S1-S4.

[5] Litovsky, R. Y., Parkinson, A., Arcaroli, J., & Sammeth, C. (2006). Simultaneous bilateral cochlear implantation in adults: A multicenter clinical study. *Ear and Hearing, 27*(6), 714-731.

[6] Mok, M., Grayden, D., Dowell, R., & Lawrence, D. (2007). Speech perception for adults who use hearing aids in conjunction with cochlear implants in opposite ears. *Journal of Speech, Language, and Hearing Research, 50*(1), 298-309.

[7] Zeng, F. G., Rebscher, S., Harrison, W., Sun, X., & Feng, H. (2008). Cochlear implants: System design, integration, and evaluation. *IEEE Reviews in Biomedical Engineering, 1*, 115-142.

[8] Dorman, M. F., Loiselle, L. H., Cook, S. J., Yost, W. A., & Gifford, R. H. (2016). Sound source localization by normal-hearing listeners, hearing-impaired listeners and cochlear implant listeners. *Audiology and Neurotology, 21*(3), 127-131.

[9] Kurz, A., Herrmann, D., Hagen, R., & Rak, K. (2023). Using anatomy-based fitting to reduce frequency-to-place mismatch in experienced bilateral cochlear implant users: a promising concept. *Journal of Personalized Medicine, 13*(7), 1109.

[10] Veugen, L. C., Chalupper, J., Snik, A. F., van Opstal, A. J., & Mens, L. H. (2016). Frequency-dependent loudness balancing in bimodal cochlear implant users. *Acta oto-laryngologica, 136*(8), 775-781.

DOI: 10.61782/fa.2025.0007

FORUM ACUSTICUM EURONOISE 2025

A COMPARATIVE STUDY OF FOUR DIRECTIONAL MICROPHONES AND DIRECTIVITY STEERING FOR BIMODAL COCHLEAR IMPLANT USERS

H. Christiaan Stronks[1,2*] **Nienke C. Langerak**[1] **Annemarie J. Schrijver**[1]
Raphael Koning[3] **Jeroen J. Briaire**[1] **Johan H. M. Frijns**[1,2,4]
[1] Otorhinolaryngology and HNS, Leiden University Medical Center, Leiden, the Netherlands
[2] Leiden Institute for Brain and Cognition, Leiden, the Netherlands
[3] Advanced Bionics, Hanover, Germany
[4] Department of Bioelectronics, Delft University of Technology, Delft, the Netherlands

ABSTRACT

Background: Cochlear implant users (CI) experience degraded speech intelligibility (SI) in noise. A contralateral hearing aid (HA) benefits listening in noise, and directional microphones and directivity steering can further enhance SI.
Objectives: Four directional microphones were evaluated for bimodal listeners, including a monaural and binaural broadband front-facing beamformer (BF_M and BF_B) and a novel monaural and binaural narrowband side-beamformer (BF_{MS}, BF_{BS}). Broadband directivity steering (DS) was also evaluated.
Methods: BF_M, BF_B, and DS were tested in diffuse noise with speech administered frontally or to the HA side (S_0N_{dif} and $S_{HA}N_{dif}$). BF_{MS} and BF_{BS} were tested with speech presented on the CI side and noise on the HA side or *vice versa* ($S_{CI}N_{HA}$, $S_{HA}N_{CI}$). SI was assessed by determining speech reception thresholds (SRTs).
Results: In the S_0N_{dif} condition, BF_B significantly improved SI by 2.9 dB SNR and BF_M by 1.3 dB SNR, but not significantly. In the $S_{HA}N_{dif}$ condition, BF_M and BF_B did not benefit SI, but DS improved SI by 3.6 dB. BF_{BS} significantly improved SI by 1.1 dB SNR, but BF_{MS} was ineffective.
Conclusion: Binaural beamformers outperform their monaural counterparts. The novel BF_{BS} is a promising technique for bimodal listeners.

Keywords: *sensorineural hearing loss; cochlear implants; hearing aids; speech in noise; asymmetric hearing loss*

1. INTRODUCTION

Unilaterally implanted cochlear implant (CI) users with contralateral residual hearing may benefit from wearing a hearing aid (HA) in the non-implanted ear, called bimodal hearing. Residual hearing in the other ear offers advantages over electrical hearing alone, including better speech understanding in quiet and noise [1-3]. The bimodal system from Advanced Bionics (Naída Link™) was developed specifically for this population. It features various speech enhancement strategies, including two noise-reduction algorithms based on monaural and binaural directional microphones called 'beamformers' (BF_M and BF_B, respectively). Beamformers are spatial filters that pass on sound from certain angles (usually from the front) while attenuating noise at angles outside of the beam. BF_M (UltraZoom™) is an adaptive beamformer that operates independently on both the CI and the HA and steers its null to the point of the lowest SNR. By contrast, BF_B (StereoZoom™) is a fixed beamformer that combines the input from the CI and HA through wireless voice streaming technology to focus the beam further [4, 5]. Polar patterns for both beamformers are compared to the omnidirectional microphone setting

[*] ***Corresponding author***: h.c.stronks@lumc.nl
Copyright: *©2025 First author et al. This is an open-access article distributed under the terms of the Creative Commons Attribution 3.0 Unported License, which permits unrestricted use, distribution, and reproduction in any medium, provided the original author and source are credited.*

in Fig. 1. It is also possible to route the signal from the HA to the CI and *vice versa*, referred to as directivity steering (DS, or ZoomControl™). This technique is akin to contralateral routing of signals (CROS), overcoming the head shadow effect by rerouting acoustic input from the HA to the typically better-hearing CI ear [5].

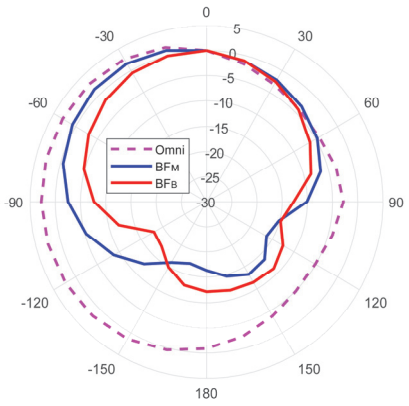


Figure 1. Polar patterns of the front-facing monaural (BF_M) and binaural beamformer (BF_B) and the default omnidirectional microphone setting (Omni) evaluated in experiment 1. The speech processor was mounted on the left ear of a KEMAR manikin. Reference: 0°.

Besides these clinically established broadband applications, a novel side-beamforming approach has been proposed based on artificially increasing interaural level differences (ILDs) at low frequencies [6]. This approach is especially relevant for bimodal listeners where residual acoustic hearing is typically confined to the lower frequencies [7]. ILDs are usually restricted to high frequencies, where the acoustic shadow imposed by the head decreases the sound level of a signal in the contralateral ear [8]. By introducing a narrow-band, side-facing beamformer active only at low frequencies, ILDs can be artificially increased without affecting the physiological ILDs at high frequencies. This technique is especially efficient when speech is present on one ear (e.g., the HA side) and noise on the other (CI side). The introduction of a side-facing beamformer on both ears in this scenario will thus increase the signal-to-noise ratio (SNR) on the HA side, where the speech is presented at the expense of the CI ear, where noise is presented. When the attention is focused on the better side (HA in this example), speech intelligibility (SI) will be enhanced. The advantage of this approach over the classical wide-band CROS or DS application is that it will benefit speech intelligibility in noise, regardless of whether the speaker is present on the CI or the HA side. Benefits can also be expected when speech comes from the front and noise from the sides [6]. As such, these side-beamformers are more versatile and may require less user intervention or rely less on automatic scene analysis than CROS or DS applications. Here, we evaluated two side-facing beamformers. One operated monaurally, i.e., on both ears individually (BF_{MS}), whereas the other operated binaurally (BF_{BS}) by combining the signals from both ears by subtracting the contralateral signal from the ipsilateral side to increase the artificial, low-frequency ILDs further. Polar patterns are shown in Fig. 2.

We performed two experiments. In the first, we evaluated the clinically established broadband, front-facing beamformers (BF_M and BF_B) and DS. In the second, we assessed the effectiveness of the two experimental narrow-band, side-facing beamformers. BF_M, BF_B, and DS were tested in a diffuse field of stationary noise with speech administered frontally (BF_M and BF_B) or to the HA side (DS, BF_M, BF_B). BF_{MS} and BF_{BS} were tested in a less challenging noise setup for a proof-of-principle approach, with speech and noise presented from a single loudspeaker on either side of the head.

2. METHODS

2.1 Participants

Experiment 1 evaluated the broadband beamformers (BF_M, BF_B) and DS in a population of 12 participants unilaterally implanted with an Advanced Bionics HiRes 90K™ device (9 biological females) with a mean age of 64 years (range: 50 – 85). Inclusion criteria were 1) pure-tone audiometric thresholds of at least 80 dB at 125, 250, and 500 Hz in the non-implanted ear; 2) a CI-aided CVC phoneme score in quiet of at least 80%, which are above-average listeners; 3) at least 6 months experience with their CI; 4) age ≥18 years. In experiment 2, the narrowband beamformers (BF_{MS} and BF_{BS}) were evaluated in 18 participants with the same inclusion criteria. However, this population included only people who used a contralateral HA in daily life, whereas the first population also included three participants who were not active HA users and were fitted with an HA for

the study. Pure-tone audiograms of the two populations are shown in Fig. 3. Written informed consent was obtained from each subject. This study was approved by the Institutional Review Board of the Leiden University Medical Center and adhered to the Declaration of Helsinki (Carlson et al., 2004).

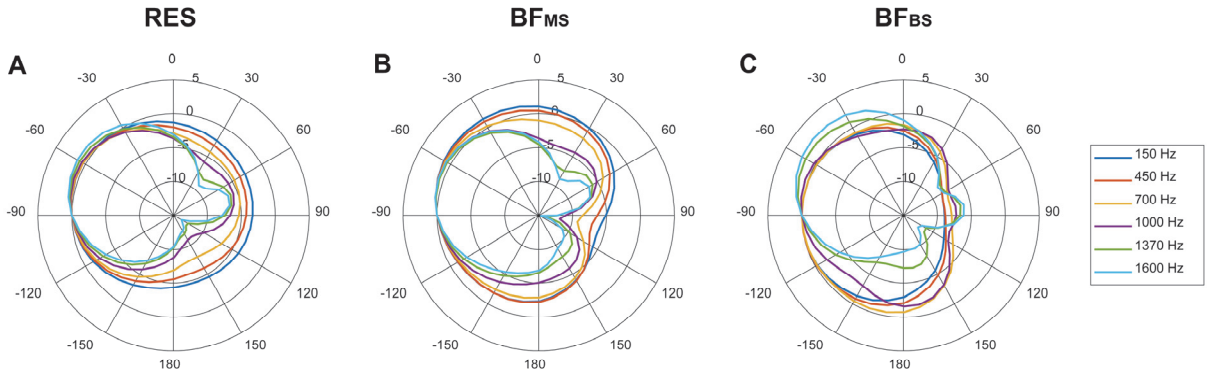


Figure 2. Polar patterns of the microphone settings evaluated in experiment 2. (A) Default microphone setting (Real Ear Sound™, RES). (B) Monaural side-facing beamformer (BF_{BM}). (C) Binaural side-facing beamformer (BF_{BS}). The speech processor was mounted on KEMAR's left ear. Reference: -90º.

2.2 CI and HA fitting

The participants in experiment 1 to evaluate BF_M, BF_B, and DS were fitted with a Q90 CI speech processor (Advanced Bionics LLC, Valencia, CA, USA) and contralaterally with a Naída S IX UP (n = 7) or Naída Link UP (n = 5) HA using PhonakTarget™ fitting software (version 3.3, Phonak, Sonova Holding AG Stäfa, Switzerland). Amplification was based on the clinical audiogram. The voice streaming technology and bimodal fitting rule are designed for the Naída Link and were fitted on the Naída S using customized fitting software (BEPSnet version 3.0.5017.18916, Advanced Bionics). The participants in experiment 1 were subsequently sent home for at least four weeks to accommodate the new fitting.

The participants in experiment 2 to evaluate BF_{MS} and BF_{BS} were fitted with a Harmony™ CI speech processor (Advanced Bionics) and an Audéo M90-312 HA (Phonak) contralaterally using PhonakTarget (version 6.2.5). HA fitting was based on an *in situ* audiogram (Phonak AudiogramDirect™). The experimental BF_{MS} and BF_{BS} algorithms could not yet be implemented on the latest generation of Advanced Bionics CI processors (Q90) available at the time of the study, and front-end processing was performed on an Audéo M90-312 HA that communicated with the Harmony CI speech processor. The pulse-width modulated HA output was converted into an analog signal suitable as auxiliary input for the Harmony CI processor using an audio transformer (Neutrik NTE1, Schaan, Liechtenstein) and a spindle potentiometer (Vishay, Malvern, PA, USA). Calibration was performed with white noise in an ACAM™ audiometry box (Acousticon Inc., Raleigh, NC, USA) using BEPSnet (version 1.14, Advanced Bionics). The HA was worn behind the ear, and the Harmony processor was clipped to the participant's clothing. A custom-made Bluetooth smartphone application (Advanced Bionics) was used to switch between microphone settings.

CI speech processors were fitted with the participant's clinical threshold and maximal comfortable stimulus levels, and HAs were fitted with the Naída bimodal fitting formula [9]. Switching off all noise-reduction algorithms other than those under investigation reduced front-end processing strategies on both devices to a minimum. The adaptive gain control remained operational.

2.3 Speech intelligibility testing in noise

Speech testing was performed in a sound-treated audiology booth. Experiment 1 was used to evaluate BF_M, BF_B, and DS by determining speech reception thresholds (SRTs) using the Leuven intelligibility sentence test (LIST) [10].

Speech was presented in a diffuse field of long-term speech-shaped (LTSS) noise using eight loudspeakers (Control 1, JBL Corp., Los Angeles, CA) as described previously [11].

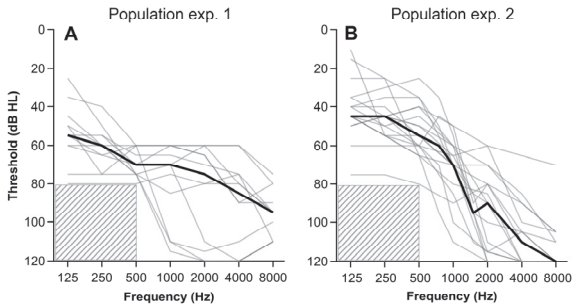


Figure 3. Pure-tone audiograms of the hearing aid ear. (A) Experiment (exp.) 1 evaluated the front-facing broadband beamformers (n = 12). Exp. 2 evaluated the side-facing narrowband beamformers (n = 18). Box: Exclusion criterion (>80 dB HL hearing loss at 125, 250, or 500 Hz). Thick black line: median.

Speech was administered through a MSP5A loudspeaker (Yamaha Corp., Japan) placed ~1 m from the listener at ear level calibrated at 65 dB SPL (Rion NA-28, Rion Co. Ltd., Tokyo, Japan). Speech was administered in front of the listener (S_0N_{dif}) or to the HA side ($S_{HA}N_{dif}$). To determine the SRT, noise levels were adaptively varied according to the LIST protocol [10]. Each listening condition was tested once. Microphone setting and speech angle were tested in a randomized block design, and LIST sentences were randomized across conditions and participants. Care was taken to deploy unique lists for each participant. Some participants found the speech testing challenging. Particularly, the $S_{HA}N_{dif}$ condition resulted in high SRTs in some participants, and we suspect that audibility, rather than noise, was the limiting factor for speech intelligibility. SRTs higher than +5 dB were excluded from the analysis. Linear mixed modeling was used for significance testing, allowing missing data to be included.

BF_{MS} and BF_{BS} were evaluated in experiment 2 by adaptively determining SRTs with the Dutch-Flemish Matrix test [12]. The speech was presented on the CI side and noise on the HA side ($S_{CI}N_{HA}$), or vice versa ($S_{HA}N_{CI}$), using two calibrated loudspeakers (KEF, Ci100QS, GP Acoustics, Kent, United Kingdom). Noise levels were kept constant at 60 dBA while speech was varied adaptively, according to Brand & Kollmeier [13]. The noise was a single male babble based on the ICRA noise [14] and time-reversed to eliminate any intelligible parts. Anecdotal reports from our lab indicate that some CI users can extract meaningful information from the original ICRA babble. Each listening condition was tested and re-tested, except for one participant who participated only in a single session. Performance was better overall than in experiment 1, and no data was excluded. Microphone setting and speech angle were tested in a randomized block design, and Matrix lists were randomized across conditions and participants.

2.4 Statistical analyses

For both experiments, linear mixed models (LMMs) were used in SPSS 29 for Windows (IBM Corp., Armonk, N.Y., USA), where SRTs were entered as the dependent variable. The microphone setting was entered as a repeated fixed variable, and the subject number was included as a random effect with a scaledID variance/covariance matrix. BF_M and BF_B were assessed using the S_0N_{dif} configuration. BF_M, BF_B, and DS were tested in the $S_{HA}N_{dif}$ listening condition. Both listening conditions were analyzed in a separate LMM. BF_{MS} and BF_{BS} were evaluated using $S_{CI}N_{HA}$ and $S_{HA}N_{CI}$ and could be analyzed in a single LMM, including microphone setting, listening condition, and test/retest as repeated fixed factors. The interaction term between the microphone setting and angle was also included.

The variance/covariance matrix for the repeated factors was chosen for each LMM individually by comparing various matrix structures befitting a repeated measures design (including, but not limited to, compound symmetry, diagonal, scaledID, and Toeplitz). Different outcomes of model fit were assessed and weighed when choosing the final variance/covariance matrix, including Akaike's information criterion, distribution of the residuals (Shapiro-Wilk's normality test, histogram), the relation between actual and predicted values, and QQ-plots.

Post hoc multiple comparisons testing was performed on the estimated marginal (EM) means relative to the omnidirectional microphone setting in experiment 1 (BF_M, BF_B, DS) or against 'Real Ear Sound' (RES, Phonak) in experiment 2 (BF_{MS} and BF_{BS}). Šidák's orrection was applied for multiple comparisons testing ($\alpha = 0.05$).

3. RESULTS

3.1 Experiment 1: Evaluation of broadband beamformers and directivity steering in diffuse noise

In the first setup of experiment 1, BF_M and BF_B were tested for their intended use when speech was administered from the front (S_0N_{dif}). The results are shown in Fig. 4A. The LMM revealed a significant main effect of beamforming ($F(2,9) = 6.9$, $p = 0.014$). Compared to omnidirectional microphone settings, BF_B significantly improved SI by 2.9 dB SNR (standard error *SE*: 0.9; 95% confidence interval (*95%CI*): 5.6 to 0.1; degrees of freedom (*df*): 9; $p = 0.042$). The effect of BF_{MS} was more moderate (1.3 dB SNR) and did not reach significance (0.6; -0.4 to 3.0; 10; $p = 0.139$).

When the speech was administered to the HA side ($S_{HA}N_{dif}$, Fig. 4B), the effect of the microphone setting was also significant ($F(3,21) = 10$, $p < 0.001$). Compared to the omnidirectional microphone setting, DS improved SI significantly by 3.6 dB SNR (*SE*: 1.2; *95%CI*: 0.2 to 7.0; *df*: 21; p = 0.032). In this listening condition, BF_M and BF_B deteriorated SI (EM means: -1.8 and -2.6, respectively) but not significantly (1.4; -5.8 to 2.1; 22; $p = 0.723$ and 1.4; -6.7 to 1.5; 21; $p = 0.401$, respectively).

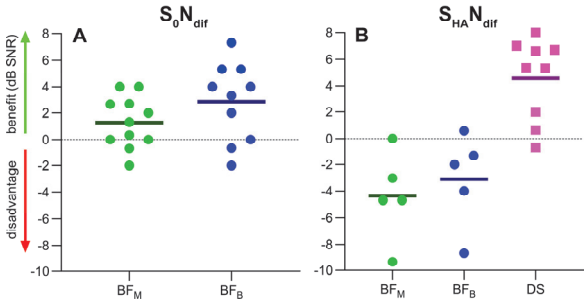


Figure 4. Evaluation of the clinically established broadband, front-facing monaural (BF_M, green symbols) and binaural beamformer (BF_B, blue), and directivity steering (DS, purple) in a diffuse noise field. (A) Effects of BF_M and BF_B when speech was administered to the front (S_0N_{dif}). (B) Effects of BF_M, BF_B, and DS with speech administered to the hearing aid side ($S_{HA}N_{dif}$). Dashed horizontal line: no effect (0 dB SNR difference on the speech recognition threshold). Thick colored lines: mean.

3.2 Experiment 2: Evaluation of side-facing narrowband beamformers

In experiment 2, two listening conditions were tested ($S_{CI}N_{HA}$ and $S_{HA}N_{CI}$), and the results are shown in Fig. 5. Microphone setting and listening condition both had a significant main effect on SRT ($F(2,29) = 5.0$, $p = 0.014$ and ($F(1,35) = 68.0$, $p < 0.001$), respectively). Their interaction was not significant ($F(2,61) = 0.2$, $p = 0.846$). Across both listening conditions, BF_{BS} modestly but significantly improved SI by 1.1 dB SNR (*SE*: 0.4; *95%CI*: 0.0 to 2.1; *df*: 19; $p = 0.046$), but BF_{MS} was ineffective with an EM mean difference of -0.1 dB SNR (0.3; -0.9 to 0.7; 45; $p = 0.985$).

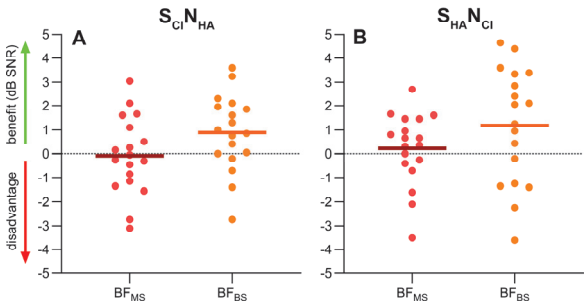


Figure 5. Evaluation of the experimental narrowband, side-facing monaural (BF_{MS}, red symbols), and binaural beamformer (BF_{BS}, orange) in a diffuse noise field. (A) Effects of BF_{MS} and BF_{BS} when speech was administered to the cochlear implant (CI) and noise to the hearing aid (HA) ($S_{CI}N_{HA}$). (B) Effects of beamforming in the $S_{HA}N_{CI}$ condition. Dashed horizontal line: no effect. Thick colored lines: mean.

To investigate the influence of the amount of residual hearing, we performed a correlation analysis by regressing the benefit of BF_{BS} against the average pure-tone threshold across 500, 1000 and 2000 Hz ($PTA_{500\text{-}2000}$) in the HA ear (Fig. 6). For the $S_{HA}N_{CI}$ condition, the correlation was significant ($F(1,16) = 6.1$, $p = 0.0252$, $r^2 = 0.28$), but not for the $S_{CI}N_{HA}$ condition ($F(1,16) = 0.0$, $p = 0.869$, $r^2 = 0.0$). This correlation was not significant for BF_{MS} in both listening conditions ($F(1,16) = 0.4$, $p = 0.550$, $r^2 = 0.0$ and $F(1,16) = 0.6$, $p = 0.451$, $r^2 = 0.0$, respectively).

4. DISCUSSION

Experiment 1 evaluated two directional microphones and directivity steering in bimodal listeners in diffuse stationary noise. The clinically established, front-facing, wideband beamformer BF_B improved SI significantly by 2.9 dB SNR, whereas BF_M resulted in a more modest and statistically insignificant benefit of 1.3 dB SNR. A previous study from

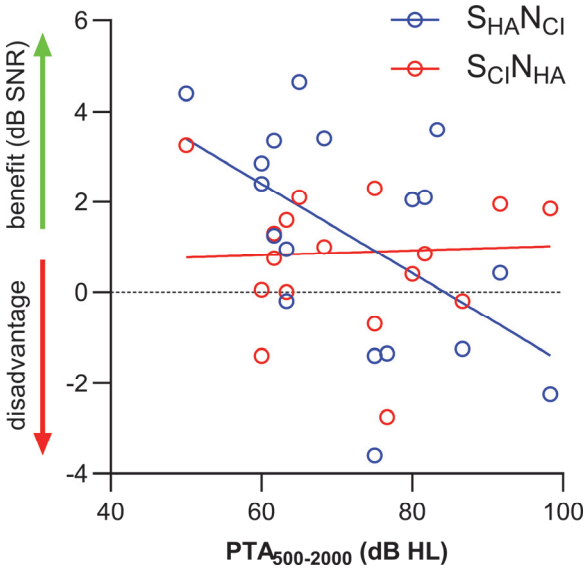


Figure 6. Correlation between the effect of binaural side-beamforming (BF_{BS}) and average pure-tone thresholds at 500, 1000, and 2000 Hz ($PTA_{500\text{-}2000}$) when speech was administered to the cochlear implant (CI) and noise to the hearing aid (HA) ($S_{CI}N_{HA}$, red symbols and line) and *vice versa* ($S_{HA}N_{CI}$, blue). The regression was significant for $S_{HA}N_{CI}$. Dashed horizontal line: no effect.

our lab evaluated the same directional microphones for bimodal users in a diffuse noise field [4]. The authors report an average benefit of BF_B that matches the current data (2.9 dB SNR), although BF_M performed substantially better in that study (2.6 dB SNR). A recent study investigating BF_B for bimodal listeners in an S_0N_{dif} measurement setup found a comparable benefit of 2.3 dB SNR [15]. Another study compared BF_M and BF_B for unilateral CI users with a CROS device in the contralateral ear, again in a diffuse noise field [5]. The reported benefit of BF_B was more modest than in the current study (1.4 dB SNR), whereas the benefit of BF_M was not significant (0.7 dB SNR). The reduced performance in the CROS configuration can be explained by the fact that BF_M and BF_B are implemented as a lighter version in the CROS device to increase battery life [5]. Other studies have investigated these two directional microphones for bimodal listeners and CI users.

As discussed elsewhere [5], the configuration of the noise sources (loudspeaker arrangement) can dramatically affect study outcomes. Front-facing beamformers attenuate noise most effectively when administered to the sides or the back. By contrast, noise sources from the front are passed through unattenuated (Fig. 1). These spatial characteristics make comparing with other studies challenging. Ernst et al. [16] used a diffuse noise setup similar to ours by implementing a ring of loudspeakers and reported benefits of 3.4 (BF_M) and 4.6 dB SNR (BF_M) for bimodal listeners. These relatively large benefits can be explained by the absence of noise from the frontal loudspeaker in their setup, which favors beamforming. By contrast, the authors report substantially reduced benefits of 1.4 (BF_M) and 2.6 dB SNR (BF_B) when a semicircle of loudspeakers was deployed in front of the listeners, again emphasizing the impact of noise administered from the front. Another study that assessed these beamformers for unilateral CI users reports benefits of 5.3 (BF_M) and 7.1 dB SNR (BF_B) [17]. In this study, noise predominantly came from the sides and the back, favoring beamforming effectivity.

Prediction of the benefits of directional microphones as based on polar patterns or manikin (KEMAR) recordings is challenging because of the adaptive behavior of BF_M and the potential overestimation of the SI benefit based on SNR effects alone [5], underscoring the importance of clinical tests for CI users.

When the speech was administered to the HA side, BF_M and BF_B did not significantly affect SI, but DS substantially and significantly improved SRTs by an average of 3.6 dB. This benefit can be attributed to reducing the head shadow effect, assuming that the CI ear was the better hearing side. The theoretical benefit of CROS with speech presented to the ear contralateral to the CI in diffuse noise equals the head shadow effect, i.e., approximately 7 dB [18]. The fact that our reported DS benefit is only about half of this can be explained by residual hearing in the HA ear that mitigates the CROS effect [19]. Further, DS is technically not CROS because attenuation is applied to the HA ear when DS is switched

on, which will somewhat reduce hearing performance in that ear. When noise is administered to the side steered to the better-hearing ear (here, the HA ear), DS will degrade SI. Further, any ILD cues between the devices are lost because of its broadband CROS steering characteristic. Therefore, we advise manual control of this feature and counseling of the end user to explain when to activate DS and when to avoid it. In the future, the automation of DS based on auditory scene analysis can be helpful.

In experiment 2, we assessed two novel, experimental directional microphones that work differently than usual beamformers by increasing low-frequency ILDs while preserving physiological ILDs at frequencies above 1500 Hz. The binaural variant BF_{BS} significantly improved SRTs by 1.1 dB, whereas BF_{MS} did not significantly improve SI. The benefit of BF_{BS} correlated significantly with residual hearing when speech was administered to the HA ear and noise to the other. Modeling studies with an algorithm very similar to $BF_{BS,}$ as used in the current study, showed that the benefit of such an approach could be expected to be up to 16 dB for bimodal listeners when speech is administered frontally, and noise is presented to the CI side, and up to 8 dB when noise is presented to the HA side. With speech also being administered to the side, the effect can be expected to be even higher [18]. One reason for the much smaller benefit found in the present study may be the amount of residual hearing. The previous modeling study simulated hearing loss in a group of typical hearing listeners through a filtering procedure. This resulted in a ski slope audiogram with normal hearing up to 500 Hz and a steeply sloping audiogram at higher frequencies. In our study population, however, the median residual hearing loss was 40 – 50 dB HL between 125-500 Hz.

Another reason for BF_{BS}'s more subtle benefit is that we used the current default microphone setting of Advanced Bionics (RES) as the reference, whereas the simulation study deployed an omnidirectional microphone. RES is also a beamformer that partially mimics, and thus mitigates, the effects of BF_{BS}.

Theoretically, the artificial inflation of low-frequency ILDs is beneficial when speech is administered to the side, regardless of whether it is the CI or the HA ear. However, it will be relevant to verify whether BFBS degrades SI in certain situations and whether it can always be switched on regardless of the auditory scene.

Conclusion

The clinically established binaural beamformer BF_B and the experimental side-facing beamformer BF_{BS} significantly improved SI. Given the insignificant benefits of the monaural counterparts BF_M and BF_{MS}, we recommend using binaural beamforming whenever feasible. DS had a significant advantage when speech was presented to the HA ear; this can also be a helpful technique when speech is administered to the lesser hearing side.

5. ACKNOWLEDGMENTS

We are grateful to the study participants for their time and dedication. This work was part of the 'INTENSE' project within the Crossover Research program funded by the Dutch Research Council (NWO) under grant number 17619. Johan H. M. Frijns and Jeroen J. Briaire are supported by a non-restrictive research grant from Advanced Bionics LLC (Valencia, CA). Johan H. M. Frijns is a European Medical Advisory Board member of Advanced Bionics.

6. REFERENCES

[1] L. G. Potts, M. W. Skinner, R. A. Litovsky, M. J. Strube, and F. Kuk, "Recognition and localization of speech by adult cochlear implant recipients wearing a digital hearing aid in the nonimplanted ear (bimodal hearing)," J Am Acad Audiol, vol. 20, no. 6, pp. 353-373, 2009.

[2] C. Morera et al., "Advantages of binaural hearing provided through bimodal stimulation via a cochlear implant and a conventional hearing aid: A 6-month comparative study," Acta Oto-Laryngologica, vol. 125, no. 6, pp. 596-606, 2005.

[3] M. Armstrong, P. Pegg, C. James, and P. Blarney, "Speech perception in noise with implant and hearing aid," Otol Neurotol, vol. 18, no. 6, pp. S140-S141, 1997.

[4] H. C. Stronks, J. J. Briaire, and J. H. M. Frijns, "Beamforming and single-microphone noise reduction effects on signal-to-noise ratio and speech recognition of bimodal cochlear implant users," Trends Hear, vol. 26, p. 23312165221112762, 2022.

[5] H. C. Stronks, J. J. Briaire, and J. H. M. Frijns, "Residual hearing does not influence the effectiveness of beamforming when using a cochlear implant in

conjunction with contralateral routing of signals," Audiol Neurootol, vol. 28, pp. 262-271, 2023.

[6] B. Dieudonné and T. Francart, "Head shadow enhancement with low-frequency beamforming improves sound localization and speech perception for simulated bimodal listeners," Hear Res, vol. 363, pp. 78-84, 2018.

[7] H. C. Stronks, J. J. Briaire, and J. H. M. Frijns, "The temporal fine structure of background noise determines the benefit of bimodal hearing for recognizing speech," J Assoc Res Otolaryngol, vol. 21, no. 6, pp. 527-544, Dec 2020.

[8] V. Pyschny, M. Landwehr, M. Hahn, R. Lang-Roth, M. Walger, and H. Meister, "Head shadow, squelch, and summation effects with an energetic or informational masker in bilateral and bimodal ci users," J Speech Lang Hear Res, vol. 57, no. 5, pp. 1942-1960, 2014.

[9] D. Cuda, A. Murri, A. Mainardi, and J. Chalupper, "Effectiveness and efficiency of a dedicated bimodal fitting formula," Audiol Res, vol. 9, no. 1, pp. 219-219, 2019.

[10] A. van Wieringen and J. Wouters, "LIST and LINT: Sentences and numbers for quantifying speech understanding in severely impaired listeners for Flanders and the Netherlands," Int J Audiol, vol. 47, no. 6, pp. 348-355, 2008.

[11] F. B. van der Beek, W. Soede, and J. H. M. Frijns, "Evaluation of the benefit for cochlear implantees of two assistive directional microphone systems in an artificial diffuse noise situation," Ear Hear, vol. 28, no. 1, pp. 99-110, 2007.

[12] H. Luts, S. Jansen, W. Dreschler, and J. Wouters, "Development and normative data for the Flemish/Dutch Matrix test," Katholieke universiteit Leuven, Belgium and Academic Medical Center Amsterdam, the Netherlands. Unpublished article, 2014.

[13] T. Brand and B. Kollmeier, "Efficient adaptive procedures for threshold and concurrent slope estimates for psychophysics and speech intelligibility tests," J Acoust Soc Am, vol. 111, no. 6, pp. 2801-2810, 2002.

[14] W. A. Dreschler, H. Verschuure, C. Ludvigsen, and S. Westermann, "ICRA noises: Artificial noise signals with speech-like spectral and temporal properties for hearing instrument assessment. International collegium for rehabilitative audiology," Audiol, vol. 40, no. 3, pp. 148-57, 2001.

[15] N. C. Langerak, H. C. Stronks, J. J. Briaire, and J. H. M. Frijns, "The benefit of bimodal hearing and beamforming for cochlear implant users," Audiol Neurootol, vol. 29, no. 4, pp. 297-305, 2024.

[16] A. Ernst, K. Anton, M. Brendel, and R.-D. Battmer, "Benefit of directional microphones for unilateral, bilateral and bimodal cochlear implant users," Cochlear Implants Int, vol. 20, no. 3, pp. 147-157, May 2019.

[17] A. Buechner, K.-H. Dyballa, P. Hehrmann, S. Fredelake, and T. Lenarz, "Advanced beamformers for cochlear implant users: Acute measurement of speech perception in challenging listening conditions," PLoS One, vol. 9, no. 4, p. e95542, 2014.

[18] C. Taal, D. van Barneveld, W. Soede, J. Briaire, and J. Frijns, "Benefit of contralateral routing of signals for unilateral cochlear implant users," J Acoust Soc Am, vol. 140, no. 1, pp. 393-401, 2016.

[19] H. C. Stronks, J. J. Briaire, and J. H. M. Frijns, "Residual hearing affects contralateral routing of signals in cochlear implant users," Audiol Neurootol, vol. 27, no. 1, pp. 75-82, 2022.

DOI: 10.61782/fa.2025.0171



FORUM ACUSTICUM
EURONOISE 2025

BETTER-EAR-LISTENING VS. COMBINED BILATERAL INFORMATION ACROSS EARS IN ASYMMETRIC HEARING

Ben Williges[1*] **Nadia Sadok**[1] **Diana Arweiler-Harbeck**[1]
Tim Jürgens[2]
[1] ENT-Department, University Hospital Essen, Germany
[2] Institute of Acoustics, University of Applied Sciences Lübeck, Germany

ABSTRACT

A growing number of cochlear implant (CI) users have asymmetric hearing, where one ear is aided with a CI, and the other ear has different degrees of useable acoustic hearing, ranging from aided with hearing aids (bimodal CI) to normal hearing (CI-Single-Sided Deaf, CI-SSD). Benefits of these combinations include improved quality of life, better speech intelligibility, and better localization abilities. To further understand the varying individual benefit, predictions from two different physiologically inspired computer model versions were compared to data previously collected from eight bimodal and eight CI-SSD users for speech-in-noise tasks (speech-reception-thresholds, SRTs). One model version predicts an SRT for each ear independently, and chooses the better SRT for each task (better-ear-listening). The other model version uses information from both acoustic and electric hearing to predict an SRT (complementary information).
Both model versions showed a satisfactory fit to the measured data (RMS-Error: 2.7 dB). The complementary information model showed a bimodal benefit (3 dB for bimodal CI, 2 dB for CI SSD), surprisingly only for lateral noise incident, but not for frontal sound incident. A better-ear-listening approach explained most of the observed data, only in few cases the complementary information model matched experimental data better.

Keywords: *Cochlear Implant, Speech intelligibility, Spatial hearing, computational model*

[*] ***Corresponding author***: *ben.williges@uk-essen.de.*
Copyright: *©2025 Ben Williges et al. This is an open-access article distributed under the terms of the Creative Commons Attribution 3.0 Unported License, which permits unrestricted use, distribution, and reproduction in any medium, provided the original author and source are credited.*

1. INTRODUCTION

Cochlear implant (CI) listeners with contralateral acoustic hearing (bimodal listeners) or single sided deaf (CI-SSD listeners) show improved speech intelligibility benefits compared to unilateral listeners, particularly in spatially separated speech and noise conditions (e.g. [1]). These benefits of having access to acoustic and electric information in opposite ears are, however, highly variable across individuals. This variability complicates an understanding about how much of the benefits are related to better ear listening, how much are related to complementary usage of information (access to acoustic and electric information), or how much is related to binaural processing. Here we employ a physiologically inspired model to predict group median spatial speech intelligibility of CI SSD and bimodal CI listeners. The model is used either in a “better ear listening” approach or a complementary usage of information approach.

2. METHODS

For comparing model results to actual patient data, patient data was taken from [2]: They measured speech in noise performance in 16 CI listeners, eight of whom were bimodally aided, and eight were CI-SSD. Additionally, eleven normal hearing listeners served as a control group. Matrix-style (e.g. Oldenburg sentence test) sentences were presented in a closed-set format, and speech-shaped noise was added to the sentences. Lists of 20 sentences were used. Spatial rendering of three different sound locations were done by convolving the wave-file with head-related-impulse-responses [3] recorded from microphones located in behind-the-ear hearing aid dummies on an artificial manikin. The three different spatial locations were noise

coming from the left (denoted N-90°), front (denoted N0°), or right (denoted N90°). Speech was always presented from the front (S0°). Target speech reception was 50%, and the SNR changes from first to last presentation of each list adaptively based on the maximum likelihood estimation procedure according to [4].
From the SRTs the following secondary measures were derived: Binaural Summation (sometimes also termed bimodal Benefit, CI-Benefit, or binaural Benefit) was calculated by subtracting the bilateral SRT from the best monaural one. Spatial release from masking (SRM) was calculated by calculating the difference in SRT between lateral noise incident and frontal sound incident.

2.1 Model Details

The model used different features for (impaired) acoustic hearing and electric hearing, which act as inputs for a speech recognition backend (FADE, [6]). The speech recognition backend had a-priori information about the speech token used (Oldenburg Sentence Test, e.g. 50 whole word tokens, with a hidden markov model for transition from silence to word token, and also knows the matrix-like structure of the sentences, thus forming a perfect listener, capable of extracting all available information). Speech and noise tokens (including HRTFs) were exactly the same as in the actual patient data. It outputs a speech reception threshold (SRT) independently for each ear ("better ear listening") or it combines the electric and acoustic feature to one feature set and predicts one SRT from this set (thereby exploiting possible "complementary usage of information").

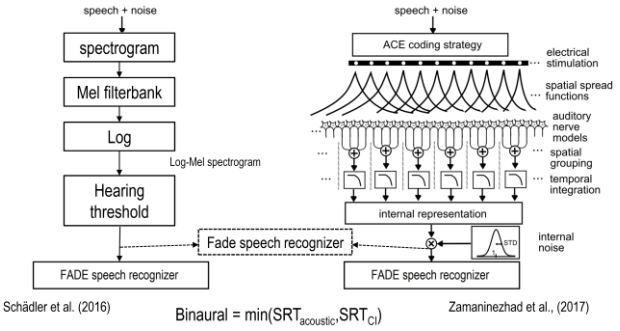


Figure 1. Overview of the model stages. Impaired acoustic model for the left ear, and CI model for the right ear. The FADE speech recognizer backend outputs a SRT using either only the internal representation from one ear as input, or uses the internal representations from both ears concatenated as input. In the case of impaired acoustic hearing, the speech + noise input signal is amplified according to the respective hearing loss.

Hearing loss on the acoustic side was modeled as increased internal noise due to the audiometric thresholds (attenuation), no supra-threshold deficits were taken into account. Aided hearing was simulated by processing the sound stimuli with the research master hearing aid [6] using CAMFIT-gain rule, as in [2]. A mild-to-severe sloping hearing loss was simulated.

CI listening was simulated using a physiologically inspired model of electric hearing [7]. The model simulated ACE coding strategy, an unrolled cochlea with a regular CI insertion, current spread, individual auditory nerve cells (leaky-integrate and fire), taking into account refractoriness, facilitation, and tonotopic organization along the cochlear. More specifically the following model parameters were chosen: Spatial spread of the electric field: 0.3mm, 2200 auditory nerve cells were simulated, and cognitive effects were simulated with a multiplicative Gaussian distributed noise with standard deviation of 0.2 applied to the internal representation. These parameters were empirically chosen such that the median SRT of the CI only data in the actual patient data for frontal sound incident (N0°) matches the corresponding predicted SRT. The acoustic hearing model parameters (default from [5]) matched NH unilateral patient data for frontal sound incident. All the other hearing configurations (bimodal CI, CI-SSD) and noise directions were predicted by the different models.

3. RESULTS

Prediction from the two models in comparison to actual patient data can be found in Fig. 2 for absolute SRTs, Fig. 3 for SRM, and Fig. 4 for binaural Summation. Overall the correlation between modelled SRTs and actual SRTs is high (R^2=0,88, $p<0.001$, for both models) with a root-mean-squared error of 2.7 dB, leading to a good match between model and actual human performance. Both models are sensitive to changes in spatial scene. For aided hearing unilaterally condition (red), the hearing thresholds are compensated for in the model, resulting in a close match to NH unilateral listening mode (black, taking the assumption that the hearing loss was completely due to audibility). For SRM, the model values are in general higher than the actual patient data, independent of listening mode (unilaterally, bilaterally, or electric side or acoustic side).

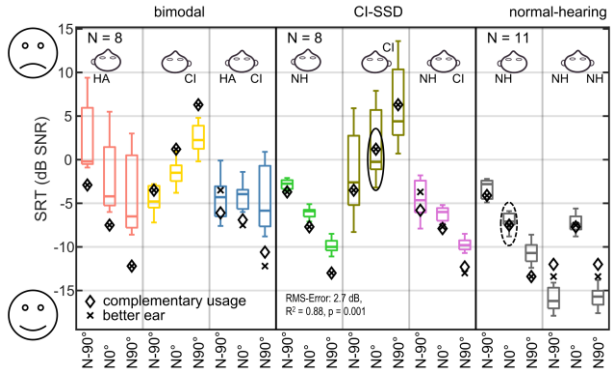


Figure 2. Absolute SRTs for the three different listening groups (bimodal CI, CI-SSD, and NH control group) compared to model predictions (diamonds for complementary use of information model, crosses for better ear listening model). On the x-axis the different noise directions are displayed.

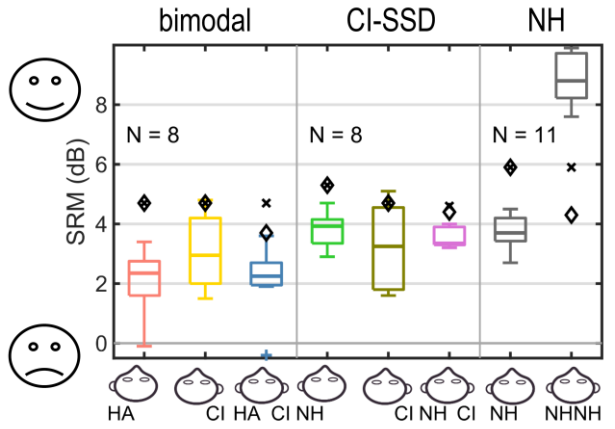


Figure 3. Spatial release from masking for the three different listening groups (bimodal CI, CI-SSD, and NH control group) compared to model predictions (diamonds for complementary use of information model, crosses for better ear listening model). On the x-axis the different hearing configurations are displayed.

For binaural summation, the better ear listening model shows no binaural summation (by design, as there is no interaction between the two ears). The complementary use of information model shows a benefit for N-90 and a decrease for N90. The decrease is of the same order as in the normal hearing control condition. The predicted benefit for N-90 is consistent for both bimodal and CI-SSD groups, and again a bit higher (1-1.5 dB in SRT) than the median of the actual patients.

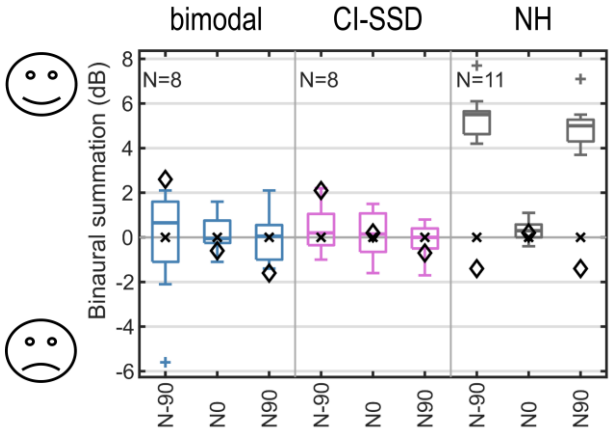


Figure 4. Binaural summation for the three different listening groups (bimodal CI, CI-SSD, and NH control group) compared to model predictions (diamonds for complementary use of information model, crosses for better ear listening model). On the x-axis the different noise directions are displayed.

4. DISCUSSION

There are several small differences between predicted data by the different models and actual patient data:
The model overestimates the SRM independent of feature, due to a "perfect" training of the speech classifier, similar to an experienced patient.
The model for acoustic hearing needs to incorporate subthreshold effects ("Audibility" is restored with MHA). This could be done using tests like tone-detection in noise. Supra-threshold effects were not taken into account here, as no additional measures were conducted during data collection from actual patients. Readily clinically available would be for instance some form of discrimination loss of monosyllabic words.
The combined usage of information model assumes equal contribution of acoustic and electric information, which might not be the best fit [8], and could explain, why there is a benefit for N-90°, and an interference for N90. The combined benefit in actual CI listeners is likely underestimated due to stationary noise masker (less "glimpsing" of acoustic information), anechoic HRTFs, and is noise-direction dependent [2].
This study did not directly investigate the use of binaural processing in bimodal CI and CI SSD. The two models proposed are quite simple, and do not assume any central

interactions or top-down processing (see [9] for a review). However, the comparison to normal hearing control data can serve as guidelines for the achieveable binaural benefit, after acoustic headshadow is accounted for:
Pure binaural processing should yield at least 2 dB SRT benefit in comparable scenarios, see for example the NH binaural summation data reaching 4 dB for lateral sound incident. This is a purely binaural effect, and needs appropiate coding of interaural cues like interaural coherence, time- and level-differences. However, speech in noise might not be the best test to use in clinical practice to show the benefit of having two ears, questionnaires,localisation tasks or binaural masking level difference tests might be more efficient.
Current provision (as of 2025) for bimodal CI for the three major CI manufacturers is in line with the presented outcomes: One manufacturer couples the hearing aid tightly with the CI including synchronizing automatic gain control, and bilateral beamformers. Another aims to minimize the interaural mismatch, and the third mainly focuses on user comfort when streaming audio.

5. CONCLUSION

The models capture the changes in SRT due to different acoustic and electric inputs and due to different spatial scenes. A simple "better ear listening" model explains most of the data in stationary noise for bimodal CI and CI SSD listeners. For noise from the acoustically aided side the complementary usage of information across ears model is more suitable.

6. ACKNOWLEDGMENTS

Simulations were performed on the HPC Cluster CARL funded by the DFG under INST 184/157 1 FUGG.

7. REFERENCES

[1] R. H. Gifford, M. F. Dorman, S. W. Sheffield, K. Teece, and A. P. Olund, 'Availability of Binaural Cues for Bilateral Implant Recipients and Bimodal Listeners with and without Preserved Hearing in the Implanted Ear', *Audiology and Neurotology*, vol. 19, no. 1, pp. 57–71, 2014, doi: 10.1159/000355700.

[2] B. Williges, T. Wesarg, L. Jung, L. I. Geven, A. Radeloff, and T. Jürgens, 'Spatial Speech-in-Noise Performance in Bimodal and Single-Sided Deaf Cochlear Implant Users', *Trends in Hearing*, vol. 23, p. 233121651985831, Jan. 2019, doi: 10.1177/2331216519858311.

[3] H. Kayser, S. D. Ewert, J. Anemüller, T. Rohdenburg, V. Hohmann, and B. Kollmeier, 'Database of Multichannel In-Ear and Behind-the-Ear Head-Related and Binaural Room Impulse Responses', *EURASIP Journal on Advances in Signal Processing*, vol. 2009, no. 1, p. 298605, 2009, doi: 10.1155/2009/298605.

[4] T. Brand and B. Kollmeier, Efficient adaptive procedures for threshold and concurrent slope estimates for psychophysics and speech intelligibility tests. The Journal of the Acoustical Society of America, 111(6), 2801–2810, 2002 doi:10.1121/1.1479152

[5] M. R. Schädler, A. Warzybok, S. D. Ewert, and B. Kollmeier, 'A simulation framework for auditory discrimination experiments: Revealing the importance of across-frequency processing in speech perception', *The Journal of the Acoustical Society of America*, vol. 139, no. 5, pp. 2708–2722, May 2016, doi: 10.1121/1.4948772.

[6] G. Grimm, T. Herzke, D. Berg, and V. Hohmann, 'The Master Hearing Aid: A PC-Based Platform for Algorithm Development and Evaluation', *Acta Acustica united with Acustica*, vol. 92, no. 4, pp. 618–628, Jul. 2006.

[7] S. Fredelake and V. Hohmann, 'Factors affecting predicted speech intelligibility with cochlear implants in an auditory model for electrical stimulation', *Hearing Research*, vol. 287, no. 1–2, pp. 76–90, May 2012, doi: 10.1016/j.heares.2012.03.005

[8] A. Zedan, B. Williges, and T. Jürgens, 'Modeling Speech Intelligibility of Simulated Bimodal and Single-Sided Deaf Cochlear Implant Users', *Acta Acustica united with Acustica*, vol. 104, no. 5, pp. 918–921, Sep. 2018, doi: 10.3813/AAA.919256.

[9] SR Anderson, E Burg, L Suveg, RY Litovsky, 'Review of Binaural Processing With Asymmetrical Hearing Outcomes in Patients With Bilateral Cochlear Implants.' *Trends in Hearing*, 2024 Jan-Dec;28:23312165241229880. doi: 10.1177/23312165241229880

DOI: 10.61782/fa.2025.0822

FORUM ACUSTICUM EURONOISE 2025

SPEECH PERCEPTION AND SOUND LOCALIZATION IN CI SUBJECTS WITH ELECTRIC-ACOUSTIC STIMULATION AND CONTRALATERAL NORMAL HEARING

Tobias Weissgerber[1*] **Mariana Bandeira**[1] **Timo Stöver**[2] **Uwe Baumann**[1]

[1] Audiological Acoustics, ENT Department, University Hospital, Goethe-University, Frankfurt am Main, Germany

[2] ENT Department, University Hospital, Goethe-University, Frankfurt am Main, Germany

ABSTRACT

In unilateral deafness or unilateral partial deafness with contralateral normal hearing, the lack of ability to localize sound, decreased speech perception in noise, and increased hearing effort lead to the desire for cochlear implantation. The aim of the present study was to assess hearing abilities in subjects using electric-acoustic stimulation (EAS) with contralateral normal hearing.

16 subjects with EAS in the ipsilateral ear and normal hearing in the contralateral ear were implanted at our department. Speech reception thresholds (SRTs) in noise were assessed in different spatial noise conditions and for different noise characteristics with and without reverberation. Mean error in sound localization was measured with an LED pointer method.

Improved SRTs with EAS stimulation in simultaneous and spatially separated masker conditions were observed. In more diffuse noise conditions and in the presence of reverberation, no benefit on SRTs was found. Mean localization error using EAS was in the range of normal hearing listeners.

Even for patients with contralateral normal hearing, EAS can improve speech perception in noise and restore sound localization in everyday life. While sound localization abilities in the horizontal plane were comparable to normal hearing, SRTs were still worse than in normal hearing participants.

Keywords: *cochlear implant, electric-acoustic stimulation (EAS), unilateral normal hearing, speech perception in noise, sound localization.*

[*] ***Corresponding author***: *weissgerber@med.uni-frankfurt.de*

Copyright: *©2025 weissgerber et al. This is an open-access article distributed under the terms of the Creative Commons Attribution 3.0 Unported License, which permits unrestricted use, distribution, and reproduction in any medium, provided the original author and source are credited.*

1. INTRODUCTION

Cochlear implant (CI) users often perform well in speech perception under quiet conditions, but their ability to understand speech is notably diminished in the presence of background noise and/or reverberation. In addition, CI users oftentimes have difficulties with sound localization. Individuals with severe to profound high-frequency hearing loss and significant residual low-frequency hearing benefit from soft CI surgery with preserving the residual hearing and using combined electric-acoustic stimulation (EAS).

In the population of EAS subjects, a very rare subpopulation has normal or close to normal hearing in the contralateral ear (EAS-NH) and could, unlike bimodal or bilateral CI recipients, potentially benefit by binaural cues from interaural time differences. Only few studies were published on auditory performance of this population so far [1-3]. In particular, there is a lack of data on speech perception in everyday listening environments, which typically cannot be captured in clinical routine. Furthermore, sound localization performance was not compared with results of other groups of CI users so far.

The aim of this study was to investigate speech perception in noise in different listening conditions and to compare

sound localization abilities with normal hearing subjects and different groups of cochlear implantees.

2. MATERIAL AND METHODS

Experiments were conducted in an anechoic chamber (size: 4.1m x 2.6m x 2.1 m) equipped with a horizontal sound reproduction system with 128 loudspeakers (see [4] for further details on the sound reproduction system).

2.1 Participants

Six EAS-NH subjects (mean age 60±8.5 years) performed study tests. The pure-tone audiograms of the implanted ear measured at study visit are shown in Figure 1.

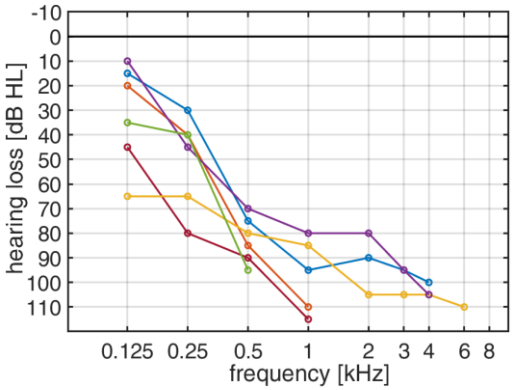


Figure 1. Pure-tone audiograms of the implanted ear measured at study visit (n=6).

2.2 Speech perception test in noise

Speech reception thresholds (SRTs) in noise were measured using the German Matrix Test (Oldenburg Sentence Test) for five different test conditions, which varied in (1) position of speech and noise and (2) in modulation characteristics of the noise:

- S0N30 continuous: speech from 0°, continuous noise at 30° towards the NH ear,
- S0N30 modulated: speech from 0°, modulated noise at 30° towards the NH ear,
- MSNF modulated: speech from 0°, modulated noise presented from 4 virtual noise sources (Multi-Source Noise Field, MSNF according to [5]),
- S-30N30 reverb continuous: speech from 30° towards the EAS ear, continuous noise at 30° towards the NH ear,
- S-30N30 reverb modulated: speech from 30° towards the EAS ear, modulated noise at 30° towards the NH ear.

Details on the technical realization of the room simulation for the conditions "reverb" are described in [6].
For the study, the individual clinical mapping of the EAS sound processors was used. Tests were conducted with EAS fitting ("EAS on" condition) and with deactivated acoustic component while occluding the ear (electric only, "EAS off" condition).
Results were compared to a group consisting of seven normal hearing (NH) subjects (mean age: 26.7±8.0 years)

2.3 Sound Localization

The sound localization test was carried out in the same anechoic chamber using the same sound reproduction system. Sound localization was assessed for seven frontal loudspeaker positions in the horizontal plane between ±60°. The stimuli consisted of five white noise bursts (according to [7]) presented at a level of 65 dB SPL. Test participants used a rotary encoder to indicate the perceived angle of the sound on a LED chain. The mean localization error was determined as the median error over all sound directions.

3. RESULTS

3.1 Speech perception in noise

SRT results for the EAS users with either EAS "on" or "off" compared with NH subjects were shown in Figure 2. SRTs in the EAS-NH group were significantly worse than in the NH group for all five test conditions ($p<0.001$).
SRTs in the EAS-NH group were improved by 0.7 dB (condition S0N30 in modulated noise) to 2.9 dB (condition S0N30 in continuous noise) when the acoustic component of the EAS processor was active.

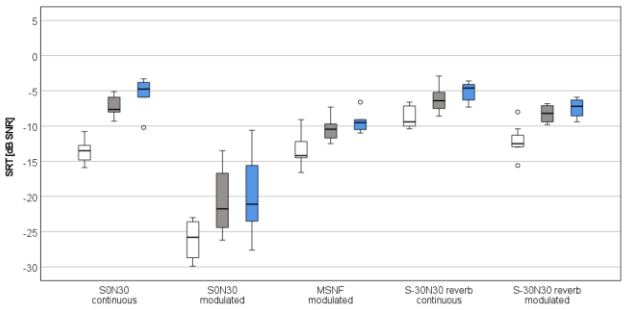


Figure 2. Speech reception thresholds (SRT) in five test conditions with different spatial conditions and

noise modulation characteristics for normal hearing (white boxes), EAS users with EAS on (grey boxes) and EAS off (electric only, blue boxes).

3.2 Sound localization

Mean localization error (MLE) in the EAS-NH group was 8.4°. MLE in the EAS-NH group was 6.1° worse than for subjects with normal hearing (MLE: 2.3°). However, localization performance of the EAS-NH group was 3.5° better than in bilateral CI users and even 10.1° better than in bimodal CI users with a hearing aid in the contralateral ear.

4. DISCUSSION AND CONCLUSION

A beneficial effect of acoustic hearing compared to the electric only condition on speech perception in different complex listening conditions and on sound localization was observed in EAS users with contralateral normal hearing. Sound localization results in the group of EAS-NH were superior compared to all other CI groups.

The results are in line with the results from a study in which greater subjective hearing benefits by using the EAS system compared to other CI groups were reported using a questionnaire [17]. Another study found significant improvements in speech perception in noise and in subjective hearing abilities in EAS-NH users within the first few months of EAS use compared to their preoperative performance [19].

Consequently, it is recommended that CI candidates with residual hearing undergo hearing preservation surgery to enable the use of EAS.

5. REFERENCES

[1] A. Lorens, A. Obrycka A, P.H. Skarzynski et al.: “Benefits of Binaural Integration in Cochlear Implant Patients with Single-Sided Deafness and Residual Hearing in the Implanted Ear” *Life*, 11(3), 2021.

[2] A. Lorens, P.H. Skarzynski, A. Obrycka et al.: “Can an individual with low frequency hearing in the candidate ear benefit from a cochlear implant even if they have normal hearing in the other ear?” *European Archives of Oto-Rhino-Laryngology*, 280(11): 4895–4902, 2023.

[3] M.T. Dillon, E. Buss, N.J. Thompson et al.: “Speech Recognition and Subjective Hearing Abilities for Electric-Acoustic Stimulation Users With Unilateral Hearing Loss” *Otol Neurotol*, 45(9):1006-1011, 2024.

[4] T. Weissgerber: [“A playback system with wave field synthesis to simulate everyday listening environments”] *HNO*, 67: 265–271, 2019.

[5] T. Rader, H. Fastl, U. Baumann: “Speech perception with combined electric-acoustic stimulation and bilateral cochlear implants in a multisource noise field” *Ear Hear*., 34: 324–332, 2013.

[6] A. Eichenauer, U. Baumann, T. Stöver, T. Weissgerber: “Interleaved Acoustic Environments: Impact of an Auditory Scene Classification Procedure on Speech Perception in Cochlear Implant Users." *Trends Hear*, 2021, 25: 1-14, 2021.

[7] B. Seeber B: “A new method for localization studies” *Acta Acust United Ac.*,88: 446–450, 2002.

DOI:

Main theme: A13 Physiological Acoustics and Audiology

Session A13.06 Audiology diagnostic techniques

Chair(s): J. A. Undurraga Lucero, M. Temboury Gutiérrez

DOI: 10.61782/fa.2025.0359



FORUM ACUSTICUM
EURONOISE 2025

EVALUATING TEST TIME IN SIMULTANEOUSLY RECORDED ABRs

Sinnet G. B. Kristensen[1*] Søren Laugesen[1] Torsten Dau[2]
Jaime Andres Undurraga Lucero[1,3]

[1] Interacoustics Research Unit, c/o: Technical University of Denmark, Kgs. Lyngby, Denmark
[2] Hearing Systems, Department of Health Technology, Technical University of Denmark, Kgs. Lyngby, Denmark
[3] Department of Linguistics, 16 University Avenue, Macquarie University, NSW 2109, Australia

ABSTRACT

Currently, the gold standard procedure for objectively evaluating hearing in infants is the auditory brainstem response (ABR). We have previously explored a novel approach that involves recording multiple ABRs simultaneously in response to narrowband (NB) CE-Chirps centered at 500, 1000, 2000, and 4000 Hz in both ears. In the current study, we investigated the overall testing time when recording ABRs simultaneously compared to consecutively at the clinical discharge levels of 30 and 40 dB estimated hearing level (eHL) to the 4 NB CE-Chirps.

Simultaneous and consecutive ABRs were obtained from 21 young normal-hearing participants within one recording session. Response presence was determined using the recently developed Fmpi, an objective statistical detection method. Testing time was estimated as the total time to reach 95% probability of response present.

The results showed that, for each NB CE-Chirp considered individually, simultaneous ABRs had on average longer testing times compared with consecutive ABRs, a consequence of the overall reduced ABR wave V amplitude evoked by the novel more frequency-specific simultaneous approach. However, the total testing time (8 ABR measurements) was significantly shorter for the simultaneous than that of the consecutive approach.

Keywords: *electrophysiology, simultaneous, auditory brainstem response, test time*

1. INTRODUCTION

The incidence of hearing loss in newborns is approximately 1 to 3 per 1000 newborns, which makes hearing loss one of the most common birth disorders [1-4]. Newborn hearing screening programs have been employed to identify newborns who require follow-up diagnostic testing, to ensure necessary intervention and treatment facilitating language and cognitive development [5-6]. The Joint Committee on Infant Hearing [4] recommends that the diagnosis of hearing loss is made within the first 3 months of life. The current gold-standard diagnostic evaluation employes the Auditory brainstem response (ABR), where 4 separate audiometric frequencies are evaluated in each ear [7-8]. However, the time required to obtain the 4 frequency-specific thresholds in both ears often exceeds the available test time in the infant population [9]. This limitation often results in the necessity of more ABR sessions to obtain the full hearing assessment. Enhancements in the speed of the ABR test could potentially reduce the test time. A recent study has introduced a novel ABR method, where multiple ABRs can be obtained in both ears in parallel, named pABR [10]. The authors demonstrated the feasibility of recording ABRs in response to five tone bursts at 500, 1000, 2000, 4000, and 8000 Hz simultaneously. In their study, they also evaluated the acquisition time of the pABR and compared it to consecutive presentation [10]. A residual

[*] ***Corresponding author***: *sbkr@iru.interacoustics.com*
Copyright: *©2025 Kristensen et al. This is an open-access article distributed under the terms of the Creative Commons Attribution 3.0 Unported License, which permits unrestricted use, distribution, and reproduction in any medium, provided the original author and source are credited.*

noise criterion of 20 nV was employed as stopping criterion. Averaging all 10 (5 per ear) tone-burst waveforms down to 20 nV residual noise required a median test time of 30.1 minute, whereas obtaining the 10 tone-burst waveforms using pABR only required 4.6 minutes. Further, when using a Signal-to-Noise Ratio (SNR)-based criterion to evaluate test time, five out of the nine test subjects had faster acquisition time with pABR, with a median pABR speed-up ratio of 1.45 at a high level of 75 dB peSPL (52 to 59 dB nHL), and of 2.99 at 45 dB peSPL (22 to 29 dB nHL).

In a recent study [11-12] we demonstrated that it is possible to obtain multiple frequency specific ABRs to NB CE-Chirp stimuli (mbABR) simultaneously at clinical stimulation levels.

The purpose of this study was to determine and compare the effectiveness—in terms of acquisition time— of the mbABR approach using the data collected in [11-12]. As mbABR and pABR have many similarities, we hypothesized that mbABR would yield an acquisition time advantage over consecutive ABR similar to pABR.

2. METHOD

2.1 Participants

Twenty-four normal-hearing participants (10 males) aged from 20 to 29 years (average age 25), participated in the study. All subjects had pure-tone audiogram thresholds equal to or better than 20 dB HL across the 125 to 8000 Hz range. Otoscopy was conducted to ensure that there was no wax obstruction and that the ear canal was suitable for insert earphone placement. The study was conducted under approval from the Science-Ethics Committee for the Capital Region of Denmark (H-1-2013-138).

2.2 Stimuli and procedure

Four frequency specific NB CE-Chirps LS [13-14] were presented at their corresponding clinical discharge levels of 30 dB estimated hearing level (eHL) and at 10 dB above (40 dB eHL). For adult participants, this corresponded to a 500 Hz NB CE-Chirp presented at 45 and 55 dB nHL, a 1000 Hz NB CE-Chirp presented at 40 and 50 dB nHL, and 2000 Hz and 4000 Hz NB CE-Chirp at 35 and 45 dB nHL, respectively [7, table 7]. The NB CE-Chirps were presented in both consecutive and simultaneous mode at a nominal rate of 40/sec. Jitter was introduced around the nominal rate from a uniform distribution spanning from -67% to +67% of the nominal stimulus interval. NB CE-Chirps had a 200 ms duration and were presented using alternating polarity.

All recordings were obtained in a sound treated and electrically shielded test booth, where the participants were instructed to relax on a bed. First, simultaneous ABRs were acquired at both the discharge and discharge level +10 dB, with a balanced testing order across participants. Then, consecutive ABRs were obtained in a balanced order for the four NB CE-Chirps at both the discharge level and discharge level +10 dB. Lastly, a retesting of simultaneous ABRs was conducted at the discharge level. For the purpose of this study, only the retest data set was used because of a lower residual noise.

At discharge level all ABRs were obtained in both ears on all participants (N = 48 ears). However, only 20 subjects had consecutive and simultaneous ABRs collected at discharge level +10 dB (N = 40 ears).

2.3 Apparatus

ABRs were recorded using a clinical Interacoustics Eclipse system paired with an RME Fireface UC soundcard and custom MATLAB interface [15-16] for control of both stimulus presentation and the collection of ABRs into distinct buffers for each NB CE-Chirp, aligned with the jittered stimulus presentation. EEG activity was captured using disposable surface electrodes at Fz to M1 or M2, with an electrode placed on the cheek serving as ground. For offline analysis, the EEG was band-pass filtered from 83 to 3000 Hz (finite impulse response Kaiser filter, 65 dB stop-band attenuation and 1 Hz transition between pass and stop bands).

RadioEar IP30 insert earphones were used for stimulus presentation. Calibration of NB CE-Chirps was performed using the root-mean-square sound pressure levels defined by [17] for each NB CE-Chirp presented at a rate of 20/sec.

2.4 Data Analysis

21 complete data sets were available for comparison of simultaneous and consecutive ABR at discharge level and 19 data sets at discharge level +10 dB.

The Fmpi-detector was chosen as the objective statistical detector and applied to all data [18]. The Fmpi builds on the clinically well-known Fmp-detector [19] and statistically assesses whether the F-value—a proxy of the SNR—is significantly different from what would be expected from a noise-only recording. If the estimated F-value is high, there is a high probability that a response is present. While Fmp assumes a general (conservative) criterion value for determining significance, the Fmpi estimates the correct criterion value for the individual recording from the noise

properties, leading to faster detections. For this analysis, the stopping criteria was a 95% probability of a response being present. For the consecutive method, per participant total test times were derived by adding the individual test times (i.e., the time to reach a 95% response probability of each individual condition) for each frequency and ear, whereas the maximum test time across all NB CE-Chirps was used for the simultaneous method. Per participant total test times were then used to perform an Analysis of variance (ANOVA) via a Linear mixed effects (LME) model. Here, the total test time (in a log-scale) was set as the dependent variable, the *Condition* (with levels: *Simultaneous* and *Consecutive*) and *Presentation level* (with levels: *Discharge* and *Discharge +10 dB*) as the independent factors, and the *Participant* as the random factor.

3. RESULTS

In Figure 1a, the total test time for each subject is presented for both consecutive (black points) and simultaneous ABR (pink points) at discharge level and discharge level +10 dB. At discharge level the median total test times were 3.25 min for consecutive and 2 min for simultaneous. At discharge level +10 dB the median total test times were 3 and 2.40 min, respectively. On average, simultaneous ABR is 1.55 times faster than consecutive ABR. In the statistical analysis, only the factor *Condition* was significant, confirming a significantly higher performance (lower total test time) for simultaneous than consecutive recordings ($F(1, 55) = 15.49$, $p < 0.001$).

Figure 1b, shows a scatterplot comparing the total test times for simultaneous and consecutive ABRs at both discharge level (orange points) and discharge level +10 dB (magenta points). Points above the identity line correspond to cases where the consecutive total test time was shorter than simultaneous one. However, the vast majority of points fell under the identity line, indicating faster ABR detections for simultaneous testing.

To further examine the test time required for each individual frequency, ear, method, and stimulation level, Figure 2 shows the normalized test time distribution, in which 100% corresponds to the maximum test time across all measurements, for all these variables and for each participant. Here, it can be seen that the lower frequencies (500 and 1000 Hz) took longer for the simultaneous than the consecutive (Interquartile range for consecutive and simultaneous in Figure 2). Despite the simultaneous having this extra measurement time at the low frequencies, which drives the overall test time in the simultaneous recording, the full test is much shorter than in the consecutive mode (Figure 2 top panels).

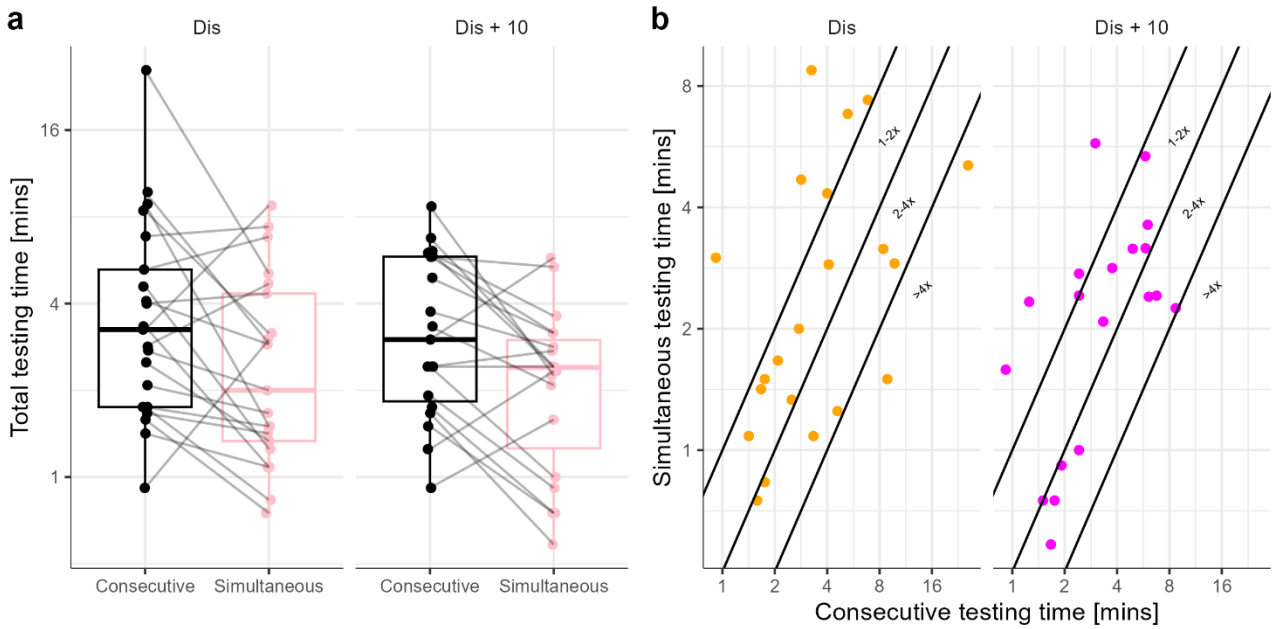


Figure 1 (a): Total test time for consecutive (black points) and simultaneous ABR (pink points) at discharge level and discharge level +10 dB. Boxplots show the median (bold vertical lines), Q1-Q3 interquartile ranges (boxes), and whiskers for 1.5 interquartile range from the hinge. **(b)** Scatterplot of acquisition times for simultaneous and consecutive ABR at both

discharge level (left panel, orange points) and discharge level +10 dB (right panel, magenta points). Points above the identity line correspond to cases where the consecutive total test time was shorter than simultaneous one, while when data points fall below the identity line the total test time was shorter with simultaneous testing. In both panels, each point corresponds to a single-subject measurement.

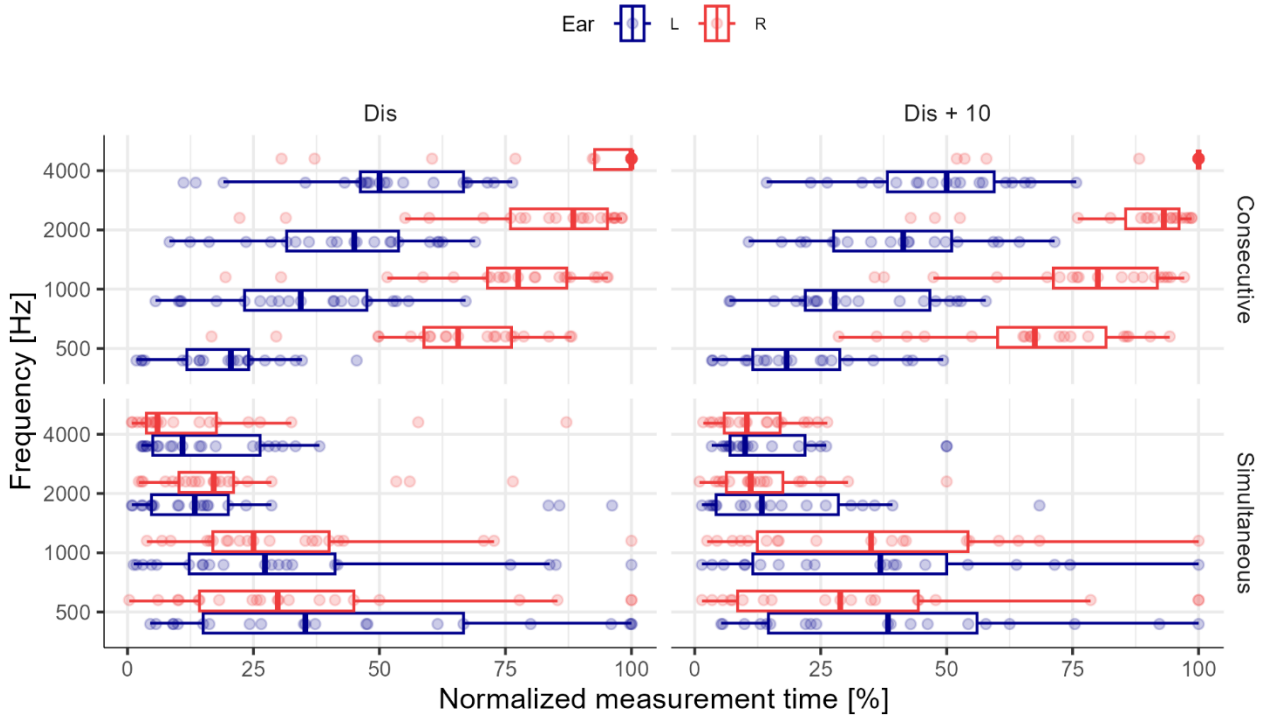


Figure 2: Normalized measurement time (in %) at both discharge level (left panels) and discharge level +10 dB (right panels) for consecutive (top panels) and simultaneous (bottom panels) recordings. The individual center frequencies of the NB CE Chirp are indicated in the vertical axes. A normalized scale was used, such that the longest test time across subjects represents 100%. Red represents the right ear and blue the left ear. Individual points correspond to single-subject data. Boxplots show the median (bold vertical lines), Q1-Q3 interquartile ranges (boxes), and whiskers for 1.5 interquartile range from the hinge. For the purpose of graphical representation, consecutive measurements are shown first for the left ear and then for the right ear, from low to high center frequencies.

4. DISCUSSION

In this study, it was demonstrated that using a simultaneous ABR collection approach in response to NB CE-Chirps results in significantly reduced test time compared to classic consecutive ABR data collection. However, speeding up the test by presenting 8 NB CE-Chirps (4 in each ear) instead of one at a time in each ear, does not speed up the test by a factor of 8. The result from this study shows that on average it takes 1.55 times longer to reach all 8 Fmpi-detection criteria for the consecutive than for the simultaneous ABR. This result is in line with findings from pABR using 0 dB SNR as stopping criterion [10].

In Figure 1a it was observed that the lower level (discharge level) showed a larger difference in median values between simultaneous and consecutive, than at the higher level (discharge level +10 dB). The larger difference at the low level was expected, based on pABR, which showed a larger speed-up ratio at a low level of 45 dB peSPL compared to 75 dB peSPL [10]. In pABR and mbABR, previous experimental and modeling studies have shown that presenting multiple stimuli together has the advantage that they act as maskers for each other [10, 11-12, 20-21]. This changes the ABR waveform morphology especially at the

lowest test frequency, where smaller wave V responses are observed compared to consecutive presentation. As the intensity is increased, the spread of excitation on the basilar membrane broadens towards higher frequencies [23]. This leads to a larger masking effect at higher levels resulting in larger difference in response amplitudes between consecutive and simultaneous stimuli presentation. In turn, this greater masking effect reduces the speed-up benefit from simultaneous presentation, as is seen in the present study as well as those from pABR.

In Figure 2 it was observed that the recording at 500 Hz drives the total test time for simultaneous ABR. This result indicates that further time optimization could be gained in threshold seeking by applying a level-varying approach. In this scenario, data collection at higher frequencies could be continued at other levels, while the 500 Hz is still averaging to a satisfied criterion. However, the interaction among frequency bands, that provides a positive effect in terms of more place-specific response, could be reverted to a negative effect if a change in level of one stimulus, and the concomitant change in spread of excitation, affects the underlying response waveform of another frequency ABR still in progress. This suggests a recommended maximum level difference among stimuli presented simultaneously.

The target population for simultaneous ABR is infants referred for diagnostic evaluation. Infants exhibit distinct waveform morphologies due to the ongoing maturation of the auditory system [24-25]. Therefore, the time advantage of using simultaneous ABR demonstrated here requires validation in the infant population.

5. CONCLUSION

The present study investigated whether there were observable and significant changes in test time when presenting NB CE-Chirps simultaneously compared to consecutively, using clinically relevant repetition rates, presentation levels, and an Fmpi-detector for response evaluation. The results showed a significantly reduced test time when recording the NB CE-Chirps simultaneously.

6. REFERENCES

[1] Bussé, A. M. L., Hoeve, H. L. J., Nasserinejad, K., Mackey, A. R., Simonsz, H. J., & Goedegebure, A. "Prevalence of permanent neonatal hearing impairment: Systematic review and Bayesian meta-analysis," *International Journal of Audiology*, 59(6), 475–485, 2010.

[2] Mackey, A. R., Bussé, A. M. L., Hoeve, H. L. J., Goedegebure, A., Carr, G., Simonsz, H. J., Uhlén, I. M., & for the EUSCREEN Foundation. "Assessment of hearing screening programmes across 47 countries or regions II: Coverage, referral, follow-up and detection rates from newborn hearing screening," *International Journal of Audiology*, 1–10, 2021.

[3] Morton, C. C., & Nance, W. E. "Newborn Hearing Screening—A Silent Revolution," New England *Journal of Medicine*, 354(20), 2151–2164, 2006.

[4] Task Force on Newborn and Infant Hearing. "Newborn and Infant Hearing Loss: Detection and Intervention," *Pediatrics*, 103(2), 527–530, 1999.

[5] Walker, E. A., Holte, L., McCreery, R. W., Spratford, M., Page, T., & Moeller, M. P. "The Influence of Hearing Aid Use on Outcomes of Children With Mild Hearing Loss," *Journal of Speech, Language, and Hearing Research,* 58(5), 1611–1625, 2015.

[6] Yoshinaga-Itano, C. "Fast Facts: Early Hearing Detection and Intervention," *Karger Medical and Scientific Publishers,* 2022.

[7] British Society of Audiology. "Guidelines for the Early Audiological Assessment and Management of Babies Referred from the Newborn Hearing Screening Programme," *Available at: https://www.thebsa.org.uk/resources [Accessed June 6, 2024]*, 2021.

[8] British Society of Audiology. "Recommended Procedure Auditory Brainstem Response (ABR) Testing in Newborns," *Available from: Https://Www.Thebsa.Org.Uk/Guidance-and-Resources/Current-Guidance/. [February 20, 2025],* 2025.

[9] Sininger, Y. S., Hunter, L. L., Hayes, D., Roush, P. A., & Uhler, K. M. "Evaluation of Speed and Accuracy of Next-Generation Auditory Steady State Response and Auditory Brainstem Response Audiometry in Children With Normal Hearing and Hearing Loss" *Ear and Hearing*, 1, 2018.

[10] Polonenko, M. J., & Maddox, R. K. "The Parallel Auditory Brainstem Response," *Trends in Hearing*, 23, 233121651987139, 2019.

[11] Kristensen, S. G. B. "Simultaneous electrophysiological measurements with auditory narrow-band stimuli" PhD Thesis. Kgs. Lyngby, Denmark, Technical University of Denmark, 2024.

[12] Kristensen, S. G. B., S. Laugesen, and T. Dau. "Simultaneous Recording of Auditory Brainstem Responses at Clinical Discharge Level".

International Symposium on Auditory and Audiological Research (ISAAR), 2023.
[13] Speidel, D., & Beck, D. L. "Demystifying the CE-Chirp," *Hearing Review*, *23*(2), 28, 2016.
[14] Elberling, C., & Don, M. "A direct approach for the design of chirp stimuli used for the recording of auditory brainstem responses," *The Journal of the Acoustical Society of America*, *128*(5), 2955, 2010.
[15] Laugesen, S., Rieck, J. E., Elberling, C., Dau, T., & Harte, J. M. "On the Cost of Introducing Speech-Like Properties to a Stimulus for Auditory Steady-State Response Measurements," *Trends in Hearing*, 22, 233121651878930, 2018.
[16] Watson, S., Laugesen, S., & Epp, B. "Potential Destructive Binaural Interaction Effects in Auditory Steady-State Response Measurements," *Trends in Hearing*, 25, 233121652110311, 2021.
[17] Elberling, C., & Esmann, L. C. "Calibration of brief stimuli for the recording of evoked responses from the human auditory pathway," *The Journal of the Acoustical Society of America*, 141(1), 466–474, 2017.
[18] Undurraga, J. A., Chesnaye, M., Simpson, D., Harte, J., & Laugesen, S. "A novel method for individualized detection of Auditory Evoked responses in real-time—The Fmpi," *International Symposium on Auditory and Audiological Research (ISAAR),* 2023.
[19] Don, M., & Elberling, C. "Evaluating residual background noise in human auditory brain-stem responses," *The Journal of the Acoustical Society of America,* 96(5), 2746–2757, 1994.
[20] Stoll, T. J., & Maddox, R. K. "Enhanced Place Specificity of the Parallel Auditory Brainstem Response: A Modeling Study," *Trends in Hearing*, 27, 23312165231205720, 2023.
[21] Stoll, T. J., & Maddox, R. K. "Enhanced Place Specificity of the Parallel Auditory Brainstem Response: An Electrophysiology Study". *bioRxiv: the preprint server for biology,* 2024.
[22] Temboury-Gutiérrez, M. "Modeling human auditory evoked brain responses to complex sounds". PhD Thesis. PhD thesis. Kgs Lyngby, Denmark: Technical University of Denmar, 2024.
[23] Robles, L., & Ruggero, M. A. Mechanics of the Mammalian Cochlea. Physiological Reviews, 81(3), 2001.
[24] Eggermont, J. J. "On the rate of maturation of sensory evoked potentials," *Electroencephalography and Clinical Neurophysiology*, 70(4), 293–305, 1988.
[25] Ponton, C. W., & Eggermont, J. J. "Electrophysiological measures of human auditory system maturation: Relationship with neuroanatomy and behavior." In R. Burkard, M. Don, & J. J. Eggermont (Eds.), Auditory evoked potentials: Basic principles and clinical application (pp. 385–402). *Lippincott Williams & Wilkins*, 2007.

DOI: 10.61782/fa.2025.0298

FORUM ACUSTICUM EURONOISE 2025

DIAGNOSING HEARING LOSS USING AIR- AND BONE-CONDUCTED PARALLEL AUDITORY BRAINSTEM RESPONSES

Melissa J. Polonenko[1*] **Ross K. Maddox**[2]

[1] Department of Speech-Language-Hearing Sciences, University of Minnesota, United States
[2] Kresge Hearing Research Institute, Department of Otolaryngology – Head & Neck Surgery, University of Michigan, United States

ABSTRACT

The auditory brainstem response (ABR) is an essential tool in screening for and diagnosing infant hearing loss to support optimal language acquisition through early intervention. The parallel ABR (pABR) paradigm measures responses to frequencies from 500–8000 Hz in both ears all at once, rather than the traditional methods of single-frequency measurements in one ear at a time. Our preliminary work in ten adults with maximally varying configurations of sensorineural hearing loss shows that the pABR provides highly accurate thresholds more than twice as fast as serial ABR. Furthermore, our recent work in a group of twenty adults with normal hearing shows that bone conduction pABR measurements are feasible, which is also a necessary part of diagnosing hearing loss by determining the relative contributions of conductive and sensorineural hearing loss. Given these air- and bone-conduction results, the pABR holds promise as a viable clinical tool for objective threshold estimation and diagnosis of hearing loss.

Keywords: *evoked potentials, hearing loss, diagnostics*

1. INTRODUCTION

Early diagnosis of and intervention for hearing loss are critical for facilitating language acquisition. Many countries worldwide use the auditory brainstem response (ABR) to estimate hearing thresholds in infants and other people who cannot complete standard behavioral audiometry. Although the ABR is effective for diagnosing hearing loss [1,2], the auditory-specific responses recorded on the scalp are small compared to the background noise, so the infant must be resting quietly, constraining the exam's duration. Exams often finish with incomplete information, requiring the family to return, further delaying diagnosis and risking attrition. Therefore, faster tests are needed.

The parallel ABR (pABR) was created to address this time constraint by measuring responses to all frequencies in both ears all at once [3]. Compared to traditional methods of single-frequency measurements in one ear at a time, the pABR is a median of 3x faster at a soft level (51 dB peSPL) in adults with normal hearing. Previous studies have also shown better place specificity for the pABR's responses than serial methods [4,5], which may improve estimates of severe hearing losses that require the use of higher levels.

The pABR's accuracy and speed, however, have not yet been tested in people with hearing loss. Neither has the pABR been tested through bone conduction, which is also an essential part of diagnosing the conductive versus sensorineural components of hearing loss. This paper presents preliminary findings for all three: the accuracy and timing of air conduction testing in adults with hearing loss and bone conduction testing in adults with normal hearing.

2. METHODS

2.1 Air conduction testing in adults with hearing loss

Seventy adults with widely varying sensorineural hearing loss configurations were recruited under an approved sIRB protocol between the Universities of Minnesota and Michigan. This paper presents findings from a subset of ten

*Corresponding author: mpolonen@umn.edu
Copyright: ©2025 Melissa Polonenko & Ross Maddox. This is an open-access article distributed under the terms of the Creative Commons Attribution 3.0 Unported License, which permits unrestricted use, distribution, and reproduction in any medium, provided the original author and source are credited.

adults chosen based on maximally different audiometric configurations, who first underwent pABR testing and then returned for testing using traditional serial ABR methods with clinical equipment. Ages ranged from 29 to 69 years.

In the first session, a threshold search was done using the pABR with a real-time custom interface before determining behavioral thresholds with standard audiometry. pABR thresholds were estimated using a leave-one-out regression between the pABR threshold levels in dB nHL and behavioral thresholds in dB HL, a correction step that is routinely done in the clinic. For the second session, the experimenter was blinded to the participant's hearing loss. A threshold search was conducted for each frequency in each ear separately using clinical protocols that were matched as closely as possible to the pABR stimuli. Time to diagnose 10 (pABR, 0.5–8 kHz in both ears) or 8 (clinical, 0.5–4 kHz in both ears) thresholds was compared.

2.2 Bone conduction in adults with normal hearing

Twenty young adults with normal hearing (aged 19 to 31 years) were recruited under the same sIRB protocol. To keep the session under 3 hours, bone conduction was only completed in one ear. Both the ear and order of air- and bone-conduction were counterbalanced across participants.

Air- and bone-conduction behavioral thresholds to the pABR stimuli were measured to determine the correction factors to match levels in dB sensation level (SL) due to the different voltage output for the two transducers. Then ABRs (Fz referenced to A1 and A2, ground at Fpz) were recorded to pABR stimuli (~40 stimuli/second) while participants reclined and rested in a darkened sound booth. An intensity series from 20–70 dB peSPL (~0–50 dB nHL calibrated to an air-conducted 1 kHz tone) was completed using ER2 insert earphones (air) or a B71 bone vibrator (bone) with contralateral masking (400 stimuli/second) through an earphone. Ten minutes of data were collected for each intensity and transducer, totaling 120 minutes. Waveform morphologies for each transducer were compared by their wave V amplitudes and latencies at similar dB SL levels.

3. RESULTS

3.1 The pABR is accurate and faster than serial ABR

Overall, the pABR provided highly accurate thresholds (Fig. 1). There was a 95% confidence interval of 0.78–0.93 for the correlation between behavioral and pABR-estimated thresholds (Fig. 1A). Fig. 1B shows the distribution of threshold differences—most differences (72%) were within one step size (±10 dB), and 90% were within ±15 dB.

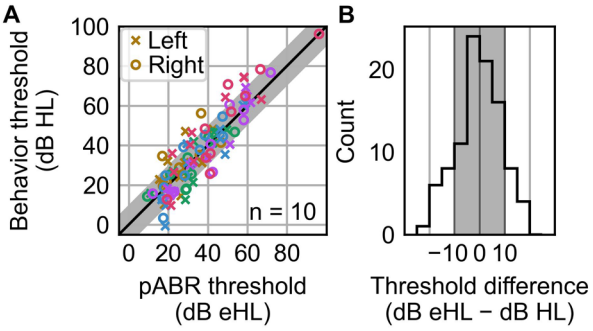


Figure 1. (A) pABR-estimated thresholds are highly correlated with behavioral audiometric thresholds. Jitter applied for visualization (±2.5 dB). Shaded regions represent differences within a step size of ±10 dB. Colors represent frequency: 0.5 kHz (gold), 1 kHz (green), 2 kHz (blue), 4 kHz (purple), 8 kHz (pink). (B) Histogram of pABR-behavioral threshold differences.

Next, the time required to obtain a complete set of thresholds was calculated (Fig. 2). The pABR was faster in all participants, with a mean ± SD testing time of 27.8 ± 8.2 minutes to estimate 10 thresholds versus 69.7 ± 20.9 minutes to estimate 8 serial thresholds, for a significant time reduction of 41.9 ± 20.0 minutes (paired t-test, $t(9) = -6.6$, $p < 0.001$). The median speedup ratio was 2.5x (ranged from 1.4x to 4.2x).

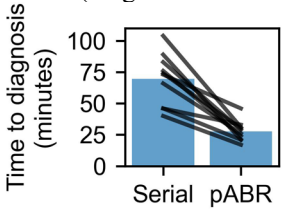


Figure 2. pABR versus serial ABR threshold estimation times. Lines show individuals and bars show the mean.

3.2 pABRs are similar for air- and bone-conduction

Sound played with the same output voltages from the headphone amplifier produced higher behavioral thresholds for bone- vs air-conduction, consistent with the higher force levels required to drive the vibrator. Insufficient force was generated to obtain clear responses above threshold for 8 kHz, which was consequently removed from the analysis. The mean correction factor to convert levels to dB SL was 35 dB for bone- and 25 dB for air-conduction. The levels for bone-conduction were ~5 dB quieter at 0.5 and 4 kHz.

Clear responses were obtained with both transducers at 4 levels (5, 15, 25, 35 dB SL). Wave V peak amplitudes and latencies across all participants and levels are shown in Fig. 3. Wave V metrics correlated between air- and bone-conduction, with a 95% confidence interval of 0.59–0.82 for amplitude and 0.91–0.96 for latency. Overall, compared to air-, the mean ± SE wave V peaks for bone-conduction were smaller by 0.014 ± 0.002 µV ($t(278) = -6.2$, $p < 0.001$) and shorter by 0.198 ± 0.068 ms ($t(278) = -2.9$, $p = 0.004$).

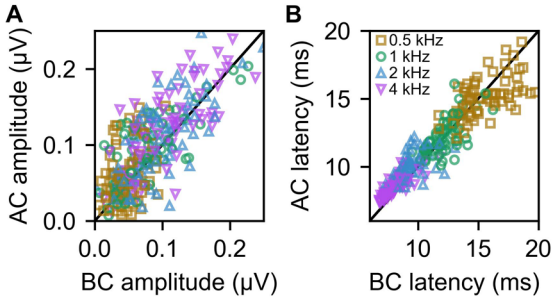


Figure 3. Wave V peak (A) amplitude and (B) latency across participants for stimuli conducted through air (AC) and bone (BC) across 5–35 dB SL levels.

4. DISCUSSION

Preliminary work from the two studies presented in this paper show the feasibility of using air- and bone-conducted pABR stimuli for accurately diagnosing hearing loss.

The pABR provides highly accurate threshold estimates in a subset of adults with widely varying hearing loss (Fig. 1) that are on par with serial ABR [2]. It is also substantially faster in a clinical-like setup than the current serial ABR (Fig. 2), which could facilitate the collection of more complete information during clinical translation of this method. Together with previous work in adults with normal hearing [3], data from all seventy adults in the study will provide further support for the pABR as a viable method for objective threshold estimation across the range of hearing.

Preliminary work in adults with normal hearing shows that bone-conduction pABR measurements are also feasible. Although air- and bone-conduction wave V metrics differed overall (Fig. 3), their responses generally aligned given the 10-dB step sizes. Due to the different voltages required to drive the bone vibrator, the actual dB SL levels were ~5 dB quieter for some frequencies (halfway between step sizes), which could contribute to the smaller responses. Further analyses of the data will reveal the necessary corrections that can be applied to future experimental paradigms to ensure similar output levels are used for both transducers. The larger study provides the necessary behavioral threshold and ABR response information to adjust the frequency-specific stimulus voltage outputs to adequately drive the bone vibrator to produce similarly sized responses. This work represents an important step towards creating a pABR paradigm that includes both air- and bone-conduction so that both the sensorineural and conductive components of hearing loss can be diagnosed.

Given these air- and bone-conduction results in adults, the pABR holds promise as a viable clinical tool for objective threshold estimation and diagnosis of hearing loss while addressing the primary drawback of current methods: speed. This preliminary work represents an important step towards translating the pABR for diagnosing hearing loss and taking the next steps to validating the method for use in infants and other populations that require objective testing.

5. ACKNOWLEDGMENTS

This work was funded by NIDCD R01DC017962. Katherine Teece assisted with recruitment. Isabel Herb and Eric Mitchell assisted with recruitment and data collection.

6. REFERENCES

[1] Joint Committee on Infant Hearing: "Year 2019 position statement: principles and guidelines for early hearing detection and intervention programs," *Journal of Early Hearing Detection and Intervention*, vol. 4, no. 2, pp. 1–44, 2019.

[2] D.R. Stapells and P. Oates: "Estimation of the pure-tone audiogram by the auditory brainstem response: a review," *Audiology and Neurotology*, vol. 2, pp. 257–280, 1997.

[3] M. J. Polonenko and R. K. Maddox: "The parallel auditory brainstem response," *Trends in Hearing*, vol. 23, pp. 2331216519871395, 2019.

[4] T. Stoll and R. Maddox: "Enhanced place specificity of the parallel auditory brainstem response: an electrophysiological study," *Journal of the Association for Research in Otolaryngology*, vol. 25, no. 5, pp. 477–489, 2024.

[5] T.J. Stoll and R.K. Maddox: "Enhanced place specificity of the parallel auditory brainstem response: a modeling study," *Trends in Hearing*, vol. 27, 23312165231205719, 2023.

DOI: 10.61782/fa.2025.0856

FORUM ACUSTICUM EURONOISE 2025

THE BINAURAL INTERACTION COMPONENT IS ENHANCED WITH CHIRPS RELATIVE TO CLICKS AND PRODUCES BETTER BEHAVIORAL LATERALIZATION

Kerry A. Walker[1*] **Carol A. Sammeth**[1] **Matthew Mavandi**[2]
Nathaniel T. Greene[3] **Daniel J. Tollin**[1,3]

[1] Department of Physiology & Biophysics, University of Colorado Anschutz Medical Campus, Aurora, USA
[2] Kansas City University, Kansas City, USA
[3] Department of Otolaryngology, University of Colorado Anschutz Medical Campus, Aurora, USA

ABSTRACT

The binaural interaction component (BIC) of the auditory brainstem response (ABR) is obtained by subtracting a binaurally-evoked ABR from the sum of monaural left and right ear ABRs. BIC amplitude is modulated by interaural time differences (ITDs) and has been proposed as a biomarker of binaural hearing ability. Traditionally, clicks are used to evoke ABRs; however, chirps are recommended to compensate for the cochlear traveling wave and enhance wave V. Whether chirps improve BIC measurements has not been systematically examined. Here, ABRs and BICs were measured in subjects (n = 6; 21-29 years) for three stimuli; 1) 100-µsec clicks, 2) level-independent CE chirps, and 3) Level-Specific (LS) chirps at four intensities ranging from 65-40 dB nHL. Subjects also completed behavioral testing measuring ITD discrimination thresholds. Compared to clicks, chirps generally elicited larger monaural and binaural wave V and larger BIC amplitudes, particularly at lower intensities. Subjects also exhibited lower ITD thresholds for chirps than clicks, mainly at lower stimulus levels. Chirps may provide an enhancement to ABR wave V and BIC, improving signal-to-noise ratio and reliability. The improved behavioral sensitivity to ITDs with chirps supports the hypothesis that BIC arises from binaural brainstem nuclei that are important for binaural hearing.

Keywords: *auditory brainstem response, binaural interaction component, binaural hearing, interaural time difference*

1. INTRODUCTION

The auditory brainstem response (ABR) is an electrophysiological measure widely used both clinically and in research to investigate the integrity of the auditory system pathway. A binaural interaction component (BIC) can be obtained by subtracting a binaurally evoked ABR from the sum of the monaural right and left ear ABRs [1]. If there were two independent monaural pathways, the resulting difference waveform would be zero (minus any measurement artifact or noise); However, a small negative component appears at approximately the latency of ABR wave V or its roll-off slope in human subjects. This indicates a different amount of synchronous neural activity occurring in the brainstem during binaural stimulation than during monaural. In the literature, this most prominent BIC component has been called “DN1” [2-6].

The ABR BIC has been measured in a number of animal models [2], [7], [8], as well as in normal-hearing human subjects [6], [9-16]. The BIC has been reported to be abnormal in the elderly [17], in persons with multiple sclerosis [18], in specific language disorder [19], and in children diagnosed with CAPD [20], [21]. The ABR BIC is thought to be generated at the level of the lateral superior

[*] ***Corresponding author**: Kerry.walker@cuanschutz.edu*

***Copyright**: ©2025 Walker et al. This is an open-access article distributed under the terms of the Creative Commons Attribution 3.0 Unported License, which permits unrestricted use, distribution, and reproduction in any medium, provided the original author and source are credited.*

olive of the brainstem ([1], [8], [22]), an area that has been associated with neural processing of interaural sound cues.

The BIC has received increasing attention as a non-invasive biomarker of binaural processing. For example, researchers have observed systematic changes in the amplitude and latency of the BIC DN1 component when interaural cues that control perceptual lateralization are varied in normal hearing adults. Specifically, latency of DN1 systematically alters with increasing interaural level difference (ILD) and/or interaural time difference (ITD) cues [3], [6], [12], [23], [24], [25]. In addition, BIC amplitude has been found to correspond with a behaviorally measured ability to lateralize sound as a function of ITD and ILD and its presence is assumed to indicate fusion of binaural stimuli [12], [23], [26]. Recently, Brown et al. [27] and Sammeth et al. [16] reported that BIC amplitude also varies systematically with interaural frequency mismatch and corresponds to ITD sensitivity measured behaviorally.

Unfortunately, however, the ABR BIC has not proven to date to be useful as a potential clinical diagnostic indicator for suprathreshold hearing ability because it is not always obtained reliably in human subjects. While the BIC is readily obtained in sedated animals, it is time consuming and difficult to obtain a clear, replicable response in awake human subjects [6], [28]. This is mostly due to its very small size relative to the size of myogenic (muscle) and other noise artifacts in the waveform, and also because the larger head size in humans than in animal models (such as rodents) results in a surface electrode measurement that is farther away from the neural generators for the BIC [8]. In ongoing efforts to find a means to more reliably obtain the ABR BIC, members of our research lab recently showed that the use of an alternative to a standard ABR click stimulus, namely, a rising frequency "chirp" stimulus, optimizes recordings of the BIC in chinchillas [29]. The current experiment was designed to determine if this stimulus advantage is also seen in human subjects.

The stimuli typically used for measurement of ABRs and BIC is the acoustic click. However, some researchers have suggested that this might not always be the best stimulus choice to obtain a robust auditory electrophysiologic response [30], [31], [32], [33], [34]. This is because the traveling wave on the basilar membrane elicits an auditory system response first from high frequencies, then from progressively lower frequencies [35]. Cochlear tonotopicity reduces temporal response synchrony to a click stimulus, resulting in reduced ABR amplitude. Therefore, chirp stimuli have been developed that compensate for the dispersion of the traveling wave by presenting low frequencies first, then progressively higher frequencies in an upward sweep, and that have been found to produce larger ABR wave V amplitude at least at a moderately/high stimulus level ([24], [31], [33], [34], [36]. As BIC DN1 arises at a similar latency as ABR wave V, we hypothesize that chirps might produce a larger BIC response.

Chirps are now widely used clinically in ABR measurements, but to our knowledge only one publication has directly explored the use of chirps versus clicks to measure BIC DN1 in humans. Reidel and Kollmeier [24] reported that, compared to clicks, chirps designed to enhance monaural ABR wave V also produced larger BIC at low to moderate sound levels, although the enhancement was not as great as seen for wave V.

A chirp stimulus now commonly used in clinical auditory evoked potential measurement equipment that was empirically derived is the "CE-Chirp®" [33], [34]. Because derivation of the standard CE-Chirp is based only on the cochlear traveling wave delay at a moderate/high stimulation level (~60 dB nHL), it is considered a "level-independent" chirp [37]. However, it has been found that the frequency sweep rate of chirps should vary by stimulation level for optimal results [36], [38], [39]. As a consequence, so-called level-dependent chirps, or "Level-Specific (LS) CE-Chirps®", which compensate for this level effect were developed [39], [40].

Of note is that both standard CE-Chirps and LS-Chirps were designed to optimize ABRs measured monaurally, while BIC is derived from binaural versus monaural stimulation. In our study, Owrusky et al. [29] considered that a chirp stimulus specifically derived from BIC DN1 latency for different frequencies of stimulation might be optimal to enhance BIC response amplitude. In their results, however, no additional DN1 amplitude enhancement was found for the DN1 latency-derived chirps compared to LS-Chirps, and therefore in the current study we chose here to only use the standard CE-Chirp and LS-Chirps.

Specifically, the current study compared the ABR BIC measured in normal-hearing young adults across multiple stimulation levels for three stimuli: 1) a standard click, 2) the level-independent CE-Chirp, and 3) the level-dependent LS-Chirps. The purpose was to build on the work of Reidel and Kollmeier [24] and Owrusky et al. [29] to evaluate our hypothesis that LS-Chirps will generate significantly higher response amplitude for the ABR BIC in human subjects across stimulus levels than will either the standard CE-Chirp or a click. In this short paper, our main objectives were to investigate if 1) chirps improve BIC measurement in humans, and if 2) chirps alters ITD sensitivity compared to traditional click stimuli.

2. METHODS

Approval was obtained from the Colorado Multiple Institutional Review Board for human subjects. All subjects had bilateral hearing thresholds < 10 dB HL at frequencies from 250 Hz to 4000 Hz and < 15 dB HL for extended high frequencies of 6000 to 16000 Hz, with symmetrical hearing thresholds between the ears (< 10 dB difference at a given audiometric frequency). None of the subjects had a history of otologic or neurological disorder. Subjects were paid for participation in the study. Subjects were 6 normal hearing adults (4 females) aged 21 to 30 years.

2.1 ABR measurements

ABR measurements were completed across six, 2-hour sessions for each subject, completed on different days. Two sessions were used for each of the three stimulus types. For example, in the first session, measurements were obtained at four stimulus levels, and in the second session, the measurements were replicated.

ABR waveform acquisition was accomplished using the commercially available International Hearing System (IHS) Duet AEP measurement system with research module. EEG was amplified by 100,000 and were bandpass filtered 100-3000 Hz. Artifact rejection threshold was set to ± 20 µV. Three different stimuli were used: 1) 100-µs clicks, 2) CE chirp, and 3) Level Specific (LS) chirp. ABRs and BICs were measured with each stimulus at stimulus levels of 65, 60, 50 and 40 dB HL. For each ABR, 4000 total sweeps were averaged across two runs. The BIC was calculated post-hoc as the binaurally stimulated ABR minus the sum of the right and left ear monaural ABRs. Two complete BIC measurements were completed for each stimulus at each level, to confirm replicability of the DN1.

Stimulus level was calibrated via a 2cc coupler attached to a Larson-Davis sound level meter and Tektronix oscilloscope for determination of peak equivalent SPL of the stimuli compared to a 1000 Hz calibration tone. The stimulus repetition rate was ~11.1 per second and was presented in rarefaction. Stimuli were presented via ER-2 insert earphones. ABRs were recorded from Ambu Neuroline 720 disposable surface electrodes (Ambu Inc., Columbia, MD).

Following skin preparation, electrodes were placed according to the International 10-20 Electrode System [41] using a midline montage: Fz (high forehead) was referenced to the nape of the neck (just above the 7th cervical vertebra), with Fpz (low forehead) as the ground. Electrode impedances were < 5 kΩ (typically 2-3 kΩ) and balanced between electrode pairs within 1 kΩ. Subjects were seated comfortably with a neck pillow in a slightly reclining chair in a darkened room and asked to close their eyes, relax, and sit quietly or sleep during measurements.

2.1.1 Marking of the Waveforms

Marked and labeled peaks (Fig. 1) were initially placed on the waveforms by the first author, who is an experienced audiologist who did all the electrophysiological testing for this study, but were then reviewed by the second author, who is also an audiologist experienced in these

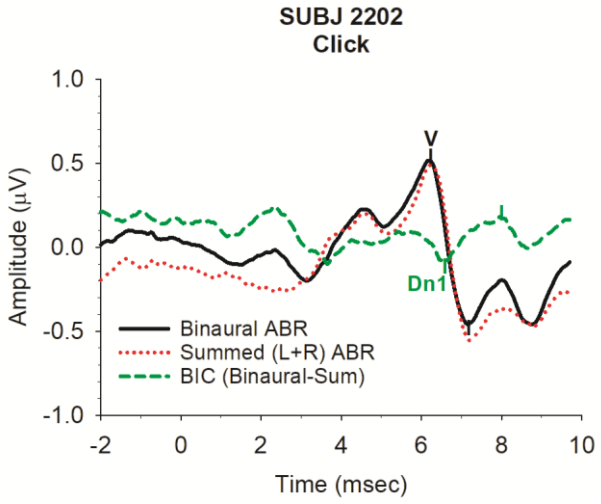


Figure 1. Example Binaural/Summed ABR and calculated BIC using clicks. Wave V was marked from the peak to following trough. BIC DN1 was marked as the most prominent trough and following peak occurring near ABR Wave V.

measures. In all cases, markings were agreed upon by both authors. All identifiable latencies and peak-to-trough amplitudes of waves I through VI of the monaural and binaural ABR waveforms were first marked, to aid in identification of the DN1 component of the BIC in the difference traces. The DN1 component of the BIC was identified as the most prominent negative peak in the temporal region of the difference waveform that corresponded to wave V and its roll-off slope and was only accepted as a valid response if it was replicable across both BIC traces for a given stimulus type and level. DN1 was marked both for latency of the negative trough, and for relative amplitude (negative peak to the

following positive peak) amplitude. When the positive peak following BIC was equivocal (e.g., as sometimes occurred in the presence of multiple fluctuations or a shallow rising slope), it was marked as the most prominent positive point occurring prior to the latency of an identifiable wave VI peak.

2.2 Behavioral ITD discrimination task

Behavioral measurements were completed across multiple sessions. The task measured both ITD discrimination threshold and subjective lateralization of each of the stimuli at four levels, 10, 20, 40 and 60 dB HL. The method was based on that used by Brown and Tollin [42], [43]. This task was implemented in a separate MATLAB program, with stimuli delivered via the playback system and insert earphones described above.

During testing, subjects sat at a desk in a lighted sound booth and responded using a large touch screen monitor (Fig. 2). On the screen was a schematic illustration of a head, with horizontal bars indicating the right and left sides of the head. Each trial consisted of presentations of two sequential sets of tone pips. A train of 5 stimuli (e.g, the CE chirp) at 14/sec was first presented simultaneously to each ear (ITD=0 µs) and this was followed by a train of 5 stimuli with a non-zero ITD. Left-favoring ITDs were imposed by delaying the stimulus to the right ear, and right-favoring ITDs imposed by delaying the stimulus to the left. The subject's task was to discriminate whether the second stimulus (target) fell perceptually to the left or the right of the first stimulus (reference). If the target set was perceived as falling to the right of the reference, the subject was instructed to touch the bar that was on the right side of the screen, and vice versa. Further, subjects were asked to indicate on the bar how far to the right or to the left the target appeared relative to the reference, i.e., a subjective lateralization task. Subjects received immediate feedback regarding the left/right discrimination response, via a green asterisk flashing on the bar if their response was correct, and a red asterisk flashing if their response was incorrect (these colors were readily discriminable by all subjects).

Each run started with the ITD for the second binaural stimulus train at 800 µs. ITD was then changed adaptively depending on the subject's response. A 3-down, 1-up procedure was used, i.e., three consecutive correct responses were required for the ITD to decrease, but one incorrect response resulted in an increase in the ITD, targeting a 79.4% correct threshold (Levitt, 1971). Step size was initially large but then rapidly decreased over a run, so that the task became increasingly difficult. Specifically, a log step size adjustment was used (1/100.2, then 1/10.05); i.e., the adjustment magnitude was a fixed percentage of the ITD magnitude so that step size decreased as subjects approached threshold. Within a run, two separate 3-down 1-up tracks were initialized and run simultaneously. Testing continued until 8 reversals were observed. The first 4 reversals were discarded, and the geometric mean of the last 6 reversals averaged to determine the ITD discrimination threshold for that condition.

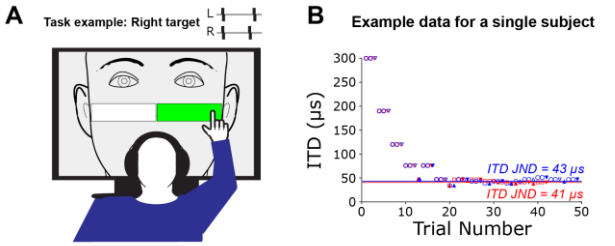


Figure 2. A) Subjects responded using a touch screen monitor and received feedback regarding the left/right response. B) A 3-down, 1-up procedure was used. Testing continued until 10 reversals were observed and the last 6 averaged to determine the ITD discrimination threshold (i.e,. ITD JND).

Practice runs were completed to familiarize and train subjects on the task. Subsequently, three runs were completed for each of the four stimulus levels, randomly ordered, and the average of the ITD discrimination thresholds for the three runs per frequency condition and stimulus level was used for final analysis.

3. RESULTS

3.1 ABR measurements

ABR measurements, and subsequent BIC, were obtained in 5 subjects in response to 1) click, 2) CE Chirp, and 3) LS Chirp stimuli presented at 65, 60, 50, 40 dB nHL. Replicable BIC detection rates ranged from 100% (50 dB CE Chirp) to 20% (65 dB LS Chirp) (Fig. 3).

As ABR BIC is derived from ABR wave V, peak-to-peak amplitudes of binaural and summed ABRs were examined to characterize enhancements to wave V, and subsequent DN1, due to differing stimuli (Fig. 4). Statistical analyses using paired t-tests revealed significantly larger binaural and summed wave V amplitudes to CE Chirp stimuli at 40 dB nHL compared to LS Chirp and Click stimuli ($p<0.05$). For summed monaural waveforms, wave V amplitude to CE Chirp stimuli at 50 dB nHL was also significantly larger than wave V evoked from LS Chirp

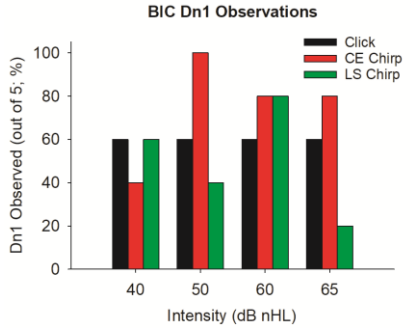


Figure 3. Percentage of replicable BIC DN1 observed from 5 subjects for each test condition.

stimuli ($p<0.05$). All other conditions did not reveal significant wave V amplitude differences between stimulus type. DN1 amplitudes also were not statistically different across all stimulus types ($p>0.05$ for all).

3.2 Behavioral ITD discrimination task

Behavioral testing was completed by 6 subjects using the same stimulus type as ABR with additional high-pass filtered stimuli at 2 kHz and a reverse chirp stimulus (Fig. 5). The high-pass condition was completed to remove the dominance of low frequency fine structure ITD cues [44]. Intensity levels included 60, 40, 20, and 10 dB nHL. Paired t-tests revealed enhanced ITD discrimination to unfiltered LS Chirp stimuli compared to Click at 10 dB nHL ($p<0.0001$) and CE Chirp ($p<0.05$). ITD discrimination was similar across stimulus types at higher intensities. With regards to filtered stimuli, high-pass at 2 kHz to remove low-frequency fine structure cues, similar statistical differences were observed as ITD discrimination was significantly better to LS Chirp at 20 dB nHL compared to click at 20 dB nHL ($p<0.0001$) and CE Chirp compared to click at 10 dB nHL ($p<0.001$).

4. CONCLUSIONS

Overall, a replicable BIC was observed in all participants for at least one stimulus type, however, the use of chirp had variable effects on BIC producibility. As expected, use of chirps generally enhanced ABR wave V, specifically at lower intensities, however, this difference was not observed for both chirp types. With regards to behavioral data, clicks yielded poorest performance compared to chirps at lower intensities. As high pass filtering eliminated an ITD

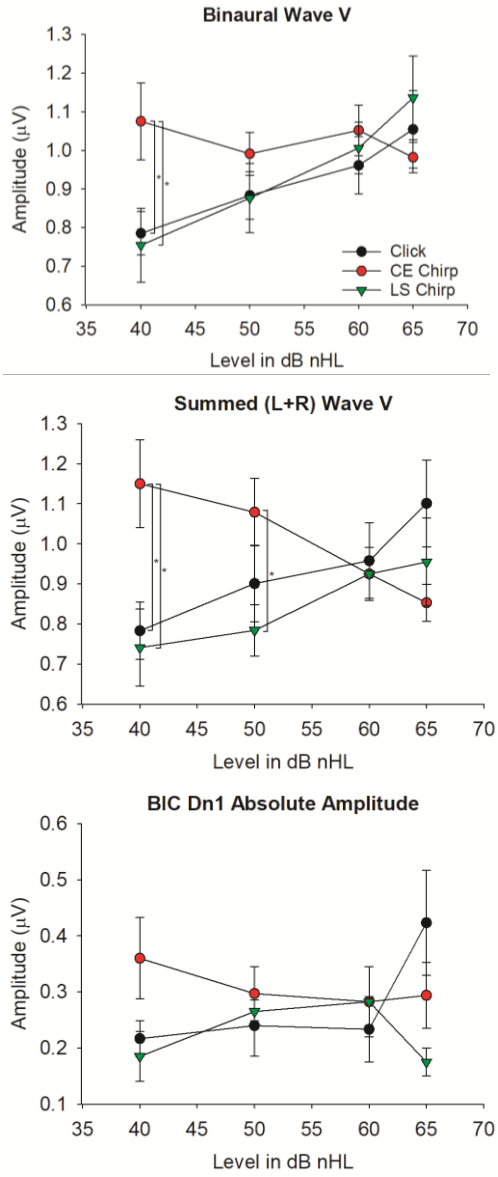


Figure 4. Average Wave V (Top, Middle) and DN1 (bottom) peak-to-peak Amplitude +/- 1 SE as a function of intensity for each stimulus. Statistics: t-tests:*$p<0.05$. Top)

dominant region (around 750 Hz;), we see significant differences between chirp and click extend to both 10 and 20 dB nHL conditions. However, no difference was observed between chirp types for filtered conditions. Across both electrophysiological and behavioral experiments, a chirp advantage over traditional click stimuli occurs at

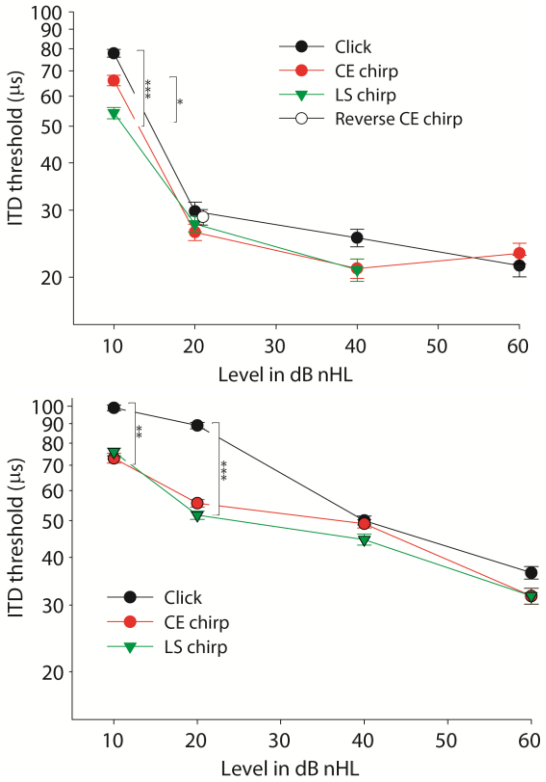


Figure 5. ITD thresholds as a function of intensity for each stimulus. Top) unfiltered stimuli. Bottom) 2 kHz High pass filtered stimuli. Paired t-tests: * $p < 0.05$; ** $p < 0.001$ and *** $p < 0.0001$

lower intensities improving perceptual lateralization and wave V characteristics. These finding support the use of chirp stimuli particularly at lower, near-threshold intensities for binaural hearing assays. To date, 5 subjects have completed both electrophysiological and behavioral measurements and future research will examine relationships between measured outcomes to investigate the utility of BIC as a marker of binaural hearing.

5. ACKNOWLEDGMENTS

This work is supported by NIH-NIDCD R01DC017924 awarded to co-author Daniel Tollin and Achim Klug. Portions of this work were completed as part of Graduate Experiences for Multicultural Students (GEMS) program, R25HL103286-07.

6. REFERENCES

[1] G. Laumen, A. T. Ferber, G. M. Klump, and D. J. Tollin, "The Physiological Basis and Clinical Use of the Binaural Interaction Component of the Auditory Brainstem Response.," *Ear Hear*, vol. 37, no. 5, pp. e276–e290, Oct. 2016, doi: 10.1097/AUD.0000000000000301.

[2] R. A. Dobie and C. I. Berlin, "Binaural Interaction in Brainstem-Evoked Responses," *Archives of Otolaryngology*, vol. 105, no. 7, pp. 391–398, Jul. 1979, doi: 10.1001/archotol.1979.00790190017004.

[3] H. Riedel and B. Kollmeier, "Interaural delay-dependent changes in the binaural difference potential of the human auditory brain stem response.," *Hear Res*, vol. 218, no. 1–2, pp. 5–19, Aug. 2006, doi: 10.1016/j.heares.2006.03.018.

[4] D. Junius, H. Riedel, and B. Kollmeier, "The influence of externalization and spatial cues on the generation of auditory brainstem responses and middle latency responses," *Hearing Research*, vol. 225, no. 1, pp. 91–104, Mar. 2007, doi: 10.1016/j.heares.2006.12.008.

[5] A. T. Ferber, V. Benichoux, and D. J. Tollin, "Test-Retest Reliability of the Binaural Interaction Component of the Auditory Brainstem Response.," *Ear Hear*, vol. 37, no. 5, pp. e291-301, Oct. 2016, doi: 10.1097/AUD.0000000000000315.

[6] C. A. Sammeth, N. T. Greene, A. D. Brown, and D. J. Tollin, "Normative Study of the Binaural Interaction Component of the Human Auditory Brainstem Response as a Function of Interaural Time Differences.," *Ear Hear*, vol. 42, no. 3, pp. 629–643, Jun. 2021, doi: 10.1097/AUD.0000000000000964.

[7] S. Wada and A. Starr, "Anatomical bases of binaural interaction in auditory brain-stem responses from guinea pig.," *Electroencephalogr Clin Neurophysiol*, vol. 72, no. 6, pp. 535–544, Jun. 1989, doi: 10.1016/0013-4694(89)90231-9.

[8] V. Benichoux, A. Ferber, S. Hunt, E. Hughes, and D. Tollin, "Across Species 'Natural Ablation' Reveals the Brainstem Source of a Noninvasive Biomarker of Binaural Hearing," *J. Neurosci.*, vol. 38, no. 40, p. 8563, Oct. 2018, doi: 10.1523/JNEUROSCI.1211-18.2018.

[9] P. J. Ainslie and J. R. Boston, "Comparison of brain stem auditory evoked potentials for monaural and binaural stimuli.," *Electroencephalogr Clin Neurophysiol*, vol. 49, no. 3–4, pp. 291–302, Aug. 1980, doi: 10.1016/0013-4694(80)90223-0.

[10] R. A. Dobie and S. J. Norton, "Binaural interaction in human auditory evoked potentials.," *Electroencephalogr Clin Neurophysiol*, vol. 49, no. 3–4, pp. 303–313, Aug. 1980, doi: 10.1016/0013-4694(80)90224-2.

[11] C. G. Fowler and J. S. Leonards, "Frequency dependence of the binaural interaction component of the auditory brainstem response.," *Audiology*, vol. 24, no. 6, pp. 420–429, 1985, doi: 10.3109/00206098509078361.

[12] D. L. McPherson and A. Starr, "Auditory time-intensity cues in the binaural interaction component of the auditory evoked potentials.," *Hear Res*, vol. 89, no. 1–2, pp. 162–171, Sep. 1995, doi: 10.1016/0378-5955(95)00134-1.

[13] Z. D. Jiang, "Binaural interaction and the effects of stimulus intensity and repetition rate in human auditory brain-stem.," *Electroencephalogr Clin Neurophysiol*, vol. 100, no. 6, pp. 505–516, Nov. 1996, doi: 10.1016/s0168-5597(96)96519-3.

[14] M. H. Stollman, A. F. Snik, G. C. Hombergen, R. Nieuwenhuys, and P. ten Koppel, "Detection of the binaural interaction component in the auditory brainstem response.," *Br J Audiol*, vol. 30, no. 3, pp. 227–232, Jun. 1996, doi: 10.3109/03005369609079043.

[15] L. N. Van Yper, K. Vermeire, E. F. J. De Vel, R.-D. Battmer, and I. J. M. Dhooge, "Binaural interaction in the auditory brainstem response: a normative study.," *Clin Neurophysiol*, vol. 126, no. 4, pp. 772–779, Apr. 2015, doi: 10.1016/j.clinph.2014.07.032.

[16] C. A. Sammeth, A. D. Brown, N. T. Greene, and D. J. Tollin, "Interaural frequency mismatch jointly modulates neural brainstem binaural interaction and behavioral interaural time difference sensitivity in humans.," *Hear Res*, vol. 437, p. 108839, Sep. 2023, doi: 10.1016/j.heares.2023.108839.

[17] L. N. Van Yper, K. Vermeire, E. F. J. De Vel, A. J. Beynon, and I. J. M. Dhooge, "Age-Related Changes in Binaural Interaction at Brainstem Level.," *Ear Hear*, vol. 37, no. 4, pp. 434–442, Aug. 2016, doi: 10.1097/AUD.0000000000000274.

[18] R. A. Levine *et al.*, "Binaural auditory processing in multiple sclerosis subjects," *Hearing Research*, vol. 68, no. 1, pp. 59–72, Jun. 1993, doi: 10.1016/0378-5955(93)90065-9.

[19] E. M. Clarke and C. Adams, "Binaural interaction in specific language impairment: an auditory evoked potential study.," *Dev Med Child Neurol*, vol. 49, no. 4, pp. 274–279, Apr. 2007, doi: 10.1111/j.1469-8749.2007.00274.x.

[20] W. Delb, D. J. Strauss, G. Hohenberg, and P. K. Plinkert, "The binaural interaction component (BIC) in children with central auditory processing disorders (CAPD).," *Int J Audiol*, vol. 42, no. 7, pp. 401–412, Oct. 2003, doi: 10.3109/14992020309080049.

[21] K. V. Gopal and K. Pierel, "Binaural interaction component in children at risk for central auditory processing disorders.," *Scand Audiol*, vol. 28, no. 2, pp. 77–84, 1999, doi: 10.1080/010503999424798.

[22] S. Tolnai and G. M. Klump, "Evidence for the origin of the binaural interaction component of the auditory brainstem response.," *Eur J Neurosci*, vol. 51, no. 2, pp. 598–610, Jan. 2020, doi: 10.1111/ejn.14571.

[23] M. Furst, R. A. Levine, and P. M. McGaffigan, "Click lateralization is related to the beta component of the dichotic brainstem auditory evoked potentials of human subjects.," *J Acoust Soc Am*, vol. 78, no. 5, pp. 1644–1651, Nov. 1985, doi: 10.1121/1.392802.

[24] H. Riedel and B. Kollmeier, "Comparison of binaural auditory brainstem responses and the binaural difference potential evoked by chirps and clicks," *Hearing Research*, vol. 169, no. 1, pp. 85–96, Jul. 2002, doi: 10.1016/S0378-5955(02)00342-8.

[25] H. Riedel and B. Kollmeier, "Auditory brain stem responses evoked by lateralized clicks: is lateralization extracted in the human brain stem?," *Hear Res*, vol. 163, no. 1–2, pp. 12–26, Jan. 2002, doi: 10.1016/s0378-5955(01)00362-8.

[26] M. Furst, S. Eyal, and A. D. Korczyn, "Prediction of binaural click lateralization by brainstem auditory evoked potentials.," *Hear Res*, vol. 49, no. 1–3, pp. 347–359, Nov. 1990, doi: 10.1016/0378-5955(90)90113-4.

[27] A. D. Brown, K. L. Anbuhl, J. I. Gilmer, and D. J. Tollin, "Between-ear sound frequency disparity modulates a brain stem biomarker of binaural hearing.," *J Neurophysiol*, vol. 122, no. 3, pp. 1110–1122, Sep. 2019, doi: 10.1152/jn.00057.2019.

[28] N. R. Haywood, J. A. Undurraga, T. Marquardt, and D. McAlpine, "A Comparison of Two Objective Measures of Binaural Processing: The Interaural Phase Modulation Following Response and the Binaural Interaction Component.," *Trends Hear*, vol. 19, Dec. 2015, doi: 10.1177/2331216515619039.

[29] Z. L. Owrutsky, J. Peacock, and D. J. Tollin, "Investigating the optimal stimulus to evoke the

binaural interaction component of the auditory brainstem response.," *Hear Res*, vol. 440, p. 108896, Dec. 2023, doi: 10.1016/j.heares.2023.108896.

[30] S. E. Shore and A. L. Nuttall, "High-synchrony cochlear compound action potentials evoked by rising frequency-swept tone bursts.," *J Acoust Soc Am*, vol. 78, no. 4, pp. 1286–1295, Oct. 1985, doi: 10.1121/1.392898.

[31] T. Dau, O. Wegner, V. Mellert, and B. Kollmeier, "Auditory brainstem responses with optimized chirp signals compensating basilar-membrane dispersion.," *J Acoust Soc Am*, vol. 107, no. 3, pp. 1530–1540, Mar. 2000, doi: 10.1121/1.428438.

[32] O. Wegner and T. Dau, "Frequency specificity of chirp-evoked auditory brainstem responses.," *J Acoust Soc Am*, vol. 111, no. 3, pp. 1318–1329, Mar. 2002, doi: 10.1121/1.1433805.

[33] C. Elberling, M. Don, M. Cebulla, and E. Stürzebecher, "Auditory steady-state responses to chirp stimuli based on cochlear traveling wave delay.," *J Acoust Soc Am*, vol. 122, no. 5, pp. 2772–2785, Nov. 2007, doi: 10.1121/1.2783985.

[34] C. Elberling and M. Don, "Auditory brainstem responses to a chirp stimulus designed from derived-band latencies in normal-hearing subjects.," *J Acoust Soc Am*, vol. 124, no. 5, pp. 3022–3037, Nov. 2008, doi: 10.1121/1.2990709.

[35] S. T. Neely, S. J. Norton, M. P. Gorga, and W. Jesteadt, "Latency of auditory brain-stem responses and otoacoustic emissions using tone-burst stimuli.," *J Acoust Soc Am*, vol. 83, no. 2, pp. 652–656, Feb. 1988, doi: 10.1121/1.396542.

[36] O. Fobel and T. Dau, "Searching for the optimal stimulus eliciting auditory brainstem responses in humans.," *J Acoust Soc Am*, vol. 116, no. 4 Pt 1, pp. 2213–2222, Oct. 2004, doi: 10.1121/1.1787523.

[37] S. G. B. Kristensen and C. Elberling, "Auditory brainstem responses to level-specific chirps in normal-hearing adults.," *J Am Acad Audiol*, vol. 23, no. 9, pp. 712–721, Oct. 2012, doi: 10.3766/jaaa.23.9.5.

[38] M. Cebulla and C. Elberling, "Auditory brain stem responses evoked by different chirps based on different delay models.," *J Am Acad Audiol*, vol. 21, no. 7, pp. 452–460, Aug. 2010, doi: 10.3766/jaaa.21.7.4.

[39] C. Elberling, J. Callø, and M. Don, "Evaluating auditory brainstem responses to different chirp stimuli at three levels of stimulation.," *J Acoust Soc Am*, vol. 128, no. 1, pp. 215–223, Jul. 2010, doi: 10.1121/1.3397640.

[40] C. Elberling and M. Don, "A direct approach for the design of chirp stimuli used for the recording of auditory brainstem responses.," *J Acoust Soc Am*, vol. 128, no. 5, pp. 2955–2964, Nov. 2010, doi: 10.1121/1.3489111.

[41] G. H. Klem, H. O. Lüders, H. H. Jasper, and C. Elger, "The ten-twenty electrode system of the International Federation. The International Federation of Clinical Neurophysiology.," *Electroencephalogr Clin Neurophysiol Suppl*, vol. 52, pp. 3–6, 1999.

[42] A. D. Brown and D. J. Tollin, "Slow Temporal Integration Enables Robust Neural Coding and Perception of a Cue to Sound Source Location.," *J Neurosci*, vol. 36, no. 38, pp. 9908–9921, Sep. 2016, doi: 10.1523/JNEUROSCI.1421-16.2016.

[43] A. D. Brown and D. J. Tollin, "Effects of interaural decoherence on sensitivity to interaural level differences across frequency," *The Journal of the Acoustical Society of America*, vol. 149, no. 6, pp. 4630–4648, Jun. 2021, doi: 10.1121/10.0005123.

[44] M. J. Goupell, G. C. Stecker, B. T. Williams, A. Bilokon, and D. J. Tollin, "The rapid decline in interaural-time-difference sensitivity for pure tones can be explained by peripheral filtering.," Jan. 10, 2024, *United States*. doi: 10.1101/2023.08.04.551950.

DOI: 10.61782/fa.2025.0025

FORUM ACUSTICUM EURONOISE 2025

A PILOT STUDY ON ASSESSING AUDITORY MASKING USING AUDITORY STEADY-STATE RESPONSES

Anna Sergeeva* **Preben Kidmose**
Department of Electrical and Computer Engineering, Aarhus University, Denmark

ABSTRACT

Auditory masking is important in the characterization of human hearing and hearing impairment. Traditionally, masking is assessed through behavioral methods, witch requires active participant engagement. This study investigates the potential of using Auditory Steady-State Response (ASSR) to assess auditory masking, enabling masking assessment without requiring active participation.

ASSRs were measured in response to a 40-Hz amplitude-modulated probe signal with and without the presence of a masker. The probe signals were 1/3-octave bandwidth Gaussian noise centered at 891 and 1414 Hz (center frequency, CF) and presented at 10, 20, 30, and 40 dB above individual behavioral masking thresholds (MT). The masker was lowpass Gaussian noise (cut-off 707 Hz) presented at 65 and 85 dB SPL (masker level, ML).

The ASSR amplitude increased with presentation level (PL) and decreased in the presence of a masker, confirming a masking effect on ASSR. At 65 dB ML, ASSRs did not differ between center frequencies when probe signals were presented relative to MT, suggesting a simple relationship between MT and ASSR. At 85 dB ML, an effect of CF was observed, suggesting that the relationship between MT and ASSR is more complex than initially anticipated, and involving all the experimental parameters (CF, PL, and ML).

Keywords: *auditory masking, electroencephalography, auditory steady-state response*

**Corresponding author*: *ans@ece.au.dk.*

***Copyright**: ©2025 Sergeeva et.al. This is an open-access article distributed under the terms of the Creative Commons Attribution 3.0 Unported License, which permits unrestricted use, distribution, and reproduction in any medium, provided the original author and source are credited.*

1. INTRODUCTION

Auditory masking is a fundamental concept in audiology, describing the phenomenon where the perception of one sound (the probe-signal) is influenced by the presence of another sound (the masker). It is typically assessed through behavioral tests, where individuals are tasked with detecting the probe signal. The behavioral masking threshold refers to the minimum level of a probe signal allowing behavioral detection of the probe in the presence of a masker. Behavioral masking thresholds are commonly studied in psychoacoustic experiments and serve as the basis for models widely employed in hearing aid fitting [1]. Psychoacoustic models of masking have described frequency-specific masking effects and the critical band theory, which explains masking in terms of auditory filters and their bandwidths [2]. However, behavioral measurements are inherently subjective and depend on the participant's attention, motivation, and cognitive state. Furthermore, significant variability in masking thresholds exists among individuals, particularly those with hearing loss [3]. This variability creates challenges for accurately predicting and compensating for masking effects in hearing aid algorithms.

Auditory Steady-State Response (ASSR) is widely used in clinical practice for hearing assessment, particularly in estimating frequency-specific hearing thresholds in individuals unable to perform behavioral tasks. ASSR reflects the neural system's entrainment to the stimulus, and is typically measured in response to an amplitude modulated stimulus [4, 5]. This neural entrainment can be influenced by external factors, such as the presence of a masking sound. Masking affects the signal-to-noise ratio (SNR) of the auditory stimulus, and increased masking reduces SNR, resulting in decreased ASSR amplitude.

Evidence of the effects of masking on ASSR and other electrophysiological measurements has been reported in various contexts. Several studies have shown that masking

noise applied contralaterally can suppress ASSR amplitudes [6–8]. Furthermore, contralateral noise, even at levels that do not cause significant behavioral threshold elevation, has been shown to significantly elevate the thresholds of the 40-Hz ASSR [9]. Similar effects of masking have been observed in other auditory measures, such as the Auditory Brainstem Response (ABR). For instance, the latency of wave V in the ABR increases with rising levels of broadband white noise masker, while the amplitudes of both wave I and wave V decrease [10].

Masking effects on the ASSR can be considered as an undesirable factor that negatively impacts its estimation. However, the masking effects can also be utilized to study the masking phenomenon itself. Unlike behavioral methods, this approach enables an objective assessment of masking effects without requiring active participation from the subject. To our knowledge, ASSR-based estimation of masking thresholds has not been previously explored.

This study examines the masking effect on the ASSR and its relationship to the behavioral masking threshold. The masker is a low-pass noise signal presented at two intensity levels. There were two probe signals, each a one-third octave amplitude-modulated noise, centered at different frequencies above the masker's cutoff. Each probe was presented at four levels relative to the behavioral masking threshold. This experimental design allows us to quantify the masking effect on the ASSR as a function of presentation level and spectral distance from the masker.

In designing this study, we hypothesized that ASSR amplitude would increase monotonically with probe intensity, enabling masking threshold estimation using a methodology similar to ASSR-based hearing threshold estimation. Additionally, we expected the masking effect on the ASSR to be independent of the probe signal's center frequency, provided the probe levels were set relative to the behavioral masking threshold.

By exploring the relationship between behavioral masking threshold and ASSR, this study aims to enhance our understanding of physiological masking mechanisms and assess the potential of ASSR as an objective tool for estimating masking thresholds.

2. METHOD

2.1 Subjects

Six participants (4 women, mean age: 33.2 years) with normal hearing thresholds (<20 dB HL for octave frequencies between 500 and 4000 Hz) and no history of hearing disorders were included in the study. Behavioral hearing thresholds for each ear were measured using the ascending method as outlined in ISO 8253-1:2010 [11].

This study was conducted as a preliminary pilot investigation to refine experimental procedures and assess feasibility. Participants were staff or students from our department who voluntarily agreed to participate based on informed consent.

2.2 Measurement setup

EEG was recorded concurrently from four scalp electrodes and 16 ear electrodes. The scalp electrodes were placed at left (M1) and right (M2) mastoids, Fpz and AFz according to the 10-20 EEG electrode system [12], and attached to the skin using custom designed electrode holders made of silicone with double adhesive pads. Prep pads were used to clean the skin prior to the attachment of the scalp electrodes. A small amount of gel (Electro-Gel, Electro-Cap International, Inc., USA) was applied on the scalp electrodes. The data recorded from ear-electrodes were not used in this study.

The EEG recordings were acquired with a sampling rate of 1000 Hz by a 32 channel portable MOBITA EEG amplifier (TMSi B.V., The Netherlands). The recording electrodes were Ag/AgCl electrodes with a diameter of 4 mm [13]. The ground electrode was placed on the neck using a disposable wet gel electrode (Ambu WS, Ambu A/S, Denmark). The auditory stimuli were presented to the test subjects using insert earphones (3M E-A-RTONE for ABR, 50 Ohm, 3M, USA) via an RME soundcard (Fireface UC, RME, Germany) with a sampling frequency of 48 kHz.

Synchronization of the auditory stimuli and EEG recordings was achieved using a trigger signal generated by the soundcard. The trigger signal, periodic at 0.1 Hz, was sent to the EEG amplifier's trigger input via a g.TRIGbox (g.tec medical engineering GmbH, Austria).

2.3 ASSR stimuli and recordings

The probe signal consisted of 40-Hz amplitude-modulated (AM) 1/3-octave Gaussian noise (GN) signals with center frequencies of 891 Hz and 1414 Hz. The masker was low-pass GN with a cut-off frequency of 707 Hz. Both the probes and the masker were filtered in the frequency domain. Initially, the GN signals in its entirely length were transformed to the frequency domain using a Discrete Fourier Transform (DFT). A window function was then applied to set frequencies outside the band of interest

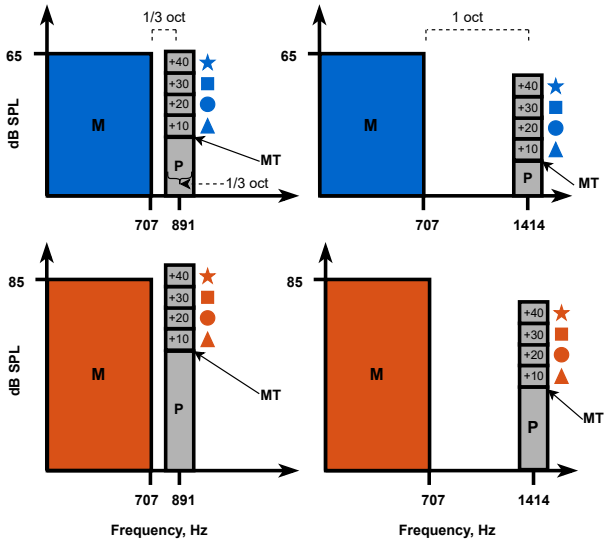


Figure 1. Schematic representation of the paradigm. The masker (M) was presented at levels 65 dB SPL (blue) and 85 dB SPL (orange). The probes (P) were presented at levels10 dB (triangles), 20 dB (circles), 30 dB (squares) and 40 dB (stars) above the behavioral masking threshold (MT), which were determined for each center frequency and masker level.

to zero. Finally, the complex spectrum was transformed back into the time domain using the Inverse DFT. This filtering method ensures a filter characteristic with steeper slopes than the auditory-filter bank. The masker was presented at levels of 65 and 85 dB SPL, while the stimuli levels were set at 10, 20, 30, and 40 dB above individual behavioral masking thresholds (MT). Stimuli were presented diotically. A schematic representation of the paradigm is shown in Figure 1.

Behavioral masking thresholds were determined for each masker level and center frequency (500-ms 1/3-octave GN centered at 891 and 1414 Hz served as probe-signals) using a three-alternative forced-choice paradigm with a 1-up, 3-down adaptive procedure. The initial step size was 5 dB. After four reversals, the step size was reduced to 2 dB and the test proceeded until 12 reversals were reached. The threshold was calculated as the average of the last 8 reversals. A computer monitor displayed a response box with three buttons representing the stimulus intervals in each trial. During stimulus presentation, the buttons were highlighted successively in sync with the corresponding intervals. The subjects were instructed to press the button corresponding to the interval containing the probe and received immediate feedback indicating whether the response was correct or incorrect.

ASSR measurements were conducted for each combination of masker level, probe level and center frequency. In the presence of a masker, EEG was recorded for 20, 20, 10, and 10 minutes for stimuli presented at 10, 20, 30, and 40 dB above MT, respectively. Similarly, for reference without masker, EEG was recorded for 10, 10, 5, and 5 minutes at 10, 20, 30, and 40 dB above MT, respectively. Longer recording times were used at lower stimulus levels to account for the lower ASSR amplitudes, ensuring sufficient data to achieve a significant response.

The total recording time was 6 hours, distributed over three days. On the first day, recordings were conducted at a center frequency of 891 Hz with two masker levels and four probe levels, totaling eight recordings (2 hours). The same procedure was followed on the second day for a center frequency of 1414 Hz, also resulting in eight recordings (2 hours). On the third day, recordings were performed without the masker (16 trials, 2 hours). Within each recording day, stimuli were presented in randomized order.

Both behavioral tests and EEG recordings took place in a double-walled sound-attenuating room. During EEG recordings, participants were seated in a comfortable chair and instructed to relax but remain awake and to have open eyes. They were offered the option to watch a silent, subtitled movie of their choice to avoid becoming drowsy during the experiment.

2.4 Data analysis of EEG

Analysis of the EEG data was performed offline after the recordings were completed. ASSRs were estimated from the average of the mastoids with reference to Fpz. The data was band-pass-filtered using an 8th order, zero-phase filter with passband between 10 and 100 Hz and Butterworth characteristic. A notch filter was applied to remove 50 Hz line noise. The trigger signal was used to split the dataset into epochs of 10 seconds length and the epochs were averaged using weighted averaging [14].

The averaged epoch was transformed into the frequency domain by means of a DFT. The ASSR was determined as the amplitude at the modulation frequency bin, and the background noise was calculated as the root-mean-square in the frequency band ±6 Hz relative to the modulation frequency (excluding the modulation frequency) [4].

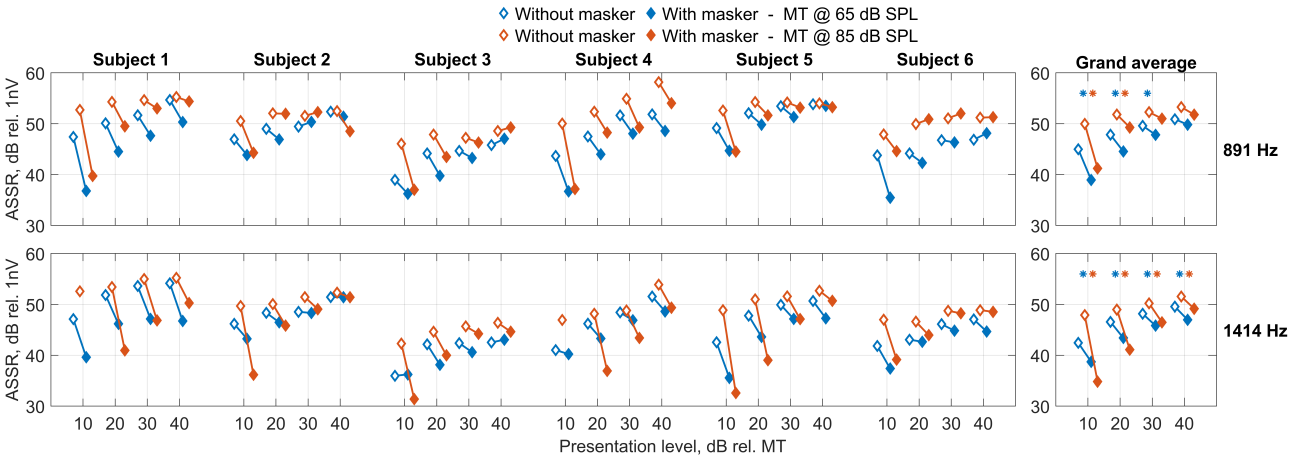


Figure 2. ASSR as a function of the presentation level for each CF (891 Hz – upper subplots, 1414 Hz – lower subplots) and masker level (blue for 65 dB SPL, orange for 85 dB SPL). Data is shown with (filled rhombs) and without (empty rhombs) the masker. Left: individual subject data; right: grand average across subjects. Asterisks indicate significant difference between ASSR with and without the masker (blue for 65 dB SPL, orange for 85 dB SPL).

Statistical significance of the ASSR amplitude was determined based on an F-test [15]. The F-ratio was calculated as the ratio between the power at the modulation frequency and the average power in the frequency band ±6 Hz relative to the modulation frequency (excluding the modulation frequency). An F-ratio with a p-value ≤ 0.05 was regarded as statistically significant. Only statistically significant ASSRs were included in the subsequent statistical analysis.

2.5 Statistical analysis of the recorded ASSR

Differences between ASSRs in the presence and absence of the masker were evaluated using a paired permutation test [16] with 1000 permutations. For the statistical analysis of ASSRs in the presence of the masker, mixed-effects models were employed in R (lme4, version 1.1.35.5, Rstudio R-4.4.2) [17]. The model included *Center Frequency* (*CF*: 891 and 1414 Hz), *Masker Level* (*ML*: 65 and 85 dB SPL), *Presentation Level* (*PL*: 10, 20, 30 and 40 dB MT) and all their interactions as fixed effects. *Subject* (*S*) was included as a random effect to account for inter-subject variability. Statistical significance of the fixed effects was assessed through model reduction based on likelihood ratio test using the `anova` function in R. Post hoc analyses were conducted using estimated marginal means (EMMs) computed with the emmeans R package [18], with Bonferroni correction applied to adjust p-values for multiple comparisons.

3. RESULTS

Table 1 presents the mean and standard deviation of behavioral masking thresholds (MT) in dB SPL (relative to 20 μPa) across six subjects for each masker level (ML) and carrier frequency (CF). For comparison, it also includes the mean and standard deviation of behavioral thresholds measured without a masker using the same procedure.

For each subject, ASSR was recorded in 32 different conditions (2 CF $\times$ 4 PL $\times$ 2 ML $\times$ with/without masker). Six subjects were included in the study, yielding a total of 192 ASSR recordings, of which 2 recordings were not

Table 1. Mean (standard deviation) of the behavioral masking thresholds in dB SPL across the subjects for each masker level and without the masker.

Center Frequency	Masker Level		
	65 dB SPL	85 dB SPL	Without
891 Hz	29.8 (4.7)	55.7 (2.3)	7.6 (4.1)
1414 Hz	18.8 (2.9)	39.5 (3.5)	9.6 (2.2)

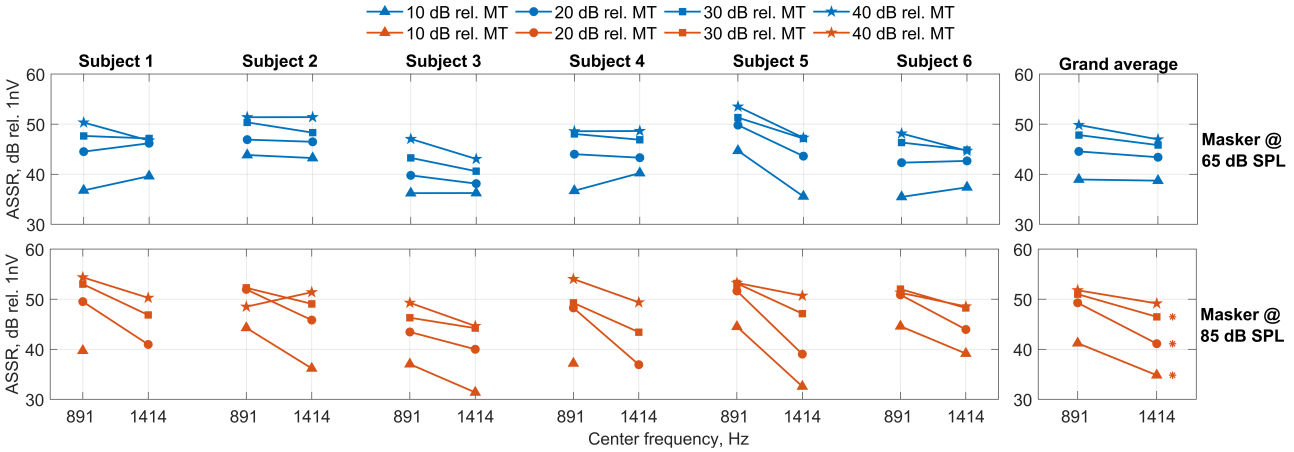


Figure 3. ASSR as a function of the CF for stimuli presented 10 dB (triangles), 20 dB (circles), 30 dB (squares) and 40 dB (stars) relative to masking threshold. Data is shown for masker levels of 65 dB SPL (blue, upper subplots) and 85 dB SPL (orange, lower subplots). Left: individual subject data; right: grand average across subjects. Asterisks indicate significant difference in ASSR amplitude between 891 Hz and 1414 Hz.

significant. Thus 190/192, corresponding to 99 % of all recordings, were significant.

Figure 2 illustrates the relationship between ASSRs to different stimuli in the experimental design, both with and without the masker. The data is shown for each individual subject followed by the grand average (only significant data points are shown). The figure reveals a reduction in ASSR amplitude in the presence of the masker, particularly at lower presentation levels. This difference diminishes as the presentation level increases.

Table 2 provides p-values from permutation tests comparing ASSRs with and without the masker. Significant differences are marked with asterisks in the grand average plots shown in Figure 2.

Figure 3 illustrates the relationship between ASSR and center frequency (891 and 1414 Hz) for stimuli presented with masker at two levels (65 and 85 dB SPL) across various presentation levels relative to the masking threshold. The data points represent the same ASSR measurements with masker shown in Figure 2, but they are visualized in a different way. Data is shown both for individual subjects and as the grand average across all subjects. The figure demonstrates that when the probe signal is presented relative to the masking threshold, ASSR amplitudes remain relatively stable across center frequencies when the masker level is 65 dB SPL. In contrast, for masker level of 85 dB SPL, a noticeable reduction in ASSR amplitude is observed at 1414 Hz compared to 891 Hz.

A full mixed-effects model was fitted to the ASSRs with the masker: $ASSR \sim CF + ML + PL + CF{:}ML + CF{:}PL + ML{:}PL + CF{:}ML{:}PL + (1|S)$

Residuals met model assumptions for normality (Shapiro-Wilk test: w = 0.989, p = 0.678) and homogeneity of variance (Bartlett's test: $\chi^2(15) = 22.996$, p = 0.084). Likelihood ratio tests during model reduction revealed a significant three-way interaction (*CF:ML:PL*, $\chi^2(3) = 12.1$, p = 0.007), indicating that the model could not be simplified.

Table 3 presents the post hoc analysis of estimated marginal means comparing ASSRs at center frequencies 891 Hz and 1414 Hz. Significant reductions at 1414 Hz are marked by red asterisks in Figure 3.

4. DISCUSSION

The behavioral masking thresholds presented in Table 1 align with previous empirical findings and established auditory system theories [1]. Initially, we observe a a clear increase in the threshold when a 65 dB masker is present compared to the without-masker condition. This confirms that the masker has an effect and that the measured threshold is a masking threshold rather than a hearing threshold. At both center frequencies (891 Hz and 1414 Hz), thresholds were higher at a masker level of 85 dB SPL than at 65 dB SPL, confirming that masking thresholds increase with masker level. Notably, consistent

Table 2. p-values from paired permutation tests, comparing ASSR with and without the masker for each masker level, center frequency and presentation level.

		Presentation Level			
Center Frequency	**Masker Level**	10 dB MT	20 dB MT	30 dB MT	40 dB MT
891 Hz	65 dB SPL	0.001	0.001	0.049	0.303
891 Hz	85 dB SPL	0.001	0.049	0.227	0.110
1414 Hz	65 dB SPL	0.013	0.001	0.001	0.045
1414 Hz	85 dB SPL	0.001	0.001	0.001	0.001

Table 3. Post hoc analysis of estimated marginal means comparing ASSR at different center frequencies for each masker level and presentation level, SE - standard error of mean.

Masker Level	**Presentation Level**	**$ASSR_{891Hz} - ASSR_{1414Hz}$**	**SE**	**t.ratio**	**p-value**
65 dB SPL	10 dB MT	0.234	1.25	0.188	1.000
65 dB SPL	20 dB MT	1.159	1.25	0.930	1.000
65 dB SPL	30 dB MT	2.008	1.25	1.611	0.881
65 dB SPL	40 dB MT	2.871	1.25	2.304	0.186
85 dB SPL	10 dB MT	6.458	1.40	4.604	<.001
85 dB SPL	20 dB MT	8.167	1.25	6.553	<.001
85 dB SPL	30 dB MT	4.522	1.25	3.628	0.003
85 dB SPL	40 dB MT	2.635	1.25	2.114	0.147

with established masking theories, a 20 dB increase in masker level resulted in a more than 20 dB increase in masking threshold. Additionally, in this study, where the masker was low-pass filtered noise with a 707 Hz cutoff frequency, the masking threshold was higher at 891 Hz than at 1414 Hz. This finding supports the auditory filter bank theory, which suggests that masker penetration decreases as the detection band is further away from the masker bands [1, 2].

Figure 2 illustrates the ASSR amplitudes as a function of presentation level for each center frequency (CF) and masker level (ML), with data shown both with and without the masker. The results indicate that ASSR amplitudes are generally lower in the presence of a masker compared to when a masker is absent, which is consistent with findings previously observed in the literature [6, 7]. This masking effect is particularly prominent at lower presentation levels, where the difference between ASSR with and without the masker is most pronounced. As the presentation level increases, the masking effect diminishes, and ASSR amplitudes with the masker approach those observed without it.

These findings are statistically supported by the paired permutation test results presented in Table 2. At 1414 Hz, significant differences were observed at all presentation levels for both masker levels. At 891 Hz, the effect was significant at 10, 20, and 30 dB MT for the 65 dB SPL masker, and at 10 and 20 dB MT for the 85 dB SPL masker, with no significant difference at higher presentation levels. This pattern further confirms that the masking effect is stronger at low probe levels and becomes less pronounced as the probe level increases. We hypothesize that, when the probe is near the masking threshold, the probe signal - and consequently, its modulation - is masked by the masker signal to a high degree. However, as the probe level increases, an increasingly larger part of its modulation surpasses the masking threshold, resulting in a stronger neural representation of the modulation.

Additionally, Figure 2 demonstrates a clear monotonic increase in ASSR amplitude with increasing presentation level, both in the presence and absence of a masker. This trend is consistent across subjects and frequencies. The observed increase in ASSR amplitude aligns with previous studies showing that higher presentation levels recruit a greater neural population, leading to stronger responses [19–21]. Although the presence of a masker reduces the ASSR amplitude, the relationship between ASSR and presentation level continues to exhibit a monotonic increasing pattern as a function of presentation level. This suggests that ASSR can serve as an objective measure for predicting behavioral thresholds. Specifically, in the absence of a masker, the threshold

corresponds to the hearing threshold, whereas in the presence of a masker, it corresponds to the masking threshold.

Figure 3 illustrates ASSR amplitudes as a function of center frequency (891 Hz vs. 1414 Hz) for different presentation levels relative to masking threshold (MT) and masker levels (65 dB SPL and 85 dB SPL). The figure shows that with a 65 dB SPL masker, ASSR amplitudes remain relatively stable across frequencies at all presentation levels. In contrast, with an 85 dB SPL masker, ASSR amplitudes at 1414 Hz are notably lower than at 891 Hz, with this effect being most pronounced at lower presentation levels. This pattern suggests a complex interplay between masker level, center frequency, and presentation level, indicating that physiological masking is not simply a linear function of these parameters.

A mixed-model reduction procedure confirmed this complexity by revealing a significant interaction between masker level, presentation level, and center frequency. To further examine this interaction, post hoc analyses were conducted. At 65 dB SPL, no significant differences were found between 891 Hz and 1414 Hz across all presentation levels, suggesting that there is the same relationship between ASSR and behavioral masking threshold across probe frequencies.

However, at 85 dB SPL ASSR amplitudes at 1414 Hz were significantly lower than at 891 Hz for presentation levels of 10, 20, and 30 dB MT, indicating a stronger physiological masking effect at the higher masker level. Interestingly, no significant difference was observed at 40 dB MT. One possible explanation is that at this high presentation level, ASSR amplitudes at 891 Hz may have reached a saturation point, reducing the observable difference between the two frequencies. Previous studies have reported that ASSR amplitudes tend to saturate at levels above 80 dB SPL [22–24].

5. CONCLUSION

This study was based on the hypothesis that the ASSR amplitude depends on the probe's presentation level relative to the behavioral masking threshold. While the empirical findings strongly support such relationship, they also reveal a more complex interaction involving the masker level and the probe signal's center frequency relative to the masker's cut-of frequency. Future studies will further explore these interactions.

6. ACKNOWLEDGMENTS

This study is supported by Center for Ear-EEG at Department of Electrical and Computer Engineering, Aarhus University, Denmark.

7. REFERENCES

[1] B. C. J. Moore, *An Introduction to the Psychology of Hearing*. BRILL, 2012.

[2] H. Fletcher, "Auditory Patterns," *Reviews of Modern Physics*, vol. 12, pp. 47–65, Jan. 1940.

[3] A. R. Horwitz, J. B. Ahlstrom, and J. R. Dubno, "Individual and level-dependent differences in masking for adults with normal and impaired hearing," *The Journal of the Acoustical Society of America*, vol. 131, pp. 323–328, Mar. 2012.

[4] T. W. Picton, M. S. John, A. Dimitrijevic, and D. Purcell, "Human Auditory Steady-State Responses," *International Journal of Audiology*, vol. 42, pp. 177–219, June 2003.

[5] A. T. Herdman, O. Lins, P. Van Roon, D. R. Stapells, M. Scherg, and T. W. Picton, "Intracerebral Sources of Human Auditory Steady-State Responses," *Brain Topography*, vol. 15, no. 2, pp. 69–86, 2002.

[6] R. Galambos and S. Makeig, "Physiological studies of central masking in man. I: The effects of noise on the 40-Hz steady-state response," *The Journal of the Acoustical Society of America*, vol. 92, pp. 2683–2690, Nov. 1992.

[7] E. E. Hansen and S. A. Small, "Effective masking levels for bone conduction auditory steady state responses in infants and adults with normal hearing," *Ear and Hearing*, vol. 33, no. 2, pp. 257–266, 2012.

[8] H. Usubuchi, T. Kawase, A. Kanno, I. Yahata, H. Miyazaki, N. Nakasato, R. Kawashima, and Y. Katori, "Effects of Contralateral Noise on the 20-Hz Auditory Steady State Response - Magnetoencephalography Study," *PLOS ONE*, vol. 9, June 2014.

[9] A. Maki, T. Kawase, and T. Kobayashi, "Effects of Contralateral Noise on 40-Hz and 80-Hz Auditory Steady-State Responses," *Ear and Hearing*, vol. 30, p. 584, Oct. 2009.

[10] P. S. Gott and E. C. Hughes, "Effect of noise masking on the brain-stem and middle-latency auditory evoked potentials: Central and peripheral components," *Electroencephalography and Clinical Neurophysiology/Evoked Potentials Section*, vol. 74, pp. 131–138, Mar. 1989.

[11] ISO 8253-1:2010, "Acoustics — Audiometric Test Methods — Part 1: Pure-tone Air and Bone Conduction Audiometry," 2010.

[12] H. Jasper, "The Ten-Twenty Electrode System of the International Federation," *Electroenceph. clin. Neurophysiol.*, vol. 10, pp. 371–375, 1958.

[13] S. Kappel and P. Kidmose, "Characterization of Dry-Contact EEG Electrodes and an Empirical Comparison of Ag/AgCl and IrO 2 Electrodes," *IEEE Engineering in Medicine and Biology Society. Annual International Conference*, 2022.

[14] M. S. John, A. Dimitrijevic, and T. W. Picton, "Weighted Averaging of Steady-State Responses," *Clinical Neurophysiology*, vol. 112, pp. 555–562, Mar. 2001.

[15] P. M. Zurek, "Detectability of Transient and Sinusoidal Otoacoustic Emissions," *Ear and hearing*, vol. 13, pp. 307–310, Oct. 1992.

[16] P. Good, *Permutation Tests*. Springer Series in Statistics, New York, NY: Springer, 2000.

[17] D. Bates, M. Mächler, B. Bolker, and S. Walker, "Fitting Linear Mixed-Effects Models Using Lme4," *Journal of Statistical Software*, vol. 67, pp. 1–48, Oct. 2015.

[18] R. V. Lenth, P. Buerkner, M. Herve, J. Love, F. Miguez, H. Riebl, and H. Singmann, "Emmeans: Estimated Marginal Means, Aka Least-Squares Means." R package version 1.10.6, 2021.

[19] T. W. Picton, C. R. Skinner, S. C. Champagne, A. J. C. Kellett, and A. C. Maiste, "Potentials Evoked by the Sinusoidal Modulation of the Amplitude or Frequency of a Tone," *The Journal of the Acoustical Society of America*, vol. 82, pp. 165–178, July 1987.

[20] R. Rodriguez, T. Picton, D. Linden, G. Hamel, and G. Laframboise, "Human Auditory Steady State Responses: Effects of Intensity and Frequency," *Ear and Hearing*, vol. 7, p. 300, Oct. 1986.

[21] D. R. Stapells, D. Linden, J. B. Suffield, G. Hamel, and T. W. Picton, "Human Auditory Steady State Potentials," *Ear and Hearing*, vol. 5, no. 2, p. 105, 1984.

[22] A. Rees, G. G. R. Green, and R. H. Kay, "Steady-State Evoked Responses to Sinusoidally Amplitude-Modulated Sounds Recorded in Man," *Hearing Research*, vol. 23, pp. 123–133, Jan. 1986.

[23] R. F. Burkard, J. J. Eggermont, and M. Don, *Auditory Evoked Potentials: Basic Principles and Clinical Application*. Philadelphia: Lippincott Williams & Wilkins, 2007.

[24] T. W. Picton and M. S. John, "Human Auditory Steady-State Responses During Sweeps of Intensity," *Ear and Hearing*, vol. 28, pp. 542–557, Aug. 2007.

DOI: 10.61782/fa.2025.0432



FORUM ACUSTICUM
EURONOISE 2025

HOW FREQUENCY-BASED PROCESSING MAY HELP CLINICIANS IMPROVE SOUND QUALITY PERCEPTION IN COCHLEAR IMPLANT USERS?

Louis Villejoubert[1*] **Lorenzo Picinali**[2]
Kathleen Faulkner[3] **Deborah Vickers**[1]
[1] Department of Clinical Neurosciences, University of Cambridge, United-Kingdom
[2] Dyson School of Design Engineering, Imperial College London, United-Kingdom
[3] Oticon A/S, Smorum, Denmark

ABSTRACT

Sound quality in cochlear implants (CIs) remains a critical challenge despite advancements in speech understanding. While CI technology's impact on sound quality degradation is well-documented, less is known about specific "frequency-to-place factors" such as frequency-to-place mismatch (FTPM) and issues with the electrode-neuron interface (ENI). This study explores innovative methods to assess the relationship between sound quality and these factors. The first experiment examines vowel perception through combinations of the first and second formant frequencies varied across a spectral continuum. Participants selected vowels from a close-set list (/a/, /i/, /ɔ/, /u/, /ɜ/) and then rated their confidence of their selection. Individual vowel maps were calculated to assess shifts in internal vowel representation potentially linked to FTPM (although not accounting for other ENI aspects). The second experiment evaluates sound quality transmission across electrodes using paired chord comparisons. Participants rated sound quality between chords and their inversions, isolating electrode-specific degradation. Ten post-lingually deafened adult CI users with over 12 months of experience participated. Preliminary findings reveal good test-retest reliability. Vowel experiments showed some preference for shifted configurations, while chord tests highlighted significant variability across electrodes. These methods may serve as clinical tools to optimize CI setup, improving sound quality for users.

1. INTRODUCTION

A cochlear implant (CI) is a neuroprosthetic device designed for people with severe hearing loss. Once implanted, users must adapt to new stimulation patterns imposed by both the CI technology and individual factors. Some of these individual factors are referred to as "frequency-to-place factors" because they alter the distribution of frequency information delivered to the auditory system.

The primary individual factor of interest here is frequency-to-place mismatch (FTPM). FTPM refers to the discrepancy between the frequency information delivered by an electrode and the frequency typically processed at the location stimulated by this electrode. This phenomenon occurs mainly because electrode arrays rarely allow stimulation along the entire length of the cochlea. Specifically, electrode arrays seldom reach the apex of the cochlea, where low frequencies are usually processed. To maintain effective transmission of the frequency spectrum, fitting strategies often involve a trade-off: a wide range of frequency information is transmitted, although not always to the ideal location. For example, frequencies ranging roughly from 100 Hz to 8000 Hz are transmitted, even though the most apical electrode typically corresponds to a location associated with a characteristic frequency (CF) of approximately 290 Hz [1]

[*] ***Corresponding author***: lv362@cam.ac.uk
Copyright: *©2025 Villejoubert et al. This is an open-access article distributed under the terms of the Creative Commons Attribution 3.0 Unported License, which permits unrestricted use, distribution, and reproduction in any medium, provided the original author and source are credited.*

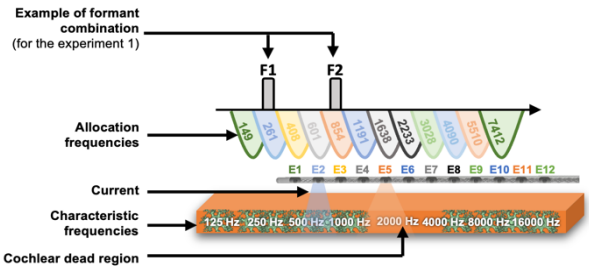


Figure 1. Simplified representation of cochlear implant processing illustrating the concepts of FTPM, poor ENI quality, and the functionality examined in Experiment 1. For FTPM, the illustration depicts a discrepancy between the allocated frequencies—the frequency information that is filtered and transmitted—and the characteristic frequencies—the cochlear regions typically responsible for processing those frequencies. Poor ENI quality is represented by missing neurons (i.e., a cochlear dead region). Its potential impact on transmission is illustrated by the wide current spread around electrode 5 (E5).

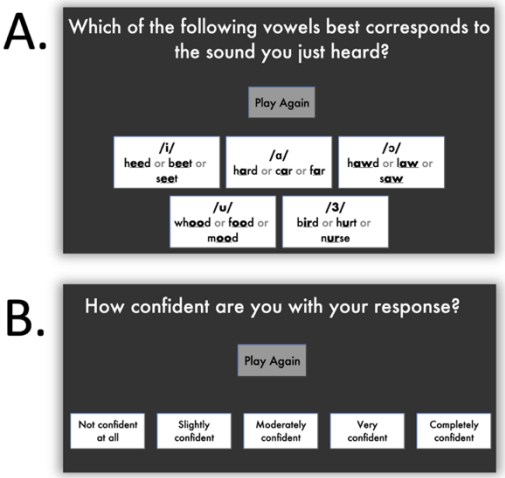


Figure 2. Illustration of the two consecutive questions presented during each trial in Experiment 1. Part A represents the identification task, while Part B assesses participants' confidence in their identification judgments.

(Figure 1). The term CF refers to the estimated frequency typically processed at a specific location within the cochlea. CF is determined through imaging methods such as computed tomography. Once estimated, the CF at the place stimulated by each electrode is compared to the allocated frequencies (AL) of each electrode—i.e., the frequencies around which information is extracted during CI processing—resulting in the FTPM value (Equation 1).

While most CI users experience some degree of FTPM, much remains unclear regarding its effects on perception and the adaptation process. This knowledge gap likely arises because the perceptual impact of FTPM varies significantly depending on the type of auditory signal. In speech understanding tasks, whether conducted in quiet or in noise, the long-term impact appears minimal [2]. However, FTPM has a more noticeable negative effect on sound quality, as indicated by one study [3]. The detrimental effects of FTPM are even more pronounced in music-related tasks such as pitch scaling, pitch discrimination, or melody recognition [4].

1.1 Experiment 1

The first experiment aims to explain how post-lingually deafened CI users with extensive implant experience process vowels in relation to the frequency distribution pattern imposed by FTPM. The experiment consisted of presenting combinations of first and second formants associated with a constant fundamental frequency (at 100 Hz). "The first formant ranged from approximately 230 Hz to 1720 Hz, and the second formant ranged from 415 Hz to 4000 Hz. Sounds were synthesized using the Parselmouth library, which enables the use of Praat directly within a Python environment.

For each combination, participants selected the perceived vowel from a closed-set list (/a/, /i/, /ɔ/, /u/, /ɜ/) and rated their confidence in their choice using a Likert scale. Using these two responses, individual perception heatmaps for each vowel were computed separately for each CI user. The same paradigm was performed with 10 normal-hearing (NH) listeners to create vowel reference heatmaps, which were then compared to CI users' individual heatmaps. The calculated shifts were then related to FTPM values to estimate the degree of adaptation to FTPM (see Equation 2).

1.2 Experiment 2

Experiment 2 builds on the findings from previous FTPM re-mapping studies that there are individual differences in the efficacy of the approach. One hypothesis is that adaptation depends not only on FTPM but also on the quality of the electrode-neuron interface (ENI).

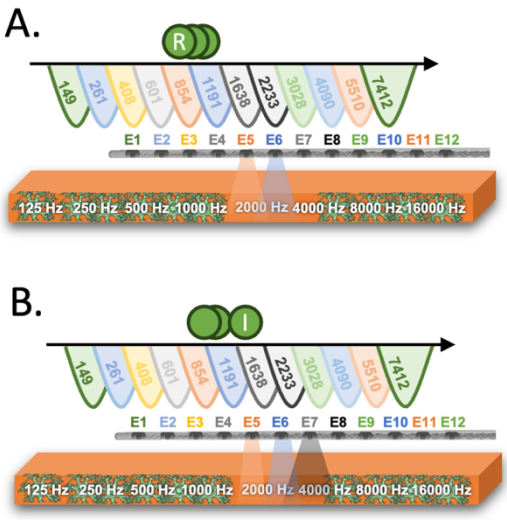


Figure 3. Illustration of an example chord pair used in Approach 2. Part A depicts the root chord, where the root note primarily stimulates electrode 5 (E5). Part B shows the inverted version of the chord, specifically stimulating electrode 7 (E7).

ENI quality describes how effectively the signal is transmitted between a specific electrode and targeted neurons. It encompasses factors such as the distance between the electrode and neurons, fibrosis around the electrode, current spread, and the number and health of stimulated neurons. Negative consequences of poor neural health have been documented for speech understanding [5].

To estimate the ENI quality of each electrode, we employed a method involving paired comparisons of chords. For each paired comparison, the root and inverted versions of a chord were presented to participants. Chords are musical units defined as combinations of notes that, when played together, are perceived as pleasant. In Western music, the most basic chord is a triad (consisting of three notes): a root note, a third interval, and a fifth interval. An inverted chord maintains the third and fifth interval notes, while the root is moved one octave higher. Theoretically, the root and its inversion differ slightly but should sound similarly pleasant. However, within paired comparisons and CI testing, differences in ENI quality at stimulation sites might influence participants' preferences between the root and inverted chords (see Figure 2). This hypothesis underlies the second approach described here: each pair of root/inverted chords was tailored to each

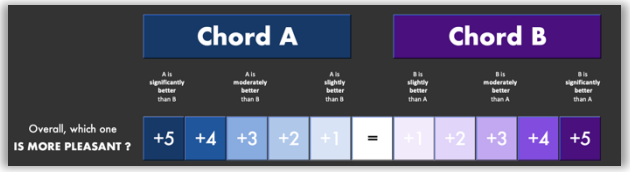


Figure 4. Illustration of the testing interface used in Experiment 2. After listening to each pair of chords—one root and one inverted—participants were asked to indicate which chord sounded more pleasant using this 10-option rating scale. Collected data were then analyzed using a Bayesian statistical model to estimate the pleasantness associated with each electrode.

CI user's mapping strategy, stimulating two different electrodes differently.

To validate this approach for estimating ENI quality, results from Experiment 2 were compared with the Panoramic ECAP (PECAP) method. The PECAP method uses forward-masked electrically evoked compound action potentials (ECAPs) to estimate neural activation patterns during CI stimulation. Specifically, PECAP provides estimations of current spread and neural health for each electrode along the cochlea.

$$FTPM = abs\left[\frac{log_{10}\left(\frac{CF}{AL}\right)}{log_{10}(2)}\right] \quad (1)$$

$$Shift = (Adaptation\ Completed) - FTPM \quad (2)$$

These experiments provide new tools for investigating how sound quality perception differs between NH and CI users. Initial results suggest that vowel perception in CI users may be shifted relative to NH listeners, potentially reflecting the influence of FTPM. The chord comparison task revealed variability across electrodes that could relate to differences in ENI quality and current spread. Further results, including detailed comparisons and relationships with neural health measures, will be presented at the conference.

2. REFERENCES

[1] M. W. Canfarotta, M. T. Dillon, E. Buss, H. C. Pillsbury, K. D. Brown, and B. P. O'Connell, "Frequency-to-Place Mismatch: Characterizing Variability and the Influence on Speech Perception

Outcomes in Cochlear Implant Recipients," *Ear and Hearing*, vol. 41, no. 5, pp. 1349–1361, Oct. 2020, doi: 10.1097/AUD.0000000000000864.

[2] A. W. Yang *et al.*, "Image-Guided Cochlear Implant Programming: A Systematic Review and Meta-analysis," *Otology & Neurotology*, vol. 43, no. 9, p. e924, Oct. 2022, doi: 10.1097/MAO.0000000000003653.

[3] J. J. Sturm, C. Ma, T. R. McRackan, and K. C. Schvartz-Leyzac, "Frequency-to-Place Mismatch Impacts Cochlear Implant Quality of Life, But Not Speech Recognition," *The Laryngoscope*, vol. n/a, no. n/a, 2024, doi: 10.1002/lary.31264.

[4] G. Creff, C. Lambert, P. Coudert, V. Pean, S. Laurent, and B. Godey, "Comparison of Tonotopic and Default Frequency Fitting for Speech Understanding in Noise in New Cochlear Implantees: A Prospective, Randomized, Double-Blind, Cross-Over Study," *Ear and Hearing*, vol. 45, no. 1, p. 35, Feb. 2024, doi: 10.1097/AUD.0000000000001423.

[5] C. J. Long *et al.*, "Examining the Electro-Neural Interface of Cochlear Implant Users Using Psychophysics, CT Scans, and Speech Understanding," *J Assoc Res Otolaryngol*, vol. 15, no. 2, pp. 293–304, Apr. 2014, doi: 10.1007/s10162-013-0437-5.

DOI: 10.61782/fa.2025.0364



FORUM ACUSTICUM
EURONOISE 2025

EVALUATION OF HYPERACUSIS AND LOUDNESS ESTIMATES AS PART OF AN EXTENDED AUDIOLOGICAL TEST BATTERY

Leny Vinceslas[1*] **Vit Drga**[1] **Jesko L. Verhey**[2] **Ifat Yasin**[1]

[1] Department of Computer Science, University College London, UK
[2] Department of Experimental Audiology, Otto von Guericke University Magdeburg, Magdeburg, Germany

ABSTRACT

Hyperacusis describes the condition in which individuals perceive mid-level sounds as uncomfortably loud, despite exhibiting normal hearing thresholds. Audiological assessments of hyperacusis commonly include the typical audiometric test battery, including uncomfortable loudness levels (ULLs), and a hyperacusis questionnaire (HQ). An estimate of the loudness growth function is often not included. This study investigated the correspondence between HQ scores, loudness functions, and key audiological measures. All twenty-two listeners had normal hearing ($<$ 20 dB HL within the range 0.25-8 kHz) and no tinnitus. Extended high-frequency thresholds (10–16 kHz) were also measured. Listeners completed a HQ and Categorical Loudness Scaling (CLS) test. ULLs were also measured using pure-tone stimuli and the audiometric standard procedure (ULL-SP) and an adaptive procedure using speech-shaped noise stimuli adapted from the CLS task (ULL-CLS). The results indicated that elevated thresholds in the 12–16 kHz range were associated with a straightening of the entire loudness function. Additionally, significant correlations were observed between HQ scores and ULL-SP at 0.5, 2, and 4 kHz. Listeners with higher HQ scores exhibited steeper lower segment of the loudness function, indicating a more rapid growth in perceived loudness for low- to mid-level stimuli.

*__Corresponding author__: l.vinceslas@ucl.ac.uk.

__Copyright__: ©2025 L.Vinceslas et al. This is an open-access article distributed under the terms of the Creative Commons Attribution 3.0 Unported License, which permits unrestricted use, distribution, and reproduction in any medium, provided the original author and source are credited.

Keywords: *Hyperacusis, High-Frequency Audiogram, Loudness, Categorical Loudness Scaling.*

1. INTRODUCTION

A three-round Delphi survey involving hearing healthcare professionals has proposed a consensus-based (90% agreement level) definition of hyperacusis as: “A reduced tolerance to sound(s) that are perceived as normal to the majority of the population or were perceived as normal to the person before their onset of hyperacusis, where “normal” refers to sounds that are generally well tolerated.” [1]. The reported prevalence of hyperacusis can vary depending on the definitions and assessments used [2] but is typically cited as ranging between 8-15% [3, 4]; with a higher prevalence associated with certain syndromes and autism spectrum disorders [5]. Hyperacusis can be associated with fear of certain acoustic and social environments, avoidance behaviours, and reduced quality of life [6]. Hyperacusis is known to often share some comorbidity with tinnitus [7], and both conditions are considered to emerge as a consequence of the brain’s attempt to compensate for cochlear trauma resulting from acoustic over-exposure. Hyperacusis may arise as a result of damage to synapses between inner hair cells and auditory nerve fibres, known as cochlear synaptopathy [8], which may manifest as a degradation in the neural coding of speech [9].

Clinical assessments of hearing are based on an assessment of hearing thresholds for sounds presented at the standard audiometric frequencies (SAF) of 0.25-8 kHz. Hyperacusis and early stages of cochlear synaptopathy may not be evident as elevated SAF thresholds [10]. Low uncomfortable loudness levels (ULLs) measured using

pure-tone signals, as part of a standard audiological hearing test battery, may also be associated with hyperacusis. However, pure-tone ULLs may be variable amongst a population that reports hyperacusis [11], so ULLs on their own may be insufficient as a psychophysical indicator of hyperacusis. For that reason, combined assessment criteria may provide an improved indicator of hyperacusis [5], for instance, combining ULLs with scores from the Hyperacusis Questionnaire (HQ) [12]. Aazh and Moore suggested a minimum average ULL of 77 dB HL (averaged across test pure-tones of 0.25, 0.5, 1, 2, 4, and 8 kHz) and a score of at least 22 at the HQ as best indicators of hyperacusis [13]. Audiological assessments commonly include measures of ULLs and/or measures of the stapedius reflex as well as the HQ, but an estimate of the loudness growth function is often not conducted. Individual loudness perception can be assessed using the Categorical Loudness Scaling (CLS) test, in which the loudness perception for stimuli of different levels is assessed [14].

There is growing evidence supporting the assessment of hearing thresholds at an extended range of audiometric frequencies (EAF), such as 9 to 20 kHz, for providing an early indication of vulnerability to risk factors such as ageing, disease, ototoxic drugs, and noise exposure [15]. Although cochlear synaptopathy may contribute to difficulties in perceiving and understanding speech in adverse listening conditions, it may not necessarily manifest as elevated hearing thresholds in a SAF audiogram [16, 17]. It has been suggested that EAF audiometry might be useful as a biomarker of cochlear synaptopathy [10, 17], but it is still unclear how, and by which mechanisms, cochlear synaptopathy and EHF hearing loss are associated with hyperacusis, despite normal thresholds in the SAF range [18].

The current study investigated the correspondence between HQ scores, loudness growth functions, ULLs, and SAF and EAF audiograms.

2. METHOD AND PROCEDURE

2.1 Participants

Twenty-two listeners participated in the measurements (14 women, 8 men; mean age 26.9 years). All provided signed consent for the study, which had been approved by the UCL Ethics Board. The test session took 1.5 hours.

2.2 Facilities and Apparatus

The measurements took place in a double-walled sound-attenuated room. Audiometric thresholds, standard audiometric ULLs, and the CLS test were measured using a calibrated clinical audiometer, Auritec Audiometer with Ear3.0 software, Earbox3.0 soundcard and Sennheiser HDA300 headphones.

2.3 Audiometry

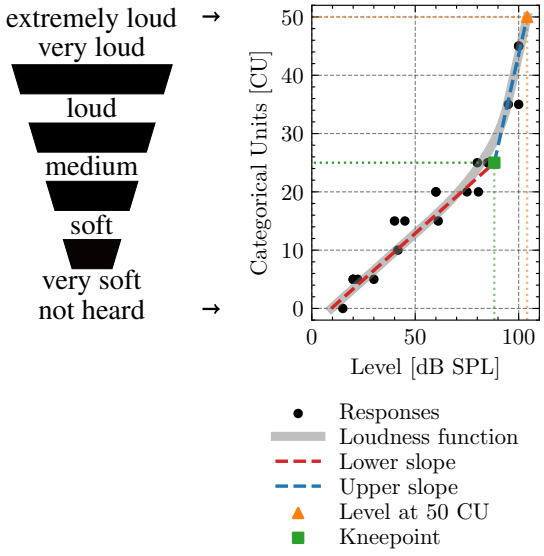
Audiometry was performed separately for listeners' right and left ears using pure-tone sound signals of 0.25, 0.5, 1, 2, 4, 6 and 8 kHz, following the British Society of Audiology (BSA) recommended procedure to obtain a SAF audiogram. All listeners had normal hearing as assessed by a SAF audiogram (i.e., hearing thresholds $<$20 dB HL) and no reported tinnitus. Listeners were also assessed with an EAF audiogram using pure-tone sound signals of 10, 12, 14 and 16 kHz.

ULLs were measured using pure-tone stimuli and following the audiometric standard procedure (ULL-SP). Aazh and Moore suggested a slight amendment to the BSA protocol when measuring ULLs using pure-tone signals for individuals with hyperacusis [19]. We followed such a protocol, which only slightly extended the overall audiological testing time. This approach allows for a more gradual exploration of the loudness space when measuring ULL-SP values in a population with hyperacusis.

The ULL-SP values were obtained separately for the right and left ears for 0.5, 2, and 4 kHz pure-tone signals, and then averaged across both ears. For comparison, ULLs were also measured using speech-shaped noise and an adaptive procedure based on the one used in the CLS test (ULL-CLS). A MatLab script was specifically created to run this adaptive CLS procedure to obtain the ULL-CLS thresholds. The ULL-CLS measurements were conducted for the right and left ears individually (monaural) and then averaged across both ears. Additionally, measurements were taken with both ears simultaneously (binaural diotic).

2.4 Categorical Loudness Scaling Test

The CLS test provides measures of loudness categorisation across an individual's dynamic range of hearing. In the CLS procedure, listeners categorised the subjectively-perceived loudness of a test signal using a pre-defined 11-point categorical scale (see Fig. 1a). Each of the categories is assigned a numerical value, referred to as a Cat-



(a) (b)

Figure 1: a) Representation of the 11-level categorical scale presented to listeners during the CLS test. Categories are mapped to categorical units (CUs) from 0 to 50. b) Example of loudness functions fitted to a participant's CLS test responses. The levels corresponding to the kneepoint at 25 CU and inferred at 50 CU, derived from the fitted functions, are indicated by the green and orange dotted lines, respectively.

egorical Unit (CU), from 0 to 50 CU. The stimuli consisted of speech-shaped noise of 1-s duration, including on- and off-ramps of 50 ms. The CLS adaptive procedure described in [14] was used to automatically adjust the stimuli presentation levels based on listeners' responses. Each listener first undertook a practice run with the CLS test followed by three recorded runs of the test.

Loudness functions were obtained by minimizing the least-square error between two linear segments intersecting at a fixed loudness level of 25 CU and the participants' responses to the CLS test. The upper and lower linear segments were smoothed between 15 and 35 CU using a quadratic Bezier curve. The fitting procedure 'BTUX' used in this study is described in [14]. Four parameters could then be derived from the loudness functions: slope values of the lower and upper linear regression segments, sound level at the point of intersection (kneepoint), and inferred level at 50 CU. The kneepoint describes the point at which the growth rate changes between the lower and upper portions of the function. For each listener, the four parameters were averaged over 3 repeated runs. Figure 1b depicts the process of defining the lower and upper function slopes, the kneepoint, and the level at 50 CU from the fitted CLS data of a single run.

2.5 Hyperacusis Questionnaire

Each listener completed the Hyperacusis Questionnaire (HQ) to quantify and evaluate potential hyperacusis symptoms. The HQ is a standardized questionnaire designed based on the literature on this pathology and consists of 14 items [12]. It was shown to be sensitive enough to discriminate between individuals based on their hyperacusis symptoms. The overall score ranges from 0 to 42, and a score greater than 28 could indicate strong auditory hypersensitivity according to [12]. Studies [13] and [20] suggested cut-off scores of 26 and 22 respectively.

3. RESULTS AND DISCUSSION

The current study investigated the correspondence between HQ scores, CLS results, and audiogram (SAF and EAF).

Figure 2 illustrates the relationship between upper and lower slopes of the loudness function and averaged audiometric thresholds, averaged across listeners' right and left ears, within each of three frequency ranges: 0.25–4 kHz, which is the main speech frequency range of the SAF; 6–10 kHz, where early indications of noise damage may be evident at the higher-frequency end of the SAF; and 12–16 kHz, an extended audiometric frequency range (EAF). This resulted in three mean thresholds per listener.

The lower slope of the loudness function shows minimal correlation with the averaged audiometric thresholds of 0.25-4 kHz and 6-10 kHz. In contrast, the lower slope of the loudness function is positively correlated (although not significantly) with the averaged audiometric thresholds at 12-16 kHz.

As listeners' thresholds increased in the 12-16 kHz EAF range, the lower slope of the loudness function became steeper. For all these listeners, thresholds were within normal limits for the SAF, indicating that for these listeners loudness perception at medium sound levels is increased compared to listeners that do not show elevated thresholds in the EAF range. The upper slope is negatively correlated (although not significantly) with the averaged audiometry thresholds at 12-16 kHz. Thus, as listen-

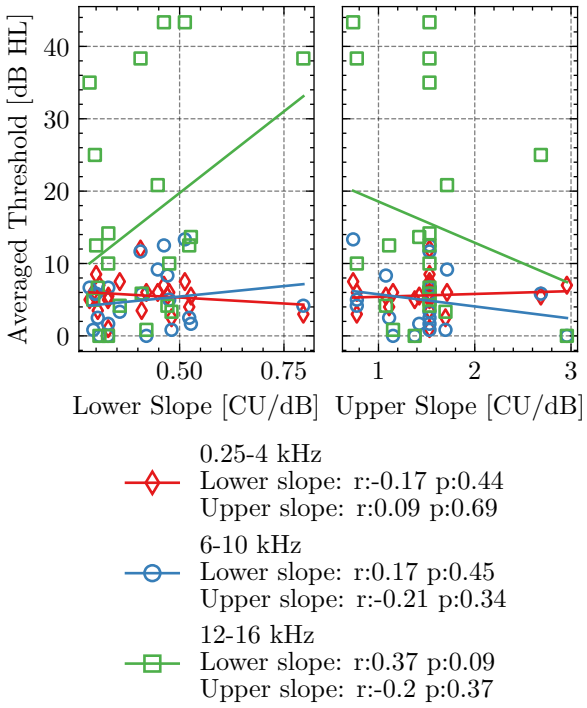


Figure 2: Data from all listeners. Averaged audiometric thresholds (across ears and within frequency ranges) as a function of CLS loudness function fit parameters, lower slope (left) and upper slope (right); and linear regressions for each frequency range.

ers' thresholds increase in the 12-16 kHz range, the upper slope of the loudness function becomes shallower. Note that a similar trend, although smaller in size, is found for the averaged thresholds in the 6-10 kHz range but is not found for the averaged thresholds of 0.25-4 kHz. This indicates the importance of the EAF audiogram in characterising early indication of a change in loudness perception. These trends suggest that for individuals with elevated audiometric thresholds in the 12-16 kHz range, the slopes of the lower and upper segments of the loudness function become more aligned.

For those individuals with audiometric thresholds within normal limits (<20 dB HL) as measured for sound frequencies of the SAF but elevated thresholds as measured for sound frequencies of the EAF, loudness perception grows more quickly with physical sound level for low- to mid-level sounds (a linearisation across both parts of the loudness function).

Some previous studies have indicated minimal or no relationship between audiometric thresholds and hyperacusis scores [7]. This may be the case for thresholds measured between 0.5 and 8 kHz, frequencies that are often tested within clinics (SAF). However, evaluation at higher signal test frequencies may be useful in monitoring and understanding the progression of altered loudness coding and its association with hyperacusis [13].

There is physiological and psychophysical evidence that assessment of hearing integrity at signal test frequencies above 8 kHz may provide a useful indicator of hearing health and an early indicator of hearing dysfunction [21]. The cochlear regions associated with the response to higher-frequency sounds are known to be especially sensitive to the effects of ageing [22], and to the use of ototoxic drugs [23]. Studies report mixed findings with respect to the relationship between high-frequency threshold elevation and noise exposure [24, 25]. Overall, elevated high-frequency thresholds may be indicative of early hearing damage prior to a noticeable perceptual change in hearing, and may be useful for early diagnosis and monitoring of hearing health [15].

Figure 3 shows the hyperacusis score per listener plotted against their ULL-SP scores (ULLs obtained using the standard audiometric procedure with pure-tone stimuli) and ULL-CLS scores (ULLs obtained using the adaptive procedure as in the CLS test with the speech-shaped noise of the CLS test). The dB HL values for ULL-SP were converted to dB SPL for comparison with the ULL-CLS values.

ULL-SP at 0.5, 2, and 4 kHz present a strong significant correlation with the HQ score (all $p<0.05$); a higher HQ score is associated with a lower ULL-SP value. One of the definitions of hyperacusis that reaching a 78.8% agreement in a three-round Delphi survey of hearing healthcare professionals suggested that hyperacusis may also be characterised by the following statement: "Hyperacusis can *sometimes* be described as a reduction in the uncomfortable loudness levels (ULL) in pure tone audiometry (PTA)" [1].

Whilst both monaural and binaural ULL-CLS are also correlated with the HQ score in the same direction, and with a correlation strength approaching that seen between the HQ score and ULL-SP, the results for ULL-CLS are not significant. The ULL-CLS binaural thresholds are observed to be lower than monaural ULL-CLS thresholds as expected due to binaural summation [26]. Overall, the binaural and monaural ULL-CLS thresholds are lower than all the ULL-SP thresholds. This is also expected for

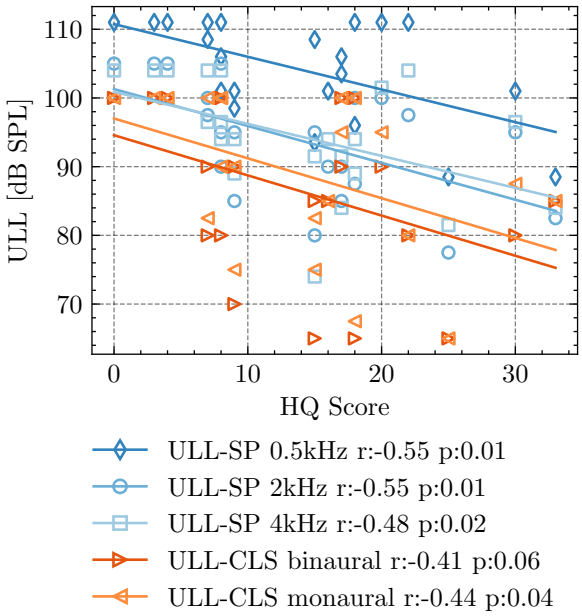


Figure 3: Data from all listeners. i) ULL-SP estimates obtained using pure tones and the BSA procedure and ii) ULL-CLS estimates obtained using the method based on the CLS adaptive procedure and CLS speech-shaped noise stimuli, with monaural (averaged across both ears) and binaural presentations. The ULLs are plotted as a function of the Hyperacusis Questionnaire (HQ) scores.

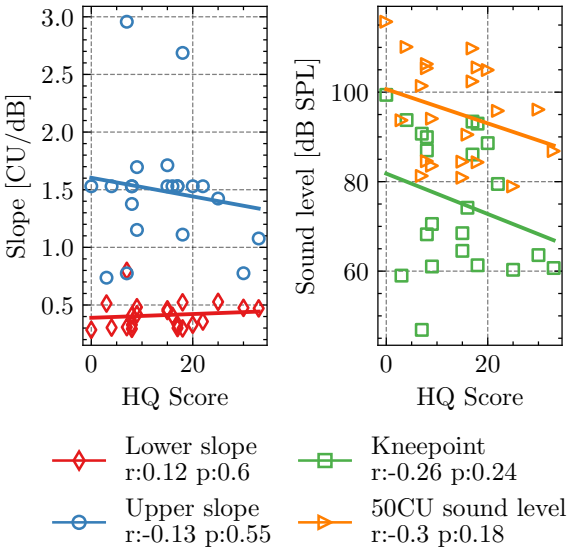


Figure 4: Data from all listeners. Loudness function parameters: lower and upper slopes (left) and kneepoint and level estimates at 50 CU (right) as a function of the Hyperacusis Questionnaire (HQ) scores.

complex sound stimuli, such as the speech-shaped noise used in this case, which inherently include modulations, compared to pure tone signals [27, 28].

Figure 4 illustrates the relationship between the CLS loudness function parameters and the HQ score. As HQ scores increase, the value of the lower slope remains essentially the same, while the upper slope tends to decrease. The values for the kneepoints and the sound levels inferred at 50 CU tend to decrease with increasing HQ scores. Note that these trends are similar to those observed for the comparison between CLS and audiometric thresholds (EAF). Individuals who scored higher on the HQ tended to demonstrate a categorical loudness function that had a steeper lower portion of the function, representing a more rapid increase in loudness with increasing sound level, and a shallower upper portion of the function. Individuals that scored higher on the HQ also displayed a lowered kneepoint of the function fit to the CLS data.

4. CONCLUSION

There is a straightening of the entire loudness function for low- to mid-level sounds for individuals with elevated thresholds for sound frequencies of 12-16 kHz. These individuals had audiometric thresholds within normal limits (<20 dB HL) for sound frequencies of 0.5-8 kHz, and no tinnitus. High frequency thresholds (>12 kHz) are informative regarding the perceptual effects of increased loudness growth which may be associated with hyperacusis. There was a strong significant correlation between the HQ score and ULL-SPs obtained at 0.5, 2, and 4 kHz (all $p<0.05$). Individuals who scored higher on the HQ tended to exhibit a categorical loudness function with a steeper lower portion, indicating a more rapid increase in perceived loudness, and a shallower upper portion of the function. Individuals who scored higher on the HQ also displayed a lower kneepoint in the function fitted to the CLS data, defined as the intersection between the lower and upper portions of the fitted curve.

5. ACKNOWLEDGMENTS

This research was funded by an Economic and Social Research Council (ESRC) grant ES/V015869/1.

6. REFERENCES

[1] B. Adams, M. Sereda, A. Casey, P. Byrom, D. Stockdale, and D. J. Hoare, "A Delphi survey to determine a definition and description of hyperacusis by clinician consensus," *International Journal of Audiology*, vol. 60, no. 8, pp. 607–613, 2021.

[2] S. N. Rosing, J. H. Schmidt, N. Wedderkopp, and D. M. Baguley, "Prevalence of tinnitus and hyperacusis in children and adolescents: a systematic review," *BMJ Open*, vol. 6, no. 6, p. e010596, 2016.

[3] A. L. Smit, I. Stegeman, R. H. Eikelboom, D. M. Baguley, R. J. Bennett, S. Tegg-Quinn, R. S. Bucks, R. J. Stokroos, M. Hunter, and M. D. Atlas, "Prevalence of hyperacusis and its relation to health: The Busselton Healthy Ageing Study," *The Laryngoscope*, vol. 131, no. 12, pp. E2887–E2896, 2021.

[4] J. Paulin, L. Andersson, and S. Nordin, "Characteristics of hyperacusis in the general population," *Noise and Health*, vol. 18, no. 83, pp. 178–184, 2016.

[5] K. Fackrell, I. Potgieter, G. S. Shekhawat, D. M. Baguley, M. Sereda, and D. J. Hoare, "Clinical interventions for hyperacusis in adults: a scoping review to assess the current position and determine priorities for research," *BioMed Research International*, vol. 2017, no. 1, p. 2723715, 2017.

[6] L. Sacchetto, E. Apa, A. Ciorba, S. Palma, V. Caragli, C. Gherpelli, D. Monzani, E. Genovese, and R. Nocini, "Psychological profile and social behaviors of patients with hyperacusis," *Journal of Clinical Medicine*, vol. 11, no. 24, p. 7317, 2022.

[7] L. Jacquemin, E. Cardon, S. Michiels, T. Luyten, A. Van Der Wal, W. De Hertogh, O. M. Vanderveken, P. Van De Heyning, M. J. W. Lammers, V. Van Rompaey, and A. Gilles, "Hyperacusis: demographic, audiological, and clinical characteristics of patients at the ENT department," *European Archives of Oto-Rhino-Laryngology*, vol. 279, no. 10, pp. 4899–4907, 2022.

[8] S. G. Kujawa and M. C. Liberman, "Synaptopathy in the noise-exposed and aging cochlea: Primary neural degeneration in acquired sensorineural hearing loss," *Hearing Research*, vol. 330, no. Pt B, pp. 191–199, 2015.

[9] E. A. Lopez-Poveda and P. Barrios, "Perception of stochastically undersampled sound waveforms: a model of auditory deafferentation," *Frontiers in Neuroscience*, vol. 7, p. 124, 2013.

[10] H. Guest, K. J. Munro, G. Prendergast, R. E. Millman, and C. J. Plack, "Impaired speech perception in noise with a normal audiogram: No evidence for cochlear synaptopathy and no relation to lifetime noise exposure," *Hearing Research*, vol. 364, pp. 142–151, Jul. 2018.

[11] J. Sheldrake, P. U. Diehl, and R. Schaette, "Audiometric characteristics of hyperacusis patients," *Frontiers in Neurology*, vol. 6, pp. 105: 1–7, 2015.

[12] S. Khalfa, S. Dubal, E. Veuillet, F. Perez-Diaz, R. Jouvent, and L. Collet, "Psychometric normalization of a hyperacusis questionnaire," *Orl*, vol. 64, no. 6, pp. 436–442, 2002.

[13] H. Aazh and B. C. Moore, "Factors related to uncomfortable loudness levels for patients seen in a tinnitus and hyperacusis clinic," *International Journal of Audiology*, vol. 56, no. 10, pp. 793–800, 2017.

[14] T. Brand and V. Hohmann, "An adaptive procedure for categorical loudness scaling," *The Journal of the Acoustical Society of America*, vol. 112, no. 4, pp. 1597–1604, 2002.

[15] M. Lough and C. J. Plack, "Extended high-frequency audiometry in research and clinical practice," *The Journal of the Acoustical Society of America*, vol. 151, no. 3, pp. 1944–1955, 2022.

[16] A. E. Hickox and M. C. Liberman, "Is noise-induced cochlear neuropathy key to the generation of hyperacusis or tinnitus?," *Journal of Neurophysiology*, vol. 111, no. 3, pp. 552–564, 2014.

[17] M. C. Liberman, M. J. Epstein, S. S. Cleveland, H. Wang, and S. F. Maison, "Toward a differential diagnosis of hidden hearing loss in humans," *PloS One*, vol. 11, no. 9, p. e0162726, 2016.

[18] Z. Jafari, D. Baguley, B. E. Kolb, and M. H. Mohajerani, "A systematic review and meta-analysis of extended high-frequency hearing thresholds in tinnitus with a normal audiogram," *Ear and Hearing*, vol. 43, no. 6, pp. 1643–1652, 2022.

[19] H. Aazh and B. C. J. Moore, "Incidence of discomfort during pure-tone audiometry and measurement of uncomfortable loudness levels among people seeking help for tinnitus and/or hyperacusis," *American Journal of Audiology*, vol. 26, no. 3, pp. 226–232, 2017.

[20] O. M. Meeus, M. Spaepen, D. D. Ridder, and P. H. V. d. Heyning, "Correlation between hyperacusis measurements in daily ENT practice," *International Journal of Audiology*, vol. 49, no. 1, pp. 7–13, 2010.

[21] C. M. Barbee, J. A. James, J. H. Park, E. M. Smith, C. E. Johnson, S. Clifton, and J. L. Danhauer, "Effectiveness of auditory measures for detecting hidden hearing loss and/or cochlear synaptopathy: a systematic review," in *Seminars in Hearing*, vol. 39, pp. 172–209, Thieme Medical Publishers, 2018.

[22] E. M. Keithley, "Pathology and mechanisms of cochlear aging," *Journal of Neuroscience Research*, vol. 98, no. 9, pp. 1674–1684, 2020.

[23] M. Mujica-Mota, S. Waissbluth, and S. J. Daniel, "Characteristics of radiation-induced sensorineural hearing loss in head and neck cancer: A systematic review," *Head & Neck*, vol. 35, no. 11, pp. 1662–1668, 2013.

[24] C. G. Le Prell, C. Spankovich, E. Lobariñas, and S. K. Griffiths, "Extended high-frequency thresholds in college students: effects of music player use and other recreational noise," *Journal of the American Academy of Audiology*, vol. 24, no. 8, pp. 725–739, 2013.

[25] S. K. Mishra, U. Saxena, and H. Rodrigo, "Extended high-frequency hearing impairment despite a normal audiogram: relation to early aging, speech-in-noise perception, cochlear function, and routine earphone use," *Ear & Hearing*, vol. 43, no. 3, pp. 822–835, 2022.

[26] P. Heil, "Towards a unifying basis of auditory thresholds: binaural summation," *Journal of the Association for Research in Otolaryngology*, vol. 15, no. 2, pp. 219–234, 2014.

[27] C. Zhang and F.-G. Zeng, "Loudness of dynamic stimuli in acoustic and electric hearing," *The Journal of the Acoustical Society of America*, vol. 102, no. 5, pp. 2925–2934, 1997.

[28] J. Hots, J. Rennies, and J. L. Verhey, "Loudness of subcritical sounds as a function of bandwidth, center frequency, and level," *The Journal of the Acoustical Society of America*, vol. 135, no. 3, pp. 1313–1320, 2014.

DOI: 10.61782/fa.2025.0109

FORUM ACUSTICUM EURONOISE 2025

ADVANCING OBJECTIVE ASSESSMENT OF SPECTRAL DISCRIMINATION USING EEG: AMPLITUDE ROVING MINIMIZES LOUDNESS CONFOUNDS

Mats Rekswinkel[1*] **Jens Hjortkjær**[1] **Abigail A. Kressner**[1,2] **Jaime A. Undurraga**[3,4]
[1] Department of Health Technology, Ørsteds Plads, Building 352, Technical University of Denmark, 2800 Kgs. Lyngby, Denmark
[2] Copenhagen Hearing and Balance Centre, Inge Lehmanns Vej 8, Rigshospitalet, 2100 København Ø, Denmark
[3] Interacoustics Research Unit, Ørsteds Plads, Building 352, Technical University of Denmark, 2800 Kgs. Lyngby, Denmark
[4] Department of Linguistics, 16 University Avenue, Macquarie University, NSW 2109, Australia

ABSTRACT

The measurement of cortical responses to frequency cues relevant for speech understanding can potentially lead to earlier and more effective clinical diagnosis and intervention in hard-to-test populations. To assess cortical responses to changes in frequency, it is important to minimize the presence of other simultaneous cues, such as loudness, which might also evoke cortical responses, potentially biasing the interpretation of the response data. To minimize this effect, we propose a new method that uses amplitude roving—commonly used in behavioral testing to ensure the cue of interest is focused on—to reduce loudness-related cortical responses. Neurophysiologically, the effect of intensity roving might translate to a form of neural adaptation to signal variance, which results in a reduced sensitivity to intensity changes.

In this study, we investigate the effects of amplitude roving on EEG responses to spectral changes in pure tones. We investigate the extent to which intensity roving can reduce cortical responses driven by intensity changes. The results show that intensity roving can significantly reduce the cortical response to amplitude changes, while responses to spectral changes remain salient.

Keywords: *acoustic change complex, amplitude roving, loudness, speech discrimination*

1. INTRODUCTION

The use of cortical auditory evoked potentials (CAEPs) as objective biomarkers of hearing in clinical practice has promising potential for guiding diagnostics in hard-to-test populations [1–3]. Cortical measures of suprathreshold discrimination can potentially supplement existing methods, particularly within the context of spectral discrimination as a proxy of perceptual vowel discrimination abilities. One such measure is the acoustic change complex (ACC), a cortical response driven by suprathreshold acoustic cue transitions. ACC responses have, for example, been demonstrated with frequency and amplitude transitions [4–8]. While the ACC is sensitive to changes in frequency, inherent simultaneous changes in loudness may also evoke neural responses [9, 10]. Cortical responses to loudness must therefore be disentangled from the compound response, and potential methods for minimizing this confound must be investigated.

In psychophysical studies, amplitude roving across trials is commonly used to reduce the perceptual weight

*__Corresponding author__: madare@dtu.dk.
__Copyright__: ©2025 Rekswinkel et al. This is an open-access article distributed under the terms of the Creative Commons Attribution 3.0 Unported License, which permits unrestricted use, distribution, and reproduction in any medium, provided the original author and source are credited.

of loudness cues [11]. Roving involves the randomization of task-irrelevant acoustic features—here, the stimulus intensity—to render them unreliable for the listener. In the neurophysiological domain, amplitude roving can be applied via random fluctuations in stimulus level across stimulus presentations and, as such, increases the stimulus level variance, which might reduce neural sensitivity to intensity changes. Animal studies indicate that neuronal adaptation to level variance occurs in the auditory cortex [12–14]. An increase in intensity variance through amplitude roving might therefore lead to reduced EEG-measured cortical sensitivity to intensity fluctuations as populations of neurons adapt their firing rate.

In this study, the concept of cortical neural adaptation is exploited through amplitude roving in a suprathreshold frequency discrimination paradigm employing pure tones. Specifically, we investigated ACC responses to periodic changes in intensity (as a proxy measure of loudness changes) as well as changes in frequency. ACCs were obtained either with or without amplitude roving in the form of random low-frequency amplitude modulations applied across the signal intervals.

2. METHODS

This paper presents a subset of the data that was obtained from a study of 26 young ($\leq$ 33 years) normal hearing participants, in which their electroencephography (EEG) responses were recorded. Recordings were carried out at the Technical University of Denmark (Kongens Lyngby, Denmark). All the experiments were approved by the Science-Ethics Committee for the Capital Region of Denmark (H-1-2013-138). All participants provided their written consent prior to taking the test.

Stimuli consisted of amplitude modulated (AM'ed; 41 Hz) loudness-balanced tones. ACC responses to the following stimulus changes were examined: (1) *intensity change*, where two 848 Hz AM'ed tones are presented with a level increment of +5 dB and (2) *frequency change*, where a 848 Hz AM'ed tone is followed by a loudness-balanced AM'ed tone of 970 Hz—i.e., with loudness cues minimized. These conditions were then presented again, but with the intensity levels roved by applying a low-frequency randomized envelope to the stimulus (envelope frequency components from 0.5 Hz to 4 Hz, fully modulated). In all conditions, the baseline intensity was set to a sound pressure level (SPL) of 65 dB. An overview of these conditions is presented in Table 1.

Cortical responses were recorded using a BIOSEMI^{TM} ActiveTwo system using a 64 + 2 external channel layout, following the 10-20 system, and responses were referenced to the Cz-electrode. Recordings lasted around 5 minutes, divided into epochs of 2 seconds (150 epochs), corresponding to the time intervals of the acoustic change in the stimuli.

EEG from the mastoid electrodes were analyzed using a statistical detection method termed the Fmpi [15]. The Fmpi measures the probability that a given F-value—the ratio between the variance of the averaged recording within a time window where the cortical response is expected (50 to 550 ms after change onset) and the variance of the post-average residual noise—is obtained by chance.

EEG processing included band-pass filtering (2-30 Hz) and weighted averaging according to [16]. To investigate how the response strength increases as more epochs are averaged together, we performed the analyses in incrementing number of epochs (step = 20 epochs).

The response detection threshold was set at an alpha level of 0.05. The total number of significant detections was then converted to a percentage of the total number of recordings per condition, denoted as detection rate.

Statistical analyses were performed via analyses of variance using a Generalized Linear Mixed Model (GLMM) with a Gamma distribution.

#	Δf [Hz]	ΔSPL [dB]	Roving
1	0	+5	No
2	122	0	No
3	0	+5	Yes
4	122	0	Yes

Table 1. Overview of experimental conditions (labeled by number). **Δf** and **ΔSPL** refer to frequency- and intensity changes respectively. The last column indicates whether roving was applied (yes/no).

3. RESULTS

Figures 1A&B show an overview of the ACC waveforms averaged across all participants and epochs. Responses to intensity changes only (Fig. 1A) are visibly smaller than ACCs to changes in frequency (Fig. 1B). Similarly, responses when the amplitude level of the stimuli was not roved (fig. 1A&B, top panels) are larger than for the roved conditions (fig. 1A&B, bottom panels). This is especially apparent in the intensity change conditions (Fig.

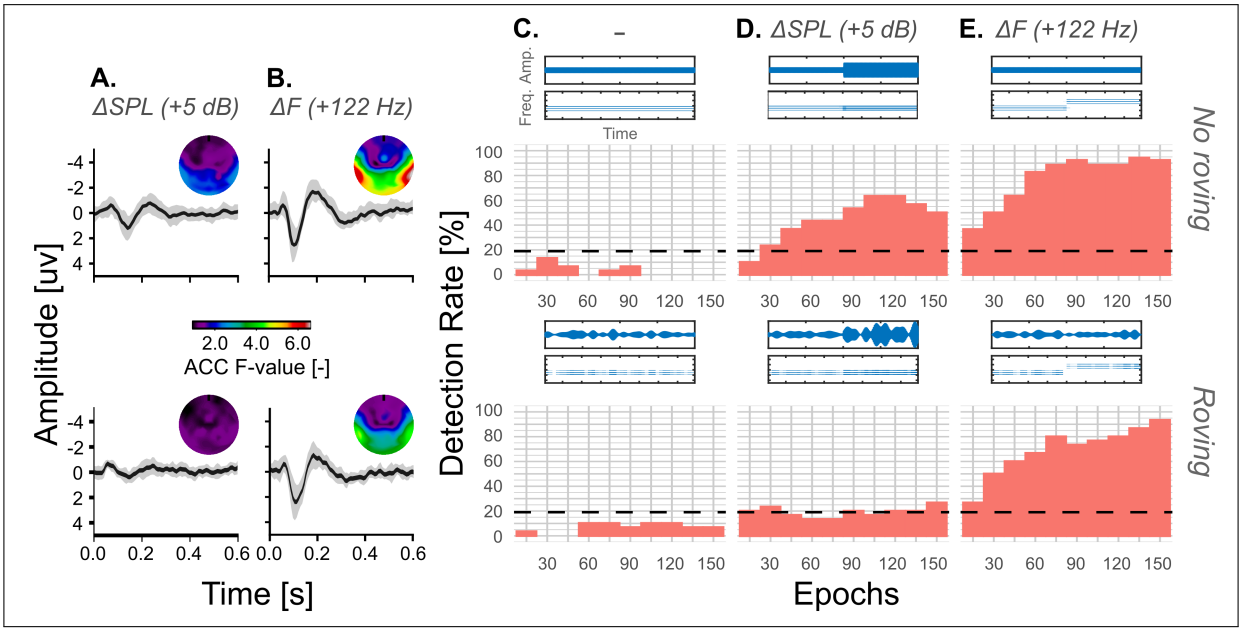


Figure 1. **A-B**: Waveforms and topographic maps of average ACCs across all participants and two mastoid channels for intensity (**A**) and frequency (**B**) conditions. Non-roved conditions are at the top, roved conditions on the bottom. Waveforms are plotted in time window 0 to 0.6 s and expressed as voltage in µV. Mean (solid) waveforms with standard deviation (shaded) are given. Additionally, topographic maps show ACC F-values from the Fmpi-detector (full recording length, number of epochs = 150) across all 64 (excluding mastoid) recorded channels along the scalp. All results are referenced to Cz. **C-E**: Results from an Fmpi-detector across varying number of epochs (time window: 50 ms to 550 ms) across all participants. Results are categorized by condition; Panel **D** shows the intensity change condition, panel **E** shows the frequency change condition. Non-roved conditions are at the top and roved conditions are on the bottom. Panel **C** shows results for the no change reference. The x-axis shows the varying number of epochs used in the detector, with the detection rate (percentage of significant responses that were obtained) on the y-axis. Dashed lines show the Bernoulli confidence interval (95%) for chance detection. The explanatory diagrams above the detection plots show the stimulus of the respective condition both in the time- and frequency domain.

1A), while this difference is less distinguishable in the frequency change condition (Fig. 1B). Topographic maps of the ACC F-value across the scalp (Fig. 1A) suggest that responses are reduced when roved in both conditions.

Detection rates across all participants (see Section 2) are shown in Figures 1C-E. By assessing detection rates in baseline recordings (i.e., a non-change reference) (Fig. 1C), the detection rates fall within the Bernoulli confidence interval (95%) for chance detection (dashed lines). For the intensity change (Fig. 1D) and frequency change (Fig. 1E), the patterns differed depending on whether roving was employed or not. In the intensity change condition without roving (Fig. 1D, top panel) the number of detections increased steadily throughout the recording. However, in the intensity change condition with roving (Fig. 1D, bottom panel), responses fluctuated roughly around chance level. In the frequency change conditions, both with and without roving, the number of detections increased steadily throughout the recording.

To provide statistical evidence on the effects of frequency, intensity and roving on the ACC we performed an analysis of variance (ANOVA) using a GLMM to predict the F-value using the following independent factors: the *acoustic cue* (frequency or intensity), *amplitude rov-*

ing (applied or not applied), and their interactions. The participant was included as a random factor. The results revealed that *acoustic cue*, ($\chi^2(1)$ = 40.60, p $<$ 0.001), *amplitude roving* ($\chi^2(1)$ = 17.91, p $<$ 0.001) and their interaction ($\chi^2(1)$ = 9.78, p = 0.0018) were significant factors.

Post-hoc analyses (Bonferroni corrected) on the model's estimated marginal means revealed a significant difference between intensity (roving vs. no roving; ΔF-value = 0.72, p $<$ 0.001), and no significant difference for the frequency condition (roving. vs. no roving; ΔF-value = 0.74, p = 0.13). Further inspections revealed that responses to the frequency change with roving were still significantly larger than responses to the loudness change without roving (ΔF-value = 1.00, p = 0.006).

4. DISCUSSION

Our results indicate that ACC responses to intensity changes decreased significantly when employing amplitude roving, whereas ACCs to frequency changes did not significantly differ when roving was applied. Moreover, the responses to frequency changes were larger compared to those in response to intensity changes. Overall, this suggests that amplitude roving effectively reduces the contributions of intensity cues in the cortical response, without compromising the response to frequency changes.

Through roving, the stimulus statistics were manipulated to increase the variance. Previously, animal studies have shown that, when subjected to a high amplitude variance context, intensity-rate decoding functions of individual cortical neurons are more adapted to the increased intensity range over which they operate, in comparison to a low amplitude variance context [12, 13]. In the present study, increasing the variance reduced the compound response to intensity changes, suggesting that like in animals, human cortical responses to changes in intensity becomes less distinct when these changes are contextualized by an increased level of variance. Since intensity changes were introduced as a proxy measure for perceptual changes in loudness, our results suggest—based on the strong reduction in responses—that cortical responses arising from changes in loudness are similarly reduced by applying amplitude roving.

5. CONCLUSIONS

Amplitude roving reduced cortical responses to loudness changes, but minimally affected responses to frequency changes. This finding can be particularly useful in the development of clinical objective methodologies of suprathreshold auditory processing. In cases where loudness cues cannot be strictly controlled for, e.g. when evaluating cortical responses to spectral changes between vowels, roving can be applied to minimize the potentially confounding loudness cue. Additionally, this method could be useful in populations where loudness perception is changed, e.g. due to hearing impairment. However, additional research is needed to confirm a reduction in loudness-driven responses via amplitude roving in these populations.

6. ACKNOWLEDGMENTS

This study was supported by the William Demant Foundation. The authors thank Ioana Stefancu, Alexandre Marc Maria and Xafsa Said for their contributions.

7. REFERENCES

[1] K. Mehta, P. Watkin, M. Baldwin, J. Marriage, M. Mahon, and D. Vickers, "Role of Cortical Auditory Evoked Potentials in Reducing the Age at Hearing Aid Fitting in Children With Hearing Loss Identified by Newborn Hearing Screening," *Trends in Hearing*, vol. 21, p. 233121651774409, Dec. 2017.

[2] S. Punch, B. Van Dun, A. King, L. Carter, and W. Pearce, "Clinical Experience of Using Cortical Auditory Evoked Potentials in the Treatment of Infant Hearing Loss in Australia," *Seminars in Hearing*, vol. 37, pp. 036–052, Feb. 2016.

[3] K. Mehta, M. Mahon, B. Van Dun, J. Marriage, and D. Vickers, "Clinicians' views of using cortical auditory evoked potentials (CAEP) in the permanent childhood hearing impairment patient pathway," *International Journal of Audiology*, vol. 59, pp. 81–89, Feb. 2020.

[4] B. A. Martin and A. Boothroyd, "Cortical, Auditory, Event-Related Potentials in Response to Periodic and Aperiodic Stimuli with the Same Spectral Envelope:," *Ear and Hearing*, vol. 20, pp. 33–44, Feb. 1999.

[5] B. A. Martin and A. Boothroyd, "Cortical, auditory, evoked potentials in response to changes of spectrum and amplitude," *J. Acoust. Soc. Am.*, vol. 107, pp. 2155–2161, Apr. 2000.

[6] A. Dimitrijevic, H. J. Michalewski, F.-G. Zeng, H. Pratt, and A. Starr, "Frequency changes in a continuous tone: Auditory cortical potentials," *Clinical Neurophysiology*, vol. 119, pp. 2111–2124, Sept. 2008.

[7] A. Dimitrijevic, A. Starr, S. Bhatt, H. J. Michalewski, F.-G. Zeng, and H. Pratt, "Auditory cortical N100 in pre- and post-synaptic auditory neuropathy to frequency or intensity changes of continuous tones," *Clinical Neurophysiology*, vol. 122, pp. 594–604, Mar. 2011.

[8] B. M. Vonck, M. J. Lammers, M. van der Waals, G. A. van Zanten, and H. Versnel, "Cortical Auditory Evoked Potentials in Response to Frequency Changes with Varied Magnitude, Rate, and Direction," *Journal of the Association for Research in Otolaryngology*, vol. 20, pp. 489–498, Oct. 2019.

[9] H. Fletcher and W. A. Munson, "Loudness, Its Definition, Measurement and Calculation," *The Journal of the Acoustical Society of America*, vol. 5, pp. 82–108, Oct. 1933.

[10] B. C. J. Moore and B. R. Glasberg, "A revision of Zwicker's loudness model," 1996.

[11] H. Dai and C. Micheyl, "On the choice of adequate randomization ranges for limiting the use of unwanted cues in same-different, dual-pair, and oddity tasks," *Attention, Perception, & Psychophysics*, vol. 72, pp. 538–547, Feb. 2010.

[12] I. Dean, N. S. Harper, and D. McAlpine, "Neural population coding of sound level adapts to stimulus statistics," *Nature Neuroscience*, vol. 8, pp. 1684–1689, Dec. 2005.

[13] N. Rabinowitz, B. Willmore, J. Schnupp, and A. King, "Contrast Gain Control in Auditory Cortex," *Neuron*, vol. 70, pp. 1178–1191, June 2011.

[14] N. C. Rabinowitz, B. D. B. Willmore, A. J. King, and J. W. H. Schnupp, "Constructing Noise-Invariant Representations of Sound in the Auditory Pathway," *PLoS Biology*, vol. 11, p. e1001710, Nov. 2013.

[15] J. A. Undurraga, M. A. Chesnaye, D. M. Simpson, J. M. Harte, and S. Laugesen, "A novel method for individualized detection of Auditory Evoked responses in real-time-The Fmpi," 2023.

[16] C. Elberling and M. Don, "Quality Estimation of Averaged Auditory Brainstem Responses," *Scandinavian Audiology*, vol. 13, no. 3, pp. 187–197, 1984. Publisher: Taylor & Francis _eprint: https://doi.org/10.3109/01050398409043059.

DOI: 10.61782/fa.2025.0720



FORUM ACUSTICUM
EURONOISE 2025

NEURAL RESPONSES AKIN TO ABRS MEASURED DURING NATURAL SPEECH LISTENING FOR HEARING AID ASSESSMENT

Florine L. Bachmann[1*] **Joshua P. Kulasingham**[2] **Kasper Eskelund**[3] **Martin Enqvist**[2]
Jens Hjortkjær[4,5] **Emina Alickovic**[1,2] **Hamish Innes-Brown**[1,4]
[1] Eriksholm Research Centre, Snekkersten, Denmark
[2] Automatic Control, Department of Electrical Engineering, Linköping University, Sweden
[3] Oticon A/S, Smørum, Denmark
[4] Hearing Systems, Department of Health Technology, Technical University of Denmark, Denmark
[5] Danish Research Centre for Magnetic Resonance, Copenhagen University Hospital, Denmark

ABSTRACT

This review outlines the current status and proposes future directions for using auditory brainstem responses (ABRs) to continuous speech as a tool in hearing aid assessment. In current clinical practice, ABRs measured via electroencephalography (EEG) in response to short stimuli, averaged across repetitions, are a cornerstone of objective hearing screening and evaluation. Recent advancements have demonstrated that ABRs can be estimated from EEG recorded during continuous speech listening by using linear models which map the auditory speech features, extracted using auditory models, to continuous EEG activity. This approach enables the simultaneous investigation of multiple auditory pathway stages using complex, ecologically valid sounds; advancing potential future hearing assessments that can be seamlessly integrated into daily life. Current findings indicate that responses similar to click-ABRs, with a salient wave V peak, can be estimated from natural continuous speech. These responses are sensitive to speech level, can be captured using insert earphones or in a sound-field environment, and can be obtained from aided older listeners with hearing impairment. While these advancements bring us closer to ecologically valid objective hearing device and fitting assessments, there are remaining hurdles to overcome, such as assessing ABRs to continuous natural speech during standard hearing device use.

Keywords: *Auditory brainstem response (ABR), speech, electroencephalography (EEG), temporal response function (TRF), hearing aid.*

*__Corresponding author__: *flln@eriksholm.com.*

__Copyright__: *©2025 Bachmann et al. This is an open-access article distributed under the terms of the Creative Commons Attribution 3.0 Unported License, which permits unrestricted use, distribution, and reproduction in any medium, provided the original author and source are credited.*

1. INTRODUCTION

Estimating brainstem responses to natural speech could potentially provide essential information on how a given hearing device processing scheme fits individual peripheral hearing abilities, offering the potential to improve hearing aid algorithms and fitting. Such assessments would require a method that can quantify *early* responses to *continuous natural speech* in a *reliable* way, is *sensitive* to changes in the incoming speech stimulus, and can be applied in *hearing aid users* while they are *using standard hearing devices*.

Current objective assessments of early sound processing do not fulfill all these requirements. The auditory brainstem response (ABR) is often employed for capturing early neural responses to sounds. Traditionally, methods to estimate ABRs measure the electroencephalogram (EEG) while the listener is exposed to many repetitions of the same sound. The EEG responses to each sound are averaged across a reasonably high number of sound repetitions (typically thousands) to estimate a transient neural response. This limits the stimuli to short duration sounds such as clicks [e.g. 1], chirps [e.g. 2–4], tones [e.g. 5, 6],

or syllables [e.g. 7, 8]. The transient stimuli are poorly suited for assessing the speech-specific hearing device signal processing algorithms [9], and the isolated speech units fail to capture the complexity of natural continuous speech [10]. However, in the past decade, approaches to estimate brainstem responses to continuous natural speech have been developed, refined, and extended [11–17].

These methodological advances enable the estimation of ABRs to continuous natural sounds, capturing the response of the brainstem to natural speech (NS-ABR). Beyond its potential in hearing aid assessment, NS-ABR also holds promising applications in research and clinical diagnostics. NS-ABR offers the potential for simultaneous estimation of speech processing in higher stages of the auditory pathway, as well as pairing with behavioral measures of speech comprehension. Initial results show intriguing patterns of brainstem and cortical processing in the presence of hearing loss and amplification [13] that could deepen our understanding of speech processing along the auditory pathway. In clinical diagnostics, NS-ABRs could add ecological relevance by providing an objective measure of peripheral auditory encoding of *speech* rather than *click* or *chirp* stimuli, supporting the identification of potential barriers to speech perception. Furthermore, presenting familiar sounds may increase measurement comfort for listeners, potentially lowering agitation which could lead to reduced movement and muscle tension artifacts and thus improve data quality [12, 13].

Here, we focus on perspectives for using NS-ABR in hearing aid assessment, where it could help evaluate the effects of device software on brainstem speech processing under different real-life conditions, offering essential feedback on algorithms and personalized fits in varied listening environments. We review current knowledge about the NS-ABR in terms of optimized response computation, understanding the response, its reliability, sensitivity to sound changes, and investigate hurdles still to overcome towards its application in hearing aid assessment.

2. COMPUTING THE ABR TO CONTINOUS SPEECH: TRFS MEET AUDITORY MODELS

NS-ABRs are typically estimated using forward linear models that map broadband speech features onto the time-lagged EEG response, estimating a temporal response function (TRF), in analogy to previous cortical analyses of continuous speech responses [e.g. 18–20]. This TRF can be interpreted as the evoked response to a unit change in the speech feature, often yielding a prominent peak at latencies similar to wave V of the click-ABR [11, 12, 16]. As linear models are unable to capture nonlinearities in the auditory periphery, this approach has recently been refined by non-linearly transforming the speech waveform into a signal simulating neural activity at the brainstem level using auditory nerve models (ANMs) [14–16]. Employing ANMs before neural response estimation via the TRF has considerably improved model performance and response signal-to-noise ratio (SNR) [15]. These improvements have led to shorter acquisition times [15] and allow for response estimation not only to continuous speech presented via insert earphones, but also to music [14], or speech presented in the sound-field [16]. While adding an ANM increases response SNR, other optimizations of the computation method, or improvements in EEG acquisition SNR for these specific signals could further reduce measurement time.

Although continuous speech and music are often encountered in daily life, a considerable share of real-life sound environments also include mixed and overlapping signals, and pauses. In conversations for example, speech often overlaps, and longer silent pauses occur [21]. In addition, sounds with very different spectrotemporal characteristics than speech or music, such as for example traffic noise, contribute to shaping real-life soundscapes. Further research could shed light on whether the current NS-ABR approach needs extension for application throughout those different and complex sound environments.

3. RESPONSE ORIGIN, SENSITIVITY, AND RELIABILITY OF THE ABR TO CONTINUOUS SPEECH

As a foundation for NS-ABR applications, it is crucial to understand the origin, sensitivity, and reliability of the response. Response analogies can facilitate interpretation and knowledge transfer from the extensive body of research on traditional brainstem measures. The estimated TRF mapping continuous broadband speech features to neural signals has been interpreted as an ABR [11, 12]. Its prominent response peak has a latency similar to ABR wave V measured to clicks [11, 12]. This short latency of less than 15 ms suggest a brainstem origin [22], as transmitting the neural signal to higher stages along the auditory pathway requires more time. The prominent peak of the NS-ABR is also positively correlated with the click-ABR wave V in both amplitude and latency [11, 12, 16], with the inferior colliculi and auditory midbrain areas thought to be the main sources of click-ABR wave V

[23–25].

When computed using a suitable auditory model, NS-ABR showed sound level sensitivity similar to click-ABRs [17]. Both showed larger amplitudes and shorter latencies at higher sound levels, and these level-dependent latency changes were consistent across the speech and click measures on an individual level [17]. This further underlines the analogies between NS-ABR and click-ABR, and suggests level sensitivity of the NS-ABR crucial for potential applications. In analogy to effects previously observed for click-ABRs [26], first results with processed 'peaky' speech stimuli show effects of energetic masking [27]. The target speech stream was presented in an increasing number of competing speech streams, leading to decreased SNR with increasing competing streams. In tact with decreasing SNR, ABR peaks to continuous 'peaky' speech occurred at longer latencies and lower amplitudes [27] - potentially indicating a similar sensitivity to masking for NS-ABR.

Another important consideration for applications is the test-retest reliability. In older aided participants with hearing-impairment, initial results indicate high test-retest reliability for identical speech stimuli, but differences for different speech material produced by the same speaker, potentially suggesting a high dependency of the response on the frequency content of the used speech signals [12]. While more work is needed for a comprehensive overview of NS-ABR test-retest reliability and its sensitivity to different abilities and sound environments, first findings on both are promising.

4. TOWARDS APPLICATION IN HEARING AID ASSESSMENT

Beyond understanding the response origin, its sensitivity, and reliability, further research is needed to lay the groundwork for use of NS-ABR as a tool in hearing aid assessment. Crucially, there is a need to understand the NS-ABR in the target group for hearing aids: people with hearing impairment - including those using their devices at the time of measurement. As the prevalence of hearing impairment shows a steep increase with age, particularly above the age of 50 [28, 29], older adults are the primary target population that could benefit from this tool. Initial findings in older adults with hearing impairment indicate that clear NS-ABRs could not be identified when presenting speech at 65 dB without any amplification [13]. Given that ABRs to clicks presented at low sensation levels relative to individual's hearing impairment are drastically reduced in amplitude [30], this suggests that the chosen 65 dB speech presentation level was too low for the participants' hearing loss and the sensitivity of the applied simpler NS-ABR method, which did not yet incorporate an auditory model [13].

The next step towards applying NS-ABR in hearing aid assessment is investigating the response in hearing impaired listeners *with amplification*. The same work that presented unamplified speech discussed above [13] also presented amplified speech to the older listeners with hearing loss, applying a linear amplification algorithm to the speech and directly presenting it via insert earphones. Findings for NS-ABR are consistent with those for click-ABR wave V, showing longer latencies and reduced amplitudes in older individuals with hearing impairment receiving amplification compared to younger normal-hearing listeners [12, 13]. More research on the NS-ABR in listeners with hearing impairment across all age groups is needed for a comprehensive understanding of the response in this diverse population.

Although these first findings are promising, evaluating hearing aid performance in real-life soundscapes requires estimating NS-ABR in listeners with hearing impairment *while providing amplification through an actual hearing aid*. This necessitates *sound-field speech presentation*. As a first step, we demonstrated that measuring NS-ABR in the sound-field was feasible in normal-hearing adults [16]. Slightly longer EEG recording time was required due to room acoustics, but this effect was migitated by pairing the TRF approach with a powerful auditory model, improving response SNR and resulting in clear NS-ABRs in all participants [16]. The next step is to integrate these elements by quantifying NS-ABRs in older individuals with hearing impairment while providing amplification through a standard hearing aid receiving sound in the sound-field.

5. OUTLOOK

ABRs measured to continuous natural speech (NS-ABR) instead of clicks and chirps is an emerging method with promise for applications. Initial research indicates that NS-ABR is reliable [13], sensitive to both speech level [17] and likely masking [27], can be quantified in older listeners with hearing impairment when presenting amplified speech [13], and when presenting speech via headphones [11–14, 17] as well as in the sound-field [16]. These findings suggest its potential for hearing aid assessment.

However, further research is needed to assess the feasibility of NS-ABR in individuals with hearing impairment while using standard hearing aids. By providing objective feedback from neural brainstem auditory processing of natural speech, the NS-ABR could help assess hearing aid software, such as noise suppression algorithms, and their adaptation to the individual listening needs in auditory scenes close to real life. This could contribute to improved hearing aid designs and better outcomes for hearing aid users.

6. REFERENCES

[1] M. Don and J. Eggermont, "Analysis of the click-evoked brainstem potentials in man using high-pass noise masking," *The Journal of the Acoustical Society of America*, vol. 63, no. 4, pp. 1084–1092, 1978.

[2] T. Dau, O. Wegner, V. Mellert, and B. Kollmeier, "Auditory brainstem responses with optimized chirp signals compensating basilar-membrane dispersion," *The Journal of the Acoustical Society of America*, vol. 107, no. 3, pp. 1530–1540, 2000.

[3] C. Elberling and M. Don, "A direct approach for the design of chirp stimuli used for the recording of auditory brainstem responses," *The Journal of the Acoustical Society of America*, vol. 128, no. 5, pp. 2955–2964, 2010.

[4] S. G. Kristensen and C. Elberling, "Auditory brainstem responses to level-specific chirps in normal-hearing adults," *Journal of the American Academy of Audiology*, vol. 23, no. 09, pp. 712–721, 2012.

[5] T. Suzuki, Y. Hirai, and K. Horiuchi, "Auditory brain stem responses to pure tone stimuli," *Scandinavian Audiology*, vol. 6, no. 1, pp. 51–56, 1977.

[6] D. R. Stapells and P. Oates, "Estimation of the pure-tone audiogram by the auditory brainstem response: a review," *Audiology and Neurotology*, vol. 2, no. 5, pp. 257–280, 1997.

[7] N. Russo, T. Nicol, G. Musacchia, and N. Kraus, "Brainstem responses to speech syllables," *Clinical Neurophysiology*, vol. 115, no. 9, pp. 2021–2030, 2004.

[8] S. Anderson, A. Parbery-Clark, H.-G. Yi, and N. Kraus, "A neural basis of speech-in-noise perception in older adults," *Ear and Hearing*, vol. 32, no. 6, pp. 750–757, 2011.

[9] S. Laugesen, J. E. Rieck, C. Elberling, T. Dau, and J. M. Harte, "On the cost of introducing speech-like properties to a stimulus for auditory steady-state response measurements," *Trends in Hearing*, vol. 22, p. 2331216518789302, 2018.

[10] L. S. Hamilton and A. G. Huth, "The revolution will not be controlled: Natural stimuli in speech neuroscience," *Language, Cognition and Neuroscience*, vol. 35, no. 5, pp. 573–582, 2020.

[11] R. K. Maddox and A. K. Lee, "Auditory brainstem responses to continuous natural speech in human listeners," *eNeuro*, vol. 5, no. 1, 2018.

[12] F. L. Bachmann, E. N. MacDonald, and J. Hjortkjær, "Neural measures of pitch processing in EEG responses to running speech," *Frontiers in Neuroscience*, vol. 15, p. 738408, 2021.

[13] F. L. Bachmann, *Subcortical electrophysiological measures of running speech [PhD Dissertation at the Technical University of Denmark]*. DTU Health Technology, 2022.

[14] T. Shan, M. S. Cappelloni, and R. K. Maddox, "Subcortical responses to music and speech are alike while cortical responses diverge," *Scientific Reports*, vol. 14, no. 789, 2024.

[15] J. P. Kulasingham, F. L. Bachmann, K. Eskelund, M. Enqvist, H. Innes-Brown, and E. Alickovic, "Predictors for estimating subcortical EEG responses to continuous speech," *Plos One*, vol. 19, no. 2, p. e0297826, 2024.

[16] F. L. Bachmann, J. P. Kulasingham, K. Eskelund, M. Enqvist, E. Alickovic, and H. Innes-Brown, "Extending subcortical EEG responses to continuous speech to the sound-field," *Trends in Hearing*, vol. 28, p. 23312165241246596, 2024.

[17] J. P. Kulasingham, H. Innes-Brown, M. Enqvist, and E. Alickovic, "Level-dependent subcortical electroencephalography responses to continuous speech," *eNeuro*, vol. 11, no. 8, 2024.

[18] E. Alickovic, T. Lunner, F. Gustafsson, and L. Ljung, "A tutorial on auditory attention identification methods," *Frontiers in Neuroscience*, vol. 13, p. 153, 2019.

[19] E. C. Lalor and J. J. Foxe, "Neural responses to uninterrupted natural speech can be extracted with precise temporal resolution," *European Journal of Neuroscience*, vol. 31, no. 1, pp. 189–193, 2010.

[20] S. Geirnaert, S. Vandecappelle, E. Alickovic, A. De Cheveigne, E. Lalor, B. T. Meyer, S. Miran, T. Francart, and A. Bertrand, "Electroencephalography-based auditory attention decoding: Toward neurosteered hearing devices," *IEEE Signal Processing Magazine*, vol. 38, no. 4, pp. 89–102, 2021.

[21] A. J. M. Sørensen, T. Lunner, and E. N. MacDonald, "Conversational dynamics in task dialogue between interlocutors with and without hearing impairment," *Trends in Hearing*, vol. 28, p. 23312165241296073, 2024.

[22] T. W. Picton, D. R. Stapells, and K. B. Campbell, "Auditory evoked potentials from the human cochlea and brainstem.," *The Journal of Otolaryngology. Supplement*, vol. 9, pp. 1–41, 1981.

[23] A. Starr, "Correlation between confirmed sites of neurological lesions and abnormalities of far-field auditory brainstem responses," *Electroencephalography and Clinical Neurophysiology*, vol. 41, no. 6, pp. 595–608, 1976.

[24] A. R. Møller and P. J. Jannetta, "Interpretation of brainstem auditory evoked potentials: Results from intracranial recordings in humans," *Scandinavian Audiology*, vol. 12, no. 2, pp. 125–133, 1983.

[25] J. K. Moore, "The human auditory brain stem as a generator of auditory evoked potentials," *Hearing Research*, vol. 29, no. 1, pp. 33–43, 1987.

[26] G. Mehraei, A. E. Hickox, H. M. Bharadwaj, H. Goldberg, S. Verhulst, M. C. Liberman, and B. G. Shinn-Cunningham, "Auditory brainstem response latency in noise as a marker of cochlear synaptopathy," *Journal of Neuroscience*, vol. 36, no. 13, pp. 3755–3764, 2016.

[27] M. J. Polonenko and R. K. Maddox, "The effect of speech masking on the human subcortical response to continuous speech," *bioRxiv*, 2024.

[28] GBD 2019 Hearing Loss Collaborators, "Hearing loss prevalence and years lived with disability, 1990–2019: Findings from the Global Burden of Disease Study 2019," *The Lancet*, vol. 397, no. 10278, pp. 966–1009, 2021.

[29] World Health Organization, *World Report on Hearing*. 2021.

[30] S. Verhulst, A. Jagadeesh, M. Mauermann, and F. Ernst, "Individual differences in auditory brainstem response wave characteristics: Relations to different aspects of peripheral hearing loss," *Trends in Hearing*, vol. 20, p. 27837052, 2016.

DOI: 10.61782/fa.2025.0661

FORUM ACUSTICUM EURONOISE 2025

OPTIMISING PARAMETERS FOR MEASURING THE ACOUSTIC CHANGE COMPLEX WITH AMPLITUDE-MODULATED STIMULI USING A CLINICAL EVOKED-POTENTIAL SYSTEM

Wayne Ellis[1, 2*] **Deborah Vickers**[2] **Nicholas Hawood**[2]
Nishchay Mehta[1,3,4] **Mahmoud Keshavarzi**[2] **Evelien De Groote**[2,5]

[1] The Royal National Ear Nose and Throat Hospital and Eastman Dental Hospital, University College Hospitals, London, United Kingdom

[2] SOUND Lab, Department of Clinical Neurosciences, University of Cambridge, Cambridge, United Kingdom

[3] National Institute for Health Care Research, University College London Hospital Biomedical Research Centre Hearing Health Theme, London, United Kingdom

[4] University College London Ear Institute, London, United Kingdom

[5] Cambridge Hearing Group, Medical Research Council Cognition and Brain Sciences Unit, University of Cambridge, Cambridge, United Kingdom

ABSTRACT

The Auditory Change Complex (ACC) is a transient cortical auditory-evoked potential, recorded via electroencephalography (EEG), and elicited by changes in an ongoing auditory stimulus. It provides insight into auditory discrimination, making it a relevant tool for evaluating cochlear implant (CI) performance. Previous studies have demonstrated that the ACC can be recorded in CI recipients, and many have reported a strong correlation with behavioural outcomes. However, these studies typically used equipment and analytical techniques not widely available in clinical settings.

As a first step toward developing a clinically feasible method for ACC recording, we adapted our EEG research protocol for amplitude-modulated (AM) rate discrimination for use with normal hearing listeners using the Eclipse system (Interacoustics). Our findings show that the ACC can be reliably recorded using this system, with good test-retest reliability. As expected, larger AM rate changes and lower carrier frequencies (CFs) elicited greater ACC amplitudes. Furthermore, increasing the presentation rate by reducing the inter-stimulus interval diminished the ACC response, and changing presentation level had minimal and inconsistent effects across participants. We are now exploring optimal AM rate changes and recording parameters for CI users, and will discuss preliminary results regarding the potential for routine clinical use in CI fittings.

Keywords: auditory change complex, cochlear implants, amplitude modulation, electroencephalography

*__Corresponding author__: wayne.ellis@nhs.net

__Copyright__: ©2025 First author et al. This is an open-access article distributed under the terms of the Creative Commons Attribution 3.0 Unported License, which permits unrestricted use, distribution, and reproduction in any medium, provided the original author and source are credited.

1. INTRODUCTION

Cochlear implants (CIs) are electronic hearing devices used to restore hearing in individuals with severe-to-profound deafness. They work by decomposing incoming sounds through a bank of bandpass filters, extracting the slowly-varying envelope cues within each filter band and using them to amplitude modulate fixed-rate electrical pulse trains presented to each electrode [1-2].

Envelope cues are crucial for speech understanding as they convey linguistic information across a range of modulation frequencies. Typical speech envelope modulations occur

within the 2-50 Hz range, with lower modulation rates (~2-5 Hz) providing syllabic and prosodic information and higher rates (~5-50 Hz) providing manner of articulation and voicing cues [3]. Modulation rates above 50 Hz provide pitch cues and the ability to discriminate periodic from aperiodic sounds. These modulation frequencies are associated with oscillatory activity in the auditory cortex. Delta (1-4 Hz), theta (4-8 Hz), and low gamma (25-50 Hz) oscillations are known to play crucial roles in processing the multi-timescale, rhythmic properties inherent in speech, facilitating the tracking of its dynamic nature [4]. These oscillatory patterns serve as foundational elements in speech and language processing, aiding in the segmentation of incoming information into units of appropriate temporal scales [4]. Slower oscillations, such as delta and theta, are implicated in phrasal and syllabic processing, while faster oscillations in the low gamma range are associated with phoneme-level processing.

Despite the success of cochlear implants, there remains significant variability in speech-perception outcomes among CI users [5-10]. One factor that contributes to this variability is the ability to accurately encode and process the temporal and spectral features of sound, which are essential for speech understanding, particularly in complex listening environments [11-13].

Although subjective speech-perception tests remain the standard method of assessing CI benefit, they are limited in scope. These behavioural measures are influenced by non-auditory factors such as attention, motivation, and cognitive ability, and are not suitable for individuals—such as young children or some adults—who cannot reliably complete listening tasks. This makes it challenging to determine whether a CI has been optimally programmed to provide access to the full range of relevant speech cues. Currently, however, there are no standardised, objective approaches to verify CI fitting. Tools such as electrically evoked compound action potentials (eCAPs) can assist in setting initial stimulation levels, but they provide only a rough indication of neural responsiveness and do not confirm functional access to speech information.

There is growing interest in using objective, neurophysiological measures to inform and verify fitting based on auditory detection and discrimination abilities in CI users. One such measure with the potential to support this goal is the Auditory Change Complex (ACC), a cortical auditory-evoked potential elicited in response to a change in an ongoing auditory stimulus [14-15]. The ACC typically exhibits the standard obligatory cortical P1–N1–P2 morphology, similar to responses evoked by sound onset, but time-locked to the point of stimulus change. This makes it a valuable tool for assessing auditory discrimination in a way that is both objective and functionally meaningful.

Previous studies have demonstrated that the ACC can be reliably recorded in CI users in response to changes in place of stimulation [16-19], indicating electrode discrimination abilities; rate of amplitude modulation—typically for rates below 50 Hz [19-22], which relates to the ability of the listener to use envelope cues—and stimulation level [23], as well as speech tokens [24-26]. Several studies have also reported correlations between ACC responses and behavioural speech perception measures [27, 28] and the development of these responses over time following device activation [29]. However, these studies have often utilised recording equipment and analytical techniques that are not typically available in clinical settings.

The primary aim of this study was to evaluate the feasibility of recording the ACC to changes in the AM rate using a clinical evoked-potential system (Eclipse, Interacoustics). We performed an initial study with normal-hearing listeners to validate our protocol and ensure that responses could be obtained for stimuli that have previously been used with the Biosemi EEG system [4]. We wanted to investigate the effects of various stimulus parameters on the ACC response amplitude, similar to the approach taken by Calcus et al [15], but using the Eclipse system. Both the N1-P2 and Root Mean Square (RMS) amplitude were evaluated. The parameters investigated were the magnitude of the AM rate change, carrier frequency (CF; equivalent to a centre frequency of a CI channel), presentation rate (adjusted by increasing the inter-stimulus interval), presentation level and direction of AM change (low to high versus high to low). We also evaluated test-retest reliability across two test sessions.

In a second phase of testing we are exploring the optimal AM rate change to use and are evaluating whether the Eclipse can be used to measure ACC responses in CI users.

2. METHODS

Two experiments were conducted using a two-channel clinical evoked potential system (Eclipse, Interacoustics). Experiment 1 investigated the effects of CF, stimulus level, AM rate change, presentation rate (adjusted by changing inter-stimulus-interval) and direction of AM rate change

(low to high or high to low) on the ACC amplitude. Test-retest reliability across sessions was also examined. Experiment 2 explores the interaction between CF and AM rate on the ACC amplitude, and testing is still ongoing.

2.1 Experiment 1

2.1.1 Participants

Twelve participants (9 females, 3 males) aged 26 to 44 years (mean age = 34.8 years) were recruited. All had normal hearing thresholds. The full experiment took two sessions to complete. The first session took two to three hours, and the follow-up session took approximately 30 minutes.

2.1.2 Stimuli and paradigm

Stimuli were 900-ms sinusoidally amplitude-modulated (AM) pure tones, created using custom MATLAB scripts. Stimulus presentation was controlled using the Eclipse EP software (Interacoustics) connected to an SP90A active loudspeaker (RadioEar). All stimuli were calibrated at 65 dB SPL prior to testing.

A total of four CFs were tested, including 626, 1438, 3313, and 5688 Hz, which correspond to the centre frequencies of electrodes 19, 13, 7 and 3 in the Cochlear Ltd device (assuming all electrodes are active). Halfway through the stimulus (at 450 ms), the AM rate was changed from 12 to 114 Hz (or vice versa). The modulation depth was 100%, and the presentation rate was set to 0.5 Hz (i.e., 1100-ms inter-stimulus interval, the quiet period between consecutive stimulus presentations). At the CF that elicited the largest ACC amplitude (usually 626 Hz), the effects of the magnitude of the AM rate change (12-40, 12-80, 12-114 Hz), presentation level (55, 65, 75 dB SPL), direction of the change (12-114 (up; low-to-high), 114-12 (down; high-to-low), and presentation rate (0.5 & 0.8 Hz with an inter-stimulus interval of 1100 ms and 350 ms respectively) were also assessed. Test-retest reliability of the ACC was evaluated by repeating the recording at the best CF and at a 12-114Hz AM rate change on Session 2. Finally, we included a 12-Hz AM no-change condition at the best CF. An example stimulus with an AM rate change is shown in Figure 1.

All conditions were presented in three blocks until 100 sweeps were accepted for each block (total of 300 sweeps per condition). Participants sat in a comfortable chair and watched a subtitled video for the duration of the experiment.

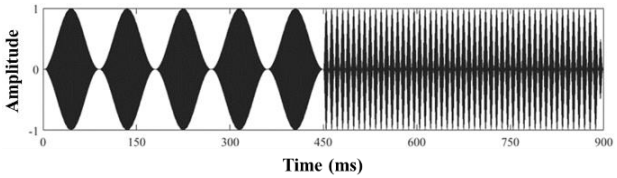


Figure 1. Example stimulus with an AM rate change. The CF for this stimulus is 1438 Hz, and the AM rate change is 12 to 114 Hz (change halfway at 450 ms).

2.1.3 EEG recording, EEG analysis, and statistical analysis

All EEG recordings were obtained using the Eclipse EP system (Interacoustics) at a sampling rate of 500 Hz. Pre-gelled disposable electrodes were placed on FPz (active), the low forehead (ground), and both mastoids (linked reference) in accordance with the standard clinical protocol. Impedances were checked prior to testing and were kept below 3 kΩ. The artefact rejection threshold was set to 40 or 80 µV depending on the participant, and the recording automatically stopped after 100 accepted sweeps. Each sweep (-90 to 810 ms post-stimulus onset) was saved for offline analysis with a 0.5-Hz high-pass hardware filter.

Individual sweeps were low-pass filtered at 30 Hz and baseline-corrected using the pre-stimulus quiet baseline period (-90 to 0 ms post-stimulus onset). For each participant and condition, all 300 sweeps were then averaged into one waveform. The amplitude of the ACC was quantified by determining the peak-to-peak amplitude for N1 and P2, which were defined as the lowest and highest amplitude values between 500-600 and 575-750 ms, respectively. The N1-P2 amplitude was chosen as the primary measure as it is the clinical standard. However, we also measured the root mean squared (RMS) amplitude within the 500-750-ms window post-stimulus onset for comparison. RMS amplitude provides an index of overall response magnitude that is less sensitive to individual differences in waveform morphology and avoids the subjectivity involved in identifying component peaks. This might make it a more suitable option for automated analysis.

Data were analysed with Repeated-Measures Analysis of Variance (RM-ANOVA) and Paired-Samples T-Tests, using jamovi (version 2.6) statistical software. Separate analyses were run to assess the effects of CF (626, 1438, 3313, 5688 Hz), magnitude of AM rate change (12-40, 12-80, 12-114 Hz), stimulus level (55, 65, 75 dB SPL), presentation rate (0.5, 0.8 Hz) and AM direction (12-114 (up), 114-12 (down)). Post-hoc pairwise comparisons were

corrected for multiple comparisons using a Bonferroni correction. Test-retest reliability (Session 1, Session 2) was assessed using a two-way random-effects intraclass correlation coefficient (ICC(2,k)) and Spearman's rank correlation.

2.2 Experiment 2

2.2.1 Participants

Four participants (2 females) aged 35 to 43 years (mean age = 39.75 years) were recruited to this pilot study. All had normal hearing thresholds. Two of the four participants had previously been tested in experiment 1.

2.2.2 Stimuli and paradigm

The stimuli were created, controlled and calibrated in the same way as in Experiment 1. Three CFs were tested (626, 1438 and 3313 Hz) at three AM rate changes (12-40, 12-80, 12-114 Hz) and a no-change condition at each CF.

2.2.3 EEG recording, EEG analysis, and statistical analysis

As per Experiment 1 (see 2.1.3).

3. RESULTS

3.1 Experiment 1

The coloured lines in Figure 2 show the group-grand-average waveforms (the average waveform computed across all participants, after first averaging each individual's responses across trials) for the largest AM rate change (i.e., 12-114 Hz) measured at four different CFs, as well as the group-grand-average waveform for the no-change condition in black. The waveforms show an initial typical onset response and an ACC after the AM change within the expected time windows.

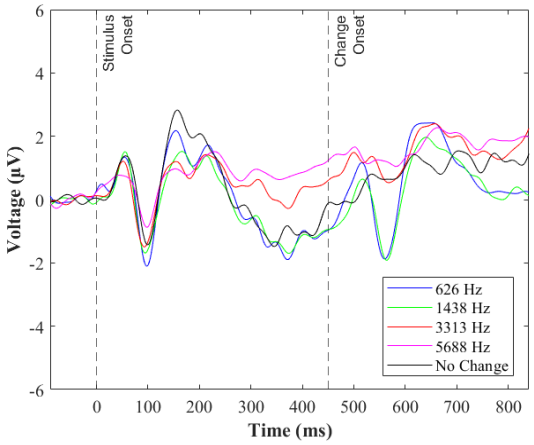


Figure 2. Group-grand-average waveforms for the change (coloured) and no-change conditions (black lines). Different colours represent different CFs. The 'change onset' at 450 ms indicates a change from 12- to 114-Hz AM rate. The group grand average refers to the average waveform computed across all participants, after first averaging each individual's responses across trials.

Figure 3 shows the mean ACC N1-P2 amplitude and standard deviation for all conditions tested in this study. Grey circles show single-participant data. Coloured bars show change conditions, and the no-change condition is shown in black. Change conditions generally evoked larger ACCs compared to the no-change condition.

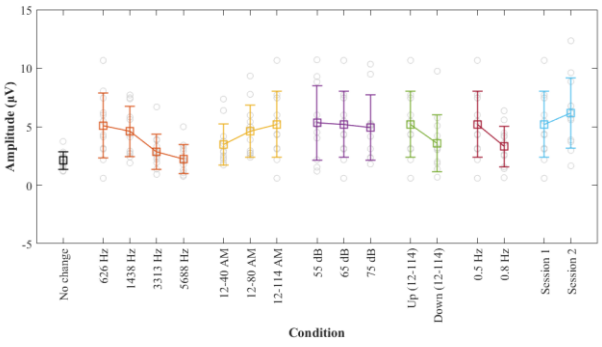


Figure 3. Mean ACC N1-P2 amplitude and standard deviations (± 1) for all conditions tested in this study. Coloured bars show change conditions grouped by their manipulation, and the no-change condition is

shown in black. Grey circles show single-participant data.

3.1.1 N1-P2 amplitude

RM-ANOVA showed a significant main effect of CF ($F(3,33) = 16.7$, $p < .001$) and AM rate change ($F(2,22) = 13.9$, $p < .001$) but no significant main effect of stimulus level ($F(2,20) = 0.512$, $p = 0.607$) on N1-P2 amplitude.

Post-hoc comparisons revealed significantly greater N1–P2 amplitudes at lower CFs: 626 Hz elicited larger responses than 3313 Hz ($p = .018$) and 5688 Hz ($p = .002$); and responses at 1438 Hz were significantly larger than those at 3313 Hz ($p = .015$) and 5688 Hz ($p = .002$). For AM rate change, amplitudes were significantly smaller at 12–40 Hz compared to both 12–80 Hz ($p = .045$) and 12–114 Hz ($p = .012$). Presentation rate also significantly affected amplitude, with larger responses at 0.5 Hz ($M = 5.20$; $SD = 2.82$) versus those at 0.8 Hz ($M = 3.30$; $SD = 1.70$), $t(11) = 2.76$, $p = .019$, Cohen's $d = 0.80$. There was no statistically significant difference in N1-P2 amplitude between upward (12-114 Hz) ($M = 5.20$; $SD = 2.82$) and downward (114-12 Hz) ($M = 3.60$; $SD = 2.43$); $t(11) = 1.95$, $p = 0.077$. direction of AM rate change. There was good test-retest reliability of N1-P2 amplitude (ICC = 0.889) and a significant positive correlation (Spearman's $\rho = 0.874$, $p < 0.001$) between sessions 1 and 2.

3.1.2 RMS amplitude

There was a significant main effect of CF ($F(3,33) = 19.5$, $p < .001$), stimulus level ($F(2,20) = 5.50$, $p < .012$) and AM rate change ($F(2,22) = 13.9$, $p < .001$) on RMS amplitude.

Post-hoc comparisons indicated significant differences in RMS amplitude between CFs 626 Hz and 3313 Hz ($p = 0.016$), 626 Hz and 5688 Hz ($p = < .001$) and 1438 Hz and 5688 Hz ($p = < .001$), AM rate changes 12-40 Hz and 12-114 Hz ($p = < .001$) and 12-80 Hz and 12-114 Hz ($p = 0.037$), and stimulus levels 55 dB SPL and 75 dB SPL ($p = 0.035$). There was also a significant effect of presentation rate 0.5 Hz ($M = 3.39$; $SD = 4.00$) and 0.8 Hz ($M = -0.36$; $SD = 3.77$); $t(11) = 2.79$, $p = 0.018$, and direction of AM change from upward (12-114 Hz) ($M = 3.39$; $SD = 4.00$) to downward (114-12 Hz) ($M = 0.038$; $SD = 4.80$); $t(11) = 2.77$, $p = 0.018$. There was good test-retest reliability of RMS amplitude (ICC = 0.877) and a significant positive correlation (Spearman's $\rho = 0.797$, $p = .0019$) between sessions 1 and 2.

3.2 Experiment 2

As testing is still ongoing (currently N = 4), statistical analyses were not performed. However, as shown in Figure 4, the general trend indicates the ACC N1-P2 amplitude diminishes as CF increases and AM rate change decreases. The ACC appears to be recordable using the clinical system at all AM rate changes tested at CF 626 Hz and 1438 Hz, although responses to the 12-40 Hz AM rate change are weak. At CF 3313 Hz it does not look possible to record the ACC for smaller AM rate change differences, despite each participant reporting that they could clearly hear the change.

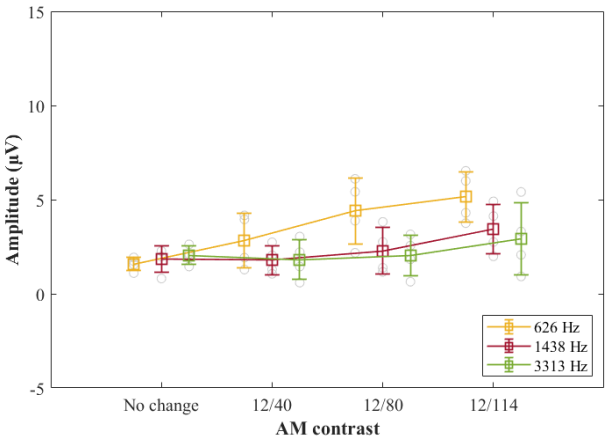


Figure 4. Mean N1–P2 amplitude (μV) as a function of AM rate change at three carrier frequencies (626 Hz, 1438 Hz, 3313 Hz). Error bars show ±1 SEM.

4. DISCUSSION

The primary aim of this study was to evaluate whether the ACC to AM rate changes can be reliably recorded using a clinical evoked-potential system (Eclipse, Interacoustics), as a step toward developing an objective measure for verifying CI fitting and informing mapping. In addition, we aimed to investigate how various stimulus parameters—including CF, AM rate change, presentation level, presentation rate, and direction of change—affect the amplitude (N1-P2 and rms) of the ACC response. In normal-hearing listeners, we found that the ACC could be robustly recorded using this system, with good test-retest reliability. These findings support the feasibility of adapting ACC protocols for clinical use, using equipment that is already available in many audiology departments.

The results of Experiment 1 suggest that several stimulus parameters significantly influenced ACC amplitude. ACCs were largest at lower CFs, with the strongest responses typically observed at 626 Hz. This is consistent with previous findings suggesting greater cortical sensitivity to lower-frequency modulation cues [20, 30, 31]. As expected, larger AM rate changes also evoked greater ACC amplitudes (N1-P2 and RMS), reflecting the increased neural response to more salient acoustic changes. This pattern aligns with prior work using research-grade EEG recording systems [15, 30]

The direction and speed of stimulus presentation also impacted response amplitude. Upward changes in AM rate (12–114 Hz) elicited stronger ACCs than downward changes (114–12 Hz), potentially reflecting perceptual asymmetries or differences in adaptation across modulation frequencies [31-33]. Faster presentation rates reduced ACC amplitude, likely due to reduced neural recovery time or attentional effects [14, 24, 34].

Notably, presentation level had only a modest and inconsistent influence on the ACC, which may be advantageous in clinical contexts where stimulus level cannot always be precisely controlled.

Importantly, ACCs were recordable across most test conditions, and test-retest reliability was high, indicating that the response is stable over time. This is a key requirement for clinical implementation, where repeatable and interpretable results are essential for guiding decisions. The ability to record robust ACCs with the Eclipse system using stimuli modelled after previous research protocols demonstrates the potential for clinical translation without the need for complex analysis pipelines or specialised hardware.

The preliminary data from Experiment 2 suggest that ACC responses are weaker at higher CFs, especially when paired with smaller AM rate changes. This trend is notable, as it may limit the clinical utility of the ACC in assessing the perception of fine-grained modulation changes in higher-frequency channels. However, responses at 626 Hz and 1438 Hz were reliably present even at smaller AM rate changes, suggesting that lower-frequency channels may provide a more consistent window into temporal processing abilities. Further work is needed to determine whether these trends hold in CI users and how best to adapt parameters for individual implant configurations.

Together, these findings suggest that the ACC has promise as a clinically feasible, objective measure to support CI programming. Unlike eCAPs, which provide only an estimate of neural excitability, the ACC reflects discrimination at the cortical level via the detection of a change in an acoustic stimulus, and it may offer more direct insight into a CI user's ability to access critical AM cues that are so important for perceiving distinctive speech features. This is especially relevant in cases where behavioural testing is not possible, such as in young children or adults with additional needs. While ACCs have been widely studied in research contexts, our study contributes to the growing evidence that they can be measured using accessible clinical systems and under test conditions that align with practical constraints.

There are several limitations to this study. First, the experiments were conducted in normal-hearing listeners, and while this allowed for controlled testing of stimulus parameters, recordings in CI users are needed to fully assess clinical applicability. Second, data collection for Experiment 2 is ongoing and currently does not allow for statistical analysis, though observed trends provide useful guidance for ongoing work. Finally, although the ACC is promising as an objective measure of auditory discrimination, further research is required to understand how it relates to real-world speech perception and functional benefit in CI users.

In the next phase of this work, we are recording ACCs in CI listeners using the Eclipse system, focusing on optimising AM rate changes and exploring the extent to which these responses may support objective verification of CI fitting. So far, we have collected data from a single CI user under two conditions, both using a 1438-Hz carrier that was amplitude-modulated at 25 Hz before switching to 80 Hz at 550 ms. First, we used the participant's clinical MAP, but with all audibility and noise reduction features disabled to ensure the processor did not alter the stimulus. Second, we set the parameters below the participant's hearing thresholds (confirmed as inaudible), enabling us to observe the CI-related artefact in the EEG without a neural response. The recording protocol extended to 900 ms, providing a 350-ms window after the modulation change (25 Hz to 80 Hz) to capture ACC. We leveraged the second (inaudible) condition to locate and characterise the CI-related artefact in the EEG. The data were first low-pass filtered below 25 Hz, then we applied a frequency-domain algorithm that detects and suppresses narrowband peaks (e.g., residual CI noise) by replacing them with the surrounding baseline in the frequency domain (calculated

via FFT). This procedure preserves the low-frequency cortical responses while minimising contamination from artefact.

If validated in this population, the ACC may offer a valuable addition to current programming tools, providing clinicians with a neurophysiological measure of auditory discrimination that is both practical and clinically meaningful.

5. ACKNOWLEDGMENTS

Dr Evelien De Groote is supported by a grant from Cochlear Corporation. Wayne Ellis is funded by the NHS National School of Healthcare Science (NSHCS) as part of the Higher Scientific Specialist Training (HSST) scheme.

6. REFERENCES

[1] B. S. Wilson et al., "Better speech recognition with cochlear implants," *Nature*, vol. 352, no. 6332, pp. 236–238, 1991.

[2] B. S. Wilson and M. F. Dorman, "Cochlear implants: a remarkable past and a brilliant future," *Hear. Res.*, vol. 242, no. 1–2, pp. 3–21, Aug. 2008.

[3] S. Rosen, "Temporal information in speech: acoustic, auditory and linguistic aspects," *Philos. Trans. R. Soc. Lond. B Biol. Sci.*, vol. 336, no. 1278, pp. 367–373, 1992.

[4] A. L. Giraud and D. Poeppel, "Cortical oscillations and speech processing: Emerging computational principles and operations," *Nat. Neurosci.*, vol. 15, no. 4, pp. 511–517, 2012.

[5] D. S. Lazard et al., "Pre-, Per- and Postoperative Factors Affecting Performance of Postlinguistically Deaf Adults Using Cochlear Implants," *PLoS One*, vol. 7, no. 11, p. 48739, Nov. 2012.

[6] D. B. Pisoni et al., "Three challenges for future research on cochlear implants," *KeAi Communications Co.*, Dec. 2017.

[7] I. Boisvert et al., "Cochlear implantation outcomes in adults: A scoping review," *PLoS One*, vol. 15, no. 5, May 2020.

[8] P. Blamey et al., "Factors affecting auditory performance of postlinguistically deaf adults using cochlear implants," *Audiol. Neurootol.*, vol. 18, no. 1, pp. 36–47, Dec. 2013.

[9] L. K. Holden et al., "Factors affecting open-set word recognition in adults with cochlear implants," *Ear Hear.*, vol. 34, no. 3, pp. 342–360, May 2013.

[10] B. Goudey et al., "A MultiCenter Analysis of Factors Associated with Hearing Outcome for 2,735 Adults with Cochlear Implants," *Trends Hear.*, vol. 25, 2021.

[11] R. V. Shannon et al., "Speech recognition with primarily temporal cues," *Science*, vol. 270, no. 5234, pp. 303–304, Oct. 1995.

[12] Q. J. Fu, "Temporal processing and speech recognition in cochlear implant users," *Neuroreport*, vol. 13, no. 13, pp. 1635–1639, Sep. 2002.

[13] Z. M. Smith et al., "Chimaeric sounds reveal dichotomies in auditory perception," 2002. [Online]. Available: www.nature.com

[14] B. A. Martin and A. Boothroyd, "Cortical, auditory, event-related potentials in response to periodic and aperiodic stimuli," *Ear Hear.*, vol. 20, no. 1, pp. 33–44, Feb. 1999.

[15] A. Calcus et al., "Simultaneous subcortical and cortical electrophysiological recordings of spectro-temporal processing in humans," *Front. Neurol.*, vol. 13, 2022.

[16] C. J. Brown et al., "The electrically evoked auditory change complex: Preliminary results from nucleus cochlear implant users," *Ear Hear.*, vol. 29, no. 5, pp. 704–717, Oct. 2008.

[17] S. He et al., "Objective measures of electrode discrimination with electrically evoked auditory change complex," *Ear Hear.*, vol. 35, no. 3, 2014.

[18] R. Mathew et al., "Objective assessment of electrode discrimination with the auditory change complex," *Hear. Res.*, vol. 354, pp. 86–101, Oct. 2017.

[19] J. A. Undurraga et al., "Neural encoding of spectro-temporal cues at slow and near speech-rate in cochlear implant users," *Hear. Res.*, vol. 403, Feb. 2021.

[20] J. H. Han and A. Dimitrijevic, "Acoustic Change Responses to Amplitude Modulation in Cochlear Implant Users," *Front. Neurosci.*, vol. 14, Feb. 2020.

[21] D. A. Vickers et al., "Electrophysiological and Psychophysical Measures of Amplitude Modulation Discrimination in Cochlear Implant Users," in *Proc. 23rd Int. Congr. Acoust. (ICA)*, Aachen, Germany, Sep.

2019. [Online]. Available: http://publications.rwth-aachen.de/record/770097

[22] N. Aldag and W. Nogueira, "Psychoacoustic and electroencephalographic responses to changes in amplitude modulation depth and frequency," *Sci. Rep.*, vol. 14, no. 1, Dec. 2024.

[23] J.-R. Kim et al., "The Effect of Changes in Stimulus Level on Electrically Evoked Cortical Auditory Potentials," *Ear Hear.*, vol. 30, no. 3, pp. 320–329, Jun. 2009.

[24] K. L. Tremblay et al., "Neural representation of amplified speech sounds," *Ear Hear.*, vol. 27, no. 2, 2006.

[25] L. M. Friesen and K. L. Tremblay, "Acoustic Change Complexes Recorded in Adult Cochlear Implant Listeners," *Ear Hear.*, vol. 27, no. 6, pp. 678–685, Dec. 2006.

[26] E. Brint, "The Acoustic Change Complex for Measuring Speech Perceptual Performance," Ph.D. dissertation, Dept. Speech and Hearing Sciences, Univ. College London, London, U.K., 2017.

[27] J. H. Han et al., "Auditory cortical activity to different voice onset times in cochlear implant users," *Clin. Neurophysiol.*, vol. 127, no. 2, pp. 1603–1617, Feb. 2016.

[28] R. Gransier et al., "Neural Modulation Transmission Is a Marker for Speech Perception in Noise," *Ear Hear.*, vol. 41, no. 3, pp. 591–602, Feb. 2020.

[29] R. Mathew et al., "Development of electrophysiological and behavioural measures of electrode discrimination," *Hear. Res.*, vol. 367, pp. 74–87, Sep. 2018.

[30] J. H. Han and A. Dimitrijevic, "Acoustic change responses to amplitude modulation," *Front. Neurosci.*, vol. 9, no. FEB, 2015.

[31] S. G. Kim et al., "Modulation change detection in human auditory cortex," *Eur. J. Neurosci.*, vol. 52, no. 2, pp. 2889–2904, Jul. 2020.

[32] F. C. Constantino et al., "Detection of Appearing and Disappearing Objects in Complex Acoustic Scenes," *PLoS One*, vol. 7, no. 9, 2012.

[33] E. Sohoglu and M. Chait, "Neural dynamics of change detection in crowded acoustic scenes," *Neuroimage*, vol. 126, 2016.

[34] J. L. Wunderlich et al., "Maturation of the cortical auditory evoked potential in infants and young children," *Hear. Res.*, vol. 212, no. 1–2, 2006.

DOI: 10.61782/fa.2025.0115

FORUM ACUSTICUM EURONOISE 2025

ALTERATIONS IN STEADY-STATE SYNCHRONISATION BETWEEN ACUTE AND CHRONIC TINNITUS SUGGESTS REDUCTION IN THE NEURAL CORRELATES OF TINNITUS OVER TIME

Abishek Umashankar[1] **William Sedley**[1] **Kai Alter**[1] **Phillip E. Gander**[2]
[1] Department of Translation and Clinical Research, Faculty of Medical Sciences, Newcastle University NE2 4HH
[2] Department of Radiology, Carver College of Medicine, University of Iowa, IA 52242

ABSTRACT

The mechanism of tinnitus remains unclear as the generation and persistence of tinnitus is not widely understood. The acute tinnitus population serves as an ideal subject for investigating the mechanisms behind the origin and persistence of tinnitus, from its initial onset to its subsequent chronification. One of the neural markers for measuring tinnitus are central gain and alterations in neural synchrony or central gain, linked to tinnitus can be measured using the Auditory Steady State Response (ASSR). The experiment was carried out on 39 participants with acute tinnitus (18 followed back six months post baseline), 30 with chronic tinnitus, and 27 controls. The results revealed cross sectionally, there were no significant differences in both absolute amplitudes of ASSR across intensities and the slope of ASSR growth function between the groups. However, longitudinally, there was a near significant increase in ASSR amplitude at low and medium intensity levels over time. Our findings indicate that the near significant differences in ASSR amplitude is attributable to changes in neural synchronisation, attentional modulation, tinnitus-related distress, and diminished GABAergic inhibition coinciding with the onset of tinnitus, which typically decreases over time. The alterations occurring at the onset may facilitate the persistence of tinnitus.

Keywords: *Neural synchronization, GABA, acute tinnitus, tinnitus generation.*

[*] ***Corresponding author***: *A.Umashankar2@newcastle.ac.uk.*
Copyright: *©2025 First author et al. This is an open-access article distributed under the terms of the Creative Commons Attribution 3.0 Unported License, which permits unrestricted use, distribution, and reproduction in any medium, provided the original author and source are credited.*

1. INTRODUCTION

Tinnitus has been found to originate most commonly because of hearing damage, which can be either an audiometrically detectable hearing loss or an undetectable kind of 'hidden' hearing loss such as cochlear synaptopathy [1]. In principle, for optimal functioning of the auditory system, each hierarchical level should have an input/output function that maintains a stable and optimum range of output values despite potentially large changes in the range of inputs. But, due to peripheral auditory insults, input to the central auditory system is reduced, thus altering the equilibrium of the input/output function. In order to maintain the input/output function, the brain typically changes the slope function by increasing the rate of excitatory to inhibitory firing to achieve homeostasis [2,3]. This alteration of slope in the input/output function is gain and helps achieve homeostatic plasticity [3].

One of the objective markers of gain is the use of Auditory Steady State Response (ASSR) [5]. Amplitude Modulation (AM) results in neurons exhibiting a *mixed coding* response at the level of primary auditory cortex, which encompasses both phase locking to the modulation frequency, and an elevated firing rate in response to the unmodulated tone [6]. The 40 Hz ASSR has been used in tinnitus studies as a potential measure of neuronal sensitivity in tinnitus [6]. The slope typically dictates the degree of excess input/output function, which cannot be fully deduced from a single data point (intensity) measurement and requires at least 2 data points (intensities). Therefore, it is necessary to do an intensity dependence analysis (across different intensities) of the steady-state response, which will provide the slope function to facilitate the determination of central gain related to the ASSR.

The generation and persistence of tinnitus has been unclear and although there have been studies that talk

about possible mechanisms of tinnitus generation and persistence, they are either from first principles, chronic tinnitus studies, or animal studies. There needs further research on acute tinnitus individuals as they are the ideal population to study how tinnitus generates and how does it transit from acute to chronic stages of tinnitus. According to the sensory precision model [3], tinnitus arises from changes in the brain's estimation of sensory precision following hearing loss. In the acute phase, reduced auditory input leads to a down-weighting of peripheral signals and an up-weighting of internal predictions, resulting in the emergence of tinnitus as a compensatory percept. Over time, if the altered sensory precision persists, the brain may recalibrate to treat the internally generated tinnitus signal as behaviorally relevant, leading to chronic tinnitus. This model suggests that persistent tinnitus reflects a maladaptive stabilization of heightened precision attributed to non-auditory predictive signals. Keeping this literature in mind, we hypothesize that central gain diminishes as a regression towards the mean from the Acute to the Chronic stage, leading us to predict a decline in ASSR slope and amplitude over time.

2. METHODS

2.1. Participants

We studied 39 participants with Acute Tinnitus (which we defined as duration 3 days to 6 weeks, with one outlier having a duration of 12 weeks), 30 participants with Chronic Tinnitus (defined as duration more than 6 months), and 27 hearing-matched (to the acute tinnitus group) non-tinnitus controls. Participants were recruited through community advertising on Google Ads, and internally within Newcastle University's research volunteer pool. The 39 Acute Tinnitus participants were invited for reassessment after a minimum of 6 months from tinnitus onset (which we took to indicate their chronic stage), and 18 of them volunteered for and completed this further testing. We refer to this as the 'Post Acute' group, to distinguish it from the group recruited during the chronic stage of tinnitus.

Control participants were matched to the acute tinnitus group for age, sex, hearing, and stimulus frequency and presentation ear.

2.2. Audiological assessment

The experimenter interviewed the subjects before the experiment, verifying a medical history consistent with subjective tinnitus and the absence of atypical symptoms or concerns regarding an undetermined underlying cause. Participants underwent a Pure Tone Audiometry (PTA) test to establish hearing thresholds at octave frequencies ranging between 250 Hz up to 8 KHz. Thresholds were estimated based on the initial presented level at either 40 dBHL or above depending on the participant's residual hearing [7]. The frequency and loudness of tinnitus were assessed using a *tinnitometry* (i.e. psychoacoustic measurement of tinnitus characteristics) approach for patients with acute or chronic tinnitus. In instances of unilateral Tinnitus, matching stimuli were delivered contralaterally, whereas in bilateral tinnitus, they were administered bilaterally. Participants initially matched the loudness of their tinnitus, followed by matching its frequency, commencing at a reference frequency of 6 kHz.

2.3. ASSR stimuli

The ASSR stimuli comprised 15 stimuli per frequency (5 stimuli for each of three intensities per frequency) within a total experiment duration of 15 minutes. These stimuli were Amplitude Modulated sounds with a modulation frequency of 40Hz and a modulation depth of 100% at 1 kHz and the participant's matched tinnitus frequency (or, for controls, the matched tinnitus participant's frequency), each lasting 30 seconds, with an interstimulus interval of 2 seconds.

For every frequency, three different intensities were presented. Stimuli were presented in one block, with intensities and frequencies fully randomized within that block. To account for hearing loss, loudness recruitment and hyperacusis, whilst keeping the stimuli clearly audible yet comfortable, stimulus intensities were presented in accordance with each participant's dynamic range, i.e. the range between their hearing threshold and uncomfortable loudness level, which were established for the specific experimental stimuli at both 1 kHz and the tinnitus frequency. Figure 1 depicts the intensity levels presented.

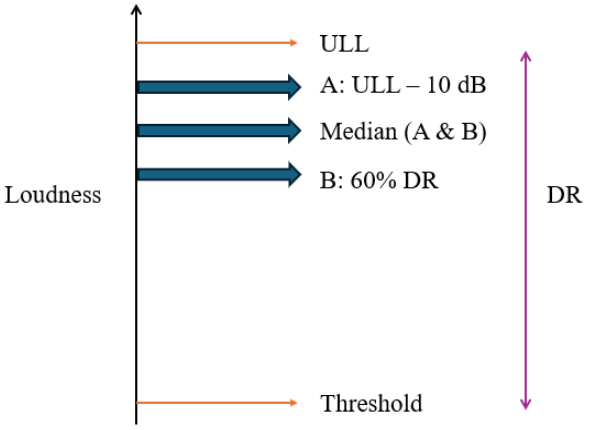


Figure 1: Stimulus presentation levels across 3 intensities based on tailored dynamic range for each subject
ULL: Uncomfortable Loudness level, DR: Dynamic Range.

2.4. EEG and Data analysis

Data were processed in MATLAB, version R2019a, using the EEGlab toolbox [8] and customized code. Data were re-referenced to the P9/P10 (Linked mastoids) montage. The data were further segmented into 30 seconds epoch around each trigger which was followed by a baseline correction. Following the segmentation of the EEG data into 50% overlapping 1s Hanning-windowed sub-epochs, a frequency analysis was conducted utilizing a Fast Fourier Transform (FFT) to transfer the time-domain data into the frequency domain, facilitating the identification and extraction of spectrum peaks, notably at 40Hz.

After pre-processing, we used customized code to perform automatic peak detection at 40Hz and signal to noise ratio calculation to determine the ASSR amplitude and signal to noise ratio. We did this using data from FCz to measure the peak amplitude for ASSR at 40Hz for both 1Khz and tinnitus frequency. Similar analysis was done for noise floor estimation, where the FFT amplitudes were averaged across the neighboring frequencies between 38 and 39, and between 41 and 43, Hz of Amplitude Modulation. The presence of a meaningful ASSR was ascertained via visual evaluation of the response at 40Hz and objectively through F-statistics [9], which analyzed the variance of peak amplitude and noise floor values; a meaningful response was judged to be present only if the ASSR response was significantly larger than the noise floor values based on a value of $p < 0.05$. Each subject had amplitude and noise floor calculated for 3 intensities across 2 frequencies of 1 kHz and tinnitus frequency. From these, the ASSR slope function at each frequency was calculated as the quotient of the Amplitude Dynamic Range (ADR: relative difference of the high and low ASSR amplitude) and Stimulus Dynamic Range (SDR: relative difference of the high and low stimulus intensity). Statistical analysis was carried out for both, across groups between acute, chronic, and controls along with a within group statistical analysis between acute and post-acute tinnitus.

3. RESULTS

3.1. ASSR Amplitude

The ASSR mean amplitude was individually evaluated among the Acute, Chronic, and Control groups for both 1 kHz and tinnitus frequencies. Before comparing amplitudes at low, medium, and high levels, we assessed the absolute stimulus presentation levels (dBSL) to establish whether possible differences in measured amplitude could be explained by stimulus presentation level. A MANOVA was carried out to establish the effect of groups (Acute, Chronic, and Controls) on the stimulus presentation levels (low, medium, and high).

3.1.1. 1 kHz

To determine the effect of group and intensities on the ASSR amplitude, we conducted a two-way Analysis of Covariance (ANCOVA) with two factors: groups (Acute, Chronic, and Controls) and intensities (low, medium, and high), with two covariates: stimulus presentation levels (low, medium, and high), and hearing thresholds at 1 kHZ. Results revealed no statistical significant main effect of intensities ($F(2,277) = 2.348$, $p = 0.097$, partial $\eta^2 = 0.017$) and statistically significant main effect of groups ($F(2,277) = 3.066$, $p = 0.048$, partial $\eta^2 = 0.022$) with near-significant difference between Chronic Tinnitus and Controls ($p = 0.055$) and no significant difference between Acute Tinnitus and Chronic Tinnitus ($p = 1$) and between Acute Tinnitus and Controls ($p = 0.142$). Controls had higher overall amplitude ($M = 1678.7$, $SE = 84.93$) when compared to Chronic Tinnitus ($M = 1388.95$, $SE = 79.62$). There was no statistically significant interaction between the groups and intensities on the amplitude ($F(4,277) = 0.279$, $p = 0.891$, partial $\eta^2 = 0.004$). With respect to the longitudinal comparison, a repeated measures 2-way ANOVA was performed to compare the effect of groups and intensities on the amplitude. Results revealed a main

effect of intensity ($F(2,16) = 23.814$, $p < 0.001$, Wilk's $A = 0.251$), no main effect for group ($F(2,16) = 2.667$, $p = 0.135$, Wilk's $A = 0.873$), and no interaction effect between groups and intensities ($F(2,16) = 0.957$, $p = 0.405$, Wilk's $A = 0.893$). We however carried out a simple main effect analysis using paired t test to determine the impact of group on amplitude for individual intensities, and the results indicated presence of near-significant difference between Acute and Post Acute Tinnitus for low intensity ($t(17) = -1.896$, $p = 0.075$) and medium intensity ($t(17) = -2.080$, $p = 0.053$) with Post Acute tinnitus (low intensity: M = 1475.97 SD = 670.05, medium intensity: M = 1674.48, SD = 771.61) having larger amplitude than Acute tinnitus (low intensity: M = 1313.82 SD = 762.2, medium intensity: M = 1456.56, SD = 809.1). No significant difference was found for the high intensity ($t(17) = -0.772$, $p = 0.451$). There was no impact of stimulus presentation levels on the obtained ASSR amplitude with no significant difference between Acute and Post Acute Tinnitus on low, mid, and high stimulus intensity presentation levels.

3.1.2. Tinnitus Frequency

Equivalent analysis was performed at tinnitus frequency and revealed no statistically significant difference for both cross sectional and longitudinal comparisons. Figure 2 depicts the cross-sectional changes in amplitude and figure 3 depicts the longitudinal changes in amplitude

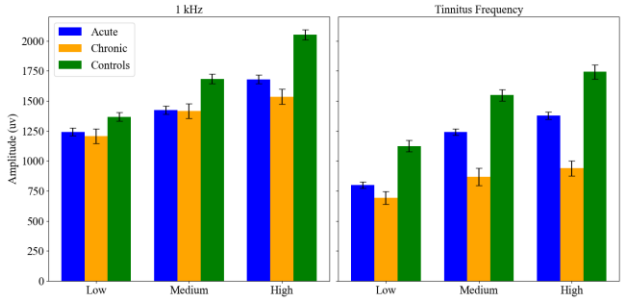


Figure 2*:* Differences in ASSR amplitude at low, medium, and high intensities between Acute, Chronic, and Controls for both 1 kHz and tinnitus frequency.

There is no statistical difference between the groups for any intensities across either frequency. However, controls show a non-significant increased amplitude when compared to both the tinnitus groups.

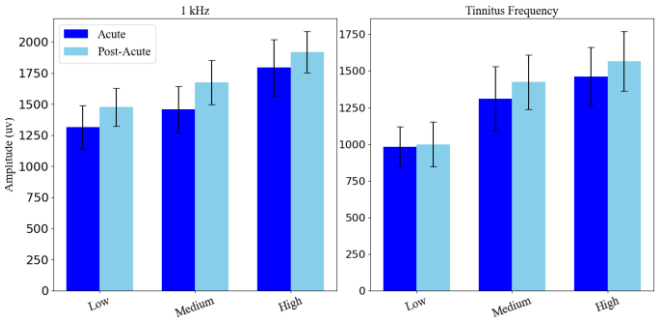


Figure 3: Differences in ASSR amplitude at low, medium, and high intensities between Acute and Post Acute Tinnitus for both 1 kHz and tinnitus frequency**.** *There is a near significant difference (increase in ASSR amplitude) between Acute and Post Acute Tinnitus for low and medium intensity at 1 kHz and none for high intensity. No differences in any loudness categories were noted for Tinnitus frequency.*

3.2. ASSR Slope

In analyzing the variations in slope among the Acute, Chronic, and Control groups, as well as between the Acute and Post Acute Tinnitus groups, we focused on three variables: the Stimulus Dynamic Range (SDR), defined as the difference between high and low stimulus presentation; the Amplitude Dynamic Range (ADR), which represents the difference between high and low ASSR amplitude; and slope, calculated as the ratio of SDR to ADR. Determining whether SDR differed will provide insight into the possible confounding factors that might affect the obtained ADR and slope. Assessing ADR in conjunction with slope will provide a comprehensive understanding of the amplitude growth function for ASSR across different groups

3.2.1. 1 kHz stimuli

A one-way MANOVA was carried out to establish the effect of group on slope, SDR, and ADR; this revealed a significant difference in overall response based on groups ($F(6,184) = 3.964$, $p < 0.001$, Wilk's $A = 0.526$, partial $\eta^2 = 0.114$). An overall main effect was seen for SDR ($F(2,94) = 10.215$, $p < 0.001$, partial $\eta^2 = 0.179$) with difference between Acute Tinnitus and Controls ($p = 0.007$), Chronic Tinnitus and Controls ($p < 0.001$), and no differences between Acute Tinnitus and Chronic Tinnitus ($p = 0.317$). Controls had higher SDR (M = 19.74, SD = 5.94) when compared to Acute (M = 15.42, SD = 5.81) and Chronic Tinnitus groups (M = 13.19, SD = 4.95). There was an overall main effect of group seen for ADR ($F(2,94) = 6.346$, $p = 0.003$, partial $\eta^2 = 0.119$)

with difference between Acute Tinnitus and Controls (p = 0.049), difference between Chronic Tinnitus and Controls (p =0.002), and no difference between Acute Tinnitus and Chronic Tinnitus (p = 0.585). Controls (M = 640.39, SD = 396.70) had higher ADR when compared to Acute Tinnitus (M = 435.73, SD = 344.19) and Chronic Tinnitus (M = 328.49, SD = 263.19). There was, however, no main effect of groups on slope (F (2,94) = 0.961, p = 0.386, partial η^2 = 0.02). There was an effect on SDR of group, which could also be a potential confound. This warranted us to carry out individual one-way ANCOVA to establish the effect of the group on ADR and slope individually, with covariates of SDR and hearing thresholds at 1 kHz. With respect to Slope and ADR, there was no significant effect of group on the values of slope (F(2,92) = 1.279, p = 0.279, partial η^2 = 0.027) and there was no significant effect of group on the values of ADR (F(2,92) = 1.774, p = 0.17, partial η^2 = 0.037) (refer figure 4.5 and 4.6). Longitudinal comparisons between Acute Tinnitus and Post Acute Tinnitus revealed no significant difference in the slope values (t(17) = 0.806, p = 0.431), ADR (t(17) = 0.319, p = 0.754), and the SDR (t(17) = -1.177, p = 0.256) values respectively.

3.2.2. Tinnitus Frequency

Similar analysis was carried out for the tinnitus frequency using nonparametric tests and yielded no statistically significant differences for both cross sectional and longitudinal comparisons. Figure 4 depicts the cross-sectional changes in slope and figure 5 illustrates the longitudinal changes in slope.

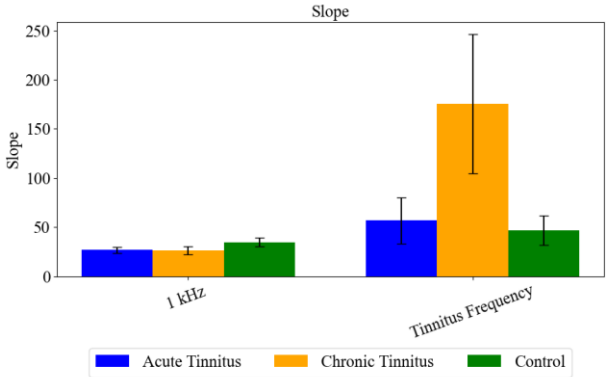


Figure 4: Slope between Acute, Chronic, and Controls at both 1 kHz and tinnitus frequency

Slope values denote Amplitude Dynamic Range/Stimulus Dynamic Range and there were no significant difference in slope across the groups for both frequencies.

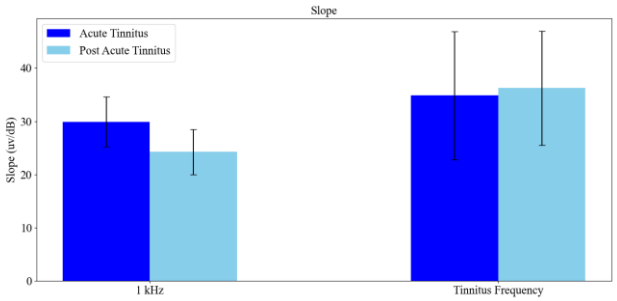


Figure 5: Slope between Acute and Post Acute Tinnitus at both 1 kHz and tinnitus frequency

There was no significant difference in slope between the groups for both frequencies.

4. DISCUSSION

The principal results indicate that there was a near significant increase in the ASSR amplitude at low and mid-level intensities for Post Acute Tinnitus when compared to Acute tinnitus at 1 kHz. Tinnitus frequency did not yield any longitudinal differences. No variations in the slope were seen in either 1 kHz or tinnitus frequency. There were no cross-sectional differences across the groups in either ASSR slope or amplitude. However, there was a non-significant increase in controls for both absolute amplitude and slope, and this finding would help us contextualize the longitudinal changes as we saw increase of amplitude over time which is in the direction toward the Controls.

4.1. No cross-sectional variations across the groups for Acute, Chronic, and Non-Tinnitus Controls

Our first findings indicate that there were no cross-sectional changes among the Acute, Chronic, and Non-Tinnitus Control groups, with respect to either slope and absolute amplitude indicating that the presence of tinnitus isn't associated with the ASSR amplitude. The customised presentation level for the subjects according to their dynamic range may have influenced the outcomes, as the level of hyperacusis has been compensated. In this case, the tailored ASSR presentation level may have curbed the influence of hyperacusis. This was in support of the findings by Paul et al. who investigated the influence of attention on the auditory steady-state response in individuals with and

without tinnitus and their results highlighted that tinnitus patients exhibited diminished attentional modulation of the 5 kHz ASSR, unlike the control group, suggesting that attentional resources may be preferentially allocated to the tinnitus percept, thus limiting further modulation [10]. The findings by Diesch et al. further suggested that the alterations of ASSR in tinnitus individuals when compared to Controls may be partially influenced by attentional processes that imply the complex interplay between tinnitus, attention, and auditory processing. The study further emphasizes the importance of considering attentional factors when interpreting ASSR findings in tinnitus research [11]. Sedley reviewed the role of gain in tinnitus mechanism and highlighted literature that tend to show an increased ASSR amplitudes for tinnitus individuals that is closer to the tinnitus frequency. In our case we did not obtain significant differences at the tinnitus frequency [12]. These studies collectively contribute to our understanding of the neural mechanisms underlying tinnitus and the potential of ASSR as a tool for assessment and treatment.

4.2. Changes between Acute and Post Acute Tinnitus

Concerning the variations seen between Acute and Post Acute, we observed a near significant rise in ASSR amplitude at low and medium intensity levels over time for Post Acute Tinnitus at 1 kHz when compared to Acute Tinnitus. We here consider this finding in the context of our hypothesis that central gain reduces over time, following the onset of tinnitus, as a regression to the mean following a period of hypersensitivity in which tinnitus first occurs. It is to be noted that the finding is in the direction of our hypothesis with reduced ASSR amplitude over time, if ASSR amplitude is interpreted as a positive indicator of central gain. Conversely, we instead interpret increased ASSR amplitude over time as a stabilizing measure as it not only trends towards the pattern of controls but also the absolute amplitude is inversely related to distress. Due to the absence of Acute Tinnitus studies concerning ASSR, we aim to compare the present findings with Chronic Tinnitus studies conducted before and after treatment, as well as the observed alterations in ASSR amplitude. Pantev et al. examined the effects of Tinnitus Retraining Therapy on ASSR and found significant reductions in tinnitus related ASSR following TRT [13]. Sadeghijam et al. utilized binaural beats in stimulating tinnitus patients over a month, measuring the changes in ASSR amplitude between the baseline and post-stimulation. Their results indicated an increase in ASSR amplitude following binaural beat stimulation when compared to baseline, which was attributed to enhanced synchronisation from repeated exposure to binaural beats and an improved temporal map that facilitated a higher stimulation rate [14]. The fact that improved synchronization increased ASSR amplitude is in support with our finding where we attribute that habituation of the tinnitus over time increased ASSR amplitude and in this instance. Further to collaborate the direction of ASSR, we would also lean towards controls as an indicator as there was a non-significant increased amplitude seen in controls.

4.3. Changes in neural synchrony and adaptation

We consider our longitudinal design to be more robust due to which we interpret the current findings based on the longitudinal designs. The generation of ASSR is thought to be a superposition of the Middle Latency Response and Auditory Brainstem Response with a predominant generation at the level of Heschl's gyrus (primary auditory cortex), and possibility of contributions from the auditory belt regions, which are secondary auditory cortical areas [15]. The generation of AM tones throughout the auditory pathway is heavily dependent on mechanisms such as phase locking, temporal envelope coding, rate coding, and population coding (group of neurons firing for different modulation frequencies) [16]. When it comes to tinnitus, it has been posited that consequently to decreased input due to hearing loss, there is aberrant (increased) neural synchrony specifically in the delta band oscillations that manifests as tinnitus [17]. The abnormal increase in neural synchrony of spontaneous activity within the cortical system may have an impact on the incoming acoustic signals, where the neural synchrony is reduced to incoming sounds due to a lack of phase locking, which is essential for the formation of auditory steady-state responses (ASSR). In our case, we attribute that the tinnitus is an ongoing neural response that increases the desynchronization causing reduction of the magnitude of ASSR.

4.4. Gamma Amino-Butyric Acid (GABA) and Tinnitus

Gamma-Aminobutyric acid (GABA) is an inhibitory neurotransmitter in the central nervous system that is an amino acid which is non-proteinogenic in nature [18]. GABAergic neurons releases GABA that plays a significant function of regulating neuronal excitability throughout the nervous system [19]. The amplitude of

ASSR has been associated with changes in GABA. Sugiyama et al. found that boosting GABAergic transmission via lorazepam, a benzodiazepine, increased the 40 Hz ASSR in the early auditory cortex [20]. However, this is an indirect effect mediated through GABA receptors, not a direct effect of GABA itself. Toso et al. further discusses how boosting GABAergic transmission increases the amplitude of the 40 Hz auditory steady-state response in the early auditory cortex [21]. They administered a GABAergic modulator, such lorazepam, and found that this neuromodulator led to a significant increase of the 40 Hz ASSR at both the early transient and later sustained components when compared to the administration of placebo and memantine [21]. This indicates that GABAergic neuronal inhibition contributes significantly to the modulation of the 40 Hz auditory steady-state response in the human auditory cortex. GABA has been linked to tinnitus. A prevailing theory is that the reduced GABAergic inhibition in the auditory pathway may contribute to the onset of tinnitus due to increase in hyperexcitability and this has reflected with the presence of lower levels of GABA at the level of the auditory cortex for tinnitus individuals [22]. However, other research suggests a more nuanced role for GABA, for example, one study found increased GABA-mediated tonic inhibition in the auditory thalami of rats with noise-induced tinnitus which further suggests that GABAergic mechanisms might also play a causative role in tinnitus, potentially by being excess and resulting in thalamocortical dysrhythmia [23]. Our overall interpretation would be that reduced ASSR amplitude during the onset of tinnitus might be attributed to reduction in GABA too which tends to gradually increase over time with increase in ASSR amplitude. However, it is to note that this finding needs more validation, and it is unclear whether GABA would be cause or effect of tinnitus or even whether it plays a role for central gain.

4.3. Summary

The current study indicates that tinnitus-related alterations in ASSR (reduction of 1 kHz amplitude compared to controls) peak at onset and thereafter diminishes, possibly impacted by alterations in neural synchronisation, tinnitus-related distress, GABAergic inhibition and/or attentional modulation. This may or may not suggest a shift in neural activity like central gain, given there were no cross-sectional differences between the groups, particularly between Acute Tinnitus and Controls. The longitudinal variations, particularly at low and medium intensity levels, suggest that the tinnitus activity in isolation diminish over time, that may or may not affect central gain. Figure 6 integrates the above-mentioned arguments and depicts the decline of neural responses linked to tinnitus with time, attributable to enhanced neural synchronisation. This activity represents a continuous stimulation that diminishes phase locking to the incoming signal, while a reduction in tinnitus enhances phase locking to the incoming signal.

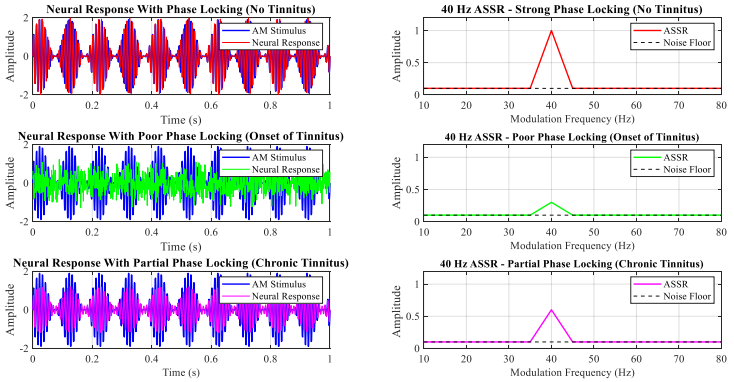


Figure 6: Differences in neural response of AM tones across 3 conditions of No Tinnitus, Acute Tinnitus, and Chronic Tinnitus.

5. REFERENCES

[1] Liberman, M.C. and Kujawa, S.G., 2017. Cochlear synaptopathy in acquired sensorineural hearing loss: Manifestations and mechanisms. *Hearing research*, *349*, pp.138-147.

[2] Auerbach, B.D., Rodrigues, P.V. and Salvi, R.J., 2014. Central gain control in tinnitus and hyperacusis. *Frontiers in neurology*, *5*, p.206.

[3] Sedley, W., Friston, K.J., Gander, P.E., Kumar, S. and Griffiths, T.D., 2016. An integrative tinnitus model based on sensory precision. *Trends in neurosciences*, *39*(12), pp.799-812.

[4] Schaette, R. and Kempter, R., 2006. Development of tinnitus-related neuronal hyperactivity through homeostatic plasticity after hearing loss: a computational model. *European Journal of Neuroscience*, *23*(11), pp.3124-3138.

[5] Stapells, D.R., Galambos, R., Costello, J.A. and Makeig, S., 1988. Inconsistency of auditory middle latency and steady-state responses in infants. *Electroencephalography and Clinical Neurophysiology/Evoked Potentials Section*, *71*(4), pp.289-295.

[6] Yin, P., Johnson, J.S., O'Connor, K.N. and Sutter, M.L., 2011. Coding of amplitude modulation in primary auditory cortex. *Journal of neurophysiology*, *105*(2), pp.582-600.

[7] Carhart, R. and Jerger, J.F., 1959. Preferred method for clinical determination of pure-tone thresholds. *Journal of speech and hearing disorders*, *24*(4), pp.330-345.

[8] Delorme, A. and Makeig, S., 2004. EEGLAB: an open source toolbox for analysis of single-trial EEG dynamics including independent component analysis. *Journal of neuroscience methods*, *134*(1), pp.9-21.

[9] Korczak, P., Smart, J., Delgado, R., Strobel, T.M. and Bradford, C., 2012. Auditory steady-state responses. *Journal of the American Academy of Audiology*, *23*(03), pp.146-170.

[10] Paul, B.T., Bruce, I.C., Bosnyak, D.J., Thompson, D.C. and Roberts, L.E., 2014. Modulation of electrocortical brain activity by attention in individuals with and without tinnitus. *Neural plasticity*, *2014*(1), p.127824.

[11] Diesch, E., Andermann, M. and Rupp, A., 2012. Is the effect of tinnitus on auditory steady-state response amplitude mediated by attention?. *Frontiers in Systems Neuroscience*, *6*, p.38.

[12] Sedley, W., 2019. Tinnitus: does gain explain?. *Neuroscience*, *407*, pp.213-228.

[13] Pantev, C., Okamoto, H. and Teismann, H., 2012. Music-induced cortical plasticity and lateral inhibition in the human auditory cortex as foundations for tonal tinnitus treatment. *Frontiers in systems neuroscience*, *6*, p.50.

[14] Sadeghijam M, Moossavi A, Akbari M, Haghani H, Yousefi A, Mohsen S. An increase in the auditory steady-state response amplitudes after a period of listening to binaural beat stimuli in tinnitus patients: a pilot study. The Egyptian Journal of Otolaryngology. 2023 Feb 23;39(1):39.

[15] Bohórquez, J. and Özdamar, Ö., 2008. Generation of the 40-Hz auditory steady-state response (ASSR) explained using convolution. *Clinical neurophysiology*, *119*(11), pp.2598-2607.

[16] Louage, D.H., van der Heijden, M. and Joris, P.X., 2004. Temporal properties of responses to broadband noise in the auditory nerve. *Journal of neurophysiology*, *91*(5), pp.2051-2065.

[17] Eggermont, J.J. and Tass, P.A., 2015. Maladaptive neural synchrony in tinnitus: origin and restoration. *Frontiers in neurology*, *6*, p.29.

[18] Hepsomali, P., Groeger, J.A., Nishihira, J. and Scholey, A., 2020. Effects of oral gamma-aminobutyric acid (GABA) administration on stress and sleep in humans: A systematic review. *Frontiers in neuroscience*, *14*, p.559962.

[19] Zhou, Y. and Danbolt, N.C., 2013. GABA and glutamate transporters in brain. *Frontiers in endocrinology*, *4*, p.165.

[20] Sugiyama, S., Ohi, K., Kuramitsu, A., Takai, K., Muto, Y., Taniguchi, T., Kinukawa, T., Takeuchi, N., Motomura, E., Nishihara, M. and Shioiri, T., 2021. The auditory steady-state response: electrophysiological index for sensory processing dysfunction in psychiatric disorders. *Frontiers in Psychiatry*, *12*, p.644541.

[21] Toso, A., Wermuth, A.P., Arazi, A., Braun, A., Grent, T., Uhlhaas, P.J. and Donner, T.H., 2024. 40 Hz steady-state response in human auditory cortex is shaped by GABAergic neuronal inhibition. *Journal of Neuroscience*, *44*(24).

[22] Sedley, W., Parikh, J., Edden, R.A., Tait, V., Blamire, A. and Griffiths, T.D., 2015. Human auditory cortex neurochemistry reflects the presence and severity of tinnitus. *Journal of Neuroscience*, *35*(44), pp.14822-14828.

[23] Sametsky, E. A., Turner, J. G., Larsen, D., Ling, L., & Caspary, D. M. (2015). Enhanced GABAA-mediated tonic inhibition in auditory thalamus of rats with behavioral evidence of tinnitus. *Journal of Neuroscience*, *35*(25), 9369-9380.

DOI: 10.61782/fa.2025.0625

FORUM ACUSTICUM EURONOISE 2025

NUMERICAL ANALYSIS OF MINIMUM RESONANCE BANDWIDTHS IN INPUT IMPEDANCES OF HUMAN EAR CANALS

Reinhild Roden[1*] **Matthias Blau**[1,2]

[1] Institut für Hörtechnik und Audiologie, Jade-Hochschule, Oldenburg, Germany.
[2] Cluster of Excellence "Hearing4All".

ABSTRACT

The acoustic input impedance of the human ear canal is a complex function of frequency, reflecting ear canal acoustics and middle and inner ear mechanics. It contains information about the sound pressure at the eardrum and is therefore useful for the individualized equalization of in-ear hearing devices. For clinical applications, it can provide insight into pathological conditions of the ear. To achieve any of the above, it is necessary to determine the ear input impedance with high accuracy. For the validation of impedance measurement system across the entire frequency range up to 16 kHz, for frequency-domain smoothing of measured impedances, as well as for the design of high-frequency couplers, knowledge of the required spectral resolution would be helpful. In this study, minimum relative bandwidths of resonance peaks across the entire frequency range for 41 digitized right ear canal geometries from the IHA database were analyzed, using 3D FEM simulations to determine the input impedance for three different residual ear canal lengths. Results indicate that minimum relative bandwidths decrease from about 0.05 at 5 kHz to around 0.01 at 16 kHz.

Keywords: *hearing acoustics, ear canal, acoustic impedance, FEM simulation*

**Corresponding author*: *reinhild.roden@jade-hs.de.*
***Copyright**: ©2025 Roden & Blau This is an open-access article distributed under the terms of the Creative Commons Attribution 3.0 Unported License, which permits unrestricted use, distribution, and reproduction in any medium, provided the original author and source are credited.*

1. INTRODUCTION

The input impedance of the ear canal can be used in different applications. A number of studies investigated the viability of employing wideband procedures as a diagnostic tool to ascertain the condition of the middle ear in clinical trials, e.g. [1], [2], [3]. Hence, established medical products integrating these procedures are already available. The main principles of these methods can be found in [4] and [5]. A second class of applications uses the input impedance to estimate the sound pressure at the eardrum, which can potentially be implemented in in-ear hearing systems for individualized equalization aiming at acoustic transparency, e.g. [6]. For the validation of impedance measurement system across the entire frequency range up to 16 kHz, for frequency-domain smoothing of measured impedances, as well as for the design of high-frequency couplers, knowledge of the required spectral resolution would be helpful. This knowledge should be based on the level of spectral detail that would be expected in real ear canal measurements. To this end, the current study analyzes the relative bandwidths of resonances in 3D FEM simulated input impedances of 41 ear canal models from the IHA database [7], [8] for different lengths.

2. METHOD

2.1 Ear canal geometry

The IHA database, containing 3D geometries of torso, head, and complete outer ears with ear canals and eardrums, is being developed. The creation of these geometries was previously described in [7]. For the present contribution, geometry models of the right ear canal of 41 subjects in the database were used. In a first step,

the centerline of each ear canal was determined using the vmtk toolbox [9]. The entrance of the ear canal was then defined as the first plane that is perpendicular to the centerline and intersects the ear canal walls in a way that a closed loop of polygon vertices was created, similar to the method described in [10]. The first and second bends were initially identified through visual inspection and then further refined by locating the nearest local torsion or curvature maximum along the centerline. Of each ear canal, three versions were derived by cuts with planes perpendicular to the centerline, located at the entrance and at the first and second bends, see fig. 1. The eardrum was identified by the following procedure: first, cross-sectional polygons of the medial end of the ear canal were interpolated, and the points with the maximum curvature in the rim region were defined as border points between ear canal wall and the eardrum. Then, the plane with the smallest possible distance to the border points of all cross-sectional polygons was calculated. The tympanic rim was then defined as the intersection of this plane with the 3D geometry. Sometimes, this resulted in unrealistically large eardrums. In these cases, the rotation of the plane was manually adjusted.

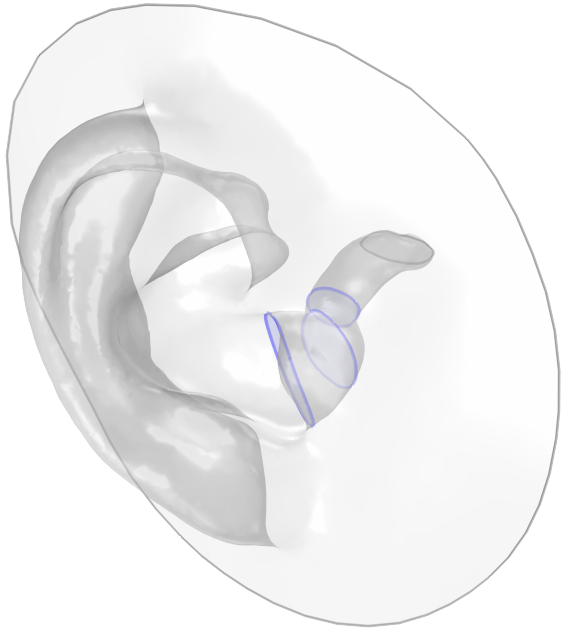


Figure 1. Right outer ear of subject 3 in the IHA database with planes at the entrance, first and second bend (marked blue) and identified eardrum.

2.2 3D FEM simulation

For the three variants of the 41 right ear canals, input impedances Z_{ec} were simulated with COMSOL Multiphysics (6.2) using the 3D finite element method. A normal velocity was assigned to the lateral surface of the residual ear canals as an excitation. Furthermore, the eardrum surface was assigned the impedance of the ear drum and the entire inner ear, according to [11] as implemented in COMSOL. The Helmholtz equation was solved, whereby thermo-viscous effects at the ear canal walls were defined as a boundary condition of the Helmholtz equation, as described in [7] on the basis of [12] and [13], and added to the skin impedance. The values for the skin impedance model are provided by COMSOL as an approximation of the experimental data obtained in [14]. For frequencies up to 20 kHz, sufficient spatial resolution of the sound field was ensured (max. element size of 0.5 mm for boundaries, 1 mm for the volume domain, quadratic (Lagrange) element order). The simulations were run at linearly distributed frequencies between 0.1 and 20 kHz with a frequency resolution of 20 Hz. This corresponds to two hundredths of an octave at 4 kHz, which is the frequency region of first resonances for longer ear canals. The input impedance Z_{ec} resulted from the ratio of the average sound pressure p_{ec} to the volume velocity on the input surface q_{ec},

$$Z_{\mathrm{ec}} = \frac{p_{\mathrm{ec}}}{q_{\mathrm{ec}}}. \tag{1}$$

2.3 Relative bandwidth calculation

All computed input impedances were interpolated to a 1 Hz resolution using a cubic spline interpolation. Subsequently, all resonances with a prominence of at least 3 dB were located. For resonances and anti-resonances, the phase response of the input impedance shows a characteristic rise and a fall, respectively, as exemplarily shown in Fig. 2. All peaks with a corresponding phase zero crossing from +25 to -25 ° were examined. In addition to the harmonics of the first resonance, less prominent side resonances without zero crossing appeared occasionally. These were removed from the analysis. The intersection points of the level of Z_{ec} with a constant line at 3 dB below the respective maximum mark the frequencies of the interval $[f_{-3\mathrm{dB,low}}\ f_{-3\mathrm{dB,high}}]$ for the absolute resonance bandwidth. The frequency f_{mid} was then defined

at the arithmetic mean of that interval. The relative resonance bandwidth was finally calculated as

$$\mathrm{BW_{rel}} = \frac{f_{-3\mathrm{dB,high}} - f_{-3\mathrm{dB,low}}}{f_{\mathrm{mid}}}. \quad (2)$$

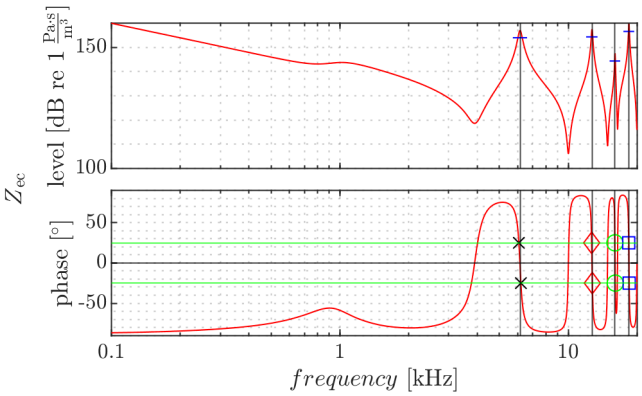


Figure 2. Input impedance for the right ear canal of subject no. 3 cut at the entrance plane.

3. RESULTS

The upper three diagrams in Fig. 3 show the relative resonance bandwidths for ear canals cut at the entrance, the first and the second bend, respectively. Resonances are numbered and sorted by color. For the longest ear canals, up to five resonances were found in the frequency range considered here. The relative resonance bandwidth appears to decay exponentially with logarithmic frequency. The bottom diagram shows all data and a fit using a nonlinear regression model given by

$$\mathrm{BW_{rel}} = 0.26 \cdot \mathrm{e}^{(-0.28\cdot 10^{-3}\cdot \mathrm{f_{mid}/Hz})} + 8.1 \cdot 10^{-3}. \quad (3)$$

This model resulted in an adjusted R^2 of 88.4%.

4. DISCUSSION

Relative resonance bandwidths were calculated for 3D FEM simulations of input impedances on 41 right ear canals of three different lengths. The first resonances occur around 4.5-5 kHz in long ear canals, with relative bandwidths varying between 0.05 and 0.12. Towards higher frequencies, relative bandwidths decay to about 0.01 with decreasing inter-individual variability. A nonlinear model was fitted to this frequency-dependent behavior. The decrease of relative bandwidths with frequency is not surprising, since skin and eardrum are acoustically effective mainly in the mid-frequency range, and their impedances increase at higher frequencies. Keeping in mind that the simulations (a) did not use the higher damping of typical ear canal walls as observed, e.g., in [11] and (b) used an eardrum model that has often been criticized for giving too high impedance values, it appears to be safe to assume a minimum relative bandwidth of 0.01 for the frequency range of human hearing, i.e., up to 16 kHz.

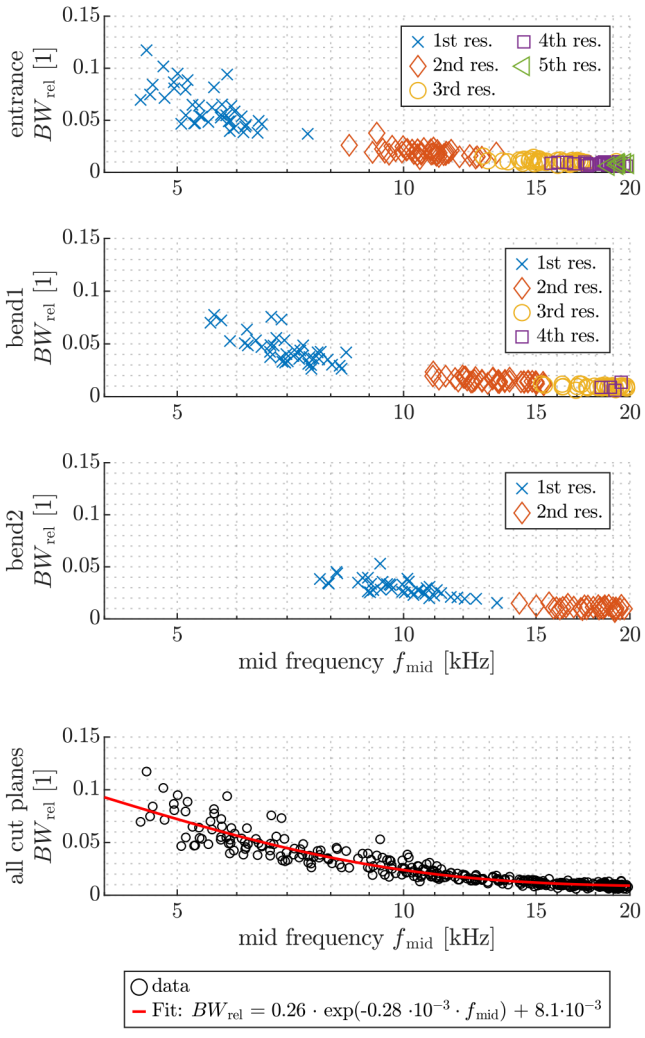


Figure 3. Relative resonance bandwidths of Z_{ec}.

5. CONCLUSION

Relative bandwidths of resonances in the input impedance of human ear canals, computed using 3D FEM simulations with highly conservative assumptions regarding damping effects, are about 0.01 at 16 kHz and larger at lower frequencies. Real ear canals can be expected to exhibit substantially larger relative bandwidths. This result can be used to define the required spectral resolution of impedance measurement systems.

6. ACKNOWLEDGMENTS

This research was partially funded by the Deutsche Forschungsgemeinschaft (DFG, German Research Foundation)—Project ID 352015383—SFB 1330 C1.

7. REFERENCES

[1] Y.-W. Liu, C. A. Sanford, J. C. Ellison, D. F. Fitzpatrick, M. P. Gorga, and D. H. Keefe, "Wideband absorbance tympanometry using pressure sweeps: System development and results on adults with normal hearing," *The Journal of the Acoustical Society of America*, vol. 124, no. 6, pp. 3708–3719, 2008.

[2] C. A. Sanford, D. H. Keefe, Y.-W. Liu, D. Fitzpatrick, R. W. McCreery, D. E. Lewis, and M. P. Gorga, "Sound-conduction effects on dpoae screening outcomes in newborn infants: test performance of wideband acoustic transfer functions and 1-khz tympanometry," *Ear and hearing*, vol. 30, no. 6, p. 635, 2009.

[3] J. J. Rosowski, H. H. Nakajima, M. A. Hamade, L. Mahfoud, G. R. Merchant, C. F. Halpin, and S. N. Merchant, "Ear-canal reflectance, umbo velocity, and tympanometry in normal-hearing adults," *Ear and hearing*, vol. 33, no. 1, pp. 19–34, 2012.

[4] D. H. Keefe, R. Ling, and J. C. Bulen, "Method to measure acoustic impedance and reflection coefficient," *The Journal of the Acoustical Society of America*, vol. 91, no. 1, pp. 470–485, 1992.

[5] S. E. Voss and J. B. Allen, "Measurement of acoustic impedance and reflectance in the human ear canal," *The Journal of the Acoustical Society of America*, vol. 95, no. 1, pp. 372–384, 1994.

[6] S. Vogl and M. Blau, "Individualized prediction of the sound pressure at the eardrum for an earpiece with integrated receivers and microphones," *The Journal of the Acoustical Society of America*, vol. 145, no. 2, pp. 917–930, 2019.

[7] R. Roden and M. Blau, "The iha database of human geometries including torso, head and complete outer ears for acoustic research," in *INTER-NOISE and NOISE-CON Congress and Conference Proceedings*, vol. 261, pp. 4226–4237, Institute of Noise Control Engineering, 2020.

[8] R. Roden and M. Blau, "The iha database of human geometries including torso, head and complete outer ears for acoustic research," 2021.

[9] L. Antiga, *Patient-specific modeling of geometry and blood flow in large arteries*. PhD thesis, Politecnico di Milano, 2002.

[10] A. P. Balouch, K. Bekhazi, H. E. Durkee, R. M. Farrar, M. Sok, D. H. Keefe, A. K. Remenschneider, N. J. Horton, and S. E. Voss, "Measurements of ear-canal geometry from high-resolution ct scans of human adult ears," *Hearing Research*, vol. 434, p. 108782, 2023.

[11] H. Hudde and A. Engel, "Measuring and modeling basic properties of the human middle ear and ear canal. part ii: Ear canal, middle ear cavities, eardrum, and ossicles," *Acta Acustica united with Acustica*, vol. 84, no. 5, pp. 894–913, 1998.

[12] M. Berggren, A. Bernland, and D. Noreland, "Acoustic boundary layers as boundary conditions," *Journal of Computational Physics*, vol. 371, pp. 633–650, 2018.

[13] J. S. Bach and H. Bruus, "Theory of pressure acoustics with viscous boundary layers and streaming in curved elastic cavities," *The Journal of the Acoustical Society of America*, vol. 144, no. 2, pp. 766–784, 2018.

[14] B. Håkansson, P. Carlsson, and A. Tjellström, "The mechanical point impedance of the human head, with and without skin penetration," *The Journal of the Acoustical Society of America*, vol. 80, no. 4, pp. 1065–1075, 1986.

DOI: 10.61782/fa.2025.0218

FORUM ACUSTICUM EURONOISE 2025

SINGLE-TRIAL ELECTROENCEPHALOGRAPHIC ANALYSIS OF FRONT-BACK CONFUSIONS IN FREE-FIELD AND HEADPHONE-BASED LISTENING CONDITIONS

Nils Marggraf-Turley[1*] **Martha Shiell**[2] **Niels Pontoppidan**[2]
Drew Cappotto[1] **Lorenzo Picinali**[1]
[1] Imperial College London, London, UK
[2] Eriksholm Research Centre, Snekkersten, Denmark

ABSTRACT

Sound source localisation relies on spatial auditory cues, which are described by the head-related transfer function (HRTF). In natural free-field listening, individuals perceive sounds filtered by their own HRTFs. Conversely, binaural (headphones-based) reproduction uses HRTFs to render virtual auditory stimuli. However, in practice, binaural reproduction typically employs non-individual HRTFs, which can impair realism and localisation accuracy, introducing phenomena such as front-back and up-down confusion. Beyond behavioural assessment, perceivable differences under the two rendering conditions can be investigated from a neurophysiological perspective. This study uses electroencephalographic data from an existing localisation study to examine disparities in front-back confusion between free-field and headphone-based (non-individual HRTF) conditions. A multilayer perceptron trained on single-trial event-related potentials classified sound source location pairs symmetric around the interaural axis. Single-trial decoding accuracy correlated with behavioural front-back confusion.

Keywords: *Electroencephalography, HRTF, Front-back confusion*

***Corresponding author**: *n.marggraf-turley23@imperial.ac.uk.*

***Copyright**: ©2025 Nils Marggraf-Turley et al. This is an open-access article distributed under the terms of the Creative Commons Attribution 3.0 Unported License, which permits unrestricted use, distribution, and reproduction in any medium, provided the original author and source are credited.*

1. INTRODUCTION

The human auditory system localises sounds using spatial auditory cues such as interaural time differences (ITD), interaural level differences (ILD), and monaural spectral cues. These cues, unique to each individual due to anatomical variability, are encapsulated within Head-Related Transfer Functions (HRTFs). Although individual HRTFs enable precise spatial auditory perception, their practical application is limited due to the complexities involved in measurement [1]. Consequently, non-individual HRTFs, often recorded using standardised mannequins such as KEMAR, are widely adopted despite potential inaccuracies, including increased rates of front-back confusion due to inadequate simulation of spectral cues.

Traditional behavioural methods assessing localisation performance with HRTFs rely heavily on subjective reports, which can have low repeatability [2]. Electroencephalography (EEG) provides an objective alternative by recording cortical neural responses associated with auditory spatial perception, potentially bypassing some limitations inherent in subjective feedback.

Previous approaches relating neural response variations to perceptual outcomes show promise [3]. Studies employing event-related potential (ERP)-based decoding have successfully discriminated horizontal and median plane sound locations [4, 5] under free-field listening. More recent work has expanded on these decoding paradigms, indicating lower decoding accuracy for non-individual HRTFs, which was correlated with front-back confusion rates [6]. However, trials were averaged to increase signal-to-noise ratio. Decoding location from a single trial is more advantageous as it paves the way for real-

time applications of EEG-based decoding.

Consequently, this study expands on the decoding approach of [6] by using single-trial decoding with a neural network instead of logistic regression with averaged trials.

2. METHOD

We re-examined EEG data from [6], where twenty-two participants localised auditory stimuli under free-field and headphone-based rendering using the KEMAR HRTF from the SONICOM database [7]. Each participant sat in the centre of a spherical loudspeaker array, stabilised with a chin rest. Stimuli comprised a 1000 ms adapter from 12 azimuthal positions (30° increments), followed by a 100 ms probe from four locations (Az. 30°, 330°, 150°, and 210°). All stimuli were presented at 65 dB SPL.

EEG data underwent band-pass filtering (0.1–40 Hz), epoching (-100 to 600 ms) and downsampling (128 Hz). To mitigate artefacts whilst maximising epochs, our artefact rejection differed from [6]. Amplitude thresholding rejected epochs with maximum amplitude above ±200 µV or below ±1 µV. Single-trial ERPs were classified using a multilayer perceptron (MLP) neural network. Feature vectors were constructed by concatenating electrodes and time points, and scaled using Z-score standardisation. The MLP architecture consisted of an input layer, a hidden layer with 512 units (ReLU activation), a dropout layer (0.4), a second hidden layer with 256 units (tanh activation), another dropout layer (0.4), and an output layer with a sigmoid activation function. Training used the Adam optimiser (learning rate of 0.00001) with binary cross-entropy loss. Model performance was evaluated through 10-fold stratified cross-validation for each subject. Data were balanced across subjects, location pairs, and spatial conditions (N=80). Separate networks were trained per subject, location pair (Az. 30 vs 150, Az. 330 vs 210), and spatial condition (Free-field, KEMAR), each for 35 epochs with a batch size of four.

3. RESULTS

Decoding accuracy data were averaged across location pairs and spatial conditions for correlation with behavioural confusion. Front-back confusion rates from behavioural responses were negatively correlated with decoding accuracy ($r = -0.51, p < 0.05$).

4. CONCLUSION

Our findings demonstrate a significant correlation between location decoding accuracy and behavioural front-back confusion rate from single-trial ERPs. This correlation from single-trial decoding highlights the potential for EEG-based approaches to inform HRTF selection or training paradigms aimed at mitigating confusion in headphone-based spatial audio applications.

5. REFERENCES

[1] L. Picinali and B. F. G. Katz, "System-to-user and user-to-system adaptations in binaural audio," in *Sonic Interactions in Virtual Environments* (M. Geronazzo and S. Serafin, eds.), Human–Computer Interaction Series, pp. 115–143, Springer, Cham, 2023.

[2] A. Andreopoulou and B. F. G. Katz, "Investigation on subjective HRTF rating repeatability," in *Proceedings of the 140th Audio Engineering Society Convention*, (Paris, France), Paper 9597, Audio Engineering Society, June 2016.

[3] M. G. Wisniewski, G. D. Romigh, S. M. Kenzig, N. Iyer, B. D. Simpson, E. R. Thompson, and C. D. Rothwell, "Enhanced auditory spatial performance using individualized head-related transfer functions: An event-related potential study," *The Journal of the Acoustical Society of America*, vol. 140, pp. EL539–EL544, December 2016.

[4] A. Bednar, F. M. Boland, and E. C. Lalor, "Different spatio-temporal electroencephalography features drive the successful decoding of binaural and monaural cues for sound localization," *European Journal of Neuroscience*, vol. 45, no. 5, pp. 679–689, 2017.

[5] O. Bialas, B. Maess, and M. Schönwiesner, "Evoked responses to localized sounds suggest linear representation of elevation in human auditory cortex," *bioRxiv preprint*, 2023. doi: 10.1101/2023.05.03.539222.

[6] N. Marggraf-Turley, M. Shiell, N. Pontoppidan, D. Cappotto, and L. Picinali, "EEG-Based Decoding of Sound Location: Comparing Free-Field to Headphone-Based Non-Individual HRTFs," 2025. arXiv:2503.10783.

[7] I. Engel, R. Daugintis, T. Vicente, A. O. T. Hogg, J. Pauwels, A. J. Tournier, and L. Picinali, "The SONICOM HRTF Dataset," *Journal of the Audio Engineering Society*, vol. 71, pp. 241–253, May 2023.

DOI: 10.61782/fa.2025.0366



FORUM ACUSTICUM
EURONOISE 2025

EVALUATION OF MICROPHONE NONLINEARITIES IN PROBES FOR MEASUREMENT OF OTOACOUSTIC EMISSIONS

Petr Honzík[1*] **Václav Vencovský**[1]
[1] Department of Radioelectronics, Faculty of Electrical Engineering,
Czech Technical University in Prague, Technická 2, 166 27 Praha, Czech Republic

ABSTRACT

Measurement of Distortion Product Otoacoustic Emissions (DPOAE) relies on evaluating the nonlinear response of the inner ear to two-tone excitation signals, specifically identifying the cubic intermodulation distortion products. However, the accuracy of these measurements can be adversely affected by nonlinear distortions within the electroacoustic measurement chain. This study examines the nonlinear behavior of microphones embedded in probes used for otoacoustic emission measurements. Nonlinearities were characterized using the source harmonic correction method reported in the literature, as there is no perfectly linear source of excitation signal. We focused on the quantification of second- and third-order harmonic distortion, which are key components of the nonlinear response of the microphone. The results are analyzed and compared to similar measurements performed on conventional and MEMS microphones, revealing specific characteristics of the probe microphone's nonlinear response. Strategies for reducing nonlinear distortion in this context, as described in the literature, are also discussed. These findings contribute to the understanding of the limitations and potential improvements in the measurement accuracy of otoacoustic emissions by addressing microphone-induced nonlinearities.

Keywords: *nonlinear distortion, OAE probe, microphone nonlinearities*

**Corresponding author*: honzikp@fel.cvut.cz.
***Copyright**: ©2025 Petr Honzík et al. This is an open-access article distributed under the terms of the Creative Commons Attribution 3.0 Unported License, which permits unrestricted use, distribution, and reproduction in any medium, provided the original author and source are credited.*

1. INTRODUCTION

Otoacoustic emissions (OAEs) are sound signals generated in the inner ear and transmitted through the middle ear to the external auditory canal [1]. While spontaneous OAEs occur without presenting evoking stimulus into the ear, clinical diagnostics primarily rely on evoked OAEs. Among these, distortion-product otoacoustic emissions (DPOAEs) are widely used [2]. DPOAEs arise from nonlinear interactions in the cochlea when stimulated with two close-frequency tones, f_1 and f_2 ($f_1 < f_2$), with the cubic distortion product at $2f_1 - f_2$ being of primary interest [3]. As a result, any nonlinearity in the measurement chain may compromise the accuracy of the recorded emissions.

The standard OAE measurement probe includes two miniature loudspeakers to separately generate f_1 and f_2, minimizing intermodulation distortion, and a miniature condenser microphone with low self-noise and a flat frequency response. The probe connects to the ear canal via a small tube. This study investigates nonlinearities in the microphone of such probes.

Accurate characterization of microphone nonlinearities is complicated by the absence of a perfectly linear acoustic reference source, making it difficult to isolate the microphone's contribution from that of the source. To overcome this, we apply a harmonic correction method for periodic signals [4], which uses predistortion and a low-distortion reference microphone to suppress source nonlinearities to the noise floor.

The following sections present the theoretical background on microphone nonlinearities, describe the experimental setup, and discuss the measured results along with possibilities for reducing nonlinear distortion.

2. NONLINEAR BEHAVIOR OF CONDENSER MICROPHONES

Nonlinearities in condenser microphones stem from factors such as variable capacitance due to membrane motion, nonlinear damping, and imperfections in mechanical or electronic components [5, 6]. The dominant source is the electrostatic transduction mechanism, which introduces both harmonic and intermodulation distortion [7, 8]. The second harmonic alone accounts for approximately 90% of total harmonic distortion [9], particularly under high sound pressure levels.

Following the model in [10], the analysis focuses on nonlinearities due to electrostatic transduction, assuming other sources are negligible. With negligible charge variation (due to a high polarization resistance), the microphone output voltage is

$$u(t) = -U_0 \frac{\mathrm{d}C(t)}{C}, \tag{1}$$

where U_0 is the polarization voltage, $\mathrm{d}C$ the time-varying change of capacitance, and $C = C_p + C_0$ is the total static capacitance composed of the parasitic capacitance C_p and the static active capacitance $C_0 = \varepsilon_0 S/h_g$ where h_g is the air gap thickness, S the electrode area, and ε_0 the vacuum permittivity.

Assuming the total time-varying capacitance due to the mean membrane displacement $\bar{\xi}(t)$

$$C(t) = C_p + \frac{\varepsilon_0 S}{h_g + \bar{\xi}(t)} = C_p + C_0 \frac{1}{1 + \bar{\xi}(t)/h_g}, \tag{2}$$

can be expressed as $C(t) = C_p + C_0 + \mathrm{d}C(t)$, the time-varying capacitance change can be approximated using Taylor series expansion as

$$\mathrm{d}C(t) = -C_0 \left[\frac{\bar{\xi}(t)}{h_g} - \left(\frac{\bar{\xi}(t)}{h_g} \right)^2 + \left(\frac{\bar{\xi}(t)}{h_g} \right)^3 - \cdots \right]. \tag{3}$$

Substituting (3) into (1), and defining $y(t) = \frac{\bar{\xi}(t)}{h_g}$ and $K_0 = U_0 \frac{C_0}{C_p + C_0}$, the output voltage becomes

$$u(t) = K_0 \left[y(t) - y^2(t) + y^3(t) - \cdots \right], \tag{4}$$

revealing the nonlinear terms. The key model parameter K_0 must be estimated from measurements.

3. MEASUREMENTS ON OAE PROBE MICROPHONE

This section describes the measurement setup and presents results for the frequency-dependent sensitivity and the levels of the first three harmonics measured at various excitation levels.

3.1 Measurement setup

The measurement setup (Fig. 1) includes the Etymotic ER10C probe with two low-noise microphones (total sensitivity 50 mV/Pa), whose signals are summed to improve accuracy, operating linearly up to 120 dB SPL. A B&K 4135 1/4" laboratory microphone serves as the low-distortion reference, and an earplug acts as the acoustic source. All components are mounted in a small plastic cavity to generate high sound pressure levels. To suppress source-induced nonlinearities, we apply a harmonic correction method for periodic signals [4] using predistortion (see "Harmonic correction" block in Fig. 1).

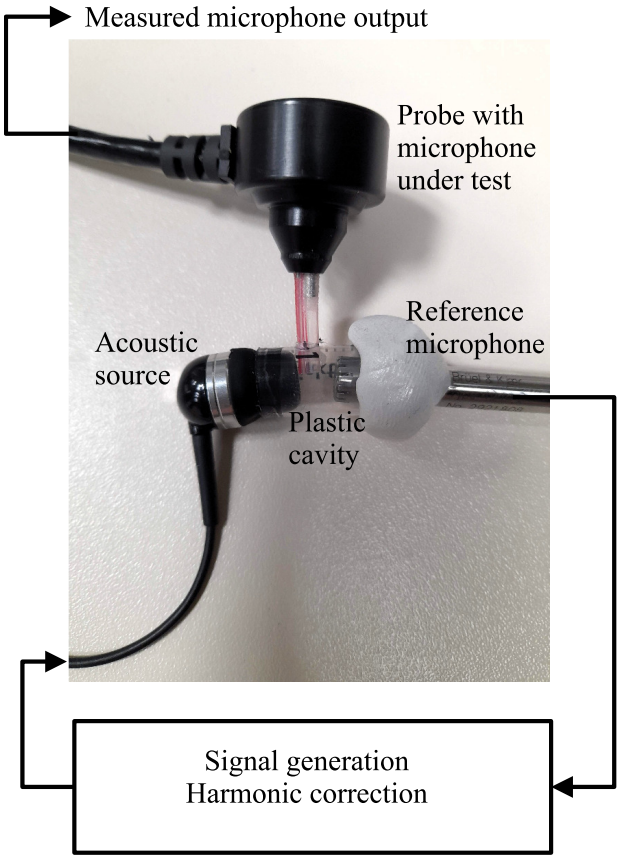


Figure 1. Schematic view of the measuremet setup.

3.2 Sensitivity

The measured frequency-dependent sensitivity is shown in Figure 2 for three different positions of the gain switch on the probe preamplifier. The frequency response is approximately flat between 100 Hz and 10 kHz. In contrast to classical condenser microphones, the phase is not quasi-constant up to the frequency of the first resonance. This is likely caused by unknown, possibly analog, signal processing in the probe preamplifier.

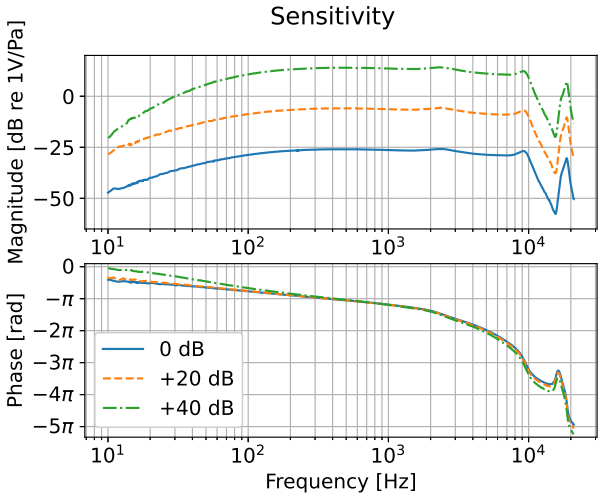


Figure 2. Measured frequency dependence of the magnitude (upper figure) and phase (lower figure) of the microphone sensitivity for the switch position 0 dB (blue solid curve), +20 dB (dashed orange curve) and +40 dB (dash-dotted green curve).

3.3 Nonlinear behavior

In line with previous research [11], the first three harmonics measured at 510 Hz for excitation levels ranging from 70 to 116 dB SPL, recalculated to sound pressure level measured by the microphone under test using its sensitivity, are shown in Figure 3 (points). The dashed lines represent theoretical predictions based on Equation (4) in Section 2, using an estimated value of the parameter $K_0 = 40\ V$. While the measured levels of the first (fundamental) and second harmonics agree well with the theoretical values, the third harmonic is significantly higher than predicted, indicating the presence of additional nonlinear effects not captured by the model. Note that similar results are obtained at higher frequencies [11].

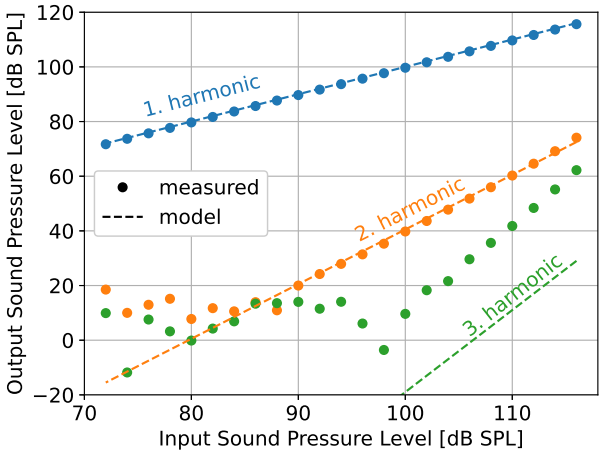


Figure 3. Measured (points) and theoretical (dashed lines) harmonics of the microphone under test at 510 Hz.

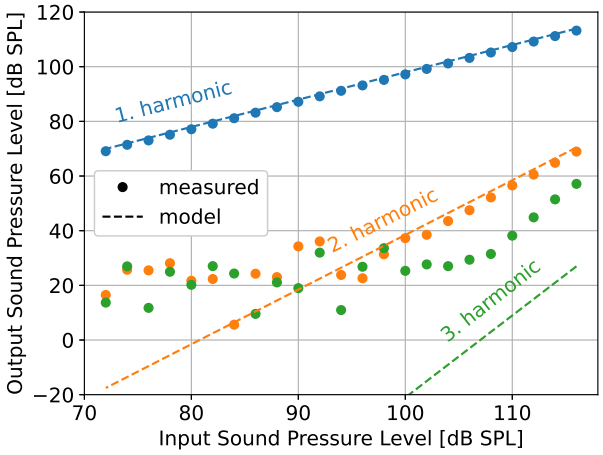


Figure 4. Measured (points) and theoretical (dashed lines) harmonics of the microphone under test at 110 Hz.

Although the frequencies used in DPOAE measurements are usually higher than 510 Hz (typically 1 to 8 kHz), methods have been proposed in the literature [12] that introduce an additional low-frequency component of relatively high amplitude in DPOAE measurements to bias the operating point of the cochlear transducer. It is therefore relevant to examine the nonlinear behavior of the probe at low frequencies. Figure 4 shows the mea-

sured and theoretical levels of the first three harmonics at 110 Hz, calculated using the same value of $K_0 = 40\ V$ and taking into account a slightly lower sensitivity (approximately 38 mV/Pa). The results are consistent with those in the previous figure, although the background noise is higher at this frequency.

4. REDUCTION OF NONLINEAR DISTORTION

Previous research [11] has shown that a low-frequency bias tone at 100 dB SPL, combined with the nonlinear distortion of the probe microphone, can generate higher harmonics of non-negligible amplitude at the microphone output. A recently published study [13] proposes a method for reducing harmonic and intermodulation nonlinear distortion in single-backplate condenser microphones by suppressing the quadratic component. This post-processing technique is based on equation (4) and utilizes the parameter K_0. The approximately linearized output voltage u_{lin} is calculated from the microphone output u as follows [13]

$$u_{lin}(t) \approx u(t) + \frac{1}{K_0} u^2(t). \tag{5}$$

In this work, we apply this simple technique to the output of the OAE probe microphone.

Figure 5 shows the level of the second harmonic component (upper plot) and the Total Harmonic Distortion (THD) parameter (lower plot) after applying the distortion reduction technique for varying values of K_0, at an excitation level of 108 dB SPL and a frequency of 510 Hz. The second harmonic exhibits a sharp minimum near the estimated value $K_0 = 40$ V, decreasing from 56 dB SPL (unprocessed value, blue solid line) to 12 dB SPL, corresponding to a reduction of 44 dB. The THD is reduced from $0.26\,\%$ to $0.026\,\%$, representing a tenfold improvement.

Figure 6 presents the same type of result at 110 Hz. Here, the second harmonic is reduced from 52 dB SPL to 42 dB SPL, resulting in a decrease of only 10 dB. Similarly, the THD parameter is reduced from $0.224\,\%$ to $0.074\,\%$, representing an improvement by approximately a factor of 3. Additionally, the positions of the minima for both the second harmonic and the THD appear to be shifted toward lower values of K_0, even though the original estimate showed good agreement between measurement and theory in Figure 4.

We propose the hypothesis that the significant change in the efficiency of the distortion reduction with frequency

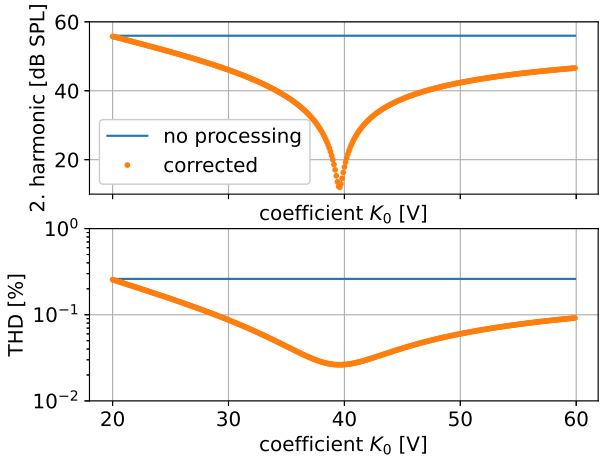


Figure 5. Reduced value of the 2^{nd} harmonic (upper figure) and THD (lower figure) at 510 Hz (orange points) compared with the unprocessed value (blue solid line).

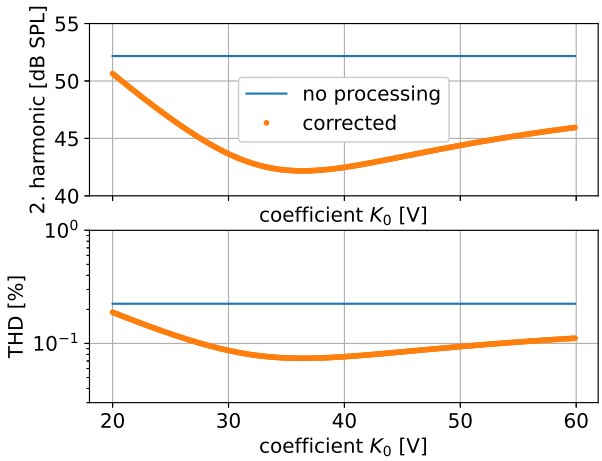


Figure 6. Reduced value of the 2^{nd} harmonic (upper figure) and THD (lower figure) at 110 Hz (orange points) compared with the unprocessed value (blue solid line).

is caused by a phase shift, possibly introduced by post-processing of the microphone output signal in the probe preamplifier. Figure 2 has shown that the phase is not quasi-constant across the entire frequency range. When the phase of the measured signal is extracted from the FFT (not unwrapped) and incorporated into the model, the

phases of the first and second harmonics are predicted correctly at 510 Hz, as shown in Figure 7. Note that the third harmonic is not predicted correctly, either in amplitude or phase, for reasons discussed in Section 3.3.

At 110 Hz, as shown in Figure 8, the phase of the second harmonic shows a discrepancy between the measured data and the model, likely due to an additional frequency-dependent phase shift originating from analog signal processing in the probe preamplifier. We hypothesize that this phase shift affects the efficiency of the distortion reduction technique, which performs better at frequencies where the additional phase shift is negligible.

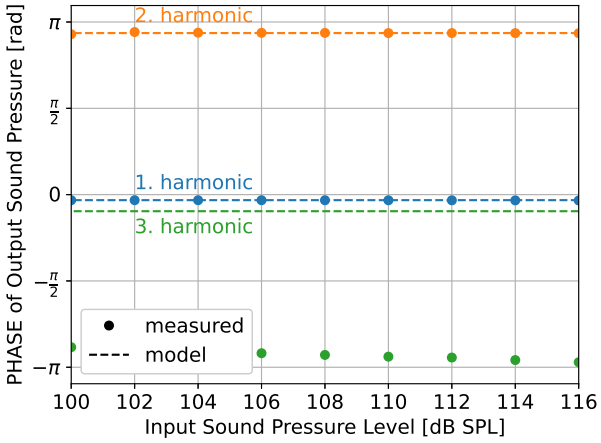


Figure 7. Phase of first three harmonics: measured (points) and theoretical (dashed lines) at 510 Hz.

5. CONCLUSION

This study examined the nonlinear behavior of condenser microphones used in otoacoustic emission (OAE) probes, focusing on its impact on measurement accuracy. A previously published analytical model based on the electrostatic transduction mechanism was applied and shown to predict the measured levels of the first and second harmonics with good accuracy. Furthermore, a distortion reduction technique from the literature, based on this model and parameterized by K_0, was evaluated. When applied as a simple post-processing step, the method significantly reduced the second harmonic component and decreased total harmonic distortion (THD), particularly at 510 Hz.

However, the efficiency of the distortion reduction technique was shown to be frequency-dependent. At 110 Hz, both the suppression of the second harmonic and

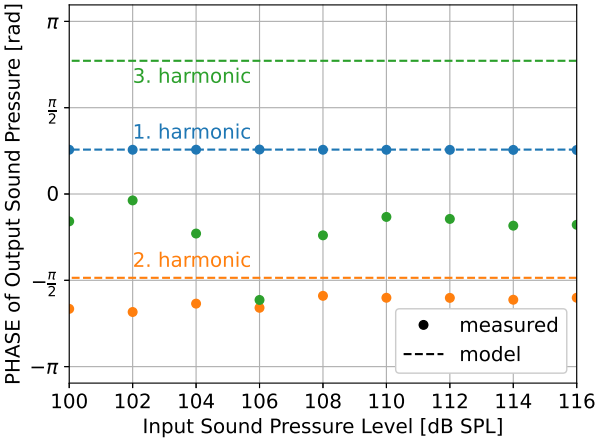


Figure 8. Phase of first three harmonics: measured (points) and theoretical (dashed lines) at 110 Hz.

THD improvement were noticeably lower. This behavior was attributed to an additional phase shift, likely introduced by analog signal processing in the probe preamplifier. Incorporating the measured signal phase into the model improved the agreement for the first and second harmonic phases at higher frequencies, while a clear discrepancy remained at lower frequencies.

These findings highlight the importance of considering frequency-dependent phase characteristics when applying nonlinear distortion reduction techniques to microphone signals. Further investigation of the internal signal processing in probe preamplifiers may help improve modeling accuracy and enable more effective compensation across a broader frequency range.

6. ACKNOWLEDGMENTS

This work was supported by the project 23-07621J of the Czech Science Foundation (GAČR) "Otoacoustic emissions in normal cochlea and cochlea with endolymphatic hydrops: modeling and experiments".

7. REFERENCES

[1] D. T. Kemp, "Stimulated acoustic emissions from within the human auditory system," *J. Acoust. Soc. Am.*, vol. 64, pp. 1386–1391, 1978.

[2] B. L. Lonsbury-Martin and G. K. Martin, "The clinical utility of distortion-product otoacoustic emissions," *Ear Hear.*, vol. 11, no. 2, pp. 144–154, 1990.

[3] M. L. Whitehead, B. B. Stagner, B. L. Lonsbury-Martin, and G. K. Martin, "Measurement of otoacoustic emissions for hearing assessment," *IEEE Eng. Med. Biol. Mag.*, vol. 13, no. 2, pp. 210–226, 1994.

[4] A. Novak, L. Simon, and P. Lotton, "A simple predistortion technique for suppression of nonlinear effects in periodic signals generated by nonlinear transducers," *J. Sound Vib.*, vol. 420, pp. 104–113, 2018.

[5] A. Dessein, *Modelling distortion in condenser microphones*. PhD thesis, Tech. Univ. Denmark DTU DK-2800 Kgs. Lyngby Denmark, 2009.

[6] S. Chowdhury, M. Ahmadi, and W. C. Miller, "Nonlinear effects in mems capacitive microphone design," in *Proc. Int. Conf. MEMS NANO Smart Syst.*, pp. 297–302, 2003.

[7] H. Pastillé, "Electrically manifested distortions of condenser microphones in audio frequency circuits," *J. Audio Eng. Soc.*, vol. 48, no. 6, pp. 559–563, 2000.

[8] M. T. Abuelma'atti, "Improved analysis of the electrically manifested distortions of condenser microphones," *Appl. Acoust.*, vol. 64, no. 5, pp. 471–480, 2003.

[9] V. Djuric, "Distortion in microphones," in *ICASSP'76. IEEE Int. Conf. Acoust. Speech Signal Process.*, vol. 1, pp. 537–539, 1976.

[10] A. Novak and P. Honzík, "Measurement of nonlinear distortion of mems microphones," *Appl. Acoust.*, vol. 175, p. 107802, 2021.

[11] P. Honzík and V. Vencovský, "Nonlinear distortion of microphone in probe for otoacoustic emission measurements," *Akustické listy*, vol. 27, no. 1-4, pp. 3–6, 2024.

[12] L. Bian, "Cochlear compression: effects of low-frequency biasing on quadratic distortion product otoacoustic emission," *J. Acoust. Soc. Am.*, vol. 116, pp. 3559–3571, 2004.

[13] P. Honzík and A. Novak, "Reduction of nonlinear distortion in condenser microphones using a simple post-processing technique," *The Journal of the Acoustical Society of America*, vol. 157, pp. 699–705, February 2025.

DOI: 10.61782/fa.2025.0563

FORUM ACUSTICUM EURONOISE 2025

METHODOLOGY FOR THE NEUROCOGNITIVE STUDY OF ACOUSTIC-PERCEPTUAL ABILITIES AND LINGUISTIC FUNCTION IN PRETERM INFANTS

Hernández-Molina, Ricardo[1*] **Varo Varo, Carmen**[1] **Rodríguez-Montaño, Víctor M.**[1]
Pérez Vargas, Rocío[1] **Fernández-Zacarías, Francisco**[1] **Puyana-Romero, Virginia**[2]
Denisenko, Tatiana[1] **Cueto-Ancela, José Luis**[1] **Zafra Rodríguez, Pamela**[3]
[1] University Institute of Research in Applied Linguistics, University of Cádiz, Cádiz, Spain
[2] Department of Sound and Acoustic Engineering, Universidad de las Américas, Quito, Ecuador
[3] Neonatology Unit, University Hospital Puerta del Mar, Cádiz, Spain

ABSTRACT

Due to the convergence of Applied Linguistics (in particular, Clinical Linguistics), Acoustic Engineering and the Neonatology Unit of the University Hospital Puerta del Mar in Cadiz, the aim of this study is to conduct a longitudinal neurocognitive study of acoustic-perceptual skills and linguistic function in preterm infants. This will allow to establish the interrelation between both aspects during the 0 to 4 years' stage, to identify possible deficiencies and their manifestation in different stages and, consequently, to achieve better diagnostic and treatment protocols for this population. For this purpose, clinical data, especially neuroimaging data, are contrasted with those derived from the evaluation of the influence of noise exposure in incubators on sensorineural hearing loss and auditory maturation by means of electrophysiological and acoustic techniques.
As for the results, it is expected that the analysis of the data obtained will shed light on the possible auditory and linguistic deficiencies observed, in addition to the design of appropriate specific audiological and speech therapy tools.

Keywords: *neonatology, linguistics, acoustic, audiology, neurocognitive study*

[*]***Corresponding author***: *ricardo.hernandez@uca.es*
Copyright: *©2025 First author et al. This is an open-access article distributed under the terms of the Creative Commons Attribution 3.0 Unported License, which permits unrestricted use, distribution, and reproduction in any medium, provided the original author and source are credited.*

1. INTRODUCTION

This study is ascribed to the project "Longitudinal and cross-sectional neurocognitive study of acoustic-perceptual abilities and linguistic function in preterm infants (PretermLA)", funded by the Research Plan of the University of Cadiz (code PR2024-010), within its call for Bridge Projects (2024/2025).
Preterm birth is associated with a spectrum of neurological, cognitive, and linguistic complications [1]. Multiple studies have documented language disorders and deficits in auditory speech processing linked to prematurity and low birth weight [2]. Research indicates that language performance in preterm children shows differences that persist over time, suggesting long-term stability of linguistic vulnerabilities [3,4].
The relationship between prematurity and language development has been extensively investigated, with findings consistently showing that premature birth poses risks for various aspects of linguistic development. These children demonstrate unique trajectories in language acquisition that differ from their full-term counterparts [4]. Neuroimaging studies have revealed altered brain connectivity in premature infants, with extremely preterm children exhibiting increased interhemispheric connectivity for language [5]. Additionally, white matter microstructure has been associated with language abilities in children born very preterm [6].
A critical element often overlooked in this context is the acoustic environment of premature infants. Exposure to incubator noise in Neonatal Intensive Care Units (NICUs) constitutes a risk factor that can lead to stress-related

functional impairments, potentially causing hearing loss [7] and affecting physiological parameters including heart rate, respiratory rate, and oxygen saturation [8]. These early acoustic experiences occur during a crucial period when language acquisition and acoustic-perceptual skills are beginning to develop, with neural encoding of voice pitch and formant structure already present at birth [9].

Despite the substantial evidence linking prematurity to language disorders, there is a significant research gap concerning the longitudinal study of language development in parallel with the perception of speech sounds during early childhood. Previous research has demonstrated through studies of Mismatch Negativity (MMN) that phonological processing at early ages can be an important prognostic factor for predicting future language development in at-risk populations [10]. However, a comprehensive approach combining acoustic assessment, language development, and neurophysiological markers throughout early childhood is still needed.

The present longitudinal study aims to address this research gap by examining the influence of the acoustic environment, particularly incubator noise, on neurocognitive development for language function in premature infants from birth to 4 years of age. By adopting a multidisciplinary approach that combines expertise in acoustic engineering, clinical linguistics, and neuropediatric, this research seeks to provide a deeper understanding of the relationship between early acoustic experiences and linguistic development in premature children.

2. METHODOLOGY

This research employs a longitudinal design with a multidisciplinary approach combining acoustic engineering, clinical linguistics, and neuropediatrics to comprehensively assess the development of language functions in premature infants.

The sample of this research is divided into two groups: an experimental group (EG) and a control group (CG). The experimental group will be composed of between 20 and 50 preterm neonates born at the Hospital Universitario Puerta del Mar during the first year of the project. The inclusion criteria for this group are birth weight less than 1,500 grams or gestational age less than 32 weeks. As for the control group, it will be made up of a similar number of full-term newborns, who will be selected without any pathological condition affecting their linguistic or neurocognitive development.

Sample size calculation was based on previous literature, aiming to detect a minimum effect size of 11.6 points on linguistic tests with 80% power and an alpha risk of 0.05, requiring at least 28 participants per group. Accounting for potential follow-up losses (10%), the target sample size is 31 participants per group.

2.1 Data collection procedures

The methodology of this research is organized in three interconnected blocks. The first, Biomedical Acoustics, focuses on the assessment of auditory thresholds and physiological responses in premature infants, taking into account factors such as stress and exposure to sounds in the incubator. This block utilizes evoked potentials, otoacoustic emissions, and electroencephalograms, employing acoustic stimuli at varying sound pressure levels to achieve this objective. The second block, Clinical Linguistics, focuses on the assessment of language development using standardized tests and the analysis of early vocal production. Speech intelligibility and neurocognitive responses to linguistic stimuli are measured using specialized tools. Early vocal production is analyzed through the recording and processing of manifestations such as crying, gurgles, babbling, and syllabic production, using specialized tools such as PRAAT. The Acoustic-Linguistic Integration block serves to synthesize the data obtained in the two preceding blocks. In this block, statistical analyses are performed to identify significant patterns in the auditory and linguistic development of preterm infants.

3. EXPECTED RESULTS

It is imperative to acknowledge that this research is still in its developmental stage; therefore, the findings obtained thus far should not be considered conclusive.

This research is expected to yield significant findings in several key areas. First, it will provide a comprehensive understanding of acoustic-perceptual and linguistic development in preterm infants, offering detailed data on the acquisition and progression of phonetic-phonological, lexical-semantic, morphosyntactic, and pragmatic skills in this population compared to full-term infants. This will enable the identification of specific developmental trajectories for preterm infants.

Second, the impact of incubator noise on neurodevelopment will be assessed by quantifying the relationship between acoustic conditions and physiological variables such as brain waves, heart rate, oxygen saturation, and sleep patterns. This analysis will be essential in defining safety

thresholds and establishing evidence-based recommendations for NICUs acoustic environments.

Consequently, the present study will concentrate on identifying specific impairments in acoustic and linguistic processing to characterize potential alterations in perceptual mechanisms among preterm infants. This will entail a meticulous examination of auditory thresholds across diverse frequency ranges and their correlation with linguistic development. Furthermore, the neuroanatomical underpinnings of language development will be investigated by integrating acoustic-perceptual and linguistic data with neuroimaging findings, particularly tractography. This comprehensive approach is expected to elucidate the functional neuroanatomical underpinnings of language acquisition in this particular population [6].

This research also aims to develop innovative assessment and intervention protocols. Utilizing the longitudinal data collected, integrated acoustic-perceptual and linguistic assessment protocols will be designed to facilitate the early identification of developmental disturbances in preterm infants, accompanied by personalized therapeutic intervention guidelines.

This research endeavors to enhance the existing body of knowledge concerning auditory maturation in preterm infants. This enhanced understanding is imperative for determining the optimal timing of interventions, such as cochlear implantation in cases of severe hearing loss [11]. Furthermore, the study will establish associations between early environmental factors and various aspects of neurobehavioral and developmental profiles in this population, thereby expanding upon previous research on very low birth weight preterm infants [12].

4. CONCLUSIONS

This longitudinal neurocognitive study addresses a critical research gap in understanding how the acoustic environment, particularly incubator noise, influences neurocognitive development for language function in premature infants. By adopting a multidisciplinary approach that combines acoustic engineering, clinical linguistics, and neuropediatrics, this study aims to provide comprehensive insights into the complex interplay between early acoustic experiences and linguistic development.

The research has significant theoretical and practical implications. From a theoretical perspective, it will contribute to linguistic theory by optimising hypotheses on the nature of the language faculty and developing connections between linguistics and other sciences. This may promote a paradigm shift within Biolinguistics and Clinical Linguistics by developing models of language and its disorders based on the interaction between biological and environmental factors.

From a practical standpoint, the findings will have immediate applications in clinical settings. The data on hearing thresholds and auditory pathway maturation would help improve protocols for early identification and treatment of hearing problems in premature children. The integrated assessment protocols and intervention guidelines developed through this research could be incorporated into routine clinical practice, potentially improving outcomes for premature infants.

The social impact of this research is substantial, as it addresses the needs of a vulnerable population. By improving our understanding of the environmental factors that affect neurodevelopment in premature infants, the investigation contributes to reducing social inequalities and enhancing early diagnosis methods. The results will be valuable not only to healthcare professionals but also to families, educators, and other stakeholders involved in supporting the development of premature children.

5. ACKNOWLEDGMENTS

This work is part of the project "Longitudinal and Cross-Sectional Neurocognitive Study of Acoustic-Perceptual Abilities and Linguistic Function in Preterm Infants (PretermLA)", funded by the Research Plan of the University of Cádiz (Project Code PR2024-010), within its Bridge Projects call (2024/2025).

6. REFERENCES

[1] LW. Doyle: “Outcome at 5 years of age of children 23 to 27 weeks’ gestation: refining the prognosis,” *Pediatrics*, vol. 108, pp. 134-141, 2001.

[2] IL. van Noort-van der Spek, MC. Franken, and N. Weisglas-Kuperus: “Language functions in preterm-born children: a systematic review and meta-analysis,” *Pediatrics*, vol. 129, no. 4, pp. 745-754, 2012.

[3] DL. Putnick, MH. Bornstein, S. Eryigit-Madzwamuse, and D. Wolke: “Long-Term Stability of Language Performance in Very Preterm, Moderate-Late Preterm, and Term Children,” *J Pediatr*, vol. 181, pp. 74-79.e3, 2017.

[4] TN. Nguyen, M. Spencer-Smith, KM. Haebich, A. Burnett, SE. Scratch, JLY. Cheong, et al.: “Language trajectories of children born very

preterm and full term from early to late childhood," *J Pediatr*, vol. 202, pp. 86-91.e1, 2018.

[5] ME. Barnes-Davis, SL. Mehar, SK. Holland, and DS. Kadis: "Extremely preterm children exhibit increased interhemispheric connectivity for language: findings from fMRI-constrained MEG analysis," *Dev Sci*, vol. 21, no. 6, 2018.

[6] IM. Mürner-Lavanchy, CE. Kelly, N. Reidy, LW. Doyle, KJ. Lee, T. Inder, et al.: "White matter microstructure is associated with language in children born very preterm," *Neuroimage Clin*, vol. 80, pp. 808-822, 2018.

[7] E. Stennert, FJ. Schulte, and M. Vollrath: "Incubator noise and hearing loss," *Early Hum Dev*, vol. 1, no. 1, pp. 113-115, 1977.

[8] SMS. Cardoso, LC. Kozlowski, ABM. de Lacerda, JM. Marques, and A. Ribas: "Newborn physiological responses to noise in the neonatal unit," *Braz J Otorhinolaryngol*, vol. 81, no. 6, pp. 583-588, 2015.

[9] S. Arenillas-Alcón, J. Costa-Faidella, T. Ribas-Prats, MD. Gómez-Roig, and C. Escera: "Neural encoding of voice pitch and formant structure at birth as revealed by frequency-following responses," *Sci Rep*, vol. 11, 2021.

[10] GN. Avecilla-Ramírez, T. Harmony, E. Porras-Katz J. Ricardo-Garcell, A. Fernández-Bouzas, and E. Santiago: "Indicadores electrofisiológicos de la percepción fonética en lactantes con riesgo de trastornos del lenguaje," *CIENCIA@UAQ*, vol. 3, no. 1, pp. 14-26, 2010.

[11] P. Salvago, A. Immordino, F. Plescia, M. Mucia, A. Albera, and F. Martines: "Risk factors for sensorineural hearing loss and auditory maturation in children admitted to neonatal intensive care units: Who recovered?," *Children*, vol. 9, no.9, 2022..

[12] MJ. Wolf, K. Koldewijn, A. Beelen, B. Smit, R. Hedlund, and IJ. de Groot: "Neurobehavioral and developmental profile of very low birthweight preterm infants in early infancy," *Acta Paediatrica*, vol. 91. no. 8, pp. 930-938, 2002.

AUTHOR INDEX

Aalmoes Roalt 5907, 5915
Abdo-Sánchez Elena 6221
Abe Keisuke 6345
Abehsera-Morell Pablo 6447
Abel Jonathan 3855
Abellan-Lopez David 155, 915, 5791
Abellera Katelyn 6511
Abhayapala Thushara 4299, 4373, 6393
Ablitzer Frédéric 2489, 2493
Ackermans Bente 6417
Acun Volkan 781, 811
Adams Christian 3601, 5325
Adasme Claudio 2821, 2827
Adelman Cahtia 3141
Adetomi Adewale 5205
Adhikary Manju 1891
Adorno Silvia 1581
Aerts Arne 2087
Afify Andrea 2171
Agrela Francisco 291
Aguado Tienda Carlos 3669
Aguirre Arturo 6125
Ahmed Feroz 1711
Ahn Chang Wook 2201
Ahn Young Eun 2039
Ahrens Jens 5669
Ahsan Noman 2375
Ahsan Noman 2393
Akbaba Andac 1095, 2289
Akemann Walther 3093
Akiwate Deepak 2447
Aklouche Omar 2489, 2493
Al-Bayyar Zinah 4577
Alakoivu Reijo 3769, 3805, 6143
Alam Md Shadab 5635
Albera Andrea 3355
Alberdie Enedina 2051
Alceu Souto Bruno 79
Aldalur Ander 567
Alessandri Elena 6377
Aletta Francesco ... 141, 163, 4657, 4699, 4761, 4767, 4889, 4909
Alexandropoulos Christos 3109
Algermissen Stephan 5301, 5317, 6353
Ali Fawad 2655
Ali Mario 1737
Ali-Maclachlan Islah 3865
Alickovic Emina 3281
Alimadhi Enkela 5023
Alloza Pablo 2605
Almagro Pastor José Antonio 4547, 4991
Almeida Raul 5037
Almunia Portoles Javier 6113
Alon David 4307, 4315, 4321
Alonso Nogales Jone 5117
Alonso-Ramos Jose Luis 3029, 3043
Alsina-Pagès Rosa Maria 1063, 2171, 3819, 4571, 4591, 6155, 6263
Alter Kai 3295
Altinsoy M. Ercan 1977, 3337, 3477, 3485, 4507, 5971
Altmann Peter 1669
Altobello Alessandra 1173
Alva Aleix 1029
Alvarez Chaia Julian 1029
Álvarez Julián 925
Alvarez Ruiz Yesika Patricia 1329
Alves Sonia 4707
Amadasi Giovanni 2647
Amado Mendes Paulo .. 2375, 2393, 2401, 3831, 4029, 4863, 5373, 5395
Amann Paul 2727
Amatriain Mikel 1079, 1099
Amielh Muriel 1879, 2619, 2655, 2683
Amiri-Simkooei Alireza 1465, 5607, 5961
Amodeo Veronica 3881, 3905, 3933
Anchustegui Paula 4817
Anda Sergio 1985
Andén Joakim 4119
Andino Cappagli Camilo Ignacio 1465
Andrade Cristobal 889
Andrejková Gabriela 3393
Andreopoulou Areti 6589
Andreou Panagiotis 1961
Andreozzi Laura 3779
Andrés Diana 3049
Andrés Julio 6497
Andrés Víctor Tomás 5859
Andrijasevic Andrea 4193
Angelini Fabio 191, 991
Angermeier Julian 3215
Anthony Michael 113
Antonacci Fabio 2787, 4079, 4397
Antonacci Fabio 6425
Antunes Sónia 503
Anwar Usman 5205
Aoki Yohko 533
Apicella Valerio 4739
Aragó Bishop Marco 2721
Aran-Ais Francisca 5791
Arana Goenaga Iñigo 519
Arana Miguel 435, 1099
Arándiga Adrián 3029, 3039
Arasan U. 2415
Arce Ruiz Rosa María 1267, 1333
Arcos Holzinger Sandra 4299
Arcos Robert 5851
Ardid Miguel 6227
Arenaz Gombau Angel 345
Arend Johannes M. 6477
Arimoto Keita 2733, 2757, 2833
Arina Renzo 1763
Ariza Alvarez Maria Luisa 1201
Ariza-Carrasco Alejandro 3035, 3067
Arizza Vincenzo 6259

Armelloni Enrico 2079
Arnela Marc 1547, 2207, 3637, 3819, 4457, 4571
Aronoff Justin 3321, 3719
Arrebola Fabian 6565
Artuso Francesco 1095, 2289, 5755, 5761, 5785
Arunagiri Sakthisandron 2073
Arvidsson Emma 3707
Arweiler-Harbeck Diana 3227
Ascari Elena 1363, 5755, 5761
Asdrubali Francesco 2335
Asensio César 3645
Asnaghi Emanuele 191
Asorey-Cacheda Rafael 6221
Aspöck Lukas 895, 3513
Aspuru Soloaga Itziar 4817
Assunta Quaglini Lara 191
Aste Patrik 2563
Astell-Burt Thomas 4761
Astolfi Arianna 775, 845, 2593, 3355, 3827, 4933
Astolfi Jacques-André 6275
Atamer Serkan 1977, 3337, 3477
Atienza Gonzalo 4095
Atzrodt Heiko 5415
Au-Yeung Hou Hin 1155
Aujogue Nicolas 1907
Aumond Pierre 1349
Aurnia Salvatore 6303
Ausejo Prieto Miguel 969
Avallone Francesco 1447, 1737, 1755, 1763, 1793, 1801, 5423
Avelar Marcio 3637
Avetisov Stepan 2485
Ayyobi Pedram 443
Azarpeyvand Mahdi 1711
Azpicueta-Ruiz Luis A. 1515, 3505, 3517, 3541, 4095, 5505
Azzaro Maurizio 6181
Babich Francesco 4001, 4905
Bachl Fabian 1573
Bachmann Florine L. 3281
Bacila Bogdan 4243
Baclet Sacha 1349, 5733
Badan Linda 4555
Bader Rolf 2767, 2877
Baek Kyungmin 5661
Baeza José 2821
Bagnus Piera 2913
Bai Mingsian R. 113
Baig Martí 5197
Bajicová Aleksandra 5287
Bakogiannis Konstantinos 6589
Baldinelli Giorgio 367
Baldovin Daniel-Catalin 1363
Ballarin Loriano 6117
Ballestero Eric 2315, 2709
Ballgjati Jona 1801
Ballout Abbas 1073, 5437
Banchero Lucas 2295, 6401
Bandeira Mariana 3231
Bang Seung-Jae 2233, 5653
Banta Gregory 3163
Bárány Mihály Tamás 885
Barbancho Ana M. 2891, 2897, 2905
Barbancho Isabel 2891, 2897, 2905
Barbaresi Luca 311, 611, 837, 3939
Barbarino Mattia 1447, 1481, 5953
Barbero Francesca 207
Bard Delphine 631
Barrigón Morillas Juan Miguel 5747
Bartha Lél 1131, 3567, 6377
Bartnitzek Jens 3589, 5839, 6545, 6549
Barton Lucy 811
Baruch-Mazur Katarzyna 2411
Baskent Deniz 5085
Basrour Skandar 1613
Bastine Amy 4299, 4373
Batet Gerard 1603
Battarra Mattia 2061
Battistini Vincenzo 1147
Baù Marco 1613
Bauer Nicole 3597
Baumann Katharina 2099
Baumann Uwe 3231
Baumgartner Mark 6199
Bazilinskyy Pavlo 5635
Bechtel Philipp 3117
Beck Augusto 5463, 5521
Becker Stefan 1689, 1867, 1965
Becuwe Sofie 471
Beddows Andrew 5693
Beer Gabriel 1965
Beevers Sean 5693
Begotti Michele 3749
Behn Maximilian 1843, 1899
Beira Jiménez Juan Luis 3897
Belenguer Rubio Paula 391, 673
Beli Danilo 79
Bellelli Francesco 1763
Belloch Jose A. 4365, 4381
Bellomini Raffaella 1181
Bellows Samuel 4473, 4481
Bellucci Patrizia 1161, 1169, 5883
Ben Jafela Nada 3017
Ben-Hur Zamir 4307, 4315, 4321
Benn Aaron 3163
Bennett Justin 4755
Benocci Roberto 991, 2171
Benz Julian 1689
Beozzo Simone 367
Beranzoli Laura 6191
Berebi Or 4307
Berg Jan 4755
Bergamini Andrea 2355, 2407
Berger Jonathan 3855
Berlec Tomaz 2225
Bernal Ortiz Francisco 5131
Bernardini Alberto 2787
Bernardini Giovanni 1421, 1683, 5441
Bertelli Andrea 6441
Bertelli Stefano 1613
Bertels Tanguy 2701
Bertotto Daniela 6195

Berzborn Marco 889, 2541, 4139
Besnea Irina 5961
Bessac Francois 797
Besse Alex 2489, 2493
Betancur Gutierrez Celeste 2929, 6519
Bettarello Federica 3987, 4223, 6075
Betton-Ployon Erwann 2285
Bevilacqua Antonella 2647
Bhatara Anjali 5975
Bhulai Sandjai 2165
Bianco Andrea 2913
Bianco Francesco 311, 2031
Bianco Lorenzo 207
Bibbó Gabriel 4983
Biberger Thomas 3399
Bieber Rebecca 3145
Bietz Heinrich 267, 2533
Binek Wojciech 1543
Binz Tina Maria 3597
Birnie Lachlan 4299
Bite Maria 943
Bjørnstad Steinar 6327
Bk Prajna 3321, 3719
Blanco José Luis 2129
Blanes Guàrdia Núria 4685
Blass Martin 1495, 3173, 4883
Blättermann Patrick 4975
Blau Matthias 3303, 6451
Blazquez Navarro Ricardo Antonio 1891
Blinet Thibaut 295, 2611
Blöcher Christian 37
Blomkvist Johan 6029
Blondé-Weinmann Cyril 3153, 3197
Boerger Marco 4739
Bogers Koen 5075
Bogey Christophe 1653
Böhme Ralf 3589, 5839, 6545, 6549
Bolognese Matteo 1197
Boman Sarah 4781
Bonanno Danilo 6131, 6251
Bonfiglio Paolo 1997
Bonnard Alexandre 2515
Bonnel Julien 6293
Bonomo Lucas 1661
Borja-Fernández Daniel 359
Bortoletti Martina 6195
Bosch Ignacio 2995
Bosia Federico 2407
Bossert Hugo 2677
Bostan Idil 5999
Botero-Bolivar Laura 1073
Bottalico Pasquale 3711, 3965, 3981
Botteldooren Dick 235, 257, 2137, 4971
Botti Tommaso 45
Bouchakour Omar 2989
Boukadia Régis 2347
Boukhemia Clara 4925
Bouley Simon 4357
Bourdieu Laurent 3093
Boutin Henri 2797
Bowers Gregory 3189
Boyle Patrick 1537
Braghin Francesco 2305
Brambilla Arianna 4761
Brambilla Giacomo 2305
Brambley Edward 1661
Brand Devora 3141
Brandão Eric 2563, 2585, 4457
Brasseur Emmanuel 2807
Bravo Teresa 2619, 2655, 2683
Breitkreutz Tabea 885
Briaire Jeroen 3219
Briguglio Andrea Sarah 6177
Brink Mark 1041, 1059, 1115, 3597
Brinkmann Fabian 889, 3457, 6597
Brokmann Holger 3773
Broneske Sylvia 1079
Brookes Mike 3449
Brooks Rory 3449
Brosig Deborah 1953
Brugnara Paola 649
Brun Maël 6275
Brungart Douglas 3145
Brunnström Jesper 4111
Buba Michael 885
Bueno Ricardo G. 3059
Buggè Valentina 2593
Bugl Benedikt 3425, 3431
Buogo Silvano 6205
Buratti Cinzia 2577
Burgess Marion 1417
Busti Martina 1173
Buzetelu Vlad Stefan 5929
Caballol Bartolomé David 683
Cabaret Jérémy 2797, 2801
Cabó Joan 4591
Cabrera Manuel 291
Cai Yinshan 5309
Calanna Momisch 1147
Calvert Simeon 2279
Calzavara Yoann 2981
Camacho Jorge 2185, 2973, 3053, 3059, 3067
Cámara Mateo 2129
Camarena Francisco 3025, 3029, 3043, 3049
Camblor Iglesias Pablo 345, 5539
Campanella Humberto 1619
Campbell Colin 3953
Campbell Murray 2721
Campello-Vicente Hector 155, 915, 5791
Campillo-Davo Nuria 155, 915, 5791
Campo-Valera María 1523, 6221
Camussi Roberto 1645, 1653, 1719
Can Arnaud 1349
Canals Santiago 3029
Candeloro Paolo 1387
Cani Alma 5023
Caniato Marco 3987, 4223, 6075
Cansu Nicole 3707, 4009
Cantalapiedra Inmaculada R. 2577
Cao Runzhen 1697
Capobianchi Giorgia 1439, 1473, 1719
Cappelletti Francesca 649, 3973, 3993

Cappelli Giuseppe 6303
Cappotto Drew 3307
Carambia Benedetto 4739
Carbajo San Martín Jesus 1553, 1559, 6083, 6135, 6213
Carcel Joan Enric 3003
Cárdenas Mansilla Jorge 4547
Cardin Vanessa 6191
Carillo Kevin 3125
Carlyon Robert P. 5193
Caronni Sarah 191
Caroppo Federico 2001
Carpentier Justine 6275
Carrascal Teresa 397, 423
Carrero-Muriel Luis 3873
Carrión Alicia 3025, 3043
Caruso Francesco 243, 6177, 6185, 6191
Carvalho André 1185
Carvalho Antonio 3657
Carvalho Maria Luiza De Ulhôa 3485
Casacci Luca Pietro 207
Casalino Damiano 1755
Casla-Herguedas Belén 397, 423
Cassens Lion 2279
Castellini Federico 2013
Castorena Carlos 2263, 2295
Castro Mota Rafael 1239
Catania Francesco Valerio 1173
Cavalieri Théo 2035
Cavallo Arianna 2013
Cavanagh Adam 2447
Cazzulani Gabriele 2305
Cebrecos Alejandro 3025, 3039
Celiker-Cenger Yagdir 867
Centeno-Cerrato María 1625, 3645
Cerchiai Mauro 1197, 1363
Cerdá Salvador 6579
Cerini Fabrizio 1581
Cerkovnik Nejc 3575
Cerwén Gunnar 4699, 5007
Cetani Davide 4933
Cetrangolo Gonzalo 5559
Chabassier Juliette 2801
Chadwick Andrew 1251
Chafe Chris 3855
Chang Kyoung-Jin 2201
Chatburn Katie 5001
Chateauvieux-Hellwig Camille 627
Chatziioannou Vasileios 2727
Cheer Jordan 3, 23
Chehami Lynda 2989, 3017
Chen Chih-Hsuan 4747
Chen Julie Chia-Ping 4747
Chen Wangqiao 1697
Chen Xiaochao 4699
Chen Xu 2457
Chen Ziqi 2501
Chetupalli Srikanth Raj 4259
Chiang Hsin-Tien 5213
Chiarella Davide 1051, 4843
Chiari Simone 1949
Chidichimo Giuseppe 1169
Chieng Julia 4941
Chisari Letizia 4739
Chizhikov Alexander 3081
Chmelík Vojtech 339, 699, 3525
Chmielewski Bartosz 713, 5337
Cho Ahhyun 689
Cho Gyumin 2201
Cho In-Je 2233, 5653
Cho Sung-Zoon 2233, 5653
Chognot Hugues 6283
Choi Jung-Woo 4073, 4337
Choi Junseok 53
Choi Sung Uk 3499
Choi Young-Ji 3735, 4013
Chojak Aleksandra 1543
Chojnacka Klara 327, 2331
Chojnacki Bartlomiej 1543
Chordekar Shai 3141, 3157
Choubey Abhishek 5983
Chowning John 3855
Choy Yat Sze 2663
Christensson Jonas 3707
Christophe Julien 1725
Chronopoulos Dimitrios 4161
Chudalla Michael 5709
Chun Youngjae 3655
Chung Jin-Yun 555, 689
Ciaburro Giuseppe 1095
Ciarallo Francesca 1161
Cibrián Rosa 6579
Cierco Ester 2383
Cimmino Gennaro 2013
Cinini Alessandra 1051, 4843
Cioffi Federico 5105
Citterio Sandra 191
Claeys Claus 933, 2355, 2415, 2423
Clairbois Jean Pierre 5869
Clar-Garcia David 155, 915
Clark Charlotte 4539
Clark Sierra Nicole 4539
Clarke Peter 4889
Clément Adrien 295
Clot Arnau 5851
Cobianchi Mattia 3925, 5045
Cobos Maximo ... 2263, 2295, 4351, 4365, 4381, 6385, 6579
Cobussen Marcel 4501, 4755
Cocconcelli Marco 2079
Cochelin Bruno 2733
Coelho Margarida 5701
Colinot Tom 2797, 2801, 2859, 2863, 2885
Collet Manuel 99
Colom Mateu 3109
Colombo Giorgio 2013
Colotto Fabio 6195
Cominelli Sebastiano 2305
Comotti Arianna 191
Company-Rubio Victor 3039
Conde Santos Luis 1185
Conoir Jean-Marc 2701

Conter Marco 5709
Contreras-Saavedra Carla E. 3443
Cook Ashley 3189
Cook Chris J.h. 3925
Cool Vanessa 933
Corallo Mario 1523
Cordioli Júlio Apolinário 1661, 1755, 1793, 5463, 5521
Corey Ryan 4087
Corigliano Alberto 1581
Corradi Roberto 2013
Corral García Gonzalo 3181, 4283, 5229
Correa Víctor 2815, 2821
Cosarinsky Guillermo ... 2179, 2185, 2241, 2973, 3053
Cosnefroy Matthias 5471
Costa Antonio 3657
Costa Gabriele 5293
Cotté Benjamin 1851
Covas Guilherme 1185
Craenen Paul 4755
Craster Richard 2713
Crispin Charlotte 585, 611
Cristofori Giulia 2061
Crivelli Bruno 2007
Crowley Danielle 249
Cruza Jorge F. 2973, 3035, 3059, 3067
Cubero-Atienza Antonio José 291
Cucharero Moya Jose 2599
Cuenca Jacques 2369, 2563
Cueto-Ancela José Luis 1329, 3315, 6169
Cuevas-Rodriguez Maria 6409, 6457, 6565
Čurović Luka 215, 803, 1019
Cutanda Henriquez Vicente 2653
Cutugno Paola 1051, 4843
Cuvillier Nicolas 3009
Czuka Martin 797, 5709
Czwielong Felix 1689, 1867
D'Adamo Amar 3517, 3541
D'Alessandro Francesco 2289, 5761
D'Olne Emilie 197
D'Orazio Dario 3787, 5501
D'Orazio Tommaso 2335
D. Ewert Stephan 6571
Da Pos Valerio 761
Da Silva Bruno 4427
Daems Walter 2087
Dagø Peter 2021
Dahham Tiba Basil 4577
Dalir Donya 4959
Dalmont Jean-Pierre 883, 2797, 2801
Dance Stephen 3961
Dannenberg Roger 6497
Daroukh Majd 1711
Dashtipour Kia 5205, 5247
Dau Torsten 3237
Däuble Lukas 547
Dauchez Nicolas 6361
Daugintis Rapolas 3421, 6483
Daumal I Domènech Francesc 4583
Davies Bill 257
Davies William 2149
Davy John Laurence 2557
Day Christopher 4043
Daydé-Thomas Vincent 5485
Daza María Pilar 2129
De Arcas Guillermo 1625
De Bie Femke 2341
De Bono Emanuele 99
De Bruijn Christel 4525
De Campos Muradas Cerântola Pedro 2461
De Diego María 149, 163
De Frutos Martin 1073, 2193
De Geetere Lieven 303
De Groote Evelien 3287
De Haas Kevin 6533
De Krom Paul 3133
De La Prida Daniel 1515, 3505, 3517, 3533, 3541, 3873, 4095, 5505
De Laciñana María Alonso 3035, 3067
De León Gonzalo 5755, 5761
De Luca Massimiliano 1201
De Luca Rosi 6259
De Marqui Jr Carlos 79
De Paola Elisa 1439, 1645, 1719
De Pastina Annalisa 1607
De Prenter Frits 1705
De Rubeis Beatrice 5441
De Ruiter Evert 3913, 5061
De Rus Juan A. 2295
De Ryck Laurent 2369
De Salvio Domenico 1193, 3933, 3939
De Sena Enzo 3413, 3457
De Souza Larissa Pereira 4917
De Vincenzi Giovanni 6181, 6191
Deacon Thomas 4983
Debevc Mark 2557
Debut Vincent 2739
Deckers Elke .. 713, 933, 2341, 2347, 2355, 2361, 2369, 2415, 2423, 2431, 4161, 5309, 5351, 5399, 6605
Decloux Antoine 4035
Dedoussi Irene 5961
Dekoninck Luc 4629
Del Duchetto Fabio 1387
Del Gaudio Francesca 6425
Del Rio Joaquin 1603
Del Val Lara 323, 4415, 4421, 4449
Delaunay Thomas 2981
Deleforge Antoine 4171
Delfrap Tim 6051
Delgado Jonathan 5153
Della Torre Sagi 4079
Delle Monache Stefano 6033, 6051
Delory Eric 6101
Denayer Hervé 933, 2341
Deng Jie 2457, 2461, 2481
Denia Francisco David 5859
Denisenko Tatiana 3315
Denzer Milenko 2827
Derré Jérémie 1907
Descamps Maxime 5485
Deschamps César José 5463, 5521
Desmet Wim 933, 5309
Despaux Gilles 2981

Devos Paul 4971
Di Bella Antonino 755, 761, 3973, 3993
Di Blasio Sonja 3779
Di Donato Balandino 4599
Di Giusto Fabio 5399, 6605
Di Marco Alessandro 1439, 1473, 1719
Di Mauro Letizia Stella 6131, 6177, 6251, 6311
Di Prisco Martina 6075
Diamantini Massimiliano 1169
Díaz Catalina 2827
Díaz César 5407
Díaz Chyla Alexander 853
Diaz Duran Joaquin Roberto 3541
Díaz Gaztelumendi Odei 4267
Díaz José Antonio 6101
Dickinson Samuel 3627
Diechmann Maike 4855
Diego-Tortosa Dídac 6131, 6227, 6251, 6303, 6311
Dietrich Felix 2099
Dietzen Thomas 4103, 4275
Díez Ramón 1123
Dijckmans Arne 585, 611
Dijkman Luc 5493
Ding Qian 2473
Dirks Coral 3157
Discetti Stefano 1809
Dobinson Nicholas 827
Doc Jean-Baptiste 2801, 2885
Doclo Simon 117, 3449
Dogan Iseri Hanife Ayca 4649
Dogu Mert 885
Dolan Tony 1285
Dolger Alexander 169
Domenichi Simone 6117
Dominguez Victor 5573
Donaldson Mark 85
Doni Serena 183
Donnerer Julia 3601
Donohue Brian 4791
Dopico Javier 1041, 1115, 3597
Dörner Lisa 249
Dosso Stan 6293
Doutres Olivier 3125
Drever John 3925, 5045
Drga Vit 3267, 3365
Drofelnik Jernej 5953
Duarte Fabio 5991
Dubno Judy 3723
Ducceschi Michele 2851
Ducousseau Mathieu 3009
Dumanowski Jakub 4823
Dumitru Vlad 6331
Dunn Malcolm 331
Duocastella Martí 3083, 3109
Dupont Samuel 3097, 3103
Duquennoy Marc 3017
Durando Giovanni 1523
Dyakonov Evgeniy 3077
Ebri Michele 5293
Eccles Jonathan 2505, 4739, 5893
Ech-Cherif El-Kettani Mounsif 3009
Echeverria Jone 207
Eckert Lucas 5101, 5167, 6331
Edworthy Judy 6007
Eerrer Esteban 1073
Egeler Jonas 3589, 5839, 6545, 6549
Eguinoa Rubén 2113
Ejiri Shinichiro 1939
El Kadmiri Pedraza Said 5301, 5317
Ellermeier Wolfgang 3583
Ellis Max W. 2121
Ellis Wayne 3287
Elsaei Ahmed 733
Elser Miriam 5627
Elvira Luis 2943, 3035, 3053, 3067
Emmenegger Silvio 3567
Emmerich Leon 2563
Ende Christoph 3589, 5839, 6545, 6549
Engel Isaac 6557
Engel Margret Sibylle 3477, 3485, 4661
Engelmann Nicole 4533
Ennis Zachariah 3189
Enqvist Martin 3281
Eom Chunwon 4967
Epure Arina 4275
Erbig Lars 1669
Erdmann Matthias 4813
Ernoult Augustin 2797, 2801
Eroles-Simó Alba 3043, 3049
Erturk Alper 2327
Escobar Nelson 705
Escudero Juan Pablo 2389
Eskelund Kasper 3281
Esperidião Aline Ramos 1063
Espinel Valdivieso Ana Esther 345, 1123
Espinosa Luis 2965
Espinosa Roselló Víctor 5359, 6259
Espinoza Carolina 2815, 2821, 2827
Esposito Antonio 601, 619
Estévez-Mauriz Laura 1379
Euler Luisa 2631
Evrard Anne-Sophie 5817
Ewers Robert 203
Ewert Stephan 3399, 6473, 6533
Expósito Paje Santiago 5601
Ezziani Youness 3009
F. Cruza Jorge 2179, 2241
Fabra-Rodriguez Miguel 155, 915, 5791
Fall Dame 3017
Fandiño-Toro Hermes 5163, 5175
Fang Xiang 4699, 4767
Fang Yihong 1677
Fanti Maria Pia 2317
Fantinelli Augusto 1547, 2207, 4457
Fantozzi Marco 1209, 1217
Farha Elie 2989
Farina Adriano 3827
Farina Angelo 3827
Farzaneh Nima 3855
Fasana Sara 2593
Fasllija Ela 3913, 5023, 5061
Fasulo Giovanni 1481, 5953

Faulkner Kathleen 3263
Fauqueux Sandrine 5485
Fausti Patrizio 1949, 1997, 2021, 2511
Favoino Fabio 775, 845
Fazi Filippo 1585, 4243, 4251
Fecht Daniela 999
Federico Luigi 1481
Fedyk Katarzyna 1321
Felcyn Jan 4823
Felix Greco Gil 3377
Félix Simon 2529
Fels Janina 895, 3513
Fenech Benjamin 383, 4539, 4941
Feng Chao 6235, 6243
Feng Sinuo 1251
Ferilli Francesca 3779
Fernández Vázquez Victoriano 5601
Fernández-Clement Raúl 2949, 2955
Fernández-Garrido Alejandro 6221
Fernandez-Grande Efren 2585, 4127, 4135, 4145, 4267, 4457
Fernández-Martínez Fernando 5179
Fernández-Zacarías Francisco 3315, 3847
Ferrari Marco 1613
Ferrari Vittorio 1613
Ferreiros-López Javier 5179
Ferrentino Agostina 3889
Ferrer Esteban 2193, 5437
Ferrer Miguel 149, 163
Ferretti Melissa 1051, 4843
Ferri Francesc J. 2295, 4351, 6385
Ferri Sara 243, 6185, 6191
Fichera Ilaria 4171, 4229, 5529
Fichna Stefan 6571
Fichtel Christoph 561
Fidecaro Francesco 2289, 5785
Fiebig André 4621, 4635, 4855, 5709
Figueroa-Duran Antonio 4127, 4135
Filiciotto Francesco 6177, 6181, 6191, 6195
Filippone Antonio 1683
Filipska Tereza 5269
Fiorella Laura 5755, 5761
Fiorini Costanza Vittoria 1147
Fisarova Zuzana 2309
Fishkin Simon 1223
Flaherty Mary M. 3981
Fleischli Silja 2515
Flores-Colen Inês 2051
Fogerty Daniel 3723
Fons-Esteve Jaume 4685
Fonseca William D'Andrea 2585
Fontana Ilaria 5565
Forcada Almarcha Aitor 6083
Fostick Leah 3157
Fox Elizabeth 3189
Foy Cédric 4171
Franceschelli Luca 1809
Frankael Rachel 3141
Franke Jörg 1689
Frasson Quaresma Sérgio Fernando 519
Fráter Attila 5189
Fratoni Giulia 3787, 5501
Frattolillo Andrea 761
Fredianelli Luca 1095, 1363, 2289, 5755, 5761
Freitas Elisabete 5037
Freixes Marc 1063, 4571, 4591, 6155
Fréour Vincent 2733, 2797, 2801, 2833, 2885
Friedrich Björn 3333, 3361
Frijns Johan 3219
Fritz Carole 3855
Fritz Claudia 2783
Froschmeir Franz 1965
Fruchart Marianne 2025, 6107
Fruncillo Felice 5945
Fu Xuehua 4799
Fuchs Andreas 1243
Fuchsluger Andreas 1607
Fuhrmann Ferdinand 4883
Fujii Shinya 6503
Fujikawa Satoshi 6013
Fürjes Andor 767, 3653
Furmanová Aneta 5269, 5287
Fusaro Gioia 837, 3939, 5865
Fuster Laura 149, 5505
G. Muñoz Javier 3035, 3067
Gabard Gwénaël 2485, 5309
Gade Anders Christian 4021
Gaggero Tomaso 6195
Gaillard Amélie 2807
Galbrun Laurent 3613
Galiana Nieves Jaime 2705, 5381, 5389
Galindo Miguel 2051, 3697
Gallagher Hilary 3189
Galland Marie-Annick 2691
Gallardo-Antolín Ascensión 5179
Galletto Andrea 3355
Gan Woon-Seng 4839
Gander Philip 3295
Ganesh Mahadevan 5573
Ganic Emir 1403
Gannot Sharon 4079
Gao Yu 1349
Garai Massimo 837, 1161, 1193, 1209, 3933, 5865, 5869
Garcén Paulina 5559
García Barrios Guillermo 5831
Garcia Beitia Sergio 6113
Garcia Charlotte 5193
García Gómez Juan Óscar 4043
Garcia Joaquín 727, 2605
Garcia Jorge Joaquin 1991
Garcia Juan 149
Garcia Lidia 1123
Garcia Luis Miguel 705
García Morales Rubén 969
García Quesada Rafael 4547, 4991
García Ugarte Iñigo 2113
García-Calderón Eugenio 359, 961
García-Garrigós Juan José 3039
García-Márquez Juan Ángel 4869
García-Martín María 1041
García-Medina Esther 3645

Gärdhagen Bo 405
Gariglio Niccolo' 1729
Garofalo Emanuele 5293
Garzón Vargas Maria Juliana 149, 163
Gashchak Sergey 2149
Gaspar Anna 3831, 4029
Gasparella Andrea 649, 3987
Gasparri Eugenia 4761
Gautier François 2485, 2489, 2493
Gauvreau Benoit 5725
Gayer Yhonatan 4321
Gazengel Bruno 2807
Gazzada Fabio 6155, 6263
Gazzola Chiara 1581
Geluykens Michiel 3525
Genell Anders 5593, 5771, 6541
Genevay Loane 2619
Gennaretti Massimo 1421, 5441
Genuit Klaus 921
Georgiou Fotis 5681
Gerasch Criostoir 1923
Gerbotto Andrea 775, 845
Geronazzo Michele 3421
Gey Flores Ricardo 1329
Ghadiri Roxana 4747
Ghani Burooj 2153, 2165
Gharbi Sirine 2099
Giannetti Flavio 5945
Giannini Daniele 471, 2361
Gianoli Pablo 1109
Giglio Andrea 5015
Giglio Federico 6181
Gil Carrillo Francisco 683
Gil-Pita Roberto 3181, 5229
Gillespie R. Brent 6511
Giménez Alicia 6579
Giner Tarazona Pablo 6259
Gino Jacopo 45
Giordano Patrizia 6181
Giovanardi Nicolas 6297
Girón Sara 3697
Givois Arthur 6361
Glé Philippe 295, 2611, 2671, 2677
Gligorijevic Mateja 5615
Gliozzi Antonio 2407
Glisser Max 949
Glorieux Christ 339, 705, 713, 741, 747, 2309
Godinho Luis 443, 2335, 2375, 2393, 2401, 3831, 4029, 4863, 5373, 5395, 5539
Gogate Mandar 5205, 5247
Gök Tokgöz Özlem 4507
Gold Martin 4713, 4721, 4725
Goldring Sapir 4315
Gölles Lukas 1565
Goman Adele 5247
Gomariz Spartacus 1603
Gomes Andrade David 443
Gomes Magda 3657
Gómez Escobar Valentín 1369, 2635
Gomez Garcia Clara 6131, 6303, 6311
Gómez Parrado Enrique 3669
Gómez Roberto 2949, 2955
Gomez Tomas Simon 705, 747
Gómez-García J.a. 5163, 5175
Gommers Diederik 3913, 5061, 5075, 5999
Gonzales Redman Yvonne G. 3965
González Alberto 149, 163
González De La Peña Penélope 391, 673
González Elizabeth 1109
González García Miguel Ángel 975, 1267
Gonzalez Nieto Jairo 345
González-Mateo Enrique 3025
González-Toledo Daniel 6409, 6457, 6565
Gosalbez Jorge 2995, 3003
Gottschalk Martin 3373
Gourdon Emmanuel 99, 2671
Gozzi Giacomo 4555, 4615
Græsbøll Christensen Mads 125
Graetzer Simone 781, 811, 3731
Graf Franz 1495, 3173, 4883
Graf Thomas 2515
Grammauta Rosario 6185
Granzow John 6511
Grasic Milan 577
Grassi Jacopo 6441
Graus Ramon 925
Gravina Nicola 3609
Grebien Stefan 1495
Greco Gioele 2787, 6385
Green Evan 4051
Green Marc C. 1409, 2121
Greene Nathaniel T. 3247
Greenland Emma 2505
Gregorac Ana 4883
Grenga Flavia 6311
Griginis Alessia 4933
Grilo Bensusan Álvaro 1087, 3669
Grimaldi Michele 4847
Grimaldi Roberto 1949
Grinstein Eric 3449
Groby Jean-Philippe 2315, 2389, 2529, 2709
Groenewoud Zoë 6199
Grozeva Ioana 4933
Gruender Andreas 1689
Gruetzner Dominik 1689
Grulkowski Ireneusz 3089
Grunder Sascha 5627
Grushko Liron 3163
Gryllias Konstantinos 933
Guagliumi Giorgia 991
Guajardo-Herrera Sebastián 2253, 2259
Gualdana Ilenia 3779
Guarnaccia Claudio 2271, 4847, 5701, 5725
Guasch Oriol 2457, 2461, 2481
Guastamacchia Angela 3355
Guattari Claudia 1147, 2335
Guðjónsson Steinar 5471
Guérin Alexandre 4291
Guérineau Cécile 6195
Guérit François 5193
Guerrero Arias Hiromy Sahory 3745
Guidorzi Paolo 1193

Guigou Carter Catherine 295, 495, 2611
Guillén Sergio 2905
Gulliver John 4539
Gulliver John 999, 5693
Gulzari Muhammad 2317
Guo Kening 4515
Gurevich Michael 6511
Gusó Enric 5197
Gustafson Andreas 5593, 5771
Gustafson Natalie 3321, 3719
Gutierrez Juan 2129
Gutierrez-Parera Pablo 6565
Gutscher Marc-André 6303
Guzman-Inigo Juan 1871
Ha Naomi 3711
Haan Chan Hoon 1375, 1501, 3681
Haberl Max 4707
Habets Emanuël 2569, 4185, 4259, 5513
Hablovicova Blanka 5797, 5803
Hafsteinsson Haukur 5471
Hagberg Klas 631
Hagmüller Martin 1529, 6331
Hahn Nara 4243, 4251, 4343
Hahn Nara 889
Haider Manfred 1243
Hajjaj Amal Z. 1961
Halimeh Mhd Modar 4259
Hall Andrew 3925
Hall Simon 3865
Hallak Simon 5983
Hamamoto Kazuhiko 5111
Hamery Pascal 3153, 3197
Hamilton Matthew 2851
Han Chae-Hyun 3681
Hansell Anna L. 999
Hansen John H.l. 5213
Hanson David 1011
Hao Siting 2473
Harbottle Charlotte 1537
Hargreaves Jonathan 811
Harry Evan 2523, 5643, 5647
Hartenstein Matthieu 4405, 4465
Harvie-Clark Jack 383, 827
Haselhoff Timo 1119, 4807
Hashim Shahis 2065
Hatheier Thomas 37
Hauptman Alon 1223, 3157
Haywood Nicholas 1537, 3287
Healy Patrick 2263
Heath Becky 203
Heggemann Louis 885
Heidegger Patrick 1867
Heigl Christoph 1689
Heimes Anne 889
Heini Gregor 1131
Heinz Johannes 5325
Heisterkamp Fabian 1953
Heldmann Janis 2599
Hellot Manuel 5811, 5817
Héllouin-De-Ménibus Arthur 2611
Hemmert Werner 3215
Herguedas Sergio 733, 4583
Hernandez Alberto 955
Hernández Guerra Alonso 6163
Hernández Lucas 5559
Hernández-Molina Ricardo 3315, 3847, 3897
Herranz-Pascual Karmele 4817
Herrera Nicolás 2375
Herrera-Leon Nicolas 2393, 5395
Herrero Saray 1123
Herrero-Durá Iván 5477
Heusser Axel 5627, 5681
Hidalgo Otamendi Antonio 955
Hilgemann Florian 61
Hill James 827
Hinton Richard 827
Hirsch Karl-Wilhelm 3117
Hjortkjær Jens 3275, 3281
Hoang Minh-Tan 2523
Hodoshima Nao 5111
Hoekstra Jurriaan 5901
Hoekstra Niels 5493
Höhle Laura 3589, 5839, 6545, 6549
Hohmann Beat W. 4641
Hollebon Jacob 1585
Holmqvist-Jämsén Sofia 3707, 4009
Holøyen Gjermund V. 353, 411
Holzmüller Felix 105
Hong Joo-Young 4833, 4835, 4839
Hongisto Valtteri . 3605, 3769, 3797, 3801, 3805, 4005, 6143
Honzík Petr 1507, 3309
Hopkins Carl 311, 3731
Horev Nitza 3141
Hörmeyer Jasmin 5477
Hornikx Maarten ... 485, 999, 4171, 4179, 4215, 4229, 5493, 5529, 6417
Horsman Sean 5875
Horvat Marko 375, 3689, 4193
Horvath Samu 1573
House-Henry Kaliyah 3711
Houtave Peter 5869
Houthuijs Danny 5901
Howell Richard 6341
Howerton Brian 1779
Hoyer Anton 889
Hruška Viktor 5269, 5287
Hu Yubo 6235
Huamani Quiquinlla Keyla Lilian 3745
Huang Weilong 4259
Hub Sandra 789
Huecas Jorge 2943, 3053
Huergo David 1073, 2193
Hummel Hilde 2165
Hussain Adeel 5205, 5247
Hussain Amir 5205, 5247
Huth Christine 3589, 5839, 6545
Hvastja Andrej 215, 2221, 2225
Ianiro Andrea 1809
Iannace Gino 1095, 2289, 2647
Iarossi Sergio 1201
Iarozinski Neto Alfredo 1063, 4591

Iatariene Taous 4291
Ibañez Alberto 3053
Ibáñez García Paula 3035, 3067
Ibanez Tania 2827
Idczak Julia 327, 1543
Idrissi Abdelghani 6131, 6251, 6303, 6311
Ikhwanuddin Rifqi 197
Imbert-Gerard Lise-Marie 5565
Immovilli Fabio 2079
Inaki Hirotsugu 6013
Innes-Brown Hamish 3281
Inoue Hiroaki 2161
Ionita Horia Sebastian 4237
Iraurgi Ioseba 4817
Isacchi Gioele 5293
Isenegger Manuel 1131, 2515, 3567, 6377
Isherwood Gary 5893
Ishida Mitsuyoshi 2161
Ishimitsu Shunsuke 2161, 3493, 6013
Ishizuka Kenji 4329
Islam Tahmida 149
Isnardo Iglesias Albert 519
Istiani Noor Fajrina Farah 3621
Iwata Kiyoaki 6013
Izquierdo Alberto 323, 4415, 4421, 4449
Izsak Marian G.s. 5453
J. Ferri Francesc 2263
J. Navarro-Brull Francisco 2949
J. Pastor-Rodríguez Francisco 2949
Jacob Marc 1891, 1915
Jacob Stefan 1239, 1923
Jäggi Jonas 1429, 5627, 5681
Jakobsson Niklas 405
Jakoby Bernhard 1607
Jambrošić Kristian 375, 3689
Jané Eduardo 1073, 2193
Janer Marcel 2383
Jang Joonghwan 5623
Januševičius Tomas 175
Jaunet Vincent 1637
Jax Peter 61
Jayanthi Anandini Sravya 5607
Jeckelmann-Imhof Christoph 3567
Jedrusiak Mikel 4807
Jensen Jesper 3449
Jeon Jae-Yun 4833, 4835
Jeon Jin Yong 3499, 4681
Jeon Wonju 2469, 2471
Jeong Cholhawn 5653
Jeong Jeongho 431, 3665
Jeong Seojin 689
Jephcote Calvin 4539
Jesus Sérgio 6283
Ji Minjung 3499
Ji Tianhang 6235
Ji Weixun 5261
Jiang Like 1489
Jiang Xing 4533, 4685
Jiménez Noé 2709, 3025, 3029, 3043, 3049
Jiménez Pérez Tamara 1329
Jiricek Ondrej 727
Jo A-Hyeon 555
Jo Hyeoncheol 2233, 5653, 5661
Jo Yeongmin 1435
Jones Ian 4731
Jordan Peter 1637
José Tomás Matus 207
Joseph Phillip 1801
Jóska Jakub 5337
Jousserand Michaël 2863
Juan Shiang-I 4747
Judd Thomas 5477
Juliust Hessel 2099
Jun David 2309
Jung Chol-Hwan 2233
Jung Jinnyon 1933, 5623
Jung Seongmo 135
Júnior Luciano Oliveira 6283
Jürgens Tim 3227
Jurkiewicz Yann 4051
Jüterbock Tobias 889
Kacem Abbes 2285
Kahle Eckhard 4051
Kaloga Yacouba 5237
Kaltbeitzel Bernd 533
Kaltenbach Hans-Jakob 5453
Kaltenbacher Manfred 1867, 3601, 5325, 5343
Kam Yui Chung 4519, 4667, 5053
Kamp Fabian 3471
Kanev Nikolay 169
Kang Boseok 5661
Kang Jeonggoo 2201
Kang Jian 141, 163, 4515, 4615, 4657, 4699, 4767, 4889, 4909
Kang Jonggyu 135
Kanka Simon 1363, 5785
Kappis Achilles 3
Karakonstantis Xenofon 889
Karaman Alara 2431
Karimi Hamid Reza 15, 31
Karimi Mahmoud 6341
Kastelik Jean-Claude 3097
Kather Vincent 2153
Katw Karam 1275
Katz Brian F. G. 3839, 4473, 6447
Kawahara Shigeto 6503
Kawai Claudia 1041, 1115
Keller Rose 4615
Kennedy John 841, 2213, 2323
Keränen Jukka 3769, 3801
Keren Nir 6409
Kersten Simon 885, 889, 3125
Keshavarzi Mahmoud 3287
Kha Jamie 6341
Khayyat Aiham 1259
Khedr Amr 1793
Kidmose Preben 3255
Kikuchi Masakazu 6013
Kılıçarslan Doğuhan 5351
Kim Byeongil 11
Kim Do-Hwan 4013
Kim Dohaeng 2471

Kim Dokyeng 4827
Kim Dokyeong 4949, 4967
Kim Doyeon 53
Kim Geonhee 4833, 4835
Kim Hyounsuk 135
Kim Hyun-Ji 4013
Kim Jeonghun 4953
Kim Jiwan 2469, 2471
Kim Juin 4681
Kim Seonghyeon 5971
Kim Seongyeol 53
Kim Suhong 4967
Kim Sunjoong 3655
Kim Yoonseong 4827, 4967
Kim Youngsun 3665
King Eoin 1007, 5685, 5875
Kirby R. Morris 5643
Kirby Ray 1239
Kirchhof Jan 163
Klein Achim 3773
Klein Florian 4489
Klein Georg 797
Kleinfeller Nikolai 5415
Kleinhenrich Christian 3117
Klenke Reinhard 257
Klin Peter 6091
Kmita Grzegorz 5337
Kobusch Michael 271
Koch Thomas 3589, 5839, 6545, 6549
Köchli Sabrina 6377
Kocsis Dénes 943, 1259, 1275
Kodama Shingo 6013
Kodrasi Ina 5237
Kolar Miriam 3855
Koldkjær Højlund Marie 4773
Kolecka Natalia 1041
Kolingba-Froidevaux Pierre 4855
Kondo Haruka 6503
Kondoh Sotaro 6503
Koning Raphael 3219
Kopco Norbert 3393
Kosowski Piotr 1977, 3337
Kostyleva Ekaterina 3077
Koyama Shoichi 4329
Kozupa Michał 5337
Kraxberger Florian 5325
Kreitzman Jordan 1779
Kressner Abigail 3275
Kreuzinger Johannes 5449
Kristensen Sinnet Greve Bjerge 3237
Krivanek Vitezslav 5797, 5803
Kroczek Leon O.h. 6451
Kroesen Maarten 2279
Kron Thorben 6549
Kropp Wolfgang 5669
Krug Dominik 1817
Kruse Tobias 541
Kryuchkov Alexander 2423
Kubiak Anna Maria 747
Kulasingham Joshua P. 3281
Kuljanin Jovana 1403
Kullukcu Berkay 3477
Kumar Manish 4299
Kuntz Matthieu 6527
Kuru Aysu 4761
Kurukose Cal Hatice 4889
Kusitzky Thomas 4707
Kuštrak Korper Ana 6029
Kuusinen Antti 3605, 3797
Kwon Miji 693
Kwon Youngmin 135
Kylliäinen Mikko 449
L. Flanagin Virginia 6571
L. Herraiz Joaquín 3035
L. Martens William 5037
L. Verhey Jesko 3267
La Magna Nicola 3465, 6483
Labraña Sebastián 2815
Lacasta Ana Maria 1029, 2577
Ladstädter Richard 4883
Laffitte Pierre 125
Lagarrigue Clément 2025, 6107
Lagosh Anton 1619
Lagrange Mathieu 4925
Lahdensivu Alina 449, 567
Lai Chung Kwan 23
Lalitte Philippe 2783
Lam Bhan 4839
Lam Lok Him 4519, 4667, 5053
Lamarque Claude-Henri 99
Lambert Isaac 4389
Lamberts Roberto 4917
Langer Jennifer 3761
Langerak Nienke 3219
Langone Leonardo 6181
Lanoye Reinhilde 593
Lapapa Josephine 3321
Larrea Marcelo 2241
Larrosa-Navarro María 2549, 3505, 3533, 3873
Larsen Bernt Mikal 277, 527
Larsson Holmgren David 6019
Lasserre Jean-Jacques 1879
Latorre Iglesias Eduardo 2549, 4207, 5407, 5831
Lattari Mateus 5463, 5521
Laudani Giuseppe 6311
Laudato Marco 4119
Laugesen Søren 3237
Laukka Johann 3769, 3805
Laurent Simon 3435
Laurijssen Dennis 2087
Lavagna Lorenzo 3827, 4933
Lavanant Romain 1851
Lavasani Majid 339
Lavia Lisa 5045
Lawson Andrew 6409
Lawson Taylor 5213
Laxmi Vijaya 5677
Lázaro Mario 2713
Lazarte Reátegui Henry Daniel 3745
Le Clézio Emmanuel 2981
Le Garrec Thomas 1711
Le Guen Lauredan 295

Le Louër Frederique 5573
Le Penru Neel 203
Le Van-Duong 2965
Le-Maoult Yannick 2965
Leal Filho Josafat 6297, 6319
Leal Gera 1341
Leão Cristina 1185
Leclère Quentin 4357
Lecoq Damien 2025
Leduc Damien 3009
Lee Dongheon 4337
Lee Haram 3499, 4681
Lee Heow Pueh 69
Lee Hyunkook 3627
Lee Jessica 4791
Lee Jongwha 1933, 5623
Lee Minsung 1933
Lee Pyoung Jik 5069
Lee Sang Kwon 53
Lee Sangil 1933, 5623
Lee Sangkyeong 2233, 5653
Lee Seung-Min 1375, 1501
Lee Songmi 4949
Lee Sungchan 3655
Legriffon Ingrid 1403
Leishman Timothy 4473
Lemke Mathias 5257
Lenzi Sara 5015, 5991
Lewenstein Maciej 3685
Lewis Heather 4781
Li Haiqin 2473
Li Joel 1417
Li Junjun 2481
Li Pengzhuo 6235
Li Sihui 4799
Li Yapeng 69
Li Ying 2663
Liang Chao 31
Licitra Gaetano .. 1161, 1197, 1341, 1363, 2289, 5755, 5761, 5785
Liepert Manfred 3589, 5839, 6545
Lietzén Jesse 449, 567
Lim Hee-Jun 4013
Lim Kian Meng 69
Limens-Pinaque Jesús 3029
Lin A Lin 5053
Lindborg Permagnus 4519, 4667, 5053
Lippold Moritz 1155
Lissek Hervé 85, 91, 1593, 3435
Liu Jingrui 1677
Liu Qianhui 6041
Liu Qin 3435
Liu Yu 6235, 6243
Liu Zhaorui 4673
Liuzzi Stefania 2031, 3793
Lladó Pedro 3405, 3413, 3457
Llorca-Bofí Josep 1155
Lloret Nuria 6497
Lluis Francesc 6605
Lo Castro Fabio 1201
Lobato Lucas 6297
Lobato Thiago 3471
Loisa Olli 6143
Lokki Tapio 2599, 4127, 6477
Lopetegi Aitor 567
Lopez Bella 3711
López Ibañez María Luisa 2549, 4207, 5407, 5831
López José Javier 2295, 6385, 6401
López-Ballester Jesús 6385, 6579
López-Jareño Aurora 5139, 5153
Lora Marco 1123
Lörcher Frieder 789
Lorenzana Antolin 323
Lorusso Lesa 4731
Lotinga Michael J. B. 1395, 2121, 3377
Lotton Pierrick 1581
Lowe Krispian 1079
Lu Austin 4087
Luan Xinmeng 2787, 5279
Lübeck Tim 889
Luberadzka Joanna 5197
Luchini Paolo 5945
Lüer Emma 4621
Luesutthiviboon Salil 1465
Lugten Martijn 1139, 4691
Luizard Paul 4405, 4465
Lüke Jonas P. 6113
Lundberg Thomas 6541
Lunde Per 6327
Lux Christian 641
Luzón-Álvarez Clara 4351
Lyberg-Åhlander Viveka 3707, 4009
Lyu Benshuai 5423
M. Arend Johannes 889
Ma Xiaochuan 6235, 6243
Ma Zhida 1697
Maaroufi Maroua 741
Machado Dario 5037
Machimbarrena Maria 733
Machner Rainer 3773
Macian Ana M. 3003
Maciel Karoline Farias Koloszuki 4661
Macwilliam Kathleen 4103
Madden Joe 1357
Maddox Ross 3243
Madrigal Javier 2995, 3003
Maeder Marcus 885, 2563
Maestro-Vallejo Rubén 2549, 4207
Maffei Luigi 3609, 3621, 4635, 5105
Mafféis Robin 5817
Maggi Elena 243
Magnini Lucia 3881
Maldonado-Ortega Sergio 3025
Malecki Pawel 4877
Malvermi Raffaele 4397
Maly Anna 4883
Mancinelli Matteo 1645
Manconi Elisabetta 2079
Maniam Arun 5415
Manni Lucia 6117
Manoha Eric 1711
Manohare Manish 5875

Mantsevich Sergey 3077
Mao Huina 5363
Marbona Himpu 1073
Marburg Steffen 2563, 5329
Marceau Sandrine 2677
Marcom Alain 295
Mardini Line 2355
Mardjono Jacky 2485, 5485
Marechal Pierre 3009
Marentakis Georgios 6033
Marescotti Cristina 1997, 2021, 2511
Mareze Paulo Henrique 2585
Marggraf-Turley Nils 3307, 6483
Marinelli Lieta 6195
Marino Oscar A. 1073, 2193, 5437
Mariotte Theo 5221
Mariotti Pierre 5363
Marisquirena Luis 1109
Markova Petra 5797, 5803
Marquis Favre Catherine 3583
Mars Jérôme 2285
Martellotta Francesco 2031, 3793
Martin Andres 4449
Martin Nadine 2285
Martin Sara 3855
Martin Vincent 6483
Martín-Castizo Manuel 3697
Martín-Nieva Helena 925
Martinelli Vito 4933
Martínez Casas José 5859
Martinez De Marcos Alvaro 417
Martínez García-Hoz Ángel María 5601
Martínez José Luis 2641
Martínez Orellanos Cristhiam Fidel 2767
Martínez Roberto Diego 4421
Martinez-Graullera Oscar 2943, 3053
Martinez-Iranzo Jose 1553, 1559
Martinez-Pia Carla 1553, 1559
Marxt Michaela 655
Marzi Arianna 3987
Marzo Asier 1609
Masci Donato 3881
Masciandaro Grazia 183
Mascolo Aurora 2271, 4847, 5701, 5725
Masmitja Ivan 1603
Masoumi Hamid 511, 519
Mastino Costantino Carlo 755, 761
Mastoori Mehrangiz 2577
Masullo Massimiliano 983, 3609, 3621, 4635, 5105
Mateos Raul 3059
Mateu-Romero Borja 5791
Mateus Diogo 3831, 4029
Matoba Yuki 2161
Matsumoto Mitsunori 6013
Maula Henna 3805
Mauri Noemi 2913
Mauro Manuela 6259
Maury Cedric 2619, 2655, 2683
Mavandi Matthew 3247
Maxit Laurent 2461
May Christina 249
Mayr Andreas 541
Mayrhofer Dominik 5343
Mazzoni Daniel 1879, 2619, 2655, 2683
Mcgregor Iain 4599
Meggitt Joshua 5851
Mehrem Ahmed 2631
Mehta Nishchay 3287
Meinke Matthias 1817
Meirelles Lucas 1793
Meiser Tomás 1465
Meiss Alberto 733
Meister Jonas 1429
Melis Aurora 4207, 5407, 5831
Melloni Arnaldo 1181
Mellot Bertrand 1729
Melo Ana Paula 4917
Melon Manuel 1581
Meloni Andrea 6195
Meloni Stefano 1653
Memoli Gianluca 2505, 4739, 5893
Mena Moreno Andrea 345
Meng Yang 2315
Menon Vyshakh Ajith 1011
Mercier Jean-François 1851
Merino-Martinez Roberto 1457, 1825, 5635, 5929, 5937
Merli Francesca 2577
Méry Fabien 1729
Messerer Theo 1007
Messerer Thomas 1007
Mestre-Tora Blanca 3109
Meyer Daniel Johannes 3589, 5839, 6545, 6549
Meyer Julie 6465, 6483
Meyer-Kahlen Nils 889
Meyer-Kahlen Nils 3405, 4127, 6477
Miao Han 91
Micheletti Cosimo 1209
Michon Romain 3855
Mietlicki Christophe 5811
Miguel-Ayala Pablo 1379
Mikama Osamu 2161
Milisenda Giacomo 6185
Miller Aaron 1011
Miller Iii Max 6369
Miller Jennifer 4731
Miotello Federico 6425
Miralles Ramón 2995
Mironovs Deniss 3949
Misaki Nitta 3493
Misdariis Nicolas 4925, 6019, 6051, 6067
Miserocchi Stefano 6181, 6191
Mishra Sitesh Kumar 2065, 2073
Mitchell Andrew 4699
Mitsuda Yasunori 6013
Mittal Manan 4087
Mittal Prateek 4699, 4767
Mitu Ana-Mari 1363
Miyabe Masahiro 1939
Mizumachi Mitsunori 5111
Mlynarczyk Dorota 2411, 4877, 5031
Mobley Frank 3189
Modica Mariasole 4933

Moebus Susanne 1119, 4807
Moghimi Mohammad 2263
Mohammadi-Firouz Reza 479
Mohammadpour Mahdi 1961
Mohapatra Abhishek Ray 207
Moingeon Hélène 4405, 4465
Molchanov Vladimir Ya. 3073, 3075, 3081
Molesworth Brett R.c. 1417
Molina-Tanco Luis 2921, 6457, 6565
Møller Martin Bo 4111
Monaco Mirko 2079
Mongillo Paolo 6195
Monk Peter 5555
Monner Hans Peter 5301, 5317
Monson Brian 3727
Montaldo Gabriel 3059
Montano Rodríguez Walter A. 901, 909, 3745
Monteleone William 819
Montenegro Alexandra 1341
Montes-Gonzáez David 5747
Montesi Marco 1209
Monticelli Alessandro 5761
Montoya Aarón 2815
Montoya Belmonte José 2143
Moñux-Bernal Alejandro 2207
Moon Hoseong 3499
Moonen Marc 4111
Moons Stijn 471, 593
Moore Brian 1537
Mora Simone 5991
Mora-Saura Elicio M. 155
Morales-Cespedes Máximo 4365
Morandi Federica 649
Morell Maxime 99
Moreno González Celia 2635
Moreno Paula 2943
Moreno Ricardo 1515
Moreno Timoteo 2827
Moresco Luiza Ternes 5521
Moretti Pier Francesco 183, 875, 6095, 6205
Morgans Aimee 1871
Mori Francesco 1949, 1997
Morin Amy 1465
Morizet David 5975
Morizet Joséphine 3093
Morlando Fabrizio 5953
Moro Antonino 5785
Moroşanu Bogdan 4237
Morris-Kirby Rod 5647
Moshona Cleopatra 5709
Mossi José Manuel 2295
Moszyński Marek 5359
Moulin Emmanuel 2989, 3017
Moussa Rita 6361
Mrabti Rhofrane 2981
Mucchi Emiliano 2061
Mueller Franz-Ullrich 3215
Mühlberger Andreas 6451
Mulas Martina 243
Mullally Darragh 841
Müller Leon 5669
Müllner Herbert 641, 3525
Mundt André 4855
Muñoz Mario 2179, 2185, 2241, 2973
Muñoz Paniagua Jorge 5831
Muñoz Sergio 5547
Muñoz-Milan Ana Belén 5791
Muñoz-Paniagua Jorge 5407
Murgia Silvia 3981
Murovec Jure 215, 1019
Murphy Enda 1007
Murray-Rust Dave 6051
Murtaza Ghulam 367
Mutel Lucien 2671, 2677
Myers Arnold 2721
Mypati Vamsi N.k. 5779
Nadagouda R V 5741
Naegelen Isabelle 1315
Naets Frank 933
Naim Faridah 999
Naranjo Valery 4095
Narimatsu Shimpei 1939
Nastro Alessandro 1613
Nataletti Pietro 1997
Naumann Juliette 5581
Naumenko Natalya 3073
Nava Baro Enrique 6169
Navacerrada Maria De Los Angeles 705, 747
Navarro Ruiz Juan Miguel 983, 2143
Navarro-Calvo Javier Ángel 3039
Navarro-Payá David 207
Nayak Sanjay 1619
Naylor Patrick A. 3449
Nazarpour Damoon 6205
Neagoe Cătălin Andrei 1363
Neidhardt Annika 3413, 3457
Neill Conor 2323
Nelson Philip 4243, 4343, 4389
Németh Zsófia 2045
Nerse Can 207
Netto Gustavo 2585
Neusser Maximilian 721
Neves E Sousa Albano 479
Neves Silvana 6101
Nhampossa Augusto Ju´nior 875
Nhancale Clotilde 875
Nicolay Pascal 2727
Nicora Chiara 2913
Niedzielczyk Michal 2439
Nieradka Paweł 5337
Nieves Francisco José 2051
Nigro Mariangela 5725
Nilsson Erik 631
Nir Fink 1223, 2775, 3141, 3157, 3163, 3349
Nistri Fabio 2407
Nolan Mélanie 2529, 2563
Nolet Stijn 5907
Nolte Alexander 4229
Nora Alessia 311, 3939
Nordblom Naomi 2877
Nosil Mešić Mateja 3689
Notley Hilary 1307

Nou-Plana Ignasi 6155, 6263
Nowicka Elzbieta 2627
Nudelman Charles J. 3711, 3965
Nuijens Helmer 6417
Nuñez Gutierrez Santiago 6147
Nusser Bernd 641
Ó Néill Eoghan 2843
O'Keefe John O'Keefe 4057
Oberman Tin 4615, 4699, 4767
Oberst Sebastian 207
Obydennov Dmitry 3081
Ochs Fabian 819
Odeh Omar 943, 1259
Ogawa Yosuke 2161
Ogun Oluwaseyi 2213
Oh Jeong-Lyul 2233, 5653
Öhler Sven 533
Öhlund-Wistbacka Greta 3707, 4009
Oiza-Zapata Irati 5179
Okei Samuel O. 5213
Oliva Alfonso 45
Oliveira Luciana 4863
Olivieri Marco 45, 5293
Ollivier François 4405, 4465
Ollivon Christian 4405, 4465
Ong Zhen-Ting 4839
Onorato Tina 1161, 5883
Ooi Kenneth 4839
Orita Mihai 4243
Orozco Tatiana 4731
Ortigoso-Narro Jorge 1515, 4365, 4381
Ortiz Miguel 2843
Osses Alejandro 6417
Ostan Paolo 6425
Østergaard Jan 4111
Österreicher Michael 5845
Östersjö Stefan 4755
Oumekloul Zakariae 3017
Outinen Okko 6143
Oyebamiji Itunu 3321
Özcan Elif . 3913, 5015, 5061, 5075, 5991, 5999, 6041, 6051
Ozcevik Bilen Asli 4649
Ozturk Zeynep Sena 4657
P V Belgaonkar 5741
P. B. Reynders Edwin 455, 471, 593, 2361
Pachale Urs 5681
Pachebat Marc 4405, 4465
Padilla-Montero Iván 1637
Paduano Angelo 1755, 1793, 5423
Paganini Lavínia 5529
Pagano Antonio 5953
Pagliaroli Tiziano 1387
Pagneux Vincent 2389
Paladini De Mendoza Francesco 6181
Palazzuoli Diego 1197
Palenda Pascal 889, 895
Palhares Teixeira Camila 257
Palleja Cabre Sergi 1801
Palma Giorgio 1653
Palomeque Váquez Sergio 1369
Palomino Franco Vera Lucia 3745
Pàmies-Vilà Montserrat 859
Panadero Soler Daniel 3029
Panagiotopoulos Dionysios 933, 4161, 5351
Panci Andrea 1197
Paredes Ruth 1123
Parisot-Dupuis Hélène 1729
Park Dongchul 2201, 4681
Park Junseo 2233, 5653
Park Kyunghwan 5661
Park Sang Hee 3583
Park Sangwon 1933, 5623
Parkinson Thomas 4761
Parnell Jeffrey 1011
Parrilla Montserrat 2943
Paruchuri Chaitanya 1801
Parzinger Michael 463
Pascal Jean-Daniel 4171
Pascale Aniello 5105
Pascale Antonio 5701
Paskiewicz Artur 889
Pastor Marie-Laetitia 2965
Pastor Sar José Daniel 6213
Pastor-Naranjo Francisco 4095
Paternain Daniel 2113
Patricio Jorge 503
Pauget Ballesteros Hugo 2783
Paul Stephan 6297, 6319
Paul Vlad 4343, 4389
Pauletto Sandra 5983, 6019, 6067
Pavan Michele 2423
Pavanello Irene 3973, 3993
Pavarin Cora 3973, 3993
Pavlov Aleksandr 3103
Pavón Ignacio 1625
Pawelczyk Marek 15, 2001
Pawlik Jan 1543
Payá Jordi 2995, 3003
Payne Jim 2557
Payne Sarah R. 3613
Payo Damián 3847
Pearce Ben 2505
Pearse John 4791
Pecchioni Gessica 1181
Pedrero Antonio 3505, 3533, 3873
Peeters Bert 1321
Pégeot Martin 2885
Pei Xingyuan 6243
Pelaez Quiñones Julián David 6327
Pelat Adrien 2485, 2489, 2493
Pellegatti Matteo 4001, 4905, 6441
Pellegrino Carmelo 6177
Pellerey Franco 3355
Peña Andrés L. 1301
Pena Manuel 5555
Pene Yves 4267
Peng Zhenjun 1697
Peral-Orts Ramon 155, 915, 5791
Perchaud Julie 2025, 6107
Pereira Andreia ... 1915, 2401, 3831, 4029, 4863, 5395
Pereira Antonio 1891

Pereira Frederico 5037
Pérez Arjona Isabel 5359, 6259
Pérez Compte Eloi 2407
Pérez Elisa 2905
Pérez Gimeno Neus 6169
Perez Guerrero Ricardo 3711
Pérez Nicolás 5559
Pérez Raposo Alvaro 683
Pérez Vargas Rocío 3315, 5125, 5147
Pérez-Liva Mailyn 3035, 3067
Peris Eulàlia 4685
Perli Filippo 1581
Perrin Marianne 2965
Peruzzi Eleonora 183
Peruzzi Laura 1217
Petiot Jean-François 2833
Petrongolo Federica 5755, 5761
Petrosino Francesco 1481, 5953
Pettoni Possenti Vincenzo 611
Pezzoli Mirco 4079, 4397, 6425
Phuleria Harish 5677
Pi-Martín Irene 3039
Piana Edoardo Alessio 727, 1991, 2605, 2871
Piątek Klaudia 5031
Piccinini Davide 183
Piccolo Andrea 1737, 1859
Picillo Marco 1447
Picinali Lorenzo 197, 203, 3263, 3307, 3421, 3465, 3557, 6457, 6465, 6483, 6487, 6557
Picker Kevin 267, 271
Picó Rubén 2317, 2705, 5381, 5389, 6221
Piechowicz Janusz 4877
Piégay Clément 2671, 2677
Pieren Reto 1429, 5627, 5681
Pietrzak Agnieszka Paula 2747
Piga Manuela 755
Pillot Yves 2347
Pind Finnur 5471
Pineda-Pardo José A. 3043
Piñero Gema 4095, 5505
Pinhède Cédric 4405, 4465
Pini Lucia 243
Pinillos Boralla Carlos 2943
Pinson Samuel 6269, 6275
Pintore Claudia 4933
Piot Adrien 1619
Pirard Ludovic 6483, 6487
Pita Lozano Antonio 2143
Pitkänen Sara 3805
Pittana Ilaria 3973, 3993
Pizzio Gastón 207
Placek Jan 1507
Placinta Claudiu 5547
Plasek Josef 2309
Pley Yann 1879
Plumbley Mark 4983
Plüss Stefan 5615
Pluymers Bert 933
Podwinska Zuzanna 1409
Poggi Caterina 1421, 1683, 5441
Poirier-Quinot David 6447
Polacsek Cyril 5485
Polikarpova Nataliya 3077
Polizzi Marta 183, 875
Poljansek Tadej 577
Pollack Katharina 3405
Polonenko Melissa 3243
Polvorinos-Fernandez Carlos 1625
Pomaro Angela 6095, 6205
Pompei Geremia 2289
Pompoli Francesco 1997, 2021, 2511
Pontalti João Vitor 2585
Pontoppidan Niels 3307
Poole Katarina 3465, 6483, 6487
Popa Bogdan 75
Popa Victor 4237
Postma Barteld 3839
Potenza Andrea 1063, 2171
Potocar Juraj 741
Pott-Pollenske Michaël 5923
Poveda Martinez Pedro 1553, 1559, 2949, 2955, 6083, 6135, 6213, 6259
Pozzi Matteo 2305
Praticò Filippo Giammaria 1161, 1169, 5779
Prawira Vanessa 4747
Prax Christian 4171
Preis Anna 4823
Preto Jorge 1185
Prezelj Jurij 215, 803, 1019, 2221, 2225, 3575
Priboi Sergiu Andrei 5937
Prieto Andrés 5553
Prinn Albert 2549, 2569, 4185, 5513
Prislan Rok 4153, 6433
Prodi Nicola 3741, 3749, 4001, 4905, 6441
Profumo Domenico 1363, 5755, 5761
Puglisi Giuseppina 3355
Puljizevic Maro 577
Puttock-Brown Mark 2505
Puyana Romero Virginia 1329, 3315
Qiu Lisha 6477
Quaranta Erika 1835
Quaranta Giulio 3637
Quaranta Luca 1147
Quaroni Luca Nicola 1457, 1825
Quesada Vázquez Leticia 5091
Quetel Lionel 6303
Quiroga Jabid 2995
Quiroz Rangel Carlos Alberto 6227
Raahede Lundgård Sissel 4773
Rachman Laura 5085
Rachman Zulfi 141
Rachman Zulfi Aulia 163
Radicchi Antonella 1063
Radun Jenni 3801, 3805, 4005
Rafaely Boaz 4307, 4315, 4321
Raffaello Possidente 755, 761
Ragni Daniele 1737
Rahmani Mohammad Mh 3541, 3549
Raiola Marco 1515, 1809
Ramachandra Rao Rakesh Rao 4489
Ramírez-Solana David 2317, 5381
Ramis-Soriano Jaime ... 1553, 1559, 6083, 6135, 6213,

6259
Ramón Martínez María 5601
Ramos Denilson 2335, 3831
Ramos Esperidião Aline 4591
Ramos-Romero Carlos 1379, 1395, 1409
Ramseier Thomas 5615
Rangaswamy Chandrashekar Shreyas 235
Rantanen Elisa 3605, 3797, 3801
Rantanen Sanna 4005
Rapino Aura 875
Rapún María-Luisa 5547
Rasmussen Birgit 665
Ravagnan Chiara 1173
Rebollo-Arjona Martí 3819
Redel-Macías María Dolores 291
Redondo Javier ... 2317, 2705, 5381, 5389, 5395, 5539
Redondo Martinez Patricia 5685
Reedijk Marije 4525, 5901
Regairaz Jean-Philippe 5817
Reicher Christa 1155
Reichl Christoph 797
Reigstad Kristian H. 4201
Rekswinkel Mats 3275
Relandini Cinzia 1217
Relandini Simone 1217
Repek Maj 4153
Resende De Souza Ébano 2751
Reserbat-Plantey Antoine 3685
Resino Viñas Alejandro 4283
Retortillo Javier 323, 4415
Rey Gozalo Guillermo 1369, 2635, 5747
Reyes-Lecuona Arcadio 6409, 6457, 6565
Ribera Marco 2401
Ricci Mattia 367
Riccobene Giorgio 6131, 6177, 6227, 6251, 6303, 6311
Richert Robin 3125
Rico Patricia 3029
Riedel Jörg 1965
Riente Fabrizio 3355
Riesco García Jose Ignacio 345, 1123
Rieß Sebastian 5415
Rijs Kelly 4525
Rindom Jensen Jesper 125
Ripamonti Francesco 31, 2013, 5293
Rittenbacher Dagmar 4731
Rittenschober Thomas 4035
Rius Clara 3889
Riva Micol 6059
Rizioli Ilaria 2061
Roa Marylin 4721, 4725
Roberts Helen 3865
Robles Arnao Encarna 6125
Roca Paz Luis Enrique 885
Rocca Sofia 191
Röck Thomas 1529
Roden Reinhild 3303
Rodrigues Vanessa 6029
Rodríguez Daniel 1637
Rodríguez Garcia Paúl 1907
Rodríguez Orlando Camargo 6283
Rodríguez Pere V. 519, 2383
Rodríguez-García Juan José 3029, 3043, 3049
Rodriguez-Manzo Fausto 4563, 4869
Rodríguez-Montaño Víctor M. 3315, 3847, 3897, 5125
Rodriguez-Pardo Jorge 3035, 3067
Rodríguez-Sendra Josep 2709, 3029
Rodriguez-Sune Laura 3109
Roel Lesur Marte 3541, 3549
Rogala Isabella 3711
Roger Sandra 2295, 6385
Rogland Latimer 6511
Rollo Milan 1465
Romagné Marc 295
Romagnoni Piercarlo 3973, 3993
Romagny Sébastien 5975
Romero Juan José 5139, 5153
Romero-Fernández Amelia 283, 315, 397, 423
Romero-García Vicent 2315, 2709, 2713
Ronneberger Dirk 1787
Röösli Martin 1041, 1115, 3597, 4533, 4685
Ropars Pierre 495
Rosa González Fernando Luis 6113
Rosales Julia 291
Rosales Manuel 291
Rosario Pedro 2641
Rosas-Pérez Carmen 3613, 3925
Rose Dawn 6377
Rossi Domenico 2271, 4847, 5701, 5725
Rossi Francesca 243
Rossignol Karl-Stephane 1387
Roßkopf Sarah 6451
Rossoni Marco 2013
Roth Sebastian 3153, 3215
Rottondi Cristina 2913
Rousou Konstantinos 4161
Roy Chowdhury Rahul 6557
Ruaud Elise 1403
Rubial Pablo 5553
Rubino Chiara 2031, 3793
Rubio Adrián 2179, 2185, 2241, 2973
Rubio Gonzalo 1073, 2193, 5437
Rubio-Garcia Sergi 2207
Rueger Theresa 227
Ruf Johannes 655
Rufer Libor 1613
Ruggeri Paolo 3973
Ruggieri Paola 3881
Ruggiero Gennaro 3621
Ruipérez Canales Irene 4755
Ruiz Arana Usue 5007
Ruiz Eduardo 6125
Ruiz Padillo Diego.p 6147
Ruiz Victor J. 2995, 3003
Ruminski Daniel 3089
Rummler Nils 4051
Rumpler Romain 1349, 5363, 5733
Russo Riccardo 2851
Ruzyla Christophe 3153
Rychtáriková Monika 339, 699, 741, 2309, 3525
Rydell Roland 3707, 4009
Ryehan Shahariar 5581
Ryu Jongkwan 4827, 4949, 4953, 4967

Saba Fabio 1523
Saba Juliana N. 5213
Sabbadin Giacomo 6117
Sacchetto Matteo 2913
Sadok Nadia 3227
Sagesser Marcel Zaes 4673, 4799
Sahai Abhishek 5901
Sahlsten Johannes 6143
Sahu Shreeniwas 5741
Said Ahmed Maamoun Khaled 15
Sáinz De La Maza Miquel 4685
Sakakibara Ken-Ichi 5111
Salazar Juan Pablo Lima Costa 5463, 5521
Saleem Nasir 5205, 5247
Salomons Erik 3133
Salorio-Corbetto Marina 1537
Samarasinghe Prasanga 4299, 4373
Sammeth Carol A. 3247
Sampedro Llopis Hermes 5471
San Martín Ricardo 2113
San Millán-Castillo Roberto 283, 359, 961
San Segundo Eugenia 5139, 5153
San-Segundo Rubén 5179
Sánchez Orgaz Eva María 5859
Sánchez-Burgos Marco Antonio 2051
Sánchez-Morcillo Víctor J. 2705, 5389
Sanders Laurent 5923
Sanfilippo Simone 6131, 6251, 6311
Sangiorgio Valentino 2317
Sangiuliano Luca 2375, 2393
Sant'Ana Luis Henrique 3637
Santika Beta Bayu 3499, 4681
Santoni Andrea 1949, 1997, 2021, 2511
Sanz Arauz David 747
Sanz Soriano Javier 331, 4043
Sarampalis Tassos 3345
Sarkar Kanad 4087
Sarria David 1603
Sarti Augusto 2787, 4397
Sastre Jorge 6497
Savan Jamie 3865
Sayin Umut 5197
Scarani Stefano 6497
Scarano Francesco 1755, 1793, 5423
Scarano Rocco 2001
Scatena Manuele 183
Scavone Gary 5279
Scavuzzo Giuseppina 6075
Schaal Jochen 1293, 5477
Schady Arthur 2099
Schäffer Beat 1041, 1059, 1115, 3597, 5615
Schanda Ulrich 463, 541, 627
Schatzmayr Welp Sa Thomas 2677
Scheck Jochen 547, 561
Scherpenhuyzen Bianca 3953
Schlecht Sebastian J. 889
Schlesinger Anton 3589, 5839, 6545, 6549
Schlittenlacher Josef 1537
Schlüter Benjamin 3589, 5839, 6545, 6549
Schmid Johannes D. 885
Schmidt Von Wolkahof Carl 3345
Schneider Martin 655
Schneider Viola I. 3425, 3431
Schoder Stefan 1867, 5325
Schoenwald Stefan 601, 619
Schöpfer Fabian 541, 627
Schopper Sebatian 5363
Schreckenberg Dirk 1059
Schrijver Annemarie J. 3219
Schröder Wolfgang 1817
Schubert Yannick 5257
Schuck Moritz 4621, 4855, 5709
Schultz Frank 889
Schulz Anita 1787
Schumann Maximilian Ulrich 3839
Schuppler Barbara 5101, 5167
Schutte Michael 6533
Schüttler Ulrike 561
Schweighardt Attila 2045
Schwertfirm Florian 5449
Sciacca Virginia 6177, 6181, 6191, 6195
Scimemi Pietro 3973, 3993
Scoczynski Ribeiro Rodrigo 3819
Scrosati Chiara 311, 2031
Scrucca Flavio 367
Sdringola Paolo 367
Secchi Simone 3881, 3905, 3933
Sedley William 3295
Seeber Bernhard 6473, 6527
Segers Laurent 4427
Segovia César 2671, 2677
Segovia-Eulogio Enrique Gonzalo ... 1553, 1559, 6213
Segura-García Jaume 6579
Sehr Armin 3425, 3431
Seiffert Gary 3731
Selgas Virginia 5555
Sentop Dumen Ayca 867
Seo Jaeyong 2233, 5653, 5661
Sequera Soto Martín 1329
Serebrenik Alexander 4229
Sergeev Stanislav 85, 91
Sergeeva Anna 3255
Serizel Romain 4291
Serre Gilles 1851
Sethi Sarab S. 197, 203
Sevenois Ruben 5431
Sgard Franck 3125, 3153
Sgroi Tiziana 6191
Shaaban Ahmed Mostafa 5329
Shabalina Elena 2631
Shafieyoon Yazdan 5851
Shaked Tom 1223
Shakya Piyush 2065, 2073
Shaporin Ruslan 2943
Sharifa Ahmad 4435
Sheehan Annalisa 5693
Sheffield Benjamin 3145
Sheikh Aziz 5247
Sheng Ping 2315
Shiell Martha 3307
Shilton Simon 1285, 1321
Shoji Tetsuro 2757

Shtrepi Louena 775, 845, 2407, 2593, 3355, 3827, 4933
Sibilio Sergio 4635
Siciliano Emanuele 3779
Siebein Gary W. 4713, 4721, 4725, 4731, 4781
Siebein Jr Gary 4721, 4725
Siebein Keely 4713, 4721, 4725, 4731, 4781
Sieben Naomi 5907, 5915
Sigcha Luis 1625
Siguas García María Fernanda 3745
Sili Ivan 207
Silva Antunes Sonia 4583
Silva Fabrice 4405, 4465
Silva Filipe Dutra 5463, 5521
Simeone Francesco 6177
Simões Da Silva Luís 443
Simona Alberti 207
Sineau Matthieu 5811, 5817
Singer Andrew 4087
Singh Arshdeep 4983
Singh Daljeet 2271
Sireteanu Tudor 1363
Širović Ana 6199
Sivula Arttu 3805
Skålevik Magne 4201
Skene Hannah 3925
Slabbekoorn Hans 249
Smagin Nikolay 3017
Smith Andrew 3757, 3761
Smith Malcolm 1835
Snellen Mirjam 1465, 5607, 5961
Soares Filipe 2733, 2739
Socoró Joan Claudi 2207
Sodum Kushal 6511
Sohn Byunggil 1933, 5623
Soma Ifat Zahan 5581
Sonderegger Martin 2515
Song Eunsung 3583
Song Guk-Gon 555, 689
Song Jaewon 11
Song Zhengxuan 1677
Song Ziwei 5069
Sontacchi Alois 37, 105
Soriano Pastor Carlos 975, 1267
Sorokin Sergey 2485
Sorrentino Gerardo 6185
Soto Molina Ignacio 969, 975, 1267, 1333
Sottek Roland 3325
Sousa Emanuel 5037
Sousa Laura 5373
Spagnol Simone 5015, 5075
Spalvier Agustin 5559
Speranza Alice 649
Spezie Roberto 1991
Srinivasan Karunya 3517
Srivastava Dr Shashank 5741
Stange-Koelling Sylvia 267
Stapelfeldt Hartmut 1315, 1321, 1357
Stärz Felix 6451
Steckel Jan 2087, 4435
Steffens Jochen 4813, 4975
Steijvers Kristof 2415
Steiner Jonas 61
Steiner Thomas 1131
Stenfeldt Liselott 4773
Stenitzer Alexander 641
Stevens Francis 1251
Stewart Mary E. 3613
Stigliano Enza 3779
Stöckl Luisa 797
Stoica Luana Georgiana 1439, 1473, 1719
Stöver Timo 3231
Stowell Dan 2153
Strazdas Edgaras 175
Strebel Romane 3583
Strigari Fabio 5709
Stronks H. Christiaan 3219
Sturm Ulrike 1131
Sü Gül Zühre 3811, 5275
Suárez David 2383
Suárez Silva Enrique 4547, 4563
Subhra Bhattacharjee Sankha 125
Subramanian Sriram 4767
Subramanyam Ramesh Raja 1923
Sumner Shannon 6511
Surdu Tatiana 3413, 4489
Suwanto Aldina 5975
Svenšek Daniel 4153
Svensson Peter 3855
Svensson U. Peter 2563, 4201
Swart Wim 5901
Sweep Rik 6417
Syed Shomaila 4897
Sygulska Anna 761, 3677
Szelag Agata 2411
Szeremeta Bani 4661
Szwarcberg Nathan 2863
T. Rocha Rodrigo 1619
Taghipour Armin 1131, 2515, 3567, 6377
Tahon Marie 2807
Tajadura-Jimenez Ana 3517, 3541, 3549
Takahashi Yu 2757
Talbot James 511
Talebzadeh Arezoo 2107, 4971, 5001
Talucci Simone 5293
Talus Lauri 449, 567
Tampone Giulia 6441
Tanaka Daisuke 2161
Tani Almona 1173
Tapken Ulf 1843, 1899
Tardón Lorenzo J. 2891, 2897, 2905
Tarsitano Anna 1147
Tavelidou Eleni 6589
Taylor Jack 6369
Taylour Jim 3761
Te Velde Kees 249
Teaca Adrian 6155
Tebaldi Luca 6441
Tejera Berengué Diana 3181, 4283, 5229
Terán Sierra Fernando José 5601
Terzakis Michail Evangelos 485, 999
Teymoori Hassan 4229
Theodossiades Stephanos 1961

Thieme Jasmin 2921
Thiergart Oliver 4259
Thisse Johan 1891
Thomas Peter James 6327
Thomas Pieter 1233, 4629
Thompson David 5831
Tiengo Massimiliano 2523
Tiffeneau Enzo 4357
Tinivella Umberta 6091
Tinney Charles 1745, 1771
Tobias Silvia 1041, 1115, 3597
Tochon-Danguy Samuel 295
Tokala Vikas 3449
Tollin Daniel J. 3247
Toma Roxana Adina 4635
Tonelli Marceau 4171
Tonetti Diego 727, 1991, 2871
Torija Martinez Antonio .. 781, 811, 1379, 1395, 1409, 2121
Torjussen Matt 3377
Torrents Pairo Ramon 3889
Torres-Aranda Ana M. 4351
Torres-Durall Jordi 3083, 3109
Torresin Simone .. 4001, 4555, 4615, 4761, 4897, 4905
Torricelli D. 5163, 5175
Toscani Andrea 2079
Tóthmérész Béla 1275
Touhafi Abdellah 4427
Tourbabin Vladimir 4321
Tournat Vincent 2315
Toward Martin 1321
Traginer Carlos 2897
Tranzi Antonio 1209
Trematerra Amelia 2647
Treybig Lukas 4489
Tricomi Alessia 6303, 6311
Trocchianesi Raffaella 6059
Trow James 1307, 1321, 1357
Truett David 2557
Trujillo José 283, 315, 3645
Tsaih Lucky 4747
Tsigklifis Kostas 6341
Tucci Maria Rosaria 207
Tudoce Juliette 3685
Tudorache Christian 249
Tughrul Arslan 5205, 5247
Tunuguntla Asritha 3711
Turcios Stephanie 3145
Ture Savadkoohi Alireza 99
Udías José M. 3035, 3067
Uhlemann Thomas 1965
Ullah Naeem 6083, 6135
Umashankar Abishek 3295
Umnova Olga 2447
Uncik Stanislav 741
Undurraga Lucero Jaime Andres 3237, 3275
Urban Camille 2807
Urbán Daniel 713, 721
Urtiaga Chasco Ion 6163
Usov Dima 1683
Utrilla-Manso Manuel 3181, 5229
Utsumi Haruto 1939
Vacalebri Francisco 2295
Vaičiūnas Juozas 755
Valdez John 1745, 1771
Valentin Luna 2929, 3855, 6519
Valério Paulo 1185
Valero-García Francisco 6497
Valgi Macheve Zaira 875
Valier-Brasier Tony 2701
Vallati Andrea 1147
Valle Pérez Carlos 6083
Vallely Sven 601, 619
Van Belle Lucas ... 933, 2347, 2361, 2369, 2415, 2431, 5399
Van Cranenburgh Sander 2279
Van Damme Bart 2035, 2355, 2401
Van De Par Steven 6451, 6473, 6571
Van De Velde Bart 455
Van Den Bosch Kirsten 3345, 5001
Van Der Eerden Frits 3133
Van Der Grift Rebekka 5607
Van Der Kassteele Jan 5901
Van Der Mei Rob 2165
Van Dort Pascal 1969
Van Egmond René 5999
Van Heijningen Ad 3133
Van Hoorickx Cédric 485, 999, 4171
Van Kempen Elise 4525
Van Keulen Wim 1037
Van Ophem Sjoerd 5309, 5333, 6605
Van Poll Ric 5901
Van Pruissen Elisabeth 3133
Van Renterghem Timothy 235, 257, 1045, 1233, 1429, 4629
Van Timmeren Arjan 1139
Van Walstijn Maarten 2843
Van Waterschoot Toon 4065, 4103, 4111, 4275
Van Wezel Cees 3921
Vande Velde Jerome 4427
Vanhamel Jurgen 3097, 3103
Vaquerizo-Serrano Jesús 2207
Varela Macarena 4443
Varo Varo Carmen 3315
Vasileva Nicheva Nadia 747
Vásquez Betsabé 949
Vassallo Rodrigo 1139, 4691
Vastiau Jasper 455
Vatteroni Davide 1197
Vazzana Mirella 6259
Veermans Marjaana 4005
Vegas-Luque Víctor 3043, 3049
Velasco-Sanchez Emilio 915
Veloso Matheus 5337
Vencovský Václav 3309
Vera-Donoso Cesar D. 3025
Verbicaro Marco 2305
Verburg Samuel A. 4127, 4135, 4267
Verdiani Giorgio 3881
Vergez Christophe 2733, 2863, 2885
Verhey Jesko 3333, 3361, 3365, 3373
Verhulst Sarah 5189

Veronesi Francesco 1585
Verreycken Erik 2087
Versaevel Marc 2485
Veršić Zoran 375, 3689
Versümer Siegbert 4813, 4975
Verza Alessandra 1669
Vesal Rahim 91, 1593
Vetterick Matthew 4731
Viala Romain 2797, 2801
Vicente Gabriel Caldeira 5463
Vickers Deborah 1537, 3263, 3287
Vida Manzano Jerónimo 4547, 4563, 4583, 4991
Vidaña-Vila Ester 1063, 2171, 2207, 4591
Vidaurre Carmen 2113
Vienneau Danielle 1041, 1115, 3597, 4533, 4685
Vílchez-Gómez Rosendo 5747
Villacorta Juan Jose 323, 4415, 4421, 4449
Villejoubert Louis 3263
Viloria-Yzquier Camila Valentina 961
Vincent Dominique 2007
Vincent Hugo 1915
Vinceslas Leny 3267, 3365
Viola Salvatore ... 6131, 6177, 6227, 6251, 6303, 6311
Visentin Chiara 3741, 4001, 4897, 4905, 6441
Visingardi Antonio 5953
Viveros-Munoz Rhoddy A. 2253, 2259, 3443
Vizzini Aiti 6259
Voltolini Emanuele 2079
Vorländer Michael 895, 2541, 3513, 4139
Vovk Tara 6433
Vugts Jeroen 3953
Wada Yohei 2757
Waddington David 257, 811
Walker Kerry A. 3247
Walther Robin 5825
Wang Chongan 2327
Wang Huiqing 4215, 4229, 5529
Wang Jiarui 6393
Wang Tingting 6041
Wang Tirui 1593
Wang Xiaomei 6235, 6243
Wang Xin 5139
Wang Yifei 1871
Wargocki Pawel Wargocki 4905
Watson John 2557
Watts Greg 4609
Watts Greg 4791
Webb Craig 2851
Webb Jack 3557, 6483
Weger Marian 3201
Weichert Frank 4807
Weigand Stefan 5477
Weinzierl Stefan 889, 6597
Weissgerber Tobias 3231
Wen Chuan 5189
Wennemann Tim-Niklas 6597
Wepner Saskia 5101
Werner Stephan 4489
Wersényi György 2045, 3385
Wesarg Thomas 3211
West Benjamin 3865
Weymar Philip 6473
Whitehead Helen 2149
Wiciak Jerzy 4877
Wie Seong-Yong 1435
Wijnant Ysbrand 359
Wilczacki Tobias 5343
Wilczek Magdalena 1321
Willemsen Silvin 4229, 5529
Williams Owen 4539, 4941
Williams Paul 1239, 6341
Williges Ben 1537, 3227
Willmann Roland 2727
Wiltshaw Richard 2713
Wingfield Carly J. 3965
Wirth Wulf-Dieter 4443
Wittebol Wouter 4215
Wittstock Volker 267, 271, 1953, 2533
Wöllstein Dominik 5681
Wong Raymond 1321
Woo Jongmun 1933
Wood Mike 257, 2149
Woodland Lisa 4941
Wouters Marjoleen 5189
Wright Matthew 3855
Wrona Stanislaw 15, 2001
Wu Xuesong 5261
Wuite Gustaf 1139, 4691
Wunderli Jean Marc 1041, 1115, 2035, 3597
Wurzinger Andreas 5325
Wuthrich Hannes 3435
Xiang Ning 2501, 5275, 6369
Xiang Qiuya 4673
Xiao Jieling 4519, 4699
Xiao Tong 117
Xie Dingding 4179
Xu Zeyu 4185, 5513
Yamada Hironori 6345
Yamada Reiko 3685
Yamamoto Mai 6013
Yamauchi Katsuya 5717
Yamazaki Toru 6345
Yami Thor 2775, 3349
Yang Hongli 6041
Yang Jaesik 5971
Yang Wonyoung 693
Yang Xufeng 1677
Yang Zhe 1817
Yarman C. Evren 4145
Yasin Ifat 3267, 3365
Yasui Nozomiko 2763
Yen Yu-Tien 4747
Yeom Insu 431
Yeon Inmo 4073
Yi Jayeon 6511
Yin Jianping 1387
Yllan Lucia 227
Yokota Kazuya 5279
Yoo Seong-Sik 2233, 5653
Yorukoglu Papatya Nur Dokmeci 4577
Yoshimura Kazuma 5717
Yossi Bar-Yosef 2775

Yossi Bar-Yosef 3349
Younis Hazem A.f. 5213
Yu Ting-Yu 4747
Yuan Zhongju 2137
Yue Ran 4667, 5053
Yuksel Dicle Seda 4761, 4909
Yumoto Seiji 2161
Yun Changyeon 4967
Yushkov Konstantin B. 3073, 3075, 3081
Zaffaroni-Caorsi Valentina 191, 6117
Zafra Rodríguez Pamela 3315
Zajacík Michal 1465
Zambila Liviu 2035, 2407
Zambon Giovanni ... 191, 991, 2171, 6117, 6155, 6263
Zampini Massimiliano 4933
Zamponi Riccardo 1725, 1737, 1859
Zannin Paulo Henrique Trombetta 4661
Zanoni Massimiliano 2913
Zarri Alessandro 1705, 1725
Zavari Mohsen 755, 761
Zea Elias 2563, 4119, 4145
Zeitler Berndt 547, 561, 655
Železnik Anže 1019
Zeng Rui 713
Zentschnig Renate 4755
Zerbinatti Marco 2593
Zese Francesco 4397
Zhang Jiahua 2369, 2401
Zhang Xin 1697
Zhang Zhicheng 1697
Zhang Zhongyu 5261
Zhao-Dubuc Yingjun 1745, 1771
Zhou Ke 4761
Zhou Peng 1697
Zhu-Zhou Fangfang 3181, 4283, 5229
Zhuang Yongjie 4087
Ziapkoff Mathias 295, 2611
Zielinski Tomasz G. 2439, 2691
Zimmer Karin 3583
Zimpfer Veronique 3197
Zirn Stefan 3215
Zollitsch Dieter 1293
Zotter Franz 1529, 1565
Zuccherini Martello Nicolò 1949
Zumelzu Antonio 1341
Zupanič Miha 5953
Zurera-Rosa Manuel 3181, 4283, 5229